John R. Haaga
Charles F. Lanzieri

CT and MR Imaging of the Whole Body

Fourth Edition

Volumes 1 & 2

CT and MR Imaging of the Whole Body

Volumes One & Two
Fourth Edition

John R. Haaga, MD, FACR
Chairman and Medical Director
Department of Radiology
University Hospitals of Cleveland
Cleveland, Ohio

Charles F. Lanzieri, MD, FACR
Professor of Radiology and Neurosurgery
Department of Radiology
University Hospitals of Cleveland/Case Western Reserve University
Cleveland, Ohio

Robert C. Gilkeson, MD
Section Head, Thoracic Radiology
Department of Radiology
Case Western Reserve University
Cleveland, Ohio

Part I

Edited by Jeffrey L. Duerk, PhD
Director, Physics Radiology
Department of Radiology
University Hospitals of Cleveland/Case Western Reserve University
Cleveland, Ohio

Part IV

Edited by Jeffrey L. Sunshine, MD, PhD
Assistant Professor of Radiology
Case Western Reserve University
Cleveland, Ohio

Part VII

Edited by Mark R. Robin, MD
Department of Radiology
University Hospitals of Cleveland/Case Western Reserve University
Cleveland, Ohio

Part VIII

Edited by Carlos J. Sivit, MD
Department of Radiology, Rainbow Babies and Children's Hospital of the University Hospitals of Cleveland and Case School of Medicine,
Cleveland, Ohio

Mosby
An Affiliate of Elsevier Science

Mosby
An Affiliate of Elsevier Science

11830 Westline Industrial Drive
St. Louis, Missouri 63146

COMPUTED TOMOGRAPHY AND MAGNETIC RESONANCE IMAGING OF THE WHOLE BODY

ISBN 0-323-01133-0

Notice

Pharmacology is an ever-changing field. Standard safety precautions must be followed, but as new research and clinical experience broaden our knowledge, changes in treatment and drug therapy become necessary or appropriate. Readers are advised to check the product information currently provided by the manufacturer of each drug to be administered to verify the recommended dose, the method and duration of administration, and the contraindications. It is the responsibility of the treating physician, relying on experience and knowledge of the patient, to determine dosages and the best treatment for the patient. Neither the publisher nor the editor assumes any responsibility for any injury and/or damage to persons or property.

The Publisher

Library of Congress Cataloging-in-Publication Data

Computed tomography and magnetic resonance imaging of the whole body/[edited by] John R. Haaga, Charles F. Lanzieri—4th ed.
p. cm.
Includes bibliographical references and index.
ISBN 0-323-01133-0
1. Tomography. 2. Magnetic resonance imaging. I. Haaga, John R. (John Robert). II. Lanzieri, Charles F.

RC78.7.T6 C6425 2002
616.07′54—dc21 2001042808

Acquisitions Editor: Janice Gaillard
Developmental Editor: Rebecca Gruliow
Project Manager: Norman Stellander
Design Coordinator: Gene Harris

MC/MVY

Printed in the United States of America.
Last digit is the print number: 9 8 7 6 5 4 3 2 1

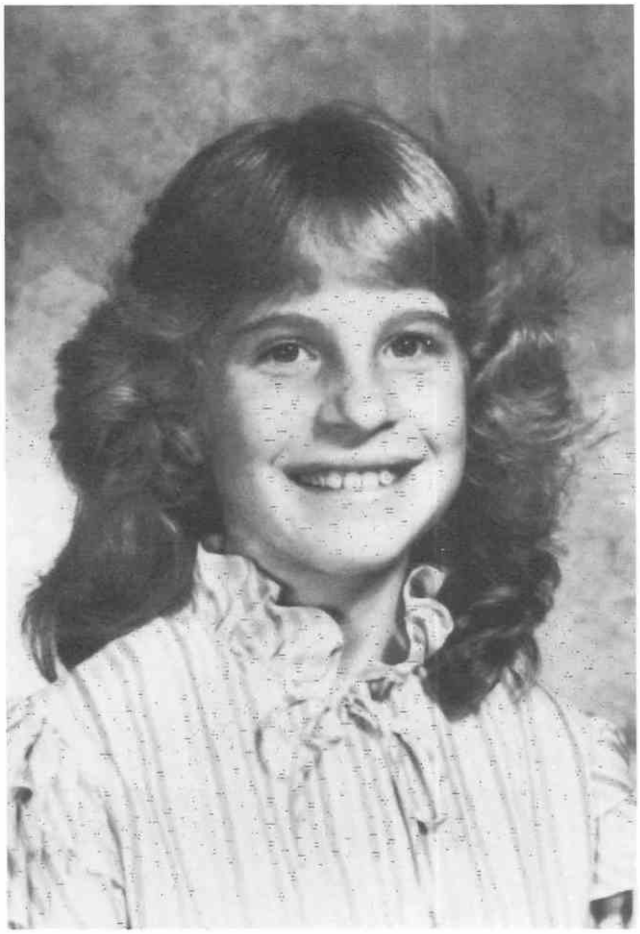

DEDICATION

This book is dedicated to Elizabeth E. Haaga, daughter of John and Ellen Haaga, who was born on August 19, 1972, and died December 9, 1985. Beth had a disseminated neuroblastoma, which was diagnosed in 1984. She was treated with a bone marrow transplant and died from graft versus host disease and infection. As her parents, we loved her dearly and cherish the memory of her early years when she was well. After the onset of her illness, we came to know that her gentle and loving nature was accompanied by a remarkably strong character. She endured her pain and suffering without bitterness and never sought to hurt those who loved her. Indeed, most incredulously, she tried to lessen our emotional pain even while enduring her physical discomforts. Many authors have marveled at the qualities of children, and although Beth's short life and premature death have left us saddened beyond comprehension, her remarkable courage and sweetness have given us a lasting pride and respect. We remember her lovingly.

Contributors

James J. Abrahams, MD
Associate Professor (Diagnostic Radiology and Surgery) and Director of Medical Studies, (Diagnostic Radiology), Section of Neuroradiology, Yale University School of Medicine, New Haven; Attending Physician, Yale–New Haven Medical Center, New Haven; West Haven Veterans Administration Hospital, West Haven, Connecticut
The Orbit

Jamshid Ahmadi, MD
Professor of Radiology, Neurology and Neurological Surgery, University of Southern California Keck School of Medicine and Los Angeles County–University of Southern California Medical Center, Los Angeles, California
Cerebral Infections and Inflammation

Kimberly E. Applegate, MD, MS
Associate Professor of Radiology, Department of Radiology, Indiana University School of Medicine and Riley Hospital for Children, Indianapolis, Indiana
Pediatric Spleen

Mark A. Augustyn, MD
Neuroradiology Fellow, University of Pennsylvania School of Medicine, Philadelphia, Pennsylvania
Temporal Bone

Errol M. Bellon, MD
Professor of Radiology, Case Western Reserve University School of Medicine; Chairman, Department of Radiology, MetroHealth Medical Center, Cleveland, Ohio
Magnetic Resonance Physics: An Introduction

Javier Beltran, MD
Clinical Professor of Radiology, New York University School of Medicine, New York; Chairman, Department of Radiology, Maimonides Medical Center, Brooklyn, New York
The Knee

Ellen C. Benya, MD
Associate Adjunct Clinical Professor of Radiology, University of Florida College of Medicine; Attending Physician, Department of Radiology, Shands Hospital at the University of Florida, Gainesville, Florida
Hepatobiliary System

Sheila C. Berlin, MD
Assistant Professor of Radiology, Case Western Reserve University School of Medicine; Staff, Division of Pediatric Radiology, University Hospital of Cleveland, Cleveland, Ohio
Heart and Great Vessels

Daniel T. Boll, MD
Resident, University Hospitals of Ulm, Ulm, Germany
Liver: Normal Anatomy, Imaging Techniques, and Diffuse Diseases

Lawrence M. Boxt, MD
Professor of Clinical Radiology, Albert Einstein College of Medicine; Chief of Cardiovascular Imaging, Beth Israel Medical Center, New York, New York
Magnetic Resonance Imaging of the Heart

Hans-Juergen Brambs, MD
Full Professor, Medical School, University of Ulm; Chairman, University Hospitals of Ulm, Ulm, Germany
Liver: Normal Anatomy, Imaging Techniques, and Diffuse Diseases

Lynn S. Broderick, MD
Associate Professor, University of Wisconsin—Madison, Madison, Wisconsin
Computed Tomography of the Heart and Pericardium

Kenneth A. Buckwalter, MD
Associate Professor of Radiology, Indiana University School of Medicine, Indianapolis, Indiana
Multislice Helical Computed Tomography: Clinical Applications

Donald W. Chakeres, MD
Professor of Radiology, Head of Neuroradiology, and Director of MRI Research, The Ohio State University College of Medicine and Public Health, Columbus, Ohio
Temporal Bone

Ja-Kwei Chang, MD
Professor of Radiology, State University of New York Upstate Medical University; Director, Division of Neuroradiology, Department of Radiology, University Hospital, Syracuse, New York
Intracranial Neoplasms

Wui K. Chong, MBBS, FRCR
Assistant Professor of Radiology, Virginia Commonwealth University School of Medicine, Richmond, Virginia; Medical College of Pennsylvania, Philadelphia, Pennsylvania; Vanderbilt University School of Medicine, Nashville, Tennessee
Thyroid and Parathyroid Glands

Richard H. Cohan, MD
Professor, University of Michigan School of Medicine and University of Michigan Hospital, Ann Arbor, Michigan
The Retroperitoneum

Hugh D. Curtin, MD
Professor and Chief of Radiology, Harvard Medical School and Massachusetts Eye and Ear Infirmary, Boston, Massachusetts
The Larynx

Murray K. Dalinka, MD
Professor of Radiology and Chief, Musculoskeletal Radiology, University of Pennsylvania School of Medicine and Hospital of the University of Pennsylvania, Philadelphia, Pennsylvania
The Shoulder

Mony J. de Leon, MD
Professor of Psychiatry and Radiology, and Director of the Neuroimaging Research Laboratory, New York University School of Medicine, New York, New York
Neurodegenerative Disorders

Pedro J. Diaz, PhD
Assistant Professor, Departments of Radiology and Biomedical Engineering, Case Western Reserve University School of Medicine and MetroHealth Medical Center, Cleveland, Ohio
Magnetic Resonance Physics: An Introduction

Huy M. Do, MD
Assistant Professor of Radiology and Neurosurgery, Stanford University Medical Center, Stanford, California
Image-Guided Spinal Interventions

Vikram Dogra, MD
Assistant Professor of Radiology, Case Western Reserve University School of Medicine; Section Head, Genitourinary Radiology, and Head, Director of Ultrasound, University Hospitals of Cleveland, Cleveland, Ohio
The Kidney

Lane F. Donnelly, MD
Professor of Radiology and Pediatrics, University of Cincinnati College of Medicine; Associate Director, Department of Radiology, Children's Hospital Medical Center, Cincinnati, Ohio
Chest

Jeffrey L. Duerk, PhD
Professor Departments of Radiology and Biomedical Engineering and Director, Physics Radiology, Department of Radiology, University Hospitals of Cleveland/Case Western Reserve University School of Medicine, Cleveland, Ohio
Magnetic Resonance Physics: An Introduction

James D. Eastwood, MD
Assistant Professor, Department of Radiology, Division of Neuroradiology, Duke University School of Medicine, Durham, North Carolina
Stroke

John C. Egelhoff, DO
Professor of Radiology and Pediatrics, University of Cincinnati College of Medicine; Staff Neuroradiologist, Children's Hospital Medical Center, Cincinnati, Ohio
Pediatric Head and Neck Imaging

Jeremy J. Erasmus, MD
Associate Professor of Radiology, Diagnostic Radiology, The University of Texas M.D. Anderson Cancer Center, Houston, Texas
Primary Pulmonary Neoplasms; The Mediastinum

Jon Mark Fergenson, MD
Neuroradiology Fellow, Yale–New Haven Medical Center, New Haven; West Haven Veterans Administration Hospital, West Haven, Connecticut
The Orbit

Thorsten R. Fleiter, MD
Associate Professor of Radiology, University of Ulm Medical School; Staff Radiologist, University Hospitals of Ulm, Ulm, Germany
Liver: Normal Anatomy, Imaging Techniques, and Diffuse Diseases; Multislice Helical Computed Tomography: Clinical Applications

Donald P. Frush, MD
Associate Professor, Department of Radiology, Duke University School of Medicine and Medical Center, Durham, North Carolina
Computed Tomography and Magnetic Resonance Imaging in the Pediatric Patient: Special Considerations

Melanie B. Fukui, MD
Formerly, Associate Professor of Radiology, University of Pittsburgh School of Medicine; Director of Neuroradiology, Allegheny General Hospital, Pittsburgh, Pennsylvania
Meningeal Processes

Amilcare Gentili, MD
Assistant Professor, Musculoskeletal Section, University of California, Los Angeles, Department of Radiological Sciences, Los Angeles, California
Musculoskeletal Tumor

Ajax E. George, MD
Professor of Radiology, New York University School of Medicine, New York, New York
Neurodegenerative Disorders

Robert C. Gilkeson, MD
Section Head, Chest Radiology, and Assistant Professor of Radiology, University Hospitals of Cleveland and Case Western Reserve University, Cleveland, Ohio
Computed Tomography and Magnetic Resonance Imaging of the Thoracic Aorta

John L. Go, MD
Assistant Professor of Radiology and Otolaryngology, University of Southern California Keck School of Medicine, Los Angeles, California
Cerebral Infections and Inflammation

Ashok K. Gupta, MD
Clinical Associate, Duke University, Durham, North Carolina
The Retroperitoneum

Hyun Kwon Ha, MD
Associate Professor, University of Ulsan College of Medicine; Staff Radiologist, Abdominal Radiology, Department of Radiology, Asan Medical Center, Seoul, Korea
The Gastrointestinal Tract

E. Mark Haacke, PhD
Director, The MRI Institute for Biomedical Research, Detroit, Michigan; Professor and Director of MRI Center of Radiology, Wayne State University; Adjunct Professor of Physics, Case Western Reserve University, Cleveland, Ohio
Magnetic Resonance Angiography: Fundamentals and Techniques

John R. Haaga, MD
Chairman and Medical Director, Department of Radiology, University Hospitals of Cleveland, Cleveland, Ohio
The Gallbladder and Biliary Tract; The Pancreas; Peritoneum and Mesentery; Image-Guided Micro Procedures: CT and MRI Interventional Procedures

Tamara Miner Haygood, PhD, MD
Radiologist, Fayette Memorial Hospital, LaGrange, Texas
The Shoulder

Thomas E. Herbener, MD
Assistant Professor, Department of Radiology, University of Ohio, Cleveland, Ohio
The Gallbladder and Biliary Tract

Leo Hochhauser, MD
Associate Professor of Radiology, State University of New York, Upstate Medical University, Syracuse, New York
Central Nervous System Trauma

Roy A. Holliday, MD
Department of Radiology, New York University School of Medicine, New York, New York
Cervical Adenopathy and Neck Masses

Andrei I. Holodny, MD
Associate Professor of Radiology, Memorial Sloane-Kettering Cancer Center, New York, New York
Neurodegenerative Disorders

David S. Jacobs, MD
Director of Neuroradiology and MRI, Hillcrest Hospital, Cleveland Clinic Health System, Mayfield Heights, Ohio
Degenerative Diseases of the Spine

Sassan Karimi, MD
Assistant Professor of Radiology, Memorial Sloane-Kettering Cancer Center, New York, New York
Neurodegenerative Disorders

Stephen A. Kieffer, MD
Professor of Radiology, University of Minnesota Medical School; Attending Neuroradiologist, Fairview-University Medical Center, Minneapolis, Minnesota
Intracranial Neoplasms

Jeong Kon Kim, MD
Fellow, University of Ulsan College of Medicine, Abdominal Radiology, Department of Radiology, Asan Medical Center, Seoul, Korea
The Gastrointestinal Tract

Paul Kim, MD
Assistant Professor of Clinical Radiology, University of Southern California Keck School of Medicine, Los Angeles, California
Cerebral Infections and Inflammation

J. Bruce Kneeland, MD
Professor, University of Pennsylvania School of Medicine, Philadelphia, Pennsylvania
The Shoulder

Barbara L. Knisely, MD
Assistant Professor of Diagnostic Radiology, University of Wisconsin Medical School, Hospital, and Clinics, Madison, Wisconsin
Pleura and Chest Wall

Scott Kolodny, MD
Assistant Professor of Radiology, Case Western Reserve University, Cleveland, Ohio
The Spinal Cord; Computed Tomography and Magnetic Resonance Imaging of the Thoracic Aorta

Kenyon K. Kopecky, MD
Professor of Radiology, Indiana University School of Medicine, Indianapolis, Indiana
Multislice Helical Computed Tomography: Clinical Applications

Janet E. Kuhlman, MD, MS
Professor of Radiology, University of Wisconsin Medical School, Hospital and Clinics, Madison, Wisconsin
Non-neoplastic Parenchymal Lung Disease

Lester Kwock, PhD
Professor of Radiology, University of North Carolina at Chapel Hill School of Medicine, Chapel Hill, North Carolina
Brain Magnetic Resonance Spectroscopy

Barton Lane, MD, FACR
Professor of Neuroradiology and Neurosurgery, Stanford University Medical School and Medical Center, Stanford; Chief of Radiology, Palo Alto Veterans Administration Medical Center, Palo Alto, California
Leukoencephalopathies and Demyelinating Disease; Image-Guided Spinal Interventions

Charles F. Lanzieri, MD, FACR
Professor of Radiology and Neurosurgury, Department of Radiology, University Hospitals of Cleveland/Case Western Reserve University School of Medicine, Cleveland, Ohio
The Sinonasal Cavity; Magnetic Resonance Imaging of Infections of the Spine

Theodore C. Larson III, MD
Associate Professor of Radiology and Radiological Sciences and Associate Professor of Otolaryngology, Vanderbilt University School of Medicine; Director of Head and Neck Radiology and Director of Interventional Neuroradiology, Vanderbilt University Medical Center, Nashville, Tennessee
Cerebral Aneurysms and Vascular Malformations; Thyroid and Parathyroid Glands

Errol Levine, MW, PhD, FACR, FRCR
Professor and Head, Sections of Computed Body Tomography, Magnetic Resonance Imaging, and Uroradiology, Department of Diagnostic Radiology, University of Kansas Medical Center, Kansas City, Kansas
The Kidney

Jonathan S. Lewin, MD
Professor of Radiology, Oncology, and Neurological Surgery, Case Western Reserve University School of Medicine; Vice Chairman, Research and Academic Affairs, and Director of Magnetic Resonance Imaging, University Hospitals of Cleveland, Cleveland, Ohio
Nasopharynx and Oropharynx

Weili Lin, PhD
Associate Professor, University of North Carolina at Chapel Hill School of Medicine, Chapel Hill, North Carolina
Magnetic Resonance Angiography: Fundamentals and Techniques

Neal Mandell, MD
Visiting Professor, Yale University School of Medicine, New Haven; Chairman, Department of Radiology, Charlotte Hungerford Hospital, Torrington, Connecticut
The Orbit

William H. Martin, MD
Assistant Professor of Radiology and Medicine, Vanderbilt University School of Medicine and Veterans Administration Medical Center, Nashville, Tennessee
Thyroid and Parathyroid Glands

H. Page McAdams, MD
Associate Professor, Department of Radiology, Duke University Medical Center; Staff Radiologist, Duke University Hospital, Durham, North Carolina
Primary Pulmonary Neoplasms; The Mediastinum

Jeffrey D. McTavish, MD
Instructor in Radiology, Harvard Medical School; Director of Body MRI, Brigham & Women's Hospital, Boston, Massachusetts
Hepatic Mass Lesions

Carolyn Cidis Meltzer, MD
Associate Professor of Radiology and Psychiatry, University of Pittsburgh School of Medicine; Medical Director, Positron Emission Tomography Facility, University of Pittsburgh Medical Center, Pittsburgh, Pennsylvania
Meningeal Processes

Elmar M. Merkle, MD
Associate Professor of Radiology, Medical School, Case Western Reserve University; Director of Body MR Imaging, Department of Radiology, University Hospitals of Cleveland, Cleveland, Ohio
Liver: Normal Anatomy, Imaging Techniques, and Diffuse Diseases

Floro Miraldi, MD, PhD
President, Neo-pet, LLC, Cleveland Heights, Ohio
Imaging Principles in Computed Tomography

Mark D. Murphey, MD
Chief, Musculoskeletal Radiology, Department of Radiologic Pathology, Armed Forces Institute of Pathology, Washington, D.C.; Associate Professor, Uniformed Services University of the Health Sciences, Departments of Radiology and Nuclear Medicine, Bethesda; Clinical Professor, University of Maryland School of Medicine, Department of Radiology, Baltimore, Maryland
The Hip

M. Hossain Naheedy, MD
Associate Professor of Radiology, Case Western Reserve University School of Medicine; Director, Radiology, at Louis Stokes Cleveland Veterans Affairs Medical Center, Cleveland, Ohio
Normal Computed Tomography and Magnetic Resonance Imaging Anatomy of the Brain and the Spine

Dean A. Nakamoto, MD
Assistant Professor, Department of Radiology, Case Western Reserve University School of Medicine and University Hospitals of Cleveland, Cleveland, Ohio
The Spleen

Sherif Gamal Nour, MD
MRI Research Associate, School of Medicine, Case Western Reserve University; Research Fellow of Interventional MRI, Department of Radiology, University Hospitals of Cleveland/Case Western Reserve University, Cleveland, Ohio; Assistant Lecturer of Diagnostic Radiology, Department of Diagnostic Radiology, Cairo University Hospitals, Cairo, Egypt
Nasopharynx and Oropharynx

Raymond P. Onders, MD
Assistant Professor, Department of Surgery, University Hospitals at Cleveland and Case Western Reserve University School of Medicine, Cleveland, Ohio
The Spleen

Eric K. Outwater, MD
Professor of Radiology, University of Arizona School of Medicine; Attending Physician, University Medical Center, Veterans Hospital, and Kino Community Hospital, Tucson, Arizona
Magnetic Resonance Imaging of the Pelvis

Kathleen Gallagher Oxner, MD
Radiologist, Greenville Radiology, Greenville, South Carolina
The Shoulder

Cheryl A. Petersilge, MD
Assistant Clinical Professor of Radiology and Orthopedic Surgery, Case Western Reserve University School of Medicine; Director, Musculoskeletal and Emergency Radiology, Hillcrest Hospital, Cleveland, Ohio
The Hip

Jay J. Pillai, MD
Associate Professor of Radiology, Medical College of Georgia School of Medicine; Staff Attending Neuroradiologist, Medical College of Georgia Hospital and Clinics, Angusta, Georgia
Brain Magnetic Resonance Spectroscopy

Donna M. Plecha, MD
Assistant Professor of Radiology, Case Western Reserve University School of Medicine and University Hospitals of Cleveland, Cleveland, Ohio
Extramedullary Spinal Tumors

Deborah L. Reede, MD
Long Island College of Medicine, Brooklyn, New York
Cervical Adenopathy and Neck Masses

Pablo R. Ros, MD, MPH
Professor of Radiology, Harvard Medical School; Executive Vice Chair, Department of Radiology, Brigham & Women's Hospital, Boston, Massachusetts
Hepatic Mass Lesions

Santiago E. Rossi, MD
Jefe de Trabajos Practicos, Universidad de Buenos Aires and Universidad de Ciencias Biomedicas Rene Tavaloro; Hospital Universitario de Clinicas Jose de San Martin; Director, Centro de Diagnostico Dr. Enrique Rossi, Buenos Aires, Argentina
Primary Pulmonary Neoplasms

Anna Rozenshtein, MD
Assistant Professor of Clinical Radiology, College of Physicians and Surgeons of Columbia University; Director of Thoracic Radiology, St. Luke's–Roosevelt Hospital Center, New York, New York
Magnetic Resonance Imaging of the Heart

Jonas Rydberg, MD
Associate Professor of Radiology, Indiana University School of Medicine, Indianapolis, Indiana
Multislice Helical Computed Tomography: Clinical Applications

Ken L. Schreibman, PhD MD
Associate Professor of Radiology, University of Wisconsin School of Medicine, Madison, Wisconsin
The Foot and Ankle

Hervey D. Segall, MD
Professor of Radiology, University of Southern California Keck School of Medicine and Los Angeles County–University of Southern California Medical Center, Los Angeles, California
Cerebral Infections and Inflammation

Steven Shankman, MD
Vice-Chairman, Department of Radiology and Resident Program Director, Maimonides Medical Center, Brooklyn, New York
The Knee

Patrick F. Sheedy II, MD
Professor, Department of Radiology, Mayo Medical School; Department of Radiology, Mayo Clinic and Mayo Foundation; Department of Radiology, Saint Marys Hospital and Rochester Methodist Hospital, Rochester, Minnesota
The Adrenal Glands

Marilyn J. Siegel, MD
Professor of Radiology, Mallinckrodt Institute of Radiology, Washington University School of Medicine, St. Louis, Missouri
Pediatric and Adolescent Pelvis

Michael S. Sims
President and CEO, UltraGuide, Inc., Cleveland, Ohio
Imaging Principles in Computed Tomography

Carlos J. Sivit, MD
Professor of Radiology and Pediatrics, Case Western Reserve University; Director of Pediatric Radiology, Rainbow Babies and Childrens Hospital, Cleveland, Ohio
Pancreas; Gastrointestinal Tract, Peritoneal Cavity, and Mesentery

Michelle M. Smith, MD
Department of Radiology, Froedtert Hospital, Milwaukee, Wisconsin
Thyroid and Parathyroid Glands

John A. Spencer, MA, MD, MRCP, FRCR
Consultant Radiologist, St. James's University Hospital, Leeds, United Kingdom, and Röntgen Professor of the Royal College of Radiologists
Computed Tomography of the Pelvis

Charles E. Spritzer, MD
Professor, Department of Radiology, Duke University, School of Medicine and Medical Center; Staff Radiologist, Duke University Hospital, Durham, North Carolina
The Mediastinum

Peter J. Strouse, MD
Assistant Professor, Section of Pediatric Radiology, Department of Radiology, University of Michigan Medical School; Attending Physician, C. S. Mott Children's Hospital, Ann Arbor, Michigan
Musculoskeletal System

Jeffrey L. Sunshine, MD, PhD
Assistant Professor of Radiology, Case Western Reserve University, Cleveland, Ohio
The Spinal Cord

Sarah E. Swift, MR, MRCP, FRCR
Consultant Radiologist, St. James's University Hospital, Leeds, United Kingdom
Computed Tomography of the Pelvis

Robert D. Tarver, MD
Professor, Department of Radiology, Indiana University School of Medicine, Indianapolis, Indiana
The Mediastinum

John J. Wasenko, MD
Associate Professor of Radiology and Director of Magnetic Resonance Imaging, State University of New York Upstate Medical University, Syracuse, New York
Central Nervous System Trauma

Timothy J. Welch, MD
Associate Professor, Mayo Medical School; Consultant, Mayo Clinic, Rochester, Minnesota
The Adrenal Glands

Ernest J. Wiesen, BSEE
Formerly, Assistant Professor, Department of Radiology, Case Western Reserve University School of Medicine; Radiologic Physicist, Department of Radiology, MetroHealth Medical Center, Cleveland, Ohio
Imaging Principles in Computed Tomography

Wade H. Wong, MD
Professor of Radiology, University of California, San Diego, California
Image-Guided Spinal Interventions

Chi-Shing Zee, MD
Professor of Radiology and Neurosurgery and Director of Neuroradiology, University of Southern California Keck School of Medicine, Los Angeles, California
Cerebral Infections and Inflammation

J. Michael Zerin, MD
Professor of Radiology, Wayne State University School of Medicine; Director of Ultrasound Imaging, Department of Pediatric Imaging, Children's Hospital of Michigan, Detroit, Michigan
Kidneys and Adrenal Glands

Preface

The progress in computed imaging over the past 25 years has been remarkable, to say the very least. These new modalities have revolutionized the delivery of health care around the world and improved the lives of innumerable citizens of the planet. The astonishing development of technology has truly spread worldwide so that even people in the remotest country or island have the benefit of imaging (albeit the highest technology still is present in the developed countries). A graphic demonstration of this spread of technology and medical knowledge can be appreciated by noting the new trend to have international interpretation of night-time studies around the world. Medicine now chases the sun in its use of computerized imaging and beams the images between countries so that night-hawk reading services help rationalize radiology care by making the best use of manpower around the world.

The impact of computed tomography (CT) and magnetic resonance imaging (MRI) on medicine can be further appreciated by noting a recent survey of physicians' views on the importance of 30 medical innovations. Fuchs and Sox published an article, titled "Physicians' Views of the Relative Importance of Thirty Medical Innovations in Health Affairs," in September/October 2001. In their survey of 225 leading internists in the United States, the replies showed that 75% of respondees believed CT and MRI were the most significant innovation, followed by ACE inhibitors, angioplasties, statins, and mammography.

The acceptance and wide application have come at a philosophical and pragmatic price and risk to the profession of radiology. While government planners and HMOs have tried to stem the tide of imaging progress, the science and technology have moved ahead with unstoppable momentum. The result of the attempts of these organizations to prevent the application of these new modalities was an ill-conceived movement to limit the training of radiologists during the era of primary-care physician promotion.

By attempting to prevent the use of imaging in health care, they interfered with the natural market forces of manpower supply and demand. The result is the current manpower shortage at a time when the need for imaging grows on a daily basis. The shortage has impaired training programs because faculty required to train radiologists have been enticed into more lucrative positions in the marketplace.

It is quite evident that the role of imaging will continue to grow and provide a positive impact on the health of all citizens. Its future is ensured by the new emphasis by the National Institutes of Health (NIH) on molecular imaging and also the image-guided microsurgery procedures performed with CT and MRI. We are quite proud to note that a radiologist, Elias Zerhouni, MD, has been appointed as current director of the NIH. Furthermore, we are proud that Dr. Zerhouni was a section editor in the third edition of this text.

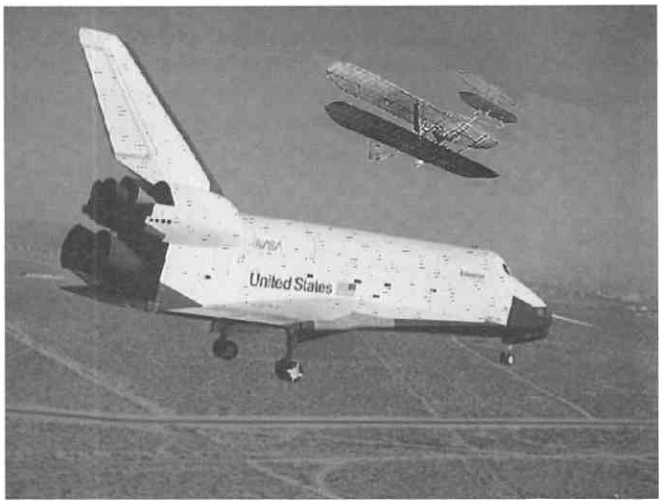

Figure 1

It is exciting to reflect back on other high technology developments that have occurred, such as aviation (Fig. 1). If one looks at the progress made in aviation since the first flight of the Wright flyer and contrast it with the Space Shuttle, there was an increase in speed of approximately 600 times (42 mph compared to 25,000 mph) in a 100-year period. With CT scanning (Fig. 2), there has been an increase in scan time of almost 1200 times in a 25-year period (7 minutes per single scan compared to 300 msec on current multislice devices).

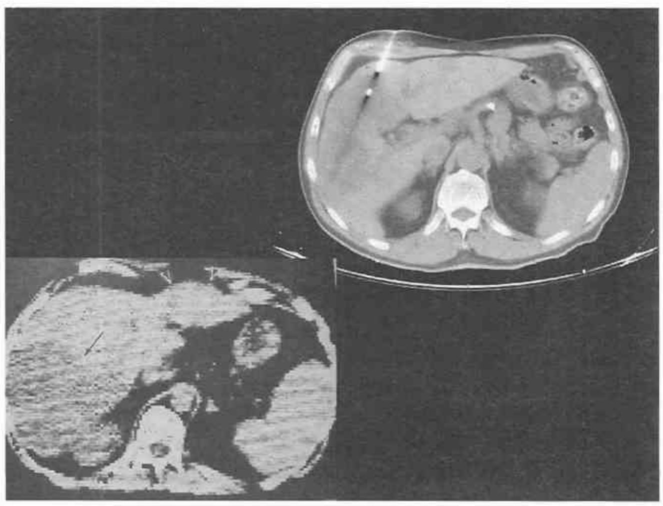

Figure 2

We are pleased to note the wide application of the new image-guided microsurgical procedures (the term *interventional radiology* is not specific enough or a unique descriptor). Progress in this area will continue and further improve the delivery of health care. Indeed, at the time of publication of this edition, we are even working on methodology using CT procedures to treat mediastinal collections of anthrax-laden lymph nodes in patients with inhalational anthrax. Data are very preliminary, but it seems that the heat from radiofrequency can be used to kill the vegetative forms of anthrax, and other strategies can be used to stimulate spores to germinate and become susceptible to local instillation of polymer-containing antibiotics.

We are especially grateful to all of our colleagues who have contributed to this edition because of the many difficulties they have overcome. Historically, it has always been difficult for authors to find time to contribute high-quality work. During this current period of faculty shortage at university centers, the commitment and dedication to our project required even more effort by our contributors.

We are delighted with the content of this fourth edition and believe it provides the most up-to-date information on MRI and CT. Information about the new, fast-sequence MRI and multislice scanners is provided. We are confident that the readers of this book will be intellectually rewarded.

Preface to First Edition

Since the introduction of computed tomography (CT) in 1974, there has been a remarkable revolution in the medical treatment of patients. The clinical use of CT has had a broad positive impact on patient management. Literally thousands of patients have been saved or their quality of life improved as a result of the expeditious and accurate diagnosis provided by CT. This improvement in diagnosis and management has occurred in all medical subspecialties, including neurological, pulmonary, cardiac, gastrointestinal, genitourinary, and neuromuscular medicine. Aside from the imaging advantages provided, the role of CT in planning and performing interventional procedures is now recognized. It is the most accurate method for guiding procedures to obtain cytological, histological, or bacteriological specimens and for performing a variety of therapeutic procedures.

The evolution and refinement of CT equipment have been as remarkable as the development of patient diagnosis. When we wrote our first book on CT, the scanning unit used was a 2-minute translate-rotate system. At the time of our second book the 18-second translate-rotate scanning unit was in general use. Currently standard units in radiological practice are third and fourth generation scanners with scan times of less than 5 seconds. All modern systems are more reliable than the earlier generations of equipment. The contrast and spatial resolution of these systems are in the range of 0.5% and less than 1 mm, respectively. The sophistication of the computer programs that aid in the diagnosis is also remarkable. There are now programs for three-dimensional reconstructions, quantitation of blood flow, determination of organ volume, longitudinal scans (Scoutview, Deltaview, Synerview, and Topogram), and even triangulation programs for performing percutaneous biopsy procedures.

CT units are now being installed in virtually every hospital of more than 200 beds throughout the United States. Most radiologists using these units are generalists who scan all portions of the anatomy. Because of the dissemination of this equipment and its use in general diagnosis, there exists a significant need for a general and complete textbook to cover all aspects of CT scanning. Our book is intended to partially supplement the knowledge of this group of physicians. We have attempted to completely and succinctly cover all portions of CT scanning to provide a complete general reference text. In planning the book, we chose to include the contributions of a large number of talented academicians with expertise different from and more complete than our own in their selected areas. By including contributors from outside our own department, we have been able to produce an in-depth textbook that combines the academic strengths of numerous individuals and departments.

The book is divided into chapters according to the organ systems, except for some special chapters on abscesses and interventional procedures. In each of the chapters the authors have organized the material into broad categories, such as congenital, benign, or neoplastic disease. Each author has tried to cover the major disease processes in each of the general categories in which CT diagnosis is applicable. Specific technical details, including the method of scanning, contrast material, collimation, and slice thickness, are covered in each chapter. The interventional chapter extensively covers the various biopsy and therapeutic procedures in all the organ systems. Finally, the last chapter presents an up-to-the-minute coverage of current and recent developments in the CT literature and also provides extensive information about nuclear magnetic resonance (NMR) imaging. At this time we have had moderate experience with the NMR superconducting magnetic device produced by the Technicare Corporation and have formulated some initial opinions as to its role relative to CT and other imaging modalities. A concise discussion of the physics of NMR and a current clinical status report of the new modality are provided.

We would like to thank all those people who have worked so diligently and faithfully for the preparation of this book. First, we are very grateful to our many contributors. For photography work, we are deeply indebted to Mr. Joseph P. Molter. For secretarial and organizational skills, we are indebted especially to Mrs. Mary Ann Reid and Mrs. Rayna Lipscomb. The editorial skills of Ms. B. Hami were invaluable in preparing the manuscript. Our extremely competent technical staff included Mr. Joseph Agee, Ms. Ginger Haddad, Mrs. E. Martinelle, Mr. Mark Clampett, Mrs. Mary Kralik, and numerous others.

Finally, we are, of course, very appreciative of the support, patience, and encouragement of our wonderful families. In the Haaga family this includes Ellen, Elizabeth, Matthew, and Timothy, who provided the positive motivation and support for this book. Warm gratitude for unswerving support is also due to Rose, Sue, Lisa, Chris, Katie, Mary, and John Alfidi.

John R. Haaga
Ralph J. Alfidi

Preface to First Edition

Contents

Part V Imaging of the Chest

Edited by John R. Haaga

VOLUME TWO

Part VI Imaging of the Abdomen and Pelvis

Edited by John R. Haaga

Part VII Imaging of the Musculoskeletal System

Edited by Mark Robbin

Part VIII Pediatric Radiology

Edited by Carlos J. Sivit

Part IX Special Considerations

Part I

Principles of Computed Tomography and Magnetic Resonance Imaging

Edited by
Jeffrey L. Duerk

1 Imaging Principles in Computed Tomography

Floro Miraldi, Michael S. Sims, Ernest J. Wiesen

A computed tomography (CT) image is a display of the anatomy of a thin slice of the body developed from multiple x-ray absorption measurements made around the body's periphery. Unlike conventional tomography, in which the image of a thin section is created by blurring out the information from unwanted regions, the CT image is constructed mathematically using data arising only from the section of interest. Generating such an image is confined to cross-sections of the anatomy that are oriented essentially perpendicular to the axial dimension of the body (Fig. 1–1). Reconstruction of the final image can be accomplished in any plane, but conventionally it is performed in the transaxial plane.

In its most basic form, the fundamental principles of CT are the same as those for radiography and tomography. Each approach directs a source of ionizing radiation through an object to recreate an image of the original object based on the x-ray absorption of the object. The basic equation used is the same for each,

$$I = I_0 e^{-\mu x} \tag{1}$$

where

- I_0 is the incident intensity of an x-ray beam on the surface of an object of thickness, x
- I is the transmitted intensity
- e is Euler's constant (2.718)
- μ is the linear attenuation coefficient (Fig. 1–2)[7, 19]

Attenuation is dependent on (1) the atomic number and density of the material through which the x-rays pass and (2) the energy spectrum of the incident x-ray beam.[19] With conventional radiography and tomography, the differential absorption of x-rays passing through an object is recorded on film, a qualitative measurement that cannot accurately reflect subtle differences in object contrast. On the other hand, differential absorption for CT is recorded by special detectors, which are quantitative and can measure subtle changes in x-ray attenuation. Radiography's most major shortfall is the superimposition of the structures on film, which has been only partially overcome by conventional tomography.

The earliest CT was designed by Godfrey Hounsfield to overcome the visual representation challenges in radiography and tomography by collimating the x-ray beam and transmitting x-rays only through small cross-sections of an object. The idea revolutionized the practice of radiology and helped win Hounsfield a share of the Nobel Prize. More recent CT developments since the mid-1980s have advanced CT from a radiology tool limited to anatomic representations to a tool capable of demonstrating physiologic and pathogenic information.

This chapter presents the physics of CT image production in qualitative terms to familiarize the practicing radiologist with the basic principles of CT. Equipment and factors that affect CT image quality are discussed, and an introduction to emerging applications using CT is provided.

Basic Principles

The fundamental concept of CT is that the internal structure of an object can be reconstructed from multiple projections of the object (Fig. 1–3). The object in Fig. 1–3*A* is composed of a number of equal blocks from which the central four have been removed to represent an internal structure. For the sake of simplicity, assume that an x-ray beam is passed through each row and column of blocks and the transmitted radiation is measured. Since each block is the same, the measured attenuation is proportional to the number of blocks encountered in each row or column.

The numbers shown at the right and beneath the object represent the relative measured attenuation (i.e., the number of blocks in each row or column). These attenuation measurements are then added (Fig. 1–3*B*) to produce a numeric representation of the object (Fig. 1–3*C*). Although this array of numbers contains all the information of the process, it is difficult to interpret; thus, the array is converted into picture form by assigning a gray scale to the numbers. Large numbers are represented by light shades of gray, and small numbers are represented by dark shades of gray. The result is the image shown in Figure 1–3*D*. The resultant image can then be manipulated to highlight certain areas. For example, if the gray scale is narrowed to include only black and white, a perfect reproduction of the object is obtained by assigning black to all numbers equal to four or less and white to all numbers greater than four.

In Figure 1–3*E*, an imperfect representation is obtained because the gray scale is chosen so that values of six and lower are black and values above six are white. In CT, the method of obtaining the array of numbers is more complex

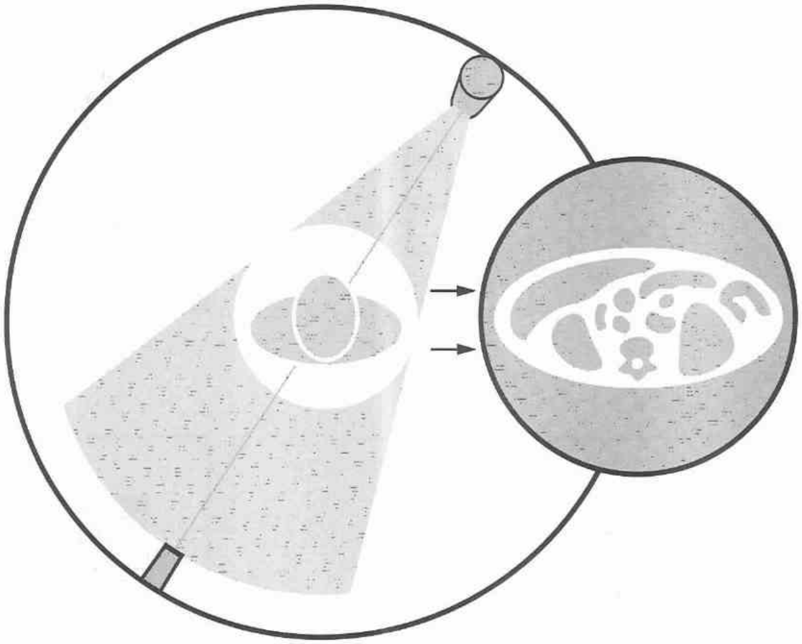

Figure 1–1. A CT image represents anatomy of a transaxial slice of the body obtained from many transaxial attenuation measurements.

and the number of projections obtained is much greater; however, the principle is the same.

The example of Figure 1–3 also provides a basis for a number of definitions of CT terms. Each of the blocks in Figure 1–3*A* represents a small attenuating volume of material and is referred to as a *voxel*. The numbers at the side and bottom of Figure 1–3*A* represent single attenuation measurements and are called *ray projections*, or *ray sums*. The array of numbers in Figure 1–3*C* is a *matrix*, and the individual numbers are elements of that matrix.

Each of the blocks of gray that are used for the construction of the images in Figure 1–3*D–F* is a picture element *(pixel)*. The process of choosing the number of gray shades for a display is referred to as "selecting a window." The width of the window (Fig. 1–3*E* and *F*) is narrow because it only contains two shades of gray (black and white) compared with the wider window in Figure 1–3*D*, which contains three shades of gray. The number at which the window setting is centered is called the *window level*. In Figure 1–3*E*, the level is set at four; in Figure 1–3*F*, it is set at six.

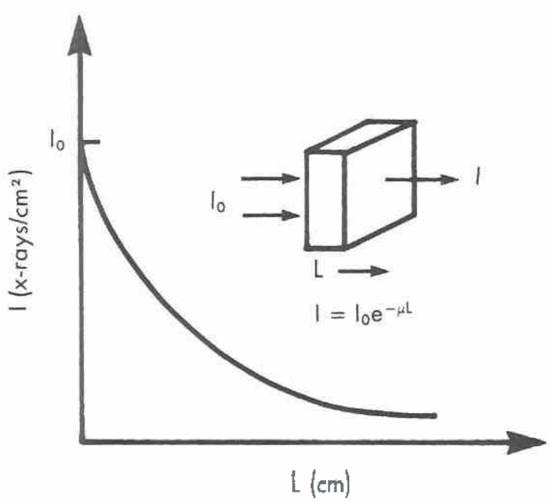

Figure 1–2. Exponential behavior of x-ray beam attenuation.

To present attenuation data (either I or μ) at every point throughout the body would be ideal in an x-ray examination. The degree to which this is attained depends on the manner in which the measured intensities, I and I_0, are registered or manipulated. In conventional radiography, the transmitted intensity (I) is seen as the darkening of a film. Because x-ray exposure of the film blackens it, the image of a dense object is lighter on the film than the image of a less dense material. In a typical radiographic film of the chest, for example, the image is light where many x-rays are absorbed or scattered (large μ), such as in bone, and dark where many x-rays are transmitted because of low absorption (small μ), such as in the regions of the lung parenchyma.

Two different areas of such a chest film may show the same darkening and therefore demonstrate equal total attenuation of the beam in the two positions. However, the attenuation profile through the body may be quite different. This is diagrammatically shown in Figure 1–4, with one beam passing through a region of relatively uniform density and the other beam passing through a region of nonuniform densities.

In conventional radiography, therefore, the different shades of gray seen on the film represent the differences in the transmission of an x-ray beam as it passes through the body. CT, however, approaches the ideal by presenting the average attenuation of each small volume element that comprises the body slice. Thus, CT unscrambles the attenuation information of the x-ray beam and presents it quantitatively with accuracy far greater than that accomplished by conventional techniques. This is equivalent to providing the individual values μ_1, μ_2, and μ_3 of Figure 1–4 rather than the total value described for conventional radiography.

All CT systems use a similar three-step process to generate a CT image: (1) scan, or data acquisition, (2)

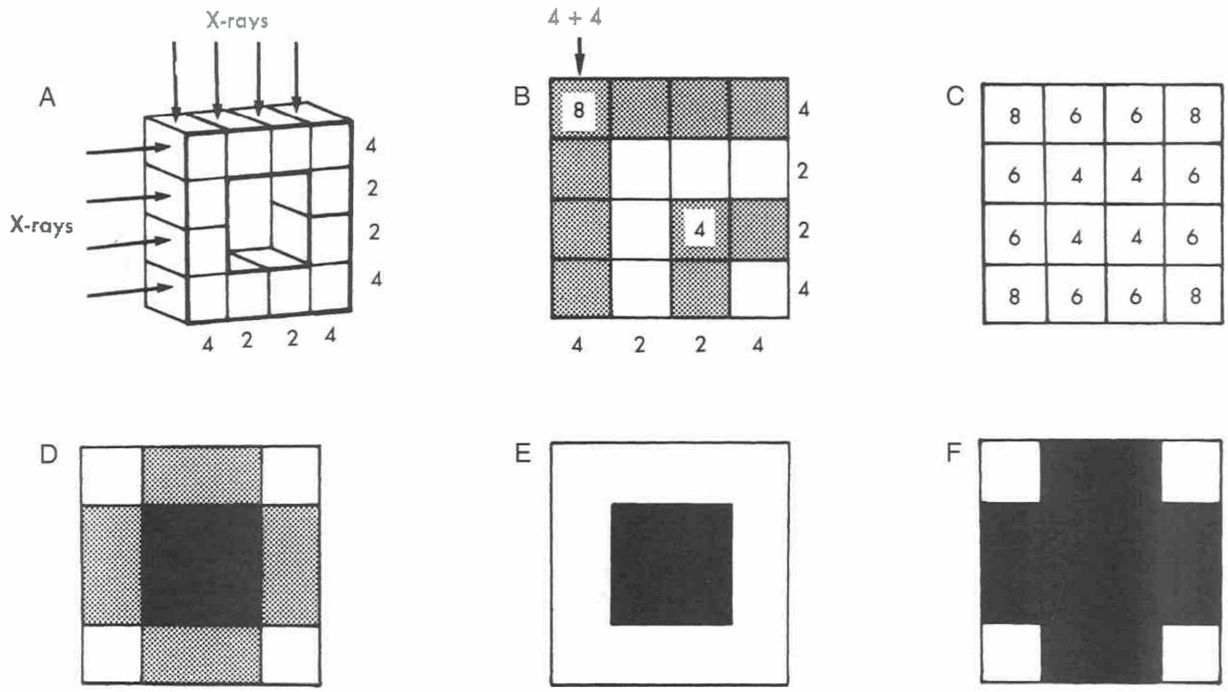

Figure 1–3. Principle of image reconstruction. (From Christensen EE, Curry TS III, Dowdey JE: An Introduction to the Physics of Diametric Radiology, 2nd ed. Philadelphia, Lea & Febiger, 1978.)

reconstruction, and (3) display; each process is considered separately throughout this chapter. In the most basic form, the flow of all CT systems includes the conversion of an x-ray source consisting of a collection of rays (*projection* or *view*). A single ray is considered the portion of the x-ray beam that falls onto one detector.

Data Acquisition

The scanning process begins with data acquisition. CT scanning is the systematic collection of projection data. Data collection encompasses all of the geometric properties of the x-ray beam and the relationship of the x-ray tube to the detector, including all of the beam-shaping devices and conversion of transmitted x-rays to digital signals for use by the reconstruction system. Since Hounsfield's invention, CT scanning geometry has evolved considerably. Before we address the evolution of CT data acquisition and CT scanning geometry, it is valuable to review the basic components of every CT data acquisition system.

Components of a Data Acquisition System

Scan Frame

Early CT scanners (in the 1980s) deployed rotating frames and recoiling system cables. This design was limited to step-and-shoot scan methods and considerably limited scanner rotation times. Current systems employ slip rings, electromechanical devices that transmit electrical energy across a rotating surface. Slip rings permit the scan frame to rotate continuously, enabling spiral or helical CT scanning and eliminating the need to rewind system cables.

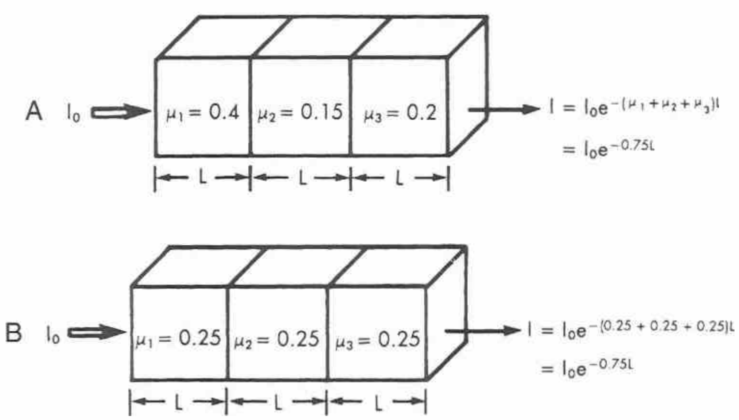

Figure 1–4. Total attenuation of equal amount in two different cases. *A,* Nonuniform attenuation coefficients. *B,* Uniform medium.

X-ray Generators

Most CT scanners today use high-frequency generators to produce x-ray quanta required for today's demanding CT protocols. Typical operating frequencies range from 5 to 50 kHz. Generator power can range from as low as 15 kilowatts (kW) to as high as 60 kW, and recent developments are likely to support ranges as high as 70 to 80 kW. In any case, most generators support a wide range of exposure techniques from 80 to 140 kilovolts (kV) and 30 to 500 milliamperes (mA). The generators are located on rotating scan frames within the CT gantry to accommodate new spiral scanning requirements.

X-ray Tubes

Early-generation CT technology used fixed-anode, oil-cooled x-ray tubes with fairly limited capability. Today's x-ray tubes include rotating anodes with unique cooling methods designed to enhance a system's ability to cover large areas of anatomy at diagnostic levels of x-ray output. Tube ratings typical in CT scanners today vary from 2 million heat units (2 MHU) of storage capability, with 300 thousand heat units (kHU)/minute cooling, up to 7 MHU of anode heat storage capability and cooling rates as fast as 1 million heat units (MHU)/minute. Future enhancements will not preclude tubes with greater than 10 MHU capacity and continuous output power capability of 60 kW. Both x-ray generator and x-ray tube developments are expected to open up the door for true volumetric CT applications with large area detectors designed to cover entire sections of patient anatomy within one revolution of the CT scanner's rotating frame.

X-ray Beam Filtration System

It is assumed that CT employs a monochromatic beam. The opposite is true; radiation from CT x-ray tubes is polychromatic. To compensate for this fact, the x-ray beam is shaped by *compensation filters*. The filters serve two purposes:

1. They remove the long-wavelength x-rays, which do not contribute to the CT image but do contribute to patient dose as these so-called soft rays are absorbed by the patient.
2. They serve to minimize the effects of beam hardening and provide a more uniform beam, as seen from the perspective of the detector.

Different filters are used for half-field (head) scanning and full-field (body) scanning. Additional corrections for beam hardening are made during the CT reconstruction process with software.

Data Acquisition Systems

Data acquisitions systems are the heart of a CT scanner. They include (1) the detector system, (2) analog-to-digital conversion, and (3) some data preprocessing for use by the scanners reconstruction system. The major functions are as follows[34]:

- To convert x-ray flux to electric current
- To convert electric current to voltage
- To convert analog voltage to digital form
- To subtract background offset signal
- To provide logarithmic conversion of data
- To transmit data to the preprocessing system

Early data acquisition systems employed xenon (gas ionization detectors). These detectors directly convert x-ray energy to electrical energy but are inefficient. Most modern systems include the use of solid-state detectors. Two primary crystal materials are in use today, cadmium tungstate and gadolinium oxysulfide. The crystals convert the x-rays to light proportional to the quantity of photons striking the crystal. The light is converted to current and hence a voltage across a resistance and then to digital data for use by the reconstruction system.

The conversion of analog signals to digital data (A to D conversion) by the data acquisition system creates a *quantization error*. Sampling speed of the A to D converter and the number of digital output combinations available determine quantization error. This quantization error, along with electronic noise in the amplifier, generally characterizes the performance of the data acquisition system. The system's ability to measure low-level signals accurately over a wide dynamic range largely contributes to CT's overall image quality capabilities per a given x-ray flux.

Evolution of Data Acquisition Systems and CT System Geometry

First-Generation System

First-generation CT data acquisition was based on parallel-beam geometry with a translate-rotate principle of the tube/detector combination. The x-ray beam was collimated to dimensions of roughly 2 × 13 mm. The 13-mm dimension corresponded to the slice thickness (voxel length). Small detectors monitored the intensity of the beam before entering the body to yield the value of the incident intensity (I_0). After passing through the body, the beam was detected by a scintillation crystal, collimated to receive, primarily, those photons that were not scattered or absorbed. The amount of transmitted intensity (I) was then recorded and stored in the computer memory.

The x-ray tube and detector system were moved continuously across the patient, making 160 multiple measurements during the translation. At the end of each translation, the x-ray tube and detector system were rotated 1 degree and the translation repeated. The translate-rotate process was repeated for 180 translations, yielding 28,800 (160 × 180) measurements. The 160 measurements made during one complete translation are called a *profile* or *view*.

From a clinical standpoint, the first-generation machine had the major disadvantage of long scanning times. Image quality severely suffered from the effects of patient motion, since 5 minutes was required to gather the 28,800 ray sums. This disadvantage limited use to body parts such as the head, which can be made immobile.

Second-Generation System

Second-generation data acquisition and scanner geometry included fan-beam reconstruction with a linear detector array. The x-ray beam was converted to a fan shape with a

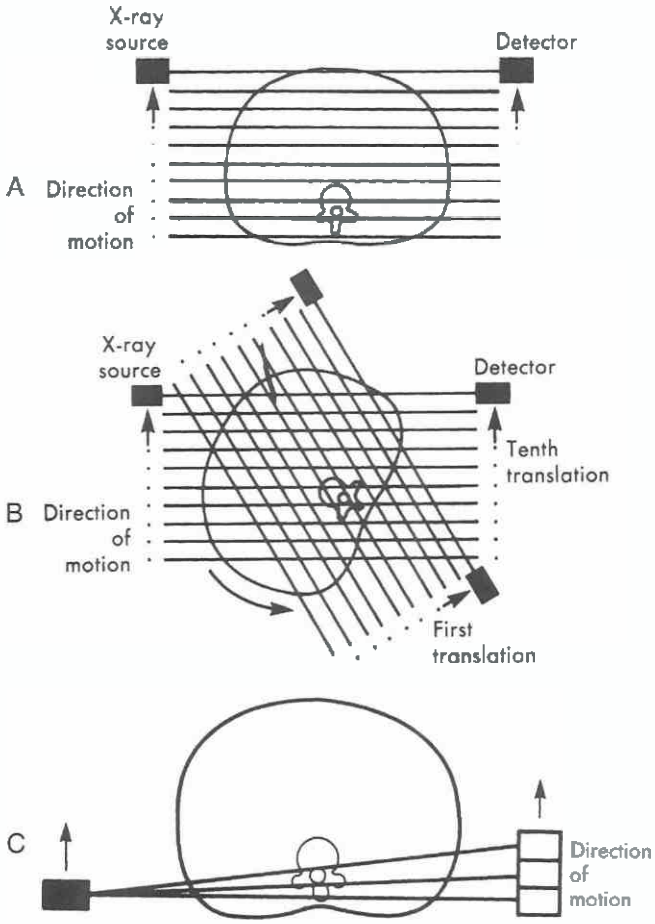

Figure 1–5. Translate-rotate scanner. *A*, Original single-detector system, single translation. *B*, Two separate translations. *C*, Second-generation system with fan beam source and multiple detectors.

diverging angle of between 3 and 10 degrees (Fig. 1–5). Multiple x-ray detectors were then placed adjacent to each other to intercept this beam. Because more x-ray detectors were used with this system, the number of angular rotations could be decreased and an adequate number of views obtained in much shorter intervals. With second-generation data acquisition, scanners could obtain a scan in periods as short as 18 seconds. From Figure 1–5, it is obvious that each detector obtains a different view during a translation because the rays from the x-ray tube to the detectors are not parallel.

The next few developments in CT involved a widening of the fan beam so that it encompasses the object entirely.

Third-Generation System

Third-generation data acquisition and scanner geometry use wide-angle fan beam geometry (50 to 55 degrees); an arc of detectors and an x-ray tube rotate continuously around the patient for 360 degrees. As the x-ray tube and detector arc are rotated, projection data (or data samples) are obtained, and for every fixed point of the tube and detector, a view is created (Fig. 1–6).

As Figure 1–6 demonstrates, the detectors are fixed radially and do not view the scan area uniformly. Only the center detectors in the array "see" the pixels at the center of the *field of view* (FOV). However, this fixed relationship allows the detectors to be highly collimated, which greatly reduces scatter radiation; as discussed later, this also reduces "image noise" (mottle, or grainy background) and improves image quality.

As a result of the fixed position of the tube/detector combination the associated detectors and electronics system must be stable, uniform, and capable of tracking over a wide dynamic range. Noncompensation for errors as small as a few thousandths of 1% can cause visible (ring) artifacts (see Fig. 1–39). In addition, spatial resolution, a key image quality parameter of CT (see later), can be limited by the data sampling. In this geometric relationship, the number of detectors in the arc or array determines data sampling; that is, spatial resolution depends on how closely spaced the rays are in each view.

The typical number of detectors ranges from about 600 to more than 900. These numbers result in a limiting spatial resolution of approximately 5 to 10 line pairs per centimeter (lp/cm), depending on the reconstruction matrix size and scan FOV. Sampling theory (Nyquist) requires that to visualize a particular frequency, the sampling frequency must be at least twice that value. In practice, even higher sampling rates are desirable. Axial resolution of greater than 5 to 10 lp/cm (0.5 to 1.0 mm) may be limiting for specific clinical applications.

To overcome this challenge, manufacturers have introduced various methods. One method of increasing sampling (and spatial resolution) is to offset the detector array relative to the center of rotation by a quarter-ray or eighth-ray. This permits data collected during the second half of a 360-degree rotation to be interleaved with that of the first half, effectively doubling the sampling and resolution. Unfortunately, patient motion can minimize this effect. In addition, this method is restricted with spiral CT scanning (see later) to certain modes in which 360 degrees of data is available for interleaving.

Another more effective method of increasing data sampling is to scan or oscillate the x-ray tube focal spot a few millimeters during a scan (Fig. 1–6*B*) in order to achieve interleaved data samples. The position of the focal spot is accurately controlled and synchronized with rotational speed and position of the rotating frame.

Spatial resolution also requires adequate view sampling to prevent "aliasing" artifacts. Views in this case are limited by the electronic measurement capability of the scanner, which is typically not the gating factor for maximum resolution. These factors vary for every CT manufacturer, which can dramatically affect the overall performance of a scanner.

Fourth-Generation System

Fourth-generation data acquisition and scanner geometry (Fig. 1–7) also use a wide-angle rotating fan beam (50 to 55 degrees); in this case, though, the tube rotates within a 360-degree arc of stationary detectors. Instead of the focal spot as the focus of views, as in a third-generation system, views are seen from the perspective of the detector. With

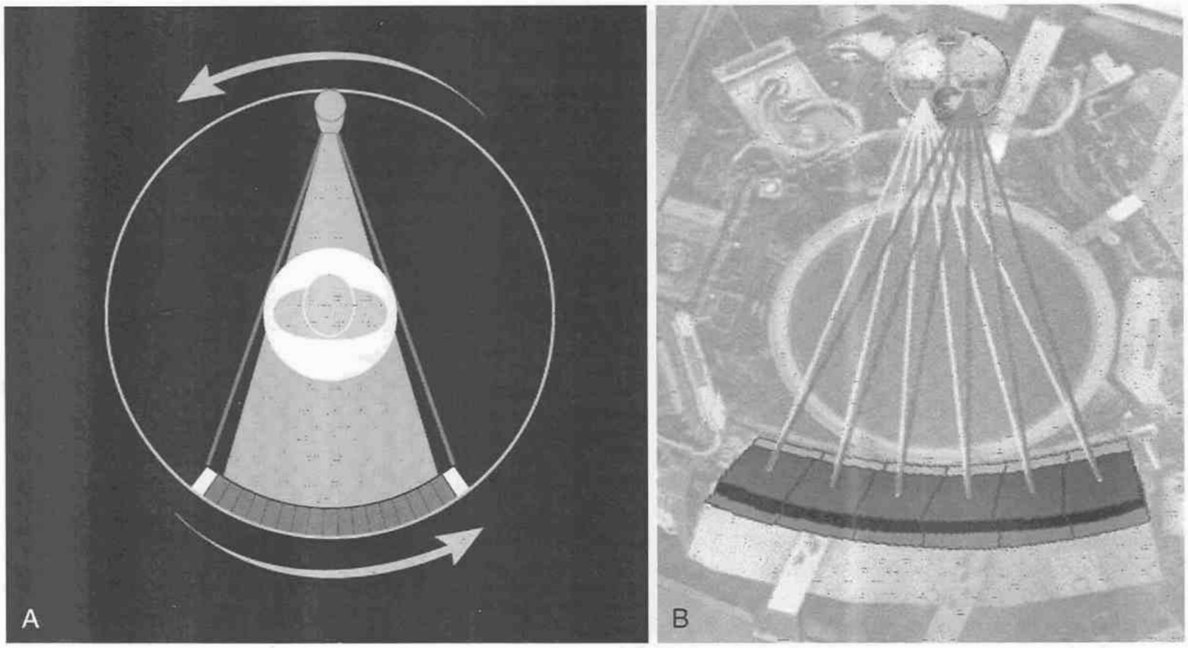

Figure 1–6. *A,* Third-generation rotate-only scanner geometry showing fixed relationship of x-ray tube and detectors. *B,* Dynamic focal spot technology (Marconi Medical Systems) effectively doubles the data sampling rate.

this approach, data samples are obtained over the width of the fan angle and several data samples are acquired per detector. The output of each detector constitutes a view. Therefore, views are limited to the number of detectors in the 360-degree arc.

In this geometric configuration, data sampling is limited by the system electronics, not by the number of detectors. The collection of equivalent, closely spaced ray sums using this geometry permits a very high spatial resolution (>20 lp/cm) (Fig. 1–8),[28] although it forces a wider collimation of the detector, which in turn can cause an increase in detection of scattered radiation. Several techniques are employed to minimize the effect of scattered radiation. Most important, natural rejection of scatter is minimized with appropriate distance between the patient and detectors.

With fourth-generation geometry, small, closely spaced

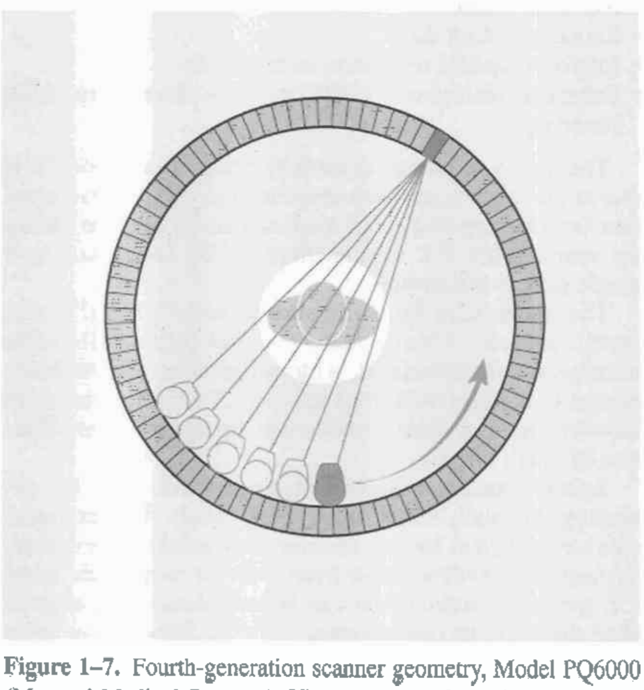

Figure 1–7. Fourth-generation scanner geometry, Model PQ6000 (Marconi Medical Systems). Views are seen from the perspective of the detector.

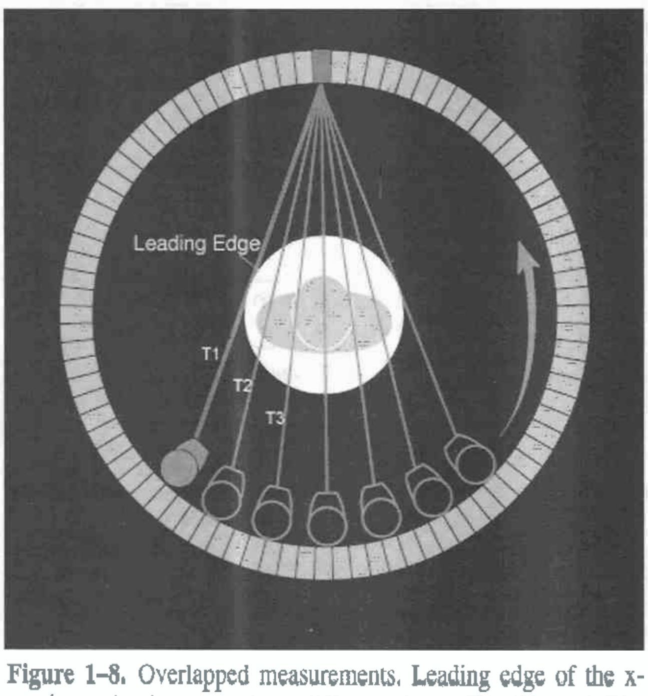

Figure 1–8. Overlapped measurements. Leading edge of the x-ray beam is shown at three different times (T1, T2, and T3), representing small, closely spaced data samples during a scan.

data samples require many individual measurements, which can affect reconstruction time. To overcome this challenge, views are averaged to reduce this effect. Most systems have many more detectors and views available to exceed the limiting resolution of the system.

There are unique advantages and disadvantages to today's CT geometry beyond spatial resolution, including (1) detected quantum efficiency, (2) noise, and (3) contrast resolution. The performance of each system depends largely on the manufacturer and not the scanning geometry used.

Spiral/Helical Computed Tomography

Until the late 1980s, CT scanners, regardless of system geometry (third or fourth generation), acquired data in discrete slices of patient anatomy in a method commonly called *axial scanning*. In axial (cross-sectional) CT, each revolution of the x-ray tube around the patient produced a single data set *(slice)*. During data collection, the patient table is motionless. To create an additional slice, the table is indexed a given amount and the x-ray tube is once again rotated around the patient. Each rotation or slice produces a single image. The advent of slip ring technology and new data reconstruction techniques provided a gateway to the data acquisition currently in use namely, (1) spiral/helical CT and (2) multislice spiral or multidetector/multirow CT data acquisition systems.

In spiral/helical CT, the patient table translates through the gantry while the x-ray tube (fourth generation) or the x-ray tube/detector combinations (third generation) rotate continuously around the patient, creating a volume of data. This permits new options in reconstruction. For example, once a volume of data is collected, an image can be reconstructed at any point along the effective path traced by the x-ray tube. At this point, it may be helpful to define the terms associated with spiral scanning (Table 1–1):

Acquisition is the entire volume of data collected during a continuous spiral scan.

Revolutions refer to the number of 360-degree rotations of the x-ray tube during a single acquisition.

Pitch is the distance the couch travels during one 360-degree revolution of the x-ray tube.

Table 1–1. Spiral Scanning Terms in Computed Tomography

Acquisition (spiral)	The process by which a single, continuous volume of computed tomography data are acquired without a pause
Revolution	One per each 360-degree rotation of the x-ray tube around the patient or object of interest
Pitch	The distance the couch or patient travels through the gantry during one 360-degree beam rotation
Pitch factor	A unitless parameter in which pitch can be designated. This is defined as the pitch (mm) divided by the collimated slice thickness (mm)
Interpolation	A mathematical technique used to estimate the value of a function from values on either side of it

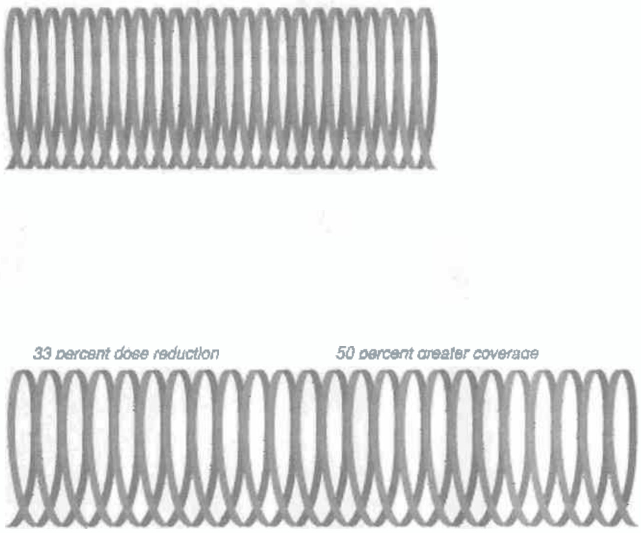

Figure 1–9. Extending the pitch factor from 1:1 to 1.5:1 increases volume coverage by 50% and decreases patient dose by 33%.

Pitch factor is the pitch divided by the collimated slice thickness, or effective width of the beam at the isocenter of the gantry. The term "pitch" has become synonymous with "pitch factor."

Interpolation is a reconstruction method (most accurately described as "deconvolution") that permits the realignment of spiral/helical scan data for reconstruction of an axial (cross-sectional) slice.

Spiral CT has many advantages over conventional or axial CT, including[30]:

- The ability to minimize motion artifacts
- Decreased incidence of misregistration between consecutive axial slices
- Reduced patient dose
- Improved spatial resolution in the z-axis
- Enhanced multiplanar (MPR) or three-dimensional (3D) renderings

The ability to minimize motion artifacts in spiral CT is due to the faster scan times associated with every examination (versus step-and-shoot axial scanning) and the ability for many spiral CT examinations to be completed in a single patient breath-hold.

The faster scan times associated with spiral CT also permit accurate slice-to-slice registration and eliminate misregistration associated with inconsistent breath-holds related to conventional axial scanning. Reconstructions can be overlapped or ideally positioned for accurate visualization of small lesions.

Spiral scanners achieve reduced patient dose by extending the pitch factor for a given study. For example, consider a typical thorax, abdomen, or pelvis examination. Typical slice widths range from 5 to 10 mm. With spiral CT, the same examination can be completed with a given slice thickness as conventional CT with 50% greater table speed using a pitch of 1.5; this results in a 33% reduction in patient dose (Fig. 1–9). The nominal downside to this

approach is a slight broadening of the slice sensitivity profile (effective axial slice thickness) based on the type of spiral reconstruction chosen. The slice thickness formula is given as[32]

$$\sigma = \frac{D^2}{12} + \frac{T^2}{24} \tag{2}$$

where

D is detector collimation
T is table speed
σ is the standard deviation (SD) of the slice sensitivity profile

See "Reconstruction" for further details.

With continuous collection of data, as just described, spiral CT enables a reduction in image-to-image separation, thus improving spatial resolution in the z-axis. Although conventional CT might overcome this challenge by overlapping consecutive axial slices, this would increase the patient radiation dose and would lengthen scan times to cover a given region of patient anatomy.

Multiplanar and 3D renderings are enhanced as a result of the ability of spiral CT to reconstruct overlapped planar and axial slices from a continuous volume of data. The optimal number is two to three transverse slices per detector collimation[32] and is given as the formula

$$n = \frac{3}{\pi\sqrt{\frac{1}{12} + \frac{p^2}{24}}} \tag{3}$$

where

n is the slice number per collimation
p is pitch (table speed over collimation)

Spiral CT data acquisition systems must be capable of collecting large volumes of data at extremely fast data rates. Data sampling for most systems is in the range of 3 kHz and can provide up to nearly 2400 projections or views per rotation of the gantry. Data rates for many new systems exceed 200 megabits/second. This extremely fast sampling capability enables high spatial resolution and enhanced z-axis sampling of patient anatomy.

The increased speed of data acquisition systems and a number of other technologic developments paved the way for data acquisition at subsecond rotation speeds of the rotating frame. Subsecond spiral data acquisition permits temporal resolution on the order of 250 to 480 msec, depending on the manufacturer. Temporal resolution of this magnitude enables more examinations to be accomplished within a single breath-hold and dramatically improves the anatomy that can be covered in a single scan. This improves clinical applications such as CT angiography, which requires precise timing of a bolus injection and rapid acquisition during the arterial phase. Subsecond data acquisition also can improve the z-axis resolution (slice thickness) for a given study by covering the same amount of anatomy in the same time with thinner slices, However, spiral CT is not without limitations and many examinations might benefit from an even more dramatic increase in data acquisition rates.

Multislice Spiral CT

The latest development in data acquisition—multislice spiral CT—overcomes the limits of spiral CT. All multislice spiral CT systems today use third-generation geometry (rotate only) with the added dimension of multiple arcs of detectors. The first deployment of this technology included a dual-arc detector (Fig. 1–10).[38] In this configuration, two parallel arcs of detectors are used to simultaneously acquire data during a single revolution of the scan frame, dividing the total x-ray beam into two equal beams described by the detector aperture of each row of detectors. Considering small gaps between rows, which can be ignored from the perspective of data acquisition, the total x-ray beam collimation now becomes the sum of detector row collimations (Fig. 1–11) and is described as

$$d(\text{mm}) = \frac{D(\text{mm})}{2} \tag{4}$$

where

d is the detector row collimation
D is the x-ray beam collimation
2 is the number of detector rows

This can be extended to include n rows of detectors.

Four-Slice Design

Since the introduction of dual-detector technology in the early 1990s, other manufacturers have introduced four-slice configurations. Two four-slice design approaches are described.

Equal-Width Detector

As with the dual-beam array, detectors of equal widths are stacked back to back in the z-axis (Fig. 1–12). In the case of one manufacturer, 16 rows of 1.25-mm detectors (effective width at isocenter) are aligned in the z-axis. To achieve different slice widths, the detectors are electronically coupled at the beginning of each scan according to the requested slice width. The total z-axis dimension of the detector covers 20 mm. This approach limits the minimal z-axis resolution to the nominal width (at isocenter) of the individual detectors. Figure 1–13 demonstrates the use of multiple detector combinations per requested slice width.

Variable-Width Detector

A second approach (Fig. 1–14) combines fewer detectors of variable widths and a postpatient collimator to define slice widths. This approach is more geometrically efficient because there is less unusable space in the z-axis (Fig. 1–15*A*). This combination also permits slice widths as small as 0.5 mm, enabling isotropic imaging (submillimeter voxel dimensions are equal in all planes) (Fig. 1–15*B*).

In either case, the clinical benefits of multislice CT can best be described by comparing clinical protocols versus single-ring spiral CT. For a given protocol, multislice CT is more efficient by the number of detector rings used. Consider a typical single-slice spiral CT protocol of 40 seconds, at 1 second per revolution (scan time), with a slice thickness of 5 mm, using 200 mA, with 200 mm of

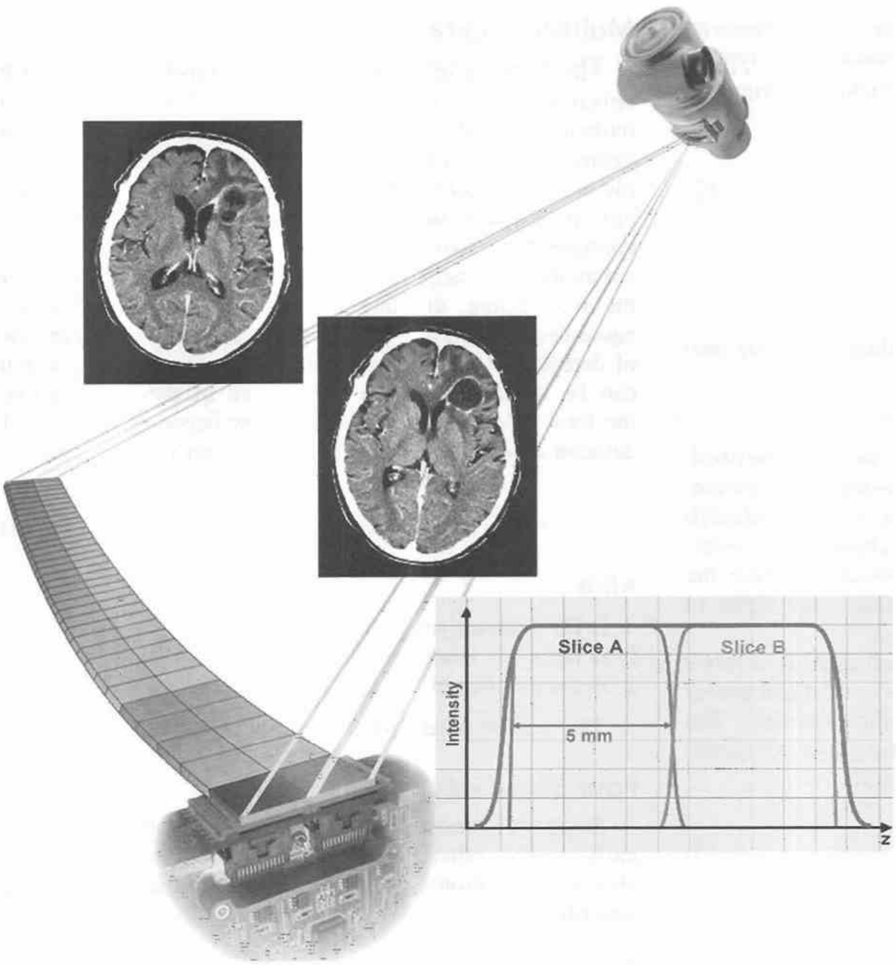

Figure 1–10. The first multislice detector system (Marconi Medical Systems dual-arc detector). Two detectors are aligned consecutively in the z-axis, creating a 2D detector matrix/array and two images per gantry revolution. (Courtesy of J. S. Arenson.)

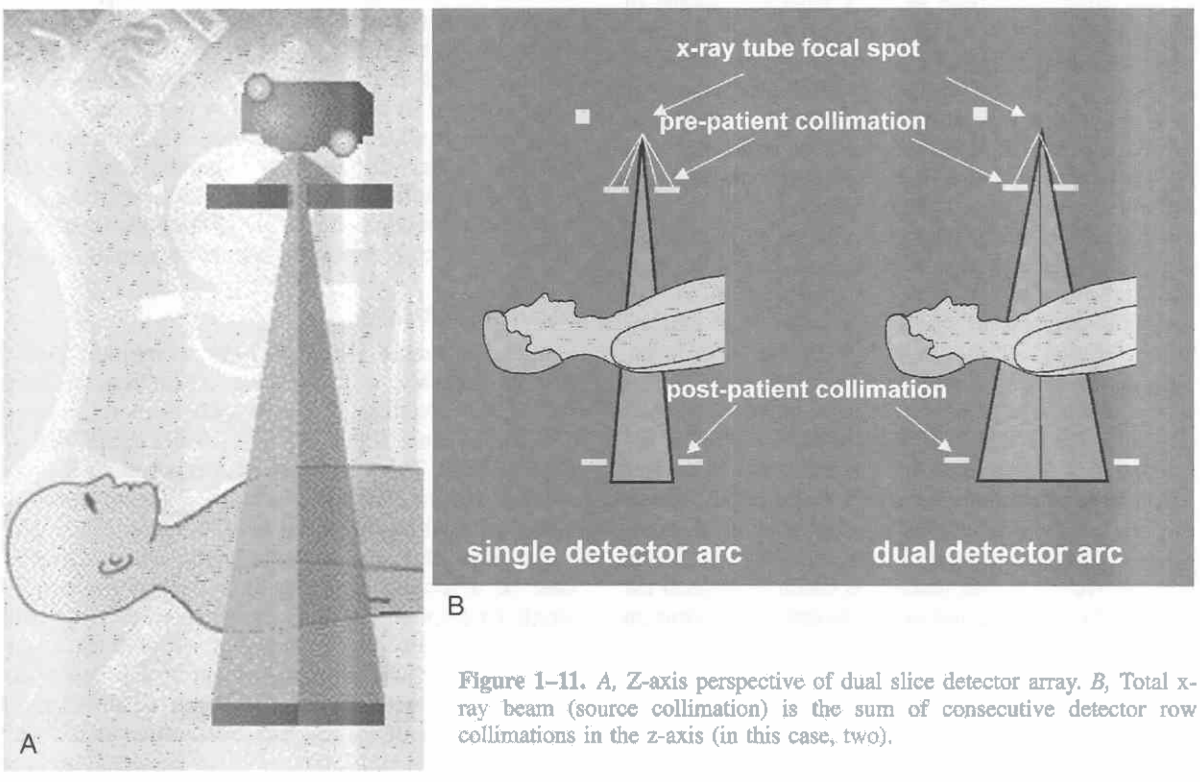

Figure 1–11. *A,* Z-axis perspective of dual slice detector array. *B,* Total x-ray beam (source collimation) is the sum of consecutive detector row collimations in the z-axis (in this case, two).

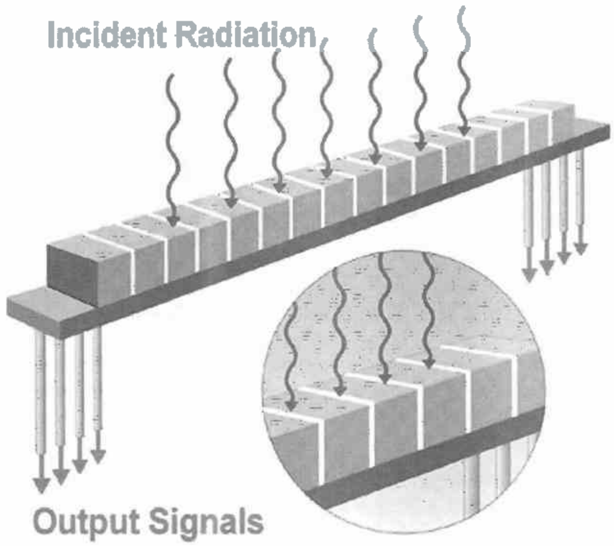

Figure 1–12. Multislice spiral CT Matrix detector (GE Medical Systems) with 16 rows of equal width (1.25 mm at isocenter) detector elements.

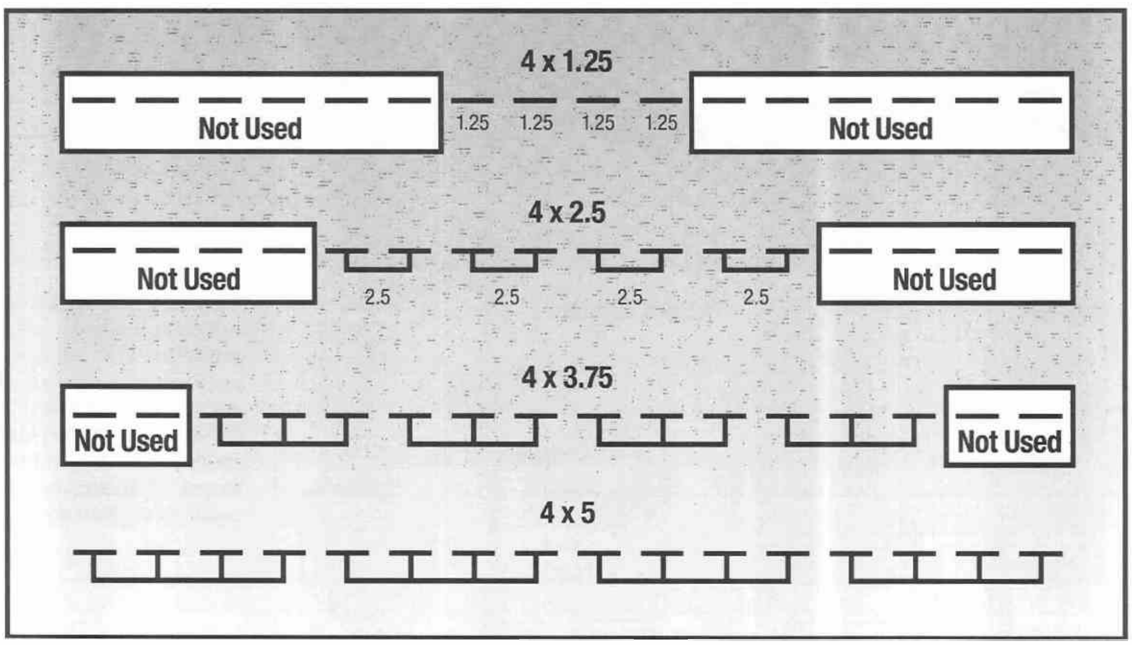

Figure 1–13. Matrix detector. Electronic combination of individual elements produces slice collimation configurations of 4 × 1.25 mm, 4 × 2.5 mm, 4 × 3.75 mm, and 4 × 5 mm.

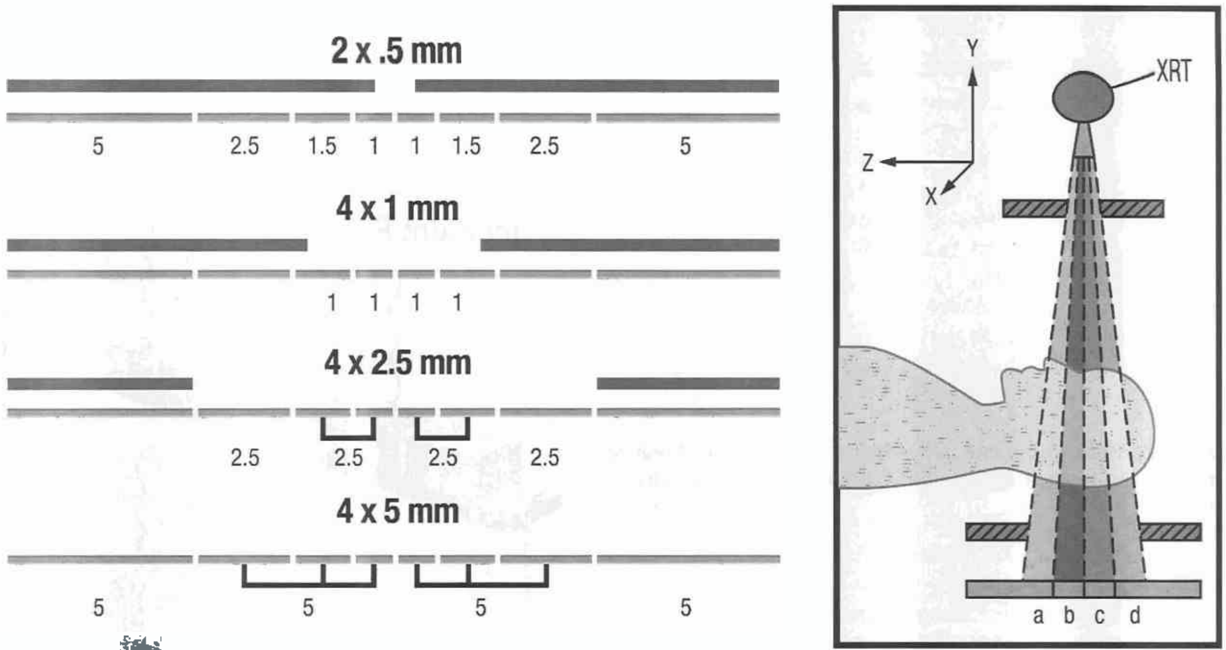

Figure 1–14. Asymmetrix variable detector array (Marconi Medical Systems) and postpatient collimator produces slice collimation configurations of 2 × 0.5 mm, 4 × 1 mm, 4 × 2.5 mm, and 4 × 5 mm.

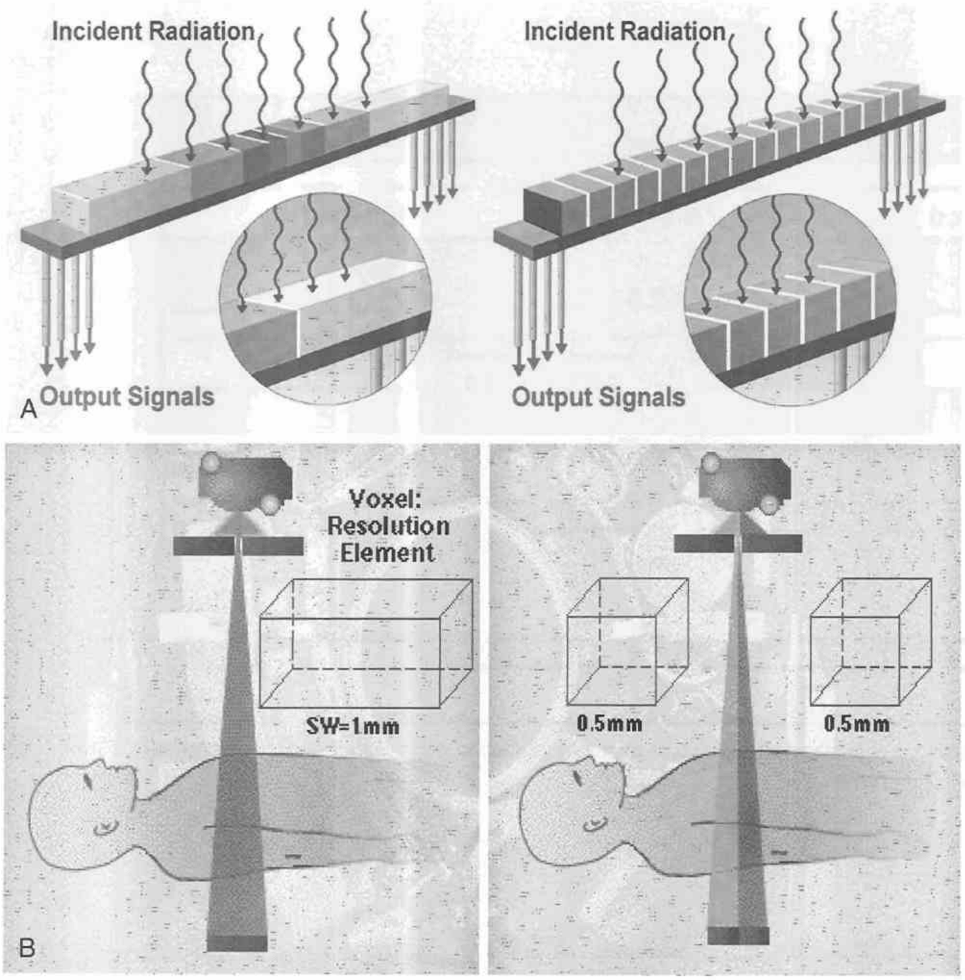

Figure 1–15. *A*, Comparison of z-axis geometric efficiency of multislice CT detectors. At wide collimations, variable detector array is more efficient. *B*, A 2- × 0.5-mm slice width with ultrahigh in-plane resolution produces isotropic imaging; voxel width is equal in all dimensions.

total anatomic coverage. Using a multislice data acquisition system with n rings, the same protocol can be modified to:

1. Enhance z-axis resolution by a factor of n. The slice thickness is divided by n rings with the same total anatomic coverage, scan time, and milliampere-seconds (mAs).
2. Enhance the speed of anatomic coverage by n. The 40-second continuous spiral run is divided by n, with the same nominal slice thickness, scan coverage, and mAs.
3. Enhance the anatomic coverage of the examination by n; 200 mm of coverage is multiplied by n using the same nominal slice thickness, scan time, and mAs.
4. Increase effective milliamperage by n. By dividing the pitch by n rings, the 200 mAs is effectively increased by a factor of n, maintaining the same nominal slice thickness, scan time, and coverage.

As described earlier, pitch or pitch factor is the distance in millimeters the couch is moved during one revolution of the gantry. Pitch is determined by dividing the movement of the table through the gantry during one 360-degree rotation by the x-ray beam collimation at the source (prepatient collimator). By segmenting the usable x-ray beam into n segments, multislice CT complicates the equation.

There are two commonly used definitions (Fig. 1–16):

1. Pitch is defined using the model described earlier; however, a prefix added to the pitch indicates the number of detector rings used (e.g., single, one ring; dual, two rings; quad, four rings). A pitch of quad-1 would refer to a scan in which the table moves the distance of the source (prepatient) collimation during one revolution of the gantry. For a given protocol, a pitch 1 scan delivers the same patient dose and fundamentally produces the same image quality in a single-slice, dual-slice, or quad-slice scanner.
2. Pitch is defined as the result of dividing the movement of the table through the gantry by the effective slice width at the isocenter of a single detector (or n rings × effective slice thickness of an individual slice). Thus, a pitch of 4 is equivalent to a quad-pitch 1 (see first definition).

An accepted convention will emerge, but at first glance it appears that the second definition is confusing and offers less information. For example, from definition 2, a pitch 2 could refer to single-pitch 2, dual-pitch 1, or quad-pitch 0.5.

As of this writing, several manufacturers have introduced four-slice models, but future configurations of 8, 16, 32, 64, and perhaps even flat panel detectors of several hundred square millimeters are on the horizon.

In each case, multislice CT complicates fan-beam reconstruction techniques by adding a divergence of the fan beam along the longitudinal axis (z-axis), creating a cone shape (cone beam) (Fig. 1–17). This new technique, *cone-beam reconstruction*, is considered later (see "Reconstruction").

Electron Beam Computed Tomography

A modification of the fourth-generation concept of data acquisition involves moving the x-ray beam electronically instead of mechanically. This scanning method reduces the scan time to approximately 0.02 second per slice and, with a small delay for consecutive slices, up to 17 slices per second.

An electron beam is accelerated along the axis of rotation of the CT scanner and is electronically deflected to any one of four fixed tungsten x-ray targets. Each target is an arc of tungsten of 210 degrees with a radius of 90 cm. The electron beam is deflected through the 210-degree arc of the target, creating the scan.

Opposite the target are two sets of stationary detectors with arcs of 216 degrees. One detector arc has 432 detectors; the other, a higher-resolution ring, has 864 detectors. Each individual detector consists of a cadmium tungstate crystal matched with a silicon photodiode and a preamplifier. Adjacent detectors of the high-resolution ring can be summed to match the other ring for dynamic imaging, or can be used singly, for high-resolution imaging.

During dynamic scanning, two slices can be acquired simultaneously. Scanning takes place over 180 degrees instead of the 360 degrees of most conventional scanners. An image can be reconstructed with 180 degrees of data.

Once the signals are generated, the remainder of the scanner is fairly conventional in design. This system design has many image quality shortfalls for routine imaging, but its superior temporal resolution has led the way for CT into the realm of cardiac imaging.[24]

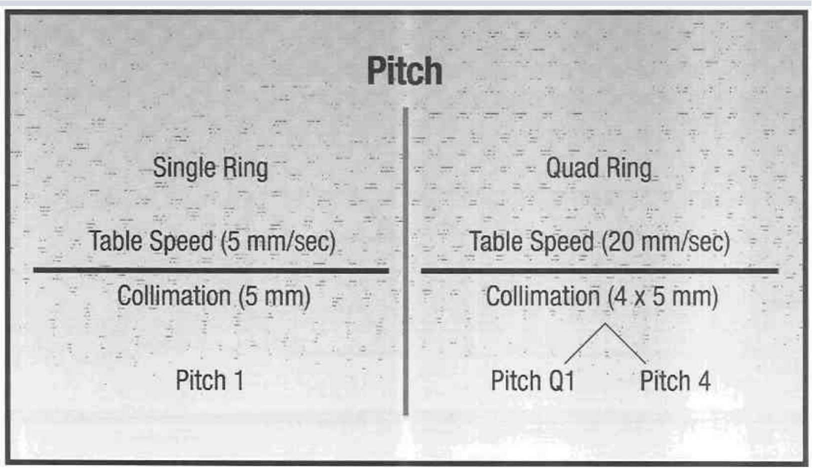

Figure 1–16. Naming conventions for pitch. *A*, Single-ring spiral CT definition in which pitch equals table speed/source collimation. *B*, Alternative definitions for multislice spiral CT, with definition 1 representing table speed/source collimation as quad-pitch 1 and definition 2 representing table speed divided by the single-slice collimation (detector collimation) as pitch 4. Both are accepted.

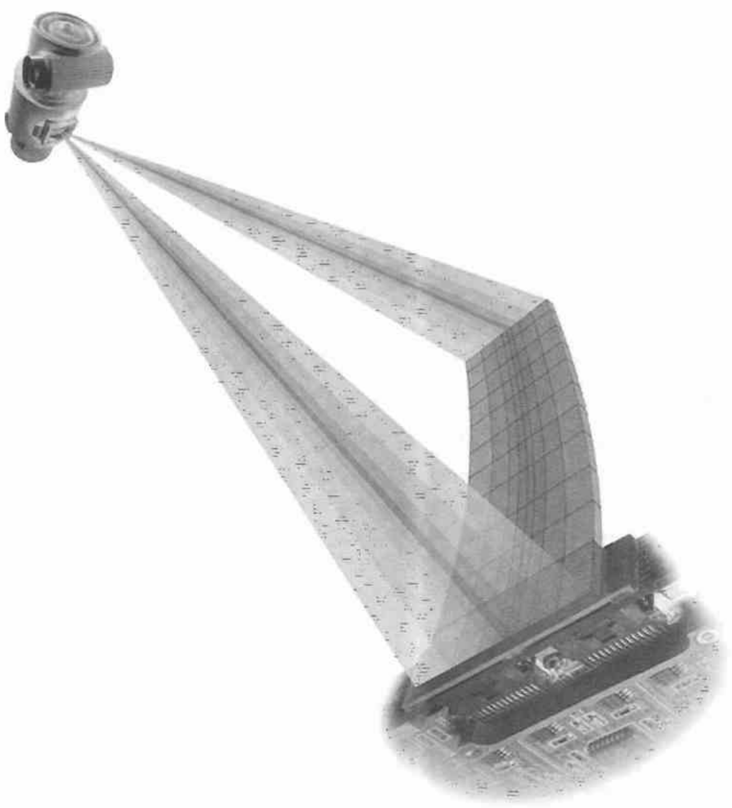

Figure 1–17. The x-ray fan beam is divergent in the z-axis, creating a cone beam.

Reconstruction

Reconstruction includes all of the system components necessary to perform the mathematical computations that are required to convert the digital data (representing the log of attenuation coefficients) provided by the data acquisition system. The reconstruction system delivers CT data to the display system in a manner that is suitable for viewing on a viewing monitor. Regardless of the scanner type, the result of a scan is a large number of individual ray sums. The reconstruction of the image from these measurements is, in principle, the same for every CT scanner.

The fundamental equation describing the behavior of the measurements is given in Equation 5, and a few simple manipulations of this relationship should help one to understand CT image reconstruction.

Figure 1–18 shows a number of thin slabs with an initial x-ray intensity (I_0) impinging on the first slab. The exit intensity from the first slab (I_1) becomes the entrance intensity for the second slab, and its exit intensity (I_2) is the entrance intensity for the third slab, and so forth. We can then write

$$\begin{aligned} I_1 &= I_0 e^{-\mu_1 L_1} \\ I_2 &= I_1 e^{-\mu_2 L_2} = (I_0 e^{-\mu_1 L_1}) e^{-\mu_2 L_2} \\ I_n &= I_{n-1} e^{-\mu_n L_n} \end{aligned} \tag{5}$$

The equation for the emergent beam after passing through n slabs can then be deduced as

$$\begin{aligned} I &= I_0 (e^{-\mu_1 L_1})(e^{-\mu_2 L_2}) \ldots (e^{-\mu_n L_n}) \\ &= I_0 e^{-\mu_1 L_1 + \mu_2 L_2 + \ldots \mu_n L_n} \end{aligned} \tag{6}$$

For simplicity, the subscript n on I_n has been dropped. Therefore, the total attenuation is equivalent to the simple equation

$$I = I_0 e^{-\mu L} \tag{7}$$

where

$$\mu L = \mu_1 L_1 + \mu_2 L_2 + \ldots \mu_n L_n \tag{8}$$

When $L_1 = L_2 = L_3 = \ldots = L_n$ (i.e., all the slabs have equal thickness), Equation 8 can be written as

$$\mu L = (\mu_1 + \mu_2 + \ldots \mu_n) L$$

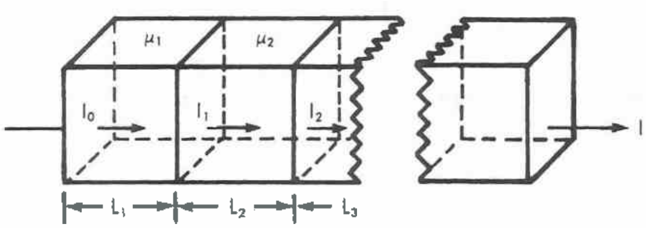

Figure 1–18. Illustration of Equation 6 (see text).

If we now take the natural logarithm (ln) of both sides of Equation 7 and rearrange it, the result is

$$\mu = (\mu_1 + \mu_2 + \ldots \mu_n) = \frac{1}{L} \ln \frac{I_0}{I} \qquad (10)$$

Equation 10 shows that, if the incident intensity I_0, transmitted intensity I, and segment length L are known, the sum of the attenuation coefficients along the path of the x-ray beam can be calculated.

Because there are n unknowns (one of each segment), each value of the attenuation coefficient cannot be determined from a single equation. Algebraic theory requires that there be n independent equations to obtain solutions for the n unknown values of μ. To get n independent equations, a number of views must be taken; it is then possible to gather sufficient data for the multiple equations.

A comparison with conventional radiography shows that because only one measurement is made in radiography, only the average value of μ or the sum of the μLs can be obtained. Thus, the information on the film is less detailed than the information on a CT image.

Reconstruction Process

For each ray projection measurement made during a CT scan, Equation 10 is generated and the complete set of such equations must then be solved to obtain the individual values of μ for each matrix element. Because thousands of ray projections are obtained for a scan, thousands of equations must be solved simultaneously and the need for high-speed computers is obvious.

Note that L is not related to the slice thickness (voxel length) and is chosen for the reconstruction process by selecting a matrix size. Provided that sufficient ray projections have been made, the image can be reconstructed in any matrix size, which is paramount to choosing any value of L. The voxel length is set by the collimation of the scanner when a slice thickness is selected. *A picture element (pixel), therefore, represents the attenuation coefficient (μ) of a volume element with length determined by the slice thickness chosen during the data acquisition and cross-sectional area that has a side dimension (L) chosen at the time of reconstruction.*

Many methods have been devised to solve the set of equations generated in a scan; however, most manufacturers have settled on the filtered back-projection method because it allows short computation time with relatively accurate solutions.[2, 4, 5, 8, 9] It also allows processing of each ray sum immediately after it is obtained while the data acquisition continues for other ray sums. This permits the final image to be available for viewing almost immediately after completion of the scanning process. It is important to understand the basic concepts underlying reconstruction procedures, since their manner of application affects the quality of the final image.

The back-projection method is an attempt to approximate the solution by projection of a uniform value of attenuation over the path of the ray such that the calculated attenuation over the path is proportional to the measured attenuation. These values are then stored in the computer for the matrix elements involved, and the process is repeated for each ray sum of the scan. Each matrix element thus receives a contribution from each ray that passes through it. For those voxels through which the beam passes obliquely, a correction is made to the contribution (Fig. 1–19). The final image obtained is rather blurred as a result of the assumption that the beam attenuation occurs uniformly over the entire path of the ray.

The process is exemplified in Figure 1–20, which demonstrates the result of applying this procedure to a uniform field with a circular object of high-density embedded in it. In the example, only a few rays are used.

Two observations should be made: (1) the procedure generates a star pattern, and (2) it tends to approximate the image better as more views are obtained.

No matter how many views are used, however, the blurring effect is never completely eliminated. Thus, a second mathematical maneuver called a *convolution operation*, or *filtering*, is used.[5, 13] The purpose of the filtering process is to modify the ray sum data such that the back-projections consist of both positive and negative values. In the example of Figure 1–21, the profile of the back-projected density is modified to look like the one in *B* rather than that in *A*. The result is the cancellation of some of the back-projected densities of other ray sums and removal of the unsharpness.

The filtering procedure involves a mathematical operation on the ray sum with a "filter function" or convolution "kernel." The filter function is a complex one that depends on many parameters, including x-ray tube geometry and

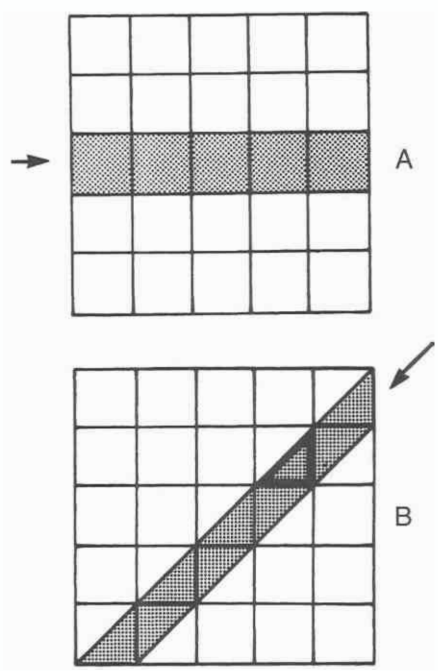

Figure 1–19. Ray projections. *A*, The projection includes only voxels parallel to the matrix representation, and entire voxels are covered. *B*, The projection is oblique to the matrix. A weighting factor must be included for the back-projections to avoid giving these pixels undue influence.

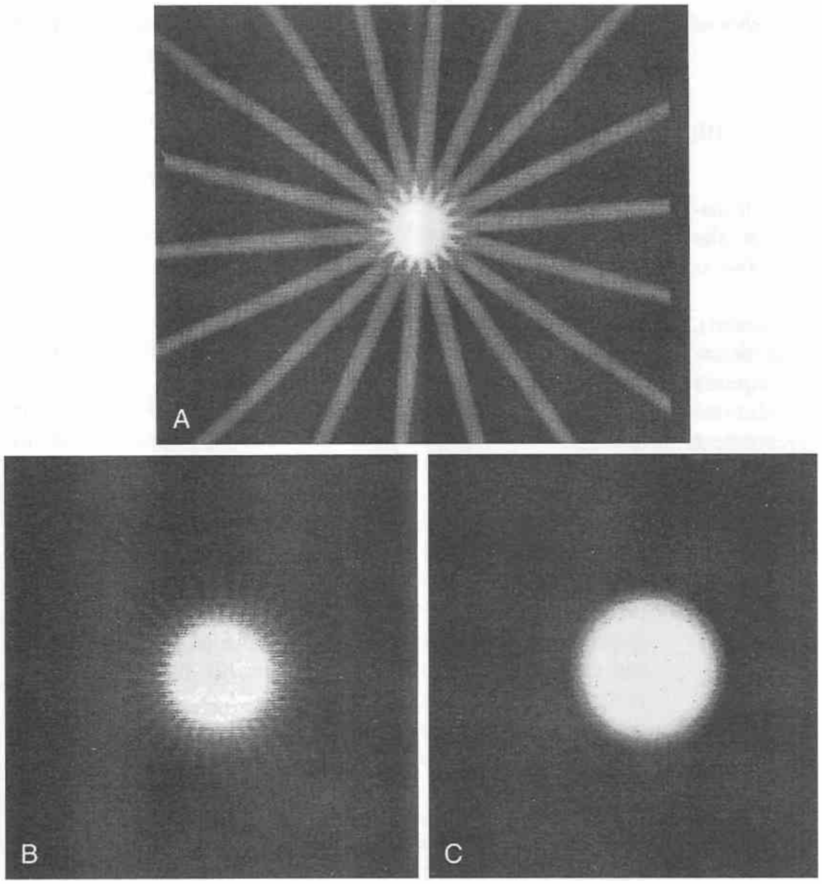

Figure 1–20. Reconstruction by back-projection of a high-density object in diffuse media. Back-projection with 18 views *(A)*, 36 views *(B)*, and 72 views *(C)*. Notice improvement of the image but persistence of star patterns with an increasing number of views. (Courtesy of Michael Mennett, Technicare Corporation, and George Kambic, Marconi Medical Systems.)

detectors. It can take on a number of forms, depending on the desired result.[3, 10] For example, one form of the filter function might enhance edges and thus sharpen the image, whereas another would blur edges for more gradual density changes. The edge-sharpening filter enhances spatial resolution but simultaneously decreases density resolution.

Thus, the choice of filter or kernel affects image quality, and the radiologist should be able to choose the best filter for a particular study. Some manufacturers automatically select the filters for particular procedures instead of requiring the radiologist to choose. Figure 1–22 illustrates the difference in applying various filter functions to the same data.

Image Reconstruction for Spiral CT

As described earlier, spiral scan data are acquired as the patient is moved continuously through the scan field by the table. If the data over a 360-degree rotation of the scan frame were reconstructed as in conventional (axial) CT, motion artifacts attributable to the movement of the table or patient would be visible.[30]

To minimize these artifacts and to reconstruct a planar image anywhere throughout the volume of collected data, some data must be synthesized or interpolated. The simplest form of interpolation is *linear*. Prior to reconstruction, projection data are weighted to produce individual sections of data at select locations. Spiral interpolators apply weighting factors to segments of the spiral data to estimate the data that would have been measured if an axial scan had occurred at a particular location.

Two common spiral linear interpolators are shown in Figure 1–23. A 360-degree interpolator uses two sets of spiral projections 360 degrees apart. This method assumes that projection data 360 degrees apart would be the exactly the same without patient motion. A 180-degree interpolator assumes that two measurements along the same path but in opposite directions would be the same without patient motion or other errors.

Generally, the more scan data that are used to reconstruct each image, the less noise, the wider the slice profile, and the longer the temporal resolution of the resulting image. Ultimately, the requested slice thickness, pitch, and spiral interpolator used for reconstruction affect the resulting z-axis resolution of spiral scan data.

As mentioned earlier, multislice CT complicates the fan-beam reconstruction techniques used by conventional and spiral CT by adding a divergence of the fan beam along the longitudinal axis (z-axis), creating a cone shape (cone beam) (see Fig. 1–17).

If the number of rows of detectors is limited to a small number (e.g., four rows), the cone-beam divergence is very small relative to the resolution of the detector element. This greatly simplifies the reconstruction of multislice data follows; just as in single-ring spiral reconstruction, only the alignment of projection rays as they cross the z-axis needs to be considered in the interpolation process. In

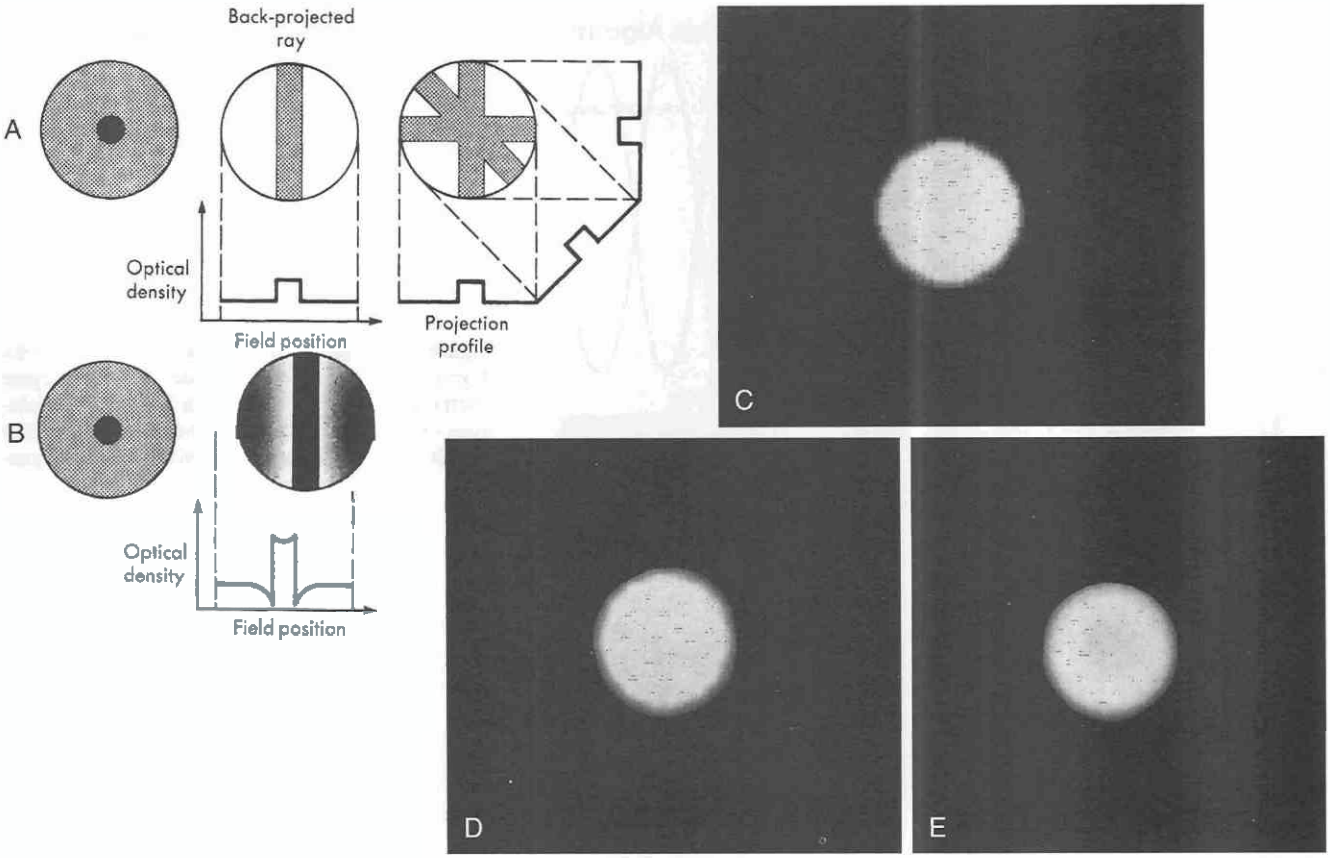

Figure 1–21. Effect of filtering in the back-projection method. *A,* Technique without filtering. *B,* Technique with filtering. The back-projected ray now has an area of decreased intensity directly adjacent to it, as shown by the profile of the back-projected ray optical density. When many projections are used, the negative aspects of the back-projections tend to smooth the image. *C–E,* Effects of performing the filtration function on the images of Figure 1–20 with 18, 36, and 72 views, respectively.

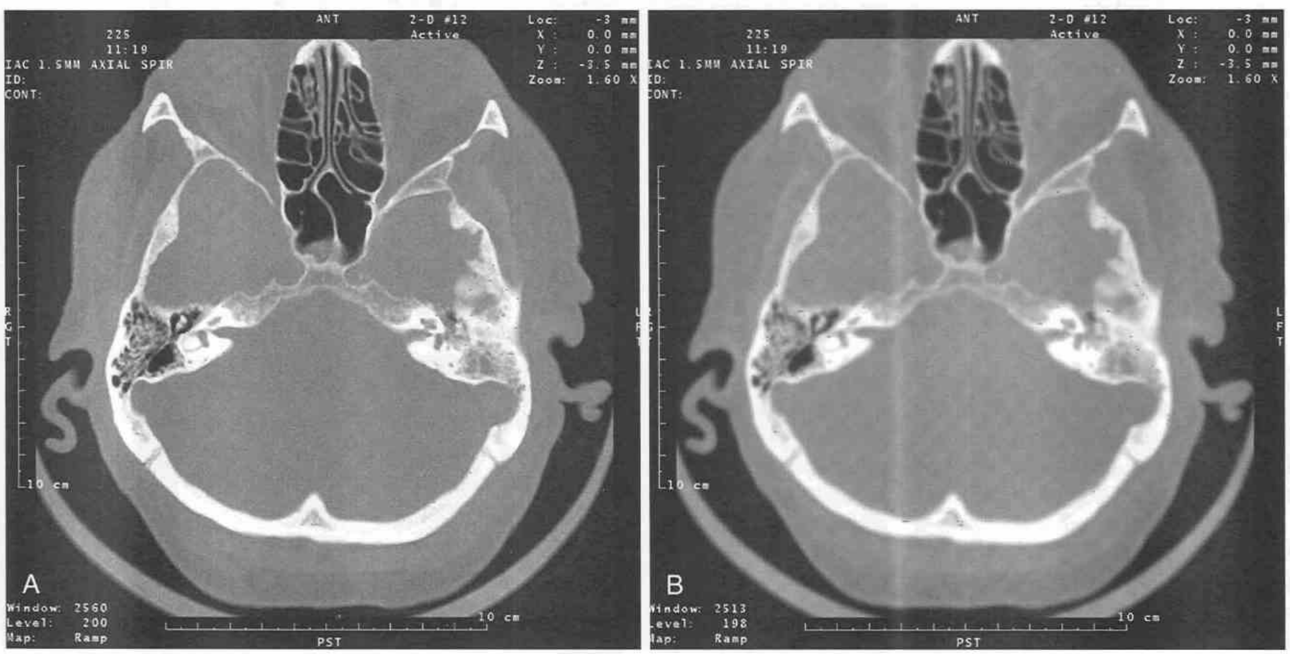

Figure 1–22. Filter effects on CT images. ***A,*** **Image with high-fre**[redacted]cy filter. Note the sharp image appearance and enhanced edge detail. *B,* Image with low-frequency (smoothing) filter. Note the blurry effects and decreased image sharpness. This filter increases density resolution at the expense of spatial resolution. (*A* and *B,* Courtesy of Marconi Medical Systems.)

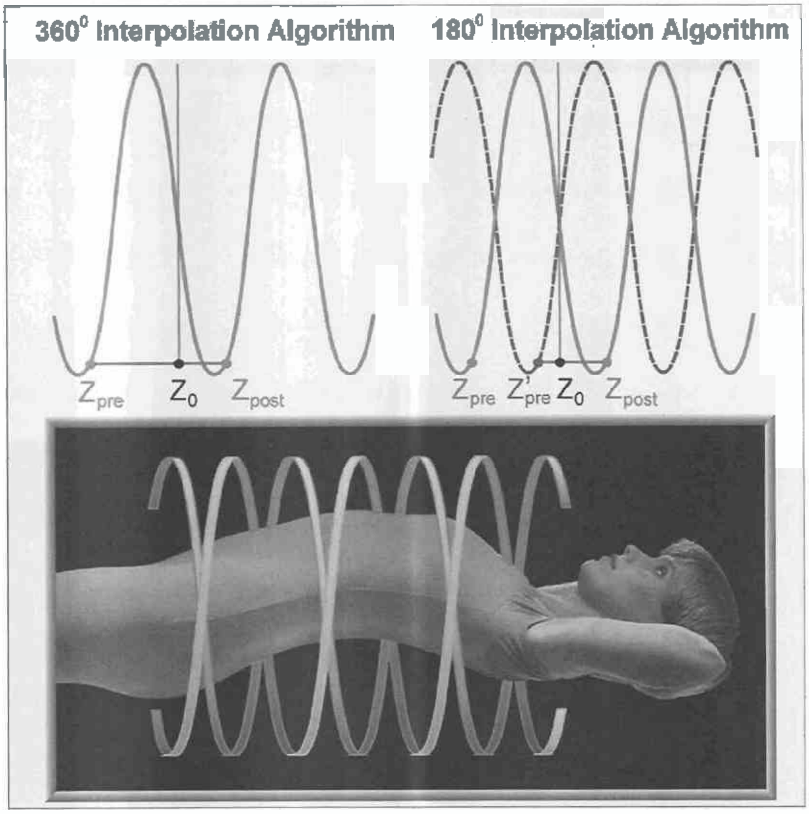

Figure 1–23. Algorithms showing 360- and 180-degree linear spiral interpolation. The 360-degree interpolator weights spiral data over two revolutions of the gantry, and the 180-degree interpolator weights spiral data over one revolution of the gantry.

the case of multislice interpolation, projection rays—either from neighboring detector rows or from rays 180 degrees apart (or more)—may be included in the interpolation.[37]

One interpolation method (spatially invariant) is described as follows:

1. For a scan with a quad-pitch factor of 0.625, up to four rays in the neighborhood of the target slice position are weighted by an interpolation function (designed to extend over the width of two detectors), synthesizing projections for the reconstructed slice.
2. For quad-pitch factors less than 1, this weighting function consistently generates slices with an effective slice width that is 30% broader than the width of one detector.
3. For quad-pitch factors greater than 1, reconstructions are generated from projections synthesized by interpolating only two neighboring projections, again resulting in an effective slice width 30% broader than the width of one detector.

This approach to multislice reconstruction maintains a more uniform resolution for different pitch factors, allowing the user to simply choose smaller pitches for higher effective milliamperage and lower spiral artifacts and larger pitches for maximum patient coverage.

Other multislice reconstruction techniques are available where the interleaving of data is best suited at optimal pitches only.[37] For example, using a linear interpolator at quad-pitch 1.5 (or pitch 6) creates slice-profile broadening of nearly 30%, whereas a quad-pitch of 0.75 (or pitch 3) creates little broadening.[37] Quad-pitches of 0.5 (2), 1 (4), 1.5 (6) and 2 (8) compare in z-axis sampling to single-ring spiral scanning with a pitch of 2.

Display

Image display includes all of the system components necessary to convert the digital data provided by the reconstruction system to electrical signals used by the CT display monitor (cathode ray tube) or flat panel (liquid crystal display), enabling a graphic display of individual CT numbers representing attenuation values of individual sections of anatomy. In addition, the display system includes the ability to display patient information, scan protocol, and reconstruction parameters, and it provides the user many graphic aids to assist in the interpretation of clinical images.

CT Number Scale

After a CT scanner reconstructs an image, the relative pixel values represent the relative linear attenuation coefficients because the process of reconstruction is not conducive to the calculation of the absolute values of the attenuation coefficients. However, it is valuable to quantify the pixel value so that the physician can compare the composition of one tissue with that of another. A CT numbering system that relates a CT number to the linear attenuation coefficients of x rays has been devised and is given by

$$\text{CT number} = \frac{K(\mu - \mu_w)}{\mu_w} \tag{11}$$

where

μ_w equals the attenuation coefficient of water
μ is the attenuation coefficient of the pixel in question

Although the original EMI CT scanner (Electronics Music Industries, Ltd.) used a value of K = 500, the value of K now used on all CT scanners is 1000. In honor of Godfrey Hounsfield, the inventor of CT scanning,[14] a CT unit is called a *Hounsfield unit* (HU). When HUs are used, air has a value of −1000; water, 0; and dense bone, +1000.

In theory, it is immaterial which value of K is used to construct a CT number scale as long as it can accommodate the accuracy of the scanner. For example, if the density resolution of the scanner is ±0.5%, the relative accuracy for density resolution is 1 part in 200 and a scale of 200 (K = 200) or greater is needed to depict the density resolution accurately. Using a value of K = 1000 expands the scale even more, representing a resolution of 1 part in 2000, or ±0.1%. Magnifying the scale does not improve the accuracy of a scanner; for example, an accuracy of ±0.5% translates to ±2.5 CT numbers with a scale of 500 and to +5 CT numbers with a scale of 1000.

As a general rule, the human eye cannot appreciate contrast differences of less than about 10%, whereas CT scanners can easily demonstrate differences of less than 1%. Thus, the small density-resolution difference measured by the CT scanner must be exaggerated to permit viewing. This is accomplished by enabling the user to select a small range of gray levels from the entire CT number scale and to reset the black and white limits.

For example, the CT numbers of liver tissues lie approximately in the range of 40 to 90 HU on a Hounsfield scale of 1000. If a portion of the scale with a CT number equal to 40 HU or lower is set at black and a CT number equal to 90 HU or greater is set at white, the scale of visualization is 50 HU and the entire range of liver tissues covers a contrast range of 100%. Now a density change of 10 HU on the original scale, which represents a true 1% contrast change, is converted to a 20% (10/50) contrast change on the adjusted range. This provides a large increase in visual contrast.

The range of CT numbers selected for gray scale amplification is called the *window width* and can generally be selected in scanners from 1 to full scale. (At the setting of 1, all pixels are either black or white.) The position describing the center of the scale is called the *window level*. Figure 1–24 shows a liver scan with different window settings. In this example, one can see the importance of the interactive display and the choice of settings by noting that in wide windows liver metastases are not well visualized.

Other display features and graphic aids assist the user in the interpretation of clinical images beyond window width and level control. For example, users have the ability to select a region of interest (ROI). Magnification of the image within the region of interest for better viewing is called *zoom reconstruction*. Some systems merely expand the image in the region of interest by expanding the pixel size on the viewing screen. This does not improve the accuracy of the scan but does allow possible visualization of some smaller structures because of better optical perception. Other systems increase image size but reconstruct the image with a smaller pixel size. This maneuver not only improves visualization of structures, because of optical reasons, but also increases spatial resolution if the pixel size is not smaller than the inherent resolution of the data (Fig. 1–25) (see "Matrix Size").

The region of interest is also used to acquire more information about pixel statistics, such as values of CT numbers in individual pixels, the average value in a number of pixels, or the number of pixels in a particular circumscribed region.

Several other display features are common to most device manufacturers, including the ability to pan and zoom images, scroll images, or view images in a cine mode. Image orientation can be inverted left to right or up and down. User-defined scales, straight or curved, may be placed anywhere on images. Finally, alphanumeric annotations may be placed anywhere on the displayed image to be filmed at a later time.

Figure 1–24. Liver scan. *A,* Wide window setting; some lesions are blurred and not visible. *B,* A more appropriate window setting enhances the presence of lesions. (MX8000 multislice CT images courtesy of Dr. John Haaga.)

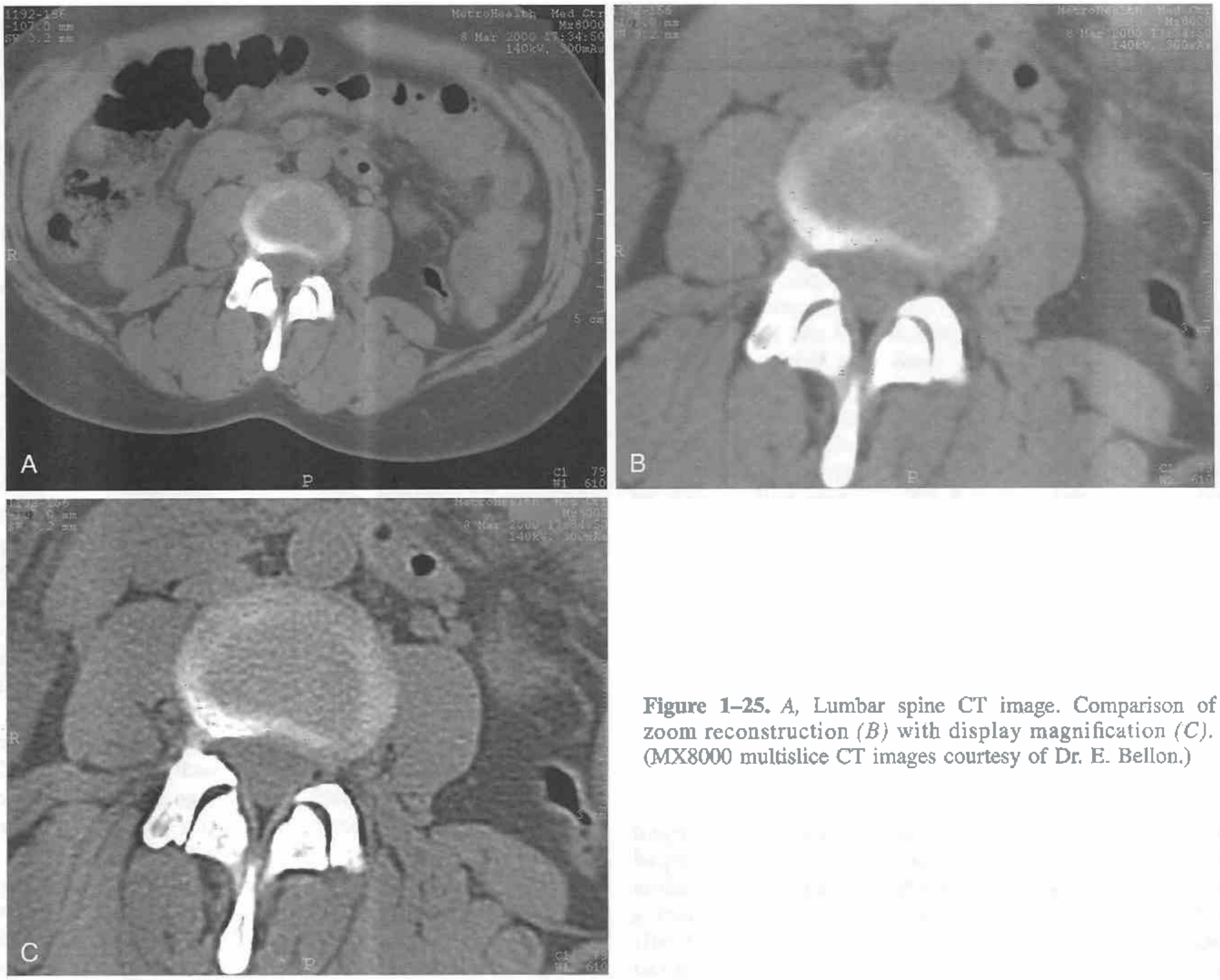

Figure 1–25. *A,* Lumbar spine CT image. Comparison of zoom reconstruction *(B)* with display magnification *(C)*. (MX8000 multislice CT images courtesy of Dr. E. Bellon.)

Advanced Display

Multiplanar Reformatting

Because a conventional CT study consists of several contiguous axial images perpendicular to the long axis of the body (see Fig. 1–1), coronal or sagittal images are not possible except when the gantry is tilted or the body is positioned to show the image in the desired plane. This limitation of CT can be overcome by image manipulation commonly referred to as *multiplanar reformatting* (MPR).

In this process, image data are taken from several axial slices and are reformatted to form images. In this viewing mode, the user defines the number of imaging planes, their position, orientation, thickness, and spacing, and the reformatted image is displayed in sagittal, coronal, or oblique planes. In the x-y plane direction, the pixel of the reformatted image has the same length as the axial image; in the z-direction, however, the pixel length is the same as the slice thickness. Since in most scans the pixel length is considerably smaller than the slice thickness, the reformatted scan can have an unusual appearance (Fig. 1–26). The resolution is quite good in one direction but very poor in another. This problem can be improved by scanning at a small-slice thickness and, as described earlier, the image is best enhanced with the use of spiral/multislice CT scanning, in which longitudinal resolution permits a slice thickness resembling minimal pixel length in the x-y plane. Scanning in this mode is commonly referred to as *isotropic imaging*. Isotropic voxels permit increased visualization of anatomy of complex shapes that do not run linearly along the z-axis (patient axis).

Multiplanar Reconstruction Viewing Mode for Interventional Procedure Guidance

With the use of spiral CT data, an interactive viewing mode consisting of axial and MPR views, as just described, can be employed in conjunction with an articulated arm to create a planning tool for image-guided CT interventional procedures. The arm is mounted on the CT gantry and is calibrated to the CT scanner's coordinate system, including integrated movement of the patient table. As an interventionist moves the arm's needle guide along the patient's skin, axial and MPR images are displayed, representing the needle guide position, trajectory, and depth of a virtual needle path in correlation with the interventional field. Correlation between actual needle placement and the virtual needle path in this method is within a radius of 2 mm (Fig. 1–27*A* and *B*).

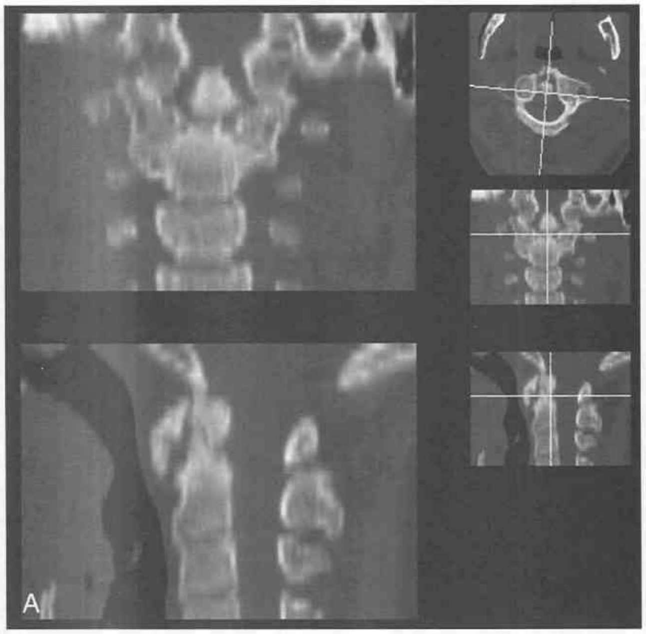

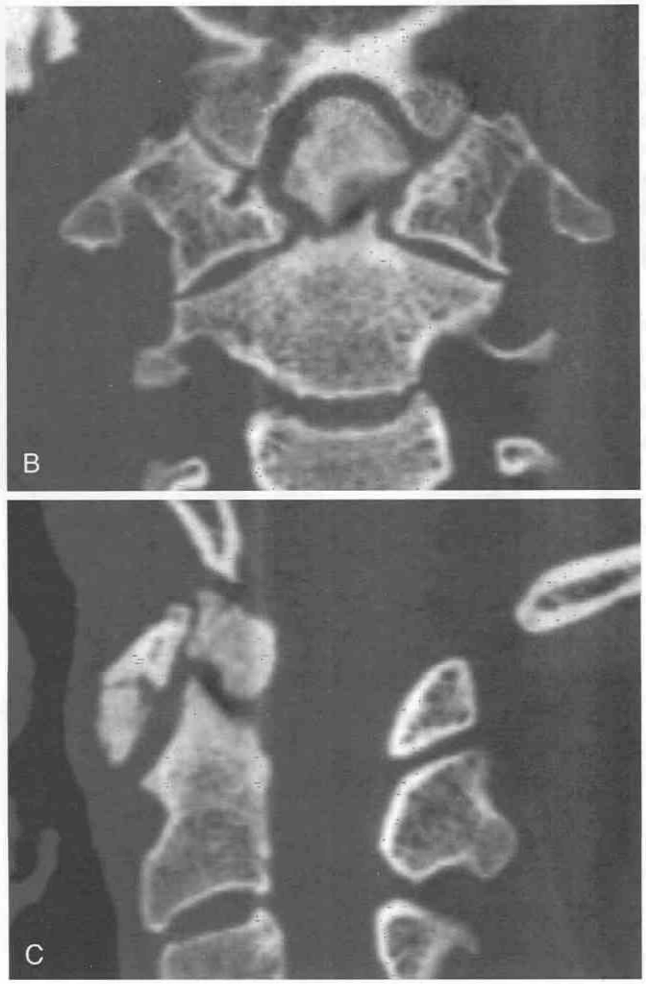

Figure 1–26. C-spine CT image. *A*, Multiplanar reformatted images acquired with a slice thickness of 2.5 mm depicting stair-stepping artifacts. *B* and *C*, Multiplanar reformat of images acquired with a slice thickness of 0.5 mm (isotropic resolution). The reduction in stair-stepping artifacts is due to the enhanced z-axis resolution of the originally acquired spiral data set. (MX8000 multislice CT images courtesy of Dr. Jay Cinnamon.)

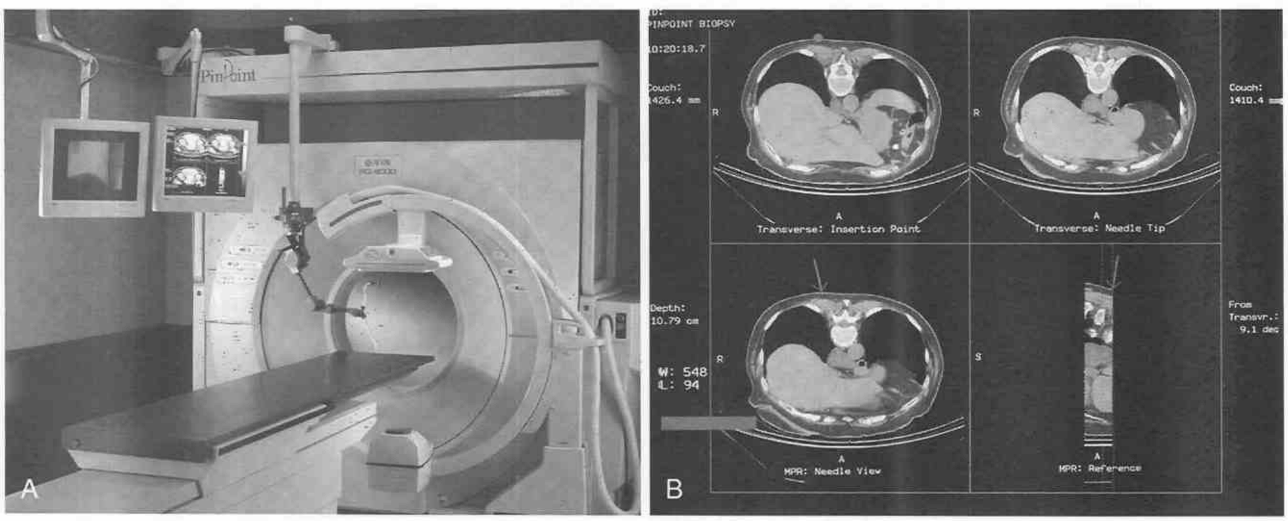

Figure 1–27. *A*, PinPoint five-point articulating arm and needle guide demonstrating relationship of arm to gantry. *B*, PinPoint multiplanar reconstruction (MPR) views used to visualize a virtual needle path to plan interventional procedures.

Data from successive slices can also be reformatted to generate other viewing modes. Three-dimensional *shaded surface, volume rendering,* and *maximum intensity projection* (MIP) are a few examples. Each of these rendering techniques is described in detail.

Figure 1–28*A* illustrates a small segment of eight voxels representing a large volume data set for demonstration purposes. Each of the eight voxels is shown with their values displayed. A *viewpoint* is defined from where imaginary rays are projected. To simplify the example, we can assume that each ray intersects two voxels, one behind the other.

Three-Dimensional Shaded Surface

For a surface rendition, the user selects a threshold range (Fig. 1–28*B*). This allows the user to select only the tissue (e.g., bone) to be rendered. The voxels with Hounsfield values within the threshold range are set to the "on" state, whereas the rest of the voxels are set to the "off" state. Depending on the number of bits used for display, "on" and "off" voxels are assigned appropriate values. For an 8-bit display, "on" would be 256 and "off" would be 0.

The second step is to project rays through the entire volume. As the rays pass through the data, they stop when they identify the first "on" voxel. For that particular ray, this first "on" voxel is part of the surface; the other voxels are ignored. This is done for all the rays, and all the "on" voxels are used to create the surface. For our example, the "on" voxels that are part of the surface would be yellow in Figure 1–29*C*. As the name suggests, only a surface is displayed in this method; there are no details within the surface. Shading the voxels enhances the effect, so that the volume image appears to be illuminated by light sources. Multiple light sources can be used, but a single light source is used in most medical applications.

Three-Dimensional Depth-Based Shading

One type of shading technique is called *depth-based shading*. With this method, those voxels that are closer to the viewer are illuminated at a greater intensity than those that are farther back. As described earlier, it is also possible for the operator to select a range of CT numbers to display. If an operator were interested in a 3D view of the skull, he or she would select the range of CT numbers of the skull. The computer would then assemble those selected voxels

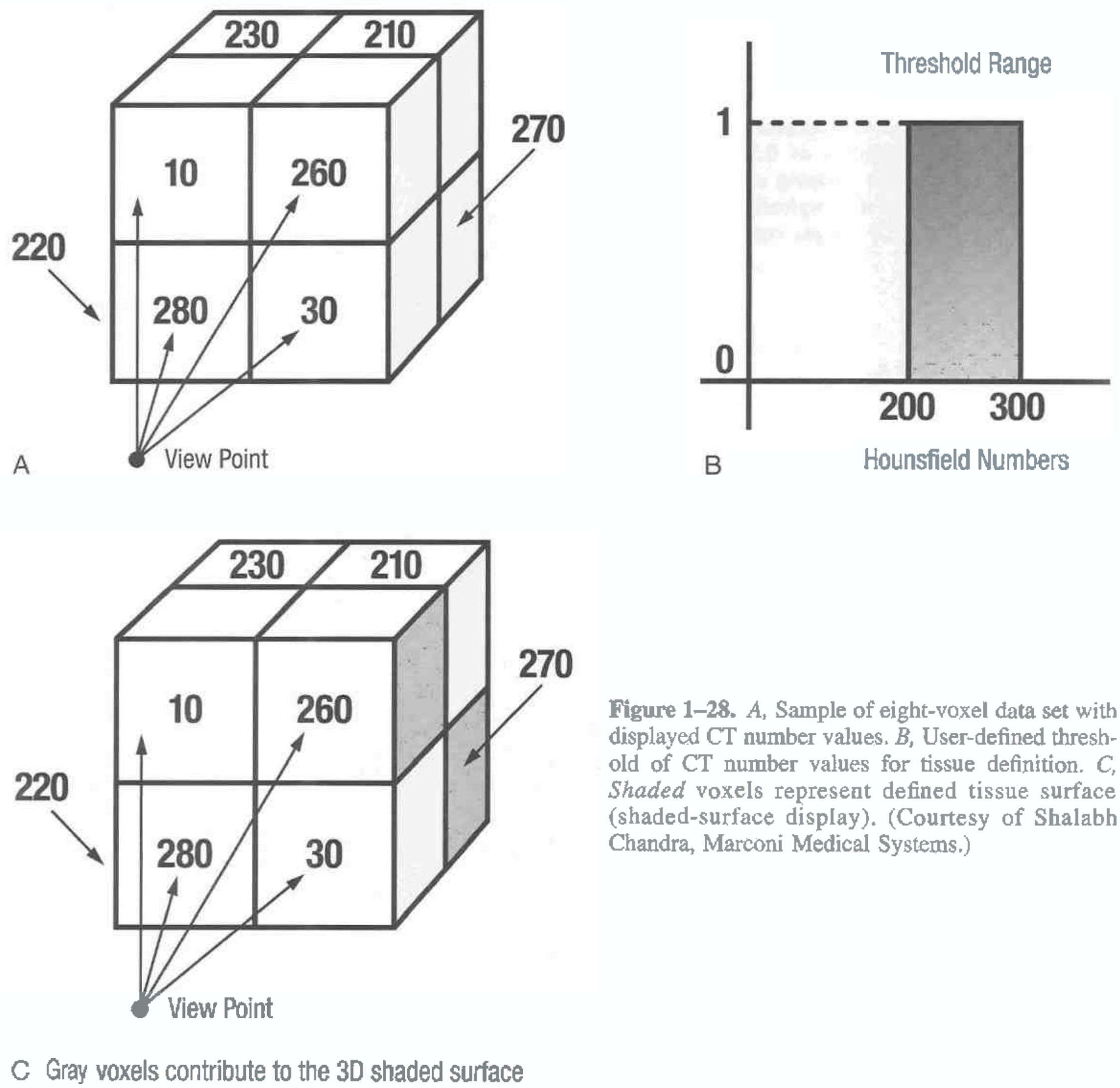

Figure 1–28. *A,* Sample of eight-voxel data set with displayed CT number values. *B,* User-defined threshold of CT number values for tissue definition. *C, Shaded* voxels represent defined tissue surface (shaded-surface display). (Courtesy of Shalabh Chandra, Marconi Medical Systems.)

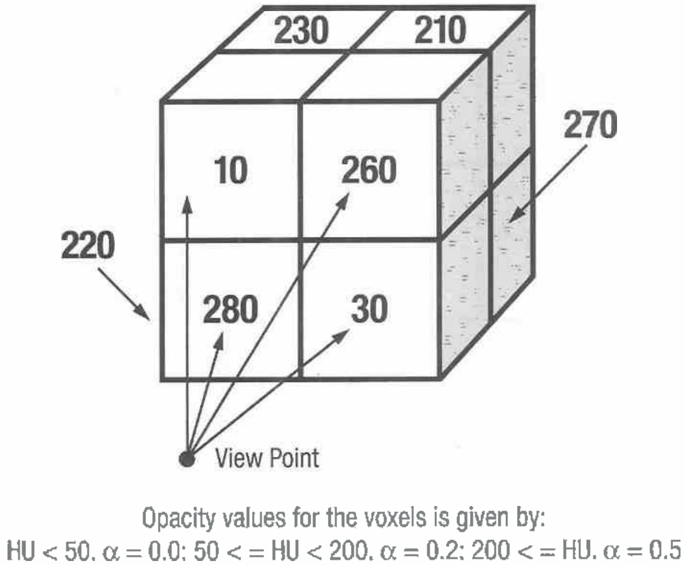

Figure 1–29. Sample of eight-voxel data set with representative opacity values assigned to various CT number ranges. (Courtesy of Shalabh Chandra, Marconi Medical Systems.)

into a 3D image. The result is a reconstructed 3D image of the skull with the soft tissue removed.

As with sagittal and coronal images, the quality of the image is improved by interpolating the data between slices to form a smooth, continuous image. When various 3D views are selected sequentially in time, the 3D image can appear to rotate. These images pose the same challenges as do sagittal and coronal images. The vertical resolution is the same as the slice thickness and not nearly as good as it is in other directions. Thus, spiral/multislice CT dramatically improves 3D viewing because of the inherent ability to cover the same anatomy as a conventional CT scanner at much thinner slice thicknesses and with overlapped image reconstructions.

Volume Rendering

Another possible viewing mode is *compositing/volume rendering* (VR). VR is an advanced rendering technique that displays an entire volume set with control of the opacity or translucency of selected tissue types. In this case, each voxel has an associated intensity in addition to an associated opacity value. Figure 1–29 shows the same 8-voxel block as Figure 1–28*A*, with each voxel having an opacity value associated with it. The user can define the opacity values for various HUs. Once the opacity values are assigned, the second step is to pass rays through the volume, accumulating values along the way. The formula for accumulating the values is given as

$$\text{final value} = I_1 \times \alpha_1 + I_2 \times \alpha_2 + \ldots + I_n \times \alpha_n \qquad (12)$$

where

$\alpha_1 + \ldots + \alpha_n \leq 1.0$
I_n is the intensity of the voxel n
α_n is the opacity associated with the voxel n
n is the number of voxels added before the opacity values sum up to 1.0, or it is the total number of voxels along that ray for that data set

Using this formula along with the voxel intensity and opacity values shown in the example, one can calculate the final image. Figure 1–30 demonstrates the results.

The obvious advantage of VR over 3D shaded-surface rendering is that it provides volume information. By using transparency, the operator can visualize information beyond the surface. For example, VR is the preferred viewing mode for stent evaluation because stents can be made transparent to view the lumen of vessels. Other clinical examples include the ability to make plaque transparent for more accurate diagnosis of vessel stenosis.

Maximum Intensity Projection

Using *maximum* or *minimum intensity projection* (MIP) for visualization permits easy viewing of vascular structures or air-filled cavities. Compared with 3D or volume-rendering techniques, MIP is a relatively simple method. Unlike 3D shaded-surface and VR displays, no preprocessing is required. The rays are cast throughout the volume, and depending on whether it is maximum or minimum intensity projection, maximum or minimum values along the rays are used in the final image display. On the basis of the 8-voxel example described earlier, Figure 1–31*A* and *B* shows the final pixel values for maximum and minimum intensity projections.

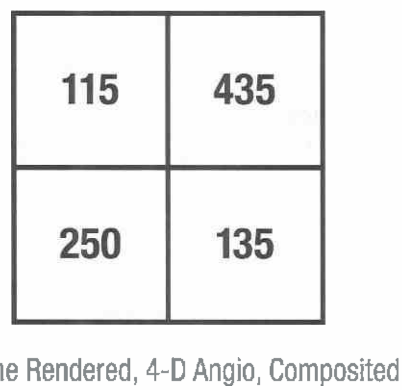

Figure 1–30. Image results for volume-rendered image of Figure 1–29.

Figure 1–31. *A*, Maximum intensity projection of a sample voxel in which only maximum values are displayed. *B*, Minimum intensity projection in which only minimum values are displayed.

MIP is a preferred method for many CT angiography applications, since visualization of contrast-filled vasculature is fast and easy. Maximum intensity projection enables easy viewing of an entire vessel in one image. This is true because voxels representing the contrast-filled vessels are most likely to be the ones with the highest values along the ray (assuming no bone along the ray). Along the same lines, minimum intensity projection can be used to demonstrate air-filled cavities.

Image Quality

Several quantitative measurements are used to define a CT system's image quality:

- Spatial resolution
- Contrast resolution
- Noise
- Slice sensitivity profile
- Temporal resolution
- Dose

Spatial Resolution

Spatial resolution is measured by the ability of a CT system to distinguish two small high-contrast objects located very close to each other under noise-free conditions. Optimal spatial resolution is required for evaluating high-contrast areas of anatomy, such as the inner ear, orbits, sinuses, and bone in general because of their complicated shapes.

Spatial resolution can be specified by spatial frequencies, which indicate how efficiently the CT scanner represents different frequencies. *Modulation transfer function* (MTF) describes this property. A 2D *Fourier transform* of the point spread function, taken with a very thin wire, provides MTF values. These concepts will be described shortly.

Consider the image of a point source that can be obtained by placing a thin wire on end in water or plastic and then scanning across the wire. Ideally, the resulting image should be a uniform background with a bright dot denoting the position of the wire. In fact, the image does demonstrate the bright dot but with a fading periphery rather than an absolutely sharp edge.

A profile across the image (i.e., a plot of the picture density along a line passing through the point source center) produces a bell-shaped distribution, called the *point response distribution*. The height of this curve represents the maximum value of the density, and the width represents the uncertainty in the measurement of the exact boundaries of the wire.

Full width at half-maximum (FWHM) is the width of the curve at the point where the attenuation values are 50% of the peak value (Fig. 1–32). The smaller the FWHM, the better the resolution. One can appreciate this fact by noting that a large FWHM reflects a larger fading periphery, which means a poorer reproduction of the actual object.

Another method of examining spatial resolution is to consider line images. This is similar to examining point images; however, the scan would be done parallel to a wire in a medium rather than across the axis. If a series of lines of different spacing or of different sizes were used, the ability to distinguish separate lines in an image would measure the spatial resolution.

With very fine lines, a measure of the resolution can be stated in terms of the number of lines that are still discernible, packed together in a given distance. Thus, one would speak of the number of lines per centimeter that could be visualized in the image. Describing the spatial resolution in terms of lines per centimeter is said to describe the resolution in the frequency domain. The frequency, in this case, is the parameter, lines per centimeter. A profile across the line image yields the *line response curve*, which is similar to the *point response curve*. Again, one can speak of FWHM, and the analysis is similar to that done with the point source. Obviously, the two response curves are related.

Performing a mathematical operation, the Fourier transform, on these response curves yields the MTF.[7, 19] The physical interpretation of the MTF is that it displays the relative fidelity of the image compared with the actual object.

Another description of MTF is shown in Figure 1–33. The rectangular profile represents the density profile of an object composed of dense lines. The density profile of the reconstructed image is shown as rectangles with rounded corners.

As the lines become closer together, the region between lines fills in because of the overlap of the response functions. The ratio of the height of the rectangles to the height

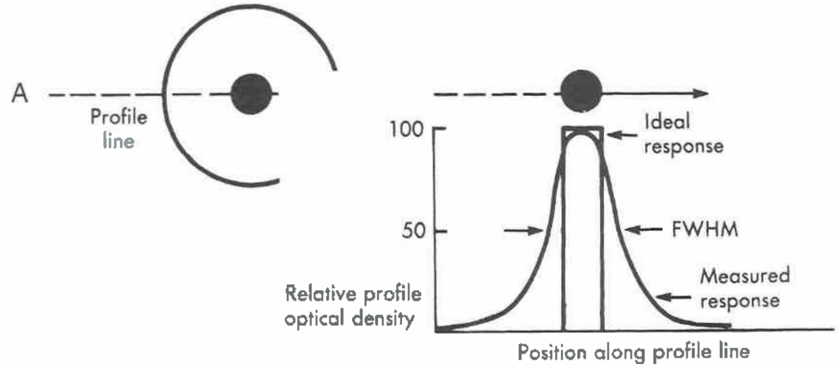

Figure 1–32. Definition of full width at half-maximum (FWHM). *A,* Solid body in uniform media. *B,* Profile across the image demonstrates the fading periphery of the image of the body. The rectangular curve represents the ideal response with sharp edges.

of the valley between lines becomes smaller as the lines become closer in the reconstructed image but, obviously, is fixed in the object. This change, or decrease, in ratio is seen as a decrease in contrast and is a manifestation of the decreasing ability of the system to resolve small objects (or small separation of objects). The MTF is basically the value of this ratio in the image divided by the value of the ratio in the object. As the frequency increases (i.e., more lines per centimeter), the ability of the system to reproduce the lines and valleys accurately is decreased and the fidelity also therefore decreases.

With widely separated lines, the MTF is 1—the maximum value; as the frequency increases, the MTF drops. Thus, the higher the MTF at a given frequency, the better the fidelity (i.e., the better the resolution).

In systems with large values of MTF at high frequencies, edges are more clearly defined; such systems produce images that appear sharp. If high frequencies are exaggerated relative to low frequencies, the result is an edge enhancement. Techniques for such high-frequency enhancement are often used to advantage in radiology, and this is the main purpose of xeroradiographic methods or subtraction methods. In Figure 1–34, curve A denotes a system with an MTF better than that shown by curve B; in this case, system A would have better resolution than system B.

The spatial resolution (composite MTF) is affected by many design parameters. The most important are as follows:

- Choice of filter used in reconstruction
  Opening size of detector aperture
- Number of projection profiles obtained
- Matrix (or pixel) size
- Focal spot size of the x-ray tube
- Relative object-to-background contrast (density)

The last two parameters in this listing are presented after the topic "Contrast/Density Resolution and Image Noise" (see later). Samples (rays and view or number of detectors), and not other parameters, gate the composite MTF for most third-generation systems. Focal spot size or detector aperture size typically gates the composite MTF of fourth-generation systems.

Filter Effects on Resolution

As discussed earlier, the major role of the convolution filter is to remove the image blurring created by the back-

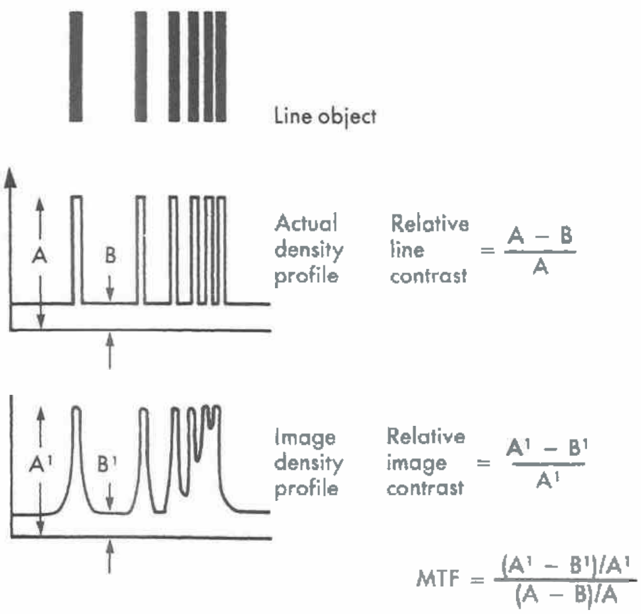

Figure 1–33. Definition of modulation transfer function (MTF). As the line frequency increases, the relative image contrast decreases, which is reflected in the fall of the MTF.

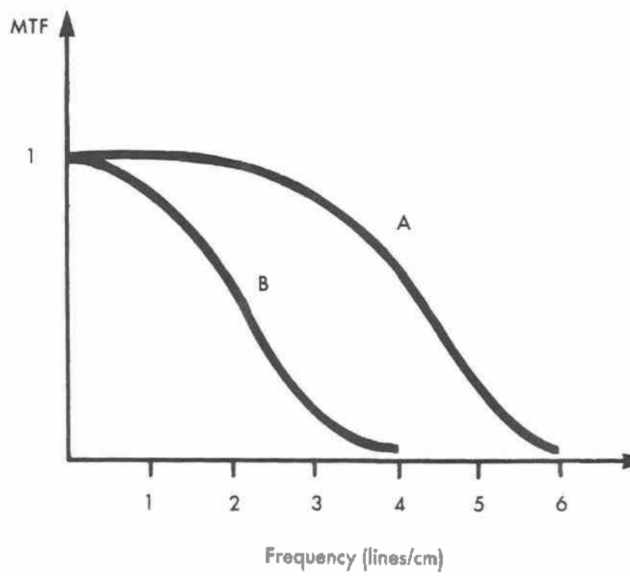

Figure 1–34. Comparison of modulation transfer function (MTF) of two theoretical systems. The system represented by *A* demonstrates a better spatial resolution than that of *B*.

projection process. Various filters control the amount of image blurring created by accentuating high-frequency components found in the data. For a crisp image, the high spatial frequencies are accentuated, and this has the effect of sharpening the edges and improving resolution. If the high spatial frequencies are not accentuated, the image of the object appears more blurred.

A tradeoff is that image noise increases and the density resolution diminishes with accentuation of high spatial frequencies. One pays for a crisp picture with a decrease in density resolution. Similarly, by increasing density resolution, one pays by loss of some spatial resolution and image crispness.

Opening Size of Detector Aperture

The detector aperture MTF curve is dependent on the magnification factor of the system (focal spot to detector distance/focal spot to object distance) and the physical size of the detector.

Consider the rotate-only scanner (Fig. 1–35). As the system rotates, the ray projection for a particular detector acts as the cord of the circle rotating about the center at a distance, R. The aperture opening for a particular detector, therefore, is associated with a particular data ring about the center. It is clear from the diagram that as the aperture size increases or decreases, the width of the data ring increases or decreases correspondingly. The width of this data ring characterizes the attenuation profile and is crucial to the spatial resolution. For example, if the object being viewed is smaller than the width of the data ring, it will be difficult to resolve because it occupies only a fraction of the space seen by the detector.

Typical detector apertures of CT systems today range from less than 1 mm to 1.5 mm, with center-to-center detector spacing of approximately 1 mm.

Number of Projection Profiles

As stated previously, to obtain a solution for the image reconstruction, Equation 10 must be obtained for each

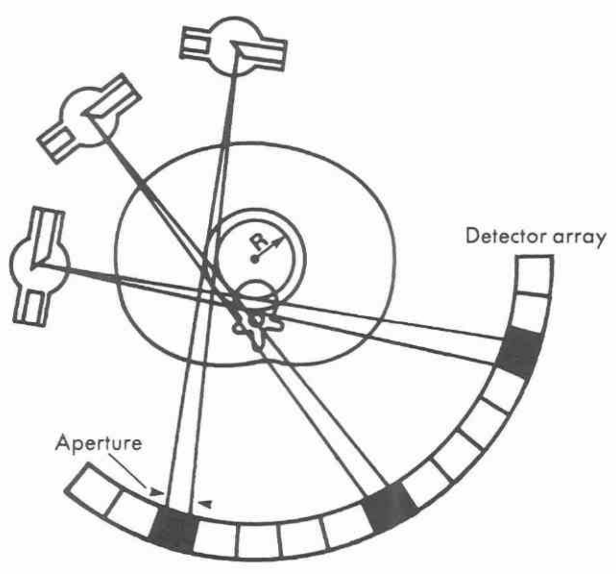

Figure 1–35. Single-ring, third-generation detector aperture. The thickness of the ring depends on the aperture opening.

value of λ needed. Therefore, if one wishes to reconstruct an image with a matrix of n columns by n rows, then n^2 measurements or ray sums must be obtained. With the large number of detectors used in present machines, this criterion is easily met. Although this criterion is necessary, it is not sufficient to guarantee the requisite resolution, and the question of optimum number of angular measurements or views must be answered.

Review Figure 1–35, and note that the resolution depends not only on the thickness of the data ring but also on the arc length of the data ring section between radiation measurements. Theoretically, this optimum number depends on required resolution and object size.[18, 26] To obtain resolution of 1 mm with small or average-sized bodies, 300 to 400 views may suffice; for larger bodies, 700 to 800 views may be needed. All current instruments of both the stationary detector type and rotate-only type have the capability of meeting these requirements. In many machines, these needs are exceeded significantly, allowing spatial resolution down to the range of 0.25 mm.

Matrix Size

It is rather obvious that the spatial resolution can be no better than the size represented by the pixel length. In reality pixel size should be 1½ to 2 times smaller than the desired resolution. Unless a matrix element exactly coincides with an object, the object representation will be averaged over two or more pixels and thus may not be visualized. It must be realized that the pixel size refers to the FOV (or body), not the viewing screen or film. For example, in a field size of 50 cm in diameter, a matrix size of 512 × 512 would indicate that each pixel represents a 0.98 × 0.98 mm area in the FOV:

$$\text{pixel size (mm)} = \frac{\text{FOV (500 mm)}}{\text{matrix (512)}} \tag{13}$$

Typical matrix sizes available in scanners today are 512 × 512 and 1024 × 1024. Most CT scanner display systems include zoom factors. If a zoom factor is used, the formula for pixel size must be modified to reflect the decreased FOV as follows:

$$\text{pixel size} = \frac{\text{scan FOV}}{\text{matrix} \times \text{zoom}} \tag{14}$$

The imaging goal is to match the pixel size with the inherent resolution of the CT system and scan protocol/filter selection for each examination. As discussed earlier, spatial resolution is measured in line pairs per centimeter. To convert this to millimeters, use the following formula:

$$\text{spatial resolution (mm)} = \frac{10}{2} \times \frac{\text{lp}}{\text{cm}} \tag{15}$$

To illustrate the concept, consider a high-resolution study with a protocol and reconstruction filter designed to achieve a spatial resolution of 20 lp/cm and an FOV of 250 mm. Converting 20 lp/cm to spatial resolution in millimeters using the preceding formula results in 0.25 mm spatial resolution.

To achieve a pixel size of 0.25 mm without zooming, the reconstructed FOV requires a matrix of 1024 × 1024 (250 mm/0.25 = 1000). To use a matrix of less than 1024 × 1024 would suggest a visual loss of spatial detail. The data are available but cannot be viewed.

Spiral and Multislice Spiral CT Effects on Spatial Resolution

Factors that affect in-plane spatial resolution for spiral and multislice spiral CT are the same as for conventional CT, although spatial resolution greater than 10 lp/cm (see third-generation CT earlier) is limited to axial modes of scanning or to manufacturers who employ special x-ray tube focal spot techniques to increase the data sampling rate during spiral scanning.

Unlike *in-plane* resolution, reconstruction in this chapter refers to a potential loss of z-dimension *(through-plane)* spatial resolution (for a given slice width) during spiral or multislice spiral CT. The loss of resolution, as measured at the FWHM of the slice sensitivity profile, is dependent on the spiral interpolation algorithm used during reconstruction and, in some cases, the pitch factor used. This phenomenon is less relevant for multislice spiral CT. This is evidenced by the fundamental clinical benefit of multislice spiral CT in covering more anatomy with thinner slices (better z-axis spatial resolution) compared with the benefits of conventional spiral CT.

The issue of degraded slice sensitivity profiles based on interpolating techniques in this case is fairly moot. For example, a best-case, single breath-hold examination, completed with the use of single-ring spiral CT at a given dose and level of image quality, may require a slice thickness of 5 mm. This same examination can be completed in less time with a slice thickness of 2.5 mm using multislice spiral CT.

Whether the slice sensitivity profile at FWHM broadens to 2.8 mm or to 3.2 mm becomes irrelevant. However, radiologists should become familiar with the typical slice broadening associated with different protocols on the CT scanner in use at their practice. Some manufacturers report the actual slice thickness, whereas others report only the requested slice thickness. It is important for radiologists to know the difference because the slice sensitivity profile indicates the CT scanner's ability to image objects within a given slice thickness. If the actual slice thickness is larger than expected, partial-volume averaging may affect the axial image quality. In addition, MPR reconstruction may be moderately affected.

Contrast/Density Resolution and Image Noise

The second major factor affecting the ability of a scanner to accurately describe anatomy is contrast, or density resolution, or the ability to differentiate the attenuation coefficients of adjacent areas of tissue. Because most soft tissues have densities that are very nearly the same, usually the differentiation of variations of a few percent or less are considered. In the computation of any single pixel value, there is error in the form of statistical variation; it is this variation that limits the ultimate contrast resolution. This variation (called image noise) is manifested as a grainy background, or mottle. The parameter used to evaluate this variation is the standard deviation (SD, or σ), and the usual procedure for evaluating a system is to obtain a scan of a uniform substance, such as water, and to compute the SD by the following formula:

$$SD = \sigma = \sqrt{\frac{\sum_{i=1}^{n}(CT_i - \overline{CT})^2}{n-1}} \qquad (16)$$

$$\overline{CT} = \frac{1}{n}(CT_1 + CT_2 + \ldots + CT_n) \qquad (17)$$

where

n is the number of pixels used in the evaluation
$\overline{CT}$ is the average pixel value for n pixels
CT_i represents individual pixel values

The meaning of the SD is that rescanning of the same water bath and a recalculation of the same pixel CT numbers would yield values in a range equal to the previously calculated value ± SD in approximately two out of three instances. The SD, therefore, describes the uncertainty in a measurement and is commonly expressed in terms of percentages. This percentage is obtained by dividing the computed SD in CT units by the range of the scale.

For example, SD equal to 5 HU on a Hounsfield scale of +1000 would translate to 5 HU/1000 HU = 0.005, or 0.5%. The interpretation is that two adjacent pixels are not significantly different if their CT numbers vary by 5 HU or less.

Since noise is the ultimate limitation in the accuracy of the density resolution, parameters that affect or induce noise need to be understood. The most important parameters are (1) photon flux, (2) x-ray scatter, (3) computation-induced error, (4) filter frequency response, and (5) voxel size. The effect of filters was discussed previously.

In any ray measurement, the statistical variation associated with that measurement is directly proportional to the number of photons detected. If I is the number of detected photons, the SD is given by the square root of I, and the relative noise in a ray measurement is given by

$$\frac{\sqrt{I}}{I}$$

which reduces to

$$\frac{1}{\sqrt{I}}$$

Because the variation in a ray measurement is propagated into every pixel computation, which involves the ray, the relative image noise is affected inversely as the square root of the detected photon flux. Large photon fluxes, or increases in milliamperes, as controlled by the radiologist, can reduce relative noise; unfortunately, they also increase radiation dose levels. Therefore, limits on CT image noise

reduction are imposed by practical limitations of increased dose to patients. The radiologist has an obligation to accept the highest noise image (lowest dose protocol) that is possible consistent with a definitive diagnosis.

The photon intensity that is detected, not the intensity impingement on the patient, must be taken into consideration, as mentioned previously. The efficiency of the detector, impinging photon flux, size of the patient, and presence of high-attenuation materials affect the detected intensity and, in turn, the uncertainty in the measurement. The image of a large patient thus has a more mottled appearance than the image of a small patient for the same tube output. Similarly, the presence of a high-contrast object, such as bone or a prosthesis, causes increased noise by reducing the transmitted photon flux.

Another aspect of noise is x-ray scatter. Because image-energy discrimination cannot be used in systems with the continuous energy spectrum obtained from an x-ray tube, no detector in particular can discriminate between a primary photon directly from the source and a scattered photon arising from an area not in the line of the ray projection. In the energy range used in scanners, many photons are scattered through small angles. The effect is to alter the recorded values in adjacent detectors. This produces a decrease in differences between adjacent measurements with a concomitant decrease in contrast resolution. The sharp interfaces between tissues also are diminished by this phenomenon, causing a reduction in spatial resolution.

The amount of scattering that is detected is controlled by collimation of the detectors. Smaller apertures reduce scattering and therefore reduce the noise component due to scattered photons. The measured intensity is also affected by the voxel length (i.e., slice thickness). If the slice thickness is reduced by 50%, the detector collimator size must be reduced accordingly, which in turn reduces the intensity by the same amount. To retain the same accuracy, one must restore the detected photon intensity, which means doubling the dose.

Similarly, decreasing pixel size increases the relative inaccuracy unless the photon flux is raised. If the pixel side length is reduced by half, the voxel volume represented by the pixel is reduced by a factor of 4. The SD of the resulting calculated CT number, shown earlier to vary as the square root, would double. The image would become more mottled in appearance, and the contrast resolution would deteriorate. To restore the uncertainty to its previous value, one would need to increase the radiation dose by a factor of 4.

These relationships between the factors of slice thickness (h), pixel size (L), SD (σ), and radiation dose (D) are shown[6] as

$$\sigma = \frac{C}{[DhL^2]^{1/2}} \tag{18}$$

where C is a constant.

This relationship also emphasizes that low contrast/density resolution (as reflected through the SD) is related to spatial resolution (as reflected through aperture opening or pixel size), and these two factors of image quality cannot be treated completely separately. Spatial resolution is usually stated for objects of high contrast. In CT scanning, attenuation coefficient differences of approximately 12% or greater are considered high contrast. As contrast differences decrease, spatial resolution also decreases. Figure 1–36 demonstrates the resolution obtained by viewing similar line phantoms but with various contrast differences.[1]

For a given dose level, regardless of the size of the object, a minimum density resolution exists, and, regardless of dose or contrast, there is a minimum size that can be resolved. Changing the dose level alters the minimum density resolution but not the spatial resolution limits[11] (Fig. 1–37).

Spiral and Multislice Spiral CT Effects on Contrast Resolution and Image Noise

The same variables that affect image noise and contrast resolution for conventional CT—slice thickness, kilovolt-

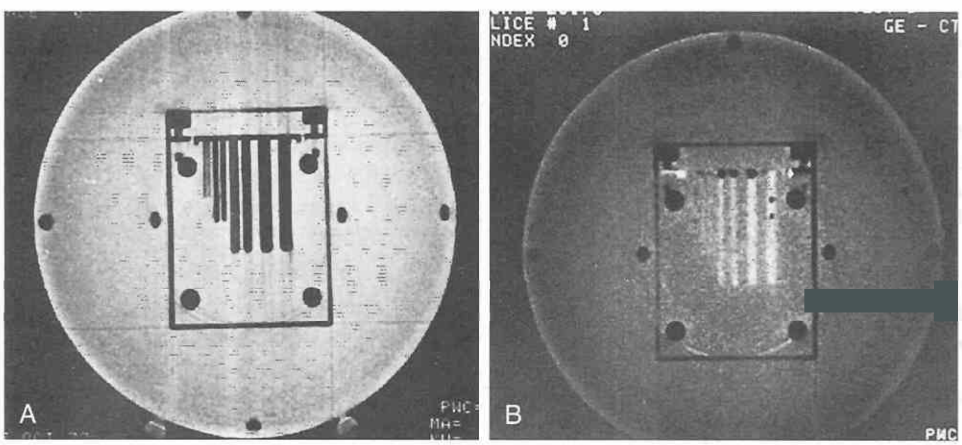

Figure 1–36. Line phantom. *A,* High-contrast line pairs; note the clarity. The diameter of the pairs and center-to-center distances are 5, 3, 2, and 1 mm. *B,* The same phantom with low contrast difference between the lines and the surrounding media. Notice the relatively poor spatial resolution, compared with *A,* and the inability to visualize the finer lines. This demonstrates the relationship between contrast and spatial resolution. (From Bellon EM, Miraldi FD, Wiesen EJ: Performance of evaluation of computed tomography scanners using a phantom model. Am J Roentgenol 132:345–352, 1979. Copyright American Roentgen Ray Society, 1979.)

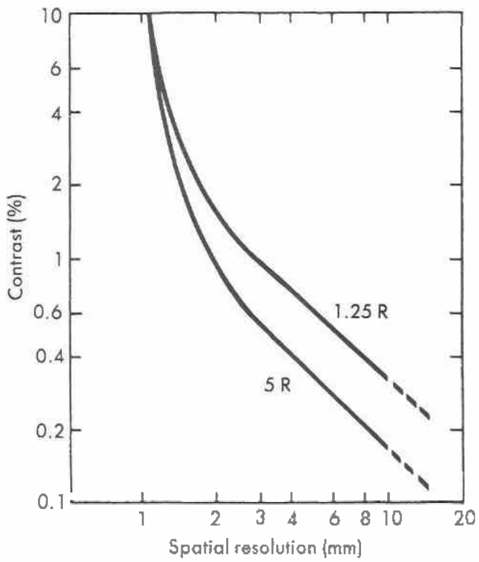

Figure 1–37. Interplay of spatial resolution, density resolution, and radiation dose. As the dose level increases, contrast resolution improves. High-contrast resolution is fixed and cannot be improved by the dose level. For a given dose level, objects with sizes and contrast that lie above the curve can be resolved; those below the curve cannot be resolved. (From CT/T Continuum: Evaluation Criteria. Milwaukee, General Electric Medical Systems,1980.)

age, milliamperage, patient size, voxel size, and convolution filter—affect spiral and multislice spiral CT, with the added variables of table speed (pitch) and spiral interpolation algorithm. For a given pitch, using more scan data to reconstruct an image (with linear interpolation) reduces noise and enhances contrast resolution at the expense of z-axis spatial resolution.[20, 29]

Temporal resolution refers to the ability of a CT scanner to capture objects that change shape or position over time and depends primarily on the gantry rotation speed and the reconstruction method used. For conventional CT using a full 360 degrees of scan data, temporal resolution is equivalent to scan time per rotation. A 1-second scan has a 1-second temporal resolution.

For spiral or multislice spiral CT, temporal resolution is dependent on the gantry rotation speed and the spiral interpolating algorithm used during reconstruction. Figure 1–38 depicts a 180-degree linear interpolator that demonstrates the relative spiral weighting values applied to projection data at the center of an axial slice. The central 180 degrees of data, including the fan angle (~50 to 55 degrees) are acquired in approximately 0.625 second for a gantry rotating at a speed of one revolution per second. The temporal resolution (FWHM) for a 360-degree linear interpolator, which uses 720 degrees of scan data, is approximately 1.25 seconds, or double that of the 180-degree interpolator.

A recent advancement that permits the reconstruction of projection data at prescribed intervals coincident with a patient's heart rate (electrocardiographic waveform) permits reconstruction techniques that can reduce effective temporal resolution to approximately 100 msec or less for data acquired using 0.5-second gantry rotation speeds. As described in Chapter 63, temporal resolution of this magnitude permits entirely new applications for CT such as cardiac and functional CT imaging.

Patient Radiation Dose

The amount of irradiation a patient receives during a CT examination is a function of many parameters. The dose can vary considerably from scanner to scanner and from image to image, depending on what is required by the radiologist (see preceding discussion). There are many methods of measuring and characterizing radiation delivered by CT.

Most methods use a standard cylindrical dosimetry phantom, with the dosimeters placed on the surface of and inside the phantom.[1, 22, 25] Measurements made on this type of phantom should not be considered a precise measurement of patient dose. True patient dose is not very well simulated by a perfectly cylindrical plastic phantom because of such factors as positioning errors, variations in patient shape, and uncertain x-ray attenuation. However, these methods are useful in demonstrating how dose varies as a function of operating conditions and between scanners.

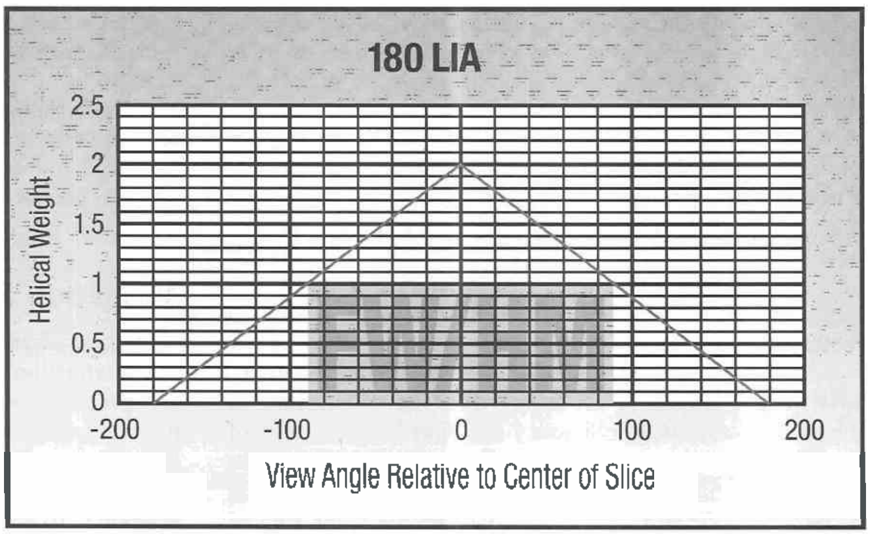

Figure 1–38. Weighting values of a 180-degree linear spiral interpolator demonstrating temporal resolution (full width at half-maximum) of approximately 0.625 second for a 1-second, 360-degree scan.

Most methods involve measuring the surface and internal doses for single slices and multiple, contiguous slices. There is a nonuniformity of absorbed dose distribution from different CT scanners because of various scanning conditions, system geometries, x-ray beam collimations, and filtration systems that make single-number dose descriptions, such as peak and average doses, inadequate.

Another concept suggested by Bureau of Radiological Health personnel to overcome some of these problems is the *computed tomography dose index* (CTDI).[25] To obtain the CTDI, a pencil-shaped ion chamber is inserted in a hole drilled in a plastic phantom. One single-slice measurement is taken. Because the ion chamber is long in relation to slice thickness, the ion chamber measures primary radiation as well as all scatter radiation. A single number that represents the average dose for a single scan is obtained. Holes may be placed at any depth along the axis of the phantom to measure the dose at any depth.

The *multiple scan average dose* (MSAD) represents the average dose delivered to a patient for a series of axial scans. This dose can be calculated by multiplying the ratio of the slice width to table index by the CTDI.

Values of skin dose can vary from a few tenths of 1 rad to high values above 15 rad and are controlled by the technique set by the operator. Depending on the x-ray beam primary energy, the amount of filtering in the beam, and the number of slices scanned, the patient internal dose may approach the skin dose for multiple slices.[25] Organs located outside the scanned volume will receive a dose because of scattered radiation from that volume and some leakage radiation from the x-ray tube housing. At distances of more than 1 cm from the scanned volume, the internal dose is relatively low.[22]

From the previous sections and as related by Equation 18, the inclination is to improve image quality by increasing the dose. Obviously, the radiologist must exercise prudence to obtain the necessary clinical information at the lowest possible radiation levels. Several published studies[16, 21, 27] have demonstrated that results of adequate clinical examinations can frequently be obtained with a great reduction in dose and with picture aesthetics as the only significant difference.

As described earlier, both spiral CT and multislice spiral CT generate axial/planar slices from a volume of data collected while the patient is continuously moved through the x-ray beam. As such, controlling the speed of table movement (pitch) can affect the average patient dose for the total examination.

As an example, consider a protocol with a slice width of 5 mm and a pitch of 5 mm, or pitch factor of 1:1. Extending the pitch factor from 1:1 to 2:1 by increasing the pitch to 10 mm effectively reduces the average patient dose in this examination by 50%. Conversely, reducing the pitch factor from 1:1 to 0.5:1 by slowing the pitch from 5 mm to 2.5 mm effectively increases the average dose by a factor of 2.

Multislice spiral CT complicates this equation somewhat, and z-axis dose efficiency must be considered. In this case, z-axis dose efficiency is defined as the ratio of the FWHM of the sensitivity profile to the FWHM of the radiation profile expressed as a percentage. For multislice systems, the FWHM of the sensitivity profile is the sum of the individual slices produced by that radiation profile. The z-axis efficiency of multislice CTs varies by manufacturer but can be expected to approach 100% at slice thicknesses between 5 and 10 mm, gradually falling off in efficiency to approximately 75% at slice thicknesses of 1mm. This falloff in efficiency is due to the penumbra-to-umbra ratio of the x-ray beam and is unique to multislice spiral CT. This is true because both the penumbra and umbra are detected with single-ring spiral CT systems but not true for today's multislice CT systems.

System geometry, x-ray tube focal spot length, and other collimation factors affect this ratio. In general, the wider the collimated beam, the smaller the penumbra-to-umbra ratio and, therefore, the lower the effect on z-axis efficiency. Manufacturers continue to develop new methods to improve z-axis efficiency with multislice spiral CT, and improvements are probable in the near term.

One final note: As the z-axis width of detectors increases from today's quad-slice systems to 8, 16, 32, 48 slices and beyond, z-axis efficiency will improve.

Image Artifacts and Their Causes

There are many causes of artifacts on an image, and it is important for the radiologist to recognize all types so that they can be eliminated or minimized.

Streak and Ring Artifacts

Streak and ring artifacts are usually the result of difficulty with the detector (Fig. 1–39*A* and *B*). With third-generation scanners, ring artifacts are seen if the x-ray detector is not properly calibrated.

In Figure 1–36, each detector is associated with a data ring. A malfunction of any one detector incorrectly back-projects along the data ring to produce the ring artifact. If a detector is not matched or is not intercalibrated accurately, the back-projection for each data ring would be slightly different, causing multiple rings. Poor alignment of tube and detector causes misplacement of calculated values, since measured values are occurring in lines different from those assumed by the reconstruction algorithm. The result can be blurring edges if the misalignment is slight or ring or streak artifact if the misalignment is great. Detectors in the center of the detector arc are most sensitive.

Fourth-generation scanners are more sensitive to streak artifacts due to failure of a detector. However, because of the large number of views available, data for the failed detector can be synthesized through interpolation.

Metal and Bone Artifacts

The presence of objects having an exceptionally high or low attenuation can create artifacts by forcing the detector to operate in a nonlinear response region. Because this incorrect response occurs at specific directions of the beam through the object, incomplete cancellation of the back-projected rays during reconstruction occurs and yields streaking artifacts. Metallic pins, for example, can give rise to streaks, as can gas (Fig. 1–40).

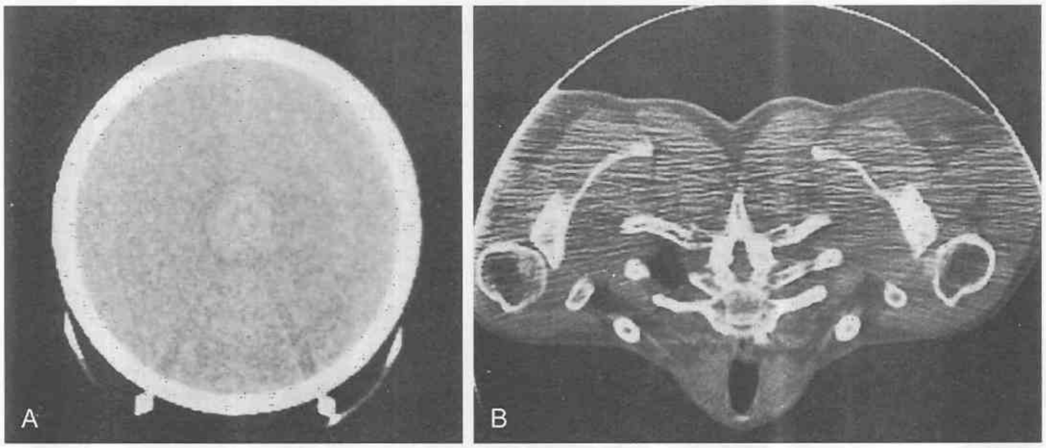

Figure 1–39. Examples of CT image artifacts. *A,* Ring artifact obtained with a third-generation CT scanner. *B,* Streak artifacts.

The range of x-ray intensity values to which the scanner can accurately respond linearly is called the *dynamic range.* The larger the dynamic range, the less prone the instrument is to creating such artifacts. In most new scanners, the dynamic range is a factor of 1 million to 1, which greatly reduces the metallic artifact problem.[12]

Beam-Hardening Artifacts

Beam-hardening artifacts result from the preferential absorption of low-energy photons from the beam. In the range of kilovoltage used in CT scanners, a prominent mode of interaction is the photoelectric process, and in this region the low-energy photons are preferentially absorbed. Thus, as a beam traverses the body, the average beam photon energy is progressively increased. Accordingly, toward the end of the x-ray path, the attenuation is less than at the beginning because the attenuation coefficient is smaller with higher energy. The reconstruction program, however, assumes a monochromatic beam and attributes any change in beam intensity to a change in tissue composition rather than to the result of a shift in average photon

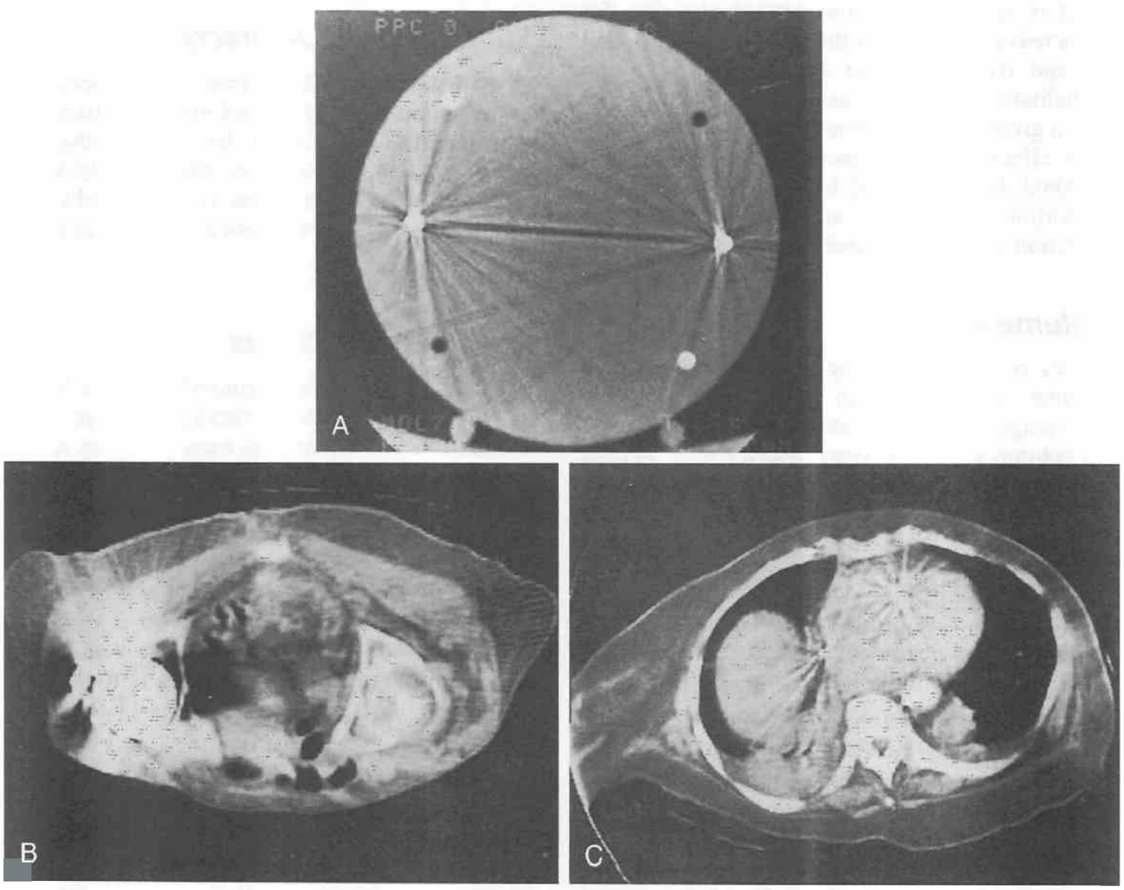

Figure 1–40. Streak artifacts. *A,* Uniform media with metallic pin; note the large amount of streak artifact. *B,* A hip prosthesis. *C,* Starburst streaks from clips in the pulsating heart of conventional (single-ring) CT scanner.

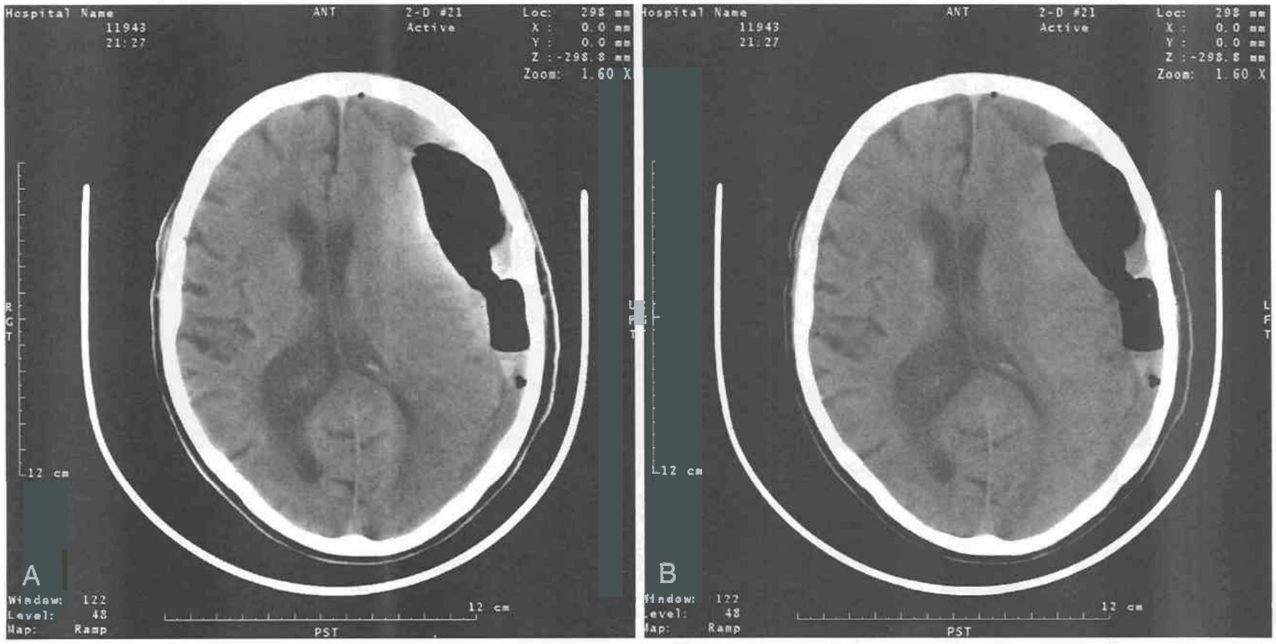

Figure 1–41. Beam-hardening artifacts. *A*, Postoperative CT image of the brain in an adult. *B*, Comparison of reductions in beam-hardening artifacts with use of iterative reconstruction technique. A corrected image using UltraImage reconstruction technique. (Courtesy of Marconi Medical Systems.)

energy. The assigned attenuation coefficients are thus in error, and the densities seen on the image are in error. The effect is most pronounced in regions of large attenuation, such as bone.

The artifact is seen as a shadow beneath the ribs, for example, or increased shadows in the mediastinum or skull (Fig. 1–41*A* and *B*). This effect occurs throughout the image, but qualitatively it is not usually perceived except where there is a great deal of hardening (e.g., in the vicinity of bone). This effect can be compensated for by use of a correction method that consists of forward-projecting only the "bone" portion of an image and by determining the required correction via a polynomial.[36]

Partial-Volume Artifacts

When tissues of widely varying absorption properties occupy the same voxel, the beam attenuation is proportional to the average value of the attenuation coefficient of the voxel. A volume average is computed for such voxels, leading to the partial-volume error. A common site of such an effect is the lung-diaphragm interface, where an increased density may be attributed to the lung base when, in reality, it does not exist (Fig. 1–42). A partial-volume artifact can be subtle and gradual, requiring care in interpretation. Another common partial-volume artifact is observed in scans of the head in the posterior fossa region.[31]

Motion Artifacts

A motion-induced artifact is usually streak or starburst in appearance and occurs where there are high-density or low-density interfaces (e.g., gas in the bowel) (Fig. 1–43). This occurs because movement during the measurement process causes structures to be in different positions when different views are taken so the back-projections are not added correctly. Artifacts can also appear as "double imaging," with the same outline shown twice.

Stair-Stepping Artifacts

Stair-stepping artifacts (see earlier) occur when in one direction the pixel of the reformatted image has the same length as the axial image but in the other direction the pixel length is the same as the slice thickness. Because pixel length in most scans is considerably smaller than slice thickness, the reformatted scan has an unusual appearance (see Fig. 1–26).

Spiral Pitch Artifacts

Pitch artifacts appear primarily because larger pitch factors are used to attain maximum coverage. Spiral artifacts exhibit similar stepping as axial scans in reformatted images, except that the steps appear as a spiral groove (Fig. 1–44).

Multislice pitch artifacts (again for large pitch factors) have a unique appearance in axial scans; a star pattern is seen off of sharp edges, where the number of spokes in the star is directly related to the number of multislice detector rows (Fig. 1–45).[35, 37] This is because each row contributes only a portion of its projection data to the multislice reconstruction.

Cone-Beam Artifacts

As the number of rows in a multislice scanner increases, the divergence of the cone beam along the z-axis becomes significant relative to the detector width. For a small num-

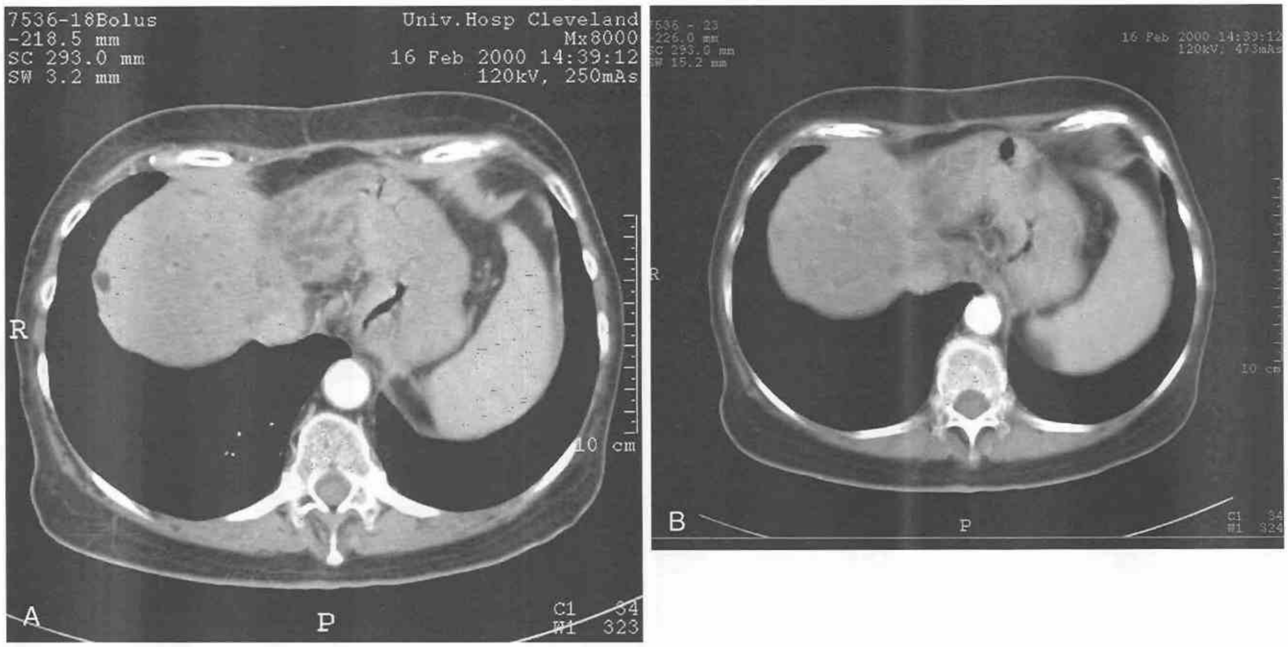

Figure 1–42. Liver scan representing enhanced lesion detection and reduced partial-volume artifacts in *A* (2.5-mm slice thickness) versus *B* (10-mm slice thickness). (Multislice CT image courtesy of Dr. John Haaga.)

ber of rows, this effect is small and noticeable only for sharp objects distant from the scan center. For scanners with eight or more rows, the cone-beam effect becomes more significant, requiring the reconstruction process to account for the divergence effect (Fig. 1–46).

Summary

The tradeoff between spatial resolution (x-y), contrast resolution, and patient dose has been optimized for CT since the early 1980s. To obtain more low-contrast resolution for a given spatial resolution, the patient dose must increase. To obtain more contrast resolution while maintaining patient dose, spatial resolution must decrease. In short, before the late 1980s, the fundamental laws of physics prevented significant improvements in 2D CT imaging without increasing patient dose. The advent of spiral and multislice spiral CT has not changed these limiting factors; however, by permitting radical improvements in z-axis spatial resolution, multislice CT enhances CT imaging of submillimeter anatomic and pathologic structures. Subsecond scanning techniques with rapid-volume coverage are enabling new functional imaging methods using CT. Finally, rapid developments of computer technology are enabling radiologists to take advantage of new 3D and 4D imaging methods, moving CT from a 2D anatomy-only tool to a 3D tool that can provide functional as well as anatomic information.

Many more clinical applications are on the horizon; this is just the beginning of a very promising future for CT as perhaps the most cost-effective, value-driven diagnostic imaging tool. Examples of many of the new CT clinical applications are described in the upcoming chapter on multislice spiral CT and are represented throughout this book.

Figure 1–43. Streak artifact (*open arrow*) caused by motion of bowel gas in a slow abdominal scan of a conventional single-ring CT scanner. Machine-caused streaks are also seen. Streak artifact shown with *solid arrow* represents a wobbly rotor in the x-ray tube.

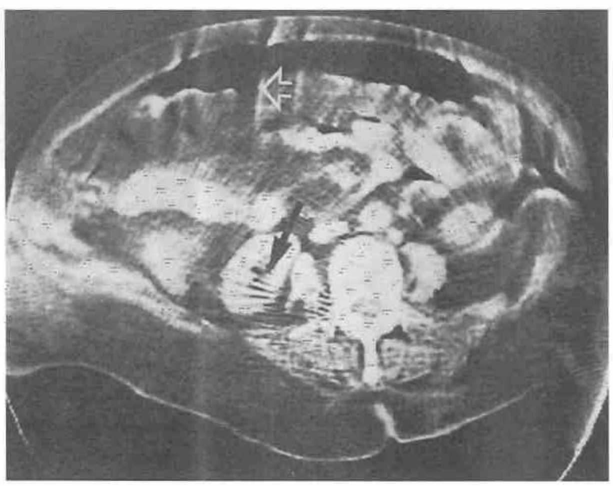

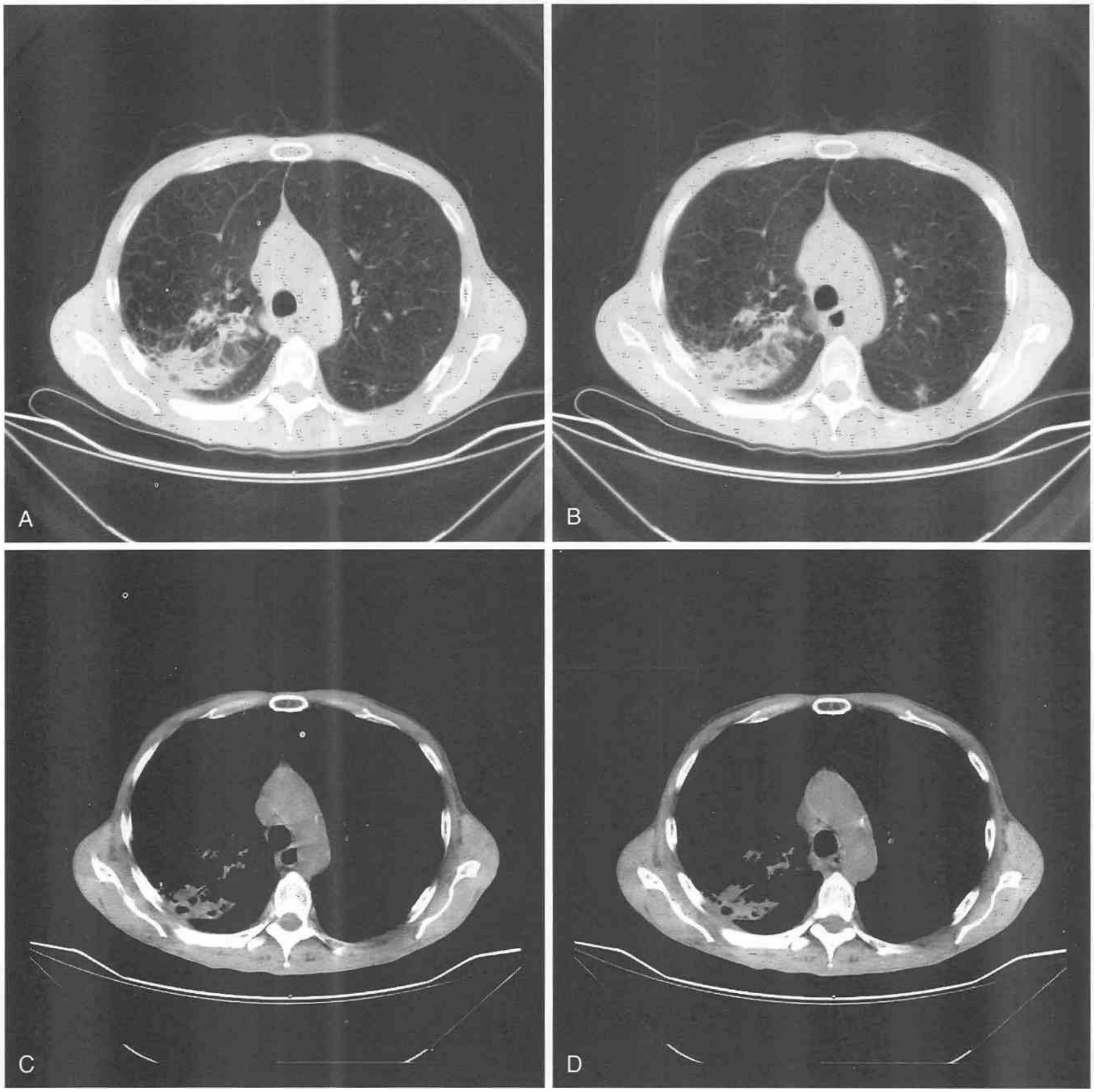

Figure 1–44. Lung scan demonstrating effects of extending spiral pitch with single-ring spiral CT. High spatial and z-axis resolution at pitch 1 *(A)* and pitch 2 *(B)*. *C*. Same scan as *B* but windowed to demonstrate spiral pitch artifacts. *D*. Same scan as *A*, but windowed to demonstrate pitch artifacts. Note the increased spiral pitch artifacts at pitch 2 *(C)* versus those at pitch 1 *(D)*.

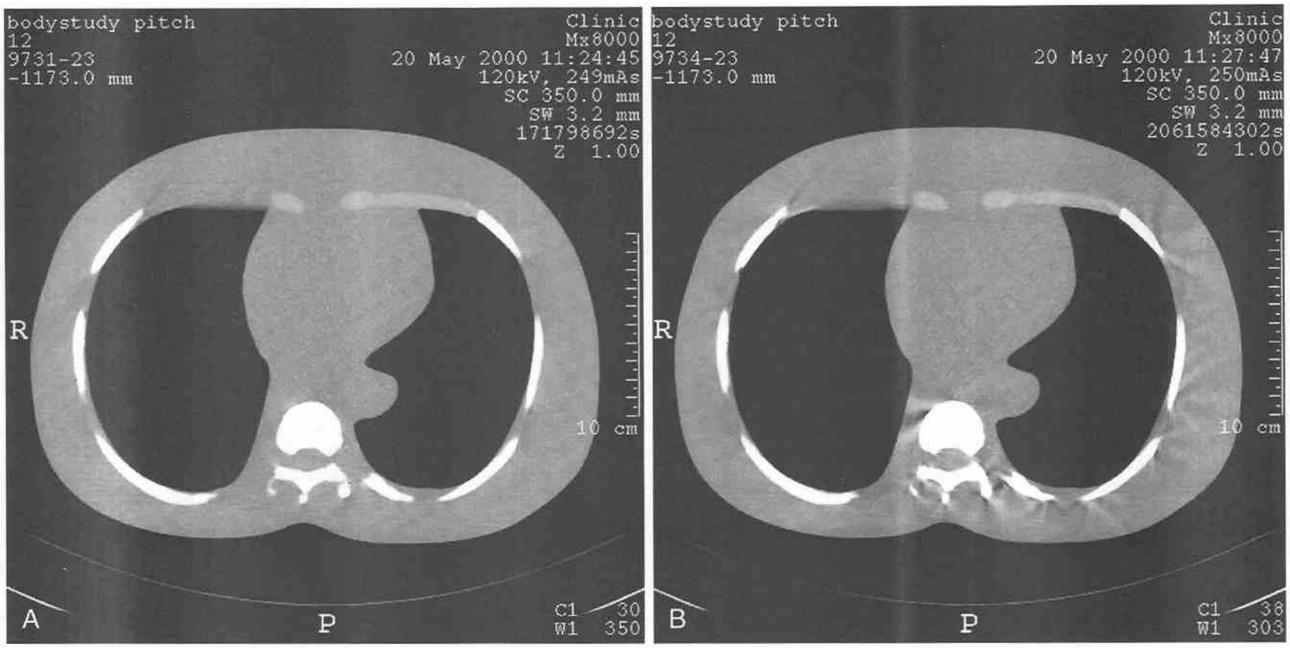

Figure 1–45. Phantom study demonstrating reduced appearance of multislice spiral CT pitch artifacts at quad-pitch 0.675 *(A)* versus quad-pitch 1.25 *(B)*. (Simulations courtesy of D. J. Heuscher and M. Vembar, Marconi Medical Systems.)

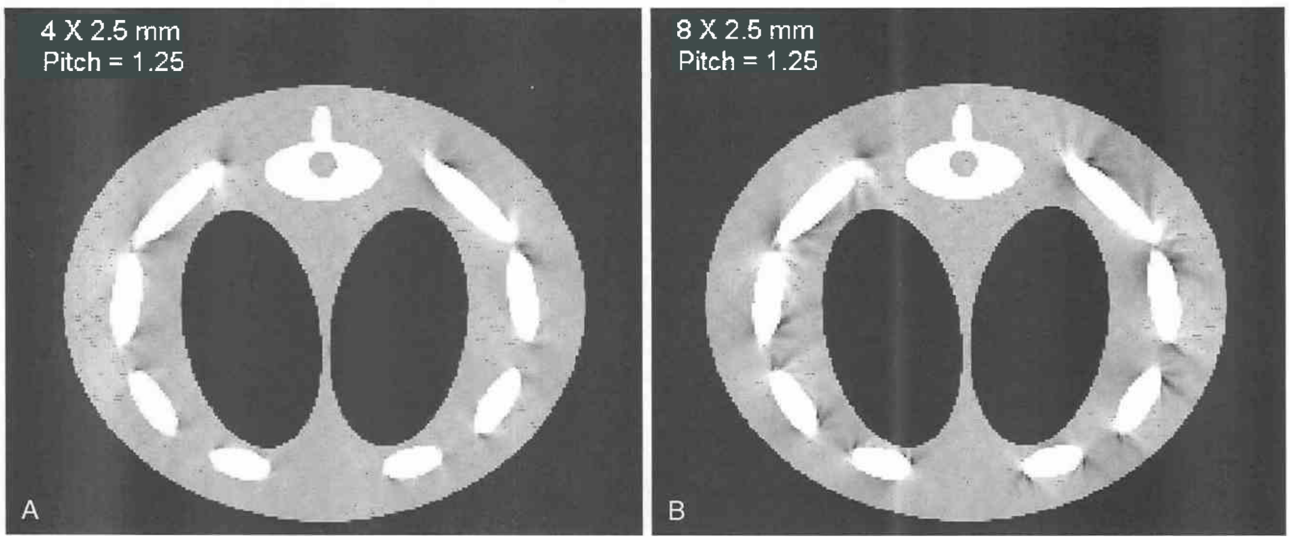

Figure 1–46. Phantom study demonstrating cone-beam artifacts. *A,* Quad slice multislice CT scanner study. The patient's ribs are positioned at a severe angle along the z-axis to demonstrate cone-beam artifact at quad-pitch 1.25. *B,* Enhanced contribution of multislice CT cone-beam artifacts caused by divergence of the x-ray beam in the z-axis when the number of detector rings used to acquire a CT image is increased from four to eight. (Simulations courtesy of D. J. Heuscher, M. Vembar, and C. Vrettos, Marconi Medical Systems.)

Acknowledgment

We thank Shalabh Chandra, M.S., Chris Vretos, M.S., and Dominic Heuscher, Ph.D., for their contributions to this chapter.

References

1. Bellon EM, Miraldi FD, Wiesen EJ: Performance evaluation of computed tomography scanners using a phantom model. Am J Roentgenol 132:345–352, 1979.
2. Brasewell RN: Strip integration in radioastronomy. Aust J Phys 9: 198–217, 1956.
3. Brasewell RN, Riddle AC: Inversion of fan-beam scans in radioastronomy. Astrophys J 150:427–434, 1967.
4. Brasewell RN, Wernealse SJ: Image reconstruction over a finite field of view. J Opt Soc Am 65:1342–1346, 1975.
5. Brooks RA, DiChiro G: Theory of image reconstruction in computed tomography. Radiology 117:561–572, 1975.
6. Brooks RA, DiChiro G: Statistical limitations in x-ray reconstructive tomography. Med Phys 3:237–240, 1976.
7. Christensen EE, Curry TS III, Dowdey JE: An Introduction to the Physics of Diagnostic Radiology, 2nd ed. Philadelphia, Lea & Febiger, 1978.
8. Cormack AM: Representation of a function by its line integrals with some radiological applications. J Appl Phys 34:2722–2727, 1963.
9. Cormack AM: Representation of a function by its line integrals with some radiological applications: II. J Appl Phys 35:2908–2913, 1964.
10. Coulam C: The Physical Basis of Medical Imaging. New York, Appleton-Century-Crofts, 1981.
11. CT/T Continuum: Evaluation Criteria. Milwaukee, General Electric Medical Systems, 1980.
12. CT9800 Computed Tomographic Systems. Milwaukee, General Electric Medical Systems, 1982.
13. Gordon R, Herman GT: Three dimensional reconstruction from projections: A review of algorithms. Int Rev Cytol 38:111–151, 1974.
14. Haaga JR, Reich NE: Computed tomography of abdominal abnormalities. St. Louis, CV Mosby, 1978.
15. Haaga JR, Alfidi RJ, MacIntyre WJ, et al: CT longitudinal scan. Am J Roentgenol 127:1059–1060, 1976.
16. Haaga JR, Miraldi F, MacIntyre W, et al: Effect of mAs variation upon computed tomography image quality as evaluated by in vivo and in vitro studies. Radiology 138:449–454, 1981.
17. Hounsfield GN: Computerized transverse axial scanning (tomography): I. Description of system. Br J Radiol 46:1016–1022, 1973.
18. Huesman RH: The effects of a finite number of projection angles and finite lateral sampling of projections on the propagation of statistical error in transverse section reconstruction. Phys Med Biol 22:511–521, 1977.
19. Johns HE, Cunningham JR: The Physics of Radiology, 3rd ed. Springfield, Ill, Charles C Thomas, 1969.
20. Kalender WA, Polacin A: Physical performance characteristics of spiral CT scanning. Med Phys 18:910–915, 1991.
21. Marmolya G, Wiesen E, et al: Paranasal sinuses: Low-dose CT. Radiology 181:689–691, 1991.
22. McCullough EC, Payne JT: Patient dosage in computed tomography radiology. Radiology 129:457–463, 1978.
23. Price J: Nuclear Radiation Detection. New York, McGraw-Hill, 1958.
24. Rumberger JA, Sheedly PE, Stanson AW: Ultrafast (cine) CT: advantages and limitations in cardiovascular assessment. Intern Med Specialist 9:1–8, 1988.
25. Shape TB, Gagne RM, Johnson GC: A method of describing the dose delivered by transmission x-ray computed tomography. Med Phys 8: 488–495, 1982.
26. Synder DL, Cox JR Jr: An overview of reconstructive tomography and limitations imposed by a finite number of projections. In Ter-Pogossian M, Phelps ME, Brownell GL (eds): Reconstruction Tomography in Diagnostic Radiology and Nuclear Medicine. Baltimore, University Park Press, 1977.
27. Wiesen E, Crass JR, Bellon EM, et al: Improvement in CT pelvimetry. Radiology 178:259–262, 1991.
28. Reynolds MD, Heuscher DJ, Vembar M: Evaluation of spiral CT on a fourth generation system. Eur J Radiol 5:102–109, 1995.
29. Heuscher DJ, Vembar M: Reduced partial volume artifacts using spiral computed tomography and an integrating interpolator. Med Phys 26:276–286, 1999.
30. *Theory of Spiral CT.* Marconi Medical Systems, 1994.
31. Glover GH, Pelc NJ: Nonlinear partial volume artifacts in x-ray computed tomography. Med Phys 7:238–248, 1980.
32. Wang G, Vannier M: Optimal pitch in spiral computed tomography. Med Phys 24:1635–1639, 1997.
33. Siebert JA, Barnes GT, Gould RG (eds): Specification, Acceptance Testing and Quality Control of Diagnostic X-ray Imaging Equipment. Woodbury, NY, American Association of Physicists in Medicine and the American Institute of Physics, 1994.
34. Vrettos C: Data Acquisition Systems in CT. Marconi Medical Systems, 1991.
35. McCullough C, Zinc F: Performance evaluation of a multislice CT system. Med Phys 26:2223–2230, 1999.
36. Newton TH, Potts DG: Radiology of the Skull and Brain: Technical Aspects of Computed Tomography, St. Louis, Mosby, 1971.
37. Hui H: Multislice helical CT: Scan and reconstruction. Med Phys 26: 5–19, 1999.
38. Arenson JS, Levinson R, Freundlich D: Dual slice scanner. U.S. Patent No. 5 228 069, 1993.

2 Magnetic Resonance Physics: An Introduction

Errol M. Bellon, Pedro J. Diaz,
Jeffrey L. Duerk

The magnetic resonance imaging (MRI) study, as seen on a computer screen or on hard-copy film, is a translation, into visual format, of numerical values residing in a computer memory. The N × M numerical values that make up the image are referred to as *pixels* (picture elements). These values are generated from MRI signals acquired during scanning in a computational process known as *Fourier transform*. Thus, MRI represents a form of computed imaging, with the numerical value of the pixel represented on the screen as a level of gray using a digital-to-analog conversion process.

The intensity of the displayed pixel is proportional to its numerical value and reflects the cumulative strength of the radiofrequency (RF) signal received from a corresponding volume element *(voxel)* within the slice of tissue examined. This RF signal is dependent on these factors:

- Strength of the magnetic field
- Size and location of the RF detector (antenna, coil, surface coil)
- Relaxation parameters (T1 and T2) of the tissue
- Amount of mobile protons in the tissue (its proton density)
- Parameters of the MRI acquisition

In an MRI experiment, or scan, the patient is placed in the external magnetic field of the MRI magnet. The magnetic dipole moment of hydrogen nuclei in the body, which are normally oriented randomly in the weak magnetic field of the earth, are affected by this much stronger external field and undergo a net alignment parallel to the field. For example, a 1.5 Tesla (T) MRI system has a magnetic field approximately 30,000 times stronger than that of the earth in most of the United States. At this field strength, only about 2 to 4 in every 2 million protons from the patient contributes to the MRI signal; all others are canceled by protons pointing in the opposite direction.

Individually, the proton magnetic moments precess about the static field, but they can be evaluated collectively such that the net magnetization is initially pointed along the static field. When subjected to brief periods of RF energy, the hydrogen nuclei in the patient's tissues absorb the RF energy and alter their orientation. In this new alignment, the net magnetization can be shown to precess about the static field. The absorbed RF energy and subsequent precession and realignment of the nuclei allow them to function as miniature RF transmitters as they return to their previous parallel alignment. Their RF signal is measured (received) by means of an external RF antenna *(coil)*.

Repetitive systematic variations in the strength of a second magnetic field (generated by gradient coils inside the magnet) during the time the nuclei are stimulated by the external RF signal makes it possible to selectively excite individual areas of the body. Recording and subsequent processing of these spatially localized data result in the clinical MRI scan.

A detailed discussion of the underlying physics of MRI is beyond the scope of this chapter. Hence, an overview of the concepts and most common technologies that are part of the process of MRI generation is presented in this chapter.

Nuclear Spin, Magnetism, and Magnets

Atomic nuclei have a property called *nuclear spin*. Nuclei, which possess an odd number of individual neutrons, protons, or both, have a net spinning charge. For the hydrogen nucleus, which consists of a solitary proton, its single moving electrical charge creates a tiny magnetic field. This magnetic field is analogous to that generated by current flowing in a wire loop, and it behaves like a small bar magnet (or magnetic *dipole)* oriented along the spin axis of the nucleus (Fig. 2–1). These magnetic dipoles, in the absence of external influences, are oriented randomly and, as such, have zero net magnetization (Fig. 2–2). In the presence of an external field, the laws governing the rotation of this spinning nucleus are analogous to those governing a spinning top. The spinning top, because of its mass and moment of inertia, precesses about the earth's gravitational field. The nucleus, because of its magnetic dipole field, precesses about the external magnetic field (Fig. 2–3).

When a hydrogen proton is placed within a magnetic field, the dipole aligns itself with the field in one of two ways: either in the direction of the field *(parallel)* or opposite to the field *(antiparallel)*. These orientations correspond to lower-energy and higher-energy states of the

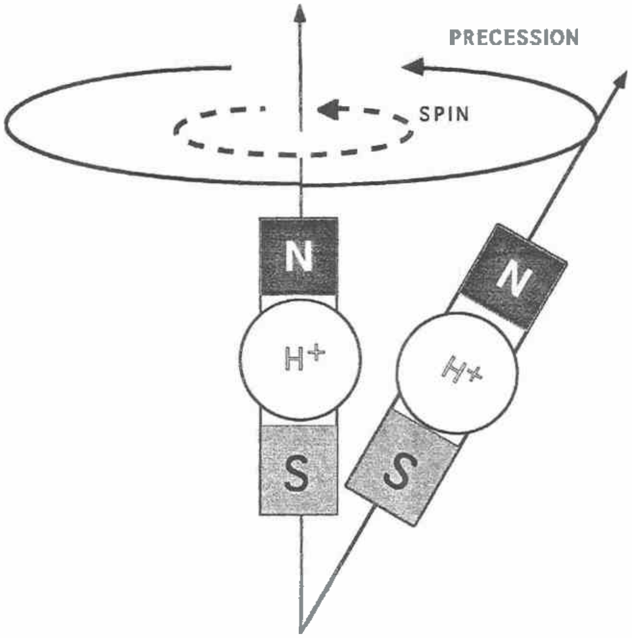

Figure 2–1. Representation of magnetic properties of the proton. The equivalent bar magnet arises as a result of nuclear spin about the axis *(dotted line)*. The introduction of an external magnetic field (B_0) causes the bar magnet to precess about its axis *(solid line)*.

frequency is specific for each nuclear species and is related to the field strength by the following formula:

$$f_{Larmor} = \gamma B_0$$

where

f_{Larmor} = the Larmor or resonance frequency
B_0 = the applied magnetic field strength
γ = the gyromagnetic ratio

The resonance frequency at 1.5 T is 64 MHz and at 1.0 T is 42.6 MHz. Hence, γ is 42.6 MHz/T for protons. Other nuclei have different gyromagnetic ratios. A shift of the net magnetization from the parallel to antiparallel state can be achieved by supplying energy to the spins in the form of an RF field at the Larmor frequency. When the applied RF field is removed, the magnetic dipoles return to their equilibrium state by releasing the previously applied RF energy. The release of this energy is also at the Larmor frequency. Prior to their return to alignment parallel to the static magnetic field, the magnetic dipoles precess about the field at the Larmor frequency, thereby creating a time varying magnetic field, much like that produced by a spinning bar magnet.

Perturbation of the net magnetization by applying an RF field at the resonance frequency and the measurement of its precession about the static field and its return to equilibrium is the underlying principle behind the MRI equipment.

dipole, respectively. By analogy, consider the task of aligning a spinning top that can be secured only at its tip, with the gravitational field of the earth. In one case, if one is very careful, the top is pointed up even though gravity is trying to pull the top over. If the top is secured at its tip, it is more likely that the top would hang down, along the gravitational field. Clearly, the top that is aligned with the gravitational field is in a lower-energy state and hence is more probable to occur in exactly the same way that the proton aligned with the magnetic field is in a lower-energy state and hence more likely to occur. The magnetic dipole of the proton is thus oriented anywhere around the surface of either one of two cones (prescribed by the precessing dipole), depending on whether the nucleus is in a parallel or antiparallel state.

Normally, a slight net excess of dipoles align in the lower-energy (parallel) direction in contrast to the higher-energy (antiparallel) direction. The excess is referred to as the *net magnetization*. This excess generates the signal measured in the MRI experiment.

Net magnetization increases with field strength, as does the difference in energy level between the parallel and antiparallel states. For these reasons, MRI signal strength increases in proportion to the external magnetic field. Thus, magnets with higher field strength are needed to increase the strength of the emitted signal. In clinical imaging, only one or two protons out of each million are in the parallel state versus the antiparallel state. Thus, only a small portion of the total pool of nuclei participate in the generation of the MRI signal.

The precession frequency of a magnetic dipole in an external field depends on the strength of the field. This

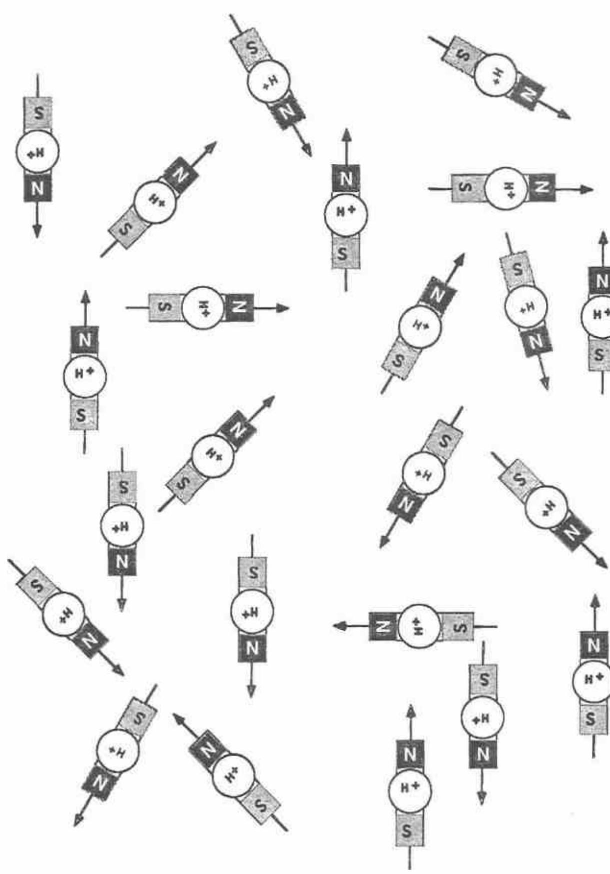

Figure 2–2. In the absence of an external magnetic field, magnetic dipoles are randomly oriented, resulting in a zero net magnetic field.

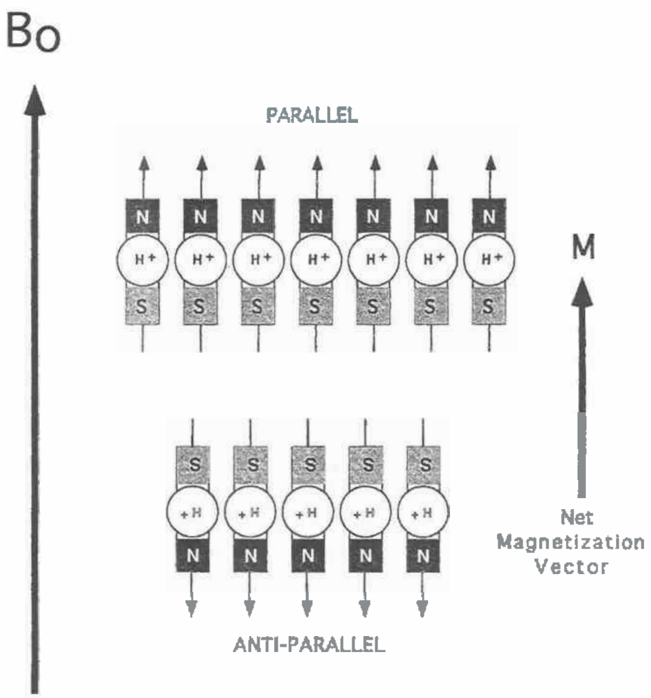

Figure 2–3. The introduction of an external magnetic field (B_0) forces the magnetic dipoles to align in one of two states: parallel (low energy) or antiparallel (high energy). A small excess in the parallel direction results in a nonzero net magnetic field (M).

Principles of Magnetic Resonance

Consider a simple analogy for the (resonance) phenomenon that underlies the MRI experiment. Resonance is manifested by enhanced and relatively abrupt absorption of energy occurring at a particular frequency.

For example, water contained in a glass goblet begins to vibrate or resonate and emits a sound if a tuning fork of the correct frequency is struck and placed near it. Imagine a goblet that contains an appropriate volume of water (e.g., 100 mL) to "ring" at pitch A. Now imagine an oscillating tuning fork, also oscillating at this frequency, placed nearby. Even though the tuning fork is not placed in contact with the goblet, the vibration of the nearby air molecules causes the goblet to also begin to vibrate because the tuning fork and the goblet have the same resonant frequency. We can observe the vibration of the water by seeing movement of the surface, heard as the sound corresponding to pitch A, or detected as a signal by an oscilloscope. The oscilloscope displays an image of what is heard in graphic form. The number of oscillations per second is a measure of the frequency of the goblet vibration, and the amplitude of the oscillation is a measure of its loudness.

If 100 goblets are placed on 10 shelves within a cabinet with opaque walls and each goblet contains 100 mL of water, as in the previous example, the peak amplitude of the signal displayed on the oscilloscope will correspond to their total loudness and will thus be a function of the entire number of goblets in the cabinet. Increasing or reducing the amount of water in the goblet modifies the resonant frequency (Fig. 2–4). However, the resonance phenomenon (i.e., vibration of the goblet) occurs only if the resonant frequency of the tuning fork matches that of the goblet.

In clinical MRI, the atomic nuclei are analogous to the goblets. The amount of water in the goblet corresponds to the strength of the external magnetic field. The tuning fork is analogous to the RF pulse. Thus, an MRI resonance, and thus the voltage, can be detected in a receiver if the frequency of the RF pulse matches the resonant frequency of the nuclei at that magnetic field strength.

The frequencies of interest in MRI are much higher than those used in our analogy and are usually expressed in megahertz (MHz) or millions of cycles per second (Hz). For example, hydrogen nuclei in a 1.0 T magnetic field resonates at a frequency of 42.6 MHz. Other MRI-sensitive nuclei have different resonant frequencies, just as differently shaped goblets, when filled with the same volume of water, also have different resonant frequencies. With the appropriate equipment, it is possible to measure signals from these other nuclei in vivo.

The initial stimulus in clinical MRI is provided by a burst or pulse of RF energy at the appropriate frequency, comparable to the effect of the tuning fork at a given tone. The nuclei resonate at that same frequency, and the amplitude of their emitted signal after removal of the stimulus reflects the number of nuclei contributing to the signal. Again, the electromagnetic oscillation induced in the receiver or detector is matched (i.e., it is tuned) to the frequency of the resonating nuclei in the same way that a radio is tuned to a specific frequency to detect a specific station.

To continue our analogy, imagine that every position, right to left, within the cabinet vibrated at a different frequency following the initial resonance phenomenon that caused it to start vibrating. Those goblets on the rightmost corner are at the highest frequency; those at the left side

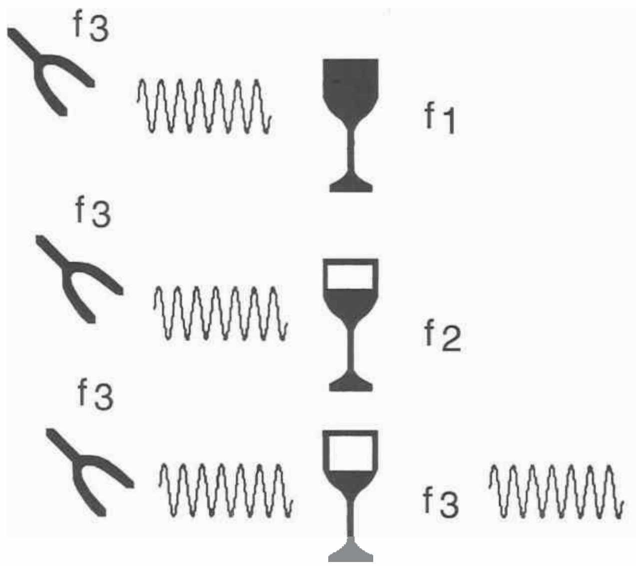

Figure 2–4. Analogy for the resonance phenomenon. Tuning forks with specific frequency (f_3) are placed in proximity to goblets with different water levels and resonance properties. Only the goblet whose resonance frequency matches frequency of the tuning forks absorbs and subsequently emits energy.

are at the lowest frequency. The sound, heard as a whole, is the sum of the component sounds emitted by each goblet at each position.

A mathematical technique, the Fourier transformation, is then employed to sort each component's amplitude and frequency. In this way, positional information regarding the location of the goblets is available because of the one-to-one relationship between spatial location and frequency of the sounds present. The number of goblets at each position is determined from the amplitude of the sound at each frequency. Thus, the positions of the goblets and number of goblets at each position can be determined even though the goblets are located in a cabinet with opaque walls and so cannot be observed directly.

The same phenomenon is used in MRI when a magnetic field gradient is applied following the resonant excitation of the RF pulse in order to establish a one-to-one mapping between position and precessional frequency. The magnetization's voltage is Fourier transformed to tell us at which locations (i.e., frequencies) protons are present and how many are at each location.

Radiofrequency and the MRI Experiment

For convenience, the direction of the external applied magnetic field (B_0) is along the z-axis. The transverse plane is perpendicular to the main field and contains the x-axis and the y-axis. The small net excess of dipoles aligned in the lower-energy parallel position are represented by a net magnetization vector (M) located along the z-axis in the direction of the field.

Application of the RF pulse causes each proton's magnetic moment aligned along the z-axis to rotate away from it, thereby causing the net magnetization vector to also rotate away from the z-axis. The amount of rotation is referred to as the *flip angle*. The greater the strength and duration (i.e., the greater the energy delivered by the RF pulse, the greater the flip angle). The flip angle is user-selectable, with the choice determined by the particular imaging sequence.

For spin-echo imaging, one would use a 90-degree RF pulse, which by definition is a pulse of sufficient strength to rotate M so that it is flipped from the z-axis to an orientation entirely in the transverse plane. This transverse component of M is entirely responsible for the MRI signal. Within this plane, M precesses around the z-axis at the Larmor frequency, returning to its equilibrium state by releasing energy to its environment in a process called *relaxation*. A receiving antenna or coil can be used to detect the time varying magnetization during precession. The resulting signal is referred to as a *free induction decay* (FID) (Fig. 2–5).

Relaxation

The maximum longitudinal magnetization along the z-axis is known as the *equilibrium magnetization*; for a given field strength and temperature, it is directly proportional to the proton density (ρ). The return of nuclear magnetization

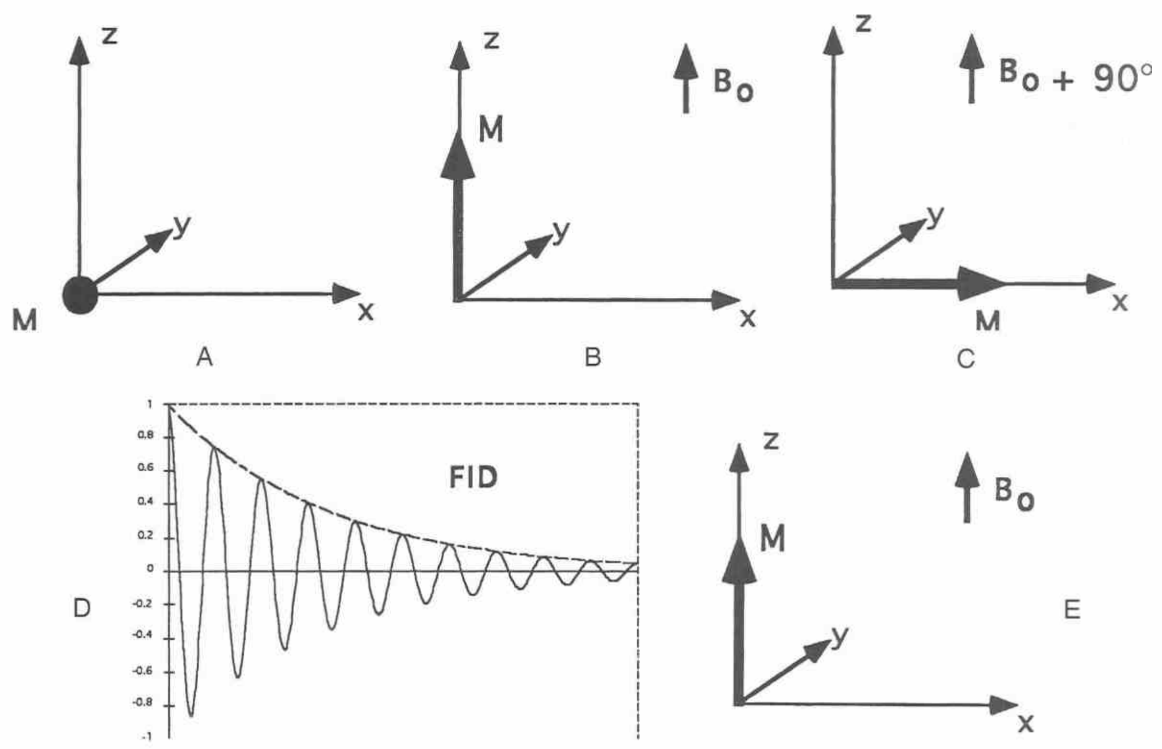

Figure 2–5. Diagrammatic representation of a basic MRI experiment. *A,* In the absence of an external magnetic field, net magnetization (M) is zero. *B,* Net magnetization is created by the application of an external static magnetic field (B_0). *C,* The application of energy, in the form of a 90-degree radiofrequency (RF) pulse, "tips" the magnetization vector onto the x-y plane. *D,* The precessing magnetization decays exponentially back to equilibrium (+z). The amplitude of the x-y component of the magnetization versus time (free induction decay [FID]) is shown. *E,* The system is back at equilibrium.

(M) after an RF pulse to its low-energy or equilibrium position along the z-axis is the result of interactions between the nuclei and the local electrochemical environment, its surrounding nuclei, and the strength of the B_0 field. The return of the magnetization to its equilibrium alignment and equilibrium value follows an exponential function of time. Because different tissues create different physical and electrochemical environments, their relaxation occurs at different rates, and their exponential recoveries are described by their relaxation times, T1. Hence, different tissues have different T1s.

As noted earlier, once the magnetization M is tipped into the transverse plane, an FID (induced voltage from the magnetization free of the RF pulse) is obtained. Careful examination of the FID reveals that its amplitude decreases exponentially with time. Hence, the transverse magnetization can be shown to also relax, and a parameter, T2, is used to describe the rate of this exponential loss of signal in the transverse plane. Different tissues have different T2s, just as they differ in T1 and proton density. Therefore, the strength of the MRI signal at any time during its induction is dependent on three parameters—proton density, T1, and T2; these parameters are responsible for the contrast in MRI images.

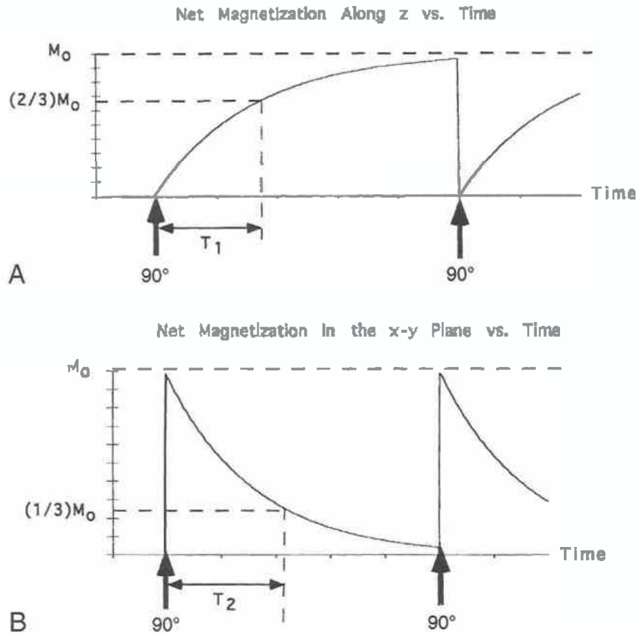

Figure 2–6. *A*, Exponential recovery of z magnetization after 90-degree pulse. The rate of recovery is dependent on T1. *B*, Exponential decay of x-y magnetization after 90-degree pulse. The rate of recovery is dependent on T2.

T1 Relaxation

Any input of RF power that tips the magnetization vector, M, away from the z-axis reduces its intensity along the z-axis to some value between the maximum and the negative of the maximum. Following cessation of the RF pulse, the nuclei return toward their equilibrium magnetization, M rotates from the x-y plane to the z-axis and M returns to the initial magnetization at some finite time later. The process of returning toward the equilibrium magnetization constitutes T1 relaxation, or *longitudinal relaxation*.

When a 90-degree RF pulse rotates M into the x-y or transverse plane, the entire vector is located in that plane, and its value along the z-axis is zero. The value slowly returns from zero to its initial strength, according to a simple exponential time constant such that its value after one T1 interval is 63% of the maximum value and reaches 99% at 5T1 (Fig. 2–6*A*). The process is caused by release of energy into the surrounding tissue (i.e., into the molecular environment or lattice around the proton). Hence T1 relaxation is also referred to as *spin-lattice relaxation*.

The return of longitudinal magnetization with time can be plotted as a curve, which has an exponential shape toward an upper limit. Thus, the difference between the curve's initial and final height is always a fixed proportion of the displacement from the maximum value, and the length of time taken to move from any point on the curve to one that is 63% closer to equilibrium is identified as the *time constant* (T1) for that curve. The Bloch equations summarize these observations and describe the regaining of *longitudinal magnetization* after an RF pulse.

Among the factors that influence the T1 value of a tissue are:

1. The particular chemical substance and its physical state.
2. Field strength (T1 increases with field strength, therefore recovery is slower).
3. Temperature (longer T1 with increased temperature in biological samples).
4. The liquid surrounding the protons.
5. The mobility of the proton; for example, protons in bone are much less mobile than those in water.

In imaging, RF pulses can be specifically designed to maximize or minimize image contrast dependence on T1 differences. The finite length of T1 limits how rapidly the RF pulses can be repeated and still yield a measurable MRI signal; that is, sufficient time must exist for longitudinal magnetization to regrow between pulses. Varying the strength and repetition time of RF pulses allows one to maximize or minimize the contrast between tissues with different T1 properties. With short *repetition times* (TRs), differences in magnetization are largely dependent on T1 differences, whereas the dependence at long TRs (hence following long recovery times) is due primarily to differences in proton density only.

T2 Relaxation

Immediately following a 90-degree RF pulse, the individual magnetic moments are all located in the transverse plane; more important, however, they are *coherent* (pointing in the same direction at nearly the same frequency). In other words, all protons have the same rotating phase.

Because the FID is the sum of voltages from many protons at each spatial location, the protons must precess at the same frequency and with the same alignment so that their magnetizations work together. As time goes on, following the RF excitation pulse the individual magnetic moments begin to become spread out in the transverse plane, much like cars of different speed on a race track. One cause of the different speeds is due to small local

variations in the static magnetic field resulting from random interactions from the magnetic moments of nearby protons. It is this spreading out that causes the vector sum to decrease. With time, therefore, the individual spins exchange energy between themselves until eventually they become completely incoherent, or *dephased*. Thus, T2 relaxation is also referred to as *spin-spin relaxation*.

The signal totally disappears when all phase coherence is lost. A curve that plots the disappearance of the signal with time shows an exponential decay toward zero, and the time taken for the signal to lose 63% of its initial intensity represents its time constant and is the T2 value for that substance, or *transverse relaxation* (Fig. 2–6*B*). T2 limits the time during which the signal is available after an RF pulse and thus limits the period of observability of the signal. This relaxation effect is also described by the Bloch equations. Thus, the dephasing resulting from interaction between adjacent spins is referred to as *T2 relaxation*.

Dephasing also occurs from local imperfections in the magnetic field and in thermal noise. All sources of dephasing—spin-spin and local inhomogeneities—are included in the single term *T2**, pronounced "tee-two-star." Fortunately, different tissues have different T2s. In clinical applications, T2 relaxation is exploited to produce image contrast.

T1 and T2 relaxations occur simultaneously, although T2 relaxation is a much more rapid process. T1 relaxation is field-dependent and increases with field strength; T2 relaxation is less dependent on field strength because it depends mainly on molecular interactions that occur at a much lower rate than the resonance frequency. Hence, imaging protocols developed at one field strength will exhibit differences in image signal-to-noise (SNR) ratio and image contrast if they are attempted at other field strengths owing to differences in T1 relaxation rates at different fields.

The phenomenon of signal decay and recovery in MRI may be summarized as follows. The T1 and T2 values for a substance are its time constants for acquiring or reacquiring its equilibrium state. The longitudinal magnetization of a substance (i.e., its ability to produce a signal) grows along the T1 curve after any disturbance in the equilibrium magnetization. A 90-degree RF pulse rotates all the longitudinal magnetization into the transverse plane, where T2 dephasing can also be observed. Basic differences in signal recovery as a result of different T1 and T2 values in the body tissues create differences in the magnetization vector of these tissues (Figs. 2–7 and 2–8).

The time constant for the substance to lose irrecoverably its transverse magnetization represents its T2 value. The loss of transverse magnetization cannot be slower than the gain in longitudinal magnetization and, in fact, can happen more rapidly, especially when there is loss of phase coherence.

The Imaging Process

The steps involved in the production of an MRI study may be summarized as follows:

1. A powerful, uniform, external magnetic field is employed to align a small but measurable fraction of the normally randomly oriented water proton's nuclear magnetic dipoles contained in the tissue being examined. Some of the randomly oriented nuclei lose energy to the lattice via T1 relaxation, causing a net magnetization to develop.
2. Next, this alignment (or magnetization) is perturbed or disrupted by introduction of external RF energy at an appropriate frequency so as to induce resonance. Spatial localization is obtained through application of a spatially dependent magnetic field *(gradient)* during the same time that RF energy is introduced into the tissue. The gradient field selectively modulates the resonant frequency of the patient in accordance to the Larmor equation (Fig. 2–9).
3. The nuclei return toward their initial alignment and precess about the static magnetic field. The magnetization along the static field grows while the precessing signal (and hence precessing magnetization) decreases through various relaxation processes. While the magnetization is precessing, the time varying magnetization induces a voltage in a receiver coil.

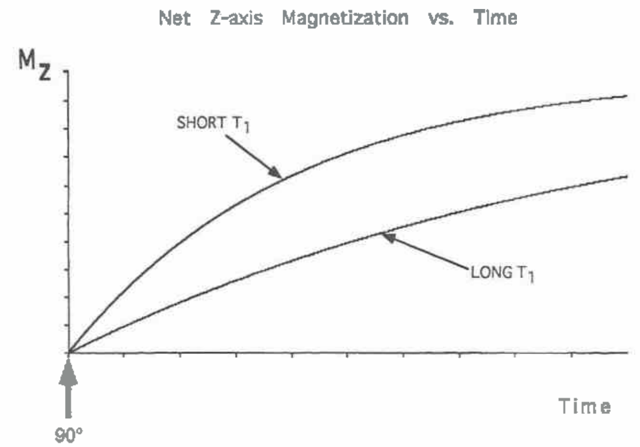

Figure 2–7. Exponential recovery of z magnetization after 90-degree pulse for two substances. The difference between the two curves determines contrast.

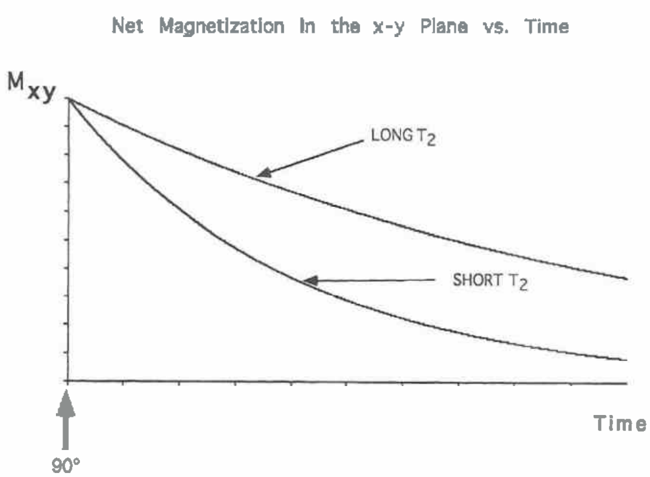

Figure 2–8. Exponential decay of x-y magnetization after 90-degree pulse for two substances. The difference between the two curves determines contrast.

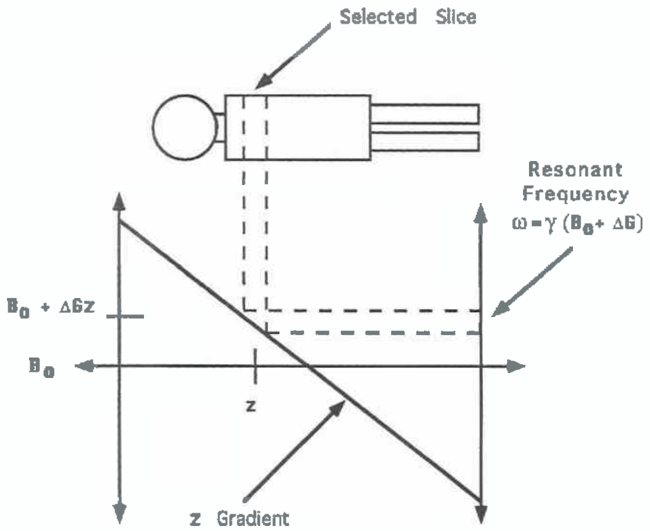

Figure 2–9. A z-axis slice selection using gradient field. Value of the net field (B_0 + gradient) at any given z value determines the resonant frequency. Radiofrequency excitation at a given frequency excites only a specific location.

4. After an appropriate period following initial RF deposition, the emitted signals are measured or read out during application of additional magnetic field gradients (typically measured in milliTesla per meter [mT/m]).
5. A mathematical process called *Fourier transformation* is used to convert the frequency information contained in the signal from each location in the imaged plane to corresponding intensity levels, which are then displayed as shades of gray in a matrix arrangement of, for example, 256 × 256 pixels.
6. Protons in the various tissues in the imaged slice realign with the magnetic field at (via T1) or decay in the transverse plane (via T2) at different rates, so that at any given moment there is a difference in signal strength between various tissues. This difference in signal strength from region to region constitutes the basis of tissue contrast and forms the substrate for interpretation of the image.

Radiofrequency Pulses

The RF energy used to perturb the protons as they align in the external magnetic field is delivered as a burst of input energy referred to as the *RF pulse*. The pulse consists of a signal at a fixed frequency, duration, and amplitude. The duration is typically a few milliseconds, and the amplitude, or power, is usually given in kilowatts. The strength of the applied RF field is on the order of microTesla (millionths of Tesla).

As the RF pulse tip angle is increased, the strength of the observed signal (i.e., the net portion of the equilibrium magnetization oriented along the x-y plane) reaches a maximum, after which further increases in the input power produce progressively less signal each time. This continues up to a point at which a pulse with a duration twice that of the one producing the maximum signal produces no signal at all.

The smallest power of the RF pulse input that produces a maximum response in the evoked signal is called the *90-degree pulse* (or a *π/2 pulse*). This pulse tips the transverse magnetization to the x-y plane.

A pulse with twice that strength that produces no evoked signal is called the *180-degree pulse* (or a *π pulse*). This pulse tips the transverse magnetization antiparallel to equilibrium (the −z direction). If the magnetization is already in the transverse plane, the 180 degree RF pulse will cause the magnetization to "pancake flip" over.

The RF transmitter is turned off or inactivated when one wishes to detect the MRI signal (on the order of nanoTesla or billionths of Tesla) so that the much stronger RF pulse does not mask the small MR signal. In the typical MRI study, several hundred signals are collected, so that the study usually consists of a series of events with the following order: RF pulse, read after some time (echo time [TE]), wait for some longitudinal recovery to occur (repetition time [TR]); RF pulse, read, wait. . . .

Each series is a repetition of the one preceding in the order and timing of the RF pulses used. The particular combination is referred to as the *RF pulse sequence*. Several pulse sequences are discussed later.

Magnets and Field Gradients

The variation of any physical quantity with distance is referred to as a *gradient*. For example, in a harp, the strings nearer the performer are shorter than those farther away. Each string is spaced at a uniform distance from the one preceding it. In the water goblet example, positional information can be derived by knowing the frequency of a signal. In MRI studies, field gradients are employed to make the MRI signal contain spatial information. The gradient magnetic field spatially alters the resonant frequency of the imaging volume in accordance to the Larmor equation (see Fig. 2–9).

A typical variation in applied field strength-static magnetic field (B_0) + gradient magnetic field-across the imaging volume is approximately 100 gauss (G) (0.01 T). Thus, for a 1.0 T magnet, the magnetic field superimposed on the main magnetic field for spatial encoding spreads the proton resonance frequency out over a range that spans 0.4 MHz or less. Recording the frequencies over this entire range and spatially decoding using the Fourier transform achieve precise localization of their source.

The gradient field is superimposed on the main magnetic field through employment of gradient coils: three orthogonal sets of coils, one each for the x-axis, the y-axis, and the z-axis. The gradients produced by these coils are spatially linear and produce a difference in field strength such that the difference between any two planes in the imaged volume is directly proportional to the distance between those planes. The nuclei at the weak end of the field resonate at a lower frequency, and those at the stronger end resonate at a slightly higher frequency. Because resonant frequency is directly proportional to field strength, imposing a linear field gradient on a magnetic field makes the resonant frequency of the nucleus vary linearly across the volume. By having an orthogonal arrangement of gradient coils, one can achieve linear gradients in any desired direc-

tion and thus can create a series of parallel planes with linearly decreasing field strength.

The amplitude and direction of the gradient are thus user-selectable. Each gradient coil is connected to an amplifier that supplies current to create the field variation. The amplifier can be turned on and off and applied at different strengths so that the gradients also become time-dependent. Because the coils are independent and used to define orthogonal scan planes, it is possible to acquire oblique scan planes electronically without physical reorientation of the patient or the hardware, simply by providing appropriate gradient waveforms to combinations of the gradient coils.

Gradients, Field of View, and Resolution

As noted earlier, each gradient coil is connected to an independent amplifier and the amount of current that the amplifier provides produces a proportionate alteration in the strength of the gradient field. It can be shown that:

1. For a fixed RF pulse, the minimum slice thickness is directly proportional to the maximum gradient strength.
2. For a fixed signal sampling time and image matrix size, the minimum field of view (FOV)—and, hence, minimum resolution—is directly proportional to the maximum gradient strength.
3. The minimum TE and minimum TR of a sequence depend on the time it takes for the gradient waveform to go from zero amplitude to its final value. The parameter that describes the MRI system's rate of change of the gradient field is the *slew rate*, given in mT/m per msec. Typical values for a common system today are near 50 mT/m per msec; typical gradient strengths for a whole body system are on the order of 25 mT/m per msec.
4. The sensitivity of the gradient coils in producing the desired field is related to the amount of field produced per unit of current. This sensitivity is related to the size of the coils, whether they are self-shielded and the spatial arrangement of the conductors that make up the coil.

These relationships establish a number of interesting possibilities. For example, the FOV along the phase encoding direction is governed by the size of the change in gradient pulse from one TR to the next. Because this is independent of the read gradient sampling, the FOV in the phase encode and read gradient can be specified independently, as can the resolution along the two axes.

Imagine that the torso is being imaged. In most people, the width of the torso (left to right [L-R]) is greater than its height. Hence, a 400-cm FOV may be required along the R-L read direction; only 300 mm is required along the anterior-posterior (A-P) phase-encode direction by acquiring a 400 × 300 mm FOV image (i.e., rectangular FOV). The phase-encoding resolution is equal to FOV/Ny, where Ny is the number of phase encoding steps. Hence, Ny can be reduced if the FOV is reduced from 400 to 300 mm, thus saving acquisition time. The only sacrifice is a small loss in the image's SNR ratio, since the SNR is proportional to $\sqrt{Ny}$ at constant resolution. Additionally, it is possible to alter the number of phase-encoding steps so as to alter the resolution such that it differs along the read and phase directions.

The gradient coils are essentially large inductors. Thus, to have the system go from zero gradient strength to the desired spatial magnetic field gradient, current must be applied to the gradient coils. The rate of change of the gradient field, or slew rate, is related to the rate of change of current. In electric circuits, the voltage across an inductor (gradient coil) is related to the inductance of the coil and the rate of change of the current (hence the slew rate of the gradient field). Thus, gradient amplifiers must produce hundreds of amps of current throughout the acquisition and at hundreds of volts during the ramping of the gradient. In very rapid sequences, such as in *echo-planar imaging*, which can achieve a complete acquisition in approximately 100 msec, the MRI gradient subsystem may be asked to produce up to 0.25 MW of power along each of the gradient axis, yet the total energy delivered may be only a few thousand kilojoules.

In many discussions of MRI pulse sequences, the various gradient lobes required are drawn as instantaneous changes in the amplitude of the gradient. In reality, however, the slew rate of the imaging system prevents this. Hence, in actual MRI pulse sequences, the gradient lobes ramp-up from some value to that required for achieving the specified field of view or slice selection thickness. Figure 2–10*A* shows the difference between real and symbolic pulse sequence gradient lobes.

Pulse Sequences

MRI pulse sequences in clinical use can be grouped into three basic classes:

- Spin-echo sequences
- Inversion recovery sequences
- Gradient-echo sequences

Many techniques have been developed using these basic sequences, thus covering a broad range of mechanisms for generating contrast between tissues.

Spin-Echo Sequences

A 90-degree pulse is applied to tip the spins into the x-y plane. As previously described, the rotating bulk magnetization vector M generates a signal (the FID). The initial strength of the FID diminishes because of loss of coherence between the precessing protons in the tissue of interest. This loss of coherence arises from spin-spin relaxation (T2) and local field inhomogeneities (T2* effects), which cause the protons to rapidly spin out of phase with each other.

In spin-echo sequences, the FID is not of interest and is ignored. A second 180-degree RF pulse is applied a short time after the 90-degree pulse. The time between these two pulses is usually referred to as tau (τ). This second 180-degree pulse rephases the portion of the protons that had lost coherence because of time-independent, static magnetic field homogeneities. The signal arising from this rephasing peaks at a time, τ, after the 180-degree pulse and is called a *spin echo*. The time between the application of the initial 90-degree pulse and the peak of the spin echo is referred to as the *echo time*, or TE (Fig. 2–10*B*). It

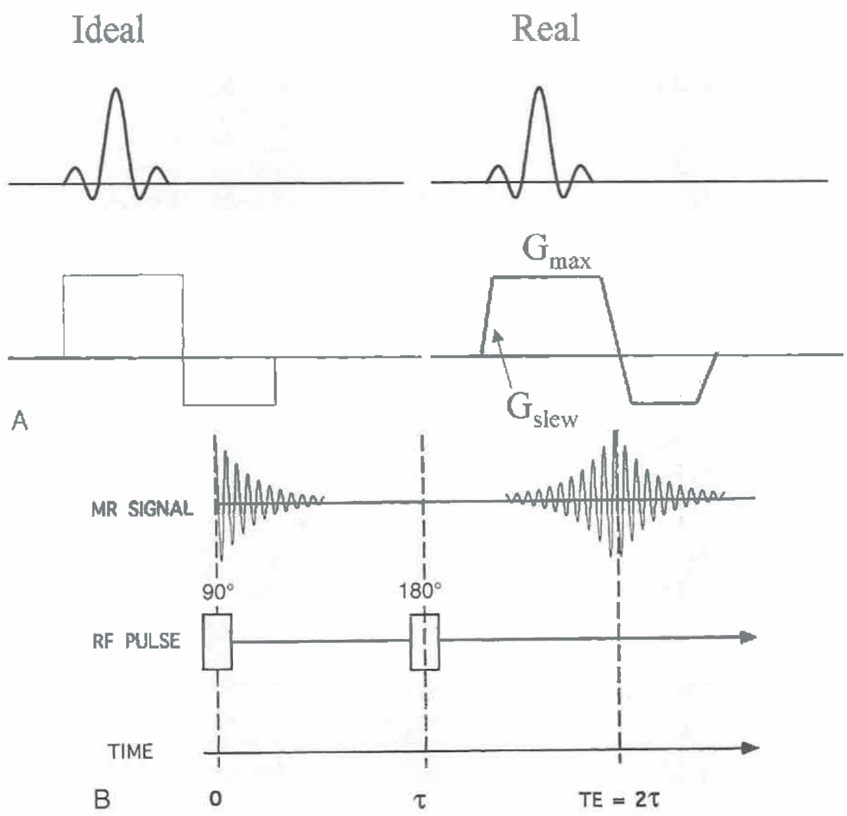

Figure 2–10. *A,* The difference between ideal and real gradient waveforms is a result of the finite slew rate of the MRI systems. Each gradient waveform takes a finite, rather than an infinitesimal, time to reach the final gradient strength. *B,* Timing diagram for spin-echo pulse sequence. TE, echo time.

essentially is equal to the time from generating the transverse magnetization until the center of the signal acquisition (see earlier).

Repeated with a long interval between the excitation pulses, the 90-τ/180-τ sequence produces an image whose strength is dependent on the proton density and the T2 of the tissue alone (T2-weighted). If the TE is short such that little dephasing occurs and with a short interval between repeated acquisitions, the image will be primarily dependent on variations in T1 between tissues (T1-weighted). Long TRs corresponding to full recovery of the magnetization (and hence limited variation due to T1 differences) and short TE corresponding to little signal loss from T2 decay, provide an image that is primarily dependent only on proton-density differences between tissues. Examples of T1, proton density, and T2-weighted images of a normal brain are shown in Figure 2–11*A–C*.

Fast (Turbo) Spin-Echo Sequences

In a conventional spin-echo pulse sequence, the 180-degree pulse allows the magnetization dephasing from field inhomogeneities to be recovered and to thus generate an echo of the initial transverse magnetization. The total imaging time is given as TR * NSA * Ny, where NSA is the number of signal repetitions that are averaged together and Ny is the number of phase-encoding steps performed.

The spatial resolution along the phase-encoding axis is given by FOV/Ny. If additional 180-degree pulses were applied, additional echoes would be obtained after the first one. These additional echoes can be combined in a few different ways. For example, if additional phase encoding is performed prior to each echo, each collected signal acquires a different one of the Ny encodings. The total imaging time is reduced because multiple phase encodings are performed after each 90-degree pulse. That is, the number of echoes (echo train length [ETL]) is acquired for each TR; echo train length is the number of echoes per TR. The total imaging time under these conditions is TR * NSA * Ny/ETL and, hence, represents a reduction in the imaging time when compared to a conventional spin-echo acquisition. These acquisitions have become known as "turbo spin-echo," or fast spin-echo scans.

A different way to use the multiple echoes is to perform no phase encoding for each echo and to collect each echo as one view for an image at a new TE. In this way, multiple images are obtained over TR * NSA * Ny, each acquired at a different TE. This technique has been widely used to acquire a short TE and a long TE acquisition at a long TR so that both proton-density weighting and T2-weighted scans are acquired in the imaging time.

Inversion Recovery Sequences

Various modifications of this standard spin-echo technique have been developed to provide enhanced contrast for many tissue and disease types. One example is the *inversion recovery* (IR) *technique*. In this sequence, a 180-degree inversion pulse is applied some time before *inversion time* (TI), the standard 90- to 180-degree spin-echo sequence previously described. The 180-degree inversion pulse flips the equilibrium magnetization vector M so that it is antiparallel to the field.

Following this pulse, the spins begin to revert to equilibrium by transferring energy to the surrounding medium (or lattice). The z-axis component of the magnetization shrinks

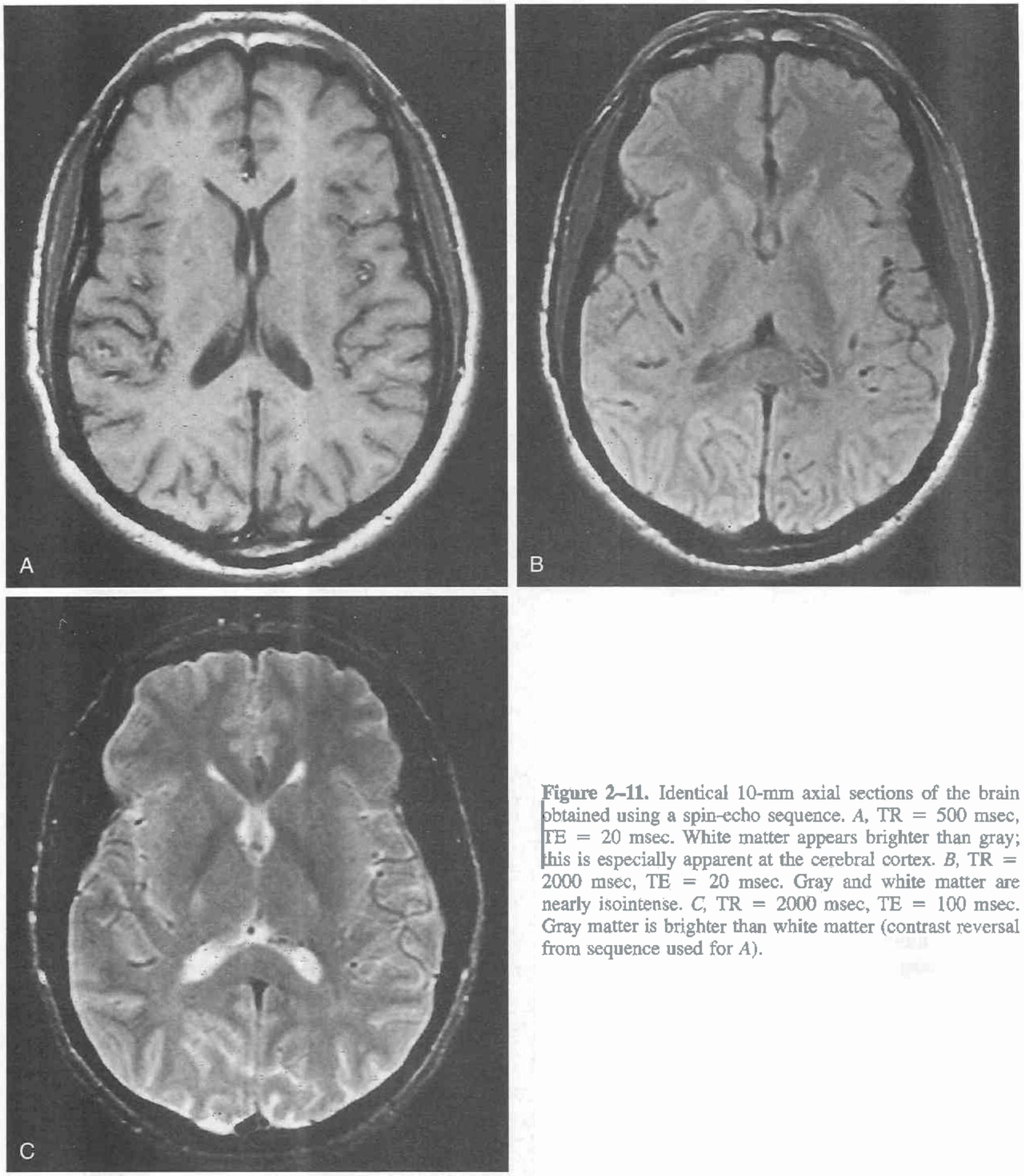

Figure 2–11. Identical 10-mm axial sections of the brain obtained using a spin-echo sequence. *A*, TR = 500 msec, TE = 20 msec. White matter appears brighter than gray; this is especially apparent at the cerebral cortex. *B*, TR = 2000 msec, TE = 20 msec. Gray and white matter are nearly isointense. *C*, TR = 2000 msec, TE = 100 msec. Gray matter is brighter than white matter (contrast reversal from sequence used for *A*).

from the antiparallel direction to zero, after which it regrows into the equilibrium (aligned) direction exponentially with the constant T1. Measurement of the magnetization M at some time TI after the initial 180-degree pulse via the 90- to 180-degree excitation of the partially recovered longitudinal magnetization and detection of the created transverse magnetization provides a measure of the T1 recovery of the tissue. Simple alteration of TI values allows for the selection of different T1 contrast points.

STIR Imaging

The time that it takes the longitudinal magnetization to reach zero is $\ln(2) * T1 \sim 0.7 * T1$. This technique to eliminate the signal from one tissue in an image has been used in two different applications. Fat, which has a T1 of approximately 240 msec at 1.5 T, can be eliminated from the image by using a TI of approximately 170 msec. Known as *short tau inversion recovery* (STIR), these acquisitions have been widely used in musculoskeletal and body MRI.

Figure 2–12*A* shows an example of a T1-weighted acquisition of the lower leg via a conventional spin-echo acquisition and an inversion recovery sequence with spin-echo read out in which the signal from fat is removed. Note the difference in contrast in the marrow, the site of the actual disease, once the fatty component is removed

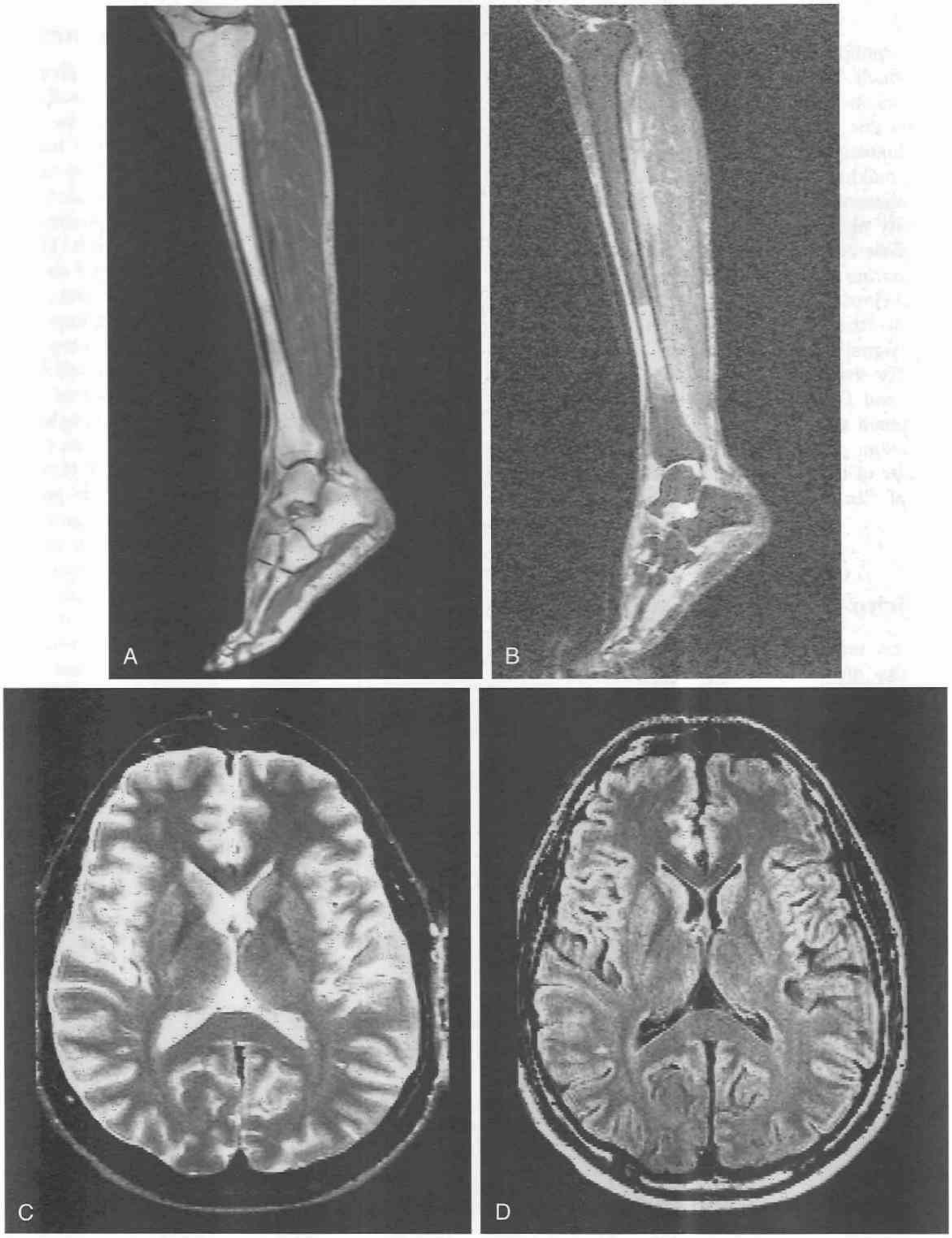

Figure 2–12. Inversion recovery sequences can be designed to generate transverse magnetization when the longitudinal magnetization has relaxed to zero following an initial inversion. *A*, Conventional T1-weighted spin echo. *B*, Conventional T1-weighted short tau inversion recovery (STIR) in which the signal from fat is removed. Note the appearance of a significant signal in the marrow once the fatty component is removed. *C*, Conventional T2-weighted spin echo. Note the high signal amplitude in the ventricles. *D*, Fluid-attenuating inversion recovery (FLAIR) acquisition in which the basic contrast between tissues in the parenchyma is unchanged from the original T2-weighted spin echo, except for the loss of the cerebrospinal fluid (CSF) signal.

via the STIR acquisition designed to eliminate the fat component (Fig. 2–12*B*).

FLAIR Imaging

The second application for signal suppression is in brain imaging, in which T2-weighted acquisitions have found great application in providing enhanced signal for pathologic processes due to edema and increased T2s in these tissues. Unfortunately, the T2 of cerebrospinal fluid (CSF) is also long, making identification of pathology in the parenchyma adjacent to the ventricles difficult as a result of high-intensity signal from both the pathology and the CSF in immediate contact.

Fluid-attenuating inversion recovery (FLAIR) methods have been developed in which the TI is approximately 2000 msec or so (the T1 of CSF is 2000 to 4000 msec) so that the CSF signal is eliminated at the time of the 90-degree pulse for the long TE spin-echo pulse sequence. Figure 2–12*C* and *D* provides a comparison of a conventional T2-weighted spin echo and a FLAIR acquisition at the same location. Adjacent to the ventricles, the high-signal amplitude of the CSF is removed and would permit visualization of "bright" signal, if present, in the brain parenchyma.

Gradient-Echo Acquisitions

Gradient-echo sequences replace the 180-degree refocusing RF pulse of the spin-echo sequence with a fast reversal of the magnetic field gradient (Fig. 2–13). The initial portion of the refocusing gradient places the protons along the applied gradient in different strength magnetic fields, causing differences in the precessional frequency and hence dephasing of the magnetization. The second portion of the gradient reverses the dephasing of the protons by rapidly reversing the gradient direction, forcing the nuclei back in phase and generating an echo.

The 90-degree RF pulse used in the initiation of the spin echo is replaced by a different (and variable) strength RF pulse. Depending on the strength of the pulse, the magnetization vector is rotated toward the x-y plane. The amount of rotation resulting from this pulse is called the *flip angle.*

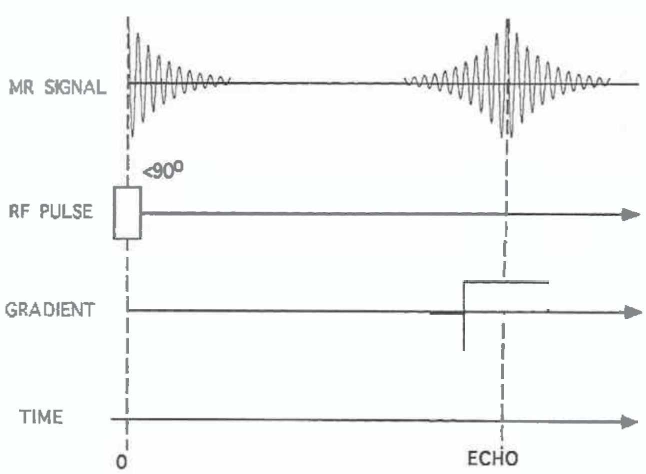

Figure 2–13. Timing diagram for gradient-echo pulse sequence.

Fast (Spoiled) Gradient-Echo Acquisitions

In normal spin-echo and IR pulse sequences, it can be safely assumed that the transverse magnetization has decayed to zero prior to the application of the next RF pulse at the end of TR. This is not necessarily true in gradient-echo acquisitions in which the TR may be very short. This has led to two types of gradient echo acquisitions: (1) those that *utilize* the residual transverse magnetization available at the end of TR and (2) those that *spoil* it. These two types of sequences have very different contrast characteristics as a function of the pulse sequence parameters.

The variation of the flip angle is an important factor in creating contrast differences and shortening imaging time. In spoiled acquisitions (e.g., FLASH, spoiled GRASS), the degree of "T2-weightedness" of the signal varies roughly with the flip angle. The smaller the flip angle, the more the gradient-echo image looks "T2-like," since the influence of spin-lattice relaxation differences is minimized. Short times between pulse repetitions are made possible also by the use of small flip angles, because longitudinal magnetization has been altered only slightly with small tip angles, sufficient time to recover and return to equilibrium.

An additional twist to the gradient-echo techniques can be achieved by using a spoiler gradient or random-phase RF pulse to eliminate the transverse component of the "steady-state" magnetization. This method results in T1-weighted images (at flip angles of 30 degrees or more). Another common name for these sequences is T1-FAST.

Short TE times are usually used in gradient-echo sequences to minimize the effect of static field inhomogeneities within the volume of interest. Unlike the spin-echo sequence, the gradient echo does not compensate for the effect of time-independent magnetic field homogeneities; hence, gradient-echo images are essentially T2*-weighted images.

Table 2–1 describes various scan sequences and their appearance for different tissues.

Unspoiled Fast Gradient-Echo Sequences

In our previous discussion, and in the presentation of contrast versus sequence parameter given in Table 2–1, it is assumed that the time between excitations is sufficiently long that transverse magnetization is sufficiently decayed (TR > T2). If this is not the case, steady-state effects must be taken into account because their effect on contrast can be significant. For these short TR cases, the RF pulse alters the residual transverse magnetization as well as the partially recovered longitudinal magnetization. A steady state of unrecovered magnetization is maintained by the fast repetition. This different (from fully recovered) initial magnetization can be manipulated to provide additional contrast possibilities. Depending on the manufacturer, these sequences go by the names FAST, GRASS, or FISP. The longitudinal component of the magnetization is dependent on the steady-state magnetization which is, in turn, dependent on the amount of T2 decay between pulses.

Table 2–1. Tissue Characteristics for Various Scan Sequences

Sequence	Parameter	Parameter	Contrast Type (Weighting)	CSF	Gray Matter	White Matter	Fat	Muscle	Disk
Spin echo	Long TR	Short TE	Spin density	Gray	Isointense	Gray-black	Bright	Isointense	Bright gray
Spin echo	Short TR	Short TE	T1	Dark	Gray	Bright gray	Bright	Isointense	Isointense
Spin echo	Long TR	Long TE	T2	Bright	Gray	Black	Gray-black	Gray-black	Bright
Inversion recovery		Long TE	T2	Bright	Gray	Black	Gray-black	Gray-black	Bright
Inversion recovery	Short T1	Short TE	T1	Dark	Gray	Bright gray	Bright	Isointense	Isointense
Gradient echo	Flip angle <20°	Long TE	T2	Bright	Gray	Dark	Gray-black	Isointense	Isointense
Gradient echo	Flip angle >45°	Short TE	T1	Dark	Gray	Bright gray	Bright	Gray-black	Bright

CSF, cerebrospinal fluid; TE, echo time; TR, repetition time.

Three-Dimensional Gradient-Echo Acquisitions

In most conventional acquisitions, the imaged volume results from signal from distinct planes excited by the selective RF pulses applied in the presence of a magnetic field gradient. At soon as the signal from one slice is collected, excitation of the next spatial location can occur. In this way, the acquisition of slice information is interleaved in time within the TR. The acquisition time largely appears independent of the number of slices acquired.

In rapid gradient-echo acquisitions, TR is very short (i.e., on the order of tens of msec versus hundreds or thousands of msec or less), thereby leaving little time for slice interleaving when multiple slices are needed. A different mechanism is used to obtain information over the image volume. In three-dimensional (3D) gradient echo acquisitions, instead of information being acquired from distinct planes, signal is obtained from the entire imaging volume for each acquisition. Frequency encoding and phase encoding are performed along the image planes as in a typical acquisition, yet an additional phase encoding is also applied along the slice select direction. Excitation is performed over a slab instead of a slice, and the phase encoding along the slice select direction subdivides the signal in this direction just as it does in conventional MRI. Thus, in 3D acquisitions, image resolution along the slab-select direction is not dependent on the slice select RF pulse bandwidth and the gradient strength but, instead, on the slab thickness and the phase-encoding gradient process, just as the phase-encoding process determines the image resolution along the phase-encoding axis in a two-dimensional (2D) image.

A 2D and a 3D pulse sequence is shown in Figure 2–14. Because phase encodings are performed along multiple axes, the total acquisition time becomes TR * Ny * NSA * Nz. Typical values for Ny in any acquisition are 128 to 512, whereas Nz for a 3D acquisition may vary from 4 to 256. Although the acquisition time in 3D acquisitions seems to be Nz times longer in a 3D gradient-echo than a spin-echo acquisition, the TRs in these sequences are typical only a few milliseconds in duration in comparison to the hundreds or thousands in spin-echo methods. The advantages of a 3D acquisition are the high spatial resolution along the slab select direction and the wide range of contrasts available from spoiled or unspoiled gradient-echo sequences.

Review and Integration

Any MRI study directly shows received signal amplitude as a function of position. For a given pixel, amplitude depends on the (1) T1, T2, and proton density of the substance being imaged; (2) motion, such as flow; (3) system noise, and (4) pulse sequence used.

Most components of the body contain approximately similar quantities of hydrogen and, therefore, have similar equilibrium magnetization. Air spaces are an exception. The MRI signal elicited in solids disappears extremely rapidly (often within microseconds) and can take hours or days to reestablish equilibrium magnetization. Thus, solids have a long T1 and a short T2. The solid tissues encountered in clinical practice are cortical bone, tooth enamel, and dentin. Conversely, in liquids potential signal can be

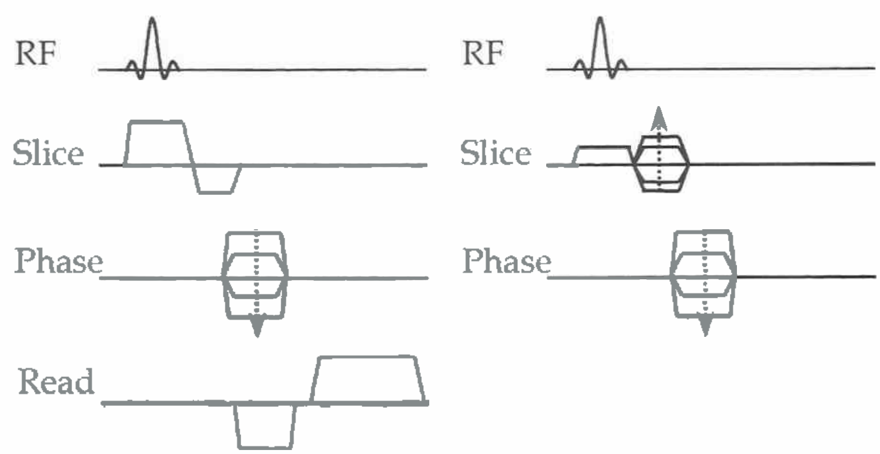

Figure 2–14. A 2D gradient-echo sequence consists of a radiofrequency (RF) slice selection and phase encoding along a separate axis. The read gradient is used for encoding along the third image axis. The RF pulse excites a thin slice of tissue, and signal only comes from that slice. In a 3D sequence, a weaker gradient pulse is used to excite a slab of tissue. The slab is then subdivided by a phase encoding, also performed along the slice direction in a manner comparable to dividing the field of view with the phase-encoding gradients in a normal sequence. A 3D Fourier transform reconstruction is used.

regained almost as quickly as actual signal is lost; that is, T2 approaches T1 and the value for both is on the order of milliseconds to seconds.

The remaining body components are tissues that are neither entirely solid nor liquid. They have a higher viscosity than liquids and less crystalline structure than solids. Making a liquid more viscous would shorten its T1. The T2 cannot be longer than T1, and thus viscous liquids have short and roughly equal T1 and T2. If the viscosity increases further, the substance becomes more like a solid, and T1 is longer than its T2. In clinical imaging most tissues have a T1 between 200 msec (fat) and 3 or 4 seconds (CSF). The T2 values lie between 30 msec (muscle) to about 2 or 3 seconds (CSF). Cortical bone and teeth are exceptions in both cases and are not typically seen in images because of low proton density and relaxation times that hinder signal detection and generation.

For a given field strength and a constant temperature, the strength of a substance's equilibrium magnetization is directly proportional to its proton density (p). In imaging objects that are not chemically uniform, such as the brain, in which all tissues have essentially the same proton density and therefore the same equilibrium magnetization, one can exploit the difference in T1 values. Plotting the curve of longitudinal magnetization versus time, all curves start at zero value following the 90-degree pulse and recover longitudinal magnetization along their own T1. After a long waiting period the magnetization will be near maximum for each; each pixel value will also be near its maximum, and the pixels will be uniformly bright over the whole image, provided that T2 differences are minimized via short TEs.

If one shortens the waiting period to an intermediate point, the signal strength will be moderately reduced; however, the signal from areas with long T1 will be more diminished than from areas with short T1. Thus, the image will reflect differences in T1 values, so that the shorter the T1 of a substance, the brighter it will appear on the image.

Finally, if the waiting period is very short, the pulses will be too close to each other to allow any significant recovery of longitudinal magnetization during the waiting period, so that signal strength is weak and the SNR ratio will be low. Thus, for T1 weighting in SE sequences, the TR should be low—but not so low as to allow an insufficient time for magnetization T1 recovery between pulses.

The difference in signal strength, as reflected by the separation between the curves of the various tissues in the previous example, constitutes the contrast in the image (see Figs. 2–7 and 2–8). Reference to the figures allows selection of an appropriate waiting time after the 90-degree pulse, at which one can obtain maximum separation between the curves and thus obtain maximum contrast between tissues in the MR image.

Because of differences in tissue composition (e.g., differences in proton density), in some circumstances the curves referred to previously do not follow the same contour but, instead, cross each other (Fig. 2–15). At such crossover points, there is no difference in perceived signal intensity, and thus the image will not show any contrast between the two tissues. Gray matter and white matter in brain are examples of this crossover phenomenon, as a function of TR. Gray matter has a longer T1 and a higher proton density than whiter matter. Thus, white matter exhibits rapid recovery of longitudinal magnetization (because of its short T1) and appears brighter than gray matter. At a slightly longer pulse delay, the gray matter and the white matter become indistinguishable; at even longer recovery times, the gray matter achieves higher equilibrium magnetization and appears brighter than white matter in the image (see Fig. 2–11*A–C*).

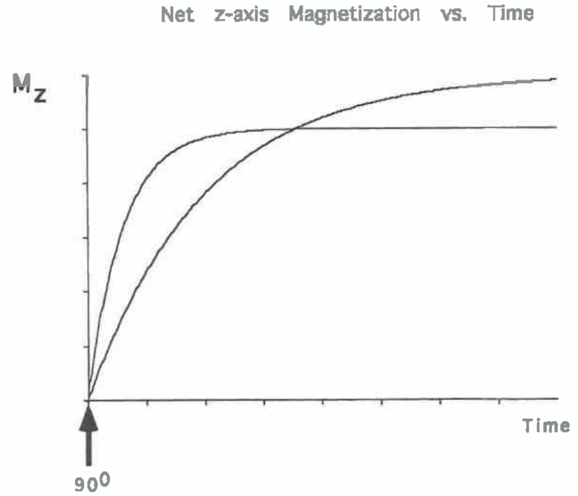

Figure 2–15. Recovery of z-axis magnetization for two substances with different proton density and T1. Note the crossover of signal difference, which results in contrast reversal.

For almost any two substances, an RF pulse sequence and TR can be selected to completely obscure any visible distinction between the two substances; however, imaging parameters that provide maximum contrast between tissues can also be found. However, maximum contrast is rarely obtained because other considerations (e.g., imaging time, slice coverage) cause compromises in one of the pulse sequence parameters so that "adequate versus optimal" contrast is obtained. In addition, the contrast observed on one side of the crossover point produces a different kind of contrast than on the other side. In similar fashion, a family of curves results as one plots transverse magnetization against time. The height of each curve is at peak amplitude initially and decays exponentially.

In spin-echo sequences, the longer the delay between the 90-degree and the 180-degree pulses, the more T2 relaxation will have occurred and the less signal there will be to recover. The signal from substances with short T2 values falls off more than from those with long T2 values (see Fig. 2–7). Eventually, all signal disappears except for the signal from substances with long T2 values. Thus, in a T2-weighted image, only substances with long T2 values remain visible. Tissues with long T2 values produce more signal than signals with short T2 values.

3 Magnetic Resonance Angiography: Fundamentals and Techniques

E. Mark Haacke, Weili Lin

Magnetic resonance angiography (MRA) has become commonplace in the last few years.[1,23,49] The improvements in pulse sequence design, hardware design, and postprocessing methods make it possible to acquire data in a short period with excellent vascular visualization in a variety of clinical applications. This chapter introduces the concepts behind MRA, the techniques used to obtain MRA studies, and its clinical applications.

Fundamentals of Imaging

Gradient Echoes

The ability to collect an image with magnetic resonance is the result of the dependence of the frequency on the local field. This relationship is governed through the Larmor equation:

$$\omega = \gamma B_0 \tag{1}$$

where

ω = the angular frequency known as the Larmor frequency
γ = the gyromagnetic ratio ($2\pi \times 42.6$ MHz/T)
B_0 = the static magnetic field

For example, for a field strength of 1.5 Tesla (T), the Larmor frequency is equal to 64 MHz.

This frequency dependence is used to spatially discriminate information by applying a gradient field (G) throughout the region of interest in one or more directions. Now the frequency response is spatially dependent (Fig. 3–1):

$$\begin{aligned} \omega(x) &= \gamma B(x)(2) \\ &= \gamma(B_0 + G \times x) \end{aligned} \tag{2}$$

If the signal is measured during the application of the gradient and subsequently Fourier transformed, the spectral amplitudes (the signal as a function of frequency) are obtained. This sampled signal is referred to as the *free induction decay* (FID) (Fig. 3–2).

The signal can also be obtained by using a bipolar gradient structure to create an echo (Fig. 3–3). However, the bipolar gradient structure is able to give only one side of the frequency spectrum (either positive or negative frequency components), which, in theory (as in the FID case) is sufficient to reconstruct an image by taking advantage of the *hermitian symmetry* (see "Partial Fourier Imaging" later on) of the Fourier transform. In practice, it is not enough to reconstruct an image by using only one side of the frequency spectrum because of signal distortion caused by local field inhomogeneities. Therefore, the second lobe of this gradient structure is lengthened by a factor of two, so that both the positive and negative frequency spectra can be obtained. Using all the data gives a more robust image when the echo is not properly centered or when local gradients are present as a result of field inhomogeneities. Further, it also gives a $\sqrt{2}$ improvement in the signal-to-noise ratio (SNR).

Phase

Relative to the echo time, for a constant gradient, the phase as a function of time is determined from

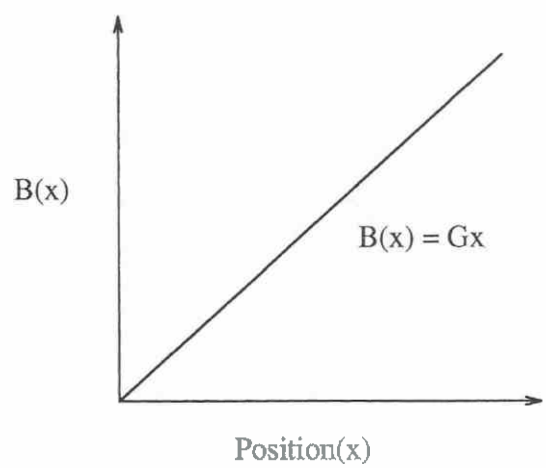

Figure 3–1. In the presence of a gradient, the magnetic field has a linear dependence on position. The horizontal axis represents the position, and the vertical axis represents the magnetic field.

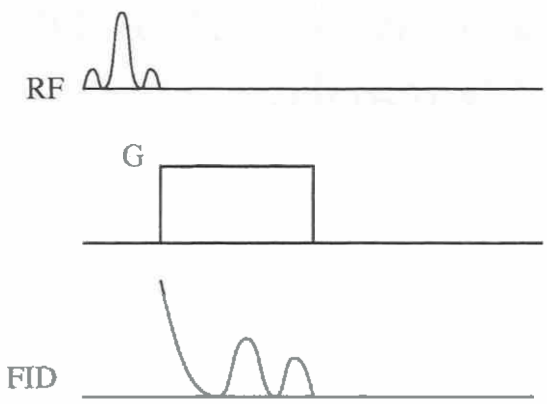

Figure 3–2. When a radiofrequency (RF) pulse is applied followed by a single-lobed gradient (G), a free induction decay (FID) of spins is formed. The time constant of the FID depends on the T2 of the material.

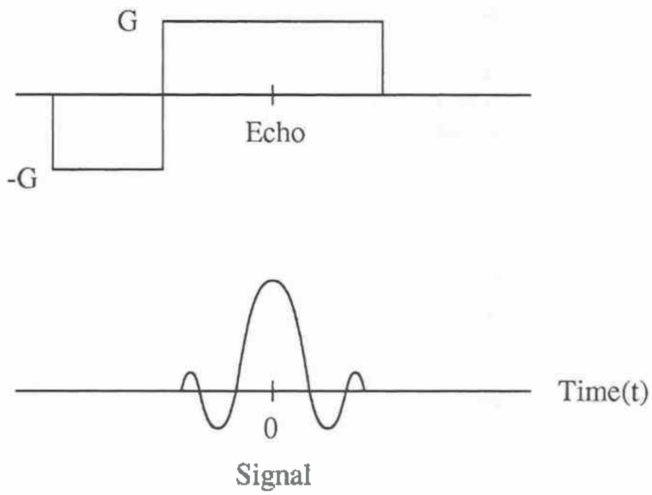

Figure 3–3. When a radiofrequency pulse is applied, followed by bipolar gradient structure, an echo is formed. At the echo the stationary tissue has accumulated a net phase of zero.

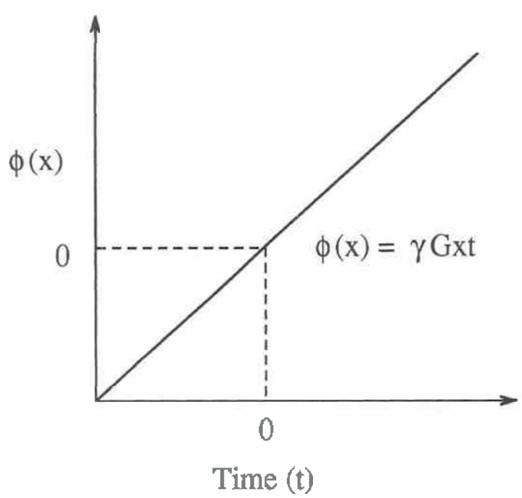

Figure 3–4. Phase behavior for stationary spins. Phase is a function of time, gradient strength, and location of spins. As shown, at $t = 0$ an echo is formed and the phase of stationary spins is zero. Here we assume x is nonzero.

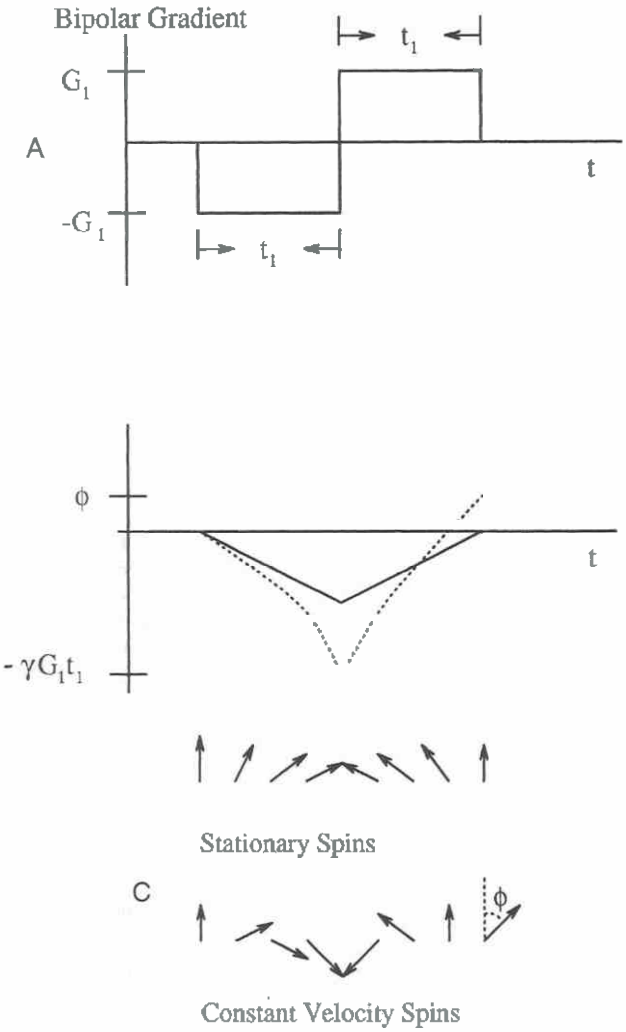

Figure 3–5. *A*, Pictorial representation of the phase for stationary and constant velocity spins as a function of time when a bipolar gradient structure is used. *B* and *C*, Graphical and vector representations of the phase, respectively. The *solid line* is for stationary spins, and the *dotted line* is for constant velocity spins. ϕ indicates the phase shift of constant moving spins at the echo.

$$\phi(t) = \omega t = \gamma Gxt \tag{3a}$$

As shown in Figure 3–4, the phase is a function of time and gradient strength. Since $G_1 = G$, $G_2 = -G$ and $t_1 = t_2$, equation 3a can be rewritten as

$$\phi(t) = \gamma x(G_1t_1 + G_2t_2) = 0 \tag{3b}$$

Therefore, the accumulated phase at the echo is always zero for these bipolar gradient structures (Fig. 3–5).

For stationary spins, the phase is generally determined from

$$\phi(t) = \gamma x \int G(t)dt \tag{4}$$

Figure 3–5*B* shows a linear growth in phase during the dephase portion of the gradient and a linear decrease in phase after the gradient is reversed for stationary tissues. No change in phase occurs when there is no gradient on. The velocity phase behavior is quadratic and overshoots the zero phase mark at the echo.

T2* Dephasing

In the presence of a local field inhomogeneity, the effective decay of the signal is quickened, and T2* is modified as

$$R2^* = R2_0 + \gamma\Delta B \tag{5}$$

where $R2^* = 1/T2^*$ and $R2_0 = 1/T2_0$ where $T2_0$ is the T2 value when no field inhomogeneities (ΔB) are present. This can be qualitatively understood, since the spins "see" different fields and become out of phase. If the time of the echo is calculated locally, it is discovered that it has shifted away from the center. The farther the echo shifts, the less signal remains in the sampling window (Fig. 3–6).

Chemical Shift

The presence of local field variations causes a shift in the frequency for different molecules. Lipids, for example, precess at a frequency (Δf), 3.35 parts per million (ppm)

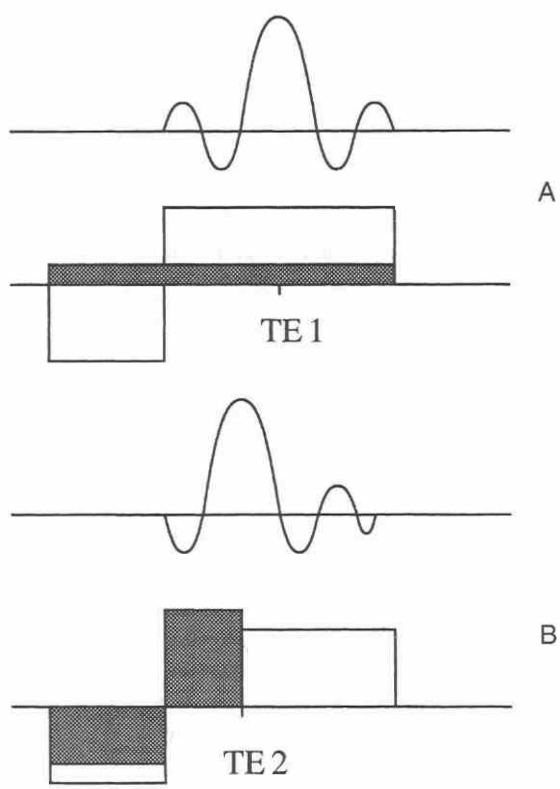

Figure 3–6. Local field inhomogeneities introduce a shift of the location of the echo. *A*, A two-lobed gradient structure is shown with an echo at the center of the second lobe (TE1); therefore, the signal is symmetrical. The gray indicates the area under the gradient from local field inhomogeneities. *B*, The location of the echo is shifted to the left (TE2) compared with *A*, and the signal becomes asymmetrical. If the shift is large enough, it will cause significant signal loss.

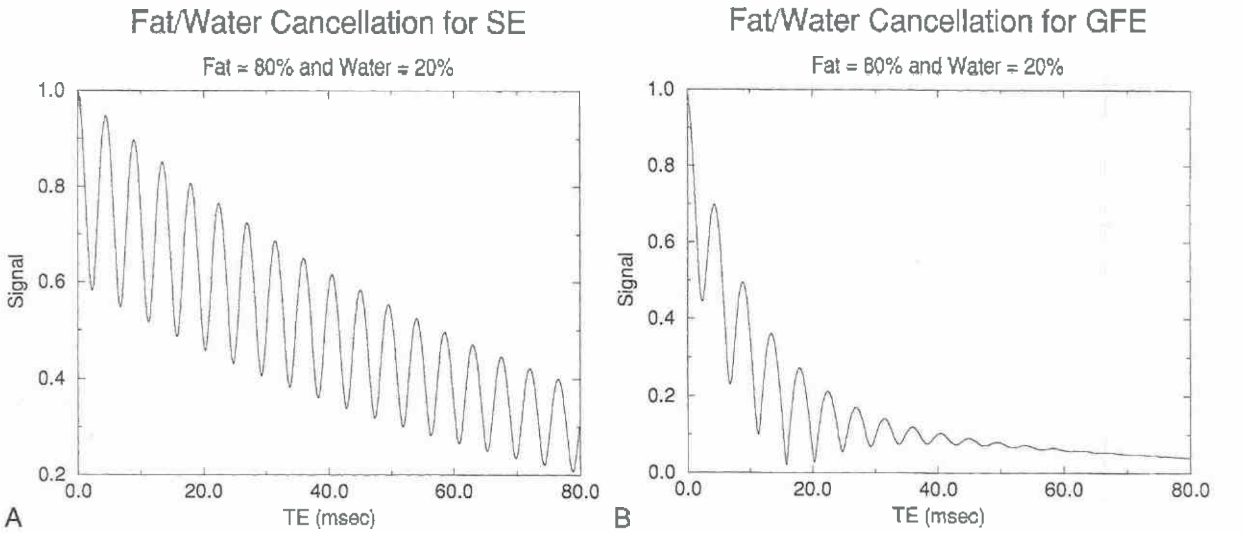

Figure 3–7. When a voxel contains water (20%) and lipid (80%) components, the signal intensity of the voxel is a function of echo time (TE). As shown in the plot, the signal intensity is modulated by a sinusoidal function with a period of 224 Hz (3.35 parts per million at 1.5 T). The spin-echo behavior is shown in *A*, and gradient field echo (GFE) behavior is shown in *B*. A T1 of 950 msec, T2 of 100 msec, and T2* of 50 msec (gray matter) are used as water relaxation parameters and T1/T2/T2* = 250/80/10 msec (fat) are used as lipid relaxation parameters. The signal behavior for a fat and water voxel is further modulated by an exponential decay (T2*). The frequency of modulation appears to be doubled at the lower values of TE because fat overwhelms the water and creates a negative signal, which is then made positive by taking the magnitude of the image. SE, spin echo.

lower than that for water. They therefore have a different phase development as a function of time and at the echo will not necessarily be in phase with water. When a voxel contains fat and water components, the signal intensity of this voxel depends on the echo time (TE) used (Fig. 3–7). At 1.5 T, for a voxel containing 50% each of water and fat, the signal intensity of this voxel will be one unit when TE = 4.5 msec (since fat and water are in phase so that the total signal is the sum of both components) and zero when TE = 6.7 msec (since fat and water are out of phase, and signal intensity is the absolute difference between these two components). To see this, note that the phase difference between the two is $\gamma\Delta B TE$, which is 2π at 4.5 msec and 3π at 6.7 msec. Consequently, the opposed phase nature can be used to suppress fat signal.[27, 60]

Resolution

The data are sampled in the read direction over n points. If the field of view (FOV) is defined as L, the resolution in the image will be (at best) L/n, or

$$\Delta x = L/n \tag{6}$$

For example, if the carotid vessel is being imaged, its lumen is 10 mm before the bifurcation and the magnetic resonance imaging (MRI) resolution is 1 mm, the smallest percentage of stenosis that can be measured is 100/10%. To detect a high percentage of stenosis, the resolution of images must be improved.

Clearly, high-resolution imaging plays an important role in MRA.[25, 37–39, 56] First, it can be used to reduce flow-related artifacts through the reduction of the intravoxel dephasing.[25, 37, 56] Second, it is able to improve the visibility of the vascular system[37, 38] (Fig. 3–8). This is especially true for the peripheral vascular system and stenotic regions. Third, the partial volume artifacts can be reduced, and hence vascular contrast is improved (Fig. 3–9). However, there are two major disadvantages associated with high-resolution imaging methods. The SNR will be reduced because of the smaller voxel size, and the minimum repetition time (TR) will be increased because the number of sampling points is increased. Therefore, when the SNR is poor, more acquisitions may be needed to compensate for the SNR lost.

Contrast

The main strength underlying the success of MRI studies is the soft tissue contrast. *Contrast* is defined as the signal difference between two tissues. *Relative contrast* is the signal difference normalized to the signal of one of the two signals. The contrast is the result of the tissue properties ρ, T1, and T2. Blood flow adds another variable to the calculation of contrast. Consider a simple imaging experiment with a very short TE and a long TR relative to the T1 values of all tissues. In this case, contrast is determined solely by spin density (Fig. 3–10). As TR is shortened to on the order of the T1 of a tissue, the image becomes T1-weighted (Fig. 3–11). For gradient-echo sequences, the TR can be shortened much below T1 and the radiofrequency (RF) pulse reduced to an angle well under 90 degrees. For no transverse magnetization before any RF pulse and after equilibrium has been reached, the signal as a function of flip angle (θ) can be expressed as

$$s(\theta) = \frac{\rho \sin\theta (1 - E1)}{1 - E1 \cos\theta} \tag{7}$$

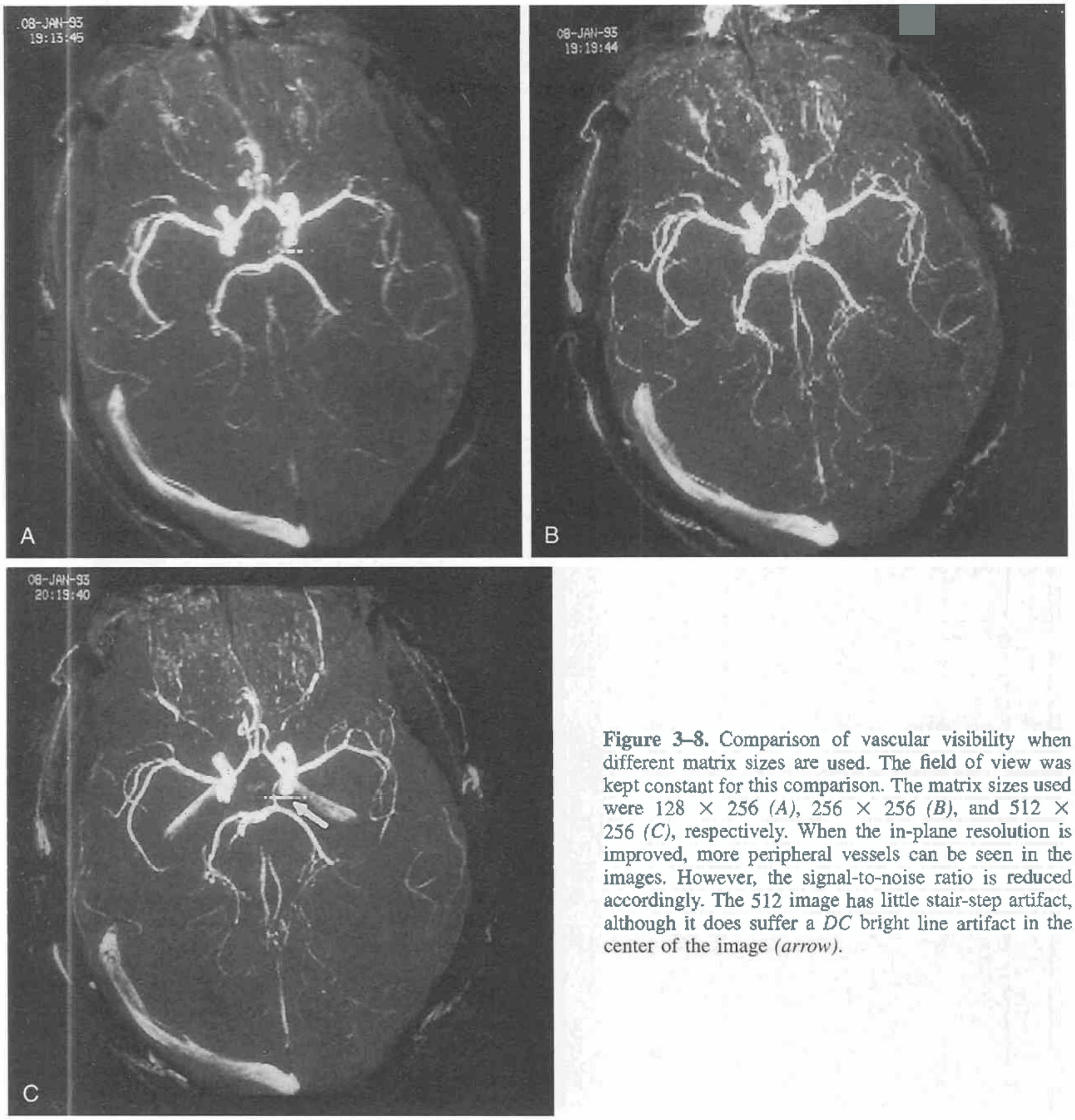

Figure 3–8. Comparison of vascular visibility when different matrix sizes are used. The field of view was kept constant for this comparison. The matrix sizes used were 128 × 256 *(A)*, 256 × 256 *(B)*, and 512 × 256 *(C)*, respectively. When the in-plane resolution is improved, more peripheral vessels can be seen in the images. However, the signal-to-noise ratio is reduced accordingly. The 512 image has little stair-step artifact, although it does suffer a *DC* bright line artifact in the center of the image *(arrow)*.

where ρ is the effective spin density and $E1 = \exp(-TR/T1)$.

The response as a function of flip angle shows why an intermediate flip angle between 0 and 90 degrees gives the best signal. The peak signal occurs when $\cos\theta = E1$; this is referred to as the *Ernst angle* (Fig. 3–12).

Two-Dimensional and Three-Dimensional Imaging

Two-dimensional (2D) and three-dimensional (3D) images can be obtained by adding a phase-encoding gradient table in each remaining direction to be imaged. The resolution in each phase-encoding direction is the FOV divided by the number of phase-encoding steps, as

$$\Delta y = L_y/n_y \tag{8}$$

for the in-plane phase encoding or

$$\Delta z = L_z/n_z \tag{9}$$

for the through-plane phase encoding (also referred to as *partition encoding*). In general, the 3D imaging method is preferable when a thinner slice is desired and flow velocity is high enough so that the flow saturation problem is not significant. Moreover, 3D imaging methods have a better SNR and are less sensitive to field inhomogeneities than

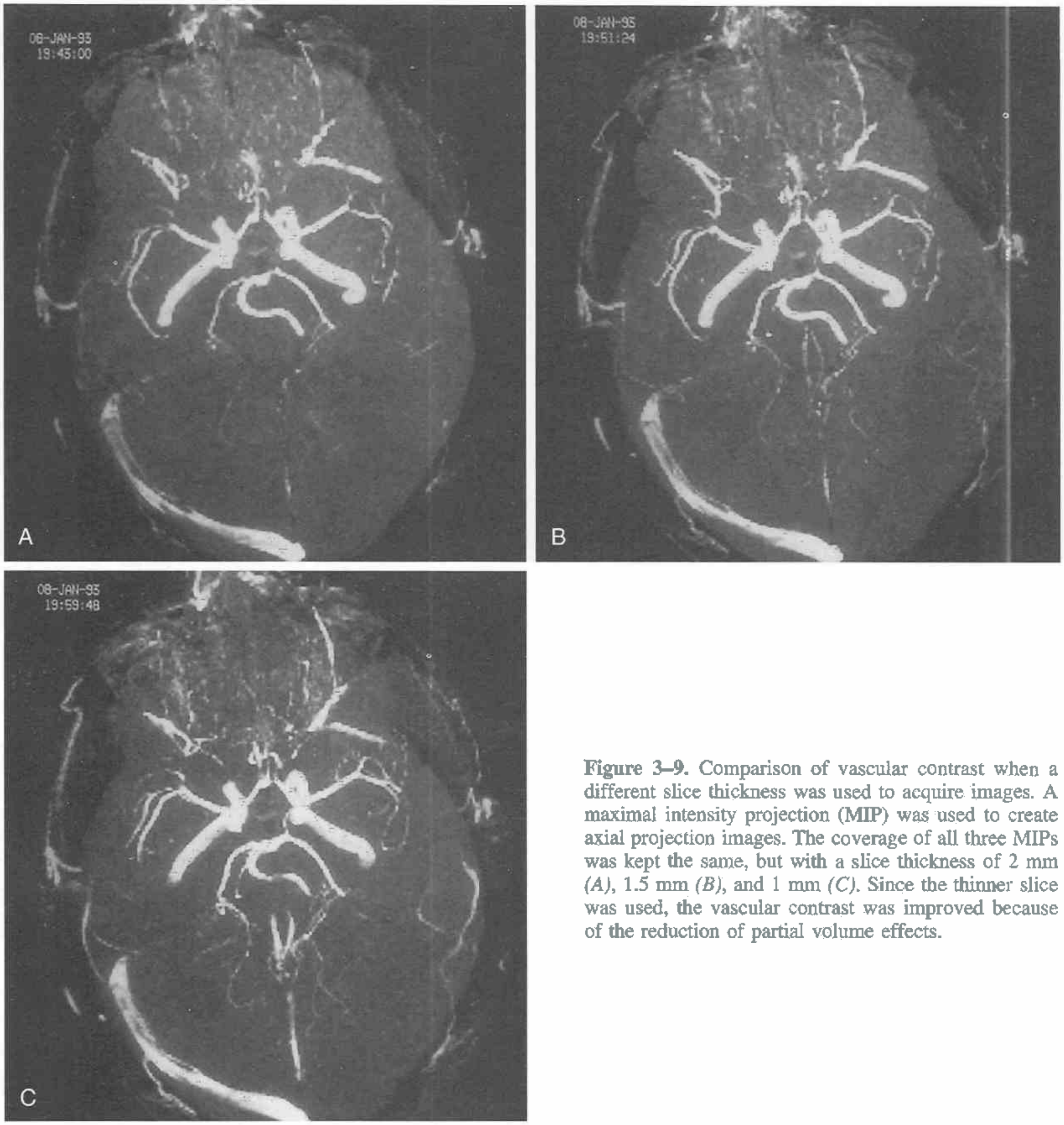

Figure 3–9. Comparison of vascular contrast when a different slice thickness was used to acquire images. A maximal intensity projection (MIP) was used to create axial projection images. The coverage of all three MIPs was kept the same, but with a slice thickness of 2 mm *(A)*, 1.5 mm *(B)*, and 1 mm *(C)*. Since the thinner slice was used, the vascular contrast was improved because of the reduction of partial volume effects.

2D imaging methods. This is easily understood from two perspectives. First, the smaller the voxel size, the less dephasing is across a pixel, since the phase error (e.g., that caused by field inhomogeneity $\phi = \gamma\Delta BTE$) is invariant spatially as the imaging parameters are changed. If there is a 2π phase variation across a voxel, this would cause complete signal loss for a uniform distribution of spins (Fig. 3–13*A*). However, for twice the resolution, the phase variation is cut in half, being 0 to pi in the first, smaller voxel and π to 2π in the second voxel (Fig. 3–13*B*). The conventional sequence diagrams for both 2D and 3D acquisition methods are shown in Figure 3–14. The phase encoding in the slice select direction is often referred to as the *partition encoding*, a term we will use here. The field-echo time (FE) refers to the time from the beginning of the gradient structure to the echo along the read direction. The echo time refers to the time from the center of the RF pulse to the echo.

Fundamentals of Flow Effects

Effects of Motion on the Phase

The previous discussion of phase needs to be modified when a spin moves. As an example, consider just the simple case of constant velocity moving spins:

$$x(t) = x_0 + vt \qquad (10)$$

where x_0, v, and t represent the initial position of the spins, constant velocity, and time, respectively.

Figure 3–10. Spin-density image of the head acquired with a 5-degree flip angle (Figure 3–11 provides imaging parameters). Because blood vessels sit in gray matter (GM) and GM and blood have the same spin density, it is not possible to distinguish between the two. The sagittal sinus *(arrow)* is saturated and isointense with GM.

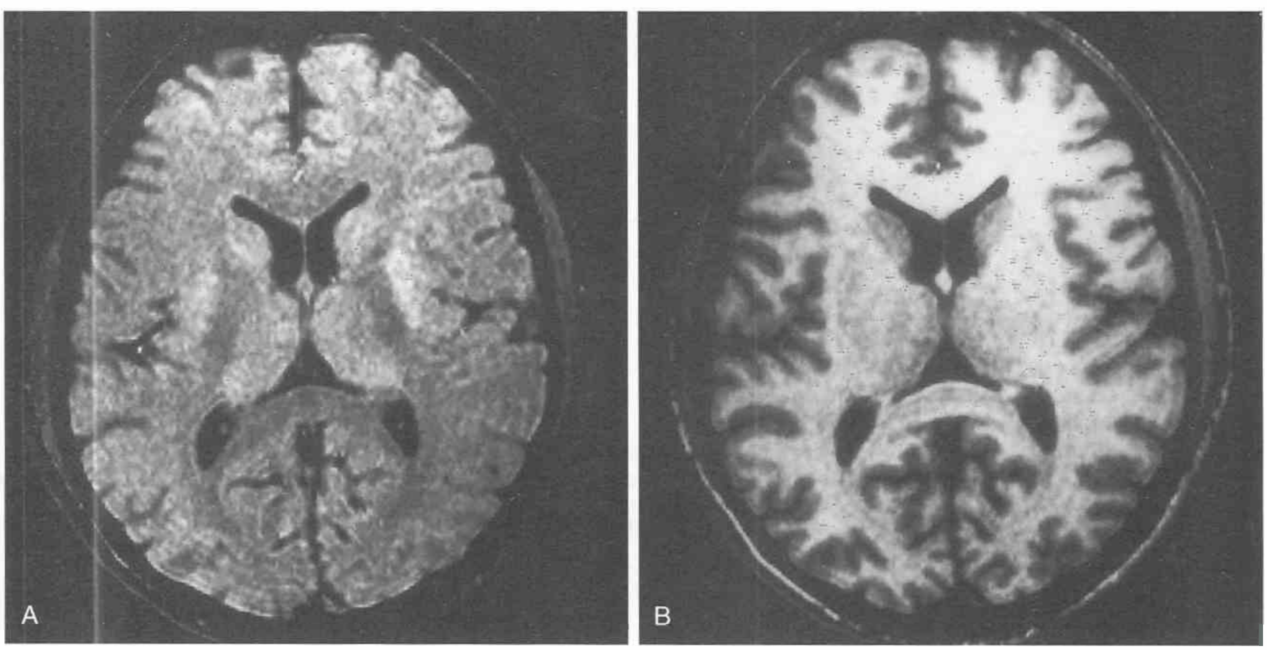

Figure 3–11. T1-weighted image of the head for *(A)* 15 degrees and *(B)* 30 degrees. Since the T1 of blood is longer than that of gray matter, it appears darker if it is saturated but may appear isointense if some inflow effect remains. Imaging parameters: TR = 40 msec, TE = 8 msec; 64 partitions, 2-mm slice thickness; matrix size, 256 × 256.

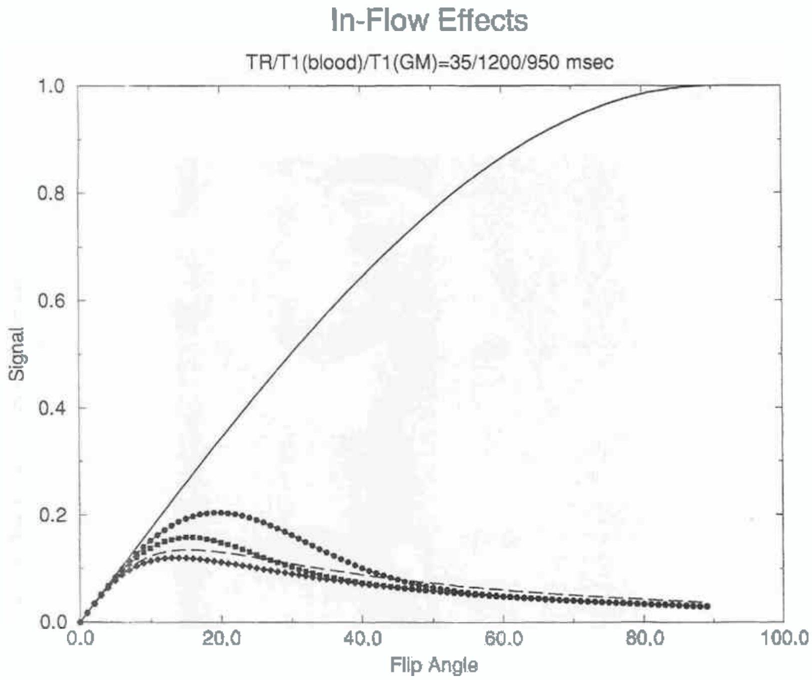

Figure 3–12. Signal intensity as a function of flip angle (see Equation 7 in text). A TR of 35 msec is used with T1 of blood equal to 1200 msec and gray matter (GM) equal to 950 msec. The *solid line* indicates the ideal case that blood experiences only one (N = 1) radiofrequency (RF) pulse. In contrast, when blood experiences more RF pulses, as when N = 5 *(line of circles)*, N = 10 *(line of squares)*, or N = 20 *(line of diamonds)*, the signal of blood is reduced. The signal behavior of GM is also plotted *(long dashed line)*. As shown, the blood may become isointense with GM at 15 degrees when N is greater than 10 and less than 20.

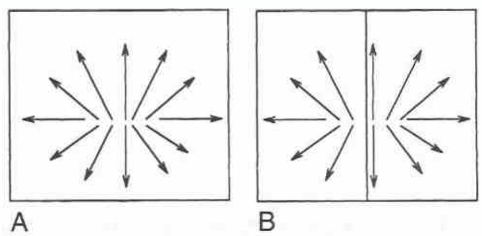

Figure 3–13. *A*, Pictorial representation of intravoxel dephasing. When a larger pixel is used, the integration of spins from 0 to 2π will give a zero signal (0). In contrast, when the resolution is reduced by a factor of 2, the integration of spins will be from 0 to π for the first pixel and π to 2π for the second pixel *(B)* and little signal loss occurs (see Table 3–1).

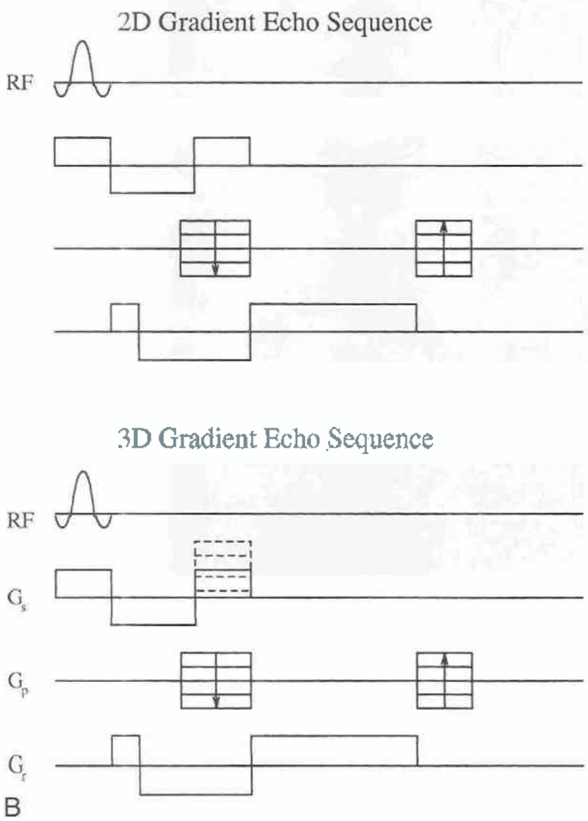

Figure 3–14. Sequence diagrams of both 2D *(A)* and 3D *(B)* sequences. The only difference between these two sequences is in the slice select direction. For the 3D sequence, an extra phase table *(dashed line)* is added to encode information along the slice select direction.

The phase during sampling is found from the expression

$$\phi(t) = \gamma \int G(t)x(t)dt \tag{11}$$

For a simple bipolar pulse as shown in Figure 3–5, the phase at the echo is

$$\phi(t) = \gamma v G(t) t_1^2 \tag{12}$$

This simple dependence of the phase on velocity is the fundamental behavior from which many MRA concepts can be understood.

Dephasing

For plug flow, all spins move in the same direction at the same speed independent of the location of the spins with respect to the vessel wall. When all the spins within a voxel are added together, they add coherently and the final signal has the same phase. In contrast, for laminar flow, the velocity of spins is dependent on the location with respect to the vessel wall (Fig. 3–15). The spins at the center of the vessel have the highest speed, and those at the edge of the vessel have the lowest. Consequently, a velocity distribution inside a given voxel causes a different phase shift for each isochromat of spins inside the voxel. The total signal in one voxel is obtained from an integration of the local signal across the entire voxel.

When the total phase shift across a voxel is uniformly distributed from 0 to 2π, there will be complete signal dropout. This phenomenon is known as *flow dephasing* or *flow void*. It usually can be seen in stenotic regions or tortuous vessels when insufficient motion compensation is used. For example, in the regions of the carotid bulb and poststenosis, a secondary flow or vortex flow is normally seen. This flow pattern also introduces signal loss (Fig. 3–16).

Table 3–1 shows the relationship between the degree of dephasing and the remaining signal.

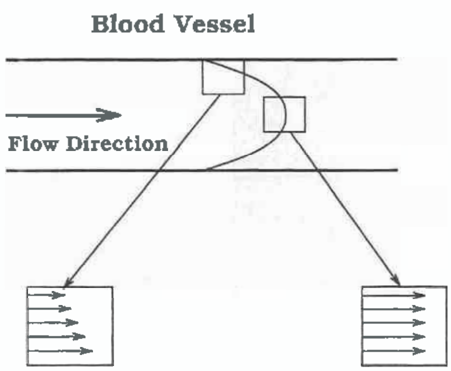

Figure 3–15. Laminar flow pattern inside a blood vessel. Because flow velocity is location-dependent, the spins have a nonuniform distribution compared with that of plug flow. As shown, the voxel close to the center of the vessel has more uniform spin distribution compared with that at the edge of the vessel. This nonuniform spread in velocity can lead to spin dephasing.

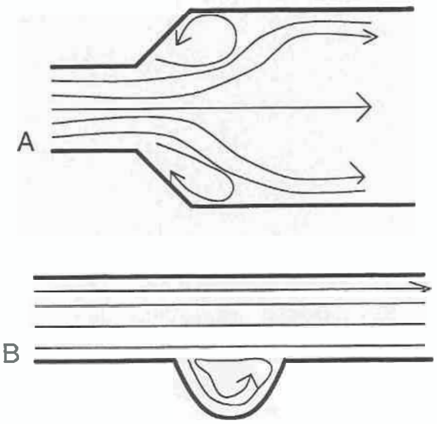

Figure 3–16. *A*, The same concept as in Figure 3–15 also holds for poststenosis regions, where secondary flow develops inside an aneurysm or beyond an aneurysm. *B*, In the region of the carotid bulb, a secondary flow pattern is normally seen because of the pressure gradient change. This causes flow dephasing as well as saturation and results in signal void in this part of the blood vessel.

Compensating Moving Spins

To eliminate or reduce the problems associated with spin dephasing, a short echo time can be used.[32, 39, 54] Alternatively, a velocity compensation gradient structure can be used.[24, 34, 44] It is possible to keep both stationary and moving spins in phase at the echo. This is accomplished by adding a third gradient lobe to the original gradient structures so that the total area still adds to zero, and the stationary spins are therefore still rephased, while the first moment of the phase is also zero for any speed. Expressed mathematically, the following conditions are applied:

$$\gamma x \int G(t)dt = 0 \tag{13}$$

and

$$\gamma v \int G(t)t dt = 0 \tag{14}$$

To compensate constant acceleration spins, four lobes are required to give three degrees of freedom so that stationary spins, constant velocity spins, and acceleration spins can all have a zero phase at the echo. The tradeoff by using a four-lobed gradient structure is that the echo time will be increased. This can cause some spin dephasing problems when higher-order motion effects are present, such as in secondary or disturbed flow, or for tortuous flow, such as in the carotid syphon.

Table 3–1. Relationship Between Degree of Dephasing and Remaining Signal

$\Delta\phi$	S/S_0
2π	0
$3\pi/2$	$2\sqrt{2}/3\pi$
π	$2/\pi$
$\pi/2$	$2\sqrt{2}/\pi$

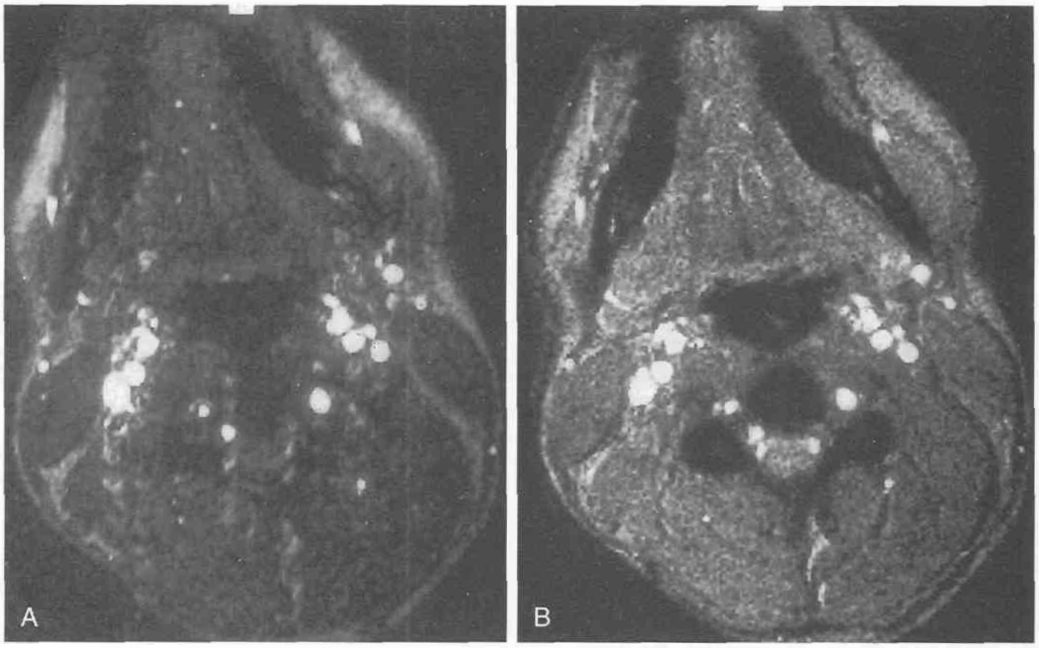

Figure 3–17. *A*, Image [redacted] the [redacted] sequence with a flip angle of 90 degrees. Because of the pulsatility of blood flow, ghosting artifacts are seen along the phase-encoding direction (y-axis). *B*, When the flip angle was decreased to 20 degrees with the same sequence, the signal intensity of the "ghosts" was decreased.

Higher-Order Terms

Even with velocity compensation, higher-order motion effects can still be seen in tortuous or stenotic flow. For the same bipolar gradient structure, acceleration compensation varies as FE^3 or as FE^2 if constant velocity spins are compensated.

Ghosting Artifacts

Ghosting artifacts are commonly seen in MRI studies. Two reasons can account for this type of artifact. First, uncompensated (or pulsatility of) moving blood causes the duplication of the blood vessels along the phase-encoding direction. The locations of the ghosting depend on the cardiac cycle and TR. This phenomenon is usually seen in peripheral MRA studies (i.e., of the legs) because of the high degree of pulsatility. When a large flip angle is used, the signal intensity of the ghosting artifacts will be significant (Fig. 3–17).

On the other hand, physiologic motion such as eye or cerebrospinal fluid (CSF) movement can also cause ghosting along the phase-encoding direction. To avoid having "ghosts" obscure other structures, the frequency and phase-encoding directions are usually swapped before any data acquisition so that the direction of ghosting becomes horizontal instead of vertical.

Inflow

Given that all spins are now rephasing at TE, any velocity profile can be imaged. The main effect of obtaining a blood signal comes from the fact that inflowing blood has experienced fewer RF pulses and has more signal than tissue with similar T1 values, which experience many RF pulses and is essentially saturated (Fig. 3–18). This phenomenon is well known as flow enhancement or an inflow effect. The MRA imaging method based on this concept is called time-of-flight (TOF) MRA to differentiate it from the phase-contrast (PC) method (see later), which uses the phase shift introduced by moving spins.

Saturation

The inflow effect makes it possible to obtain good contrast between vessels and stationary tissue because the stationary tissue experiences more RF pulses and eventu-

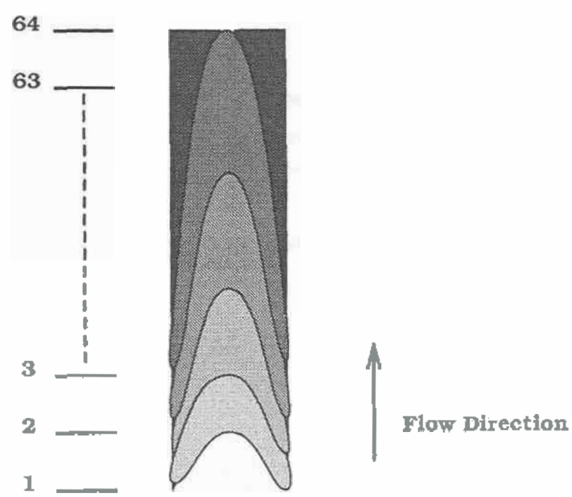

Figure 3–18. For through-plane flow with a laminar flow profile, blood will have higher signal at the entry region *(slice 1)* when compared with the region where blood flows deep into the slab. Numbers represent slice numbers.

ally the magnetization becomes saturated. Consequently, when the velocity of blood in a vessel is slow, both background tissue and blood magnetization are saturated; hence blood vessels become isointense to the stationary tissue. This is usually the case in the head because gray matter (GM) and blood have similar spin densities and T1 values. In addition, this problem is seen more in 3D TOF imaging methods, since a larger imaging volume is normally acquired.[26, 41]

Saturation Pulses

It is also possible to apply another RF pulse just before the usually low flip angle pulse to saturate the signal from stationary tissue and see fresh blood flow into this saturated band. Flow that takes place between the saturation pulse and the echo time can be seen as bright in the saturated band. This band can also be applied parallel to the usual 3D slice select direction, but offset from it, to saturate spins coming from one side of the slab to be imaged. An example is shown in Figure 3–19, in which a saturation pulse was used to saturate the venous blood magnetization and only the arteries were seen in the image (Fig. 3–19*B*).

Phase Contrast

One way to eliminate the problems associated with flow saturation is to obtain flow information by collecting two images, each of which is not perfectly compensated in one direction so that a phase shift exists at the echo along the uncompensated direction, which is different for the two sequences.[14, 15] This is the primary difference between PC methods and TOF MRA. Subtracting one image from the next eliminates the background. This can be done with the complex data or the phase images themselves. The sequence diagram of an interleaved PC method is shown in Figure 3–20. This method has the advantage that when saturation is a problem (as it is for slow flow), the background is easily removed. The resulting phase images contain values only from $-\pi$ to π as long as the peak velocity is such that $|\phi(v)| < \pi$. The velocity at which $|\phi(v)| = \pi$ is referred to as the *velocity-encoding value* (VENC).

Unfortunately, several disadvantages are associated with PC methods, which require at least four separated scans to extract flow in all three directions yet given the very short TR values that can be used, rapid acquisition of data is still possible. Because subtraction is used to remove the background signal and extract flow information from four scans, patient motion must be avoided. Eddy currents also affect the phase behavior in the images. Moreover, this method requires a choice of the maximum velocity so that aliasing will not occur in the phase images. One way to overcome the problem of the correct choice for the VENC is to use a multiple VENC in one sequence so that a wide range of velocity information can be obtained.

Finally, this method, like TOF methods, is apt to suffer from spin dephasing because of the rapid flow. A shorter TE is necessary for PC methods as well. The TOF and PC methods are likely to complement each other in the future.

Projection Images

The use of 2D TOF over thick slices is often referred to as projection imaging because of the projection of information over the slice thickness. In these methods, excellent background suppression is required. Interleaved 2D PC is the method of choice when rapid imaging is required.

Sequence Parameters

As mentioned earlier, 2D and 3D imaging methods have different advantages and disadvantages and are suitable for

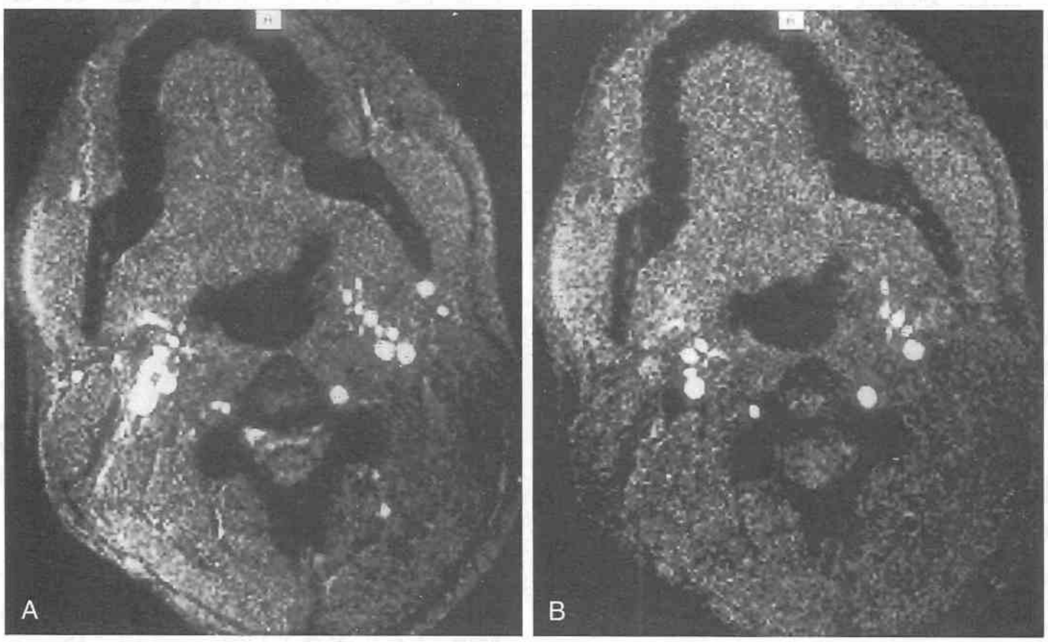

Figure 3–19. Images acquired with a conventional 2D sequence in the region of the neck. *A*, When saturation was not used, both arteries and veins were seen in the image. *B*, In contrast, when a saturation pulse was placed above the image slice, the veins were saturated and only arteries were seen in the image.

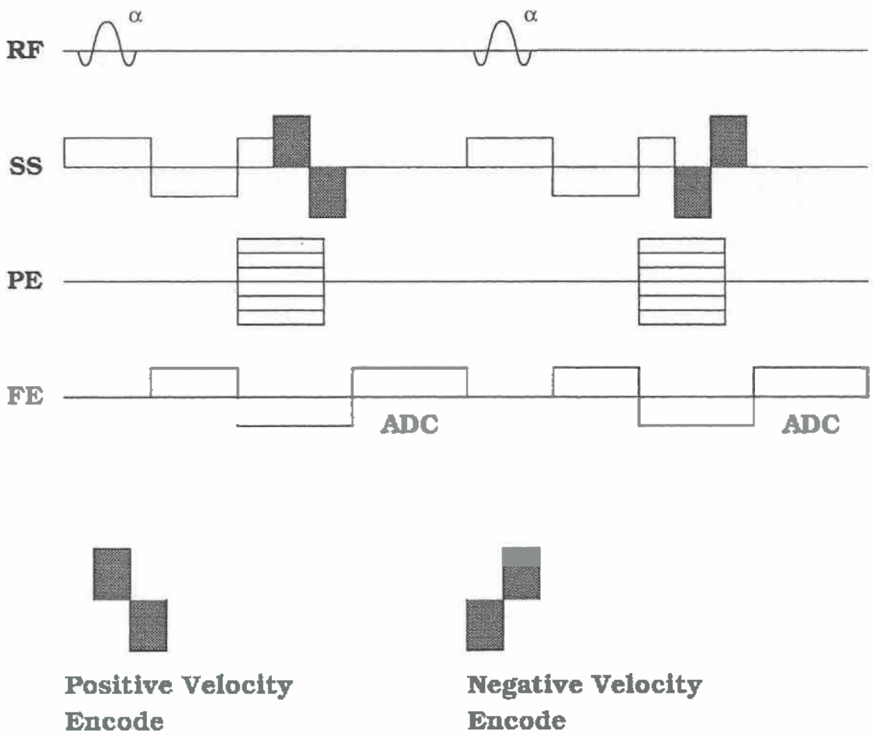

Figure 3–20. Sequence diagram for an interleaved phase contrast acquisition method. A flow-encoding gradient (bipolar gradient) shown in gray was placed along the slice select direction. As shown, the sign of this flow-encoding gradient was reversed for the second part of the data acquisition when compared with the first part. Because an interleaved data acquisition method was used, the effective TR was increased by a factor of 2. Slice select (SS), phase-encoding (PE), frequency-encoding (FE) directions; and analog-to-digital converter (ADC). RF, radiofrequency.

different applications. Consequently, the imaging parameters for 2D and 3D imaging methods are different to optimize vascular contrast.

Two-Dimensional Imaging

In general, 2D imaging is used to image slow flow because this method is less sensitive to flow saturation. Moreover, 2D imaging is also suitable for dynamic studies because of its short data acquisition time. Unfortunately, 2D imaging is highly sensitive to local field inhomogeneities. It is also more difficult to achieve high resolution along the slice select direction compared with 3D imaging.

Three-Dimensional Imaging

In contrast to 2D imaging, 3D acquisition is used to cover a large region of interest and to achieve high resolution along the slice select direction. Moreover, the SNR is normally higher than in 2D imaging because more points are acquired along the slice select direction. However, 3D TOF suffers from flow saturation effects when a large volume is covered or when slow flow is present. As discussed previously, 3D PC is less affected. General advantages of 2D versus 3D imaging are shown in Table 3–2.

Technical Developments in MRA Sequences

Saving Time

Once a good MRA scan has been collected, one can look at methods to speed up its acquisition. This will invariably mean a loss of SNR, given that resolution remains the same.

Rectangular Field of View

A simple trick is to reduce the number of phase-encoding steps while decreasing the FOV in the phase-encoding direction. For example, reducing the number of steps from 256 to 128 and reducing the FOV from 256 to 128 mm maintain the resolution, cut the imaging time in half, but reduce the SNR by a factor of $\sqrt{2}$. For imaging a child's head, this is possible; for adults, however, the reduction is usually to 192 steps—still giving a considerable savings in time of 25%. When nonintegral ratios between the original FOV and the reduced FOV are used, a careful interpolation algorithm must be employed to retain the correct aspect ratio of images. Figure 3–21 shows a comparison with (Fig. 3–21*A*) and without (Fig. 3–21*B*) the use of rectangular FOV.

Partial Fourier Imaging

Use in the Phase-Encoding Direction. There is a special symmetry property of the Fourier transform for a real object that makes it possible to design a data collection

Table 3–2. Comparison of Two-Dimensional (2D) and Three-Dimensional (3D) Imaging

2D		3D	
Advantages	*Disadvantages*	*Advantages*	*Disadvantages*
Faster	Thicker slice	Thinner slices	Slower
Better inflow	More T2* loss	Less T2* loss	Blood saturation
High CNR	Low SNR	High SNR	Low CNR

CNR, contrast-to-noise ratio; SNR, signal-to-noise ratio.

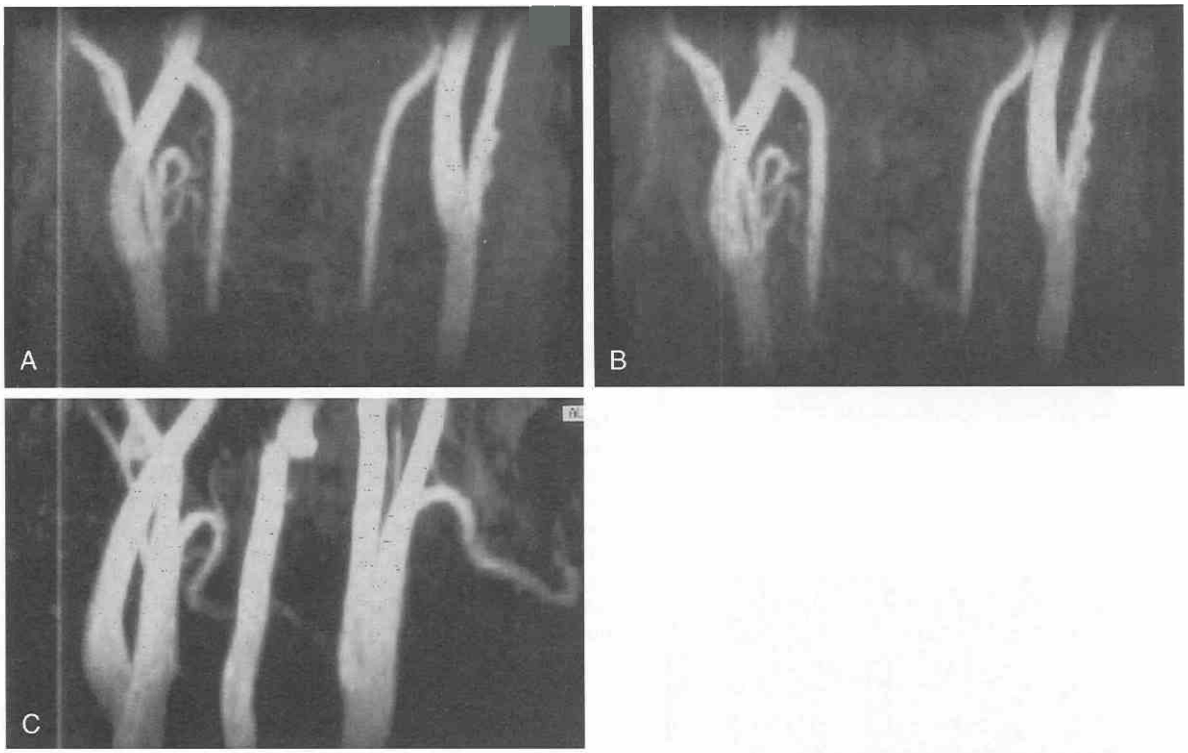

Figure 3–21. *A*, Image acquired with a conventional 3D sequence in the region of the neck. The imaging parameters are TR, 35 msec; TE, 8 msec; flip angle, 15 degrees; and matrix size, 256 × 256. The total data acquisition time is about 10 minutes. *B*, The same imaging parameters are used, except that the matrix is reduced to 160 × 256 and the rectangular field of view (FOV) is used to acquire the image. Although the signal-to-noise ratio (SNR) is reduced accordingly, the total data acquisition time is reduced to 7 minutes. *C*, At this stage, data in the neck are often collected with a 256 × 512 acquisition. Although this image was not obtained using a reduced FOV, the SNR is sufficient that it would be possible to do so if the carotid bifurcation were the region of interest.

method that in theory saves a factor of 2 in data collection time. This property, known as *hermitian symmetry*, relates the negative data to the positive data so that only the positive data, for example, need be collected and the negative data will be recreated from it. The expression is simply

$$s(-k) = s \times (k) \quad (15)$$

where

k represents the phase-encoding value
s(k) is the signal

In practice, more than half the data is collected and special algorithms are used to reconstruct the data (Fig. 3–22). Once again, a factor of nearly $\sqrt{2}$ is lost in SNR.[25] A comparison is shown in Figure 3–23 to demonstrate the partial Fourier reconstruction method.

Use in the Read Direction. This trick can also be used to reduce the echo time by putting the echo off center with respect to the data sampling window[25] (Fig. 3–24). This reduced echo time allows better suppression of the dephasing of moving spins from higher-order motion. For example, a 25% asymmetrical echo with 256 sampling points indicates 64 points before the echo and 192 points collected after the echo. Mathematically it represents a symmetrical echo multiplied by a rectangular pulse in the time domain, and it translates to a convolution of the ideal image with a complex filter function. This reduces the sharpness of the reconstructed image. Therefore, the half-Fourier reconstruction is necessary to eliminate this artifact. Figure 3–25 shows sequence diagrams of the TE = 5.1 msec sequence (even shorter echo times are available today).

To achieve high resolution, longer echo times may have to be used because of the limitation of the maximum gradient strength in the system. Consequently, the longer echo time would increase the flow-related artifact since the higher-order motion-dephasing effects increased. Alternatively, an off-center echo can be used such as 6.25%, 12.5%, or 25%, and the echo time decreases accordingly.

Overcoming Saturation Effects

Two solutions can be used to reduce the saturation problems associated with 3D TOF imaging methods: (1) increase the blood signal, and/or (2) reduce the background tissue signal so that the contrast between blood vessels and background tissue can be improved. Alternatively, postprocessing methods can be used to remove unwanted tissue structures (see "Processing and Image Display").

Increasing Signal from Blood

Central k-Space Reordering. In certain sequences, there is a wait time (TW) between application of the partition and phase-encoding loops. In this case, central reordering collects the largest signal at the lowest values

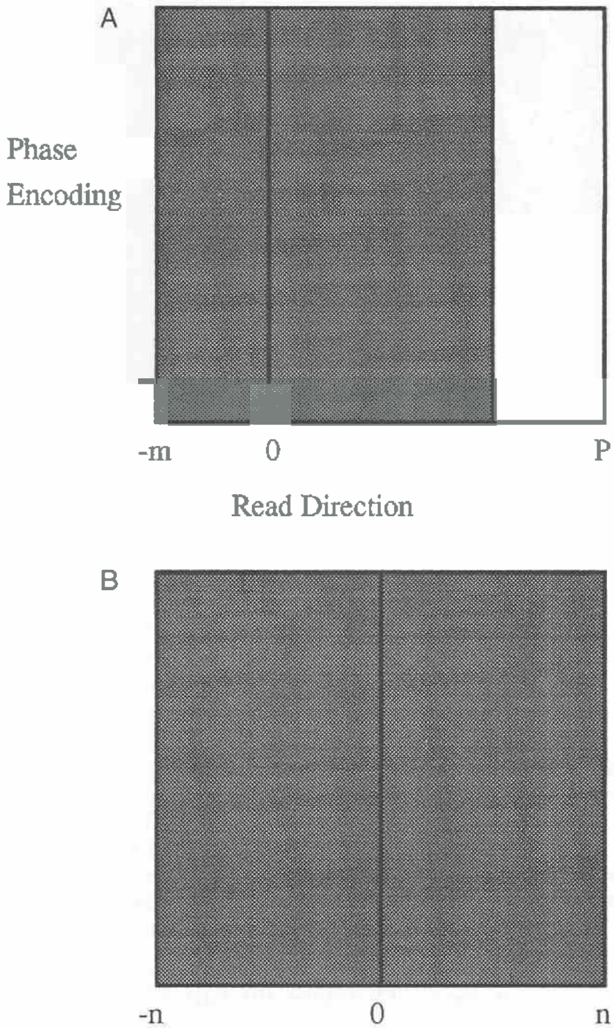

Figure 3–22. Pictorial representation of k-space coverage. Instead of collecting the entire k-space, only three fourths of the k-space was acquired along the read direction. A partial Fourier reconstruction was used to recover the lost information without blurring the image. The shaded portion represents the data used for the partial Fourier reconstruction, and the entire figure represents the data collected from the imager *(A)*. *B*, After reconstruction, data space is symmetrically covered. The data are collected with m points before the echo and P points after the echo, with $m + P - 1 = 2n$.

of the k-space or at the low spatial frequency values (Fig. 3–26). This enhances the signal not only from the fast blood but also from any blood that has this TW to regrow. In addition, when a T1 reduction contrast agent such as gadolinium–diethylenetriaminepentaacetic acid (Gd-DTPA) is administered, the centric reordered k-space scheme can be used to further improve the vascular contrast, since the half-life of Gd-DTPA is short and Gd-DTPA is most effective immediately after the injection of contrast agents.

Variable Flip Angle as a Function of Radiofrequency Pulse Number. Signal can also be enhanced by not applying a constant RF pulse angle every time. A constant RF pulse usually leads to saturation of the signal (it always does for stationary tissue if the angle is greater than the Ernst angle). If the flip angle is varied to give constant transverse magnetization each time the RF pulse is applied, the signal can be enhanced (even specifically at low k-space if desired).

Contrast Agents. One of the main difficulties associated with 3D TOF MRA studies is the saturation of slow flow. To reduce the saturation problem, a thinner 3D slab can be used so that more fresh blood can flow into the imaging volume.[6, 7, 45] However, this method requires several overlapping thin slabs to cover the region of interest, and cooperation of the patient is required. Alternatively, a contrast agent, Gd-DTPA, may be used to shorten the T1 over reasonably long periods[8, 11, 38] (its half-life in the blood is about 12 minutes). For example, when a high dose of Gd-DTPA is used, the T1 of blood may be reduced by a factor of 4 and the contrast between blood and stationary tissue will be substantially increased (Fig. 3–27). An example of preadministration and postadministration Gd-DTPA is shown in Figure 3–28. As expected, after injection (Fig. 3–28*B*), more small vessels are seen as compared with Figure 3–28*A*. It can also be used to see T2* effects during the first minute of its application, after which its concentration is so low that T2* effects disappear.

Multiple Thin-Slab Acquisition. Multiple thin-slab acquisition methods can also be used to reduce spin saturation problems because spins experience fewer RF pulses compared with single thick-slab acquisition methods (Fig. 3–29). Consequently, the region of coverage is reduced accordingly. To cover a large region of interest, several thin slabs with 25% to 50% overlap can be used. Better-quality images in the regions of overlap and in the rest of the images can then be combined using maximum intensity projection (MIP) processing to generate the projection images (see later).

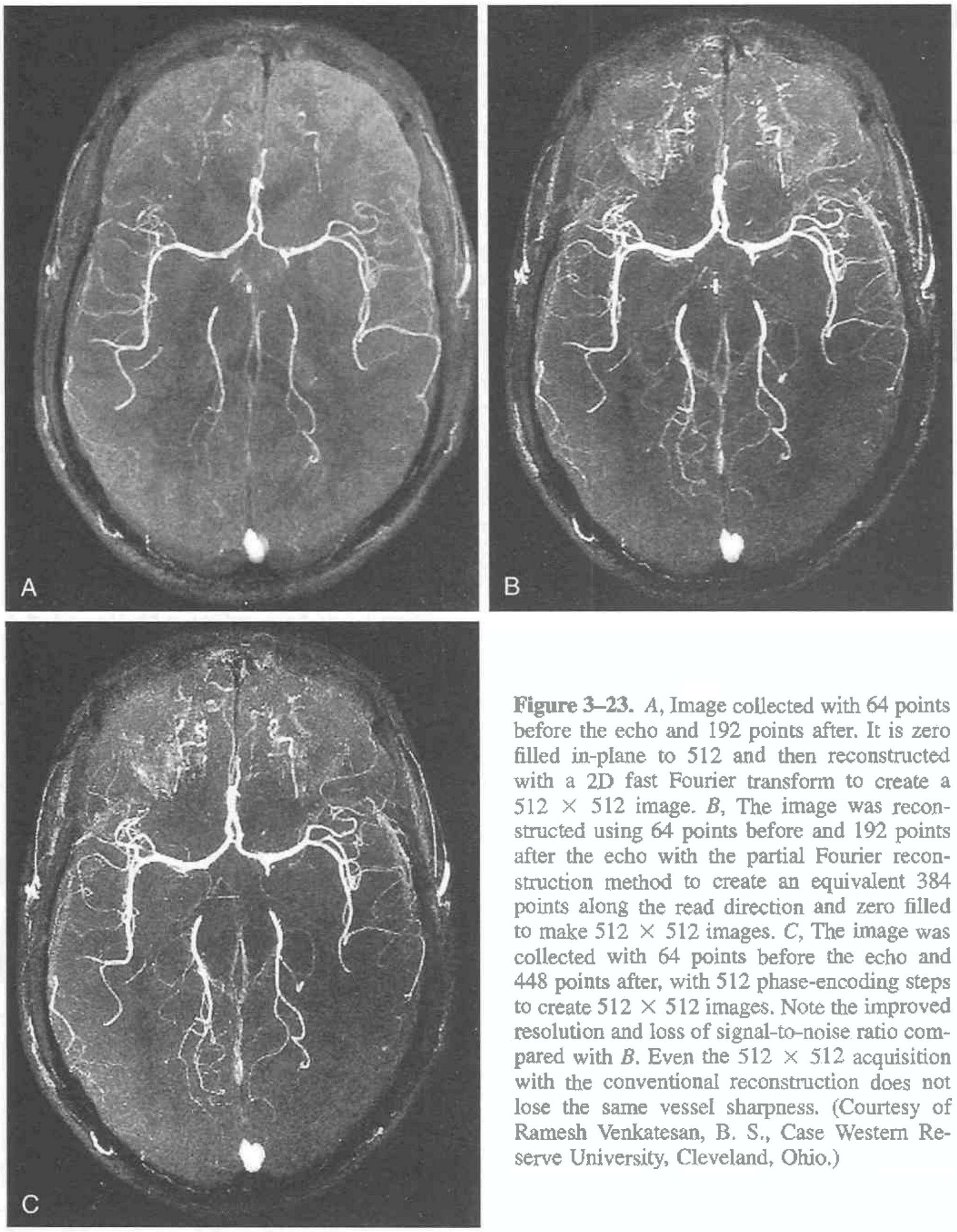

Figure 3–23. *A*, Image collected with 64 points before the echo and 192 points after. It is zero filled in-plane to 512 and then reconstructed with a 2D fast Fourier transform to create a 512 × 512 image. *B*, The image was reconstructed using 64 points before and 192 points after the echo with the partial Fourier reconstruction method to create an equivalent 384 points along the read direction and zero filled to make 512 × 512 images. *C*, The image was collected with 64 points before the echo and 448 points after, with 512 phase-encoding steps to create 512 × 512 images. Note the improved resolution and loss of signal-to-noise ratio compared with *B*. Even the 512 × 512 acquisition with the conventional reconstruction does not lose the same vessel sharpness. (Courtesy of Ramesh Venkatesan, B. S., Case Western Reserve University, Cleveland, Ohio.)

Improving Background Tissue Suppression

Too high a signal from background obscures the blood vessels. By reducing background signal, the vessels become more visible.

Spatially Variable Flip Angle or TONE Pulses. One method of keeping the signal uniform in response across the FOV in the slice select direction (for blood flow perpendicular to the imaging plane—that is, in the slice select direction) is to vary the flip angle spatially (Fig. 3–30). Using small flip angles and increasing to large flip angles keep inflowing blood fairly uniform as it passes through the volume.[35] The principle is the same as that previously described, but it is accomplished by appropriately redesigning the RF pulse to accomplish the desired shape of the RF response. This is most often useful in neck studies (Fig. 3–31).

Magnetization Transfer Saturation. Bound macromolecules have very short T2 values (<1 msec), whereas more mobile protons have much longer values (50 to 100 msec). Through a cross-relaxation mechanism, the latter exchange with the former and are dephased as a result of the local field environment. By exciting a pulse at an off-resonance value of roughly 2 kHz, those water-like tissues with a long T1 are saturated and do not contribute to the signal.[13, 62] Gray matter is affected less than white matter, but the effect is still large enough that up to a 40% drop in brain parenchyma signal has been seen.[63] This makes the vessels much easier to visualize because the partial-volume artifact is reduced. In practice, a frequency offset saturation pulse can be applied to suppress background tissue with negligible effect on the moving blood by an optimal choice of offset frequency and bandwidth of the saturation pulse.[16, 48]

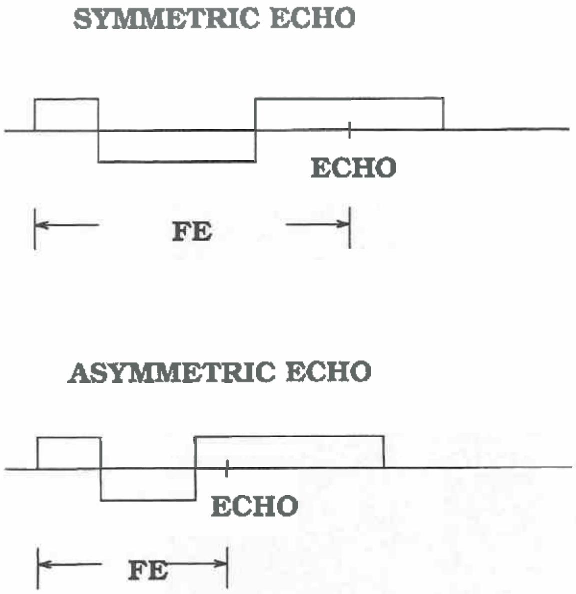

Figure 3–24. Pictorial representation of a symmetrical and an asymmetrical echo along the frequency-encoding direction. In this manner, the frequency encoding (FE) can be reduced substantially. Here the FE is defined as the duration from the beginning of the gradient to the echo.

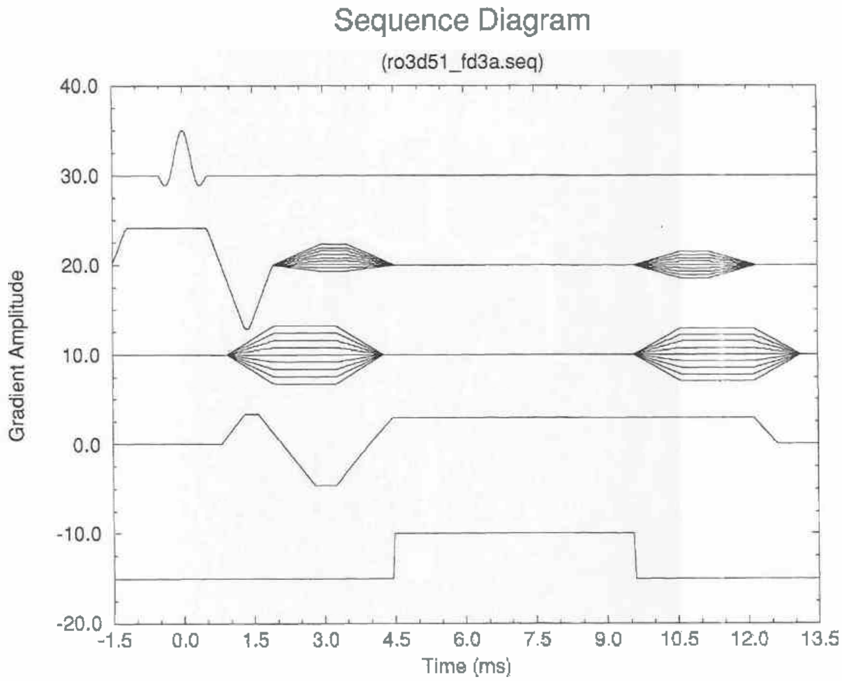

Figure 3–25. Sequence diagram of TE = 5.1 msec, which has an asymmetrical echo of 12.5% of the entire sampling window. The sequence is velocity compensated along the frequency-encoding and slice select directions. The slice select direction is also phase-encoded, and this encoding is usually referred to as "partition" encoding to distinguish it from "in-plane phase" encoding. (Courtesy Dee Wu, Ph.D., Case Western Reserve University, Cleveland, Ohio.)

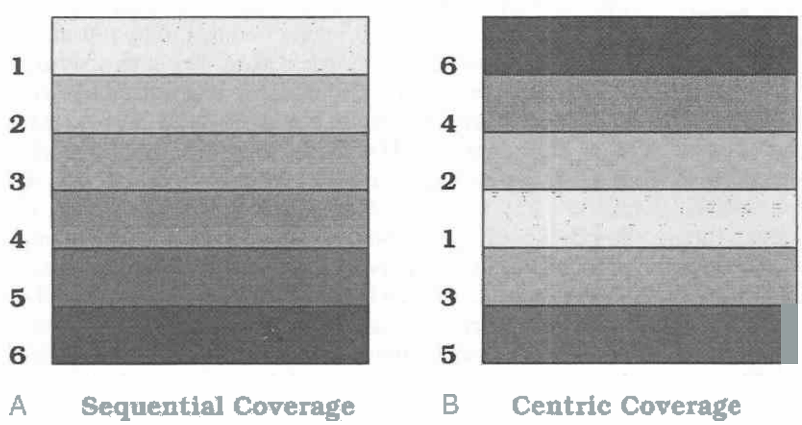

Figure 3–26. Two different methods are used to cover the k-space: sequential *(A)* and centric *(B)*. For the sequential order, either the positive or negative high-frequency components are collected first and then the lower-frequency components. The gray-scale levels indicate the time during which the data are collected. The darker the color, the later the data are collected. For centric ordering, the low-frequency components are collected before the high-frequency components.

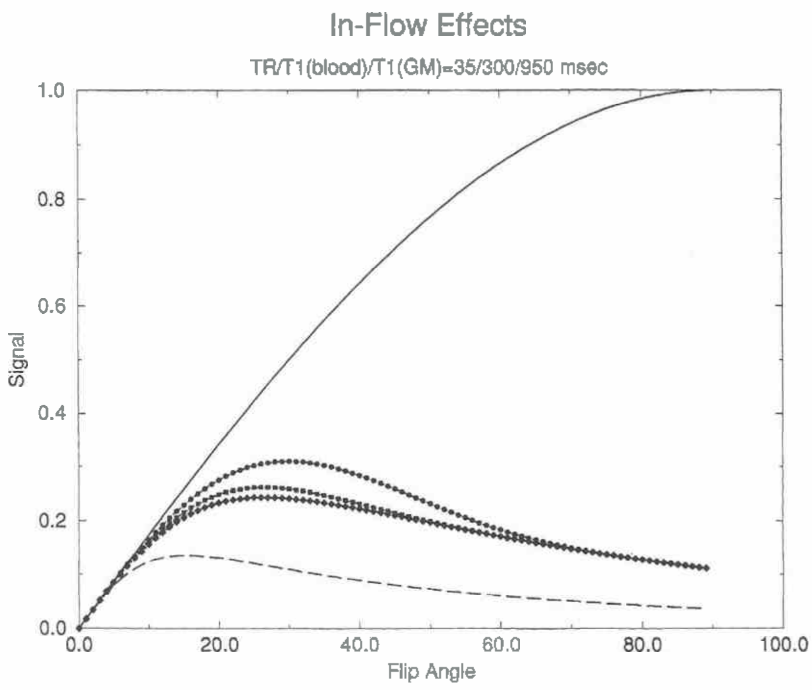

Figure 3–27. When a T1 reduction contrast agent is used, such as gadolinium-DTPA, the T1 of the blood will be reduced dramatically immediately after the injection. Here a T1 of 300 msec is used to create this plot. This plot is analogous to that in Figure 3–12. The *solid line* indicates that the blood experiences only one radiofrequency (RF) pulse (N = 1); the *line of circles* plots data for N = 5; the *line of squares*, for N = 10; and the *line of diamonds*, for N = 20, and the *dashed line* represents gray matter (GM). Even when blood experiences 20 RF pulses, the contrast between blood vessel and GM remains high.

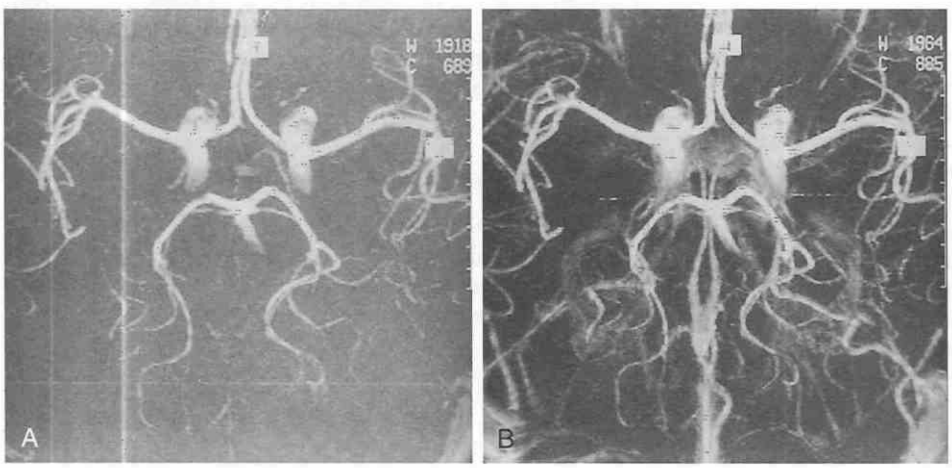

Figure 3–28. Comparison without *(A)* and with *(B)* the injection of gadolinium (Gd)-DTPA. When Gd-DTPA is used, more small vessels are seen than without injection. However, more enhanced veins are also seen in the image, which tends to obscure vessels in the maximum intensity projection images. The imaging parameters were TR = 35 msec, TE = 8 msec, 64 partitions, slab thickness 70 mm, and matrix size 256 × 512 (phase by read).

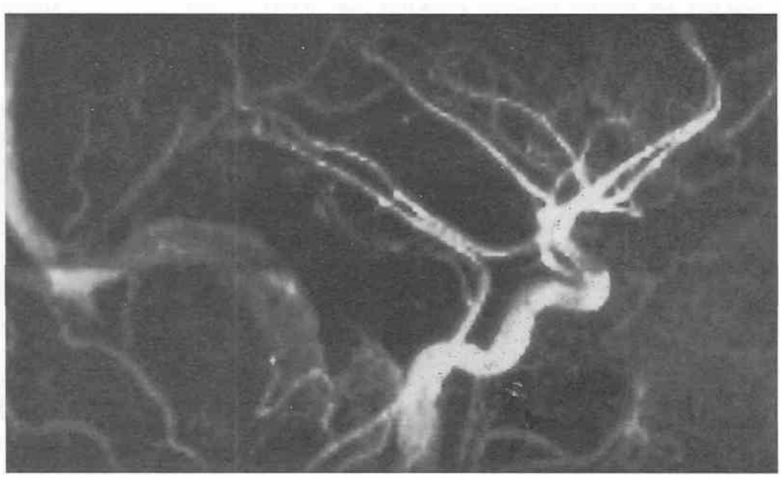

Figure 3–29. Lateral view of intracranial vessels. Images were acquired with a TE of 6.5 msec and 64 slices per slab. Two slabs with 50% overlap were combined to create the maximum intensity projection images. A large region of interest was covered without the problem of spin saturation.

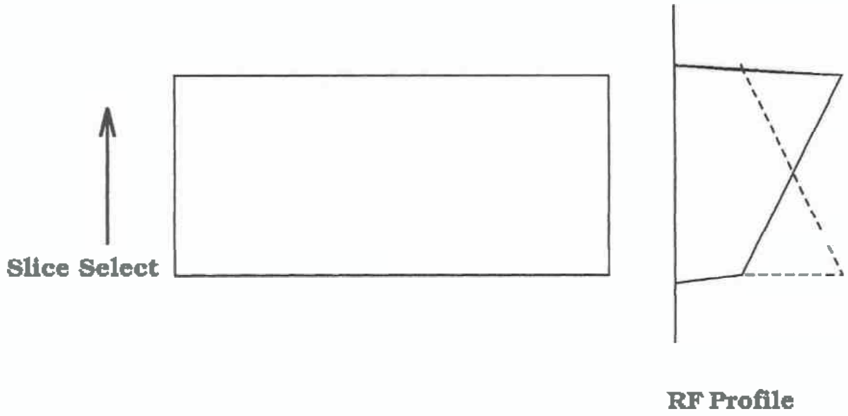

Figure 3–30. A pictorial representation of the flip angle along the slice select direction as it is varied spatially. The slope of this TONE pulse can be chosen according to the flow velocity to optimize response along the slice select direction. If the arterial flow *(dashed line)* is up, the solid line would be used to optimize arterial blood signal uniformity. RF, radiofrequency.

This contrast enhancement is especially helpful for visualizing slow flow in the regions of peripheral vessels as well as aneurysms[39] (Fig. 3–32).

Several problems are associated with this method:

1. The power deposited may be high.
2. The saturation pulse may also saturate the moving spins because of the local field change.
3. This saturation will have no effect on the fatty tissue; hence, fatty tissue will appear relatively bright compared with the background.

To overcome the problem associated with the specific absorption rate (SAR) limit, a double side band saturation pulse can be applied to achieve the same effect as that of a single side band but with half of the SAR. Moreover, a temporal variable saturation pulse can be applied so that a large saturation pulse is applied when the low spatial frequency components are collected to suppress most of the background tissue. However, a smaller saturation pulse can then be applied for the high-frequency portion. In this way, the total SAR can be reduced and yet have the same effect as that of a constant saturation pulse.[58] On the other hand, a frequency-selective fat saturation pulse can be used to suppress the unwanted fat signal[39] (see Fig. 3–32).

Fat Saturation. As mentioned earlier, fat and water have different resonant frequencies. When a frequency-selective, small bandwidth saturation pulse centered on the fat resonant frequency is used, it should be possible to suppress fat signal without affecting the water signal.[12,31] Because of the nonuniform static field, it is difficult to obtain uniform fat suppression throughout the entire imaging volume. Moreover, the choice of offset frequency and bandwidth of the fat saturation pulse requires fine-tuning so that the best combination of the parameters can be obtained.

A sequence diagram is shown in Figure 3–33. A frequency-selective fat saturation RF pulse is applied outside of the normal 3D encoding direction so that the fat saturation is applied only once every 3D encoding loop. Because the fat signal will be at a minimum immediately after the application of the fat saturation pulse, a centric reordering along the slice select direction is used so that the low-frequency component will be collected while the fat signal is at a minimum[39] (Fig. 3–32*C*).

Alternate Imaging Schemes

TOF bright blood imaging is not the only way to collect angiographic information. Bright blood techniques and PC techniques have been discussed; here we consider three other possible methods.

Black Blood

There are at least six ways to get blood to appear dark in an MRA study:

1. If the blood is not motion compensated and flow is fast enough, the signal within a voxel with a gradient large enough to create a 2π phase change across the voxel will vanish.

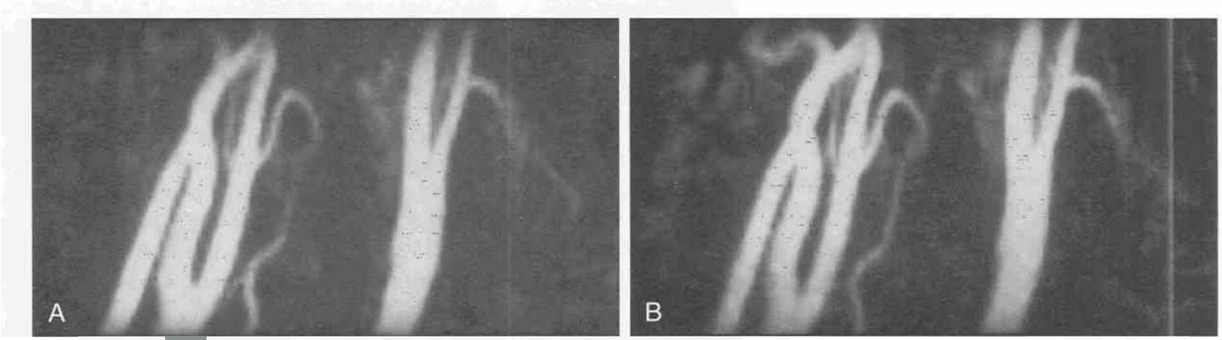

Figure 3–31. Conventional 3D MRA study with a constant radiofrequency pulse *(A)* versus a caudal to cranial increase in flip angle spatially *(B)*. Note the more uniform response along the slice selection direction when the latter, TONE, pulse is used.

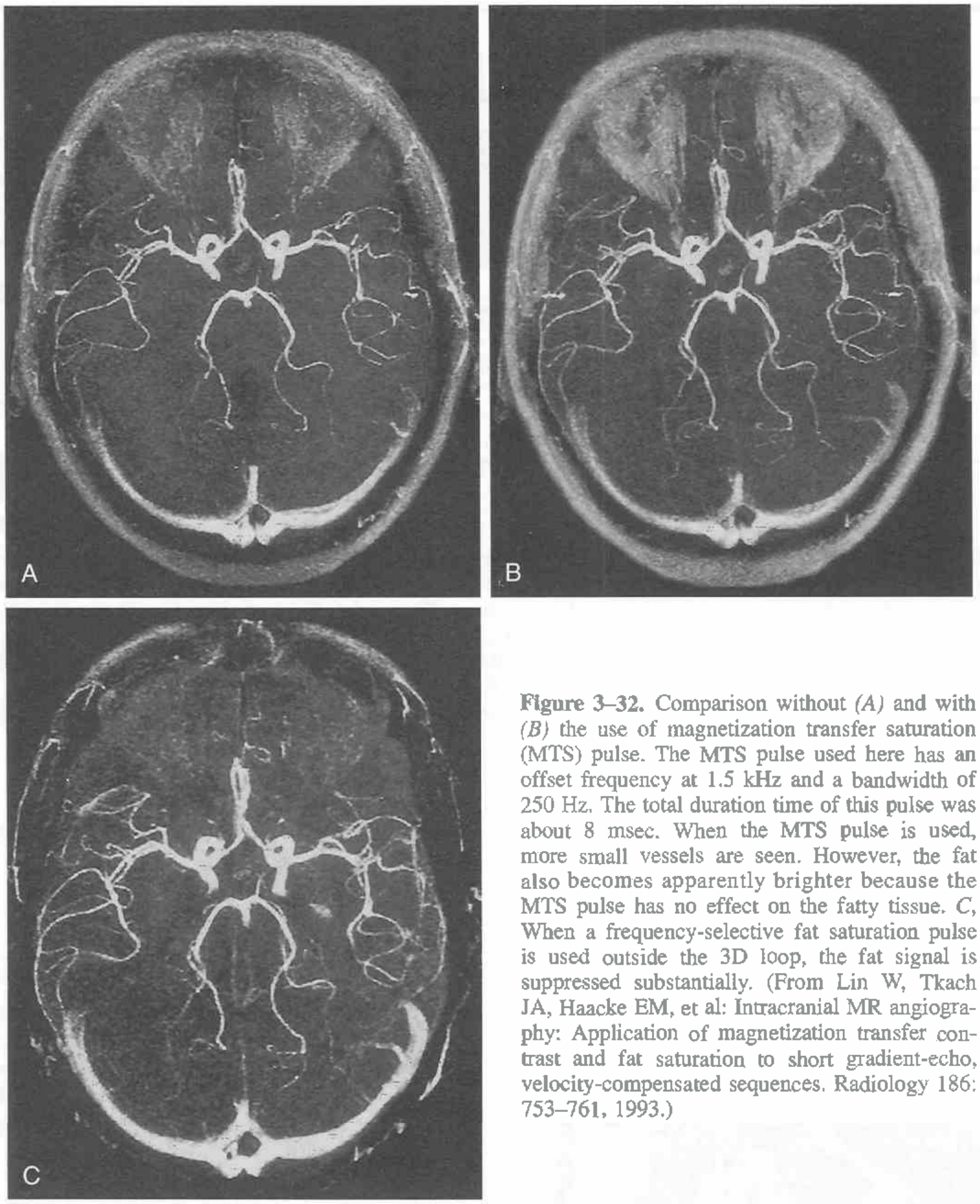

Figure 3–32. Comparison without *(A)* and with *(B)* the use of magnetization transfer saturation (MTS) pulse. The MTS pulse used here has an offset frequency at 1.5 kHz and a bandwidth of 250 Hz. The total duration time of this pulse was about 8 msec. When the MTS pulse is used, more small vessels are seen. However, the fat also becomes apparently brighter because the MTS pulse has no effect on the fatty tissue. *C*, When a frequency-selective fat saturation pulse is used outside the 3D loop, the fat signal is suppressed substantially. (From Lin W, Tkach JA, Haacke EM, et al: Intracranial MR angiography: Application of magnetization transfer contrast and fat saturation to short gradient-echo, velocity-compensated sequences. Radiology 186: 753–761, 1993.)

2. Saturation can be used to suppress the signal from the blood before it enters the imaging volume.
3. A π pulse can be used to invert the spins from blood and the signal acquired at the null point of blood (Fig. 3–34).
4. A flow-sensitive fast-imaging method can be used.
5. The old-fashioned signal void can be created by letting blood flow out of a slice between a $\pi/2$ pulse and a π pulse of a spin-echo acquisition.
6. A T2* contrast agent can be used to dephase the signal from blood.

The primary advantage of using black blood acquisition methods is to reduce the problems associated with higher-order motion artifacts (spin dephasing)[17,18] since all the blood vessels will appear dark. However, this method requires special postprocessing methods so that blood vessels can be separated from other low signal intensity structures such as sinuses.

Steady-State Free Precession Bright Blood

Steady-state free precession imaging can also play a role in bright blood MRA studies. For tissue with small T1/T2 ratios and large flip angle, short TR scans can give high SNR. Blood has a T1/T2 ratio of about 6, which is small enough that at a large flip angle it will have significantly brighter signal than that of the surrounding muscle or brain parenchyma.[49]

Spin-Density Approach

Fast imaging can also be used to highlight spin-density differences.[49] Blood has an effective spin density (i.e., spin density weighted by T2*) higher than all of muscle, fat, or brain parenchyma. Therefore, using a low flip angle (much less than the Ernst angle) can bring about excellent contrast even if the blood is not flowing (i.e., this would be good for obstructed flow studies).

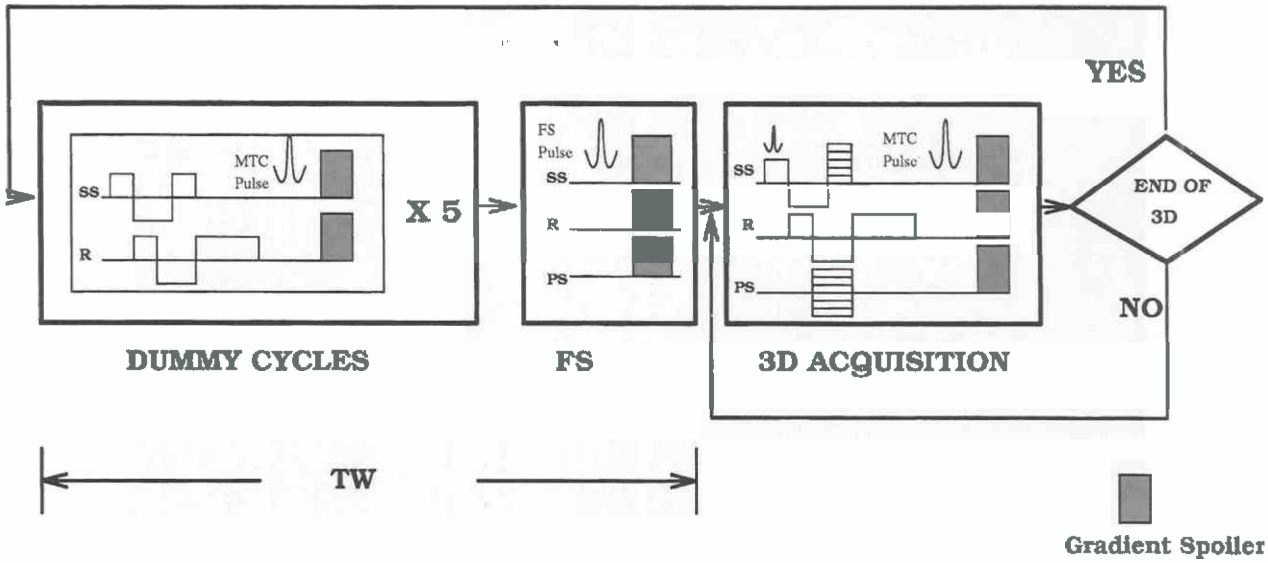

Figure 3–33. Sequence diagram showing the use of magnetization transfer saturation (MTS) and fat saturation (FS) pulses. The fat saturation pulse is applied outside the 3D loop so that it will be applied only once for one step of the 3D encoding procedure (including slice select [SS], read [R], and phase-encoding [PE] gradient timings). To acquire the data when the fat signal is at a minimum, a centric reordering scheme is used along the SS direction so that the low-frequency components are collected before the high-frequency components. There is a delay time (TW) between the end of one 3D encoding and the next phase-encoding step to apply the MTC and FS pulses and adjust contrast as desired. (From Lin W, Tkach JA, Haacke EM, et al: Intracranial MR angiography: Application of magnetization transfer contrast and fat saturation to short gradient-echo, velocity-compensated sequences. Radiology 186:753–761, 1993.)

Flow Quantification

PC methods can be used in a cine format to generate information on the flow rates throughout the cardiac cycle in just a few minutes. A variety of methods exist to do this, including a one-dimensional (1D) method called real-time acquisition and velocity evaluation (RACE), a 2D cine phase method, and a 1D or 2D projective Fourier phase method. The latter has been used to measure wave speeds.

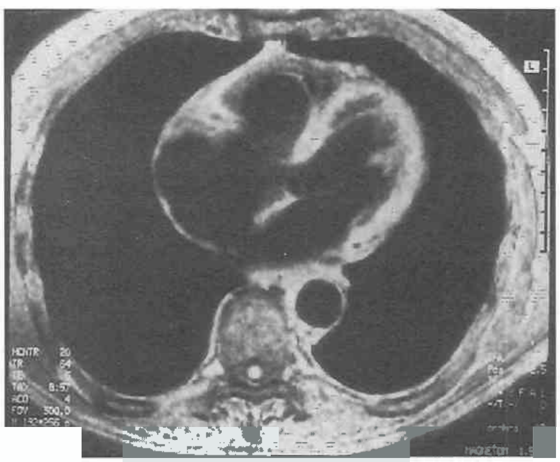

Figure 3–34. By applying an extra nonselective π pulse before collecting the data, followed by a selective π pulse to reinvert the spins in the volume to be imaged, a delay time of T1 is used to null inflowing blood while leaving stationary tissue bright. This is demonstrated in the heart from a single partition (1 of 16 collected) of 2.5-mm thickness. Note the bright wall of the aorta and myocardium. (Courtesy of Debiao Li, Ph.D., Washington University, St. Louis.)

RACE

Collecting just velocity information in one direction allows for the acquisition to be on the order of a tenth of one heartbeat. This is accomplished by projecting along the usual phase-encoding direction to examine phase changes at that position in the read direction.[43] The sequence diagram is shown in Figure 3–35. Usually a 2D plane is excited, but the method is best applied when a cylinder is excited and no partial voluming is present to degrade the signal.[28, 42]

One example of RACE is shown in Figure 3–36 in the region of the aorta. The problem associated with this method comes with the nature of the projection image. When two vessels are located in the same row (column) along the projection direction, the flow velocity information is projected into the same pixel, obscuring the velocity information. However, this method can provide very high temporal resolution (equal to TR) and can be used to monitor the dynamic change of flow velocity.

Fourier Phase

Another projection method to obtain flow velocity information is called the *Fourier phase method*.[29, 57] The sequence structure of this method is identical to a 2D sequence (Fig. 3–37). However, instead of putting the phase-encoding gradients along the phase-encoding direction, the encoding gradients are put into, for example, the slice select direction to encode flow velocity along the slice select direction. Therefore, for a Fourier phase image, one

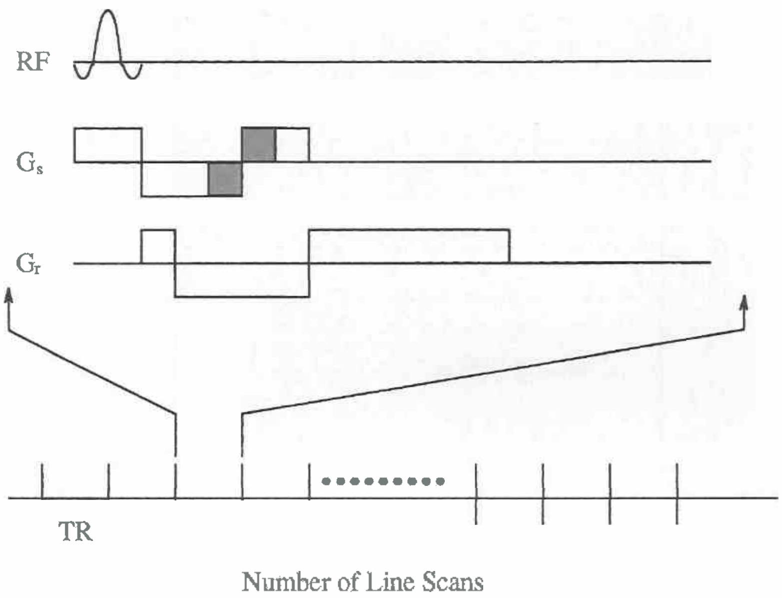

Figure 3–35. Sequence diagram for real-time acquisition and velocity evaluation (RACE). Basically this sequence is identical to a conventional 2D sequence, except that there is no phase-encoding gradient so that all the information in the image plane will collapse into one line. The temporal resolution is equivalent to TR. The shaded portion represents the velocity-encoding gradients. Velocity-compensated gradients are used along the frequency-encoding direction. (G_s and G_r represent slice select and (radio)frequency-encoding directions, respectively.) RF, radiofrequency.

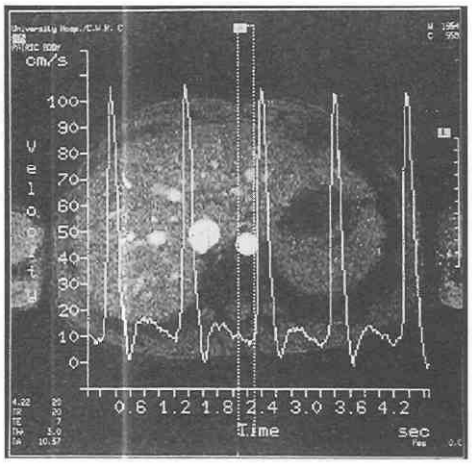

Figure 3–36. Example of a real-time acquisition and velocity evaluation (RACE) image. The velocity was measured in the region of the descending aorta. As shown, the peak velocity is about 110 cm/second, and five cardiac cycles were measured. (From Haacke EM, Smith AS, Lin W, et al: Velocity quantification in magnetic resonance imaging. Top Magn Reson Imaging 3:34–49, 1991.)

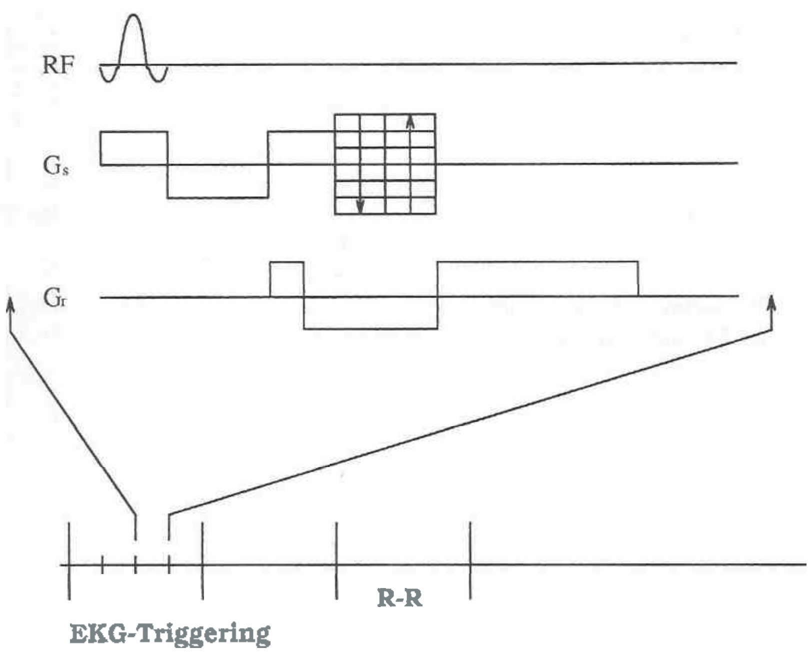

Figure 3–37. Sequence diagram of the Fourier phase method. Because this is a projection method, no phase-encoding gradient is used. However, a pair of encoding gradients are applied along the slice select direction to encode through-plane flow. G_s and G_r, slice select and (radio)frequency-encoding directions, respectively; RF, radiofrequency.

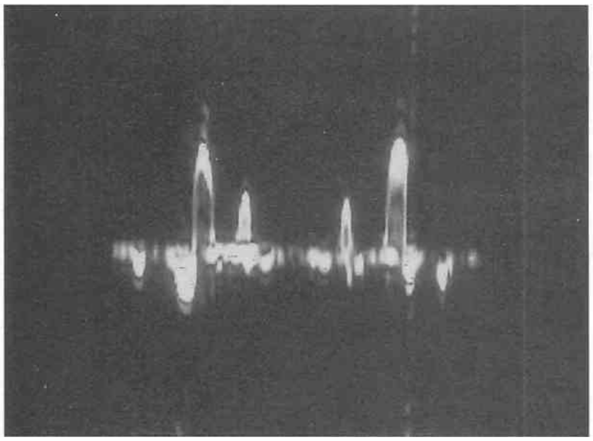

Figure 3–38. Example of the Fourier phase method. This image was obtained during diastole so that the common carotid arteries on both sides show high flow velocity (the signal extends far away from the DC line). Two vertebral arteries show slower velocity compared with the common carotid arteries. Moreover, the jugular vein shows slower negative flow.

axis represents spatial position and the other represents velocity. Unlike the preceding method, no conversion from phase to velocity is needed and the effects are clear from the image. Cardiac gating is used to collect velocity information during the cardiac cycle. Figure 3–38 illustrates an example application of this approach in the neck.

Again, this is a projection method, and overlapping vessels affect its accuracy. This problem may be completely eliminated when an echo planar method is used. Moreover, the inconsistent heart rate creates ghosting, which may obscure the measurement of the velocity. Aliasing has to be avoided by appropriate choice of the encoding gradient strength to meet the Nyquist criterion. The SNR may be too low for fast flow to be seen because of spin dephasing. For measuring slow flow, high signal from stationary tissue at the direct current (DC) line may obscure the flow information.

Two-Dimensional Cine

When cardiac gating is used along with short TR, a set of 2D images can be collected in a given cardiac cycle. For example, if the heart rate is T, the number of slices (phases) that can be imaged is T/TR. By interleaving a velocity-sensitive gradient structure with its negative structure and subtracting the former image from the latter image, a cine set of images with velocity in one direction is obtained.[5, 20, 46, 47, 59]

The number of phases that can be acquired is limited by the TR and heart rate. To improve the temporal resolution, it may be better to have a delay time after the R wave to ensure that the peak velocity during systole will be sampled.

Disadvantages associated with this method include:

1. Inconsistent heart rate affects the accuracy of the velocity measurement.
2. Eddy current effects can cause distortion of phase information and hence velocities.
3. Spin dephasing can occur from higher-order motion artifacts.
4. Aliasing may occur caused by the poor choice of maximum velocity—which is the common problem usually seen with the PC method.

Bolus Tracking

One method is to use excitation of the blood followed by a parallel multislice read to find the blood that had an increasing signal.[19, 33] Knowing the distance traveled by the blood and the time between the excitation pulse and data acquisition, it is possible to calculate the velocity of the flow. Alternatively, presaturation pulses can be applied to the normal gradient-echo sequences (2D or 3D) to saturate tissue in a fixed region but to otherwise leave the image unaffected. The dark band created by the presaturation pulse can be used as a region to view inflowing spins that enter it between the saturation pulse and data acquisition. Again, if the distance the blood travels inside the dark band and the duration between presaturation pulses and data acquisition is known, the flow velocity can be calculated (Fig. 3–39).

Several disadvantages are associated with bolus tracking methods. Motion during the sampling gradients causes distortion of the signal and, hence, of the images. Blood T2 relaxation time may affect detectability when the TE is long. Spin dephasing caused by higher-order motion artifacts may interfere with the measurement of the distance traveled by the blood. This method is also limited by the T1 relaxation of blood (which affects the appearance of the saturation band) as well as the flow profile and RF pulse profiles, which may not saturate the blood well when the profile itself is poorly defined.

Evaluating Microcirculation via Functional Images

During the past few years a great deal of interest has been generated in functional imaging in MRI.[3, 4, 21, 22] This

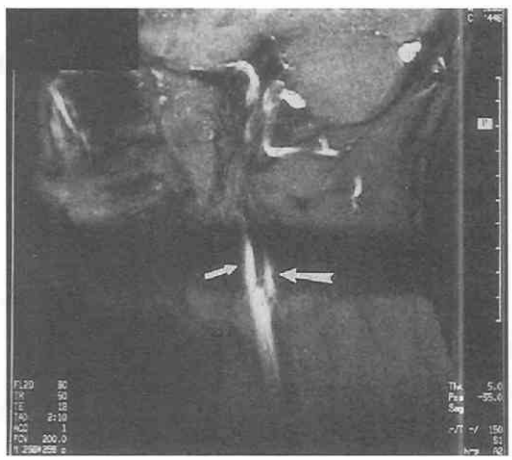

Figure 3–39. Saturation pulse is applied axially with a 2D sagittal acquisition to create a dark band in the maximum intensity projection image so that the distance that blood travels from the bottom of the dark band can be used as a means to calculate flow velocity. Note the more rapid flow in the internal carotid artery *(small arrow)* compared with that in the external carotid artery *(large arrow)*.

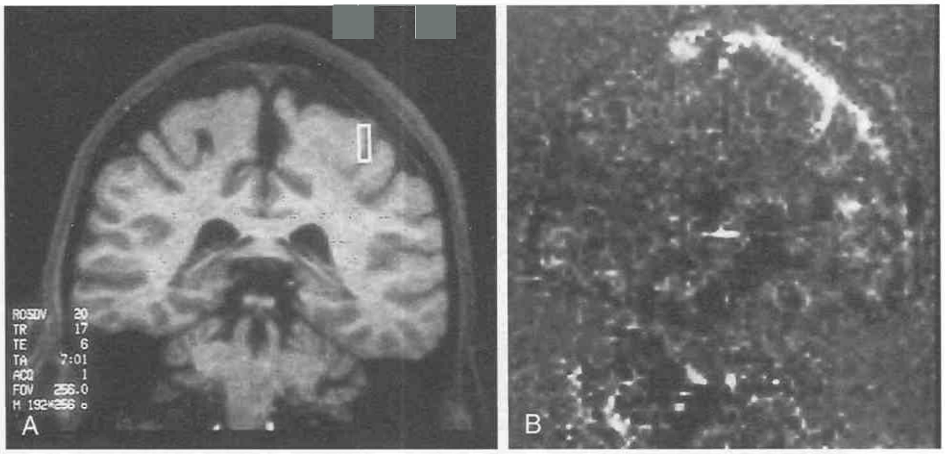

Figure 3–40. Functional imaging is possible even at 1.5 T when a long echo time (TE) sequence is used. *A*, One slice from a 3D T1-weighted scan is used to locate the central sulcus. *B*, A subtraction of poststimulation minus prestimulation by moving the right hand shows the region of the motor cortex on the left side. The motor cortex sits in the gray matter adjacent to the sulcus anteriorly.

is based on the fact that T2* is reduced when deoxyhemoglobin is present in the blood. For activation states such as motor or visual cortex stimulation, blood flow increases but the percentage of deoxyhemoglobin remains the same. Hence, T2* dephasing is not as severe and the signal increases. The subtraction of two images before and after stimulation then gives an image displaying that portion of the brain where the microcirculation increases.

An example of a 3D image used to localize the central sulcus for motor cortex studies is shown in Figure 3–40*A*. The subtraction of an image collected before moving the right-hand fingers from that collected when the right-hand fingers were moving in a sequential finger-touching mode is shown in Figure 3–40*B*. The bright region sits on the gray matter of the central sulcus. The exciting part of this research direction is that these images can be acquired with excellent resolution, and each image only takes seconds.

Processing and Image Display

To create a conventional angiography–type image from which the primary diagnosis is generally made, some special postprocessing methods and display techniques can be used. This is especially true today, thanks to the improvements in computer power; many methods are becoming more accessible because there is little waiting for the processed images to be reviewed. Having rapid image display makes it possible to modify acquisition strategy. In most of the cases, these methods can further improve the accuracy of the images for better diagnosis. These methods can be divided into two main categories: display techniques and image-processing methods.

Display Techniques

Maximum Intensity Projection

The maximum intensity projection (MIP) approach is a method to display 3D vascular data onto a 2D projection. The idea is simple; the maximum value along any ray is used as the 2D intensity value for that pixel through which the ray intersects the plane orthogonal to the viewing direction. Consequently, it can be used to create a projection at any desired angle by rotating the viewing direction (Fig. 3–41). A cine display method can then be used to generate a movie-like display of vascular information in which the vascular structures can be viewed from all angles.

Since the concept of this method is simple and does not require intensive computation, and the results can be obtained in less than a minute, it has been widely used as a regular protocol for MRA studies. However, some

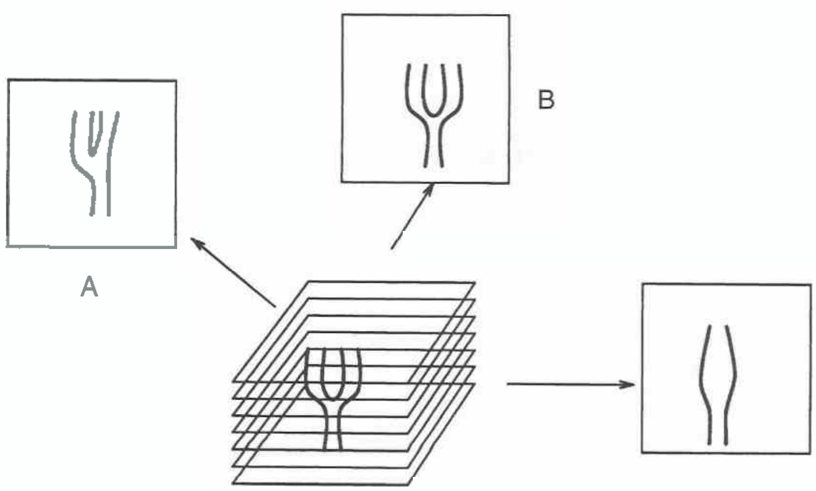

Figure 3–41. Pictorial representation demonstrating the maximum intensity projection algorithm. *A*, Oblique view. *B*, Posteroanterior view. *C*, Lateral view.

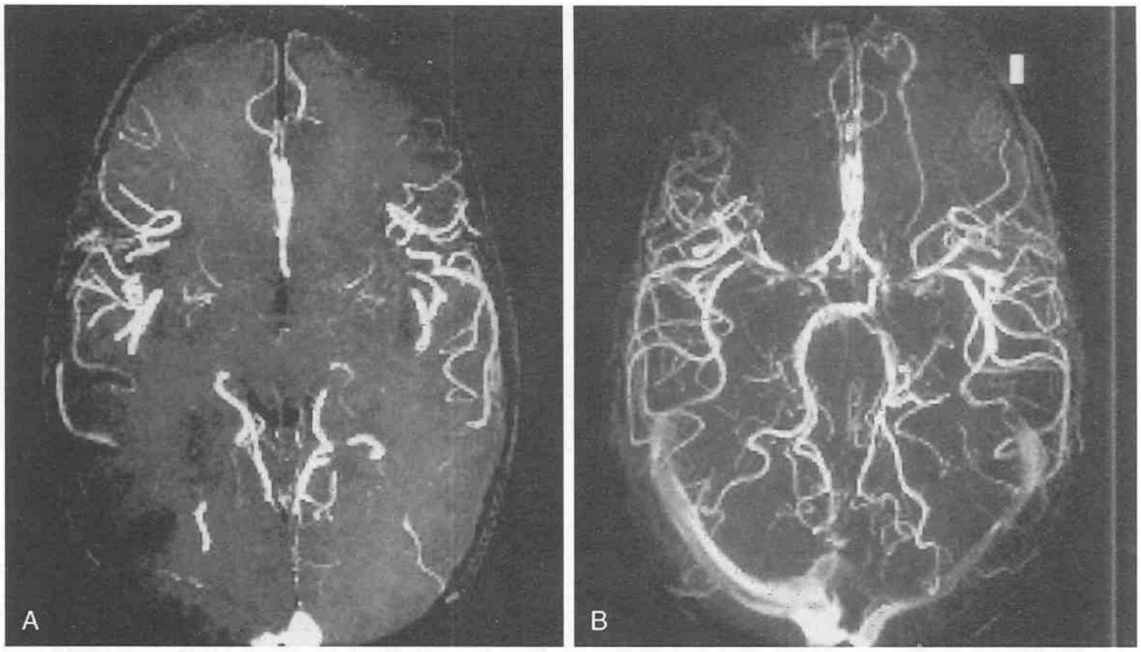

Figure 3–42. Comparison of local maximum intensity projection (MIP) and full MIP. Since the MIP algorithm tends to reduce CNR, some of the small vessels may be lost in the processing of MIP. *A*, A local MIP is one way to solve this problem, since only a few slices are used to perform MIP. However, the global vascular information is lost compared with full MIP *(B)*. (From Lin W, Haacke EM, Masaryk TJ, et al: Automated local maximum-intensity projection with three-dimensional vessel tracking. J Magn Reson Imaging 2:519–526, 1992.)

disadvantages are associated with this method.[2, 9] If MIP is done over the entire 3D space, a great deal of noise is picked up and contrast is lost between vessels and background tissue (Fig. 3–42). Also, when fat is too bright (or signal from other tissues overwhelms the blood signal), the MIP image will lose the vessels.

Summation Methods

When all intensities are summed over a vessel, the background noise is suppressed and intersections of vessels are clearly displayed as bright. One disadvantage is that background signal can become too high and overwhelm the blood signal. One way around this problem is to sum only when the signal is above some threshold or to sum over the vessel-tracked images (see next).

Optical and Shading Methods

A computer graphic method, surface rendering, can also be applied to create the surface of blood vessels so that a shading method according to a light source can then be used to generate a visual 3D perspective image. This complements the depth information loss in the MIP images. However, to do so, the vascular information must be extracted from other nonvascular structures. Some of the vascular segmentation methods are discussed next.

Processing Methods

Single Slice and Multiplanar Reconstruction

Each slice from a set of MRA images contains blood vessel information. Whenever images are postprocessed for display, it is possible that information is lost. The best images to look at from a 3D data set are the original unprocessed images. A simple processing method that can prove highly useful is reformatting the data along any plane through the volume; this is referred to as *multiplanar reconstruction* (MPR). Some interpolation of the image data is required, but it is usually a good technique if the 3D data are collected isotropically. The best results are obtained when the data are "sync" interpolated (i.e., the Fourier data are zero-filled to a larger matrix size and then transformed) until they are as close to isotropic as possible.[60]

Vessel Tracking

The basic concepts of the vessel-tracking method are based on the assumptions that all vessels are connected with each other and that blood vessels have a reasonable uniform signal distribution.[9, 10, 30, 36, 53, 55] Accordingly, we can extract vascular structures from other background tissue. This makes it possible to segment out the vessels so that they can be displayed independently of the background. After vessel-tracking processing, only the points that are classified as blood vessels will keep their original signal intensity and other points will be assigned a zero intensity. In this manner, the vascular information is extracted from other nonvascular structures.

This method is able to overcome the difficulties associated with MIP. Since only the points that contain vessel information are used to create the MIP images, the contrast is 100% and fatty structures or other bright tissues will not obscure vascular structures. Moreover, the processed images are ready for use in a surface-rendering program. The difficulties of this method are that it may not be able

to accurately extract vascular information when the SNR or CNR is low. Further, the nonperfect RF profiles and nonuniform receiver coils will affect the uniformity of vessel signal distribution. To overcome this problem, vessel tracking can be coupled with a traveling MIP (TMIP) method[55] to remove the signal variation at the edge of the vessel. This method is analogous to the vessel-tracking method. One of the difficulties of vessel tracking is to choose the optimum thresholds. TMIP serves as an alternate method that is less sensitive to the choice of thresholds or at least makes it possible to eliminate boxy artifacts and see where vessel tracking failed.

Superposition Methods

The ability to collect high-resolution 3D images makes it possible for accurate surgical information to be obtained from vessel-tracked images. Today, 1- to 2-mm^3 3D information obtained using MRI is standard (Fig. 3–43). Some applications even allow data for the larger vessels to be simultaneously acquired with a 3D T1-weighted study (Fig. 3–43). With the use of vessel tracking and 3D shading, both the vascular information and background tissue can then be superimposed onto each other.

Clinical Applications

The focus of this chapter so far has been on techniques, with the examples being in the head and neck. The major use for MRA has been in intracranial and carotid studies for evaluating stenosis (Fig. 3–44), aneurysms (Fig. 3–45), arteriovenous malformation (AVM) (Fig. 3–46), sickle cell disease (Fig. 3–47), and other vessel abnormalities (Fig. 3–48). The multislab 3D method can also be applied to the aortic arch with some success (Fig. 3–49).

In the chest wall, respiratory motion has long been the bane of MRI studies. Nevertheless, 3D MRA methods can be useful in both the lungs (Fig. 3–50) and heart (Fig. 3–51). In the latter case, both fat saturation and magnetization transfer contrast (MTC) are required for optimal visualization of the blood pool. In the abdomen, 2D TOF with breath-holding is most often used (Fig. 3–52). Still, 3D has found some application in the renal arteries (Fig. 3–53).

Peripheral vessels are often the most difficult to visualize because obstruction leads to slow flow and techniques based on moving blood are less likely to succeed. Two-dimensional TOF often works best in these cases, as illustrated in the upper legs of two patients (Figs. 3–54 and 3–55). The use of Gd-DTPA may prove most useful in the legs; a single high-resolution 3D coronal scan covering both legs can be accomplished in only 10 to 20 minutes. Tissue properties themselves can be used to discriminate blood from surrounding vessels in peripheral studies.

Dynamic Contrast-Enhanced MRA

As already mentioned, the use of T1-reducing contrast agents is an excellent means by which to enhance the blood signal. The previous discussion focused on a steady-state approach that required several minutes to acquire the data. For very-high-resolution studies, data acquisition might take up to 10 minutes for a 3D volume acquisition approach with a 512 × 512 matrix. The main disadvantage of steady-state imaging postcontrast injection is that arteries and veins are equally bright.

Dynamic contrast-enhanced imaging refers to acquiring the data rapidly immediately following injection of the contrast agent.[50, 52] The novel aspect of this method is that for roughly the first 30 seconds after injection, the contrast agent remains predominantly in the arteries.[40] Hence, this early time period is called the *arterial phase*, the best time for collecting data to avoid signal from the veins. If data are collected for longer than 30 seconds, the signal from the veins continues to increase. One way to avoid a problem from this increase in venous signal is to relegate it to the edges of k-space so that it only contributes to the high-spatial-frequency components. This can be accomplished by using a doubly centric (either square spiral or elliptical[61]) ordered k-space coverage (i.e., all data collected in the arterial phase are for the central part of k-space). After 30 seconds, the outer parts of k-space are collected from the inntermost parts at early times to the outermost parts at later times.

There are two drawbacks to this approach:

1. It is possible to miss the full effect of the arterial phase; this situation sometimes leads to an infiltration of venous signal.
2. In 30 seconds, only a limited amount of k-space can be covered in 3D; this situation leads to a low-resolution scan. Current gradient strengths have helped reduce TR and TE to 5 and 2 msec, respectively, which are helpful.

For a 200-mm FOV and 200 phase-encoding steps, only 30 slices can be collected in 30 seconds. To cover a reasonably thick slab thus requires a slice thickness of 2 to 3 mm. This makes reformatting into a rotating view of the vessels inappropriate. Also, a 30-second breath-hold is already rather long.

Despite these drawbacks, this approach is becoming the method of choice for abdominal MRA, in which speed is a priority because of respiratory and cardiac motion. For imaging of the heart and the coronary arteries in particular, data are collected for only 128 msec during the cardiac cycle. For FOV = 128 mm, TR = 4 msec, 64 phase-encoding steps, and 16 slices, only 32 seconds is needed to collect images with a resolution of 1 × 2 × 2 mm. This is not great resolution but does result in some very informative images of the proximal coronary vessels.

To demonstrate these principles, we show results of dynamic scans in the neck and aortic arch (Fig. 3–56), pulmonary system (Fig. 3–57), heart (Fig. 3–58), and peripheral vasculature (Fig. 3–59). For the pulmonary system, a later scan also reveals the entry of venous signal at this time. In the leg, for example, a very-high-resolution, steady-state image demonstrates the potential of increased resolution even though the data are acquired both during and after the arterial phase.

Venographic Imaging and Cerebral Blood Volume

The major focus of this chapter, and of the medical community for the past 100 years, has been on the side of

Text continued on page 81

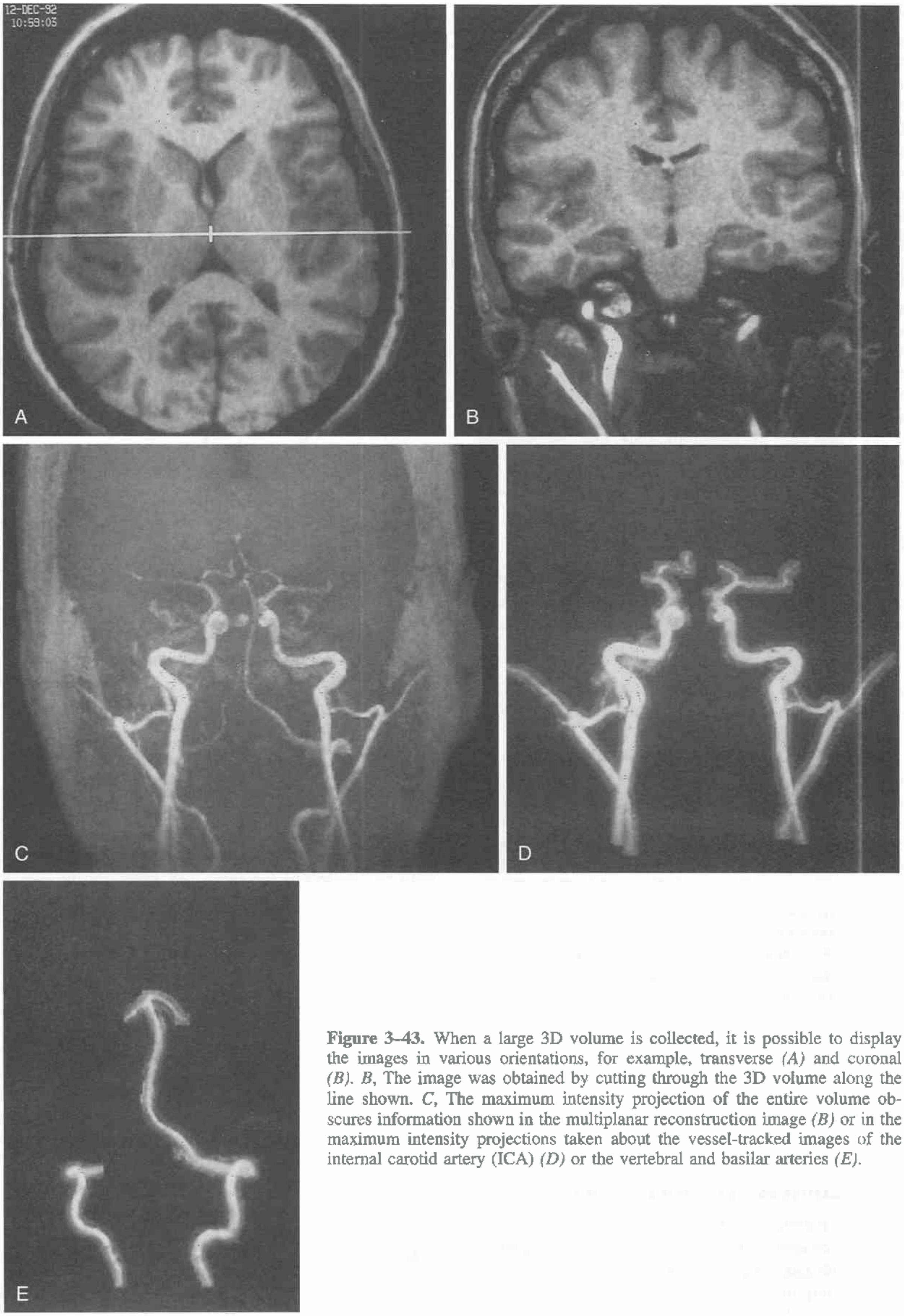

Figure 3–43. When a large 3D volume is collected, it is possible to display the images in various orientations, for example, transverse *(A)* and coronal *(B)*. *B*, The image was obtained by cutting through the 3D volume along the line shown. *C*, The maximum intensity projection of the entire volume obscures information shown in the multiplanar reconstruction image *(B)* or in the maximum intensity projections taken about the vessel-tracked images of the internal carotid artery (ICA) *(D)* or the vertebral and basilar arteries *(E)*.

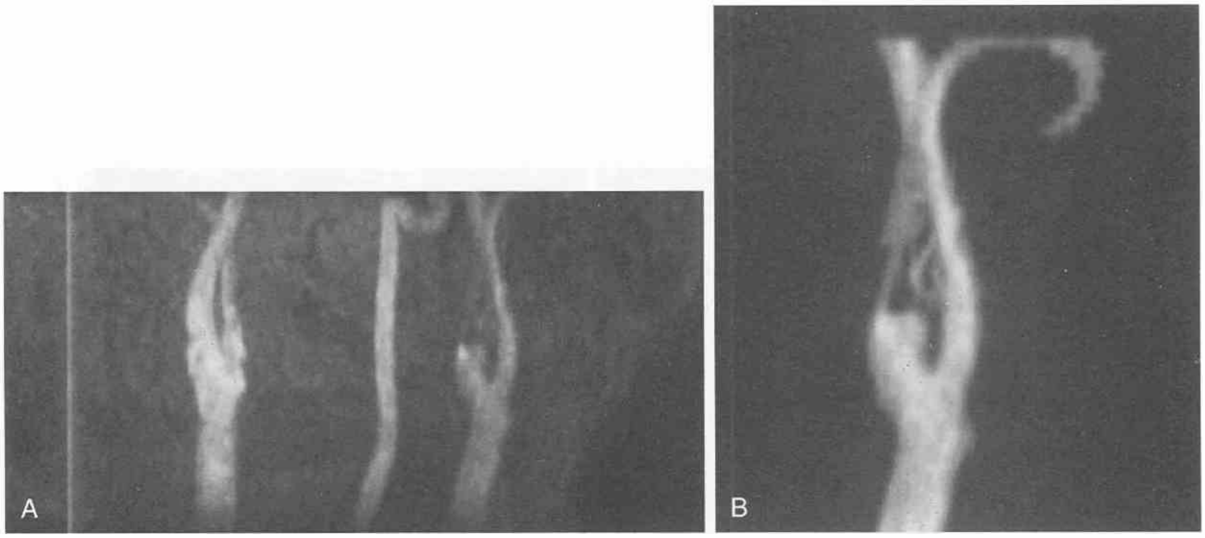

Figure 3–44. *A*, High-resolution carotid stenosis shown after taking the maximal intensity projection (MIP) of a 3D MRA study. *B*, The vessel-tracked image (similar to a local MIP) shows just the stenotic region without interference from overlapping structures. The resolution in-plane and through-plane is roughly $0.45 \times 0.9 \times 1.1$ mm³.

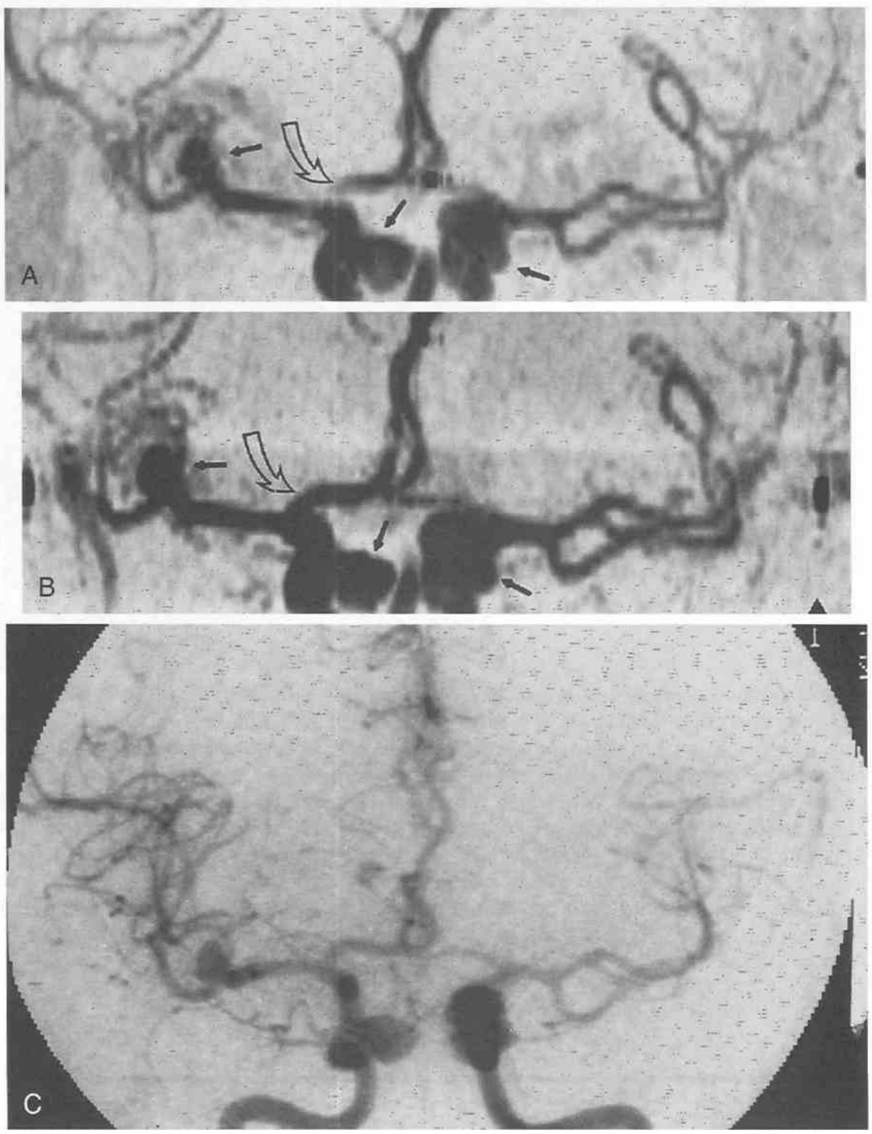

Figure 3–45. Patient study shows intracranial aneurysms. The individual images were acquired by the TE = 8 msec and TE = 5.1 msec sequences, respectively. Both sequences have a magnetization transfer contrast (MTC) pulse to suppress background tissue. Moreover, the TE = 5.1 sequence was used in the sequence structure showing in Figure 3–33. *A* and *B*, Three intracranial aneurysms are seen in both cases *(small arrows)*. However, improved aneurysm visualization and lumen definition are obtained when the TE = 5.1 msec sequence was used *(B)*. For example, the smaller aneurysm at the M2 section of the right major coronary artery (MCA) *(A)* shows flow-related dephasing and is relatively smaller as compared with that shown in *B*. In this example, the difference in sequence performance is especially striking since small aneurysms tend to have highly complex and fast flow. Moreover, *B* also shows better lumen definition and continuity at the right anterior cerebral artery (ACA) *(unfilled arrow)* compared with *A* (TE = 8 msec, *open arrow*). The digital subtraction angiography (DSA) image was available to compare with these two studies. It is evident from the comparison of *A* to *C* that the TE = 5.1 msec images and MIPs show the best correlation with the DSA image. (From Lin W, Tkach JA, Haacke EM, et al: Intracranial MR angiography: Application of magnetization transfer contrast and fat saturation to short gradient-echo, velocity-compensated sequences. Radiology 186:753–761, 1993.)

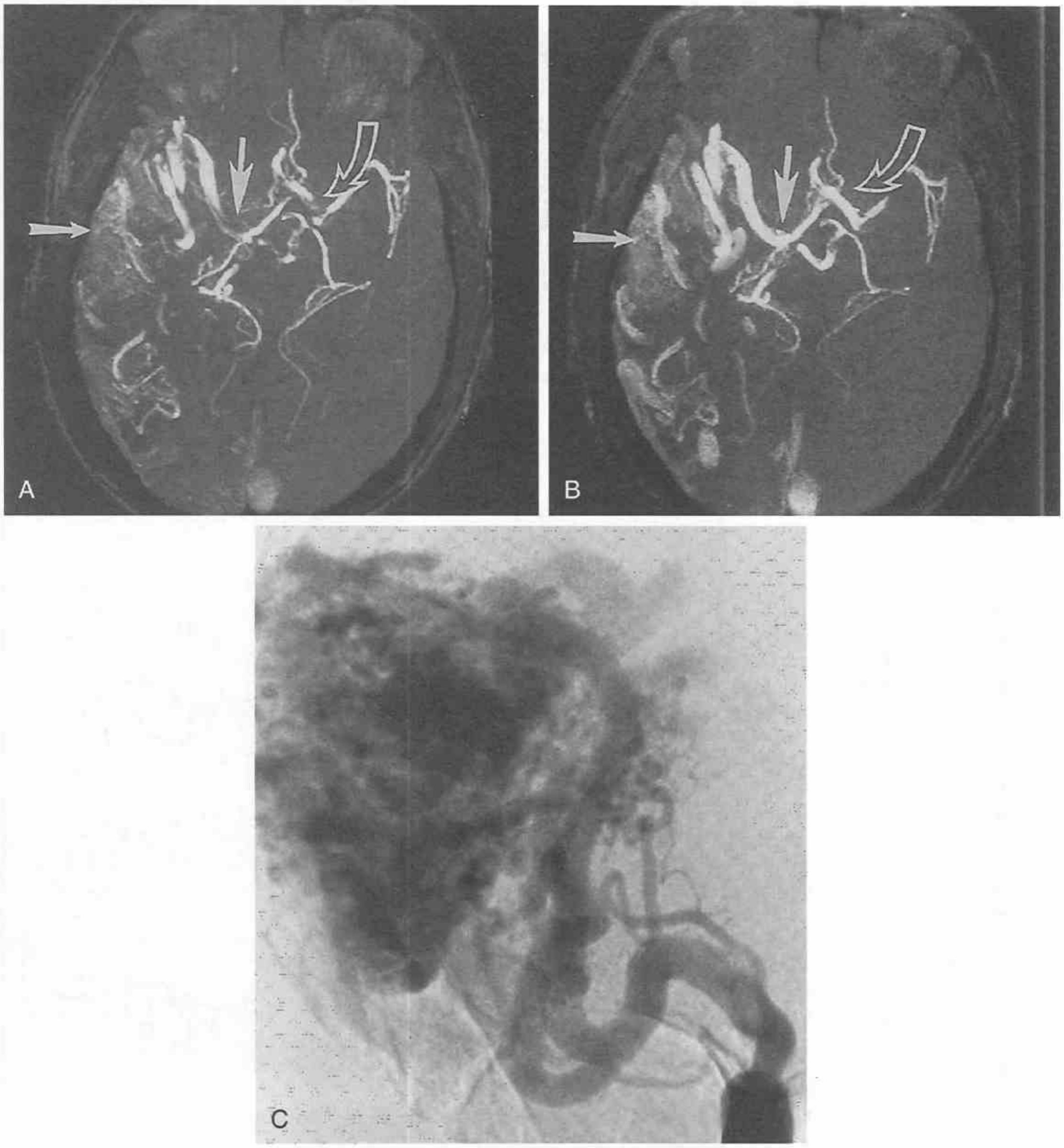

Figure 3–46. Patient study shows a large arteriovenous malformation (AVM) on the right side of brain *(small arrows)*. Maximum intensity projection images are shown to compare the lumen definition in the region of rapid flow. *A*, The TE = 8 msec sequence shows signal dropout at the right middle cerebral artery *(large solid arrow)* and left anterior cerebral artery *(unfilled arrow)* from the flow-related dephasing. However, when the TE = 5.1 msec sequence is used *(B)*, no signal dropout occurs in these regions and superior lumen definition is obtained *(large solid arrow, open arrow)*. In both cases, the AVM is clearly seen. *C*, The results were compared with digital subtraction angiography (DSA). Good correlations between TE = 5.1 msec sequence and DSA were obtained. Specifically, in the regions where the TE = 8 msec sequence showed flow dephasing, there was no evidence of vessel narrowing in the TE = 5.1 msec sequence. Again, both sequences had a magnetization transfer contrast (MTC) pulse to suppress background tissue, and the TE 5.1 sequence used the sequence structure shown in Figure 3–33. (From Lin W, Tkach JA, Haacke EM, et al: Intracranial MR angiography: Application of magnetization transfer contrast and fat saturation to short gradient-echo, velocity-compensated sequences. Radiology 186:753–761, 1993.)

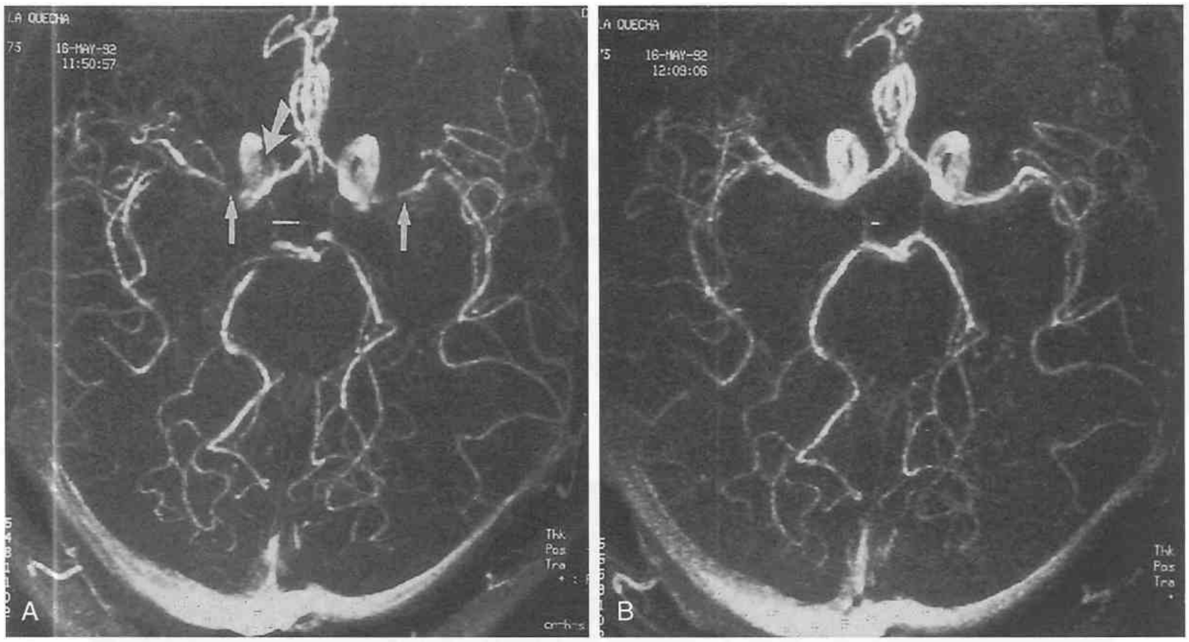

Figure 3–47. A 19-year-old female with sickle cell diseas[redacted]he resulting vessel lumen definition obtained from both the TE = 8 msec and TE = 5.1 msec sequences is shown in *A* and *B*, respectively. At both the right and left MCAs *(small arrows)* and the right internal carotid artery *(large arrow)*, the TE = 8 msec sequence shows signal dropout, which suggests a possible high-grade stenosis. In contrast, the TE = 5.1 msec sequence shows high signal intensity and good lumen definition in the same regions *(large and small arrows)*. Again, both sequences have an MTC pulse to suppress background tissue, and the TE = 5.1 sequence used the sequence structure shown in Figure 3–33. (From Lin W, Tkach JA, Haacke EM, et al: Intracranial MR angiography: Application of magnetization transfer contrast and fat saturation to short gradient-echo, velocity-compensated sequences. Radiology 186:753–761, 1993.)

Figure 3–48. Base of skull MRA study. Axial collapse image from 3D phase-contrast MRA TR/TE, 22/9, flip angle 30 degrees, all-direction flow encoding, velocity encoding (VENC) = 30 cm/second. The approximate acquisition time was 15 minutes. Each slice is 1.5 mm thick. Note the loop in the posterior inferior cerebellar artery *(open arrow)* arising from the vertebral artery. (Courtesy of Fred Steinberg, M.D., Magnetic Resonance Institute of Boca Raton, Fla.)

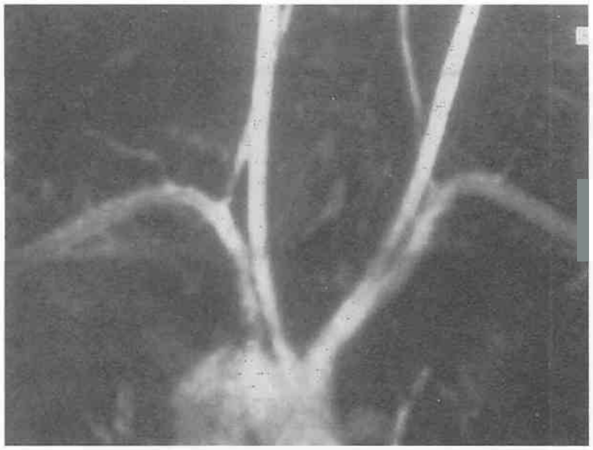

Figure 3–49. Two-slab acquisition of the aorta arch with 3D time-of-flight acquisition method. (From Lewin JS, Laub G, Hausmann R: Three-dimensional time-of-flight MR angiography: Applications in the abdomen and thorax. Radiology 179:261–264, 1991.)

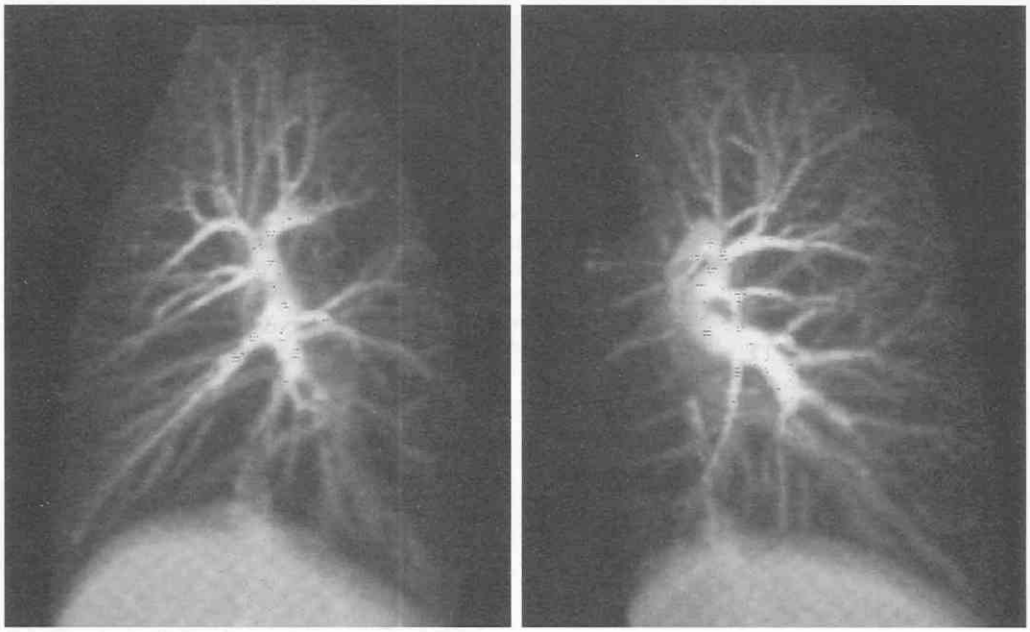

Figure 3–50. Vessels can be displayed in a maxi[redacted] intensity pr[redacted]ion format at any angle after being collected with a 3D time-of-flight sequence. (Courtesy of Piotr Wieloposki, Ph.D., Deaconess Hospital, Boston.)

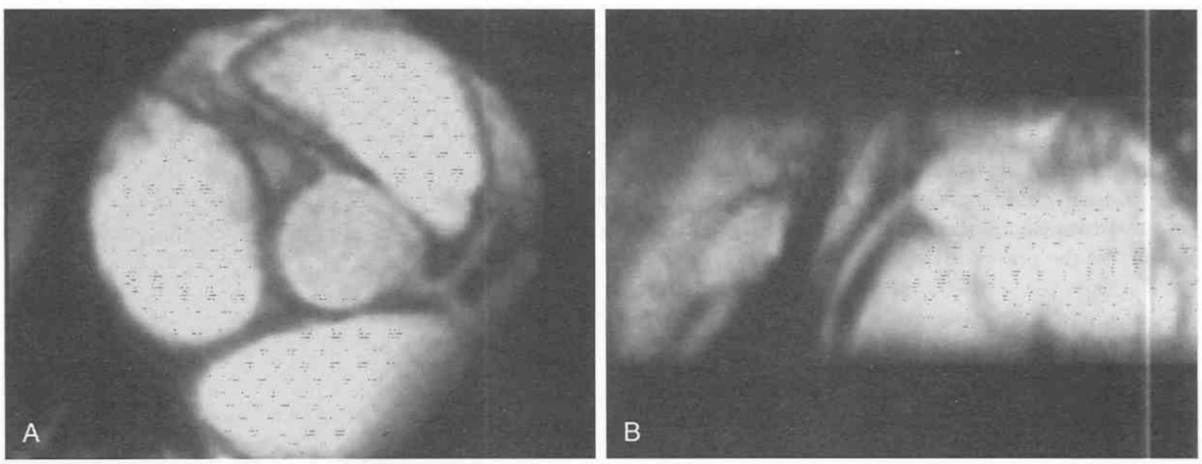

Figure 3–51. Collecting 32 slices through the heart (all at end-diastole) using a 3D method avoids misregistration artifact inherent in 2D imaging and allows a high-quality multiplanar reconstruction image to be obtained *(A)*. It is then used to search for an appropriate plane to visualize the right coronary artery *(B)*. (From Li D, Paschal CB, Haacke EM, et al: Coronary arteries: Three-dimensional MR imaging with fat saturation and magnetization transfer contrast. Radiology 187:401–406, 1993.)

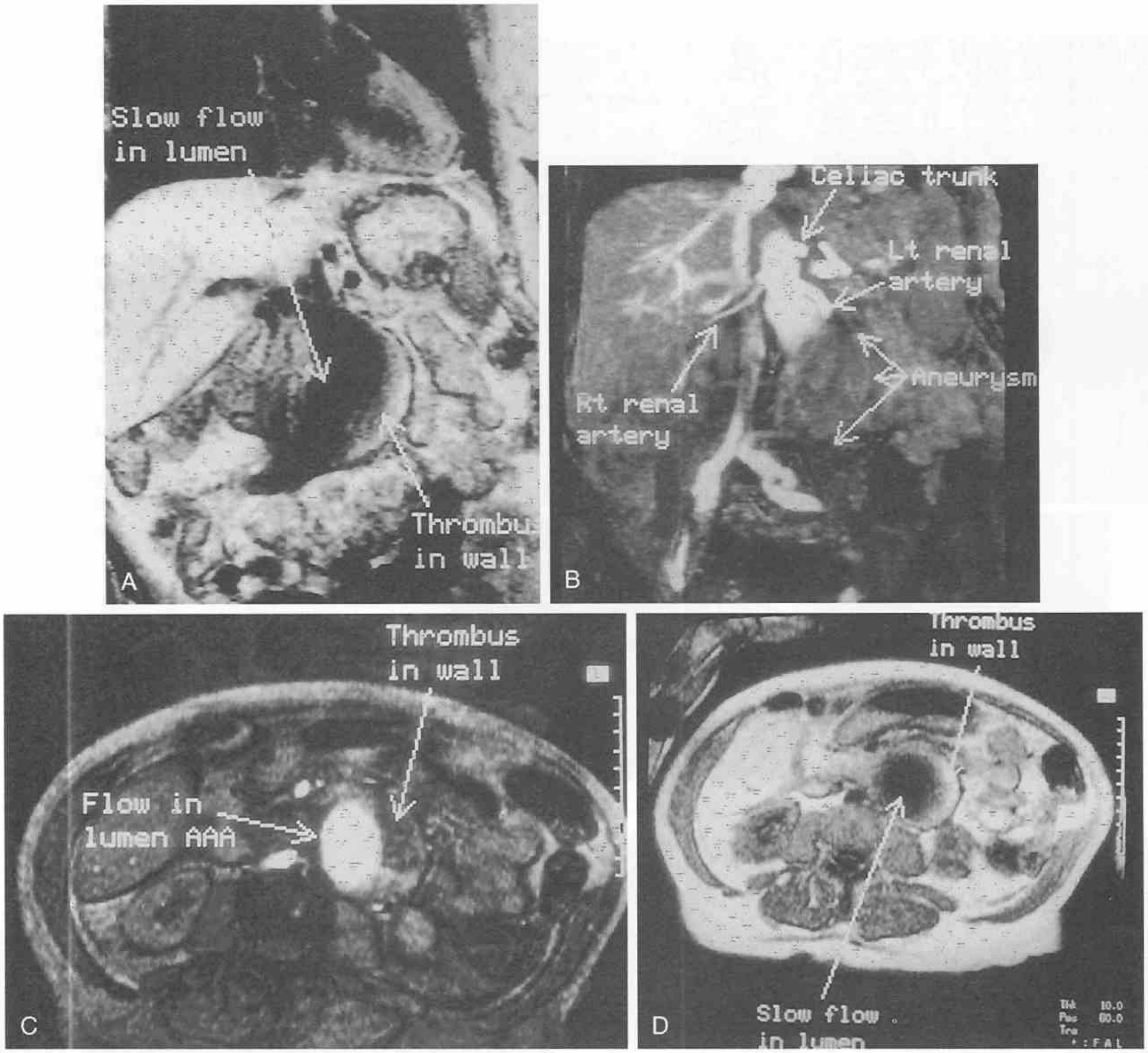

Figure 3–52. Infrarenal abdominal aortic aneurysm (AAA). *A*, Coronal black blood TurboFLASH image shows blood within the lumen (labeled) and thrombus in the wall (labeled). *B*, Coronal projection angiogram gated to systole shows both renal arteries above the aneurysm and shows poor flow enhancement downstream resulting from in-plane saturation. *C*, The same sequence in the axial plane yields good flow contrast between the lumen and thrombus in the wall, and these correlate well on the axial black blood image *(D)*. (Courtesy of Paul Finn, M.D., Northwestern University, Chicago.)

arterial imaging. Although the impetus for this method is well founded on the need to understand the delivery of oxygen-bearing blood to the tissue and to visualize the arteries themselves to discover diseased vessels, the venous blood carries with it the information about tissue function. One can consider the arterial blood as reflecting *input* function and the venous blood as reflecting *output* function. If oxygen saturation in the veins could be measured, it would serve as a means to quantify the cerebral metabolic uptake of oxygen by the brain tissue.

Today, major veins in the brain can be visualized after use of a contrast agent or with a 2D TOF approach. Still, smaller veins are difficult to see with conventional methods, because the background parenchymal signal also increases thanks to its local blood volume content after the injection of a contrast agent. By using the blood oxygenation level–dependent (BOLD) effect, however, we can design a 3D sequence to highlight the veins as dark structures while leaving the arteries with as much or more signal than the background tissue.[51] We choose an echo time in which the phase of the veins becomes opposed to that of the surrounding tissue for vessels parallel to the main magnetic field. This occurs at roughly 40 to 50 msec at 1.5 T.

Now consider a two-compartment model in which λ is the venous signal fraction of blood in that voxel. If the normalized signal at any given echo time is $1 - \lambda$ for the parenchyma and λ for the veins, then when $\varphi = \pi$, the summed signal of both components is $1 - 2\lambda$ and the veins will look darker than the surrounding tissue. The

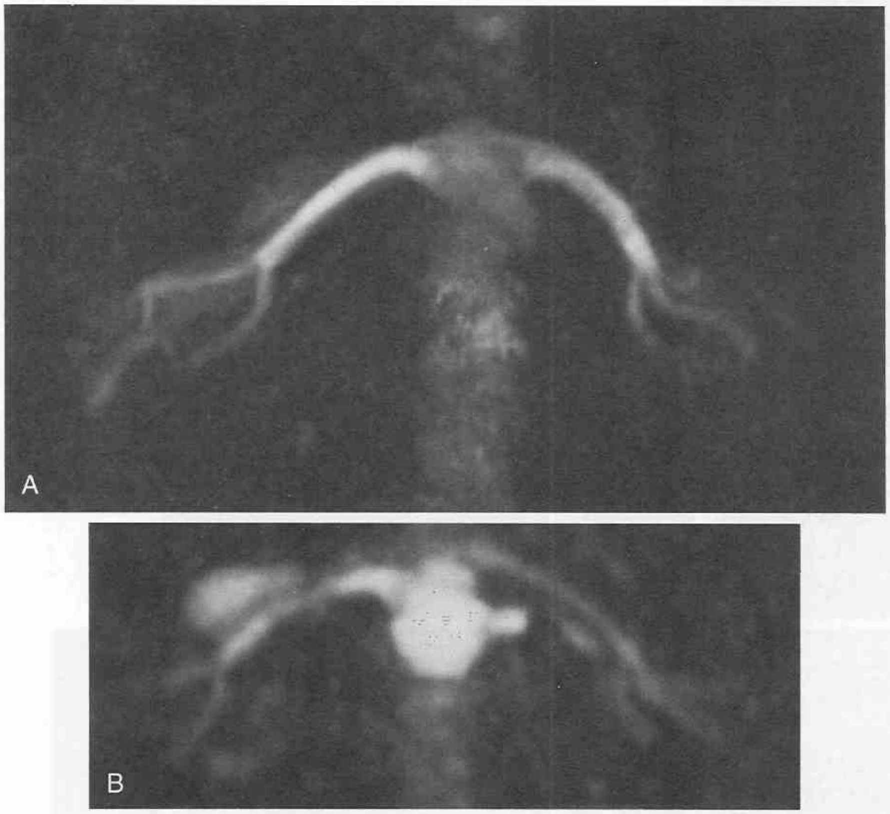

Figure 3–53. Images were obtained using a 3D phase contrast technique, which included 32 slices with 2-mm-thick partitions, a 128 × 256 matrix, and 24-cm field of view, TR = 34 msec, and TE = 9 msec. The velocity-encoding (VENC) value was equal to 40 cm/second and two averages were used. Three-directional velocity encoding was used and resulted in an 18-minute data acquisition time. *A*, A normal pair of renal arteries. *B*, Stenosis of the right renal artery. (Courtesy of Thomas M. Grist, University of Wisconsin.)

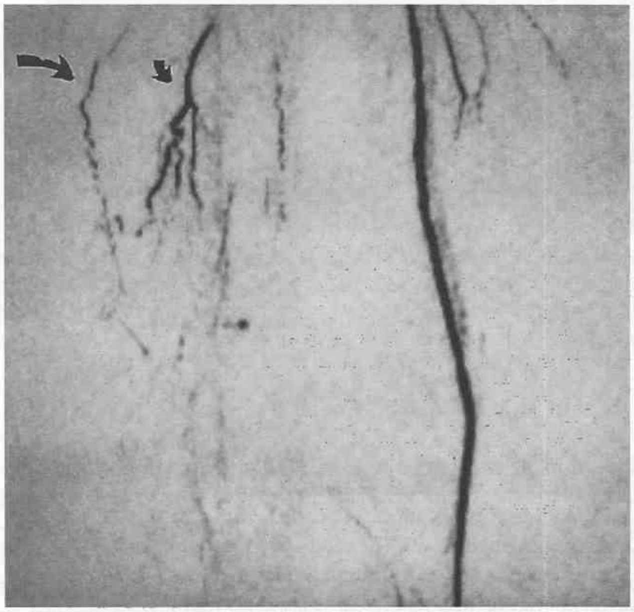

Figure 3–54. Occluded right superficial femoral artery. Coronal cine phase contrast MRA study: TR/TE, 24/11, 30 degrees, superior inferior flow encoding, velocity-encoding (VENC) value = 60 cm/second, 40 cm-field of view. The approximate acquisition time was 2 minutes 20 seconds. This image used a projection-dephasing gradient so that the slice thickness was infinite. Note the collateral flow in the right profunda femoral artery *(small arrow)* and the deep muscular branch collateral *(larger arrow)*. (Courtesy of Fred Steinberg, M.D., Magnetic Resonance Institute of Boca Raton, Fla.)

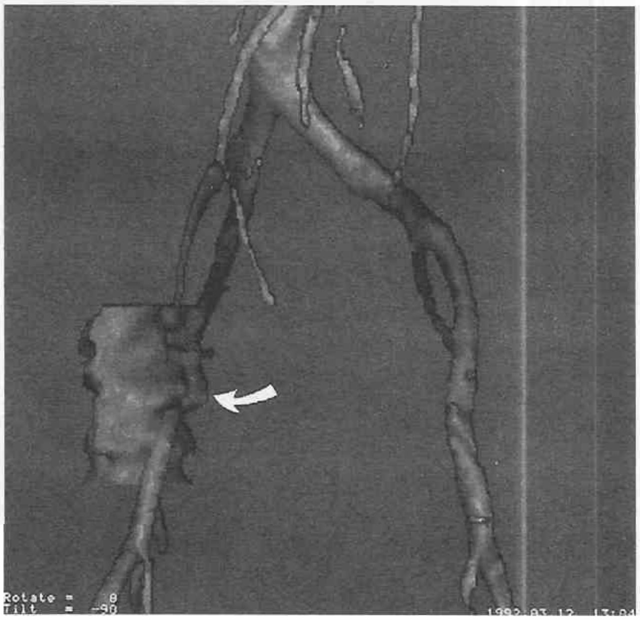

Figure 3–55. Encasement of the right iliac vein by metastatic lymph node. Coronal projection of 2D time-of-flight MRA study with arterial presaturation. This color-encoded image shows the mass *(white arrow)* encasing the iliac vein in this patient with right leg swelling. (Courtesy of Fred Steinberg, M.D., Magnetic Resonance Institute of Boca Raton, Fla.)

Figure 3–56. Dynamic contrast-enhanced image of the neck and aortic arch acquired in 18 seconds. (Courtesy of Paul Finn, M.D., Northwestern University, Chicago.)

Figure 3–58. Contrast-enhanced image of the left coronary artery system, including the left main coronary artery, a portion of the circumflex artery, and the left anterior descending artery and its first branching into secondary vessels. Other portions of the heart and pulmonary system are also visible in the image. These data were collected in a breath-hold after the injection of a T1-reducing contrast agent. (Courtesy of Debiao Li, Ph.D., Washington University, St. Louis.)

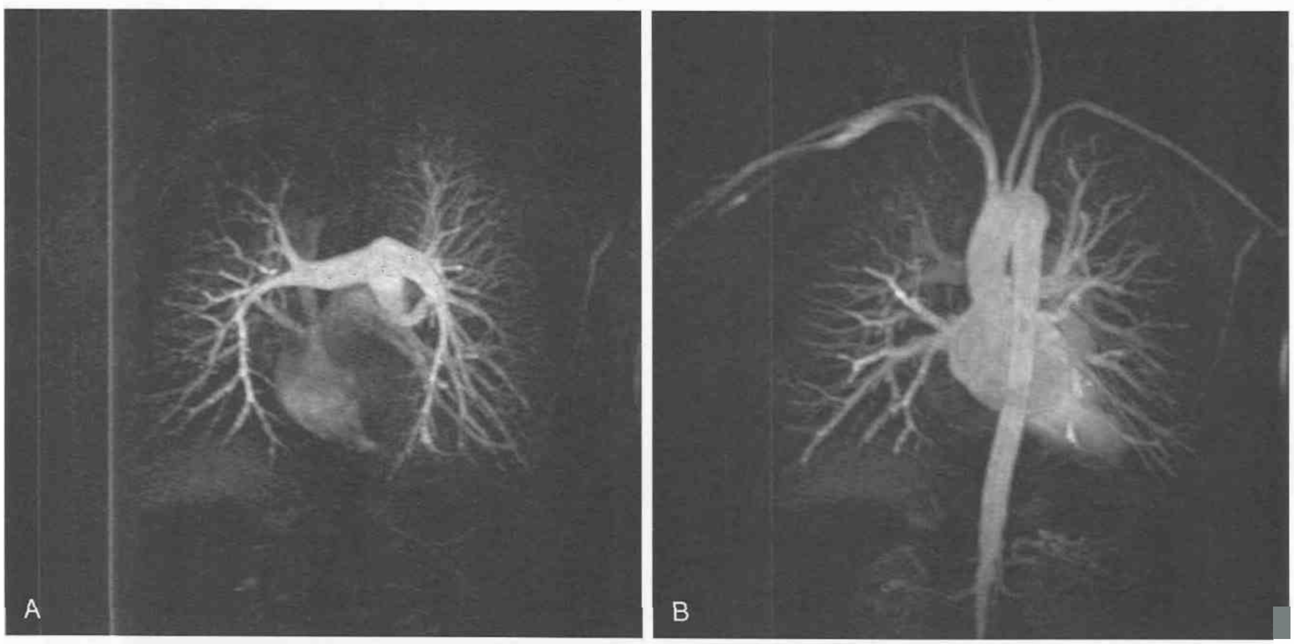

Figure 3–57. Dynamic contrast-enhanced images of the pulmonary system immediately after injection *(top)* and 10 seconds after injection *(bottom)*. Each scan is acquired in a short breath-hold. (Courtesy of Paul Finn, M.D., Northwestern University, Chicago.)

Figure 3–59. Contrast-enhanced image of the peripheral vessels. This data set has a resolution of 0.5 mm × 0.5 mm × 0.7 mm and took roughly 10 minutes to collect. Because the collection was conducted with central reordering, the veins do not show up as bright (except for their edges).

larger λ is, the stronger the cancellation. A series of these images is viewed using a minimum intensity projection to show the connectivity of the venous vessels.

An example of this method along with a contrast-enhanced image for comparison is shown in Figure 3–60. Figure 3–60*A* represents a minimum intensity projection over five 2-mm slices from this venographic technique. Figure 3–60*B* represents a maximum intensity projection over the same region from a T1-weighted data set acquired after injection of contrast material.

Future Directions

MRA has come a long way since the mid-1980s. Much of its progress is due to the ingenuity of the many investigators who have contributed to this field. A great deal is also owed to the developments of better gradients and the ability to image significantly faster than before. But the real progress comes with the combination of the hardware and the methodology with the new high-relaxivity contrast agents. This advance opens the door to continued new

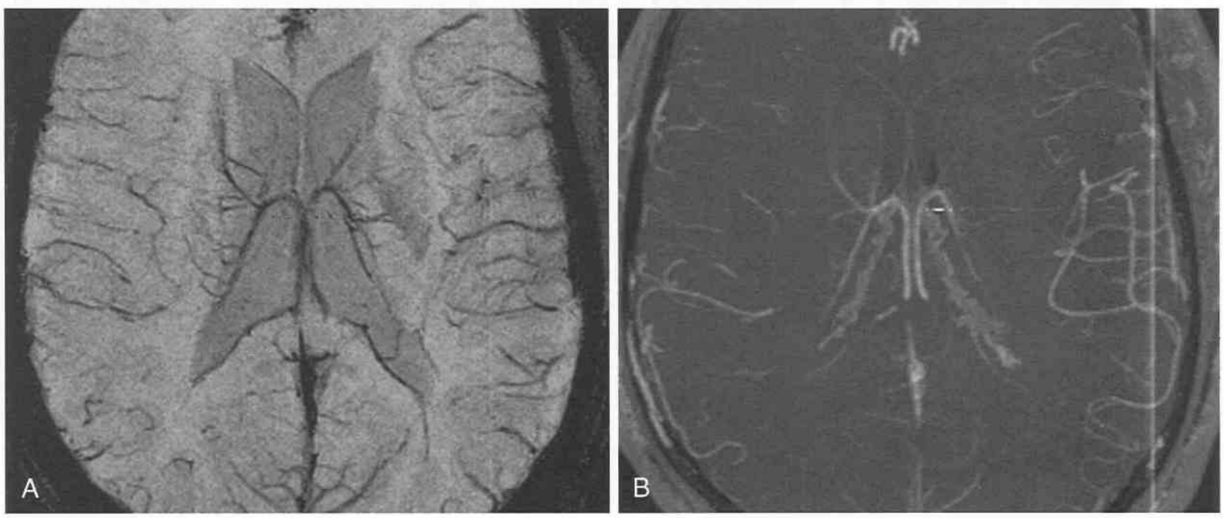

Figure 3–60. *A*, Minimum intensity projection over five 2-mm slices from the blood oxygenation level–dependent (BOLD) venographic technique. *B*, Maximum intensity projection over the same region from a T1-weighted data set acquired after contrast injection.

developments in the field, faster acquisition of data, better resolution, and availability of more functional information. From measuring flow to visualizing coronary arteries, MRI is making it possible to create the "vascular-visible" human (see www.mrimaging.com).

References

1. Anderson CM, Edelman RR, Turski PA: Clinical Magnetic Resonance Angiography. New York, Raven Press, 1993.
2. Anderson CM, Saloner D, Tsuruda JS, et al: Artifacts in maximum-intensity-projection display of MR angiograms. AJR Am J Roentgenol 154:623–629, 1990.
3. Belliveau JW, Kennedy DN, McKinstry RC, et al: Functional mapping of the human visual cortex by magnetic resonance imaging. Science 254:716–719, 1991.
4. Belliveau JW, Rosen BR, Kantor HL, et al: Functional cerebral imaging by susceptibility contrast NMR. Magn Reson Med 14:538–546, 1990.
5. Bendel P, Buonocore E, Bockisch A, et al: Blood flow in the carotid arteries: Quantification by using phase-sensitive MR imaging. AJR Am J Roentgenol 152:1307–1310, 1989.
6. Blatter DD, Parker DL, Ahn SS, et al: Cerebral MR angiography with multiple overlapping thin slab acquisition. Part II. Early clinical experience. Radiology 183:379–389, 1992.
7. Blatter DD, Parker DL, Robinson R: Cerebral MR angiography with multiple overlapping thin slab acquisition. Part I. Quantitative analysis of vessel visibility. Radiology 179:805–811, 1991.
8. Chakeres DW, Schmalbrock P, Brogan M, et al: Normal venous anatomy of the brain: demonstration with gadopentetate dimeglumine in enhanced 3D MR angiography. AJR Am J Roentgenol 156:161–172, 1991.
9. Cline HZ, Dumoulin CL, Lorensen WE, et al: Volume rendering and connectivity algorithm for MR angiography. Magn Reson Med 18: 384–394, 1991.
10. Cline HZ, Lorensen WE, Kikinis R, et al: Three-dimensional segmentation of MR images of the head using probability and connectivity. J Comput Assist Tomogr 14:1037–1045, 1990.
11. Creasy JL, Price RR, Presbrey T, et al: Gadolinium-enhanced MR angiography. Radiology 175:280–283, 1990.
12. Dixon WT: Simple proton spectroscopic imaging. Radiology 153: 189–194, 1984.
13. Dixon WT: Use of magnetization transfer contrast in gradient-recalled echo images. Radiology 179:15–16, 1991.
14. Dumoulin CL, Souza SP, Walker MF, et al: Three dimensional phase contrast angiography. Magn Reson Med 9:139–149, 1989.
15. Dumoulin CL, Souza SP, Walker MF, et al: Time-resolved magnetic resonance angiography. Magn Reson Med 6:275–286, 1988.
16. Edelman RR, Ahn SS, Chien D, et al: Improved time-of-flight MR angiography of the brain with magnetization transfer contrast. Radiology 184:395–399, 1992.
17. Edelman RR, Chien D, Kim D: Fast selective black blood imaging. Radiology 181:655–660, 1991.
18. Edelman RR, Mattle HP, Wallner B, et al: Extracranial carotid arteries: evaluation with "black blood" MR angiography. Radiology 177: 45–50, 1990.
19. Feinberg DA, Crooks LE, Hoenninger J, et al: Pulsatile blood velocity in human arteries displayed by magnetic resonance imaging. Radiology 153:177–180, 1984.
20. Feinberg DA, Crooks LE, Sheldon P, et al: Magnetic resonance imaging the velocity vector components of fluid flow. Magn Reson Med 2:555–566, 1985.
21. Frahm J, Bruhn H, Merboldt K-D, et al: Dynamic MR imaging of human brain oxygenation during rest and photic stimulation. J Magn Reson Imaging 2:501–505, 1992.
22. Frahm J, Merboldt K-D, Hanicke W: Functional MRI of human brain activation at high spatial resolution. Magn Reson Med 29: 139–144, 1992.
23. Haacke EM, Brown RW, Thompson MR, Venkatesan R. Magnetic Resonance Imaging: Physical Principles and Sequence Design. New York, John Wiley & Sons, 1999.
24. Haacke EM, Lenz GW: Improving MR image quality in the presence of motion by using rephasing gradients. AJR Am J Roentgenol 148: 1251–1258, 1987.
25. Haacke EM, Lindskog E, Lin W: Partial-Fourier imaging: a fast, iterative, POCS technique capable of local phase recovery. J Magn Reson 126–145, 1991.
26. Haacke EM, Masaryk TJ, Wielopolski PA, et al: Optimalizing blood vessel contrast in fast 3D MRI. Magn Reson Med 14:102–121, 1990.
27. Haacke EM, Patrick JL, Lenz GW, et al: The separation of water and lipid components in the presence of field inhomogeneities. Rev Magn Reson Med 1:123–154, 1986.
28. Hardy CJ, Pearlman JD, Moore J, et al: Continuous cardiography with a half-echo MR M-mode method. In SMRM 10th Annual Meeting, Book of Abstracts, vol 1. New York, 1990, p 280.
29. Henning J, Mueri M, Brunner P, et al: Quantitative flow measurement with the fast Fourier flow technique. Radiology 166:237–240, 1988.
30. Hu X, Alperin N, Levin DN, et al: Visualization of MR angiographic data with segmentation and volume-rendering techniques. J Magn Reson Imaging 1:539–546, 1991.
31. Keller PJ, Hunter WW, Schmalbrock P: Multislice fat-water imaging with chemical shift selective presaturation. Radiology 164:539–541, 1987.
32. Krug B, Kugel H, Friedmann G, et al: MR imaging of poststenotic flow phenomena: experimental studies. J Magn Reson Imaging 1: 585–591, 1991.
33. Kwait D, Elnav S, Elad D: A magnetic resonance imaging method of flow by successive excitation of moving slice. Med Phys 17: 258–263, 1990.
34. Laub GW, Kaiser WA: MR angiography with gradient motion refocusing. J Comput Assist Tomogr 12:377–382, 1988.
35. Laub GW, Purdy DE: Variable-tip-angle slab selection for improved three-dimensional MR angiography. In SMRI 10th Annual Meeting, Book of Abstracts, 1992, Chicago, p 167.
36. Lin W, Haacke EM, Masaryk TJ, et al: Automated local maximum-intensity projection with three-dimensional vessel tracking. J Magn Reson Imaging 2:519–526, 1992.
37. Lin W, Haacke EM, Smith AS: Lumen definition in MR angiography. J Magn Reson Imaging 1:327–336, 1991.
38. Lin W, Haacke EM, Smith AS, et al: High resolution magnetic resonance angiography using gadopentetate dimeglumine with adaptive vessel tracking: preliminary results in studying the intracranial circulation. J Magn Reson Imaging 2:277–284, 1992.
39. Lin W, Tkach JA, Haacke EM, et al: Intracranial MR angiography: Application of magnetization transfer contrast and fat saturation to short gradient-echo, velocity-compensated sequences. Radiology 186: 753–761, 1993.
40. Maki JH, Prince MR, Londy FJ, Chenevert TL: The effects of time varying intravascular signal intensity and k-space acquisition order on three-dimensional MR angiography image quality. J Magn Reson Imaging 6:642–651, 1996.
41. Masaryk TJ, Modic MT, Ross JS, et al: Intracranial circulation: Preliminary clinical results with three-dimensional (volume) MR angiography. Radiology 171:793–799, 1989.
42. Matsuda T, Shimizu K, Sakurai T, et al: Spin-echo M-mode NMR imaging. Magn Reson Med 27:238–246, 1992.
43. Mueller E, Laub G, Grauman R, et al: RACE—real time acquisition and evaluation of pulsatile blood flow on a whole body MRI unit. In SMRM 7th Annual Meeting, Book of Abstracts. San Francisco, 1988, p 729.
44. Nishimura DG, Macovski A, Pauly JM: Magnetic resonance angiography. IEEE Trans Med Imaging MI-5:140–151, 1986.
45. Parker DL, Yuan C, Blatter DD: MRA angiography by multiple thin slab 3D acquisition. Magn Reson Med 17:434–451, 1991.
46. Pelc NJ, Shimakawa A, Glover GH: Phase contrast cine MRI. In SMRM 8th Annual Meeting, Book of Abstracts, Amsterdam, The Netherlands, 1989.
47. Pettigrew RI, Dannels W, Galloway JR, et al: Quantitative phase-flow MR imaging by using standard comparison with in vivo flow-meter measurement. AJR Am J Roentgenol 148:411–414, 1987.
48. Pike GB, Hu BS, Glover GH, et al: Magnetization transfer time-of-flight magnetic resonance angiography. Magn Reson Med 25: 372–379, 1992.
49. Potchen EJ, Haacke EM, Siebert JE, Gottschalk A (eds): Magnetic Resonance Angiography: Concepts and Applications, St. Louis, CV Mosby, 1993.
50. Prince MR, Yucel EK, Kaufman JA, et al: Dynamic gadolinium-enhanced 3D abdominal MR arteriography. J Magn Reson Imaging 3:877–881, 1993.
51. Reichenbach JR, Venkatesan R, Schillinger D, et al: Small vessels in

the human brain: MR venography with deoxyhemoglobin as an intrinsic contrast agent. Radiology 204:272–277, 1997.
52. Revel D, Loubeyre P, Delignette A, et al: Contrast-enhanced magnetic resonance tomoangiography: A new imaging technique for studying thoracic great vessels. Magn Reson Imaging 11:1101–1105, 1993.
53. Saloner D, Hanson WA, Tsuruda JS, et al: Application of a connected-voxel algorithm to MR angiographic data. J Magn Reson Imaging 1: 423–430, 1991.
54. Schmalbrock P, Yuan C, Chakeres DW, et al: Volume MR angiography: Methods to achieve very short echo times. Radiology 175: 861–865, 1990.
55. Smith AS, Haacke EM, Lin W, et al: Carotid MR angiography: Technique for improved maximal intensity projection resolution and decreased cost. In 76th Scientific Assembly and Annual Meeting of the Radiological Society of North America, Oak Brook, Ill, Book of Abstracts, 1990, p 89.
56. Smith AS, Lin W, Haacke EM, et al: Cerebrovascular high resolution MR angiography—techniques application. In Book of Abstracts, vol 2, Tenth Annual Meeting in SMRM, 1991, p 938.
57. Thomsen C, Stahlbert F, Stubgarrd M, et al: Fourier analysis of cerebrospinal fluid flow velocities: MR imaging study. Radiology 177:659–665, 1990.
58. Tkach JA, Lin W, Masaryk TJ, et al: The use of spatial and/or temporal modulation of the excitation flip angle to reduce blood saturation in 3D TOF MRA of the ICV's. In SMRI 11th Annual Meeting, Book of Abstracts, 1992, p 3124.
59. Underwood SR, Firmin DN, Klipstein RH, et al: Magnetic velocity mapping: Clinical application of a new technique. Br Heart J 57: 404–412, 1987.
60. Venkatesan R, Haacke EM: Role of high resolution in magnetic resonance (MR) imaging: Applications to MR angiography, intracranial T1-weighted imaging, and image interpolation. Int J Imaging Systems Technol 8:529–543, 1997.
61. Wehrli FW, Perkins TG, Shimakawa A, et al: Chemical shift–induced amplitude modulations in images obtained with gradient refocusing. Magn Reson Imaging 5:157–158, 1987.
62. Wilman AH, Riederer SJ, King BF, et al: Fluorscopically triggered contrast-enhanced 3D MR angiography with elliptical centric view order: Application to the renal arteries. Radiology 205:137–146, 1997.
63. Wolff SD, Balaban RS: Magnetization transfer contrast (MTC) and tissue water proton relaxation in vivo. Magn Reson Med 10:135–144, 1989.
64. Wolff SD, Eng J, Balaban RS: Magnetization transfer contrast: Method for improving contrast in gradient-recalled echo images. Radiology 179:133–137, 1991.

Part II

Brain and Meninges

Edited by
Charles Lanzieri

4 Normal Computed Tomography and Magnetic Resonance Imaging Anatomy of the Brain and the Spine

M. Hossain Naheedy

CT and MRI Anatomy of the Brain

In this section of the chapter, a brief review of the gross surface anatomy precedes the explanation of computed tomography (CT) and magnetic resonance imaging (MRI) techniques and is followed by a discussion of sectional anatomy in multiplanar axes, as seen in these two modalities.

Overview of Surface Anatomy[10, 21, 33, 34]

Dura and Dural Structures

The brain substance is covered by cerebrospinal fluid (CSF) to allow the brain to float in the intracranial cavity of the calvarium. The brain is separated from the calvarium by pia mater, arachnoid membrane, and dura mater. The pia mater follows all the gyri and is separated from the arachnoid membrane by CSF. The outer layer of the dura is attached to the periosteum of the bony calvarium. The dura is separated from the arachnoid membrane by potential subdural space. The dural sinuses are venous structures made between the dural reflections and their opposing edges, thereby forming the superior and inferior sagittal, transverse, sigmoid, cavernous, and straight sinuses. These sinuses drain to the jugular venous system.

Ventricles

There are four ventricles within the brain that contain choroid plexus–producing CSF.

Lateral Ventricles

Traditionally, the left lateral ventricle is labeled first, followed next by the right lateral ventricle. The two lateral ventricles join to the third ventricle via the midline foramen of Monro (Fig. 4–1). The lateral ventricles are open C-shaped cavities extending from front to back within deep brain tissue. They are covered by a layer of ependymal cells, forming inner walls.

The anterior extensions into the frontal lobes are called *frontal horns*. The frontal horns are separated from each other midline by the septum pellucidum. Sometimes a cavity exists between the two layers of septum, which produces the cavum septi pellucidi, most commonly seen in early infancy. Posterior extension of this cavity between the two lateral ventricles produces the cavum vergae, which unites with the subarachnoid spaces behind the pineal region. The frontal horns are outlined laterally by the head of the caudate nuclei.

Anteriorly, the frontal horns are bound by the genu of the corpus callosum. The body of the lateral ventricles extends posteriorly over the corpus callosum and is outlined by the body of the caudate nuclei. The posterior extension of the body of the lateral ventricles forms the occipital horns.

Medially, the occipital horns are bound by the splenium of the corpus callosum, causing the peculiar shape of the occipital horns. The temporal horns are the extension of the lateral ventricles into the temporal lobes. The place where the temporal and occipital horns and the body of the lateral ventricles meet is called the *atrium* and is the most expanded part of the lateral ventricles. The main portion of the choroid plexus is located in the atrium, with some portions extending into the temporal and occipital horns.

Third Ventricle

The third ventricle is a midline structure situated between the two thalami. Anteriorly, the floor of the third ventricle is formed by the tuber cinereum; posteriorly, it is bounded by the cerebral peduncles. The roof of the third ventricle is formed by the velum interpositum. Occasionally, a cavity exists between these two layers of velum, forming the cavum velum interpositum, which is readily visible in coronal and sagittal MRI studies.

Fourth Ventricle

The fourth ventricle is located in the posterior fossa between the pons and cerebellum. The fourth ventricle is

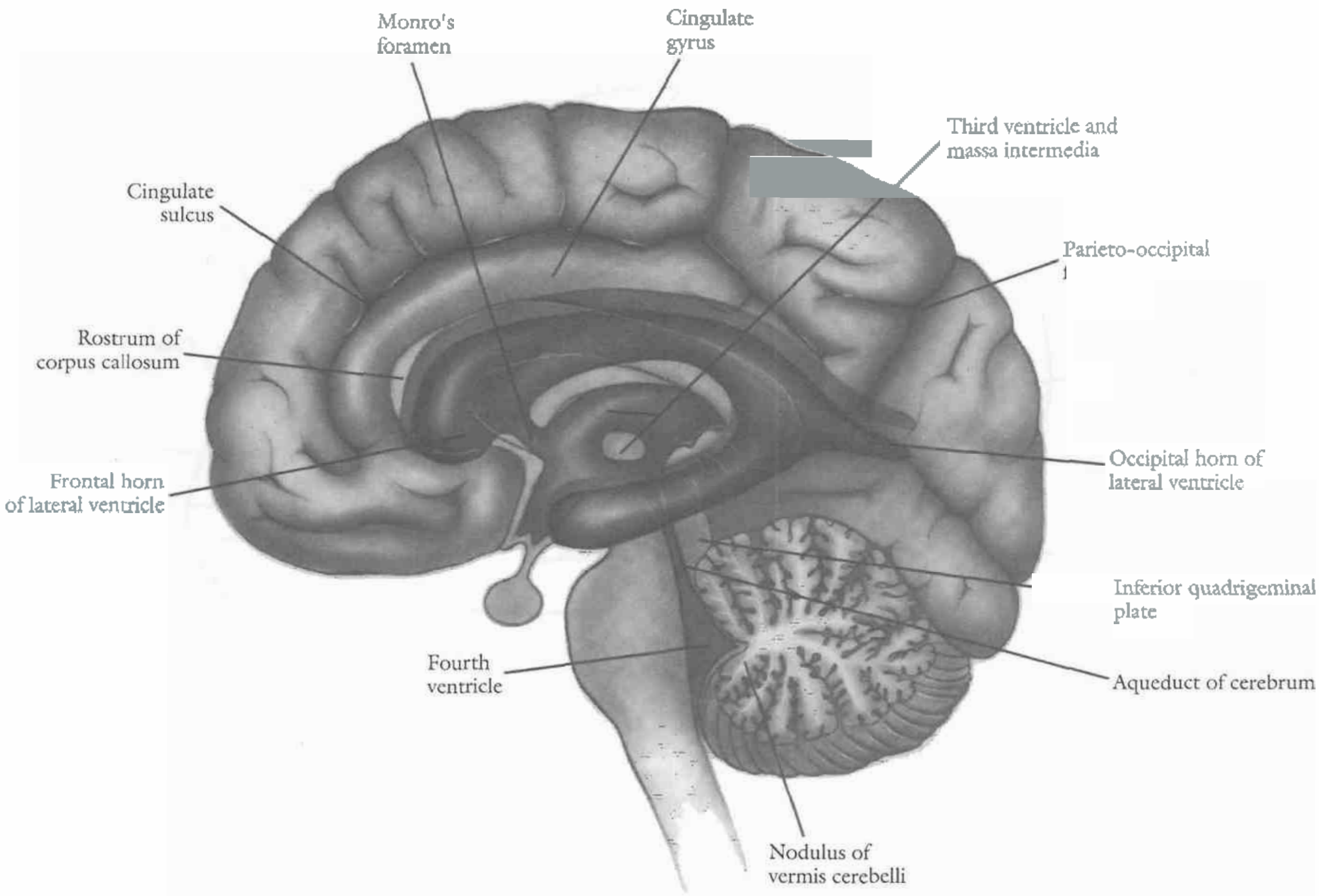

Figure 4–1. Medial surface of the brain.

connected to the third ventricle via the cerebral aqueduct. CSF, which is excreted by the choroid, flows from the lateral ventricles to the third ventricle and from there to the fourth ventricle, exiting the ventricles (via the foramen of Magendie in midline and the foramen of Luschka on either side of the fourth ventricle) to drain into the cisterna magna.

Cerebral Hemispheres[10, 15]

The two cerebral hemispheres are separated by interhemispheric fissures and falx cerebri. The deep fissures separate the lobes, and the sulci separate the adjacent gyri. On the lateral surface of the brain, the sylvian fissure begins anteriorly and inferiorly, separating the frontal lobe as it extends posteriorly and superiorly.

The rolandic fissure (central fissure) starts from the superior midhemisphere and extends anteriorly and inferiorly to separate the frontal lobe from the parietal lobe, ending at the junction of the anterior and middle thirds of the sylvian fissure over the lateral surface of the brain. There is no anatomic landmark to separate the occipital lobe from the parietal lobe. Three sulci over the lateral surface of the frontal lobe divide it into superior, middle, and inferior frontal gyri. Two small sulci divide the lower frontal lobe into the orbital, opercular, and triangular gyri.

Two transverse sulci divide the temporal lobe into superior, middle, and inferior temporal gyri. Heschl's gyrus is located anterolateral over the upper superior temporal gyrus and inferior to the sylvian fissure. The postcentral sulcus separates the postcentral gyrus from the remainder of the parietal lobe. The precentral sulcus separates the precentral gyrus from the remainder of the frontal lobe. The transverse sulcus divides the parietal lobe into superior and inferior parietal gyri.

On the medial aspect, the two hemispheres are connected by the corpus callosum. The callosal fissure separates the corpus callosum from the cingulate gyrus, and it is separated from the frontal lobe by the cingulate sulcus. On the medial aspect, the frontal lobe has several sulci separating the orbitofrontal, frontal polar, anterior inferior frontal, middle internal frontal, and posterior interior frontal gyri (Fig. 4–2). In the parietal bone, the marginal sulcus separates the paracentral lobule from the superior parietal lobe. On the medial aspect, the occipital lobe is separated from the parietal lobe by the parieto-occipital sulcus. The hippocampal gyrus is located between the medial aspect of the temporal lobe and the lateral aspect of the midbrain. The hippocampal gyrus is separated from the parahippocampal gyrus by the hippocampal sulcus. These two gyri unite to form the uncus of the temporal lobe.

Hemispheric White Matter

The axons of the neurons from the cerebral cortex and basal ganglia form the white matter. Some white matter

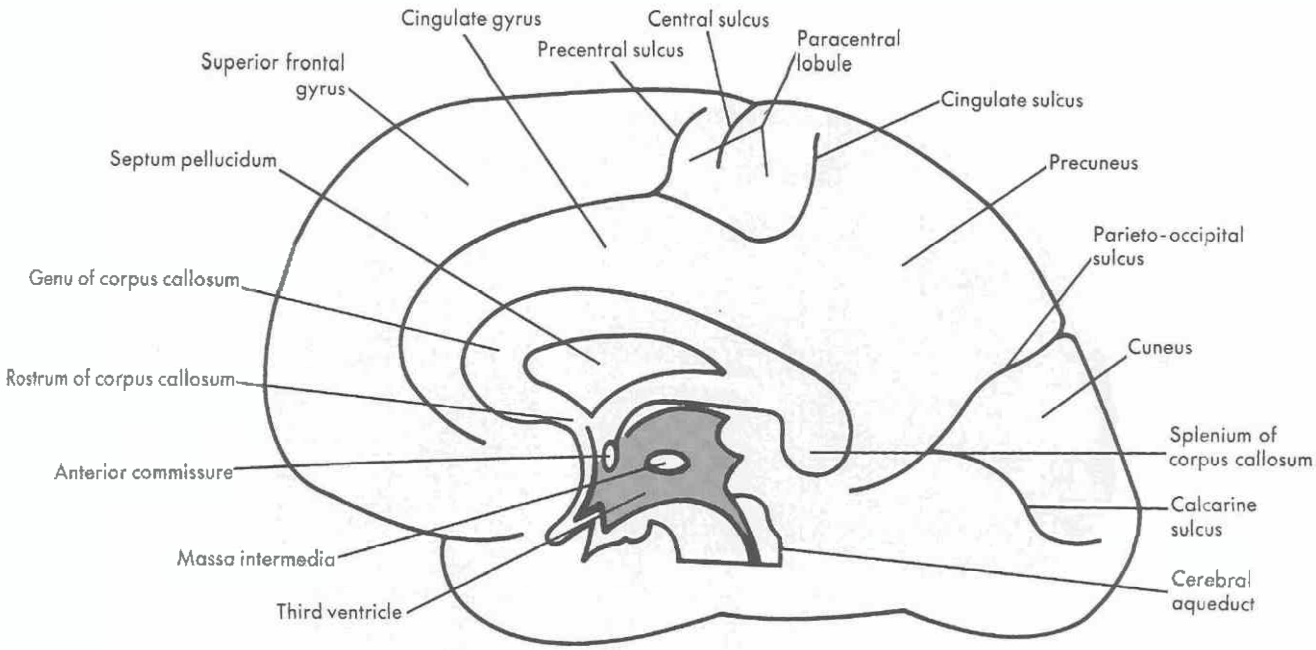

Figure 4–2. Medial surface of the cerebral hemisphere.

fibers connect the adjacent lobes, and some connect the two hemispheres.

The interhemispheric commissures are the following:

1. Anterior commissure, connecting the temporal lobes.
2. Posterior commissure, connecting the rostral midbrain nuclei, located behind the third ventricle.
3. Corpus callosum, a large commissure connecting the two hemispheres: it is located over the lateral ventricles and extends anteroposteriorly from the fornices, genu, body, and splenium.

The intrahemispheric commissures are the following:

1. Visual radiations, connecting the lateral geniculate bodies to the occipital lobes.
2. Superior longitudinal fasciculus, connecting the occipital lobes to the parietal and frontal lobes.
3. Arcuate fasciculus, connecting the temporal lobe to the superior longitudinal fasciculus.
4. Cingulate fibers, connecting the cingulate gyrus to the middle temporal gyrus.
5. Fornix, connecting the hippocampus to the ipsilateral mammillary body.

Posterior Fossa (Fig. 4–3)

The posterior fossa contains the cerebellum, brain stem, pons, and medulla, and it is outlined by the clivus, petrous, and occipital bones. The superior boundary of the posterior fossa is the tentorium cerebelli, which opens into the tentorial notch, permitting the connection of the infratentorial structures to the supratentorial structures. The posterior fossa is divided into two compartments by the fourth ventricle. Anteriorly, the brain stem occupies about one third of the posterior fossa; posteriorly, the cerebellum occupies the posterior two thirds.

The brain stem has three anatomically recognizable components: (1) midbrain, (2) pons, and (3) medulla.

The *midbrain* consists of cerebral peduncles anteriorly and colliculi posteriorly. The cerebral peduncles are separated from each other by the interpeduncular fossa, a CSF-filled space that merges with the suprasellar cistern. The basilar artery lies in this fossa. In the dorsal aspect of the cerebral peduncles are four nubbins of colliculi, outlined by the quadrigeminal cistern. This cistern extends laterally and anteriorly to merge with the perimesencephalic cistern. Superiorly, this space is limited by the tentorium and the great vein of Galen. Anteriorly, this space is connected to the velum interpositum over the top of the third ventricle. This space as well as the interpeduncular fossa should almost always be visible on axial CT or MRI scans. Any asymmetry of the quadrigeminal plate cistern is indicative of a mass effect.

The *pons* is characterized by anterior bulging, which is caused by the middle cerebellar peduncles and the pontocerebellar connections. Laterally, the pons rests against the medial posterior aspect of the petrous bone. There is a CSF-filled space between the lateral aspect of the pons and the anterior aspect of the cerebellum (floccular lobules), called the *cerebellopontine angle* (CPA). The seventh and eighth cranial nerves cross this space to enter the internal auditory meatus. In the most caudal aspect, the ninth and tenth cranial nerves cross this space; superiorly, the fifth nerve crosses it.

The *medulla* is the most caudal portion of the brain stem and connects to the cervical cord at the level of the foramen magnum. The medulla is separated from the pons by the transverse sulcus. The pyramids and other longitudinal tracts cause minimum anterior bulging in the long axis on the ventral surface of the medulla, making its appearance different from the pons. The inferior cerebellar peduncle makes the superior protrusion on the lateral aspect of the medulla.

The two cerebellar hemispheres are joined by the midline structure of the vermis. Transverse fissures and sulci

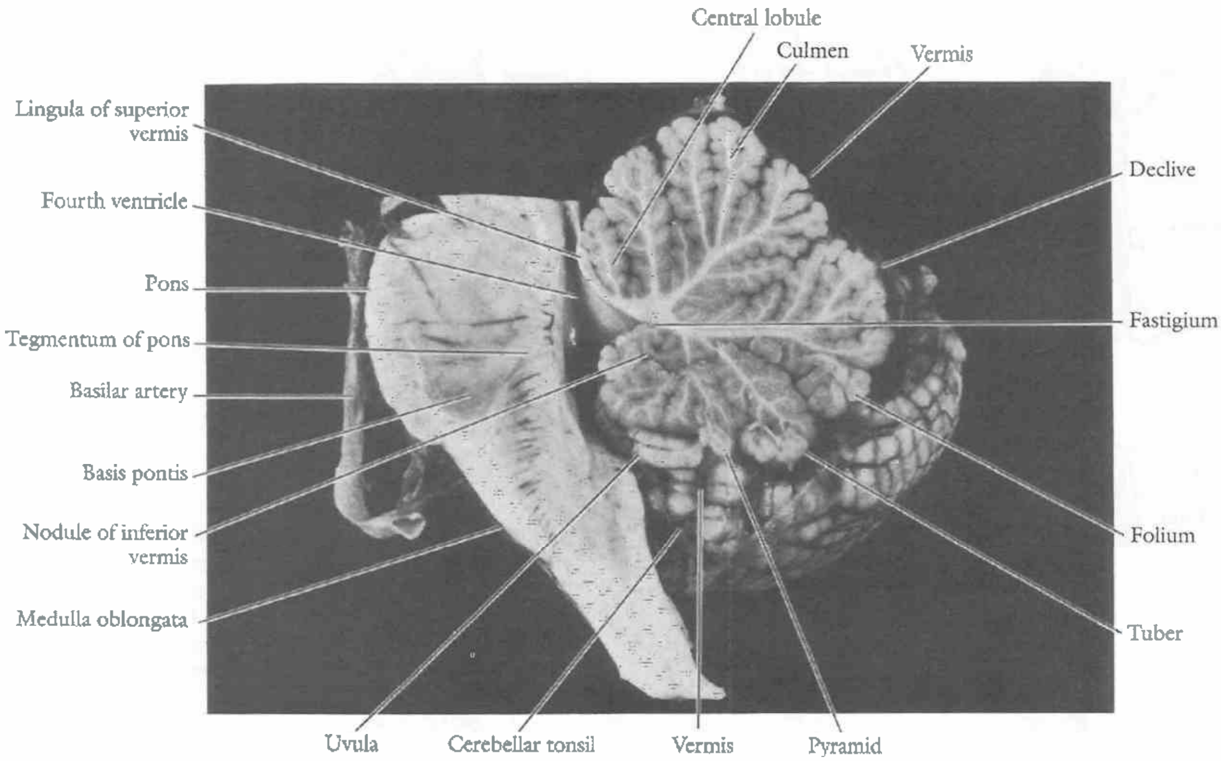

Figure 4–3. Sagittal section of the hind brain.

(cerebellar folia) separate the laminae. The anterosuperior fissure (primary fissure) divides the cerebellum into anterior and posterior lobes. The posterior lobe is divided by another major fissure (the posterolateral fissure) in the flocculonodular and nodular lobules.

Vascular Supply[1, 10, 14, 21]

The brain derives its vascular supply (Fig. 4–4) via two carotid and two vertebral arteries. The internal carotid artery, after giving off the ophthalmic branch and posterior communicating and anterior choroidal arteries in the supraclinoid portion, divides into the anterior and middle cerebral arteries. The anterior cerebral artery supplies blood mainly to the frontal lobe medially and mediolaterally, with some supply to the parasagittal parietal lobe. The lenticulostriate arteries, arising from the horizontal portion of the anterior cerebral artery, supply the medial basal ganglia and part of the internal capsule. The anterior choroidal branch of the internal carotid artery supplies the remaining portion of the internal capsule as well as the choroid plexus. The lenticulostriate arteries, arising from the horizontal portion of the middle cerebral artery, supply the lateral basal ganglia. At this juncture, the middle cerebral artery branches in the anterior inferior sylvian fissure into two or three branches that supply the temporal and parietal lobes. The posterior cerebral arteries, terminal branches of the basilar artery, supply the occipital lobes. The thalamoperforate arteries, arising from the posterior communicating artery and the most proximal portion of the posterior cerebral arteries, supply the thalami. The posterior temporal branch of the posterior cerebral artery supplies the posterior temporal lobe.

On axial CT scans, one can readily delineate the vascular territory by drawing a line along the anterior and posterior course of the lateral border of the lateral ventricles (see Fig. 4–4). The area between the anterior portion of the interhemispheric fissure and a line along the anterior lateral wall of the lateral ventricle is the anterior cerebral territory. The area between the posterior portion of the interhemispheric fissure and a line along the posterior lateral wall of the lateral ventricle is the posterior cerebral territory. The area between the lines along the lateral ventricle wall is the middle cerebral territory.

In high-convexity slices above the ventricular levels, almost all parasagittal areas of the frontal and parietal lobes are supplied by branches of the anterior cerebral artery, with the small portion in the posterior medial area supplied by the branches of the posterior cerebral artery. The ill-defined anterior area between the anterior cerebral artery and the middle cerebral artery is called the *anterior watershed region*. The posterior watershed area lies between the territory of the middle cerebral and posterior cerebral arteries. These two areas are more susceptible to hypotensive infarctions than other areas of the brain are.

In the posterior fossa, the inferior vermis, inferior cerebellar hemispheres, and choroid plexus of the fourth ventricle are supplied by the posterior inferior cerebellar artery and its branches, which arise from the vertebral artery before or at about the level of the foramen magnum. The area of the CPA and the anterior inferior cerebellar hemispheres are supplied by the branches of the anterior inferior cerebellar artery, which is a branch of the basilar artery. The perforator branches of the basilar artery supply the pons. The superior cerebellar arteries, arising from the

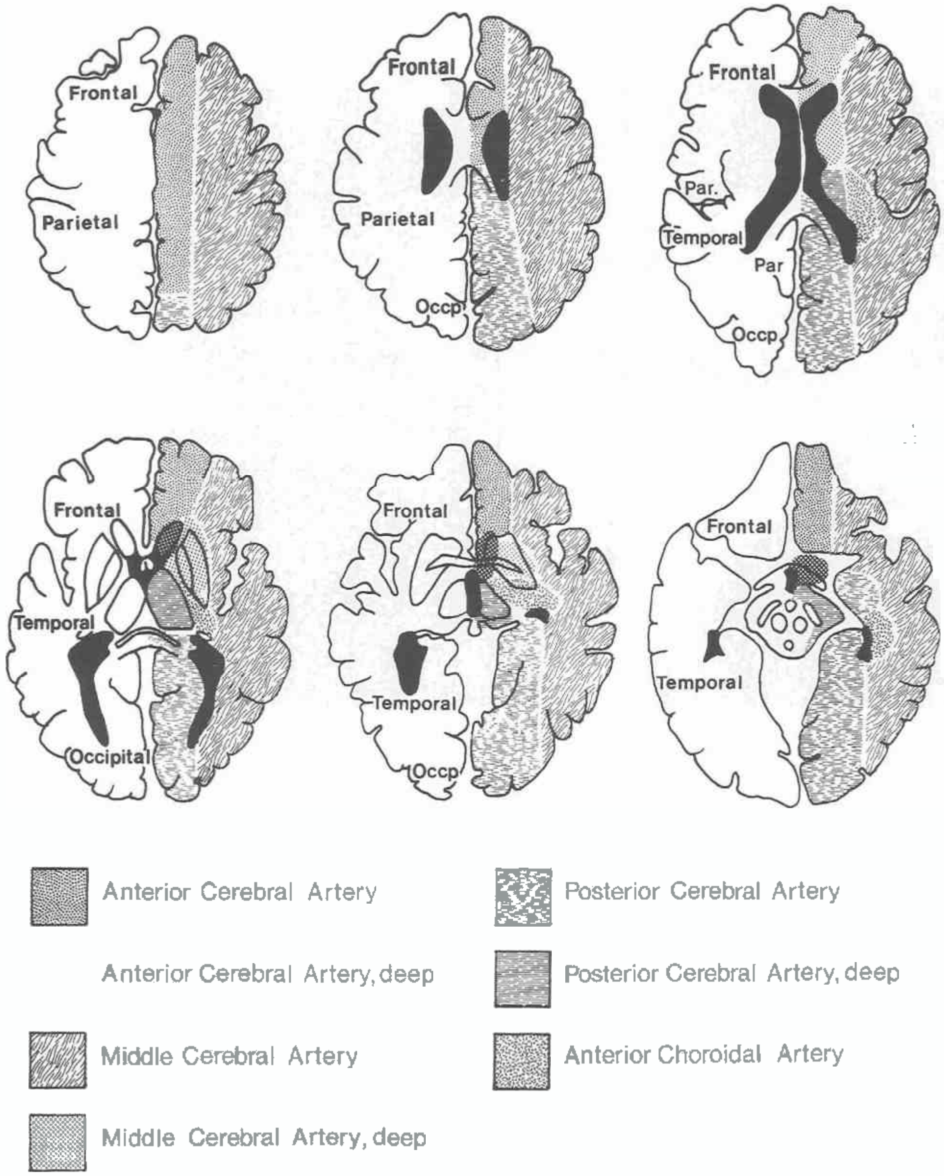

Figure 4–4. Demonstration of vascular territories on axial images. (Modified from Gonzalez C, Grossman CB, Masdeu JC: Head and Spine Imaging. New York, Churchill Livingstone, 1985, p 145.)

basilar artery, supply the superior portion of the cerebellar hemispheres.

CT Technique[11, 22, 36]

Routine head CT is performed in an axial axis with a 15- to 20-degree angulation of the gantry to the canthomeatal line. This angulation decreases radiation to the eyes. There has been a tendency, on CT scans, to reduce this angle parallel to the canthomeatal line to match the MRI slices. The latter technique is preferred in axial imaging of the orbits and the sellar region. Slice thickness varies among different scanners and can be adjusted according to the area of interest. In routine studies, slices 8 to 10 mm thick are used. In evaluation of the orbits, the pituitary gland, the suprasellar and parasellar regions, and the CPA, thinner slices—1.5 to 3 mm thick—are needed. In these situations, coronal CT scans are also essential. Using the bony algorithm is highly important to review the bony detail in evaluating trauma patients with facial bone and petrous bone diseases.

Contrast Studies

Except in acute trauma, excluding bleed in acute stroke, hydrocephalus, and follow-up of trauma patients, the use of intravenous (IV) contrast medium is routine. At least 100 mL, preferably 150 mL, of a 60% iodinated contrast agent should be given for optimal study results. In evaluating arteriovenous malformation, neoplastic disease (either primary or metastatic), the pituitary gland, or the sellar region, a contrast agent is essential unless renal disease or a history of sensitivity to contrast medium contradicts this usage.

In postcontrast studies, the following structures enhance physiologically without any break in the blood-brain barrier:

1. The pituitary gland and its stalk, which enhance homo-

geneously. Heterogeneity is an indication of pathologic processes.

2. Dural structures, including the interhemispheric falx, falx cerebelli, tentorium along the cavernous sinus, the tentorial notch.
3. Arterial structures in the suprasellar region, including the circle of Willis and proximal portions of the anterior, middle, and posterior cerebral arteries. The deep venous structures, such as the internal cerebral vein, vein of Galen, and dural sinuses, do show enhancement.
4. The choroid plexus within the lateral, third, and fourth ventricles. Care should be given not to confuse the nodular enhancement in the fourth ventricle, or a comma-shaped enhancement within the temporal horns connecting to the rest of the plexus in the atrium, with the enhancing mass.

Intrathecal use of contrast medium has become nearly obsolete in the evaluation of intracranial disease. This technique was commonly used for the evaluation of CPA masses, sellar region masses, and empty-sella syndrome.

MRI Technique

Routine MRI studies of the brain are performed in axial, coronal, and, sometimes, in sagittal axes in varying thickness from 5 to 10 mm. T1 images have a shorter repetition time (TR) of less than 1000 msec and a short echo time (TE) of less than 30 msec. The T2-weighted images have a long TR of more than 1500 msec. The first echo of T2 images with shorter TE is called *proton density*, or balanced T1 and T2 images. The second echo of T2 images with a longer TR of over 60 msec represents real T2 images. Studies have shown that most pathologic processes cause an increase in the water content of the brain. Therefore, T2 images are highly sensitive in detecting brain pathology.

Routinely, T1 and T2 axial and T2 coronal studies are performed. The T2 images contain a first echo with short TR and a second echo of long TR. In the evaluation of sellar and posterior fossa regions, sagittal and coronal images of 2 to 4 mm thick are needed. Specific techniques are needed to diagnose various pathologic processes; these are mentioned in related chapters.

The CSF has a long T1, which demonstrates low signal intensity in T1 images, but becomes slightly higher in intensity in the first echo T2 images. In real T2 (long TE and very long TR) images, the CSF has very high signal intensity. The basal ganglia, dentate nuclei of the cerebellum, and red nuclei of the midbrain have low signal intensities in T2 images because of their mineral content.[6] The gray matter has a slightly higher signal intensity in relation to white matter in almost all spin-echo images. The very high signal intensity of fat in T1 images can be appreciated within the diploic space and is outlined by the low signal intensity of cortical bone. Vascular structures show signal void in all regular T1, T2, and proton-density images because of the moving protons of circulating blood. Flowing CSF can have the same effect, demonstrating signal void in the cerebral aqueduct.[29] The appearance of the vessels can be changed if the special technique of magnetic resonance angiography (MRA) is applied.

So far, gadolinium compounds are the only contrast medium approved by the Food and Drug Administration that may be used intravenously. The regular dose is about 0.1 mmol/kg of body weight, and the agent must be injected at a slow rate. The same structures that enhance with IV use of contrast medium on CT scans enhance similarly on MRI scans.

Sectional Anatomy

Normal Axial CT and MRI Anatomy[10, 11, 21, 22]

CT scans are reviewed from the caudal to cephalic levels; the scans are obtained at a 15- to 20-degree angulation to the canthomeatal line. MRI scans are generally obtained parallel to this line. These scans are divided into posterior fossa cuts of 5-mm increments and supratentorial cuts of 8-mm increments.

Posterior Fossa Cuts

Four slices from the foramen magnum to the suprasellar region are now reviewed.

Above the Foramen Magnum Level (Fig. 4–5)

The cerebellar tonsils can be seen lateral to the medulla. Most of the structures in the anterior and middle fossa are components of the base of the skull and the orbits. In the middle fossa, the foramen ovale and spinosum can be visualized if a wide window setting is used. They transmit the third branch of the fifth cranial nerve and the middle meningeal artery, respectively. The inferior portion of the cisterna magna outlines the posterior aspect of the cerebellar hemispheres.

Level of the Fourth Ventricle (Fig. 4–6)

The lower pons is seen in front of the fourth ventricle, connecting to the cerebellar hemispheres by the middle cerebellar peduncles. The pons is outlined by the anterior and lateral mesencephalic cisterns containing CSF. On MRI examinations, the seventh and eighth cranial nerves can be seen at this level. Posteriorly, the fourth ventricle is outlined by the nodulous in the midline and cerebellar hemispheres laterally. The choroid plexus within the fourth ventricle, which may enhance, can simulate a true nodule and should not be mistaken as the true parenchymal nodule.

Above the Fourth Ventricular Level (Fig. 4–7*A–C*)

The superior cerebellar surface is seen with separation of the two hemispheres by the superior vermis. With contrast studies, the transverse sinuses can be seen joining together in the torcula. In the middle fossa, the temporal lobes are separated from the frontal lobe by the sylvian fissure. The temporal horn, seen as a comma-shaped structure in the middle of the temporal lobe, is easily visualized in patients older than 50 years of age. Sometimes enhancement of both the choroid plexus within the temporal horn, extending to the atrium and the tentorium medially, can mimic an enhancing nodule in this region. The medial aspect of the temporal lobes bounds the suprasellar cistern and contains the internal carotid artery, the optic chiasm, the infundibulum, the mammillary bodies, and the top of the basilar artery (Fig. 4–7*D–F*). In the anterior fossa, the

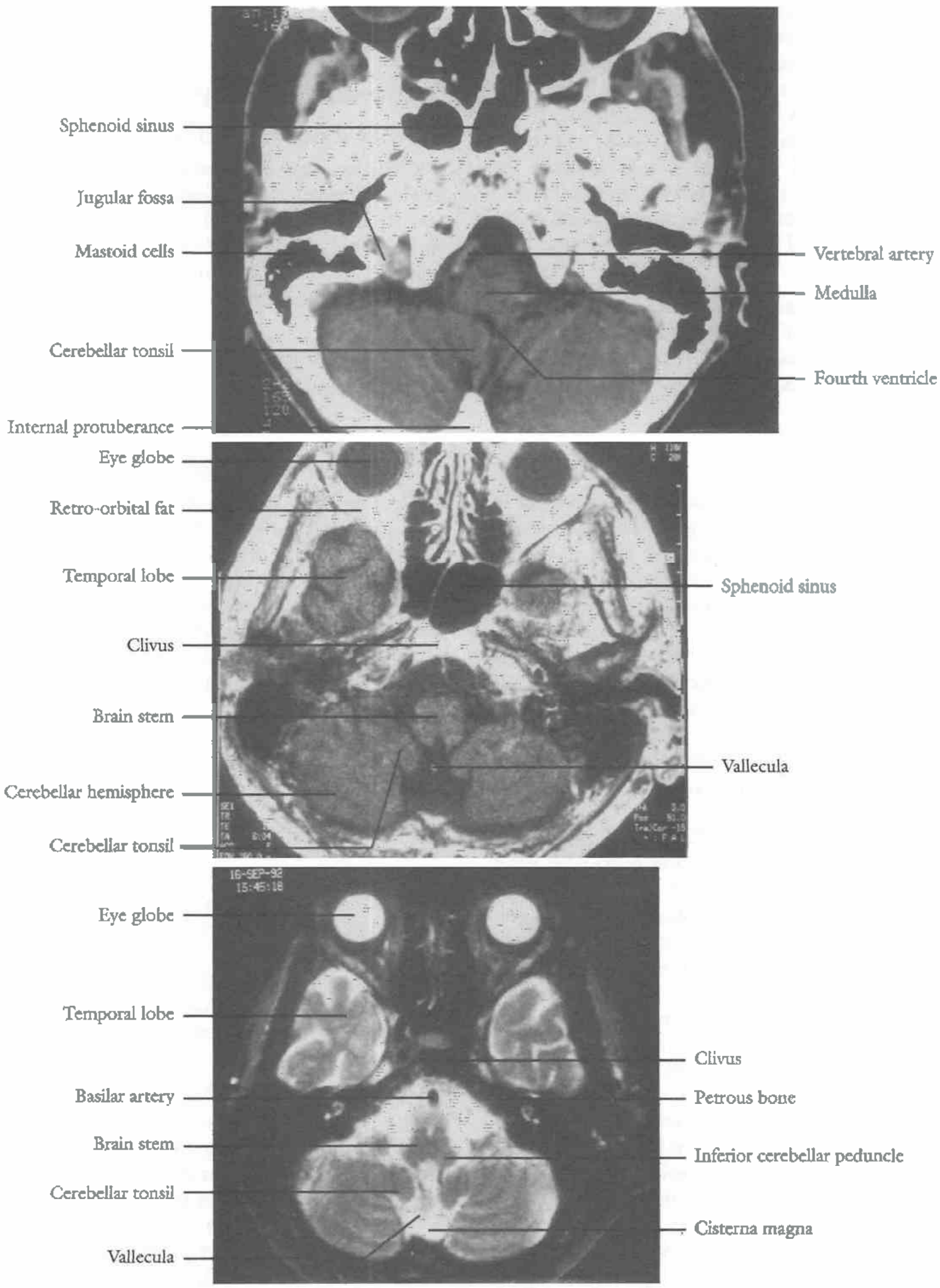

Figure 4–5. *Top*, Enhanced axial CT scan above the foramen magnum. *Center*, Axial T1 MRI scan above the foramen magnum. *Bottom*, Axial T2 MRI scan above the foramen magnum.

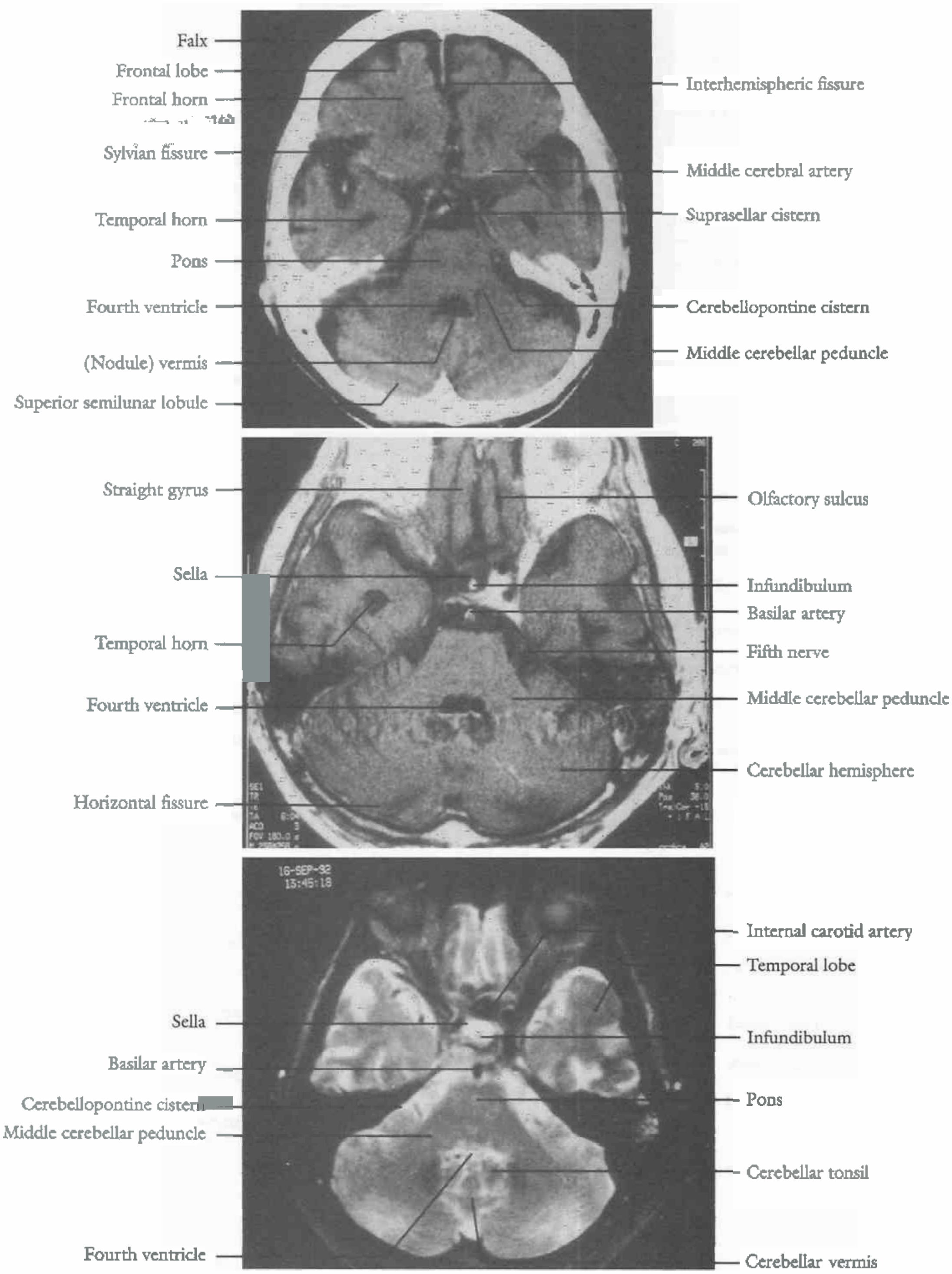

Figure 4–6. *Top*, Enhanced axial CT scan at the level of the fourth ventricle. *Center*, Axial T1 MRI scan at the level of the fourth ventricle. *Bottom*, Axial T2 MRI scan at the level of the fourth ventricle.

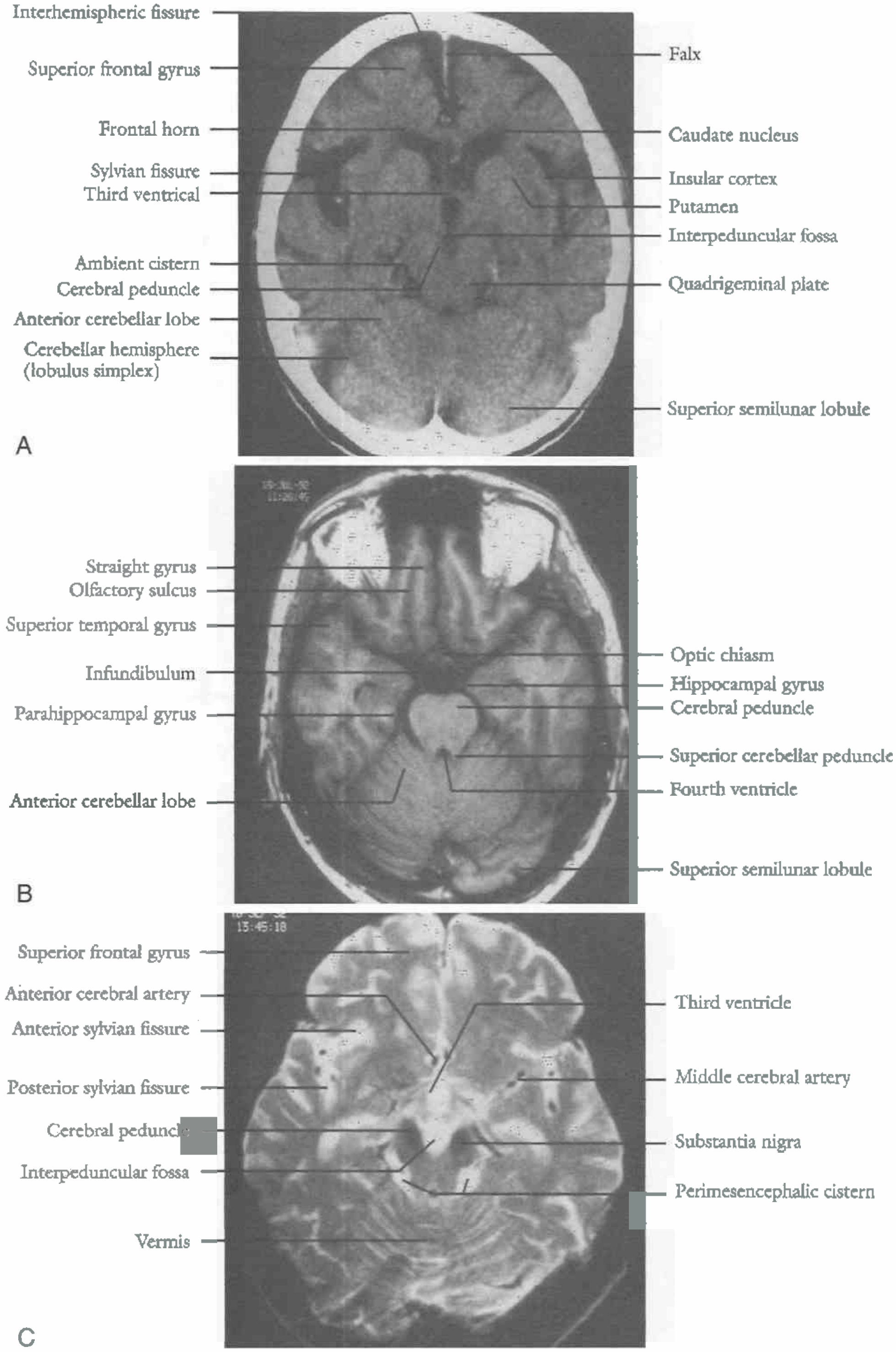

Figure 4–7. *A*, Enhanced axial CT scan at the level above the fourth ventricle. *B*, Axial T1 MRI scan at the level above the fourth ventricle. *C*, Axial T2 MRI scan at the level above the fourth ventricle.

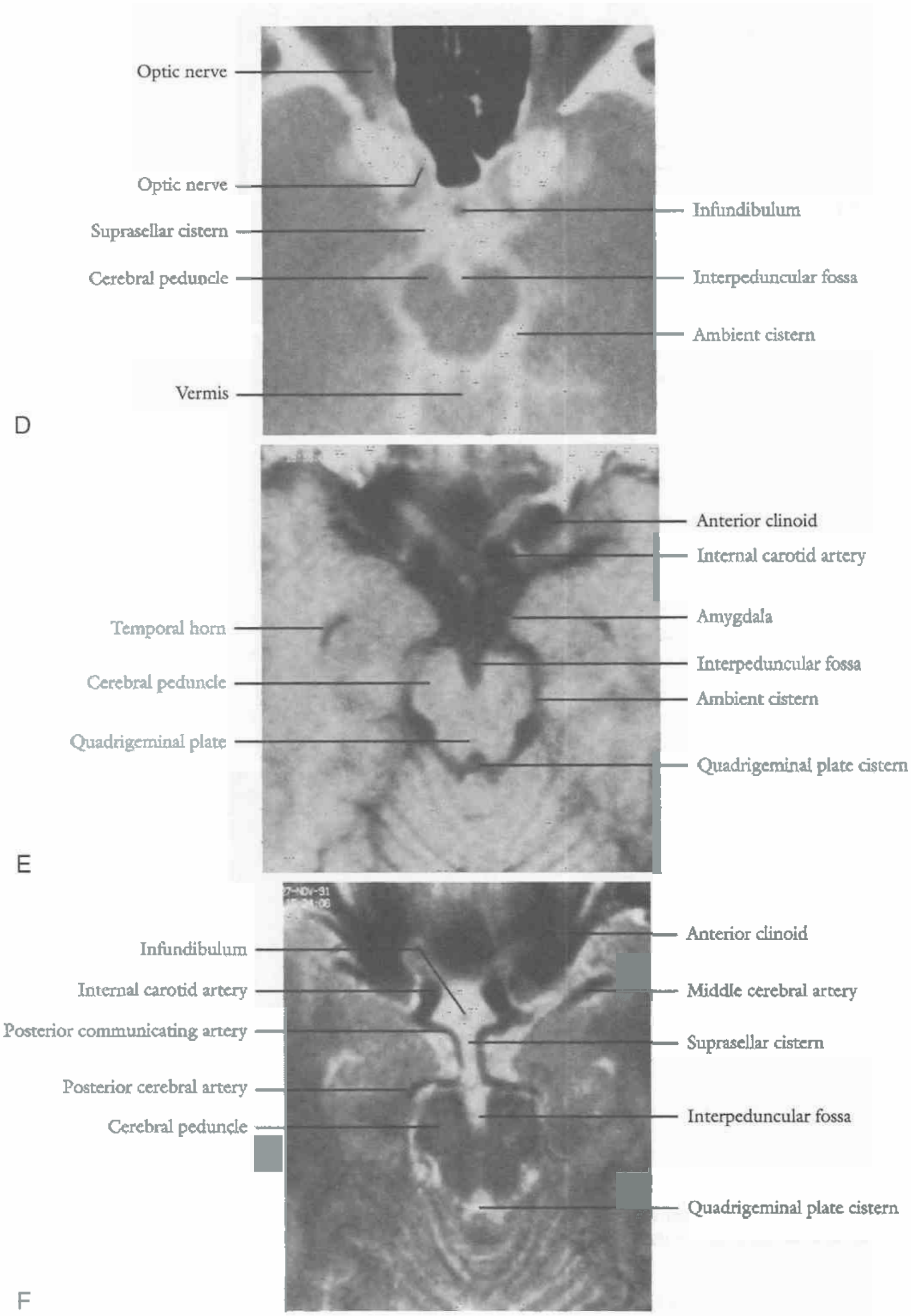

Figure 4–7 *Continued. D*, Intrathecal enhanced axial CT scan at the level of the suprasellar cistern shows the outline of the midbrain by contrast with defects of the infundibulum and optic nerves. *E*, Axial T1 MRI scan of the suprasellar cistern. *F*, Axial proton-density MRI scan through the suprasellar cistern.

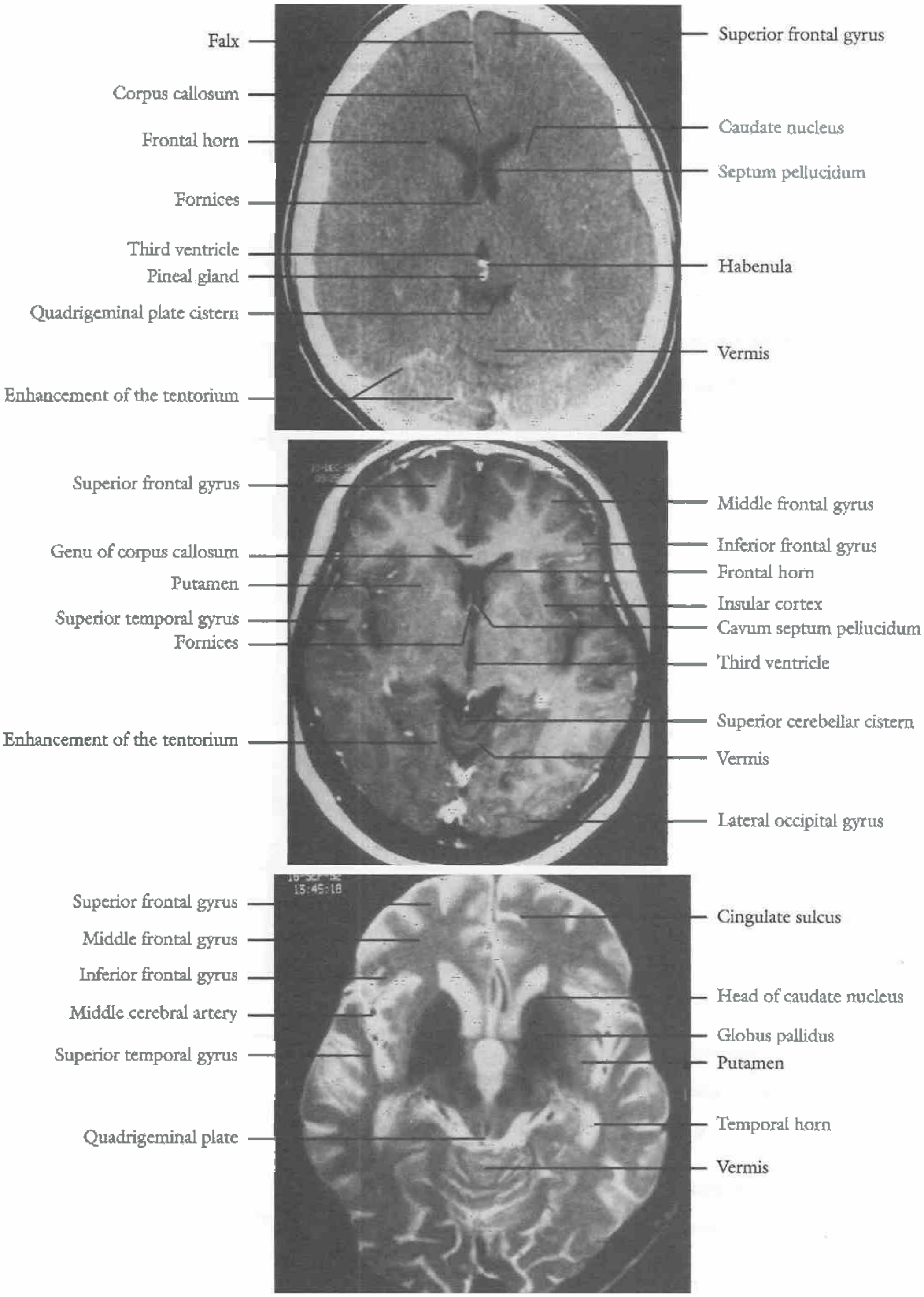

Figure 4–8. *Top*, Axial enhanced CT scan at the level of the tentorium. *Center*, Axial T1 MRI scan at the level of the tentorium. *Bottom*, Axial T2 MRI scan at the level of the tentorium.

most inferior part of the frontal lobe can be seen separated by the interhemispheric fissure.

Tentorial Level (Fig. 4–8)

The V-shaped enhancement of the tentorial notch outlines the superior vermis and junction of the pons to the midbrain. In axial scans, it is sometimes difficult to separate an infratentorial lesion from a supratentorial lesion because of partial averaging. If the lesion is lateral to the tentorial notch, it is probably supratentorial. In such circumstances MRI plays an important role in localizing these lesions in the sagittal or coronal axis.

Supratentorial Cuts

Third Ventricular Level (Fig. 4–9)

The most inferior aspects of the frontal lobes can be seen with part of the posterior inferior interhemispheric

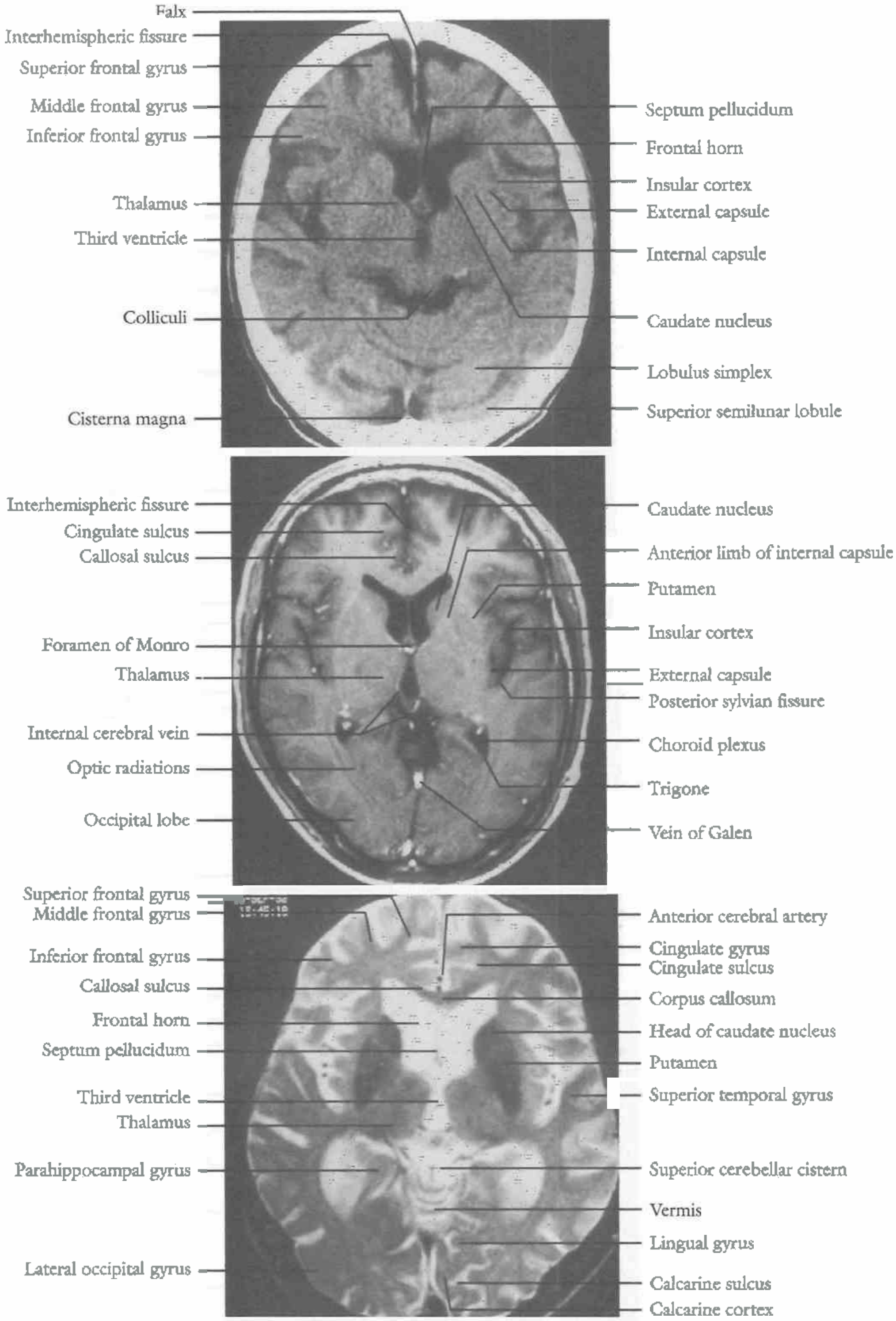

Figure 4–9. *Top*, Enhanced axial CT scan at the third ventricular level. *Center*, Axial T1 MRI scan at the third ventricular level. *Bottom*, Axial T2 MRI scan at the third ventricular level.

fissure medial to them. The third ventricle (a midline structure) is seen as a slitlike cavity. Generally, its transverse diameter should not exceed 5 mm. Superficially, the sylvian fissures can be seen extending medially to separate the frontal lobe from the temporal lobe. Medial to the medial aspect of the sylvian fissure, the insular cortex, external capsule, putamen, and globus pallidus are visualized. Behind the third ventricle, part of the upper brain stem, including the quadrigeminal plates and cistern, can be seen.

Low Ventricular Level (Fig. 4–10)

The superior portion of the frontal horns is seen outlined by the head of the caudate nuclei. Anteriorly, the frontal

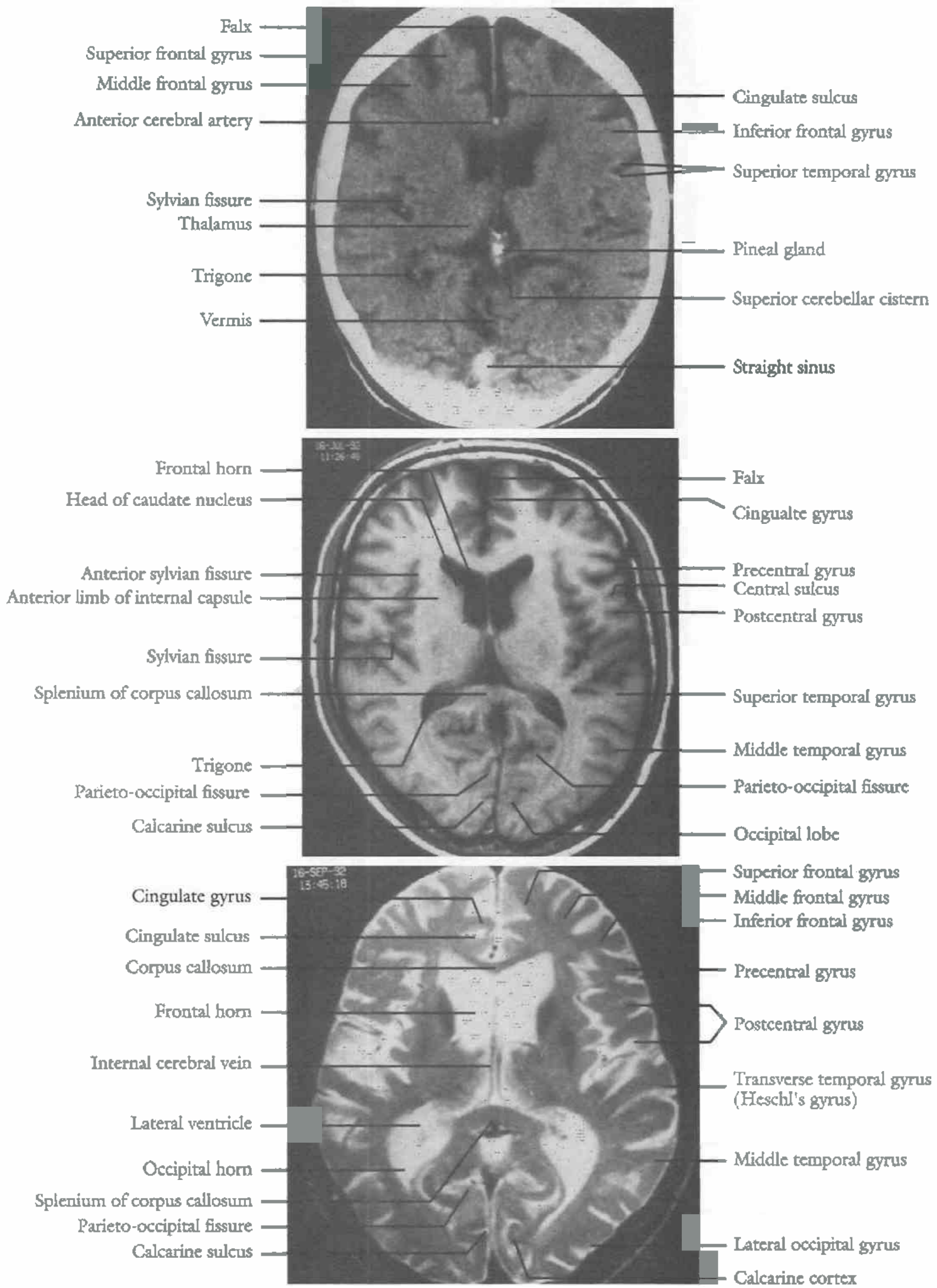

Figure 4–10. *Top*, Enhanced axial CT scan at the low ventricular level. *Center*, Axial T1 MRI scan at the low ventricular level, slightly above the CT scan level. *Bottom*, Axial T2 MRI scan at the low ventricular level, slightly above the CT scan level.

horns are shaped by indentation of the genu of the corpus callosum. The cingulate sulcus is seen separating the corpus callosum from the cingulate gyrus. With IV contrast injection, the junction of the internal cerebral vein and thalamostriate veins can be seen in the region of the foramen of Monro. Pineal gland calcification is located behind the third ventricle. Occasionally, some calcification of the habenula occurs anterior to the pineal gland calcification.

Behind the pineal gland, the great vein of Galen may show slightly increased attenuation value in precontrast studies as a result of circulating blood. With contrast injection, the vein and its junction to the straight sinus can be easily identified. The pineal gland and the vein of Galen are in the large subarachnoid space formed by the juncture of the supracerebellar cistern, the cephalic portion of the quadrigeminal cistern, and the interpositum cistern. Within the lateral ventricle, the most commonly calcified choroid plexus can be identified. On contrast studies, the anterior portion of the choroid plexus, which may not be calcified, demonstrates enhancement. The posterior horns of the lateral ventricles, including the atrium, are seen at this level.

Midventricular Level (Fig. 4–11)

The superior extension of the sylvian fissure and the superior temporal gyrus are seen. The central sulcus, slightly anterior to the sylvian fissure, separates the temporal lobe from the parietal lobe. The most superior aspect of the frontal horns is outlined anteriorly by the anterior portion of the corpus callosum, and the most superior aspect of the caudate nuclei binds them laterally. The posterior medial aspect of the occipital horns is seen bound by the white matter fibers of the splenium of the corpus callosum. The posterior portion of the cingulate sulcus, separating the cingulate gyrus from occipital lobe, can be seen connecting to the posterior interhemispheric fissure.

Above the Ventricular Level (Fig. 4–12)

The scans mainly include the frontal, the parietal, and a small portion of the occipital lobes. Because it is deep, the central sulcus can be identified in the midportion of the scan. Precentral and postcentral sulci outline motor and sensory cortices. The interhemispheric fissure can be seen in its entire length with the falx between. Generally, the falx has a higher attenuation value because of its fibrous texture and because of the presence of calcification.

Sectional Anatomy: Review of Coronal Scans

Coronal CT scanning has never equaled high-quality MRI because of significant motion artifacts and linear artifacts from dental fillings. Next, four slices are analyzed.

Frontal Horn Level (Fig. 4–13)

The frontal horns, outlined by the head of the caudate nuclei and corpus callosum, are visualized, separated by a thin layer of septum pellucidum. The sylvian fissure is seen superficially, with its superior and inferior branches separating the temporal lobe from the frontal lobe and insula.

Third Ventricular Level (Fig. 4–14)

The optic chiasm superior to the infundibulum of the pituitary gland can be identified. The suprasellar cistern outlining the optic chiasm and the superior aspect of the pituitary gland shows the CSF intensity. Some extension of this space into the interior of the pituitary fossa is now considered a normal finding rather than a manifestation of the empty-sella syndrome. In the parasellar region, the cavernous sinus is outlined by the low-intensity area of the dura, which contains the third, fourth, fifth, and sixth cranial nerves. The signal void of the internal carotid arteries within the cavernous sinus can be identified on T1 images.

Midventricular Level (Fig. 4–15)

The body of the lateral ventricles, containing portions of the choroid plexus, is seen. The precentral and postcentral sulci, the central sulcus, and the sylvian fissure are visualized, demonstrating the CSF signal in all MR images. Heschl's gyrus and the temporal lobe gyri can be easily identified. The cerebral aqueduct and midbrain structures are also visualized.

Occipital Horn Level (Fig. 4–16)

The splenium of the corpus callosum can be seen outlining the medial aspects of the occipital lobes. In the infratentorium, the cerebellar hemispheres, the fourth ventricle, the supracerebellar cistern, and the inferior, middle, and superior cerebellar peduncles are all clearly visualized on MRI studies.

Sectional Anatomy: Review of Sagittal Scans

Midsagittal Level (Fig. 4–17)

MRI has revolutionized the field by its capability to obtain sagittal and coronal images without special positioning of the patient. Therefore, patients are more comfortable, and the images are less susceptible to motion artifacts, which can arise from special positioning. Sagittal images are essential in the evaluation of sellar and parasellar lesions, posterior fossa lesions, and intraventricular lesions as well as the vascular anatomy. Sagittal images are also essential in three-dimensional (3D) visualization of intracranial lesions. At this level, the following structures can be identified:

- Venous structures—superior and inferior sagittal sinuses, the vein of Galen, and the straight sinus
- Ventricular system—third and fourth ventricles, including clear visualization of the sylvian aqueduct
- Subarachnoid spaces—suprasellar, perimesencephalic, quadrigeminal, interpeduncular supracerebellar cisterns; the cisterna magna; the central sulcus; precentral and postcentral sulci; the parieto-occipital fissure; the cingulate sulcus; and other sulci separating the frontal and parietal gyri
- Gray matter—cerebral cortices of the frontal, parietal, and occipital lobes and a comma-shaped cingulate gyrus over the corpus callosum and thalamus
- White matter—a comma-shaped corpus callosum over the lateral ventricle, the optic chiasm and optic nerves, and the pons

Text continued on page 109

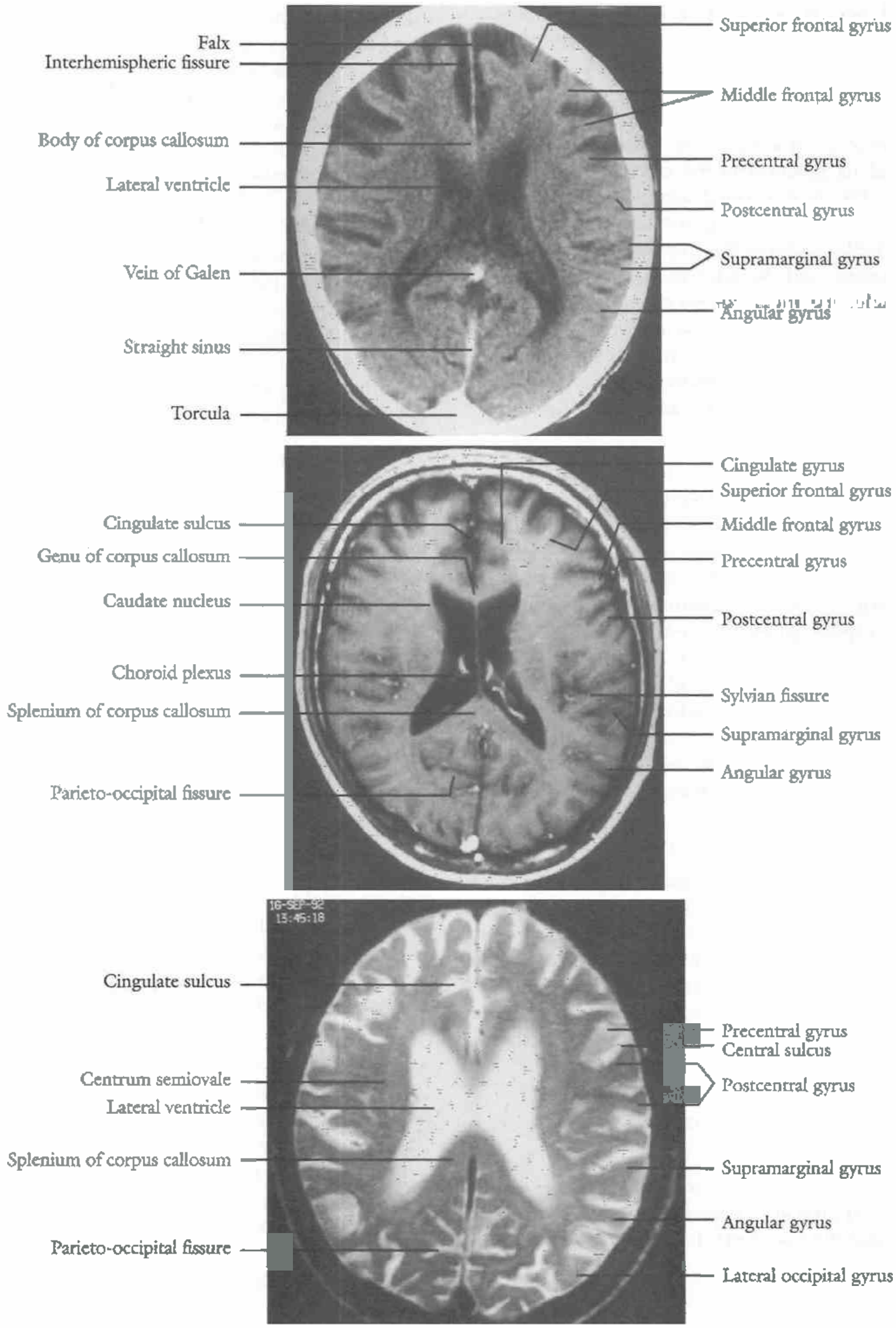

Figure 4–11. *Top*, Enhanced axial CT scan at the midventricular level. *Center*, Axial T1 MRI scan at the midventricular level. *Bottom*, Axial T2 MRI scan at the midventricular level.

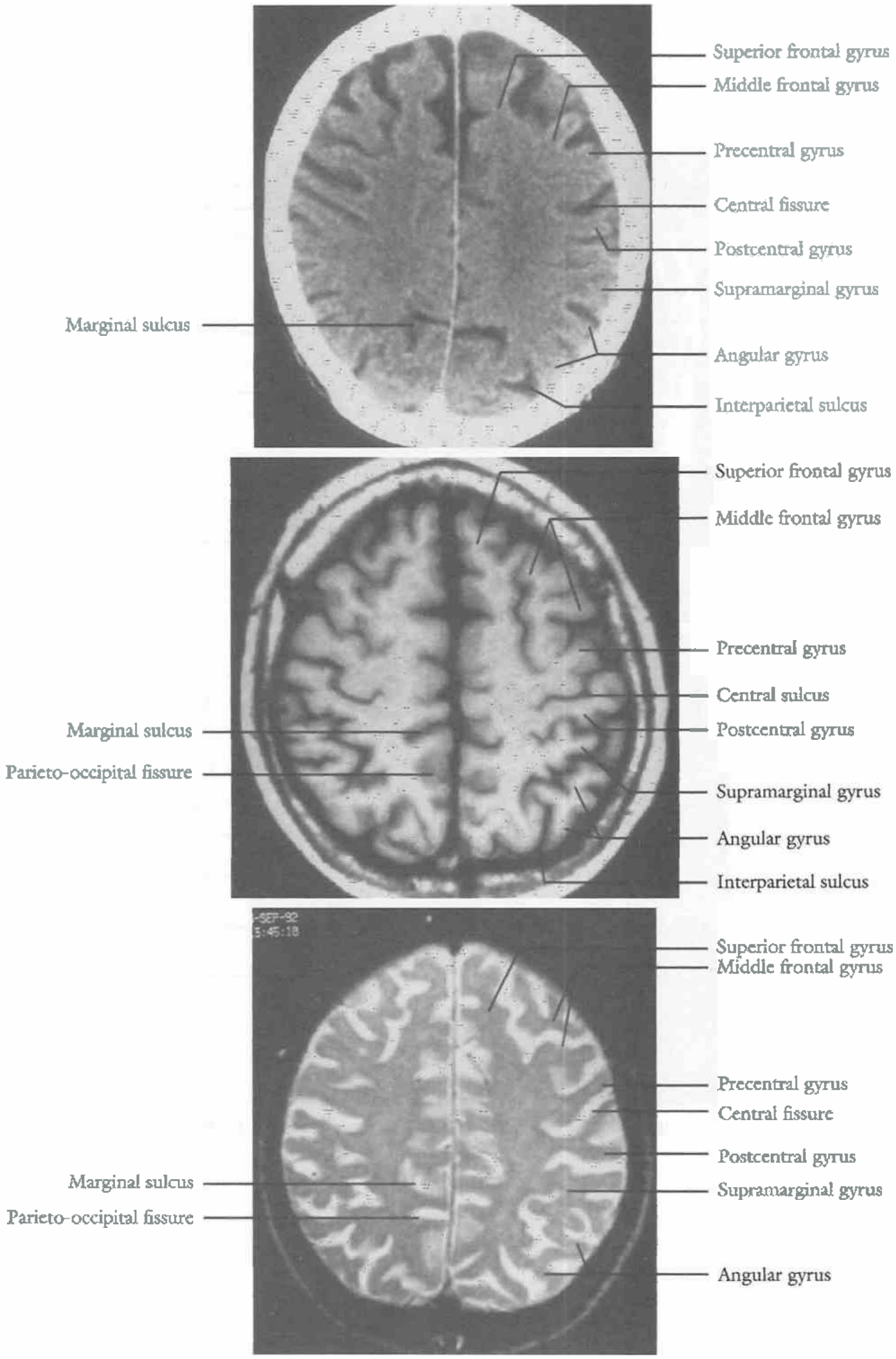

Figure 4–12. *Top*, Enhanced axial CT scan above the ventricular level. *Center*, Axial T1 MRI scan above the ventricular level. *Bottom*, Axial T2 MRI scan above the ventricular level.

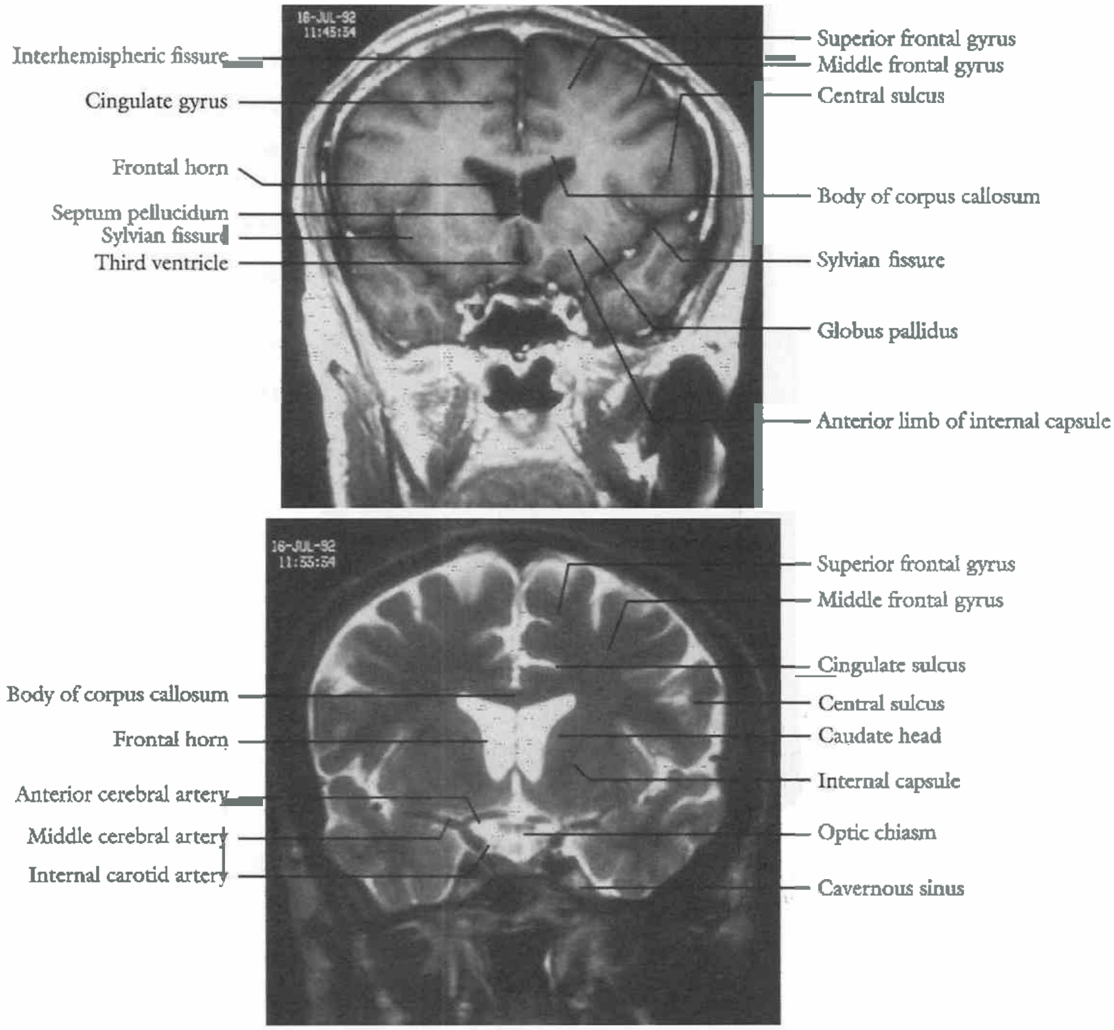

Figure 4–13. *Top*, Coronal T1 MRI scan at the level of the frontal horns. *Bottom*, Coronal T2 MRI scan at the level of the frontal horns.

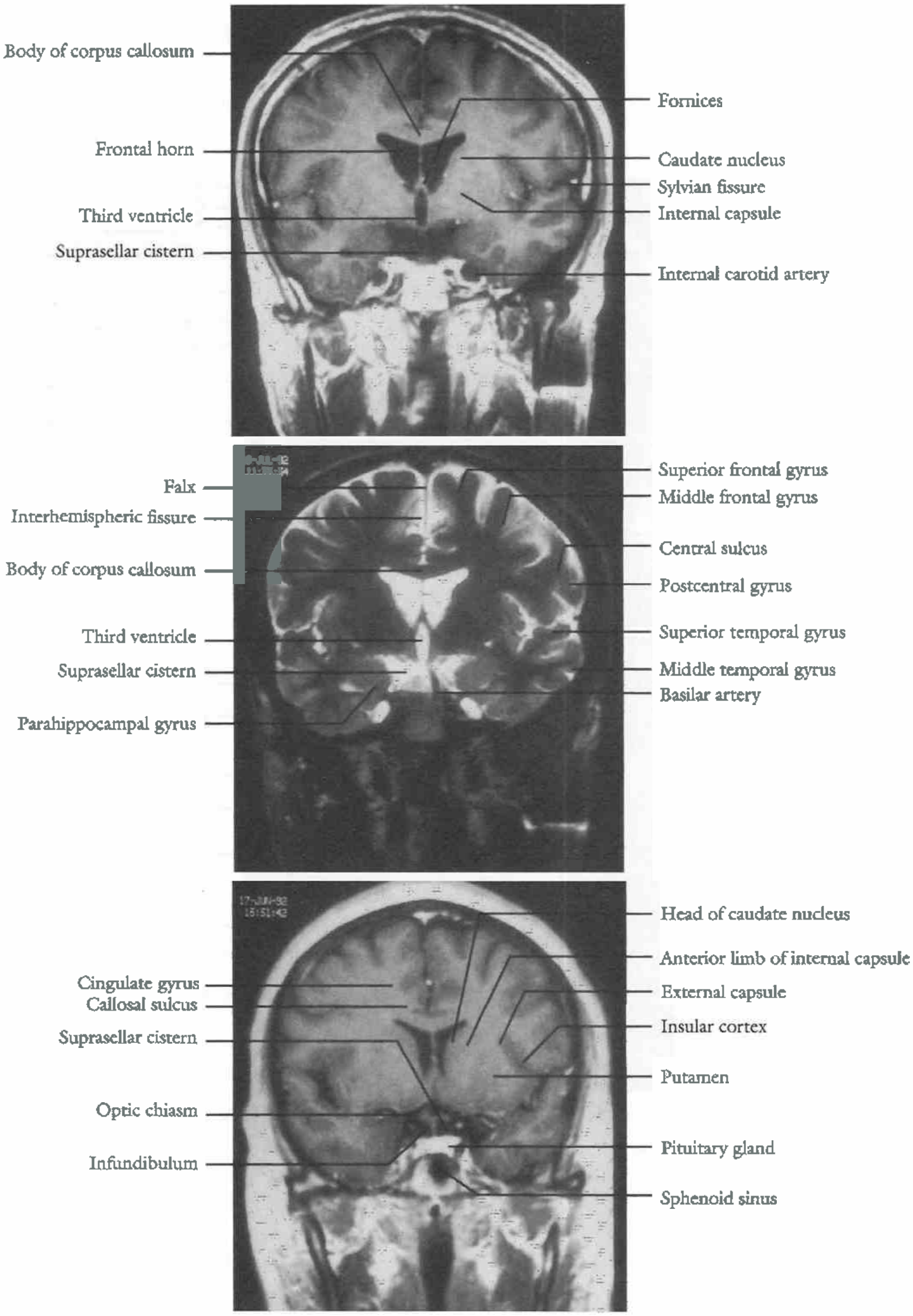

Figure 4–14. *Top*, Coronal T1 MRI scan at the level of the third ventricle. *Center*, Coronal T2 MRI scan at the level of the third ventricle. *Bottom*, Coronal T1 MRI scan through the suprasellar level.

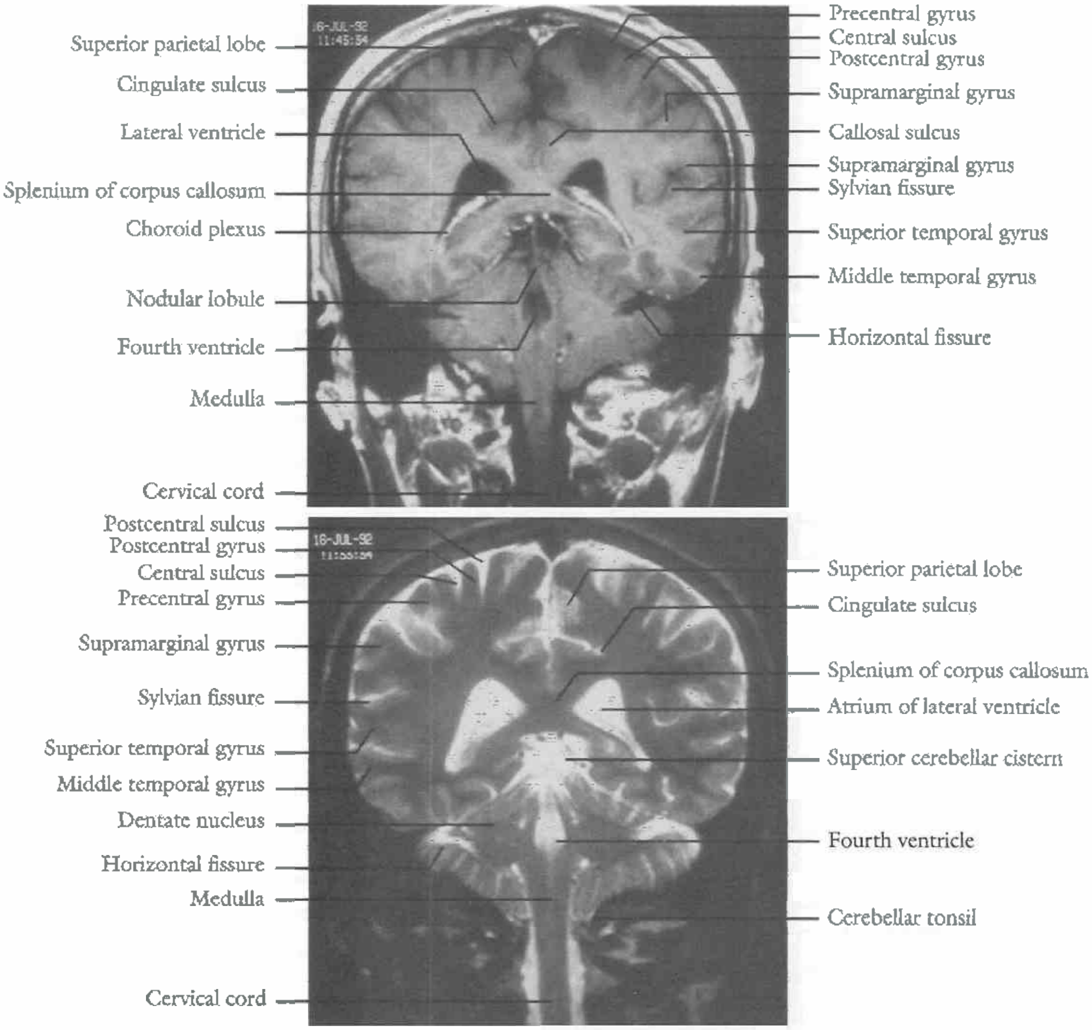

Figure 4–15. *Top*, Coronal T1 MRI scan at the mid-to-posterior ventricular level. *Bottom*, Coronal T2 MRI scan at the mid-to-posterior ventricular level.

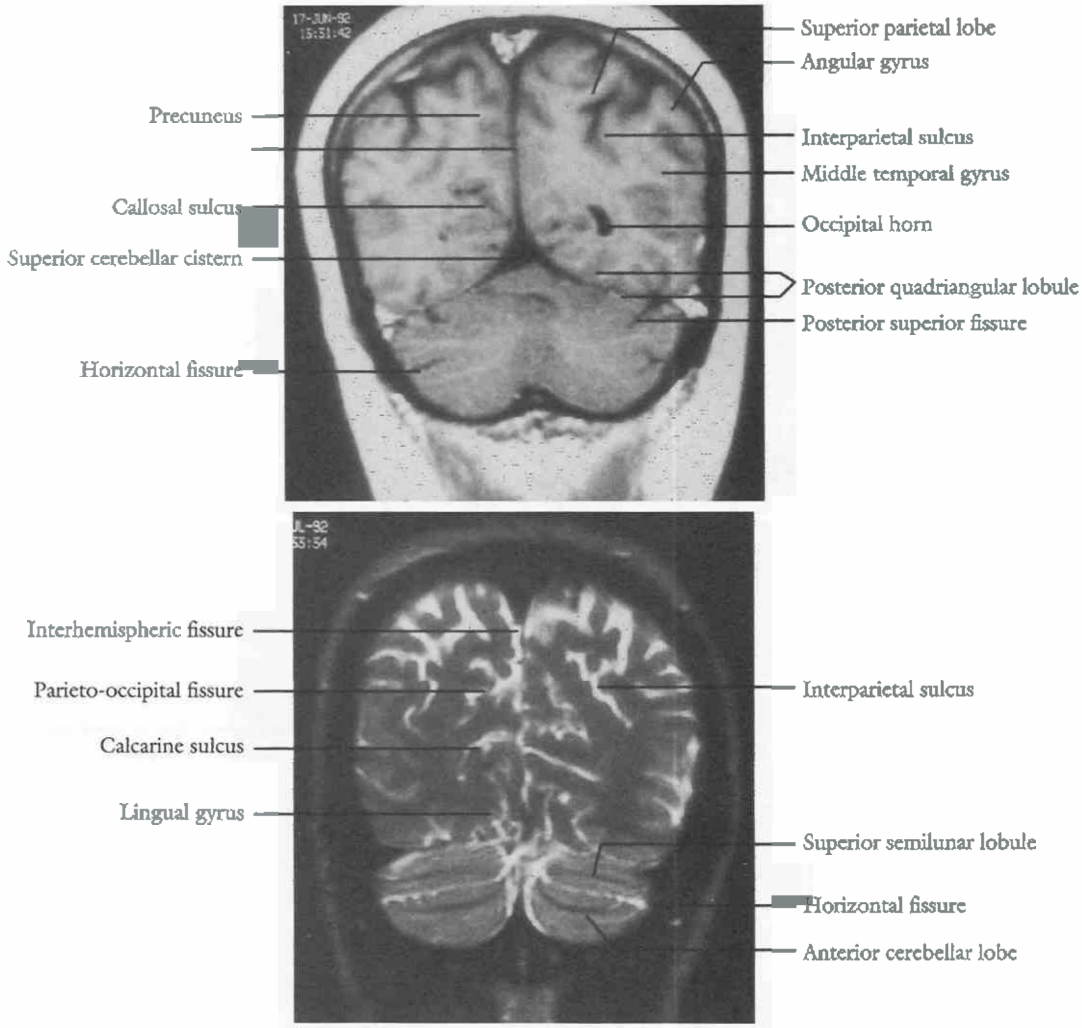

Figure 4–16. *Top*, Coronal T1 MRI scan slightly posterior to the occipital horns. *Bottom*, Coronal T2 MRI scan slightly posterior to the occipital horns.

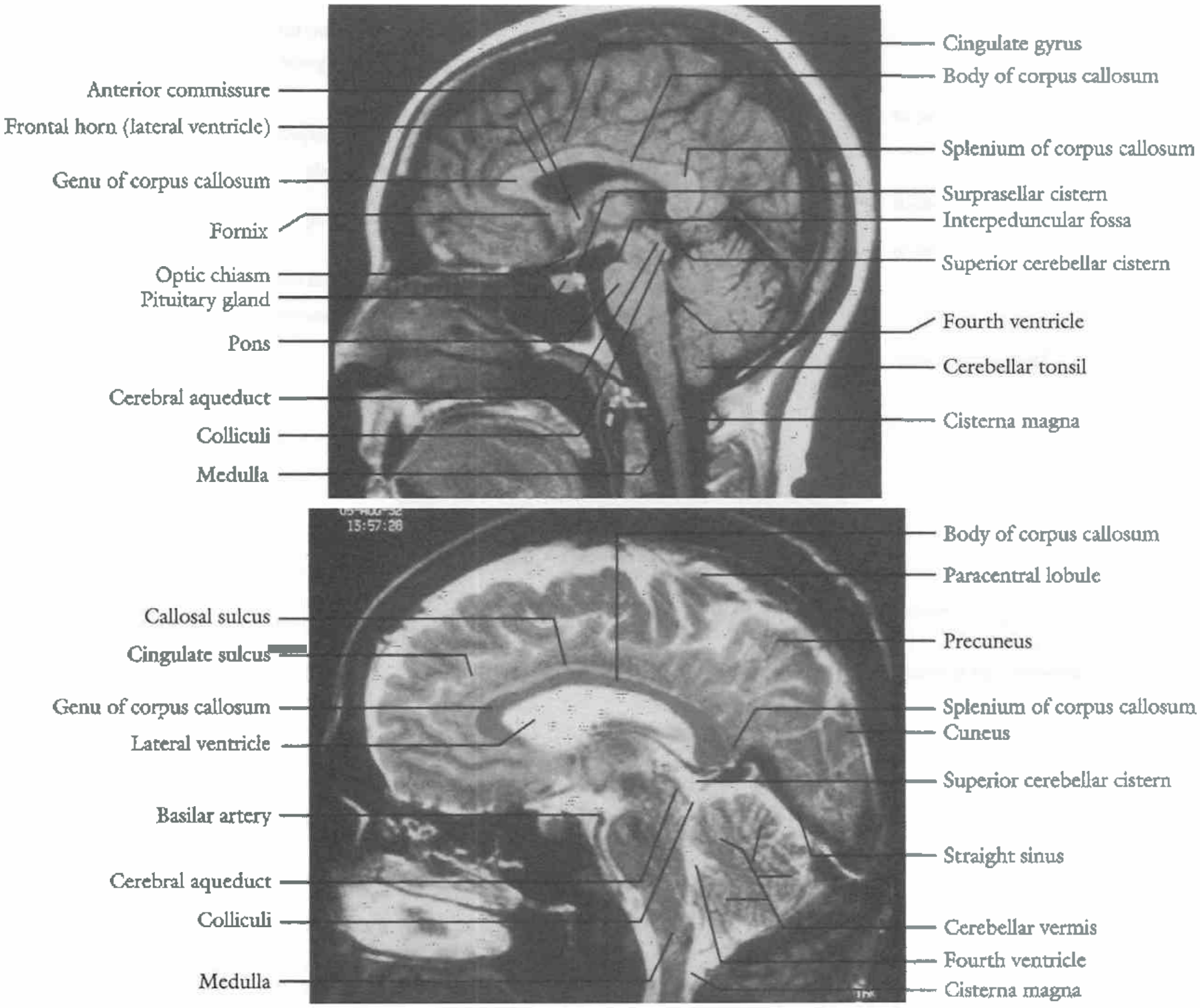

Figure 4–17. *Top*, Sagittal T1 MRI scan at the midsagittal level. *Bottom*, Sagittal T2 MRI scan at the midsagittal level.

- Other structures—the pituitary gland, the clivus, the sphenoid sinus, the frontal sinus, the cerebellar cortex and white matter, the medulla, and the cerebellar tonsils

Parasagittal Level through the Lateral Ventricular Body (Fig. 4–18)

The following structures can be identified: the central sulcus as well as the precentral and postcentral sulci; the superior frontal gyrus; the body of the caudate nucleus; the cingulate sulcus and the gyrus; the putamen; the dentate nuclei; the cerebellar peduncles; and the parieto-occipital fissure.

Lateral Orbital Level (Cortical Level) (Fig. 4–19)

The following structures can be identified: the central, precentral, and postcentral sulci; the supramarginal gyrus; the angular gyrus; the lateral occipital gyrus; the horizontal fissure of the cerebellum; the superior and inferior semilunar lobules; the middle and inferior frontal gyri; the sylvian fissure; and the superior, inferior, and middle temporal lobe gyri.

Normal Calcifications

The following calcifications seen on CT and MRI of the brain are considered to be normal.

Choroid Plexus[23, 33]

Calcification occurs mainly in the glomus located within the atrium of the lateral ventricles. Calcification of the choroid plexus in the third or fourth ventricle is rare. Within the lateral ventricles, calcification is rare under the age of 3 years. With age, the incidence increases, reaching 75% by the fifth decade.

Basal Ganglia[4]

Before the age of 9 years, calcification within the basal ganglia is uncommon but becomes frequent after age 40 years. This calcification is usually minimal. If the degree of the calcification is massive and associated with dentate nuclei calcification, the possibility of Fahr's disease should be ruled out.

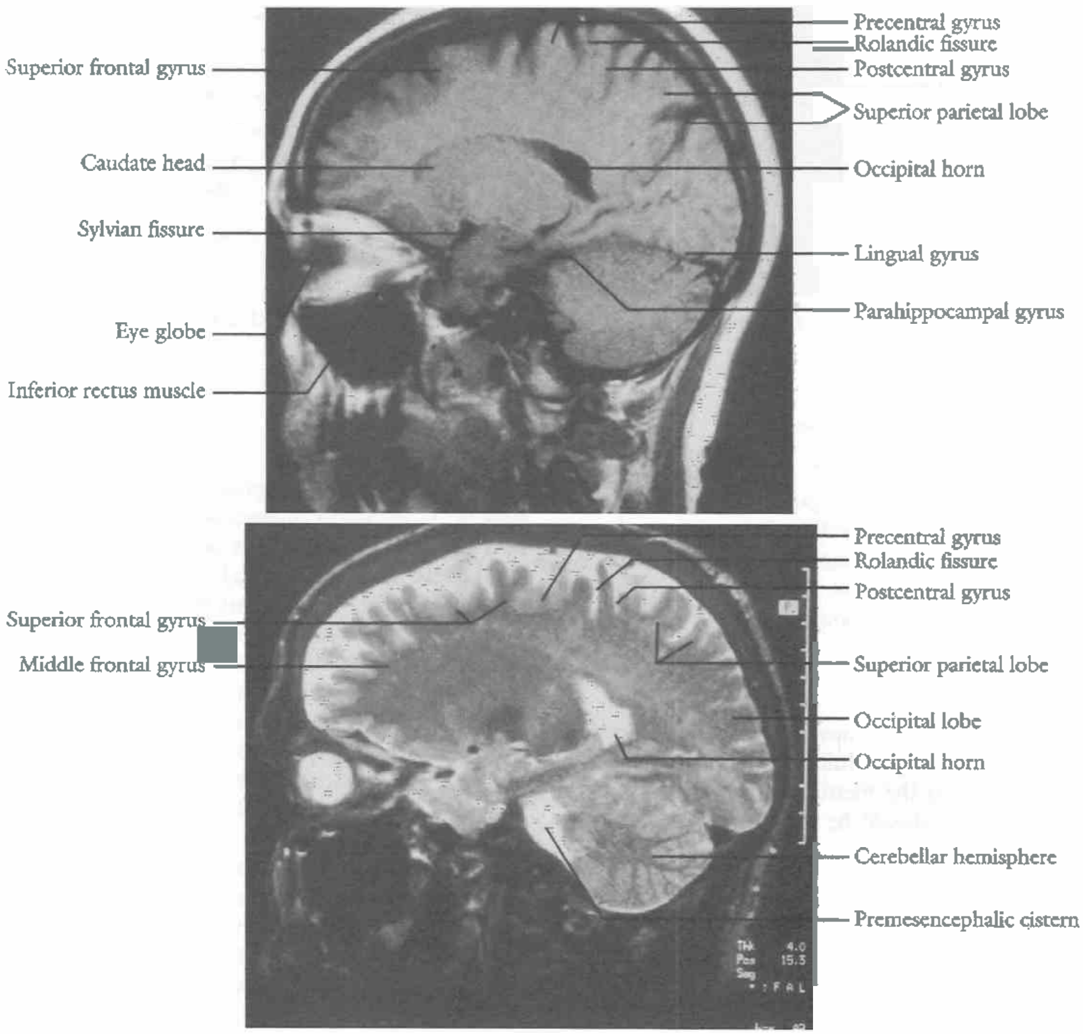

Figure 4–18. *Top*, Sagittal T1 MRI scan through the body of the lateral ventricle. *Bottom*, Sagittal T2 MRI scan through the body of the lateral ventricle.

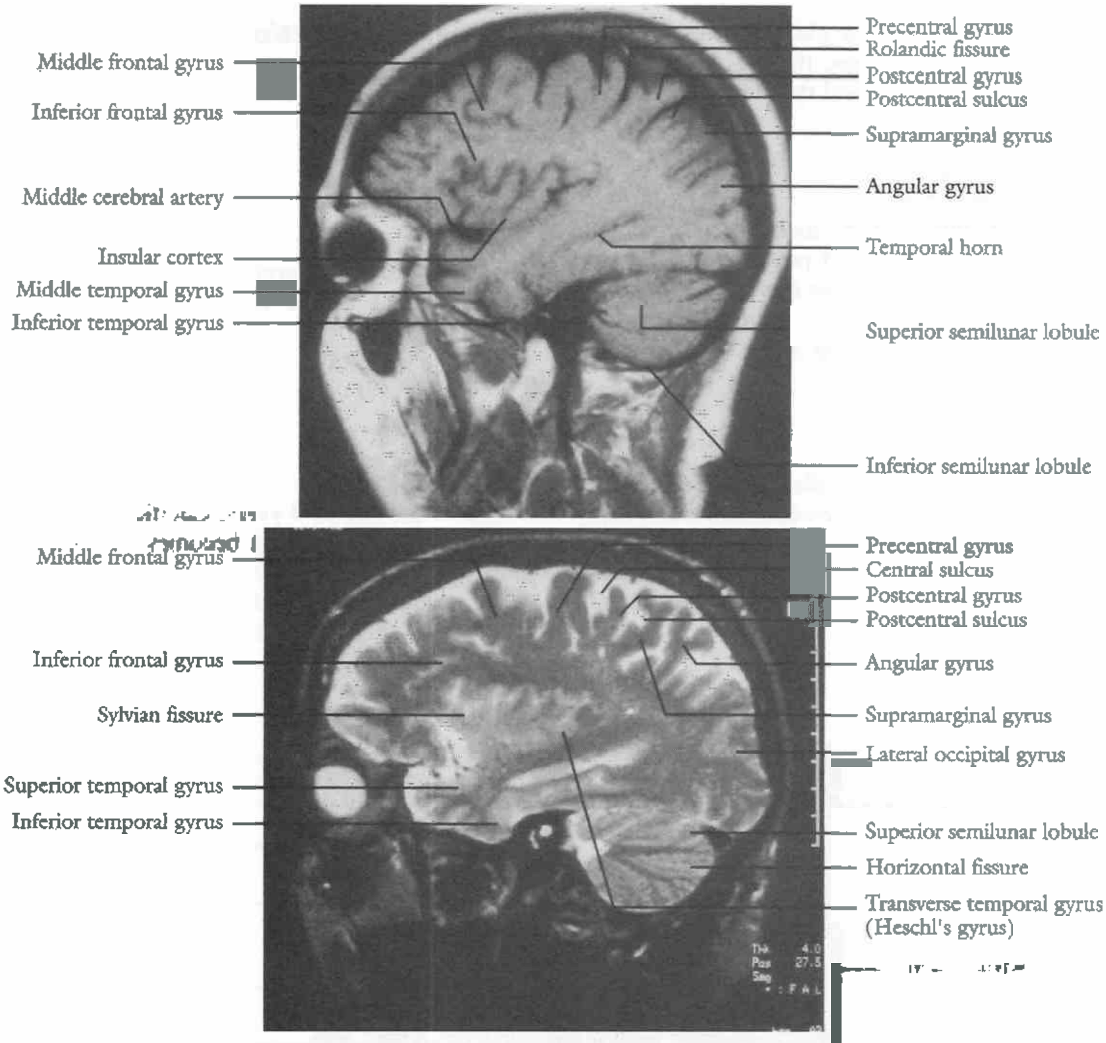

Figure 4–19. *Top*, Sagittal T1 MRI scan at the lateral orbital level. *Bottom*, Sagittal T2 MRI scan at the lateral orbital level

Pineal Gland and Habenula[23, 37]

After the age of 30 years, 15% of CT scans show habenula calcification.[10] However, pineal gland calcification is common, occurring in more than 83% of the patients older than age 30 years. If calcification of the pineal gland is larger than 12 mm × 12 mm × 12 mm, the possibility of a pineal gland region tumor should be considered.

Falx Calcification

Calcification of the falx is commonly seen in the posterior interhemispheric fissure in adults. If increased attenuation of the falx extends to the medial sulci, the possibility of subarachnoid bleeding should be excluded.

CT and MRI Anatomy of the Spine

Prior to a review of the normal anatomy, the techniques used in performing CT scans and MRI studies are discussed.

CT Technique[19, 35]

CT scanning of the spine is generally done in the axial axis in 3- to 5-mm increments. In the cervical spine, thin cuts of 1.5-mm increments are necessary to evaluate disk disease. A stacking method can be used without angling the gantry (Fig. 4–20). This method has the advantage of visualizing the entire scanned area in one column without interruption to reconstruct the images in a different orientation for further evaluation. Another method involves angling the gantry and the x-ray beam perpendicular to the disk and scanning from midbody of one vertebra to midbody of the next vertebra. At each level, scans require different angulation and thus not all of the slices can be reconstructed together.

Targeting to zoom to the spine area increases the detail and resolution of the scans. Images should be filmed at two different settings, one with a narrow window for evaluation of the soft tissue shadows and disk and the other with a wide window setting for evaluation of bony structures (Figs. 4–21 and 4–22). This is very important in postintrathecal contrast studies.

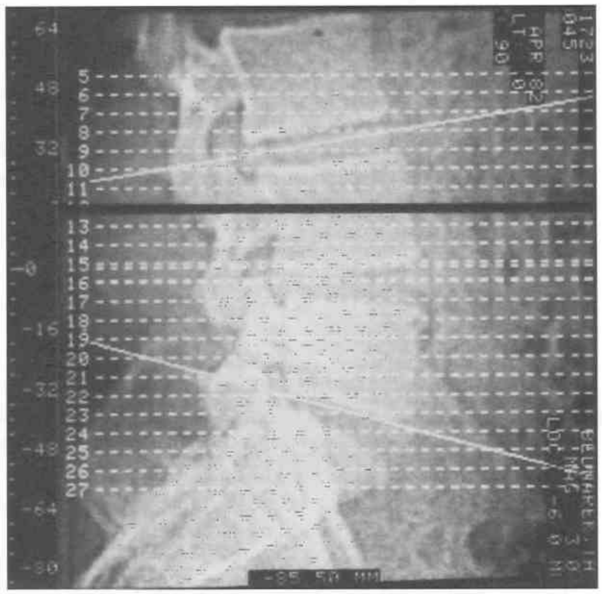

Figure 4–20. Lateral view of the lumbar spine by a scanogram showing stacking method of the axial CT scanning technique. Lines demonstrate the exact level of each side. A single angled cut can be obtained through each intervertebral disk at a perpendicular angle.

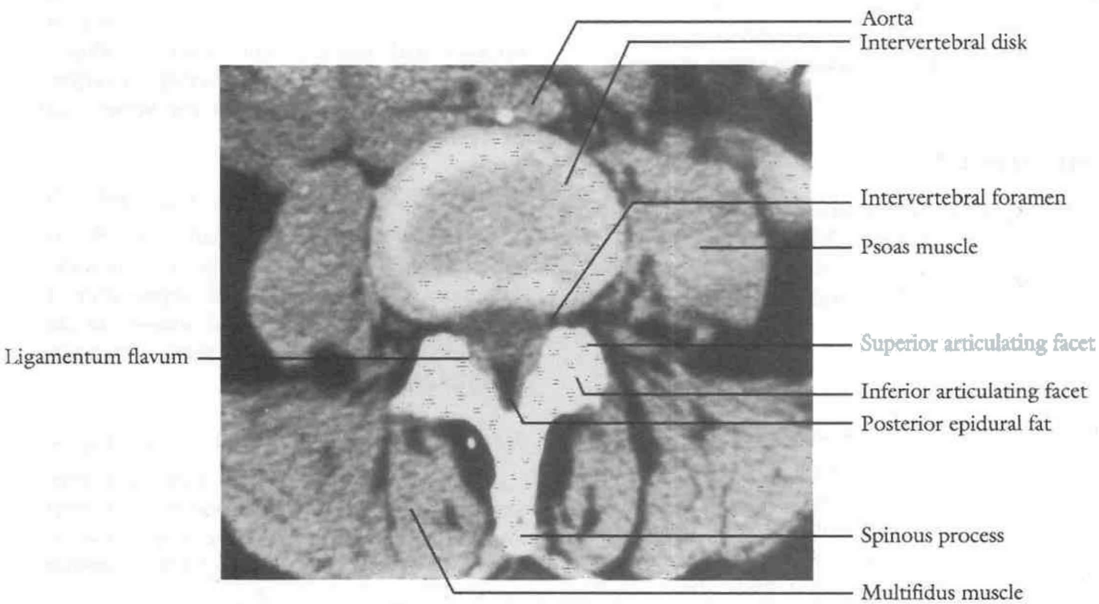

Figure 4–21. Axial CT scan through the intervertebral disk in the midlumbar region. Minimal averaging of the cortex causes increased attenuation value at the periphery. At these regular window and level settings, the facet joints cannot be readily seen. The fat in the epidural space is seen within the intervertebral foramen and posterior to the thecal sac.

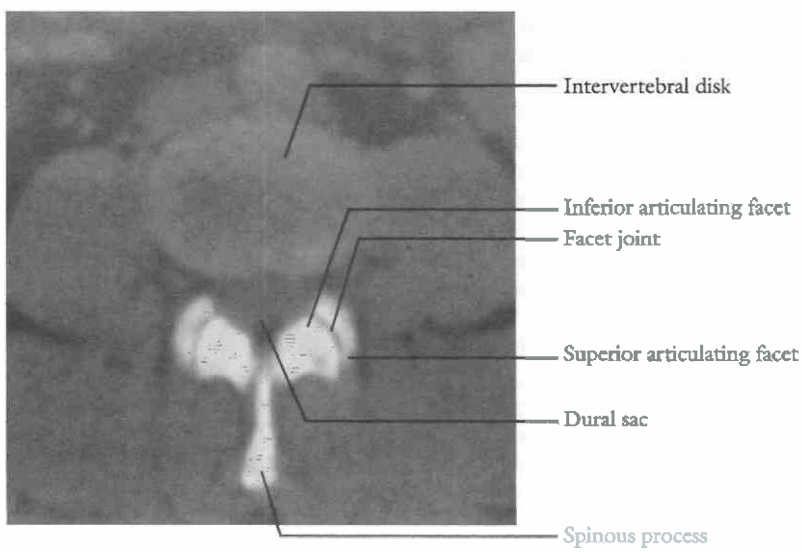

Figure 4–22. Axial CT scan through intervertebral disk. Wide window setting allows visualization of low attenuation of the facet joint between the facets.

Generally, IV contrast is not necessary unless the vascularity of a spinal lesion is to be evaluated. Prior to the advent of MRI, IV contrast was used for evaluation of both cervical disk herniation and postoperative spine in an attempt to visualize the epidural venous plexus.[27]

MRI Technique[2, 18]

MRI of the spine is routinely done in the axial and sagittal axes, rarely in the coronal axis. Our routine includes T1 and fast spin-echo images in the sagittal plane and T1 images in the axial plane in the lumbar region. In cervical spine studies, axial gradient echo is added to this menu (see Fig. 4–27). If clinically infectious diseases of the spine or intra-axial lesions are suspected, T2 axial and sagittal studies are also needed. The slice thickness is routinely 4 to 5 mm; however, it should be tailored to fit the clinical presentation. The use of IV gadolinium DTPA or DOTA is limited to evaluation of infectious disease, nonepidural neoplasms, or postoperative spine studies.[5, 27]

Normal Anatomy*

The vertebral column comprises 32 or 33 vertebrae: 7 in the cervical, 12 in the thoracic, 5 in the lumbar, 5 in the sacral, and 3 or 4 segments in the coccygeal area.

The review of CT and MRI anatomy is divided into *osseous* and *soft tissue* structures.

Osseous Structures

Vertebral Bodies (Figs. 4–23 to 4–25)

In the cervical region (Fig. 4–24), the transverse diameter is wider than the anteroposterior diameter. The uncovertebral joint is between the uncinate process and a small depression in the inferior aspect of the vertebral body above it. The vertebral bodies become wider between the C3 and C7 levels.

In the thoracic area, the transverse and anterioposterior diameters are the same (Fig. 4–25). The vertebral bodies are cone-shaped in the axial plane. In the lumbar region, the vertebral bodies become wider in the transverse diameter. They are generally larger than at the thoracic level. In the midportion of the posterior cortex, the basivertebral vein enters into the vertebral body, bifurcating into branches and making a Y-shaped defect in the axial images.

On CT studies, dense cortical bone has very high attenuation value with less attenuation in the center because of cancellous bone. On axial scans, if a slice averages through the end plate and disk space, the central part of the vertebral body will have decreased density, mimicking a destructive process (Fig. 4–23*C*).

Vertebral bodies are isointense on T1 images (Figs. 4–25, 4–26*B*, and 4–27*B*), with a decrease in signal intensity on gradient echo images. The cortex with dense bone has a low signal intensity on T1 images. On T2 images, the signal intensity of vertebral bodies decreases.

*See References 2, 5, 7–9, 12, 13, 16–18, 25, 28, 31, and 32.

Pedicles

Pedicles extend from the vertebral bodies posteriorly to reach the articular pillars. They are very short in the cervical area and increase in length cephalocaudally. In the thoracic area, the pedicles are located in the upper half of the vertebral bodies, resulting in a higher location of the intervertebral foramina in relation to disk spaces. In the lumbar region, the pedicles are larger in the superior aspect than in the inferior aspect. On axial scans, the pedicles are seen outlining the lateral borders of the spinal canal, forming a full circle of bone. In the scans above or below the pedicles, the lateral borders of the canal are interrupted by the intervertebral foramina.

Laminae (Fig. 4–26; see Fig. 4–23)

The two laminae at each level extend posteriorly and medially to meet in midline and fuse into the spinous process. The superior fusion is slightly more anterior than the inferior fusion. In the thoracic area, the laminae are broader and shorter, with some overlap. In the lumbar region, the laminae do not overlap. A larger space is found between adjacent laminae in the upper lumbar spine than in the lower lumbar spine.

Spinous Processes (see Figs. 4–23 and 4–26)

The spinous processes start from the junction of two laminae and extend posteriorly and downward. In midcervical areas, they have a bifid appearance. In the thoracic region, they are slender and longer. In the lumbar area, they are larger and taller with rectangular shape on a lateral view.

Transverse Processes (Fig. 4–27; see Fig. 4–23)

In the cervical area, the transverse processes have an anterior and posterior component that meet laterally in a horizontal plane to form the transverse foramina. These foramina permit the passage of the vertebral arteries from the C7 to the C2 level (Fig. 4–27).

In the thoracic region, the transverse processes are close to the heads, necks, and tubercles of the corresponding ribs. In the lumbar area, the transverse processes extend laterally and posteriorly. The transverse processes of L1 and L5 are thicker and shorter.

Articulating Pillars

The articulating pillar is created by the superior and inferior facets.

Intervertebral Foramina (see Figs. 4–23 and 4–27)

The foramina are bounded medially by the posterior vertebral body and the intervertebral disk space, superiorly by the inferior margin of the upper vertebral pedicle, and inferiorly by the superior pillars. The intervertebral foramina contain corresponding spinal nerve, veins, fat, arteries, and connective tissue. At the thoracic level, the foramina are at the lower half of the vertebral bodies. The neck of the rib participates in creating the boundaries of the foramen anterolaterally.

In the lumbar region, the foramina are larger and longer.

Text continued on page 116

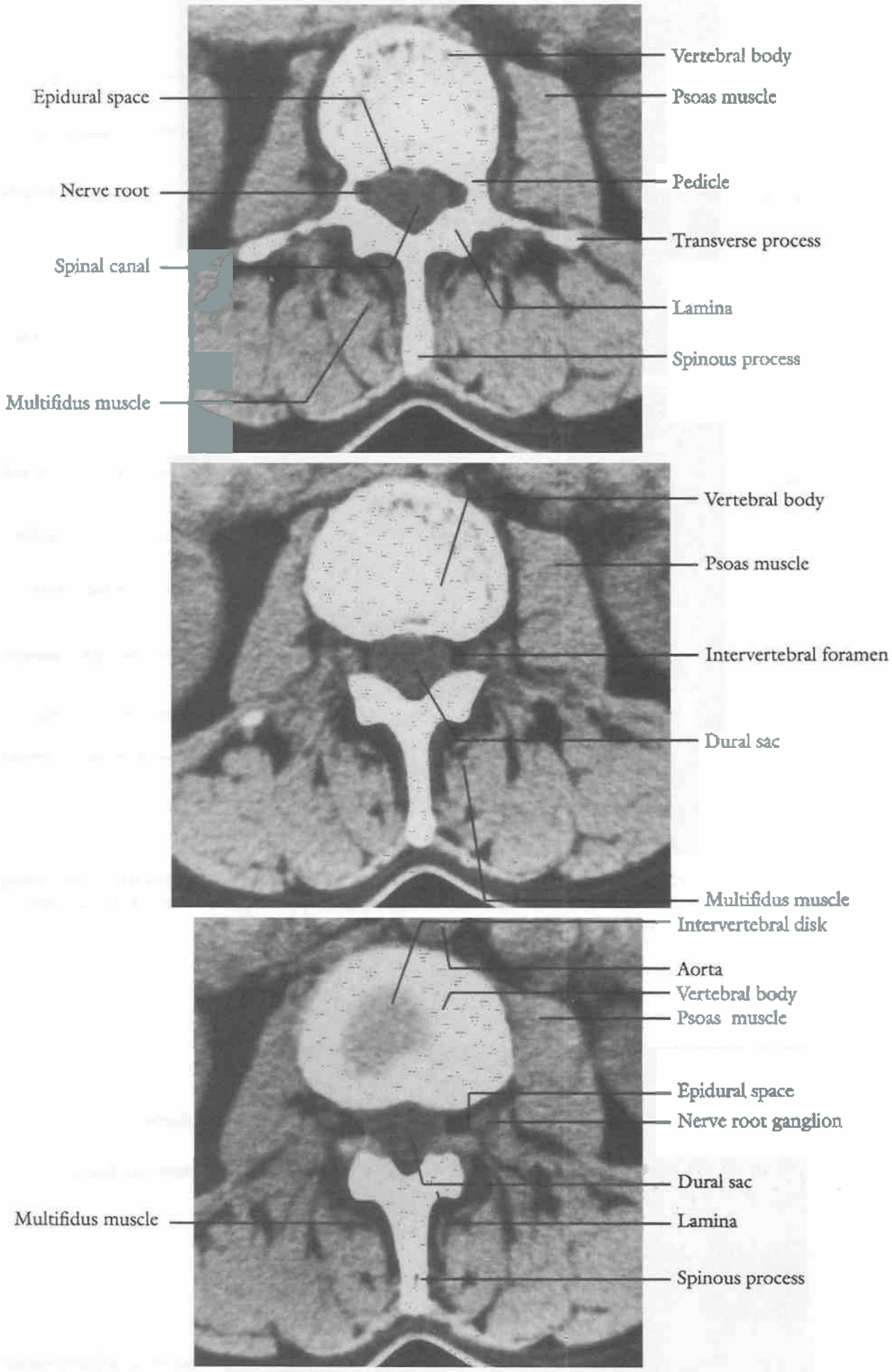

Figure 4–23. *Top*, Axial CT scan through the upper half of the vertebral body demonstrating the full circle of bony canal made by the vertebral body, pedicles, laminae, and the spinous process. *Center*, Axial CT scan through the intervertebral foramen in the midlumbar region. Low attenuation of fat and the slightly increased attenuation of ligamentum flavum help to determine the border of the thecal sac. *Bottom*, Axial CT scan through the midvertebral body in the lumbar region. The ganglion is seen in the most proximal portion of the intervertebral foramen (canal) surrounded by fat.

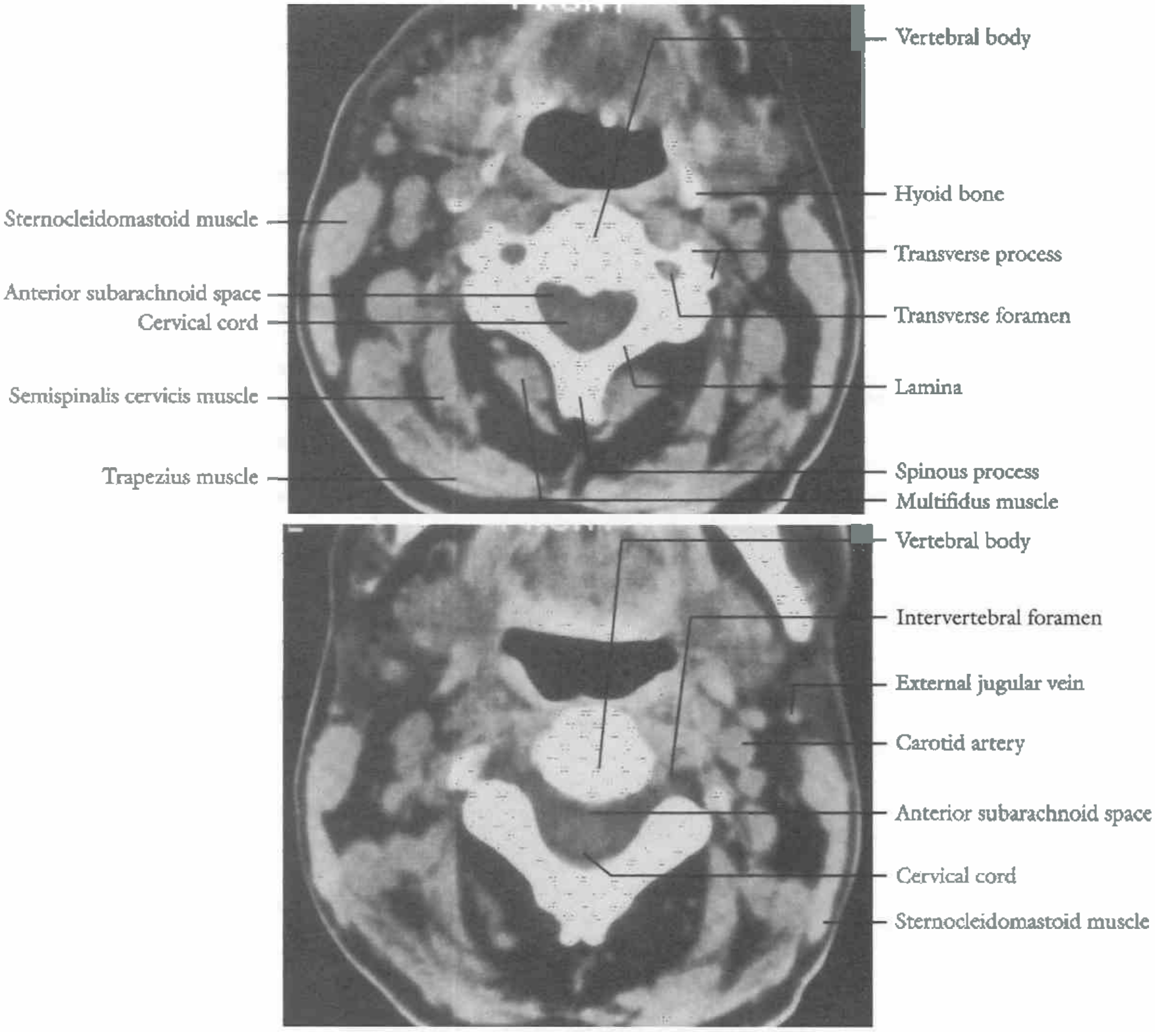

Figure 4–24. *Top*, Axial CT scan through a cervical vertebral body, showing the transverse foramina for passage of the vertebral arteries. *Bottom*, Axial CT scan through the intervertebral foramen in the midcervical region. The large amount of cerebrospinal fluid in front and back of the cervical cord helps to delineate the cervical cord and the roots.

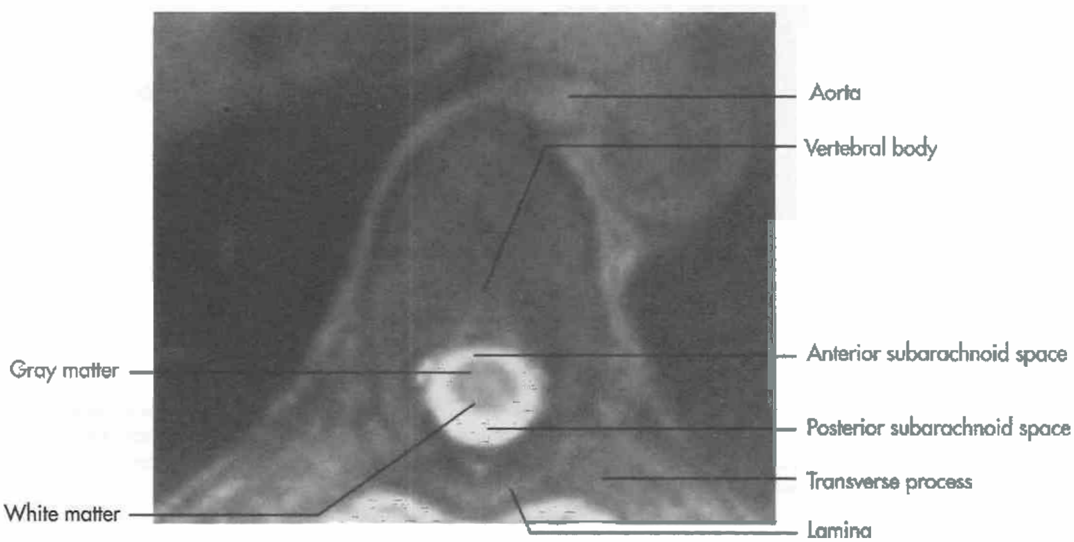

Figure 4–25. Axial T2 MRI at the midthoracic level. The thoracic cord has a more rounded appearance. Note the larger subarachnoid space posteriorly with high signal intensity in this T2 study.

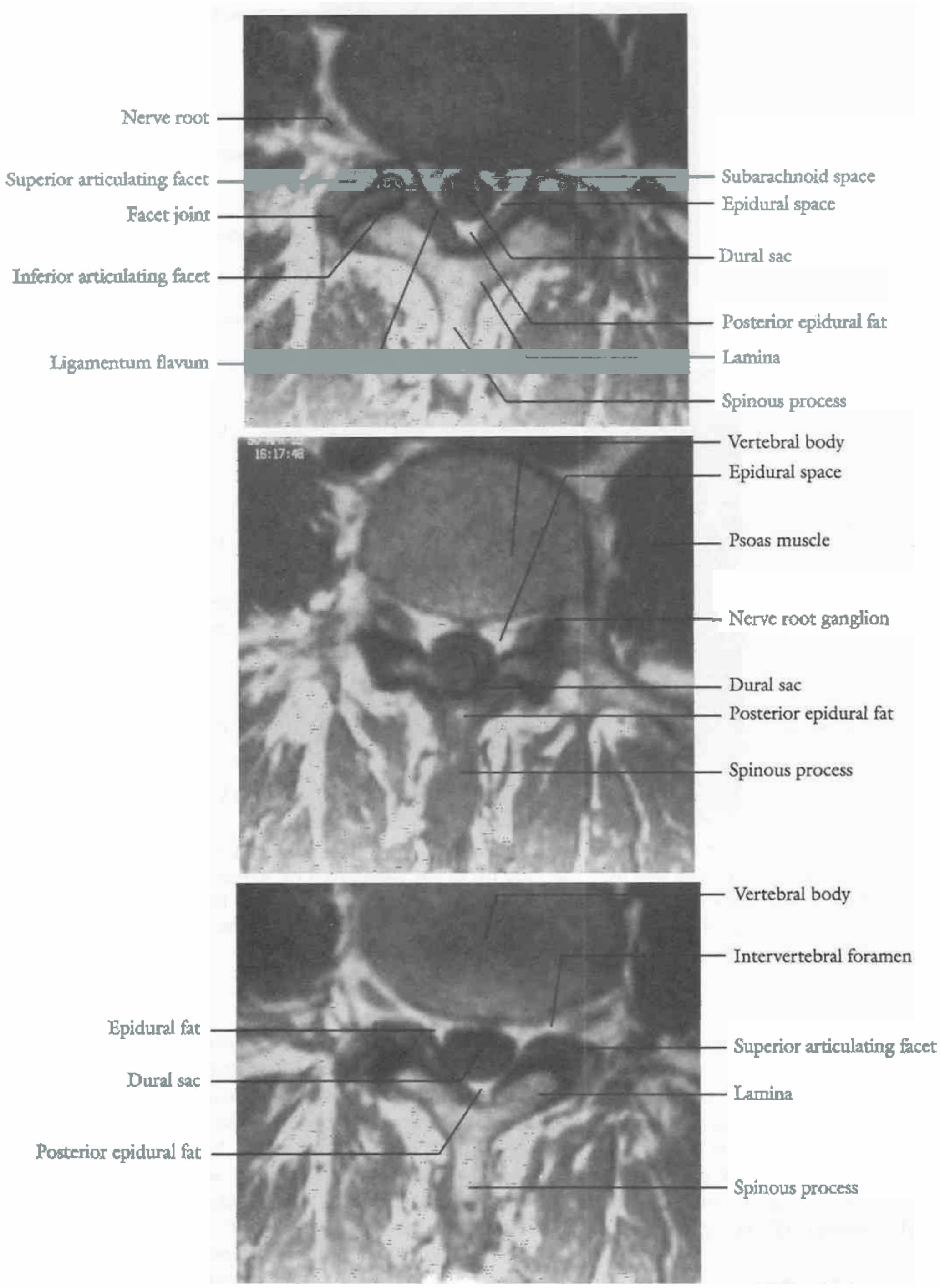

Figure 4–26. *Top*, Axial T1 MRI through the facet joints. The ligamentum flavum, medial to the lamina, is seen bordering the posterior lateral aspect of the canal. The thecal sac is separated from the ligament by fat. *Center*, Axial T1 MRI scan through midportion of the vertebral body in the lumbar region. Fat with high signal intensity is seen anterior to the thecal sac and within the intervertebral foramen. The nerve root ganglion is seen inside the foramen. Dense cortical bone has lower signal intensity relative to the rest of the vertebral body. *Bottom*, Axial T1 MRI of fat in the epidural space helps to outline the thecal sac. Ligamentum flavum, which has a low-signal-intensity border, outlines the canal posterolaterally.

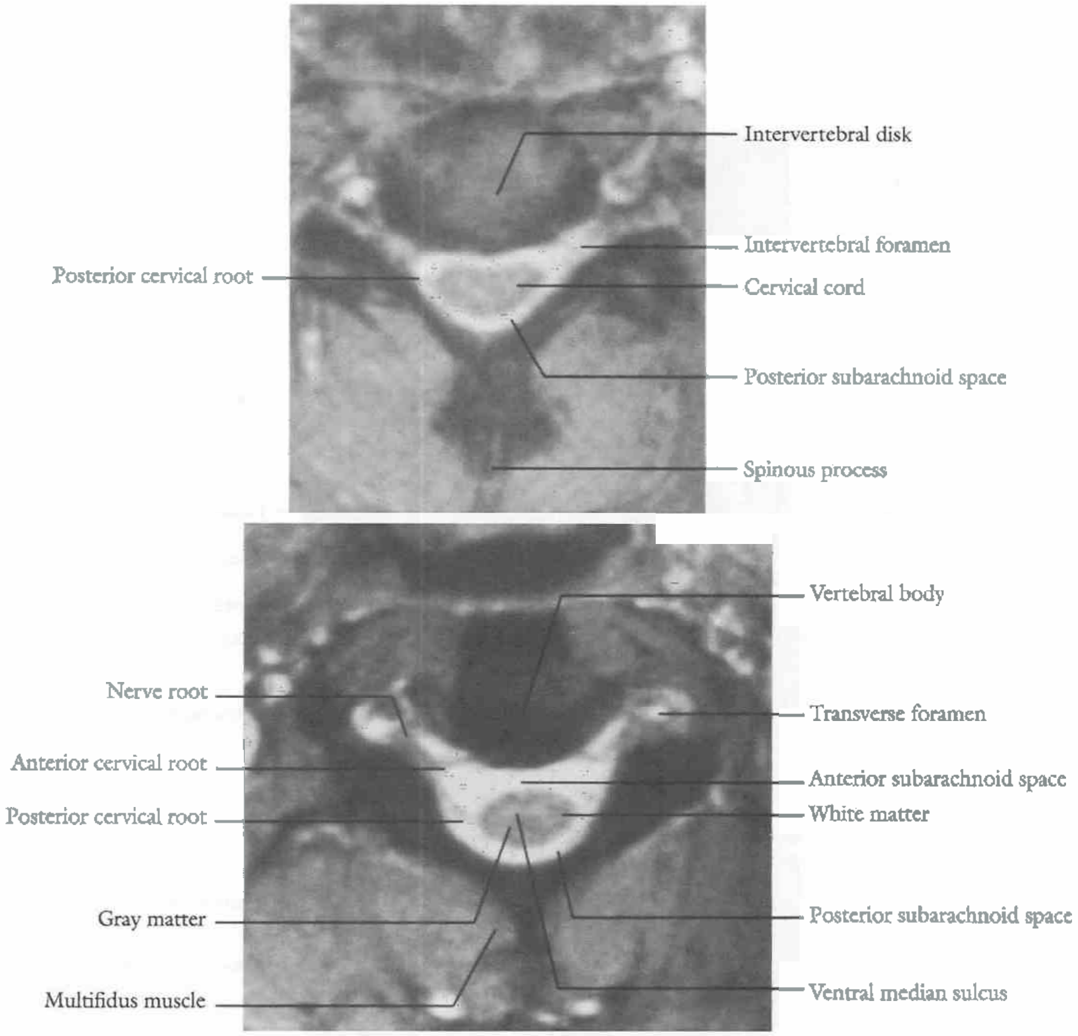

Figure 4–27. *Top*, Axial gradient-echo MRI scan through the intervertebral foramen in the midcervical region. The high-signal-intensity cerebrospinal fluid outlines the cervical cord and the roots (similar to the appearance on intrathecal contrast-enhanced CT scan). Any protrusion into the foramen by degenerative joint disease or disk herniation can be appreciated in this imaging. *Bottom*, Axial gradient-echo MRI scan in the midcervical region, just caudal to the top image, showing the distal end of the intervertebral foramen (canal). The transverse foramina are seen allowing passage of vertebral arteries.

They have a canal-like appearance and are oriented anteriorly and laterally.

On MRI studies, the high signal intensity of the fat on the T1 within the epidural space and the foramina outlines the isointense nerve root, covered by the low signal intensity of CSF (see Fig. 4–26*B*, *C*). On gradient-echo images, the CSF becomes high in signal intensity, outlining the diminished signal intensity of the spinal nerve root and cord (Fig. 4–28*B*).

On CT scans, the water attenuation value of the nerve root and ganglion are seen within the intervertebral foramina, with some low attenuation of the fat in the epidural space (see Fig. 4–23*B*, *C*). The entire length of the foramen, which is actually a canal, can be seen by following the scans from cephalic to caudal levels.

Spinal Canal[8, 35]

The canal measures about 27 mm at the C1 level and 21 mm in the lower cervical area in the sagittal midline plane. The lowest normal diameters of the canal are 12 mm in the lower cervical area and 15 to 16 mm at C1–C2.[32]

In the thoracic area, the spinal canal is completely outlined by bones in the upper half, with some discontinuity of the bone in the lower half to form the facet joints. The canal is rounded and is fairly constant in size and contour, with a triangular appearance in the lower region. In the lumbar area, the canal has a round to oval shape in the upper lumbar region and a triangular shape caudally. In the lower lumbar region, the laminae bow inward with some indentation toward the canal.

On T1 sagittal images, the canal can easily be measured in the anteroposterior diameter (Figs. 4–28 to 4–30). Anteriorly, the canal is outlined by a low signal from the posterior cortex and the posterior longitudinal ligament. The spinal cord, which is isointense on T1 images, is outlined by the low signal intensity of CSF (Figs. 4–28 and 4–29). On gradient images, the intensity of the cord and that of CSF are similar, making it very difficult to measure the spinal cord.

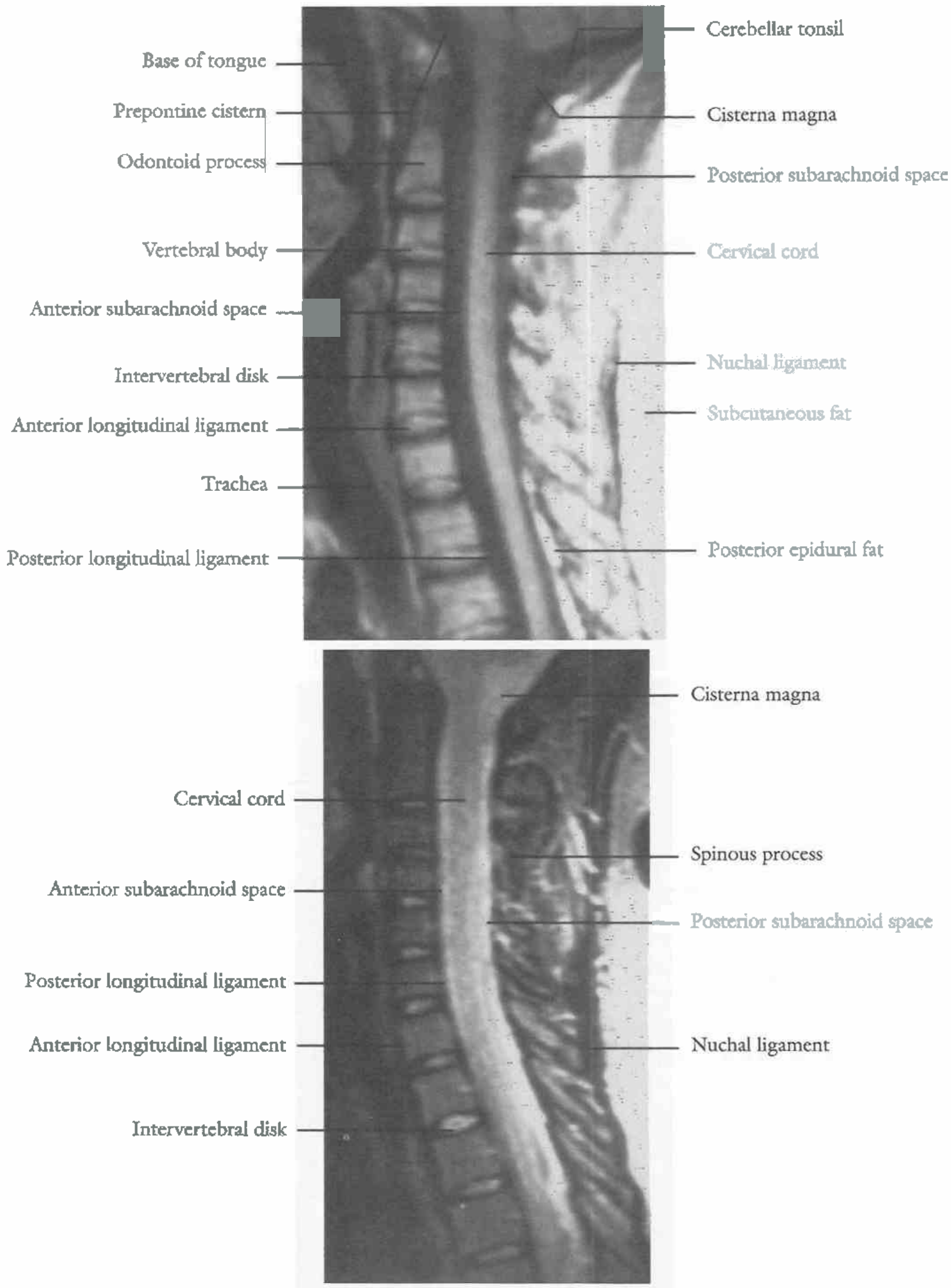

Figure 4–28. *Top*, **Sagittal T1 MRI in cervical area. The intervertebral disk** has [redacted]htly higher intensity relative to outlining cortical bone and the ligaments. The subarachnoid space is larger from C1 to C3 posteriorly, whereas it becomes larger in the midcervical and lower cervical areas anteriorly. *Bottom*, Sagittal gradient-echo study of cervical spine showing increased signal intensity of cerebrospinal fluid similar to that in a T2 study. The healthy intervertebral disk has higher signal intensity as a result of its water content. The anterior and posterior longitudinal ligaments can readily be seen outlining the spinal canal.

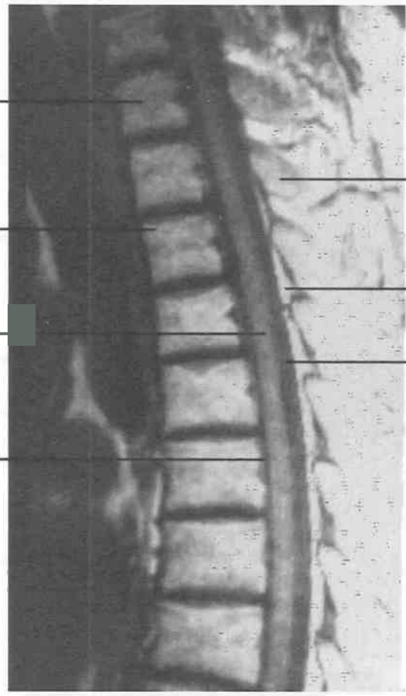

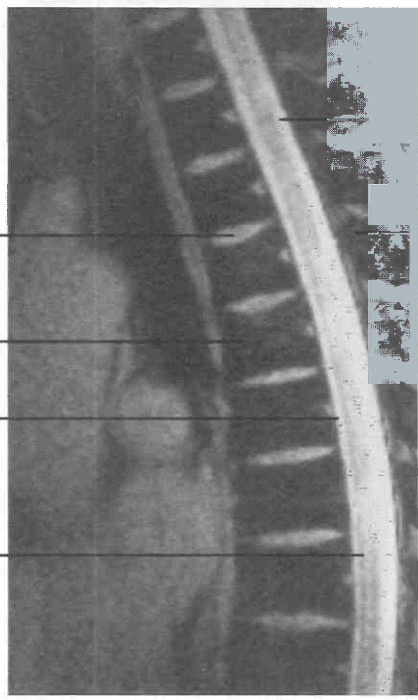

Figure 4–29. *Top*, Sagittal T1 MRI study of the thoracic spine. There is more cerebrospinal fluid posteriorly in the thoracic area. The spinal cord can be measured more accurately with this technique than with gradient-echo or T2 studies. *Bottom*, Sagittal T2 MRI of the thoracic spine. In this image, the border to the thoracic cord is not as clear as in the top image. The high signal intensity indicates a healthy disk.

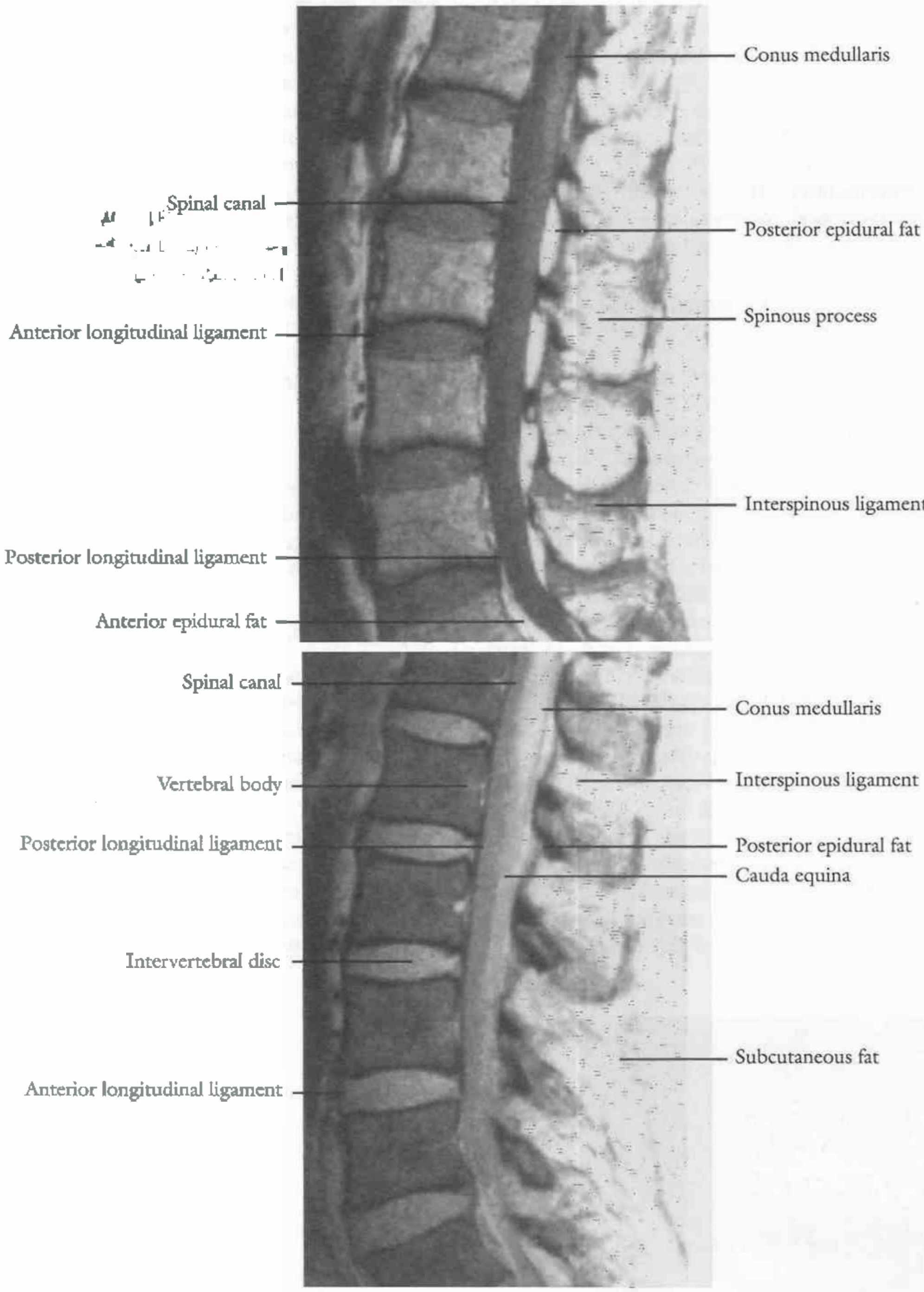

Figure 4–30. *Top*, Sagittal T1 MRI study of the lumbar spine in midline. The epidural fat behind the thecal sac and in front of the distal lumbar area shows high signal intensity. The intervertebral disk space has slightly lower intensity relative to the vertebral body. *Bottom*, Sagittal gradient-echo MRI study of the lumbar area in midline. The cerebrospinal fluid has slightly increased signal intensity. The anterior and posterior longitudinal ligaments are seen outlining the vertebral bodies and intervertebral disk spaces. The interspinous ligaments connect the two adjacent spinous processes.

On T2 images, the CSF has high signal intensity, thereby outlining the decreased intensity of the cord. Care should be taken that the cord measurements on T2 images may be less than their actual size because of partial-averaging volume of the CSF and the cord. On CT scans, the canal border can be identified by the bony margins of the spinous processes, laminae, and posterior aspects of the venous processes (see Figs. 4–22 and 4–23). The cord in the cervical region can be seen without intrathecal contrast (see Fig. 4–24). In the lumbar and thoracic areas, however, intrathecal contrast is needed to evaluate the spinal cord and intracanal abnormalities. The fat within the epidural space and the intervertebral foramina help to outline the disease processes affecting the margins of the spinal canal.

Soft Tissues, Joints, and Ligaments

Intervertebral Disk

The disk spaces separate the two adjacent vertebral bodies. No disk space exists between C1 and C2. The disk comprises the central portion of the nucleus pulposus and the peripheral segment of the annulus fibrosus. The nucleus pulposus is softer with greater water content. The annulus fibrosus comprises hard fibrous tissue surrounding the nucleus. Because of the curvature of the disk spaces in the cervical area, angulation of the gantry to cut through the disk is not always possible unless slices 1.5 mm thick are taken. In the cervical region, the disks are thinner compared to those of the thoracic and lumbar regions. The disks have an attenuation value of 50 to 110 Hounsfield units. The thoracic disks are thinner but larger in the cross-sectional area. In the thoracic area, ligaments connect the crest of the head of the ribs to corresponding disk spaces.

The lumbar disks are thicker and larger. The height of a lumbar disk varies from 8 to 12 mm. The posterior margins are concave or flat except at the level of L5–S1, and these can be convex, bulging into the canal centrally. On T1 images, a disk will have low intensity (Figs. 4–26*A* and 4–27*A*), with increased intensity on gradient-echo images (Fig. 4–30); see Figs. 4–28 and 4–29) and T2 images. Especially on T2 images, the disk should have high signal intensity (see Fig. 4–29*B*). Decreased signal intensity on T2 images is indicative of a decrease in water content, a manifestation of disk degeneration. On sagittal images, anterior and posterior disk margins appear outlined by the anterior and posterior longitudinal ligaments (see Fig. 4–30). Discontinuity of the ligament may suggest a tear resulting from a herniated disk.

On CT scans, the water attenuation of a disk is similar to that of muscle (see Fig. 4–22). The disk border should not extend beyond the posterior aspect of the adjacent vertebral bodies, except at the L5–S1 level, where the disk bulges in midline (Fig. 4–31). With degeneration, a disk will bulge diffusely, extending beyond the border of the vertebral body. Evidence of gas (air density) within a disk suggests the vacuum phenomenon or is a manifestation of an infectious process that requires further investigation. On CT scans, disks and ligaments cannot be distinguished because of their similar attenuation values.

Uncovertebral Joints[3]

In the cervical area, these joints are between the uncinate process and the adjacent vertebral body. With degenerative joint diseases and narrowing of the disk spaces, the joint space also becomes narrowed.

Facet Joints (Fig. 4–32; see also Fig. 4–26)

These are joints between the superior articulating facet of the lower vertebra and the inferior facet of the upper vertebra. They are oriented halfway in the sagittal and axial axes. The superior articulation facet of the lower vertebra is always anterior to the inferior articulating facet of the upper vertebra. The facet joints are oriented almost in the coronal plane in the thoracic region. The articular surfaces are flat, with some convex shape to the nonarticulating parts. Joint spaces are found between the heads of the ribs and the vertebral bodies as well as between the ribs and the transverse processes.

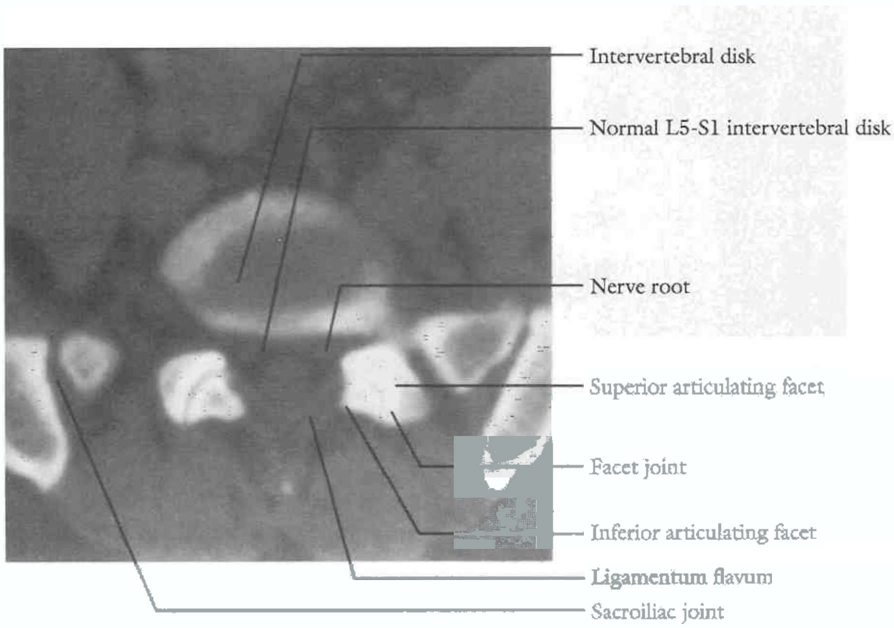

Figure 4–31. Axial CT scan through the intervertebral disk space of L5–S1, demonstrating the flat, slightly concave border of the disk posteriorly, a normal finding. The posterior aspect of the disk spaces is concave in remainder of spinal column.

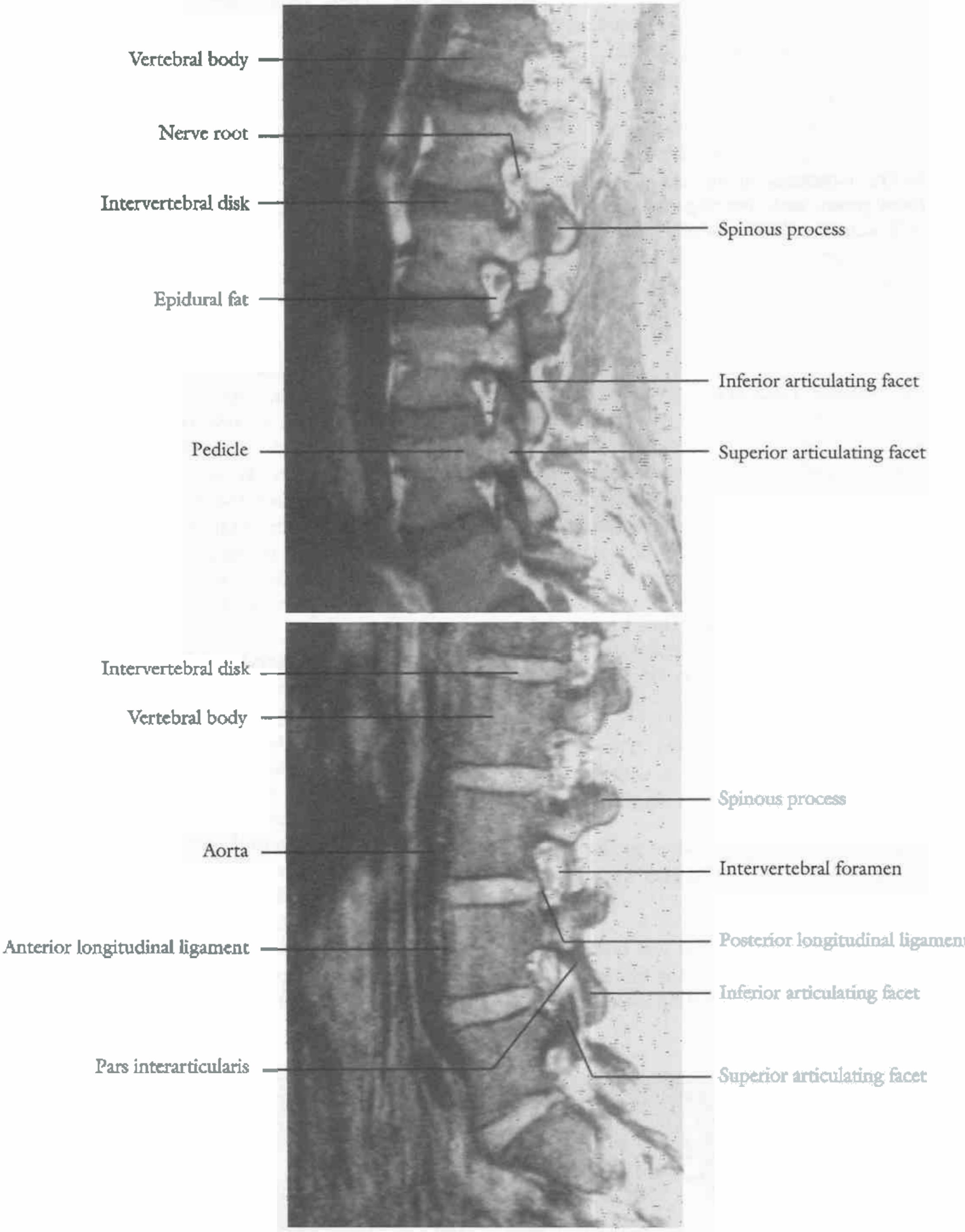

Figure 4–32. *Top*, Sagittal T1 MRI scan in the lumbar spine. The boundary of the intervertebral foramen (pedicle, posterior inferior portion of the vertebral body, intervertebral disk, anterior superior aspect of superior articulating facet) can readily be identified in this para-midline sagittal plane. *Bottom*, Sagittal MRI study of lumbar area in para-midline plane. The very low signal intensity of the cortical bone helps to visualize the upper and lower border of the intervertebral disk. The foramina and the facet joints are clearly visualized on this image. Defects within the pars interarticularis and foraminal narrowing can be appreciated in this axis.

The facet joints are oriented in a parasagittal plane in the upper lumbar area with an oblique orientation in the lower lumbar area. The joint spaces are 2 to 4 mm[3]. The synovium extends into the canal to attach to the ligamentum flavum that covers the anterior end of the joint space. Sagittal MRI studies are useful for evaluation of the facet joints and their orientation (see Fig. 4–32).

Spondylolysis defects can easily be identified on these images. In addition, the fluid within the joint space, which has signal intensity similar to that of water, can be seen outlined by the very low signal of the dense cortical bone of the facets and the isointense ligamentum flavum. Narrowing of the facet joints and spurring can easily be detected on axial CT scans or MRI studies. With CT scans, the dense cortex of the articulating facet is separated by the low attenuation value of the facet joint space (Fig. 4–22).

Ligaments

Anterior Longitudinal Ligament (see Figs. 4–28 to 4–30). This ligament starts from the axis as the anterior atlantoaxial ligament and extends to the sacral segments, connecting the anterior aspects of the vertebral bodies and disk spaces (see Fig. 4–30). On CT scans, the ligament cannot be separated from the bony structures and the disk space. Thickening of the ligament results in a narrowing of the canal in the sagittal diameter.

Posterior Longitudinal Ligament. This ligament begins on the posterior surface of the axis and extends to the sacrum to connect the posterior aspects of the vertebral bodies and disk spaces (see Fig. 4–30).

Interspinous Ligament (see Fig. 4–30). This ligament connects the spinous processes. It has a slightly higher attenuation value, making it recognizable on CT scans.

Nuchal Ligament. This ligament connects the base of the occipital bone to the spinous processes of C1 to C7 (see Fig. 4–28*B*).

Ligamentum Flavum. This ligament has both stretchability and retractability functions, and it is attached to the laminae. It does have a higher attenuation value that can be identified on CT scans. It measures 3 to 5 mm in thickness and extends to the level of the first sacral segment (see Fig. 4–21). The ligamentum flavum and interspinous ligaments can easily be seen on T1 MRI images (Fig. 4–26*A*). Their hypertrophy results in narrowing of the canal, posteriorly and laterally.

Epidural Space (see Figs. 4–23, 4–26, and 4–30). This space contains fat, vessels, and neural elements. In the cervical area, the anterior space is thinner and less visible on CT scans. The internal vertebral veins have no valves, thereby facilitating the spread of infectious processes and metastasis. The anterior and posterior epidural spaces can be visualized by IV injection of contrast medium for evaluation of extradural diseases. The basivertebral vein penetrates the vertebral body to join the internal plexus. The external vertebral plexus lying outside of the vertebral bodies is linked to the internal plexus by veins passing through the ligamentum flavum and the neural foramina.[20]

The epidural space has more fat posteriorly in the thoracic region,[13] with a minimal amount anteriorly (see Fig. 4–29*A*). The venous structures of the epidural space are similar in the cervical and thoracic areas except for a possible link between the anterior and posterior vertebral plexus with the intercostal veins and the azygous system.[30] The epidural space is larger in the lower lumbar area. This is helpful in outlining the disk border. Obliteration of fat in the epidural space is an indication of an epidural process.

Dura Mater, Intradural Space, and Spinal Cord. The dura mater is a hard membrane that forms a sleeve around the subarachnoid space to cover the cord and intracanal component of the nerve roots. It extends beyond the canal to cover the root within the foramina and fuses with the perineurium of the spinal nerves to close the extension of the subarachnoid space (see Fig. 4–27). The cervical cord is wider in the ventral surface and is indented by the anterior median fissure (see Fig. 4–27). The posterior median fissure is shallow.[31] The cervical cord is larger from C3 to C6 as identified on myelography. Because of the larger subarachnoid space in the cervical area, the cord can easily be seen on plain CT scans without intrathecal contrast (see Fig. 4–24). With intrathecal contrast, visualization

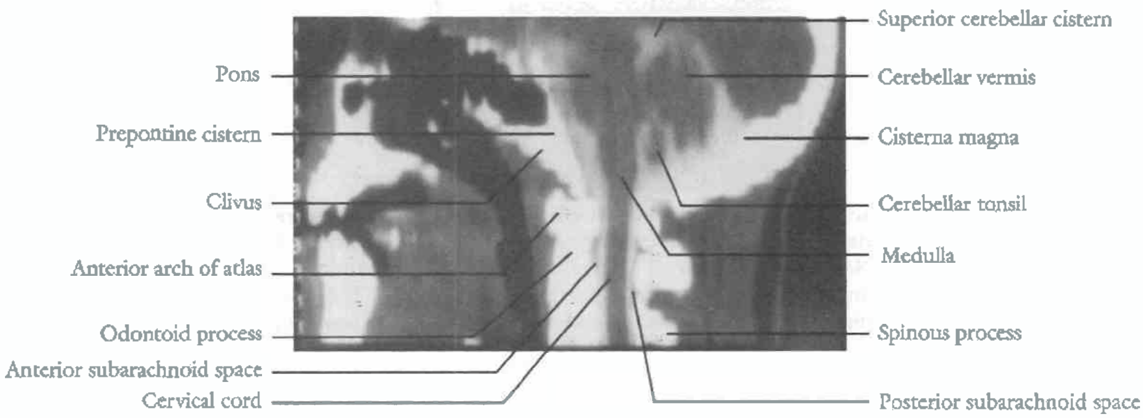

Figure 4–33. Reconstructed image of a cervical spine CT scan with enhancement by intrathecal contrast CT at the craniocervical junction. The upper cervical cord, medulla, pons, cerebellar tonsils, and vermis are surrounded by contrast material.

of the cervical cord and roots can be enhanced significantly (Fig. 4–33).

Eight pairs of cervical spine nerves exist. The first cervical spine nerve passes posterior to the atlanto-occipital joint. The remaining nerves pass through the intervertebral foramina. The number of nerve roots in the cervical region corresponds to the lower vertebral count number (e.g., the root passing through the C5–6 foramen is the C6 that lies medial to the pedicle of C5). In the thoracic area, the cord has a more rounded appearance[26, 30] (see Fig. 4–25). The cord becomes larger from T9 to T12,[32] terminating in conus with rapid tapering in its diameter.

In the upper thoracic region, the location of pathology is about two vertebrae higher than the corresponding clinical level. The discrepancy increases to three segments in the lower thorax. The spinal nerves are difficult to visualize on plain CT scans. The dura terminates at the level of S2 and fuses with the filum terminale to terminate at the coccyx. The lumbar canal contains the conus, cauda equina, and the filum terminale. The conus medullaris ends at the L1–2 disk space (see Fig. 4–30), becoming the filum terminale. In the lumbar area, the spinal nerves can be seen on plain CT scans, exiting medial to the corresponding pedicles (see Figs. 4–23*A* and 4–31).

References

1. Berman SA, Hayman LA, Hinck VC: Correlation of CT cerebral vascular territories with function: 1. Anterior cerebral artery. AJNR Am J Neuroradiol 1:259–263, 1980.
2. Berry I, Sigal R, Lebas J, et al: Magnetic resonance imaging: principles, technique and imaging protocols. In Manelfe C (ed): Imaging of the Spine and Spinal Cord. New York, Raven Press, 1992, pp 157–194.
3. Carrera GF, Haughton VM, Syvertsen A: Computed tomography of the lumbar facet joints. Radiology 134:145–148, 1980.
4. Cohen CR, Duchesneau PM, Weinstein MA: Calcification of the basal ganglia as visualized by computed tomography. Radiology 134: 97–99, 1980.
5. Donovan Post JM, Sze G, Quencer RM: Gadolinium-enhanced MR in spinal infection. J Comput Assist Tomogr 14:721–729, 1990.
6. Drayer BP, Burger P, Dawrin R, et al: MRI of brain iron. AJNR Am J Neuroradiol 7:373–380, 1986.
7. Dryer PB, Rosenbaum AE, Reigel DB: Metrizamide computed tomography cisternography: Pediatric application. Radiology 124:349–357, 1977.
8. Dryer PB, Rosenbaum AE, Higman HB: Cerebrospinal fluid imaging using serial metrizamide CT cisternography. Neuroradiology 13:7–17, 1977.
9. Epstein BS: The Spine: A Radiological Text and Atlas. Philadelphia, Lea & Febiger, 1976.
10. Goss C (ed): Gray's Anatomy, 29th ed. Philadelphia, Lea & Febiger, 1973.
11. Hanaway J, Scott W, Strother C: Atlas of the Human Brain and the Orbit for Computed Tomography. St. Louis, Warren Green, 1977.
12. Haughton VM, Syvertsen A, Williams AL: Soft tissue anatomy within the spinal canal as seen on computed tomography. Radiology 134: 649–655, 1980.
13. Haughton VM, Williams AL: CT anatomy of the spine. CRC Diagn Imaging 15:173–192, 1981.
14. Hayman LA, Berman SA, Hinck VC: Correlation of CT cerebral vascular territories with function: Posterior cerebral artery. AJNR Am J Neuroradiol 2:219–225, 1981.
15. Kido DK, LeMay M, Levinson AW, et al: Computed tomographic localization of the precentral gyrus. Radiology 135:373–377, 1980.
16. Kido DK, O'Reilly GVA, Naheedy MH: Radiological perspective on idiopathic low back pain. In White AA, Gordon SL (eds): Symposium on Idiopathic Low Back Pain. St. Louis, CV Mosby, 1982, pp 178–194.
17. Kjos BO, Norman D: Strategies for efficient imaging of the lumbar spine. In Brantzawaski M, Norman D (eds): Magnetic Resonance Imaging of the Central Nervous System. New York, Raven Press, 1987, pp 279–287.
18. Labischong P, et al: Normal anatomy of the spine, spinal cord, and nerve roots. In Manelfe E (ed): Imaging of the Spine and Spinal Cord. New York, Raven Press, 1992, pp 1–91.
19. LaMasters DL, et al: Computed tomography of the spine and spinal cord. In Newton TH, Potts DG (eds): Modern Neuroradiology, vol 1. San Anselmo, Clavadel Press, 1983, pp 53–113.
20. Lewit K, Sereght T: Lumbar epiduragraphy with special regard to the anatomy of the lumbar spine. Neuroradiology 8:233–240, 1975.
21. Masdeu JC, Grossman BC (eds): Head and Spine Imaging. New York, John Wiley & Sons, 1985.
22. Matsui T, Hirano A: An Atlas of the Human Brain for Computed Tomography. New York, Igaku-Shoin, 1978.
23. McPherson P, Matheson MS: Comparison of calcification of pineal, habenular commissure, and choroid plexus on plain films and computed tomography. Neuroradiology 18:67–72, 1979.
24. Modic MT: Calcification of the choroid plexus visualized by computed tomography. Radiology 135:369–372, 1980.
25. Naidich TP, Moran CJ, Pudlowski RM, et al: Advances in diagnosis: Cranial and spinal computed tomography. Med Clin North Am 63: 849–895, 1979.
26. Resjo IM, Harwood-Nash DC, Fitz CR: Normal cord in infants examined with computed tomographic metrizamide myelography. Radiology 130:691–696, 1979.
27. Ross JS, Modic MT, Masaryk TJ, et al: Assessment of extradural degenerative disease with Gd-DTPA-enhanced MR imaging: Correlation with surgical and pathologic findings. AJNR Am J Neuroradiol 10:1243–1249, 1989.
28. Russell EJ, D'Angelo CM, Zimmerman RD, et al: Cervical disc herniation: CT demonstration after contrast enhancement. Radiology 152:703–712, 1984.
29. Sherman JL, Citrin CM: MR demonstration of normal CSF flow. AJNR Am J Neuroradiol 7:3–6, 1986.
30. Taylor AJ, Haughton VM, Doust BD: CT imaging of the thoracic spinal cord without intrathecal contrast medium. J Comput Assist Tomogr 4:223–224, 1980.
31. Theron J, Moret J: Spinal Phlebography: Lumbar and Cervical Techniques. New York, Springer-Verlag, 1978.
32. Thijssen HO, Rombouts JJ, Walder HA: Morphology of the cervical spinal cord on computed myelography. Neuroradiology 18:57–62, 1979.
33. Truex RC, Carpenter MB: Human Neuroanatomy, 6th ed. Baltimore, Williams & Wilkins, 1969.
34. Williams PL, Warwick R: Functional Neuroanatomy of Man. Philadelphia, WB Saunders, 1975.
35. Wolpert SM: Appropriate window settings for CT anatomic measurements. Radiology 132:775, 1979.
36. Zatz LM: Basic principle of computed tomography scanning. In Newton TH, Potts DG (eds): Radiology of the Skull and Brain: Technical Aspects of Computed Tomography, vol. 5. St. Louis, CV Mosby, 1981, pp 3853–3876.
37. Zimmerman RA, Bilaniuk LT: Age-related incidence of pineal calcification detected by computed tomography. Radiology 142:659–662, 1982.

5

Intracranial Neoplasms

Stephen A. Kieffer, Ja-Kwei Chang

Primary neoplasms of the central nervous system (CNS) represent nearly 10% of all tumors reported in large autopsy series.[286] The American Cancer Society estimates that nearly 17,000 primary intracranial neoplasms were newly diagnosed in the United States in 1999.[182] The brain and meninges are also common sites of secondary tumor implantation; hematogenous metastases likely account for more intracranial tumors than primary brain neoplasms.[203, 264]

Approximately 10% of primary brain tumors occur in children. Brain tumors, the most common solid neoplasms of childhood, are second in frequency only to the leukemias among childhood malignancies.[25, 352] Although the incidence of intracranial neoplasms and the proportion of higher grade (more malignant) tumors are both considerably lower in children than in adults, primary brain tumors are nevertheless the leading cause of cancer related deaths in children younger than 15 years.[245]

In 1993, the World Health Organization (WHO) issued a major revision of its classification system for tumors of the brain and CNS.[163, 303] This system is based on the presumed cell of origin and assigns a numerical grade estimating the biologic potential of the particular neoplasm.[303] The revised classification has been widely accepted around the world. A further revision issued in 2000 serves as the basis for the organization of this chapter (Table 5–1).[164]

Approximately 40% of intracranial neoplasms are of neuroepithelial origin, including astrocytomas, glioblastomas, oligodendrogliomas, ependymomas, medulloblastomas, and less common variants and combinations of these cell types.[342] Meningiomas (15% to 18%), pituitary adenomas (7% to 8%), and schwannomas (6%) also occur relatively frequently within the cranial vault.[342]

The presenting symptoms in most patients with intracranial neoplasms are often nonspecific, initially mild, or both. Headache, reported by about 50% of patients with brain tumors, is the most common initial complaint.[85, 264] The headache is frequently described as diffuse and more severe in the morning and often dissipates in a few hours even without treatment.[85] When unilateral, it can accurately indicate the hemisphere involved by tumor.[108] Episodes of confusion or change in behavior also commonly bring the patient to the physician. Unfortunately, headache and personality change are often attributed to other causes.[263] Manifestations of focal cerebral dysfunction (e.g., unilateral weakness, aphasia) are less common presenting complaints, but a careful history often reveals the prior occurrence of less specific symptoms.

It is the progressive nature of the symptoms that eventually leads to consideration of brain tumor as a diagnostic possibility, but this is often late in the course of the tumor. An exception to this more typical pattern—insidious onset and slow progression with resultant late diagnosis of intracranial neoplasm—is the abrupt onset of seizures, which are typically focal but may become generalized and lead to loss of consciousness.[85] Seizure is the presenting complaint in 15% to 95% of patients with brain tumors, occurring more frequently in low grade gliomas and meningiomas than in higher grade gliomas and lymphomas.[85]

Intracranial neoplasms produce symptoms by three mechanisms[331]: (1) infiltration and destruction of normal tissues (e.g., by a glioblastoma), (2) localized cortical irritation or depression (e.g., by a convexity meningioma), or (3) expansion within the rigid and unyielding cranial vault. Edema of the white matter adjacent to the tumor is often extensive and may account for much of the patient's symptomatology and neurologic deficit,[106, 286] an impression that is verified by the striking improvement, both clinical and on imaging, exhibited by many patients after systemic administration of corticosteroids.[75]

An increase in intracranial pressure above the normal level of 180 mm H_2O commonly accompanies an expanding intracranial mass. Headache, nausea, vomiting, and sixth cranial nerve palsy may reflect increased intracranial pressure.[85] Prolonged or significantly elevated intracranial pressure manifests clinically as loss of attentiveness, apathy, and drowsiness.[328] These signs of depressed cerebral function are most likely caused by diminished cerebral blood flow secondary to distention of the intracranial contents. This distention also produces traction on the overlying meninges, probably accounting for the headache, nausea, and vomiting that occur with chronic intracranial hypertension.

Diagnostic Imaging

The goals of diagnostic imaging in the patient with suspected intracranial tumor include *detection* of the presence of a neoplasm, *localization* of the extent of the tumor (including definition of involvement of key structures and assessment of the presence and severity of secondary changes, e.g., edema, herniation, hemorrhage), and *characterization* of the nature of the process.

Imaging (usually magnetic resonance imaging [MRI]) is also extensively utilized in treatment planning before surgery or radiation to define the gross tumor margins and to permit selection of the safest approach to the lesion.[276]

Table 5–1. Classification of Tumors of the Nervous System

Gliomas	
Astrocytomas	
Circumscribed astrocytomas	
Juvenile pilocytic astrocytoma	
Pleomorphic xanthoastrocytoma	
Subependymal giant cell astrocytoma	
Diffuse astrocytomas	
Low grade astrocytoma	
Optic pathway glioma	
Brainstem glioma	
Anaplastic astrocytoma	
Glioblastoma multiforme	
Gliomatosis cerebri	
Gliosarcoma	
Oligodendrogliomas	
Low grade oligodendroglioma	
Anaplastic oligodendroglioma	
Ependymomas	
Ependymoma	
Subependymoma	
Choroid plexus tumors	
Choroid plexus papilloma	
Choroid plexus carcinoma	
Nonglial Tumors	
Neuronal and mixed neuronal/glial tumors	
Ganglioglioma	
Gangliocytoma	
Dysplastic gangliocytoma of the cerebellum (Lhermitte-Duclos)	
Desmoplastic infantile ganglioglioma	
Dysembryoplastic neuroepithelial tumor	
Central neurocytoma	
Pineal parenchymal tumors	
Pineoblastoma	
Pineocytoma	
Embryonal tumors	
Medulloblastoma	
Supratentorial primitive neuroectodermal tumor	
Tumors of the Cranial Nerves	
Schwannoma	
Neurofibroma	
Malignant peripheral nerve sheath tumors	
Tumors of the Meninges	
Meningioma	
Hemangiopericytoma	
Mesenchymal nonmeningothelial tumors	
Melanocytic tumor	
Hemangioblastoma	
Tumors of the Hematopoietic System	
Primary CNS lymphoma	
Secondary CNS lymphoma	
Histiocytic lesions	
Granulocytic sarcoma (chloroma)	
Germ Cell Tumors	
Germinoma	
Teratoma	
Other germ cell tumors	
Tumors of the Sellar Region	
Pituitary adenoma	
Microadenoma	
Macroadenoma	
Craniopharyngioma	
Rathke cleft cyst	
Tumors of the neurohypophysis	
Chordoma	
Metastatic Tumors	
Metastases to the brain	
Metastases to the skull and intracranial dura	
Leptomeningeal metastasis (leptomeningeal carcinomatosis)	

Based on the World Health Organization (WHO) Classification (2000 Revision). This classification has been adapted and modified from Kleihues P, Cavenee WK (eds): Pathology and Genetics of Tumours of the Nervous System. Lyon, International Agency for Research on Cancer, 2000.

Functional MRI is increasingly employed preoperatively to determine the location of functionally eloquent cortex, which can then be avoided during an operative approach.[185] Interactive computerized neuronavigational devices utilize these data (1) to allow administration of very high doses of precisely focused radiation to small (up to 3 cm) intracranial tumors while sparing the adjacent normal brain[260, 325] and (2) to accurately register the previously acquired image data set onto intraoperative space, thus enabling precise intraoperative localization of surgical instrumentation relative to tumor margins, key vascular structures, and other critical anatomy.[202, 325] A relatively new and highly promising application is image guided surgery, in which the entire surgical resection is guided by direct real time MRI in the operating room environment.[337]

Followup assessment of intracranial neoplasms utilizes CT and MRI and related techniques extensively, including MR spectroscopy and MR perfusion weighted imaging, to monitor post-treatment complications and to detect the presence of residual or recurrent tumor.[231, 276]

Computed Tomography

Before the introduction of computed tomography (CT) in the early 1970s, confirmation of the presence or absence of brain tumor involved the use of invasive diagnostic procedures (e.g., cerebral angiography or pneumoencephalography) that required hospitalization and carried some morbidity and risk. Clinicians were often reluctant to submit patients with uncertain history and findings to such risks.

The advent of CT significantly altered the method and timing of diagnostic evaluation of the patient with suspected brain tumor.[13, 14] CT evaluation of the brain is relatively noninvasive and is therefore easily and rapidly accomplished. In the mid-1970s, CT emerged as the primary diagnostic screening modality for the *detection* of intracranial disease. Areas of structural abnormality (e.g., tumors) appeared on CT as regions of altered tissue radiographic density.[15] Accuracy of *localization* with CT exceeded the accuracy that could be achieved by cerebral angiography or other invasive diagnostic procedures. Another important advantage of CT was the demonstration of *no* disease in the symptomatic patient who did not have a neoplasm or other structural abnormality, thus affording reassurance to the patient and physician and avoiding costly hospitalization and more invasive or more hazardous diagnostic procedures.[13, 355] Conversely, CT occasionally revealed abnormalities (including tumors) that were not suspected clinically in patients with relatively nonspecific complaints.[14, 346]

Magnetic Resonance Imaging (MRI)

Since its introduction as a clinically practicable diagnostic modality in the early 1980s, MRI has rapidly earned recognition as the optimal screening technique for the detection of most intracranial neoplasms.[10, 11, 37, 172, 275] Compared with CT, MRI using spin echo, gradient echo, and combination spin and gradient echo pulsing sequences before and after intravenous (IV) administration of paramagnetic contrast agents provides inherently greater contrast resolution between structural abnormalities and adjacent brain parenchyma and has proved to be even more sensitive in the detection of focal lesions of the brain.[158, 172, 275] Early experience suggested that 3% to 30% more focal intracranial lesions could be identified on MRI than on CT.[37, 100]

Lesions and tissues with increased water content appear even more conspicuous on T2-weighted MR images than on CT images obtained after IV infusion of contrast agents.[36] Delineation by MRI of normal and abnormal soft tissue anatomy in the posterior cranial fossa, near the base of the skull, and in other areas of the brain that lie adjacent to dense bone is considerably better than with CT because of MRI's lack of the beam hardening artifacts secondary to absorption of x-rays in bone seen on CT.[39] Accuracy of lesion localization on MRI is enhanced by its direct multiplanar capability, which permits acquisition of images in the coronal and sagittal planes in addition to the axial plane conventionally used in CT. MRI offers superior contrast resolution, including greater sensitivity for the detection of subacute and chronic hemorrhage in association with tumors and other structural lesions of the brain.[9, 276] The ability with MRI (using conventional anatomic imaging protocols as well as MR angiography sequences that display blood flow) to visualize vessels supplying and draining structural lesions in the brain adds yet another important dimension of information that can contribute to the diagnostic assessment.

Even with current state of the art equipment utilizing very high magnetic fields and rapidly switching gradient coils, MR nevertheless suffers two disadvantages in comparison with CT in the assessment of intracranial structural abnormalities: (1) MRI requires significantly longer image acquisition times, and (2) abnormalities involving cortical bone, intratumoral calcification, and hyperacute hemorrhage are more clearly and accurately assessed with CT. Newer multi-slice helical or spiral CT scanners are capable of providing highly collimated submillimeter thickness sectional images in extremely short acquisition times, and thus areas of hyperostosis or bone destruction, intratumoral calcifications, and early intratumoral or peritumoral hemorrhage are more completely defined with greater certainty on CT than on MRI.[36, 275] The much faster acquisition capability of current CT units strongly favors their use in patients who are critically ill or medically unstable. Also, in patients with magnetically controlled cardiac pacemakers and other internal paramagnetic metallic devices, the risk of the MRI magnet interacting with such devices may preclude the use of MRI.[297]

Given both the higher cost and more restricted availability of MR equipment to date as well as continuing improvements in CT equipment and scanning techniques that permit shorter examination times with improved spatial and contrast resolution, it is not surprising that CT remains a major imaging technique for the followup of intracranial mass lesions. In current clinical practice, initial diagnosis and localization of brain lesions are most often accomplished with MRI, but the imaging modality of convenience for followup studies is often CT.

Diagnostic Uncertainties

Resolution of soft tissue anatomy underlying thick dense bony structures remains a significant problem with CT. Small hyperdense lesions at the periphery of the brain may be overlooked on CT because they may "blend" with the adjacent bone unless relatively high center and window width settings are employed.[287]

Small lesions with a diameter less than or approximating the thickness of the CT or MR "slice" may not be accurately depicted, because the density or signal intensity reflects averaging of the lesion and the adjacent tissues included in the slice volume.[91] Unless very thin slices are employed, small tumors may thus be obscured.

Localization of a peripherally situated neoplasm as either within (intraaxial) or outside (extraaxial) the brain may be difficult on CT. The presence of inward "buckling" of the adjacent gray-white matter junction indicates that the tumor is extracerebral (see Fig. 5–36*A*); when this sign is demonstrated, it appears to be reliable and valid, but it was identified on CT in only 40% of one large group of superficially situated meningiomas.[113] In contradistinction, peripherally located intraaxial tumors tend to spread and widen the adjacent white matter, displacing the gray-white junction outwardly.[16, 276] Other factors that may aid in establishing on CT that a lesion is extraaxial are the demonstration of adjacent bone destruction or hyperostosis (see Fig. 5–36), widening of the surface subarachnoid spaces adjacent to the margins of the lesion, and continuity of the tumor with the falx or tentorium.[218, 276]

CT in the modified coronal projection and MRI in the true coronal projection have proved to be of considerable help in the evaluation of questionable areas at the periphery of the brain, where the previously described problems of volume averaging and lesion detection or localization occur.[210] Coronal MR images are also valuable in establishing whether a tumor is supratentorial or infratentorial, because the tentorium is oriented nearly horizontally, and imaging in the coronal plane allows precise determination of the relationship of adjacent mass lesions to this structure.[276] Multiplanar MRI also increases the diagnostic precision with which paraventricular masses can be differentiated from intraventricular masses. Paraventricular tumors characteristically displace the choroid plexus and compress the lateral ventricles, whereas intraventricular masses cause local ventricular expansion and generally conform to the shape of the ventricle.[173]

Contrast Enhancement

IV administration of iodinated contrast medium causes a transient increase in the attenuation coefficient of normal

gray matter and accentuates the difference in radiographic density on CT images between white matter and gray matter in the normal brain.[112] Similarly, IV administration of paramagnetic contrast agent (e.g., gadolinium chelates) transiently induces shortening of both the T1 and T2 relaxation times of normal gray matter and accentuates the difference in MR signal intensity between normal cerebral gray matter and white matter.[1] Most intracranial neoplasms also exhibit "contrast enhancement" in all or part. The presence, extent, and pattern of tumor contrast enhancement has proved to be of significant value in improving the detection, localization, and characterization of intracranial neoplasms by CT[16, 53] and MRI.[100]

Although the passage of *intravascular* contrast agent through brain parenchyma causes brief transient enhancement of the normal cerebral cortex,[1, 112] leakage of contrast material into the *extravascular* extracellular space accounts for the more pronounced and somewhat longer lasting contrast enhancement seen in many tumors and other structural abnormalities of the brain on both CT[51, 53] and MRI.[1] The mechanisms involved in contrast enhancement of intracranial neoplasms on CT and MRI and in the uptake of radionuclide by such tumors appear to be identical.[10, 53, 103, 112]

In normal brain, tight intercellular junctions between capillary endothelial cells create a "blood-brain barrier" that prevents escape of radionuclide or contrast agent from the intravascular space. In gliomas, electron microscopic studies have demonstrated that the endothelial junctions are frequently patent and that the level of junctional patency is proportional to the degree of tumor malignancy.[198] It therefore seems reasonable to postulate that the intensity of contrast enhancement in gliomas and other intracranial tumors reflects the degree of blood-brain barrier breakdown.[51, 53, 236, 289] Experimental data support this hypothesis by demonstrating that the peak intensity of tumor contrast enhancement in malignant gliomas occurs 20 to 60 minutes later than the peak serum concentration of contrast agent.[236, 293] Furthermore, glucocorticoids, which are known to diminish defects in the blood-brain barrier, also significantly reduce the extent of contrast enhancement in primary and secondary brain tumors.[75, 86, 134]

Factors involved in maximizing contrast enhancement of intracranial neoplasms on CT or MRI include the quantity of injected contrast agent and the timing of the images. Conventional protocols for IV administration of contrast media for CT use 28 to 42 grams of iodine (100 to 150 mL of 60% iodine concentration injected as a bolus or 200 to 300 mL of 30% iodine concentration delivered as an infusion). Doubling of the dose of contrast material has been reported to significantly increase the incidence, extent, and intensity of contrast enhancement in both gliomas and metastases on CT images obtained 60 to 90 minutes after injection,[137, 294, 299] without permanent alteration of serum creatinine levels.[136] Not only are more lesions identified with this delayed double dose technique but also hypodense centers within "ring" lesions have been observed to gradually opacify.[236, 294] Because of the potential for permanent renal damage with such high doses of iodinated contrast agents and because the serum creatinine concentration does not assay all aspects of renal function, use of this double dose technique should be restricted to situations in which the clinical suspicion of one or more focal lesions is high and results of previous studies have been equivocal or negative.

The standard dose of paramagnetic contrast agent (typically a chelate of gadolinium) administered intravenously for MRI is 0.1 millimoles per kilogram of body weight.[100] In a comparative study, the sensitivity of contrast enhanced MRI using conventional single dose technique for the detection of cerebral metastases exceeded that of contrast enhanced CT, even with double dose of contrast material and delayed imaging.[82]

The diagnostic efficacy of a double dose of gadolinium (0.2 mmol/kg) has been open to question, and few centers currently use it. A triple dose (0.3 mmol/kg) has also been advocated, with some evidence that its use demonstrates more lesions in the brain.[135, 359]

Contrast enhancement on MRI is usually assessed on T1-weighted images obtained with fat saturation. However, enhancement is also demonstrated on T2-weighted images obtained with fluid attenuated inversion recovery (FLAIR); this latter technique has proved to be advantageous in the evaluation of peripherally located superficial lesions of the brain and in meningeal disease.[211]

Application of a strong radiofrequency pulse that is slightly offset from the resonance frequency of water protons before initiation of the standard T1-weighted spin-echo pulsing sequence produces saturation of protons in macromolecules, which is then transferred to the free water protons, thus diminishing their signal intensity. Because this maneuver does not affect the T1 shortening caused by IV administration of gadolinium, the intensity and conspicuity of resultant contrast enhancement are increased.[105] This phenomenon is known as *magnetization transfer* (MT), and its application in brain tumor MRI has been judged as equivalent to the improvement gained with administration of high doses of gadolinium.[1] However, because of greater suppression of white matter signal, magnetization transfer alters tissue contrast relationships such that certain structures (basal ganglia, pulvinar, substantia nigra) become more conspicuous on noncontrast MT images, whereas other structures that normally enhance (choroid plexus, cerebral veins and dural venous sinuses, body of caudate nucleus, pituitary gland) do so more conspicuously on MT images acquired after contrast administration.[1] The reader must therefore exercise caution in interpreting areas of apparent contrast enhancement as possibly signifying disease.

Newer Diagnostic Techniques

Accumulated experience together with continuing improvements in contrast discrimination and spatial resolution have permitted highly accurate correlation between CT and MRI appearance and histologic grading of supratentorial gliomas.[10, 51, 84, 191, 276] However, noninvasive differentiation between high grade glioma with a cystic or necrotic center, solitary metastatic carcinoma with central necrosis, resolving hematoma, resolving infarction, atypical masslike presentation of a tumefactive multiple sclerosis plaque, and cerebral abscess on the basis of CT or MRI findings remains a difficult task.[5, 38, 348] Also, precise and accurate

separation of infiltrating high grade glioma from surrounding edema is not currently attainable with either conventional MRI or CT, even after IV administration of contrast medium.[45, 95] Differentiation between recurrent tumor and radiation necrosis is another major diagnostic problem in the management of the patient with malignant glioma who has already undergone surgical resection with postoperative radiation therapy.[89] Newer diagnostic techniques based on magnetic resonance are addressing these problems (see later).[23, 183]

Magnetic Resonance Spectroscopy (MRS)

In magnetic resonance spectroscopy (MRS), the resonance signal that is utilized to generate an image in MRI is instead used to generate a frequency spectrum reflecting the components that make up that image.[179] In normal brain tissue, these components reflect both the water content of the brain and the metabolism of the normal neurons and glial cells. If the signal from water is suppressed, the frequency spectrum (expressed in parts per million [ppm]) reflects the cellular metabolism of the brain in the voxel or section of tissue being interrogated.

The highest peak amplitude in the normal brain frequency spectrum is that of *N*-acetyl aspartate (NAA), which occurs at a frequency of 2.0 ppm. NAA is a specific marker of neuronal density and viability. The next highest peak in the normal brain spectrum is that of creatine (Cr), at 3.03 ppm; creatine is involved in energy dependent processes of cellular metabolism in many different types of cells. The third highest peak of the normal brain spectrum is that of choline (Cho), which is involved in and reflects the metabolism of cellular membrane turnover; its frequency peak is 3.2 ppm. In normal brain, the ratio of the height of the choline peak to that of the creatine peak (Cho/Cr) is less than 1.0.

Another important metabolite peak occurs at approximately 1.32 ppm and reflects both lipids and lactate. Lactate is not a normal constituent of brain metabolism; its presence indicates that the normal cellular oxidative metabolism has been altered and that glycolysis is taking place via anaerobic pathways. An elevated lactate peak is seen in the presence of cellular necrosis and reflects lesions that have outgrown their blood supply—for example, the central portions of abscesses, malignant gliomas, lymphomas, and carcinomatous metastases. Lipids resonate at a similar frequency and are also found in highly malignant tumors.[60]

When the interrogating voxel is placed on the peripheral contrast enhancing rim of a rounded intracerebral mass with central hypointensity on T1-weighted MRI, the MR spectroscopic pattern demonstrating elevation of the choline peak with depression of the NAA and creatine peaks is typical for both primary and secondary malignant tumors of the brain and does not aid in their differentiation (see Fig. 5–14*B*).[60, 262] MRS of the central hypointense region of such a mass demonstrates elevated lactate and lipid signals, which indicate only the presence of necrosis and do not provide differential information. However, the choline peak in peripheral viable tissue is not elevated in inflammatory processes such as fungal, parasitic, and bacterial abscesses, possibly representing an important differential finding.[131, 262]

It is clearly established that in malignant gliomas, infiltrating tumor cells are present well beyond the contrast enhancing tumor margins seen on CT scans and MR images.[45, 49] However, in metastasis, the peritumoral region contains no infiltrating tumor cells.[49] Studies involving MR spectroscopic interrogation of the peritumoral region in patients with solitary brain tumors have documented elevated choline levels with reversal of the normal Cho/Cr ratio in the peritumoral region in patients who have infiltrating high grade gliomas but not in patients who have metastases.[23, 183] This finding on MRS may enable the discrimination between malignant glioma and metastasis and suggests that the peritumoral hyperintensity on T2-weighted images and the peritumoral hypointensity on T1-weighted images seen in association with malignant gliomas may reflect not only vasogenic edema (see later) but also tumor infiltration, whereas the lack of reversal of the Cho/Cr ratio in the peritumoral tissue surrounding metastases suggests that the similar MRI appearance of this tissue is likely due to edema or gliosis.[183]

Perfusion-Weighted MRI

Another difference between patients with malignant glioma and those with metastasis has been noted on dynamic contrast enhanced perfusion-weighted MRI utilizing a first pass image acquisition protocol after bolus IV administration of gadolinium.[183] One study has demonstrated a significant increase in relative cerebral volume (rCBV) in the peritumoral region in patients with malignant gliomas, and a diminished rCBV in the peritumoral region in patients with metastases.[183] Increased peritumoral perfusion in patients with malignant gliomas is presumed to be due to tumor infiltration into the peritumoral region with associated loss of blood-brain barrier integrity. Diminished peritumoral perfusion in the tissue surrounding a metastasis may reflect an intact blood-brain barrier with the vasogenic edema causing local compression of the microcirculation.[183]

Positron Emission Tomography

Studies of cerebral oxygen metabolism using the positron-emitting isotope fluorine-18 (^{18}F) tagged to fluorodeoxyglucose (FDG), an analogue of glucose, have established that most malignant brain tumors have increased glucose uptake and metabolism compared with normal brain parenchyma,[88] that the level of ^{18}FDG uptake correlates well with histologic grade in cerebral gliomas,[88] and that ^{18}FDG positron emission tomography (PET) is a good predictor of prognosis in these tumors.[17]

Differentiation between recurrent tumor and radiation necrosis remains a major unsolved problem in the management of patients with malignant gliomas.[89] Both processes can present the heterogeneous appearance of a growing infiltrative mass with irregularly marginated contrast enhancement on CT and MRI. Early work suggested that necrotic tissue failed to take up the radioactivity and appeared hypometabolic and that actively growing tumor demonstrated strong hypermetabolic uptake.[89] This finding was verified on a subsequent study demonstrating high sensitivity and specificity for ^{18}FDG PET.[161] However, other

studies have questioned the accuracy and specificity, and therefore the utility, of ^{18}FDG PET for this indication.[275]

Complications of Brain Tumors

Brain Edema

Edema or swelling of the brain is a common accompaniment of many brain tumors and other structural abnormalities of the brain. When sufficiently severe, edema may be responsible for both focal and generalized signs of brain dysfunction.[106, 286] Edema is not a single pathologic response to a variety of insults but rather occurs in at least three different forms,[162] vasogenic (secondary to tumor, inflammation, hemorrhage, extensive infarction, or contusion), cytotoxic (in response to hypoxia, early infarction, or water intoxication), and interstitial (resulting from acute obstruction to the flow or absorption of cerebrospinal fluid [CSF]).

Vasogenic edema is the form of brain swelling most typically associated with intracranial neoplasms. It is caused by a breakdown in the blood-brain barrier with seepage of a plasma filtrate containing plasma proteins through patent junctions between capillary endothelial cells.[106] Gray matter is relatively resistant to the development of edema, and the extracellular plasma filtrate mainly accumulates in the white matter, extending along the major white matter fiber tracts. The subcortical arcuate (U) fibers between adjacent gyri offer greater resistance to the spread of edema than the long white matter tracts and are therefore involved relatively later and in more severe cases.

The severity of edema associated with various brain tumors varies widely, even between lesions of identical histology. In general, white matter swelling is greatest in association with carcinomatous metastases, and it is not unusual for a small metastasis to provoke a disproportionately large amount of edema.[286, 364] In order of declining severity, edema is associated with metastases, glioblastomas, meningiomas, and low grade gliomas, but exceptions to this order are common.[219] Rarely, a low grade glioma may be surrounded by extensive edema, whereas occasional metastases or meningiomas may have little associated white matter swelling.

On CT, vasogenic edema appears as widening and diminished density of the major white matter tracts with finger-like extensions into the arcuate fibers in each gyrus.[94, 219] The overlying cortical gray matter is compressed and thinned by the expanded pseudopods of edematous white matter (see Figs. 5–12 and 5–17).

On noncontrast enhanced MRI, the high water content in the edematous peritumoral white matter causes prolonged T1 and T2 relaxation in the involved white matter; these findings manifest as an increase in signal intensity on T2-weighted images and as a less conspicuous decrease in signal intensity on T1-weighted images (see Figs. 5–1*A*, 5–13, 5–20*B*).[175] It is often difficult to delineate the boundary between tumor and edema on these nonenhanced images; IV administration of paramagnetic contrast agent permits gross demarcation on T1-weighted (see Fig. 5–20*C*) and FLAIR images in many tumors (e.g., metastases) but not in malignant gliomas, as noted previously.[45, 95]

Systemic administration of glucocorticoids minimizes the blood-brain barrier defect inherent in most higher grade brain tumors, with resultant reduction in fluid and protein extravasation. Diminution in peritumoral white matter swelling as well as in the volume and intensity of tumor contrast enhancement is often evident on followup imaging studies within a few days after institution of steroid therapy.[75, 134]

Interstitial edema secondary to obstruction of CSF pathways appears on CT as poorly circumscribed periventricular hypodensity[94] and on T2-weighted MRI as bandlike periventricular hyperintensity of varying thickness and margination.[175, 374] These findings are often symmetrical and are most evident surrounding the anterosuperior margins of the dilated frontal horns of the lateral ventricles (see Fig. 5–2*D*) and the posterior margins of the occipital horns.[175] Fluid accumulates in the periventricular white matter as a result of transependymal seepage of ventricular fluid across microscopic breaks in the ependymal lining of the ventricles. Systemic glucocorticoids do not affect this type of edema, but surgical insertion of a shunt catheter above the level of obstruction usually results in prompt decompression of the ventricles and disappearance of the periventricular hypodensity/hyperintensity.[94]

Herniations

An expanding mass within the rigid cranial vault, whether due to tumor, edema, or a combination of both processes, compresses and distorts the adjacent normal brain, producing internal herniation of the brain under the relatively rigid falx or through the tentorial incisura.

Laterally placed masses in the cerebral hemispheres, particularly those located in the superior temporal, midfrontal, or frontoparietal regions, displace the deep central structures (basal ganglia, thalamus, third ventricle, lateral ventricles, septum pellucidum) medially.[280] The ipsilateral cingulate gyrus is compressed and displaced across the midline under the free edge of the falx (*subfalcial herniation*). Medially located high frontoparietal (parasagittal) masses depress and also displace the cingulate gyrus contralaterally but without significantly affecting the deep central structures. Subfalcial herniation is most clearly depicted on coronal CT scans and MR images, which also demonstrate depression and contralateral displacement of the corpus callosum and the underlying body of the ipsilateral ventricle (Fig. 5–1). The septum pellucidum and third ventricle are bowed away from the side of the mass. On axial CT scans and MR images, the ipsilateral ventricle appears compressed and displaced contralaterally.

Tumors of the temporal lobe and middle cranial fossa displace the uncus and parahippocampal gyrus on the medial aspect of the temporal lobe toward the midline, with resultant encroachment on the lateral aspect of the suprasellar and ambient (circummesencephalic) cisterns and the tentorial incisura (*descending transtentorial herniation*) (see Figs. 5–7 and 5–18*A*).[280, 286, 331] The ipsilateral margin of the midbrain is compressed, displaced contralaterally, and rotated by the impinging temporal lobe. Noncontrast MRI, contrast enhanced CT, or both may demonstrate medial displacement of the posterior communicating and posterior cerebral arteries, narrowing of the contralateral crural

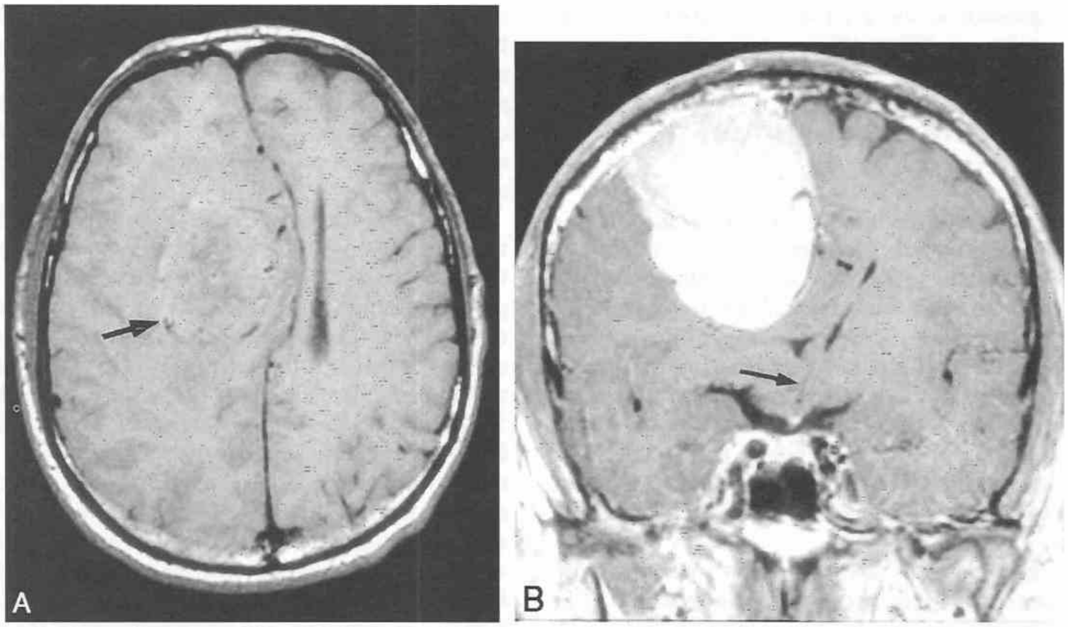

Figure 5–1. Right high frontal convexity meningioma causing subfascial herniation. *A,* Axial T1-weighted noncontrast MR image at the level of the cingulate gyri. The right cingulate gyrus is displaced to the left of the midline under the free edge of the falx cerebri by a large lobulated rounded heterogeneous hypo- and isointense parasagittal mass *(arrow).* Note that the mass is surrounded by focal signal voids representing enlarged vessels on the surface of this extraaxial tumor. A wide band of slight hypointensity surrounding the mass represents vasogenic edema of the peritumoral white and gray matter. *B,* Coronal T1-weighted postintravenous gadolinium image through the level of the mid third ventricle demonstrates marked downward and medial displacement of the right side of the corpus callosum and the frontal horn of the right lateral ventricle. The third ventricle *(arrow)* is bent and displaced across the midline by this large homogeneously contrast enhancing dural based tumor.

and circummesencephalic cisterns, and widening of their ipsilateral counterparts behind the impinging temporal lobe.[312] Late secondary signs include hemorrhages in the compressed midbrain and unilateral or bilateral medial occipital infarctions (due to occlusion of one or both posterior cerebral arteries).[286, 312] Large centrally located cerebral masses for which the primary vector of force is directly downward may cause bilateral transtentorial herniation.

Ascending transtentorial herniation with upward displacement of the superior cerebellar vermis through the posterior aspect of the tentorial incisura is caused by expanding masses in the superior portion of the posterior compartment of the posterior cranial fossa, including the upper half of the cerebellum.[286] As the superior cerebellar vermis is forced anteriorly and superiorly into the incisura, it protrudes into and compresses the superior cerebellar cistern from below and flattens the normal posterior convexity of the quadrigeminal cistern from behind.[239] Increasing severity of herniation leads to reversal of that convexity and eventually to obliteration of the quadrigeminal and superior cerebellar cisterns (Fig. 5–2*A* and *B*) with flattening of the posterior margin of the third ventricle.

Tumors of the lower half of the cerebellum and other masses in the inferior portion of the posterior compartment of the posterior fossa may produce downward displacement of the cerebellar tonsils through the foramen magnum (*tonsillar herniation*).[286] This situation can be visualized directly on T1-weighted MRI in the sagittal plane (see Fig. 5–2*A* and *C*) and can be suggested on axial CT or MRI if the cisterna magna and upper cervical posterior subarachnoid spaces are encroached on and partially or completely obliterated by soft tissue density.

Hemorrhage

Hemorrhage is not a common accompaniment of most intracranial neoplasms at initial presentation. In a series of 973 intracranial tumors, CT demonstrated acute intratumoral bleeding in 28 patients (3%) at the time of initial diagnosis and in 7 additional patients (0.7%) who experienced clinical deterioration during their subsequent course.[369] In Cushing and Eisenhardt's[78] meticulously reported experience, hemorrhage was found in association with intracranial gliomas in 31 of 832 cases (3.7%). Acute hemorrhage was demonstrated on CT in 6 of a series of 131 meningiomas (4.6%).[287]

Intratumoral bleeding is more common in certain tumors, notably metastases from choriocarcinoma, melanoma (see Fig. 5–62), carcinomas of the lung and thyroid, and renal cell carcinoma,[12, 205] as well as in neuroblastoma, lymphoma, and medulloblastoma.[362] In metastatic melanoma and choriocarcinoma, the typically hyperdense appearance of the metastatic nodules on CT has been attributed to the presence of acute hemorrhage or hemosiderin within the tumor.[116]

Because many of the breakdown products of blood have paramagnetic properties, MRI provides a unique and highly sensitive method for detection of subacute or chronic intracranial bleeding.[12, 122] Hemorrhage associated with intra-

cranial tumors may occur centrally within a necrotic tumor cavity (in glioblastoma [see Fig. 5–12] and some metastases) or peripherally around the tumor (seen in other metastases and meningiomas). Signal intensity (MR) or density (CT) is typically more heterogeneous in tumor bleeds than in benign intracranial hemorrhage.[9, 12] On occasion, hemorrhage may completely mask the presence of the underlying neoplasm, but images obtained after injection of contrast medium may demonstrate enhancement of tumor along a margin of the hematoma or in other locations within the brain.[10, 369] Hemorrhage into a pituitary adenoma is a common cause of "pituitary apoplexy" and may obliterate not only the entire tumor but also the normal pituitary (see Figs. 5–55 and 5–56).[267, 316] Intracranial hemorrhage not related to underlying tumor may occur in patients receiving systemic chemotherapy for acute leukemia who demonstrate bone marrow depression with low levels of circulating platelets.[246]

Resolution and organization of acute intratumoral and peritumoral hematomas are often somewhat delayed in comparison with those of other intracranial hematomas.[9, 10] In fact, high signal intensity on T1- and T2-weighted MR images in an area of parenchymal hemorrhage that persists beyond the expected time of hematoma resolution should raise the possibility that the hemorrhage has occurred within tumor tissue.[10] It is probable that atypical hypodense regions on CT within some meningiomas and pituitary adenomas represent foci of necrosis or cystic change secondary to old hemorrhage.[267, 287]

Gliomas

Gliomas represent 40% to 45% of all intracranial tumors.[286, 344] They include all primary brain tumors of astrocytic, oligodendroglial, or ependymal origin—astrocytomas, oligodendrogliomas, and ependymomas as well as choroid plexus papillomas and carcinomas.

Astrocytomas

Astrocytomas (tumors derived from astrocytes) are the most common of all primary intracranial neoplasms.[303] They account for approximately 60% of all primary tumors of the brain.[61] In the 1993 revision of the WHO classification of brain neoplasms, astrocytomas were subdivided into four histologic grades.[163] This histologic grading system has demonstrated a high positive correlation with the biologic potential and behavior of tumors. Tumors of lower histologic grades (I and II) demonstrate few mitoses, little cellular structural variation (pleomorphism), and no vascular proliferation or necrosis. Tumors in grades III (anaplastic astrocytoma) and IV (glioblastoma multiforme) are characterized by more frequent mitoses, higher degrees of cellular dedifferentiation, and increasing angioneogenesis at the tumor periphery and by necrosis within the more central portion of the tumor.

Astrocytomas are characterized on both gross dissection and diagnostic imaging into two groups, circumscribed and diffuse. Generally speaking, the diffuse astrocytomas are more common, tend to occur more in adulthood, and are more infiltrative or aggressive with spread along the white matter tracts.[61]

Circumscribed Astrocytomas

Three histologic types of astrocytoma are assigned to the circumscribed group. They are the juvenile pilocytic astrocytoma (JPA), the pleomorphic xanthoastrocytoma (PXA), and the subependymal giant cell astrocytoma (SCGA).[47, 303] All three types occur mainly in children and have a less aggressive biologic potential than the diffuse astrocytomas.

Juvenile Pilocytic Astrocytoma. The most common type of circumscribed astrocytoma, JPA represents 2% to 6% of all primary brain tumors.[303] It most commonly (60% of cases) occurs in the cerebellum (hemispheres more often than vermis) in children (Figs. 5–2 and 5–3), with a peak age distribution between 5 and 15 years. JPA is also frequently found, however, in the intracranial optic nerves and chiasm and the adjacent hypothalami (Fig. 5–4), usually in slightly younger children (2 to 3 years) and often in association with neurofibromatosis type I (NF1, also known as von Recklinghausen's disease).[6, 47, 303]

JPA is the classic well circumscribed brain neoplasm, but it lacks a true tumor capsule. It grows mainly by expansion rather than by infiltration. It is widely considered to be a benign (biologically stable) neoplasm and is classified as histologic grade I.[47] It may be densely cellular or more loosely arranged with intervening microcysts, and both patterns may coexist in different portions of the same tumor. Mitoses are rare in this lesion, and necrosis is not seen. Most often, the tumor represents a mural nodule in the wall of a well circumscribed cyst. The origin and nature of the cyst are not well understood, but the cyst fluid is proteinaceous and is probably secreted from coiled capillaries found in the midst of the nodular tumor. With the exception of the mural tumor nodule, the wall of the cyst consists of compacted normal brain or nonneoplastic gliotic tissue.[47] Intratumoral calcification is occasionally identified (5% to 25% of cases), but hemorrhage into or adjacent to the tumor is rare.[303]

The clinical presentation of children with JPA depends on the tumor site. The cerebellar tumors typically manifest with headache, nausea, and vomiting because of hydrocephalus secondary to obstruction of the fourth ventricle.[56] Weakness and loss of equilibrium are not uncommon. The optic tumors typically cause difficulties with vision, but signs of hydrocephalus may appear if the tumor has extended into the hypothalamus and is obstructing the third ventricle.[6]

On CT, the typical JPA appears as a smoothly marginated, hypodense cystlike mass with a well defined, less hypodense tumor nodule on one wall (see Fig. 5–3*A*). The nodule may contain one or more areas of dense calcification. The cyst fluid is less hypodense than the CSF (15–25 Hounsfield units [HU]) because of the high protein concentration.[226] Typically, after IV administration of a contrast agent, dense homogeneous contrast enhancement of the tumor nodule, but not of the other walls of the cyst, is seen (see Fig. 5–3*B, C*).[190, 200, 226] More extensive enhancement of the cyst walls suggests a more aggressive (higher histologic grade) tumor.[56]

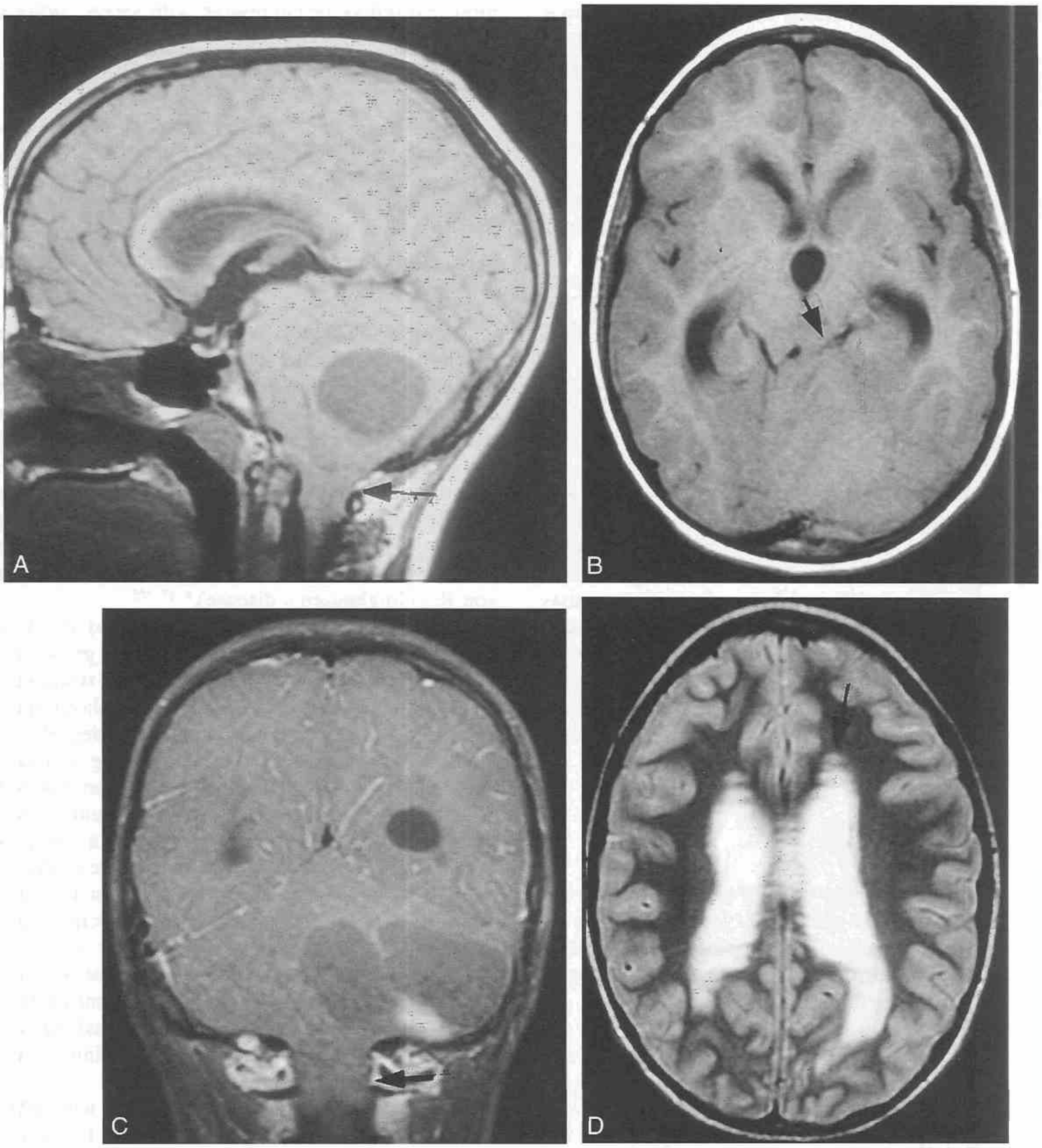

Figure 5–2. Juvenile pilocytic astrocytoma of the cerebellum causing interstitial edema and upward transtentorial herniation and tonsillar herniation. *A,* Left parasagittal T1-weighted MR image without intravenous contrast. A large sharply marginated cyst in the left cerebellar hemisphere causes downward herniation of the cerebellar tonsils into the upper cervical spinal canal *(arrow).* The cystic mass compresses the fourth ventricle and pons from behind and displaces the superior vermis upward through the tentorial notch, obliterating the superior cerebellar and quadrigeminal cisterns and elevating and displacing forward the floor and posterior wall of the third ventricle. *B,* Axial T1-weighted noncontrast image at the level of the quadrigeminal cistern demonstrates forward displacement and compression of the quadrigeminal plate and cistern on the left *(arrow)* by the upwardly herniating superior cerebellar vermis and hemisphere. Note enlargement of the aqueduct, third ventricle, and temporal horns of the lateral ventricles secondary to obstruction of the fourth ventricle. *C,* Coronal T1-weighted image at the level of the posterior aspect of the foramen magnum following intravenous administration of gadolinium. Both cerebellar tonsils have herniated downward through the foramen magnum *(arrow).* Note homogeneous contrast enhancement of a solid tumor nodule in the floor of the left cerebellar hemisphere cystic mass. *D,* Axial T2-weighted image at the level of the superior aspect of the lateral ventricles. The ventricles are markedly distended, and cerebrospinal fluid has dissected across the ependymal margins of the ventricles into the adjacent periventricular white matter anteriorly *(arrow)* and in the corpus callosum.

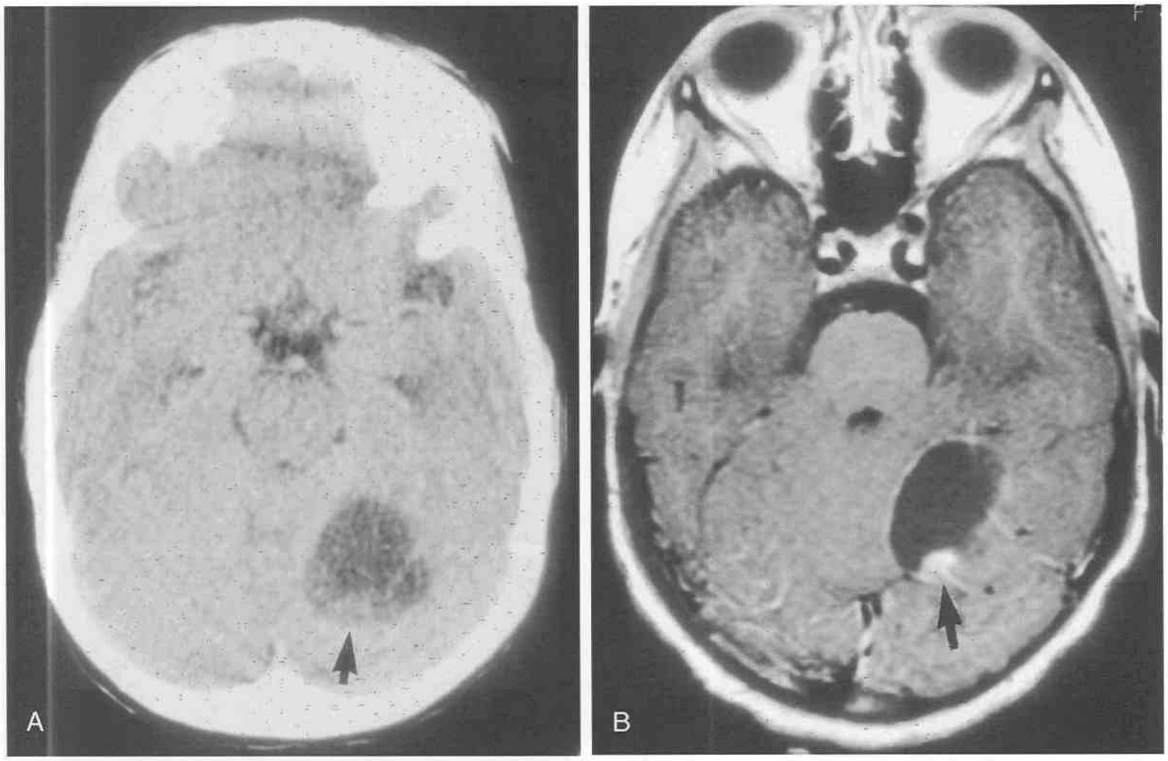

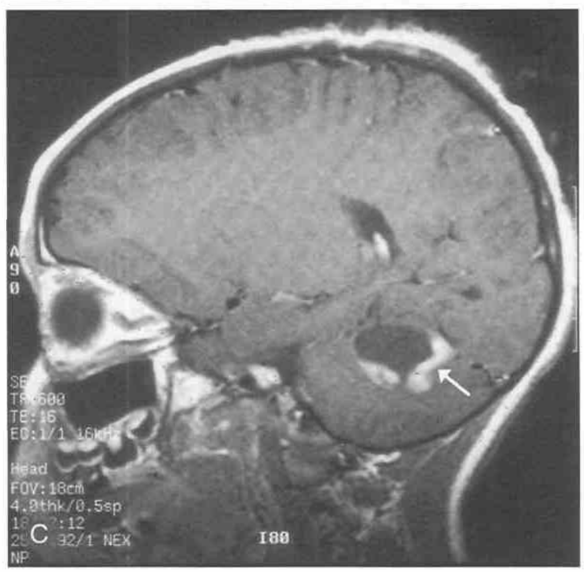

Figure 5–3. Juvenile pilocytic astrocytoma of the cerebellum. *A,* Axial CT image without intravenous contrast. A large well circumscribed hypodense mass is noted in the left cerebellar hemisphere. A flat nodular density is seen on the posteromedial wall of this cystic hypodensity *(arrow).* Axial *(B)* and parasagittal *(C)* T1-weighted MR images following intravenous administration of gadolinium demonstrate intense homogeneous contrast enhancement of the mural nodule *(arrows)* within the cystic hypointense mass.

On MRI, the mural nodule appears homogeneously hyperintense to gray matter on T2-weighted images and hypointense to isointense on T1-weighted images.[190, 200, 226] Intratumoral calcification may cause a more heterogeneous appearance. The associated cyst is even more hyperintense on T2-weighted images and even more hypointense on T1-weighted images (see Fig. 5–2*A*). Edema of the adjacent white matter is usually minimal. Homogeneous contrast enhancement of the tumor nodule is characteristic (see Figs. 5–2*C* and 5–3*B* and *C*), although a calcific focus, if present, does not demonstrate enhancement.

The clinical prognosis of JPA is guardedly optimistic. The cerebellar tumor nodule can often be totally excised, and 5- and 10-year survival rates exceeding 75% are commonly reported.[47, 56] The location and extent of the optic-chiasmatic-hypothalamic tumors typically preclude total excision, but irradiation and chemotherapy often achieve long-term tumor control.[47, 368]

Pleomorphic Xanthoastrocytoma. PXA was newly designated in the 1993 WHO revised classification.[163, 303] The number of cases documented in the literature is still small. PXA is presumed to arise from subpial astrocytes near the surface of the cerebral hemispheres.[70, 159] Rare tumors have also been described in the posterior cranial fossa and in the spinal cord. The gross morphology resem-

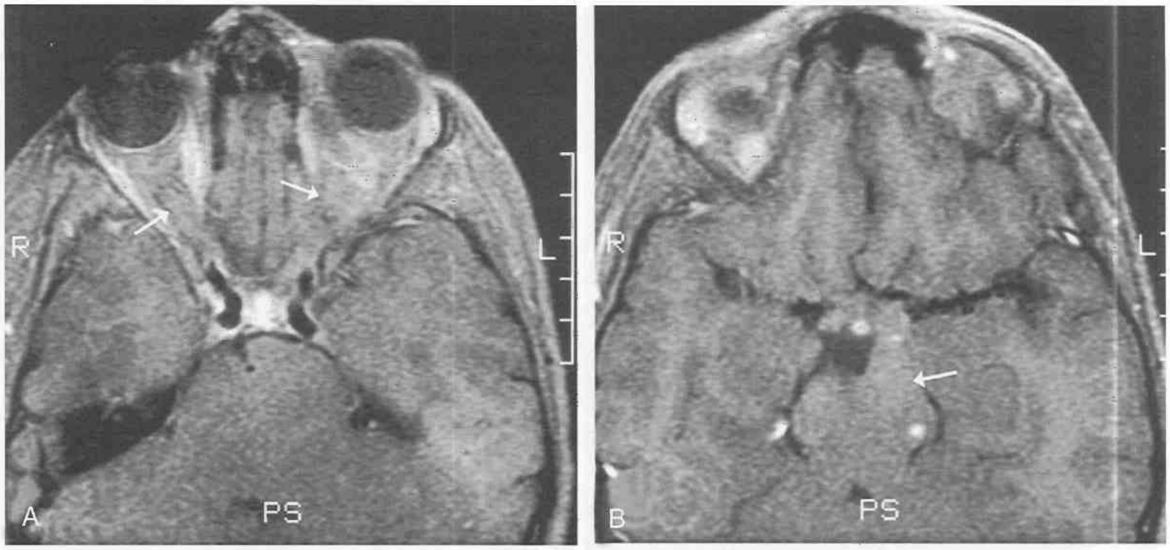

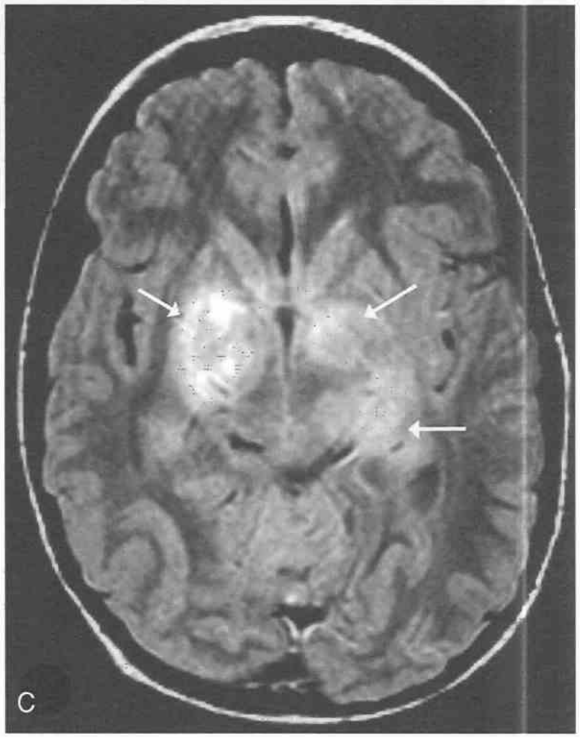

Figure 5–4. Juvenile pilocytic astrocytoma of the optic chiasm and hypothalamus with spread along visual pathways. Axial T1-weighted MR images obtained with fat saturation following intravenous gadolinium. *A,* At the level of the mid orbits, arrows indicate contrast enhancement in and marked widening of the intraorbital optic nerves bilaterally due to tumor spread. *B,* At the level of the optic chiasm, note widening of the chiasm and extension of the contrast enhancing tumor into the left optic tract *(arrow)*. *C,* At the level of the mid third ventricle, intense homogeneous contrast enhancement indicates tumor extension into the basal ganglia bilaterally *(arrows)*.

bles the nodule and cyst appearance of the pilocytic astrocytoma. The nodule is often based on the pial surface of the brain.

On CT and on MRI, the appearance is similar to that of the pilocytic astrocytoma: well circumscribed, hypodense to isodense on CT, hypointense on T1-weighted and hyperintense on T2-weighted MR images, often with cystic component (Fig 5–5*A*). However, the location is supratentorial (order of descending frequency: temporal, frontal, parietal) and superficial with little or no mass effect.[195, 333] Although the tumor presents a circumscribed appearance, it usually grows slowly and may infiltrate the overlying pia, even causing focal thickening of the meninges (dural tail). Intense homogeneous contrast enhancement of the tumor nodule is the rule (Fig. 5–5*B, C*).

Histologically, as the name implies, the tumor nodule is pleomorphic, but cells with a foamy myxoid cytoplasm are common.[70] PXA is usually classified as grade II, but later dedifferentiation into higher grade neoplasm may occur.[70, 159] The clinical presentation most commonly consists of seizures that may be intractable. Most reported cases have been in adolescents or young adults; the median age at diagnosis is 14 years.[303]

Subependymal Giant Cell Astrocytoma. This low-grade (WHO grade I) astrocytic tumor occurs almost exclusively in patients with tuberous sclerosis in their late teens or 20s.[298] It is estimated that 10% to 15% of patients with tuberous sclerosis develop this grade I **neoplasm.**[301, 303] These tumors arise from subependymal nodules located on

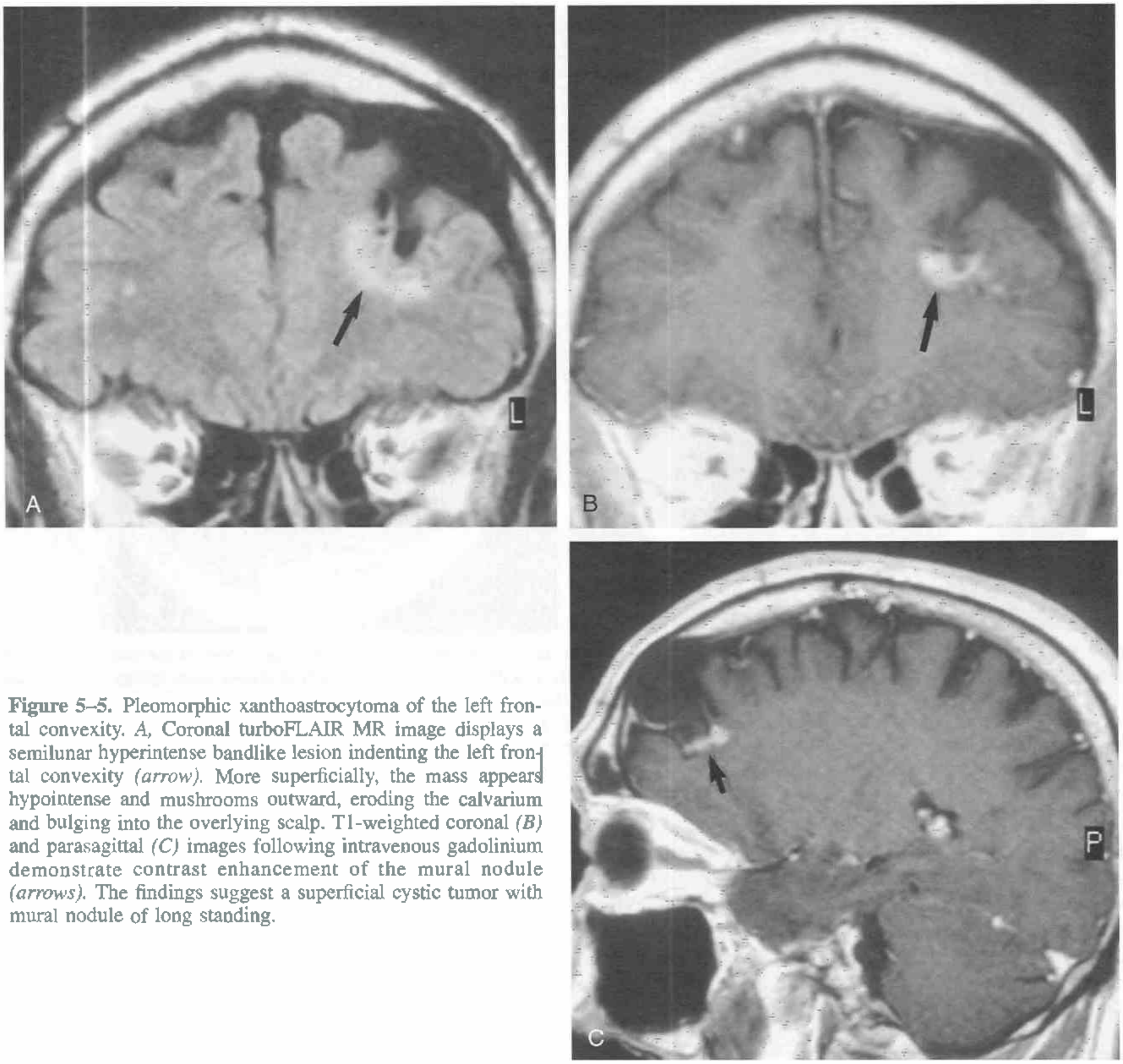

Figure 5–5. Pleomorphic xanthoastrocytoma of the left frontal convexity. *A*, Coronal turboFLAIR MR image displays a semilunar hyperintense bandlike lesion indenting the left frontal convexity *(arrow)*. More superficially, the mass appears hypointense and mushrooms outward, eroding the calvarium and bulging into the overlying scalp. T1-weighted coronal *(B)* and parasagittal *(C)* images following intravenous gadolinium demonstrate contrast enhancement of the mural nodule *(arrows)*. The findings suggest a superficial cystic tumor with mural nodule of long standing.

the lateral wall of the lateral ventricle overlying the head of the caudate nucleus.[298, 349] By convention, subependymal nodules that are more than 1 cm in diameter or that become symptomatic are considered giant cell astrocytomas.[349] The tumor does not invade into the underlying caudate head but rather grows outward into the ventricular lumen near the foramen of Monro, which may be obstructed either unilaterally or bilaterally. Despite this tendency for intraventricular growth, the overlying ependyma remains intact, and dissemination via the CSF is rare.[303] Intratumoral calcification is common and may be heavy.

Histologically, the tumor is seen to contain large multinucleated giant cells of uncertain origin.[25, 349] On cytochemical analysis, some of these cells display GFAP (glial fibrillary acidic protein) reactivity, a feature consistent with an astrocytic origin, whereas others contain neuron-specific enolase, a finding consistent with neuronal origin.[25]

Subependymal giant cell astrocytomas present a characteristic appearance on CT.[200, 226, 303] They appear as large, hypodense, polypoid, sharply marginated intraventricular masses at the level of the foramen of Monro (Fig. 5–6*A*). The tumor may be heavily calcified and may obstruct the foramen unilaterally or bilaterally, causing gross enlargement of one or both lateral ventricles. Other manifestations of tuberous sclerosis are usually evident, including cortical tubers and subependymal hamartomatous nodules.[226] On MRI, subependymal giant cell astrocytoma appears as a heterogenous, sharply demarcated intraventricular mass that is mildly hyperintense on T2-weighted images and hypointense or isointense on T1-weighted images. It is located within the frontal horn of the left ventricle without evidence for deep invasion or spread within the basal ganglia.[200, 303] On both CT and MRI, intense but heterogeneous contrast enhancement is often demonstrated (Fig. 5–6*B*). The heterogeneous signal on MRI both with and without contrast enhancement reflects the presence of dense

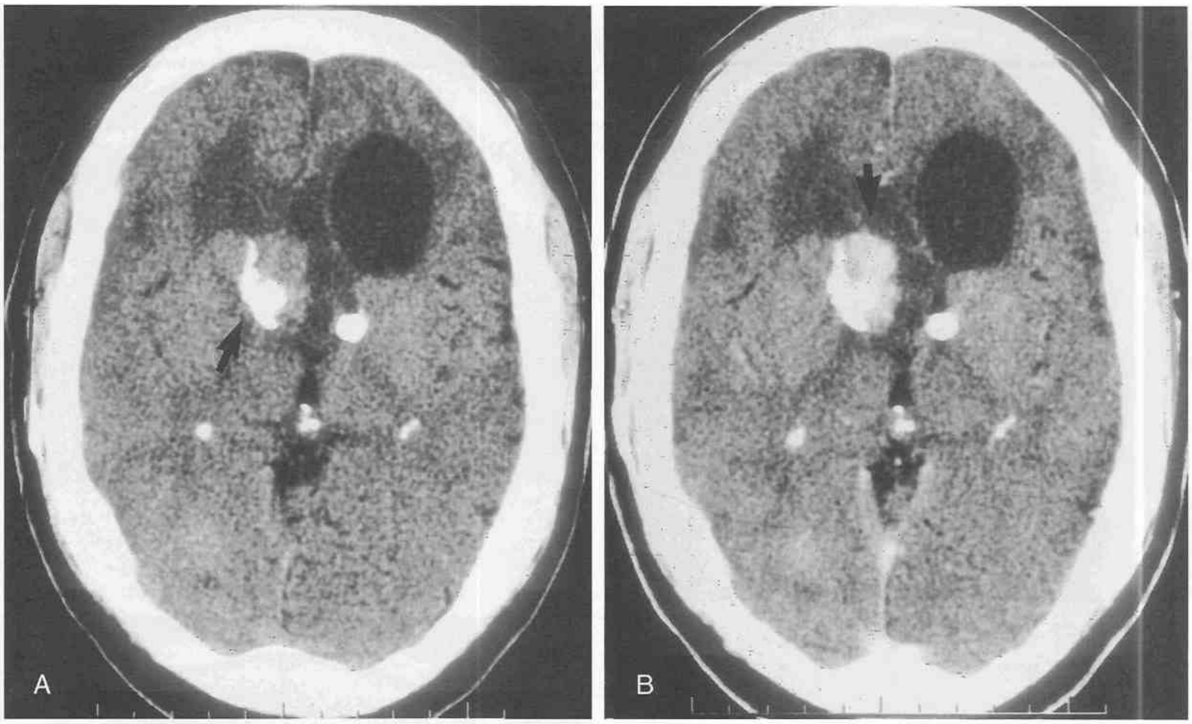

Figure 5–6. Subependymal giant cell astrocytoma in a patient with tuberous sclerosis. Axial CT images prior to *(A)* and following *(B)* intravenous administration of iodinated contrast medium. A partially calcified (*arrow* in *A*) multilobulated mass arising on the medial surface of the head of the right caudate nucleus fills and obscures the frontal horn of the right lateral ventricle. On the left, a calcified tuber (not neoplastic) obstructs the foramen of Monro; the dilated left frontal horn is compressed and displaced by a cyst, which is likely secondary to previous ventriculostomy complication. The noncalcified portion of the right frontal intraventricular tumor demonstrates homogeneous contrast enhancement (*arrow* in *B*).

calcification in these tumors. Differentiation of this tumor from the subependymal hamartomatous nodules that are so ubiquitous in patients with tuberous sclerosis is sometimes problematic, but the factors usually considered are the characteristic tumor location, its larger size, and the presence of contrast enhancement (not seen in the nontumorous nodules).[200, 303]

Diffuse Astrocytomas

Poorly marginated diffuse astrocytomas demonstrate much more aggressive infiltrative behavior than circumscribed astrocytomas. Progression from lower histologic grade (astrocytoma, WHO grade II) to higher grades (anaplastic astrocytoma, WHO grade III; glioblastoma multiforme, WHO grade IV) is common.[286, 303]

Low Grade Astrocytoma. Low grade (WHO grade II) supratentorial astrocytomas are hypercellular tumors that demonstrate few mitoses and moderate pleomorphism but no vascular proliferation or necrosis.[61, 165] On immunohistochemistry studies, they demonstrate strong affinity for GFAP.[165] These tumors, often simply labeled astrocytomas without any modifier, constitute 10% of all intracranial tumors and 15% to 20% of all gliomas.[191, 303, 342, 345] They arise in white matter and grow by infiltration, predominantly along white matter tracts, extending between and separating anatomic landmarks. The involved area of the brain eventually appears larger than its contralateral counterpart. Cerebral astrocytomas are usually solid masses that, because of their infiltrative characteristics, are poorly circumscribed and blend imperceptibly with the adjacent cerebral parenchyma. Small and large cysts are occasionally found within these tumors,[286] but hemorrhage is rare.

Low grade astrocytomas arise mainly in the frontal, parietal, and temporal lobes (Fig. 5–7). They typically provoke little or no edema in the surrounding tissues. Because such a tumor begins in the white matter without affecting the more eloquent cortical centers, symptoms are usually vague and nonlocalizing until the lesion gains sufficient size, extends into eloquent cortex, or undergoes dedifferentiation into a grade III or IV tumor.[304] The peak age range for occurrence of low grade astrocytoma is the third through fifth decades of life.

Some diffuse (initially low grade) astrocytomas occur in childhood, notably involving the optic nerves and chiasm, optic tracts, and visual pathways as well as the hypothalamus and thalamus. More than half of the optic pathway gliomas of early childhood involve the optic chiasm and hypothalamus, and 40% of these are diffuse fibrillary astrocytomas.[4] In contradistinction to the young children with neurofibromatosis type I in whom more circumscribed pilocytic astrocytomas of the visual pathways develop,[6] the more solid and diffuse astrocytomas arise in a similar age group (peak age 2 to 3 years) but without any identifiable genetic predilection.[61] However, the diffuse fibrillary tumors share with their adult counterparts a more aggressive biologic progression and thus merit a more aggressive course of management.[4]

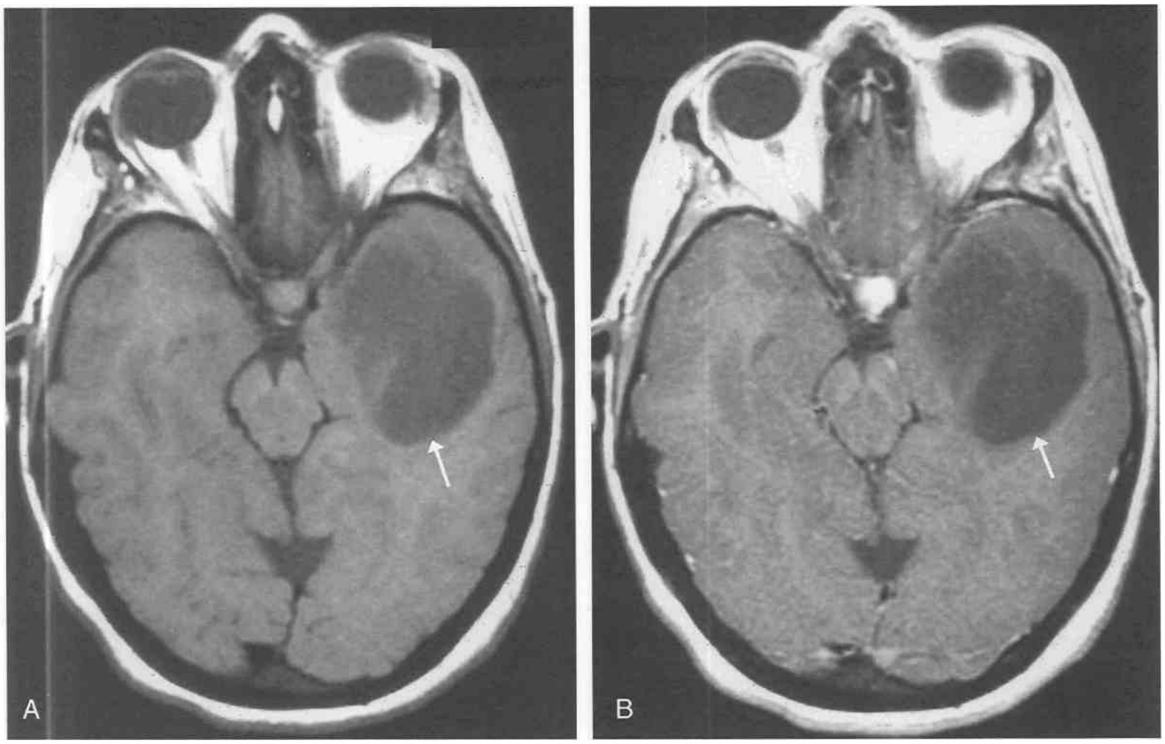

Figure 5–7. Low grade astrocytoma of the temporal lobe. Axial T1-weighted MR images prior to *(A)* and following *(B)* intravenous administration of gadolinium. A mostly ill defined homogeneously hypointense mass expands the left anterior temporal lobe *(arrow).* There is no contrast enhancement and no surrounding edema. Note medial displacement of the medial margin (uncus and parahippocampal gyrus) of the left temporal lobe indicating early transtentorial herniation with compression of the left ambient cistern and the anterolateral aspect of the left cerebral peduncle.

Another relatively common location of diffuse low grade astrocytoma in childhood is in the brain stem. Brain stem gliomas constitute 10% to 20% of all pediatric brain tumors.[200] The peak age of occurrence is 5 to 10 years. These tumors arise mainly in the pons but commonly involve the midbrain and medulla.[366] Despite their proximity to the aqueduct and fourth ventricle, considerable tumor growth may take place without causing obstruction of the ventricular system. Cranial nerve deficits, long tract signs, and ataxia are the most common presenting findings.[200, 206, 366] Although these tumors are often regarded as low grade lesions, histologic heterogeneity with intermixed areas of higher grade neoplastic change is common.[3] Approximately 60% demonstrate foci of glioblastomatous change with central necrosis.[286] Five year survival rates range from 15% to 30%.[200]

On CT scans, low grade diffuse cerebral astrocytomas appear most commonly as poorly marginated areas of decreased attenuation involving the white matter of one or more lobes of the brain with mild to moderate mass effect.[53, 191, 208, 275, 303] A more heterogeneous appearance with patchy areas of normal or slightly higher tissue density intermixed with hypodensity is seen in a small number of cases. Contrast enhancement is usually absent, reflecting a lack of tumor vascularity, blood-brain barrier breakdown, or both.[303]

Because low grade astrocytomas are predominantly hypodense (15 to 30 HU) and usually do not exhibit contrast enhancement, it is often not possible to differentiate the margin of the tumor from the adjacent white matter with CT. However, because the blood-brain barrier is intact, extensive peritumoral edema is unusual in low grade astrocytomas.[5, 191, 303] Grossly identifiable areas of intratumoral hemorrhage or necrosis are also not seen on CT or MRI studies in these lesions. Calcification is identified in 20% of these tumors, and cysts are occasionally demonstrated.[275] The presence of hemorrhage, necrosis, edema, and/or contrast enhancement suggests progression to a higher tumor grade.

Optic chiasm–hypothalamic diffuse astrocytomas appear on CT as rounded or lobulated thickening of the optic chiasm that appears homogeneously hypodense; the tumor may encase the arteries of the circle of Willis and invade the floor of the third ventricle, causing obstructive hydrocephalus.[4, 165, 303] Necrosis and hemorrhage are uncommon; the demonstration of contrast enhancement in these solid tumors suggests a transition to a higher tumor grade.

Brain stem gliomas typically appear on CT as ill defined diffuse heterogeneously hypodense and isodense expansions of the pons and medulla with dorsal displacement of the floor of the fourth ventricle and aqueduct and ventral encroachment upon the pontine cistern (Fig. 5–8*A*, *B*).[3, 28, 303, 366] Despite the impression of the tumor on the aqueduct and the floor of the fourth ventricle, hydrocephalus is a relatively late finding. Approximately 50% of brain stem gliomas exhibit some contrast enhancement on CT and MRI after IV administration of contrast medium (Fig. 5–8*C*). Enhancement is usually patchy and heterogeneous.[28, 197]

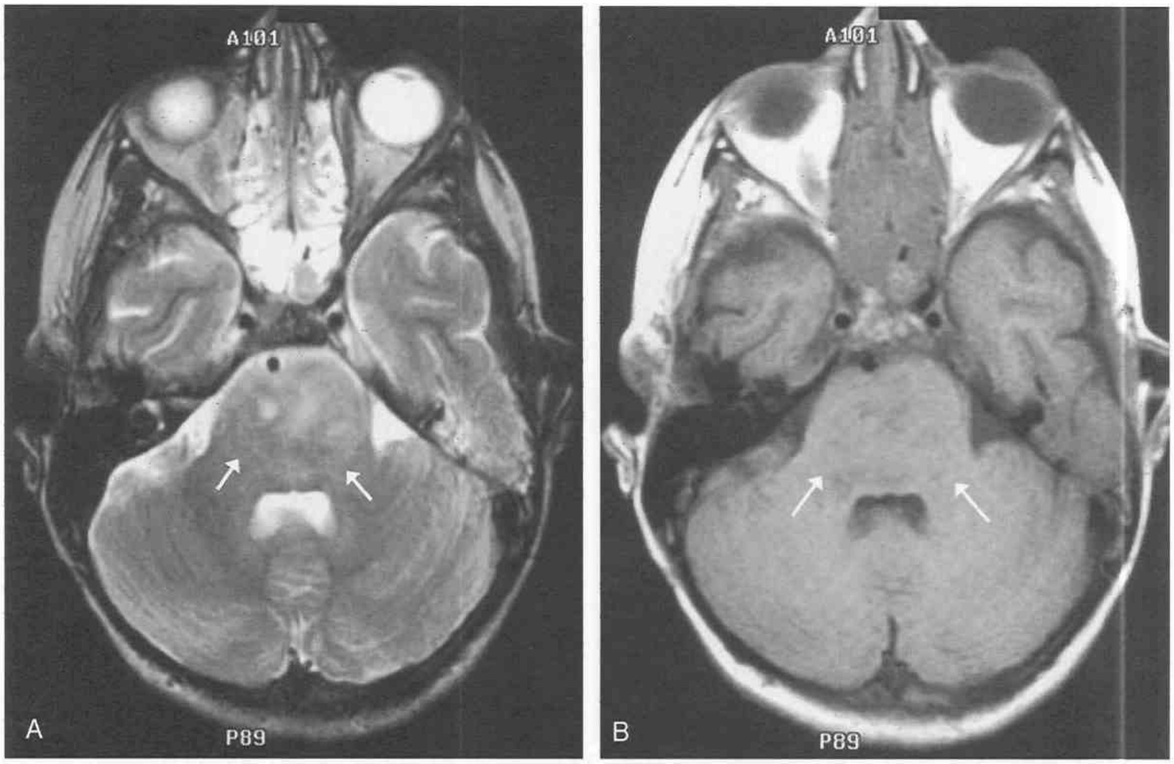

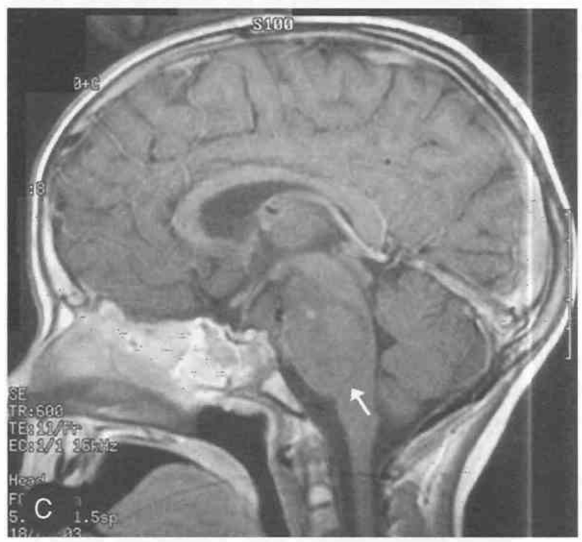

Figure 5–8. Brain stem glioma. Axial T2-weighted *(A)* and T1-weighted *(B)* noncontrast MR images through the midpons demonstrate a poorly circumscribed mass with heterogeneous signal intensity involving the pons, which is larger on the left than on the right *(arrows)*. This expansile and invasive tumor causes thinning of the prepontine cistern and flattening and posterior displacement of the floor of the fourth ventricle. *C,* On this midsagittal T1-weighted image following intravenous gadolinium, note the extension of the tumor *(arrow)* superiorly into the midbrain with posterior bowing of the aqueduct and floor of the fourth ventricle and patchy intratumoral contrast enhancement.

On MR images, diffuse low grade astrocytomas appear relatively homogeneous and demonstrate varying degrees of prolonged T1 and T2 relaxation. They therefore appear homogeneously hypointense on T1-weighted images and hyperintense on T2-weighted images in comparison with normal brain (see Figs. 5–7*A* and 5–8*A*, *B*).[10, 95, 275] Because of the inherently higher contrast resolution of MRI, astrocytomas are often better demarcated from adjacent normal white matter on MRI than on CT, reflecting their higher water content. Nevertheless, as on CT, the apparent margins of the lesion on the MRI (with or without contrast enhancement) do not closely correlate with histopathologic evidence of tumor extent.[95, 175] As on CT, contrast enhancement on MRI is absent in diffuse low grade cerebral astrocytomas (Fig. 5–7*B*); the demonstration of contrast enhancement should raise the strong suspicion of a higher tumor grade.[51, 100, 125, 275, 303]

The differential imaging diagnosis of low grade diffuse astrocytoma on CT and MRI is ubiquitous. Principal considerations are cerebral infarction, cerebritis, and higher grade gliomas (e.g., anaplastic astrocytoma). Infarctions generally (but not always) have less mass effect, tend to involve adjacent cortical gray matter more extensively, and are often more sharply delineated from the adjacent cerebral parenchyma.[219] Inflammatory processes and higher grade gliomas are often associated with blood-brain barrier

breakdown and exhibit contrast enhancement and surrounding edema.[275]

The prognosis in low grade astrocytoma is guarded. Most of these tumors in young adults progress to a higher grade.[213] Median survival has been reported as 5 to 8 years.[213, 275]

Anaplastic Astrocytoma. As the name implies, anaplastic astrocytomas (WHO grade III) exhibit considerable variation in cellular morphology, with high cellularity, frequent mitoses, and foci of vascular proliferation, findings that are not present in low grade (grade II) astrocytomas.[303] However, no necrosis is present in anaplastic astrocytomas, on either gross inspection or microscopic evaluation.[275] These tumors tend to occur in a slightly older age group (peak age mid-40s) than the grade II lesions and, in many cases (some estimates are as high as 75%), represent a progressive dedifferentiation of a previously low grade tumor.[247]

Reflecting the increased histologic variation, the imaging findings are also less homogeneous than in the lower grade tumors (Fig. 5–9*A*). On T2-weighted MRI, anaplastic astrocytomas are most often heterogeneously hyperintense and are associated with a greater degree of vasogenic edema and overall mass effect. Contrast enhancement on both CT and T1-weighted MRI is common (Fig. 5–9*B*); compared with glioblastoma (grade IV), the enhancement pattern is not ringlike but, rather, more patchy.

Current estimates indicate that anaplastic astrocytomas represent about 25% of all primary gliomas of the brain.[240] Median survival for patients with anaplastic astrocytoma is 2 to 3 years. Most tumors progress relatively rapidly to frank glioblastoma with intratumoral necrosis.

Glioblastoma Multiforme. Glioblastoma multiforme (WHO grade IV) is the most common primary tumor of the CNS, accounting for more than half of all intracranial gliomas.[342] It is biologically the most aggressive of the gliomas, with rapid progression of clinical signs and symptoms and a mean survival time in the range of 12 months. Like all other astrocytomas, glioblastoma characteristically involves the cerebral white matter, but this highly malignant process readily infiltrates and destroys the gray matter with loss of gray-white differentiation.[286] As their name implies, these highly malignant tumors have a variegated histologic appearance, with interspersed areas of hypercellularity, cellular pleomorphism, endothelial proliferation, and intratumoral necrosis.[49]

It is probable that most glioblastomas arise by anaplastic change within preexisting low grade cerebral astrocytomas, although some likely occur de novo.[286] Although most commonly focal and singular in their presentation, glioblas-

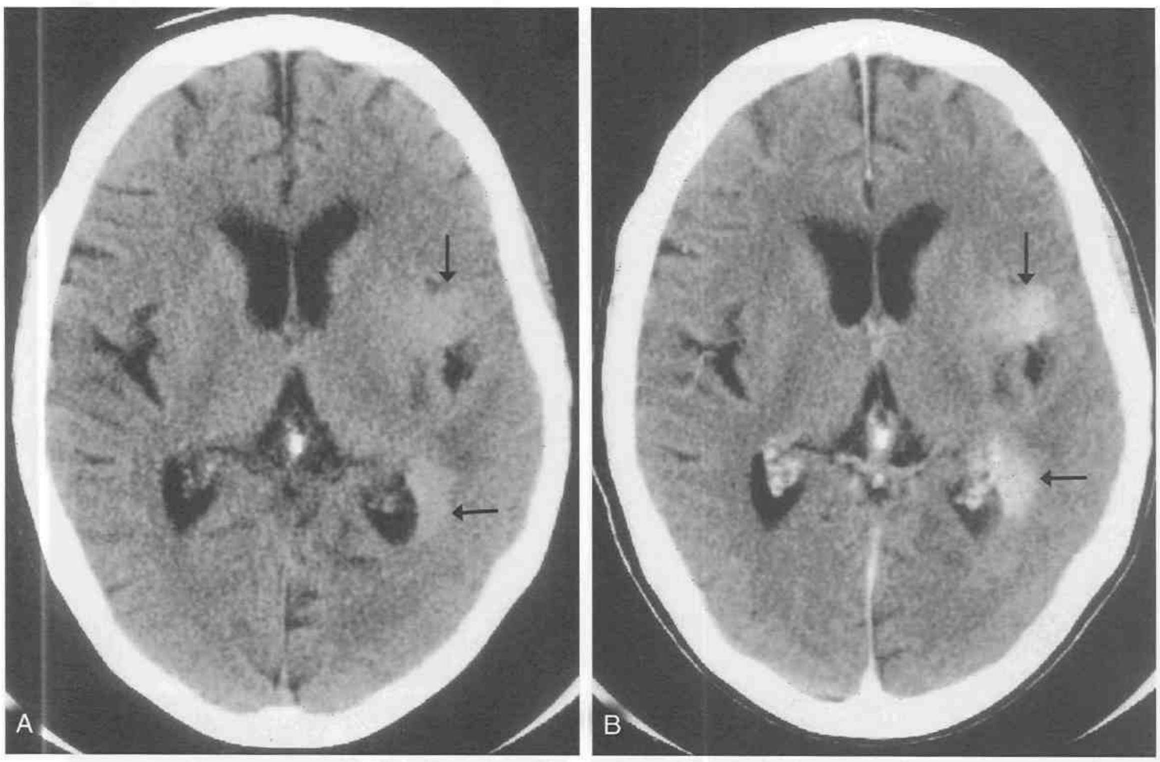

Figure 5–9. Anaplastic astrocytoma, left frontotemporal. Axial CT images prior to *(A)* and following *(B)* the intravenous administration of iodinated contrast medium. On the noncontrast image *(A)*, patchy areas of hyperdensity *(arrows)* are noted on both sides of the left sylvian fissure, involving the medial (insular) and lateral (temporal) aspects. There is mild mass effect on the lateral margin of the atrium of the left lateral ventricle by the posterior extension of this tumor *(posterior arrow)*. Note the ill defined diffuse hypodensity extending between and surrounding the hyperdense regions; this likely represents a mixture of infiltrating tumor cells and reactive edema. *B*, On the postcontrast image, there is diffuse contrast enhancement of the previously hyperdense regions *(arrows)*. Note that the enhancement reaches the ependymal surface of the left atrium. There is no evidence of intratumoral necrosis.

tomas may be multifocal or multicentric in origin.[20] The peak age of incidence of glioblastoma is during the fifth and sixth decades of life, some 10 to 20 years later than the peak age for astrocytoma. However, glioblastoma is not rare in younger adults or even in children; of all glioblastomas, approximately 3% occur in childhood, mainly in the brain stem and cerebellum. Studies indicate that the incidence of malignant gliomas is increasing significantly in the elderly.[80]

On gross inspection, glioblastomas appear more or less spherical when confined to one lobe of a cerebral hemisphere. However, these rapidly growing neoplasms invariably infiltrate into adjacent lobes, the corpus callosum ("butterfly gliomas"), and the contralateral hemisphere. Tumors that have extended widely tend to have more irregular configurations with lobulated margins. Infiltration of the ependyma of the lateral and third ventricles and penetration of the cerebral cortex with invasion of the overlying meninges occur commonly and may lead to seeding through the CSF pathways.[214, 286] Vascular endothelial proliferation with formation of large sinusoidal channels (angioneogenesis) is a typical finding in glioblastomas, and intratumoral hemorrhage is not rare.[366] The central portions of these tumors frequently undergo ischemic coagulative necrosis, leaving only a peripheral rim of viable tumor of variable thickness.[286] Cysts of varying size representing the residua of central necrosis may be found within the more solid portions of many glioblastomas.

The gross pathologic findings previously described are accurately portrayed on CT and MRI. Although smaller tumors are generally rounded, more extensive lesions have irregular configurations indicating their spread along white matter pathways and penetration into and through cerebral cortex. These tumors typically appear on CT as heterogeneous masses with irregular borders of normal or slightly increased density intermixed with or surrounding cystlike areas of diminished attenuation (see Fig. 5–12).[191]

Findings on MRI parallel those on CT. Because of the greater inherent sensitivity of MRI for the detection of subacute and chronic hemorrhage and for the demonstration of tumor hypervascularity (curvilinear and racemose signal voids), the overall appearance of the lesion is even more heterogeneous on MRI than on CT.[175] Areas of intratumoral necrosis, which tend to dominate the appearance of the most aggressive of these tumors, appear notably hyperintense on T2-weighted images except where interrupted by more solid masses of cellular debris (Fig. 5–10*A*). Compared with this central necrotic hyperintensity, the surrounding rim of viable and growing tumor appears significantly less hyperintense (owing to its hypercellularity), with unsharp margins, and may blend with or be indistinguishable from the peritumoral edema.

Virtually all glioblastomas are associated with vasogenic edema in the surrounding peritumoral white matter, usually graded as moderate or severe (Figs. 5–11*A* and 5–13*A*).[5, 191] The origin of this edema is uncertain; it may reflect production of a vascular permeability factor by the tumor cells.[10] Grossly evident mildly hyperdense or hyperintense

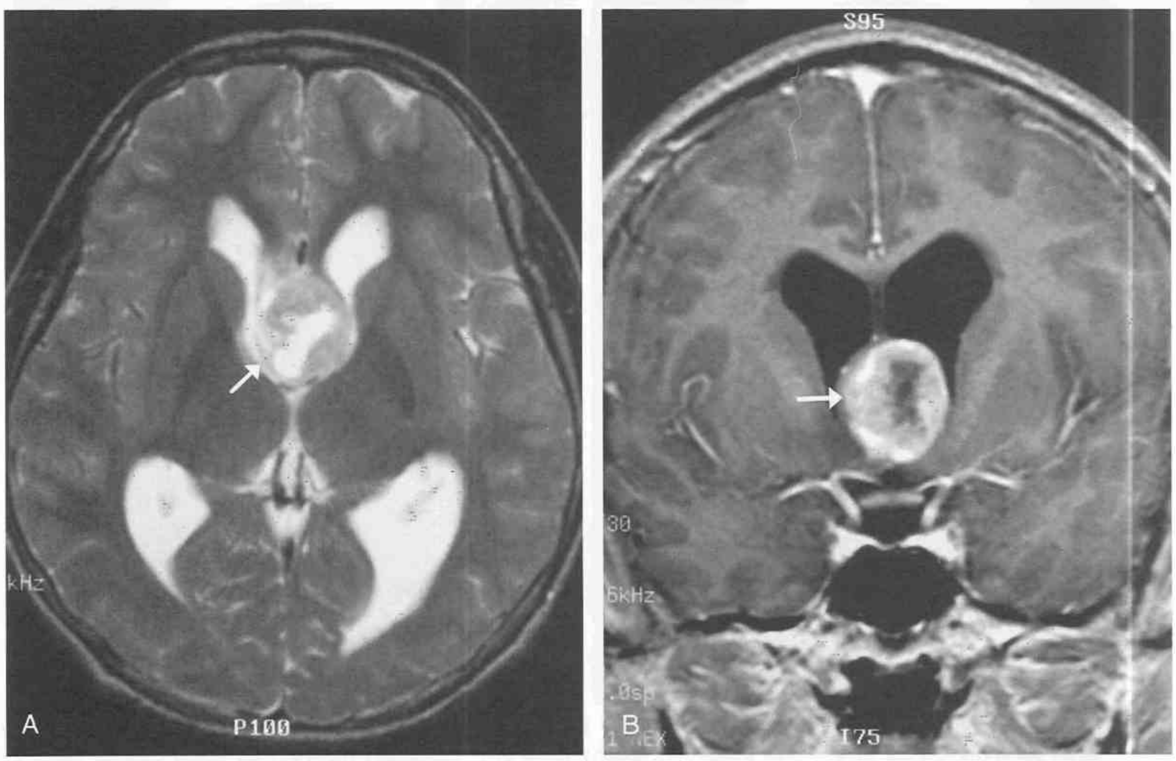

Figure 5–10. Glioblastoma multiforme involving the septum pellucidum. *A*, Axial T2-weighted MR image through the inferior aspect of the frontal horns of the lateral ventricles. An ovoid heterogeneously hyperintense mass *(arrow)* arising from the inferior aspect of the septum pellucidum indents and partially occludes the frontal horns bilaterally. Note the irregularly marginated intratumoral marked hyperintensity suggesting central necrosis. *B*, Following intravenous administration of gadolinium, a coronal T1-weighted image demonstrates intense contrast enhancement *(arrow)* of the thick peripheral rind with nonenhancement of the central cavity.

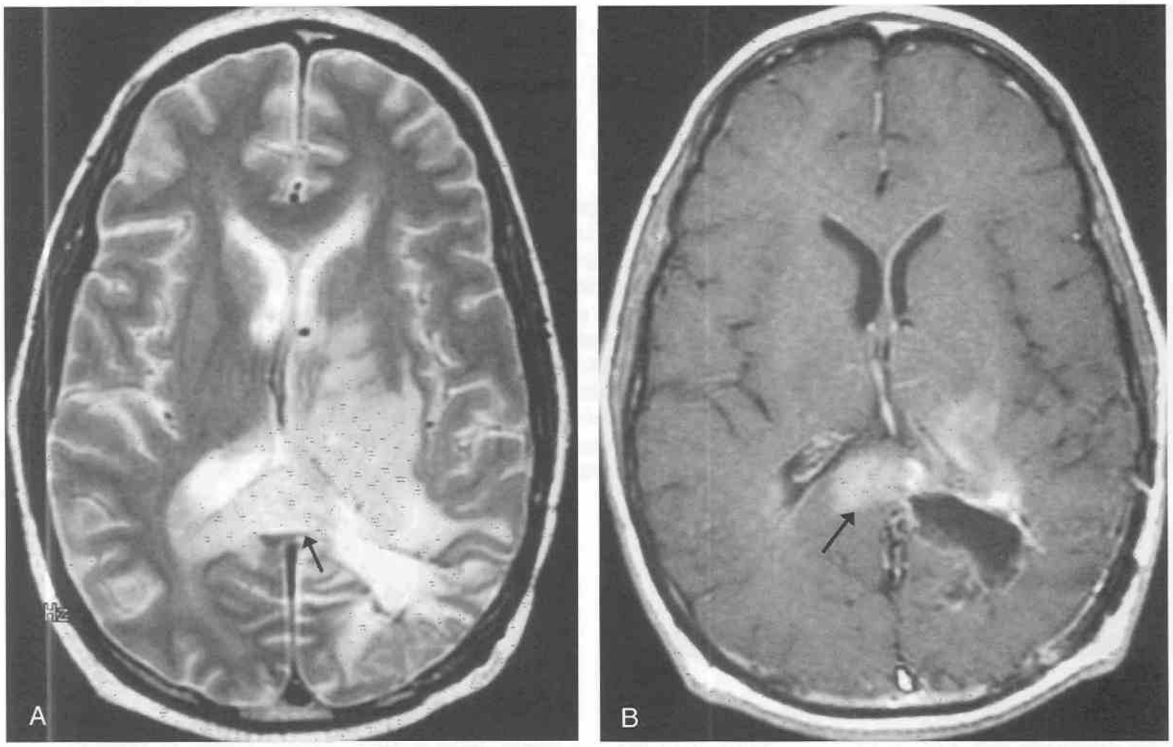

Figure 5–11. Left deep frontoparietal glioblastoma with extension through corpus callosum. *A*, Axial T2-weighted MR image through the level of the upper third ventricle. A large area of diffuse hyperintensity involves the left posterior thalamus and basal ganglia and extends posteriorly to involve the subcortical white matter in the left parietooccipital convexity. It is not possible on this image to either define the tumor margins or to separate gross tumor from surrounding edema. The third ventricle and the flow voids of the two parallel internal cerebral veins are bowed to the right of the midline secondary to the left sided deep mass effect. Note that this hyperintensity also extends into and widens the splenium of the corpus callosum *(arrow)*, crossing the midline into the contralateral hemisphere and creating a "butterfly glioma" pattern. *B*, Axial T1-weighted image following intravenous gadolinium demonstrates patchy heterogeneous contrast enhancement within the splenium *(arrow)* and surrounding the dilated and posteriorly displaced atrium of the left lateral ventricle; the tumor has blocked the posterior portion of the ventricle, and the marginal contrast enhancement of the atrium suggests subependymal tumor spread.

tumor margins are typically unsharp, but they stand out in contrast to the surrounding hypodense or hypointense edematous white matter on CT and on T1-weighted MRI, respectively, after IV administration of a contrast agent.[38, 51, 95, 111]

Hemorrhage within the tumor is common in these aggressive tumors with extensive angioneogenesis. The appearance of hemorrhage in glioblastoma on both CT and MRI differs from that seen in nonneoplastic intracerebral hemorrhage, in that the former is more heterogeneous because of the surrounding and intermixed tumor and necrotic debris (Fig. 5–12).[215] Also, evolution of intratumoral hemorrhage usually proceeds more slowly compared with hypertensive, posttraumatic, or other nonneoplastic types of parenchymal hematomas.[9]

Contrast enhancement of viable tumor, including the peripheral rim and the intratumoral solid portions, is nearly universal in glioblastomas (Figs. 5–10*B*, 5–11*B*, and 5–13*B*).[5, 51, 52, 191, 208] The opacifying tumor ring is typically irregular and of varying thickness. The intensity of the enhancement is often significant and correlates with the level of cellular anaplasia,[51] but it does not accurately reflect the extent of microscopic tumor infiltration.[44, 95] Careful imaging–histopathologic correlation studies have conclusively established the presence of viable tumor cells well beyond the margin of contrast enhancement, and the zone of apparent edema in the surrounding white matter must be understood as including foci of microscopic tumor infiltration.[45, 46, 95]

Differentiation by CT or MR among glioblastoma (or other grade IV gliomas), carcinomatous metastasis, and lymphoma is often difficult. All three processes may appear as irregularly rounded, contrast enhancing, ringlike masses with walls of varying thickness. In all, the viable tumor rim is typically irregular and nonuniform in thickness, and histologic examination is usually required for definitive diagnosis. Primary CNS lymphoma is typically more central in location and homogeneously solid (see Fig. 5–45), but central necrosis, infiltration into the corpus callosum and other major white matter pathways, and tumor extension into the meninges and along the ependyma (all common late manifestations in glioblastoma) are not rare occurrences with lymphoma. Occasionally, a large area of active demyelination with inflammation and edema secondary to previously undiagnosed multiple sclerosis may also simulate a glioblastoma on CT or MRI.[35]

When images demonstrate multiple nodular or ringlike masses, multicentric glioblastoma must be included in the

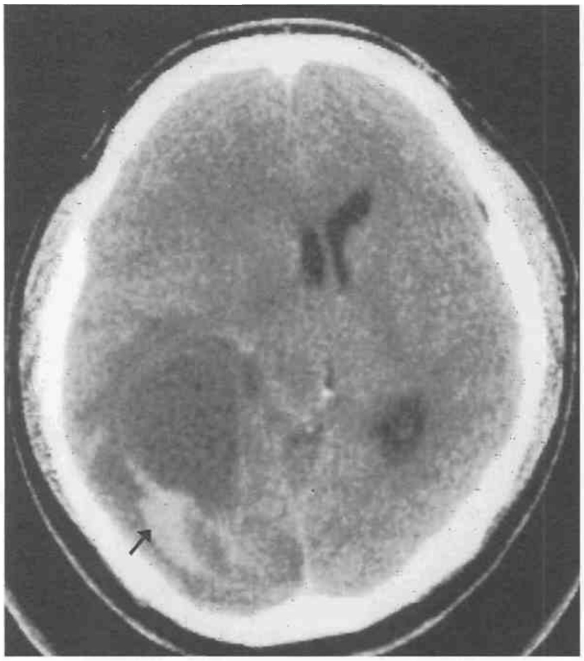

Figure 5–12. Intratumoral hemorrhage into large right posterior fronto-parietal glioblastoma. Axial CT image without intravenous contrast. A large well demarcated hypodense cystic cavity in the deep right fronto-parietal white matter is surrounded by poorly defined hypodensity. On the posterior margin of this cavity, there is a sharply defined scythelike hyperdense collection *(arrow)* representing intratumoral hemorrhage. Note the considerable mass effect secondary to diffuse edema in the right frontal lobe with shift of the lateral and third ventricles and the septum pellucidum to the left of the midline. The atrium of the left lateral ventricle is compressed and displaced anteromedially by this cavitated tumor.

differential diagnosis (see Fig. 5–13),[160,271] along with metastases and pyogenic cerebral abscesses.[268] The peripheral rim of an abscess is typically (but not always) thinner and more uniform than that of a glioblastoma or a metastasis.[50,348] MRS has been suggested as a method for differentiating abscess from glioblastoma or metastasis with central necrosis; the chemical shift spectrum in the center of the lesion reflects high lactate signal in both necrotic tumor and abscess. Sampling of the peripheral rim and adjacent edematous white matter, however, typically demonstrates depressed NAA and elevated choline levels in the case of tumor (Fig. 5–14*B*), compared with normal choline and NAA levels in the abscess margin.[131] Our experience to date with MR spectroscopy has supported this differentia-

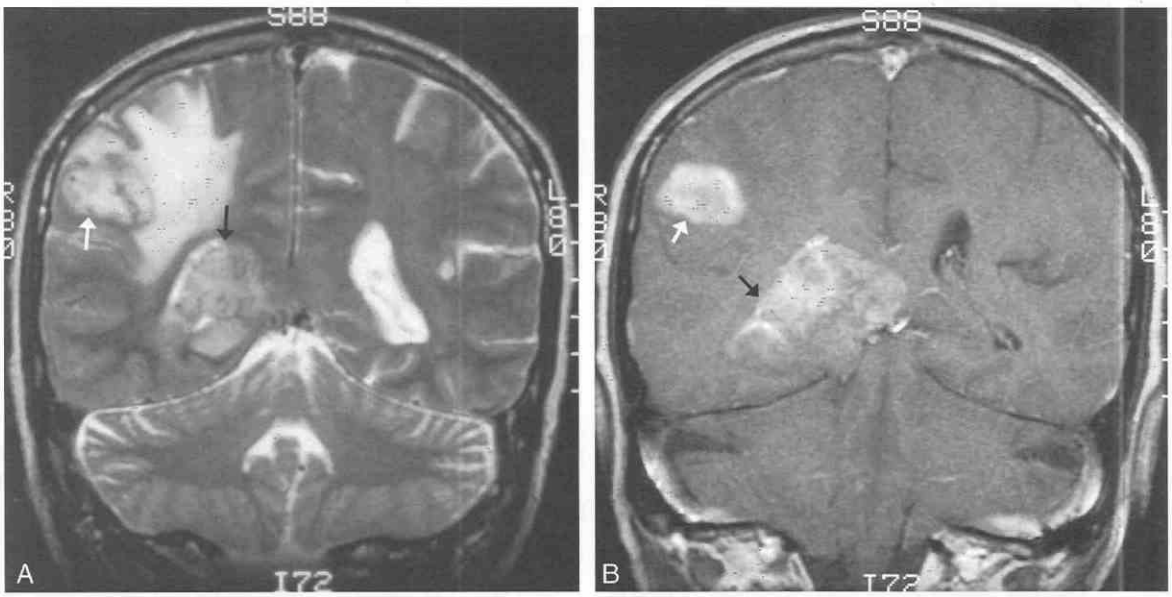

Figure 5–13. Multicentric glioblastoma. Coronal MR images through the posterior atrial region. *A,* T2-weighted image demonstrates a hyperintense rounded mass in and deep to the high right frontoparietal convexity *(upward pointing white arrow)* and a second similar mass in the inferomedial right temporooccipital cortex and white matter *(downward pointing black arrow)*. Between these masses is a large area of greater hyperintensity, likely representing edema with probable microscopic tumor infiltration, which effaces the overlying convexity cortex and severely compresses and obscures the atrium of the right lateral ventricle. *B,* On a T1-weighted image following intravenous gadolinium administration, both lesions demonstrate inhomogeneous contrast enhancement. The inferomedial tumor has invaded the splenium of the corpus callosum, extending across the midline into the left hemisphere. Note also extension of this tumor inferiorly, protruding into the tentorial notch and impinging on the right side of the superior cerebellar vermis.

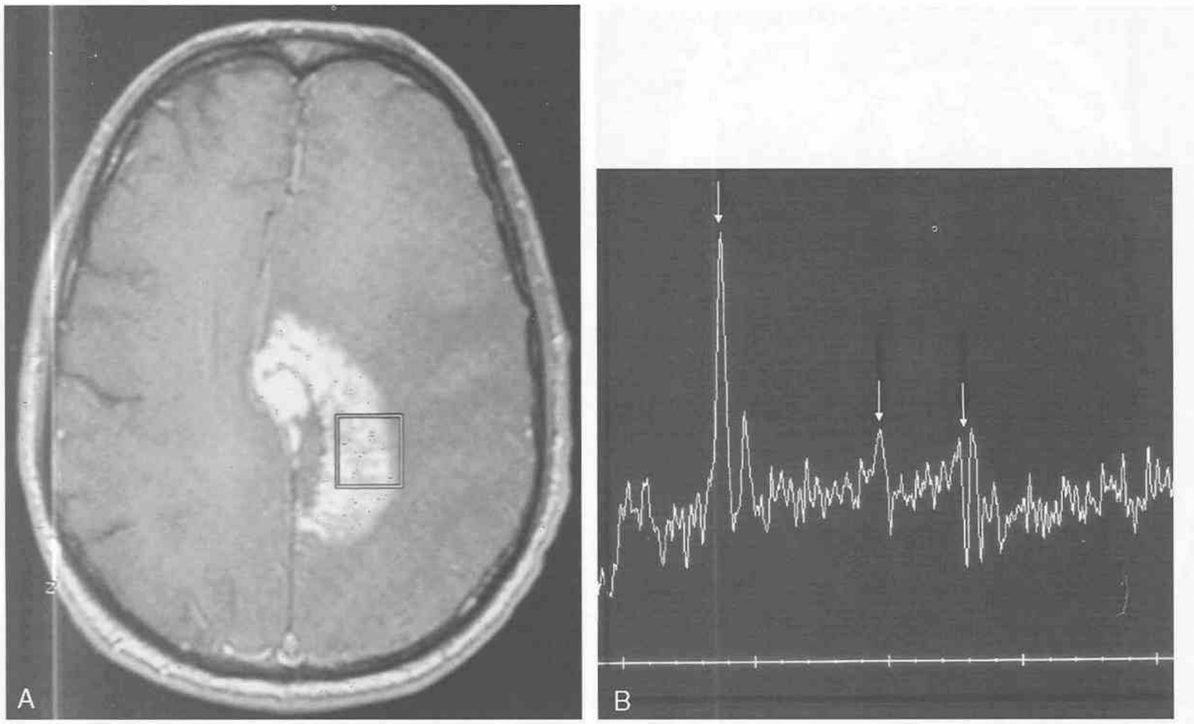

Figure 5–14. Glioblastoma with MR spectroscopic correlation. *A*, Axial T1-weighted postgadolinium MR image demonstrates an irregularly marginated contrast enhancing left posterior frontal parasagittal tumor involving the white and gray matter of the left cingulate gyrus with associated subfalcine herniation. The square outline overlying the midportion of the enhancing mass indicates the voxel selected for spectroscopic interrogation. *B*, Graphic display of proton spectroscopic interrogation of the tissue included within the voxel outlined on *A* demonstrates markedly reduced concentration of n-acetyl aspartate (NAA) *(middle arrow)* with slight elevation of lactate peak *(right arrow)* and marked elevation of choline *(left arrow)*. The elevation in lactate reflects tissue necrosis, while the markedly elevated choline peak indicates increased cell membrane turnover. These findings support the diagnosis of a malignant glioma.

tion. However, needle biopsy under imaging guidance remains the most definitive method for establishing the diagnosis and instituting definitive treatment.[220]

A commonly encountered clinical problem is the need to differentiate radiation necrosis from recurrent glioblastoma in a patient who has undergone surgical resection and a complete course of radiation therapy and now, several months after the radiation therapy, demonstrates a change in neurologic status. If the followup imaging study demonstrates increases in the size of the apparent tumor mass and the extent of contrast enhancement, differentiation of recurrent tumor from radiation necrosis on the basis of CT or MRI is not possible. In such circumstances, ^{18}FDG PET studies of brain glucose metabolism have shown the level of glucose utilization to be a valid measure of tumor growth,[89] although one study has challenged these results.[276] MRS may be able to provide similar prognostic information (Fig. 5–15), but clinical experience to date is limited.[183]

Gliomatosis Cerebri. A comparatively uncommon pattern of glial neoplasia, gliomatosis cerebri is characterized by widespread diffuse neoplastic infiltration in multiple lobes and both cerebral hemispheres. The extent of infiltration is disproportionate with the other histopathologic features, such as the level of anaplasia and the relative lack of destruction of normal tissues. Despite the extent of tumor infiltration, neural connections are preserved, and the clinical signs and symptoms are relatively mild. Nevertheless, the clinical course is relentlessly progressive over periods varying from weeks to years.

The process tends to extend along the white matter tracts but also involves the adjacent gray matter with loss of clear gray-white distinction. Grossly, the involved parenchyma is both expanded and distorted by the tumor infiltration. Microscopically, the tumor cells infiltrate between myelinated fibers without destroying them, much like in a low grade astrocytoma, but there is greater cellular atypia and mitotic frequency, and foci of necrosis are occasionally seen.

Diagnostic imaging studies demonstrate the extensive and scattered areas of parenchymal involvement with multiple ill defined areas of hyperintensity on T2-weighted MR images and subtle hypodensity on CT scans (Fig. 5–16*A*).[309] Focal expansion and distortion are seen as areas of diffuse effacement of sulci and compression and displacement of the adjacent ventricles and cisterns. The incidence and level of contrast enhancement are often less than the extent of apparent tumor infiltration (Fig. 5–16*B*), because enhancement relates closely to the degree of cellular dedifferentiation.[10] Clinically, the principal differential diagnosis is with multiple sclerosis, but the imaging pattern of multiple widespread areas of expansion and distortion as well as the relatively rapid and consistent progressive clinical course favor a diagnosis of neoplasm.

Gliosarcoma. A rare tumor, gliosarcoma consists of

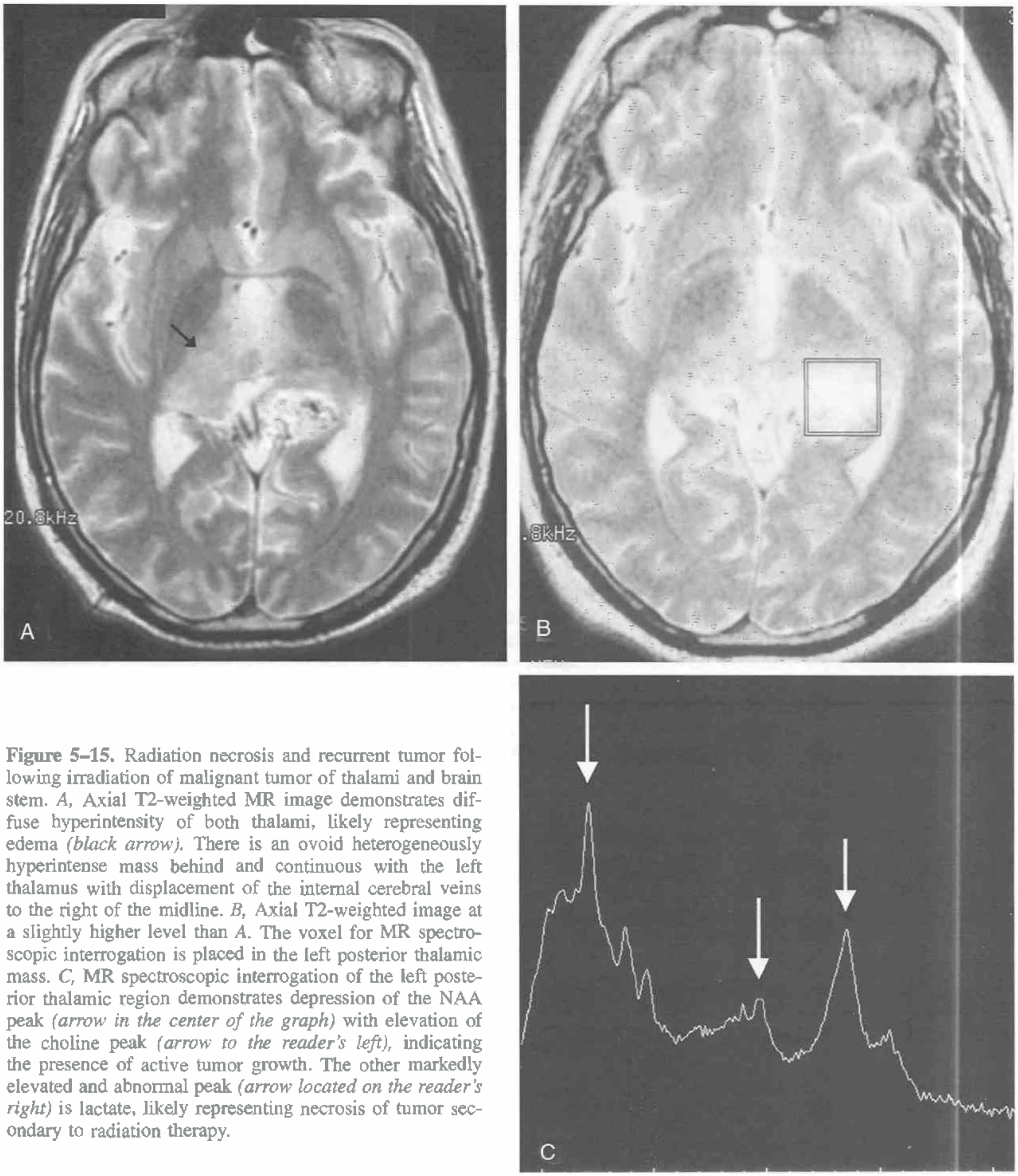

Figure 5–15. Radiation necrosis and recurrent tumor following irradiation of malignant tumor of thalami and brain stem. *A*, Axial T2-weighted MR image demonstrates diffuse hyperintensity of both thalami, likely representing edema *(black arrow)*. There is an ovoid heterogeneously hyperintense mass behind and continuous with the left thalamus with displacement of the internal cerebral veins to the right of the midline. *B*, Axial T2-weighted image at a slightly higher level than *A*. The voxel for MR spectroscopic interrogation is placed in the left posterior thalamic mass. *C*, MR spectroscopic interrogation of the left posterior thalamic region demonstrates depression of the NAA peak *(arrow in the center of the graph)* with elevation of the choline peak *(arrow to the reader's left)*, indicating the presence of active tumor growth. The other markedly elevated and abnormal peak *(arrow located on the reader's right)* is lactate, likely representing necrosis of tumor secondary to radiation therapy.

both glial and mesenchymal elements. Most reported patients have been between 50 and 70 years old. The origin of the mesenchymal element remains uncertain and controversial; it presumably arises from spontaneous neoplastic transformation of vascular elements within the glial neoplasm, but prior radiation therapy has been implicated in a few case reports. The mesenchymal element is usually a fibrosarcoma, but other sarcomas have been reported. Immunohistochemistry studies demonstrate both GFAP reactivity, confirming the astrocytic nature of the glial component, and positive staining for collagen and reticulin, confirming the mesenchymal component.[70]

The glial component of these mixed tumors is typically glioblastoma, and gross pathology as well as both CT and MRI demonstrate the variegated pattern of that tumor with areas of central necrosis and peripheral infiltration both along white matter tracts and into adjacent gray matter (Fig. 5–17). Invasion into and involvement of the overlying meninges are often noted (Fig. 5–17*B*); invasion into bone and extracranial soft tissue likely reflects the sarcomatous

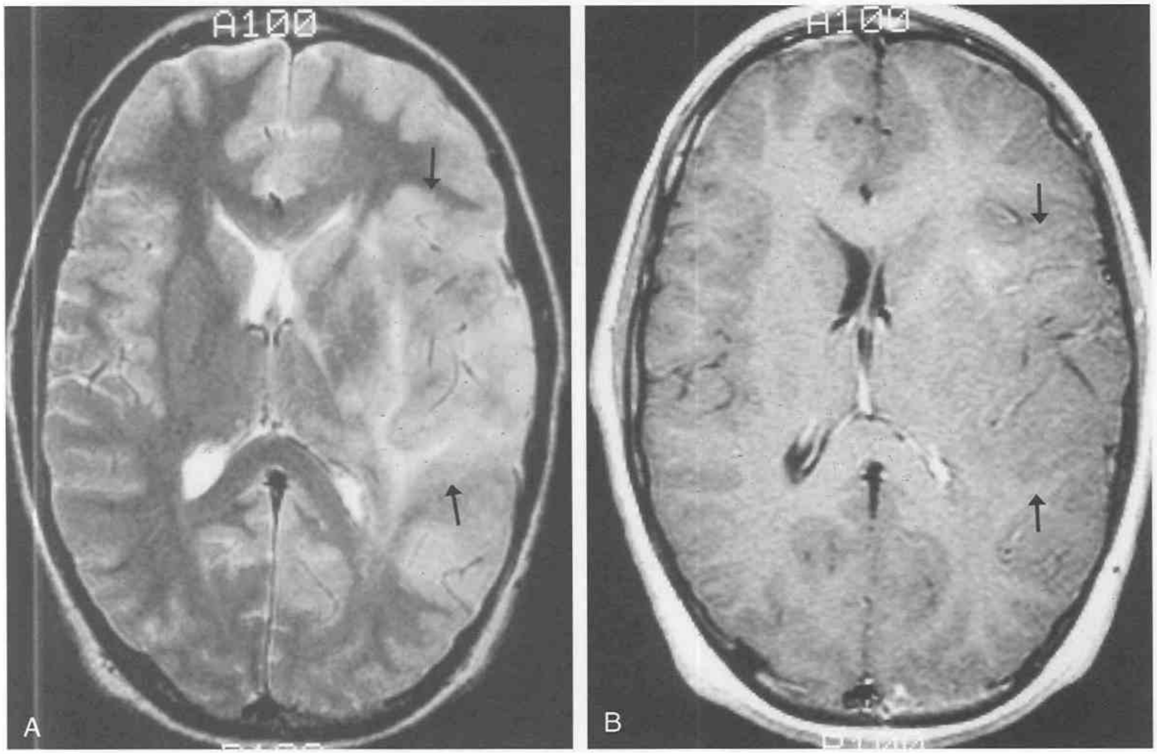

Figure 5–16. Gliomatosis cerebri in the left cerebral hemisphere. *A,* On this axial T2-weighted MR image, there is evidence of diffuse enlargement of the left frontal, temporal, and parietal lobes with extensive but ill defined hyperintensity involving the temporoparietal convexity cortex and adjacent white matter *(arrows). B,* Axial T1-weighted image following intravenous gadolinium demonstrates widely separated patchy areas of faint contrast enhancement *(arrows),* which represent scattered foci of malignant gliomatous infiltration.

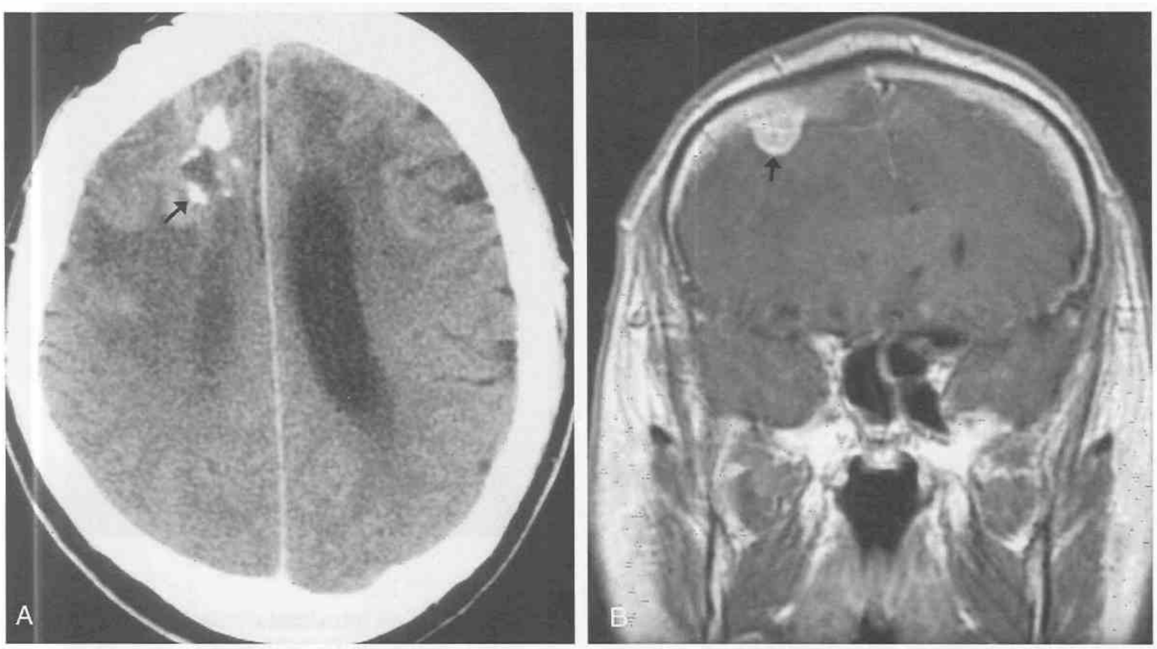

Figure 5–17. Gliosarcoma. *A,* Axial CT image following intravenous contrast demonstrates a lobulated mass with variegated contrast enhancement in the high right frontal convexity with multiple intratumoral calcifications *(arrow)* surrounding an area of central hypodensity that likely represents necrosis. The contrast enhancement crosses the midline into the high left frontal convexity. Extensive white matter hypodensity, likely representing edema, involves the surrounding frontal lobe white matter bilaterally. *B,* Coronal T1-weighted MR image post intravenous gadolinium confirms the presence of a lobulated high right frontal convexity contrast enhancing tumor and also clearly demonstrates the extensive spread of this tumor along the inner table of the skull bilaterally with bandlike meningeal thickening over the convexities of both cerebral hemispheres.

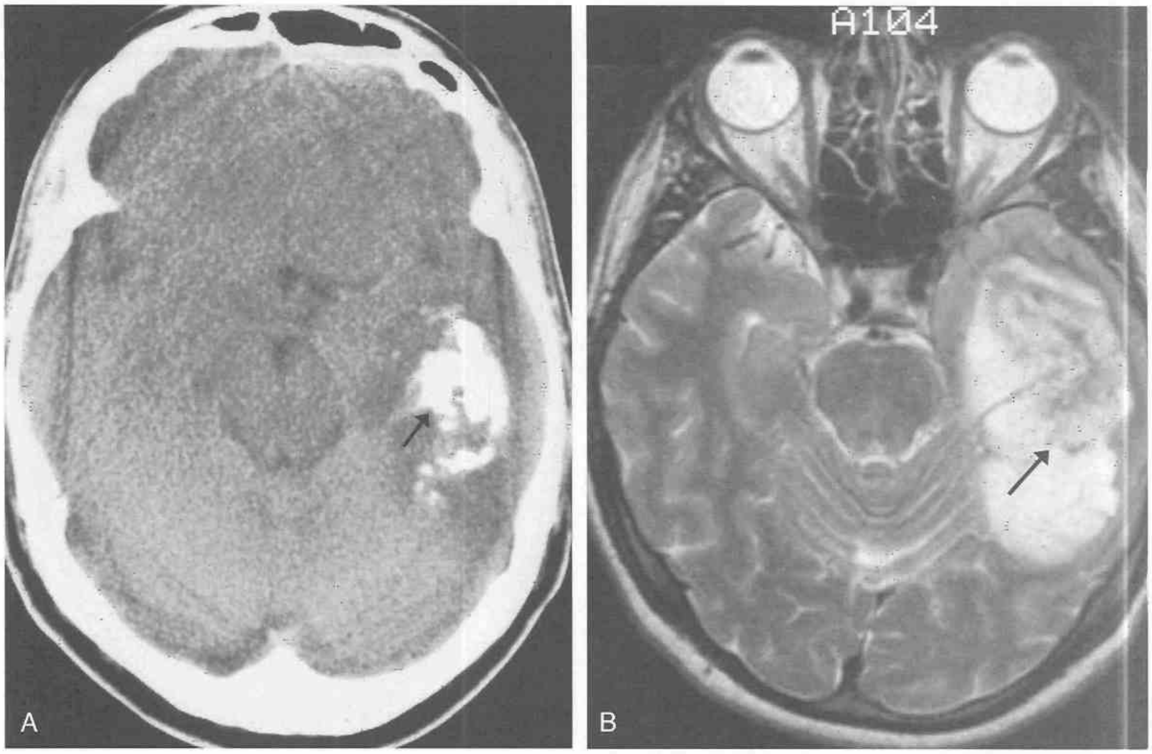

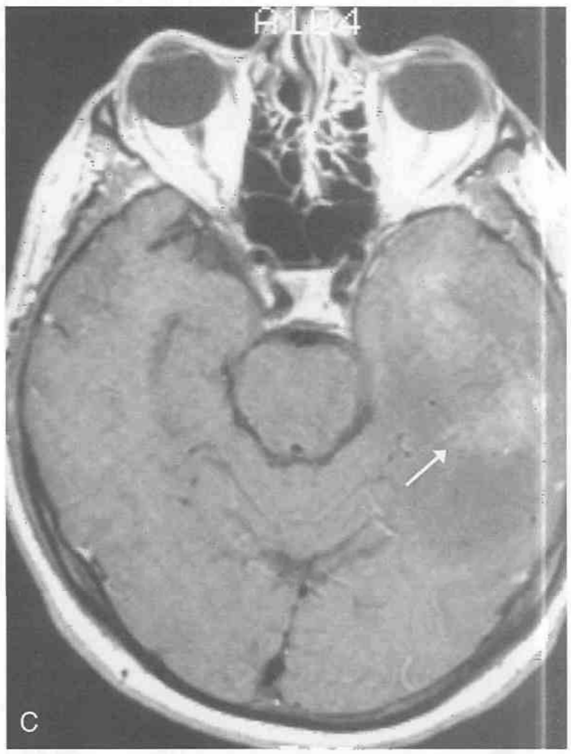

Figure 5–18. Oligodendroglioma. *A,* Axial noncontrast CT image demonstrates a large mass with poorly defined margins in the left midtemporal lobe *(arrow)*. The mass is predominantly hypodense, with a large amorphous central calcification, and involves the convexity cortex as well as the underlying white matter. The expanded left temporal lobe herniates across the tentorial margin and compresses the lateral aspect of the left cerebral peduncle. *B,* On this axial T2-weighted image, the large intratemporal tumor appears heterogeneously hyperintense, with the calcified portion *(arrow)* exhibiting lesser intensity. *C,* Axial T1-weighted MR image following intravenous administration of gadolinium. The tumor appears predominantly hypointense, has ill defined margins, and involves mainly white matter but also extends into the convexity cortex and demonstrates faint heterogeneous contrast enhancement *(arrow)*.

element within the tumor, and systemic metastasis (a rare occurrence in glioblastoma) is well described for gliosarcoma.[48, 70, 187]

Oligodendrogliomas

Oligodendrogliomas (tumors derived from oligodendrocytes) represent 15% to 20% of intracranial gliomas and 5% to 10% of all intracranial neoplasms.[71, 376] The diagnosis is made much more commonly now than in the past, reflecting a reevaluation of the histologic and immunochemical criteria that define the distinction between oligodendroglioma and astrocytoma.[70, 71] These tumors occur principally in the supratentorial white matter. Like low grade astrocytomas, they tend to infiltrate along white matter tracts in a nondestructive manner. However, more

commonly than astrocytomas, oligodendrogliomas may also invade the adjacent cortex, and involvement of deep structures is also common.[286] Eighty-five percent occur in the cerebral hemispheres, more than half in the frontal lobes.[81, 191, 296]

The peak age of incidence of oligodendrogliomas is in the fourth and fifth decades of life; these tumors are much less common in childhood or adolescence.[70, 273] The initial clinical presentation is most often a seizure.[274] Tumor growth is generally slower than in astrocytomas of similar grade, but a more biologically aggressive category is now recognized in the revised WHO classification as anaplastic oligodendroglioma.[70, 71, 168, 274] Cytogenetic studies have noted loss of the 1p and 19q chromosomes in approximately half of patients with anaplastic oligodendroglioma; on imaging studies, patients with loss of 1p have demonstrated a significant association with positive response to multiagent nitrosourea-based chemotherapy.[54]

Oligodendrogliomas are typically densely cellular and solid, contain multiple irregular masses of dystrophic calcification, and grow very slowly. They can attain considerable size before they produce symptoms.[70] Areas of cystic degeneration are found in 20% of cases, mainly in the larger tumors.[189] Intratumoral hemorrhage is also a frequent finding.[189]

Foci of astrocytoma are frequently found in association with oligodendroglioma, and when these are prominent, the tumor is termed a *mixed glioma*.[365] When there is a clear preponderance of neoplastic oligodendrocytes (75% to 90%), the tumor is classified as an oligodendroglioma.[303]

On CT, oligodendrogliomas most often appear as masses of heterogeneous density (predominantly hypodense) in the frontal lobe with irregular and poorly defined margins involving the more superficial white matter and frequently infiltrating into the overlying cortex and obscuring the gray-white interface. The characteristic feature in the great majority of cases is the presence of large irregular calcifications, sometimes described as ribbonlike or gyriform in character, within the tumor (Fig. 5–18*A*).[341] The frequency of intratumoral calcification in oligodendrogliomas (70% to 90%) is the highest of any cerebral neoplasm,[341] but overall, intratumoral calcification is most common in astrocytomas (frequency, 25%) because of the much greater prevalence of that lesion.[168] Intratumoral cyst formation is common (20%),[189] but frank intratumoral necrosis is unusual and indicates a poor prognosis.[42] Contrast enhancement is noted in approximately two thirds of oligodendrogliomas (Fig. 5–18*C*), but the degree of enhancement is variable and appears to correlate with higher histologic grade and lower survival.[303, 341]

On MRI, oligodendrogliomas appear heterogeneous on both T1- and T2-weighted spin-echo images because of the presence of intratumoral cysts and calcifications.[145] On T1-weighted images, the tumors appear predominantly hypointense to gray matter, and on T2-weighted images, they are most often hyperintense, with small intratumoral cysts and focal calcifications and hemorrhages contributing to the overall heterogeneity (Fig. 5–18*B*).[168, 189] Peritumoral edema is noted in about a third of cases, but erosion of the overlying calvaria may be identified on both CT and MRI when the lesion is peripheral; this finding indicates the long-standing course commonly associated with oligodendrogliomas.[189]

Ependymoma

The ependyma lining the floor of the fourth ventricle is the most common site of origin of intracranial ependymomas (65%). Nevertheless, approximately 30% occur above the tentorium, arising from the walls of the lateral or third ventricles or from ependymal cell rests in the cerebral white matter adjacent to the lateral ventricles.[226, 286, 303, 315] Infratentorial ependymomas occur predominantly in children between the ages of 1 and 6 years; supratentorial ependymomas occur mainly in the second through the fourth decades of life.[7, 110, 315]

Posterior fossa ependymomas compose approximately 10% to 15% of all primary CNS neoplasms of childhood and approximately 5% to 10% of all intracranial neoplasms.[141, 286, 341] They are the fourth most common posterior fossa tumor of childhood,[18, 22] exceeded only by medulloblastoma, juvenile pilocytic astrocytoma, and brain stem glioma.[228] Ependymomas are usually slow growing tumors of moderate malignancy (WHO grade II), but the prognosis is guarded because of their notable tendency to recur locally and to disseminate via the subarachnoid spaces. The incidence of seed metastases via the CSF is approximately 10% overall but is considerably higher in the infratentorial tumors of early childhood; tumor seeding into the subarachnoid spaces is found initially or on followup studies in approximately a third of fourth ventricle ependymomas.[101, 226, 286]

Supratentorial ependymomas are commonly paraventricular, located most frequently within cerebral parenchyma near the atrium of the lateral ventricle or the foramen of Monro and presumably arising from ependymal cell rests.[226] Infratentorial ependymomas are lobulated, well circumscribed, exophytic masses that expand within the cavity of the fourth ventricle rather than infiltrate into the surrounding parenchyma. They often extend in a tonguelike fashion through the lateral recesses into the lateral medullary and cerebellopontine angle cisterns (15%) or through the foramen of Magendie into the vallecula (10%).[18, 226, 286, 303] Tumor growth within the fourth ventricle eventually leads to occlusion of the ventricle with resultant obstructive hydrocephalus.

These tumors are highly cellular, with uniform cells that tend to form characteristic perivascular pseudorosettes.[25] Although they do not invade through the ventricular walls, they are firmly attached to the ventricular floor, and complete resection of the tumor base is frequently not possible. The rate of local tumor recurrence after surgical resection is 90% to 95% within 3 years, and the 5 year survival is currently 45% to 70%.[138, 141, 228, 273, 304] Furthermore, about 25% of ependymomas exhibit features of anaplasia with a high mitotic rate, cellular pleomorphism, and intratumoral necrosis; these are considered WHO grade III.[25, 70]

Intratumoral calcification and cyst formation are common in ependymomas (20% to 50% of reported cases).[7, 226, 315, 361] Peritumoral edema is a prominent and frequent finding in association with both cerebellar and cerebral ependymomas.

On noncontrast CT, ependymomas appear as hypodense or isodense, heterogeneous, midline, rounded masses within the fourth ventricle that partially or completely obliterate it.[200, 226, 303, 315, 361] The tumor is typically well defined by a prominent hypodense halo of peritumoral edema. Aggregates of calcification, usually small and round but sometimes quite large, are found in up to half of these lesions, and focal lucencies resulting from cyst formation are nearly as common.[200] In supratentorial tumors, the cysts are both larger and more frequent (up to 80%) than in the fourth ventricle ependymomas (see Fig. 5–20*A*).[7] Intratumoral hemorrhage is relatively less common, with reported frequency of 20% or less.[200] After IV administration of contrast agent, the solid portions and cyst walls of the tumor mass exhibit moderate but variable and heterogeneous enhancement.[7, 110, 200, 315, 361]

The MRI appearance of ependymomas is heterogeneous, reflecting mixed signals from intratumoral calcification, cysts, and hemorrhage. Usually, these tumors are isointense to hypointense relative to white matter on T1-weighted

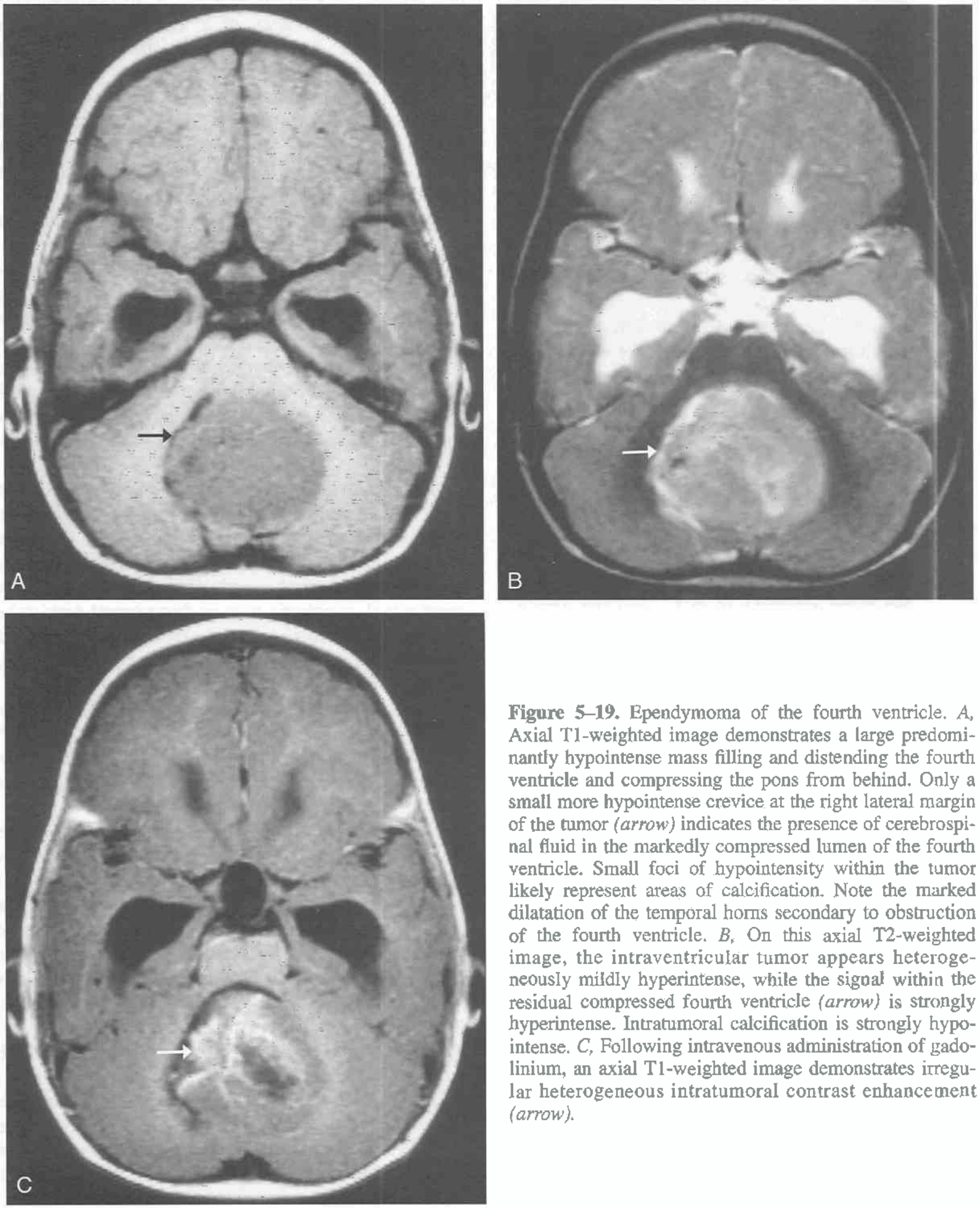

Figure 5–19. Ependymoma of the fourth ventricle. *A,* Axial T1-weighted image demonstrates a large predominantly hypointense mass filling and distending the fourth ventricle and compressing the pons from behind. Only a small more hypointense crevice at the right lateral margin of the tumor *(arrow)* indicates the presence of cerebrospinal fluid in the markedly compressed lumen of the fourth ventricle. Small foci of hypointensity within the tumor likely represent areas of calcification. Note the marked dilatation of the temporal horns secondary to obstruction of the fourth ventricle. *B,* On this axial T2-weighted image, the intraventricular tumor appears heterogeneously mildly hyperintense, while the signal within the residual compressed fourth ventricle *(arrow)* is strongly hyperintense. Intratumoral calcification is strongly hypointense. *C,* Following intravenous administration of gadolinium, an axial T1-weighted image demonstrates irregular heterogeneous intratumoral contrast enhancement *(arrow).*

images and isointense to hyperintense to white matter on T2-weighted images (Figs. 5–19*A*, *B*, and 5–20*B*).[110, 200, 311] As on CT, contrast enhancement is the rule for MRI, but it is variable in degree and typically not uniform (Figs. 5–19*C* and 5–20*C*). Although the MRI features of ependymoma are nonspecific,[18, 128, 311] the multiplanar capabilities of this modality offer unique visualization of infratentorial tumor extent within the cranial vault and the region of the cervicocranial junction.[10]

On both CT and MRI as well as in the clinical setting, the presentation of ependymoma of the fourth ventricle may closely resemble that of medulloblastoma and of JPA. The incidence and extent of intratumoral calcification, heterogeneity of density or signal intensity, and propensity for

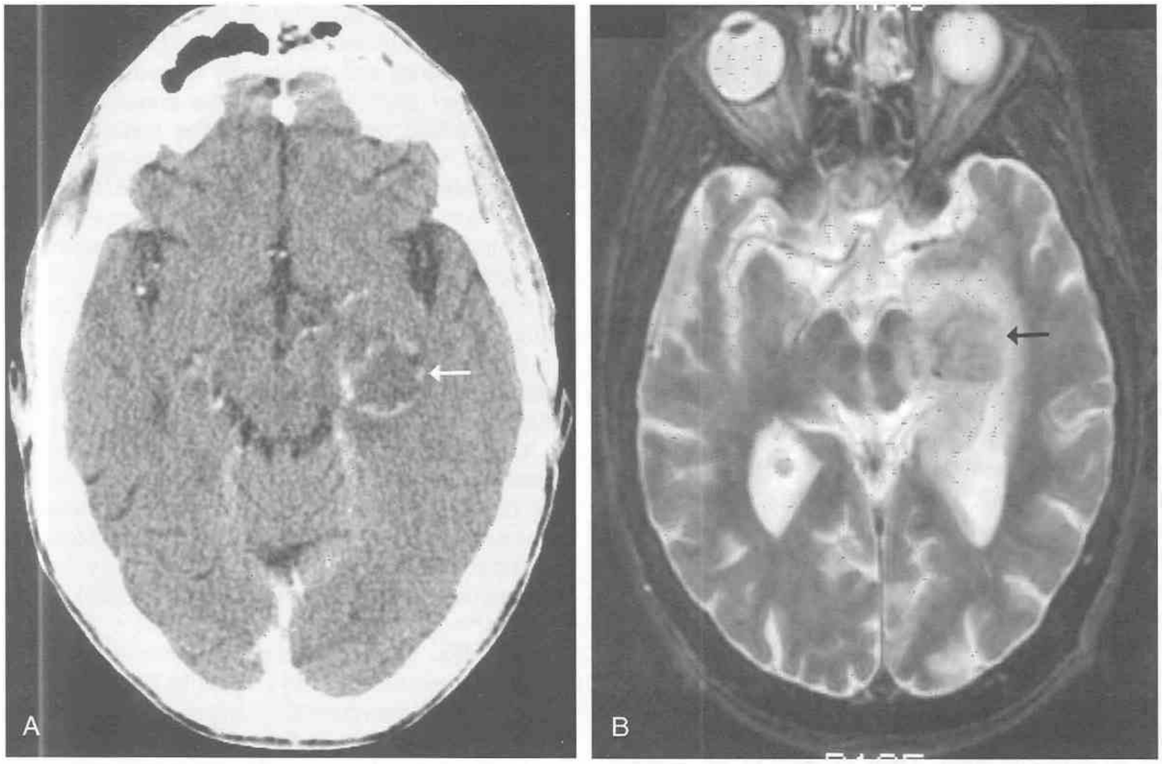

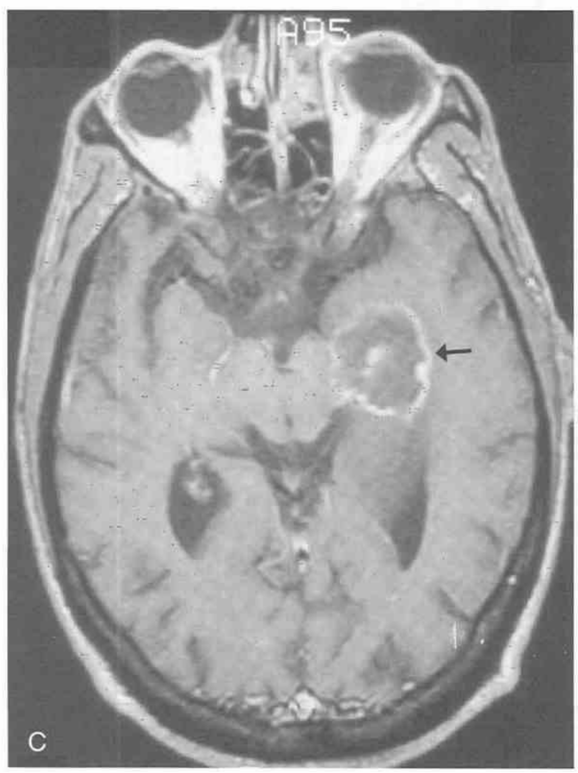

Figure 5–20. Supratentorial ependymoma. *A,* Axial CT image post intravenous contrast demonstrates a cystic appearing hypodense mass with irregular rimlike contrast enhancement *(arrow)* in the medial aspect of the left temporal lobe. *B,* On this axial T2-weighted MR image, the tumor *(arrow)* exhibits mixed signal intensity; it is predominantly isointense with gray matter and hypointense to cerebrospinal fluid. A tiny ovoid hypointensity in its posteromedial surface likely represents calcification. There is extensive surrounding edema in the temporal lobe and in the lateral aspect of the left cerebral peduncle. *C,* Axial T1-weighted postgadolinium image demonstrates irregular rimlike and central contrast enhancement *(arrow)* with medial extension into the lateral margin of the midbrain.

tumor extension into the fourth ventricular recesses are greater in ependymomas than in medulloblastomas or astrocytomas. In general, medulloblastomas appear more dense on CT with a lower frequency of intratumoral calcification, and they exhibit more homogeneous contrast enhancement than ependymomas. Definitive differentiation in a given case on the basis of CT or MRI findings may not, however, be possible.[200] Astrocytomas tend to occur in slightly older patients and are much less frequently centered in the midline.

Subependymoma

A rare variant of ependymoma that actually consists of both highly differentiated ependymal cells and astrocytes, subependymoma is classified as a benign (WHO grade I) glial neoplasm. It is considered to arise from beneath the ventricular lining and projects into the ventricular cavity as a sharply outlined intraventricular mass but does not extend deeply from its base into the adjacent brain parenchyma (Fig. 5–21). Subependymomas are typically solid and homogeneous, although larger tumors may contain calcifications, microcystic changes, and evidence of intratumoral hemorrhage.[10]

Subependymomas occur mainly in the fourth ventricle in older adults; they are often asymptomatic and found incidentally at autopsy.[10] Those that become symptomatic (causing obstructive hydrocephalus) occur mostly in the lateral ventricle in relation to the septum pellucidum and foramen of Monro and much less commonly in the region of the aqueduct.

On CT and MRI, symptomatic lesions in the lateral ventricles usually arise from the septum pellucidum and appear homogeneous in density and signal intensity. On T2-weighted MRI, the tumor appears homogeneously hyperintense to adjacent brain. There is little or no tumoral enhancement after IV administration of contrast medium (Fig. 5–19*C*). However, larger tumors may exhibit internal heterogeneity of density and signal owing to intratumoral calcification and hemorrhage.[110, 311]

The differential diagnosis includes central neurocytoma, ependymoma, and subependymal giant cell astrocytoma. Patient age, the nature of the symptoms, the presence of associated disease, tumor size, the presence and extent of calcification, cystic change, evidence of hemorrhage, and contrast enhancement are the key factors in making the differentiation.

Choroid Plexus Papilloma and Carcinoma

Papillomas arising in the choroid plexus are benign intraventricular neoplasms that locally expand the involved ventricle and cause hydrocephalus, which may be secondary to ventricular obstruction, overproduction of CSF, or impairment of CSF absorption. Choroid plexus papillomas represent less than 1% of all brain tumors but are more common in young children (3% of all pediatric brain tumors), particularly in the neonatal period; 85% occur in the first 5 years of life, and these tumors represent 40% of all brain tumors in the first 60 days of life.[200, 270, 303]

The atria of the lateral ventricles and the fourth ventricle are the most common sites of involvement. An age disparity exists with regard to tumor location, the lateral ventricle tumors occurring mainly in young children and the fourth ventricle papillomas appearing more commonly in adults.[11, 286] It is not uncommon for the fourth ventricle tumors to extend through the lateral recesses and protrade into the cerebellopontine angle cisterns.[253]

Histologically, choroid plexus papillomas consist of well differentiated proliferation of both the surface epithelium of the choroid plexus and the underlying vascular connective tissue core and are usually classified as WHO grade I.[70, 286] They grow slowly and are noninvasive, tending to expand within the confines of the ventricle or its outlet foramina.[70, 253, 303] Occasionally, however, the epithelium may exhibit malignant change, and in such cases, the tumors are classified as carcinomas; they may extend into the adjacent brain parenchyma.[221] The prognosis in these malignant choroid plexus tumors depends on the completeness of surgical resection, but overall, the 5 year survival ranges from 26% to 40%.[254]

Because of the friability and high vascularity of choroid plexus papillomas, intratumoral and intraventricular hemorrhage are common.[70, 201, 304]

On CT, choroid plexus papillomas appear as large, rounded or lobulated, isodense or hyperdense intraventricular masses that engulf and separate the normal choroid plexus calcifications and exhibit intense homogeneous contrast enhancement.[166, 221, 370] Small hypodense, nonenhancing foci are occasionally identified within these tumors.[166, 370]

On MRI, choroid plexus papillomas are usually isointense or hypointense with respect to brain on T1-weighted images and heterogeneously hyperintense relative to brain on T2-weighted images (Fig. 5–22*A*, *B*);[65, 200] the heterogeneity of signal intensity within the tumor mass may be due to areas of vascularity, calcification, or previous hemorrhage (Fig. 5–22*A*). As noted previously, the tumor typically expands the ventricle locally at the site of origin and may obstruct ventricular drainage, causing dilatation (entrapment) of the more proximal portion of the affected ventricle.[11] On both CT and MRI, these tumors usually demonstrate intense contrast enhancement (Fig. 5–22*C*), which may be homogeneous or heterogeneous, depending on the tumor contents.

The differential diagnosis of choroid plexus papilloma on imaging studies usually includes ependymoma in older children and adults and meningioma in adults. The lobulated tumor margins, the lack of invasion of brain parenchyma despite the large tumor size, and the heterogeneous signal pattern within the tumor all aid in distinguishing this lesion.

Nonglial Tumors

Neuronal and Mixed Neuronal and Glial Tumors

In this group of tumors of neuroepithelial origin, neuronal and glial differentiation are present in varying degrees. The 1993 revised WHO classification of tumors of the CNS includes the following recognized entities:

Figure 5–21. Subependymoma of the fourth ventricle and vestibular schwannoma in the right cerebellopontine angle. Axial T1-weighted *(A)* and T2-weighted *(B)* MR images demonstrate a small sharply marginated isointense (T1-weighted)/hyperintense (T2-weighted) nodular intraventricular mass in the central and left lateral aspects of the fourth ventricle *(white arrows)*. The mass appears continuous with the left lateral wall of the ventricle. Also evident is a rounded heterogeneously hypointense (T1-weighted)/hyperintense (T2-weighted) mass in the right cerebellopontine angle and internal auditory canal that indents the lateral aspect of the pons and middle cerebellar peduncle and the anterior margin of the right cerebellar hemisphere *(black arrows)*. *C,* Axial T1-weighted image post intravenous gadolinium administration demonstrates nearly homogeneous contrast enhancement of both lesions; the uptake of contrast in the intraventricular nodule is more subtle than in the cerebellopontine angle lesion.

ganglioglioma, gangliocytoma, dysplastic gangliocytoma of the cerebellum (Lhermitte-Duclos disease), desmoplastic infantile ganglioglioma, dysembryoplastic neuroepithelial tumor, and central neurocytoma.[163, 303]

Ganglioglioma and Gangliocytoma

Gangliogliomas are uncommon low grade tumors consisting of a mixture of neoplastic astrocytes and dysplastic neurons. Slow growing neoplasms with well differentiated ganglion cells and a low grade astrocytomatous stroma,[286] these tumors are considered WHO grade I or II.[70, 168] Gangliocytomas (also known as ganglioneuromas) are relatively less common and contain only neuronal elements; they are classified as WHO grade I.[200] Together, these tumors account for 1.3% of all primary brain tumors.[168]

Gangliogliomas and gangliocytomas occur in young

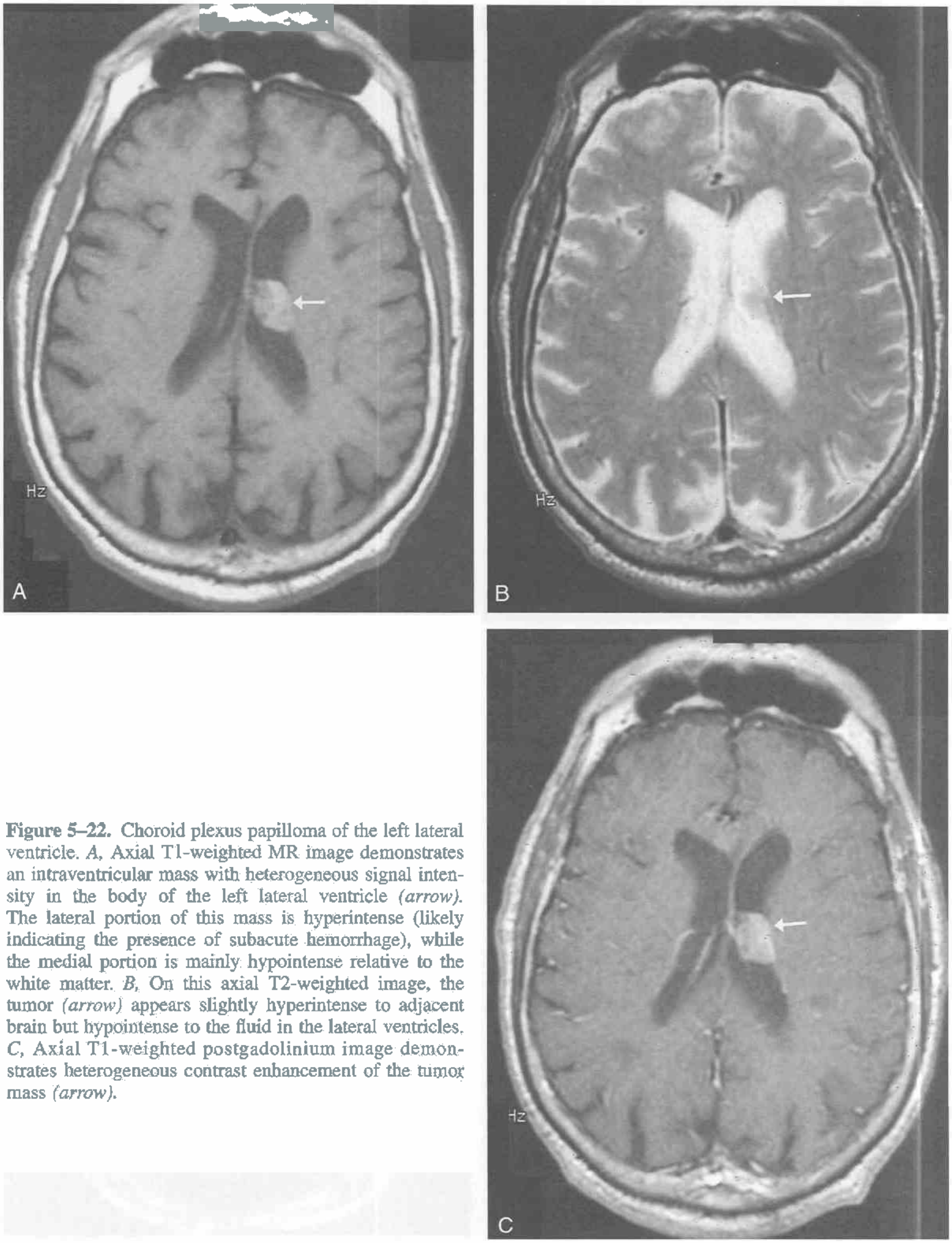

Figure 5–22. Choroid plexus papilloma of the left lateral ventricle. *A*, Axial T1-weighted MR image demonstrates an intraventricular mass with heterogeneous signal intensity in the body of the left lateral ventricle *(arrow)*. The lateral portion of this mass is hyperintense (likely indicating the presence of subacute hemorrhage), while the medial portion is mainly hypointense relative to the white matter. *B*, On this axial T2-weighted image, the tumor *(arrow)* appears slightly hyperintense to adjacent brain but hypointense to the fluid in the lateral ventricles. *C*, Axial T1-weighted postgadolinium image demonstrates heterogeneous contrast enhancement of the tumor mass *(arrow)*.

people (peak incidence in the second decade of life) and constitute approximately 3% to 4% of primary brain tumors in children.[155, 226] They are found most commonly in the temporal lobes but may occur anywhere in the cerebral hemispheres.[229, 363] The clinical presentation is usually with seizures of long duration, and gangliogliomas are considered the most common cause of chronic temporal lobe epilepsy.[229] These tumors are usually well circumscribed solid masses but may include one or more cysts.[59, 70] Gross total resection of a tumor is the treatment of choice. Overall, gangliogliomas and gangliocytomas have a 92% 3 year survival.[155] In approximately 10% of cases, however, the tumor is more aggressive; in these cases, the malignant element is always glial.[70]

Diagnostic imaging findings are relatively nonspecific and are similar to those in other low grade intracerebral

neoplasms.[168, 200] Noncontrast CT scans demonstrate relatively well circumscribed hypodense (occasionally isodense with adjacent brain) lesions typically located in the periphery of the hemisphere with little associated mass effect or surrounding vasogenic edema. Foci of calcification are identified in a third to 40% of cases and cysts in half of cases.[155, 226, 363, 371] Calcification is less common in the noncystic tumors.[168] Rarely, a peripherally located indolent tumor may erode the inner table of the overlying skull.[226] Hemorrhage is rare in these tumors.[226] Contrast enhancement is observed in about 50% of cases and may be homogeneous or heterogeneous, depending on the presence and size of cystic and calcific changes.[59, 155, 363]

On MRI, these tumors (like many other intracerebral neoplasms) are usually heterogeneous in appearance, predominantly hypointense to gray matter on T1-weighted images and hyperintense on T2-weighted images (Fig. 5–23*A*).[59, 155, 323, 364, 368] Mild to moderate contrast enhancement of the solid noncystic portion of the tumor is found in the majority of cases on both CT and MRI (Fig. 5–23*B*).[59]

The findings on CT and MRI in these ganglion cell tumors are not characteristic; oligodendroglioma is a common differential consideration. However, in a young patient with a protracted history of seizures and a relatively well circumscribed cystic tumor containing calcification in the periphery of the temporal lobe with little or no associated mass effect, ganglioglioma should be strongly considered.[59, 155, 275, 314, 363]

Dysplastic Gangliocytoma of the Cerebellum

A rare lesion, dysplastic gangliocytoma of the cerebellum (Lhermitte-Duclos disease) is considered a complex hamartoma or malformation and is classified as WHO grade I.[350] Dysplastic gangliocytoma may exist as an isolated entity or as part of Cowden's disease, a rare syndrome with multiple mucosal hamartomas.[178, 350] The clinical presentation is usually ataxia and signs of increased intracranial pressure in a young adult. A large dysplastic mass occupies most or all of the cerebellar hemisphere with thickening of the granular and molecular layers of the overlying cerebellar cortex (Fig. 5–24*A*). The enlarged mass causes displacement and compression of the fourth ventricle. On MRI, the mass is poorly demarcated, hypointense on T1-weighted images and hyperintense on T2 weighted images, and the thickened folia present a distorted striate pattern (Fig. 5–24*B*).[307] Contrast enhancement of either the tumor or the thickened cerebellar folia is unusual (Fig. 5–24*C*).[177]

Desmoplastic Infantile Ganglioglioma

Desmoplastic infantile ganglioglioma (DIG) is an unusual lesion that occurs in young infants. It consists of immature neurons and astrocytes together with extensive fibrocollagenous (desmoplastic) thickening and cyst formation. The solid desmoplastic portion is often located adja-

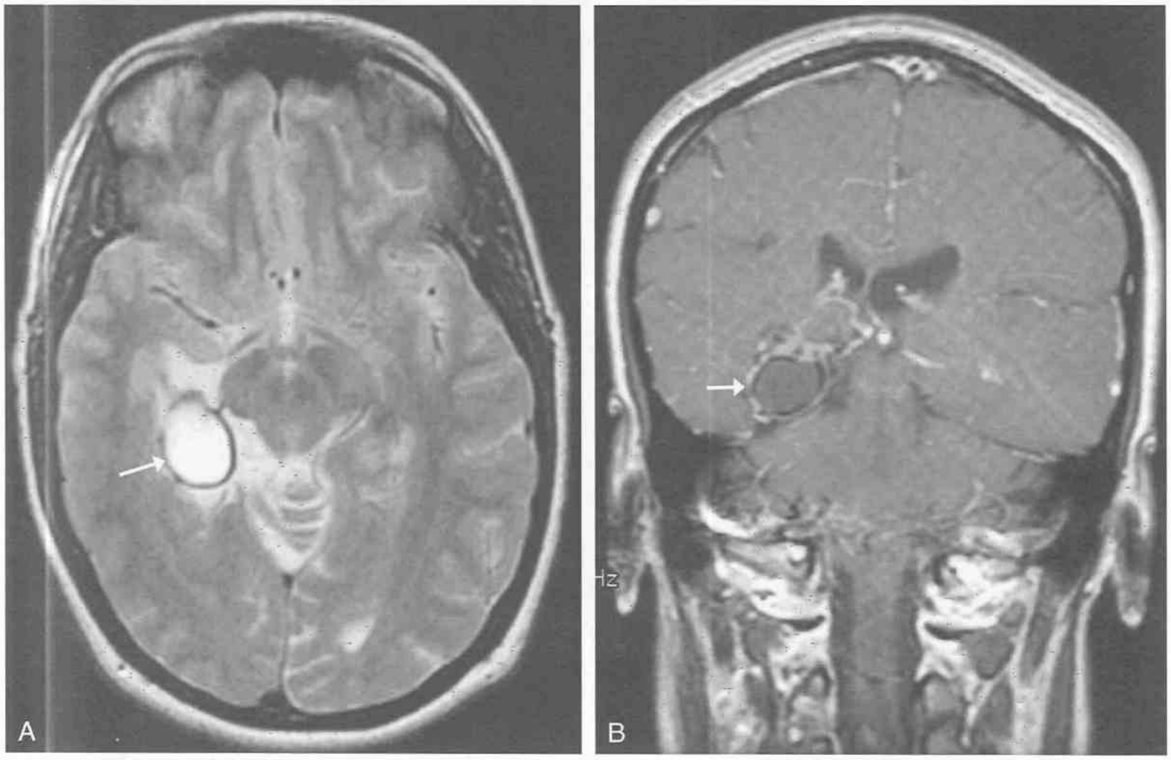

Figure 5–23. Ganglioglioma of the right temporal lobe. *A,* Axial T2-weighted MR image demonstrates a well circumscribed cystic mass *(arrow)* with a hypointense rim (secondary to calcification) in the region of the right parahippocampal gyrus and surrounding hyperintensity (due to edema). There is associated mass effect with effacement of the sulci of the right temporooccipital convexity, but there is no evidence of tentorial herniation. *B,* On this postgadolinium T1-weighted coronal image, peripheral rimlike contrast enhancement *(arrow)* outlines the margins of this cystic tumor, which is located immediately above the right leaf of the tentorium. The contents of the cyst are slightly hyperintense relative to cerebrospinal fluid, reflecting a higher protein content.

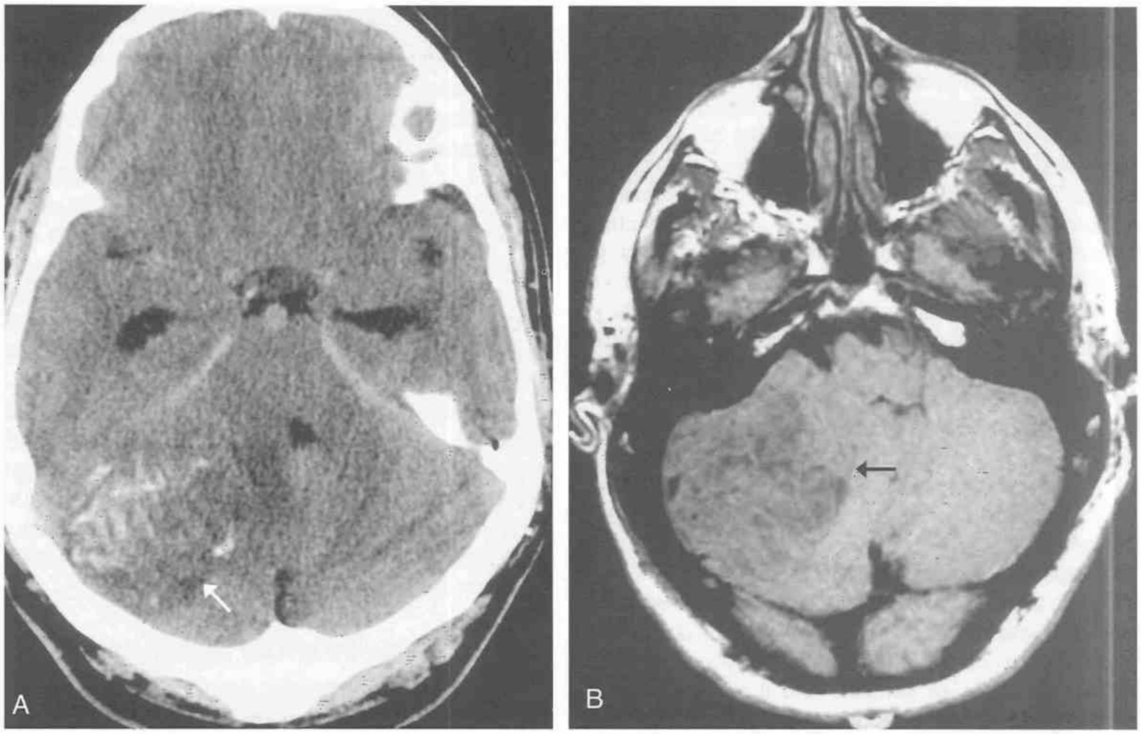

Figure 5–24. Dysplastic gangliocytoma of the cerebellum (Lhermitte-Duclos). *A,* Axial CT image without intravenous contrast demonstrates a poorly marginated heterogeneous predominantly hypodense mass *(arrow)* occupying most of the right cerebellar hemisphere and displacing the fourth ventricle to the right of the midline. A striate pattern of calcification is noted within this process. *B,* On this T1-weighted axial noncontrast MR image, the poorly marginated hypointense mass presents a distorted internal architecture *(arrow)* and compresses and displaces the pons anteriorly and to the left. *C,* Axial T1-weighted image post intravenous gadolinium: there is no evident contrast enhancement of this hamartomatous process *(arrow).*

cent to the meninges. Despite its variegated appearance, this tumor is classified as WHO grade I and has a favorable long term prognosis after complete excision.[155]

DIGs are large and superficial hemispheric tumors that occur mainly in the frontal and parietal lobes and present a markedly heterogeneous appearance on both gross inspection and MRI (Fig. 5–25).[155, 209, 326] The solid portions of this tumor are hypointense relative to normal brain on T2-weighted images and frequently demonstrate intense contrast enhancement.[155, 326] DIG differs from the usual ganglioglioma in that it presents in infancy, is predominantly frontoparietal in location, and has dense desmoplasia.[200] On MRI, the intermixed collagenous and multicystic pattern of this lesion most resembles that of a primitive neuroectodermal tumor (PNET), which carries a much less favorable prognosis; however, PNET is also

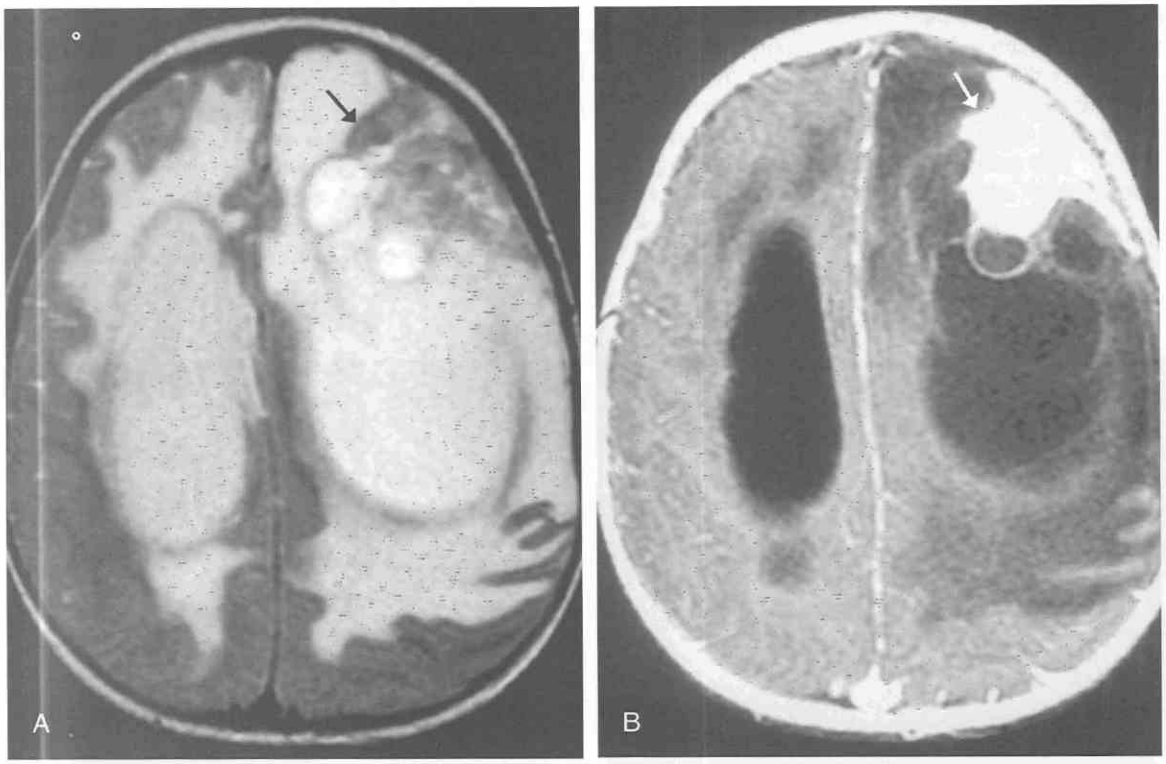

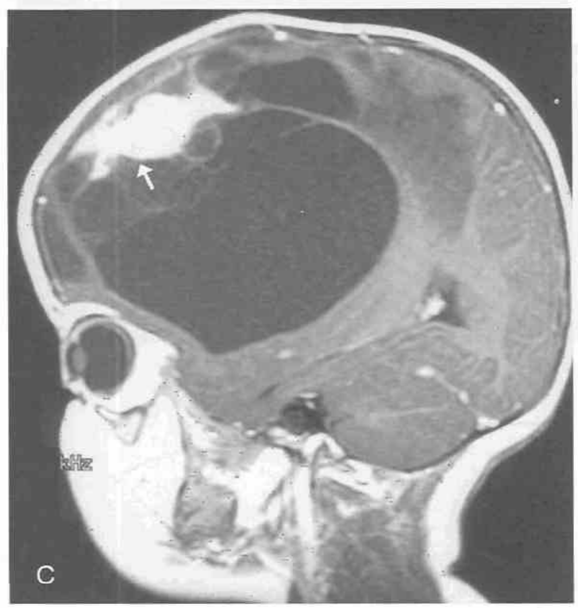

Figure 5–25. Desmoplastic infantile ganglioglioma (DIG). *A*, Axial T2-weighted MR image demonstrates a well circumscribed heterogeneous left high frontal convexity tumor that is predominantly hypointense to adjacent brain *(arrow)*. On its posteromedial aspect, there are two small cysts and one large ovoid cyst on the left and a single large cyst on the right, all with hyperintense contents. There is extensive white matter edema bilaterally, surrounding the large cysts and extending into the left frontoparietal convexity gyri. Following intravenous administration of gadolinium, axial *(B)* and left parasagittal *(C)* T1-weighted images demonstrate intense contrast enhancement of the superficial solid area of this tumor *(arrows)*, which consists of thick dense fibrocollagenous (desmoplastic) tissue. Contrast enhancement is also seen to a variable degree in the rims of the cystic elements of this lesion. On *C*, note the posteroinferior displacement and compression of the atrium and temporal horn of the left lateral ventricle by the large left cystic mass.

characterized by the common presence of intratumoral calcification, hemorrhage, and necrosis, findings that are uncommon in DIG.[200]

Dysembryoplastic Neuroepithelial Tumor

Dysembryoplastic neuroepithelial tumors (DNETs) are uncommon benign intracortical tumors that characteristically occur in young patients (<20 years) above the tentorium, mainly in the temporal lobe (60% to 80%) or frontal lobe.[79, 80, 168, 169, 303] They can be multifocal and rarely arise in the deep cortical structures. The patients typically present with intractable partial seizures. Partial or complete excision is the treatment of choice, and no recurrences have been reported.[80] The tumor is termed "dysembryoplastic" because of its multinodularity, with areas of cortical dysplasia at the margins between the tumor nodules and the adjacent brain.[79, 80]

DNETs are lesions of long standing that most frequently involve the convexity cortex and often protrude beyond the adjacent cortical margin, eroding the overlying inner table of the calvarium.[168, 169, 303] The imaging findings, except for the superficial cortical location, are similar to those of other low grade glial tumors (astrocytoma, oligodendroglioma). On CT, DNET typically appears as a well circumscribed hypodense superficial mass, occasionally with intratumoral

calcification, or cystic change, or both.[168, 242, 303] MRI demonstrates a mass centered in the convexity cortex and bulging externally that is hypointense to adjacent brain on T1-weighted images (Fig. 5–26*B*) and hyperintense on T2-weighted images (Fig. 5–26*A*) with no surrounding edema.[168, 169, 303] The protruding external margin may present a "soap bubble" appearance, reflecting internal cystic change.[178] Contrast enhancement is seen in only a minority of these lesions (Fig. 5–26*C*).[169, 178, 242]

Central Neurocytoma

A relatively rare, benign, slow growing (WHO grade II) intraventricular tumor, central neurocytoma has now been recognized as a separate entity.[70, 303] It occurs almost exclusively in the anterior portion of the lateral ventricle, arising from the superolateral ventricular wall and extending medially adjacent to the septum pellucidum and the foramen of Monro; extension through the foramen into the third ventricle is unusual. No such tumors have been

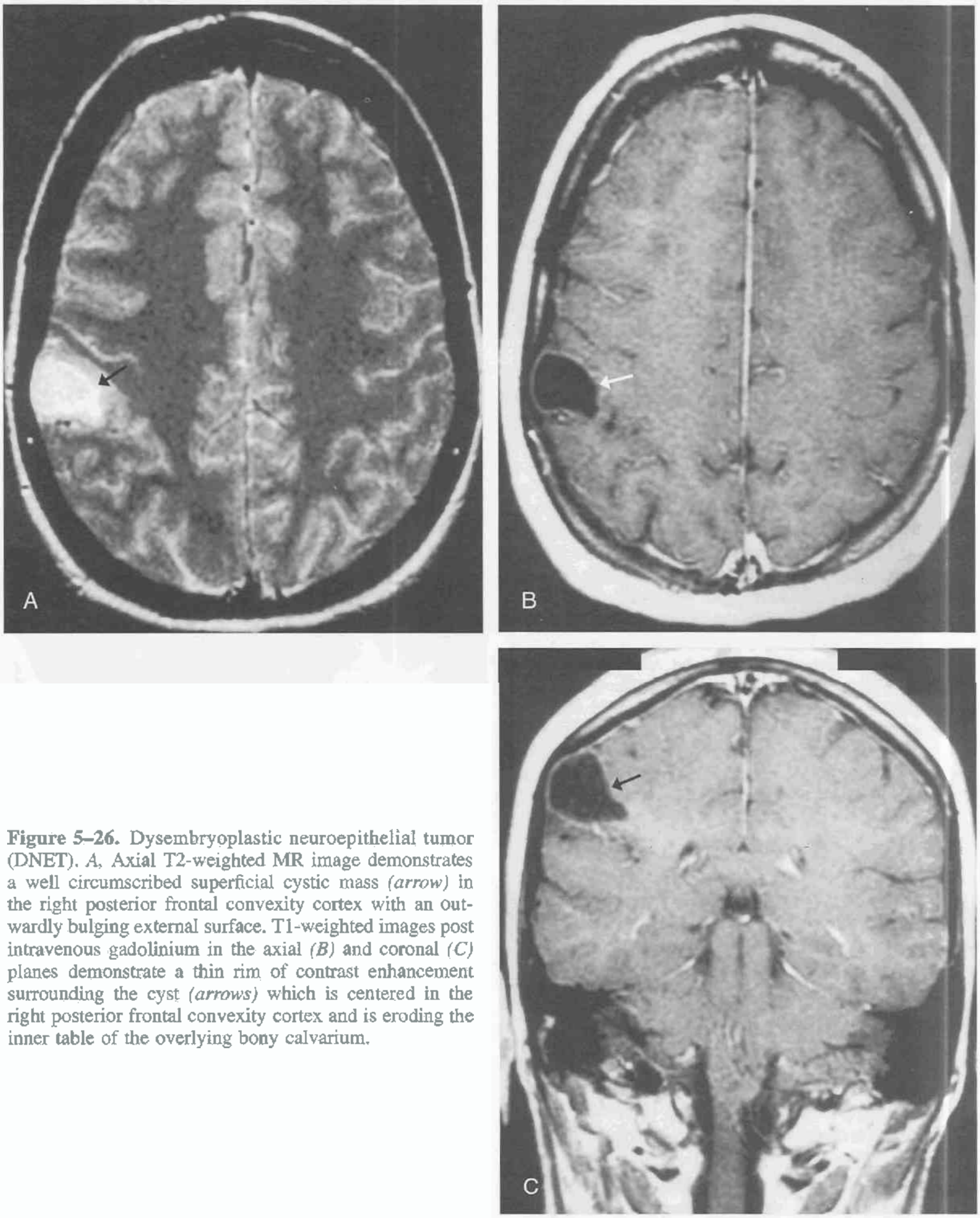

Figure 5–26. Dysembryoplastic neuroepithelial tumor (DNET). *A,* Axial T2-weighted MR image demonstrates a well circumscribed superficial cystic mass *(arrow)* in the right posterior frontal convexity cortex with an outwardly bulging external surface. T1-weighted images post intravenous gadolinium in the axial *(B)* and coronal *(C)* planes demonstrate a thin rim of contrast enhancement surrounding the cyst *(arrows)* which is centered in the right posterior frontal convexity cortex and is eroding the inner table of the overlying bony calvarium.

reported arising in the third or fourth ventricles, and only a few hemispheric lesions have been found.[241] Central neurocytomas are tumors of young adults and are rare in children and the elderly. Patients typically present clinically with headache and signs of increased intracranial pressure secondary to ventricular obstruction.[70, 241] Partial or complete surgical excision is the treatment of choice, and no deaths from tumor growth or recurrence have been reported.[356]

Histologically, central neurocytoma is identical to oligodendroglioma. It is characterized by nests of small well differentiated cells separated by thin fibrovascular septa.[10, 356] Intratumoral calcification and multiple small cysts are common findings, but hemorrhage (either intratumoral or intraventricular) is unusual. It is only with electron microscopy and immunohistochemistry that its neuronal origin can be determined.[70]

CT scans demonstrate a sharply marginated, inhomogeneous, isodense to slightly hyperdense intraventricular mass with a broad-based attachment to the wall of the frontal horn or anterior body of the lateral ventricle and abutting the septum pellucidum. Calcifications, either coarse or globular, and multiple small intratumoral hypodense cysts are found in 50% or more of central neurocytomas. Mild to moderate contrast enhancement of the isodense to hyperdense regions is common.[33, 119, 356]

The findings on MRI are similar. The tumor demonstrates a heterogeneous pattern with intermixed foci of isointensity (compared with adjacent gray matter) and hypointensity (due to calcifications and cysts) on T1-weighted images and isointensity to hyperintensity on T2-weighted images (Fig. 5–27*A*). Inhomogeneous mild contrast enhancement is common (Fig. 5–27*B*).[33, 119, 356]

The differential diagnosis is that of a well circumscribed intraventricular mass at or near the foramen of Monro and includes ependymoma and subependymoma. The absence of both deep extension into adjacent brain parenchyma and intratumoral hemorrhage as well as the relatively young age of the patient favors the diagnosis of central neurocytoma.[10, 241]

Pineal Parenchymal Tumors

Tumors arising within the parenchyma of the pineal gland constitute less than 1% of all primary brain tumors in adults.[70] However, pineal tumors represent nearly 10% of all pediatric brain tumors.[200] The most common tumors to involve the pineal gland are the germ cell tumors, which constitute 50% to 70% of pineal region tumors and are discussed elsewhere in this chapter.

Pineal parenchymal tumors represent only 15% to 30% of pineal region neoplasms.[305, 360] They include a range from primitive undifferentiated (pineoblastoma) through

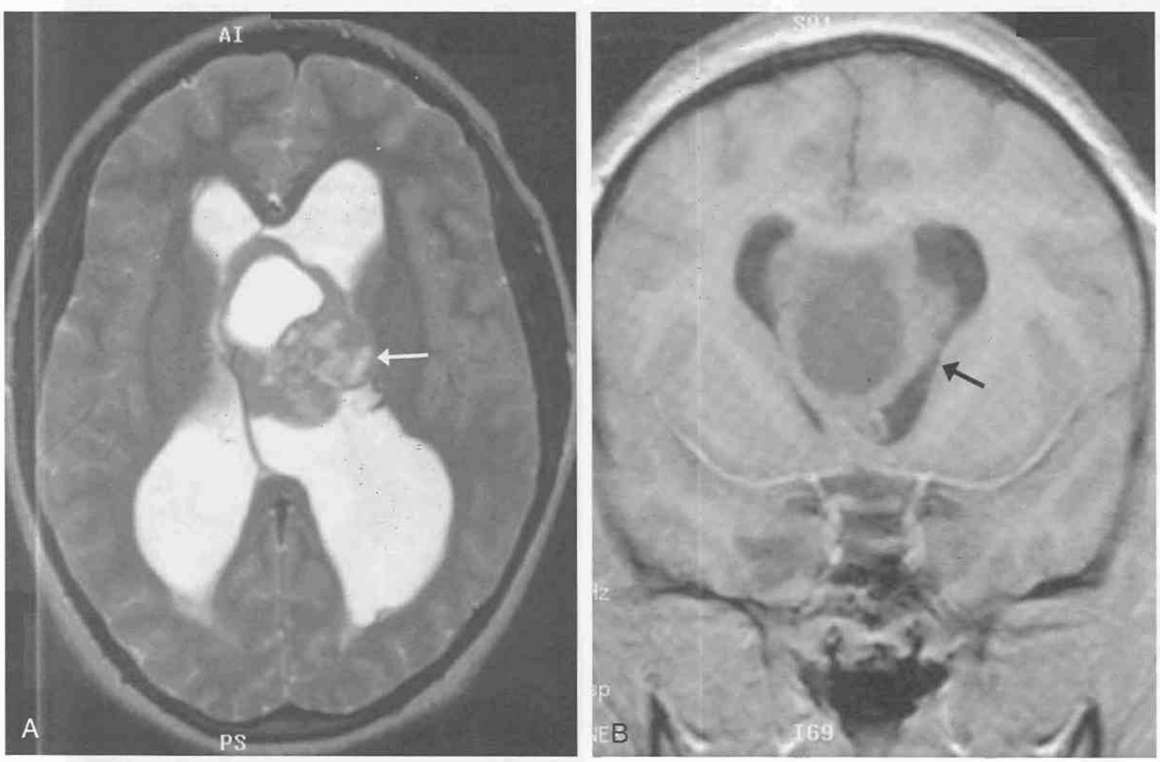

Figure 5–27. Central neurocytoma in the anterior body and frontal horn of the left lateral ventricle. *A*, Axial T2-weighted MR image demonstrates a large multilobulated heterogeneous but predominantly isointense (with gray matter) intraventricular mass arising from the lateral wall of the left lateral ventricle *(arrow)* with multiple small hyperintense foci and one large intratumoral hyperintense cyst. The tumor expands the left lateral ventricle. Enlargement of both lateral ventricles is likely secondary to obstruction of the foramen of Monro by this mass. *B*, Coronal T1-weighted spoiled gradient echo image following intravenous gadolinium: the plane of section passes through the anterior portion of the tumor. The more solid portion of this tumor demonstrates faint contrast enhancement. Note the extension of the tumor inferiorly and medially at a level just anterior to the foramen of Monro.

transitional forms to moderately mature and well differentiated (pineocytoma).[200, 292]

Pineoblastoma

Pineoblastomas are pediatric tumors with a peak incidence in the first two decades of life and rarity after age 30. These malignant, highly cellular, undifferentiated small cell tumors are histologically and histochemically identical with other primitive neuroectodermal tumors and exhibit similar biologic behavior. They are locally invasive and may spread into the third ventricle, the thalami, and the quadrigeminal plate. Pineoblastomas frequently contain areas of hemorrhage and necrosis, and intratumoral calcification is common.[10, 292] Presenting symptoms include precocious puberty (possibly related to destruction of normal pineal tissue with loss of melatonin secretion),[25] Parinaud's syndrome and other cranial nerve deficits, and obstructive

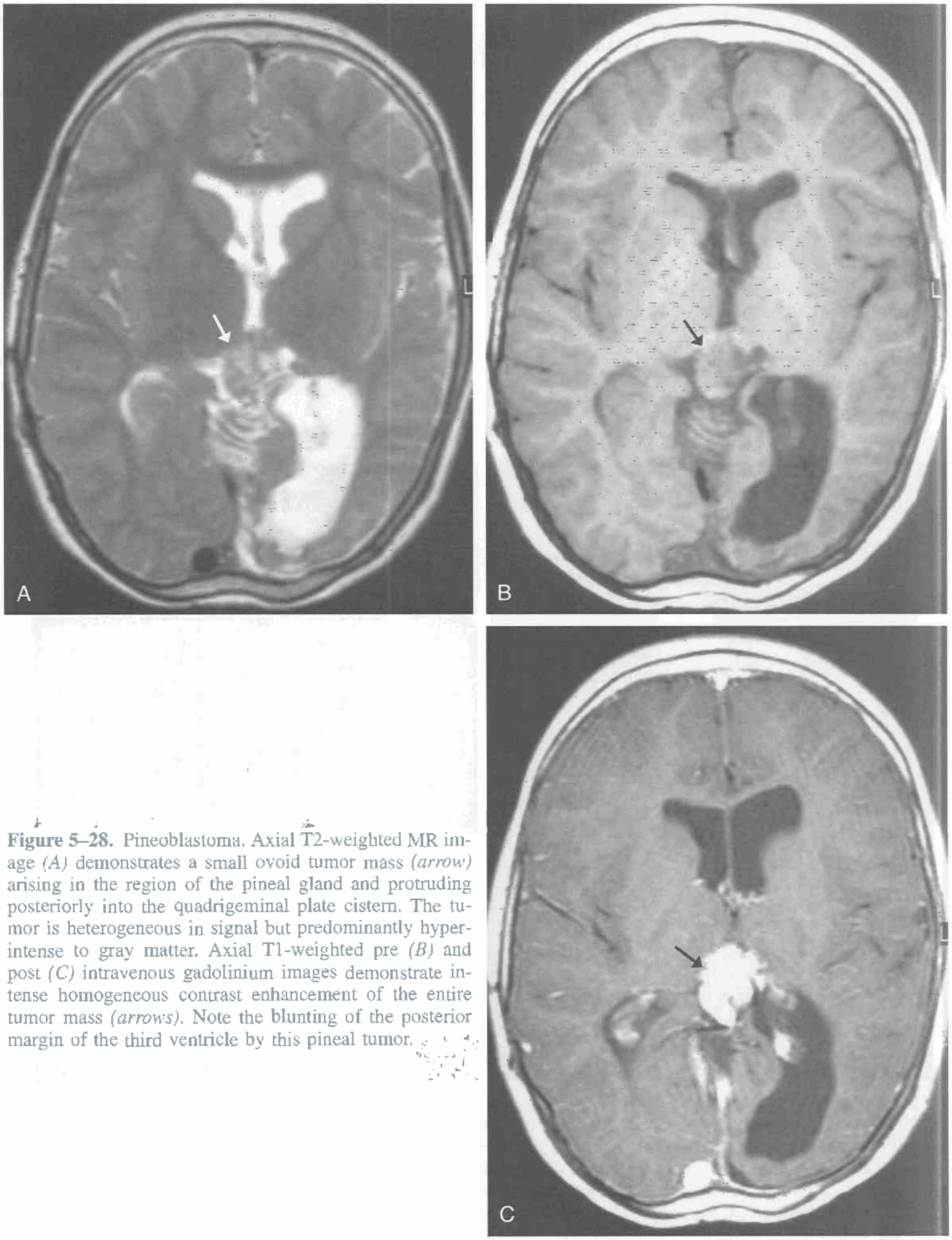

Figure 5–28. Pineoblastoma. Axial T2-weighted MR image *(A)* demonstrates a small ovoid tumor mass *(arrow)* arising in the region of the pineal gland and protruding posteriorly into the quadrigeminal plate cistern. The tumor is heterogeneous in signal but predominantly hyperintense to gray matter. Axial T1-weighted pre *(B)* and post *(C)* intravenous gadolinium images demonstrate intense homogeneous contrast enhancement of the entire tumor mass *(arrows)*. Note the blunting of the posterior margin of the third ventricle by this pineal tumor.

hydrocephalus. Dissemination via the CSF with leptomeningeal and ependymal metastases occurs in 10% of cases and may be found at the time of initial diagnosis. The 5-year survival rate is 58%.[292]

On CT, pineoblastomas appear hyperdense with irregular intratumoral calcification, infiltration into neighboring structures, and mass effect upon the posterior aspect of the third ventricle and the tectum of the midbrain. They demonstrate dense contrast enhancement. On MRI, pineoblastomas appear heterogeneous in signal, predominantly hypointense to gray matter on T1-weighted images and isointense with gray matter on T2-weighted images, with interspersed foci of hypointensity secondary to intratumoral necrosis and calcification (Fig. 5–28*A, B*).[10, 305, 332, 360] As on CT, contrast enhancement of the solid portion of the tumor is the rule (Fig. 5–28*C*). The chief differential consideration is germinoma, which may look identical on CT and MRI.

A rare occurrence that is nevertheless important for recognition and management is the association of bilateral retinoblastomas with pineoblastoma, often termed *trilateral retinoblastoma*. This condition, an inherited disorder occurring in very young children (<2 years), is found in 3% of patients with bilateral retinoblastomas.[269]

Pineocytoma

Pineocytomas are tumors of adults with a mean age of presentation of 36 years. Compared with pineoblastomas, these lesions are less densely cellular with well differentiated cells that have more cytoplasm arranged in lobules in an architecture similar to that of the normal pineal gland.[25, 292] They tend to follow a slower and more benign clinical course, but transitional tumors intermediate in cellularity and mitotic activity also exist.[70, 292] Intratumoral calcification is present in more than 50%. Subarachnoid seeding is not seen in the more benign neoplasms. The 5 year survival for pineocytomas is 67%.[292]

On CT, the typical appearance is of a rounded, well circumscribed, homogeneously hyperdense, lobulated expansile mass with intratumoral calcification situated at and often obstructing the posterior margin of the third ventricle (Fig. 5–29*A*).[200, 269] There is no evidence of invasion of neighboring structures. Multiplanar MRI demonstrates a rounded or ovoid mass compressing the posterior margin of the third ventricle and the superior aspect of the quadrigeminal plate. The mass is homogeneously hypointense to isointense on T1-weighted images and hyperintense relative to gray matter on T2-weighted images.[200, 305, 332, 360] The signal characteristics reflect the higher water content of these more mature tumors compared with pineoblastomas.[10] Contrast enhancement of all or a major portion of a pineocytoma is the rule on both CT (Fig. 5–29*B*) and MRI.

Embryonal Tumors

The terminology regarding primitive or embryonal tumors of neuroepithelial origin has been a source of controversy for nearly two decades. Gradually, however, a con-

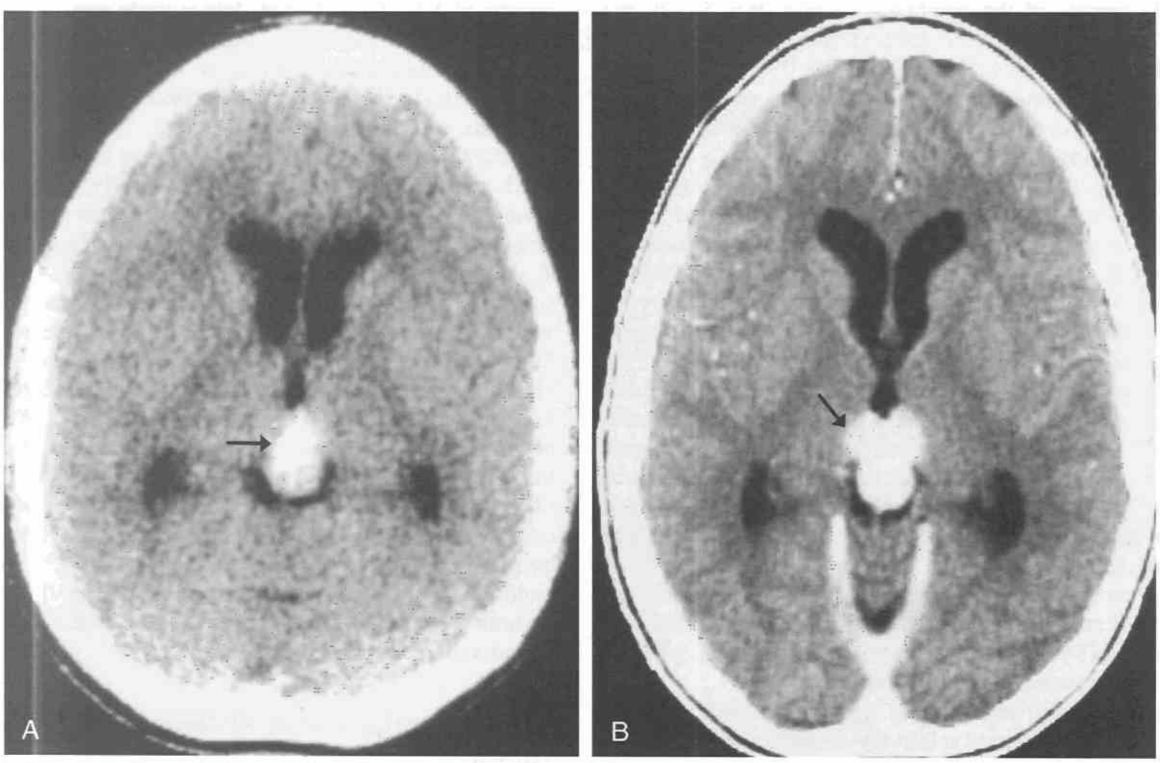

Figure 5–29. Pineocytoma. Axial noncontrast *(A)* and postcontrast *(B)* CT images demonstrate a well circumscribed markedly hyperdense mass in the midline (*arrow* in *A*) in the pineal region with bilateral lobulated intense contrast enhancement impinging on the medial aspects of both thalami (*arrow* in *B*). The tumor is partially obstructing the posterior aspect of the third ventricle, accounting for the enlarged lateral and anterior third ventricles.

sensus appears to be emerging concomitant with advances in applied molecular biology.[25] Primitive neuroectodermal tumors (PNETs) of the CNS appear to be one group of a larger category of embryonal tumors that occur throughout the body (e.g., neuroblastomas of the adrenal and sympathetic ganglia).[25, 281] These are the second most common intracranial tumors of childhood, representing approximately 15% to 20% of all childhood brain tumors and exceeded in frequency only by the astrocytomas.[25] They have a common histology, consisting of densely packed undifferentiated round cells with a high nuclear-to-cytoplasmic ratio and high mitotic activity but follow divergent patterns of differentiation.[281]

The classic PNET is the medulloblastoma of the cerebellar vermis, which constitutes 85% of this group of tumors.[25] The remaining 15%, almost all supratentorial, include pineoblastomas (see earlier), ependymoblastomas, and medulloepitheliomas. The histogenesis of PNETs is undetermined, but one hypothesis is that they arise from immature pluripotential precursor cells in the subependymal layers of the developing ventricular system and in the external granular layer of the cerebellum.[25, 281]

Medulloblastoma

An invasive and highly malignant tumor (WHO grade IV), medulloblastoma is the second most common primary brain tumor of childhood and the most common pediatric posterior fossa neoplasm.[115, 168] Although medulloblastomas may occur at any age, 75% present clinically before age 15 years. There are two distinct age peaks, at 4 to 8 years and 15 to 35 years.[168] In children, medulloblastomas are primarily tumors of the cerebellar vermis (Fig. 5–30), but in adults, they tend to be located more laterally in the cerebellar hemispheres (Fig. 5–30).[48, 167, 281, 286, 372] The typical clinical presentation consists of signs of obstructive hydrocephalus, cerebellar dysfunction, or both—headache, nausea, vomiting, and ataxia.[168]

These aggressive tumors grow rapidly, with extension from the vermis into the fourth ventricle, and spread inferiorly into its recesses and outlet foramina and superiorly into the aqueduct.[303, 335] More than 90% present clinically with hydrocephalus.[200] They have a strong tendency to seed via the CSF, and approximately 40% demonstrate subarachnoid or retrograde ependymal metastases at the time of initial diagnosis.[96, 176] They are highly radiosensitive, and the standard treatment approach is gross total resection plus chemotherapy and total craniospinal axis irradiation.[176] Ten year survival rates are in the range of 50% to 70%, but the prognosis is poorer in children younger than 3 years.[34, 92, 200] Recurrence after the initial treatment regimen is about equally distributed between local regrowth at the primary tumor site and distant metastasis.[34] Systemic metastasis, a highly unusual occurrence with most CNS primary neoplasms, is identified in approximately 5% of patients, mainly to bone.[168]

Compared with other highly aggressive brain tumors, medulloblastomas appear relatively discrete and solid with convex margins on gross inspection but may contain foci of necrosis and hemorrhage.[25, 200] Microscopically, the tumor cells tend to be arranged in pseudorosettes, and areas of vascular proliferation, cellular pleomorphism, and calcification are occasionally identified. Electron microscopy and immunostaining usually confirm neuronal differentiation.[25] Approximately 15% of medulloblastomas contain a significant amount of collagen and reticulin and may demonstrate a nodular pattern; designated desmoplastic medulloblastomas, these tumors are relatively more common in the cerebellar hemispheres in adolescents and young adults.[25, 193]

On noncontrast CT scans, medulloblastomas appear as rounded or oblong, mainly homogeneous, isodense to slightly hyperdense masses centrally located in the inferior vermis and cavity of the fourth ventricle (Fig. 5–30*A*).[19, 226, 320, 372] Differentiation of medulloblastoma from diffuse solid cerebellar astrocytoma is most reliably made on noncontrast CT.[372] The solid hyperdense appearance of medulloblastoma reflects the dense cellular nature of this tumor, whereas astrocytomas are typically rather uniformly hypodense.[109, 112] Obstruction of the fourth ventricle, inferior aqueduct, or both with resulting enlargement of the third and lateral ventricles is commonly seen on CT at the time of clinical presentation. Punctate or nodular intratumoral calcifications are identified in 10% to 20% of cases.[167, 168, 335, 362] Hypodense intratumoral foci of necrosis and cysts are found in up to 50% of medulloblastomas (see Fig. 5–30*A*).[226, 320, 362] Many medulloblastomas are surrounded by a thick, poorly marginated, hypodense halo representing extensive peritumoral edema. The imaging findings in young adults are similar, except for the more lateral (hemispheric) location of the tumor.[372]

After IV administration of contrast medium, moderate to intense homogeneous enhancement of the solid tumor mass is the rule in medulloblastomas,[19, 167, 335, 372] although approximately 10% do not demonstrate contrast enhancement on CT.[226] Areas of tumor seeding in the posterior fossa cisterns or in the third or lateral ventricles exhibit similar homogeneous contrast enhancement in a nodular or sheetlike configuration.[320, 372]

The appearance of medulloblastomas is less specific on MRI than on CT. The tumors are mildly hypointense to isointense relative to the adjacent cerebellar vermis on T1-weighted images and isointense to slightly hyperintense on T2-weighted images (Figs. 5–30*B*, *C* and 5–31*A*). Isointensity (or even hypointensity) of the tumor matrix on T2-weighted images are likely due to the hypercellularity and high nuclear-to-cytoplasmic ratio of this tumor.[22, 83, 128, 197] However, heterogeneity of signal intensity is often seen on the T2-weighted images (Figs. 5–30*C* and 5–31*B*) secondary to intratumoral cysts, necrosis, vascular flow voids, and hemorrhage.[168, 200, 335] Contrast enhancement of the solid portions of the tumor, seen in more than 90% of patients, is typically intense and homogeneous (Fig. 5–31*B*) but may be irregular and patchy (Fig. 5–30*D*).[168, 173, 278, 335] MRI with gadolinium enhancement is very sensitive for the detection of tumor spread and metastatic seeding in the cranial and spinal subarachnoid spaces.[173, 278, 303, 335]

Supratentorial Primitive Neuroectodermal Tumor

Fifteen percent of all PNETs of the CNS occur above the tentorium.[25] However, they represent less than 1% of all pediatric brain tumors. Like their infratentorial counter-

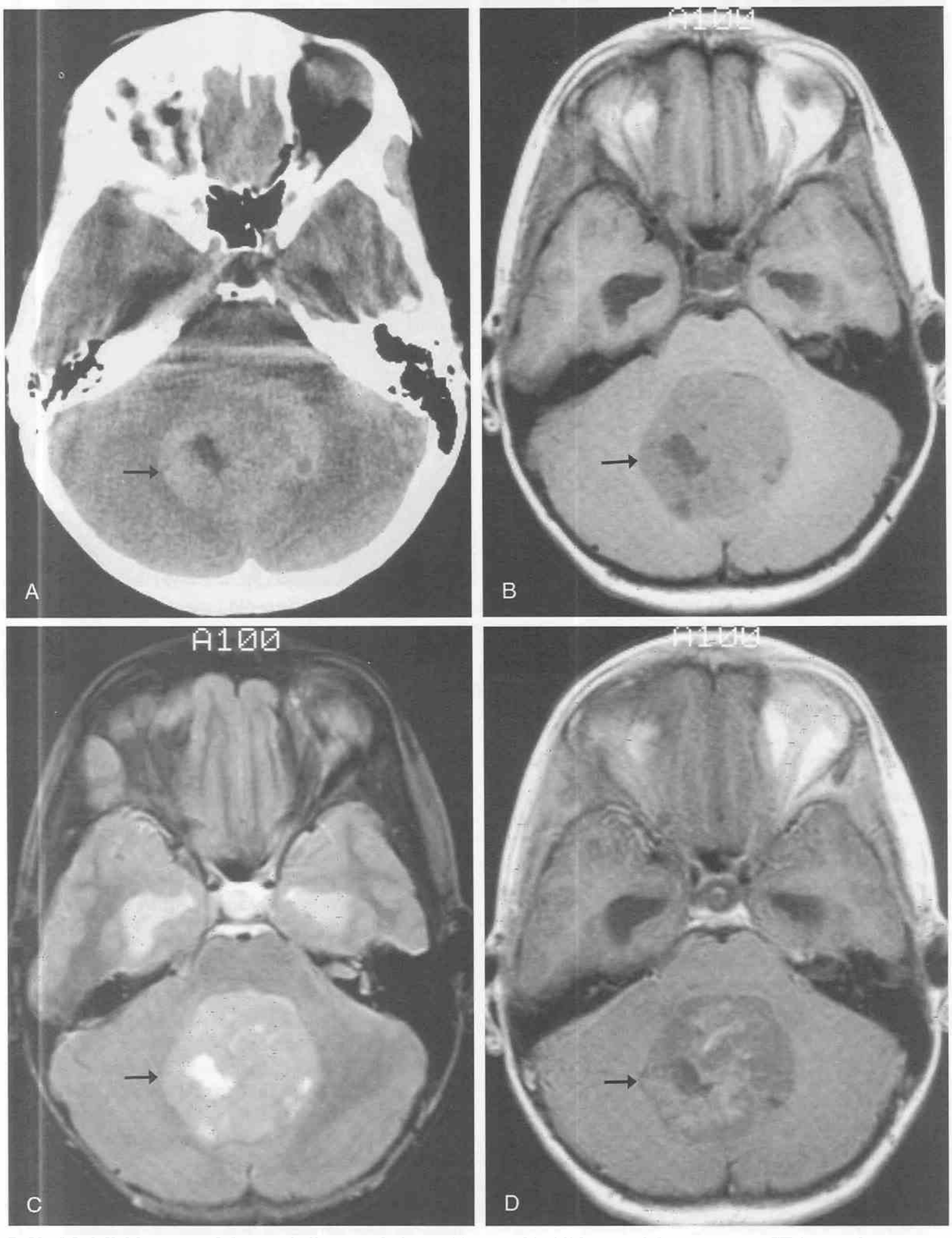

Figure 5–30. Medulloblastoma of the cerebellar vermis in an 11-year-old child. *A*, Axial noncontrast CT image demonstrates a large lobulated hyperdense round tumor *(arrow)* with an internal hypodense cavity to the right of the midline that compresses the fourth ventricle from behind. An ill defined faintly hypodense band surrounding the hyperdense mass represents white matter edema. The intratumoral area of marked hypodensity to the right of the midline likely represents necrosis. A smaller focus of lesser hypodensity on the left posterolateral tumor margin suggests an intratumoral cyst. These findings are confirmed on noncontrast axial T1-weighted *(B)* and T2-weighted *(C)* MR images; the solid portion of the tumor appears mildly hypointense on T1-weighting and mildly hyperintense on T2-weighting *(arrows)*. Following intravenous gadolinium, an axial T1-weighted image *(D)* demonstrates irregular patchy contrast enhancement of the solid areas of the tumor *(arrow)*.

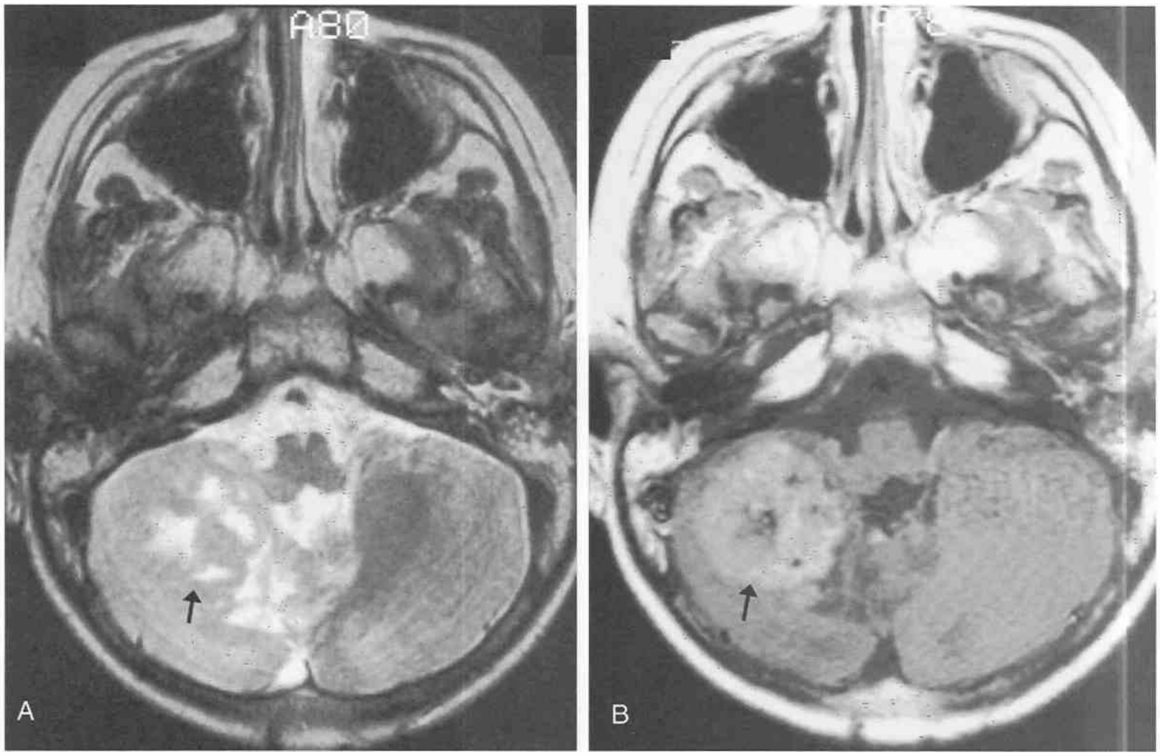

Figure 5–31. Medulloblastoma of the anteroinferior right cerebellar hemisphere in a 26-year-old patient. *A,* Axial T2-weighted MR image demonstrates a poorly circumscribed mass with a heterogeneous signal pattern in the anteroinferior portion of the right cerebellar hemisphere. Irregular areas of pronounced hyperintensity *(arrow)* are interspersed in a mildly hyperintense background that likely represents surrounding edema. The tumor extends medially into the inferior vermis. *B,* After intravenous administration of gadolinium, the tumor demonstrates homogeneous contrast enhancement with well circumscribed margins *(arrow).* Punctate intratumoral hypointensities represent enlarged vascular channels and/or focal calcifications.

parts, they occur mainly in the very young (65% of patients <5 years, 85% <10 years).[62] Patients may present clinically with seizures or with symptoms and signs of increased intracranial pressure. The distribution of these aggressive tumors within the cerebral hemispheres is, in diminishing order of frequency, frontal, parietal, temporal, and occipital.[200] Approximately one third are pineoblastomas; the remainder are central neuroblastomas,[62, 83] ependymoblastomas,[92] ganglioneuroblastomas, medulloepitheliomas, and other rare immature round cell tumors.[281]

On CT scans, supratentorial PNETs appear heterogeneous and well circumscribed. The heterogeneity reflects cystic or necrotic changes and intratumoral hemorrhage.[201] The solid elements are hyperdense because of their high cellularity and demonstrate contrast enhancement. Coarse calcifications are described in 50% to 70%, a much higher proportion than in cerebellar medulloblastomas.[200, 281] Supratentorial PNETs share with their infratentorial counterparts a strong propensity for spread via CSF.[83]

MRI also demonstrates heterogeneity of signal intensity on both T1-weighted and T2-weighted images (Fig. 5–32). They are often large tumors with relatively lesser degrees of surrounding edema.[83, 92] The differential diagnosis includes other large well circumscribed supratentorial tumors, such as ependymomas and oligodendrogliomas.[200] As on CT, the solid portions of the tumor demonstrate strong contrast enhancement, a feature that may aid in the differentiation.

Tumors of the Cranial Nerves

Approximately one third of all intracranial masses are nonglial primary neoplasms of the CNS, almost all of which are extraaxial in origin and location.[302] The most common of these are schwannomas of the cranial nerves and meningiomas.

Within the brain and spinal cord, the nerve fiber tracts are surrounded by oligodendrocytes. However, as the cranial nerves emerge from the brain, there is a transition zone beyond which the oligodendrocytes do not extend but are instead replaced by Schwann cells (also called neurilemmal cells), which surround and ensheath the extraaxial portions of the cranial nerves, the spinal nerve roots and nerves, and the peripheral nerves. Within the cranial vault, tumors arising from these nerves nearly all represent schwannomas.

The other major primary tumor of the cranial nerves is neurofibroma. Neurofibromas differ from schwannomas not only in site of origin but also in histology and natural history.[48, 354] Malignant degeneration is essentially unknown in schwannomas, but both malignant degeneration of neurofibromas and primary malignant peripheral nerve sheath tumors are recognized but uncommon occurrences.[339, 354]

Schwannoma

Schwannoma is a benign (WHO grade I) encapsulated tumor that arises from the Schwann cells of the nerve

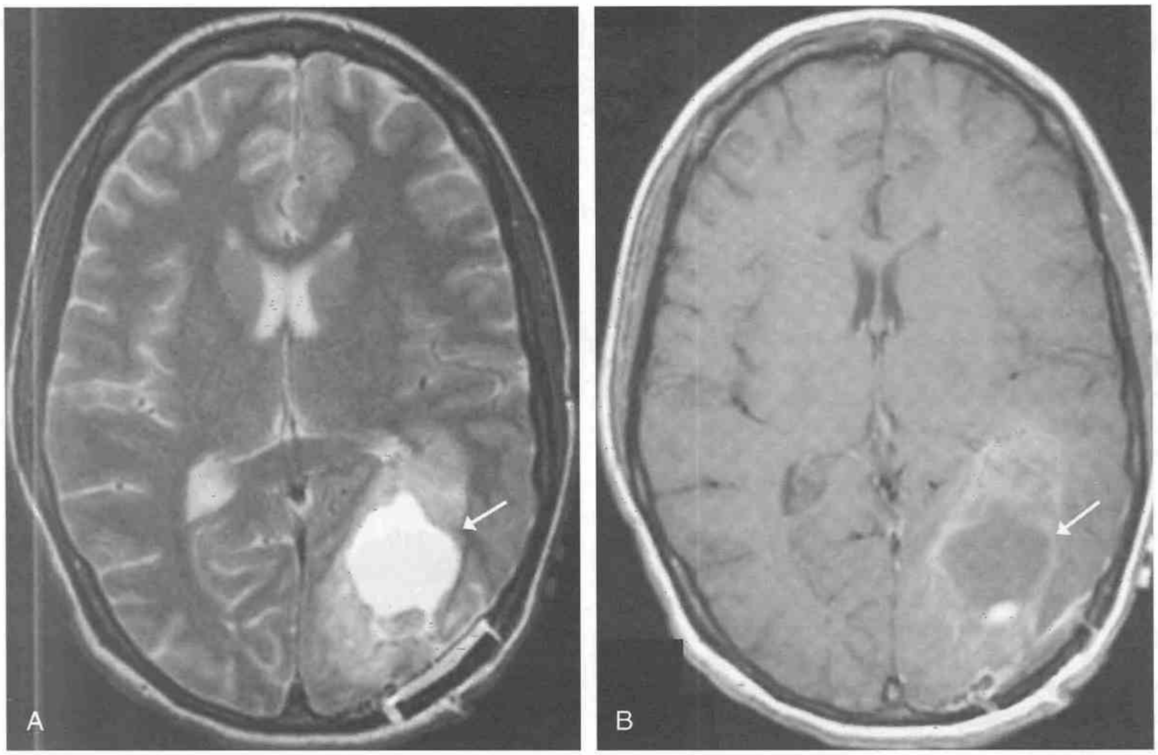

Figure 5–32. Primitive neuroectodermal tumor in the left parietooccipital region (postcraniotomy). *A,* Axial T2-weighted MR image demonstrates an ovoid heterogeneously hyperintense mass in the left parietooccipital white matter with extension into the overlying convexity cortex and a single large intratumoral sharply marginated central collection of marked hyperintensity, likely representing a combination of necrosis, surgical resection cavity, and/or cyst formation *(arrow).* The mass compresses and displaces the atrium of the left lateral ventricle from behind. *B,* Following intravenous gadolinium, an axial T1-weighted image demonstrates irregular contrast enhancement within the tumor interstices without enhancement of the central cavity *(arrow).*

sheaths of cranial and spinal nerves.[354] It is estimated to account for between 5% and 10% of primary intracranial neoplasms and for nearly 30% of intraspinal tumors.[57, 302]

Intracranial schwannomas occur in all age groups, but the peak incidence is in the fourth through the seventh decades of life.[57, 302, 354] There is a distinct sex predilection with a female-to-male ratio of 2:1, although no such predilection exists in regard to spinal schwannomas.[57, 302]

By far the most common site of intracranial involvement is the superior vestibular division of the eighth cranial nerve.[207, 302] Trigeminal nerve schwannomas are much less common, with facial, trochlear, and abducens nerve tumors only rarely reported.[241] Only the first (olfactory) and second (optic) cranial nerves lack Schwann cell sheaths and are therefore not potential sites of origin. The clinical presentation varies according to the site of origin. Vestibular schwannoma (also called acoustic neuroma or neurinoma) typically presents with symptoms of a mass in the cerebellopontine angle, including tinnitus, sensorineural hearing loss, and facial paresthesias.[241, 302, 354] Despite the tumor's origin from the vestibular nerve, symptoms and signs of vestibular dysfunction do not become manifest until relatively late. These tumors have a distinct propensity to involve the sensory nerve roots, and motor symptoms are uncommon.[354]

Multiplicity of intracranial schwannomas strongly suggests the presence of neurofibromatosis 2 (NF2), a congenital inherited disorder associated with a mutation on the long arm of chromosome 22.[223] The occurrence of bilateral acoustic schwannomas (see Fig. 5–34) is pathognomonic of this disorder, which has also been termed MISME (multiple inherited schwannomas, meningiomas, and ependymomas).[304] In fact, labeling this disorder neurofibromatosis is a misnomer, because neurofibromas are not a part of its constellation of abnormalities. Patients with this disorder typically present clinically in the second and third decades of life, much earlier than those with the sporadic intracranial schwannoma.[302]

On gross inspection, schwannomas appear as focal, well circumscribed, globular or ovoid masses that do not infiltrate the nerve but rather arise and grow eccentrically, displacing the uninvolved portion of the cranial nerve of origin to the side.[48, 241, 302] As the tumor grows and matures, it may undergo cystic degeneration or develop patchy areas of lipid accumulation.[48, 354] Vestibular schwannomas typically enlarge within the cerebellopontine angle cistern and may displace and compress the adjacent pons, medulla, and fourth ventricle. They can attain considerable size before becoming clinically evident. Obstruction of the ipsilateral cerebellopontine angle cistern may occur, with formation of one or more extratumoral arachnoid cysts.[241, 306] Trigeminal schwannomas tend to occur more commonly in the parasellar region of the middle cranial fossa than in the posterior fossa, although approximately 25% extend through the tentorial notch, involving both fossae.[241]

Microscopic evaluation of a schwannoma typically dem-

onstrates a well encapsulated tumor containing collections of spindle-shaped Schwann cells in both compact cellular (Antoni A) and less cellular, more loosely textured (Antoni B) arrangements.[48, 354] Histologic variations are commonly encountered in larger tumors, including intratumoral clusters of lipid-laden cells, confluent microcysts and larger cysts, and dilated vascular sinusoids surrounded by foci of hemorrhage.[354]

The diagnosis of vestibular schwannoma on CT rests on the demonstration of a well circumscribed, globular or ovoid, hypodense to isodense (with respect to the adjacent pons and cerebellum) extraaxial mass in the cerebellopontine angle cistern with its base on the posterior aspect of the petrous temporal bone in the region of the internal auditory meatus. Images displayed in a bone window may demonstrate fusiform widening of the internal auditory canal with erosion of its bony margins. However, soft tissue detail within the cisternal portion of the tumor is often obscured by beam hardening artifacts caused by the adjacent dense cortical bone and pneumatized air cells of the petrous pyramid. Tumors up to about 1 cm in diameter typically demonstrate homogeneous density and homogeneously strong contrast enhancement, but larger tumors often demonstrate heterogeneity of both density and contrast enhancement because of the presence of intratumoral cystic degeneration, xanthomatous change, or intermixed areas of hypercellularity and hypocellularity.[66, 241, 302]

On MRI, smaller tumors can be more reliably detected, especially within the internal auditory canal, because of the lack of bone induced artifact and the multidimensional capability of this modality. The transition zone between the central (oligodendroglial) and peripheral (Schwann cell) portions of the eighth (vestibulocochlear) nerve, the presumed site of origin of schwannomas of this nerve, occurs within the canal. Tumors less than 5 mm in diameter can be reliably identified on thin section T1-weighted MRI, appearing as homogeneously mildly hypointense or isointense (to adjacent brain) ovoid or tubular intracanalicular masses with intense homogeneous contrast enhancement (Fig. 5–33).[222, 241, 275, 302, 306] On T2-weighted pulsing sequences, small vestibular schwannomas appear mildly to markedly hyperintense and may be obscured by the similarity in signal intensity to that of the surrounding CSF.[11]

As these tumors enlarge, the intratumoral degenerative changes previously described cause increasing heterogeneity of signal within the main tumor mass in the cerebellopontine angle cistern.[241, 302] On axial images, the tumor often has a commalike shape with a globular cisternal mass medially and a short tapered fusiform extension laterally into the internal auditory canal. Contrast enhancement is seen in nearly all schwannomas and may be homogeneous (two thirds of cases) or heterogeneous (see Figs. 5–21, 5–33, and 5–34).[241, 302, 306] Larger tumors compress and displace the adjacent anterolateral margin of the cerebellar hemisphere posteromedially, displace, compress, and rotate the pons and medulla, and narrow the fourth ventricle, elongating it in the anteroposterior direction (Figs. 5–21 and 5–34). Peritumoral vasogenic edema is frequently observed, and (as noted previously) associated arachnoid cysts are visualized in 5% to 10% of cases.[222]

Vestibular schwannomas represent 80% to 85% of cerebellopontine angle masses.[275, 306] The major differential di-

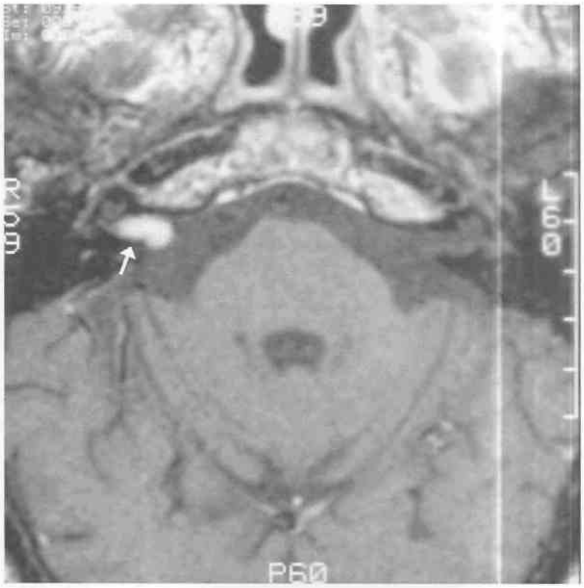

Figure 5–33. Vestibular schwannoma. Axial T1-weighted image of the posterior fossa and skull base following intravenous administration of gadolinium. A small intensely enhancing intracanalicular ovoid mass protrudes slightly medially into the cerebellopontine angle cistern on the right *(arrow)*.

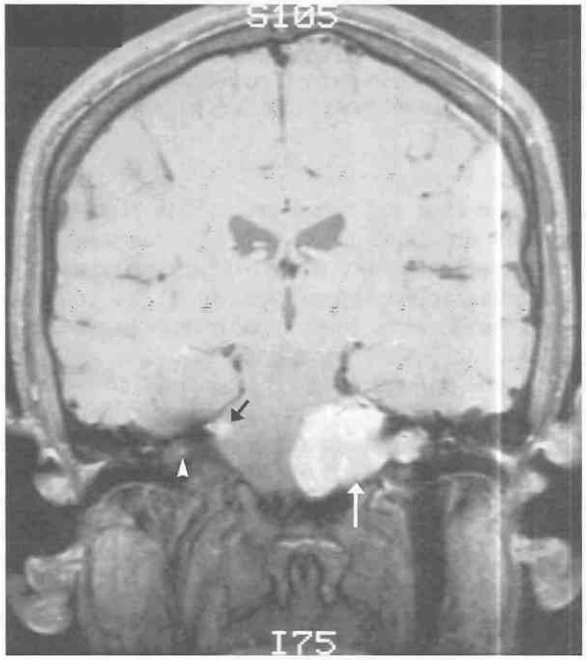

Figure 5–34. Bilateral vestibular schwannomas and right trigeminal schwannoma in a patient with neurofibromatosis type 2. Coronal postgadolinium T1-weighted MR image demonstrates three intensely contrast enhancing lesions in the posterior cranial fossa. The large left sided lobulated vestibular schwannoma fills the left cerebellopontine angle cistern *(white arrow)*, compresses, indents and displaces the left lateral margin of the pons inward, and extends laterally into the widened left internal auditory canal. A tiny punctate focus of contrast enhancement in the right petrous temporal region *(white arrowhead)* represents a small intracanalicular vestibular schwannoma. A third focus of contrast enhancement abuts and indents the right lateral margin of the pons *(black arrow)*; this is a trigeminal (fifth cranial nerve) schwannoma.

agnostic considerations include meningioma and epidermoid tumor.[241, 275, 306] Meningioma involving the dura of the posterior margin of the petrous temporal bone can project posteriorly into the cerebellopontine angle and simulate a vestibular schwannoma (Fig. 5–35). Such lesions represent about 10% of cerebellopontine angle masses.[306] Although meningiomas are typically more dense on CT, these two neoplasms may have identical signal intensity characteristics on MRI. Intense homogeneous or slightly heterogeneous contrast enhancement is another shared characteristic (Fig. 5–35*B*).[275] However, meningiomas are usually situated eccentric to the internal auditory canal and form a more obtuse angle with the petrous ridge than schwannomas.[181] Extension of meningioma into the internal auditory canal is uncommon but not unknown,[275] and rarely, schwannoma may simulate the appearance of a dural tail on contrast enhanced images.[252]

Epidermoid may resemble vestibular schwannoma on noncontrast CT but typically appears more lobulated and more hypodense and tends to insinuate more extensively into the subarachnoid spaces adjacent to the pons without causing major compression of the pons and fourth ventricle. On both CT and MRI, epidermoid does not demonstrate contrast enhancement. On MRI, larger epidermoids appear more homogeneous than schwannomas of similar size and may mimic CSF in intensity, with high T2 signal and low T1 signal.[11, 275, 306, 322]

Neurofibroma

Neurofibromas are well demarcated infiltrative intraneural or diffusely infiltrative extraneural benign tumors that consist of a mixture of neoplastic Schwann cells, perineurial cells, and fibroblasts in a collagenous and mucoid matrix.[241, 354] They are histologically benign and considered WHO grade I. With only extremely rare exception, neurofibromas do not arise within the intracranial portions of the cranial nerves.[241, 354] However, they can arise peripherally and extend retrogradely into the cranial vault, notably in the facial nerve (CN VII) and the ophthalmic division of the trigeminal nerve (CN V_1).[241]

The tumors exhibiting this retrograde intracranial extension are usually plexiform neurofibromas, which involve multiple nerve fascicles or trunks with fusiform multinodular enlargement often described as ropelike. On noncontrast CT, they appear isodense with adjacent muscle, and on MRI they are isointense with adjacent muscle on T1-weighted images and hyperintense on T2-weighted images.[241] Contrast enhancement is variable, with areas of moderate to strong enhancement after IV administration of gadolinium.

Multiple neurofibromas are typically associated with NF1 (also known as von Recklinghausen disease), an autosomal dominant congenital disorder associated with a gene defect on the long arm of chromosome 17.[339] Approximately 50% of patients report no family history and are presumed to represent new spontaneous germline mutations.[241, 339] In addition to multiple neurofibromas of the spinal and peripheral nerves, NF1 also includes optic nerve and chiasm gliomas, foci of "hamartomatous" change of uncertain etiology in the region of the basal ganglia and in the optic tracts and radiations, cerebral peduncles, and brain stem, astrocytomas of the spinal cord, multiple café au lait spots, axillary and inguinal freckling, malignant

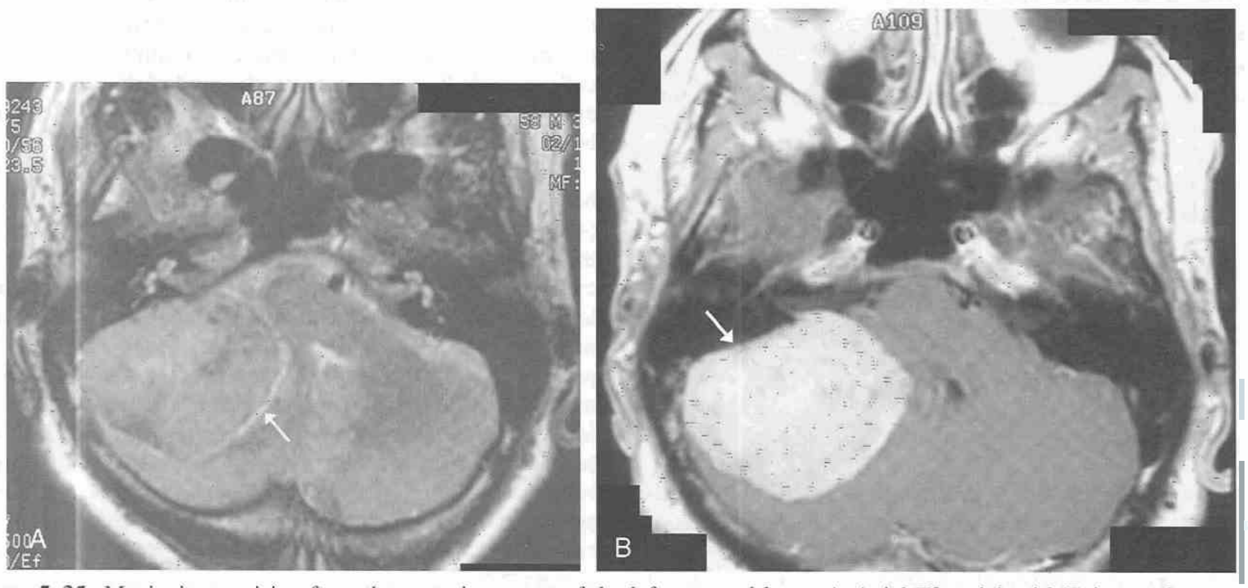

Figure 5–35. Meningioma arising from the posterior aspect of the left temporal bone. *A*, Axial T2-weighted MR image demonstrates a large rounded extraaxial tumor mass in the right side of the posterior fossa with its base on the posterior dura of the left temporal bone. The mass is slightly hyperintense relative to gray matter and compresses and displaces the right cerebellar hemisphere posteriorly and medially. A narrow cleft of cerebrospinal fluid *(arrow)* separates the medial margin of the tumor from the adjacent compressed cerebellum and pons. Note that the internal auditory canals bilaterally are filled with cerebrospinal fluid. *B*, Following intravenous administration of gadolinium, an axial T1-weighted image demonstrates intense homogeneous contrast enhancement of this large dural-based tumor *(arrow)*.

peripheral nerve sheath tumors, iris hamartomas, and dysplastic osseous lesions (sphenoid wing dysplasia, pencil-like thinning of the long bones).[223, 321, 339] Patients with NF1 usually present clinically very early in life, whereas those with sporadic solitary neurofibroma involving a cranial nerve may present in later youth and adult life.

On noncontrast CT, plexiform neurofibroma appears as a poorly circumscribed irregular widening of the involved root, which is isodense with adjacent muscles. Erosion of adjacent bone with widening of bony foramina may be evident. MRI demonstrates the widened nerve, which is isointense with adjacent muscle on T1-weighted images and hyperintense on T2-weighted images. Contrast enhancement after IV administration of gadolinium is the rule, varying from moderate to intense.[25, 241]

Malignant Peripheral Nerve Sheath Tumors

Malignant peripheral nerve sheath tumors are rare tumors that appear to arise de novo in the cranial nerves, the fifth cranial nerve being more frequently involved than any other.[354] Elsewhere in the body, almost two thirds of reported cases of malignant peripheral nerve sheath tumors have arisen from preexisting neurofibromas, often plexiform and in the setting of NF1.[354] Approximately 50% occur in association with NF1. The incidence of malignant progression in patients with plexiform neurofibroma is approximately 5%. Imaging findings include irregularity and loss of clear tumor margins together with inhomogeneous contrast enhancement. Evidence of diffuse invasion of the skull base may also be present.[241]

Tumors of the Meninges

A wide variety of primary tumors can arise from and develop within the meninges.[199] By far the most common is meningioma. Another important meningeal tumor, until 1993 considered a variant of meningioma, is the hemangiopericytoma. Additionally, nonmeningothelial mesenchymal tumors, both benign (lipoma, chondroma, benign fibrous histiocytoma) and malignant (chondrosarcoma, osteosarcoma), can originate in the meninges. Also, tumors of melanocytic origin can rarely arise within the intracranial meninges. Finally, although the histogenesis is uncertain, neuropathologists usually assign hemangioblastomas to this category.

Meningioma

Meningiomas are solid, well circumscribed, highly cellular, slow growing tumors that are usually benign histologically (WHO grade I). These spherical and sometimes lobulated tumors are composed of neoplastic meningothelial cells originating from the arachnoid layer of the meninges with a broad attachment to the adjacent dura. Most commonly, they project inward from the dura, indenting and compressing the underlying brain, causing neurologic symptoms and signs through compression of the adjacent cortex.

Meningiomas are the most common primary extracerebral tumors of the CNS, accounting for approximately 20% of primary brain tumors.[184, 199] They occur mainly in middle and old age, with a peak incidence in the fifth through seventh decades of life[277]; these tumors can, however, be found in all age groups. Meningiomas exhibit a strong sex predilection, occurring preponderantly in females, with a female-to-male ratio of at least 2:1.[302] However, meningiomas associated with hereditary tumor syndromes, such as NF2, generally occur in younger patients and do not demonstrate a female predilection.[199]

Common sites of origin are the frontal and parietal convexities and the parasagittal region, often in close association with the falx cerebri (about 50%), as well as the sphenoid wings, olfactory grooves, sylvian fissures, and parasellar regions (about 35%).[120, 199] Less than 10% arise below the level of the tentorium, mainly from the clivus, the leaves and free edge of the tentorium, and the petrous pyramid.[282] Multiple meningiomas are reported in 6% to 9% of cases,[286] occurring both as a component of NF2[223] and, less commonly, sporadically.

Although most meningiomas are slow growing and well encapsulated globular masses, variations in shape and histology are not unusual. Invasion of the dura and encasement or invasion of the nearby dural venous sinuses are common.[199] Tumors arising in relation to the sphenoid wing are frequently flat (en plaque) and tend to invade through both layers of the cranial dura into the adjacent bone, provoking a notable bony reaction with thickening and sclerosis (meningioma bone).[120, 277] Such bony changes are a source of considerable controversy; many clinical neuroscientists regard bony sclerosis and thickening as highly indicative of tumor infiltration into the haversian canals of the calvaria,[199] whereas others state that such hyperostosis can also occur without histologic evidence of bone infiltration by tumor.[277] Meningiomas arising adjacent to the cribriform plate and planum sphenoidale and those occurring over the high cerebral convexities are more typically rounded and invaginate the underlying brain; however, they also show a propensity for stimulating adjacent bony thickening and sclerosis (Fig. 5–36).[120]

Several different histologic types of meningioma have been described.[31, 199, 257, 286] A small but significant minority (4% to 8%) of meningiomas are identified as atypical on the basis of increased mitotic activity and high nuclear-to-cytoplasmic ratio. The most aggressive exhibit the histologic features of frank malignancy (anaplastic and malignant meningiomas) and may invade the adjacent cerebral parenchyma.[199] Atypical and anaplastic meningiomas occur more frequently in the high cerebral convexities and the falx. Most meningiomas are homogeneously solid tumors, but foci of necrosis and scarring (probably secondary to ischemia), microcystic change or areas of heavy lipid storage (lipomatous/lipoblastic meningiomas) (see Fig. 5–38) can be identified in approximately 5% to 15% of excised tumors.[99, 204, 287]

Approximately three quarters of meningiomas appear on noncontrast CT as sharply circumscribed, rounded and sometimes lobulated, homogeneous masses of slightly increased density (40 to 50 HU) compared with adjacent brain.[5, 40, 233] The hyperdensity is related to the dense cellularity of these tumors and does not reflect psammomatous

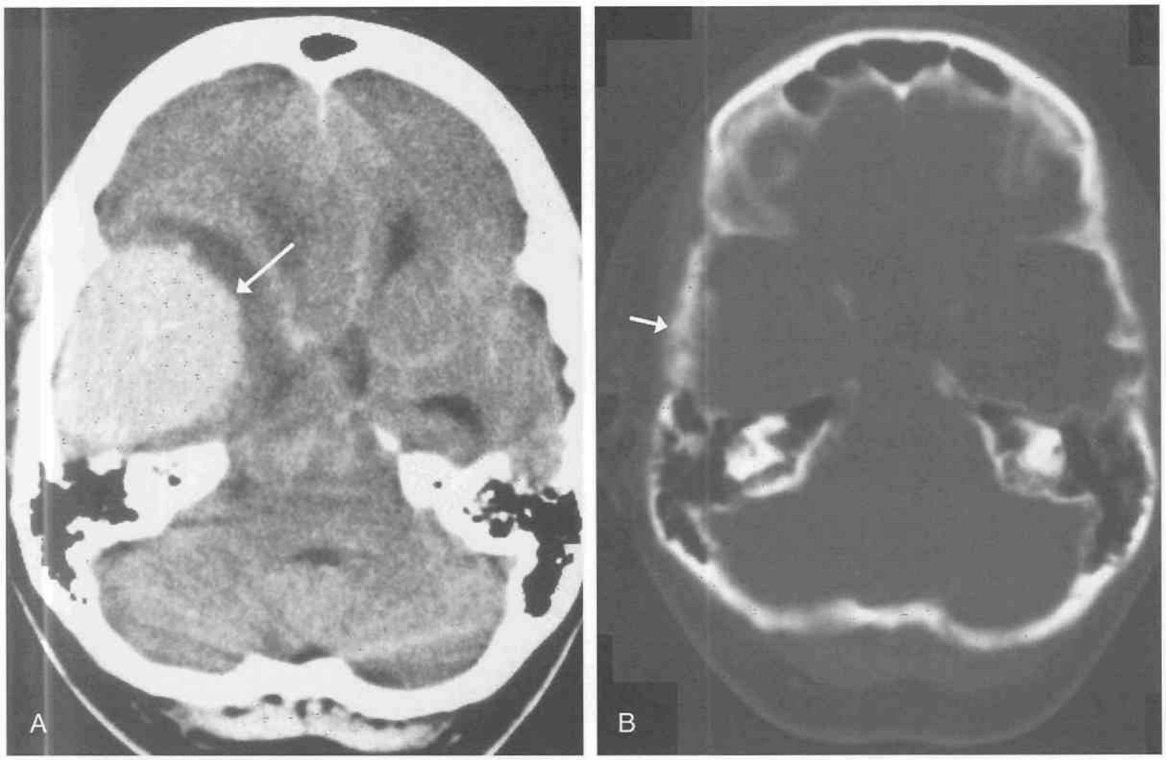

Figure 5–36. Sphenoid wing meningioma with underlying hyperostosis ("meningioma bone"). *A,* Axial postcontrast CT image demonstrates intense homogeneous contrast enhancement of a large round extracerebral tumor with its base on the right greater sphenoid wing *(arrow).* On its inner aspect, the tumor is surrounded by a thick band of hypodensity representing edema of the adjacent cerebral cortex and white matter. There is a marked shift of the midline vessels to the left. *B,* On an axial CT image displayed in a bone window setting, the underlying greater sphenoid wing and squamous portion of the temporal bone demonstrate heterogeneous bony thickening *(arrow).*

change within the tumor. Meningioma typically has a broad base on a dural surface. The invaginating mass displaces and compresses the underlying brain and causes flattening of the adjacent cerebral cortex (Fig. 5–36*A*). Inward buckling of the white matter can be identified in about 40% of meningiomas.[113] A hypodense rim (representing trapped CSF) may be insinuated between the invaginating mass and the invaginated cerebral parenchyma; cystic changes in the arachnoid may also be identified adjacent to the tumor margins.[287] About 10% of meningiomas appear isodense with the adjacent brain on noncontrast CT,[233] and an occasional tumor contains areas of hypodensity that correlate pathologically with foci of ischemic scar, microcysts, or lipoblastic change.[40, 99, 204, 287]

Vasogenic edema of the adjacent cerebral white matter is identified in 50% to 75% of meningiomas.[5, 302] The mechanism responsible for the occurrence of peritumoral intracerebral edema is uncertain, and there is no correlation between tumor size and extent of edema.[233] Significant edema is found more commonly in patients with lateral convexity tumors than in those with tumors in other sites.[233] The occurrence of intracerebral edema appears to correlate with a poorer prognosis, a correlation that may be related to reduced resectability.[302] Hyperostosis and thickening of adjacent bone in sphenoid wing, skull base, and high convexity meningiomas, as described previously, can be clearly delineated on CT if high center and wide window settings are employed (Fig. 5–36*B*).

After IV administration of contrast medium, a meningioma typically displays a striking homogeneous enhancement (increase of 40 to 50 HU or more) (see Fig. 5–36*A*).[5, 302] Even the occasional isodense meningiomas exhibit this intense opacification. However, meningiomas that are predominantly microcystic may not enhance strongly or uniformly.[199] In 5% to 15% of cases, focal areas of nonenhancement can be identified within the tumor mass.[233, 287] These areas have been correlated pathologically with regions of necrosis, old hemorrhage, scarring, cystic degeneration, and lipoblastic change[287]; they usually do not interfere with the accuracy of diagnosis. Occasionally, however, the heterogeneity of contrast enhancement may be sufficient to raise the question of glioblastoma.[5, 233, 287]

Parasagittal meningiomas of sufficient size may compress (Fig. 5–37*A, B*) or invade the adjacent superior sagittal sinus; interruption of the sinus can be identified on coronal postcontrast CT or noncontrast MR images and is an important preoperative finding for which the radiologist must search. Indistinct irregular tumor margins, a mushroomlike extension of opacified tumor well away from the main ovoid tumor mass, and prominent venous drainage centrally from the tumor are CT and MRI signs that may suggest an aggressive anaplastic or malignant meningioma invading the brain.[234, 295]

In a multiinstitutional prospective study, the sensitivity of contrast enhanced CT for detection of an intracranial mass in patients with meningioma was 96%.[233] Ten percent

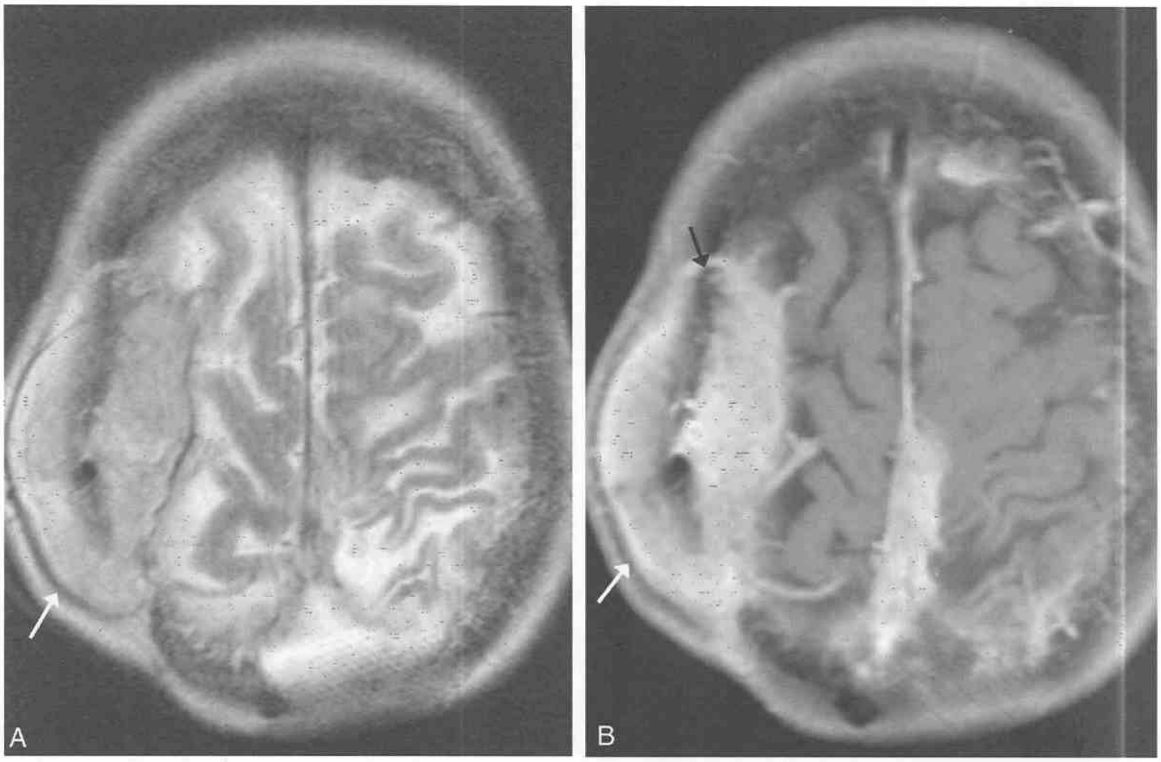

Figure 5–37. Multiple meningiomas. Transcalvarial tumor extension with subgaleal mass and dural tail. Axial T2-weighted *(A)* and post intravenous gadolinium T1-weighted *(B)* images demonstrate a large right frontoparietal convexity extracerebral tumor that is homogeneously mildly hyperintense to gray matter on T2-weighting and intensely and homogeneously enhances following intravenous gadolinium. This aggressive tumor extends through the calvaria (*black arrow* in *B*) and presents as a broad based mass under the scalp (*white arrows* in *A* and *B*). Note also the presence of a second similar tumor arising in the high posterior falx cerebri on its left lateral aspect and displacing the superior sagittal sinus posterosuperiorly and to the right of the midline. *C*, Coronal T1-weighted postgadolinium image demonstrates intense homogeneous contrast enhancement of both the convexity and the parasagittal tumors and also of a third large similarly enhancing tumor in the left cerebellopontine angle. Note the "dural tail" of tumor extension over the right frontal convexity *(arrow)*.

of the masses were not detected on the noncontrast scans. The differential diagnosis of a hyperdense or isodense peripherally situated extracerebral mass with homogeneous contrast enhancement includes metastatic malignancy (particularly, carcinoma of the lung and melanoma),[116, 268] acute leukemia,[347] systemic lymphoma,[11] and (at the skull base) schwannoma of a cranial nerve.[286] Criteria for differentiation are lesion location and configuration, definition of margins, and presence or absence of associated bony changes (erosion or hyperostosis).

On noncontrast MRI, the majority of meningiomas present a homogeneous appearance similar to that seen on CT. Tumor signal intensity on T1-weighted images tends to approximate that of the adjacent cerebral cortex in about

50% of cases and to be hypointense to cortex in 50%. On T2-weighted images, about 50% are mildly hyperintense relative to adjacent gray matter (see Fig. 5–37*A*) and 50% are isointense with the cortex (see Fig. 5–35*A*).[11, 99] On T2-weighted images, comparison of signal intensity of tumor with that of cortex may have histologic correlation; in one reported series, hyperintensity correlated strongly with either syncytial or angioblastic types of meningioma, whereas fibroblastic and transitional meningiomas failed to demonstrate hyperintensity.[99] A minority of meningiomas appear heterogeneous on both T1- and T2-weighted images because of the presence of intratumoral lipoblastic or cystic changes (Figs. 5–1*A* and 5–38*A*, *B*), calcifications, or prominent vessels.[11, 100]

MRI enables more accurate localization and evaluation of these extracerebral tumors than CT. This superiority is

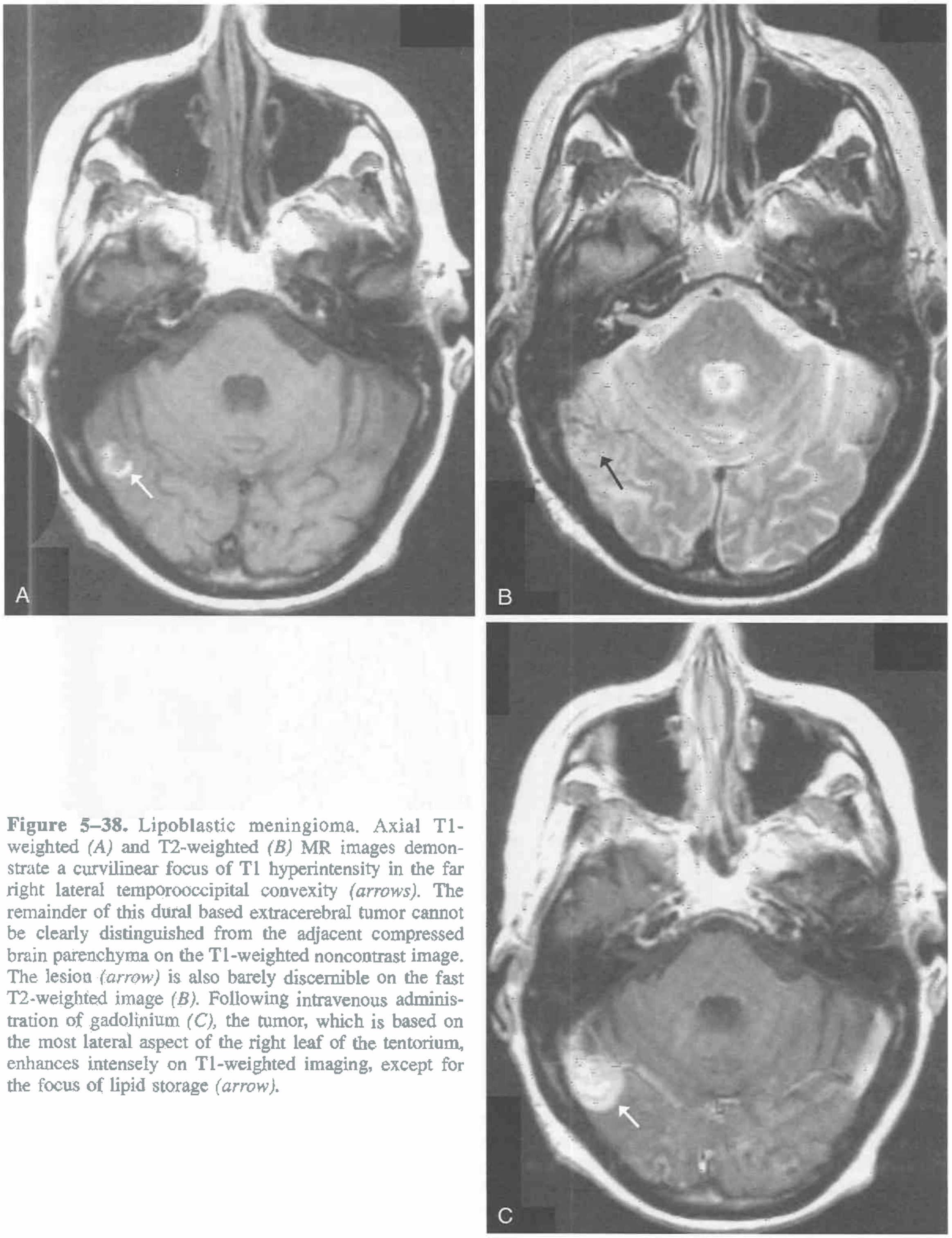

Figure 5–38. Lipoblastic meningioma. Axial T1-weighted *(A)* and T2-weighted *(B)* MR images demonstrate a curvilinear focus of T1 hyperintensity in the far right lateral temporooccipital convexity *(arrows)*. The remainder of this dural based extracerebral tumor cannot be clearly distinguished from the adjacent compressed brain parenchyma on the T1-weighted noncontrast image. The lesion *(arrow)* is also barely discernible on the fast T2-weighted image *(B)*. Following intravenous administration of gadolinium *(C)*, the tumor, which is based on the most lateral aspect of the right leaf of the tentorium, enhances intensely on T1-weighted imaging, except for the focus of lipid storage *(arrow)*.

due not only to the visualization of the mass in all three dimensions and the lack of beam bardening artifact at the base of the brain with MR. In approximately two thirds of cases, the interface between the inner margin of the extracerebral tumor mass and the invaginated or displaced cortex can be recognized on MRI from the presence of a cleft of CSF (see Fig. 5–35*A*) or the interposition of vascular flow voids of the displaced arteries and veins on the pial surface of the brain (see Fig. 5–1*A*).[11] Also, invasion of adjacent brain by meningiomas arising from the tentorium, the falx, and the dura of the lateral wall of the cavernous sinus can be recognized as a breech in the hypointense dural rim at the tumor margin.[11] Finally, arterial encasement and partial dural venous sinus invasion are more readily and accurately depicted by the contrast between the flow void and the tumor tissue.[11]

As on CT, meningiomas usually demonstrate rapid and pronounced contrast enhancement after IV administration of paramagnetic contrast agent, and the strong, often striking, homogeneous contrast enhancement seen in most meningiomas enables their accurate detection and localization (Figs. 5–1*B*, 5–35*B*, 5–37*B*, *C*, 5–38*C*, and 5–39*B*).[11, 158, 275]

A thickened tapered extension of contrast enhancing dura is commonly identified at the margins of the tumor (Fig. 5–35*C*). This *dural tail* may indicate the presence of tumor infiltration[121] or may be due to dural reaction.[225] Because a major prognostic factor in the recurrence of meningiomas after surgery is the extent of tumor resection,[199] careful assessment must be made of preoperative postcontrast MR images for the presence of a dural tail.

The arachnoid contributes embryologically to the formation of the choroid plexuses, so intraventricular meningiomas may arise within the choroid plexus of the lateral ventricle and locally expand the ventricle to conform to the size and shape of the tumor (Fig. 5–39).[221, 300, 302] These tumors share the imaging characteristics of extracerebral meningiomas as previously described. The normally compact choroid glomus calcifications may be fragmented and spread by the expanding tumor mass.[300] Differentiation from choroid plexus papilloma is based on (1) patient age (papillomas of the lateral ventricles occur mainly in infants and very young children), (2) tumor surface characteristics (papillomas tend to have a nodular irregular margin, whereas meningiomas tend to be smoothly rounded), and (3) size and shape of the cerebral ventricles (papillomas are often associated with diffuse enlargement of all ventricles, whereas meningiomas cause only focal enlargement).[11]

Hemangiopericytoma

Hemangiopericytoma is now recognized in the WHO classification of tumors of the CNS as a distinct entity separate from meningioma.[147] This dural based tumor was formerly considered an "angioblastic" meningioma be-

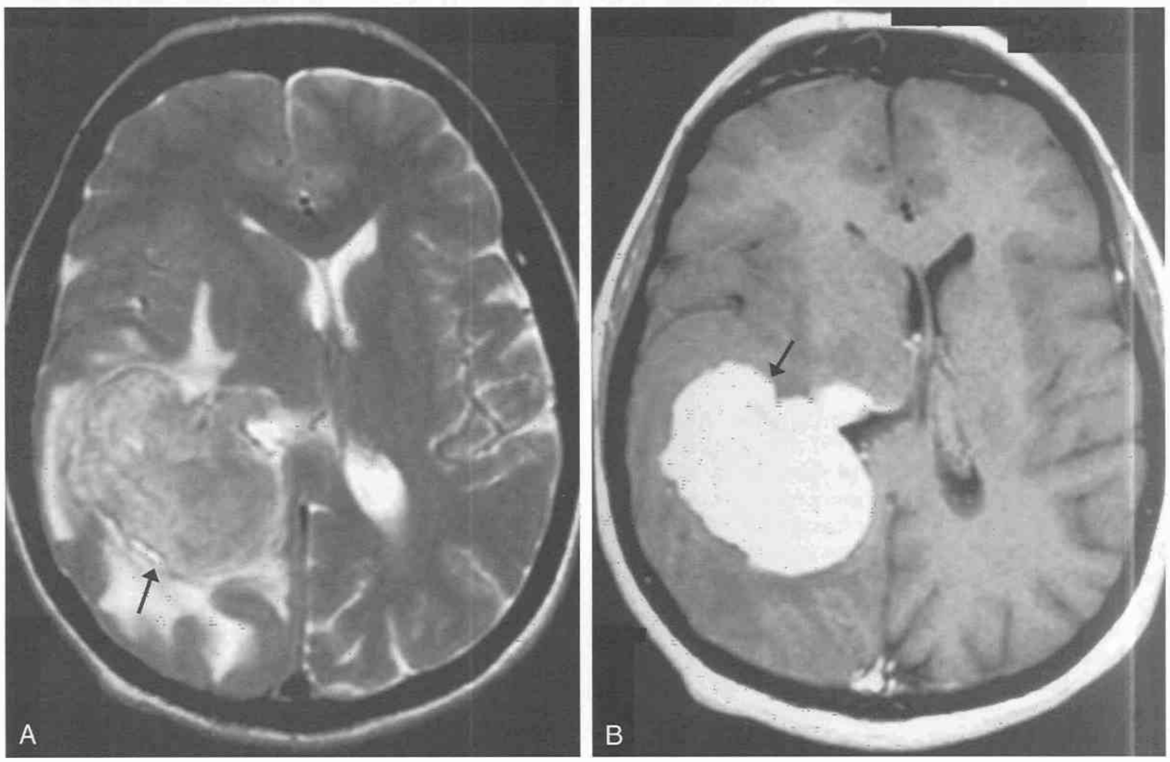

Figure 5–39. Intraventricular meningioma. *A*, A large round mildly hyperintense (to gray matter) tumor fills and distends the atrium of the right lateral ventricle *(arrow)* on this axial T2-weighted MR image. Note the dilatation of the anterior right temporal horn proximal to the obstruction caused by this mass. Edema of the surrounding white matter contributes to the right sided mass effect, which causes compression of the right frontal horn and marked shift of the septum pellucidum to the left of the midline. *B*, An axial T1-weighted postgadolinium image demonstrates intense homogeneous contrast enhancement of this large multilobulated intraventricular meningioma *(arrow)*.

cause of its hypervascularity. However, despite many gross pathologic. histopathologic, and imaging similarities to meningioma, the aggressive clinical behavior of hemangiopericytomas differs considerably from the majority of meningiomas, and it is now possible to distinguish the two entities immunohistochemically.[147] The cell of origin is the pericyte, a perivascular cell of mesenchymal origin, and the intracranial tumors are identical histologically to their counterparts in the somatic soft tissues.[147]

Like meningiomas, hemangiopericytomas are dural based, extraaxial rounded masses, well circumscribed and highly cellular. They are often more lobulated in contour than the typical meningioma and are more commonly located in the occipital region near the confluence of the dural venous sinuses, to which they are often attached.[148] They are comparatively rare, with a ratio of 1 hemangiopericytoma to 40 or 50 meningiomas.[129, 148] They tend to occur in younger patients, typically in their 40s, and the sex distribution (male-to-female ratio = 1.4:1) differs markedly from that of meningiomas.[147]

Histologically, hemangiopericytomas appear highly cellular with moderate nuclear atypia and prominent mitotic activity comparable to that of anaplastic meningiomas.[147] They are richly vascular tumors with arterial supply from both the meningeal and cerebral arteries, and numerous large and branching vascular channels ("staghorn sinusoids") with perivascular fibrosis are a prominent microscopic finding.[147] Invasion and destruction of overlying bone is not unusual, but these tumors do not provoke a hyperostotic ("meningioma bone") response. Infiltration of underlying brain parenchyma can also occur. Hemangiopericytomas exhibit a marked tendency to recur locally despite apparently complete surgical excision and postoperative irradiation of the former tumor bed; in one large series, the 15 year recurrence rate was 85%.[129] They also tend to metastasize beyond the cranial cavity; in the same large series,[129] 60% of tumors had metastasized after 15 years, mainly to bone, lung, and liver.

The findings on diagnostic imaging tend to mimic those of meningiomas. These sharply circumscribed extraaxial masses appear hyperdense on noncontrast CT and are generally homogeneous and hypointense to white matter and isointense with gray matter on T1-weighted noncontrast MRI (Fig. 5–40*A*). On T2-weighted images, hemangiopericytomas typically are slightly hyperintense and more heterogeneous in appearance (Fig. 5–40*B*). As noted previously, hemangiopericytomas often appear more lobulated and exhibit a higher incidence and degree of heterogeneity of attenuation (CT) and signal intensity (MRI) than meningiomas owing to the presence of multiple flow voids.[302] Contrast enhancement of hemangiopericytomas is usually intense and homogeneous (Fig. 5–40*C*). Points of differentiation from meningioma include a greater frequency of internal heterogeneity and external lobulation, a tendency toward a more narrow base of dural attachment, and absence of tumor calcification and hyperostosis of adjacent bone.[53]

Mesenchymal Nonmeningothelial Tumors

A diverse group of relatively rare tumors, mesenchymal nonmeningothelial tumors may arise within the cranial vault, either in the skull base, the calvaria and sutures, the meninges, or (most rarely) within the cerebral parenchyma. They may be of primitive mesenchymal origin but have not differentiated along the meningothelial line. Rather, these unusual lesions exhibit fibrous, fibrohistiocytic, adipose, myoid, endothelial, chondroid, or osseous differentiation and cannot be distinguished histologically from their more common counterparts in the somatic soft tissues.[251]

These tumors vary widely in location, histology, pathologic grade, and clinical behavior. Some (e.g., lipomas and hemangiomas) are benign (WHO grade I) and mainly asymptomatic, and some (e.g., osteosarcomas and rhabdomyosarcomas) are highly malignant (WHO grade IV) and highly invasive. Tumors arising in the meninges are more common than those originating within cerebral parenchyma. Although most of these lesions occur supratentorially in adults, many rhabdomyosarcomas occur below the tentorium in young children. Lipomas typically occur in or near the midline and are associated with malformations of the corpus callosum, whereas chondrosarcomas arise most commonly in the skull base off the midline (e.g., the petroclival suture).

Lipomas are not true neoplasms but instead likely represent congenital malformations.[356] They enlarge only with somatic growth. Intracranial lipomas are usually subarachnoid in location and occur most commonly in the pericallosal sulcus. Other sites are the chiasmatic, circummesencephalic, interpeduncular, and quadrigeminal cisterns and, in the posterior fossa, the cerebellopontine angle cistern.[11] More than 50% of pericallosal lipomas are associated with partial agenesis or dysgenesis of the adjacent corpus callosum, with the rostrum, genu, and anterior portion of the body more commonly affected than the posterior body or splenium.[356]

Two types of pericallosal lipomas are recognized. The tubonodular lipomas are large and rounded, are located anteriorly, and have a high incidence of associated corpus callosal dysgenesis as well as anomalies of the frontal lobes.[239] The curvilinear type tend to be more posteriorly situated, appear long and thin, curve around the splenium, and are associated with a normal or only slightly dysgenetic corpus callosum (Fig. 5–41).[238] These lesions are tightly adherent to the adjacent brain, and lipoma in the cerebellopontine angle cistern may envelop and compress the seventh and eighth cranial nerves where they pass through the cistern.[67]

Lipomas are typically asymptomatic and discovered only incidentally when the head is imaged for other reasons. Even on plain skull radiographs, the tubonodular masses are recognized from their well demarcated homogeneous lucency in the midline anteriorly, often associated with marginal curvilinear calcification bilaterally (see Fig. 5–41). On CT scans, the smoothly demarcated mass appears more hypodense than CSF (−50 to −100 HU) and is often marginated laterally by nodular or curvilinear calcification (see Fig. 5–41). On MRI, lipomas appear mainly homogeneously hyperintense on both T1-weighted and fast spin-echo T2-weighted images, but areas of low signal, secondary to the marginal calcification, are commonly noted peripherally.[114] Central flow voids, representing pericallosal arteries coursing through the substance of the tumor, are prominent within the tumor mass.

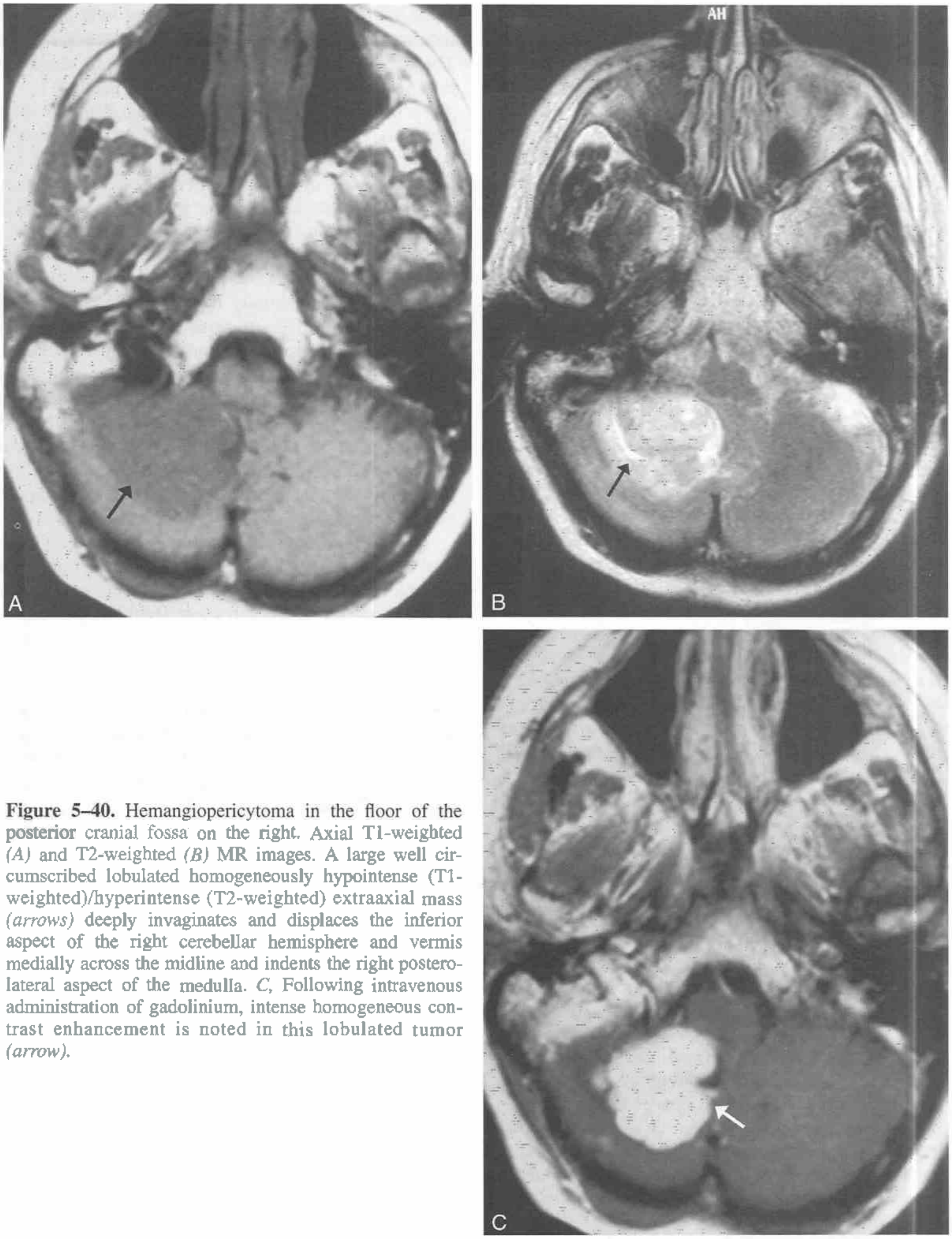

Figure 5–40. Hemangiopericytoma in the floor of the posterior cranial fossa on the right. Axial T1-weighted *(A)* and T2-weighted *(B)* MR images. A large well circumscribed lobulated homogeneously hypointense (T1-weighted)/hyperintense (T2-weighted) extraaxial mass *(arrows)* deeply invaginates and displaces the inferior aspect of the right cerebellar hemisphere and vermis medially across the midline and indents the right posterolateral aspect of the medulla. *C,* Following intravenous administration of gadolinium, intense homogeneous contrast enhancement is noted in this lobulated tumor *(arrow).*

Osteocartilaginous tumors occasionally arise within dural structures such as the falx. The CNS is the most common site of occurrence of extraosseous *chondrosarcoma*.[251] This mesenchymally derived malignancy occurs more frequently in the skull base, notably in the region of the intrasphenoid synchondrosis or the adjacent petroclival suture, and it may invade the overlying brain (Fig. 5–42). Whether arising from dura or from skull base structures, chondrosarcomas manifest as soft tissue masses with focal bone destruction. Intratumoral calcifications, identified in about half of tumors, contribute to a heterogeneous appearance on MRI, with intratumoral nodules which appear hypointense to isointense with adjacent brain on T1-weighted images and hyperintense to brain on T2-weighted images.[216] Intense contrast enhancement of the soft tissue mass is the rule (Fig. 5–42*B*).

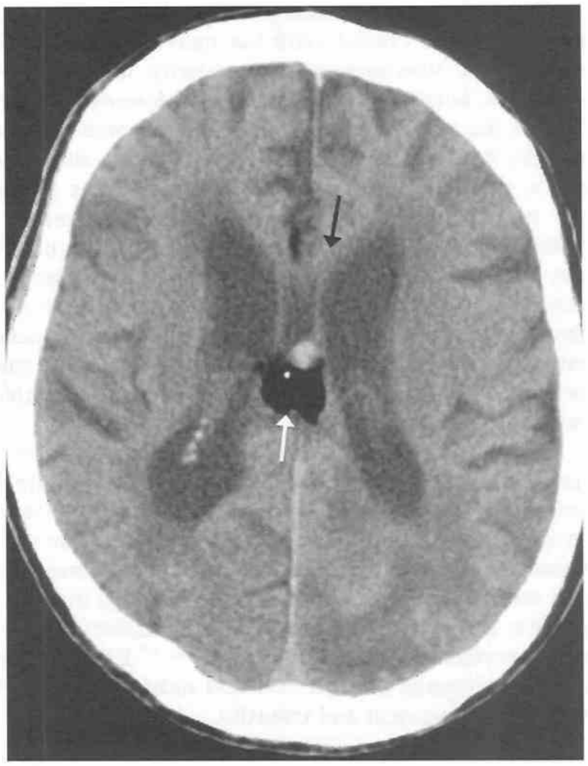

Figure 5–41. Pericallosal lipoma and partial agenesis of the corpus callosum. Axial noncontrast CT image demonstrates widely separated and parallel bodies of the lateral ventricles with an intervening elevated and dilated third ventricle *(black arrow);* these findings are consistent with partial agenesis of the anterior portion of the corpus callosum. In the midline more posteriorly, a markedly hypodense rhomboid-shaped curvilinear lipoma *(white arrow)* with two internal foci of calcification separates the lateral ventricles.

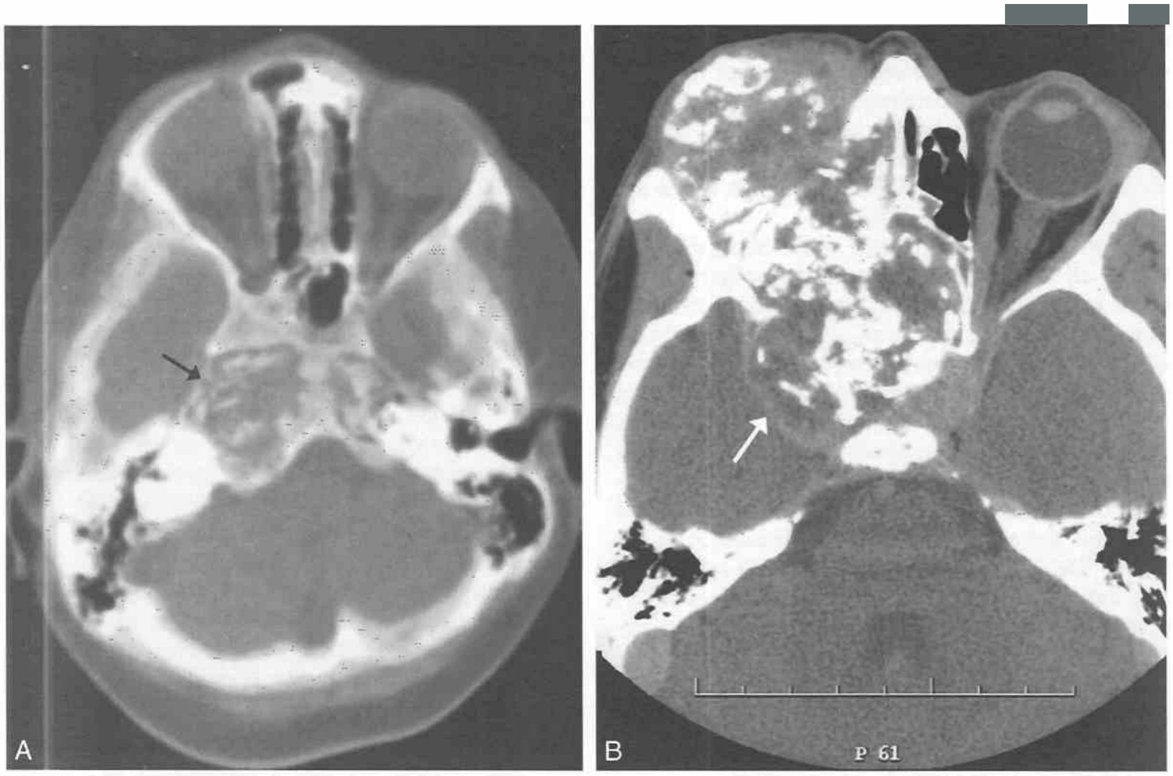

Figure 5–42. Chondrosarcomas of the skull base. *A,* Axial noncontrast CT image displayed in a bone window demonstrates bilateral irregularly marginated areas of bone destruction in the region of the intrasphenoid synchondrosis with multiple intratumoral hyperdensities respresenting foci of calcification and/or bony sequestra. The bony destruction involves the right lateral margin of the clivus *(arrow)* and the right petrous apex. *B,* In another patient, an axial CT image following intravenous contrast displayed in a soft tissue window demonstrates more extensive bone destruction involving the entire body of the sphenoid bone, the right ethmoid sinus, and the right orbit with foci of intratumoral calcification and/or bony sequestra. The soft tissue components of this tumor demonstrate heterogeneous contrast enhancement *(arrow)* with multiple ill defined areas of nonenhancement.

Other mesenchymal malignancies may also rarely originate within the cranial vault but more commonly arise in extracranial structures and secondarily invade the skull and brain, notably the *embryonal rhabdomyosarcoma*.[237, 251] This is the most common soft tissue sarcoma in children, and the head and neck are the most common site of occurrence, especially the orbit and the nasopharynx as well as the middle ear.[237] The tumor is almost uniformly fatal within 2 years of presentation, despite intensive chemotherapy and radiotherapy.[251] An extremely aggressive neoplasm, embryonal rhabdomyosarcoma commonly invades through the skull base into the adjacent brain. Evidence of invasion of the anterior skull base, the cavernous sinuses, or both is identified on MRI in 35% of embryonal rhabdomyosarcomas originating in the nasopharynx.[180]

Perineural and meningeal spread of tumor is also common in this tumor.[238] Imaging studies demonstrate large soft tissue masses with evidence of aggressive bone destruction. On MRI, these lesions appear isointense with muscle on T1-weighted images and hyperintense to brain and muscle on T2-weighted images, findings that are nonspecific and similar to those seen in nasopharyngeal carcinoma, myeloma, and neuroblastoma.[180, 237] Embryonal rhabdomyosarcomas exhibit contrast enhancement, which varies in both extent and intensity.

Melanocytic Tumors

A wide spectrum of tumors of melanocytic origin, varying from benign and diffuse (melanocytosis) to benign and well circumscribed (melanocytoma) to malignant (primary malignant melanoma), can originate within the meninges and the CNS.[151] They are thought to arise from leptomeningeal melanocytes derived from the neural crest. These tumors are all uncommon lesions, but the benign forms are less rare than the primary malignancies.

Melanocytomas of the meninges, which represent less than 0.1% of all brain tumors, present as solitary solid, round or flat extraaxial masses occurring mainly near the foramen magnum or in the region of Meckel's cave. Histologically, they demonstrate monomorphic cells with variable melanin content in their cytoplasm and a low mitotic rate.[151] Immunohistochemical studies show most tumors reacting to antimelanosomal antibody.[151] Presenting symptoms are those related to local compression of the underlying brain or obstruction of CSF flow. They can be found in patients of all age groups, with a peak incidence in the fifth decade of life.[151] Females are affected more commonly than males, with a reported 2:1 ratio.[227] On MRI, melanocytomas of the meninges appear as well-circumscribed extraaxial masses that are isointense to hyperintense, depending on the quantity of melanin in the tumor cells on T1-weighted images and hypointense to gray matter on T2-weighted images. Like the majority of meningeal tumors, they exhibit homogeneous contrast enhancement.[196, 338]

Hemangioblastoma

Hemangioblastomas are benign (WHO grade I) vascular neoplasms of uncertain origin that consist of abundant endothelial pericytes forming a rich capillary network intermixed with vacuolated (lipid-containing) stromal cells.[32] Although relatively uncommon overall (1% to 2.5% of all primary CNS tumors), hemangioblastoma is the most common primary intraaxial posterior fossa tumor in adults.[168, 186, 286] The great majority (80% to 85%) of CNS hemangioblastomas occur in the cerebellum, 2% to 3% in the medulla, and only 1% to 1.5% above the tentorium.[142, 286] The remainder (10% to 15%) arise within the spinal cord.[142]

Seventy-five percent to 85% of hemangioblastomas are sporadic in occurrence and solitary. They typically present clinically in young adults with peak incidence in the third to fifth decades of life and are rare in children. The natural history is that of a slow growing mass in the cerebellum that is frequently associated with a cyst. Approximately 60% of these tumors are cystic at the time of clinical presentation.[142] Symptoms are usually related to obstruction of CSF flow in the fourth ventricle by the solid tumor or the associated cyst.[32] Hemorrhage is uncommon in hemangioblastoma despite the prominent vascularity, and necrosis is rare. The advent of microsurgical excision techniques has significantly improved the prognosis in patients with sporadically occurring hemangioblastomas; mortality is low, and permanent neurologic deficits are rare.[32]

On gross inspection, hemangioblastomas are well demarcated, highly vascularized, small (5 to 10 mm), rounded solid lesions located peripherally within the cerebellum, brain stem, or spinal cord, usually abutting a pial surface (Fig. 5–43).[32, 104] The most striking lesions are those associated with well circumscribed cysts in which the solid tumor is a mural nodule.[286] Like the cyst associated with juvenile pilocytic astrocytoma of the cerebellum with a mural nodule, the cyst associated with a hemangioblastoma is essentially extratumoral, lacking any tumor tissue in its margin except for the eccentrically located solid nodule.[286] The cyst wall is composed of compressed brain parenchyma or reactive gliosis.[142]

Approximately 25% of hemangioblastomas are associated with von Hippel–Lindau disease, a phakomatosis that is inherited as an autosomal dominant trait caused by a germline mutation of a suppressor gene on the 3p chromosome.[32] Lindau[194] originally described this disease complex in 1926; it is characterized by the development of capillary hemangioblastomas in the CNS in association with identical tumors in the retina (originally described by von Hippel[340] in 1906); clear cell renal carcinomas, pheochromocytomas, and pancreatic, renal, and hepatic cysts are also frequently found in patients with the disease.

Multiplicity of hemangioblastomas of the cerebellum, brain stem, and spinal cord is common (10% to 40% of cases) in patients with von Hippel–Lindau disease,[104] and multiple tumors are found almost exclusively in patients with the disease (Fig. 5–44).[32, 232] Patients with von Hippel–Lindau disease become symptomatic at an earlier age (mean age at diagnosis, 29 years) than those with solitary sporadically occurring tumors.[32] Despite improved surgical techniques, the most common cause of death in patients with von Hippel–Lindau disease is hemangioblastoma.[157]

Noncontrast CT scans usually demonstrate a large, sharply marginated, hypodense, cystic cerebellar hemi-

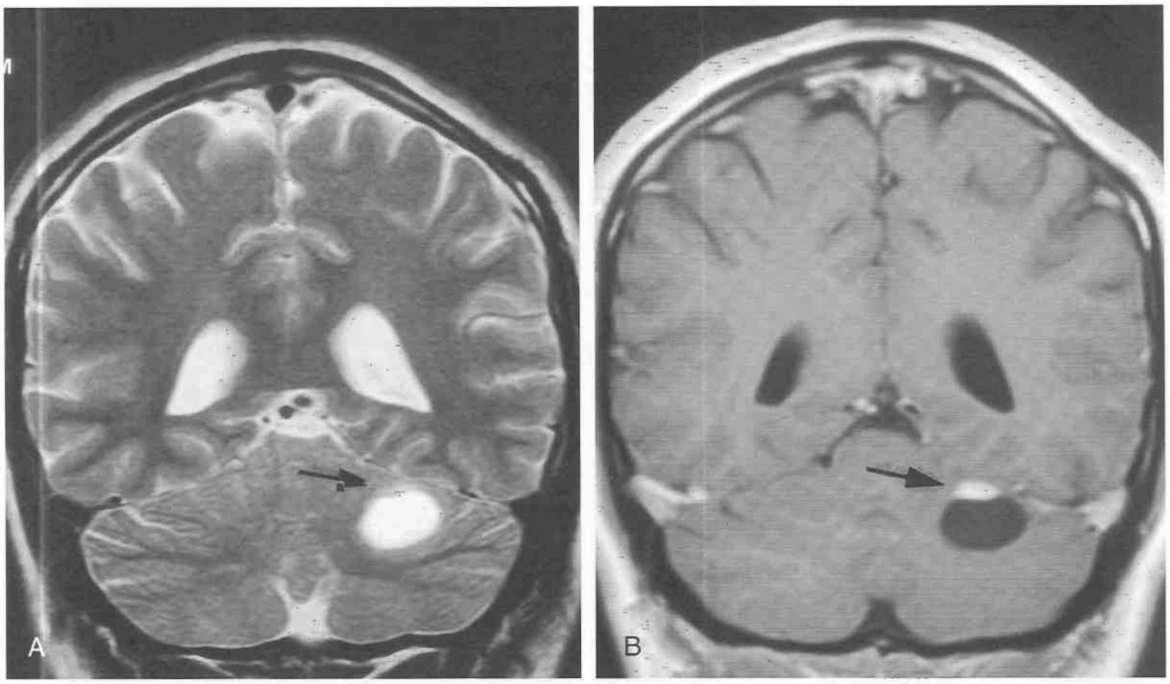

Figure 5–43. Hemangioblastoma of the cerebellum. *A,* A coronal T2-weighted MR image demonstrates a sharply marginated ovoid hyperintense mass in the superior aspect of the left cerebellar hemisphere. On the superior margin of this cystic mass, a flat nodule that is isointense to adjacent gray matter is identified *(arrow). B,* Following intravenous administration of gadolinium, a coronal T1-weighted image demonstrates intense homogeneous contrast enhancement of the mural nodule *(arrow),* which is located on the superior surface of the cerebellum. The adjacent cyst is hypointense, and its margins do not demonstrate contrast enhancement.

spheric mass with a slightly more dense rounded mural nodule. There is typically little or no peritumoral edema, and the solid lesion or mural nodule may not be distinguishable from surrounding normal cerebellar parenchyma, particularly if the lesion is located inferiorly within the posterior fossa, where it may be masked by dense adjacent bone and beam hardening artifact.[157] Calcifications have not been detected in these tumors.[168] After IV administration of a contrast agent, the solid tumor or mural nodule enhances homogeneously and intensely adjacent to a pial surface.[241] Because of the intense vascularitv of even the smallest solid tumor nodules, angiography may be more sensitive than CT or MRI in the detection of hemangioblastoma.

On MRI, the cysts typically are sharply and smoothly marginated and homogeneously hypointense relative to adjacent brain parenchyma on T1-weighted images and hyperintense on T2-weighted images (Fig. 5–43*A*).[142, 241] The solid tumors and mural nodules are usually inhomogeneous in signal pattern but predominantly isointense with normal gray matter on T1-weighted images and slightly hyperintense on T2-weighted images. Areas of increased signal within the nodule or the cyst on T1-weighted images are occasionally noted secondary to hemorrhage.[142, 168, 186] Serpentine signal voids due to enlarged vessels supplying and draining the tumor may be identified at the periphery of the mass or nodule, a finding that should strongly suggest the diagnosis in the appropriate clinical setting.[186, 241] As with CT, contrast enhancement of the solid tumor or mural nodule on T1-weighted MRI is characteristically homogeneous and intense (see Figs. 5–43*B* and 5–44).[10, 142, 241]

Tumors of the Hematopoietic System

During the last two decades of the 20th century, tumors and tumor-like conditions of the hematopoietic system involving the CNS increased in both frequency and clinical and societal significance. Most notable in this regard was a greater than 10-fold increase in incidence of primary CNS non-Hodgkin's lymphoma in the United States.[217] The vast majority of these tumors are malignant B-cell lymphomas, which carry a poor prognosis.[249] Their site of origin is unknown, because the normal brain lacks lymphatics and lymphoid tissue. The rise in incidence of these tumors has been associated with the human immunodeficiency virus (HIV) epidemic; up to 10% of patients in the terminal stages of acquired immunodeficiency syndrome (AIDS) experience an Epstein-Barr virus–associated B-cell malignant cerebral lymphoma.[249] The concomitantly growing number of non–HIV-positive immunocompromised patients who have primary cerebral lymphoma, notably those undergoing long term immunosuppressive therapy after allograft organ transplantation, has also contributed to the higher incidence of primary CNS lymphoma.[10, 143, 254, 286]

Lymphomas arising systemically may involve the brain and meninges secondarily. They include T-cell lymphoma, plasmacytoma, angiotropic lymphoma, and Hodgkin's disease. In current practice, secondary involvement of the CNS by systemic lymphoma is much less common than the primary intracranial malignant B-cell variety.[217]

A heterogeneous group of tumors and tumor-like pro-

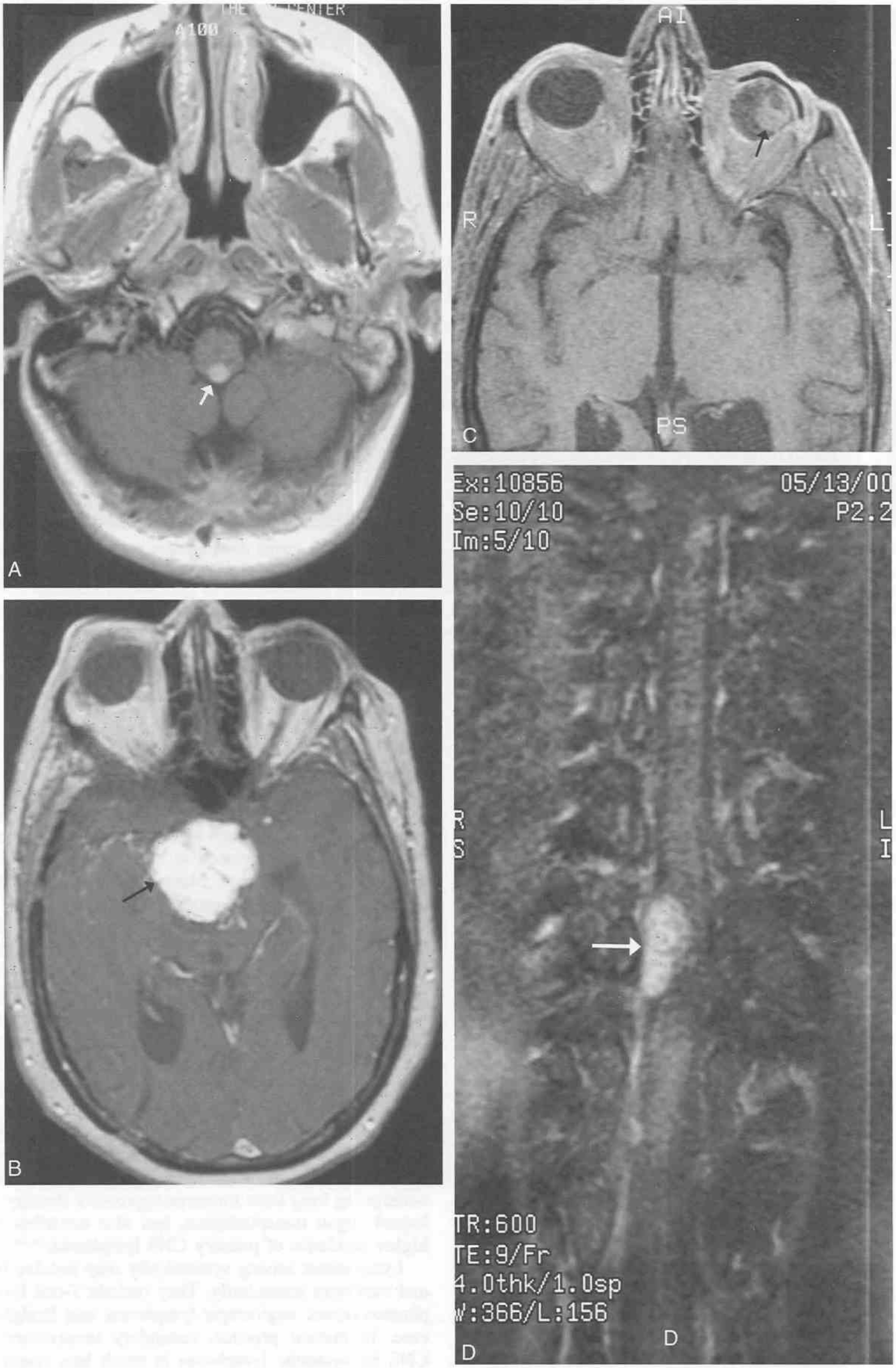
A
AI
R
L
C
PS
B
Ex:10856
05/13/00
Se:10/10
P2.2
Im:5/10
R
S
L
I
TR:600
TE:9/Fr
4.0thk/1.0sp
W:366/L:156
D
D

cesses of histiocytic origin rarely involve the brain, notably Langerhans cell histiocytosis.[250] Although the leukemias in their advanced stages may involve the meninges, leading to detection of malignant cells on CSF cytology, radiologically detectable dural based or intracerebral masses are rare.[248]

Primary Central Nervous System Lymphoma

Primary malignant lymphomas of the CNS are extranodal tumors arising in the CNS in patients with no obvious lymphoma outside the nervous system at the time of initial diagnosis.[217] Historically, this entity constituted about 1% of all primary tumors of the CNS; by the early 1990s, however, this proportion had increased to 6.6%,[217] mainly as a consequence of the AIDS epidemic. The incidence of this neoplasm in the AIDS population (4.7 per 1000 person-years) is approximately 3600 times that in the general population.[73] Approximately 10% of patients with AIDS experience primary CNS lymphoma, mainly during the late stages of their illness.[55] In transplant recipients who are immunosuppressed, the incidence of primary CNS lymphoma exceeds 20%.[255]

Primary CNS lymphoma affects all ages, but the peak incidence in immunocompetent individuals is in the sixth and seventh decades. In patients who have AIDS or have received organ transplants and are receiving immunosuppressive therapy, the median age of onset is in the late 30s. This tumor shows a definite sex predilection, with a 3:2 male-to-female ratio in immunocompetent patients and a 9:1 ratio in patients with AIDS.[217] The presenting symptoms and signs are nonspecific; focal neurologic deficits are most common, but seizures, signs of increased intracranial pressure, neuropsychological symptoms, and visual disturbances are also frequent.[217] Primary CNS lymphoma carries a guarded prognosis in immunocompetent patients and a poor prognosis in immunocompromised and immunosuppressed patients. In immunocompetent patients, the initial response rate to radiotherapy, chemotherapy, or both is 85%, but the survival rate is 40% to 70% at 2 years and 25% to 45% at 5 years; in patients with AIDS, the median survival after multimodal therapy is 13.5 months.[217]

On gross inspection, primary CNS lymphoma presents as one or more (usually multiple) firm or friable, centrally located, deep seated masses with variable demarcation from adjacent cerebral parenchyma. The tumors are often located in close proximity to the ventricles and may infiltrate through and along the ependymal ventricular walls (Fig. 5–45).[70] The corpus callosum and the basal ganglia are common sites of involvement. Intratumoral hemorrhage and necrosis are uncommon, and peritumoral edema is usually mild in immunocompetent patients, but in immunocompromised patients, lesion growth is more rapid, hemorrhage and necrosis are much more common, and edema of the surrounding white matter is often extensive.[70, 217] Involvement of the leptomeninges is a common but late finding.

Histologically, 98% of primary CNS lymphomas are high grade B-cell tumors that characteristically demonstrate an angiocentric infiltration pattern, in which collars of small neoplastic lymphocytes surround and infiltrate the walls of the small penetrating vessels of the brain and the perivascular (Virchow-Robin) extensions of the subarachnoid space.[70, 217] From these perivascular foci, tumor cells invade the adjacent neural parenchyma and coalesce, forming diffuse masses. In AIDS-associated cases, the diffuse masses tend to be multifocal with intervening areas of necrosis.[70, 217]

CT shows that the tumor masses involve the deep gray matter structures, the periventricular white matter, and the corpus callosum; they appear homogeneously isodense to moderately hyperdense (reflecting dense packing of small tumor cells with a high nuclear-to-cytoplasmic ratio), have relatively ill defined margins, and demonstrate diffuse strong homogeneous contrast enhancement (see Fig. 5–45).[10, 149, 241, 310] Peritumoral edema is less extensive than that seen in association with primary gliomas and metastases of similar size.[10] Central necrosis with peripheral ring-like contrast enhancement is uncommon in immunocompetent patients but is noted more frequently and involves wider areas with larger lesions in immunocompromised patients.[10, 149, 241] Extension along the ventricular walls with ependymal contrast enhancement (Fig. 5–45*C*) and leptomeningeal tumor spread, with hyperdensity in and contrast enhancement of the cisterns and sulci, are common late findings.[143]

On MRI, the deeply seated tumor nodules exhibit a variable signal intensity pattern. Most often, the tumors are homogeneously isointense with gray matter on both T1- and T2-weighted images, findings that are similar to those for other small cell hypercellular tumors.[10, 241, 279] However, some lesions may exhibit marked T2 hyperintensity. Almost all primary CNS lymphomas demonstrate intense contrast enhancement after IV administration of gadolin-

Figure 5–44. Multiple hemangioblastomas in a patient with von Hippel–Lindau disease. *A,* Axial T1-weighted MR image following intravenous administration of gadolinium demonstrates a sharply defined round homogeneously contrast enhancing nodule on the dorsal aspect of the lower medulla *(arrow).* Note the absence of a surrounding cyst. *B,* Axial T1-weighted postgadolinium image at the level of the suprasellar cistern. A large lobulated homogeneously intensely contrasting hypothalamic tumor protrudes inferiorly, filling and distending the suprasellar cistern *(arrow)* and insinuating into the interpeduncular cistern with spreading apart of the cerebral peduncles. Intratumoral hypointense linear and round foci likely represent flow voids within the rich tumor vasculature. This is a most unusual location for a hemangioblastoma. Also, the comparatively large size of this mass without an associated cyst is unusual. *C,* Axial T1-weighted postgadolinium image of the orbits and anterior brain obtained with fat saturation. A relatively large contrast enhancing nodule is identified within the lateral aspect of the left globe *(arrow);* a partially intranodular cyst is visualized anteriorly. *D,* Coronal T1-weighted postgadolinium image of the thoracic spine demonstrates an elongated nodular homogeneously enhancing tumor located eccentrically within the lower thoracic spinal cord on the right and protruding into and widening the right lateral subarachnoid space *(arrow);* the differential diagnosis of this lesion would include meningioma, schwannoma, and leptomeningeal metastasis.

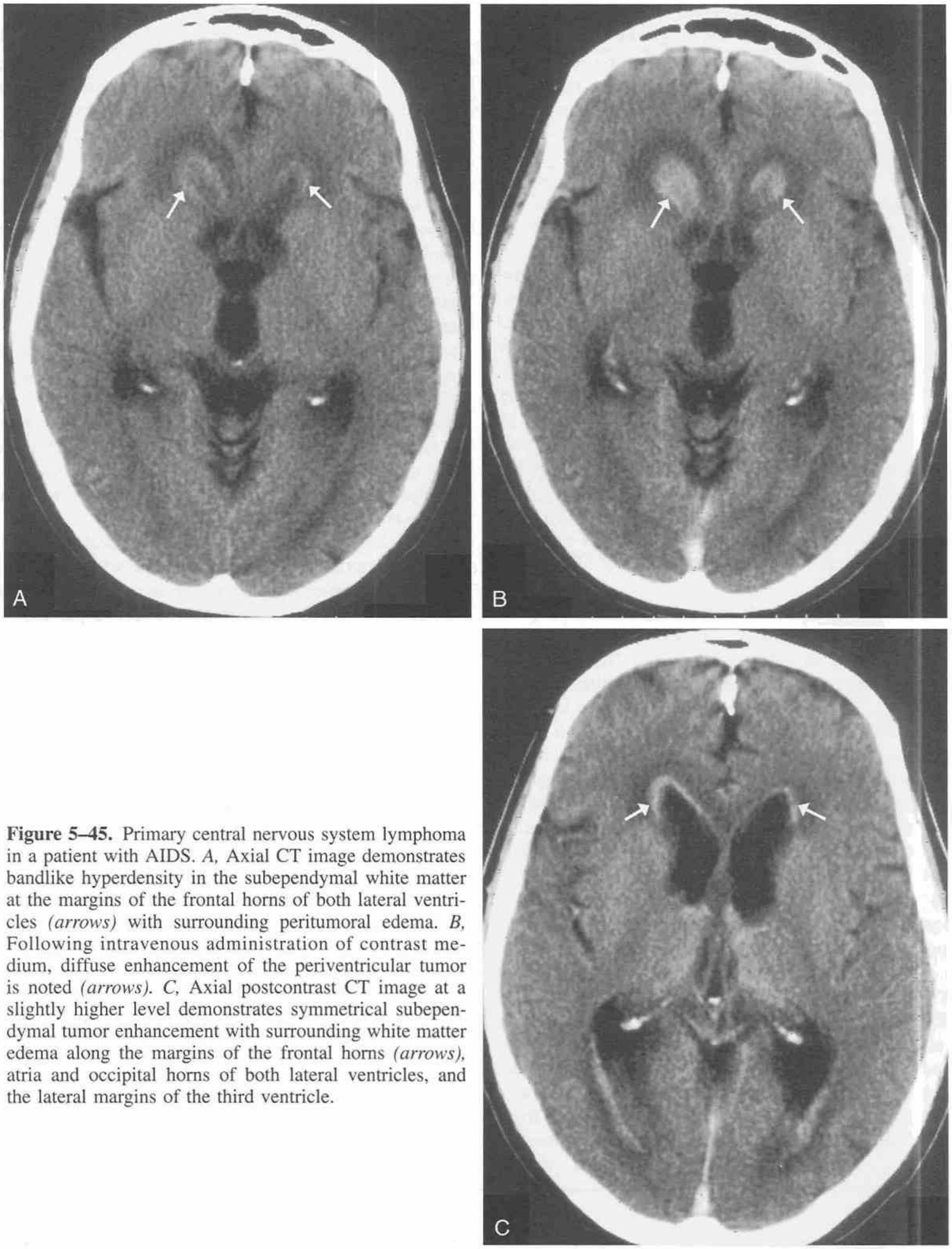

Figure 5–45. Primary central nervous system lymphoma in a patient with AIDS. *A,* Axial CT image demonstrates bandlike hyperdensity in the subependymal white matter at the margins of the frontal horns of both lateral ventricles *(arrows)* with surrounding peritumoral edema. *B,* Following intravenous administration of contrast medium, diffuse enhancement of the periventricular tumor is noted *(arrows). C,* Axial postcontrast CT image at a slightly higher level demonstrates symmetrical subependymal tumor enhancement with surrounding white matter edema along the margins of the frontal horns *(arrows),* atria and occipital horns of both lateral ventricles, and the lateral margins of the third ventricle.

ium. In immunocompromised patients, this enhancement is often ringlike (reflecting central necrosis) and associated with extensive peritumoral edema, and the clinical and radiologic presentation can simulate that of toxoplasmosis, a common occurrence in patients with AIDS.[90] The differential diagnosis favors toxoplasmosis if there is associated hemorrhage, whereas the presence of subependymal extension with contrast enhancement of the ventricular walls favors lymphoma.[10] In such circumstances, a short trial of anti-*Toxoplasma* therapy followed by evaluation of the clinical and imaging response may be sufficient to avoid invasive biopsy.

Leptomeningeal seeding occurs in up to 60% of patients with primary CNS lymphoma, generally late in the course of the disease. Although malignant cells may be readily detected on CSF cytology, detection of subarachnoid tumor

spread on imaging studies has been problematic. Imaging verification of leptomeningeal neoplasm, which is visible as parallel linear streaklike contrast enhancement, may be more easily and reliably detected on T1-weighted postgadolinium MRI than on contrast enhanced CT.[143, 318]

An unusual form of presentation of primary CNS lymphoma simulates diffuse white matter disease, with patchy and diffuse infiltration of deep white matter as well as deep gray matter. Poorly marginated areas of T2 hyperintensity are seen scattered through the deep cerebral white and gray matter and in the pons. The pattern is similar to that of gliomatosis cerebri. This entity has been termed *lymphomatosis cerebri*.[241]

In an immunocompetent patient, the differential diagnosis of solitary or multiple deep seated tumors that are relatively homogeneous, appear isointense with gray matter on MRI and hyperdense on CT, and demonstrate dense contrast enhancement with mild surrounding edema would include, in addition to primary CNS lymphoma, high grade glioma (e.g., anaplastic astrocytoma), sarcoid, and intraventricular meningioma.

Secondary CNS Lymphoma

Approximately one third of patients with systemic lymphoma demonstrate secondary brain or spinal involvement.[21] The majority of secondary CNS lymphomas are T-cell lymphomas with a propensity to first involve the leptomeninges surrounding the brain and then extend into cerebral parenchyma along the Virchow-Robin spaces in the periphery of the cerebral hemispheres. Both focal and diffuse thickening of the arachnoid occurs, and infiltration also extends into the overlying dura. As in the primary CNS lymphomas, multicentricity is common, but the masses are predominantly peripherally rather than deeply situated. Thick plaques of tumor on the brain surface that are isointense with the adjacent brain on T1- and T2-weighted images and demonstrate homogeneous contrast enhancement (Fig. 5–46) may simulate the appearance of meningioma; in general, the tumor masses of lymphoma are more numerous and more extensive than those of meningioma and often extend into the subarachnoid space and underlying brain parenchyma.[10]

Histiocytic Lesions

Histiocytic lesions represent a heterogeneous group of tumors and tumor-like masses of the brain of unknown etiology that are composed of histiocytes (macrophages) and are often but not always associated with histologically identical extracranial lesions.[250] The most common of these disorders is *Langerhans cell histiocytosis (LCH)*, a disease that usually occurs in children and causes solitary (eosinophilic granuloma) or multifocal (Hand-Schüller-Christian) osteolytic lesions of the skull base and membranous skull.[126] In the multifocal form, there is often irregularly marginated bone destruction in the region of the sella turcica with associated thickening of the pituitary stalk and hypothalamus. The lesions, whether in brain or in bone, appear to be granulomatous infiltrates composed mainly of Langerhans cell histiocytes in an admixture of lymphocytes, macrophages, plasma cells, and eosinophils.[250] Very rarely, multiple foci of demyelination and gliosis with minimal or no granular parenchymal infiltrates may be found within the cerebral or cerebellar white matter in patients with cranial and extracranial LCH; these appear as small poorly marginated areas of hypodensity on CT scans and of hyperintensity on T2-weighted MR images (Fig. 5–47).[259]

Leukemia

Granulocytic sarcoma (formerly known as *chloroma*) is a focal collection of leukemic cells that form a solid mass projecting inward from the meninges or within the brain parenchyma contiguous with the ventricular wall ependyma in patients with systemic leukemia, typically acute or chronic myelogenous leukemia.[117, 127, 241] In approximately one third of cases, the tumor may actually precede the development of the systemic disease.[117] On CT, the lesion appears hyperdense or isodense relative to brain parenchyma with unsharp margins. On MRI, it demonstrates heterogeneous isointensity or hypointensity relative to gray matter on T1-weighted images and isointensity to hyperintensity on T2-weighted images. Homogeneous contrast enhancement of the tumor is the rule (Fig. 5–48).[117, 127, 248]

Germ Cell Tumors

Tumors arising from primordial germ cells represent only 0.3% to 0.5% of all primary intracranial neoplasms, although in Asia the figure is 2%.[284] Germ cell tumors represent about 3% of primary pediatric intracranial neoplasms, except in Asia, where the proportion has been reported as 10% to 15%.[212] These tumors are the intracranial morphologic homologues of germinal neoplasms arising in the gonads and in other sites. They present mainly in children and adolescents, with an age peak of 10 to 12 years.[284] Approximately 90% arise in patients younger than 20 years with a strong (2:1) male predilection.

Intracranial germ cell tumors occur mainly in or near the midline in the vicinity of the third ventricle. The most common sites of occurrence are the pineal region (65%) and the suprasellar region (30%).[154] Nearly two thirds (65%) of intracranial germ cell neoplasms are germinomas, the intracranial morphologic equivalent of the testicular seminoma, whereas 16% represent teratomas, 6% are endodermal sinus (yolk sac) tumors or embryonal cell carcinomas, 4% are choriocarcinomas, and the remaining 9% are mixed tumors incorporating elements of two or more germ cell types.[250] These lesions may be multifocal with involvement of both the pineal and suprasellar regions.

The clinical presentation depends on the location of the tumor mass.[284] Patients with pineal region tumors typically present with complaints of headache, because the tumor compresses and obstructs the aqueduct, causing a noncommunicating hydrocephalus. Compression on or invasion of the quadrigeminal plate causes a Parinaud syndrome, with paralysis of upward gaze and convergence. Tumors in the floor of the third ventricle or the suprasellar region typi-

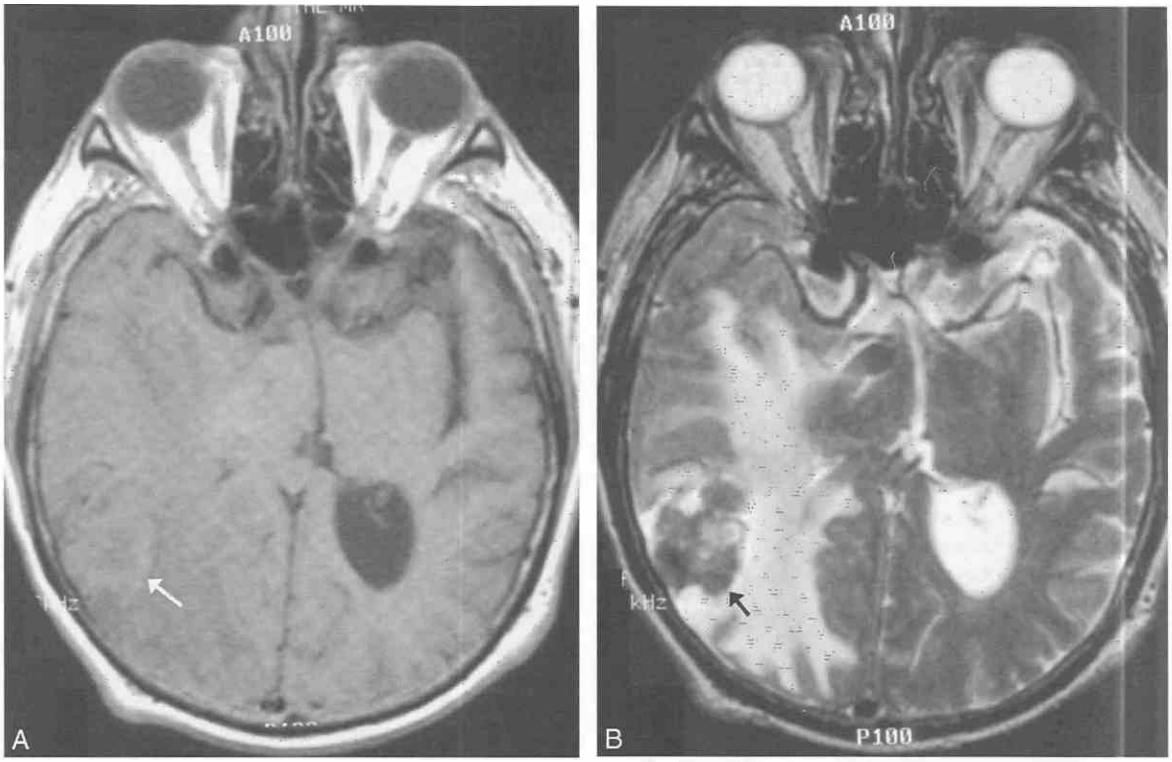

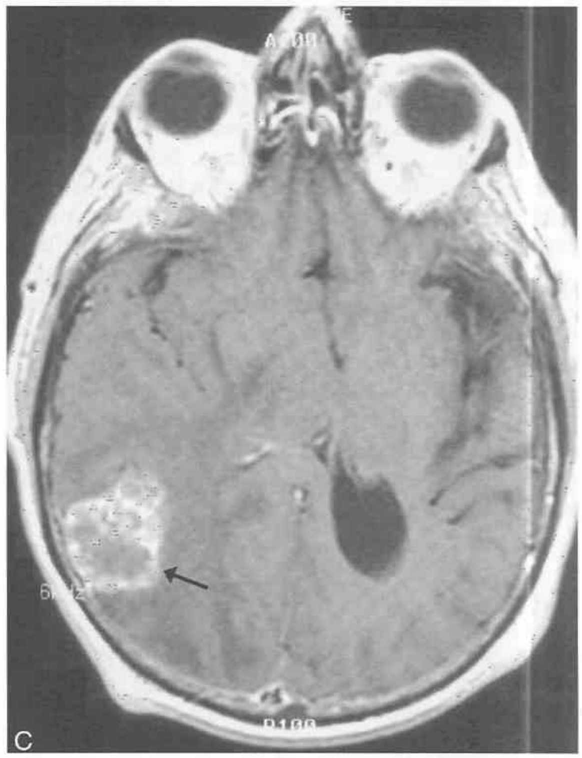

Figure 5–46. Systemic lymphoma with secondary central nervous system involvement. *A,* An ill defined isointense (with gray matter) mass involves the right posterior temporooccipital convexity cortex *(arrow)* and the adjacent white matter on this axial T1-weighted MR image. *B,* An axial T2-weighted image at the same level demonstrates a multilobulated right temporooccipital convexity tumor with extensive surrounding edema. Like a meningioma, this heterogeneous tumor is based on the convexity dura, but the deep extension *(arrow)* suggests spread into the cerebral parenchyma via the perivascular (Virchow-Robin) spaces. There is extensive edema of the adjacent forceps major white matter resulting in considerable mass effect with compression of the right sylvian fissure and atrium of the right lateral ventricle, bowing of the third ventricle across the midline, and effacement of the sulci of the right temporal and occipital lobes. *C,* Following intravenous administration of gadolinium, an axial T1-weighted image demonstrates heterogeneous contrast enhancement in this peripheral multilobulated tumor *(arrow).*

cally impinge upon the optic chiasm (causing visual field defects) or the hypothalamic-pituitary pathways (causing diabetes insipidus, growth retardation, or precocious puberty).

Examination of the serum and CSF for the presence of certain oncoproteins elaborated by germ cell tumors often provides valuable differential diagnostic information and is also useful in monitoring the course of treatment.[284] Elevation of placental alkaline phosphatase (PLAP) in these fluids favors the diagnosis of germinoma, whereas a rise in concentration of alpha-fetoprotein (AFP) suggests the presence of yolk sac endoderm, as in an endodermal sinus (yolk sac) tumor or an immature teratoma. Human chorionic gonadotropin (β-HCG) is elaborated by syncytial tro-

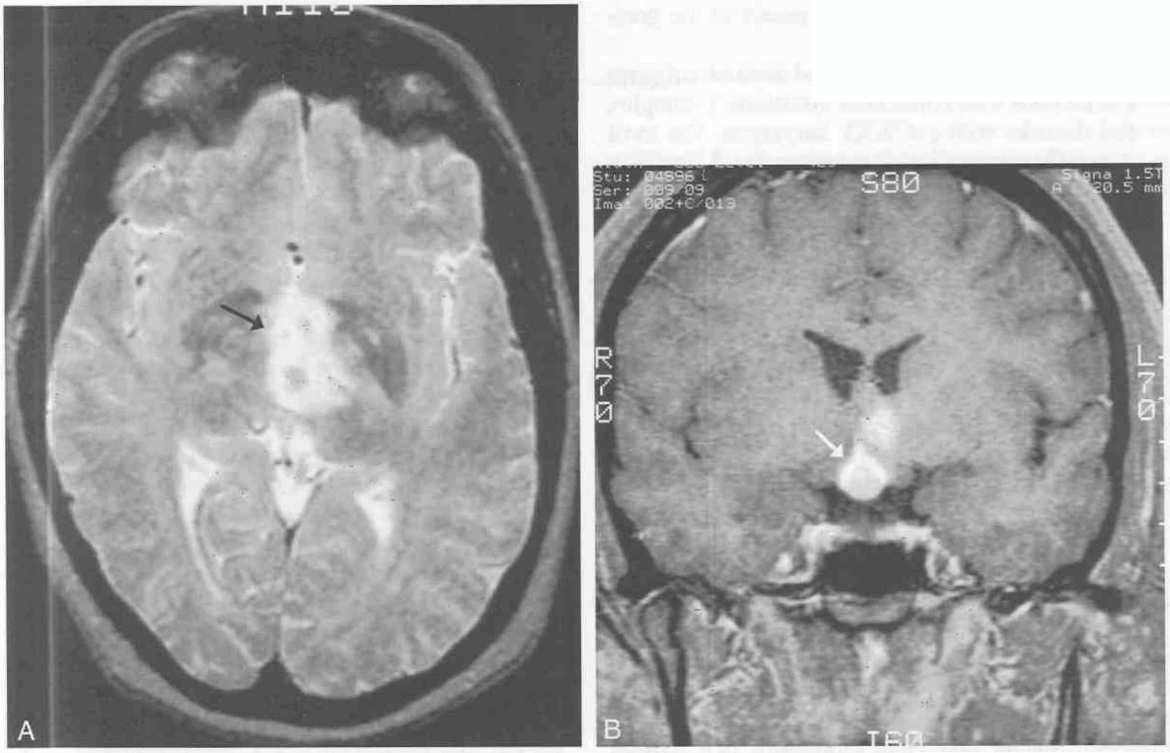

Figure 5–47. Langerhans cell histiocytosis of the hypothalamus and pituitary stalk. *A,* Axial T2-weighted MR image displays a large ill defined area of hyperintensity (likely representing edema) in the region of the hypothalamus *(arrow).* Within this hyperintensity can be seen two smaller isointense (with gray matter) foci. *B,* Coronal T1-weighted postgadolinium image demonstrates homogeneous contrast enhancement of the two foci; the larger lesion *(arrow)* extends into and widens the pituitary stalk.

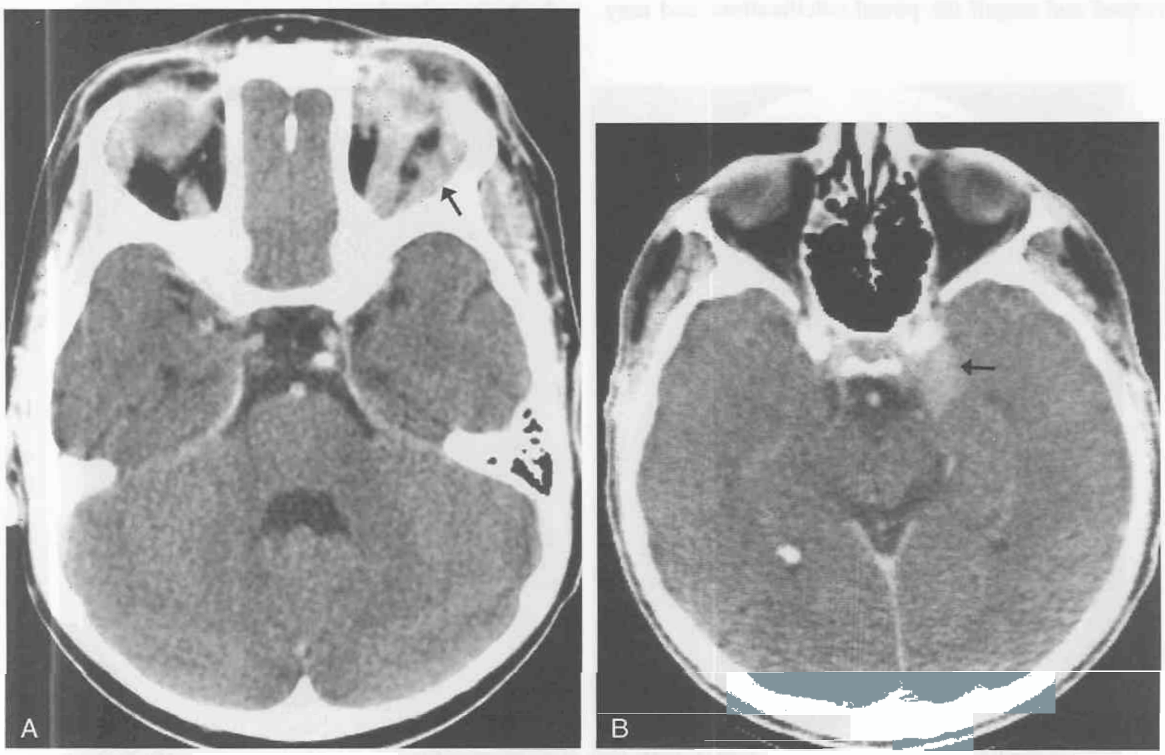

Figure 5–48. Granulocytic sarcoma (formerly known as chloroma) involving the left orbit and cavernous sinus. *A* and *B,* Axial CT images following intravenous contrast administration. In *A,* a sharply outlined irregular contrast enhancing mass is seen in the the lateral aspect of the left orbit *(arrow).* The mass slightly displaces the superior aspect of the left globe and the composite density of the levator palpebrae superioris and superior rectus muscles medially. At a slightly lower level *(B),* the tumor extends into and diffusely widens the left cavernous sinus *(arrow).*

phoblasts, and elevation of this marker points to the presence of choriocarcinoma.

There is a higher risk of intracranial and mediastinal germ cell tumors in patients with Klinefelter syndrome, a complex chromosomal disorder with a 47XXY karyotype. The most common cause of hypogonadism in young males, Klinefelter syndrome is characterized by testicular atrophy, gynecomastia, and lack of secondary sex characteristics.[152, 284] Affected individuals are also at greater risk for development of breast carcinoma. Histopathologic examination of tumor tissue is essential for treatment planning and prognosis.[102, 284] Although germinomas and teratomas often occur as pure tumor types, the nongerminomatous neoplasms are often of mixed cellular composition, and immunohistochemical studies performed on excised tissue to detect and localize the oncoproteins expressed by these tumors (mentioned in the preceding paragraph) are valuable for their characterization.

Germinoma

Germinomas are usually solid tumors that may contain cystic foci. The most common germ cell tumor is a pure germinoma, composed of sheets or lobules of uniform cells with large nuclei and clear cytoplasm that exhibit immunohistochemical labeling for PLAP on their cell membrane surfaces.[284] Mitoses are common, but intratumoral hemorrhage and necrosis are uncommon. These tumors are not encapsulated, and they tend to grow by invasion of neighboring structures. In the pineal region, they surround and engulf the pineal calcifications and may invade the adjacent thalami and quadrigeminal plates.[109, 305] In the suprasellar region, these tumors appear as rounded or lobulated masses in the floor of the third ventricle, compressing and invading the optic chiasm and surrounding the pituitary stalk[19]; they may also extend superiorly, infiltrating the walls of the third ventricle. Seeding of tumor cells may occur into the CSF with both ependymal and subarachnoid spread of tumor.

More than 90% of pineal region germinomas occur in males, whereas for tumors in the suprasellar region, the sex distribution is approximately equal.[19, 360]

Pure germinomas are highly radiosensitive, and 5 year survival rates of 65% to 95% are reported.[284] Adjuvant chemotherapy may permit reduction in radiation dosage with comparable survival rates. Extent of disease at the time of diagnosis is an important prognostic factor.[152]

On both CT and MRI, germinomas in the pineal and suprasellar regions appear as well circumscribed and mostly homogeneous rounded or lobulated masses.[19, 109, 305, 360] Their hypercellularity explains their notable hyperdensity on CT (Fig. 5–49*A*) and their isointensity to gray matter and hypointensity relative to CSF on T2-weighted MR images (Fig. 5–50*A*, *B*). Intratumoral cysts are occasionally found and are easily distinguished from the surrounding solid tumor. Intratumoral hemorrhage and necrosis are rare occurrences. CT visualization of intratumoral calcification in a cluster likely signifies engulfment or displacement of the normal calcified pineal gland; widely dispersed calcifications favor a diagnosis of a primary pineal cell neoplasm.[284] The solid parts of these tumors exhibit uniform contrast enhancement, and spread of tumor from the pineal region into the quadrigeminal plate or

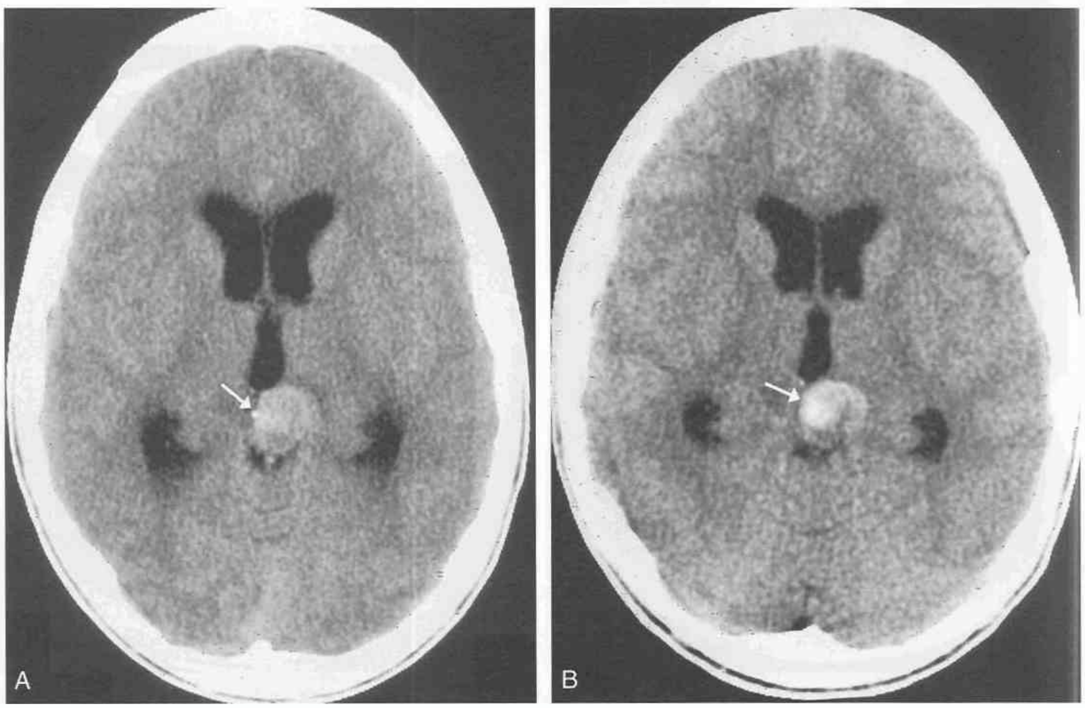

Figure 5–49. Germinoma of the pineal region. *A*, Axial CT image demonstrates a well circumscribed round hyperdense mass in the pineal region extending slightly to the left and indenting the posteromedial aspect of the left thalamus *(arrow)* with a thin hypodense rim (likely representing edema) at the interface with the left thalamus. *B*, Following intravenous contrast administration, the mass demonstrates diffuse contrast enhancement *(arrow)*.

thalami or from the floor of the third ventricle into the optic chiasm and pituitary stalk can be clearly delineated on either CT or MRI images after IV administration of contrast medium (Figs. 5–49*B* and 5–50*C*).[19, 241] Differentiation of suprasellar germinoma from JPA on either CT or MRI may be difficult, but clinical differences in age and presenting symptoms usually permit accurate characterization.[19]

Teratoma

Teratomas are the second most common germ cell tumors. They originate from multipotential germ cells that recapitulate normal somatic development by developing elements of the three embryonic germ layers—ectoderm, endoderm, and mesoderm.[284] They are subdivided pathologically into mature and immature teratomas. *Mature teratomas* are composed entirely of fully differentiated tissue elements that may be arranged in patterns simulating those of normal organogenesis and originating from ectoderm (skin, brain, choroid), mesoderm (bone, tooth, cartilage, fat, muscle), and endoderm (intestine, respiratory).[284] *Immature teratomas* occur more commonly,[200] demonstrate greater hypercellularity and mitotic activity, and are composed of incompletely differentiated tissue elements resembling fetal tissues (e.g., the developing neural tube).[284] An occasional teratoma contains a malignant component, such as rhabdomyosarcoma, undifferentiated sarcoma, squamous cell carcinoma, or adenocarcinoma.[284]

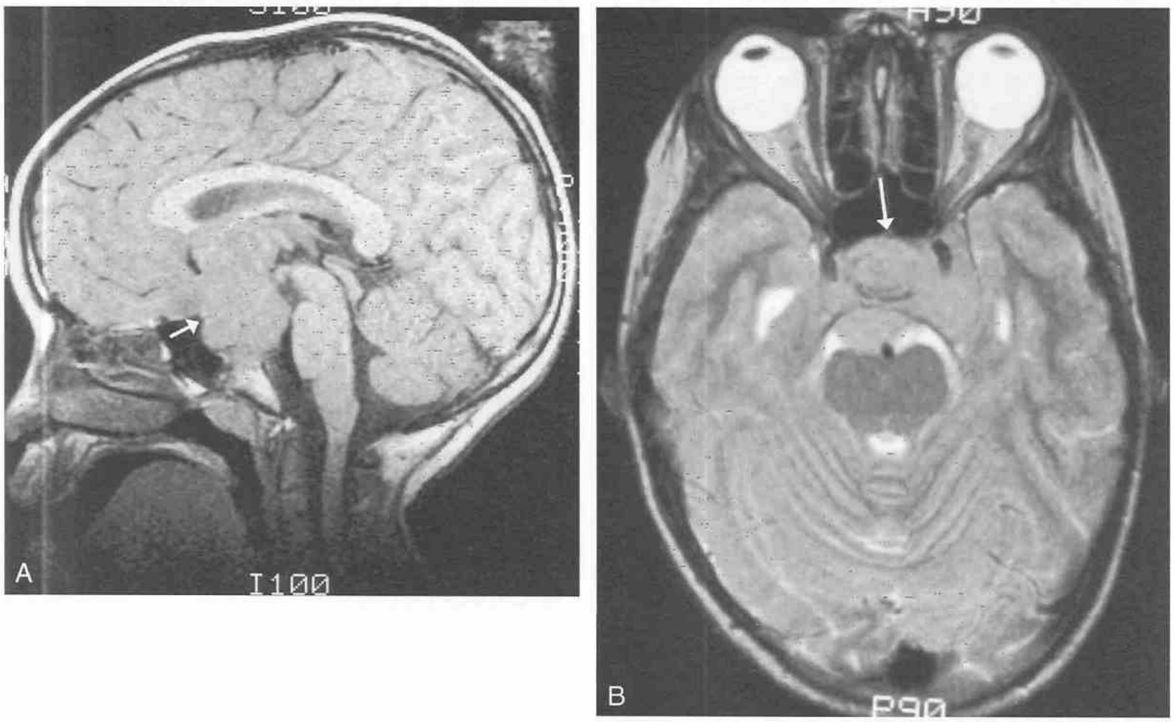

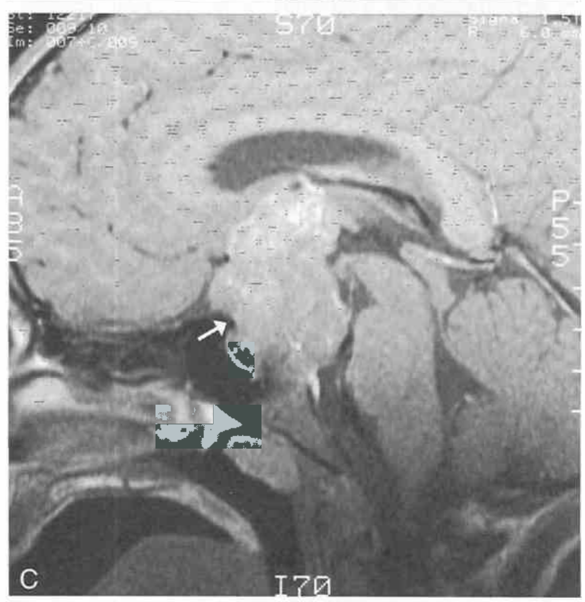

Figure 5–50. Germinoma of the suprasellar region. *A*, Sagittal T1-weighted MR image demonstrates a bulky lobulated ill defined isointense (with gray matter) tumor that nearly completely fills the third ventricle and extends downward into the sella *(arrow)* and posteriorly into the prepontine cistern. The belly of the pons is flattened and displaced posteriorly by this extensive tumor. *B*, Axial T2-weighted image through the level of the sella. The homogeneously isointense intrasellar tumor *(arrow)* extends bilaterally to encase the adjacent internal carotid arteries and posteriorly into the prepontine cistern, abutting the ventral surface of the pons on the right. *C*, Following intravenous administration of gadolinium, a sagittal T1-weighted image demonstrates patchy contrast enhancement of this extensive tumor *(arrow)*.

Teratomas occur almost exclusively in males in the pineal, parapineal, and suprasellar regions. The clinical presentation for these lesions is earlier than for germinomas, usually during the first decade of life.[10, 144, 200] On gross inspection, teratomas are typically well defined lobulated masses containing multiple structures, including mucus-filled cysts, nodules of cartilage and bone, and, rarely, teeth and hair.[284] In the pineal region, these tumors are not usually invasive.[19] For mature teratomas that can be completely excised, the 5-year survival rate is 80% to 90%.[200]

On both CT and MRI, teratomas are characterized by their striking heterogeneity in density and signal.[10, 19, 109, 241, 305, 360] Intratumoral cysts with well-defined margins and variable density or signal of contents (watery, proteinaceous, lipid) are intermixed with calcifications or ossifications and areas of variegated soft tissue appearance, including hemorrhage. Dilatation of the lateral and third ventricles may indicate compression of the cerebral aqueduct by the tumor mass. Contrast enhancement is variable and, when patchy or ringlike, raises the possibility of malignant degeneration (Fig. 5–51).[19] Invasion of neighboring structures can best be assessed on postcontrast images.

Other Germ Cell Tumors

Endodermal sinus (yolk sac) tumor is characterized by the accumulation of a myxoid matrix within a meshwork of primitive epithelial cells. *Embryonal carcinoma* is composed of large primitive cells that form abortive papillae and may attempt to replicate the structure of the early embryo. *Choriocarcinoma* consists of very large multinucleated trophoblastic cells that attempt to simulate placental tissue and include ectatic vascular channels that are prone to hemorrhage. Elements of these tumors may be found in germinomas or teratomas, and such tumors are then classified as mixed germ cell tumors.[102, 284] Approximately 10% of germ cell tumors contain more than one cell type.[19, 102]

All of these neoplasms, including the mixed germ cell tumors, have a high mitotic rate and a worse prognosis than pure germinomas or teratomas.[152, 212, 284] These lesions exhibit a strong propensity for seeding via the CSF, for hematogenous metastasis to lung and bone, and even for spread of tumor via a ventriculoperitoneal shunt catheter into the peritoneal cavity.

Differentiation of these lesions on CT or MRI studies from pure germinoma or teratoma depends on demonstration of a pineal region or suprasellar region mass with areas of intratumoral necrosis and hemorrhage. Hemorrhage is particularly common in choriocarcinoma, reflecting the vascular stroma of that tumor. However, these findings are nonspecific, and individual tumor type is best established with immunohistochemical evaluation of excised tumor tissue.[19, 241, 284, 305]

Tumors of the Sellar Region

Tumors of the pituitary gland and adjacent structures reflect the variety of tissues involved in the formation of these structures. Intrasellar, suprasellar, and parasellar tumors affect the CNS by expansion, with resultant compression of cranial nerves and the base of the brain, or by interference with the hypothalamic-neurohypophyseal pathway. Alternatively, certain neoplasms, mainly intrasellar, may become clinically manifest because of endocrine hyperfunction.

The most common neoplasms in this region are pituitary adenomas and craniopharyngiomas, both of which are considered to arise from derivatives of Rathke's pouch, the embryonic infolding of endoderm that extends superiorly from the stomodeum and gives rise in early fetal development to the adenohypophysis (anterior lobe of the pituitary gland). The anterior lobe constitutes 75% of the volume of the pituitary gland.[237] The posterior lobe of the pituitary gland is of neuroectodermal origin, extending inferiorly from the hypothalamus through the pituitary stalk (infundibulum). Neoplasms arising in the posterior pituitary are extremely rare.

Less common masses in the sellar region, all of nonhypophyseal origin, are chordomas, meningiomas, gliomas of the optic pathways, germinomas, teratomas, and metastases.

Pituitary Adenoma

Adenomas of the anterior pituitary are relatively common benign neoplasms, representing 10% to 15% of all intracranial tumors.[171] They are mainly tumors of adulthood, with less than 3% occurring in individuals younger than 18 years.[237] Pituitary adenomas vary greatly in size, but the vast majority are less than 10 mm in diameter and are designated by convention as *microadenomas*. In a series of 1000 unselected autopsy specimens, 3.1% of pituitary glands contained microadenomas, all from individuals older than 40 years.[237]

Microadenoma

Microadenomas are typically well demarcated lesions. Although they lack a definite capsule, they can be distinguished on gross inspection from the normal pituitary gland because they have a pseudocapsule of compressed pituitary tissue.[201] Approximately 75% of pituitary adenomas are hormonally active; compared with nonfunctional (endocrinologically inactive) adenomas, hormonally active adenomas usually present earlier in their course of evolution when they are much smaller, with symptoms and signs of endocrine hyperfunction.[201] They are generally classified on the basis of the hormone produced—for example, lactotroph (prolactin), somatotroph (growth hormone), corticotroph (ACTH), thyrotroph (TSH), and gonadotroph (FSH).[171] Cells that secrete prolactin and growth hormone and the tumors arising from them tend to be located in the lateral portions of the gland, whereas cells that secrete ACTH, TSH, and FSH and the tumors arising from them tend to be located centrally.[171, 201, 237]

Approximately 50% of hormonally active adenomas are prolactinomas.[201] They arise mainly in women (female-to-male ratio, 4–5:1), who typically present in young adulthood with amenorrhea, galactorrhea, and infertility.[237] Loss of libido and impotence are the most common presenting symptoms in males. The symptoms and signs are less

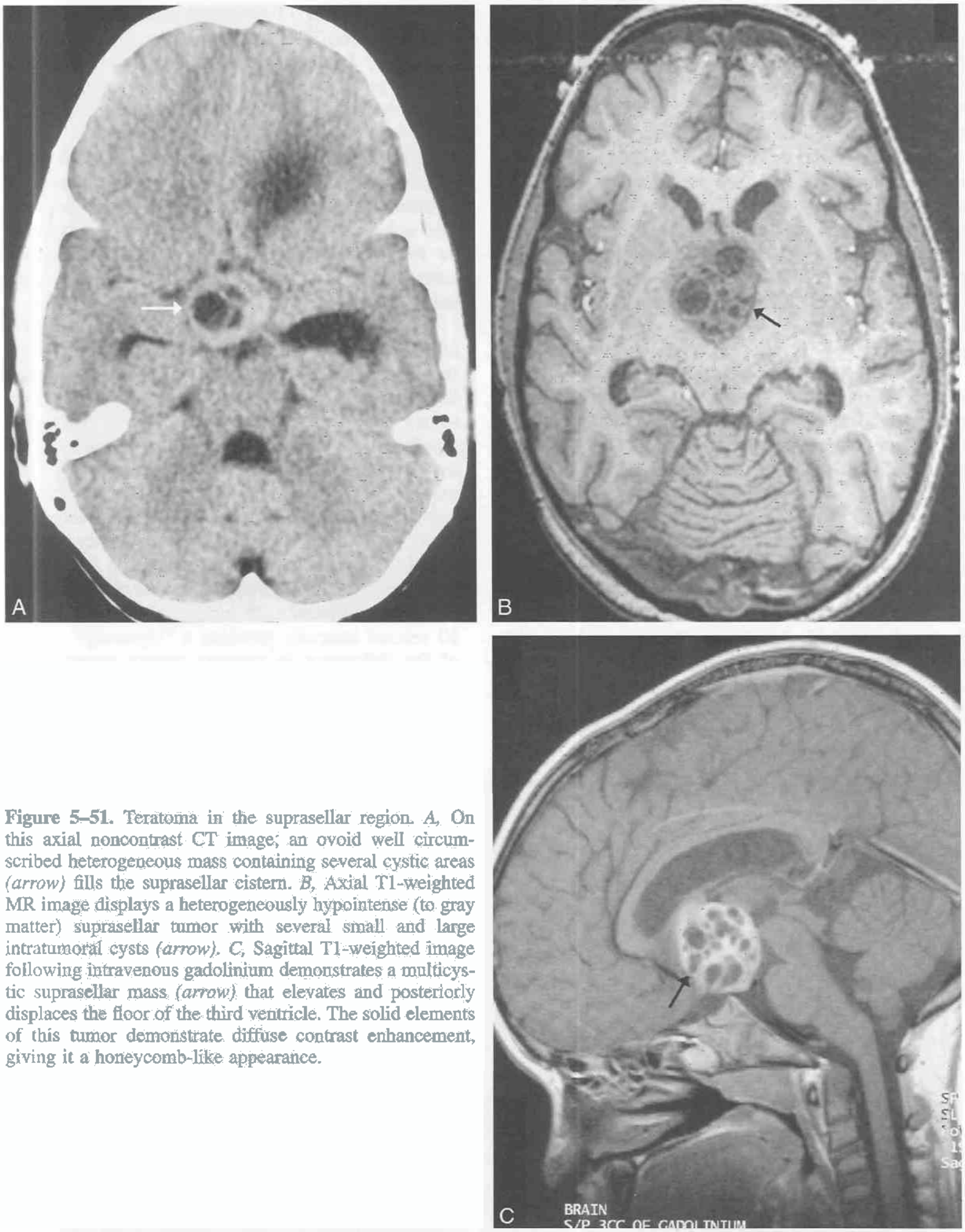

Figure 5–51. Teratoma in the suprasellar region. *A,* On this axial noncontrast CT image, an ovoid well circumscribed heterogeneous mass containing several cystic areas *(arrow)* fills the suprasellar cistern. *B,* Axial T1-weighted MR image displays a heterogeneously hypointense (to gray matter) suprasellar tumor with several small and large intratumoral cysts *(arrow)*. *C,* Sagittal T1-weighted image following intravenous gadolinium demonstrates a multicystic suprasellar mass *(arrow)* that elevates and posteriorly displaces the floor of the third ventricle. The solid elements of this tumor demonstrate diffuse contrast enhancement, giving it a honeycomb-like appearance.

pronounced in postmenopausal women and in men, in whom the tumors may manifest clinically only when they have become large enough to compress the visual pathways or cause pituitary hypofunction.[201] The great majority of prolactin-secreting tumors lie in the lateral aspect of the anterior pituitary.

Elevation of the serum prolactin concentration above the normal upper limit of 20 ng/mL raises the level of suspicion for the presence of prolactinoma, but elevated serum prolactin values can also be associated with ingestion of certain drugs (notably the phenothiazines and the tricyclic antidepressants), the presence of a suprasellar mass compressing the hypothalamus or pituitary stalk, and primary hypothyroidism.[201] Although markedly elevated serum prolactin values (>150 ng/mL) are almost always due to the presence of a prolactinoma, many patients with this

tumor present with prolactin values between 20 and 150 ng/mL; in this group, diagnostic imaging often provides evidence allowing differentiation of prolactinoma from nonneoplastic causes of hyperprolactinemia.

Somatotrophic and corticotrophic tumors each account for approximately 15% of microadenomas.[98] The former cause gigantism in children and acromegaly in adults and are usually located laterally within the pituitary gland. The latter are located centrally, cause Cushing's disease, and are typically very small. The great majority (75%) of patients presenting with Cushing's disease are female. Thyrotrophic and gonadotrophic tumors are relatively rare. About 10% of microadenomas secrete more than one hormone, most commonly prolactin and growth hormone.[171]

Approximately 25% of pituitary adenomas are nonfunctional, that is, they do not cause nor are they directly associated with endocrine hyperfunction.[98] These tumors are detected accidentally as microadenomas when patients undergo diagnostic imaging for other clinical indications, are discovered incidentally at autopsy, or present clinically at a later stage as macroadenomas when they are large enough to compress the pituitary stalk, the optic chiasm, the cranial nerves in the cavernous sinus or suprasellar cistern, or the base of the brain.[98, 201]

On CT and MRI, the pituitary gland is best visualized in the coronal plane. Because of the lack of bone artifact and the greater intrinsic soft tissue contrast on MRI, this modality has largely supplanted CT for the initial detection and localization of pituitary microadenoma. Approximately 80% to 85% of these tumors demonstrate focal subtle hypointensity on T1-weighted images and focal mild hyperintensity on T2-weighted images. However, the differential signal intensity between the tumor and surrounding normal pituitary tissue is often very slight (Fig. 5–52*A*), thus explaining the 15% to 20% false-negative rate for MRI evaluation.[174]

Intratumoral calcification occurs only rarely in pituitary adenomas and even more rarely in the microadenomas.[237] Intratumoral necrosis, cyst formation, and hemorrhage are also infrequent occurrences that are much more likely to be found in the larger tumors. These changes typically cause heterogeneity of the density or signal pattern within the lesion.

The use of thin section T1-weighted images obtained after IV bolus administration of gadolinium improves the sensitivity and specificity of MRI for the detection and localization of pituitary microadenomas.[235] The normal pituitary gland lacks a blood-brain barrier and thus opacifies rapidly and homogeneously after IV administration of contrast medium. The uptake of contrast agent by microadenomas is slower than that of the gland, and this difference provides greater conspicuity of the relatively hypointense tumor over the first 1 to 2 minutes after injection (Fig. 5–52*B*). Rapid sequence coronal single slice T1-weighted imaging of the sella immediately after IV bolus administration of gadolinium with images obtained consecutively at 10 second intervals provides a "dynamic" demonstration of the difference in contrast uptake between tumor and normal pituitary (Fig. 5–53).[201] A similar result can be obtained on CT with the use of thin-section coronal scans

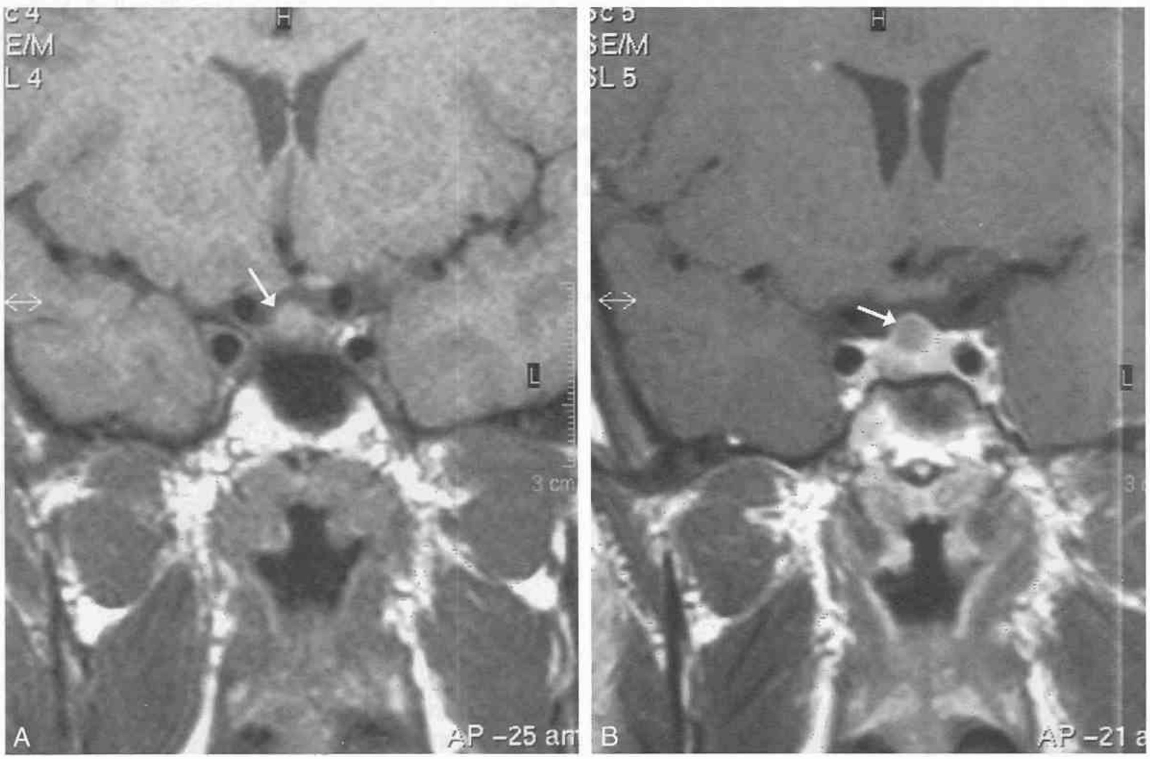

Figure 5–52. Prolactin secreting pituitary microadenoma. *A*, Coronal T1-weighted thin section MR image through the midsella demonstrates a round isointense mass arising from the right side of the pituitary gland and projecting upward into the suprasellar cistern *(arrow)*. *B*, Coronal T1-weighted image obtained shortly following intravenous gadolinium administration. Normal pituitary tissue demonstrates homogeneous contrast enhancement, while the round mass shows little or no enhancement.

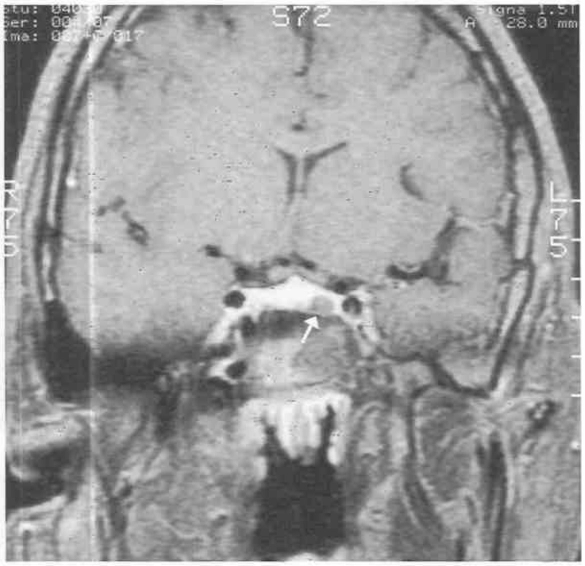

Figure 5–53. Pituitary microadenoma. Coronal T1-weighted MR image obtained during a dynamic scanning sequence following bolus intravenous administration of gadolinium. A 5 mm in diameter ovoid hypointense lesion in the left inferior aspect of the pituitary gland *(arrow)* fails to take up the contrast medium as rapidly as the surrounding normal pituitary tissue.

obtained after IV bolus administration of iodinated contrast medium; on early rapid sequence serial images, the microadenoma appears hypodense relative to the homogeneously contrast enhancing normal pituitary tissue. This difference in contrast enhancement effect fades after several minutes, and later or delayed images may mask the presence of the tumor or rarely may demonstrate reversal of the image contrast pattern, with the adenoma enhancing more strongly than the surrounding tissue.[201]

Laterally placed microadenomas may cause either unilateral upwardly convex bulging of the overlying superior margin of the pituitary gland into the suprasellar cistern or downward protrusion of the inferior margin into the floor of the sella, or both. Also, the pituitary stalk may be displaced contralaterally by the expanding microadenoma. However, these findings are inconstant, depending on the size of the tumor and the location of its epicenter; when present, they may raise the level of confidence in the diagnosis of microadenoma, but their absence does not detract from the significance of an intrasellar hypodense or hypointense mass. Also, pituitary stalk deviation can be seen in individuals without symptoms, signs, or imaging evidence of intrasellar or suprasellar tumor.[2]

The differential diagnosis of pituitary microadenoma on MRI or CT is limited. Pituitary adenomas may contain cells that are undergoing mitosis or may demonstrate dural invasion without being classified as malignant. The diagnosis of primary pituitary carcinoma is made only rarely and then usually in the circumstance of distant metastasis.[330] Most malignancies occurring within the gland are metastases from primary carcinomas of the breast, lung, kidney, and gastrointestinal tract,[156, 330] although metastases account for only about 1% of intrasellar and parasellar tumors.[237] Often multiple and tiny, metastases are demonstrated only on postcontrast high resolution images.

Nonneoplastic inflammatory entities that may involve the anterior lobe of the pituitary gland include lymphocytic hypophysitis and sarcoidosis. Lymphocytic hypophysitis is a rare disorder, likely autoimmune, that occurs mainly in young women during late pregnancy or postpartum. It is characterized by diffuse lymphocytic infiltration of the anterior pituitary. On imaging studies, the pituitary gland appears diffusely enlarged and demonstrates contrast enhancement.[192] Sarcoidosis, another autoimmune disorder, affects the CNS in about 5% of cases, notably involving the meninges and parenchymal structures at the base of the brain. On imaging studies, multiple foci of ill-defined contrast enhancement are seen within and enveloping the surfaces of the hypothalamus, optic chiasm, and pituitary stalk (Fig. 5–54).[72]

Intrapituitary focal abnormalities are commonly identified on MRI of asymptomatic volunteers[130] and as incidental findings in large autopsy series.[171] These include not only microadenomas but also Rathke's cleft cysts (see Fig. 5–59) (see later) and other benign cysts of uncertain origin. The incidence of such cysts on autopsy series varies from 5.8% to 8.3% of individuals older than 30 years.[171] In one double-blinded series of asymptomatic adult volunteers, MRI demonstrated intrapituitary focal hypointensities on T1-weighted imaging that were consistent with microadenoma or benign pituitary cyst in 15% of subjects.[130] Another possible explanation proposed for these "incidentalomas" is magnetic susceptibility induction of signal distortion in the floor of the sella near the junction with

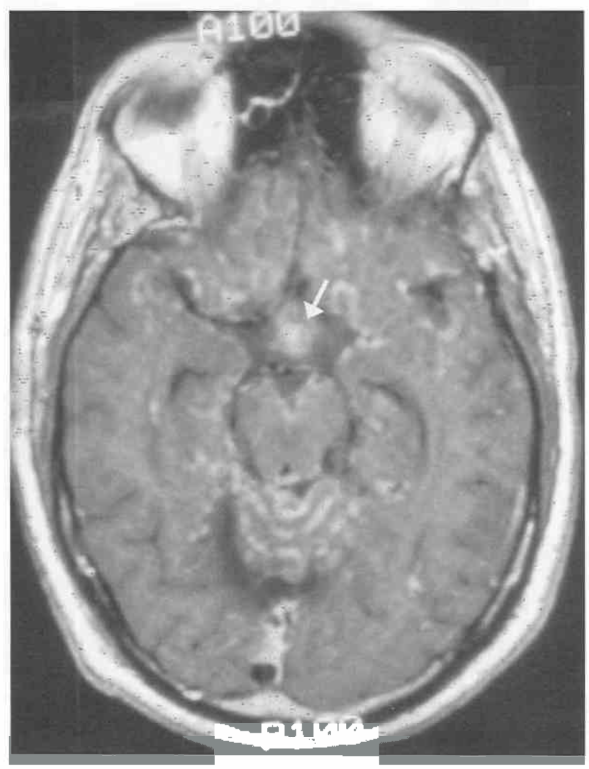

Figure 5–54. Sarcoidosis involving the base of the brain. Axial postgadolinium T1-weighted MR image demonstrates patchy diffuse contrast enhancement of the leptomeninges enveloping the base of the brain. A large focus *(arrow)* involves the pituitary stalk.

the sphenoid sinus.[201] Most of these lesions, apparent or real, are very small (<3 mm) and, in the absence of correlating clinical symptoms or signs, can be followed with periodic monitoring on an annual or biannual basis.[201]

Macroadenoma

When an adenoma of the pituitary gland reaches or exceeds 10 mm in diameter, it is designated by convention a *macroadenoma*. The great majority of such lesions are endocrinologically nonfunctional, although immunohistochemical and electron microscopic studies now suggest that these "null cell" tumors may be elaborating proteins that are involved in the formation or control of hormones.[329] The tumors often become clinically evident in middle age, when they reach sufficient size to compress the optic chiasm, causing a disturbance in vision, typically an asymmetric bitemporal hemianopsia. Detailed clinical and laboratory evaluation may reveal evidence of hypopituitarism due to compression of the normal pituitary gland or stalk, but this is rarely a presenting symptom.[330]

Macroadenomas originate as intrasellar masses that slowly expand in all directions, notably upward out of the sella, protruding into the suprasellar cistern and eventually elevating and compressing the optic chiasm, the hypothalamus, and the floor of the third ventricle (Fig. 5–55*B, C*). They also spread laterally and can invade across dura into the cavernous sinus and partially or completely encase the internal carotid artery.[201] Slow tumor growth in the inferior direction leads to thinning and erosion of the floor of the sella with protrusion into the underlying sphenoid sinus. On plain films and CT images this chronic slow enlargement causes expansion of the sellar cavity with thinning of the bony cortex of the dorsum, floor, and anterior wall of the sella.

Histologically, pituitary adenomas consist of small oval or polyhedral cells in a sheetlike monomorphous array, which contrasts markedly with the pleomorphic acinar pattern of the normal anterior pituitary gland.[329] Cellular pleomorphism and even occasional mitoses may be seen in pituitary adenomas but do not indicate aggressive biologic behavior.[97] Calcification in these tumors is rare (in the range of 1%)[237] but may be more common in prolactin-secreting tumors.[97]

Intratumoral necrosis, cystic change, and hemorrhage all occur more frequently in macroadenomas than in microadenomas.[201] Hemorrhage is present in 20% to 30% of macroadenomas; it may be associated with pituitary apoplexy, an

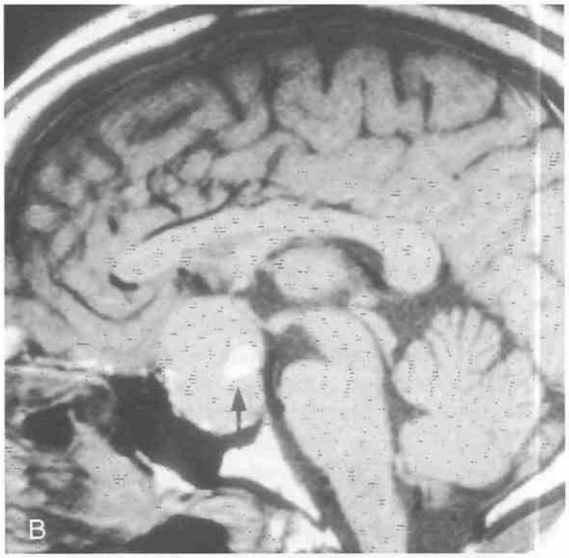

Figure 5–55. Pituitary macroadenoma with intratumoral hemorrhage and cystic changes. *A*, Axial noncontrast CT image demonstrates a soft tissue mass filling the suprasellar cistern. The tumor is mainly isodense with adjacent brain, but a faintly hyperdense focus at the right lateral margin *(arrow)* suggests recent hemorrhage. On a sagittal T1-weighted MR image *(B)*, the tumor is seen to enlarge the sella and extend into the suprasellar cistern, elevating and slightly posteriorly displacing the optic chiasm and the anterior floor of the third ventricle. It is mainly homogeneously isointense with adjacent brain, but contains several hyperintense foci (the largest is located in the posterior portion of the tumor and is indicated by an *arrow*) which likely represent subacute hemorrhage.

Illustration continued on opposite page

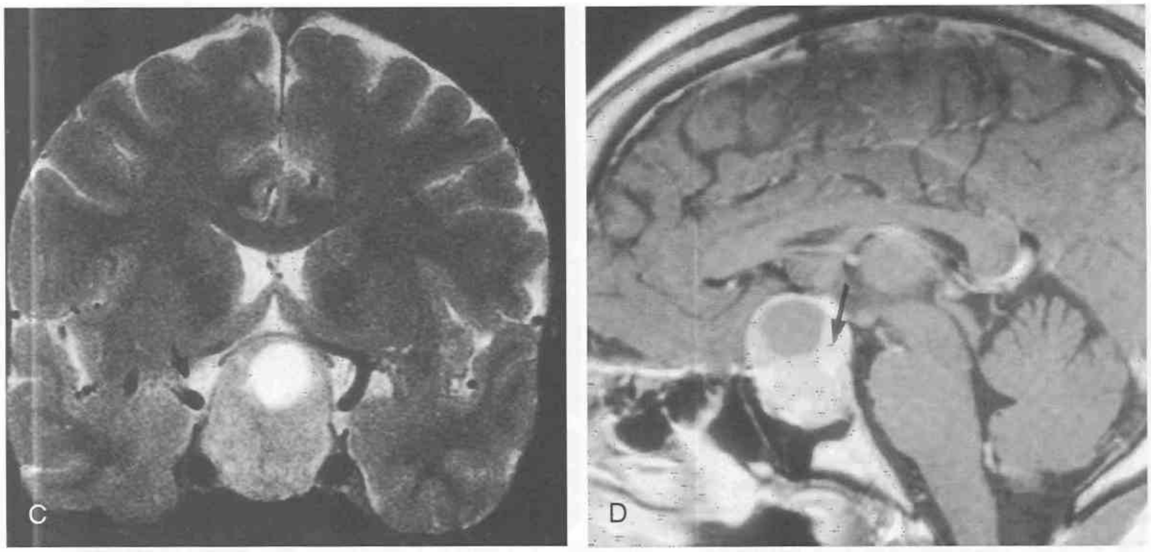

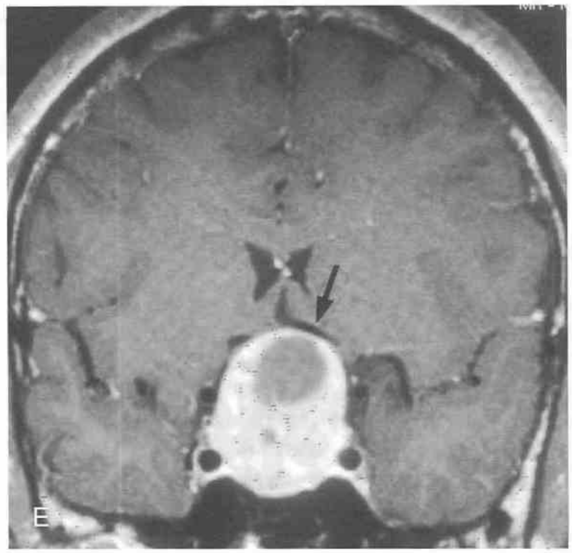

Figure 5–55. *Continued. C,* Coronal T2-weighted image at a level through the anterior third ventricle. The dome of the tumor contains a large cyst. The mass displaces the supraclinoid internal carotid arteries laterally *(arrow)* and elevates and flattens the floor of the third ventricle. Sagittal *(D)* and coronal *(E)* T1-weighted images following intravenous gadolinium demonstrate homogeneous contrast enhancement of the solid portions of this large tumor. The arrow in *D* delineates the large focus of subacute hemorrhage in the posterior aspect of the tumor. The arrow in *E* demonstrates elevation and stretching of the proximal (A1) segment of the left anterior cerebral artery by this large intra- and suprasellar mass.

acute clinical event characterized by sudden onset of severe headache, visual loss, and hypotension. More often, however, intratumoral hemorrhage is subclinical and discovered incidentally on MRI (Figs. 5–55*B* and 5–56*A*).[201, 243] Hemorrhage occurs even more commonly in patients with prolactinomas who are being treated with bromcriptine.[357]

On CT, macroadenomas often appear as large, homogeneously isodense, rounded midline masses arising out of the sella and insinuating upward to elevate and compress the optic chiasm and overlying third ventricle (Fig. 5–55*A*).[237] On occasion, a tumor may grow so large as to invaginate the floor and walls of the third ventricle and obstruct the foramen of Monro. Areas of intratumoral necrosis or cystic degeneration appear as hypodensities within the tumor mass, whereas acute or subacute hemorrhage causes focal intratumoral hyperdensity.

Because MRI offers multiplanar imaging capabilities and is not degraded by beam hardening artifacts due to adjacent bone, it is the preferred modality for visualizing the pituitary gland. Pituitary macroadenomas appear hypointense relative to gray matter on T1-weighted images and hyperintense on T2-weighted images (Figs. 5–55*B, C* and 5–56*A*).[237] The T2 hyperintensity appears to correlate with softening of the tumor observed at the time of surgical removal and may reflect intratumoral necrosis.[201, 308] Normal pituitary tissue is usually severely compressed downward into the sellar floor by these bulky tumors and cannot be recognized.[201]

After IV administration of a contrast agent, delayed moderate contrast enhancement of the solid portions of the tumor mass appears on both CT and MRI (Figs. 5–55*D, E* and 5–56*B*).[174, 201, 235, 237] A major advantage of MRI is the ability to demonstrate the location and status of the internal carotid arteries relative to the tumor. Lateral tumor extension into the cavernous sinus may displace the carotid flow void laterally (Figs. 5–55*C* and 5–56). Further tumor extension may surround the flow void, indicating the presence of vessel encasement.[68] In contradistinction to meningioma, such encasement by macroadenoma rarely causes arterial constriction or occlusion.

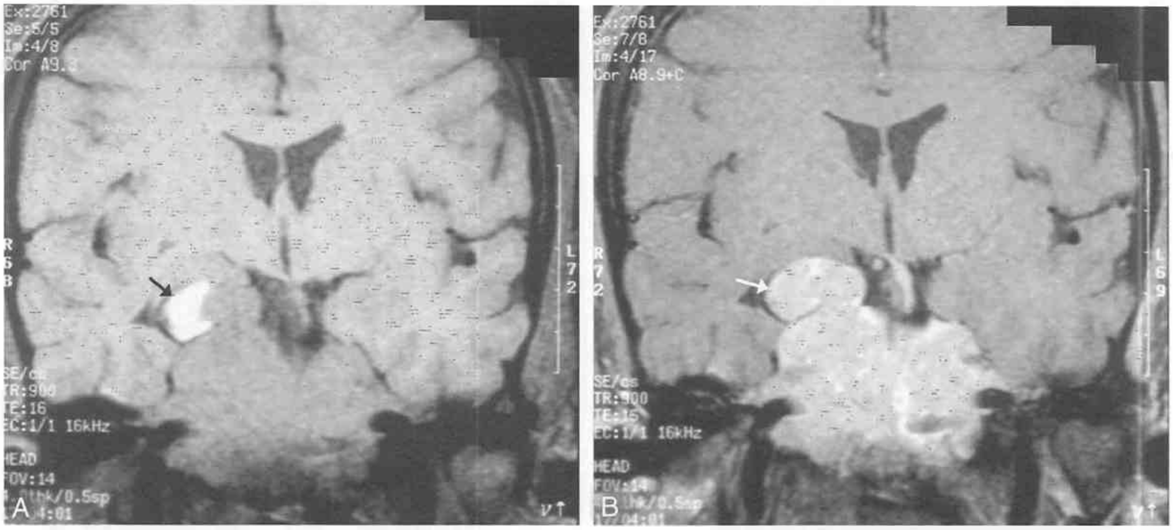

Figure 5–56. Pituitary macroadenoma with intratumoral hemorrhage. *A,* Coronal T1-weighted MR image demonstrates a very large multilobulated well circumscribed homogeneously hypointense tumor widening the sella and extending superiorly and bilaterally, more to the right than to the left. The most superolateral extension of this mass contains a large focal hyperintensity representing late subacute hemorrhage *(arrow).* The pituitary stalk is deviated to the left of the midline by the predominantly right sided tumor. Note that the supraclinoid internal carotid arteries on both sides are compressed and displaced far laterally, as are the medial aspects of both temporal lobes. *B,* Following intravenous administration of gadolinium, an axial T1-weighted image demonstrates diffuse homogeneous contrast enhancement of this multilobulated tumor *(arrow).*

Craniopharyngioma

Craniopharyngiomas are benign, partly cystic, epithelial tumors that occur almost exclusively in the sellar region and are presumed to arise from remnants of Rathke's pouch epithelium.[150] They represent 1.2% to 4.6% of all intracranial tumors but are more common in children, in whom they represent 5% to 10% of intracranial neoplasms.[43] They are most frequently suprasellar in location with an intrasellar component; less commonly (about 20% of cases), they may be entirely suprasellar, and approximately 5% are purely intrasellar.[133, 150]

These tumors have a bimodal age distribution that largely corresponds to two clinicopathologic forms, adamantinomatous and papillary.[150] Approximately two thirds of cases of craniopharyngioma occur in the first two decades of life, mainly between ages 5 and 14 years; the great majority of these are of the adamantinomatous variety.[150, 202, 369] The second age peak is in middle age (40 to 50 years); almost all papillary craniopharyngiomas occur in this group.[76, 150] Craniopharyngioma has no sex predilection.

Craniopharyngiomas are slow growing tumors that extend superiorly and often insinuate into the third ventricle. They may also expand anteriorly under the frontal lobes (30%), posteriorly into the interpeduncular cistern with impingement on and posterior displacement of the ventral margins of the midbrain and upper pons (20%), and laterally into the medial aspect of the middle cranial fossa (20%).[133, 150] The adamantinomatous tumors provoke an intense gliosis in the adjacent brain and become firmly adherent to adjacent brain and vessels. On gross inspection, they have a multilobulated inner aspect with nodules of solid tissue separated by cysts of varying size.[150] The cystic component is usually predominant in the adamantinomatous tumors and much less prominent in the papillary variety.[201] The papillary tumors often involve the third ventricle.[150]

Calcification is present in the solid portions of nearly 90% of adamantinomatous craniopharyngiomas but is much less common in the papillary tumors.[201, 291, 369] The cyst contents have a "machine oil" color and consistency and frequently contain suspended debris with a high cholesterol content.[150] Microscopically, the adamantinomatous tumors consist of broad strands and cords of stratified squamous epithelium with nodules of keratin and dystrophic calcification.[150] In the papillary tumors, sheets of squamous epithelium form papillae with a fibrovascular stroma, but keratin, cholesterol deposits, and calcification are typically lacking.[76, 150]

Like pituitary macroadenomas, these slow growing tumors present clinically most commonly with visual disturbances secondary to compression of the optic chiasm, nerves, or tracts.[150, 201, 369] Endocrine deficiencies are slightly less frequent. Compression of the neurohypophysis leads to diabetes insipidus in up to 15% of children and up to 30% of adults.[150] Symptoms and signs of increased intracranial pressure (headache, nausea, vomiting, papilledema) secondary to third ventricular obstruction are also common presenting findings that may lead to cognitive impairment and personality changes.[150, 201]

On CT, these tumors typically appear as heterogeneously hypodense suprasellar masses with nodular solid areas intermixed with cystic areas of varying size. The cyst contents are more dense than CSF. More than 80% of craniopharyngiomas in children (usually of the adamantinomatous variety) demonstrate nodular and curvilinear calcifications in the solid nodules and in the cyst walls (Fig. 5–57*A*).[133, 238, 369] Papillary craniopharyngiomas in adults appear more solid and rarely demonstrate calcification.[76]

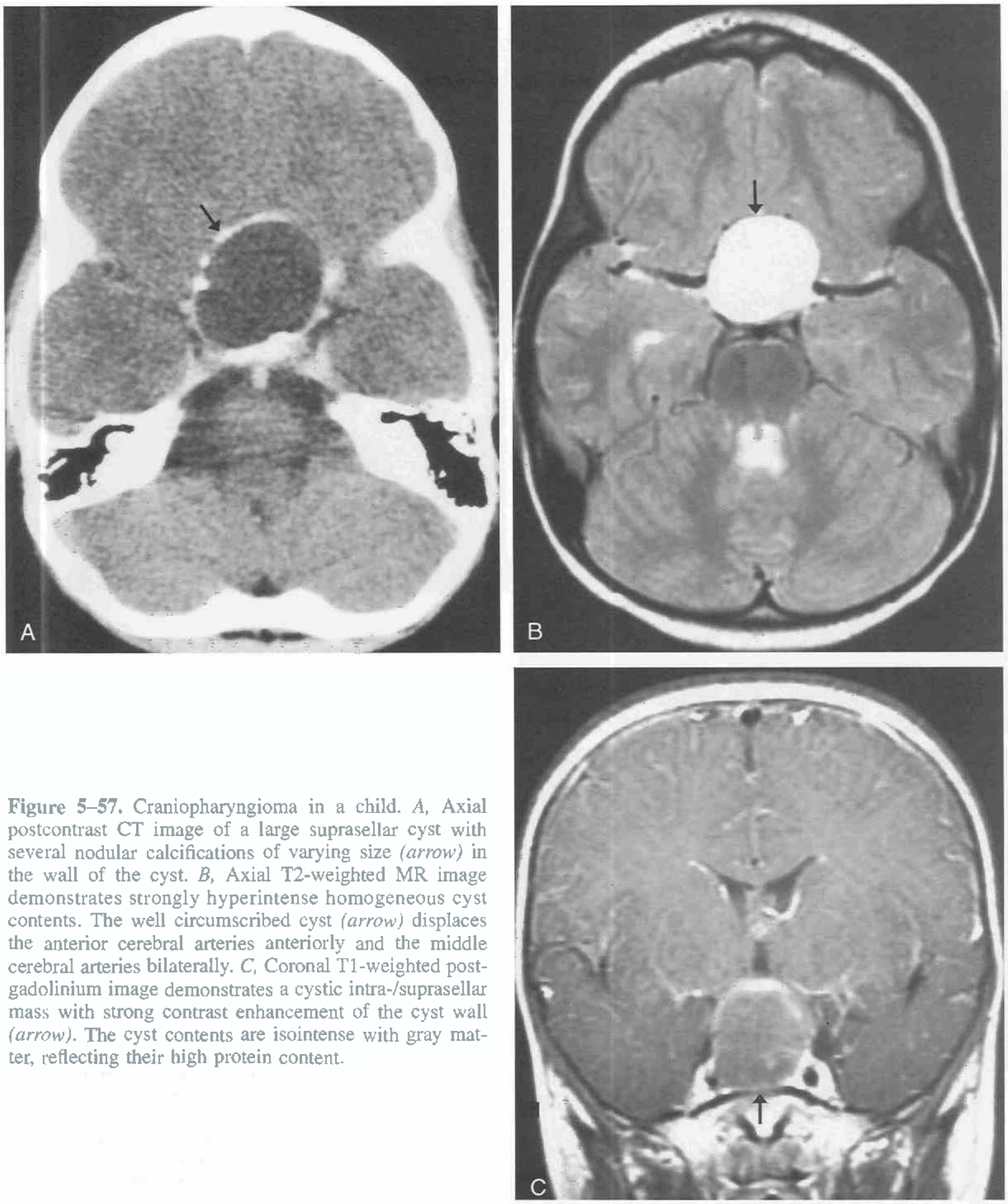

Figure 5–57. Craniopharyngioma in a child. *A,* Axial postcontrast CT image of a large suprasellar cyst with several nodular calcifications of varying size *(arrow)* in the wall of the cyst. *B,* Axial T2-weighted MR image demonstrates strongly hyperintense homogeneous cyst contents. The well circumscribed cyst *(arrow)* displaces the anterior cerebral arteries anteriorly and the middle cerebral arteries bilaterally. *C,* Coronal T1-weighted post-gadolinium image demonstrates a cystic intra-/suprasellar mass with strong contrast enhancement of the cyst wall *(arrow).* The cyst contents are isointense with gray matter, reflecting their high protein content.

Cysts are found in approximately 50% of papillary tumors versus about 90% of adamantinomatous neoplasms.[291] In contrast to pituitary adenomas, slow growing craniopharyngiomas do not usually enlarge the sella but rather gradually erode the posterior clinoid processes and the upper portion of the dorsum sellae.

The adamantinomatous suprasellar tumors appear as heterogeneous masses of variable intensity on T1-weighted MR images.[201] Areas containing calcification usually appear more hypointense. The cystic components are well marginated and vary in signal but are commonly hyperintense relative to gray matter, reflecting high concentration of protein in the cyst contents (Figs. 5–57*C* and 5–58*B, C*).[291] On T2-weighted images, the solid areas vary from hypointense to mildly hyperintense as compared with gray matter, whereas the cysts present a more internally uniform, hyperintense appearance (Figs. 5–57*B* and 5–58*A*).[201] The papillary tumors have a more uniform and homogeneous appearance.[201, 237, 291]

On both CT and MRI, after IV administration of contrast agents, enhancement of the noncalcified solid components of the adamantinomatous tumors and of the solid papillary tumors is typically intense and uniform (Figs. 5–57*C* and 5–58*B, C*).[76, 133, 203, 237, 291, 369]

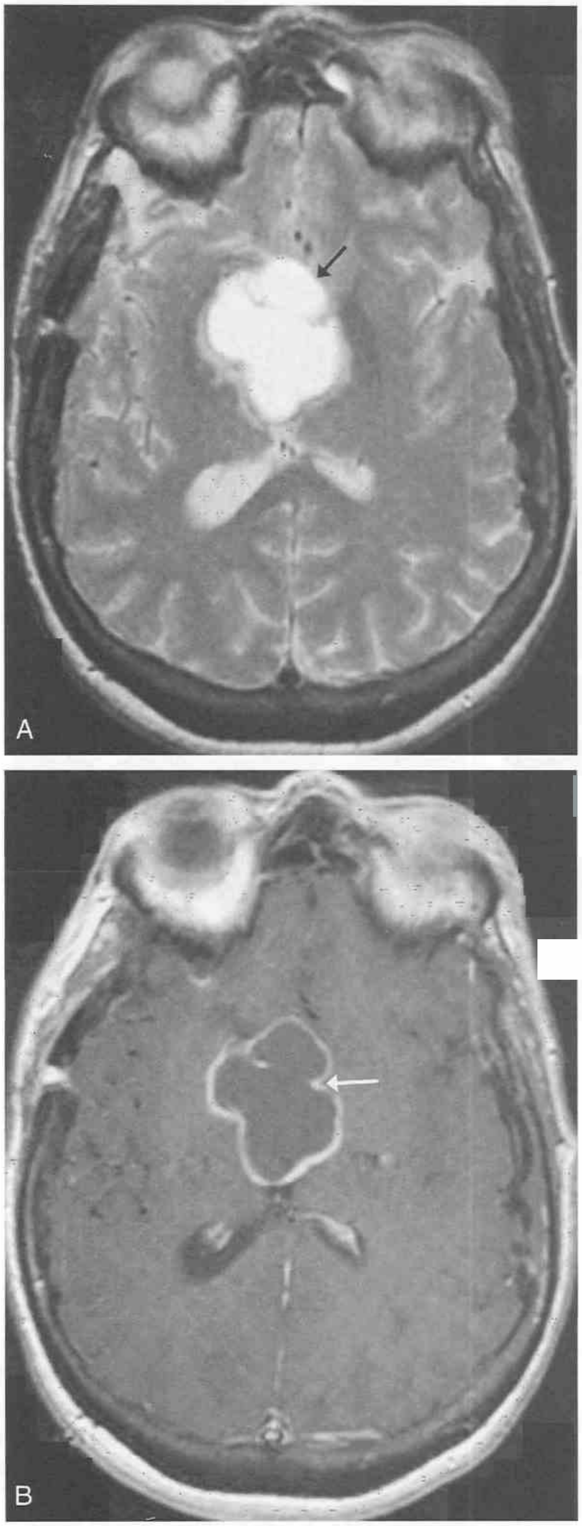

Figure 5–58. Craniopharyngioma in an adult. *A,* Axial T2-weighted MR image demonstrates a multilobulated multicystic hyperintense midline tumor *(arrow)* with irregular margins that has insinuated itself between the basal ganglia of the two cerebral hemispheres. The tumor extends more to the right than to the left of the midline, and the right globus pallidus is compressed and displaced laterally. The cyst contents are more hyperintense than the solid tumor rim in this papillary tumor. Axial *(B)* and right parasagittal *(C)* T1-weighted images following intravenous gadolinium demonstrate contrast enhancement of the solid tumor rim *(arrow)*. The cyst contents are hyperintense relative to cerebrospinal fluid, reflecting their high protein content. On the sagittal image, note that this cystic tumor extends into and nearly obliterates the third ventricle with its superior margin projecting into the floor of the right lateral ventricle; posteroinferiorly, the tumor projects into the interpeduncular cistern and displaces the midbrain posteriorly.

Both adamantinomatous and papillary craniopharyngiomas are managed surgically. Ten-year recurrence free survival rates vary from 64% to 96%.[76, 150] The extent of surgical resection is the most important factor in predicting recurrence; because of the intense gliotic reaction provoked by the tumor as it impinges on adjacent brain and the adhesion of large tumors to vascular structures in the suprasellar region, incomplete surgical resection remains a significant problem, especially in tumors larger than 5 cm in diameter.[150]

Rathke Cleft Cyst

Both Rathke cleft cysts and craniopharyngiomas are considered to arise from embryonic rests of Rathke's pouch.[290] In normal embryonic development, Rathke's pouch regresses by the sixth week of gestation into a narrow cleft. Persistence and enlargement of that cleft is believed to be the cause of Rathke cleft cysts, which are lined by cuboidal or columnar epithelium and are usually located in the pars intermedia between the anterior lobe (adenohypophysis) and posterior lobe (neurohypophysis) of the pituitary gland.[97]

Rathke cleft cysts are typically small (2 to 10 mm), thin-walled, smoothly marginated intrapituitary cysts with mucinous contents.[97] Less commonly, the contents may be serous.[74] They are usually asymptomatic and found incidentally on MRI or at autopsy. In an unselected series of 1000 cases, incidental Rathke cleft cysts were found in 11.3%.[327] Nearly 90% occur in the center of the pituitary gland.[327] Larger cysts may be both intrasellar and suprasellar and may become symptomatic if they compress the pituitary gland, pituitary stalk, or optic chiasm, but such compression is unusual. They are found in patients in all age groups but are usually identified in adults. A 2:1 to 3:1 female predominance has been reported,[285] but this figure may reflect selection bias, because more women than men undergo pituitary imaging, mainly for menstrual problems, hyperprolactinemia, and infertility.

On CT, 75% of Rathke cleft cysts appear as round, well-marginated, hypodense intrapituitary lesions.[285] The density of the cyst likely reflects the concentration of mucoprotein in the cyst contents. Calcification is not found in these cysts.[201, 237] On MRI also, they appear discrete and sharply marginated. On T1-weighted images, approximately two thirds of Rathke cleft cysts appear hyperintense and one third hypointense relative to gray matter (Fig. 5–59*B*)[285]; this variance is also likely related to the protein content of the cyst fluid. On T2-weighted MR images, approximately 50% exhibit moderate to strong hyperintensity relative to gray matter (Fig. 5–59*A*), another 25% appear isointense, and a like number are hypointense.[285] After IV administration of contrast agent, Rathke cleft cyst does not enhance on either CT or MRI, although the surrounding compressed pituitary tissue may exhibit rimlike enhancement.[238]

Tumors of the Neurohypophysis

Neoplasms arising in the posterior lobe of the pituitary gland or the pituitary stalk are very uncommon.

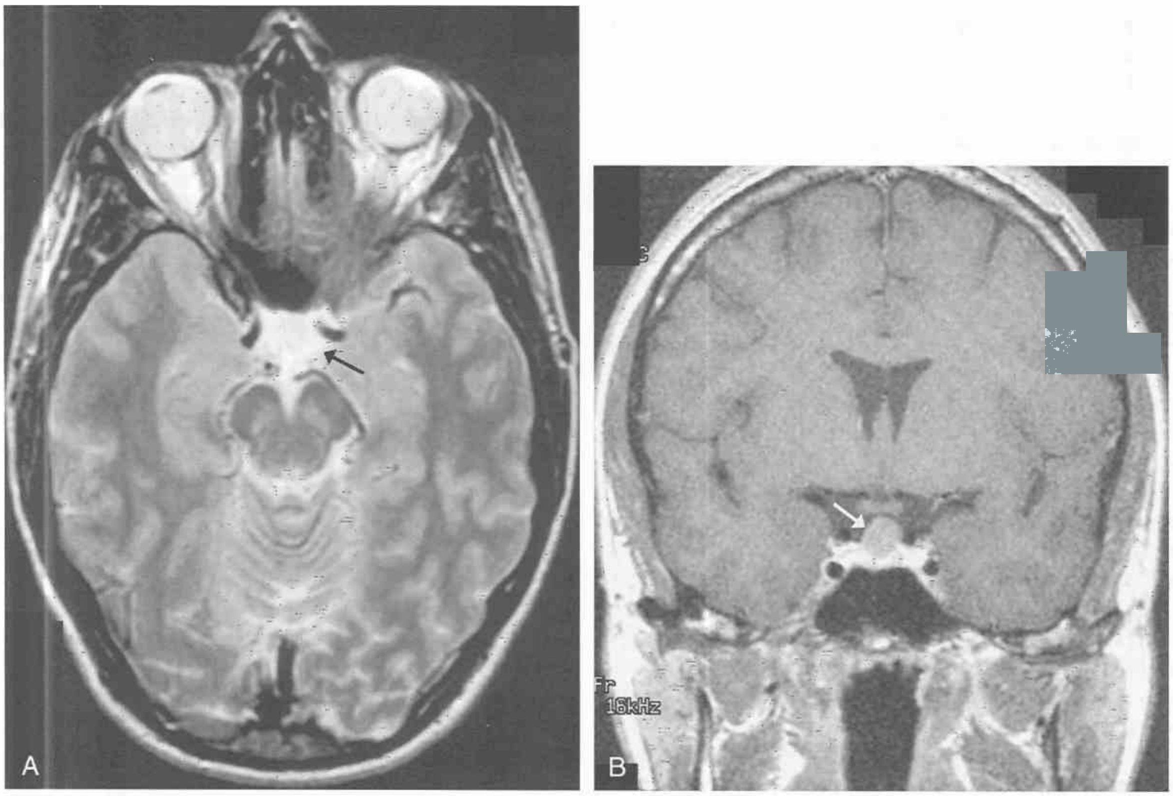

Figure 5–59. Rathke cleft cyst. Axial T2-weighted *(A)* and coronal postgadolinium T1-weighted *(B)* images demonstrate a small smoothly marginated cystic mass *(arrows)* within and projecting above the pituitary gland. The cyst appears slightly hyperintense relative to gray matter on both T1-weighting *(B)* and T2-weighting *(A)*. There is no contrast enhancement of its contents or margins.

Granular cell tumor of the neurohypophysis (also known as choristoma or pituicytoma) is a rarely occurring, benign, slow growing intrasellar or suprasellar mass that originates within the posterior pituitary or the pituitary stalk and presents as a well defined rounded mass composed of densely packed nests of large cells with a granular cytoplasm.[343] These tumors, considered to be of neural crest or glial origin, exhibit intense immunoreactivity for the S-100 tumor marker.[124] Like many intrasellar and suprasellar neoplasms, granular cell tumors usually develop insidiously and present with hormonal and visual disturbances secondary to compression of normal pituitary and optic pathway structures. On imaging studies, they appear as well circumscribed round masses within the posterior pituitary or on the posterior aspect of the pituitary stalk. The tumors are isodense with brain on CT and isointense with gray matter on T1- and T2-weighted MR images.[69, 201, 237] The posterior pituitary "bright spot" on T1-weighted images is effaced or absent.[343] Granular cell tumors are described as richly vascular and demonstrate strong contrast enhancement.[238, 343]

Langerhans cell histiocytosis involves the sellar region as a component of the Hand-Schüller-Christian syndrome; granulomas may be found in the pituitary stalk, hypothalamus, or both in association with destruction of the bony margins of the sella (see above). Imaging studies may demonstrate thickening and contrast enhancement of these structures (see Fig. 5–47).[334]

Chordoma

Chordomas are histologically benign neoplasms derived from remnants of the embryonic notochord. Despite their benign histology, they are locally invasive and destructive, behaving clinically like low grade malignancies.[132] These tumors arise in or near the midline and occur most commonly at the proximal (clivus-basisphenoid) and distal (sacrum) ends of the notochord. Approximately 40% of chordomas arise in the basisphenoid region.[70] They are uncommon tumors, representing less than 0.2% of all intracranial neoplasms.[132] Chordomas can present clinically in any age group, but their peak incidence is in patients between 20 and 50 years, and less than 5% are identified in children.[70, 132]

Chordomas arising in the upper clivus expand slowly and inexorably in all directions, infiltrating and eroding the surrounding bone. Posterior extension leads to the presence of a bulky lobulated mass in the prepontine cistern, compressing and displacing (but not invading) the pons and midbrain posteriorly. Anterior extension may manifest as a nasopharyngeal mass.[77, 201] Upward growth causes destruction of the walls of the sella with extension of tumor into and above the sella. Tumor infiltration into the cavernous sinuses with encasement of arteries and nerves is common. Sequestra of intratumoral necrotic bone and calcification and foci of intratumoral hemorrhage are common findings.[77, 132, 201] Histologically, chordoma consists of clusters of large vacuolated physaliferous (Greek for "bubble-bearing") cells interspersed with abundant extracellular mucinous material and separated into lobules by fibrous septa.[70, 132]

The clinical presentation of this slowly expanding neoplasm is insidious and depends on its precise location. The majority of patients present with head or neck pain and cranial nerve deficits.[132] The most common presenting complaint is diplopia, noted in 60% to 90% of cases.[107] Upward extension of chordoma causes visual disturbances and hypopituitarism, whereas posterior extension leads to extraocular nerve palsies.[201] Hearing loss and dysphagia are relatively common presenting findings that correlate with downward and anterior spread of tumor.

CT of clival chordoma demonstrates irregularly marginated erosion and destruction of the bony clivus with heterogeneous attenuation of the associated intraosseous and extraosseous lobulated soft tissue mass.[132] The heterogeneity is due to the presence of hyperdense intratumoral bony sequestra and calcifications intermixed with areas of hypodensity and hyperdensity secondary to cystlike mucinous collections as well as intratumoral hemorrhage.[77] On T1-weighted MR images, the infiltrating tumor appears isointense with gray matter in 75% of patients and mildly hypointense in the remaining 25% (Fig. 5–60*A*, *C*). In either case, the tumor presents a striking contrast to the diffusely hyperintense T1 signal of the adjacent normal marrow fat of the clivus.[201, 319] On T2-weighted images, chordoma demonstrates moderate heterogeneity of signal with areas of hyperintensity intermixed with linear strands of hypointensity (Fig. 5–60*B*).[201, 216, 319] After IV administration of contrast material, varying and heterogeneous contrast enhancement is seen within the tumor mass on both CT and MRI (Fig. 5–60*C*).[93]

Differentiation of chordoma from *chondrosarcoma*, both on imaging and gross and microscopic examination, may be very difficult.[77, 132] There is considerable overlap of both imaging and histological appearances between these two tumors. Tumor location may be of limited help in this differentiation; chordoma arises in or near the midline, whereas the majority of chondrosarcomas of the skull base tend to arise laterally in or near the petroclival junction. However, chondrosarcomas often spread medially into the clivus and posteriorly into the cerebellopontine angle, extending into the ipsilateral cavernous sinus and encasing the arteries of the circle of Willis in a manner similar to chordoma.[93] Immunohistochemical studies also aid in this differentiation; chordoma is of neural crest origin and stains positively for epithelial membrane antigen (EMA) and cytokeratin, but chondrosarcoma, being of mesodermal origin, does not take up these markers.[283]

Other neoplasms occurring in or metastasizing to the sellar region, including meningiomas, gliomas of the optic pathways, epidermoid tumors, germ cell tumors, and carcinomatous metastases, are considered elsewhere in this chapter.

Metastatic Tumors

Hematogenous metastases from extracranial primary malignant neoplasms may involve the skull, the dura, the leptomeninges, or the brain parenchyma. In adults, metastasis to the brain is most common.

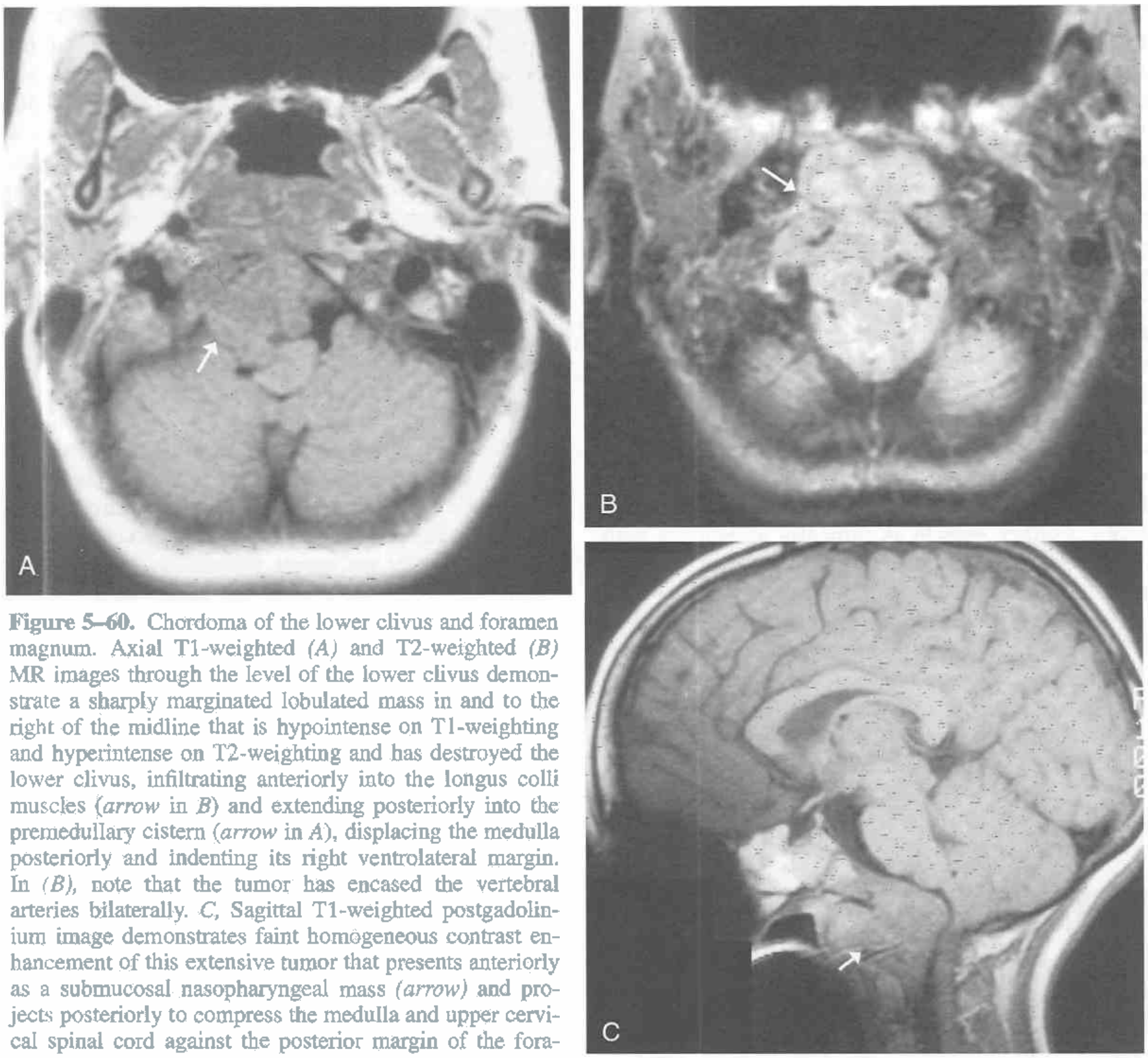

Figure 5–60. Chordoma of the lower clivus and foramen magnum. Axial T1-weighted *(A)* and T2-weighted *(B)* MR images through the level of the lower clivus demonstrate a sharply marginated lobulated mass in and to the right of the midline that is hypointense on T1-weighting and hyperintense on T2-weighting and has destroyed the lower clivus, infiltrating anteriorly into the longus colli muscles (*arrow* in *B*) and extending posteriorly into the premedullary cistern (*arrow* in *A*), displacing the medulla posteriorly and indenting its right ventrolateral margin. In *(B)*, note that the tumor has encased the vertebral arteries bilaterally. *C,* Sagittal T1-weighted postgadolinium image demonstrates faint homogeneous contrast enhancement of this extensive tumor that presents anteriorly as a submucosal nasopharyngeal mass *(arrow)* and projects posteriorly to compress the medulla and upper cervical spinal cord against the posterior margin of the foramen magnum.

Metastases to the Brain

More than 30% of intracranial tumors detected in a multi-institutional prospective CT study were metastatic malignancies.[16] Autopsy studies have demonstrated the presence of intracranial metastasis in approximately 25% of patients with cancer.[266] The incidence of intracranial metastasis is rising because of (1) the wider availability and greater refinement of cross-sectional diagnostic imaging and (2) continuing improvements in other diagnostic and treatment modalities with resultant prolonged survival of patients with systemic tumors.[230, 263]

The most common sources of intracranial metastasis, in order of decreasing frequency, are carcinomas of the lung and breast, malignant melanoma, and carcinomas of the kidney and gastrointestinal tract.[10, 230, 268, 286] Certain primary malignancies, particularly bronchogenic carcinoma,[52, 321, 324] carcinoma of the breast,[231, 322] choriocarcinoma,[286] and melanoma,[41, 116] have a notable propensity to metastasize to the brain. Between 30% and 65% of patients with carcinoma of the lung exhibit cerebral metastases at autopsy, many of which were not clinically evident during life.[154, 286, 321, 353] The most common cause of death in patients with melanoma is metastasis to the brain; autopsy studies reveal cerebral metastases in up to 90% of patients with melanoma.[41]

Cerebral metastases occur most frequently at the junction of cortex and underlying white matter,[268] a finding likely related to obstruction by circulating tumor cell emboli of the penetrating arteries, which abruptly narrow as they enter the subcortical white matter.[87, 230, 286] Eighty percent of brain metastases are located in the arterial distribution zones of the cerebral hemispheres, with 3% in the basal ganglia and 15% in the cerebellum.[230] A notable departure from this pattern occurs in the case of mucinous adenocarcinomas of gastrointestinal origin; although these tumors represent only 5% of intracranial metastases, approximately 50% occur in the posterior fossa, mainly in the cerebellum.[87] Metastasis to the cerebellum occurs mainly at the junction of the superior and inferior cerebellar artery distributions.[230]

Differentiation between solitary and multiple cerebral metastases has a major impact on the further management of the patient. The relative ratio of solitary-to-multifocal

cerebral metastases in autopsy series has been reported as approximately 50:50.[230] However, experience with advances in diagnostic imaging, particularly with contrast enhanced MRI, suggests that about 70% of patients with cerebral metastasis demonstrate more than one lesion.[10, 153, 238]

On gross inspection, small metastases are usually discrete, spherical, well circumscribed tumors (Fig. 5–61).[230] However, microscopic examination often reveals tumor cell infiltration into the adjacent surrounding normal tissue with angioneogenesis, perivascular invasion, and reactive gliosis.[230, 286] Histologically, metastases typically recapitulate the pattern of the tumor of origin.[153] These are markedly malignant neoplasms with high rates of mitotic activity.[153] Edema of the adjacent white matter is often disproportionately extensive in comparison with the small size of the tumor and may spread along white matter fiber tracts for a considerable distance.[10, 230, 286, 321] As the tumor implant grows, it penetrates and distorts the surrounding gray and white matter. Further growth is typically associated with central necrosis like that seen in glioblastoma, leaving recognizable tumor tissue only at the periphery and around the blood vessels.[230] Intratumoral hemorrhage is found in about 20% of cerebral metastases, notably in melanomas (Fig. 5–62), choriocarcinomas, and carcinomas of the lung, kidney, and thyroid.[10, 205]

Although metastases to the CNS can occur in all age groups, more than 75% are found in older patients. The age-specific incidence rises steeply after age 45 years.[27, 256] Approximately 30% of patients with cerebral metastases are asymptomatic at the time of initial diagnosis—that is, the tumors are discovered incidentally during evaluation for other causes (e.g., head trauma) or are found on screening imaging surveys of patients who have primary tumors with a known high incidence of hematogenous seeding to the brain.[27] When symptoms occur, they are usually of insidious onset and slow progression and relate either to increased intracranial pressure or to localized mass effect; they include headache (in approximately 50%), nausea and vomiting, mental status or behavioral change, progressive neurologic deficit, and seizures. These symptoms do not differ from those caused by primary gliomas in the same area.[27]

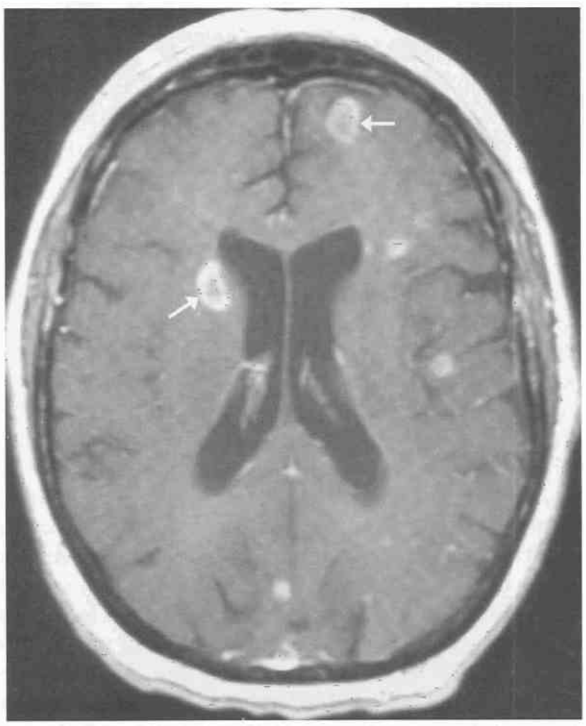

Figure 5–61. Hematogenous metastases of small cell carcinoma of the lung to the brain. Axial T1-weighted postgadolinium image demonstrates multiple contrast enhancing ring and ovoid lesions of varying size *(arrows)* at the junction of gray and white matter in both cerebral hemispheres. Although numerous, these tumors are relatively small and have not yet provoked grossly evident surrounding white matter edema.

Mean survival time after pathologic confirmation of the diagnosis of cerebral metastasis is 1 to 3 months.[30] Despite advances in surgery, irradiation, and chemotherapy, the prognosis for patients with cerebral metastases from extracranial primary malignant neoplasms has only minimally improved, with survival in the range of 3 to 6 months.[58] When only a solitary parenchymal lesion of the brain can be identified and the extent of the disease in other organs is not progressing, surgical excision of the cerebral metastasis correlates with improvement in both quality and length of life.[313]

The appearance of hematogenous cerebral metastasis on noncontrast CT scans corresponds closely to the gross pathologic changes already described. Small tumors appear as rounded homogeneously isodense or, less commonly, slightly hyperdense nodules relative to adjacent normal brain.[5, 10, 52, 153, 268] The isodense lesions merge imperceptibly with the adjacent cortex and may be detected only when they distort the inner margin of the cortex. The hyperdense nodules typically represent small round cell tumors or other tumors with high nuclear-to-cytoplasmic ratios.[153] However, most metastases from melanoma and choriocarcinoma as well as some metastases from carcinomas of the thyroid and kidney appear hyperdense because of hemorrhage within the tumor (Fig. 5–62*A*). Some small lesions and virtually all large metastases have undergone central necrosis by the time they are detected and appear as ringlike masses with central lucency and a peripheral isodense or slightly hyperdense rim of irregular thickness.[268] As already noted, edema (hypodensity) of the surrounding white matter is usually extensive and produces considerable mass effect (see Fig. 5–62). Calcification is rarely found in association with intracerebral metastases because of their rapid growth; however, it may occasionally be found in metastases originating from carcinoma of the breast or gastrointestinal tract.[87]

Contrast enhancement is virtually universal in these tumors. Less than 4% of the metastases in a multiinstitutional prospective CT study did not demonstrate contrast enhancement of the viable peripheral tumor rim (in lesions with central necrosis) or of the entire tumor (in small solid lesions of homogeneous density).[268] The enhancement is typically intense and fairly uniform within viable portions of the neoplasm, enabling clear separation of small tumor foci that are isodense on precontrast CT images from surrounding edema. The use of a double dose of iodinated contrast agent in combination with delayed image acquisi-

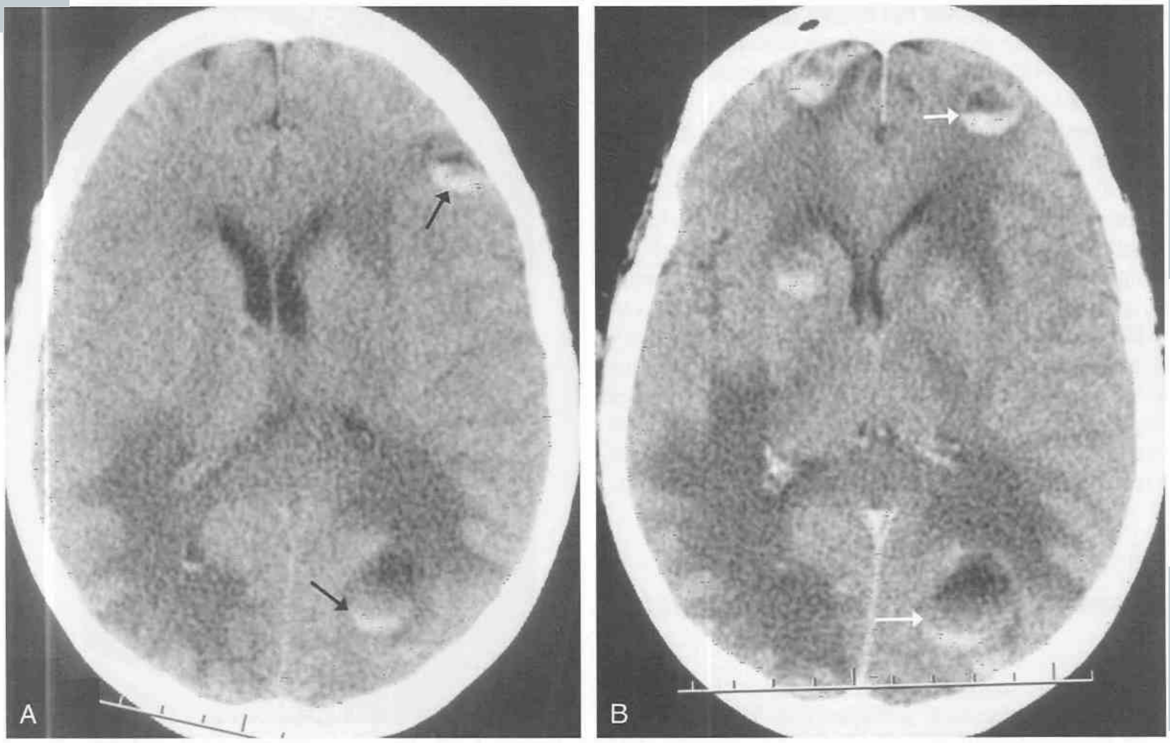

Figure 5–62. Hematogenous metastases of melanoma to the brain with intratumoral hemorrhage. *A,* An axial noncontrast CT image demonstrates at least four foci of varying size located at gray/white junctions in both cerebral hemispheres. All four lesions contain blood/fluid levels *(arrows)* indicating the presence of intratumoral hemorrhage. The lesions in the frontoparietal regions bilaterally and the left deep frontal area have provoked considerable surrounding edema. *B,* An axial CT image at an adjacent level following intravenous contrast injection demonstrates faint ringlike contrast enhancement of the margins of several of these tumors *(arrows).*

tion increases the conspicuity of small tumor foci that might otherwise be overlooked and further improves both the sensitivity and the specificity of the examination.[82, 294]

Definitive preoperative differentiation of metastasis from glioblastoma with CT is often not possible in an individual case, even though larger metastases generally retain a spherical or ovoid outline and extensive glioblastomas most commonly have much more irregular lobulated configurations and exhibit greater heterogeneity of density on contrast enhanced images. Definitive differentiation of multiple metastases from multiple pyogenic cerebral abscesses also is not usually possible with CT; although virtually all abscesses demonstrate uniformity and smoothness of contrast enhancing wall thickness, so may many small metastases. Extensive surrounding edema is also characteristic of both processes.

As noted previously, CT with contrast injection has been used for the preoperative screening evaluation of patients with carcinoma of the lung,[53] malignant melanoma,[116] and choriocarcinoma who have no cerebral symptoms or neurologic deficit. In one study of individuals without clinical evidence of brain involvement, cerebral metastases were found on CT in 40% of patients with adenocarcinoma of the lung and 11% of patients with oat cell carcinoma of the lung[324]; in another study, 11% of patients with melanoma were found on CT to have metastatic intracranial lesions.[116] Demonstration of unsuspected cerebral metastases in such patients may eliminate unnecessary surgery and permit earlier institution of more appropriate forms of treatment.

On evaluation with MRI, most intracerebral metastatic lesions have prolonged relaxation times (diminished signal on T1-weighted images and increased signal on T2-weighted images compared with normal brain).[10] As with CT, differentiation of the lesion or lesions from surrounding white matter edema is often problematic on noncontrast images. Additionally, signal intensity of the tumor can be highly variable, depending on the tumor constituents; the signal characteristics in a given metastasis depend on the cellularity of the lesion, the extent of intratumoral necrosis, the presence and age of hemorrhage, the presence and extent of calcification, and the severity of surrounding edema.[8–10, 153] Melanoma has a somewhat characteristic appearance if there has not been previous hemorrhage; the lesion is hyperintense on T1-weighted images and isointense with brain on T2-weighted images, most likely because of the free radical content of the melanin.[8, 9] Metastases from mucinous adenocarcinomas of gastrointestinal origin often appear hypointense on T2-weighted images because of the high protein content of the mucin.[10] If intratumoral hemorrhage has occurred, the signal pattern is determined by the nature of the blood degradation products, i.e., the age of the hemorrhage.[9, 123]

Contrast enhanced MRI has proven even more sensitive than contrast enhanced CT for detection of intracranial metastatic disease.[8, 140, 288] Multiplanar T1-weighted MR images obtained after IV administration of gadolinium, usually in a dose of 0.1 mmol per kg of body weight, are currently the most sensitive method for evaluation of intracranial metastatic disease.[10, 238] As on CT, contrast

enhancement on MRI allows the reader to distinguish the gross margins of the metastasis from the surrounding edema (see Fig. 5–61), a differentiation not often permitted on precontrast T1- or T2-weighted MR images.

Several investigators have suggested that higher doses of gadolinium (0.2 to 0.3 mmol/kg) further improve the sensitivity of this examination for the detection of additional lesions, although (unlike CT) delayed MR images do not increase the contrast between the tumor and the surrounding brain.[135, 359] In patients with known extracranial primary malignancy in whom standard dose contrast enhanced MRI of the brain appears to demonstrate a solitary parenchymal enhancing metastasis, it would seem appropriate and cost effective to repeat the postcontrast images with a higher dose of gadolinium, so as to more conclusively exclude the possibility of more metastases before surgical resection of the apparent solitary lesion is undertaken.

Metastases to the Skull and Intracranial Dura

Metastasis to the cranial vault or the base of the skull is associated with intracranial metastasis in 5% to 10% of cases.[139, 286] Hematogenous metastasis to the calvarial diploë often leads to destruction of the internal and external tables and extension of tumor into the adjacent epidural space. In one autopsy series of patients with primary extracranial malignancy and intracranial metastasis, 18% demonstrated dural involvement (including epidural or subdural neoplasm) as the only site of intracranial metastasis.[11, 266] Occasionally, dural metastasis may occur without an associated calvarial lesion, either as a nodular plaquelike focus or as a more extensive diffuse thickening of the dura.[82, 230] Epidural or dural metastasis is most often secondary to carcinoma of the breast, lymphoma, carcinoma of the prostate, and neuroblastoma.[266] Other common sources are carcinomas of the lung and kidney.[11] Although the dura is usually an effective barrier to further deep invasion, spread of tumor in the epidural space with nodular or bandlike soft tissue thickening is common. Symptoms usually relate to compression of the underlying brain parenchyma.[11]

Irregularly marginated focal osseous destruction of the bony calvaria or the skull base caused by metastasis to the diploë or marrow can be best defined on noncontrast CT scans obtained through the use of a bone targeting algorithm with wide window and high center settings.[238] Destruction of the inner table of the skull allows extension of tumor into the intracranial epidural space, which can be demonstrated on CT scans obtained after IV administration of iodinated contrast medium with the use of a soft tissue algorithm and appropriate ("subdural window") soft tissue window and center settings. These tumors typically demonstrate intense contrast enhancement, but recognition of the enhancing biconvex epidural tumor mass can be masked by the adjacent bone unless relatively wide window and high center settings are employed.

In current practice, early detection of small metastases in the diploë or in the dura can best be accomplished by utilizing T1-weighted MR images both before and after IV administration of gadolinium.[11] Small foci of intradiploic metastasis appear hypointense on noncontrast T1-weighted images and differ sharply from the adjacent hyperintense fatty marrow in the diploic space (Fig. 5–63). Postgadolinium T1-weighted images obtained with fat suppression typically demonstrate intense contrast enhancement of tumor in the epidural space or dura, which appears as nodular or curvilinear, bandlike thickening (see Fig 5–63); the underlying cerebral cortex is displaced inward, and (unlike leptomeningeal metastasis) the enhancing tumor does not extend into the cerebral sulci.[317] The findings may simulate those of meningioma, but epidural or dural metastasis typically appears hyperintense to adjacent cerebral cortex on T2-weighted images, whereas meningioma is nearly isointense with cortex on this pulsing sequence.[11, 238, 317]

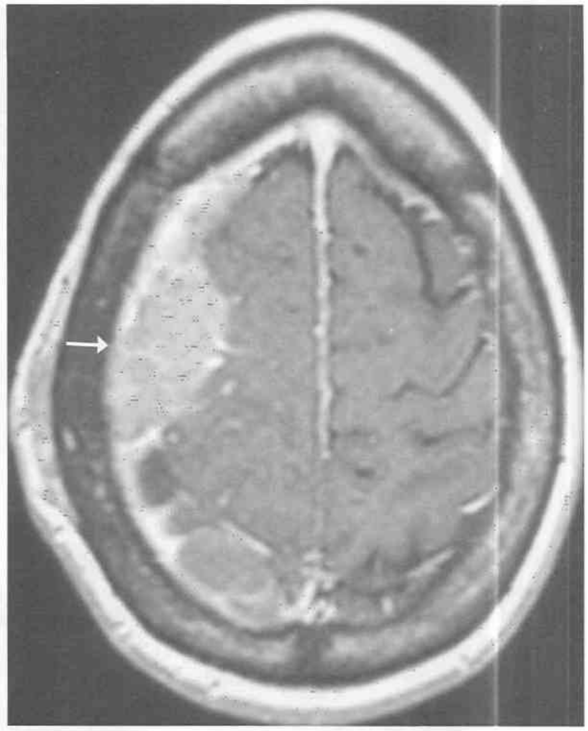

Figure 5–63. Diffuse pachymeningeal and calvarial metastasis from carcinoma of the breast. Axial T1-weighted postgadolinium MR image demonstrates diffuse nodular and bandlike contrast enhanced thickening of the dura over the high right frontoparietal convexity. The process extends into the falx and across the midline into the high left frontal convexity dura. Several ovoid and plaquelike masses in the right frontoparietal convexity represent outcroppings of dural metastasis *(arrow)* and compress the underlying frontal and parietal lobes with resultant effacement of the sulci. Note the loss of normal fatty marrow signal in the diploë of the overlying right parietal bone, indicating the presence of calvarial tumor involvement. Immediately posterior and lateral to the arrow is a focal plaque of tumor extension into the subgaleal space, with elevation of the overlying subcutaneous fat of the scalp.

Leptomeningeal Metastasis (Leptomeningeal Carcinomatosis)

Hematogenous metastasis from primary extracranial malignant tumors may occur directly to the meninges, but

leptomeningeal carcinomatosis may also result from parenchymal neoplasm that breaches either the ependymal lining of the ventricles or the pia overlying the cortex, with seeding of tumor cells into the CSF and subsequent spread by implantation on meningeal surfaces.[170, 286] These metastases tend to occur most commonly in the basal cisterns and in areas of relative CSF stasis.[317] The malignant infiltrate induces a reactive inflammatory response of the leptomeninges, and communicating hydrocephalus may develop as a result of obstruction of the basal cisterns or the pacchionian granulations.[11, 286] Sources include most primary parenchymal neoplasms of the brain, even relatively low grade gliomas,[64] as well as carcinomas of the breast, lung, and gastrointestinal tract, melanoma, lymphoma, and leukemias, notably acute lymphatic leukemia.[230, 286, 317] Of the secondary causes, carcinomas of the breast and lung are most common; in as many as 50% of patients with small cell carcinoma of the lung, leptomeningeal metastasis may be found at autopsy.[317]

Leptomeningeal metastasis is nearly always symptomatic, and the simultaneous presentation of signs and symptoms in widely scattered areas of the CNS is typical.[344] Headache is the most common initial complaint, occurring in 50% of patients, and weakness is found on clinical examination in 80%.[344] Cranial nerve palsies are presenting complaints in 40% of patients, and lethargy and confusion are found in 20%.[344] Although on occasion, the diagnosis of leptomeningeal metastasis may be established before the primary tumor becomes symptomatic, the interval between primary diagnosis of neoplasm and diagnosis of leptomeningeal involvement is typically between 6 months and 3 years; at this stage, most patients also have evidence of metastatic disease outside the CNS.[317] The diagnosis is usually established by lumbar puncture and microscopic examination of the CSF; abnormal cytologic results are obtained in approximately 50% of patients on the initial analysis and in 95% after six lumbar punctures.[344] Supporting findings include elevation of CSF pressure above 160 mm Hg, increase in protein concentration above 20 gm/L, and elevated white blood cell count (usually lymphocytes), all of which are found in at least one half of patients.[224]

Although CT has proved highly sensitive for the detection of cerebral parenchymal metastases, leptomeningeal metastasis has been demonstrated on contrast enhanced CT images in less than a third of patients with cytologic evidence of CSF seeding.[16, 116, 188] The sensitivity of MRI without and with paramagnetic contrast enhancement for detection of leptomeningeal metastasis appears to be approximately twice that of CT.[118, 317, 318, 358] MRI findings strongly suggestive of leptomeningeal metastasis include (1) nodular or plaquelike thick curvilinear hyperintensity of the involved subarachnoid cisterns and spaces on FLAIR images and (2) homogeneous contrast enhancement on postcontrast T1-weighted images that diffusely involves one or more subarachnoid cisterns, coats the surfaces of the adjacent brain parenchyma, and extends into the sulci (Fig. 5–64).[11, 118, 317, 358] The leptomeningeal tumor may also invade the underlying brain parenchyma and infiltrate the perivascular spaces surrounding the penetrating vessels.[317] The greater sensitivity of MRI for detecting leptomeningeal tumor spread has established this technique as the diagnostic modality of choice for the evaluation of possible leptomeningeal carcinomatosis.[11]

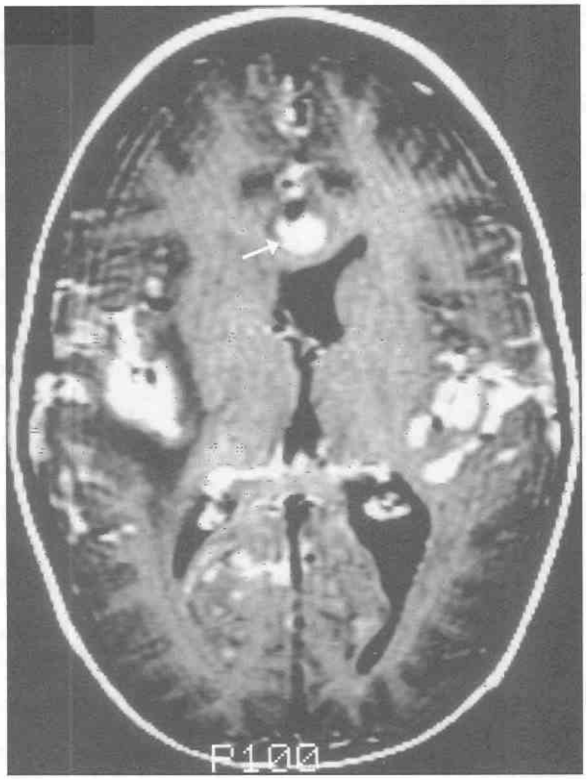

Figure 5–64. Leptomeningeal metastasis/carcinomatosis from carcinoma of the breast. Axial T1-weighted postgadolinium MR image. Numerous and diffuse nodular foci of leptomeningeal thickening with intense contrast enhancement are seen in the sylvian fissures, over the convexity surfaces, and in the convexity and parasagittal sulci bilaterally. A large nodule fills the pericallosal sulcus anteriorly *(arrow)*. There is associated mass effect in the right frontotemporal region with resultant compression of the frontal horn of the right lateral ventricle and slight displacement of the third ventricle to the left of the midline.

The differential diagnosis of leptomeningeal contrast enhancement includes bacterial and fungal meningitis, sarcoid (see Fig. 5–54), and postoperative inflammatory changes in the meninges.[11, 118, 258, 317] On the basis of imaging alone, definitive differentiation of tumor from inflammation or infection is not possible. Local or diffuse meningeal contrast enhancement at the site of previous craniotomy or at the site of insertion of a ventriculostomy shunt catheter reflects an inflammatory response of the traumatized dura and leptomeninges with eventual fibrosis.[146] Nodularity of the contrast enhancing tissue may favor neoplastic over inflammatory processes, but by no means is this true in all cases.[146, 258, 317]

References

1. Abdullah ND, Mathews VP: Contrast issues in brain tumor imaging. Neuroimaging Clin North Am 9:733–749, 1999.
2. Ahmadi H, Larsson EM, Jinkins JR: Normal pituitary gland: Coronal MR imaging of infundibular tilt. Radiology 177:389–392, 1990.
3. Albright AL, Guthkelch AN, Packer RJ, et al: Prognostic factors in pediatric brain-stem gliomas. J Neurosurg 65:751–755, 1986.
4. Alshail E, Rutka JT, Becker LE, et al: Optic chiasmatic-hypothalamic glioma. Brain Pathol 7:799–806, 1997.

5. Amundsen P, Dugstad G, Syvertsen AH: The reliability of computer tomography for the diagnosis and differential diagnosis of meningiomas, gliomas, and brain metastases. Acta Neurochirurg 41:177–190, 1978.
6. Aoki S, Barkovich AJ, Nishimura K, et al: Neurofibromatosis types I and II: Cranial MR findings. Radiology 172:527–534, 1989.
7. Armington WG, Osborne AG, Cubberly DA, et al: Supratentorial ependymoma: CT appearance. Radiology 157:367–372, 1985.
8. Atlas SW: Adult supratentorial tumors. Semin Roentgenol 25:130–154, 1990.
9. Atlas SW, Grossman RI, Gomori JM, et al: Hemorrhagic intracranial malignant neoplasms: Spin-echo MRI. Radiology 164:71–77, 1987.
10. Atlas SW, Lavi E, Fisher PG: Intraaxial brain tumors. In Atlas SW (ed): Magnetic Resonance Imaging of the Brain and Spine, 3rd ed. Philadelphia, Lippincott Williams & Wilkins, 2002, pp 565–693.
11. Atlas SW, Lavi E, Goldberg HI: Extraaxial brain tumors. In Atlas SW (ed): Magnetic Resonance Imaging of the Brain and Spine, 3rd ed. Philadelphia, Lippincott Williams & Wilkins, 2002, pp 695–772.
12. Atlas SW, Thulborn KR: Intracranial hemorrhage. In Atlas SW (ed): Magnetic Resonance Imaging of the Brain and Spine, 3rd ed. Philadelphia, Lippincott Williams & Wilkins, 2002, pp 773–832.
13. Baker HL Jr: The impact of computed tomography on neuroradiologic practice. Radiology 116:637–640, 1975.
14. Baker HL Jr, Campbell JK, Houser OW, et al: Computer assisted tomography of the head: An early evaluation. Mayo Clin Proc 49: 17–27, 1974.
15. Baker HL Jr, Campbell JK, Houser OW, et al: Early experience with the EMI scanner for the study of the brain. Radiology 116: 327–333, 1975.
16. Baker HL Jr, Houser OW, Campbell JK: National Cancer Institute study: Evaluation of computed tomography in the diagnosis of intracranial neoplasms. I: Overall results. Radiology 136:91–96, 1980.
17. Barker FG 2nd, Chang SM, Valk PE, et al: 18-Fluorodeoxyglucose uptake and survival of patients with suspected recurrent malignant glioma. Cancer 79:115–126, 1997.
18. Barkovich AJ: Brain tumors of childhood. In Pediatric Neuroimaging, 2nd ed. New York, Raven Press, 1995, pp 321–437.
19. Barkovich AJ: Germ cell tumors. In Pediatric Neuroimaging, 2nd ed. New York, Raven Press, 1995, pp 397–403.
20. Barnard R, Geddes J: The incidence of multifocal cerebral gliomas: A histologic study of large hemispheric sections. Cancer 60:1519–1531, 1987.
21. Barnard RO, Scott T: Patterns of proliferation in cerebral lymphoreticular tumors. Acta Neuropathol (Suppl vi):125–130, 1975.
22. Barnes PD, Kupsky WJ, Strand RD: Cranial and intracranial tumors. In Wolpert SM, Barnes PD (eds): MRI in Pediatric Neuroradiology. St. Louis, Mosby-Year Book, 1992, pp 204–298.
23. Bartscher IM, Skageberg G, Geijer B, et al: Proton MR spectroscopy and preoperative diagnostic accuracy: An evaluation of intracranial mass lesions characterized by stereotaxic biopsy findings. AJNR Am J Neuroradiol 21:84–93, 2000.
24. Batzdorf U, Malamud N: The problem of multicentric gliomas. J Neurosurg 20:122–136, 1963.
25. Becker LE: Pathology of pediatric brain tumors. Neuroimaging Clin North Am 9:671–690, 1999.
26. Beges C, Revel MP, Gaston A, et al: Trigeminal neuromas: Assessment of MRI and CT. Neuroradiol 34:179–183, 1992.
27. Bentson JR, Steckel RJ, Kagan AR: Diagnostic imaging in clinical cancer management: Brain metastases. Invest Radiol 23:335–341, 1988.
28. Bilaniuk LT, Zimmerman RA, Littman P, et al: Computed tomography of brain stem gliomas in children. Radiology 134:89–95, 1980.
29. Bilaniuk LT: Adult infratentorial tumors. Semin Roentgenol 25: 155–173, 1990.
30. Bindal RK, Sawaya R, Leavens ME, et al: Surgical treatment of multiple brain metastases. J Neurosurg 79:210–216, 1993.
31. Black PM: Brain tumors. N Engl J Med 324:1471–1476, 1555–1564, 1991.
32. Bohling P, Plate KH, Haltio MJ, et al: Von Hippel-Lindau disease and capillary hemangioblastoma. In Kleihues P, Cavenee WK (eds): Pathology and Genetics of Tumours of the Nervous System. Lyon, International Agency for Research on Cancer, 2000, pp 223–226.
33. Bolen JW Jr, Lipper MH, Caccamo D: Intraventricular central neurocytoma: CT and MR findings. J Comput Assist Tomogr 13:495–497, 1989.
34. Bouffet E, Doz F, Demaille MC, et al: Improving survival in recurrent medulloblastoma: Earlier detection, better treatment or still an impasse? Br J Cancer 77:1321–1326, 1998.
35. Brant-Zawadzki M: Multiple sclerosis and its imitators. In Huckman MS (ed): Neuroradiology Categorical Course Syllabus. Detroit, American Roentgen Ray Society, 1992, pp 229–232.
36. Brant-Zawadzki M, Badami JP, Mills CM, et al: Primary intracranial tumour imaging: A comparison of magnetic resonance and CT. Radiology 150:435–440, 1984.
37. Brant-Zawadzki M, Norman D, Newton TH, et al: Magnetic resonance of the brain: The optimal screening technique. Radiology 152: 71–77, 1984.
38. Braun IF, Chambers E, Leeds NE, et al: The value of unenhanced scans in differentiating lesions producing ring enhancement. Am J Neuroradiol 3:643–647, 1982.
39. Brooks RA, DiChiro G: Beam hardening in x-ray reconstructive tomography. Phys Med Biol 21:390–398, 1976.
40. Buetow MP, Buetow PC, Smirniotopoulos JG: Typical, atypical and misleading features in meningioma. Radiographics 11:1087–1106, 1991.
41. Bullard DE, Cox EB, Seigler HF: Central nervous system metastases in malignant melanoma. Neurosurgery 8:26–30, 1981.
42. Bullard DE, Rawlings CE III, Phillips B, et al: Oligodendroglioma: An analysis of the value of radiation therapy. Cancer 60:2179–2188, 1987.
43. Bunin GR, Surawicz TS, Witman PA, et al: The descriptive epidemiology of craniopharyngioma. J Neurosurg 89:547–551, 1998.
44. Burger PC, Dubois PJ, Schold C Jr, et al: Computerized tomographic and pathologic studies of the untreated, quiescent, and recurrent glioblastoma multiforme. J Neurosurg 58:159–169, 1983.
45. Burger PC, Heinz ER, Shibata T, et al: Topographic anatomy and CT correlations in the untreated glioblastoma multiforme. J Neurosurg 68:698–704, 1988.
46. Burger PC, Scheithauer BW: Tumors of neuroglia and choroid plexus epithelium. In Tumors of the Central Nervous System. Washington, DC, Armed Forces Institute of Pathology, 1994, pp 25–161.
47. Burger PC, Scheithauer BW, Paulus W, et al: Pilocytic astrocytoma. In Kleihues P, Cavenee WK (eds): Pathology and Genetics of Tumours of the Nervous System. Lyon, International Agency for Research on Cancer, 2000, pp 45–51.
48. Burger PC, Scheithauer BW, Vogel FS: Brain tumors. In Surgical Pathology of the Nervous System and Its Coverings, 3rd ed. New York, Churchill Livingstone, 1991, pp 193–437.
49. Burger PC, Vogel FS, Green SB, et al: Glioblastoma multiforme and anaplastic astrocytoma: Pathologic criteria and prognostic implications. Cancer 56:1106–1111, 1985.
50. Burrows EH, Leeds NE: Neuroradiology. New York, Churchill Livingstone, 1981, pp 252–253.
51. Butler AR, Horii SC, Kricheff II, et al: Computed tomography in astrocytomas: A statistical analysis of the parameters of malignancy and the positive contrast-enhanced CT scan. Radiology 129:433–439, 1978.
52. Butler AR, Leo JS, Lin JP, et al: The value of routine cranial computed tomography in neurologically intact patients with primary carcinoma of the lung. Radiology 131:399–401, 1979.
53. Butler AR, Passalaqua AM, Berenstein A, et al: Contrast enhanced CT scan and radionuclide brain scan in supratentorial gliomas. Am J Roentgenol 132:607–611, 1979.
54. Cairncross JG, Ueki K, Zlatescu MC, et al: Specific genetic predictors of chemotherapeutic response and survival in patients with anaplastic oligodendrogliomas. J Natl Cancer Inst 90:1473–1479, 1998.
55. Camilleri-Broet S, Davi F, Feuillard J, et al: AIDS-related primary brain lymphomas: Histopathologic and immunohistochemical study of 51 cases. The French study group for HIV-associated tumors. Hum Pathol 28:367–374, 1997.
56. Campbell JW, Pollack IF: Cerebellar astrocytomas in children. J Neurooncol 28:223–231, 1996.
57. Casadei GP, Komori T, Scheithauer BW, et al: Intracranial parenchymal schwannoma: A clinicopathological and neuroimaging study of nine cases. J Neurosurg 79:217–222, 1993.
58. Cascio TL: Neurologic complications of systemic cancer. Med Clin North Am 77:265–279, 1993.
59. Castillo M, Davis PC, Takei Y, et al: Intracranial ganglioglioma: MR, CT, and clinical findings in 18 patients. Am J Roentgenol 154: 607–612, 1990.

60. Castillo M, Kwock L: Proton MR spectroscopy of common brain tumors. Neuroimaging Clin North Am 8:733–752, 1998.
61. Cavenee WK, Furnari FB, Nagane M, et al: Diffusely infiltrating astrocytomas. In Kleihues P, Cavenee WK (eds): Pathology and Genetics of Tumours of the Nervous System. Lyon, International Agency for Research on Cancer, 2000, pp 10–21.
62. Chambers EF, Turski PA, Sobel D, et al: Radiologic characteristics of primary cerebral neuroblastomas. Radiology 139:101–104, 1981.
63. Chiechi MV, Smirniotopoulos JG, Mana H: Intracranial hemangiopericytomas: MR and CT features. AJNR Am J Neuroradiol 17:1365–1371, 1996.
64. Civitello LA, Packer RJ, Rorke LB, et al: Leptomeningeal dissemination of low-grade gliomas in childhood. Neurology 38:562–566, 1988.
65. Coates TL, Hinshaw DB Jr, Peckman N, et al: Pediatric choroid plexus neoplasms: MR, CT, and pathologic correlation. Radiology 173:81–88, 1989.
66. Cohen LM, Schwartz AM, Rockoff SD: Benign schwannomas: Pathologic basis for CT inhomogeneities. Am J Roentgenol 147:141–143, 1986.
67. Cohen TI, Powers SK, Williams DW III: MR appearance of intracanalicular eighth nerve lipoma. AJNR Am J Neuroradiol 13:1188–1190, 1992.
68. Coltier J, Destrieux C, Brunereau L, et al: Cavernous sinus invasion by pituitary adenoma: MR imaging. Radiology 215:463–469, 2000.
69. Cone L, Srinivasan M, Romanul FCA: Granular cell tumor (choristoma) of the neurohypophysis: Two cases and a review of the literature. AJNR Am J Neuroradiol 11:403–406, 1990.
70. Coons SW, Ashby LS: Pathology of intracranial neoplasms. Neuroimaging Clin North Am 9:615–649, 1999.
71. Coons SW, Johnson PC, Scheithauer BW, et al: Improving diagnostic accuracy and interobserver concordance in the classification and grading of primary gliomas. Cancer 79:1381–1393, 1997.
72. Cooper SD, Brady MB, Williams JP, et al: Neurosarcoidosis: Evaluation using CT and MRI. J Comput Assist Tomogr 12:96–99, 1988.
73. Cote TR, Manns A, Hardy CR, et al: Epidemiology of brain lymphoma among people with or without acquired immunodeficiency syndrome. AIDS/Cancer Study Group. J Natl Cancer Inst 88:675–679, 1996.
74. Crenshaw WB, Chew FS: Rathke's cleft cyst. Am J Roentgenol 158:1312, 1993.
75. Crocker EF, Zimmerman, RA, Phelps ME, et al: The effect of steroids on the extravascular distribution of radiographic contrast material and technetium pertechnetate in brain tumors as determined by computed tomography. Radiology 119:471–474, 1976.
76. Crotty TB, Scheithauer BW, Young WF Jr, et al: Papillary craniopharyngiomas: A clinicopathological study of 48 cases. J Neurosurg 83:206–214, 1995.
77. Curtin HD: The skull base. In Atlas SW (ed): Magnetic Resonance Imaging of the Brain and Spine, 3rd ed. Philadelphia, Lippincott Williams & Wilkins, 2002, pp 1283–1362.
78. Cushing H, Eisenhardt L: Meningiomas: Their Classification, Regional Behavior, Life History, and Surgical End Results. Springfield, Ill, Charles C Thomas, 1938.
79. Daumas-Duport C: Dysembryoplastic neuroepithelial tumors. Brain Pathol 3:283–295, 1993.
80. Daumas-Duport C, Pietsch T, Lantos PL: Dysembryoplastic neuroepithelial tumour. In Kleihues P, Cavenee WK (eds): Pathology and Genetics of Tumours of the Nervous System. Lyon, International Agency for Research on Cancer, 2000, pp 103–106.
81. Daumas-Duport C, Tucker ML, Kolles H, et al: Oligodendrogliomas. Part II: A new grading system based on morphological and imaging criteria. J Neurooncol 34:61–78, 1997.
82. Davis PC, Hudgins PA, Peterman SB, Hoffman JC Jr: Diagnosis of cerebral metastases: Double-dose delayed CT vs contrast-enhanced MR imaging. AJNR Am J Neuroradiol 12:293–300, 1991.
83. Davis PC, Wichman RD, Takei Y, et al: Primary cerebral neuroblastoma: CT and MR findings in 12 cases. AJNR Am J Neuroradiol 11:115–120, 1990.
84. Dean BL, Drayer B, Bird CR, et al: Gliomas: Classification from MR imaging. Radiology 174:411–415, 1990.
85. DeAngelis LM: Brain tumors. N Engl J Med 344:114–123, 2001.
86. Deck MDF, Messina AV, Sackett JF: Computerized transaxial tomography in metastatic disease of the brain. Radiology 119:115–120, 1976.
87. Delattre JY, Krol G, Thaler HT, et al: Distribution of brain metastases. Arch Neurol 45:741–744, 1988.
88. Di Chiro G, De La Paz RL, Brooks RA, et al: Glucose utilization of cerebral gliomas measured by [18F] fluorodeoxyglucose and positron emission tomography. Neurology 32:1323–1329, 1982.
89. Di Chiro G, Oldfield E, Wright DC, et al: Cerebral necrosis after radiotherapy and/or intraarterial chemotherapy for brain tumors: PET and neuropathologic studies. Am J Roentgenol 150:189–197, 1988.
90. Dina T: Primary central nervous system lymphoma versus toxoplasmosis in AIDS. Radiology 179:823–828, 1991.
91. Dohrmann GJ, Geehr RB, Robinson F: Small hemorrhages vs. small calcifications in brain tumors: Difficulty in differentiation by CT. Surg Neurol 10:309–312, 1978.
92. Dorsay TA, Rovira MJ, Ho VB, et al: Ependymoblastoma: MR presentation. Pediatr Radiol 25:433–435, 1995.
93. Doucet V, Peretti-Viton P, Figarella-Branger D, et al: MRI of intracranial chordomas: Extent of tumour and contrast enhancement: Criteria for differential diagnosis. Neuroradiology 39:571–576, 1997.
94. Drayer BP, Rosenbaum AE: Brain edema defined by cranial computed tomography. J Comput Assist Tomogr 3:317–328, 1979.
95. Earnest F IV, Kelly PJ, Scheithauer BW, et al: Cerebral astrocytomas: Histopathological correlation of MR and CT contrast enhancement with stereotactic biopsy. Radiology 166:823–827, 1988.
96. Edwards MSB, Hudgins RJ: Medulloblastomas and PNET of the posterior fossa. In McLaurin RL, Schut L, Venes JL, Epstein F (eds): Pediatric Neurosurgery, ed 2. Philadelphia, WB Saunders, 1989, pp 346–356.
97. Ellison D, Love S, Chimelli L, et al: Rathke cleft cyst. In Neuropathology: A Reference Text of CNS Pathology. St. Louis, Mosby, 1998, pp 44.1–44.11.
98. Elster AD: Modern imaging of the pituitary. Radiology 187:1–14, 1993.
99. Elster AD, Challa VR, Gilbert TH, et al: Meningiomas: MR and histopathologic features. Radiology 170:857–862, 1989.
100. Elster AD, Moody DM, Ball MR, et al: Is Gd-DTPA required for routine cranial MRI? Radiology 173:231–238, 1989.
101. Enzmann DR, Norman D, Levin V, et al: Computed tomography in the follow-up of medulloblastomas and ependymomas. Radiology 128:57–63, 1978.
102. Felix I, Becker LE: Intracranial germ cell tumors in children: An immunohistochemical and electron microscopic study. Pediatr Neurosci 16:156–162, 1990–1991.
103. Felix R, Schorner W, Laniado M, et al: Brain tumors: MR imaging with gadolinium-DTPA. Radiology 156:681–688, 1985.
104. Filling-Katz MR, Choye PL, Oldfield E, et al: Central nervous system involvement in von Hippel-Lindau disease. Neurology 41:41–46, 1991.
105. Finelli DA, Hurst GC, Gullapali RP, et al: Improved contrast of enhancing brain lesions on postgadolinium T1-weighted spin-echo images with use of magnetization transfer. Radiology 190:553–559, 1994.
106. Fishman RA: Brain edema. N Engl J Med 293:706–711, 1975.
107. Forsyth PA, Cascino TL, Shaw EG, et al: Intracranial chordomas: A clinicopathological and prognostic study of 51 cases. J Neurosurg 78:741–747, 1993.
108. Forsyth PA, Posner JB: Headaches in patients with brain tumors: A study of 111 patients. Neurology 43:1678–1683, 1993.
109. Fujimaki T, Matsutani M, Funada N, et al: CT and MRI features of intracranial germ cell tumors. J Neurooncol 19:217–226, 1994.
110. Furie DM, Provenzale JM: Supratentorial ependymomas and subependymomas: CT and MR appearances. J Comput Assist Tomogr 19:518–526, 1995.
111. Gado M, Huete I, Mikhael M: Computerized tomography of infratentorial tumors. Semin Roentgenol 12:109–120, 1977.
112. Gado MH, Phelps MB, Coleman RE: An extravascular component of contrast enhancement in cranial computed tomography. I: The tissue-blood ratio of contrast enhancement. Radiology 117:589–593, 1975.
113. George AE, Russell EJ, Kricheff II: White matter buckling: CT sign of extraaxial intracranial mass. Am J Neuroradiol 1:425–430, 1980.
114. Georgy BA, Hesselink JR, Jernigan TL: MR imaging of the corpus callosum. Am J Roentgenol 160:949–955, 1993.
115. Giangasparo F, Bigner SH, Kleihues P, et al: Medulloblastoma. In Kleihues P, Cavenee WK (eds): Pathology and Genetics of Tumours

of the Nervous System. Lyon, International Agency for Research on Cancer, 2000, pp 129–137.
116. Ginaldi S, Wallace S, Shalen P, et al: Cranial computed tomography of malignant melanoma. Am J Neuroradiol 1:531–535, 1980.
117. Ginsberg LE, Leeds NE: Neuroradiology of leukemia. Am J Roentgenol 165:525–534, 1995.
118. Ginsberg LE: Contrast enhancement in meningeal and extra-axial disease. Neuroimaging Clin North Am 4:133–152, 1994.
119. Goergen SK, Gonzales MF, McLean CA: Intraventricular neurocytoma: Radiologic features and review of the literature. Radiology 182:787–792, 1992.
120. Gold LHA, Kieffer SA, Peterson HO: Intracranial meningiomas: A retrospective analysis of the diagnostic value of plain skull films. Neurology 19:873–878, 1969.
121. Goldsher D, Litt AW, Pinto RS, et al: Dural tail associated with meningiomas on Gd-DTPA enhanced MR images: Characteristics, differential diagnostic value, and possible implications for treatment. Radiology 176:447–450, 1990.
122. Gomori JM, Grossman RI, Goldberg HI, et al: Intracranial hematomas: Imaging by high field MR. Radiology 157:83–93, 1985.
123. Gomori JM, Grossman RI: Mechanisms responsible for the MR appearance and evolution of intracranial hemorrhage. Radiographics 8:427–440, 1988.
124. Gonzales MF: Classification and pathogenesis of brain tumors. In Kaye AH, Laws ER Jr (eds): Brain Tumors: An Encyclopedic Approach. London, Churchill Livingstone, 2001, pp 29–49.
125. Graif M, Bydder GM, Steiner RE, et al: Contrast-enhanced MR imaging of malignant brain tumors. Am J Neuroradiol 6:855–862, 1985.
126. Grois N, Broadbent V, Favara BE, et al: Report of the Histiocyte Society workshop on central nervous system (CNS) disease in Langerhans cell histiocytosis (LCH). Med Pediatr Oncol 29:73–78, 1997.
127. Guermazi A, Feger C, Rousselot P, et al: Granulocytic sarcoma (chloroma): Imaging findings in adults and children. Am J Roentgenol 178:319–325, 2002.
128. Gusnard DA: Cerebellar neoplasms in children. Semin Roentgenol 25:263–278, 1990.
129. Guthrie BL, Ebersold MJ, Scheithauer BW, et al: Meningeal hemangiopericytoma: Histopathological features, treatment and long-term follow-up of 44 cases. Neurosurgery 25:514–522, 1989.
130. Hall WA, Lucciano MG, Doppman JL, et al: A prospective double-blind study of high resolution MRI in normal human subjects: Occult pituitary adenomas in the general population. J Neurosurg 92:342A, 1990.
131. Hansman Whiteman ML, Bowen BC, Donovan Post MJ, Bell MD: Intracranial infection. In Atlas SW (ed): Magnetic Resonance Imaging of the Brain and Spine, 3rd ed. Philadelphia, Lippincott Williams & Wilkins, 2002, pp 1099–1175.
132. Harsh GR IV: Chordomas and chondrosarcomas of the skull base. In Kaye AH, Laws ER Jr (eds): Brain Tumors: An Encyclopedic Approach, 2nd ed. London, Churchill Livingstone, 2001, pp 857–868.
133. Harwood-Nash DC: Neuroimaging of childhood craniopharyngioma. Pediatr Neurosurg 21(Suppl 1):2–10, 1990.
134. Hatam A, Bergstrom M, Yu Z-Y, et al: Effect of dexamethasone treatment on volume and contrast enhancement of intracranial neoplasms. J Comput Assist Tomogr 7:295–300, 1983.
135. Haustein J, Laniado M, Niendorf H-P, et al: Triple-dose versus standard-dose gadopentetate meglumine: A randomized study in 199 patients. Radiology 186:855–860, 1993.
136. Hayman LA, Evans RA, Fahr LM, et al: Renal consequences of rapid high dose contrast CT. Am J Neuroradiol 1:9–11, 1980.
137. Hayman LA, Evans RA, Hinck VC: Delayed high iodine dose contrast computed tomography: Cranial neoplasms. Radiology 136: 677–684, 1980.
138. Healey EA, Barnes PD, Kupsky WJ, et al: The prognostic significance of postoperative residual tumor in ependymoma. Neurosurgery 28:666–672, 1991.
139. Healy JF, Marshall WH, Brahme FJ, et al: CT of intracranial metastases with skull and scalp involvement. Am J Neuroradiol 2:335–338, 1981.
140. Healy ME, Hesselink JR, Press GA, et al: Increased detection of intracranial metastases with intravenous Gd-DTPA. Radiology 165: 619–624, 1987.
141. Hendrick EB, Raffel C: Tumors of the fourth ventricle: Ependymomas, choroid plexus papillomas and dermoid cysts. In McLaurin RL, Schut L, Venes JL, Epstein F (eds): Pediatric Neurosurgery, ed 2. Philadelphia, WB Saunders, 1989, pp 366–372.
142. Ho VB, Smirniotopoulos JG, Murphy FM, et al: Radiologic-pathologic correlation: Hemangioblastoma. AJNR Am J Neuroradiol 13: 1343–1352, 1992.
143. Hochberg FH, Miller CD: Primary central nervous system lymphoma. J Neurosurg 68:835–853, 1988.
144. Hoffman HJ, Otsubo H, Hendrick EB, et al: Intracranial germ-cell tumors in children. J Neurosurg 74:545–551, 1991.
145. Holland BA, Kucharcyzk W, Brant-Zawadzki M, et al: MR imaging of calcified intracranial lesions. Radiology 157:353–356, 1985.
146. Hudgins PA, Davis PC, Hoffman JC: Gadopentetate dimeglumine-enhanced MR imaging in children following surgery for brain tumor: Spectrum of meningeal findings. AJNR Am J Neuroradiol 12:301–307, 1991.
147. Jaaskelainen J, Louis DN, Paulus W, et al: Haemangiopericytoma. In Kleihues P, Cavenee WK (eds): Pathology and Genetics of Tumours of the Nervous System. Lyon, International Agency for Research on Cancer, 2000, pp 190–192.
148. Jaaskelainen J, Servo A, Haltia M, et al: Meningeal haemangiopericytoma. In Schmidek H (ed): Meningiomas and Their Surgical Treatment. Orlando, WB Saunders, 1991, pp 73–82.
149. Jack CR, O'Neill BP, Banks PM, Reese DF: Central nervous system lymphoma: Histologic types and CT appearance. Radiology 167: 211–215, 1988.
150. Janzer RC, Burger PC, Giangaspero F, Paulus W: Craniopharyngioma. In: Kleihues P, Cavenee WK (eds): Pathology and Genetics of Tumours of the Nervous System. Lyon, International Agency for Research on Cancer, 2000, pp 244–246.
151. Jellinger K, Chou P, Paulus W: Melanocytic lesions. In Kleihues P, Cavenee WK (eds): Pathology and Genetics of Tumours of the Nervous System. Lyon, International Agency for Research on Cancer, 2000, pp 193–195.
152. Jennings MT, Gelman R, Hochberg F: Intracranial germ-cell tumors: Natural history and pathogenesis. J Neurosurg 68:155–167, 1985.
153. Johnson BA: Central nervous system metastases. In Drayer BP, Enzmann DR, Smirniotopoulos JG, Lukin RR (eds): Core Curriculum Course in Neuroradiology. Part II: Neoplasms and Infectious Diseases. Oak Brook, Ill, American Society of Neuroradiology, 1996, pp 23–31.
154. Johnson DH, Windham WW, Allen JH, et al: Limited value of CT brain scans in the staging of small cell cancer. Am J Neuroradiol 3: 649–652, 1982.
155. Johnson JH, Hariharan S, Berman J, et al: Clinical outcome of pediatric gangliogliomas: Ninety-nine cases over 20 years. Pediatr Neurosurg 27:203–207, 1997.
156. Juneau P, Schoene WC, Black P: Malignant tumors in the pituitary gland. Arch Neurol 49:555–558, 1992.
157. Karsdorp N, Elderson A, Wittebol P, et al: Von Hippel-Lindau disease: New strategies in early detection and treatment. Am J Med 97:158–168, 1994.
158. Kelly WM, Brant-Zawadzki M: Magnetic resonance imaging and computed tomography of supratentorial tumors. In Taveras JM, Ferrucci JT (eds): Radiology—Diagnosis, Imaging, Intervention, vol 3. Philadelphia, JB Lippincott, 1986, pp 1–21.
159. Kepes JJ, Louis DN, Giannini C, Paulus W: Pleomorphic xanthoastrocytoma. In Kleihues P, Cavenee WK (eds): Pathology and Genetics of Tumours of the Nervous System. Lyon, International Agency for Research on Cancer, 2000, pp 52–54.
160. Kieffer SA, Salibi N, Kim RC, et al: Multifocal glioblastoma: Diagnostic implications. Radiology 143:709–710, 1982.
161. Kim EE, Chung SK, Haynie TP, et al: Differentiation of residual or recurrent tumors from post-treatment changes with F-18 FDG PET. Radiographics 12:269–279, 1992.
162. Klatzo I: Neuropathological aspects of brain edema. J Neuropathol Exp Neurol 26:1–14, 1967.
163. Kleihues P, Burger PC, Scheithauer BW: Histological classification of CNS tumours. In Sobin LH (ed): Histologic Typing of Tumours of the Central Nervous System, 2nd ed. Berlin, Springer-Verlag, 1993, pp 1–105.
164. Kleihues P, Cavenee WK (eds): Pathology and Genetics of Tumours of the Nervous System. Lyon, International Agency for Research on Cancer, 2000.

165. Kleihues P, Davis RL, Ohgaki H, et al: Diffuse astrocytoma. In: Kleihues P, Cavenee WK (eds): Pathology and Genetics of Tumours of the Nervous System. Lyon, International Agency for Research on Cancer, 2000, pp 22–26.
166. Klibanski A, Zervas NT: Diagnosis and management of hormone-secreting pituitary adenomas. N Engl J Med 324:822–831, 1991.
167. Koci TM, Chiang F, Mehringer CM, et al: Adult cerebellar medulloblastoma: Imaging features with emphasis on MR findings. AJNR Am J Neuroradiol 13:1319–1325, 1992.
168. Koeller KK: Central nervous system neoplasms: Intraaxial. In Smirniotopoulos JG (ed): Categorical Course in Diagnostic Radiology: Neuroradiology, 2000 Syllabus. Oak Brook, Ill, Radiological Society of North America, 2000, pp 105–121.
169. Koeller KK, Dillon WP: Dysembryoplastic neuroepithelial tumors: MR appearance. AJNR Am J Neuroradiol 13:1319–1325, 1992.
170. Kokoris CP: Leptomeningeal carcinomatosis: How does cancer reach the pia-arachnoid? Cancer 51:154–160, 1983.
171. Kovacs K, Horvath E, Asa SL: Classification and pathology of pituitary tumors. In Wilkins RH, Rengachary SS (eds): Neurosurgery. New York, McGraw-Hill, 1985, pp 834–842.
172. Kramer ED, Rafto S, Packer RJ, et al: Comparison of myelography with computed tomography follow-up vs. gadolinium magnetic resonance imaging for subarachnoid metastatic disease of children. Neurology 41:46–50, 1991.
173. Kricheff II: Strategies for the evaluation of supratentorial brain neoplasms. In Huckman MS (ed): Neuroradiology Categorical Course Syllabus. Detroit, American Roentgen Ray Society, 1992, pp 9–12.
174. Kucharczyk W, Davis DO, Kelly WM, et al: Pituitary adenoma: High resolution MRI at 1.5T. Radiology 161:761–765, 1986.
175. Kucharczyk W, Kelly WM, Chuang SH, et al: The brain. In Kucharczyk W (ed): MRI: Central Nervous System. Philadelphia, JB Lippincott, 1990, pp 1.1–1.78.
176. Kuhl J: Modern treatment strategies in medulloblastoma. Child Nerv Syst 14:2–5, 1998.
177. Kulkantrakorn K, Awwad EE, Levy B, et al: MRI in Lhermitte-Duclos disease. Neurology 48:725–731, 1997.
178. Kuroiwa T, Bergey GK, Rothman MI, et al: Radiologic appearance of the dysembryoplastic neuroepithelial tumor. Radiology 197:233–238, 1995.
179. Kwock L: Localized MR spectroscopy: Basic principles. Neuroimaging Clin North Am 8:733–752, 1998.
180. Laine FJ, Nadel L, Braun IF: CT and MR imaging of the central skull base. Radiographics 10:797–821, 1990.
181. Lalwani AK, Jacklen RK: Preoperative differentiation between meningioma of the cerebellopontine angle and acoustic neuroma using MRI. Otolaryngol Head Neck Surg 109:88–95, 1993.
182. Landis SH, Murray T, Bolder S, Wingo PA: Cancer statistics, 1999. CA Cancer J Clin 49:8–31, 1999.
183. Law M, Cha S, Knopp EA, et al: High-grade gliomas and solitary metastases: Differentiation by using perfusion and proton spectroscopic MR imaging. Radiology 222:715–721, 2002.
184. Laws ER, Thapar K: Brain tumors. CA Cancer J Clin 43:263–271, 1993.
185. Lee CC, Ward HA, Sharbrough FW, et al: Assessment of functional MR imaging in neurosurgical planning. AJNR Am J Neuroradiol 20:1511–1519, 1999.
186. Lee SR, Sanders J, Mark AJ, et al: Posterior fossa hemangioblastomas: MR imaging. Radiology 171:463–468, 1989.
187. Lee Y-Y, Castillo M, Nauert C, et al: Computed tomography of gliosarcoma. Am J Neuroradiol 6:527–531, 1985.
188. Lee Y-Y, Glass JP, Geoffrey A, et al: Cranial computed tomographic abnormalities in leptomeningeal metastasis. Am J Neuroradiol 5: 559–563, 1984.
189. Lee Y-Y, van Tassel P: Intracranial oligodendrogliomas: Imaging findings in 35 untreated cases. AJNR Am J Neuroradiol 10:119–127, 1989.
190. Lee Y-Y, van Tassel PV, Bruner JM, et al: Juvenile pilocytic astrocytomas: CT and MR characteristics. AJNR Am J Neuroradiol 10: 363–370, 1989.
191. Leeds NE, Elkin CM, Zimmerman RD: Gliomas of the brain. Semin Roentgenol 19:27–43, 1984.
192. Levine SN, Benzel EC, Fowler MR, et al: Lymphocytic hypophysitis: Clinical, radiological, and magnetic resonance imaging characteristics. Neurosurgery 22:987–941, 1988.
193. Levy RA, Bliavas M, Muraszko K, et al: Desmoplastic medulloblastoma: MR findings. AJNR Am J Neuroradiol 18:1364–1366, 1997.
194. Lindau R: Studien uber kleinhirncysten: Bau, pathogenese und bezeihungen zur angiomatosis retinae. Arch Pathol Microbiol Scand Suppl 1, 1926.
195. Lipper MH, Eberhard DA, Phillips CD, et al: Pleomorphic xanthoastrocytoma, a distinctive astroglial tumor: Neuroradiologic and pathologic features. AJNR Am J Neuroradiol 14:1397–1404, 1993.
196. Litofsky NS, Zee C-S, Breeze RE, et al: Meningeal melanocytoma: Diagnostic criteria for a rare lesion. Neurosurgery 31:945–948, 1992.
197. Lizak PF, Woodruff WW: Posterior fossa neoplasms: Multiplanar imaging. Semin Ultrasound CT MR 13:182–206, 1992.
198. Long DM: Capillary ultrastructure and the blood-brain barrier in human malignant brain tumors. J Neurosurg 32:127–144, 1970.
199. Louis DN, Scheithauer BW, Budka H, et al: Meningiomas. In Kleihues P, Cavenee WK (eds): Pathology and Genetics of Tumours of the Nervous System. Lyon, International Agency for Research on Cancer, 2000, pp 176–184.
200. Luh GY, Bird CR: Imaging of brain tumors in the pediatric population. Neuroimaging Clin North Am 9:691–716, 1999.
201. Lum C, Kucharczyk W, Montanera WJ, Becker LE: The sella turcica and parasellar region. In Atlas SW (ed): Magnetic Resonance Imaging of the Brain and Spine, 3rd ed. Philadelphia, Lippincott Williams & Wilkins, 2002, pp 1283–1362.
202. Maciunas RJ, Berger MS, Copeland B, et al: A technique for interactive image-guided neurosurgical intervention in primary brain tumors. Neurosurg Clin North Am 7:245–266, 1996.
203. Mahaley MS Jr, Mettlin C, Natarajan N, et al: National survey of patterns of care for brain-tumor patients. J Neurosurg 71:826–836, 1989.
204. Maiuri F, Iaconetta G, de Divitis O, et al: Intracranial meningiomas: Correlations between MR imaging and histology. Eur J Radiol 31: 69–75, 1999.
205. Mandybur TI: Intracranial hemorrhage caused by metastatic tumors. Neurology 27:650–655, 1977.
206. Mantravardi RVP, Phatak R, Bellur S, et al: Brainstem glioma: An autopsy study of 25 cases. Cancer 49:1294–1296, 1982.
207. Mark AS: Contrast-enhanced magnetic resonance imaging of the temporal bone. Neuroimaging Clin North Am 4:117–131, 1994.
208. Marks JE, Gado M: Serial computed tomography of primary brain tumors following surgery, irradiation, and chemotherapy. Radiology 125:119–125, 1977.
209. Martin DS, Levy B, Awwad EE, et al: Desmoplastic infantile ganglioglioma: CT and MR features. AJNR Am J Neuroradiol 12:1195–1197, 1991.
210. Mass S, Norman D, Newton TH: Coronal computed tomography: Indications and accuracy. Am J Roentgenol 131:875–879, 1978.
211. Mathews VP, Caldemeyer KS, Lowe MJ, et al: Gadolinium enhanced fast FLAIR imaging of the brain. Radiology 211:257–263, 1999.
212. Matsutani M, Sano K, Takakura K, et al: Primary intracranial germ cell tumors: A clinical analysis of 153 histologically verified cases. J Neurosurg 86:446–455, 1997.
213. McCormack BM, Miller DC, Budzilovich GN, et al: Treatment and survival of low-grade astrocytoma in adults: 1977–1988. Neurosurgery 31:636–642, 1992.
214. McGeachie RE, Gold LHA, Latchaw RE: Periventricular spread of tumor demonstrated by computed tomography. Radiology 125: 407–410, 1977.
215. Meyer JR, Gorey MT: Differential diagnosis of nontraumatic intracranial hemorrhage. Neuroimaging Clin North Am 8:263–293, 1998.
216. Meyers SP, Hirsch WL Jr, Curtin HD, et al: Chondrosarcomas of the skull base: MR imaging features. Radiology 184:103–108, 1992.
217. Miller DC, Hochberg FH, Harris NL, et al: Pathology with clinical correlations of primary central nervous system non-Hodgkin's lymphoma: The Massachusetts General Hospital experience 1958–1989. Cancer 74:1383–1397, 1994.
218. Miller EM, Newton TH: Extra-axial posterior fossa lesions simulating intra-axial lesions on computed tomography. Radiology 127: 675–679, 1978.
219. Monajati A, Heggeness L: Patterns of edema in tumors vs. infarcts: Visualization of white matter pathways. Am J Neuroradiol 3:251–255, 1982.
220. Moran CJ, Naidich TP, Gado MH, et al: Central nervous system lesions biopsied or treated by CT-guided needle placement. Radiology 131:681–686, 1979.

221. Morrison G, Sobel DF, Kelley WM, et al: Intraventricular mass lesions. Radiology 153:435–442, 1984.
222. Mulkens TH, Parizel PM, Martin J-J, et al: Acoustic schwannoma: MR findings in 84 tumors. AJR Am J Roentgenol 160:395–398, 1993.
223. Mulvihill JJ, Parry DM, Sherman JL, et al: NIH conference: Neurofibromatosis 1 (Recklinghausen disease) and neurofibromatosis 2 (bilateral acoustic neurofibromatosis)—an update. Ann Intern Med 113:39–52, 1990.
224. Murray JJ, Greco FA, Wolff SN, Hainsworth JD: Neoplastic meningitis: Marked variations of cerebrospinal fluid composition in the absence of extradural block. Am J Med 75:289–294, 1983.
225. Nagele T, Petersen D, Klose U, et al: The "dural tail" adjacent to meningiomas studied by dynamic contrast-enhanced MRI: A comparison with histopathology. Neuroradiology 36:303–307, 1994.
226. Naidich TP, Zimmerman RA: Primary brain tumors in children. Semin Roentgenol 19:100–114, 1984.
227. Naul LG, Hise JH, Bauserman SC, et al: CT and MR of meningeal melanocytoma. AJNR Am J Neuroradiol 12:315–316, 1991.
228. Nazar GB, Hoffman HJ, Becker LE, et al: Infratentorial ependymoma in childhood: Prognostic factors and treatment. J Neurosurg 72:408, 1990.
229. Nelson JS, Bruner JM, Wiestler OD, et al: Ganglioglioma and gangliocytoma. In Kleihues P, Cavenee WK (eds): Pathology and Genetics of Tumours of the Nervous System. Lyon, International Agency for Research on Cancer, 2000, pp 96–102.
230. Nelson JS, von Deimling A, Petersen I, Janzer RC: Metastatic tumours of the CNS. In Kleihues P, Cavenee WK (eds): Pathology and Genetics of Tumours of the Nervous System. Lyon, International Agency for Research on Cancer, 2000, pp 249–253.
231. Nelson SJ: Imaging of brain tumors after therapy. Neuroimaging Clin North Am 9:801–819, 1999.
232. Neumann HPH, Eggert HR, Scheremat R, et al: Central nervous system lesions in von Hippel-Lindau syndrome. J Neurol Neurosurg Psychiatry 55:898–901, 1992.
233. New PFJ, Aronow S, Hesselink JR: National Cancer Institute study: Evaluation of computed tomography in the diagnosis of intracranial neoplasms. IV: Meningiomas. Radiology 136:665–675, 1980.
234. New PFJ, Hesselink JR, O'Carroll CP, et al: Malignant meningiomas: CT and histologic criteria, including a new CT sign. Am J Neuroradiol 3:267–276, 1982.
235. Newton DR, Dillon WP, Norman D, et al: Gd-DTPA-enhanced MR imaging of pituitary adenomas. AJNR Am J Neuroradiol 10: 949–954, 1989.
236. Norman D, Stevens EA, Wing D, et al: Quantitative aspects of contrast enhancement in cranial computed tomography. Radiology 129:683–688, 1978.
237. Osborn AG, Rauschning W: Brain tumors and tumorlike masses: Classification and differential diagnosis. In Osborn AG (ed): Diagnostic Neuroradiology. St. Louis, Mosby, 1994, pp 401–528.
238. Osborn AG: Miscellaneous tumors, cysts, and metastases. In Osborne AG (ed): Diagnostic Neuroradiology. St. Louis, Mosby, 1994, pp 626–670.
239. Osborn AG, Heaston DK, Wing SD: Diagnosis of ascending transtentorial herniation by cranial CT. Am J Roentgenol 130:755–760, 1978.
240. Osborn AG: Astrocytomas and other glial neoplasms. In Osborne AG (ed): Diagnostic Neuroradiology. St. Louis, Mosby, 1994, pp 529–578.
241. Osborn AG: Meningiomas and other nonglial neoplasms. In Osborne AG (ed): Diagnostic Neuroradiology. St. Louis, Mosby, 1994, pp 579–625.
242. Ostertun B, Wolf HK, Campos MG, et al: Dysembryoplastic neuroepithelial tumors: MR and CT evaluation. AJNR Am J Neuroradiol 17:419–430, 1996.
243. Ostrov SG, Quencer RM, Hoffman JC, et al: Hemorrhage within pituitary adenomas: How often associated with pituitary apoplexy syndrome? AJNR Am J Neuroradiol 10:503–510, 1989.
244. Packer RJ: Childhood medulloblastoma: Progress and future challenges. Brain Dev 21:75–81, 1999.
245. Packer RJ: Childhood tumors. Curr Opin Pediatr 9:551–557, 1997.
246. Pagani JJ, Libshitz HI, Wallace S, et al: Central nervous system leukemia and lymphoma: Computed tomographic manifestations. Am J Neuroradiol 2:397–403, 1981.
247. Parisi JE, Scheithauer BW: Glial tumors. In Nelson JS, Parisi JE, Scheithauer BW (eds): Principles and Practice of Neuropathology. St. Louis, Mosby, 1993, pp 123–183.
248. Parker K, Hardjasudarma M, McLellan RL, et al: MR features of an intracerebellar chloroma. AJNR Am J Neuroradiol 17: 1592–1594, 1996.
249. Paulus W, Jellinger K, Morgello S, Deckert-Schluter M: Malignant lymphomas. In Kleihues P, Cavenee WK (eds): Pathology and Genetics of Tumours of the Nervous System. Lyon, International Agency for Research on Cancer, 2000, pp 198–203.
250. Paulus W, Kepes JJ, Jellinger K: Histiocytic tumors. In Kleihues P, Cavenee WK (eds): Pathology and Genetics of Tumours of the Nervous System. Lyon, International Agency for Research on Cancer, 2000, pp 204–206.
251. Paulus W, Scheithauer BW: Mesenchymal, non-meningothelial tumours. In Kleihues P, Cavenee WK (eds): Pathology and Genetics of Tumours of the Nervous System. Lyon, International Agency for Research on Cancer, 2000, pp 185–189.
252. Paz-Fumagalli R, Daniels DL, Millen SJ, et al: Dural "tail" associated with an acoustic schwannoma in MR imaging with gadopentetate dimeglumine. AJNR Am J Neuroradiol 12:1206, 1991.
253. Pencalet P, Sainte-Rose C, Lelauch-Tubiana A, et al: Papillomas and carcinomas of the choroid plexus in children. J Neurosurg 88: 521–528, 1998.
254. Penn I: Development of cancer as a complication of clinical transplantation. Transplant Proc 9:1121–1127, 1977.
255. Penn I, Porat G: Central nervous system lymphomas in organ allograft recipients. Transplantation 59:240–244, 1995.
256. Percy AK, Elveback LR, Okazaki H, Kurland LT: Neoplasms of the central nervous system: Epidemiologic considerations. Neurology 22:40–48, 1972.
257. Perry A, Stafford SL, Scheithauer BW, et al: Meningioma grading: An analysis of histologic parameters. Am J Surg Pathol 21:1455–1465, 1997.
258. Phillips ME, Ryals TJ, Kambhu SA, Yuh WTC: Neoplastic vs inflammatory meningeal enhancement with Gd-DTPA. J Comp Assist Tomogr 14:536–541, 1990.
259. Poe LB, Dubowy RL, Hochhauser L, et al: Demyelinating and gliotic cerebellar lesions in Langerhans cell histiocytosis. AJNR Am J Neuroradiol 15:1921–1928, 1994.
260. Pollock BE, Lunsford LD, Kondziolka D, et al: Outcome analysis of acoustic neuroma management: A comparison of microsurgery and stereotactic radiosurgery. Neurosurgery 36:215–224, 1995.
261. Poon T, Matoso I, Tchertkoff V, et al: CT features of primary cerebral lymphoma in AIDS and non-AIDS patients. J Comp Assist Tomogr 13:6–9, 1989.
262. Poptani H, Gupta RK, Roy R, et al: Characterization of intracranial mass lesions with in vivo proton MR spectroscopy. AJNR Am J Neuroradiol 16:1593–1603, 1995.
263. Posner JB: Brain tumors. CA Cancer J Clin 43:261–262, 1993.
264. Posner JB: Neurologic Complications of Cancer. Philadelphia, FA Davis, 1995.
265. Posner JB: Neurological complications of systemic cancer. Med Clin North Am 63:783–800, 1979.
266. Posner JB, Chernik NL: Intracranial metastases from systemic cancer. Adv Neurol 19:579–592, 1978.
267. Post MJD, David NJ, Glaser JS, et al: Pituitary apoplexy: Diagnosis by computed tomography. Radiology 134:665–670, 1980.
268. Potts DG, Abbott GF, von Sneidern JV: National Cancer Institute study: Evaluation of computed tomography in the diagnosis of intracranial neoplasms. III: Metastatic tumors. Radiology 136:657–664, 1980.
269. Provenzale JM, Weber AL, Klinworth GK, et al: Radiologic-pathologic correlation: Bilateral retinoblastoma with coexistent pineoblastoma (trilateral retinoblastoma). AJNR Am J Neuroradiol 16:157–165, 1995.
270. Radkowski MA, Naidich TP, Tamita T, et al: Neonatal brain tumors: CT and MR findings. J Comput Assist Tomogr 12:10–20, 1988.
271. Rao KCVG, Levine H, Itani A, et al: CT findings in multicentric glioblastoma: Diagnostic-pathologic correlation. J Comput Tomogr 4:187–192, 1980.
272. Rawlings CE, Giangaspero F, Burger PL, et al: Ependymomas: A clinicopathologic study. Surg Neurol 29:271–281, 1988.
273. Razack N, Baumgartner J, Bruner J: Pediatric oligodendrogliomas. Pediatr Neurosurg 28:121–129, 1998.
274. Reifenberger G, Kros JM, Burger PC, et al: Oligodendroglioma. In Kleihues P, Cavenee WK (eds): Pathology and Genetics of Tumours of the Central Nervous System. Lyon, International Agency for Research on Cancer, 2000, pp 56–61.

275. Ricci PE: Imaging of adult brain tumors. Neuroimaging Clin North Am 9:651–669, 1999.
276. Ricci PE, Karis JP, Heiserman JE, et al: Differentiating recurrent tumor from radiation necrosis: Time for reevaluation of positron emission tomography? AJNR Am J Neuroradiol 19:407–413, 1998.
277. Rohringer M, Sutherland G, Louis D, et al: Incidence and clinicopathological features of meningioma. J Neurosurg 71:665–672, 1989.
278. Rollins N, Mendelsohn D, Mulne A, et al: Recurrent medulloblastoma: Frequency of tumor enhancement on Gd-DTPA MR imaging. AJNR Am J Neuroradiol 11:583–587, 1990.
279. Roman-Goldstein SM, Goldman DL, Howieson J, et al: MR in primary CNS lymphoma in immunologically normal patients. AJNR Am J Neuroradiol 13:1207–1213, 1992.
280. Ropper AH: Lateral displacement of the brain and level of consciousness in patients with an acute hemispheral mass. N Engl J Med 314:953–958, 1986.
281. Rorke LB, Trojanowski JQ, Lee VMY, et al: Primitive neuroectodermal tumors of the central nervous system. Brain Pathol 7:765, 1997.
282. Rosenbaum AE, Rosenbloom SB: Meningiomas revisited. Semin Roentgenol 19:8–26, 1984.
283. Rosenberg AE, Nielsen GP, Keel SB, et al: Chondrosarcoma of the base of the skull: A clinicopathological study of 200 cases with emphasis on its distinction from chordoma. Am J Surg Pathol 23: 1370–1378, 1999.
284. Rosenblum MK, Matsutani M, Van Meir EG: CNS germ cell tumors. In Kleihues P, Cavenee WK (eds): Pathology and Genetics of Tumours of the Nervous System. Lyon, International Agency for Research on Cancer, 2000, pp 207–214.
285. Ross DA, Norman D, Wilson CB: Radiologic characteristics and results of surgical management of Rathke's cysts in 48 patients. Neurosurgery 30:173–179, 1992.
286. Russell DS, Rubinstein LJ: Pathology of tumours of the nervous system, ed 5. Baltimore, Williams & Wilkins, 1989.
287. Russell EJ, George AE, Kricheff II, et al: Atypical computed tomographic features of intracranial meningioma: Radiological-pathological correlation in a series of 131 consecutive cases. Radiology 135: 673–682, 1980.
288. Russell EJ, Geremia GK, Johnson CE, et al: Multiple cerebral metastases: Detectability with Gd-DTPA-enhanced MR imaging. Radiology 165:609–617, 1987.
289. Sage MR: Blood-brain barrier: Phenomenon of increasing importance to the imaging clinician. Am J Neuroradiol 3:127–138, 1982.
290. Samii M, Tatagiba M: Craniopharyngioma. In Kaye AH, Laws ER Jr (eds): Brain Tumors: An Encyclopedic Approach, 2nd ed. London, Churchill Livingstone, 2001, pp 945–964.
291. Sartoretti-Schefer S, Wichmann W, Aguzzi A, Valavanis A: MR differentiation of adamantinomatous and squamous-papillary craniopharyngiomas. AJNR Am J Neuroradiol 18:77–87, 1997.
292. Schild SE, Scheithauer BW, Schomberg PJ, et al: Pineal parenchymal tumors. Cancer 72:870–880, 1993.
293. Schorner W, Laniedo M, Niendorf HP, et al: Time-dependent changes in image contrast in brain tumors after gadolinium-DTPA. Am J Neuroradiol 7:1013–1020, 1986.
294. Shalen PR, Hayman LA, Wallace S, et al: Protocol for delayed contrast enhancement in computed tomography of cerebral neoplasia. Radiology 139:397–402, 1981.
295. Shapir J, Coblentz C, Melanson D, et al: New CT finding in aggressive meningioma. Am J Neuroradiol 6:101–102, 1985.
296. Shaw EG, Scheithauer BW, O'Fallon JR, et al: Oligodendrogliomas: The Mayo Clinic experience. J Neurosurg 76:428–434, 1992.
297. Shellock FG (ed): Magnetic Resonance Procedures: Health Effects and Safety. Boca Raton, Fla, CRC Press, 2001.
298. Shepherd CW, Scheithauer BW, Gomez MR, et al: Subependymal giant cell astrocytoma. Neurosurgery 28:864–868, 1991.
299. Sighvatsson V, Ericson K, Tomasson H: Optimising contrast-enhanced cranial CT for detection of brain metastases. Acta Radiol 39:718–722, 1998.
300. Silver AJ, Ganti SR, Hilal SK: Computed tomography of tumors involving the atria of the lateral ventricles. Radiology 145:71–78, 1982.
301. Sinson G, Sutton LN, Yachnis AT, et al: Subependymal giant cell tumor in children. Pediatr Neurosurg 20:233–239, 1994.
302. Smirniotopoulos JG: Extraaxial masses of the central nervous system. In Smirniotopoulos JG (ed): Categorical Course in Diagnostic Radiology: Neuroradiology. Oak Brook, Ill, Radiological Society of North America, 2000, pp 123–132.
303. Smirniotopoulos JG: The new WHO classification of brain tumors. Neuroimaging Clin North Am 9:595–613, 1999.
304. Smirniotopoulos JG, Murphy FM: The phakomatoses. AJNR Am J Neuroradiol 13:725–746, 1992.
305. Smirniotopoulos JG, Rushing EJ, Mena H: Pineal region masses: Differential diagnosis. Radiographics 12:577–596, 1992.
306. Smirniotopoulos JG, Yue NC, Rushing EJ: Cerebellopontine angle masses: Radiologic-pathologic correlation. Radiographics 13:1131–1147, 1993.
307. Smith RR, Grossman RI, Goldberg HI, et al: MR imaging of Lhermitte-Duclos disease: A case report. AJNR Am J Neuroradiol 10: 187–189, 1989.
308. Snow RB, Johnson CE, Morgello S, et al: Is magnetic resonance imaging useful in guiding the operative approach to large pituitary tumors? Neurosurgery 26:801–803, 1990.
309. Spagnoli MV, Grossman RI, Packer RJ, et al: Magnetic resonance imaging determination of gliomatosis cerebri. Neuroradiology 29: 15–18, 1987.
310. Spillane JA, Kendall BE, Moseley IF: Cerebral lymphoma: Clinical radiological correlation. J Neurol Neurosurg Psychiatry 45:199–208, 1982.
311. Spoto GP, Press GA, Hesselink JR, et al: Intracranial ependymoma and subependymoma: MR manifestations. AJNR Am J Neuroradiol 11:83–91, 1990.
312. Stovring J: Descending tentorial herniation: Findings on computed tomography. Neuroradiology 14:101–105, 1977.
313. Sundaresan N, Galicich JH: Surgical treatment of brain metastases: Clinical and computerized tomography evaluation of the results of treatment. Cancer 55:1382–1388, 1985.
314. Sutton LS, Packer RJ, Rorke LB, et al: Cerebral gangliogliomas during childhood. Neurosurgery 13:124–128, 1983.
315. Swartz JD, Zimmerman RA, Bilaniuk LT: Computed tomography of intracranial ependymomas. Radiology 143:97–101, 1982.
316. Symon L, Mohanty S: Hemorrhage in pituitary tumors. Acta Neurochir 65:41–49, 1982.
317. Sze G: Meningeal carcinomatosis. In Drayer BP, Enzmann DR, Smirniotopoulos JG, Luken RR (eds): Core Curriculum Course in Neuroradiology. Part II: Neoplasms and Infectious Disease. Oak Brook, Ill, American Society of Neuroradiology, 1996, pp 145–150.
318. Sze G, Soletsky S, Bronen R, et al: MR imaging of the cranial meninges with emphasis on contrast enhancement and meningeal carcinomatosis. AJNR Am J Neuroradiol 10:965–975, 1989.
319. Sze G, Uichanco LS, Brant-Zawadski MN, et al: Chordomas: MRI. Radiology 166:187–191, 1988.
320. Tadmor R, Harwood-Nash DCF, Savoiardo M, et al: Brain tumors in the first two years of life: CT diagnosis. Am J Neuroradiol 1: 411–417, 1980.
321. Tally PW, Laws ER, Scheithauer BW: Metastases of central nervous system neoplasms. J Neurosurg 68:811–816, 1988.
322. Tampieri D, Melanson D, Ethier R: MR imaging of epidermoid cysts. AJNR Am J Neuroradiol 10:351–356, 1989.
323. Tampieri D, Moumdjian R, Melanson D, et al: Intracerebral gangliogliomas in patients with partial complex seizures: CT and MR imaging findings. AJNR Am J Neuroradiol 12:749–755, 1991.
324. Tarver RD, Richmond BD, Klatte EC: Cerebral metastases from lung carcinoma: Neurological and CT correlation. Radiology 153: 689–692, 1984.
325. Tatter SB: Neurosurgical management of brain tumors. Neuroimaging Clin North Am 9:779–799, 1999.
326. Tenreiro-Picon OR, Kamath SV, Knorr JR, et al: Desmoplastic infantile ganglioglioma: CT and MRI features. Pediatr Radiol 25: 540–543, 1995.
327. Teramoto A, Hirakawa K, Sanno N, et al: Incidental pituitary lesions in 1000 unselected autopsy specimens. Radiology 193:161–164, 1994.
328. Tew JM Jr, Feibal JH, Sawaya R: Brain tumors: Clinical aspects. Semin Roentgenol 19:115–128, 1984.
329. Thapar K, Kovacs K: Tumors of the sellar region. In Bigner DD, McLendon RE, Bruner JM (eds): Russell and Rubinstein's Pathology of Tumors of the Nervous System. Baltimore, Williams & Wilkins, 1998, pp 561–677.
330. Thapar K, Laws ER Jr: Pituitary tumors. In Kaye AH, Laws ER Jr (eds): Brain Tumors: An Encyclopedic Approach, 2nd ed. London, Churchill Livingstone, 2001, pp 803–853.

331. Thomas LM: Acute increased intracranial pressure and the pathophysiology of mass lesions. In Youmans JR (ed): Neurological Surgery. Philadelphia, WB Saunders, 1973.
332. Tien RD, Barkovich AJ, Edwards MSB: MR imaging of pineal tumors. AJNR Am J Neuroradiol 11:557–565, 1990.
333. Tien RD, Cardenas CA, Rajagopalan S: Pleomorphic xanthoastrocytoma of the brain: MR findings in six patients. Am J Roentgenol 159:1287–1290, 1992.
334. Tien RD, Newton TH, McDermott MW, et al: Thickened pituitary stalk on MR images in patients with diabetes insipidus and Langerhans' cell histiocytosis. AJNR Am J Neuroradiol 11:703–708, 1990.
335. Tortori-Donati P, Fondelli MP, Rossi A, et al: Medulloblastoma in children: CT and MRI findings. Neuroradiology 38:352–359, 1996.
336. Truwit CL, Barkovich AJ: Pathogenesis of intracranial lipomas: An MR study in 42 patients. AJNR Am J Neuroradiol 11:665–674, 1990.
337. Tummala RP, Chu R, Liu H, et al: Optimizing brain tumor resection: High-field interventional MR imaging. Neuroimaging Clin North Am 11:673–683, 2001.
338. Uematsu Y, Yukawa S, Yokoto H, et al: Meningeal melanocytoma: Magnetic resonance imaging characteristics and pathological features: Case report. J Neurosurg 76:705–709, 1992.
339. Von Deiming A, Foster R, Krone W: Neurofibromatosis type 1. In Kleihues P, Cavenee WK (eds): Pathology and Genetics of Tumours of the Nervous System. Lyon, International Agency for Research on Cancer, 2000, pp 216–218.
340. Von Hippel E: Uber eine sehr selbene Erkrankung der Netzhaub. Graefe's Arch 59:83–86, 1904.
341. Vonofakos D, Marcu H, Hacker H: Oligodendrogliomas: CT patterns with emphasis on features indicating malignancy. J Comput Assist Tomogr 3:783–788, 1979.
342. Walker MD: Malignant Brain Tumors. New York, American Cancer Society, 1975.
343. Warzok RW, Vogelgesang S, Faiden W, Shuangshoti S: Granular cell tumour of the neurohypophysis. In Kleihues P, Cavenee WK (eds): Pathology and Genetics of Tumours of the Nervous System. Lyon, International Agency for Research on Cancer, 2000, pp 247–248.
344. Wasserstrom WR, Glass JP, Posner JB: Diagnosis and treatment of leptomeningeal metastases from solid tumors: Experience with 90 patients. Cancer 49:759–772, 1982.
345. Weir B, Grace M: The relative significance of factors affecting postoperative survival in astrocytomas, grades one and two. Can J Neurol Sci 3:47–50, 1976.
346. Weisberg LA: Incidental focal intracranial computed tomographic findings. J Neurol Neurosurg Psychiatry 45:715–718, 1982.
347. Wendling LR, Cromwell LD, Latchaw RE: Computed tomography of intracerebral leukemic masses. Am J Roentgenol 132:217–220, 1979.
348. Whelan MA, Hilal SK: Computed tomography as a guide in the diagnosis and follow-up of brain abscesses. Radiology 135:663–671, 1980.
349. Wiestler OD, Lopes BS, Green AJ, Vinters HV: Tuberous sclerosis complex and subependymal giant cell astrocytoma. In Kleihues P, Cavenee WK (eds): Pathology and Genetics of Tumours of the Nervous System. Lyon, International Agency for Research on Cancer, 2000, pp 227–229.
350. Wiestler OD, Padberg GW, Steck PA: Cowden disease and dysplastic gangliocytoma of the cerebellum/Lhermitte-Duclos disease. In Kleihues P, Cavenee WK (eds): Pathology and Genetics of Tumours of the Nervous System. Lyon, International Agency for Research on Cancer, 2000, pp 235–237.
351. Wiestler OD, Schiffer D, Coons SW, et al: Ependymoma. In Kleihues P, Cavenee WK (eds): Pathology and Genetics of Tumours of the Nervous System. Lyon, International Agency for Research on Cancer, 2000, pp 72–76.
352. Wilson CB: Current concepts in cancer: Brain tumors. N Engl J Med 300:1469–1471, 1979.
353. Winstanley DP: Fruitless resection. Thorax 23:327, 1968.
354. Woodruff JM, Kourea HP, Louis DN, et al: Tumours of cranial and peripheral nerves. In Kleihues P, Cavenee WK (eds): Pathology and Genetics of Tumours of the Nervous System. Lyon, International Agency for Research on Cancer, 2000, pp 163–174.
355. Wortzman G, Holgate RC, Morgan PP: Cranial computed tomography: An evaluation of cost effectiveness. Radiology 117:75–77, 1975.
356. Yasargil M, von Ammon K, von Deimling A, et al: Central neurocytoma: Histopathological variants and therapeutic approaches. J Neurosurg 76:32–37, 1992.
357. Yousem DM, Arrington JA, Zinreich SJ, et al: Pituitary adenomas: Possible role of bromocriptine in intratumoral hemorrhage. Radiology 170:239–243, 1989.
358. Yousem DM, Patrone PM, Grossman RI: Leptomeningeal metastases: MR evaluation. J Comput Assist Tomogr 14:255–261, 1990.
359. Yuh WT, Fisher DJ, Runge VM, et al: Phase III multicenter trial of high-dose gadoteridol in MR evaluation of brain metastases. AJNR Am J Neuroradiol 15:1037–1051, 1994.
360. Zee CS, Segall H, Apuzzo M, et al: MR imaging of pineal region neoplasms. J Comput Assist Tomogr 15:56–63, 1991.
361. Zee CS, Segall HD, Ahmadi J, et al: Computed tomography of posterior fossa ependymomas in childhood. Surg Neurol 20:221–226, 1983.
362. Zee CS, Segall HD, Miller C, et al: Less common CT features of medulloblastoma. Radiology 144:97–102, 1982.
363. Zentner J, Wolf HK, Ostertun B, et al: Gangliogliomas: clinical, radiological, and histopathological findings in 51 patients. J Neurol Neurosurg Psychiatry 57:1497–1502, 1994.
364. Zhang M, Olsson Y: Hematogenous metastases of the human brain: Characteristics of peritumoral brain changes—a review. J Neurooncol 35:81–89, 1997.
365. Zimmerman HM: The pathology of brain tumors. Semin Roentgenol 19:129–138, 1984.
366. Zimmerman RA: Neuroimaging of primary brainstem gliomas: Diagnosis and course. Pediatr Neurosurg 25:45–53, 1996.
367. Zimmerman RA: Pediatric supratentorial tumors. Semin Roentgenol 25:225–248, 1990.
368. Zimmerman RA: Supratentorial pediatric brain tumors, In Drayer BP, Enzmann DR, Smirniotopoulos JG, Lukin RR (eds): Core Curriculum Course in Neuroradiology. Part II: Neoplasms and Infectious Diseases. Oak Brook, Ill, American Society of Neuroradiology, 1996, pp 103–111.
369. Zimmerman RA, Bilaniuk LT: Computed tomography of acute intratumoral hemorrhage. Radiology 135:355–359, 1980.
370. Zimmerman RA, Bilaniuk LT: Computed tomography of choroid plexus lesions. J Comput Tomogr 3:93–102, 1979.
371. Zimmerman RA, Bilaniuk LT: Computed tomography of intracerebral gangliogliomas. J Comput Tomogr 3:24–30, 1979.
372. Zimmerman RA, Bilaniuk LT, Pahlajani H: Spectrum of medulloblastomas as demonstrated by computed tomography. Radiology 126:137–141, 1978.
373. Zimmerman RA, Bilaniuk LT, Dolinskas C: Cranial computed tomography of epidermoid and congenital fatty tumors of maldevelopmental origin. J Comput Tomogr 3:40–50, 1979.
374. Zimmerman RD, Fleming CA, Lee BCP, et al: Periventricular hyperintensity as seen by magnetic resonance: Prevalence and significance. Am J Neuroradiol 7:13–20, 1986.
375. Zulch KJ: Tumors of neuroepithelial tissue. In Brain Tumors: Their Biology and Pathology, 3rd ed. Berlin, Springer-Verlag, 1986, pp 210–343.

6

Cerebral Infections and Inflammation

Chi-Shing Zee, John L. Go, Paul Kim,
Hervey D. Segall, Jamshid Ahmadi

Since the advent of computed tomography (CT) scanning and magnetic resonance imaging (MRI), a significant decrease has occurred in the morbidity and mortality of patients with intracranial infections.[123] Although conventional cerebral angiography may be required in selected circumstances to confirm suspected vasculitis or mycotic aneurysm, CT and MRI studies are generally the modalities of choice in the evaluation of intracranial infection. CT and MRI, with stereotactic devices, have permitted biopsy of the intracranial focus of infection to identify the pathogen and subsequent drainage of abscesses through needle aspiration.[148] Recent advances in technology have allowed us to utilize additional imaging modalities in the evaluation of intracranial infection, such as positron emission tomography (PET), single photon emission computed tomography (SPECT), diffusion imaging, and magnetic resonance proton spectroscopy (MRS).

Two main sources of intracranial infection exist:

1. *Hematogenous*, in which infectious agents are carried to the meninges, corticomedullary junction, and choroid plexus by way of the bloodstream from a remote focus such as a lung infection; for instance, children with cyanotic heart disease have a high incidence of intracranial infection because of a right-to-left shunt. Retrograde venous spread can also occur via anastomotic connections between superficial veins of the face and scalp and cortical veins.
2. *Direct extension,* resulting from otitis media, mastoiditis, sinusitis, and open wounds from the trauma. In addition, certain viral infections can occur by spreading along the nerve in retrograde fashion.

Certain external factors appear to enhance the risk of intracranial infections (e.g., diabetes mellitus, alcoholism, malignancy, agammaglobulinemia, radiation or chemotherapy, steroid therapy). Patients with acquired immunodeficiency syndrome (AIDS) now account for a significant number of cases of intracranial infection, but the disease spectrum in these individuals is different. Various infectious processes involve the central nervous system (CNS). Pyogenic infection is discussed in detail in this chapter with categorization according to the anatomic site of involvement. Other infectious processes are also discussed, including viral infections, granulomatous disease, spirochete infections, fungal diseases, and parasitic diseases.

Meningitis

Meningitis is an inflammation of the dura, leptomeninges (the pia mater and the arachnoid membrane), and the adjacent subarachnoid space.[72] The diagnosis is usually made clinically. The role of neuroimaging is to exclude complications of meningitis (e.g., abscess, ventriculitis, empyema) that may call for different treatment. With appropriate window settings, CT scans may provide information regarding diseases of the paranasal sinuses or mastoids, which may be a source of intracranial infection. MRI studies are extremely sensitive in detecting diseases in the paranasal sinuses and the mastoids, especially on T2-weighted images.

In older people, *Streptococcus pneumoniae* and *Listeria monocytogenes* are often the causative agents. In young adults and older children, purulent meningitis is caused mainly by *Neisseria meningitidis.* In young children and infants, the cause may be *Haemophilus influenzae, S. pneumoniae,* and *N. meningitidis.* In infants younger than 1 month of age, causes include *Streptococcus agalactiae* (group B) and *Escherichia coli.*[36]

The initial pathologic responses of the dura and leptomeninges to infection include vascular congestion, edema, and minute hemorrhages. CT and MRI findings may be normal early in the disease process[21, 170] and remain normal with prompt and adequate treatment.

Once infection progresses, unenhanced CT scans frequently show obliteration of the basal cisterns. This probably results from a combination of hypervascularity in the acutely inflamed leptomeninges and exudate in the subarachnoid space. Diffuse cerebral swelling may be seen. Contrast-enhanced CT scans may show enhancement in the basal cisterns and sylvian fissure, regardless of the causative organism.

Routine MRI scans show obliteration of the basal cisterns on T1-weighted images. Contrast-enhanced MRI studies may show basal cisternal and sylvian enhancement as well as enhancement deep within the cortical sulci. Enhancement can be seen along the tentorium, falx, and the convexities—which can be better appreciated with MRI because of its greater contrast resolution[20, 112, 138] (Fig. 6–1).

Early complications of meningitis include abscess, subdural empyema, ventriculitis, and infarction. Late complications include subdural effusion, encephalomalacia, hydrocephalus, and atrophy.[21, 129]

On contrast-enhanced CT scans, the differential diagnosis includes meningeal carcinomatosis and subacute stage of subarachnoid hemorrhage. The clinical histories, however, are entirely different in these disease entities. The MRI differential diagnosis includes only meningeal carcinomatosis, since subacute subarachnoid hemorrhage shows

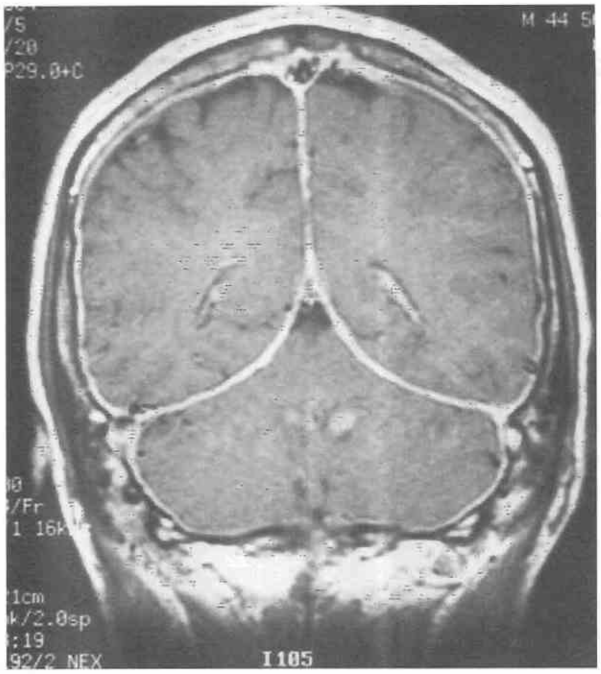

Figure 6–1. Meningitis. Gadolinium-enhanced MRI study shows enhancement along the tentorium, falx, and convexities.

distinct hyperintensity on T1-weighted images before injection of contrast material.

Contrast-enhanced MRI has been shown to be more sensitive than contrast-enhanced CT in detection of meningitis and its complications in experimental studies.[93] The radiology literature reports that abnormal contrast enhancement on intravenous (IV) gadolinium-enhanced MRI is seen in only 55% to 70% of patients with the clinical diagnosis of meningitis. The fluid attenuation inversion-recovery (FLAIR) technique is very sensitive and relatively specific in the diagnosis of intracranial subarachnoid space disease and meningeal disease.[135]

Subdural Effusion

Subdural effusions are believed to be caused by irritation of the dura by the infectious agents or its by-products or by inflammation of subdural veins with loss of fluid and albumin into the subdural space.[17] *H. influenzae* is a common pathogen associated with subdural effusion.[12] On neuroimaging, these effusions have a similar appearance to cerebrospinal fluid (CSF) and are frequently seen in the frontal region.[138] On contrast-enhanced imaging studies, there is no evidence of abnormal enhancement seen in the adjacent brain parenchyma. The subdural effusion usually resolves spontaneously without any treatment unless there is superimposed infection.

Subdural Empyema

Subdural empyema accounts for about 13% to 20% of all cases of intracranial infection. Subdural empyema is a collection of pus between the dura and the leptomeninges, which often occurs as a complication of meningitis, paranasal sinusitis, otitis media, osteomyelitis, or a penetrating wound of the skull.[73, 125]

Frontal sinusitis is the most common cause of subdural empyema. Infective organisms probably enter the subdural space in a retrograde fashion through a dural sinus or through bridging veins.[125] Occasionally, a subdural effusion induced by meningitis may become infected. Subdural empyemas, even when small, usually cause focal neurologic deficits in addition to acute febrile illness. Subdural empyema is considered a neurosurgical emergency because of its progressive clinical course. Despite recent improvement in surgical technique and antibiotics, mortality remains high (25% to 40%).[125]

Complications of subdural empyema include venous thrombosis and infarction. On a CT scan, subdural empyema appears as a hypodense or isodense crescentic or lenticular area adjacent to the inner table of the skull.[83, 99] On a contrast-enhanced CT scan, enhancement of the medial rim may be seen. Empyemas are better visualized with MRI than with CT. Empyemas show slightly higher intensity, compared with CSF, on both T1-weighted and T2-weighted images, which can help to differentiate them from sterile subdural effusion. The higher signal intensity is caused by the increased protein content of the empyema. On T2-weighted images, adjacent cerebritis or infarction may present as high-signal-intensity areas with irregular margins[138] (Fig. 6–2*A*). Enhancement of the medial rim is invariably seen (Fig. 6–2*B* and *C*); enhancement of the lateral rim adjacent to bony calvarium may sometimes be visible. Subdural empyemas may also be parafalcine,[54] and they may occur over the tentorium. Occasionally, enhancement of the subjacent cerebral cortex may be seen in a gyriform pattern in contrast-enhanced CT or MRI scans, suggesting the presence of concomitant cerebritis or infarction.

Epidural Empyema

Epidural empyema, a collection of pus between the dura and calvaria, occurs as a complication of otitis media, mastoiditis, sinusitis, or osteomyelitis of the skull.[59] Generally, infection in these patients is not as toxic as that in patients with subdural empyema. In addition to the presence of an extracerebral collection, imaging studies may show displacement of the falx and dural sinuses away from the inner table of the skull, which is an important and useful sign indicating the epidural location of a collection.[78]

A hypointense rim, representing inflamed dura, is seen on T2-weighted MR images in an epidural, but not a subdural, empyema.[151] Contrast-enhanced CT or MRI scans show a reasonably well-demarcated rim of enhancement representing inflamed dura. Because the dura usually acts as a barrier to organisms, the cerebral cortex beneath an epidural empyema is generally normal, and no enhancement in the underlying brain is seen.

Ten percent of epidural empyemas may be associated with subdural empyema (Fig. 6–3). An unenhanced CT scan shows a lentiform hypodense or isodense collection. MRI shows a slightly higher-signal-intensity collection, compared with CSF, on both T1-weighted and T2-weighted images because of the increased protein content of the pus.

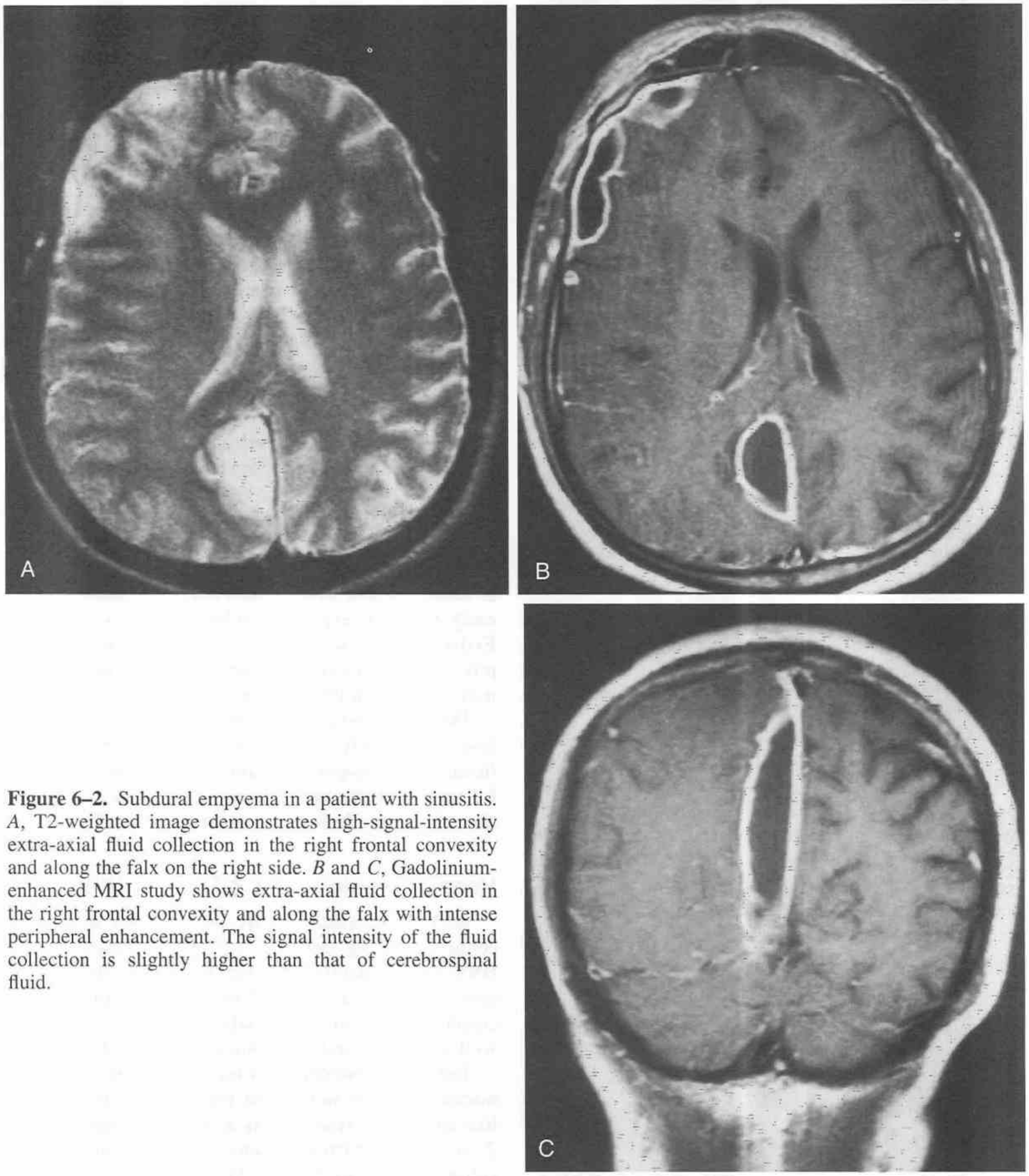

Figure 6–2. Subdural empyema in a patient with sinusitis. *A*, T2-weighted image demonstrates high-signal-intensity extra-axial fluid collection in the right frontal convexity and along the falx on the right side. *B* and *C*, Gadolinium-enhanced MRI study shows extra-axial fluid collection in the right frontal convexity and along the falx with intense peripheral enhancement. The signal intensity of the fluid collection is slightly higher than that of cerebrospinal fluid.

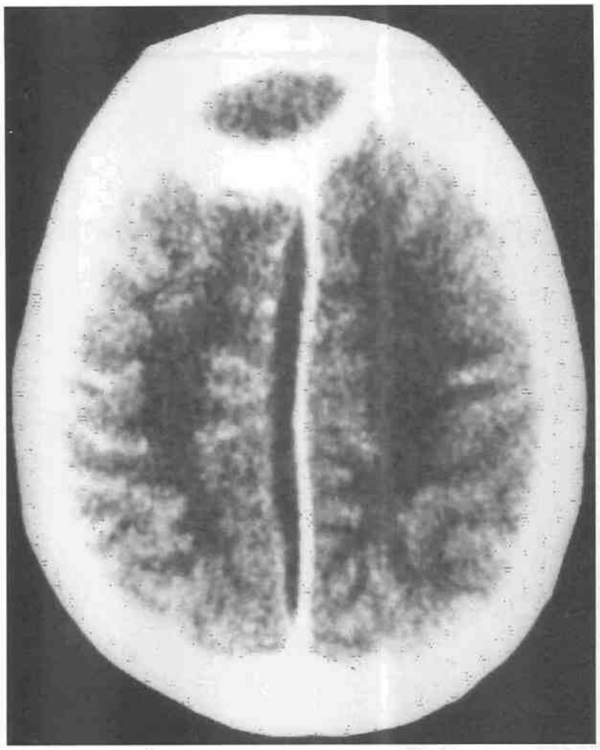

Figure 6–3. Frontal epidural empyema and interhemispheric fissure subdural empyema. Lentiform low-density collection is seen in the frontal region with displacement of the sagittal sinus away from the inner table of skull. An interhemispheric subdural collection is also seen.

Encephalitis

Encephalitis refers to diffuse inflammation of the brain with a parenchymal infiltration of inflammatory cells, usually caused by a virus. The brain damage caused by acute infective encephalitis is due to a combination of intracellular viral growth and the host's inflammatory response.

The most common viral agents are herpes simplex virus type 1 (HSV-1) and type 2 (HSV-2). Other causes include herpes zoster, arbovirus, and enteroviruses. Viral encephalitis in immunosuppressed patients can result from the human immunodeficiency virus (HIV), cytomegalovirus (CMV), and papovavirus. Other nonviral agents of encephalitis in immunosuppressed patients include *Toxoplasma*, *Aspergillus*, and *L. monocytogenes*.

Herpes Simplex Encephalitis

Herpes Simplex Type 1 Encephalitis

HSV-1 most commonly affects adults, whereas HSV-2 affects neonates. HSV-1 is the cause of 95% of all cases of herpetic encephalitis and is the most common cause of sporadic encephalitis. HSV-1 encephalitis is a fulminating, necrotizing meningoencephalitis that characteristically involves the temporal lobes and frontal lobes.

In the adult form, unenhanced CT scans show hypodense areas with mass effect in both temporal lobes and frontal lobes; these changes are less likely to be observed in parietal lobes. The findings are often asymmetrical.[27, 84] Sparing of the lenticular nucleus is said to be characteristic,[173] although such sparing may be observed in patients with infarction or glioma. An unenhanced CT scan infrequently shows hemorrhage in the low-density area early in the disease process, even though petechial hemorrhage is a frequent finding pathologically.

Contrast enhancement is a later finding in the disease process. Many published reports have documented uptake of technetium Tc 99m pertechnetate in various parts of the brain but most commonly in the temporal lobes. However, the scans become positive only at 2 days after the onset of clinical symptoms.[44, 50, 58] There are published reports that hexamethyl-propyleneamineoxime (HM-PAO)–SPECT is capable of detecting increased activity early on in the disease process.[44]

Enhanced CT scans show streaky, linear enhancement in the region of the sylvian fissure and the island of Reil[97] (Fig. 6–4). Unfortunately, CT studies, even high-resolution ones, show minimal changes, or results may be normal in the first 5 days despite the presence of obvious clinical symptoms. CT scans must be studied carefully to detect subtle changes that support the clinical diagnosis and to allow the institution of early antiviral therapy.

MRI studies show hypointensity on T1-weighted images and hyperintensity on T2-weighted images (Fig. 6–5). The temporal lobes and insular cortex are the areas of early involvement. The frontal lobe and the cingulate gyrus are involved later.[61] The contrast enhancement pattern of MRI is similar to that of CT. MRI is more sensitive than CT for early findings, especially when FLAIR imaging is used.[3] End-stage disease consists of encephalomalacia and atrophy in the previously involved areas; later, calcification may develop in these areas.

Definitive diagnosis is made either with positive fluorescein antibody staining or with a culture of the virus from a brain biopsy. Mortality is high, up to 70%. Successful treatment depends on early diagnosis and early institution of therapy before the onset of coma.[158]

Herpes Simplex Type 2 Encephalitis

HSV-2 encephalitis may be acquired through the placenta or during delivery.[41, 126] During the first trimester, HSV-2 encephalitis infection may have significant teratogenic effects on the fetal nervous system, including microphthalmia, encephalomalacia, and retinal dysplasia as well as mental and developmental retardation.[102, 136, 139]

Initial CT abnormalities include low density in the white matter diffusely, not just in the temporal lobes, and fingerlike areas of increased cortical density on unenhanced scans 2 to 30 days after presentation. A gyriform pattern of enhancement may be seen later.

MRI shows hypointensity in the white matter on T1-weighted images and hyperintensity on T2-weighted images. The enhancing pattern in MRI studies is similar to that on contrast-enhanced CT scans.

End-stage HSV-2 encephalitis may be characterized by cystic encephalomalacic change and cortical calcification.[62] Periventricular calcification and parenchymal calcification

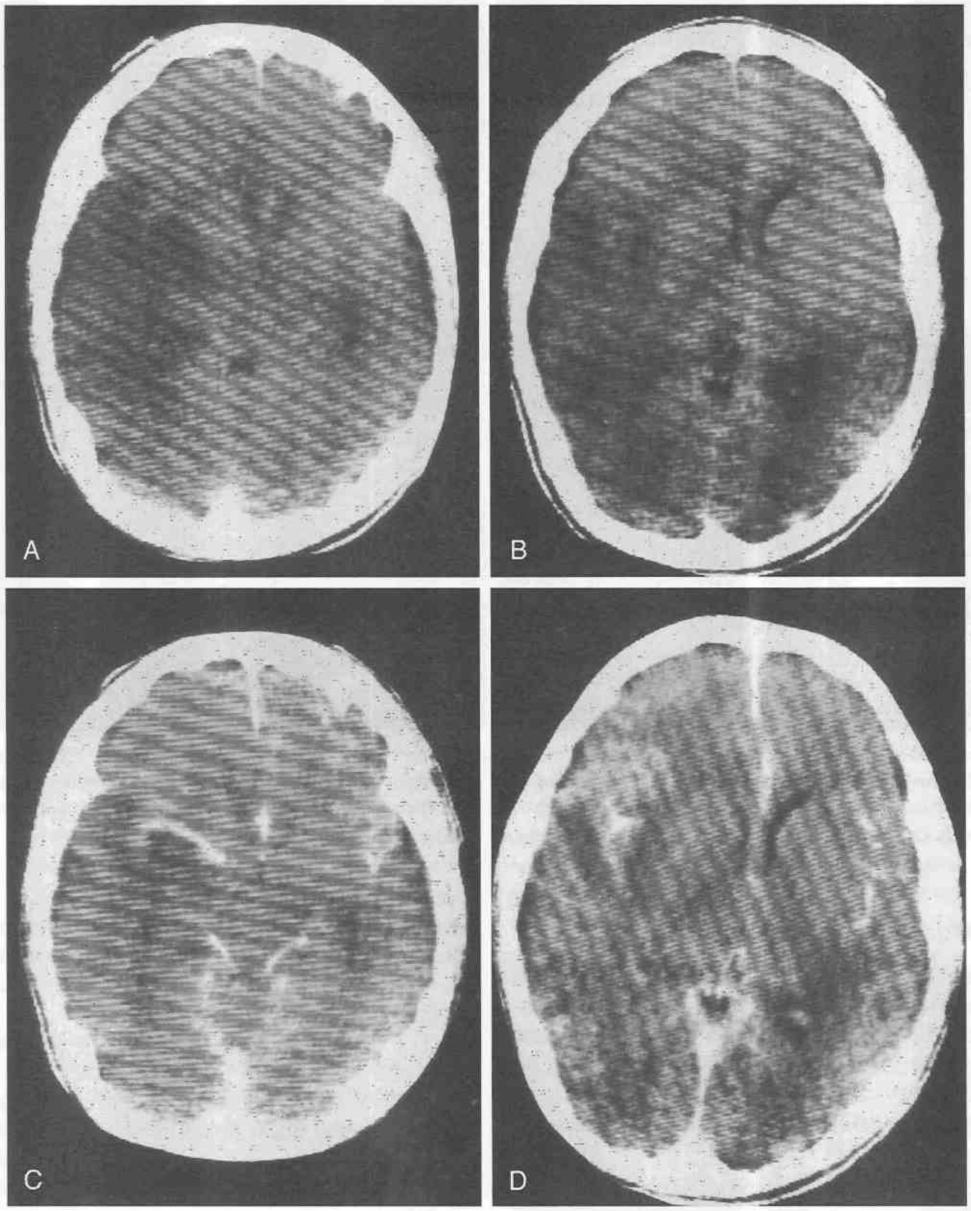

Figure 6–4. Herpes simplex encephalitis. *A* and *B*, A large low-density area is seen in the right temporal lobe with sparing of the lenticular nucleus. Significant mass effect has occurred with compression of the right lateral ventricle. *C* and *D*, Postcontrast scans show streaky linear enhancement in the region of the sylvian fissure.

are better seen on unenhanced CT scans than in MRI studies.[34] Mortality and morbidity rates are high.[158]

Herpes Zoster Encephalitis

Herpes zoster encephalitis is thought to be secondary to reactivation of a latent viral infection of earlier chickenpox. It is more commonly seen in immunosuppressed patients.[33, 65] CNS involvement is frequently seen in patients with skin lesions.

CT scans show multiple low-density lesions in the deep white matter. Hemorrhage may be seen as areas of poorly defined high density within the low density. MRI studies show hyperintensity in the deep white matter on T2-weighted images.

Herpes zoster virus has been implicated in the cause of granulomatous angiitis.[85, 125] Small cerebral arteries are typically involved, although large vessels may also be affected (Fig. 6–6). Cerebral infarction or aneurysm formation may be seen.

Arbovirus Encephalitis

Human infection caused by arbovirus is transmitted from birds through ticks and mosquitoes. There are more than 250 types of arbovirus, including eastern and western equine encephalitis, St. Louis encephalitis, Japanese encephalitis, and so on. CT and MRI may show abnormalities intracranially without the propensity to involve any specific region.[128, 132]

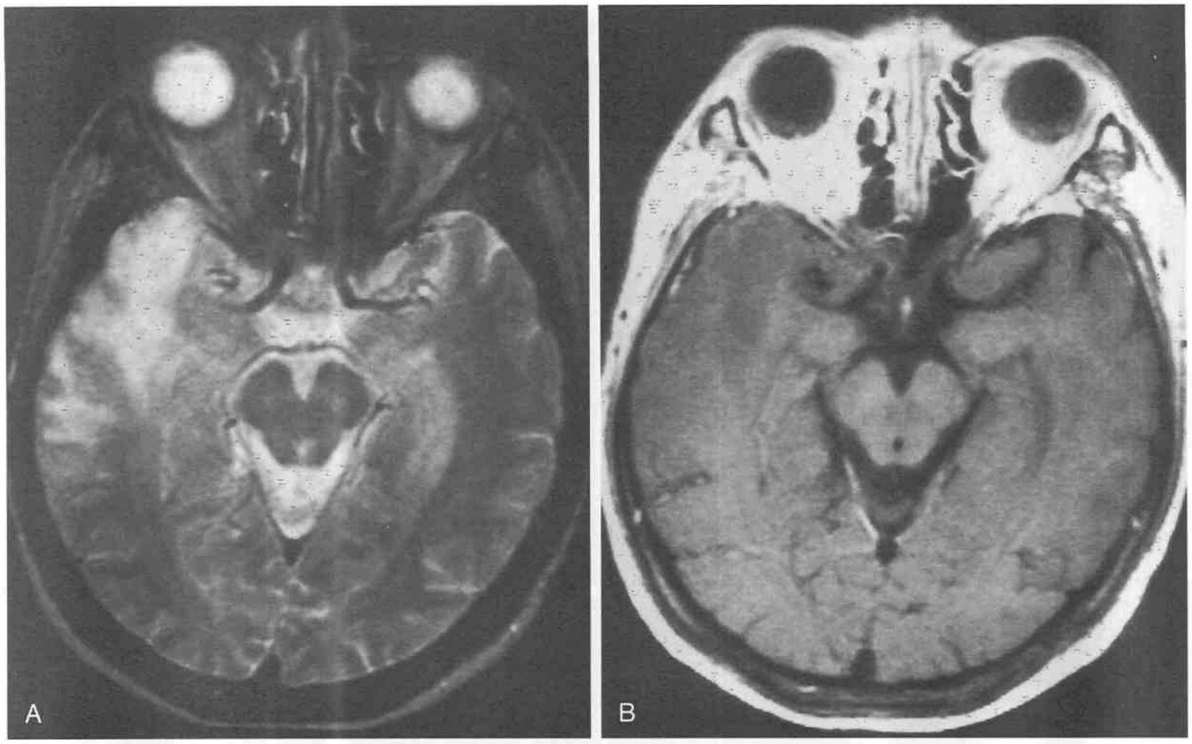

Figure 6–5. Herpes simplex encephalitis. *A*, T2-weighted image shows high signal intensity involving the gray and white matter of the right temporal lobe. Note the effacement of the adjacent cortical sulci, indicating the presence of mass effect. *B*, Gadolinium-enhanced image demonstrates no definite contrast enhancement in the early stage of disease. Low signal intensity with mass effect in right temporal lobe is obvious.

Acute Disseminated Encephalomyelitis

Acute disseminated encephalomyelitis is caused by an immune response to a preceding viral infection or vaccination. Patients usually present with neurologic signs and symptoms 5 days to 2 weeks later. Both humoral and cell-mediated immunity are implicated as the cause of pathologic changes. Vasculitis is thought to be caused by complement activation as a result of antigen-antibody complexes. A hypersensitivity reaction to a myelin protein is thought to cause demyelination. Perivenous demyelination is the hallmark of the disease.

The disease primarily involves white matter, but change may also be apparent in gray matter and brain stem. CT may show low density in the periventricular white matter, and MRI may show hyperintensity in the white matter on T2-weighted images.[67, 75, 89, 104] Some of the lesions may exhibit contrast enhancement following IV injection of gadolinium.

The differential diagnosis include multiple sclerosis, vasculitis, and embolic infarction. In later stages of the disease, encephalomalacia, ventriculomegaly, and atrophy may be seen.

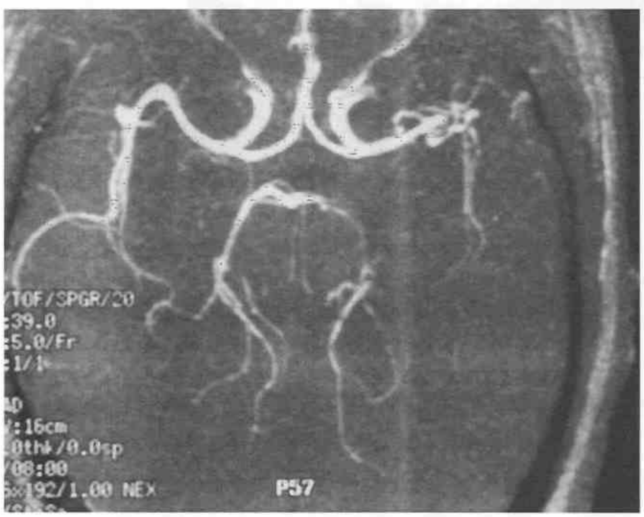

Figure 6–6. Herpes zoster vasculitis. Magnetic resonance angiogram demonstrates narrowing of the left middle cerebral artery branches as well as the proximal left posterior cerebral artery. There is a small infarct in the left middle cerebral artery territory.

Other Encephalitides

Creutzfeldt-Jakob Disease

Creutzfeldt-Jakob disease is a human spongiform encephalopathy that results from an infection by a "slow virus." The mode of transmission has been traced to inoculations by injections of human growth hormone, transplantation of corneas, and implantation of cerebral electrodes.[118] In addition, butchers and meat handlers are at greater risk of contracting the disease. A new variant of Creutzfeldt-Jakob disease is due to bovine spongiform encephalopathy (so-called mad cow disease).

The infective prion is a proteinaceous particle that contains little or no nucleic acid. The disease occurs in adults

in their late 50s. However, the new variant of the disease can affect all age groups. Dementia with rapid progression to stupor is seen clinically. CT and MRI studies are useful to document the rapid progression of atrophy.[78, 147] Cortical gray matter involvement without cerebral atrophy may represent an early phase of the disease.[45] Hyperintensity may be seen in cortical gray matter on T2-weighted images or FLAIR images, and on diffusion-weighted images, which may reflect areas of gliosis and microvacuolization pathologically.[6, 28, 44]

Subacute Sclerosing Panencephalitis

Subacute sclerosing panencephalitis is caused by the measles virus. Elevated levels of a neutralizing antibody to the virus can be detected in the blood and CSF. The disorder is usually seen in children and young adults. CT scans may show low-density changes in subcortical white matter as well as in basal ganglia. MRI studies show hyperintensity in the periventricular white matter and basal ganglia on T2-weighted images.[146] Atrophy is a late-stage finding.

Reye's Syndrome

Reye's syndrome is a disease of unknown etiology in children. It usually follows a viral infection such as type A or B influenza and varicella. Exogenous toxins, such as salicylates, and intrinsic metabolic defects have been implicated as being other factors associated with the disease.

Gross pathologic specimens demonstrate diffusely swollen brain. CT scans show diffuse low density of the supratentorial structures, a finding consistent with diffuse cerebral edema.[124]

Rasmussen's Encephalitis

Rasmussen's encephalitis is a childhood disease. The child presents with severe epilepsy and progressive neurologic deficits.[143] Seizures are usually of the partial motor seizure type and tend to be intractable. The intractable nature of the seizure may make hemispherectomy necessary if medical therapy is ineffective.

Early in the disease process, CT and MRI findings may be normal. MRI may reveal hyperintensity in the white matter and putamen on T2-weighted images.[143] PET imaging using fluorodeoxyglucose-18 (FDG-18) may show decreased hemispheric activity.

Encephalitis in Immunocompromised Patients

Human Immunodeficiency Virus Encephalitis

HIV is a neurotropic virus, which typically causes a subacute form of encephalitis. CT scans may show low density in the periventricular white matter. MRI may show hyperintensity in the periventricular white matter on T2-weighted and FLAIR images.[114] Normal neuroimaging studies do not exclude HIV encephalitis.

Progressive Multifocal Leukoencephalopathy

Progressive multifocal leukoencephalopathy is caused by papovavirus. It is uncertain whether it represents a reactivation of a latent infection. Pathologically, the major target cell is the oligodendrocyte. Because this cell is responsible for myelin maintenance, its destruction leads to demyelination.

CT scans characteristically show low density in the parietal and occipital white matter. Frontal involvement is seen later on. Early involvement may assume an asymmetrical pattern, but the changes in later disease are highly symmetrical and diffuse. Contrast enhancement is usually absent but may occur.[155] The presence of contrast enhancement may actually suggest the relative presence of host immunity and thus indicates a better prognosis.

MRI shows hypointensity in the white matter on T1-weighted images and hyperintensity on T2-weighted images (Fig. 6–7). MRI is more sensitive than CT in detecting abnormalities.[56]

Cytomegalovirus Encephalitis

In immunocompromised patients, CMV may cause meningoencephalitis or subacute encephalitis.[106] CMV can produce demyelination and necrosis within the white matter.

CT scans show low density in the white matter, which may or may not enhance with contrast agents. MRI shows high signal intensity in the white matter on T2-weighted images and is more sensitive than CT in detecting leukoencephalitis.[92]

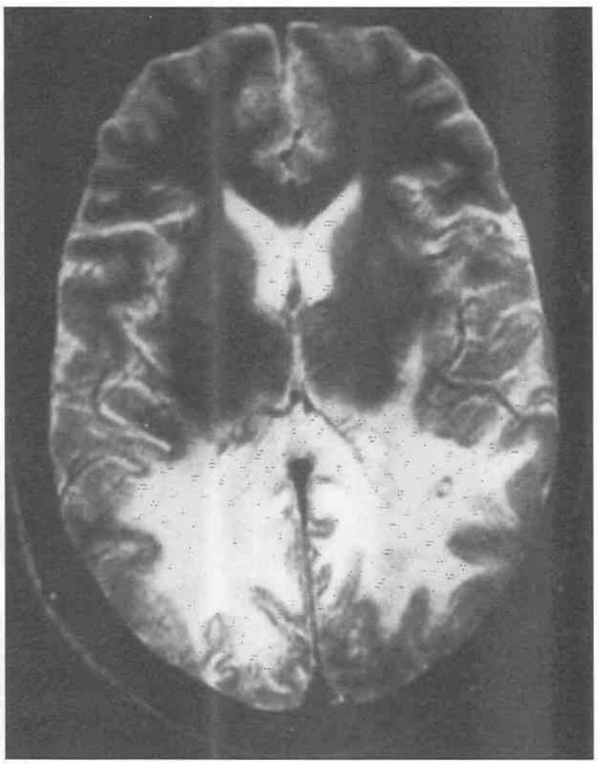

Figure 6–7. Progressive multifocal leukoencephalopathy. T2-weighted image shows high signal intensity in the parieto-occipital white matter bilaterally.

Neonatal cytomegalic inclusion disease is a severe disseminated necrotizing encephalitis with a tendency to involve the periventricular tissue. Unenhanced CT scans show periventricular calcification with ventricular dilatation[4] (Fig. 6–8).

Cerebritis and Abscess

Pathologically, there are four stages in the evolution of cerebral abscess as demonstrated by experimental studies by Enzmann and colleagues[38]:

1. *Acute cerebritis* (the first 4 to 5 days). The organism grows in the parenchyma. Acute inflammatory cells, particularly polymorphonuclear leukocytes, migrate into the parenchyma to ingest or destroy bacteria. Opening of the blood-brain barrier produces edema. Microscopic hemorrhage may be seen during the acute cerebritis stage but is unusual later.
2. *Late cerebritis* (at 7 to 10 days). The small areas of necrosis coalesce into one large focus filled with necrotic debris. Granulation tissue forms at its margin, containing macrophages. Edema and small foci of cerebritis are seen surrounding this area. These small foci later form satellite lesions adjacent to the large abscess.
3. *Early abscess* (at 10 to 14 days). Formation of a collagenous capsule by fibroblasts is seen. The central necrotic area is liquefied. Surrounding edema persists.
4. *Mature abscess* (>14 days). A decrease in surrounding edema is seen. A gliotic reaction develops at the outer margin of the abscess capsule. The wall of the mature abscess consists of three layers: (1) an inner inflammatory layer of granulation tissue containing macrophages, (2) a middle collagenous layer, and (3) an outer gliotic layer.[172]

Acute cerebritis is not often identified on neuroimaging studies because symptoms do not usually develop until later.[139] Initially, acute cerebritis usually manifests in white matter with vascular congestion and edema, so that ill-defined areas of low density and mass effect in the white matter are noted on unenhanced CT scans.[21, 101] On MRI studies, edema is seen as hypointensity on T1-weighted images and hyperintensity on T2-weighted images. MRI is superior to CT in detecting cerebral edema and subtle mass effect.[57, 128]

In early cerebritis, mild central nodular enhancement may be seen on contrast-enhanced CT or MRI scans (Fig. 6–9). In the late cerebritis stage, experimental studies of the evolution of brain abscess following inoculation of organisms have demonstrated brain enhancement on CT scans.[38] On MRI studies, the enhancing pattern is similar to that with CT. A relatively thick, slightly irregular, ringlike enhancement is seen interposed between the peripheral edema and central necrosis (Fig. 6–10).

As the lesion matures, the ringlike enhancement becomes thinner and smoother. The most distinctive feature of abscess on imaging is the presence of a smooth, thin capsule with a moderate amount of cerebral edema.[57] It is located at the corticomedullary junction and usually extends into the white matter. The abscess cavity has necrosis and liquefaction within its center. Unenhanced CT scans show a low-density area with mass effect and compression of the ventricular system. Between the central low-density area (representing the cavity) and the surrounding low-density edematous zone, a ring of higher density may be seen.[70, 137, 153] Visualization of spontaneous gas within the

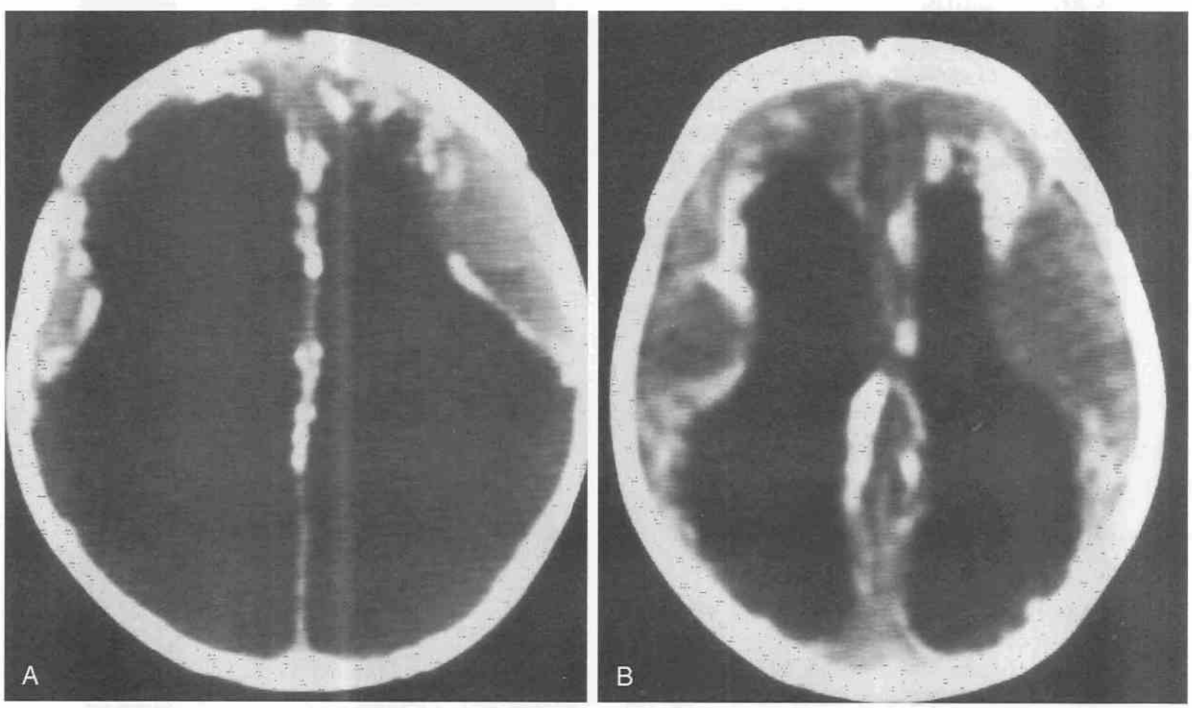

Figure 6–8. *A* and *B*, Cytomegalic inclusion disease. Unenhanced CT scan in a newborn shows periventricular calcification and ventricular dilatation.

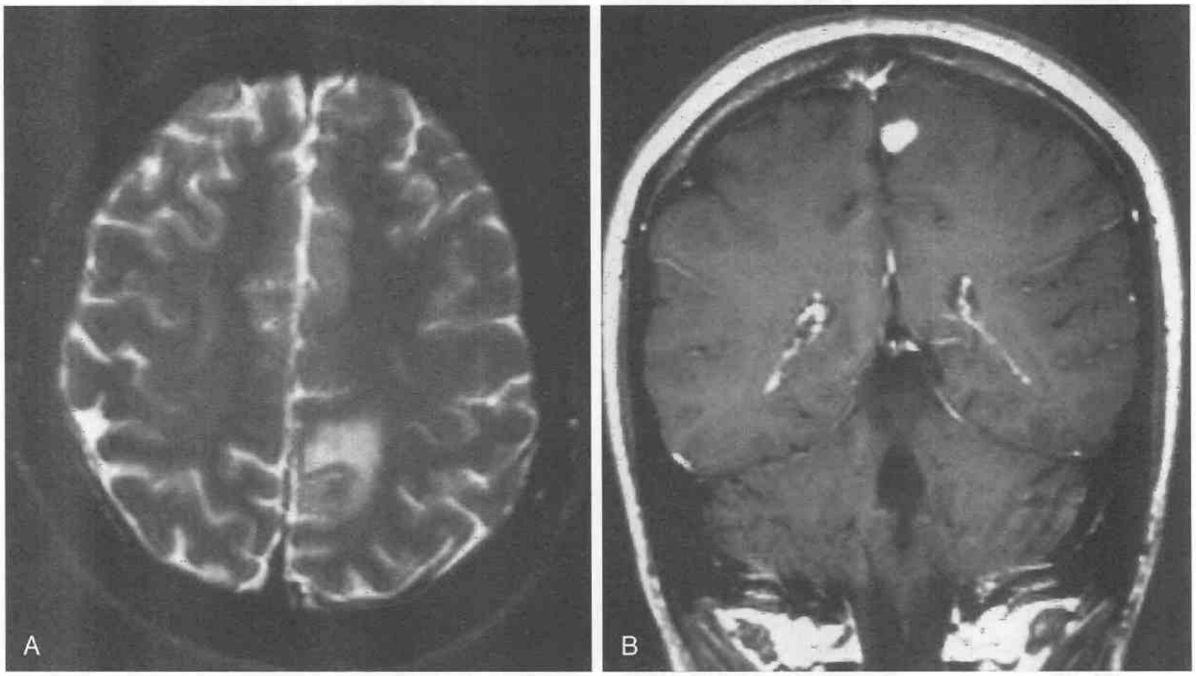

Figure 6–9. Early cerebritis. *A*, T2-weighted image demonstrates a low-signal-intensity focus with surrounding high-signal-intensity edema. *B*, Gadolinium-enhanced MRI study shows nodular enhancement with surrounding edema.

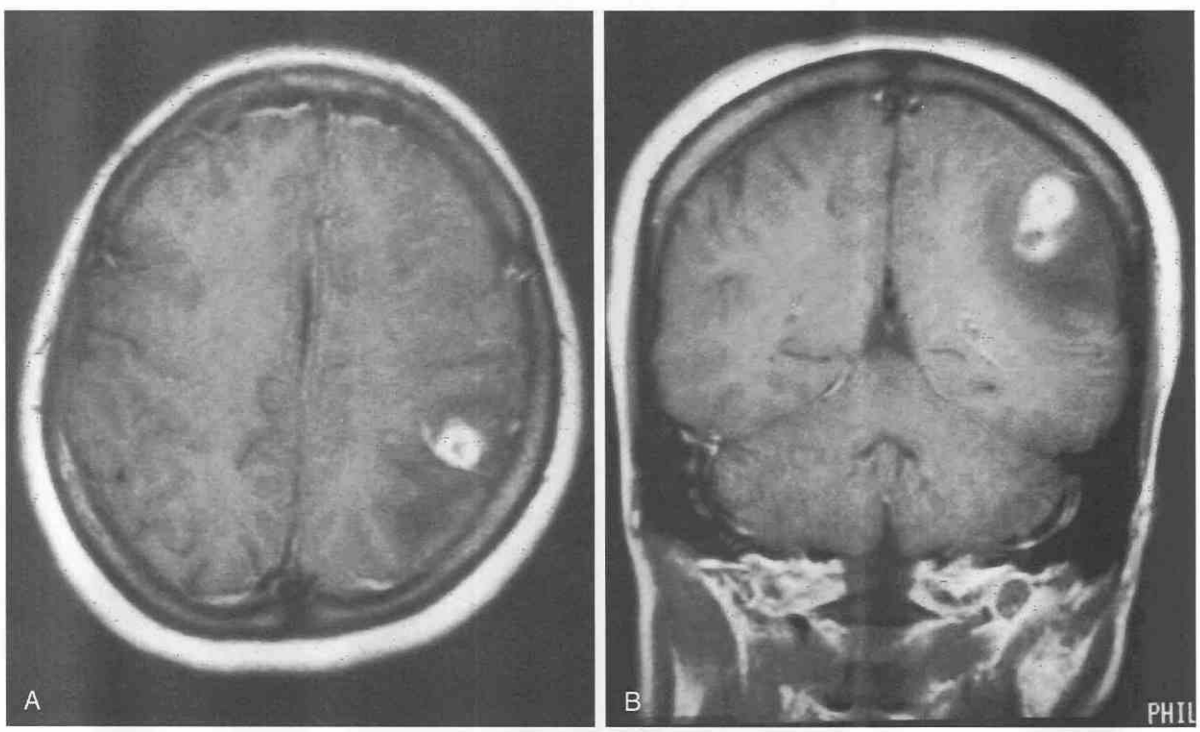

Figure 6–10. Late cerebritis. *A*, Gadolinium-enhanced MRI study shows thick, smooth, ringlike enhancement with surrounding edema. *B*, Gadolinium-enhanced MRI study (coronal view) shows a second, small, adjacent ringlike enhancement.

abscess cavity indicates the presence of gas-forming organisms[99, 101] (Fig. 6–11). Contrast-enhanced CT scans show ringlike enhancement, which is usually thin and uniform in thickness. Occasionally, thick irregular ring enhancement may be seen—especially following partial treatment—and may mimic neoplasm.

The CT features of abscess vary, depending on the function of the host reaction to infection and different stages in the evolution of the abscess.[97, 172] On MRI scans, the capsule is better visualized as compared with CT. The capsule is isointense to hyperintense to gray matter on T1-weighted images and hypointense on T2-weighted images. The hypointensity on the abscess capsule is consistently seen with abscess and may be useful in characterizing the lesion[57] (Fig. 6–12*A*). However, other lesions, such as metastasis, glioma, and cysticercosis, may show a similar hypointense ring on T2-weighted images. The capsule enhances with IV administration of contrast material on CT or MRI studies.

The presence of satellite lesions is a unique feature of cerebral abscess (Fig. 6–12*B*). Firmness of the capsule wall depends on how long the lesion has been present. Usually, more than 2 weeks is required to form a firm capsule. Clinical improvement with medical therapy has been correlated with a decrease in both the degree of ring enhancement and the amount of surrounding edema (Fig. 6–13).[71, 121]

A serious fulminating complication is rupture of the abscess into an adjacent ventricle. Abscesses tend to rupture medially into the ventricular system because the medial wall is thinner than the lateral wall.[153] This is related to the white matter having less vascular supply than gray matter. A more intense perivascular response is seen at the site of gray matter.[137]

The differential CT diagnosis of cerebral abscess includes primary or metastatic neoplasm, subacute infection, and resolving hematoma. The enhancing ring of an abscess is usually thinner and more uniform than that found in the neoplasm. Granulomatous abscesses tend to have a thicker ring than pyogenic abscesses and have less surrounding edema. Infarcts often show gyral enhancement, occasionally mimicking ring enhancement. Resolving hematoma may have a dense center with ringlike enhancement and much less surrounding edema.

The MRI differential diagnosis of abscess is similar to the CT diagnosis except for hematomas, which can be recognized by their characteristic MRI signal intensity patterns, depending on the age of the hematomas.

Various authors have given different explanations of capsular hypointensity.[68, 139, 171] The most plausible hypothesis seemed to suggest that macrophages within the granulation layer of the abscess capsule are the cause of the hypointensity. Macrophages kill bacteria with respiratory burst, during which molecular oxygen is converted into atomic oxygen, which then generates a series of short-lived highly reactive oxygen free radicals that interact with the bacteria. Because these free radicals are intracellular, they may be capable of producing similar susceptibility effects as intracellular methemoglobin or deoxyhemoglobin with resultant T2 shortening.[68, 139, 171]

The features of abscess tend to differ in immunocompromised patients receiving steroids. In such patients, edema may be minimal and the abscess capsule may be thick and irregular. Hypointensity of the capsule seen on T2-weighted images may not be obvious. Extraparenchymal spread into the ventricles and meningitis are more common.

The differential diagnosis of brain abscesses is quite

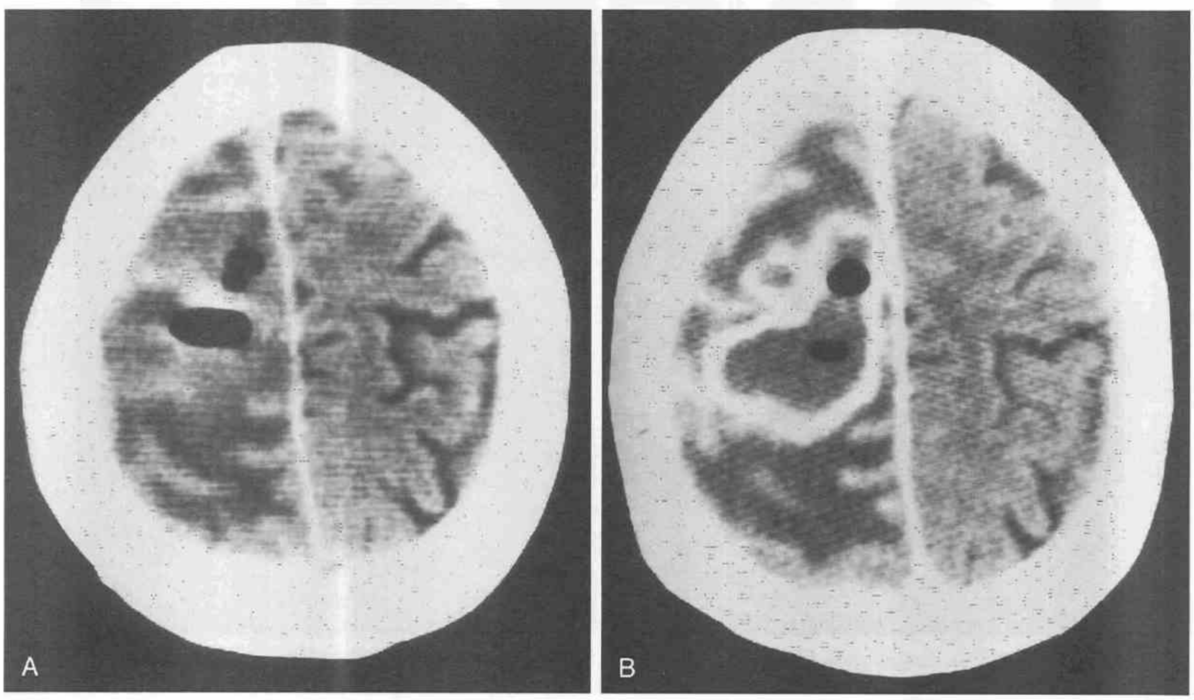

Figure 6–11. Abscess caused by gas-forming organism. *A*, Gas is seen with a surrounding low-density area on noncontrast CT scan. *B*, Contrast CT scan shows irregular, ringlike enhancement; gas is visible within the cavity. The causative organism was *Escherichia coli*.

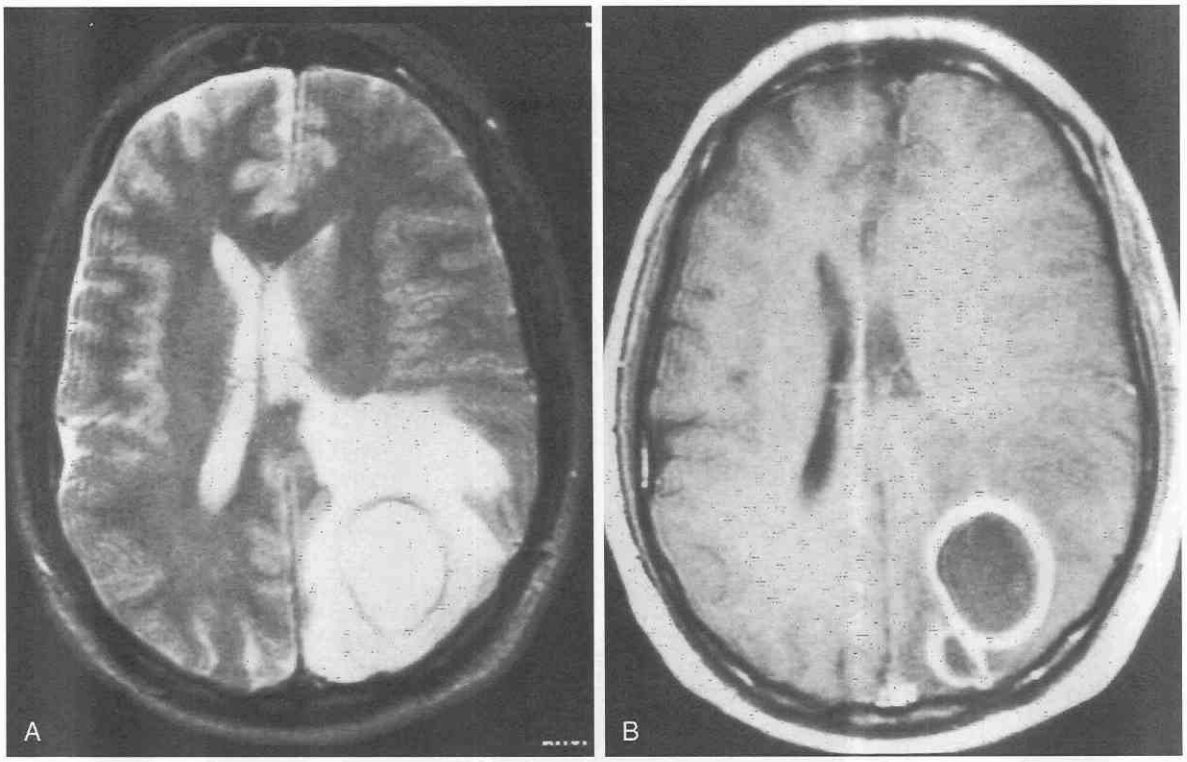

Figure 6–12. Mature abscess. *A*, T2-weighted image shows a mature abscess with hypointense rim, central cavity, and adjacent surrounding edema. A small satellite lesion is also seen. *B*, Gadolinium-enhanced MRI study demonstrates smooth, ringlike enhancement corresponding to the hypointense rim seen on T2-weighted images.

extensive and includes necrotic primary brain tumor, cystic metastatic tumor, infarction, resolving hematoma, cysticercosis, and thrombosed aneurysm. Thallium 201 SPECT or PET may be useful in differentiating an abscess from a necrotic tumor. Preferential uptake of thallium is seen in tumor, especially high-grade tumor, but not in abscess.[44] Tumor has higher glucose utilization than that of abscess, as shown on FDG PET imaging.

Recently, much work has been done with advanced imaging techniques such as diffusion-weighted imaging and proton MRS. The central portion of an abscess cavity tends to show depression of apparent diffusion coefficient, thus increased signal intensity on diffusion-weighted images (Fig. 6–14), whereas tumor necrosis exhibits an increase in apparent diffusion coefficient.

A significant number of studies of proton MRS have been performed in differential diagnosis of abscess and necrotic brain tumors. It is well documented that abscess cavities contain amino acids, succinate, and acetate, which are not seen in the necrotic center of the tumor.[30] Furthermore, MRS may be useful as the follow-up examination in evaluation of the response to therapy.[31]

Mycotic Aneurysm

Intracranial septic emboli may lead to the formation of mycotic aneurysms, usually seen in patients with a history of IV drug abuse, cyanotic heart disease, and subacute bacterial endocarditis. Mycotic aneurysms probably result from infarction of the arterial wall secondary to infected emboli. Mycotic aneurysms may be solitary or multiple, and they usually involve middle cerebral artery branches. The relative frequency of middle cerebral artery branch involvement is probably explained by the likelihood of emboli being carried into this territory.

Rupture of a mycotic aneurysm may produce an intracerebral or subdural hematoma[134] (Fig. 6–15). An unruptured mycotic aneurysm may occasionally be detected by contrast-enhanced CT or MRI studies.[2] Associated infarction or small areas of cerebritis or abscess formation may be seen on imaging. Follow-up imaging studies can be useful when mycotic aneurysms are being treated medically with antibiotics. A single mycotic aneurysm may warrant surgical extirpation.

Ependymitis

Ventriculitis, or ependymitis, is an inflammation of the ependymal lining of the ventricular system. Spread of infection to the ventricles may result from rupture of a periventricular abscess or from retrograde spread of infection from the basal cisterns by way of the fourth ventricle. Hydrocephalus may result from intraventricular adhesions and septation caused by organization of intraventricular exudate and debris, resulting in blockage of the interventricular foramina.[129, 166] A trapped fourth ventricle may result from obstruction of its outlets and the aqueduct because of ependymitis.[169]

The noncontrast CT scan may be normal or may show only slightly increased density in the region of the affected

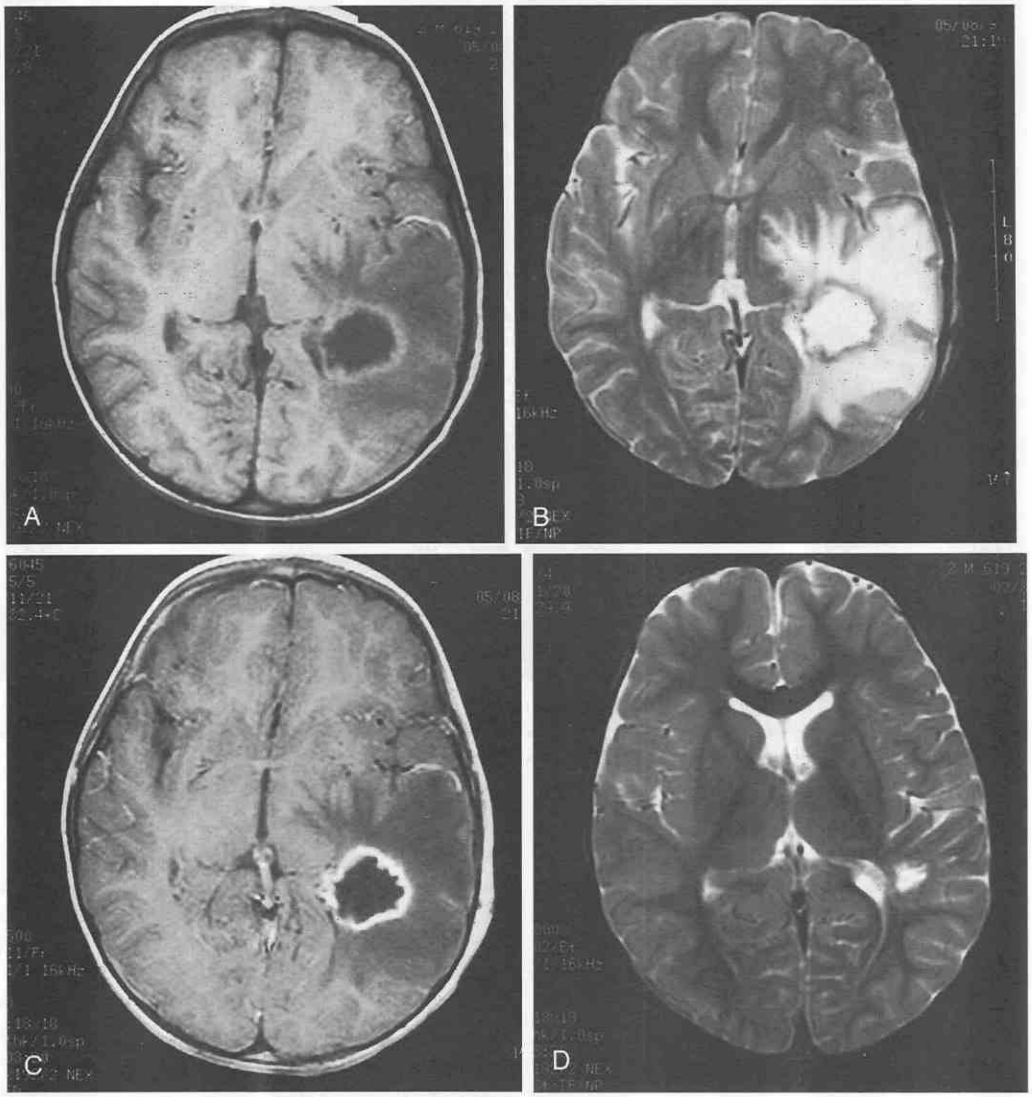

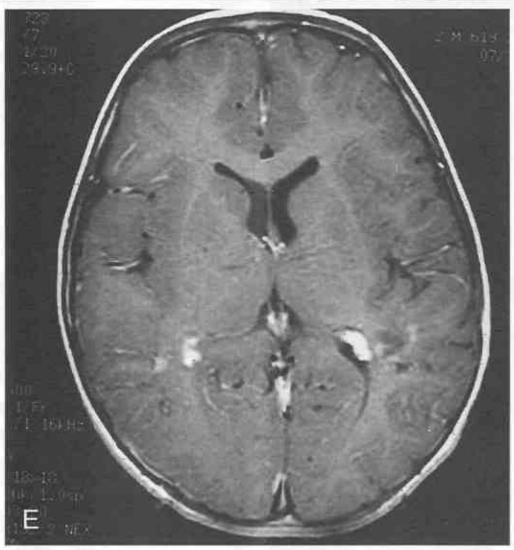

Figure 6–13. Abscess treated conservatively with antibiotics. *A*, T1-weighted image shows a low-signal-intensity mass with an isointense ringlike rim and surrounding edema in the left posterior temporal lobe. *B*, T2-weighted image shows a high-signal-intensity mass with low-signal-intensity rim and marked surrounding edema. *C*, Gadolinium-enhanced image demonstrates avid ringlike enhancement of the ringlike rim with a central cavity and surrounding edema. *D*, Follow-up T2-weighted image obtained 8 weeks later reveals a significant decrease in the size of the abscess and surrounding edema. *E*, Follow-up gadolinium-enhanced image demonstrates minimal residual enhancement.

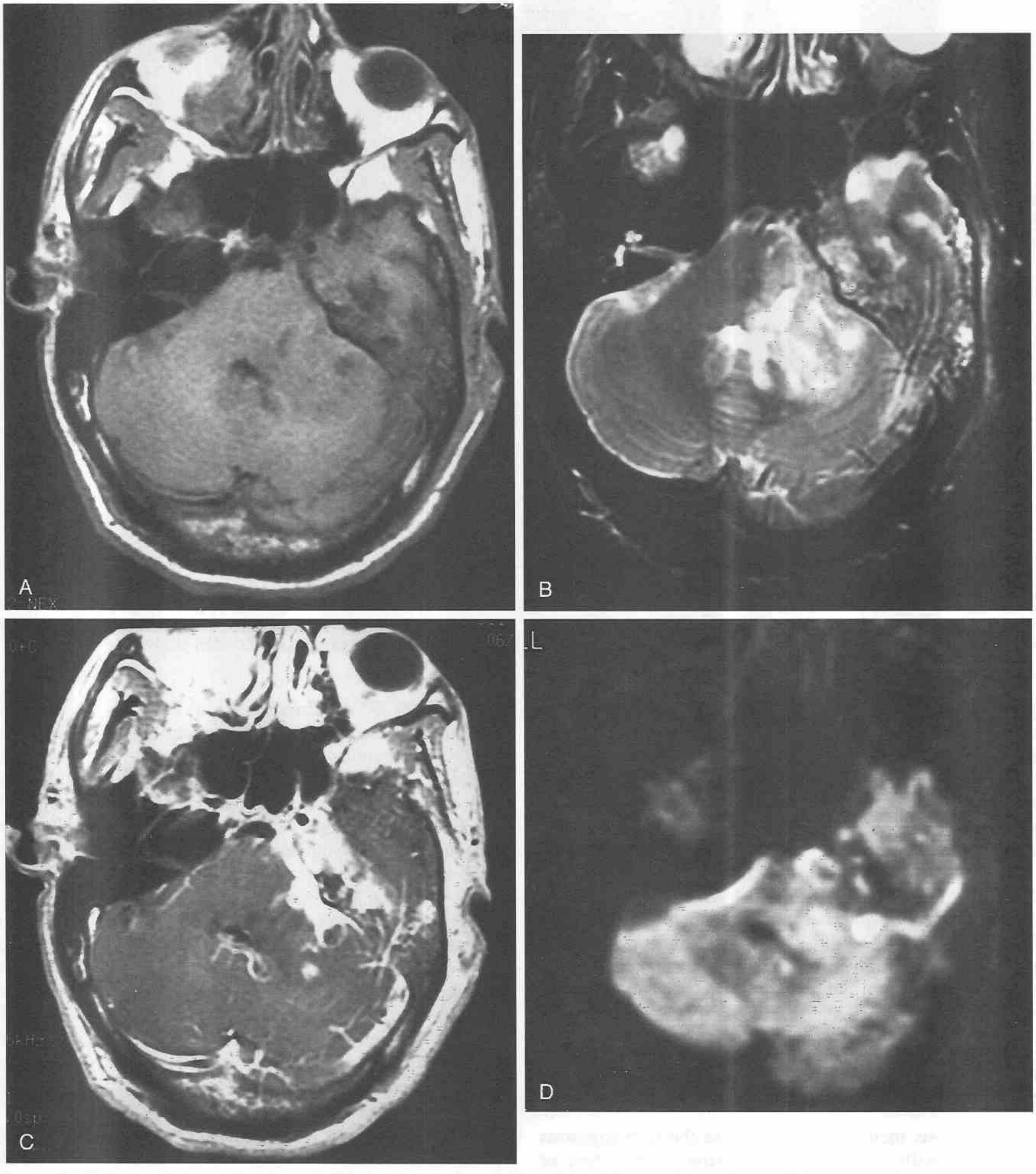

Figure 6–14. Mastoiditis, cerebritis, and abscess formation. *A*, T1-weighted image shows abnormal low signal intensity in the left temporal lobe, left brachium pontis, and left mastoid. *B*, T2-weighted image shows heterogeneous high signal intensity involving the left temporal lobe, left brachium pontis, and left mastoid. *C*, Gadolinium-enhanced image demonstrates abnormal enhancement involving the left temporal lobe, left brachium pontis, and left mastoid. Note the presence of a small ringlike enhancement in the posterior aspect of the brachium pontis. *D*, Diffusion-weighted image reveals a focal area of increased signal intensity, corresponding to the ringlike enhancement. This is consistent with restricted diffusion in an abscess.

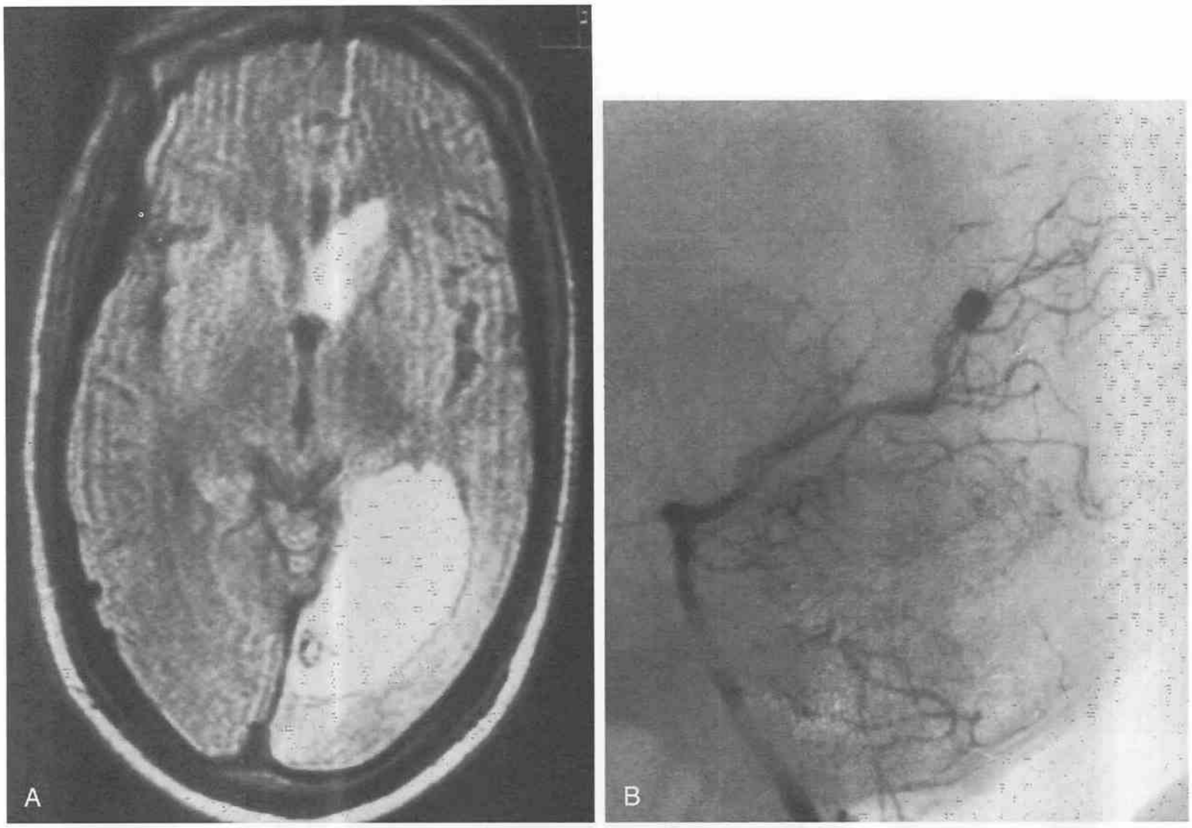

Figure 6–15. Mycotic aneurysm. *A*, Proton-density–weighted image shows high-signal-intensity hemorrhage in the left occipital lobe as well as in the ventricle. A small, ringlike, low-signal-intensity area is seen within the hemorrhage. *B*, A mycotic aneurysm was found on cerebral angiogram, corresponding to the small, ringlike, low-signal-intensity area seen on the MRI study.

ependyma.[101, 170] MRI studies may show marginal ventricular abnormality or only slightly increased signal intensity in the region of affected ependyma on proton-density–weighted images. The fluid within the ventricles may show slightly increased intensity, indicating the presence of cells and inflammatory debris as well as increased protein concentration in the CSF.

Contrast-enhanced CT or MRI studies show uniform, thin ependymal enhancement (Fig. 6–16).

The differential diagnosis on CT and MRI studies includes ependymal seeding of intracranial neoplasm. The ependymal enhancement may be irregular or nodular if it is secondary to seeding of neoplasm. Obviously, the clinical history may be helpful in arriving at the correct diagnosis.

Granulomatous Infection

Tuberculosis

Tuberculosis meningitis results from the hematogenous spread of bacilli from a primary lesion in the chest or genitourinary tract or from direct extension from an intracerebral focus. Primarily, very young and very old persons are affected, with the highest incidence in the first 3 years of life.[111] More recently, an increased incidence of tuberculosis has been seen in immunocompromised patients. In the patient with tuberculous meningitis, the exudate, which is commonly seen in the basal cisterns, tends to be thick and adhesive. Communicating hydrocephalus may result from obstruction at the level of the basal cisterns. Vascular involvement of the arteries at the base of the brain or sylvian fissures may result from vasculitis and surrounding meningeal inflammation.

On noncontrast CT or MRI studies, the basal cisterns and sylvian fissures may be partially or completely obscured by the presence of purulent exudate and inflammatory tissue, which appears to have a density or signal intensity similar to that of the adjacent brain on CT scans or T1-weighted MRI studies, respectively.

On contrast-enhanced CT or MRI studies, the involved cisterns show intense enhancement[5, 16, 138, 154] (Fig. 6–17). MRI studies are more sensitive than CT scans for detection of tuberculous meningitis.[14] Ischemic infarcts, meningeal enhancement, and ventriculitis are better shown by MRI than by CT. Gadolinium injection is essential in evaluation of patients with intracranial tuberculosis. Calcification in the basal cisterns has been demonstrated a few years after the onset of disease and is better shown with CT scans.[87] Cerebral infarction may result from arterial or venous involvement. Middle cerebral artery territory is a common location[9] (Fig. 6–18).

Arriving at a definitive diagnosis of tuberculoma may be difficult because 52% of patients with intracranial tuberculomas have no extracranial disease.[94] Tuberculomas may be found in any portion of the intracranial compartment. Histologically, tuberculomas consist of a central zone of caseous material surrounded by reactive epithelial cells, Langhans' giant cells, polymorphonuclear cells, plasma cells, and lymphocytes.[154]

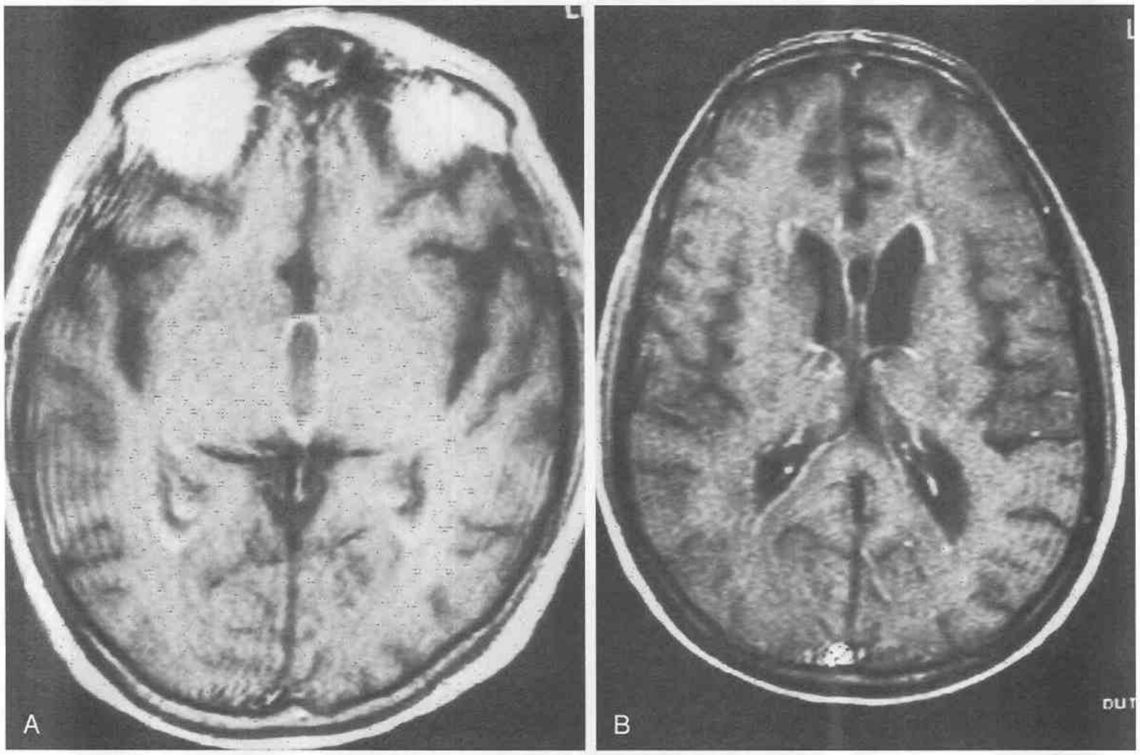

Figure 6–16. Ependymitis. *A* and *B*, Gadolinium-enhanced MRI study shows thin, smooth ependymal enhancement in an AIDS patient with cytomegalovirus ependymitis.

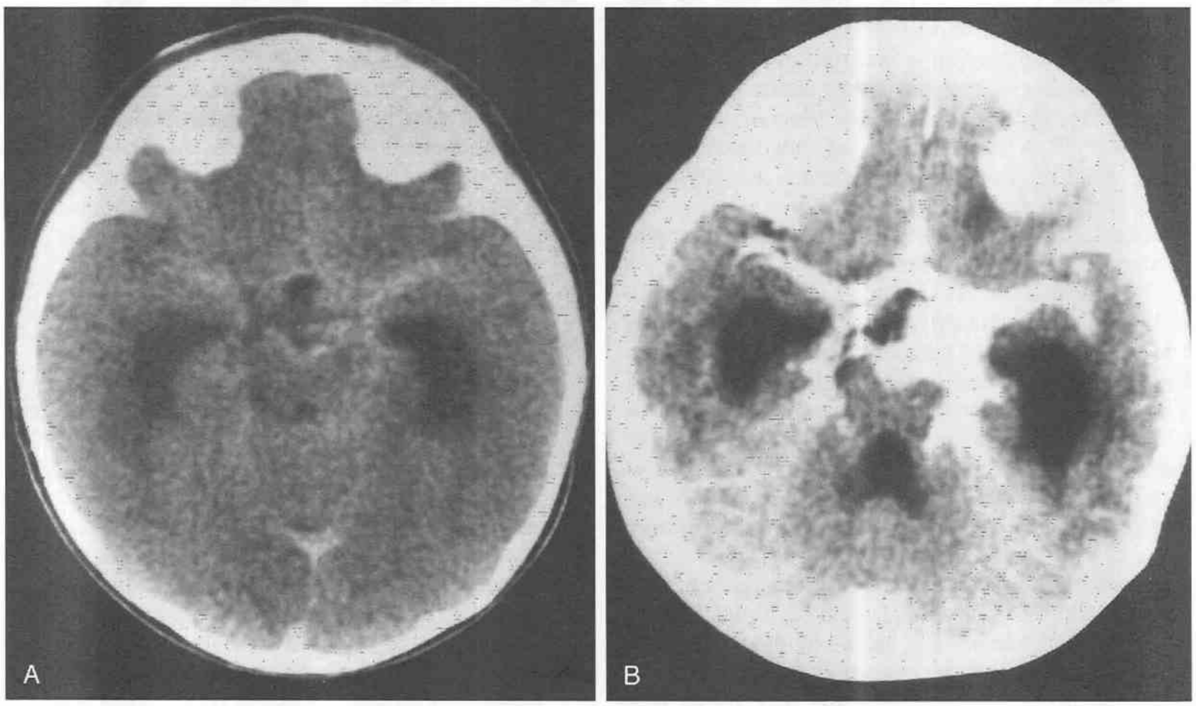

Figure 6–17. Tuberculous meningitis. *A*, Noncontrast CT scan shows high-density material in the suprasellar cistern, sylvian cistern, and perimesencephalic cistern. Dilation of both temporal horns is seen. *B*, Contrast CT scan shows diffuse intense enhancement in the involved cisterns.

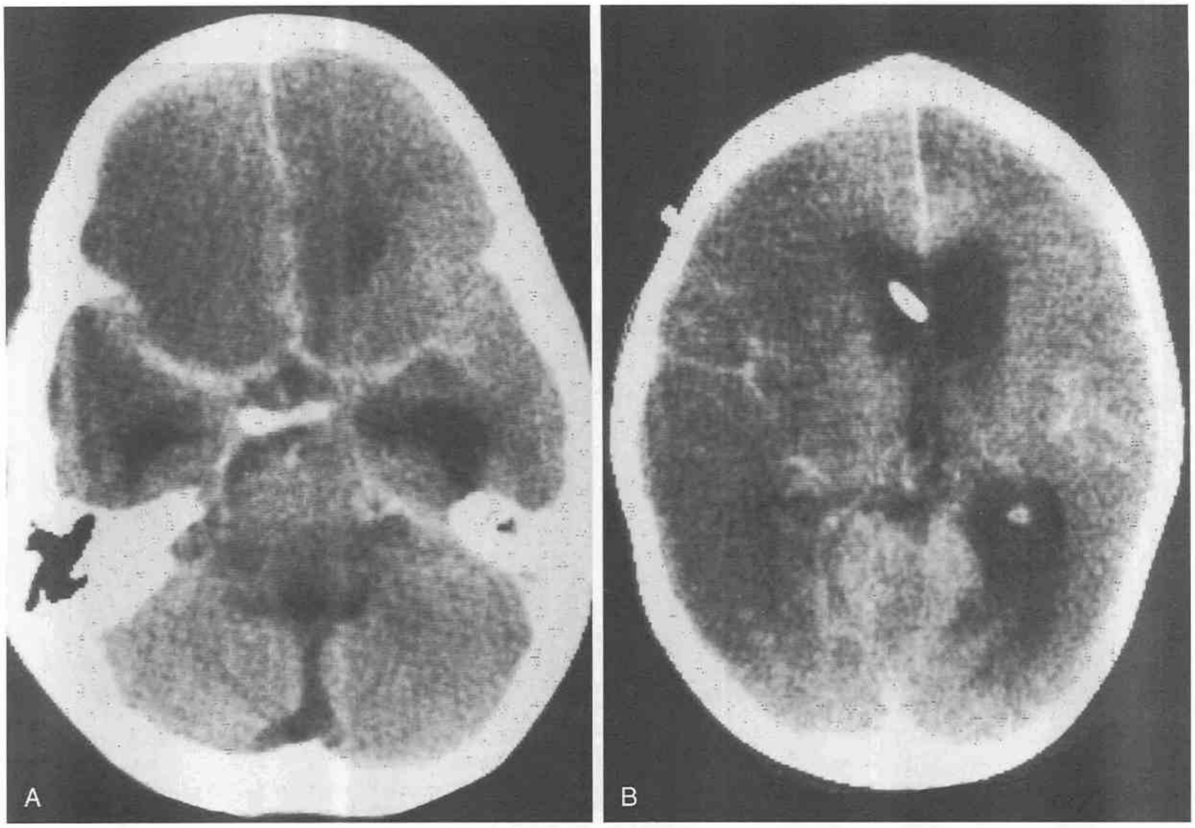

Figure 6–18. Cerebral infarction as a complication of tuberculous meningitis. *A,* Large low-density area is seen in the right temporal frontoparietal region in the right middle cerebral artery distribution, consistent with an infarct. *B,* Enhancement is seen in the sylvian fissures and along the tentorial margin, consistent with meningitis.

On unenhanced CT scans, tuberculomas may be isodense, hyperdense, or of mixed density. On contrast-enhanced CT scans, tuberculomas may present a pattern of ringlike enhancement[152] or, less likely, areas of nodular enhancement (Fig. 6–19) or irregular nonhomogeneous enhancement.[21, 109, 116] A central nidus of calcification with surrounding ringlike enhancement, known as the *target sign*, suggests tuberculoma.[152]

Gadolinium-enhanced MRI studies show enhancing patterns similar to those on contrast-enhanced CT scans[20, 29] (Fig. 6–20). Unenhanced MRI studies show mixed, predominantly low-signal-intensity lesion with a central zone of high signal intensity and surrounding high-signal-intensity edema on T2-weighted images or FLAIR images. A central high-signal-intensity zone on T2-weighted or FLAIR images corresponds to caseating necrosis. The low signal intensity of the capsule may be related to a layer of collagenous fibrosis with high protein concentration and low water content and a layer of outer inflammatory cells.[130]

On MRS, tuberculomas show only lipid resonance, with specific components of serine and phenolic lipids.[130] Follow-up CT or MRI studies are useful in monitoring the response to medical treatment.

Parenchymal infection of tuberculosis may occur with or without meningitis. Tuberculosis cerebritis or abscess may have an appearance on neuroimaging studies similar to that of pyogenic bacterial infection. Tuberculous abscess is rare and is characterized by a central area of liquefaction with pus (Fig. 6–21). These abscesses should not be confused with tuberculomas with central caseation and liquefaction mimicking pus.[52, 156]

Continued growth of tuberculoma with unresponsiveness to therapy, despite adequate medical treatment, is a known phenomenon called *paradoxical expansion.* Various immunologic mechanisms have been advanced as explanations, including defective local tissue immune response and poor penetration of drugs.[130]

Sarcoidosis

The intracranial compartment is involved in 15% of patients with known sarcoidosis.[24, 120, 133, 150] On rare occasions, CNS involvement may be the sole manifestation of sarcoidosis.[13, 53] Sarcoid is more prevalent in the 3rd and 4th decades of life. It may present as leptomeningitis or intracerebral granulomas. A third form of sarcoidosis, meningoencephalitis, is rarely seen.[96] Granulomatous meningitis often involves the basal cisterns in the region of the optic chiasm and hypothalamic-pituitary axis. Hydrocephalus may occur as a result of obstruction at the aqueduct, fourth ventricle, or leptomeninges.[80, 90]

Contrast-enhanced MRI is the imaging modality of choice for evaluation of meningeal sarcoidosis. Solitary or multiple lesions involving the meninges may be seen, and occasionally they may present as a large extra-axial mass (Fig. 6–22). The lesions are hypointense to isointense to

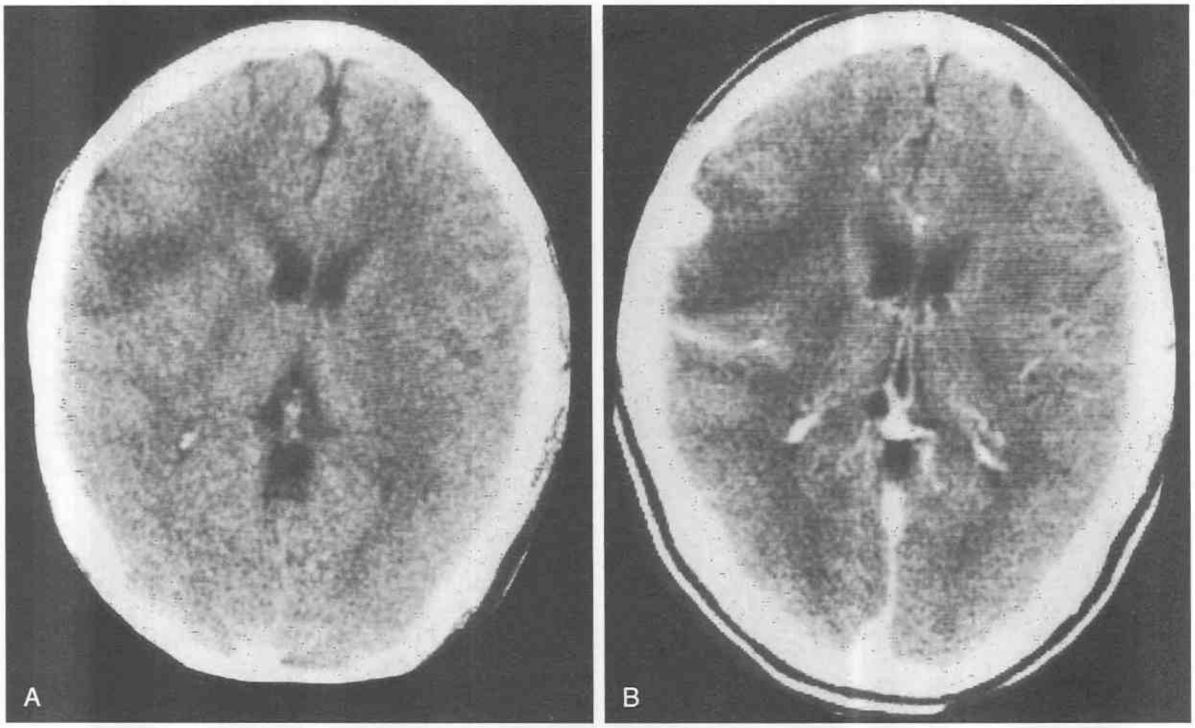

Figure 6–19. Tuberculoma. *A*, Noncontrast CT scan shows an isodense area with surrounding edema in the right frontal region. *B*, Contrast CT scan demonstrates nodular homogeneous enhancement.

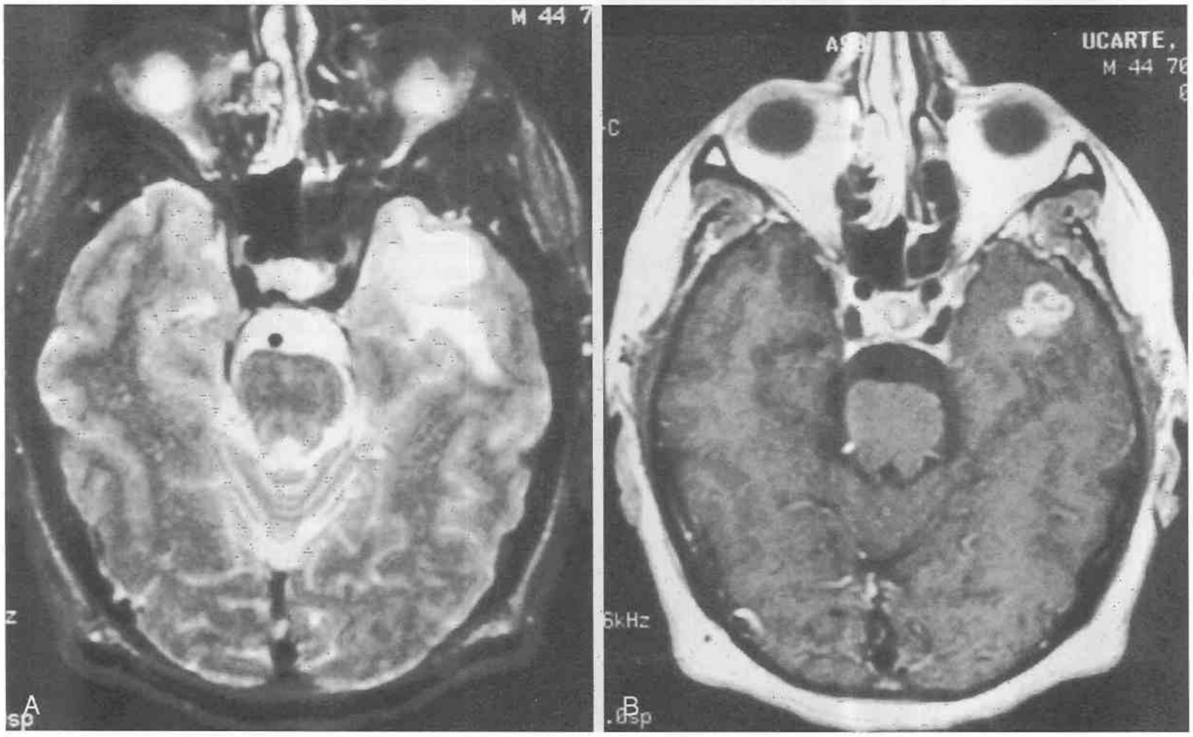

Figure 6–20. Tuberculoma. *A*, T2-weighted image shows an area of high signal intensity in the left temporal lobe. *B*, Gadolinium-enhanced MRI study demonstrates multiring enhancement with surrounding edema.

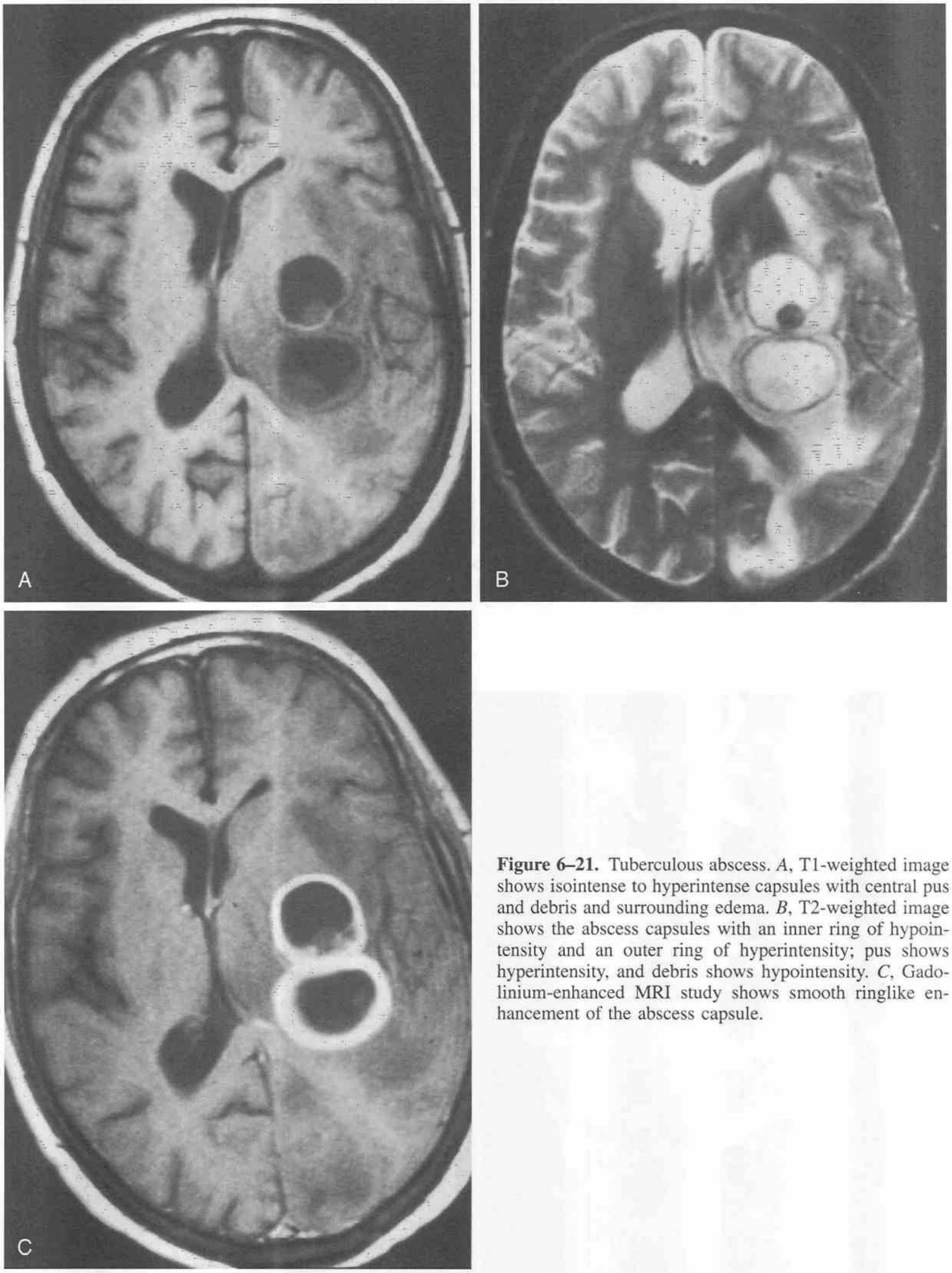

Figure 6–21. Tuberculous abscess. *A*, T1-weighted image shows isointense to hyperintense capsules with central pus and debris and surrounding edema. *B*, T2-weighted image shows the abscess capsules with an inner ring of hypointensity and an outer ring of hyperintensity; pus shows hyperintensity, and debris shows hypointensity. *C*, Gadolinium-enhanced MRI study shows smooth ringlike enhancement of the abscess capsule.

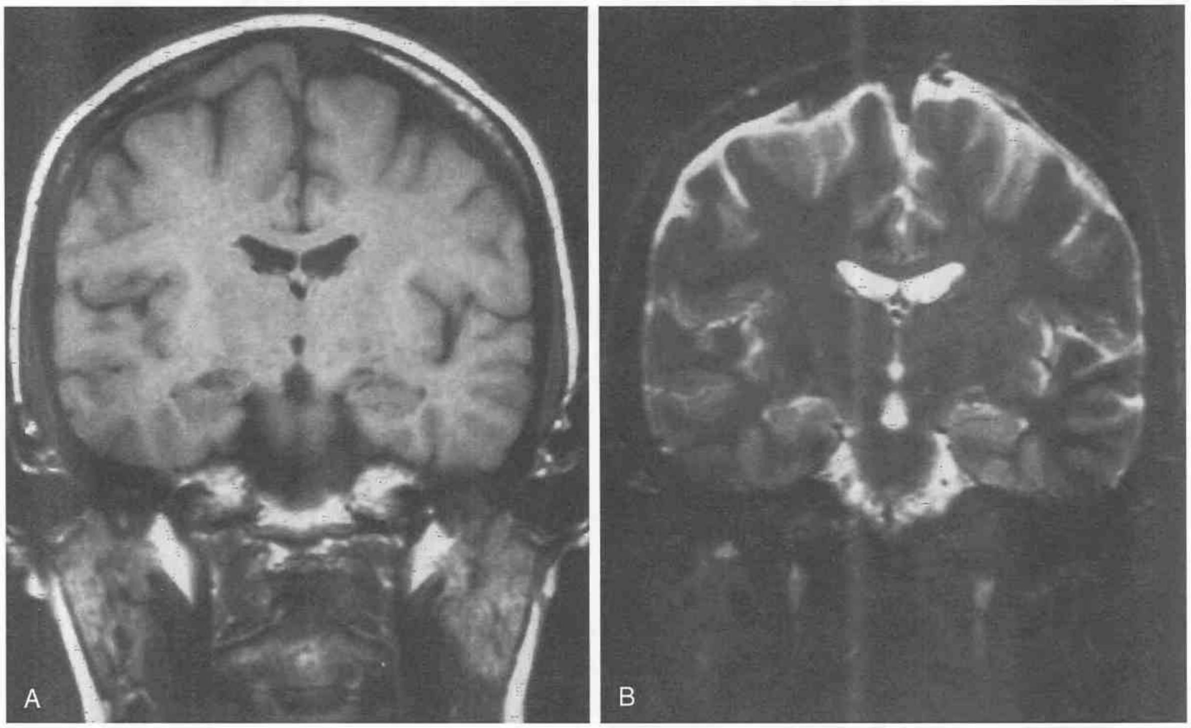

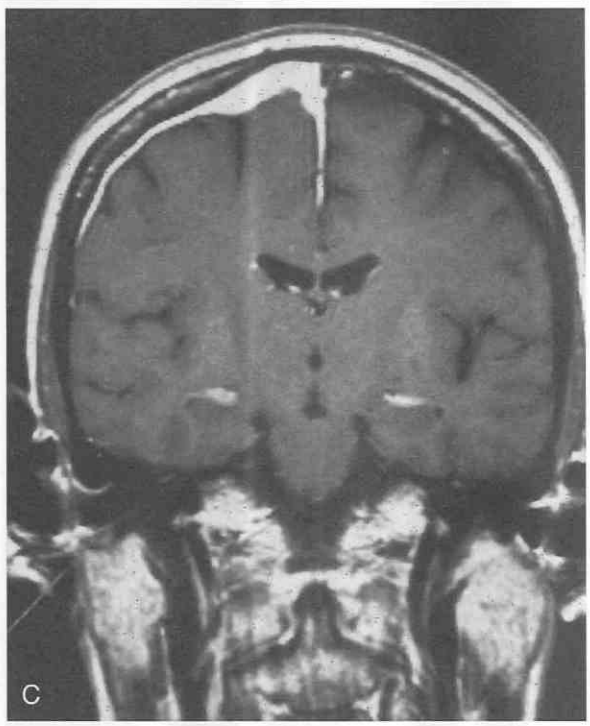

Figure 6–22. Sarcoid. *A*, T1-weighted image shows an isointense extra-axial lesion near the vertex. *B*, T2-weighted image shows the lesion to be of low signal intensity. *C*, Gadolinium-enhanced MRI study demonstrates intense enhancement of the lesion, which is better shown as compared with unenhanced images.

brain on T1-weighted images and are of variable but frequently low signal intensity on T2-weighted images. Homogeneous enhancement is seen with contrast-enhanced MRI as with contrast-enhanced CT.

The differential diagnosis may include meningiomas, metastatic disease, and lymphoma. Diffuse meningeal disease is more common than focal disease in sarcoidosis. Leptomeningeal enhancement involving the basal cisterns can be seen on contrast-enhanced MRI studies (Fig. 6–23).[131] However, a normal contrast-enhanced MRI study does not exclude the possibility of meningeal sarcoidosis.

The differential diagnosis of basal leptomeningeal enhancement may include bacterial, tuberculous, fungal, or cysticercal meningitis and meningeal seeding from metastasis, lymphoma, or leukemia. The noncaseating granulomas may be single or multiple, sometimes mimicking primary or metastatic neoplasm.[53, 127, 133]

On unenhanced CT scans, the granulomatous lesion shows hyperdense or isodense areas with minimum surrounding edema. Contrast-enhanced CT scans reveal homogeneous enhancement of these lesions.[74] Improvement with a decrease in size and number of lesions may be observed following steroid treatment. The intracranial granulomas may be single or multiple in the cortical or subcortical region.

On MRI studies, the lesions show heterogeneous and hyperintense signal pattern on T2-weighted images. Contrast-enhanced MRI studies show homogeneous enhancement.[60, 131] The differential diagnosis may include primary or metastatic neoplasms. Occasionally, meningeal disease extends into the deep cortical tissue and may mimic a parenchymal lesion. Diffuse periventricular white matter high-signal-intensity lesions on T2-weighted images are among the most common findings in neurosarcoidosis. The areas of involvement may show enhancement following IV injection of gadolinium. These lesions are probably secondary to involvement of the small arteries in the white matter.[60, 76, 131]

In the rare form of meningoencephalitis, contrast-enhanced CT scans may show linear and nodular meningeal enhancement extending into the parenchyma through the Virchow-Robin spaces.[96] Hypodense lesions in the white matter have been described and are probably secondary to involvement of the small arteries in the white matter.[76]

SPIROCHETE INFECTION

Lyme Disease

Lyme disease is caused by the spirochete *Borrelia burgdorferi* and is transmitted by deer ticks.[107] *Borrelia* is a neurotrophic bacterium that can produce acute neurologic symptoms or can remain dormant for many years.

Like syphilis, Lyme disease presents clinically in stages. The characteristic finding in the *early* stage is the skin rash known as erythema chronicum migrans seen at the site of tick bite.[79] Flulike symptoms and arthralgia associated with regional lymphadenopathy are also seen in the early stage. A disseminated form of early Lyme disease can occur in

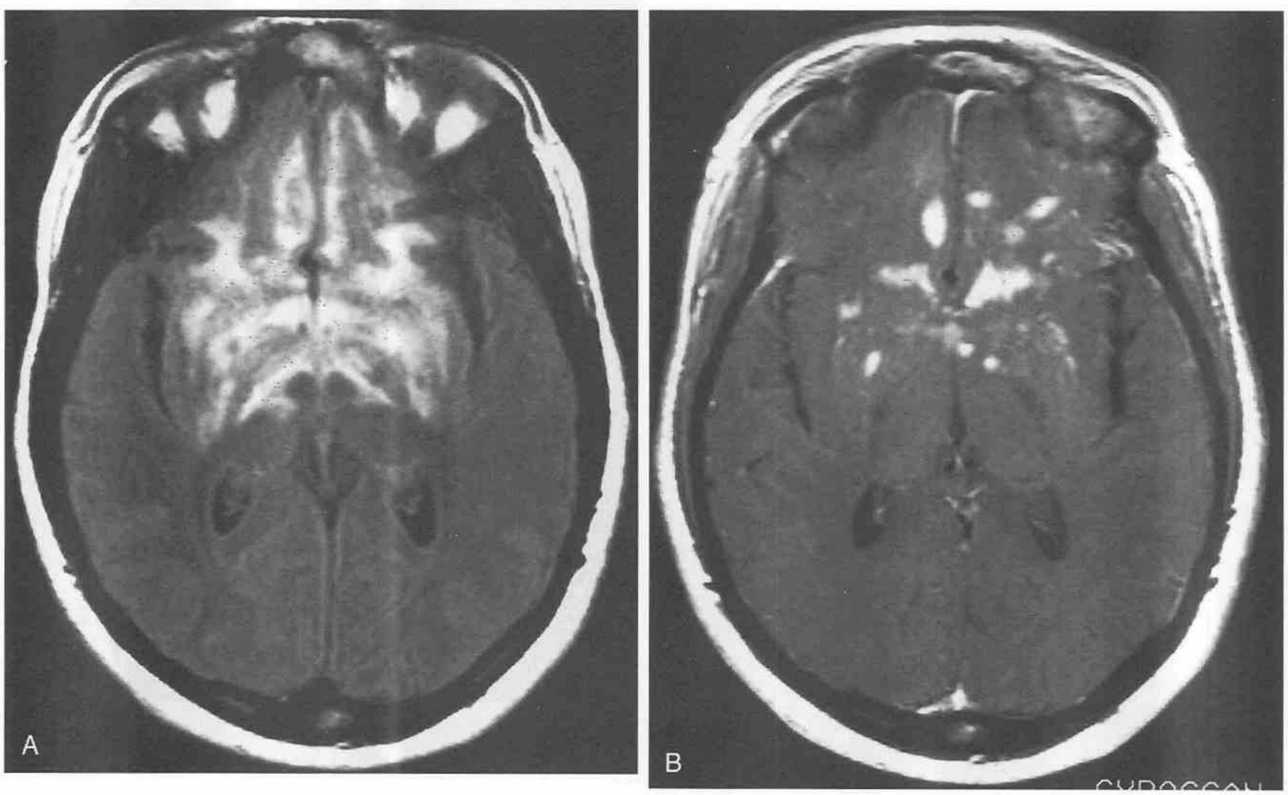

Figure 6–23. Sarcoidosis. *A*, Fluid-attenuating inversion recovery (FLAIR) image shows diffuse, irregular, abnormal high signal intensity extending from the subarachnoid space into the brain parenchyma of frontal lobes and basal ganglia. *B*, Gadolinium-enhanced image demonstrates patchy contrast enhancement involving the frontal lobes and basal ganglia.

which the organs primarily involved are skin, joints, heart, and nervous system.

Late symptoms occur in approximately 10% of untreated patients. Signs and symptoms of chronic neurologic damage include headache, memory impairment, papilledema, irritability, facial palsy, and peripheral neuropathies.

In many patients, neuroimaging studies may be normal. MRI findings, when present, include multiple bilateral periventricular, subcortical white matter, basal ganglia, and brain stem hyperintense lesions seen on T2-weighted or FLAIR images. The lesions are said to resemble multiple sclerosis plaques.[46, 119] Peripheral enhancement of these lesions may be seen. In some patients, diffuse meningeal enhancement is seen, indicating the presence of an encephalopathic process.

Syphilis

Syphilis is usually a sexually transmitted disease caused by *Treponema pallidum*, and CNS involvement occurs in the tertiary stage. Patients with AIDS usually show CNS involvement earlier, within 3 to 18 months. Acute syphilitic meningitis is a common manifestation in HIV-positive patients who are infected by *T. pallidum*.

Neurosyphilis can be divided into (1) meningovascular syphilis and (2) syphilitic gumma.

Meningovascular Syphilis

Pathologically, meningovascular syphilis is manifested by widespread thickening of the meninges, with lymphocytic infiltration involving the meninges and around the small vessels.[108] CT shows multiple low-density areas involving both gray and white matter.[48] Contrast-enhanced CT scans show linear, nonhomogeneous enhancement.

MRI is superior to CT scans in demonstrating additional foci of abnormality.[64] Contrast-enhanced MRI studies may demonstrate meningeal enhancement in addition to a gyriform pattern of enhancement.

Syphilitic Gumma

Gummas consist of masses of granulation tissue and are rare. They originate in the meninges and blood vessels and spread into the brain parenchyma.

On CT scans, gummas are well-delineated masses with ringlike or nodular enhancement. On MRI scans, gumma shows a high-signal-intensity ring on T1-weighted images and low signal intensity with surrounding high-signal-intensity edema on T2-weighted images. On contrast-enhanced MRI, gumma shows nodular or ringlike enhancement. Cerebral atrophy may develop in patients with neurosyphilis.[51]

Fungal Disease

Fungal infection may involve intracranial blood vessels, leptomeninges, and brain parenchyma. Intracranial infection is frequently secondary to pulmonary disease. Prior to the era of immunosuppressive therapy in organ transplant patients and the increase in HIV infection, fungal infection of the CNS was rare. Other conditions that predispose patients to fungal infection include diabetes, pregnancy, and malignancy.

Depending on the genera, fungi may exist as single cells (yeast) or in a branched appearance (hyphal form). The yeast and hyphal forms may coalesce and form mycelia. The fungi of yeast forms tend to spread hematogenously to the meningeal microcirculation, with resultant leptomeningitis attributable to their smaller size; the larger hyphal form more commonly involves the brain parenchyma, with resultant cerebritis or encephalitis.

The genera that are present predominantly as yeast forms include *Blastomyces, Candida, Coccidioides, Cryptococcus, Histoplasma, Paracoccidioides,* and *Torulopsis*. Hyphal forms include *Aspergillus, Mucor* and other agents of mucormycosis, and *Pseudoallescheria*.[49]

CNS fungal infection displays neuroimaging features similar to those seen with tuberculosis. It is known that CT scanning underestimates the extent of the disease in patients with widespread fungal infection, and MRI probably better represents the extent of the disease. CT or MRI findings are not specific for various types of fungal infection.

Aspergillosis

Aspergillus fumigatus infection is seen predominantly in immunocompromised patients.[26] CNS aspergillosis is more commonly caused by hematogenous spread of pulmonary disease and less commonly caused by direct extension of disease in the nasal cavity and paranasal sinuses. Pathologically, diffuse vascular invasion with thrombosis of cerebral vessels occurs.[161] Necrotizing arteritis of small vascular channels is also seen.

CT scans show low-density areas with little or no contrast enhancement and mass effect, representing areas of infarction.[40, 55] At times, hemorrhagic infarction may be seen. Cerebritis or abscess formation may also be seen secondary to hematogenous spread of the disease. CT scans show a slightly hyperdense, ringlike lesion with central low density and surrounding edema. Some contrast enhancement may be seen.[77] Focal areas of hemorrhage within the lesion may be seen.[148]

MRI studies demonstrate a peripheral ring of low signal intensity with an isointense (to gray matter) center and high signal surrounding edema on T2-weighted images. The ring of low signal intensity corresponds to a dense population of *Aspergillus* hyphal elements and small areas of hemorrhage histologically.

Coccidioidomycosis

Coccidioidomycosis is caused by the airborne fungus *Coccidioides immitis*. This fungus is endemic in the southwestern United States as well as in portions of Mexico and central South America.

Pathologically, coccidioidomycosis is characterized by thickened, congested leptomeninges and multiple granulomas in the basal cisterns. Meningitis is most intense at the base of the brain. Hydrocephalus is seen as a result of

granulomatous meningitis.[10] Meningeal involvement is the most common manifestation of CNS disease, occurring in up to 50% of the patients with disseminated systemic disease. Males are affected five to seven times more commonly than females. Adult nonwhites often have acute, rapidly fatal meningitis, whereas children and adult whites usually have subacute or chronic meningitis.

Unenhanced CT or MRI studies show isodense or isointense granulomatous tissue filling the basal cisterns. Contrast-enhanced CT or MRI studies show extensive basal cisternal or convexity enhancement (Fig. 6–24). Parenchymal granulomas occur infrequently; ringlike enhancement with minimum surrounding edema may be seen on contrast-enhanced CT or MR studies[35, 40, 98] (Fig. 6–25).

A lytic lesion involving the calvarium may be seen without parenchymal disease. Hydrocephalus may be secondary to meningitis or ependymitis. Small-vessel arteritis occurs in 40% of patients with meningitis, resulting in cerebral ischemia or infarction.[49]

Cryptococcosis

Cryptococcosis is a systemic infection that is worldwide in distribution. Despite the high prevalence of cryptococci in the environment, cryptococcal infection is uncommon but commonly occurs in immunocompromised patients. A selective impaired lymphocyte response to cryptococci in otherwise healthy patients has been demonstrated.[111] Cryptococcosis is the most common fungal infection in patients with AIDS.

CNS infection is usually secondary to pulmonary infection. Cryptococcosis is the most frequent clinically encountered CNS fungal infection. CNS cryptococcosis may present as meningitis, meningoencephalitis, or cryptococcal mass. Meningitis is the most common presentation. Hydrocephalus is seen as a result of the meningitis. Meningeal infection may extend from the basal cistern via dilated Virchow-Robin spaces into the basal ganglia and thalami.[144] Visual symptoms are common in patients with cryptococcal meningitis.

Two mechanisms have been implicated in patients with visual loss and optic atrophy: (1) increased intracranial compression with resultant damage to the optic nerve, and (2) direct cryptococcal involvement of the optic nerve.[103, 140]

Contrast-enhanced CT or MR studies may show meningeal enhancement involving the basal cisterns, sylvian fissure, and cortical sulci; nodular or ringlike enhancement may be seen[25] (Fig. 6–26). Dilated Virchow-Robin spaces may be seen on CT scanning or MR imaging, which is highly suggestive of cryptococcosis.[144]

On contrast-enhanced MR images, enhancement within the Virchow-Robin space may be seen (Figs. 6–27 and 6–28) . However, similar findings may be seen in coccidioidomycosis and candidiasis. Optic atrophy is better demonstrated by MRI than by CT.

Mucormycosis

Mucormycosis occurs in immunocompromised patients, most often in patients with poorly controlled diabetes. There are two forms of CNS mucormycosis:

1. The common form is rhinocerebral infection, with or without intracranial extension, with a predilection for patients with diabetes.[43]
2. The rare form is focal intracerebral infection in the absence of sinus disease. It is most often encountered in IV drug users. Anatomically, there is a predilection for the basal ganglia.[141]

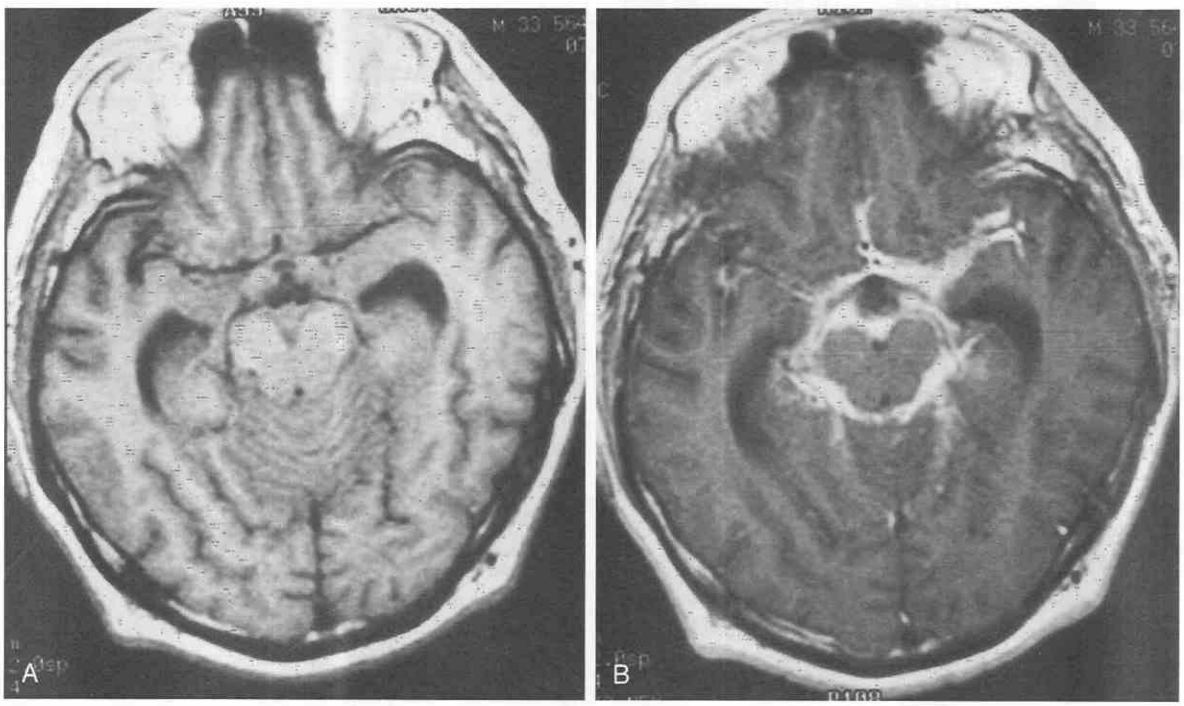

Figure 6–24. Coccidioidomycosis meningitis. *A*, T1-weighted image shows isointense granulomatous tissue in the suprasellar cistern. *B*, Gadolinium-enhanced image demonstrates intense enhancement in the basal cisterns.

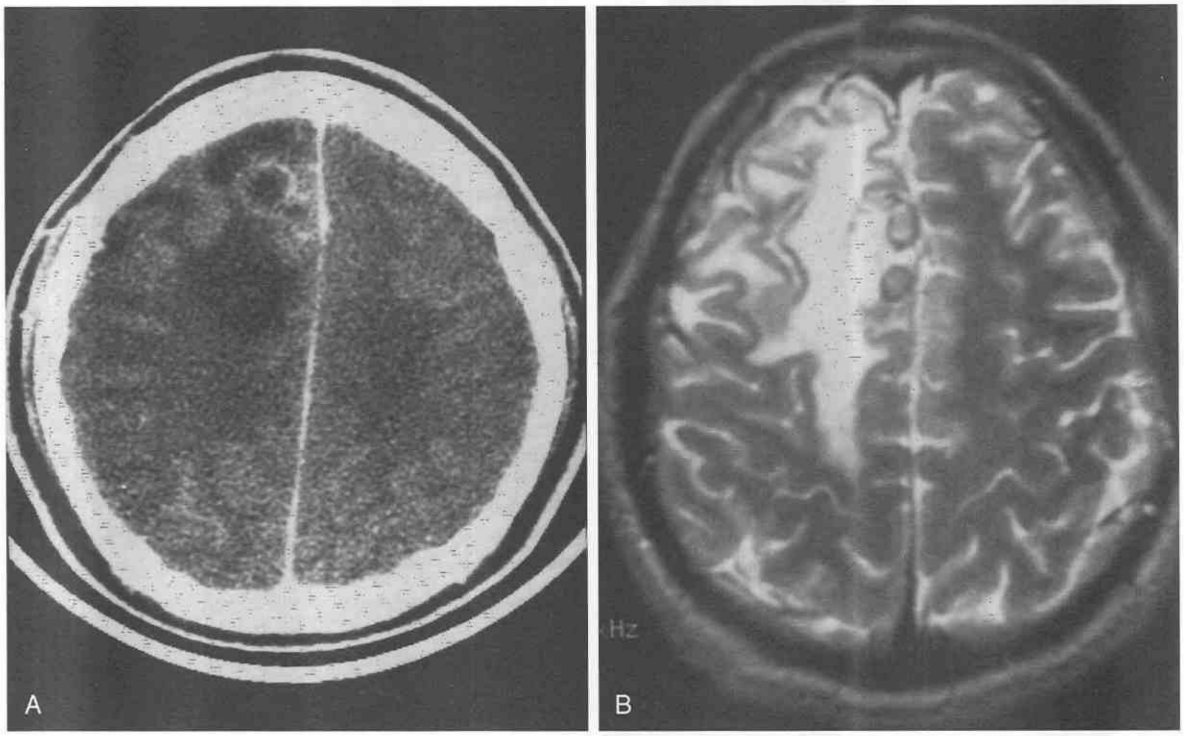

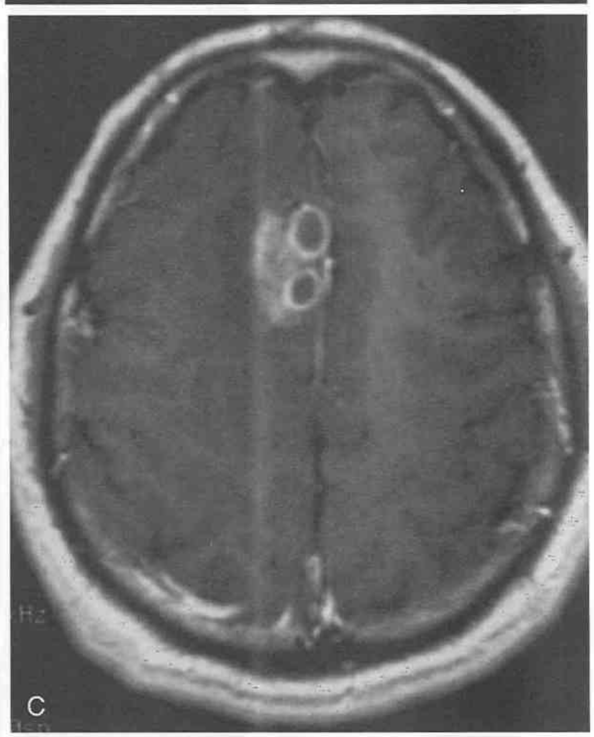

Figure 6–25. Coccidioidomycosis. *A*, Contrast-enhanced CT scan shows small lesions with ringlike enhancement. *B*, T2-weighted image shows two small low-signal rings with intermediate center and high-signal adjacent edema. *C*, Gadolinium-enhanced MRI study shows small lesions with ringlike enhancement and an adjacent area of patchy enhancement. The lesions are better shown with MRI than with CT.

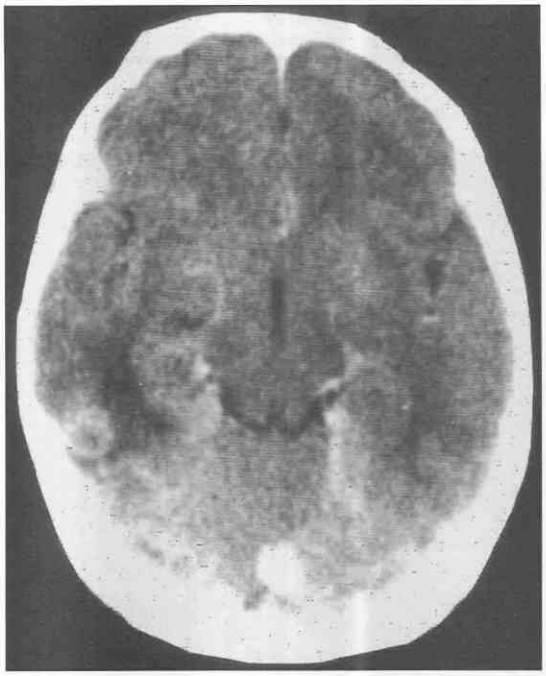

Figure 6–26. Cryptococcosis. Contrast CT scan shows a ringlike enhancement in the right posterior temporal lobe with surrounding edema.

Rhinocerebral mucormycosis spreads from the nasal cavity and paranasal sinuses by means of perivascular perineural channels through the cribriform plate into the frontal lobe and through the orbital apex into the cavernous sinus.[82] Pathologically, there is a predilection for the vasculature, particularly the arteries. It proliferates along the internal elastic lamina of the arterial walls, and hyphae may penetrate through the endothelium into the lumen, causing thrombosis with resultant infarction.

In the appropriate clinical setting, extensive paranasal sinus disease, with or without intracranial or nasopharyngeal extension, on CT or MRI studies should suggest mucormycosis. Extension of mucormycosis through bony partitions may occur without radiologic evidence of bone destruction.[47] Unenhanced CT scans may show low-density areas intracranially.

Contrast-enhanced CT scans may show ringlike enhancement with little surrounding edema. On MRI studies, sinus disease may exhibit near signal void (similar to air) on T2-weighted sequences, indistinguishable from normal aerated sinuses, which some suggest is the result of a high concentration of iron and manganese within the fungal mass.[141]

Primary intracerebral mucormycosis may reveal low density on unenhanced CT scans. Patchy, irregular enhancement is seen on contrast-enhanced CT scans. Focal

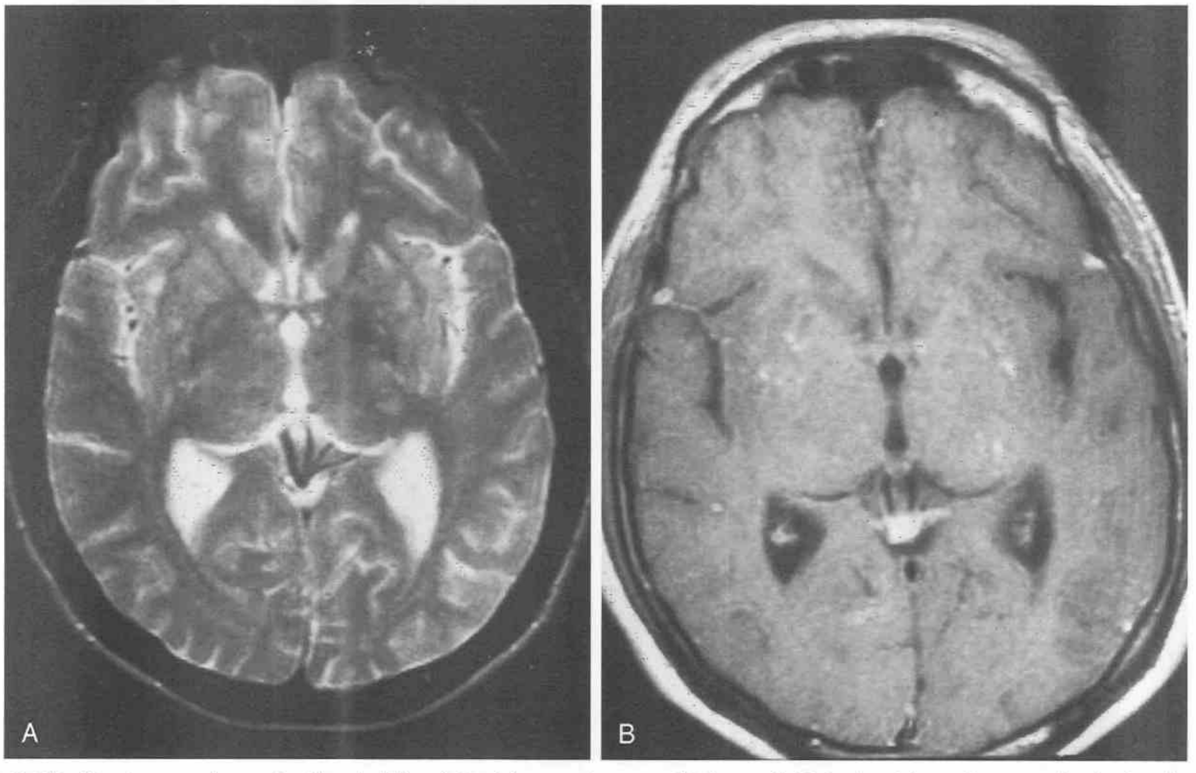

Figure 6–27. Cryptococcosis meningitis. *A*, T2-weighted image shows multiple small high-signal-intensity areas in the basal ganglia, consistent with a dilated Virchow-Robin space. *B*, Gadolinium-enhanced MRI study demonstrates small nodular enhancement, corresponding to the high signal intensity seen on T2-weighted images.

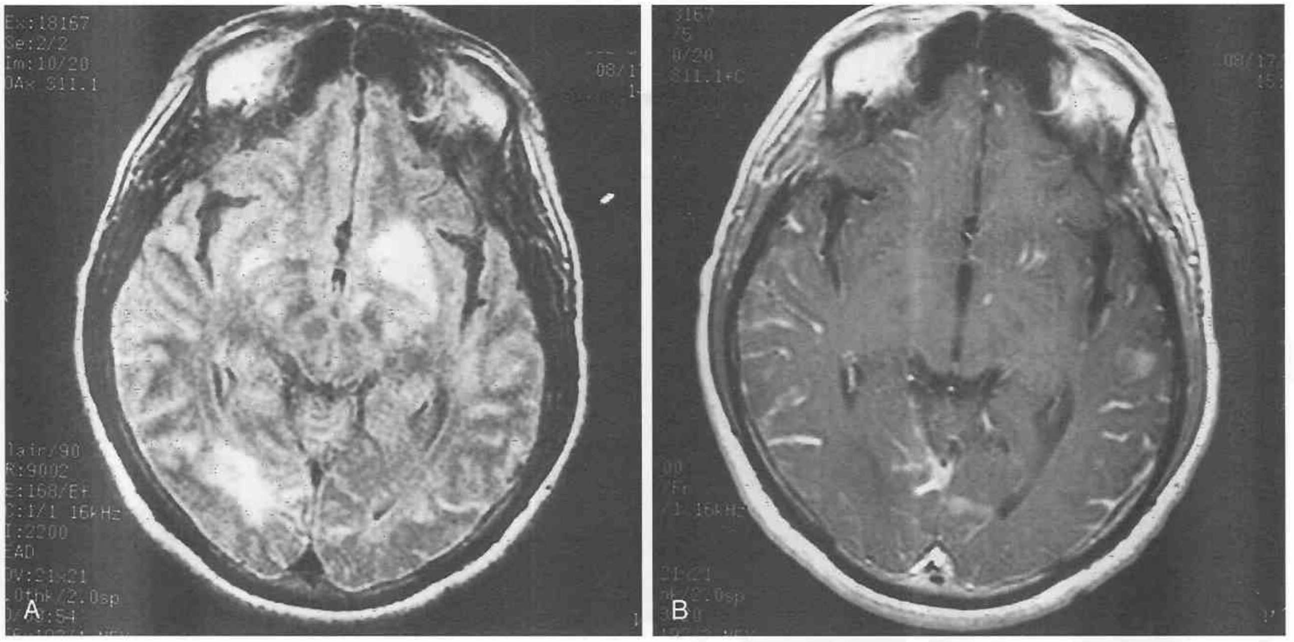

Figure 6–28. Cryptococcosis meningitis. *A*, Fluid-attenuating inversion recovery (FLAIR) image shows multiple high-signal areas in the basal ganglia as well as in the cortical sulci and subcortical white matter. *B*, Gadolinium-enhanced image demonstrates curvilinear abnormal enhancement in the basal ganglia and cortical sulci.

areas of hemorrhage may be seen within the lesion. With MRI, low signal intensity is seen on T1-weighted images, and areas of high signal intensity, mixed with very low signal intensity (near signal void), are seen on T2-weighted images. Patchy enhancement may be seen on contrast-enhanced MR images[128] (Fig. 6–29).

Candidiasis

Candida albicans is part of the normal flora in the gastrointestinal (GI) tract and mucocutaneous regions. *Candida* is also present in the vagina of healthy nonpregnant females and, more frequently, in pregnant females. *C. albicans* is the most common cause of human fungal infection[8] and represents 75% of the fungal infections in patients with neoplasm. Candidiasis occurs in immunocompromised patients. Systemic candidiasis is an opportunistic mycosis, with the GI tract being the usual portal of entry. Any organ may be involved in systemic candidiasis including kidney, GI tract, brain, and respiratory system. CNS involvement occurs as a result of hematogenous spread or direct invasion from the oral cavity or orbit. There is a higher incidence of renal and cardiac candidiasis in patients with intracranial disease. Approximately 80% of patients with myocardial or valvular involvement have had cerebral candidiasis. Candidiasis may present as meningitis, granuloma, or microabscess.

Unenhanced CT scans usually show low-density areas. Contrast-enhanced CT scans may show little or no enhancement or irregular, ringlike enhancement.[18, 37, 142] Mycotic aneurysms associated with candidiasis have been reported.[86] Calcification in healed lesions has also been reported.[66]

Nocardiosis

Nocardiosis is an uncommon bacterial disease that has traditionally been included in medical mycology. *Nocardia asteroides* is usually the causative organism. *Nocardia* is found in the soil worldwide. Nocardiosis occurs mostly in immunocompromised patients, patients with diabetes, and those with collagen-vascular disease or preexisting pulmonary disease. The organism is airborne, and the primary focus of infection is usually pulmonary. CNS involvement is usually secondary to hematogenous spread of pulmonary disease, and occurs in about 25% of patients.[157] The most common manifestation is abscess formation, which may be multiple. Pathologically, polymorphonuclear cells are primarily responsible for the inflammatory response. Granuloma formation is rare.

Unenhanced CT scans show low-density areas. MRI studies show low-signal-intensity areas on T1-weighted images and high-signal-intensity areas on T2-weighted images. Contrast-enhanced CT scanning or MRI shows ringlike enhancement, which may be multiple or multiloculated.[37]

Parasitic Disease

Cysticercosis

Cysticercosis is one of the most common parasitic diseases involving the brain. It is caused by ingesting the ova of the pork tapeworm *(Taenia solium),* usually on unwashed, fecally contaminated vegetables or water. The human being serves as the intermediate host of the pork tapeworm, and the main intermediate host of *T. solium* is the pig. By ingesting poorly cooked pork infected with cysticercosis, the human becomes the definitive host for *T.*

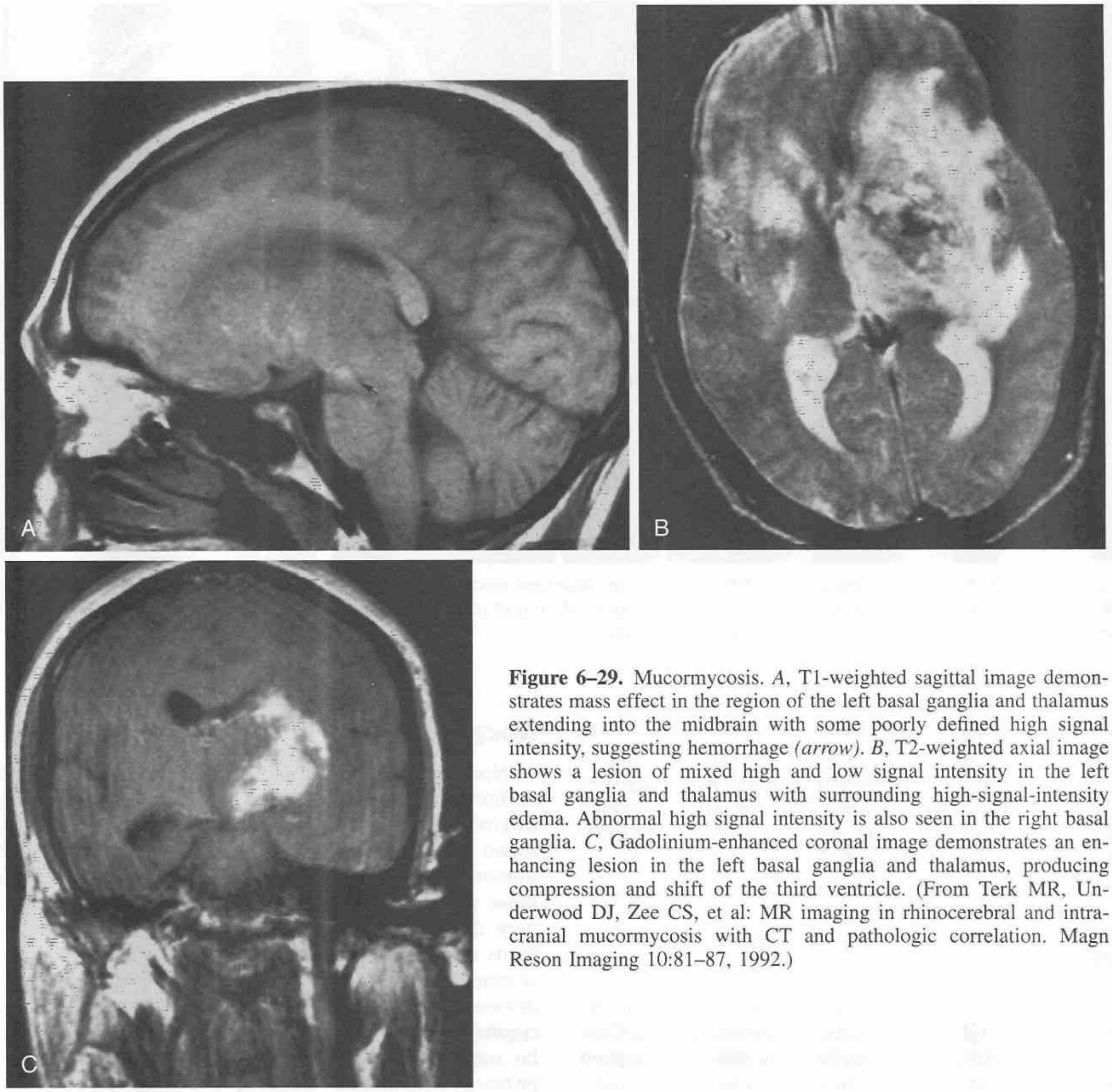

Figure 6–29. Mucormycosis. *A*, T1-weighted sagittal image demonstrates mass effect in the region of the left basal ganglia and thalamus extending into the midbrain with some poorly defined high signal intensity, suggesting hemorrhage *(arrow)*. *B*, T2-weighted axial image shows a lesion of mixed high and low signal intensity in the left basal ganglia and thalamus with surrounding high-signal-intensity edema. Abnormal high signal intensity is also seen in the right basal ganglia. *C*, Gadolinium-enhanced coronal image demonstrates an enhancing lesion in the left basal ganglia and thalamus, producing compression and shift of the third ventricle. (From Terk MR, Underwood DJ, Zee CS, et al: MR imaging in rhinocerebral and intracranial mucormycosis with CT and pathologic correlation. Magn Reson Imaging 10:81–87, 1992.)

solium. Humans infected with *T. solium* tapeworm excrete eggs of the tapeworm in the fecal material, which then contaminates water and vegetables in areas with poor hygiene. Of course, it is easy for a person with tapeworm in the intestine to become infected with cysticercosis through the anus-finger-mouth route. The disease has been reported to be endemic in parts of Latin America, Eastern Europe, Asia, and Africa. A recent increase in incidence has been noted in the southern and southwestern United States because of immigration.

The intracranial compartment is involved in 60% to 90% of patients with cysticercosis. The location of involvement can be meningobasal, parenchymal, intraventricular, or a combination of these sites.[95] Parenchymal cysticercosis has a varied appearance on neuroimaging. Following arrival in the brain parenchyma, the precysticercosis embryo transforms into an encysted larva that contains liquid and is covered by a thin membrane. Initially, this cysticercosis embryo is a living organism, exhibiting morphologic features to signify that it is viable. Similarly, certain morphologic alterations may indicate that the parasite is dead.

Pathologists have identified a series of alterations occurring within and surrounding the larva from its earliest viable stage to its final stage. Escobar,[42] in providing an interesting account of the disease, has identified four stages that the parasite undergoes within the brain parenchyma.

In the *vesicular stage*, the tiny (4 to 5 mm) live spherical larva appears as a whitish nodule invaginated into a small cyst containing transparent fluid. The cyst has a thin, friable, translucent whitish capsule. The larva can still be found in the colloidal vesicular stage, but it already shows signs of hyalin degeneration and early mineralization. In this stage, the fluid becomes turbid or jelly-like. The capsule steadily thickens with each succeeding phase, so that its walls are noticeably thicker and collagenous by the time the cyst has reached the granular nodule stage. The cyst

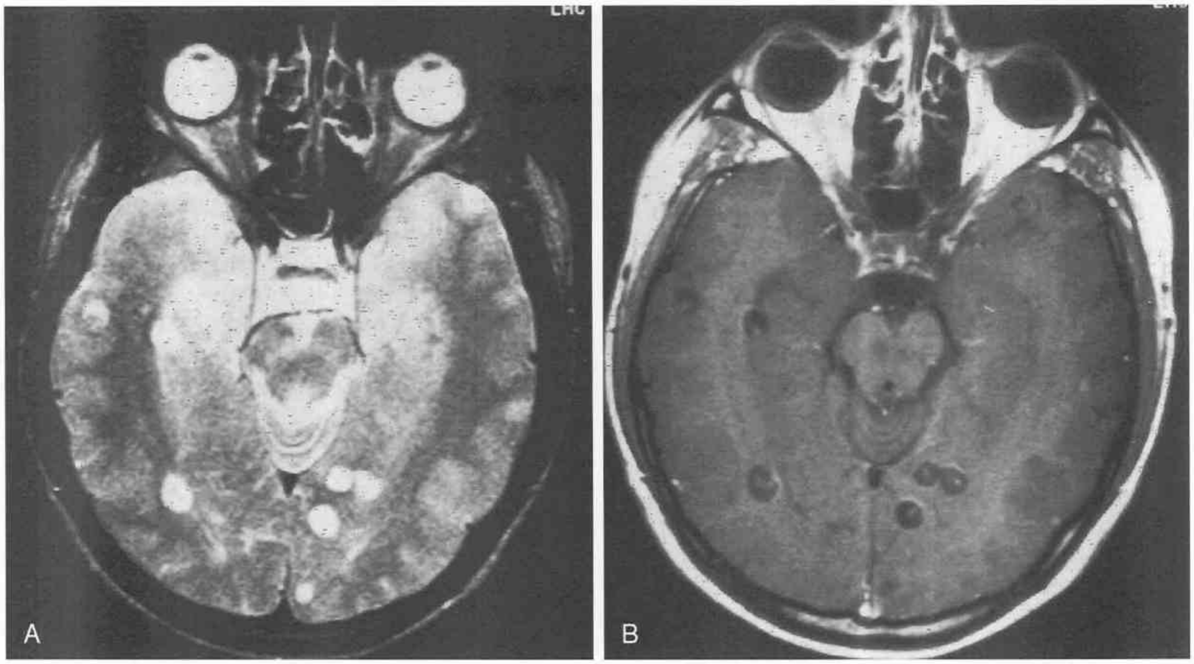

Figure 6–30. Parenchymal cysticercosis. *A*, T2-weighted image shows multiple high-signal-intensity lesions. *B*, Gadolinium-enhanced image shows multiple low-signal-intensity lesions with an eccentric isointense scolex. A few of the cysts show partial enhancement of the cyst wall.

reduces its size, and its content changes into coarse granules that are mineralized with calcium salts.

In the *nodular calcified stage*, this granular material appears completely mineralized, with the lesion having shrunk to one half or one quarter of the size of the original live cysticercosis embryo.

On the basis of the preceding data, it seems likely that a cysticercal lesion in the vesicular stage would be identified as such on imaging studies. The cyst fluid would be isodense to CSF on CT and isointense to CSF on MRI studies. The scolex is isodense to brain parenchyma on CT and hyperintense on MRI studies (Fig. 6–30).

With aging, the parenchymal cysts evolve into the *colloidal vesicular stage*. The cyst wall may show enhancement on contrast-enhanced CT or MRI studies (Fig. 6–31). The cyst fluid may show increased density with CT and intensity with MRI. The scolex begins to degenerate and shrink.

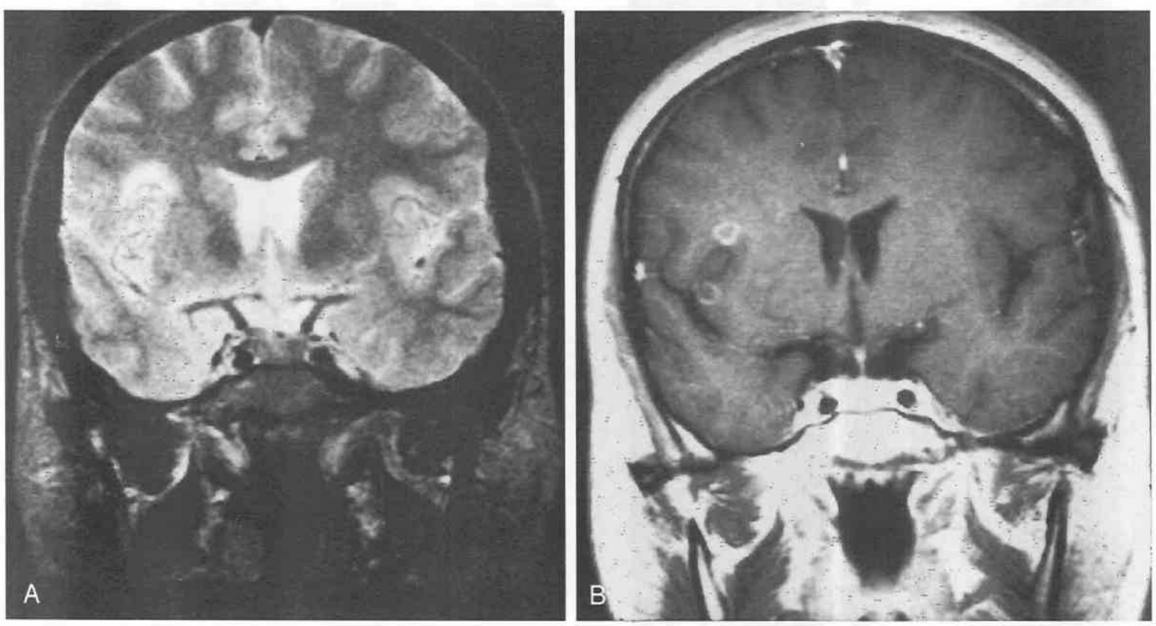

Figure 6–31. Parenchymal cysticercosis. *A*, T2-weighted image shows no definite abnormality. *B*, Gadolinium-enhanced image shows two ringlike enhancing lesions in the right insular cortex.

In the *granular nodular stage*, calcification may be identified within the scolex and along the cyst wall on CT scans. A nodular type of enhancement may be seen on contrast-enhanced CT or MRI. Calcification is much better demonstrated on CT than on MRI.

In the nodular calcified stage, calcification may be seen within the dead larva (Fig. 6–32). Surrounding edema is seen in the colloidal vesicular and granular nodular stages.[15, 164, 166] Note that evolution of cysticercosis is a dynamic process, and cysts do not change from one stage to another in an abrupt fashion. It is possible to observe cysts in transition from one stage to another.[163]

Intraventricular cysticercosis is potentially lethal; in our series, 6 of 46 patients with intraventricular cysticercosis cysts died of acute obstructive hydrocephalus shortly after hospital admission.[168] The need for early diagnosis of intraventricular cysticercosis cysts cannot be overemphasized. The cysts can be identified by CSF density or signal intensity. Cyst fluid surrounded by a thin wall is a high-density or high-signal-intensity scolex seen on CT or MRI scans (Figs. 6–33 and 6–34). Depending on the stage of the cyst, enhancement of the cyst wall may be identified on the contrast-enhanced CT or MRI study. A thick, ringlike enhancement associated with intraventricular cysticercosis cysts has been correlated with the finding of granular ependymitis in surgical patients (Fig. 6–35). Cysticercosis cysts may migrate within the ventricular system (Fig. 6–36). If time has elapsed since the initial diagnosis, reconfirmation of the location of the intraventricular cysticercosis cyst is advisable before surgery. Metrizamide entrance into an intraventricular cysticercosis cyst has been described.[167]

Cysticercosis cysts are seen in the basal cisterns and sylvian fissure. If large enough, these cysts may expand and distort the basal cisterns. MRI studies are more sensitive than CT scans in demonstrating cisternal cysts, which tend to agglomerate in a racemose form, and the body or scolex of the parasite is usually not recognizable (Fig. 6–37). It is interesting to consider why cysticercosis cysts present as a racemose form in the basal cisterns. Trelles and coworkers[145] suggested that disordered perforation of the cyst wall is associated with disappearance of the scolex. Martinez[91] held that the racemose cysts are an arrested form in the development of the cyst, the scolex never being formed. Adhesive arachnoiditis develops as a local inflammatory meningeal reaction in the basal cisterns. Contrast-enhanced MRI may show basal meningeal enhancement (Fig. 6–38). Communicating hydrocephalus may also develop as a result of basal arachnoiditis. The inflammatory reaction may involve the adjacent blood vessels and cranial nerves. The walls of the arteries are invaded by inflammatory cells, leading to vasculitis, which can lead to cerebral infarction or mycotic aneurysm formation.[151] Spinal cysticercosis cysts can be secondary to intracranial cisternal cysts.[164]

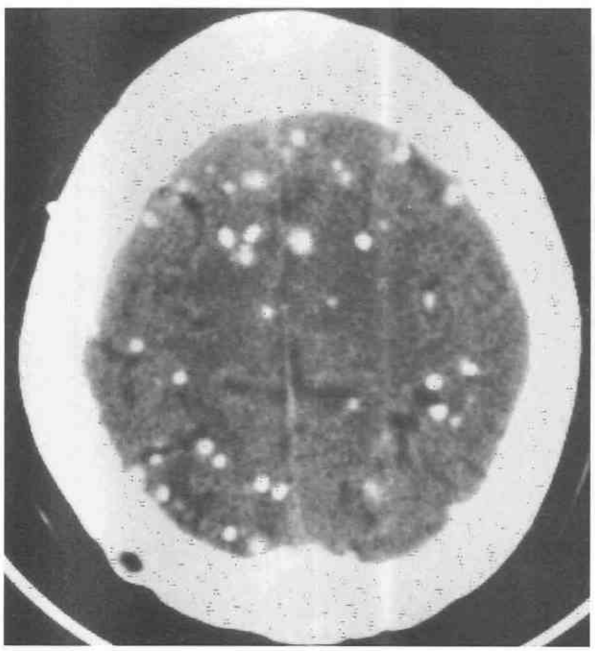

Figure 6–32. Cysticercosis. Noncontrast CT scan reveals multiple intracranial calcifications, consistent with dead larvae.

Echinococcosis

Hydatid disease, or echinococcosis, is the larval stage of *Echinococcus granulosus*. The definitive host of *E. granulosus* is the dog, and the intermediate hosts are sheep, cattle, and camels. Human infection occurs by accidental ingestion of contaminated dog feces containing ova of a dog tapeworm. The disease is endemic in many sheep-raising and cattle-raising countries in the world.[22] Hydatid disease frequently involves the liver and lung. CNS involvement is rare.[28] Hydatid cysts of the brain are usually large and spherical, and they may be solitary or multiple.

Extradural cysts have been reported.[106] On unenhanced CT or MRI studies, they appear as large intraparenchymal cystic lesions with sharp margins (Fig. 6–39). Cyst fluid is of CSF density or signal intensity. The lack of surrounding edema is an important feature that serves to differentiate this lesion from cerebral abscess.[1] Contrast enhancement may be seen partially or completely involving the wall. Calcification of the wall may also be seen (Fig. 6–40). Recurrent disease following surgery may present with intense enhancement of the cyst wall and surrounding edema (Fig. 6–41).

Paragonimiasis

Paragonimiasis is the result of infestation by *Paragonimus westermani* in freshwater crabs and crayfish. It is endemic in East and Southeast Asia, West Africa, and Latin America.[63] The lungs are the most common site of infestation. Cerebral infection occurs in approximately 1% of patients with pulmonary paragonimiasis.[19]

Plain films show characteristic "soap bubble" intracranial calcifications. CT scans show multiple, densely calcified areas with various nodular shapes around and within the lateral ventricles and high over the cerebral convexities.[160]

Toxoplasmosis

Toxoplasmosis is caused by infestation with the parasite *Toxoplasma gondii*, a protozoan. The adult form usually

Text continued on page 240

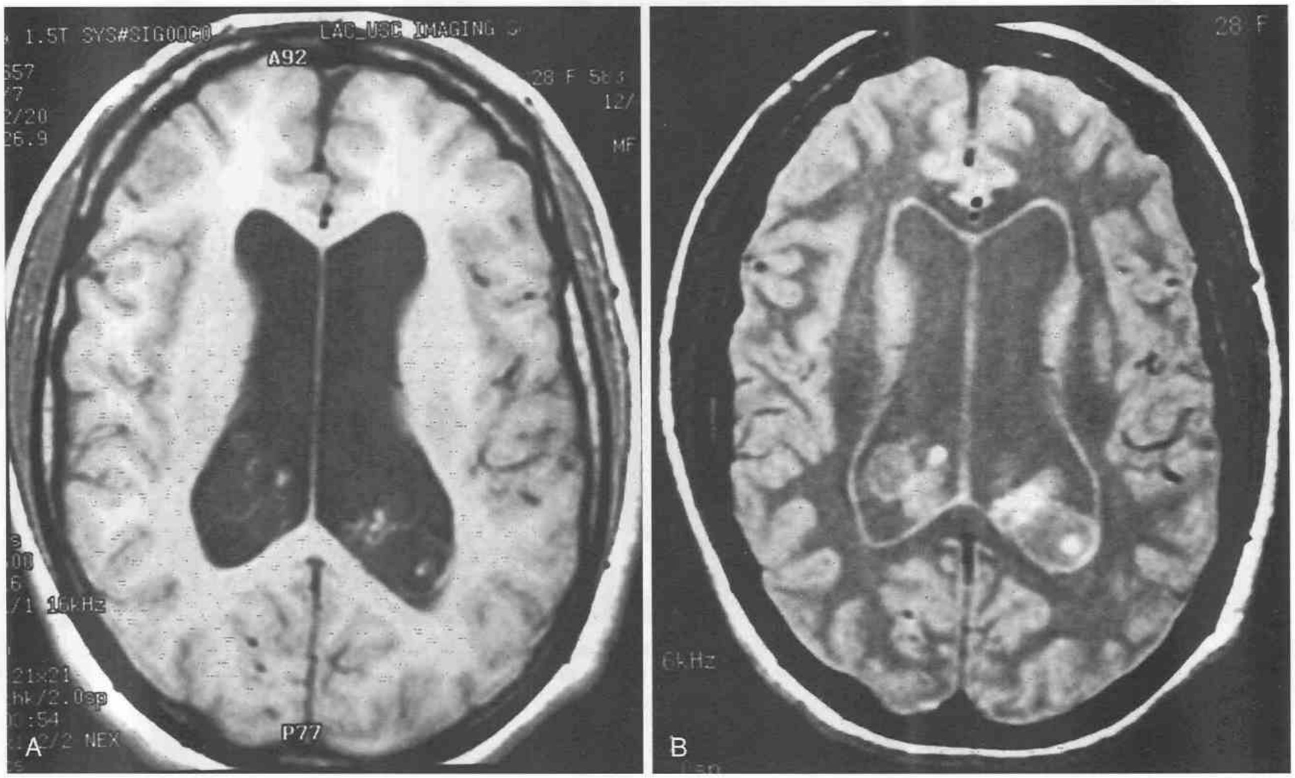

Figure 6–33. Intraventricular cysticercosis. *A*, T1-weighted image shows multiple cysts in the dependent portions of the lateral ventricles. *B*, The proton-density–weighted image shows the presence of scolices in some of the cysts better than the T1-weighted image does.

Figure 6–34. Intraventricular cysticercosis. A thin-walled cyst is seen expanding the fourth ventricle. An isointense, eccentrically located scolex is seen.

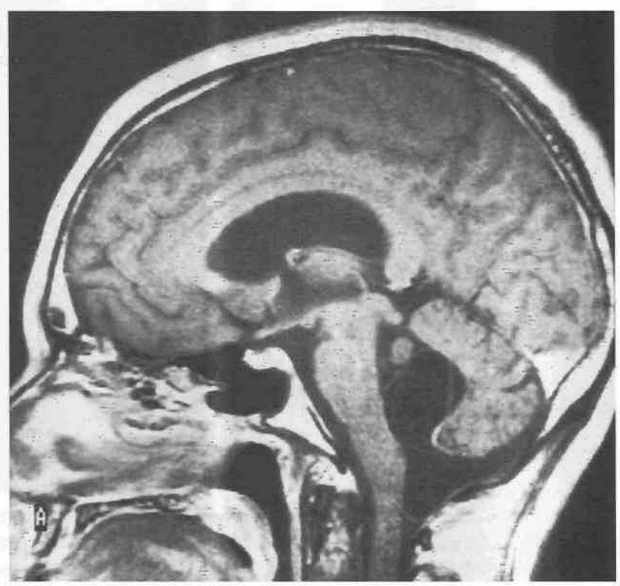

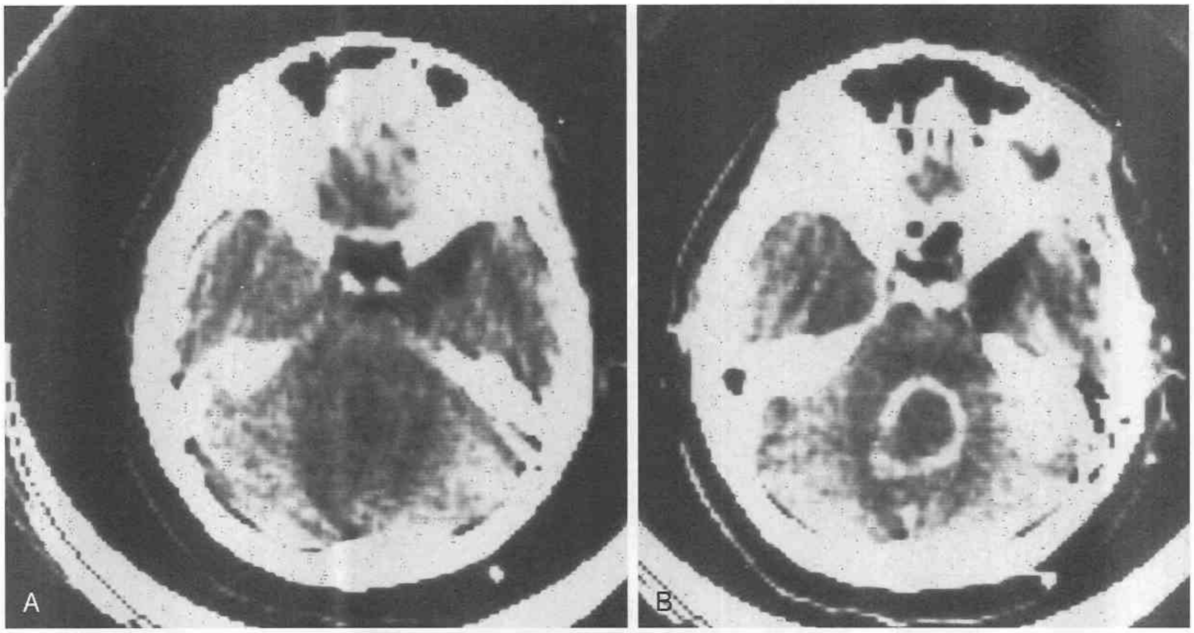

Figure 6–35. Enhancing intraventricular cysticercosis cyst. *A*, Noncontrast CT scan shows a low-density area in the region of the fourth ventricle. The fourth ventricle is obliterated. *B*, Contrast CT scan demonstrates a ringlike enhancement. (From Zee C, et al: Unusual neuroradiological feature of intracranial cysticercosis. Radiology 137:397–407, 1980.)

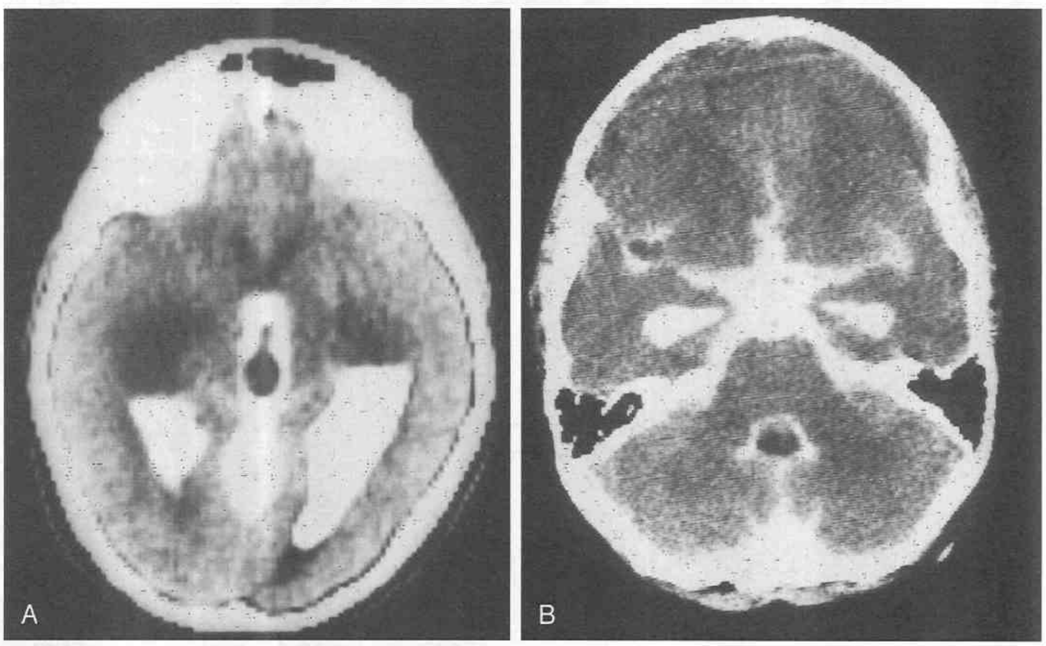

Figure 6–36. Cyst mobility in cysticercosis. *A*, Initial CT ventriculogram shows a cyst in the third ventricle. *B*, The cyst moved into the fourth ventricle on the metrizamide CT ventriculogram performed on the morning of surgery. (From Zee C, et al: Intraventricular cysticercal cysts: Further neuroradiologic observations and neurosurgical implications. AJNR Am J Neuroradiol 5:727–730, 1984. Copyright American Society of Neuroradiology, 1984.)

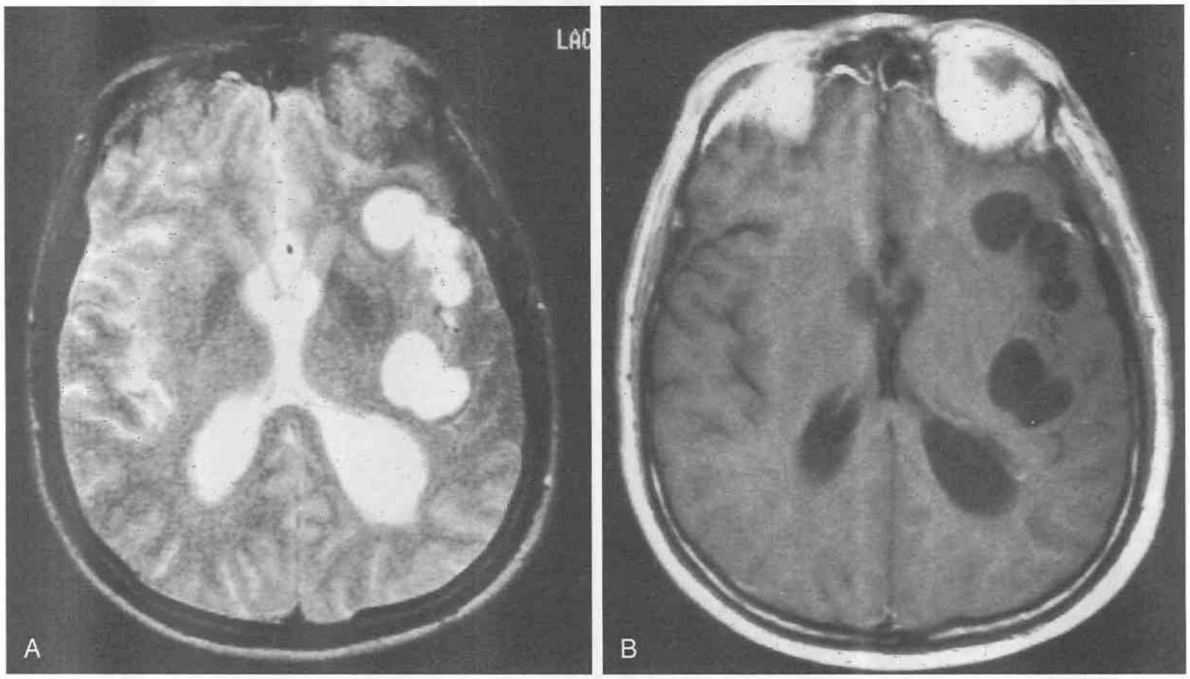

Figure 6–37. Cisternal cysts and intraventricular cyst. *A*, T2-weighted image shows multiple cisternal cysts in the region of the left sylvian fissure. *B*, Gadolinium-enhanced image shows multiple cisternal cysts in the region of the left sylvian fissure. No enhancement of these cysts is seen in this case. Incidentally, a cyst is seen in the atrium of the left lateral ventricle.

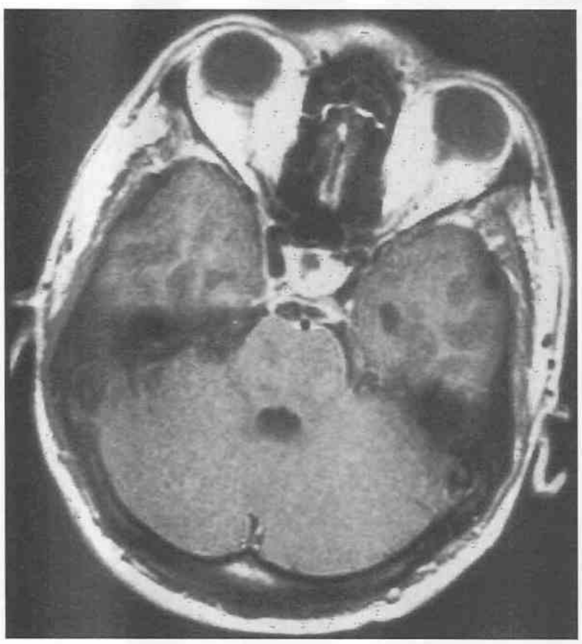

Figure 6–38. Cisternal cyst with basal meningeal enhancement. Gadolinium-enhanced MRI study shows ovoid ringlike enhancement in the pontine cistern and enhancement at the left ambient cistern.

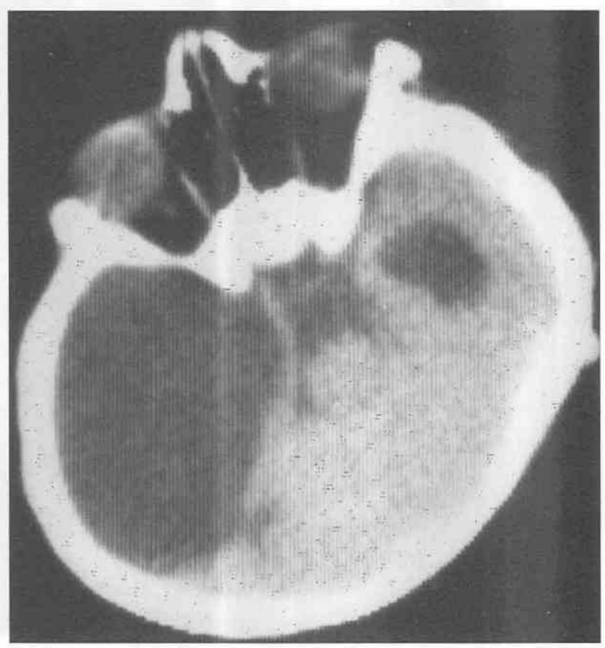

Figure 6–39. Echinococcosis. Large echinococcal cyst is seen in the right temporal lobe in this child. The left temporal horn is dilated. (Courtesy of Dr. Lawrence O'Connor.)

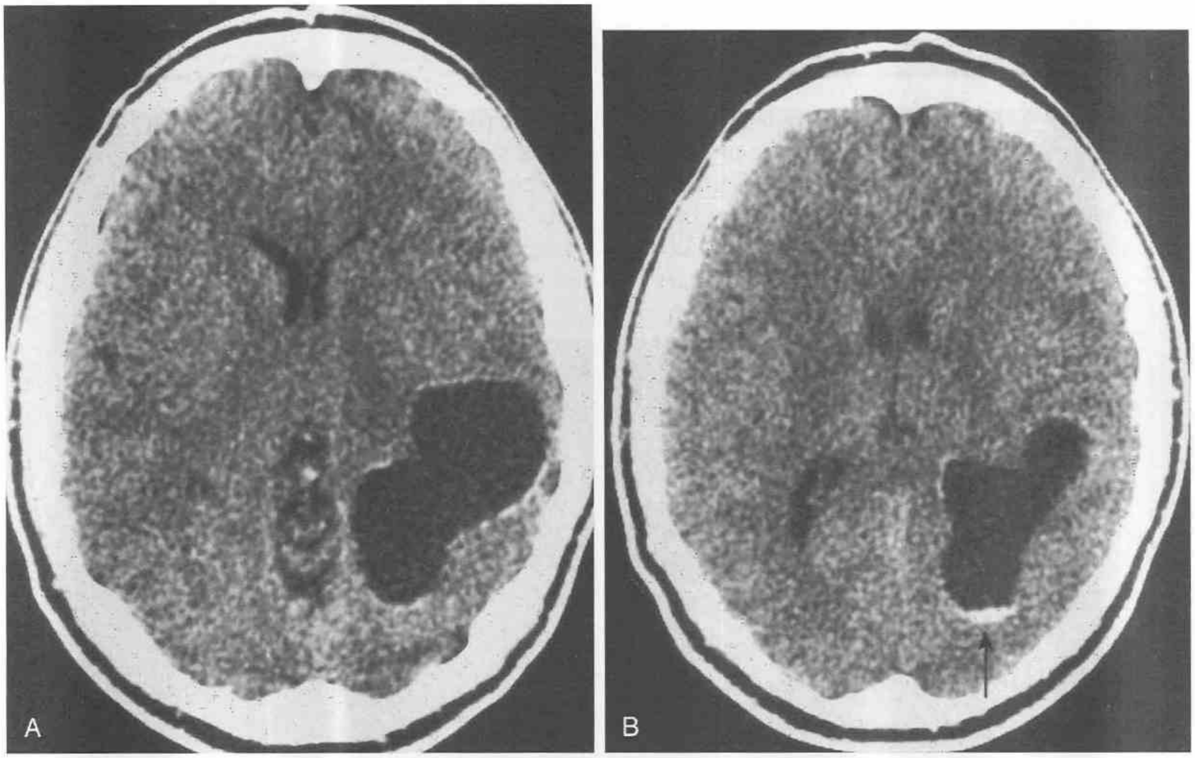

Figure 6–40. Echinococcosis. *A* and *B*, Contrast-enhanced CT scans show a large lobulated cyst with marginal calcification *(arrow* in *B)* and minimum cyst wall enhancement.

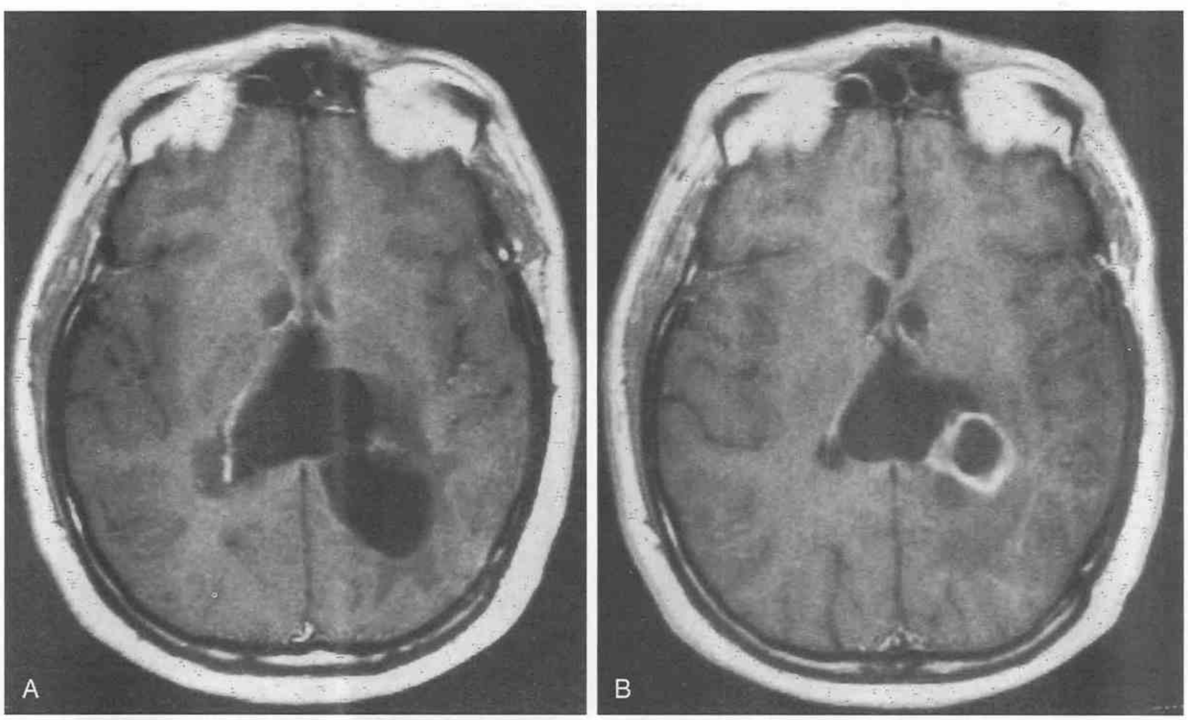

Figure 6–41. Recurrent echinococcosis. *A*, Gadolinium-enhanced MRI study shows recurrent cysts. No contrast enhancement is seen at this stage. *B*, Gadolinium-enhanced MRI study obtained a year later shows a decrease in the size of these cysts and contrast enhancement of one of the cysts.

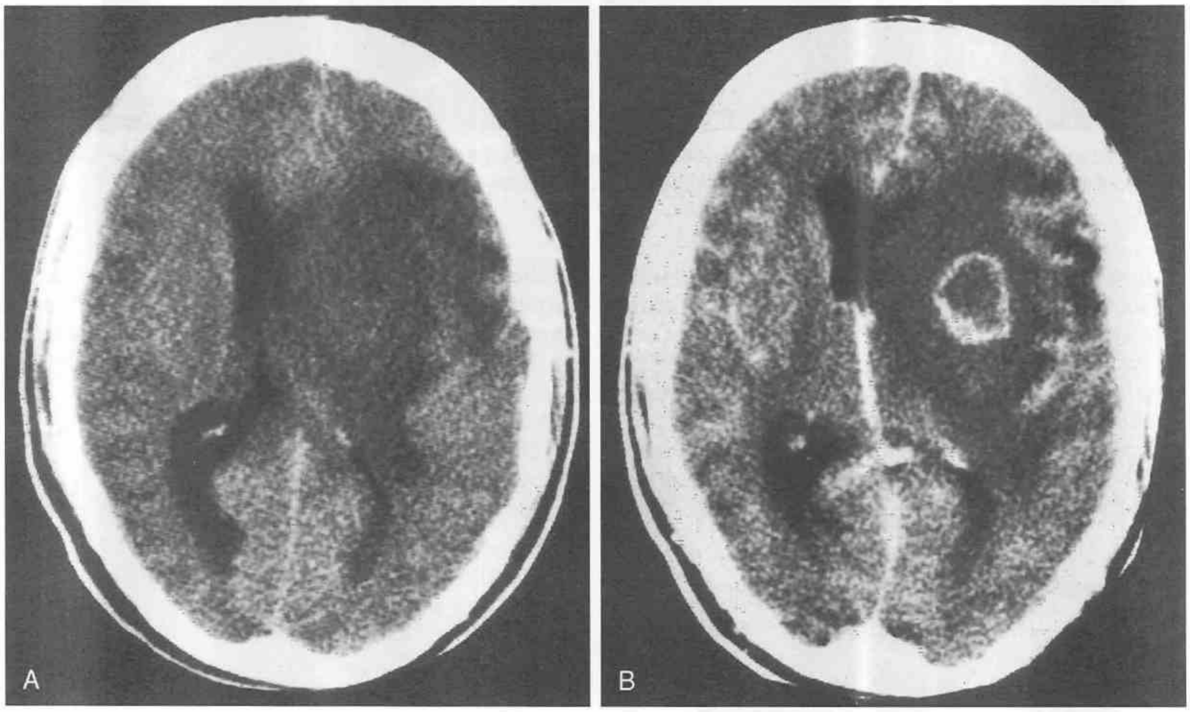

Figure 6–42. Toxoplasmosis. *A*, Noncontrast CT scan shows a large low-density area in the left frontoparietal region and left basal ganglion, with significant mass effect in a patient with acquired immunodeficiency syndrome. *B*, Contrast CT scan demonstrates a ringlike enhancing lesion.

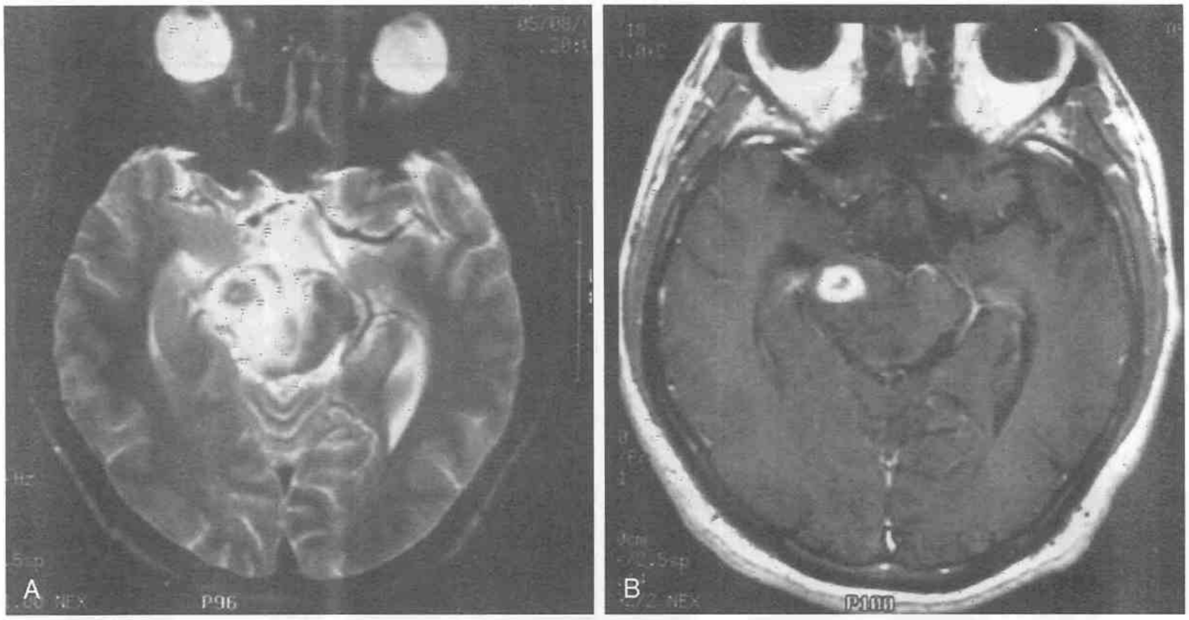

Figure 6–43. Toxoplasmosis. *A*, T2-weighted image shows a low-signal-intensity lesion in the right cerebral peduncle with surrounding edema. *B*, Gadolinium-enhanced MRI study shows a ringlike enhancing lesion in the right side of the midbrain.

occurs in immunocompromised patients or in patients with AIDS. Toxoplasmosis may appear as meningoencephalitis or as granulomas. In patients with AIDS, *Toxoplasma* encephalitis is the most common opportunistic infection. The granulomas may be situated at the corticomedullary junction or in the periventricular areas.

Noncontrast CT scans show multiple low-density areas. Contrast CT scans may show no enhancement, nodular enhancement, or ringlike enhancement (Fig. 6–42). MRI studies are more sensitive in detecting the *Toxoplasma* lesions than contrast-enhanced CT scans.[165] They exhibit hypointensity on T1-weighted images and variable intensity on T2-weighted images. Gadolinium-enhanced MRI studies show enhancing patterns similar to those seen on contrast-enhanced CT scans (Fig. 6–43).[114]

The differential diagnosis includes lymphoma and progressive multifocal leukoencephalopathy.[81] When treated, healed *Toxoplasma* lesions become calcified. These calci-

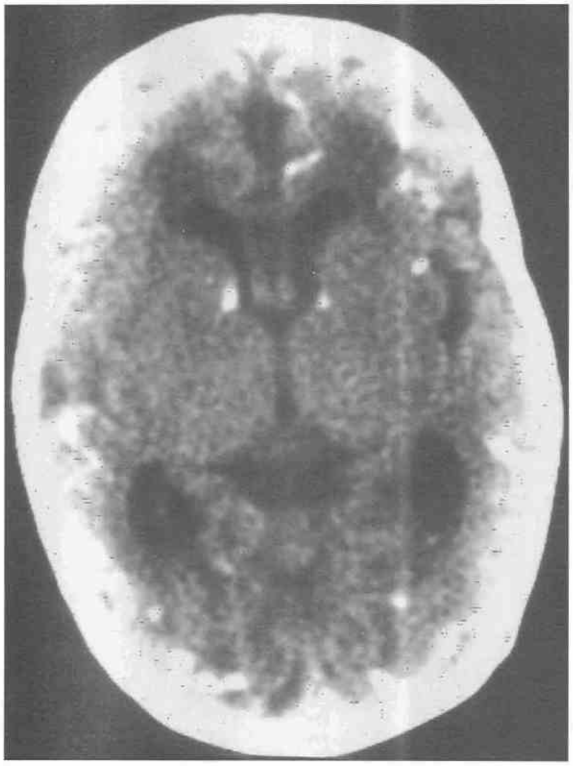

Figure 6–44. Neonatal toxoplasmosis. Noncontrast CT scan shows hydrocephalus and scattered intracranial calcifications, with a few seen in the periventricular region.

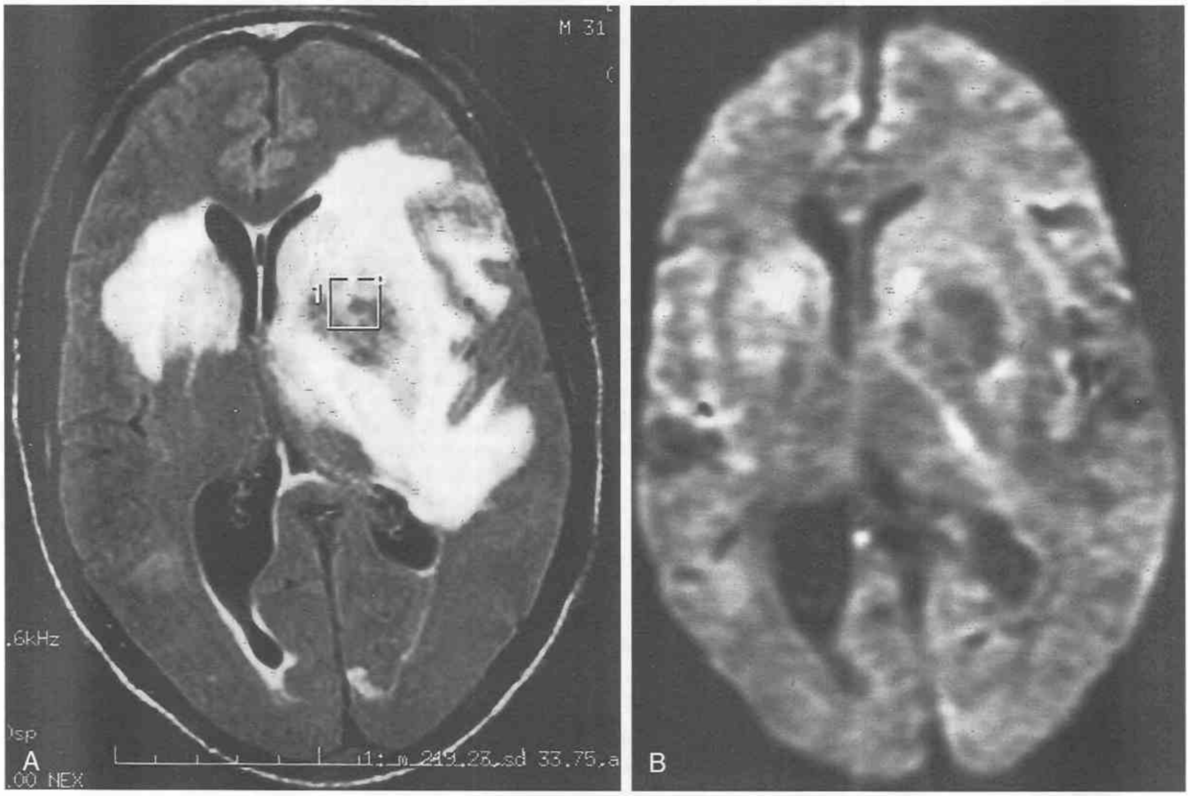

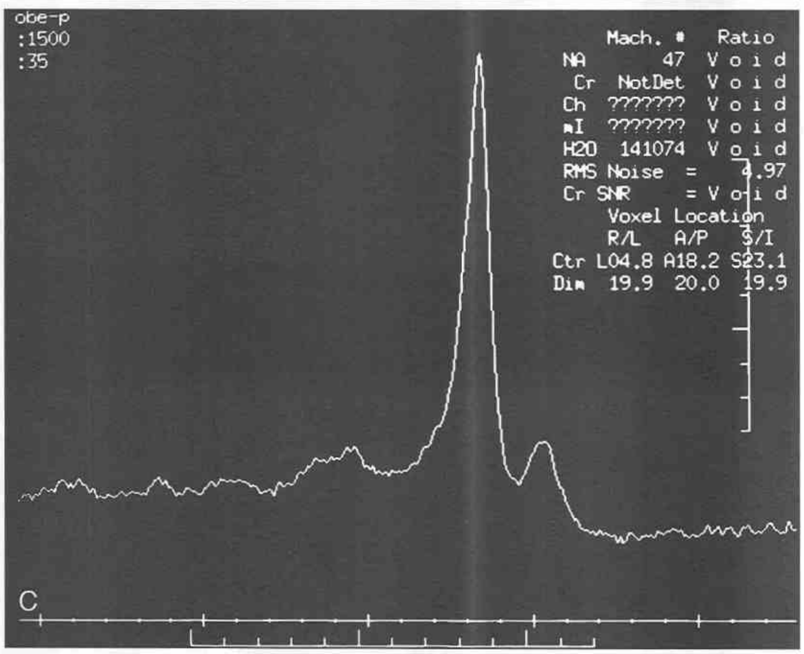

Figure 6–45. Toxoplasmosis. *A*, Fluid-attenuating inversion recovery (FLAIR) image shows an irregular mixed-signal-intensity lesion in the left basal ganglia with marked surrounding edema. *B*, Diffusion-weighted image shows the lesion to be of low signal intensity, indicating no evidence of restricted diffusion. *C*, MR proton spectroscopy shows high lipid/lactate at 0.9 to 1.5 ppm and no choline at 3.2 ppm, excluding the diagnosis of lymphoma in a patient with acquired immunodeficiency syndrome.

fications are revealed more effectively by CT than by MRI. In newborns with toxoplasmosis, noncontrast CT scans may show hydrocephalus and scattered calcifications in the parenchyma as well as in the periventricular region (Fig. 6–44). These findings may be seen in cytomegalic inclusion disease, herpes encephalitis, and congenital rubella involving newborns. With cytomegalic inclusion disease, however, calcifications are seen predominantly in the periventricular region.

Various noninvasive methods have been used to differentiate toxoplasmosis and lymphoma in AIDS patients, including SPECT, PET, and MRS. On PET imaging using FDG-18, increased tracer activity is seen in lymphoma as a result of hypermetabolic activity, but it is not seen in toxoplasmosis. On SPECT imaging, thallium 201 uptake also reflects hypermetabolism. On MRS, increased lipid and lactate peaks with a decrease in other metabolites are characteristic for toxoplasmosis (Fig. 6–45). Lymphoma shows a large increase in choline peak with only a mild increase in lipid and lactate peaks. The increased choline peak in lymphoma is believed to be due to increased cell membrane turnover and high cellularity of the lymphoma.[117]

References

1. Abbassioun K, Rahmat H, Ameli NO, et al: Computerized tomography in hydatid cyst of the brain. J Neurosurg 49:408–411, 1978.
2. Ahmadi J, Segall HD, Zee CS: Computed tomography in childhood intracranial infections. Semin Neurol 2:166–188, 1982.
3. Albertyn LE: Magnetic resonance imaging in herpes simplex encephalitis. Australas Radiol 34:117–121, 1990.
4. Anders BJ, Lauer BA, Foley LC: Computerized tomography to define CNS involvement in congenital cytomegalovirus infection. Am J Dis Child 134:795–797, 1980.
5. Arimitsu T, Jabbari B, Buckler RE, et al: Computed tomography in a verified case of tuberculosis meningitis. Neurology 29:384–386, 1979.
6. Bahn MM, Parchi P: Abnormal diffusion weighted magnetic resonance images in Creutzfeldt-Jakob disease. Arch Neurol 56:577–583,1999.
7. Bentson JR, Wilson GH, Helmer E: CT in intracranial cysticercosis. J Comput Assist Tomogr 1:464–471, 1977.
8. Black JT: Cerebral candidiasis: Case report of brain abscess secondary to *Candida albicans* and review of literature. J Neurol Neurosurg Psychiatry 33:864–870, 1970.
9. Bonafe A, Mnelfe C, Gomez MC, et al: Tuberculous meningitis: Contribution of computerized tomography to its diagnosis and prognosis. J Neuroradiol 12:302, 1985.
10. Bouza E, Dreyer JS, Hewitt WL, et al: Coccidioidal meningitis: An analysis of thirty-one cases and review of the literature. Medicine 60:139–172, 1981.
11. Brooks ML, Wang A, Black P, et al: Subdural mass lesion secondary to sarcoid granuloma MR and CT findings and differential diagnosis. Comput Med Imaging Graph 13:199, 1989.
12. Cabral DA, Flodmark O, Farrell K, et al: Prospective study of computed tomography in acute bacterial meningitis. J Pediatr 111: 201–205,1987.
13. Cahill DW, Salchuman M: Neurosarcoidosis—a review of the rare manifestation. Surg Neurol 15:204–211, 1981.
14. Caparros-Lefebvre D, Salomez JL, Petit H: Multiple intracranial tuberculomas: Magnetic resonance imaging and ofloxacin efficacy. Ann Med Interne (Paris) 140:699, 1989.
15. Carbajal JR, Palacio E, Azar-Kia B, et al: Radiology of cysticercosis of the CNS, including CT. Radiology 125:127–131, 1977.
16. Casselman ES, et al: CT of tuberculous meningitis in infants and children. J Comput Assist Tomogr 4:211–216, 1980.
17. Centeno RS, Winter J, Bentson JR, et al: CT evaluation of *Haemophilus influenzae* meningitis with clinical and pathologic correlation. Comput Radiol 7:243–249, 1983.
18. Chaabane M, Krifa H, Ladeb MF, et al: Cerebral candidiasis: Computed tomography appearance. Pediatr Radiol 19:436, 1989.
19. Chang KH, Cho SY, Hesselink JR, et al: Parasitic diseases of the central nervous system. Neuroimaging Clin North Am 1:159–178, 1991.
20. Chang KH, Han MH, Roh JK, et al: Gd-DTPA-enhanced imaging of brain in patients with meningitis: Comparison with CT. AJNR Am J Neuroradiol 11:69–76, 1990.
21. Claveria LE, Du Boulay GH, Moseley IF: Intracranial infections: Investigations by C.A.T. Neuroradiology 12:59–71, 1976.
22. Coates R, von Sinner W, Rahm B: MR imaging of an intracerebral hydatid cyst. AJNR Am J Neuroradiol 11:1249–1250, 1990.
23. Cockrill HH, et al: CT in leptomeningeal infections. Am J Roentgenol 130:511–515, 1978.
24. Colover J: Sarcoidosis with involvement of the nervous system. Brain 71:451–475, 1948.
25. Cornell SA, Jacoby CG: The varied computed tomographic appearance of intracranial cryptococcosis. Radiology 143:703–707, 1982.
26. Danziger A, Price H: Computed axial tomography in intracranial aspergillosis—a report of two cases. S Afr Med J 54:706–708, 1978.
27. Davis JM, Darris KR, Kleinman GM, et al: CT of herpes simplex encephalitis with clinicopathological correlation. Radiology 129: 409–417, 1978.
28. Demaerel P, Heiner L, Robberecht W, et al: Diffusion weighted MRI in sporadic Creutzfeldt-Jakob disease. Neurology 52:205–208, 1999.
29. Demaerel P, Wilms G, Marchal G: MRI findings in tuberculous meningo-encephalitis. Fortschr Rontgenstr 152:384–387, 1990.
30. Desprechins B, Stadnik T, Koerts G, et al: Use of diffusion weighted MR imaging in differential diagnosis between intracerebral necrotic tumors and cerebral abscesses. AJNR Am J Neuroradiol 20:1252–1257, 1999.
31. Dev R, Gupta RK, Poptani H, et al: Role of in vivo proton magnetic resonance spectroscopy in the diagnosis and management of brain abscess. Neurosurgery 42:37–42, 1998.
32. Dew HR: Hydatid disease of the brain. Surg Gynecol Obstet 59: 312–319, 1934.
33. Dolin R, Reichman RC, Mazur MH, et al: Herpes zoster varicella infections in immunosuppressed patients. Ann Intern Med 89:375–388, 1978.
34. Dublin AB, Merten DF: CT in the evaluation of herpes simplex encephalitis. Radiology 125:133–134, 1977.
35. Dublin AB, Phillips HE: CT of disseminated cerebral coccidioidomycosis. Radiology 135:361–368, 1980.
36. Durack DT, Perfect JR: Acute bacterial meningitis. In Wilkins RH, Rengachary SS (eds): Neurosurgery. New York, McGraw-Hill, 1985.
37. Enzmann DR, Brant-Zawadzki M, Britt RH: Computed tomography of central nervous system infections in immunosuppressed patients. AJNR Am J Neuroradiol 1:2349–243, 1980.
38. Enzmann DR, Britt RH, Yeager AS: Experimental brain abscess evolution: Computed tomographic and neuropathologic correlation. Radiology 133:113–122, 1979.
39. Enzmann DR, Chang Y, Augustyn G: MR findings in neonatal herpes simplex encephalitis type 2. J Comput Assist Tomogr 14: 453–457, 1990.
40. Enzmann DR, Norman D, Mani J, et al: CT of granulomatous basal arachnoiditis. Radiology 120:341–344, 1976.
41. Enzmann DR, Ranson B, Norman D, et al: CT of herpes simplex encephalitis. Radiology 129:419–425, 1978.
42. Escobar A: The pathology of neurocysticercosis. In Palacios E, Rodriguez-Carbajal J, Taveras J (eds): Cysticercosis of the Central Nervous System. Springfield, Ill, Charles C Thomas, 1983, pp 27–54.
43. Estrem SA, Tully R, Davis WE: Rhinocerebral mucormycosis: Computed tomographic imaging of cavernous sinus thrombosis. Ann Otol Rhinol Laryngol 99:160–161, 1990.
44. Falcone S, Donovan Post MJ: Encephalitis, cerebritis, and brain abscess. Neuroimaging Clin North Am 10:333–353, 2000.
45. Falcone S, Quencer RM, Bowen B, et al: Creutzfeldt-Jakob disease: Focal symmetrical cortical involvement demonstrated by MR imaging. AJNR Am J Neuroradiol 13:403–406, 1992.
46. Fernandez RE, Rothberg M, Ferencz G, et al: Lyme disease of the CNS: MR imaging findings in 14 cases. AJNR Am J Neuroradiol 11:479–481, 1990.

47. Gamba JL, et al: Craniofacial mucormycosis: Assessment with CT. Radiology 160:207–212, 1986.
48. Ganti SR, et al: Computed tomography of cerebral syphilis. J Comput Assist Tomogr 5:345–347, 1981.
49. Go JL, Kim PE, Ahmadi J, et al: Fungal infections of the central nervous system. Neuroimaging Clin North Am 10:409–425, 2000.
50. Go RT, Yousef MM, Jacoby CG: The role of radionuclide brain imaging and computed tomography in the early diagnosis of herpes simplex encephalitis. J Comput Tomogr 3:286–296, 1979.
51. Godt P, et al: The value of computed tomography in cerebral syphilis. Neuroradiology 18:197–200, 1979.
52. Gonzalez PRM, Herro CV, Joachim GF, et al: Tuberculous brain abscess: Case report. J Neurosurg 52:419, 1980.
53. Griggs RC, Manesberry WR, Condemi JJ: Cerebral mass due to sarcoidosis: Regression during corticosteroid therapy. Neurology 23: 981–989, 1973.
54. Grinnell VS, et al: Diagnosis of interhemispheric subdural empyema by CT. J Comput Assist Tomogr 1:99–105, 1977.
55. Grossman RI, Davis KR, Taveras JM, et al: Computed tomography of intracranial aspergillosis. J Comput Assist Tomogr 5:646–650, 1981.
56. Guilleux MH, Steiner RE, Young IR: MR imaging in PML. AJNR Am J Neuroradiol 7:11033–11035, 1986.
57. Haimes AB, Zimmerman RD, Morgello S, et al: MR imaging of brain abscesses. AJNR Am J Neuroradiol 10:279, 1989.
58. Halpern SE, Smith CW Jr, Ficken V: ^{99m}Tc brain scanning in herpes virus type I encephalitis. J Nucl Med 11:548–550, 1970.
59. Handel SF, Klein WC, Kim YU: Intracranial epidural abscess. Radiology 111:117–120, 1974.
60. Hayes WS, Sherman JL, Stern BJ, et al: MR and CT evaluation of intracranial sarcoidosis. AJR Am J Roentgenol 149:1043, 1987.
61. Healton EB, Zito G, Chauhan P, et al: Intracranial subdural sarcoid granuloma. J Neurosurg 56:728, 1982.
62. Herman TE, et al: CT of neonatal herpes encephalitis. AJNR Am J Neuroradiol 6:773–775, 1985.
63. Higashi K, Aoki H, Tatebayashi K, et al: Cerebral paragonimiasis. J Neurosurg 34:515–527, 1971.
64. Holland BA, Perret LV, Mills CM: Meningovascular syphilis: CT and MR findings. Radiology 158:439–442, 1986.
65. Horten B, Price RW, Jimenez D: Multifocal varicella zoster virus: Local encephalitis temporally remote from herpes zoster. Ann Neurol 9:251–266, 1981.
66. Ikeda K, Yamashita J, Fujisawa H, et al: Cerebral granuloma and meningitis caused by *Candida albicans:* Useful monitoring of mannan antigen in cerebrospinal fluid. Neurosurgery 26:860–863, 1990.
67. Johnsen SD, Sidell AD, Bird CR: Subtle encephalitis in children: A variant of acute disseminated encephalomyelitis. J Child Neurol 4: 214–217, 1989.
68. Johnston RB: Oxygen metabolism and the microbicidal activity of macrophages. Fed Proc 37:2759, 1978.
69. Jordan J, Enzmann DR: Encephalitis. Neuroimaging Clin North Am 1:17–38, 1991.
70. Joubert MD, Stephanov S: CT and surgical treatment in intracranial suppuration. J Neurosurg 47:73–78, 1977.
71. Kamin M, Biddle D: Conservative management of focal intracerebral infection suppuration. J Neurosurg 47:73–78, 1977.
72. Kanamalla US, Ibarra RA, Jinkins R: Imaging of cranial meningitis and ventriculitis. Neuroimaging Clin North Am 10:309–331, 2000.
73. Kaufman DM, Leeds NE: CT in the diagnosis of intracranial abscesses. Neurology 27:1069–1073, 1977.
74. Kendall BE, Tateler GLV: Radiological findings in neurosarcoidosis. Br J Radiol 51:81–92, 1978.
75. Kesselring J, Miller DH, Robb SA, et al: Acute disseminated encephalomyelitis: MRI findings and the distinction from multiple sclerosis. Brain 113:291–302, 1990.
76. Ketonen L, et al: Hypodense white matter lesions in computed tomography of neurosarcoidosis. J Comput Assist Tomogr 10:181–183, 1986.
77. Klein HJ, Richter HI, Schachenmayr W: Intracerebral *Aspergillus* abscess: Case report. Neurosurgery 13:306–309, 1983.
78. Kovanen J, Erkinguntti T, Iivaananninen M, et al: Cerebral MR and CT imaging of Creutzfeldt-Jakob disease. J Comput Assist Tomogr 9:125–128, 1983.
79. Kornbluth CM, Dastian S: Imaging of rickettsial, spirochetal, and parasitic infections. Neuroimaging Clin North Am 10:375–390, 2000.
80. Kumpe DA, et al: Intracranial neurosarcoidosis. J Comput Assist Tomogr 3:324–330, 1979.
81. Kupfer MC, Zee CS, Colletti PM, et al: MRI evaluation of AIDS-related encephalopathy: toxoplasmosis vs. lymphoma. Magn Reson Imaging 8:51–57, 1990.
82. Lazo A, Wilner HI, Metes JJ: Craniofacial mucormycosis: Computed tomographic and angiographic findings in two cases. Radiology 139: 623–629, 1981.
83. Lee SH: Infectious diseases. In Lee SH, Rao KCVG (eds): Cranial Computed Tomography. New York, McGraw-Hill, 1983.
84. Leo JS, Weiner RL, Lin JP, et al: Computed tomography in herpes simplex encephalitis. Surg Neurol 10:313–317, 1978.
85. Linnemann CC Jr, Alvira MN: Pathogenesis of varicella zoster angiitis in the CNS. Arch Neurol 37:239–240, 1980.
86. Lipton SA, Hickey WF, Morris JH, et al: Candidal infection in the central nervous system. Am J Med 76:101–108, 1984.
87. Lorber J: Intracranial calcification following tuberculous meningitis in children. Acta Radiol 50:204–210, 1958.
88. Lott T, et al: Evaluation of brain and epidural abscess by CT. Radiology 122:371, 1977.
89. Lukes SA, Norman D: CT findings in acute disseminated encephalomyelitis. Ann Neurol 13:567–572, 1983.
90. Lukin RR, Chambers AA, Soleimanpour M: Outlet obstruction of the fourth ventricle in sarcoidosis. Neuroradiology 10:65–68, 1975.
91. Martinez A: Anatomia patologica dela cisticercosis cerebral. Neurochirurgie 19:191–201, 1961.
92. Masdeu JC, Small CB, Weiss L, et al: Multifocal cytomegalovirus encephalitis in AIDS. Ann Neurol 23:97–99, 1988.
93. Mathews VP, Kuharik MA, Edwards MK: Gd-DTPA enhanced MR imaging of experimental bacterial meningitis: Evaluation and comparison with CT. AJNR Am J Neuroradiol 9:1045–1050, 1988.
94. Mayers MM, Kaufmann DF, Miller MM: Recent cases of intracranial tuberculomas. Neurology 28:256–260, 1978.
95. McCormick GF, Giannotta S, Zee CS, et al: Carotid occlusion in cysticercosis. Neurology 33:1078–1080, 1983.
96. Mirfakhraee M, et al: Virchow-Robin space: A path of spread in neurosarcoidosis. Radiology 158:715–720, 1986.
97. Nahser HC, et al: Development of brain abscesses—CT compared with morphological studies. Adv Neurosurg 9:32–35, 1981.
98. Nakazawa G, Lulu RE, Koo AH: Intracerebellar coccidioidal granuloma. AJNR 4:1243–1244, 1983.
99. New PFJ, Davis KR: The role of CT scanning in diagnosis of infections of the central nervous system. In Remington J, Swartz M (eds): Current Clinical Topics in Infectious Diseases, New York, McGraw-Hill, 1980.
100. New PFJ, Davis KR, Ballantine HT: Computed tomography in cerebral abscess. Radiology 121:641–646, 1976.
101. Nielsen H, Gyldenstadt C: CT in the diagnosis of cerebral abscess. Neuroradiology 12:207–217, 1977.
102. Noorbehesht B, Enzmann DR, Sullendar W, et al: Neonatal herpes simplex encephalitis: Correlation of clinical and CT findings. Radiology 162:813–819, 1987.
103. Ofner E, Butler WT: Ophthalmologic complications of cryptococcal meningitis. J Clin Neuro Ophthalmol 7:45–48, 1987.
104. Okuno T, Fuseya Y, Ito M, et al: Reversible multiple hypodense areas in the white matter diagnosed as acute disseminated encephalomyelitis. Case report. J Comput Assist Tomogr 5:119–121, 1981.
105. Osenbach RK, Blumenkopf B, Ramirez H, et al: Meningeal neurosarcoidosis mimicking convexity en-plaque meningioma. Surg Neurol 26:387, 1986.
106. Ozgen T, Erbengi A, Bertan V, et al: The use of computerized tomography in the diagnosis of cerebral hydatid cysts. J Neurosurg 50:339–342, 1979.
107. Pachner AR, Duray P, Steere AC: Central nervous system manifestations of Lyme disease. Arch Neurol 46:790–795, 1989.
108. Parker JC Jr, Dyer MC: Neurologic infections due to bacteria, fungi, and parasites. In Doris RL, Robertson DM (eds): Textbook of Neuropathology. Baltimore, Williams & Wilkins, 1985, pp 632–703.
109. Pearfield RC, Shawdon HH: Five cases of intracranial tuberculoma followed by serial CT. J Neurol Neurosurg Psychiatry 42:373–379, 1979.
110. Perfect JR, Kurack DT, Gallis HA: Cryptococcemia. Medicine 62: 98–109, 1993.
111. Pfuetze KH, Radner DB (eds): Clinical Tuberculosis: Essentials of Diagnosis and Treatment. Springfield, Ill, Charles C Thomas, 1966.
112. Philips ME, Ryals YJ, Kambhu SA, et al: Neoplastic vs. inflamma-

tory meningeal enhancement with Gd-DTPA. J Comput Assist Tomogr 14:536–541, 1990.
113. Post MJD, Kursunoglu SJ, Hensley GT, et al: Cranial CT in acquired immunodeficiency syndrome: Spectrum of diseases and optimal contrast enhancement technique. AJNR Am J Neuroradiol 6:743–754, 1985.
114. Post MJD, Tate LG, Wuencer RM, et al: CT, MR, and pathology in HIV encephalitis and meningitis. AJR Am J Roentgenol 151: 373–380, 1988.
115. Post MJD, et al: Cytomegalic inclusion virus encephalitis in patients with AIDS: CT, clinical and pathologic correlation. AJNR Am J Neuroradiol 7:275–280, 1986.
116. Price HI, Danziger A: CT in cranial tuberculosis. Am J Roentgenol 130:769–771, 1978.
117. Provenzale JM, Jinkins RJ: Brain and spine imaging findings in AIDS patients. Radiol Clin North Am 35:1997.
118. Prusiner SB: Prions and neurodegenerative diseases. N Engl J Med 317:1571–1581, 1987.
119. Rafto SE, Milton WJ, Galetta SL, et al: Biopsy confirmed CNS Lyme disease at 1.5 T. AJNR Am J Neuroradiol 11:482–484, 1990.
120. Ricker W, Clark M: Sarcoidosis: A clinicopathologic review of 300 cases, including 22 autopsies. Am J Clin Pathol 19:725–749, 1949.
121. Robertheram EB, Kessler LA: Use of computerized tomography in non-surgical management of brain abscess. Arch Neurol 36: 25–26, 1979.
122. Rodriguez-Carbajal J, Salgado P, Gutierrez-Alvarado R: The acute encephalitic phase of neurocysticercosis: Computed tomographic manifestations. AJNR Am J Neuroradiol 4:51–55, 1983.
123. Rosenbaum ML, Hoff JT, Norman D, et al: Decreased mortality from brain abscesses since the advent of computerized tomography. J Neurosurg 49:658, 1978.
124. Russet EJ, Zimmerman RD, Leeds NE: Reye's syndrome: CT documentation of disordered intracerebral structure. J Comput Assist Tomogr 3:217–220, 1979.
125. Sadhu VK, Handel SF, Pinto RS, et al: Neuroradiologic diagnosis of subdural empyema and CT limitations. AJNR Am J Neuroradiol 1:39–44, 1980.
126. Sage MR, et al: Rapid development of cerebral atrophy due to perinatal herpes simplex encephalitis. J Comput Assist Tomogr 7: 763–766, 1981.
127. Saltzman GF: Roentgenologic changes in cerebral sarcoidosis. Acta Radiol (Diagn) (Stockh) 50:235–241, 1958.
128. Schroth G, Kretzschmar K, Gawehn J, et al: Advantage of MRI in the diagnosis of cerebral infections. Neuroradiology 29:120–126, 1987.
129. Schultz P, Leeds NE: Intraventricular septations complicating neonatal meningitis. J Neurosurg 38:620–626, 1973.
130. Shah R: Tuberculosis. Neuroimaging Clin North Am 10:355–374, 2000.
131. Sherman JL, Stern BJ: Sarcoidosis of the CNS: Comparison of unenhanced and enhanced MR images. AJNR Am J Neuroradiol 11: 915, 1990.
132. Shoji H, Murakami T, Murai I, et al: A follow-up study by CT and MRI in 3 cases of Japanese encephalitis. Neuroradiology 32: 215–219, 1990.
133. Silverstein A, Feuer MM, Siltzbach LE: Neurologic sarcoidosis: Study of 18 cases. Arch Neurol 12:1–11, 1965.
134. Simmons KC, Sage MR, Reilly PL: CT of intracerebral hemorrhage due to mycotic aneurysms—case report. Neuroradiology 19:215–217, 1980.
135. Singer MB, Atlas SW, Drayer BP: Subarachnoid space disease: Diagnosis with fluid-attenuated inversion recovery MR imaging and comparison with gadolinium-enhanced spin echo MR imaging—blinded reader study. Radiology 208:417–422, 1998.
136. South MA, et al: Congenital malformation of the CNS associated with genital type (type 2) herpes virus. Pediatr 75:13–18, 1969.
137. Stevens EA, Norman D, Kramer RA: CT brain scanning in intraparenchymal pyogenic abscesses. Am J Roentgenol 130:111–114, 1978.
138. Sze G, Soloetsky S, Bronen R, et al: MR imaging of the cranial meninges with emphasis on contrast enhancement and meningeal carcinomatosis. AJNR Am J Neuroradiol 10:965–975, 1989.
139. Sze G, Zimmerman RD: The magnetic resonance imaging of infections and inflammatory diseases. Radiol Clin North Am 26:839–859, 1988.
140. Tan CT: Intracranial hypertension causing visual failure in *Cryptococcus* meningitis. J Neurol Neurosurg Psychiatry 51:944–946, 1988.
141. Terk MR, Underwood DJ, Zee CS, et al: MR imaging in rhinocerebral and intracranial mucormycosis with CT and pathologic correlation. Magn Reson Imaging 10:81–87, 1992.
142. Thron A, Wietholter H: Cerebral candidiasis: CT studies in a case of brain abscess and granuloma due to *Candida albicans*. Neuroradiology 23:223–225, 1982.
143. Tien RD, Ashdown BC, Lewis DV, et al: Rasmussen's encephalitis: Neuroimaging findings in four patients. AJR Am J Roentgenol 158: 1329–1332,1992.
144. Tien RD, Chu PK, Hesselink JR, et al: Intracranial cryptococcosis in immunocompromised patients: CT and MR findings in 29 cases. AJNR Am J Neuroradiol 12:283–289, 1991.
145. Trelles JO, Rocca E, Pavens R: Estudios sobre neurocisticercosis: Sobre la fina estructura de la membrana vesicula quistica y racemosa-deducciones pathologicas. Rev Neurol Psiquist 15:1–35, 1952.
146. Tsuchiya K, Yamauchi T, Furui S, et al: MR imaging versus CT in subacute sclerosing panencephalitis. AJNR Am J Neuroradiol 9: 943–946, 1988.
147. Uchino A, Yoshinaga M, Shiokawa O, et al: Serial MR imaging in Creutzfeldt-Jakob disease. Neuroradiology 33:364–367, 1991.
148. Visudhiphan P, et al: Cerebral aspergillosis: Report of 3 cases. J Neurosurg 39:472–476, 1973.
149. Walker RJ, El Gammal T, Allen MB Jr: Cranial arteritis associated with herpes zoster: Case report with angiographic findings. Radiology 107:109–110, 1973.
150. Weiderholt WC, Siekert RG: Neurological manifestations of sarcoidosis. Neurology 15:1147–1154, 1965.
151. Weingarten K, Zimmerman RD, Becker RD, et al: Subdural and epidural empyemas: MR imaging. AJNR Am J Neuroradiol 10: 81–87, 1989.
152. Welchman JM: CT of intracranial tuberculomata. Clin Radiol 30: 567–573, 1979.
153. Whelan MA, Hilal SK: Computed tomography as a guide in the diagnosis and follow-up of brain abscesses. Radiology 135:663–671, 1980.
154. Whelan MA, Stern J: Intracranial tuberculoma. Radiology 138: 75–81, 1981.
155. Whiteman MLH, Post MJ, Berger J, et al: PML in 45 HIV positive patients: Neuroimaging with pathologic correlation. Presented at the 77th Scientific Assembly and Annual Meeting of the Radiological Society of North America, November 1991.
156. Whitener DR: Tuberculous brain abscess: Report of a case and review of the literature. Arch Neurol 35:148, 1978.
157. Wood M, Anderson M (eds): Neurological Infections. Philadelphia, WB Saunders, 1988.
158. Whitley RJ: Herpes simplex virus infections of the central nervous system in children. Semin Neurol 2:87–96, 1982.
159. Whitley RJ, Soong SJ, Dolin R, et al: Adenine arabinoside therapy of biopsy-proven herpes simplex encephalitis. N Engl J Med 297: 289–294, 1977.
160. Yoshida M, Moritaka K, Kuga S, et al: CT findings of cerebral paragonimiasis in the chronic state. J Comput Assist Tomogr 6: 195–196, 1982.
161. Young RC, Bennett JE, Vogel CL, et al: Aspergillosis: The spectrum of the disease in 98 patients. Medicine 49:147–173, 1970.
162. Zee CS, Apuzzo MJ, Segall HD: Neuroradiology for imaging-directed stereotactic biopsy. In Chandrasoma PT, Apuzzo MJ (eds): Stereotactic Brain Biopsy. New York, Igaku-Shoin, 1992.
163. Zee CS, Go JL, Kim P, et al: Imaging of neurocysticercosis. Neuroimaging Clin North Am 10: 391–407, 2000.
164. Zee CS, Segall HD, Boswell W, et al: MR imaging of neurocysticercosis. J Comput Assist Tomogr 12:927–934, 1988.
165. Zee CS, Segall RD, Roger C, et al: MR imaging of cerebral toxoplasmosis: Correlation of computed tomography and pathology. J Comput Assist Tomogr 9:797–799, 1985.
166. Zee CS, Segall HD, Ahmadi J, et al: Unusual neuroradiological feature of intracranial cysticercosis. Radiology 137:397–407, 1980.
167. Zee CS, Segall HD, Ahmadi J, et al: Entrance of metrizamide into an intraventricular cysticercosis cyst. AJNR Am J Neuroradiol 2: 189–191, 1981.

168. Zee CS, Segall HD, Ahmadi J, et al: Intraventricular cysticercal cysts: Further neuroradiologic observations and neurosurgical implications. AJNR Am J Neuroradiol 5:727–730, 1984.
169. Zimmerman RA, Bilaniuk LT, Gallo E: CT of the trapped fourth ventricle. Am J Roentgenol 130:503–506, 1978.
170. Zimmerman RA, Patel S, Bilaniuk LT: Demonstration of purulent bacterial intracranial infections by computed tomography. Am J Roentgenol 127:155–165, 1976.
171. Zimmerman RD, Weingarten K: Neuroimaging of cerebral abscess. Neuroimaging Clin North Am 1:1–16, 1991.
172. Zimmerman RA, Bilaniuk LT, Shipkin PM, et al: Evolution of cerebral abscess: Correlation of clinical features with computed tomography. Neurology 27:14–19, 1977.
173. Zimmerman RD, Russell EJ, Leeds NE, et al: CT in the early diagnosis of herpes simplex encephalitis. AJNR Am J Neuroradiol 134:61–66, 1980.

7 Stroke

James D. Eastwood

Worldwide, stroke is the second leading cause of death,[54] and it is the leading cause of permanent disability.[7] Stroke is also among the most common indications for diagnostic imaging of the brain.

The term *stroke* is most accurately used to describe a clinical event that consists of the sudden onset of neurologic symptoms, and use of the term implies that symptoms are caused by cerebrovascular disease (i.e., a "cerebrovascular accident"). *Cerebral infarction,* by contrast, is a term that describes a lethal tissue-level ischemic event that may or may not cause symptoms. Cerebral infarction accounts for approximately 85% of all strokes.[4] *Primary* cerebral hemorrhages (e.g., subarachnoid hemorrhage and intraparenchymal hemorrhage) account for most of the remainder.

A number of practical topics are related to clinical imaging of ischemic stroke, and physicians who interpret imaging studies of the brain should be familiar with them. These practical topics form the basis of this chapter.

Etiology of Ischemic Stroke

Ischemic stroke is most often caused by obstruction of cerebral arteries or cerebral veins, although stroke due to obstruction of cerebral *arteries* is substantially more common than stroke due to obstruction of cerebral *veins.* It is useful to consider strokes that are caused by obstruction of *large* cerebral arteries separately from those that are caused by obstruction of *small* cerebral arteries, because the locations and extents of brain tissue involved by these two types of stroke are different. Similarly, the locations and extents of stroke that are caused by obstruction of cerebral veins are generally different than the locations and extents of stroke that are caused by obstruction of cerebral arteries.

In certain situations, cerebral infarction occurring without obstruction of cerebral arteries or veins may also occur, for example, cerebral infarction that is associated with a toxic or an anoxic insult or stroke caused by slow flow, such that seen in patients who experience sustained arterial hypotension. In this chapter, nonocclusive strokes are considered separately from strokes caused by vascular occlusion.

Risk Factors for Stroke

A number of medical conditions are associated with atherosclerotic disease and stroke. Hypertension, smoking, obesity, hyperlipidemia, diabetes mellitus, and homocystinemia are all examples of such conditions that are risk factors for atherosclerosis and stroke.[14, 43]

Atherosclerosis of the carotid artery is one of the most important conditions that predisposes to stroke.[6] Indeed, it has been implicated as the etiologic mechanism in approximately one third or more cases of ischemic stroke.[57] Many types of cardiac disease (e.g., valvular and ischemic heart disease, dysrhythmia, and right-to-left intracardiac shunting of blood) predispose to embolic stroke.[76] Atrial fibrillation, in particular, causes a substantial number of cardiogenic strokes.[23] Aortic arch atherosclerotic disease is also significantly associated with stroke, presumably as a result of associated thrombotic emboli.[27]

Many other conditions are often associated with stroke. For example, patients with conditions that predispose to hypercoagulable states, such as those patients with increased levels of factor V Leiden or antiphospholipid antibodies, are at increased risk.[29, 62] Cerebral ischemia and stroke due to vasospasm are the most important causes of morbidity and mortality in patients with subarachnoid hemorrhage. In addition, about 15% of children with sickle cell disease are afflicted by cerebral infarction.[5] Stroke may also afflict those with other vasculopathic conditions, such as fibromuscular dysplasia and the vasculopathy associated with neurofibromatosis type 1.

Pathophysiology in Ischemic Stroke

Knowledge of some of the pathophysiologic changes that occur in acute stroke can be helpful to understanding the imaging findings present in patients with acute stroke. Likewise, some of the histopathologic findings that are seen in the first days and weeks after stroke are relevant to an understanding of the imaging findings seen in these patients. A brief discussion of the most essential elements is provided.

Cytotoxic Edema

One concept that is helpful to understanding the changes that are seen in stroke is the development of *cytotoxic edema* associated with ischemia. When regional cerebral blood flow (CBF) falls below about 15 to 18 mL/100 g per minute, electrical activity within human neurons ceases.[2, 21] With further decreases in CBF (i.e., below about 8 mL/100 g per minute), the associated decrease in availability of oxygen and glucose results in decreased production of adenosine triphosphate (ATP).[38] With the loss of ATP production, Na^+/K^+ ATPase, an enzyme that is important to cell homeostasis, fails. This event permits the unbalanced influx of extracellular calcium and sodium and, secondarily, the influx of extracellular water into cells. This

increased intracellular water is termed cytotoxic edema. The formation of cytotoxic edema is postulated to be the cause of most of the computed tomography (CT) and magnetic resonance imaging (MRI) findings seen in acute ischemic stroke.

Effects of Cytotoxic Edema on CT and MRI Studies

Because water is lower in density than normal brain tissue, one effect of edema on the appearance of the brain on CT images is a decreased density of brain tissues. This decrease has two primary (albeit related) effects on the appearance of the brain on CT scans (Fig. 7–1):

1. A diminished difference in density that normally exists between gray and white matter. This decrease in contrast may be seen in cortical regions and also at the base of the brain.
2. An overall decreased density in a region of the brain.

Water is also associated with longer T1 and T2 relaxation times than those for normal brain tissue. Therefore, one effect of cytotoxic edema on MRI scans is to increase the T1 and T2 relaxation times of involved tissues. Although regions of the brain that are involved with ischemic stroke may be depicted as areas of relative T1 and T2 prolongation, the changes on a T1-weighted image are not usually seen as early as the changes on T2-weighted images. In the acute stroke patient, the earliest findings on conventional MRI scans are regions of increased signal intensity on long repetition time (TR) images.

Cytotoxic edema can also influence the appearance of brain tissues on imaging studies by creating regional *mass effect*. In acute stroke cases involving the cortex of the brain, stroke-related edema is commonly associated with swelling of the cortical gyri. Gyral swelling is typically identified on imaging studies by the observation that the sulci between the gyri are effaced (i.e., narrowed). Regional sulcal effacement is, therefore, a sign that can be used to detect the changes of acute stroke (see Fig. 7–1).

Mass effect that is associated with acute stroke usually peaks at about 72 hours after the initial ischemic insult, with a gradual decrease in mass effect beginning after that time. When the extent of cerebral infarction is great, the possibility exists that mass effect from brain edema will result in *brain herniation*. Brain herniation represents an important complication of stroke because compression of brain tissues and vascular structures against nonmobile cranial structures (e.g., falx, tentorium, skull base) can result in new neurologic deficits and may exacerbate ischemia and elevate intracranial pressure. Brain herniation can also result in obstruction of cerebral ventricles (i.e., *ventricular trapping*), a problem that also increases intracranial pressure.

When stroke-related edema is extensive and life-threatening, it is sometimes called *malignant brain edema*.[64] The use of the word *malignant* to describe brain edema associated with stroke should not be confused with the type of brain edema associated with brain neoplasms (i.e., *vasogenic* edema). Life-threatening brain edema that is associated with stroke occurs most commonly in patients with extensive ischemia in the territory of a middle cerebral artery (MCA). Patients with cardiac embolus, internal ca-

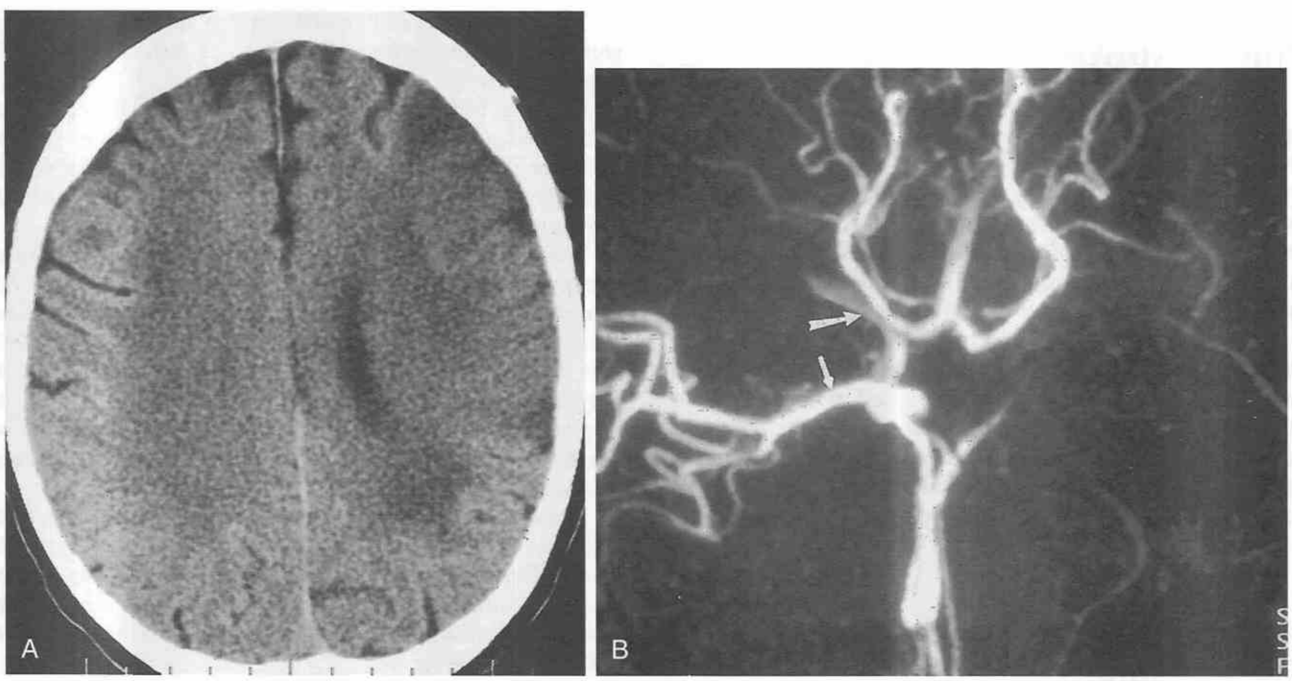

Figure 7–1. Acute aphasia and right-sided weakness. *A,* Unenhanced CT scan shows low density, loss of gray matter–white matter contrast, and effacement of sulci within the territory of the left middle cerebral artery. *B,* Maximum intensity projection image (anterior displayed at the bottom of the image) from intracranial 3D time-of-flight MRA shows no signal within the left middle cerebral artery or the left internal carotid artery. The normal appearance of the right internal carotid artery *(arrow)* and the middle cerebral artery *(small arrow)* is well visualized by comparison.

rotid artery (ICA) occlusion, and ICA dissection appear to be at highest risk for development of life-threatening brain edema from stroke.[9] When necessary, control of intracranial pressure may initially be attempted with the use of cerebrospinal fluid (CSF) diversion (e.g., with ventriculostomy catheters). In some cases, severe stroke-related edema may be managed by ipsilateral decompressive craniectomy to reduce intracranial pressure.[18]

In addition to the effects on brain CT density, MRI relaxation rates, and local mass effect, the formation of cytotoxic edema may also be related to the changes that are seen on DW magnetic resonance images in acute stroke patients. Such changes may be mediated by an increase in intracellular water with or without a secondary effect on extracellular water diffusion.[75, 77] DW changes in acute stroke are detailed later (see "Time Course of Diffusion-Weighted Images in Stroke").

T2 Fogging in Late Subacute Infarction

In some patients, during the 3rd week following a stroke, the typical hyperintense signal that is associated with ischemic stroke may regress. In some cases, signal intensity that appears normal may be seen transiently during this period. Such a decrease in signal intensity on a T2-weighted image (T2WI) is called "fogging." The causes of fogging are not clear, but it has been proposed that a decrease in edema, accompanied by increased macrophage activity, may be responsible.[1, 68] In such cases, parenchymal enhancement on T1-weighted images is typically seen after injection of gadolinium contrast material.

Chronic Stroke

After about 4 weeks, brain tissue that has undergone infarction has completed most of the pathologic changes related to reparation and resorption. Glial scar and areas of cystic necrosis typically have replaced neural tissue. If the volume of infarcted tissue was substantial, there may be evidence of volume loss, such as enlargement of adjacent sulci, cisterns, and ventricles. CT density is typically low, and MRI signal intensities reflect prolonged T1 and T2.

In some cases, areas of gyral increased density and increased signal on T1-weighted images may appear to reflect mineralization (i.e., calcification) within areas of cortical necrosis.[8] Gyral signal changes may be the most easily identified imaging feature associated with remote infarction, or signal changes associated with chronic stroke may be minimal, with regional volume loss representing the most readily detected evidence of prior ischemia.

Hemorrhage Associated with Cerebral Infarction

Hemorrhage that is associated with ischemic stroke may be symptomatic or asymptomatic. Cerebral hemorrhage that occurs secondary to ischemia is often called a *hemorrhagic infarction* or a *hemorrhagic transformation*. By comparison, cerebral hemorrhage that is the result of a process other than ischemia (e.g., cerebral hematoma or subarachnoid hemorrhage) can, like ischemic stroke, be associated with abrupt onset of neurologic symptoms. When this occurs, a primary cerebral hemorrhage is sometimes called a *hemorrhagic stroke*.

Because these two types of cerebral hemorrhage that are associated with stroke symptoms have different causes and are often treated differently, the imaging specialist should exercise care when using these terms. Furthermore, the diagnostic investigations undergone by patients with primary hemorrhages of the brain (e.g., MRI, cerebral angiography) are often substantially different from the diagnostic investigations undergone by patients with infarction (e.g., echocardiography, carotid ultrasonography). Because distinguishing primary cerebral hemorrhage from cerebral hemorrhage secondary to ischemic stroke can be of clinical importance, care should be taken to communicate (to the extent possible) whether the primary event appears to be hemorrhage or ischemia.

Evidence that ischemic cerebral hemorrhage is secondary to ischemic stroke is the absence of such hemorrhage on the initial imaging study obtained after the onset of symptoms (Figs. 7–2 and 7–3). Imaging findings suggestive of an ischemic cause of stroke (e.g., dense artery or parenchymal abnormality within a vascular territory) on the initial scan are also helpful. It is typically during the subacute, or reparative, phase (beginning after about 24 hours following the onset of initial symptoms) that hemorrhage may be seen in association with ischemic stroke. By contrast, primary cerebral hemorrhage is typically seen on imaging studies that are obtained at the time of initial symptoms. Primary hemorrhages are discussed in Chapter 16.

Two main forms of hemorrhage may be seen on imaging studies after an ischemic stroke: (1) *petechial* and (2) *space-occupying*.

Petechial hemorrhages are not associated with new mass effect and are often limited to the cortical gray matter. They are thought to be caused by red blood cell diapedesis through small breaches that occur in the endothelium following a stroke (Fig. 7–4).

When greater disruption of blood vessels occurs, space-occupying hemorrhages may occur (see Fig. 7–3). Although the exact cause of these hemorrhages (i.e., hematomas) that occur secondary to ischemic stroke is not certain, it is thought that reperfusion of ischemic tissue, such as may be seen after lysis of a proximal embolus, may be responsible. The use of anticoagulant therapy may also be a risk factor for symptomatic, space-occupying hemorrhage following stroke.

Hemorrhage is also common in stroke caused by venous obstruction. However, the pattern of such hemorrhages often differs from the pattern associated with stroke due to arterial obstruction. In stroke due to venous obstruction, associated hemorrhage is more commonly found in subcortical locations (Fig. 7–5).

On CT scans, the appearance of hemorrhage caused by ischemic stroke is that of increased density. On MRI scans, the appearance of hemorrhage due to ischemic stroke varies with time, but petechial hemorrhages due to ischemic stroke are usually detected as areas of hyperintense signal

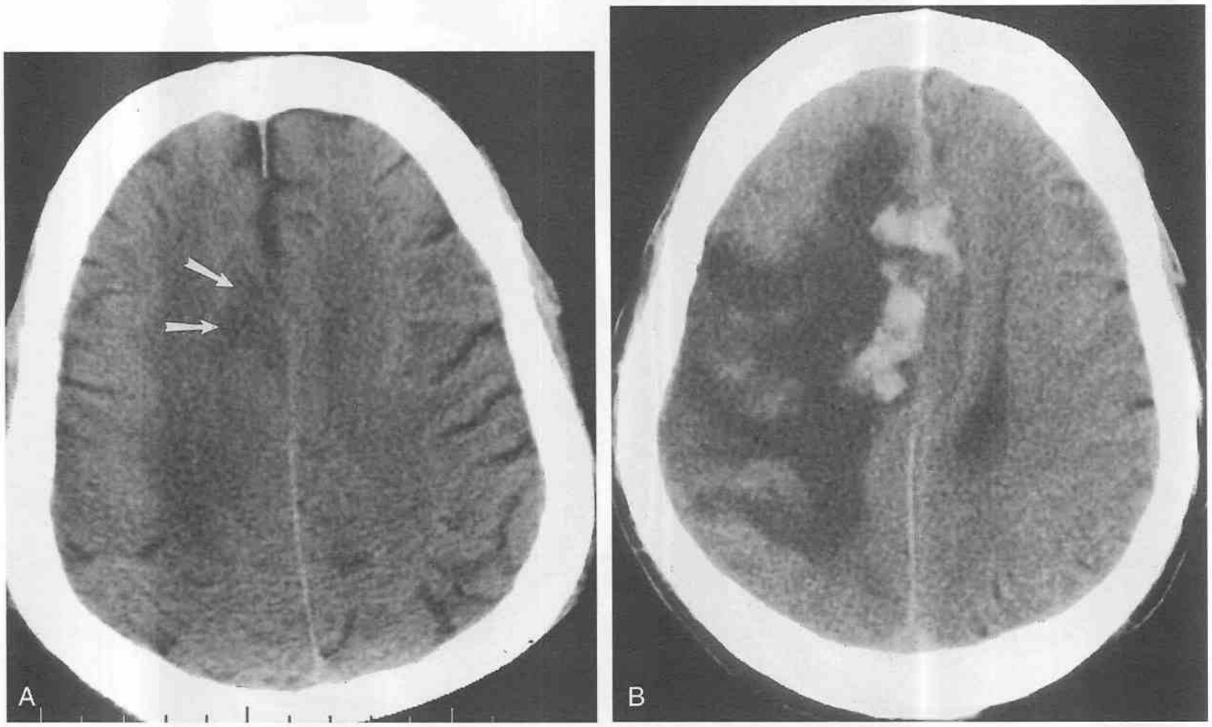

Figure 7–2. Hemorrhagic infarction. *A,* Unenhanced axial CT shows low density in the right anterior cerebral artery territory *(arrows)*. *B,* Three days later, low density has extended into the middle cerebral artery territory (MCA), and the anterior cerebral artery territory infarct shows evidence of new hemorrhage. *C,* Lateral catheter angiogram shows occlusion of the right internal carotid artery proximally with a small patent stump *(arrow)*.

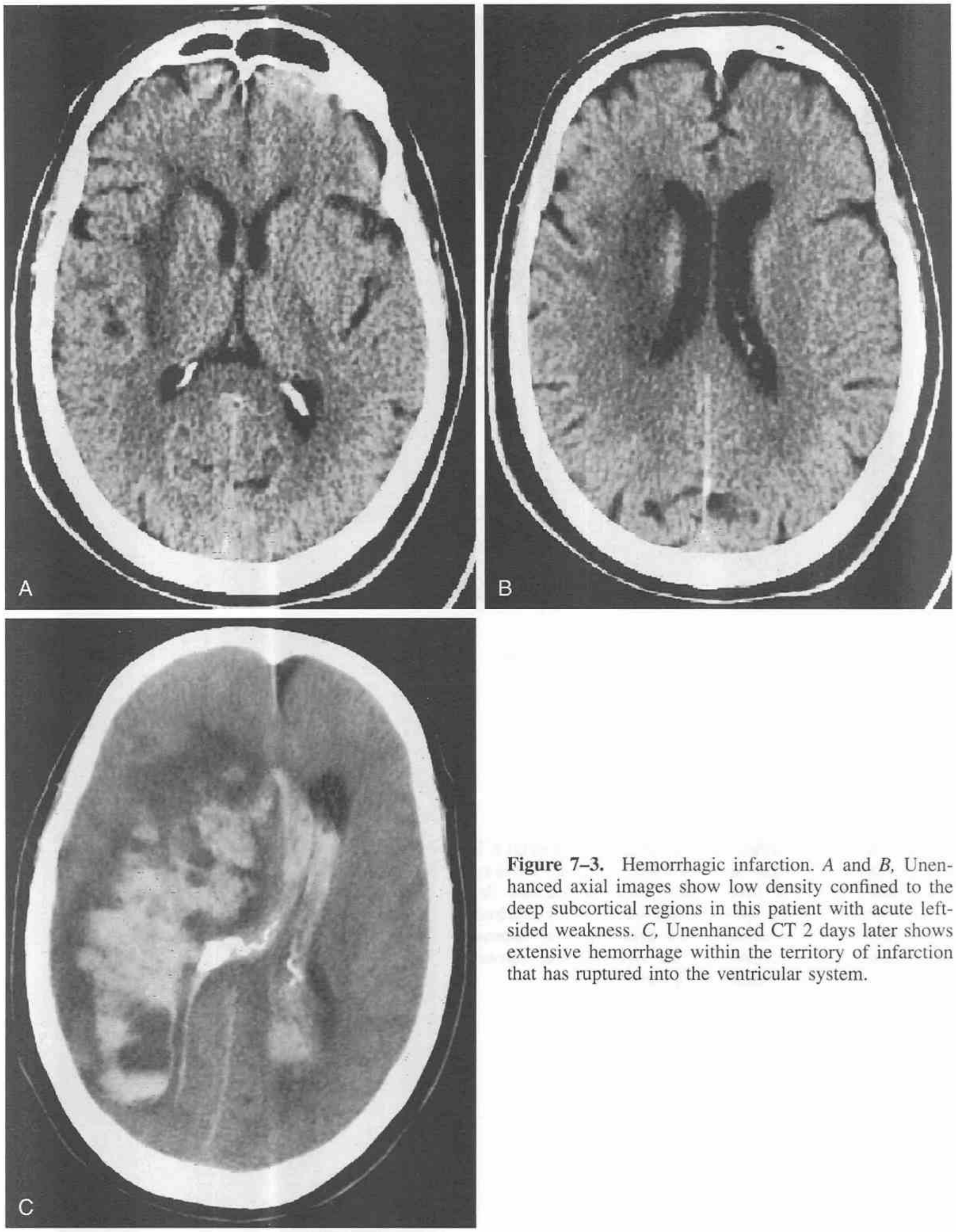

Figure 7–3. Hemorrhagic infarction. *A* and *B*, Unenhanced axial images show low density confined to the deep subcortical regions in this patient with acute left-sided weakness. *C*, Unenhanced CT 2 days later shows extensive hemorrhage within the territory of infarction that has ruptured into the ventricular system.

RoshanKetab Medical Publishers TEHRAN - IRAN Tel: +98 (21) 66950639 TelFax: +98 (21) 66963783-6

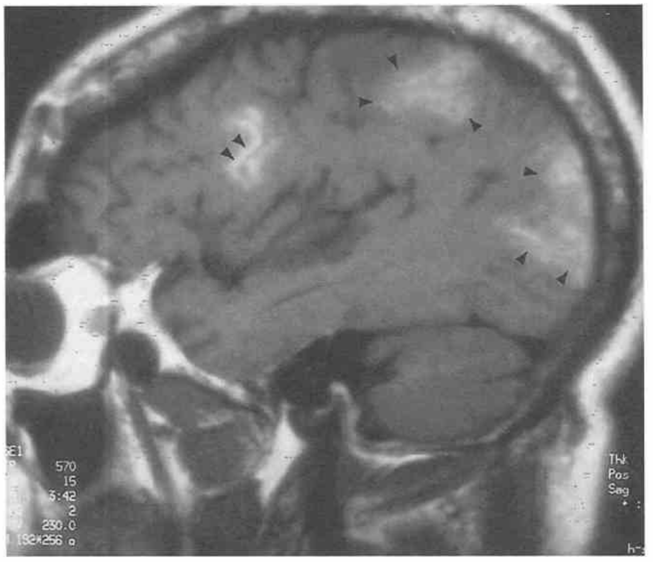

Figure 7–4. Multiple hemorrhagic infarctions. T1-weighted sagittal image shows several areas of gyral high signal *(arrowheads)* compatible with petechial hemorrhage.

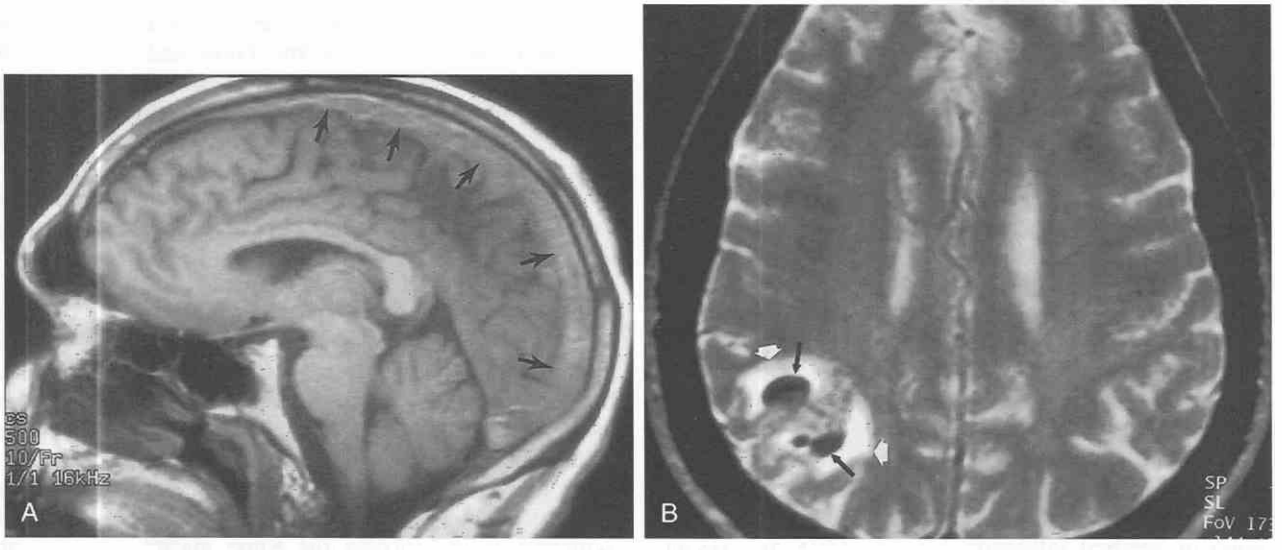

Figure 7–5. Superior sagittal sinus thrombosis. *A,* T1-weighted sagittal image (unenhanced) shows mild increased signal in the superior sagittal sinus *(arrows)*. *B,* T2-weighted axial image shows subcortical decreased signal *(black arrows)* surrounded by increased signal edema *(small arrows)*. The subcortical location of hemorrhage is characteristic of venous infarction.

on T1-weighted images (see Fig. 7–4), whereas acute hematomas are often depicted as regions of low signal intensity on T2-weighted images (see Fig. 7–5).

Time Course of Contrast Enhancement in Ischemic Stroke

Changes in brain enhancement can be associated with ischemia and infarction. One of the earliest changes in enhancement that can be seen on MRI scans in patients with acute stroke is increased enhancement in the cortical vessels and meninges overlying an ischemic region of the brain (Fig. 7–6). This can be seen in the first hours after onset of symptoms. The precise cause of this increased intravascular enhancement associated with ischemic stroke is not known, but one possibility is delayed wash-out of contrast material due to slow flow. Another possibility is autoregulatory vasodilation. These possible mechanisms would be expected to increase the enhancement seen in vessels by increasing the concentration of contrast material and the size of blood vessels, respectively.

Parenchymal enhancement associated with ischemic stroke, by comparison, is most commonly seen in the subacute time frame and, using standard techniques (i.e., 0.1 mmol/kg gadolinium contrast material and no magnetization transfer pulse), is seen to some degree in most patients by 7 days following an ischemic stroke (Fig. 7–7). Studies have shown that enhancement of the parenchyma can be demonstrated in the acute setting with the use of magnetization transfer (MT) techniques or with high-dose gadolinium injections.[45] The added clinical value of MT in stroke remains to be determined.

When mass effect and parenchymal enhancement are present in a case of subacute infarction, one must occasionally differentiate infarction from brain neoplasm, such as primary cerebral glioma. Often, simply observing that a given lesion conforms to the expected territory of supply of a cerebral artery (e.g., MCA) can be helpful (see Fig. 7–7). Additionally, apparent diffusion coefficient (ADC) analysis of diffusion-weighted (DW) MR images may also provide evidence of restricted diffusion in a region of enhancement. In such cases, the diagnosis of infarction should be favored. After 5 to 7 days, however, infarction is typically associated with normal to increased ADC values. If clinical suspicion of infarction is high, another MRI scan in 2 to 4 weeks can document decreasing enhancement and mass effect.

Alternatively, magnetic resonance spectroscopy (MRS) can be used to document low *N*-acetyl-aspartate (NAA) peak and increased lactate peak that would be expected in a region of cerebral infarction.[13, 20] The MRS findings in neoplasms are discussed in Chapter 11. Biopsy should only rarely be necessary to distinguish infarction from tumor. Enhancement due to infarction decreases after 4 to 6 weeks.

CT Versus MRI in the Setting of Acute Stroke

MRI is more sensitive than CT in the setting of acute stroke.[65] This advantage has increased with the recent clinical availability of DW MRI. DW MR images have the highest sensitivity and specificity for acute cerebral infarction of any imaging tool presently available.[36] Nonetheless, CT remains the first imaging test performed at many institutions, even when MRI is subsequently performed. CT is the only imaging test performed in the setting of acute stroke at other institutions. The reasons for this appear to be the high sensitivity of CT for detecting hemorrhage and its greater availability at many institutions.

Small-Artery Stroke

Occlusion of the small end-arteries that penetrate the brain results in focal, deeply located areas of infarction. Such infarctions can be multiple and can occur in the absence of significant disease involving the large arteries. Areas of infarction in the territories of small arteries are frequently called *lacunar* infarctions (Fig. 7–8). It is often assumed that patient histories of hypertension and diabetes mellitus are associated with lacunar infarction more frequently than with other stroke subtypes. However, this concept has recently been challenged.[58] Locations that are commonly involved with small-artery stroke are as follows:

- Basal ganglia and internal capsule (lenticulostriate arteries)
- Thalamus (thalamoperforate arteries)
- Deep hemispheric white matter (deep cortical perforators)
- Brain stem (pontine perforators and other small brain stem perforating arteries)

Occasionally, a large perivascular space (Virchow-Robin space) may mimic the appearance of a small-artery infarction.[25] However, perivascular spaces are most prominent near the surfaces of the brain and have imaging features typical of CSF. A proton-density–weighted image and/or a fluid-attenuated inversion recovery (FLAIR) image can be used to separate infarction (bright) from CSF (dark) (Fig. 7–9).

The imaging specialist can often differentiate infarction in the territory of pontine perforating arteries from other lesions that involve the pons by noting that infarctions in the territories of the paramedian arteries typically have medial margins that approach, but do not cross, the plane of midline (Fig. 7–10). Findings of ischemia that are due to disease involving the small perforating arteries are not limited to lacunar infarctions. Regions of T1 and T2 prolongation (or CT hypodensity) that are larger and less well defined than regions of lacunar infarction may be seen in many elderly patients as well as in patients with a history of hypertension or diabetes. These regions are commonly symmetrical and involve the white matter of the central pons (see Fig. 7–8).

Large-Artery Stroke

Occlusions of large cerebral arteries generally result in regions of ischemic involvement that differ substantially in extent than those produced by occlusion of small cerebral arteries. Nonetheless, it is useful to note that ischemic stroke in the territory of a large cerebral artery may result

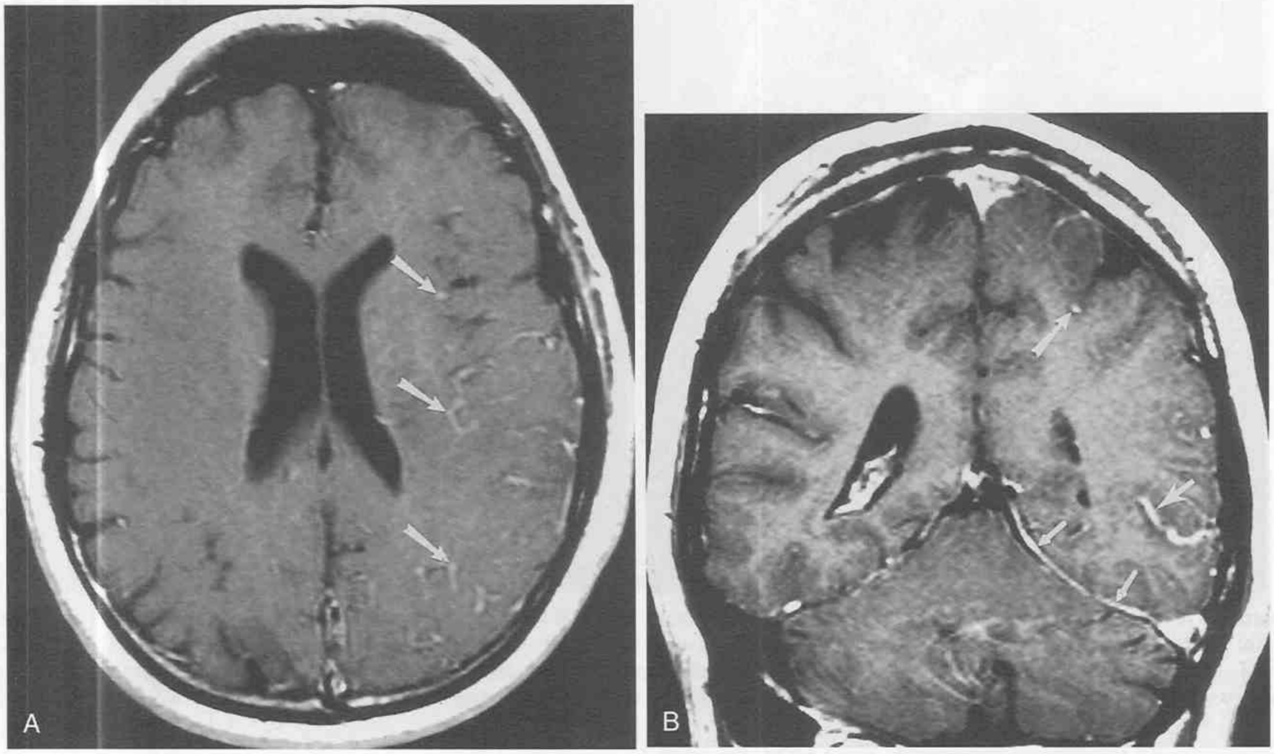

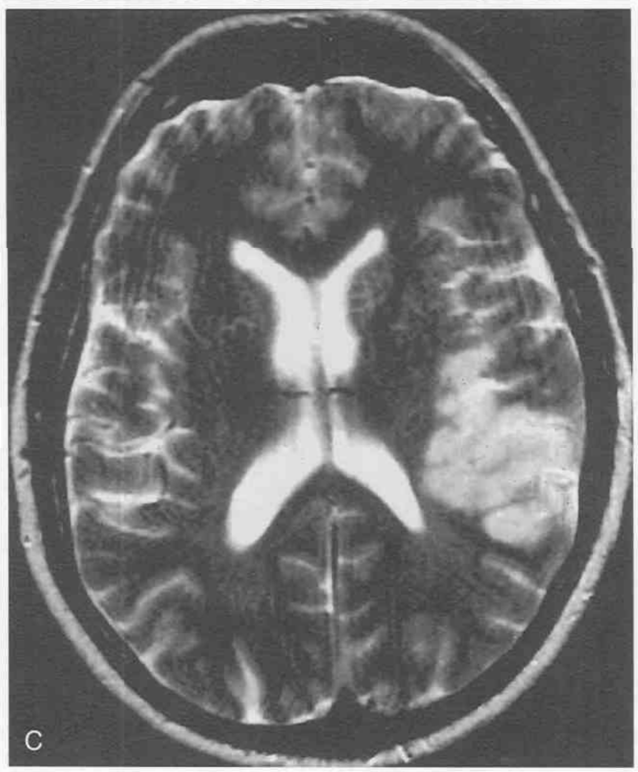

Figure 7–6. Acute right-sided weakness. *A,* T1-weighted axial image following intravenous gadolinium (0.1 mmol/ kg) shows prominent intravascular enhancement *(arrows)*. *B,* T1 postcontrast coronal image shows asymmetrical enhancement of the left tentorium *(small arrows)*. *C,* T2-weighted axial image shows high signal in the territory of the left middle cerebral artery (inferior division), consistent with infarction.

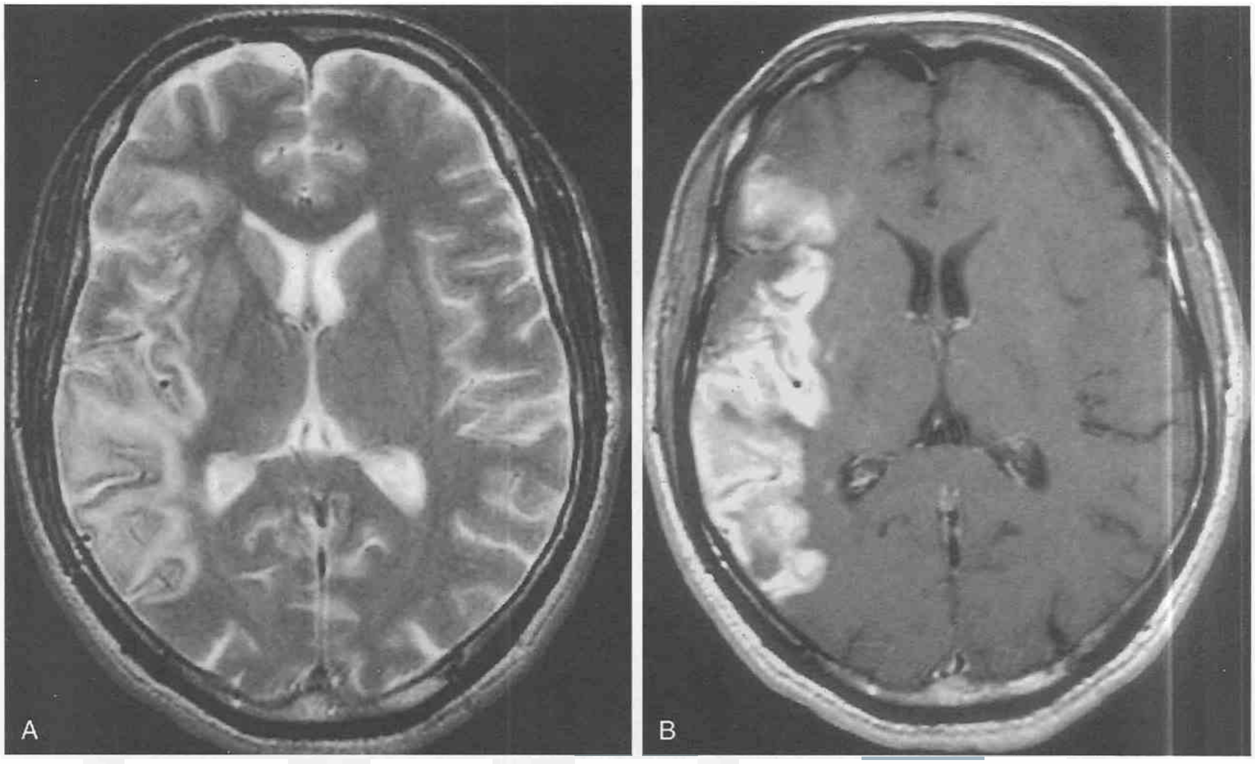

Figure 7–7[redacted]Enhancing infarct[redacted]week after s[redacted] onset). *A*, T[redacted]eighted axial image shows increased signal within the cortical territories of the right middle cerebral artery. *B*, T1-weighted axial image following intravenous gadolinium (0.1 mmol/kg) reveals gyral and subcortical enhancement. An enhancing infarct can often be differentiated from tumor by clinical information (e.g., acute onset of symptoms) and extent that conforms to the territory of a cerebral vessel.

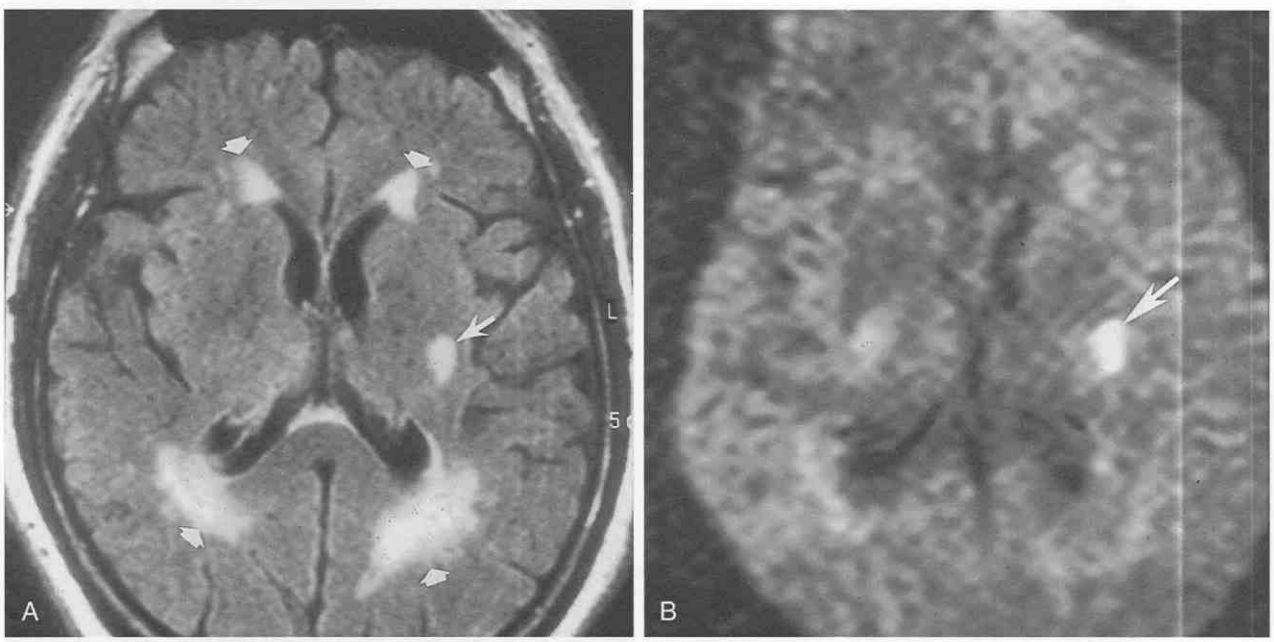

Figure 7–8. Acute right hemiparesis. *A*, Fluid-attenuated inversion recovery (FLAIR) MR image (TI = 2000) shows high signal in the periventricular regions *(small arrows)* and posterior limb of the left internal capsule *(arrow)*. *B*, Axial diffusion-weighted image (b = 980) shows increased signal only in the left internal capsule, consistent with acute stroke *(arrow)*. Other areas that were hyperintense on the FLAIR image presumably represent older ischemic changes.

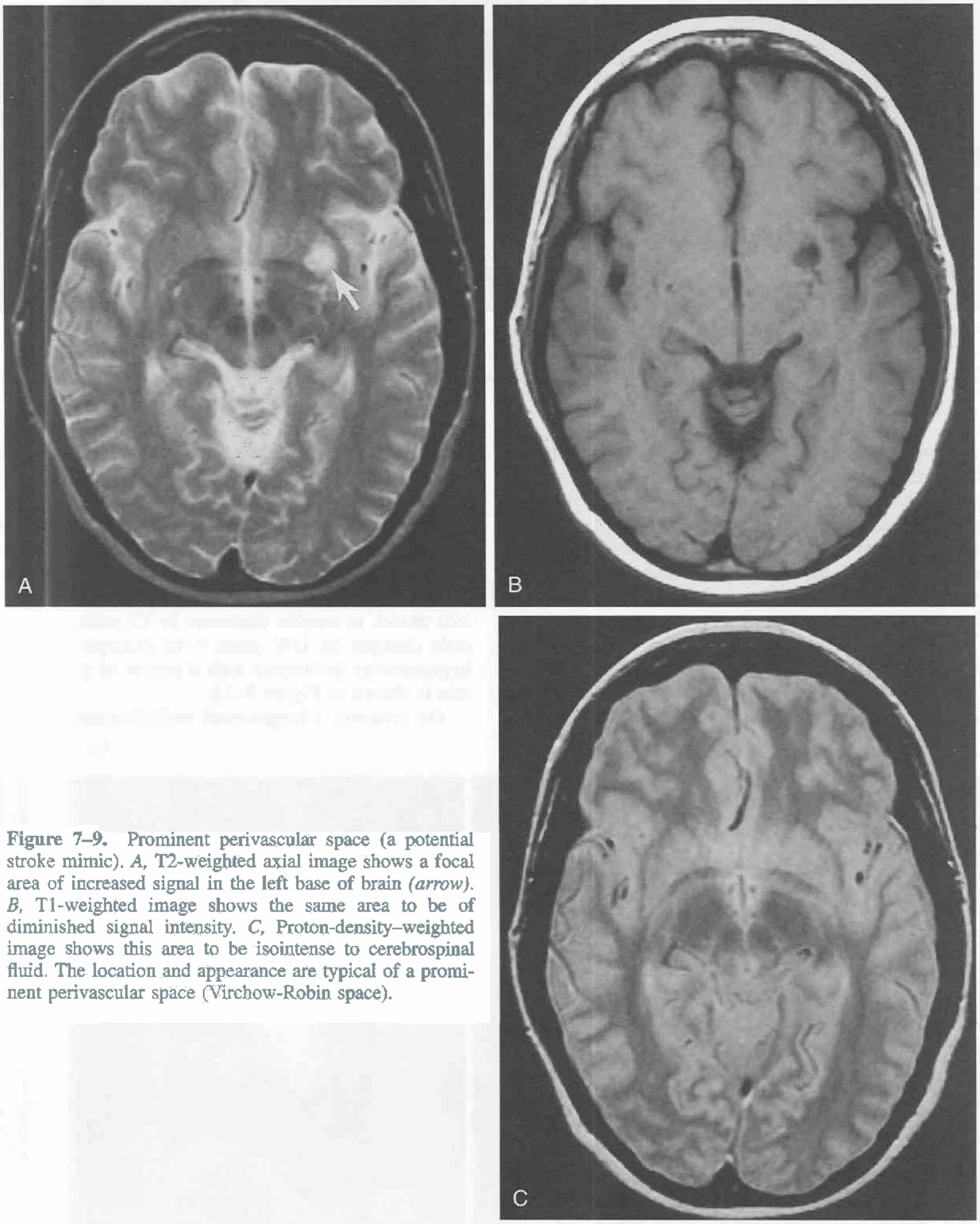

Figure 7–9. Prominent perivascular space (a potential stroke mimic). *A,* T2-weighted axial image shows a focal area of increased signal in the left base of brain *(arrow)*. *B,* T1-weighted image shows the same area to be of diminished signal intensity. *C,* Proton-density–weighted image shows this area to be isointense to cerebrospinal fluid. The location and appearance are typical of a prominent perivascular space (Virchow-Robin space).

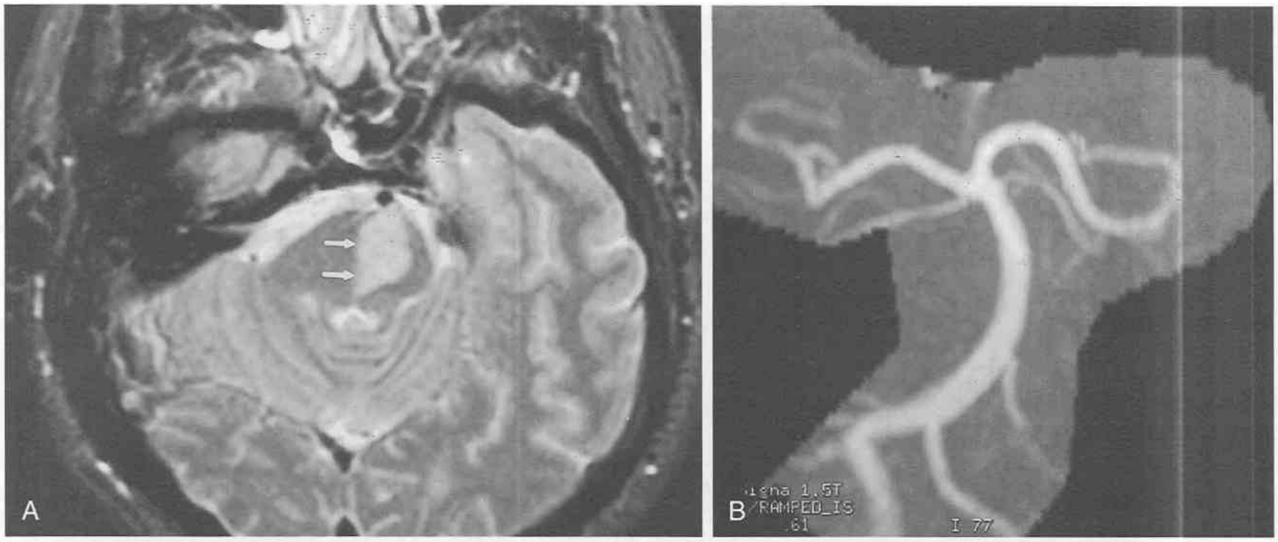

Figure 7–10. Acute pontine perforator infarct. *A*, T2-weighted axial image shows increased signal within the central pons. The medial border of this infarct does not cross the plane of the midline. This tendency to respect the midline is typical of paramedian branch infarction. *B*, Three-dimensional time-of-flight MRA shows no narrowing of the basilar artery in this patient with small-vessel infarction.

in infarctions in the territories of multiple small arteries that receive their supply from the large artery in question. A common example of this phenomenon is the extensive basal ganglia infarctions that may occur in proximal MCA occlusion as a result of loss of supply to the lenticulostriate arteries. Occasionally, the territories of supply of the lenticulostriate arteries may be the only regions that undergo infarction in MCA stroke (Fig. 7–11).

On imaging studies, one feature that can help to differentiate large-artery from small-artery stroke is involvement of cortical gray matter. With large-artery stroke, the earliest changes that are apparent on T2 and proton-density–weighted images typically are seen in the cortex. As time passes, subcortical hyperintensity becomes more evident and is usually well visualized at 24 hours.

One exception to the rule that cortical findings precede subcortical findings in large-vessel stroke, however, may occur when subcortical low signal intensity accompanies acute cortical hyperintense changes.[22] In an animal ischemia model, reversible decreases in T2 relaxation may precede changes on DW scans.[15] An example of subcortical hypointensity associated with a region of presumed ischemia is shown in Figure 7–12.

On occasion, a large-vessel occlusion can result in deep

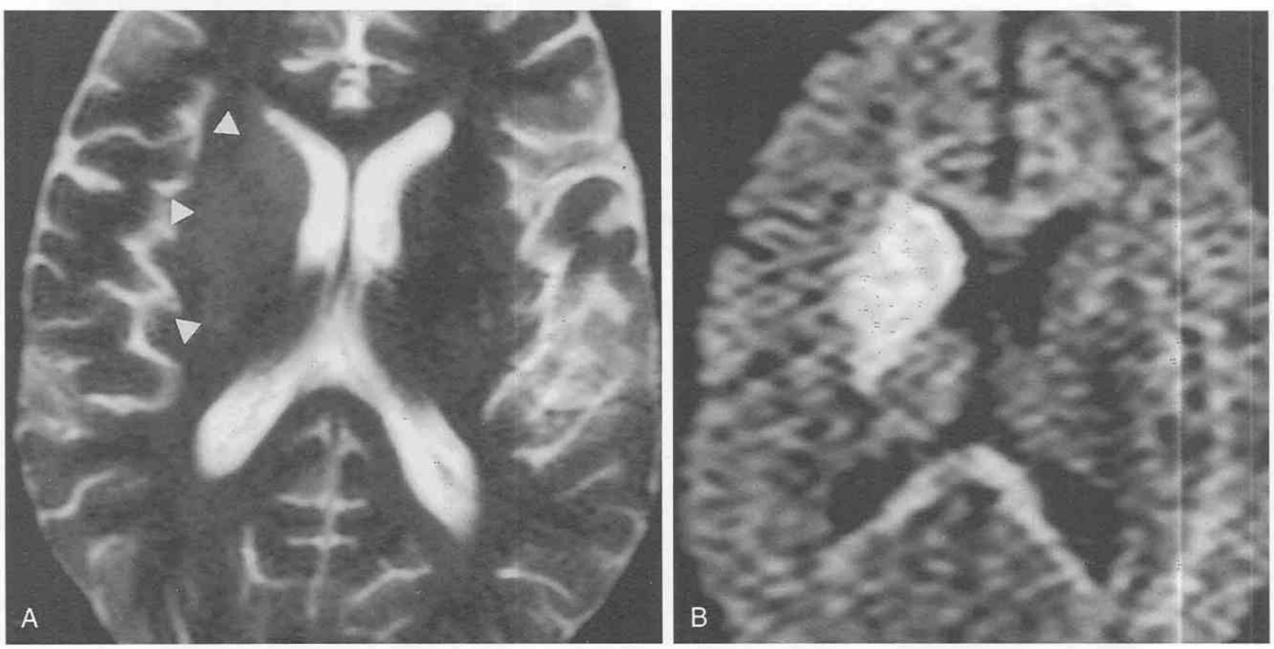

Figure 7–11. Acute dissection of the internal carotid artery. *A*, T2-weighted axial image shows minimal increased signal within the right basal ganglia (triangles). *B*, Diffusion-weighted (b = 970), echo-planar image shows hyperintensity within the same region that is substantially more conspicuous. Diffusion-weighted images have greater sensitivity for acute infarction.

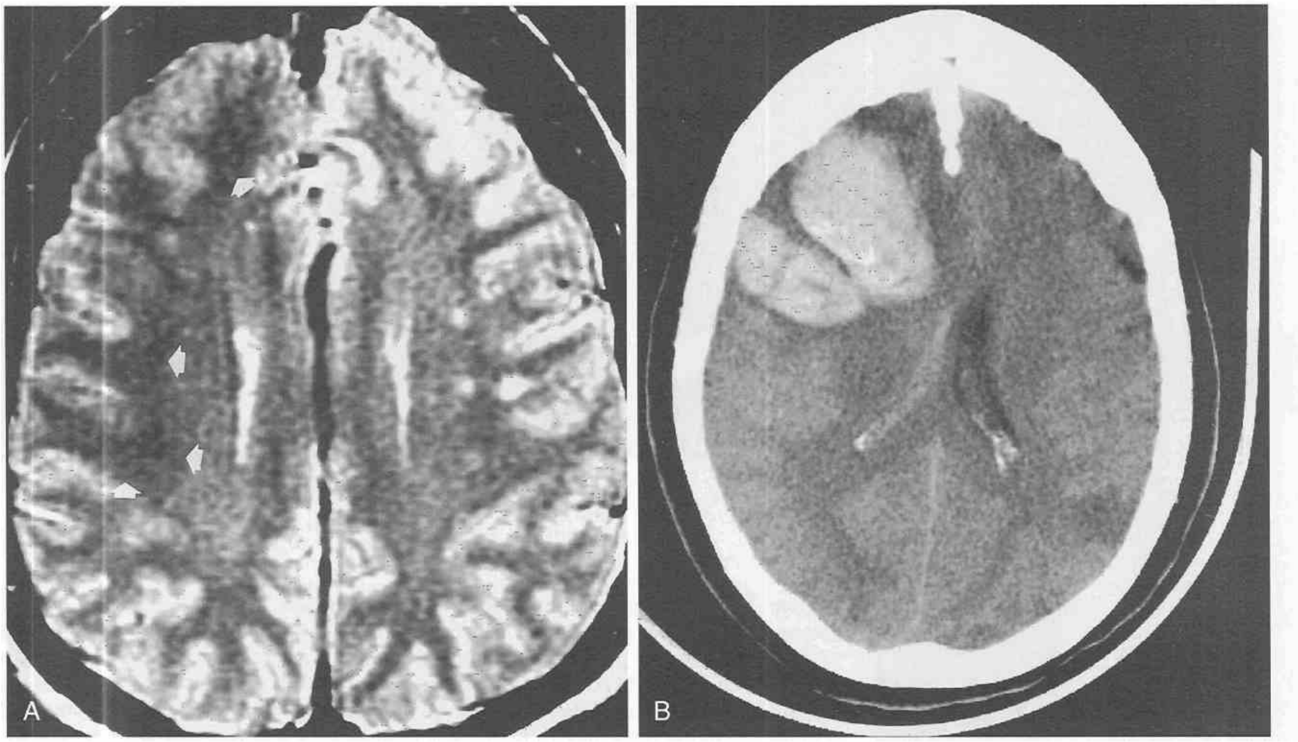

Figure 7–12. Acute left-sided weakness. *A,* T2-weighted axial image shows extensive subcortical low signal in the right frontal lobe *(arrows). B,* Unenhanced CT 36 hours later shows development of right frontal hematoma. Hypointense changes on T2-weighted images appear to have preceded hemorrhagic infarction.

subcortical white matter infarction with relative sparing of the cortex. This is presumably a hemodynamic phenomenon caused by a low rate of flow that is not sufficient to supply the territories of the deep perforating arteries (see Fig. 7–3). The terms *internal watershed stroke* and *deep watershed stroke* apply to this pattern of infarction. In such cases, it is the extent of abnormality that helps to distinguish regional subcortical ischemia from other lesions.

Stroke Caused by Internal Carotid Artery Disease

It is thought that diseases resulting in narrowing of the lumen of the ICA can lead to stroke by two likely interrelated mechanisms:

1. *Hemodynamic compromise by obstruction of flow.* Hemodynamic compromise of brain tissues may be minimal when adequate collateral flow is present. Because gradual occlusion of the ICA (e.g., because of atherosclerosis or fibromuscular disease) often allows time for adequate collateral development, gradual occlusion is often clinically better tolerated by patients than sudden occlusion (e.g., acute arterial dissection). Furthermore, in some cases gradual carotid occlusion does not result in neurologic symptoms or brain infarction.
2. *Thrombotic emboli.* In arteries that are irregular or very narrowed, emboli that involve vessels such as the MCA and the anterior cerebral artery (ACA) may be produced.[78] This concept is supported by diminished stroke rates in patients with carotid artery disease treated with antiplatelet agents, such as aspirin, as compared with the rates in control patients.[17]

The most important disease of carotid arteries that can lead to stroke is atherosclerosis of the ICA (Fig. 7–13). Stenosis due to atherosclerotic plaque most commonly occurs at the level of the carotid bulb. By contrast, stenosis of the carotid artery by fibromuscular dysplasia is more likely to occur distal to the bulb, above the level of the C3 vertebral body.[70] Type II fibromuscular dysplasia is associated with a characteristic appearance on conventional catheter angiograms consisting of alternating narrowing and dilation, the appearance of which has been likened to a "string of beads."

Acute dissection of the extracranial cerebral vessels is another relatively common cause of stroke that often occurs following trauma, though some cases occur spontaneously in patients with hypertension or in patients with various arteriopathies (e.g., fibromuscular dysplasia, Ehlers-Danlos syndrome). Patients with dissection of the ICA frequently present with ipsilateral cerebral or retinal symptoms.

Alternatively, patients with carotid dissection may present with ipsilateral Horner's syndrome, consisting classically of ptosis, meiosis, and anhidrosis of the affected eye. Horner's syndrome due to dissection is thought to be related to disruption of the postganglionic sympathetic plexus that is associated with the cervical carotid artery.

Characteristic locations for cervical arterial dissection include the distal cervical ICA and the cervical loop of the vertebral artery (at the C1 and C2 levels), although other locations may be involved. Vertebral artery injuries, including dissection, may occur in association with cervical spine


Figure 7–13. Atherosclerotic stenosis of the internal carotid artery. *A,* Maximum intensity projection image from 2D time-of-flight MRA shows focal loss of signal ("flow gap") in the proximal left internal carotid artery *(arrow)*, suggestive of flow-limiting stenosis. *B,* Maximum intensity projection image from intracranial 3D time-of-flight MRA shows diminished signal in the left M2 branches *(small arrows)*. The diminished signal is thought to be a result of slow flow and resultant spin saturation.

trauma.[79] Fractures involving the transverse foramina raise concern for associated vertebral artery injury, including dissection.[81]

MRI scans and CT angiograms obtained in patients with extracranial dissection may reveal tapered or irregular narrowing of the affected vessel, with or without evidence of an intimal flap on magnetic resonance angiography (MRA) source images (Figs. 7–14 and 7–15). T1-weighted axial MRI may also reveal hyperintense thrombus within the false lumen of the artery. In cases of suspected dissection, evidence of pseudoaneurysm complicating dissection should be sought. Any evidence of focal outpouching should be confirmed angiographically.

Diseases of the ICA that predispose to embolus formation may result in embolic occlusion of any of the intracranial arteries that receive all or most of their supply from the ICA. Stroke in the territories of the ophthalmic artery, ACA, and MCA are commonly associated with ICA disease.

The anterior choroidal artery also arises from the ICA. It originates at the posterior aspect of the distal ICA, usually just beyond the junction of the ICA with the posterior communicating (PCom) artery. The territory of the anterior choroidal artery includes several regions that can give rise to focal neurologic symptoms, and occlusion of this artery may produce infarction in the optic tract, cerebral peduncle, and posterior limb of the internal capsule. The anterior choroidal artery is not usually seen directly on MRI or CT scans; instead, it is identified angiographically.

Middle Cerebral Artery Stroke

Stroke in the territory of the MCA is associated with the greatest degree of morbidity and mortality and is among the most common types of ischemic stroke. For the purposes of hyperacute stroke management, a thorough understanding of acute MCA stroke imaging is needed for optimal patient care.

In general, the most important initial goal of acute stroke imaging is to exclude hemorrhage as the cause of new neurologic symptoms. Acute primary intracerebral hematoma and subarachnoid hemorrhage are conditions that represent absolute contraindications to thrombolytic and anticoagulation (e.g., heparin) therapies.

Once hemorrhage has been excluded (typically by CT imaging), the next goals are (1) to help confirm the clinical diagnosis of stroke and (2) to determine the extent of irreversible ischemia. When extensive, irreversible ischemia is associated with a poor prognosis and an increased rate of hemorrhage related to thrombolysis.

Confirming the diagnosis of stroke, by observing the earliest imaging signs associated with stroke and excluding other possible causes of symptoms, can be of value in choosing optimal therapy and minimizing complications.[16]

Middle Cerebral Artery Territory

Knowledge of the usual territory of supply of the MCA is essential to understanding the changes seen in acute MCA stroke. The territory of supply of the MCA artery

Figure 7–14. Acute dissection of the internal carotid artery. *A,* Maximum intensity projection image from 3D time-of-flight MRA shows a focal area of irregularity in the distal portion of the cervical segment of the right internal carotid artery *(arrow)*. *B,* Axial "source" image from the same sequence shows diminished signal in the petrous segment of the right internal carotid artery *(small arrow)*. *C,* Unenhanced axial T1-weighted image obtained through the upper neck with fat saturation shows crescentic hyperintense signal representing thrombus *(arrow)*. A small, flow-related signal void represents the residual lumen at this point *(arrowhead)*. [redacted]

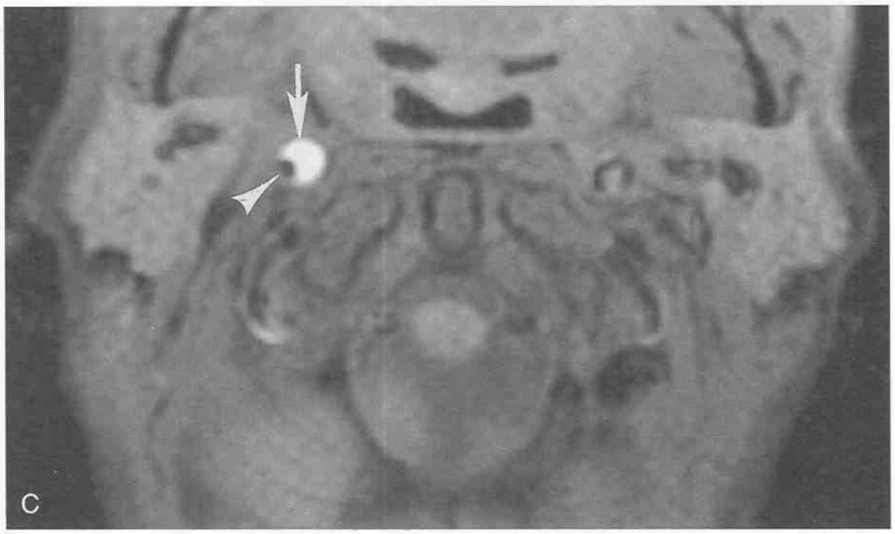

can be considered to consist of a cortical territory and subcortical territory (i.e., that territory supplied by lenticulostriate perforator arteries). The cortical territory of supply of the MCA is reciprocal with that of the posterior cerebral artery (PCA) and the ACA.

The cortical territory of the MCA can be understood to be composed of two main parts: (1) a more anterior part that supplies the frontal lobe and (2) a more posterior part that supplies the parietal and temporal surfaces of the brain.

In common clinical use, the territory of the MCA that is more anterior is said to be supplied by the *superior division* of the MCA; the territory of the MCA that is more posterior is said to be supplied by the *inferior division* of the MCA. This separation of the MCA into two major divisions is based on the proximal branching of the MCA into (usually) two dominant segments. For practical purposes, it is useful to recognize that one main MCA division may become occluded (e.g., by embolus), whereas the other main division remains patent and that the imaging findings of ischemia may reflect this separation.

Substantial variation in territory of supply may occur among patients. Nonetheless, the cortical extent of the MCA territory may, for practical purposes, be approximated as the insula, the anterior and lateral portions of the temporal lobe, the frontal and parietal opercula, and most of the frontal and parietal convexities. At the level of the ventricles, the MCA territory is approximately delimited by imaginary lines that connect the frontal horns and atria with the cortical surfaces of the frontal and occipitotemporal lobes, respectively. Furthermore, these imaginary lines approximate the hemodynamic watershed zones that lie between the major vascular territories. The concept of a hemodynamic watershed has been proposed to be the basis of a specific type of stroke associated with low flow. So-called watershed strokes are discussed later.

In addition to the cortical branches of the MCA, numerous small perforating arteries originate from the proximal (horizontal) segment of the MCA (the M1 segment). These small arteries are collectively known as the lenticulostriate arteries. Their territories of supply include the basal ganglia, the internal capsule, and portions of the overlying cerebral white matter.

Infarction in the territory of a single lenticulostriate artery results in a lacunar infarct, an event that commonly

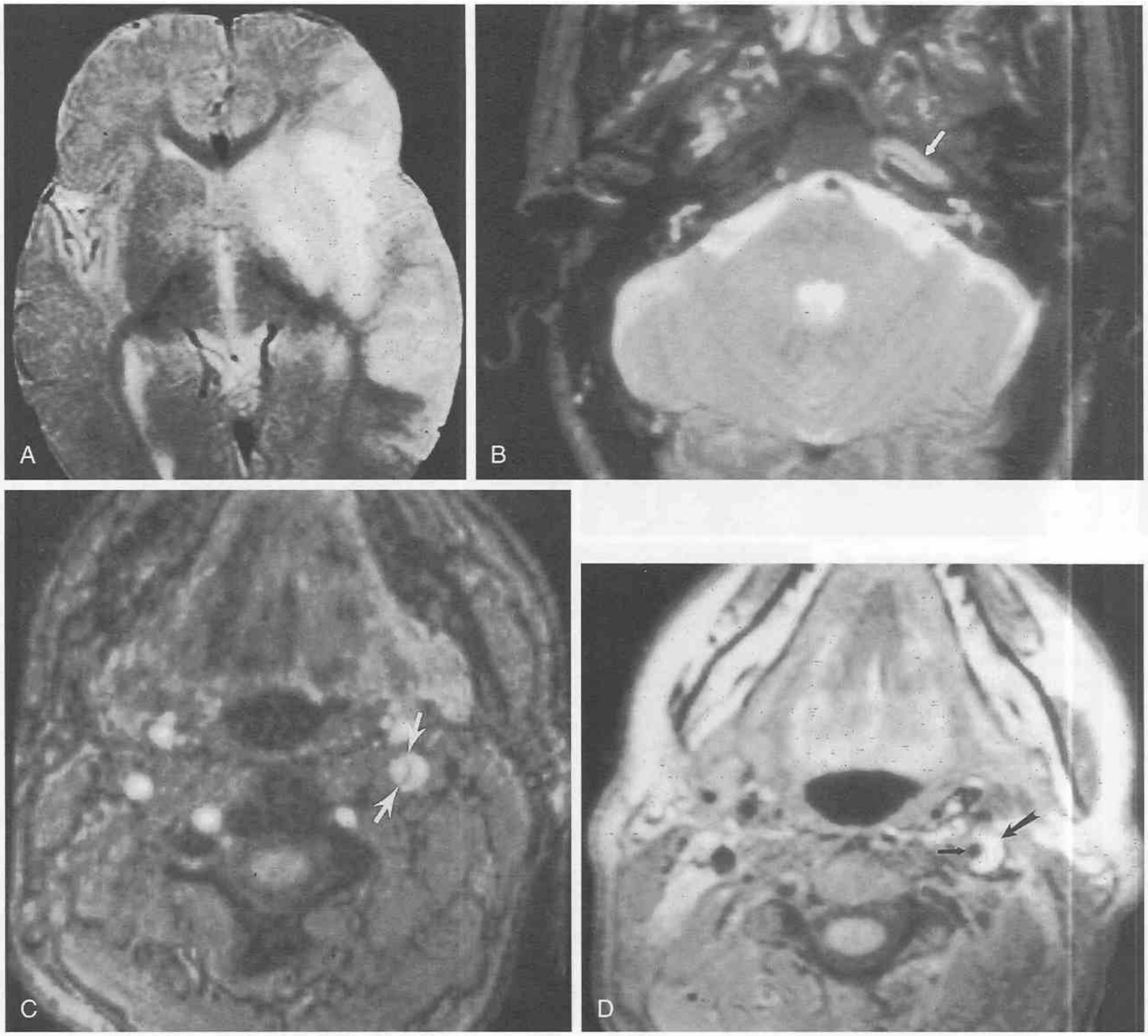

Figure 7–15. Acute left internal carotid artery dissection. *A,* Axial T2-weighted image shows extensive infarction in the territory of the left middle cerebral artery. *B,* Axial T2-weighted image through the left of the temporal bone shows abnormal increased signal within the petrous segment of the internal carotid artery *(small arrow). C,* Axial "source" image from 3D time-of-flight MRA shows the presence of a low-signal intimal flap *(arrows)* within the upper cervical internal carotid artery. *D,* Unenhanced axial T1-weighted image through the same level reveals a crescentic area of high signal representing thrombus *(arrows).* A small focus of flow-related signal void represents the remaining portion of the lumen.

occurs independently of MCA stroke. Nonetheless, occlusion of the M1 artery typically results in infarction in the territories of multiple lenticulostriate arteries (i.e., striatocapsular infarction). Infarction in the basal ganglia due to MCA occlusion can occur with or without infarction in the territories of the cortical MCA branches (see Fig. 7–11). When occlusion of the MCA occurs distal to the M1 segment (and thus distal to the origins of the lenticulostriate arteries), infarction in the cortical territory of the MCA may occur without infarction of the basal ganglia.

Imaging Findings in Acute Middle Cerebral Artery Stroke

The most important early CT evidence of irreversible brain tissue damage after a hyperacute stroke is hypodensity.[44] Early CT hypodensity, when extent is greater than or equal to one third of the expected MCA territory, is associated with unfavorable risk of symptomatic hemorrhage following thrombolytic therapy.[16]

It is often assumed that changes seen on DW MR scans after a hyperacute stroke reflect irreversible ischemia (i.e., infarction). Although this assumption may be valid in many cases, recent evidence suggests that with human stroke at least some early changes that are depicted on DW images may be reversed following thrombolytic therapy.[30] With additional study, criteria may be developed that would allow irreversible ischemia to be reliably distinguished from reversible ischemia, perhaps with the use of DW imaging or DW imaging in combination with another modality, such as perfusion imaging. Because such criteria have not yet been developed and accepted, the following

discussion focuses on the role of early CT imaging in the diagnosis and management of acute MCA stroke.

A number of early CT signs of MCA ischemia have been reported and may be used to confirm clinically suspected stroke of the MCA. One helpful CT sign, when present, is hyperdensity within the MCA.[59] This finding, in the setting of clinical signs of stroke in the territory of the dense vessel, signifies thrombus within the lumen of the artery (Fig. 7–16). However, a unilateral dense MCA should always be correlated with patient symptoms, since the specificity of this finding alone is not high.[63]

An important pitfall to avoid is comparing the density of a cerebral artery (e.g., the MCA) with adjacent brain tissue rather than with other vascular structures. The density of the MCA should be compared with that of other vascular structures of similar size, such as the opposite MCA, the ICA, the basilar artery, the large veins, and the dural venous sinuses. Although the hyperdense MCA sign can sometimes assist in the diagnosis of stroke, identification of a hyperdense MCA has some prognostic value and may predict increased morbidity, mortality, and increased risk of life-threatening brain edema.[39]

Two other helpful early CT signs of acute MCA stroke are obscuration of the lentiform nucleus and loss of the insular ribbon.[72, 73] These signs are, presumably, the result of ischemia in the territory of the lenticulostriate arteries arising from the M1 segment. The confirmation of these findings, therefore, suggests the presence of proximal occlusion of the MCA. Normally, the insula may be distinguished from the adjacent external capsule by their differing densities. In early MCA stroke, the contrast between these structures may be lost, presumably as a result of early cytotoxic edema (Fig. 7–17). Decreased density of the basal ganglia, also assumed to be caused by cytotoxic edema, results in obscuration of the lentiform nucleus (see Fig. 7–16).

Although observation of the hyperdense MCA sign, obscuration of the lentiform nucleus, and loss of the insular ribbon signs can help confirm the diagnosis of proximal MCA occlusion, careful examination of the cortical territory of the MCA is also important. Hypodensity, loss of gray matter to white matter contrast, and sulcal effacement should all be sought in the cortical territories. Manual adjustment of the display window and level settings may assist in detecting regions of hypodensity related to early stroke.[42]

Additional Findings in Chronic Middle Cerebral Artery Stroke

In the chronic stage, infarction in the territory of the MCA (and, to a lesser degree, elsewhere along the corticospinal pathways) may affect the appearance of the brain elsewhere. A common example is wallerian degeneration. When the corticospinal fibers are interrupted, as often happens in MCA stroke, the corticospinal fibers inferior to the lesion may undergo degeneration. The appearance of wallerian degeneration consists of volume loss and increased signal on T2-weighted images (Fig. 7–18).

Another example of change in the appearance of regions

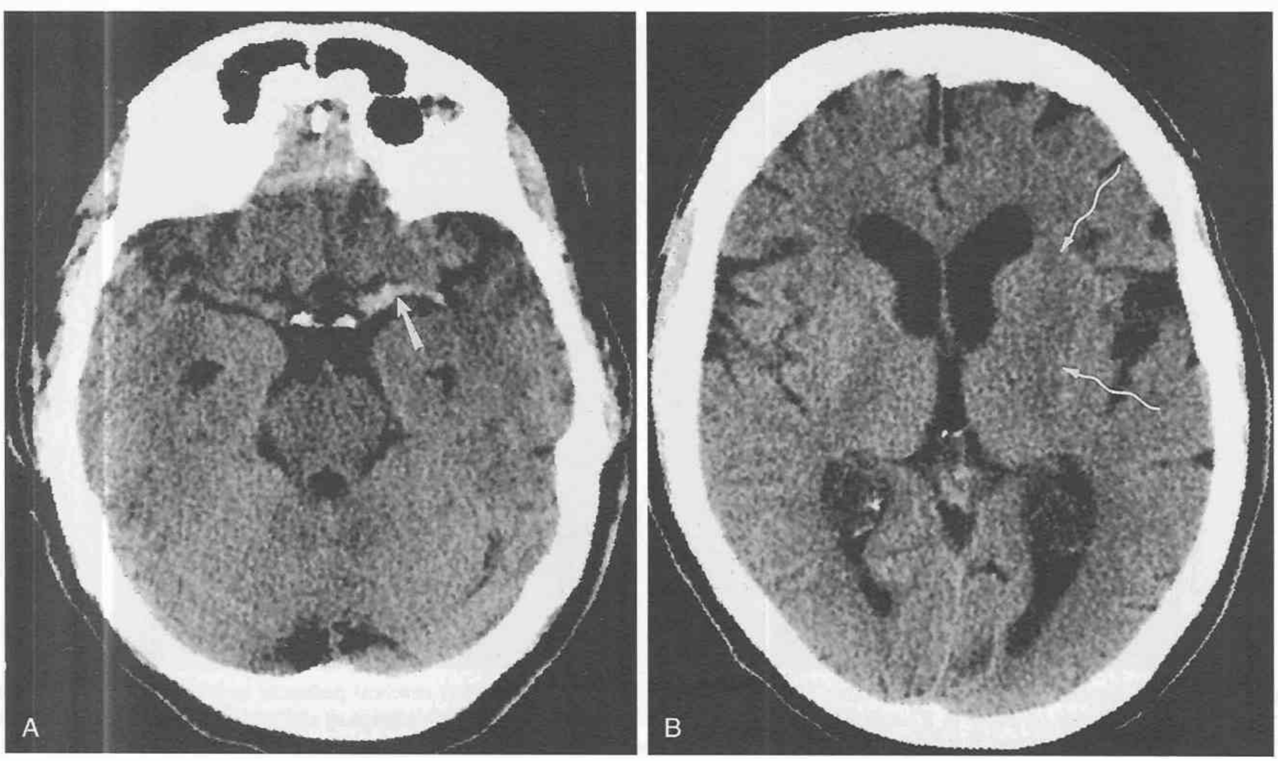

Figure 7–16. Obscuration of the lentiform nucleus. *A*, Unenhanced axial CT scan shows hyperdensity within the proximal (M1) segment of the middle cerebral artery *(arrow)*. *B*, There is decreased density with loss of definition within the left basal ganglia *(wavy arrow)*. Obscuration of the lentiform nucleus and hyperdense middle cerebral artery is one of the earliest signs of stroke on an unenhanced CT scan.

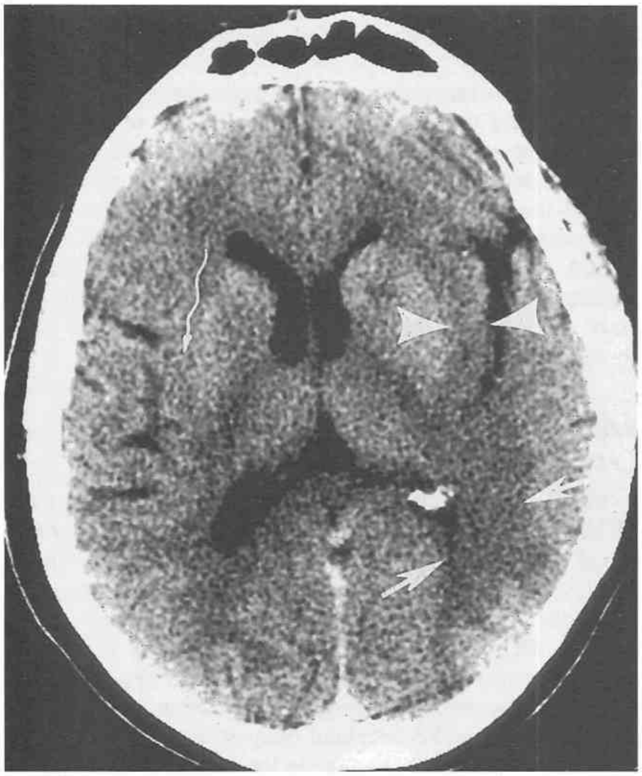

Figure 7–17. Loss of the insular ribbon. Unenhanced axial CT scan in a patient with acute right hemiparesis. There is decreased density with loss of distinction of the insular gray matter from the underlying external capsule *(large arrowheads)*. Diminished density is also present in the posterior left temporal lobe *(arrows)*. The right insular ribbon appears normal *(wavy arrow)*.

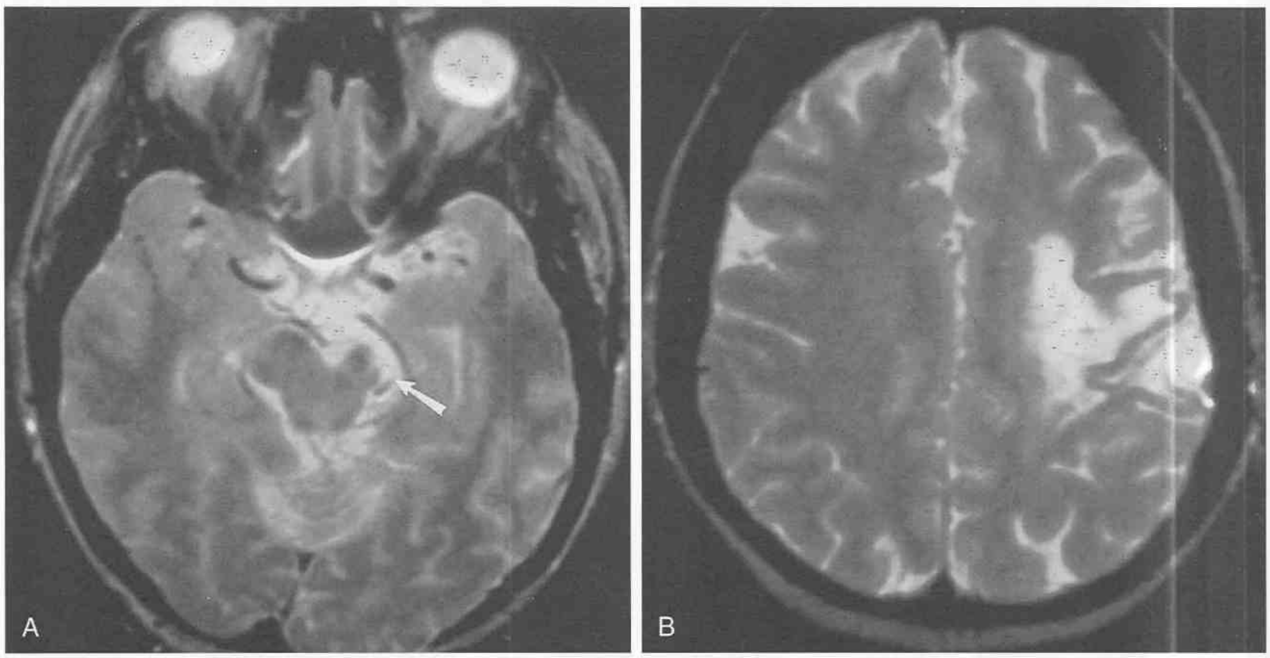

Figure 7–18. Wallerian degeneration. *A,* Axial T2-weighted MR image shows the left cerebral peduncle to be of decreased size and increased signal intensity *(arrow)*. *B,* T2-weighted image located more superiorly shows evidence of old middle cerebral artery territory infarction. Axonal degeneration is thought to produce the remote subcortical changes.

of the brain outside the territory of ischemia is known as *crossed cerebellar diaschisis*. In general, these changes are seen mainly on hemodynamic (i.e., perfusion) or metabolic studies. In patients with a cerebral injury, diaschisis may be considered to be functional impairment at an anatomic location that is remote from the area that sustained the injury. Diaschisis is thought to occur because of a loss of afferent input to the remote (noninjured) site. In the case of cerebral hemisphere injury, the opposite cerebellar hemisphere may show evidence of decreased blood flow,[56] decreased blood volume,[82] and decreased metabolism.[89] In the case of crossed cerebellar diaschisis, it is thought that the fibers that are interrupted are those within the corticopontocerebellar tract.

Anterior Cerebral Artery Stroke

The territory of the ACA is typically the anterior medial surface of the hemisphere and a small but variable amount of the frontal convexity and inferior frontal lobe (Fig. 7–19). Infarction in the territory of the ACA may occur in isolation (e.g., because of embolus or vasospasm following aneurysm rupture) or in combination with infarction in the territory of the ipsilateral MCA. This latter situation occurs most often with ICA occlusion when the anterior communicating artery (ACoA) is small or absent. Infarction in the territory of Heubner's artery may accompany ACA infarction because the origin of this vessel arises from the ACA in the vicinity of the ACoA. Heubner's artery is a

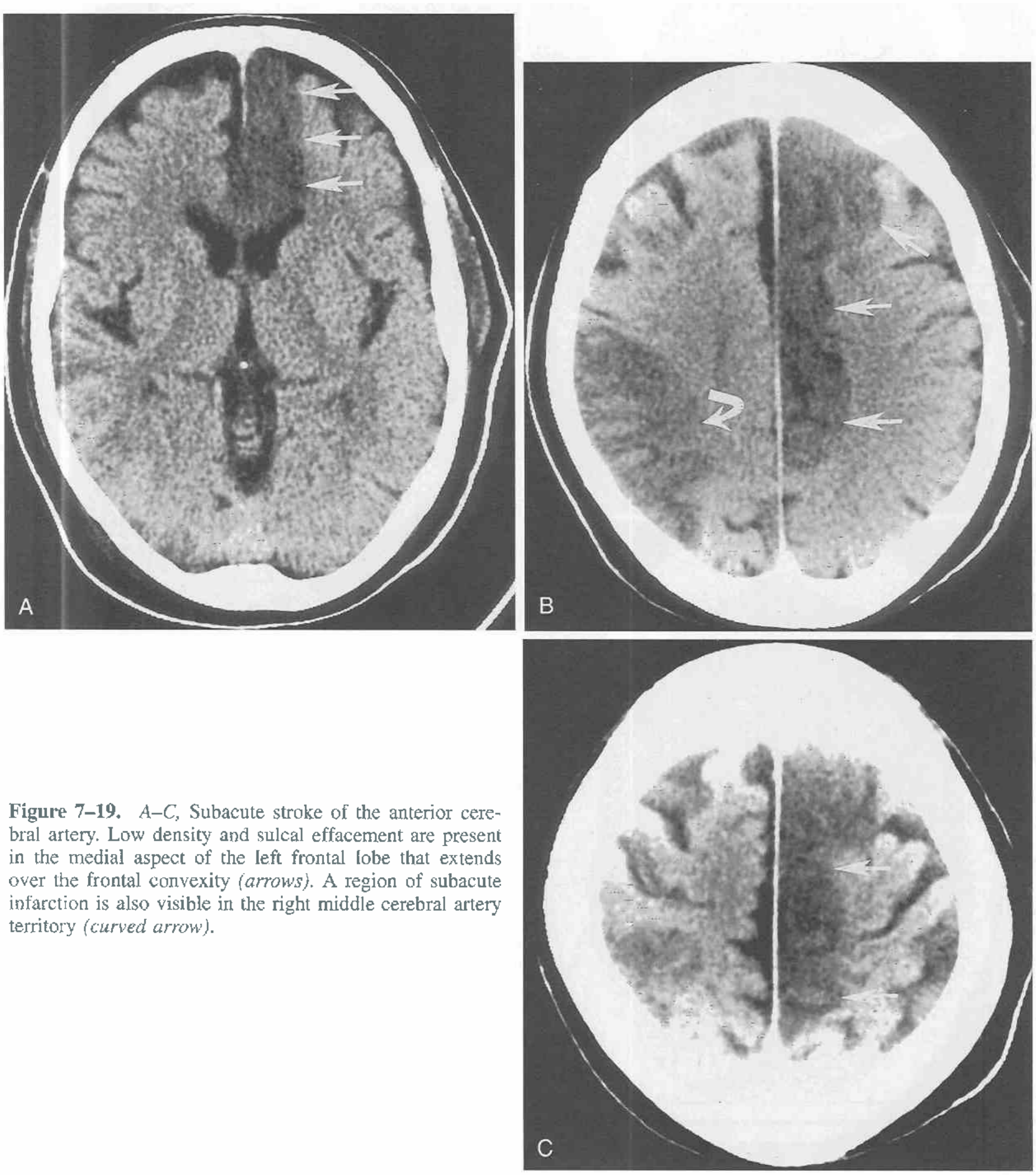

Figure 7–19. *A–C,* Subacute stroke of the anterior cerebral artery. Low density and sulcal effacement are present in the medial aspect of the left frontal lobe that extends over the frontal convexity *(arrows).* A region of subacute infarction is also visible in the right middle cerebral artery territory *(curved arrow).*

small perforating artery that usually supplies the head of the caudate nucleus and the anterior limb of the internal capsule.

Posterior Cerebral Artery Stroke

The cortical territory of the PCA includes the occipital lobes, the medial and inferior temporal lobes, and the posterior and medial portions of the parietal lobes (Figs. 7–20 and 7–21). The thalamoperforate arteries are small end-arteries that arise from the proximal PCA and the PCom artery. A consequence of this relationship is that infarction in the territory of the PCA may be associated with lacunar infarctions of the thalamus[9] (Fig. 7–22). Other small perforating arteries from the proximal PCA supply the cerebral peduncles and upper midbrain.

The PCA usually arises from the basilar artery. Because of this, disease in the vertebral and basilar arteries may result in infarction in the territory of the PCA. However, a common variant of the PCA is an origin from the ICA. In such a case, the vessel is described as having a *fetal origin.* This common variant is associated with severe hypoplasia or absence of the P1 segment (i.e., the segment of the PCA

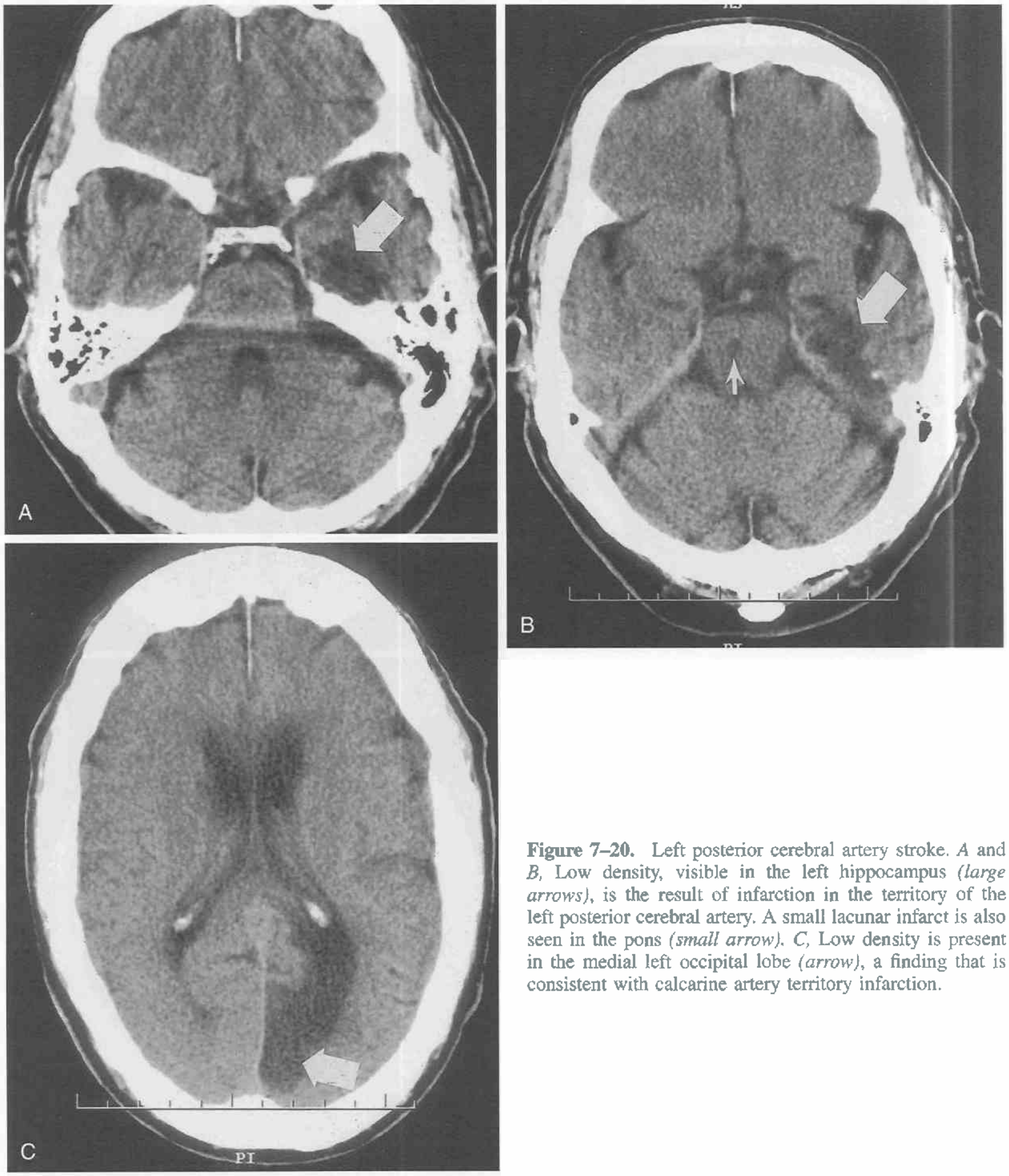

Figure 7–20. Left posterior cerebral artery stroke. *A* and *B*, Low density, visible in the left hippocampus *(large arrows)*, is the result of infarction in the territory of the left posterior cerebral artery. A small lacunar infarct is also seen in the pons *(small arrow)*. *C*, Low density is present in the medial left occipital lobe *(arrow)*, a finding that is consistent with calcarine artery territory infarction.

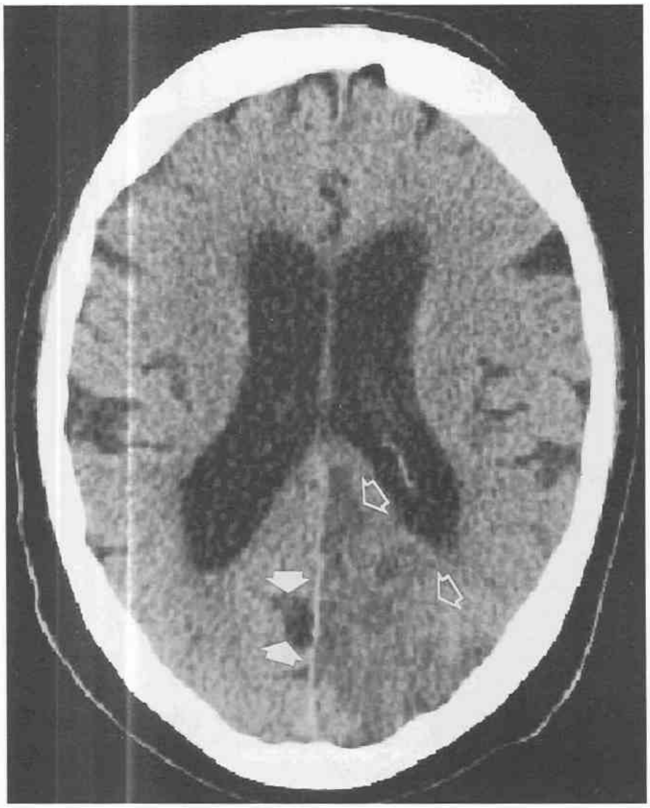

Figure 7–21. Infarct of the posterior cerebral artery (parietal-occipital branch). There is a wedge-shaped area of decreased attenuation in the medial portions of the parietal and occipital lobes *(open arrows)*. The parietal-occipital sulcus contains the parietal occipital branch of the posterior cerebral artery. The normal location and appearance of the right parietal occipital sulcus are shown *(small solid arrows)*.

between the basilar artery and the PCom artery). In patients with this variant, anterior circulation (i.e., carotid) disease can sometimes result in PCA infarction.

Posterior Fossa Stroke

The basilar artery is the sole source of blood supply to the brain stem. Occlusion of the basilar artery is poorly tolerated and can result in rapid progression of ischemic neurologic deficits and infarction (Fig. 7–23). Sometimes collateral supply to the distal basilar artery territory may be present in cases of occlusion of the proximal segment of the basilar artery via retrograde flow from one or both PCAs.

Basilar artery thrombosis can be detected on CT scans by the appearance of hyperdense clot within this artery and variable ischemic hypodensity in the brain stem, cerebellum, thalami, and PCA territory. Careful clinical correlation is recommended when the diagnosis of basilar artery thrombosis is suggested on the basis of unenhanced CT findings, since the appearance of basilar artery thrombosis in some older patients may be mimicked by increased arterial density related to atherosclerotic calcification.

The diagnosis of basilar artery thrombosis may be confirmed with CT angiography or MR angiography, or, more commonly, with conventional catheter angiography. Basilar artery thrombosis may produce complete or incomplete occlusion of the basilar artery with variable visualization of intraluminal thrombus.

Three arteries provide most of the blood supply to the cerebellum. The posterior inferior cerebellar arteries (PICAs) arise from the intracranial portions of the vertebral arteries. The PICAs supply the posterior-lateral aspects of the medulla, the cerebellar tonsils, and the inferior and posterior surfaces of the cerebellar hemispheres. Occlusion of the proximal PICA can cause infarction of the lateral medulla and tonsil, whereas a more distal occlusion results in infarction mainly along the inferior cerebellar hemisphere (Figs. 7–24 and 7–25).

The anterior inferior cerebellar arteries (AICAs) are usually small vessels that provide reciprocal supply of the cerebellum along with the PICAs. The AICAs are occasionally duplicated and may arise together from a common trunk with the PICA. The AICA gives rise to the artery of the internal auditory canal. Therefore, in addition to causing inferior cerebellar infarction, occlusion of the AICA can result in sensorineural hearing loss, nausea, vertigo, and facial paralysis.

The superior cerebellar arteries (SCAs) arise from the distal basilar artery and supply the superior portions of the cerebellar hemispheres. They often appear duplicated (or triplicated) on angiograms. Infarction of the SCA territory may involve a variable amount of the superior portion of the hemisphere (Fig. 7–26).

The pontine perforator arteries include about 15 to 20 small paired vessels that arise from either side of the basilar artery. Infarction in the paramedian branches of these arteries may result in a centrally located area of abnormal low density or increased signal on long TR images. Infarctions in the territory of paramedian branches of the pontine perforator arteries typically do not cross the plane of midline This feature can be helpful in the differential diagnosis of deep pontine lesions (see Fig. 7–10). The anterolateral surface of the pons is supplied by the short circumferential branches of the pontine arteries.

An unusual arterial variant whose territory should be recognized is the artery of Percheron.[41] This small artery usually arises from the terminal portion of the basilar artery, then bifurcates to produce two small median thalamoperforate arteries that supply small portions of the medial aspects of both thalami (Fig. 7–27). Knowledge of the territory of supply of this artery, along with the MR appearance of a given lesion, can encourage the imaging specialist to suggest the vascular nature of a lesion in this location.

Infarction Caused by Venous Occlusion

Occlusion of cerebral venous structures may lead to increased intracranial pressure and nonfocal neurologic symptoms, such as headache and seizure, without resulting cerebral infarction. Occlusion of venous structures may also lead to focal cerebral infarction associated with focal or nonfocal neurologic symptoms. Since local cerebral perfusion pressure is related to the difference between local

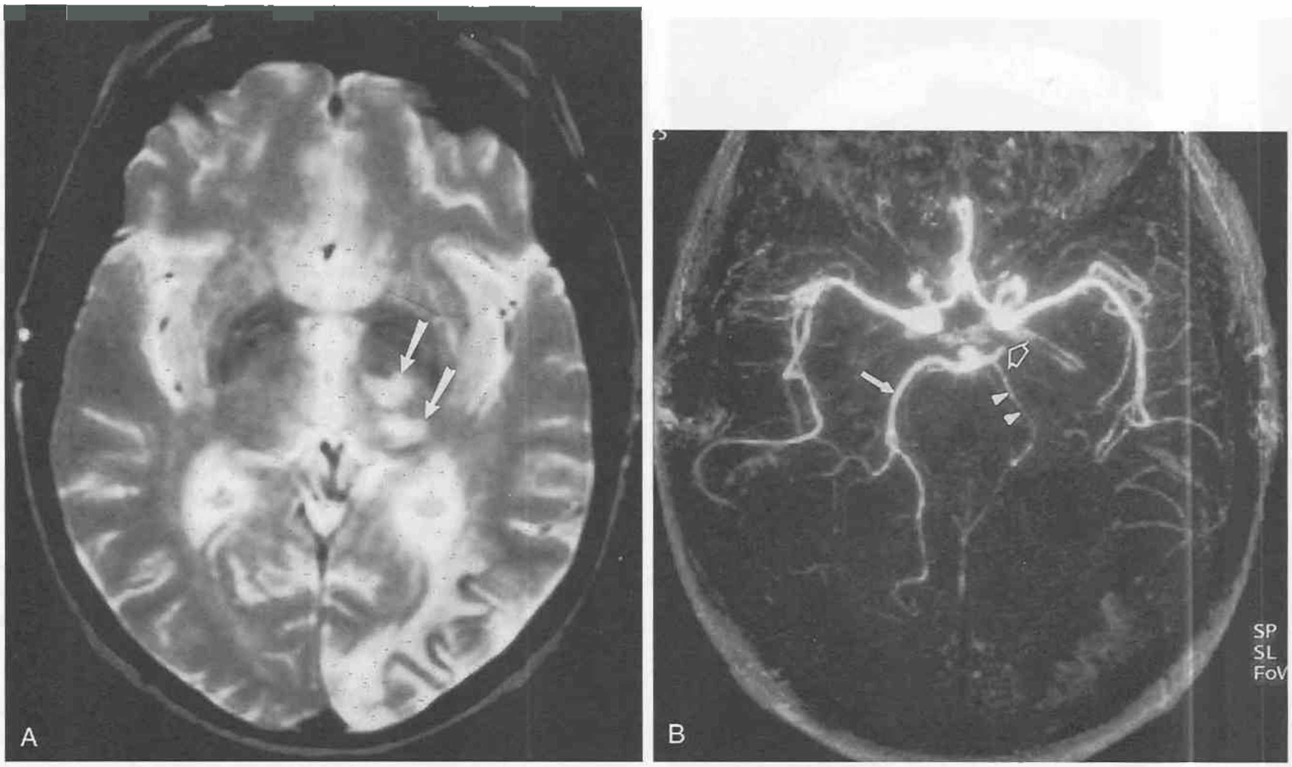

Figure 7–22. Left posterior cerebral artery (PCA) stroke. *A,* T2-weighted axial image shows increased signal in the left occipital lobe. Focal areas of increased signal are also seen in the left thalamus *(arrows).* Infarction of the thalamus may accompany PCA stroke as a result of occlusion of thalamoperforate arteries originating from the proximal PCA. *B,* Maximum intensity projection image (viewed from beneath) from 3D time-of-flight MRA. The left PCA is occluded proximally *(open arrow).* The right PCA has a normal appearance *(arrow).* The left superior cerebellar artery is visible *(arrowheads).*

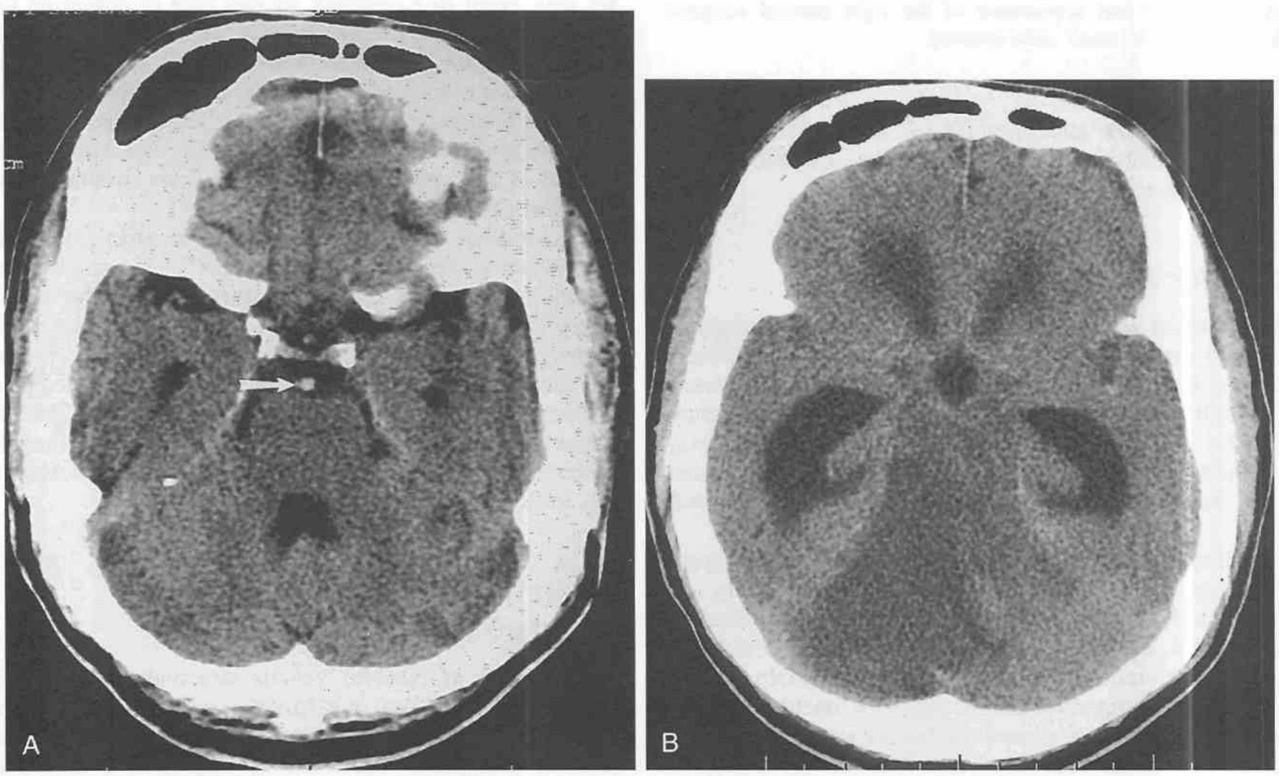

Figure 7–23. Basilar artery thrombosis. *A,* Unenhanced axial CT image shows increased density within the basilar artery *(arrow). B,* Unenhanced axial CT the following day shows extensive cerebellar hypodensity and hydrocephalus due to fourth ventricular and aqueductal compression.

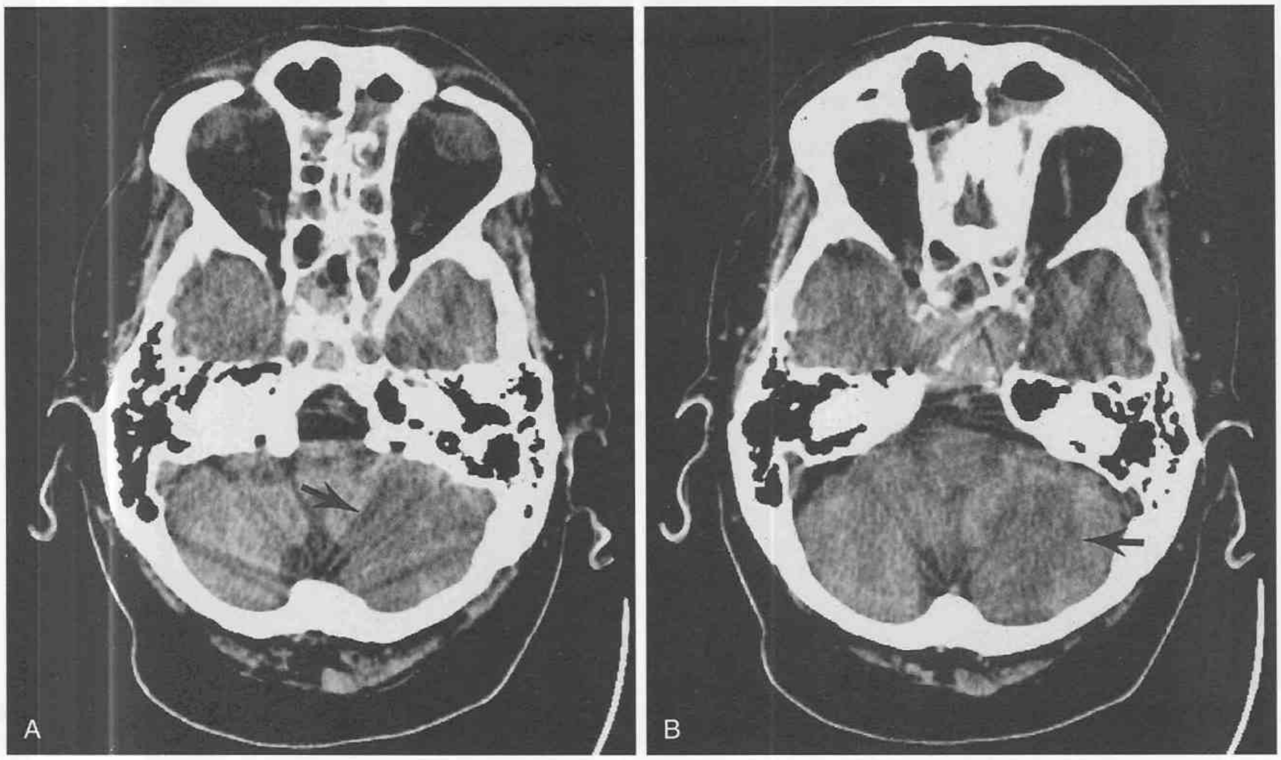

Figure 7–24. Stroke of the posterior inferior cerebellar artery. *A* and *B*, Unenhanced CT scan shows well-defined hypodensity in the distal territory of this artery *(arrows)*.

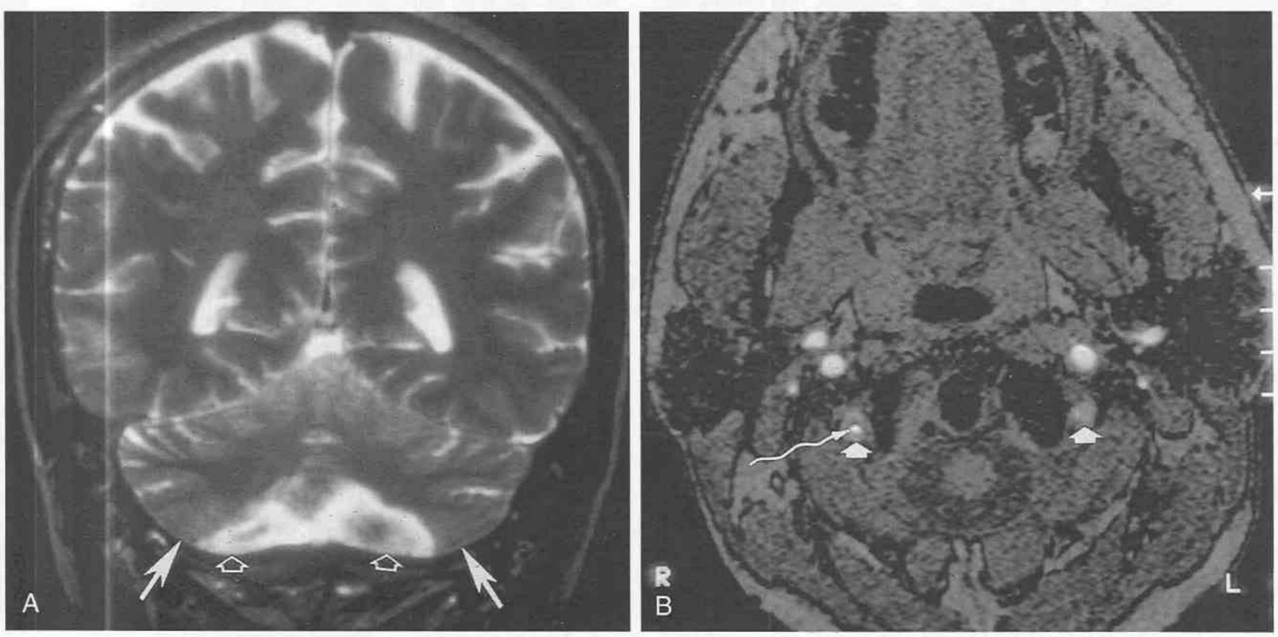

Figure 7–25. Bilateral stroke of the posterior inferior cerebellar artery (PICA). *A*, T2-weighted coronal MR image shows high signal in the territories of this artery bilaterally *(open arrows)*. The territories of the anterior inferior cerebellar arteries are spared *(arrows)*. *B*, Axial source image from a 2D time-of-flight MRA study shows diminished signal within both vertebral arteries *(short arrows)*. A small channel of flow is present in the right vertebral artery *(long wavy arrow)*. The findings are those of bilateral vertebral artery thrombosis.

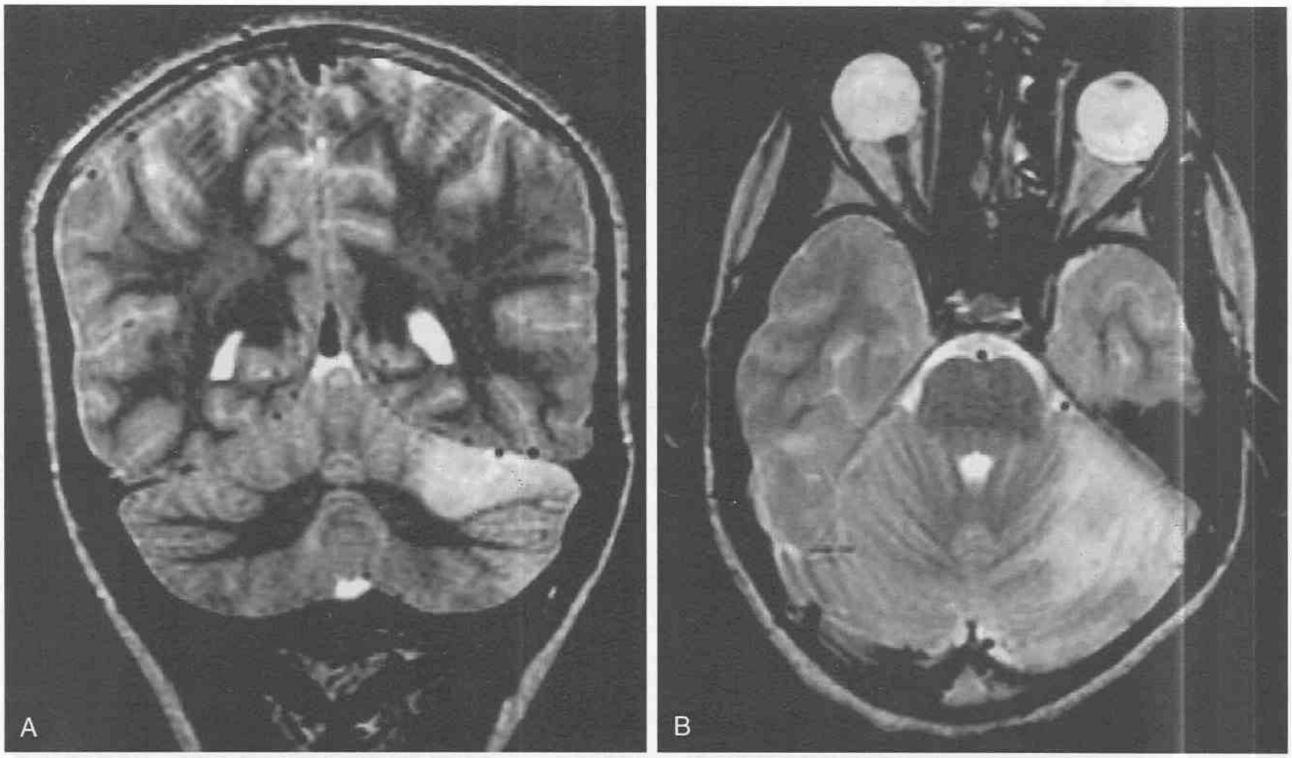

Figure 7–26. Ataxia in an 8-year-old girl. *A,* Coronal T2-weighted MR image shows a wedge-shaped area of increased signal in the superior left cerebellar hemisphere. *B,* Axial T2-weighted image confirms abnormality in the territory of the superior cerebellar artery. Biopsy showed evidence of evolving infarction.

arterial and venous pressures, the probable mechanism of ischemia in venous infarction is a regional decrease in perfusion pressure that is due to regional elevation of venous pressures.

In most cases, the cause is thrombosis of one or more veins or dural venous sinuses. Cerebral vein and dural sinus thrombosis are often associated with certain predisposing conditions such as dehydration, infection, polycythemia, and sickle cell disease. The presence of a hypercoagulable state also appears to be an important risk factor.[11, 61] Intracranial venous thrombosis may also occur in the peripartum period[37] and may be seen in nonpregnant women taking oral contraceptive medications.

Compared with the location and extent of strokes resulting from arterial occlusion, the location and extent of strokes due to venous occlusion are much more variable. Nonetheless, location and extent of ischemia reflect, to some degree, the location and extent of venous occlusion. For example, when venous occlusion is limited to a cortical vein, findings of infarction may be unilateral and limited in extent to the region of the occluded vein. When venous thrombosis is more extensive, such as when extensive thrombus is present within a major dural sinus structure (e.g., the superior sagittal sinus), the findings of brain ischemia may be bilateral and more extensive. Hemorrhage is frequently associated with venous infarction, although the precise reasons are not known. Furthermore, the hemorrhages that are seen in ischemia as a result of venous occlusion are commonly subcortical in location.[28]

The imaging signs that are often most helpful for diagnosis of venous occlusion are those that indicate the presence of thrombus within a venous structure. On CT scans, the presence of hyperdense material within a venous channel and lack of appropriate central enhancement with contrast material are the most important signs (Fig. 7–28). MR images may show increased T1 signal within venous structures occluded by thrombus (see Fig. 7–5). Lack of appropriate flow-related signal void within the venous structure on T2-weighted images and lack of enhancement within the venous structure following injection of gadolinium-containing contrast agents are also typical (Fig. 7–29). Flow-sensitive sequences, such as time-of-flight and phase-contrast MR venograms, can be used to document the presence and extent of venous occlusion.[3]

A number of pitfalls must be recognized when one is evaluating an MRI scan (including MR venogram studies) for the presence of venous thrombus.[3] First, thrombus that is hyperintense on T1-weighted images may be mistaken for flow on time-of-flight images. The imaging specialist can minimize this pitfall by carefully inspecting the unenhanced T1- and T2-weighted images for evidence of clot and by using phase-contrast MR venography alone or in combination with time-of-flight methods. Phase-contrast methods are affected not by the relaxation properties (e.g., T1) of the imaged tissues; they are influenced only by the net displacement (i.e., flow) of spins.

Interpretation of MR scans performed for the evaluation of the dural venous sinuses can also be affected by the fact that flowing blood can appear hyperintense on T1-weighted images, potentially mimicking hyperintense signal due to thrombus. Flowing blood is typically brightest near the edges of the imaged volume, an artifact that can be helpful

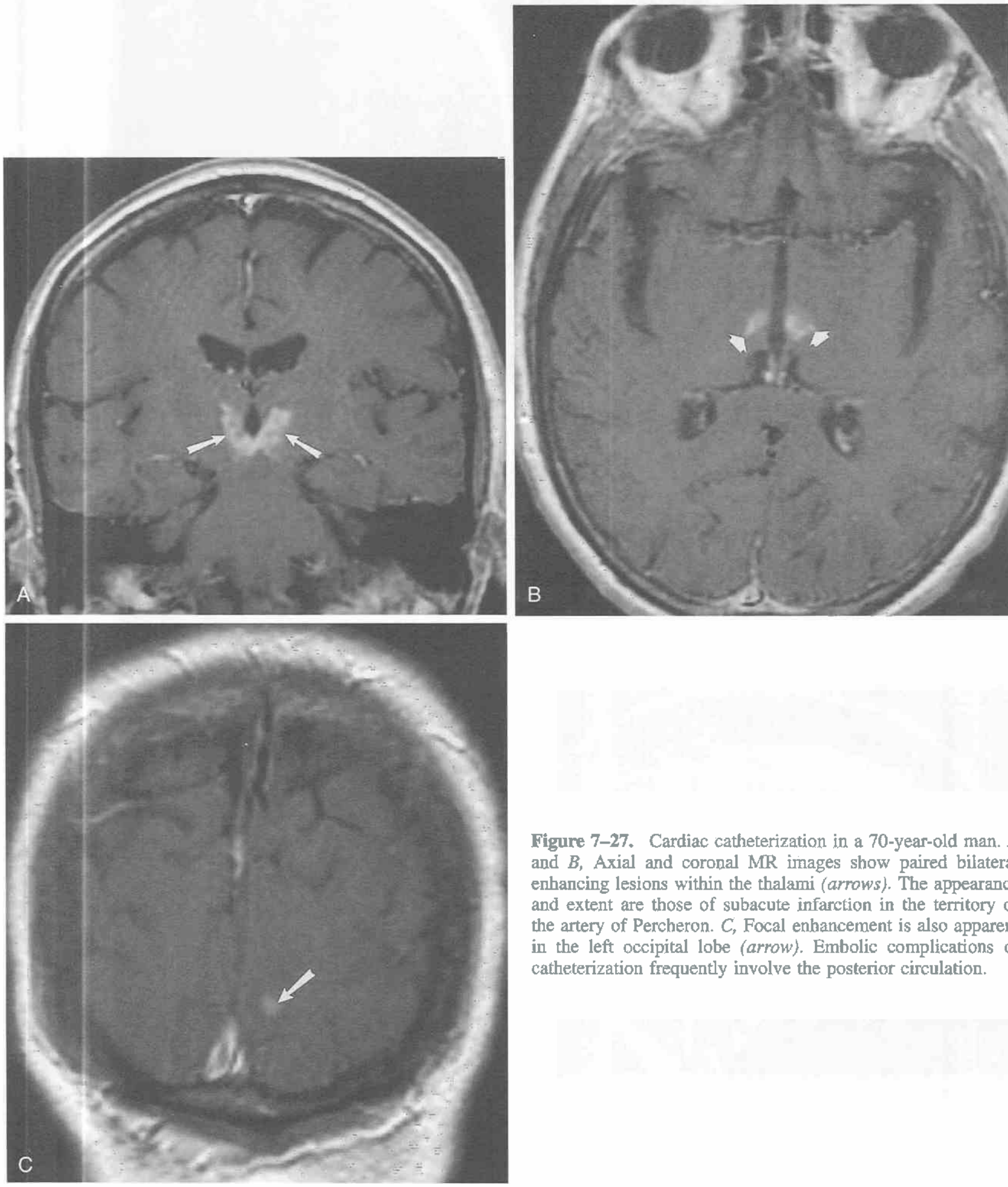

Figure 7–27. Cardiac catheterization in a 70-year-old man. *A* and *B*, Axial and coronal MR images show paired bilateral enhancing lesions within the thalami *(arrows)*. The appearance and extent are those of subacute infarction in the territory of the artery of Percheron. *C*, Focal enhancement is also apparent in the left occipital lobe *(arrow)*. Embolic complications of catheterization frequently involve the posterior circulation.

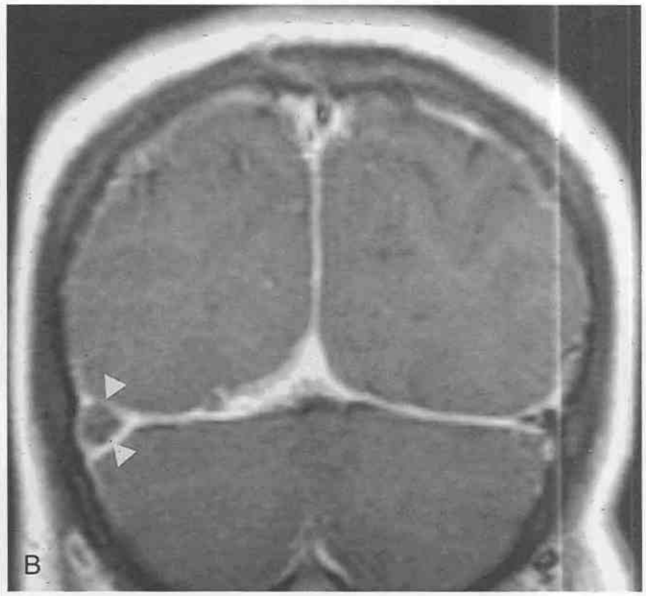

Figure 7–28. Transverse sinus thrombosis. *A,* Unenhanced axial CT image shows increased density within the right transverse sinus *(small arrows).* The left transverse sinus is of normal density *(larger arrows). B,* T1-weighted coronal image following contrast shows absent enhancement in the right transverse sinus *(triangles).*

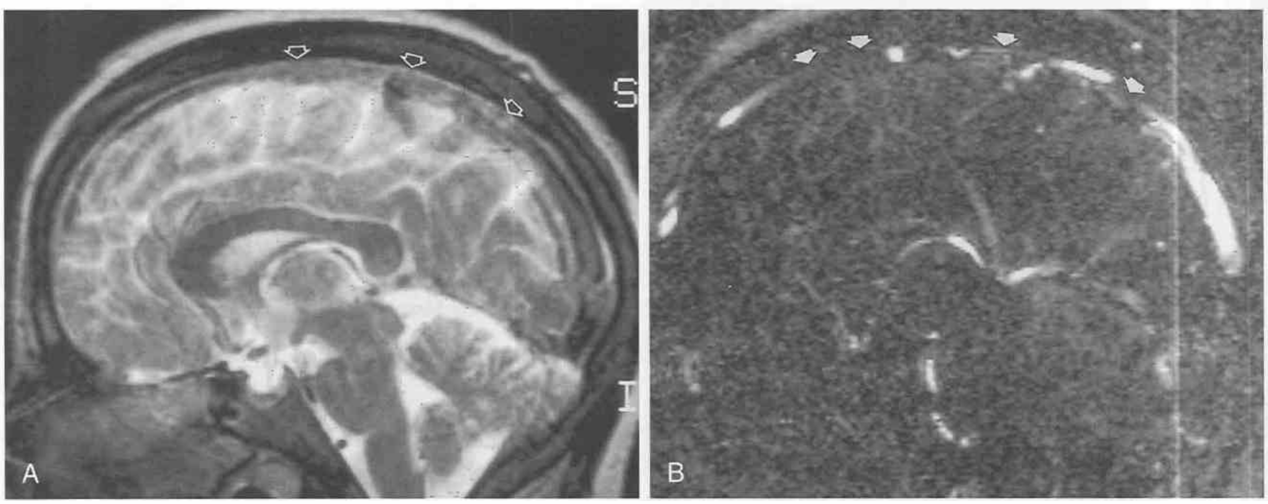

Figure 7–29. Superior sagittal sinus thrombosis. *A,* T2-weighted sagittal MR image shows increased signal in the superior sagittal sinus *(open arrows). B,* Partition image from a phase-contrast MR venogram study (VENC = 5 cm/second) shows regions of absent flow within the superior sagittal sinus *(small arrows).*

in analysis of the findings in a given case. Inspection of the T2-weighted image can also be helpful because absence of signal on long echo-time (TE) images usually suggests that flow is present.

Many patients have congenital absence or hypoplasia of one transverse venous sinus (most often the left), which can mimic occlusion of the sinus on MR venogram studies. In addition, flow gaps within one or both transverse sinuses may be a normal finding in about 30% of patients and should not be mistaken for clot.[3] In addition, small papillary arachnoid villi may project into the lumina of dural sinuses and thus may appear as small filling defects that can mimic clot on MR venogram studies. These villi typically appear hyperintense on T2-weighted images, allowing them to be distinguished, in some cases, from thrombus.

Thrombosis of the deep cerebral veins produces a devastating clinical course and characteristic appearance on imaging studies.[35] Thrombosis of the internal cerebral veins, the vein of Galen, and the straight sinus may also be accompanied by occlusion of the basal veins (of Rosenthal). Infarction of the thalami, midbrain, and basal ganglia may occur, often associated with hemorrhage (Fig. 7–30).

CT venography is a relatively new but promising modality that provides an alternative to MR venography for the evaluation of the cerebral venous system.[77] This study is performed with the use of helical acquisition with thin collimation and rapid, continuous infusion of iodinated contrast material. Available commercial postprocessing software can provide surface-shaded renderings and projection-type images of the cerebral venous system. The most important clinical application of this modality is for the investigation of the cerebral venous system for occlusion (Fig. 7–31).

Nonocclusive Stroke and Other Problems

Purely hemodynamic stroke can occur in patients without sources of emboli and with episodic hypotension.[6] In such cases, the extent of abnormality on imaging studies depends on the degree and duration of systemic hypotension. When hypotension has been relatively mild in degree or short in duration, ischemic changes may be seen in the territories of the watershed zones between major vascular territories or in the deep watershed zones that correspond to the deep cerebral white matter.[51] A parasagittal location, a chainlike pattern, and a deep location all suggest infarction caused by low flow (Fig. 7–32).

Cerebral infarction may also occur in patients who have suffered toxic or anoxic insult. Hypoxemia, carbon monoxide poisoning, and hypoglycemia all have the potential to result in selective or global infarction. Metabolic enzyme and mitochondrial defects can also lead to ischemia and infarction (Fig. 7–33). Selective involvement of the basal ganglia may be seen in many of the processes described. In particular, carbon monoxide poisoning is associated with selective infarction of the globus pallidus, whereas Leigh's disease, a mitochondrial enzyme abnormality, most commonly affects the striatum.[74] Hypoglycemia can cause a pattern of diffuse ischemia that predominantly affects the parietal and occipital regions.[53]

Hypoxic-ischemic encephalopathy (HIE) can result in a diffuse or focal infarction in young children and infants (Fig. 7–34). Especially vulnerable are the deep periatrial white matter regions, areas that form part of the deep watershed in infants. On postnatal MRI or CT scans, end-stage periventricular leukomalacia (PVL) is depicted as the symmetrical pattern of periatrial white matter abnormality and volume loss (Fig. 7–35). A number of causes other than hypoxia or ischemia can produce PVL, including infectious and metabolic abnormalities.

Other commonly encountered stroke mechanisms include vasospasm and vasculitis. Following aneurysm rupture, vasospasm of the intracranial arteries is the cause of a substantial part of the morbidity and mortality caused by subarachnoid hemorrhage. Typically, CT or MRI signs of infarction are seen in the territory of arterial insufficiency (Fig. 7–36).

Vasculitis of the cerebral arteries may be primary or secondary to a systemic problem, such as systemic vasculitis or lupus erythematosus. Patients with lupus erythematosus have a particularly high incidence of secondary CNS vasculitis. On CT and MRI studies, the presence of multiple areas of ischemia suggests vasculitis, especially when a substantial number of small cortical and subcortical lesions are present (Fig. 7–37). CT and MRA can depict vasculitic changes in the medium-sized vessels of the circle of Willis; however, visualization of the small cortical arteries is limited with these techniques. Catheter angiography is considered to be the imaging test with the highest degree of sensitivity and specificity for CNS vasculitis.

Cortical laminar necrosis is a histologic, pathologic term that also can be used to describe a particular type of postischemic pattern of injury on CT and MR images. Ischemic injury, occasionally, can be limited to one or more cell layers of the cortex without involvement of the remaining layers. When this occurs, mineralization may develop within the affected layers, producing a gyriform pattern of increased density or signal intensity (on T1-weighted images) (Fig. 7–38).

Diffusion-Weighted Imaging in Acute Stroke

DW images are MR images that are created by applying a pair of magnetic gradient pulses that sensitize the sequence to motion. By applying very large gradients and allowing sufficient time to pass between gradient lobes (pulses), one can sensitize the scan to microscopic motions that are occurring within the imaging voxel.[48]

The amount of diffusion weighting of a DW image is determined by the magnitude of the applied gradients, how long they are switched on, and the time between the two lobes. The magnitude of diffusion weighting is connoted by the "b" value of the image. Typical "b" values (in seconds per square millimeter) for imaging stroke are on the order of 400 to 1000 seconds/mm^2. By comparing a diffusion-sensitized image (or images) to a similar scan without diffusion-sensitizing gradients (i.e., the "b zero" image), one can compute the amount of diffusion that appears to have occurred.[40] If this is done on a pixel-by-

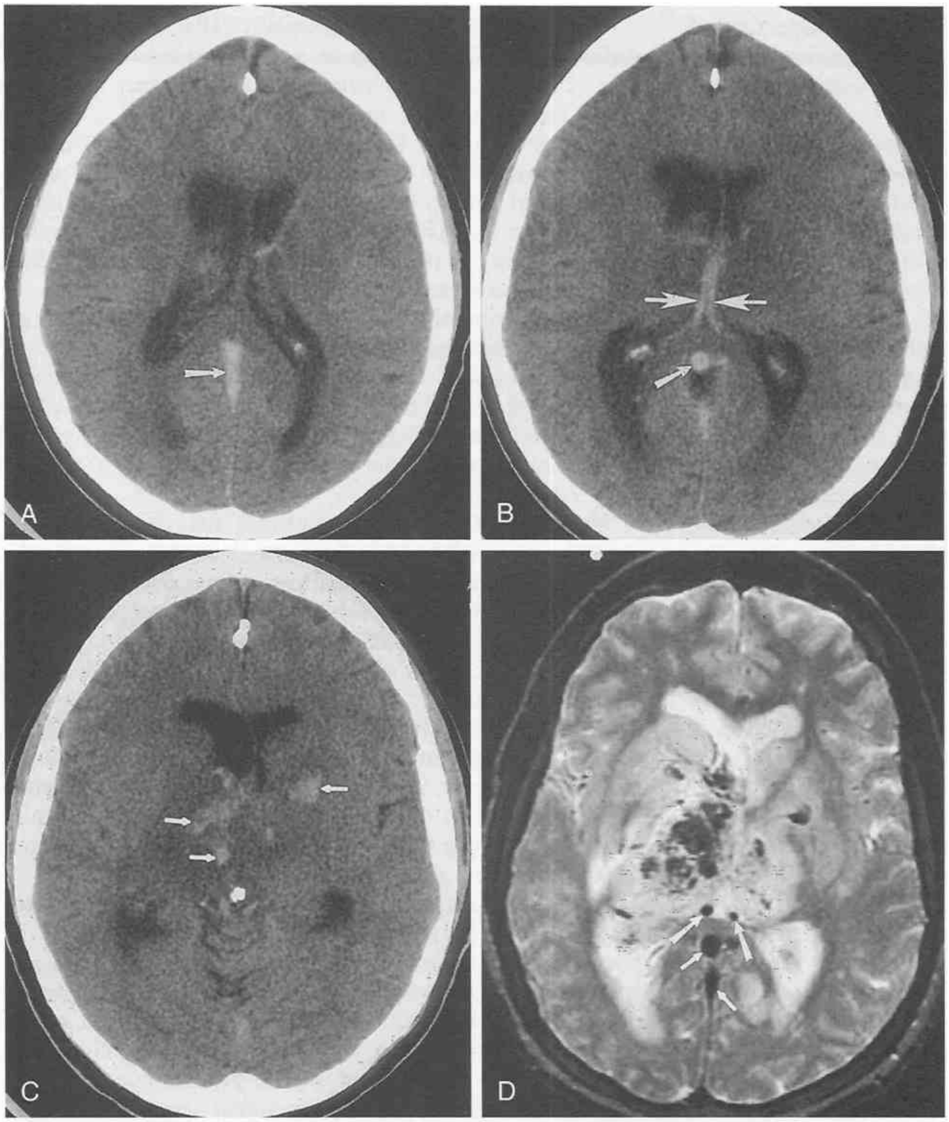

Figure 7–30. Deep cerebral venous thrombosis. *A–C,* Unenhanced axial CT images show extensive low density in the basal ganglia, thalami, and upper brain stem. Foci of hemorrhage are also seen within the brain *(small arrows).* Increased density is seen within the internal cerebral veins, the vein of Galen, and the straight sinus *(larger arrows). D,* T2-weighted MR image 2 hours later shows low signal in the internal cerebral veins *(larger arrows)* and in the vein of Galen and the straight sinus *(small arrows).* Acute thrombus can sometimes appear as low signal, mimicking flow-related signal void. *E,* Time-of-flight MR venogram shows no signal in the straight sinus *(small arrows).*

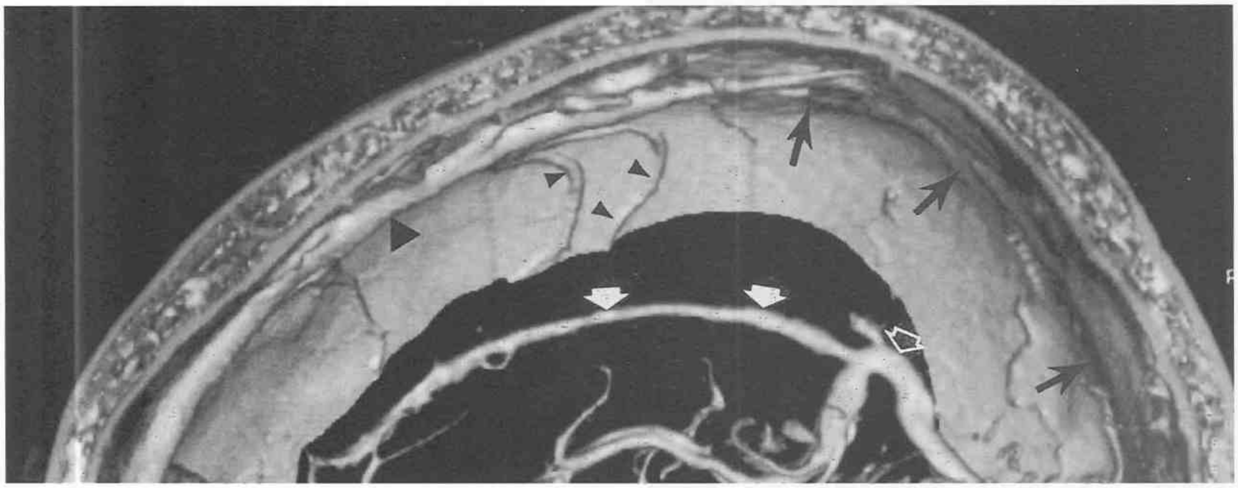

Figure 7–31. **Superior s**[redacted]**nus** thrombosis. Surface-rendered CT venogram study shows absent opacification in the posterior portion of the superior sagittal sinus *(black arrows)*. The anterior portion of the superior sagittal sinus is patent *(triangle)*. Small cortical veins are depicted *(arrowheads)*. The inferior sagittal sinus *(small arrows)* and the vein of Galen are also seen *(open arrow)*.

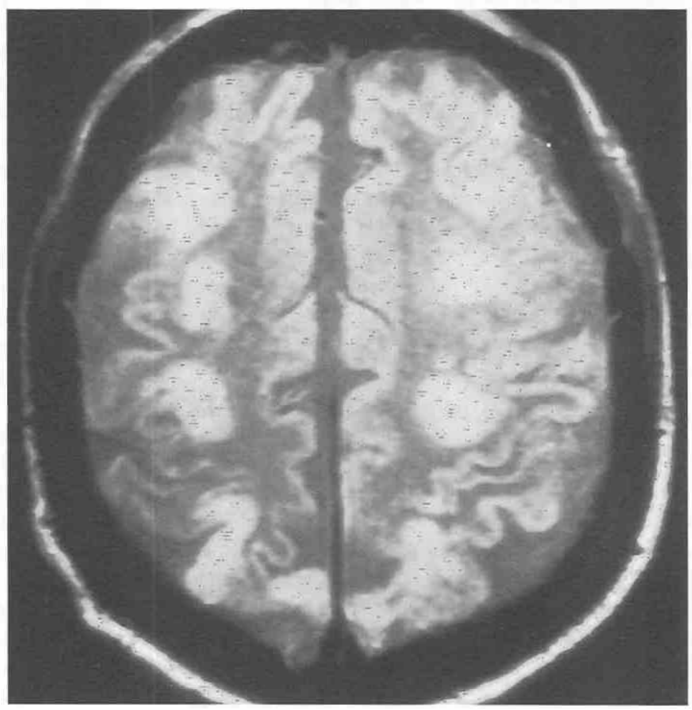

Figure 7–32. Watershed stroke. Intermediate-weighted axial image in a child shows bilateral, symmetrical parasagittal increased signal. The "chainlike" appearance depicted here is often seen with hemodynamic stroke.

Figure 7–33. Leigh's disease in an 18-month-old child. T2-weighted axial image shows increased signal in the basal ganglia bilaterally. Some toxic and anoxic injuries can produce a similar pattern of ischemic injury.

pixel basis, the result is a computed map of apparent diffusion known as an "ADC map."

DW images are highly sensitive to the diffusion restriction that occurs in acute stroke.[24] Regions of acute cerebral ischemia are typically hyperintense on DW images and result in diminished ADC values of up to 40%. In experimental stroke models, hyperintensity on DW images can be seen before changes on T2-weighted images are visible.[49]

It is often assumed that hyperintense signal on DW images represents irreversible ischemia. However, studies of experimental stroke and some reports in humans suggest that some changes in diffusion depicted on imaging studies represent potentially reversible ischemia.[30, 57]

Artifacts on Diffusion-Weighted Images

Acute stroke is characterized by high signal intensity on DW images (Fig. 7–39); however, there are other causes of high signal intensity on these images. Knowing these other causes can be helpful in assessing the likelihood that a given patient has evidence of cerebral ischemia.

One commonly seen artifact that can mimic the appearance of acute stroke is known as *T2 shine-through*. Because DW scans also typically have substantial spin density and T2 weighting, areas of T2 prolongation may result in carryover of hyperintense signal to the DW image. Careful comparison with a reference image (i.e., the "b zero" image) or another type of T2-weighted image can be helpful in recognizing this artifact.

Another artifact that can mimic the appearance of acute stroke on DW images is hyperintensity due to white matter diffusion anisotropy. If one reviews DW images that have been sensitized to diffusion in only one direction (e.g., the phase-encoding direction), the white matter tracts that run orthogonal to the direction of sensitization appear relatively bright. This artifact can be recognized with experience, although comparison with DW images obtained with the diffusion-sensitizing gradients applied in other directions can also be helpful. One can eliminate this artifact completely by reviewing only images that have isotropic weighting (i.e., DW images that have been combined so that weighting is applied in all three cardinal directions). Such images are also called *trace-weighted* or, simply, *trace* images. Both expressions refer to the diagonal numerical terms that are part of a 3 × 3 (nine-element) tensor matrix of data that expresses the diffusion properties of an object.[80]

Another artifactual cause of hyperintense signal on DW scans is related to magnetic susceptibility artifacts. Most DW scans are made using *echo-planar imaging* techniques. These very rapid MRI methods are commonly used for DW images because DW scans are highly sensitive to patient motion.

One potential problem with echo-planar images is that they are very sensitive to susceptibility artifacts at soft tissue/bone and soft tissue/air interfaces. Foreign bodies (e.g., shunt catheters) may also produce susceptibility artifacts on DW echo-planar images. Susceptibility artifacts are usually easy to recognize because:

1. They occur in locations (e.g., calvarium and skull base) that are prone to such artifacts.
2. They are often flame-shaped.
3. When severe, they can cause regional anatomic distortion in addition to causing increased signal intensity.

Text continued on page 279

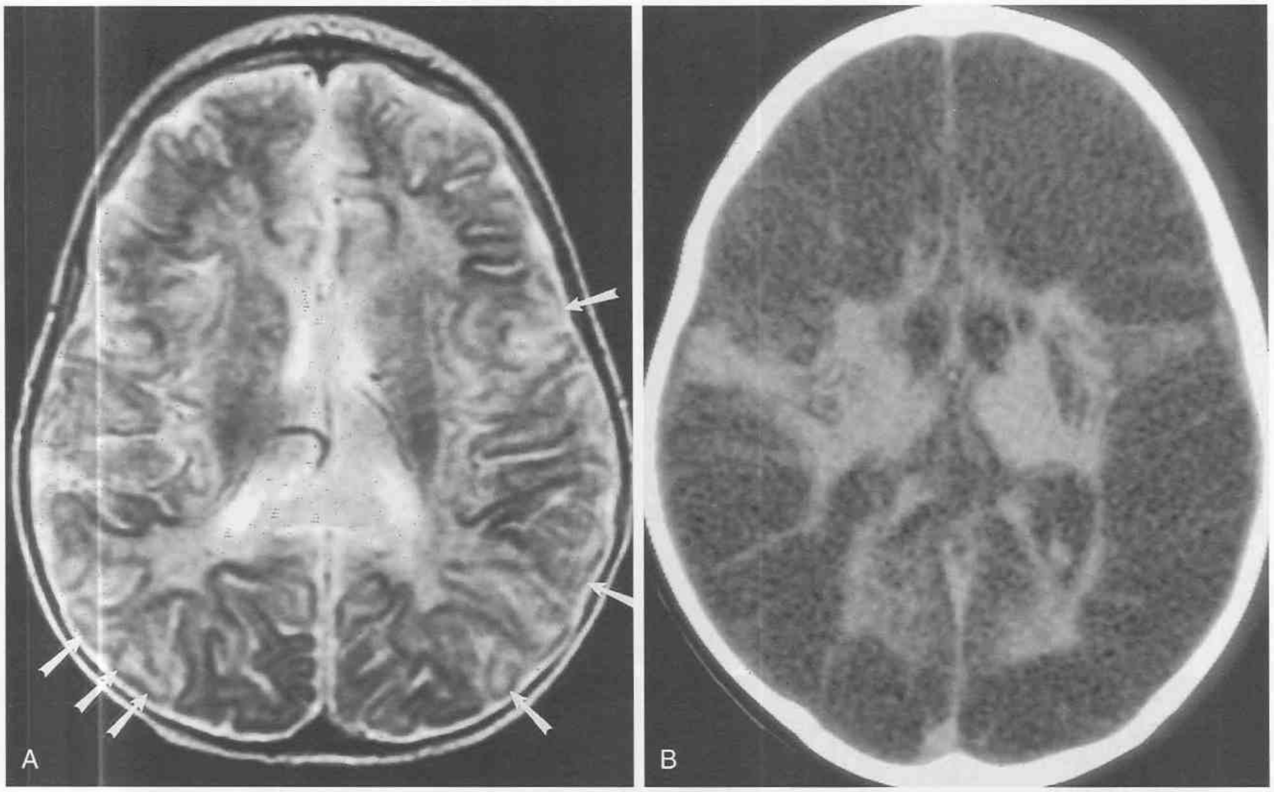

Figure 7–34. Seizure in a 3-month-old girl. *A,* T2-weighted axial image shows areas of cortical and subcortical increased signal involving extensive areas in both hemispheres *(arrows)*. *B* and *C,* Axial unenhanced CT scans 12 months later show extensive hypodensity and volume loss involving much of the hemispheric regions bilaterally. The injury was presumed to be hypoxic or ischemic in nature.

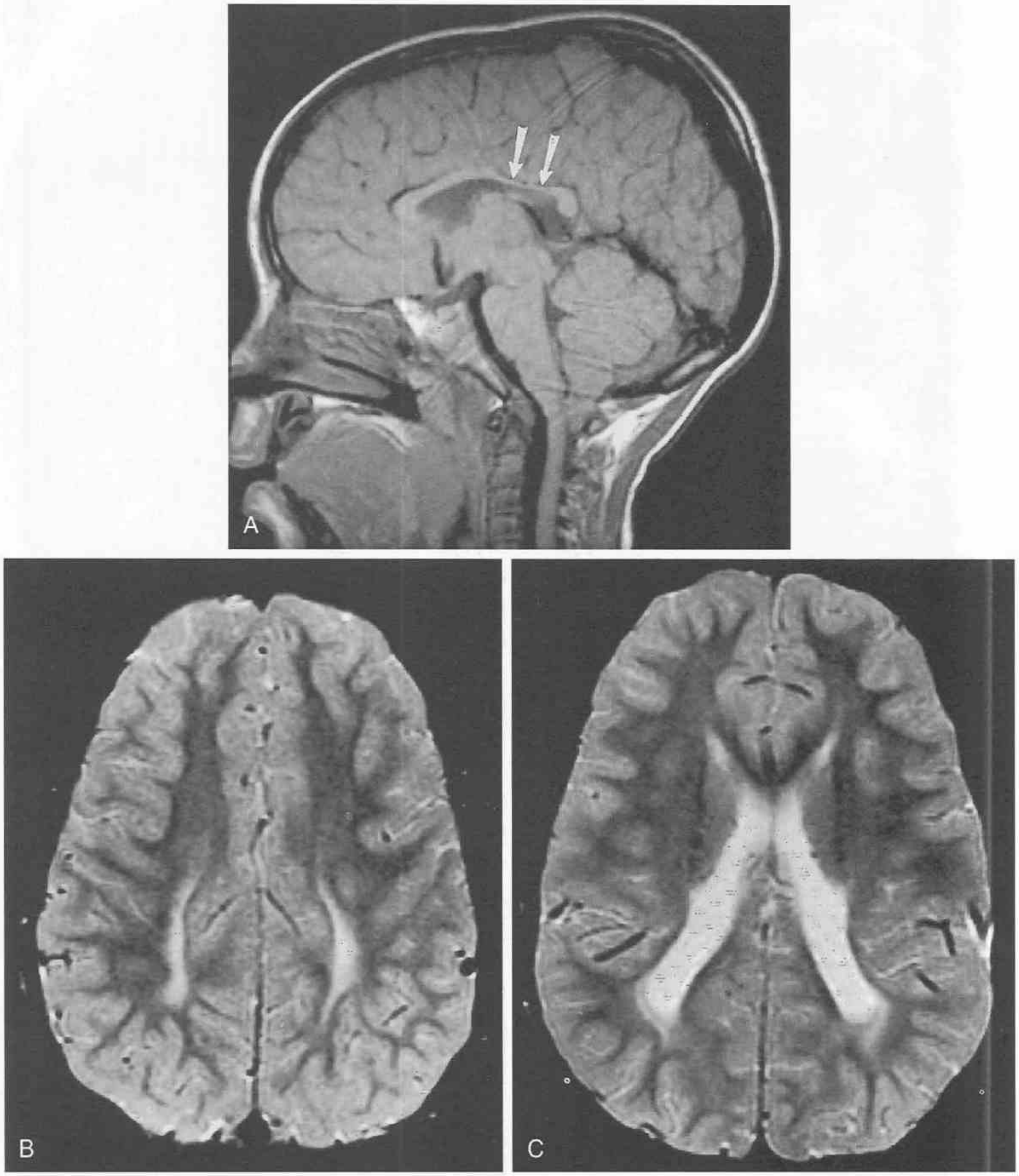

Figure 7–35. End-stage periventricular leukoma[redacted]. *A,* [redacted]ghted sagittal image shows fo[redacted]he posterior portion of the body of the corpus callosum *(arrows)*. *B* and *C,* T2-weighted axial images show dilation of the atria of the lateral ventricles and increased signal in the deep periventricular white matter. There are a number of causes of periventricular leukomalacia, one of which is hypoxic-ischemic encephalopathy.

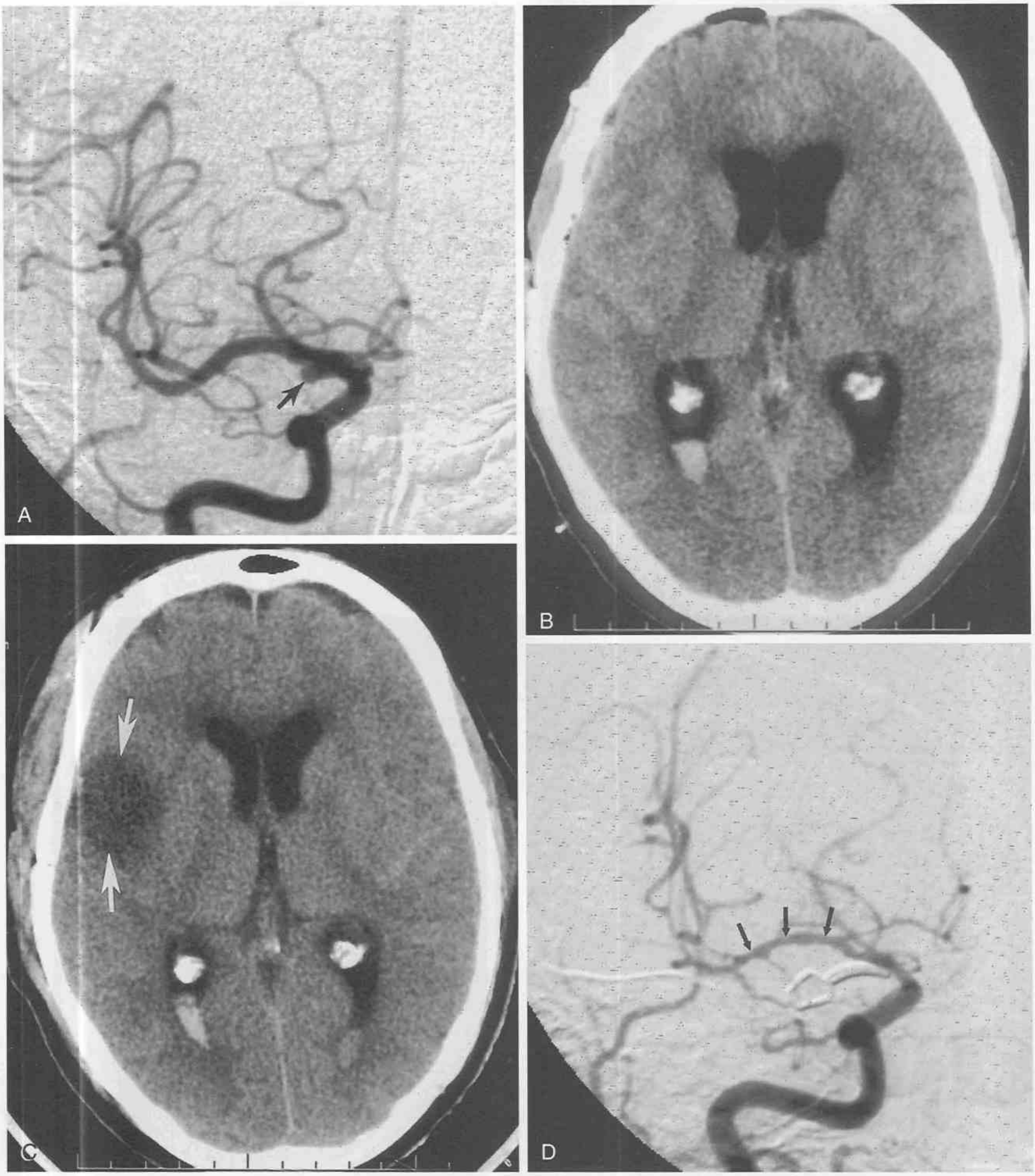

Figure 7–36. Ischemia caused by vasospasm. *A,* Digital subtraction catheter angiogram in a patient with subarachnoid hemorrhage. A ruptured posterior communicating artery–internal carotid artery junction aneurysm is seen *(arrow). B,* Unenhanced axial CT image immediately following ligation of the aneurysm shows postoperative changes but no evidence of infarction. *C,* Unenhanced CT 3 days later, after the onset of left-sided weakness, shows new focal hypodensity *(arrows). D,* A subsequent angiogram shows significant vasospasm in the right M1 segment *(small arrows).*

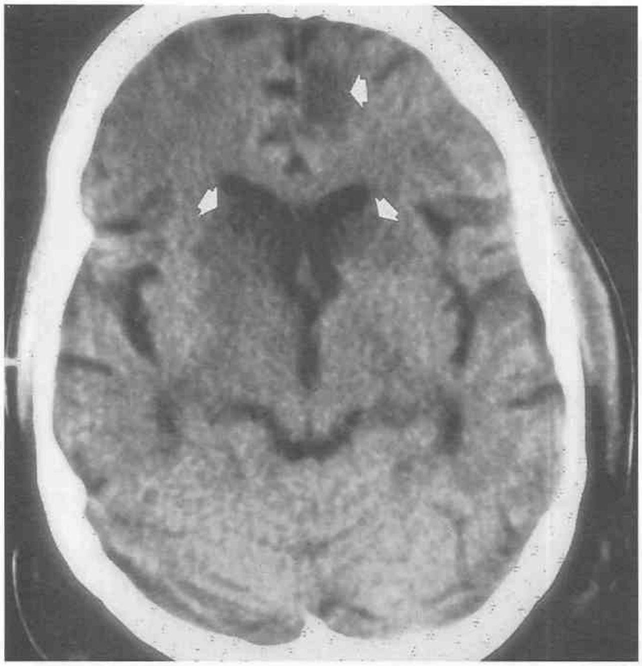

Figure 7–37. Vasculitis. Unenhanced axial CT image shows abnormal low density in the basal ganglia bilaterally and in the left frontal lobe *(arrows)*. Multiple areas of cortical and subcortical infarction may be seen in patients with vasculitis.

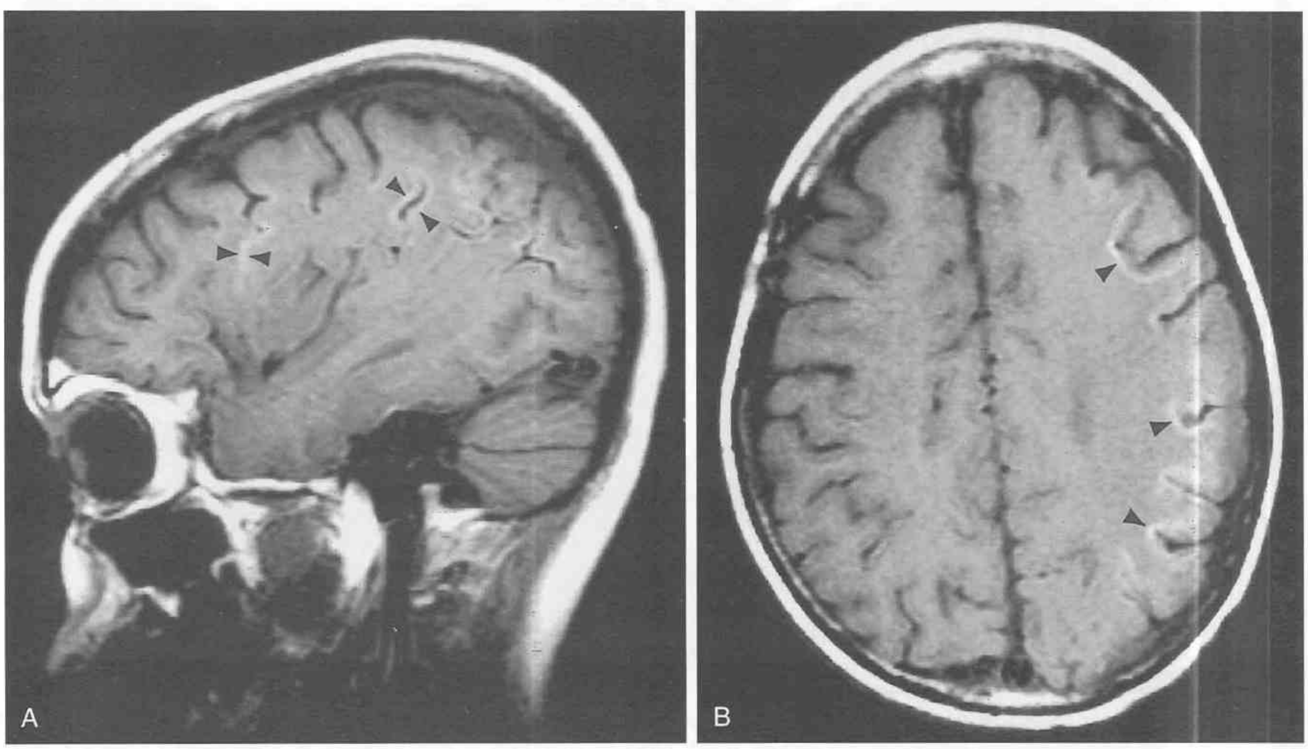

Figure 7–38. Cortical laminar necrosis. *A* and *B*, T1-weighted sagittal and axial images show cortical gyral increased signal *(arrowheads)* without substantial volume loss. The extent matches the expected left cortical middle cerebral artery territory. The signal changes are thought to represent mineralization within tissue damaged by ischemia.

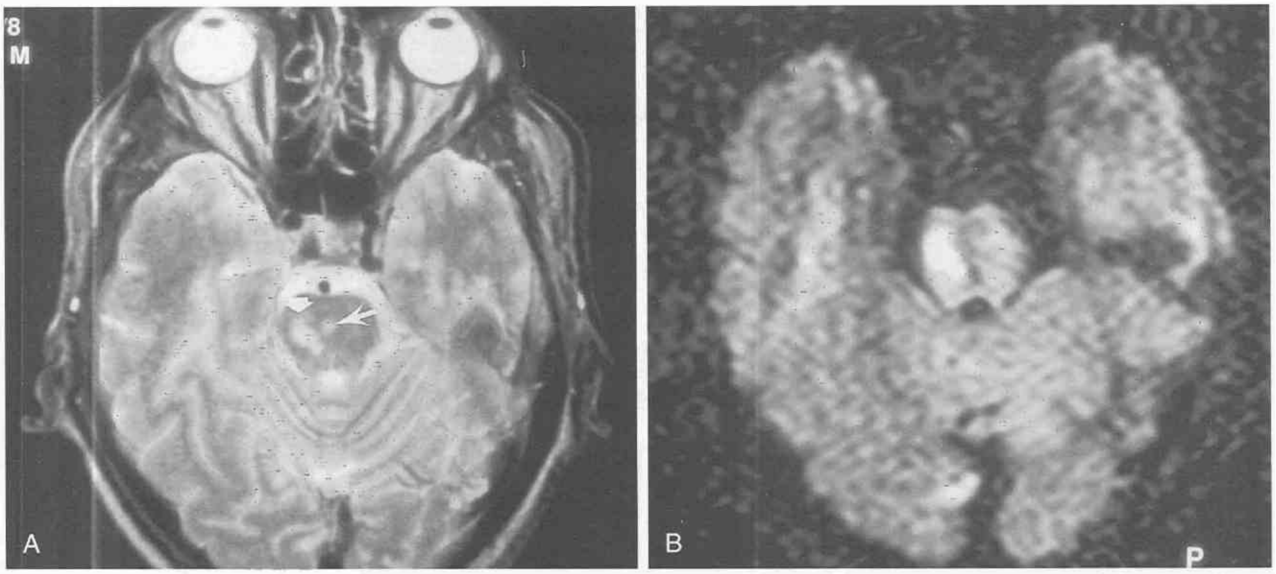

Figure 7–39. The patient is a 59-year-old man with acute stroke. *A,* T2-weighted axial image shows increased signal focally within the central *(arrow)* and lateral *(small arrow)* portions of the pons. *B,* Axial diffusion-weighted image shows hyperintense signal within the lateral abnormality, suggesting that only this area represents acute infarct. The smaller, central hyperintensity, presumably, represents a more remote ischemic lesion.

Finally, some conditions other than stroke can be associated with diffusion restriction, for example, cerebral abscess.[31] Cerebral trauma resulting in diffuse axonal injury can also result in foci of hyperintensity on DW scans.[42a]

Time Course of Diffusion-Weighted Images in Stroke

The very earliest change that can be seen on DW images after an acute stroke is minimal hyperintensity. As mentioned, some early hyperintense changes on DW images may be reversible, both in human stroke patients and in animal subjects. Such findings suggest that separate thresholds of ischemia may exist for early diffusion changes and irreversible cell damage.

ADC values vary with the age of ischemic stroke,[60] a fact that can influence the analysis of clinical cases. In the first hours after the onset of ischemia, ADC values decrease rapidly, often to 30% or more below normal. ADC values lower than about 60×10^{-4} mm²/second are usually seen in ischemia, and values below 50×10^{-4} mm²/second are often seen. After about 24 hours, ADC values begin to increase again, approaching normal values at about 5 to 7 days. This tendency for ADC values to increase and return to the normal range after the initial decrease that occurs in acute cerebral infarction is termed *pseudonormalization.* After about 2 weeks, ADC values are typically increased within the territory of infarction.

One can often distinguish acute stroke from other diagnoses that are associated with T2 prolongation by measuring diminished brain ADC values within the lesion (i.e., many disease processes are associated with *increased* ADC values). Because ADC values increase with the age of a given infarction, one cannot reliably use ADC measurements to distinguish subacute and chronic infarction from other diagnoses.

Despite these changes in ADC values that occur after a stroke, cerebral infarction on DW images often remains hyperintense throughout most of the time course of stroke. The reason that the appearance of stroke remains hyperintense on DW images throughout its time course is presumably related to T2 shine-through. That is, the fact that the region of infarction is bright on T2-weighted images influences the appearance of the stroke on DW images (which typically have substantial T2 weighting).

In addition to standard DW images and ADC maps, a third type of diffusion image can be created that combines some of the advantages of each. If one divides the DW image by the "b zero" reference image, one can create a calculated image known as the *ratio image,* or *exponential image.*[47] Such an image is similar to standard DW scans, in that areas of acute ischemia appear hyperintense. Unlike standard DW images, however, so-called exponential images do not have any T2 weighting and thus do not show the effects of T2 shine-through (Fig. 7–40).

Cerebral Perfusion Imaging

Hemodynamic Pathophysiology in Cerebral Ischemia

The cerebral perfusion parameters CBF and cerebral blood volume (CBV) are related by the central volume principle, which is expressed as the relation

$$CBF = \frac{CBV}{MTT}$$

where MTT is the mean transit time of a nondiffusible tracer in a volume of brain tissue.[34]

The pathophysiology of ischemia can be considered in four stages, based on autoregulatory physiology:

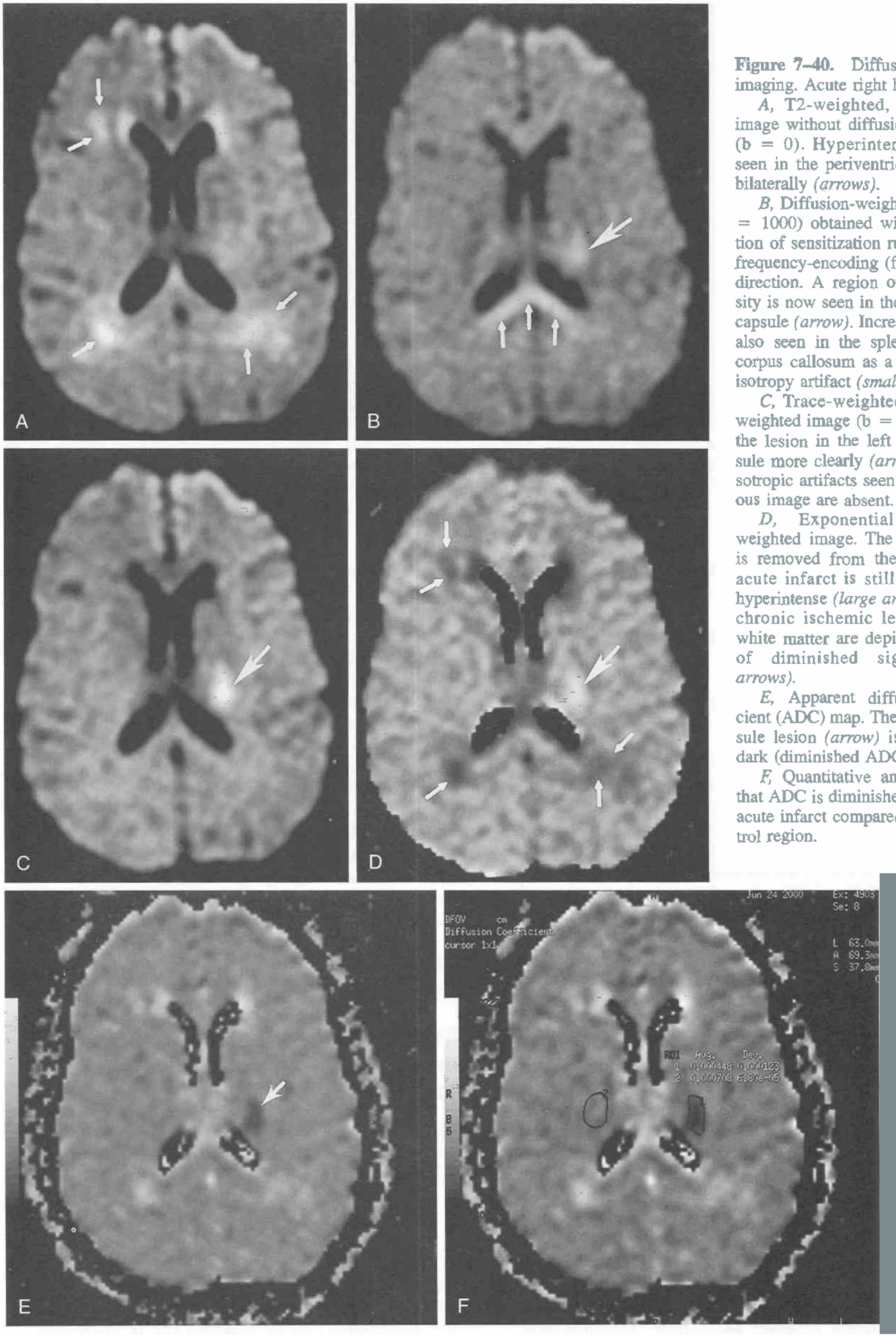

Figure 7–40. Diffusion-weighted imaging. Acute right hemiparesis.

A, T2-weighted, echo-planar image without diffusion weighting (b = 0). Hyperintense signal is seen in the periventricular regions bilaterally *(arrows).*

B, Diffusion-weighted image (b = 1000) obtained with the direction of sensitization running in the frequency-encoding (front to back) direction. A region of hyperintensity is now seen in the left internal capsule *(arrow).* Increased signal is also seen in the splenium of the corpus callosum as a result of anisotropy artifact *(small arrows).*

C, Trace-weighted, diffusion-weighted image (b = 1000) shows the lesion in the left internal capsule more clearly *(arrow)*; the anisotropic artifacts seen in the previous image are absent.

D, Exponential diffusion-weighted image. The effect of T2 is removed from the image. The acute infarct is still depicted as hyperintense *(large arrow),* but the chronic ischemic lesions in the white matter are depicted as areas of diminished signal *(small arrows).*

E, Apparent diffusion coefficient (ADC) map. The internal capsule lesion *(arrow)* is depicted as dark (diminished ADC).

F, Quantitative analysis shows that ADC is diminished 37% in the acute infarct compared with a control region.

- *First stage,* normal hemodynamics.
- *Second stage,* characterized by an initial decrease in perfusion pressure. Initially, autoregulatory vasodilation preserves CBF, at the same time increasing CBV. MTT is also typically increased.
- *Third stage,* characterized by greater decrease in perfusion pressure and by an initial decrease in CBF value. CBV typically remains increased.
- *Fourth stage,* characterized by further decrease in perfusion pressure and decreases in both CBF and CBV. This stage is associated with tissue ischemia and hemodynamic failure.

Perfusion Imaging in Stroke

An important goal of hemodynamic stroke imaging is the depiction of tissue at risk for infarction that might be saved though intervention. In the setting of acute stroke, if the location and extent of viable tissue at risk for infarction were known, such knowledge could help clinicians to weigh the risks associated with stroke therapies. Viable tissue that is at risk for infarction is commonly called the *ischemic penumbra,* or the tissue outside the (nonviable) core of infarction that is nonetheless underperfused. It is postulated that the ischemic penumbra differs from viable tissue that is not at risk by the (decreased) amount of blood flow that it receives.

A number of methods of imaging cerebral perfusion are available. Imaging with radioisotopes is possible with single-photon emission computed tomography (SPECT) and positron emission tomography (PET). It is also possible to image CBF with CT using inhaled stable xenon.[10] This method is capable of depicting extent of hemodynamic abnormality in stroke.[71] Although xenon CT remains an attractive tool for the assessment of CBF, this method has not yet achieved widespread clinical use. One possible reason may be the requirement for specialized equipment to administer and ventilate the gas.

It is now possible to obtain dynamic, contrast-enhanced perfusion scans using either CT or MR scanners[32, 66] (Figs. 7–41 and 7–42). Generally, a volume of contrast material is injected rapidly into an arm vein by an automatic (power) injector, and the bolus of contrast material is tracked by the scanner through a slice or slab of brain tissue that is repeatedly scanned over the course of about 45 to 60 seconds. For best results, temporal resolution of 2 seconds or faster is needed.

It has been proposed that MR perfusion imaging may complement DW imaging in depicting the region of penumbra.[26] The premise is that DW imaging is thought to depict the region of core infarction, whereas the region of perfusion abnormality represents both the core and the penumbra. The difference between the extent of the diffusion abnormality and the extent of perfusion abnormality is thus thought to represent penumbra.

An alternate approach for determining the extent of penumbra is to use perfusion maps alone to distinguish the core of infarction from the penumbra, usually with the use of perfusion parameter value thresholds. The most commonly used perfusion parameter is the mean CBF value. Earlier work with xenon CT in stroke patients has

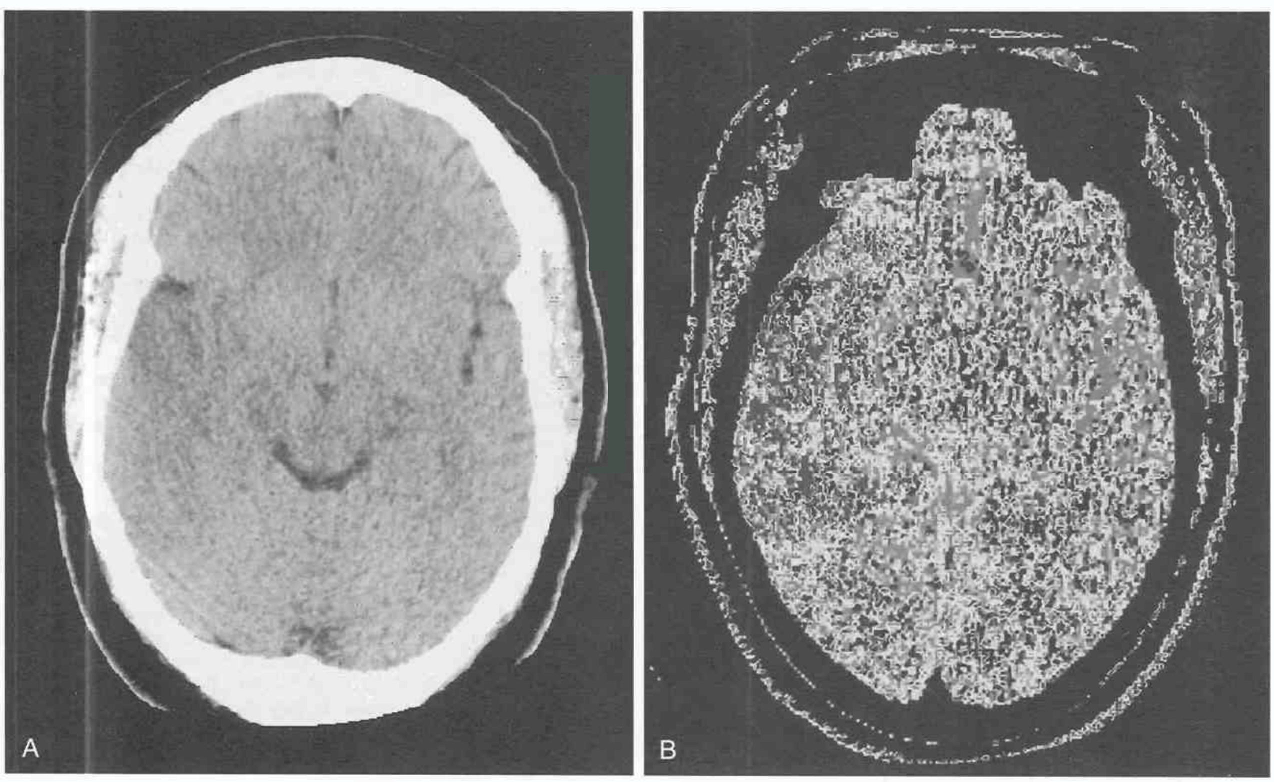

Figure 7–41. Acute stroke of the right middle cerebral artery. *A,* Unenhanced axial CT scan of the brain shows no substantial abnormalities. *B,* Mean transit time (MTT) map from dynamic CT perfusion scan depicts a well-defined region of MTT prolongation. The extent and degree of regional hemodynamic abnormalities can be determined by perfusion imaging techniques.

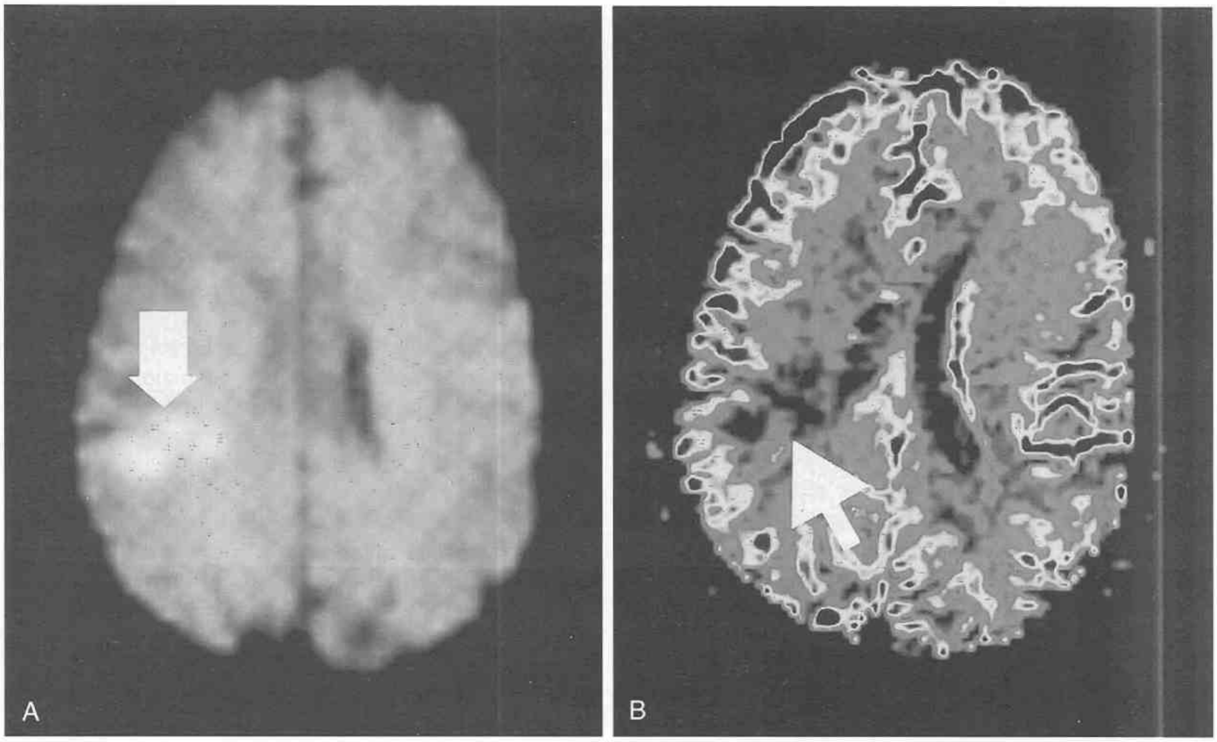

Figure 7–42. Acute dissection of the right internal carotid artery. *A,* Trace-weighted, diffusion-weighted image (b = 1000) shows cortically based region of hyperintense signal consistent with acute middle cerebral artery territory infarction *(arrow). B,* Negative enhancement integral image (relative cerebral blood volume) from gadolinium-enhanced dynamic sequence. The extent of a region of *(arrow)* diminished perfusion is identical to the diffusion-weighted image abnormality *(arrow).* This represents a "matched" perfusion and diffusion defect.

described thresholds for infarct core (CBF values < 7 mL/100 g per minute) and penumbra (CBF values between 7 and 20 mL/100 g per minute).[18]

The perfusion parameter CBV may provide additional information about tissue viability that CBF alone cannot provide. Studies using MRI with SPECT and xenon CT with dynamic CT have shown that for tissues associated with moderately low CBF values, CBV value can help to predict tissue viability.[50] These studies suggest that moderately decreased CBF values and increased CBV values may carry a better prognosis than that for tissues in which both CBF and CBV values are diminished.

References

1. Asato R, Okumura R, Konishi J: "Fogging effect" in MR of cerebral infarct. J Comput Assist Tomogr 15:160–162, 1991.
2. Astrup J, Siesjo B, Symon L: Thresholds in cerebral ischemia—the ischemic penumbra. Stroke 12:723–725, 1981.
3. Ayanzen RH, Bird CR, Keller PJ, et al: Cerebral MR venography: Normal anatomy and potential diagnostic pitfalls. AJNR Am J Neuroradiol 21:74–78, 2000
4. Bamford J, Sandercock P, Dennis M, et al: A prospective study of acute cerebrovascular disease in the community: The Oxfordshire Community Stroke Project, 1981–1986: Part 2. Incidence, case fatality rates, and overall outcome at one year of cerebral infarction, primary intracerebral and subarachnoid hemorrhage. J Neurol Neurosurg Psychiatry 53:16–22, 1990.
5. Bernaudin F, Verlhac S, Freard F, et al: Multicenter prospective study of children with sickle cell disease: Radiographic and psychometric correlation. J Child Neurol 15:333–343, 2000.
6. Bladin CF, Chambers BR: Frequency and pathogenesis of hemodynamic stroke. Stroke 25:2179–282, 1994.
7. Bonita R: Epidemiology of stroke. Lancet 339:343–344, 1992.
8. Boyko OB, Burger PC, Shelbourne JD, Ingram P: Non-heme mechanisms for T1 shortening: Pathologic, CT, and MR elucidation. AJNR Am J Neuroradiol 13:1439–1445, 1992.
9. Brandt T, Steinke W, Thie A, et al: Posterior cerebral artery territory infarcts: Clinical features, infarct topography, causes, and outcome. Cerebrovasc Dis 10:170–182, 2000.
10. Caille JM, Constant P, Renou AM, Billerey J: Prognostic value of rCBF measurements and CT in focal cerebral ischemia. Neuroradiology 16:238–241, 1978.
11. Dulli DA, Luzzio CC, Williams EC, Schutta HS: Cerebral venous thrombosis and activated protein C resistance. Stroke 27:1731–1733, 1996.
12. Fisher M: Occlusion of the internal carotid artery. Arch Neurol Psychiatry 65:346–377, 1951.
13. Ford CC, Griffey RH, Matwiyoff NA, Rosenberg GA: Multivoxel ^{1}H-MRS of stroke. Neurology 42:1408–1412, 1992.
14. Gerhard GT, Duell PB: Homocysteine and atherosclerosis. Curr Opin Lipidol 10:417–428, 1999.
15. Grohn OH, Lukkarinen JA, Oja JM, et al: Noninvasive detection of cerebral hypoperfusion and reversible ischemia from reductions in the magnetic resonance imaging relaxation time, T2. J Cereb Blood Flow Metab 18:911–920, 1998.
16. Hacke W, Kaste M, Fieschi C, et al: Intravenous thrombolysis with recombinant tissue plasminogen activator for acute hemispheric stroke: The European Cooperative Acute Stroke Study. JAMA 274:1017–1025, 1995.
17. Hankey GJ, Sudlow CL, Dunbabin DW: Thienopyridines or aspirin to prevent stroke and other serious vascular events in patients at high risk of vascular disease? A systematic review of the evidence from randomized trials. Stroke 31:1779–1784, 2000.
18. Hatazawa J, Shimosegawa E, Toyoshima H, et al: Cerebral blood volume in acute brain infarction: A combined study with dynamic susceptibility contrast MRI and ^{99m}Tc-HMPAO-SPECT. Stroke 30:800–806, 1999.
19. Heinsius T, Bogousslavsky J, Van Melle G: Large infarcts in the middle cerebral artery territory: Etiology and outcome patterns. Neurology 50:341–350, 1998.

20. Henriksen O, Gideon P, Sperling B, et al: Cerebral lactate production and blood flow in acute stroke. J Magn Reson Imaging 2:511–517, 1992.
21. Hossmann KA: Viability thresholds and the penumbra of focal ischemia. Ann Neurol 36:557–565, 1994.
22. Ida M, Mizunuma K, Hata Y, Tada S: Subcortical low intensity in early cortical ischemia. AJNR Am J Neuroradiol 15:1387–1393, 1994.
23. Johnson WD, Ganjoo AK, Stone CD, et al: The left atrial appendage: Our most lethal human attachment! Surgical implications. Eur J Cardiothorac Surg 17:718–722, 2000.
24. Jones SC, Perez-Trepichio AD, Xue M, et al: Magnetic resonance diffusion-weighted imaging: Sensitivity and apparent diffusion constant in stroke. Acta Neurochir Suppl (Wien) 60:207–210, 1994.
25. Jungreis CA, Kanal E, Hirsch WL, et al: Normal perivascular spaces mimicking lacunar infarction: MR imaging. Radiology 169:101–104, 1988.
26. Kaufmann AM, Firlik AD, Fukui MB, et al: Ischemic core and penumbra in human stroke. Stroke 30:93–99, 1999.
27. Kazui S, Levi CR, Jones EF, et al: Risk factors for lacunar stroke: A case-control transesophageal echocardiographic study. Neurology 54: 1385–1387, 2000.
28. Keiper MD, Ng SE, Atlas SW, Grossman RI: Subcortical hemorrhage: Marker for radiographically occult cerebral vein thrombosis on CT. J Comput Assist Tomogr 19:527–531, 1995.
29. Kenet G, Sadetzki S, Murad H, et al: Factor V Leiden and antiphospholipid antibodies are significant risk factors for ischemic stroke in children. Stroke 31:1283–1288, 2000.
30. Kidwell CS, Saver JL, Mattiello J, et al: Thrombolytic reversal of acute human cerebral ischemic injury shown by diffusion/perfusion magnetic resonance imaging. Ann Neurol 47:462–469, 2000.
31. Kim YJ, Chang KH, Song IC, et al: Brain abscess and necrotic or cystic brain tumor: Discrimination with signal intensity on diffusion-weighted MR imaging. AJR Am J Roentgenol 171:1487–1490, 1998.
32. Koenig M, Klotz E, Luka B, et al: Perfusion CT of the brain: Diagnostic approach for early detection of ischemic stroke. Radiology 209:85–93, 1998.
33. Koh MS, Goh KY, Tung MY, Chan C: Is decompressive craniectomy for acute cerebral infarction of any benefit? Surg Neurol 53:225–230, 2000.
34. Kohlmeyer K, Graser C: Comparative studies of computed tomography and measurements of regional cerebral blood flow in stroke patients. Neuroradiology 16:233–237, 1978.
35. Lafitte F, Boukobza M, Guichard JP, et al: Deep cerebral venous thrombosis: Imaging in eight cases. Neuroradiology 41:410–418, 1999.
36. Lansberg MG, Albers GW, Beaulieu C, Marks MP: Comparison of diffusion-weighted MRI and CT in acute stroke. Neurology 54: 1557–1561, 2000.
37. Lanska DJ, Kryscio RJ: Risk factors for peripartum and postpartum stroke and intracranial venous thrombosis. Stroke 31:1274–82, 2000.
38. Lassen NA, Astrup J: Ischemic penumbra. In Wood JH (ed): Cerebral Blood Flow: Physiologic and Clinical Aspects. New York, McGraw-Hill, 1987, 1994.
39. Launes J, Ketonen L: Dense middle cerebral artery sign: An indicator of poor outcome in middle cerebral artery area infarction. J Neurol Neurosurg Psychiatry 50:1550–1552, 1987.
40. Le Bihan D, Breton E, Lallemand D, et al: Separation of diffusion and perfusion in intravoxel incoherent motion MR imaging. Radiology 168:497–505, 1988.
41. Lepore FE, Gulli V, Miller DC: Neuro-ophthalmological findings with neuropathological correlation in bilateral thalamic-mesencephalic infarction. J Clin Neuroophthalmol 5:224–228, 1985.
42. Lev MH, Farkas J, Gemmete JJ, et al: Acute stroke: Improved nonenhanced CT detection—benefits of soft-copy interpretation by using variable window width and center level settings. Radiology 213:150–155, 1999.
42a. Liu AY, Maldjian JA, Bagley LJ, et al: Traumatic brain injury: Diffusion-weighted MR imaging findings. AJNR Am J Neuroradiol 20:1636–1641, 1999.
43. MacWalter RS: Secondary prevention of stroke. Thromb Haemost 82(Suppl):95–103, 1999.
44. Marks MP, Holmgren EB, Fox AJ, et al: Evaluation of early computed tomographic findings in acute ischemic stroke. Stroke 30:389–392, 1999.
45. Mathews VP, King JC, Elster AD, Hamilton CA: Cerebral infarction: Effects of dose and magnetization transfer saturation at gadolinium-enhanced MR imaging. Radiology 190:547–552, 1994.
46. Mattle HP, Wentz KU, Edelman RR, et al: Cerebral venography with MR. Radiology 178:453–458, 1991.
47. Meier P, Zierler KL: On the theory of the indicator-dilution method for measurement of blood flow and volume. J Appl Physiol 6: 731–744, 1954.
48. Merboldt KD, Bruhn H, Frahm J, et al: MRI of "diffusion" in the human brain: New results using a modified CE-FAST sequence. Magn Reson Med 9:423–429, 1989.
49. Mosely ME, Kucharczyk J, Mintorovitich J, et al: Diffusion-weighted MRI of acute stroke: Correlation with T2-weighted and magnetic susceptibility-enhanced MRI in cats. AJNM Am J Neuroradiol 11: 423–429, 1990.
50. Muizelaar JP, Fatouros PP, Schroder ML: A new method for quantitative regional cerebral blood volume measurements using computed tomography. Stroke 28:1998–2005, 1997.
51. Mull M, Schwarz M, Thron A: Cerebral hemispheric low-flow infarcts in arterial occlusive disease: Lesion patterns and angiomorphological conditions. Stroke 28:118–123, 1997.
52. Muller TB, Haraldseth O, Jones RA, et al: Combined perfusion and diffusion-weighted magnetic resonance imaging in a rat model of reversible middle cerebral artery occlusion. Stroke 26:451–457, 1995.
53. Murakami Y, Yamashita Y, Matsuishi T, et al: Cranial MRI of neurologically impaired children suffering from neonatal hypoglycaemia. Pediatr Radiol 29:23–72, 1999.
54. Murray CJ, Lopez AD: Mortality by cause for eight regions of the world: Global Burden of Disease Study. Lancet 349:1269–1276, 1997.
55. Norris DG, Niendorf T, Leibfritz D: Healthy and infarcted brain tissues studied at short diffusion times: The origins of apparent restriction and the reduction in apparent diffusion coefficient. NMR Biomed 7:304–310, 1994.
56. Pantano P, Lenzi GL, Guidetti B, et al: Crossed cerebellar diaschisis in patients with cerebral ischemia assessed by SPECT and ^{123}I-HIPDM. Eur Neurol 27:142–148, 1987.
57. Pessin MS, Duncan GW, Mohr JP, Poskanzer DC: Clinical and angiographic features of carotid transient ischemic attacks. N Engl J Med 296:358–362, 1977.
58. Petty GW, Brown RD, Whisnant JP, et al: Ischemic stroke subtypes: A population-based study of incidence and risk factors. Stroke 30: 2513–2516, 1999.
59. Pressman BD, Tourje EJ, Thompson JR: An early CT sign of ischemic infarction: Increased density in a cerebral artery. AJR Am J Roentgenol 149:583–586, 1987.
60. Provenzale JM, Engelter ST, Petrella JR, et al: Use of MR exponential diffusion-weighted images to eradicate T2 "shine-through" effect. AJR Am J Roentgenol 172:537–539, 1999.
61. Provenzale JM, Loganbill HA: Dural sinus thrombosis and venous infarction associated with antiphospholipid antibodies: MR findings. J Comput Assist Tomogr 18:719–723, 1994.
62. Rademacher J, Sohngen D, Specker C, et al: Cerebral microembolism, a disease marker for ischemic cerebrovascular events in the antiphospholipid syndrome of systemic lupus erythematosus? Acta Neurol Scand 99:356–361, 1999.
63. Rauch RA, Bazan C 3d, Larsson EM, Jinkins JR: Hyperdense middle cerebral arteries identified on CT as a false sign of vascular occlusion. AJNR Am J Neuroradiol 14:669–673, 1993.
64. Rudolf J, Grond M, Stenzel C, et al: Incidence of space-occupying brain edema following systemic thrombolysis of acute supratentorial ischemia. Cerebrovasc Dis 8:166–171, 1998.
65. Salgado ED, Weinstein M, Furlan AJ, et al: Proton magnetic resonance imaging in ischemic cerebrovascular disease. Ann Neurol 20: 502–507, 1986.
66. Schlaug G, Benfield A, Baird AE, et al: The ischemic penumbra: Operationally defined by diffusion and perfusion MRI. Neurology 53: 1528–1537, 1999.
67. Schlaug G, Siewert B, Benfield A, et al: Time course of the apparent diffusion coefficient (ADC) abnormality in human stroke. Neurology 49:113–119, 1997.
68. Scuotto A, Cappabianca S, Melone MB, Puoti G: MRI "fogging" in cerebellar ischemia: Case report. Neuroradiology 39:785–787, 1997.
69. Shamoto H, Chugani HT: Glucose metabolism in the human cerebellum: An analysis of crossed cerebellar diaschisis in children with unilateral cerebral injury. J Child Neurol 12:407–414, 1997.

70. So EL, Toole JF, Dalal P, Moody DM: Cephalic fibromuscular dysplasia in 32 patients: Clinical findings and radiologic features. Arch Neurol 38:619–622, 1981.
71. Sorensen AG, Copen WA, Ostergaard L, et al: Hyperacute stroke: Simultaneous measurement of relative cerebral blood volume, relative cerebral blood flow, and mean tissue transit time. Radiology 210: 519–527, 1999.
72. Tomura N, Uemura K, Inugami A, et al: Early CT finding in cerebral infarction: Obscuration of the lentiform nucleus. Radiology 168: 463–467, 1988.
73. Truwit CL, Barkovich AJ, Gean-Marton A, et al: Loss of the insular ribbon: Another early CT sign of acute middle cerebral artery infarction. Radiology 176:801–806, 1990.
74. Valanne L, Ketonen L, Majander A, et al: Neuroradiologic findings in children with mitochondrial disorders. AJNR Am J Neuroradiol 19:369–377, 1998.
75. van Gelderen P, de Vleeschouwer MH, DesPres D, et al: CT: Water diffusion and acute stroke. Magn Reson Med 31:154–163, 1994.
76. Wein TH, Bornstein NM: Stroke prevention: Cardiac and carotid-related stroke. Neurol Clin 18:321–341, 2000.
77. Wetzel SG, Kirsch E, Stock KW, et al: Cerebral veins: Comparative study of CT venography with intraarterial digital subtraction angiography. AJNR Am J Neuroradiol 20:249–255, 1999.
78. Wijman CA, Babikian VL, Winter MR, Pochay VE: Distribution of cerebral microembolism in the anterior and middle cerebral arteries. Acta Neurol Scand 101:122–127, 2000.
79. Willis BK, Greiner F, Orrison WW, Benzel EC: The incidence of vertebral artery injury after midcervical spine fracture or subluxation. Neurosurgery 34:435–441, 1994.
80. Wong EC, Cox RW, Song AW: Optimized isotropic diffusion weighting. Magn Reson Med 1995 34:139–143, 1995.
81. Woodring JH, Lee C, Duncan V: Transverse process fractures of the cervical vertebrae: Are they insignificant? J Trauma 34:797–802, 1993.
82. Yamauchi H, Fukuyama H, Nagahama Y, et al: Decrease in regional cerebral blood volume and hematocrit in crossed cerebellar diaschisis. Stroke 30:1429–1431, 1999.

8 Cerebral Aneurysms and Vascular Malformations

Theodore C. Larson III

Cerebral Aneurysms

Incidence and Natural History

Cerebral aneurysms are found in approximately 0.5 to 5% of the population.[130a, 139, 193, 242, 255, 261, 262, 326, 339a] Women have a variably greater incidence of cerebral aneurysms compared with men, and aneurysm development increases with advancing age.[15, 139, 242, 297, 326] Some families demonstrate a genetic predisposition to develop cerebral aneurysms.[43, 214, 305] The risk of new aneurysm development is approximately 2% per year.[139] Subarachnoid hemorrhage, the most common presenting symptom of a cerebral aneurysm, is the second most common cause of subarachnoid hemorrhage, after trauma.[261] Eighty percent to 90% of nontraumatic subarachnoid hemorrhages are due to a ruptured cerebral aneurysm, a far more common cause than an arteriovenous malformation, which accounts for 15% of subarachnoid hemorrhages.[301] Other, less common presenting signs and symptoms, which are due to mass effect or neighboring inflammation, aneurysm thrombosis, or aneurysm-generated emboli, are cranial nerve palsy, headache, seizure, and transient or permanent neurologic dysfunction.[242] These nonhemorrhagic symptoms can be seen with aneurysms of any size but occur more commonly with posterior circulation or internal carotid aneurysms.[242]

The annual incidence of rupture of an asymptomatic cerebral aneurysm has been estimated at approximately 0.5% to 2%, or roughly 10 cases per 100,000 population.[135, 139, 255, 273, 326] Symptomatic intact aneurysms have a higher rate of bleeding—4% or more per year. Some studies have suggested that for aneurysms less than 1 cm in diameter, the incidence of annual rupture is less than 0.1%.[315a, 326] Other reports, however, have documented that the majority of ruptured aneurysms are less than 9 to 10 mm in diameter,[130a, 141, 255] and that even small (2 to 3 mm) aneurysms may cause subarachnoid hemorrhage.[10a, 273, 288, 340] The presence of a daughter sac probably raises the likelihood of rupture.[273, 326] Younger patients may have a greater propensity for aneurysmal hemorrhage, especially if they have multiple aneurysms.[139]

A ruptured cerebral aneurysm carries significant morbidity and mortality, the 30-day mortality traditionally being stated as 40% to 60%.[139, 141, 255, 262] Untreated patients with ruptured cerebral aneurysms have a rebleeding rate of 10% to 50% in the first 2 weeks to 6 months. The rebleeding rate is highest in the first day, with a 50% mortality[5, 40a, 135, 141, 231a, 236a, 297]; thereafter, the bleeding rate is approximately 3% per year.[135, 139] Initial aneurysm size is not a prognostic factor influencing rebleeding in the acute period.[141] Approximately 14% to 23% of survivors of rupture of a cerebral aneurysm are left with significant morbidity[255, 267]; in 13% to 32% of cases, the morbidity is the direct result of delayed vasospasm-caused ischemia.[193, 231a, 236a, 267] Twenty-one percent of patients who enter the hospital for treatment of subarachnoid hemorrhage eventually die.[267] Surgical clipping of acutely ruptured aneurysms results in improved functional outcome compared with delayed intervention.[218] These data also argue for elective treatment of an unruptured aneurysm.

Unruptured cerebral aneurysms are most often asymptomatic but can cause local mass effect and headache. Focal mass effect can compress adjacent cranial nerves or brain parenchyma, a typical example being third nerve palsy due to a posterior communicating aneurysm. Other diseases can cause neurologic deficits similar to those due to aneurysms, however. For example, third nerve palsy could be caused by diabetes or microvascular disease instead of a posterior communicating aneurysm. When magnetic resonance imaging (MRI) and MR angiography (MRA) fail to diagnose the cause of the patient's third nerve palsy, catheter cerebral angiography may be required to exclude a cerebral aneurysm, because the morbidity and mortality associated with cerebral aneurysms are so significant. When catheter cerebral angiography does not demonstrate an aneurysm in a patient with no history of subarachnoid hemorrhage, the patient can be assumed to have small-vessel cerebrovascular disease. Sometimes the angiogram supports this diagnosis by showing other areas of atherosclerotic disease.

Types of Aneurysms, Etiology, and Pathology

Aneurysms may be divided into different classifications according to morphology, size, location, or etiology. Most cerebral aneurysms are acquired lesions and are saccular or fusiform. Older medical reports proposed that saccular or berry cerebral aneurysms were due to an embryologic abnormality of the walls of cerebral vessels.[221] Stehbens[293] and others have refuted this theory. Most cerebral aneurysms develop from hemodynamic stresses,[143a, 262, 293] which typically occur at vessel bifurcations or terminations, or

along the outer curvature of looping vessels.[143a, 197, 244, 273, 293] The aneurysm's location is a continuation of the primary flow direction in the parent vessel, especially if the parent vessel is tortuous.[244] Rupture and thrombosis of cerebral aneurysms are also believed to be due to hemodynamic forces.[97, 293] Supporting this theory of an underlying etiology is the higher incidence of cerebral aneurysms in patients with intracranial vascular anomalies, including fenestrations and congenital or iatrogenic vascular variants of the circle of Willis (e.g., persistent trigeminal artery, unilateral absence of the A1 segment of an anterior cerebral artery, azygous proximal anterior cerebral artery, and occlusion or absence of an internal carotid artery).[205, 236, 264, 272] Primary causes of aneurysms are as follows: (1) atherosclerosis, (2) hypertension, (3) smoking, (4) abuse of cocaine, methamphetamine, ephedrine, heroin, and other drugs with resultant arteritis or hypertension,[132, 139, 206, 230] (5) vascular malformations (approximately 6% to 10% incidence of aneurysm, both proximal flow–related and nidal[11, 44, 60, 90, 148, 186, 204]), (6) specific vascular diseases, such as fibromuscular dysplasia (20% to 50% incidence of aneurysm[113, 272]), spontaneous cervical carotid or vertebral artery dissection (more commonly seen in women[272]), Takayasu's arteritis,[111] polycystic kidney disease (10% incidence of aneurysm), and neurofibromatosis,[117] and (7) the connective tissue disorders, such as Marfan's syndrome and Ehlers-Danlos syndrome (in which aneurysms of the carotid siphon to supraclinoid segment are more common).[272] The walls of saccular cerebral aneurysms contain intima and adventitia but the media and internal elastic membrane are thinned or absent.[49, 50]

A number of patients with cerebral aneurysms demonstrate collagen type III abnormalities.[272] Most cerebral aneurysms arise from the circle of Willis and middle cerebral artery bifurcations. Ninety percent involve the anterior circulation, and 10% the posterior circulation.[11, 221] The most common sites are the anterior communicating artery at its junction with the adjacent anterior cerebral artery (30% to 35%), the posterior communicating artery at its union with the internal carotid artery (30% to 35%), the middle cerebral artery bifurcation (20% to 25%), the basilar terminus (5%), the carotid terminus (5%), and the origin of the ophthalmic artery (5%).[227] Less commonly, aneurysms occur along the course of the anterior cerebral arteries, particularly at the origin of the callosomarginal artery, the middle cerebral arteries, posterior cerebral arteries, superior cerebellar arteries, anterior inferior cerebellar arteries, and posterior inferior cerebellar arteries.[15, 115, 130a, 244, 259]

In 15% to 30% of patients, multiple aneurysms are found, more often in women than in men by a 5:1 ratio,[139, 141, 297, 297a, 307a, 316] and most frequently involving the middle cerebral artery.[340] Of the patients with multiple cerebral aneurysms, 75% have two, 15% have three, and 10% have four or more.[297] When one of multiple aneurysms ruptures and causes subarachnoid hemorrhage, it is most often the largest[340] although this is not always the case. For instance, Nehls and colleagues[209] have reported the propensity for anterior communicating aneurysms to rupture when several are present simultaneously. Vasculopathies, such as fibromuscular dysplasia and connective tissue disorders, as well as syndromes such as polycystic kidney disease are associated with a higher incidence of multiple cerebral aneurysms. Bilateral symmetrical aneurysms are called *mirror aneurysms*, and they most often involve the internal carotid arteries or the middle cerebral artery bifurcations.[297]

Other causes of cerebral aneurysms, identified in less than 5% of patients, are (1) penetrating and nonpenetrating trauma, (2) dissection (post-traumatic or otherwise), (3) inflammation or mycosis due either to septic emboli causing destruction of the endothelium or to spread of infection to the vasa vasorum with subsequent vessel wall destruction and focal dilatation, and (4) neoplasm; rarely, cerebral aneurysms may be congenital.[5, 139, 161, 170, 212] Except for congenital aneurysms, aneurysms with these uncommon causes often develop in unusual locations that are distal to the circle of Willis.

Trauma typically results in a pseudoaneurysm rather than a true aneurysm, because no normal vascular components constitute the sac within a hematoma that communicates with the injured vessel. Post-traumatic pseudoaneurysms occur in locations not common for other cerebral aneurysms, including the proximal internal carotid artery, particularly at the skull base[280]; the meningeal vessels, which often are associated with overlying skull fractures and epidural hematomas[311]; the posterior cerebral or anterior cerebral arteries, caused by tentorial or falcine impaction, respectively[170, 205, 212, 280]; and in extracranial vessels within the scalp, such as the superficial temporal artery and the occipital artery.[281] Penetrating, high-velocity trauma, such as from gunshot wounds, is more likely to produce a traumatic aneurysm if the entrance site is in the temporal or peritemporal region, if fragments cross the midline, and if the pseudoaneurysm is surrounded by hematoma. The surrounding anterior and middle cerebral arteries are most often involved.[9] Initially, traumatic pseudoaneurysms may not be visualized, but then they rapidly enlarge.[205, 280] Fifty percent of untreated, post-traumatic aneurysms bleed, with an almost uniformly fatal outcome.[9, 205]

Uncommon neoplastic aneurysms are also pseudoaneurysms, resulting from primary or metastatic tumor invasion of a vessel or metastatic emboli to the vessel lumen or its vasa vasorum.[92, 116a] Pituitary adenomas are associated with a higher incidence of cerebral aneurysms, acromegaly-producing adenomas theorized to sometimes produce diffuse cerebrovascular ectasia and unilateral or bilateral cavernous carotid aneurysms due to growth hormone secretion.[11, 327]

Dissection of the internal carotid artery or more commonly the vertebral artery can be spontaneous, post-traumatic, or secondary to disease of the vessel wall such as fibromuscular dysplasia.[200a] A pseudoaneurysm accompanies up to a third of internal carotid dissections and 7% of vertebral artery dissections.[5, 289] Dissecting pseudoaneurysms may manifest as ischemic symptoms due to emboli or small arterial branch occlusion in addition to subarachnoid hemorrhage.[5] Dissecting pseudoaneurysms more commonly present as subarachnoid hermorrhage when occurring in the posterior circulation.[85a] Rebleed rates are particularly high with accompanying significant mortality.[200a]

Fusiform aneurysms are vascular ectasias due to advanced focal atherosclerotic disease that has degraded the vessel's media.[5, 293] The vertebrobasilar system is more commonly affected than the anterior circulation. The involved vessel is frequently elongated and tortuous, so that

in effect, the native vessel is replaced by aneurysmal dilatation with no neck. Although fusiform aneurysms may rupture, thrombosis due to blood stagnation may be the mode of presentation. Local mass effect, ischemia due to penetrating vessel occlusion, and cranial nerve palsies are other pathologic sequelae.[5, 302]

An infundibulum represents the residua of a developmental vessel that has undergone incomplete regression. It most commonly involves the junction of the internal carotid artery and posterior communicating artery, and less commonly the origin of the anterior choroidal artery from the internal carotid artery. Infundibula are usually 3 mm or less in diameter. They can be difficult to differentiate from cerebral aneurysms unless the characteristic origination of the emerging vessel from the dome of the infundibulum is identified.

Imaging Evaluation of Cerebral Aneurysms

Imaging objectives for the identification of a cerebral aneurysm are (1) visualization of subarachnoid hemorrhage, (2) confirmation of the size, location, and morphology of the cerebral aneurysm, (3) evaluation of the adjacent cerebral vasculature, including evidence of spasm, atherosclerosis, displacement, and incorporation into the aneurysm's wall, and (4) demonstration of any accompanying adjacent brain pathology.

The typical patient with a ruptured cerebral aneurysm is a woman between 40 and 60 years old who presents with "the worst headache of my life," with or without a neurologic deficit. Clinical assessment of the patient classifies into Hunt and Hess grades I through V (Table 8–1).[124a] CT scan of the head identifies subarachnoid hemorrhage, and the patient undergoes catheter angiography, which is timed to precede surgical treatment with either craniotomy or endovascular coiling. In patients in whom CT scan shows no hemorrhage, lumbar puncture should be performed. Patients with a positive lumbar puncture result then undergo catheter cerebral angiography, unless the lumbar tap was traumatic. In some situations, MRI and MRA may be performed to evaluate the subarachnoid hemorrhage and to identify a cerebral aneurysm, for example, when the suspicion for a cerebral aneurysm is low or the patient is a poor candidate for cerebral angiography or aneurysm intervention (i.e., is elderly or severely injured). MRI and MRA may also be employed as screening tests in populations known to have a higher incidence of cerebral aneurysms (see preceding discussion) or for monitoring known, untreated aneurysms. Although the permanent neurologic risk of catheter cerebral angiography is low—approximately 0.8% in the usual patient population with ruptured cerebral aneurysms—one should always keep in mind the morbidity of stroke when deciding whether a particular patient should undergo the procedure.

TABLE 8–1. Hunt and Hess Grading Scale for Subarachnoid Hemorrhage

Grade I	Asymptomatic or minimal headache
Grade II	Moderate to severe headache, nuchal rigidity, oculomotor palsy, normal level of consciousness
Grade III	Confusion, drowsiness, mild focal neurologic deficit
Grade IV	Stupor or hemiparesis
Grade V	Comatose or moribund with decerebrate posturing

Computed Tomography

The most important role for CT in the patient with a cerebral aneurysm is in the identification of acute subarachnoid hemorrhage, which is demonstrated as increased density within a cisternal space (Fig. 8–1). The location of the subarachnoid hemorrhage may help determine the location of the underlying cerebral aneurysm.[1, 5, 259, 277, 297] For example, blood in the sylvian fissure most likely has arisen from a middle cerebral aneurysm, and blood in the fourth ventricle is a common sign of rupture of a posterior inferior cerebellar artery aneurysm.[259] Some subarachnoid hemorrhage patterns are not diagnostic of aneurysm location, and none is foolproof.

The CT demonstration of subarachnoid hemorrhage progressively decreases until it disappears by approximately 3 weeks,[107, 259] depending on the initial amount of subarachnoid hemorrhage. In 5% to 10% of CT scans, subarachnoid hemorrhage is not identifiable. For this reason, any patient in whom acute subarachnoid hemorrhage is suspected but CT scanning does not demonstrate intracranial blood should undergo lumbar puncture.

A small amount of aneurysmal subarachnoid hemorrhage adjacent to the brain stem may be mistaken for perimesencephalic (prepontine and interpeduncular) hemorrhage, a finding believed to be due to the rupture of small perimesencephalic veins[139a, 248] and usually resulting in a good outcome, unlike an aneurysm rupture.

Fig. 8–1. CT demonstrating subarachnoid hemorrhage (*arrow*) from aneurysm rupture.

CT is also excellent for identifying intraventricular hemorrhage (seen in 13% to 28% of cases[259]), parenchymal hematoma (20% to 30%), and the occasional subdural hematoma, findings that often help localize the underlying aneurysm.

CT examination is secondarily important to identify cerebral aneurysms, typically 5 mm or larger in diameter. The rate of identification of cerebral aneurysms by thin-section, high-resolution, contrast-enhanced CT scanning has been reported to be at least 67% for aneurysms 3 to 5 mm in diameter and to approach 100% for larger aneurysms.[271, 274] Focal, slightly dense areas of luminal blood in typical locations where aneurysms arise,[342] focal globular or elongated areas of contrast enhancement,[210] variable calcification involving the aneurysm's walls, and clot within larger aneurysms characterize cerebral aneurysms.[108] Large aneurysms have a transverse dome diameter of 1.0 to 2.4 cm, and giant aneurysms are 2.5 cm or more in diameter. Large and giant cerebral aneurysms are typically more easily identifiable because of their conspicuous size but also often from the presence of internal clot and peripheral wall calcifications, especially in giant aneurysms (Fig. 8–2). Giant aneurysms are most commonly identified in middle-aged women, are typically located in the extradural

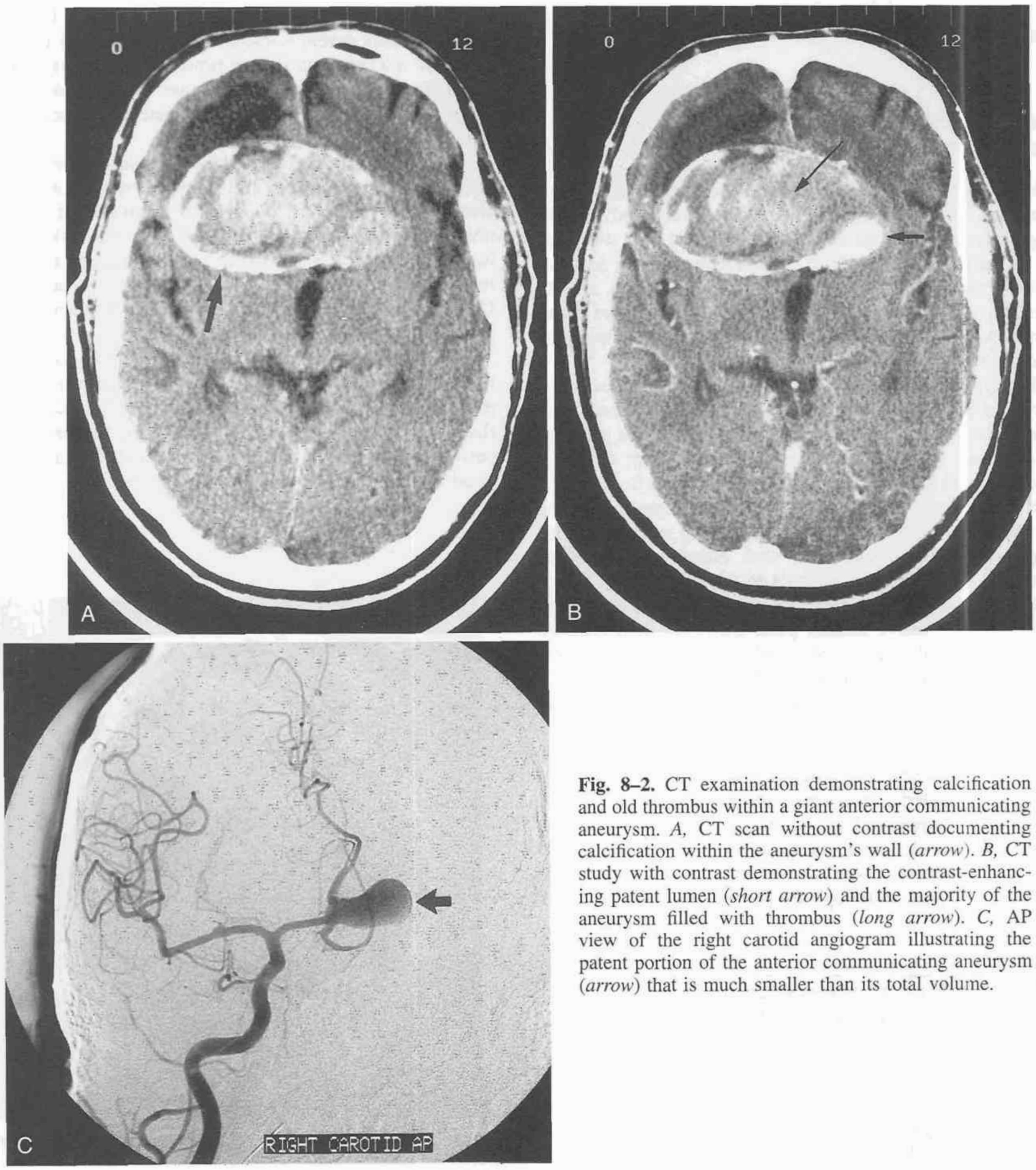

Fig. 8–2. CT examination demonstrating calcification and old thrombus within a giant anterior communicating aneurysm. *A,* CT scan without contrast documenting calcification within the aneurysm's wall (*arrow*). *B,* CT study with contrast demonstrating the contrast-enhancing patent lumen (*short arrow*) and the majority of the aneurysm filled with thrombus (*long arrow*). *C,* AP view of the right carotid angiogram illustrating the patent portion of the anterior communicating aneurysm (*arrow*) that is much smaller than its total volume.

carotid artery, the middle cerebral artery bifurcation, or the basilar summit, and usually manifest with a mass effect but can present as subarachnoid hemorrhage.[48, 69, 141] Any large aneurysm can have a mass effect on adjacent brain or cranial nerves. CT is excellent for identifying skull base erosion due to large or giant aneurysms, especially if thin sections (3 mm or less) are obtained.

Brain parenchymal hemorrhage, which may be associated with any of the cerebral aneurysms, is thought to occur from acute or chronic rupture of the cerebral aneurysm into adjacent brain substance after the blood passes through overlying pia. Both parenchymal and subarachnoid hemorrhages often obscure an underlying ruptured cerebral aneurysm.

MRI

The identification of acute subarachnoid hemorrhage by routine MRI has been notoriously poor,[19, 217] although there are reports that claim otherwise.[136] The following two reasons have been postulated for the lack of visualization of acute subarachnoid hemorrhage on MRI[104] (1) normal P_{O_2} (partial pressure of oxygen) in CSF inhibits the development of deoxyhemoglobin and (2) lysis of red blood cells in subarachnoid CSF prevents heterogenous magnetic susceptibility. However, with the employment of pulse sequences including intermediate-weighted spin-echo with TE (echo time) values of 22 to 45 msec, T1 weighting, FLAIR (fluid-attenuated inversion recovery) imaging, and gradient-echo imaging, acute subarachnoid hemorrhage can frequently be identified. Other imaging problems can obscure precise identification of subarachnoid hemorrhage on MRI, including CSF and vascular pulsation artifact and magnetic susceptibility artifact along the skull base. Significant experience is therefore required to correctly identify acute subarachnoid hemorrhage on MRI. Subarachnoid hemorrhage older than 12 to 24 hours can routinely be identified on MR images, often helping pinpoint the underlying ruptured cerebral aneurysm by a collection of blood.

Thin-section MRI examination can often identify cerebral aneurysms more than 3 mm in diameter.[197] The identification may be easier if the aneurysm is unruptured. It may be difficult, however, to differentiate normal vascular tortuous anatomy or bone such as the anterior clinoid process from a cerebral aneurysm. When large enough, cerebral aneurysms can be positively identified on MRI as flow artifacts or characteristic findings with the use of different pulse sequences. Phase-encoding artifact due to flow-producing signal mismapped in the phase-encoding direction is optimally seen on the short TE, long TR, spin-echo pulse sequence, which may be the best sequence for positive identification of aneurysms (Fig. 8–3). Other flow effects, such as a swirling appearance inside the aneurysm due to spin dephasing, rephasing, and turbulence, even-echo or gradient rephasing, diastolic pseudogating, slow flow, variable intraluminal flow rates, entry slice enhancement, and signal void due to rapidly flowing blood on all pulse sequences except those using short TE, short TR, relatively large flip angle gradient echo scans that are typically employed for time-of-flight (TOF) MRA studies, are often also helpful to identify cerebral aneurysms.[12, 39, 252a, 321]

Contrast enhancement of the aneurysm highlights its central lumen and can exaggerate the aforementioned artifacts, particularly the phase mismapping effects. For instance, these clues can often reliably diagnose cavernous carotid segment aneurysms and differentiate them from pituitary masses. A partially thrombosed aneurysm contains peripheral layers of clot of different ages, usually with the oldest clot located most peripherally.[13, 108, 302] MRI may identify intramural thrombus in dissecting aneurysms, aiding in their distinction from fusiform aneurysms.[5] The signal intensities of intraluminal clot correspond to the expected age of hemorrhage on MRI according to the magnetic field strength employed.[13, 108] Fibrosis and cellular infiltration can accompany the clot.

Completely thrombosed aneurysms or aneurysms with extremely slow flow can rarely mimic tumors, including sellar and parasellar masses. Catheter cerebral angiography should be undertaken in these problematic cases, to prevent "surprises" during craniotomy and potentially catastrophic hemorrhage during trans-sphenoidal or other operations.

The brain parenchymal changes adjacent to cerebral aneurysms may be absent unless the aneurysm is large enough to cause edema and localized mass effect. MRI is superior for evaluating the relationship of the aneurysm with adjacent brain structures because of the inherent soft tissue contrast limitations to and posterior fossa beam-hardening artifact seen with CT. If the aneurysm has ruptured, an adjacent intraparenchymal or subarachnoid clot may be identified. This finding is especially useful for determining which aneurysm has ruptured in a patient with multiple aneurysms, especially when clinical localizing signs are not helpful.[107, 297] The imaging location of the clot can subsequently guide treatment.[107] Chronic changes include gliosis and deposition of hemosiderin or ferritin; the latter two substances represent hemorrhagic breakdown products, which are best demonstrated on long TE, long TR, T2-weighted spin-echo or T2* gradient-echo MRI sequences. Superficial siderosis represents intracellular (most often macrophage) and extracellular hemosiderin or ferritin coating the leptomeninges, cranial nerves, and superficial central nervous system parenchyma.[95] The siderosis is secondary to any cause of subarachnoid hemorrhage, usually repetitive, but can also occur on the ventricular ependymal surfaces.[95] Focal or generalized neurologic deficits correspond to the location and extent of central nervous system involvement.[95]

MRI is superior to CT for the localization of cerebral aneurysms, their relationship with adjacent structures, and associated changes in neighboring brain tissue.

MRA and CT Angiography

MRA has made tremendous strides in the identification of cerebral aneurysms. Between 55% and 86% of cerebral aneurysms may be identified with routinely available MRA.[17, 128a, 240, 256, 275] Sensitivity of MRA for detection of aneurysms can be increased when MRA is combined with MRI,[256, 275] thereby overcoming the inherent difficulties of imaging slow flow, turbulent flow, or intraluminal clot with MRA. Because almost all aneurysms larger than 3 mm

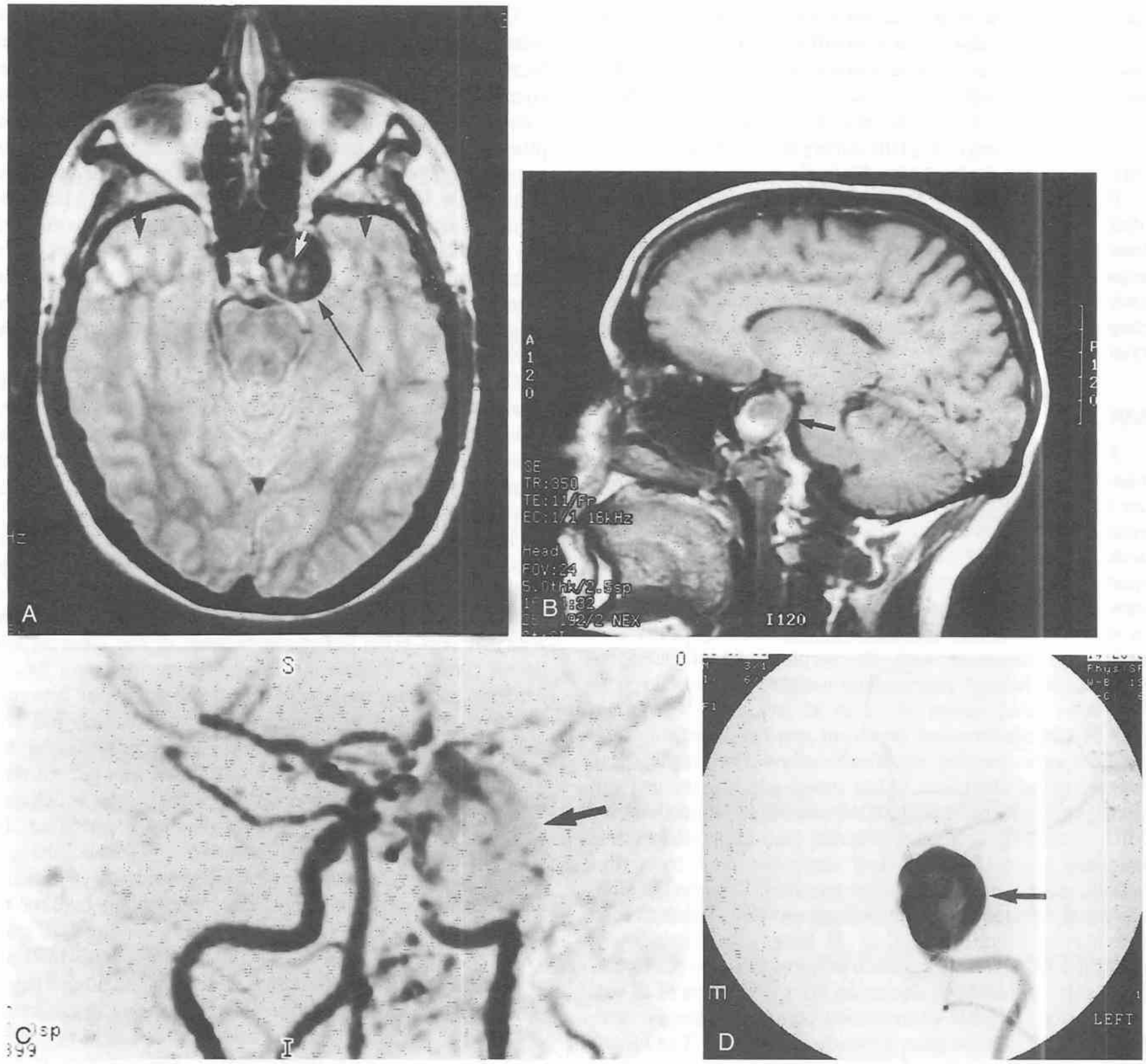

Fig. 8–3. MRI and MRA examination demonstrating flow effects associated with a giant left cavernous carotid aneurysm. *A,* Axial short TE, long TR MR image demonstrating the aneurysm (*long arrow*) with internal and external phase encoding artifact (*short arrows*) due to mismapped flow. *B,* Sagittal T1-weighted image falsely gives the appearance of thrombus within the aneurysm (*arrow*) due to slow flow. *C,* Three-dimensional time-of-flight MRA poorly outlines the aneurysm (*arrow*) because of internal slow flow. *D,* AP view of left carotid angiogram confirms giant left cavernous carotid aneurysm (*arrow*). (Case courtesy of Daryl Harp, MD.)

can be visualized,[149] MRA can function as a screening examination.[45, 240]

The most commonly employed sequence is TOF three-dimensional (3D) MRA, which typically provides submillimeter in-plane resolution. A variant of this is MOTSA (multiple overlapping thin-slab acquisition),[33, 34, 232] which attempts to combine the advantages of 3D with two-dimensional (2D) MRA. MOTSA is especially helpful when the slow flow in an aneurysm located distally within the imaging slab is not imaged on a 3D TOF study because of flow saturation. The T1 shortening effect of subacute subarachnoid blood or intraluminal or perianeurysmal clot can obscure an aneurysm or mimic flowing blood on a TOF imaging sequence.[126]

An alternative pulse sequence is phase-contrast (PC) MRA, which has excellent background, susceptibility artifact, and stagnant blood suppression and may help image in-plane flow and slow flow, two causes of flow saturation degradation of TOF MRA.[73, 127] It can be combined with cardiac gating using electrocardiogram leads or peripheral photoplethysmography to create cine PC MRA, a technique that has been used to document a greater pulsatility change in aneurysm size with ruptured than with unruptured aneurysms.[302] PC MRA has poorer spatial resolution, depends on a prescribed velocity encoding gradient with the potential for aliasing, can be altered by complex flow, and requires longer imaging and processing times than TOF MRA.[127] Although PC MRA may identify fewer aneurysms

than TOF MRA,[137] the slow flow within fusiform aneurysms is often better imaged with PC MRA. A patent double lumen in a dissecting aneurysm would also be best imaged with PC MRA.

MRA combined with MRI can often demonstrate internal flow patterns within large and giant cerebral aneurysms; faster flow is located more peripherally, and stagnant flow more centrally.[97, 102, 298] Vascular loops may be confused with cerebral aneurysms on MRA. Gadolinium-based intravenous contrast agents are not typically employed in the identification of cerebral aneurysms but can be helpful to highlight aneurysms that are small, are in atypical locations, or have slow or stagnant flow or to document the residual patent lumen in an incompletely thrombosed aneurysm.[252a] The use of contrast enhancement with MRI or MRA increases flow-dependent artifact and can obscure cerebral aneurysms because of enhancement of dural sinuses, intracranial veins, and extracranial structures,[59] unless a PC MRA technique is utilized.[127] In large or giant, partially or completely thrombosed aneurysms, the aneurysmal wall may show enhancement.

Special MRI techniques may help in the positive identification of cerebral aneurysms; they include magnetization transfer pulses,[75, 146] progressive increases in radiofrequency pulse flip angles, and multiple postprocessing algorithms.[21, 123, 169] It is important that both the 3D reconstructed MRA images and the source, 2D planar images are scrutinized, so that small aneurysms and aneurysms with slow flow are not missed. Standard maximum intensity projection (MIP) images have some artifact-derived limitations.[3] Targeted MIPs select a region of interest and help exclude confounding extraneous vessels and other structures.[127] Review of the source images also best demonstrates the neck of the aneurysm and its relationship to the parent vessel. Vessel loops and magnetic susceptibility artifact from air-filled sinuses or bone at the skull base may obscure aneurysms.

CT angiography (CTA) is a relatively new development that can well demonstrate the morphology and location of cerebral aneurysms. Thin-section spiral CT slices are acquired during rapid intravenous infusion of a contrast agent. The axial images and the reconstructed 3D images, created with MIP and other processing methods, reproduce the proximal cerebral vasculature for analysis.[207, 216, 217] Both the source images and the reconstructed images should be reviewed.[345] The exclusion of adjacent skull base bone and the contrast enhancement of nonarterial structures can be problematic.[274]

3D CTA has a reported sensitivity of 67% to 90% for identifying cerebral aneurysms.[274, 345] Aneurysms less than 5 mm in diameter may be missed.[345] CTA has some benefits over MRA for evaluation of calcified atherosclerotic disease of adjacent vessels and, in some instances, for visualization of the aneurysm neck or dome and their relationship to osseous skull base structures such as the anterior clinoid process. 3D rotational views of both CT angiograms and MR angiograms help elucidate the precise anatomic relationships of cerebral aneurysms with adjacent vessels. Software reconstruction enhancements can provide endoscopic views of the dome and neck of an aneurysm.[188a]

Catheter cerebral angiography remains the standard for evaluation of cerebral aneurysms. Catheter-based angiography has better spacial resolution than MRA or CTA, but it evaluates only the intraluminal portion of the aneurysm that contains flowing blood. The inability of catheter cerebral angiography to demonstrate aneurysmal clot can lead to underestimation of the size of the aneurysm. This deficiency of catheter cerebral angiography is significant in comparison with MRI, which can demonstrate not only clot but also its age as well as the relationship of the aneurysm with adjacent brain structures. Cerebral angiography has the benefit, however, of better demonstrating cerebral vasospasm, the aspects of the aneurysm's morphology, such as dome irregularity or lobulation, which are possible predictors of hemorrhage, and a focal tit or dimple indicating the site of recent aneurysmal hemorrhage.[340] Aneurysms evaluated soon after rupture often are smaller than when intact, because of clot compression and spasm of either the aneurysm or adjacent artery, but they subsequently enlarge if surgery is delayed.[141, 209, 273, 326]

Cerebral Aneurysm Evaluation after Surgery

Controversy has arisen regarding the use of MRI to evaluate patients who have undergone cerebral aneurysm clipping. Most cerebral aneurysm clips are currently MRI compatible[281a] but create local ferromagnetic artifact on MRI that obscures precise evaluation of the neck of the clipped aneurysm (Fig. 8–4).[103] Issues have been raised regarding clip-to-clip variability, distortion of the aneurysm clip during surgical application, manufacturer liability, warnings from the U.S. Food and Drug Administration regarding rotational and translational aneurysm clip motion in a magnetic field, and the necessity of institutional assurance that all aneurysm clips are MR compatible.[139b] Because of these issues, many facilities have denied MRI to patients with cerebral aneurysm clips, even though an MRI permits better evaluation of brain parenchyma than CT. In fact, fatal cerebral hemorrhage attributed to the MR's magnetic field has been reported in a patient in whom a stainless steel, MRI-incompatible aneurysm clip had been placed on a middle cerebral artery aneurysm.[146]

Gugliemi detachable platinum coils, which are used to treat cerebral aneurysms endovascularly, are MRI compatible.[67a, 281a] However, localized artifact caused by the platinum coils on either MRI or CT often do not permit precise evaluation of the aneurysm.[66a, 96a, 313] Less metallic artifact is present in both the endovascularly treated and surgically clipped aneurysm patient than CT.[136] Catheter angiography remains the only method to determine whether the aneurysm has been completely clipped or coiled.

Cerebral Vascular Malformations

Cerebral vascular malformations can be divided into four primary types[38, 194, 258]:

- Arteriovenous malformation (AVM)
- Cavernous angioma
- Capillary telangiectasia
- Venous angioma

These types of vascular malformations can also be mixed—incorporating elements of two or more types.[23, 74, 98, 219, 246, 247, 305] The four classic types of cerebral vascular

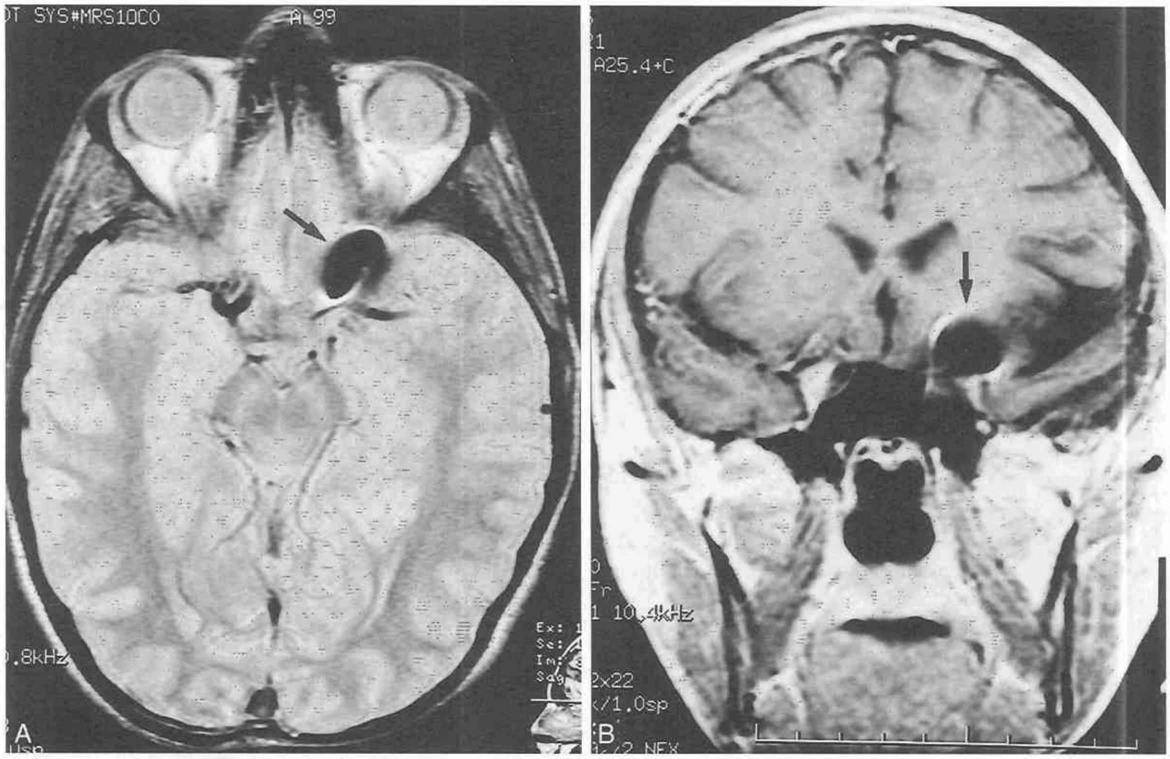

Fig. 8–4. Ferromagnetic artifact produced by cerebral aneurysm clip on MRI. Short TE, long TR (*A*) and coronal post-contrast T1-weighted (*B*) images demonstrating an ophthalmic aneurysm clip (*arrows*).

malformations are based on their congenital origin and do not include acquired arteriovenous cerebral fistulas, which are dural in location, or acquired or congenital direct arteriovenous fistulas. The term *occult cerebral vascular malformations* has been used to describe cavernous angiomas, capillary telangiectasias, and thrombosed AVMs because they could not be visualized with catheter cerebral angiography. Because all of these lesions, except some capillary telangiectasias, can be demonstrated on MRI, they are no longer truly "occult," and the term therefore has little current relevance.

The overall incidence of vascular malformations of all types in the general population is estimated to be 2%.

Arteriovenous Malformations

Incidence and Pathology

Approximately 0.1% of the general population harbor a cerebral AVM, the most common symptomatic cerebral vascular malformation.[235] AVMs are most commonly identified in women in the second to fourth decades.[332] Roughly 30% to 55% of patients present with intracranial hemorrhage,[2, 43, 58, 223, 237] a heralding event that is also most common in children with cerebral AVMs. Seventy percent of patients with intracranial hemorrhage due to AVMs present prior to age 40.[20a, 43, 94] Intracranial hemorrhage is most commonly intraparenchymal but may be intraventricular or subarachnoid. Nontraumatic subarachnoid and intraventricular hemorrhages are more commonly due to rupture of cerebral aneurysms. Spontaneous thrombosis of a draining vein and rupture of a nidal aneurysm are believed to be the most common causes of AVM hemorrhage. Exclusive central venous drainage and a periventricular or intraventricular location have been reported as other characteristics indicating a propensity for AVM hemorrhage. Peripheral venous drainage or mixed peripheral and central venous drainage, along with angiomatous change, dilated arterial collaterals that pass through brain to supply the AVM, have been correlated with a decreased incidence of AVM hemorrhage.[185, 186] AVMs 3 cm or less in diameter have been reported to bleed more frequently and to produce larger hematomas than larger AVMs.[135, 238] The rate of hemorrhage of a cerebral AVM is estimated to be 2% to 3.5% per year and to increase with advancing age; this figure is higher than the yearly rupture rate for cerebral aneurysms.[20a, 43, 58, 99, 116, 223, 294] Mortality of 10% to 30% is associated with each instance of hemorrhage, for an overall annual mortality rate of less than 1%. The risk of permanent neurologic deficit is 20% to 30% with each AVM hemorrhage,[20a, 43, 94] resulting in an annual incidence of approximately 1%. The risk of rebleeding after a first hemorrhage is approximately 6% in the first year[99] and subsequently decreases to an annual rate of 3%.[43, 235, 303, 309]

The second most common clinical presentation of cerebral AVMs is seizures, which are reported in 22% to 60% of cases.[99, 196, 235, 237, 322] Seizures manifest more commonly in patients who are younger than 30 years and with AVMs that are large or diffuse. Large AVMs are also more commonly identified with progressive neurologic deficit. The overall risk of a seizure disorder in a patient with an AVM is 18%, and the risk of a neurologic deficit is 25% to 30%.[4, 43, 53] There is an approximately 1 in 4 risk that a patient will become intellectually disabled because of a brain AVM, without or with previous hemorrhage.

Brain AVMs cause nonhemorrhagic symptoms because of (1) blood flow steal from adjacent normal territories and

(2) regional venous hypertension due to the engorged, high-flow, draining veins of the AVM. Clinical sequelae are seizures, neurologic deficit, and headache. Acute neurologic deficits, however, are most commonly associated with intracranial hemorrhage due to an AVM. Occasionally, brain AVMs can result in mass effect or hydrocephalus due either to vascular compression of CSF pathways or communicating hydrocephalus secondary to previous hemorrhage. Headache is identified in more than 50% of patients with brain AVMs.[341] Thirty percent of patients report a bruit, which is due to transmission of blood pulsations from the AVM.[43] Calvarial auscultation of a cranial bruit is unusual, however. Occasionally, an AVM may cause either hemifacial spasm or cranial nerve neuralgia or palsy if the AVM in whole or in part is located in the basilar cisterns[341] or if subarachnoid hemorrhage has occurred previously.

More than 80% of cerebral AVMs are located supratentorially, and the remainder within the posterior fossa. AVMs may be multiple in up to 2% of patients,[263] often as part of Rendu-Osler-Weber disease,[2] an autosomal dominant inherited condition in which mucosal, skin, gastrointestinal, and cerebral hereditary hemorrhagic telangiectasias, brain cavernous angiomas, and pulmonary AVMs are also found (Fig. 8–5), and in the Wyburn-Mason syndrome (also termed mesencephalo-occulofacial angiomatosis), which is signified by the presence of cutaneous nevi and retinal angiomas together with brain AVMs.[201, 336] AVMs may also be located extracranially or intracranial AVMs may be associated with additional extracranial AVMs.

Pathologically, the cerebral AVM represents a direct communication between arteries and veins without intervening capillaries,[10a, 140, 221] the communicating vascular channels being larger than capillaries yet arbitrarily smaller than fistulas. Fistulas often reside within the AVM nidus, however. The nidus represents the central compact tangle of low-resistance vessels constituting the junction of the feeding arteries and draining veins. The nidus does not contain normal brain parenchyma, although the enlarged feeding arteries and draining veins can traverse normal tissue.[49] Large, diffuse AVMs may contain normal neurons and white matter, however.[54a] Brain AVMs may be located in the subarachnoid space, intraparenchymally, or intraventricularly or may transgress several spaces, including the cranial vault. The AVM nidus volume together with characteristics such as the presence of fistulas, the chronicity of the lesion (the age of the patient), and the rate of flow through the AVM determine the size and tortuosity of feeding arteries and draining veins.

AVMs may be supplied by any of the cerebral vessels, including meningeal contributors in 15% to 50% of cases.[198] Approximately 10% of AVMs have an arterial feeder, nidus, or remote arterial aneurysm,[186, 232, 339] the flow-related aneurysms most often located on feeding vessels.[60, 148, 199, 232] Some of these flow-related aneurysms are pseudoaneurysms.[234] The aneurysms contribute to the incidence of hemorrhage from AVMs.[339] Varices can develop in draining veins and can become quite large. Areas of stenosis, thrombosis, or occlusion can occur in supplying arteries or exiting veins. The findings of vascular stenoses and aneurysm formation are attributed to local hemodynamic stresses.[234]

Histologic examination of cerebral AVMs demonstrate thickened walls of both variably enlarged feeding arteries and draining veins, the walls demonstrating smooth muscle hyperplasia, fibroblast infiltration, and increased connective tissue. Arteries are differentiated from veins on the basis

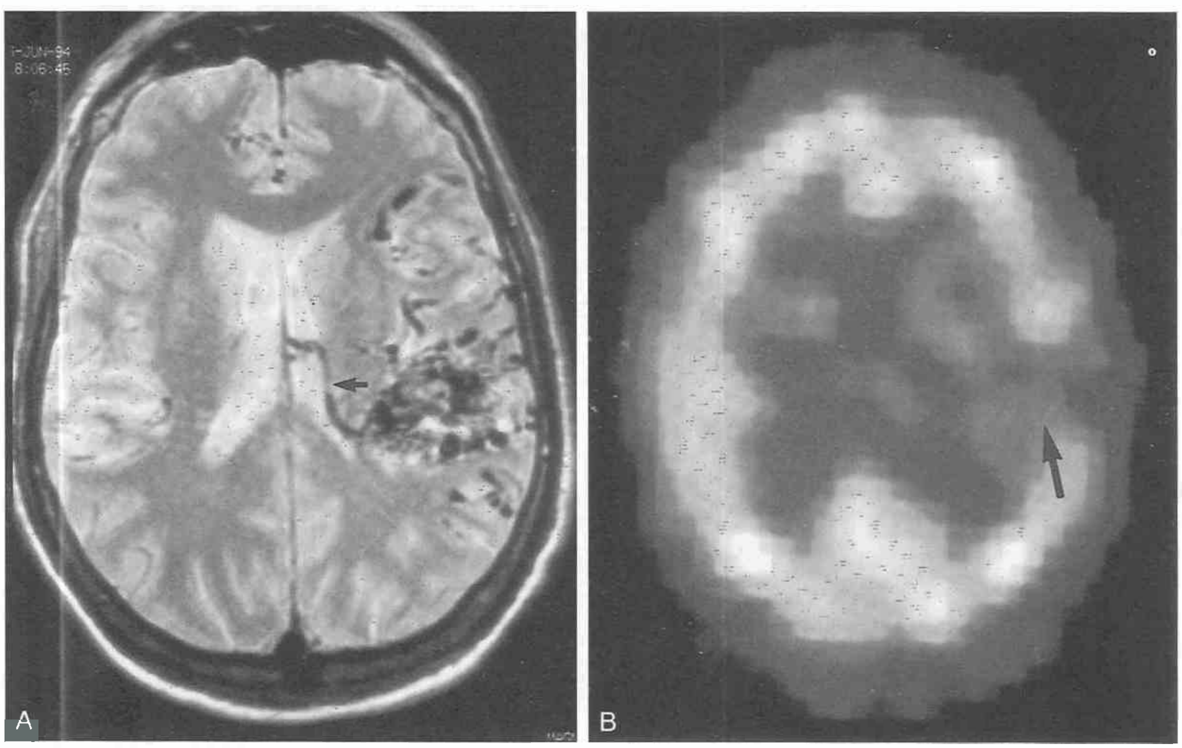

Fig. 8–5. *A,* Axial T2-weighted MR image demonstrates an AVM with venous drainage to an enlarged left thalamostriate vein (*arrow*). *B,* Axial Cerectec SPECT brain scan demonstrating diminished cerebral perfusion within the AVM (*arrow*).

TABLE 8–2. Cerebral AVM Grade

	Assigned Points
Nidus size	
Small (<3 cm)	1
Medium (3–6 cm)	2
Large (>6 cm)	3
Adjacent brain eloquence	
Noneloquent	0
Eloquent	1
Venous Drainage	
Superficial only	0
Deep	1
Total number of points = Grade I–V	

of the presence of elastic lamina and muscular layers within arteries. Adjacent brain parenchyma may exhibit atrophy, gliosis, and demyelinization[49, 220, 222] due to ischemic steal by the AVM,[52] compressive mass effect, venous hypertension, and prior hemorrhage. If previous hemorrhage has occurred, ferritin and hemosiderin staining of brain will be demonstrated. Calcification may be identified within component vessel walls as well as in adjacent brain parenchyma because of chronic venous hypertension or hemorrhage. Overlying leptomeninges may be thickened by venous engorgement or as a result of previous hemorrhage, which is also denoted by hemosiderin or ferritin staining.[50a]

The most commonly used AVM grading system was proposed by Spetzler and Martin.[291] This system assigns a numerical grade to the AVM on the basis of the size of the nidus, the location of the nidus in relationship to eloquent functional brain, and the venous drainage (superficial or deep) (Table 8–2). The intent of such a grading system is to predict therapeutic risk and outcome, and its application is fairly simple; the details of many AVMs are not completely explained by this classification system, however.

The therapy of brain AVMs is based on one of the following four options: conservative observation, surgical resection, radiosurgery, and endovascular embolization. The various treatment options may be combined. Complete surgical resection has been reported in approximately 80% of brain AVMs, with morbidity and mortality rates reaching approximately 10% regardless of AVM grade.[116] Radiosurgery is typically employed for brain AVMs that are 3 cm or less in diameter, but it can be used for an AVMs whose nidus is larger. Radiosurgery has obliterated AVMs at 3-year follow-up in more than 80% of reported series. The procedure has a complication rate of less than 3%, adverse events being most often due to radiation necrosis.[79, 174, 175, 294, 295] Embolization is often performed to reduce the flow and size of brain AVMs prior to surgical resection or radiosurgery, but in a few instances, complete cure can be achieved with embolization alone.[30]

CT and MRI

CT imaging of brain AVMs demonstrates a focal collection of isointense to slightly hyperintense vessels on unenhanced scans but may be completely unremarkable without the administration of a contrast agent. Acute hemorrhage is well documented when present.[23] Occasionally, mass effect, surrounding edema, calcification (25% to 30% of cases), or adjacent brain atrophy may be identified.[153] Intravenous contrast enhancement is essential for identifying the typical "bag of worms" appearance of a brain AVM as well as its enlarged supplying arteries and draining veins.

MRI examination is, for the most part, superior to CT for identifying and evaluating cerebral AVMs. MRI not only outlines the nidus and permits evaluation of its size but also identifies supplying arteries and draining veins. A cluster of vessels of variable signal intensities, depending upon the imaging sequences used, characterize the AVM nidus. Flow-dependent phenomena such as dephasing, rephasing, slow flow, entry slice enhancement, and phase encoding mismapping may all be demonstrated (Fig. 8–6).[39] Most often, the nidus vessels demonstrate signal void on spin-echo pulse sequences and bright signal intensity on gradient-echo sequences, findings that are also typical within enlarged feeding arteries and draining veins. Adjacent brain parenchyma can be well evaluated for edema or gliosis, which has bright signal intensity on T2-weighted spin-echo studies (Fig. 8–7).[50a, 287] MRI is crucial for localizing the AVM in relationship to eloquent cortex or deeper gray matter structures and significant white matter fiber tracts as well as demonstrating any mass effect. MRI well demonstrates the expected evolutionary appearance of acute, subacute, and chronic hemorrhage. Chronic hemorrhage with resultant ferritin- or hemosiderin-stained brain, including superficial or ependymal hemosiderosis,[50a, 95, 287] is displayed as areas of parenchymal decreased signal intensity on T2-weighted spin-echo and T2*-weighted gradient-echo sequences.[52] Gadolinium-based contrast agents are of limited if any utility in the MRI evaluation of cerebral AVMs because of inconsistent enhancement and the production of excessive flow artifact. Functional MRI utilizes cortical blood flow changes based on deoxyhemoglobin levels to create activation maps, which may be used to evaluate brain function adjacent to an AVM before therapeutic interventions are undertaken.[122, 178] In some instances, the tested neurologic function is expressed in an unexpected cerebral region secondary to neural plasticity, a consequence of the congenital nature of the AVM and the development of alternative neural circuits.[178]

MRA and CTA can help in the evaluation of cerebral AVMs, but these studies may be nonrevealing for AVMs that are small or have slow flow. CTA and MRA of the circle of Willis as well as the territory containing the nidus must be performed so that all critical features of the AVM are imaged. Evaluation of the source planar images acquired during MRA may reveal a small AVM as bright vessels differentiated from intravascular or extravascular clot, which may obscure an AVM on conventional MRI and the reconstructed 3D MRA. Both TOF and PC methods can be used in MRA examinations.[188] MOTSA and PC MRA are better suited to diagnose AVMs with slow flow.[33, 188] MRA is notorious for incompletely visualizing AVMs because of variable flow effects and related artifact. Aneurysms are frequently unidentifiable. Both MRA and CTA have difficulty discriminating the AVM's supplying arteries from draining veins. The precise angioarchitecture of cerebral AVMs is best demonstrated with traditional catheter angiography, which can identify flow-related and nidal aneurysms, the rate of AVM flow, characteristic early

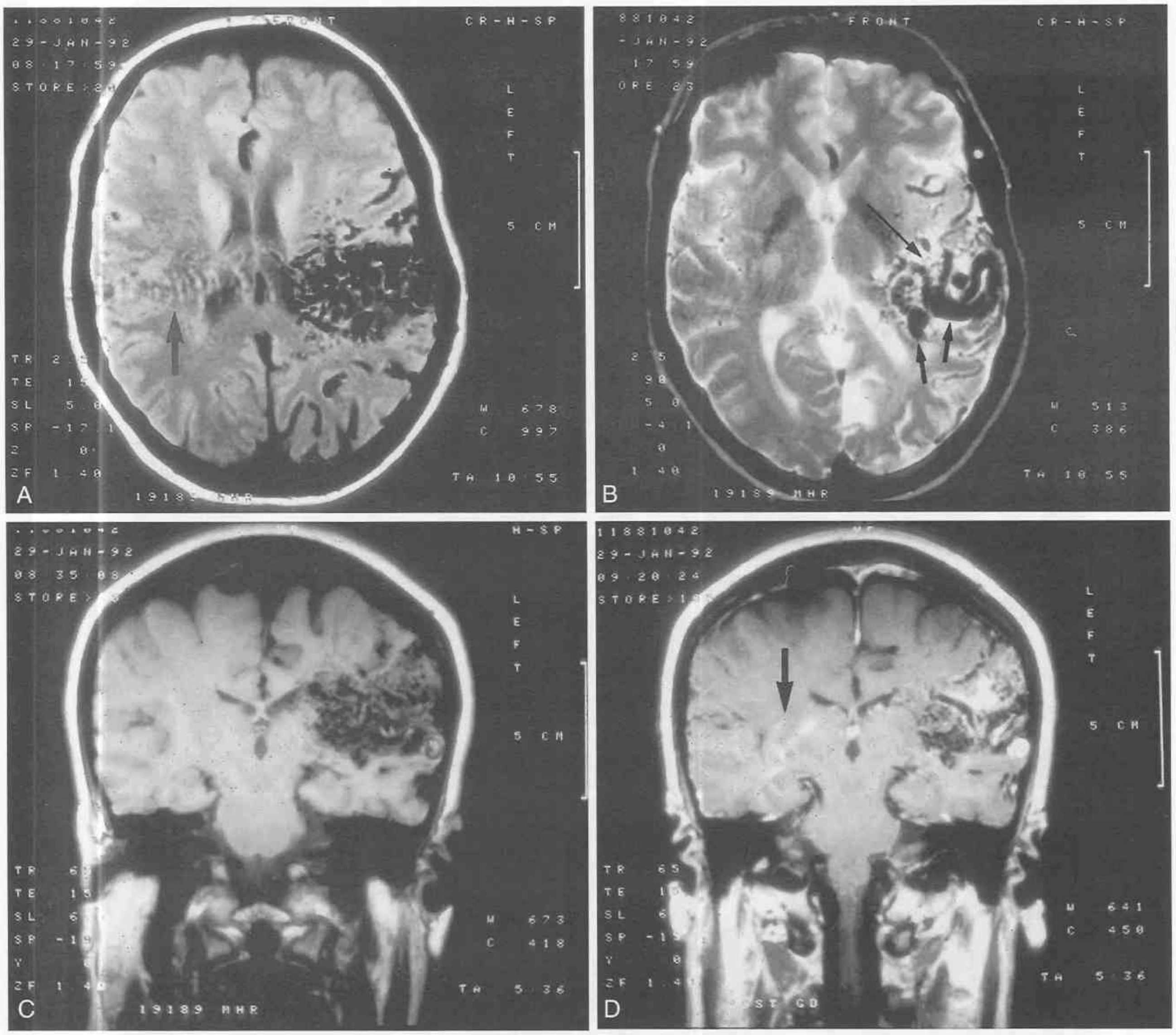

Fig. 8–6. *A,* Shor[redacted]ial MR [redacted]ereb[redacted]VM[redacted]ending f[redacted]cort[redacted] ventricle. The AVM nidus is of decreased signal intensity due to rapid flow, which produces phase encoding artifact (*arrow*). *B,* Axial T2-weighted MR image demonstrates some of the AVM's draining veins (*short arrows*) and less uniform decreased signal intensity in smaller nidus vessels, some of which have increased signal intensity (*long arrow*). *C,* Coronal T1-weighted MR image illustrates the triangular shape of the AVM. *D,* Coronal T1-weighted contrast-enhanced image illustrates variable contrast enhancement of the AVM's nidus due to differential flow rates, faster flow producing less enhancement. Note the phase encoding artifact (*arrow*).

filling veins, all of the contributing arteries and draining veins, and arterial and, particularly, venous stenoses.

The differential diagnosis of cerebral AVMs is limited. Incompletely or totally thrombosed AVMs can appear similar to other masses, including vascular neoplasms such as hemangioblastoma. When a thrombosed AVM has an accompanying intraparenchymal hematoma, differentiating it from a hemorrhagic metastasis, a high-grade glioma, or a nonmalignant cause of hemorrhage, such as hypertension or amyloid angiopathy, can be difficult.

Occasionally, moyamoya can mimic basilar cistern or basal ganglia AVMs. An unusual occurrence in North America, moyamoya is more commonly identified in Japan. It may manifest as intraparenchymal (60%), intraventricular (40%), or, rarely, subarachnoid hemorrhage,[300, 344] transient or permanent ischemic stroke, or seizures and is seen in both children and adults. The most typical age at presentation in adults is in the fourth decade. Moyamoya is characterized by progressive obliteration of large proximal anterior circulation vessels with the development of small "puff of smoke" arterial collaterals. Causes of findings similar to those of moyamoya include neurofibromatosis, sickle cell disease, prior radiation therapy, and Down syndrome. The MRI appearance of moyamoya is notable for the numerous small vessels seen within the inferior brain substance, which represent the collaterals for severely narrowed or occluded distal internal carotid or proximal anterior or middle cerebral arteries.[86, 112] Hemorrhage or infarction may also be demonstrated.

MRI examination is also well suited to evaluate cerebral

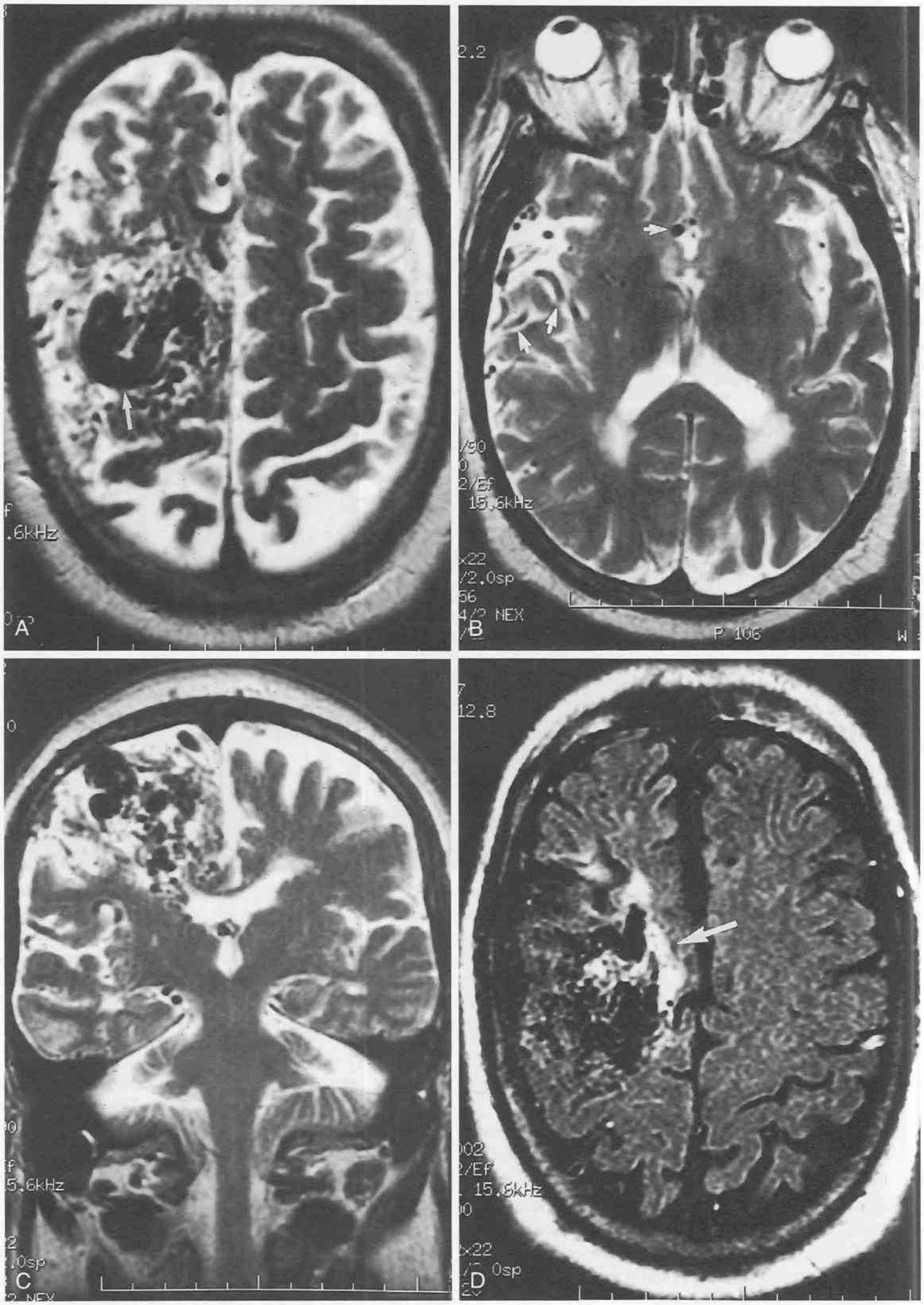

Fig. 8–7. Brain AVM with bordering reactive astrocytosis (gliosis). *A,* T2-weighted axial MR study demonstrating a high flow right frontoparietal AVM. Draining vein (*arrow*). *B,* More inferior T2-weighted axial section reveals enlarged right MCA and ACA branches (*arrows*) supplying the AVM. *C,* Coronal T2-weighted image illustrating the AVM's extent from cortex to ventricle. *D,* FLAIR image highlighting reactive astrocytosis (gliosis) bordering the AVM, seen as bright signal intensity (*arrow*).

AVMs after therapy, particularly radiosurgery or embolization,[145, 287] to demonstrate decreased size and reduced flow.[174, 182, 183] The use of a contrast agent is helpful for identifying any residual AVM nidus; however, contrast enhancement may also be secondary to postoperative gliosis, radiation necrosis, or infarction. Hemorrhage may sometimes occur as a component of radiation necrosis, which may develop as soon as 3 months after radiation therapy. Perinidal edema after radiosurgery, seen as increased signal intensity on T2-weighted spin-echo MR images, is expected and does not necessarily indicate impending radiation necrosis.

Cavernous Angioma

Cavernous angiomas account for approximately 10% to 15% of all cerebral vascular malformations,[229] and are found in approximately 0.4% of the general population.[234] They are the second most common type of symptomatic vascular malformation. Cavernous angiomas typically present as focal parenchymal intracranial hemorrhages between the third and fifth decades of life. Those found in the brain occur equally in males and females. The most common location is in the cerebral hemispheres, with only 10% identified in deep gray matter or white matter tracts. Approximately 25% are found infratentorially, in equal numbers within the brain stem and cerebellum. The pons is the most common location in the brain stem. Unusual cases may arise from the leptomeninges,[276, 285] dura, ependyma, choroid plexus, or cranial nerves, or extradurally. In 30% to 50% of cases, cavernous angiomas are multiple. Spinal cord cavernous angiomas may be isolated or may be associated with cerebral cavernous angiomas.[37] A genetic predisposition manifests when cavernous angiomas are found in 10% to 15% of family members in addition to the index case.[31, 57, 245] When a familial tendency exists, the propensity for multiple cavernous angiomas rises to 80%.[346] Multiple cavernous angiomas can be seen in Rendu-Osler-Weber disease.

The clinical presentation of cavernous angiomas typically consists of seizure activity or of acute or progressive neurologic deficit due to cerebral hemorrhage,[247] but in one study, only 61% of patients were symptomatic.[49, 55, 250, 346] Seizures, the most common symptom, occur in approximately 50% of patients. Seizures are believed to be secondary to mass effect from the cavernous angioma and adjacent brain parenchymal hemosiderin or ferritin and gliosis. Symptomatic hemorrhage manifesting as headache, seizures, or acute neurologic deficit most often occurs in the second and third decades of life and has an incidence of approximately 0.5% to 1% per year.[28, 61, 250] Subclinical hemorrhage is not uncommon, and clinically significant hemorrhage occurs in only 10% to 13% of cases.[49] Hemorrhage from a cavernous angioma uncommonly extends into the ventricular system or the subarachnoid space. It is unclear whether cavernous angiomas, once having bled, have a propensity for subsequent hemorrhage. Cavernous angiomas may initially be tiny and grossly unrecognizable, then suddenly enlarge because of new hemorrhage and thrombosis. They often change over time in size, shape, and character because of intermittent and recurrent hemorrhage and thrombosis, recannulization, vascular ingrowth, and granulation tissue.[37, 284] When an angioma is large enough, mass effect can produce cranial nerve palsies and focal neurologic deficits. Cranial radiation therapy may cause thrombosis and hemorrhage to develop in preexistent, unrealized cavernous angiomas, making them appear as new findings on serial MRI studies.

On pathologic examination, cavernous angiomas are well circumscribed and have a mulberry configuration. The lesions are not encapsulated but contain a compact or sometimes racemose network of multiple endothelium-lined, sinusoidal, nonuniform vascular channels containing thrombosed blood of varying ages.[49, 220] Compartment walls are irregularly thickened with collagen, hyalin, and scattered calcium deposition and contain no muscularis or elastic lamina layers. No interposed brain tissue is identified within the cavernous angioma. Adjacent brain may be calcified, laden with hemosiderin or ferritin, atrophic, and gliotic. Cavernous angiomas are typically parenchymal lesions sometimes marginating a pial or ependymal surface. Capillary telangiectasias may coexist with or may be mixed with the cavernous angioma.[23, 210] Venous angiomas may also coexist.[98, 247, 305]

CT and MRI

CT scans of cavernous angiomas typically demonstrate an isodense to hyperdense focal area within the brain parenchyma that may or may not contain calcification (Fig. 8–8). They may or may not enhance after intravenous administration of an iodinated contrast agent.[269] Mass effect

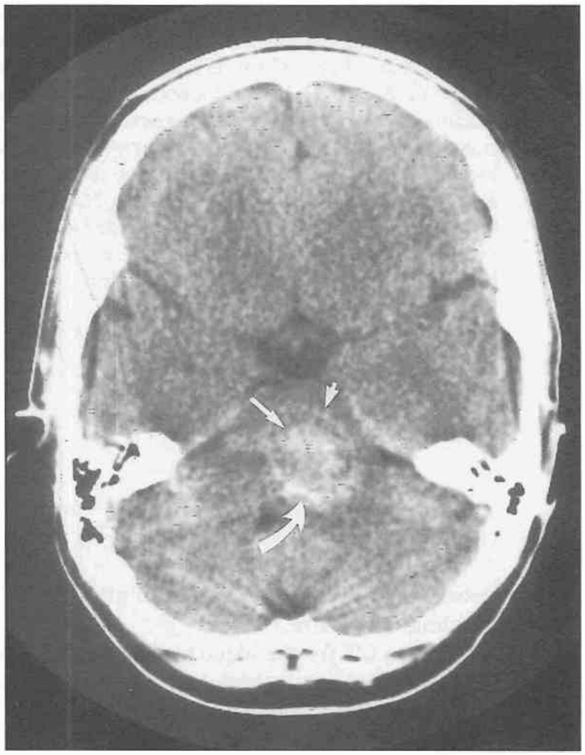

Fig. 8–8. CT examination without contrast of a pontine cavernous angioma demonstrating focal calcification (*curved arrow*) and peripheral (*short arrow*) and central (*long arrow*) hemorrhagic degradation products.

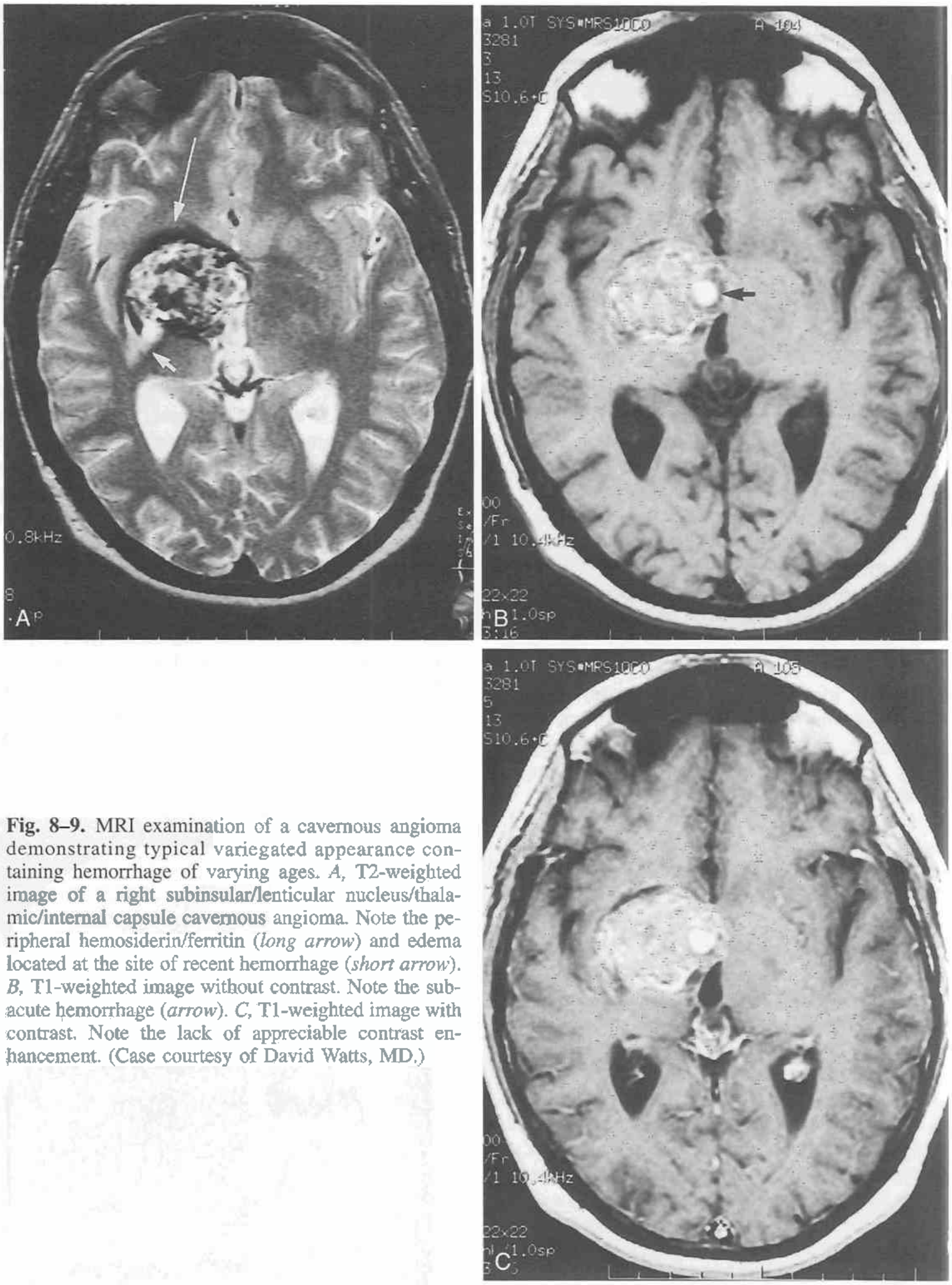

Fig. 8–9. MRI examination of a cavernous angioma demonstrating typical variegated appearance containing hemorrhage of varying ages. *A,* T2-weighted image of a right subinsular/lenticular nucleus/thalamic/internal capsule cavernous angioma. Note the peripheral hemosiderin/ferritin (*long arrow*) and edema located at the site of recent hemorrhage (*short arrow*). *B,* T1-weighted image without contrast. Note the subacute hemorrhage (*arrow*). *C,* T1-weighted image with contrast. Note the lack of appreciable contrast enhancement. (Case courtesy of David Watts, MD.)

and edema associated with the cavernous angioma may be present, depending on its size.[152]

MRI is superior to CT for the identification of cavernous angiomas.[245] It typically demonstrates a mass characterized as popcorn in appearance owing to the varying ages of internal hemorrhages.[96] The margin of the cavernous angioma is of decreased signal intensity on T2*-weighted gradient-echo and T2-weighted spin-echo images if chronic hemorrhage is present.[96] This finding is due to the magnetic susceptibility–caused phase incoherence created by the hemosiderin and ferritin residua from previous hemorrhage (Fig. 8–9).[37] The signal intensity of the rim of the cavernous angioma is also decreased because of fibrin and collagen deposition. T2*-weighted gradient-echo scans, which are best for the identification of hemosiderin and ferritin, should always be performed in the evaluation for intracranial hemorrhage. In some cases, the T2* gradient-echo study reveals multiple cavernous angiomas when the T2-weighted spin-echo study illustrates only a solitary lesion. Hemosiderin and ferritin may cause a dark flaring appear-

ance extending into the adjacent brain parenchyma because macrophages and astrocytes remove blood breakdown products, including hemosiderin and ferritin, along white matter fibers.[49] Owing to MRI's exquisite sensitivity for blood degradation products, cavernous angiomas may be incidentally discovered as asymptomatic lesions.[245] Gadolinium-based contrast agents typically produce some enhancement of the cavernous angioma.

Unusual extra-axial cavernous angiomas may have a typical or atypical MRI appearance. Extra-axial cavernous angiomas may resemble meningiomas with homogeneous, intense contrast enhancement but bright signal intensity on T2-weighted spin-echo images.[142, 150, 171]

Catheter cerebral angiography is indicated only to exclude a true arteriovenous malformation as the cause of intracranial hemorrhage when the diagnosis of cavernous angioma using MRI is uncertain. Catheter angiography displays cavernous angiomas as avascular masses, occasionally demonstrating very late capillary staining without arteriovenous shunting.[269] When present, an associated venous angioma may be demonstrated.

Therapy for cavernous angiomas consists of medical treatment for seizure control, surgical excision when the lesion is accessible and clinically indicated, and radiosurgery.

The differential diagnosis of cavernous angiomas includes previous hypertensive hemorrhage, treated toxoplasmosis, previous radiation therapy, amyloid angiopathy, and disseminated intravascular coagulopathy. The demonstration of a lesion containing hemorrhages of multiple ages, a complete peripheral hemosiderin/ferritin ring with flaring into neighboring brain, and the lack of surrounding edema help differentiate cavernous angioma from hemorrhagic metastasis; in some instances, however, particularly with melanoma, only follow-up MRI examinations documenting typical hemorrhage evolution confirm the diagnosis of cavernous angioma.

Capillary Telangiectasia

Capillary telangiectasias are small, usually clinically silent lesions that most commonly occur in the pons or cerebellum but can occur in other locations in the brain parenchyma. They are the second most common cerebral vascular malformation, after venous angiomas, and are usually multiple.[222] The histology of capillary telangiectasias is characterized by dilated, thin-walled capillaries. Unlike cavernous angiomas, normal brain parenchyma is identified within the capillary telangiectasia.[49, 220] Adjacent brain is most often normal but may contain gliosis or hemosiderin/ferritin from previous hemorrhage.[49] Capillary telangiectasias are believed to bleed rarely, however.

Other types of cerebral vascular malformations can be found together with capillary telangiectasias, especially cavernous angiomas.[247] Cerebral capillary telangiectasias can be found in Rendu-Osler-Weber disease, also known as hereditary hemorrhagic telangiectasias, along with telangiectasias in other visceral, mucosal, and cutaneous sites plus pulmonary and cerebral true AVMs. Approximately 28% of patients with Rendu-Osler-Weber disease have cerebral AVMs, with cerebral capillary telangiectasias being less common.[2, 167] Cerebellar capillary telangiectasias may also be a component of the ataxia-telangiectasia syndrome.

CT and MRI

Capillary telangiectasias are most often not identified on unenhanced MRI studies using all available pulse sequences. Rare capillary telangiectasias that have hemorrhaged demonstrate expected MR findings of blood. Most often the hemorrhage is minor and remote, best demonstrated on T2*-weighted gradient-echo studies. Enhancement with gadolinium-based contrast agents demonstrates a lacy network of vessels constituting the capillary telangiectasia (Fig. 8–10). A coexisting cavernous angioma may

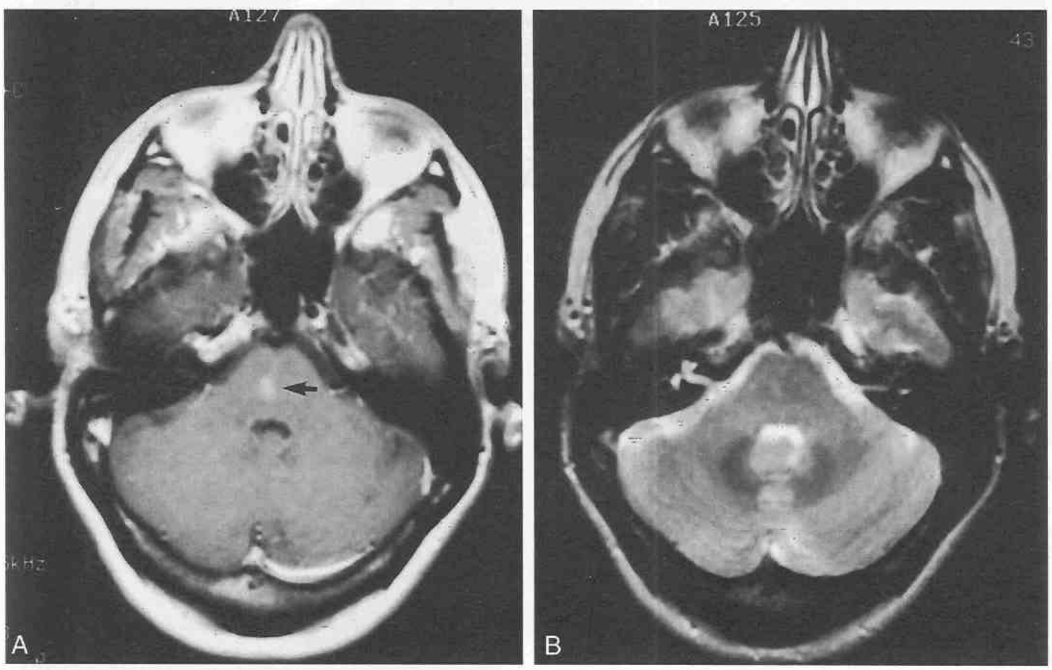

Fig. 8–10. Contrast-enhanced T1-weighted MRI examination (*A*) demonstrating a pontine capillary telangiectasia (*arrow*) that is not well visualized on the T2-weighted study (*B*).

obscure identification of the capillary telangiectasia.[23] CT usually demonstrates no abnormality.

Venous Angiomas

Venous angiomas are the most common cerebral vascular malformation, accounting for almost two thirds of the total and having an incidence in the general population of approximately 2%.[156, 222, 266, 312] This vascular malformation represents a developmental variant of normal venous drainage,[156] composed entirely of venous elements, and some writers prefer to call them "developmental venous anomalies," dropping the term "angioma."[156] The association of venous angiomas with neuronal migration anomalies and the absence of normal venous drainage from regional brain containing the venous angioma emphasizes their embryologic origin (Fig. 8–11).[156, 312] Typically solitary and located in any part of the brain parenchyma, although most often in the frontal lobe, then the cerebellum,[229, 318] venous angiomas range in size from small to large enough to drain an entire hemisphere.[312] Multiple venous angiomas are not rare, particularly when they occur bilaterally in the cerebellum,[312] and their multiplicity has been described in the blue rubber bleb nevus syndrome.

Venous angiomas are characterized by a medusa head of enlarged medullary veins draining to a collector vein, which continues to either the superficial or subependymal cerebral venous drainage system or a combination of these.[98, 312, 318, 329] Venous angiomas are occasionally found intraventricularly. An unusual case of a venous angioma draining to the foramen of Monro and resulting in obstructive hydrocephalus has been reported.[312, 318] The brain parenchyma through which the venous angioma passes is typically normal and shows no evidence of previous bleeding.

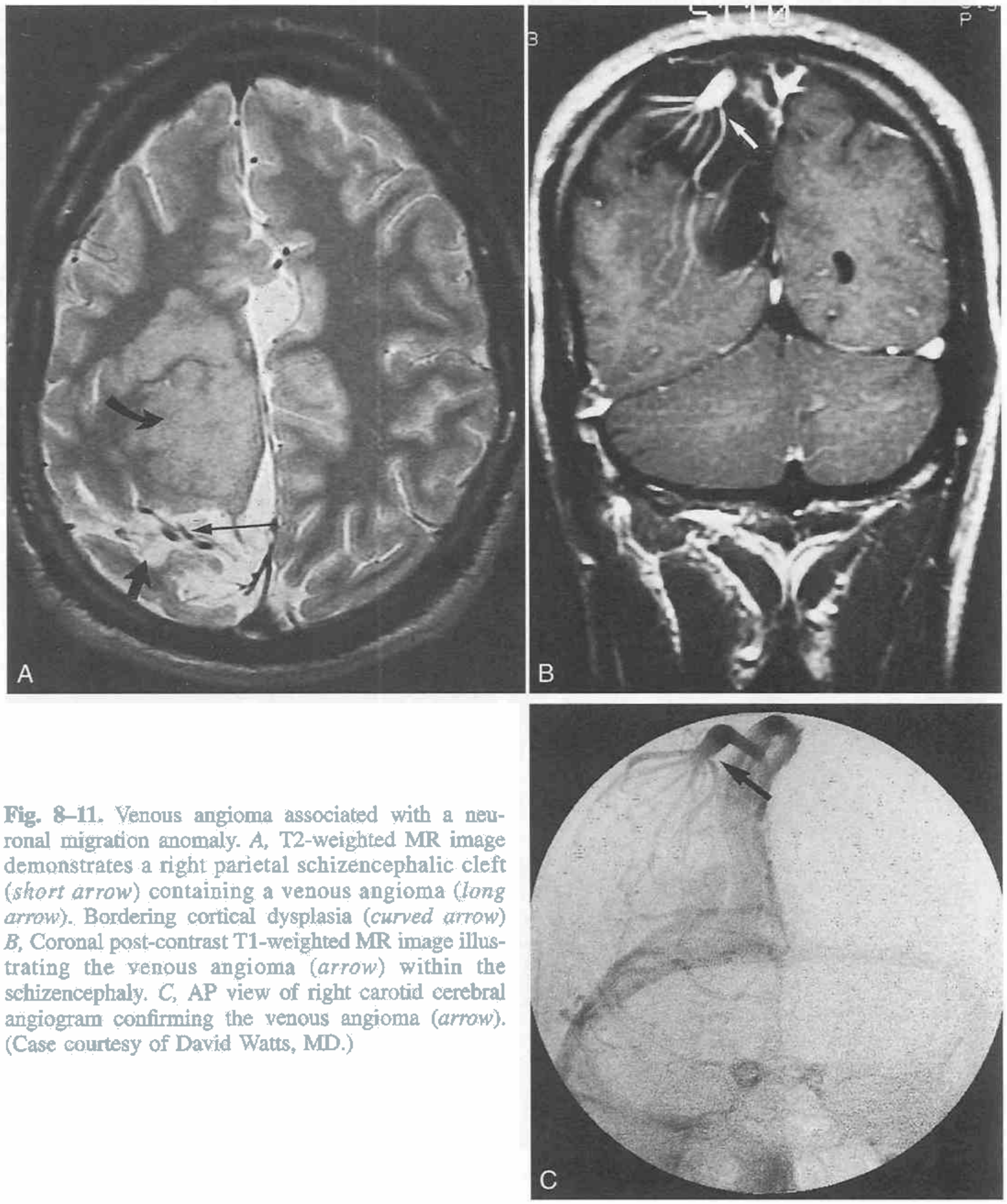

Fig. 8–11. Venous angioma associated with a neuronal migration anomaly. *A,* T2-weighted MR image demonstrates a right parietal schizencephalic cleft (*short arrow*) containing a venous angioma (*long arrow*). Bordering cortical dysplasia (*curved arrow*) *B,* Coronal post-contrast T1-weighted MR image illustrating the venous angioma (*arrow*) within the schizencephaly. *C,* AP view of right carotid cerebral angiogram confirming the venous angioma (*arrow*). (Case courtesy of David Watts, MD.)

Some writers believe that venous angiomas may rarely cause venous infarction with or without hemorrhage, or hemorrhage alone, more often subarachnoid than parenchymal[155, 160, 314, 318, 337, 339] the hemorrhage is possibly due to acquired venous outflow restriction by stenosis or thrombosis[68, 156] secondary to hemodynamic stresses. A venous varix or ectatic component is rarely seen and is explained by similar obstructive mechanisms or hemodynamic forces.[156] The higher incidence of associated contiguous cavernous angiomas in as many as one third of cases,[98, 229] however, is often used to explain any clinically significant hemorrhage being derived from the cavernous angiomas (Fig. 8–12).[23, 170, 192, 247, 312] Rarely, seizures, focal neurologic deficit, cerebellar signs, tinnitus, and headache have been

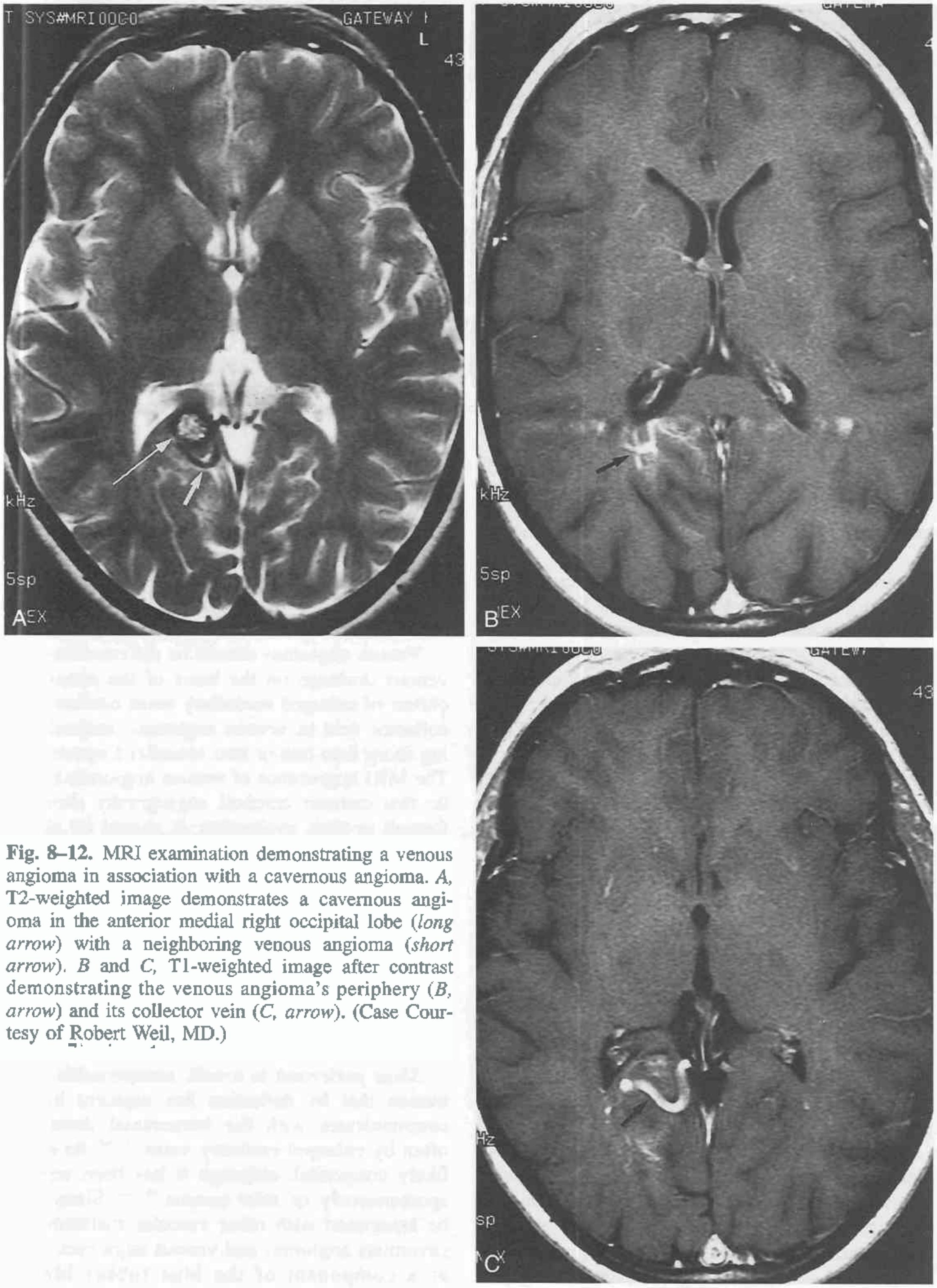

Fig. 8–12. MRI examination demonstrating a venous angioma in association with a cavernous angioma. *A,* T2-weighted image demonstrates a cavernous angioma in the anterior medial right occipital lobe (*long arrow*) with a neighboring venous angioma (*short arrow*). *B* and *C,* T1-weighted image after contrast demonstrating the venous angioma's periphery (*B, arrow*) and its collector vein (*C, arrow*). (Case Courtesy of Robert Weil, MD.)

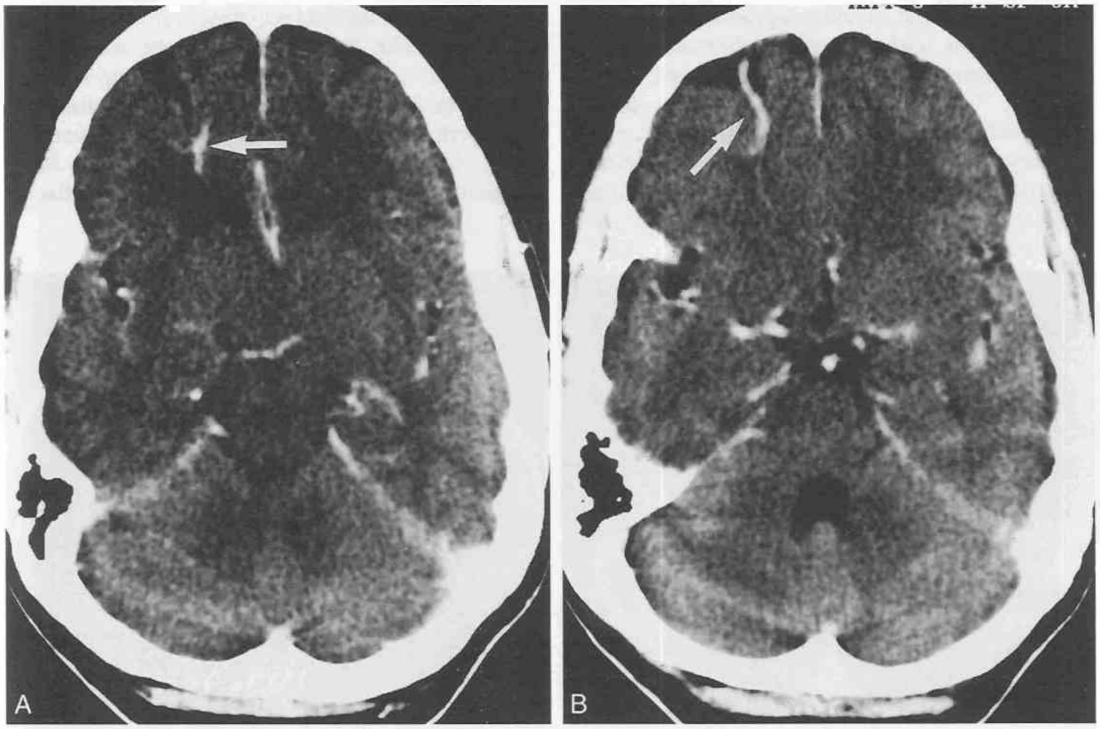

Fig. 8–13. Contrast-enhanced CT examination demonstrating a frontal lobe venous angioma (*A, arrow*). Note the collector vein (*arrow*) illustrated in *B*.

ascribed to venous angiomas,[32, 156, 229, 314, 318, 337, 339] depending on their location, but these clinical presentations are controversial.

CT scanning of a venous angioma demonstrates a contrast-enhancing vascular structure with a thistle-shaped collection of veins coursing to a single dominant draining vein (Fig. 8–13).[312, 318] Calcification of these lesions is unusual, and without calcification, they are typically not identified on unenhanced CT scans. A large venous angioma, however, may be demonstrated by CT as a slightly dense solitary vessel or collection of vessels.[318]

MRI best demonstrates venous angiomas and has revealed their true incidence in the general population. A venous angioma appears as a cluster of small vessels with signal void if flow within them is rapid or dephased; or the vessels may produce increased signal intensity due to slow flow, entry slice phenomena, even-echo rephasing, or when gradient-moment nulling techniques are utilized. Spatial misregistration artifact occurs in venous angiomas when gradient-moment nulling techniques are used on T2-weighted spin-echo images.[154] T2*-weighted gradient-echo techniques or TOF or PC MRA can demonstrate venous angiomas as a bright grouping of veins if the flow is fast enough or if MRA techniques crafted to take advantage of slow flow, such as thin-slice, 2D TOF, oriented perpendicular to venous inflow are employed (Fig. 8–14).[229]

MRA is typically not necessary to image venous angiomas, however. The rate of blood flow within the venous angioma usually depends on its overall size and determines its signal intensity on MRI[337] together with its orientation to the plane of acquisition. Contrast-enhanced T1-weighted spin-echo or gradient-echo MRI sequences best demonstrate venous angiomas and their relationship to adjacent brain parenchyma.[229, 337, 339] Contrast-enhanced CT or MRI may reveal a focal parenchymal stain around the venous angioma's caput medusa. Frequently, venous angiomas are imaged on MRI as incidental findings because most are clinically silent. They also can be overlooked on MRI scans if small and similar to normal venous drainage.

Venous angiomas should be differentiated from aberrant venous drainage on the basis of the classic findings of a cluster of enlarged medullary veins continuing into a larger collector vein in venous angiomas, anomalous veins lacking more than one or two visualized upstream small veins. The MRI appearance of venous angiomas is so characteristic that catheter cerebral angiography should not be performed in their evaluation. It should be noted that small venous angiomas can be overlooked on catheter cerebral angiography, being thought another example of variant venous drainage, although characteristically they appear later and persist longer than normal veins.[229]

Sinus Pericranii

Sinus pericranii is a soft, compressible venous malformation that by definition lies adjacent to the skull and communicates with the intracranial dural sinuses, most often by enlarged emissary veins.[35, 260] Its etiology is most likely congenital, although it has been reported to occur spontaneously or after trauma.[35, 260] Sinus pericranii may be associated with other vascular malformations, such as cavernous angiomas and venous angiomas, or may be seen as a component of the blue rubber bleb nevus syndrome.[35, 260]

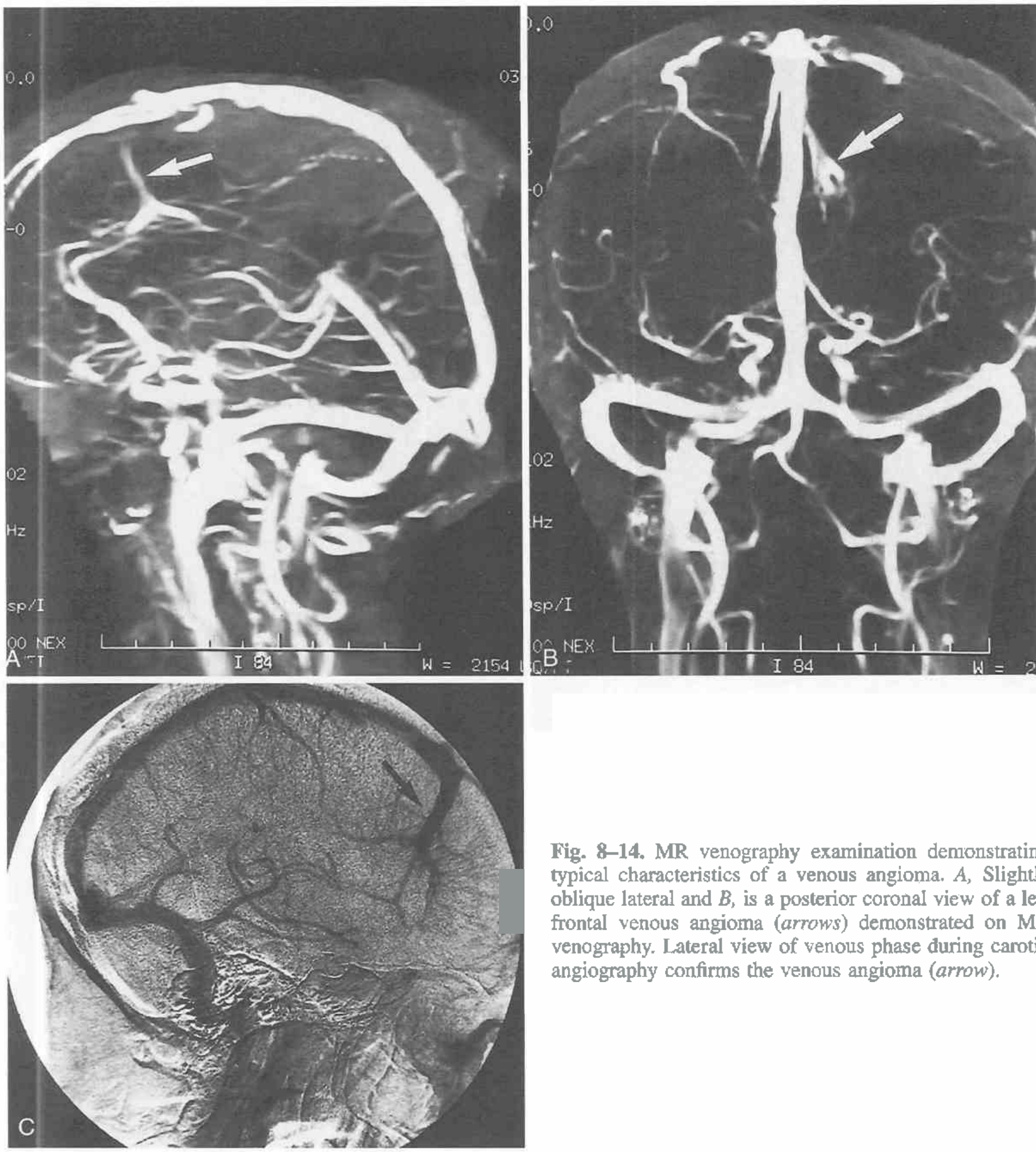

Fig. 8–14. MR venography examination demonstrating typical characteristics of a venous angioma. *A,* Slightly oblique lateral and *B,* is a posterior coronal view of a left frontal venous angioma (*arrows*) demonstrated on MR venography. Lateral view of venous phase during carotid angiography confirms the venous angioma (*arrow*).

Sinus pericranii most commonly occurs in the frontal scalp near the midline.[35, 260] An asymptomatic cosmetic scalp lump is found typically in a patient younger than 30 years. The lesion is twice as common in men as in women and is remarkable for its enlargement with Valsalva maneuvers.[260]

On imaging, sinus pericranii has been described as a vascular soft tissue scalp mass that is slightly hyperdense on unnenhanced CT, demonstrates flow on MRI, and enhances strongly with use of a contrast agent on both CT and MRI.[35, 260] CT best identifies associated osteolytic changes from the vascular mass and its associated diploic veins.[35, 260]

Arteriovenous Fistulas

Terminology

Arteriovenous fistulas (AVFs) are usually acquired[53] but may be congenital in some instances. Congenital fistulas most often represent an anomaly of cerebral vascular development and are part of a spectrum of cerebral vascular disorders. Single or multiple arterial venous connections or a true AVM nidus with one or more associated arterial venous fistulae illustrates the variety of pathologic presentations (Fig. 8–15). AVFs may be located intracranially or extracranially within the scalp or facial structures. The arterial venous shunting with increased venous pressure

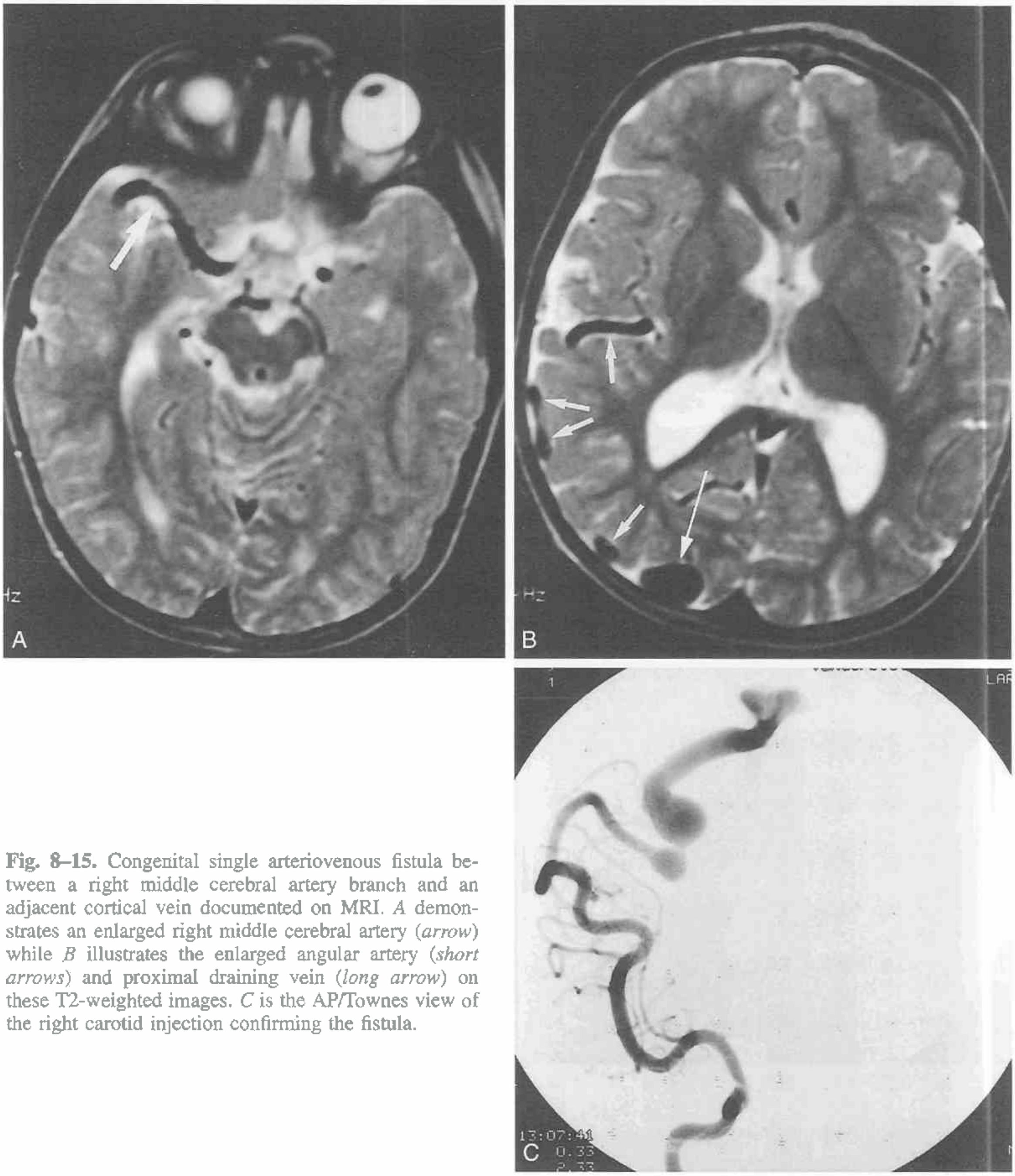

Fig. 8–15. Congenital single arteriovenous fistula between a right middle cerebral artery branch and an adjacent cortical vein documented on MRI. *A* demonstrates an enlarged right middle cerebral artery (*arrow*) while *B* illustrates the enlarged angular artery (*short arrows*) and proximal draining vein (*long arrow*) on these T2-weighted images. *C* is the AP/Townes view of the right carotid injection confirming the fistula.

and flow within any of the AVFs can result in variably sized varices that, when large enough, can produce mass effect such as brain parenchymal or cranial nerve compression or obstructive hydrocephalus.[65, 120, 121, 157, 179, 319, 320]

Most dural arterial venous fistulae are spontaneous and are believed to be acquired after thrombosis of the draining dural sinus with the subsequent development of multiple fistulous shunts to the involved sinus.[121, 133] Chronic venous hypertension without dural sinus thrombosis has also been postulated.[307] Other causes of dural AVFs are trauma, surgery, infection, systemic hypertension, and hypercoagulable states, including pregnancy, contraception pills, and dehydration.[27, 120, 121, 179] Another type of acquired AVF is best illustrated by the post-traumatic direct carotid cavernous fistula.

Dural AVFs are characterized pathologically by abnormal, direct communications between normal sinus wall arteries and veins.[211] Hemodynamic stresses lead to pathologic disorganization and thickening (less commonly, thinning) of the walls of supplying arteries, draining cortical and medullary veins, and the dural sinus wall at the site of the fistula as well as thrombosis, stenosis, and occlusion of

the involved vascular elements, most commonly the dural sinus itself and least commonly the feeding arteries.[121, 179, 211] Angiogenesis factors are probably involved in the propagation of dural AVFs.[179]

Dural AVFs represent approximately 10% to 15% of intracranial vascular malformations[45, 120, 190, 320] and are more common in women than men.[320] Most often, the dural AVF involves a single sinus, sometimes with involvement of contiguous sinuses. Multiple disparate dural AVFs are rare[45] and are typically in close proximity,[179] even the bilateral dural carotid cavernous fistulas possibly related by the interconnecting circular sinus and clival veins.

Dural AVFs may spontaneously obliterate[15, 179]; however, closure of such a lesion may be associated with intracranial hemorrhage.[157] Approximately 15% of patients present with intraparenchymal, subarachnoid, or subdural hemorrhage, listed in decreasing order of frequency.[45, 120, 157] Significant in the production of intracranial hemorrhage is reversal of flow within the involved dural sinus into variably dilated cortical veins, which results in venous rupture or venous hypertension in the involved cerebral territory.[120, 157, 238] The risk of hemorrhage from a dural AVF is 1.8% per year, with a 20% mortality for each hemorrhage.[45] Risk factors for producing hemorrhage include AVF location in the anterior cranial fossa (ethmoidal), superior petrosal sinus, or deep veins, leptomeningeal venous drainage, draining vein stenosis, and a venous varix.[45, 110, 179, 190, 320]

Dural AVFs have been categorized on the basis of their venous drainage pattern (Table 8–3).[55a] Over time, dural AVFs may change and so be assigned to a different type.[179] Symptomatology and risk of hemorrhage roughly correspond to more abnormal venous drainage.[179]

Dural AVFs may also cause seizures or neurologic deficits owing to venous hypertension-caused hemorrhage or ischemia/infarction or, less commonly, to arterial steal.[45, 121, 157, 304, 315, 320] Pulsatile tinnitus and headache, the most common complaints,[45, 320] may be mild enough and of such chronicity that the patient does not seek medical attention until other symptoms develop, such as cranial nerve palsies due to arterial steal or abnormal venous drainage and congestion.[157] Dural AVFs most often become symptomatic in patients between 40 and 60 years of age.[225]

Communicating hydrocephalus may be the result of the dural AVF producing dural sinus hypertension, dural sinus thrombosis, or prior subarachnoid hemorrhage.[157] Increased intracranial pressure without communicating hydrocephalus may be due to cerebral venous congestion, increased cerebral blood volume, elevated intrasinus pressure, and impaired cerebral venous drainage.[121, 320]

TABLE 8–3. Classification of Dural AVFs

Type I	
Antegrade drainage into sinus	
Type II	
II a	Antegrade and retrograde drainage into sinus
II b	Antegrade drainage into sinus and retrograde drainage into cortical veins
II a & b	Antegrade drainage into sinus and retrograde drainage into sinus and cortical veins
Type III	
Retrograde drainage into cortical veins	
Type IV	
Retrograde drainage into cortical veins with venous ectasia	
Type V	
Drainage into spinal veins	

Arterial supply to dural AVFs is from meningeal branches of the external carotid artery (e.g., the middle meningeal, ascending pharyngeal, and occipital arteries), the internal carotid artery (e.g., the tentorial artery of the meningohypophyseal trunk), and the vertebral artery (e.g., the posterior meningeal artery).[45, 226] Pial arteries derived from the carotid or vertebrobasilar system can also supply dural arteriovenous fistulae.

In one third to two thirds of cases, dural AVFs involve the sigmoid and transverse sinuses.[45, 49] The cavernous sinus is the second most common location, accounting for 12% to 20% of AVFs and being most common in middle-aged women.[45, 65] The symptoms of cavernous sinus dural AVFs include palsies of cranial nerves III, IV, and VI, which produce diplopia, proptosis, conjunctival engorgement, retro-orbital or cranial nerve V pain, increased intraocular pressure and secondary glaucoma; all of these are due to the abnormal venous hypertension within the cavernous sinus and retrograde venous drainage into the involved orbit.[120, 147, 306] More ominous consequences are papilledema, choroidal or retinal detachment, central retinal vein thrombosis, and diminished visual acuity.[179] Other sites of dural AVF are the tentorium and its incisura, the superior and inferior petrosal sinuses, the occipital and marginal sinuses, the superior and inferior sagittal sinuses, the straight sinus, the vein of Galen, and the anterior and middle cranial fossae.[65, 190] Adjacent cortical veins may also incorporate AVFs within their walls.[179]

Unenhanced CT scans of dural AVFs are normal unless intracranial hemorrhage, edema or infarction from venous hypertension, or thrombosis of a dural sinus or draining vein is identified. Contrast-enhanced scans may occasionally demonstrate enlarged cortical or medullary veins or stenotic or enlarged dural sinuses (Fig. 8–16). These findings are noted in up to half of patients with dural carotid cavernous fistulas, with expansion of the involved cavernous sinus and increased size of the draining superior ophthalmic vein.

MRI demonstration of cerebral AVFs depends on the type of fistula encountered. With congenital direct AVF, MRI demonstrates an enlarged supplying artery that communicates directly within an enlarged draining vein (see Fig. 8–15). In a post-traumatic direct carotid cavernous fistula, MRI shows enlargement of the cavernous sinus containing diminished signal intensity due to excessive blood flow within the sinus, and dilated superior and inferior ophthalmic veins as well as other smaller orbital veins with accompanying orbital proptosis and extraocular muscle enlargement. Dural carotid cavernous fistulas often show similar but less dramatic findings.[147] Either type of carotid cavernous fistula may produce bilateral cavernous sinus and orbital findings on MRI because of intersinus midline venous communications. The MRI findings with dural AVFs are more subtle if the more easily appreciated findings of intracranial hemorrhage, edema, or infarction are not present.

MRI and MRA are notorious for missing uncomplicated dural AVF unless the venous drainage into enlarged cortical or medullary veins is demonstrated.[65] In such instances,

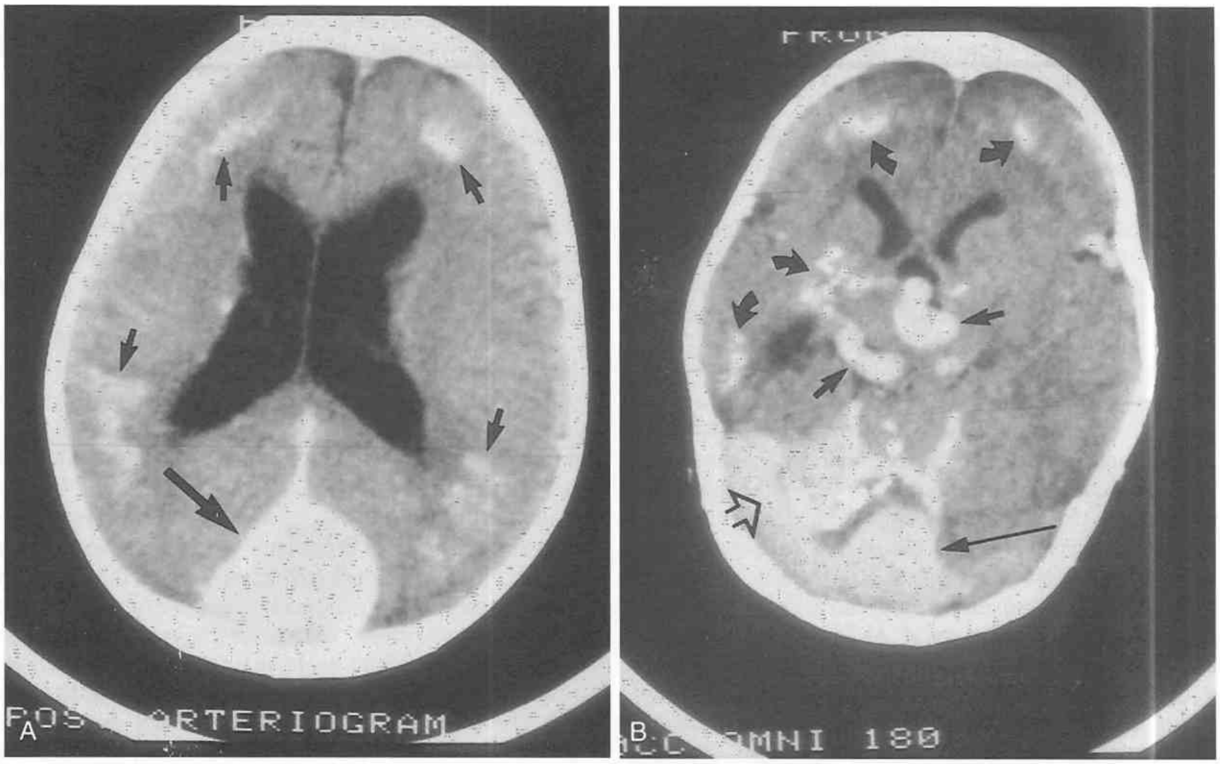

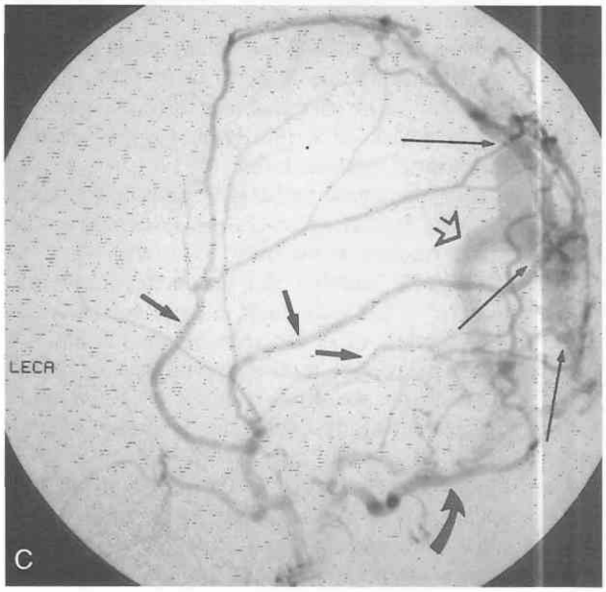

Fig. 8–16. Contrast-enhanced CT examination of a congenital superior sagittal sinus dural arterial venous fistula demonstrating (*A*) an enlarged superior sagittal sinus (*arrow*) and subcortical calcifications (*small arrows*) and (*B*) an enlarged torcula (*long arrow*), right transverse sinus and tentorial veins (*open arrow*), and deep perimesencephalic veins (*small arrows*). Note also the subcortical and lenticular nuclei calcifications (*small curved arrows*). *C*, Lateral left external carotid angiogram illustrates left middle meningeal branches (*arrows*) and left occipital branches (*curved arrow*) supplying the congenital superior sagittal sinus dural arteriovenous fistula (*long arrows*). Note the fenestration of the superior sagittal sinus (*open arrow*).

venous varices may also be identified. Although MRI can be used to document an occluded or stenosed dural sinus or vein,[268] the evaluation can be problematic because of typically encountered variable venous signal intensity, caused by flowing blood within dural sinuses on various spin-echo pulse sequences, and the changing appearance of clot depending on its age. Other difficulties with MRI are the small caliber of the feeding arteries in dural arteriovenous malformations and the focal or diffuse rather that masslike site of the abnormal dural shunts, which are often located next to flowing blood and near cortical bone making their distinction difficult. MR venography can be used to define patent, occluded, or stenotic dural sinuses.

Catheter cerebral angiography is always necessary for full evaluation of the angioarchitecture of cerebral AVFs.

Vein of Galen Malformations

The vein of Galen malformation is a congenital anomaly in which AVFs supply the embryologic precursor to the

vein of Galen. Some writers have divided vein of Galen malformations into two types, choroidal and mural. The choroidal type (Type I), which is more common, consists of one or more anterior and posterior choroidal, distal pericallosal, thalamoperforating, and sometimes superior cerebellar arteries directed to the dorsal vein of the prosencephalon, which continues into the median prosencephalic vein. With this type, the posterior choroidal vessels are typically the dominant supply. The mural type (Type II) of malformation consists of collicular and posterior choroidal arteries supplying the wall of the median prosencephalic vein, although additional arteries, such as the thalamoperforators, may also be contributors. These features distinguish the vein of Galen malformation from congenital parenchymal AVMs, acquired dural AVFs, and vein of Galen or straight sinus stenoses, which feature a dilated vein of Galen. The primitive median prosencephalic vein, the precursor of the vein of Galen, is usually abnormally dilated in vein of Galen malformations. Normal deep veins drain not into the median prosencephalic vein but through alternate routes, because the true vein of Galen is absent. The persistent median prosencephalic vein drains to a falcine sinus rather than the straight sinus, and the straight sinus is often absent. Venous outflow restriction is common in the vein of Galen malformation and contributes to further dilatation of the median prosencephalic vein, also commonly referred to as a dilated vein of Galen. Other venous anomalies are often associated with the vein of Galen malformation, including absence of or hypoplastic sigmoid or jugular sinuses, duplicated sinuses, and persistent marginal or occipital sinuses.[89] Venous-to-arterial shunting through a patent foramen ovale or persistent ductus arteriosus may coexist.[59a, 176, 191a]

The venous drainage of the enlarged median prosencephalic vein or vein of Galen typically demonstrates a dilated venous varix continuing into an accessory or inferior falcine sinus. If the venous outflow stenosis is severe enough, some Vein of Galen malformations have been documented to proceed to thrombosis which may lead to spontaneous cure but also can result in acute hydrocepha-

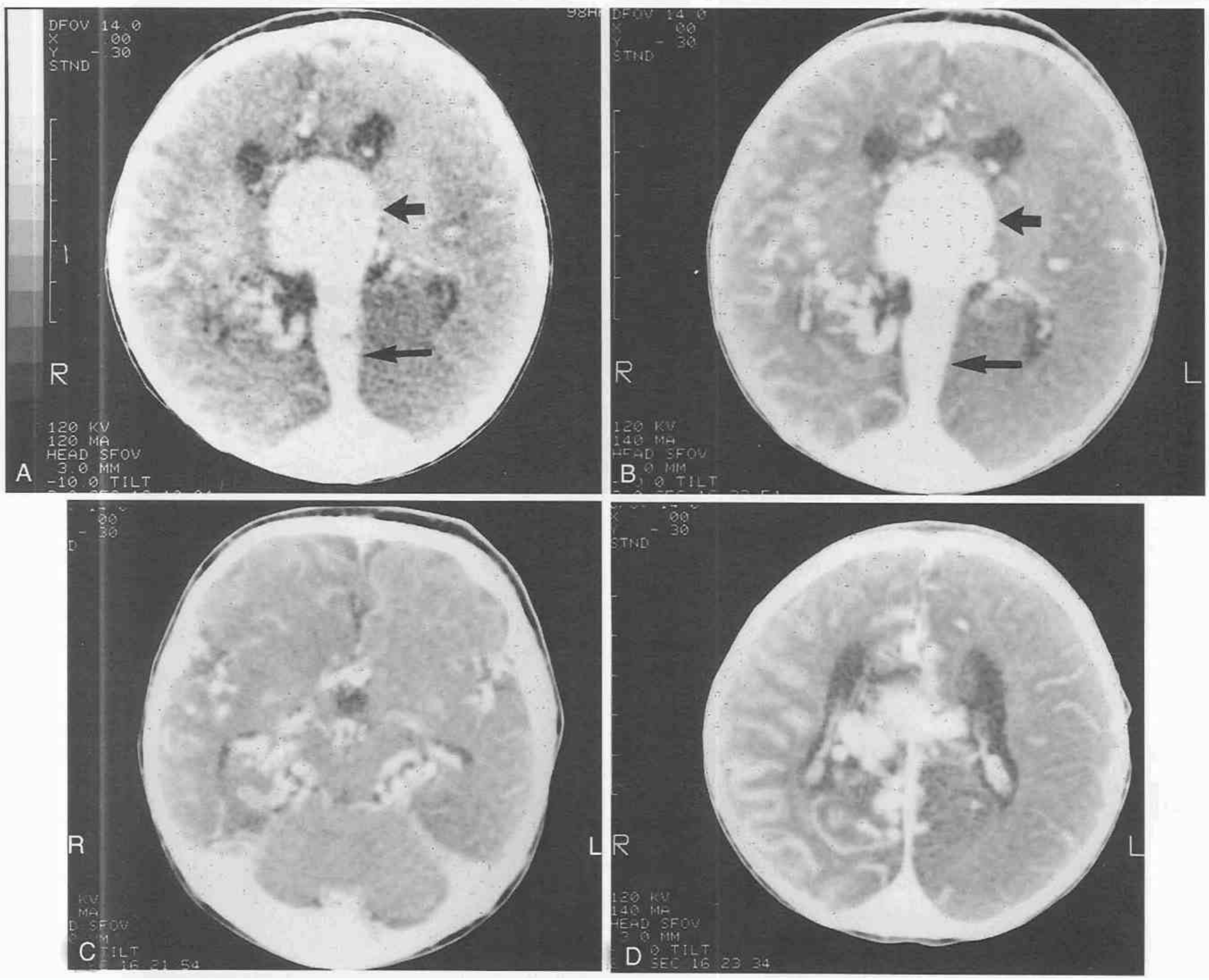

Fig. 8–17. CT examination of a vein of Galen malformation before (*A*) and after (*B*) contrast. *B, C, D,* Note the enlarged primitive median prosencephalic vein (*short arrow*) continuing to the falcine sinus (*long arrow*). Both structure are dense without contrast in an infant. *C* and *D* illustrate numerous enlarged arteries supplying this choroidal type of vein of Galen malformation.

lus, intracranial hemorrhage, or central venous hypertension.

The extent of high-flow shunting and the amount of venous outflow restriction in a vein of Galen malformation determine the age of the patient at presentation. Patients with high-flow multiple fistulas and no venous outflow stenosis (usually type I) are often identified at birth with high-output congestive heart failure, intracranial bruit, macrocephaly, and hydrocephalus. If the vein of Galen shunt is severe enough, the infants can demonstrate metabolic lactic acidosis due to multiorgan hypoperfusion and quickly progress to death. Patients who have decreased flow through the a vein of Galen malformation, typically those with high-grade venous outflow restriction (usually type II), may present later in childhood, even as adults. In such patients, cardiomegaly may be asymptomatic, and developmental delay and ocular symptoms are more common. Seizures, enlarging head circumference, intracranial hemorrhage that may be parenchymal, subarachnoid, or intraventricular, focal neurologic deficit, pulsatile tinnitus, and cranial bruit can be seen in any patient with a vein of Galen malformation, although hemorrhage is rare and is usually seen only with venous drainage thrombosis.

CT and MRI

CT scans clearly demonstrate the enlarged primitive median prosencephalic vein, which appears as a mass in the tentorial incisura of slightly increased density on unenhanced scans and markedly enhances with use of an iodinated contrast agent (Fig. 8–17). Intravenous contrast administration also may demonstrate the feeding arteries as well as the disproportionate outflow restriction, which is often characterized by diffuse or focal narrowing of the falcine sinus or, less commonly, of the straight sinus. Unenhanced CT scanning is valuable for identifying brain parenchymal calcifications located in the hemispheric venous watershed zones owing to chronic deep venous hypertension.

MRI provides a 3D display of the vein of Galen malformation, documenting the dilated primitive median prosencephalic vein, the falcine sinus, and the abnormal arterial supply (Fig. 8–18). Flow-related artifacts are related to the size of and rate of flow through the vein of Galen malformation. MRA can also display the malformation.

MRI, CT, and ultrasonography can demonstrate brain parenchymal encephalomalacia, atrophy, hemorrhage, thrombosis, and ischemic changes. Each modality's efficacy depends on the patient's age at presentation and the corresponding degree of brain myelination or, in the case of ultrasonography, the size of the skull fontanels. Each imaging technique also accurately depicts hydrocephalus. The enlargement of the ventricular system is due to venous hypertension and impedance of CSF resorption (communicating hydrocephalus) or, less commonly, to obstruction of the aqueduct of Sylvius by the enlarged vein of Galen (obstructive hydrocephalus). In utero, hydrocephalus may produce cerebral developmental dysplasia.

Transcranial ultrasound examination in the fetus or neonate is often used to provide the initial diagnosis of vein of Galen malformations. Catheter cerebral angiography is

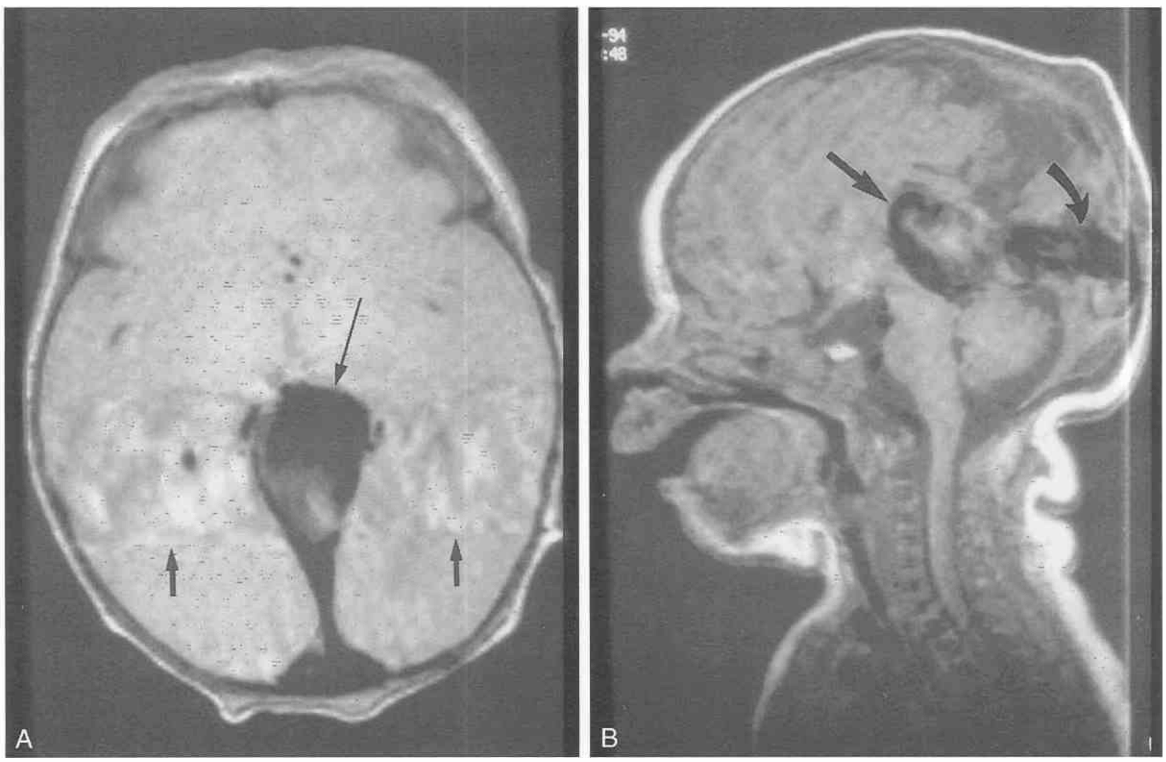

Fig. 8–18. Short TE, long TR axial MRI of a vein of Galen malformation. Note the enlarged vein of Galen (primitive median prosencephalic vein) (*long arrow*) producing flow artifact (*short arrows*). *B,* Sagittal T1-weighted MRI illustrates the vein of Galen malformation including the enlarged vein of Galen (primitive median prosencephalic vein) (*straight arrow*) and a low falcine vein (*curved arrow*). (Case courtesy of Michelle Smith, MD.)

necessary to define the angioarchitecture of the malformations and to correctly categorize it.

Vein of Galen malformations are typically treated with endovascular or combined operative transtorcular and endovascular methods.

References

1. Aalmaani WS, Richardson AE: Multiple intracranial aneurysms: Identifying the ruptured lesion. Surg Neurol 9:303–305, 1978.
2. Aesch B, Lioret E, de Toffol B, Jan M: Multiple cerebral angiomas and Rendu-Osler-Weber disease: Case report. Neurosurgery 29:599–602, 1991.
3. Anderson CM, Saloner D, Tsuruda JS, et al: Artifacts in maximum intensity projection display of MR angiograms. AJR Am J Roentgenol 154:623–629, 1990.
4. Anderson BB, Petersen J, Mortensen EL, Udesen H: Conservatively treated patients with cerebral arteriovenous malformation: Mental and physical outcome. J Neurol Neurosurg Psychiatry 51:1208–1212, 1988.
5. Andoh T, Shirakami S, Nakashima T, et al: Clinical analysis of a series of vertebral aneurysm cases. Neurosurgery 31:987–993, 1992.
6. Anson J, Cromwell RM: Craniocervical arterial dissection. Neurosurgery 29:89–96, 1991.
7. Anzalone N, Triulzi F, Scotti G: Acute subarachnoid hemorrhage: 3D time-of-flight MR angiography versus intra-arterial digital angiography. Neuroradiology 37:257–261, 1995.
8. Aoki S, Sasaki Y, Machida T, et al: Cerebral aneurysms: Detection and delineation using 3-D-CT angiography. AJNR Am J Neuroradiol 13:1115–1120, 1992.
9. Arabi B: Traumatic aneurysms of brain due to high velocity missile head wounds. Neurosurgery 22:1056–1063, 1988.
10. Armstrong DC: Presented at the 29th Annual Scientific Meeting of the American Society of Neuroradiology, Washington, DC, May 1991.
11. Atkinson JLD, Sundt TM Jr, Houser OW, et al: Angiographic frequency of anterior circulation intracranial aneurysms. J Neurosurg 70:551–555, 1989.
12. Atlas SW, Fram EK, Mark AS, Grossman RI: Vascular intracranial lesions: Applications of fast scanning. Radiology 169:455–461, 1988.
13. Atlas SW, Grossman RI, Goldberg HI, et al: Partially thrombosed giant intracranial aneurysms: Correlation of MR and pathologic findings. Radiology 162:111–114, 1987.
14. Atlas SW, Grossman RI, Gomori JM, et al: Hemorrhagic intracranial malignant neoplasms: Spin-echo MR imaging. Radiology 164:71–77, 1987.
15. Atlas SW, Listerud J, Chung W, Flamm E: Intracranial aneurysms: Depiction on MR angiograms with a multi-feature extraction postprocessing algorithm. Radiology 192:129–139, 1994.
16. Atlas SW: Intracranial vascular malformations and aneurysms: Current imaging applications. Radiol Clin North Am 26:821–837, 1988.
17. Atlas SW: MR angiography in neurological disease: State of the art. Radiology 193:1–16, 1994.
18. Atlas SW: Imaging vascular intracranial disease: Current status. Curr Opin Radiol 2:18–25, 1990.
19. Atlas SW: MR imaging is highly sensitive to acute subarachnoid hemorrhage . . . not! Radiology 186:319, 1993.
20. Atlas S (ed): Intracranial Vascular Malformations and Aneurysms: Magnetic Resonance Imaging of the Brain and Spine, 2nd ed. Philadelphia, Lippincott-Raven, 1996.

20a. Auger RG, Wiebers DO: Management of unruptured intracranial arteriovenous malformations: A decision analysis. Neurosurgery 30: 561–569, 1992.

21. Augustyn G, Scott J, Olson E, et al: Cerebral venous angiomas: MR imaging. Radiology 156:391–395, 1985.
22. Awad I, Little J: Dural arteriovenous malformations. In Barrow D (ed): Intracranial Vascular Malformations. Park Ridge, Ill, AANS, 1990, pp 219–226.
23. Awad I, Robinson J, Mohanty S, Estes M: Mixed vascular malformations of the brain: Clinical and pathogenetic considerations. Neurosurgery 33:179–188, 1993.
24. Axel L: Blood flow effects in magnetic resonance imaging. AJR Am J Roentgenol 143:1157–1166, 1984.
25. Baenziger O, Martin E, Willi V, et al: Prenatal brain atrophy due to a giant vein of Galen malformation. Neuroradiology 35:105–106, 1993.
26. Barker CS: Peripheral cerebral aneurysm associated with a glioma. Neuroradiology 34:30–32, 1992.
27. Barnwell SL, Halbach VV, Dowd CF, et al: Multiple dural arteriovenous fistulas of the cranium and spine. AJNR Am J Neuroradiol 12: 441–445, 1991.
28. Barrow D, Krisht A: Cavernous malformations and hemorrhage. In Awad I, Barrow D (eds): Cavernous Malformations. Park Ridge, Ill, AANS, 1993, pp 65–80.
29. Belliveau J, Kennedy D, McKinstry R, et al: Functional mapping of the human visual cortex by magnetic resonance imaging. Science 254:716–719, 1991.
30. Berenstein A, Lasjaunias P: Surgical Neuroangiography. New York, Springer-Verlag, 1992.
31. Bicknell J, Carlow T, Kornfield M, et al: Familial cavernous angiomas. Arch Neurol 35:746–749, 1978.
32. Blackmore CC, Mamourian AC: Compression from venous angioma: MR findings. AJNR Am J Neuroradiol 17:458–460, 1996.
33. Blatter DD, Parker DL, Ahn SS, et al: Cerebral MR angiography with multiple overlapping thin slab acquisition. Part II: Early clinical experience. Radiology 183:379–389, 1992.
34. Blatter DD, Parker DL, Robison RO: Cerebral MR angiography with multiple overlapping thin slab acquisition. Part I: Quantitative analysis of vessel visibility. Radiology 179:805–811, 1991.
35. Bollar A, Allut AG, Prieto A, et al: Sinus pericranii: radiological and etiopathological considerations. J Neurosurg 77:469–472, 1992.
36. Bosmans H, Marchal G, Van Hecke P, Vanhoenacker P: MRA review. Clin Imaging 16:152–167, 1992.
37. Bourgouin PM, Tampieri D, Johnston W, et al: Multiple occult vascular malformations of the brain and spinal cord: MRI diagnosis. Neuroradiology 34:110–111, 1992.
38. Burger P, Scheithauer B, Bernd, Vogel FS: Surgical Pathology of the Nervous System and Its Covering, 3rd ed. New York, Churchill Livingstone, 1991.
39. Bradley WG, Waluch V: Blood flow: Magnetic resonance imaging. Radiology 154:443–450, 1985.
40. Bradley WG, Widoff BE, Yan K, et al: Comparison of routine and gadodiamide-enhanced 3D time-of-flight MR angiography in the brain. RSNA Book of Abstracts 122, 1992.

40a. Brott T, Mandybur TI: Case-control study of clinical outcomes after aneurysmal subarachnoid hemorrhage. Neurosurgery 19:891–895, 1986.

41. Brown BM, Soldevilla F: MR angiography and surgery for unruptured familial intracranial aneurysms in persons with a family history of cerebral aneurysms. AJR Am J Roentgenol 173:133–138, 1999.
42. Brown E, Prager J, Lee H-Y, Ramsey RG: CNS complications of cocaine abuse: Prevalence, pathophysiology, and neuroradiology. AJR Am J Roentgenol 159:137–147, 1992.
43. Brown RD Jr, Wiebers DO, Forbes G, et al: The natural history of unruptured intracranial arteriovenous malformations. J Neurosurg 68:352–357, 1988.
44. Brown RD, Wiebers DO, Forbes GS: Unruptured intracranial aneurysms and arteriovenous malformations: Frequency of intracranial hemorrhage and relationship of lesions. J Neurosurg 73:859–863, 1990.
45. Brown RD Jr, Wiebers DO, Nichols DA: Intracranial dural arteriovenous fistulae: Angiographic predictors of intracranial hemorrhage and clinical outcome in nonsurgical patients. J Neurosurg 81:531–538, 1994.
46. Brunereau L, Cottier JP, Sonier CB, Medioni B, et al: Prospective evaluation of time-of-flight MR angiography in the follow-up of intracranial saccular aneurysms treated with Guglielmi detachable coils. J Comput Assist Tomogr 23:216–223, 1999.
47. Brust JCM, Richtor RW: Stroke associated with cocaine abuse? NY State J Med 77:1473–1475, 1989.
48. Bull J: Massive aneurysms at the base of the brain. Brain 92: 535–570, 1969.
49. Burger PC, Schuthauer BW: Vascular tumors and tumor-like lesions. In Tumors of the Central Nervous System. Washington, DC, Armed Forces Institute of Pathology, 1994, pp 287–299.
50. Burger PC, Schuthaver BW, Vogel FS: Surgical Pathology of the Nervous System and its Coverings, 3rd ed. New York, Churchill Livingstone, 1991, pp 439, 443.

50a. Burger PC, Schuthauer BW, Vogel FS: Surgical Pathology of the Nervous System and Its Coverings, 3rd ed. New York, Churchill Livingstone, 1991.
51. Camarata PJ, Latchaw RE Jr, Rüffenacht DA, Heros RC: Intracranial aneurysms. Invest Radiol 28:373–382, 1993.
52. Chappell PM, Steinberg GK, Marks MP: Clinically documented hemorrhage in cerebral arteriovenous malformations: MR characteristics. Radiology 183:719–724, 1992.
53. Chaudhary MY, Sachdev VP, Cho SH, et al: Dural arteriovenous malformations of the major venous sinuses: An acquired lesion. AJNR Am J Neuroradiol 3:13–19, 1982.
54. Chen JC, Tsuruda JS, Halbach VV: Suspected dural arteriovenous fistula: Results with screening MR angiography in seven patients. Radiology 183:265–271, 1992.
54a. Chin LS, Raffel C, Gonzales-Gomez, et al: Diffuse arteriovernous malformations: A clinical, radiological, and pathological description. Neurosurgery 31:863–868, 1992.
55. Churchyard A, Khangure M, Grainger K: Cerebral cavernous angioma: A potentially benign condition? Successful treatment in 16 cases, J Neurol Neurosurg Psychiatry 55:1040–1045, 1992.
55a. Cognard C, Gobin YP, Picrot L, et al: Cerebral dural arteriovenous fistulas: Clinical and angiographic correlation with a revised classification of venous drainage. Radiology 194:671–680, 1995.
56. Cohen HCM, Tucker WS, Humphreys RP, et al: Angiographically cryptic histologically verified cerebrovascular malformations. Neurosurgery 10:704–714, 1982.
57. Cosgrove R, Bertrand G, Fontaine S, et al: Cavernous angiomas of the spinal cord. J Neurosurg 68:31–36, 1988.
58. Crawford PM, West CR, Chadwick DW, Shaw MDM: Arteriovenous malformations of the brain: Natural history in unoperated patients. J Neurol Neurosurg Psychiatry 49:1–10, 1986.
59. Creasy J, Price RR, Presbrey T, et al: Gadolinium-enhanced MR angiography. Radiology 175:280–283, 1990.
60. Cunha e Sa MJ, Stein BM, Solomon RA, McCormick PC: The treatment of associated intracranial aneurysms and arteriovenous malformation. J Neurosurg 77:853–859, 1992.
61. Curling O, Kelly D: The natural history of intracranial cavernous and venous malformations. Persp Neurol Surg 1:19–39, 1990.
62. Curling OP, Kelly DL, Elster AD, Craven TE: An analysis of the natural history of cavernous hemangiomas. J Neurosurg 75: 702–708, 1991.
63. Davis JM, Zimmerman RA: Injury of the cortical and vertebral arteries. Neuroradiology 25:55–69, 1983.
64. Davis WL, Warnock SH, Harnsberger HR, et al: Intracranial MRA: single volume vs. multiple thin slab 3D time-of-flight acquisition. J Comput Assist Tomogr 17:15–21, 1993.
65. De Marco JK, Dillon WP, Halback VV, Tsuruda JS: Dural arteriovenous fistulas: Evaluation with MR imaging. Radiology 175:193–199, 1990.
66. DeMarco JK, Dillon WP, Halback VV, Tsuruda JS: Dural arteriovenous fistulas: Evaluation with MR imaging. Radiology 175:193–199, 1990.
67. deTilly, LN, Willinsky R, Ter Brugge K, et al: Cerebral arteriovenous malformation causing epistaxis. AJNR Am J Neuroradiol 13: 333–334, 1992.
68. Dillon WP: Venous angiomas. Presented at the 29th Annual Meeting of the American Society of Neuroradiology, Washington, DC, June 9–14, 1991.
69. Drake CG: Giant intracranial aneurysms: Experience with surgical treatment in 174 patients. Clin Neurol 26:12–95, 1979.
70. Dross P, Raji MR, Dastur KJ: Cerebral varix associated with a venous angioma. ANJR Am J Neuroradiol 8:373–374, 1987.
71. Dumoulin CL, Hart HR: Magnetic resonance angiography. Radiology 161:717–720, 1986.
72. Dumoulin CL, Souza SP, Hart HR: Rapid scan magnetic resonance angiography. Magn Reson Imaging 5:238–245, 1987.
73. Dumoulin CL, Souza SP, Walker MF, et al: Three-dimensional phase contrast angiography. Magn Reson Med 9:139–149, 1989.
74. Ebeling JD, Tranmer BI, Davis KA, et al: Thrombosed arteriovenous malformations: A type of occult vascular malformation. Neurosurgery 23:605–610, 1988.
75. Edelman RR, Ahn SS, Chien D, et al: Improved time-of-flight MR angiography of the brain with magnetization transfer contrast. Radiology 184:395–399, 1992.
76. Eng J, Ceckler TL, Balaban RS: Quantitative 1H magnetization transfer imaging in vivo. Magn Reson Med 17:304–314, 1991.
77. Enomoto H, Goto H: Spinal epidural cavernous angioma. Neuroradiology 33:462–465, 1991.
78. Evans AJ, Blinder RA, Herfkens RJ, et al: Effects of turbulence on signal intensity in gradient echo images. Invest Radiol 23:512–518, 1988.
79. Fabrikant J, Levy R, Steinberg G, et al: Charged particle radiosurgery for intracranial vascular malformations. Neurosurg Clin North Am 3:99–139, 1992.
80. Farres MT, Ferraz-Leite H, Schindler E, Muhlbauer J: Spontaneous subarachnoid hemorrhage with negative angiography: CT findings. J Comput Assist Tomogr 16:534–537, 1992.
81. Firmin DN, Nayler GL, Underwood SR, et al: MR angiography, flow velocity, and acceleration measurements combined using a field even-echo rephasing (FEER) sequence. Chicago, 127, 1986.
82. Fogelholm R: Subarachnoid hemorrhage in middle Finland: Incidence, early prognosis and indication for neurosurgical treatment. Stroke 12:296–301, 1981.
83. Fox PT, Raichle ME, Mintun MA, Dence C: Nonoxidative glucose consumption during focal physiologic neural activity. Science 241: 462–464, 1988.
84. Fox PT, Raichle ME: Focal physiological uncoupling of cerebral blood flow and oxidative metabolism during somatosensory stimulation in human subjects. Proc Natl Acad Sci U S A 83:1140–1144, 1986.
85. Fram EK, Dimick R, Hedlund LW, et al: Parameters determining the signal of flowing fluid in gradient refocused MR imaging: Flow velocity, TR and flip angle (abstract). Abstracts of the Fifth Annual Meeting, SMRM, 84–85, 1986.
85a. Friedman AH, Drake CG: Subarachnoid hemorrhage from intracranial dissecting aneurysm. J Neurosurg 60:325–334, 1984.
86. Fujisawa I, Asato R, Nishimura K, et al: Moyamoya disease: MR imaging. Radiology 164:103–105, 1987.
87. Fujiwara T, Mino S, Nagao S, Ohmoto T: Metastatic choriocarcinoma with neoplastic aneurysms cured by aneurysm resection and chemotherapy: Case report. J Neurosurg 76:148–151, 1992.
88. Fukusumi A, Okudera T, Huang YP, et al: Neuroradiological analysis of medullary venous malformations in the cerebellar hemisphere. Neuroradiology 33:359, 1991.
89. Garcia-Monaco R, Lasjaunias P, Berenstein A: Therapeutic management of vein of Galen aneurysmal malformations in interventional neuroradiology. In Vinvela F, Halback VV, Dion JE (eds): Endovascular Therapy of the Central Nervous System. New York, Raven Press, 1992.
90. Garcia-Monaco R, Rodesch G, Alvarez H, et al: Pseudoaneurysms within ruptured intracranial arteriovenous malformations: Diagnosis and early endovascular management. AJNR Am J Neuroradiol 14: 315–321, 1993.
91. Gerosa MA, Cappellotto P, Licata C, et al: Cerebral arteriovenous malformations in children (56 cases). Childs Brain 8:356–371, 1981.
92. Giannakapoulos G, Nair S, Snider C, Amenta DS: Implications for the pathogenesis of aneurysm formation: Metastasis choriocarcinoma with spontaneous splenic rupture. Surg Neurol 38:236–240, 1992.
93. Goldwyn D, Cardenas C, Murtagh F, et al: MRI of cervical extradural cavernous hemangioma. Neuroradiology 34:68–69, 1992.
94. Golfinos JG, Wascher TM, Zabramski JM, Spetzler RF: The management of unruptured intracranial vascular malformations. BNI Q 8:2–11, 1992.
95. Gomori JM, Grossman RI, Bilaniuk LT, et al: High-field MR imaging of superficial siderosis of the central nervous system. J Comput Assist Tomogr 9:972–975, 1985.
96. Gomori JM, Grossman RI, Goldberg HI, et al: Occult cerebral vascular malformations: High-field MR imaging. Radiology 158: 707–713, 1986.
97. Gonzales CF, Cho YI, Ortega HV, Moret J: Intracranial aneurysms: Flow analysis of their origin and progression. AJNR Am J Neuroradiol 13:181–1888, 1992.
98. Goulao A, Alvarez H, Monaco RG, et al: Venous anomalies and abnormalities of the posterior fossa. Neuroradiology 31:476–482, 1990.
99. Graf CJ, Perret GE, Torner JC: Bleeding from cerebral arteriovenous malformations as part of their natural history. J Neurosurg 58: 331–337, 1990.
100. Graves VB, Duff TA: Intracranial arteriovenous malformations: Current imaging and treatment. Invest Radiol 25:952–960, 1990.

101. Graves YB, Duff TA: Intracranial arteriovenous malformations: Current imaging and treatment. Invest Radiol 25:952, 1990.
102. Graves VB, Strother CM, Partington CR, Rappi A: Flow dynamics of lateral carotid artery aneurysms and their effect on coils and balloons: An experimental study in dogs. AJNR Am J Neuroradiol 13:189–196, 1992.
103. Grieve JP, Stacey R, Moore E, et al: Artefact of MRA following aneurysm clipping: An in vitro study and prospective comparison with conventional angiography. Neuroradiology 41:680–686, 1999.
104. Grossman RI, Kemp SS, Yu IC, et al: The importance of oxygenation in the appearance of acute subarachnoid hemorrhage on high-field magnetic resonance imaging. Acta Radiol (Suppl) 369:56–58, 1986.
105. Guo W-Y, Lindquist M, Lindquist C, et al: Sterotaxic angiography in gamma knife radiosurgery of intracranial arteriovenous malformations. AJNR Am J Neuroradiol 13:1107–1114, 1992.
106. Haase A, Frahm J, Matthaei D, et al: Rapid NMR imaging using low flip-angle pulses. J Magnet Reson 67:258–266, 1986.
107. Hackney DB, Lesnick JE, Zimmerman RA, et al: MR identification of bleeding site in subarachnoid hemorrhage with multiple intracranial aneurysms. J Comput Assist Tomogr 10:878–880, 1986.
108. Hahn FJ, Chg E, McComb R, Leibrock L: Peripheral signal void ring in giant vertebral aneurysm: MR and pathology findings. J Comp Asst Tomogr 10:1036–1038, 1986.
109. Halback VV, Barkovich AJ: Anomalies of cerebral vasculature. In Barkovich AJ (ed): Pediatric Neuroimaging, 2nd ed. New York, Raven Press, 1995.
110. Halback VV, Higashida RT, Heishima GB, et al: Transvenous embolization of dural fistulas involving the transverse and sigmoid sinuses. AJNR Am J Neuroradiol 10:385–392, 1989.
111. Hargraves RW, Spetzler RF: Takayasu's arteritis: Case report. BNI Q 7:20–23, 1991.
112. Hasuo K, Tamura S, Kudo S, et al: Moyamoya disease: The use of digital subtraction angiography in its diagnosis. Radiology 157: 107–111, 1985.
113. Healton EB: Fibromuscular dysplasia. In Barnett HJM (ed): Stroke, vol 2. New York, Churchill Livingstone, 1986, pp 831–843.
114. Heiserman JE, Drayer BP, Fram EK, Keller PJ: MR angiography of cervical fibromuscular dysplasia. AJNR Am J Neuroradiol 13: 1454–1457, 1992.
115. Herneshiemi J, Tapaninaho A, Vapalahti M, et al: Saccular aneurysms of the distal anterior cerebral artery and its branches. Neurosurgery 31:994–999, 1992.
116. Heros RC, Korosue K: Arteriovenous malformations of the brain. Curr Opin Neurol Neurosurg 3:63–67, 1990.
117. Hoffmann KR, Hosten N, Liebig T, et al: Giant aneurysm of the vertebral artery in neurofibromatosis type 1: Report of a case and review of the literature. Neuroradiology 40: 245–248, 1998.
118. Holtas S, Olsson M, Romner B, et al: Comparison of MR imaging and CT in patients with intracranial aneurysm clips. AJNR Am J Neuroradiol 9:891–897, 1988.
119. Hormann E, Becker T, Romberg-Hahnloser R, et al: Cranial MRI and CT in patients with left atrial myzoma. Neuroradiol 34:57–61, 1992.
120. Houser O, Baker HJ, Rhoton AJ, et al: Intracranial dural arteriovenous malformations. Radiology 163:55–64, 1972.
121. Houser O, Campbell J, Campbell R, Sundt T: Arteriovenous malformation affecting the transverse dural venous sinus: An acquired lesion. Mayo Clin Proc 54:651–661, 1979.
122. Howard RS, Maldjian J, Alsop D, et al: Functional MRI in the assessment of cerebral gliomas and AVMs prior to surgical or endovascular therapy (abstract). SMR Annual Meeting Book of Abstracts, San Francisco, 1994.
123. Hu X, Alperin N, Levin DN, et al: Visualization of MR angiographic data with segmentation and volume-rendering techniques. J Magn Reson Imaging 1:539–546, 1991.
124. Huk WJ: Vascular malformations. In Huk WJ, Gademann G, Friedmann G (eds): MRI of the Central Nervous System. Berlin, Springer-Verlag, 1990, pp 325–346.
124a. Hunt WE, Hess RM: Surgical risks as related to time of intervention in the repair of intracranial aneurysms. J Neurosurg 28:14–20, 1968.
125. Hurst RW, Kagetser NJ, Berenstein A: Angiographic findings in two cases of aneurysmal malformation of vein of Galen prior to spontaneous thrombosis: Therapeutic implications. AJNR Am J Neuroradiol 13:1446–1450, 1992.
126. Huston J III, Ehman RL: Comparison of time-of-flight and phase-contrast MR neuroangiographic techniques. Radio-Graphics 13:5–19, 1993.
127. Huston J III, Rufenacht DA, Ehman RL, Wiebers DO: Intracranial aneurysms and vascular malformations: Comparison of time-of-flight and phase-contrast MR angiography. Radiology 181:721–730, 1991.
128. Huston J III, Nichols DA, Leutrer PH, et al: Blinded prospective evaluation of sensitivity of MR angiography to known intracranial aneurysms: Importance of aneurysm size. AJNR Am J Neuroradiol 15:1607–1614, 1994.
129. Iizuka Y, Lasjaunias P, Garcia-Monaco R, et al: Multiple cerebral arteriovenous malformations in children (15 patients). Neuroradiology 33:538, 1991.
130. Ikawa F, Sumida M, Uozumi T, et al: Comparison of three-dimensional phase-contrast magnetic resonance angiography with three-dimensional time-of-flight magnetic resonance angiography in cerebral aneurysms. Surg Neurol 42:287–292, 1994.
131. Iwata K, Misu N, Terada K, et al: Screening for unruptured asymptomatic intracranial aneurysms in patients undergoing coronary angiography. J Neurosurg 75:52–55, 1991.
132. Jacobs IG, Roszler MH, Kelly JK, et al: Cocaine abuse: Neurovascular complications. Radiology 170:223–227, 1989.
133. Jacobs J: Angiography in intracranial hemorrhage. Neuroimaging Clin North Am 2:89–106, 1992.
134. Jafar JJ, Davis AJ, Berenstein A, et al: The effect of embolization with *N*-butyl cyanoacrylate prior to surgical resection of cerebral arteriovenous malformations. J Neurosurg 78:60–69, 1993.
135. Jane JA, Kassell NF, Torner JC, Winn HR: The natural history of aneurysms and arteriovenous malformations. J Neurosurg 62: 321–323, 1985.
136. Jenkins A, Hadley DM, Teasdale GM, et al: Magnetic resonance imaging of acute subarachnoid hemorrhage. J Neurosurg 68:731–736, 1988.
137. Jinkins JR, Dadsetan MR, Sener RN, et al: Value of acute-phase angiography in the detection of vascular injuries caused by gunshot wounds to the head: Analysis of 12 cases. AJNR Am J Neuroradiol 169:365–368,1992.
138. Johnston IH, Whittle IR, Besser M, et al: Vein of Galen malformation: Diagnosis and management. Neurosurgery 20:747–758, 1987.
139. Juvela S, Porras M, Heiskanen O: Natural history of unruptured intracranial aneurysms: A long-term follow-up study. J Neurosurg 79:174–182, 1993.
140. Kaplan HA, et al: Vascular malformations of the brain: An anatomical study. J Neurosurg 27:630, 1961.
141. Kassel NJ, Torner JC: Size of intracranial aneurysms. Neurosurgery 12:291–297, 1983.
142. Katayama Y, Tsubokawa T, Miyasaki S, et al: Magnetic resonance imaging of cavernous sinus cavernous hemangioma. Neuroradiology 33:118–122, 1991.
143. Kaufman SL, White RI Jr, Harrington DP, et al: Protean manifestations of mycotic aneurysms. Am J Roentgenol 131:1019–1025, 1978.
144. Kim J, Kucharczyk W, Henkelman R: Cavernous hemangiomas: Dipolar susceptibility artifacts at MR imaging. Radiology 187:735–741, 1993.
145. Kjellberg RN, Hanamura T, Davis KR, et al: Bragg-peak proton beam therapy for arteriovenous malformations of the brain. N Engl J Med 309:269–274, 1983.
146. Klucznik R, Carrier D, Pyka R, Haid R: Placement of a ferromagnetic intracerebral aneurysm clip in a magnetic field with a fatal outcome. Radiology 187:612–614, 1993.
147. Komiyama M, Fu Y, Yagura H, et al: MR imaging of dural AV fistulas at the cavernous sinus. J Comp Asst Tomogr 14:397–401, 1990.
148. Kondiziolka D, Nixon BJ, Lasjaunas P, et al: Cerebral arteriovenous malformations with associated arterial aneurysms: Hemodynamic and therapeutic considerations. Can J Neurol Sci 15:130–134, 1988.
149. Korogi, Y, Takahashi M, Mabuchi N, et al: Intracranial aneurysms: Diagnostic accuracy of the three dimensional, Fourter transform, time-of-flight MR angiography. Radiology 193: 181–186, 1994.
150. Krief O, Sichez JP, Chedid G, et al: Extraaxial cavernous hemangioma with hemorrhage. AJNR Am J Neuroradiol 12:988–990, 1990.
151. Krysl J, de Tilly LN, Armstrong D: Pseudoaneurysm of the internal carotid artery: Comparison of deep neck space infection. AJNR Am J Neuroradiol 14:696–698, 1993.

152. Kucharczyk W, Lemme-Pleghos L, Uske A, et al: Intracranial vascular malformations: MR and CT imaging. Radiology 156:383–389, 1985.
153. Kumar AJ, Vinuela F, Fox AJ, Rosenbaum AE: Unruptured intracranial arteriovenous malformations do cause mass effect. AJNR Am J Neuroradiol 6:29–32, 1985.
154. Larson TC III, Kelly WM, Ehman RL, Wehrili FW: Spatial misregistration of vascular flow during MR imaging of the CNS: Cause and clinical significance. AJNR Am J Neuroradiol 11:1041–1048, 1990.
155. Lasjaunias P, Berenstein A: Functional Vascular Anatomy of Brain, Spinal Cord, and Spine. New York, Springer-Verlag, 1990.
156. Lasjaunias P, Burrows P, Planet C: Developmental venous anomalies (DVA): The so-called venous angioma. Neurosurg Rev 9:233–244, 1986.
157. Lasjaunias P, Chue M, TerBrugge K: Neurological manifestations of intracranial dural arteriovenous malformations. J Neurosurg 64: 724–730, 1986.
158. Lasjaunias P, Garcia-Monaco R, Rodesch G, TerBrugge K: Deep venous drainage in great cerebral vein (vein of Galen) absence and malformations. Neuroradiology 33:234–238, 1991.
159. Lasjaunias P, TerBrugge K, Ibor LL, et al: The role of dural anomalies in vein of Galen aneurysms: Report of six cases and review of the literature. AJNR Am J Neuroradiol 8:185–192, 1987.
160. Latchaw RE, Truwit CL, Heros RC: Venous angioma, cavernous angioma, and hemorrhage. AJNR Am J Neuroradiol 15:1255–1257, 1994.
161. Lawrence-Friedl D, Bauer KM: Bilateral cortical blindness: An unusual presentation of bacterial endocarditis. Ann Emerg Med 21: 1502–1504, 1992.
162. Lazar EB, Russell EJ, Cohen BA, et al: Contrast-enhanced MR of cerebral arteritis: Intravascular enhancement related to flow stasis within areas of focal arterial ectasia. AJNR Am J Neuroradiol 13: 271–276, 1992.
163. Lazinski D, Willinsky RA, TerBrugge K, Montanera W: Dissecting aneurysms of the posterior cerebral artery: Angioarchitecture and a review of the literature. Neuroradiology 42:128–133, 2000.
164. Leavine SR, Brust JCM, Futrell N, et al: A comparative study of the cerebrovascular complication of cocaine: Alkaloidal versus hydrochloride—a review. Neuroradiology 41:1173–1177, 1991.
165. Lee KS, Liu SS, Spetzler RF, Rekate HL: Intracranial mycotic aneurysms in an infant: Report of a case. Neurosurgery 26:129–133, 1990.
166. Lewin JS, Laub G: Intracranial MR angiography: Direct comparison of three time-of-flight techniques. AJNR Am J Neuroradiol 12: 1133–1139, 1991.
167. Licata C, Pasqualin A, Freschini A, et al: Management of associated primary cerebral neoplasms and vascular malformations. 1: Intracranial aneurysms. Acta Neurochir (Wien) 82:28–38, 1986.
168. Lichtenfeld PJ, Rubin DB, Feldman RS: Subarachnoid hemorrhage precipitated by cocaine snorting. Arch Neurol 41:223–224, 1984.
169. Lin W, Haacke EM, Smith AS, Clampitt ME: Gadolinium-tracking: Preliminary results in the intracranial circulation. Magn Reson Imaging 2:277–284, 1992.
170. Lindquist C, Guo W-Y, Karlsson B, Steiner L: Radiosurgery for venous angiomas. J Neurosurg 78:531–536, 1993.
171. Linsky ME, Sekhar LN: Cavernous sinus hemangioma: A series, a review, and an hypothesis. Neurosurgery 3:101–108, 1992.
172. Luessenhop A, Gennarelli T: Anatomical grading of supratentorial arteriovenous malformations for determining operability. Neurosurgery 1:30–35, 1977.
173. Luessenhop A, Rosa L: Cerebral arteriovenous malformations. J Neurosurgery 60:14–22, 1984.
174. Lunsford L, Flickinger J, Coffey R: Stereotactic gamma knife radiosurgery: Initial North American experience in 207 patients. Arch Neurol 7:169–175, 1990.
175. Lunsford L, Kondziolka D, Bissonette D, et al: Stereotactic radiosurgery of brain vascular malformations. Neurosurg Clin North Am 3: 79–98, 1992.
176. Lylyk P, March AD, Kohan GA, Vinuela F: Alternative therapeutic approaches in intravascular embolization of vein of Galen vascular malformations. In Vinvela F, Halback VV, Dion JE (eds): Endovascular Therapy of the Central Nervous System. New York, Raven Press, 1992.
177. Mabuchi S, Kamiyama H, Abe H: Distal aneurysms of the superior cerebellar artery and posterior inferior cerebellar artery feeding an associated arteriovenous malformation: Case report. Neurosurgery 30:284–287, 1992.
178. Maldjian J, Howard R, Alsop DA, et al: Functional MRI in AVMs prior to surgical or endovascular therapy (abstract). In Book of Abstracts, Annual Meeting of the Radiological Society of North America, 1994.
179. Malek AM, Halbach VV, Dowd CF, Higashida RT: Diagnosis and treatment of dural arteriovenous fistulas. Neuroimaging Clin North Am 8:445–468, 1998.
180. Malik GM, Morgan JK, Boulos RS, Ausman JI: Venous angiomas: An underestimated cause of intracranial hemorrhage. Surg Neurol 30:350–358, 1988.
181. Mann CI, Dietrick RB, Schrader MT, et al: Posttraumatic carotid artery dissection in children: Evaluation with MR imaging. AJR Am J Roentgenol 160:134–136, 1993.
182. Marks MP, DeLapaz RL, Fabrikant JI, et al: Intracranial vascular malformations: Imaging of charged-particle radiosurgery. Part I: Results of therapy. Radiology 168:447–455, 1988.
183. Marks MP, DeLapaz RL, Fabrikant JI, et al: Intracranial vascular malformations: Imaging of charged-particle radiosurgery. Part II: Complications. Radiology 168:457–462, 1988.
184. Marks MP, Lane B, Steinberg G, Chang P: Vascular characteristics of intracerebral arteriovenous malformations in patients with clinical steal. AJNR Am J Neuroradiol 12:489–496, 1991.
185. Marks MP, Lane B, Steinberg GK, Chang PJ: Hemorrhage in intracerebral arteriovenous malformations: Angiographic determinants. Radiology 176:807–813, 1990.
186. Marks MP, Lane B, Steinberg GK, Snipes GJ: Intracranial aneurysms in cerebral arteriovenous malformations: Evaluation and endovascular treatment. Radiology 183:355–360, 1992.
187. Marks MP, Lane B, Steinberg GK, Chang PJ: Hemorrhage in intracerebral aneurysms and arteriovenous malformations: Frequency of intracranial hemorrhage and relationship of lesions. J Neurosurg 73: 859–863, 1990.
188. Marks MP, Pelc MJ, Ross MR, Enzmann DR: Determination of cerebral blood flow with a phase-contrast cine MR imaging technique: Evaluation of normal subjects and patients with arteriovenous malformation. Radiology 182:467–476, 1992.
189. Martelli A, Scotti G, Harwood-Nash DC, et al: Aneurysm of the vein of Galen in children: CT and angiographic correlations. Neuroradiology 20:123–133, 1980.
190. Martin N, King W, Wilson C, et al: Management of dural arteriovenous malformations of the anterior cranial fossa. J Neurosurg 72: 692–697, 1990.
191. Masaryk TJ, Ross JS, Modic MT, et al: Carotid bifurcation: MR imaging: Work in progress. Radiology 166:461–466, 1988.
192. McCormick P, Michelson W. Management of cavernous and venous malformations. In Barrow D (ed): Intracranial Vascular Malformations. Park Ridge, Ill, AANS, 1990, pp 197–217.
193. McCormick PW, McCormick J, Zimmerman R, et al: The pathophysiology of acute subarachnoid hemorrhage. BNI Q 7:18–26, 1991.
194. McCormick WF: The pathology of vascular ("arteriovenous") malformations. J Neurosurg 24:807–816, 1966.
195. McCormick WF, Acosta-Rua GJ: The size of intracranial saccular aneurysms: An autopsy study. J Neurosurg 33:422–427, 1970.
196. Mendalow A, Erfurth A, Grossary K, et al: Do cerebral arteriovenous malformations increase in size? J Neurol Neurosurg Psychiatry 50:980–987, 1987.
197. Meyer FB, Huston J III, Reiderer SS: Pulsatile increases in aneurysm size determined by cine phase-contrast MR angiography. Neurosurgery 78:879–883, 1993.
198. Miyachi S, Negoro M, Harda T, Sugita K: Contribution of meningeal arteries to cerebral arteriovenous malformations. Neuroradiology 35: 205–209, 1993.
199. Miyasaka K, Wolpert SM, Prager RJ: The association of cerebral aneurysms, infundibula and intracranial arteriovenous malformations. Stroke 13:196–203, 1982.
200. Miyasaka Y, Yada K, Ohwada T, et al: Pathophysiologic assessment of stagnating arteries after removal of arteriovenous malformations. AJNR Am J Neuroradiol 14:15–18, 1993.
200a. Mizutani T, Aruga T, Kirino T, et al: Recurrent subarachnoid hemorrhage from untreated ruptured vertebrobasilar dissecting aneurysms. J Neurosurg 36:905–913, 1995.
201. Mizutani T, Tanaka H, Aruza T: Multiple arteriovenous malforma-

tions located in the cerebellum, posterior fossa, spinal cord, dura, and scalp with associated port wine stain and supratentorial venous anomaly. Neurosurgery 31:137–141, 1992.
202. Mohr J, Kistler J, Zambranski J, et al: Intracranial aneurysms. In Barnett H, Mohr J, Stein B, Yatsu F (eds): Stroke: Pathophysiology, Diagnosis, and Management. New York, Churchill Livingstone, 1986, pp 643–677.
203. Mokri B: Traumatic and spontaneous extracranial internal carotid artery dissection. J Neurol 237:356–361, 1990.
204. Monaco RG, Alvarez H, Goulao A, et al: Posterior fossa arteriovenous malformations: Angioarchitecture in relation to their hemorrhagic episodes. Neuroradiology 31:471–475, 1990.
205. Nakstad P, Nornes H, Hauge HN: Traumatic aneurysms of the pericallosal arteries. Neuroradiology 28:335–338, 1986.
206. Nalls G, Disher A, Darybagi J, et al: Subcortical cerebral hemorrhages associated with cocaine abuse: CT and MR findings. J Comp Asst Tomor 13:1–5, 1989.
207. Napel S, Marks MP, Rubin GP, et al: CT angiography with spiral CT and maximum intensity projection. Radiology 185:607–610, 1992.
208. Nayler GL, Firmin GL, Longmore DB: Blood flow imaging by cine magnetic resonance. J Comput Assist Tomogr 10:715, 1986.
209. Nehls DG, Flom RA, Carter LP, Spetzler RF: Multiple intracranial aneurysms: Determining the site of rupture. J Neurosurg 63:342–348, 1985.
210. Newell DW, LeRoux PD, Dacey RG Jr, et al: CT infusion scanning for the detection of cerebral aneurysms. J Neurosurg 71:175–179, 1989.
211. Nishijima M, Takaku A, Endo S, et al: Etiological evaluation of dural arteriovenous malformations of the lateral and sigmoid sinuses based on histopathological examinations. J Neurosurg 76:600–606, 1992.
212. Nov AA, Cromwell LD: Traumatic pericallosal artery aneurysm. J Neuroradiol 11:3–8, 1984.
213. Nussel F, Wegmuller H, Huber P: Comparison of magnetic resonance angiography, magnetic resonance imaging, and conventional angiography in cerebral arteriovenous malformations. Neuroradiology 33:56–61, 1991.
214. Obuchowski NA, Modic MT, Magdinec M: Current implications for the efficacy of noninvasive screening for occult intracranial aneurysms in patients with a family history of aneurysms. J Neurosurg 83:42–49, 1995.
215. O'Neill M, Hope T, Thompson G: Giant intracranial aneurysms: Diagnosis with special reference to computerized tomography. Clin Radiol 31:27–39, 1980.
216. Ogawa S, Lee TM, Kay AR, Tank DW: Brain magnetic resonance imaging with contrast dependent on blood oxygenation. Proc Natl Acad Sci U S A 87:9868–9872, 1990.
217. Ogawa T, Inugami A, Shimosegawa E, et al: Subarachnoid hemorrhage: Evaluation with MR imaging. Radiology 186:345, 1993.
218. Ohman J, Heiskanen O: Timing of operation for ruptured supratentorial aneurysms: A prospective randomized study. J Neurosurg 70: 55–60, 1989.
219. Okazaki H, Scheithauer B: Atlas of Neuropathology. New York, Gower Medical, 1988.
220. Okazaki H: Fundamentals of Neuropathology. New York, Igaku-Shoin, 1983.
221. Okazaki H: Malformative vascular lesions. In Fundamentals of Neuropathology, 2nd ed. New York, Igaku-Schoin, 1989, pp 70–74.
222. Okazaki H: Cerebrovascular disease. In Fundamentals of Neuropathology, 2nd ed. New York, Igaku-Shoin, 1989, pp 27–94.
223. Ondra S, Troupp H, George E, Schwab K: The natural history of symptomatic arteriovenous malformations of the brain. J Neurosurg 73:387–391, 1990.
224. Osborn AG: Intracranial aneurysms. In Handbook of Neuroradiology. St. Louis, Mosby-Year Book, 1991, pp 79–84.
225. Osborn AG: Intracranial vascular malformations. In Introduction to Cerebral Angiography. St. Louis, Mosby-Year Book, 1991, pp 85–91.
226. Osborn AG: Introduction to Cerebral Angiography. Harper and Row, 1980, pp 49–86.
227. Osborn A: Intracranial aneurysms. In Diagnostic Neuroradiology, St. Louis, Mosby-Year Book, 1994.
228. Osborn A: Intracranial vascular malformations. In Diagnostic Neuroradiology. St. Louis, Mosby-Year Book, 1994.
229. Osterton B, Solymosi L: Magnetic resonance angiography of cerebral developmental anomalies: Its role in differential diagnosis. Neuroradiology 35:97–104, 1993.
230. Oyesiku N, Colohan ART, Barow DL, Reisner A: Cocaine-induced aneurysmal rupture: An emergent negative factor in the natural history of intracranial aneurysms? Neurosurgery 32:518–526, 1993.
231. Parent AD, Harkey HL, Touchstone DA, et al: Lateral cervical spine dislocation and vertebral artery injury. Neurosurgery 31:501–509, 1992.
232. Parker DL, Yuan C, Blatter DD: MR angiography by multiple thin slab 3D acquisition. Magn Reson Med 17:434–451, 1991.
233. Pellitieri L, Carlsson C, Grevsten S, et al: Surgical versus conservative treatment of intracranial arteriovenous malformations: A study in surgical decision making. Acta Neurochir (Wien) 29(Suppl):1–86, 1979.
234. Perata HJ, Tomsick TA, Tew JM Jr: Feeding artery pedicle aneurysms: Association with parenchymal hemorrhage and arteriovenous malformation in the brain. J Neurosurg 80:631–634, 1994.
235. Perret G, Nishioka H: Arteriovenous malformations: An analysis of 545 cases for craniocerebral arteriovenous malformations and fistulae reported to the cooperative study. J Neurosurg 25:467–490, 1966.
236. Picard L, Roy D, Bracard S, et al: Aneurysm associated with a fenestrated basilar artery: Report of two cases treated by endovascular detachable balloon embolization. AJNR Am J Neuroradiol 14: 591–594, 1993.
237. Piepgras DG, Sundt TM Jr, Ragoowansi AT, Stevens L: Seizure outcome in patients with surgically treated cerebral arteriovenous malformations. J Neurosurg 78:5–11, 1993.
238. Pierot L, Chiras J, Meder J-F, et al: Dural arteriovenous fistulas of the posterior fossa draining into subarachnoid veins. AJNR Am J Neuroradiol 13:315–323, 1992.
239. Prayer L, Wimberger D, Kramer J, et al: MRI—a noninvasive tool for evaluating therapeutic embolization of cerebral arteriovenous malformations. Eur Radiol 1:51–57, 1991.
240. Raaymakers TW, Buys PC, Verbeeten B Jr, et al: MR angiography as a screening tool for intracranial aneurysms: Feasibility, test characteristics and interobserver agreement. AJR Am J Roentgenol 173: 1469–1475, 1999.
241. Rao KCVG, Chiantella NM, Arora S, Gellad F: Intracranial venous aneurysms: Vein of Galen and other similar vascular anomalies. J Comp Tomogr 7:345–350, 1983.
242. Raps EC, Rogers JD, Galeta SL, et al: The clinical spectrum of unruptured intracranial aneurysms. Arch Neurol 50:265–268, 1993.
243. Raybaud CA, Strother CM, Hald JK: Aneurysms of the vein of Galen: Embryonic considerations and anatomical features relating to the pathogenesis of the malformations. Neuroradiology 31:109–128, 1989.
244. Rhoton A: Anatomy of saccular aneurysms. Surg Neurol 14:59–66, 1980.
245. Rigamonti D, Hadley MN, Drayer BP, et al: Cerebral cavernous malformations: Incidence and familial occurrence. N Engl J Med 319:343–347, 1988.
246. Rigamonti D, Johnson PC, Spetzler RF, et al: Cavernous malformations and capillary telangiectasia: A spectrum within a single pathological entity. Neurosurgery 28:60–64, 1991.
247. Rigamonti D, Spetzler D: The association of venous and cavernous malformations: Report of form cases and discussions of the pathophysiological, diagnostic and therapeutic implications. Acta Neurochir (Wien) 92:100–105, 1988.
248. Rinkel GJE, Wijdicks EFM, Vermeulen M, et al: Nonaneurysmal perimesencephalic subarachnoid hemorrhage: CT and MR patterns that differ from aneurysmal rupture. AJNR Am J Neuroradiol 12: 829–834, 1991.
249. Rinkel GJE, Wijdicks EFM, Hasan D, et al: Outcome in patients with subarachnoid haemorrhage and negative angiography according to pattern of haemorrhage on computed tomography. Lancet 338: 964–968, 1991.
250. Robinson J, Awad I, Little J: Natural history of the cavernous angioma. J Neurosurg 75:709–714, 1991.
251. Robinson JR Jr, Awad IA, Magdinec M, Paranandi L: Factors predisposing to clinical disability in patients with cavernous malformations of the brain. Neurosurgery 32:730–736, 1993.
252. Rodesch G, Lasjaunias P: Physiopathology and semeiology of dural arteriovenous shunts. Riv di Neuroradiol 5:11–21, 1992.
253. Ronleainem A, Puranen MI, Hernesniemi JA, et al: Intracranial aneurysms: MR angiographic screening in 400 asymptomatic individuals with increased familial risk. Radiology 195: 35–40, 1995.

254. Rosenorn J, Eskesen V, Madsen F, Schmidt K: Importance of cerebral pan-angiography for detection of multiple aneurysms in patients with aneurysmal subarachnoid haemorrhage. Acta Neurol Scand 87: 215–218, 1993.
255. Rosenorn J, Eskesen V, Schmidt K: Unruptured intracranial aneurysms: An assessment of the annual risk of rupture based on epidemiological and clinical data. Br J Neurosurg 2:369–378, 1988.
256. Ross JS, Masaryk TJ, Modic MT, et al: Intracranial aneurysms: Evaluation by MR angiography. AJNR Am J Neuroradiol 11:449–456, 1990.
257. Ruggieri PM: Presented at the 78th Annual Scientific Assembly of the Radiological Society of North America, Chicago, Nov 29–Dec 4, 1992.
258. Russell DS, Rubinstein LJ: Pathology of Tumors of the Nervous System, 5th ed. Baltimore, Williams & Wilkins, 1989.
259. Sadato N, Numaguchi T, Rigamonti D, et al: Bleeding patterns in ruptured posterior fossa aneurysms: a CT study. J Comp Asst Tomogr 15:612–617, 1991.
260. Sadler LR, Tarr RW, Jungreis CA, Sekhar L: Sinus pericranii: CT and MR findings. J Comp Asst Tomogr 14:124–127, 1990.
261. Sahs AL, Perret GE, Locksley HB, et al: Intracranial Aneurysms and Subarachnoid Hemorrhage: A Cooperative Study. Philadelphia, JB Lippincott, 1969.
262. Sakaki T, Tominaga M, Miyamoto K, et al: Clinical studies of de novo aneurysms. Neurosurgery 32:512–517, 1993.
263. Salcman M, Scholtz H, Numaguchi Y: Multiple intracerebral arteriovenous malformations: Report of three cases and review of the literature. Surg Neurol 38:121–128, 1992.
264. Sanders WP, Sorek PA, Mehta BA: Fenestration of intracranial arteries with special attention to associated aneurysms and other anomalies. AJNR Am J Neuroradiol 14:675–680, 1993.
265. San-Galli F, Leman C, Kein P, et al: Cerebral arterial fenestrations associated with intracranial saccular aneurysms. Neurosurgery 30: 279–283, 1992.
266. Sarwar M, McCormick W: Intracerebral venous angioma: Case report and review. Arch Neurol 35:323–325, 1978.
267. Saveland H, Hillman J, Brandt L, et al: Overall outcome in aneurysmal subarachnoid hemorrhage. J Neurosurg 76:729–734, 1992.
268. Savino PJ, Grossman RI, Schatz NJ, et al: High-field magnetic resonance imaging in the diagnosis of cavernous sinus thrombosis. Arch Neurol 43:1081–1082, 1986.
269. Savoiardo M, Strada L, Passerini A: Intracranial cavernous hemangioma: Neuroradiologic review of 36 operated cases. AJNR Am J Neuroradiol 4:945–950, 1983.
270. Scazzeri F, Prosetti D, Nenci R, et al: Angioma venoso. Riv di Neuroradiol 4:201–208, 1991.
271. Schievink WI, Limburg M, Dreissen J Jr, et al: Screening for unruptured familiar aneurysms: Subarachnoid hemorrhage 2 years after angiography negative for aneurysms. Neurosurg 29:434–438, 1991.
272. Schievink WI, Mokri B, Piepgras DG: Angiographic frequency of saccular intracranial aneurysms in patients with spontaneous cervical arterial dissection. J Neurosurg 76:62–66, 1992.
273. Schievink WI, Piepgras DG, Wirth FP: Rupture of previously documented small asymptomatic saccular intracranial aneurysms. J Neurosurg 76:1019–1024. 1992.
274. Schmid UD, Steiger HJ, Huber P: Accuracy of high resolution computed tomography in direct diagnosis of cerebral aneurysms. Neuroradiology 29:152–159, 1987.
275. Schuierer G, Huk WJ, Laub G: Magnetic resonance angiography of intracranial aneurysms. Neuroradiology 35:50–54, 1992.
276. Scott RM, Barnes P, Kupsky W, Adelman LS: Cavernous angiomas of the central nervous system in children. J Neurosurg 76:38–46, 1992.
277. Scotti G, Ethier R, Melancon D, et al: Computed tomography in the evaluation of intracranial aneurysms and subarachnoid hemorrhage. Radiology 123:85–90, 1977.
278. Seidenwurm D, Berenstein A, Hyman A, Kowalsla H: Vein of Galen malformation: Correlation of clinical presentation, arteriography, and MR imaging. AJNR Am J Neuroradiol 12:347–345, 1991.
279. Seidenwurm D, Berenstein A: Vein of Galen malformation: Clinical relevance of angiographic classification, and utility of MRI in treatment planning. Neuroradiology 33(Suppl): 153–155, 1991.
280. Senegor M: Traumatic pericallosal aneurysm in a patient with no major trauma. J Neurosurg 75:475–477, 1991.
281. Sharma A, Tyagi G, Sahai A, Baijal SS: Traumatic aneurysm of superficial temporal artery: CT demonstration. Neuroradiol 33:510–512, 1991.
282. Sherry RG, Walker ML, Olds MV: Sinus pericranii and venous angioma in the blue-rubber bleb nevus syndrome. AJNR Am J Neuroradiol 5:832–834, 1984.
283. Shi YQ, Chen XC: A proposed scheme for grading intracranial arteriovenous malformations. J Neurosurg 65:484–489, 1986.
284. Sigal R, Krief O, Houtteville JP, et al: Occult cerebrovascular malformations: Follow-up with MR imaging. Radiology 176:815–819, 1990.
285. Simard JM, Garcia-Bengochea F, Ballinger WEJ, et al: Cavernous angioma: A review of 126 collected and 12 new clinical cases. Neurosurgery 18:162–172, 1986.
286. Sisti MD, Kader A, Stein BM: Microsurgery for 67 intracranial arteriovenous malformations less than 3 cm in diameter. J Neurosurg 79:653–660, 1993.
287. Smith HJ, Strother CM, Kikuchi Y, et al: MR imaging in the management of supratentorial intracranial AVMs. AJNR Am J Neuroradiol 9:225–235, 1988.
288. Solomon RA, Fink ME, Pile-Spellman J: Surgical management of unruptured intracranial aneurysms. J Neurosurg 80:440–446, 1994.
289. Sorek PA, Silbergleit R: Multiple asymptomatic cervical cephalic aneurysms. AJNR Am J Neuroradiol 14:31–33, 1993.
290. Spetzler RF, Hargraves RW, McCormick PW, et al: Relationship of perfusion pressure and size to risk of hemorrhage from arteriovenous malformation. J Neurosurg 76:918–923, 1992.
291. Spetzler RF, Martin NA: A proposed scheme for grading intracranial arteriovenous malformations. J Neurosurg 65:476–483, 1986.
292. Spetzler RF, Wilson CB, Weinstein P, et al: Normal perfusion pressure breakthrough theory. Clin Neurosurg 25:651–672, 1978.
293. Stehbens WE: Etiology of intracranial berry aneurysms. J Neurosurg 70:823–831, 1989.
294. Steiner L, Lindquist C, Adler JR, et al: Clinical outcome of radiosurgery for cerebral arteriovenous malformations. J Neurosurg 77:1–8, 1992.
295. Steiner L: Radiosurgery in cerebral arteriovenous malformations. In Flamm E (ed): Cerebrovascular Surgery. New York, Springer-Verlag, 1986.
296. Steinmeier R, Schramm J, Muller H, Fahlbush R: Evaluation of prognostic factors in cerebral arteriovenous malformations. Neurosurgery 24:193–200, 1989.
297. Stone JL, Crowell RM, Gandhi YN, Jafar JJ: Multiple intracranial aneurysms: Magnetic resonance imaging for determination of the site of rupture. Neurosurgery 23:97–100, 1988.
298. Strother CM, Graves VB, Rappe A: Aneurysm hemodynamics: An experimental study. AJNR Am J Neuroradiol 13: 1089–1095, 1992.
299. Sugita K, Kobayashi S, Takemae T, et al: Giant aneurysm of the vertebral artery. J Neurosurg 68:960–966, 1988.
300. Suzuki J, Kodama N: Moyamoya disease: A review. Stroke 14: 104–109, 1983.
301. Suzuki S, Kayama T, Sakurai Y, et al: Subarachnoid hemorrhage of unknown origin. Neurosurg 21:310–313, 1987.
302. Symon L: Surgical experiences with giant intracranial aneurysms. Acta Neurochir (Wien) 118:53–58, 1992.
303. Szabo M, Crosby G, Sundaram P, et al: Hypertension does not cause spontaneous hemorrhage of intracranial arteriovenous malformations. Anesthesiology 70:761–763, 1989.
304. Takahashi S, Tomura N, Watarai J, Mizoi K, Manabe H: Dural arteriovenous fistula of the cavernous sinus with venous congestion of the brain stem: report of two cases, AJNR Am J Neuroradiol 20: 886–888, 1999.
305. Takamiya Y, Takayama H, Kobayashi K, et al: Familial occurrence of multiple vascular malformations of the brain. Neurol Med Chir (Tokyo) 24:271–277, 1984.
306. Taniguchi RM, Goree JA, Odom GL: Spontaneous carotid cavernous shunts presenting diagnostic problems. J Neurosurg 35:384–391, 1971.
307. Terada T, Higashida R, Halbach VV, et al: Development of acquired arteriovenous fistulas in rats due to venous hypertension. J Neurosurg 80:884–889, 1994.
308. Tien RD, Wilkins RH: MRA delineation of the vertebrovascular system in patients with hemifacial spasm and trigeminal neuralgia, AJNR Am J Neuroradiol 14:34–36, 1993.
309. Toffol GJ, Gruener G, Naheedy MH: Early-filling cerebral veins. J Am Osteopath Assoc 88:1007–1009, 1988.

310. Tomlinson FH, Howser OW, Scheithauer BW, et al: Cavernous angioma: Angiographically occult vascular malformations: A correlative MR imaging and histological study. J Neurosurg 78:328, 1993.
311. Toro VE, Fravel JF, Weidman TA: Posttraumatic pseudoaneurysm of the posterior meningeal artery associated with intraventricular hemorrhage. AJNR Am J Neuroradiol 14:264–266, 1993.
312. Truwit CL: Venous angioma of the brain: History, significance and imaging findings. AJR Am J Roentgenol 159:1299–1307, 1992.
313. Tsuruda J, Saloner D, Norman D: Artifacts associated with MR neuroangiography. AJNR Am J Neuroradiol 13:1411–1422, 1992.
314. Uchino A, Imador H, Ohno M: Magnetic resonance imaging of intracranial venous angioma. Clin Imaging 14:309–314, 1990.
315. Uchino A, Kato A, Kuroda Set al: Pontine venous congestion caused by dural carotid-cavernous fistula: Report of two cases. Eur Radiol 7:405–408, 1997.
315a. Unruptured intracranial aneurysms—Risk of rupture and risks of surgical intervention. N Engl J Med 339:1725–1733, 1998.
316. Vajda J: Multiple intracranial aneurysms: A high-risk condition. Acta Neurochir (Wien) 118:59–75, 1992.
317. Valavanis A, Schubiger O, Wichmann W: Classification of brain arteriovenous malformation nidus by magnetic resonance imaging. Acta Radiol Suppl 369:86–89, 1986.
318. Valavanis A, Wellauer J, Yasargil MG: The radiological diagnosis of cerebral venous angioma: Cerebral angiography and computed tomography. Neuroradiology 24:193–199, 1983.
319. Vinuela F, Drake CG, Fox AJ, Pelz DM: Giant intracranial varices secondary to high-flow arteriovenous fistulae. J Neurosurg 66:198–203, 1987.
320. Vinuela F, Fox AJ, Pelz DM, Drake CG: Unusual clinical manifestations of dural arteriovenous malformations. J Neurosurg 64:554–558, 1986.
321. von Schulthess GK, Higgins CB: Blood flow imaging with MR: Spin-phase phenomena. Radiology 157:687–695, 1985.
322. Waltimo O: The relationship of size, density and localization of intracranial arteriovenous malformations to the type of the initial symptom. J Neurol Sci 19:13–19, 1973.
323. Wascher TM, Golfinos J, Zabramski JM, Spetzler RF: Management of unruptured intracranial aneurysms. BNI Q 8:2–7, 1992.
324. Wedeen VJ, Rosen BR, Chesler D, Brady TH: MR velocity imaging by phase display. J Comput Assist Tomogr 9:530–536, 1985.
325. Wehrli FW, Shimakawa A, Gullberg GT, MacFall JR: Time-of-flight MR flow imaging: Selective saturation recovery with gradient refocusing. Radiology 160:781–785, 1986.
326. Weibers DO, Whisnant JP, Sundt T, et al: The significance of unruptured intracranial aneurysms. J Neurosurg 66:23–29, 1987.
327. Weir B: Pituitary tumors and aneurysms: Case report and review of the literature. Neurosurgery 30:585–591, 1992.
328. Weir BKA: Intracranial aneurysms. Curr Opin Neurol Neurosurg 3: 55–62, 1990.
329. Wendling LR, Moore JS Jr, Kieffer SA, et al: Intracerebral venous angioma. Radiology 119:141–147, 1976.
330. Westra SJ, Curran JG, Duckwiler GR, et al: Pediatric intracranial vascular malformations: Evaluation of treatment results with color doppler US. Radiology 186:775–783, 1993.
331. Wiebers DO, Torner JC, Meissner I: Impact of unruptured intracranial aneurysms on public health in the United States. Stroke 23: 1416–1419, 1992.
332. Wilkins RH, Rengachary SS: Vascular malformations. In Neurosurgery. New York, McGraw-Hill, 1985, pp 1448–1473.
333. Willinsky R, TerBrugge K, Montanera W, et al: Microarteriovenous malformations of the brain: Superselective angiography in diagnosis and treatment. AJNR Am J Neuroradiol 13:325–330, 1992.
334. Willinsky R, TerBrugge K, Montanera W, et al: Venous congestion: an MR finding in dural arteriovenous malformations with cortical venous drainage. AJNR Am J Neuroradiol 15:1501–1507, 1994.
335. Willinsky RA, Fitzgerald M, TerBrugge K, et al: Delayed angiography in the investigation of intracranial intracerebral hematomas caused by small arteriovenous malformations. Neuroradiology 35: 307–311, 1993.
336. Willinsky RA, Lasjaunias P, TerBrugge K, Burrows WP: Multiple cerebral arteriovenous malformations (AVMs): Review of our experience from 203 patients with cerebral vascular lesions. Neuroradiology 32:207–210, 1990.
337. Wilms G, Demaerel P, Marchi G, et al: Gadolinium-enhanced MR imaging of cerebral venous angiomas with emphasis on their drainage. J Comput Assist Tomogr 15:199–206, 1991.
338. Wilms G, Goffin J, VanDriessche J, Demaerel P: Posterior fossa venous anomaly and ipsilateral acoustic neuroma: Two cases. Neuroradiology 34:337–339, 1992.
339. Wilms G, Marchal G, Vas Hecke P, et al: Cerebral venous angioma: MR imaging at 1.5 tesla. Neuroradiology 32:81–85, 1990.
340. Wood EH: Angiographic identification of the ruptured lesion in patients with multiple cerebral aneurysms. J Neurosurg 21:182–198, 1964.
341. Woodard E, Barrow D: Clinical presentation of intracranial arteriovenous malformations. In Barrow D (ed): Intracranial Vascular Malformations. Park Ridge, Ill, AANS, 1990, pp 53–61.
342. Yamamoto Y, Asari S, Sunami N et al: Computed angiotomography of unruptured cerebral aneurysms. J Comp Assist Tomogr 10:21–27, 1986.
343. Yapor WY, Gutierrez FA: Cocaine-induced intratumoral hemorrhage: Case report and review of the literature. Neurosurgery 30:288–291, 1992.
344. Yonakawa Y, Handa J, Okuno T: Moyamoya disease: Diagnosis, treatment, and recent achievement. In Barnett HJ, Stein BM, Mohr JP, Yatsu FM (eds): Stroke: Pathophysiology, Diagnosis, and Management, 2nd ed. New York, Churchill Livingstone, 1985, pp 805–831.
345. Young N, Dorsch NW, Kingston RJ: Pitfalls in the use of spiral CT for identification of intracranial aneurysms. Neuroradiology 41: 93–99, 1999.
346. Zambramski JM, Wascher TM, Spetzler RF, et al: The natural history of familial cavernous malformations: Results of an ongoing study. J Neurosurg 80:422–432, 1994.

9 Central Nervous System Trauma

John J. Wasenko
Leo Hochhauser

The neuroradiology of trauma has undergone dramatic changes since the advent of computed tomography (CT) and more recently with the establishment of magnetic resonance imaging (MRI) as a diagnostic imaging tool. With the ubiquitous availability of CT in the 1970s, the diagnosis and management of head trauma have changed significantly. Elaborate neurologic testing to appropriately localize a space-occupying lesion such as an intracerebral hemorrhage is no longer of paramount importance, because CT precisely defines the nature and location of the lesion, thus facilitating rapid implementation of treatment. Since the early days of CT scanning, when the contents of the skull were imaged noninvasively for the first time, CT has been the primary modality for evaluating patients with acute head injuries.[1, 52] The ability of CT scans to rapidly demonstrate a surgically correctable lesion, fracture, and subarachnoid hemorrhage (SAH) makes it the modality of choice in the evaluation of acute head injury. CT scans delineate acute hemorrhage from brain edema and allow one to determine whether a hematoma is intracerebral or extracerebral. Modern high-resolution CT scanning, with the direct display of axial anatomy, has replaced angiography as the prevalent method of demonstrating the indirect sign of intracerebral, epidural, or subdural hematomas (SDHs). Although the extent and multiplicity of lesions can be well evaluated by CT scans, MRI, with its greater sensitivity, frequently shows additional areas of contusion and shear injury.

MRI is playing an increasingly important role in the evaluation of head trauma. It has proved more sensitive than CT in the detection of diffuse axonal (shear) injury, nonhemorrhagic contusions, and SDHs and is equivalent to CT in the depiction of hemorrhagic contusions.[37–39, 50, 136] The development of MRI-compatible life-support equipment, such as nonferromagnetic ventilators, allows the severely injured, comatose patient to be evaluated with MRI. The use of adequate sedation minimizes patient discomfort and motion, which may severely degrade image quality. Disadvantages of MRI that preclude its use in the evaluation of acute head injury include long scan time and the inability to detect fractures, SAH, and hyperacute hemorrhage. MRI is the modality of choice in the subacute and chronic stages of head injury because it is more sensitive than CT in the detection of both hemorrhagic and nonhemorrhagic lesions.

Technique

Computed Tomography

Ten-millimeter scans without interslice gap are made at an angle of 15 to 20 degrees to the canthomeatal line and parallel to the skull base. To reduce beam-hardening artifacts and increase the conspicuity of small lesions, the posterior fossa may be studied with 5-mm slices from the Cl arch, through the level of the posterior clinoids, followed by 10-mm slices from the sella through the vertex. From the array of image-processing algorithms, the one specially designed for soft tissue densities or a combination of soft tissues and bone is best suited for making a diagnosis and establishing appropriate management in the acute trauma situation. Algorithms for high spatial resolution imaging are necessary for trauma to regions with great density differences such as the face (air–soft tissue and air-bone interfaces), the skull base and the temporal bone, and occasionally, the cranial vault.

We frequently use the intermediate algorithm ("Detail," GE; "High," Siemens; "Soft," Picker) because it provides good resolution for soft tissues, gives excellent resolution for edema and hemorrhage, and defines fractures well without blooming artifact from bone (which often occurs with the soft tissue algorithms). Therefore, this algorithm is particularly well suited to image associated facial injuries in which density differences range from air to bone densities. Specific algorithms for bone densities are well suited to examine fracture sites of the facial bones, skull base, and cranial vault.

Hard copies are printed in the following three different window settings to allow for routine viewing of three different areas of interest: (1) the soft tissues of the brain for infarct or hemorrhage, (2) the extracerebral spaces to detect hematomas adjacent to the dense bone of the skull vault and skull base, and (3) the bones for the detection of fractures. Intravenous contrast agent usually not required. If, however, there is unexplainable mass effect or the study is normal but the patient is comatose or lethargic or presents with a focal neurologic deficit, the administration of intravenous contrast material may become necessary. Often, MRI, with its inherent greater sensitivity, may be required for these patients. Small SDHs are difficult to visualize with CT, whereas they pose no difficulty with MRI. Isodense SDHs can usually be visualized with current third- and fourth-generation CT imaging equipment. Intravenous contrast agents may facilitate their detection by

increasing the density of the cortical vessels, thus creating a density interface between blood and the diffusely enhancing cortex or cortical vessels, which are displaced from the inner table of the skull.

Axial CT scans performed with current high image resolution scanners provide exquisite image detail and are usually sufficient in the emergency situation. Imaging in the coronal plane is frequently better for the evaluation of fractures of the skull base but may not be feasible because of the patient's condition. Coronal reconstructions are adequate only when thin slices ($\leq$3 mm) are used, but they usually lack the rich detail of direct coronal scans.

Magnetic Resonance Imaging

Conventional T1- and T2-weighted spin-echo (SE) images are used in the evaluation of head trauma. Proton-density and T2-weighted sequences are sensitive in the detection of nonhemorrhagic lesions such as contusions and diffuse axonal (shear) injury, because of the sensitivity of these sequences to the presence of extracellular free water. The T2-weighted sequences are also sensitive in the detection of acute and chronic hemorrhage, especially at high field strength (1.5 T).[44] The use of T1-weighted sequences readily allows the detection of subacute hemorrhagic lesions. Acute hemorrhagic lesions are poorly seen on T1-weighted images because they are isointense or slightly hypointense. Conventional SE sequences may be supplemented with T2* gradient-recalled echo (GRE) sequences, which are highly sensitive in the detection of small acute and chronic hemorrhagic lesions.[3, 28] Fast spin-echo (FSE) sequences may be used in place of conventional SE sequences, resulting in much faster scan time, which is an important consideration in critically injured patients. FSE sequences offer similar lesion conspicuity in the visualization of nonhemorrhagic lesions.[58] Magnetic susceptibility effects are less evident on FSE images, and as a result, hemorrhagic lesions are not as hypointense as with SE sequences. Although the hemorrhagic lesions are not as hypointense on FSE images, they are still evident and almost equivalent to that noted on SE images.[57] The multiplanar imaging capability and superior contrast resolution of MRI are advantages over CT in that they allow the accurate localization and characterization of intracranial injuries.[39] Sagittal T1-weighted and axial T2-weighted sequences supplemented with a T2* GRE sequence enable the detection and localization of both nonhemorrhagic and hemorrhagic lesions.

Image parameters for T1-weighted images (TR = 500 msec, TE = 20 msec, 2 excitations), for proton-density images (TR = 2000 msec, TE = 30 msec, 1 excitation), and for T2-weighted images (TR = 2000 msec, TE = 80 msec, 1 excitation) achieve a high enough signal-to-noise ratio to allow the detection of small lesions. T2* GRE image parameters (TR = 500 to 700 msec, TE = 20 to 25 msec, flip angle 15 to 20 degrees) provide sufficient sensitivity to magnetic susceptibility effects. FSE proton-density (TR = 2500 msec, TE = 17 msec, 1 excitation), echo train 4 sequences and T2-weighted (TR = 3500 msec, TE = 102 msec, 1 excitation), echo train 8 sequences, acquired separately, may be used in place of conventional SE sequences with a decrease in scan time. Images with higher signal-to-noise ratio, contrast, and spatial resolution values may also be obtained in a comparable scan time with the use of more excitations. A 5-mm slice thickness with a 2.5-mm gap and a 256 × 192 matrix provides adequate signal-to-noise ratio and spatial resolution.

Fractures

Demonstration of a fracture on skull radiographs indicates that a significant force has been applied to the bony vault. However, the lack of visualization of a fracture does not exclude significant injury to the underlying brain. CT evaluation of the skull and brain has therefore superceded the primary evaluation with skull films. In the emergency room assessment of a trauma victim, the primary concern is the diagnosis of injury to the brain and life-threatening post-traumatic changes of intracranial hemorrhage and vascular spasm. Fractures may involve the skull vault, the skull base, or both.

Linear Fracture

Linear fractures that run parallel in the axial plane are easily missed on CT scans, and are usually negligible if no associated brain injury is demonstrated (Fig. 9–1).

Depressed Fracture

A fragment is considered depressed when its outer table is displaced below the level of the inner table of the skull (Fig. 9–2). Although skull films are frequently diagnostic,

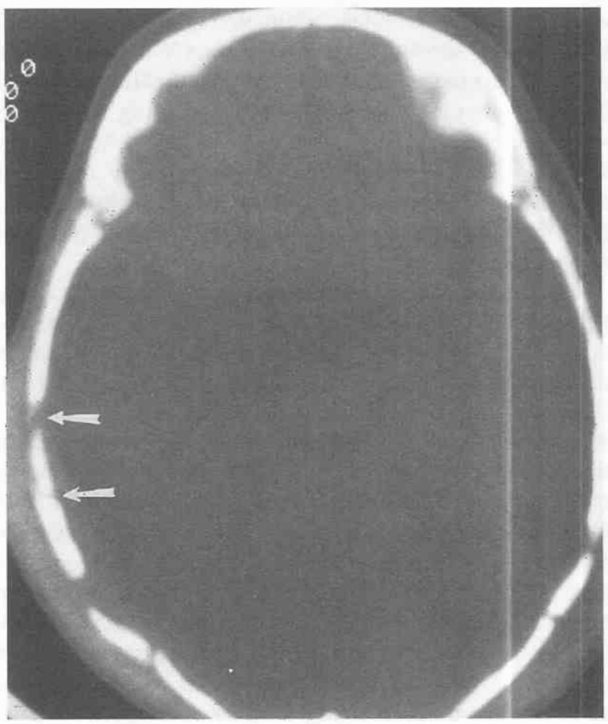

Figure 9–1. Axial CT scan with bone window setting shows nondepressed fractures of the right temporal bone (*arrows*).

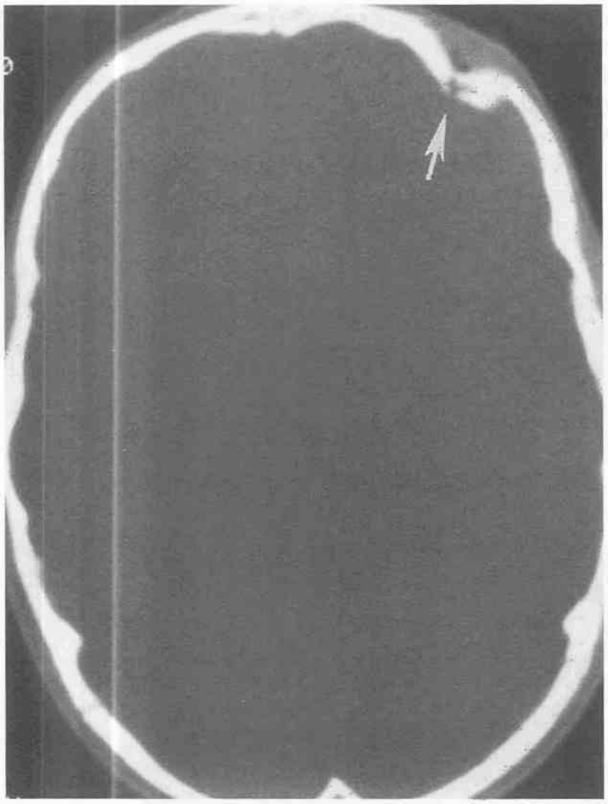

Figure 9–2. Depressed fracture with fragment of the left frontal bone (*arrow*).

the depression can usually be identified during CT on the preliminary computer generated scout image of the skull. Depressed fractures near the vertex or the skull base require direct coronal imaging or reconstructions in a plane parallel to the vector of impact. Delineation of a depressed fracture is important because it may be the cause for an underlying dural tear, extracerebral hematoma, or brain contusion. Although compound depressed fractures frequently require surgical treatment, the majority of such injuries are managed conservatively. The goals of treatment are the prevention of infection and post-traumatic epilepsy and the amelioration of neurologic deficits.[125] Depressed fractures adjacent to venous sinuses are usually left in place because of the danger of uncontrollable hemorrhage when fragments are removed.

Basilar Skull Fracture

If a basilar skull fracture is clinically suspected, high spatial resolution CT scans with a thickness of 3 mm or less are required to delineate a fracture of the chondrocranium. Alternatively, CT scans may suggest a basilar skull fracture before it becomes clinically evident. An air-fluid level in the paranasal sinuses or the mastoid in cells should be viewed as secondary to a basilar skull fracture until proven otherwise.

Frontal Sinus Fracture

It is important to visualize fractures of the posterior wall of the frontal sinus because they frequently require surgical closure of the disrupted dura to prevent cerebrospinal (CSF) leakage and infection. Some surgeons treat only the severely comminuted fracture or when there is overt CSF leakage or pneumocephalus, and "simple" comminuted fractures are treated conservatively.[125] Fractures of the cribriform plate are commonly associated with anosmia.

Pneumocephalus

Air locules in the extracerebral spaces usually indicate traumatic air entry resulting from fracture of a paranasal sinus or mastoid air cells abutting the dura (Fig. 9–3). When associated with a dural tear, they may be complicated by CSF leakage, empyema, meningitis, or brain abscess. Most post-traumatic CSF leaks cease spontaneously, and the responsible fractures may never be visualized.[123]

Growing Fracture

Enlarging skull fractures have been described in 0.75% of skull fractures in children. Most cases are associated with a history of significant trauma, such as experiencing a motor vehicle accident, being struck by a train, or falling out of a window, that causes a skull fracture and contusion of the underlying brain. Growing fractures commonly occur in the growing skull, although occasional reports of such lesions in adults are on record.[71] The ongoing normal growth of the child's brain is considered an aggravating factor.[126] Children with growing fractures present weeks to

Figure 9–3. Pneumocephalus. Collections of air overlie the frontal lobes and extend along the anterior interhemispheric fissure (*arrows*).

years after injury with a pulsatile mass or rarely with a depressed calvarial defect.[75] Kingsley and coworkers reported 10 cases in children seen over 10 years.[64] The lesions seem to occur when a skull fracture in childhood is accompanied by a dural tear or rent, with focal protrusion of the arachnoid membrane into the fracture gap. The unabating CSF pulsations transmitted to the entrapped arachnoid protrusion result in the remodeling of bone of the growing skull at the fracture site, causing enlargement of the fracture line (Fig. 9–4). The frequently underlying porencephaly or encephalomalacia appears to be the result of an associated contusion from the initial trauma rather than the pathogenetic factor in the enlargement of the fracture. The term "leptomeningeal cyst" is obsolete.[54, 71]

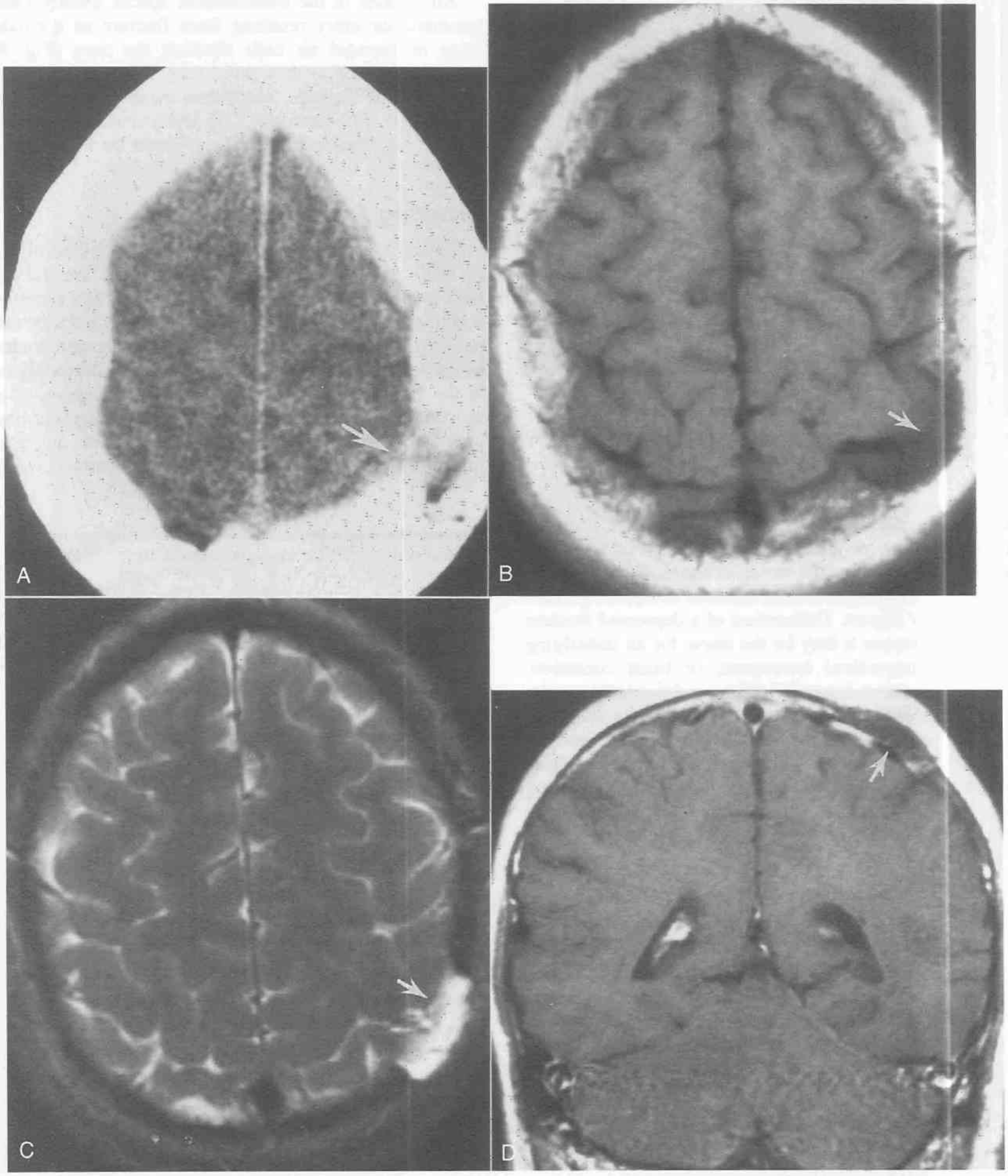

Figure 9–4. *A,* Growing fracture. Unenhanced CT can shows a defect in the left parietal bone (*arrow*). *B* and *C,* Axial T1-weighted (500/15) and T2-weighted (2500/80) MR images reveal mass isointense with CSF (*arrows*). *D,* Coronal enhanced T1-weighted (500/15) image shows no enhancement of lesion (*arrow*).

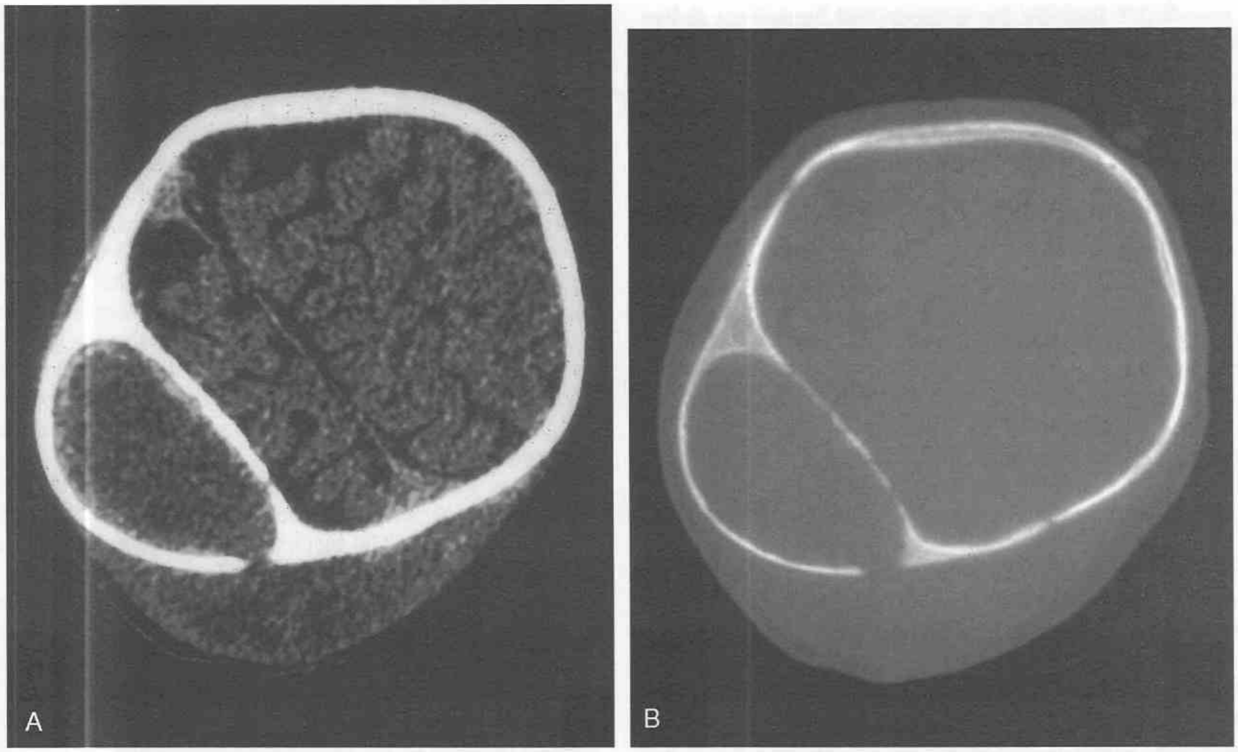

Figure 9–5. *A* and *B*, Cephalhematoma. CT scans with soft tissue and bone windows show partially ossified cephalhematoma overlying the right parietal bone. Note remodeling of the underlying parietal bone. Soft tissue swelling is present, overlying and posterior to the cephalhematoma.

Cephalhematoma may occur as a result of a difficult labor and delivery. A shell of cortical bone forms around the periphery of a subperiosteal hematoma, which may result in deformity of the calvarium (Fig. 9–5).

Intracerebral Hematoma

Intracerebral hematomas are differentiated from hemorrhagic contusions in that the former are homogeneously hyperdense, sharply marginated, and surrounded by a rim of decreased density (Fig. 9–6).[66] Considerable mass effect may be present, depending on the size of the lesion. The most common sites of involvement are the frontal and temporal lobes.[66, 132] Other rare sites of involvement are the basal ganglia and posterior fossa.[60, 119] Hematomas may be bilateral or multiple and are frequently associated with other lesions, such as SAH and SDHs.[26, 66, 132] Not infrequently there is associated rupture of the hematoma into the ventricular system.[132]

Intracerebral hematomas occur most commonly at the time of injury; however, they may be delayed, with most appearing within 48 hours following head injury.[73] Rarely an intracerebral hematoma appears several weeks after the episode of trauma. Possible etiologies of a delayed intracerebral hematoma include focal loss of autoregulation in an area of brain contusion and surgical evacuation of a lesion such as an SDH with relief of a tamponade effect and subsequent hemorrhage into the area of traumatized brain.[73]

Intracerebral hematomas demonstrate a typical pattern of evolution as blood products are gradually broken down

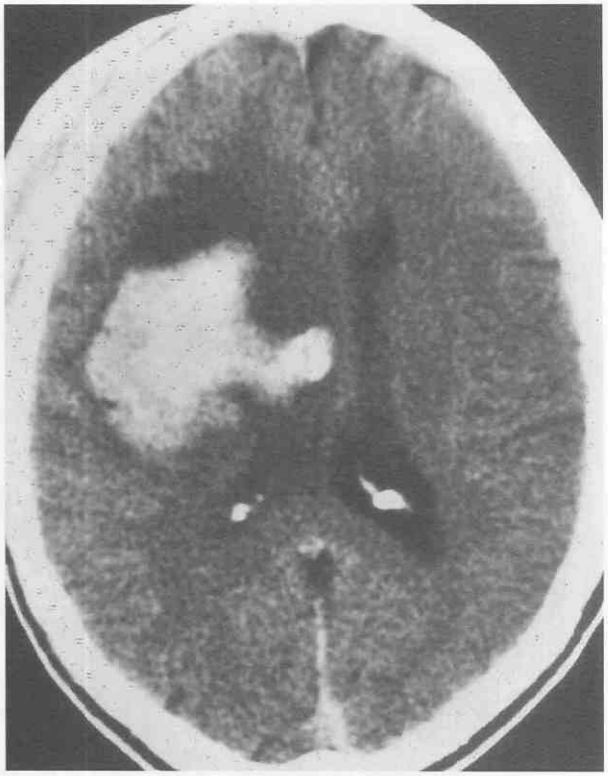

Figure 9–6. Intracerebral hematoma. Large, well-marginated hematoma in the right parietal lobe with rupture into the ventricular system.

and resorbed.[82] Initially the intracerebral hematoma is hyperdense from clotted blood with surrounding edema and mass effect. Enhancement may be evident within or around the hematoma with the administration of intravenous contrast material.[120] The hematoma gradually becomes isodense with brain parenchyma over several weeks to a month.[23, 82] Mass effect persists after the hematoma has become isodense because the decrease in mass effect does not occur simultaneously with decrease in the density of the hematoma.[23, 82] At this time, the hematoma exhibits ringlike enhancement from the surrounding capillary proliferation.[120] Decreased density eventually appears over 1 to several months. Encephalomalacia is evident as low density with adjacent sulcal enlargement and ventricular dilatation.

The MRI appearance of intracerebral hematoma has been described at low and high field strengths.[21, 25, 44, 110, 137] The following description of the evolution of intracerebral hematomas is at a field strength of 1.5 T.[44, 45] *Acute hematomas* are less than 1 week old, *subacute hematomas* are more than 1 week and less than 4 weeks old, and *chronic hematomas* are more than 1 month old. Acute hematomas are isointense or slightly hypointense on T1-weighted images and very hypointense on T2-weighted images. The extreme hypointensity is caused by preferential T2 proton relaxation enhancement (PRT2PRE) of intracellular deoxyhemoglobin, which is dependent on the square root of the magnetic field strength and the interecho interval. The PRT2PRE phenomenon is caused by the dephasing of water protons in areas of local magnetic field inhomogeneity. As the echo time lengthens, signal loss increases as water protons experience the local field inhomogeneity for a longer period. Acute hemorrhage is therefore slightly hypointense on a proton-density–weighted image and very hypointense on a T2-weighted image.

Subacute hematomas have a variable appearance at high field strength.[45] The hematoma in the subacute state is composed of methemoglobin, a paramagnetic material. Paramagnetic materials produce T1 and T2 shortening, which theoretically results in hyperintensity on T1-weighted images and hypointensity on T2-weighted images. The concentration of methemoglobin, however, determines the signal intensity present on any image sequence. Concentrated (undiluted) intracellular methemoglobin acts as a true paramagnetic material and appears hyperintense on T1-weighted images and very hypointense on T2-weighted images. Undiluted extracellular methemoglobin is hyperintense on T1-weighted images and slightly hypointense on T2-weighted images. Dilute extracellular methemoglobin is hyperintense on both T1- and T2-weighted images (Fig. 9–7). The mechanism of relaxation for methemoglobin is proton-electron dipole-dipole relaxation enhancement (PEDDRE). The hyperintense signal is present initially at the periphery of the hematoma and gradually progresses toward the center of the hematoma. Chronic hematomas are isointense to slightly hypointense on T1-weighted images and very hypointense on T2-weighted images because of the presence of hemosiderin. The signal intensity of the chronic hematoma is similar to that of acute hematoma because of a similar mechanism of relaxation—PRT2PRE.

GRE acquisition imaging is highly sensitive to the detection of acute and chronic hemorrhage,[3, 28, 103, 122] because

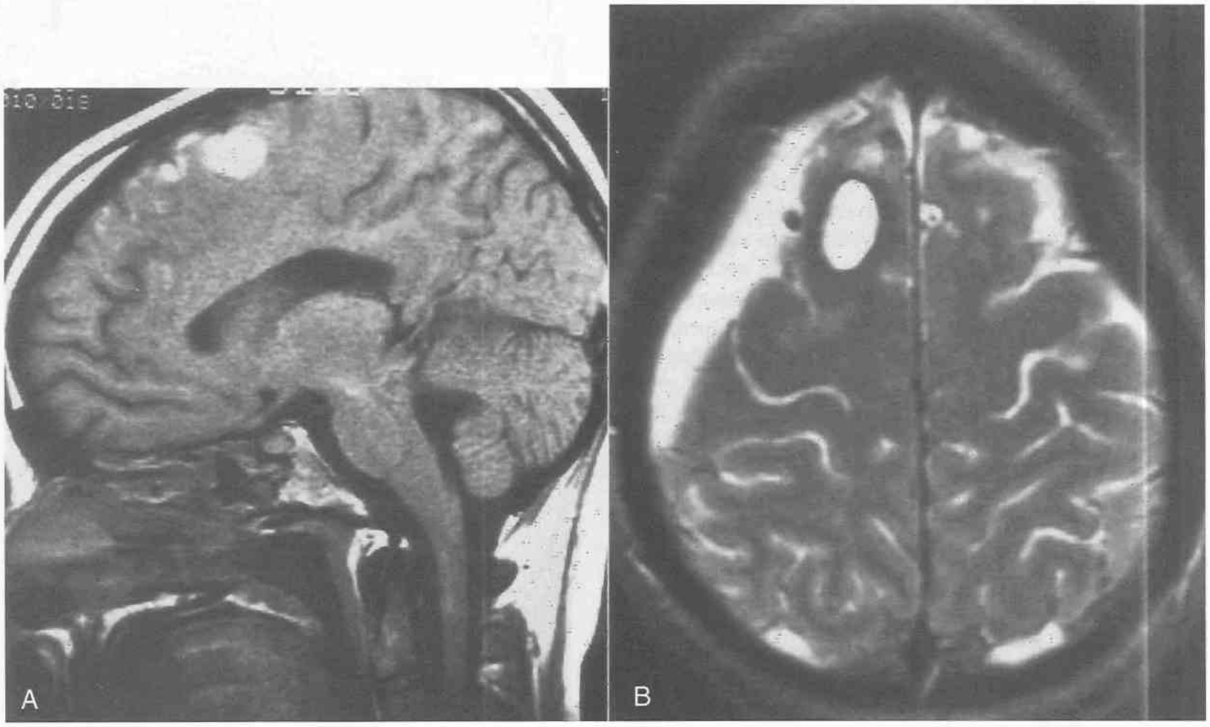

Figure 9–7. *A* and *B,* Right frontal lobe subacute intracerebral hematoma is hyperintense on sagittal T1-weighted (500/15) and axial T2-weighted (2500/80) MR images. The hyperintensity reflects the presence of dilute intracellular methemoglobin. Note the right convexity subacute subdural hematoma.

of the sensitivity of GRE sequences to the magnetic susceptibility effects of acute and chronic hemorrhage.[28] Hemorrhagic lesions are more evident, and more are detected with GRE than with conventional SE sequences.[31] The conspicuity of hemorrhagic lesions on SE sequences is superior at 1.5 T than at 0.5 T. The addition of a GRE sequence at lower field strength provides depiction of a hemorrhagic lesion equal to that obtained at higher field strength.[103]

The development of FSE sequences results in decreased scan time and motion artifact. Lesion conspicuity with FSE sequences is similar to that obtained with SE sequences.[58] FSE sequences are, however, less sensitive in the detection of hemorrhage because they are not as sensitive to magnetic susceptibility effects as conventional SE sequences.[80] Despite the relative lack of sensitivity of FSE sequences to the presence of hemorrhage, they are comparable to SE sequences in hemorrhage detection.[57] The addition of a GRE sequence allows the detection of small foci of hemorrhage that may not be visualized on FSE images.

Epidural Hematoma

Epidural hematomas are characteristically biconvex or lentiform (Fig. 9–8).[25] Uncommonly, epidural hematomas may be bilenticular, crescentic, or irregular.[19] The shape is determined by the dura, which is firmly adherent to the inner table of the skull. A blow to the calvarium results in damage to the underlying vessel, with subsequent displacement of the dura away from the inner table of the skull. The vessel may be damaged, even without fracture of the adjacent bone, as is commonly seen in children. Fracture of the adjacent bone is, however, common.[128] The most common location for epidural hematomas is over the temporal lobe, followed by the parietal, frontal, and occipital lobes with the posterior fossa the least common location.[19] Damage to the middle meningeal artery is responsible for most epidural hematomas; however, they may occur as a result of laceration of diploic veins or dural sinuses.[128]

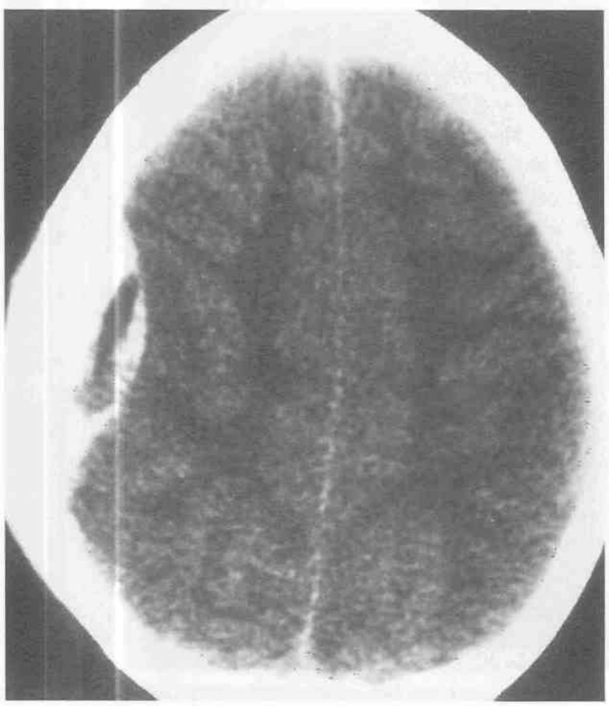

Figure 9–8. Typical biconvex epidural hematoma is present over the right parietal lobe.

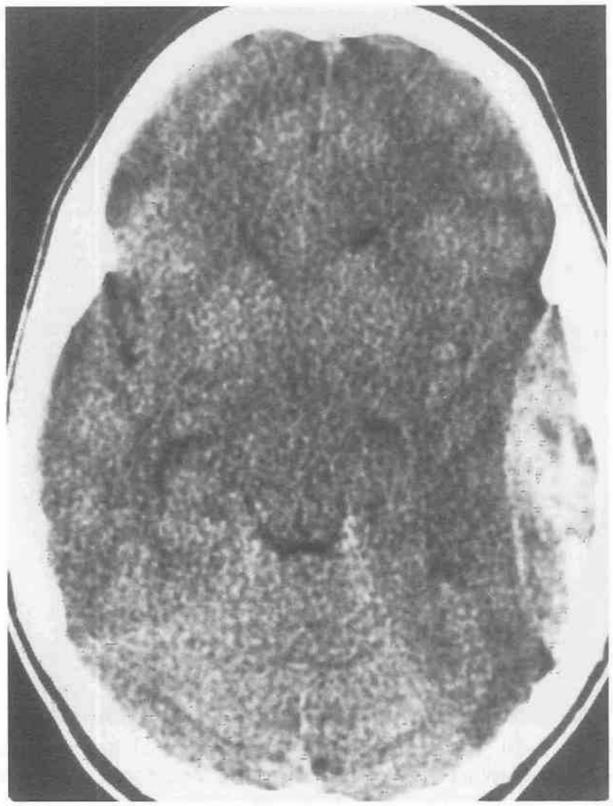

Figure 9–9. Heterogeneous left temporal convexity epidural hematoma exhibits considerable mass effect. Heterogeneous areas represent unclotted blood.

Epidural hematomas may be classified as acute, subacute, and chronic. An acute epidural hematoma is heterogeneous in attenuation, containing areas of hyperdense blood and isodense serum (Fig. 9–9). Subacute epidural hematoma is homogeneously hyperdense in attenuation, consisting of solid blood clot (Fig. 9–10). Heterogeneous or decreased attenuation, as well as an enhancing membrane, are characteristics of chronic epidural hematoma, as a result of degradation of blood products.[128] Peripheral enhancement representing dura and membrane formation between the epidural hematoma and adjacent brain parenchyma may be seen in chronic epidural hematomas with the use of intravenous contrast.[90] Delayed epidural hematoma is most commonly from slow venous bleeding from rupture of a dural sinus (Fig. 9–11).[54, 90, 110] Other causes of delayed epidural hematoma are pseudoaneurysm rupture of an epidural vessel and arteriovenous fistula.[84] In some instances, when minimal neurologic signs and symptoms are present, epidural hematoma may undergo spontaneous resolution, which is visualized on serial CT scanning.[124] Some hematomas expand 1 to 2 weeks after injury and then gradually resolve. This expansion correlates with an increase in or persistence of symptoms.[92] The imaging

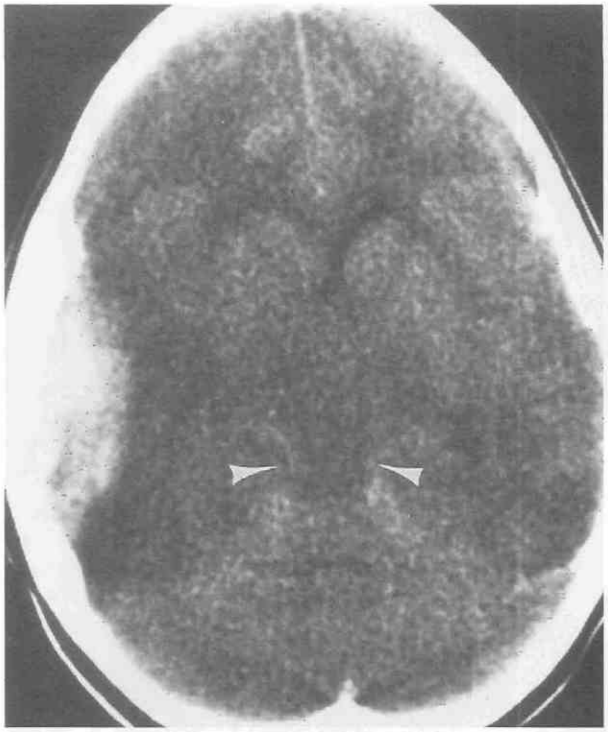

Figure 9–10. Right temporal convexity epidural hematoma is largely homogeneous in density, indicating the presence of clotted blood. Note the effacement of the basal cisterns (*arrowheads*).

criteria in determining whether an epidural hematoma may be treated conservatively are (1) a diameter of less than 1.5 cm and (2) a minimal midline shift of less than 2 mm. The patient must be neurologically intact without focal deficit.[48,104] Parenchymal abnormalities are not present as frequently with epidural hematomas as with acute SDHs. Surgical evacuation of the hematoma results in marked clinical improvement. Little or no residual hematoma is evident on postoperative scans.[24]

Posterior fossa epidural hematomas are rare; however, delay in detection may result in fatal brain stem injury.[119] Many posterior fossa epidural hematomas are not readily visualized on CT because of beam-hardening artifact. The use of contrast material facilitates the detection by demonstrating displacement of the dural sinuses, the torcular herophili, or both as well as displacement of the dura away from the calvarium.[119]

MRI studies allow the distinction between epidural hematomas and SDHs, which may not be possible with CT scans when a hematoma is small or is not typically biconvex. In epidural hematomas, the dura is seen as a curvilinear band of decreased signal intensity between the hematoma and brain parenchyma (Figs. 9–12 and 9–13).[39] Venous epidural hematomas may be differentiated from arterial hematomas on the basis of the former's proximity to a dural sinus and displacement of the involved sinus away from the inner table of the skull.[36, 84] The majority of posterior fossa epidural hematomas are of venous origin and may not be well visualized with CT scans because of beam-hardening artifact from adjacent bone structure.[128]

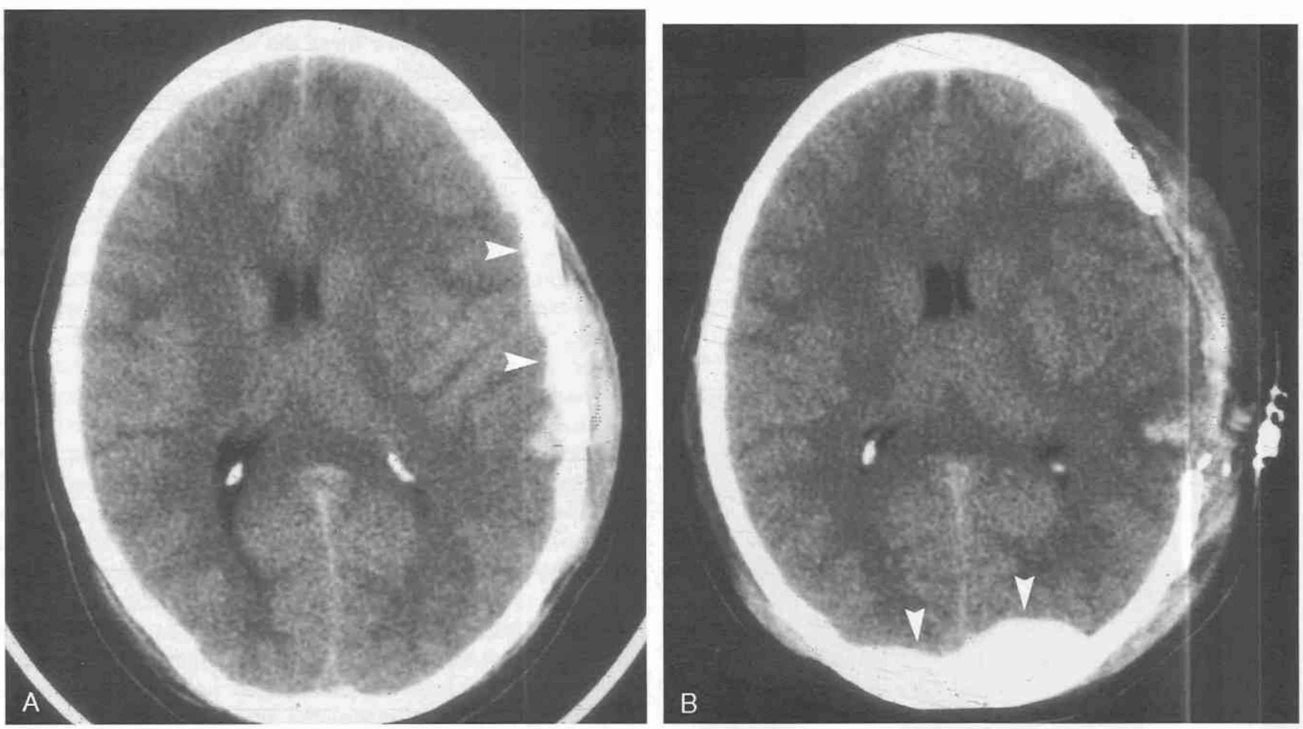

Figure 9–11. Delayed epidural hematoma. *A,* Acute subdural hematoma is present over the left parietal convexity (*arrowheads*). Note the small hemorrhagic contusion in the left parietal lobe. *B,* The patient has undergone craniectomy and drainage of the subdural hematoma. Note the new posterior parieto-occipital epidural hematoma (*arrowheads*).

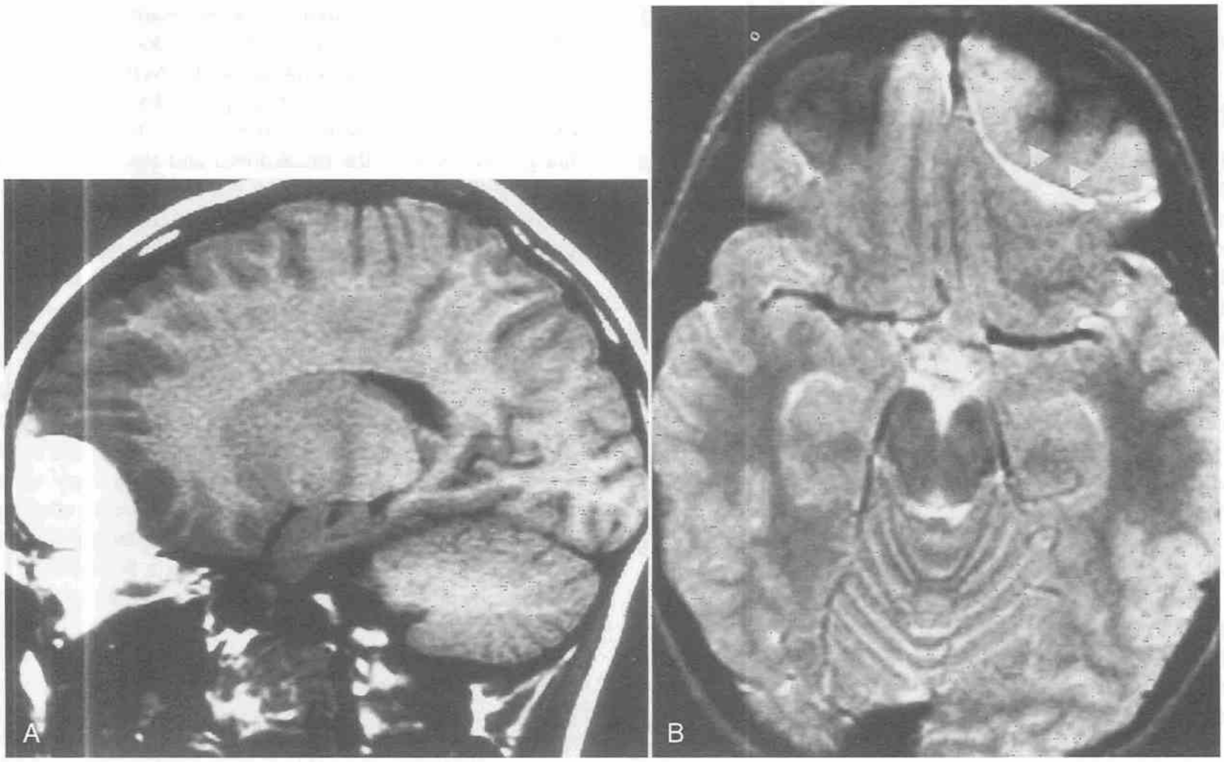

Figure 9–12. *A* and *B*, Sagittal T1-weighted (500/15) and axial T2-weighted (2500/80) MR images show large subacute epidural hematoma overlying the left frontal lobe. Note the displacement of the hypointense dura away from the inner table of the calvarium (*arrowheads*).

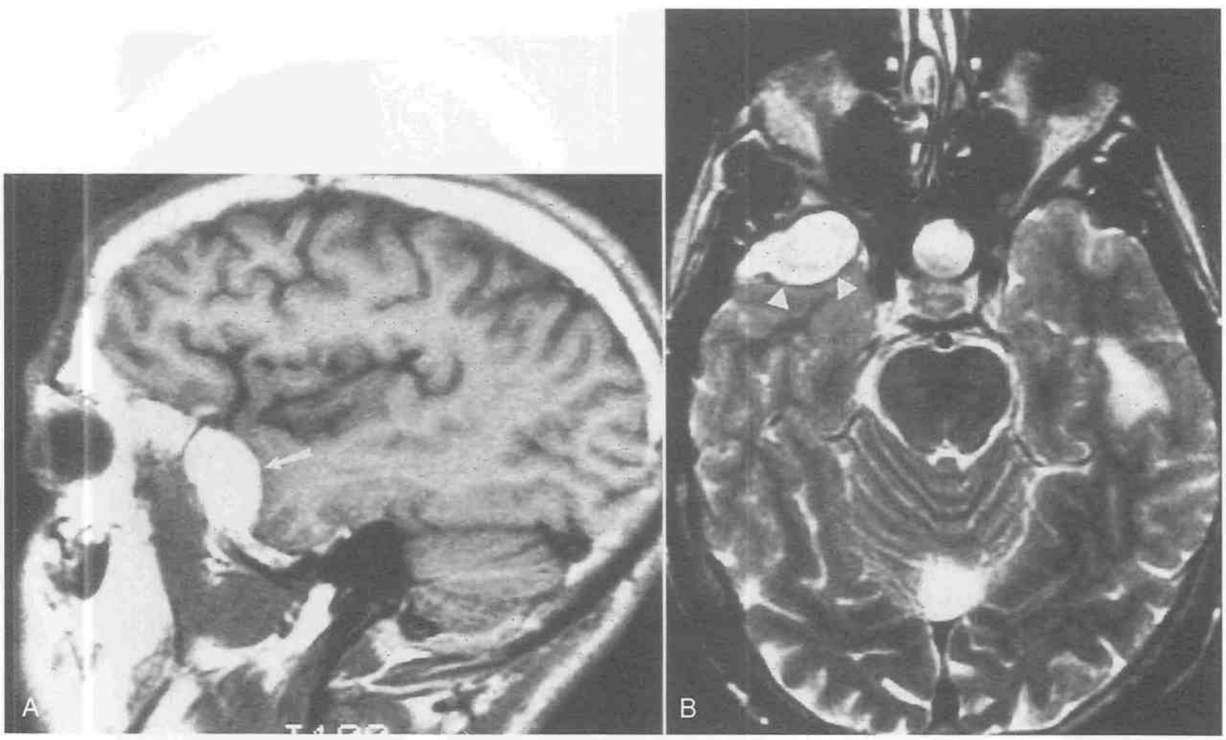

Figure 9–13. *A* and *B*, Subacute right temporal convexity epidural hematoma is hyperintense on both sagittal T1-weighted (500/15) (*arrow*) and axial fast spin-echo T2-weighted (4000/108) MR images (*arrowheads*). The band of hypointensity corresponds to the displaced dura (*arrowheads*). Retention cyst is present in the sphenoid sinus.

The lack of artifact from bone on MRI studies readily enables the detection of a small epidural hematoma.

Subdural Hematoma

SDHs are most commonly caused by shear forces that result in the tearing of the bridging veins present in the subdural space.[35] Laceration of cortical arteries and parenchymal contusions are other causes of SDHs.[105] Rarely, an SDH may be caused by rupture of an aneurysm or arteriovenous malformation.[96] Unlike an epidural hematoma, which is focal, an SDH is diffuse and may overlie an entire cerebral hemisphere. The potential subdural space offers little or no resistance to the expansion of the hematoma within the subdural space.

Underlying brain injury, such as hemorrhagic contusion and edema, are frequently seen with acute SDH.[26,132] These injuries are seen more commonly with SDH than with epidural hematoma.[24] The degree of mass effect seen with SDH is often out of proportion to the size of the hematoma. This mass effect is from the presence of hemorrhagic contusions and edema rather than the SDH.[24,132]

The typical appearance of an acute SDH is a hyperdense crescent-shaped collection with a convex lateral border and concave medial border overlying the cerebral convexity (Fig. 9–14).[26,132] Occasionally the hematoma may be biconcave, simulating the appearance of an epidural hematoma.[12] This biconcavity can be seen particularly when the hematoma is large.[34] The majority of acute SDHs are hyperdense because of the attenuating properties of the hemoglobin molecule. In one report, SDHs were found to be hyperdense in all patients with a history of acute injury.[102] An acute SDH may be isodense with brain parenchyma in patients with anemia as a result of a reduced concentration of hemoglobin.[113] The typical acute SDH gradually approaches the density of brain parenchyma and appears isodense with brain over an interval of 1 to 5 weeks.[26] This change occurs from the breakdown and absorption of blood products.

The classic homogeneous, hyperdense appearance of acute SDH is not always present. The hematoma may appear mixed rather than homogeneous in attenuation.[95] It may have one of three patterns: marginal hypodensity, central irregular areas of hypodensity, or laminar areas of hypodensity (Figs. 9–15 and 9–16). The low density may be secondary to unclotted blood or possibly CSF resulting from arachnoid tears. The mixed SDH is usually larger and has more mass effect than the classic hyperdense SDH.

SDHs located adjacent to the tentorium may simulate an intra-axial lesion. Several features serve to distinguish the subdural location of the lesion. Supratentorial SDHs located adjacent to the tentorium have a well-defined medial margin corresponding to the edge of the tentorium. A sheetlike area of increased density that slopes laterally is present, and the trigone of the lateral ventricle is rotated anteriorly and superiorly.[69] When the hematoma is located below the tentorium, the lesion has a sharp lateral margin corresponding to the tentorium and increased density that slopes medially (Fig. 9–17).

Interhemispheric SDHs occur in the posterosuperior aspect of the interhemispheric fissure (Fig. 9–18).[135] Anterior extension of the lesion occurs less commonly. This lesion may be differentiated from a normal or calcified falx and SAH. SDH in the interhemispheric location has a character-

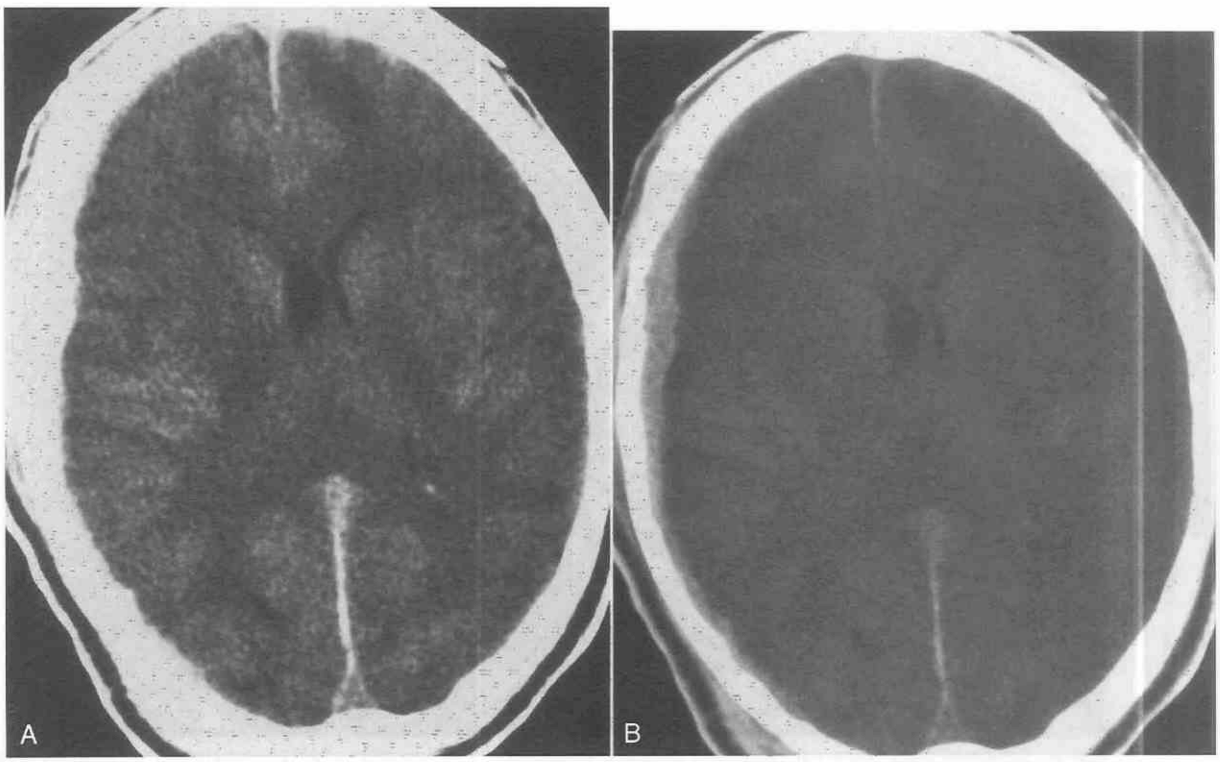

Figure 9–14. *A,* Crescentic right convexity acute subdural hematoma is evident from the irregular contour on the brain window setting. *B,* The subdural hematoma is better demonstrated with an intermediate window setting.

Figure 9–15. Acute left convexity subdural hematoma has marginal hypodensity, representing unclotted blood or cerebrospinal fluid.

Figure 9–16. Irregular areas of hypodensity indicate that unclotted blood or cerebrospinal fluid is present in this acute left convexity subdural hematoma.

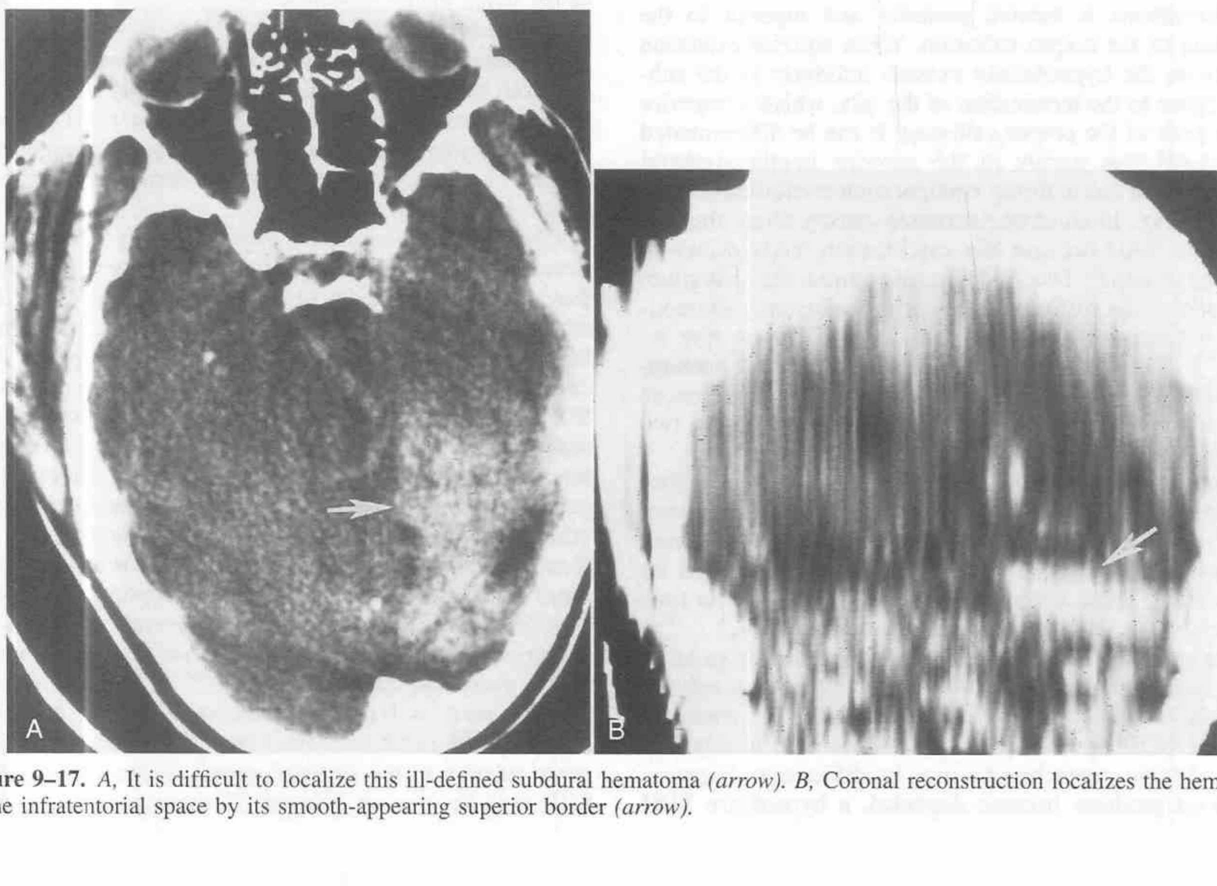

Figure 9–17. *A,* It is difficult to localize this ill-defined subdural hematoma *(arrow). B,* Coronal reconstruction localizes the hematoma to the infratentorial space by its smooth-appearing superior border *(arrow).*

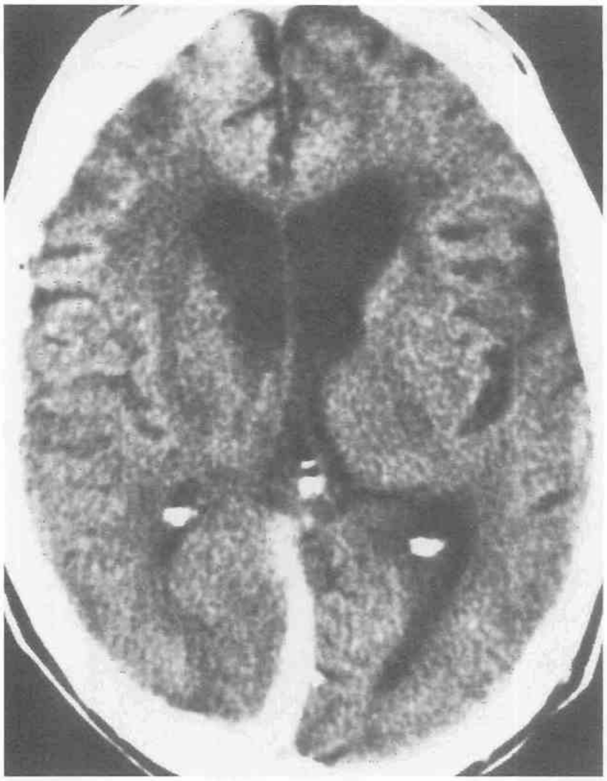

Figure 9–18. Interhemispheric subdural hematoma. The flat medial border of this acute hematoma localizes it to the subdural space above the tentorium.

istic crescentic shape with a flat medial border that abuts the falx and a convex lateral border that abuts the brain. The hematoma is located posterior and superior to the splenium of the corpus callosum. When anterior extension is present, the hyperdensity extends inferiorly in the subdural space to the termination of the falx, which is superior to the genu of the corpus callosum. It can be differentiated from SAH that occurs in the anterior interhemispheric fissure, which has a zigzag configuration conforming to the cortical sulci. In children, increased density along the falx represents SAH because falx calcification rarely occurs in this age group.[22] The SAH extends from the calvarium inferiorly to the rostrum of the corpus callosum, differentiating it from an SDH. Posterior fossa SDHs are rare lesions.[119] Distinction between SDHs and epidural hematomas may be accomplished with the use of intravenous contrast agents that allow differentiation between the two lesions.[119]

Postoperatively, residual SDH may be seen from failure to find the origin of bleeding and difficulty in removing blood clot adherent to the arachnoid (Fig. 9–19).[31] Small SDHs are not surgically evacuated and are managed by observation. These lesions are gradually resorbed over time as fibrinolysis and absorption of blood clot occurs.[5]

The majority of SDHs differ in attenuation from adjacent brain, being either hyperdense or hypodense relative to brain, and are readily diagnosed with CT scanning. Isodense SDHs—with attenuation values near or equal to those of brain parenchyma—may be difficult to diagnose. As blood products become degraded, a hyperdense SDH gradually decreases in attenuation, becoming isodense with brain. Occasionally, rebleeding into a chronic SDH results in an isodense lesion.[26] Acute isodense SDH may rarely be seen, occurring in patients with anemia.[113] Other possible causes of isodense SDH are dilution with CSF secondary to arachnoidal tear and local or disseminated coagulopathy.[8, 61]

Effacement of the cortical sulci over the cerebral convexity and mass effect on the ventricular system or midline shift indicate the presence of an isodense SDH (Fig. 9–20).[2] Mass effect on the ventricular system may be negligible or absent when bilateral collections are present.[34] Delayed contrast-enhanced CT scans performed 4 to 6 hours after injection of the contrast agent reveal enhancement of the subdural collection.[2, 82] Contrast-enhanced CT scans may also demonstrate enhancement of cortical veins that are displaced medially from the inner table of the calvarium; however, this enhancement is not seen in all cases.[63] The use of rapid high-dose contrast enhancement allows the more accurate detection of an isodense SDH.[49] The majority of patients with an isodense SDH may have three or four of the following signs: posterior displacement of the ipsilateral anterior horn of the lateral ventricle, compression of the ipsilateral posterior and temporal horns, anterior displacement of the ipsilateral posterior and temporal horns, anterior displacement of the ipsilateral glomus calcification, and widening of the contralateral ventricle.[85] In a patient with a history of head trauma, the presence of small compressed ventricles with the absence of cortical sulci should raise the possibility of bilateral isodense SDH.[63] High-resolution CT scans allow the differentiation of gray matter from white matter. The presence of an extra-axial mass displaces the gray-white matter interface medially, producing buckling of the central white matter.[40] Buckling of the white matter is virtually diagnostic of an extra-axial mass (see Fig. 9–20).

Chronic SDHs are most commonly caused by trauma; however, the traumatic episode is frequently so minor that it is forgotten or ignored.[16, 59] The chronic SDH is caused by a torn bridging vein in the subdural space through which venous blood slowly flows.[24] In one series, no acute SDH evolved into a chronic SDH.[24]

Chronic SDHs are most commonly hypodense on CT scans (Fig. 9–21).[66] The are typically crescentic, however, they may be biconcave or lentiform as a result of fluid absorption into the hematoma.[34] Another possible cause is the formation of adhesions. A capsule composed of a capillary-rich membrane develops and surrounds the SDH.[59] This capillary-rich membrane is responsible for repeated episodes of rebleeding and subsequent increase in size of the hematoma. As the hematoma enlarges, the patient becomes symptomatic, showing signs of increased intracranial pressure, hemiparesis, or intellectual and personality change.[16] Repeated episodes of rebleeding may result in a mixed-density collection containing areas of hypodense, isodense, and increased attenuation (Fig. 9–22). A chronic SDH may appear hyperdense from acute hemorrhage, simulating an acute process.[26, 102] Fluid-fluid levels may be seen as blood products settle in the dependent aspect of the subdural collection, which becomes hyperdense relative to the superior aspect. Enhancement of the SDH may be seen on delayed CT scans obtained 3 and 6

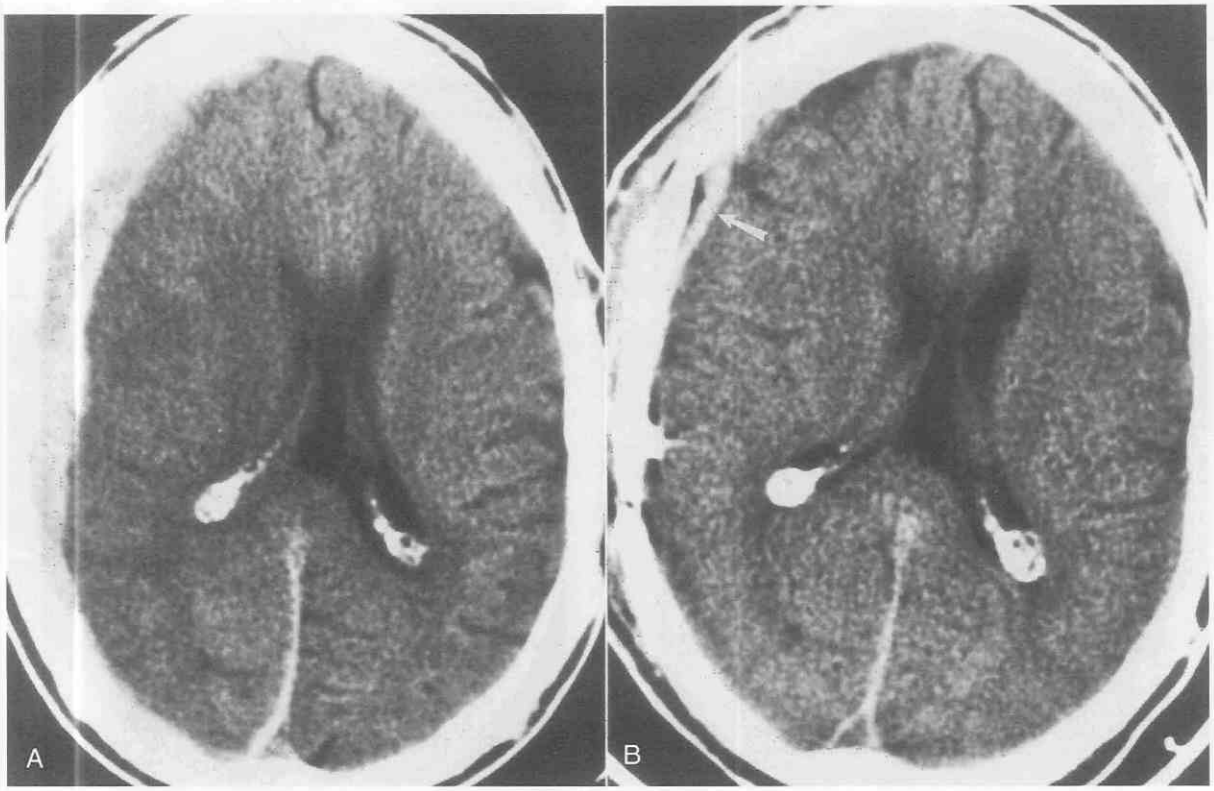

Figure 9–19. *A,* Acute subdural hematoma is present over the right cerebral convexity with extension into the interhemispheric fissure posteriorly. *B,* Postoperative scan reveals small residual hematoma *(arrow).*

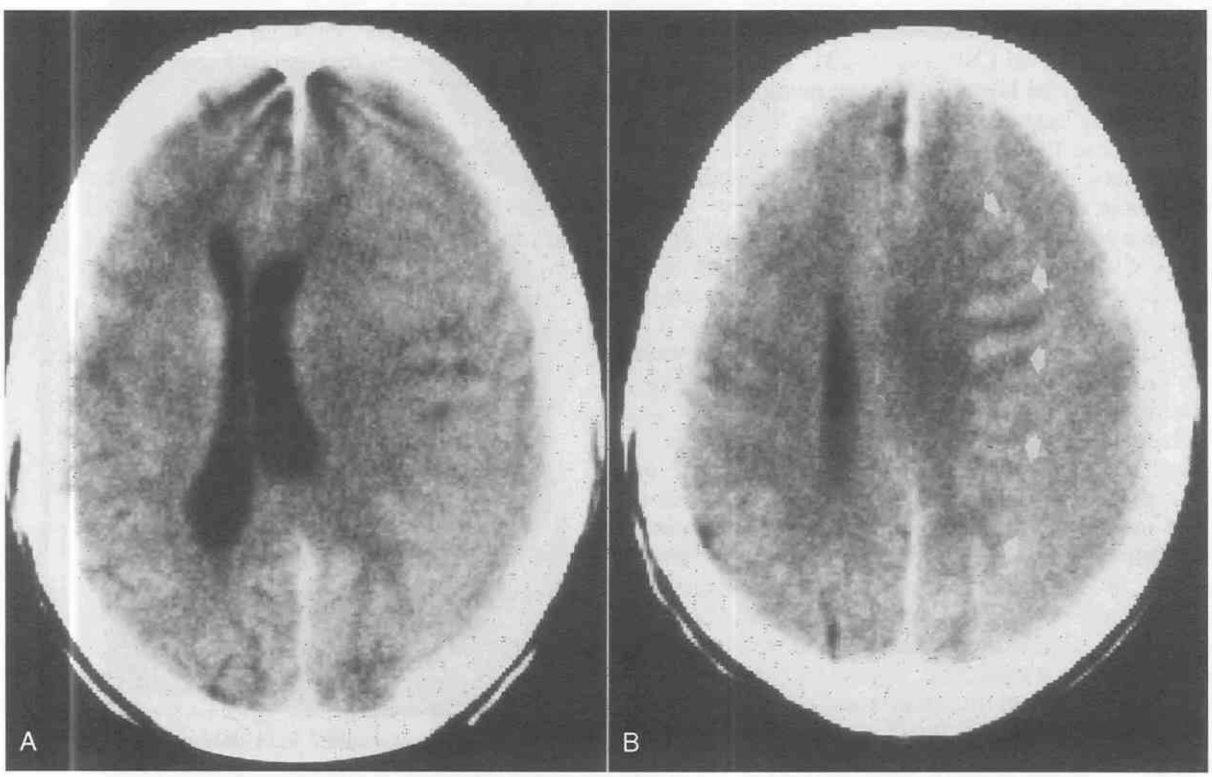

Figure 9–20. *A,* Left convexity isodense: subdural hematoma causes mass effect on and shift of the left lateral ventricle. *B,* White matter buckling *(arrows)* indicates the presence of the extra-axial subdural collection.

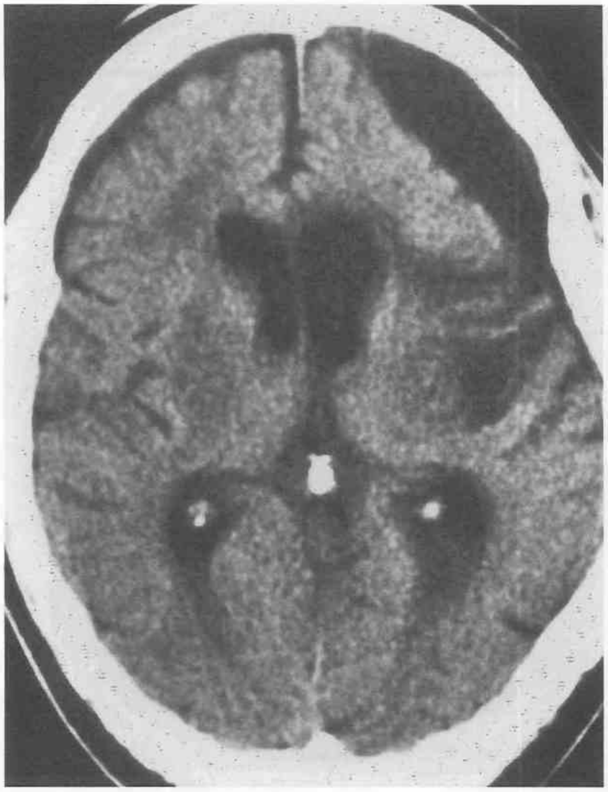

Figure 9–21. Bilateral frontal convexity chronic subdural hematomas are present. Note the slight shift of the septum pellucidum to the right.

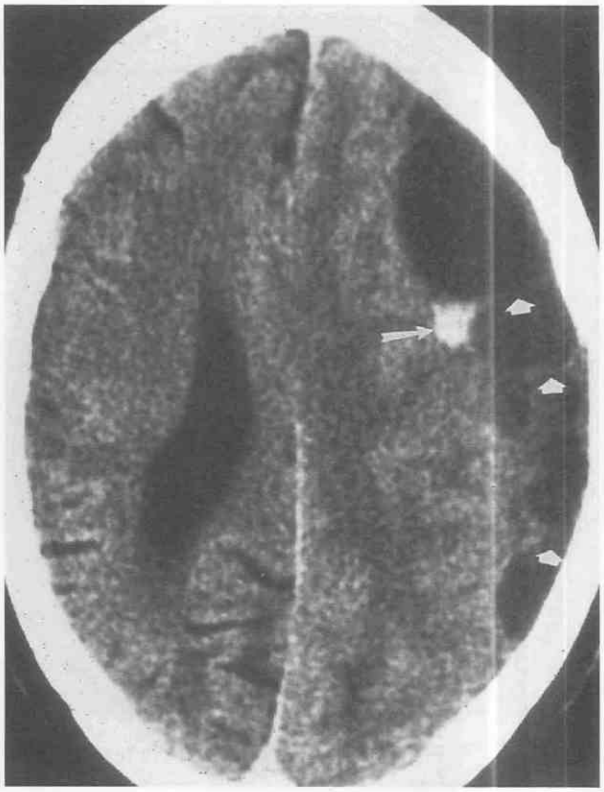

Figure 9–22. Large chronic subdural hematoma overlies the left cerebral convexity. The hyperdense area represents recurrent hemorrhage *(long arrow)*. Note the septations within the hematoma *(small arrows)*.

hours after intravenous administration of contrast material.[59]

A subdural hygroma is a hypodense extracerebral collection equal in density to CSF (Fig. 9–23). The lesions are crescentic and may be bilateral. It is not possible to distinguish a subdural hygroma from a chronic SDH with CT scanning, because the two lesions are identical in appearance. At surgery, clear fluid and lack of a membrane allow the diagnosis of a subdural hygroma.[51,102]

The MRI appearance of SDH has been well documented.[33, 86,111] In the acute phase (<1 week old), an SDH is isointense or slightly hypointense relative to gray matter on T1-weighted images and very hypointense on T2-weighted images. Early subacute hematomas (>1 one week and <2 weeks old) are characterized by a rim of hyperintensity surrounding a center of hypointensity on T1- and T2-weighted images. In the late subacute hematoma (>2 weeks and <1 month old), the lesion is hyperintense on both T1- and T2-weighted images (Fig. 9–24). Chronic SDH (>1 month old) are isointense relative to gray matter on T1-weighted images and hyperintense on T2-weighted images (Fig. 9–25). Usually no hypointensity is evident in chronic SDHs on T2-weighted images, most likely because of the lack of a blood-brain barrier and resorption of hemosiderin from the collection. Occasionally hemosiderin may be seen in thickened membranes and areas of rehemorrhage. Fluid-fluid levels of different signal intensity suggest rebleeding. It is possible to distinguish a chronic subdural hygroma from a chronic SDH because the hygroma is of CSF signal intensity on all pulse sequences (Fig. 9–26).[33]

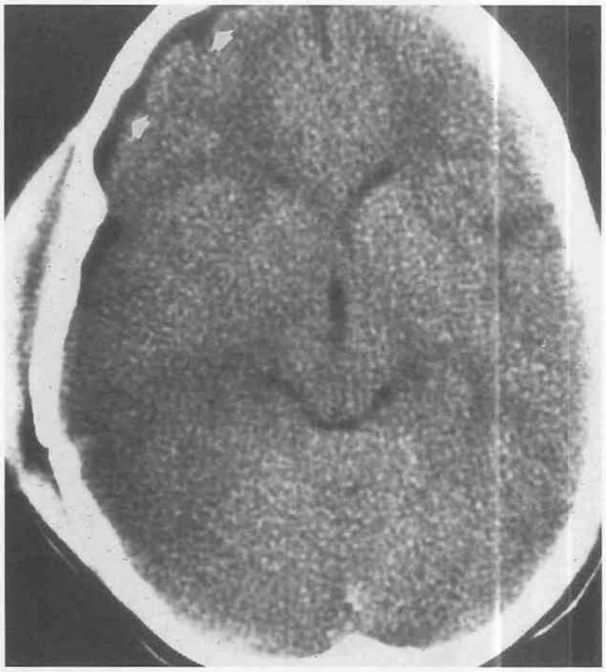

Figure 9–23. Cerebrospinal fluid–density collection representing a cerebrospinal fluid hygroma is present over the right frontal convexity *(arrows)*. The initial CT scan 3 days earlier showed no subdural collection.

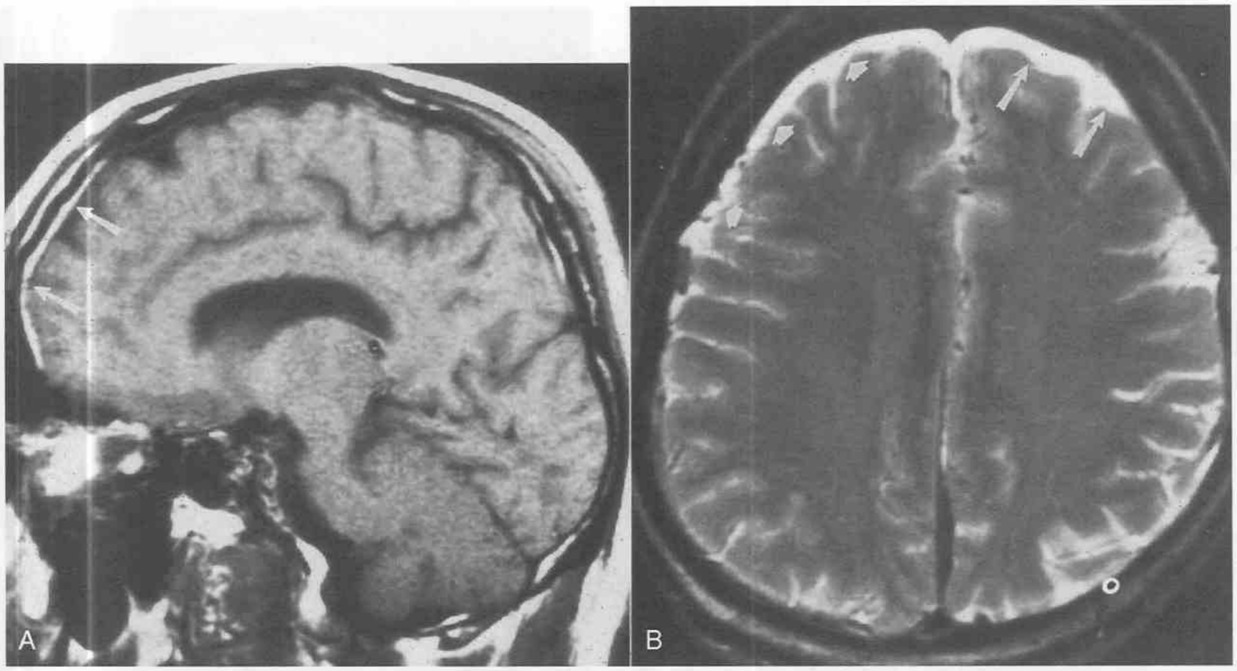

Figure 9–24. *A* and *B,* Sagittal T1-weighted (500/15) and axial T2-weighted (2500/80) MR images demonstrate hyperintense left frontal convexity subacute subdural hemorrhage. Right frontal convexity subacute hematoma is seen on the axial T2-weighted image *(small arrows).*

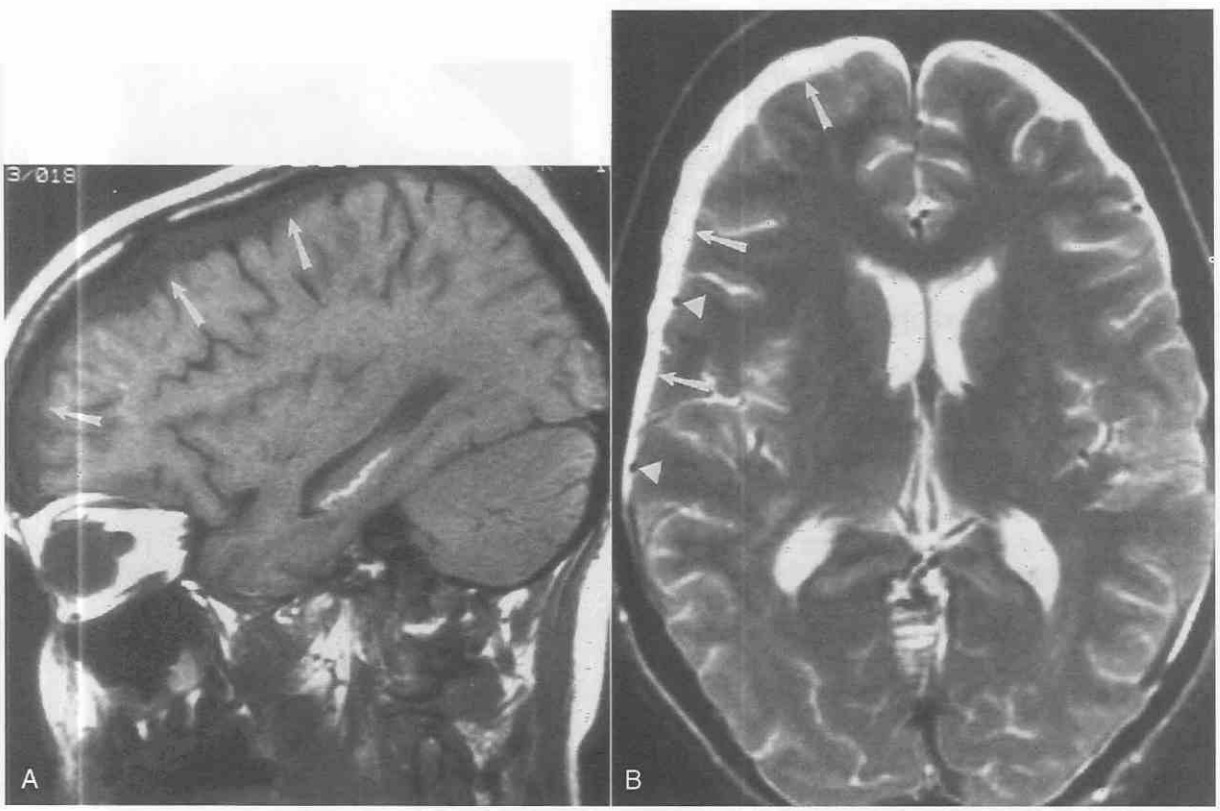

Figure 9–25. *A* and *B,* Right frontal convexity chronic subdural hematoma is slightly hyperintense on sagittal T1-weighted (500/15) and isointense on axial T2-weighted (2500/80) MR images relative to cerebrospinal fluid *(arrows).* Note displacement of the subdural veins away from inner table of the calvarium *(arrowheads).* A small left frontal convexity subdural hemorrhage is present.

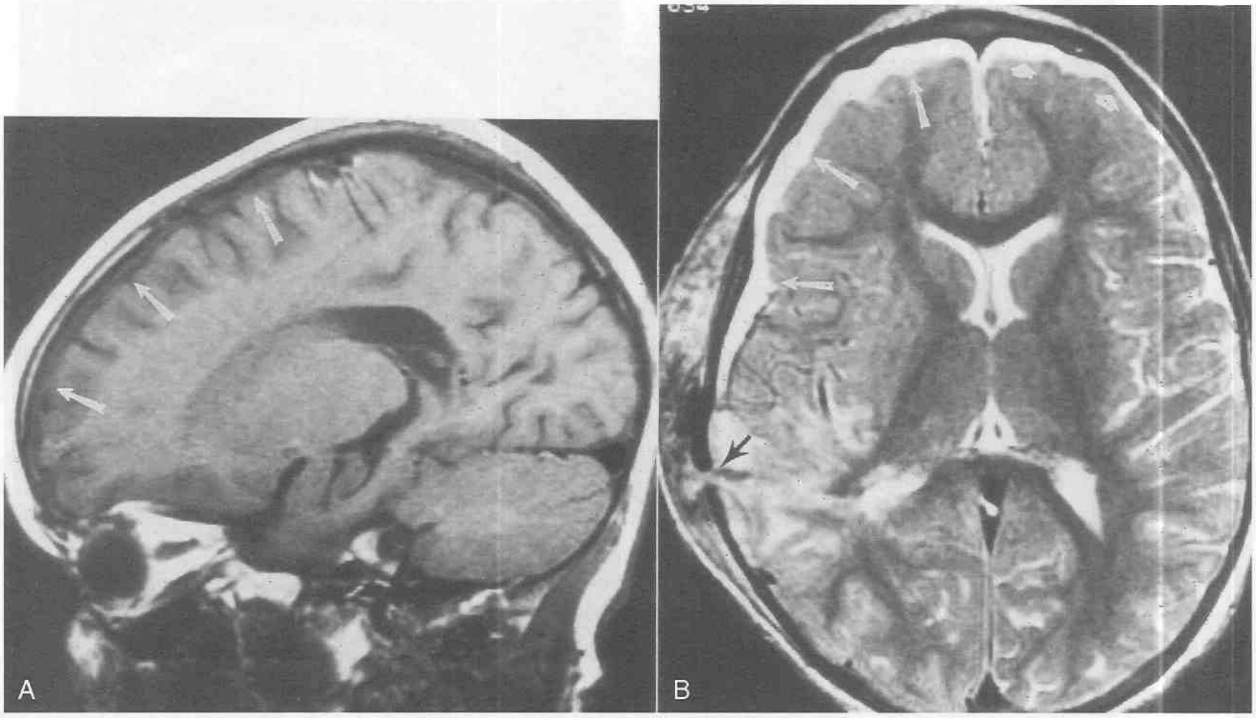

Figure 9–26. *A* and *B*, Same case as shown in Figure 6–23. Sagittal T1-weighted (500/15) and axial fast spin-echo/T2-weighted (3500/108) MR images show cerebrospinal fluid hygroma over right frontotemporoparietal convexity *(arrows)*. The small left frontal convexity hygroma not evident on the CT scan is well visualized on the MRI study *(small arrows)*. Note the right temporal lobe contusion and herniation of the temporal lobe through the temporal bone fracture *(black arrow)*.

It is not always possible to distinguish a subdural hygroma from atrophy because the findings of mass effect and sulcal effacement associated with subdural hygroma may be subtle. Visualization of cortical veins adjacent to displaced cortex is indicative of subdural hygroma. A diagnosis of atrophy is made when cortical veins are seen traversing a widened subarachnoid space.[79]

Subarachnoid Hematoma

SAH is frequently present in the acutely injured patient. It is often associated with other lesions, such as intracerebral hematoma. SAH is caused by damage to blood vessels on the pia-arachnoid. Intraparenchymal hematoma with rupture into the ventricular system may gain access to the subarachnoid space via the foramina of Mangendie and Luschka. On CT scans, hyperdensity representing acute hemorrhage is visualized in the sulci overlying the cerebral convexities, within the sylvian fissures, basal cisterns, and interhemispheric fissure (Fig. 9–27). Hemorrhage is rapidly cleared from the subarachnoid space. The majority of CT scans performed within 1 week appear normal.[66]

CT is the modality of choice in the evaluation of SAH because of the hyperdensity of clotted blood. It is difficult to visualize with MRI studies because the high oxygen concentration in CSF prevents the degradation of oxyhemoglobin to deoxyhemoglobin.[10, 21, 39] This process has been described in detail in both clinical and experimental situations.[10, 17] SAH may be seen on MRI studies only when large volumes of clot are present.[39] Acute SAH is isointense

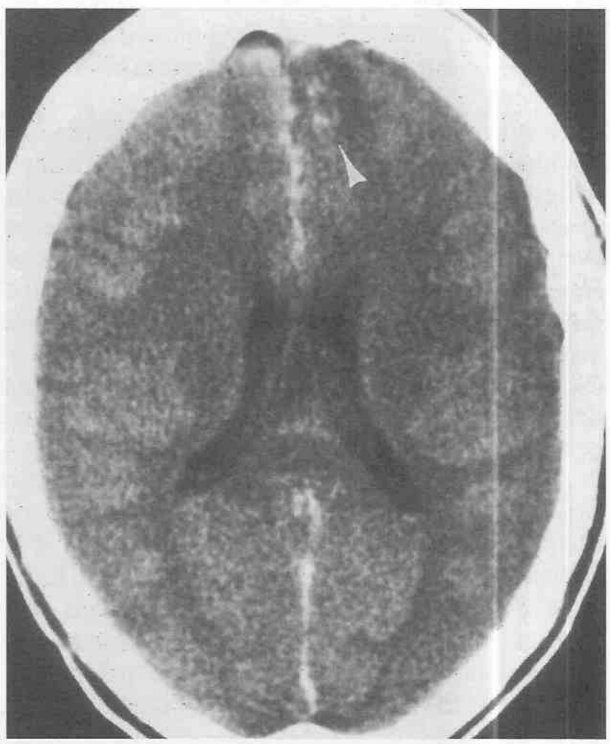

Figure 9–27. Subarachnoid hematoma is present along the interhemispheric fissure. Blood in the sulci is responsible for the zigzag appearance of the interhemispheric hemorrhage. Hemorrhagic contusion is present adjacent to the falx in the left frontal lobe *(arrowhead)*.

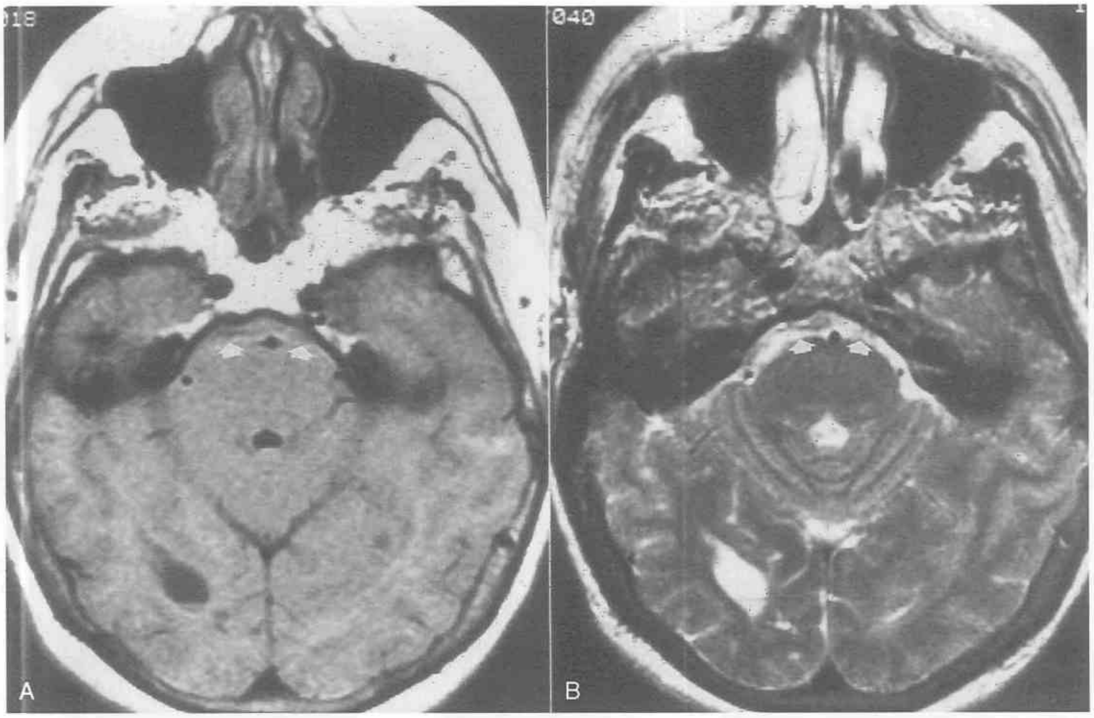

Figure 9–28. *A,* Acute subarachnoid hemorrhage in pontine cistern is isointense on axial T1-weighted (500/15) MR image (*arrows*). *B,* Hypointense hemorrhage is poorly seen on axial fast spin-echo T2-weighted (3900/108) image (*arrows*) because it is masked by hyperintense cerebrospinal fluid.

on T1-weighted images and hypointense on T2-weighted images with respect to brain (Fig. 9–28). Toward the end of the first week, the SAH exhibits T1 shortening and appears hyperintense on T1-weighted images.[10] Subacute SAH does not evolve like intraparenchymal hematoma, which as stated previously becomes isointense or slightly hypointense on T1-weighted images and very hypointense on T2-weighted images in the chronic stage. This may be from the high oxygen concentration of CSF, which may prevent the further degradation of methemoglobin to hemosiderin, or from CSF pulsation, which may aid in clot dissolution and resorption. The residual of SAH may be evident as hypointensity in the leptomeninges because of hemosiderin deposition present in macrophages.[43] This reflects the preferential T2 shortening that occurs as water protons precess through a local heterogeneous magnetic field and lose signal intensity. The effect is more evident at high field strength.[44] A T2* GRE sequence with a short flip angle and relatively long TE has been utilized in the improved detection of intraparenchymal hemorrhage.[28, 122] The improved ability of these sequences to detect hemorrhage stems from their sensitivity to inhomogeneities in the magnetic field that are produced by paramagnetic blood products. The use of GRE sequences may allow improved detection of acute SAH. Fast fluid-attenuated inversion recovery (FLAIR) sequences have proved to be sensitive in the detection of SAH. It is, however, nonspecific as leptomeningeal carcinomatosis and meningitis can have a similar appearance.[109a]

Contusion

Contusions are the most commonly encountered lesions due to head trauma.[26, 66, 130] The lesions are characterized pathologically as areas of hemorrhage, necrosis, and edema. The mechanism of contusion production is complex and depends on many factors, with lesions occurring at the site of impact as well as at sites remote from impact; they are referred to as coup and contrecoup lesions, respectively. A *coup* lesion is produced by transient inbending of the calvarium with resultant compression of the underlying brain. Fracture of the calvarium is not always present. The *contrecoup* lesion is produced when the calvarium decelerates but the brain continues in motion and strikes the irregular inner surface of the calvarium.[46]

Contusions appear as areas of heterogeneous increased density mixed with or surrounded by areas of decreased or normal density (Figs. 9–29 to 9–31).[26, 66, 130, 132] Mass effect may or may not be present, depending on the size of the lesion. The frontal lobe convexity and the lateral temporal areas are the most common sites for coup injury.[130] Contrecoup injuries typically involve the inferior surface of the frontal and temporal lobes.[130]

Hemorrhagic contusions have a typical pattern of evolution that occurs over several months.[130] The initial area of heterogeneous increased density progresses to an area of decreased density within 1 week. At 2 weeks, the contusion is not visualized because it is isodense with brain parenchyma. Enhancement occurs during the acute and subacute stages.[120, 130] Focal encephalomalacia becomes evident by 1 month after injury. Contusions may be isodense if they consist of equal amounts of hemorrhage and edema. The use of intravenous contrast material allows the detection of these isodense lesions as contrast material accumulates in areas of blood-brain barrier breakdown.[117, 120]

In the posterior fossa, contusions may be difficult to detect because of beam-hardening artifact from adjacent

Figure 9–29. *A,* Hemorrhagic contusions with surrounding edema are evident in the inferior left frontal and anterior right temporal lobe (*arrowheads*). *B,* CT scan at higher level reveals additional cortical hemorrhagic contusions in the frontal lobe (*arrowheads*).

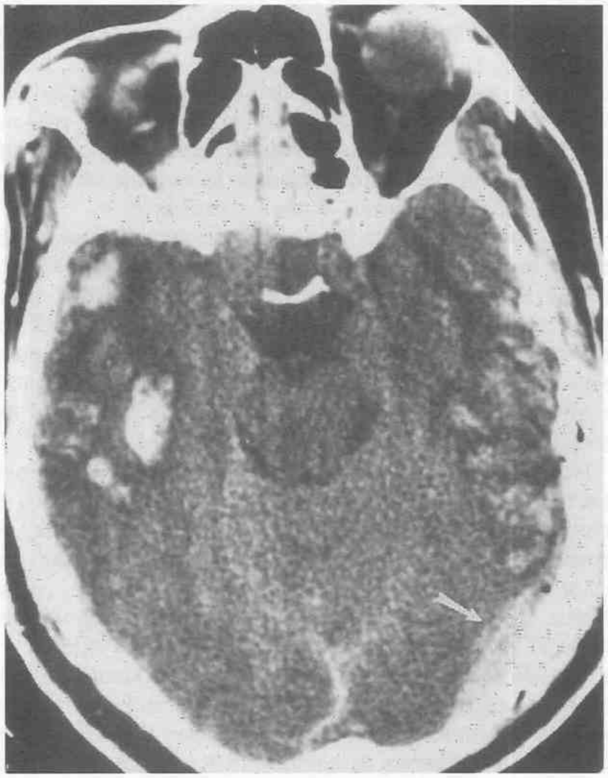

Figure 9–30. Axial CT scan demonstrates multiple hemorrhagic contusions in the temporal lobes. Note the small left occipital lobe convexity subdural hematoma (*arrow*).

Figure 9–31. Deep gray matter contusion. Hemorrhagic contusion involves the right lentiform nucleus (*arrow*).

bony structure (Fig. 9–32). In some instances, no lesion can be identified, and the presence of indirect signs such as effacement of the pontine, cerebellopontine angle, and perimesencephalic cisterns must be used to suggest the presence of brain stem injury.[118] Isodense contusions not visualized on unenhanced CT scans will become evident with the use of intravenous contrast material.[118] Brain stem injuries may be primary, occurring at the time of injury, or secondary, occurring at a later time from downward transtentorial herniation or direct compression by other lesions.[118] Hemorrhagic lesions in the rostral midbrain may also occur at the time of injury (Fig. 9–33).[83] Injury to the brain stem carries a grave prognosis and is associated with a high mortality.[119]

MRI studies are equivalent to CT scans in the detection of hemorrhagic cortical contusions but are more sensitive in the detection of nonhemorrhagic contusions.[39,136] In some cases, acute hemorrhagic contusions visible on CT scans may not be visualized with MRI.[50] As the hemorrhagic contusion evolves, it becomes isodense and finally hypodense on CT scans and is poorly seen. It is in the subacute and chronic stages that MRI studies are more sensitive than CT in the detection of contusions.[50] MRI studies also allow the contusions to be better characterized.[62] Contusions tend to be multiple and to involve the cortex with sparing of the underlying white matter. A hemorrhagic component is evident in many lesions.[37]

Acute hemorrhagic contusions are isointense or slightly hypointense in signal on T1-weighted images and very hypointense on T2-weighted images (Fig. 9–34). This feature reflects the preferential T2 shortening of intracellular deoxyhemoglobin. Subacute lesions are hyperintense on

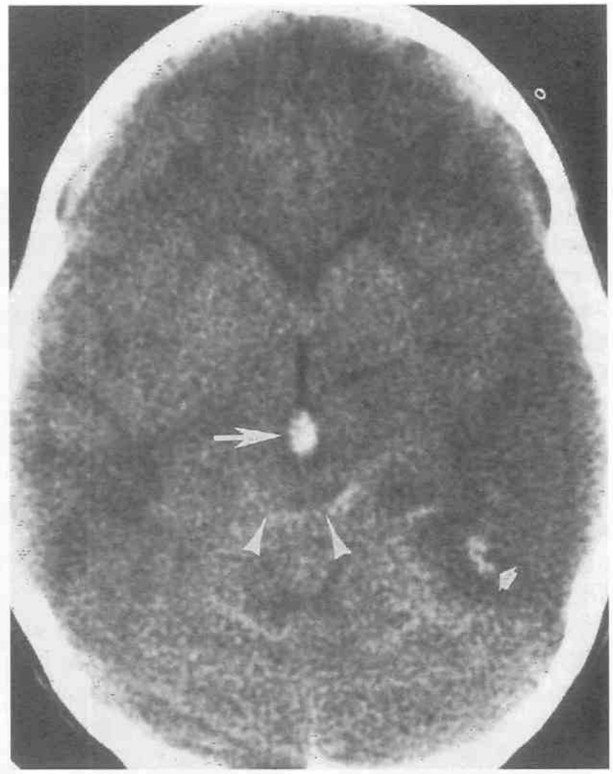

Figure 9–33. Acute hemorrhagic contusion is demonstrated in the rostral midbrain (*arrow*). Note the effacement of the quadrigeminal cistern (*arrowheads*) and the left temporal lobe contusion (*small arrow*).

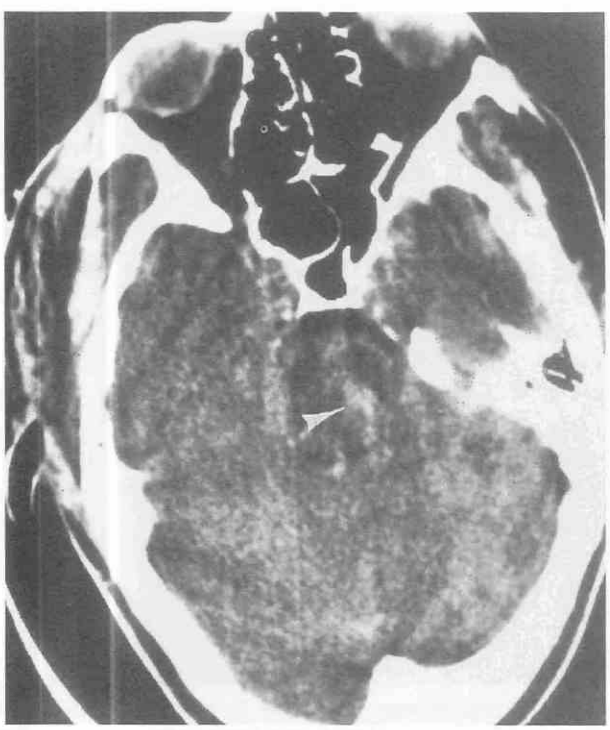

Figure 9–32. Pontine contusion. Hemorrhagic contusion is seen in the left posterolateral pons (*arrowhead*).

T1- and T2-weighted images because of the effect of extracellular methemoglobin (Fig. 9–35).[44] Hypointensity from hemosiderin and encephalomalacia are evident in chronic lesions. The discrepancy between CT and MRI in the detection of nonhemorrhagic contusions is due to the superior spatial resolution of MRI and its sensitivity in the detection of changes in water content in damaged tissue. The use of supplemental T2* GRE sequences should allow the detection of small hemorrhagic contusions that are visualized on CT scans but not with conventional SE MRI studies (Fig. 9–36).

In the posterior fossa, contusions typically occur along the posterolateral aspect of the midbrain and lateral aspect of the cerebral peduncle.[38] They are primary injuries occurring at the time of injury. Secondary injuries occur later in the ventral, ventrolateral, and paramedian aspects of the brain stem.[38] MRI studies are more sensitive than CT scans in the detection of contusions in the posterior fossa because of the lack of artifact from the adjacent bone. Indirect signs of brain stem injury, which may be the only abnormalities present on the CT scan, are well demonstrated in addition to intrinsic lesions.[38,50] Secondary foci of hemorrhage, located in the midline of the rostral midbrain, occur from tearing of penetrating arteries that supply the brain stem.[38] Although a high percentage of patients with brain stem contusions and normal CT findings have a good clinical outcome, 20% with normal CT scans do poorly because of undetected lesions or secondary complications.[74] MRI stud-

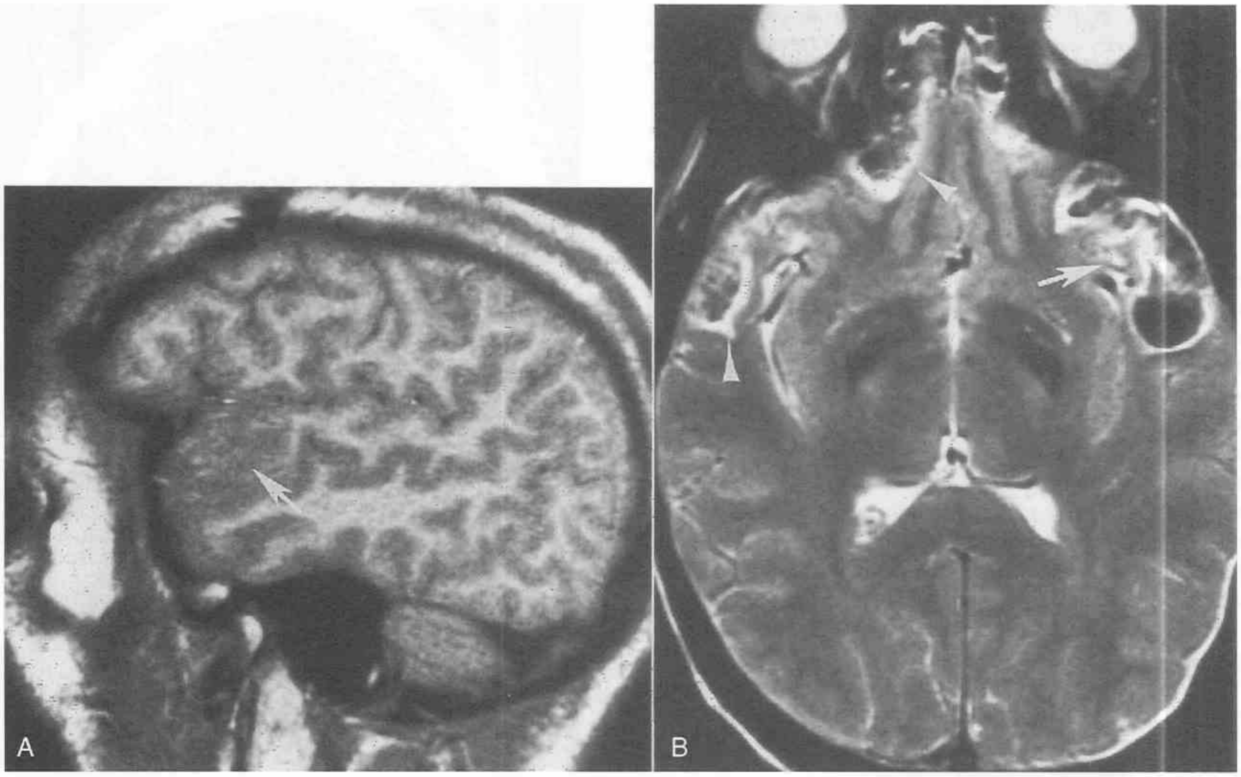

Figure 9–34. *A,* Acute left temporal lobe hemorrhagic contusion is isointense with gray matter on sagital T1-weighted (500/15) MR image (*arrow*). *B,* Hemorrhagic contusion is hypointense on axial T2-weighted (2500/80) image (*arrow*). Note additional hemorrhagic contusions in the right frontal and temporal lobes (*arrowheads*).

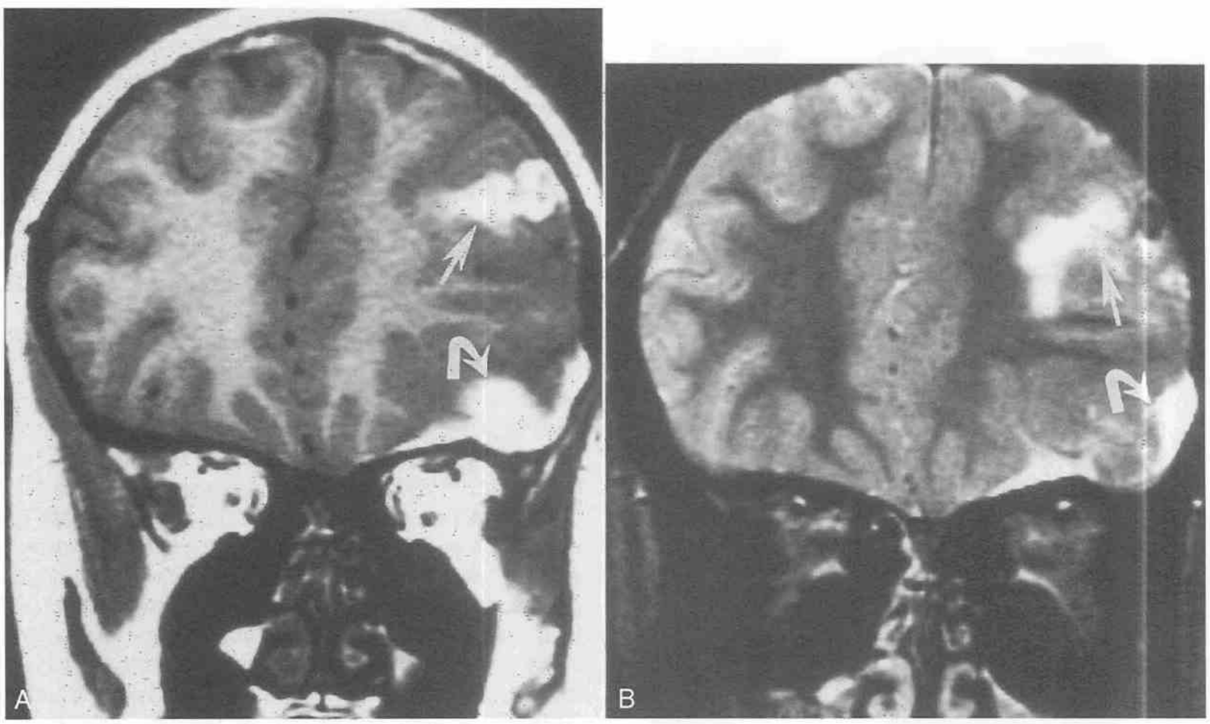

Figure 9–35. *A* and *B,* Subacute hemorrhagic contusion in left frontal lobe is hyperintense on coronal T1-weighted (500/15) and largely hyperintense on coronal T2-weighted (2500/80) MR images, indicating the presence of methemoglobin (*arrows*). In addition, there is a small left frontal, convexity subacute subdural hematoma (*curved arrows*).

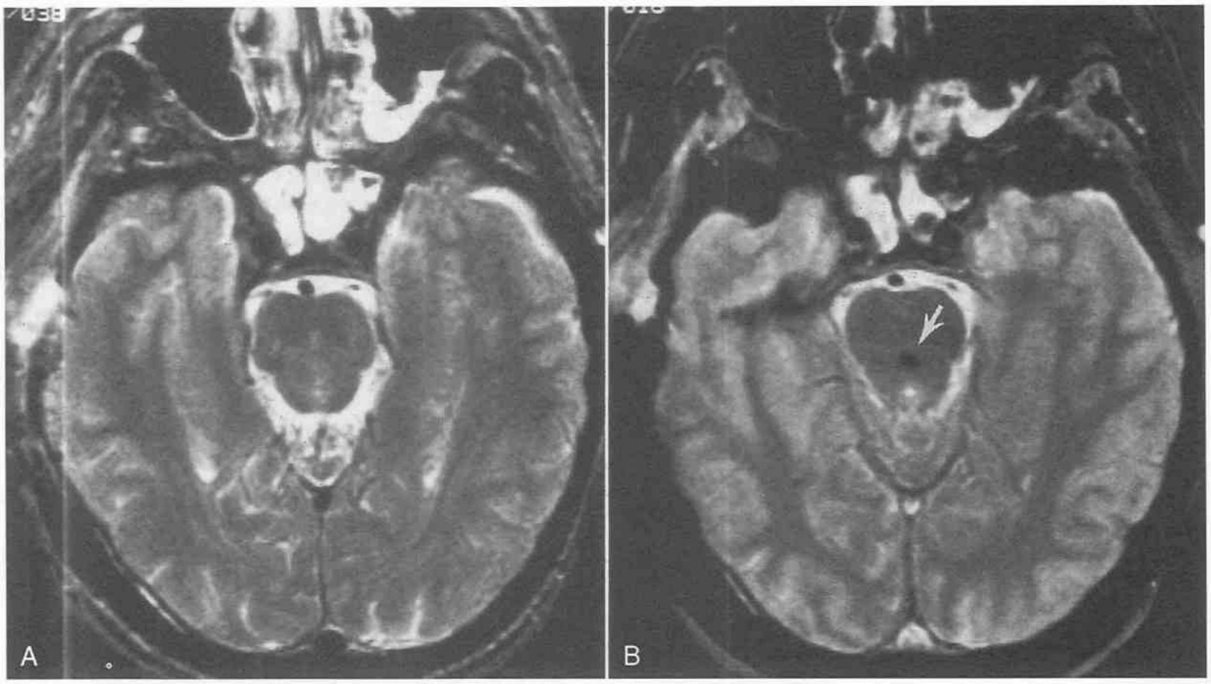

Figure 9–36. *A,* Axial T2-weighted (2600/80) MR image shows no abnormality in a comatose patient. *B,* Axial T2* gradient-recalled echo (600/17), 20-degree flip-angle image reveals a small acute hemorrhagic contusion in the pons (*arrow*).

ies are more accurate in the assessment of subacute and chronic injuries and may provide a more reliable correlation with clinical findings to better predict clinical outcome.

Diffuse Axonal (Shear) Injury

Diffuse axonal (shear) injury is frequently encountered in patients with head trauma.[39] Shearing injuries to the white matter were first described in the CT literature in 1978[129] and have been described extensively in the neuropathological literature in the past. A study by Strich and Oxon[115] in 1961 described these injuries as axonal tears with or without microscopically visible hematoma. They reported on five patients who sustained head injury, died of brain swelling, and were found at autopsy to have white matter degeneration. Midbrain damage in patients with closed head injury has been frequently described at autopsy. In another study, 80% of patients dying of injuries resulting from head trauma had midbrain lesions at autopsy that were not visualized by CT scans.[98] Although blunt head trauma has been associated with a significant number of hemorrhagic foci in the corpus callosum at autopsy,[72] the outcome of corpus callosum hematoma is not invariably dismal, because many patients with such lesions diagnosed by CT scans have been shown to survive.

Coma, decerebrate posturing, vegetative state, and no increase in intracranial pressure are present in many patients with diffuse axonal injury.[129] This injury is caused by rotational forces that produce shear strain, resulting in tissue damage. Shear strain is maximum at the junction of tissues with different densities such as the gray-white junction.[37] The presence of diffuse axonal injury is of great prognostic significance because the lesions are often associated with a poor outcome.[129]

CT findings in diffuse axonal injury include diffuse cerebral swelling, corpus callosal hemorrhage, and SAH. Hemorrhage may also be present in the area of the third ventricle and hemispheric white matter.[132] Although CT scans do not reveal the actual axonal lesion demonstrated with histology, they do show the associated edema and hemorrhage (Fig. 9–37).[128]

MRI studies are more sensitive than CT scans in the detection of diffuse axonal injury. Lesions are readily demonstrated by MRI in patients in whom the CT scan shows no abnormality.[37–39,136] The injuries are demonstrated with CT only when greater than 1.5 cm or when present in the corona radiata or internal capsule.[39]

Diffuse axonal injury lesions are usually multiple, range from 0.5 to 1.5 cm, and are typically oval or elliptical. The lesions are most commonly located in the subcortical white matter of the frontal and temporal lobes, splenium of the corpus callosum, corona radiata, and internal capsule (Figs. 9–38 and 9–39). The parieto-occipital lobes and cerebellum are less commonly involved.[37] In the brain stem, the lesions are located in the dorsolateral aspect of the midbrain and upper pons (Fig. 9–40). More than 80% of the lesions are nonhemorrhagic, being most evident as foci of hyperintensity on T2-weighted images.[38]

Brain Swelling and Edema

Brain swelling and edema occur commonly in patients with head trauma. Brain swelling is observed more commonly in children than in adults.[131] Minor episodes of trauma may result in brain swelling. Patients may experience a lucid interval after the episode of trauma, followed by the sudden onset of headache, nausea, vomiting, and

Figure 9–37. Diffuse axonal injury. CT scan demonstrates small hemorrhagic diffuse axonal injuries in the deep white matter and corpus callosum.

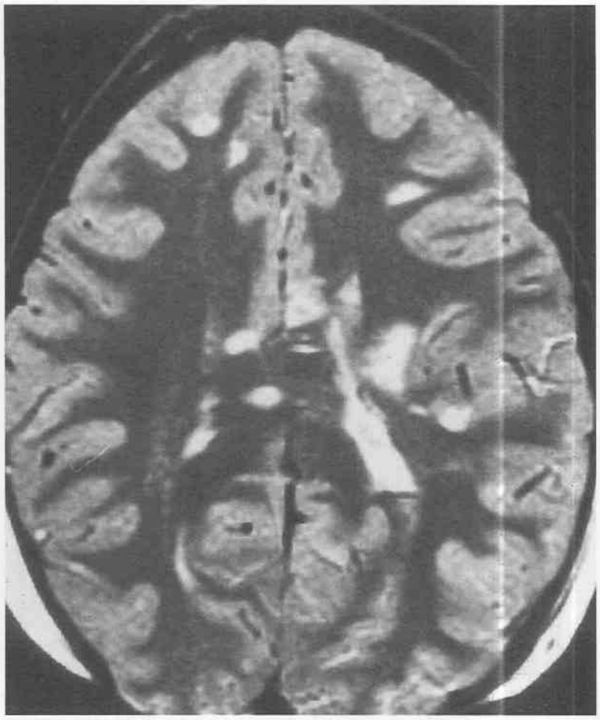

Figure 9–38. Diffuse axonal injury. Axial T2-weighted (2500/80) MR image demonstrates typical locations of diffuse axonal injury: subcortical white matter, corpus callosum, and corona radiata.

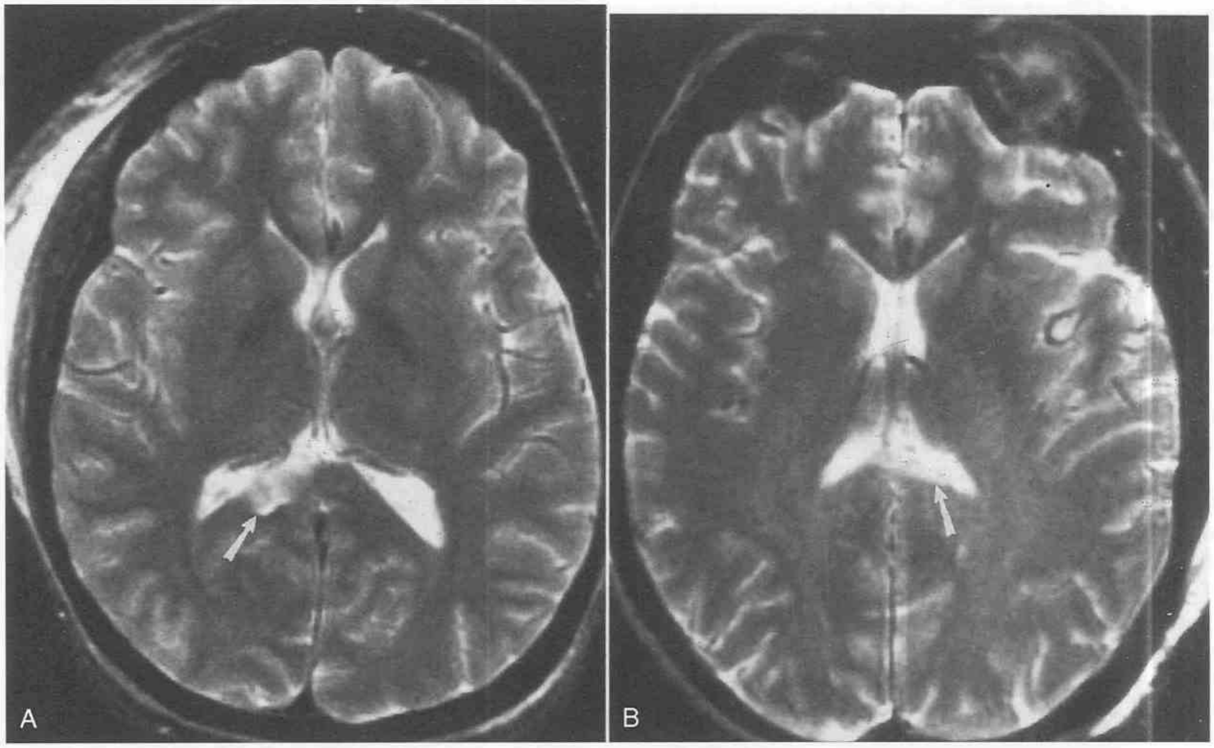

Figure 9–39. *A* and *B,* Diffuse axonal injury in two different patients. Hyperintense lesions are present in the splenium of the corpus callosum on axial T2-weighted (2500/80) MR images (*arrows*).

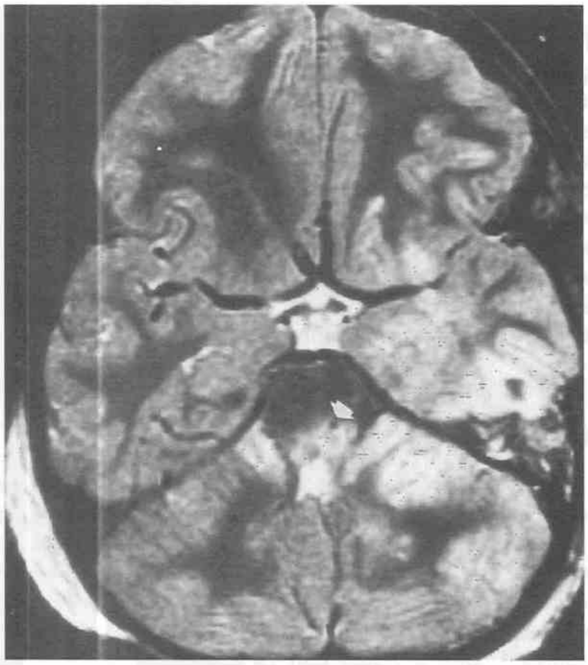

Figure 9–40. Axial T2-weighted (2500/80) MR image shows areas of diffuse axonal injury in the pons, middle cerebellar peduncles, and left-cerebellar hemisphere. The pontine lesion contains a focus of acute hemorrhage (*small arrow*). Hemorrhagic contusion is present in the left temporal lobe.

loss of consciousness.[131] SAH and contusions are often seen in association with this type of abnormality.[14, 55]

Brain swelling is evident in the majority of patients with head trauma, occurring at the time of injury or several hours afterwards.[55] CT findings consist of compression of the lateral and third ventricles and perimesencephalic cistern (Figs. 9–41 and 9–42). There is an associated increase in density of the white matter from transient hyperemia.[131] It is thought that loss of autoregulation results in an increase in cerebral blood flow and blood volume. This increase in blood flow forces CSF out of the ventricles and subarachnoid space, resulting in the compressed appearance. Serial CT scans show the gradual resolution of brain swelling over a period of 3 to 5 days.[55] The initial white matter hyperdensity gradually returns to normal as the swelling subsides. In more than one third of cases in children, extracerebral collections and sulcal and ventricular enlargement are seen to develop on follow-up CT scans.[131]

Cerebral edema may be cytotoxic, interstitial, or vasogenic in origin. In the immediate post-traumatic interval, cerebral edema is vasogenic, reflecting breakdown of the blood-brain barrier with leakage of intravascular contents into and around areas of damaged tissue. Edema is evident as decreased density within and surrounding areas of contusion and intraparenchymal hematoma.[26, 66, 82] Edema may occur as an isolated finding, appearing as an area of decreased density.[66] Cerebral edema typically appears 24 hours after injury, then increases and becomes maximum at 3 to 5 days and then gradually resolves.

Brain swelling and edema are evident with MRI stud-

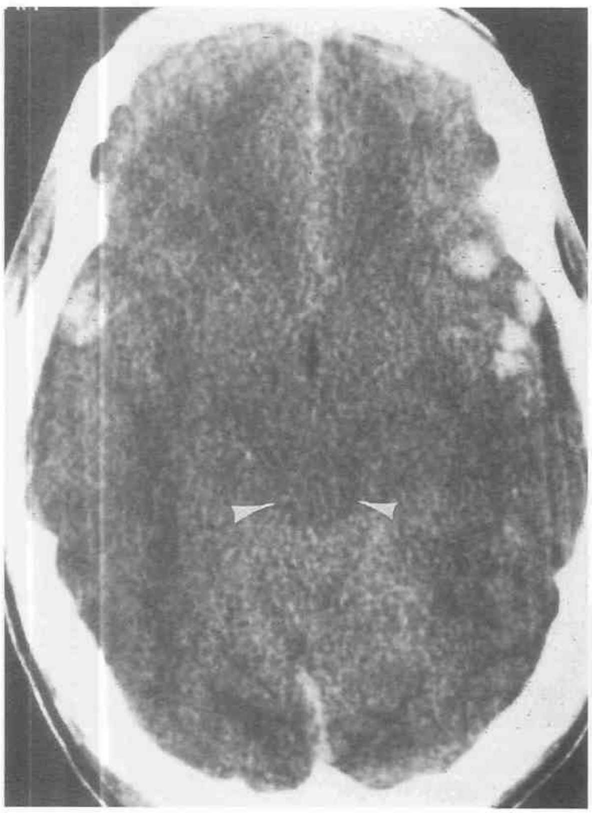

Figure 9–41. Brain swelling. Effacement of the perimesencephalic cistern indicates brain swelling (*arrowheads*). Note the bilateral temporal lobe contusions.

Figure 9–42. Axial CT scan shows effacement of basal cisterns, and third ventricle representing brain swelling. Note pneumocephalus overlying the right frontotemporal convexity (*arrowheads*).

ies.[37, 50, 62, 136] The exquisite sensitivity of MRI to the presence of extracellular free water enables the detection and visualization of small regions of edema, particularly on T2-weighted images.

Penetrating Injury

Gunshot wounds are a common cause of penetrating head injury. CT scans allow one to rapidly locate the position of a missile and determine the extent of intracranial injury.[4, 109] The missile, its track and fragments, as well as skull fracture and displaced intraparenchymal bone fragments are readily identified (Fig. 9–43). Hematoma along the missile track, intraventricular hemorrhage and SAH, diffuse edema, and pneumocephalus, both extracerebral and intracerebral, are frequently seen on CT scans.[109] Laceration of a major blood vessel may result in massive intraparenchymal hemorrhage, which is an indication for early surgical intervention.[109] Injuries beyond the missile track may sometimes be seen if the missile is of a large-caliber or high-velocity type.[4] Prognosis is best when damage is limited to a single lobe, worse with unilateral multilobe injury, and poorest with bilateral hemispheric injury.[88] Damage to vital structures such as the diencephalon and mesencephalon is also associated with a poor prognosis.[109] Complications of penetration injuries include CSF leak, osteomyelitis, abscess, and seizures.[88] Repeat CT scans may reveal the development of encephalomalacia along the missile track and intraparenchymal cystic areas of CSF density.[4] The presence of metal projectiles is a relative contraindication to an MRI study because projectiles containing steel are deflected when placed in a magnetic field. Nonferromagnetic missiles are a contraindication to MRI when they contain ferromagnetic contaminants.[112] Any metal distorts the local magnetic field, the magnitude of which depends on the degree of ferromagnetism of the metal alloy. In addition to undergoing deflection, stainless steel or alloys with ferromagnetic contaminants distort the local magnetic field to a greater degree than titanium compounds and, if in the region of interest, severely degrade image quality.

Vascular Injury

Injury to the carotid or vertebral arteries may be produced by blunt force, penetrating injury, strangulation, and hyperextension.[41] Dissection, laceration, thrombosis, and pseudoaneurysm or arteriovenous fistula formation may occur.[20] The site of injury depends on the nature of the forces on the vessels and the occurrence of nearby skull fractures.[87] Arterial injury may be diagnosed with CT scanning; however, angiography remains the modality that best defines the site of arterial injury.

An intimal tear in the arterial wall may result in dissection and thrombus formation.[87] Although one third of patients are symptomatic at the time of injury, the majority experience a lucent interval varying from hours to days before the onset of symptoms.[87] Symptoms are variable and

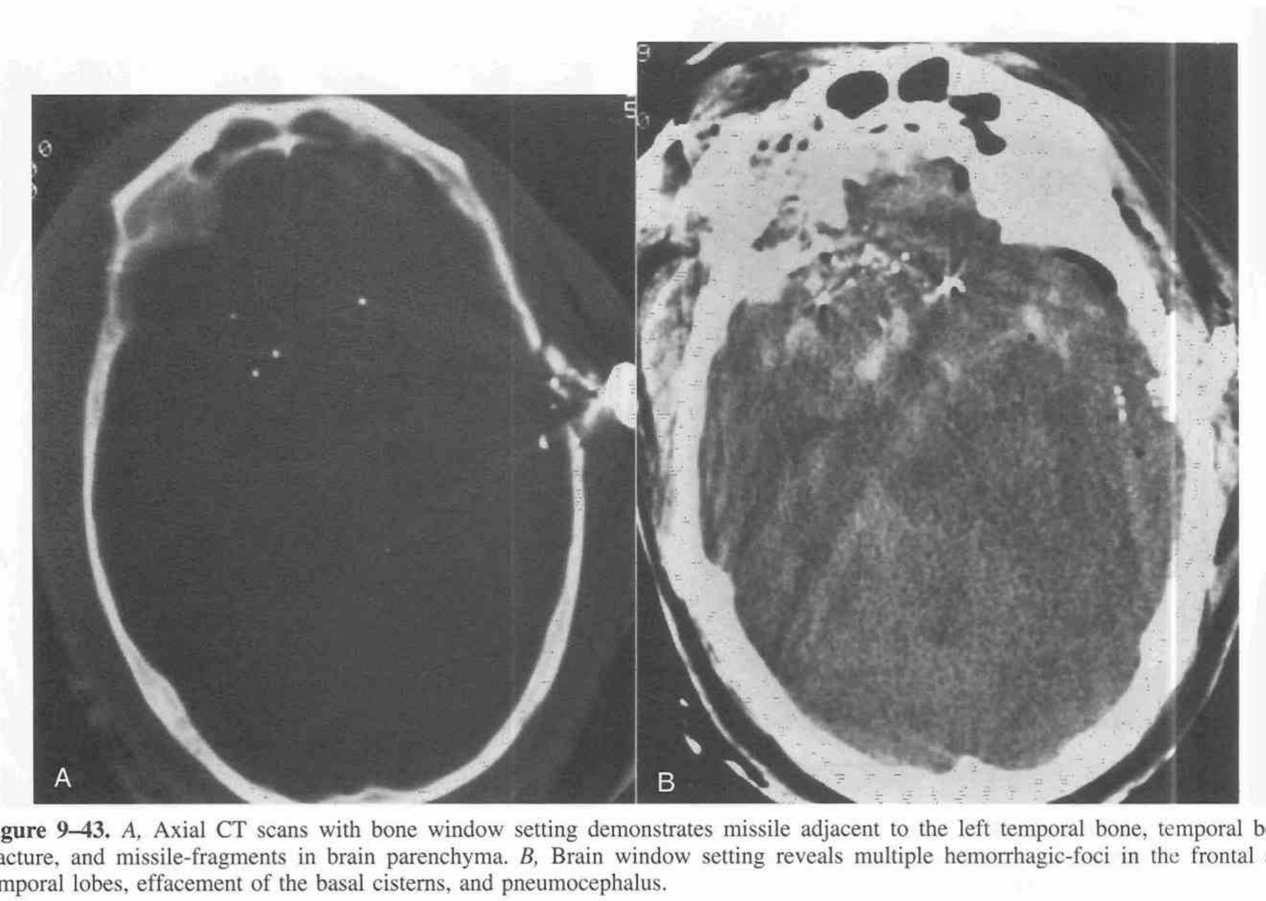

Figure 9–43. *A,* Axial CT scans with bone window setting demonstrates missile adjacent to the left temporal bone, temporal bone fracture, and missile-fragments in brain parenchyma. *B,* Brain window setting reveals multiple hemorrhagic-foci in the frontal and temporal lobes, effacement of the basal cisterns, and pneumocephalus.

include headache, Horner's syndrome, transient ischemic attacks, and completed stroke.

The diagnosis of arterial dissection may also be accomplished with MRI studies.[42] Abnormal signal intensity representing hemorrhage is seen in a thickened arterial wall on all pulse sequences. The signal intensity depends on the age of the hematoma. The hematoma is usually contained by a thin rim of hypointensity that represents the adventitia. In addition, the arterial lumen appears narrow. Arteries normally appear hypointense or demonstrate flow void phenomena on MRI.[9] In arterial dissection, the slow flow distal to the area of dissection produces hyperintense signal within the vessel lumen. However, the hyperintense signal is not specific for dissection and may be the result of slow flow from stenosis caused by atherosclerotic disease. The hyperintensity of slow arterial flow must be differentiated

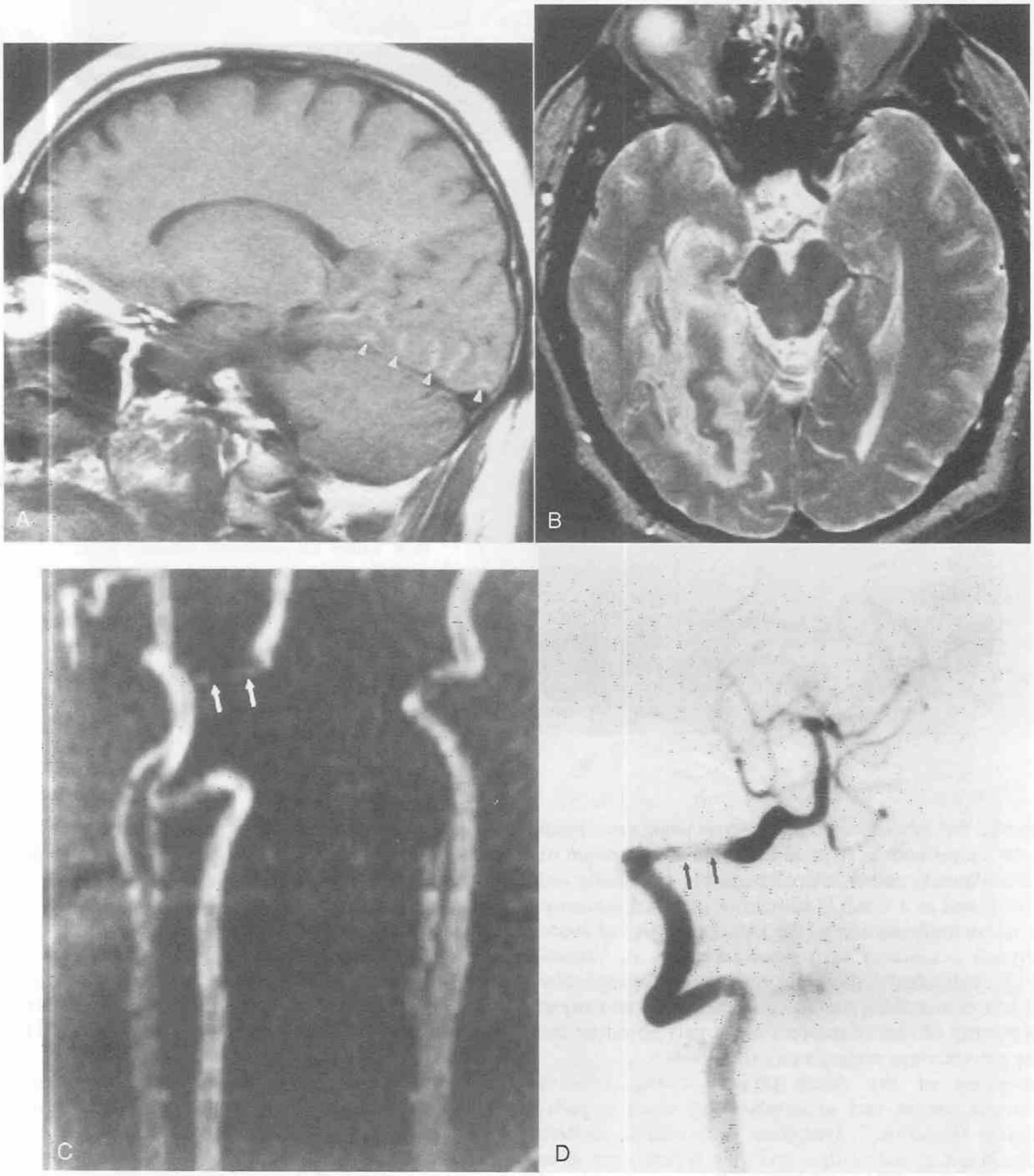

Figure 9–44. *A,* Arterial dissection. Sagittal T1-weighted (500/15) MR image shows cortical ribbon of hyperintensity representing subacute hemorrhage in the right temporal lobe (*arrowheads*). *B,* Hyperintense signal is evident on axial T2-weighted (2500/80) image. Findings are consistent with acute infarction. *C,* Two-dimensional time-of-flight MR angiography study demonstrates irregular narrowing of the right vertebral artery consistent with dissection (*arrows*). *D,* Intraarterial digital subtraction angiogram of the right vertebral artery confirms the dissection (*arrows*).

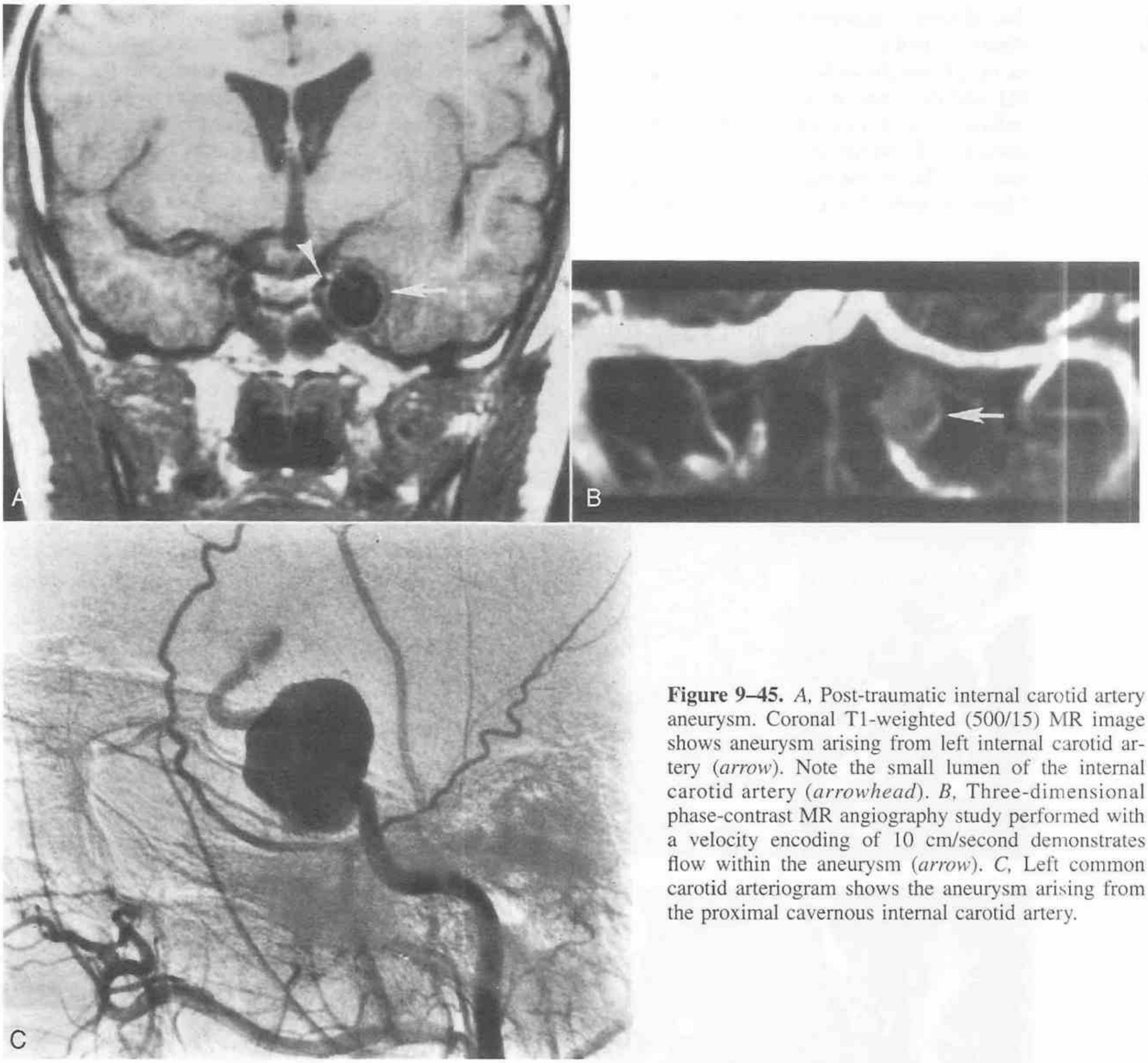

Figure 9–45. *A,* Post-traumatic internal carotid artery aneurysm. Coronal T1-weighted (500/15) MR image shows aneurysm arising from left internal carotid artery (*arrow*). Note the small lumen of the internal carotid artery (*arrowhead*). *B,* Three-dimensional phase-contrast MR angiography study performed with a velocity encoding of 10 cm/second demonstrates flow within the aneurysm (*arrow*). *C,* Left common carotid arteriogram shows the aneurysm arising from the proximal cavernous internal carotid artery.

from arterial thrombosis, which appears as isointense signal within the vessel lumen. Arterial thrombus is composed of fibrin and platelets, rather than hemoglobin containing red blood cells, and as a result is isointense in signal intensity. This is in contradistinction to the signal intensity of intraparenchymal hematoma or venous thrombus in various stages of evolution.[67] Magnetic resonance angiography (MRA) can demonstrate the concentric luminal narrowing and irregularity of carotid dissection and may eliminate the need for conventional angiography (Fig. 9–44).

Disruption of the three layers of the arterial wall—intima, media, and adventitia—may result in pseudoaneurysm formation.[87] Symptoms are variable, include headache, tinnitus, and vertigo, and may appear years after injury.[20] Although CT and MRI studies are capable of demonstrating a pseudoaneurysm, angiography is required to accurately depict the lesion. The MRI appearance of a pseudoaneurysm is variable, depending on the size and presence of thrombus. Areas of signal void, representing residual lumen, and areas of mixed signal intensity, representing thrombus of variable age, may be seen. An advantage of MRI is that it demonstrates the true size of the aneurysm, including the patent lumen as well as intraluminal thrombus, whereas conventional angiography demonstrates only the patent lumen (Fig. 9–45).

MRA has the capability to demonstrate both small and large aneurysms. Aneurysms as small as 3 mm may be visualized with current imaging techniques.[1a] The three-dimensional time-of-flight technique is sensitive to the detection of small aneurysms, whereas the phase-contrast technique is better able to depict large aneurysms.[53,99]

Laceration of the intracavernous carotid artery with rupture into the cavernous sinus results in traumatic carotid cavernous fistula.[89] Symptoms and signs include orbital bruit, proptosis, conjunctival redness and swelling, blurred vision, pain, and pulsatile exophthalmos. CT and MRI studies demonstrate proptosis, enlargement of the rectus muscles, superior ophthalmic vein, and cavernous sinus

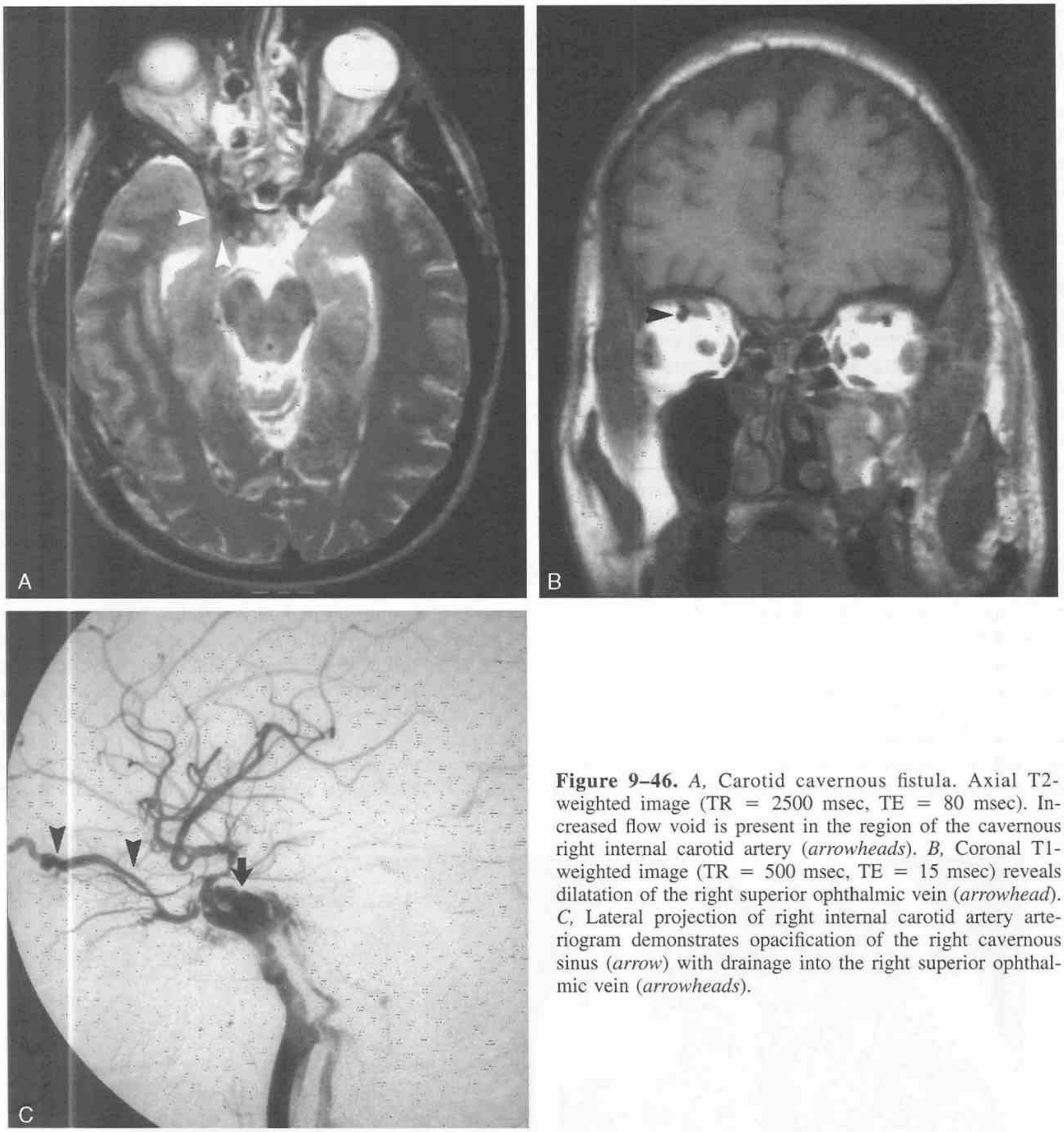

Figure 9–46. *A,* Carotid cavernous fistula. Axial T2-weighted image (TR = 2500 msec, TE = 80 msec). Increased flow void is present in the region of the cavernous right internal carotid artery (*arrowheads*). *B,* Coronal T1-weighted image (TR = 500 msec, TE = 15 msec) reveals dilatation of the right superior ophthalmic vein (*arrowhead*). *C,* Lateral projection of right internal carotid artery arteriogram demonstrates opacification of the right cavernous sinus (*arrow*) with drainage into the right superior ophthalmic vein (*arrowheads*).

(Fig. 9–46). MRI shows flow void within the enlarged superior ophthalmic vein and cavernous sinus. Angiography is, however, necessary to visualize the site of the fistula. Phase-contrast MRA studies show promise in the detection of the fistulous communication.[121]

Child Abuse

Child abuse is a major cause of morbidity and mortality. Most victims of child abuse are younger than 2 years, with the majority younger than 1 year; however, older children up to adolescence may also be victims.[18,134] The abused child may present with a variety of symptoms, including breathing difficulty, irritability, lethargy, poor feeding, and seizures.[27] The clinical outcome depends on the severity of the injuries sustained. Minor disabilities may be present, such as visual disturbance, extremity weakness, and seizures.[18] Children with severe impairment, such as mental retardation, or those existing in a vegetative state require institutional placement. It is important to recognize the CT findings encountered in child abuse; these findings may be the only signs of abuse because commonly there is no external evidence of injury.[13] Clinical features may not allow the differentiation of the abused child from the child injured in an accident.

The mechanism of injury in child abuse was previously thought to be caused by shaking—the so-called shaken

baby syndrome. Shaking alone, however, does not generate the force required to produce head injury.[26] Rather, most victims of child abuse have evidence of blunt trauma to the head, and it is the force of the blunt impact that is responsible for the observed head injuries.[27] The child is likely first shaken and subsequently thrown, and the head strikes an object—the so-called shaken impact syndrome.[13]

The most common CT finding seen in child abuse on early-generation CT scanners was an acute interhemispheric SDH located in the parieto-occipital area (Fig. 9–47). The SDH is secondary to tearing of the bridging cerebral veins at their attachment to the falx. Infarction or cerebral swelling in the parieto-occipital lobes was a frequent associated abnormality.[133,134] The most common finding observed on later-generation CT scanners is SAH.[18] Other findings frequently seen include cerebral edema, intraparenchymal hemorrhage, SDH, infarction, and skull fracture. It may sometimes be difficult to differentiate interhemispheric SDH from SAH, and in some instances, they may coexist.[18] In children who are victims of strangulation, large infarctions and SDHs may be present, usually involving the supratentorial brain.[16] Skull radiographs should be obtained in victims of child abuse because fractures may not be evident on CT scans. Radiographic features of skull fractures may allow the differentiation of the abused child from the child injured in an accident.[81] These features are multiple, bilateral fractures that cross suture lines. Focal or diffuse atrophy with sulcal and ventricular enlargement is evident on repeat CT scans in all patients; infarction is evident in some patients.[18,134]

Although CT scans are performed in acutely injured patients to exclude a surgical lesion, MRI studies should be used when the clinical symptoms do not correlate with the CT findings. MRI is also more useful in the evaluation of subacute and chronic head injury because the technique is more sensitive than CT scans in the detection of small SDH, cortical contusion, and diffuse axonal injury. The advantage of MRI lies in the ability to determine the age of subdural blood on the basis of signal intensity. The presence of SDHs in various stages of evolution, signifying a difference in age, may be an indicator of child abuse.[100]

Complications of Central Nervous System Trauma

Hydrocephalus

Hydrocephalus is a possible complication of head injury. Diffuse brain injury or obstruction of CSF pathways results in enlargement of the ventricular system. In the former, as diffuse edema resolves, there is a gradual enlargement of the ventricular system, which retains a normal configuration.[26] Noncommunicating hydrocephalus may be evident initially or shortly after injury, with intraventricular hemorrhage impeding the outflow of CSF at the level of obstruction.[26] Communicating hydrocephalus is the result of decreased absorption of CSF at the level of the arachnoid villi over the cerebral convexities. This may be observed as a gradual enlargement of the ventricular system on serial CT scan.[66] Enlargement of the ventricular system occurs in the majority of patients within 2 weeks of injury, however, it may rarely develop over several months to 1 year after injury.[65] The clinical outcome in patients who experience

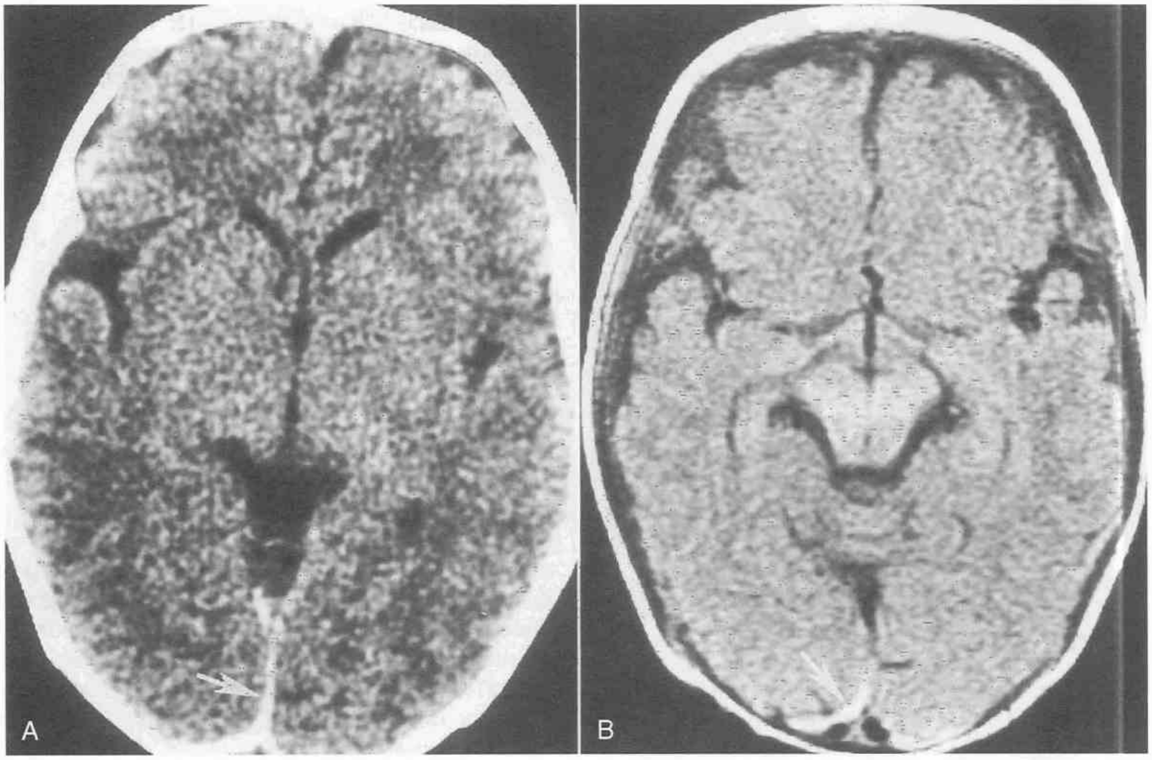

Figure 9–47. *A* and *B*, Child abuse. Axial CT scans show an acute posterior interhemispheric subdural hemorrhage in the occipital area (*arrows*).

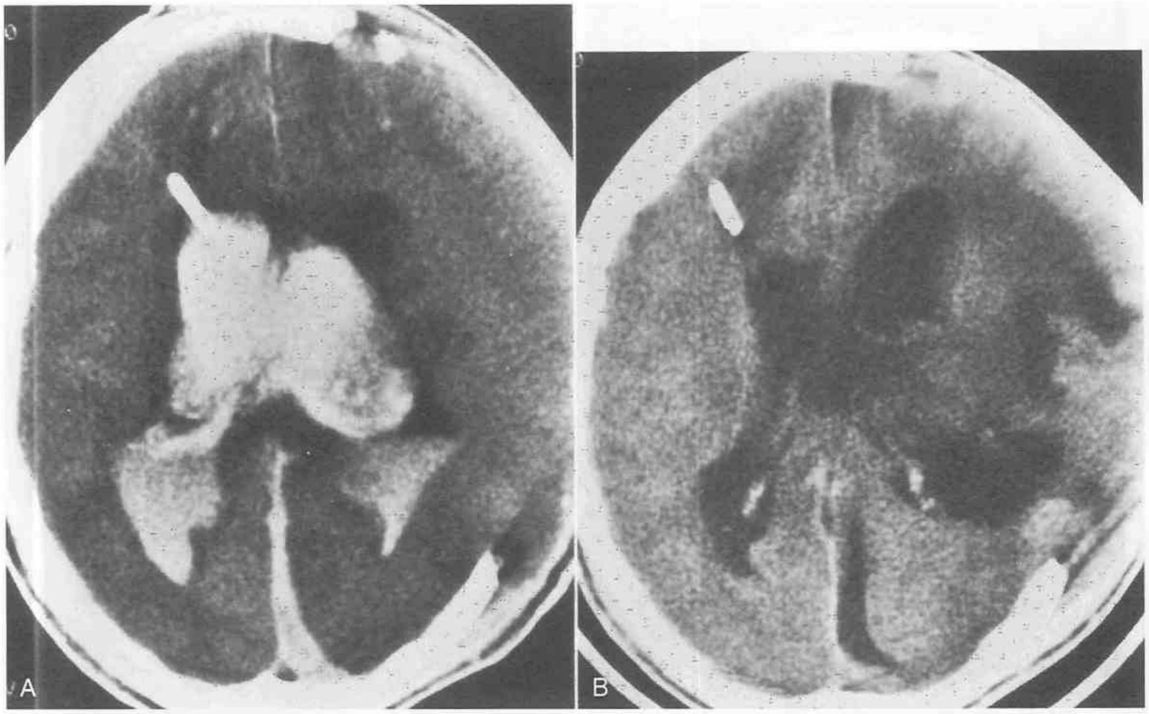

Figure 9–48. *A,* Hydrocephalus. Axial CT scan shows ventricular enlargement with massive intraventricular hemorrhage. A shunt tube is present in the right lateral ventricle. Posterior interhemispheric subdural hematoma and frontal lobe contusions are present. *B,* Ten days later, the intraventricular hemorrhage has resolved, and the ventricles have decreased in size but remain enlarged.

hydrocephalus is much worse than in those who do not, with the majority sustaining moderate to severe disability.[65]

The CT appearance of communicating hydrocephalus consists of dilatation of the ventricular system and effacement of the cortical sulci (Fig. 9–48). In the acute stage, decreased density representing transependymal fluid shift is present in the periventricular white matter. The transependymal fluid shift is visible as a thin rim of hyperintensity in the periventricular white matter on proton-density and T2-weighted MR images. Other findings that may be observed are dilatation of the anterior third ventricle, inferior displacement of the hypothalamus, depression of the posterior fornix, and elevation of the corpus callosum—which are seen on sagittal T1-weighted images.[29]

The CSF flow void sign is from the turbulent flow of CSF and indicates the presence of flow in the aqueduct of Sylvius and third and fourth ventricle.[106] Absence of the flow void sign in the aqueduct in the presence of hydrocephalus is an indication of obstruction or stenosis at the level of the aqueduct.[107] Intraventricular hemorrhage within the aqueduct results in absence of the flow void sign. The flow void sign is present in normal individuals as well as in patients with normal-pressure hydrocephalus, acute communicating hydrocephalus, and atrophy.[11] Although the flow void sign is present in all of these conditions, it is most evident in normal-pressure hydrocephalus and is not as evident in atrophy and acute communicating hydrocephalus.[31] However, it cannot be used to differentiate acute communicating hydrocephalus from atrophy.[108]

Atrophy

Areas of porencephaly may result from head trauma at the site of intracerebral hematoma or infarction. Porencephaly is a cystic defect that may or may not communicate with the ventricular system. In the communicating type, the defect communicates with the ventricular system or is separated from it by only a thin layer of tissue. In closed porencephaly, the cyst does not communicate with the ventricular system. The CT appearance is that of a well-defined area of CSF density with no contrast enhancement.[94] Shift of the midline structures and the ventricular system is usually toward and rarely away from the defect. MRI studies demonstrate the porencephalic defect to be of CSF signal intensity on all pulse sequences.

Infarction

Infarction may be a sequela of head trauma secondary to vasospasm, vascular occlusion, or direct vessel damage.[66] In the acute stage, decreased density or isodense cerebral swelling with mass effect and midline shift may be seen on CT scans (Fig. 9–49).[18,134] The use of intravenous contrast material demonstrates luxury perfusion around areas of infarction.[18] Focal encephalomalacia or porencephaly with ventricular and sulcal dilatation are seen in the chronic stage.[66] MRI is more sensitive than CT in the detection of infarction. Brain swelling is seen on T1-weighted images within several hours after the onset of symptoms, before any signal change is evident on T2-weighted images.[127] Hyperintense signal may be evident between 8 and 24 hours on T2-weighted images, whereas the CT scan may be normal up to 2 days after the onset of symptoms. Intravascular and meningeal enhancement may be present within the first several days after administration of gadopentetate dimeglumine.[30,127]

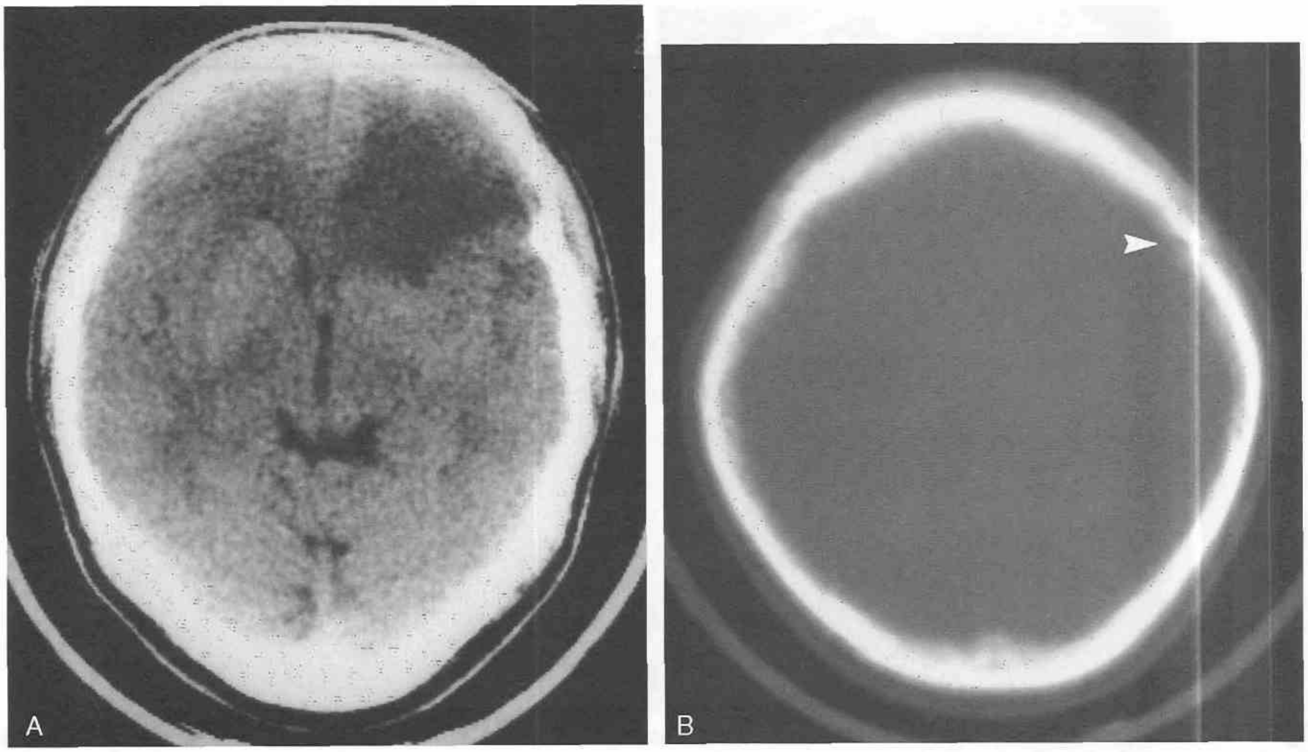

Figure 9–49. *A,* Infarction secondary to assault with a hammer. Unenhanced CT scan shows acute left frontal lobe infarction in the distribution of the left anterior cerebral artery. *B,* CT scan with bone window reveals nondepressed fracture of the left frontal bone (*arrowhead*).

Post-traumatic Leak

A CSF leak indicates abnormal communication between the intracranial and extracranial environments. It most commonly occurs after penetrating injury or fracture along the skull base and usually involves the cribriform plate or the temporal bone. CSF leak indicates communication with the paranasal sinuses and, less likely, the mastoid air cells or the middle ear cavity. The clinical significance ranges from entirely benign, because it is frequently self-limited, to infection and brain abscess if it is associated with persistent extracerebral communication.[97]

The most common sites of fractures and CSF leaks are in the sphenoethmoid region of the anterior cranial fossa. Leakage may occur through the nose, mouth, or the middle ear and depends on the location of the fracture. Precise detection of the sites of leakage is difficult. An air-fluid level in the sphenoid sinus suggests a fracture of the cribriform plate, although a CSF leak from anywhere between the frontal sinus and sphenoid bone may result in retrograde flow of CSF into the sphenoid ostium.[116] Most CSF leaks are related to high-velocity trauma.[68, 70, 97]

The demonstration of a post-traumatic leakage site requires thin-section, high-spatial resolution[68, 70, 97] direct coronal scans. Such scans may demonstrate a bony dehiscence of the skull base near a sinus or an air cell and, thus, localize the level of air entry. A cisternogram may be of help if there is an active leak at the time of the study but is otherwise not necessary, particularly when high-spatial-resolution, direct coronal scanning is performed (Fig. 9–50).[77]

Infection

Infection of the central nervous system may uncommonly occur as a complication of trauma associated with fracture. Direct extension of microorganisms through a

Figure 9–50. Post-traumatic cerebrospinal fluid leak. High-resolution direct coronal CT cisternogram demonstrates leakage of contrast material in the right ethmoid sinus (*arrowhead*) and the fracture site in the right cribriform plate (*arrow*).

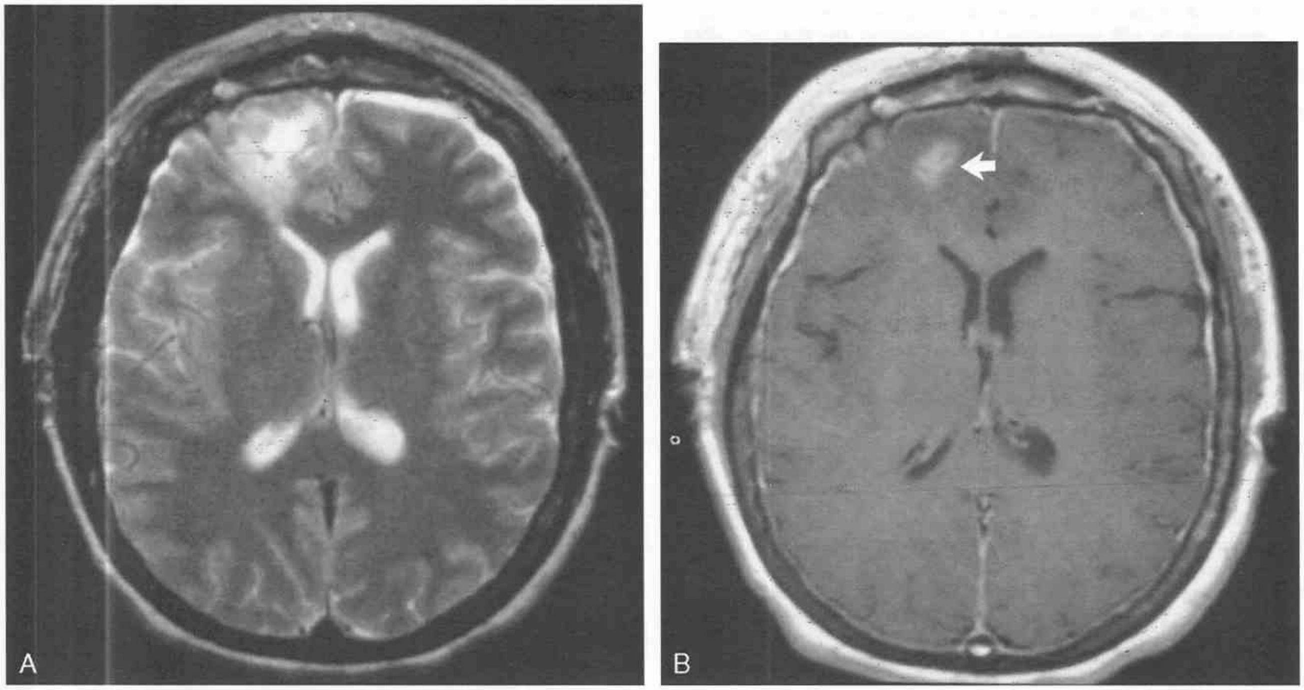

Figure 9–51. *A,* Cerebritis. Axial T2-weighted image (TR = 2500 msec, TE = 80 msec) shows edema in the right frontal lobe. Small, bilateral, convexity subdural hematomas are present. *B,* Contrast-enhanced T1-weighted image (TR = 500 msec, TE = 15 msec) reveals focus of nodular enhancement (*arrow*).

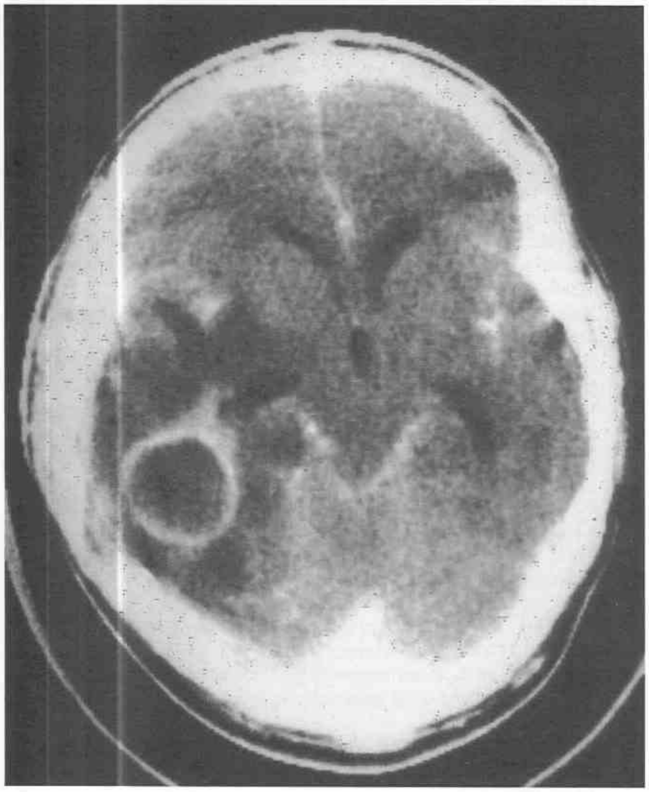

Figure 9–52. Abscess secondary to right temporal bone fracture. Contrast-enhanced CT scan shows ring enhancing abscess caused by *Staphylococcus* in the right temporal lobe.

fracture site may result in meningitis, cerebritis, abscess, or, less commonly, subdural or epidural empyema. The initial CT scan is often normal with meningitis. A second CT scan may demonstrate hydrocephalus, effacement of the basal cisterns secondary to inflammatory exudate, and enhancement of the basal cisterns and meninges with intravenous contrast material.[15] Contrast-enhanced MRI is more sensitive than contrast-enhanced CT in detecting meningeal enhancement.[78] Cerebritis is more readily demonstrated with MRI than with CT.[47,101] Hyperintense edema is evident on T2-weighted images, whereas nodular enhancement can be seen on contrast-enhanced T1-weighted images (Fig. 9–51). Contrast-enhanced CT and MRI depict intraparenchymal abscess as a ring enhancing mass with surrounding edema (Fig. 9–52).

Tension Pneumocephalus

Air may enter the cranial cavity through a fistulous connection in sufficient amounts to cause mass effect.[7,32,91] Its mechanism is poorly understood. This is a rare complication usually caused by trauma or surgery to the skull base, it has also been described after infection with gas-forming organisms or congenital defects of the skull base.[76]

References

1. Ambrose J: Computerized transverse axial scanning (tomography). Part 2: Clinical application. *Br J Radiol* 46:1023–1047, 1973.
1a. Adams WM, Laitt RD, Jackson A: The role of MR angiography in the pretreatment assessment of intracranial aneurysms: A comparative study. *AJNR Am J Neuroradiol* 21:1618–1628, 2000.
2. Amendola MA, Ostrum BJ: Diagnosis of isodense subdural hematomas by computed tomography. *AJR* 129:693–697, 1977.

3. Atlas SW, Mark AS, Grossman RI, et al: Intracranial hemorrhage: gradient-echo MR imaging at 1.5 T. *Radiology* 168:803–807, 1988.
4. Bakay L: The value of CT scan in gunshot injuries of the brain. *Acta Neurochir (Wien)* 71:189–204, 1984.
5. Bergstrom AS, Ericson K, Levander B, et al: Computed tomography of cranial subdural and epidural hematomas: Variation of attenuation related to time and clinical events such as rebleeding. *J Comput Assist Tomogr* 1:449–455, 1977.
6. Bird CR, McMahan JR, Gilles FH, et al: Strangulation in child abuse: CT diagnosis. *Radiology* 163:373–375, 1987.
7. Black PM, Davis JM, Kjellberg RN, Davis KR: Tension pneumocephalus of the cranial subdural space: A case report. *Neurosurgery* 5:368–370, 1979.
8. Boyko OB, Cooper DF, Grossman CB. Contrast-enhanced CT of acute isodense subdural hematoma. *AJNR Am J Neuroradiol* 12: 341–343, 1991.
9. Bradley WG Jr: Carmen lecture: Flow phenomena in MR imaging. *AJR* 150:983–994, 1988.
10. Bradley WG Jr, Schmidt PG: Effect of methemoglobin formation on the MR appearance of subarachnoid hemorrhagic. *Radiology* 156: 99–103, 1985.
11. Bradley WG Jr, Kortman KE, Burgoyne B: Flowing cerebrospinal fluid in normal and hydrocephalic states: Appearance on MR images. *Radiology* 159:611–616, 1986.
12. Braun J, Borovich B, Guilburd JN, et al: Acute subdural hematoma mimicking epidural hematoma on CT. *AJNR Am J Neuroradiol* 8: 171–173, 1987.
13. Bruce DA, Zimmerman RA: Shaken impact syndrome. *Pediatr Ann* 18:482–494, 1989.
14. Bruce DA, Alavi A, Bilanluk L, et al: Diffuse cerebral swelling following head injuries in children: The syndrome of "malignant brain edema." *J Neurosurg* 54:170–178, 1981.
15. Cabral DA, Flodmark O, Farrell K, et al: Prospective study of computed tomography in acute bacterial meningitis. J Pediatr 111: 201–205, 1987.
16. Cameron M: Chronic subdural haematoma: A review of 114 cases. *J Neurol Neurosurg Psychiatry* 41:834–839, 1978.
17. Chakeres DW, Bryan RN. Acute subarachnoid hemorrhage: In vitro comparison of magnetic resonance and computed tomography. *AJNR Am J Neuroradial* 7:223–228, 1986.
18. Cohen RA, Kaufman RA, Myers PA, et al: Cranial computed tomography in the abused-child with head injury. *AJNR Am J Neuroradiol* 6:883–888, 1985.
19. Cordobes F, Lobato RD, Rivas JJ, et al: Observations on 82 patients with extradural hematoma. Comparison of results before and after the advent of computerized tomography. *J Neurosurg* 54:179–186, 1981.
20. Davis JM, Zimmerman RA: Injury of the carotid and vertebral arteries. *Neuroradiology* 25:55–69, 1983.
21. DeLa Paz RL, New PF, Buonanno FS, et al: NMR imaging of intracranial hemorrhage. *J Comput Assist Tomogr* 8:599–607, 1984.
22. Dolinskas CA, Zimmerman RA, Bilaniuk LT: A sign of subarachnoid bleeding on cranial computed tomograms of pediatric head trauma patients. *Radiology* 126:409–411, 1978.
23. Dolinskas CA, Bilaniuk LT, Zimmerman RA, et al: Computed tomography of intracerebral hematomas. I. Transmission CT observations on hematoma resolution. *AJR* 129:681–688, 1977.
24. Dolinskas CA, Zimmerman RA, Bilaniuk LT, Gennarelli TA: Computed tomography of post-traumatic extracerebral hematomas: Comparison to pathophysiology and responses to therapy. *J Trauma* 19: 163–169, 1979.
25. Dooms GC, Ustse A, Brant-Zawadski M, et al: Spin-echo MR imaging of intracranial hemorrhage. *Neuroradiology* 28:132–138, 1986.
26. Dublin B, French BN, Rennick JM: Computed tomography in head trauma. *Radiology* 122:365–369, 1977.
27. Duhaime AC, Gennarelli TA, Thibault LE, et al: The shaken baby syndrome: A clinical pathological, and biomechanical study. *J Neurosurg* 66:409–415, 1987.
28. Edelman RR, Johnson K, Burton R, et al: MR of hemorrhage: A new approach. *AJNR Am J Neuroradiol* 7:751–756, 1986.
29. El Gammal T, Allen MB Jr, Brooks BS, Mark EK: MR evaluation of hydrocephalus. *AJR* 149:807–813, 1987.
30. Elster AD, Moody DM: Early cerebral infarction: Gadopentetate dimeglumine enhancement. *Radiology* 177:627–632, 1990.
31. Fell DA, Fitzgerald S, Moiel RH, Caram P: Acute subdural hematoma. Review of 144 cases. *J Neurosurg* 42:37–42, 1975.
32. Findler G, Hoffman HJ, Munro IR: Tension pneumocephalus complicating craniofacial surgery in a shunted hydrocephalic patient: case report. *Neurosurgery* 7:525–528, 1980.
33. Fobben ES, Grossman RI, Atlas SW, et al: MR characteristics of subdural hematomas and hygromas at 1.5 T. *AJNR Am J Neuroradiol* 10:687–693, 1989.
34. Forbes GS, et al: Computed tomography in die evaluation of subdural hematomas. *Radiology* 126:143–148, 1978.
35. Gennarelli TA, Thibault LE: Biomechanics of acute subdural hematoma. *J Trauma* 22:680–685, 1982.
36. Gentry LR: Head trauma. In Atlas SW (ed): *Magnetic Resonance Imaging of the Brain and Spine*. New York, Raven Press, 1991.
37. Gentry LR, Godersky JC, Thompson BH: MR imaging of head trauma: Review of the distribution and radiopathologic features of traumatic lesions. *AJNR Am J Neuroradiol* 9:101–110, 1988.
38. Gentry LR, Godersky JC, Thompson BH: Traumatic brain stem injury: MR imaging. *Radiology* 171:177–187, 1989.
39. Gentry LR, Godensky JC, Thompson B: Prospective comparative study of intermediate-field MR and CT in the evaluation of closed head trauma. *AJNR Am J Neuroradiol* 9:91–100, 1988.
40. George AE, Russell EJ, Kricherf IL: White matter buckling. CT sign of extraaxial intracranial mass. *AJR* 135:1031–1036, 1980.
41. Glickman MG: Angiography in head trauma. In Newton TH, Potts DG (eds): *Radiology of the Skull and Brain*. St. Louis, CV Mosby, 1974.
42. Goldberg HI, Grossman RI, Gomori JM, et al: Cervical internal carotid artery dissecting hemorrhage: Diagnosis using MR. *Radiology* 158:157–161, 1986.
43. Gomori JM, Grossman RI, Bilanluk LT, et al: High-field MR imaging of superficial siderosis of the central nervous system. *J Comput Assist Tomogr* 9:972–975, 1985.
44. Gomori JM, Grossman RI, Goldberg HI, et al: Intracranial hematomas: Imaging by high-field MR. *Radiology* 157:87–93, 1985.
45. Gomori JM, Grossman RI, Hackney DB, et al: Variable appearances of subacute intracranial hematomas on high-field spin-echo MR. *AJR* 150:171–178, 1988.
46. Gurdjian ES, Gurdjian ES. Cerebral contusions: Re-evaluation of the mechanism of their development. *J Trauma* 16:35–51, 1976.
47. Haimes AB, Zimmerman RD, Morgello S, et al: MR imaging of brain abscesses. AJNR Am J Neuroradiol 10:279–291, 1989.
48. Hamilton M, Wallace C: Nonoperative management of acute epidural hematoma diagnosed by CT: the neuroradiologist's role *AJNR* 13:853–859, 1992.
49. Hayman LA, Evans RA, Hinck VC: Rapid high dose contrast computed tomography of isodense subdural hematoma and cerebral swelling. *Radiology* 131:381–383, 1979.
50. Hesselink JR, Dowd CF, Healy ME, et al: MR imaging of brain contusions: a comparative study with CT. *AJNR Am J Neuroradiol* 9:269–278, 1988.
51. Hoff J, Bates E, Bames B, et al: Traumatic subdural hygroma. *J Trauma* 13:870–876, 1973.
52. Hounsfield GN: Computerized transverse axial scanning (tomography). Part I: Description of system. *Br J Radiol* 46:1016–1022, 1973.
53. Huston J III, Rufenacht DA, Ehman RL, Wiebers DO: Intracranial aneurysms and vascular malformations: Comparison of time-of-flight and phase-contrast MR angiography. *Radiology* 181:721–730, 1991.
54. Ito H, Miwa T, Onodra Y: Growing skull fracture of childhood. *Child's Brain* 3:116–126, 1977.
55. Ito U, Tomita H, Yamazaki SH, et al: Brain swelling and brain oedema in acute head injury. *Acta Neurochir (Wien)* 79:120–124, 1986.
56. Iwakuma T, Brunngraher CV: Chronic extradural hematoma: A study of 21 cases. *J Neurosurg* 38:488–493, 1973.
57. Jones KM, et al: Brain hemorrhage: Evaluation with fast spin-echo and conventional dual spin-echo images. *Radiology* 182:53–58, 1992.
58. Jones KM, Multkern RV, Schwartz RB, et al: Fast spin-echo MR imaging of the brain and spine: Current concepts. *AJR* 158:1313–1320, 1992.
59. Karasawa H, Tomira S, Suzuki S: Chronic subdural hematoma: Time-density curve and iodine concentration in enhanced CT. *Neuroradiology* 29:36–39, 1987.

60. Katz DI, Alexander MP, Seliger GM, Bellas DN: Traumatic basal ganglia hemorrhage: Clinicopathologic features and outcome. *Neurology* 39:897–904, 1989.
61. Kaufman HH, Singer JM, Sadhu VK, et al: Isodense acute subdural hematoma. *J Comput Assist Tomogr* 4:557–559, 1980.
62. Kelly AB, Zimmerman RD, Snow RB, et al: Head trauma: Comparison of MR and CT—experience in 100 patients. *AJNR Am J Neuroradiol* 9:699–708, 1988.
63. Kim KS, Hemmati M, Weinberg PE: Computed tomography in isodense subdural hematoma. *Radiology* 128:71–74, 1978.
64. Kingsley D, Till K, Hoare R: Growing fractures of the skull. *J Neurol Neurosurg Psychiatry* 41:312–318, 1978.
65. Kishore PRS, Lipper MH, Miller JD, et al: Post-traumatic hydrocephalus in patients with severe head injury. *Neuroradiology* 16: 261–265, 1978.
66. Kon AH, LaRoque RL: Evaluation of head trauma by computed tomography. *Radiology* 123:345–350, 1977.
67. Lane JL, Flanders AE, Doan HT, Bell RD: Assessment of carotid artery parency on routine spin-echo MR imaging of the brain. *AJNR Am J Neuroradiol* 12:819–826, 1991.
68. Lantz EJ, Forbes GS, Brown ML, Laws ER Jr: Radiology of cerebrospinal fluid rhinnorhea. *AJR* 135:1023–1030, 1980.
69. Lau LSW, Pike JW: The computed tomographic findings of peritentorial subdural hemorrhage. *Radiology* 146:699–701, 1983.
70. Leech PJ, Patterson A: Conservative and operative management for cerebrospinal fluid leakage after closed head injury. *Lancet* 1: 1013–1016, 1973.
71. Lende RA: Enlarging skull fractures of childhood. *Neuroradiology* 7:119–124, 1974.
72. Lindenberg R, Fischer RS, Durlacher SH, et al: Lesions of the corpus callosum following blunt mechanical trauma to the head. *Am J Pathol* 31:287–317, 1955.
73. Lipper MH, Kishore PRS, Girevendulis AK, et al: Delayed intracranial hematoma in patients with severe head injury. *Radiology* 133:645–649, 1979.
74. Lipper MH, Kishore PRS, Enas GG, et al: Computed tomography in the prediction of outcome in head injury. *AJNR Am J Neuroradiol* 6:7–10, 1985.
75. Luerssen TG. Heart injuries in children. *Neurosurg Clin North Am* 2:399–410, 1991.
76. Lunsford LD, Maroon JC, Sheptak PE, Albin MS, et al: Subdural tension pneumacephalus. *J Neurosurg* 50:525–527, 1979.
77. Manelfe C, Cellerier P, Sobel D, et al: Cerebrospinal fluid rhinorrhea: evaluation with metrizamide cisternography. *AJR Am J Roentgenol* 138:471–476, 1982.
78. Mathews VP, Kuharik MA, Edwards MK: Gd-DTPA enhanced MR imaging of experimental bacterial meningitis: Evaluation and comparison with CT. *AJNR Am J Neuroradiol* 9:1045–1050, 1988.
79. McCluney KW, Yeakley JW, Fenstermacher MJ, et al: Subdural hygromas versus atrophy on MR brain scans: "The cortical vein sign." *AJNR Am J Neuroradiol* 13:1335–1339, 1992.
80. Melki PS, Mulkern RV, Panych LP, Jolesz FA: Comparing the FAISE method with conventional dual-echo sequences. *JMRI* 1: 319–326, 1991.
81. Meservy CJ, Tabin R, McLaurin RL, et al: Radiographic characteristics of skull fractures resulting from child abuse. *AJR* 149:173–175, 1987.
82. Messina AV, Chernik NL: Computed tomography: the "resolving" intracerebral hemorrhage. *Radiology* 118:609–613, 1975.
83. Meyer CA, Mirvis SE, Wolf AL, et al: Acute traumatic midbrain hemorrhage: Experimental and clinical observations with CT. *Radiology* 179:813–818, 1991.
84. Milo R. Razon N, Schiffer J: Delayed epidural hematoma: A review. *Acta Neurochir (Wien)* 84:13–23, 1987.
85. Moller A, Ericson K: Computed tomography of isoattenuating subdural hematomas. *Radiology* 130:149–152, 1979.
86. Moon KL Jr, Brant-Zawadzki M, Pitts LH, Mills CM: Nuclear magnetic resonance imaging of CT-isodense subdural hematomas. *AJNR Am J Neuroradiol* 5:319–322, 1984.
87. Morgan MK, Besser M, Johnston I, Chaseling R: Intracranial carotid artery injury in closed head trauma. *J Neurosurg* 66:192–197, 1987.
88. Nagib MG, Rockswold GL, Sherman RS, Lagaard MW: Civilian gunshot wounds to the brain: Prognosis and management. *Neurosurgery* 18:533–536, 1986.
89. Newton TH, Troost BT: Arteriovenous malformations and fistulae. In Newton TH, Potts DG (eds): *Radiology of the Skull and Brain.* St. Louis, CV Mosby, 1974.
90. Omar MM, Binet EF: Peripheral contrast enhancement in chronic epidural hematomas. *J Comput Assist Tomogr* 2:332–335, 1978.
91. Osborn AG, Daines JH, Wing SD, Anderson RE: Intracranial air on computerized tomography. *J Neurosurg* 48:355–359, 1978.
92. Pang D, Horton JA, Herron JM, et al: Nonsurgical management of extradural hematomas in children. *J Neurosurg* 59:958–971, 1983.
93. Pozzati F, Tognetti F, Cavallo M, Acciarri N: Extradural hematomas of the posterior cranial fossa: Observations on a series of 32 consecutive cases treated after the introduction of computed tomography scanning. *Surg Neurol* 32:300–303, 1989.
94. Ramsey RG, Huckman MS: Computed tomography of porencephaly and other cerebrospinal fluid–containing lesions. *Radiology* 123: 73–77, 1977.
95. Reed D, Robertson WD, Graeb DA, et al: Acute subdural hematomas: Atypical CT findings. *AJNR Am J Neuroradiol* 7:417–421, 1986.
96. Rengachary SS, Szymanski DC: Subdural hematomas of arterial origin. *Neurosurgery* 8:166–171, 1981.
97. Robinson J, Donald PJ: Management of associated cranial lesions. In Pitts L, Wagner FC (eds): *Craniospinal Trauma.* New York, Thieme Medical, 1989.
98. Rosenblum WI, Greenberg RP, Seelig JM, Becker DP: Midbrain lesions: Frequent and significant prognostic feature in closed head injury. *Neurosurgery* 9:613–620, 1981.
99. Ross JS, Masaryk TJ, Modic MT, et al: Intracranial aneurysms: Evaluation by MR angiography. *AJNR Am J Neuroradiol* 11:449–456, 1990.
100. Sato Y, Yuh WC, Smith WL, et al: Head injury in child abuse: Evaluation with MR imaging. *Radiology* 173:653–657, 1989.
101. Schroth G, Kretzschmar K, Gawehn J, et al: Advantage of magnetic resonance imaging in the diagnosis of cerebral infections. Neuroradiology 29:120–126, 1987.
102. Scotti G, Terbrugge K, Melancon D, Belanger G: Evaluation of the age of subdural hematomas by computerized tomography. *J Neurosurg* 47:311–315, 1977.
103. Seidenwurm D, Meng TK, Kowalski H, et al: Intracranial hemorrhagic lesions: Evaluation with spin-echo and gradient-refocused MR imaging at 0.5 and 1.5 T. *Radiology* 172:189–194, 1989.
104. Servadei F, Faccani G, Roccella P, et al: Asymptomatic extradural haematomas: Results of a multicenter study of 158 cases in minor head injury. *Acta Neurochir (Wien)* 96:39–45, 1989.
105. Shenkin HA: Acute subdural hematoma: Review of 39 consecutive cases with high incidence of cortical artery rupture. *J Neurosurg* 57: 254–257, 1982.
106. Sherman JL, Citrin CM: Magnetic resonance demonstration of normal CSF flow. *AJNR Am J Neuroradiol* 7:3–6, 1986.
107. Sherman JL, Citrin CM, Bowen BJ, Gangarosa RE: MR demonstration of altered cerebrospinal fluid flow by obstructive lesions. *AJNR Am J Neuroradiol* 7:571–579, 1986.
108. Sherman JL, Citrin CM, Gangarosa RE, Bowen BJ: The MR appearance of CSP flow in patients with ventriculomegaly. *AJR Am J Roentgenol* 148:193–199, 1987.
109. Shoung HM, Sichez JP, Pertuiset B: The early prognosis of craniocerebral gunshot wounds in civilian practice as an aid to the choice of treatment. *Acta Neurochir (Wien)* 74:27–30, 1985.
109a. Singer MB, Atlas SW, Drayer BP: Subarachnoid space disease: Diagnosis with fluid-attenuated inversion-recovery MR imaging and comparison with gadolinium-enhanced spin-echo MR imaging—blinded reader study. *Radiology* 208:417–422, 1998.
110. Sipponen JT, Sepponen RE, Sivula A: Nuclear magnetic resonance (NMR) imaging of intracerebral hemorrhage in the acute and resolving phases. *J Comput Assist Tomogr* 7:954–959, 1983.
111. Sipponen JT, Sepponen RE, Sivula A: Chronic subdural hematoma: Demonstration by magnetic resonance. *Radiology* 150:79–85, 1984.
112. Smith AS, Hurst GC, Duerk JL, Diaz PJ: MR of ballistic materials: imaging artifacts and potential hazards. *AJNR Am J Neuroradiol* 32: 567–572, 1991.
113. Smith WP Jr, Batnitzky S, Rengachary SS: Acute isodense subdural hematomas: a problem in anemic patients. *AJNR Am J Neuroradiol* 2:37–40, 1981.
114. Sparacio RR, Khatib R, Chiu J, Cook AW: Chronic epidural hematoma. *J Trauma* 12:435–439, 1972.
115. Strich SJ, Oxon DM: Shearing of nerve fibres as a cause of brain

damage due to head injury: A pathological study of twenty cases. *Lancet* 2:443–448, 1961.
116. Tamakawa Y, Hanafee WN: Cerebrospinal fluid rhinorrhea: The significance of an air-fluid level in the sphenoid sinus. *Radiology* 135:101–103, 1980.
117. Tsai FY, Huprich JE: Further experience with contrast-enhanced CT in head trauma. *Neuroradiology* 16:314–317, 1978.
118. Tsai FY, Teal JS, Quinn MF, et al: CT of brainstem injury. *AJNR Am J Neuroradiol* 1:23–29, 1980.
119. Tsai FY, Teal JS, Itabashi HH, et al: Computed tomography of posterior fossa trauma. *J Comput Assist Tomogr* 4:291–305, 1980.
120. Tsai FY, Huprich JE, Gardner FC, et al: Diagnostic and prognostic implications of computed tomography of head trauma. *J Comput Assist Tomogr* 2:323–331, 1978.
121. Turski PA, Korosec F: Technical features and emerging clinical applications of phase-contrast magnetic resonance angiography. *Neuroimaging Clin North Am* 2:785–800, 1992.
122. Unger EC, Cohen MS, Brown TR: Gradient-echo imaging of hemorrhage at 1.5 Tesla. *Magn Reson Imaging* 7:163–172, 1989.
123. Van den Heever CM, Van der Merwe DJ: Management of depressed skull fractures: Selective conservative management of nonmissle injuries. *J Neurosurg* 71:186–190, 1989.
124. Weaver D, Pobereskin L, Jane JA: Spontaneous resolution of epidural hematomas: Report of two cases. *J Neurosurg* 54:248–251, 1981.
125. Wilberger J, Chen DA: The skull and meninges. *Neurosurg Clin North Am* 2:341–350, 1991.
126. Winston KR, Beatty RM, Fischer EG: Consequences of dural defects acquired in infancy. *J Neurosurg* 59:839–846, 1983.
127. Yuh WTC, Crain MR, Loes DJ, et al: MR imaging of cerebral ischemia: Findings in the first 24 hours. *AJNR Am J Neuroradiol* 12:621–629, 1991.
128. Zimmerman RA, Bilaniuk LT: Computed tomographic staging of traumatic epidural bleeding. *Radiology* 144:809–812, 1982.
129. Zimmerman RA, Bilaniuk LT, Gennarelli T: Computed tomography of shearing injuries of the cerebral white matter. *Radiology* 127: 393–396, 1978.
130. Zimmerman RA, Bilaniuk LT, Dolinska C, et al: Computed tomography of acute intracerebral hemorrhagic contusion. *Comp Ax Tomogr* 1:271–279, 1977.
131. Zimmerman RA, Bilaniuk LT, Bruce D, et al: Computed tomography of pediatric head trauma: Acute general cerebral swelling. *Radiology* 126:403–408, 1978.
132. Zimmerman RA, Bilaniuk LT, Gennarelli T, et al: Cranial computed tomography in diagnosis and management of acute head trauma. *AJR* 131:27–34, 1978.
133. Zimmerman RA, Bilaniuk LT, Bruce D, et al: Interhemispheric acute subdural hematoma: A computed tomographic manifestation of child abuse by shaking. *Neuroradiology* 16:39–40, 1978.
134. Zimmerman RA, Bilaniuk LT, Bruce D, et al: Computed tomography of craniocerebral injury in the abused child. *Radiology* 130:687–690, 1979.
135. Zimmerman RA, Russell EJ, Yurberg E, Leeds NE, et al: Falx and interhemispheric fissure on axial CT. II: Recognition and differentiation of interhemispheric subarachnoid and subdural hemorrhage. *AJNR Am J Neuroradiol* 3:635–642, 1982.
136. Zimmerman RA, Bilaniuk LT, Hackney DB, et al: Head injury: Early results of comparing CT and high-field MR. *AJNR* 7:757–764, 1986.
137. Zimmerman RD, Heier LA, Snow RB, et al: Acute intracranial hemorrhage: Intensity changes on sequential MR scans at .5T. *AJR* 150:651–661, 1988.

10 Neurodegenerative Disorders

Andrei I. Holodny, Ajax E. George,
Mony J. de Leon, Sassan Karimi

Advances in magnetic resonance imaging (MRI) have significantly improved the assessment of neurodegenerative disorders, including the dementias, hydrocephalus, and movement disorders. Often it is difficult to differentiate clinically between various neurodegenerative disorders and even between pathologic processes and the normal aging process. In recent years, specific and sensitive radiologic criteria have been developed to accurately establish the correct diagnosis in these disorders. MRI, with its ability to image the structure and function of the living brain, has become an invaluable tool. The value of understanding the MRI appearance of neurodegenerative disorders will increase as the population ages and as new therapies for these disorders are developed.

Normal Aging

The brain changes that occur as part of normal aging include ventricular and sulcal dilatation due to cerebral atrophy (Fig. 10–1).[21, 26, 27, 46, 67, 75, 88, 102, 111] Despite these structural changes, cerebral metabolism, as measured by positron emission tomography (PET) with the glucose analogues fluorine deoxyglucose (18-FDG) and carbon deoxyglucose (^{11}C-2DG) does not decline with age.[24, 25] The severity of normally occurring brain atrophy is variable, ranging from minimal to moderately severe. Sulcal dilatation is a prominent feature of the aging process, even in the absence of ventricular enlargement. Some subjects over 60 years of age show no ventricular enlargement and demonstrate only mild or no sulcal dilatation. These subjects may be more appropriately considered "supernormals" because of the minimal structural changes that are present despite their age.

On average, ventricular volume increases approximately twofold between young (ages 20 to 30) and elderly (ages 60 to 80) normal subjects. The ventricular volume remains relatively stable up to age 60 years, after which time there is an accelerated increase in size. MRI quantification studies of this type have confirmed the findings reported in the literature on computed tomography (CT) showing that in young normal subjects sulcal volume is approximately equal to that of the ventricular system. In normal subjects over age 60, sulcal volume is greater than that of ventricular volume.[102] MRI-based measurements have shown that in normal healthy volunteers the volumes of the hippocampus, amygdala, and temporal horn remain stable until age 60, with progressive volume loss seen with more advanced age.[86]

Dementia

Dementia can be caused by myriad pathologic processes: (1) *anatomic* (e.g., tumor, subdural hematoma, or normal-pressure hydrocephalus), (2) *physiologic* (electrolyte imbalance), or (3) *psychiatric* (depression). It is often difficult to establish the cause by clinical examination alone. During radiologic assessment, it is imperative to rule out the presence of treatable causes of dementia. The advent of new pharmacologic agents and neurosurgical techniques has increased the number of dementias, which are at least potentially treatable, making the accurate radiologic assessment even more important.

Alzheimer's Disease

Alzheimer's disease (AD)[6, 7] has been recognized as one of the most significant health problems of the 20th century.[73] AD is estimated to afflict 10% of people over 65 years of age and 50% of individuals over age 85 years.[37] It is the most common dementing disorder of the elderly.[119] According to the *Diagnostic and Statistical Manual of Mental Disorders* (*DSM-IV*)[29] patients with AD present with "a multifaceted loss of intellectual abilities, such as memory, judgment, abstract thought, and other higher cortical functions, and changes in personality and behavior." However, these clinical findings are not specific for AD and often are seen with other causes of dementia.

In up to 40% of cases, genetic factors have been implicated in the etiology of AD. Three genes, when mutated, have been identified to cause AD. Some cases of AD are inherited as autosomal dominant trait. In addition, sporadic cases have been identified and account for up to 20% of cases of AD.[22]

A number of pharmacologic trials have been undertaken to improve or stem the advancement of the clinical symptoms of AD. Some have been encouraging. Cholinergic enhancement achieved by pharmacotherapy improves cognitive and noncognitive abilities in a number of patients.[42]

With the introduction of CT in the 1970s, investigators tried to correlate the degree of cerebral atrophy to the degree of dementia in patients with AD. Several early CT studies reported ventricular and sulcal enlargement in association with AD.[21, 26, 27, 46, 75, 79, 80, 111, 114] These atrophic changes, therefore, accentuate those of normal aging. However, there was a large overlap between patients with AD and normal age-matched controls. Some patients with severe cortical atrophy had normal cognition, whereas some patients with severe dementia had minimal cortical atrophy.

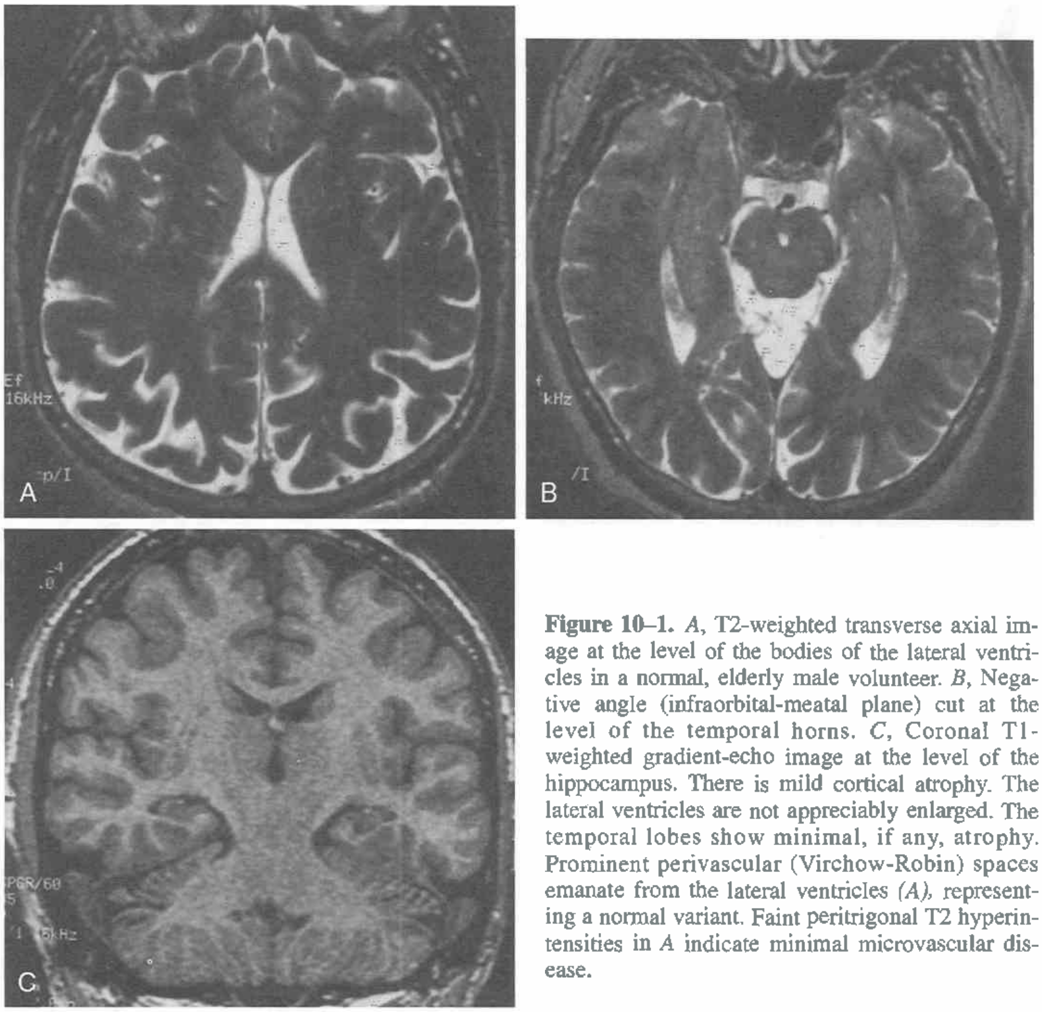

Figure 10–1. *A*, T2-weighted transverse axial image at the level of the bodies of the lateral ventricles in a normal, elderly male volunteer. *B*, Negative angle (infraorbital-meatal plane) cut at the level of the temporal horns. *C*, Coronal T1-weighted gradient-echo image at the level of the hippocampus. There is mild cortical atrophy. The lateral ventricles are not appreciably enlarged. The temporal lobes show minimal, if any, atrophy. Prominent perivascular (Virchow-Robin) spaces emanate from the lateral ventricles *(A)*, representing a normal variant. Faint peritrigonal T2 hyperintensities in *A* indicate minimal microvascular disease.

Neuropathologic evidence has shown severe focal cell loss and neurofibrillary tangle formation of the subiculum and entorhinal cortex in AD.[88] The focal pattern of pathology in this region apparently isolates the hippocampal formation from much of its output and input, thereby contributing to the memory disorder characteristic of AD patients. The pathologic changes include senile plaques, neurofibrillary tangles, and granulovacuolar degeneration with progressive neuronal loss and atrophy of the hippocampal formation.[10, 64, 74, 121] There are also neural transmitter deficits and a severe loss in the density of synaptic terminals.[57] In view of the involvement of this region, AD has been characterized as a hippocampal dementia.[10]

In view of this neuropathologic evidence, imaging studies, including our own,[21, 26, 27, 46, 75, 76, 79, 80, 111, 114] have focused on specific evaluation of the temporal lobes. These studies strongly suggest that AD may be diagnosed in life by MRI or CT. Thus, the role of neuroimaging and the diagnosis of this process, which has long been based on the method of exclusion, is now changing.

The transverse fissure of Bichat separates the telencephalon from the diencephalon. A medial part separates the thalamus from the fornix and corpus callosum, and a lateral part is situated between the thalamus and the parahippocampal gyrus. Medially the transverse fissure communicates with the perimesencephalic cistern[60] (Figs. 10–2 and 10–3).

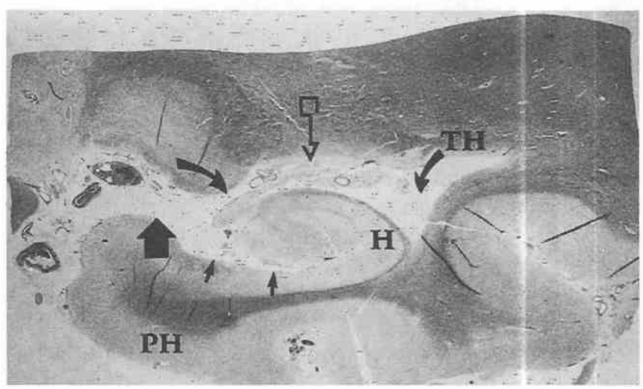

Figure 10–2. Normal anatomy of the brain Coronal pathologic section through the medial temporal lobe, including the hippocampus (H). The perihippocampal fissures, including the transverse fissure of Bichat (*large arrow*), the hippocampal fissure (*small arrows*), and the choroidal fissure (*curved arrows*) are seen. The transverse fissure of Bichat communicates with the perimesencephalic cistern (*lower left*). The choroid plexus and the fimbria (*arrow with square*) form a physical barrier between the temporal horn (TH) and the choroidal fissure. PH, parahippocampal gyrus. (From Holodny AI, George AE, Golomb J, et al: The perihippocampal fissures: Normal anatomy and disease states. Radiographics 18:653–665, 1998.)

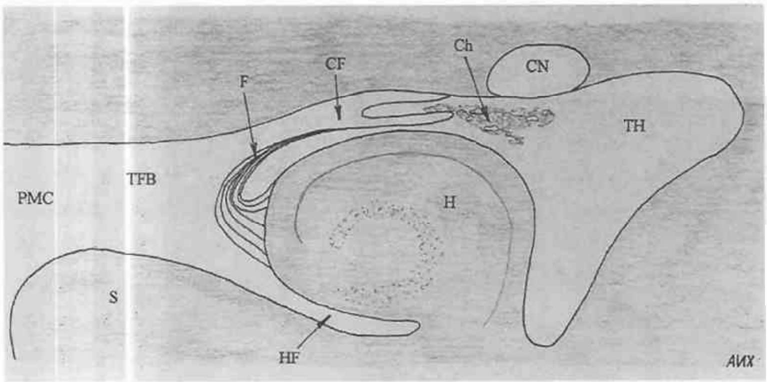

Figure 10–3. Normal brain anatomy. Coronal diagram shows the medial temporal lobe structures, including the perihippocampal fissures. The medial aspect is to the left and the lateral aspect is to the right. The perihippocampal fissures are visible but are not dilated. The choroid plexus (Ch) and the fimbria (F) form a physical barrier between the temporal horn (TH) and the choroidal fissure (CF). CN, caudate nucleus; H, hippocampus; HF, hippocampal fissure; PMC, perimesencephalic cistern; S, subiculum; TFB, transverse fissure of Bichat. (From Holodny AI, George AE, Golomb J, et al: The perihippocampal fissures: Normal anatomy and disease states. Radiographics 18:653–665, 1998.)

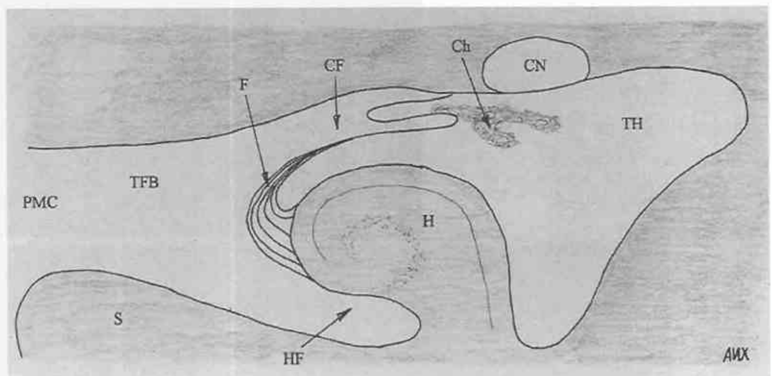

Figure 10–4. Anatomic changes in a patient with Alzheimer's disease. Coronal diagram shows the medial temporal lobe structures, including the perihippocampal fissures. Compared to the normal individual in Figure 10–3, there is volume loss of the hippocampus and corresponding dilatation of the perihippocampal fissures. The choroid plexus (Ch) and the fimbria (F) form a physical barrier between the temporal horn (TH) and the choroidal fissure (CF). CN, caudate nucleus; H, hippocampus; HF, hippocampal fissure; PMC, perimesencephalic cistern; S, subiculum; TFB transverse fissure of Bichat. (From Holodny AI, George AE, Golomb J, et al: The perihippocampal fissures: Normal anatomy and disease states. Radiographics 18:653–665, 1998.)

Temporal lobe changes are highly sensitive markers of AD.[27, 46, 61] The use of either CT or MRI negative-angle thin-section cuts that parallel the temporal lobes or coronal thin-section MRI scans perpendicular to the axial plane maximizes the demonstration of temporal lobe pathology. Almost all patients with AD show at least a moderate degree of hippocampal atrophy as well as atrophy of the parahippocampal gyrus, dentate gyrus, and subiculum. These atrophic changes lead to enlargement of the transverse fissure of Bichat and the hippocampal and choroidal extensions as well as dilatation of the temporal horn (Fig. 10–4). Although high-resolution coronal images display this anatomy optimally, even mild hippocampal atrophy and the resultant dilatation of the perihippocampal fissures can be seen on standard MRI and CT images[27] (see Figs. 10–5 and 10–6).

The longitudinal study of normal subjects and patients with AD for structural brain changes shows a greatly increased rate of change in the AD patients as compared with normal subjects.[26, 41] We found that 90% of patients with AD showed progressive atrophy of the temporal lobes when they were longitudinally studied over a 3-year period[26] (see Fig. 10–12). More important is that the presence of medial temporal lobe atrophy in **normal individuals**[49] may represent a significant risk factor for the subsequent development of AD.[27]

In addition, it appears that an atrophic hippocampus not only is a radiologic marker for the presence of AD but also may actually serve as a predictor for the future development of this disorder. In a landmark study by de Leon and coworkers,[27] 86 older adult patients who were either normal

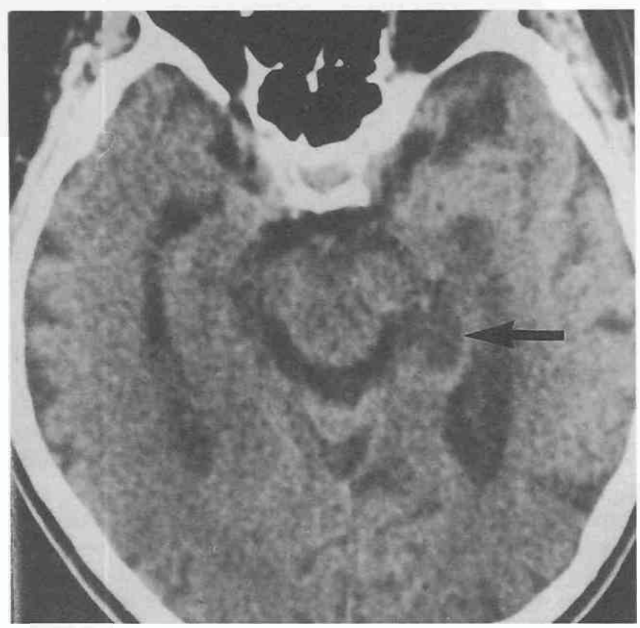

Figure 10–5. Clinical Alzheimer's disease. Reverse-angle CT scan (angled parallel to the hippocampus) demonstrates an area of decreased density in the medial aspect of the temporal lobe (*arrow*). The density of this area approaches that of cerebrospinal fluid. This corresponds to dilatation of the perihippocampal fissures and is an accurate indicator of hippocampal atrophy. (From Holodny AI, George AE, Golomb J, et al: The perihippocampal fissures: Normal anatomy and disease states. Radiographics 18: 653–665, 1998.)

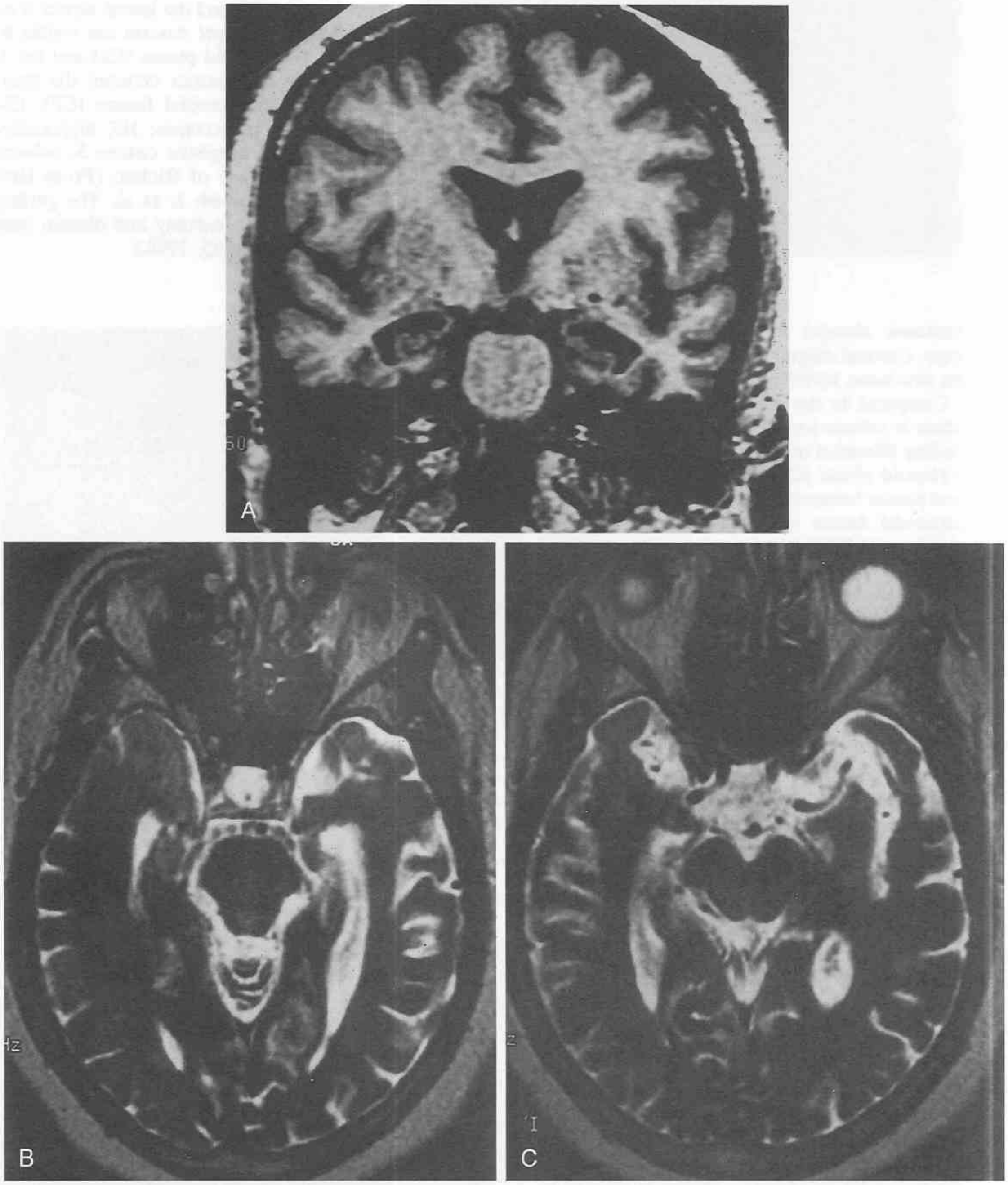

Figure 10–6. Presumed Alzheimer's disease in a 60-year-old woman. *A*, Coronal T1-weighted MR image demonstrates severe atrophy of the hippocampus and dilatation of the perihippocampal fissures. *B* and *C*, Reverse-angle axial T2-weighted images in the same patient. These images demonstrate the importance of evaluating for prominence of the perihippocampal fissures and hippocampal atrophy in the correct plane. *B* is inferior to *C*. In *B*, the left medial temporal lobe demonstrates prominent perihippocampal fissures (the area of increased signal intensity between the temporal horn and the pons). The right medial temporal lobe on image B fails to demonstrate this area of increased signal intensity. This is because the patient is slightly tilted and one is actually scanning through the area of the parahippocampal gyrus (see Fig. 10–1), not the atrophic hippocampus. An analogous situation exists in *C*. The dilated perihippocampal fissures are seen on the right. The scanning plane on the left side is directed superior to the perihippocampal fissures and therefore does not demonstrate the area of increased signal intensity associated with dilated perihippocampal fissures. (From Holodny AI, George AE, Golomb J, et al: The perihippocampal fissures: Normal anatomy and disease states. Radiographics 18: 653–665, 1998.)

or who had minimal cognitive impairment were monitored for four years. Dilatation of the perihippocampal fissures at the time of entry into the study was a predictor of future deterioration and development of AD, with a sensitivity of 91% and a specificity of 89%.

Hydrocephalus

Classification

Hydrocephalus, from the Greek *hydro* (water) and *cephalus* (brain) is an abnormal accumulation of intracranial fluid (i.e., water on the brain) resulting from a structural or functional block to the normal flow of cerebrospinal fluid (CSF). The ventricles may become significantly enlarged.

The diagnosis of hydrocephalus in patients under age 60 years is usually straightforward. In patients over age 60, however, often confounding superimposed changes of atrophy are caused by normal aging and possible coexisting AD.[48] Hydrocephalus is initially associated with increased intracranial pressure, but it may later reach a state of equilibrium known as *arrested*, or *normal-pressure*, *hydrocephalus*.

When the block to the flow of CSF occurs along the ventricular system, the condition is known as *obstructive hydrocephalus*. Since all hydrocephalus is obstructive, the term *intraventricular obstructive hydrocephalus* has been proposed as a more accurate description for this type of obstruction. If the block to CSF is distal to the ventricular system, either at the base of the skull or as distal as the level of the pacchionian granulations, the hydrocephalus is described as *communicating* (i.e., the ventricular system communicates with the extraventricular subarachnoid space). A more accurate term for this condition would therefore be *extraventricular obstructive hydrocephalus*. The term *hydrocephalus ex vacuo* is sometimes used to refer to cerebral atrophy; this term is best avoided, however, because of its confusing implications.

The terms *communicating hydrocephalus* and *noncommunicating* (or *obstructive*) *hydrocephalus* have prevailed since the early days of neuroradiologic diagnosis. Dandy and Blackfan[23] introduced a color dye (phenolsulfonphthalein) by ventricular catheter into the hydrocephalic ventricular system. If the color dye could be extracted by lumbar spinal tap within 2 to 3 minutes, the hydrocephalus was then described as "communicating." If the dye did not appear on spinal tap or was greatly delayed, the hydrocephalus was considered obstructive, or "noncommunicating."

The CT and MRI features of communicating hydrocephalus are as follows:

1. *Early dilatation and rounding of the temporal horns.* These features may be the earliest manifestation of ventricular obstruction and may be seen before obvious enlargement of the bodies of the lateral ventricles. In contradistinction, temporal horn dilatation as a manifestation of temporal lobe atrophy occurs later in the progression of a degenerative brain disease and is invariably associated with the presence of enlargement of the perihippocampal fissures (the transverse fissure of Bichat, and the choroidal and hippocampal fissures). The cisternal spaces and their extensions (the perihippocampal fissures) do not communicate with the temporal lobe; therefore, the dilatation of the temporal horn caused by obstructive hydrocephalus may actually displace the hippocampus medially and cause compression of the perihippocampal fissures[59] (Figs. 10–7 and 10–8).
2. *Rounding and enlargement of the frontal horns.* Figure 10–8 shows the MRI scan of a 47-year-old woman with hydrocephalus. The scan shows severe lateral and third ventricular dilatation. The frontal horns are ballooned, and the angle formed by their medial walls (the septal angle) is acute. In atrophy, the frontal horns are typically enlarged but not ballooned. The septal angle is often obtuse.
3. *Enlargement and ballooning of the third ventricle.* In atrophy, the third ventricle tends to enlarge by increasing the distance between its walls, which tend to remain parallel to each other. Ballooning and rounding of the third ventricle are characteristic of hydrocephalus. In the sagittal projection, the roof of the third ventricle may be flattened by the often huge lateral ventricular bodies.
4. *Severe dilatation of the bodies of the lateral ventricles and increased height of the ventricles.* The degree of dilatation of the lateral ventricles in hydrocephalus is typically notably greater than that occurring secondary to atrophy. The corpus callosum is thinned and bowed, forming an arch. Interpeduncular height may be decreased.[35] Typically, a patient with severe ventricular

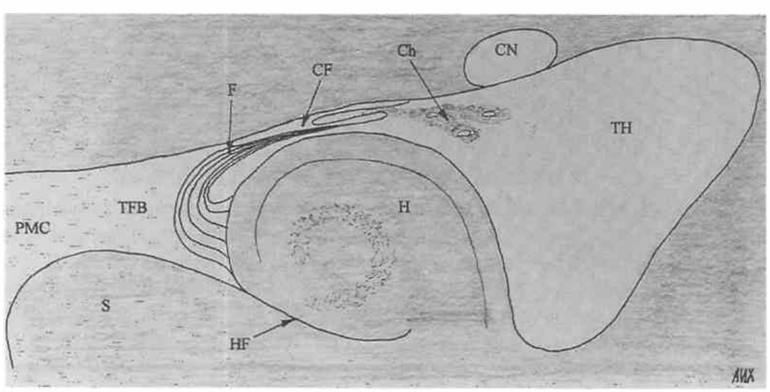

Figure 10–7. Anatomic changes in hydrocephalus. Coronal diagram shows the structures of the medial temporal lobe, including the perihippocampal fissures. Compared to the normal individual in Figure 10–3, there is dilation of the temporal horn of the lateral ventricle. The hippocampus is displaced medially, and the perihippocampal fissures are compressed. The choroid plexus (Ch) and the fimbria (F) form a physical barrier between the temporal horn (TH) and the choroidal fissure (CF). CN, caudate nucleus; H, hippocampus; HF, hippocampal fissure; PMC, perimesencephalic cistern; S, subiculum; TFB, transverse fissure of Bichat. (From Holodny AI, George AE, Golomb J, de Leon MJ, Kalnin AJ: The perihippocampal fissures: Normal anatomy and disease states. Radiographics 18:653–665, 1998.)

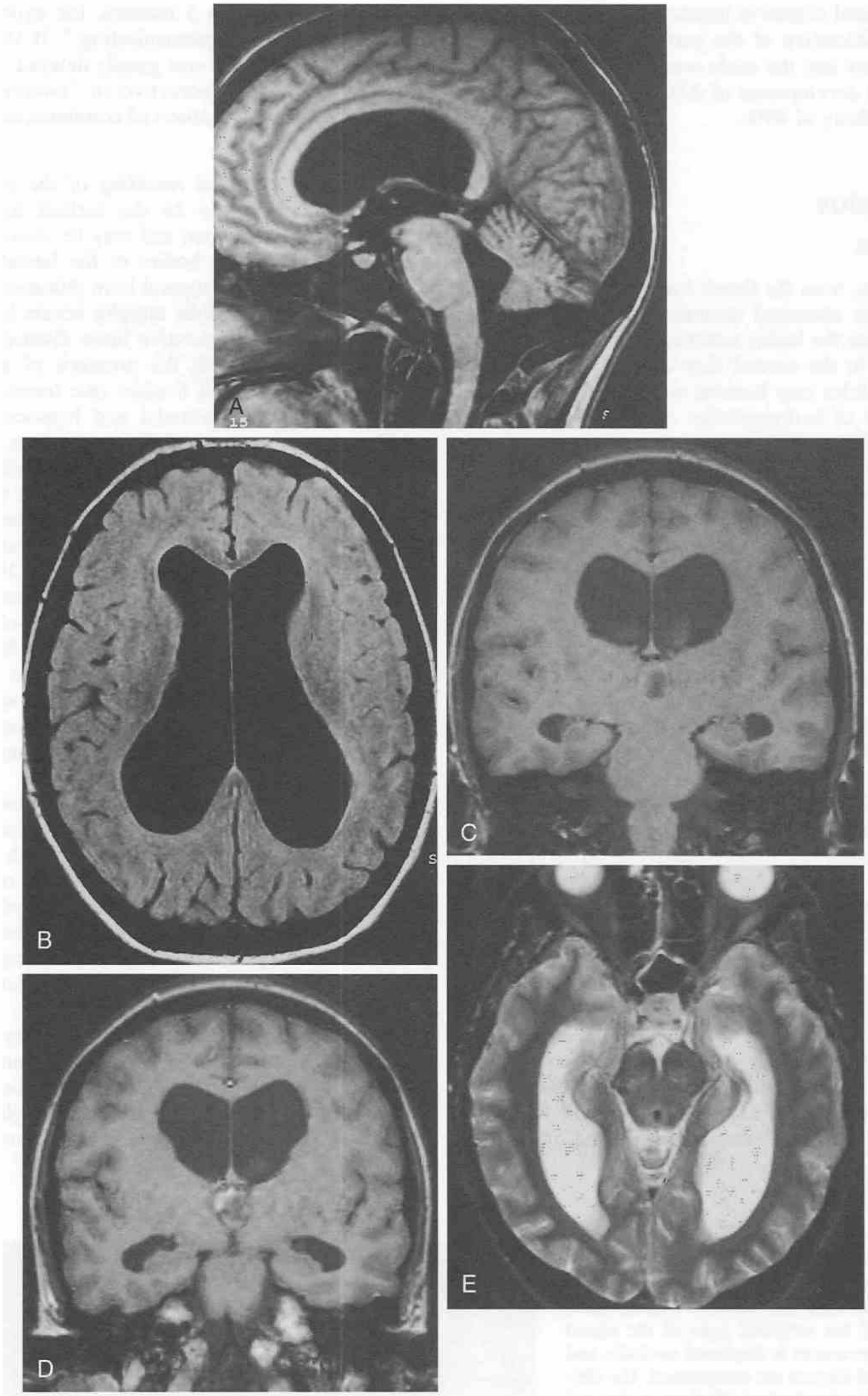

Figure 10–8. Hydrocephalus in a 47-year-old patient. *A,* Sag[redacted] T1-weighted image demonstrates dilatation of the lateral, third, and fourth ventricles. There is bowing of the corpus callosum. *B,* Axial fluid-attenuated inversion recovery (FLAIR) image demonstrates marked dilatation of the ventricles out of proportion to the sulci. *C* and *D,* Coronal T1-weighted images demonstrate marked dilatation of the lateral ventricles, including the temporal horns. There is no hippocampal atrophy. *E,* Hydrocephalus is confirmed on this axial T2-weighted image. (From Holodny AI, George AE, Golomb J: Neurodegenerative disorders. In Edelman R, Hesselink JR (eds): Clinical Magnetic Resonance Imaging, 2nd ed. Philadelphia, WB Saunders, 1996.)

dilatation caused by hydrocephalus may show a minimal cognitive deficit. In contrast, a patient with comparably severe ventricular dilatation caused by atrophy usually shows profound cognitive impairment. Note the relatively modest ventricular enlargement in patients with severe dementia. A motoric deficit, especially gait impairment, is a characteristic feature of hydrocephalus. The motoric deficit may be severe to the point that patients may be wheelchair-bound or bed-bound. Ventricular shunting in these patients may have dramatic results, with significant improvement in gait and motor function.

5. *Enlargement of the fourth ventricle.* This finding presupposes that the hydrocephalus is communicating. In chronic obstructive hydrocephalus, however, the fourth ventricle may also enlarge secondarily from incisural obstruction created by the enlarged ventricles, dilated temporal horns, and swollen temporal lobes, which tend to herniate into the incisural notch. When present, dilatation of the fourth ventricle can be helpful in establishing the diagnosis of hydrocephalus. However, fourth-ventricular enlargement may be absent or minimal despite the presence of definite hydrocephalus.
6. *Sulcal effacement.* When present, sulcal effacement is usually diagnostic of hydrocephalus in the elderly age group because cortical atrophy is almost invariably present as part of the normal aging process. Hydrocephalus, however, may coexist with large sulci and, in particular, with large sylvian fissures. This occurs when the block is at the level of the high convexity or the pacchionian granulations. Consequently, the sulci and fissures dilate because of the damming of fluid proximal to the block. In effect, the sulci and fissures dilate in the same way as the ventricular system because of the distal obstruction. In such patients, ventricular shunting may lead to collapse of the sylvian fissures, the sulci, and other convexity CSF collections.[60]
7. *Periventricular edema.* This finding is seen especially in the periventricular white matter of the frontal horns in acute and subacute phases of hydrocephalus. In older people, however, it is usually not possible to distinguish between periventricular T2 changes resulting from microvascular parenchymal disease (see later) and the periventricular edema of hydrocephalus. In fact, hydrocephalus may lead to chronic microvascular changes, as shown in animal hydrocephalus models.[59] It was initially thought that MRI might help identify ventricular enlargement due to hydrocephalus by the presence of a periventricular high-signal halo on T2-weighted images. Because periventricular high-signal changes as a result of microvascular disease are also seen, the finding is therefore nonspecific and not helpful.[97] Furthermore, in chronic stages of hydrocephalus, periventricular edema resolves and is not visualized by either CT or MRI.

Obstructive Hydrocephalus

The sites where the ventricular system is normally narrow (i.e., the foramina) are particularly vulnerable to obstruction. Causes of intraventricular obstruction at the level of the foramen of Monro include (1) colloid cyst of the third ventricle, (2) ependymoma, (3) teratoma, (4) congenital atresia, and (5) involvement by adjacent glioma.

The posterior third ventricle may be obstructed by pinealomas and aneurysms of the vein of Galen. Aqueductal obstruction can also occur in association with aqueductal stenosis, periaqueductal gliomas, arteriovenous malformations, and cysts of the quadrigeminal region.

Communicating Hydrocephalus

Communicating hydrocephalus may result from previous infection such as meningitis or may be secondary to previous hemorrhage caused by trauma, surgery, or rupture of an aneurysm with subarachnoid hemorrhage. It is also seen in association with Arnold-Chiari malformation and in the presence of subarachnoid seeding of tumor (meningiocarcinomatosis). A functional hydrocephalus in the presence of elevated CSF protein is seen in association with spinal cord tumors, typically ependymomas. Overproduction of CSF caused by choroid plexus papilloma or carcinoma may also result in hydrocephalus.

Normal-Pressure Hydrocephalus

An idiopathic form of communicating hydrocephalus, usually seen in older adults and known as normal-pressure hydrocephalus (NPH), was described originally by Adams and Hakim and their colleagues.[3, 56] These authors reported a clinical triad of gait impairment characterized as magnetic gait, dementia, and urinary incontinence. Symptoms can be relieved by ventricular shunting, with the most dramatic improvement usually seen in gait. The typical patient with NPH who is likely to respond to a shunt exhibits a mild cognitive impairment along with a significant gait disturbance.

Differentiating NPH from cerebral atrophy can be extremely difficult. Initial enthusiasm for the concept of NPH as a treatable cause of dementia and gait impairment resulted in shunt procedures in patients who either failed to respond or showed an initial improvement but subsequently continued to deteriorate. Because of these discouraging results, the number of shunt procedures for NPH in the elderly has significantly decreased. The failure of patients to respond to the shunt procedure probably resulted from erroneous diaguosis of hydrocephalus in patients who were suffering from degenerative brain disease such as cerebral atrophy associated with AD. This has led to more stringent criteria to identify potential shunt candidates. These criteria include (1) radioisotope cisternography,[84] (2) continuous intracranial pressure recordings,[98] (3) spinal effusion,[90] and (4) CT cisternography with intrathecal iodinated contrast material.[36] Despite these criteria, a reliable study predicting shunt outcome has not been established.

In terms of MRI, two approaches can be used to differentiate NPH from cerebral atrophy: the anatomic approach and the functional approach. Anatomically, in patients with AD, volume loss of the hippocampus develops and resultant dilatation of the perihippocampal fissures ensues (see Fig. 10–4). Patients with NPH have dilation of the temporal horn (Fig. 10–7).[61] Although the hippocampus and the

Figure 10–9. Clinical Alzheimer's disease in a woman. Reverse-angle axial T1-weighted MR image (Global Deterioration Scale = 5). There is decreased signal intensity between the temporal horns and the perimesencephalic cistern. This represents dilatation of the perihippocampal fissures (PHFs) and atrophy of the structures of the medial temporal lobe, including the hippocampus. The size of the PHFs was assessed as moderately dilated. Compare with Figures 10–11 and 10–12. (From Holodny AI, Waxman R, George AE, et al: MR differential diagnosis of normal-pressure hydrocephalus and Alzheimer disease: Significance of the perihippocampal fissures. AJNR Am J Neuroradiol 19:813–819, 1998.)

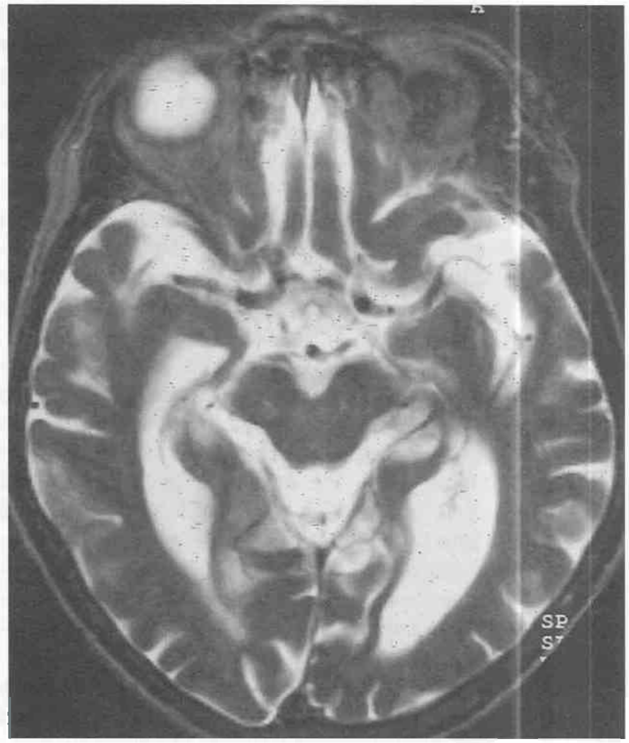

Figure 10–10. Alzheimer's disease in a 73-year-old patient. Axial T2-weighted images angled parallel to the hippocampi demonstrate marked atrophy of the hippocampus and marked dilatation of the perihippocampal fissures. By comparison, the ventricles and cortical sulci are only mildly dilated. Compare with Figures 10–11 and 10–12. (From Holodny AI, Waxman R, George AE, et al: MR differential diagnosis of normal-pressure hydrocephalus and Alzheimer disease: Significance of the perihippocampal fissures. AJNR Am J Neuroradiol 19:813–819, 1998.)

Figure 10–11. Reverse-angle axial T1-weighted MR image of normal-pressure hydrocephalus in a 72-year-old man who improved after the placement of a ventriculoperitoneal shunt. There is no abnormally decreased signal intensity of the structures of the medial temporal lobes; therefore, there is no dilatation of the perihippocampal fissures or atrophy of the structures of the medial temporal lobe, including the hippocampus. The size of the perihippocampal fissures was graded as normal. This is in contrast to the patients from the group with Alzheimer's disease in Figures 10–9 and 10–10. There is dilatation of the temporal horns to a degree similar to patients from the Alzheimer group. (From Holodny AI, Waxman R, George AE, et al: MR differential diagnosis of normal-pressure hydrocephalus and Alzheimer disease: Significance of the perihippocampal fissures. AJNR Am J Neuroradiol 19:813–819, 1998.)

perihippocampal fissures are best seen in the coronal plane on MRI, it is important to stress that the anatomic changes occurring in NPH and AD can be appreciated to a large degree on axial MRI and CT (Figs. 10–9 to 10–12).[59]

Occasionally, patients with NPH present with dilated sylvian fissures and rarely with focally dilated cortical sulci.[60] In a number of cases of shunt-proven NPH, there was actually paradoxical decrease in the size of the dilated cortical fissures and sulci that paralleled the decrease in the size of the lateral ventricles following successful shunting. Therefore, sulcal dilatation (especially when focal) should not be taken to imply cortical atrophy, and the maxim that hydrocephalus is defined as ventricles dilated out of proportion to the sulci does not always apply (Figs. 10–13 and 10–14).

Because AD is rather prevalent in the elderly, it can occasionally coexist with NPH. Earlier literature suggested that patients with dementia due to AD are not candidates for intraventricular shunting. However, more recent work suggests that for patients with accurately diagnosed NPH, concomitant AD does not strongly influence the clinical response to shunt placement.[50]

Another MRI approach to the diagnosis of NPH is the quantification of CSF flow in the aqueduct. Work by Bradley and coworkers[14] has demonstrated that in patients with shunt-proven NPH, the CSF stroke volume and CSF velocity in the aqueduct are both increased. However, the presence or absence of a flow void in the aqueduct does not appear to be an accurate predictor of shunt response.[14]

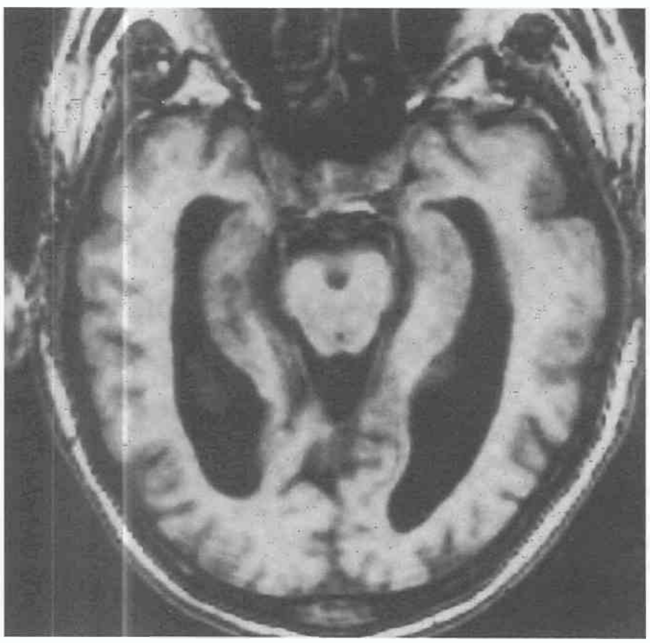

Figure 10–12. Reverse-angle axial T1-weighted MR image of a patient with normal-pressure hydrocephalus. There is a mild degree of decreased signal intensity of the structures of the medial temporal lobes. Therefore, the size of the perihippocampal fissures was graded as mildly dilated. Compare with Figures 10–9 and 10–10. (From Holodny AI, Waxman R, George AE, et al: MR differential diagnosis of normal-pressure hydrocephalus and Alzheimer disease: Significance of the perihippocampal fissures. AJNR Am J Neuroradiol 19:813–819, 1998.)

In summary, using the combination of radiologic and clinical criteria in conjunction with the results of measurements of cerebral blood flow and cerebral metabolism, we may more reliably and with greater accuracy identify patients with hydrocephalus who are likely to respond to shunt. Functional MRI techniques now becoming available may noninvasively provide similar functional information as that derived from PET and single photon emission computed tomography (SPECT). As a result of these advances, interest has been renewed in the surgical management of patients with hydrocephalus.

Pick's Disease

Pick's disease, another cause of dementia in adults, was first described in 1892.[97] The onset of dementia is often in the presenile age group, and a familial occurrence has been reported.[54] Pick's disease is much less prevalent than AD. The clinical presentation in most patients is suggestive of frontal lobe damage. There is an insidious deterioration in intellectual capacity and difficulty in concentration and memory. There is a slow but steady progression to marked dementia, which is usually more rapidly progressive than with AD.

On pathologic examination, there is atrophy of the brain, particularly of the frontal lobes and the anterior aspects of the temporal lobes. The parietal and occipital lobes are usually spared. Histologically, there is an intense loss and misalignment of neurons as well as subcortical gliosis in the affected areas of the brain. Many of the remaining neurons are small and contain characteristic intracytoplasmic, argentophilic inclusion bodies (Pick's bodies), which are well seen with Bielschowsky silver stain and antibody immunostaining.[2]

Prior to the advent of cross-sectional imaging, Pick's disease could be definitively diagnosed only at autopsy; however, the introduction of CT and MRI has allowed for the accurate diagnosis of Pick's disease in vivo and to differentiate it from other neurodegenerative disorders.[40] Radiographically, Pick's disease parallels the findings seen on pathologic studies, and marked atrophy of the anterior temporal and frontal lobes are characteristics. The sulci of these lobes become so atrophic that they have been described as icicle-like. There is usually a sparing of the posterior aspect of the superior frontal gyrus and the brain posterior to it.[33]

Leukoencephalopathy of Aging, Multi-Infarct Dementia, and Binswanger's Disease

MRI is exquisitely sensitive to the detection of white matter disease. As in the atrophic changes described in the first part of this chapter, understanding the MRI characteristics and the underlying pathophysiology can allow one to arrive at the accurate diagnosis. Since this chapter focuses on neurodegenerative diseases, it covers only the limited number of white matter diseases that apply to this category.

Long repetition time (TR) (T2, proton-density) and fluid-attenuating inversion recovery [FLAIR] hyperintensities are common in the elderly.[45] These white matter lesions

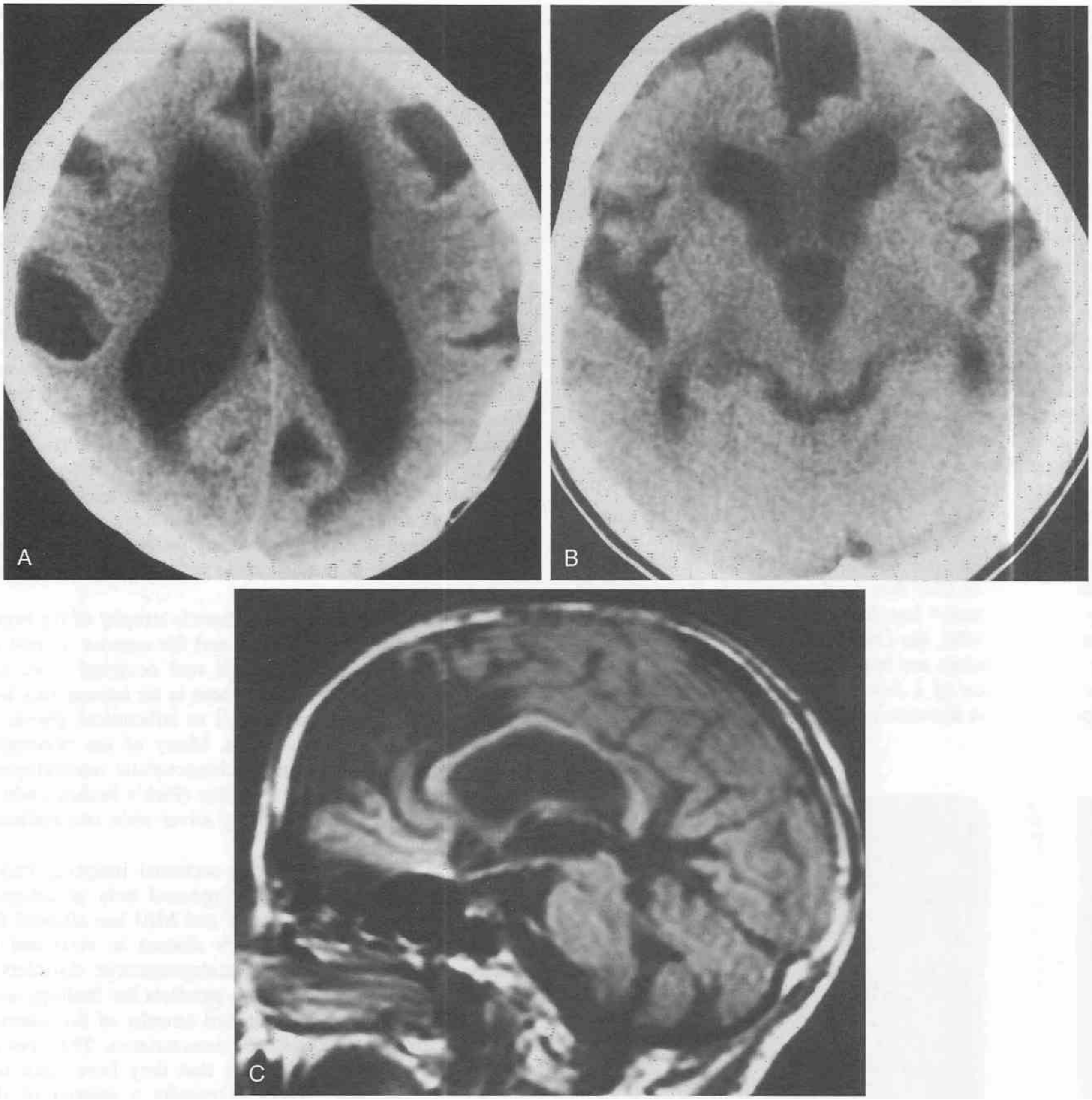

Figure 10–13. Shunt-proven normal-pressure hydrocephalus in a patient with prominent focal sulcal dilatation. Axial CT scans through the bodies of the lateral ventricles *(A)* and third ventricle *(B)* and midsagittal MR image *(C)* demonstrate marked dilatation of the lateral ventricles. The temporal horns are moderately enlarged. The third ventricle is severely dilated and rounded. There is marked dilatation of the following sulci: the sylvian fissures bilaterally, the central sulci bilaterally, the anterior aspect of the interhemispheric fissure, the left parieto-occipital fissure and the left calcarine fissure. In addition, there is marked focal dilatation of the cingulate sulcus on the right, the precentral sulcus on the left, and the frontal sulci bilaterally. There is also dilatation of the suprasellar and quadrigeminal plate cisterns. The remaining sulci are compressed. There is no evidence of dilatation of the choroidal and parahippocampal fissures, hippocampal atrophy, or cerebellar or brain stem abnormalities. (From Holodny AI, George AE, de Leon MJ, et al: Focal dilatation and paradoxical collapse of cortical fissures and sulci in patients with normal-pressure hydrocephalus. J Neurosurg 89:742–747, 1998.)

are typically patchy or punctate and involve the peritrigonal region preferentially. The second most common area involves the white matter adjacent to the frontal horns. Brain stem lesions are less common. Typically, this process spares the arcuate fibers and the corpus callosum. Variously termed *leukoencephalopathy, leukoaraiosis,*[16, 55] *deep white matter ischemia*, or *white matter hyperintensities of aging*, the lesions are strongly related to age and have increasing prevalence in individuals over age 60 years.[44] It is also seen earlier and to a greater degree in patients with microvascular diseases, such as diabetes and hypertension. White matter is more susceptible than gray matter to chronic ischemic changes because it is supplied by long, small-caliber vessels, which are affected these diseases.

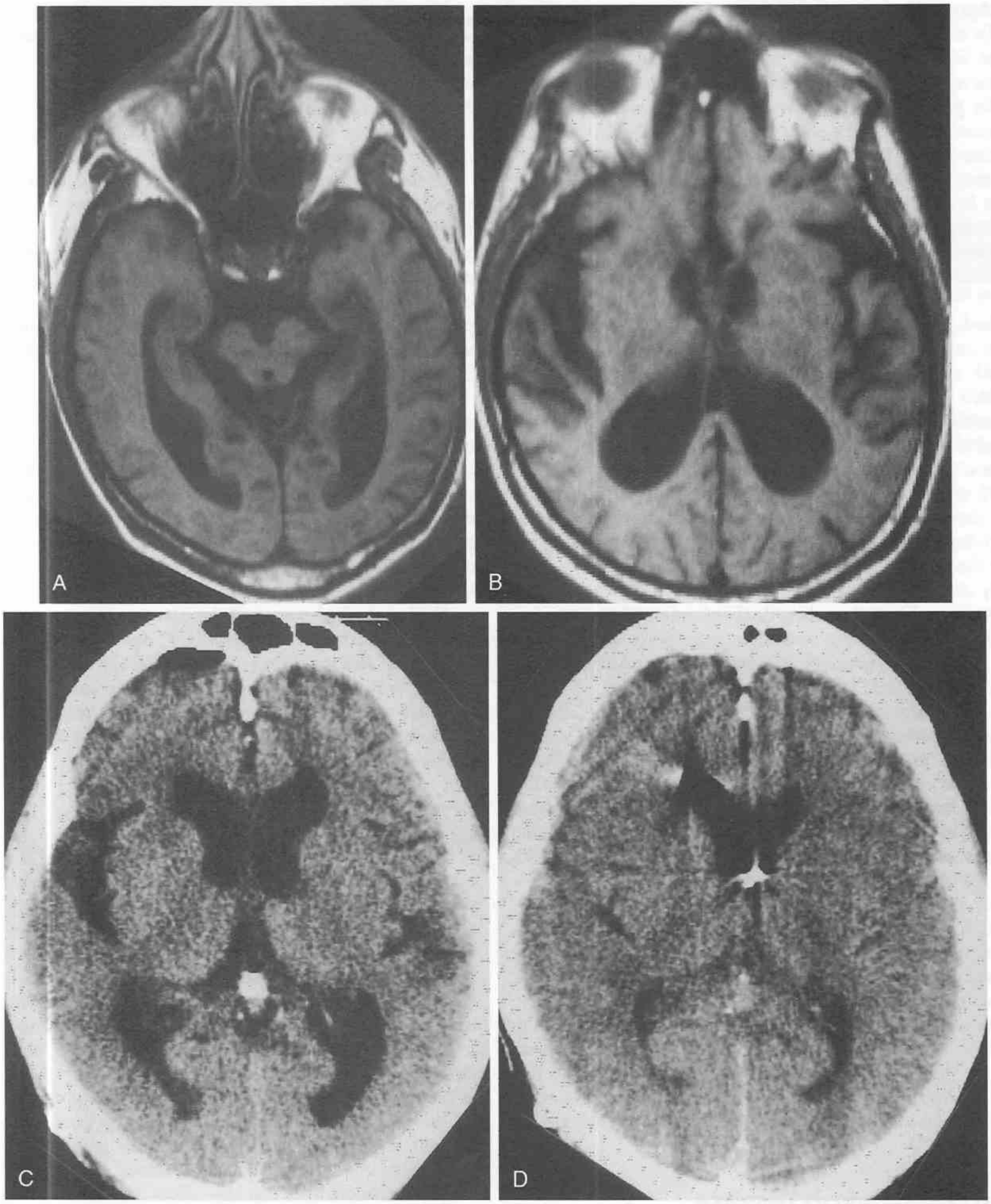

Figure 10–14. Normal-pressure hydrocephalus in a 68-year-old man with paradoxical collapse of the sylvian fissures. *A* and *B*, Axial T1-weighted images demonstrate enlarged lateral ventricles, including the temporal horns as well as moderately distended sylvian fissures. Several months after successful shunting, the patient returned with recurrent symptoms. *C*, A CT scan demonstrated evidence of shunt failure with distention of the lateral ventricles. Sylvian fissure dilatation was also present. *D*, Following shunt revision, a CT scan demonstrated a decrease in the size of the lateral ventricles as well as a decrease in the size of the sylvian fissures. (From Holodny AI, George AE, de Leon MJ, et al: Focal dilatation and paradoxical collapse of cortical fissures and sulci in patients with normal-pressure hydrocephalus. J Neurosurg 89:742–747, 1998.)

Leukoencephalopathy cannot be considered a benign entity.[16] We and others have found that these brain changes are related to gait disturbances and increased incidence of falls in the elderly,[83] deficits of fine motor coordination,[77] and an increased frequency in cerebral infarcts.[44, 45, 69, 122] The increased incidence of falls is particularly of concern in older people.[83] The microvascular lesions themselves are not associated with dementia; however, the cognitive deficit associated with preexisting AD or other dementing disorders may be potentiated by the presence of the white matter lesion.[44]

Autopsy work, including our own, has shown changes of the hypertensive type in the white matter associated with hyalinosis of arterioles and rarefaction of the white matter.[19, 44, 52, 82, 100] In addition, mild gliosis, increased interstitial fluid, and "myelin pallor" are seen. Frank infarction occurs in more advanced cases and can be seen as well-defined areas of decreased signal intensity on the T1-weighted images. The T1 characteristics allows one to differentiated leukoencephalopathy from frank infarction.

Multiple-infarct dementia (MID) is the second most common cause of dementia in the elderly representing 10% to 20% of cases in patients over 65 years old.[121] Clinically, these patients present with a sudden onset of dementia, day-to-day fluctuation, and spontaneous improvement early in the disease. These patients present radiographically with focally dilated fissures and multiple areas of focal cortical volume loss. Multiple subcortical infarcts and infarcts involving certain strategic structures (e.g., parts of the thalamus, caudate, or genu of the internal capsule) can also result in dementia.[81]

In 1894, Binswanger[6] described a slowly progressive disease characterized by loss of memory and intellectual impairment associated with recurring neurologic deficits. Binswanger was apparently describing a type of multi-infarct dementia with severe hypertensive type microvascular changes, multiple subcortical infarcts, and dementia. The presence of periventricular T2 hyperintensities on MRI scans should not prompt a diagnosis of *Binswanger's disease* or multi-infarct dementia unless evidence clearly shows that infarcts are also present and that dementia is clinically present. Multiple infarcts, whether cortical or subcortical and especially when bilateral, may be associated with dementia. One should also keep in mind that even numerous subcortical infarcts may lead to only mild dementia. Because periventricular white matter hyperintensities are widely prevalent, especially in the elderly, the terms *multi-infarct dementia* and *Binswanger's disease* should not be used to describe these radiologic findings.[95]

Creutzfeldt-Jakob Disease

Creutzfeldt-Jakob disease (CJD) is a rare cause of rapidly progressive dementia and is one of several associated neurodegenerative illnesses whose pathogenesis is related to a small, nonviral, 30- to 35-kD proteinaceous infectious particle known as a *prion*. The loci of pathology involve the cerebral and cerebellar cortices as well as the basal ganglia, where neuronal loss, reactive astrocytosis and the formation of cytoplasmic vacuoles within the glia and neurons give the tissue a characteristic spongiform appearance on light microscopy. All of these changes occur in the absence of an inflammatory response.

The clinical syndrome is typically one of rapid cognitive decline, often with psychosis and delirium. Motor abnormalities of cerebellar dysfunction can appear, and almost all patients evidence pronounced myoclonus prior to the final phase of deepening unresponsiveness and coma. The time course of the disease from presentation until death is usually less than 1 year.

In the very early stages of the disease, CT and even MRI findings may be normal.[125] Early changes are symmetrical increased signal intensity in the basal ganglia[11, 30, 85, 118] and occasionally in the white matter.[131] Occasionally, the changes in the basal ganglia occur before the typical clinical and neurophysiologic signs of CJD develop.[101] In three patients, cortical diffusion-weighted imaging abnormalities were reported to occur before the onset of abnormal signal in the basal ganglia on routine sequences.

The year 1986 heralded the appearance of a new form of CJD—bovine spongiform encephalitis (BSE), or "mad cow disease." This new variant (nvCJD) was first detected in humans in 1996. The possibility of direct transmission of BSE from cows to humans has raised serious concerns, especially in Europe.[127] nvCJD tends to affect a younger population, with a median age at death of 29 years.[129] The earliest MRI findings are abnormal signal intensity on the long TR-weighted images of the pulvinar.[129, 132]

During the late stages of the disease, significant atrophy develops and progresses rapidly.[125] Symmetrical increased T2 signal abnormality with mass effect in the occipital cortex, predominantly in a gray matter distribution, has been reported.[38] A study using magnetic resonance spectroscopy (MRS) detected a decrease in *N*-acetylaspartate (NAA) and other metabolites in late CJD.[53]

Huntington's Disease

Huntington's disease (HD) is a degenerative neurologic disease that is inherited in an autosomal dominant fashion with complete penetrance. It is determined by a gene localized to the short arm of chromosome 4. Patients usually become symptomatic before age 50 and tend to present with abnormalities of affect and personality. Within time, dementia becomes evident, accompanied by gradual disintegration of motor control and the emergence of choreoathetoid movements. Occasionally, rigidity rather than chorea is the most salient motor abnormality (Westphal variant).

Neuropathologically, the most conspicuous finding in patients with HD is atrophy of the basal ganglia, generally proceeding medial to lateral and dorsal to ventral.[58, 99, 126] Degenerative changes can also affect the frontal and temporal cortices. The degenerative process is accompanied by diminished neurotransmitter concentrations of acetylcholine and gamma-aminobutyric acid (GABA). In early cases, neuronal loss is generally first appreciated in the head of the caudate.[126] This has been confirmed by a number of MRI studies showing atrophy of the basal ganglia in patients with HD, which is most prominent in the head of the caudate, appearing as focal enlargement of frontal horns on imaging. The atrophy of these structures worsens as the disease progresses.[9] MRS studies indicate a decrease in

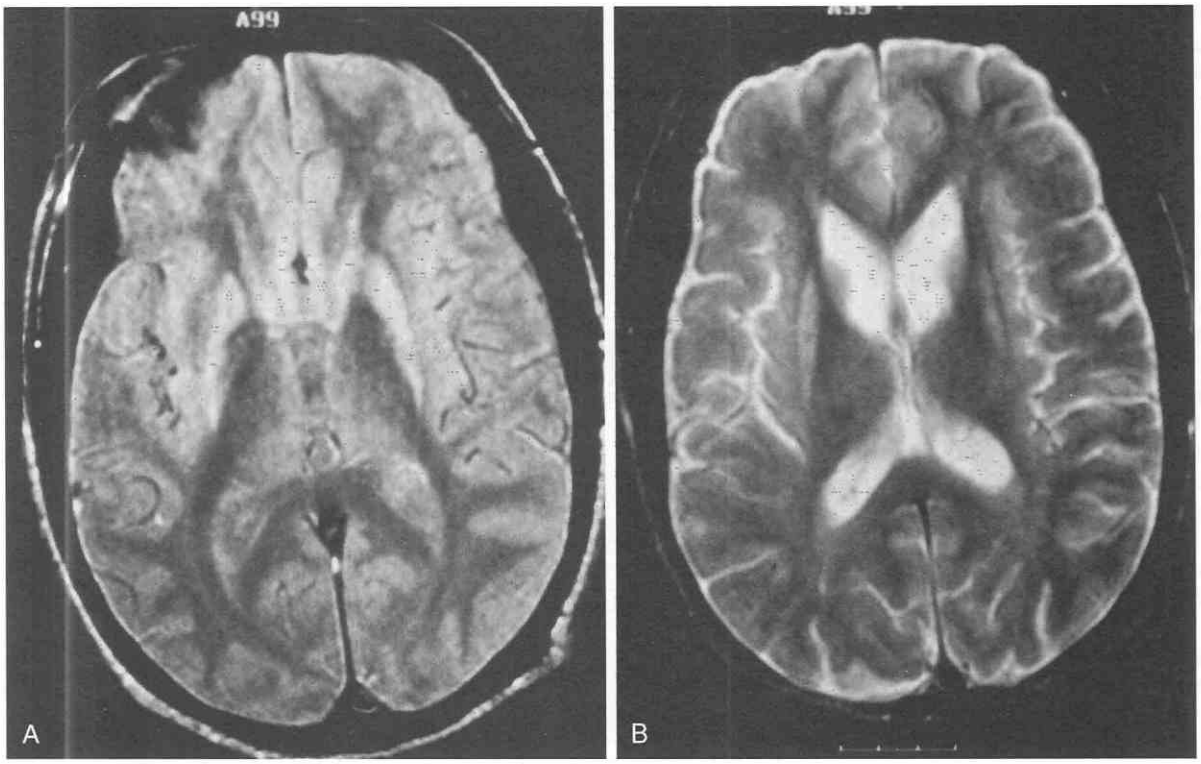

Figure 10–15. Huntington's disease in a 33-year-old man. Axial proton-density (*A*) and T2-weighted (*B*) images demonstrate abnormal signal intensity in the putamen and caudate nuclei. (From Sclar G, Kennedy CA, Hill JM: Cerebellar degeneration associated with HIV infection [letter]. Neurology 54:1012–1013, 2000.)

NAA and creatine in the basal ganglia of 60% in symptomatic patients and a decrease of 30% in presymptomatic gene carriers.[114]

A number of investigators have reported that in addition to atrophic changes, patients with HD present with areas of abnormal T2 signal hyperintensity in the basal ganglia (Fig. 10–15). Two groups have reported that such changes are present in all patients with the rigid form of HD but only occasionally in the classic hyperkinetic form.[93, 107]

More advanced cases of HD present with atrophy of other parts of the central nervous system, including the olives, pons, and cerebellum[108]; the thalamus, mesial temporal lobe and white matter tracts[70]; and the cerebral cortex.[115] Cortical atrophy, as seen on the MRI scan, has been shown to correlate well with specific neuropsychological deficits.[115]

Parkinson's Disease

Parkinson's disease (PD) affects approximately 1% of the population over 50 years of age and is perhaps the most common neurologic explanation of progressive motor impairment among older adults. Onset of symptoms is typically seen between 40 and 70 years of age. The disease is caused by an acceleration of the normal age-dependent depletion of dopamine synthesizing pigmented cells within the pars compacta of the substantia nigra. The loss of dopaminergic input to the striatum caused by this cell loss produces a characteristic syndrome, of which the most salient features are progressive bradykinesis, rigidity, masked facies, hypophonia, festinating gait with stooped posture, and a coarse resting tremor. Dementia may occur in up to 30% of patients, which may reflect the concomitant presence of AD. In addition to the substantia nigra, patients at autopsy reveal a loss of pigmented cells within the locus ceruleus and the dorsal motor nucleus of the vagus. These regions exhibit reactive astrocytosis, and some of the remaining neurons contain eosinophilic cytoplasmic inclusions called Lewy bodies.

Radiographs show a significant narrowing of the pars compacta of the substantia nigra, best visualized on T2-weighted sequences. Multiple studies have demonstrated very little overlap between patients with PD and normal age-matched controls.[15, 34] Early PD has been reported to show a loss of signal in a lateral to medial gradient of the pars compacta, thereby indicating the potential for detecting presymptomatic disease.[63] The diagnostic role of MRI in patients with suspected PD is to exclude other neurodegenerative syndromes with a clinical presentation similar to that of PD.[17, 110]

With the advent of deep brain stimulator (DBS) implants, which have been successful in treatment of medically refractory tremor, MRI plays an important role in targeting the nucleus ventralis intermedius (Vim) of the thalamus during the stereotactic implantation of the device.[5]

Multiple-System Atrophy

In contrast to PD, in which extrapyramidal clinical manifestations result from a loss of dopaminergic input to the

striatum, other diseases produce progressive motor dysfunction by means of primary degenerative processes that simultaneously affect groups of several subcortical anatomic structures. This group of disorders has been referred to by the clinical term *Parkinson's plus syndrome* or by the anatomic term *multiple-system atrophy* (MSA). Various forms of MSA can present with a clinical picture similar to that of PD. These two disorders can be especially difficult to differentiate clinically early on in the presentation.

Neurologically, MSA is suspected when patients presumed to have PD do not respond to L-dopa therapy. Anatomically, the patient's disease is due to the involutional change undergone by various combinations of striatal, cerebellar, pontine, brain stem, and spinal cord nuclei. With the growing ability of MRI to show detailed anatomy, a number of recent investigators have demonstrated the atrophic and signal abnormality changes in patients with the various forms of MSA, which allows differentiation from PD.

One neuropathologic pattern of MSA is termed *striatonigral degeneration* (SND). In patients with this condition, a PD-like syndrome results from a progressive atrophy and neuronal depletion of the putamen and caudate, accompanied by cell loss within the zona compacta of the substantia nigra without Lewy body deposition. Radiographically, patients with SND also exhibit thinning of the pars compacta of the substantia nigra, a presentation similar to that seen in PD.[8, 116] This is expected from the histopathology of the disease. However, SND also exhibits a number of specific findings that allows one to differentiate it from PD radiographically.

The most prominent distinguishing feature of SND is the presence of hypointensities in the putamen,[78, 92, 117, 120, 123] thought to be due to increased iron deposition.[28, 103] Focal atrophy in the quadrigeminal plate[104] and putamen[92] has also been reported. These findings are not seen in PD. When MSA patients present with hemiparkinsonism, MRI findings have consistently demonstrated abnormalities, including (1) T2 hypointensity of the posterior lateral putamen and (2) atrophy of the putamen, caudate nucleus, and pars compacta of the substantia nigra on the contralateral side.[71, 78]

Another form of MSA is olivopontocerebellar atrophy (OPCA) in which degeneration involves the pontine nuclei, transverse pontine fibers, middle cerebellar peduncles, cerebellar cortex, and inferior olives. Clinically, the syndrome results in progressive ataxia and bulbar dysfunction. OPCA is typically a disorder of adult onset and can be both familial (usually autosomal dominant) as well as sporadic.

Radiographically, patients present with atrophy of the transverse fibers of the pons, cerebellum,[87, 120] and middle cerebellar peduncles[106] (Fig. 10–16). There is a mild decrease in the width of the pars compacta of the substantia nigra.[9] The T2 hypointensity seen in SND is not seen in OPCA.[123] These radiographic findings are in concert with the histopathology. They appear to be specific for the disease and should be identified before the diagnosis of OPCA is made.

Other cases have been identified in which the anatomic loci of degenerative change are even more widespread and involve brain stem motor nuclei, corticospinal pathways, and such spinal cord structures as the dorsal columns, anterior horns, and spinocerebellar tracts. OPCA can occur independently or in tandem with SND.

Many patients with MSA undergo cell loss within the autonomic intermediolateral nuclei of the spinal cord, producing symptoms of orthostatic hypotension, anhidrosis, incontinence, and sexual dysfunction in addition to the those of MSA. This is known as *Shy-Drager syndrome* (SDS). MRI findings reflect the atrophic changes and T2 abnormalities seen in MSA.[96, 105]

Progressive Supranuclear Palsy

Progressive supranuclear palsy (PSP) is a neurodegenerative disorder without known familial predilection that affects middle-aged and older adults. The pathologic changes involve neuronal loss and astrocytosis within the globus pallidus, dentate nucleus, and several diencephalic structures, including the subthalamic nucleus, periaqueductal gray matter, and pretectal regions. Single-stranded neurofibrillary pathology is a distinctive histopathologic feature of this condition. The clinical presentation is characterized by pseudobulbar signs, supranuclear oculomotor disturbances, axial dystonia, gait dysfunction, and dementia.

Radiographically, patients with PSP present with atrophy of the pretectum, dorsal pons, tectum and midbrain.[4] In addition, decreased T2 relaxation times have been reported in the superior colliculi, globus pallidus, and putamen, which are more pronounced than in patients with MSA.[33] These radiographic findings are confirmed by the histopathology of the disease and are useful in distinguishing PSP from clinically similar entities such as PD.[33, 109]

Friedreich's Ataxia

Friedreich's ataxia (FA) is a progressive spinocerebellar degeneration transmitted both by autosomal dominant and recessive modes of inheritance that affect both children and young adults. Spinal cord degeneration involves the dorsal columns, lateral corticospinal tracts, Clarke's column, and spinocerebellar tracts. Degeneration also occurs within the dorsal root ganglia, dentate nucleus, cerebellar vermis, and inferior olive. Children typically present with ataxia and are often incapable of walking by 5 years of age. Later, bilateral Babinski signs with areflexia, tremor, slurred speech, and nystagmus appear. Other associated abnormalities include pes cavus deformity, kyphoscoliosis, and cardiomyopathy.

Radiographic findings include FA spinal cord atrophy, which is often severe[128] and which is seen even in early cases.[89] Moderate cerebellar or bulbar atrophy is occasionally seen.[128] In advanced cases, atrophy of the cerebellar vermis and medulla has been reported (Fig. 10–17).[94]

Amyotrophic Lateral Sclerosis

Amyotrophic lateral sclerosis (ALS), is the most common form of a broader class of motor system diseases characterized by primary degeneration of the motor neurons within the brain, brain stem, and spinal cord. Patients

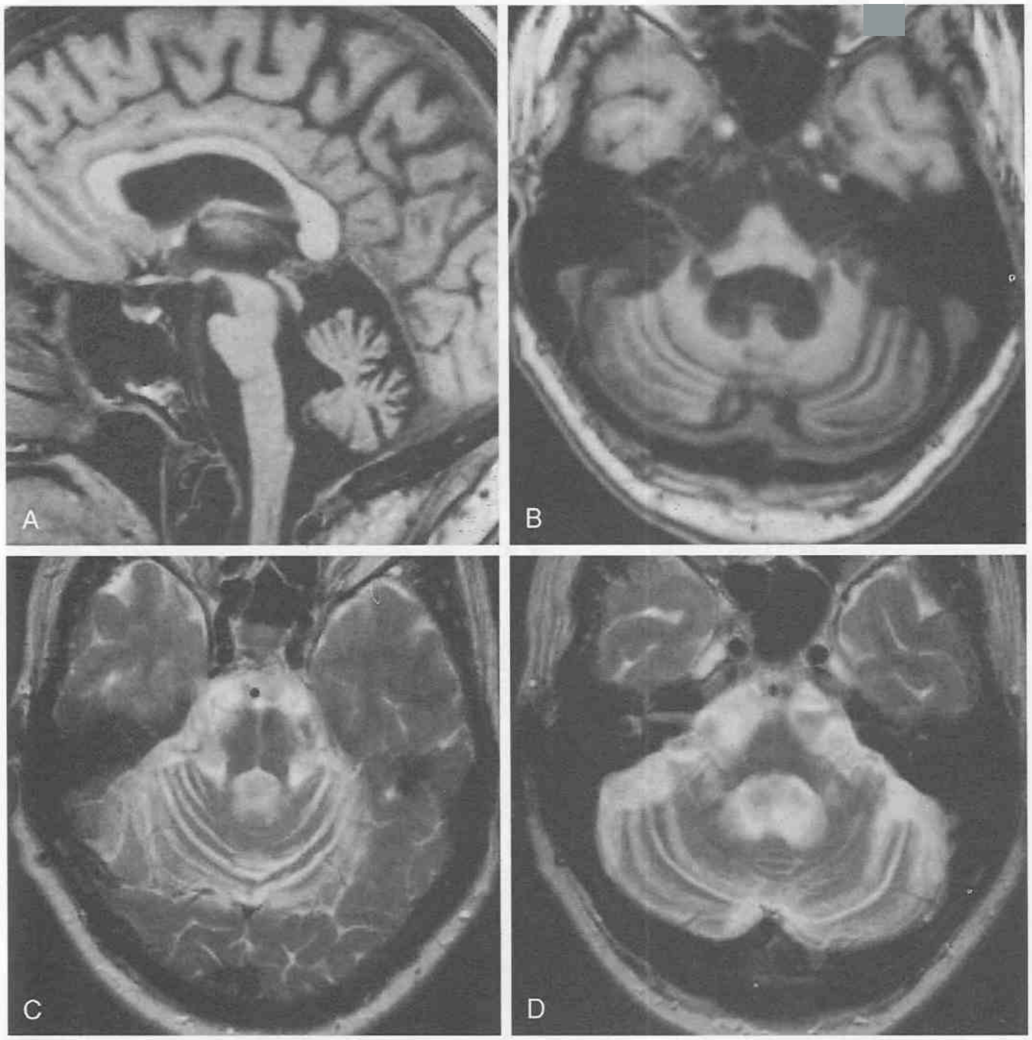

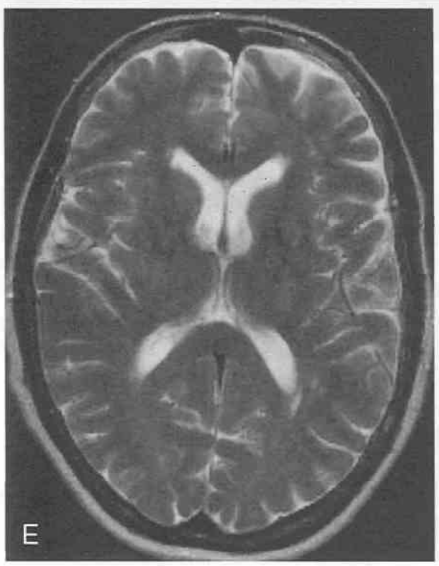

Figure 10–16. Olivopontocerebellar atrophy in a 57-year-old woman who presented with slight unsteadiness 2 years earlier. The symptoms have since progressed. At the time of this MRI study, she was experiencing swallowing difficulties, abnormal eye movements, and severe difficulty walking. Sagittal T1-weighted *(A)*), axial T1-weighted *(B)*, and two axial T2-weighted (*C* and *D*) images demonstrate atrophy of the transverse fibers of the pons, the cerebellum, the middle cerebellar peduncles, and the inferior olives. *E*, Axial T2-weighted image through the lateral ventricles fails to demonstrate atrophy or hydrocephalus. (From Holodny AI, George AE, Golomb J: Neurodegenerative disorders. In Edelman R, Hesselink JR [eds]: Clinical Magnetic Resonance Imaging, 2nd ed. Philadelphia, WB Saunders, 1996.)

typically present with progressive muscle weakness and limb and truncal atrophy combined with signs of spacticity. Mean age at the time of diagnosis is 55 years, and the incidence of new cases is 1 per 100,000 population.[18] Familial transmission is seen in 10% of the cases as both autosomal dominant and recessive traits and sporadic in the remaining 90% of the cases.[112] Prognostically, about 50% of patients die within 3 years and 90% die within 6 years following onset of symptoms.

In ALS, both anterior horn neurons in the spinal cord

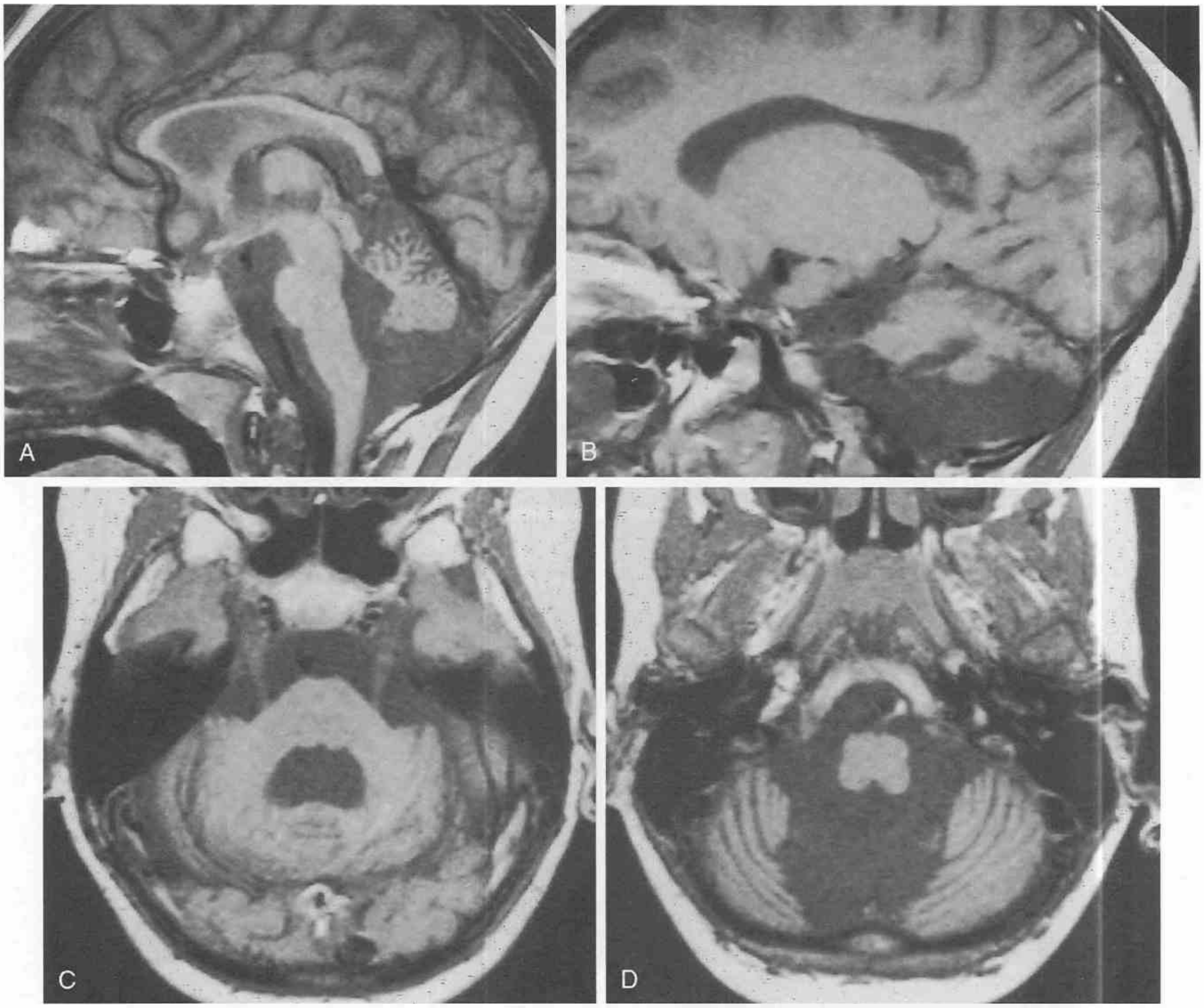

Figure 10–17. Progressive Friedreich's ataxia in a 4-year-old girl. Two sagittal (*A* and *B*) and two axial (*C* and *D*) T1-weighted images demonstrate severe atrophy of the cerebellum. (From Holodny AI, George AE, Golomb J: Neurodegenerative disorders. In Edelman R, Hesselink JR [eds]: Clinical Magnetic Resonance Imaging, 2nd ed. Philadelphia, WB Saunders, 1996.)

as well as pyramidal Betz cells within the primary motor cortex (precentral gyrus) undergo progressive involutional change. Histopathologic features include astrocytosis, lipofuscin deposition, and, occasionally, the accumulation of intracytoplasmic inclusion bodies. Secondary degeneration of the descending corticospinal fibers occurs with variable demyelination and lipid-filled macrophage buildup. Corticospinal tract involvement is most evident within the lateral and anterior columns of the lower spinal cord but can also affect the cerebral white matter of the internal capsule, corona radiata, and centrum semiovale.

MRI reveals abnormal signal intensity along the motor pathways. In the precentral gyrus (i.e., the location of the perikarya of the motor neurons, which are affected by ALS), T2 hypointensity is thought to represent increased deposition of iron.[91, 130] In the subcortical white matter tracts, patients with ALS typically demonstrate abnormal hyperintensity on long TR images (T2, proton-density, and FLAIR). These areas of signal abnormality extend from the motor cortex to the centrum semiovale, the corona radiata, the posterior third quarter of the internal capsule, and the pons.[1, 51, 65, 66, 124] Radiologic-pathologic studies have shown that these signal abnormalities represent degeneration of the corticospinal tract and myelin pallor.[65] These signal abnormalities are distinctly different from normally appearing areas of hypointensity on T1 and hyperintensity on T2, which represent normal fibers of the corticospinal tract traversing the internal capsule. Similar areas of T2 hyperintensity have been identified in the corticospinal tracts in the spinal cord.[39]

MRI shows an increase in the mean choline and myo-inositol and a decrease in glutamine and *N*-acetyl in the precentral gyrus.[13] Magnetization transfer measurements have also been reported to be sensitive in the early identification of ALS.[71]

References

1. Abe K, Yorifuji S, Nishikawa Y: Reduced isotope uptake restricted to the motor area in patients with amyotrophic lateral sclerosis. Neuroradiology 35:410–411, 1993.

2. Adams JH, Duchen LW: Greenfield's Neuropathology. New York, Oxford University Press, 1992.
3. Adams RD, Fisher CM, Hakim S: Symptomatic occult hydrocephalus with "normal" cerebrospinal fluid pressure: A treatable syndrome. N Engl J Med 273:117–126, 1965.
4. Aiba I, Hashizume Y, Yoshida M, et al: Relationship between brainstem MRI and pathological findings in progressive supranuclear palsy—study in autopsy cases. J Neurol Sci 152:210–217, 1997.
5. Alterman RL, Reiter GT, Shils J, et al: Targeting for thalamic deep brain stimulator implantation without computer guidance: Assessment of targeting accuracy. Stereotact Funct Neurosurg 72:150–153, 1999.
6. Alzheimer A: Über eine eigenartige Erkrankung der Hirnrinde. Allg Z Psychiatr Psych Med 64:146, 1907.
7. Alzheimer A: Über eine eigenartige Erkrankung der Hirnrinde. Zentralb gesamte Neurologie Psychiatrie, 18:177–179, 1907.
8. Aotsuka A, Shinotoh H, Hirayama K, et al: Magnetic resonance imaging in multiple system atrophy. Rinsho Shinkeigaku 32(8): 815–821, 1992.
9. Aylward EH, Li Q, Stine OC, et al: Longitudinal change in basal ganglia volume in patients with Huntington's disease. Neurology 48:394–399, 1997.
10. Ball MJ, Fishman M, Hachinski V, et al: A new definition of Alzheimer's disease: A hippocampal dementia. Lancet 1:14–16, 1985.
11. Barboriak DP, Provenzale JM, Boyko OB: MR diagnosis of Creutzfeldt-Jakob disease: Significance of high signal intensity in the basal ganglia. AJR Am J Roentgenol 162:137–140, 1994.
12. Baron SA, Jacobs L, Kinkel W: Changes in size of normal lateral ventricles during aging determined by computerized tomography. Neurology 26:1011–1013, 1976.
13. Bowen BC, Pattany PM, Bradley BG, et al: MR imaging and localized proton spectroscopy of the precentral gyrus in amyotrophic lateral sclerosis. AJNR Am J Neuroradiol 21:647–658, 2000.
14. Bradley WG, Scalzo D, Queralt J, et al: Normal-pressure hydrocephalus: Evaluation with cerebrospinal fluid flow measurements at MR imaging. Radiology 198:523–529, 1996
15. Braffman BH, Grossman RI, Goldberg HI, et al: MR imaging of Parkinson's disease with spin-echo and gradient-echo sequences. AJR Am J Roentgenol 152:159–195, 1989.
16. Briley DP, Haroon S, Sergent SM, Thomas S: Does leukoaraiosis predict morbidity and mortality? Neurology 54:90–94, 2000.
17. Brooks DJ: Morphological and functional imaging studies on the diagnosis and progression of Parkinson's disease. J Neurol 247 (suppl 2):II11–II18, 2000.
18. Brown RH: Amyotrophic lateral sclerosis: Insights from genetics. Arch Neurol 54:1246–1250, 1997.
19. Burger PC, Burch JG, Kunze U: Subcortical arteriosclerotic encephalopathy (Binswanger's disease): A vascular etiology of dementia. Stroke 7:626–631, 1976.
20. Cala LA, Thickbroom GW, Black JL, et al: Brain density and cerebrospinal fluid space size: CT of normal volunteers. Am J Neuroradiol 2:41–47, 1981.
21. Convit A, de Leon MJ, Golomb J, et al: Hippocampal atrophy in early Alzheimer's disease: Anatomic specificity and validation. Psychiatr Q 64:371–387, 1993.
22. Cruts M, Van Broeckhoven C: Molecular genetics of Alzheimer's disease. Ann Med 30:560–565, 1998.
23. Dandy WE, Blackfan DK: An experimental and clinical study on internal hydrocephalus. JAMA 61:2216, 1913.
24. de Leon MJ, George AE, Ferris SH, et al: Positron emission tomography and computed tomography assessments of the aging human brain. J Comput Assist Tomogr 8:88–94, 1984.
25. de Leon MJ, George AE, Tomanelli J, et al: Positron emission tomography studies of normal aging: A replication of PET III and 18-FDG using PET VI and 11C-2DG. Neurobiol Aging 8: 319–323, 1987.
26. de Leon MJ, George AE, Reisberg B, et al: Alzheimer's disease: Longitudinal CT studies of ventricular change. AJNR Am J Neuroradiol 10:371–376, 1989.
27. de Leon MJ, Golomb J, George AE, et al: The radiologic prediction of Alzheimer disease: The atrophic hippocampal formation. AJNR Am J Neuroradiol 14:897–906, 1993.
28. De Volder AG, Francart J, Laterre C, et al: Decreased glucose utilization in the striatum and frontal lobe in probable striatonigral degeneration. Ann Neurol 26:239–247, 1989.
29. Diagnostic and Statistical Manual of Mental Disorders, 4th ed. Washington, DC, American Psychiatric Association, 1994.
30. Di Rocco A, Molinari S, Stollman AL, et al: MRI abnormalities in Creutzfeldt-Jakob disease. Neuroradiology 35:584–585, 1993.
31. Drayer BP, Olanow W, Burger P, et al: Parkinson plus syndrome: Diagnosis using high field MR imaging of brain iron. Radiology 159:493–498, 1986.
32. Drayer BP: Imaging of the aging brain: I. Normal findings. Radiology 166:785–796, 1988.
33. Drayer BP: Imaging of the aging brain: II. Pathological conditions. Radiology 166:797–806, 1988.
34. Duguid JR, De La Paz R, DeGroot J: Magnetic resonance imaging of the midbrain in Parkinson's disease. Ann Neurol 20:744–747, 1986.
35. El Gammal T, Allen MB Jr, Brooks BS, et al: Evaluation of hydrocephalus. AJNR Am J Neuroradiol 8:591–597, 1987.
36. Enzmann DR, Norman D, Price NC, Newton TH: Metrizamide and radionuclide cisternography in communicating hydrocephalus. Radiology 13:681–686, 1979.
37. Evans DA, Funkenstein HH, Albert MS, et al: Prevalence of Alzheimer's disease in a community population of older persons: Higher than previously reported. JAMA 262:2551–2556, 1990.
38. Falcone S, Quencer RM, Bowen B, et al: Creutzfeldt-Jakob disease: Focal symmetrical cortical involvement demonstrated by MR imaging. AJNR Am J Neuroradiol 13:403–406, 1992.
39. Freidman DP, Tartaglino LM: Amyotrophic lateral sclerosis: Hyperintensity of the corticospinal tracts on MR images of the spinal cord. AJR Am J Roentgenol 160:604–606, 1993.
40. Fukui J, Kertesz A: Volumetric study of lobar atrophy in Pick's complex and Alzheimer's disease. J Neurol Sci 174:111–121, 2000.
41. Gado M, Patel J, Hughes CP, et al: Brain atrophy in dementia judged by CT scan ranking. Am J Neuroradiol 4:499–500, 1983.
42. Gauthier S: Do we have a treatment for Alzheimer's disease? Yes. Arch Neurol 56:738–739, 1999.
43. George AE, de Leon MJ: Computed tomography and positron emission tomography in aging and dementia. In Latchaw RE (ed): MR and CT Imaging of the Head, Neck, and Spine, 2nd ed. Chicago, Year Book Medical Publishers, 1991, pp 413–442.
44. George AE, de Leon MJ, Gentes CJ, et al: Leukoencephalopathy in normal and pathologic aging: Part 1. CT of brain lucencies. Am J Neuroradiol 7:567–570, 1986.
45. George AE, de Leon MJ, Kalnin A, et al: Leukoencephalopathy in normal and pathologic aging: Part 2. MRI of brain lucencies. Am J Neuroradiol 7:567–570, 1986.
46. George AE, de Leon MJ, Stylopoulos LA, et al: CT diagnostic features of Alzheimer disease: Importance of the choroidal/hippocampal fissure complex. AJNR Am J Neuroradiol 11:101–107, 1990.
47. Glydenstead C, Kosteljanetz M: Measurements of the normal ventricular system with computed tomography. Neuroradiology 10:205–215, 1976.
48. Golomb J, de Leon MJ, George AE, et al: Hippocampal atrophy correlates with severe cognitive impairment in elderly patients with suspected normal pressure hydrocephalus. J Neurol Neurosurg Psychiatry 57:590–593, 1993.
49. Golomb J, de Leon MJ, Kluger A, et al: Hippocampal atrophy in normal aging: An association with recent memory impairment. Arch Neurol 50:967–976, 1993.
50. Golomb J, Wisoff J, Miller DC, et al: Alzheimer's disease comorbidity in normal pressure hydrocephalus: Prevalence and shunt response. J Neurol Neurosurg Psychiatry 68:778–781, 2000.
51. Goodin DS, Rowley HA, Olney RK: Magnetic resonance imaging in amyotrophic lateral sclerosis. Ann Neurol 23:418–420, 1988.
52. Goto K, Ishii N, Fukasawa H: Diffuse white matter disease in the geriatric population: A clinical neuropathological and CT study. Radiology 141:687–695, 1981.
53. Graham GD, Petroff OA, Blamire AM, et al: Proton magnetic resonance spectroscopy in Creutzfeldt-Jakob disease. Neurology 43: 2065–2068, 1993.
54. Groen JJ, Hekster RE: Computed tomography of Pick's disease: Findings in a family affected in three consecutive generations. J Comput Assist Tomogr 6:907–911, 1982.
55. Hachinski VC, Potter P, Merskeu H: Leuko-araiosis. Arch Neurol 44:21–23, 1987.
56. Hakim S, Adams RD: The special clinical problem of symptomatic hydrocephalus with normal cerebrospinal fluid pressure. J Neurol Sci 2:307–327, 1965.

57. Hamos JE, DeGennaro LJ, Drachman DA: Synaptic loss in Alzheimer's disease and other dementias. Neurology 39:355–361, 1989.
58. Harris GJ, Pearlson GD, Peyser CE, et al: Putamen volume reduction on magnetic resonance imaging exceeds caudate changes in mild Huntington's disease. Ann Neurol 31:69–75, 1992.
59. Holodny AI, George AE, Golomb J, et al: The perihippocampal fissures: Normal anatomy and disease states. Radiographics 18: 653–665, 1998.
60. Holodny AI, George AE, de Leon MJ, et al: Focal dilatation and paradoxical collapse of cortical fissures and sulci in patients with normal-pressure hydrocephalus. J Neurosurg 89:742–747, 1998.
61. Holodny AI, Waxman R, George AE, et al: MR differential diagnosis of normal-pressure hydrocephalus and Alzheimer disease: Significance of the perihippocampal fissures. AJNR Am J Neuroradiol 19:813–819, 1998.
62. Hughes CP, Gado M: Computed tomography and aging of the brain. Radiology 139:391–396, 1981.
63. Hutchinson M, Raff U: Structural changes of the substantia nigra in Parkinson's disease as revealed by MR imaging. AJNR Am J Neuroradiol 21:697–701, 2000.
64. Hyman BT, Van Horsen GW, Damasio AR, Barnes CL: Alzheimer's disease: Some specific pathology isolates the hippocampal formation. Science 22:1168–1170, 1984.
65. Ishikawa K, Nagura H, Yokota T, Yamanouchi H: Signal loss in the motor cortex on magnetic resonance images in amyotrophic lateral sclerosis. Ann Neurol 33:218–222, 1993
66. Iwasaki Y, Kinoshita M, Ikeda K, et al: MRI in patients with amyotrophic lateral sclerosis: Correlation with clinical features. Int J Neurosci 59:253–258, 1991.
67. Jack CR Jr, Peterson RC, O'Brien PC, Tangalos EG: MR based hippocampal volumetry in the diagnosis of Alzheimer's disease. Neurology 42:183–188, 1992.
68. Jacoby RJ, Levy R, Dawson JM: Computed tomography in the elderly: I. The normal population. Br J Psychiatry 136:249, 1980.
69. Janota I: Dementia, deep white matter damage and hypertension: "Binswanger's disease." Psychol Med 11:39–48, 1981.
70. Jernigan TL, Salmon DP, Butters N, Hesselink JR: Cerebral structure on MRI: Part II. Specific changes in Alzheimer's and Huntington's diseases. Biol Psychiatry 29:68–81, 1991.
71. Kato T, Kume A, Ito K, et al: Asymmetrical FDG-PET amd MRI findings of striatonigral system in multiple system atrophy with hemiparkinsonism. Radiat Med 10:87–93, 1992.
72. Kato Y, Matsumura K, Kinosada Y, et al: Detection of pyramidal tract lesions in amyotrophic lateral sclerosis with magnetization transfer measurements. AJNR Am J Neuroradiol 18:1541–1547, 1997.
73. Katzman R: Alzheimer's disease. N Engl J Med 314:964–973, 1986.
74. Kemper T: Neuroanatomical and neuropathological changes in normal aging and in dementia. In Albert ML (ed): Clinical Neurology of Aging. New York, Oxford University Press, 1984, pp 9–52.
75. Kesslak JP, Nalcioglu O, Cotman CW: Quantification of magnetic resonance scans for hippocampal and parahippocampal atrophy in Alzheimer's disease. Neurology 41:51–54, 1991.
76. Kido DK, Caine ED, LeMay M, et al: Temporal lobe atrophy in patients with Alzheimer disease: A CT study. AJNR Am J Neuroradiol 10:551–555, 1989.
77. Kluger A, Gianutsos J, de Leon MJ, et al: Significance of age-related white matter lesions. Stroke 19:1054–1055, 1988.
78. Kume A, Shiratori M, Takahashi A, et al: Hemi-parkinsonism in multiple system atrophy: A PET and MRI study. J Neurol Neurosurg Psychiatry 52:1221–1227, 1989.
79. LeMay M: CT changes in dementing diseases: A review. Am J Neuroradiol 7:841–853, 1986.
80. LeMay M, Stafford JL, Sandor T, Albert M, et al: Statistical assessment of perceptual CT scan ratings in patients with Alzheimer type dementia. J Comput Assist Tomogr 10:802–809, 1986.
81. Loeb C, Meyer JC: Vascular dementia. J Neurol Sci 143:31–40, 1996.
82. Lotz PR, Ballinger WE Jr, Quisiling RG: Subcortical arteriosclerotic encephalopathy: CT spectrum and pathologic correlation. Am J Neuroradiol 7:817–822, 1986.
83. Masdeu J, Lantos G, Wolfson L: Periventricular white matter lesions correlate with falls in the elderly. Acta Radiol Suppl 369:392, 1986.
84. McCullough DC, Harbert JC, Di Chiro G, Ommaya AK: Prognostic criteria for cerebrospinal shunting from isotope cisternography in communicating hydrocephalus. Neurology 20:594–598, 1970.
85. Milton WJ, Atkas SW, Lavi E, Mollman JE: Magnetic resonance imaging of Creutzfeldt-Jakob disease. Ann Neurol 29:438–440, 1991.
86. Mu Q, Xie J, Wen Z, et al: A quantitative study of the hippocampal formation, the amygdala and the temporal horn of the lateral ventricle in healthy subjects 40 to 90 years of age. AJNR Am J Neuroradiol 20:207–211, 1999.
87. Mukai E, Makino N, Fujishiro K: Magnetic resonance imaging of parkinsonism. Rinsho Shinkeigaku 29:720–725, 1989.
88. Narkiewicz O, de Leon MJ, Convit A, et al: Dilatation of the lateral part of the transverse fissure of the brain in Alzheimer's disease. Acta Neurobiol Exp 53:457–465, 1993.
89. Nicolau A, Diard F, Fontan D, et al: Magnetic resonance imaging in spinocerebellar degenerative diseases. Pediatrie 42:359–365, 1987.
90. Nosaka Y: Hydrocephalus associated with subarachnoid hemorrhage: Clinical study of computed tomography, radioisotope cisternography and constant infusion test. Acta Med Okayama 35:45–60, 1981.
91. Oba H, Araki T, Ohtomo K, et al: Amyotrophic lateral sclerosis: T2 shortening in motor cortex at MR imaging. Radiology 189: 843–846, 1993.
92. O'Brien C, Sung JH, McGeachie RE, Lee MC: Striatonigral degeneration: Clinical, MRI and pathological correlation. Neurology 40: 710–711, 1990.
93. Oliva D, Carella F, Savoiardo M, et al: Clinical and magnetic resonance features of the classical and akinetic-rigid variants of Huntington's disease. Arch Neurol 50:17–19, 1993.
94. Ormerud IE, Harding AE, Miller DH, et al: Neuropsychological deficits accompanying striatonigral degeneration. J Clin Exp Neuropsychol 13:773–788, 1991.
95. Pantoni L, Garcia JH: The significance of cerebral white matter abnormalities 110 years after Binswanger's report: A review. Stroke 26:1293–1301, 1996.
96. Pastakia B, Polinsky R, Di Chiro G, et al: Multiple system atrophy (Shy-Drager syndrome): MR imaging. Radiology 159:499–502, 1986.
97. Pick A: Ueber die Benziehungen der senile n Hirnat ophiel zur Aphasie. Prager Med Wochenschr 17:165, 1892.
98. Pickard JD: Adult communicating hydrocephalus. Br J Hosp Med 27:35–40, 1982.
99. Roos RAC, Pruyt JFM, de Vries J, Bots GTA: Neuronal distribution in the putamen in Huntington's disease. J Neurol Neurosurg Psychiatry 48:422–425, 1985.
100. Rosenberg GA, Kornfeld M, Stouring J, Bicknell JM: Subcortical arteriosclerotic encephalopathy (Binswanger): Computerized tomography. Neurology 29:1102–1106, 1979.
101. Rother J, Schwartz A, Harle M, et al: Magnetic resonance imaging follow-up in Creutzfeldt-Jakob disease. J Neurol 239:404–406, 1992.
102. Rusinek H, de Leon MJ, George AE, et al: Alzheimer disease: Measuring loss of cerebral gray matter with MR imaging. Radiology 78:109–114, 1991.
103. Rutledge JN, Hilal SK, Silver AJ, et al: Study of movement disorders and brain iron by MR. AJNR Am J Neuroradiol 8:397–411, 1987.
104. Sanchez-Pernaute R, Garcia-Segura JM, del Barrio Alba A, et al: Clinical correlation of striatal 1H MRS changes in Huntington's disease. Neurology 53:806–812, 1999.
105. Savoiardo M, Strada L, Girotti F, et al: MR imaging in progressive supranuclear palsy and Shy-Drager syndrome. J Comput Assist Tomogr 13:555–560, 1989.
106. Savoiardo M, Strada L, Girotti F, et al: Olivopontocerebellar atrophy: MR diagnosis and relationship to multisystem atrophy. Radiology 174:693–696, 1990.
107. Savoiardo M, Strada L, Oliva D, et al: Abnormal MRI signal in the rigid form of Huntington's disease. J Neurol Neurosurg Psychiatry 54:888–891, 1991.
108. Sax DS, Bird ED, Gusella JF, Myers RH: Phenotypic variation in 2 Huntington's disease families with linkage to chromosome 4. Neurology 39:1332–1336, 1989.
109. Schrag A, Good CD, Miszkiel K, et al: Differentiation of atypical parkinsonian syndromes with routine MRI. Neurology 54:697–702, 2000.
110. Schultz JB, Skalej M, Wedekind D, et al: Magnetic resonance imaging-based volumetry differentiates idiopathic Parkinson's syndrome from multiple system atrophy and progressive supranuclear palsy. Ann Neurol 45:65–74, 1999.

111. Seab JP, Jagust WS, Wong SFS, et al: Quantitative NMR measurements of hippocampal atrophy in Alzheimer's disease. Magn Reson 8:200–228, 1988.
112. Siddique T, Nijhawan D, Hentati I: Familial amyotrophic lateral sclerosis. J Neural Trans Suppl 49:219–233, 1997.
113. Soininen R, Puranen M, Riekkinen PJ: Computed tomography findings in senile dementia and normal aging. J Neurol Neurosurg Psychiatry 45:50–54, 1982.
114. Squire LR, Amaral DG, Press GA: Magnetic resonance imaging of the hippocampal formation and mammillary nuclei distinguish medial temporal lobe and diencephalic amnesia. J Neurosci 10:3106–3117, 1990.
115. Starkstein SE, Brandt J, Bylsma F, et al: Neuropsychological correlates of brain atrophy in Huntington's disease: A magnetic resonance imaging study. Neuroradiology 34:487–489, 1992.
116. Stern MB, Braffman BH, Skolnick BE, et al: Magnetic resonance imaging in Parkinson's disease and parkinsonian syndromes. Neurology 39:1524–1526, 1989.
117. Sullivan EV, De La Paz R, Zipursky RB, Pfefferbaum A: Neuropsychological deficits accompanying striatonigral degeneration. J Clin Exp Neuropsychol 13:773–778, 1991.
118. Tartaro A, Fulgente T, Delli Pizzi C, et al: MRI alterations as an early finding in Creutzfeldt-Jakob disease. Eur J Radiol 17: 155–158, 1993.
119. Terry RD: Senile dementia of the Alzheimer type. Ann Neurol 14: 497–506, 1983.
120. Testa D. Savoiardo M, Fetoni V, et al: Multiple system atrophy. Clinical and MR observations on 42 cases. Ital J Neurol Sci 14: 211–216, 1993.
121. Tomlinson BE, Corsellis JAN: Ageing and dementias. In Adams JH, Corsellis JAN (eds): Greenfield's Neuropathology, 4th ed. New York, LW Duchen Wiley, 1984, pp 951–1025.
122. Tomonaga M, Hiroski Y, Tohgi H: Clinicopathologic study of progressive subcortical vascular encephalopathy (Binswanger type) in the elderly. J Am Geriatr Soc 30:524–529, 1982.
123. Tsuchiya K: High-field MR findings of multiple system atrophy. Nippon Igaku Hoshasen Gakkai Zasshi 50:772–779, 1990.
124. Udaka F, Sawada H, Seriu N, et al: MRI and SPECT findings in amyotrophic lateral sclerosis. Neuroradiology 34:389–393, 1992.
125. Urchino A, Yoshinaga M, Shiokawa O, et al: Serial MR imaging in Creutzfeldt-Jakob disease. Neuroradiology 33:364–367, 1991.
126. Vonsattel JP, Meyers RH, Stevers TJ: Neuropathologic classification of Huntington's disease. J Neuropathol Exp Neurol 44:559–577, 1985.
127. Weber T, Otto M, Bodemer M, Zerr I: Diagnosis of Creutzfeldt-Jakob disease and related human spongiform encephalopathies. Biomed Pharmacother 51:381–387, 1997.
128. Wessel K, Schroth G, Diener HC, et al: Significance of MRI-confirmed atrophy of the cranial spinal cord in Friedreich's ataxia. Eur Arch Psychiatry Neurol Sci 238:225–230, 1989.
129. Will RG, Zeidler M, Stewart GE, et al: Diagnosis of new variant Creutzfeldt-Jakob disease. Ann Neurol 47:575–582, 2000.
130. Yagashita A, Nakano I, Oda M, Hirano A: Location of the corticospinal tract in the internal capsule at MR imaging. Radiology 191: 455–460, 1994.
131. Yamamoto K, Morimatsu M: Increased signal in the basal ganglia and white mater on magnetic resonance imaging in Creutzfeldt-Jakob disease. Ann Neurol 32:114, 1992.
132. Zeidler M, Sellar RJ, Collie DA, et al: The pulvinar sign on magnetic resonance imaging in variant Creutzfeldt-Jakob disease. Lancet 355: 1412–1418, 2000.

11

Brain Magnetic Resonance Spectroscopy

Jay J. Pillai, Lester Kwock

A Brief History

Magnetic resonance spectroscopy (MRS) is a means of noninvasive physiologic imaging of the brain that measures relative levels of various tissue metabolites. Absolute quantitation of these metabolites is also possible, although in standard clinical practice ratios are commonly used to describe relative concentrations of these metabolites. MRS enables evaluation of metabolic derangements that are specific to certain central nervous system (CNS) diseases or categories of disease. Thus, MRS may aid in the diagnosis of various CNS diseases when standard structural magnetic resonance imaging (MRI) findings may be nonspecific. MRS may also be used to monitor therapy and to provide prognostic information in certain conditions. This chapter presents the basic principles of MRS, followed by a discussion of basic clinical applications.

The discovery of the phenomenon of nuclear magnetic resonance (NMR) can be traced to Purcell and coworkers and Bloch and coauthors in 1946, who found that magnetic dipoles of atomic nuclei resonated when placed in an external magnetic field and demonstrated nuclear induction (induction of an electromotive force in a surrounding recording coil).[20, 116, 185] MRS, in the 1970s, involved phosphorus (^{31}P) spectroscopy in animals, including evaluation of red blood cells and rat leg muscle tissue.[101, 116, 161] Human applications became possible in the early 1980s, when larger-bore magnets became available; applications in the extremities were followed by applications in the CNS.[116] The first human brain applications involved ^{31}P spectroscopy in infants.[32, 99, 116, 197] Bottomley and Radda and their coauthors then described applications of in vivo ^{31}P spectroscopy in the adult brain, followed in 1985 by the earliest in vivo brain hydrogen (^{1}H) spectroscopic studies.[22, 23, 116, 186]

With the advent of technical advances that allowed for improved spatial localization and water suppression, MRS has rapidly progressed in clinical utility and acceptance in the late 1980s to near its current status. Today MRS—in particular, ^{1}H MRS—has become a valuable physiologic imaging tool with wide clinical applicability.

Technical Considerations

Basic Principles

What is the difference between MRS and MRI? The answer to this most frequently asked question is that basically there is no difference, because both techniques are governed by the same physical principles of magnetism. MRS and MRI differ only in the manner in which the data are processed and presented. With MRI, the data collected are analyzed in the time domain (free induction decay [FID] signal) to obtain information about the nuclear relaxation time (namely, T1 and T2), which is processed to generate an anatomic image. In MRS, time domain information is converted to frequency domain information via Fourier transformation of the FID time domain signal.

What is the frequency domain, and why do the protons of water resonate at a different frequency (H_2O, 4.7 parts per million at pH = 7.4) from that of the protons located in other metabolites, such as the following?

1. The *N*-acetyl methyl group of *N*-acetylaspartate ($CH_3C{=}ONH{-}R$; 2.0 ppm).
2. The *N*-methyl groups of choline ($(CH_3)_3N{-}$); 3.2 ppm).
3. The *N*-methyl group of creatine ($CH_3{-}NH{-}R$).

As presented in a number of reviews, NMR is based on the principle that some nuclei have associated magnetic spin properties that allow them to behave like small magnets.[123, 206, 213] In the presence of an externally applied magnetic field, the magnetic nuclei interact with that field and distribute themselves to different energy levels. With protons having a magnetic spin number of 1/2, the nuclei distribute themselves into two energy states. Conceptually, these energy states correspond to the proton nuclear spins, either aligned in the direction of (low-energy spin state) or against the applied magnetic field (high-energy spin state).

If energy is applied to the system in the form of a radiofrequency (RF) pulse that exactly matches the energy between both states, a condition of *resonance* occurs. That is, nuclei in the lower-energy state can absorb this energy and are promoted to the higher-energy state. The Larmor frequency equation describes this phenomenon:

$$\Delta E = h\omega_0 = h/2\pi\gamma B_0$$

where

ω_0 is the Larmor precessional frequency (cycles/second [Hz])
h is Planck's constant
γ is the gyromagnetic ratio for that nucleus (MHz/Tesla [T])
B_0 is the applied magnetic field (T)

This equation states that the resonance frequency of a

magnetic nucleus (the RF needed to excite a given nucleus to the higher spin state) is directly proportional to the magnetic field environment it experiences. Chemical elements having different atomic numbers such as hydrogen (^1H) and phosphorus (^{31}P) resonate at different Larmor RFs because of the differences in the magnetic properties in the nucleus of these atoms; that is, at 1.5 T the Larmor RF for ^1H is 63.86 MHz; for ^{31}P it is 25.85 MHz.

This difference in the Larmor RF has been used to identify magnetic nuclei having different atomic numbers. Even for a given magnetic nucleus having the same atomic number, however, chemical compounds containing this nucleus can have slightly different Larmor RFs. The reason for this is due to the electrons (negatively charged subatomic particles) that surround the nucleus of the atom. The circulating electrons form an "electron cloud" that surrounds the nucleus. Like protons and neutrons in the nucleus of the atom, electrons have magnetic spin properties. Thus, when exposed to an externally applied magnetic field, electrons precess and produce a small magnetic field, B*, around the nucleus. These local magnetic fields generated by the electrons (normally in the range of parts per million of B_0) can add or subtract from the applied magnetic field, B_0. Consequently, the nucleus of the atom experiences a slightly different magnetic field from B_0. This field is defined as $B_{effective}$ and is equal to (B_0 − B*).

Because of this small change in the local magnetic field, the nucleus of the atom resonates at a shifted Larmor RF; i.e.,

$$\Delta E = h2/\pi\,(B_0 - B^*) = h(\omega_0 - \omega^*)$$

This phenomenon is called the chemical shift and is the basis of MRS.

Single-Volume versus Multivolume MRS Techniques

Single-Volume Proton Magnetic Resonance Spectroscopy

At present, two single-volume proton localization techniques are employed in clinical MRS studies[24]:

- Stimulated echo acquisition mode (STEAM)
- Point-resolved spectroscopy (PRESS)

Both methods are highly effective, each with its advantages and disadvantages.

Advantages of STEAM

STEAM enables observation of proton metabolites that have short T2 relaxation processes, such as *myo*-inositol (MI), glutamate (Glu), and glutamine (Gln), because echo times (TEs) less than 20 msec can be used; with PRESS, they cannot. STEAM also affords more effective suppression of the water resonance signal because water suppression *chemical shift–selective* (CHESS) pulses can be placed not only at the preparation phase of the volume localization pulse sequence but also within the localization sequence (at the TM phase of the STEAM sequence) without penalty to the TE being used. This is a major advantage, especially when short TEs (<20 msec) are used. At short TEs, the signal intensity of the water resonance can be severalfold greater than at higher TEs; thus, higher or more water suppression pulses must be used to attenuate the water signal.

In PRESS, the water suppression CHESS pulses can be placed only at the beginning of the localization pulse sequence.

Disadvantages of STEAM

There are two major disadvantages of STEAM:

1. There is a theoretical factor-of-2 loss in signal intensity.
2. STEAM is much more susceptible to motion, multiple quantum effects (i.e., homonuclear coupling), and diffusion processes that lead to difficulties in phasing and baseline corrections in the spectrum.[162]

The twofold signal loss in signal intensity in the STEAM sequence is due to the imperfect refocusing of the spin magnetization when the second 90-degree pulse is applied, which rotates only half the spins of interest into the longitudinal axis; this part of the magnetization eventually generates the stimulated echo. The other half of the spin magnetization that remains in the transverse axis is dephased by the TM spoiling gradient and does not lead to any rephased magnetization at the time of acquisition.

Advantage of PRESS

The major advantage of the PRESS sequence is the theoretical twofold gain in signal intensity compared to the STEAM sequence. PRESS is also much less sensitive to patient motion, homonuclear coupling effects, and eddy current effects.[162]

Multivolume Magnetic Resonance Spectroscopy

Multivolume MRS is normally called either *chemical shift imaging* (CSI) or *spectroscopic imaging* (SI) because the signal intensity, peak resonance areas, or ratios of peak areas or signal intensities of the metabolites can be converted to an image format and overlaid onto anatomic magnetic resonance (MR) images, thus showing a qualitative or quantitative distribution of the metabolite within the brain area examined.[179] Utilizing the CSI/SI multivolume technique, one can obtain spectroscopic information from multiple adjacent volumes over a large region of interest in a single measurement. Volume elements as small as 1 mL can be examined in reasonable acquisition times, namely, 6 to 12 minutes.[26, 74, 250]

The MRS pulse and gradient sequences used to obtain the localized multivolume spectroscopic data are similar to MRI sequences except that no readout gradient is applied during the data collection.[132] Either PRESS or STEAM pulse sequences are used for volume selective pulse sequences for the CSI/SI multivolume technique, which defines a large slice. Spatial localization is achieved by phase encoding in one dimension (1D CSI/SI), two dimensions (2D CSI/SI), or three dimensions (3D CSI/SI):

The 1D CSI/SI generates a column of *n* volume elements within the defined slice (*n* = number if phase-encoding steps in a defined phase-encoding direction).

The 2D CSI/SI generates $n_1 \times n_2$ adjacent volume elements within a defined slice plane.
The 3D CSI/SI generates multiple defined adjacent slice planes with $n_1 \times n_2 \times n_3$ spectroscopic volume elements or voxels.

Practical Considerations in Spatially Localized Magnetic Resonance Spectroscopy

Suppression of Water Peak in Localized Proton Magnetic Resonance Spectroscopy

The concentration of protons of water is 110 molar, whereas the concentrations of tissue proton metabolites are typically in the millimolar concentration range. This difference in concentration between water protons and tissue metabolites leads to a large dynamic concentration range effect on the observed signal intensity in the MR spectrum.

If the water peak is not suppressed or attenuated, the spectrum is dominated by the water resonance and no other resonances can be observed. This is due to the fact that when the analogue-to-digital conversion of the time domain signal occurs within the receiver of the spectrometer, the intensity of the peaks are scaled relative to the most intense signal found in the frequency domain. Thus, because of the large difference in the concentrations between water and tissue metabolites, if the water signal is not selectively suppressed or attenuated, only the water signal will be observed.

Additionally, a water suppression pulse sequence that only partially suppresses the water signal can lead to residual eddy current effects that can severely distort the phase of the signals and baseline of the spectrum. These distortions may not be corrected for by the postprocessing procedures used to correct for the phase of the signals and the baseline of the spectrum and thus will render the spectrum uninterpretable.

One usually accomplishes suppression of the water peak by using a frequency-selective pulse, centered over the resonance frequency of the water protons, and increasing the amplitude of this pulse until maximal attenuation of the water peak is achieved via a peak saturation process. The water-selective frequency pulse is applied before the beginning of the volume localization pulse sequence.[132]

Field Homogeneity

The magnetic field homogeneity of the volume being analyzed should be as uniform as possible. In most cases, the water shim should be less than 0.2 ppm (~12 Hz at 1.5 T), as judged by measuring the width of the water signal at half-peak height.

Inhomogeneities in the magnetic field of the volume lead to slightly different Larmor frequencies for proton nuclei from the same molecule in different parts of the volume. This leads to observation of broader peak signals because the signal observed is an average of the peak signal at different Larmor frequencies throughout the volume. This line broadening is undesirable because it not only reduces the signal to noise ratio but also can make it more difficult to distinguish between two closely neighboring resonance peaks. This can lead to errors in determining peak areas or signal intensities used for quantification of metabolite levels.

Choice of Echo Time

In MRI, the contrast observed in the anatomic images is dependent on the TE and the time between repetition times (TRs) used. If a short TE and a long TR are used, the image contrast becomes more dependent upon the total number of spins or density of protons in each pixel. If a long TE and TR are used, the contrast in each pixel forming the image is more dependent on the T2 or spin-spin relaxation time of the proton nuclei.

Similarly, in MRS, changing the TE changes the type of information obtained as well as the appearance of the frequency domain spectrum. *The choice of TE or TEs to be used should be decided by the clinical question being asked.*

For instance, if a patient is thought to have Alzheimer's disease, MRS should be performed using a short TE (<30 msec), because the *myo*-inositol/creatine (MI/Cr) ratio would be significantly elevated in this patient.[217] MI can be observed with only short TEs.

To determine whether a hypoxic event is occurring, a TE = 135 msec should be used because the major question is whether lactate (Lac) is present. At a TE of 135 msec, an inverted doublet should be observed in the spectrum centered at 1.3 ppm, which suggests the presence of Lac.[244]

Finally, to determine whether the lesion is a tumor, a TE of 270 msec should be used because we are interested in examining differences in the *N*-acetylaspartate/creatine (NAA/Cr) and choline/creatine (Cho/Cr) ratios. At this long TE, differences between NAA, Cho, and Cr signal intensities are maximized because of the differences in the concentration of these metabolites and T1 relaxation times in tumor versus normal tissue.[183]

Clinical Applications of Proton Magnetic Resonance Spectroscopy

Important Metabolites

Several important metabolites are evaluated in long TE (135 to 288 msec) proton MR spectra (Fig. 11–1):

- *N*-acetylaspartate (NAA)
- Choline (Cho)
- Creatine/phosphocreatine (Cr)
- Lactate (Lac)

When short TEs (20 to 30 msec) are used, a greater number of metabolites can be identified in the MR spectra; in addition to NAA, Cho, Cr, and Lac, the following may be identified[18, 35, 102, 163, 182, 193, 200, 251]:

- Glx (glutamate [Glu])
- Glutamine (Gln)
- Gamma-amino butyric acid (GABA)
- MI
- Alanine (Ala)
- Glucose (Gc)

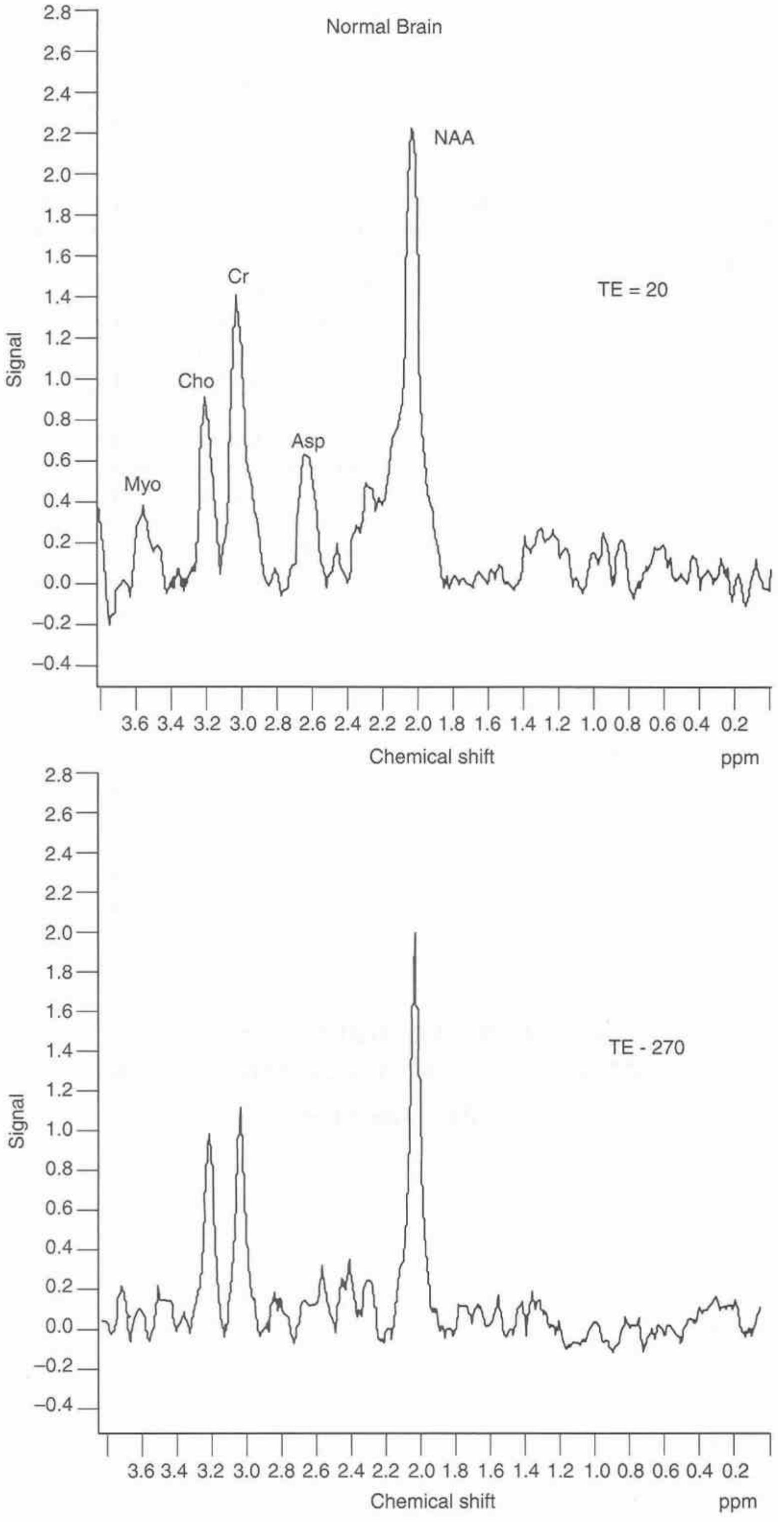

Figure 11–1. Normal adult brain, proton MR spectra. Example of normal single-voxel spectra obtained with echo time (TE) values of 20 and 270. Asp, aspartate; Cho, choline; Cr, creatine; Myo, *myo*-inositol; NAA, *N*-acetylaspartate.

- Lipids and proteins
- Scyllo-inositol/taurine (scyMI/Tau)

Although it may appear advantageous to obtain spectra routinely at only short TEs to distinguish among different clinical entities, some disadvantages of short TE studies exist. For example, short TE spectra display greater baseline distortion, and estimating peak areas calls for more sophisticated processing software algorithms.[169] Methods of absolute measurement of peak areas have been developed and are rapidly gaining acceptance,; however, most proton MR spectra today are described in terms of metabolite ratios, with creatine often used as the reference standard.[14]

NAA

NAA accounts for the majority of the NAA resonance at 2.01 ppm; this peak is the most prominent one in normal adult brain proton MRS and is used as a reference for determination of chemical shift.[12, 125, 126] The NAA peak also contains contributions from other *N*-acetyl groups, such as *N*-acetylaspartylglutamate (NAAG), glycoproteins, and amino acid residues in peptides.[12, 125, 126] NAA is second only to Glu as the most abundant free amino acid in the normal adult brain.[144] The function of this amino acid is not fully understood despite its early discovery in 1956 by Tallan.[229, 230]

From animal studies, NAA is believed to be involved in coenzyme A (CoA) interactions and in lipogenesis within the brain.[8, 16, 29, 60] Specifically, such studies suggest that NAA is synthesized in the mitochondria from aspartate and acetyl CoA and transported into the cytosol, where it is converted by aspartoacylase into aspartate and acetate.[16, 40, 60] Although NAA is widely regarded as a nonspecific neuronal marker, it has also been detected in immature oligodendrocytes and astrocyte progenitor cells.[200, 243]

Normal absolute concentrations of NAA in the adult brain are generally in the range of 8 to 9 mmol/kg, although regional and age-related variations in NAA concentration have been noted by Kreis and others.[127, 153, 182] In normal adults, NAA concentrations in cortical gray matter are higher than those in white matter; in infants, the concentrations in gray and white matter are similar (highly active lipid synthesis in immature white matter accounts for this difference from the adult pattern).[29, 157] NAA concentrations are decreased in many brain disorders, resulting in neuronal and/or axonal loss, such as in neurodegenerative diseases, stroke, brain tumors, epilepsy, and multiple sclerosis, but are increased in Canavan's disease.[21]

Creatine

The main Cr peak is present at 3.03 ppm and demonstrates major contributions from methyl protons of creatine and phosphocreatine as well as minor contributions from GABA, lysine, and glutathione.[125, 126] A second, usually smaller Cr peak is seen at 3.94 ppm. Cr is probably involved in maintenance of energy-dependent systems in brain cells by serving as a reserve for high-energy phosphates in muscle cells and neurons and as a buffer in cellular adenosine triphosphate/diphosphate (ATP-ADP) reservoirs.[38, 40, 127, 155] Thus, this Cr peak is an indirect indicator of brain intracellular energy stores.

The Cr peak is often used as an internal reference standard for characterizing other metabolite signal intensities, because it tends to be relatively constant in each tissue type in normal brain; however, this is not always true in abnormal brain tissue, particularly in areas of necrosis.[139] Cr concentrations in the brain are relatively high, with progressive increases noted from white matter to gray matter to cerebellum.[182, 200] Kreis and coworkers noted a mean absolute Cr concentration in normal adult brains of 7.49 $\pm$ 0.12 mmol/kg on the basis of a sample of 10 normal subjects,[127, 202] whereas Michaelis and colleagues reported a similar value of 5.3 mmol/kg.[115, 153] Cr values tend to be abnormally reduced in all brain tumors, particularly malignant ones.[36]

Choline

The Cho resonance is present at 3.2 ppm and is attributable to trimethylammonium residues of free choline as well as phosphocholine, phosphatidylcholine, and glycerophosphocholine. This peak reflects cell membrane synthesis and degradation.[21] Thus, all processes resulting in hypercellularity (e.g., primary brain neoplasms or gliosis) or myelin breakdown (demyelinating diseases) lead to locally increased Cho concentration, whereas hypomyelinating diseases result in decreased Cho levels.[21, 36] Kreis and coworkers have described a mean absolute Cho concentration in normal adult brain tissue of 1.32 $\pm$ 0.07 mmol/kg.[127, 202] Michaelis and others have reported a similar value of 1.6 mmol/kg.[115, 153]

Myo-inositol

MI produces two peaks, noted at 3.56 ppm and 4.06 ppm. MI is the major component of the peak at 3.56 ppm, although contributions from MI-monophosphate and glycine are also present.[193] MI is believed to be a glial marker because it is present primarily in glial cells and is absent in neurons.[25]

A role in osmotic regulation of the brain has been attributed to MI.[200] In addition, MI may represent both a storage pool for membrane phosphoinositides involved in synaptic transmission and a precursor of glucuronic acid, which is involved in cellular detoxification.[35, 38, 104, 128] A derivative, MI-1,4,5-triphosphate, may act as a second messenger of intracellular calcium-mobilizing hormones.[38, 43]

The mean absolute concentration of MI in normal brain tissue obtained in the Kreis series was 6.56 $\pm$ 0.43 mmol/kg.[127, 198] MI concentrations are abnormally increased in patients with demyelinating diseases and in those with Alzheimer's disease.[38, 153]

Lactate

Lac resonance is identified as a doublet (splitting into two distinct resonant peaks separated by 0.2 ppm, produced by magnetic field interactions among adjacent protons (referred to as J-coupling) centered at 1.32 ppm. A second Lac peak is present at 4.1 ppm but tends to be inconspicuous on spectra obtained with water suppression owing to its proximity to the water peak.[38] Because Lac levels in normal brain tissue are absent or extremely low ($<$0.5 mmol/L), they are essentially undetectable on normal spectra.[200] The presence of a visible Lac peak constitutes a

nonspecific indicator of cellular anaerobic glycolysis, which may be seen with brain neoplasms, infarcts, hypoxia, metabolic disorders, or seizures.[200] Lac may also accumulate within cysts or foci of necrosis.[38, 200]

Changing the TE using a PRESS sequence enables confirmation of the presence of an abnormal Lac doublet and differentiation from lipid peaks; at TE = 272 msec, the Lac doublet projects above baseline; at TE = 136 msec, the doublet is inverted below the baseline.[38] In encephalopathic neonates, however, a doublet very similar to Lac may be seen at 1.15 ppm, which corresponds to propan-1,2-diol and which may be easily mistaken for Lac; propan-1,2-diol is a solvent commonly used for administration of anticonvulsant medications to neonates.[14]

Glutamate, Glutamine, and GABA

The Glx peaks are a complex set of resonances noted between 2.1 and 2.5 ppm and consist of Glu, Gln, and GABA components. Glutamate is an excitatory neurotransmitter involved in neuronal mitochondrial metabolism and is the most abundant amino acid in the human brain.[38, 40, 247] Glutamine is involved in both cellular detoxification and regulation of neurotransmitter activities.[38, 153] GABA is a product of Glu and serves as an inhibitory neurotransmitter.[200] Abnormalities in this peak complex have been noted in schizophrenia and epilepsy.[40]

Alanine

The Ala resonance is present between 1.3 and 1.5 ppm and is easily overshadowed by the Lac resonance when also present. Ala is a nonessential amino acid with no known specific function.[38, 200] However, its elevation is frequently noted in meningiomas.[35]

Fats and Proteins

Lipids produce multiple resonances, the most important of which are noted at 0.8 to 0.9 and 1.2 to 1.3 ppm because of methyl and methylene protons, respectively.[38, 110, 181, 200] Membrane lipids are not usually identified unless very short TEs are employed, since they have very short relaxation times.[38] Although artifactual accentuation of these peaks may be seen with voxel contamination by adjacent subcutaneous fat, it may also be noted in high-grade gliomas, meningiomas, demyelination, necrotic foci, and inborn errors of metabolism.[200]

Scyllo-inositol

Scyllo-inositol is a nonmetabolized isomer of MI that may inhibit the incorporation of MI into phospholipids. It demonstrates a single peak at 3.35 ppm.[14] Most authorities in the field believe that this peak results from scyllo-inositol rather than from taurine (Tau), as had been thought in the past.[14]

Normal Brain Development During Childhood

Although most neurons are formed during intrauterine life, proliferation of dendrites, astroglia, and oligodendroglia continues after birth.[212] In particular, the processes of myelination and neuronal and dendritic development are associated with changes in various brain metabolites during infancy and early childhood, which are demonstrated by MRS.[107, 118, 127, 245]

NAA is present in very low concentrations in the newborn brain, compared to those in the adult brain, but levels rapidly increase during the first 2 to 3 years of life and may even double according to one study.[107] Preterm infants were noted to have lower brain NAA levels than full-term infants.[200]

MI forms the most prominent peak in the newborn MR spectrum, whereas Cho dominates the spectrum of older infants.[21] The reason for the prominence of these two components of the infant spectrum is presumed to be the presence of active myelination.[212] In fact, MRS may enable earlier detection of white matter myelination abnormalities in infants than is possible with conventional MRI sequences because changes in the Cho and NAA peaks occur before white matter signal abnormalites on standard imaging sequences.[212]

Although NAA and Cr levels increase during the first few weeks of life, Cho and MI levels decrease.[21] In fact, the MI peak declines rapidly in the first 3 to 4 months and decreases to adult levels by approximately 1 year of age.[200] Cr levels rise to adolescent levels by 4 months of age, presumably as a result of increasing energy demands of the developing brain.[187, 237] The spectral pattern stabilizes during early adulthood, and NAA levels then begin to decrease with advancing age.[21]

The Cr/Cho ratio increases in gray matter during the first 2 years of life, whereas the ratio remains nearly constant in white matter.[14] The scyllo-inositol peak is also highest in newborns and decreases over time.[96, 104, 152]

Lac peaks are normally seen in preterm and small-for-gestational-age infants.[14, 200] However, in appropriate-for-gestational-age term infants, it is abnormal to find higher than trace amounts of Lac, particularly following the first few hours of life; such abnormal amounts of Lac signify brain injury.[14] In preterm infants, the levels of Lac decrease progressively until the age of 40 postconceptional weeks.[14, 136, 176]

Significant regional heterogeneity in spectral patterns has been noted in both the developing brain and in mature brains.[4, 83, 255] In the developing brain, proton MR spectra demonstrate that different parts of the brain mature at different rates and at different times and that the more metabolically mature areas demonstrate lower MI and higher NAA levels than those in less mature regions of brain; specifically, the basal ganglia, perirolandic cortex, and visual cortex mature before areas such as the prefrontal cortex and temporal cortex.[14, 108, 140]

Tedeschi and colleagues[232] have noted significant regional variations in metabolite ratios in young adults; NAA/Cho and NAA/Cr ratios varied by more than a factor of 2 for different brain regions with particularly high levels of Cho and Cr and low levels of NAA found in the cerebellar vermis.[255] In addition, Ando and coworkers noted that NAA/Cho ratios in the frontal region were lower than those in the parietal lobe at birth with subsequent increase during the first 6 months of life.[4]

Grachev and Apkarian have demonstrated metabolic

heterogeneity in normal brain tissue that appears to be age-dependent and gender-dependent as well as specific for brain region.[83] For example, in their series they noted that the total metabolite concentrations were highest in the prefrontal regions in all subjects studied and that higher metabolite concentrations were present in the orbital frontal cortex and sensorimotor cortex in the 25- to 31-year age group than in the 19- to 20-year age group.[83] Furthermore, they observed that women demonstrated higher metabolite concentrations in these two areas than men did.[83]

Brain Tumors

To date, a wide variety of brain tumors have been studied with MRS, and the numerous studies published in this area have demonstrated certain consistent patterns of metabolic abnormalities in both glial and nonglial tumors.* Proton MRS allows reliable differentiation of tumor margins from adjacent brain parenchymal edema, which is not possible with conventional gadolinium-enhanced MRI.[36] In fact, conventional MRI underestimates or overestimates tumor size in approximately 40% of cases.[172]

Although it is possible to clearly distinguish glial neoplasms from normal brain tissue by MRS, controversy exists regarding the reliability of MRS in distinguishing among different histologic grades of astrocytomas and other brain tumors.[38, 129, 168, 215] For example, Shimizu and associates[215] demonstrated that through semiquantitation of MRS peak intensities as a ratio to that of an external reference, it was possible to predict tumor malignancy; higher-grade brain tumors were associated with higher Cho/reference and lower NAA/reference values in their series.[220]

In another series involving children, linear discriminant analysis and proton MRS demonstrated an 83% success rate in establishing the correct diagnosis of histologic grade of brain tumors.[253] In their series of 27 patients with biopsy-confirmed brain tumors, Meyerand and colleagues[150] showed that the combination of Lac/water and choline/water ratios obtained from regions of contrast-enhancing brain tumor (with normalization of each metabolite peak area to the area of the unsuppressed water peak) permitted differentiation of low-grade astrocytomas from anaplastic astrocytomas and glioblastoma multiforme (GBM). In a multicenter study involving 86 cases of glial tumors, however, Negendank and coauthors showed that each type and grade of tumor was a metabolically heterogeneous group with significant overlap in spectral NAA/Cr and Cho/Cr ratios with tumors in other categories; all tumors demonstrated abnormally decreased NAA/Cr and increased Cho/Cr ratios with respect to normal brain parenchyma.[168]

Burtscher and colleagues have described a series of 26 intracranial tumors in which MRS allowed differentiation of infiltrative processes from circumscribed lesions but did not allow differentiation of different types of lesions within each category.[30]

Astrocytomas typically demonstrate reduced NAA levels, moderately reduced Cr levels, and elevated Cho levels compared to normal brain parenchyma[27] (Figs. 11–2 to 11–4). These absolute reductions result in abnormally low NAA/Cr ratios and elevated Cho/Cr ratios.[200] In fact, the NAA level in astrocytomas is reduced to 40% to 70% of that of normal brain parenchyma.[148] Furthermore, Cho has been reported to be substantially elevated in the more malignant astrocytomas, and this elevation may reflect increased cellularity and cell membrane synthesis.[148, 245] There is evidence to suggest that the elevation of Cho is proportional to the degree of tumor malignancy.[36] However, highly malignant primary brain tumors with extensive necrosis may actually demonstrate decreased levels of Cho. Elevated Cho levels are seen more consistently in anaplastic astrocytomas, which do not demonstrate histologic evidence of necrosis, than in GBM, and ependymomas display higher Cho/Cr ratios than those noted for astrocytomas in general.[36, 253]

Lac levels may be elevated in some astrocytomas as well. However, a higher incidence of Lac in more aggressive or higher-grade astrocytomas is controversial because Lac may also be present in benign pilocytic astrocytomas.[74, 111, 168, 172, 242] It is thought that Lac may be present across the entire spectrum of grades of astrocytomas because Lac may arise not only from hypoxia developing within the tumor itself as a result of disruption of normal vascular networks but also from necrosis or cysts within the tumor.[36, 38, 215] In fact, Lac levels may be elevated in all cysts regardless of etiology.[36]

The presence of Lac has been attributed to (1) the extent of anaerobic glycolysis, (2) the efficiency of electron transport, and (3) the rate of washout from tumor tissue.[111, 138, 200] In highly vascular tumors, Lac may be rapidly removed from the tumor as a result of increased blood flow; even in high-grade vascular tumors, therefore, Lac may not be present in the MR spectra.[36]

The value of Lac identification following radiation therapy or surgery is controversial, but the Lac concentration may be proportional to tumor size.[36, 236] Lac has been reported following radiation therapy and surgery, including stereotactic biopsy, although postsurgical porencephaly may lead to artifactual increases in Lac levels, since cerebrospinal fluid (CSF) is known to be rich in Lac.[36, 74, 141]

The presence of elevated lipid levels has also been used to differentiate low-grade from high-grade neoplasms.[138, 168, 172, 181, 242] Some studies suggest that mobile lipids tend to be present in higher-grade neoplasms, with highest levels noted in GBM; however, although high levels of mobile lipids may be specific for anaplastic astrocytoma or GBM, their absence in MR spectra does not exclude the possibility of such high histologic grades.[168] Lipids may originate from tumor cells within high-grade astrocytomas, macrophages along the tumor periphery, or areas of necrosis.[36] Lipids may be present as a result of microscopic cellular necrosis, which may not be apparent on conventional MR images.[36]

It must be understood that in adults the biologic behavior of low-grade astrocytomas with identical histologic grades is heterogeneous, with more than half of low-grade tumors eventually recurring as or evolving into more aggressive tumors.[164] Some investigators believe that differences in MR spectral ratios of various metabolites, like differences in glucose metabolism in positron emission tomography (PET), may be of prognostic significance even if they are not of diagnostic value in such cases of low-

*See References 36, 38, 63, 111, 168, 172, 180, 183, 200, 215, 221, 225, 241, 242, and 252.

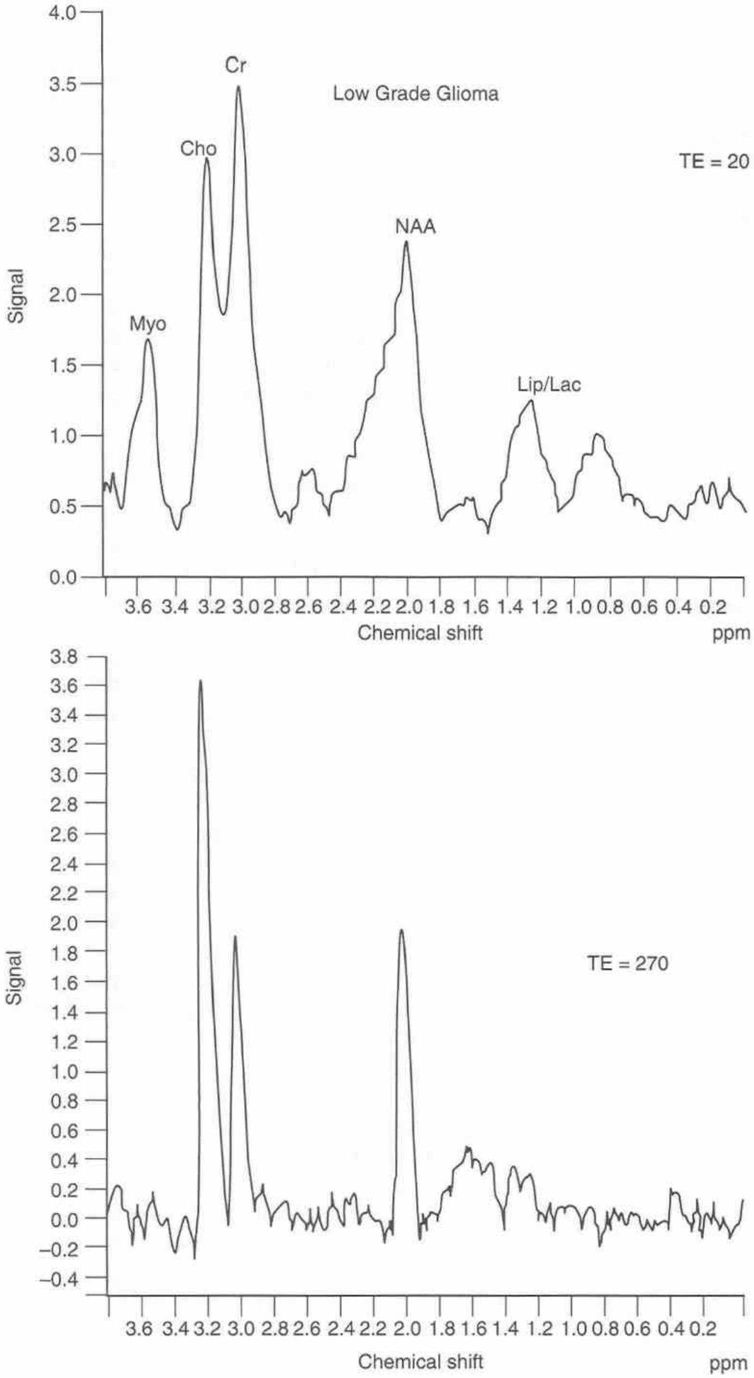

Figure 11–2. Low-grade glioma. A representative single-volume proton MR spectrum of a histologically proven low-grade glioma was examined using a STEAM (stimulated echo acquisition mode) sequence for the TE = 20 msec spectrum and a PRESS (point-resolved spectroscopy) sequence for the TE = 270 msec spectrum. The TR used was 1500 msec in both the TE = 20 and the TE = 270-msec studies. Note the intensity of the *myo*-inositol (3.56 ppm) and choline (3.2 ppm) resonances at a TE = 20 msec in the low-grade lesions compared to the higher-grade lesions.

grade neoplasms.[98, 117, 168, 173] In addition, proton MRS may be used to monitor responses of astrocytomas to therapy[38, 245] (Figs. 11–5 to 11–7). Proton MRS may allow detection of tumor recurrence before abnormalities can be identified on conventional MRI.[38]

Meningiomas have also been studied extensively with proton MRS, and they display certain characteristic features on MR spectra. Marked elevation of Cho levels up to 300 times that of normal brain parenchyma has been reported, particularly in recurrent meningiomas.[36, 38, 129] The Cho/Cr ratio has been reported to be higher in malignant meningiomas than in benign meningiomas.[36, 172]

Theoretically, NAA is not present in meningiomas, which arise from arachnoid structures and not from within the CNS; however, in clinical experience it is not uncommon to detect NAA in these extra-axial tumors, particularly in atypical and malignant varieties.[27, 36, 38, 79] The reason for the presence of NAA in these tumors may be contamination of the voxel by adjacent normal brain parenchyma, use of large voxels, or inadequate voxel placement.[36] In addition, mobile lipids have been reported in meningiomas, and this may be due to fatty degeneration or contamination of the MRS voxel from subcutaneous tissues or fat at the skull base.[27, 36, 172] Furthermore, the presence of alanine, although not invariably present, is considered to be characteristic of meningiomas.[27, 36, 38, 172]

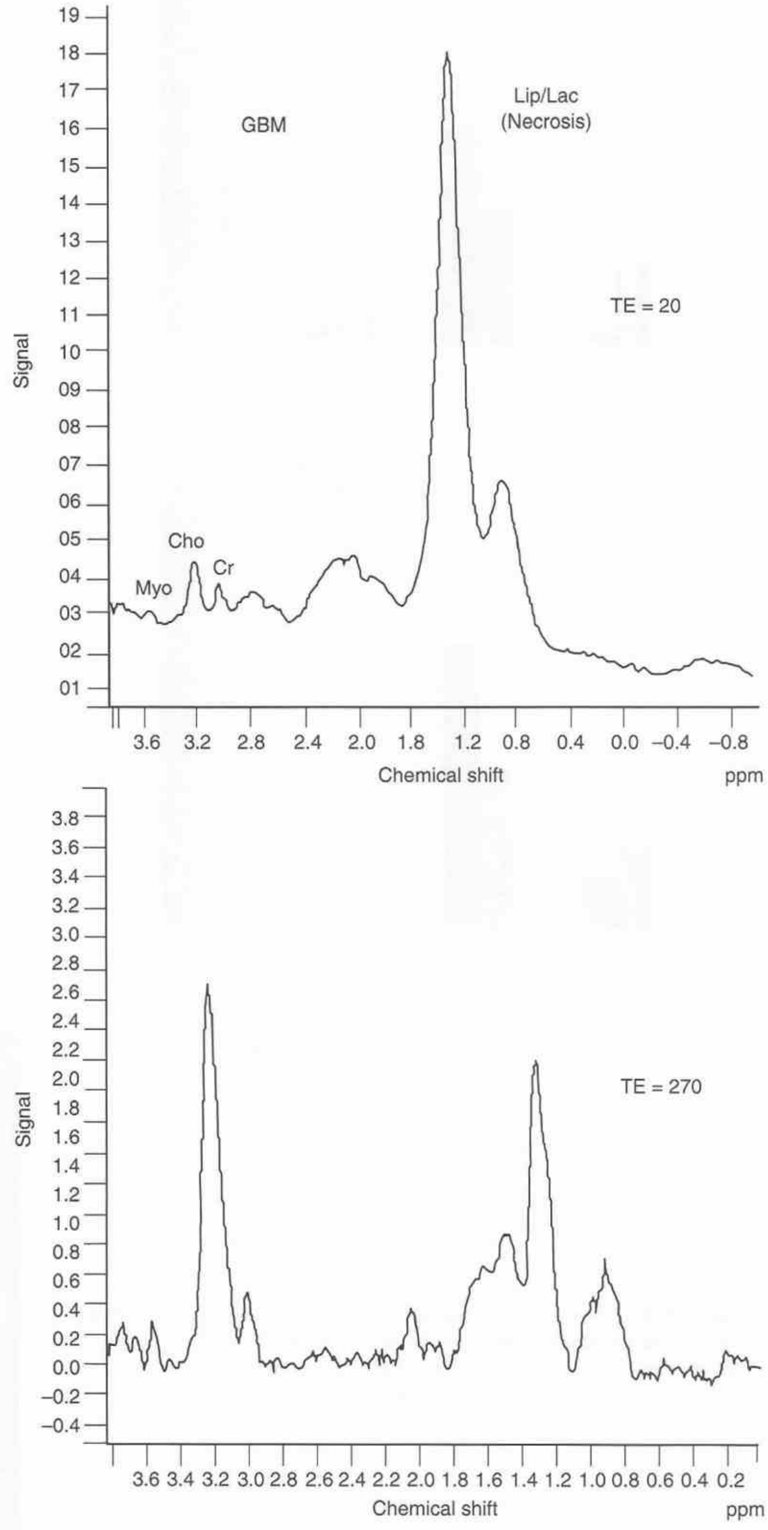

Figure 11–3. Glioblastoma multiforme (GBM). Representative single-volume proton MR spectra of a histologically proven GBM using a STEAM sequence for the TE = 20 msec spectrum and a PRESS sequence for the TE = 270 msec spectrum and a TR = 1500 msec for both studies. Note the large lipid/lactate (Lip/Lac) peak between 0.4 and 1.8 ppm, which probably represents the necrotic core of the tumor, and the lower *myo*-inositol resonance, compared with the lower-grade brain tumors and the elevated choline peak intensity relative to creatine peak intensity for the GBMs.

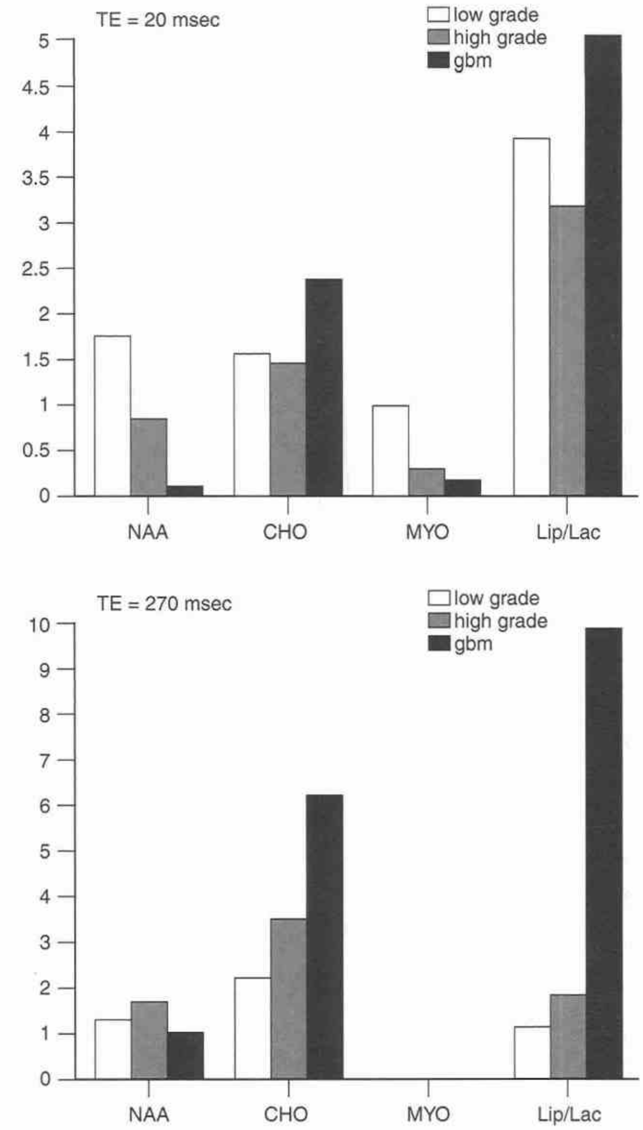

Figure 11–4. Table of relative brain metabolite levels in brain tumors. The bar graph represents the average of the relative levels of *N*-acetylaspartate (NAA), choline (CHO), *myo*-inositol (MYO), and lipase/lactate (Lip/Lac) found in 10 histologically proven cases of low-grade glioma, high-grade glioma, and glioma multiforme. The relative values were determined by dividing the peak resonance area of each metabolite found in the tumor volume by the peak resonance area of Cr found in the tumor volume examined. Ratios were determined on single-volume MRS studies conducted at both a TE = 20 and a TE = 270 msec with a TR = 1500 msec.

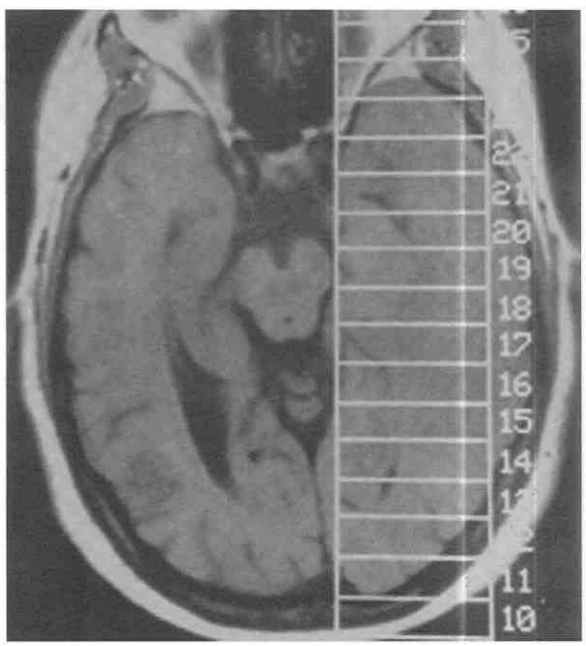

Figure 11–5. Chemical shift imaging Planscan of tumor region. MRI is used to plan the multivolume 1D proton spectroscopic imaging study of a 49-year-old man with a histologically proven high-grade anaplastic astrocytoma located in the left temporal lobe.

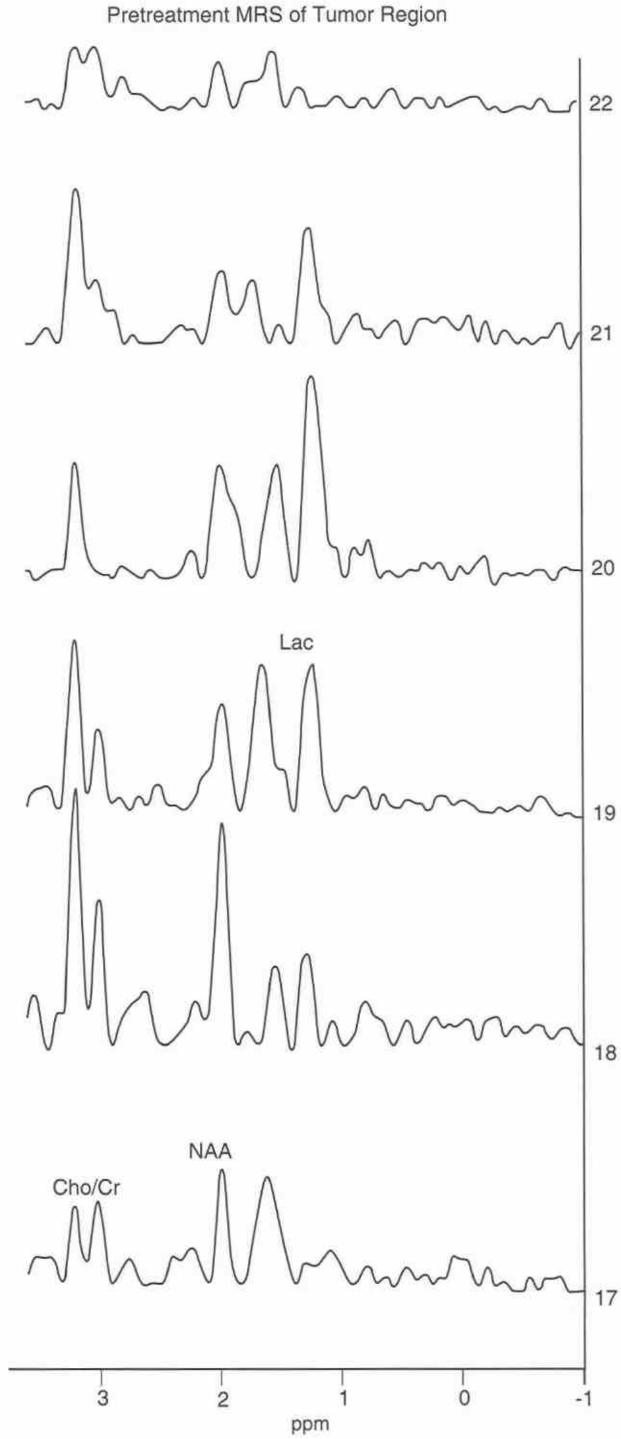

Figure 11–6. Chemical shift imaging pretreatment of tumor. Multivolume one-dimensional spectroscopic image (1D SI) of high-grade anaplastic astrocytoma located in the left frontotemporal lobe before treatment with a chemotherapy (BCNU) regimen. The patient did not respond to a complete course of radiation therapy and two courses of intra-arterial cisplatin. Volume elements are 1 × 2 × 3 cm in size, and studies were performed using a 1D PRESS sequence, with TE = 272 msec and TR = 1600 msec. Note the presence of elevated choline resonances (3.2 ppm) in volumes 18 to 21.

Lac levels may be elevated in some meningiomas.[27, 38] However, Castillo and colleagues have reported that in their experience meningiomas may be indistinguishable from astrocytomas on the basis of their proton MR spectra and only rarely display an identifiable alanine peak.[38] Although characteristic conventional MRI features usually allow confident diagnosis of these tumors (which are the most common adult extra-axial neoplasms), proton MRS is very helpful in atypical cases.

Metastases are another class of intracranial neoplasms that have been studied with proton MRS. Although they usually do not pose much of a diagnostic challenge when they are multiple, based on conventional MRI, metastases can be problematic when they are solitary because it may be difficult to distinguish them from primary brain neoplasms.[36] Unfortunately, the proton MR spectra of intracranial metastases are often nonspecific and indistinguishable from those of primary brain tumors; using long TE PRESS technique, they display low NAA levels, low Cr levels, and elevated Cho levels.[35, 36, 38, 129, 172]

Although in theory NAA should not be present in metastases because of their lack of neural or glial components, it

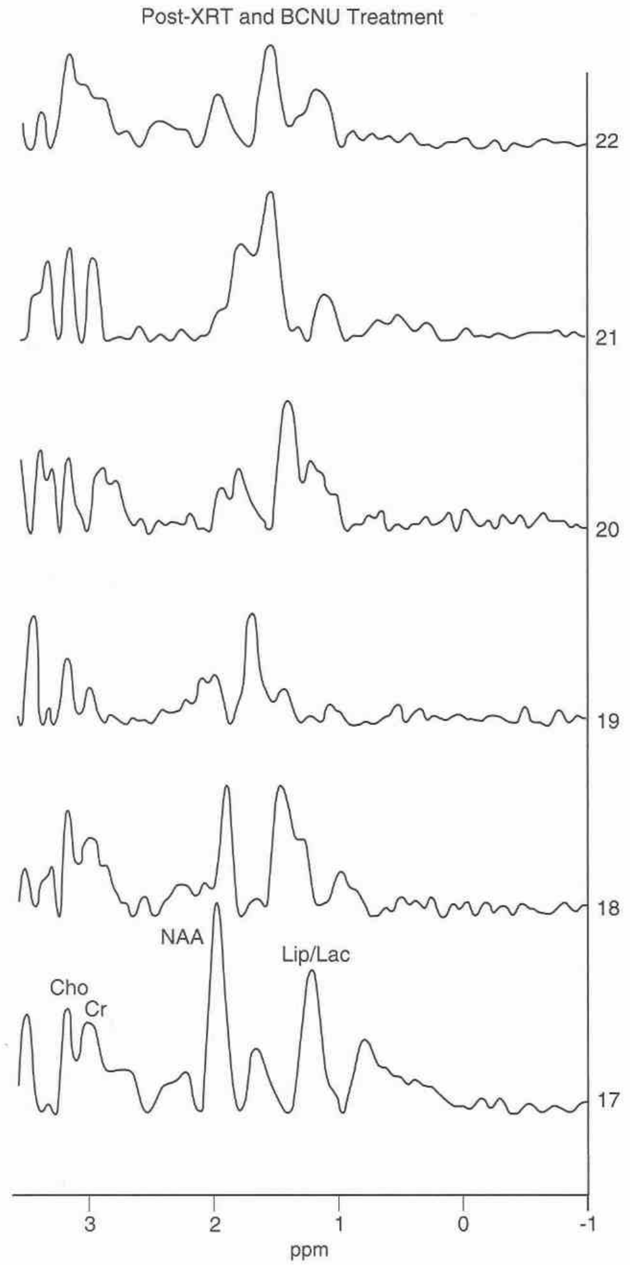

Figure 11–7. Chemical shift imaging of tumor after treatment. Multivolume one-dimensional spectroscopic image (1D SI) of high-grade anaplastic astrocytoma 3 months after completion of BCNU chemotherapy rounds. Note the marked decreases in choline resonances at 3.2 ppm in volumes 18 to 21. The patient was alive 5 years after treatment of his brain tumor.

frequently is present in proton MR spectra, presumably secondary to voxel contamination with adjacent brain parenchyma or due to the presence of *N*-acetylated metabolites on their cell membranes.[36] One study indicated that although no statistically significant difference existed between peak areas of Cho, Cr, and NAA in spectra of metastases and those of high-grade astrocytomas, a trend toward higher Cho/Cr and Cho/NAA ratios in astrocytomas did exist, and lipid and Lac peaks were more common in intracranial metastatic lesions[36] (Figs. 11–8 and 11–9). Another study suggested that lipid peaks were often present in metastases, particularly those from breast carcinoma.[38, 220]

Kinoshita and colleagues suggested that glycine levels may be used to distinguish metastatic tumors from glial tumors or neuroectodermal tumors; glycine levels were noted to be markedly elevated in GBMs, high-grade astrocytomas, an ependymoma, and a medulloblastoma, whereas they were low in metastatic tumors.[115, 121]

One study has evaluated the MR spectrum of acoustic schwannomas, and absence of Cr, marked reduction in NAA, and increased lipids were noted.[27, 36] Other MRS studies have attempted to distinguish astrocytomas from ependymomas and primitive neuroectodermal tumors (PNETs); these studies have demonstrated reduced NAA/Cho and elevated Lac/Cho ratios in astrocytomas and ependymomas in comparison with PNETs.[200, 225, 226, 241, 252]

One report described MRS findings in gliomatosis cerebri; these cases all demonstrated elevated Cho/Cr and Cho/NAA levels as well as varying degrees of decreased NAA/Cr ratios.[15] This study demonstrated a maximum Cho/NAA ratio of 1:3 in low-grade lesions, compared with 2.5 for anaplastic tumors; in addition, Lac peaks were noted in grade III and IV lesions.[15]

MRS may be able not only to facilitate diagnosis and accurate classification of de novo brain tumors but also to allow differentiation of recurrent tumor and tumor progression from radiation necrosis, post-treatment effects, or edema.[21, 36, 38, 200] Thus, MRS may be useful in evaluating the response to therapy in patients with brain tumors. Radiation necrosis occurs from approximately 6 to 24 months after completion of therapy, is seen more commonly with high-grade astrocytomas, and may be indistinguishable from recurrent tumor by conventional gadolinium-enhanced MRI.[38] Elevated Lac levels are seen in proton MR spectra of patients who have received 40 Gy or more of radiation to the brain, even when the conventional MRI study does not yet demonstrate any structural abnormality within the resection bed.[38]

One study involving 25 patients with cerebral astrocytomas who received a combination of radiation and chemotherapy demonstrated increased Cho/NAA and Cho/Cr ratios as well as the presence of Lac, in cases of recurrent tumor, compared to markedly decreased levels of NAA, Cho, and Cr and the presence of a broad intense peak between 0 and 2.0 ppm in cases of radiation necrosis.[38, 67] This broad peak, between 0 and 2.0 ppm, consists of free fatty acids, Lac, and amino acids.[38, 67] However, because most therapy-induced tissue damage occurs in combination with areas of viable tumor, single-voxel techniques are not optimal for evaluation of these patients; 3D MR spectroscopic imaging (MRSI) is preferable for distinguishing among areas of residual or recurrent tumor, radiation necrosis, and viable normal brain tissue.[36] Sensitivity and specificity of proton MRS for the detection of residual/recurrent tumor in radiated patients in one series were 71% and 100%, respectively, and serial MRS in the same series allowed differentiation of necrosis and tumor progression; progressive decreases in Cho levels and mild increases in NAA levels correlated well with therapy success.[36, 231]

Other groups have reported similar success in distinguishing radiation necrosis from recurrent tumor with proton MRS, although a few have reported contradictory re-

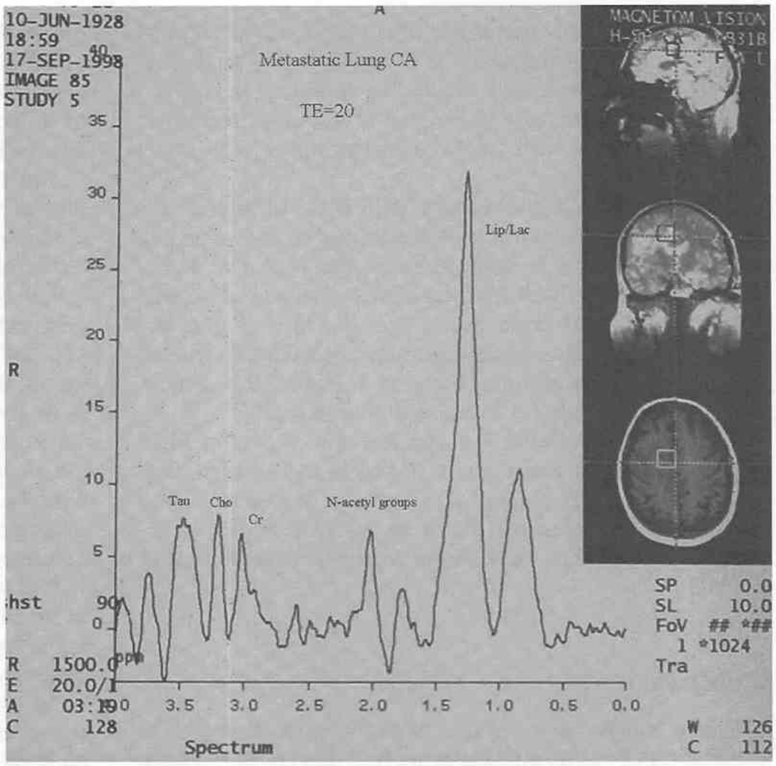

Figure 11–8. Metastatic lung carcinoma (CA). A single-volume brain proton MR spectrum was obtained using a TE = 20 msec in a 70-year-old patient presumed to have metastatic lung carcinoma. The definitive diagnosis was primary lung carcinoma.

sults; the reasons for differences in results may include the fact that Cho levels may be elevated in early radiation-induced lesions because of demyelination and reactive astrocytosis.[44, 49, 56, 74, 113, 200] In addition, Bizzi and coworkers reported that MRS is useful in the surveillance of lymphoma following treatment.[19, 36] Furthermore, Tedeschi and coauthors demonstrated that interval changes in Cho levels during long-term (3.5 years) follow-up with MRS allow differentiation of stable from progressive varieties of glioma.[21, 235] A recent study by Henry and associates suggested

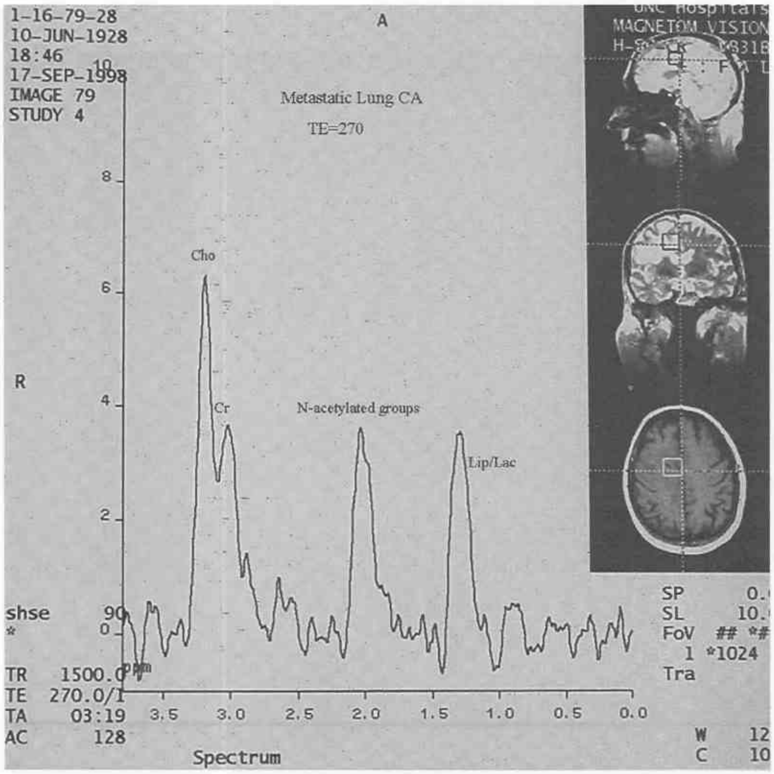

Figure 11–9. Metastatic lung carcinoma (CA). A single-volume brain proton MR spectrum was obtained using a TE = 270 msec in a 70-year-old patient with a presumed metastatic lung carcinoma.

that MRS and MR perfusion imaging (relative cerebral blood volume mapping) may be complementary modalities that, when combined, may be able to noninvasively differentiate tumor from necrosis, post-treatment effects, or edema in patients with treated gliomas better than either modality alone.[94]

Another application of proton MRS is the differentiation of gliomas from hamartomas, particularly in the setting of phakomatoses such as neurofibromatosis, type I.[200] NAA/Cho, NAA/Cr, and Cr/Cho ratios in hamartomas are closer to those of normal brain tissue than to those of gliomas; specifically, studies have demonstrated Cho/Cr ratios greater than 2.0 in gliomas, between 1.3 and 2.0 in hamartomas, and less than 1.3 in normal brain tissue.[33, 81, 200]

Therefore, a multitude of applications of proton MRS exist in the field of brain tumor diagnosis and management, and MRS is clearly playing an increasingly valuable clinical role that complements the roles of conventional structural MRI and other physiologic imaging modalities such as PET.

Epilepsy

Proton MRS has a major clinical application in the localization of subtle epileptogenic foci that are not evident on conventional structural MRI sequences as well as in the prognostication and planning of epilepsy surgery. Specifically, single-voxel MRS may confirm a structurally abnormal epileptogenic focus, whereas MRSI may detect foci that appear normal on conventional structural MR images but demonstrate definite metabolic abnormalities, such as those associated with very subtle malformations of cortical development.[54, 169] In fact, one study suggested that the sensitivity of MRS for the detection of subtle neuronal dysfunction was greater than that of PET.[2, 200] The advent of viable surgical approaches to the management of epilepsy, as well as the potential for future less invasive treatment modalities such as Gamma knife radiosurgery, has made precise localization of seizure foci critical.[169]

Most of the applications of MRS in epilepsy have been involved with temporal lobe epilepsy (TLE), the most common type of partial epilepsy, and many cases have been refractory to medical therapy.[21] The most common lesion associated with TLE is mesial temporal sclerosis (also called hippocampal sclerosis), noted in approximately 65% of cases of TLE.[9, 21, 54] Although in classic cases of mesial temporal sclerosis (MTS) the involved hippocampus is easily identified by a combination of volume loss and signal hyperintensity on T2-weighted and fluid-attenuated inversion recovery (FLAIR) sequences, 20% of patients with TLE have normal structural MRI scans and the findings in children generally tend to be more subtle than those in adults.[169, 200] NAA, NAA/Cho, NAA/Cr, and NAA/(Cho + Cr) all are decreased in atrophic hippocampi, as well as in nonatrophic hippocampi with abnormal electroencephalographic (EEG) findings, according to the results from the series by Ende and coworkers[21, 68] (Figs. 11–10 and 11–11).

In addition, even when seizure onset and structural MRI abnormalities are clearly unilateral, MRS has shown that bilateral temporal lobe abnormalities are present; bilateral metabolic abnormalities are found in approximately 40% to 50% of TLE cases, and in such cases these abnormalities appear to be more diffuse than the corresponding structural abnormalities would suggest.[53, 54, 58, 68, 95, 170]

Kuzniecky and colleagues also argued that the lack of correlation between structural hippocampal volume loss and proton MRSI metabolic abnormalities reflects the presence of distinct pathophysiologic processes that are coexistent in cases of MTS.[131] Gadian's investigators, examining

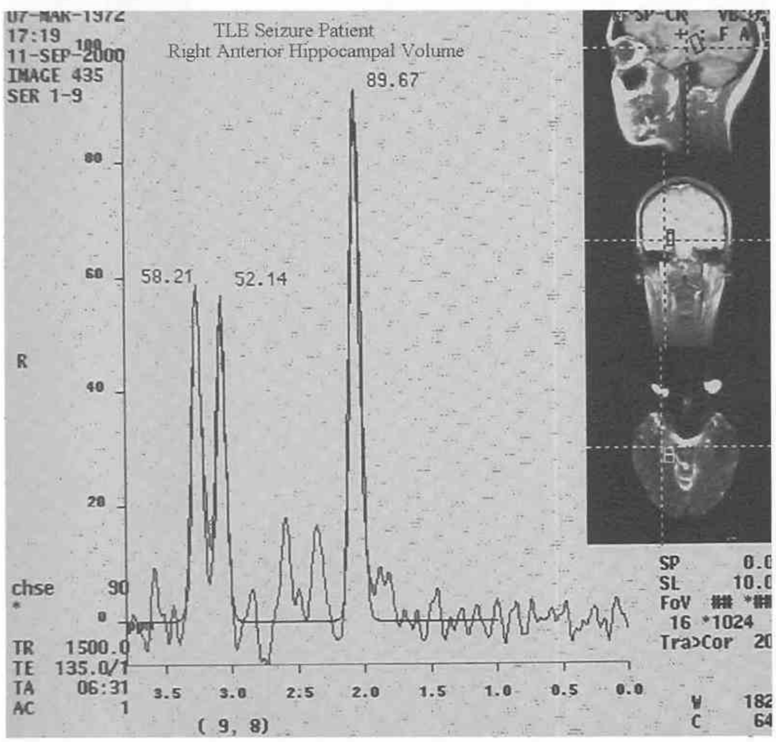

Figure 11–10. Study of temporal lobe epilepsy (TLE), right anterior hippocampal volume. Oblique spectroscopic imaging (SI) study of the hippocampus of a 28-year-old patient with TLE. This volume represents the peak resonance area of the metabolites of the normal right hippocampus. A TE = 135 msec and a TR = 1500 msec were used. The SI study used an angled SI region of interest of 25 degrees, which was parallel to and covered both the left and right hippocampal regions. Each volume element was 1 × 1 × 1.5 cm in dimensions.

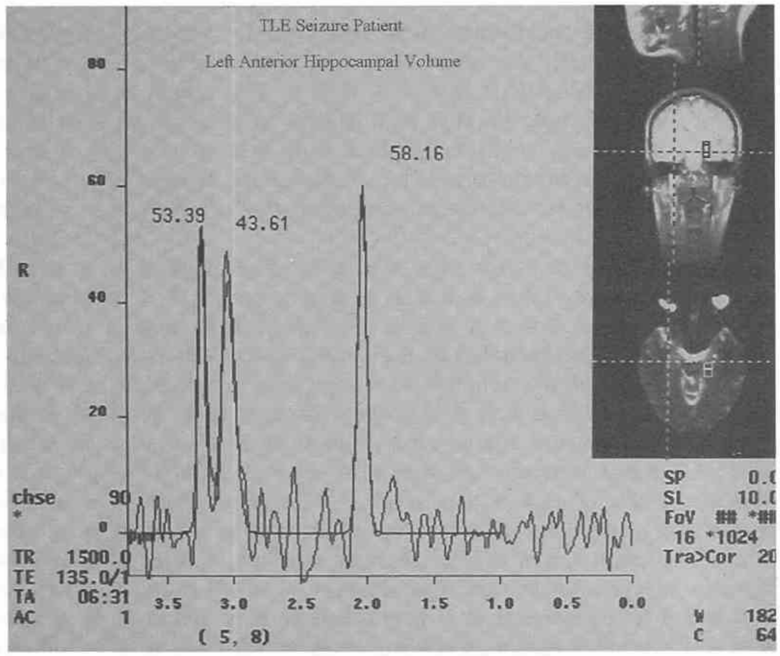

Figure 11–11. Study of temporal lobe epilepsy (TLE), left anterior hippocampal volume. Oblique spectroscopic imaging (SI) study of the hippocampus of a 28-year-old patient with TLE. This left anterior SI volume of the hippocampus was found to have an approximately 40% decrease in *N*-acetylaspartate (NAA) peak resonance area compared to the volume examined on the contralateral right hippocampus and coincided with the electroencephalographic findings indicating a left temporal lobe seizure focus.

a mixed group of patients with partial seizures, mostly with TLE, reported a 9% decrease in the NAA content of the epileptogenic temporal lobe, with an increase of 14% and 17%, respectively, in the levels of Cr and Cho.[75, 120]

Additional multivoxel MRS studies have shown not only reduced NAA levels in the diseased hippocampus but also the presence of Lac peaks in the spectra of epileptogenic foci when studied within 6 hours of seizure activity.[41, 50, 170, 200, 223] The postictal Lac peak has been described as having potential lateralizing value, since only one side demonstrates a peak in Lac, even in patients with bilateral disease.[50, 223]

Cendes and associates noted that correct lateralization of the seizure focus in patients with TLE was possible in 83% of cases in their large series with MR volumetry and 86% with MRSI.[42, 120] Ende and coauthors found that the NAA/(Cho + Cr) ratio was the most sensitive measure for lateralization compared with ictal EEG[68, 120]; they also noted that in unilateral TLE, the reduced levels of NAA in the hippocampus contralateral to the atrophic one predicted poor clinical outcome following surgical resection of the epileptic focus.[21, 68] Thus, MRS may provide important prognostic as well as diagnostic information.

MRS has also shown promise in the evaluation of patients with extratemporal epilepsy, including those with neocortical epilepsy. This class includes the second largest group of patients with complex partial seizures refractory to medical therapy—those with frontal lobe epilepsy.[1]

Garcia and coworkers[76] reported that, in a series of eight patients with frontal lobe epilepsy, the mean NAA/Cr ratio in the epileptogenic frontal lobe was decreased by 27%, compared with that of the contralateral frontal lobe, with decreases of at least 5% in each individual.[1] In addition, in patients with structural MR evidence of malformations of cortical development (MCD) or neuronal migration disorders (NMD), MRS provides insight into both the pathophysiology and true spatial extent of the disease processes.

Li and coworkers[137] showed that the maximal NAA/Cr ratio decrease, indicative of metabolic dysfunction, localized to the structural malformation noted on conventional MRI in 23 cases of MCD (including focal cortical dysplasia, heterotopia, polymicrogyria, and tuberous sclerosis); however, less impressive decreases also extended to normal-appearing areas of brain tissue adjacent to the structural lesion.

Simone and colleagues,[222] in their series of 15 patients with NMD, noted abnormally decreased NAA/Cr and Cho/Cr ratios in these lesions when compared with gray and white matter of neurologic controls; they also noted abnormally decreased Cho/Cr ratios in the normal-appearing brain contralateral to the identified NMD, when compared with gray and white matter of neurologic controls. The absence of correlation between the NAA/Cr decrease, EEG abnormalities, and NMD lateralization suggested that the metabolic abnormality may be related more to the underlying structural and functional alterations within the focus of NMD than to actual epileptic activity in the lesions, and that the Cho/Cr ratio decreases may reflect more extensive diffuse hypomyelination than what the structural MRI had suggested.[222]

Alzheimer's Disease

Alzheimer's disease is the most common form of dementia in older adults and represents approximately 40% to 60% of all such dementias.[21, 38] The disease is characterized by decreased cortical acetylcholine, neuronal loss, amyloid deposits, and neurofibrillary tangles. Diagnosis, which may be difficult, is based primarily on clinical criteria, and imaging has been used primarily for excluding other possible causes of dementia, such as intracranial mass lesions and subcortical vascular disease. Nevertheless, structural MRI can confirm clinical findings in Alzheimer's disease by demonstrating preferential atrophy of the hippocampi and temporoparietal cortices. MRS, however, may enable earlier diagnosis of this disease.

The proton MR spectrum in Alzheimer's disease demonstrates an abnormally elevated MI/Cr ratio and an abnormally decreased NAA/Cr ratio.[156, 158, 159, 197, 217] This combination of spectroscopic findings distinguishes Alzheimer's disease from normal conditions in the elderly, whereas the elevated MI/Cr ratio distinguishes Alzheimer's disease from other dementias, with the possible exception of Pick's disease.[197]

Reduced levels of NAA are noted in the frontoparietal regions and temporal lobes, including the hippocampi.[21, 209, 234] In Pick's disease, however, decreased NAA levels and elevated MI levels are noted in the frontal lobes, and no such similar metabolic abnormalities are present in these brain regions in those with Alzheimer's disease; thus, the differentiation between Alzheimer's disease and Pick's disease was made correctly on the basis of proton MRS findings in 92% of cases in one series.[21, 69] However, many confounding metabolic disorders can also result in abnormal MI/Cr ratios: renal failure, diabetes mellitus, chronic hypoxic encephalopathy, and hypernatremia can all result in elevated MI concentrations, whereas hepatic encephalopathy and hyponatremia can result in decreased MI concentrations.[124–126, 135, 154, 197, 249]

Degenerative and Metabolic Brain Disorders

Various brain metabolic disorders, including primary leukodystrophies and mitochondrial disorders, have been studied with proton MRS. Although the MR spectral findings, conventional imaging findings, and clinical symptoms of most of these degenerative brain disorders (many of which present in childhood) are nonspecific, MRS can sometimes be useful in distinguishing the various clinical entities.

Wang and Zimmerman[255] have divided brain metabolic disorders into five general categories:

1. Disorders of lipid metabolism.
2. Disorders of carbohydrate metabolism and respiratory chain.
3. Disorders of amino acid metabolism and the urea cycle,
4. Primary white matter disorders.
5. Miscellaneous metabolic disorder not fitting into the previously described categories.

Furthermore, peroxisomal and mitochondrial disorders may be considered to be subcategories of these five categories.[255]

Disorders of lipid metabolism include the following[255]:

1. Abnormalities of long-chain fatty acid metabolism (peroxisomal diseases), such as Zellweger's syndrome (in which peroxisomes are deficient or absent).
2. Rhizomelic chondrodysplasia punctata (in which several peroxisomal enzymes are absent).
3. Adrenoleukodystrophy (in which a single peroxisomal enzyme is deficient).

Adrenoleukodystrophy is unique, in that among hereditary leukodystrophies it is the only one associated with an increased Cho signal at times other than during the early stage of acute demyelination.[21] In childhood adrenoleukodystrophy, decreased NAA/Cr and increased Cho/Cr ratios are present in addition to elevated Lac, Glu, Gln, and MI peaks.[38, 240] The decline in the NAA/Cr ratio in X-linked adrenoleukodystrophy both parallels disease progression and can predate emergence of white matter hyperintensities on conventional T2-weighted MRI scans.[51, 214]

Disorders of carbohydrate metabolism include diabetes mellitus and galactosemia. In diabetes mellitus, MR spectra reveal elevated glucose signal and an acetone peak at 2.2 ppm owing to hyperglycemia and ketogenesis.[194] In addition, it is suggested that the extent of brain injury in severe diabetic ketoacidosis may be evaluated with MRS because elevated Lac levels have been noted in individuals eventually dying of cerebral herniation and cardiac arrest.[255] Furthermore, in galactosemia, a condition in which one of various inborn errors of metabolism prevents normal conversion of galactose to glucose, neonates demonstrate elevated brain galactitol peaks in proton MR spectra at 3.67 and 3.74 ppm at the time of symptom onset; this corresponds to elevated levels of galactitol in brain autopsy specimens in fatal cases.[254, 257]

Disorders of the respiratory chain include mitochondrial disorders such as mitochondrial myopathy, encephalopathy, lactic acidosis, and strokes (MELAS) and myoclonic epilepsy with ragged red fibers (MERRF), Kearns-Sayre syndrome, and pyruvate dehydrogenase deficiency (PDD). MRS may provide useful information regarding the extent of metabolic derangement, severity of disease, and response to therapy.[64, 92, 119, 255] All of these diseases are characterized by brain Lac accumulation secondary to impaired mitochondrial oxidative phosphorylation.[255] Figure 11–12 illustrates an example of a MELAS spectrum.

MRSI is the preferred approach of evaluating distributions of cerebral metabolites in these disorders, since the distribution of Lac in the brain may vary significantly across different anatomic regions and since metabolic abnormalities may be present even when no corresponding conventional brain MRI abnormalities are present.[34, 146] The most striking Lac elevations are noted in regions of brain displaying the most marked structural abnormalities on conventional MR studies. The peaks have been noted in the parieto-occipital gray and white matter in MELAS; occipital cortex in MERRF; brain stem, basal ganglia, and occipital cortex in Leigh's syndrome; and cortical gray matter in Kearns-Sayre syndrome.[200] All of these syndromes are also associated with decreased NAA/Cr ratios, presumably related to neuronal loss or dysfunction.[89, 146] However, PDD has been associated more marked reductions in NAA/Cr ratios in addition to elevated Lac levels and decreased Cho/Cr ratios; in fact, Zimmerman and Wang have noted one case in which NAA was completely absent from the spectrum.[214, 255, 262]

Disorders of amino acid metabolism include entities such as phenylketonuria (PKU), the most prevalent of this class of disorders, and maple syrup urine disease (MSUD).

PKU results from a deficiency of the hepatic enzyme phenylalanine hydroxylase and demonstrates an autosomal recessive mode of inheritance.[210] In patients with PKU, the proton MR spectrum is remarkable only for an abnormal elevation of the phenylalanine signal at 7.3 ppm, which is a finding that is specific for this disease.[255]

In patients with MSUD, long TE proton MR spectra

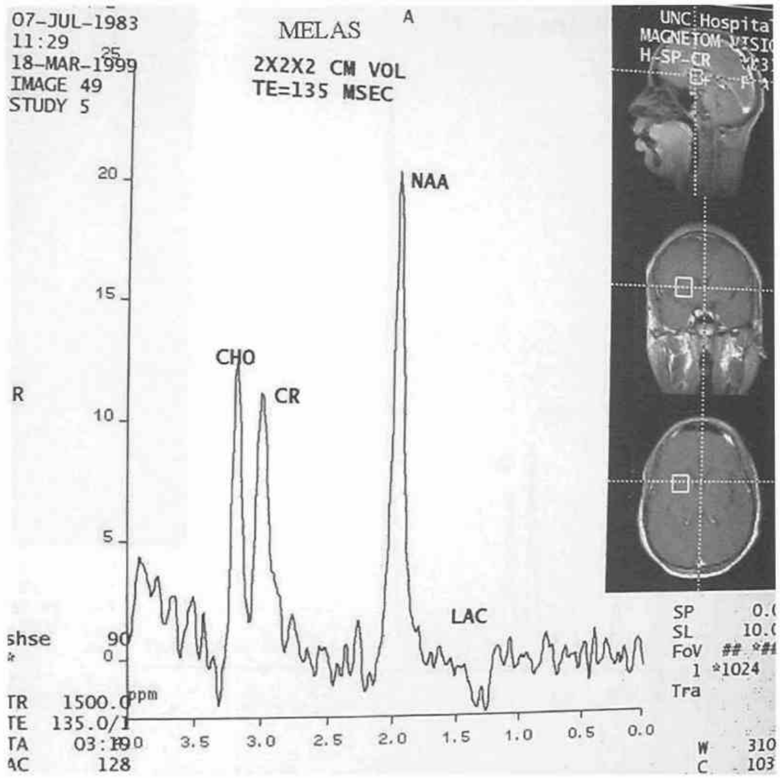

Figure 11–12. Mitochondrial encephalomyelopathy–lactic acidosis–and stroke-like symptoms syndrome (MELAS) in a 16-year-old patient. Single-volume proton MRS study (2 × 2 × 2 cm) over the basal ganglia. A TE of 135 msec was used to determine the presence of an inverted peak at 1.3 ppm. Both the left and right basal ganglia area showed the presence of an inverted lactate peak, centered at 1.3 ppm.

reveal a peak at 0.9 to 1.0 ppm in addition to a reversible decrease in the NAA/Cr ratio during acute metabolic decompensation.[71, 253, 255] Abnormal accumulation of valine, leucine, and isoleucine occurs in the CSF, blood, and tissues as a consequence of defective oxidative decarboxylation.[65, 255]

Ornithine transcarbamylase deficiency is the most common disorder of the urea cycle and is inherited in an X-linked dominant fashion. In patients with this condition, hyperammonemia and intracerebral glutamine accumulation lead to cerebral edema, neuronal loss, and white matter gliosis.[122, 255] Reported MR spectral abnormalities include elevated glutamine levels in a case of hyperammonemia and decreased MI with a normal glutamine level in one patient with a normal serum ammonia level.[52, 194]

The primary white matter disorders include Canavan's disease, Alexander's disease, and Pelizaeus-Merzbacher disease, among others. In patients with Canavan's disease, which is the only primary white matter disorder with truly specific findings on MRS, markedly increased NAA levels have been noted, probably secondary to impaired NAA breakdown related to a deficiency in the enzyme aspartoacyclase[21, 38, 89, 143] (Fig. 11–13). Canavan's disease is the only metabolic disorder that is associated with an elevated NAA level.[253, 255, 259] Other findings in Canavan's disease include elevated MI levels and decreased Cho and Cr peaks; the decreased Cho is probably due to failure of myelination, whereas a decreased Cr level may reflect spongy degeneration.[255]

In patients with Alexander's disease, decreased NAA levels and elevated Lac levels are observed, most prominently in the frontal lobe; the structural white matter abnormality extends from the frontal lobes posteriorly.[89, 255]

Pelizaeus-Merzbacher disease may be characterized by normal spectra or slight decreases in NAA in the basal ganglia in the early stages and by more prominent NAA decreases and Cho increases in advanced disease.[89, 133, 228]

Several as-yet unclassified primary white matter diseases have also been reported. For example, van der Knaap and coauthors[248] have reported a new leukoencephalopathy in nine children manifested by severe white matter degeneration with elevated Lac and Glu and virtual disappearance of most other metabolites in MR spectra.[255] In addition, the studies of Tedeschi and associates[21, 233] have described a new white matter syndrome resulting from a metabolic defect producing hypomyelination and secondary axonal dysfunction characterized by a prominent decrease in NAA, Cho, and Cr levels and an increase in Lac.

In general, childhood demyelinating disorders and neuronal degenerative disorders typically demonstrate decreased NAA/Cr ratios, with the degree of decrease corresponding to the extent of white matter disease and degree of cortical atrophy, respectively, depicted on conventional MR images.[38, 246] Decreased NAA levels and elevated Lac levels are noted in Schilder's and Cockayne's diseases in addition to the disorders described earlier.[38, 89]

Still other metabolic disorders are characterized by specific pathologic changes in proton MR spectra. For example, abnormal lipid peaks are seen in Niemann-Pick disease type C (a lysosomal disorder), low Cr levels are present in guanidinoacetate methyltransferase deficiency, and elevated Gly levels are present in nonketotic hyperglycinemia.[199] Furthermore, in adult hepatic encephalopathy, increased levels of Glu and decreased levels of MI and Cho in proton MR spectra have been described; the Glu elevation is thought to be secondary to hyperammonemia.[196, 255] MRS

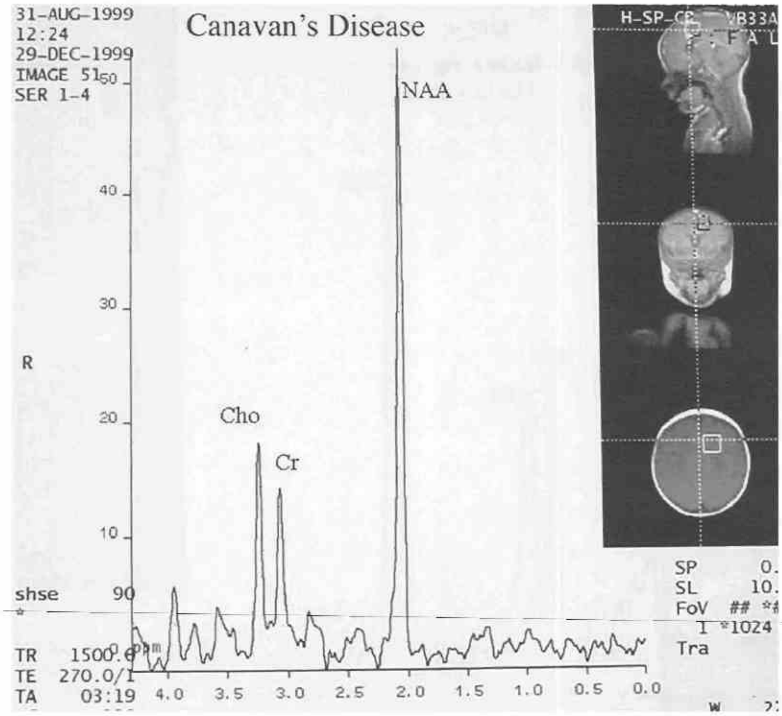

Figure 11–13. Canavan's disease. A single-volume proton, TE = 270 msec MRS study of a 4-month-old baby with a diagnosis of Canavan's disease. Note the level of *N*-acetylaspartate (NAA), which was found to be three times higher than that found in the normal frontal lobe of age-matched infants using TE = 20 msec STEAM proton MR spectrum of Canavan's disease. (See Wang ZJ, Zimmerman RA: Proton MR spectroscopy of pediatric brain metabolic disorders. Neuroimaging Clin North Am 8:781–807. 1998.)

may even be able to detect subclinical encephalopathy, since the reduction in MI level may occur even in patients with hepatic disease without neurologic symptoms.[38, 126, 195] The specificity of these abnormalities may be useful in both diagnosis and monitoring of therapeutic efficacy in these conditions.

Stroke

Stroke is another clinical condition in which MRS has been applied. Although the utility of MRS in the acute stroke setting may be less than that of diffusion and perfusion MRI, or even noncontrast CT, since a critical need for rapid imaging exists in the hyperacute and acute setting for decision making regarding need for thrombolysis, MRS may be very useful in the chronic phase and for monitoring recovery from stroke.[169, 175]

The first detectable change in the MR spectrum that occurs following the onset of cerebral ischemia is the appearance of the Lac doublet.[189] The Lac peak has been noted within minutes of induction of ischemia in animal models, and its level tends to rise over the first few hours after onset.[3, 160, 165, 189] A blood flow threshold of 20 mL/100 g of brain tissue per minute has been described in animal models for the appearance of Lac, but whether a similar threshold exists for humans is not certain.[57]

Studies in humans have also noted the presence of Lac during the first few days following symptom onset, correlated with ischemia and resultant edema[169, 256] (Fig. 11–14). Not only does MRS demonstrate spectral changes before comparable changes in signal intensity of ischemic tissue on conventional T2-weighted MR images occur, but also the extent of cerebral tissue displaying metabolic abnormalities exceeds the extent of signal hyperintensity on the T2-weighted images.[10, 80, 160, 165, 189] In addition, the concentration of Lac in ischemic tissue is not homogeneous; rather, the center of the infarct tends to demonstrate higher concentrations than the infarct periphery.[77] Concentrations of Lac during the evolution of an infarct also demonstrate temporal as well as spatial variability.[84, 189] Although the presence of Lac signifies ischemia, it does not necessarily signify actual irreversible infarction.[10, 17, 80, 189]

A later and more specific spectral change signifying actual cerebral infarction that occurs during the evolution of a clinical stroke is a reduced NAA concentration.[189] Several studies have demonstrated both a reduction in NAA and appearance of Lac in human stroke.[10, 86, 207, 256] The reduced NAA level is thought to be related to actual neuronal damage (neuronal cell death or replacement by non–NAA-containing cells, such as glial cells, which occurs in a delayed fashion relative to the changes seen in Lac levels) and is correlated highly with clinical outcome.[165, 166, 169, 189]

Pereira and coworkers studied a series of 31 patients with new middle cerebral artery distribution infarcts within the first 72 hours following clinical onset of stroke symptoms with proton MRS and T2-weighted structural MRI. The authors noted that the combination of infarct volume and NAA concentration could accurately predict clinical outcome.[178]

Decreases in NAA levels can often be identified in initial MR spectra; in fact, one study using an animal model demonstrated NAA reduction within 30 to 60 minutes following induction of cerebral infarction.[96, 174, 189] Regional variability in NAA concentrations is noted, just as with Lac, and the areas demonstrating the greatest elevation of Lac within an infarct also demonstrate the most marked NAA depression.[10, 70, 84, 189]

Changes in Cho and Cr concentrations during acute infarction are more variable than changes involving Lac and NAA. Many studies have reported decreases in Cr levels.[28, 70, 72, 77, 85, 207] Nevertheless, a few studies docu-

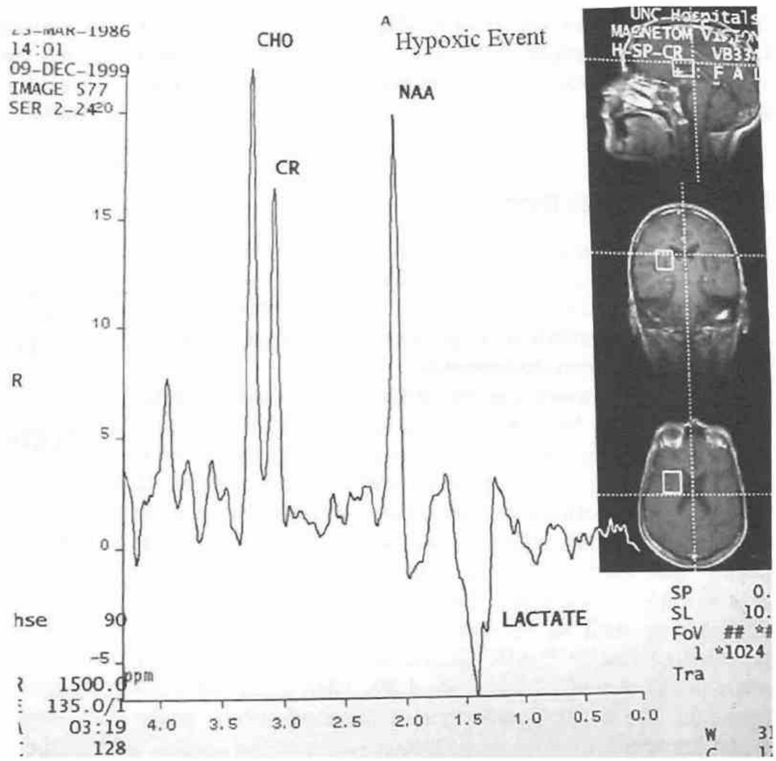

Figure 11–14. Hypoxic event/mitochondrial disorder in a 13-year-old patient. A single-volume, TE = 135 msec PRESS proton MRS study showed the presence of an inverted lactate peak in the basal ganglia. Lactate was found in both the left and right basal ganglia areas and also in various areas of the left and right frontal lobes.

mented no consistent change in Cr levels,[72, 77, 84, 207] and two studies have even noted increased levels of Cr.[10, 80]

Variability in Cho levels has been equally problematic. Elevated Cho levels have been reported in acute infarction, and this elevation may be related to ischemic demyelination.[10, 80, 189] However, this finding is not consistent, since several studies have noted decreased[28, 84] or unchanged[72, 77, 207] Cho levels.

In the subacute stage, Lac levels decrease progressively from the peak levels that are present in the acute stage with an approximately 36% reduction in Lac levels noted per week.[85] Lac may disappear or persist in low levels in the chronic stage; it may also disappear in the subacute stage and recur in the chronic stage.[10, 78, 84, 85, 100, 204] The reasons for the persistence of Lac peaks into the subacute and chronic phases are not entirely clear.[189]

In the chronic stage, NAA, Cr, and Cho levels all decrease.[189, 207] Specifically, the NAA level decreases in an irreversible fashion at an average rate of approximately 29% per week.[10, 70, 77, 85, 100] The rate of decrease of Cr and Cho is less than that of NAA, although these levels also decrease in the subacute and chronic phases.[66, 70, 77, 189] The smaller relative decrease of Cho and Cr is probably related to both the relatively decreased vulnerability of glial cells to ischemia compared to neurons and the reactive gliosis that occurs as a result of ischemic brain injury.[85, 189]

Hypoxic-Ischemic Injury

MRS has been used to evaluate brain damage due to perinatal asphyxia, or hypoxic-ischemic injury (HIE).[11, 87, 90, 208] HIE is the main cause of developmental injury that leads to cerebral palsy. In many cases, the most severe damage (selective neuronal necrosis) involves the occipital gray matter and is manifested as a reduction in NAA and Cr levels and a proportional increase in Cho levels.[208] This suggests that significant astrocyte survival may be present in these cases of neuronal necrosis secondary to HIE.[208]

In particularly severe cases, a Lac peak may also be present, with the Lac peak appearing during the first 24 hours and persisting for at least 48 hours.[177] This finding often precedes the reduction in the NAA/Cr ratio and the increase in the Cho/Cr ratio, both of which have been noted on MRS studies performed 1 to 2 weeks after the initial insult.[214] The severity of the MRS changes appears to be well correlated with the severity of the initial insult and the clinical outcome; persistent NAA and Cho peak abnormalities and the presence of Lac are associated with poor prognosis.[13, 90, 97, 208, 218] Specifically, the presence of Lac in the acute phase has been associated with poor neurocognitive status at 1 year of age.[13] Barkovich and coauthors[13] have demonstrated that Lac/Cho ratios in the basal nuclei had particularly highly statistically significant associations with clinical outcome.

The distribution of Lac elevation in the brain also correlates well with the severity of the injury; in severe asphyxia, the basal ganglia demonstrate greater Lac elevation than the arterial watershed regions; in mild to moderate asphyxia, the watershed regions demonstrate greater Lac elevation.[14] Penrice and colleagues have shown that Lac/NAA ratios in the thalami, in particular, correlate highly with degree of severity of asphyxia; the ratios in normal infants were less than 0.3, the ratios in infants with asphyxia were greater than 0.4, and the ratios in severely affected infants were greater than 0.5.[14, 176]

Finally, Pu and others have shown that cases of moderate to severe HIE display detectable brain glutamate/gluta-

mine (Glx) peaks on proton MR spectra.[184] Elevated Glx/(Cr + PCr) ratios in these cases correlated positively with the Sarnat stage of HIE on both initial and follow-up MRS studies.[184]

Cerebral Infections

Most of the applications of proton MRS in evaluation of intracranial infections have involved the study of acquired immunodeficiency syndrome (AIDS) and AIDS-related conditions. Nevertheless, evaluation of cerebral abscesses with MRS has been documented.

Cerebral abscesses can be differentiated from necrotic brain neoplasms by MRS. Grand and coworkers, in their series of 34 cystic intracranial lesions, showed that at a TE of 136 msec, the detection of an amino acid resonance at 0.9 ppm in bacterial abscesses allows differentiation from necrotic neoplasms, which do not demonstrate this spectral peak.[88] MR spectra of brain abscesses demonstrate absent or low Cho and Cr levels and a relatively decreased level of NAA as well as the possible presence of substantial amounts of Lac.[38, 188] MR spectra of abscesses may show other peaks at 0.97, 1.24, 1.36, 1.50, 1.89, 2.02, and 2.14 ppm, and the exact significance of these additional peaks is not known.[38]

Various studies have shown resonances from acetate, succinate, and some amino acids (peaks not seen in brain neoplasms), in addition to Lac, Ala, and lipid peaks (which may also be seen with certain brain tumors).[39] Similar findings have been reported by Castillo and colleagues and others in cases of toxoplasmosis and cysticercosis[38, 39] (Figs. 11–15 and 11–16).

The few reports in the literature regarding MR spectra of other infectious processes include studies of intracranial tuberculomas, Creutzfeldt-Jakob disease, and herpes simplex encephalitis.[39] Prominent lipid resonances have been noted in intracranial tuberculomas, with particularly important peaks at the 1.3 and 0.9 ppm, corresponding to the methylene and terminal methyl groups of fatty acids, respectively.[39] Abnormally decreased NAA levels in both white matter and gray matter, as well as abnormally increased levels of MI in the white matter, have been noted in Creutzfeldt-Jakob disease, whereas reductions in the NAA/Cho and NAA/Cr ratios and the presence of Lac peaks have been noted in herpes encephalitis[39] (Figs. 11–17 and 11–18).

Acquired Immunodeficiency Syndrome

Various studies of applications of MRS to the evaluation of metabolic disturbances related to HIV infection have been recently performed; these studies have demonstrated reduced NAA concentrations in HIV-positive patients,[45–48, 112, 155, 203, 227, 239] including those who are asymptomatic[151] or who display normal structural MRI findings.[239] Increases in Cho and progressive decreases in NAA levels have been noted with disease progression[45–48, 112, 155, 169, 203, 227, 239]

Increased levels of glutamine and MI have been noted in the late stages of HIV dementia.[46] One study reported a decrease of both NAA and Cr along with increases in Cho and MI both in structural brain lesions and in normal-appearing areas of brain (on conventional MRI) in patients with AIDS.[21, 149] It is not clear whether the metabolic abnormalities in AIDS are due directly to the virus or whether they represent secondary effects related to opportunistic infection or AIDS-related neoplasms.[21] Nevertheless, it appears that MRS may be able to detect subclinical metabolic abnormalities prior to clinical and brain struc-

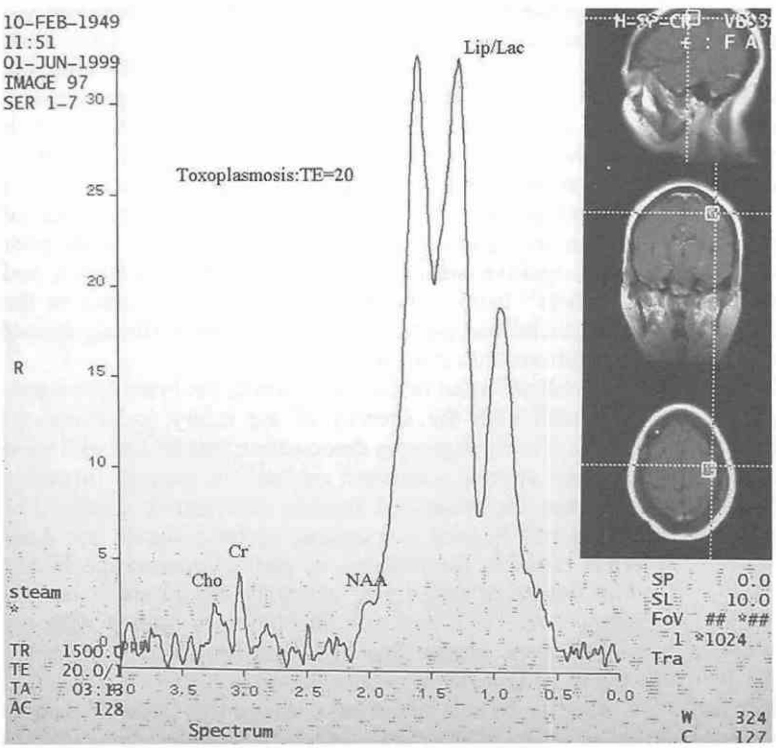

Figure 11–15. Toxoplasmosis. This was a single-volume STEAM MRS study (TE = 20 msec) of a 50-year-old patient with human immunodeficiency virus (HIV) infection with proven toxoplasmosis. Note the large decrease in metabolites and the presence of a large lipid or cellular breakdown peak between 0.5 and 1.8 ppm.

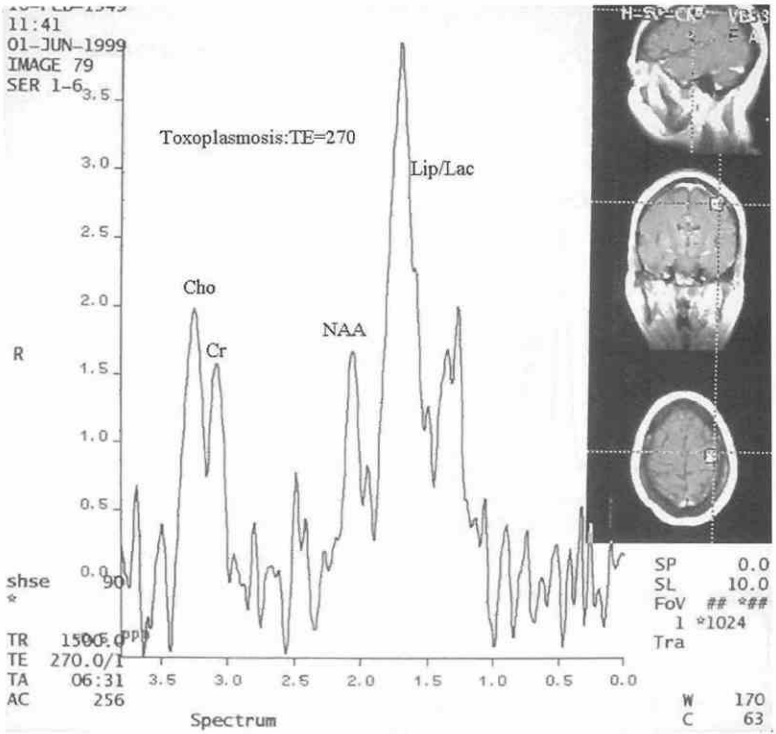

Figure 11–16. Proven toxoplasmosis in a 50-year-old patient with human immunodeficiency virus (HIV) infection. The MRS study used a TE = 270 msec PRESS. Again, note the decreased levels of brain metabolites and the presence of lipids and cellular breakdown peaks. Note the relationship between the choline and creatine peak in toxoplasmosis versus viral encephalitis. Normally, these peak ratios (TE = 270 msec, between 1.2 and 1.4) in patients with toxoplasmosis are much less than those observed in the active viral inflammatory processes. (Normally, choline-to-creatine peak area ratios using a TE = 270 msec are greater than 1.5 in viral inflammatory processes.)

tural manifestations of the disease.[199] The diffuse cortical atrophic changes and white matter hyperintensities noted on T2-weighted images are late findings in the AIDS dementia complex.

MRS may be particularly useful in the evaluation of infants of HIV-infected mothers; it may be able to demonstrate abnormalities in the infant brain as early as 10 days after birth, whereas seroconversion is difficult to determine during the first 6 months and conventional brain MR images may be normal.[38, 55]

MRS may also prove to be a useful means of monitoring both disease progression and treatment effects in patients with AIDS.[48, 169, 203] Specifically, it has been suggested that monitoring of the efficacy of antiretroviral therapy—and even prediction of a patient's response to therapy—may be performed with MRS.[199, 258]

Multiple Sclerosis

Multiple sclerosis (MS) is a disease that is manifested primarily as multifocal demyelination, although significant axonal injury and wallerian degeneration are usually present as well.[7, 109, 145, 169, 199] In fact, the axonal loss, rather than

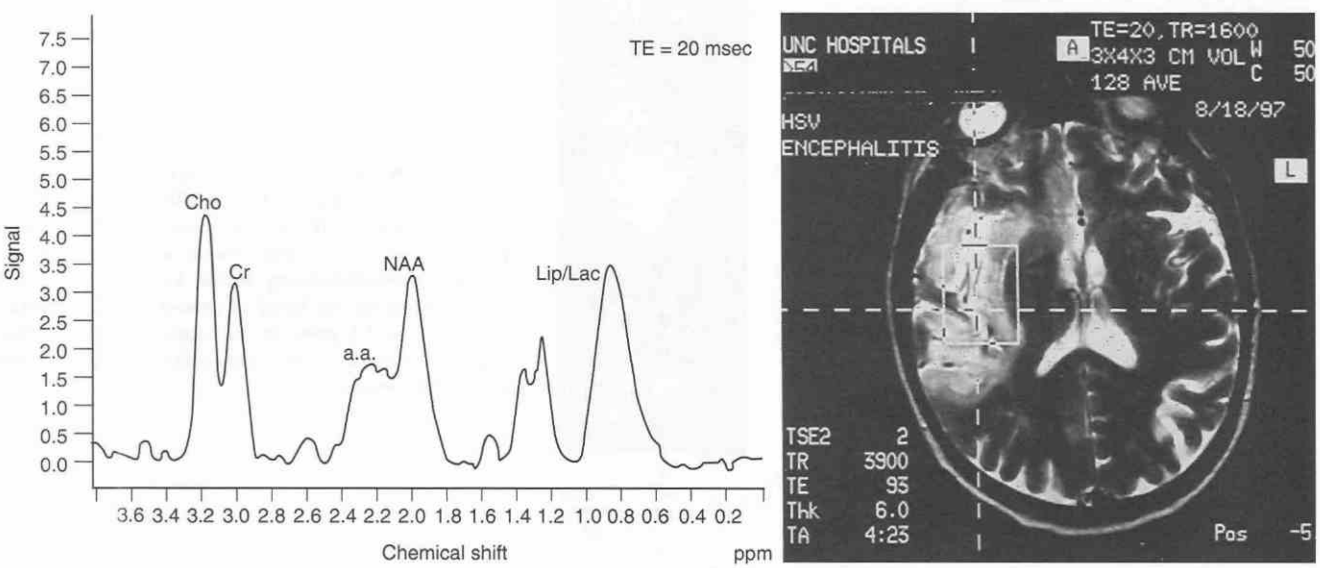

Figure 11–17. Herpes simplex viral (HSV) encephalitis in a 55-year-old patient. A 3 × 4 × 3 cm volume was used. The MRS study used a STEAM TE = 20 msec sequence. a.a., amino acids.

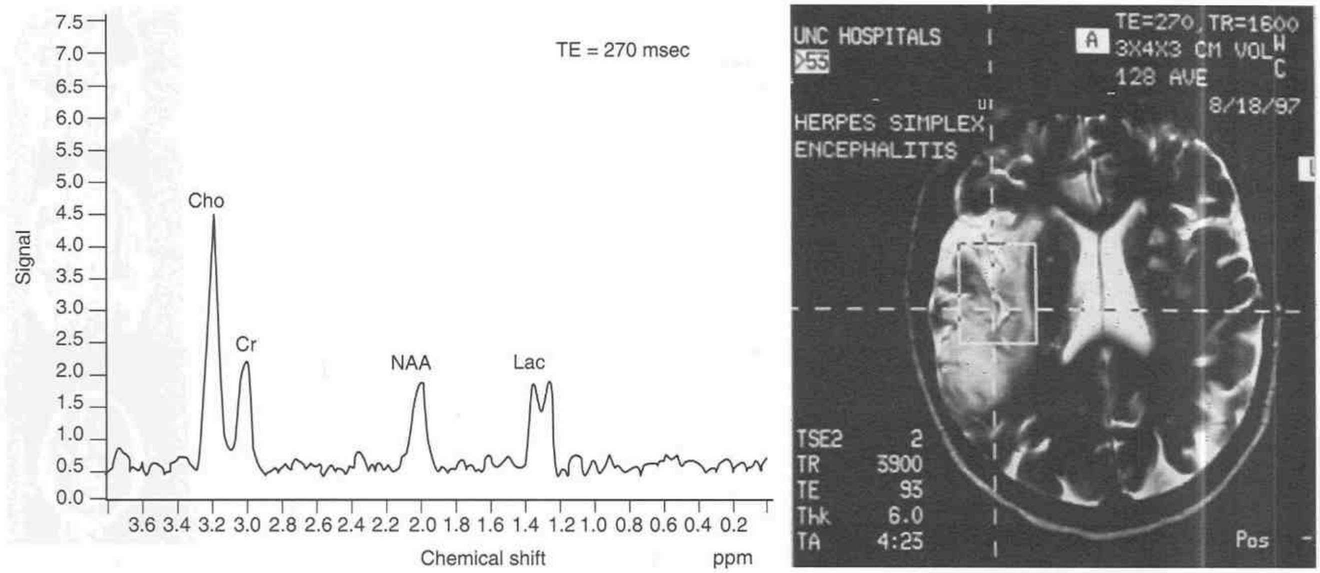

Figure 11–18. Active case of herpes simplex viral (HSV) encephalitis in a 55-year-old patient. This was a PRESS MRS study (TE = 270 msec).

the demyelination, may be responsible for the neurologic impairment seen in patients with MS.[147, 199]

Active demyelinating plaques generally demonstrate enhancement on gadolinium-enhanced MR scans in addition to displaying hyperintensity on T2-weighted and FLAIR conventional MR sequences.[38] Substantial reductions in NAA concentration are noted in acute (active) MS lesions, and these reductions correlate highly with clinical neurologic impairment; partial recovery of NAA levels is also not uncommon, and these changes are also reflected in clinical improvement.[199] Whether the partial recovery of NAA levels is due to reduction of edema or to actual recovery of neuronal function is not clear.[33, 199]

In the acute phase, marked increases in Cho concentration, moderate increases in Lac, and increases in mobile lipid peaks and "marker peaks" in the range of 2.0 to 2.6 ppm may be present.[7, 21, 91] The increase in Cho levels is due to release of phosphocholine and glycerophosphocholine during active demyelination.[21] The mobile lipid peaks are products of myelin breakdown, and the "marker peaks" are of uncertain etiology but appear to be typical of demyelinating conditions in general.[21, 38] One study even suggested that lipid concentration increases may precede signal hyperintensity development on T2-weighted conventional MR sequences.[167, 199]

The presence of Lac may be related to local inflamma-

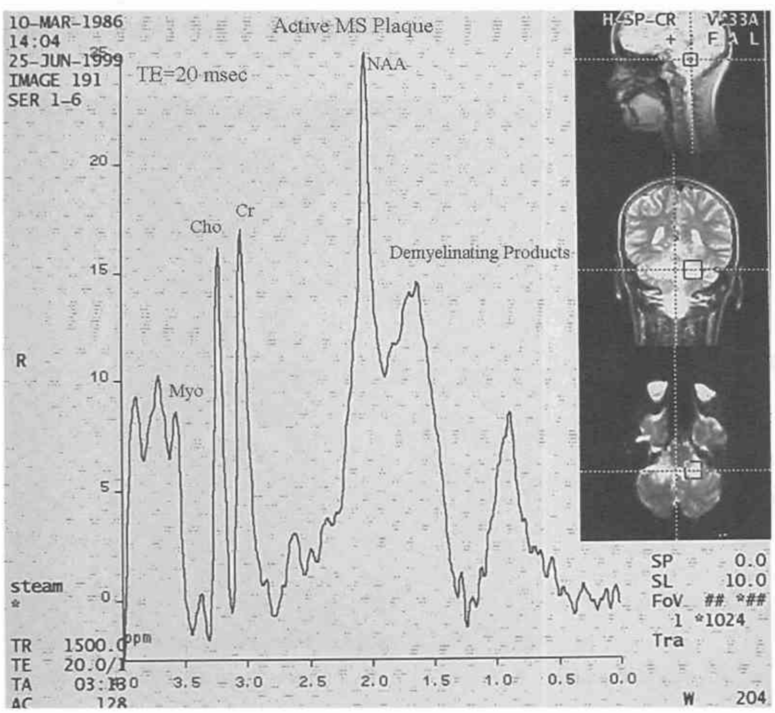

Figure 11–19. Active multiple sclerosis (MS) plaque. A single-volume proton STEAM MR study used a TE of 20 msec and a TR of 1500 msec in a patient with MS. The 2 × 2 × 2 cm volume was centered over the gadolinium-enhancing lesion located in the left cerebellum. Note the level of *myo*-inositol and other sugars (3.5 to 3.8 ppm) in the active plaque volume compared to the level in a non–gadolinium-enhancing inactive MS lesion.

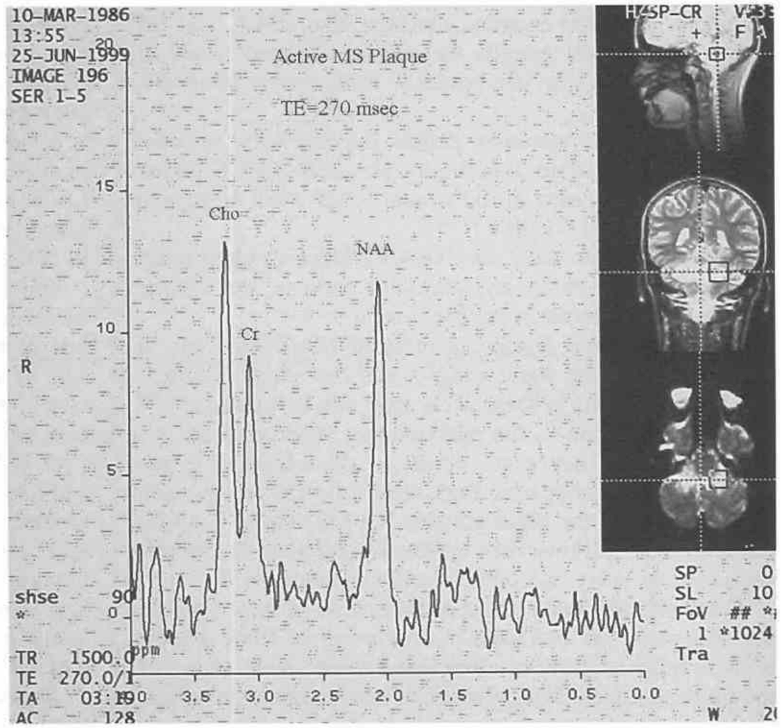

Figure 11–20. Active multiple sclerosis (MS). This was a single-volume proton PRESS MRS study (TE = 270 msec) of a patient with a gadolinium-enhancing MS lesion.

tory infiltrates associated with the demyelinating plaques and their effects on local cerebral vasculature.[7, 199]

A transient but significant decrease in Cr levels in the hyperacute stage may revert to normal in the subacute and chronic stages.[199]

Increases in MI concentrations may be seen on short TE spectra; MI is usually detected when the demyelinating process is severe[21, 61, 199] (Figs. 11–19 and 11–20).

Reduction of NAA/Cr ratios has been noted not only in structural lesions (visible demyelinating plaques) but even in white matter, which appears normal by conventional T2-weighted MRI; thus, these MRS findings suggest that conventional MR sequences may underestimate the true extent of brain tissue involvement by MS.[21, 62, 73, 196] Although much of the reduction has been attributed to decreases in absolute concentrations of NAA, controversy exists regarding possible increases in Cr levels as well.[62, 169, 192] Actually, the metabolite changes noted in MRS may be better correlated with actual clinical status than the number or volume of hyperintense structural brain lesions on conventional T2-weighted sequences.[5, 210, 238] In fact, the reduction in NAA in the normal-appearing white matter correlates best with the degree of clinical disability.[199] Furthermore, preliminary data suggest that MRS may be used to monitor responses to therapy in patients with MS.[169, 209] Gonen and colleagues[82] have suggested that measurement of whole brain NAA concentration may serve as an effective and reproducible measure of disease load in MS and may be used to measure disease progression.

In the chronic phase of MS, axonal loss and mild cortical atrophy may occur. Although acute plaques demonstrate edema and demyelination, chronic plaques demonstrate gliosis and mild associated neuronal loss.[21]

Incomplete recovery of axonal damage leads to irreversible clinical disabilities. NAA levels are decreased in both the structural lesions identified on conventional MR sequences and in surrounding normal-appearing white matter in the chronic phase, and this NAA decrease corresponds to the axonal and mild neuronal loss.[199] In addition, the fact that NAA levels may be normal in the acute phase of MS suggests that the axons in these cerebral regions have not yet sustained permanent damage, whereas in the chronic phase, when axonal loss has occurred, NAA levels are decreased.[38] Free mobile lipids and "marker peaks" may also be seen in MR spectra in the chronic phase in MS.[38]

Because MRS provides valuable insight into the various stages of the evolution of MS plaques and the physiologic and metabolic changes associated with this evolution, in the near future it may also provide a reliable means of effectively monitoring responses to new therapeutic interventions. A recent study has already explored serial spectroscopic changes in active MS plaques during pharmacologic intervention.[142] These interventions may be designed to target particular stages in the development and maturation of these plaques and thus may prevent progression of the disease.

Other Applications of Proton Magnetic Resonance Spectroscopy in the Central Nervous System

Other CNS applications of proton MRS include the study of psychiatric diseases, upper motor neuron disease (e.g., amyotrophic lateral sclerosis [ALS]), Huntington's disease, and parkinsonian syndromes, among other clinical entities.

In patients with schizophrenia, the most consistent findings include decreased NAA levels in the temporal lobes.[116]

In bipolar affective disorder, elevated Cho, NAA, and MI levels in the basal ganglia as well as elevated levels of glutamate (Glu) in the parietal lobes have been described.[37, 212]

Children with attention deficit hyperactivity disorder (ADHD) demonstrate abnormally elevated NAA/Cr, Glu/Cr, and Cho/Cr ratios in the frontal lobes when compared with age-matched controls.[37]

In patients with ALS, the NAA/Cr ratio is significantly decreased in the motor and premotor cortices, and similar decreases are present in the brain stem.[21, 59]

In Huntington's disease, a reduced NAA/Cho ratio is present in both the basal ganglia and the cerebral cortex, and Lac elevations in these areas may also be present.[114, 199]

MRS evaluation of the parkinsonian syndromes has revealed typical absence of metabolic abnormalities in the basal ganglia in idiopathic Parkinson's disease, as opposed to reductions in the basal ganglia NAA/Cr and NAA/Cho ratios in other parkinsonian syndromes such as progressive supranuclear palsy and corticobasal degeneration.[199]

Certainly, the range of applications of proton MRS in the diagnosis and therapeutic monitoring of CNS disease will continue to grow as clinicians become more aware of the tremendous clinical potential of this imaging technique.

Phosphorus Magnetic Resonance Spectroscopy

Although much work has been performed to date utilizing ^{31}P MRS, applications to the CNS have constituted only a small fraction of this work; applications involving muscle tissue, liver, heart, and even other organs have been studied. Since a thorough discussion of phosphorus MRS is beyond the scope of this chapter and since the overall clinical utility of this modality is much lower than that of proton MRS because of a decreased signal-to-noise ratio and poorer spatial resolution, only a brief introduction to its applications to the study of the brain is provided.

The seven major metabolite peaks that can be detected in phosphorus MR spectra of the brain include the following[116]:

- Three peaks of ATP, seen at approximately −7.8, −16.3, and −2.7 ppm (known as alpha, beta, and gamma ATP peaks, respectively)
- Phosphocreatine (PCr) peak, seen at 0 ppm
- Phosphodiester (PDE) compounds peak, seen at 2.6 ppm
- Inorganic phosphate (Pi) peak, seen at 4.9 ppm
- Phosphomonoester (PME) compounds peak, seen at 6.5 ppm

All of these are markers of energy utilization and transfer within the cells, and levels of these compounds are affected by intracellular energy balance. PCr serves as a high-energy phosphate storage compound in brain and muscle tissue, whereas PME and PDE compounds are found in membrane phospholipids and are involved in cell membrane synthesis and degradation. Elevations in PME compounds have been noted in cases of rapid cell membrane synthesis, such as in tumors and in normal developing infant brain (levels of PDE compounds are low in infants). Levels of PME compounds decrease whereas PDE compounds increase from birth to approximately 3 years of age, when these levels stabilize.

The chemical shift of the Pi peak relative to the PCr peak has been used to determine intracellular pH, since it is pH-dependent. Multiple studies have shown that the pH of normal brain varies from 6.95 to 7.03.[6, 31, 93, 103, 106, 115, 224] Little variation in pH between gray and white matter is noted, and brain tumors consistently demonstrate elevations in pH relative to normal brain tissue.[31, 115]

Several studies have shown that tumor differentiation based on tissue pH is not possible.[6, 31, 93, 224] Findings regarding alteration of the concentrations of the metabolites PCr and Pi in gliomas have been inconsistent and inconclusive.[115] However, PDE is decreased in all gliomas relative to normal brain tissue, and its levels are higher in patients with GBM than in those with lower-grade tumors.[6, 103] In addition, markedly elevated PME levels have been described in GBM.[6, 31, 93, 171, 211] In addition, both the PME:ATP and PDE:ATP ratios tend to be elevated in glial tumors, particularly in GBM.[31, 115, 201] Higher-grade tumors also demonstrate relatively elevated PME peaks and relatively decreased PDE peaks, which probably signify increased cell turnover.[115]

Studies utilizing ^{31}P MRS in patients with epilepsy have shown ictal increases in Pi and Lac and decreases in PCr and pH in TLE.[120, 216, 260] Postictally, pH is noted to increase with development of alkalosis prior to Lac normalization.[120, 219] Interictal increased pH in the temporal lobe ipsilateral to the seizure onset has been noted in adults with TLE.[223] In addition, ipsilaterally increased Pi and decreased PME without significant differences in other metabolites have been noted in TLE.[105, 134, 223] In neonates, Younkin and coworkers have noted a 50% decrease in the PCr/Pi ratio in the seizure region with reestablishment of normal ratio postictally.[261] Studies of frontal lobe epilepsy have shown elevated pH and decreased PME in the affected frontal lobe.[130]

Additional applications of ^{31}P MRS have been described, particularly in pediatric neuroradiology. These and additional applications of phosphorus MRS, undoubtedly, will continue to evolve in the near future in light of the unique metabolic information that can be provided by this physiologic MR modality.

Other Nuclei and Functional Magnetic Resonance Spectroscopy

Spectroscopy using nuclei other than ^{1}H and ^{31}P has been performed for the study of CNS disease. The nuclei that have been used for this purpose include carbon 13 (^{13}C), sodium 23 (^{23}Na), and fluorine 19 (^{19}F). However, since none of these nuclei has been used widely for clinical applications, they are not discussed in this chapter.

Another exciting research application of MRS is functional MRS, which enables evaluation of temporal changes in metabolite concentrations during visual and auditory stimulation or performance of language tasks.[195] A special fast spectroscopic imaging technique, called proton echo-planar spectroscopic imaging (PEPSI), has been used by Richards and colleagues to study language activation during performance of a silent verb generation task.[190] In-

creases in Lac and Cr have been noted in the left temporal lobe during this language task, and transient elevation of Lac has also been noted during visual and auditory stimulation in the respective sensory cortices.[190, 195] Functional MRS is a promising new method for studying brain activation that may complement other techniques, such as functional MRI, magnetoencephalography, and PET, which are currently in widespread use for the study of transient physiologic changes in the brain.

References

1. Achten E: Aspects of proton MR spectroscopy in the seizure patient. Neuroimaging Clin North Am 8:849–862, 1998.
2. Achten E, Santens P, Boon P, et al: Single-voxel proton MR spectroscopy and positron emission tomography for lateralization of refractory temporal lobe epilepsy. AJNR Am J Neuroradiol 19: 1–8, 1998.
3. Allen K, Busza AL, Crockard HA, et al: Acute cerebral ischaemia: Concurrent changes in cerebral blood flow, energy metabolites, pH, and lactate measured with hydrogen clearance and ^{31}P and ^{1}H nuclear magnetic resonance spectroscopy: III. Changes following ischaemia. J Cereb Blood Flow Metab 8:816–821, 1988.
4. Ando K, Ishikura R, Morikawa T, et al: Regional differences of in vivo proton MR spectroscopy in developing human brain. Nippon Igaku Hoshasen Gakkai Zasshi 60:199–204, 2000.
5. Arnold DL, Matthews PM, Francis GS, Antel JP: Proton magnetic resonance spectroscopy of human brain in vivo in the evaluation of multiple sclerosis: Assessment of the load of the disease. Magn Reson Med 14:154–159, 1990.
6. Arnold DL, Emrich JF, Shoubridge EA, et al: Characterization of astrocytomas, meningiomas, and pituitary adenomas by phosphorus magnetic resonance spectroscopy. J Neurosurg 74:447–453, 1991.
7. Arnold DL, Matthews PM, Francis GS, et al: Proton magnetic resonance spectroscopic imaging for metabolic characterization of demyelinating plaques. Ann Neurol 31:235–241, 1992.
8. Austin SJ, Connelly A, Gadian DG, et al: Localized ^{1}H NMR spectroscopy on Canavan's disease: A report of two cases. Magn Reson Med 19:439–445, 1991.
9. Babb TL, Brown WJ: Pathological findings in epilepsy. In Engel J Jr (ed): Surgical Treatment of the Epilepsies. New York, Raven Press, 1987, pp 511–540.
10. Barker PB, Gillard JH, van Ziji PCM, et al: Acute stroke: Evaluation with serial proton MR spectroscopic imaging. Radiology 192:723–732, 1994.
11. Barkovich AJ, Westmark K, et al: Perinatal asphyxia: MR findings in the first 10 days. AJNR Am J Neuroradiol 16:427–438, 1995.
12. Barkovich AJ: Pediatric Neuroimaging, 2nd ed. Philadelphia, Lippincott-Raven, 1996, pp 47–52.
13. Barkovich AJ, Baranski K, Vigneron D, et al: Proton MR spectroscopy for the evaluation of brain injury in asphyxiated term neonates. AJNR Am J Neuroradiol 20:1399–1405, 1999.
14. Barkovich AJ: Pediatric Neuroimaging, 3rd ed. Philadelphia, Lippincott Williams & Wilkins, 2000, pp 55–59, 168, 199–202.
15. Bendszus M, Warmuth-Metz M, Klein R, et al: MR spectroscopy in gliomatosis cerebri. AJNR Am J Neuroradiol 21:375–380, 2000.
16. Benuck M, D'Adamo JAF: Acetyl transport mechanisms: Metabolism on *N*-acetyl-L-aspartic acid in the non-nervous tissues of the rat. Biochem Biophys Acta 152:611–618, 1968.
17. Berkelbach van der Sprenkel JW, Luyten PR, et al: Cerebral lactate detected by regional proton magnetic resonance spectroscopy in a patient with cerebral infarction. Stroke 19:1556–1560, 1988.
18. Birken DL, Oldendorf WH: *N*-acetyl-L-aspartic acid: A literature review of a compound prominent in ^{1}H-NMR spectroscopic studies of brain. Neurosci Biobehav Rev 13:23–31, 1989.
19. Bizzi A, Movsas B, Tedeschi G, et al: Response of non-Hodgkin lymphoma to radiation therapy: Early and long-term assessment with H-1 spectroscopic imaging. Radiology 194:271–276, 1995.
20. Bloch F, Hansen WW, Packard ME: Nuclear induction. Phys Rev 69:127, 1946.
21. Bonavita S, Di Salle F, Tedeschi G: Proton MRS in neurological disorders. Eur J Radiol 30:125–131, 1999.
22. Bottomley PA, Hart HR, Edelstein WA, et al: Anatomy and metabolism of the normal human brain studied by magnetic resonance at 1.5 Tesla. Radiology 150:441–446, 1984.
23. Bottomley PA, Edelstein WA, Foster TH, Adams WA: In vivo solvent-suppressed localized hydrogen nuclear magnetic resonance (NMR): A new window to metabolism? Proc Natl Acad Sci U S A 82:2148–2152, 1985.
24. Bottomley PA: Spatial localization in NMR spectroscopy in vivo. Ann N Y Acad Sci 508:376–385, 1987.
25. Brand A, Richter-Landsberg C, Leibfritz D: Multinuclear NMR studies on the energy metabolism of glial and neuronal cells. Dev Neurosci 15:289–98, 1993.
26. Brown TR, Kincaid BM, Ugurbil K: Chemical shift imaging in 3 dimensions. Proc Natl Acad Sci U S A 79:3523–3526, 1982.
27. Bruhn H, Frahm J, Gyngell ML, et al: Noninvasive differentiation of tumors with use of localized H-1 MR spectroscopy in vivo: Initial experience in patients with cerebral tumors. Radiology 172: 541–548, 1989.
28. Bruhn H, Frahm J, Gyngell ML, et al: Cerebral metabolism in man after acute stroke: New observations using localized proton NMR spectroscopy. Magn Reson Med 9:126–131, 1989.
29. Burri R, Steffen C, Herschkowitz N: *N*-acetyl-L-aspartate is a major source of acetyl groups for lipid synthesis during rat brain development. Dev Neurosci 13:403,1991.
30. Burtscher IM, Skagerberg G, Geijer B, et al: Proton MR spectroscopy and preoperative diagnostic accuracy: An evaluation of intracranial mass lesions characterized by stereotactic biopsy findings. AJNR Am J Neuroradiol 21:84–93, 2000.
31. Cadoux-Hudson TA, Blackledge MJ, Rajagopalan B, et al: Human primary brain tumor metabolism in vivo: A phosphorus magnetic resonance spectroscopy study. Br J Cancer 60:430–436, 1989.
32. Cady EB, Costello AM, Dawson MJ: Noninvasive investigation of cerebral metabolism in newborn infants by phosphorus nuclear magnetic resonance spectroscopy. Lancet i:1059–1063, 1983.
33. Castillo M, Green C, Kwock L, et al: Proton MR spectroscopy in patients with neurofibromatosis type I: Evaluation of hamartomas and clinical correlation. AJNR Am J Neuroradiol 16:141–147, 1995.
34. Castillo M, Kwock L, Green C: MELAS syndrome: Imaging and proton MR spectroscopic findings. AJNR Am J Neuroradiol 16: 233–239, 1995.
35. Castillo M, Kwock L, Mukherji SK: Clinical applications of proton MR spectroscopy. AJNR Am J Neuroradiol 17:1–15, 1996.
36. Castillo M, Kwock L: Proton MR Spectroscopy of common brain tumors. Neuroimaging Clin North Am 8:733–752, 1998.
37. Castillo M, Kwock L, Courvoisie HE, et al: Proton MR spectroscopy in psychiatric and neurodevelopmental childhood disorders: Early experience. Neuroimaging Clin North Am 8:901–912, 1998.
38. Castillo M, Kwock L, Scatliff J, Mukherji SK: Proton MR spectroscopy in neoplastic and non-neoplastic brain disorders. Magn Res Imaging Clin North Am 6:1–20, 1998.
39. Cecil KM, Lenkinski RE: Proton MR spectroscopy in inflammatory and infectious brain disorders. Neuroimaging Clin North Am 8: 863–880, 1998.
40. Cecil KM: Technical Aspects of Performing and Interpreting Proton MR spectroscopy (syllabus, Advanced Imaging Symposium: Preparing the neuroradiologist for the new millennium, pp 29–36). Paper presented at Annual Meeting of the American Society of Neuroradiology, April 2000, Atlanta.
41. Cendes F, Andermann F, Preul MC, et al: Lateralization of temporal lobe epilepsy based on regional metabolic abnormalities in proton magnetic resonance spectroscopic images. Ann Neurol 35:211–216, 1994.
42. Cendes F, Caramano Z, Andermann F, et al: Proton magnetic resonance spectroscopic imaging and magnetic resonance imaging volumetry in the lateralization of temporal lobe epilepsy: A series of 100 patients. Ann Neurol 42:737–746, 1997.
43. Ceodan S, Parrilla R, Santoro J, et al: H-1 NMR detection of cerebral myo-inositol. FEBS Lett 187:167–172, 1985.
44. Chan Y-l, Yeung DKW, Leung S-F, et al: Proton magnetic resonance spectroscopy of late delayed radiation-induced injury of the brain. J Magn Reson Imaging 10:130–137, 1999.
45. Chang L: In vivo magnetic resonance spectroscopy in HIV and HIV-related brain diseases. Rev Neurosci 6:365–378, 1995.
46. Chang L, Ernst T: MR spectroscopy and diffusion-weighted MR imaging in focal brain lesions in AIDS. Neuroimaging Clin North Am 7:409–426, 1997.

47. Chang L, Ernst T, Tornatore C, et al: Metabolite abnormalities in progressive multifocal leukoencephalopathy by proton magnetic resonance spectroscopy. Neurology 48:836–845, 1997.
48. Chang L, Ernst T, Leonido-Yee M, et al: Cerebral metabolite abnormalities correlate with clinical severity of HIV-1 cognitive motor complex. Neurology 52:100–108, 1999.
49. Chiang CS, McBride WH, Withers HR: Radiation-induced astrocytic and microglial responses in mouse brain. Radiother Oncol 29:60–68, 1998.
50. Comair YG, Ng T, Xue M, et al: Early post-ictal lactate detection in temporal lobe epilepsy for localization of seizure focus: A chemical shift imaging study (abstract). In Book of Abstracts. San Francisco, Society of Magnetic Resonance in Medicine, 1994, p 401.
51. Confort-Gouny S, Vion-Dury J, Chabrol B, et al: Localized proton magnetic resonance spectroscopy in X-linked adrenoleukodystrophy. Neuroradiology 37:568–575, 1995.
52. Connelly A, Cross J, Gadian D, et al: Magnetic resonance spectroscopy shows increased brain glutamine in ornithine carbamoyl transferase deficiency. Pediatr Res 33:77–81, 1993.
53. Connelly A, Jackson GD, Duncan JS, Gadian DG: Proton MRS in temporal lobe epilepsy. Neurology 44:1411–1417, 1994.
54. Connelly A, Paesschen WV, Porter DA, et al: Proton magnetic resonance spectroscopy in MRI-negative temporal lobe epilepsy. Neurology 51:61–66, 1998.
55. Cortey A, Jarvik JG, Lenkinski RE, et al: Proton MR spectroscopy of brain abnormalities in neonates born to HIV-positive mothers. AJNR Am J Neuroradiol 15:1853–1859, 1994.
56. Cousins JP, Seymour PA, Weaver S, et al: Clinical differentials of CNS tumors and radiation necrosis using single voxel H1-MRS correlated with pathology. Proceedings of the 5th Annual Scientific Meeting of the International Society for Magnetic Resonance in Medicine, 1997, Vancouver, p 1126.
57. Crockard HL, Gadian DG, Frackowiak SJ, et al: Acute cerebral ischaemia: Concurrent changes in cerebral blood flow, energy metabolites, pH, and lactate measured with hydrogen clearance and ^{31}P and ^{1}H nuclear magnetic resonance spectroscopy: II. Changes during ischaemia. J Cereb Blood Flow Metab 7:394–402, 1987.
58. Cross JH, Connelly A, Jackson GD, et al: Proton magnetic resonance spectroscopy in children with temporal lobe epilepsy. Ann Neurol 39:107–113, 1996.
59. Cwik VA, Hanstock CC, Allen PS, et al: Estimation of brainstem neuronal loss in amyotrophic lateral sclerosis with in vivo proton magnetic resonance spectroscopy. Neurology 50:72–77, 1998.
60. D'Adamo AF, Jr, Smith JC, Woiler C: The occurrence of *N*-acetylaspartate amidohydrolase (aminoacylase II) in the developing rat. J Neurochem 20:1275–1278, 1973.
61. Davie CA, Hawkins CP, Barker GJ, et al: Serial proton magnetic resonance spectroscopy in acute multiple sclerosis lesions: Part 1. Brain 117:49–58, 1994.
62. Davie CA, Barker GJ, Webb S, et al: Persistent functional deficit in multiple sclerosis and autosomal dominant cerebellar ataxia is associated with axon loss: Part 6. Brain 118:1583–1592, 1995.
63. Demaerel P, Johannik K, van Heche P, et al: Localized H-1 NMR spectroscopy in fifty cases of newly diagnosed intracranial tumors. J Comput Assist Tomogr 15:67–76, 1991.
64. De Stefano N, Matthews P, Ford B, et al: Short-term dichloroacetate treatment improves indices of cerebral metabolism in patients with mitochondrial disorders. Neurology 45:1193–1198, 1995.
65. Diezel P, Martin K: Die Ahornsirupkrankheit mit familarem Befall. Virchows Arch Pathol Anat 337:425–445, 1964.
66. Duijn JH, Matson GB, Maudsley AA, et al: Human brain infarction: Proton MR spectroscopy. Radiology 183:711–718, 1992.
67. Ende J, Scatliff JH, Powers S, et al: Spectral proton and P-31 MR spectroscopy patterns of treated human brain tumors. Paper presented at the Annual Meeting of the Society of Magnetic Resonance in Medicine, 1992.
68. Ende G, Laxer K, Knowlton R, et al: Temporal lobe epilepsy: Bilateral hippocampal metabolite changes revealed at proton MR spectroscopic imaging. Radiology 202:809–817, 1997.
69. Ernst T, Chang L, Melchor R, et al: Frontotemporal dementia and early Alzheimer disease: Differentiation with frontal lobe H-1 MR spectroscopy. Radiology 203:829–836, 1997.
70. Felber SR, Aichner FT, Sauter R, et al: Combined magnetic resonance imaging and proton magnetic resonance spectroscopy of patients with acute stroke. Stroke 23:1106–1110, 1992.
71. Felber SR, Sperl W, Chemelli A, et al: Maple syrup urine disease: Metabolic decompensation monitored by proton magnetic resonance imaging and spectroscopy. Ann Neurol 33:396–401, 1993.
72. Fenstermacher MJ, Narayana PD: Serial proton magnetic resonance spectroscopy of ischemic brain injury in humans. Radiology 25: 1034–1039, 1990.
73. Fu L, Matthews PM, De Stefano N, et al: Imaging axonal damage of normal appearing white matter in multiple sclerosis. Brain 121: 103–113, 1998.
74. Fulham MJ, Bizzi A, Dietz MJ, et al: Mapping of brain tumor metabolites with proton spectroscopic imaging: Clinical relevance. Radiology 185:675–686, 1992.
75. Gadian DF, Connelly A, Duncan JS, et al: ^{1}H magnetic resonance spectroscopy in the investigation of intractable epilepsy. Acta Neurol Scand Suppl 152:116–121, 1994.
76. Garcia PA, Laxer KD, van der Grond J, et al: Proton magnetic resonance spectroscopic imaging in patients with frontal lobe epilepsy. Ann Neurol 37:279–281, 1995.
77. Gideon P, Henriksen O, Sperling B, et al: Early time course of *N*-acetylaspartate, creatine, and phosphocreatine, and compounds containing choline in the brain after acute stroke: A proton magnetic resonance spectroscopy study. Stroke 23:1566–1572, 1992.
78. Gideon P, Sperling B, Arlien-Soborg P, et al: Long-term follow-up of cerebral infarction patients with proton magnetic resonance spectroscopy. Stroke 25:967–973, 1994.
79. Gill SS, Thomas DGT, Van Bruggen N, et al: Proton MR spectroscopy of intracranial tumors: In vivo and in vitro studies. J Comput Assist Tomogr 14:497–504, 1990.
80. Gillard JH, Barker PB, van Zijl PCM, et al: Proton MR spectroscopy in acute middle cerebral artery stroke. AJNR Am J Neuroradiol 17: 873–886, 1996.
81. Gonen O, Wang ZJ, Viswanathan AK, et al: Three-dimensional multivoxel proton MR spectroscopy of the brain in children with neurofibromatosis type I. AJNR Am J Neuroradiol 20:1333–1341, 1999.
82. Gonen O, Catalaa I, Babb JS, et al: Total brain *N*-acetylaspartate: A new measure of disease load in MS. Neurology 54:15–19, 2000.
83. Grachev ID, Apkarian AV: Chemical heterogeneity of the living human brain: A proton MR spectroscopy study on the effects of sex, age, and brain region. Neuroimage 11(5 Part 1):554–563, 2000.
84. Graham GD, Blamire AM, Howseman AM, et al: Proton magnetic resonance spectroscopy of cerebral lactate and other metabolites in stroke patients. Stroke 23:333–340, 1992.
85. Graham GD, Blamire AM, Rothman DL, et al: Early temporal variation of cerebral metabolites after human stroke. Stroke 24: 1891–1896, 1993.
86. Graham GD, Kalvach P, Blamire AM, et al: Clinical correlates of proton magnetic resonance spectroscopy findings after acute cerebral infarction. Stroke 26:225–229, 1995.
87. Graham SH, Meyerhoff DJ, Bayne L, et al: Magnetic resonance spectroscopy of *N*-acetylaspartate in hypoxic-ischemic encephalopathy. Ann Neurol 35:490–494, 1994.
88. Grand S, Passaro G, Ziegler A, et al: Necrotic tumor versus brain abscess: Importance of amino acids detected at ^{1}H MR spectroscopy—initial results. Radiology 213:785–793, 1999.
89. Grodd W, Krageloh-Mann W, Klose U, et al: Metabolic and destructive brain disorders in children: Findings with localized proton MR spectroscopy. Radiology 181:173–181, 1991.
90. Groenendaal F, Veenhoven RH, et al: Cerebral lactate and *N*-acetylaspartate/choline ratios in asphyxiated full-term neonates demonstrated in vivo using proton magnetic resonance spectroscopy. Pediatr Res 35:148–151, 1994.
91. Grossmann RI, Lenkinski RE, Ramer KN, et al: MR proton spectroscopy in multiple sclerosis. AJNR Am J Neuroradiol 13:1535–1543, 1992.
92. Harada M, Tanouchi M, Arai K, et al: Therapeutic efficacy of a case of pyruvate dehyrogenase complex deficiency monitored by localized proton magnetic resonance spectroscopy. Magn Reson Imaging 14:129–133, 1996.
93. Heindel W, Bunke J, Glathe S, et al: Combined ^{1}H-MR imaging and localized ^{31}P-spectroscopy of intracranial tumors in 43 patients. J Comput Assist Tomogr 12:907–916, 1988.
94. Henry RG, Vigneron DB, Fischbein NJ, et al: Comparison of relative cerebral blood volume and proton spectroscopy in patients with treated gliomas. AJNR Am J Neuroradiol 21:357–366, 2000.

95. Hetherington H, Kuzniecky R, Pan J, et al: Proton nuclear magnetic resonance spectroscopic imaging of human temporal lobe epilepsy at 4.1 T. Ann Neurol 38:396–404, 1995.
96. Hida K: In vivo ^{1}H and ^{31}P NMR spectroscopy of the developing rat brain. Hokkaido J Med Sci 67:272–281, 1992.
97. Holshouser BA, Ashwal S, Luh GY, et al: Proton MR spectroscopy after acute nervous system injury: Outcome prediction in neonates, infants, and children. Radiology 202:487–496, 1997.
98. Holzer T, Herholz K, Jeske J, et al: FDG-PET as a prognostic indicator in radiochemotherapy of glioblastoma. J Comput Assist Tomogr 17:681–687, 1993.
99. Hope PL, Costello AM, Cady EB, et al: Cerebral energy metabolism studied with phosphorus NMR spectroscopy in normal and birth-asphyxiated infants. Lancet ii:366–370, 1984.
100. Houkin K, Kamada K, Kamiyama H, et al: Longitudinal changes in proton magnetic resonance spectroscopy in cerebral infarction. Stroke 24:1316–1321, 1993.
101. Hoult DI, Busby SJW, Gadian DG, et al: Observation of tissue metabolites using phosphorus nuclear magnetic resonance. Nature 252:285–287, 1974.
102. Howe FA, Maxwell RJ, Saunders DE, et al: Proton spectroscopy in vivo. Magn Reson Q 9:31–59, 1993.
103. Hubesch B, Sappey-Marinier D, Roth K, et al: P-31 MR spectroscopy of normal human brain and brain tumors. Radiology 174: 401–409, 1990.
104. Hueppi PS, Posse S, Lazeyras F, et al: Developmental changes in 1H spectroscopy in human brain. In Lafeber HN (ed): Fetal and Neonatal Physiological Measurements. New York, Elsevier, 1991, pp 33–41.
105. Hugg JW, Laxer KD, Matson GB, et al: Lateralization of human focal epilepsy by ^{31}P magnetic resonance spectroscopic imaging. Neurology 42:2011–2018, 1992.
106. Hugg JW, Matson GB, Twieg DB, et al: Phosphorus-31 MR spectroscopic imaging (MRSI) of normal and pathological human brains. Magn Reson Imaging 10:227–243, 1992.
107. Huppi P, Posse S, et al: Magnetic resonance in preterm and term newborns: H spectroscopy in developing human brain. Pediatr Res 30:574–578, 1991.
108. Huppi PS, Fusch C, Boesch C, et al: Regional metabolic assessment of human brain during development by proton magnetic resonance spectroscopy in vivo and by high-performance liquid chromatography/gas chromatography in autopsy tissue. Pediatr Res 37:145–150, 1995.
109. Husted CA, Goodin DS, Hugg JW, et al: Biochemical alterations in multiple sclerosis lesions and normal-appearing white matter detected by in vivo ^{31}P and ^{1}H spectroscopic imaging. Ann Neurol 36: 157–165, 1994.
110. Hwang J-H, Graham GD, Behar KL, et al: Short echo time proton magnetic resonance spectroscopic imaging of macromolecule and metabolite signal intensities in the human. Magn Reson Med 35: 633–639, 1996.
111. Hwang J-H, Egnaczyk GF, Ballard E, et al: Proton MR spectroscopic characteristics of pediatric pilocytic astrocytomas. AJNR Am J Neuroradiol 19:535–540, 1998.
112. Jarvik JG, Lenkinski RE, Saykin AJ, et al: Proton spectroscopy in asymptomatic HIV-infected adults: Initial results in a prospective cohort study. J Acquir Immune Defic Syndr Hum Retrovirol 13: 247–253, 1996.
113. Jaysundar R, Bakshi A, Singh VP, et al: Diagnostic potential of proton MRS in differentiating between tumor recurrence and radiation necrosis? Paper presented at the Fifth Annual Scientific Meeting of the International Society for Magnetic Resonance in Medicine, 1997, Vancouver, BC, p 1142.
114. Jenkins BG, Koroshetz WJ, Beal MF, Rosen BR: Evidence for impairment of energy metabolism in vivo in Huntington's disease using localized ^{1}H NMR spectroscopy. Neurology 43:2689–2695, 1993.
115. Kaibara T, Tyson RL, Sutherland GR: Human cerebral neoplasms studied using MR spectroscopy: A review. Biochem Cell Biol 76: 477–486, 1998.
116. Kegeles LS, Humaran TJ, Mann JJ: In vivo neurochemistry of the brain in schizophrenia as revealed by magnetic resonance spectroscopy. Biol Psychiatry 44:382–398, 1998.
117. Kim CK, Alavi JB, Alavi A, et al: New grading system of cerebral gliomas using positron emission tomography with F-18 fluorodeoxyglucose. J Neurooncol 10:85–91, 1991.
118. Kimura H, Fujii Y, Matsuda T, et al: Metabolic alterations in the neonate and infant brain during development: Evaluation with proton MR spectroscopy. Radiology 194:483–489, 1995.
119. Kimura S, Ohtuki N, Nezu A, et al: Clinical and radiologic improvements in mitochondrial encephalomyelopathy following sodium dichloroacetate therapy. Brain Dev 19:535–540, 1997.
120. King D, Baltuch GH: Magnetic resonance imaging and temporal lobe epilepsy. Acta Neurol Scand 98:217–223, 1998.
121. Kinoshita Y, Kajiwara H, Yokota A, Koga Y: Proton magnetic resonance spectroscopy of brain tumors: An in vitro study. Neurosurgery 35:606–614, 1994.
122. Kornfeld M, Woodfin B, Papile L, et al: Neuropathology of ornithine carbamyl transferase deficiency. Acta Neuropathol 65:261–264, 1985.
123. Koutcher JA, Burt CT: Principles of nuclear magnetic resonance. J Nucl Med 25:101–111, 1984.
124. Kreis R, Farrow NA, Ross BD: Localized ^{1}H NMR spectroscopy in patients with chronic hepatic encephalopathy: Analysis of changes in cerebral glutamine, choline and inositols. NMR Biomed 4:109–116, 1991.
125. Kreis R, Ross BD: Cerebral metabolic disturbances in patients with subacute and chronic diabetes mellitus: Detection with proton MR spectroscopy. Radiology 184:123–130, 1992.
126. Kreis R, Ross BD, Farrow NA, Ackerman Z: Metabolic disorders of the brain in chronic hepatic encephalopathy detected with H-1 MR spectroscopy. Radiology 182:19–27, 1992.
127. Kreis R, Ernst T, Ross BD: Development of the human brain: In vivo quantification of metabolite and water content with proton magnetic spectroscopy. Magn Reson Med 30:424–437, 1993.
128. Kreis R, Ernst T, Ross BD: Absolute quantitation of water and metabolites in the human brain: II. Metabolite concentrations. J Magn Reson 102:9–15, 1993.
129. Kugel H, Heindel W, Ernestus RI, et al: Human brain tumors: Spectral patterns detected with localized H-1 MR spectroscopy. Radiology 183:701–709, 1992.
130. Kuzniecky R, Elgavish GA, Hetherington HP, et al: In vivo ^{31}P nuclear magnetic resonance spectroscopy of human temporal lobe epilepsy. Neurology 42:1586–1590, 1992.
131. Kuzniecky R, Hugg JW, Hetherington H, et al: Relative utility of ^{1}H spectroscopic imaging and hippocampal volumetry in the lateralization of mesial temporal lobe epilepsy. Neurology 51:66–71, 1998.
132. Kwock L: Localized MR spectroscopy. Neuroimaging Clin North Am 8:713–731, 1998.
133. Lam WWM, Wang ZJ, Zhao H, et al: ^{1}H MR spectroscopy of the basal ganglia in childhood: A semiquantitative analysis. Neuroradiology 40:315–232, 1998.
134. Laxer KD, Hubesch B, Sappey-Marinier D, Weiner MW: Increased pH and inorganic phosphate in temporal seizure foci demonstrated by ^{31}P MRS. Epilepsia 33:618–623, 1993.
135. Lee JH, Arcinue E, Ross BD: Organic osmolytes in the brain of an infant with hypernatremia. N Engl J Med 331:439–442, 1994.
136. Leth H, Toft PB, Pryds O, et al: Brain lactate in preterm and growth-retarded neonates. Acta Pediatr 84:495–499, 1995.
137. Li LM, Cendes F, Bastos AC, et al: Neuronal metabolic dysfunction in patients with cortical developmental malformations: A proton magnetic resonance spectroscopic imaging study. Neurology 50: 755–759, 1998.
138. Lichter T, Dohrman GJ, Gets GS: Respiratory deficiency and increased glycolysis in benign human tumors. Surg Forum 35:486–488, 1994.
139. Lowry OH, Berger SJ, Chi M-Y, et al: Diversity of metabolic patterns in human brain tumors: I. High energy phosphate compounds and basic composition. J Neurochem 29:959–977, 1977.
140. Lu D, Pavlakis SG, Frank Y, et al: Proton MR spectroscopy of the basal ganglia in healthy children and children with AIDS. Radiology 199:423–428, 1996.
141. Luyten PR, Marien AJH, Heindel W, et al: Metabolic imaging of patients with intracranial tumors: H-1 MR spectroscopic imaging and PET. Radiology 176:791–799, 1990.
142. Mader I, Roser W, Kappos L, et al: Serial proton MR spectroscopy of contrast-enhancing multiple sclerosis plaques: Absolute metabolic values over 2 years during a clinical pharmacological study. AJNR Am J Neuroradiol 21:1220–1227, 2000.
143. Marks HG, Caro PA, Wang Z, et al: Use of computed tomography,

magnetic resonance imaging, and localized [1]H magnetic resonance spectroscopy in Canavan's disease: A case report. Ann Neurol 30: 106–110, 1991.
144. Matalon R, Michals K, Sevesta D, et al: Asparto-acylase deficiency and *N*-acetylaspartic aciduria in patients with Canavan's disease. Am J Med Genet 20:463–471, 1988.
145. Matthews PM, Francis G, Antel J, Arnold DL: Proton magnetic resonance spectroscopy for metabolic characterization of plaques in multiple sclerosis Neurology 41:1251–1256, 1991 (correction in Neurology 41:1828, 1991).
146. Matthews PM, Andermann F, Silver K, et al: Proton MR spectroscopic characterization of differences in regional brain metabolic abnormalities in mitochondrial encephalomyopathies. Neurology 43: 2484–2490, 1993.
147. Matthews PM, De Stefano N, Narayanan S, et al: Putting magnetic resonance spectroscopy studies in context: Axonal damage and disability in multiple sclerosis. Semin Neurol 18:327–336, 1998.
148. Maudsley AA, Twieg DB, Sappey-Marinier D, et al: Spin echo [31]P spectroscopic imaging in the human brain. Magn Reson Med 14: 415–422, 1990.
149. Menon DK, Baudouin CJ, Tomlinson D, et al: Proton MR spectroscopy and imaging of the brain in AIDS: Evidence of neuronal loss in regions that appear normal with imaging. J Comput Assist Tomogr 14:882–885, 1990.
150. Meyerand ME, Pipas JM, Mamourian A, et al: Classification of biopsy-confirmed brain tumors using single-voxel MR spectroscopy. AJNR Am J Neuroradiol 20:117–123, 1999.
151. Meyerhoff DJ, Bloomer C, Cardenas V, et al: Elevated subcortical choline metabolites in cognitively and clinically asymptomatic HIV+ patients. Neurology 52:995–1003, 1999.
152. Michaelis T, Helms KD, Merboldt W, et al: First observation of scyllo-inositol in proton NMR spectra of human brain in vitro and in vivo. Paper presented at Annual Meeting of the Society of Magnetic Resonance in Medicine, Berlin, 1992.
153. Michaelis T, Merboldt KD, Bruhn H, et al: Absolute concentrations of metabolites in the adult human brain in vivo: Quantification of localized proton MR spectra. Radiology 187:219–227, 1993.
154. Michaelis T, Videen J, Linsey MS, et al: Cerebral abnormalities in end stage renal disease. Paper presented at the Second Annual Meeting of the Society of Magnetic Resonance in Medicine, 1994, San Francisco, p 306.
155. Miller B: A review of chemical issues in [1]H NMR spectroscopy: *N*-acetyl-aspartate, creatine and choline. NMR Biomed 4:47–52, 1991.
156. Miller BL, Moats R, Shonk T, et al: Alzheimer disease: Depiction of increased cerebral myo-inositol with proton MR spectroscopy. Radiology 187:433–437, 1993.
157. Miyake M, Kakimoto Y: Developmental changes of *N*-acetyl-L-aspartic acid, *N*-acetyl-L-aspartylglutamic acid, and beta-citryl-L-glutamic acid in different brain regions and spinal cords of rat and guinea pig. J Neurochem 37:1064–1067, 1981.
158. Moats RA, Ernst T, Kreis R, et al: Well-localized standardized, quantitized short TE [1]H MRS permits new diagnostic accuracy in patients with Alzheimer disease. TAMU Newsletter 413:13–14, 1993.
159. Moats RA, Ernst T, Shonk TK, et al: Abnormal cerebral metabolite concentrations in patients with probable Alzheimer disease. Magn Reson Med 32:110–115, 1994.
160. Monsein LH, Mathews VP, Barker PB, et al: Irreversible regional ischemia: Serial MR imaging and proton MR spectroscopy in a nonhuman primate model. AJNR Am J Neuroradiol 14:963–970, 1993.
161. Moon RB, Richards JH: Determination of intracellular pH by [31]P magnetic resonance. J Biol Chem 248:7276–7278, 1973.
162. Moonen CTW, van Zijl PCM, Frank JA, et al: Comparisons of single shot localization methods (STEAM and PRESS) for in vivo proton NMR spectroscopy. NMR Biomed 2:201–208, 1989.
163. Moore GJ: Proton magnetic resonance spectroscopy in pediatric neuroradiology. Pediatr Radiol 28:805–814, 1998.
164. Morantz RA: The management of the patient with low-grade cerebral astrocytomas. In Morantz, RA, Walsh JW (eds): Brain Tumors: A Comprehensive Text. New York, Marcel Dekker, 1994, pp 387–415.
165. Moseley ME, Cohen Y, Mintorovitch J, et al: Early detection of regional ischemia in cats: Comparison of diffusion- and T2-weighted MRI and spectroscopy. Magn Reson Med 14:330–346, 1990.
166. Nagatomo Y, Wick M, Prielmeier F, et al: Dynamic monitoring of cerebral metabolites during and after transient global ischemia in rats by quantitative proton NMR spectroscopy in vivo. NMR Biomed 8: 265–270, 1995.
167. Narayana PA, Doyle TJ, Lai D, Wolinsky JS: Serial proton magnetic resonance spectroscopic imaging, contrast-enhanced magnetic resonance imaging, and quantitative lesion volumetry in multiple sclerosis. Ann Neurol 43:56–71, 1998.
168. Negendank WG, Sauter R, Brown TR, et al: Proton magnetic resonance spectroscopy in patients with glial tumors: A multicenter study. J Neurosurg 84:449–458, 1996.
169. Nelson SJ: MR Spectroscopy in adults: Current and future applications (syllabus, Advanced Imaging Symposium: Preparing the neuroradiologist for the new millennium, pp 37–43). Presented at the American Society of Neuroradiology Annual Meeting, April 2000, Atlanta.
170. Ng TC, Comair YG, Xue M, et al: Temporal lobe epilepsy: Presurgical localisation with proton chemical shift imaging. Radiology 193: 465–472, 1994.
171. Oberhaensli RD, Hilton-Jones D, Bore PJ, et al: Biochemical investigation of human tumors in vivo with phosphorus-31 magnetic resonance spectroscopy. Lancet 2(8497):8–11, 1986.
172. Ott D, Hennig J, Ernst T: Human brain tumors: Assessment with in vivo proton MR spectroscopy. Radiology 186:745–752, 1993.
173. Patronas NJ, Di Chiro G, Kufta C, et al: Prediction of survival in glioma patients by means of positron emission tomography. J Neurosurg 62:816–822, 1985.
174. Peeling J, Wong D, Sutherland GR: Nuclear magnetic resonance study of regional metabolism after forebrain ischemia in rats. Stroke 20:633–640, 1989.
175. Pendlebury ST, Blamire AM, Lee MA, et al: Axonal injury in the internal capsule correlates with motor impairment after stroke. Stroke 30:956–962, 1999.
176. Penrice J, Cady EB, Lorek A, et al: Proton magnetic resonance spectroscopy of the brain in normal preterm and term infants and early changes after perinatal hypoxia-ischemia. Pediatr Res 40:6–14, 1996.
177. Penrice J, Lorek A, Cady EB, et al: Proton magnetic resonance spectroscopy of the brain during acute hypoxia-ischemia and delayed cerebral energy failure in the newborn piglet. Pediatr Res 41:795–802, 1997.
178. Pereira AC, Saunders DE, Doyle VL, et al: Measurement of initial *N*-acetyl aspartate concentration by magnetic resonance spectroscopy and initial infarct volume by MRI predicts outcome of patients with middle cerebral artery territory infarction. Stroke 30:1577–1582, 1999.
179. Pfefferbaum A, Adalsteinsson E, Spielman D, et al: In vivo spectroscopic quantification of the *N*-acetyl moiety, creatine, and choline from large volumes of brain gray and white matter: Effects of normal aging. Magn Res Med 41:276–284, 1999.
180. Poptani H, Gupta RK, Roy R, et al: Characterization of intracranial mass lesions with in vivo proton MR spectroscopy. AJNR Am J Neuroradiol 16:1593–1603, 1995.
181. Posse S, Schuknecht B, Smith ME, et al: Short echo time proton MR spectroscopic imaging. J Comput Assist Tomogr 17:1–14, 1994.
182. Pouwels PJW, Frahm J: Regional metabolite concentrations in human brain determined by quantitative localized proton MRS. Magn Reson Med 39:53–60, 1998.
183. Preul MC, Caramanos Z, Collins DL, et al: Accurate, noninvasive diagnosis of human tumors by using proton magnetic resonance spectroscopy. Nature Med 2:323–325, 1996.
184. Pu Y, Li QF, Zeng CM, et al: Increased detectability of alpha brain glutamate/glutamine in neonatal hypoxic-ischemic encephalopathy. AJNR Am J Neuroradiol 21:203–212, 2000.
185. Purcell EM, Torrey HC, Pound RV: Resonance absorption by nuclear magnetic moments in a solid. Phys Rev 69:37–38, 1946.
186. Radda GK, Bore PJ, Rajagopalan B: Clinical aspects of [31]P NMR spectroscopy. Br Med Bull 40:155–159, 1984.
187. Rakic P, Bourgeois JP, Eckenhoff MF et al: Concurrent overproduction of synapses in diverse regions of the primate cerebral cortex. Science 232:232–235, 1986.
188. Remy C, Grand S, Lai ES, et al: [1]H MRS of human brain abscesses in vivo and in vitro. Magn Reson Med 34:508–514, 1995.
189. Ricci PE: Proton MR spectroscopy in ischemic stroke and other vascular disorders. Neuroimaging Clin North Am 8:881–900, 1998.
190. Richards TL, Dager SR, Panagiotides HS, et al: Functional MR

spectroscopy during language activation: A preliminary study using proton echo-planar spectroscopic imaging (PEPSI). Int J Neuroradiol 3:490, 1997.

191. Richards TL, Dager SR, Posse S: Functional MR spectroscopy of the brain. Neuroimaging Clin North Am 8:823–834, 1998.
192. Rooney WD, Goodkin DE, Schuff N, et al: H MRS of normal appearing white matter in multiple sclerosis. Mult Scler 3:231–237, 1997.
193. Ross BD: Biochemical considerations in ^{1}H spectroscopy. Glutamate and glutamine: Myo-inositol and related metabolites. NMR Biomed 4:59–63, 1991.
194. Ross B, Kreis R, Ernst T: Clinical tool for the 90s: Magnetic resonance spectroscopy and metabolite imaging. Eur J Radiol 14: 128–140, 1992.
195. Ross BD, Jacobson S, Villamil F, et al: Subclinical hepatic encephalopathy: Proton MR spectroscopic abnormalities. Radiology 193: 457–463, 1994.
196. Ross B, Danielsen E, Bluml S: Proton magnetic resonance spectroscopy: The new gold standard for diagnosis of clinical and subclinical hepatic encephalopathy? Dig Dis 14(suppl 1):30–39, 1996.
197. Ross BD, Bluml S, Cowan R, et al: In vivo MR spectroscopy of human dementia. Neuroimaging Clin North Am 8:809–822, 1998.
198. Ross BD: A biochemistry primer for neuroradiologists (syllabus, Advanced Imaging Symposium: Preparing the neuroradiologist for the new millennium, pp 13–27). Paper presented at the Annual Meeting of the American Society of Neuroradiology, April 2000, Atlanta.
199. Rudkin TM, Arnold DL: Proton magnetic resonance spectroscopy for the diagnosis and management of cerebral disorders. Arch Neurol 56:919–926, 1999.
200. Ruggieri PM: Practical MR spectroscopy in pediatric neuroradiology (syllabus, Advanced Imaging Symposium: Preparing the neuroradiologist for the new millennium, pp 45–53). Paper presented at the Annual Meeting of the American Society of Neuroradiology, April 2000, Atlanta.
201. Rutter A, Hugenholtz H, Saunders JK, Smith IC: One-dimensional phosphorus-31 chemical shift imaging of human brain tumors. Invest Radiol 30:359–366, 1995.
202. Salibi N, Brown MA: Clinical MR Spectroscopy. New York, Wiley-Liss, 1998.
203. Salvan AM, Vion-Dury J, Confort-Gouny S, et al: Brain proton magnetic resonance spectroscopy in HIV-related encephalopathy: Identification of evolving metabolic patterns in relation to dementia and therapy. AIDS Res Hum Retroviruses 13:1055–1066, 1997.
204. Sappey-Marinier D, Calabrese G, Hetherington HP, et al: Proton magnetic resonance spectroscopy of the human brain: Applications to normal white matter, chronic infarction, and MRI white matter signal hyperintensities. Magn Reson Med 26:313–327, 1992.
205. Sarchielli P, Presciutti O, Tarducci R, et al: H-MRS in patients with multiple sclerosis undergoing treatment with interferon β-1a: Results of a preliminary study. J Neurol Neurosurg Psychiatry 64:204–212, 1998.
206. Sarchielli P, Presciutti O, Pelliccioli GP, et al: Absolute quantification of brain metabolites by proton magnetic resonance spectroscopy in normal-appearing white matter of multiple sclerosis patients. Brain 121:513–521, 1999.
207. Saunders DE, Howe FA, Van Den Boogaart: Continuing ischemic damage after acute middle cerebral artery infarction in humans demonstrated by short-echo proton spectroscopy. Stroke 26:1007–1013, 1995.
208. Scarabino T, Popolizio T, Bertolino A, Salvolini U: Proton magnetic resonance spectroscopy of the brain in pediatric patients. Eur J Radiol 30:142–153, 1999.
209. Schuff N, Amend D, Ezekiel BA, et al: Changes of hippocampal *N*-acetyl aspartate and volume in Alzheimer's disease: A proton MR spectroscopic imaging and MRI study. Neurology 49:1513–1521, 1997.
210. Scriver C, Kaufman S, Woo S: The hyperphenylalaninemias. In Scriver CR, Beaudet AL, Sly WS, et al (eds): The Metabolic Basis of Inherited Disease. New York, McGraw-Hill, 1989, pp 495–546.
211. Segebarth CM, Baleriaux DF, de Beer R, et al: ^{1}H image-guided localized ^{31}P MR spectroscopy of human brain: Quantitative analysis of ^{31}P MR spectra measured on volunteers and on intracranial tumor patients. Magn Reson Med 11:349–366, 1989.
212. Sharma R, Venkatasubramanian PN, Barany M, et al: Proton MRS of the brain in schizophrenia and affective disorders. Schizophr Res 8:43–49, 1992.
213. Shaw D: The fundamental principles of nuclear magnetic resonance. In Wehrli FW, Shaw D, Kneeland JB (eds): Biomedical Magnetic Resonance Imaging. New York, VCH Publishers, 1988, pp 1–45.
214. Shevell MI, Ashwal S, Novotny E: Proton magnetic resonance spectroscopy: Clinical applications in children with nervous system diseases. Semin Pediatr Neurol 6:68–77, 1999.
215. Shimizu H, Kumabe T, Tominaga T, et al: Noninvasive evaluation of malignancy of brain tumors with proton MR spectroscopy. AJNR Am J Neuroradiol 17:737–747, 1996.
216. Shnall MD, Yoshizaki K, Chance B, Leigh JS: Triple nuclear NMR studies of cerebral metabolism during generalized seizure. Magn Reson Med 6:15–23, 1988.
217. Shonk TK, Moats RA, Gifford P, et al: Probable Alzheimer disease: Diagnosis with proton MR spectroscopy. Radiology 195:65–72, 1995.
218. Shu SK, Ashwal S, Holshouser BA, et al: Prognostic value of ^{1}H MRS in perinatal CNS insults. Pediatr Neurol 17:309–318, 1997.
219. Siesjo BK, von Hanwehr R, Nergelius G, et al: Extra- and intracellular pH in the brain during seizures and in the recovery period following arrest of seizure activity. J Cereb Blood Flow Metab 5: 47–57, 1985.
220. Sijens PE, van Dijk P, Oudkerk M: Correlation between choline level and Gd-DTPA enhancement in patients with brain metastases of mammary carcinomas. Magn Reson Med 32:549–555, 1994.
221. Sijens PE, Knopp MV, Brunetti A, et al: H-1 spectroscopy in patients with metastatic brain tumors: A multicenter study. Magn Reson Med 33:818–826, 1995.
222. Simone IL, Federico F, Tortorella C, et al: Metabolic changes in neuronal migration disorders: Evaluation by combined MRI and proton MR spectroscopy. Epilepsia 40:872–879, 1999.
223. Sitoh Y, Tien RD: Neuroimaging in epilepsy. J Magn Reson Imaging 8:277–288, 1998.
224. Sutton LN, Lenkinski RE, Cohen BH, et al: Localized ^{31}P magnetic resonance spectroscopy of large pediatric brain tumors. J Neurosurg 72:65–70, 1990.
225. Sutton LN, Wang Z, Gusnard D, et al: Proton magnetic resonance spectroscopy of pediatric brain tumors. Neurosurgery 31:195–202, 1992.
226. Sutton LN, Wehrli SL, Gennareli L, et al: High-resolution ^{1}H-magnetic resonance spectroscopy of pediatric posterior fossa tumors in vitro. J Neurosurg 81:443–448, 1994.
227. Swindells S, McConnell JR, McComb RD, Gendelman HE: Utility of cerebral proton magnetic resonance spectroscopy in differential diagnosis of HIV-related dementia. J Neurovirol 1:268–274, 1995.
228. Takanashi J-I, Sugita K, Osaka H, et al: Proton MR spectroscopy in Pelizaeus-Merzbacher disease. AJNR Am J Neuroradiol 18:533–535, 1997.
229. Tallan HH: Studies on the distribution of *N*-acetyl-L-aspartic acid in brain. J Biol Chem 224:41–45, 1956.
230. Tallan HH, Moore S, Stein WH: *N*-acetyl-L-aspartic acid in brain. J Biol Chem 219:257–264, 1956.
231. Taylor JS, Langston JW, Reddick WE, et al: Clinical value of proton magnetic resonance spectroscopy for differentiating recurrent or residual brain tumor from delayed cerebral necrosis. Int J Radiat Oncol Biol Phys 36:1251–1261, 1996.
232. Tedeschi G, Bertolino A, Righini A, et al: Brain regional distribution pattern of metabolite signal intensities in young adults by proton magnetic resonance spectroscopic imaging. Neurology 45:1384–1391, 1995.
233. Tedeschi G, Schiffmann R, Barton NW, et al: Proton magnetic resonance spectroscopic imaging in childhood ataxia with diffuse white matter hypomyelination. Neurology 45:1526–1532, 1995.
234. Tedeschi G, Bertolino A, Lundbom N, et al: Cortical and subcortical chemical pathology in Alzheimer's disease as assessed by multislice proton magnetic resonance spectroscopic imaging. Neurology 47: 696–704, 1996.
235. Tedeschi G, Lundbom N, Raman R, et al: Increase of choline signal coincides with malignant degeneration of cerebral gliomas: A serial proton magnetic resonance spectroscopic imaging study. J Neurosurg 87:516–524, 1997.
236. Tien RD, Lai PH, Smith JS, et al: Single-voxel proton brain spectroscopy exam (PROBE/SV) in patients with primary brain tumors. AJR Am J Roentgenol 167:201–209, 1996.

237. Toft PB, Leth H, Lou HC, et al: Metabolite concentrations in the developing brain estimated with proton MR spectroscopy. J Magn Reson Med 4:674–680, 1994.
238. Tourbah A, Stievenart JL, Gout O, et al: Localized proton magnetic resonance spectroscopy in relapsing remitting versus secondary progressive multiple sclerosis. Neurology 53:1091–1097, 1999.
239. Tracey I, Lane J, Chang I, et al: ^{1}H magnetic resonance spectroscopy reveals neuronal injury in a simian immune deficiency virus macaque model. J Acquir Immune Defic Syndr Hum Retrovirol 15: 21–27, 1997.
240. Tzika AA, Ball WS, Vigneron DB, et al: Childhood adrenoleukodystrophy: Assessment with proton MR spectroscopy. Radiology 189: 467–480, 1993.
241. Tzika AA, Vigneron DB, Dunn RS, et al: Intracranial tumors in children: Small single-voxel proton MR spectroscopy using short- and long-echo sequences. Neuroradiology 38:254–263, 1996.
242. Tzika AA, Vajapeyam S, Barnes PD: Multivoxel proton MR spectroscopy and hemodynamic MR imaging of childhood brain tumors: Preliminary observations. AJNR Am J Neuroradiol 18:203–218, 1997.
243. Urenjak J, Williams SR, Gadian DG, et al: Specific expression of *N*-acetylaspartate in neurons, oligodendrocyte-type 2 astrocyte progenitors, and immature oligodendrocytes in vitro. J Neurochem 59:55–61, 1992.
244. van der Grond J, van Everdingen KJ, Eikelboom BC, et al: Assessment of borderzone ischemia with a combined MR imaging–MR angiography–MR spectroscopy protocol. J Magn Reson Imaging 9: 1–9, 1999.
245. van der Knaap MS, vanderGrond J, van Rijen PC, et al: Age-dependent changes in localized proton and phosphorus MR spectroscopy of the brain. Radiology 176:509–515, 1990.
246. van der Knaap MS, van der Grond J, Luyten PR, et al: H-1 and P-31 magnetic resonance spectroscopy of the brain in degenerative cerebral disorders. Ann Neurol 31:202–211, 1993.
247. van der Knaap MS, Ross B, Valk J: Uses of MR in inborn errors of metabolism. In Kucharczyk J, Mosely M, Barkovich AJ (eds): Magnetic Resonance Neuroimaging. Boca Raton, Fla, CRC Press, 1994, pp 245–318.
248. van der Knaap MS, Barth P, Gabreels F, et al: A new leukoencephalopathy with vanishing white matter. Neurology 48:845–855, 1997.
249. Videen JS, Michaelis T, Pinto P, et al: Human cerebral osmolytes during chronic hyponatremia: A proton magnetic resonance spectroscopy study. J Clin Invest 95:788–793, 1995.
250. Vigneron DB, Nelson SJ, Kurhanewicz J: Proton chemical shift imaging of cancer. In Higgins CB, Hricak H, Helms CA (eds): Magnetic Resonance of the Body. Philadelphia, Lippincott-Raven, 1997, pp 205–220.
251. Vion-Dury J, Meyerhoff DJ, Cozzone PJ, et al: What might be the impact on neurology of the analysis of brain metabolism by in vivo magnetic resonance spectroscopy? J Neurol 241:354–371, 1994.
252. Wang Z, Sutton LN, Cnaan A, et al: Proton MR spectroscopy of pediatric cerebellar tumors. AJNR Am J Neuroradiol 16:1821–1833, 1995.
253. Wang Z, Zimmerman RA, Sauter R: Proton MR spectroscopy of the brain: Clinically useful information obtained in assessing CNS diseases in children. AJR Am J Roentgenol 167:191–199, 1996.
254. Wang ZJ, Berry GT, Dreha SF, et al: In vivo proton brain MRS of galactosemia. Paper presented at the Sixth Annual Meeting of the International Society of Magnetic Resonance in Medicine, 1998, Sydney, Australia, p 538.
255. Wang ZJ, Zimmerman RA: Proton MR spectroscopy of pediatric brain metabolic disorders. Neuroimaging Clin North Am 8:781–807, 1998.
256. Wardlaw JM, Marshall I, Wild J, et al: Studies of acute ischemic stroke with proton magnetic resonance spectroscopy: Relation between time from onset, neurological deficit, metabolite abnormalities in the infarct, blood flow, and clinical outcome. Stroke 29:1618–1624, 1998.
257. Wells W, Pittman T, Wells H, et al: The isolation and identification of galactitol from the brains of galactosemia patients. J Biol Chem 240:1002–1004, 1965.
258. Wilkinson ID, Lunn S, Miszkiel KA, et al: Proton MRS and quantitative MRI assessment of the short term neurological response to antiretroviral therapy in AIDS. J Neurol Neurosurg Psychiatry 63: 477–482, 1997.
259. Wittsack H, Kugel H, Roth B, et al: Quantitative measurements with localized ^{1}H MR spectroscopy in children with Canavan's disease. J Magn Reson Imaging 6:889–893, 1996.
260. Yaksh TL, Anderson RE: In vivo studies on intracellular pH, focal flow and vessel diameter in the cat cerebral cortex: Effects of altered CO_2 and electrical stimulation. J Cereb Blood Flow Metab 7:332–341, 1987.
261. Younkin DP, Delivoria PM, Maris J, et al: Cerebral metabolic effects of neonatal seizures measured with in vivo ^{31}P NMR spectroscopy. Ann Neurol 20:513–519, 1986.
262. Zimmerman RA, Wang Z: Proton spectroscopy of the pediatric brain. Riv Neuroradiol 5(suppl 1):5–8, 1992.

12 Meningeal Processes

Melanie B. Fukui, Carolyn Cidis Meltzer

Anatomy and Embryology

Meninges

The meninges, which form the coverings of the brain and spinal cord, develop from the meninx primitiva.[68] The neural tube is surrounded by this dense cellular layer, the meninx primitiva, shortly after the neural tube closes.[122] As early as 32 days and as late as 44 of gestation, the primitive meninx begins to cavitate to form the cerebral cisterns by gradually decreasing its cellular component and enlarging its intercellular space.[122] The periphery of the meninx primitiva, however, develops more dense cellularity to become the primitive dura mater.[122]

The earliest subarachnoid space (SAS) is that ventral to the brain stem.[122] As this space expands, the prepontomedullary cisterns and anterior spinal SAS are formed.[122, 155] At approximately 41 days, the space is extended to create perimesencephalic and dorsal mesencephalic cisterns.[121, 122, 155] The primitive meninx is composed of totipotential mesenchymal cells of neural crest origin.[68] The remnants of incomplete differentiation of these pluripotential cells may be seen as deposits of fat, or lipomas, in and around the basal cisterns, corpus callosum, and cavernous sinuses.[155] The order of regression of the primitive meninx is reflected in the distribution of lipomas, as described by Salvi.[155] Thus, intracranial lipomas are thought most appropriately to represent developmental, rather than neoplastic, pathology of the meninges.[155]

This network of concentric membranes consists of the pachymeninx (dura mater) and the leptomeninges (arachnoid and pia mater) (Fig. 12–1). The dura mater is the most superficial membrane, a thick, tough structure composed of dense connective tissue.[21] The dura is composed of 2 layers: (1) an outer periosteal layer, which is highly vascularized, serves as the true periosteum of the inner table of the calvaria, and is not of meningeal origin,[142] and (2) an inner meningeal layer, derived from the meninx. The cranial dural layers split to form the venous sinuses.

The term *dura* (from Latin, *durus*, meaning "hard") is an apt descriptor of the structure that maintains the position of the cerebral hemispheres and posterior fossa structure by its reflections, such as the falx cerebri and tentorium cerebelli. The arachnoid and pia mater constitute the leptomeninges (from Greek, *lepto* and *meninx*, meaning slender membrane). The delicate arachnoid is adjacent to the inner surface of the dura and is thinner over the convexities than at the base of the brain. The pia mater is a fine membrane that extends into the depths of the sulci.

Extra-axial Spaces

The meninges delimit the extra-axial compartments of the central nervous system (CNS). The epidural space is created when the dura is separated from the calvaria. Although the subdural space (between the dura and arachnoid membranes) has conventionally been characterized as a potential space containing minimal fluid, cells of the arachnoid actually form an intimate network with those of the meningeal dural layer.[46] Electron microscopy has provided evidence that cells belonging to the inner dural layer may be found on *both* sides of this space when collections form in the subdural space.[46, 64] The subdural space, therefore, is formed by cleavage through the inner layer of the dura rather than by a true separation of dura and arachnoid and, as such, probably exists only in pathologic states.[64]

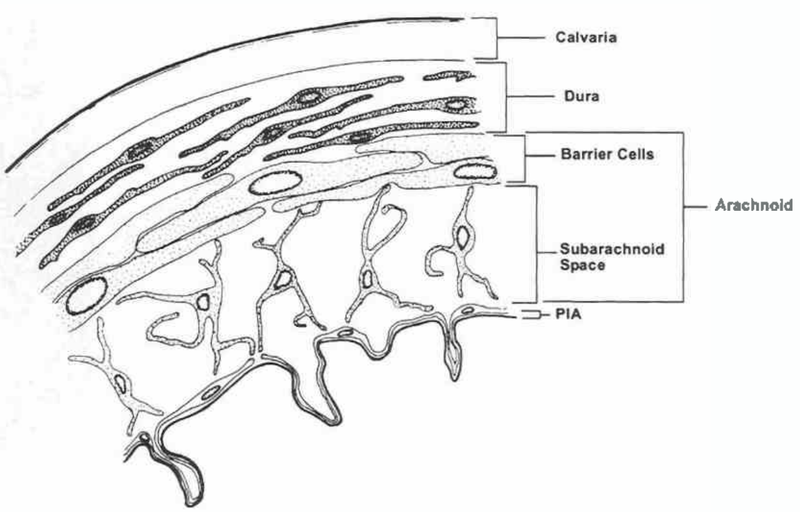

Figure 12–1. Schematic representation of the dura and leptomeninges. PIA, pia mater. (From Meltzer CC, Fukui MB, Kanal E, Smirniotopoulos JG: MR imaging of the meninges: Part 1. Normal anatomic features and nonneoplastic disease. Radiology 201: 297–308, 1996.)

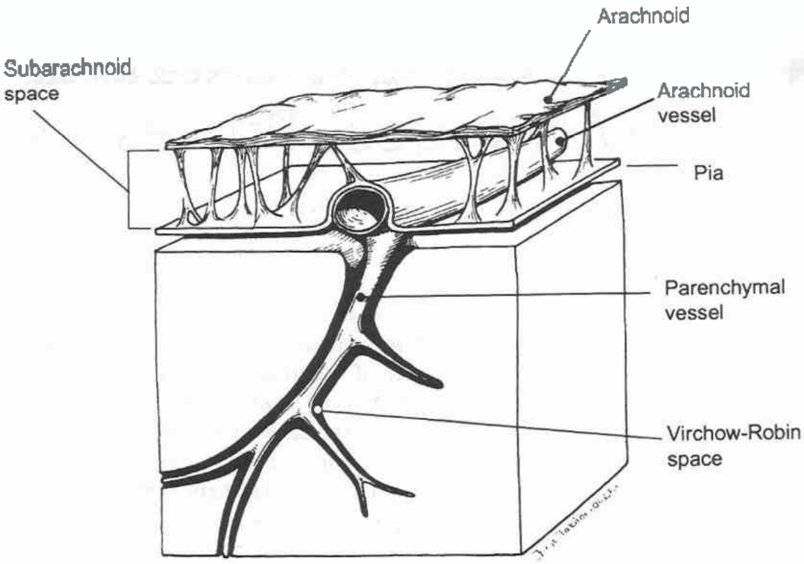

Figure 12–2. Diagram illustrating the anatomy of the perivascular (Virchow-Robin) space with respect to the pia mater and the subarachnoid space. (Modified from Fukui MB, Meltzer CC, Kanal E, Smirniotopoulos JG: MR imaging of the meninges: Part 2. Neoplastic disease. Radiology 201:605–612, 1996.)

The SAS (between the arachnoid and pia mater) contains cerebrospinal fluid (CSF) that flows throughout the CNS and drains into the venous sinuses through the valves of the arachnoid granulations.[142] The pia and the arachnoid are joined by fine connective tissue and cellular septa that traverse the SAS.[19] Near the base of the brain, though, the pia and arachnoid widely separate to accommodate the basal cisterns. Perivascular, or Virchow-Robin, spaces were originally thought to be potential pathways connecting the CSF and deep brain structures by virtue of continuity with the SAS.[41] More recent studies, however, have concluded that perivascular spaces are within the subpial space, separated from the SAS by pia mater[3] (Fig. 12–2).

Extra-axial Collections

Fluid collections in the epidural space assume a localized biconvex configuration as a result of the strong force needed to detach the firmly adherent dura from the inner table of the calvaria. The outer dural layer is most tightly adherent at sutures; classic teaching therefore holds that epidural collections do not cross suture lines.[60] Uncommon exceptions to this rule do occur, however. After administration of paramagnetic contrast medium, the dura adjacent an epidural hematoma (EDH) has a curvilinear, enhancing appearance. An inflammatory reaction, with formation of granulation tissue on the outer surface of the dura, may produce increased thickness and intensity of enhancement in the dura immediately subjacent to an EDH, as demonstrated in Figure 12–3.[67]

Greater tissue contrast and multiplanar imaging capability contribute to the superior sensitivity of magnetic resonance imaging (MRI) compared with computed tomography (CT) in detecting small subdural fluid collections.[85] MRI is especially useful in cases of subacute subdural hematoma (SDH), which may appear isodense to cortex on CT. Subdural hygromas result from leakage of CSF into the subdural space, probably after a tear in the arachnoid. MRI can distinguish subdural hematoma from subdural hygroma by improved detection of blood products, which are absent in a hygroma, but it cannot distinguish simple from infected subdural fluid, however, since peripheral dural enhancement may be seen in both infected and noninfected subdural collections (Fig. 12–4). A diffusely enhancing, infected subdural collection may mimic an en plaque meningioma.[102]

Imaging

Imaging Modalities

MRI is substantially more sensitive than CT for visualizing both normal and abnormal meninges[37, 55, 70, 104, 152, 154]

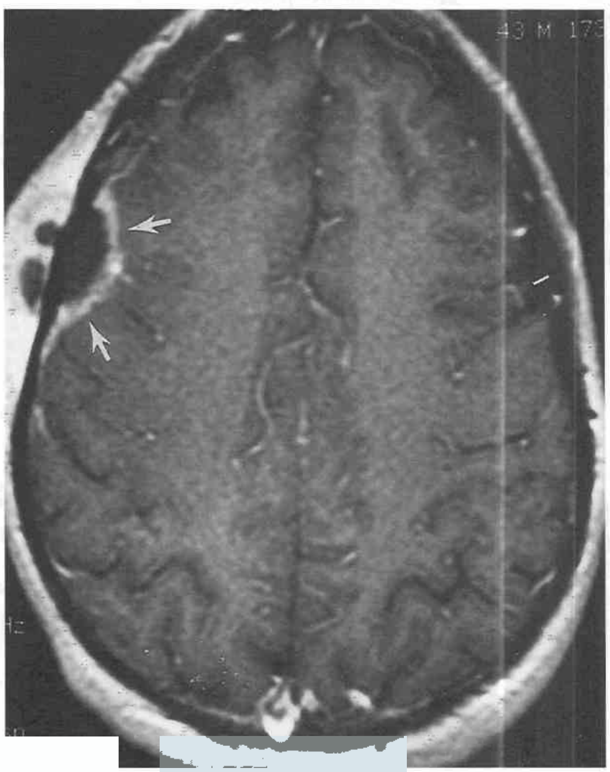

Figure 12–3. Epidural abscess. Enhanced axial T1-weighted image shows a lentiform epidural collection of pus with dural enhancement *(arrows)* that could mimic an epidural hematoma.

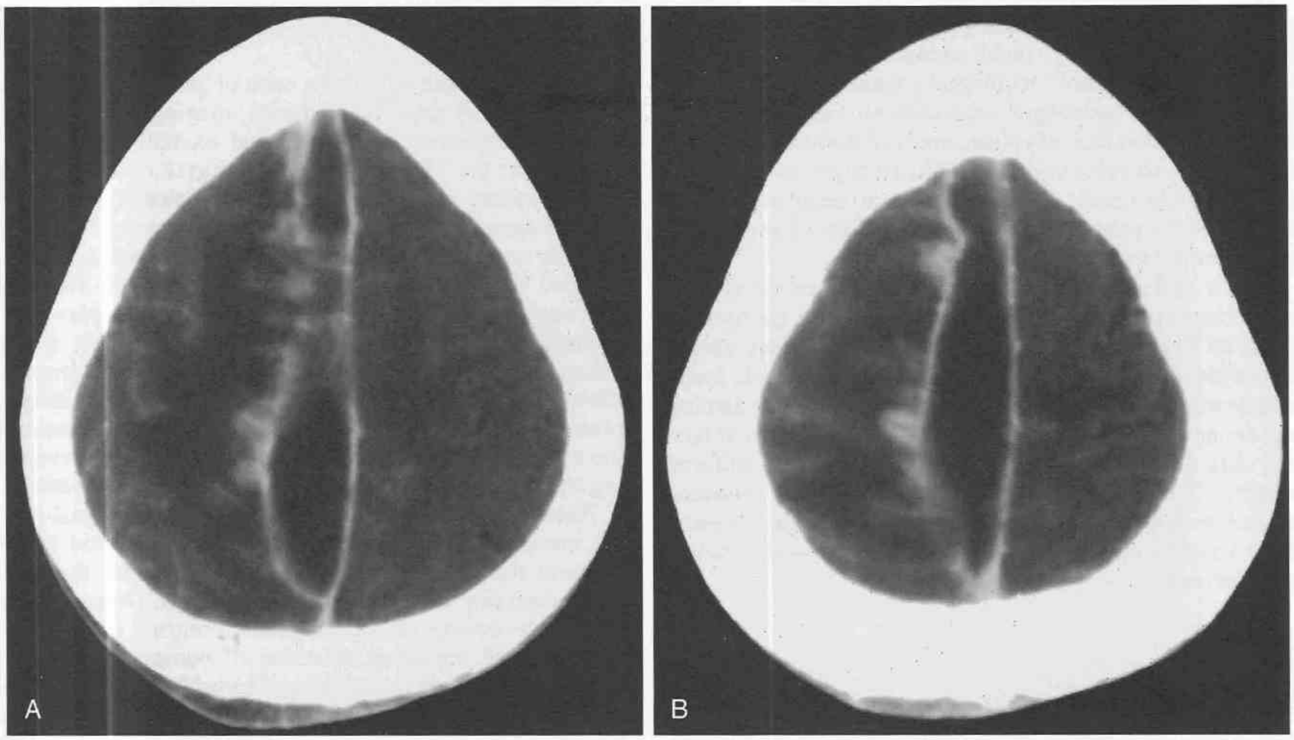

Figure 12–4. Subdural empyema. *A* and *B*, Enhanced axial CT images at the level of the falx cerebri show dural enhancement surrounding a subdural empyema.

(Fig. 12–5). Beam-hardening and other artifacts adjacent the calvaria may be partly responsible for the diminished detection of meningeal enhancement with CT. Experimental evidence suggests, in addition, that more intense enhancement results in areas of blood-brain barrier disruption with gadolinium-DTPA–enhanced MRI than with CT performed after iodinated contrast.[92, 136]

It has been suggested that MRI may be equally sensitive or even superior to CT in detecting subarachnoid hemorrhage (SAH) in the subacute and chronic phases and when a fluid-attenuated inversion recovery (FLAIR) pulse sequence is used.[115, 117] Other evidence suggests that FLAIR sequences may result in false-negative interpretations in the setting of SAH.[167]

Normal Meninges on Magnetic Resonance Imaging

The normal meninges may demonstrate short segments of thin, low signal intensity on standard spin-echo sequences.[43] Intravenous (IV) administration of gadolinium-DTPA results in enhancement of the normal cranial dura, which lacks a blood-brain barrier, in an interrupted pattern of short linear

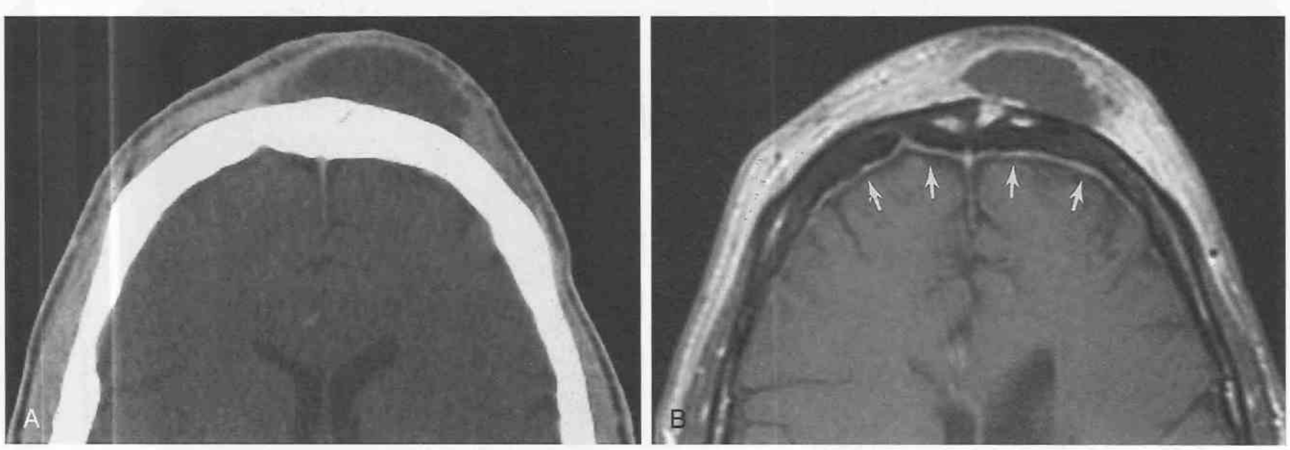

Figure 12–5. Superior sensitivity of MRI over CT in detection of meningeal disease: Pott's puffy tumor. *A*, Enhanced axial CT image at the level of an extracranial subperiosteal collection of pus. *B*, Enhanced axial MR image obtained after administration of gadolinium at the same level shows enhancement of the subjacent dura/arachnoid *(arrows)*. Detection of this meningeal enhancement prompted a change of antibiotics to improve cerebrospinal fluid drug penetration.

segments that is typically most prominent parasagittally[27, 152] (Figs. 12–6 and 12–7). Field strength may influence the conspicuity of "normal" meningeal enhancement as well as the detection of pathologic enhancement. Earlier literature reported a distinct lack of enhancement of normal meningeal structures with relatively low-field-strength MRI.[20] The greater signal-to-noise levels achieved at relatively higher field strengths potentiate increased detection of meningeal enhancement (see Fig. 12–6).

Cohen and colleagues[27] reported that when meningeal enhancement was present on more than three contiguous 1.5 Tesla (T) spin-echo MR images, it was highly correlated with significant intracranial abnormality. Thick, long, or intensely enhancing segments, as well as nodular meningeal enhancement, are particularly suspect. The normal falx and dura may occasionally enhance in a thin uniform pattern.[86] The typical lack of normal meningeal enhancement observed in MRI of the spine may reflect the absence of the vascular outer dural layer that is found in the cranial pachymeninx.

Technique

The selection of MRI has a significant impact upon the conspicuity of normal meningeal enhancement and sensitivity in detecting meningeal disease (see Figs. 12–6 and 12–7). Numerous factors influence the appearance of the meninges on MR images, including (1) the presence and amount of MR contrast agent administered, (2) the type of pulse sequence performed, and (3) the exact pulse sequence parameters.

For partial saturation (spin echo or gradient echo), short echo time (TE) sequences, crucial imaging parameters include the repetition time (TR) and excitation flip angle. The shorter the TR, the greater the degree of saturation of magnetization (i.e., decreased signal intensity) from all imaged tissues. As a result, contrast-enhancing tissue will be more conspicuous against the more saturated (i.e., hypointense) background tissues on a typical short TR, large flip angle gradient-echo study than on a spin-echo study. Therefore, the normal meninges usually exhibit diffuse enhancement on such ultrashort TR, large flip angle gradient-echo imaging sequences[43] (see Fig. 12–7). Imaging plane also affects visualization of meningeal enhancement; the coronal plane is preferred to axial MRI data for evaluating meningeal enhancement over the cerebral convexity.

Similarly, factors that either increase the signal from the meninges or decrease signal from background tissues enhance the contrast-to-noise ratio (CNR) and, therefore, the conspicuity of the enhancing meninges. Double-dosing and triple-dosing of paramagnetic contrast agents have demonstrated improved detection of parenchymal lesions with MRI,[69] and there is evidence to support a similar dose effect for enhanced MRI of meningeal disease.[82, 83, 137] More recently, cases of leptomeningeal metastases that had been diagnosed by MRI and high-dose (0.3 mmol/kg) gadolinium have been reported that were not visualized with standard dose (0.1 mmol/kg) technique (Fig. 12–8).[59, 83] Also, the use of fat saturation or magnetization transfer

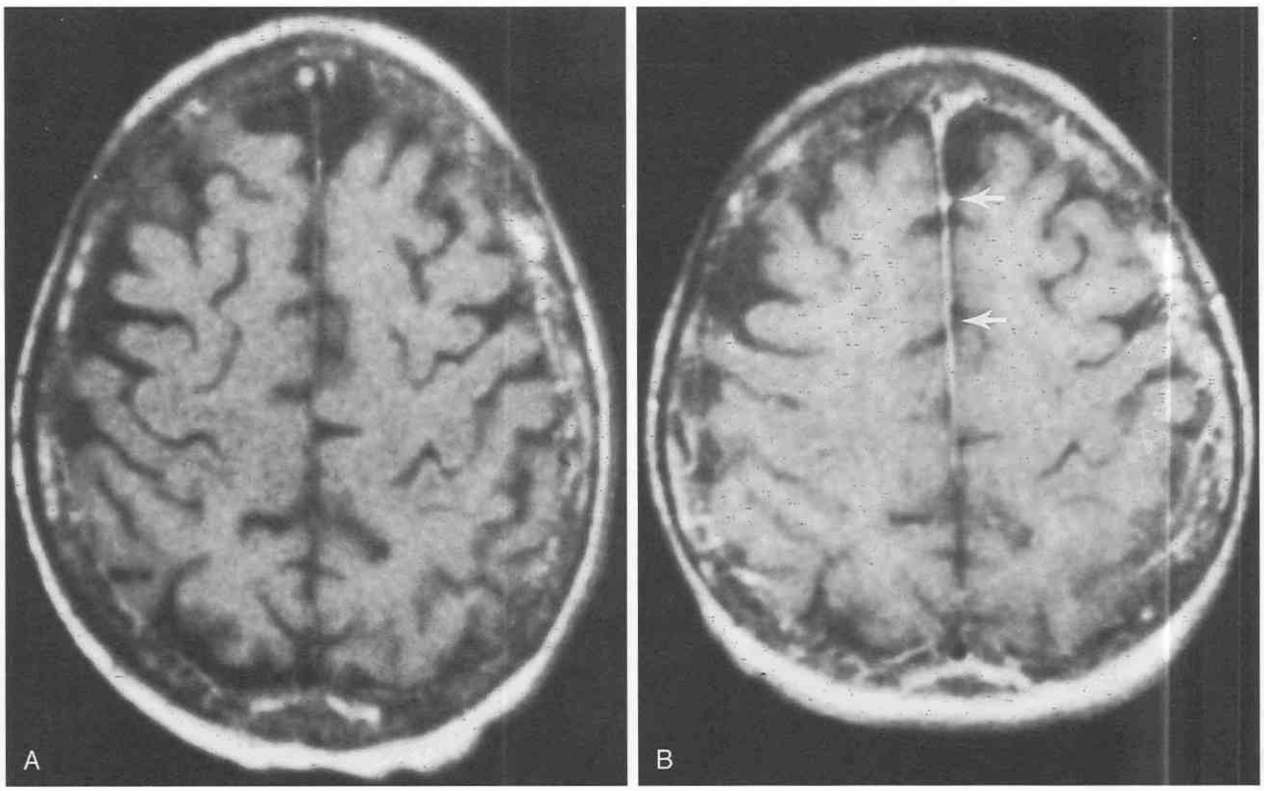

Figure 12–6. Effects of field strength on conspicuity of normal meningeal enhancement. *A*, Axial T1-weighted image acquired at 0.5 T immediately after injection of 0.1 mmol/kg gadolinium. *B*, Axial T1-weighted image acquired at 1.5 T, one day later, in the same patient, immediately after injection of the same dose of gadolinium shows more prominent enhancement of the falx *(arrows)* than in *A*. (From Meltzer CC, Fukui MB, Kanal E, Smirniotopoulos JG: MR imaging of the meninges: Part 1. Normal anatomic features and nonneoplastic disease. Radiology 201:297–308, 1996.)

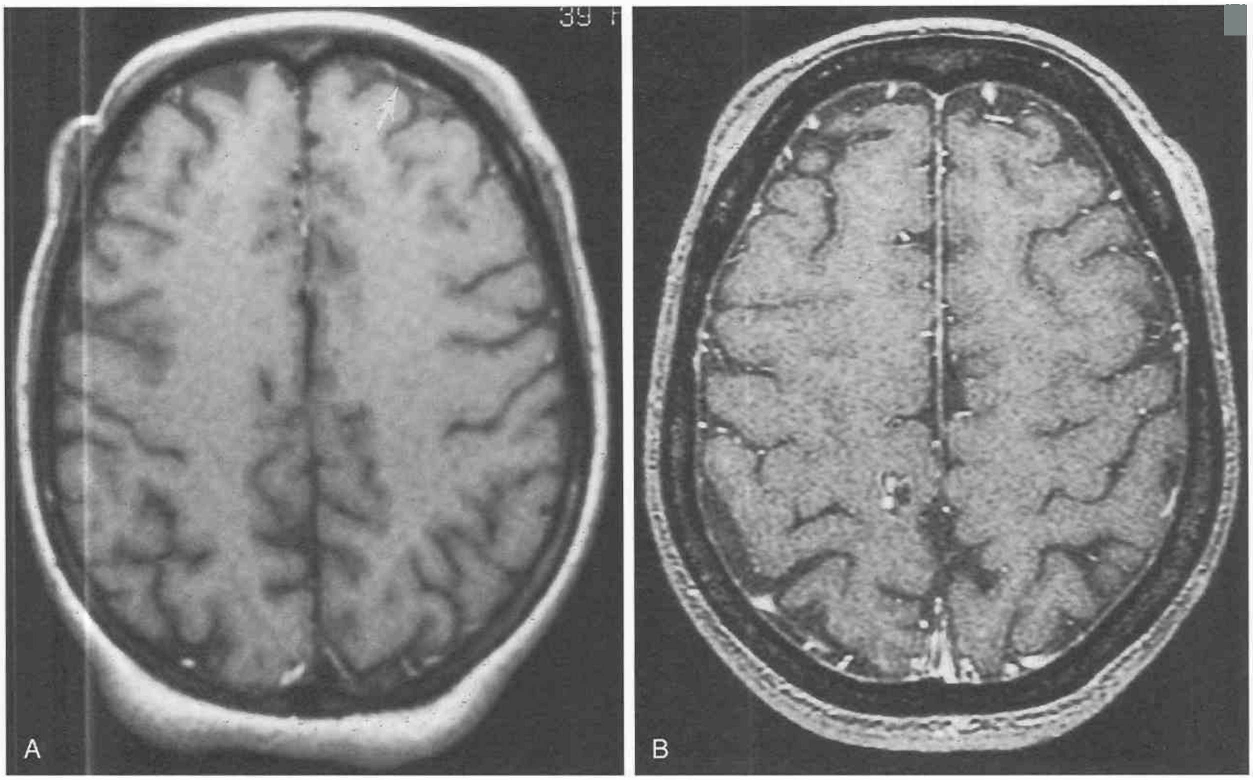

Figure 12–7. Effects of and pulse sequence on conspicuity of normal meningeal enhancement. *A,* Axial T1-weighted spin-echo image in another patient shows faint, short segment meningeal enhancement *(arrow). B,* Axial, spoiled-gradient, recalled-echo image in the same patient shows thin, continuous enhancement in a dura/arachnoid pattern. (From Meltzer CC, Fukui MB, Kanal E, Smirniotopoulos JG: MR imaging of the meninges: Part I. Normal anatomic features and nonneoplastic disease. Radiology 201:297–308, 1996.)

options increases the CNR by decreasing the signal from the background tissues.[38, 137]

The optimal imaging protocol for detection of meningeal disease is based on (1) sensitivity, (2) technique, (3) role, (4) cardinal signs, and (5) principal patterns (Table 12–1).

Sensitivity of Magnetic Resonance Imaging

In the past, unenhanced spin-echo MRI was insensitive in detecting meningeal disease.[104] The advent of the FLAIR sequence has greatly improved the sensitivity of MRI performed in the absence of gadolinium to detect meningeal and SAS abnormalities.[145, 167] Singer and coworkers evaluated the use of FLAIR MRI in 62 patients (21 with proven SAS or meningeal disease) and 41 control patients.[145] The sensitivity, specificity, and accuracy of FLAIR for SAS disease were 85%, 93%, and 90%, respectively.[145] Although all six cases of acute SAH were interpreted as abnormal on FLAIR images in the Singer series, this was a source of false-negative interpretation in the series by Williams and associates.[145, 167]

Poor detection of SAH has been attributed to the relatively high oxygen tension in the SAS, which does not permit evolution to deoxyhemoglobin[62] and to the diluting effect of CSF. In 24 patients who underwent both FLAIR and gadolinium-enhanced T1-weighted MRI, FLAIR imaging (sensitivity, specificity, and accuracy, 86%, 91%, and 89%, respectively) was superior to gadolinium-enhanced T1-weighted imaging (43%, 88%, and 74%).[145]

Williams and coauthors[167] prospectively evaluated 376 consecutive cases performed with FLAIR imaging and showed that FLAIR may result in false-negative diagnoses of meningeal or SAS disease in cases of infectious meningitis, carcinomatosis, and SAH.[167] In this series, a false-positive diagnosis of meningeal or SAS pathology was made in the presence of normal and hyperintense cortex, susceptibility artifact, prominent pial vessels, concatenated saturation pulse, or flow artifact.[167] Neoplastic or inflammatory processes involving the SAS are best evaluated with paramagnetic contrast agents for visualization of enhancement of the accompanying meningeal involvement (Fig. 12–9).

Table 12–1. Protocol for Magnetic Resonance Imaging Performed at 1.5 Tesla

Axial FLAIR image
Axial T1-weighted image
Axial and coronal T1-weighted image after administration of a double or a triple dose of gadolinium with a fat-saturation pulse or magnetization transfer

FLAIR, fluid-attenuated inversion recovery.

Role of Imaging

Before and after gadolinium administration, MRI plays an important role in the diagnosis of meningeal neoplasm

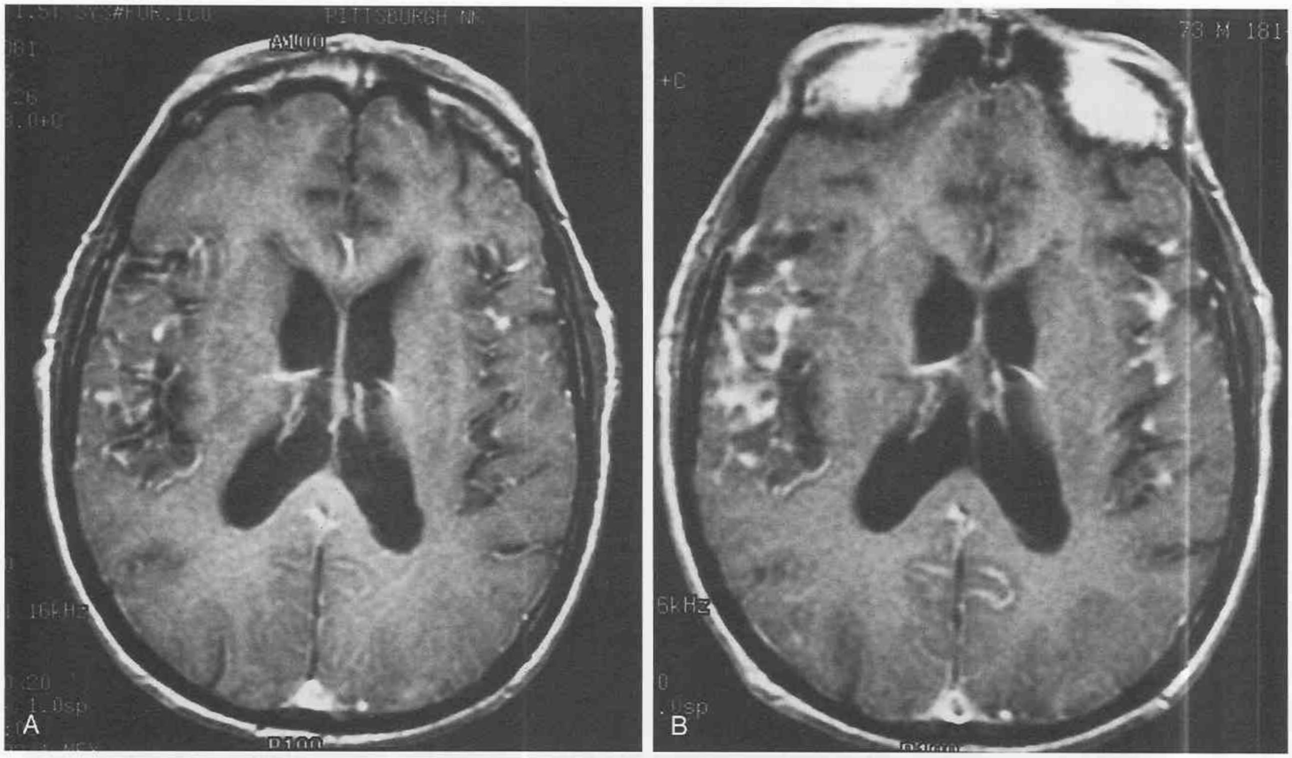

Figure 12–8. Effect of contrast dose on meningeal enhancement. Axial T1-weighted images obtained after administration of 0.1 mmol/kg *(A)* and 0.2 mmol/kg *(B)* doses of gadolinium show increased enhancement in a pia/subarachnoid space pattern at the higher dose in this patient with carcinomatosis of the meninges from gastric carcinoma.

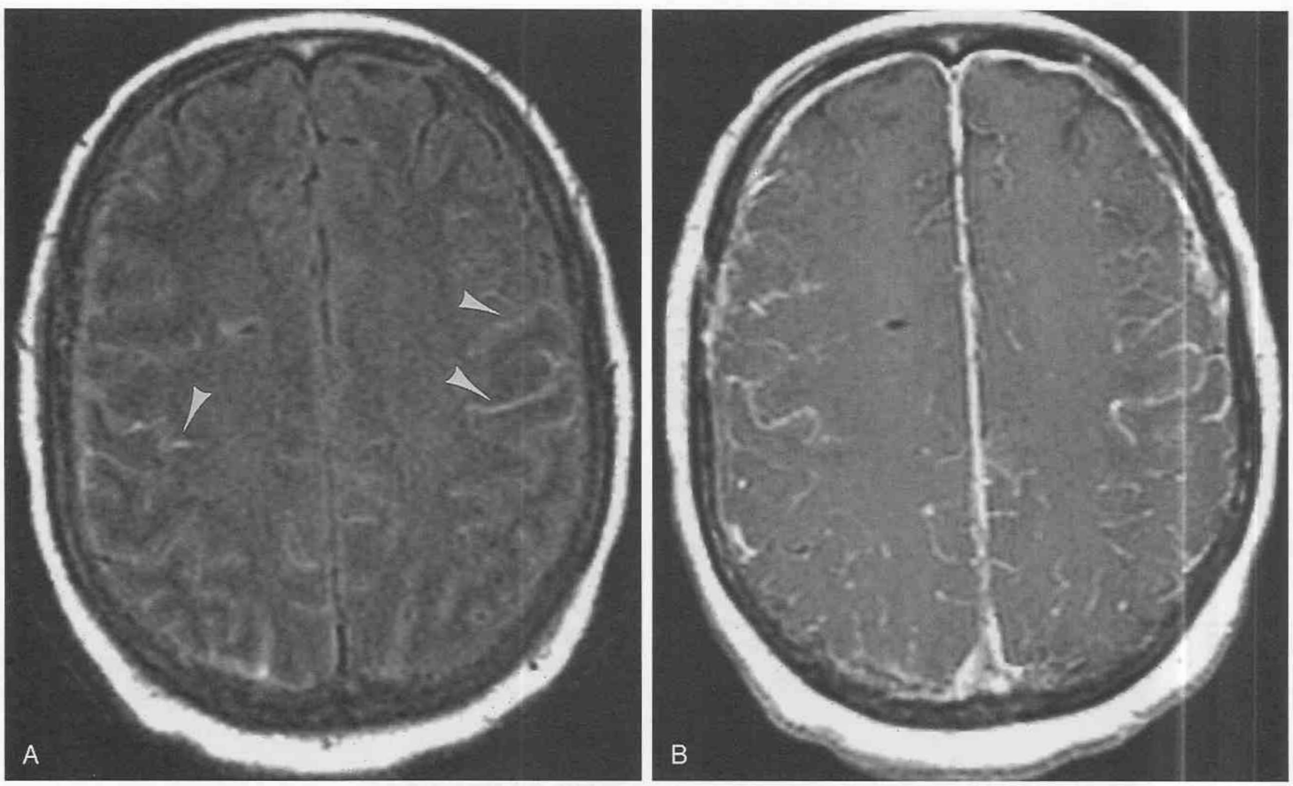

Figure 12–9. Axial fluid-attenuated inversion recovery (FLAIR) image in a patient with leptomeningeal spread of breast carcinoma *(A)* shows signal abnormality in a pia/subarachnoid space pattern *(arrowheads)* that enhances on the T1-weighted image after administration of gadolinium *(B)*.

in the asymptomatic patient when CSF cytologic examination results are equivocal, or when lumbar puncture is contraindicated.[23, 47, 52, 152] Imaging, however, does not replace CSF examination in diagnosis of meningeal neoplasm.

The limited sensitivity of CSF cytologic examination continues to be a significant obstacle and reinforces the complementary role of imaging.[53] The percentage of positive spinal CSF cytology in cases of primary CNS tumors with histologically confirmed meningeal involvement varies from 12% to 63% and is increased in symptomatic patients.[6, 56, 89, 112] With meningeal metastases from non-CNS neoplasms, CSF cytology was positive in between 45% and 80% of cases with higher yields after multiple spinal taps.[118, 161] The modest sensitivity of CSF cytology has fueled the search for CSF tumor markers to detect dissemination of neoplasm. Like CSF cytology, tumor detection with CSF markers is also restricted by suboptimal sensitivity and specificity.[114, 157]

The sensitivity of MRI in detecting meningeal neoplasm was originally reported to be lower than that of CSF cytology, with high false-negative rates: 30 to 33% for MRI and 58% for CT.[24, 173] The early studies, however, may have unwittingly introduced a selection bias by using positive cytology as an inclusion criterion.[24, 173] Later series comparing CT myelography with MRI showed an increased detection rate of CSF metastases with MRI (65% to 72%) compared with CT myelography (45% to 47%) and with cytology (29%).[70, 91]

A more recent Memorial Sloan-Kettering Cancer Center study[47] showed that when the patient cohort was not restricted to patients with positive cytologic findings, the rate of detection of meningeal carcinomatosis was increased. This study examined 137 patients with signs and symptoms of meningeal disease.[47] CT and MRI were assessed for signs of meningeal or SAS neoplasm, including hydrocephalus, enhancement of the dura, leptomeninges, and cranial nerves.[47] Leptomeningeal metastases were identified in 77 of 137 patients.[47] The diagnosis of leptomeningeal metastases was based on the clinical and imaging findings *alone*, in 31% of those cases.[47] Abnormal imaging findings were reported much more frequently in cases of solid tumor primaries (90%) than in hematologic neoplasms (55%).[47] A caveat in using MRI for the diagnosis of leptomeningeal tumor involvement, then, is that MRI is less sensitive in detecting involvement of the meninges resulting from hematologic malignancies in contrast to detecting solid tumors.[24, 47, 173]

When the distinction between meningeal neoplasm and inflammatory meningeal disease cannot be established by CSF and clinical data, MRI can support the diagnosis of neoplasm and guide meningeal biopsy.[80, 96] Although infectious meningitides are often uncovered by CSF analysis, MRI may be used to target meningeal biopsies when needed.

Cheng and coworkers[26] reported an improved yield from meningeal biopsy specimens in cases of chronic meningitis when tissue specimens were obtained from enhancing regions identified on MRI (Fig. 12–10). MRI has an advantage over CSF examination in its ability to characterize bulky neoplastic disease that may be more responsive to radiation therapy.[23] Because CSF cytologic examination

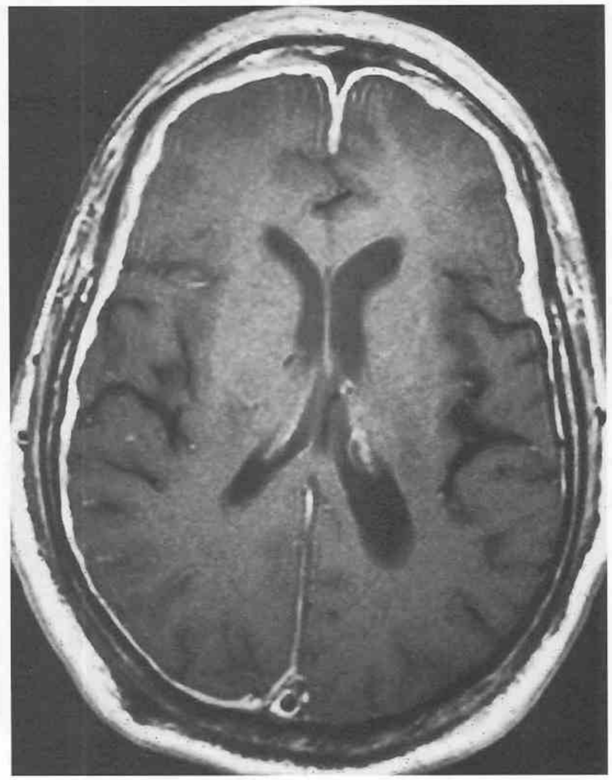

Figure 12–10. Chronic meningitis. Thick, slightly irregular dura/arachnoid enhancement on axial T1-weighted imaging proved to be idiopathic hypertrophic pachymeningitis on biopsy.

produces a higher false-negative rate in focal (rather than diffuse) disease,[13, 53] imaging may be of particular value in detecting focal spread of neoplasm to the meninges or SAS. MRI also has the potential to allow noninvasive monitoring of treatment response, although it is conceivable that the imaging abnormalities may persist beyond the eradication of neoplastic cells in the CSF.[169] In a series of patients with coccidioidal meningitis, diminution of meningeal enhancement was seen in treated patients with improving CSF profiles.[171] Therefore, MRI also may be useful as a means of monitoring a response to therapy in fungal meningeal disease.[171]

Imaging is a useful adjunct for the diagnosis of neoplastic meningeal disease in the appropriate clinical setting along with CSF examination to exclude infectious or noninfectious processes of the meninges.[47]

Finally, imaging may allow the clinician to assess outcome, since diffuse leptomeningeal involvement confers a poor prognosis.[14]

Cardinal Signs

The main imaging findings that have been associated with meningeal pathology are as follows[30, 40, 47, 78, 91, 132, 151, 152, 173]:

- Hydrocephalus (Fig. 12–11)
- Dura and arachnoid enhancement or signal abnormality (see Fig. 12–10)
- Pia and SAS enhancement or signal abnormality (see Fig. 12–11)

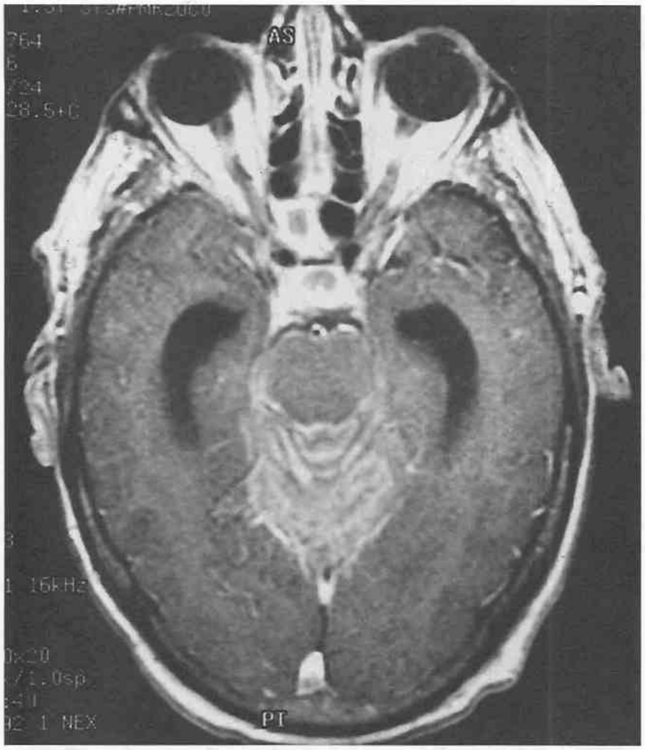

Figure 12–11. Hydrocephalus and pia/subarachnoid space abnormality. Enlargement of the temporal horns of the lateral ventricles and a pia/subarachnoid enhancement pattern over the cerebellum indicates meningeal spread of lung carcinoma.

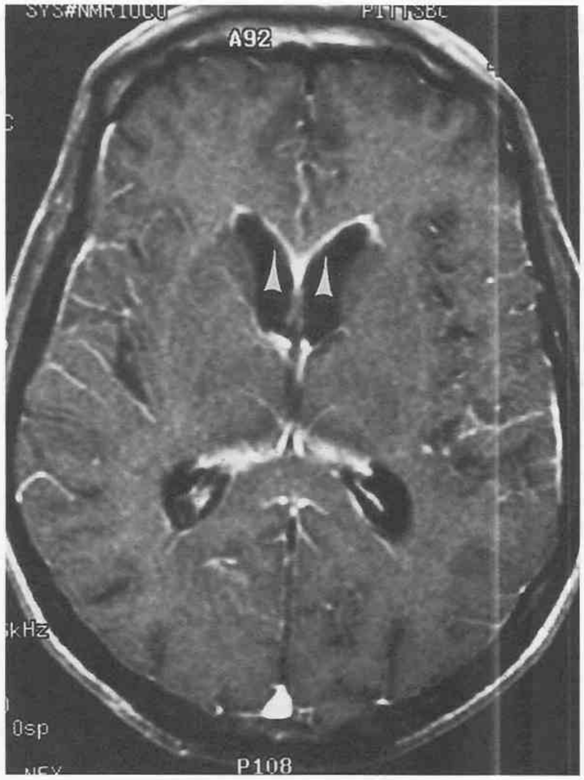

Figure 12–12. Ependymal enhancement. Thin, linear enhancement of ependyma *(arrowheads)* on T1-weighted imaging in addition to pia/subarachnoid enhancement is present in this patient with disseminated small-cell lung carcinoma.

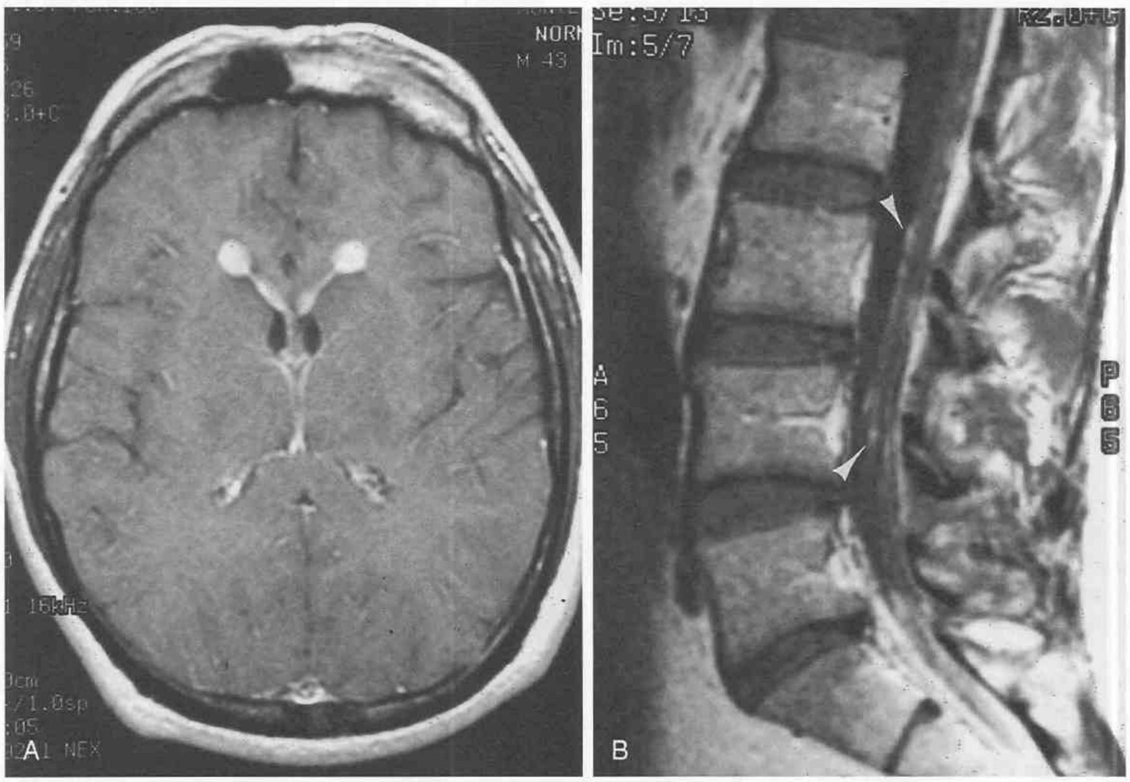

Figure 12–13. Focal, nodular ependymal enhancement. *A,* Nodular enhancement of the ependyma of the frontal horns was the probable entry point for subarachnoid spread of melanoma. *B,* Sagittal T1-weighted image of the lumbar spine shows nodular, enhancing drop metastases to the cauda equina *(arrowheads).*

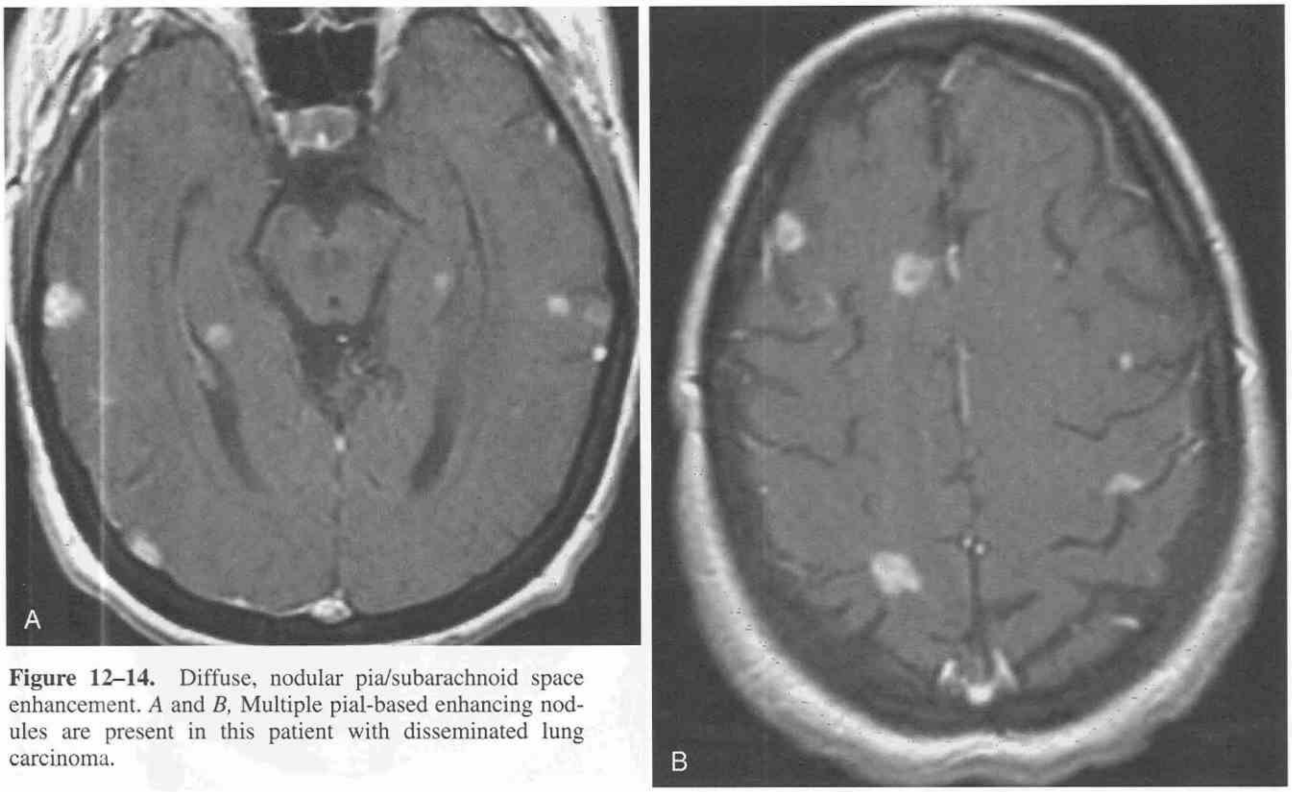

Figure 12–14. Diffuse, nodular pia/subarachnoid space enhancement. *A* and *B,* Multiple pial-based enhancing nodules are present in this patient with disseminated lung carcinoma.

- Subependymal enhancement or signal abnormality (Fig. 12–12)

Hydrocephalus may or may not be associated with enhancement of the meninges or ependyma. In this setting, hydrocephalus alone implies a resorptive block to CSF flow. Hydrocephalus may occur in the setting of SAH, infectious or noninfectious meningitis, and, of course, neoplasm. In the patient with neoplastic meningeal disease, hydrocephalus is more likely when leptomeningeal invasion or SAS has occurred rather than when neoplasm is limited to the dura.[162]

Enhancement of the meninges may occur in the spine or brain. Meningeal or subependymal enhancement may be focal (Fig. 12–13) or diffuse (see Fig. 12–12) and may have either a smooth or nodular contour (Fig. 12–14; see Fig. 12–13). Diffuse leptomeningeal involvement is a harbinger of a worse prognosis than focal disease.[14] Although a nodular pattern of enhancement may suggest neoplasm, it is not specific, since non-neoplastic entities such as sarcoidosis may also produce nodular thickening of the meninges (Fig. 12–15B). Infiltration of the leptomeninges overlying the convexities or in the basal cisterns may result in sulcal or cisternal obliteration on a non-contrast T1-weighted image (Fig. 12–16) or a FLAIR sequence (see Fig. 12–9). Minimal shortening of T1 and T2 relaxation times in the cisternal CSF ("dirty CSF sign") may be seen on unenhanced MR images[16] (see Fig. 12–16). In rare instances, subarachnoid tumor or inflammatory exudates may result in distention of the SAS (Fig. 12–17).

Imaging Patterns

Two distinct patterns of meningeal enhancement or signal abnormality may be observed with MRI. The *dura/arachnoid* pattern follows the inner contour of the calvaria (Fig. 12–18), whereas the *pia mater/SAS* abnormality extends into the depths of the sulci (Fig. 12–19). Enhancement or signal abnormality surrounding the brain stem is always of the pia mater/SAS type, since the arachnoid is clearly separated from the pia mater by the intervening basal cisterns in this region. Although pia mater/SAS enhancement does occur more commonly in the setting of meningitis than with tumor involvement, both inflammatory and neoplastic processes may demonstrate either pattern.[87, 128] A diffuse appearance favors an inflammatory etiologic mechanism, whereas nodular meningeal enhancement suggests a neoplasm (Tables 12–2 to 12–6).

Table 12–2. Differential Diagnosis: Focal Dura/Arachnoid Pattern

Infectious
Adjacent petrous apicitis/sinusitis/mastoiditis
Adjacent abscess or cerebritis
Fungal infection (*Aspergillus*)
Noninfectious Inflammatory
Reactive
Calvarial metastasis
Subdural or epidural hematoma
Acute infarction
Iatrogenic
Catheter or craniotomy
Sarcoidosis
Neoplastic
Meningioma
Breast carcinoma
Prostate carcinoma
Lymphoma
Post-transplant lymphoproliferative disorder (PTLD)

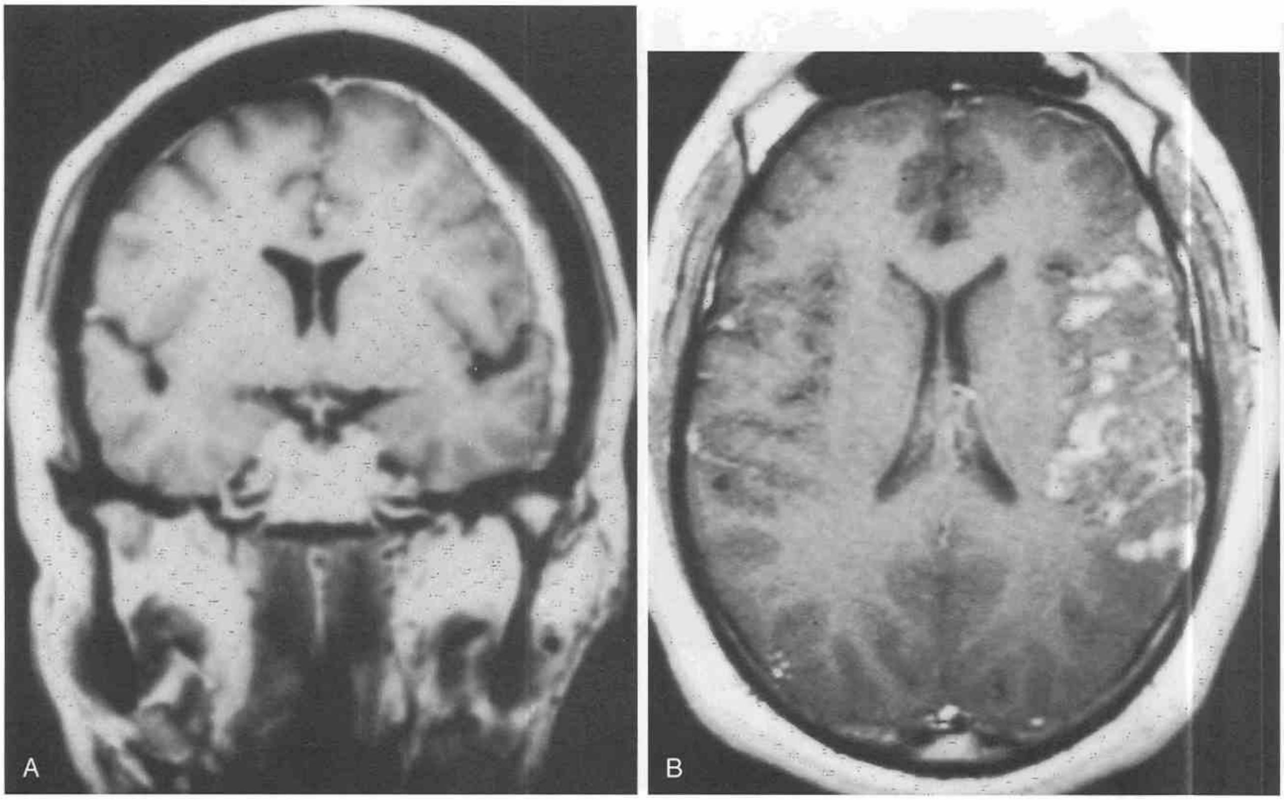

Figure 12–15. Non-neoplastic focal nodular and linear meningeal enhancement. *A,* Focal, linear enhancement in a dura/arachnoid pattern in sarcoidosis. (From Meltzer CC, Fukui MB, Kanal E, Smirniotopoulos JG: MR imaging of the meninges: Part 1. Normal anatomic features and nonneoplastic disease. Radiology 201:297–308, 1996.) *B,* Focal, nodular enhancement in a pia/subarachnoid pattern mimics neoplasm in another case of sarcoidosis. (Courtesy of Robert L. Williams, M.D., University of Pittsburgh Medical Center, Pittsburgh, Pa.)

Dura/Arachnoid Pattern

Because the dura and arachnoid are closely approximated, the distribution of meningeal enhancement does not reliably distinguish purely pachymeningeal (dural) from leptomeningeal (arachnoidal and pial) involvement. As a result, the dura/arachnoid pattern of enhancement does not imply that the leptomeninges or the SAS is spared. This fact has practical importance because some authors report a lower incidence of positive CSF cytologic findings with the dural pattern, in contrast to the pial pattern, implying a lack of subarachnoid space neoplasm.[123]

Table 12–3. Differential Diagnosis: Diffuse Dura/Arachnoid Pattern

Infectious
Bacterial (unusual)
Noninfectious Inflammatory
Reactive
Diffuse calvarial metastases
Extensive subdural hematoma
Iatrogenic
Response to catheter or craniotomy
Low intracranial pressure states
Cerebrospinal fluid leak
After lumbar puncture (unusual)
Spontaneous intracranial hypotension (rare)
Hypertrophic cranial pachymeningitis (rare)
Wegener's granulomatosis (rare)
Multiple sclerosis (rare)
Neoplastic
Breast carcinoma
Prostate carcinoma

A surprisingly moderate rate (55%) of positive CSF cytologic results was reported in a subset of 11 patients with a dura/arachnoid enhancement pattern on MRI.[47] The presence of malignant cells in the CSF of patients in this subgroup implies neoplastic involvement of the arachnoid and SAS. This confirms the limitation of MRI in distinguishing abnormal enhancement of the dura from that of the arachnoid.[47] When restricted to the dura, however, meningeal carcinomatosis often results in negative CSF cytology; in this setting, MRI can play an important role in disease detection.

The dural tail sign, once considered specific for meningioma, may be observed in a wide variety of other extra-axial lesions, including schwannoma (Fig. 12–20), dural metastases (Fig. 12–21), lymphoma, tuberculoma, and sarcoidosis.[106] Occasionally, a dural tail may be seen in association with intra-axial mass lesions, such as gliomas or non-CNS metastases.[106] Although this imaging feature has been useful in suggesting the diagnosis of meningioma, its lack of specificity may occasionally cause misleading interpretation of MR images.[106] Similar signal, shape, and enhance-

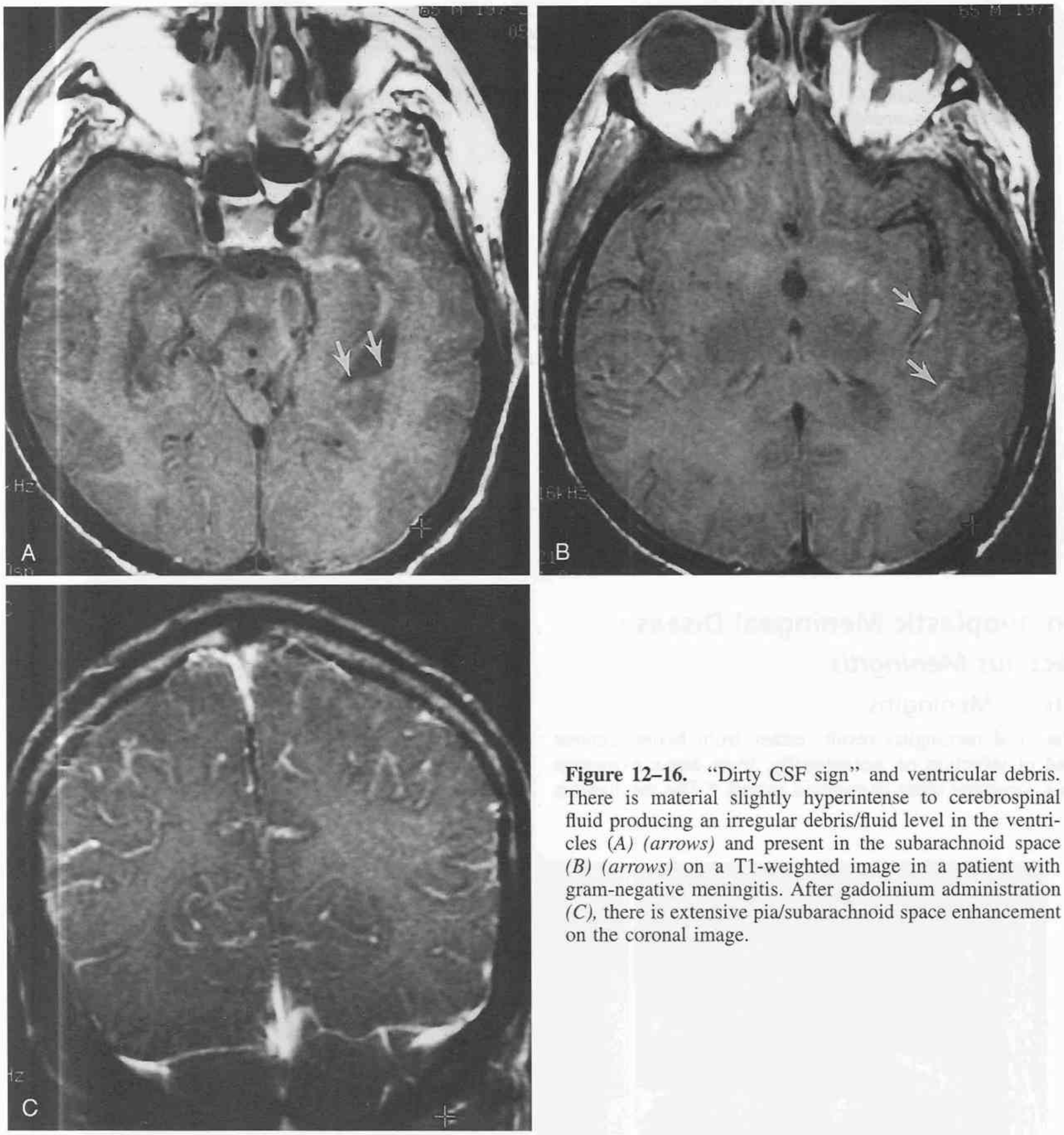

Figure 12–16. "Dirty CSF sign" and ventricular debris. There is material slightly hyperintense to cerebrospinal fluid producing an irregular debris/fluid level in the ventricles *(A) (arrows)* and present in the subarachnoid space *(B) (arrows)* on a T1-weighted image in a patient with gram-negative meningitis. After gadolinium administration *(C)*, there is extensive pia/subarachnoid space enhancement on the coronal image.

ment characteristics found with several of these lesions may further confound the distinction between meningiomas and other entities.[106]

Pia Mater/Subarachnoid Space Pattern

Similarly, the pia mater/SAS pattern of enhancement may reflect neoplasm within the SAS, tumor infiltration of the pia mater, or both.[173] The pia mater/SAS pattern is more common in patients with infectious meningitis than in those with a neoplasm,[87, 128] although the pia mater/SAS distribution is not at all specific for inflammation.

A higher rate of positive CSF cytologic findings has been reported in conjunction with the pia mater/SAS pattern than with the dura/arachnoid pattern of enhancement in cases of neoplasm.[123] This may reflect the anatomy of the blood-brain barrier with respect to the meninges.[87] The dura lacks a blood-brain barrier, since its capillary endothelium has a discontinuous cell layer, whereas the outer layer of the arachnoid has capillaries with a continuous cell layer and tight junctions.[139, 140] Bloodborne neoplastic cells, therefore, may gain access to the dura more easily than to the SAS.[87] A pia mater/SAS pattern may reflect SAS enhancement, pial enhancement, or both.[45] Gadolinium may leak through capillary tight junctions that have been disrupted by neoplastic invasion of the meninges[45] and directly enter the CSF.

Table 12–4. Differential Diagnosis: Focal Pia Mater/Subarachnoid Space Pattern

Infectious	**Neoplastic**
Bacterial meningitis	Primary CNS
Tuberculous meningitis (basal)	Glioblastoma multiforme
Fungal (*Aspergillus, Cryptococcus, Coccidioides*)	Astrocytoma
Viral (herpes)	Primitive neuroectodermal tumor
Adjacent abscess or cerebritis	Medulloblastoma
Spirochetal (neurosyphilis)	Germinoma
Noninfectious Inflammatory	Ependymoma
Reactive	Secondary neoplasm
Sarcoid	Melanoma
Subarachnoid hemorrhage	Breast carcinoma
Multiple sclerosis (rare)	Lung carcinoma
Vascular	False-positive on FLAIR image
Pial vascular malformation (e.g., Sturge-Weber syndrome)	Normal, hyperintense cortex (especially at convexities)
Subarachnoid hemorrhage	Susceptibility artifact
Superficial siderosis	Prominent pial vessels
Granulomatous angiitis	Flow artifact (especially in basal cisterns)
Hamartomatous	
Meningioangiomatosis	

CNS, central nervous system; FLAIR, fluid-attenuated inversion recovery.

Non-neoplastic Meningeal Disease

Infectious Meningitis

Bacterial Meningitis

Bacterial meningitis results either from hematogenous spread of infection or, occasionally, from direct extension from a paranasal sinus or mastoid source.[88] The mechanism of entry of bacteria from the intravascular space into the CSF is not well understood.

Animal studies have suggested that bacterial cell wall elements provoke an inflammatory response that brings about opening of tight intercellular junctions in the arachnoidal capillary bed.[87] This breakdown in the leptomeningeal blood-brain barrier allows the bacteria to gain access to the SAS. Early congestion and hyperemia of the lepto-

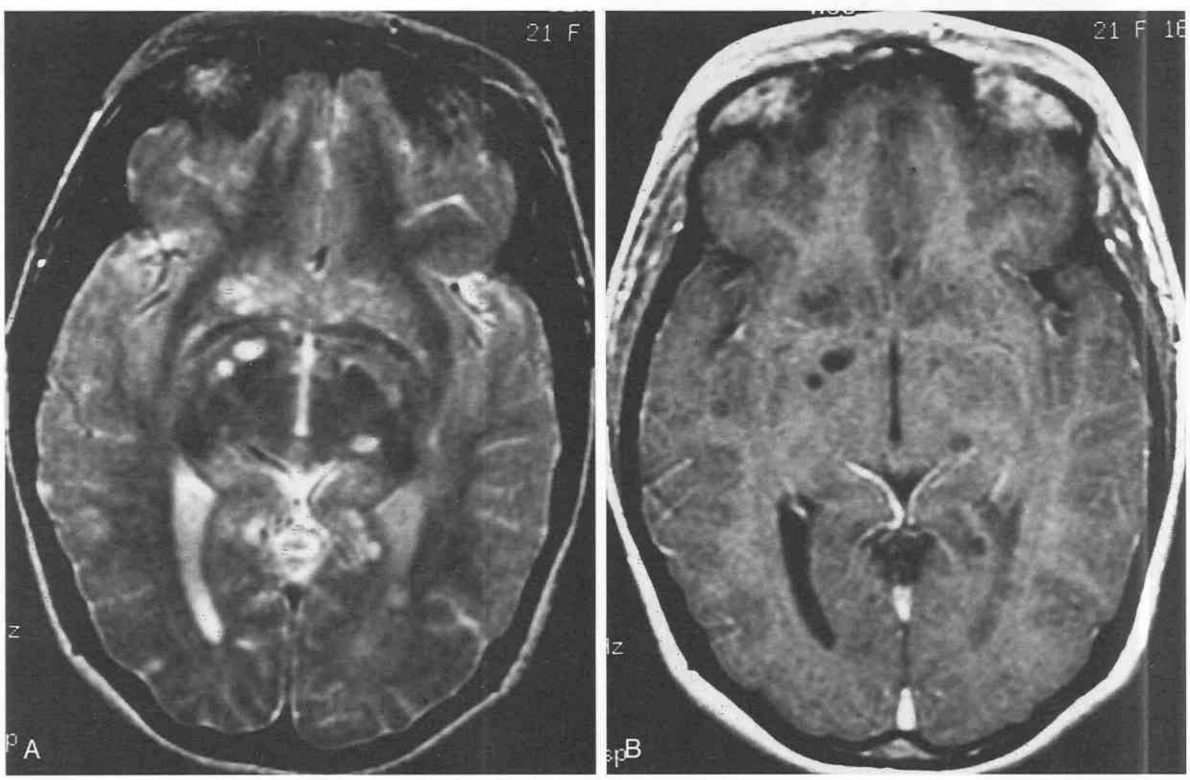

Figure 12–17. Perivascular space pattern. Axial T2-weighted image *(A)* and enhanced T1-weighted image *(B)* show distention of the perivascular spaces at the base of the brain by the gelatinous, nonenhancing pseudocysts of cryptococcosis.

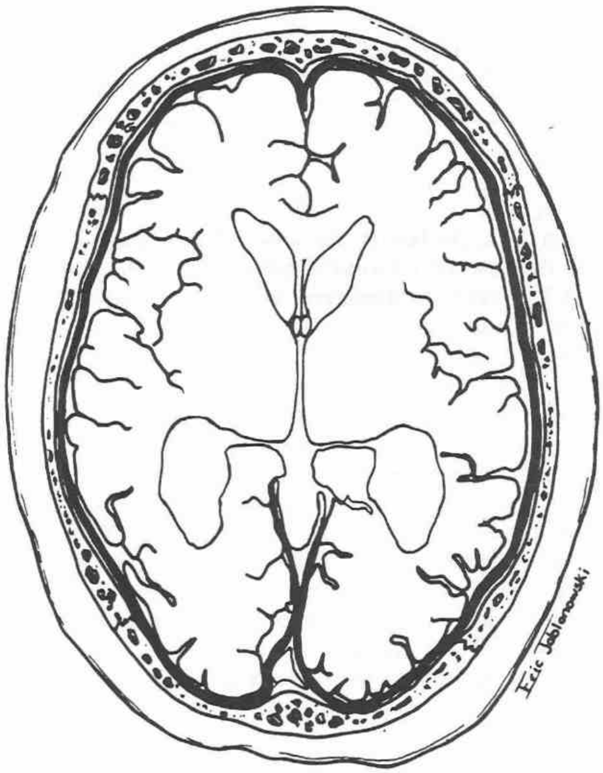

Figure 12–18. Diagram illustrating the dura/arachnoid pattern of meningeal abnormality that follows the inner table of the skull and the dural reflections. (From Meltzer CC, Fukui MB, Kanal E, Smirniotopoulos JG: MR imaging of the meninges: Part 1. Normal anatomic features and nonneoplastic disease. Radiology 201:297–308, 1996.)

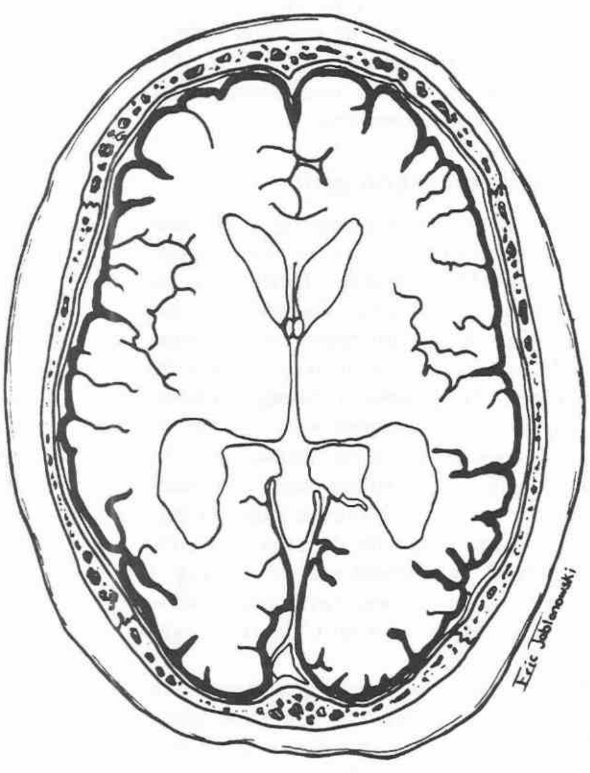

Figure 12–19. Diagram illustrating the pia/subarachnoid space pattern of meningeal abnormality that invaginates into sulci. (From Meltzer CC, Fukui MB, Kanal E, Smirniotopoulos JG: MR imaging of the meninges: Part 1. Normal anatomic features and nonneoplastic disease. Radiology 201:297–308, 1996.)

Table 12–5. Differential Diagnosis: Perivascular Space Pattern

Infectious	Neoplastic
Enhancing	Carcinomatosis
Tuberculosis	Breast carcinoma
Nonenhancing	Lung carcinoma
Cryptococcosis	

meninges are succeeded by mixed inflammatory cell infiltration with exudate in the subarachnoid space, especially over the cerebral convexity (see Fig. 12–16).

A link between meningeal enhancement and the degree of inflammatory cell infiltration of the leptomeninges has been proposed by Mathews and coworkers.[104] The lack of gadolinium enhancement in some areas of minimal inflammation suggests a threshold effect, whereby a critical degree of inflammatory reaction is required before meningeal enhancement may be observed.[104] MRI is superior to CT in the evaluation of complications of meningitis, including subdural empyemas, dural venous thrombosis, secondary ischemia, and parenchymal lesions.[25] Septic thrombosis of the superior sagittal sinus, although uncommon since the advent of antibiotics, may complicate bacterial meningitis[147] (Fig. 12–22).

When thrombosis is suspected, MRI is the imaging modality of choice for confirming the presence of thrombus. Absent flow may be detected as lack of a normal flow void in the sagittal sinus on short TR images and optimally demonstrated by magnetic resonance angiography (MRA) using two-dimensional (2D) phase-contrast techniques.[81] Conversely, localized meningeal enhancement may also be seen overlying an adjacent parenchymal infectious process, such as a brain abscess or encephalitis. Bacterial meningitis may result in ventriculitis, especially in the setting of gram-negative and iatrogenic infections.[48] An early finding in ventriculitis may be that of irregular debris in the dependent portions of the ventricles[48] (see Fig. 12–16). Infectious meningeal processes may occasionally spread across the pial barrier to cause cerebritis.

Table 12–6. Differential Diagnosis: Diffuse Pia Mater/Subarachnoid Space Pattern

Infectious
Bacterial
Spirochetal
Neurosyphilis
Lyme disease
Viral ("aseptic") meningitis
CMV
Varicella-zoster (spinal in AIDS)
Noninfectious Inflammatory
Reactive
Irritative ("aseptic") meningitis
Response to foreign material:
Contrast agents
Chemical (e.g., ruptured dermoid)
Subarachnoid hemorrhage
Vascular
Subarachnoid hemorrhage
Neoplastic
Primary CNS
AIDS lymphoma
Glioblastoma multiforme
Astrocytoma
Primitive neuroectodermal tumor
Primary leptomeningeal gliomatosis (very rare)
Secondary neoplasm
Melanoma
Breast carcinoma
Lung carcinoma
False-positive result on FLAIR image
Concatenated saturation pulse

AIDS, acquired immunodeficiency syndrome; CMV, cytomegalovirus; CNS, central nervous system; FLAIR, fluid-attenuated inversion recovery.

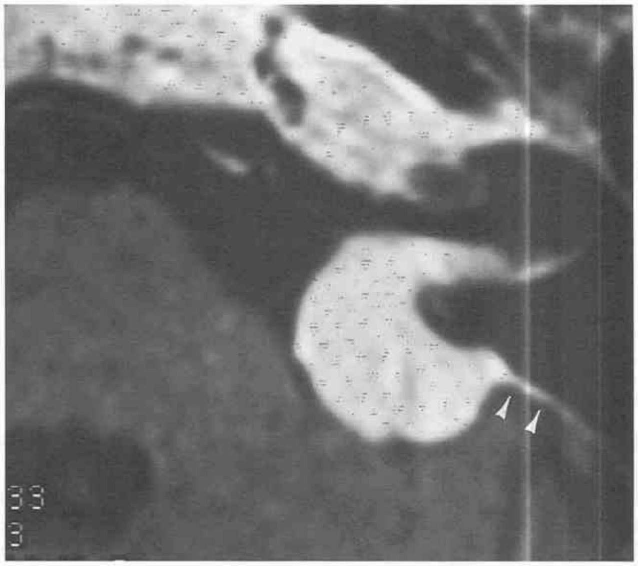

Figure 12–20. Focal dura/arachnoid enhancement. A dural tail *(arrowheads)* adjacent a left acoustic schwannoma illustrates the nonspecificity of this sign as an indicator of meningioma on an enhanced axial T1-weighted image.

Mycobacterial Meningitis

CNS tuberculosis is increasing in frequency, partly as a result of its proclivity to occur with human immunodeficiency virus (HIV) infection. Tuberculous meningitis commonly occurs as a result of disseminated pulmonary infection, usually along with parenchymal brain involvement, although it rarely may be seen as the sole manifestation of the disease.[107] In contrast to bacterial meningitis, tuberculous infection is associated with a more insidious onset, fewer changes in the CSF profile, and higher rates of mortality and complications, such as infarction. Although tuberculosis tends to involve the basal meninges, tuberculomas may occur within the brain parenchyma or subarachnoid, subdural, or epidural spaces[16, 129] (Fig. 12–23). In one series, meningeal enhancement was observed in 36% of HIV-infected patients with CNS tuberculosis evaluated with MRI.[165]

MRI of tuberculous meningitis demonstrates meningeal enhancement, most often in the basal cisterns, reflecting the known predilection of tuberculosis for the base of the brain. Calcification of the basal meninges may also be seen and is more easily appreciated with CT than with MRI.

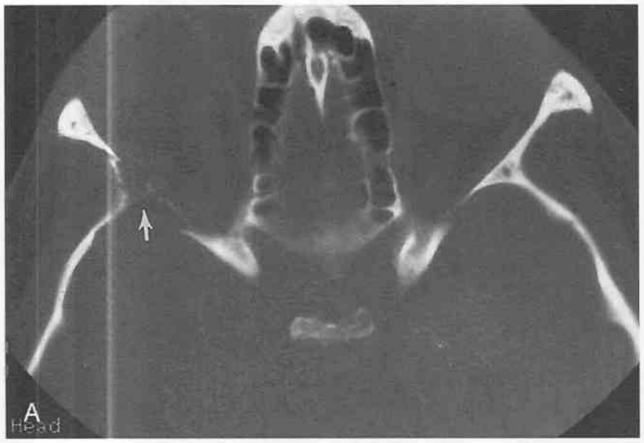

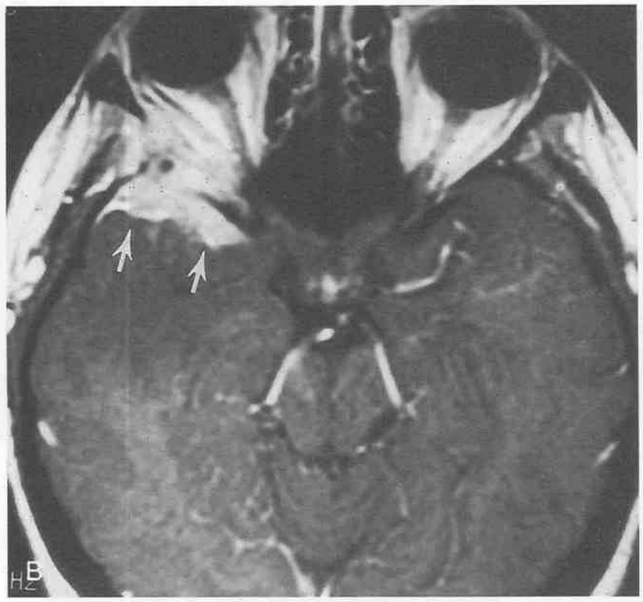

Figure 12–21. Focal dura/arachnoid mass. CT scan *(A)* shows metastatic breast carcinoma to the calvaria *(arrow)* extending to the dura on an enhanced axial T1-weighted image *(B)* *(arrows)*.

Focal or diffuse dura/arachnoid enhancement may be observed on contrast-enhanced MRI scans of the spine in cases of suspected active tuberculous meningitis.[93] Thickening, inflammation, and fibrosis of the leptomeninges are commonly seen at histopathologic examination.

Meningitis may also be caused by a virus or fungus, a fact that is of particular importance in immunocompromised patients. In patients with acquired immunodeficiency syndrome (AIDS), a polyradiculomyelitis may develop, in rare circumstances, as a result of cytomegalovirus (CMV) or varicella-zoster virus infection.[51] Diffuse enhancement of the cauda equina on MRI should alert the clinician to exclude these causes in AIDS patients.[164]

Fungal Meningitis

Fungal meningitis usually results from hematogenous dissemination of disease and is also often seen in immunosuppressed hosts. Fungal meningitides, such as those caused by *Aspergillus*, *Cryptococcus*, and *Coccidioides*, may be demonstrated by contrast-enhanced MRI.[105, 110, 171]

Aspergillosis is an important cause of morbidity and mortality in organ transplant recipients and may be associated with focal, thick dura/arachnoid enhancement that resolves with treatment.[110]

Cryptococcus frequently infects patients with AIDS, but meningeal enhancement is seen only occasionally in cryptococcal meningitis, probably because of the blunted host response.[105, 141] Meningeal enhancement was observed in only one in five autopsy-proven cases of AIDS-related cryptococcosis studied with gadolinium-enhanced MRI.[105] Cryptococcal infection tends to spread from the basal cisterns via perivascular spaces to the basal ganglia, brainstem, internal capsule, and thalamus.[163] This produces a characteristic appearance on MRI scans of nonenhancing,

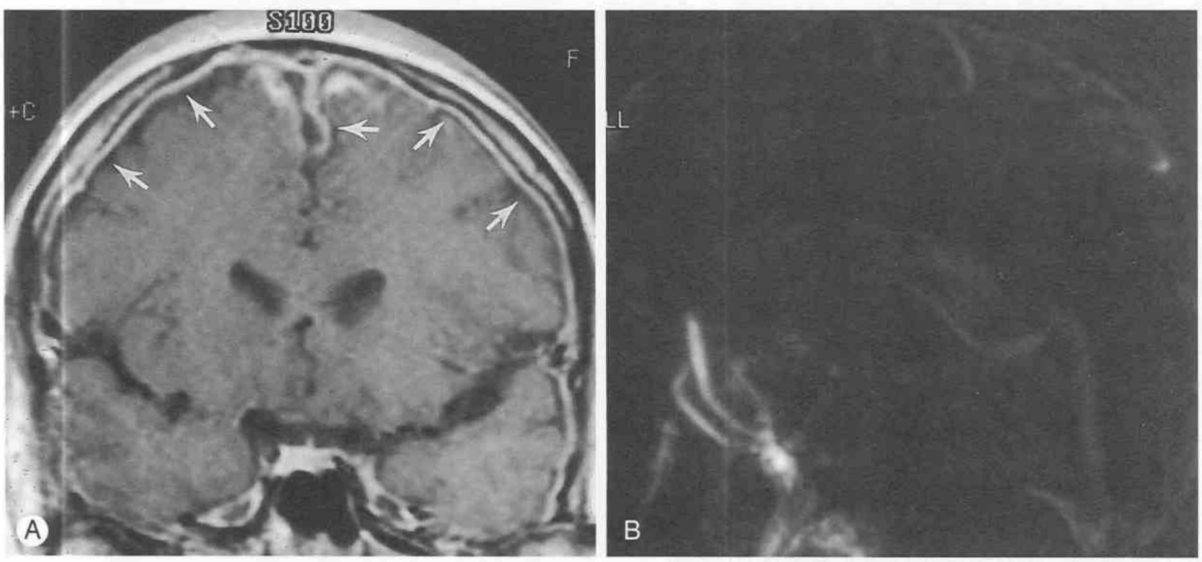

Figure 12–22. Diffuse dura/arachnoid enhancement. *A,* Coronal T1-weighted image shows dura/arachnoid enhancement *(arrows)* in a patient with meningitis and subsequent superior sagittal sinus thrombosis. *B,* There is an absence of flow in the superior sagittal sinus on a sagittal phase-contrast MR angiogram.

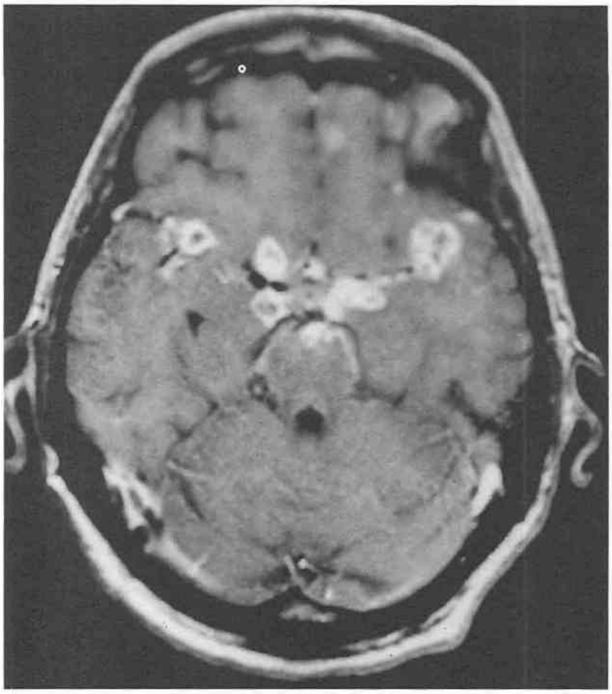

Figure 12–23. Multiple ring-enhancing tuberculomas are distributed throughout the perivascular spaces and basal pial surfaces on an axial T1-weighted image after administration of gadolinium.

dilated perivascular spaces, caused by infestation with the gelatinous pseudocysts of cryptococcal material (see Fig. 12–17).

In contrast to the pattern seen with *Cryptococcus*, Wrobel and colleagues[171] reported MRI enhancement of the meninges in 7 of 11 patients with coccidioidal meningitis. Enhancement was most prominent in the basilar cisterns, the sylvian and interhemispheric fissures, and the upper cervical SAS. Spirochetal infections may exhibit both localized and diffuse meningeal enhancement.[18] Similarly, smooth, diffuse pia/SAS enhancement of the brain stem and the entire spinal cord has been reported in Lyme disease, even in the absence of MRI evidence of parenchymal disease.[33]

Aseptic Meningitis

Meningitis is designated "aseptic" when CSF cultures are sterile. Aseptic meningitis may have a variety of causes, including viral infection and irritation after introduction of foreign substances into the CSF (e.g., blood, chemical agents, or contrast materials), or it may be seen against the backdrop of connective tissue disorders.[107] MRI may demonstrate meningeal enhancement or subarachnoid signal abnormality (Fig. 12–24). In cases of suspected aseptic meningitis, performing MRI after administration paramagnetic contrast medium may help prevent delays in diagnosis.[42]

Noninfectious Inflammatory Meningitis

Noninfectious granulomatous disease can also involve the meninges. Approximately 5% of patients with sarcoidosis have neurologic manifestations; of those, the most common sign is that of cranial nerve palsies.[150] Gadolinium-enhanced MRI is the study of choice to document meningeal involvement and may show either the pia mater/SAS or the dura/arachnoid[143, 144, 174] (see Fig. 12–15). Striking thickening of the meninges may also be demonstrated. Sarcoid was present in 31% of 37 patients with chronic meningitis of unknown etiology examined with enhanced MRI and meningeal biopsy and, as such, was the most frequent cause of chronic meningitis in that series.[26]

Meningeal abnormality may also occur in Wegener's granulomatosis[131] (Fig. 12–25). Thickened, nodular meninges on both enhanced CT and MR images in a patient with Wegener's granulomatosis were reported by Tishler and colleagues.[153] The imaging features reflect the histopathologic findings of dural and brain biopsies that revealed granulomatous infiltration of the dura and development of fibrosis and granulomas of the pia mater and arachnoid.

Hypertrophic cranial pachymeningitis is a rare type of diffuse granulomatous inflammation that produces thickening, chronic inflammation, and fibrosis of the dura.[101, 103] Common presenting symptoms include headache, cranial nerve palsies, and ataxia. Diffuse dural enhancement (on enhanced T1-weighted images) or hypointense and thickened dura (on T2-weighted images) may be demonstrated on MRI (see Fig. 12–10). Diagnosis requires confirmation with dural biopsy. The disease may progress despite corticosteroid therapy.

In rare instances, meningeal enhancement has been reported to accompany demyelinating disease. We are aware of two reports of meningeal enhancement on MRI in cases of multiple sclerosis (MS). One case displayed a diffuse dura/arachnoid pattern; the other showed focal pial enhancement.[9, 32] Serial MRI of MS plaques suggests that parenchymal lesion enhancement is related to the inflammatory process associated with active demyelination.[9] Analogously, meningeal enhancement in MS may result from extension of perivascular lymphoplasmacytic infiltration into the leptomeninges, found in 41% of autopsy cases.[63] A similar inflammatory etiology was proposed by Fulbright and coauthors[49] in describing enhancement of multiple cranial nerves in Guillain-Barré syndrome, a disorder characterized by peripheral demyelination.

Iatrogenic Meningeal Enhancement

Benign meningeal enhancement on MRI may result from mechanical disruption of the meninges from a variety of causes. Localized or diffuse dural enhancement may occur after craniotomy and may persist indefinitely[20, 37] (Fig. 12–26). It may be difficult to distinguish normal reactive postoperative enhancement from meningeal tumor involvement following craniotomy for tumor resection. Postoperative meningeal enhancement usually regresses over time, often resolving between 1 and 2 years after craniotomy.[37] In addition, the distribution of enhancement may support a benign etiologic mechanism.

In contrast to the typically basilar pattern of neoplastic meningitis, postoperative enhancement occurs more often over the convexities.[20] The morphology of enhancement may also provide clues as to the cause. A nodular dural

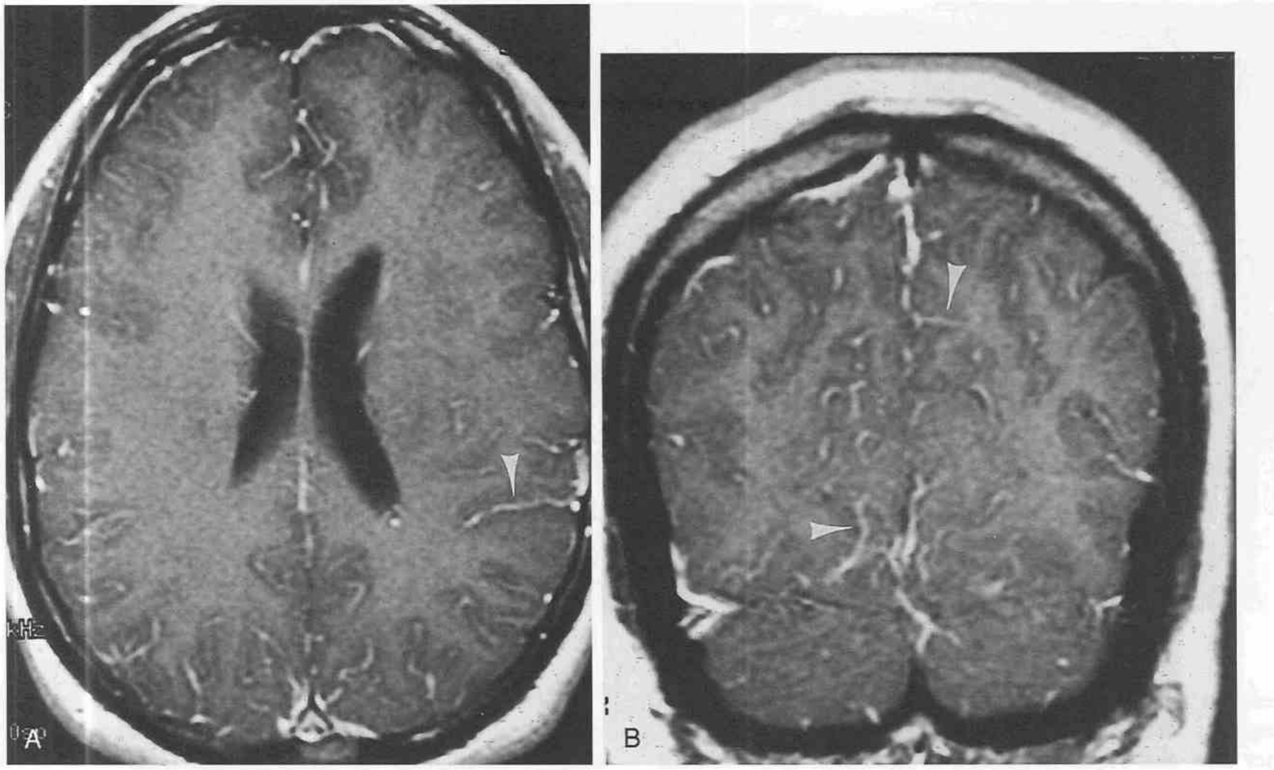

Figure 12–24. Aseptic meningitis. *A* and *B,* Thin, linear pia/subarachnoid space enhancement *(arrowheads)* is seen in a patient with headache and no organism growth on cerebrospinal fluid culture on axial and coronal enhanced T1-weighted images.

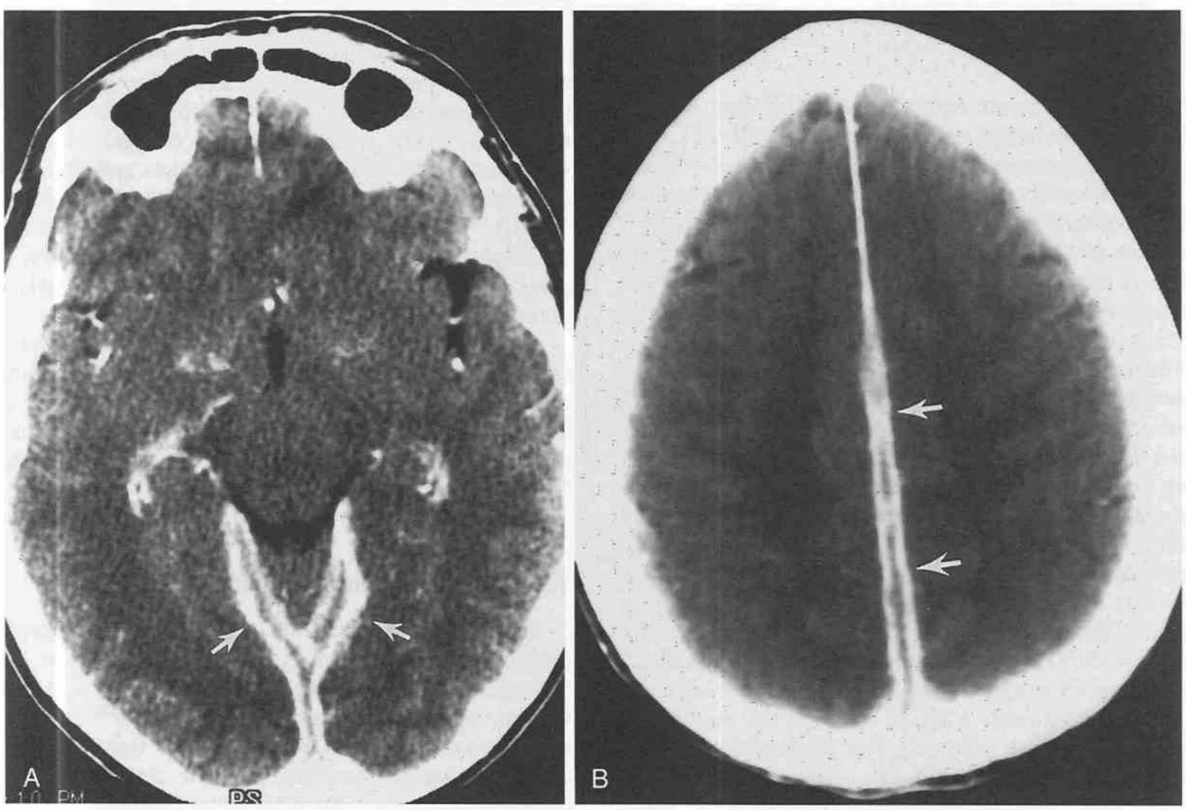

Figure 12–25. Wegener's granulomatosis. *A* and *B,* Diffuse thickening and enhancement of the meninges in a dura/arachnoid pattern *(arrows)* are present in a patient with biopsy-proven Wegener granulomatosis on a contrast-enhanced CT scan.

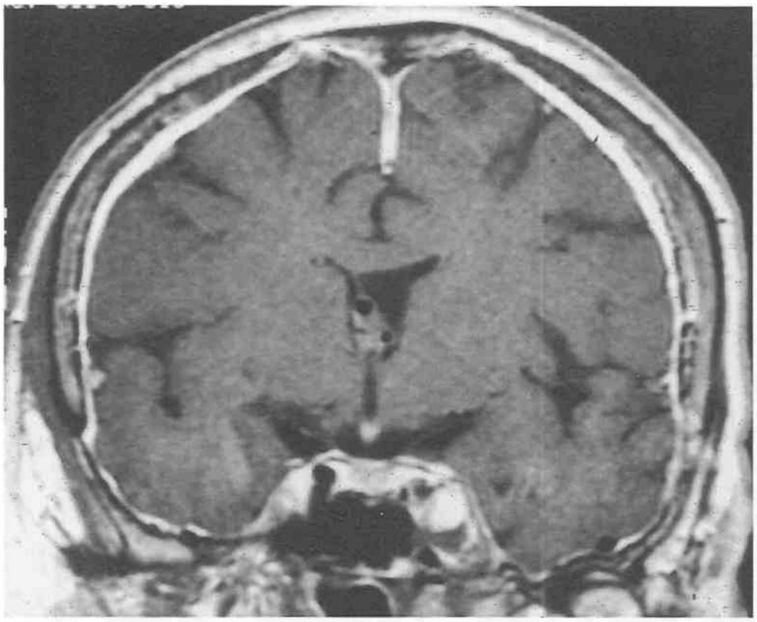

Figure 12–26. Postoperative meningeal enhancement. Coronal T1-weighted image shows diffuse, linear enhancement in a patient who had undergone previous craniotomy for meningioma.

enhancement pattern or thick pia mater/SAS enhancement suggests recurrent tumor.[75] Placement of a ventricular catheter may also result in diffuse or localized dural enhancement. In rare instances, dura/arachnoid enhancement may result from uncomplicated lumbar puncture.[108] Dural enhancement after lumbar puncture occurs more commonly, however, when intracranial hypotension results, suggesting a CSF leak.[15]

Vascular Disease

Occasionally, an acute cerebral infarction may demonstrate adjacent meningeal enhancement (Fig. 12–27). This "meningeal enhancement sign" occurs between day 2 and day 6 after infarction. It is seen with large supratentorial infarcts and usually has a dura/arachnoid configuration.[36, 39] Although the cause of meningeal enhancement in cerebral infarction is not established, possible contributing factors include reactive hyperemia and local inflammation following meningeal irritation.[36]

Hemorrhage into the SAS also irritates the leptomeninges, causing inflammation of the pia mater and arachnoid.[66] In severe cases, fibrosis may ensue and, eventually, may obliterate the SAS. Superficial siderosis is a rare condition resulting from deposition of hemosiderin in the leptomeninges and surface of the brain following recurrent SAH and is a cause of hearing loss.[22, 76, 79] The leptomeninges are thickened and pigmented on pathologic examination. A characteristic hypointense rim is observed along the brain surface on T2-weighted images[17, 22] (Fig. 12–28). This hypointense border of hemosiderin deposits in superficial siderosis becomes exaggerated, and thus more readily detected, on gradient-echo MRI as a result of augmented magnetic susceptibility effects.[79] The thickened meninges may also enhance with gadolinium. Vasculitis rarely involves the meninges. Preferential involvement of small leptomeningeal vessels in granulomatous angiitis may result in meningeal enhancement.[113]

MRI is the modality of choice for evaluation of Sturge-Weber syndrome, a phakomatosis characterized by deranged vasculature of the face, brain, and meninges.[146] Poor venous drainage and chronic ischemic damage to the underlying cortex develop as a result of the leptomeningeal vascular malformation that originates in the subarachnoid space. MRI of the brain shows superficial gyriform enhancement. This enhancement likely results from slow flow within the leptomeningeal vascular malformation with or without enhancement of ischemic[11, 160] (Fig. 12–29).

Meningioangiomatosis is a rare hamartomatous disorder of the leptomeninges, distinguished by meningovascular proliferation and leptomeningeal calcification.[2, 65, 126] A cortical mass with meningeal extension and heterogeneous signal intensity on T2-weighted images and demonstrating contrast enhancement on MRI has been reported (Fig. 12–30).[126, 166] Halper and coworkers[65] have theorized that meningioangiomatosis is caused by a proliferation of both meningothelial cells and leptomeningeal vessels within perivascular spaces as they penetrate the cortex.

A combined pia mater/SAS and dura/arachnoid pattern of enhancement has been rarely reported in association with migraine headaches.[29, 97] This unusual finding is attributed to hyperperfusion, documented on single photon emission computerized tomography (SPECT) or transcranial Doppler imaging.[29, 97]

Toxic Meningeal Enhancement

Chemical meningitis may arise following rupture of dermoid or epidermoid cyst. This inflammation is likely provoked by the irritating effect of cholesterin crystals and keratin material discharged into the CSF.[31, 98] In such cases, the diagnosis of ruptured dermoid is usually verified by demonstration of droplets of high signal lipid material dispersed throughout the SAS on unenhanced T1W MR images.

Meningeal irritation resulting in contrast enhancement

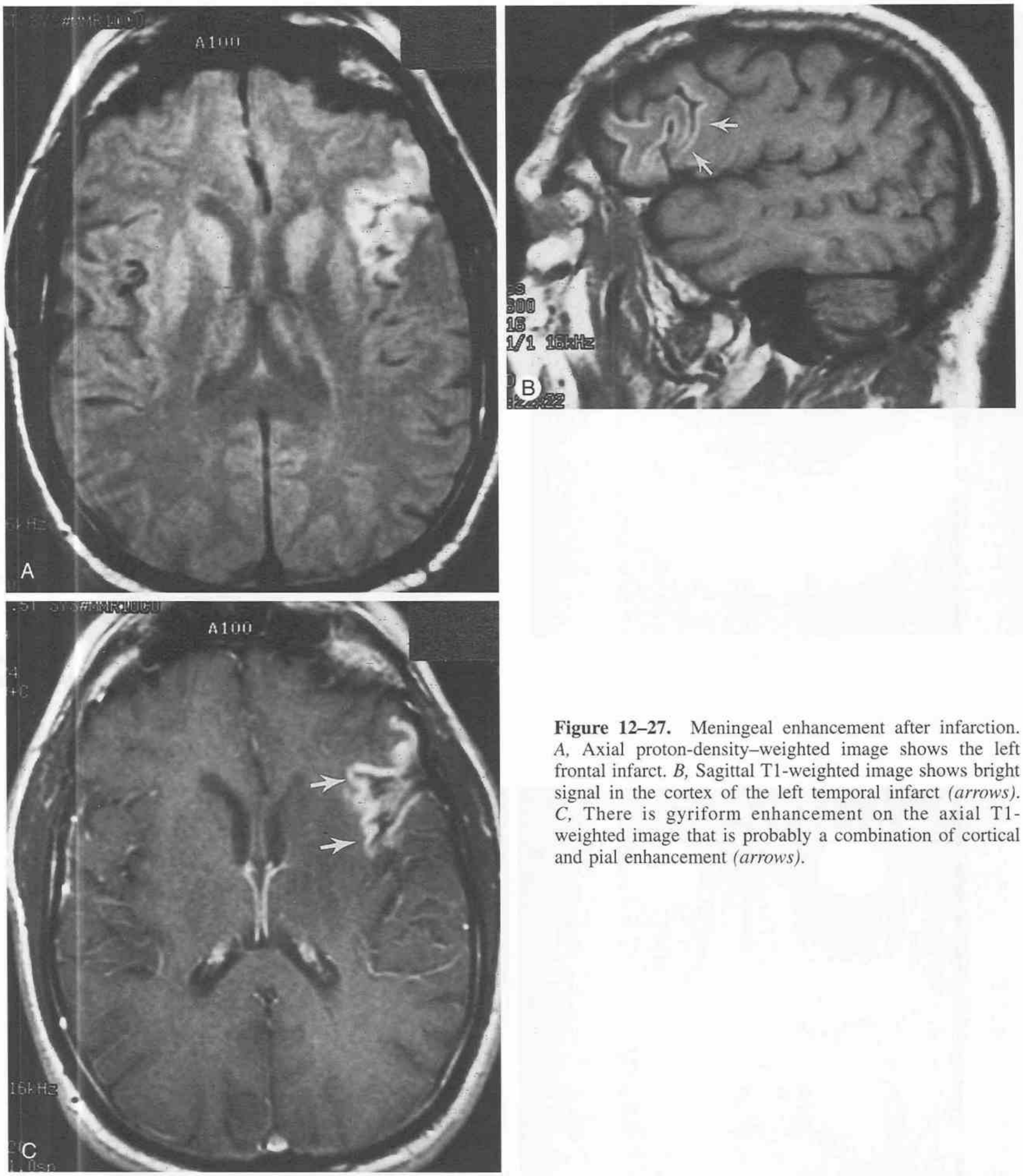

Figure 12–27. Meningeal enhancement after infarction. *A,* Axial proton-density–weighted image shows the left frontal infarct. *B,* Sagittal T1-weighted image shows bright signal in the cortex of the left temporal infarct *(arrows)*. *C,* There is gyriform enhancement on the axial T1-weighted image that is probably a combination of cortical and pial enhancement *(arrows)*.

on MRI has also been reported in the setting of adverse drug reactions. Eustace and Buff[42] reported a case of ibuprofen-induced meningitis depicted by meningeal enhancement on MRI. Meningeal enhancement persisted on repeated MRI scans 1 week later despite resolution of symptoms within 12 hours of drug cessation.

Spontaneous Intracranial Hypotension

Like the low intracranial pressure headache after complicated lumbar puncture, spontaneous intracranial hypotension is identified by a postural headache that resolves after placement of an epidural blood patch.[135] A CSF pressure of less than 60 mm of water in the absence of previous lumbar puncture establishes the diagnosis.

MRI has shown striking, thick, diffuse dural/arachnoid enhancement.[44, 74] Subdural fluid collections may occur in conjunction with this low-pressure state.[135] An unsuspected, spontaneous CSF leak may be the inciting factor (Fig. 12–31), and thus recognition of this combination of imaging and clinical findings should prompt a search for the source of leak. Identification of this treatable cause of

Figure 12–28. Siderosis. The dark signal from hemosiderin outlines the pial surface of the cerebellum in this patient with superficial siderosis in an axial T2-weighted image.

Figure 12–29. Sturge-Weber syndrome. Gyriform enhancement defines the pial vascular malformation and adjacent ischemic occipital cortex on an axial T1-weighted image.

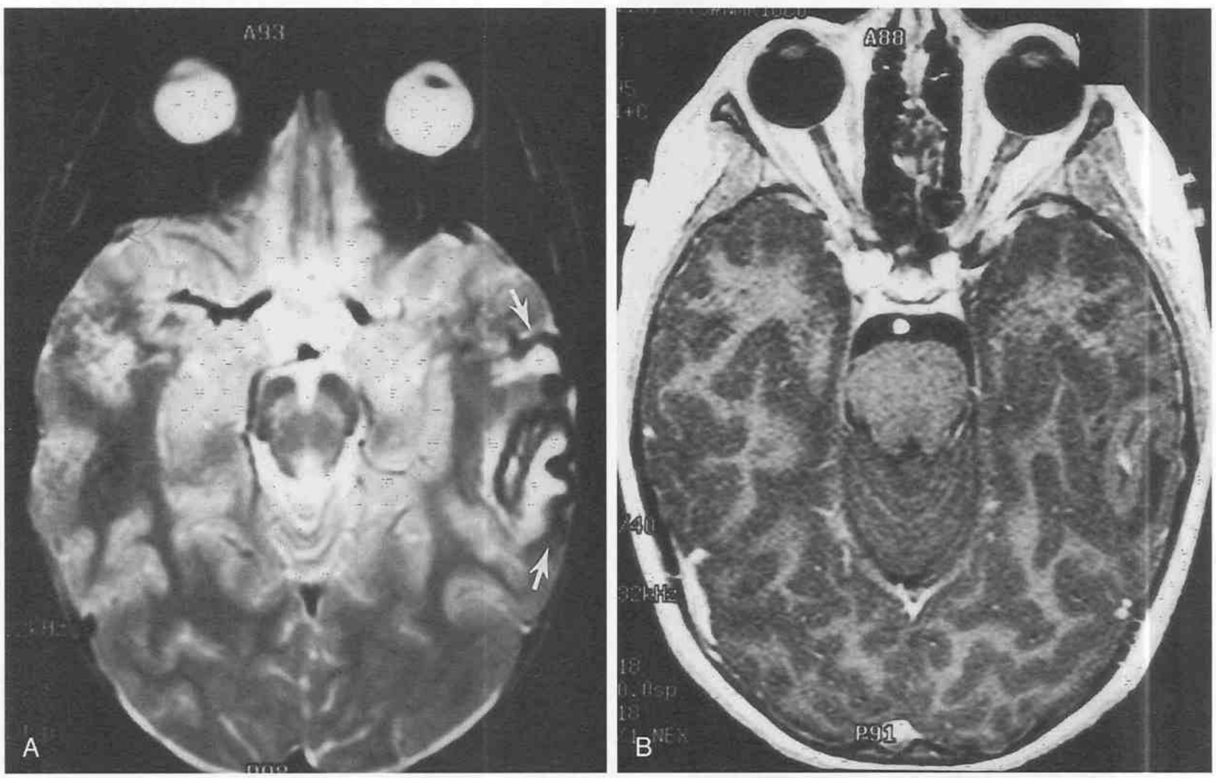

Figure 12–30. Meningioangiomatosis. *A,* Axial T2-weighted image reveals left temporal gyriform hypointensity with subcortical hyperintensity *(arrows)* that may represent the meningovascular proliferation. *B,* This axial spoiled GRASS image does not reveal enhancement. GRASS, gradient-recalled acquisition in a steady state.

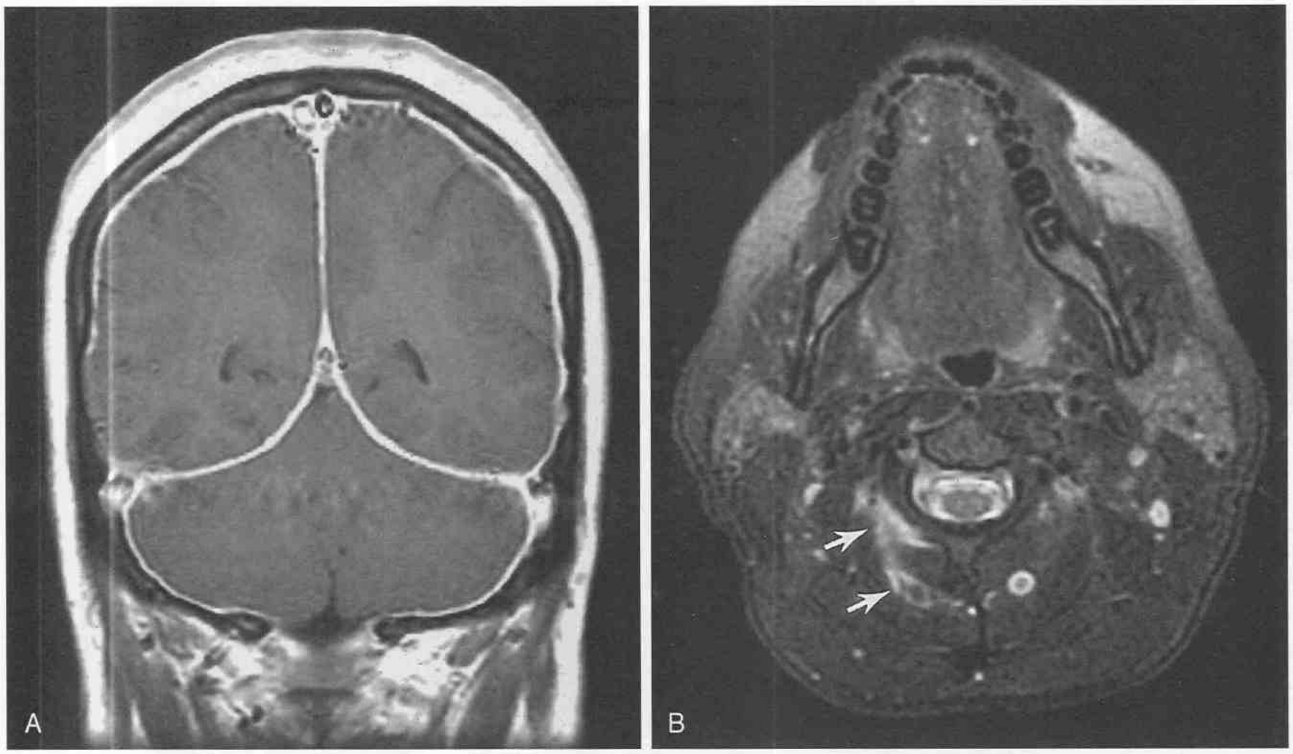

Figure 12–31. Intracranial hypotension. Coronal T1-weighted image demonstrates diffuse dura/arachnoid enhancement in this patient who presented with severe headaches and whose CSF pressure was low on lumbar puncture. The axial T2-weighted image shows fluid, presumed to be cerebrospinal fluid in the soft tissues of the upper neck *(arrows)*. The patient recovered after surgery despite the fact that, although myelography revealed a leak, the exact site could not be found at operation.

meningeal abnormality in association with the germane clinical features may prevent diagnostic delay and unnecessary meningeal biopsy.

Neoplastic Meningeal Disease

Primary Involvement

Primary dural neoplasms are rare. Neoplasms arising from the dura are mesenchymal in origin because the dura is composed of fibrous tissue.[138] Primary dural tumors bridge the entire range of benign (fibromas) to intermediate (fibromatosis) to malignant (sarcomas).[134] An assortment of dural sarcomas has been reported, including chondrosarcoma, fibrosarcoma, and malignant fibrous histiocytoma.[5, 95, 100] Previous radiation therapy for another disease has been connected with some sarcomas.[5]

The most common primary tumor arising from the leptomeninges is meningioma (Figs. 12–32 and 12–33).[138] Meningiomas originate from meningothelial cells of the arachnoid.[138] A hormonal influence has been implicated in the pathogenesis of meningiomas because they are more common in women than in men, occur more often in patients with breast cancer, and may become symptomatic during pregnancy.[12, 77, 138] Radiation therapy has also been implicated as a causative factor in meningioma,[50, 149] especially in patients treated for tinea capitis or vascular nevi in childhood. Fifty percent of meningiomas are isointense with gray matter on T1-weighted and T2-weighted imaging; the remaining half vary in signal intensity.[148] Heterogeneous signal intensity on MRI may result from calcification, vascular, or cystic components.[148]

Additional primary leptomeningeal neoplasms, such as glioma (Fig. 12–34),[34, 73, 96, 125] melanoma,[4] melanocytoma

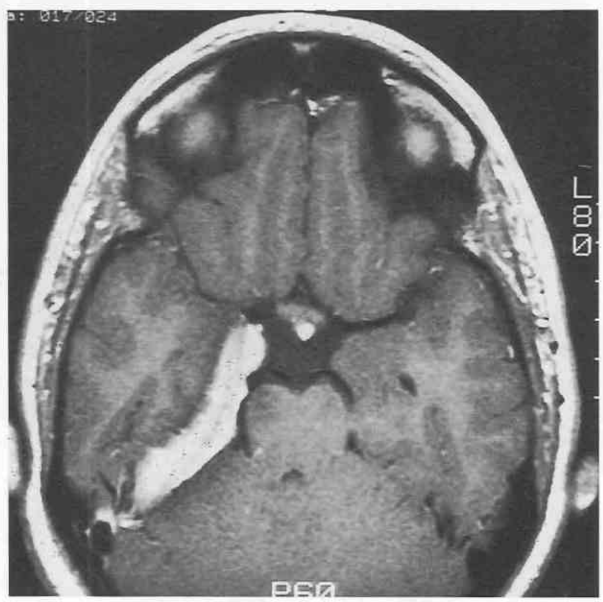

Figure 12–32. Focal, linear dura/arachnoid enhancement characterizes this right tentorial en plaque meningioma.

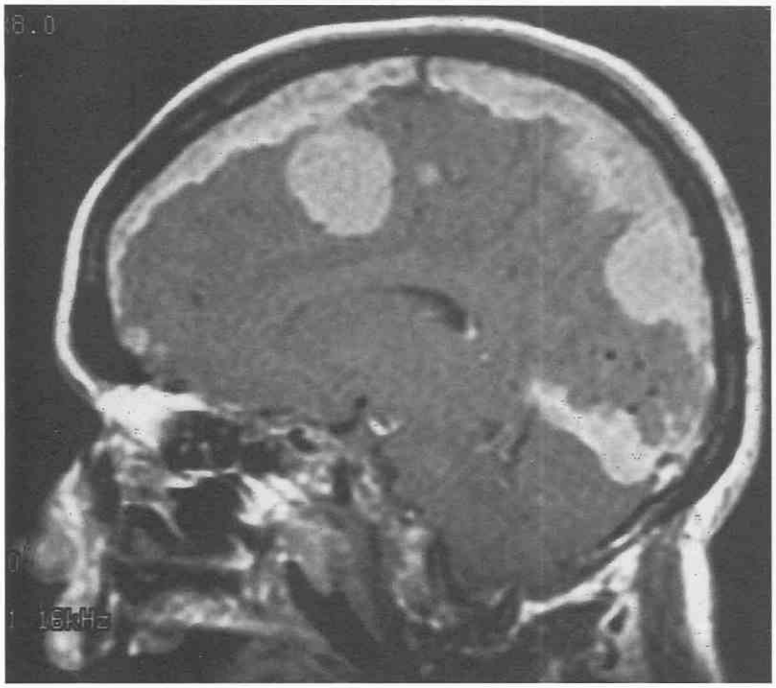

Figure 12–33. Meningiomatosis in neurofibromatosis, type 2 (NF 2). Meningiomatosis (multiple meningiomas) was found in this patient with diffuse, nodular dura and arachnoid enhancement.

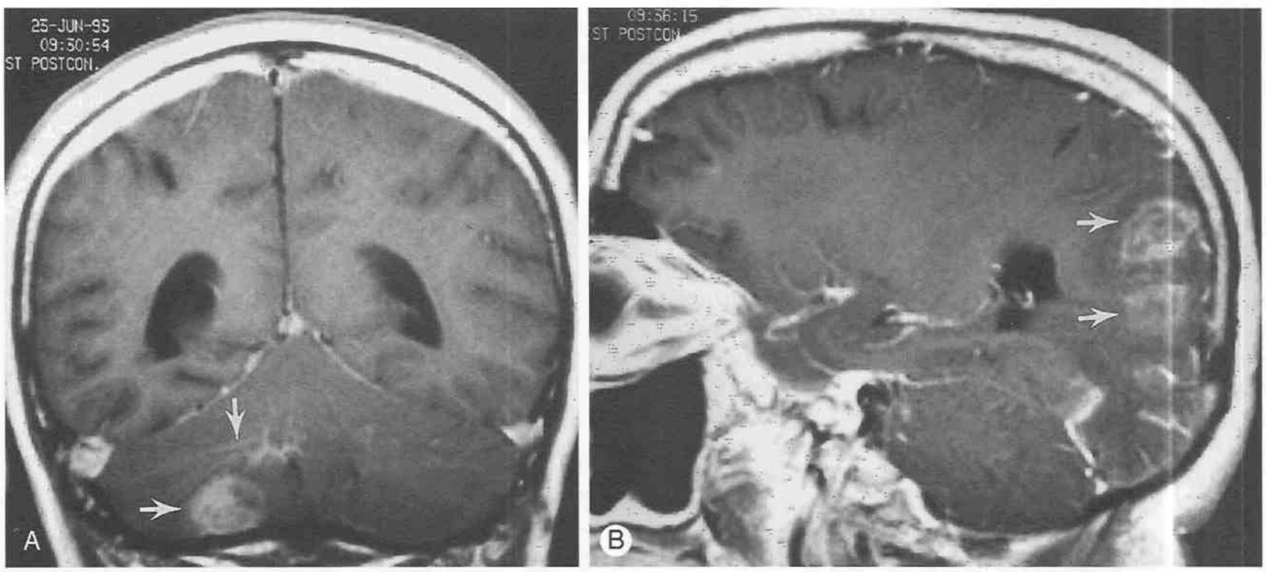

Figure 12–34. Primary leptomeningeal gliomatosis. This rare primary malignant meningeal neoplasm was diagnosed only at autopsy. There is both linear and nodular enhancement in a pia/subarachnoid space pattern *(arrows)* on a coronal image *(A)* and a sagittal enhanced T1-weighted image *(B)*. (Courtesy of Bernhard C. Sander, M.D., and Tibor Mitrovics, M.D., Freie Universitatsklinikum Rudolf Virchow, Berlin, Germany.)

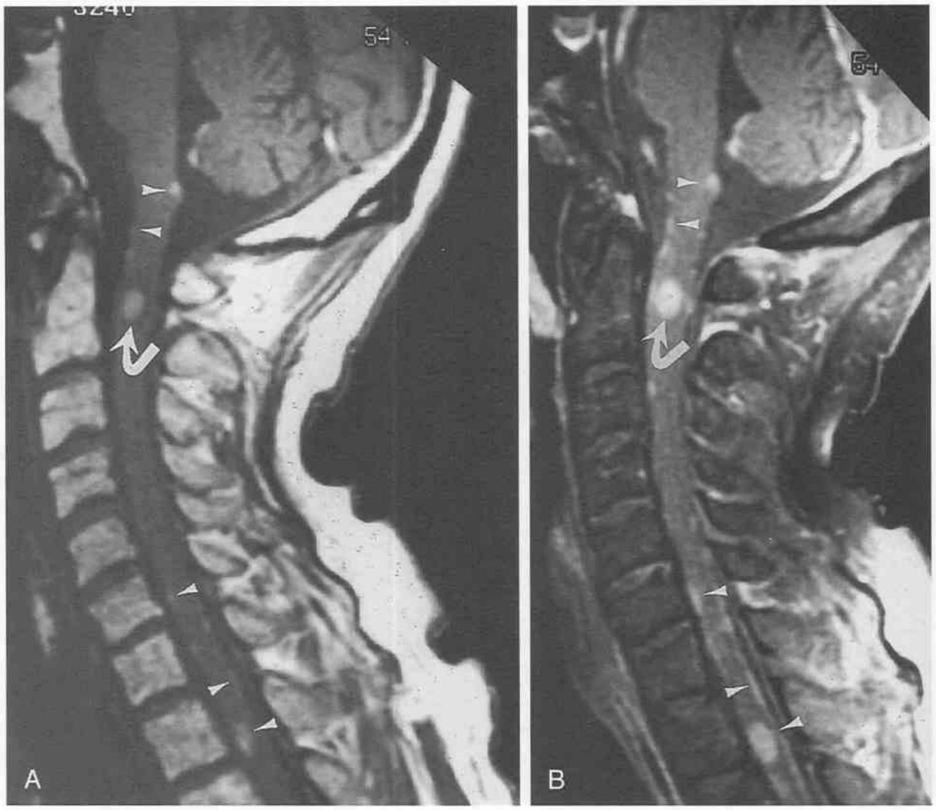

Figure 12–35. Primary leptomeningeal melanocytosis. Sagittal T1-weighted images obtained before *(A)* and after *(B)* administration of gadolinium show multiple, tiny nodular foci of hyperintensity *(arrowheads)* along the pial surface of the cervical spinal cord with enhancement in this case of primary leptomeningeal melanocytosis. There is also an intramedullary lesion *(curved arrow)*.

(Fig. 12–35),[111] sarcoma,[127, 138] and lymphoma,[94] are very rare. Primary leptomeningeal gliomas probably originate from heterotopic rests of glial tissue within the meninges and SAS.[28, 170]

Secondary Involvement

Breast carcinoma (CA), lymphoma, leukemia, lung CA, malignant melanoma, gastrointestinal CA, and genitourinary CA are the most common neoplasms to progress to meningeal dissemination.[71, 118, 161] Primary CNS neoplasms, such as medulloblastoma and primitive neuroectodermal tumor (PNET), pineoblastoma (Fig. 12–36), ependymoma, germ cell tumor (Fig. 12–37), astrocytoma (Fig. 12–38), and glioblastoma (Fig. 12–39), also have a propensity for meningeal spread.[6, 7, 119, 120, 124] Most tumors tend to produce focal involvement in a dura/arachnoid or pia/SAS distribution. Exceptions to this are very aggressive tumors, such as lung and breast CA, that may result in diffuse meningeal neoplasm.

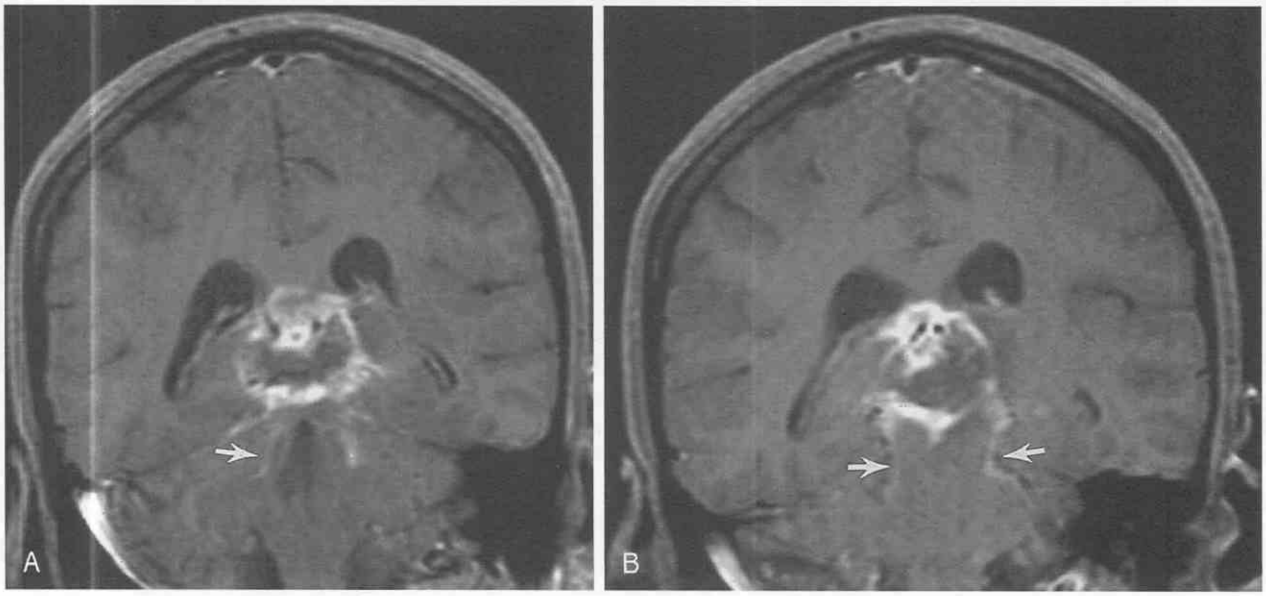

Figure 12–36. Subarachnoid spread of pineoblastoma. *A* and *B*, Coronal enhanced T1-weighted images show the pineal region mass with pia/subarachnoid space enhancement *(arrows)* in this patient with cerebrospinal fluid dissemination of pineoblastoma.

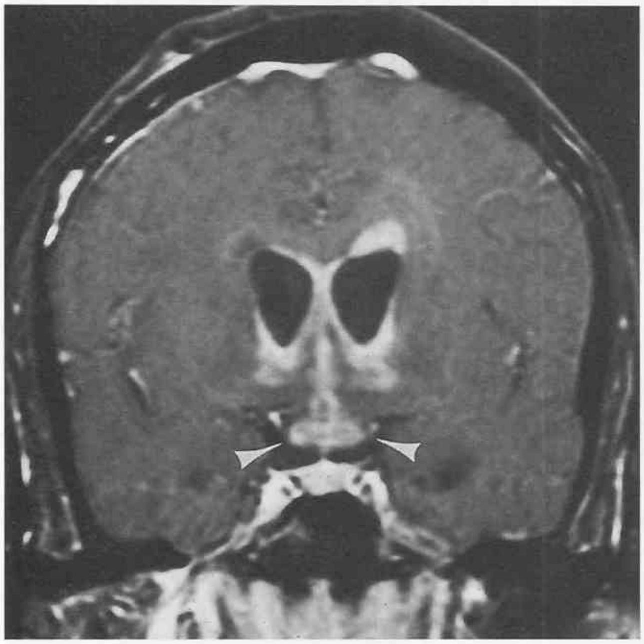

Figure 12–37. Disseminated germ cell tumor. This pineal region neoplasm demonstrates ependymal and subarachnoid spread involving the optic chiasm *(arrowheads)* on an enhanced coronal T1-weighted image.

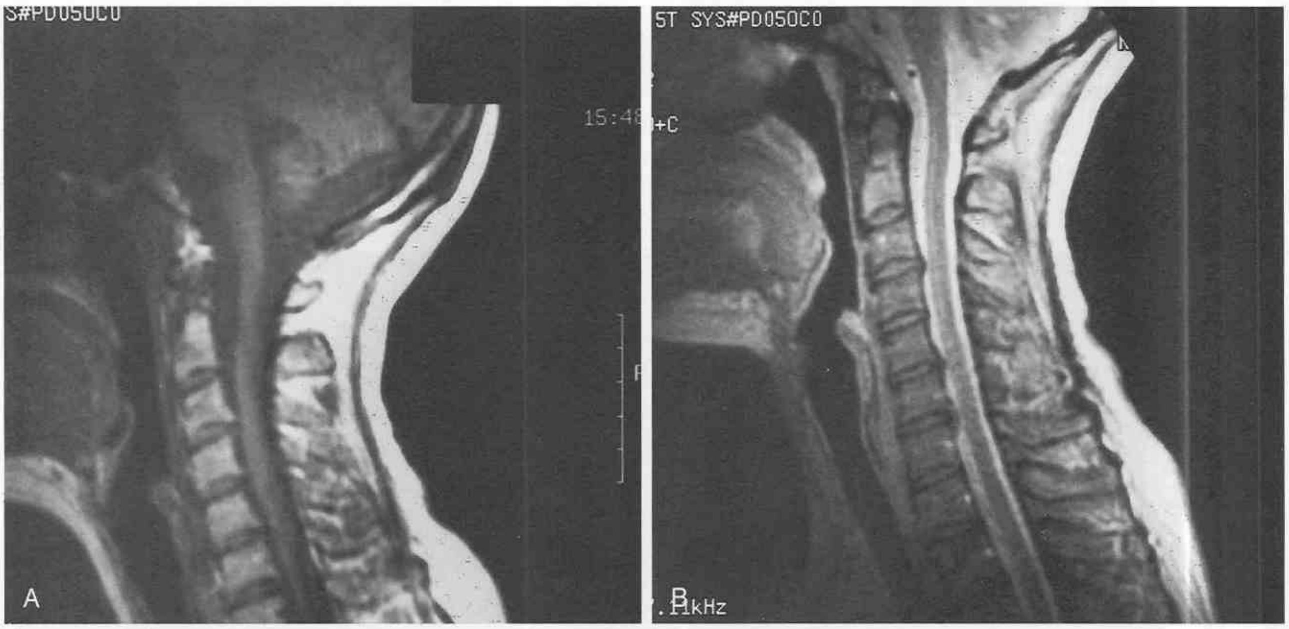

Figure 12–38. Cerebrospinal fluid spread of astrocytoma in a 30-year-old patient. Sagittal T1-weighted images obtained before *(A)* and after *(B)* gadolinium administration show such extensive enhancement of the subarachnoid space that the enhanced T1-weighted image mimics a T2-weighted sequence. The patient had been treated for astrocytoma 3 years earlier.

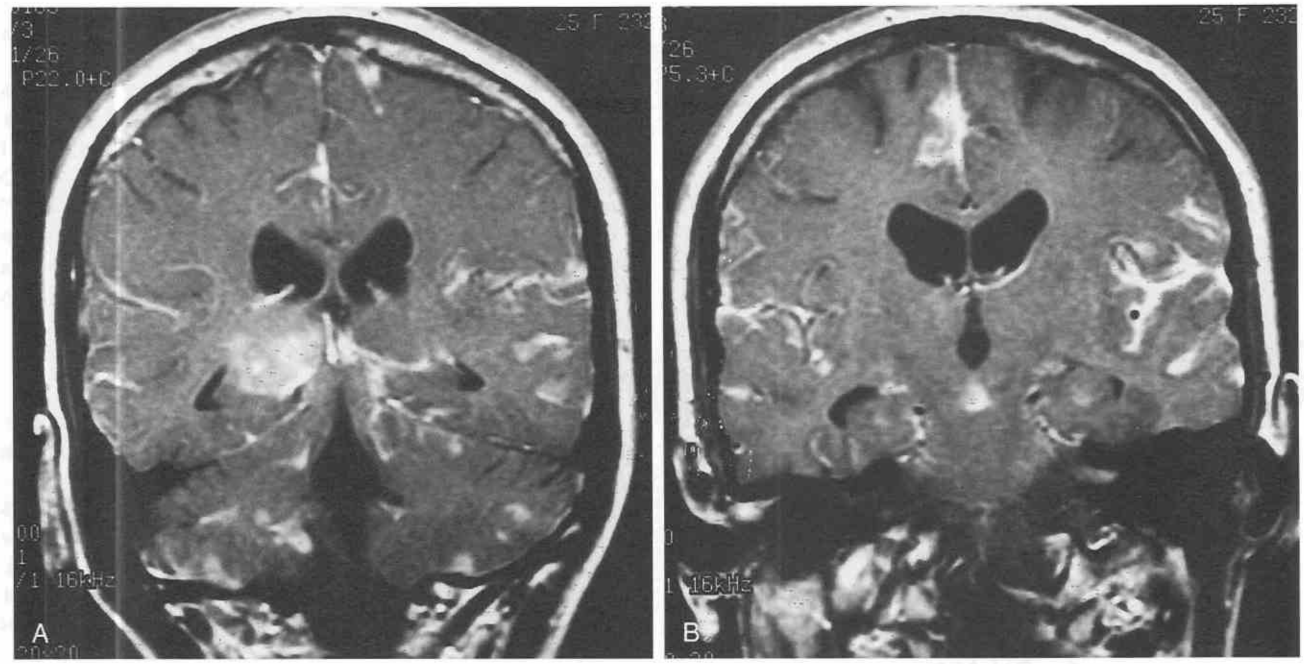

Figure 12–39. Cerebrospinal fluid spread of glioblastoma multiforme after biopsy in a 40-year-old patient. Six weeks after stereotactic biopsy, an enhanced coronal T1-weighted image shows the primary right thalamic glioblastoma and extensive, thick dissemination of neoplasm in a pia/subarachnoid space pattern.

Risk Factors for Leptomeningeal Dissemination of Neoplasm

The risk factors for leptomeningeal dissemination differ somewhat for primary CNS and non-CNS neoplasms but are largely related to tumor dedifferentiation and proximity to CSF spaces.

Characteristics of primary CNS neoplasms that correlate highly with a tendency to CSF spread are (1) poor glial fibrillary acidic protein (GFAP) staining, indicating poor differentiation of neoplasm,[119] and (2) close proximity to CSF spaces.[57, 158] Patient risk factors for leptomeningeal dissemination of primary CNS neoplasm include extended survival[7] and previous operation (see Fig. 12–39).[6, 8]

In cases of non-CNS neoplasm, prolonged survival[116, 118, 172] and the presence of other metastatic foci[14, 116, 156] increase the probability of meningeal dissemination. Dispersion of non-CNS neoplastic cells is likely a multistep process, according to the analysis of the pathways of metastases performed by Viadana and colleagues.[159] This "cascade" phenomenon postulates that spread of the primary tumor occurs to at least one intermediate organ, from which it may disseminate widely.[159] The observation that vertebral body (especially in breast CA),[14, 156] bone marrow, and liver metastases (especially in lung CA)[116] are commonly present in cases of meningeal carcinomatosis lends credence to this predisposition of tumors to first spread to an intervening organ before disseminating widely. The breast, lung, and stomach, in addition to melanoma, are primary sites of solid tumors that tend to metastasize to the leptomeninges.[71, 72, 118, 161] Hematologic neoplasms such as leukemia and lymphoma are also inclined to CSF spread.[72]

Mechanisms of Meningeal Neoplastic Dissemination

Dura

The two major mechanisms of spread of neoplasm to the dura are (1) hematogenous dissemination and (2) direct extension.

Hematogenous Spread

One pathway for neoplasm to reach the dura is as a sequela of bone metastases; this route is common in patients with breast CA. Vertebral bone metastases disseminate hematogenously through Batson's plexus and then to the intracranial dural venous sinuses[156] (Fig. 12–40). For example, dural metastases are as likely as parenchymal brain metastases in cases of disseminated breast CA, reflecting the high incidence of vertebral involvement.[156]

Direct Extension

A second route is dural infiltration, with neoplasm extending directly from vertebral or calvarial lesions[1] (Fig. 12–41).

Leptomeninges

The major mechanisms of seeding into the CSF and leptomeninges are also hematogenous spread and direct extension, but these may take a variety of forms.

Hematogenous Spread

There are three main modes by which neoplasm is spread hematogenously to the leptomeninges and CSF.

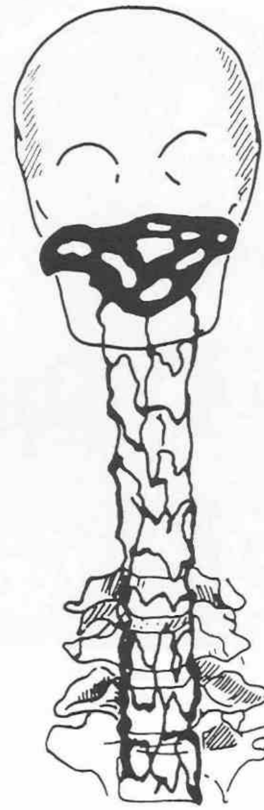

Figure 12–40. Diagram of the route of hematogenous spread to dura via Batson plexus. (From Fukui MB, Meltzer CC, Kanal E, Smirniotopoulos JG: MR imaging of the meninges: Part 2. Neoplastic disease. Radiology 201:605–612, 1996.)

First, the choroid plexus may become seeded hematogenously that results in tumor deposits that are then sloughed into the CSF.[35, 58, 71, 72] This pathway is presumably more common than is clinically evident. The frequency of choroid metastases is likely to be underestimated on MRI because the normal choroid plexus is irregular in contour. Metastases occur frequently when the choroid plexus is sectioned at pathologic examination; however, the choroid plexus may not be examined routinely.[109, 118]

The second hematogenous route is via parenchymal blood vessels in the Virchow-Robin (perivascular spaces) to the pia mater and then into the SAS[54, 72] (see Fig. 12–2). This mechanism of seeding of the leptomeninges and SAS may result in tumor spread either *to* or *from* the SAS.[54, 72, 109]

Third, neoplasm may interrupt the thin walls of microscopic vessels in the arachnoid to enter the SAS[130] (see Fig. 12–2). This pathway of spread occurs more commonly in leukemia and lymphoma than in solid tumors.[130]

Direct Extension

Direct extension, the other major means by which neoplasm gains access to the leptomeninges, can also take one of three forms.

First, parenchymal neoplasm close to CSF borders, such as cortical or subependymal tumor, may shed cells into the CSF[35, 168] (see Fig. 12–13). Non-CNS neoplasms may induce a fibrous reaction that tends to prevent CSF spread; thus, this pathway may be more common among tumors of CNS origin.[71, 118]

Second, an overlying dural neoplasm may invade the leptomeninges directly.[61, 71, 72]

Third, spinal epidural neoplasm can spread contiguously along nerve roots or their lymphatics.[10, 14, 35, 90, 118, 156] This route of spread is somewhat controversial; some authors assert that the frequency of leptomeningeal carcinomatosis would be greater if this were an important pathway, considering the common occurrence of vertebral metastases.[71]

Complications of Meningeal Neoplasms

Once the CSF has been seeded, neoplasm has the potential to disseminate widely from a focus in the leptomeninges, throughout the arachnoid and pia mater, through the perivascular (Virchow-Robin) spaces, or along the sleeves of cranial nerves and spinal nerve roots.[58] Extension into the perivascular spaces or partial obstruction of the vessel lumen by tumor cells can result in ischemic complications

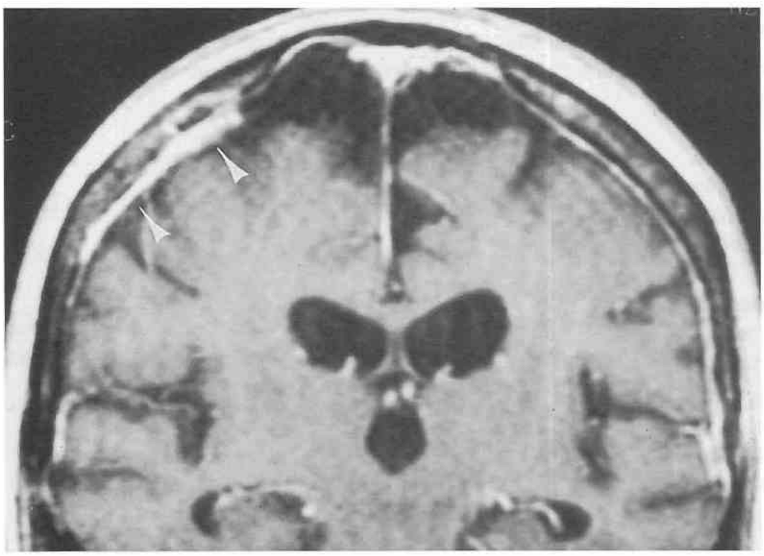

Figure 12–41. Focal, direct extension of breast carcinoma calvarial metastasis to dura. Coronal enhanced T1-weighted image shows focal dural thickening *(arrowheads)* and enhancement deep to a calvarial focus of breast carcinoma (see also Fig. 12–21).

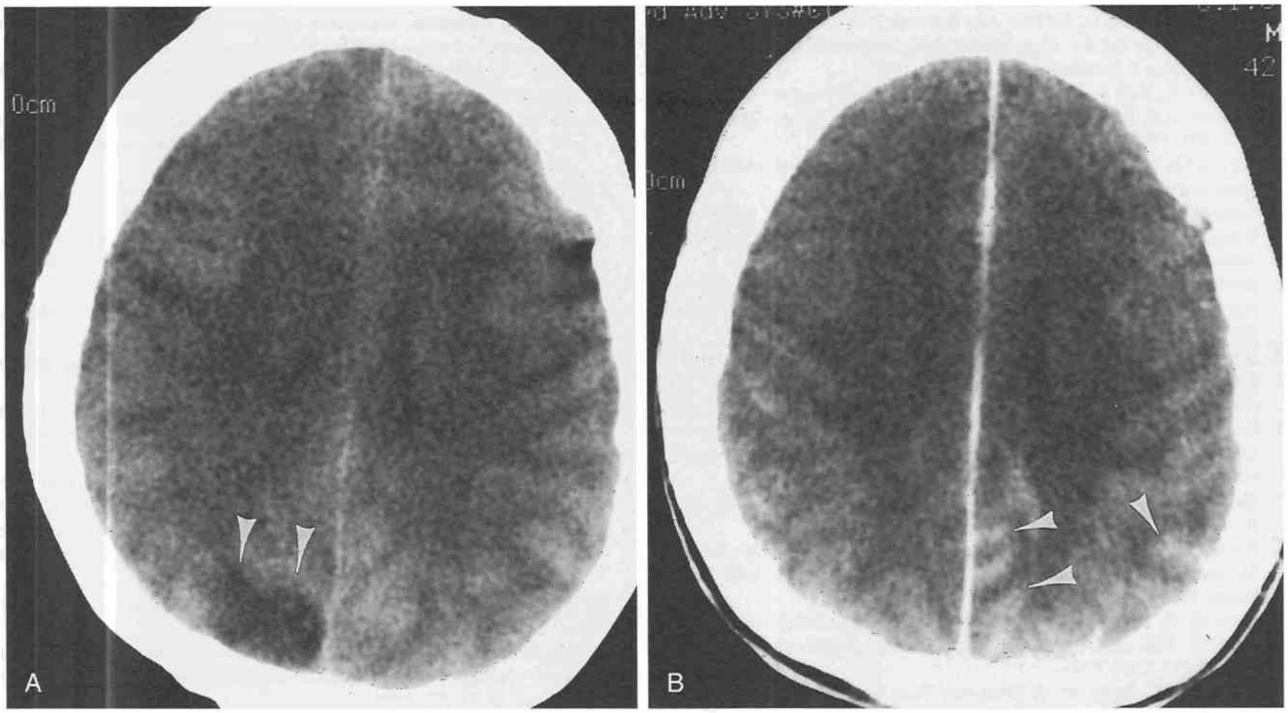

Figure 12–42. Carcinomatous encephalitis. *A,* Axial CT of the head obtained before contrast medium shows hypoattenuation in the posterior parietal lobe *(arrowheads)* in a 42-year-old patient who presented with a 4-month history of seizures. *B,* After contrast administration, pial enhancement is minimal *(arrowheads).* The patient was initially thought to have subarachnoid hemorrhage, but autopsy showed extensive adenocarcinoma in the perivascular spaces and meninges, with multiple ischemic foci in the brain and a primary focus in the lung.

of leptomeningeal carcinomatosis (Fig. 12–42).[118, 161] The term "carcinomatous encephalitis" refers to the rare occurrence of diffuse perivascular (Virchow-Robin space) infiltration resulting in ischemia.[71, 99] Neoplasm adjacent to the meninges or a small site of meningeal tumor involvement may also provoke a diffuse fibrous response of the meninges.[118] Since both the meningeal reaction to neoplasm and the neoplasm itself usually enhance on MRI, this finding is not specific.

Summary

A wide spectrum of non-neoplastic and neoplastic conditions may affect the meninges. MRI with FLAIR sequences or enhanced T1-weighted images is an effective modality for characterizing meningeal pathology. The cardinal MRI findings in meningeal disease are hydrocephalus and smooth or nodular enhancement or signal abnormality of the dura/arachnoid, the pia mater/SAS, and the ependyma of the brain or spine.

Two major patterns of disease are identified: (1) a dura/arachnoid pattern, which follows along the inner table of the calvarium, and (2) a pia mater/SAS pattern, which extends into the sulcal spaces. Nodular disease, in particular, may suggest neoplasm. Meningeal neoplasm may be clinically silent, and false-negative results on CSF cytologic study are common.[6, 8, 13, 118] The addition of MRI to the clinical data and CSF examination may increase the detection of meningeal involvement and may allow tumor staging.

Understanding the routes of neoplastic spread to the meninges permits identification of imaging features of the primary tumor that predispose to CSF dissemination, such as proximity to the SAS or ventricles. Although there is considerable overlap in the MR appearance of meningeal involvement in various diseases, the pattern and distribution of enhancement may provide guidance for diagnosis, management, and treatment monitoring of disorders affecting the meninges. Correlation of imaging findings with clinical and CSF data is essential to ensure that treatable disease is not overlooked.

References

1. Ahmadi J, Hinton D: Dural invasion by craniofacial and calvarial neoplasms: MR imaging and histopathologic evaluation. Radiology 188:747–749, 1993.
2. Aizpuru R, Quencer R, Norenberg M, et al: Meningioangiomatosis: Clinical, radiologic, and histopathologic correlation. Radiology 179: 819–821, 1991.
3. Alcolado R, Weller R, Parrish E, Garrod D: The cranial arachnoid and pia mater in man: Anatomical and ultrastructural observations. Neuropathol Appl Neurobiol 14:1–17, 1988.
4. Allcutt D, Michowitz S, Weitzman S, et al: Primary leptomeningeal melanoma: An unusually aggressive tumor in childhood. Neurosurgery 32:721–729, 1993.
5. Anonymous: Case records of the Massachusetts General Hospital: Weekly clinicopathological exercises. Case 26–1988. A 40-year-old man with a persistent dural abnormality after treatment for an astrocytoma. N Engl J Med 318:1742–1750, 1988.
6. Arita N, Taneda M, Hayakawa T: Leptomeningeal dissemination of malignant gliomas, incidence, diagnosis and outcome. Acta Neurochir 126:84–92, 1994.
7. Awad I, Bay J, Rogers L: Leptomeningeal metastasis from supratentorial malignant gliomas. Neurosurg 19:247–251, 1986.

8. Balhuizen J, Bots G, Schaberg A, Bosman F: Value of cerebrospinal fluid cytology for the diagnosis of malignancies in the central nervous system. J Neurosurg 48:747–753, 1978.
9. Barkhof F, Valk J, Hommes O, Scheltens P: Meningeal Gd-DTPA enhancement in multiple sclerosis. AJNR Am J Neuroradiol 13: 397–400, 1992.
10. Batson O: The function of the vertebral veins and their role in the spread of metastases. Ann Surg 112:138–149, 1940.
11. Benedikt R, Brown D, Walker R, et al: Sturge-Weber syndrome: Cranial MR imaging with Gd-DTPA. AJNR Am J Neuroradiol 14: 409–415, 1993.
12. Bickerstaff E, Small J, Guest I: The relapsing course of certain meningiomas in relation to pregnancy and menstruation. J Neurol Neurosurg Psychiatry 21:89–91, 1958.
13. Bigner S, Johnston W: The cytopathology of cerebrospinal fluid: II. Metastatic cancer, meningeal carcinomatosis and primary central nervous system neoplasms. Acta Cytol 25:461–479, 1981.
14. Boogerd W, Hart A, van der Sande J, Engelsman E: Meningeal carcinomatosis in breast cancer: Prognostic factors and influence of treatment. Cancer 67:1685–1695, 1991.
15. Bourekas E, Wildenhain P, Lewin J, et al: The dural tail sign revisited. AJNR Am J Neuroradiol 16:1514–1516, 1995.
16. Bowen B, Donovan Post M: Intracranial Infection. In Atlas S (ed): Magnetic Resonance Imaging of the Brain and Spine. New York, Raven Press, 1991, pp 501–538.
17. Bracchi M, Savoiardo M, Triulzi F, et al: Superficial siderosis of the CNS: MR diagnosis and clinical findings. AJNR Am J Neuroradiol 14:227–236, 1993.
18. Brightbill T, Ihmeidan I, Donovan Post M, et al: Neurosyphilis in HIV-positive and HIV-negative patients: Neuroimaging findings. AJNR Am J Neuroradiol 16:703–711, 1995.
19. Brodal P: The Central Nervous System. New York, Oxford University Press, 1992, p 464.
20. Burke J, Podrasky A, Bradley W: Meninges: Benign postoperative enhancement on MR images. Radiology 174:99–102, 1990.
21. Carpenter MB: Meninges and cerebrospinal fluid. In Wilkins W (ed): Core Text of Neuroanatomy, 2nd ed. Baltimore, Williams & Wilkins, 1978, pp 1–14.
22. Castelli M, Husband A: Superficial siderosis of the central nervous system: An underestimated cause of hearing loss. J Laryngol Otol 111:60–62, 1997.
23. Chamberlain M: Current concepts in leptomeningeal metastasis. Curr Opin Oncol 4:533–539, 1992.
24. Chamberlain M, Sandy A, Press G: Leptomeningeal metastasis: A comparison of gadolinium-enhanced MR and contrast-enhanced CT of the brain. Neurology 40:435–438, 1990.
25. Chang K, Han M, Roh J, et al: Gd-DTPA-enhanced MR imaging of the brain in patients with meningitis: Comparison with CT. AJNR Am J Neuroradiol 11:69–76, 1990.
26. Cheng T, O'Neill B, Scheithauer B, Piepgras D: Chronic meningitis: The role of meningeal or cortical biopsy. Neurosurgery 34:590–596, 1994.
27. Cohen J, Quint D, Eldevik O: Patterns of normal meningeal enhancement on 1.5-T MR imaging. American Roentgen Ray Society Proceedings Book, 1995, p 127.
28. Cooper I, Craig M, Kernohan J: Tumors of the spinal cord: Primary extramedullary gliomas. Surg Gynecol Obstet 92:183–190, 1951.
29. Crawford J, Konkol R: Familial hemiplegic migraine with crossed cerebellar diaschisis and unilateral meningeal enhancement. Headache 37:590–593, 1997.
30. Davis P, Friedman N, Fry S, Malko J, et al: Leptomeningeal metastasis: MR imaging. Radiology 163:449–454, 1987.
31. De Klerk D, Spence J: Chemical meningitis with intracranial tumours. S Afr Med J 48:131–135, 1974.
32. Demaerel P, Robberecht W, Casteels I, et al: Focal leptomeningeal MR enhancement along the chiasm as a presenting sign of multiple sclerosis. J Comput Assist Tomogr 19:297–298, 1995.
33. Demaerel P, Wilms G, Van Lierde S, et al: Lyme disease in childhood presenting as primary leptomeningeal enhancement without parenchymal findings of MR. AJNR Am J Neuroradiol 15:302–304, 1994.
34. Dietrich P-Y, Aapro M, Pizzolato G: Primary diffuse leptomeningeal gliomatosis (PDLG): A neoplastic cause of chronic meningitis. J Neurooncol 15:275–283, 1993.
35. Dinsdale H, Taghavy A: Carcinomatosis of the meninges. Can Med Assoc J 90:505–512, 1964.
36. Elster A: Magnetic resonance contrast enhancement in cerebral infarction. Neuroimaging Clin North Am 4:89–100, 1994.
37. Elster A, DiPersio D: Cranial postoperative site: Assessment with contrast-enhanced MR imaging. Radiology 174:93–98, 1990.
38. Elster A, Mathews V, King J, Hamilton C: Improved detection of gadolinium enhancement using magnetization transfer imaging. Neuroimaging Clin North Am 4:185–399, 1994.
39. Elster A, Moody D: Early cerebral infarction: Gadopentetate dimeglumine enhancement. Radiology 177:627–632, 1990.
40. Enzmann D, Krikorian J, Yorke C, Hayward R: Computed tomography in leptomeningeal spread of tumor. J Comput Assist Tomogr 2: 448–455, 1978.
41. Esiri M, Gay D: Immunological and neuropathological significance of the Virchow-Robin space. J Neurol Sci 100:3–8, 1990.
42. Eustace S, Buff B: Magnetic resonance imaging in drug-induced meningitis. Can Assoc Radiol J 45:463–465, 1994.
43. Farn J, Mirowitz S: MR imaging of the normal meninges: Comparison of contrast-enhancement patterns on 3D gradient-echo and spin-echo images. AJR Am J Roentgenol 162:131–135, 1994.
44. Fishman R, Dillon W: Dural enhancement and cerebral displacement secondary to intracranial hypotension. Neurology 43:609–611, 1993.
45. Frank J, Girton M, Dwyer A, et al: Meningeal carcinomatosis in the VX2 rabbit tumor model: Detection with Gd-DPTA–enhanced MR imaging. Radiology 167:825–829, 1988.
46. Frederickson R: The subdural space interpreted as a cellular layer of meninges. Anat Rec 230:38–51, 1991.
47. Freilich R, Krol G, DeAngelis L: Neuroimaging and cerebrospinal fluid cytology in the diagnosis of leptomeningeal metastasis. Ann Neurol 38:51–57, 1995.
48. Fukui M, Williams R, Mudigonda S: CT and MR imaging signs of pyogenic ventriculitis. Paper presented at Proceedings of the American Society of Neuroradiology (ASNR), 1999, San Diego.
49. Fulbright R, Erdum E, Sze G, Byrne T: Cranial nerve enhancement in the Guillain-Barré syndrome. AJNR Am J Neuroradiol 16:923–925, 1995.
50. Giaquinto S, Massi G, Ricolfi A, Vitali S: On six cases of radiation meningiomas from the same community. Ital J Neurol Sci 5:173–175, 1984.
51. Gilden D, Beinlich B, Rubenstien E, et al: Varicella-zoster virus myelitis: An expanding spectrum. Neurology 44:1818–1823, 1994.
52. Ginsberg L, Leeds N: Neuroradiology of leukemia. AJR Am J Roentgenol 165:525–534, 1995.
53. Glass J, Melamed M, Chernik N, Posner J: Malignant cells in cerebrospinal fluid (CSF): The meaning of a positive CSF cytology. Neurology 29:1369–1375, 1979.
54. Globus J, Meltzer T: Metastatic tumors of the brain. Arch Neurol Psychiatry 48:163–226, 1942.
55. Goldsher D, Litt A, Pinto R, et al: Dural "tail" associated with meningiomas on Gd-DTPA–enhanced MR images: Characteristics, differential diagnostic value, and possible implications for treatment. Radiology 176:447–450, 1990.
56. Gondos B, King E: Cerebrospinal fluid cytology: Diagnostic accuracy and comparison of different techniques. Acta Cytol 20:542–547, 1976.
57. Grabb P, Albright A, Pang D: Dissemination of supratentorial malignant gliomas via the cerebrospinal fluid in children. Neurosurgery 30:64–71, 1992.
58. Grain G, Karroo J: Diffuse leptomeningeal carcinomatosis: Clinical and pathologic characteristics. Neurology 5:706–722, 1955.
59. Gray L, Macula J, Provenzale J, et al: High dose MR contrast agent for the diagnosis of leptomeningeal disease (abstract). Radiology 197(P):410, 1995.
60. Greenberg R, Lane E, Cinnamon J, et al: The cranial meninges: Anatomic considerations. Semin Ultrasound CT MRI 15:454–465, 1994.
61. Griffin J, Thompson R, Mitchinson M, et al: Lymphomatous leptomeningitis. Am J Med 51:200–208, 1971.
62. Grossman R, Kemp S, Yu I, et al: The importance of oxygenation in the appearance of acute subarachnoid hemorrhage on high-field magnetic resonance imaging. Acta Radiol (Suppl) 369:56–58, 1986.
63. Guseo A, Jellinger K: The significance of perivascular infiltrations in multiple sclerosis. J Neurol 211:51–60, 1975.
64. Haines D: On the question of a subdural space. Anat Rec 230: 3–21, 1991.
65. Halper J, Scheithauer B, Okazaki H, Laws E: Meningioangio-

matosis: A report of six cases with special reference to the occurrence of neurofibrillary tangles. J Neuropathol Exp Neurol 45:426–446, 1986.
66. Hammes E: Reaction of the meninges to blood. Arch Neurol Psychiatry 52:505–514, 1944.
67. Hardman J: Cerebrospinal trauma. In Davis R, Robertson D (eds): Textbook of Neuropathology, 2nd ed. Baltimore, Williams & Wilkins, 1991, pp 962–1002.
68. Harvey S, Burr H: The development of the meninges. Arch Neurol Psychiatry 15:545–567, 1926.
69. Haustein J, Laniado M, Niendorf H-P, et al: Triple-dose versus standard-dose gadopentetate dimeglumine: A randomized study in 199 patients. Radiology 186:855–860, 1993.
70. Heinz R, Wiener D, Friedman H, Tien R: Detection of cerebrospinal fluid metastasis: CT myelography or MR? AJNR Am J Neuroradiol 16:1147–1151, 1995.
71. Henson R, Urich H: Carcinomatous meningitis. In Henson R, Urich H (eds): Cancer and the Nervous System. Boston, Blackwell Scientific, 1982, pp 101–119.
72. Henson R, Urich H: Diffuse infiltration by lymphoma and leukemia. In Henson R, Urich H (eds): Cancer and the Central Nervous System. Boston, Blackwell Scientific, 1982, pp 227–267.
73. Ho K-L, Hoschner J, Wolfe D: Primary leptomeningeal gliomatosis: Symptoms suggestive of meningitis. Arch Neurol 38:662–666, 1981.
74. Hochman M, Naidich T, Kobetz S, Fernandez-Maitin A: Spontaneous intracranial hypotension with pachymeningeal enhancement on MRI. Neurology 42:1628–1630, 1992.
75. Hudgins P, Davis P, Hoffman J Jr: Gadopentetate dimeglumine–enhanced MR imaging in children following surgery for brain tumor: Spectrum of meningeal findings. AJNR Am J Neuroradiol 12:301–307, 1991.
76. Hughes J, Oppenheimer D: Superficial siderosis of the central nervous system. Acta Neuropathol (Berl) 13:56–74, 1969.
77. Jacobs D, McFarlane M, Holmes F: Female patients with meningioma of the sphenoid ridge and additional primary neoplasms of the breast and genital tract. Cancer 60:3080–3082, 1987.
78. Jaeckle K, Krol G, Posner J: Evolution of computed tomographic abnormalities in leptomeningeal metastases. Ann Neurol 17:85–89, 1985.
79. Janss A, Galetta S, Freese A, et al: Superficial siderosis of the central nervous system: Magnetic resonance imaging and pathological correlation. J Neurosurg 79:756–760, 1993.
80. Jennings M, Slatkin N, D'Angelo M, et al: Neoplastic meningitis as the presentation of occult primitive neuroectodermal tumors. J Child Neurol 8:306–312, 1993.
81. Johnson B, Fram E: Cerebral venous occlusive disease: Pathophysiology, clinical manifestations, and imaging. Neuroimaging Clin North Am 2:769–783, 1992.
82. Kallmes D, Gray L, Brown M, Glass J: Triple dose gadolinium in the diagnosis of leptomeningeal metastases. American Society of Neuroradiology (ASNR) Proceedings Book, 1994, p 208.
83. Kallmes D, Gray L, Glass J: High-dose gadolinium-enhanced MRI for diagnosis of meningeal metastasis. Neuroradiology 40:23–26, 1998.
84. Katz D, Taubenberger J, Raine C, et al: Gadolinium-enhancing lesions on magnetic resonance imaging: Neuropathologic findings (abstract). Ann Neurol 28:P92, 1990.
85. Kelly A, Zimmerman R: Head trauma: Comparison of MR and CT: Experience in 100 patients. AJNR Am J Neuroradiol 9:699–708, 1988.
86. Kilgore D, Breger R, Daniels D, et al: Cranial tissues: Normal MR appearance after intravenous injection of Gd-DTPA. Radiology 160: 757–761, 1986.
87. Kioumehr F, Dadsetan M, Feldman N, et al: Postcontrast MRI of the cranial meninges: Leptomeningitis versus pachymeningitis. J Comput Assist Tomogr 19:713–720, 1995.
88. Kirkpatrick J: Neurologic infections due to bacteria, fungi, and parasites. In Davis R, Robertson D (eds): Textbook of Neuropathology, 2nd ed. Baltimore, Williams & Wilkins, 1991, pp 719–803.
89. Kline T: Cytological examination of the cerebrospinal fluid. Cancer 15:591–597, 1962.
90. Kokkoris C: Leptomeningeal carcinomatosis: How does cancer reach the pia-arachnoid? Cancer 51:154–160, 1983.
91. Kramer E, Rafto S, Packer R, Zimmerman R: Comparison of myelography with CT follow-up versus gadolinium MRI for subarachnoid metastatic disease in children. Neurology 41:46–50, 1991.
92. Krol G, Sze G, Malkin M, Walker R: MR of cranial and spinal meningeal carcinomatosis: Comparison with CT and myelography. AJR Am J Roentgenol 151:583–588, 1988.
93. Kumar A, Montanera W, Willinsky R, et al: Case report: MR features of tuberculous arachnoiditis. J Comput Assist Tomogr 17: 127–130, 1993.
94. Lachance D, O'Neill B, Macdonald D, et al: Primary leptomeningeal lymphoma: Report of 9 cases, diagnosis with immunocytochemical analysis, and review of literature. Neurology 41:95–100, 1991.
95. Lee Y-Y, Van Tassel P, Raymond A: Intracranial dural chondrosarcoma. AJNR Am J Neuroradiol 9:1189–1193, 1988.
96. Leproux F, Melanson D, Mercier C, et al: Leptomeningeal gliomatosis: MR findings. J Comput Assist Tomogr 17:317–320, 1993.
97. Lindner A, Reiners K, Toyka K: Meningeal hyperperfusion visualized by MRI in a patient with visual hallucinations and migraine. Headache 36:53–57, 1996.
98. Lunardi P, Missori P, Rizzo A, Gagliardi F: Chemical meningitis in ruptured intracranial dermoid: Case report and review of the literature. Surg Neurol 32:449–452, 1989.
99. Madow L, Alpers B: Encephalitic form of metastatic carcinoma. Arch Neurol Psychiatry 65:161–173, 1951.
100. Malat J, Virapongse C, Palestro C, Richman A: Primary intraspinal fibrosarcoma. Neurosurgery 19:434–436, 1986.
101. Mamelak A, Kelly W, Davis R, Rosenblum M: Idiopathic hypertrophic cranial pachymeningitis: Report of three cases. J Neurosurg 79: 270–276, 1993.
102. Mark A: Nondegenerative, non-neoplastic diseases of the spine and spinal cord. In Atlas S (ed): Magnetic Resonance Imaging of the Brain and Spine. New York, Raven Press, 1991, pp 967–1011.
103. Martin N, Masson C, Henin D, et al: Hypertrophic cranial pachymeningitis: Assessment with CT and MR imaging. AJNR Am J Neuroradiol 10:477–484, 1989.
104. Mathews V, Kuharik M, Edwards M, et al: Gd-DTPA–enhanced MR imaging of experimental bacterial meningitis: Evaluation and comparison with CT. AJR Am J Roentgenol 152:131–136, 1989.
105. Mathews VP, Alo PL, Glass JD, et al: AIDS-related CNS *Cryptococcus:* Radiologic-pathologic correlation. AJNR Am J Neuroradiol 13: 1477–1486, 1992.
106. Meltzer C, Smirniotopoulos J, Fukui M: The dural tail. Int J Neuroradiol 4:33–40, 1998.
107. Miller J, Jubelt B: Bacterial infections. In Rowland L (ed): Merritt's Textbook of Neurology, 8th ed. Philadelphia, Lea & Febiger, 1989, pp 63–96.
108. Mittl R, Yousem D: Frequency of unexplained meningeal enhancement in the brain after lumbar puncture. AJNR Am J Neuroradiol 15:633–638, 1994.
109. Moberg A, Reis G: Carcinosis meningeum. Acta Med Scand 170: 747–755, 1961.
110. Murai H, Kira J, Kobayashi T, et al: Hypertrophic cranial pachymeningitis due to *Aspergillus flavus*. Clin Neurol Neurosurg 94:247–250, 1992.
111. Naul L, Hise J, Bauserman S, Todd F: CT and MR of meningeal melanocytoma. AJNR Am J Neuroradiol 12:315–316, 1991.
112. Naylor B: The cytologic diagnosis of cerebrospinal fluid. Acta Cytol 8:141–148, 1964.
113. Negishi C, Sze G: Vasculitis presenting as primary leptomeningeal enhancement with minimal parenchymal findings. AJNR Am J Neuroradiol 14:26–28, 1993.
114. Newton H, Fleisher M, Schwartz M, Malkin M: Glucose phosphate isomerase as a CSF marker for leptomeningeal metastasis. Neurology 41:395–398, 1991.
115. Noguchi K, Ogawa T, Inugami A, et al: MR of acute subarachnoid hemorrhage: A preliminary report of fluid-attenuated inversion-recovery pulse sequences. AJNR Am J Neuroradiol 15:1940–1943, 1994.
116. Nugent J, Bunn P, Matthews M, et al: CNS metastases in small cell bronchogenic carcinoma. Cancer 44:1885–1893, 1979.
117. Ogawa T, Inugami A, Fujita H, et al: MR diagnosis of subacute and chronic subarachnoid hemorrhage: Comparison with CT. AJR Am J Roentgenol 165:1257–1262, 1995.
118. Olson M, Chernik N, Posner J: Infiltration of the leptomeninges by systemic cancer. Arch Neurol 30:122–137, 1974.
119. Onda K, Tanaka R, Takahashi H, et al: Cerebral glioblastoma with cerebrospinal fluid dissemination: A clinicopathological study of 14 cases examined by complete autopsy. Neurosurgery 25:533–540, 1989.

120. Onda K, Tanaka R, Takahashi H, et al: Symptomatic cerebrospinal fluid dissemination of cerebral glioblastoma. Neuroradiology 32: 146–150, 1990.
121. O'Rahilly R, Muller F: The meninges in human development. J Neuropathol Exp Neurol 45:588–608, 1986.
122. Osaka K, Handa H, Matsumoto S, Yasuda M: Development of the cerebrospinal fluid pathway in the normal and abnormal human embryos. Childs Brain 6:26–38, 1980.
123. Paako E, Patronas N, Schellinger D: Meningeal Gd-DTPA enhancement in patients with malignancies. J Comput Assist Tomogr 14: 542–546, 1990.
124. Packer R, Siegel K, Sutton L, et al: Leptomeningeal dissemination of primary central nervous system tumors of childhood. Ann Neurol 18:217–221, 1985.
125. Park J, Van den Noort S, Kim R, et al: Primary diffuse leptomeningeal gliomatosis with signs of increased intracranial pressure and progressive meningeal enhancement on MRI. J Neuroimaging 6: 250–254, 1996.
126. Partington C, Graves V, Hegstrand L: Meningioangiomatosis. Am J Neuroradiol 12:549–552, 1991.
127. Pfluger T, Weil S, Weis S, et al: MRI of primary meningeal sarcomas in two children: Differential diagnostic considerations. Neuroradiology 39:225–228, 1997.
128. Phillips M, Ryals T, Kambhu S, Yuh W: Neoplastic vs. inflammatory meningeal enhancement with Gd-DTPA. J Comput Assist Tomogr 14:536–541, 1990.
129. Praharaj S, Sharma M, Prasad K, et al: Unilateral meningeal thickening: A rare presentation of tuberculous meningitis. Clin Neurol Neurosurg 99:60–62, 1997.
130. Price R, Johnson W: The central nervous system in childhood leukemia: I. The arachnoid. Cancer 31:520–533, 1973.
131. Provenzale J, Allen N: MR findings in Wegener's granulomatosis. American Society of Neuroradiology (ASNR) Proceedings Book, 1995, p 130.
132. Pui M, Langston J, Arai Y: Gd-DTPA enhancement of CSF in meningeal carcinomatosis. J Comput Assist Tomogr 17:940–944, 1993.
133. Quagliarello V, Scheld W: Bacterial meningitis: Pathogenesis, pathophysiology, and progress. N Engl J Med 327:864–872, 1992.
134. Quest D, Salcman M: Fibromatosis presenting as a cranial mass lesion. J Neurosurg 44:237–240, 1976.
135. Rando T, Fishman R: Spontaneous intracranial hypotension: Report of two cases and review of the literature. Neurology 42:481–487, 1992.
136. Runge V, Clanton J, Price A, et al: Evaluation of contrast-enhanced MR imaging in a brain-abscess model. AJNR Am J Neuroradiol 6: 139–147, 1985.
137. Runge V, Wells J, Williams N, et al: Detectability of early brain meningitis on MR images with pathologic correlation (abstract). Radiology 197P: 480, 1995.
138. Russell D, Rubinstein L: Pathology of Tumours of the Nervous System, 5th ed. London, Edward Arnold, 1989, p 1012.
139. Sage M: Blood-brain barrier: Phenomenon of increasing importance to the imaging clinician. AJNR Am J Neuroradiol 3:127–138, 1982.
140. Sage M, Wilson A: The blood-brain barrier: An important concept in neuroimaging. AJNR Am J Neuroradiol 15:601–622, 1994.
141. Sakamoto S, Kitagaki H, Ishii K, et al: Gadolinium enhancement of the cerebrospinal fluid in a patient with meningeal fibrosis and cryptococcal infection. Neuroradiology 39:504–505, 1997.
142. Sarnat H, Netsky M: Evolution of the Nervous System, 2nd ed. New York, Oxford University Press, 1981, p 504.
143. Seltzer S, Mark A, Atlas S: CNS sarcoidosis: Evaluation with contrast-enhanced MR imaging. AJNR Am J Neuroradiol 12:1227–1233, 1991.
144. Sherman J, Stern B: Sarcoidosis of the CNS: Comparison of unenhanced and enhanced MR images. AJNR Am J Neuroradiol 11: 915–923, 1990.
145. Singer M, Atlas S, Drayer B: Subarachnoid space disease: Diagnosis with fluid-attenuated inversion-recovery MR imaging and comparison with gadolinium-enhanced spin-echo MR imaging—blinded reader study. Radiology 208:417–422, 1998.
146. Smirniotopoulos J, Murphy F: The phakomatoses. AJNR Am J Neuroradiol 13:725–746, 1992.
147. Southwick F, Richardson E, Swartz M: Septic thrombosis of the dural venous sinuses. Medicine 65:82–106, 1986.
148. Spagnoli M, Goldberg H, Grossman R, et al: Intracranial meningiomas: High-field MR imaging. Radiology 161:369–375, 1986.
149. Spallone A, Gagliardi F, Vagnozzi R: Intracranial meningiomas related to external cranial radiation. Surg Neurol 12:153–159, 1979.
150. Stern B, Krunholz A, Johns C, et al: Sarcoidosis and its neurological manifestations. Arch Neurol 42:909–917, 1985.
151. Sze G: Diseases of the intracranial meninges: MR imaging features. AJR Am J Roentgenol 160:727–733, 1993.
152. Sze G, Soletsky S, Bronen R, Krol G: MR imaging of the cranial meninges with emphasis on contrast enhancement and meningeal carcinomatosis. AJNR Am J Neuroradiol 10:965–975, 1989.
153. Tishler S, Williamson T, Mirra S, et al: Wegener granulomatosis with meningeal involvement. AJNR Am J Neuroradiol 14:1248–1252, 1993.
154. Tokumaru A, O'uchi T, Tsuneyoshi E, et al: Prominent meningeal enhancement adjacent to meningioma on Gd-DTPA–enhanced MR images: Histopathologic correlation. Radiology 175:431–433, 1990.
155. Truwit C, Barkovich A: Pathogenesis of intracranial lipoma: An MR study in 42 patients. AJR Am J Roentgenol 155:855–864, 1990.
156. Tsukada Y, Fouad A, Pickren J, Lane W: Central nervous system metastasis from breast carcinoma: Autopsy study. Cancer 52:2349–2354, 1993.
157. Twijnstra A, Van Zanten A, Nooyen W, et al: Cerebrospinal fluid beta$_2$-microglobulin: A study in controls and patients with metastatic and non-metastatic neurological disease. Eur J Cancer Clin Oncol 22:387–391, 1986.
158. Vertosick F, Selker R: Brainstem and spinal metastases of supratentorial glioblastoma multiforme: A clinical series. Neurosurgery 27: 516–522, 1990.
159. Viadana E, Bross I, Pickren JW: Cascade spread of blood-borne metastases in solid and nonsolid cancers of humans. In Weiss L, Gilbert HA (eds): Pulmonary Metastasis. Boston, GK Hall, 1978, pp 142–167.
160. Vogl T, Stemmler J, Bergman C, et al: MR and MR angiography of Sturge-Weber syndrome. AJNR Am J Neuroradiol 14:417–425, 1993.
161. Wasserstrom W, Glass J, Posner J: Diagnosis and treatment of leptomeningeal metastases from solid tumors: Experience with 90 patients. Cancer 49:759–772, 1982.
162. Watanabe M, Tanaka R, Takeda N: Correlation of MRI and clinical features in meningeal carcinomatosis. Neuroradiology 35:512–515, 1993.
163. Wehn S, Heinz E, Burger P, Boyko O: Dilated Virchow-Robin spaces in cryptococcal meningitis associated with AIDS: CT and MR findings. J Comput Assist Tomogr 13:756–762, 1989.
164. Whiteman M, Dandapani B, Shebert R, Donovan Post M: MRI of AIDS-related polyradiculomyelitis. J Comput Assist Tomogr 18: 7–11, 1994.
165. Whiteman M, Espinoza L, Post M, et al: Central nervous system tuberculosis in HIV-infected patients: Clinical and radiographic findings. AJNR Am J Neuroradiol 16:1319–1327, 1995.
166. Wiebe S, Munoz D, Smith S, Lee D: Meningioangiomatosis: A comprehensive analysis of clinical and laboratory features. Brain 122:709–726, 1999.
167. Williams R, Fukui M, Tishkoff N, et al: MR imaging of the subarachnoid space utilizing FLAIR: Pathology and pitfalls. Radiology 213:552, 1999.
168. Willis R: Pathology of Tumours, 4th ed. New York, Appleton-Century-Crofts, 1967, p 1019.
169. Witham T, Fukui M, Meltzer C, et al: Survival using intrathecal thiotriethylenephosphoramide (thio-TEPA) for the treatment of ependymal or leptomeningeal gliomatosis in patients with high grade gliomas. Cancer 86:1347–1353, 1999.
170. Wolbach S: Congenital rhabdomyoma of the heart: Report of a case associated with multiple nests of neuroglial tissue in the meninges of the spinal cord. J Med Res 16:495–519, 1907.
171. Wrobel C, Meyer S, Johnson R, Hesselink J: MR findings in acute and chronic coccidioidomycosis meningitis. AJNR Am J Neuroradiol 13:1241–1245, 1992.
172. Yap H-Y, Yap B-S, Tashima C, et al: Meningeal carcinomatosis in breast cancer. Cancer 42:283–286, 1978.
173. Yousem D, Patrone P, Grossman R: Leptomeningeal metastases: MR evaluation. J Comput Assist Tomogr 14:255–261, 1990.
174. Zouaoui A, Maillard J-C, Dormont D, et al: MRI in neurosarcoidosis. J Neuroradiol 19:271–284, 1992.

13 Leukoencephalopathies and Demyelinating Disease

Barton Lane

The cerebral (and cerebellar) white matter may be affected by various disease processes. With its ability to detect these alterations in white matter, neuroimaging contributes to the diagnosis and management of these disorders.

It is useful to briefly consider the underlying mechanisms that account for the changes seen on magnetic resonance (MR) images and computed tomography (CT) scans in white matter disease. Demyelinating disorders result in increased water content of the white matter because myelin (rich in solids) is lost, leaving behind more hydrated material. This water is found in extracellular fluid; astrocytes; and, possibly, inflammatory cells. The magnitude of the change depends on the severity of the disease. The abnormally increased water content causes reduced attenuation on CT scans and prolongation of T1 and T2 values on MR scans. In the late stages of demyelination, extreme shrinkage of the affected white matter, accompanied by gross cerebral atrophy, may result.[6]

Cerebral edema, trauma, ischemic lesions, and infection are among the causes of abnormal white matter, as visualized by CT and magnetic resonance imaging (MRI), and may therefore be included in the differential diagnosis of primary myelin disorders. Further, secondary myelin (wallerian) degeneration[84] occurs when axons are severed or destroyed. This chapter emphasizes primary diseases of white matter or those disorders in which the white matter is the primary focus of the pathologic process.

The classification of white matter disease may seem confusing and arbitrary; it can be undertaken on biochemical, etiologic, clinical, pathologic, or radiologic bases. Some diseases cross nosologic lines; an example is progressive multifocal leukoencephalopathy (PML), in which myelin is destroyed as a result of viral infection, which is in turn secondary to immune compromise. The classification in this chapter is based on that of Waxman.[95]

Normal White Matter

CT Appearance

Normal cerebral white matter in the adult has an x-ray attenuation coefficient 0.5% to 0.8% less than normal gray matter of the cerebral cortex. Average values of 35 to 40 Hounsfield units (HU) for adult human gray matter and 29 to 33 HU for white matter have been derived from clinical studies. These figures agree with in vitro studies performed on human and primate brains. This small attenuation difference (5 to 7 HU) is detectable on CT as a relative lucency of white matter, as compared with gray matter.

The cause of the lower attenuation in white matter is its myelin content. Myelin accounts for the whitish appearance, the high lipid content, and the relatively low water content of white matter when compared with gray matter (72% versus 82%).[9, 10] Although white matter is less vascular than gray matter, the low blood content of white matter accounts for only a small fraction of the attenuation difference. Contrast infusion increases the differences in density only slightly. This difference is probably caused by the higher cerebral blood volume in gray versus white matter.

White matter in the infant differs significantly from that in the adult. It is known that complex biochemical and morphologic changes occur in the white matter in utero and throughout the first years of life. Extensive myelination occurs in the first few months after birth and is virtually complete by the end of the second year. Some slower myelination continues throughout childhood and adolescence. Thereafter, the white matter is relatively stable during adulthood.

Immature myelin, compared with the adult form, has a much greater water content. As myelination proceeds in the brain, the white matter loses water and gains lipids and proteolipids until, in the adult, white matter has three times as much lipid as does gray matter. CT density measurements show an average linear increase in brain density from term to 20 weeks, after which the density increases only slightly.[63]

This high water content of immature myelin has a predictable effect, as seen on CT scans. The white matter in premature and normal full-term infants shows greater lucency (i.e., lesser attenuation) than in adults (Figs. 13–1 and 13–2). This finding must not be mistaken for a pathologic process.[22, 49, 66] (The thinner neonatal calvaria may also contribute to better gray-white discrimination, since there is less beam-hardening and a better signal-to-noise ratio.)

When the patient is about 6 months of age, the difference in gray-white matter is similar to that in the adult. From ages 2 to 17 years, the normal white matter density values are identical to those of adults.

Constant identifiable changes in white matter in aging human brains have been described. After middle age, the total amount of certain myelin lipids decreases and the

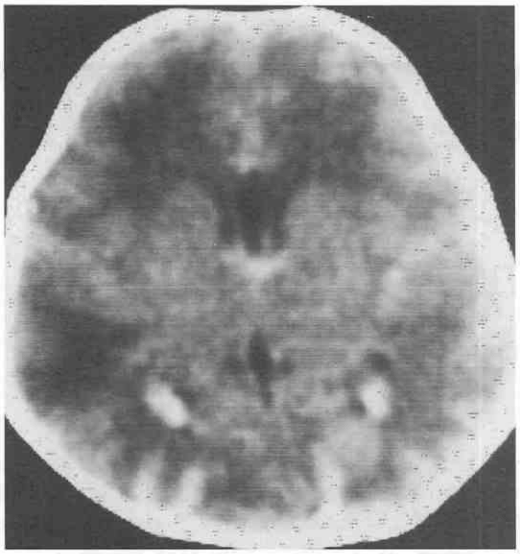

Figure 13–1. Immature myelination in a premature infant. CT scan, obtained at 1 month of age, demonstrates the typical lucency of incompletely myelinated white matter in premature infants. The internal capsules that myelinate first are not visible.

cerebral hemispheres show increased water content. These changes appear as decreased attenuation of the cerebral white matter in CT scans of older patients.[9] This generalized decrease in white matter density has been correlated with dementia and other clinical symptomatology[83]; however, the imaging specialist must be cautious when interpreting CT scans in the very aged (as well as the very young) because the observed white matter differences may be a part of the maturation or aging process.

MRI Appearance

On the basis of the neuropathologic differences in the water and lipid content of white matter versus gray matter (as just explained), MRI can be used to exploit these differences in imaging the brain.

T1 and T2 relaxation values in normal white matter are shorter than in gray matter. Thus, on T1-weighted images, white matter is relatively brighter in signal intensity; on T2-weighted images, white matter is less intense, or darker. In general, MRI is superior to CT in delineating differences in white and gray matter, the various gray matter nuclei, and white matter tracts. MRI is more sensitive than CT in demonstrating accurately the extent and distribution of histologically verified central nervous system (CNS) disease, and for that reason MRI should be the imaging procedure of choice in suspected white matter abnormalities. Still, familiarity with the CT findings is important because some patients may undergo CT as the initial imaging procedure or may, for whatever reason, be unable to undergo MRI.

Assessment of myelination patterns in the newborn and in the developing brain by MRI has been well addressed by several MRI investigators.[2, 5, 20, 34] Myelination of the brain occurs in a more or less orderly fashion, proceeding caudal to rostral, and with more primitive structures myelinating before "newer" ones. Timetables for myelination of specific structures have been published and are useful in assessment of pediatric brain MR images. Generally, nonmyelinated tissue is *hypointense* (darker) on T1-weighted sequences but *hyperintense* (brighter) on T2-weighted sequences; as structures myelinate, they become hyperintense (bright) on T1-weighted sequences but hypointense (dark) on T2-weighted sequences (Figs. 13–3 and 13–4).

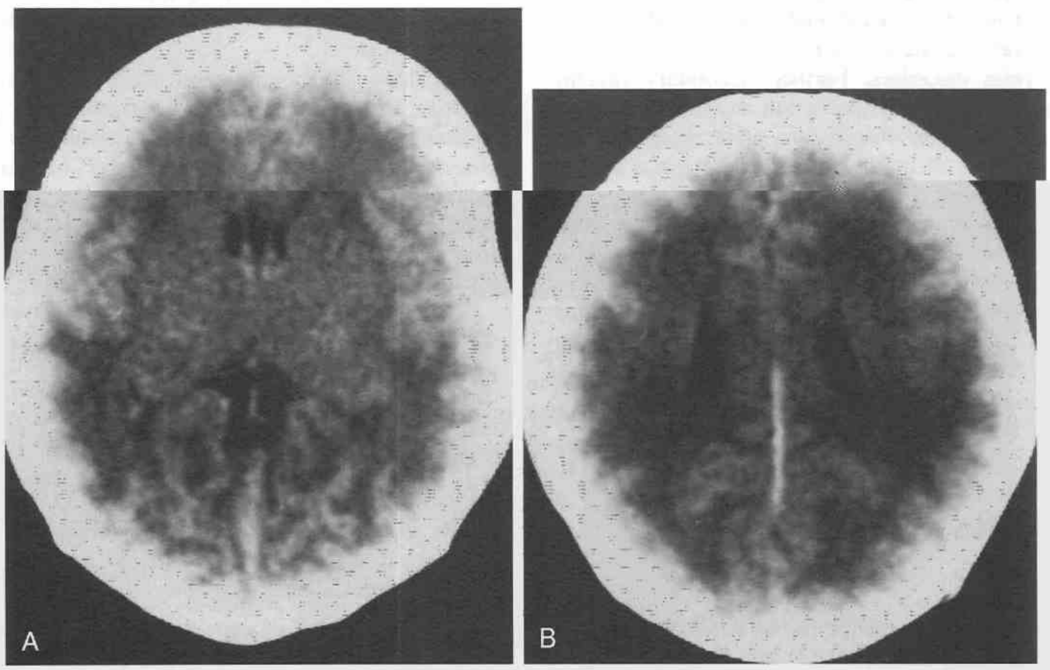

Figure 13–2. CT scans of myelin in a normal neonate. The immature myelin with its high water content imparts a generalized lucency to the central white matter. Note especially the discrete border with overlying cortical tissue. The internal capsule, however, having more mature myelination, is not visualized separately.

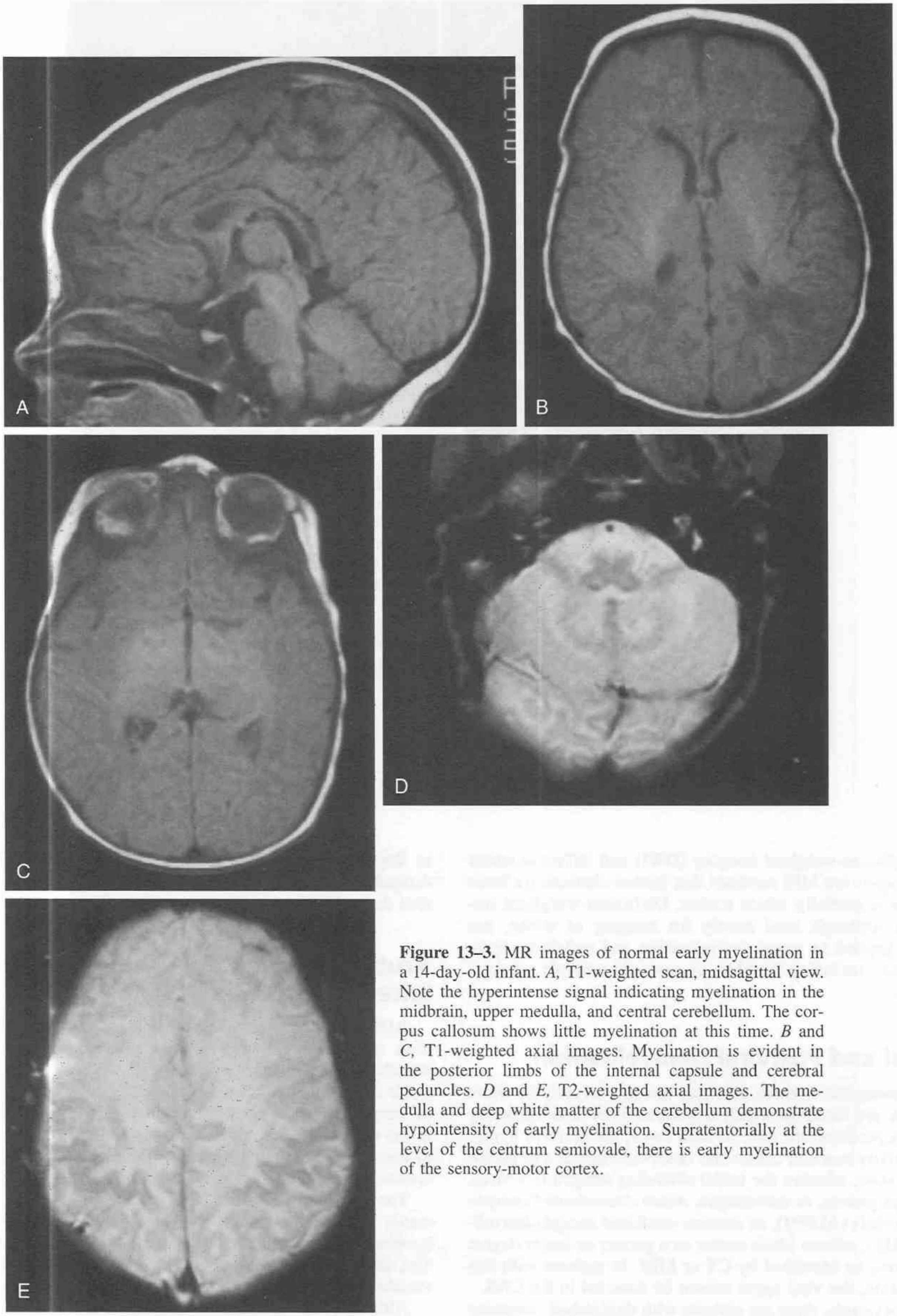

Figure 13–3. MR images of normal early myelination in a 14-day-old infant. *A,* T1-weighted scan, midsagittal view. Note the hyperintense signal indicating myelination in the midbrain, upper medulla, and central cerebellum. The corpus callosum shows little myelination at this time. *B* and *C,* T1-weighted axial images. Myelination is evident in the posterior limbs of the internal capsule and cerebral peduncles. *D* and *E,* T2-weighted axial images. The medulla and deep white matter of the cerebellum demonstrate hypointensity of early myelination. Supratentorially at the level of the centrum semiovale, there is early myelination of the sensory-motor cortex.

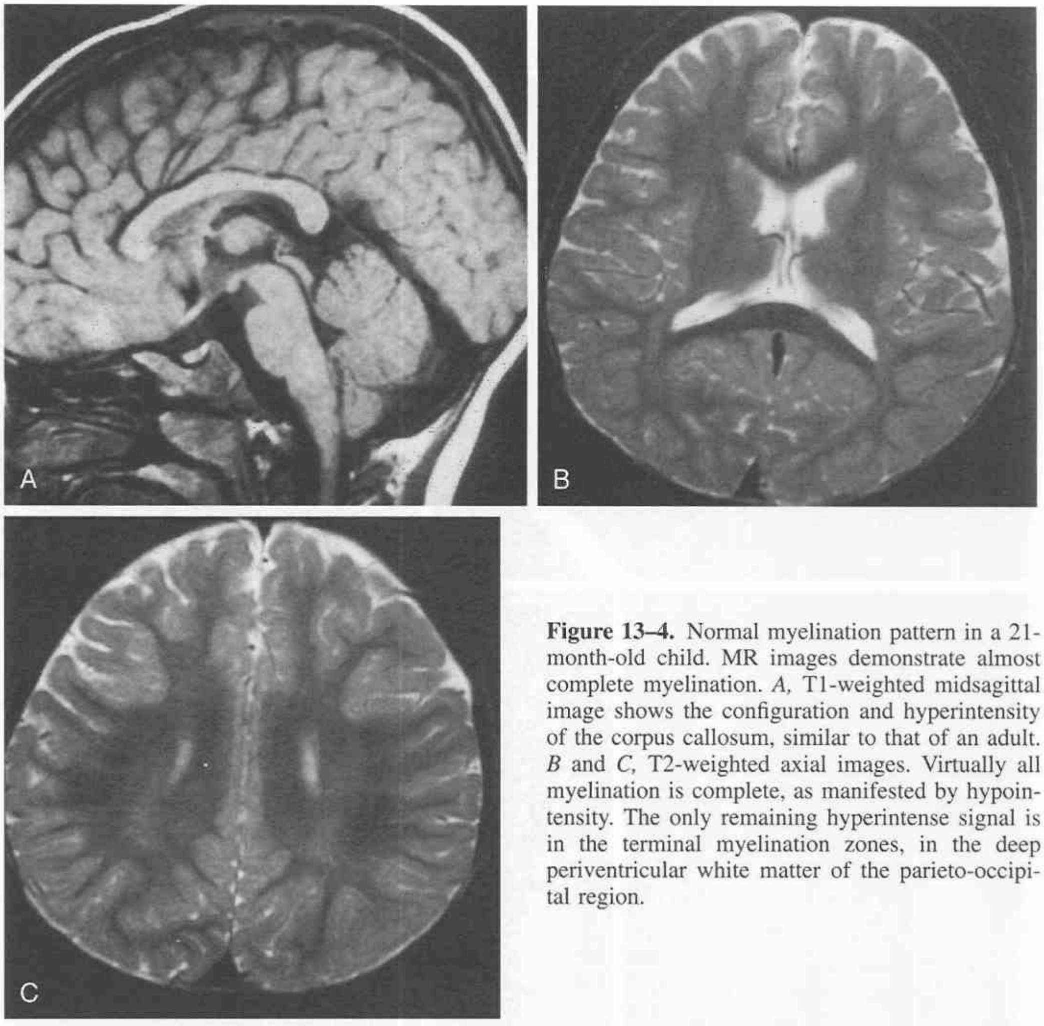

Figure 13–4. Normal myelination pattern in a 21-month-old child. MR images demonstrate almost complete myelination. *A,* T1-weighted midsagittal image shows the configuration and hyperintensity of the corpus callosum, similar to that of an adult. *B* and *C,* T2-weighted axial images. Virtually all myelination is complete, as manifested by hypointensity. The only remaining hyperintense signal is in the terminal myelination zones, in the deep periventricular white matter of the parieto-occipital region.

Diffusion-weighted imaging (DWI) and diffusion tensor techniques are MRI methods that further characterize brain tissue, especially white matter. Diffusion-weighted imaging, although used mostly for imaging of stroke, has been applied to many demyelinating and metabolic brain diseases, including Krabbe's disease and multiple sclerosis (MS).[31, 78]

Viral and Postviral Demyelination

Among the diseases that may directly involve the white matter are those in which hypersensitivity and immunity play a predominant role. In such cases, the cerebral hypersensitivity reaction causes the observed clinical and pathologic state, whether the initial offending antigen is a virus, foreign protein, or autoantigen. *Acute disseminated encephalomyelitis* (ADEM), or *immune-mediated encephalomyelitis* (IME), affects white matter to a greater or lesser degree and may be identified by CT or MRI. In patients with this condition, the viral agent cannot be detected in the CNS.

Conversely, there are patients with diminished immunity in whom a virus, which normally cannot gain a foothold in the CNS, propagates there unchecked and results in demyelination; such a disease is PML. Some virus-associated demyelinating conditions are described next.

Acute Disseminated Encephalomyelitis

ADEM has been associated with varicella zoster infections and measles as well as with rubella, influenza, and possibly infectious mononucleosis. The postvaccinal types result from inoculation for rabies, yellow fever, or influenza or from other brain-derived vaccines.[77] In some subacute forms of ADEM, the onset is slower and the course of the disease is prolonged. Corticosteroid medication may be beneficial in these conditions.[71]

The distribution of the encephalomyelitis is predominantly in the white matter, characterized pathologically by lymphocytic and mononuclear perivenous inflammation. The demyelination may be local or diffusely confluent, and variable degrees of edema may be present.

Although low-attenuation lesions in the white matter have been described on CT scans,[50] MRI is much more

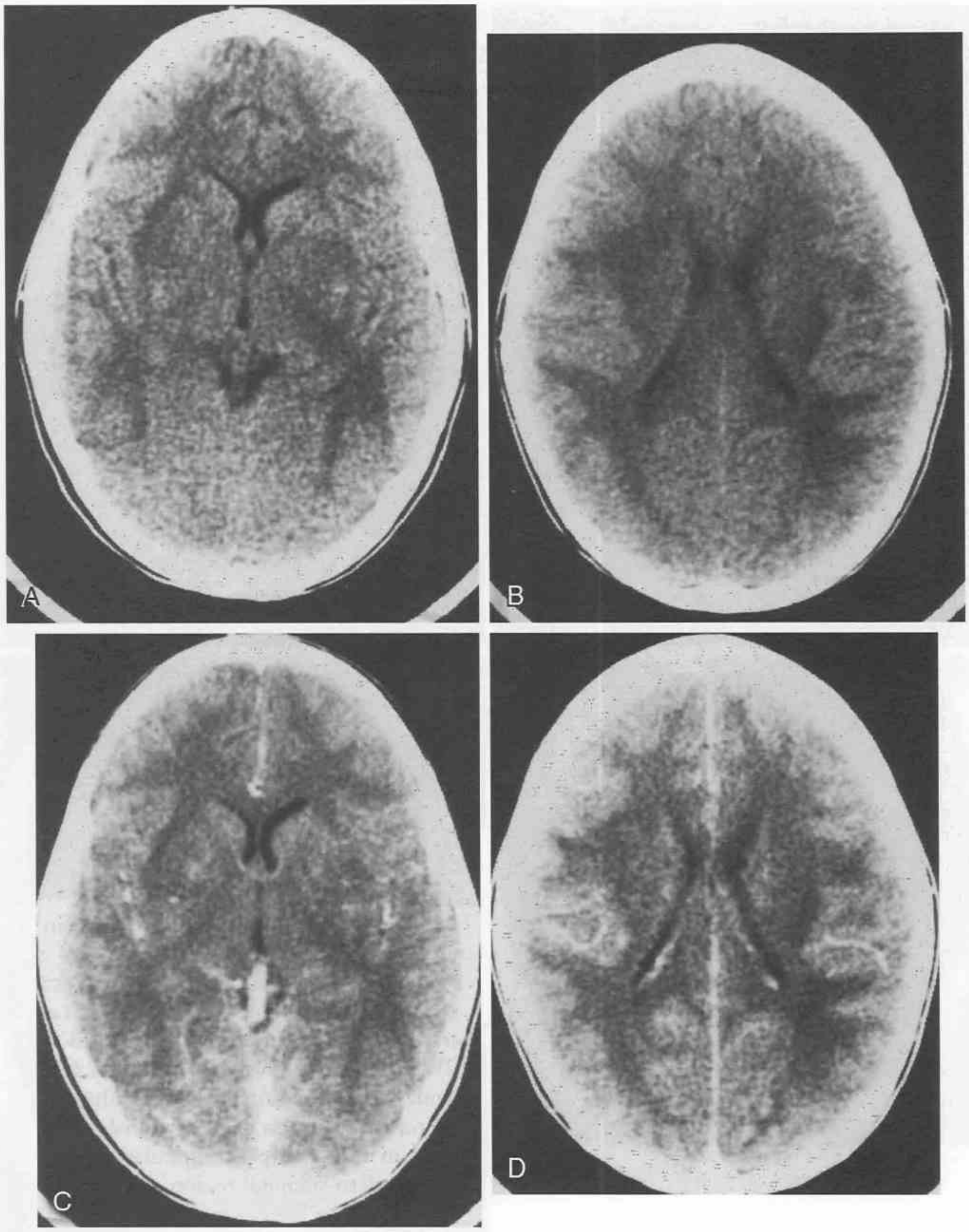

Figure 13–5. Acute disseminated encephalomyelopathy (ADEM). *A* and *B,* Non–contrast-enhanced CT scans demonstrate multifocal white matter lucencies, most visible in the basal ganglia bilaterally as well as in the parieto-occipital white matter. *C* and *D,* There is no contrast enhancement. The multiplicity of lesions is typical.

sensitive and is the imaging method of choice in demonstrating the lesions of ADEM (Figs. 13–5 and 13–6). T2-weighted MR images are the most sensitive, with asymmetrical white matter foci of hyperintensity. The size and number of lesions are variable. Even gray matter may be involved.

Enhancement with gadolinium may be prominent, either as punctate foci or, less commonly, as ringlike lesions.[12] Corresponding lesions may be also be seen in the spinal cord and less commonly in the optic nerves. An important differential diagnostic consideration is MS, but fortunately the time course of the two diseases differs.[41] MS is relapsing-remitting, whereas ADEM is a monophasic illness. Another important diagnostic consideration is vasculitis, which may mimic the lesions of ADEM. ADEM usually resolves, and the prognosis for recovery is good.

Progressive Multifocal Leukoencephalopathy

A compromised immune system may predispose to viral replication in the brain, resulting in leukoencephalopathy.

PML is a rare, subacute demyelinating disease caused by replication of polyoma virus in the brain of an individual with immunosuppression, first reported with malignant

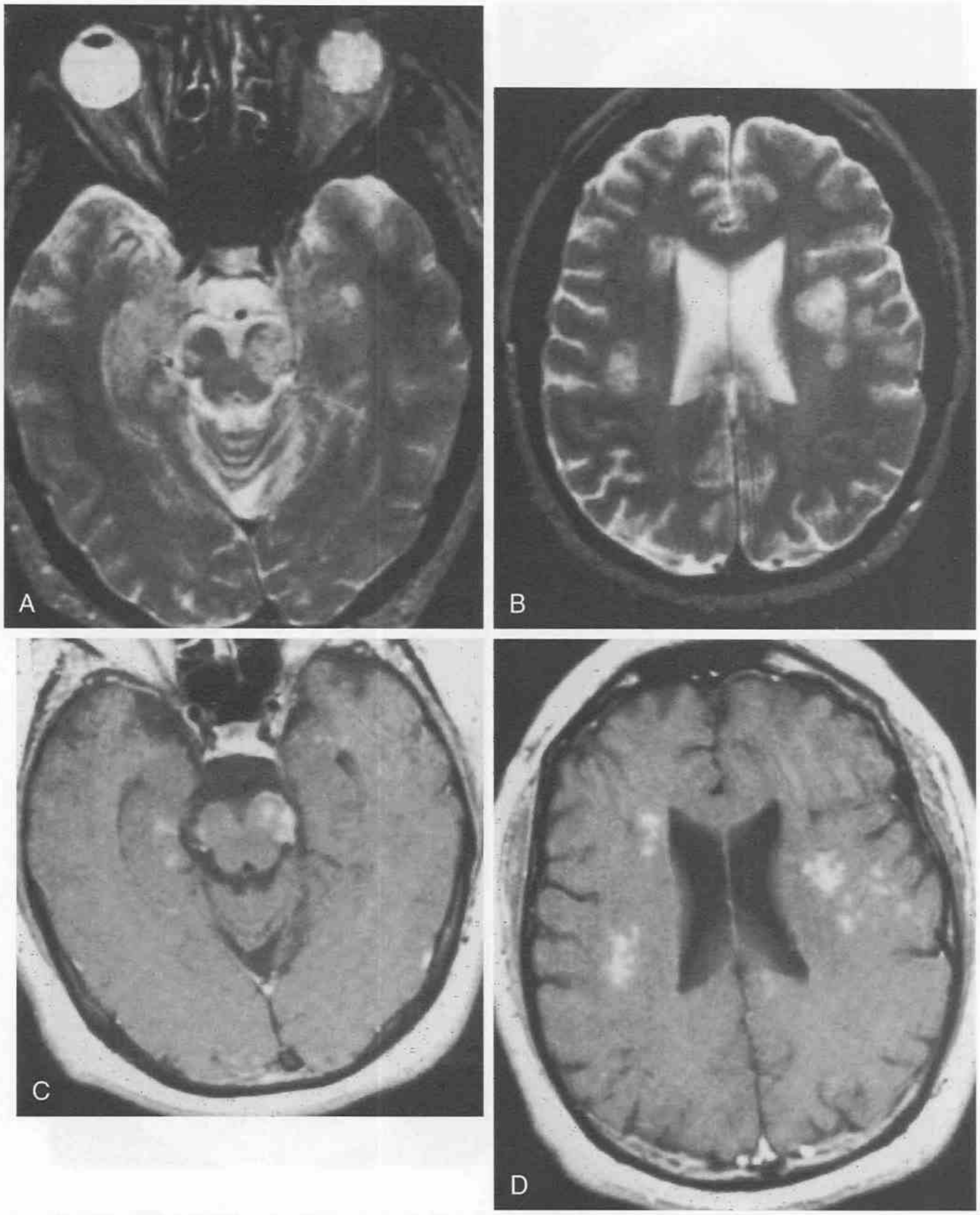

Figure 13–6. Acute disseminated encephalomyelopathy (ADEM) in a 52-year-old man with memory loss, apathy, and inflammatory cells in the cerebrospinal fluid. *A* and *B,* Cranial MR T2-weighted axial images show multiple, hyperintense lesions involving the right medial temporal lobe, both cerebral peduncles, and the mesencephalic deep white matter. *C* and *D,* Gadolinium contrast-enhanced, T1-weighted MR images at the same levels show patchy multinodular contrast enhancement within the lesions.

lymphoproliferative disease.[65, 92] PML has been associated with acquired immunodeficiency syndrome (AIDS) and is now the most frequently encountered predisposing disease.[47]

PML has a characteristic radiographic appearance on CT and MRI scans (Figs. 13–7 to 13–12).[53, 97] Subcortical foci of demyelination are seen with scalloped lateral borders following the outline of the intact overlying cortex. With CT, the lesions show decreased attenuation; with MRI, they are correspondingly intense on proton-density and T2-weighted images. In my experience, there is a predilection for the parieto-occipital region. The corpus callosum, the internal and external capsules, and the posterior fossa structures are less commonly involved. The disease is progressive, and early minimal lesions can be followed temporally by CT and MRI as they become larger and coalesce.

Mass effect is usually absent on both pathologic and radiologic examinations and radiographically. In rare cases, the lesions are edematous and swollen, making the imaging diagnosis more problematic. Contrast enhancement, which helps to distinguish this disease from toxoplasmosis and other opportunist infections and acute MS, is not usually present. In later stages of the disease, shrinkage of the affected white matter may cause ipsilateral atrophic changes.

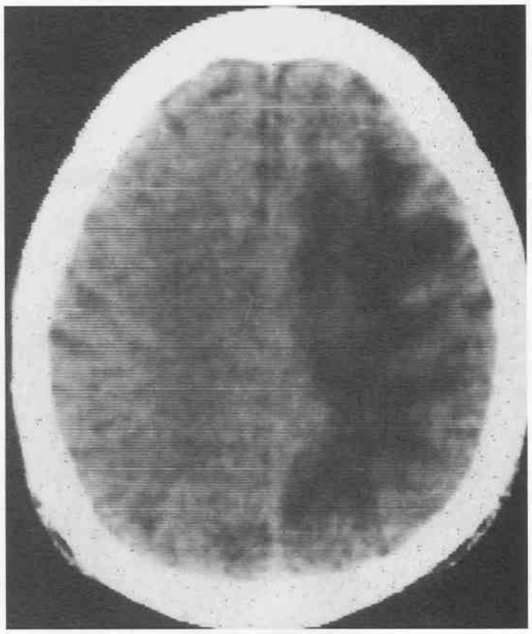

Figure 13–7. Progressive multifocal leukoencephalopathy (PML) in a 63-year-old man with worsening right hemiparesis and a lung nodule. On the basis of this CT scan, a left frontal brain biopsy, which was diagnostic of PML, was performed. A large, low-density lesion occupies the entire left centrum semiovale. Other, lower sections showed the lesion extending down into the internal capsule; a second, much smaller lesion was also visible in the right parietal white matter. The clearly defined borders of the lesion, the absence of contrast enhancement, and the lack of mass effect, despite the lesion's considerable extent, are typical of PML.

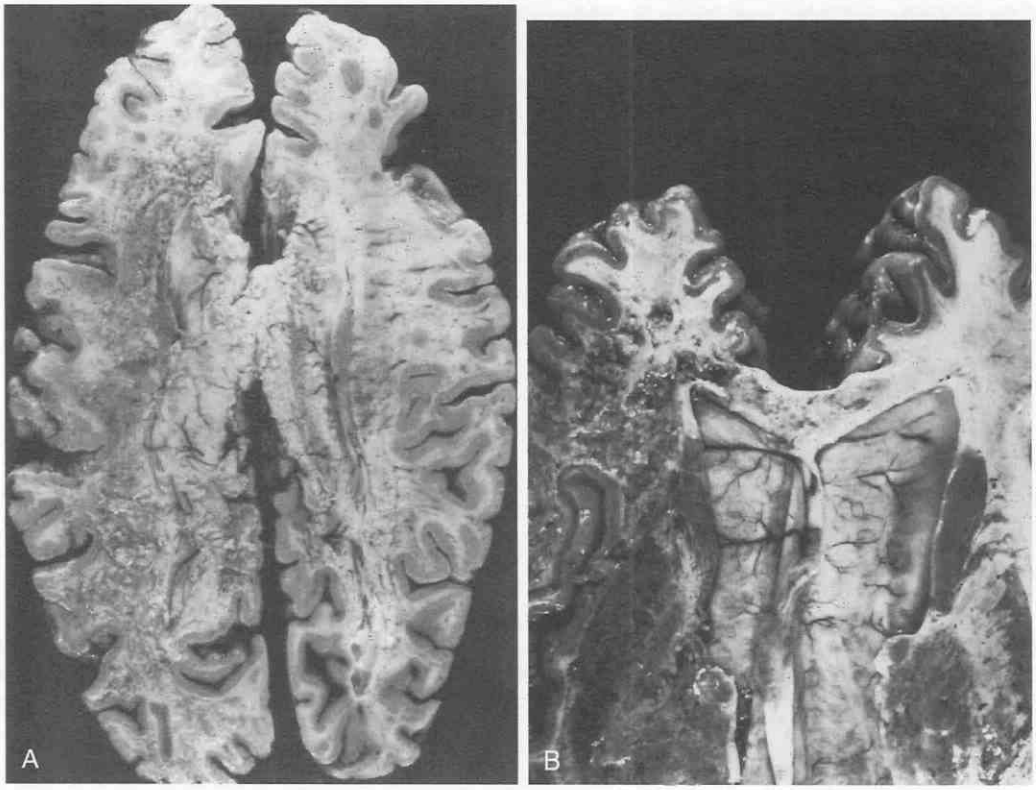

Figure 13–8. Progressive multifocal leukoencephalopathy (PML), typical pathologic specimen. The patient is a 51-year-old woman with a 7-month history of personality changes, blindness, dementia, and eventual coma. *A* and *B,* Horizontal brain sections obtained at autopsy. Almost the entire right hemispheric white matter has been replaced by a granular necrotic process. A similar process has begun in the left hemisphere. *B,* Close-up view of unfixed right frontal lobe. The typical lesion of PML has destroyed the central white matter and extends across the corpus callosum. Note the spared cortical mantle.

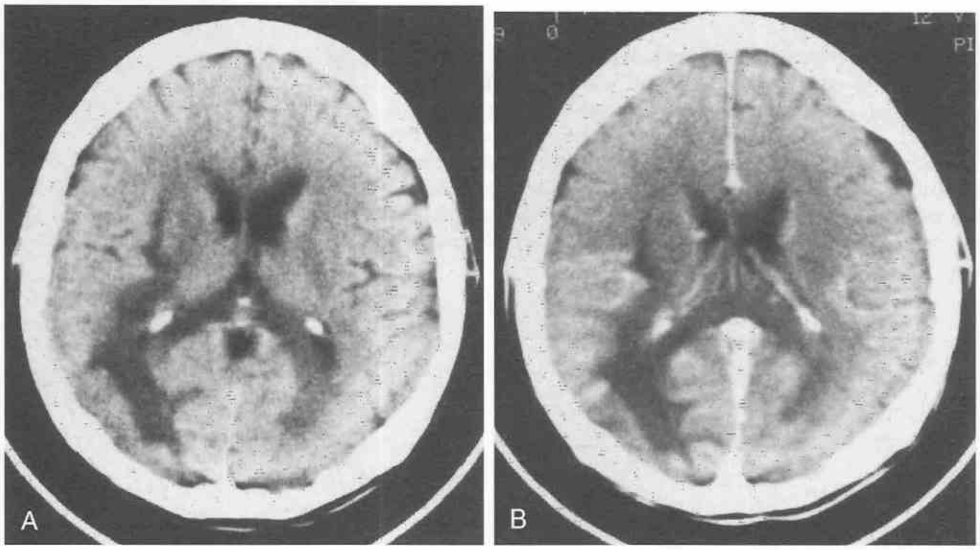

Figure 13–9. Progressive multifocal leukoencephalopathy (PML) associated with acquired immunodeficiency syndrome (AIDS). *A,* This non–contrast-enhanced CT scan, in this patient with rapidly progressive neurologic disease, shows a well-defined area of lucency in the right parieto-occipital white matter extending forward into the external capsule and medially into the splenium of the corpus callosum. Lesser involvement in the opposite occipital lobe is also present. *B,* Postcontrast image at the same level shows nonspecific enhancement of the overlying cortex but none within the white matter lesions. The diagnosis of PML was confirmed by biopsy.

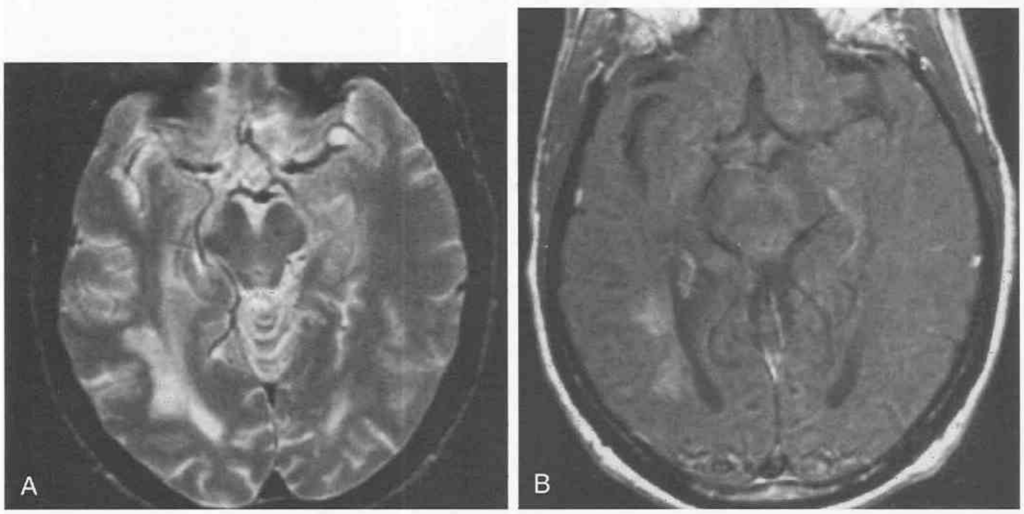

Figure 13–10. Progressive multifocal leukoencephalopathy (PML) in a 56-year-old man with human immunodeficiency virus infection and hemiparesis. *A,* Cranial T2-weighted axial MR image shows a confluent hyperintense white matter lesion adjacent laterally to the right occipital horn. Note the sparing of the overlying gray matter cortex. *B,* Magnetization transfer (MT) postgadolinium-enhanced MR axial image. Note the minimal contrast enhancement, which was not seen on CT or standard T1-weighted MR images.

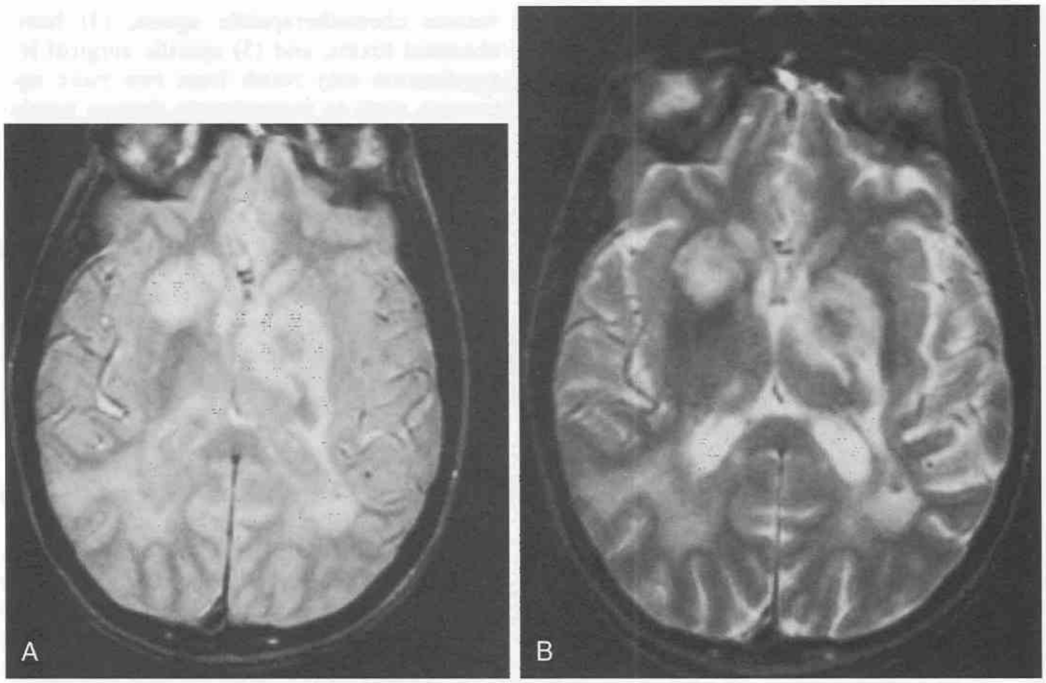

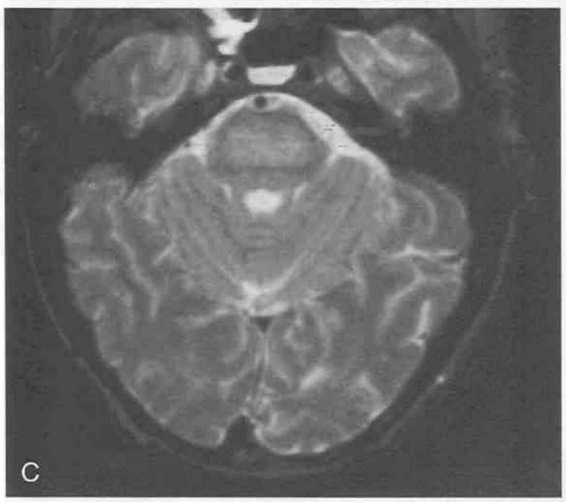

Figure 13–11. Progressive multifocal leukoencephalopathy (PML) and toxoplasmosis in a 46-year-old man with acquired immunodeficiency syndrome (AIDS). *A* and *B,* Proton-density and T2-weighted axial images at the level of the thalami. Bilateral, edematous basal ganglia lesions are typical of toxoplasmosis. Bilateral, deep white matter hyperintense lesions are also seen in both occipital lobes, compatible with a diagnosis of PML. The thalamic lesions enhanced with contrast medium; the occipital lesions did not. *C,* T2-weighted axial image demonstrates presumed PML of the pons.

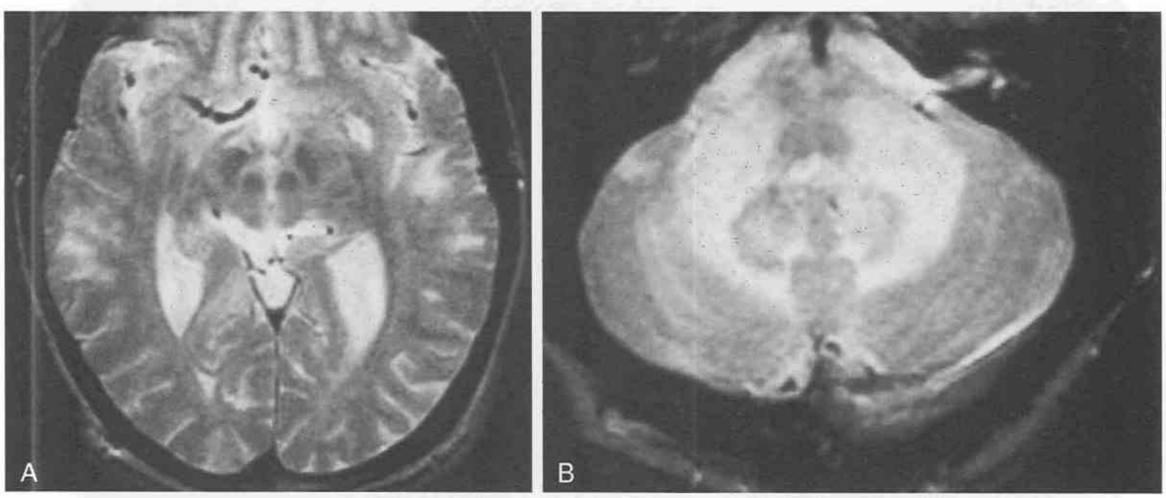

Figure 13–12. Progressive multifocal leukoencephalopathy (PML) in a 44-year-old man with chronic lymphocytic leukemia. Cranial T2-weighted axial MR images. *A,* At the level of the midbrain, there are bilateral temporal white matter lesions, with complete sparing of the overlying cortex. *B,* Symmetrical, hyperintense cerebellar white matter lesions are seen in the brachium pontis and corpus medullaris. The diagnosis of PML was confirmed by biopsy.

In the appropriate clinical setting, MRI or CT can be of value in confirming the clinical suspicion of PML when radiographic findings are typical. Equally valuable is the exclusion of underlying tumor or abscess.

AIDS-Related Leukoencephalitis

It is now known that the human immunodeficiency virus (HIV) is not only lymphotrophic but also neurotropic. It replicates in multinucleated giant cells within the CNS, resulting eventually in demyelination. This demyelination is characterized by negligible edema and a lack of inflammation. Neuroimaging of HIV encephalitis, whether by CT or MRI, tends to lag behind the pathologic involvement. Generalized atrophy is the most common abnormality that is nonspecific. With more severe involvement, CT discloses symmetrical white matter hypodensity, usually seen bifrontally. There is no contrast enhancement or mass effect.

With MRI, there is greater sensitivity, with diffuse increase in signal on T2-weighted and proton-density images (Fig. 13–13). Patchy white matter lesions may become confluent and extensive; this may cause diagnostic confusion with PML, also commonly associated with AIDS.[60, 70] Patients with PML are usually much more symptomatic, with more rapid deterioration.

Toxic and Traumatic Encephalomyelopathies

Many toxic and traumatic processes may selectively damage or destroy the myelinated portions of the brain. Among the agents implicated are (1) gamma radiation, (2) various chemotherapeutic agents, (3) heavy metals, (4) chemical toxins, and (5) specific surgical lesions. The demyelination may result from two more agents acting in concert, such as methotrexate therapy combined with cranial irradiation.

Radiation-Induced Demyelination

Radiation to the brain may cause *radiation necrosis* (radionecrosis) or *diffuse leukoencephalopathy.* These two types differ in their clinical course and in their pathologic and radiographic appearance.

Radiation Necrosis

Radiation necrosis is characterized by coagulative destruction of the white matter, accompanied by fibrinoid necrosis of the capillary blood vessels. The lesion is the result of high-dose focal radiation therapy to the brain, usually appearing after a latent period of 4 months to several years. Characteristically, radionecrosis appears on CT scan as abnormal low-density white matter with mass effect and may have a higher density central core that enhances (Fig. 13–14).

MRI is more sensitive and specific than CT and shows prominent white matter edema on T2-weighted and proton-density images. A core of enhancing mass may be present, and the differential diagnosis from recurrent tumor may be difficult. Often the distinction can be made only by positron emission tomography (PET) or by magnetic resonance spectroscopy (MRS) to distinguish the metabolically active tumor from the inactive radiation necrosis. Stereotactic biopsy may be necessary in selected cases.

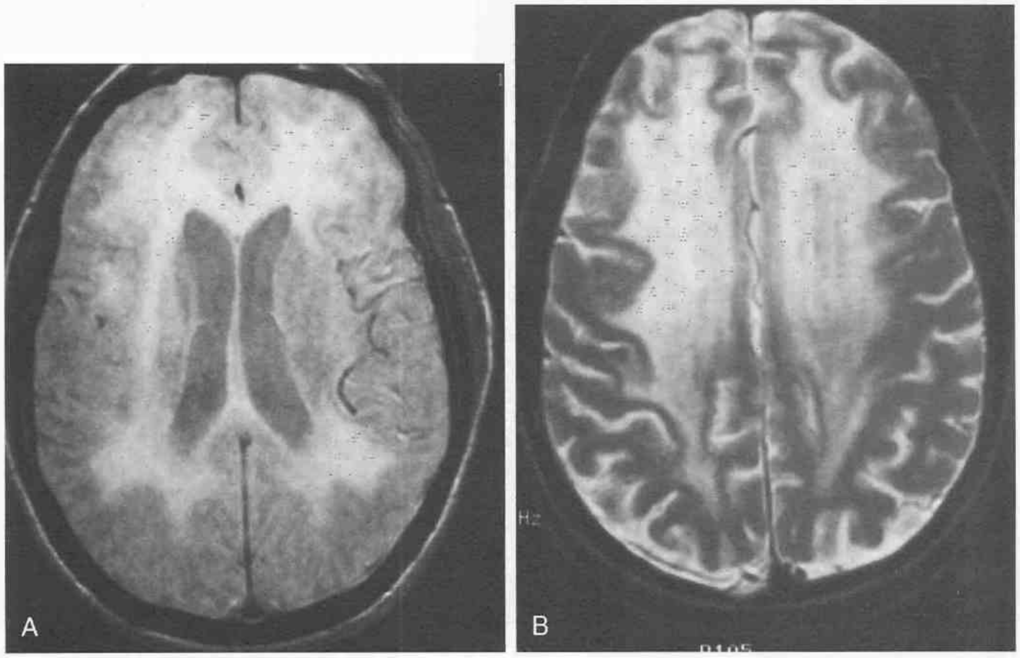

Figure 13–13. Human immunodeficiency virus encephalitis in a 39-year-old patient with acquired immunodeficiency syndrome (AIDS) and rapidly worsening dementia. *A* and *B,* Proton-density and T2-weighted axial MR images show widespread diffuse hyperintensity of the deep cerebral white matter. Not shown is similar involvement of the pons and mesencephalon.

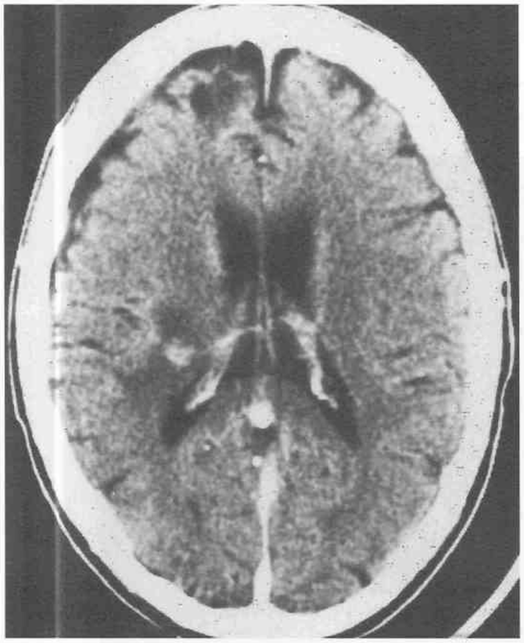

Figure 13–14. Radiation necrosis, contrast-enhanced CT scan. A small, enhancing focus within the right posterior corona radiata is surrounded by white matter lucency. (The right frontal pole encephalomalacia resulted from a previous biopsy establishing the diagnosis of intracranial lymphoma.) The differential diagnosis of the contrast-enhancing lesion includes infection or recurrent tumor. At autopsy, radiation necrosis was found without lymphoma or abscess.

Diffuse Radiation-Induced Leukoencephalopathy

Diffuse radiation-induced leukoencephalopathy is more common than radiation necrosis.[74, 87] This diffuse leukoencephalopathy may involve all visible cerebral white matter when whole brain irradiation has been given, or it may correspond closely to irradiated volumes after treatment for a solitary brain tumor.

CT scans show diffuse, low-density white matter without contrast enhancement and no mass effect. The surrounding cortical gray matter ribbon is preserved. Correspondingly, MRI shows abnormal signal intensity in the white matter on T2-weighted and proton-density images (Fig. 13–15). The lesions may start as small foci, which then coalesce to become symmetrical. Some of the most symmetrical white matter involvement in any disease category is seen in diffuse radiation-induced leukoencephalopathy.

Patients may have dementia or may have focal neurologic findings, but MRI is so sensitive that the lesions may be discovered incidentally during follow-up examinations of relatively asymptomatic individuals. In some patients, the changes are stable; in others, they may progress. Changes are more severe with advancing age and an increasing radiation dose.

Disseminated Necrotizing Leukoencephalopathy

Disseminated necrotizing leukoencephalopathy (DNL), or *subacute leukoencephalopathy*, closely related to radiation necrosis, is an iatrogenic complication of intensive chemotherapy directed to CNS malignancy.[27] Responsible agents appear to be combined whole brain irradiation with chemotherapy, most commonly methotrexate.

DNL has been associated with multiagent chemotherapy without irradiation in such conditions as adult leukemia and bone marrow transplantation for breast cancer.[91] On pathologic examination, the lesions consist of discrete multifocal necrosis disseminated randomly in the white matter and becoming confluent and extensive in extreme cases.

CT and MRI findings are similar to those seen with postradiation encephalopathy (Fig. 13–16). In milder forms, CT and MRI show diffuse symmetrical white matter lesions similar to those seen with radiation alone.[62, 74] Again, as in radiation-induced injury, the most severe cases lead to swelling with ventricular compression and midline shift and to contrast enhancement.

Mineralizing Microangiopathy

Another sequela of radiation treatment and chemotherapy results in intracerebral calcifications, commonly located in the subcortical zones and basal ganglia, and, less commonly, in the cortex. These findings are usually associated with generalized atrophy and diffuse white matter disease, seen as lucency on CT scans and hyperintensity on MR images. This is one entity in which CT scanning may be more diagnostic, since MRI is relatively insensitive to the calcifications unless gradient techniques are used (Figs. 13–17 and 13–18).

Marchiafava-Bignami Disease

Marchiafava-Bignami disease (MBD), originally described in Italian alcoholic patients, is characterized by toxic demyelination of the corpus callosum and, frequently, by extension to the centrum semiovale.

Pathologically, the myelin loss may be striking and may be accompanied by axonal degeneration. Acute deterioration is common, but survival with little permanent deficit is possible. Both CT and MRI show prominent involvement of the corpus callosum, resulting in lucency on CT scans and hyperintensity on T2-weighted and proton-density MR images (Fig. 13–19). MRI is superior to CT in demonstrating the extracallosal sites of involvement.[16, 25, 75, 100]

Hypoxic-Ischemic Leukoencephalopathies

The white matter of the brain is susceptible to hypoxic-ischemic events and may be involved even when the insult is systemic and generalized. Thus, a leukoencephalopathy can be the end result of long-standing hypertension or a single hypotensive episode (e.g., perinatal hypoxia).[8, 11] These and other related disorders are considered in the following sections.

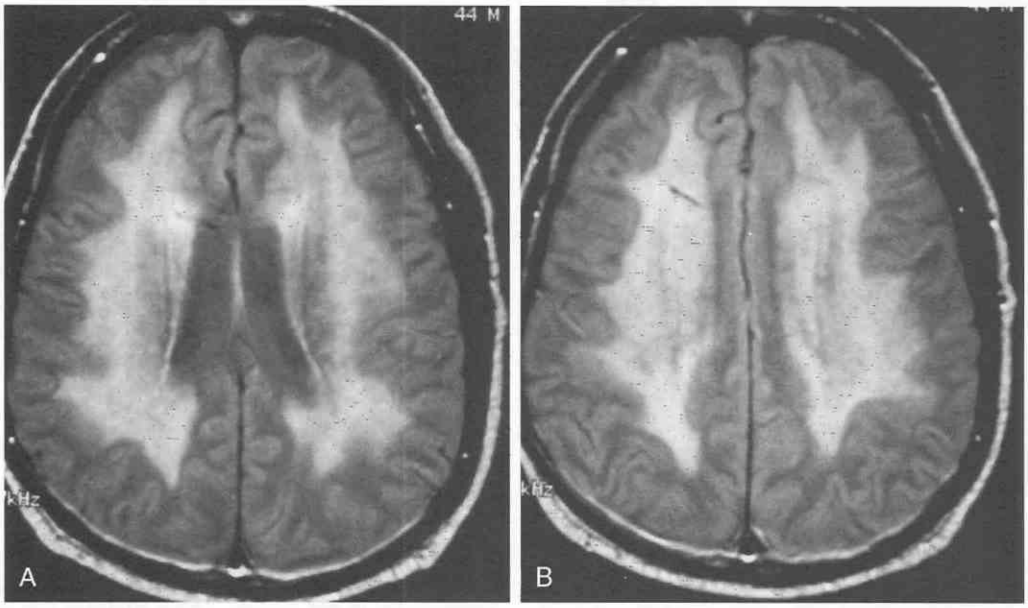

Figure 13–15. Leukoencephalopathy secondary to radiation and intraventricular methotrexate chemotherapy. *A* and *B,* Proton-density axial cranial MR image. There is extensive diffuse, confluent white matter hyperintensity.

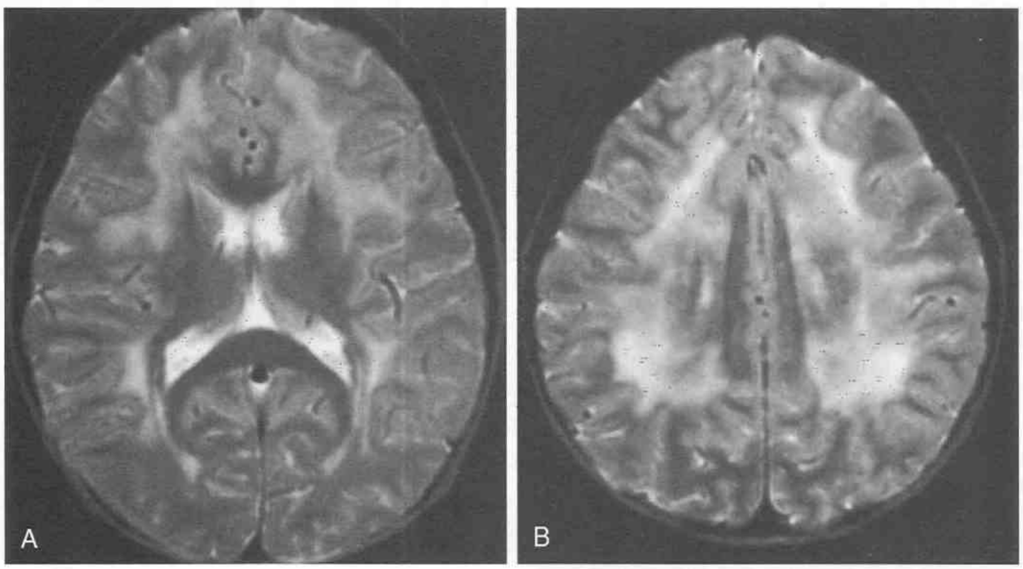

Figure 13–16. Leukoencephalopathy secondary to multiagent chemotherapy for acute lymphocytic leukemia without radiotherapy. *A* and *B,* T2-weighted axial cranial MR images show diffuse, mild hyperintensity in the deep white matter bilaterally. Despite the MR appearance, this patient had minimal neurologic signs and was doing well in school.

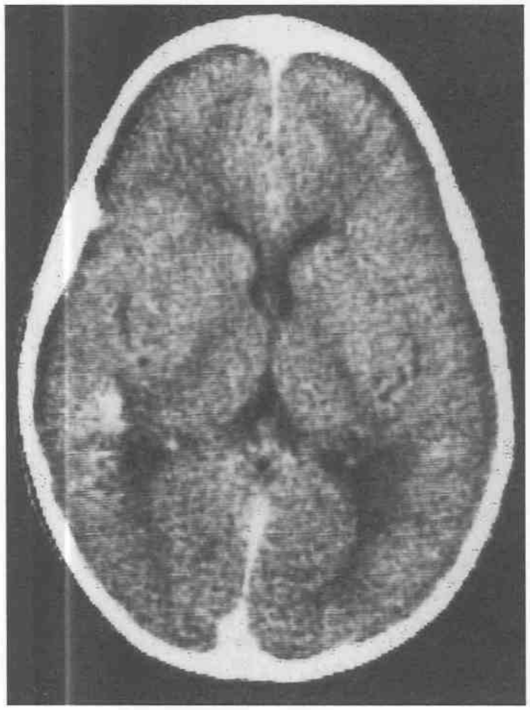

Figure 13–17. CT scan shows calcification with leukoencephalopathy (mineralizing microangiopathy). The patient is a 7-year-old girl who, 1 year previously, had received 55 Gy to the posterior fossa for a cerebellar astrocytoma. At the time of the scan, she was asymptomatic. The heavily calcified focus in the right parietotemporal region is typically situated at the interface between the cortex and white matter; the latter is abnormally lucent just medial to the calcification. Similar subtle changes are mirrored in the opposite hemisphere.

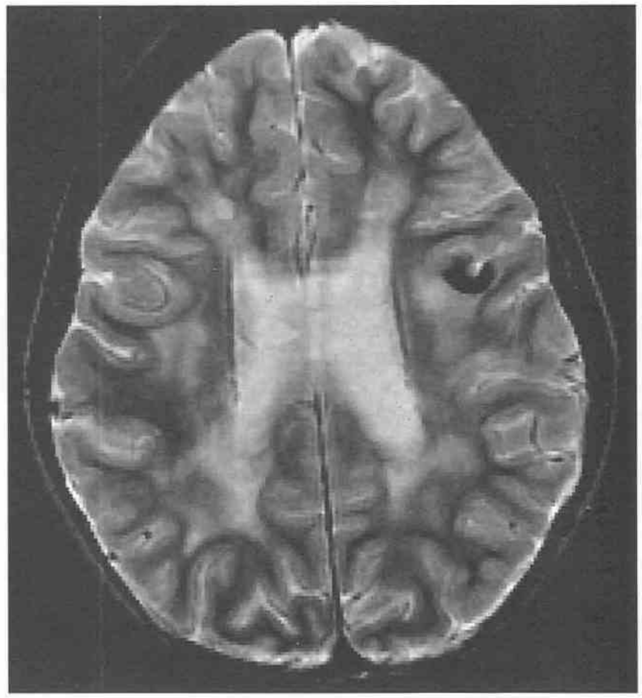

Figure 13–18. Diffuse necrotizing leukoencephalopathy (DNL) in a 20-year-old man with acute lymphoblastic leukemia several years after intrathecal methotrexate therapy and craniospinal irradiation. This T2-weighted axial MR image demonstrates widespread demyelination; there also is a focus of T2-weighted hypointensity in the left frontal deep cortex, indicating dystrophic calcification (mineralizing microangiopathy).

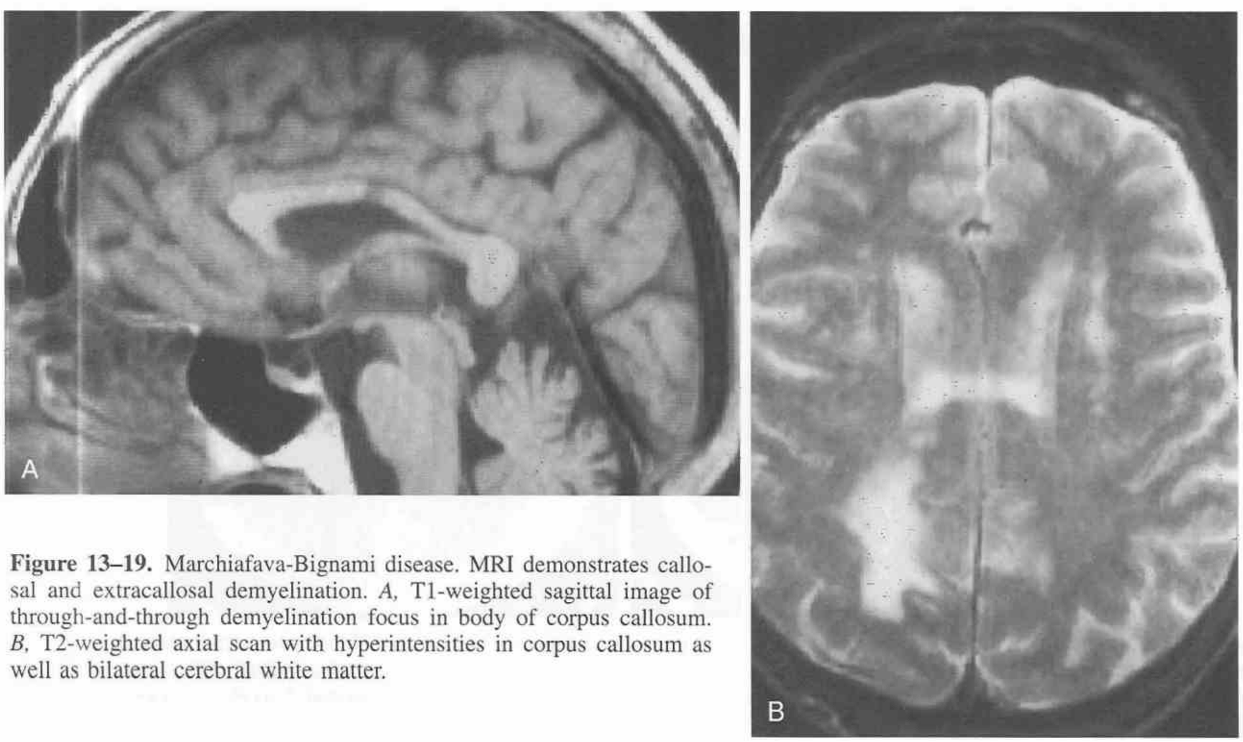

Figure 13–19. Marchiafava-Bignami disease. MRI demonstrates callosal and extracallosal demyelination. *A,* T1-weighted sagittal image of through-and-through demyelination focus in body of corpus callosum. *B,* T2-weighted axial scan with hyperintensities in corpus callosum as well as bilateral cerebral white matter.

Global Hypoperfusion Syndromes

Prolonged hypoxia with accompanying systemic hypotension and acidosis can cause selective injury to cerebral white matter. Common etiologic factors include drug overdose, cardiac and respiratory arrest, anesthesia accidents, profound hypoglycemia, strangulation, postoperative shock, carbon monoxide poisoning, status epilepticus, and vasospasm from a ruptured aneurysm.[14] Selective cerebral edema, elevated venous pressure, and structural peculiarities in the microvascularity of white matter have been proposed as causes for the apparently greater vulnerability of myelinated brain to hypoxic insults.

The damage to white matter ranges from myelinopathy to patchy or confluent frank necrosis. The severity of the lesion seems to correlate with the degree of systemic metabolic acidosis and systolic hypotension associated with the hypoxia.[42]

Lesions in cerebral cortex and basal ganglia are often observed in contiguity with the leukoencephalopathy. These changes are especially prominent in arterial boundary watershed zones, which may make differentiation from infarction difficult (Fig. 13–20). The gray matter, however, may be unaffected in the presence of severe white matter damage. Sparing of gray matter is particularly likely in so-called delayed hypoxic encephalopathy, observed in some patients who survive the initial insult and then develop subsequent neurologic signs.

The imaging appearance of global hypoperfusion states is therefore variable.[42] Symmetrical hypodensity of the white matter and lentiform nuclei has been reported in CT scans of patients after anoxia or cardiac arrest. Diffusion-weighted MRI can be of value in characterizing global cerebral anoxia and hypoxic-ischemic brain injury in neonates.[1, 98]

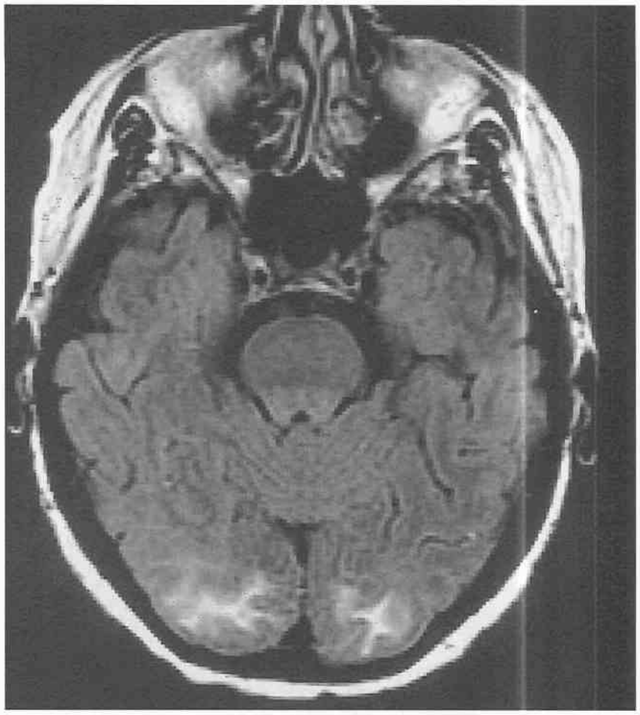

Figure 13–21. Hypertensive encephalopathy (reversible posterior leukoencephalopathy syndrome). T2-weighted axial MR scan shows symmetrical hyperintensity of occipital lobe white matter. The patient, a 52-year-old woman, experienced visual changes and acutely elevated blood pressure.

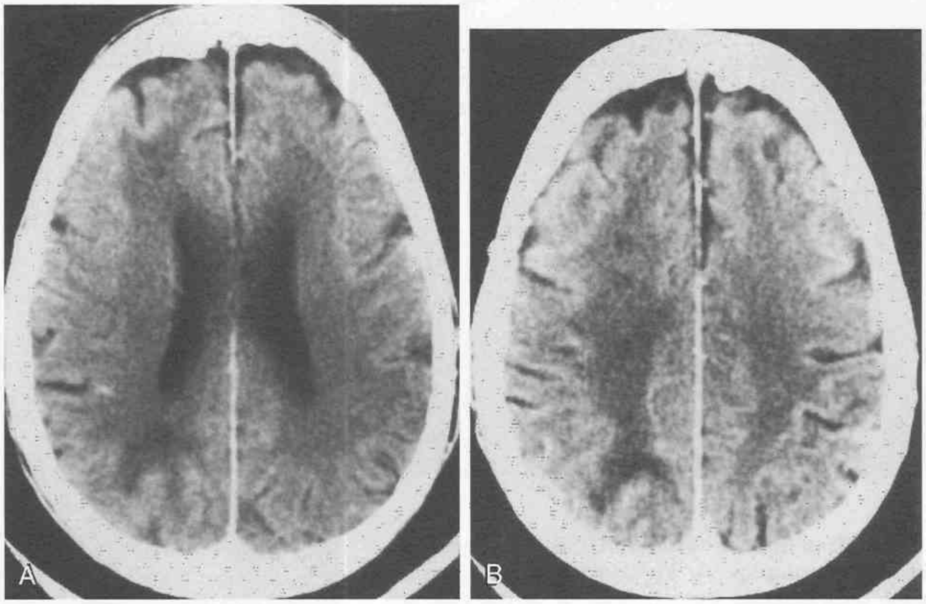

Figure 13–20. Deep watershed infarction mimicking primary leukoencephalopathy. Two CT images demonstrate right-sided white matter lesions, most prominent in the frontal and occipital region but confluent in the corona radiata. This represents ischemic leukoencephalopathy, secondary to acute deep watershed infarction. The CT scan had been normal 1 week previously at the onset of symptoms.

The following topics consider the CT and MRI findings in ischemia-related leukoencephalopathies. Primary gray matter (cortex and basal ganglia) lesions and syndromes are beyond the scope of this chapter and are not included. Even though some overlap exists with toxic encephalopathies, the major causative factor in the examples discussed here is vascular pathology.

Hypertensive Encephalopathy

An encephalopathy may develop in hypertensive patients with a rapidly rising blood pressure. This encephalopathy is caused by vascular alterations, which in turn lead to widespread cerebral edema, parenchymal microinfarcts, and even petechial hemorrhages. CT scans of patients with clinical hypertensive encephalopathy show extensive, symmetrical, well-defined hypodensity in the centrum semiovale, internal and external capsules, and periventricular white matter.[45, 69, 96] MR images are even more revealing, with T2-weighted and proton-density sequences more sensitive for the edema (Figs. 13–21 and 13–22).

Eclampsia

A specialized type of hypertensive disorder occurs in pregnancy, usually in the last trimester. Neurologic complications may include seizures, focal neurologic deficits, and even decreased level of consciousness. Most commonly, the posterior hemispheres are involved, often in a symmetrical fashion. On CT scans, the white matter shows symmetrical decreased density[26]; on MR images, long repetition time (TR) images show hyperintensity in the deep white matter of the occipital lobes.[7, 24] In other cases, scattered subcortical white matter lesions may also appear, and even basal ganglia involvement has been reported. Fortunately, with aggressive clinical treatment, most patients recover (Figs. 13–23 and 13–24).

A similar mechanism may explain the *reversible posterior leukoencephalopathy syndrome*, which affects some

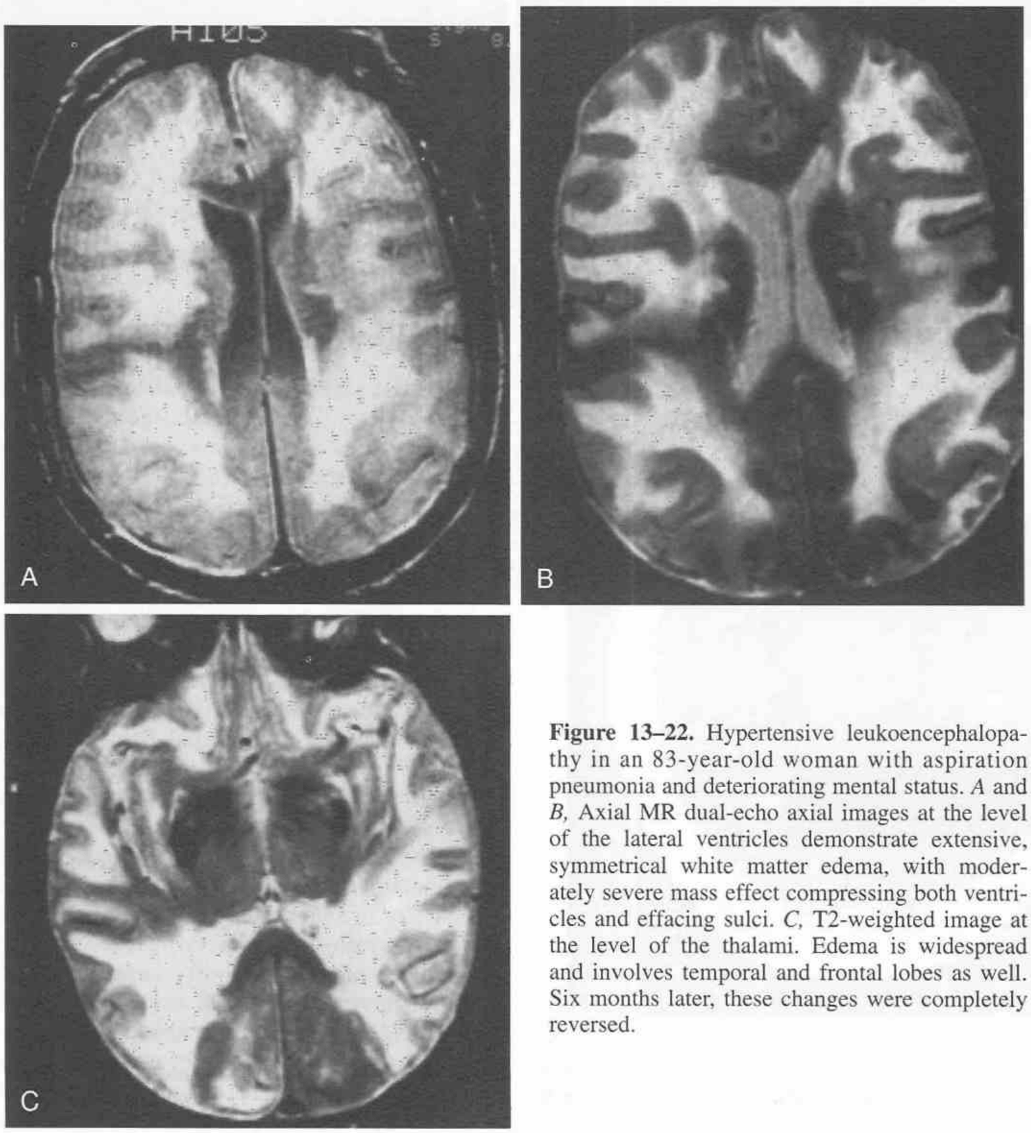

Figure 13–22. Hypertensive leukoencephalopathy in an 83-year-old woman with aspiration pneumonia and deteriorating mental status. *A* and *B*, Axial MR dual-echo axial images at the level of the lateral ventricles demonstrate extensive, symmetrical white matter edema, with moderately severe mass effect compressing both ventricles and effacing sulci. *C*, T2-weighted image at the level of the thalami. Edema is widespread and involves temporal and frontal lobes as well. Six months later, these changes were completely reversed.

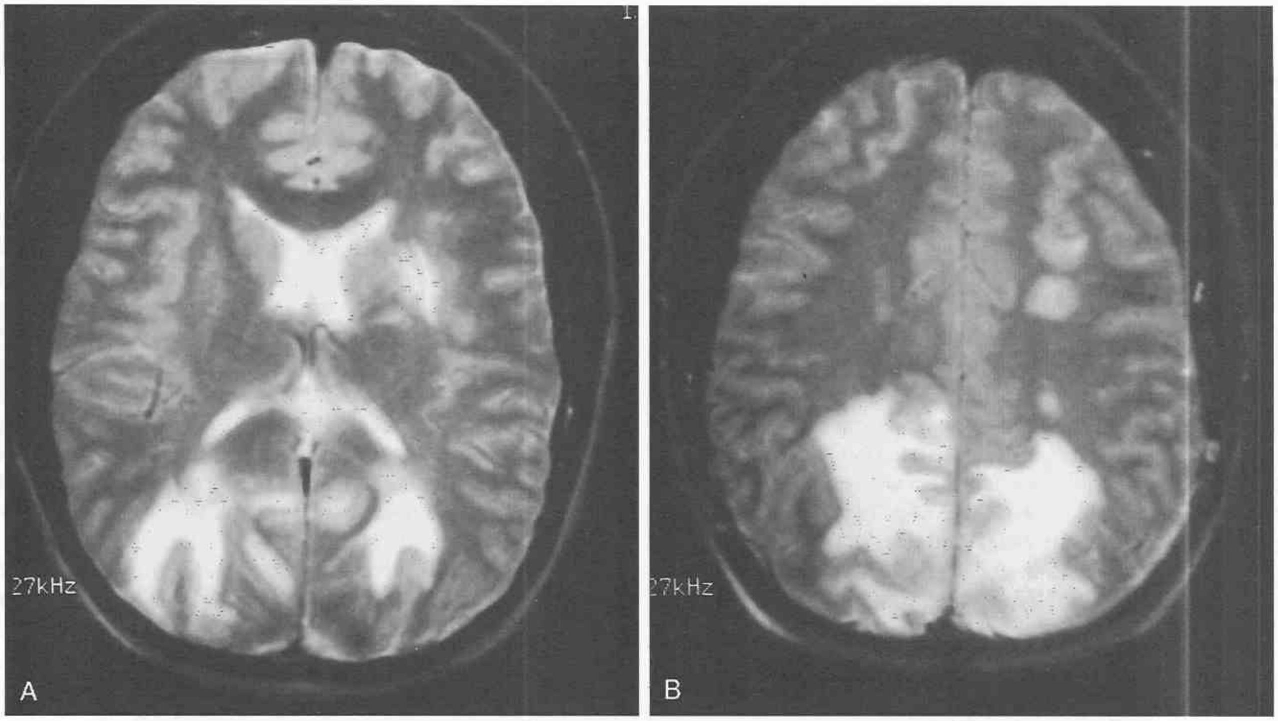

Figure 13–23. Eclampsia (reversible posterior leukoencephalopathy syndrome). *A* and *B*, T2-weighted MR axial images show the predominantly occipital white matter swelling. Cortical and left basal ganglia involvement are present.

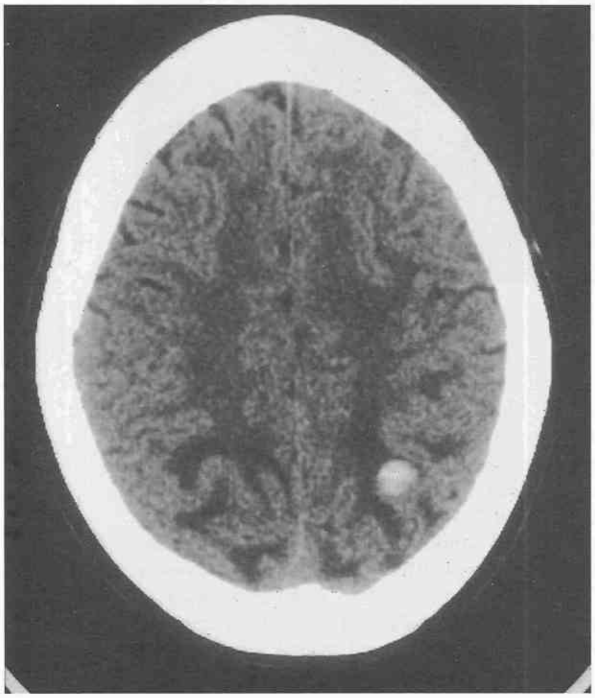

Figure 13–24. HELLP syndrome (hemolysis, elevated liver enzymes, low platelets), a severe form of eclampsia. Axial CT scan demonstrates bilateral occipital vasogenic edema and a small subcortical hemorrhage.

patients treated with cyclosporine or combination chemotherapy.[13, 36]

Binswanger's Disease

Binswanger's disease, or *subcortical arteriosclerotic encephalopathy* (SAE), is another ischemia-related leukoencephalopathy. It is now considered to be a diffuse or multifocal destructive process in the central white matter that results from generalized ischemic or vascular conditions.

Pathologically, the symmetrical and diffuse white matter lesions are associated with severe arteriosclerosis of the small penetrating arteries, which are thickened, hyalinized, stenotic, or even occluded. In most patients, multiple lacunar infarcts are also present in the basal ganglia, thalami, and pons *(état lacunaire)*. The lacunar state in white matter *(état criblé)* may be the same disorder or at least a variant thereof.[89]

In affected patients, CT reveals a diffuse, severe, incompletely symmetrical hypodensity of the central white matter, especially prominent in the frontal lobes and the centrum semiovale.[29, 103] MRI changes are much more striking, consisting of subcortical and periventricular lesions visible on fluid-attenuated inversion recovery (FLAIR), T2-weighted, and proton-density sequences. The areas are irregular, commonly grouped around the frontal and occipital horns, and in the centrum semiovale. Moderate, generalized cerebral atrophy is invariably present, and lacunar infarcts in the basal ganglia and thalami are common.

Although logical proof is lacking in many instances,

since the disease is nonfatal and chronic, often lasting for 10 years or more, sufficient case descriptions confirm that at autopsy some of these patients do have the typical neuropathologic features of SAE.[48, 89] The radiologic diagnosis of SAE may be suspected if diffuse or confluent hypodensity of the white matter, moderate cerebral atrophy, and lacunar infarcts are seen on CT or MRI scans of a hypertensive patient with clinical features of the disease. An interesting genetically transmitted form of the disease is known as *familial arteriopathic leukoencephalopathy*, or *CADASIL* (cerebral autosomal dominant arteriopathy with strokes, ischemia, and leukoencephalopathy) (Fig. 13–25).[28]

A milder white matter change may be noted in some elderly individuals.[32] These foci of increased MRI signal intensity are located in the immediate periventricular white matter extending from the frontal horns along the bodies of the lateral ventricles and also involving the trigones. This white matter abnormality is smooth and continuous and may be thin to more than a few millimeters thick. This entity appears to be different from ischemic leukoencephalopathy, since it is found in normal individuals, is accentuated with age, and is not necessarily associated with dementia or clinical symptomatology. Lacunar infarcts are not usually present. Rather than demyelination, the most likely explanation for this white

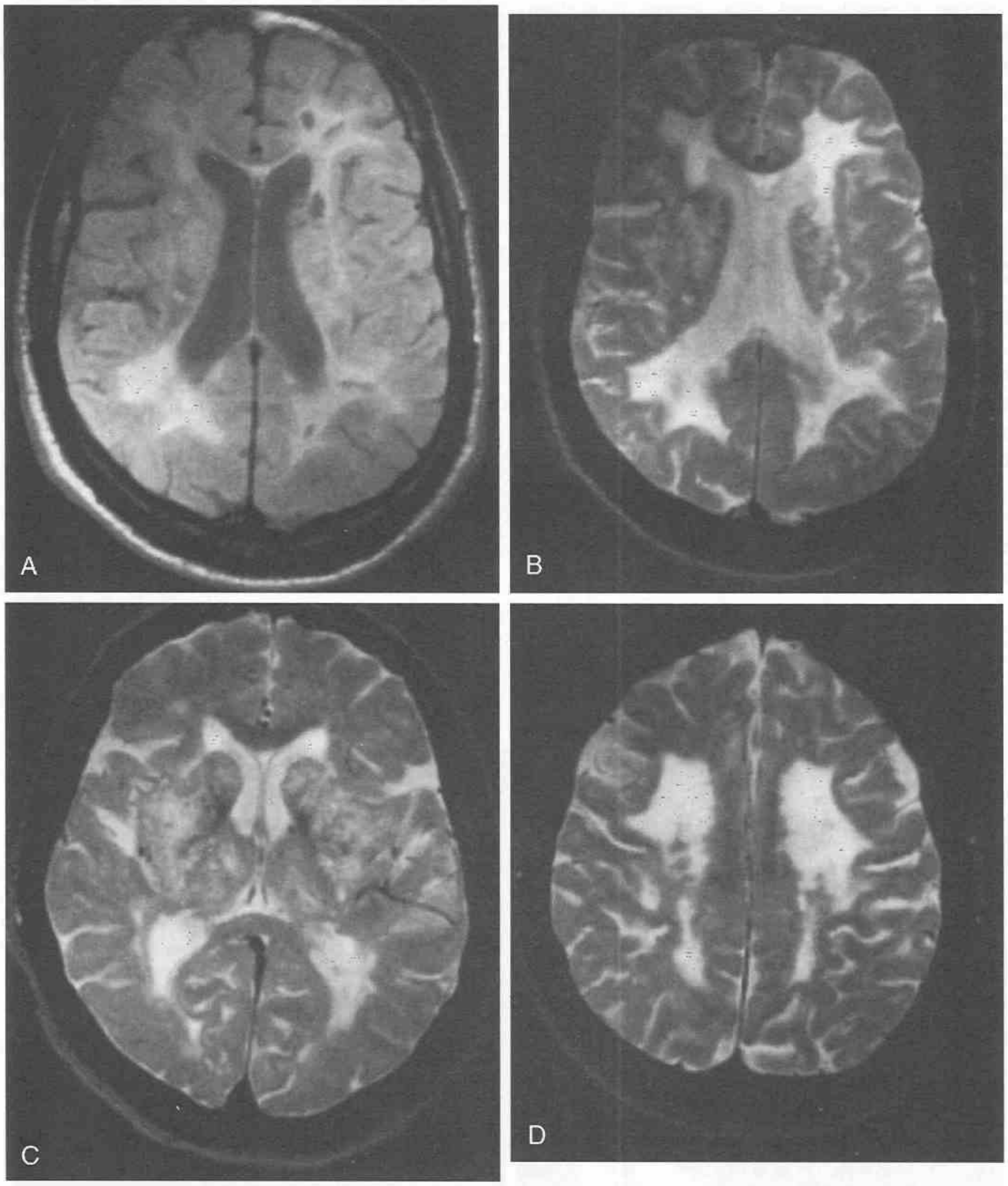

Figure 13–25. Familial arteriopathic leukoencephalopathy in two family members who were nonhypertensive with dementia. Cranial MR images are shown. Cerebral autosomal dominant arteriopathy with strokes, ischemia, and leukoencephalopathy (CADASIL) was confirmed at autopsy. *A* and *B*, Proton-density and T2-weighted axial images of diffuse symmetrical demyelination with cystic components in a 52-year-old man. *C* and *D*, T2-weighted axial MR images demonstrate extensive cribriform hyperintense signal in the basal ganglia and confluent demyelination in the centrum semiovale in a 70-year-old woman.

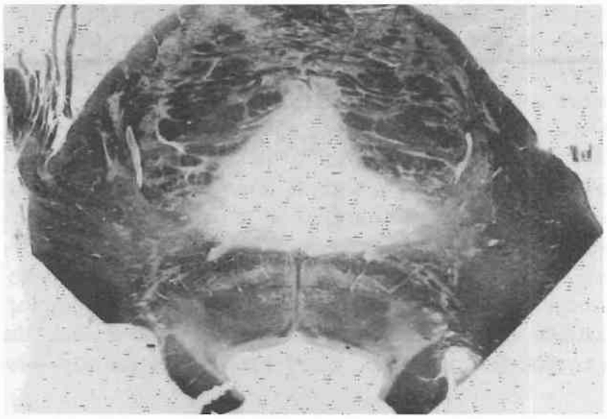

Figure 13–26. Central pontine myelinolysis (CPM), pathologic specimen. The patient is middle-aged, with chronic alcoholism and progressively impaired mental status. At autopsy, the classic triangular demyelinative lesion of CPM was found.

matter change is an aging process resulting in subependymal accumulation of fluid.

Central Pontine Myelinolysis

Central pontine myelinolysis (CPM) is a syndrome of acute pontine demyelination. Most patients with this disorder have a history of alcoholism associated with hyponatremia and exacerbated by overhydration and administration of diuretic medications. Other etiologic factors include systemic hypotension, cerebral edema, and drug-induced, inappropriate antidiuretic hormone secretion. The typical clinical presentation is a rapidly progressive, pontine-level, neurologic deficit (i.e., quadriparesis and pseudobulbar symptoms) that often progresses to a "locked-in" syndrome. Permanent and irreversible neurologic damage may result if appropriate treatment is not instituted early in the course. Partial or full recovery has been reported.[68]

Pathologically, the classic picture is edematous demyelination of the central ventral pons, with characteristic sparing of the tegmentum (Fig. 13–26). The demyelination may extend cephalocaudad from the superior cerebellar peduncle to the inferior olive. It is postulated that either the grid arrangement of descending and crossing tracts in the pons or perhaps its vulnerable vascularity is responsible for the peculiar focality of the lesion.

Although CT scans of patients with clinically apparent CPM may show central pontine radiolucency,[85] MRI is much more sensitive and is the imaging method of choice. Even on T1-weighted images, a low-signal-intensity lesion in the central pons may be seen (Fig. 13–27); however, T2-weighted images are much more preferable. The classic appearance is a triangle- or trident-shaped, central pontine hyperintensity seen in the axial plane (Fig. 13–28; see Fig. 13–27).

In more severe disease, almost the entire central pons may be involved with only a rim of normal signal around it (see Fig. 13–28). Peripheral contrast enhancement has been reported but is not a prominent imaging feature. The abnormality may regress with clinical treatment, leaving little or no residuum.

The differential diagnosis must include a variety of brain stem lesions, including ADEM, vasculitis, MS, Lyme disease, and, in rare cases, brain stem tumor.[37, 56] The clinical setting and the central symmetry of the lesion are usually sufficient for the imaging diagnosis of CPM.

Leukodystrophies and Dysmyelinating Disorders

The term *leukodystrophy* includes a heterogeneous group of heredofamilial diseases characterized by meta-

Figure 13–27. Central pontine myelinolysis (CPM) in a 56-year-old man. *A,* Midsagittal T1-weighted cranial MR image shows a triangular hypointense lesion in the midpons. *B,* Axial T2-weighted MR image at the midpontine level. Note the classic trident-shaped hyperintense lesion, characteristic of CPM.

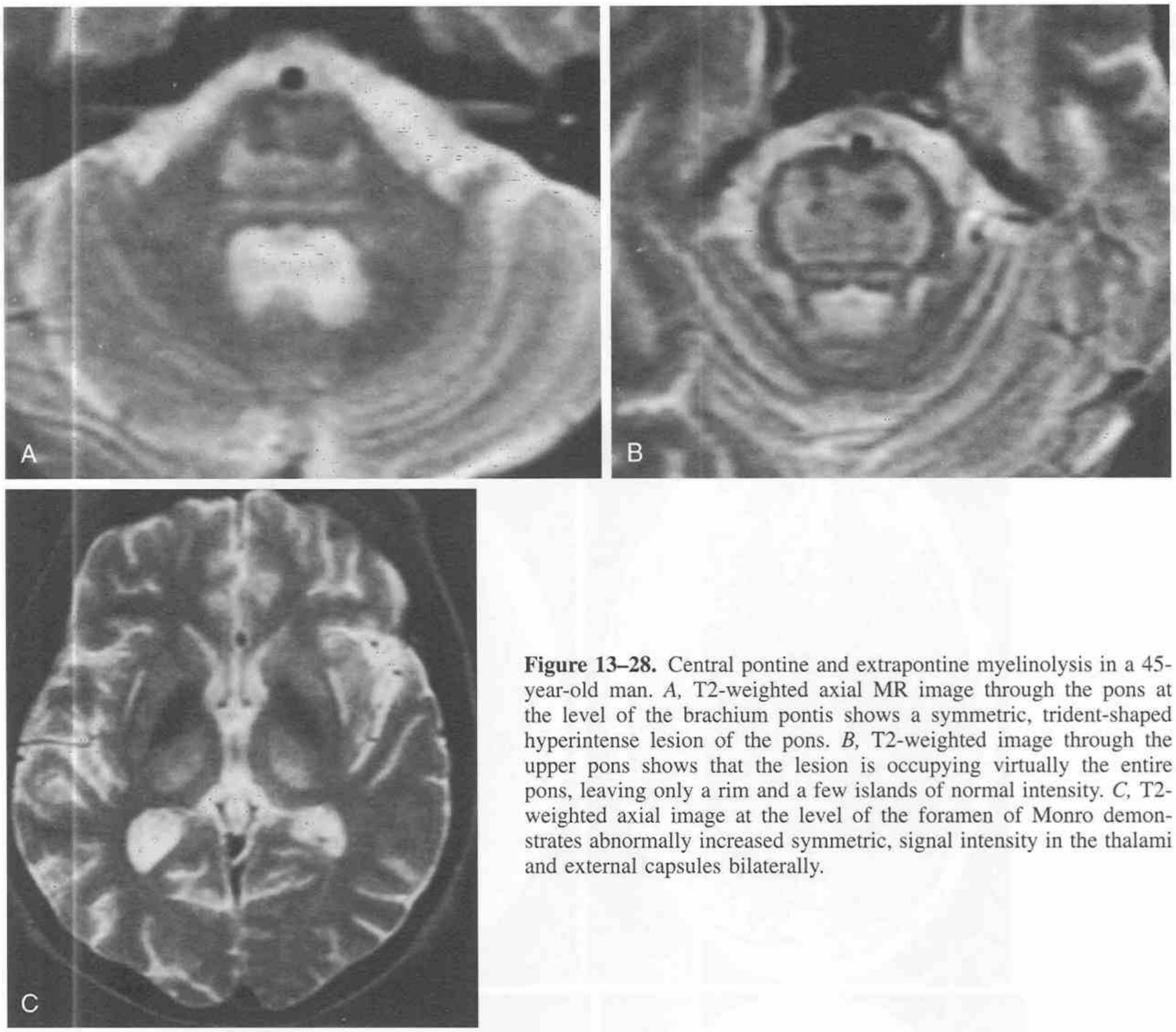

Figure 13–28. Central pontine and extrapontine myelinolysis in a 45-year-old man. *A,* T2-weighted axial MR image through the pons at the level of the brachium pontis shows a symmetric, trident-shaped hyperintense lesion of the pons. *B,* T2-weighted image through the upper pons shows that the lesion is occupying virtually the entire pons, leaving only a rim and a few islands of normal intensity. *C,* T2-weighted axial image at the level of the foramen of Monro demonstrates abnormally increased symmetric, signal intensity in the thalami and external capsules bilaterally.

bolic defects that principally affect the CNS myelin sheath. The concept of *dysmyelination* was introduced by Poser to delineate those diseases in which myelin does not form properly, is delayed or arrested in development, or is not maintained. When *demyelination* (myelinoclasis) occurs, normal myelin is destroyed, as in MS.

Included in the leukodystrophies are the following major subtypes:

- Adrenoleukodystrophy
- Metachromatic leukodystrophy
- Globoid cell leukodystrophy (Krabbe's disease)
- Neutral fat (sudanophilic and orthochromatic) leukodystrophy
- Mitochondrial disorders (Leigh's disease, MELAS syndrome, MERRF, Kearns-Sayre syndrome) (see "Mitochondrial Cytopathies" later)
- Aminoacidopathies (maple syrup urine disease, phenylketonuria, Wilson's disease)
- Mucopolysaccharidoses (Hurler's syndrome)
- Megaloencephalic leukodystrophies (Canavan's disease, Alexander's disease)

Adrenoleukodystrophy

Adrenoleukodystrophy (ALD) is a hereditary dysmyelinating disease associated with adrenocortical insufficiency and melanoderma. Its primary clinical manifestation is progressive neurologic dysfunction. The disease, caused by a deficiency of the enzyme acyl-coenzyme A synthetase, is transmitted as an X-linked recessive gene and is therefore almost exclusively confined to males, although a few sporadic cases involving females do occur.

The onset is usually in childhood, with characteristic signs of progressive behavioral aberrations, visual loss, and ataxia; there may be no clinical signs of adrenal hypofunction. The patient can live for several years, but a vegetative state leading to death is the almost inevitable outcome. Rare cases of remission, long-term survival, and response to steroid medications have been reported.[93, 102] Various subtypes involve multiple enzymatic defects, including adrenomyeloneuropathy, affecting the spinal cord and peripheral nerves, and a neonatal form.

Pathologically, the cerebral lesions are most severe in the parietal, occipital, and posterior temporal white matter,

invariably sparing the overlying cortex. The lesions are confluent and often extend in continuity across the corpus callosum. The fornix, hippocampal commissure, and posterior cingulum are also usually affected. Whereas the disease is symmetrical and widespread posteriorly, frontal involvement is more asymmetrical and variable. Cerebellar white matter lesions are common.

Histopathologically, the white matter lesions of ALD are interesting for their significant inflammatory changes and for the sequential zones of involvement in a caudal-rostral distribution. The frontal advancing zone of demyelination is followed closely by a zone of inflammatory response, in turn followed by the largest zone of complete destruction of white matter. ALD is one of the dysmyelinating diseases with a characteristic imaging appearance.[19, 61, 88]

Lesions demonstrable by CT and MRI correlate closely with the known neuropathologic alterations (Fig. 13–29). MRI is more sensitive than CT and shows earlier changes (Fig. 13–30).[43] The typical appearance is symmetrical white matter hyperintensity on T2-weighted images in the parieto-occipital regions, adjacent to the atria of the lateral

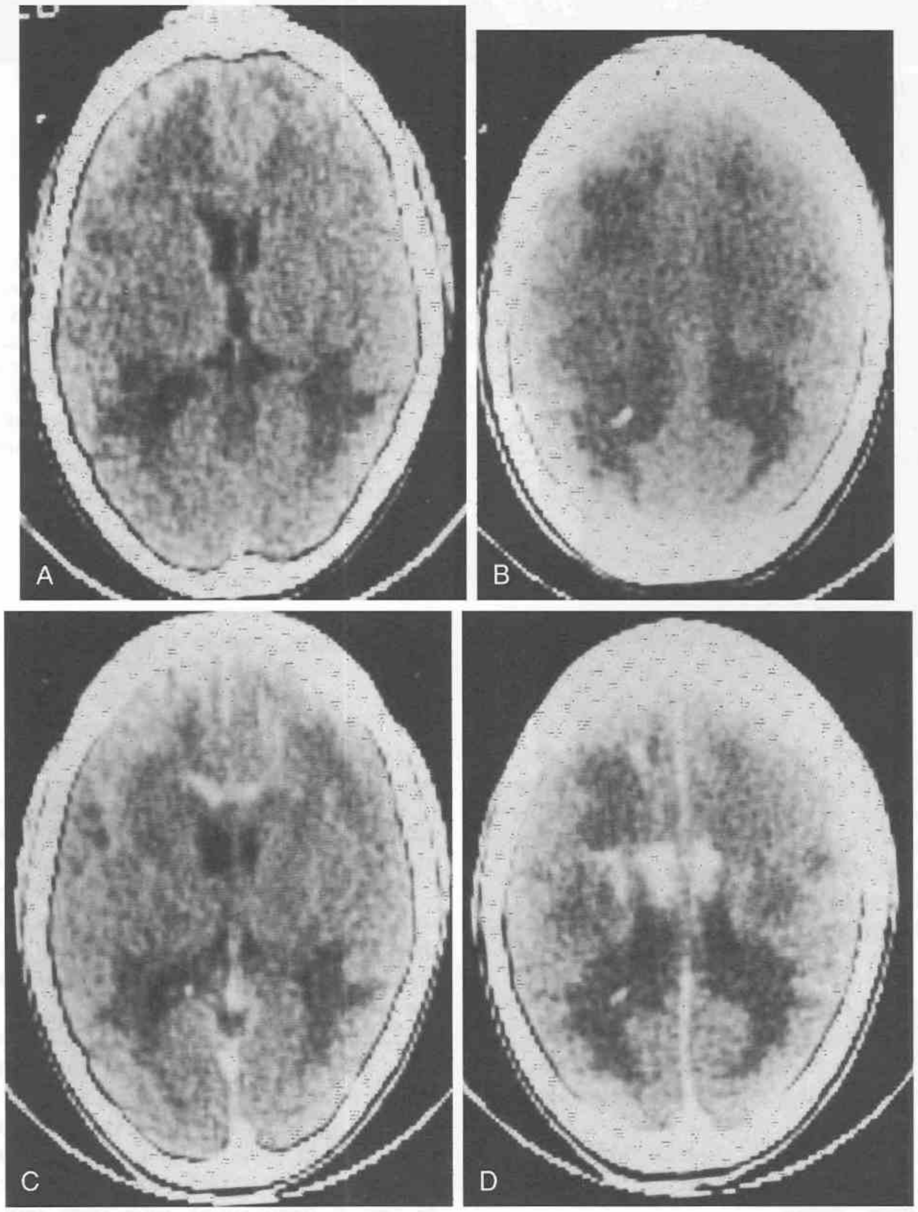

Figure 13–29. Adrenoleukodystrophy (ALD). The patient is a 13-year-old boy who had behavior problems since age 7 years and who recently experienced seizures. *A* and *B*, Precontrast CT images show white matter lucency surrounding the occipital horns and trigones of the lateral ventricles. Less severe white matter abnormalities are present bilaterally in the frontal lobes. *C* and *D*, Corresponding postcontrast sections demonstrate the peripheral serpiginous enhancement around the frontal lobe lesions and crossing the rostrum of the corpus callosum. Note the lack of contrast enhancement in the older, "burned out" posterior lesions. (Courtesy of Valley Radiologic Associates of San Jose, Calif.)

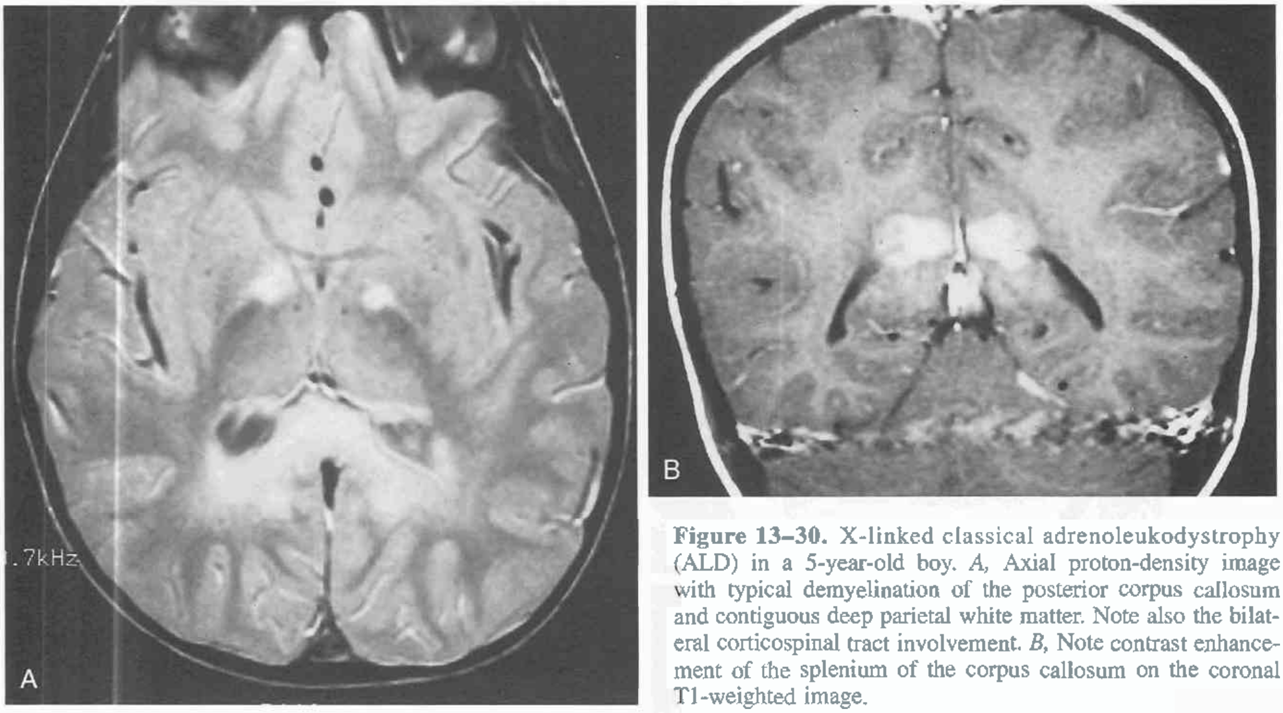

Figure 13–30. X-linked classical adrenoleukodystrophy (ALD) in a 5-year-old boy. *A,* Axial proton-density image with typical demyelination of the posterior corpus callosum and contiguous deep parietal white matter. Note also the bilateral corticospinal tract involvement. *B,* Note contrast enhancement of the splenium of the corpus callosum on the coronal T1-weighted image.

ventricles and splenium. These appear as hypointense lesions on T1-weighted images and as lucency on CT images. The overlying gray matter is entirely spared.

With contrast infusion, serpiginous, garland-shaped enhancement may be visible in the anteriormost periphery of the lesions.[55] This finding may be subtle early in the course of the disease. Mild to moderate ventricular dilatation may result from the damage caused by the disease. If the patient survives for several years, the extensive demyelinated lesions shrink, causing gross central and peripheral atrophy. Contrast enhancement is not seen at this later stage of disease.

ALD may be difficult to diagnose with confidence on MR or CT scans if imaging is performed very early or very late in the disease, and variant appearances have been described with more or less involvement of the frontal lobes. At the usual time of diagnostic workup several weeks to months after the appearance of the first neurologic symptoms, however, the combination of clinical and imaging features should be highly suggestive.

Metachromatic Leukodystrophy

Metachromatic leukodystrophy (MLD) is the most common of all the familial leukodystrophies. *Metachromatic* refers to the histologic staining characteristic caused by abnormal accumulations of sulfatides in the white matter. Sulfatide excess is caused by a deficiency of the enzyme arylsulfatase.

The disease is subclassified either clinically or biochemically. The clinical groups include (1) infantile, (2) juvenile, (3) late juvenile, and (4) adult forms. The biochemical variants are (1) arylsulfatase A deficiency (classic MLD) and (2) multiple sulfatase deficiencies. Inheritance is autosomal recessive; the diagnosis is confirmed by demonstration of absent or low levels of sulfatase in urine, leukocytes, or cultured fibroblasts.

In the most common form of MLD, symptoms begin in the second or third year of life and progress insidiously. Irritability, frequent crying, and anorexia herald the subsequent manifestations of hypotonicity and lack of truncal control. Further deterioration is accompanied by hypertonicity, extensor postural abnormalities, and intellectual decline. In the later stages of the disease, the patient may be blind, spastic, and unresponsive.

At autopsy the surface of the brain appears atrophic, the white matter is shrunken and sclerotic, and the ventricles are dilated. Changes in the peripheral nerve myelin explain the polyneuropathy often noted in MLD.

Although the diagnosis of MLD is usually established by enzymatic assay for arylsulfatase A deficiency or by peripheral nerve biopsy, MRI and CT have proved useful in suggesting the presence of leukodystrophy in early, undiagnosed cases and in excluding other processes, such as hydrocephalus or intracranial masses.

The typical CT appearance of MLD is a symmetrical lucency of the white matter, especially prominent in the centrum semiovale and the corpus callosum (Fig. 13–31).[94] There is no evidence of inflammation or contrast enhancement, and the cortical gray matter is spared.

MRI shows symmetrical areas of hypointensity on T1-weighted and hyperintensity on T2-weighted images (Fig. 13–32).[4, 40] Although the lesions are symmetrical, they may be patchy and there may be cerebellar white matter involvement as well. In the later stages, considerable atrophic dilatation of the lateral ventricles appears. Atrophy may be the only finding in late adult onset cases.

Although MLD has one of the more nonspecific appearances of a leukodystrophy, the diagnosis is usually considered from the combination of clinical and imaging appearances and can then be confirmed by a biochemical analysis.

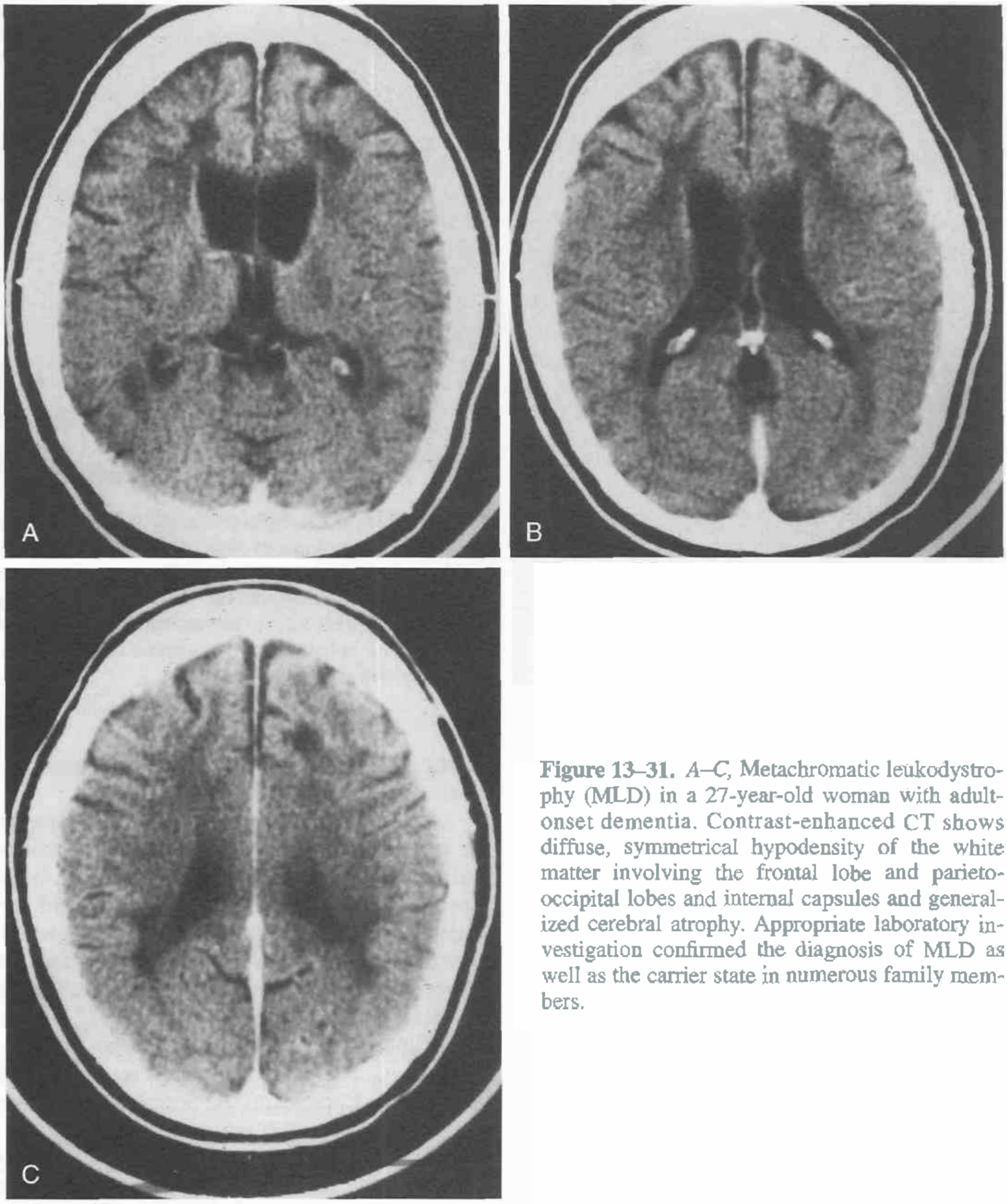

Figure 13–31. *A–C,* Metachromatic leukodystrophy (MLD) in a 27-year-old woman with adult-onset dementia. Contrast-enhanced CT shows diffuse, symmetrical hypodensity of the white matter involving the frontal lobe and parieto-occipital lobes and internal capsules and generalized cerebral atrophy. Appropriate laboratory investigation confirmed the diagnosis of MLD as well as the carrier state in numerous family members.

Globoid Cell Leukodystrophy

Globoid cell leukodystrophy (GLD), or *Krabbe's disease* (globoid body leukodystrophy), is a rare dysmyelinating disorder that is inherited as an autosomal recessive gene.

The clinical course of the disease may closely mimic that of MLD, with irritability and hypotonicity progressing to spasticity, myoclonus, and seizures. Unlike MLD, the onset of symptoms is usually earlier (<6 months of age), and the duration of the illness is shorter. Peripheral neuropathy is prominent in both diseases, a feature not present in most other cerebral lipidoses.

The deficient enzyme in GLD is β-galactocerebrosidase. This deficiency results in excessive accumulation of galactocerebrosides in myelin, found in the so-called globoid cells that are characteristic of the disease.

At autopsy, the brain of a GLD victim is shrunken because of the diffuse central myelin abnormality. The entire cerebral white matter, including the centrum semiovale, internal capsule, pons, and cerebellum, is firm, rubbery, and grayish, although areas of cystic softening may be present within. The subcortical U-shaped fibers and gray matter are unaffected. In the earlier stages of the disease, the white matter lesions would presumably be less significant. The histologic picture is dominated by the presence of globoid cells and complete myelin destruction with loss of oligodendroglia.

The CT findings in GLD range from white matter lucency to diffuse cerebral atrophy (Fig. 13–33).[3, 44] Well-defined and symmetrical decreased attenuation in the central white matter may be especially prominent in the frontal periventricular region and in the centrum semiovale.

This appearance is much more characteristic of the disease if accompanied by increased density of the thalami,

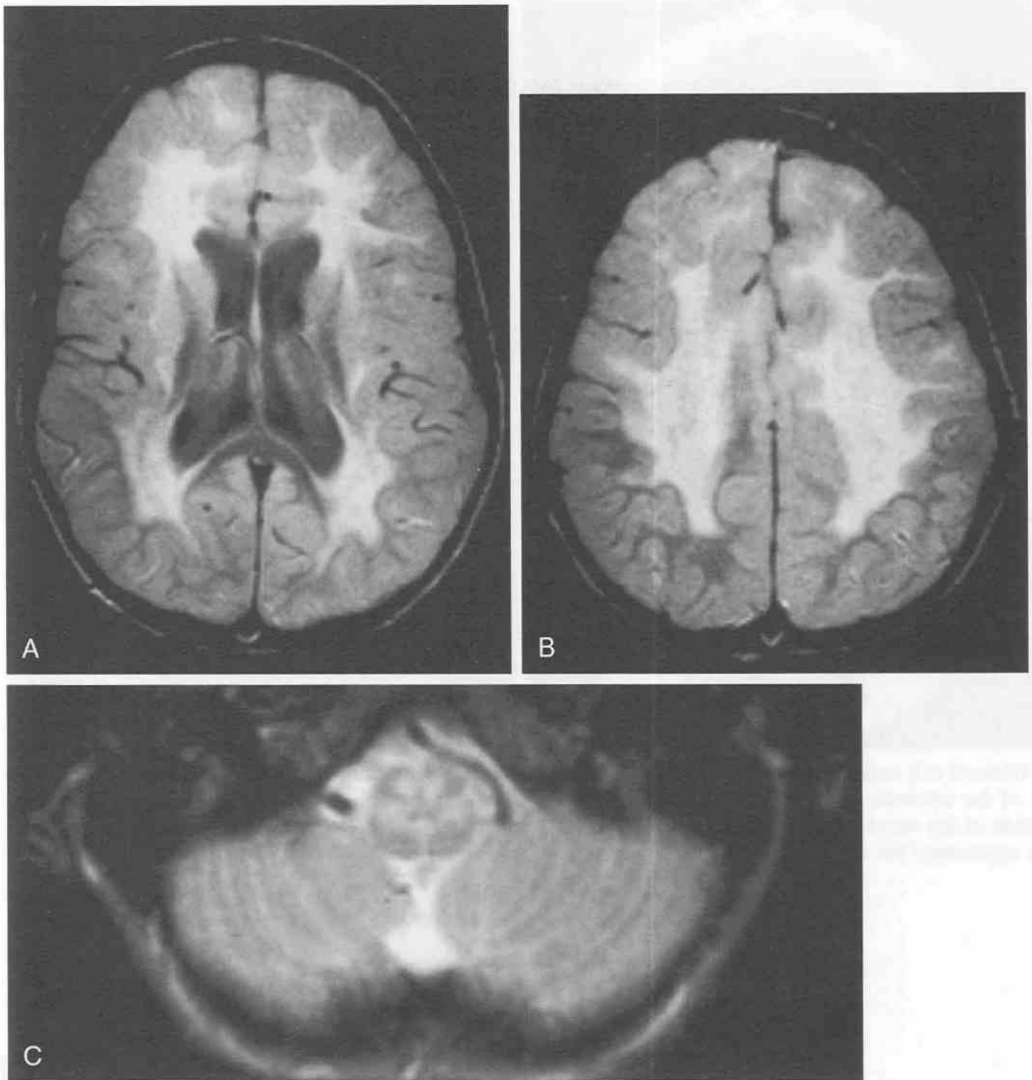

Figure 13–32. Metachro[redacted]ukodystrophy (MLD) in a 6-year-old boy. *A* and *B*, Cranial MR axial proton-density images show severe demyelination inv[redacted]e deep white matter of both hemispheres with well-defined borders at the subcortical U-fiber junction. The corpus callosum and internal capsules retain some normal hypointense myelin signal. *C*, Axial T2-weighted MR image at the level of the medulla depicts significant demyelination.

caudate nuclei, and cerebellar cortex. MRI shows prolongation of T2-weighted signal in the deep white matter and thalamic and cerebellar white matter hyperintensity (Fig. 13–34).[18] Contrast enhancement has not been demonstrated. In later stages of the disease, cerebral atrophy may be the predominant imaging feature.

Sudanophilic (Neutral Fat and Orthochromatic) Leukodystrophies

The sudanophilic (neutral fat and orthochromatic) leukodystrophies are difficult to classify. All cases show the accumulation of liberated sudanophilic myelin breakdown products. Several diseases of both sporadic and familial origin may lead to this end. The continuing advances in neurochemistry and neuropathology have served to separate and reclassify some of the entities. It is hoped that, eventually, the neutral fat leukodystrophies will be more accurately characterized. Of these, *Pelizaeus-Merzbacher disease* has been studied extensively, and its imaging features are discussed here. A remaining, less homogeneous group of sudanophilic leukodystrophies is poorly understood and is considered briefly.

Pelizaeus-Merzbacher Disease

Pelizaeus-Merzbacher (PM) disease is a rare familial leukodystrophy in which the affected child or infant shows progressive signs of neurologic dysfunction similar to the signs of MLD or GLD. Ataxia, hyperreflexia, seizures, and mental deterioration eventually result in death.

The laboratory examination is only of limited value and mainly serves to exclude MLD and GLD, since enzyme assays are normal. The definitive diagnosis rests on histologic examination of the affected brain. In PM disease, there is extensive and severe demyelination, with a peculiar, unique, patchy, tigroid appearance. Sudanophilic

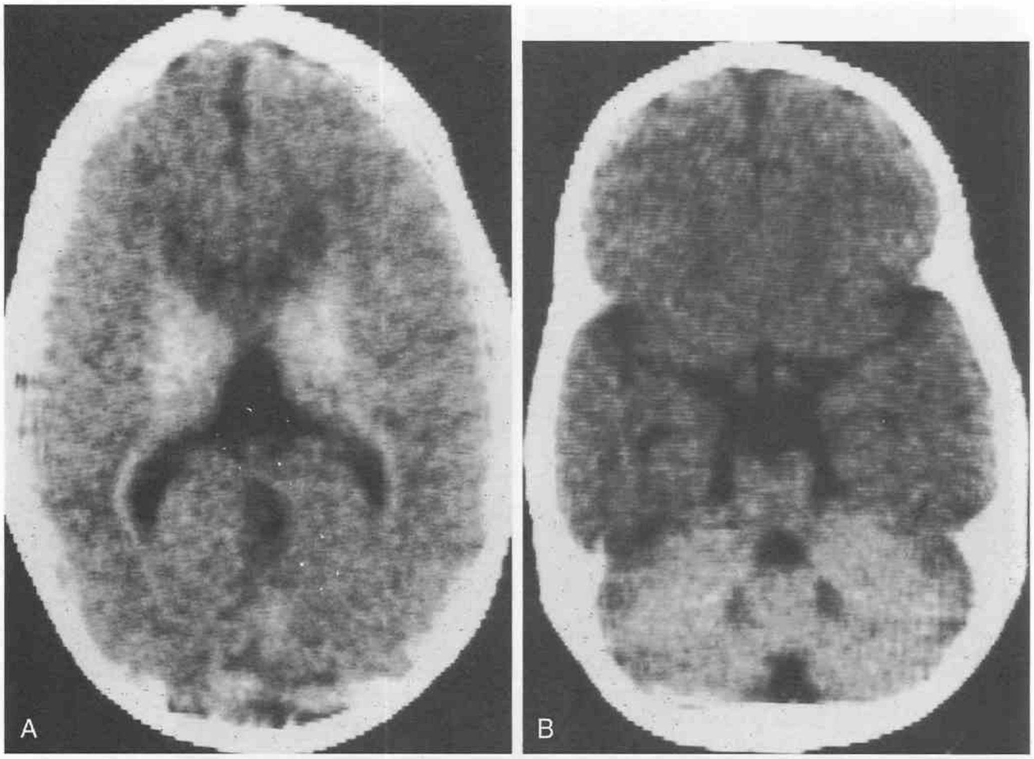

Figure 13–33. Globoid cell leukodystrophy (GLD), or Krabbe's disease, in a 3-month-old girl. Two representative CT sections disclose relative density of the cerebellum, thalami, and periventricular regions. Attenuation measurements of these regions confirm a slightly higher density than in the normal cortex. The remainder of the brain shows uniform attenuation without white matter lucency. This is a representative appearance for early GLD, with later scans usually showing minimal white matter changes but severe cortical atrophy.

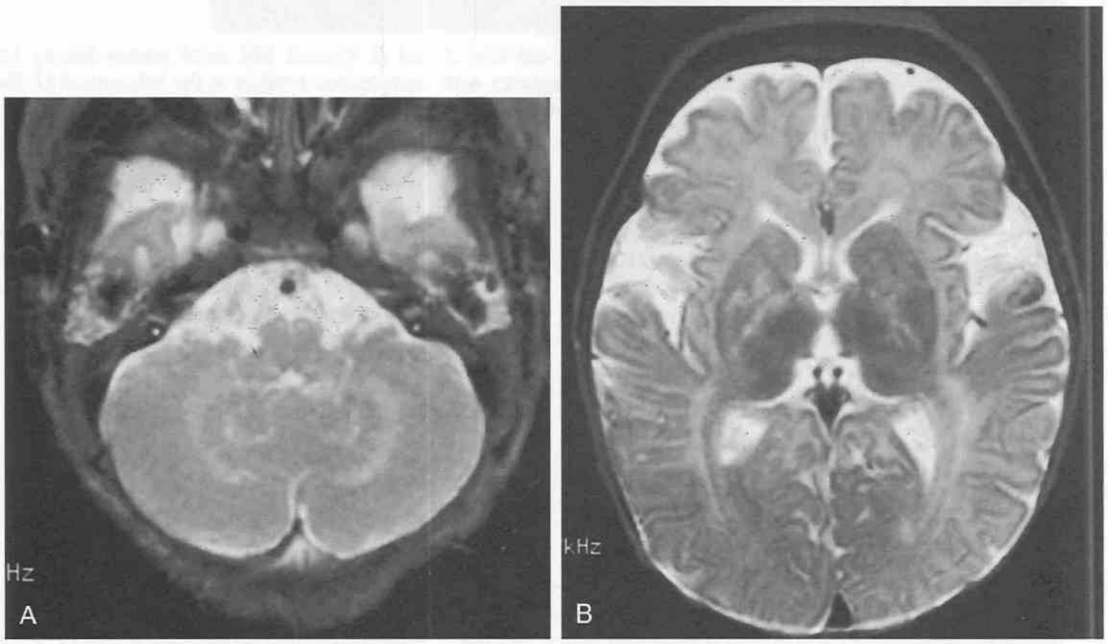

Figure 13–34. Globoid cell leukodystrophy (Krabbe's disease) in a 5-month-old infant with total body spasticity and high levels of protein in the cerebrospinal fluid. T2-weighted axial MR images. *A,* Abnormal high intensity cerebellar white matter changes. *B,* There is both white matter generalized hyperintensity as well as early T2 hyperintensity in the deep gray matter nuclei (lenticular nuclei, thalami).

breakdown products are present, but inflammation and metachromasia are absent.

The CT appearance of PM disease is nonspecific, with low density in the central white matter and with variable degrees of white matter atrophy. This pattern is diagnostic for a leukodystrophy but is not distinguishable from MLD or GLD by CT alone. On MR images, however, the predominant appearance is lack of myelination without definite evidence of white matter destruction (Fig. 13–35).[39, 64] Therefore, the brain retains the appearance of a newborn with distinct absence of myelination. Barkovich and colleagues suggest that this absence of myelination is specific for PM disease.[5] Because CT scans may be normal in early stages,[82] MRI is recommended as the imaging modality of choice whenever this or other leukodystrophies are suspected.

Cockayne's Syndrome

Cockayne's syndrome is a complex, hereditary, autosomal recessive demyelinating disorder with clinical features of dwarfism, microcephaly, retinal atrophy, deafness, and progeria (accelerated aging). Basal ganglia calcifications are a known neuropathologic feature of Cockayne's syndrome and can be detected on CT scans. The few MRI reports suggest that the changes are similar to those in PM disease, with the added feature of calcification in the basal ganglia manifesting as decreased signal intensity (Fig. 13–36). The combination of demyelination and basal ganglia calcification may therefore be helpful in the imaging of this entity.

Spongiform Encephalopathy (Canavan's Disease)

Familial spongy degeneration of the CNS (Canavan's disease) is a well-documented disease affecting infants of Ashkenazi Jewish extraction, transmitted as an autosomal recessive trait. Symptoms usually begin at 1 to 3 months of age, and the patient usually dies before the age of 4.

The infants have severe motor and mental deterioration, accompanied by hypotonia, decorticate posturing, and blindness. Progressive megalencephaly caused by enlarge-

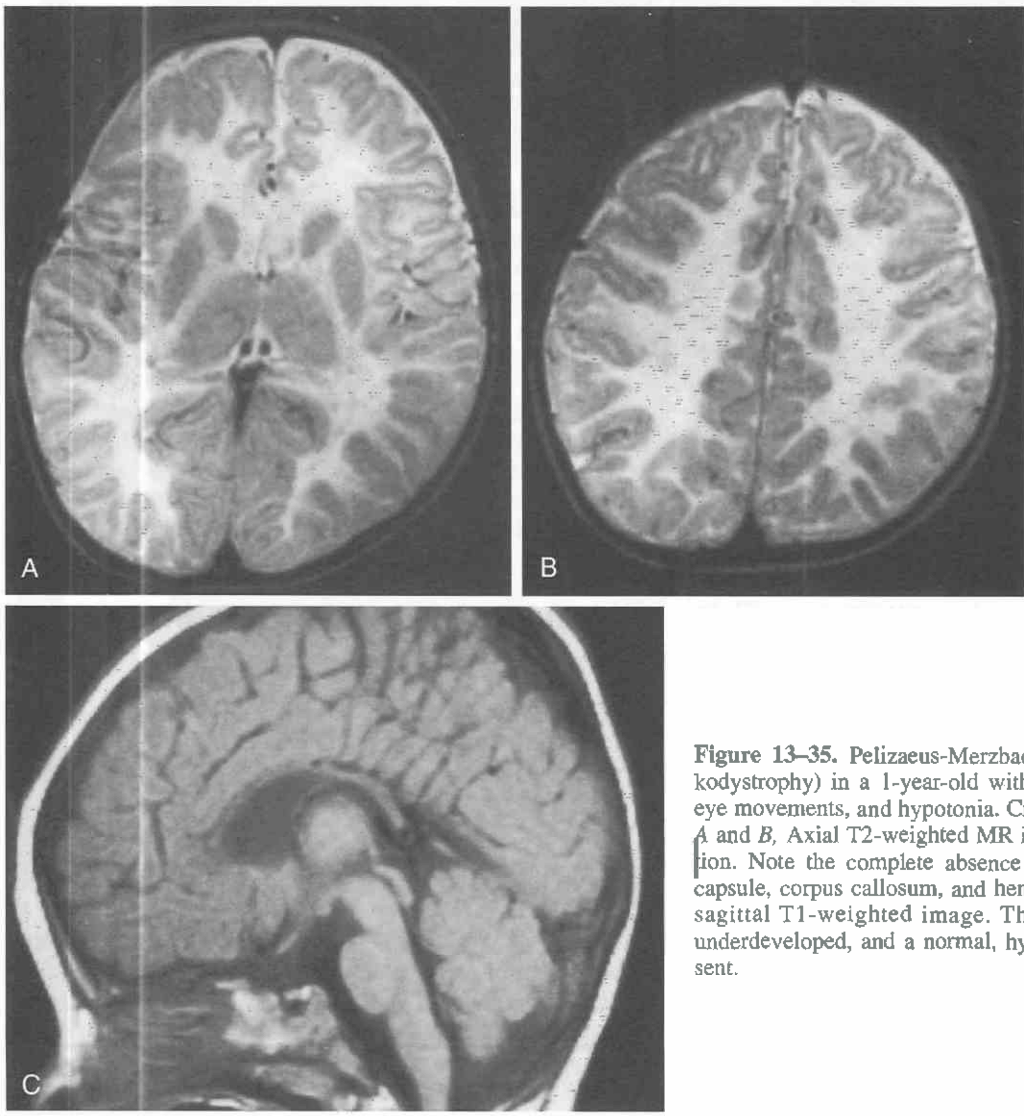

Figure 13–35. Pelizaeus-Merzbacher disease (sudanophilic leukodystrophy) in a 1-year-old with marked retardation, abnormal eye movements, and hypotonia. Cranial MR images at age 1 year. *A* and *B,* Axial T2-weighted MR images. Profound hypomyelination. Note the complete absence of myelination in the internal capsule, corpus callosum, and hemispheric white matter. *C,* Midsagittal T1-weighted image. The corpus callosum is notably underdeveloped, and a normal, hyperintense myelin signal is absent.

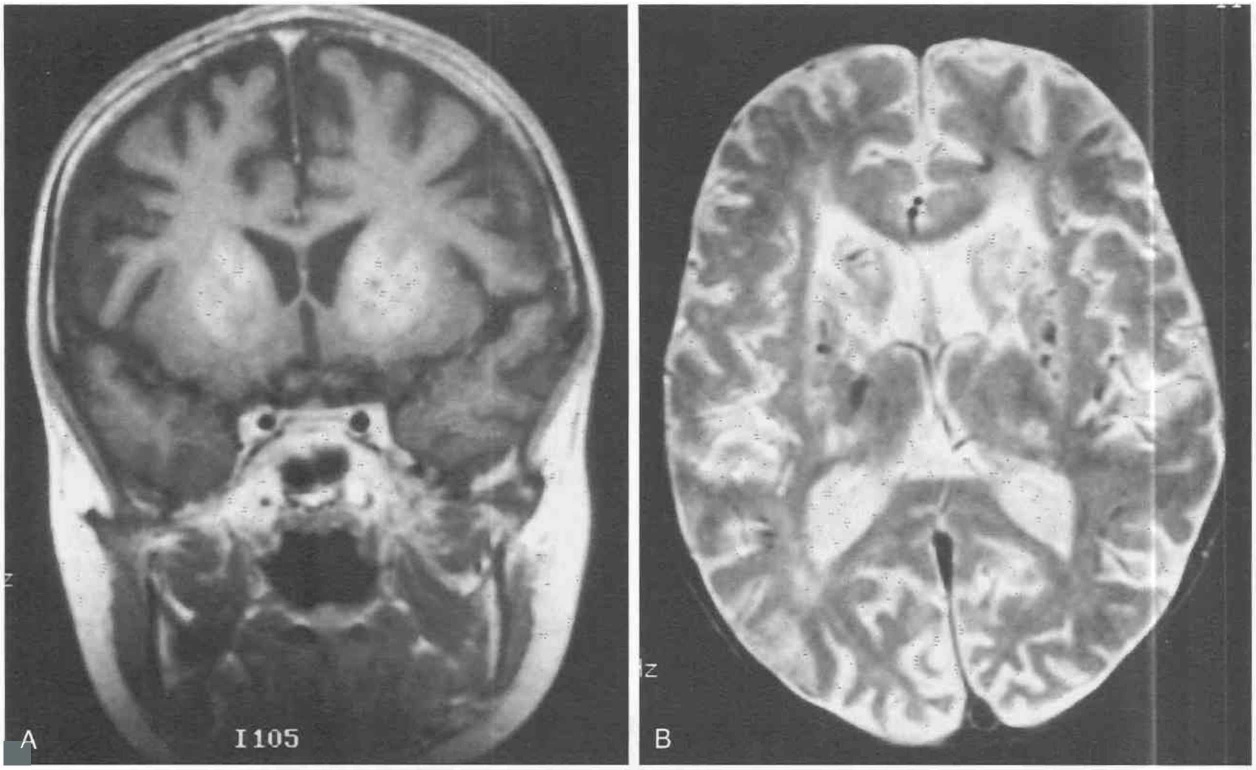

Figure 13–36. Cockayne's disease in an 11-year-old boy. *A,* T1-weighted coronal MR image demonstrates the prominent basal ganglia hyperintensity, presumably T1 shortening caused by extensive calcification. *B,* T2-weighted axial MR image, with the findings of atrophy, generalized demyelination, and signal dropout in basal ganglia from calcifications.

ment of the brain is an important differential diagnostic feature, since there are few other leukodystrophies (e.g., fibrinoid leukodystrophy, or *Alexander's disease*) in which macrocephaly is found.

The enzymatic defect in Canavan's disease is a deficiency of *N*-aspartoacylase, and the disease is classified as a metabolic disorder.

Widespread sponginess of the cerebral myelin, more pronounced in the outer zone of white matter and also affecting the subcortical U-shaped fibers and deep cortical layers, is noted pathologically. No abnormal myelin-breakdown products, globoid cells, or inflammatory changes are present.

The edematous sponginess of the white matter causes a characteristically low radiographic attenuation on CT so that it stands out in relief from the relatively unaffected gray matter (Fig. 13–37). A similar finding on MR images is extremely widespread and symmetrical low intensity on T1-weighted images, and even more prominent high signal on T2-weighted sequences.[54] Canavan's disease shows some of the most extensive white matter abnormalities, and in a child with progressive megalencephaly this can be almost pathognomonic of the disease. In very late stages, atrophic dilatation is seen, but the white matter abnormality remains. MRI also shows involvement of brain stem and cerebellum, which is difficult to identify with CT.

Fibrinoid Leukodystrophy (Alexander's Disease)

Alexander's disease, a very rare sporadic dysmyelinating disease, is a form of spongy sclerosis, similar to spongiform encephalopathy (Canavan's disease), in that there is megalencephaly. The distinguishing feature of fibrinoid leukodystrophy is the histologic feature of fibrinoid astroglia changes, the so-called Rosenthal fibers. The demyelination involves almost the entire cerebral white matter.

Changes on CT and MR images are widespread but have a predilection for the frontal lobes, which may help to distinguish the entity from Canavan's disease.[70] In addition, significant cystic change is a late feature in the frontal white matter. Contrast enhancement is rare but has been reported[35] (Fig. 13–38). Atrophy is notable in later stages.

Miscellaneous Neurodegenerative Disorders

Various rare hereditary and spontaneous neurodegenerative diseases may cause pathologic white matter changes that are visible on MR and CT scans.[33] A brief review of some of the more important entities follows.

Gangliosidoses

Tay-Sachs disease (GM_2 gangliosidosis) is associated with a form of dysmyelination. The loss of myelin cannot be accounted for solely on the basis of secondary wallerian degeneration. There is an abnormality of myelin sphingolipid metabolism, even though Tay-Sach's disease is classified not as leukodystrophy but as a lipidosis.

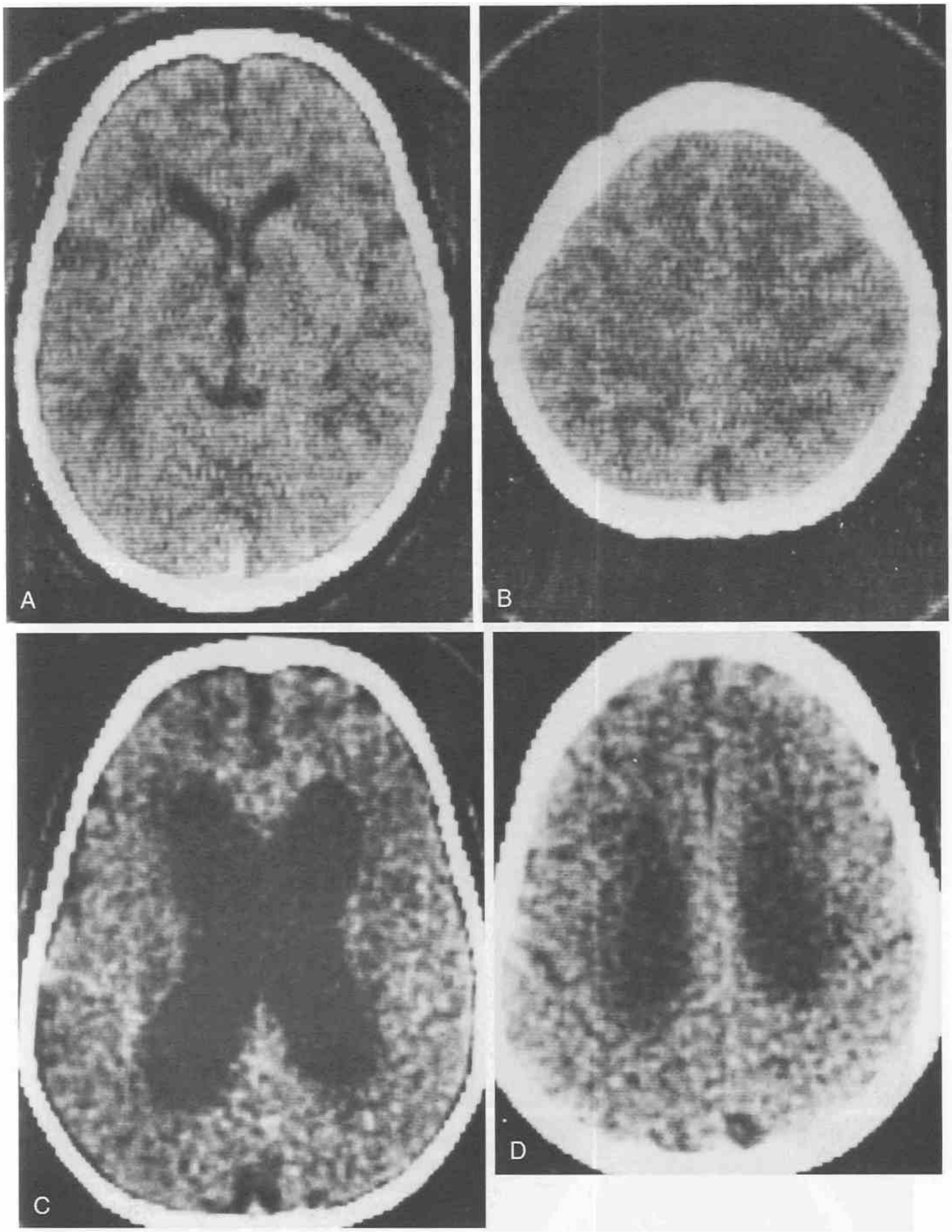

Figure 13–37. Spongiform encephalopathy (Canavan's disease). *A* and *B,* CT scans of a 2½-year-old boy with progressive neurologic deterioration and an enlarging head. There is diffuse, symmetrical, generalized lucency of the white matter. *C* and *D,* A repeated CT scan performed 2 years later, when the patient was 4½ years old and in a vegetative state. Significant ventricular dilatation has supervened. The white matter has become shrunken, resulting in central cerebral atrophy. At this final stage of the disease, the CT appearance is nonspecific. (*A–D,* From Moss AA, Goldberg I [eds]: Computed Tomography, Ultrasound, and X-ray: An Integrated Approach. San Francisco, University of California, San Francisco, Department of Radiology, 1980.)

Macrocephaly and diminished attenuation of the entire cerebral white matter have been reported on CT scans in patients with GM_1 and GM_2 gangliosidoses.[4]

With MRI, deep white matter demyelination may be prominent; thalami may show changes consistent with calcification. No abnormal contrast enhancement is described (Fig. 13–39).

Mitochondrial Cytopathies[38]

Leigh's disease (subacute necrotizing encephalomyelopathy) is a rare, inherited disorder in which multiple biochemical defects are found. The most striking neuropathologic change is symmetrical vacuolation of the basal ganglia, the brain stem, the cortex, and, to a lesser degree,

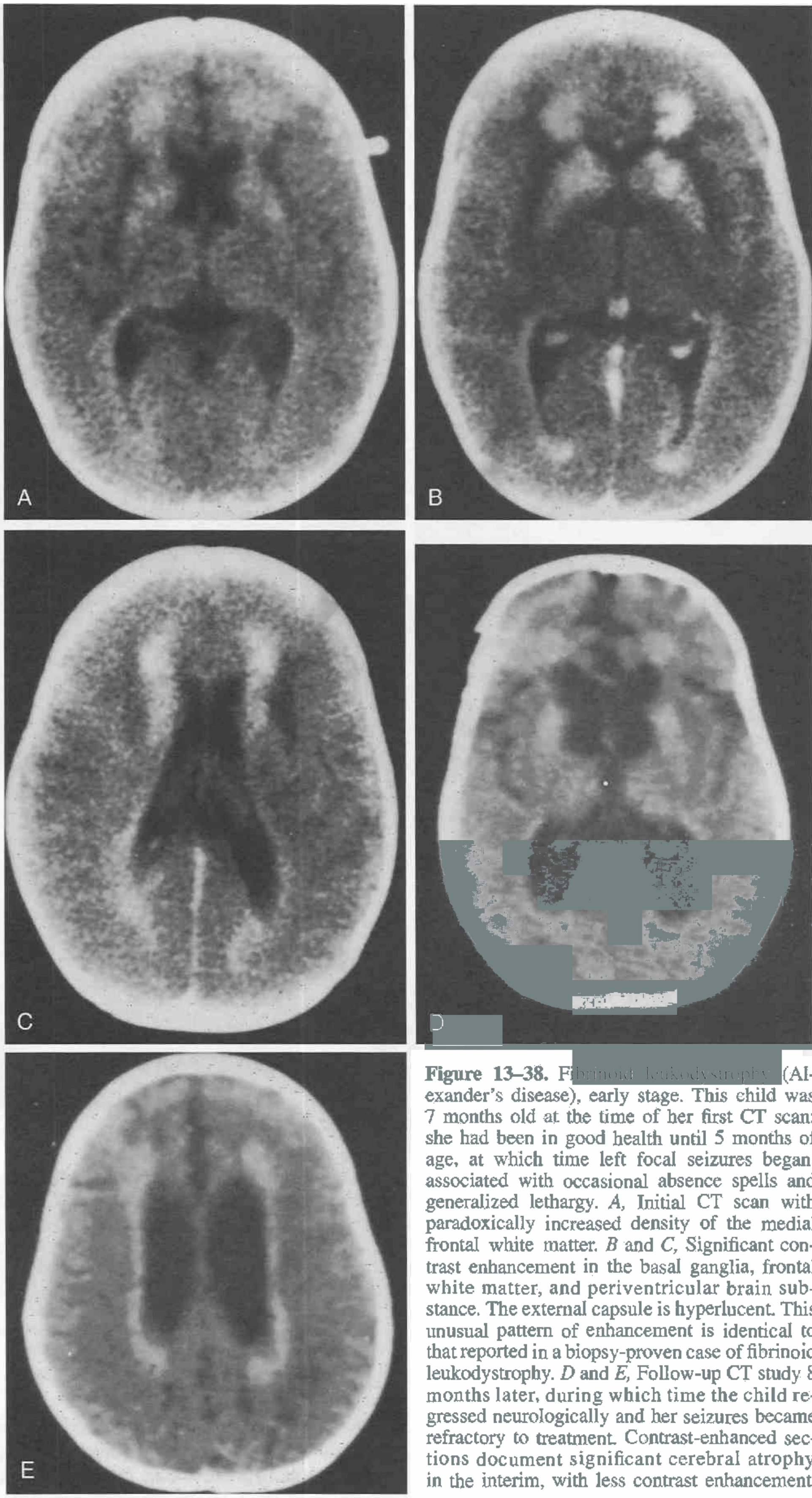

Figure 13–38. Fibrinoid leukodystrophy (Alexander's disease), early stage. This child was 7 months old at the time of her first CT scan: she had been in good health until 5 months of age, at which time left focal seizures began, associated with occasional absence spells and generalized lethargy. *A*, Initial CT scan with paradoxically increased density of the medial frontal white matter. *B* and *C*, Significant contrast enhancement in the basal ganglia, frontal white matter, and periventricular brain substance. The external capsule is hyperlucent. This unusual pattern of enhancement is identical to that reported in a biopsy-proven case of fibrinoid leukodystrophy. *D* and *E*, Follow-up CT study 8 months later, during which time the child regressed neurologically and her seizures became refractory to treatment. Contrast-enhanced sections document significant cerebral atrophy in the interim, with less contrast enhancement.

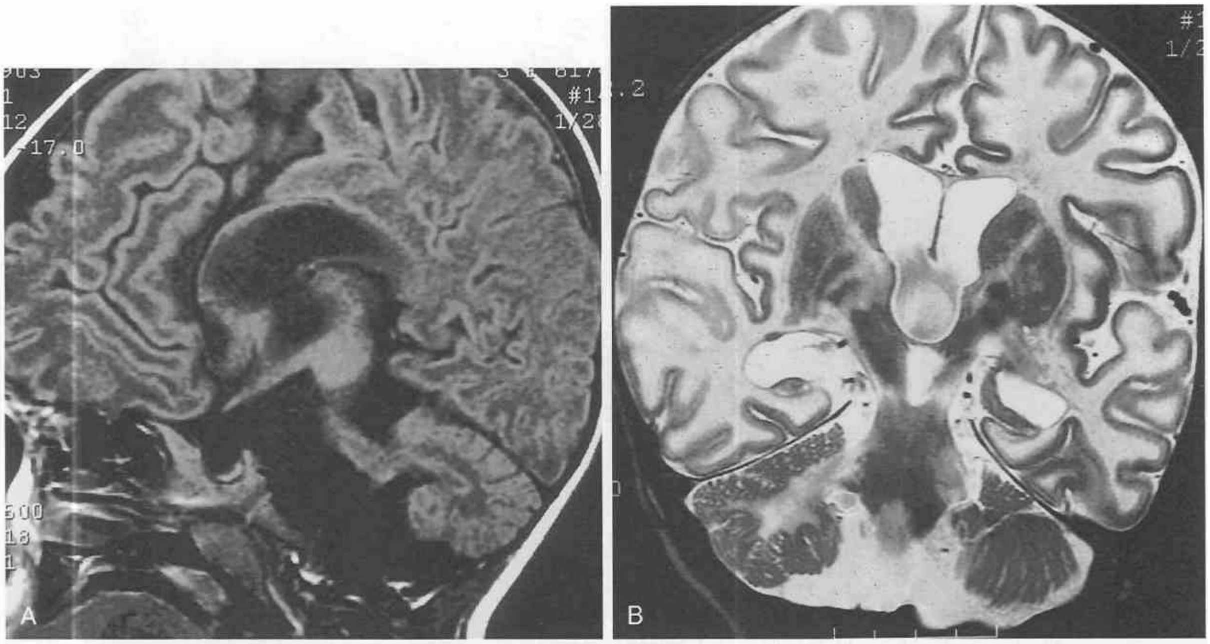

Figure 13–39. Tay-Sachs disease (hexosaminidase deficiency) in a 3-year-old girl with megalencephaly. *A*, T1-weighted sagittal MR image shows generalized white matter hypoattenuation and extreme hypogenesis of the corpus callosum (a nonspecific finding). *B*, T2-weighted axial MR shows extreme demyelination of virtually all white matter as well as characteristic T2 prolongation in thalami and lenticular nuclei.

the white matter. Low attenuation in the basal ganglia, brain stem, or central white matter may be seen on CT scans but is much better delineated on T2-weighted MR images (Fig. 13–40).[15, 17, 86] The most characteristic foci of demyelination are in the lentiform nuclei, the cerebral peduncles, the periaqueductal gray matter, the pons, and the medulla. Contrast enhancement may be seen in the acute stages.

Other mitochondrial cytopathies that have shown abnormalities on imaging are *MELAS syndrome* (mitochondrial myopathy, encephalopathy, lactic acidosis, and strokes), *MERRF* (myoclonic epilepsy with ragged red fibers), and *Kearns-Sayre syndrome* (Figs. 13–41 and 13–42).[73, 99]

Aminoacidopathies

Aminoacidopathies constitute another class of neurodegenerative disorders. Heritable disorders of amino acid

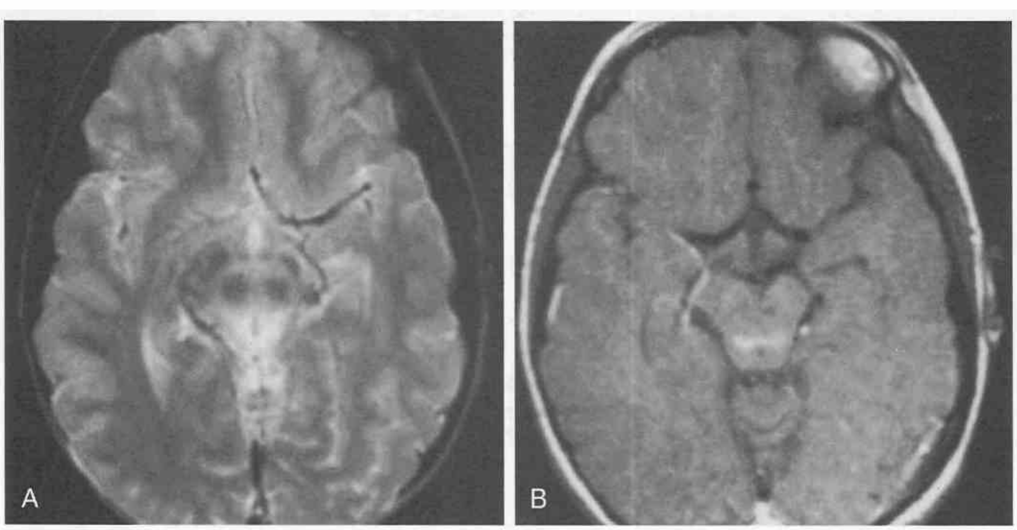

Figure 13–40. Leigh's disease (subacute necrotizing encephalomyelopathy) in a 10-year-old girl with developmental delay and slow neurologic deterioration. *A* and *B*, Initial MR scans. *C* and *D*, Follow-up scan 3 years later. *A*, T2-weighted axial MR image at the level of the midbrain. Hyperintensity of the entire mesencephalic tectum is visible, with lesser involvement of the cerebral peduncles. *B*, Postgadolinium-enhanced, T1-weighted image at the same level demonstrates symmetrical enhancement just anterior to the aqueduct.

Illustration continued on following page

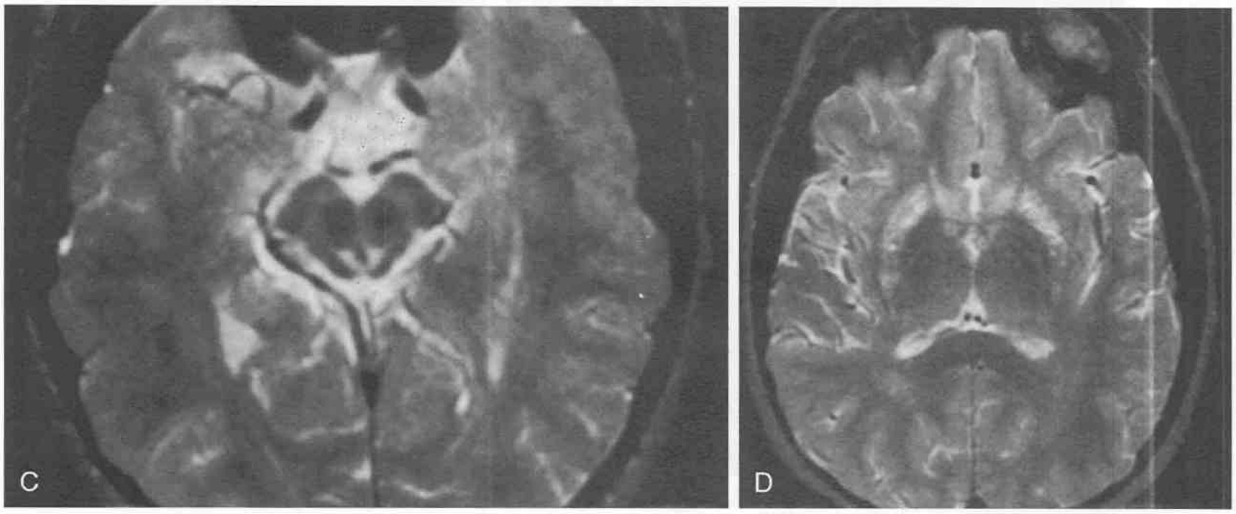

Figure 13–40. *Continued. C,* T2-weighted axial image at the midbrain level. The previously seen hyperintensities have resolved almost completely, leaving only small periaqueductal foci. *D,* There is residual persistent hyperintensity in the putamina bilaterally.

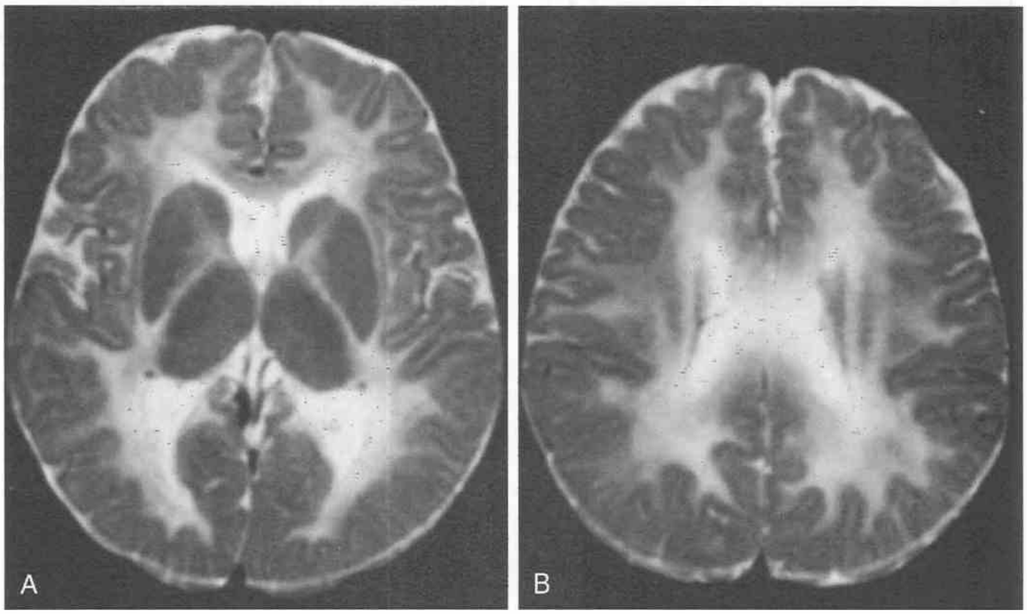

Figure 13–41. Mitochondrial depletion syndrome in an 8-month-old boy with hypoglycemia, liver failure, and pancreatic insufficiency. *A* and *B,* Cranial MR axial T2-weighted images. There is hyperintensity of virtually the entire cerebral white matter, including internal and external capsules, compatible with severe hypomyelination and demyelination.

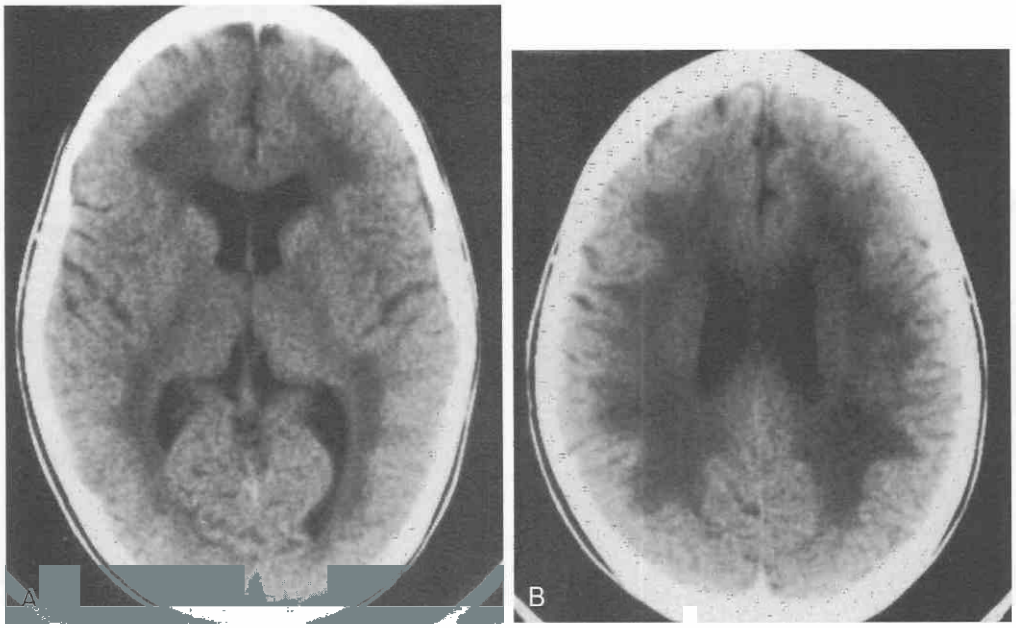

Figure 13–42. Myopathic carnitine deficiency in a 10-year-old boy with myopathy. Non–contrast-enhanced CT scans show diffuse, widespread, symmetrical lucency of the white matter, suggestive of demyelination.

metabolism may be accompanied by neurologic dysfunction, ranging from mild to severe, acute or chronic.

Some affected infants die of edema brought on by hyperammonemia or anoxia; others have been shown at autopsy to have spongy degeneration of the white matter, demyelination, or hypomyelination.

The more well-known aminoacidopathies include maple syrup urine disease (MSUD), phenylketonuria, the ketotic hyperglycinemias, urea cycle enzyme errors (ornithine transcarbamylase deficiency or citrullinemia), and nonketotic hyperglycinemias. More than 50 subtypes have been described. Depending on the time of imaging, an affected child with one of these aminoacidopathies may show cerebral edema, hypomyelination, or diffuse white matter atrophy (Fig. 13–43).[6, 51] A characteristic diagnostic feature is the demonstration of white matter edema in the neonatal period, since this excludes most classic leukodystrophies.

Wilson's Disease

Wilson's disease is a rare autosomal recessive disorder of copper metabolism. Although basal ganglia are predominantly affected, white matter tract abnormalities have been routinely characterized by MRI.[90]

Mucopolysaccharidoses

Six well-recognized syndromes are caused by enzyme defects resulting in accumulation of glycosaminoglycans in many organs. *Hurler's syndrome* is the prototype. Although demyelination is not a prominent neuropathologic feature, diffuse white matter changes simulating demyelination have been reported (Fig. 13–44).[40, 58]

Multiple Sclerosis

The most common demyelinating disease seen in adult neurologic practice is MS. Clinically, it may present in acute, chronic, or relapsing forms. The common neurologic signs are optic neuritis, paralysis, numbness, ataxia, and tremor. Repeated remissions and exacerbations are characteristic, and the average duration of disease is many years.[67, 95]

The gross pathologic features of MS have been well documented over many decades. The in vivo demonstration of demyelinated plaques was first made possible with the advent of CT, but MRI is clearly the imaging method of choice, with superior sensitivity, specificity, and characterization of the disease process.[72, 76] In many studies, MRI not only is the most accurate imaging method but also is even more sensitive than other nonimaging tests such as oligoclonal bands, somatosensory evoked potentials, and visual evoked potentials.[80]

The sensitivity of MRI has been as high as 85% in patients with clinically definite MS, and the figure is probably even higher if serial studies are performed.[59] CT, however, has probably less than half the sensitivity of MRI; nonetheless, a brief description of CT abnormalities is in order, if only for historical interest.

Three CT features are typical of MS:

1. Most characteristic is focal decreased attenuation in the periventricular white matter.
2. Another type of focal abnormality in CT scans of MS is contrast-enhancing plaque. These enhancing lesions have been shown to correspond to the acute phase of demyelination, and the blood-barrier breakdown resolves within a few weeks (Fig. 13–45).[57] The contrast enhancement may be ameliorated or abolished by the administration of corticosteroids, although the long-term

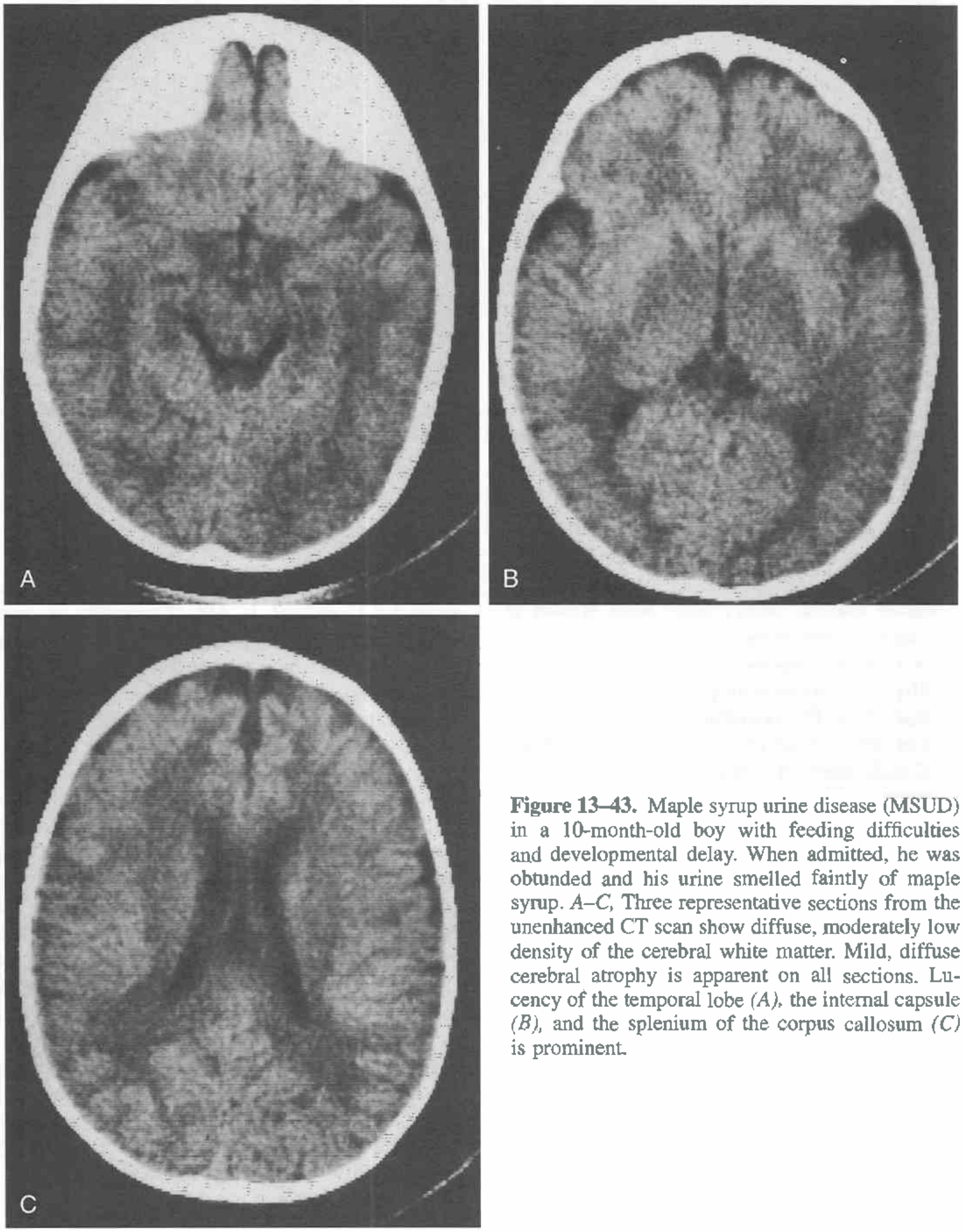

Figure 13–43. Maple syrup urine disease (MSUD) in a 10-month-old boy with feeding difficulties and developmental delay. When admitted, he was obtunded and his urine smelled faintly of maple syrup. *A–C,* Three representative sections from the unenhanced CT scan show diffuse, moderately low density of the cerebral white matter. Mild, diffuse cerebral atrophy is apparent on all sections. Lucency of the temporal lobe *(A),* the internal capsule *(B),* and the splenium of the corpus callosum *(C)* is prominent.

Figure 13–44. Mucopolysaccharidosis (Hurler's syndrome) in a 7-year-old girl with mild macrocephaly. CT scan demonstrates the multiple periventricular cysts, characteristic of this disease, as well as more subtle generalized white matter hypodensity. Unusual skull defects with brain herniations are also shown.

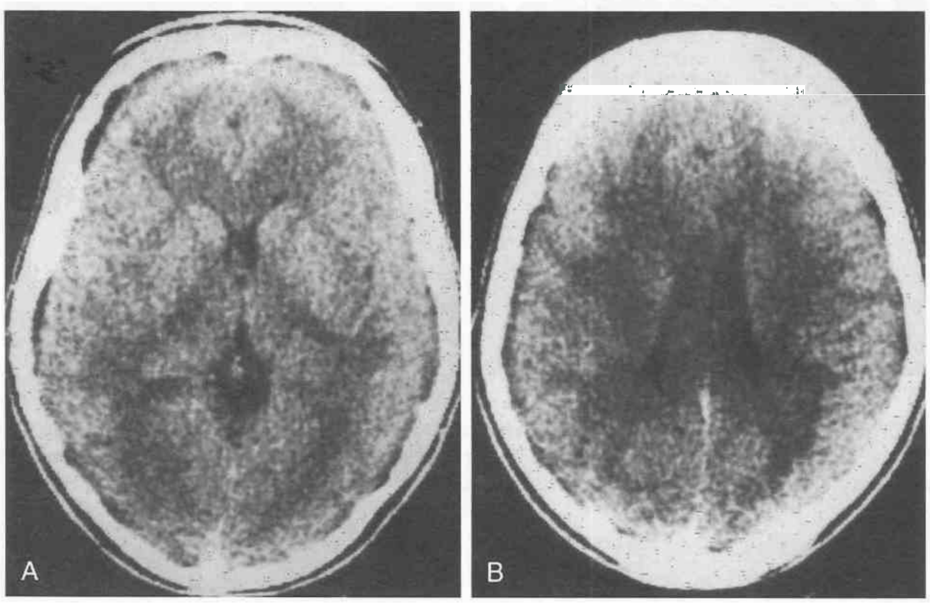

Figure 13–45. Multiple sclerosis, acute phase, in a 19-year-old woman with extremity numbness, difficulty in walking, blurred vision, and slurred speech. *A–C,* Precontrast CT sections are abnormal, with diffuse, patchy hypodensity of the white matter.

Illustration continued on following page

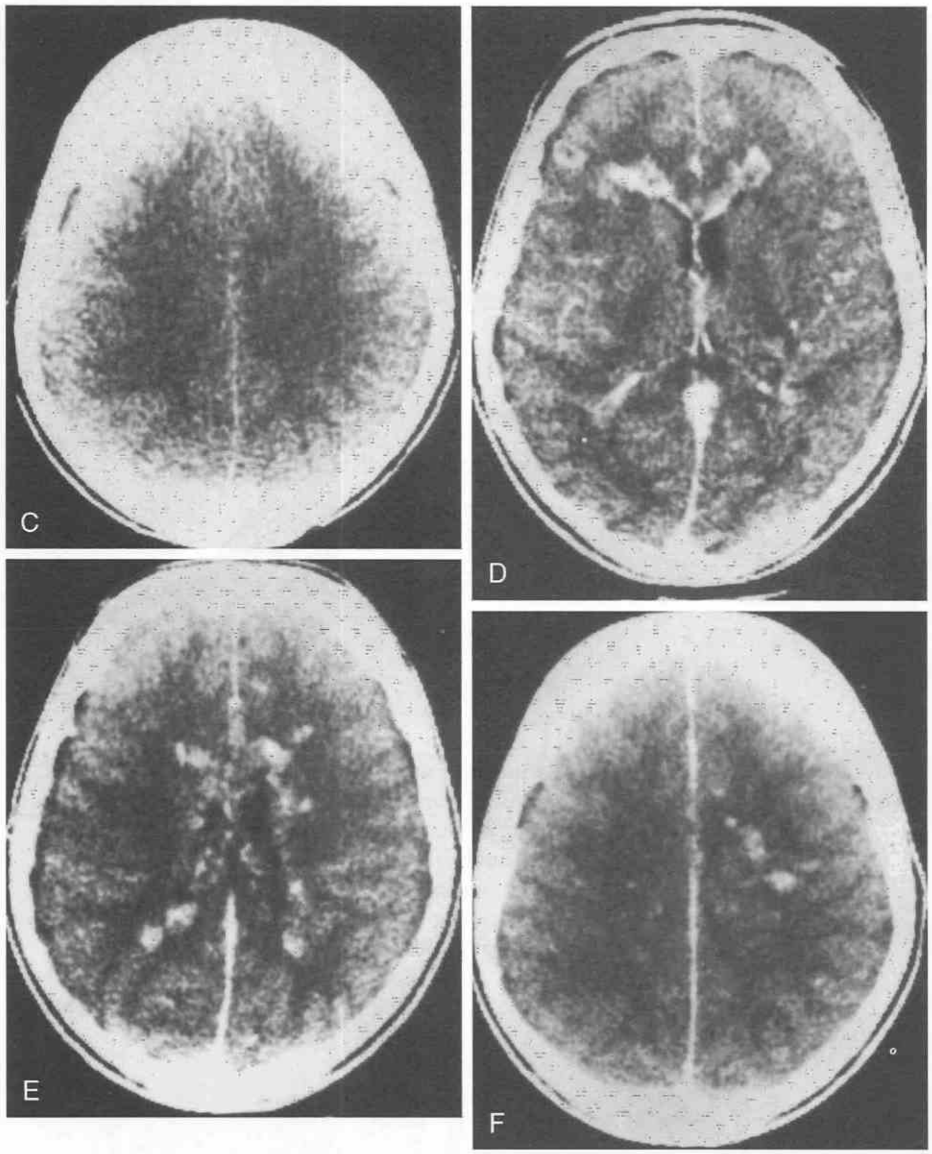

Figure 13–45. *Continued. D–F,* Corresponding sections after administratio[redacted] intravenous contra[redacted] is prominent patchy enhancement of the periventricular white matter bilaterally. Occasionally, as in this case, a few contrast-enhancing plaques may be found in the cerebral cortex, but the periventricular lesions predominate.

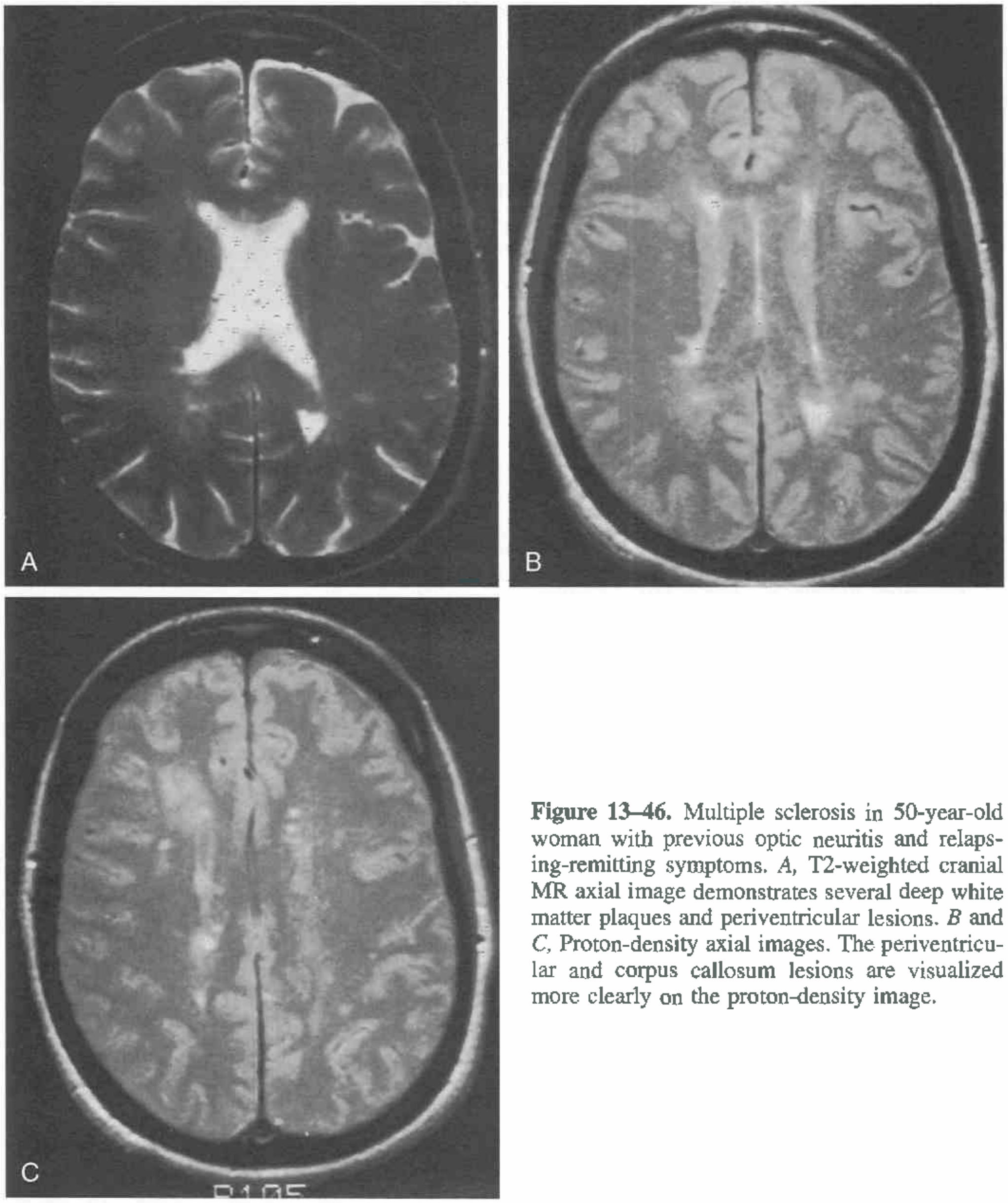

Figure 13–46. Multiple sclerosis in 50-year-old woman with previous optic neuritis and relapsing-remitting symptoms. *A*, T2-weighted cranial MR axial image demonstrates several deep white matter plaques and periventricular lesions. *B* and *C*, Proton-density axial images. The periventricular and corpus callosum lesions are visualized more clearly on the proton-density image.

course of the disease does not appear to be altered by this regimen.

3. A less common CT finding in MS is cerebral atrophy, caused by large-scale white matter shrinkage. This results in generalized ventricular and sulcal dilatation.

The foregoing discussion notwithstanding, MRI is the imaging method of choice in cases of suspected MS of the brain and spinal cord. The emphasis is not only on supporting the diagnosis of MS but on the fact that MRI is effective in differentiating MS from other processes, such as slowly growing tumors, brain stem vascular malformations, and vasculitis. The most widely used sequences for detection of MS are the T2-weighted and proton-density sequences. These are rapidly being supplemented by fast spin-echo imaging. Other techniques that may prove to be extremely useful are magnetization transfer; FLAIR; and, possibly, high-dose contrast-enhancement schemes.[21] Although magnetic resonance spectroscopy is beyond the scope of this chapter, it is evident that it is a powerful technique for the study of MS and other white matter diseases.[23]

On standard T2-weighted sequences, MS plaques appear as high-intensity lesions, usually ovoid, elongated, or round. The proton-density and FLAIR scans are very useful because high-signal plaques adjacent to ependymal surfaces may be obscured by high-signal cerebrospinal fluid on standard T2-weighted images (Figs. 13–46 to 13–49).[81]

In general, T1-weighted images are much less sensitive, but it is noteworthy that chronic plaques of MS are often well shown, especially in the corpus callosum, on T1-weighted sequences, appearing as low-signal lesions surrounded by a very thin halo of mildly increased signal intensity (Fig. 13–50). Hemorrhage is not seen in MS lesions; edema and mass effect are distinctly uncommon (see later).

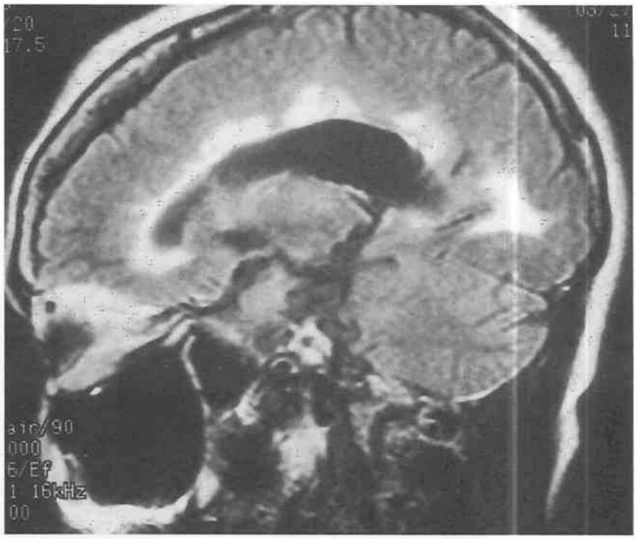

Figure 13–48. Multiple sclerosis (MS). Fluid-attenuated inversion recovery (FLAIR) parasagittal MR image depicts the extensive demyelinated plaques of progressive MS.

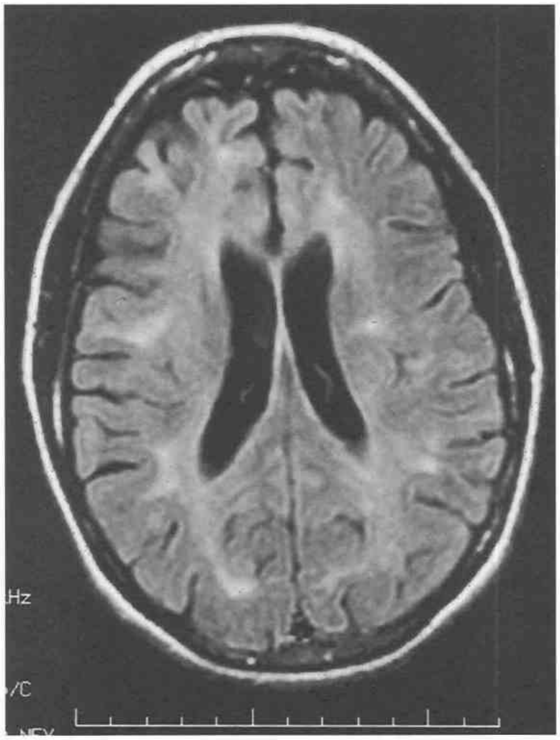

Figure 13–47. Multiple sclerosis (MS), as shown on a fluid-attenuated inversion recovery (FLAIR) MR image; the patient is a 36-year-old woman with relapsing-remitting MS. Note the conspicuity of the numerous bilateral periventricular white matter lesions.

The most characteristic diagnostic feature of MS plaques on MR images is not their signal intensity but their anatomic distribution. There is a predilection for periventricular distribution and ependymal surfaces, especially along the occipital horns and, to a lesser degree, the frontal horns. If not pathognomonic, corpus callosum lesions are so characteristic of MS as to be almost specific.[81] Other MS sites commonly affected are the corona radiata, internal capsule, and centrum semiovale. In the posterior fossa, MS plaques are quite common, with a predilection for the surface of the pons, especially near the fifth cranial nerve entry zone, the middle cerebral peduncle (brachium pontis), the floor of the fourth ventricle, and the colliculi.

Contrast enhancement is an important part of MRI technique.[30] It is known that acute lesions of MS are accompanied by transient breakdown of the blood-brain barrier, which may be demonstrated with use of gadolinium contrast enhancement. While T1-weighted images are the standard practice, magnetization transfer may show greater detectability of these lesions because of its background suppression (Fig. 13–51; see Fig. 13–49).[21] Serial studies have demonstrated that contrast enhancement in acute lesions of MS may persist for 6 to 8 weeks after acute demyelination.[46] The enhancement may be punctate, nodular, or ringlike. In rare cases, there may be single or multiple large foci of MS with mass effect and significant contrast enhancement simulating a tumor (Fig. 13–52).[52, 101]

Although many cases of MS have these characteristic imaging features, rendering differential diagnosis relatively unimportant, MS lesions may occur anywhere in the CNS, including the cortex and other gray matter nuclei.

The lesions may be few or may be present in otherwise uncharacteristic locations. A differential diagnosis in these

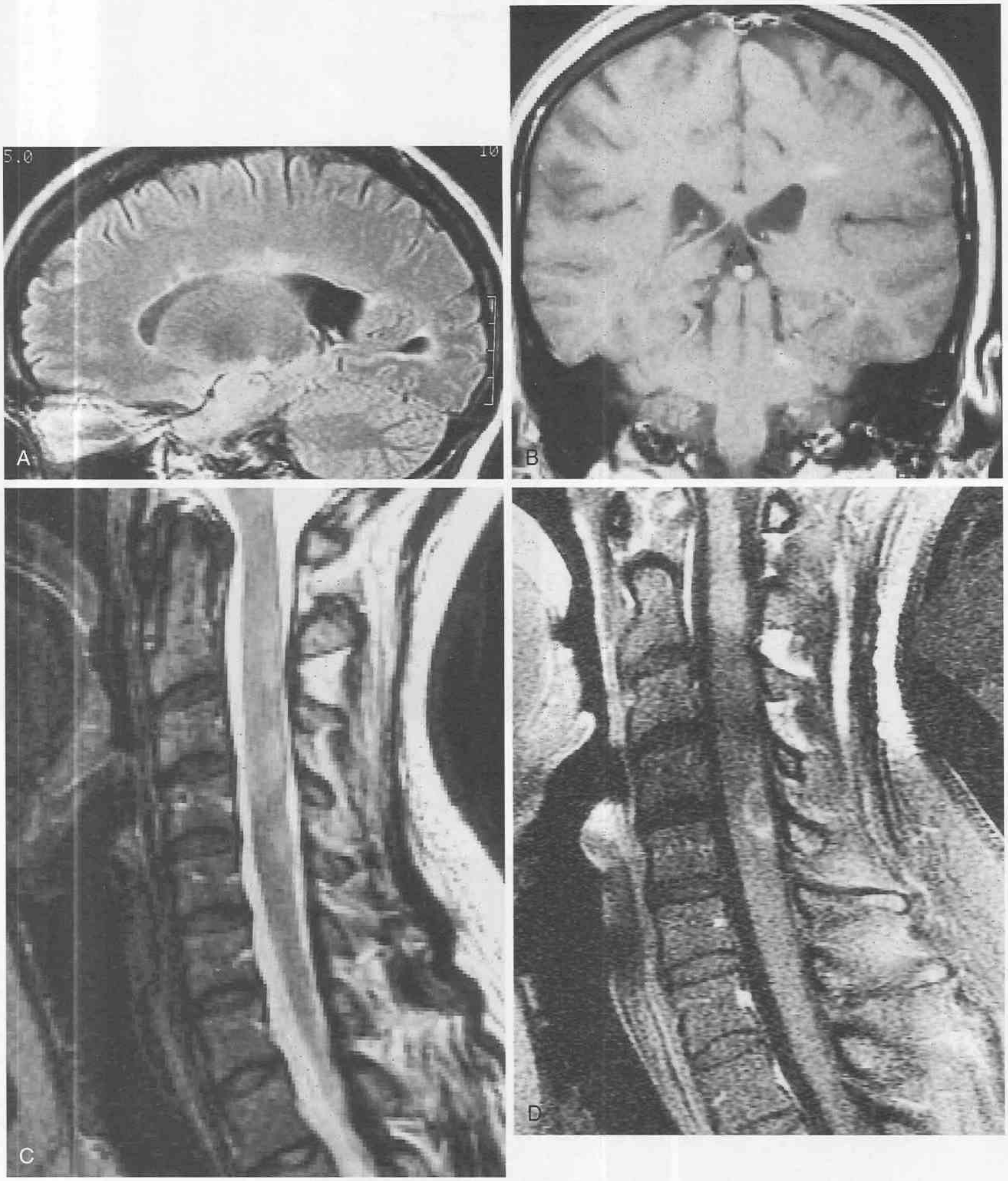

Figure 13–49. MRI features in a 32-year-old woman with spinal and cerebral multiple sclerosis (MS). *A,* Parasagittal fluid-attenuated inversion recovery (FLAIR) sequence. Numerous hyperintense plaques are clustered on the inferior surface of the corpus callosum, highly correlated with the diagnosis of MS. *B,* Contrast-enhanced, T1-weighted, magnetization-transfer coronal image; two enhancing plaques are visible, indicating active demyelination: one in the corona radiata, the other in the brachium pontis. *C,* Sagittal T2-weighted, fast spin-echo MRI of the cervical spinal cord. Numerous plaques are visible, some with evident swelling (edema). *D,* Fat-suppressed, contrast-enhanced image at the same level as in *C*; one of the lesions has ringlike enhancement.

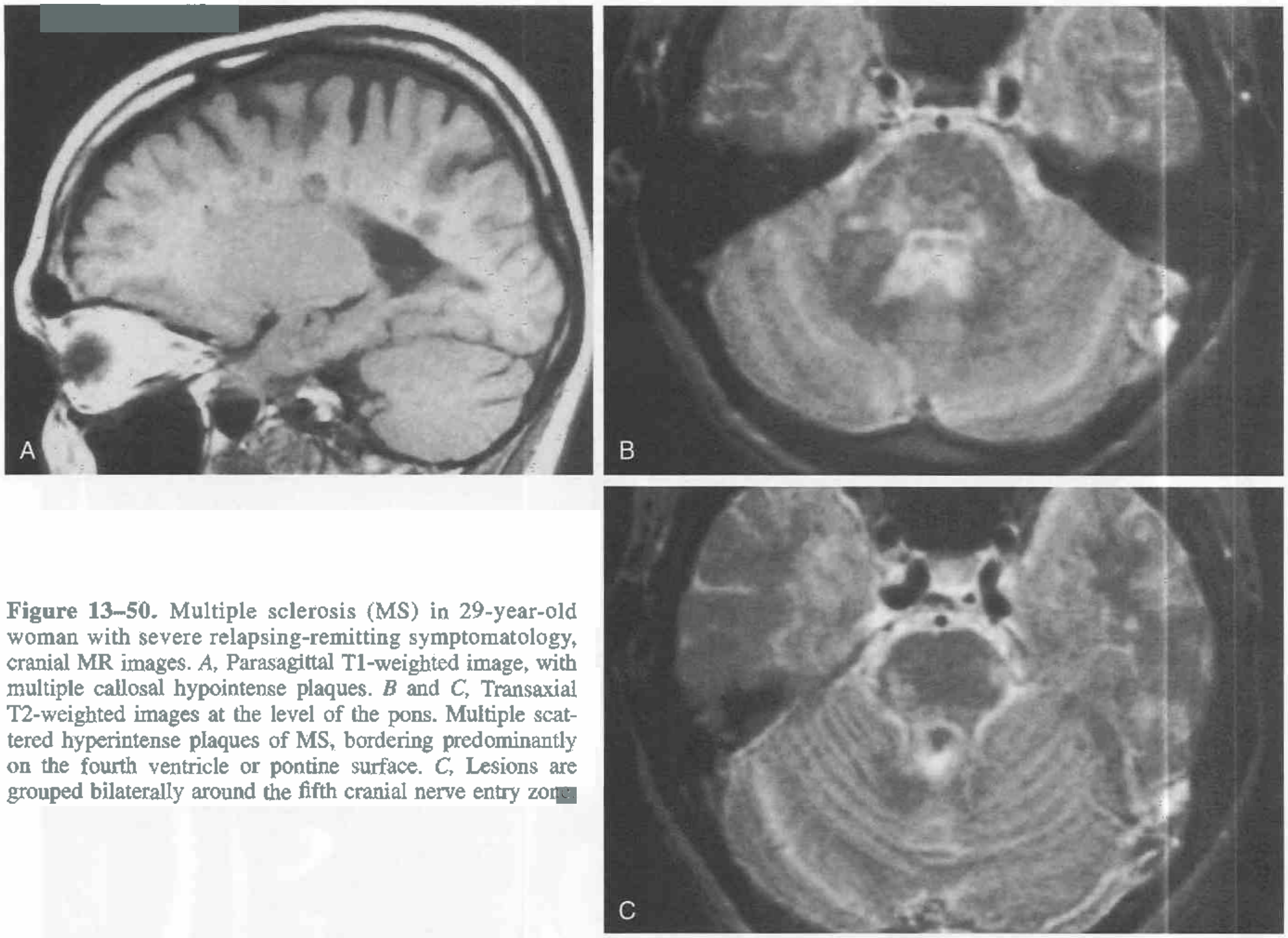

Figure 13–50. Multiple sclerosis (MS) in 29-year-old woman with severe relapsing-remitting symptomatology, cranial MR images. *A*, Parasagittal T1-weighted image, with multiple callosal hypointense plaques. *B* and *C*, Transaxial T2-weighted images at the level of the pons. Multiple scattered hyperintense plaques of MS, bordering predominantly on the fourth ventricle or pontine surface. *C*, Lesions are grouped bilaterally around the fifth cranial nerve entry zone

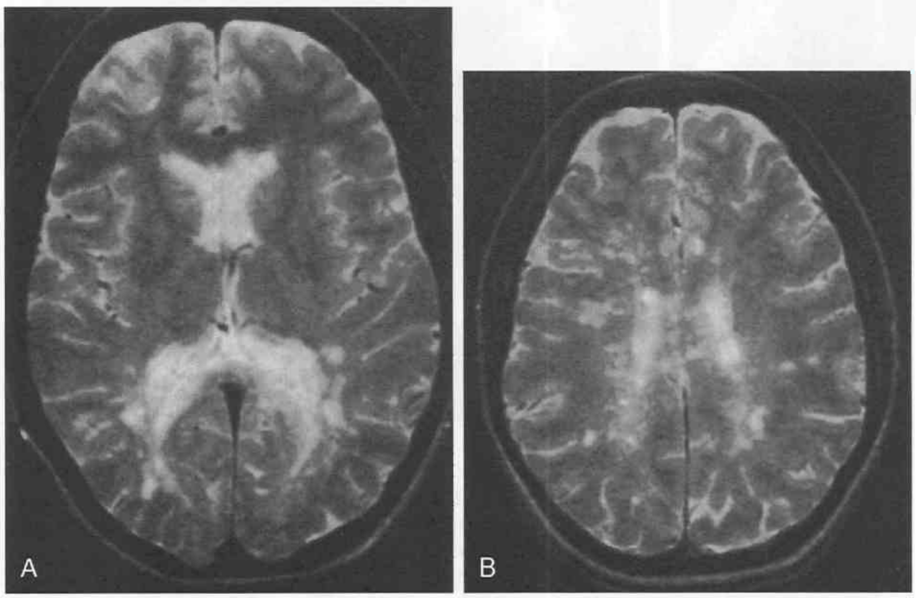

Figure 13–51. Multiple sclerosis (MS) in 37-year-old woman presenting with thoracic myelopathy. *A* and *B*, Cranial T2-weighted axial MR images show multiple, hyperintense plaques distributed bilaterally in the centrum semiovale and periventricular regions and especially grouped around the trigones. Note especially the characteristic corpus callosum lesions.

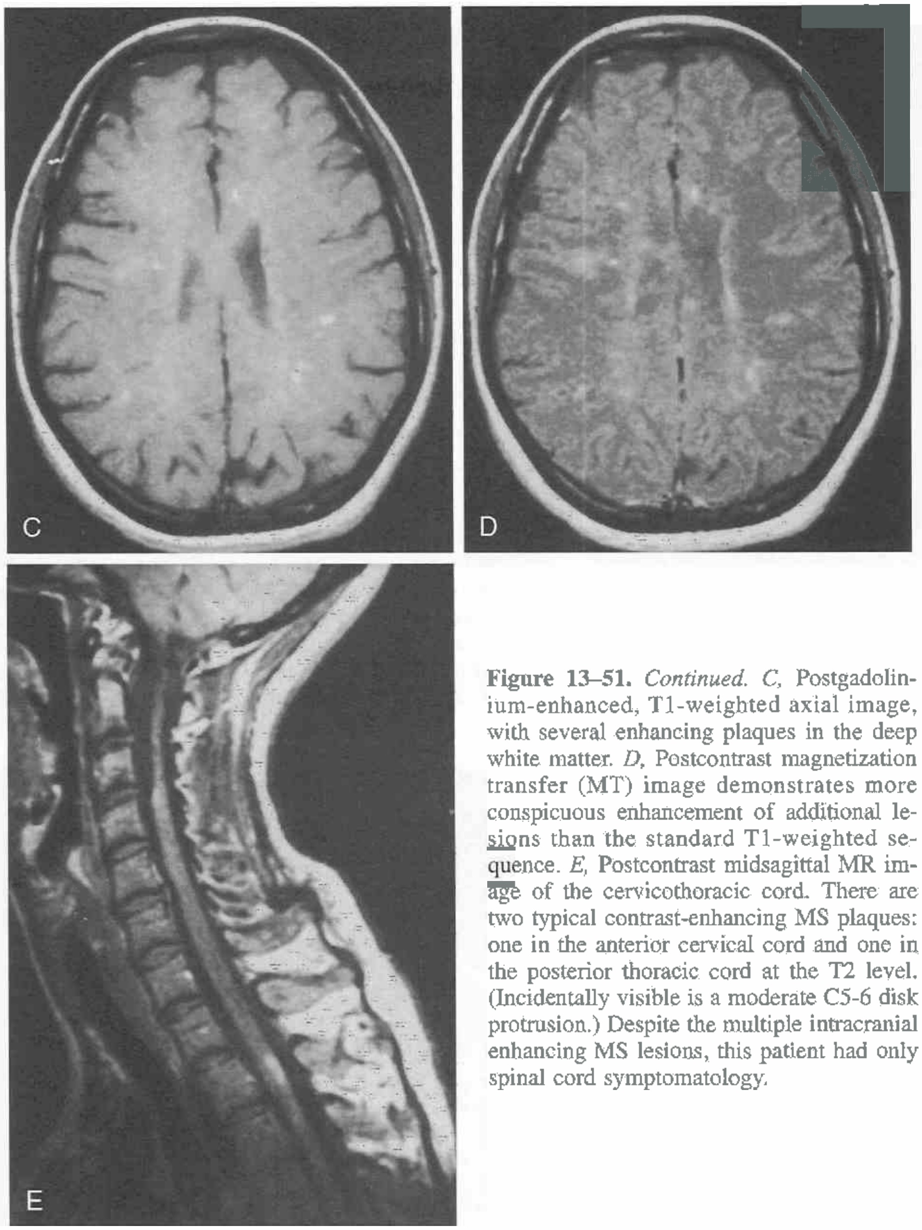

Figure 13–51. *Continued. C,* Postgadolinium-enhanced, T1-weighted axial image, with several enhancing plaques in the deep white matter. *D,* Postcontrast magnetization transfer (MT) image demonstrates more conspicuous enhancement of additional lesions than the standard T1-weighted sequence. *E,* Postcontrast midsagittal MR image of the cervicothoracic cord. There are two typical contrast-enhancing MS plaques: one in the anterior cervical cord and one in the posterior thoracic cord at the T2 level. (Incidentally visible is a moderate C5-6 disk protrusion.) Despite the multiple intracranial enhancing MS lesions, this patient had only spinal cord symptomatology.

cases must include demyelination secondary to ADEM, vasculitis, Lyme disease, sarcoidosis, ischemic disease, and, in rare cases, tumors.

As previously described, multiple ischemic white matter foci are usually seen in older patients, are associated with cardiovascular risk factors, are not located in the immediate periventricular white matter in most cases, and rarely involve the corpus callosum. Also, infratentorial ischemic lesions tend to have a different distribution than does MS in the pons and cerebellum. Despite all of these clues, some MR images are indeterminate, and the final diagnosis must await clinical confirmation or serial studies.

Spinal Cord Multiple Sclerosis

Some of the false-negative MRI diagnoses of MS are attributable to cases with only spinal cord involvement. The spinal cord is much more of a challenge in MRI diagnosis, but newer techniques are yielding more rapid and detailed examinations of such cord lesions. These include multiarray receiver coils, fast spin-echo imaging, and the FLAIR sequence. Reports suggest that cord lesions may be detected in a majority of MS patients using such techniques. Characteristically, the cord lesions of MS appear as high signal intensity on T2-weighted sequences, with the cervical cord involved about twice as often as the thoracic cord. The lesions range from a few millimeters to extension over one or more vertebral segments (Fig. 13–53; see Figs. 13–49 and 13–51).

The most common location is lateral and posterior in the cord, but MS may involve both gray and white matter and may occupy the entire transverse diameter. Swelling of the cord is reported in a minority of cases, with diminished signal intensity on T1-weighted images sometimes

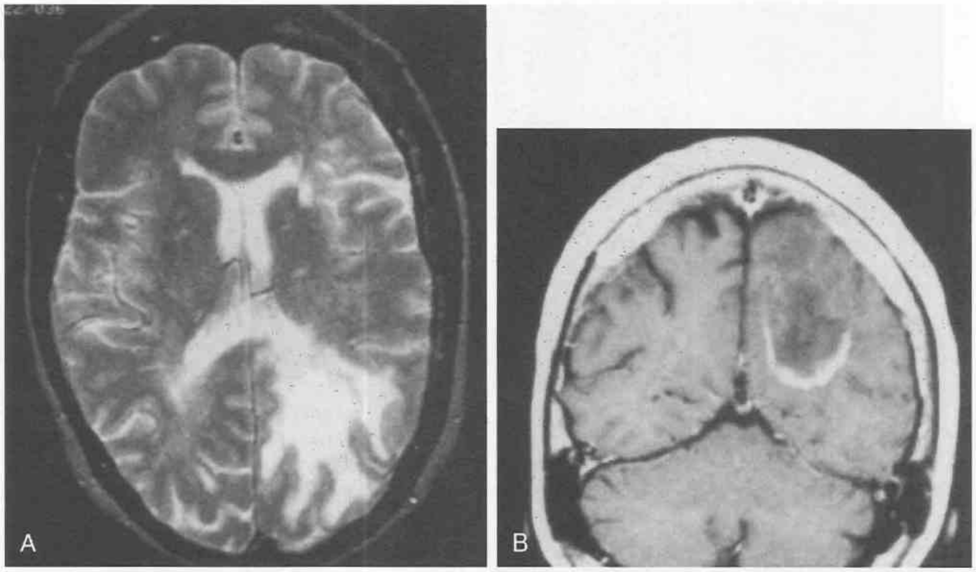

Figure 13–52. Demyelinating disease presenting as a mass. *A,* T2-weighted cranial MR axial image. There is a hyperintense masslike lesion in the left parieto-occipital lobe, surrounded by edema. A few scattered periventricular and deep white matter lesions are also visible bilaterally. *B,* Postgadolinium-enhanced, T1-weighted coronal MR image. Incomplete ringlike enhancement outlines the lesion. Biopsy showed nonspecific demyelination. Follow-up MR several months later showed almost complete spontaneous resolution of this mass. (From Jordan JE, Lane B: MRI characteristics of demyelinating disease mimicking brain tumor. Appl Radiol, December 1992, pp 36–38.)

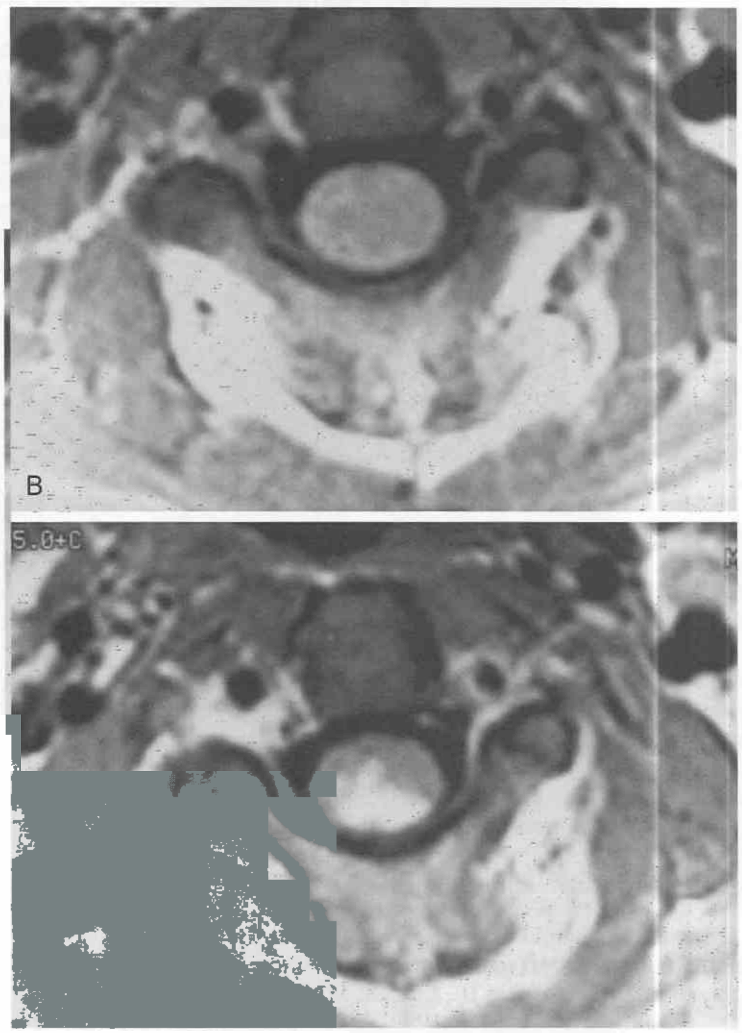

Figure 13–53. Multiple sclerosis (MS) in a 26-year-old woman with myelopathy. *A,* Fast spin-echo, midsagittal T2-weighted cervicothoracic MR image shows extensive, high-intensity demyelination involving the cervical and thoracic spinal cord. The cord appears mildly swollen. *B,* Axial T1-weighted cervical cord MR image at the C2-3 level. The spinal cord appears mildly enlarged. *C,* Postgadolinium-enhanced, T1-weighted MR image at the C2-3 level shows extensive plaque enhancement in the posterior spinal cord. The clinical diagnosis is MS.

visible. Gadolinium enhancement parallels that of MS brain lesions.

The differential diagnosis includes transverse myelitis, other inflammations, and intrinsic cord tumor. The final diagnosis is accomplished, preferably, by serial imaging studies and clinical correlation rather than by biopsy.

References

1. Arbelaez A, Castillo, M: Diffusion-weighted MR imaging of global cerebral anoxia. AJNR Am J Neuroradiol 20:999, 1999.
2. Ballesteros MC, Hansen PE, Soila K: MR imaging of the developing human brain. Part 2. Postnatal development. Radiographics 13:611, 1993.
3. Baram TZ, Goldman AM, Percy AK: Krabbe disease: Specific MRI and CT findings. Neurology 36:111, 1986.
4. Barkovich AJ: Metabolic and destructive brain disorders. In Pediatric Neuroimaging. New York, Raven Press, 1990, p 39.
5. Barkovich AJ, Lyon G, Evrard P: Formation, maturation and disorders of white matter. AJNR Am J Neuroradiol 13:447, 1992.
6. Barnes CM, Enzmann DR: The evolution of white matter disease as seen on computed tomography. Radiology 138:379, 1981.
7. Bozzo M, Capriani G, Leo L, et al: HELLP syndrome and factor V Leiden. Obstet Gynecol Reprod Biol 95:55, 2001.
8. Braffman BH, Zimmerman RA, Trojanowski JQ, et al: Brain MR: Pathologic correlation with gross and histopathology. Part 2. Hyperintense white matter foci in the elderly. AJNR Am J Neuroradiol 9: 629, 1988.
9. Brant-Zawadzki M, Enzmann DR: Using computed tomography of the brain to correlate low white matter attenuation with early gestational age in neonates. Radiology 139:105, 1981.
10. Brooks RA, Di Chiro G, Keller MR: Explanation of cerebral white-gray contrast in computed tomography. J Comput Assist Tomogr 4: 489, 1980.
11. Cajade-Law AG, Cohen JA, Heirer LA: Vascular causes of white matter disease. Neuroimaging Clin North Am 3:361, 1993.
12. Caldemeyer KS, Harris TM, Smith RR, et al: Gadolinium enhancement in acute disseminated encephalomyelitis. J Comput Assist Tomogr 15:673, 1991.
13. Casey SO, Sampaio RC, Michel E, Trunit CL: Posterior reversible encephalopathy syndrome. AJNR Am J Neuroradiol 21:1199, 2000.
14. Chang KH, Han MH, Kim HS, et al: Delayed encephalopathy after acute carbon intoxication: MR imaging features and distribution of cerebral white matter lesions. Radiology 184:117, 1992.
15. Chi JG, Yoo HW, Chang KH, et al: Leigh's subacute necrotizing encephalomyelopathy: Possible diagnosis by CT scan. Neuroradiology 22:141, 1981.
16. Clavier E, Thiebot J, Delangre T, et al: Marchiafava-Bignami disease: A case studied by CT and MR imaging. Neuroradiology 28: 376, 1986.
17. Davis PC, Hoffman JC Jr, Braun IF, et al: MR of Leigh's disease (subacute necrotizing encephalomyelopathy). AJNR Am J Neuroradiol 8:71, 1987.
18. Demaerel P, Wilms G, Verdru P, et al: MR findings in globoid leukodystrophy. Neuroradiology 32:520, 1990.
19. Di Chiro G, Eiben RM, Manz HJ, et al: A new CT pattern in adrenoleukodystrophy. Radiology 137:687, 1980.
20. Dietrich RB, Bradley WG, Zaragoza EJ, et al: MR evaluation of early myelination patterns in normal and developmentally delayed infants. AJNR Am J Neuroradiol 9:69, 1988.
21. Dousset V, Grossman RI, Ramer KN, et al: Experimental allergic encephalomyelitis and multiple sclerosis: Lesion characterization with magnetization transfer imaging. Radiology 182:483, 1992.
22. Estrada M, El Gammal T, Dyken PR: Periventricular low attenuations: A normal finding in computerized tomographic scans of neonates. Arch Neurol 37:754, 1980.
23. Falini A, Calbrese G, Filippi M, et al: Benign versus secondary-progressive multiple sclerosis: The potential role of proton MR spectroscopy in defining the nature of disability. AJNR Am J Neuroradiol 19:223, 1998.
24. Feske SK, Speling RA, Schwartz RB: Extensive reversible brain magnetic resonance lesion in a patient with HELLP syndrome. Neuroimaging 7:247, 1997.
25. Friese SA, Bitzer M, Freudenstein D, et al: Classification of acquired lesion of the corpus callosum with MRI. Neuroradiology 42:795, 2000.
26. Gaitz JP, Bamford CR: Unusual computed tomographic scan in eclampsia. Arch Neurol 39:66, 1982.
27. Glass JP, Lee YY, Bruner J, Fields WS: Treatment-related leukoencephalopathy: A study of three cases and literature review. Medicine (Baltimore) 65:154, 1986.
28. Glusker P, Horoupian DS, Lane B: Familial arteriopathic leukoencephalopathy: Imaging and neuropathologic findings. AJNR Am J Neuroradiol 19:469, 1998.
29. Goto K, Ishii N, Fukasawa H: Diffuse white matter disease in the geriatric population. Radiology 141:687, 1981.
30. Grossman RI, Gonzalez-Scarano F, Atlas SW, et al: Multiple sclerosis: Gadolinium enhancement in MR imaging. Radiology 161:721, 1986.
31. Guo A, Petrella J, Kurtzberg J, Provenzale J: Evaluation of white matter anisotropy in Krabbe disease with diffusion tensor MR imaging: Initial experience. Radiology 218:809, 2001.
32. Hoffman E, Sedaghat-Kerdar M, Becker T, et al: Unspecific white matter lesions: Prevalence, number and distribution in cranial MRI. Eur Radiol 2:154, 1992.
33. Hokezu Y, Kuriyama M, Kubota R, et al: Cerebrotendinous xanthomatosis: Cranial CT and MRI studies in eight patients. Neuroradiology 34:308, 1992.
34. Holland BA, Haas DK, Norman D, et al: MRI of normal brain maturation. Am J Neuroradiol 7:201, 1986.
35. Holland I, Kendall BM: Computed tomography in Alexander's disease. Neuroradiology 20:103, 1980.
36. Honkaniemi J, Kahara V, Latvala M, et al: Reversible posterior leukoencephalopathy after combination chemotherapy. Neuroradiology 42:895, 2000.
37. Imiya M, Ichikawa K, Matsushima H, et al: MR of the base of the pons in Wilson disease. AJNR Am J Neuroradiol 13:1009, 1992.
38. Johns D: Mitochondrial DNA and disease. N Engl J Med 333: 638, 1995.
39. Journel H, Roussey M, Gaudon Y, et al: Magnetic resonance imaging in Pelizaeus-Merzbacher disease. Neuroradiology 29:403, 1987.
40. Kendall BE: Disorders of lysosomes, peroxisomes, and mitochondria. AJNR Am J Neuroradiol 13:621, 1992.
41. Kesselring J, Miller DH, Robb SA, et al: Acute disseminated encephalomyelitis: MRI findings and the distinction from multiple sclerosis. Brain 113:291, 1990.
42. Kjos BO, Brant-Zawadzki M, Young RG: Early CT findings of global central nervous system hypoperfusion. Am J Roentgenol 141: 1227, 1983.
43. Kumar AJ, Rosenbaum AE, Naidu S, et al: Adrenoleukodystrophy: Correlation MR imaging with CT. Radiology 165:497, 1987.
44. Kwan E, Drace J, Enzmann D: Specific CT findings in Krabbe disease. Am J Neuroradiol 5:453, 1984.
45. Kwong YL, Yu YL, Lam KS, et al: CT appearance in hypertensive encephalopathy. Neuroradiology 29:215, 1987.
46. Lee KH, Hashimoto SA, Hooge JP, et al: Magnetic resonance imaging of the head in the diagnosis of multiple sclerosis: A prospective 2-year follow-up with comparison of clinical evaluation, evoked potentials, oligoclonal banding, and CT. Neurology 41:657, 1991.
47. Levy RM, Rosenbloom S, Perrett LV: Neuroradiologic findings in AIDS: A review of 200 cases. Am J Neuroradiol 7:833, 1986.
48. Lotz PR, Ballinger WE, Quisling RG: Subcortical arteriosclerotic encephalopathy: CT spectrum and pathologic correlation. Am J Roentgenol 147:1209, 1986.
49. Ludwig B, Brand M, Brockerhoff P: Postpartum CT examination of the heads of full term infants. Neuroradiology 20:145, 1980.
50. Lukes SA, Norman D: Computed tomographic findings in acute disseminated encephalomyelitis. Ann Neurol 13:567, 1983.
51. Mantovani JF, Naidich TP, Prensky AL, et al: Maple syrup urine disease: Presentation with pseudotumor cerebri and CT abnormalities. J Pediatr 96:279, 1980.
52. Marano GD, Goodwin CA, Ko JP: Atypical contrast enhancement in computerized tomography of demyelinating disease. Arch Neurol 37:523, 1980.
53. Mark AS, Atlas SW: Progressive multifocal leukoencephalopathy in patients with AIDS: Appearance on MR images. Radiology 173: 517, 1989.
54. McAdams H, Geyer CA, Done SL, et al: CT and MR imaging of Canavan disease. AJNR Am J Neuroradiol 11:397, 1990.

55. Melhem E, Loes D, Georgiades S, et al: X-linked adrenoleukodystrophy: The role of contrast-enhanced MR imaging in predicting disease progression. AJNR Am J Neuroradiol 21:839, 2000.
56. Miller GM, Baker HL Jr, Okazaki H, et al: Central pontine myelinolysis and its imitators. Radiology 168:795, 1988.
57. Morariu MA, Wilkins DE, Patel S: Multiple sclerosis and serial computed tomography: Delayed contrast enhancement of acute and early lesions. Arch Neurol 37:189, 1980.
58. Murata R, Nakajima S, Tanaka A, et al: MR imaging of the brain in patients with mucopolysaccharidosis. AJNR Am J Neuroradiol 10:1165, 1989.
59. Mushlin AI, Detsky AS, Phelps CE, et al: The accuracy of magnetic resonance imaging in patients with suspected multiple sclerosis. JAMA 269:3146, 1993.
60. Olsen WL, Longo FM, Mills CM, et al: White matter disease in AIDS: Findings at MR imaging. Radiology 169:445, 1988.
61. O'Neill BP, Forbes GS: Computerized tomography and adrenoleukomyeloneuropathy: Differential appearance in disease subtypes. Arch Neurol 38:293, 1981.
62. Pederson H, Clausen N: The development of cerebral CT changes during treatment of acute lymphocytic leukemia in childhood. Neuroradiology 22:79, 1981.
63. Penn RD, Trinko B, Baldwin L: Brain maturation followed by computed tomography. J Comput Assist Tomogr 4:614, 1980.
64. Penner MW, Li KC, Gebarski SS, et al: MR imaging of Pelizaeus-Merzbacher disease. J Comput Assist Tomogr 11:591, 1987.
65. Peters AC, Versteeg J, Bots GT, et al: Progressive multifocal leukoencephalopathy. Arch Neurol 37:497, 1980.
66. Picard L, Claudon M, Roland J, et al: Cerebral computed tomography in premature infants, with an attempt at staging developmental features. J Comput Assist Tomogr 4:435, 1980.
67. Poser CM: Exacerbation, activity and progression in multiple sclerosis. Arch Neurol 37:471, 1980.
68. Ragland RL, Duffis AW, Gendelmal S, et al: Central pontine myelinolysis with clinical recovery: MR documentation. J Comput Assist Tomogr 13:316, 1989.
69. Rail RL, Perkin GD: Computerized tomographic appearance of hypertensive encephalopathy. Arch Neurol 37:310, 1980.
70. Ramsey RG, Geremia GK: CNS complications of AIDS: CT and MR findings. AJR 151:449, 1988.
71. Reik L Jr: Disseminated vasculomyelinopathy: An immune complex disease. Ann Neurol 7:291, 1980.
72. Reisner T, Maida E: Computerized tomography in multiple sclerosis. Arch Neurol 37:475, 1980.
73. Rowland LP: "Ophthalmoplegia plus" or Kearns-Sayre syndrome. Arch Neurol 37:256, 1980.
74. Rowley HA, Dillon WP: Iatrogenic white matter diseases. Neuroimaging Clin North Am 3:379, 1993.
75. Ruiz-Martinez J, Martinez Perez-Basal A, Ruibal M, et al: Marchiafava-Bignami disease with widespread extracallosal lesions and favourable course. Neuroradiology 41:40, 1999.
76. Runge VM, Kirsch JE, Lee C, et al: MRI of multiple sclerosis in the brain. MRI Decisions 6(4):2, 1992.
77. Saito H, Endo M, Takase S, Itahara K: Acute disseminated encephalomyelitis after influenza vaccination. Arch Neurol 37:564, 1980.
78. Scanberger A, Tomaiuolo F, Sabatini U, et al: Demyelinating plaques in relapsing-remitting and secondary-progressive multiple sclerosis: Assessment with diffusion MR imaging. AJNR Am J Neuroradiol 21:862, 2000.
79. Shah M, Ross J: Infantile Alexander disease: MR appearance of a biopsy-proved case. AJNR Am J Neuroradiol 11:1105, 1990.
80. Sheldon JJ, Siddharthan R, Tobias J, et al: MR imaging of multiple sclerosis: Comparison with clinical and CT examination in 74 patients. Am J Neuroradiol 6:683, 1985.
81. Simon JH, Holtas SL, Schiffer RB, et al: Corpus callosum and subcallosal-periventricular lesions in multiple sclerosis: Detection with MR. Radiology 160:363, 1986.
82. Statz A, Boltshauser E, Schinzel A, Spiess H: Computed tomography in Pelizaeus-Merzbacher disease. Neuroradiology 22:103, 1981.
83. Steingart A, Hachinski VC, Lau C, et al: Cognitive and neurologic findings in demented patients with diffuse white matter lucencies on computed tomographic scan (leukoaraiosis). Arch Neurol 44:36, 1987.
84. Stovring J, Fernando LT: Wallerian degeneration of the corticospinal tract region of the brain stem: Demonstration by computed tomography. Radiology 149:717, 1983.
85. Thompson DS, Hutton JT, Stears JC, et al: Computerized tomography in the diagnosis of central and extrapontine myelinolysis. Arch Neurol 38:243, 1981.
86. Topcu M, Saatci I, Apak A, et al: Leigh syndrome in a 3-year-old boy with brain MR imaging and pathologic findings. AJNR Am J Neuroradiol 21:224, 2000.
87. Tsuruda JS, Kortman KE, Bradley WG, et al: Radiation effects on cerebral white matter: MR evaluation. AJNR Am J Neuroradiol 8:431, 1987.
88. Uchimaya M, Hata Y, Tada S: MR imaging in adrenoleukodystrophy. Neuroradiology 33:25, 1991.
89. Valentine AR, Moseley IF, Kendall BE: White matter abnormality in cerebral atrophy: Clinicoradiological correlations. J Neurol Neurosurg Psychiatry 43:139, 1980.
90. van Wassenaer–van Hall H, van den Heuvel G, Jansen G, et al: Cranial MR in Wilson disease: Abnormal white matter in extrapyramidal and pyramidal tracts. AJNR Am J Neuroradiol 16:2021, 1995.
91. Vaughn DJ, Jarvik JG, Hackney D: High-dose cytarabine neurotoxicity: MR findings during the acute phase. AJNR Am J Neuroradiol 14:1014, 1993.
92. Walker DL: Progressive multifocal leukoencephalopathy. In Vinken PJ, Bruyn GW, Klawaus HL (eds): Handbook of Clinical Neurology. New York, Elsevier, 1985, p 503.
93. Walsh PJ: Adrenoleukodystrophy: Report of two cases with relapsing and remitting courses. Arch Neurol 37:448, 1980.
94. Waltz G, Harik SI, Kaufman B: Adult metachromatic leukodystrophy. Arch Neurol 44:225, 1987.
95. Waxman S: The demyelinating diseases. In Rosenberg RN (ed): The Clinical Neurosciences, vol 1. New York, Churchill Livingstone, 1983.
96. Weingarten KL, Zimmerman RD, Pinto RS, Whelan MA: Computed tomographic changes of hypertensive encephalopathy. Am J Neuroradiol 6:395, 1985.
97. Whiteman MLH, Post MJD, Berger JL, et al: Progressive multifocal leukoencephalopathy in 47 HIV-seropositive patients: Neuroimaging with clinical and pathological correlation. Radiology 187:233, 1993.
98. Wolf R, Zimmerman R, Clancy R, Haselgrove J: Quantitative apparent diffusion coefficient measurements in term neonates for early detection of hypoxic-ischemic brain injury: Initial experience. Radiology 218:825, 2001.
99. Wray S, Provenzale J, Johns D, Thulborn K: MR of brain in mitochondrial myopathy AJNR Am J Neuroradiol 16:1167, 1995.
100. Yamamoto T, Ashikaga R, Araki Y, Nishimura Y: A case of Marchiafava-Bignami disease: MRI findings on spine-echo and fluid attenuated inversion recovery (FLAIR) images. Eur J Radiol 34:141, 2000.
101. Yetkin FZ, Haughton VM: Common and uncommon manifestations of MS on MRI. MRI Decisions 6:13, 1992.
102. Young RSK, Osbakken MD, Alger PM, et al: Magnetic resonance imaging in leukodystrophies of childhood. Pediatr Neurol 1:15, 1985.
103. Zeumer H, Schonsky B, Sturm KW: Predominant white matter involvement in subcortical arteriosclerotic encephalopathy (Binswanger disease). J Comput Assist Tomogr 4:14, 1980.

Part III

Imaging of the Head and Neck

Edited by
Charles F. Lanzieri

14 The Orbit

Jon Mark Fergenson, Neal Mandell,
James J. Abrahams

Magnetic resonance imaging (MRI) and computed tomography (CT) have revolutionized diagnostic imaging of the orbit and its contents. With its superb soft tissue contrast and ability to image in multiple planes, MRI provides excellent rendering of the orbital anatomy. CT also shows the soft tissues within the orbit very well and is best at displaying anatomy and pathology of the bony orbit.

The fine structures within the orbit require more attention to imaging protocol than many other regions of the body to ensure optimal diagnostic information.

This chapter discusses technique for the more commonly used imaging issues, presents an overview of pertinent anatomy, and touches on a cross-section of orbital pathology, including some familiar and some unusual lesions.

Anatomy

The anatomy of the orbit consists of a bony cavity within which the globe, muscle cone, optic nerve–sheath complex, lacrimal apparatus, and various vascular and nerve structures are packed into a cushion of fat.

The bony orbit is a conical structure that consists of the orbital plate of the frontal bone, the maxilla, the greater and lesser wings of the sphenoid bone, the ethmoid bone, and the lacrimal bone. The inferior and medial walls are quite thin and prone to fracture. The medial wall is named the lamina papyracea, in recognition of its paper-thin nature. Multiple foramina transmit vessels and nerves. The most prominent among these include the superior and inferior orbital fissures, the optic canal, the infraorbital and supraorbital foramina, and the lacrimal duct foramen. Other tiny foraminal spaces are not usually appreciated in imaging because of their size. The contents of the major foramina are listed in Box 14–1.

Box 14–1. Major Foramina of the Orbit

Optic Canal

Optic nerve
Ophthalmic artery

Superior Orbital Fissure

III, IV, VI, V_1 cranial nerves
Lacrimal and frontal nerves
Superior and inferior ophthalmic veins

Inferior Orbital Fissure

V_2 cranial nerve
Infraorbital vessels, zygomatic nerve

The muscle cone consists of seven extraocular muscles: the superior, medial, lateral, and inferior recti as well as the superior and inferior obliques, and the levator palpebrae superioris. All but the inferior oblique muscle originate at the orbital apex at Zinn's ring and pass anteriorly to form tendinous attachments to the globe. The inferior oblique muscle originates on the inferomedial aspect of the orbit and passes in a somewhat lateral course to attach to the posterolateral aspect of the globe. The cone of the muscle has been designated a relative boundary or demarcation in addressing the position of several pathologic processes, with the orbit divided into *intraconal* and *extraconal* spaces. In general, processes involving the intraconal space require surgical attention, whereas extraconal processes are often amenable to medical management.

The globe is approximately spherical, with only a few readily visualized structures: the cornea, lens, anterior chambers, vitreous, and the retina-sclera-choroid complex. None of the conventional imaging modalities is able to visualize the retina from the choroid separately in the healthy patient. When an intervening process does occur, it causes separation of these thin membranes.

Proptosis is evaluated by axial scanning, with a line connecting the lateral orbital walls at the level of the lens and with the imaging specialist measuring from that line to the anterior aspect of the globe.[31] This measurement should not exceed 21 mm.[31]

The optic nerve–sheath complex consists of the optic nerve, its surrounding meningeal sheath, and the cerebrospinal fluid (CSF), which separates them. The sheath extends from the optic canal to the globe. The normal diameter of the nerve is up to 4 mm. The diameter of the complex may vary from 4 to 6 mm. The amount of visualized subarachnoid fluid is also variable.

Occasionally, the presence of CSF makes it possible to determine whether a tumor arises from the sheath or from the nerve itself. Tumors arising from the sheath, such as meningiomas, form a "tram track" appearance in which the outer layer is thickened but remains separated from the normal-sized nerve by a layer of fluid. Because the nerve takes a sigmoid course from apex to globe, coronal imaging is essential for assessing the optic nerve–sheath complex.

The lacrimal apparatus consists of the lacrimal gland, its secretory duct, and the ductal system, which drains these secretions into the nasal cavity. The gland lies in the superolateral aspect of the orbit. The draining ductal system lies near the medial canthus and consists of the superior and inferior puncta, their associated ducts, the lacrimal sac, lacrimal duct, and the valve of Hasner, a draining orifice inferolateral to the inferior nasal turbinate.

The anterior border of the orbit is formed by the orbital

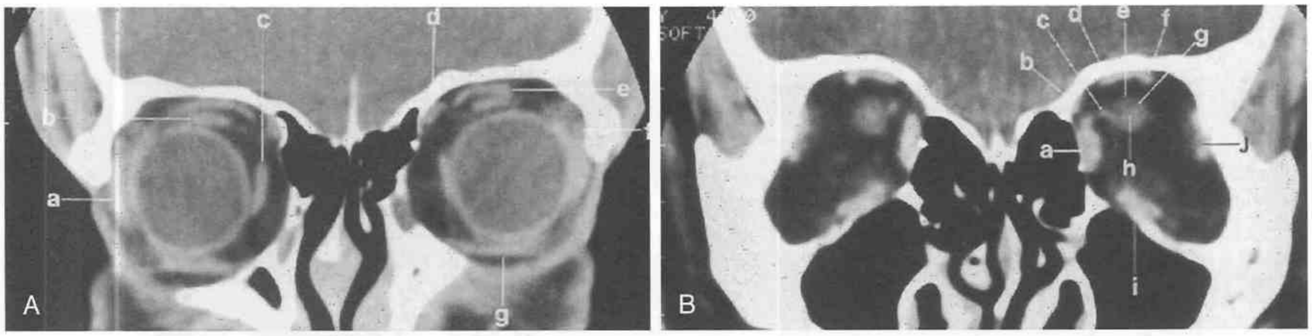

Figure 14–1. *A,* Coronal CT scan: normal anatomy. Lateral rectus (a), superior rectus (b), medial rectus (c), superior oblique (d), levator palpebrae superioris (e), lacrimal gland (f), inferior oblique (g). *B,* Medial rectus (a), superior oblique (b), ophthalmic artery (c), superior rectus/levator palpebrae superioris complex (d), dural sheath (e), superior ophthalmic vein (f), subarachnoid space (g), optic nerve (h), inferior rectus (i), lateral rectus (j).

septum, a fibrous structure adherent to the inner margin of the orbital rim with central portions that extend into the tarsus of the eyelids. Although there are a few orifices for passage of vessels, nerves, and ducts, the septum forms an effective barrier to prevent superficial processes from extending into the orbit proper. A pathologic process such as cellulitis may be designated *preseptal* or *postseptal.*

Technique

Computed Tomography

Intraorbital fat provides a natural source of contrast on CT scans. Most lesions within the orbit, whether inflammatory, infectious, or neoplastic, are relatively radiodense in comparison to the surrounding fat, and they are easily distinguished by CT. CT is rapid, and the images are obtained incrementally. Therefore, patient cooperation is less crucial than in MRI.

Commonly accepted protocols call for both axial and coronal images with the potential for multiplanar reconstruction. For most orbital studies, 3-mm sections in the axial and coronal planes are adequate. Coronal sections should be initiated at the lateral orbital rim (to lessen exposure to the radiosensitive lens[80]) and continued to the posterior aspect of the optic canals, with the anterior clinoid or dorsum sella used as landmarks. The axial sections should include images of the entire brain, specifically to include the retro-orbital optic apparatus, with additional retrospective magnified views of the orbits.

Coronal images are especially important in that cross-sectional evaluation of all of the intraorbital structures is optimal (e.g., extraocular muscles, optic nerve–sheath–nasal complex, vessels, and globe) (Fig. 14–1). This plane is also imperative for assessing spread of processes from surrounding structures (e.g., paranasal sinuses, trauma, tumor). The prone patient position is ideal, especially with sinus-related disease,[2] but supine positioning is also acceptable.

Occasionally, a patient may be unable to tolerate positioning for direct coronal imaging. This occurs most commonly with elderly patients with severe degenerative disease of the cervical spine and in the setting of acute trauma. Recent developments in multislice CT technology allow for faster thin-slice imaging. As a result, axial thin-section images can be obtained for coronal reconstruction in these patients (Fig. 14–2).

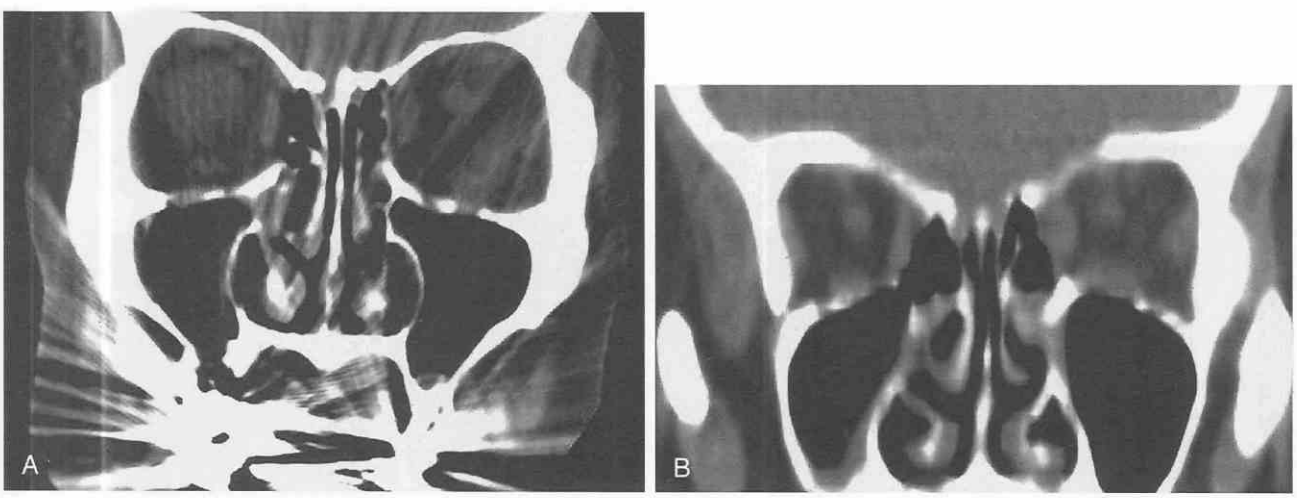

Figure 14–2. *A,* Coronal CT scan in a patient whose extensive dental hardware obscures detail in the orbits. *B,* Reformatted coronal view shows enlargement of the extraocular muscles on the left side. In view of the patient's known hyperthyroidism, this finding was thought to represent Graves' disease.

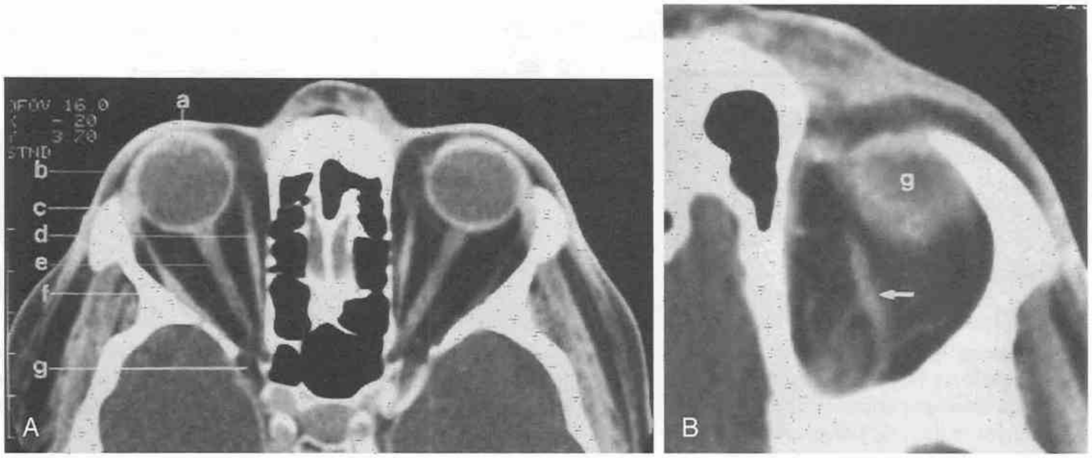

Figure 14–3. *A,* Axial CT scan: normal anatomy. Lens (a), lid (b), lacrimal gland (c), medial rectus (d), optic nerve-n-sheath complex (e), lateral rectus (f), superior orbital fissure (g). *B,* Axial CT scan: normal anatomy. Superior ophthalmic vein *(arrow)*, globe (g).

Intravenous (IV) contrast material is a necessary addition to most orbital examinations, although it is not necessary in the setting of trauma. IV contrast can increase the sensitivity and sometimes specificity of distinguishing between various entities–whether inflammatory, infectious, neoplastic, or vascular. The contrast agent can be administered by either IV drip or by mechanical injector. A single dose (e.g., 150 mL) can be used, or split doses, one for each plane or section, depending on the lesion. *Windowing* is also critical to assessing pathologic changes and should include both soft tissue and bone windows (Fig. 14–3).

Thin-section CT may be performed following the administration of contrast material into the nasolacrimal duct to evaluate patency. These CT dacrocystograms are often performed in conjunction with an ophthalmologist, who cannulates the duct and administers the contrast agent. Coronal reconstructions of the axial data can be helpful (Fig. 14–4).

Magnetic Resonance Imaging

Although MRI is relatively new, compared with CT, this modality has rapidly gained ground in the assessment of orbital disease. The capacity to produce images without ionizing radiation and in any plane of section without a change in patient position has made MRI an important tool in orbital imaging. The absence of bony artifact is an advantage over CT, especially in the orbital apex, optic canal, and parasellar regions.

MRI uses the physical properties of the proton, the hydrogen atom's nucleus, to generate imaging data. Because hydrogen is an abundant component of the water and the macromolecules in all tissues, MRI can be used to examine any body part.

The patient is placed in a strong unidirectional magnetic field, and a small population of protons become aligned with that field. The region of interest is subjected to pulsed radiofrequency (RF) energy. This serves to change the orientation of the spinning proton. The natural tendency of the perturbed proton is to realign with the overall magnetic field. This is referred to as the *T1* characteristic of the tissue. By definition, T1 is that time for which protons in a particular tissue have regained approximately 63% of the original alignment.

When the protons are "tipped" by the RF pulse, they

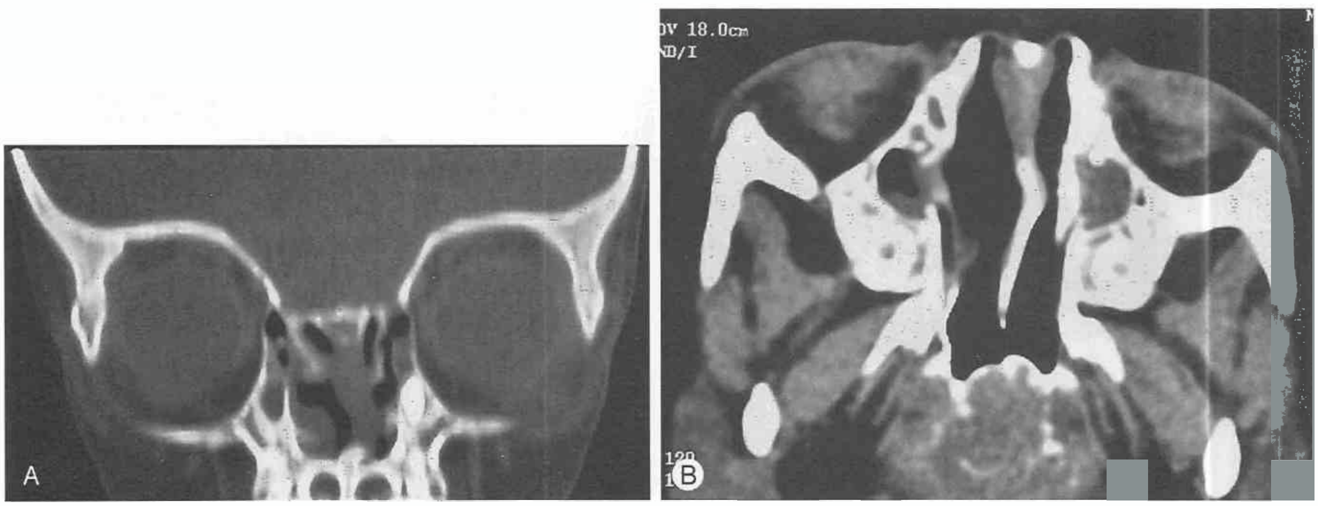

Figure 14–4. *A,* Coronal reformatted image from a CT dacrocystogram shows dilation of the lacrimal duct. The nasal septum and inferior turbinate are deviated leftward and cause obstruction at the valve of Hasner. *B,* The obstruction is only partial, as evidenced by the presence of contrast material in the posterior nasopharynx.

are initially "in phase," or are spinning together coherently in the 90-degree frame of reference. Over time, they lose cohesion and become "out of phase," called *T2 relaxation.*

T1 and T2 are inherent tissue characteristics and are not produced by the magnetic resonance itself. One uses the T1 and T2 of various tissues being imaged to enhance and accentuate contrast differences between those tissues.

Magnetic gradients are superimposed on the overall magnetic field to spatially "encode" the position of each spinning proton in space. One can obtain spatial information using the frequency of the spinning protons or their relative phase.

The most commonly used protocols today involve (1) *spin-echo* imaging and (2) *gradient-echo* imaging.

Spin-echo imaging involves an additional 180-degree pulse to "rephase" the protons to produce an "echo" at a specified time: TE, or *echo time*. The sequence is repeated as many times as needed to obtain information about the anatomic area of interest. TR, or *repetition time*, refers to those repeated intervals. For a more detailed review of MRI physics, see References 3, 15, 22, 45, 53, and 71.

Gradient-echo imaging involves the actual reversal of the image gradients used for spatial encoding in the region of interest. Acquisition imaging data can be obtained rapidly, either in a slice-by-slice format or volumetrically.

Shallow flip angles (<90 degrees) and faster techniques have been developed for even faster image acquisition (see specific articles on these techniques).

Gadolinium–diethylene-triamine-penta-acetic acid (Gd-DTPA) is an IV contrast agent that shortens the T1 relaxation time of the tissues it penetrates. This results in higher T1 signal, or "brighter" areas on the scan images. Gadolinium contrast is analogous to the iodinated contrast material used in CT scanning and identifies tissues with greater perfusion. Within the brain, gadolinium enhancement results from breakdown of the blood-brain barrier.

As in CT scans, multiple planes are important to assess the orbit. Standard protocols usually include coronal and axial T1-weighted images as well as T2-weighted axial and coronal images (Figs. 14–5 to 14–7). The imaging specialist should include the brain posterior to the orbital area in order to evaluate the cavernous sinus, optic chiasm, optic radiations, and the nuclei of the oculomotor, abducens, and trochlear nerves in the midbrain and pons.

MRI offers the ability to suppress the normally strong T1 signal of fat. Precontrast T1 imaging should be performed without fat suppression because fat suppression diminishes the inherent contrast between the high signal of fat and the lower signal of most pathologic processes. Postcontrast imaging should be performed with fat suppression techniques to increase the difference in signal between an enhancing pathologic process and its surroundings (Fig. 14–8).

Pathology

Trauma

Traumatic lesions of the orbit can involve any or all of the orbital structures. Treatment is determined by proximity to, or disruption of, key anatomic elements.

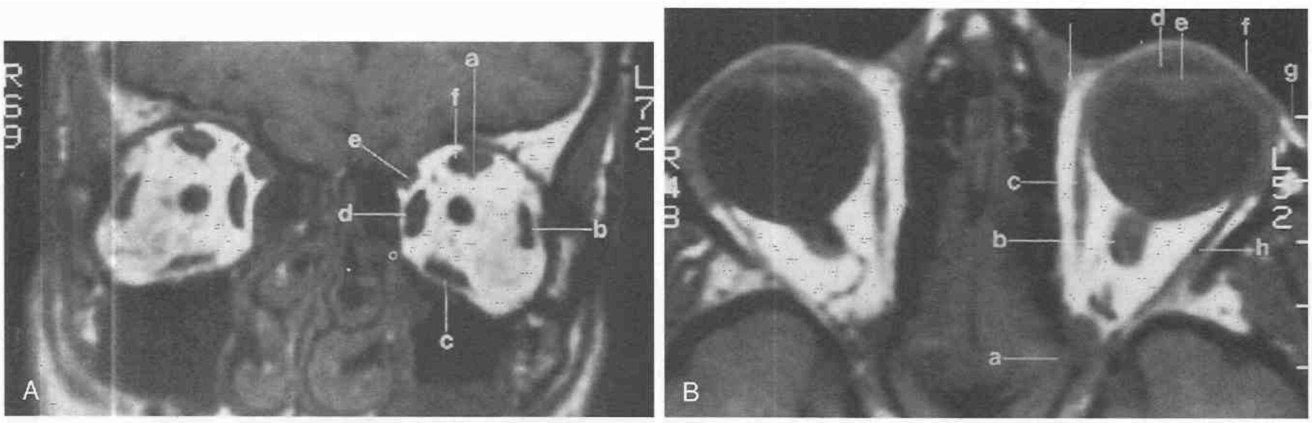

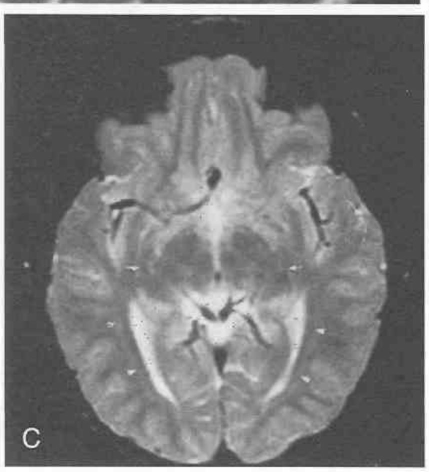

Figure 14–5. *A,* Coronal T1-weighted MRI study: normal anatomy. Superior ophthalmic vein (a), lateral rectus (b), inferior rectus (c), medial rectus (d), superior oblique (e), superior rectus–levator palpebrae superioris complex (f). *B,* Axial T1-weighted MRI study: normal anatomy. Optic nerve in the optic canal (a), optic nerve sheath complex (b), medial rectus (c), anterior chamber (d), lens (e), lid (f), medial and lateral aspects of the orbital septum *(arrows;* g), lateral rectus (h). *C,* Axial T2-weighted MRI study: posterior visual apparatus. Position of lateral geniculate body *(arrows;* a), path of optic radiations *(arrowheads).*

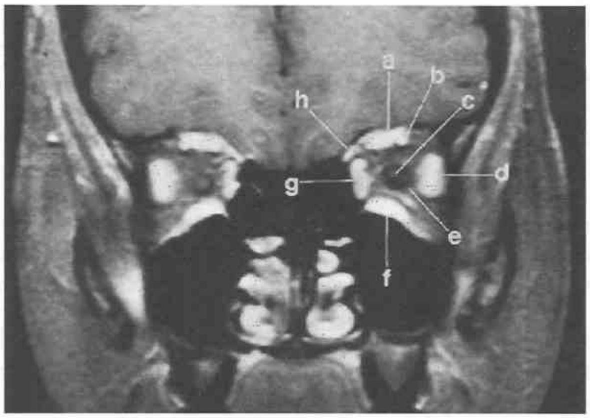

Figure 14–6. Coronal T1-weighted MRI study with fat saturation: normal anatomy. *A,* Superior rectus/levator palpebrae superioris complex. *B,* Superior ophthalmic vein. *C,* Optic nerve. *D,* Lateral rectus. *E,* Dural sheath. *F,* Inferior rectus. *G,* Medial rectus.

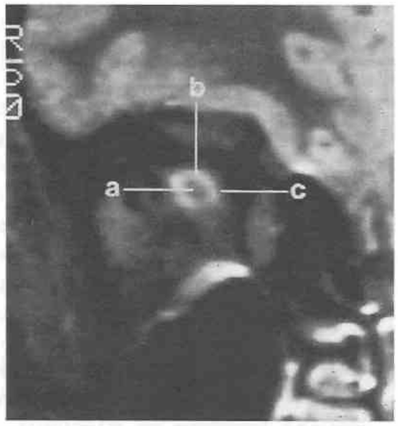

Figure 14–7. Coronal inversion [redacted]overy, fast spin-echo MRI study: normal anatomy. *A,* Optic nerve. *B,* Subarachnoid space with cerebrospinal fluid. *C,* Optic nerve sheath.

One of the more common entities is disruption of an orbital wall with the potential for entrapment of extraocular muscles, the so-called "blowout" fracture. The mechanism of injury is usually blunt trauma to the anterior orbit. The increased intraorbital pressure is transmitted to the walls, resulting in fracture. The inferior and medial walls, which are thinnest, are the most vulnerable. Orbital contents are often seen to herniate through the fracture. Because of its superior bone detail, CT is the study of choice in the setting of trauma. Coronal images are essential for optimal assessment of the orbital floor. The lacrimal apparatus can also be evaluated, since it is commonly affected in trauma.[73]

Because the extra-ocular muscles are tethered to the walls of the orbit by tiny fibrous strands that are too small to image on CT or MR, muscle entrapment can occur in the presence of an orbital blowout fracture, even without herniation of the muscle itself (Fig. 14–9).[34]

Foreign body evaluation usually necessitates thin-section CT scanning (1.5 mm) to rule out clinically important objects (Fig. 14–10). Wood fragments can be particularly difficult to identify because of hydrational differences of various woods or air content. Because wood can have a variety of densities, especially on CT scans, special care should be taken to evaluate both dense foci and lucent foci within the orbit if the presence of a wood fragment is suspected.[62]

Phthisis bulbi represents the end stage of traumatic or inflammatory injury to the globe. The result is a shrunken, atrophic, and usually heavily calcified globe.

Infection

Infection most commonly affects the orbit by extension from adjacent structures. Contiguous spread of sinusitis or a superficial periorbital cellulitis of the face is the most

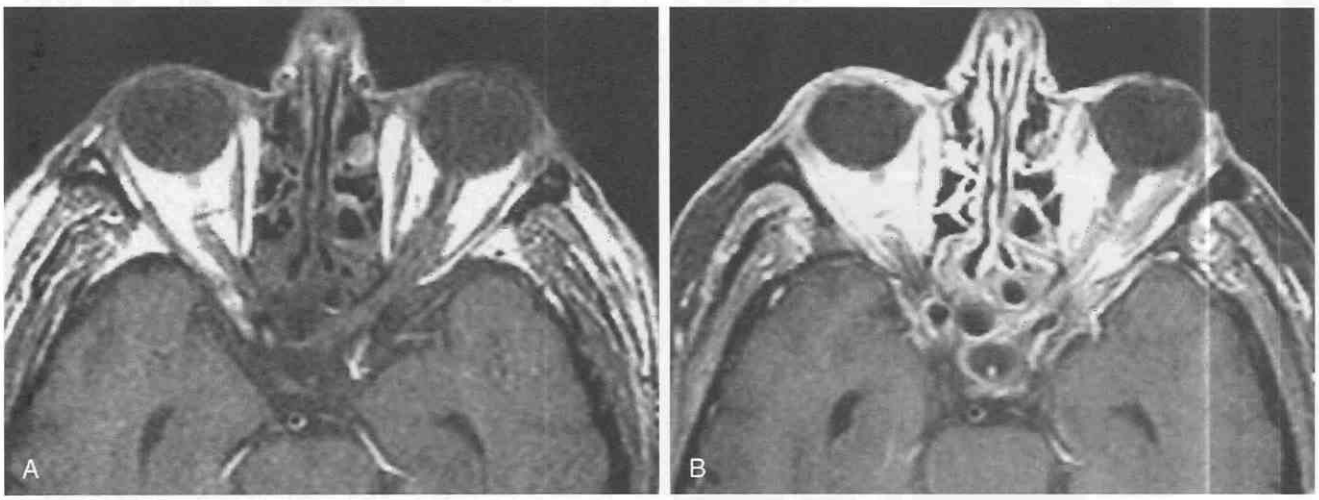

Figure 14–8. *A,* Precontrast axial T1-weighted image performed without fat suppression demonstrates a mass at the left orbital apex in a patient with known cutaneous lymphoma. *B,* Postcontrast T1-weighted image of the same patient in which the fat saturation pulse failed to suppress the orbital fat (this may be due to dental artifact). The lesion demonstrates marked contrast enhancement and is now indistinguishable from the high signal of the orbital fat. This case illustrates the importance of performing nonsuppressed precontrast images and fat-suppressed postcontrast studies.

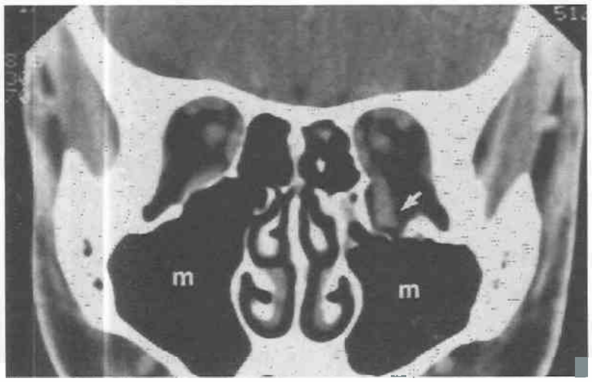

Figure 14–9. CT scan shows blowout fracture of the left orbital floor with herniation of extraconal fat and inferior rectus muscle *(arrow)*. m, maxillary sinus.

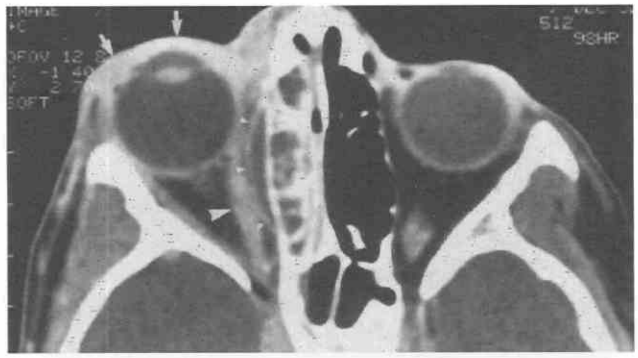

Figure 14–11. CT scan shows an extraconal subperiosteal abscess *(small arrowhead)*. This is a complication of ethmoid sinusitis. A thickened, displaced medial rectus *(large arrowhead)* and preseptal soft tissue swelling *(arrows)* are seen.

common scenario. Hematogenous infection is less common. The specific location of an orbital cellulitis is important for prognostic and therapeutic reasons. When possible, it should be determined whether a process is (1) preseptal or postseptal or (2) intraconal or extraconal.[22]

Extension of infection from the paranasal sinuses occurs most commonly from the ethmoid air cells (Fig. 14–11) in children and from the frontal sinuses (Fig. 14–12) in adults.[68] CT continues to be the examination of choice because it demonstrates not only the fluid and/or soft tissue component of the inflammatory process but also any bony changes. Findings range from mild mucoperiosteal thickening or elevation to frank intraorbital abscesses. The amount of periosteal elevation may dictate whether the patient is managed conservatively or surgically. The most common organisms in acute sinusitis are *Streptococcus pneumoniae,* beta-hemolytic streptococci, and *Haemophilus influenzae.* Staphylococci and anaerobes are less common.[68]

A mucocele is the expansion of a paranasal sinus that results from trapped mucus secretions. The expanding sinus can cause mass effect and distortion of the orbit (Fig. 14–13). MRI studies complement CT scans in this setting. In the absence of superimposed infection, the fluid is homogeneous in appearance. The fluid can have a variety of signal intensities as a result of differences in protein content from lesion to lesion. Mucoceles are seen most often in the frontal sinuses but may be found in the other paranasal sinuses as well.[68]

Inflammation

Graves' Ophthalmopathy

Graves' disease is one entity in the spectrum of hyperthyroidism. It is thought to be caused by a circulating stimulator of thyroid function, so-called long-acting thyroid stimulator (LATS).[32] Orbital involvement demonstrates inflammatory cells that enlarge the extraocular muscles and infiltrate the retro-orbital fat. Involvement of the globe and optic nerve is rare.

The imaging findings demonstrate fusiform enlargement of the extraocular muscles, which is classically found in the belly of the muscle (Fig. 14–14; see Fig. 14–2). Typically, the tendonous attachments at the ring of Zinn are spared, which helps to differentiate Graves' disease from orbital pseudotumor. Most commonly affected is the inferior rectus muscle, both in isolation and in association with multiple muscular involvement.[54] The lack of tendonous involvement may be difficult to demonstrate in cases of massive muscle enlargement. It is important to assess for compression of the optic nerve–sheath complex, especially near the orbital apex.

In some cases, orbital involvement precedes clinically

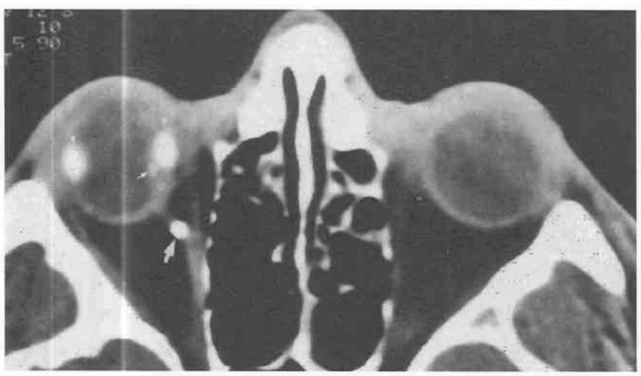

Figure 14–10. CT scan shows intraconal, metallic, foreign bodies just medial to the medial rectus *(large arrow)* and intraocular *(small arrow)*. Scleral band in place right *(arrowheads)*.

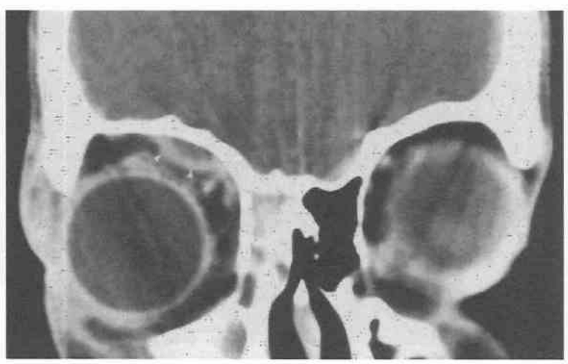

Figure 14–12. CT scan shows subperiosteal abscess of the superior orbit *(arrowheads)* from ethmoid or frontal sinus disease.

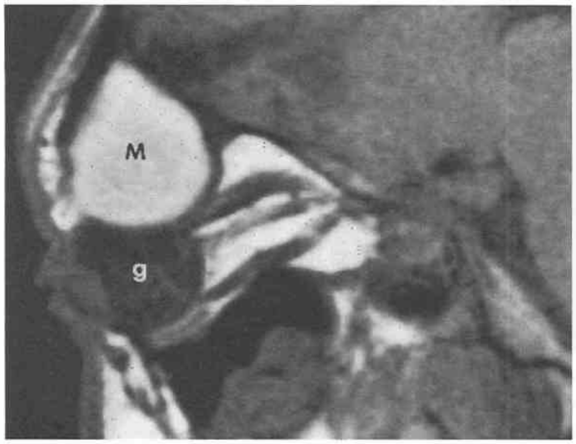

Figure 14–13. Sagittal T1-weighted MRI study shows mucocele (M) of the frontal sinus with inferior displacement of the globe (g).

apparent thyroid disease. In these circumstances, differentiation from pseudotumor can be difficult, especially when the involvement is unilateral.

Orbital Pseudotumor

Orbital pseudotumor is an idiopathic inflammatory process that may involve the extraocular muscles, orbital fat, and less commonly, other intraorbital structures.[12] The two most common appearances are a solitary intraorbital mass and diffuse muscle thickening.

The inflammation may involve any or all parts of the orbit and is usually unilateral. The diagnosis is usually based on a good clinical response to steroids[50] plus the exclusion of other inflammatory lesions of the orbit (e.g., sarcoid, Wegener's granulomatosis, multiple sclerosis). CT evaluation in the assessment of orbital pseudotumor most commonly demonstrates contrast enhancement of the involved structures, extraocular muscle enlargement, retrobulbar fat infiltration, and proptosis (Fig. 14–15*A* and *B*).

The muscular involvement in pseudotumor is classically diffuse, with extension to the tendonous attachments (Fig. 14–16). As mentioned earlier, tendonous involvement can help to differentiate pseudotumor from Graves' disease. Tumefactive or tumor-like inflammatory masses may also occur, and differentiation from a neoplastic, infectious, or vascular process is required.

Imaging of pseudotumor and Graves' ophthalmopathy is usually accomplished with a contrast-enhanced CT scan, again with coronal and axial views essential.[17, 46] MRI studies are also useful in evaluating involvement of the optic nerve–sheath complex.

Sarcoid

Sarcoid is a noninfectious granulomatous disease that can have manifestations in almost any part of the optic pathway, from the globe to the optic radiations. The lacrimal gland and anterior layer of the globe (Fig. 14–17) and eyelids are common areas of involvement.[11] This entity shows increased signal on T1-weighted images in MRI studies.[52] Intracranial involvement by sarcoid, especially in the region of the sella turcica, is seen optimally with MRI (Fig. 14–18), although specificity and differentiation from other lesions can be difficult.

Optic Neuritis

Optic neuritis is an inflammation of the optic nerve that can have many causes, including infections (e.g., viral, bacterial, fungal, parasitic), granulomatous diseases, and demyelinating diseases such as multiple sclerosis.[68] Imaging characteristics of optic nerve inflammation are often subtle. Faint enhancement or slightly increased T2 signal may be seen. These changes are nonspecific.

Inversion recovery sequences (Fig. 14–19) are highly sensitive to increased water content, which often accompanies inflammatory processes. Increased signal on these images may be seen in optic neuritis, but this finding is also nonspecific.[18]

Neoplasms

Lymphoma

The most common neoplasm in the orbit is lymphoma, which accounts for just over half of all cases.[74] B-cell lymphomas of the non-Hodgkin's type are by far the most common. T-cell lineages are uncommon but have been described.[9] Usually, orbital lymphomas are primary to the orbit, but occasionally orbital manifestation of a systemic

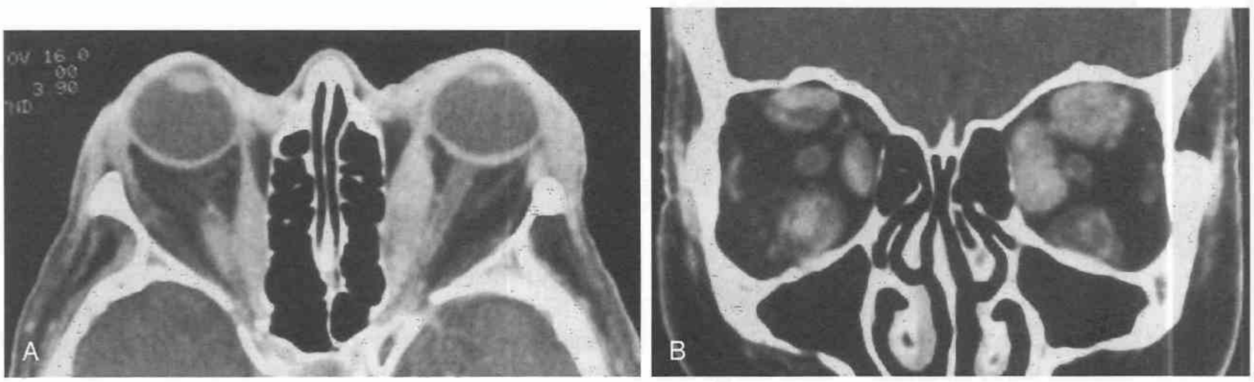

Figure 14–14. *A*, Axial contrast-enhanced CT scan shows Graves' ophthalmopathy characterized by enlarged superior, medial, and inferior recti with compromise of the orbital apex. *B*, Coronal contrast-enhanced CT scan of the same patient shown in *A*.

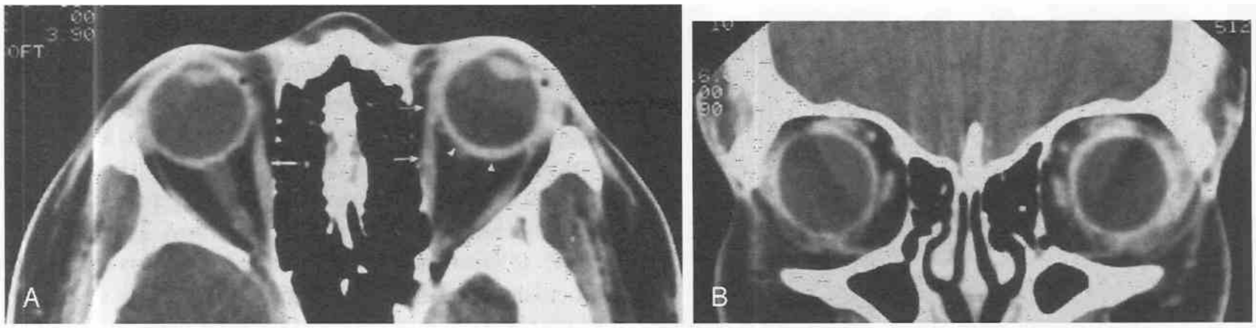

Figure 14–15. *A,* Axial CT scan shows pseudotumor of the orbit with swollen bilateral medial rectus *(arrows),* which includes tendinous insertion on the globe. Thickening and enhancement of the globe *(arrowheads)* are also shown. *B,* Coronal CT scan shows pseudotumor of the orbit (same patient as in *A*).

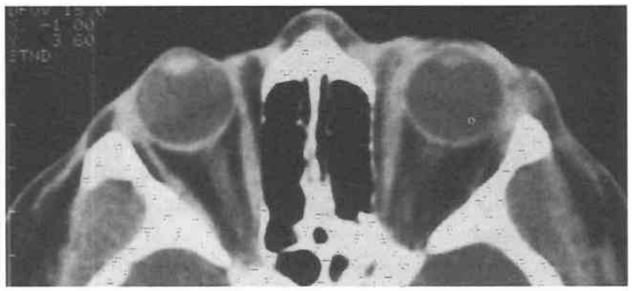

Figure 14–16. CT scan of orbital pseudotumor with bilateral medial rectus and left lacrimal involvement.

Figure 14–17. Axial T1-weighted MRI study with gadolinium shows sarcoid of the anterior left globe.

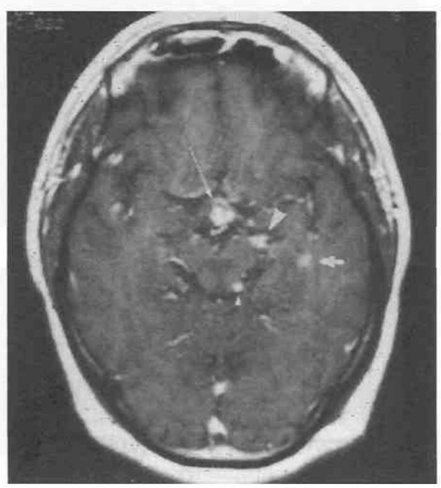

Figure 14–18. Axial T1-weighted MRI study with gadolinium shows sarcoid of the chiasm *(long arrow),* left cerebral peduncle *(large arrowhead),* lateral geniculate body *(short arrow),* and superior colliculus *(small arrowhead).*

Figure 14–19. Coronal MRI study, inversion recovery fast spin echo, shows left optic neuritis with increased signal at the left optic nerve.

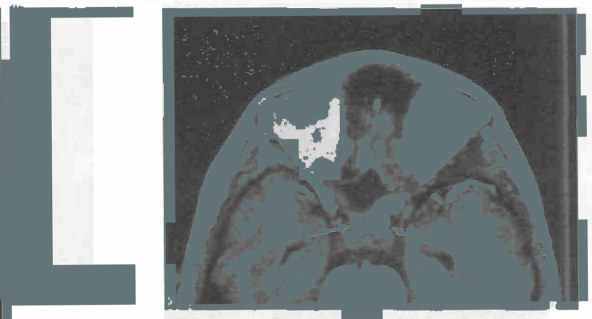

Figure 14–21. Axial T1-weighted MRI study shows optic glioma, bilateral optic nerves, with involvement of the chiasm *(arrows)* in a patient with neurofibromatosis.

lymphoproliferative process is seen. The usual appearance is a well-defined mass within the muscle cone (Fig. 14–20). Less frequently, extraconal masses or diffuse infiltration of the orbital fat can be seen.

The differential diagnosis includes pseudotumor and metastasis. Lacrimal gland involvement can be seen either in isolation or in combination with the other manifestations of lymphoma within the orbit.

Optic Glioma

Primary tumors of the optic nerve or nerve sheath are relatively uncommon. Optic gliomas most often occur in children, especially between the ages of 2 and 6 years, and are usually benign. This lesion usually involves the anterior optic apparatus (e.g., optic nerves, chiasm, and optic tracts) and causes enlargement and often tortuosity of these struc-

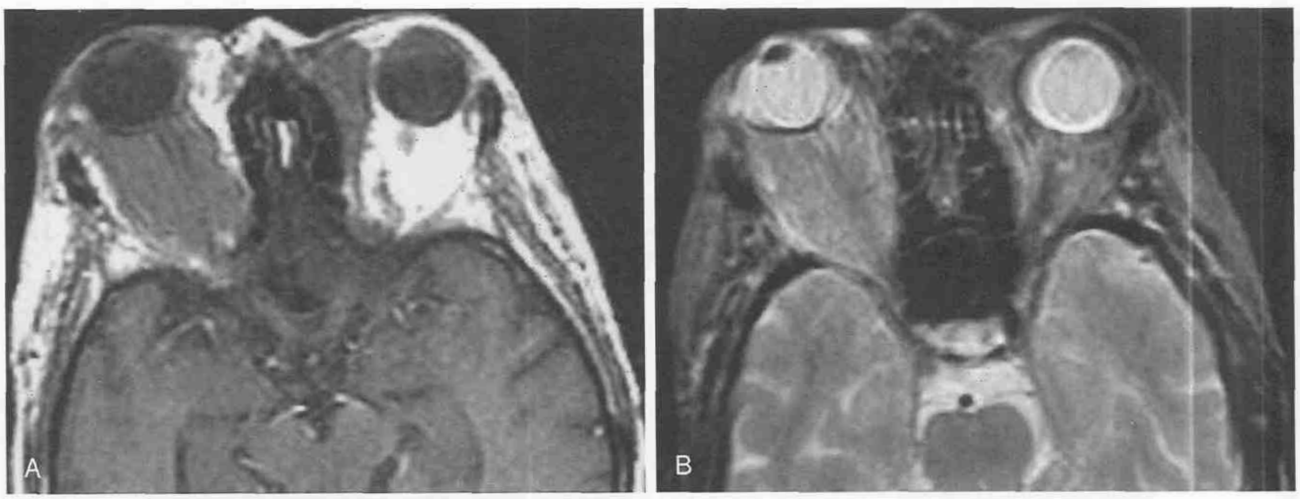

Figure 14–20. *A,* T1-weighted axial MRI study shows a large mass replacing the intraconal fat in the right orbit. *B,* T2-weighted axial image of the same patient. *C,* Gadolinium-enhanced axial T1-weighted image of the same patient demonstrates marked enhancement. Fat suppression allows the smaller lesion to be visible at the apex of the left orbit.

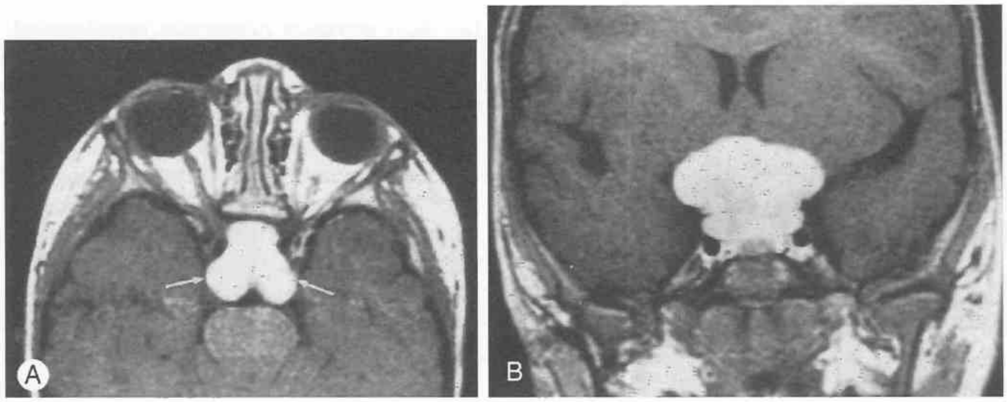

Figure 14–22. *A,* T1-weighted axial MRI study with gadolinium enhancement shows optic glioma of the optic chiasm *(arrows)*. *B,* T1-weighted coronal MRI study with gadolinium shows same patient as in *A*.

tures. The incidence is increased in neurofibromatosis I (Fig. 14–21). These lesions do not calcify.[10]

MRI has become the modality of choice, given the necessity of evaluating the intracranial extent of the tumor (Fig. 14–22*A* and *B*). Optic gliomas are typically either nonenhancing or weakly enhancing. The lesions are generally isointense to slightly hypotense on T1-weighted images and hyperintense on T2-weighted images.[21]

CT can help in assessing bony changes and is especially valuable in detecting expansion of the optic canal. CT thus complements MRI in evaluation of these lesions.

Nerve Sheath Meningioma

The differential diagnosis of optic nerve and sheath lesions also includes meningiomas. Meningiomas tend to occur in middle-aged women rather than in children. These lesions can cause enlargement of the optic nerve sheath (Fig. 14–23*A* and *B*) or the entire complex (Fig. 14–24). Calcification is common, which helps to differentiate meningiomas from gliomas. Extension into the optic canal is rare, and extension to the chiasm is extremely rare.[25]

MRI studies are the best modality for evaluation of these lesions, but CT can be helpful for the same reasons as with gliomas, and can also show calcifications.[39] Because meningiomas tend to grow outward from the nerve sheath, they are less likely to efface the CSF layer between the nerve and sheath. This property sometimes helps to distinguish meningioma from glioma.

Melanoma

Melanoma is a malignant tumor that usually originates in the uveal layers of the globe. It can extend posteriorly to the rest of the orbit. MRI studies have been used to evaluate the intraorbital extent of melanoma and to search for metastatic disease.[57]

On MRI studies, the amount of melanin contained in the lesion determines the signal characteristics. Melanin shortens T1 and T2, thereby causing increased signal on T1-weighted images and decreased signal on T2-weighted images[19] (Fig. 14–25).

Signal is also affected by hemorrhage, which is not uncommon in patients with melanotic lesions. With hemorrhage, the differential diagnosis includes retinal and choroid detachments from other causes (Fig. 14–26). Detachments are usually distinguished clinically and radiographically.[43] Gadolinium enhancement increases the sensitivity in the detection of lesions[6] but does not increase specificity.

As previously stated, melanotic lesions have characteristic appearances, but nonpigmented melanomas cannot be reliably differentiated from other masses.[61] CT can also be used to evaluate these lesions (Fig. 14–27).

Metastatic Disease

The most common tumor to metastasize to the orbit is carcinoma of breast. Other primary sites include lung, colon, and prostate (Fig. 14–28). Metastatic lesions may

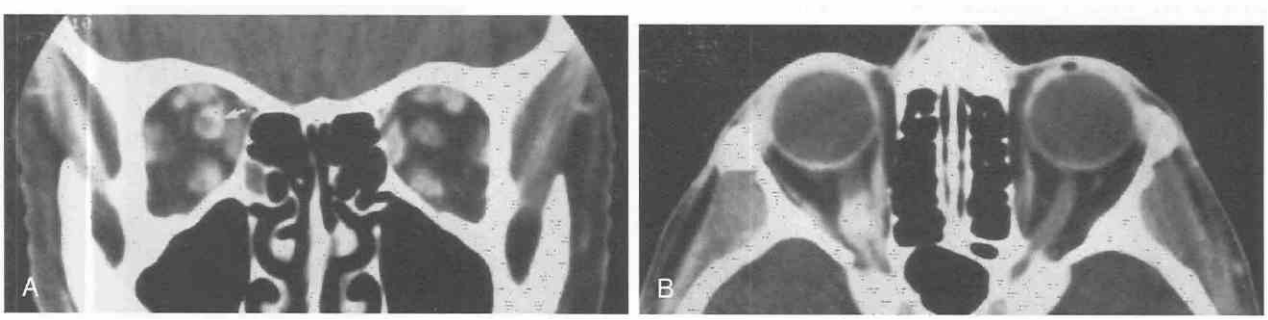

Figure 14–23. *A,* Coronal contrast-enhanced CT scan shows optic nerve sheath meningioma *(arrow)*. *B,* Axial contrast-enhanced CT scan shows same patient as in *A*.

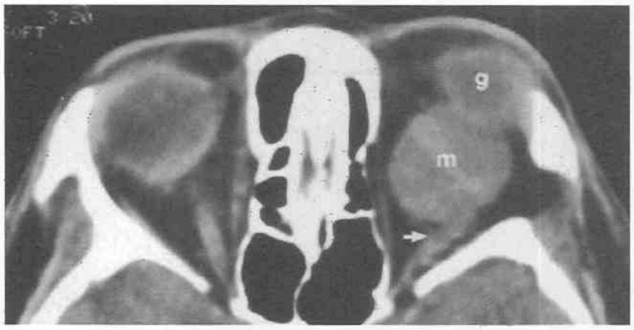

Figure 14–24. Axial contrast-enhanced CT scan shows optic nerve sheath meningioma. m, meningioma; g, globe; arrow, displaced optic nerve sheath complex emerging from mass.

affect any of the intraorbital structures as well as the bony orbit itself[30, 66] (Fig. 14–29). With a known distant primary site, a metastatic lesion should be considered. However, none of the available imaging techniques offers specificity to differentiate metastases from the many other orbital lesions. The findings may be subtle, with small areas of focal thickening of the globe, or large destructive lesions.[24] In addition, extension of tumor from an adjacent structure (e.g., the paranasal sinuses) may occur (Fig. 14–30*A* and *B*).

Cavernous Hemangioma and Lymphangioma

Cavernous hemangioma and lymphangioma are benign lesions that can be difficult to differentiate.[44]

Cavernous Hemangioma

Cavernous hemangiomas are usually discovered in young to middle-aged adults. The lesions tend to be well encapsulated with distinct margins, are usually intraconal,[55] and grow slowly. CT demonstrates a well-marginated soft tissue mass with mild or heterogeneous enhancement. MRI studies also demonstrate a well-defined intraconal lesion with isointense to slightly increased signal, when compared with the extraocular muscles on T1-weighted images. These lesions demonstrate marked signal intensity on T2-weighted images[40] (Fig. 14–31*A* and *B*).

Lymphangioma

Orbital lymphangioma presents at an earlier age, from infancy through the first decade. This lesion tends to occur either in the intraconal or extraconal compartment. Lymphangiomas are usually lobulated, with ill-defined borders, and may contain septations.[26] Multilocular or cystic blood collections are common.

These lesions are commonly hemorrhagic. CT scanning shows lobular heterogeneous masses with varying degrees of contrast enhancement. MRI characteristics include increased signal on T1-weighted images and marked signal intensity on T2-weighted images[20] (Fig. 14–32).

Retinoblastoma

Retinoblastoma is a malignant lesion with prominent tumor calcification. In its familial form, which results from loss of one copy of the Rb tumor suppressor gene,[35] it is the most common intraocular neoplasm of children under 2 years of age. Inheritance is autosomal dominant. Metastasis may occur via direct spread along the optic nerve, hematogenously, or via lymphatics.

CT is the examination of choice because the hallmark finding is retinal calcification, for which MRI is less sensitive[58] (Fig. 14–33). MRI should be used as an additional modality, especially to detect extension into the region of the optic canal as well as to accomplish a more sensitive evaluation of parenchymal disease. Rarely, retinoblastoma may be seen in the pineal gland as well as in the eyes, the so-called "trilateral" retinoblastoma.

Indirect Involvement of the Orbit and Optic Pathways

The orbit or any part of the optic pathways may be affected by adjacent intracranial lesions. The most common lesions arise from the sella turcica and parasellar regions. The differential diagnosis includes pituitary macroadenoma (Fig. 14–34), meningioma, craniopharyngioma, metastasis, aneurysm, chordoma, and other less common entities. The posterior optic apparatus—superior colliculi, lateral geniculate bodies (see Fig. 14–18), optic radiation, and occipital lobes—may be affected by any infiltration or mass lesion (e.g., tumor, infarction, or inflammatory process).

Meningioma

One of the more common locations of an intracranial meningioma is the sphenoid wing. Visual symptoms can

Figure 14–25. Ocular melanoma of the inferior aspect of the globe. *Top,* T1-weighted coronal MRI study. *Bottom,* T2-weighted coronal MRI study.

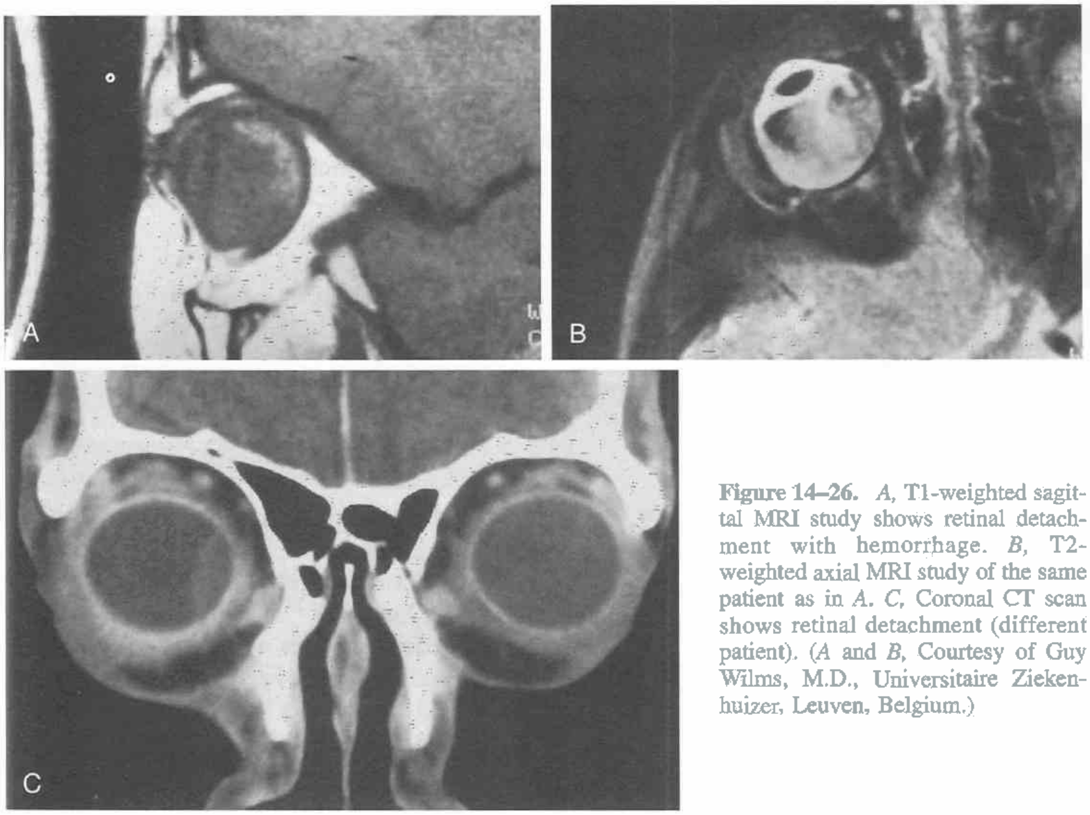

Figure 14–26. *A,* T1-weighted sagittal MRI study shows retinal detachment with hemorrhage. *B,* T2-weighted axial MRI study of the same patient as in *A*. *C,* Coronal CT scan shows retinal detachment (different patient). (*A* and *B*, Courtesy of Guy Wilms, M.D., Universitaire Ziekenhuizer, Leuven, Belgium.)

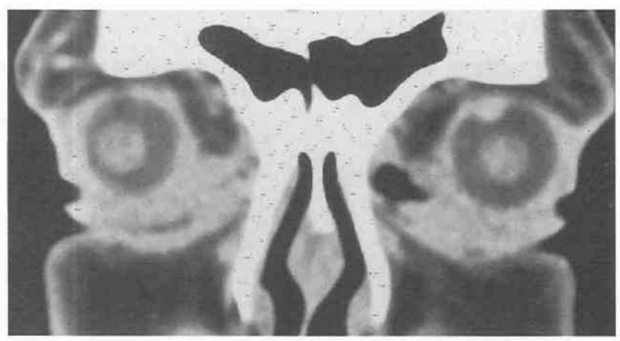

Figure 14–27. Coronal contrast-enhanced CT scan shows melanoma of the left ciliary body.

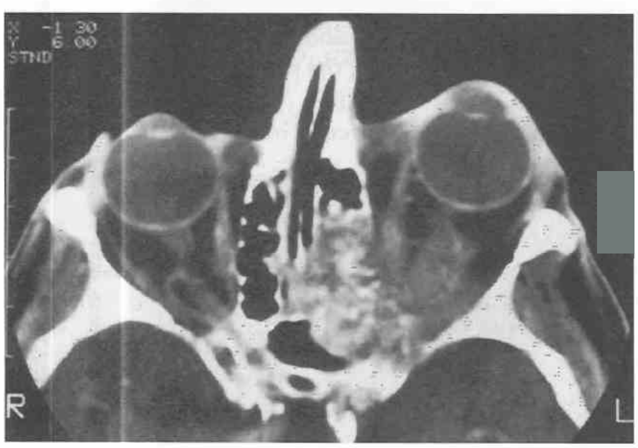

Figure 14–28. Axial contrast-enhanced CT scan shows prostate metastasis to the left orbit roof.

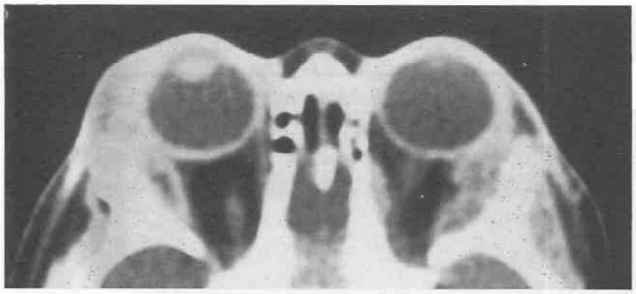

Figure 14–29. Axial contrast-enhanced CT scan shows bilateral neuroblastoma metastasis.

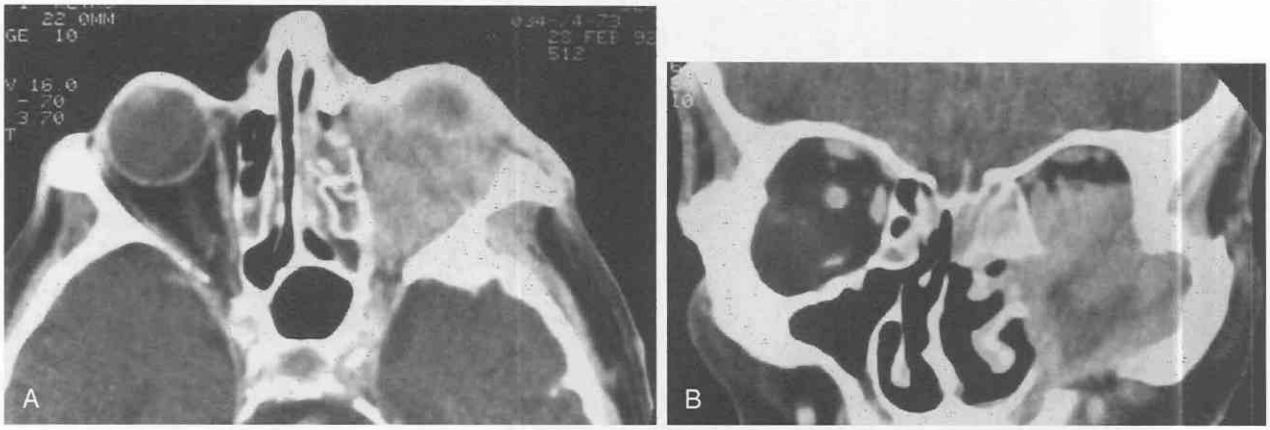

Figure 14–30. *A*, Axial contrast-enhanced CT scans shows extension of squamous cell carcinoma of the maxillary sinus to the orbit. *B*, Coronal contrast-enhanced CT scan shows the same patient as A.

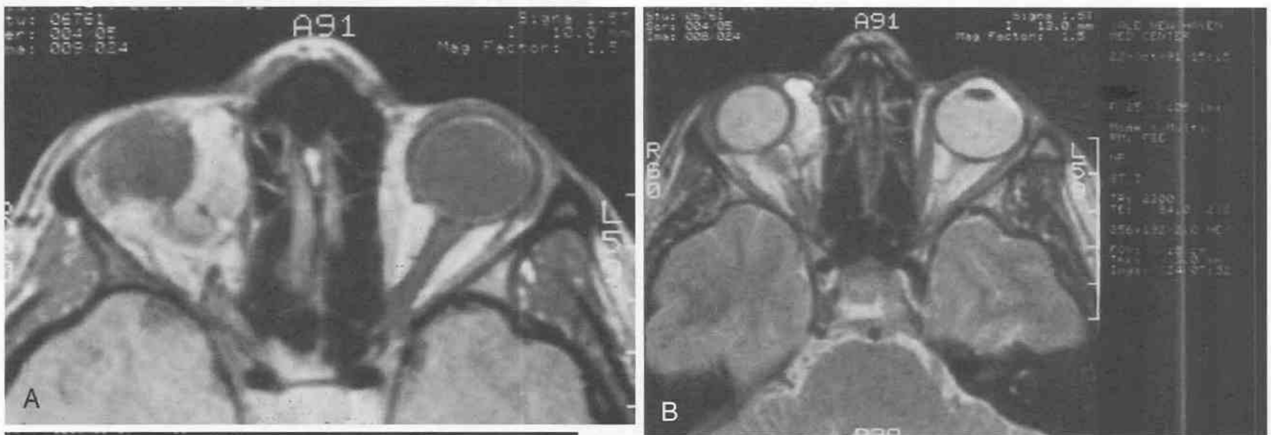

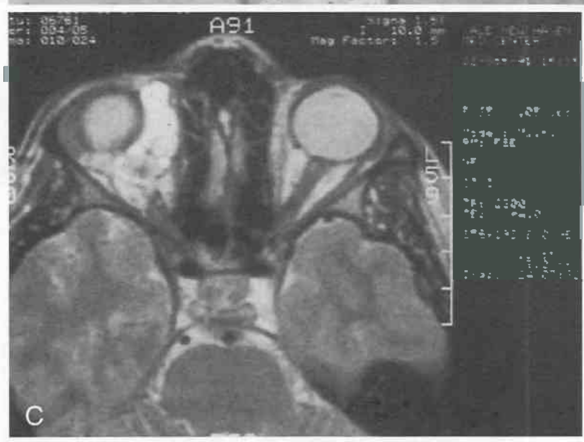

Figure 14–31. *A*, Axial T1-weighted MRI study shows cavernous hemangioma of the medial right orbit. *B*, Axial T2-weighted MRI study shows the same patient as in *A*.

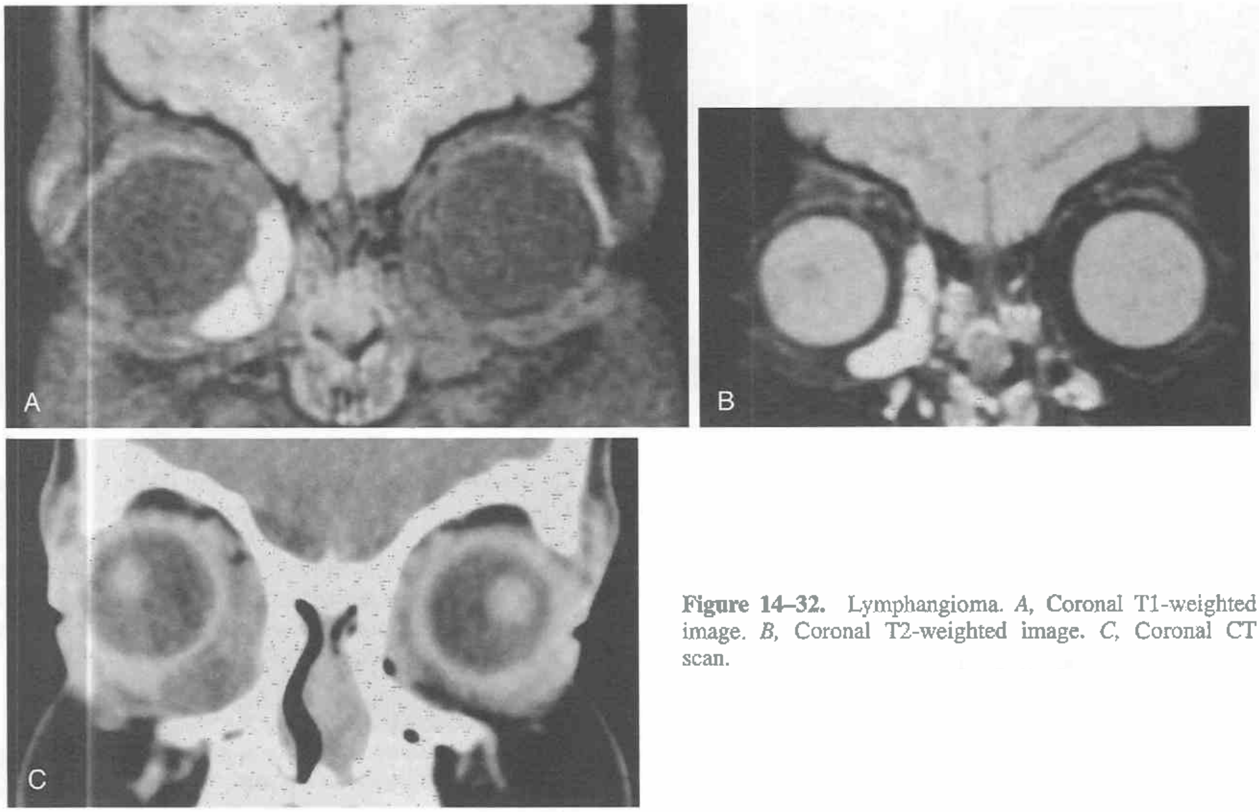

Figure 14–32. Lymphangioma. *A,* Coronal T1-weighted image. *B,* Coronal T2-weighted image. *C,* Coronal CT scan.

result from proximity to the optic canal or by mass effect on the anterior optic apparatus. Direct extension into the orbit is also possible (Fig. 14–35). On MRI studies, meningiomas are generally isointense to brain on T1-weighted and T2-weighted images with uniform, often very intense contrast enhancement.[83] However, signal and enhancement can be affected by the amount of calcification, vascularity, and heterogeneity of the lesion. The lesion can also show a variable amount of associated edema in the adjacent brain parenchyma.

Craniopharyngioma

Craniopharyngiomas are generally tumors of children, with a second peak in the middle-aged population. They most commonly present as a suprasellar mass. These tumors are often well circumscribed and lobulated, often with cystic components. There may be a spectrum in signal characteristics on MRI scans, depending on whether the tumor is cystic or solid and whether the cysts contain high concentrations of cholesterol or hemorrhagic debris. Generally, the lesions are low to isointense on T1-weighted images and hyperintense on T2-weighted images.[33, 59] Gadolinium enhancement of the cyst walls and solid components have been demonstrated[78] (Fig. 14–36).

Craniopharyngiomas commonly calcify. CT and MRI are complementary studies for evaluation of these lesions.

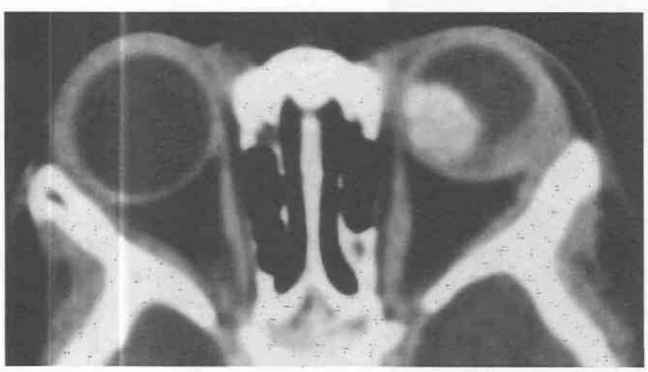

Figure 14–33. Axial contrast-enhanced CT scan shows calcified retinoblastoma of the left eye.

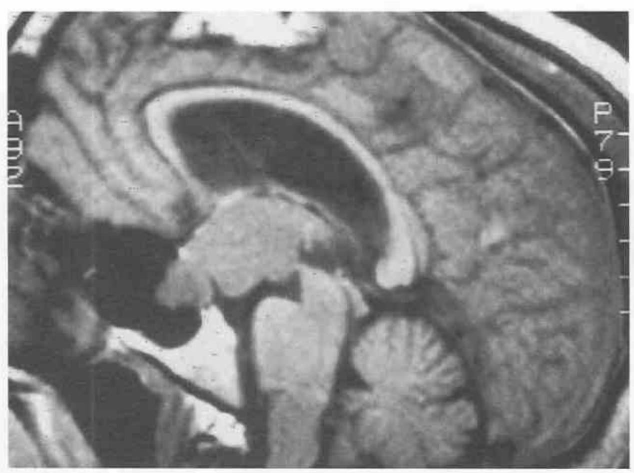

Figure 14–34. T1-weighted sagittal MRI study shows macroadenoma with suprasellar mass extension and superior displacement of the optic chiasm.

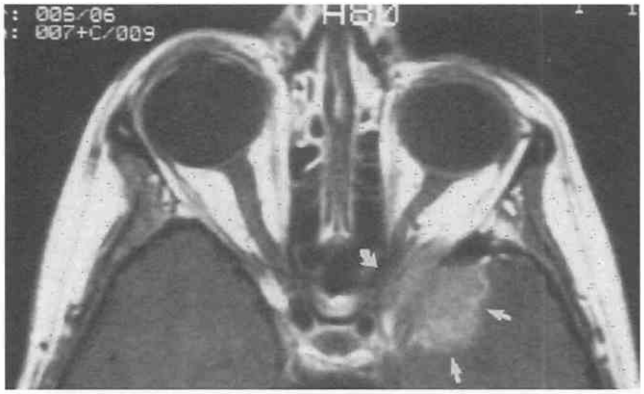

Figure 14–35. Axial T1-weighted MRI study with gadolinium shows left sphenoid wing meningioma *(arrows)*, with compromise of the optic canal *(curved arrow)*.

Lacrimal Gland and Apparatus

The most common lesions affecting the lacrimal gland are benign inflammatory processes, with tumors less common.[41]

Inflammatory, neoplastic, and traumatic processes can affect the lacrimal gland. The patient can present with deviation of the globe, proptosis, or conjunctival injection, depending on the extent of the lesion. With the possible exception of traumatic disruption, glandular enlargement is common to most lesions. Contrast enhancement does not distinguish between inflammation and neoplasia.

In the acute setting, viral adenitis accounts for most of the benign lesions and tends to affect a younger population. Chronic disease is usually secondary to granulomatous disease (e.g., sarcoid or Wegener's) or autoimmune disease (e.g., Sjögren's syndrome). Orbital pseudotumor may affect the lacrimal gland. Unilateral or bilateral glandular enlargement as well as variability of enhancement may be seen. The chronic entities tend to be more well marginated than the acute inflammatory processes.[41]

Tumors of the lacrimal gland may be either benign or malignant.[65] Approximately half of the lacrimal neoplasms are tumors of epithelial origin represented by pleomorphic adenoma (also known as *benign mixed tumor*) and adenoid cystic carcinoma (Fig. 14–37). Mucoepidermoid carcinoma and adenocarcinoma are also seen. Lymphocytic hyperplasia and lymphoma (Fig. 14–38) make up the bulk of additional tumors.[29]

CT scanning may demonstrate bone involvement in several lesions, including adenocarcinoma and mucoepidermoid carcinoma.[29] A study by Hesselink and coworkers[29] also revealed variable enhancement in both inflammatory (Fig. 14–39) and neoplastic lesions. The malignant mucoepidermoid demonstrated marked enhancement, but the adenocarcinoma showed no enhancement.

Calcified Orbital Lesions

There are many causes of orbital calcification, including such previously described entities as retinoblastoma and meningioma.[72]

Optic Drusen

One of the more common calcified lesions is optic drusen, usually seen in adults. The cause is uncertain. Drusen occur at the junction of the nerve with the globe. Drusen are composed of complex hyaline-like collections that frequently calcify.[7] Although these lesions may present with prominence of the optic disk, so-called pseudopapilledema,[63] the actual lesion is invisible funduscopically. CT scanning is used to identify drusen[60, 72] (Fig. 14–40).

Phthisis Bulbi

Phthisis bulbi is the degenerative end-stage of prior injury to the globe from trauma or infection. The globe is small, usually misshapen, and commonly densely calcified.

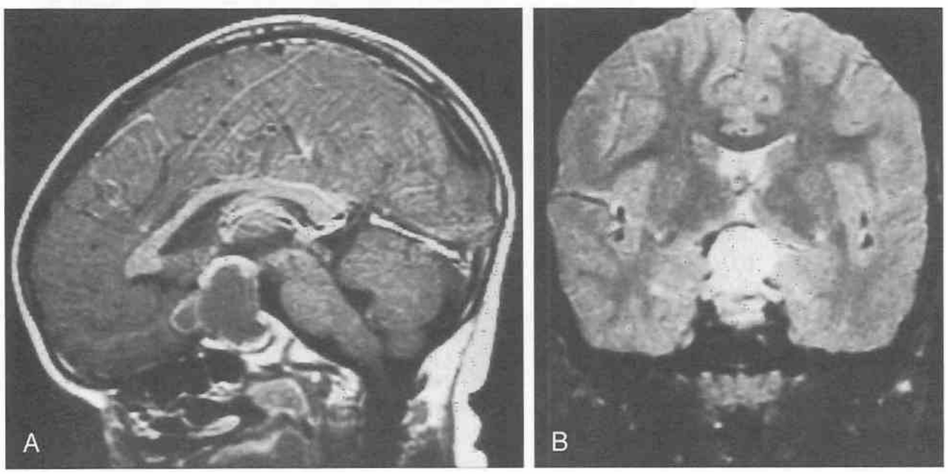

Figure 14–36. *A,* T1-weighted sagittal MRI study with gadolinium shows craniopharyngioma, mostly cystic, with sellar extension, and marked elevation of the chiasm, nerves, and tracts. *B,* Coronal T2-weighted MRI study shows the same patient as in *A.*

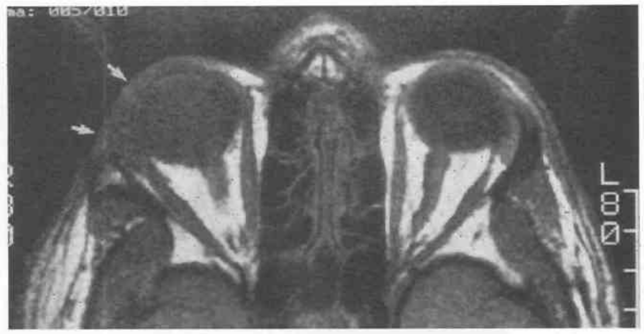

Figure 14–37. T1-weighted axial MRI study shows adenoid cystic carcinoma in the right lacrimal gland with extension to preseptal soft tissues *(arrows)*.

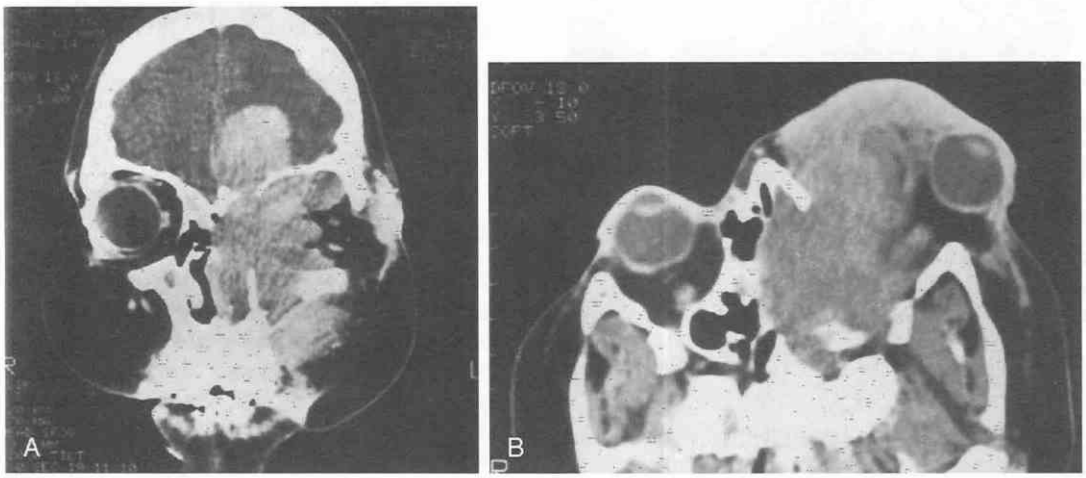

Figure 14–38. *A,* Coronal contrast-enhanced CT scan shows left lymphoma with extension into the sinuses and anterior cranial fossa. *B,* Axial contrast-enhanced CT scan shows the same patient as in *A.*

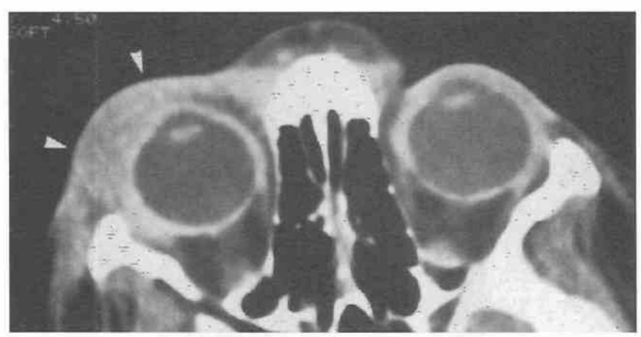

Figure 14–39. Axial contrast-enhanced CT study shows lacrimal gland pseudotumor with extension to preseptal soft tissues on the right *(arrowheads)*.

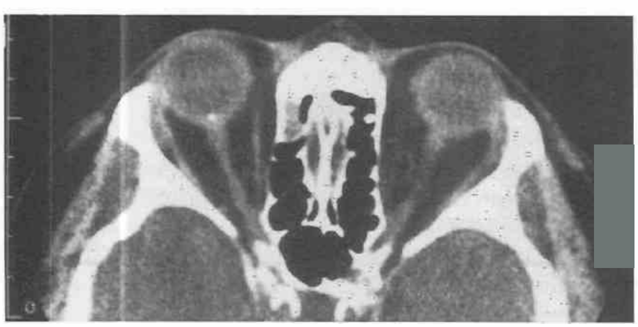

Figure 14–40. Axial CT scan shows optic disk drusen, right optic nerve head calcification, and optic nerve atrophy.

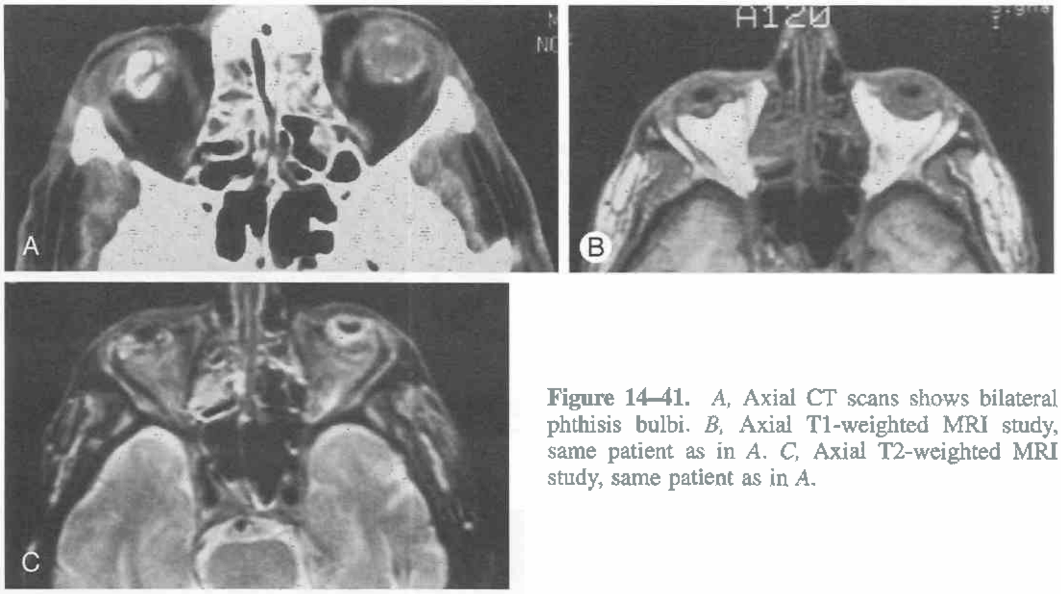

Figure 14–41. *A*, Axial CT scans shows bilateral phthisis bulbi. *B*, Axial T1-weighted MRI study, same patient as in *A*. *C*, Axial T2-weighted MRI study, same patient as in *A*.

This entity can be identified by either CT or MRI, but confirmation of calcification is made with CT (Fig. 14–41). Trochlear calcification has also been seen both with increasing patient age and with diabetes mellitus in younger patients.[27]

Teratoma

The teratoma is a rare benign lesion that contains mixed endodermal, mesodermal, and ectodermal elements. It usually calcifies. Because the teratoma is usually seen in neonates, knowing a patient's age can help one decide whether to include this entity on a differential diagnosis[28, 81] (Fig. 14–42).

Calcified Ciliary Muscle Insertions

Calcification of the insertions of the ciliary muscles of the pupil can be seen in elderly patients, which is often an incidental finding on CT studies of the head performed for reasons other than suspected orbital pathology.

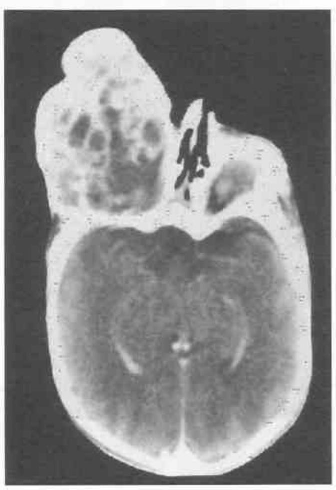

Figure 14–42. Axial contrast-enhanced CT scan shows calcified teratoma with areas of enhancement.

Vascular Lesions

A carotid cavernous fistula is an abnormal high flow communication between the arterial and venous circulations. The most common cause is post-traumatic.[53] Other causes include spontaneous fistulas, possibly related to atherosclerotic disease and rupture of an aneurysm of the intracavernous portion of the carotid artery.[14] Clinical findings include bruit, chemosis, exophthalmos (which can be pulsatile), visual loss, and swelling of the eyelid. Cranial nerve palsies are also seen, which may affect any of the nerves coursing through the cavernous sinus (III, IV, V1, V2, and VI).

Arteriography has been considered the "gold standard" for delineating the vascular anatomy and the site of fistulous communication.[13] However, CT and MRI studies also have adjunctive roles in suggesting the diagnosis and also as follow-up examinations, especially after embolization.[13] Imaging findings include proptosis, asymmetry, and distention of the affected cavernous sinus, and congestion and (usually) asymmetrical dilation of the venous structures that drain the cavernous sinus, especially the superior ophthalmic vein (Fig. 14–43*A* and *B*). Contrast enhancement, to evaluate the vascular structures, and bone windows, to evaluate fracture, are essential.[37]

The orbital varix is a venous malformation that may be represented by a large, tortuous vein or a masslike confluence of small veins, which may markedly enlarge with changes in venous pressure (e.g., Valsalva's maneuver, straining, and exertion). The changes in venous pressure and subsequent venous distention cause a painful intermittent exophthalmos.

In the past, orbital venography was the imaging procedure of choice.[36] However, contrast-enhanced CT scans are currently the ideal diagnostic test. The examination is best performed with a technique for increasing orbital pressure, such as Valsalva's maneuver[77] (Fig. 14–44*A* and *B*) or even with a gentle venous compression on the neck.[64] In addition, color flow Doppler imaging may be useful as a screening examination for a varix.[76]

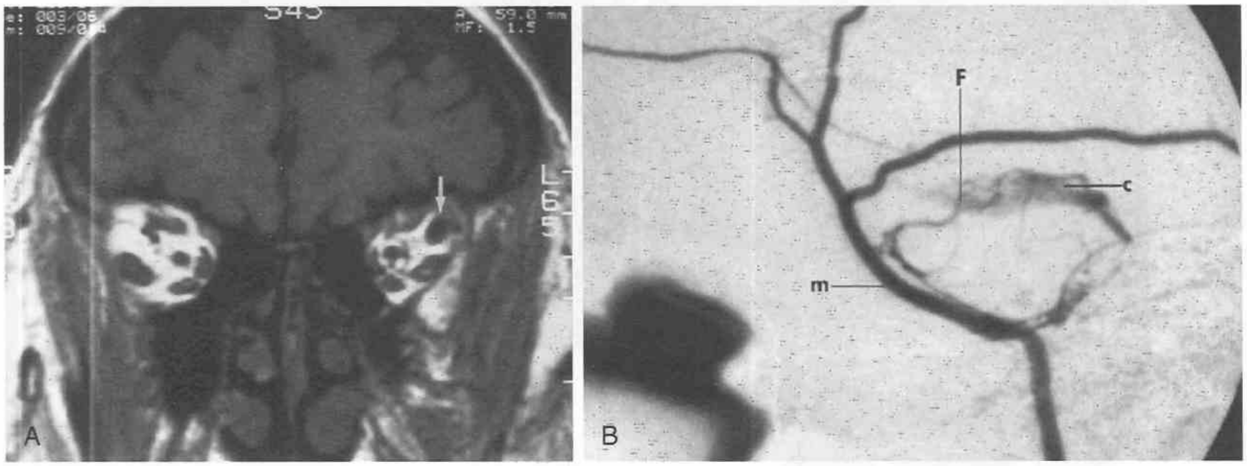

Figure 14–43. Carotid cavernous fistula. *A,* Coronal T1-weighted MRI study shows marked enlargement of the left superior ophthalmic vein *(arrow)*. *B,* Lateral digital subtraction angiogram shows fistulous communication between branches of the external carotid and the cavernous sinus. m, middle meningeal artery; F, fistula; c, cavernous sinus.

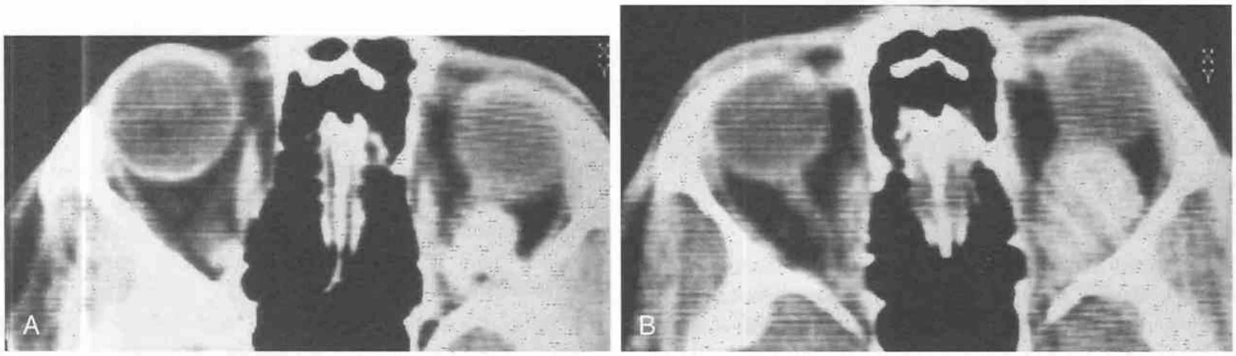

Figure 14–44. Axial contrast-enhanced CT scan. Orbital varix both before *(A)* and during *(B)* Valsalva's maneuver demonstrates the increase in size of the lesion. (Courtesy of Robert E. Peyster, M.D., Hahnemann Hospital, Philadelphia.)

Figure 14–45. Axial CT scan shows left orbit coloboma.

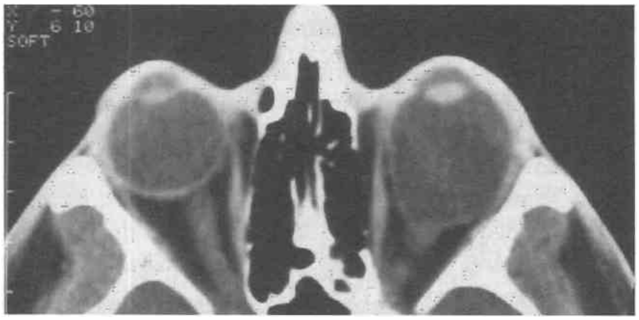

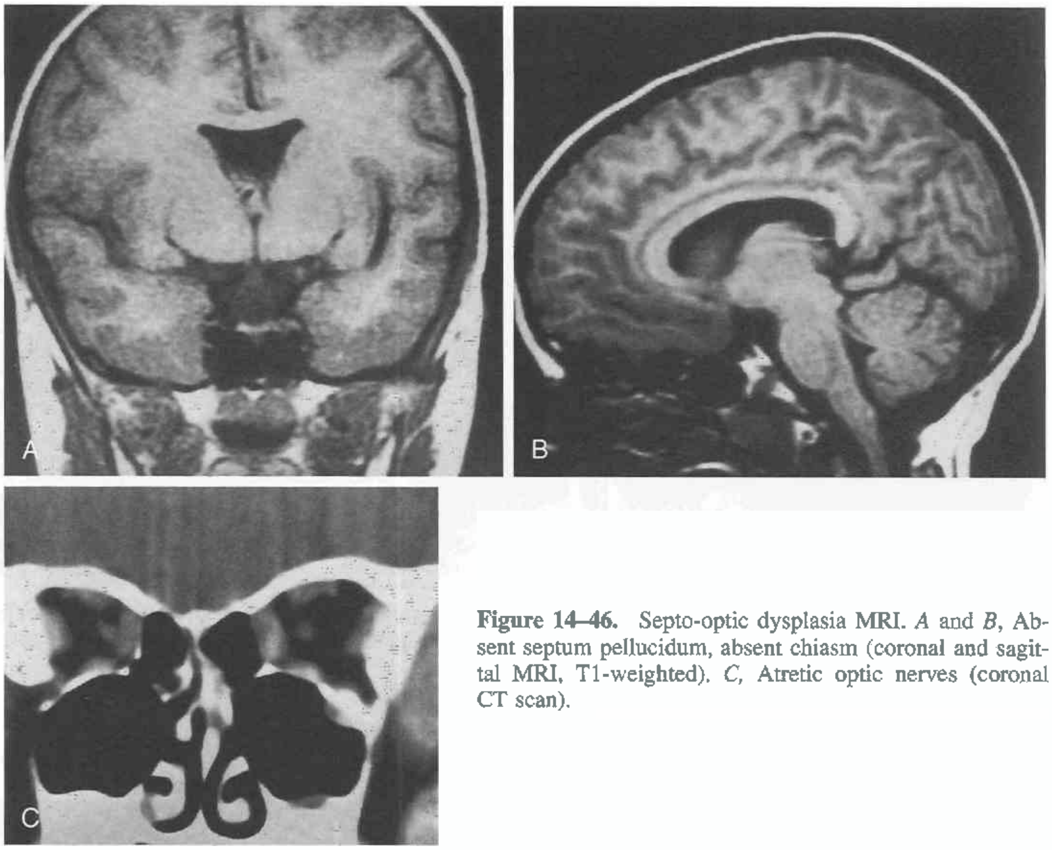

Figure 14–46. Septo-optic dysplasia MRI. *A* and *B*, Absent septum pellucidum, absent chiasm (coronal and sagittal MRI, T1-weighted). *C*, Atretic optic nerves (coronal CT scan).

Congenital Abnormalities and Anomalies

Coloboma

Optic nerve colobomas are congenital defects in the optic nerve usually near the optic disc. These lesions represent a spectrum of developmental abnormalities that result from incomplete or inadequate fusion of the optic fissure during embryogenesis and occur along the inferomedial aspect of the globe and nerve.[45] The defects can be bilateral and can be transmitted as an autosomal dominant trait.[64] They may present as a small cone-shaped defect at the optic disc or as a large retinal cyst. CT scans have been used to delineate the various elements of this lesion,[66] and thin-section axial scans through the region of the optic disc, in particular, are suggested[42] (Fig. 14–45).

Septo-optic Dysplasia

Septo-optic dysplasia is the mildest form of a spectrum of developmental abnormalities that includes holoprosencephaly. These abnormalities result from abnormal ventral induction and mesodermal differentiation. In septo-optic dysplasia, absence of the septum pellucidum and hypoplasia of the optic nerves is sometimes accompanied by pituitary or hypothalamic endocrine dysfunction.[49]

These abnormalities are often accompanied by or associated with other congenital and migrational defects.[8] MRI is therefore the modality of choice in evaluating these lesions,[5] especially because of the multiplanar capabilities and superior visualization of the sellar region, optic nerves and chiasm, and the septum pellucidum. Coronal views are especially important for evaluating the septum[78] (Fig. 14–46). Optic nerve hypoplasia may be present *without* an absent septum.

Summary

Imaging of the orbit by CT and MRI has undergone many recent technologic advances. With attention to technique, the localization and characterization of lesions can be made without difficulty. However, specificity is still an issue with many of the described lesions, and clinical correlation is essential for diagnosis.

References

1. Anzai Y, Lufkin RB, Jabour BA, Hanafee WN: Fat-suppression failure artifacts simulating pathology on frequency-selective fat-suppression MR images of the head and neck. AJNR Am J Neuroradiol 13:879–884, 1992.
2. Babbel RW, Harnsberger HR: A contemporary look at the imaging issues of sinusitis: Sinonasal anatomy physiology and computed tomography techniques. Semin Ultrasound CT MRI 12:526–540, 1991.
3. Balter S: An introduction to the physics of magnetic resonance imaging. Radiographics 7:371, 1987.
4. Barkovitch AJ: Contemporary Neuroimaging: Pediatric Neuroradiology, vol 1. New York, Raven Press, 1990, pp 106–108.
5. Barkovich AJ, Fram EK, Norman D: Septo-optic dysplasia: MR imaging. Radiology 171:189–192, 1989.
6. Bond JB, Haik BG, Mihara F: Magnetic resonance imaging of choroidal melanoma with and without gadolinium contrast enhancement. Ophthalmology 98:459–466, 1991.
7. Boyce SW, Platia EV, Green WR: Drusen of the optic nerve head. Ann Ophthalmol 10:645–704, 1978.
8. Byrd SE, Naidich TP: Common congenital brain anomalies. Radiol Clin North Am 26:755–772, 1988.

9. Coupland SE: T-cell and T/natural killer cell lymphomas involving ocular and ocular adnexal tissues: A clinicopathologic, immunohistochemical, and molecular study of seven cases. Ophthalmology 106: 2109–2120, 1999.
10. Chutorian AM, Schwartz JF, Evans RA, et al: Optic gliomas in children. Neurology 14:83–95, 1964.
11. Collison JMT, Miller NR, Green WR: Involvement of orbital tissues by sarcoid. Am J Ophthalmol 102:302–307, 1986.
12. Curtin HD: Pseudotumor. Radiol Clin North Am 25:583–599, 1987.
13. Debrun G: Management of traumatic carotid-cavernous fistulas. In Viñuela F, Halbach VV, Dion JE, et al (eds): Interventional Neuroradiology: Endovascular Therapy of the Central Nervous System. New York, Raven Press, 1992, pp 107–112.
14. Dohn DF: Carotid aneurysms and arteriovenous fistulae of the cavernous sinus. In Youmans JR (ed): Neurological Surgery, vol 2. Philadelphia, WB Saunders, 1973, pp 870.
15. Flanders AE, Mafee MF, Rao VM, Choi KH: CT characteristics of orbital pseudotumor and other orbital inflammatory processes. J Comput Assist Tomogr 13:40–47, 1989.
16. Fullerton GD: Magnetic resonance imaging signal concepts. Radiographics 7:579–596, 1987.
17. Gibby WA, Cohen MS, Goldberg HI, Sergott RC: Pseudotumor cerebri: CT findings and correlation with vision loss. AJR Am J Roentgenol 160:143–146, 1993.
18. Glassberg R, Abrahams JJ: Optic neuritis evaluation with inversion recovery fast spin echo (IRFSE) work in progress (personal communication). New Haven, Yale Department of Radiology.
19. Gomori JM, Grossman RI, Shields JA, et al: Choroidal melanomas: Correlation of NMR spectroscopy and MR imaging. Radiology 158: 443–445, 1986.
20. Graeb DA. Rootman J, Robertson WD, et al: Orbital lymphangiomas: Clinical, radiologic, and pathologic characteristics. Radiology 175: 417–421, 1990.
21. Haik BG, Saint Louis L, Bierly J, et al: Magnetic resonance imaging in evaluation of optic nerve gliomas. Ophthalmology 94:709–717, 1987.
22. Handler LC, Davey IC, Hill JC, Lauryssen C: The acute orbit: Differentiation of orbital cellulitis from subperiosteal abscess by computed tomography. Neuroradiology 33:15–18, 1991.
23. Harms SE, Siemers PT, Hildebrand P, Plum G: Multiple spin echo magnetic resonance imaging of the brain. Radiographics 6:117–134, 1986.
24. Harnsberger HR: Head and Neck Imaging: Handbooks in Radiology. Chicago, Year Book Medical Publishers, 1990, p 358.
25. Harnsberger HR: Head and Neck Imaging: Handbooks in Radiology. Chicago, Year Book Medical Publishers, 1990, p 363.
26. Harris GJ. Sakol PJ, Bonavolonta G, et al: An analysis of thirty cases of orbital lymphangioma: Pathophysiologic considerations and management recommendations. Ophthalmology 97:1583–1592, 1990.
27. Hart BL, Spar JA, Orrison WW: Calcification of the trochlear apparatus of the orbit: CT appearance and association with diabetes and age. AJR Am J Roentgenol 159:1291–1294, 1992.
28. Henderson JW: Orbital cysts. In Orbital Tumors, 2nd ed. New York, BC Decker, 1980, pp 75–115.
29. Hesselink JR, Davis KR, Dallow RL, et al: Computed tomography of masses in the lacrimal gland region. Radiology 131:143–147, 1979.
30. Hesselink JR, Davis KR, Weber AL, et al: Radiologic evaluation of orbital metastasis, with emphasis on computed tomography. Radiology 137:363–366, 1980.
31. Hilal SK, Trokel SL: Computerized tomography of the orbit using thin sections. Semin Roentgenol 12:137–147, 1977.
32. Ingbag SH, Woebar KA: Diseases of the thyroid. In Petersdorf RG, et al (eds): Harrison's Principles of Internal Medicine, 10th ed. New York, McGraw-Hill, 1983, pp 611–634.
33. Johnson LN, Hepler RS, Yee RD, et al: Magnetic resonance imaging of craniopharyngioma. Am J Ophthalmol 102:242–244, 1986.
34. Koornneef L, Zonneveld F: The role of direct multiplanar high resolution CT in the assessment and management of orbital trauma. Radiol Clin North Am 25:753–766, 1987.
35. Korsmeyer SJ: Genes and neoplasia. In Isselbacher KJ, et al (eds): Harrison's Principles of Internal Medicine, 13th ed. New York, McGraw-Hill, 1994, p 378.
36. Kubin DA, Amundsen P, Newton TH: Orbital venography in the diagnosis of intermittent exophthalmos. Radiology 88:930–934, 1967.
37. Lasjaunias P, Berenstein A: Surgical Neuroradiology: Endovascular Treatment of Craniofacial Lesions, vol 2. New York, Springer-Verlag, 1987, pp 176–211.
38. Lee DH, Simon JH, Szumowski J, et al: Optic neuritis and orbital lesions: Lipid-suppressed chemical shift MR imaging. Radiology 179: 543, 1991.
39. Lindblow B, Truwit C, Hoyt WF: Optic nerve sheath meningioma: Definition of intraorbital, intracanalicular, and intracranial components with magnetic resonance imaging. Ophthalmology 99:560–566, 1992.
40. Mafee MF: The orbit proper. In Som PM, Bergeron TA (eds): Head and Neck Imaging, 2nd ed. St. Louis, Mosby–Year Book, 1991, pp 800–801.
41. Mafee MF: The orbit proper. In Som PM, Bergeron TA (eds): Head and Neck Imaging, 2nd ed. St. Louis, Mosby–Year Book, 1991, pp 805–810.
42. Mafee MF, Jampol LM, Langer BG, et al: Computed tomography of optic nerve colobomas, morning glory anomaly, and colobomatous cyst. Radiol Clin North Am 25:693–699, 1987.
43. Mafee MF, Peyman GA: Retinal and choroidal detachments: Role of magnetic resonance imaging and computed tomography. Radiol Clin North Am 25:487–507, 1987.
44. Mafee MF, Putterman A, Valvassori GE, et al: Orbital space occupying lesions: Role of computed tomography and magnetic resonance imaging. An analysis of 145 cases. Radiol Clin North Am 25:529–559, 1987.
45. Mann I: Developmental Abnormalities of the Eye, 2nd ed. Philadelphia, JB Lippincott, 1957, pp 68–94.
46. McNichols MMJ, Power WJ, Griffen JF: Idiopathic inflammatory pseudotumor of the orbit: CT features correlated with clinical outcome. Clin Radiol 44:3–7, 1991.
47. Merandi SF, Kudryk BT, Murtagh FR, et al: Contrast-enhanced MR imaging of optic nerve lesions in patients with acute optic neuritis. AJNR Am J Neuroradiol 12:923–926, 1991.
48. Merritt CRB: Magnetic resonance imaging: A clinical perspective—image quality, safety and risk management. Radiographics 7:1001–1016, 1987.
49. Morishima A, Aronoff GS: Syndrome of septo-optic-pituitary dysplasia: The clinical spectrum. Brain Dev 8:233–239, 1986.
50. Motton-Lippa L, Jakobiec FA, Smith M: Idiopathic inflammatory orbital pseudotumor in childhood: II. Results of diagnostic tests and biopsies. Ophthalmology 88:565–574, 1981.
51. Munk PL, Vellet AD, Levin M, et al: Sonography of the eye. AJR Am J Roentgenol 157:1079–1086, 1991.
52. Naheedy MH, Haaga JR, Azar-Kia B, et al: MRI and CT of sellar and parasellar disorders. Radiol Clin North Am 25:819–847, 1987.
53. Newton TH, Troost BT: Arteriovenous malformations and fistulae radiology of the skull and brain: Angiography. In Newton TH, Potts DG (eds): Radiology of the Skull and Brain, vol 2. St. Louis, CV Mosby, 1971, pp 2420–2565.
54. Nugent RA, Belkin RI, Meigel JM, et al: Graves orbitopathy: Correlation of CT and clinical findings. Radiology 177:675–682, 1990.
55. Orcutt JC, Wulc AE, Mills RP, et al: Asymptomatic orbital cavernous hemangiomas. Ophthalmology 98:1257–1260, 1991.
56. Pavlicek W: MR instrumentation and image formation. Radiographics 7:809–814, 1987.
57. Peyman GA, Mafee MF: Uveal melanoma and similar lesions: The role of magnetic resonance imaging and computed tomography. Radiol Clin North Am 25:471–486, 1987.
58. Price HI, et al: The neuroradiology of retinoblastoma. Radiographics 2:7–23, 1982.
59. Pusey E, Kortman KE, Flannigan BD, et al: MR of craniopharyngiomas: Tumor delineation and characterization. AJR Am J Roentgenol 149:383–388, 1987.
60. Ramirez H, Blatt ES, Hibri HS: Computed tomography identification of calcified optic nerve drusen. Radiology 148:137–139, 1983.
61. Raymond WR, Char DH, Norman D, et al: Magnetic resonance imaging evaluation of uveal tumors. Am J Ophthalmol 111:633–641, 1991.
62. Roberts CF, Leehey PJ III: Intraorbital wood foreign body mimicking air at CT. Radiology 185:507–508, 1992.
63. Rosenberg MA, Savino PJ, Glaser JS: A clinical analysis of pseudopapilledema: I. Population, laterality, acuity, refractive error, ophthalmoscopic characteristics and coincident disease. Arch Ophthalmol 97: 65–70, 1979.
64. Savell J, Cook JR: Optic nerve colobomas of autosomal dominant heredity. Arch Ophthalmol 94:395–400, 1976.

65. Shnier R, Parker GD, Hallinan JM, et al: Orbital varices: A new technique for noninvasive diagnosis. AJNR Am J Neuroradiol 12: 717–718, 1991.
66. Shields JA, Bakewell B, Augsburger JJ, et al: Classification and incidence of space-occupying lesions of the orbit: A survey of 645 biopsies. Arch Ophthalmol 102:1606–1611, 1984.
67. Simmons JS, Lamasters D, Char D: Computed tomography of ocular colobomas. Am J Roentgenol 141:1223–1226, 1983.
68. Som P: Sinonasal cavity. In Som PM, Bergeron TA (eds): Head and Neck Imaging, 2nd ed. St. Louis, Mosby–Year Book, 1991, pp 150–159.
69. Spencer WM: Ophthalmologic Pathology: An Atlas and Textbook, vol 3. Philadelphia, WB Saunders, 1986, pp 2391–2409.
70. Sullivan JA, Harms SE: Characterization of orbital lesions by surface coil MR imaging. Radiographics 7:9–28, 1987.
71. Tien RD: Fat suppression MR imaging in neuroradiology: Techniques and clinical application. AJR Am J Roentgenol 158:369–379, 1992.
72. Turner RM, Gutman I, Hilal SK, et al: CT of drusen bodies and other calcified lesions of the optic nerve: Case report and differential diagnosis. Am J Neuroradiol 4:175–178, 1983.
73. Unger JM: Fractures of the nasolacrimal fossa and canal: A CT study of appearance, associated injuries, and significance in 25 patients. AJR Am J Roentgenol 158:1321–1324, 1992.
74. Valvassori GE: Imaging of orbital lymphoproliferative disorders. Radiol Clin North Am 37:135–50, 1999.
75. Wehrli FW, MacFall JR, Newton TH: The parameters determining the appearance of NMR images. In Newton TH, Potts DG (eds): Advanced Imaging Techniques. San Anselmo, Calif, Clavadel, 1984.
76. Wildenhain PM, Lehar SC, Dastur KJ, et al: Orbital varix: Color flow imaging correlated with CT and MR studies. J Comput Assist Tomogr 12:171–173, 1991.
77. Winter J, Centeno RS, Bentson JR: Maneuver to aid diagnosis of orbital varix by computed tomography. Am J Neuroradiol 3:39–40, 1982.
78. Wolpert SM, Barnes PD: MRI in Pediatric Neuroradiology. St. Louis, Mosby–Year Book, 1992, p 101.
79. Wolstencroft, SJ: Orbital metastasis due to interval lobular carcinoma of the breast: A potential mimic of lymphoma. Arch Ophthalmol 117: 14, 19–21, 1999.
80. Yeoman LJ, Howarth L, Britten A, et al: Gantry angulation in brain CT: Dosage implications, effect on posterior fossa artifacts, and current international practice. Radiology 184:113–116, 1992.
81. Youssef B: J Pediatr Ophthalmol 6:177–81, 1969.
82. Zimmerman RA: Imaging of intrasella, suprasella and parasella tumors. Semin Roentgenol 25:174–197, 1990.
83. Zimmerman RD, Fleming CA, Saint Louis LA, et al: Magnetic resonance imaging of meningiomas. AJNR Am J Neuroradiol 6: 149–157, 1985.
84. Zonneveld FW: Normal direct multiplanar CT anatomy of the orbit with correlative anatomic cryosections. Radiol Clin North Am 25: 381–407, 1987.

15 Temporal Bone

Donald W. Chakeres, Mark A. Augustyn

Many imaging modalities are available for the evaluation of the temporal bone, including plain radiographs, angiography, cerebrospinal fluid (CSF) analysis, air and non-ionic contrast cisternography, computed tomography (CT), and magnetic resonance imaging (MRI). CT and MRI are currently the most widely used techniques and have largely replaced the other modalities.[2, 3, 5, 8–10, 12, 14, 31, 57, 67] Plain films remain an inexpensive survey of large bony and air-filled structures although they often result in inaccurate diagnosis.

CT scanning excels in the evaluation of bone and air space anatomy and disorders. Because CT scans are more accurate in identifying many soft tissue abnormalities and are much less prone to artifacts,[16] they have largely replaced polytomography; there is also less radiation to the lens of the globe with CT scans than with polytomography.[14] With advances in MR technology, MRI has surpassed CT in certain areas of spatial and contrast resolution.[7]

MRI has expanded the range of pathology that can be accurately evaluated because it can image many soft tissue entities not visible by other techniques. MRI studies can also be extremely useful in the evaluation of blood vessel–related disorders of the temporal bone and is much better than CT in characterizing the CSF, brain, and cranial nerves.

Angiography is still the "gold standard" for vascular evaluation, and interventional angiography can be used in treatment of vascular lesions of the temporal bone. Each technique has its own advantages and disadvantages, and often more than one examination is necessary for a complete temporal bone evaluation.[39]

Normal Temporal Bone

Embryology and Development

The development of the *inner ear* structures (vestibule, semicircular canals, internal auditory canal [IAC], cochlea) is independent of the *middle ear* (ossicles, mastoid antrum, tympanic membrane, middle ear air spaces) and *external ear* (external auditory canal [EAC], temporomandibular joint) structures. This explains why developmental abnormalities of the inner ear are usually not seen with deformities of the external ear and middle ear, and vice versa.[23] The mechanical sound-conducting structures of the external ear and middle ear develop from the first and second branchial arches. The neural sound-perceiving apparatus of the inner ear develops from the ectodermal otocyst. Adjacent mesenchyme contributes to the development of the inner ear, middle ear, and external ear.

The first and second branchial arches mold two significant cartilaginous structures. The first arch forms Meckel's cartilage, from which the head of the malleus and short process of the incus develop. The second arch forms Reichert's cartilage, from which the remainder of the malleus and incus, styloid process, and stapes superstructure develop.[55] The stapes footplate is a bilaminar structure, with an outer portion developing from Reichert's cartilage and an inner portion developing from the ectodermal otocyst.

The middle ear cavity and mastoid antrum are fluid-filled until birth. The neonate's initial crying and breathing fill the eustachian tube system and the middle ear with air. The mastoid air cells develop as saclike extensions from the mastoid antrum, commencing at about the time of birth and continuing for several years. There is extensive variation in the degree of pneumatization. Incomplete pneumatization of the mastoid air cells may be caused by a lack of proper function of the eustachian tube during early life.[47]

Normal Anatomy (Figs. 15–1 to 15–15)

External Auditory Canal

The external auditory canal consists of a funnel-shaped, undulating, cartilaginous lateral portion and an osseous medial segment (see Figs. 15–3, 15–9, and 15–10).[11] The cartilaginous portion is continuous with the pinna. These structures are flexible and are surrounded by fat. The osseous portion constitutes two thirds of the length of the external auditory canal and is covered by skin and periosteum only.

Tympanic Cavity

The tympanic cavity is the air space between the eustachian canal and the mastoid air cells (see Figs. 15–7 and 15–8) that contains the ossicles. The *hypotympanum* is the most inferior portion of the tympanic cavity and connects anteromedially to the osseous orifice of the eustachian canal. The semicanal for the tensor tympani muscle parallels the eustachian canal. The protympanum forms the anterior triangular portion of the tympanic cavity adjacent to the carotid canal.

The *mesotympanum*, the central portion of the tympanic cavity, is bordered laterally by the scutum (or spur) and tympanic membrane and medially by the otic capsule. The scutum is a bony crest separating the external auditory canal from the epitympanic space. The tympanic membrane attaches to the scutum superiorly and to the limbus inferiorly.[22]

The *post-tympanum*, the posterior portion of the cavity, contains the facial recess laterally and the sinus tympani

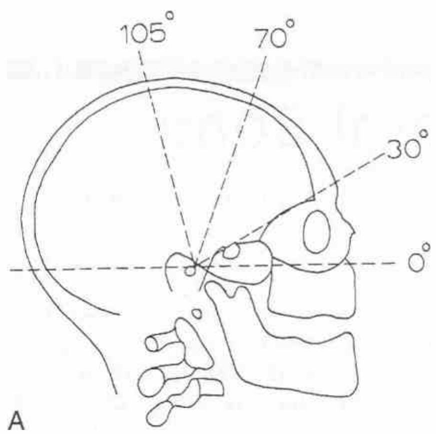

A

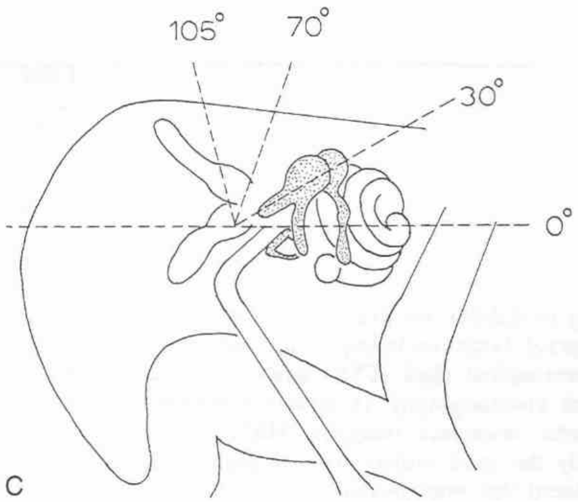

C

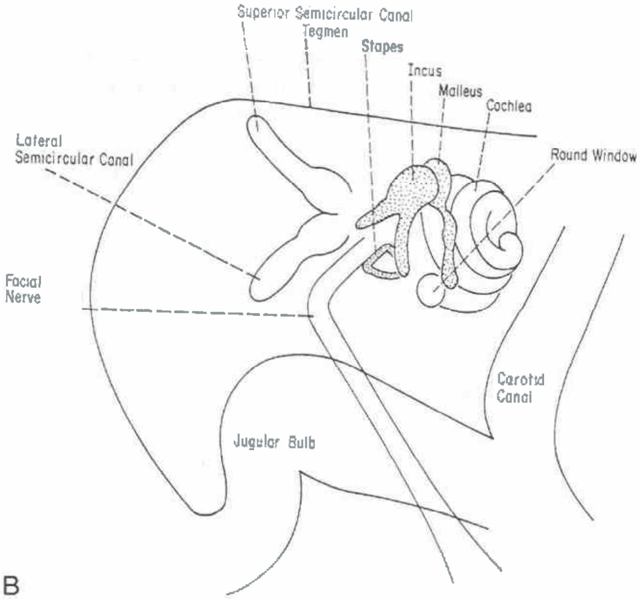

B

Figure 15–1. Temporal bone, diagram of normal anatomy.

A, Diagram simulating a lateral CT scout view of the skull. The 0-degree plane represents the anthropological baseline (through the external auditory canal and inferior orbital rim). The recommended CT planes (30 and 105 degrees) are illustrated. The internal temporal bone structures are consistently oriented to these external landmarks.

B, Schematic of the lateral view of the temporal bone that depicts the normal relationship of several major temporal bone structures.

C, Spatial relationship of the normal temporal bone structures to the anthropologic baseline. The four recommended tomographic planes (0, 30, 70, and 105 degrees) correspond to the scan planes through the temporal bone based on the scout positioning.

(*A–C*, From Chakeres DW, Spiegel RK: A systematic technique for comprehensive evaluation of the temporal bone by computed tomography. Radiology 146:97, 1983.)

medially. The triangular epitympanum forms the superior portion of the middle ear and contains the massive portions of the malleus (head) and the incus (body and short process). The epitympanic space is linked to the mastoid antrum by a narrow hourglass-shaped isthmus called the aditus ad antrum.

Mastoid Antrum

The cone-shaped antrum is interposed between the aditus ad antrum and the mastoid air cells (see Fig. 15–6). The size of the antrum varies considerably as a result of the alterations in pneumatization of the air cells that drain into it.

Ossicles

The ossicles are suspended by the tympanic membrane, the ligaments to the epitympanic walls, and the oval window (see Figs. 15–5, 15–7, and 15–13). The long process of the malleus attaches to the tympanic membrane. The neck of the malleus is connected to the tensor tympani ligament. The circular head of the malleus articulates with the triangular body of the incus. The short process of the incus is suspended within the epitympanic space, pointing toward the aditus ad antrum. The long process of the incus articulates with the stapes.

The stapes consists of two crura and one footplate. The footplate of the stapes attaches to the oval window of the vestibule and is secured by the annular ligament.[24]

Internal Auditory Canal

The internal auditory canal is a bony conduit that transmits cranial nerves VII (facial) and VIII (vestibulocochlear) from the pontomedullary junction of the brain stem to the inner ear (see Figs. 15–5 and 15–8). Its medial orifice is the porus acusticus. The internal auditory canal is partially divided by a central anterior bony lamina called the *falciform crest* (Fig. 15–15*A*), which runs parallel to the long axis of the canal. The falciform crest divides the canal into a smaller superior portion containing the superior vestibular and facial nerves and a larger inferior portion containing

Text continued on page 506

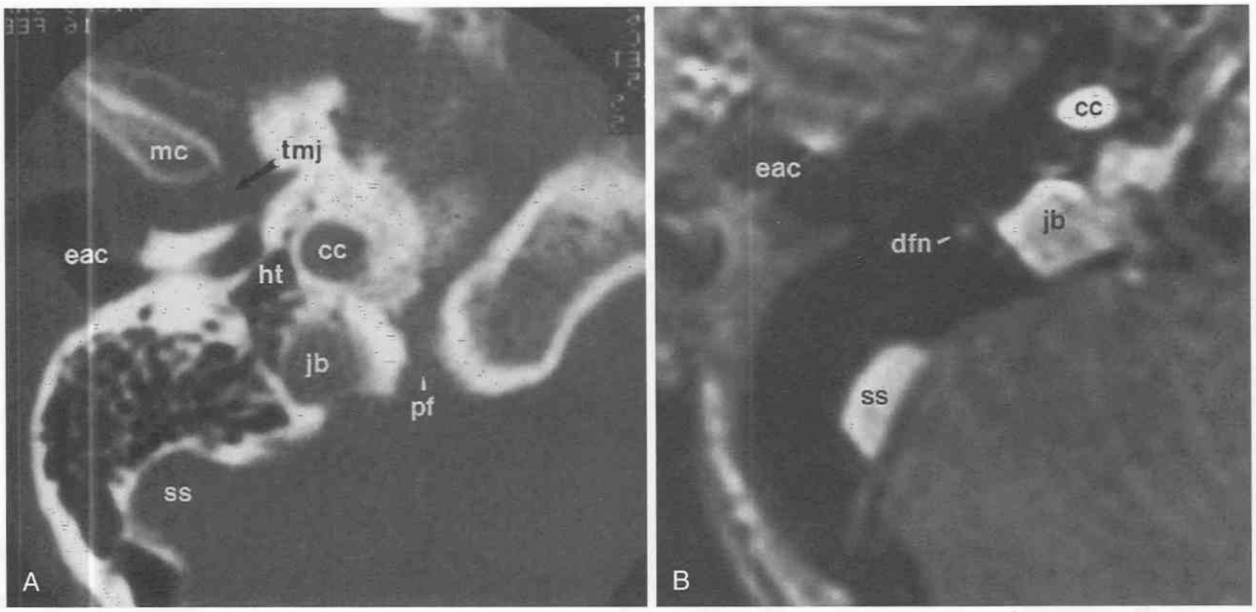

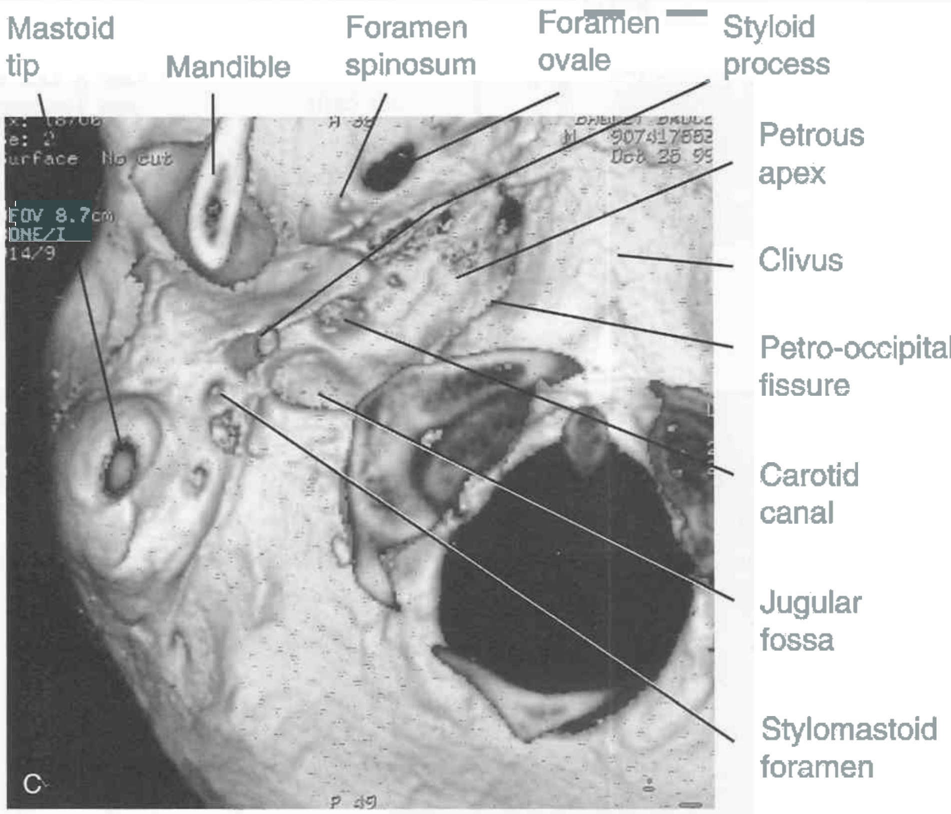

Figure 15–2. Hypotympanic jugular foramen level.

A, Axial CT section acquired through the right temporal bone.

B, High-resolution time-of-flight MRI study at a similar level where the vessels demonstrate a high signal intensity. cc, vertical carotid canal; dfn, descending facial nerve; eac, external auditory canal; ht, hypotympanum; jb, jugular bulb; mc, mandibular condyle; pf, petro-occipital fissure; ss, sigmoid sinus; tmj, temporomandibular joint.

C, Surface CT reconstruction, inferior view of temporal bone. This surface reconstruction of the inferior skull base has been processed from axial CT images. The openings for the carotid canal, jugular fossa, foramen ovale, foramen spinosum, and the stylomastoid foramen are all visible. The mandible, mastoid tip, cut end of the styloid process, external auditory canal, petrous apex, clivus, petro-occipital fissure, and stylomastoid foramen are shown.

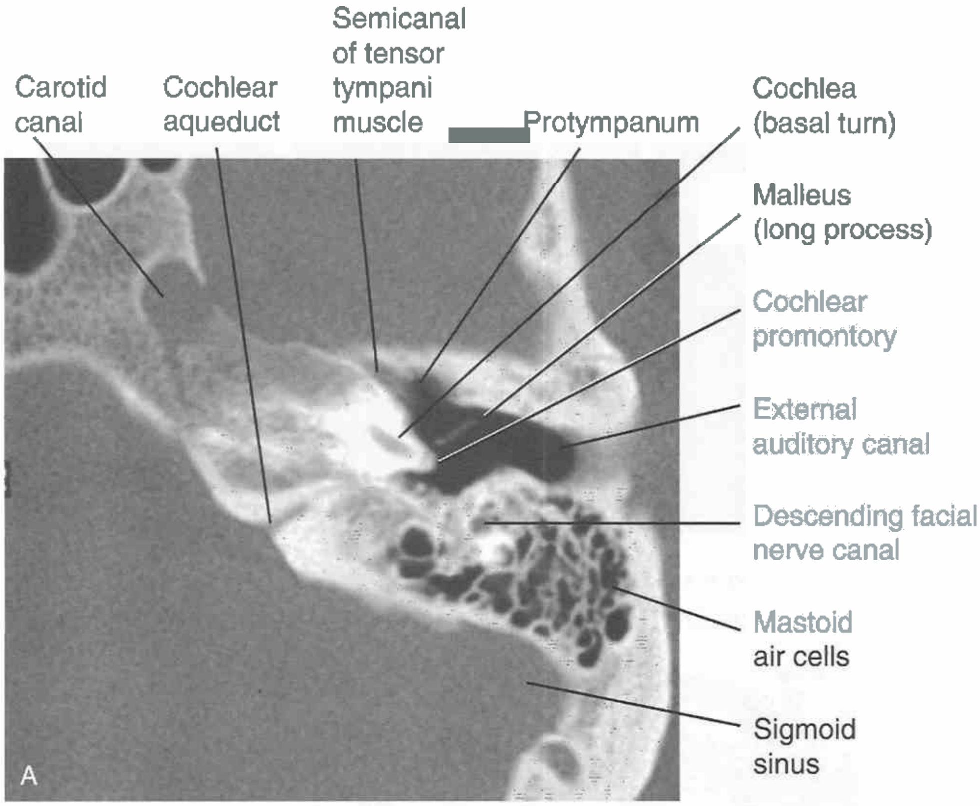

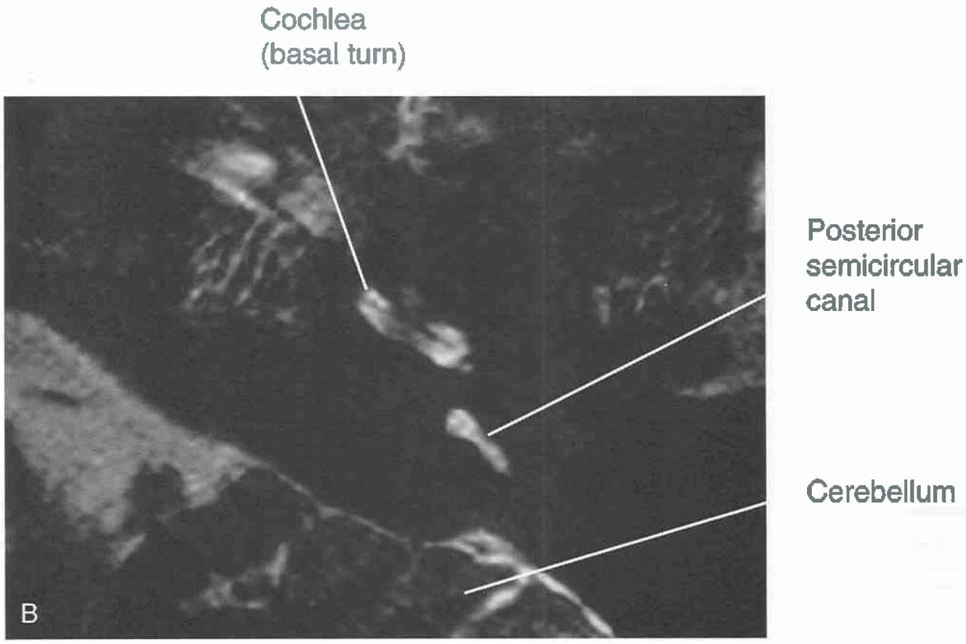

Figure 15–3. Axial views, normal anatomy.

A, Axial CT section. This is the most inferior CT axial section of the temporal bone. The external auditory canal and the long process of the malleus are seen. The tympanic membrane is too thin to be visible. The cochlear promontory and basal turn of the cochlea are visible. The thin, linear semicanal of the tensor tympani muscle is seen interposed between the protympanum and the carotid canal. The cochlear duct is seen arching from the posterior fossa toward the basal turn of the cochlea. The descending facial nerve canal, sigmoid sinus, and the mastoid air cells are shown.

B, Axial MRI section.

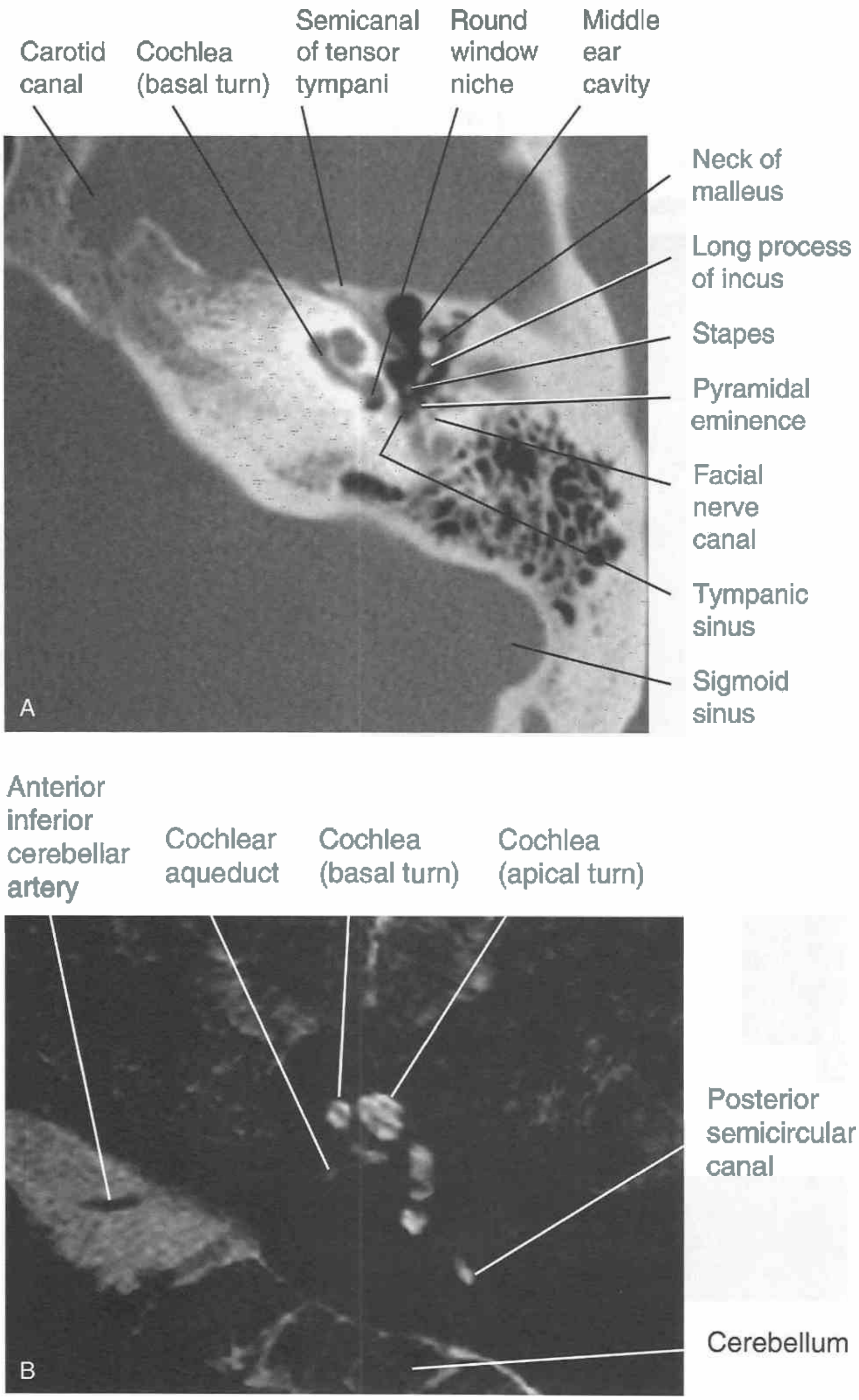

Figure 15–4. Axial views, normal anatomy.

A, Axial CT scan of the left temporal bone centered at the neck of the malleus in the epitympanic space. The adjacent long process of the malleus and the stapes are both visible posteriorly. The semicanal of the tensor tympani muscle is seen as a linear lucency just lateral to the cochlea. The ligaments are not visible. The three turns of the cochlea are all visible as well as the air space related to the round window niche. The descending facial nerve canal is seen posterior to the tympanic sinus and anterior to the mastoid air cells. Other labeled structures include the petrous apex, carotid canal, and the sigmoid sinus.

B, Axial MR image.

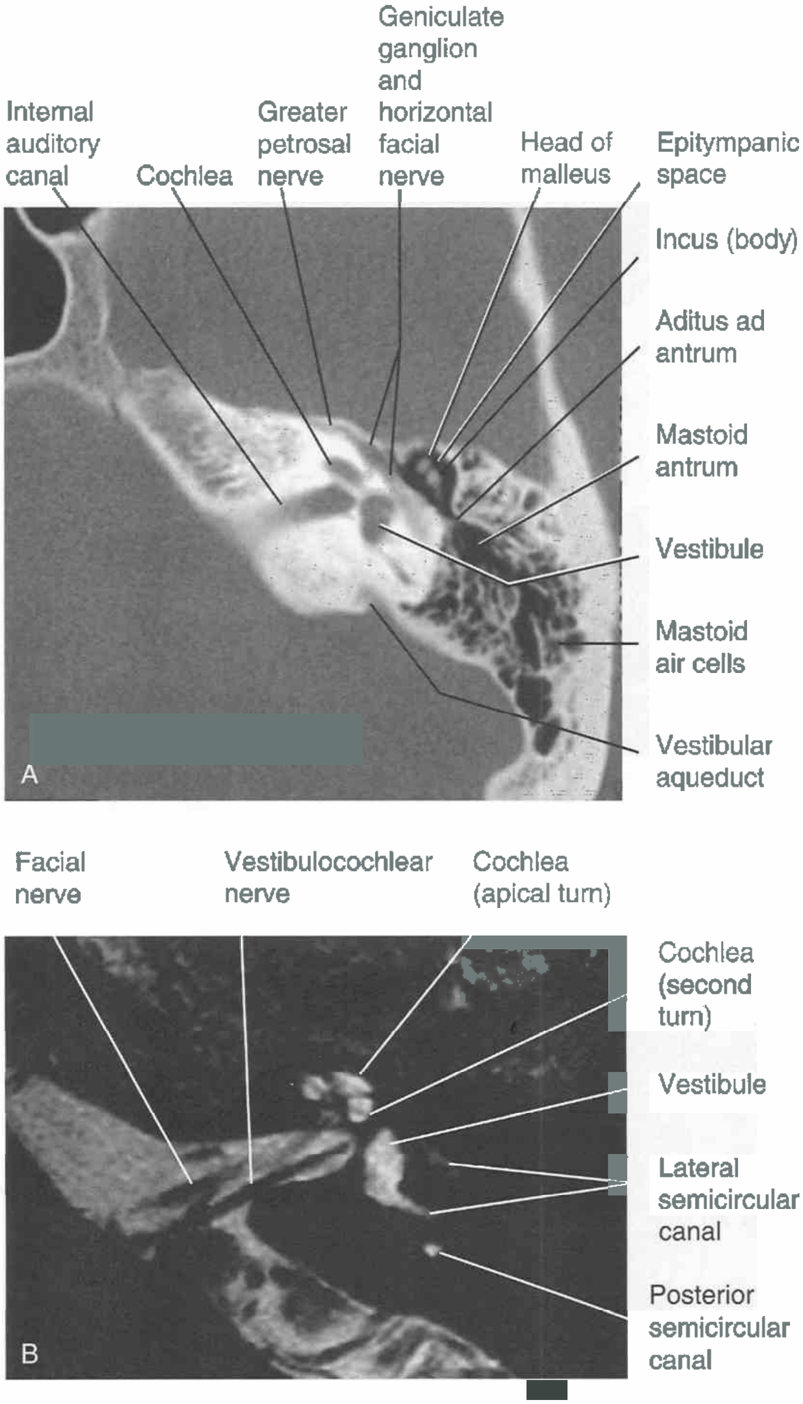

Figure 15–5. Axial views, normal anatomy.

A, Axial CT image centered over a long segment of the facial nerve canal. The geniculate ganglion and horizontal portions of the facial nerve canal are seen continuous with the internal auditory canal. The superior portion of the cochlea and the vestibule are visible. The opening of the vestibular aqueduct and endolymphatic sac is seen as a thin slit along the posterior margin of the temporal bone just medial to the mastoid air cells. The epitympanic space holds the head of the malleus and the body of the incus and is continuous posteriorly with the aditus ad antrum and the mastoid antrum.

B, Axial MR image

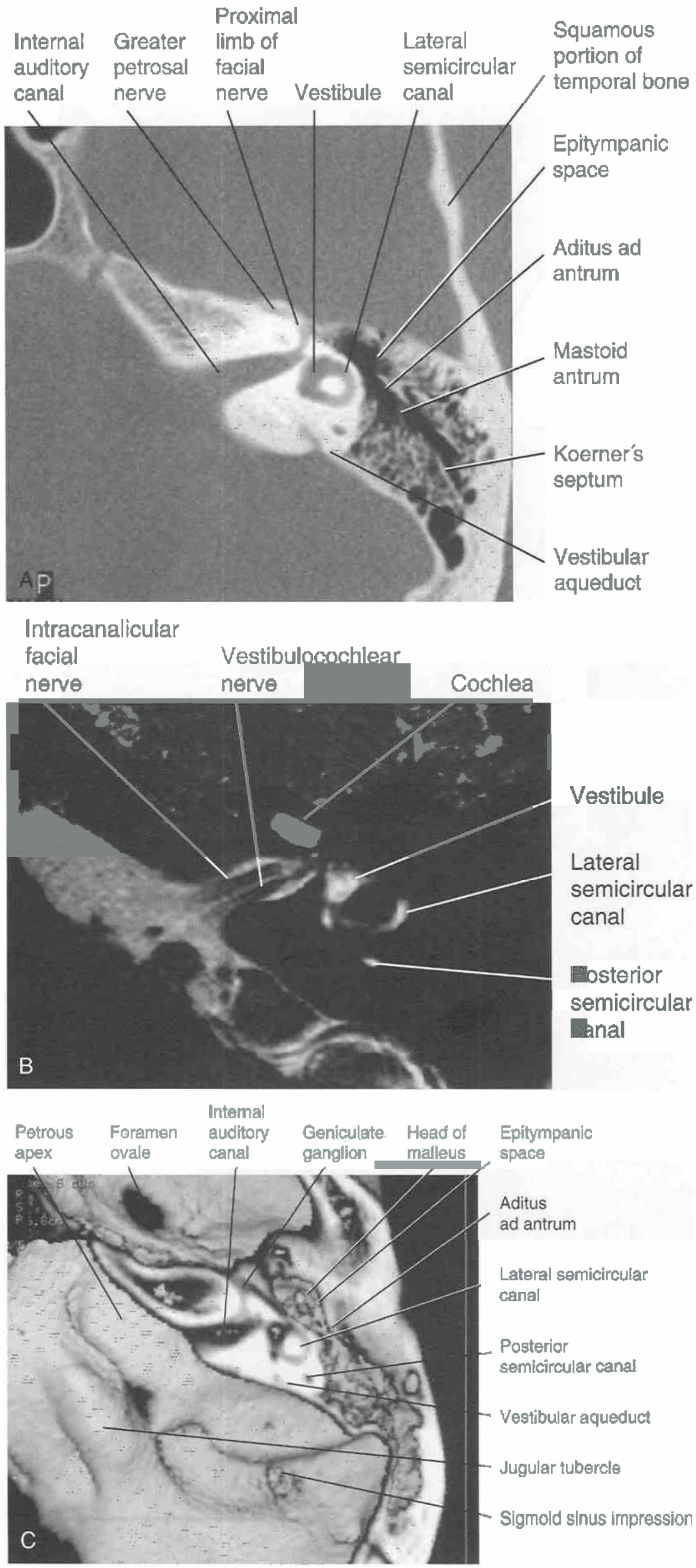

Figure 15–6. Axial views, normal anatomy.

A, Axial CT section of the complete internal auditory canal, ending in the proximal limb of the geniculate segment of the facial nerve canal anteriorly. The vestibule and complete lateral semicircular canal are visible. The posterior semicircular canal and the vestibular aqueduct are seen posteriorly. Portions of the epitympanic space, the aditus ad antrum, and the mastoid antrum are seen in continuity. Koerner's septum is also visible. The squamous portion of the temporal bone is seen anterior to the mastoid and petrous segments.

B, Axial MR section.

C, Axial 3D reconstruction of the interior of the skull base clipped at the level of the internal auditory canal. The relationship of the temporal inner and the middle ear structures to the skull base is shown.

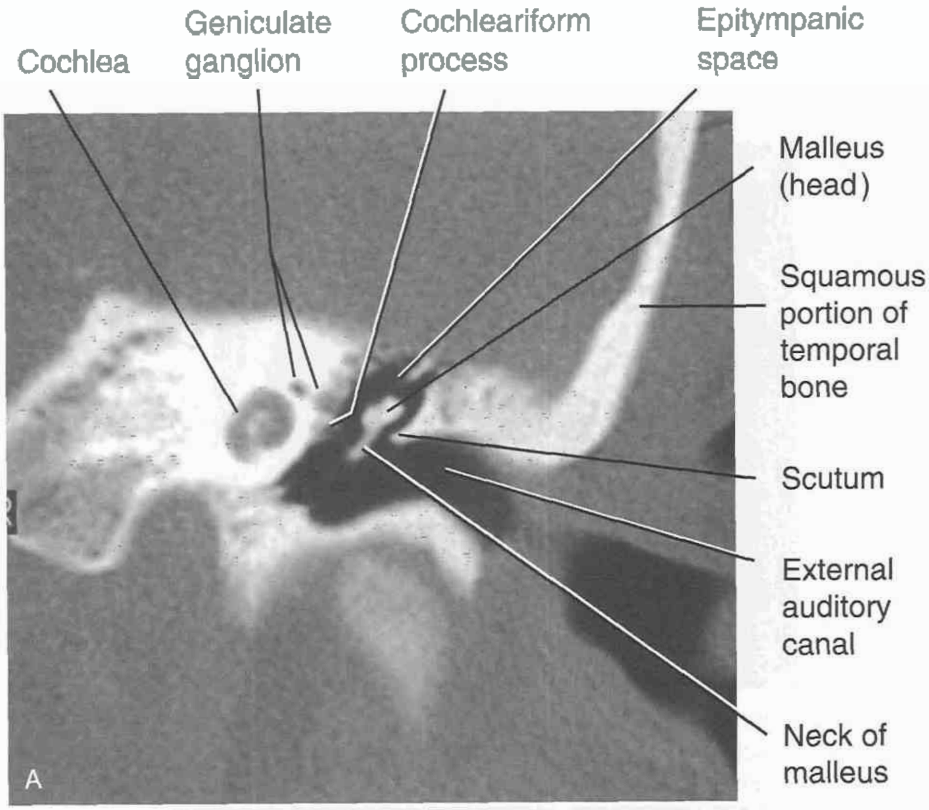

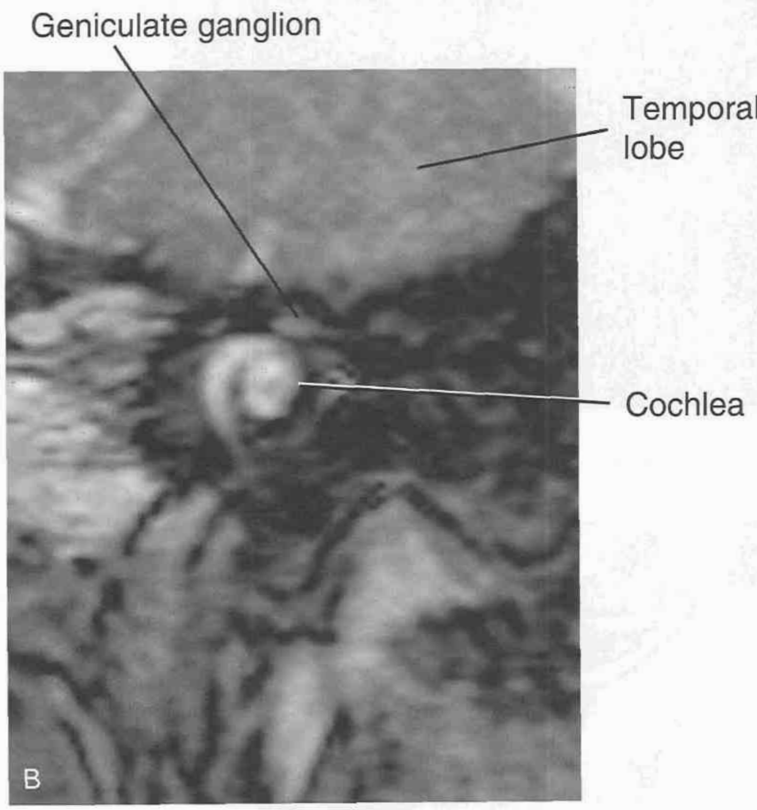

Figure 15–7. Normal anatomy.

A, Coronal CT section. This is the most anterior CT section of the left temporal bone. The scutum forming the medial margin of the external auditory canal and adjacent head of the malleus and the long process of the malleus are seen. The epitympanic space supports the ossicles. The external auditory canal appears continuous with the middle ear cavity; the tympanic membrane is frequently not visible when normal. Abnormal thick tympanic membranes are easier to image. Three small canals are just medial and superior to the anterior cochlea. These include the proximal limb of the geniculate ganglion, the distal limb of the geniculate ganglion, and the semicanal of the tensor tympani muscle.

B, Axial MR section.

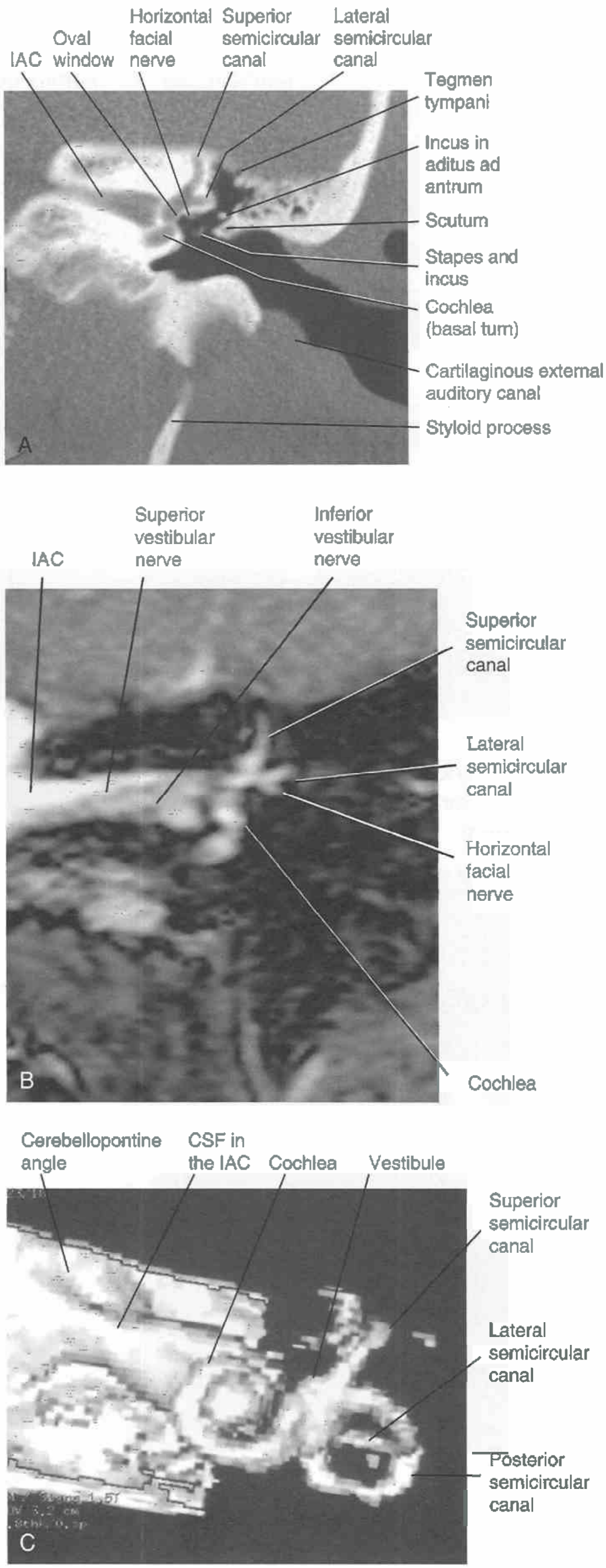

Figure 15–8. Normal anatomy.

A, Coronal CT section made at the level of the oval window. The adjacent stapes and incudostapedial joint are visible as an L-shaped structure overlying the oval window. The horizontal portion of the facial nerve is just below the lateral semicircular canal. The short process of the incus is interposed between the scutum and the lateral semicircular canal. The internal auditory canal (IAC), middle ear, external auditory canal (EAC), stapes, and the basal turn of the cochlea are shown. Note the absence of visible soft tissues over the medial EAC, which is normal. Only the cartilaginous segment of the EAC is seen as a soft tissue component.

B, Coronal MR section.

C, Surface MRI reconstruction. This is an oblique view of the left otic capsule structures imaged by high-resolution 3D Fourier transform MRI T2-weighting and postprocessing with a surface algorithm. The three turns of the cochlea are clearly seen, with the basal turn merging with the vestibule. The superior, lateral, and posterior semicircular canals are all well visualized. The cerebrospinal fluid (CSF) in the internal auditory canal is seen as a tubular structure extending back toward the cerebellopontine angle. The anatomy appears as a "plaster cast" of the otic capsule.

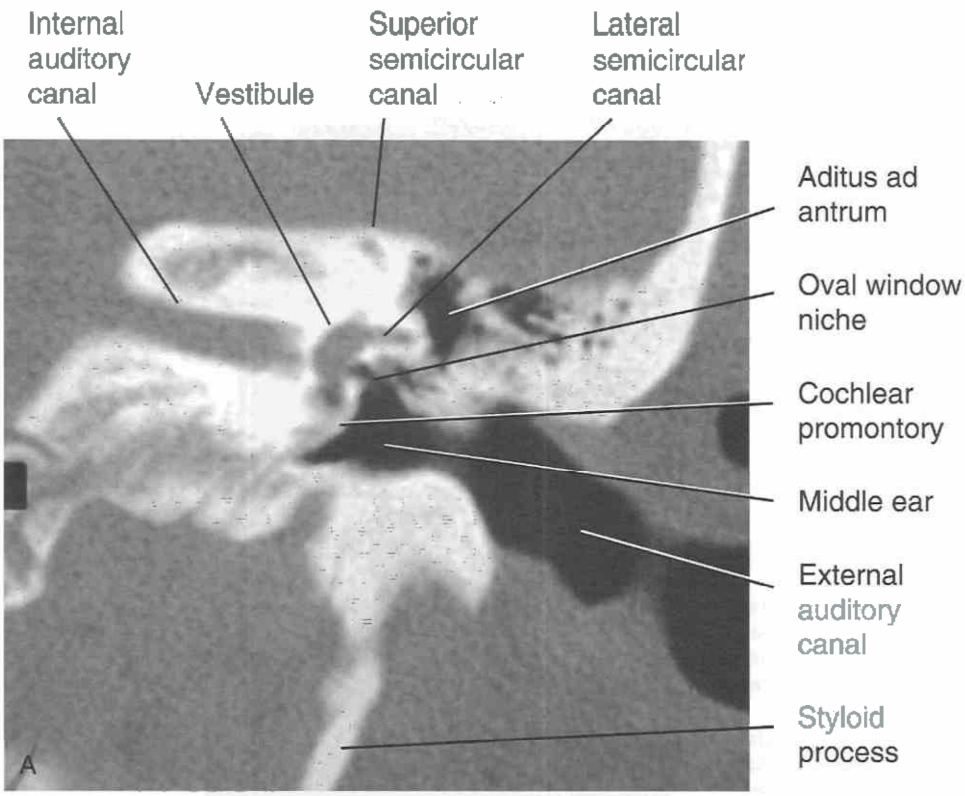

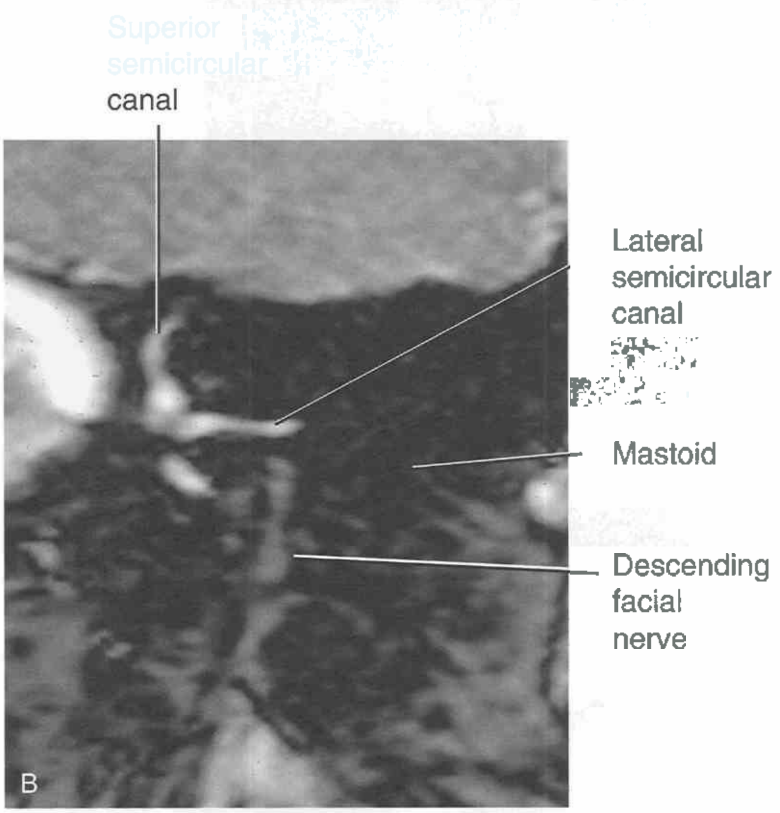

Figure 15–9. Coronal views, normal anatomy. *A*, Coronal CT section of the left temporal bone, made through the vestibule and the posterior portion of the oval window. The basal turn of the cochlea and cochlear promontory are seen. The aditus ad antrum is seen just lateral to the lateral semicircular canal. A short portion of the superior semicircular canal is visible. The internal auditory canal, middle ear, styloid process, and external auditory canal are shown. *B*, Coronal MR section.

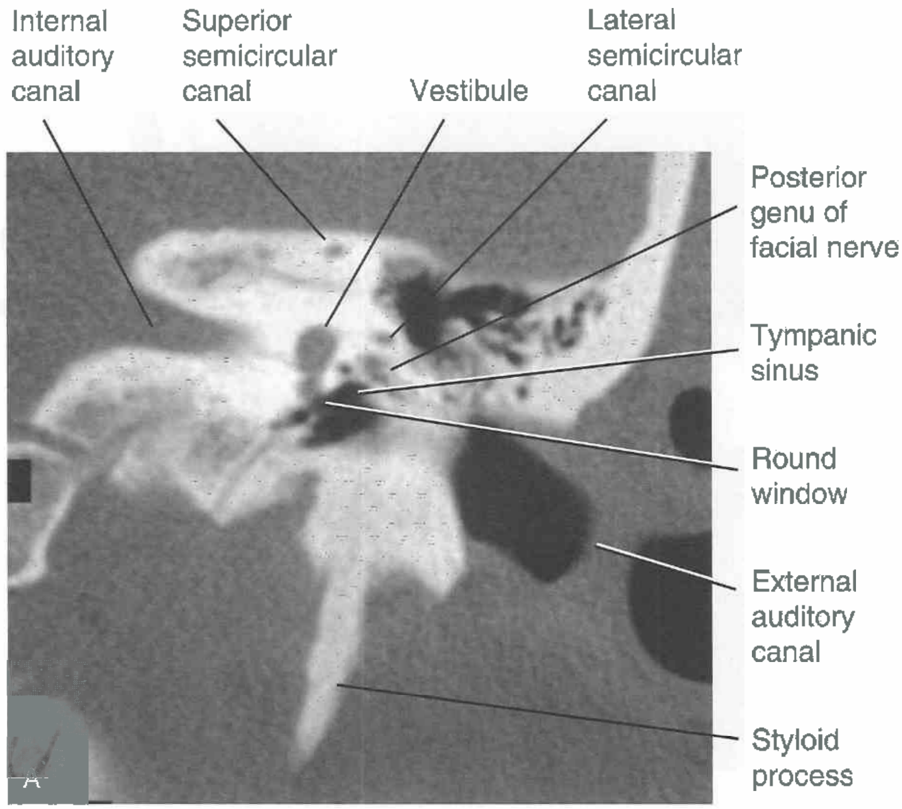

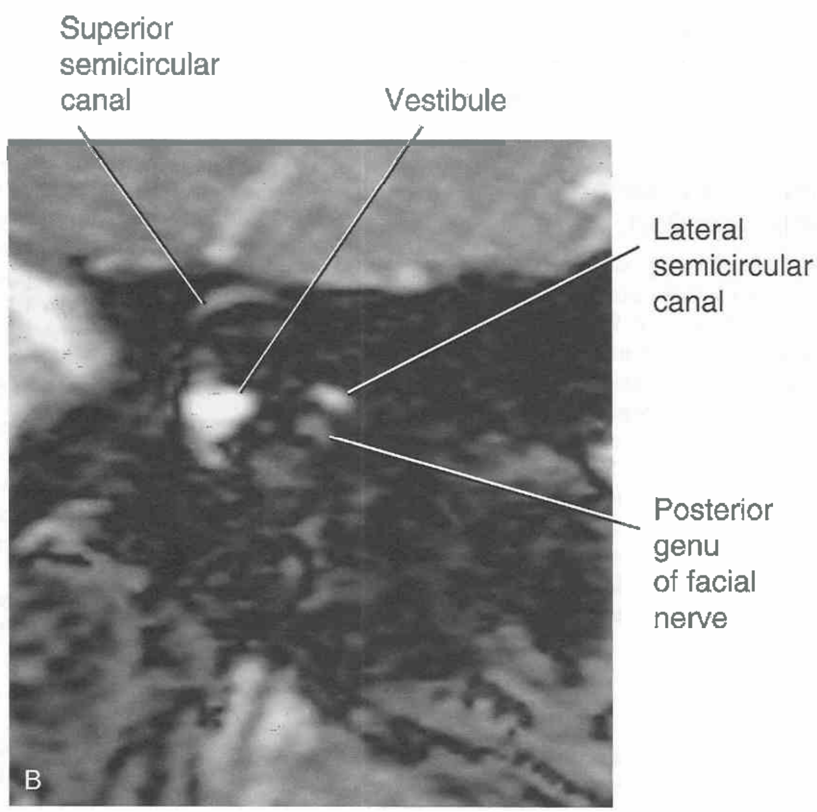

Figure 15–10. Coronal views, normal anatomy. *A*, Posterior coronal CT section of the temporal bone centered at the level of the round window and the tympanic sinus. The air spaces extend all the way to the otic capsule membrane surfaces. The adjacent posterior genu of the facial nerve and vestibule are seen. Other depicted structures include the posterior internal auditory canal, superior semicircular canal, lateral semicircular canal, styloid process, and external auditory canal. *B*, Coronal MR section.

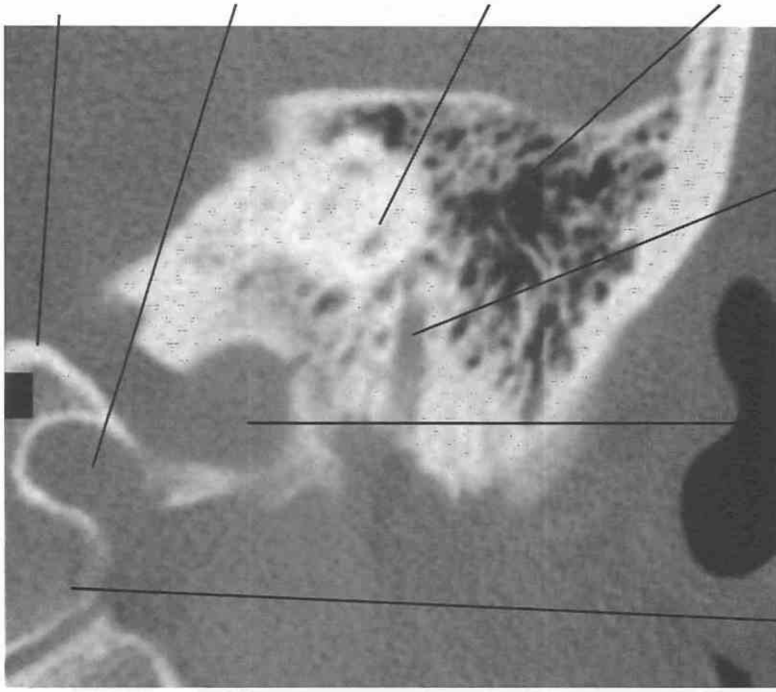

Figure 15–11. Coronal CT section. This is the most posterior section of the temporal bone. The descending facial nerve canal is seen between the mastoid air cells and the more medial jugular fossa. The jugular tubercle, hypoglossal canal, and occipital condyle all appear medial to the jugular fossa. Short segments of the posterior semicircular canal are seen.

the inferior vestibular and cochlear nerves.[23] The lateral portion of the canal is perforated by the cranial nerves where they enter the cochlea, vestibule, and facial nerve canal.

Vestibule, Vestibular Aqueduct, Endolymphatic Duct, and Sac

The vestibular cavity is the central portion of the membranous labyrinth that communicates with the semicircular canals and cochlea (see Figs. 15–6, 15–10, and 15–14). The vestibule lies immediately lateral to the fundus of the internal auditory canal, and the oval window of the middle ear forms its lateral margin. The vestibular aqueduct is a narrow bony canal that contains the small endolymphatic duct and sac (see Fig. 15–14). The endolymphatic duct originates from the posteromedial aspect of the vestibule, courses past the common crus,[5] and assumes a hockey stick shape. The endolymphatic sac, an extension of the endolymphatic duct, is a dead-end fluid space arising from the vestibule that lies beneath the dura of the posterior temporal bone.

Semicircular Canals

The semicircular canals are three orthogonally arranged circular structures of the membranous labyrinth arising from the vestibule (Figs. 15–6, 15–8, and 15–13). The lateral semicircular canal approximates the horizontal plane. The posterior and superior semicircular canals share a common crus posteriorly.

Cochlea and Cochlear Aqueduct

The spiral cochlear apparatus contains the membranous labyrinth components for hearing (see Fig. 15–4). The cochlea lies anterior to the vestibule and has 2½ to 2¾ turns around its modiolus, the central bony spiral axis. The most lateral portion of the basal turn of the cochlea projects into the tympanic cavity, forming a promontory of bone.[30]

The cochlear aqueduct, a channel that connects the cochlea near the round window with the subarachnoid space just superior to the jugular tubercle, lies inferior to the internal auditory canal.

Oval and Round Windows

The oval window of the vestibule is the interface between the mechanical and neural elements of the ear (see Fig. 15–8). It lies just inferior to the horizontal facial nerve canal and the lateral semicircular canal. It is covered by the annular ligament, which surrounds the footplate of the stapes.[23]

The round window is the bony opening of the basal turn of the cochlea and is covered by a fibrous membrane (see Fig. 15–10). It lies inferior and slightly posterior to the oval window and is adjacent to the inferior tympanic sinus.

Facial Nerve and Facial Nerve Canal (Fallopian Canal)

The facial nerve has a highly tortuous course and comes in close contact with almost every other important component of the temporal bone (Figs. 15–5, 15–8, and 15–12). The labyrinthine (cochlear) portion of the facial nerve

Text continued on page 511

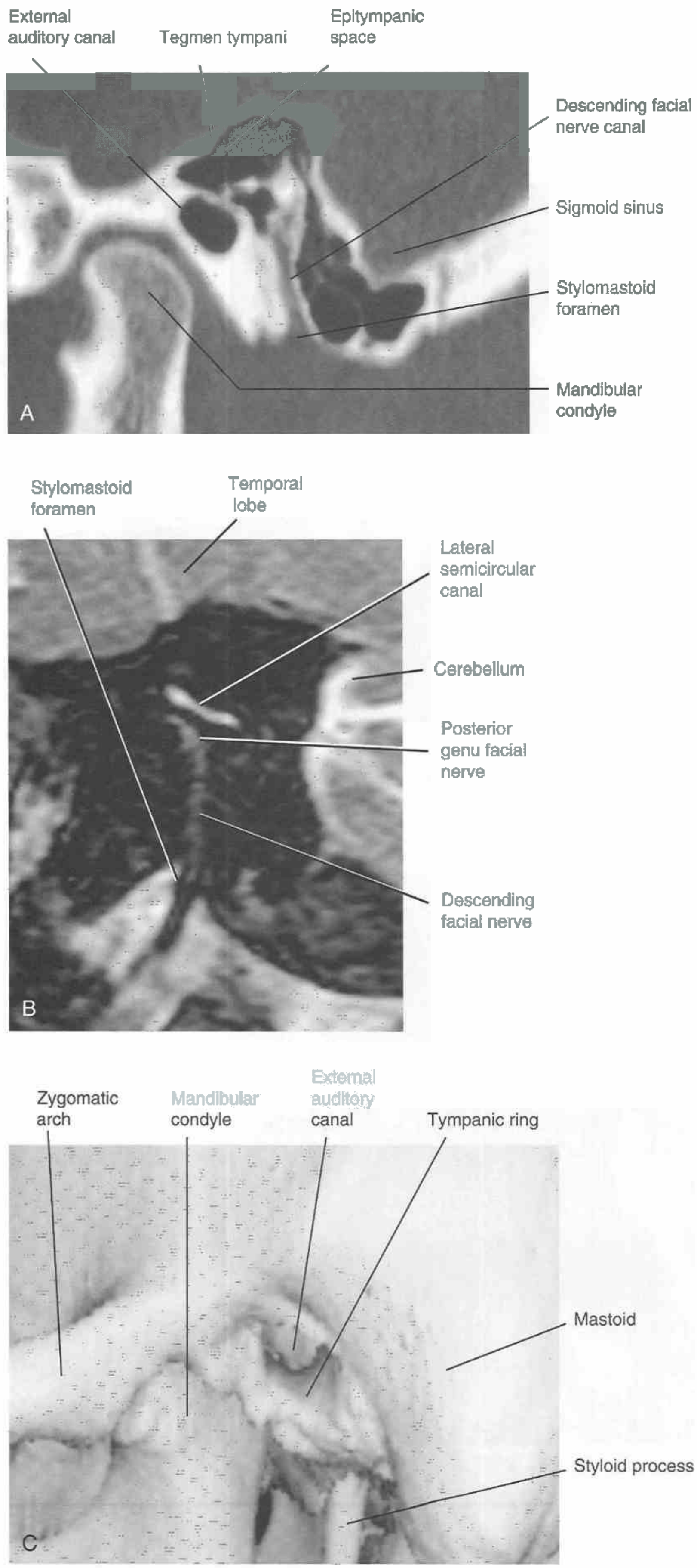

Figure 15–12. Sagittal views, normal anatomy. *A,* Sagittal CT reconstruction through the descending facial nerve canal and stylomastoid foramen. The mastoid air cells and sigmoid sinus lie just posterior to the facial nerve. The mandibular condyle, mandibular fossa, external auditory canal, and epitympanic space are visible. *B,* Sagittal MRI section. *C,* CT surface reconstruction of the lateral skull and mandible centered over the external auditory canal.

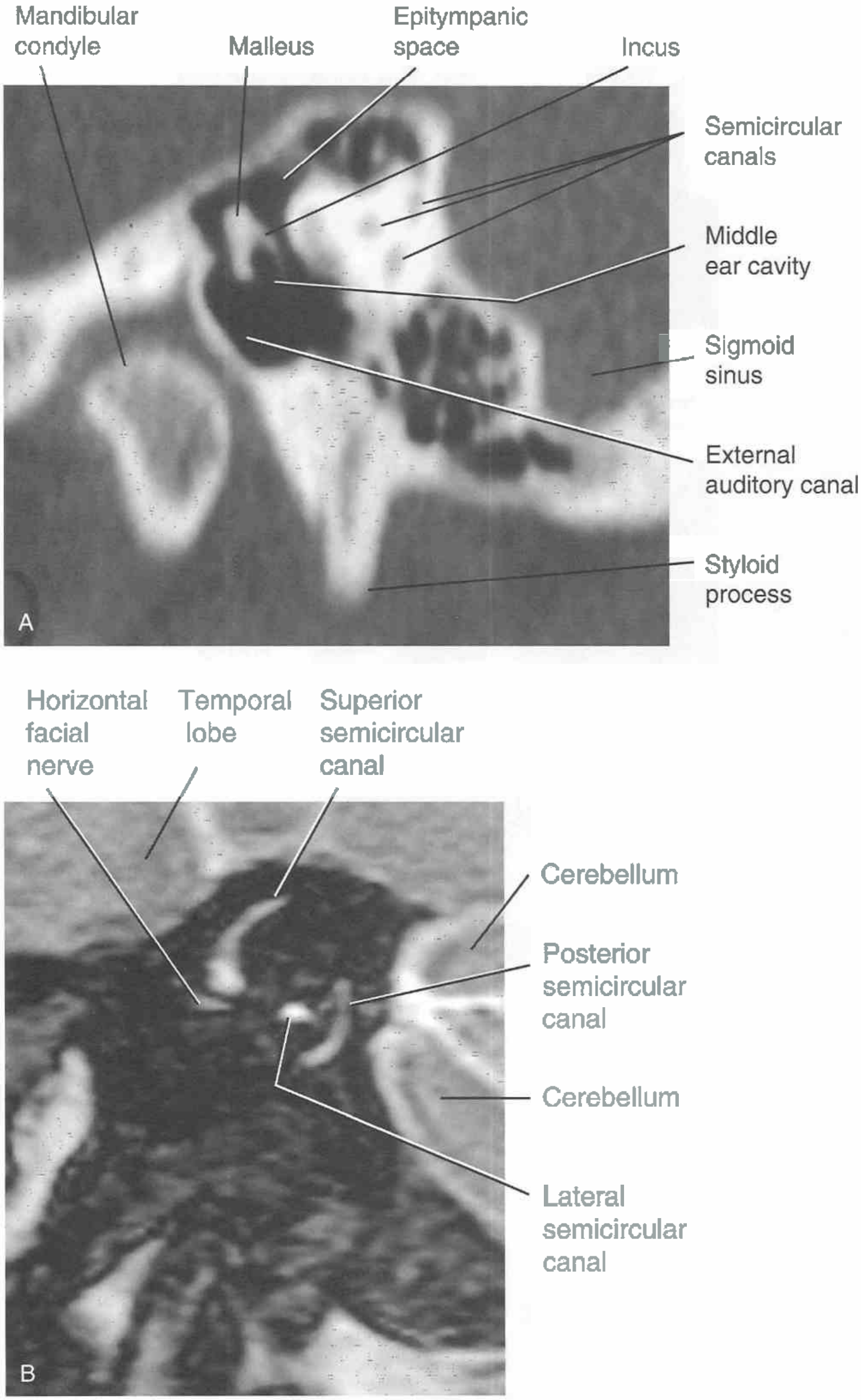

Figure 15–13. Sagittal views, normal anatomy. *A*, Sagittal CT reconstruction made at the level of the epitympanic space. The most medial portion of the mandibular condyle and the mandibular fossa are seen. The styloid process and the mastoid air cells are visible. The head of the malleus and the long process of the incus are visible in the epitympanic space. The thin wall of the epitympanic space, the semicircular canals, and a portion of the facial nerve canal in the middle ear are visible. *B*, Sagittal MR section.

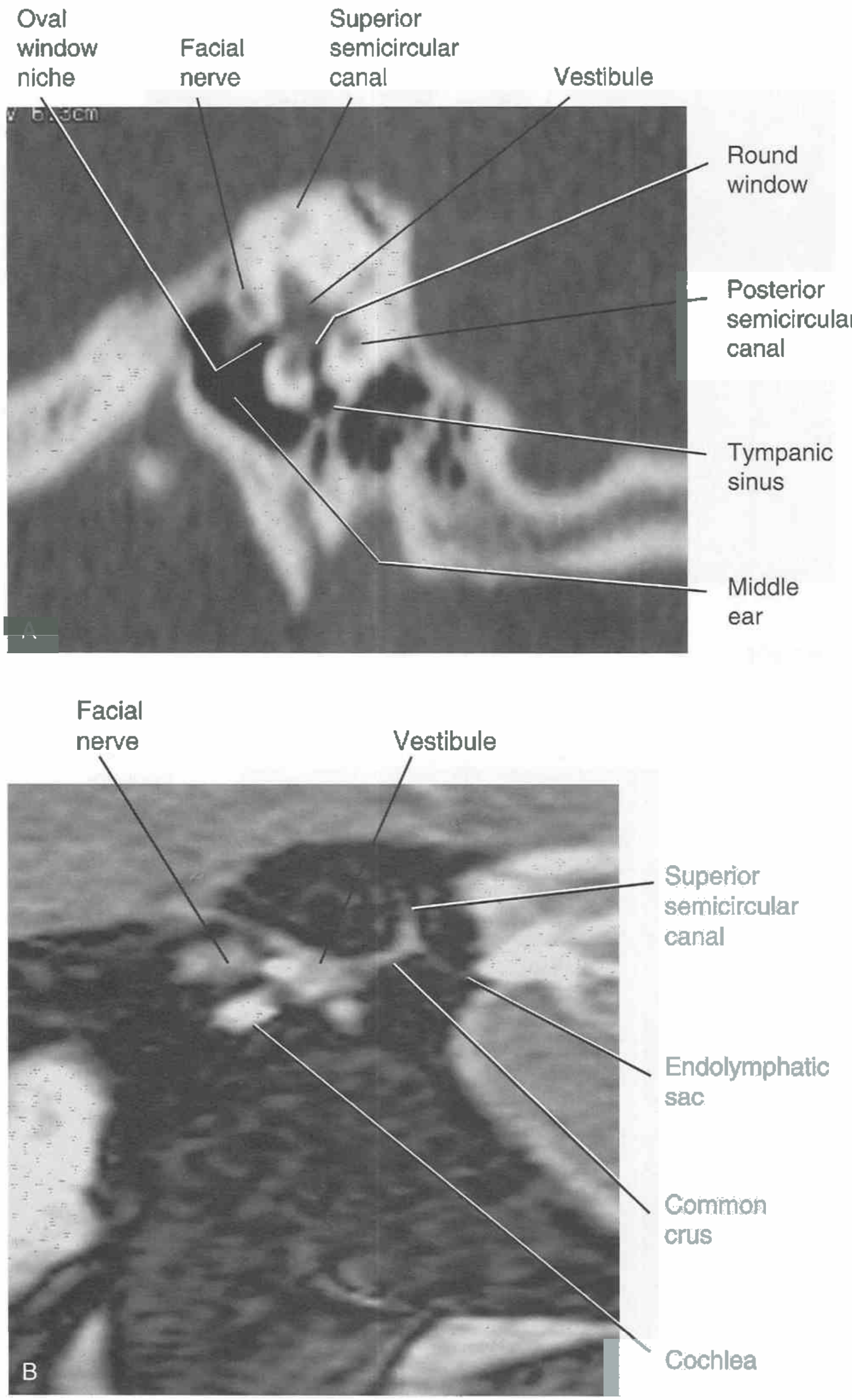

Figure 15–14. Sagittal views, normal anatomy. *A*, Sagittal CT reconstruction centered at the level of the middle ear. The oval and round windows are seen with their associated niches. The vestibule and the basal turn of the cochlea are seen as well. The superior and posterior semicircular canals are visible. The tympanic sinus is continuous with the round window. *B*, Sagittal MR section.

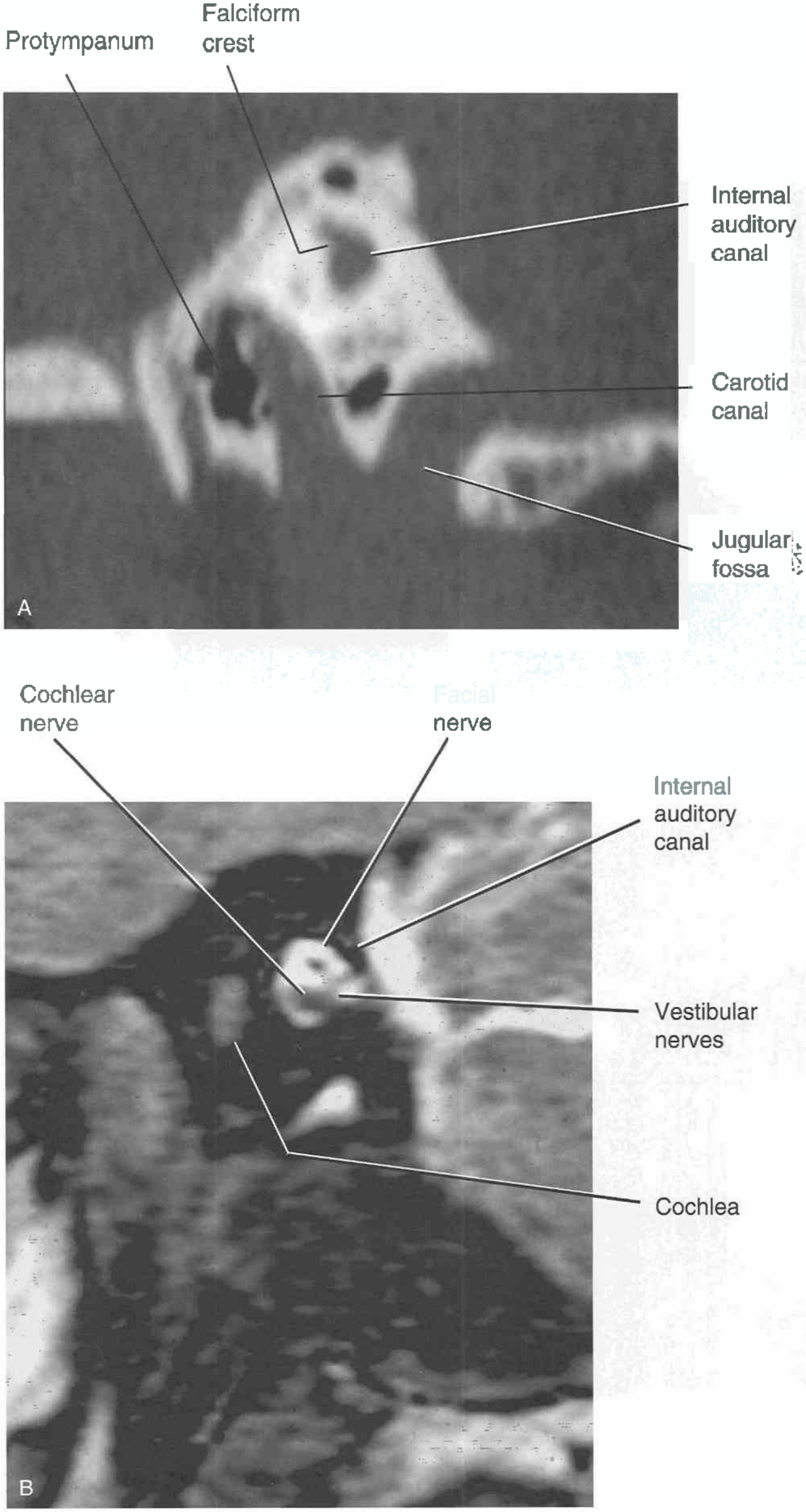

Figure 15–15. Sagittal views, normal anatomy. *A,* This sagittal CT reconstruction is the most medial section and is centered at the protympanum, carotid canal, internal auditory canal, and jugular fossa. Note the close association of the protympanum and the carotid canal. The internal auditory canal demonstrates a small anterior pointed indentation resulting from the falciform crest that separates the facial and cochlear nerves. *B* and *C,* Sagittal MR sections.

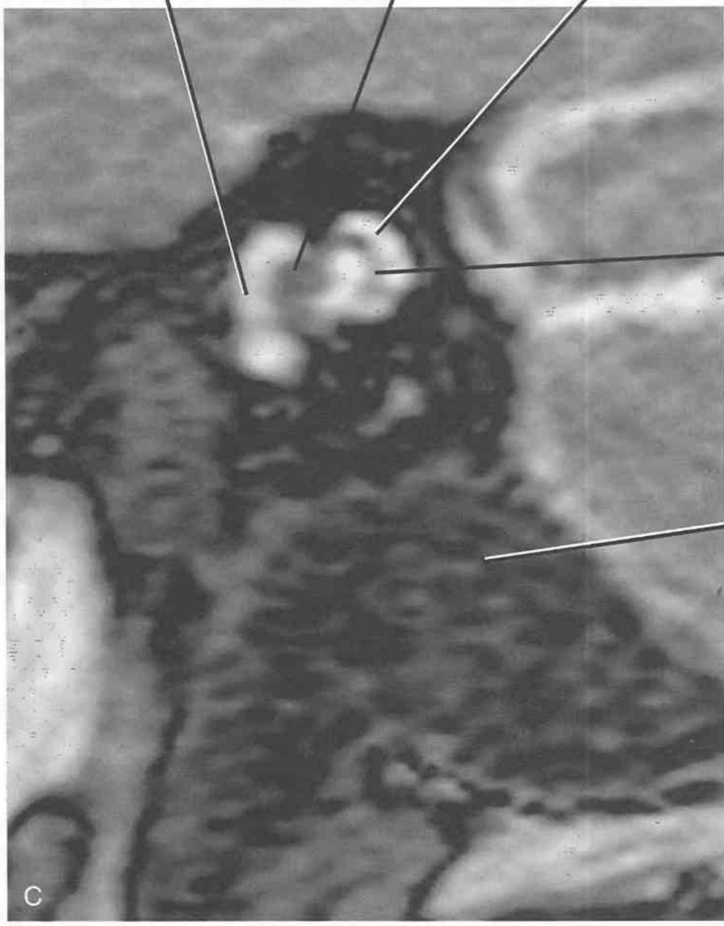

Figure 15–15 *Continued*

exits the superior anterior portion of the internal auditory canal fundus.

At the geniculate ganglion, an acute reverse (inverted V) angle of the nerve and canal is seen. The distal limb of the geniculate ganglion doubles back posteriorly to become the horizontal segment in the medial wall of the tympanic cavity. This portion of the facial nerve canal has a thin inferior bony covering that may be dehiscent.

The horizontal portion of the facial nerve runs directly inferior to the lateral semicircular canal. The facial nerve then abruptly turns inferiorly (at an angle of 95 to 125 degrees) to form the posterior genu near the tympanic sinus and the pyramidal eminence.[53]

The vertical, or descending, facial nerve in the mastoid portion of the facial nerve canal runs vertically just posterior to the external auditory canal. In this vertical portion, the nerve to the stapedius muscle and the chorda tympani (first and second branches, respectively, of the facial nerve distal to the geniculate ganglion) arise. The facial nerve then exits from the mastoid portion of the temporal bone via the funnel-shaped, fat-filled stylomastoid foramen.

Carotid Canal

The carotid canal enters the base of the skull, ascends vertically, then turns horizontally and medially toward the petrous apex (see Figs. 15–2 and 15–15). This canal lies anterior and inferior to the cochlea and is separated from the protympanum by a thin bony plate.

Jugular Foramen and Fossa

The jugular foramen is divided into a smaller anteromedial neural compartment (pars nervosa) containing cranial nerves IX, X, and XI, and a larger posterolateral vascular compartment (the pars vascularis) containing the jugular vein (see Fig. 15–11). The floor of the tympanic cavity normally forms the roof of the jugular fossa. The jugular bulbs are frequently asymmetrical, and there may be a small diverticulum from their apices.

CT and MRI Anatomy

CT scans and MRI studies are complementary. On CT scans, bony structures are demonstrated by high density

and CSF by low density, and air spaces appear black. The brain and vascular structures are intermediate in density. CT is not ideal for evaluating detail of the soft tissues of the otic capsule contents, brain, and vessels. In contrast, MRI studies receive no signal from dense bone or air spaces and thus cannot be used to evaluate these components accurately in the absence of pathology. MRI, however, is superior to CT in characterizing the CSF, brain, cranial nerves, and blood vessels.

CT Techniques

The temporal bone has a high inherent radiation attenuation contrast, having both the most dense bone in the body as well as air-filled spaces. High-resolution CT images are usually acquired with thin sections (1 to 2 mm) and special bone algorithms for high detail.[14] CT scans of the temporal area can be obtained rapidly, with relatively low radiation doses, compared with many other types of CT examinations. Contrast enhancement is not essential for evaluation of pathology isolated to bone or air spaces. Intravenous (IV) contrast material is often used to assess vascular lesions, areas of breakdown in the blood-brain barrier, or soft tissue changes. CT is less expensive than MRI, although CT is limited by scan artifacts, radiation exposure, and fewer scanning planes (because of the limitations in gantry and in patient positioning).

Multiplanar CT reformations can display the complex anatomy of the temporal bone in all of the conventional polytomography projections while exposing the patient to radiation only once.[25] However, even slight motion by the patient is intolerable because the small bony structures of the temporal bone are in such close proximity that motion artifacts may obscure significant detail.[63] In addition, reformation results in slight image degradation and loss of resolution. The longitudinal oblique plane (Stenvers projection) is parallel to the long axis of the petrous bone and is ideal for the study of longitudinal temporal bone fractures.[60]

MRI Techniques

Many different techniques can be used to acquire MR images, depending on the suspected abnormality and the equipment available. T1-weighted (TR = 600 msec, TE = 20 msec) spin-echo coronal or axial images are usually acquired without contrast medium. The fat spaces have high signal intensity, and the brain has intermediate signal intensity. CSF demonstrates low signal intensity, and air and bone spaces appear as voids. This sequence also helps to differentiate fat from subacute hemorrhage.

T2-weighted (TR = 3000 or longer msec, TE = 80 or longer msec) axial spin-echo images accurately display the CSF spaces and many disease processes as high-signal-intensity regions. High-resolution, thin-section (1.5 mm or less), three-dimensional (3D) Fourier transform (3D FT) T1-weighted, gradient-echo (TR = 50 msec, TE = 7 msec; flip-angle, 30 degrees) images can be acquired with paramagnetic contrast agents. Gradient images have the advantage of high resolution, very thin sections, and blood flow information (phase or time-of-flight effects).[15, 59]

Various image contrasts are also possible, including T1, free precession, or proton-density weighting. T2-weighted, spin-echo 3D FT imaging using multiple echo times (TE) in for each repetition time (TR) generate excellent quality images. T2-weighted or free precession at steady-state gradient-echo 3D FT imaging (SIMCAST*) with very high resolution displays the otic capsule structures as high-signal-intensity regions surrounded by signal void.[7] Three-dimensional data can also be computer-processed into maximum pixel signal intensity ray projections, planar sections, or surface reconstructions.[57]

MRI is outstanding for its ability to evaluate blood vessel–related disorders of the temporal bone.[48, 59] With many gradient-echo techniques, flowing blood can be seen as a high-intensity-signal region,[15] and phase imaging can be used to quantify velocity and flow volumes.[59] Gadolinium-diethylenetriamine-penta-acetic acid (Gd-DTPA) contrast-enhanced MRI studies using T1-weighted images are particularly sensitive for evaluating abnormalities that alter the blood-brain barrier or that are vascular, such as inflammatory disease (Bell's palsy, vestibulitis, otitis, granulation tissue, meningitis), carcinomatosis, posterior fossa infarcts, tumors,[6, 38] and demyelination.[50] Frequently, the findings of contrast enhancement are more obvious on MR images than on CT scans. MRI studies, compared with CT, also have higher resolution and are more sensitive to alteration in the fluid spaces of the inner ear and the cerebellopontine angle.

Normal Temporal Bone Images

Axial Sections

Caudad to Cephalad (see Figs. 15–1 to 15–6)

The axial or transverse plane is most suitable for a survey study of the temporal bone.[68] This suitability is based on the ease by which axial CT sections may be obtained.[63] The structures within the temporal bone are consistently oriented to the external landmarks of the skull. Axial CT sections made 30 degrees above the anthropologic baseline are parallel to the lateral semicircular canal and optimally display many structures.[14] The axial plane is of special interest for the visualization of the incudomalleolar and incudostapedial articulations, facial nerve canal, internal auditory canal, vestibular aqueduct, lateral semicircular canal, and the oval and round windows.

Axial Hypotympanic-Jugular Foramen Level (see Fig. 15–2)

The carotid canal lies just anterior to the jugular fossa, forming a "snowman"-like configuration. The carotid canal is usually smaller than the jugular fossa, and both demonstrate sharp cortical margins. Inferiorly, only a small spine separates the two as they converge to enter the carotid sheath. The hypotympanum is adjacent to these structures. The opening of the eustachian canal is triangular, with the apex extending parallel to the carotid canal.[9] The petro-occipital fissure separates the temporal bone from the occiput.

The mandibular condyle and temporomandibular joint

*SIMCAST, segmented interleaved motion compensated acquisition in the steady-state technique.

can also be seen on CT scans. On MRI gradient-echo studies, the descending portion of the facial nerve can be seen just lateral to the jugular bulb, and the blood vessels can be seen as high-signal-intensity regions because of flow effects.

Axial Inferior Tympanic Level (see Fig. 15–3)

On CT scans, the anterior and posterior walls of the bony external auditory canal demonstrate dense sharp cortical margins without soft tissue covering. The anterior margin of the external auditory canal forms the posterior lip of the temporomandibular joint. The cartilaginous segment is surrounded by fat that is of low density on CT scans and of high signal intensity on T1-weighted MRI studies.

The descending facial nerve canal is easily identified on CT scans as a well-marginated circular lucency in the temporal bone posterior to the external auditory canal. On MRI studies, the facial nerve is seen as an intermediate-signal-intensity to high-signal-intensity circular structure, surrounded by a large area of signal void of the temporal bone and mastoid air spaces.

The carotid canal can be seen early in its anteromedial course through the skull base, parallel and medial to the semicanal of the tensor tympani muscle at this level. On CT scans, the medial funnel-shaped opening of the cochlear aqueduct can be seen as a triangular lucency facing the cerebellopontine angle. Its apex points toward the round window. The opening of the duct may be large and mimic the internal auditory canal. The long process of the malleus parallels the tympanic membrane.

Axial Midtympanic Level (see Fig. 15–4)

The middle ear cavity is highly complex but is constant in size and configuration among patients. The normally thin tympanic membrane is often invisible on axial CT sections. The long process of the malleus lies parallel and anterior to the long process of the incus.

The axial projection is ideally suited for demonstrating the cochlear aqueduct as a thin canal within the dense cortical bone, progressively enlarging from lateral to medial. The duct is demonstrated on CT scans but not well seen on MRI studies, possibly because of the combination of its small diameter and CSF motion artifacts.

The complex medial margin of the middle ear includes the cochlear promontory, oval and round windows, cochleariform process, tensor tympani tendon, pyramidal eminence, stapedial tendon, and lateral semicircular canal. Unless there is fluid or a mass within the middle ear, MRI cannot be used to depict these structures. On CT scans, the apical, second, and basal cochlear turns are seen at this level. On MRI studies, these fluid-filled structures are identified by their intermediate signal intensity.

Axial Epitympanic Internal Auditory Canal Level (see Fig. 15–5)

CT images at this level display the round head of the malleus and triangular body of the incus in the characteristic "ice cream cone" configuration (incudomalleolar articulation). The stapedial superstructure is occasionally seen, forming an arch over the oval window on high-resolution CT scans. The internal auditory canal is slightly funnel-shaped and ends in an ovoid vestibule.

These canals should be nearly symmetrical. Although there is wide variation in the exact shape and size of the canals, asymmetry of greater than 2 mm suggests pathology. Lower-resolution MRI studies can demonstrate CSF in the canal, and high-resolution MRI studies can actually demonstrate the individual nerves as filling defects within the CSF.

On CT scans, the descending facial nerve canal is seen just lateral to the sinus tympanum. On MRI studies, the cochlear fluid contents, labyrinthine and horizontal segments of the facial nerve, and the geniculate ganglion are all seen as intermediate-signal-intensity structures surrounded by the signal void resulting from their bony walls.

Axial Lateral Semicircular Canal Level (see Fig. 15–6)

The axial projection is excellent for visualizing the entire lateral semicircular canal, since both are 30 degrees above the anthropologic baseline. The vestibular aqueduct is seen as a thin, hockey stick–shaped bony lucency. On MRI studies, the endolymphatic duct and sac appear as thin, high-signal-intensity regions. The endolymphatic duct extends posteriorly from the region of the common crus. It then abruptly turns laterally between the posterior margin of the temporal bone and the posterior semicircular canal.[9]

The mastoid antrum lies posterior and lateral to the aditus ad antrum and opens into many mastoid air cells. It is bordered superiorly by the tegmen tympani, which may be extremely thin and not well visualized on CT scans. The medial margin of the antrum is the promontory formed by the otic capsule of the lateral semicircular canal. On CT scans, the posterior semicircular canal and its ampulla are demonstrated.

Coronal Sections

Anterior to Posterior (see Figs. 15–1 and 15–7 to 15–11)

Coronal CT sections are particularly useful in the evaluation of the ossicles, geniculate ganglion, oval window, stapes, jugular fossa, middle ear walls, and roof (tegmen tympani) of the tympanic cavity.[4] The internal auditory canal and vestibule as well as Koemer's septum, which separates the squamous and petrous portions of the temporal bone, may also be identified.

Coronal Anterior Tympanic Level (see Fig. 15–7)

This plane offers excellent visualization of the superior and inferior walls of the external auditory canals. The tympanic membrane often is not visible, but it may be identified as a thin, filamentous structure extending from the scutum superiorly and coursing parallel to the plane of the long process of the malleus to attach to the limbus inferiorly.[11] The head of the malleus can be seen in the epitympanic space, and the floor and roof (tegmen) of the middle ear are also well visualized on CT scans.

The basal and second turn of the cochlea, geniculate ganglion, and internal auditory canal are identified on CT scans, surrounded by the dense bone of the otic capsule.

The cochlea and geniculate ganglion can be directly viewed on MRI studies by their fluid and soft tissue signal intensity.

Coronal Midtympanic Level (see Fig. 15–8)

The CT image at this level shows the body of the incus and incudostapedial articulation as an L-shaped configuration. The stapes projects medially and superiorly from the body of the incus toward the oval window (above the cochlear promontory). The proximal limb of the geniculate ganglion is seen just superior and lateral to the cochlea.

Beneath the lateral semicircular canal, the horizontal portion of the facial nerve canal appears as a small circular structure.[53] The floor and roof (tegmen) of the middle ear are well visualized on CT scans. On MRI studies, the facial (VII) and vestibulocochlear (VIII) nerves can be seen together in the internal auditory canal, diverging laterally.

Coronal Oval Window Level (see Fig. 15–9)

The full extent of the internal auditory canal, which often includes the central crista falciformis dividing the canal into two portions, is well visualized at this level. On CT scans, the oval window is seen as a bony defect of the lateral portion of the vestibule. The stapes is oriented slightly superiorly toward the oval window, just inferior to the lateral semicircular canal and the horizontal facial nerve.

Coronal Posterior Middle Ear Level (see Fig. 15–10)

The posterior middle ear has several small niches. One of the niches is the tympanic sinus, which extends between the vestibule and the pyramidal eminence. The second niche extends toward the round window. The epitympanic space lies just lateral to the lateral semicircular canal.

Coronal Jugular Foramen Level (see Fig. 15–11)

The jugular foramen and bulb frequently have a dome-shaped outline. The descending portion of the facial nerve canal may be identified running nearly vertical, directly inferior to the lateral semicircular canal. The mastoid antrum is seen superiorly and laterally. On CT scans, this section reveals various segments of the semicircular canals as well as the articulation of the occipital bone and atlas. Just lateral to this, the descending facial nerve is seen over a long section coursing toward the stylomastoid foramen.

Sagittal Images (see Figs. 15–12 to 15–15)

Direct sagittal images or reformations[25] can show the relationship of the mandibular condyle to the glenoid fossa and external auditory canal. The external auditory canal may be seen lateral to the tympanic membrane or long process of the malleus. The aditus ad antrum, mastoid antrum, and tegmen tympani are all well demonstrated.

The third portion of the facial nerve canal, the internal and external auditory canals, and the vestibular aqueduct are also well visualized on sagittal images.[11] MRI studies can demonstrate the individual nerves in the internal auditory canal, with the facial nerve superior and anterior, the cochlear nerve inferior and anterior, and the vestibular nerves posterior.

Sagittal Descending Facial Nerve Level (see Fig. 15–12)

The circular external auditory canal lies just below the ossicles in the epitympanic space. On CT and MRI scans, the descending facial nerve and posterior genu form an upside-down hockey stick shape. On MRI studies, the soft tissue components are easily seen.

Sagittal Vestibular Level (see Fig. 15–13)

Sagittal sections through the lateral vestibule demonstrate the multiple small components of the individual semicircular canals.

Sagittal Common Crus Level (see Fig. 15–14)

The vestibule, cochlea, and semicircular canals form an "x"-like configuration on sagittal sections. The vestibule is central, and the common crus of the superior and inferior semicircular canals can be seen just posterior and superior to the vestibule on both CT scans and MRI studies. The vestibular aqueduct appears as a thin, linear structure underlying a flange of the posterior petrous bone on CT scans, and the contained endolymphatic duct and sac can be seen on MR images. On MRI studies, the endolymphatic sac can be seen as a triangular area of increased signal at the distal end of the endolymphatic duct.

Sagittal Internal Auditory Canal Level (see Fig. 15–15)

On sagittal sections, the petrous apex has a triangular configuration. On CT scans, the circular internal auditory canal may demonstrate a small ridge anteriorly, related to the falciform crest. On high-resolution MRI studies, the individual nerves can be seen as filling defects. The carotid canal and the jugular fossa are directly inferior to the other otic capsule structures.

Abnormal Temporal Bone

Congenital Malformations

Evaluation of the congenitally deaf child is very difficult. Audiologic testing, although frequently not specific, is imperative to distinguish neurosensory defects from conductive hearing problems. Neurosensory defects occur medial to the oval window and are caused by maldevelopment of the otocyst. Conductive defects occur in the external and middle ears as a result of anomalies of the branchial arch derivatives.

CT scanning is essential in evaluation of the patient with known or suspected structural deformities of the external or middle ear. If the anomaly appears to be surgically correctable, identification of associated inner malformations is essential, since the anomaly may be inoperable. MRI studies can be used to directly evaluate the fluid spaces within the otic capsule.

Middle Ear and External Ear Malformations[41]

The most common anomaly of the middle ear and the external ear is *atresia* (also called *microtia*, or absence of the external ear) (Fig. 15–16).[55] Isolated anomalies of the ossicles can occur but are less common.

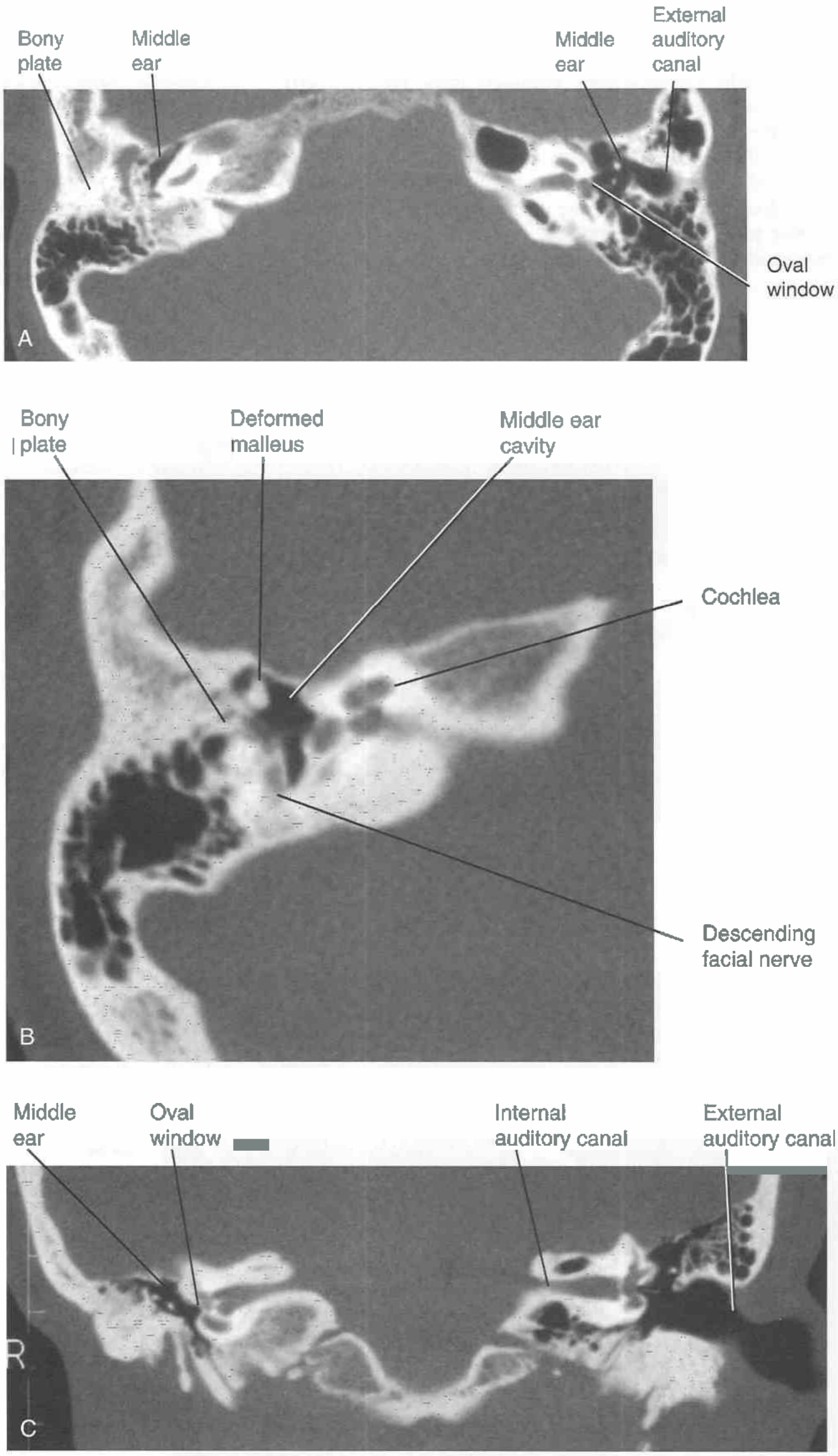

Figure 15–16. Atresia of the external auditory canal.

A, Axial CT scan showing a normal external auditory canal (EAC), middle ear, and oval window on the left. The right temporal bone is sectioned slightly more inferior in location and shows no external auditory canal. A thick bony plate completely covers the small middle ear cavity, centered at the cochlear promontory on the right.

B, Axial magnification view of the right ear. The deformed malleus is seen adjacent to the bony plate covering the EAC. The middle ear cavity is smaller than normal. The descending facial nerve is in a normal location. The mastoid air cells are well pneumatized.

C, Coronal CT scan showing a normal left EAC, internal auditory canal, and oval window. On the right, the otic capsule structures are intact but the EAC is completely replaced with thick bone. The descending facial nerve canal is somewhat anterior in location as it tracks toward the stylomastoid foramen.

Microtia may be associated with narrowing or agenesis of the bony external auditory canal. The degree of distortion can range from a web or small band of soft tissue partially covering the external auditory canal to complete absence.[11] Microtia is also associated with a number of other middle ear anomalies, including those seen in Pierre Robin and Apert's syndromes.

Numerous ossicular anomalies may be associated with atresia of the external auditory canal. The most common is fusion of the malleus and incus to the lateral epitympanic wall. Bony ankylosis of the neck of the malleus to the atresia plate is also common. Anomalies of the second branchial arch result in deformities of the long process of the incus, stapes superstructure, and a portion of the footplate of the stapes. Combined ossicular anomalies are common. The stapes is most often involved in cases of isolated deformity.

The facial nerve canal must be carefully evaluated in all cases of suspected external and middle ear anomalies, particularly if surgery is planned, because anomalous development of the middle ear may alter the course of the facial nerve. In anomalies of the second branchial arch, the facial nerve canal may be positioned within the floor of the tympanic cavity or may cross the oval window. Occasionally, the facial nerve branches into two or three portions within the temporal bone.

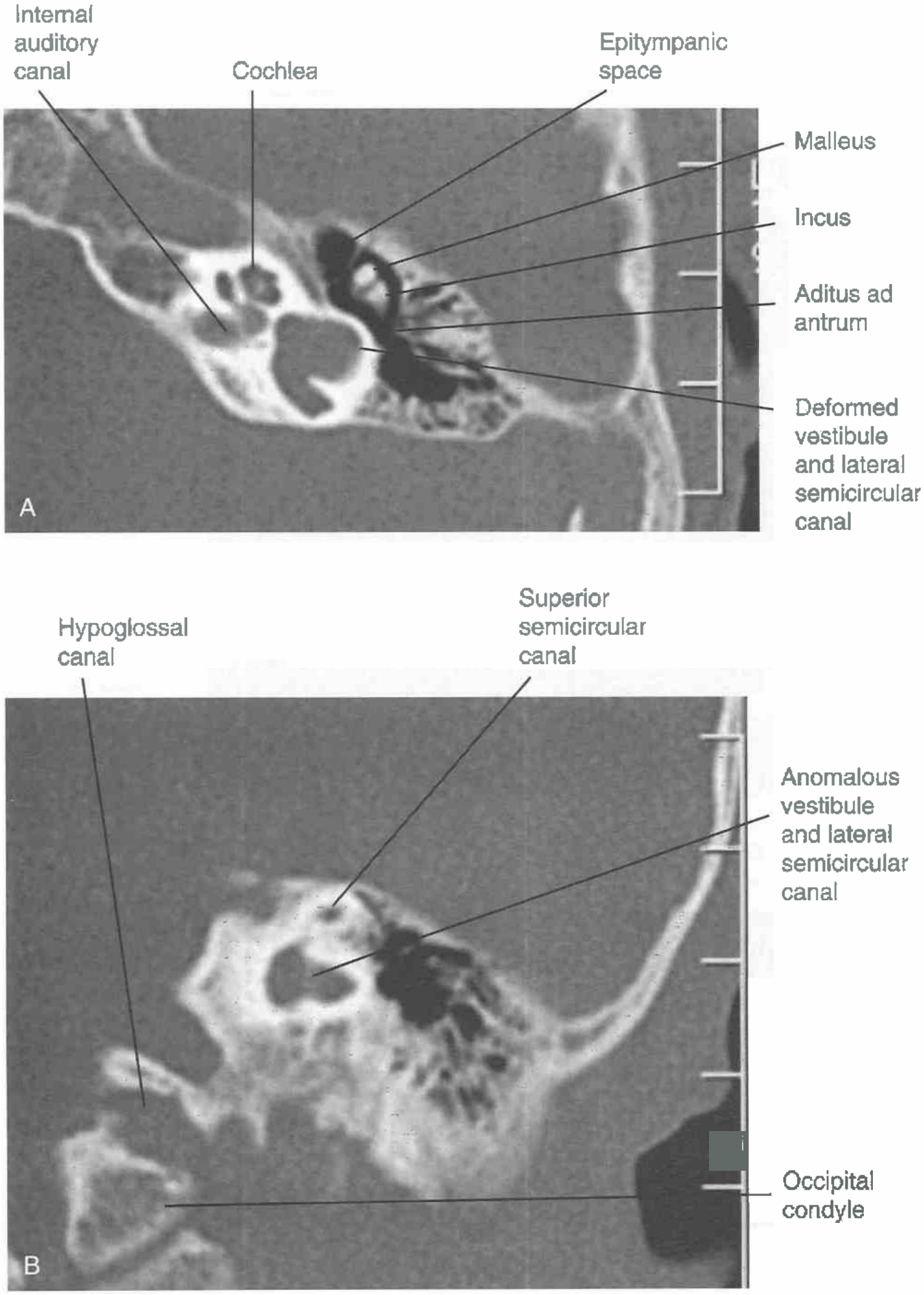

Figure 15–17. Vestibular anomaly. *A,* Axial CT image at the level of the vestibule, epitympanic space, and cochlea. The ossicles and middle ear are normal. The cochlea is dysplastic. The vestibule is deformed with a bulbous configuration. The vestibule fuses with the lateral semicircular canal. The posterior semicircular canal is also enlarged. It is important to exclude an abnormal fistulous connection between an otic capsule abnormality and the middle ear. *B,* Coronal CT slice sectioned through the anomalous bulbous vestibule. The hypoglossal canal, superior semicircular canal, and occipital condyle are normal.

Inner Ear Malformations

Severe hearing loss secondary to malformations of the membranous labyrinth may coincide with entirely normal CT findings. A subtle finding associated with hearing loss is a lateral semicircular canal diameter less than 6 mm.[44] In contrast, some patients with CT evidence of minor dysplasias of the osseous labyrinth involving the cochlea, vestibule, or semicircular canals may have no clinical evidence of deafness.

The *Mondini malformation* is associated with hypoplasia, absence, or the presence of only a rudimentary coil of the cochlea. Generally, there is a central cavity that contains the remnants of the modiolus. The defect is usually bilateral and associated with dilatation of the vestibular aqueduct. More complex anomalies of the cochlea, with dilatation of the vestibule and partial or complete absence of the semicircular canals may also occur (Fig. 15–17).[2]

A complete lack of inner ear development is the *Michel defect*. A single labyrinthine cavity with no distinct vestibule, cochlea, or semicircular canals may be seen, or petrous development may be totally absent. Occasionally, the internal auditory canal is absent.[19, 32]

CT evaluation of congenital inner ear malformations should include evaluation of the cochlear and vestibular aqueducts. In patients with large cochlear aqueducts, there is a high incidence of CSF leaks near the oval window (stapes "gusher" syndrome). There is a known association between cochlear abnormalities and dilatation of the vestibular aqueduct. Many patients with the Mondini or Michel malformation have enlarged vestibular aqueducts. This implies a deformity of the membranous labyrinth. Dilatation of the vestibular aqueduct may also occur as an isolated event, leading to fluctuating hearing loss (Fig. 15–18).

Before placement of cochlear implants, patients are often studied with CT to more fully characterize the inner ear anomaly.[67] Following inflammation, the membranous labyrinth may be fibrotic and the cochlea may not accept the implant. There may be complete obliteration of the bony cochlea. MRI studies can confirm that the space within the bony otic capsule is filled with fluid when there is a question of fibrous obliteration of the otic capsule.

Vascular Anomalies

Many of the anomalies of the vascular structures of the temporal bone that were previously visible only on angiograms are now readily recognizable on high-resolution CT scans and MR images. If the surgeon is aware of the anomalous vasculature, vessel injury may be avoided during surgery or biopsy.

The development of the intrapetrous portion of the internal carotid artery is independent of that of the remaining ear. Because a vessel must be present before its canal forms, the carotid canal does not develop in cases of agenesis of the carotid artery. Agenesis of the intrapetrous carotid artery is thus identified on CT scans by absence of the carotid canal and carotid sulcus.

An ectopic intratympanic carotid artery (Fig. 15–19) may occur when there is alteration in carotid development.[54] The carotid canal may be partially absent, resulting in dehiscence of the bony margins and ectopic placement of the vessels into the middle ear. Pulsation tinnitus or conductive hearing loss, or both, may occur.[2] An intratym-

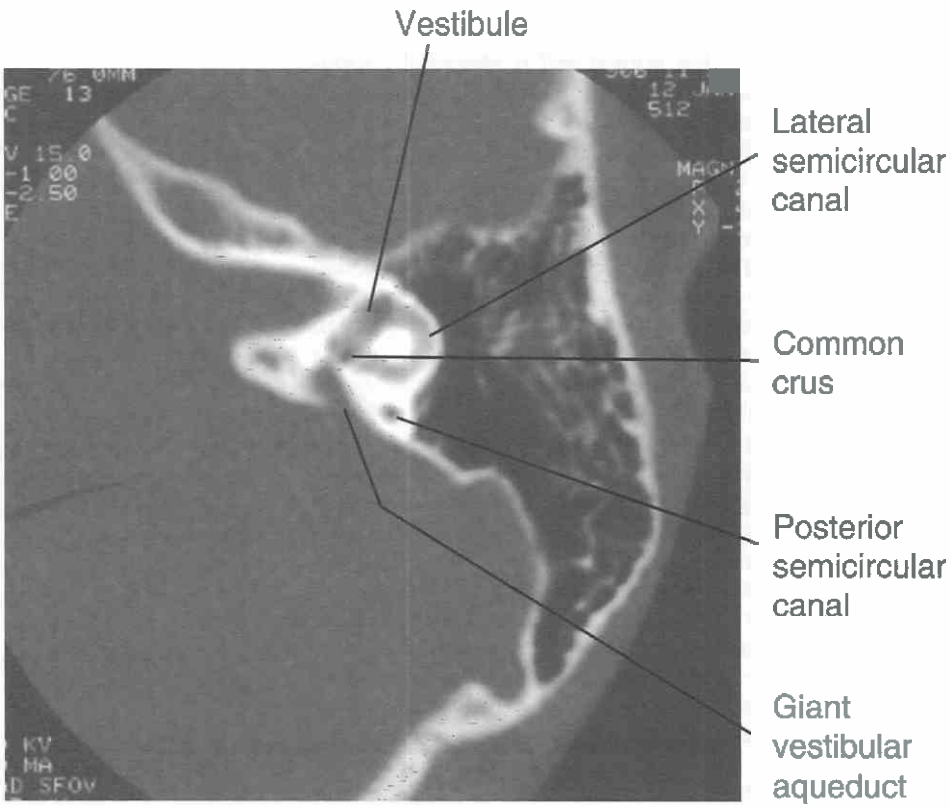

Figure 15–18. Giant vestibular aqueduct. This axial CT section is centered at the internal auditory canal and the lateral semicircular canal. The vestibular aqueduct is more than 2 mm in thickness. It is seen extending back toward the region of the vestibule and the common crus. Usually, the vestibular aqueducts are seen only as thin slits. This is a common congenital anomaly and suggests that other anomalies may be present, including those of the cochlea. The process may be bilateral as well.

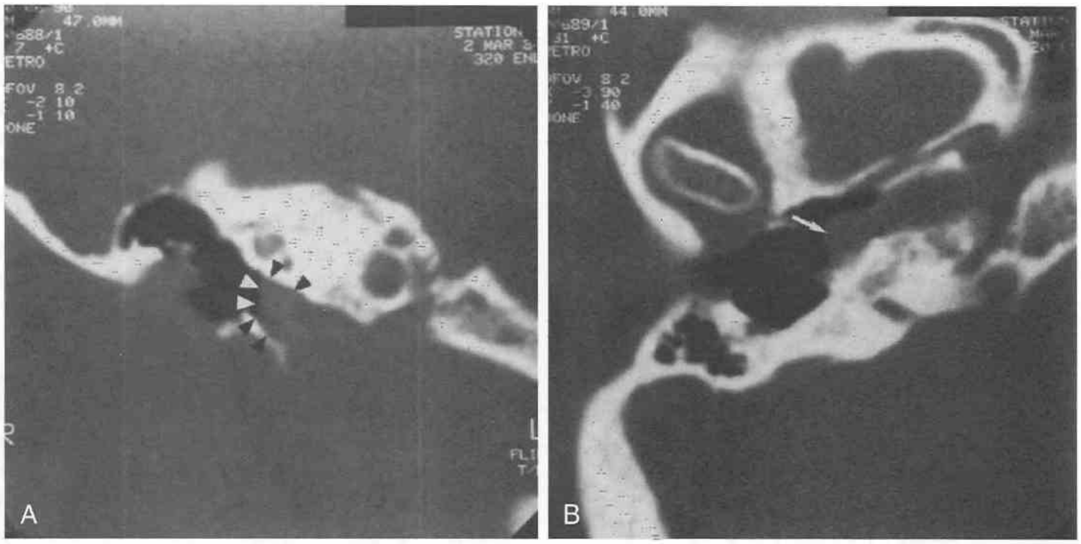

Figure 15–19. Ectopic intratympanic carotid artery in a young adult presenting with a pulsating mass behind the right eardrum. *A,* Coronal CT scan of the right ear. There is a dehiscence *(white arrowheads)* in the floor of the tympanic cavity inferior to the cochlea. The ectopic carotid artery *(black arrowheads)* bulges into the hypotympanum through this bony dehiscence. *B,* Axial CT scan through the right hypotympanum. The vessel *(arrow)* simulates a soft tissue mass in the hypotympanum. The anterior lateral portion of the bony carotid canal is absent. (Courtesy of Dr. C. Roger Bird.)

panic, ectopic carotid artery may actually represent the inferior tympanic branch of the ascending pharyngeal artery secondary to agenesis of a segment of the internal carotid artery during early development. The aberrant vessel thus takes over as a source of blood flow to the brain. In either case, high-resolution CT or MRI studies can be used to differentiate these arterial vascular anomalies from a middle ear tumor. Angiography is generally not necessary but can be useful in questionable instances. On CT or MRI studies, the first genu of the ectopic carotid artery is usually located more lateral than normal and is abnormally tortuous. With dehiscence of the carotid canal, the carotid artery fills the anterior medial middle ear. The ectopic carotid artery is commonly small and tortuous. On angiography, the genu is lateral to the vestibule.

Another type of intratympanic vascular anomaly involves substitution of the stapedial artery for the middle meningeal artery. The intratympanic course of the stapedial artery is seen with enlargement of the tympanic portion of the facial nerve canal and absence of the ipsilateral foramen spinosum. Involvement of the facial nerve canal is seen in this defect because the development of the facial nerve canal closely parallels that of the middle meningeal artery. In this substitution anomaly, the stapedial artery originates from the intrapetrous internal carotid artery, runs with the facial nerve through the tympanic cavity, and then exits into the middle cranial fossa to supply the dura of the cerebral hemisphere.

Anomalies of the jugular vein and bulb are common. A defect in the bony plate separating the jugular bulb from the hypotympanum may result in a high jugular bulb that protrudes into the middle ear (Fig. 15–20). With other jugular bulb lesions, there is loss of the normal smooth margin of the osseous bulb because of irregular bony destruction.[12, 17]

A high jugular bulb may also give rise to a jugular bulb diverticulum (see Fig. 15–20). A diverticulum is distinct from a large jugular bulb because the diverticulum is usually posterior to the internal auditory canal and does not affect the middle ear.[3] The diverticulum is recognizable on CT scans and should not be mistaken for a tumor.[34] MRI signal from slow flow in a diverticulum may mimic a mass. Two-dimensional gradient-echo or phase-flow images are particularly sensitive to slow flow abnormalities of the venous system.[15]

Inflammatory Lesions

Both CT and MRI are important in staging the primary changes and identifying complications of temporal bone inflammatory disease. CT has proved effective in detecting bony erosions and soft tissue masses associated with middle ear inflammatory disease. Contrast-enhanced MRI studies can be used to differentiate fluid and cholesteatoma from enhancing granulation tissue or tumor.[40]

Acute and Subacute Otitis Media

Acute otitis media is associated with middle ear opacification.[56] Concomitant mastoiditis is evidenced by opacification or fluid levels in the mastoid air cells. The fluid in serous otitis media cannot be distinguished from the pus seen with purulent otitis. Subacute otitis media shows similar findings in the mastoid air cells and middle ear, with the additional finding of focal or diffuse mucosal thickening.

Chronic Otitis Media and Chronic Mastoiditis

Chronic otitis media (Fig. 15–21) results in the formation of granulation tissue that may become heaped up, obscuring the margins of the middle ear contents.[64] This

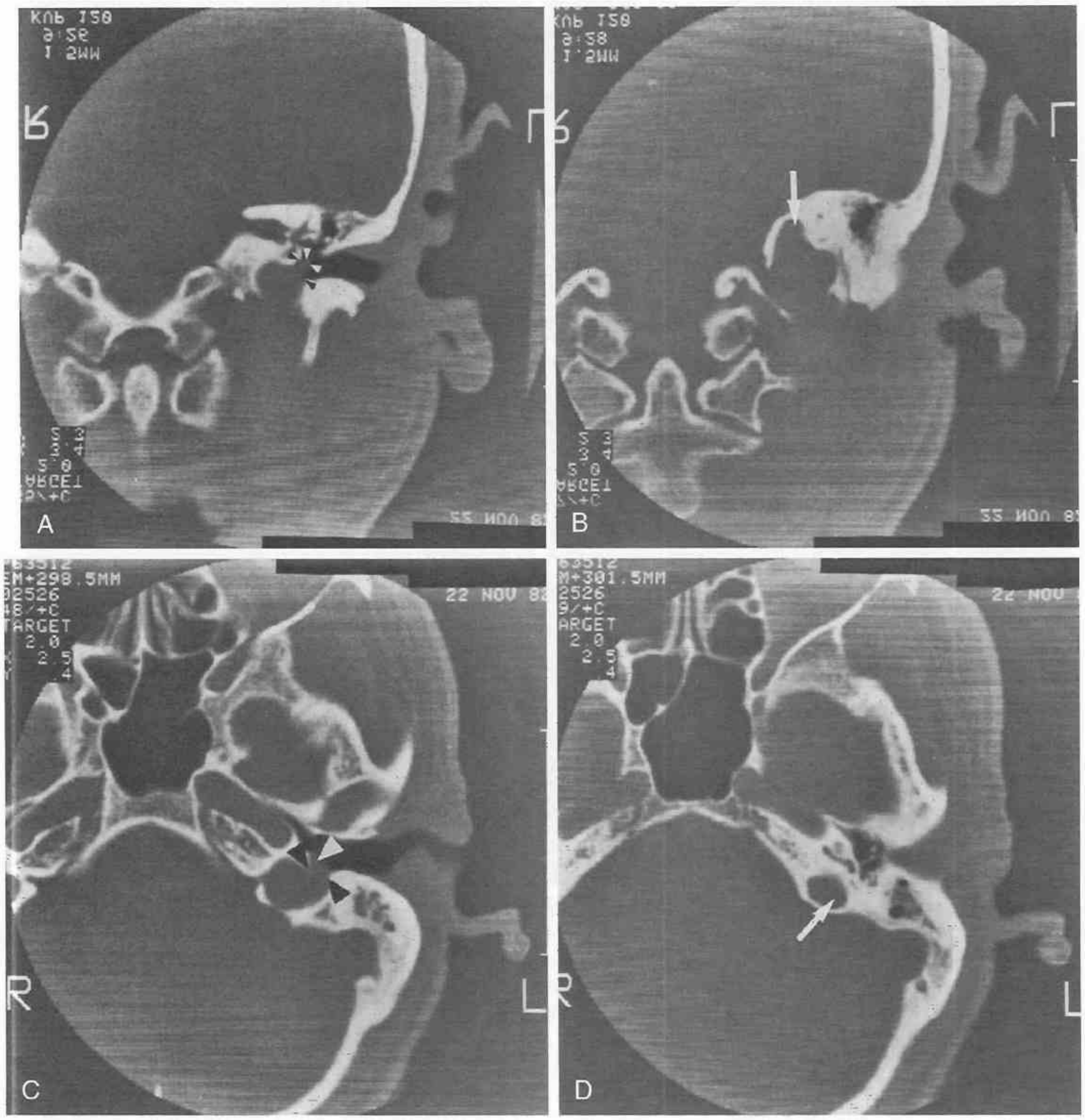

Figure 15–20. Dehiscent jugular bulb with diverticulum in an adult presenting with a pulsating bluish mass behind the left eardrum.

A and *B*, Coronal CT scans of the left ear. There is a dehiscence in the floor *(white arrowheads)* of the tympanic cavity, with extension of a portion of the jugular bulb *(black arrowheads)* into the hypotympanum *(A)*. The remaining jugular fossa is sharply defined. A small diverticulum of the jugular fossa *(white arrow)* protrudes superiorly toward the roof of the petrous temporal bone *(B)*.

C and *D*, Axial CT scans of the left ear. Note the dehiscence *(black arrowheads)* of the jugular fossa with extension of the jugular bulb simulating a mass into the hypotympanum *(white arrowhead) (C)*. The diverticulum *(white arrow)* extends superiorly to the level of the osseous labyrinth *(D)*. The ipsilateral sigmoid sinus impression is also large, suggesting a developmental variation rather than tumor.

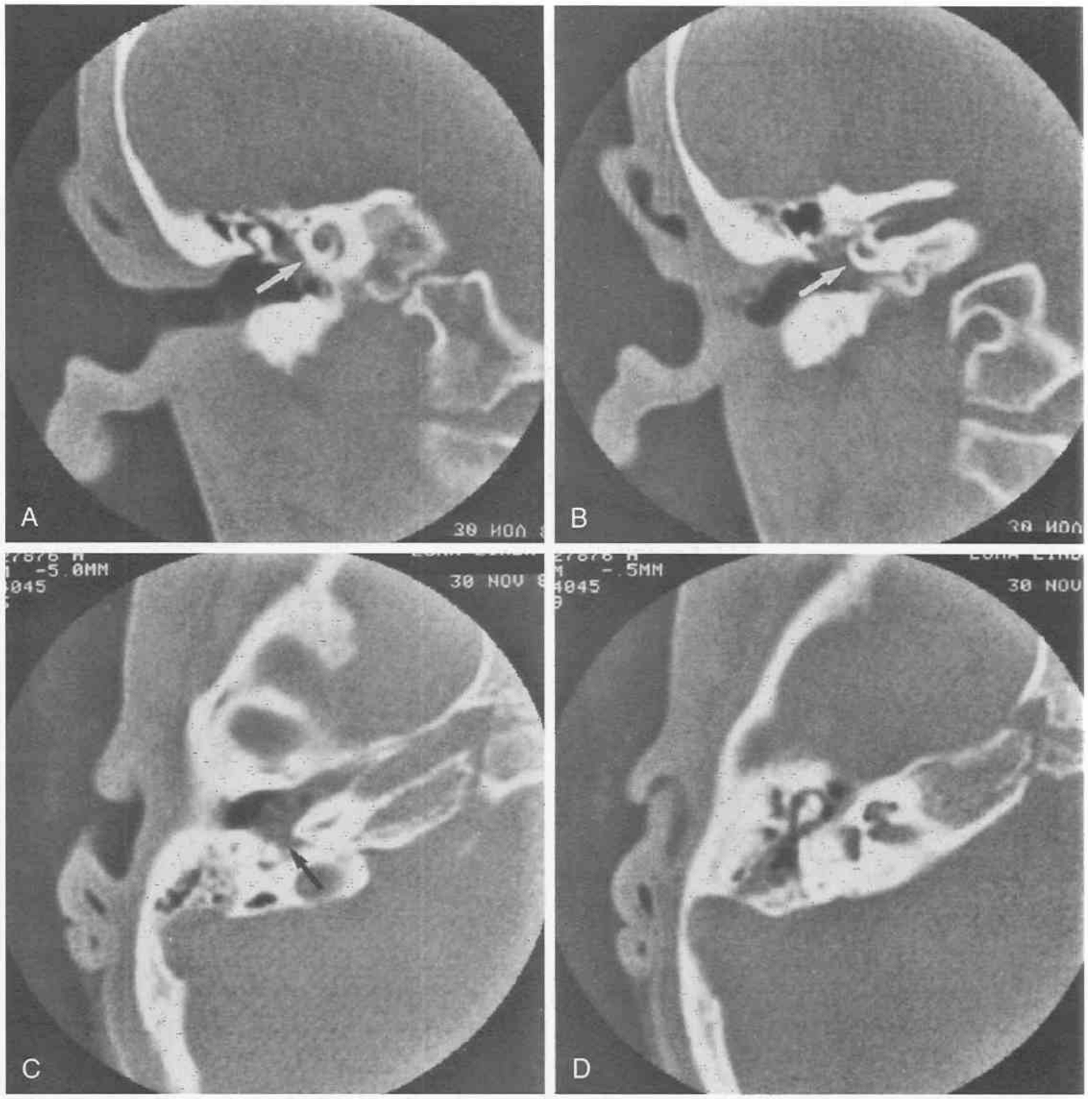

Figure 15–21. Chronic otitis media in a young child with a long history of right-sided conductive hearing loss.

A and *B*, Coronal CT scans of the right ear. There is a soft tissue density within the tympanic cavity *(arrows)*. The tympanic membrane is retracted medially. The ossicles are intact and show no evidence of bone destruction.

C and *D*, Axial CT scans of the right ear. The middle ear cavity is largely opacified. The sinus tympani is involved *(arrow)*. The mastoid air cells are poorly developed. The nasopharynx should be evaluated to rule out an obstructive lesion. In children, the nasopharyngeal process is commonly an adenoid enlargement.

process results in areas of nondependent radiodensities within the middle ear. The tympanic membrane is usually retracted inward in patients with chronic otitis media. The mastoid may be poorly developed and sclerotic, since this process begins in childhood.

Chronic mastoiditis (Fig. 15–22) follows repeated bouts of otitis media and accompanying mastoid infections. There is a gradual reduction in the number of mastoid air cells, with thickening of the mucous membrane and reactive sclerosis of the bony septa. Persistent suppuration leads to mucosal destruction and subsequent granulation tissue formation. Erosion of mastoid air cell walls rarely occurs without the presence of cholesteatoma.

Cholesteatoma

Cholesteatomas develop in patients with chronic perforations of the tympanic membrane, usually from eustachian tube dysfunction. Most perforations occur at the pars flaccida segment of the tympanic membrane (Fig. 15–23). Perforations of the pars tensa membranae tympani are rare. In these patients, the cholesteatoma extends directly into the central portion of the middle ear (Fig. 15–24).

Histologically, cholesteatomas consist of an inner layer of desquamated, stratified squamous epithelium apposed on an outer layer of subepithelial connective tissue. The subepithelial connective tissue layer is formed by a chronic inflammatory process that deposits cholesterol crystal clusters, giant cells, and round cells. Accumulation of epithelial debris within the lumen leads to progressive enlargement of the epithelial soft tissue mass. As the lesion enlarges, it contacts the contiguous bony structures of the middle ear, mastoid air cells, and petrous pyramid, causing erosion from pressure necrosis and enzymatic lysis of bone. Cholesteatomas typically originate in the middle ear but

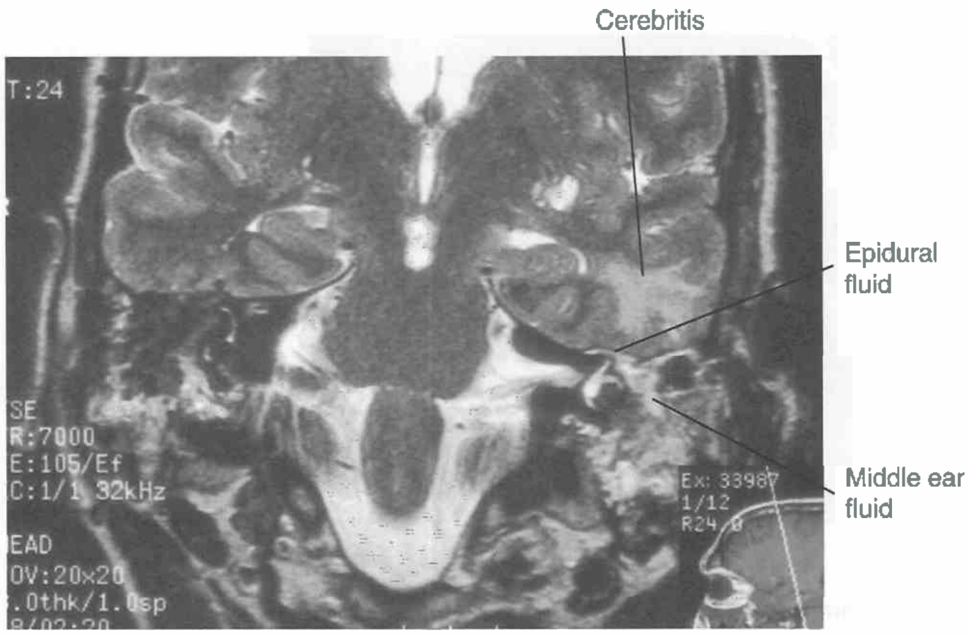

Figure 15–22. Cerebritis and mastoiditis in a young man who presented with a seizure and left ear drainage. This coronal T2-weighted, high-resolution, spin-echo MR image demonstrates a region of edema related to brain infection in the inferior portion of the left temporal lobe. In the adjacent left temporal bone, there is opacification of the middle ear cavity due to septic mastoiditis. Note the small fluid collection (epidural) along the superior portion of the left temporal bone related to the infection. In patients with temporal lobe pathology, a careful review of the temporal bones should always be made to exclude an extra-axial source.

may extend into mastoid air cells and, occasionally, into the petrous pyramid.

Pus within a denuded mucosal cavity results in proteolytic erosion of the ossicles and walls of the middle ear. Chronic otitis media and cholesteatoma are thus characterized by a combination of focal or diffuse soft tissue densities in association with focal or diffuse bone destruction. This process leads to rarefying osteitis or erosive otitis media. The erosions typically involve the lateral wall of the tympanic cavity, including the scutum and the ossicles.[26] The facial nerve canal and lateral semicircular canal are rarely affected.[29] Differentiation from cholesteatoma may be impossible.

Classically, cholesteatomas expand into the antrum and mesotympanum, resulting in medial displacement of the ossicles away from Prussak's space. From the mesotympanum, the extension may be posterior into the sinus tympani or inferior into the hypotympanum. Further growth may be in several directions, most commonly into the posterolateral attic and then through the aditus into the antrum and mastoid air cells.[52]

The diagnosis of cholesteatoma is based on the identification of a sharply demarcated soft tissue mass in the middle ear and bony destruction. Most of the time, the diagnosis is clear and is based on physical examination. The purpose of imaging is to stage the lesion. Continual

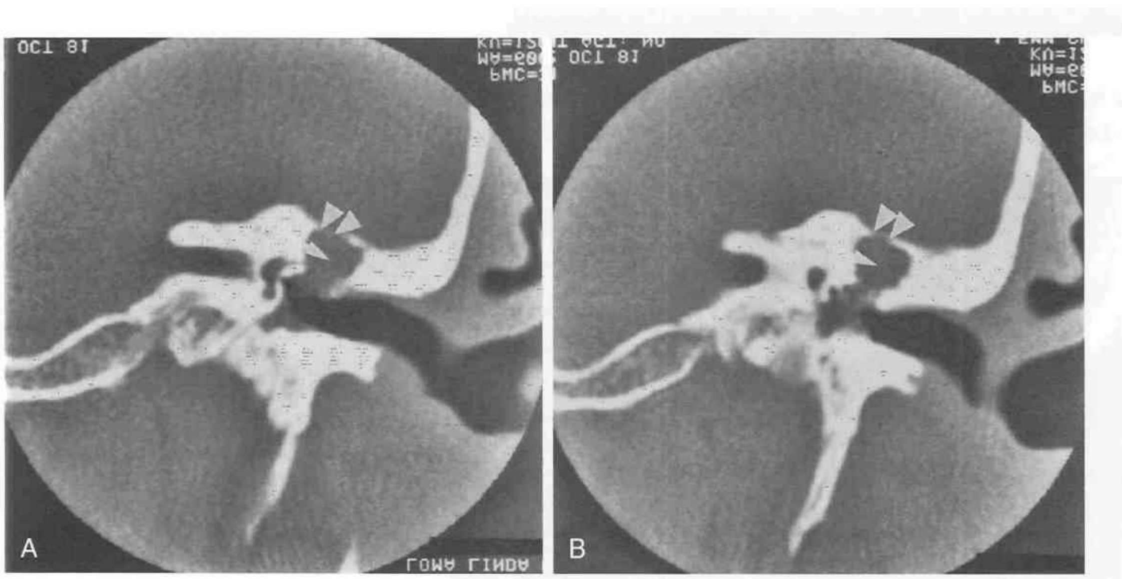

Figure 15–23. Epitympanic cholesteatoma in an elderly woman with a [illegible]ar histor[illegible] vertigo and left-sided hearing loss. *A* and *B*, Coronal CT scans of the left ear show a large, destructive soft tissue mass in the tympanic cavity, epitympanic space, attic, and antrum *(arrows)*. The scutum is thinned. The walls of the middle ear cavity are expanded and amorphous. There is erosion of the cholesteatoma into the lateral semicircular canal. The tympanic membrane is retracted. The tegmen antri is thin, but there is no evidence of intracranial extension *(arrowheads)*.

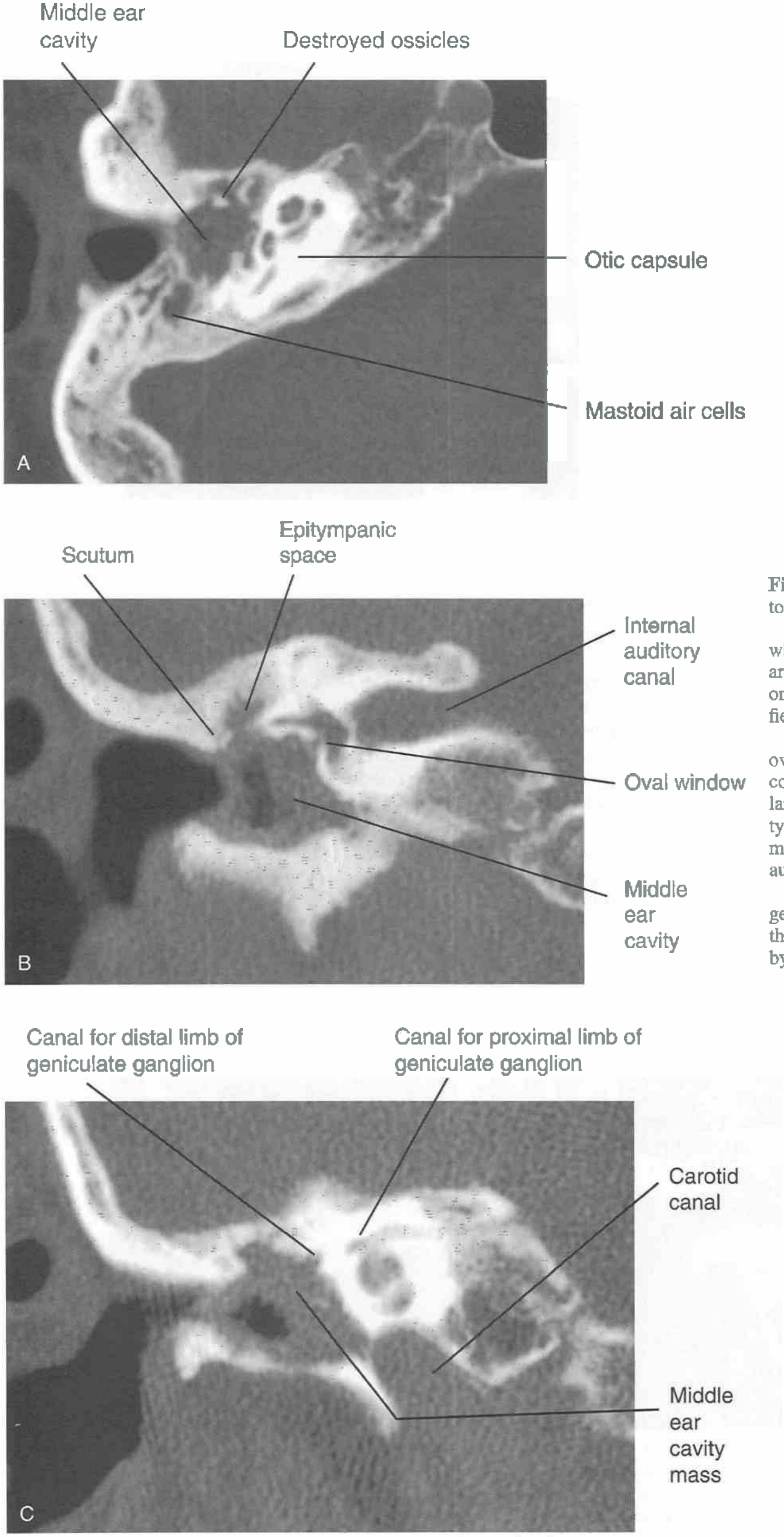

Figure 15–24. Inflammatory cholesteatoma.

A, Axial CT through the middle ear, which is largely opacified. The ossicles are partially destroyed and pushed anteriorly. The mastoid air cells are also opacified. There is no otic capsule destruction.

B, Coronal CT image through the oval window. The middle ear is almost completely opacified. The normal ossicular structures have been eroded. The epitympanic space is opacified as well. The mass does not protrude into the external auditory canal, but the scutum is blunted.

C, Coronal CT image centered at the geniculate ganglion. The distal limb of the geniculate ganglion canal is eroded by the middle ear mass.

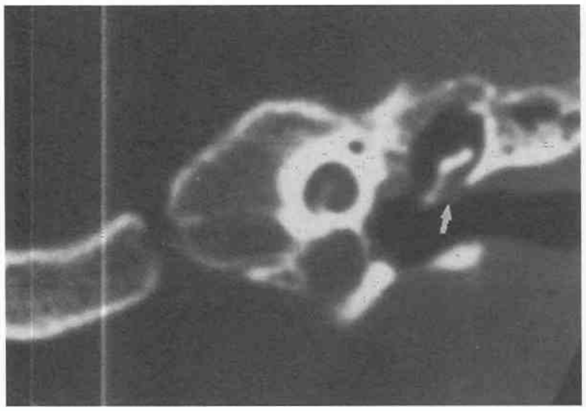

Figure 15–25. Small early cholesteatoma. Coronal CT scan of the left temporal bone shows a small soft tissue mass *(arrow)* just lateral to the malleus and medial to the scutum. There is no bone destruction. This is consistent with an early deformity of the pars flaccida and a cholesteatoma.

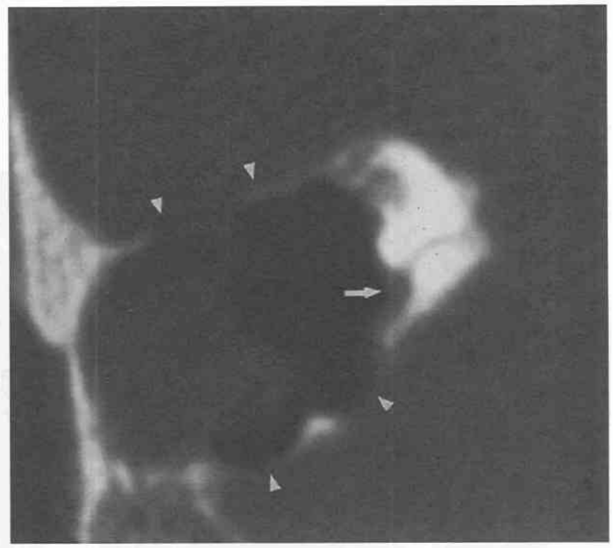

Figure 15–26. Autoantrectomy. Axial CT section through the right superior temporal bone. There is a large defect in the mastoid with thinning of the bony margins *(arrowheads)*. A central soft tissue mass partially fills the space. This patient did not have surgery, but the cholesteatoma has almost completely emptied the mastoid space as a result of chronic bone destruction. There is erosion of the superior semicircular canal *(arrow)*.

pressure on the ossicles may lead to necrosis or dislocation. The most common type of ossicular destruction involves the short and long processes of the incus, followed by destruction of the body of the incus and the head of the malleus.[52] Early small cholesteatomas (Fig. 15–25) may be associated with no bony change.

Patients with facial nerve palsy may have erosion of the facial nerve canal and compression of the facial nerve. Labyrinthine fistulas may form when there is erosion into the lateral or posterior semicircular canals. In rare instances, a cholesteatoma may extend into the otic capsule or the middle cranial fossa through the tegmen antri or tegmen tympani.

The cholesteatoma may be extruded spontaneously through an acquired osseous defect, usually associated with a large bony defect of the external auditory canal and mastoid (autoantrectomy) (Fig. 15–26).[28] Such an osseous defect may appear similar to a surgical defect. The residual cavity may have circumferential mural cholesteatomatous material, with an empty, air-filled central cavity.

Malignant External Otitis

Malignant external otitis (Fig. 15–27) is most often associated with a *Pseudomonas* infection in elderly, diabetic, or immunosuppressed patients. These patients complain of severe otalgia and purulent discharge from the external auditory canal.

More extensive disease causes necrosis of the adjacent soft tissues, with extensive bony destruction. The bony destruction may involve the walls of the external auditory canal and may extend into the tympanic cavity and inner ear, leading to hearing loss and facial nerve dysfunction.

The necrotizing soft tissue infection may also spread along Santorini's fissures (small clefts in the cartilaginous portion of the external auditory canal) into the soft tissues of the nasopharynx and oropharynx. Both the osseous and soft tissue spread may lead to intracranial extension. If left untreated, the disease progresses, leading to meningitis, cerebritis, and osteomyelitis of the skull base. The disease can be fatal in a short period, thus earning the term *malignant external otitis*.

Early findings include soft tissue thickening of the external auditory canal with clouding of the middle ear and mastoid air cells. There are varying degrees of surrounding bone destruction involving the temporomandibular joint, petrous pyramid, tympanic cavity, or mastoid process.

CT scanning with IV contrast material is needed to define the extent of disease within the soft tissues of the head and neck. There may be widespread enhancement with multiple focal abscesses. CT and MRI studies optimally demonstrate the fat and muscle planes, illustrating the extent of the disease in the soft tissues of the pinna, parapharyngeal space, clivus, infratemporal fossa, and carotid sheath.[11] Involvement of the subtemporal fossa is evidenced by obliteration of the normal fat planes, whereas involvement of the parapharyngeal space is evident by loss of the characteristic CT low density within the space and presence of a mass lesion.[18] Marrow involvement and vessel occlusion are best seen on MR images.

CT is excellent for following the progression of the bone and soft tissue involvement after treatment. The bone erosions are usually constant. If there is no resolution after appropriate antibiotic therapy, surgery may be necessary for adequate drainage of soft tissue abscesses and removal of destroyed bone.[42]

Infection of the Endolymphatic Sac

MRI is sensitive to subtle changes of the membranes of the otic capsule structures. Transient enhancement may commonly involve the vestibule (Fig. 15–28) and is generally thought to represent a viral infection or another inflammatory process. In rare instances, enhancement of the endolymphatic duct and cochlea is seen. Suppurative infections (e.g., syphilitic, staphylococcal) produce enhancement as well, but the findings are more persistent. These infec-

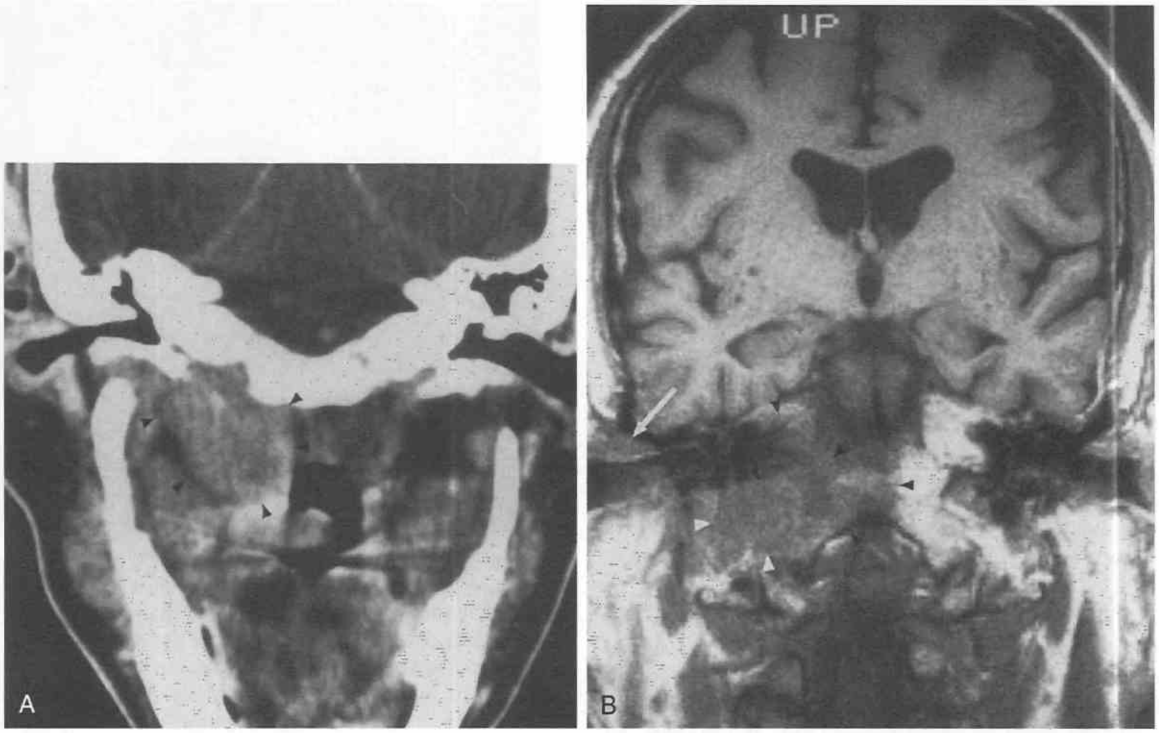

Figure 15–27. Malignant external otitis.

A, Coronal CT section through the external auditory canals. There is slight loss of the fatty interfaces surrounding the soft tissue portion of the right external auditory canal. The bulk of the pathology is centered in the parapharyngeal space and the nasopharynx. There is obliteration of the normal fat planes in the infratemporal fossa and an ill-defined soft tissue mass *(arrowheads)*.

B, Coronal T1-weighted MRI study at a similar location. The fat planes directly parallel to the right external auditory canal *(white arrow)* are partially obliterated. The fatty marrow spaces of the clivus *(black arrowheads)* and the adjacent fatty soft tissue space *(white arrowheads)* have been replaced by lower-signal inflammatory tissue. The ascending internal carotid artery is enveloped by these infiltrative changes.

(*A* and *B*, Courtesy of Barbara Carter, M.D.)

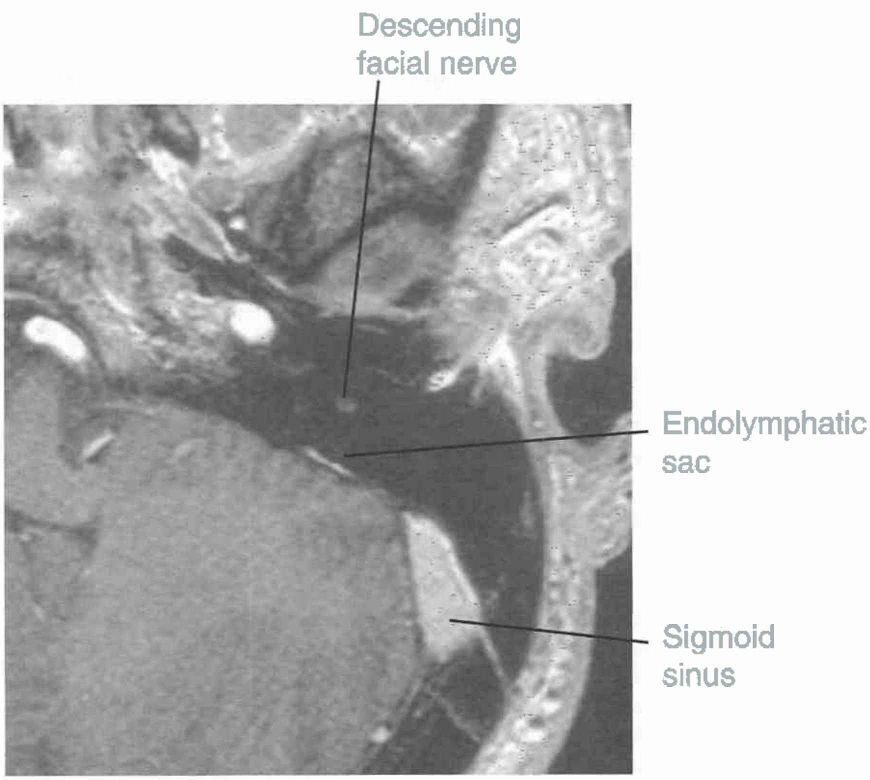

Figure 15–28. Endolymphatic sac inflammation in a young male who presented with severe hearing loss and vertigo, probably related to a viral infection. This is an axial 3D Fourier transform T2-weighted, high-resolution MR image through the descending facial nerve and the lower endolymphatic duct. Note the abnormal enhancement of the sac. Unlike a congenital anomaly or a tumor, the sac is not enlarged. This type of finding suggests an inflammatory process and has been described in association with Meniere's disease.

tions demonstrate other more aggressive findings such as bone destruction and mass effect. Occasionally, sarcoid, metastasis, lymphoma, or eosinophilic granuloma may mimic an infection early in their course.[33, 51, 65]

Brain Abscess

Brain abscesses may develop from temporal bone inflammatory processes by several mechanisms. Petrositis of the apical air cells can extend into the epidural and skull base spaces. In these instances, CT scanning shows the bony destruction with dural enhancement adjacent to the temporal bone. This is called *Gradenigo's syndrome.* Cholesteatomas can erode through the tegmen tympani or tegmen antri into the middle cranial fossa or through the mastoid into the posterior cranial fossa. CT or MRI with contrast enhancement shows elevation and enhancement of the dura with extension of pus into the epidural space (see Fig. 15–22). Classic ring-enhancing lesions can also be seen. In patients with recurrent cholesteatomas after radical mastoidectomies, intracranial spread of the infection may develop. This occurs when the bony barriers have been surgically removed.

Meniere's disease is a poorly understood disorder of the temporal bone consisting of intermittent severe vertigo with progressive hearing loss. Some believe that it is related to inflammation of the membranes of the otic capsule leading to obliteration of the endolymphatic duct. In the active phase, enhancement of the endolymphatic sac may be seen. Later on, the endolymphatic sac may be asymmetrical or not visible. The imaging diagnosis is complicated by the fact that there are many variations in the sacs among patients and from side to side in the same patient.[66]

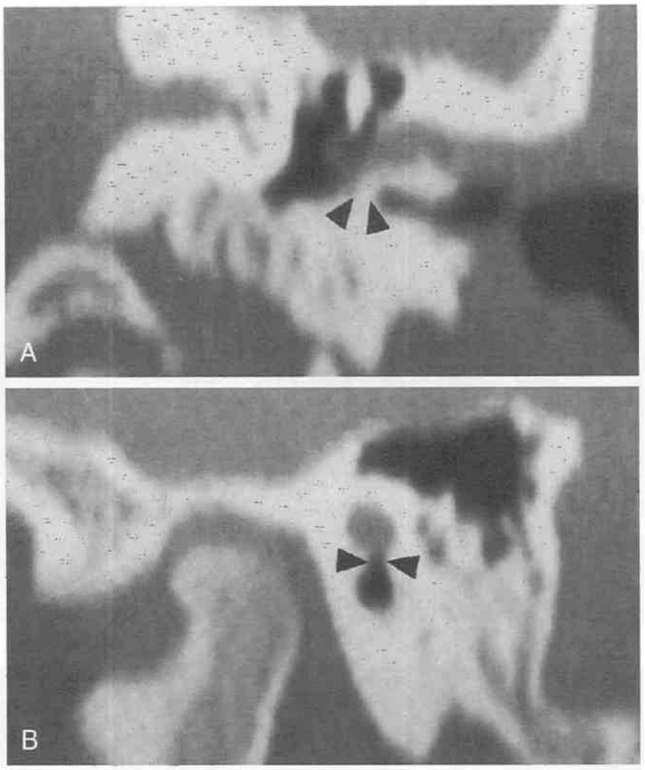

Figure 15–29. Osteoma of the left external auditory canal (EAC) in a 13-year-old boy with a history of cold-water swimming and a chronic deformity of the EAC. Coronal *(A)* and sagittal *(B)* reformatted CT images through the left EAC. The EAC is opacified, with osseous constriction of its medial portion. The osteoma *(arrowheads)* is completely incorporated into the adjacent bone *(A)*. Note the keyhole constriction *(arrowheads)* of the EAC, best seen in the sagittal reformatted image *(B)*. Within the stenotic EAC is a soft tissue mass that represents a secondary EAC cholesteatoma.

Neoplastic Lesions

Benign Neoplasms

Osteomas

Osteomas (Fig. 15–29) are common benign tumors of the temporal bone. Some osteomas are large enough to occlude osseous foramina such as the external auditory canal or the eustachian canal. Osteomas may also develop in the mastoid process after trauma. Bony thickening of the external auditory canal is commonly associated with prolonged exposure to cold water and is usually seen in swimmers. CT scanning demonstrates an osteoma as an area of dense thickening of compact bone.

Acoustic Schwannomas

Acoustic schwannomas are benign tumors of cranial nerve VIII, usually located within the internal auditory canal and cerebellopontine angle cistern. They classically arise at the junction of the neuroglial and Schwann cell sheaths, commonly near the porus acusticus. The vestibular nerve is the most common site of origin.

Symptoms are directly related to the size and location of the tumor. Growth of acoustic schwannomas in the internal auditory canal causes compression of the cochlear and vestibular nerves. This results in progressive neurosensory loss and tinnitus. Early vestibular dysfunction is uncommon, probably resulting from the slow growth of the tumor, which allows for central compensation of the progressive peripheral dysfunction.[23] Facial nerve paresis or palsy is a rare event but may occur with large masses. Clinical symptoms from the fifth cranial nerve are actually more common than the seventh cranial nerve.

The imaging presentations of acoustic schwannomas vary widely. Some of these tumors are only a few millimeters in dimension (Fig. 15–30), and are difficult to identify, whereas others are so massive (Fig. 15–31) that they are life-threatening. They rarely occur within the vestibule or cochlea (Fig. 15–32). Some tumors cross from the internal auditory canal into the otic capsule regions, but this is uncommon.

CT scans can be used in diagnosis, as large tumors can be seen directly. Small tumors of the internal auditory canal that do not affect the bony margins necessitate either air-contrast cisternography or MRI studies. The bony changes of the internal auditory canal, porus acusticus, and otic capsule are common and help to differentiate acoustic tumors from other cerebellopontine angle masses (Fig. 15–33).[58] It is extremely uncommon for a nonacoustic tumor to expand or to erode the auditory meatus. Asymmetry of the internal auditory canals of more than 2 mm suggests the presence of a mass. IV contrast enhancement may

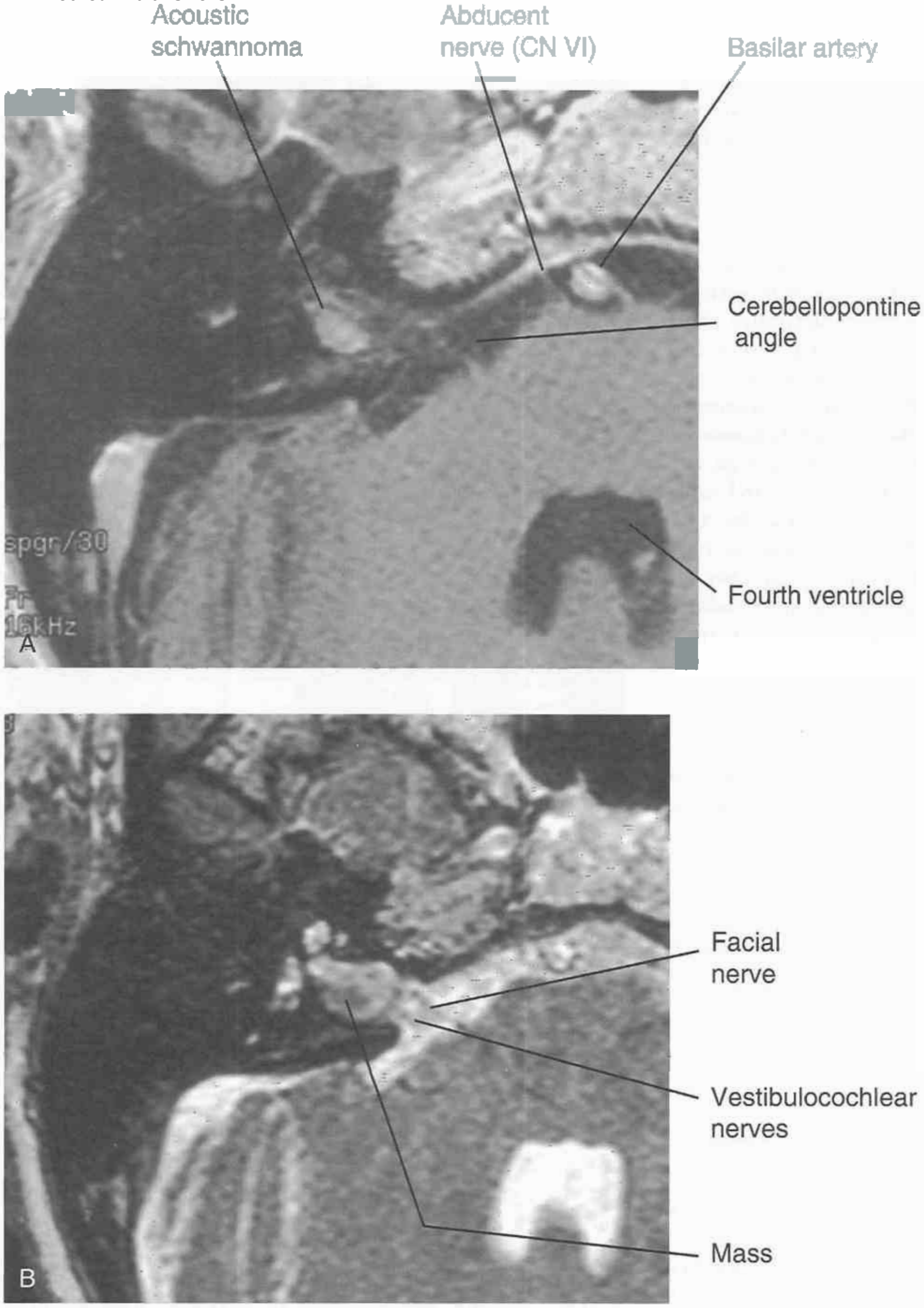

Figure 15–30. Small right acoustic schwannoma.

A, Axial T1-weighted, 3D Fourier transform, contrast-enhanced MR section through the internal auditory canal (IAC). The posterior portion of the IAC is filled with a small enhancing mass, which does not protrude into the cerebellopontine angle (CPA). There is some remodeling of the posterior margin of the IAC. Other structures depicted include the fourth ventricle, basilar artery, and sixth cranial nerve.

B, Axial T2-weighted, 3D Fourier transform, high-resolution, gradient-echo, non–contrast-enhanced image at a site similar to that in *A*. The seventh and eighth cranial nerves are seen in the CPA and the IAC. There is a small posterior filling defect related to the small tumor. The more lateral segments of the cranial nerves in the IAC are visible.

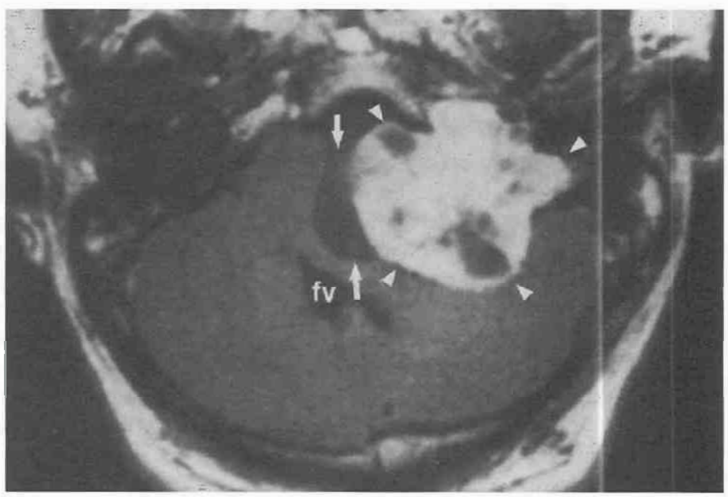

Figure 15–31. Large acoustic schwannoma. Axial T1-weighted, contrast-enhanced, spin-echo MRI study shows a large, lobulated left anterolateral posterior fossa mass *(arrowheads)*. The lesion enhances inhomogeneously. A medial cyst is adjacent to the lesion *(arrows)*. The acoustic schwannoma displaces the fourth ventricle (fv) to the right. There is massive erosion of much of the medial temporal bone, with replacement by schwannoma.

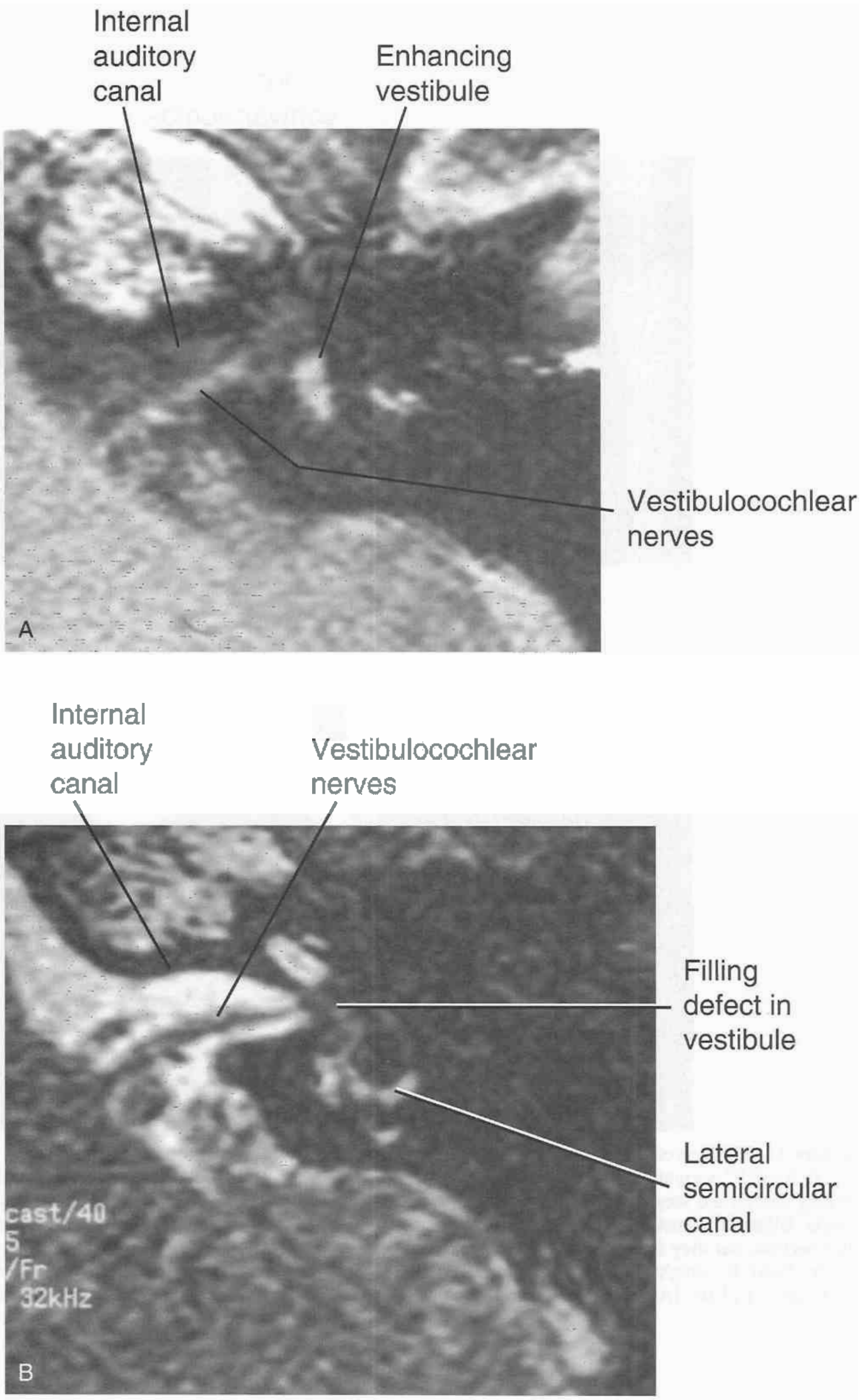

Figure 15–32. Vestibular schwannoma in a patient presenting with symptoms suggesting an acoustic schwannoma; however, no lesion was seen in the internal auditory canal (IAC).

A, Axial contrast-enhanced, high-resolution, 3D Fourier transform, T1-weighted MR image through the vestibule and the IAC. The normal eighth cranial nerve is seen in the IAC. There is abnormal enhancement of the normal-sized vestibule. This was able to be seen with vestibulitis, but this finding did not resolve in a few weeks. The imaging properties of an otic capsule schwannoma are identical to those in the IAC, but the location is different.

B, MR scan made at the same level as in *A* but with a high-resolution, 3D Fourier transform, gradient-echo, T2-weighted MR sequence. Again, the IAC and the eighth cranial nerve are normal. A filling defect is seen where the enhancing mass was centered on the contrast study. Filling defects are more likely to be tumors than inflammatory changes.

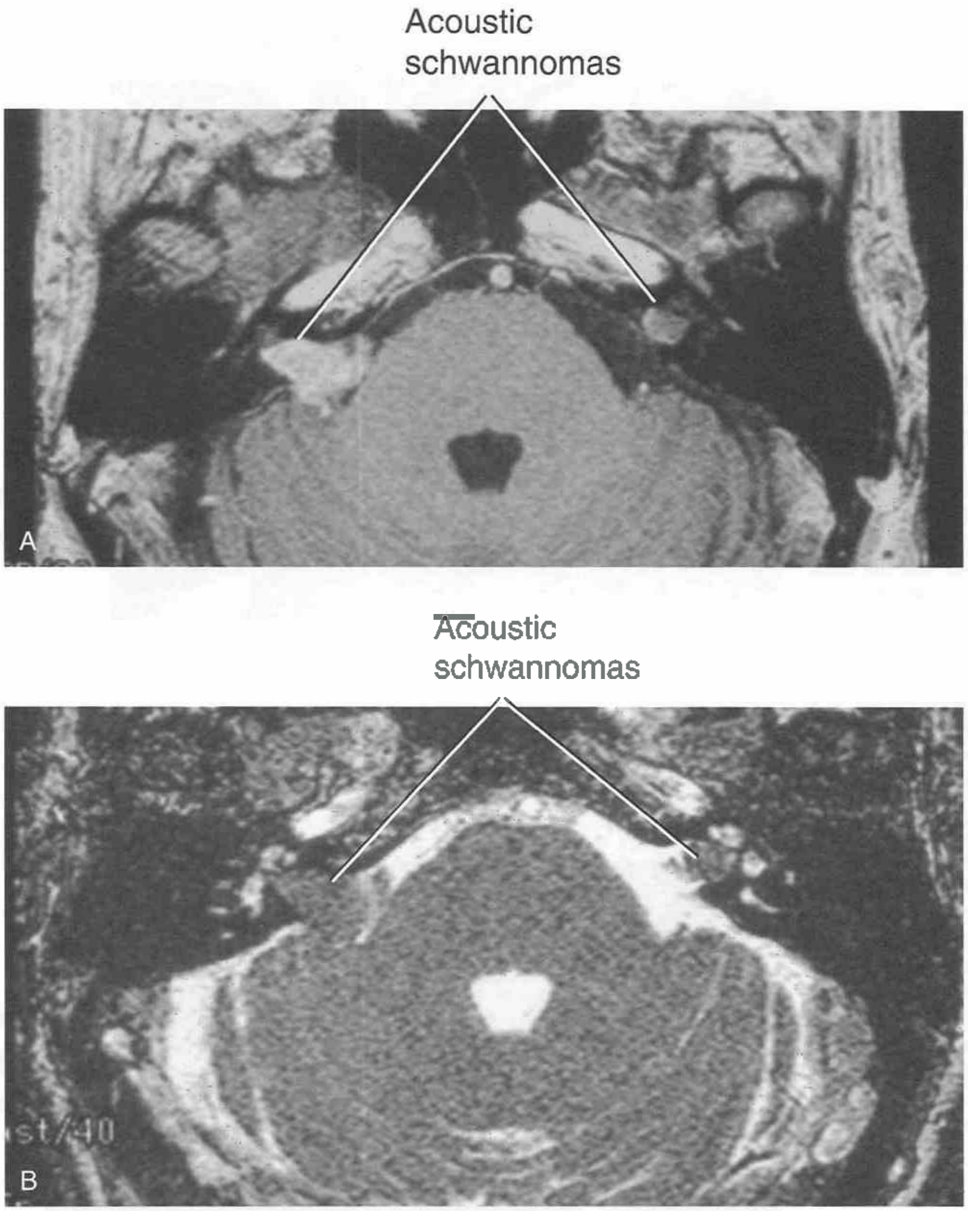

Figure 15–33. Neurofibromatosis type 2.

A, Axial T2-weighted, 3D Fourier transform, high-resolution, gradient-echo MR image acquired through the internal auditory canals. Filling defects are seen in both internal auditory canals (IACs). The mass on the right is larger and extends out into the cerebellopontine angle. Bilateral acoustic tumors suggest neurofibromatosis type 2 or carcinomatosis. No other meningiomas or neuromas are seen on this section, but they should be sought.

B, Axial T1-weighted, 3D Fourier transform, high-resolution, gradient-echo MR image acquired after contrast through the IACs. Both tumors of the IACs are seen as enhancing small masses. The mass on the right shows greater enhancement.

reveal a classic mushroom-shaped mass centered at the internal auditory canal.

Massive tumors (see Fig. 15–31) may cause severe distortion of the posterior fossa, with brain stem herniation, hydrocephalus, and displacement and compression of the fourth ventricle. Some acoustic schwannomas can be cystic. Bilateral acoustic schwannomas are associated with neurofibromatosis type 2 (Fig. 15–34; see Fig. 15–33).

In general, MRI is better than CT in the diagnosis of acoustic schwannomas. Enhancement and enlargement of the eighth cranial nerve within the internal auditory canal (or even the otic capsule) can be seen. Small lesions are visible on survey examinations without the need for cisternography. MRI can differentiate small acoustic tumors from the nerves themselves. Smaller tumors can be seen to displace the nerves in the internal auditory canal. The nerve can be seen crossing small tumors. This is important for surgical planning and usually implies a better prognosis for hearing salvage after surgery. Larger tumors totally fill the internal auditory canal and obscure the other anatomic structures. The other characteristic findings of larger tumors can also be appreciated. Careful review of other cranial nerves is important to rule out neurofibromatosis.

The rate of growth of acoustic schwannomas is variable. Accurate follow-up is important because many tumors do not grow and may not warrant therapy, particularly in the case of older patients. High-resolution imaging is essential to aid in recognition of subtle changes in tumor volume. Better evaluation of these tumors is more important now that there are many different management possibilities, including waiting, surgery, and focused radiation.

Facial Nerve Schwannomas

Facial nerve schwannomas (Figs. 15–35 and 15–36) may be located anywhere along the course of cranial nerve VII. These tumors are gray, firm, lobulated masses that may be either schwannomas or neurilemmomas. Both originate from Schwann cell sheaths. These tumors most frequently involve the geniculate ganglion and tympanic mastoid portions of the facial nerve. Although facial schwannomas are commonly associated with facial nerve palsy, they account for only about 5% of all peripheral facial palsies. Inflammation (Bell's palsy) (Fig. 15–37), trauma, infection, and neoplasm are more common causes of cranial nerve VII dysfunction.[22]

The location of the schwannoma determines the constellation of clinical findings. Neurosensory hearing loss resulting from compression of adjacent cranial nerve VIII is seen with cerebellopontine angle and internal auditory canal tumors or erosion into the cochlea. Conductive hearing loss may be seen in tympanic cavity schwannomas associated with ossicular dysfunction.

Although the CT findings of an intracanalicular or cerebellopontine facial schwannoma are similar to those of acoustic schwannomas, erosion of the anterosuperior por-

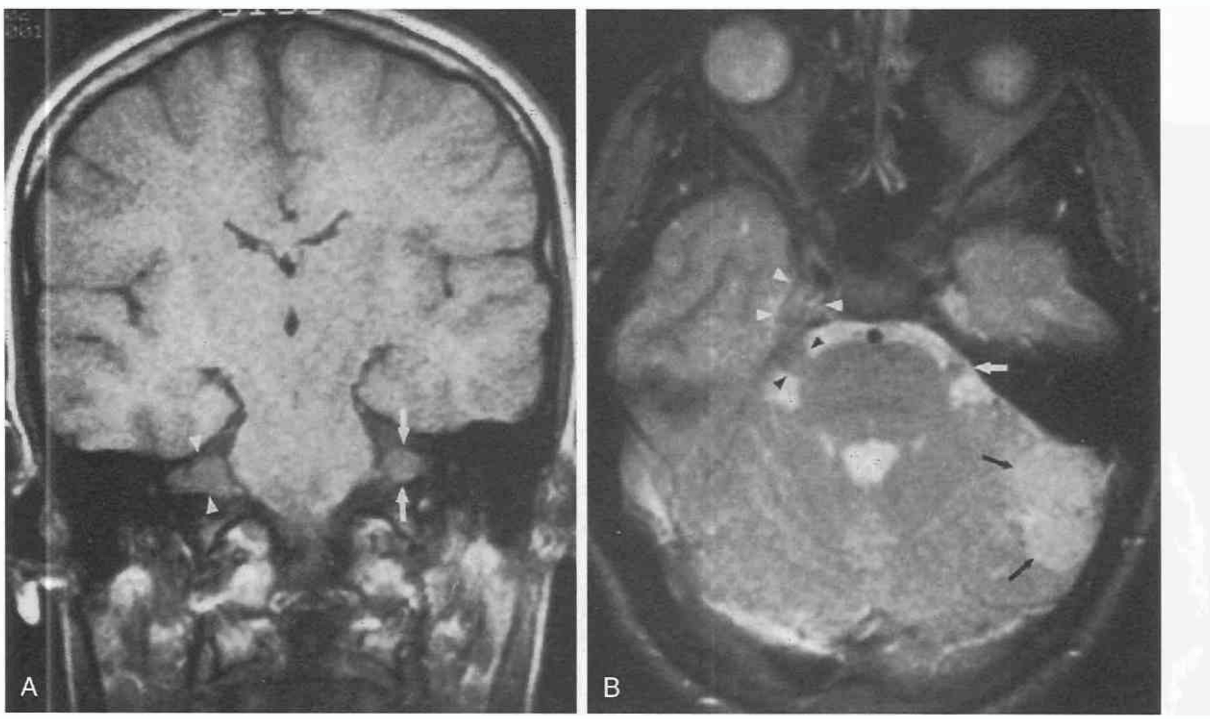

Figure 15–34. Bilateral acoustic schwannoma in a young female with a history and the stigmata of neurofibromatosis.

A, Coronal noncontrast, T1-weighted MRI study shows bilateral lobulated smoothly marginated masses in the cerebellopontine angles. The mass on the right *(arrowheads)* expands the internal auditory canal. The mass on the left is circular and isodense and is in the cerebellopontine angle *(arrows).*

B, Axial T2-weighted section superior to the internal auditory canals. There is enlargement of the right fifth cranial nerve *(black arrowheads)* and filling of Meckel's cave by a neurofibroma of the trigeminal nerve *(white arrowheads).* There is also thickening of the proximal portion of the left fifth cranial nerve *(white arrow).* A nearly isointense mass at the surface of the lateral hemisphere relating to meningioma can also be seen *(black arrows).*

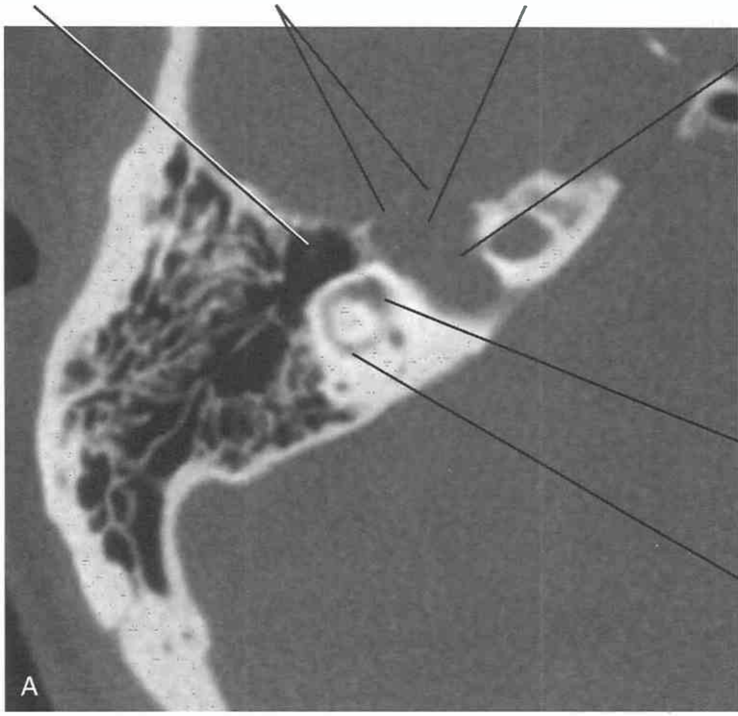

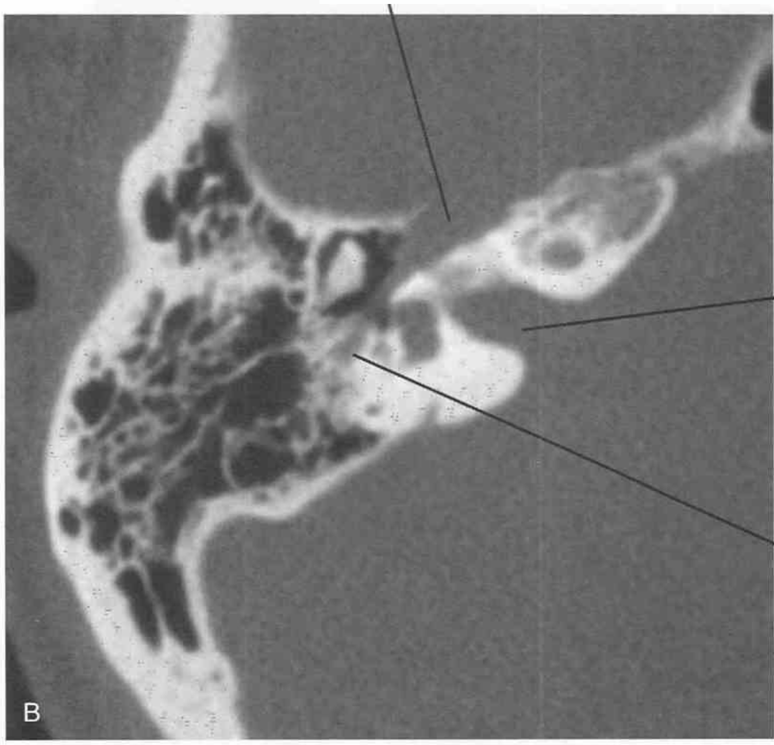

Figure 15–35. Facial schwannoma.

A, Axial CT image of the right temporal bone in a patient presenting with a long history of facial palsy that did not improve. The lateral internal auditory canal (IAC) is expanded. There is a broad opening of the IAC and the geniculate ganglion related to the schwannoma. There is erosion of the bone facing the middle cranial fossa.

B, Axial CT image, slightly inferior in relation to *A*. The geniculate ganglion is clearly expanded, with erosion of the anterior portion of the facial canal. This type of pattern can be seen with a hemangioma or with perineural spread of tumor.

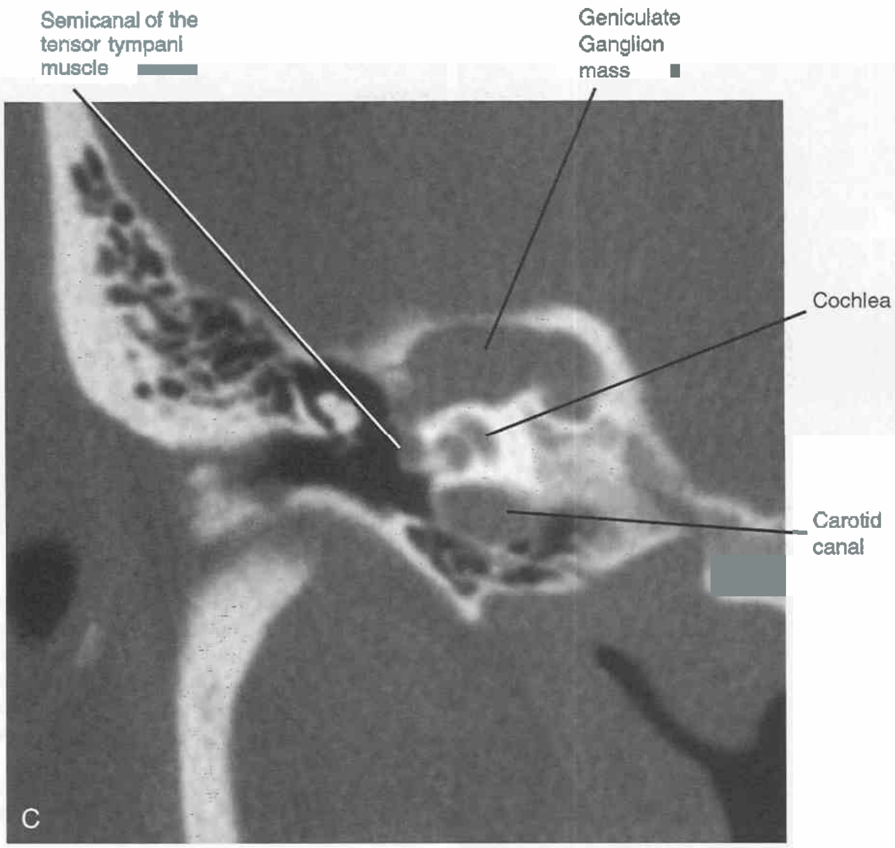

Figure 15–35 *Continued C,* Coronal CT image through the geniculate ganglion region. Note the massive enlargement of the canal superior and medial to the cochlea and carotid canal. The bony canal is smoothly enlarged, a common finding with facial schwannomas and acoustic schwannomas. The location of the bony expansion is centered anteriorly and superiorly in the IAC and along the facial nerve canal.

tion of the internal auditory canal and the geniculate ganglion region in particular may distinguish proximal facial schwannomas from acoustic schwannomas.[31] Tumors originating within the facial nerve canal cause enlargement and erosion of the involved segment.[61] Extracanalicular expansion of schwannomas may be evidenced by eccentric location of the tumor mass beyond the facial nerve canal, in the supralabyrinthine area, the middle ear cavity, the mastoid segment, or the parotid gland. Involvement of the geniculate ganglion is easy to detect on CT scans because of enlargement of the geniculate fossa on axial images. Most of these tumors enhance on MRI studies and have a characteristic tubular shape following the complex curves of the nerve.

Meningiomas

Most meningiomas (Fig. 15–38) arise outside the middle ear from the meninges covering the posterior petrous bone. Some meningiomas may subsequently invade the temporal bone, producing primarily otologic symptoms. Meningiomas arising within the cerebellopontine angle cause varying symptoms, including deafness, tinnitus, posterior fossa herniation, and facial paresis, although most are not symptomatic until they are large, in contrast to most acoustic schwannomas. Meningiomas rarely originate within the internal auditory canal. When this does occur, it may simulate an acoustic tumor with vestibular and otologic symptoms. In a few instances, meningiomas may arise from ectopic arachnoid granulations within the middle ear cleft.[63] They may also be seen in neurofibromatosis.

Meningiomas of the cerebellopontine angle are classically semicircular dura-based lesions that protrude posteriorly. On CT scans, some are partially calcified and usually enhance. Hyperostosis of the posterior margin of the temporal bone is difficult to recognize because it is already highly dense, but air spaces changes are more sensitive. The internal auditory canal is usually not affected, or it is covered. Large lesions deform the adjacent brain and tract along the adjacent dural (Meckel's cave, petroclinoid ligament) structures.

On MRI studies, the lesions may be isointense with brain without contrast. The junction of the meningioma and temporal bone usually forms an obtuse angle, whereas an acoustic schwannoma usually forms an acute angle with the temporal bone.[17] In rare circumstances, the meningioma involves the mastoid and middle ear structures, either as en bloc cerebellopontine angle lesions or arising centrally without a dural surface involved. On CT scans, sclerosis

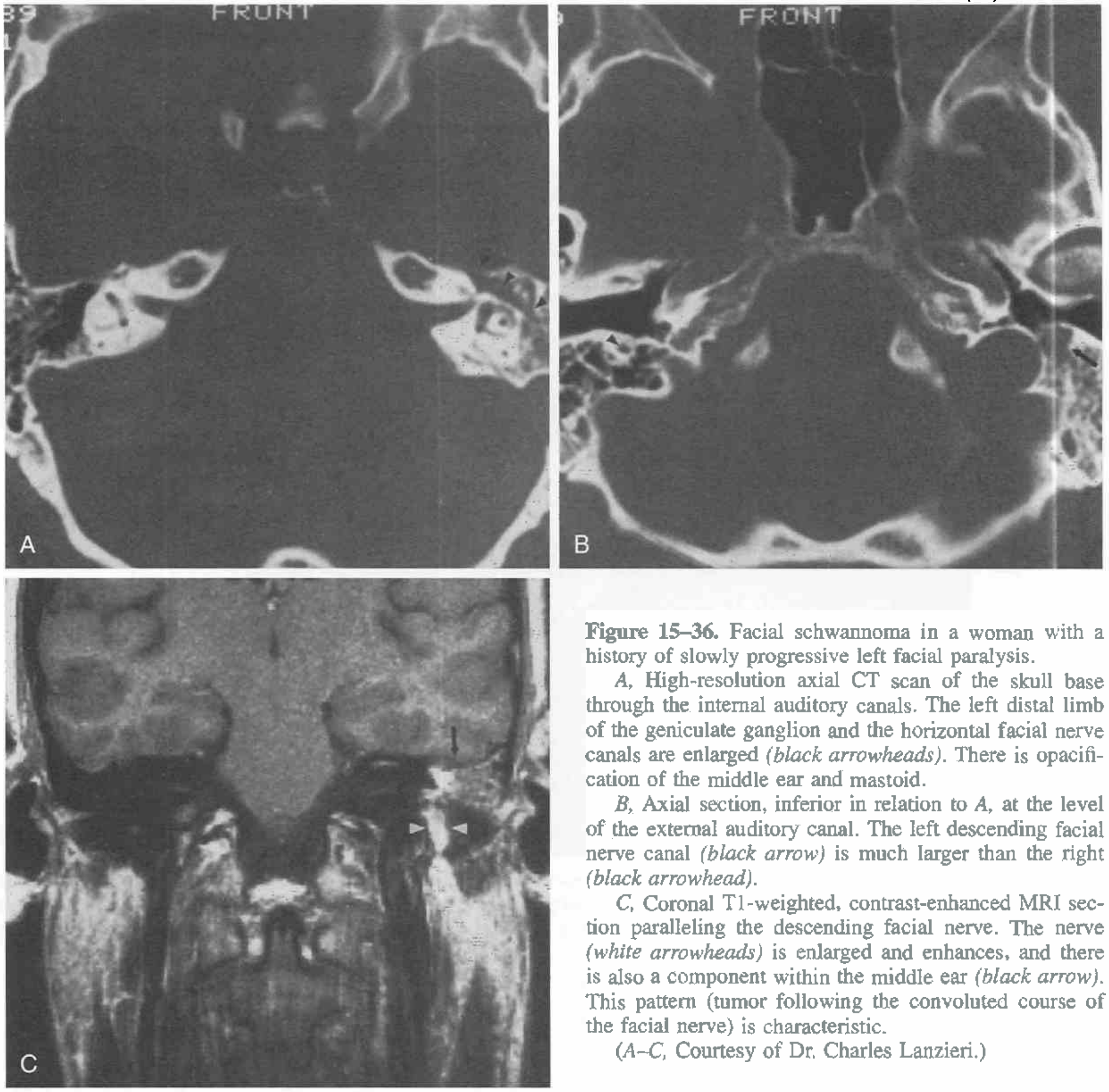

Figure 15–36. Facial schwannoma in a woman with a history of slowly progressive left facial paralysis.

A, High-resolution axial CT scan of the skull base through the internal auditory canals. The left distal limb of the geniculate ganglion and the horizontal facial nerve canals are enlarged *(black arrowheads).* There is opacification of the middle ear and mastoid.

B, Axial section, inferior in relation to *A,* at the level of the external auditory canal. The left descending facial nerve canal *(black arrow)* is much larger than the right *(black arrowhead).*

C, Coronal T1-weighted, contrast-enhanced MRI section paralleling the descending facial nerve. The nerve *(white arrowheads)* is enlarged and enhances, and there is also a component within the middle ear *(black arrow).* This pattern (tumor following the convoluted course of the facial nerve) is characteristic.

(*A–C,* Courtesy of Dr. Charles Lanzieri.)

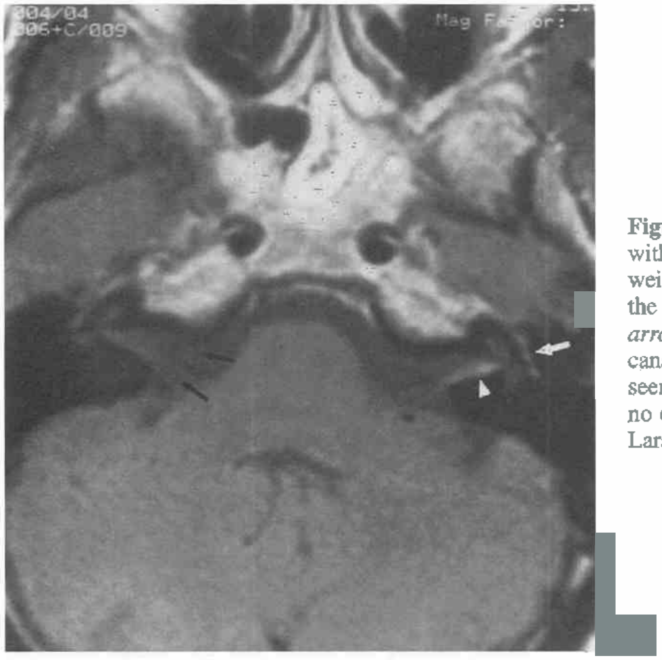

Figure 15–37. Bell's palsy in a middle-aged woman who presented with acute left facial palsy that gradually improved. This axial T1-weighted, contrast-enhanced MRI study shows linear enhancement of the seventh cranial nerve within the internal auditory canal *(white arrowhead)* and the horizontal portion of the facial nerve (fallopian) canal *(white arrow).* The seventh and eighth cranial nerves are easily seen in the cerebellopontine angle on the right *(black arrows).* There is no enlargement of the canal or bone destruction. (Courtesy of Theodore Larson, M.D.)

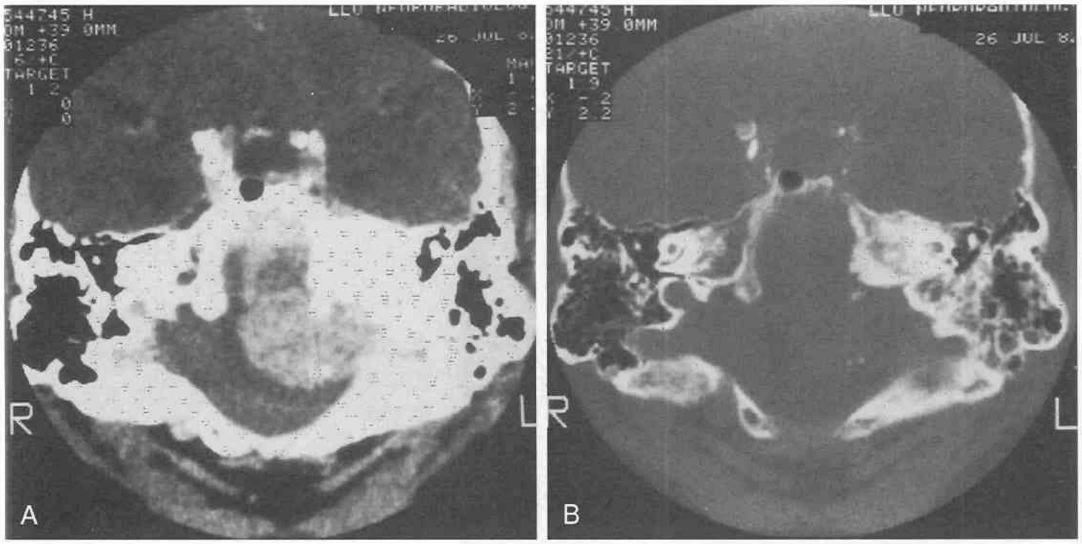

Figure 15–38. Meningioma in a middle-aged woman with multiple lower left cranial nerve deficits. *A,* Steeply angled axial CT scan of the skull base after contrast infusion. A large, enhancing, dura-based mass extends along the clivus and the left petrous bone. The tumor mass contains scattered calcifications. The adjacent brain structures are extensively deformed. *B,* High-resolution CT image at same level as in *A*. There is extensive sclerosis of the left petrous bone with partial opacification of the mastoid air cells.

and soft tissue opacification may be seen. On MRI studies, the infiltrative tumor may enhance.

Paragangliomas (Glomus Tumors)

Paragangliomas (Figs. 15–39 and 15–40), also referred to as *glomus tumors*, are slow-growing, purple-red vascular tumors that arise from chemoreceptor cells.[12, 62] They are histologically related to pheochromocytomas, are of mesenchymal or neuroectodermal origin, and secrete catecholamines in approximately 10% of instances. Arising from the ninth and tenth cranial nerves, paragangliomas are the most common tumor of the middle ear and the second most common tumor of the temporal bone after acoustic schwannoma. They occur most frequently in middle-aged women. They may be multicentric in up to 10% of patients and are commonly familial.[22] Even though most of the paragangliomas are benign and solitary, they are locally highly aggressive, simulating a malignant tumor in their local behavior. Some are malignant and metastasize.

Histologically and biologically, the lesions are similar, but historically they have unique names associated with their locations. Glomus tumors (paragangliomas) typically develop in the jugular bulb (glomus jugulare), the middle ear (glomus tympanicum), the carotid body (carotid body tumor), and the ganglion of the vagus nerve (glomus vagale).[12] Jugulotympanic glomus tumors involve both the middle ear and jugular bulb.

Symptoms are based on the location and size of the tumor. Tumors of the middle ear typically cause pulsating tinnitus, with subsequent conductive hearing loss. Paragangliomas cause permeative bone destruction; surprisingly, however, they often spare the ossicles. Erosion of the promontory or invasion into the cochlea leads to progressive neurosensory hearing loss. Vertigo may accompany the hearing loss as the tumor advances into the labyrinth. Involvement of the facial and lower cranial nerve canals may result in cranial nerve dysfunction. Extension superiorly into the middle cranial fossa may occur as the tumor erodes the tegmen. Because many of the tumors arise within the jugular fossa, extension intracranially or inferiorly into the upper neck with venous occlusion is common. Most posterior cranial fossa involvement is extradural. A nodular appearance of the medial intracranial border indicates intradural extension.[62]

Differentiation of these lesions is usually not possible by otoscopy alone unless the glomus tympanic mass is small enough so that its circumference is visible.[35] High-resolution cross-sectional imaging is effective in staging these tumors. Vascular anomalies as well as some other nonvascular lesions in the differential diagnosis may be accurately assessed by CT and MRI studies. Angiography is still important in their evaluation. Differentiation of paragangliomas from vascular malignant tumors (renal cell metastasis) may be difficult.

Glomus tympanicum tumors (see Fig. 15–39) are isolated to the middle ear cavity. They usually arise on the cochlear promontory and extend into the middle ear and mastoid air cells. The most common CT finding is the presence of a small soft tissue density protruding from the cochlear promontory without bony destruction.[12, 45] CT and MRI studies with IV contrast agents demonstrate a homogeneous, densely enhancing soft tissue mass within the tympanic cavity. These tumors may also fill the middle ear cavity but rarely cause ossicular destruction. The highly vascular nature of the lesions can be confirmed with angiography.

Glomus jugulare tumors (see Fig. 15–40) show bony destructive distortion at the separation of jugular fossa and hypotympanum.[12] The tumors commonly invade the hypotympanum. There may be displacement of the tympanic membrane and the long process of the malleus and erosion of the basal turn of the cochlea. On CT scans, invasion into the infralabyrinthine compartment results in a mottled appearance.[62] Infralabyrinthine involvement may

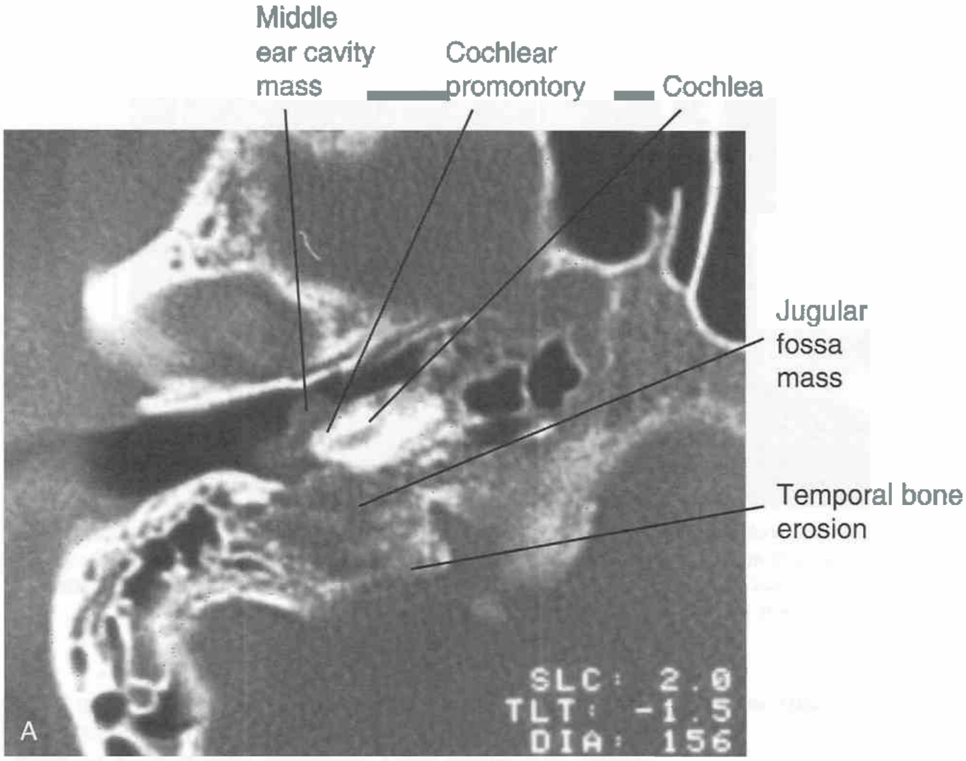

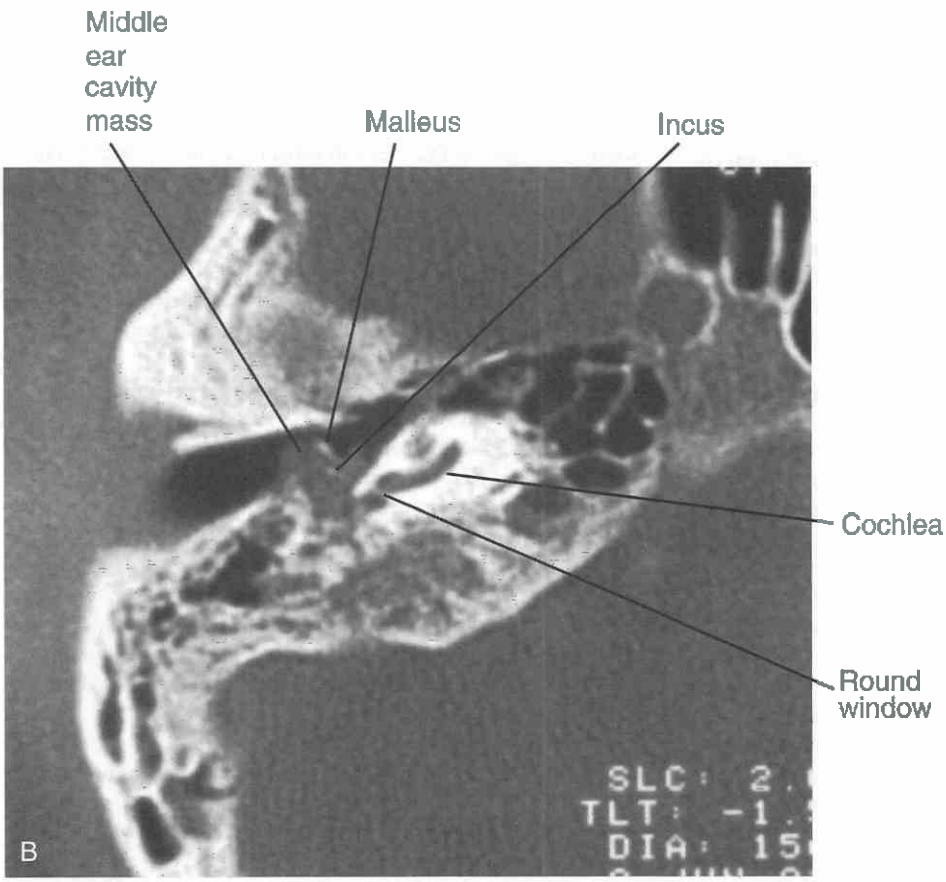

Figure 15–39. Glomus jugulare paraganglioma in a patient presenting with pulsatile tinnitus.

A, Axial CT image through the basal turn of the cochlea. A small, hypotympanic, soft tissue mass in the middle ear overlies the cochlear promontory. The adjacent temporal bone is eroded near the jugular fossa. The erosion is very near the descending facial nerve canal. This combination of a destructive mass arising near or in the jugular fossa and extending into the middle ear is characteristic of paragangliomas.

B, Axial CT section, slightly superior in relation to *A,* shows the mass in contact with the round window, the long process of the malleus, the long process of the incus, and the tympanic membrane. There is no destruction of the ossicles, which is typical. There is some minor opacification of the mastoid.

Figure 15–39 *Continued C,* Lateral angiogram of the internal maxillary artery showing enlargement of the many feeding vessels (including the ascending pharyngeal artery) extending to the jugular fossa. The highly vascular tumor is characteristic of a paraganglioma.

destroy the vertical and horizontal portions of the carotid canal. In these patients, preoperative balloon occlusion of the carotid artery may be necessary. The examination should extend inferiorly to include the upper neck, and intracranially, since these tumors commonly follow the jugular venous system from the torcular Herophili to the lower cervical jugular vein. On MRI studies, the vascular nature of the lesion is demonstrated by the presence of small tortuous signal voids.

Angiography is still important in the preembolization workup to define various vascular pedicles so that each pedicle can be individually catheterized and embolized. Catheter or magnetic resonance venography may be needed to confirm the patency of the venous structures.

Epidermoidomas (Epidermoid Cysts)[49]

Epidermoidomas *(primary congenital cholesteatomas)* consist of masses of embryonic ectodermal rests and are thus distinct from true cholesteatomas, whose formation is a reaction to inflammation and trapped squamous epithelium. These lesions may be found in several areas within the temporal bone. They can arise in the external auditory canal, leading to chronic obstruction (Fig. 15–41), termed *keratosis obturans.* Some lesions originate in the middle ear, with subsequent erosion of the ossicles, facial nerve canal, or lateral semicircular canal. Patients usually have unilateral serous otitis or unexplained unilateral conductive hearing loss. Some epidermoidomas originate in the osseous structures, typically in a supralabyrinthine location. The lesions show sharp outlines with distinct edges and appear as expansile cystic lesions along the superior portions of the temporal bone.

Typically, the lesions exhibit a "punched-out" appearance. Thy may erode into the facial nerve canal or internal auditory canal, causing facial nerve palsy or hearing loss. They may also arise in the petrous apex, forming an expansile, sharply marginated destructive lesion that can affect the clivus (Fig. 15–42).

Epidermoidomas may also originate in the cerebellopontine angle. These masses can demonstrate a wide range of imaging characteristics. On CT scans, they are frequently low density structures and may mimic a subarachnoid cyst. They can be solid or even calcified and usually do not significantly enhance. Contrast cisternography characteristically shows a frondlike pattern as the contrast enters many small channels at the irregular surface of the lesion. On MRI scans, a wide range of findings may also be seen, including expansion out of the cerebellopontine angle into Meckel's cave or the ambient cistern. These tumors do not tend to invade the brain.

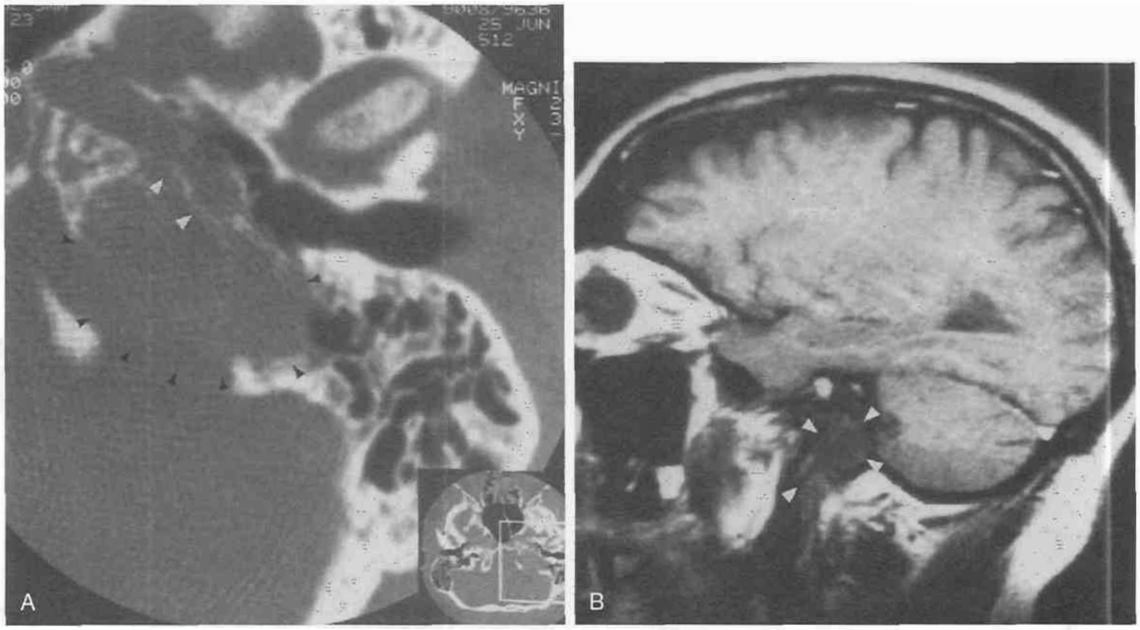

Figure 15–40. Glomus jugulare in a 40-year-old woman presenting with multiple lower cranial nerve palsies and a visible blue middle ear mass.

A, Magnified axial CT scan of the left temporal bone through the hypotympanum. The left jugular fossa is massively enlarged *(black arrowheads)* with destructive margins. A mass extends into the petrous apex. A thin margin of bone outlines the carotid canal *(white arrowheads).* The separation of the mass and the middle ear is poorly defined.

B, Sagittal non–contrast-enhanced, T1-weighted MR image through the jugular fossa. The jugular fossa is usually seen as a signal void as a result of cortical bone and blood flow. In this instance, a low-signal-intensity soft tissue mass is seen expanding the jugular fossa *(white arrowheads)* but does not extend through the dura.

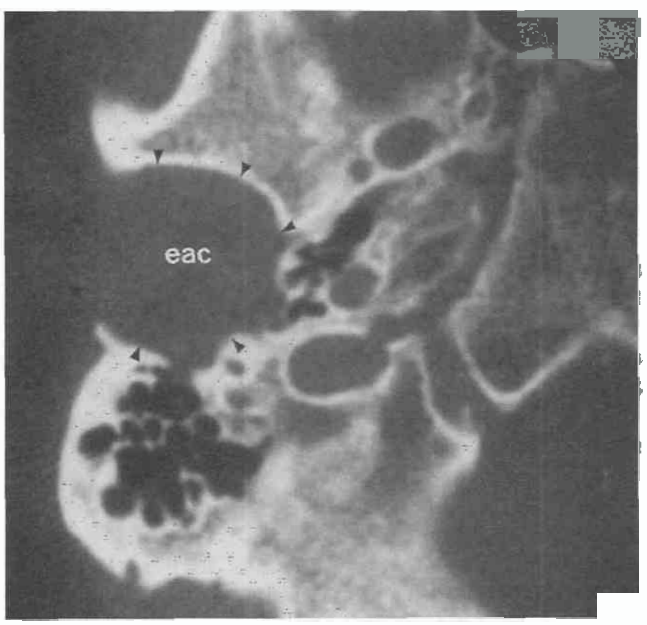

Figure 15–41. Epidermoid of the external auditory canal in a young man presenting with a chronic history of bilateral external canal obstruction. He had no history of chronic infection or tympanic membrane rupture (as would be seen with cholesteatoma). The axial CT scan through the right external auditory canal (eac) shows a smoothly marginated mass *(arrowheads)* expanding the canal. The mastoids and protympanum are intact without inflammatory changes.

Hemangiomas of the Facial Nerve

Small hemangiomas of the facial nerve are actually as common as facial schwannomas. These benign tumors most commonly affect the geniculate ganglion, but they occasionally involve the internal auditory canal. Patients usually present with progressive facial paralysis. Most of these tumors are not extremely vascular but, instead, are partially calcified. On CT scans, one sees a small lesion of mixed sclerosis with erosion of the facial nerve canal. On MRI studies, hemangiomas may display slight contrast enhancement (Fig. 15–43).

Miscellaneous Benign Lesions

A variety of neoplastic and non-neoplastic lesions occasionally involve the cerebellopontine angle and the temporal bone. Other cranial nerve tumors may occur in addition to acoustic schwannomas.

Trigeminal schwannomas typically follow the course of the nerve from the anterior pons into Meckel's cave and then into the subtemporal fossa.[3] The foramen ovale and rotundum as well as the superior orbital canal may be enlarged.

Schwannomas of lower cranial nerves IX, X, XI, and XII may mimic paragangliomas by forming a dumbbell-shaped mass that enlarges the jugular fossa (Fig. 15–44).[12] On angiograms, however, they are often less vascular.

Lipomas and some *epidermoid* or *dermoid tumors* of the cerebellopontine angle may be readily identified by CT as low-density fatty masses.[21] On MRI studies, if the masses are composed predominantly of triglyceride, they

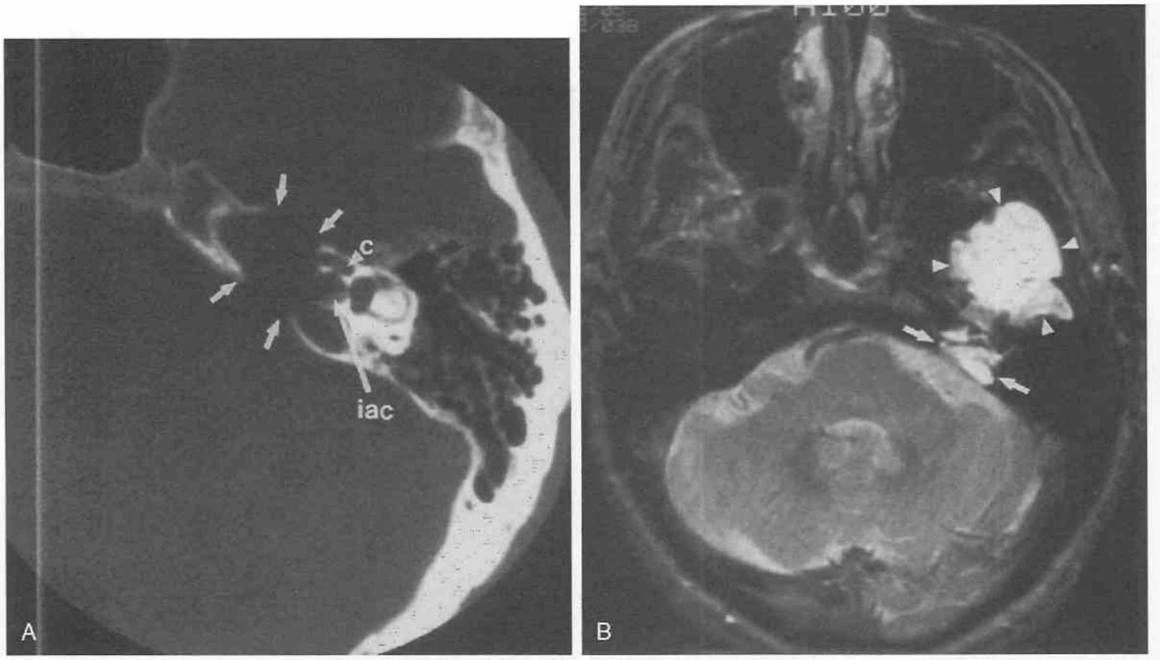

Figure 15–42. Epidermoid of the petrous apex in a 40-year-old man presenting with symptoms similar to those of an acoustic schwannoma. *A,* Axial CT image through the left internal auditory canal shows a large destructive lesion *(arrows)* involving the petrous apex, internal auditory canal (iac), and cochlea (c). The lesion is rather sharply marginated. The mastoid and middle ear are intact. *B,* Axial T2-weighted MR image demonstrates that the lesion has a very high signal (consistent with a high water content). One component is within the petrous apex *(arrows)*, and a second larger area involves the anterior portion of the middle cranial cavity *(arrowheads)*. There is little reaction of the adjacent brain.

Figure 15–43. Facial nerve hemangioma in a patient with slowly progressive facial paralysis. The axial CT section through the left temporal bone shows mixed sclerosis and destruction of the geniculate ganglion region *(arrowheads)*. The normal smoothly marginated canal is not visible and is replaced with an irregular cluster of calcification. There is no soft tissue component within the middle ear.

may have high signal intensity on T1-weighted images and may demonstrate chemical shift artifacts. If the fat is not triglyceride in nature, it appears as a low-density mass on CT scans but not as a high-signal-intensity mass on T1-weighted MR images.

Several non-neoplastic lesions may appear similar to their neoplastic counterparts. An *arachnoid cyst* of the posterior fossa can mimic a cystic cerebellopontine angle tumor (epidermoid). The CT appearance is that of a CSF-density mass filling the cerebellopontine angle cistern, with slight distortion of the adjacent brain structures. Scalloping of the petrous bone suggests a chronic process. It may be difficult to differentiate cystic epidermoids and dermoids from arachnoid cysts unless there is evidence of arachnoiditis. MRI is superior to CT in its capacity to help confirm the nature of cystic lesions.

Cholesterol granulomas of the petrous apex (Fig. 15–45) are slow-growing collections of blood products. These lesions are non-neoplastic. The etiology is not clear but may be related to chronic obstruction. These granulomas are common incidental findings on MRI studies that are seen as high-signal-intensity regions of subacute hemorrhage on all pulse sequences involving the petrous apex. There may be no expansion, and the CT findings are essentially normal. A minority of these lesions expand to erode the petrous apex. Most patients present with symptoms similar to those of an acoustic schwannoma. CT scanning typically shows a circular soft tissue density mass expanding the apex. There may also be involvement of the clivus and internal auditory canal. On MRI studies, the lesions are seen as expansile high-signal-intensity masses centered in the petrous apex.

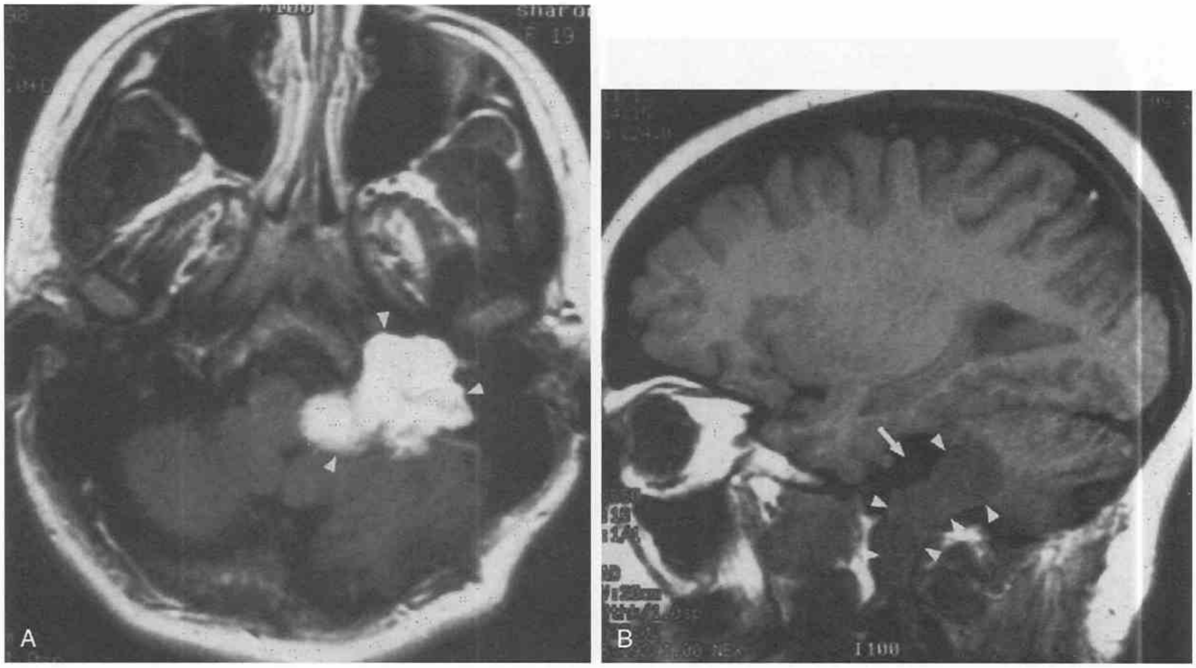

Figure 15–44. Jugular fossa schwannoma in a teenaged girl thought to have neurofibromatosis and who presented with a recurrent jugular fossa schwannoma.

A, Axial contrast-enhanced, T1-weighted, spin-echo MRI study at a level inferior to that of the internal auditory canal. A large, lobulated, enhancing mass *(arrowheads)* is centered in the left jugular fossa region. The bony margins are eroded. The mass protrudes into the posterior fossa.

B, Sagittal, non–contrast-enhanced, T1-weighted MRI study through the jugular fossa. The slightly low-signal-intensity posterior fossa mass *(arrowheads)* extends from the cerebellum through the expanded jugular fossa into the superior neck. The adjacent internal auditory canal *(arrow)* is intact.

Malignant Neoplasms

Primary malignant neoplasms of the temporal bone are relatively uncommon. When they do occur, they are most often squamous or basal cell carcinomas. These tumors usually originate from mucosal epithelium of the external auditory canal, middle ear, or mastoid air cells and are usually aggressive. Patients who have primary squamous cell carcinomas of the external auditory canal may have a history of chronic external otitis. Symptoms may also include otalgia, bleeding, otorrhea, dizziness, deafness, and facial nerve palsy. They may extend locally into the parotid gland and the temporomandibular joint. More medial invasion is associated with a worse prognosis. Lymphatic invasion and subsequent distant metastasis are rare.

The most important CT finding suggesting a diagnosis of carcinoma is erosion of the walls of the bony external auditory canal or middle ear by a soft tissue mass in a patient who does not have a history of cholesteatoma.[46] CT scanning can outline the bony erosion and can show the extension of the soft tissue mass into the adjacent normal soft tissues.[28, 64] On MRI studies, there may be edema and abnormal soft tissue with irregular enhancement after IV contrast infusion as well as distortion of the surrounding soft tissue planes (Fig. 15–46). In some patients, it is difficult to differentiate between tumor and secondary infection (malignant external otitis) because in both cases there may be soft tissue enhancement with the presence or absence of bony erosion.

Glandular neoplasms, such as adenoma and adenocarcinoma, account for about 14% of primary temporal bone masses. The clinical and CT findings of glandular carcinoma are similar to those of squamous cell carcinomas, except that metastasis to regional lymph nodes may occur. For this reason, the lymph nodes at the skull base and upper neck should be evaluated on CT scans. Lymph node involvement is evidenced by peripheral soft tissue enhancement with central necrosis on IV contrast-enhanced CT studies.[11]

Embryonal rhabdomyosarcoma (Fig. 15–47) is the most frequently encountered malignant middle ear neoplasm in children. Involvement of the temporal bone by rhabdomyosarcoma is relatively common. The tumor is highly aggressive, and bone destruction associated with a middle ear soft tissue mass occurs quite often. The patient may also have cranial nerve deficits. Intracranial spread secondary to direct epidural extension may be seen on CT or MRI studies as an enhancing mass in continuity with the ear mass. CT scanning is the ideal examination for monitoring recurrence after surgical resection, radiation, or chemotherapy.[22] Eosinophilic granuloma may have a very similar appearance.

Malignant tumors from adjacent structures may secondarily involve the temporal bone from several avenues, including through the foramina and fissures of the skull base and from the soft tissues of the external auditory canal. The most common extensions are from nasopharyngeal cancer (Fig. 15–48) and skin and salivary gland cancers, via the eustachian canal and external auditory canal,

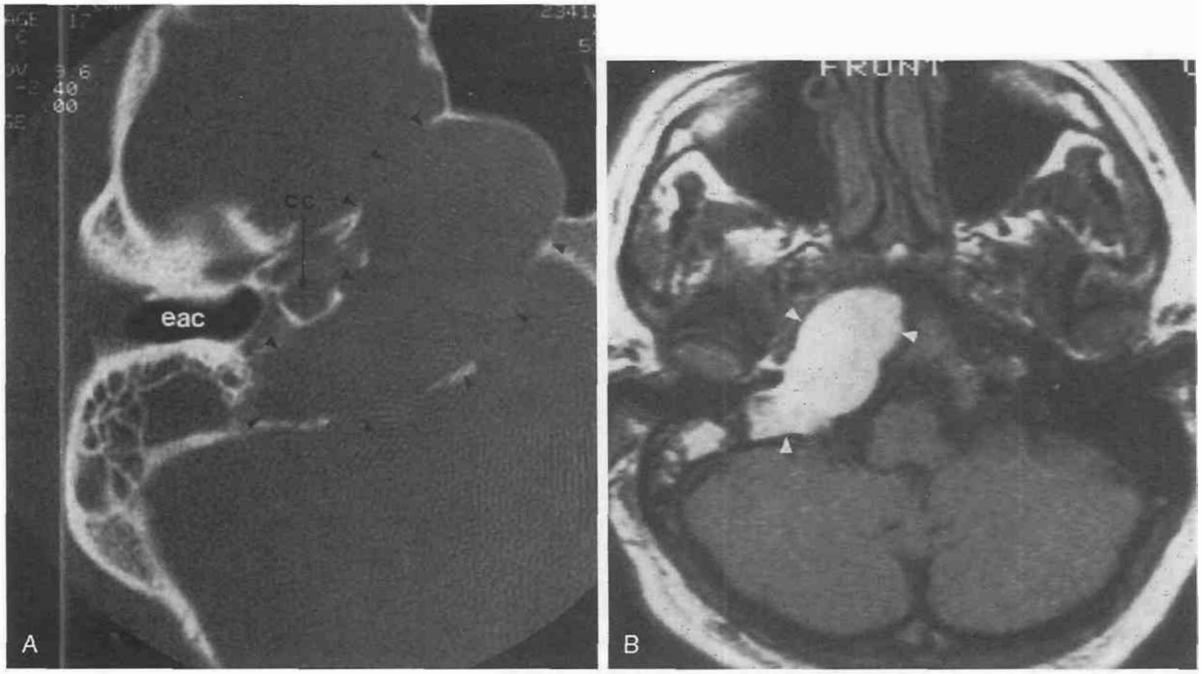

Figure 15–45. Cholesterol granuloma in a patient presenting with symptoms similar to those of an acoustic schwannoma.

A, Axial CT section through the right external auditory canal (eac) and carotid canal (cc). A large expansile mass is in the petrous apex. The margins of the surrounding bone are thinned. There is remodeling of the sphenoid sinus and the posterior margin of the temporal bone *(black arrowheads).* The mastoid is opacified. The external auditory canal is intact.

B, Axial T1-weighted, non–contrast-enhanced MRI study at the same level as in *A.* A large mass with very high signal intensity caused by subacute hemorrhage can be seen *(arrowheads).* The margins of the lesion are smooth, with displacement of adjacent structures rather than invasion. The lesion is centered at the petrous apex and involves the clivus. This lesion was of high signal intensity on all imaging sequences.

(*A* and *B,* Courtesy of William Lo, M.D.)

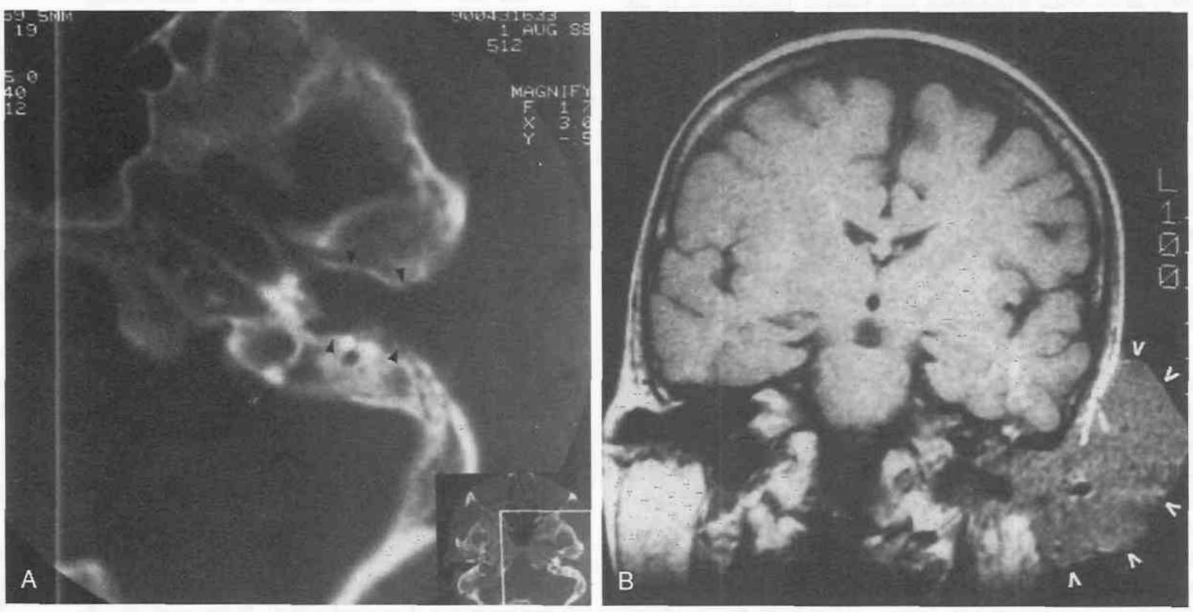

Figure 15–46. **Basal cell carcinoma of the external auditory canal.** *A,* Axial CT section through the left external auditory canal shows a soft tissue mass *(black arrowheads)* filling the canal and middle ear. Irregular destruction and expansion of the bony canal are shown. *B,* Coronal T1-weighted MRI study shows a large mushroom-shaped mass *(white arrowheads)* extending external from the auditory canal to involve the adjacent soft tissues. The normal fatty structures have been invaded.

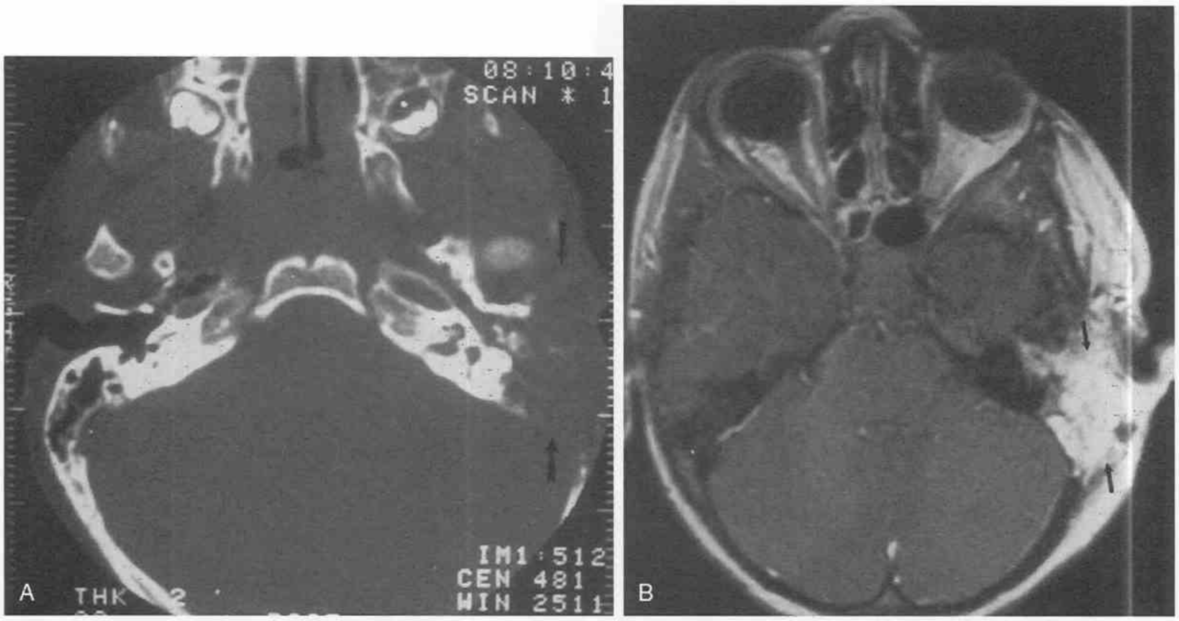

Figure 15–47. Rhabdomyosarcoma in a 5-year-old girl who presented with rapidly progressive pain and swelling of the left mastoid, mimicking an acute infection. Biopsy showed an invasive rhabdomyosarcoma.

A, Axial bone window CT scan made through the internal auditory canals. The right ear is normal. The left ear shows a large destructive lesion *(black arrows)* involving the mastoid, external auditory canal, and middle ear.

B, Axial contrast-enhanced, T1-weighted, spin-echo MRI study at approximately the same level as in *A.* A large, enhancing soft tissue mass *(black arrows)* extends laterally from the region of bone destruction. There is secondary edema and thickening of the soft tissues overlying the calvarium on the left.

respectively.[23] Perineural spread occurs when malignant tumors track along the course of normal nerves (Fig. 15–49). This is a very subtle but important finding, since the tumor may appear to spread in a discontinuous manner and to recur a long distance from the primary site. This is most frequently seen with squamous cell cancer because it is the most common head and neck malignancy. Perineural spread is especially prevalent with adenoid cystic carcinoma and lymphoma. The facial nerve is most often affected. Perineural spread through the facial nerve can arise from tumors involving the parotid region or from small interconnecting branches of the fifth cranial nerve.[20]

CSF carcinomatosis is a relatively common complication of systemic cancers (Fig. 15–50). The metastases can occur in the internal auditory canal and may mimic benign acoustic tumors transiently. When single lesions are seen, the findings are nonspecific; however, when multiple lesions are in the CSF or brain or when multiple cranial nerves are affected and dural enhancement is present, the diagnosis is clear. The prognosis for a patient with carcinomatosis is poor.

The temporal bone is susceptible to any neoplasm that typically metastasizes to bone. Hematogenous spread typically occurs from tumors of the breast, lung, stomach, prostate gland (Fig. 15–51), or kidney. These lesions cause a diffuse or focal osteolytic destructive pattern. There may be postcontrast enhancement, especially if both the epidural space and the bone are involved. Differentiation of glomus tumors from renal carcinoma metastases may be difficult, since both tumors are highly vascular. Prostatic tumors may cause osteoblastic changes that simulate a sclerosing inflammatory process, a meningioma, or Paget's disease.

Traumatic Injuries

The common local serious consequences of temporal bone trauma are hearing loss, CSF fistula, and facial nerve palsy. CT is the best diagnostic modality for identification of fractures.[27] Routine head CT examinations of trauma patients should include accurate surveys of the temporal bones. Follow-up detailed, high-resolution images can be acquired if indicated. MRI studies can be of value for vascular and brain injuries.[48, 59]

Fractures[1]

Longitudinal Fractures

Longitudinal fractures (Fig. 15–52) occur along the long axis of the petrous pyramid, which extends parallel to the external and internal auditory canal toward the petrous apex. These fractures typically extend from the temporal squamosa across the roof or posterior wall of the external auditory canal into the tympanic cavity and tegmen tympani. There may be rupture of the tympanic membrane, with hemorrhage in the external auditory canal and middle ear.[11]

Conductive hearing loss is common and may be caused by ossicular dislocation or fracture or by the presence of intratympanic hemorrhage.[47] Neurosensory hearing loss is rare with longitudinal fractures but can result from a labyrinthine injury. Facial nerve paralysis occurs in about 20% of instances. Common sites of injury include the geniculate ganglion and the posterior genu.

Axial CT sections favor the visualization of longitudinal

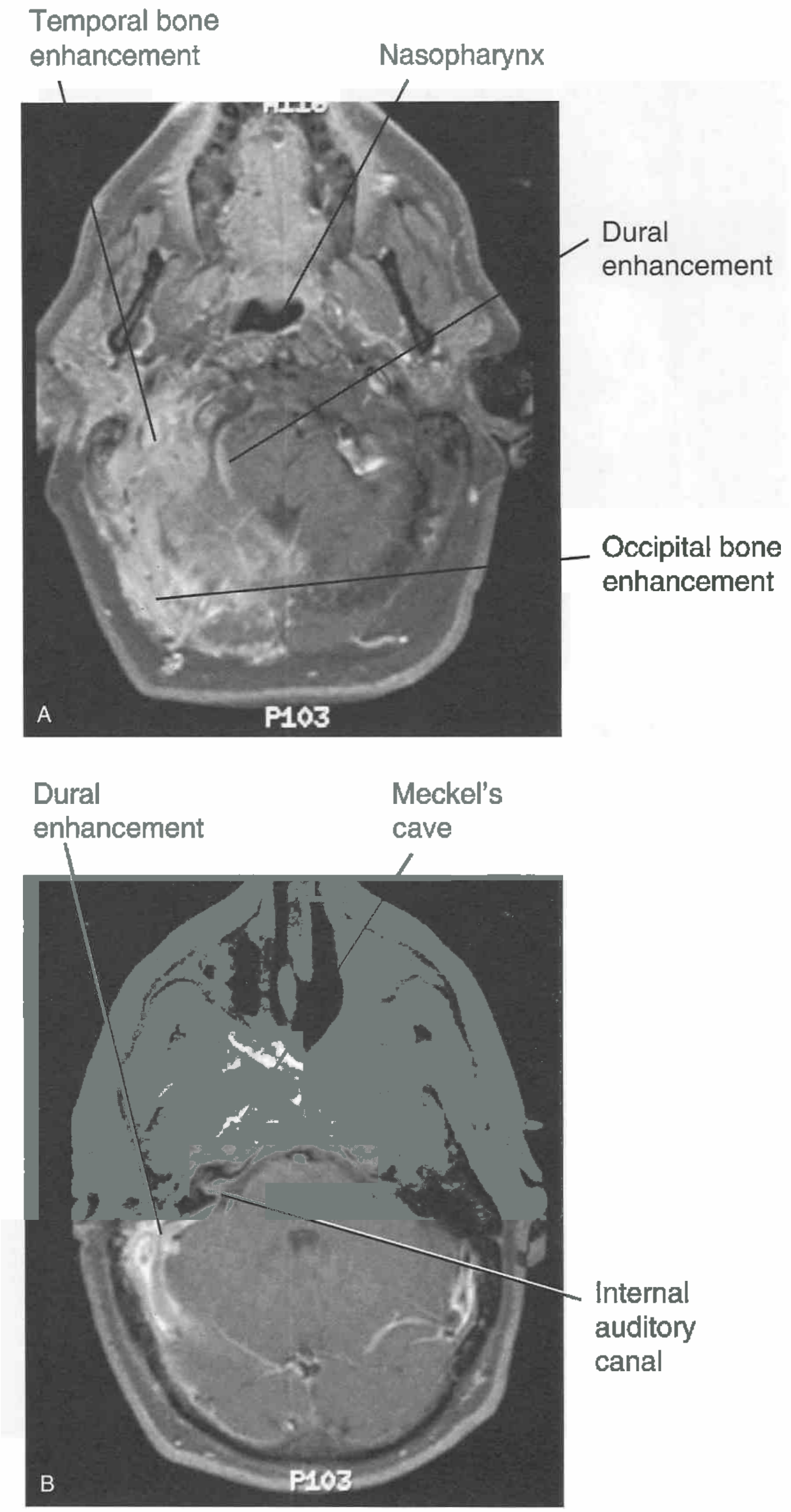

Figure 15–48. Invasive nasopharyngeal carcinoma in a young man with a very aggressive invasive carcinoma of the nasopharynx that has spread into the adjacent skull base, temporal bone, occipital bone, and posterior fossa. *A,* Axial T1-weighted, spin-echo image with fat saturation. A large arching region of tumor infiltration extends from the posterior margin of the nasopharynx all the way back to near the midline occipital bone. *B,* Axial T1-weighted spin-echo image with fat saturation centered more cephalad than in *A*. There is extensive enhancement of Meckel's caves, the right internal auditory canal, and the dural surfaces of the posterior right temporal bone.

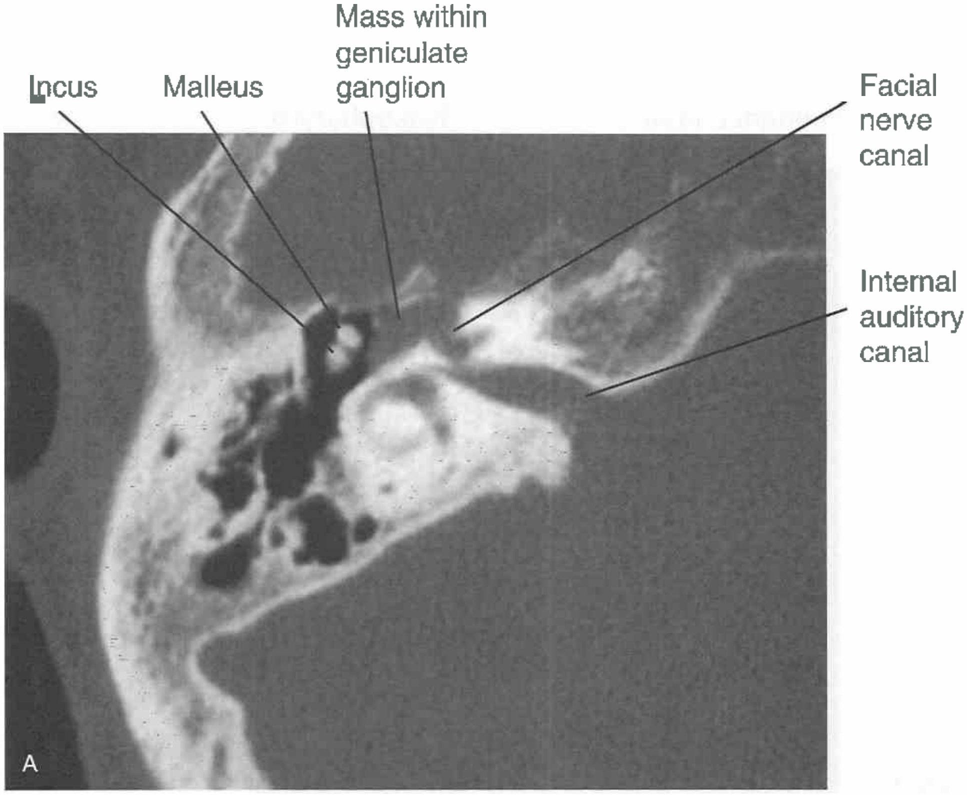

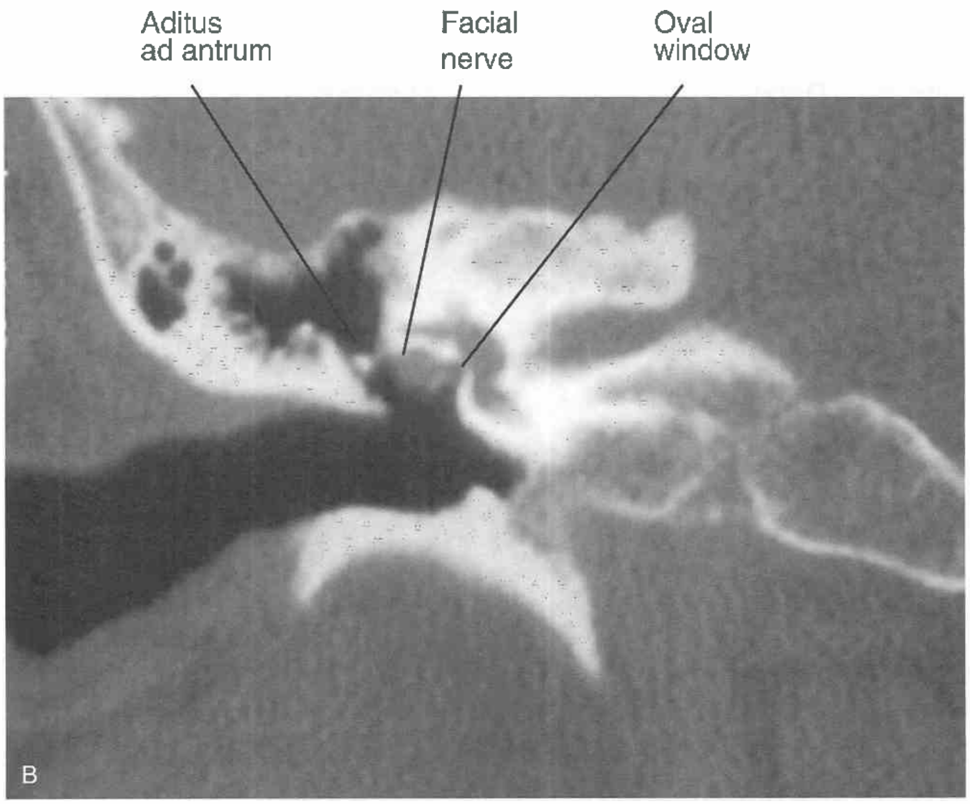

Figure 15–49. Perineural spread into geniculate ganglion in a middle-aged woman presenting with a long history of progressive right facial palsy. A CT-directed needle biopsy of the parotid showed carcinoma.

A, Axial CT image through the geniculate ganglion and internal auditory canal portions of the facial nerve canal. There is bulbous expansion of the geniculate ganglion canal. A small soft tissue component protrudes into the epitympanic space just medial to the head of the malleus and the body of the incus.

B, Coronal section through the right temporal bone at the level of the horizontal middle ear segment of the facial nerve, the oval window, and the aditus ad antrum. Note the expansion of the facial nerve that protrudes inferiorly overlying the oval window.

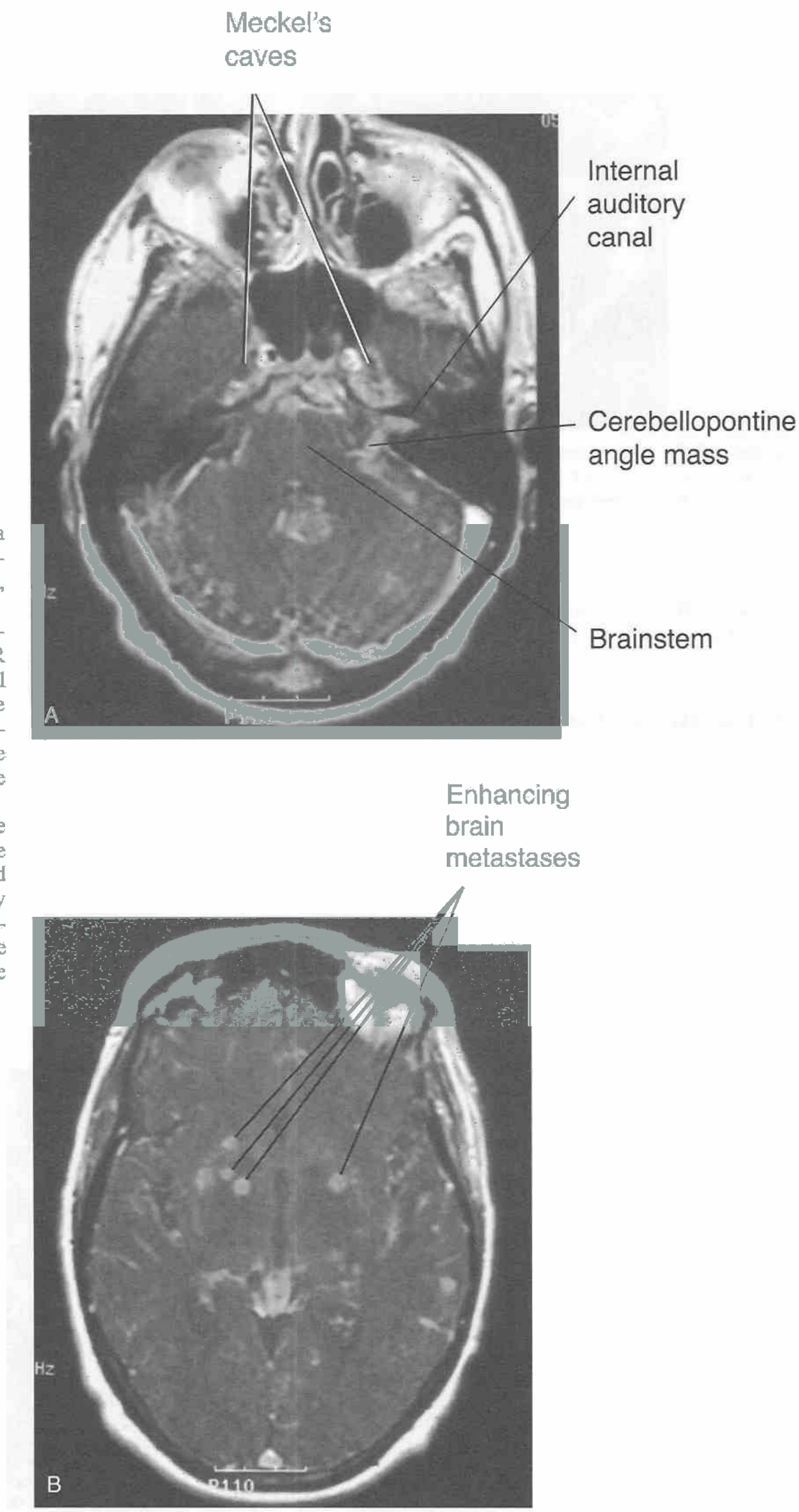

Figure 15–50. Metastatic carcinomatosis in a patient with a known primary tumor and presenting with multiple cranial nerve problems, including hearing loss.

A, Axial T1-weighted, 3D Fourier transform, high-resolution, contrast-enhanced MR image through the left internal auditory canal (IAC). The left IAC, cerebellopontine angle (CPA), and surface of the brain stem all enhance. Multiple other small lesions overlie the surface of the cerebellum. Meckel's caves are involved as well.

B, Axial T1-weighted, spin-echo MR image shows "miliary" enhancing metastases of the brain in addition to CPA disease. Isolated involvement of the IAC by carcinomatosis may mimic a small acoustic schwannoma, but frequently other lesions are imaged or multiple clinical findings may suggest a more diffuse process.

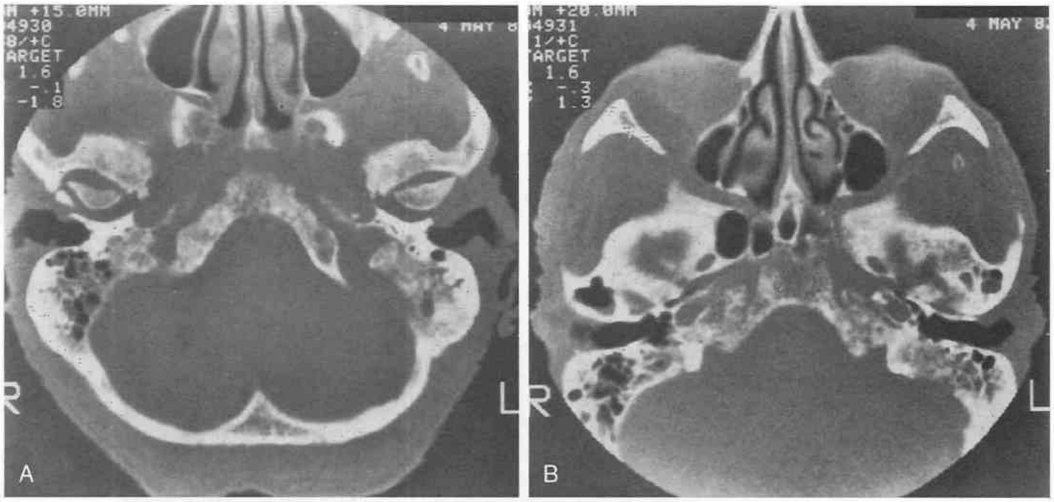

Figure 15–51. Metastatic prostatic carcinoma in an elderly man with a history of severe headaches, ear pain, and known prostate cancer. *A* and *B*, Axial CT scans of the skull base show extensive mixed lytic and blastic metastases involving the clivus and petrous apices. There is moderate destruction of the inferior portions of the petrous bones bilaterally, with patchy opacification of the mastoid air cells.

fractures. However, subtle ossicular disruptions with small bony fragments may be more readily seen on coronal images.

Transverse Fractures

Transverse fractures (Fig. 15–53) cross the temporal bone from a posterior to an anterior direction. This type of injury is less common, occurring in approximately 20% of instances. There may be associated traumatic lesions involving the temporomandibular joint, mandibular condyle, or skull base.

Transverse fractures frequently cause labyrinthine dysfunction, resulting in a totally "dead" ear whenever the fracture traverses the vestibule, semicircular canals, or cochlea. Bony fragments may impinge on the facial nerve canal. Facial nerve palsy is commonly present and is the usual reason for radiographic investigation. CT scanning can be used to explore the facial nerve canal and to illustrate the precise site of injury.[58]

Complex Fractures

A variety of comminuted fractures (Fig. 15–54) may affect the temporal bone. Other fractures of the skull base are common, since the skull base acts as a ring. Severe trauma may be associated with the presence of CSF otorrhea or rhinorrhea. Patients with persistent otorrhea or rhinorrhea can be investigated with CT scans after injection of intrathecal water-soluble contrast material. The site of leakage through the temporal bone may thus be identified, facilitating surgical repair. Vascular injuries, such as carotid

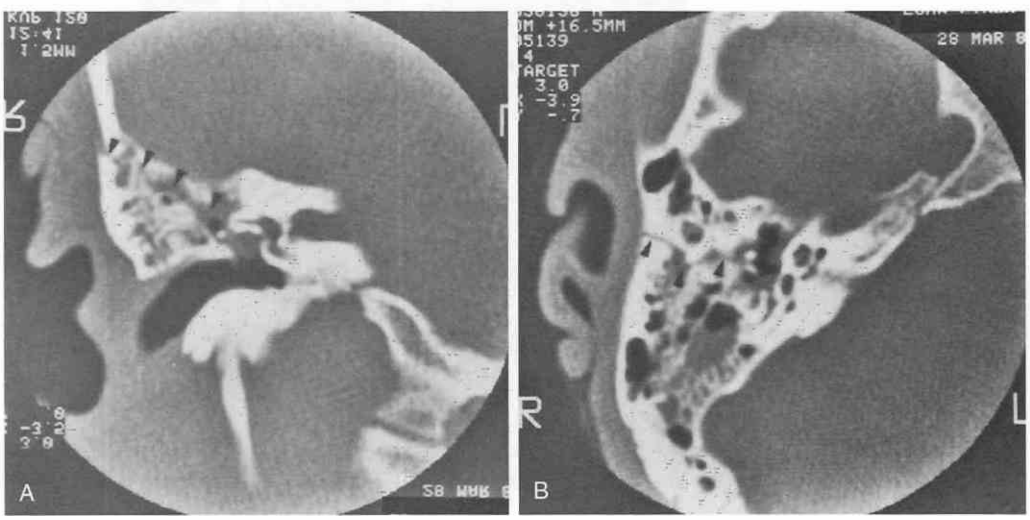

Figure 15–52. Longitudinal fracture in a young man presenting with right-sided conductive hearing loss following skull trauma. Coronal *(A)* and axial *(B)* CT scans of the right temporal bone show a fracture line *(arrowheads)* extending obliquely from the superior lateral portion of the mastoid air cells into the tympanic cavity. There is patchy air-fluid level opacification of the tympanic cavity and mastoid air cells because of hemorrhage and fluid. The ossicles are not displaced.

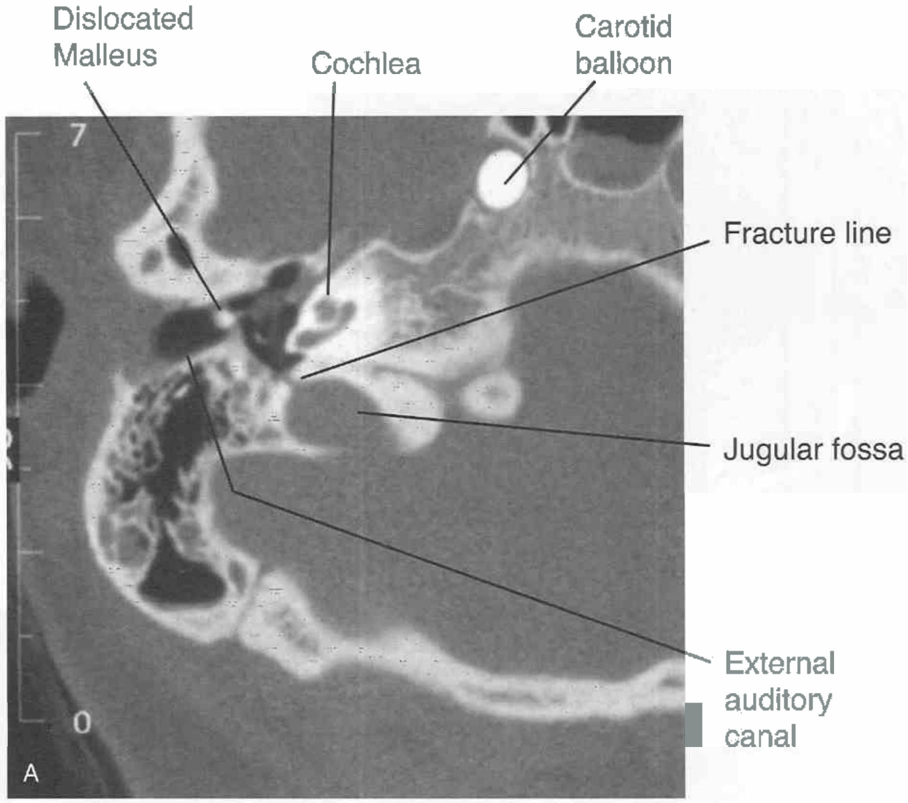

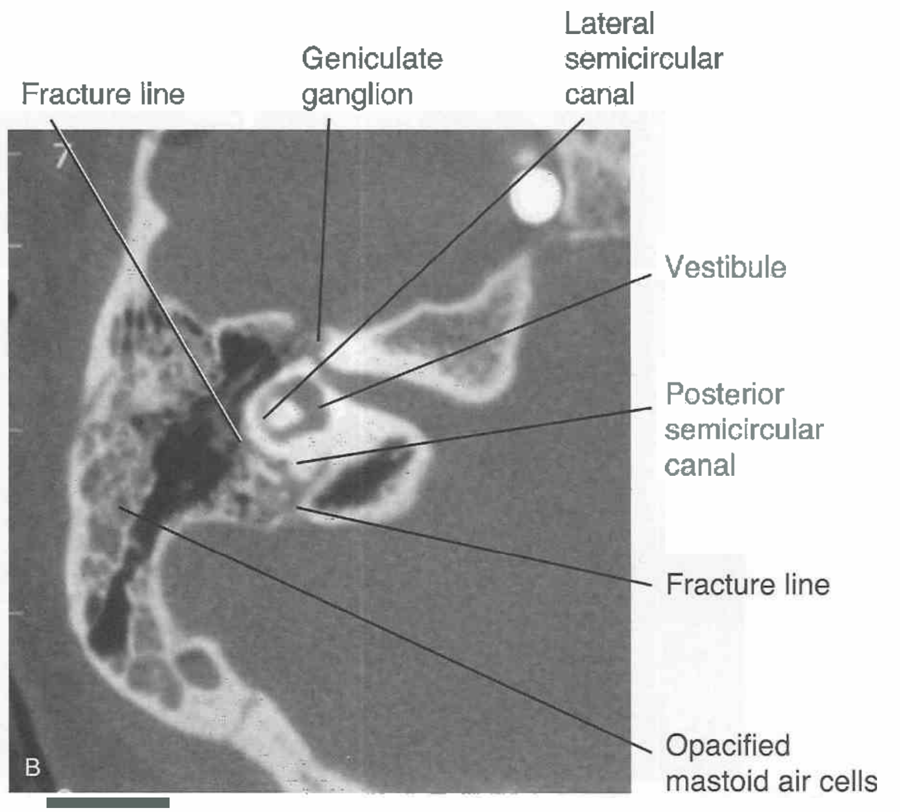

Figure 15–53. Transverse fracture. *A,* Axial CT image through the cochlea demonstrates dislocation of the ossicles (head of the malleus) into the external auditory canal and tympanic membrane. The normal position of the long process of the malleus is not seen. A linear fracture crosses obliquely into the jugular fossa. *B,* CT section through the epitympanic space demonstrates an absence of the head of the malleus and the body of the incus; they have been dislocated inferiorly. An oblique transverse fracture runs posterior to the posterior semicircular canal. A fracture of the geniculate ganglion canal is too wide to be normal. The mastoid air cells are partially opacified. A balloon is present in the carotid canal as a result of a carotid-cavernous fistula.

Figure 15–54. Comminuted fracture in a young man who sustained a severe traumatic skull and brain injury. Axial CT image through the right internal auditory canal (iac) shows multiple longitudinal *(black arrowheads)* and transverse *(black arrows* and *white arrowheads)* comminuted fractures. The lateral semicircular canal *(double-headed arrows)* is avulsed, and the malleus *(white arrow)* and incus are dislocated from the epitympanic space. The air spaces are opacified with fluid. Cerebrospinal fluid or otic capsule fistula could not be excluded.

Figure 15–55. [redacted]eral cochlear otosclerosis[redacted]dult wit[redacted]history of progressive[redacted]ateral neurosensory hearing loss. *A* and *B*, Coronal CT scans of the left ear show a rim of hypodensity paralleling the left cochlea *(arrowheads)*. This lucency represents an area of the enchondral layer of bone formation. *C* and *D*, Axial CT scans of the right ear show similar findings *(arrowheads)*. (*A–D*, Courtesy of Dr. Galdino Valvassori.)

dissection and carotid cavernous fistulas, may also be seen. Both MRI and angiography are of value.

Facial Nerve Injury

Transient facial nerve paralysis may occur after temporal bone injury as a result of edema (see Fig. 15–53). Contusion of the facial nerve occurs at the site of greatest narrowing. Whenever there is persistent dysfunction, surgical exploration of the facial nerve may be indicated.[60] Preoperative CT examination can identify the site of injury.[27]

Metabolic and Dysplastic Lesions

The petrous temporal bone may be affected by a variety of primary bone diseases that can involve other portions of the skeleton. When they involve the temporal bone, the significance is related to disturbances of hearing, balance, or facial nerve function. Thus, these afflictions usually require detailed, high-resolution CT evaluation of the temporal bones.

Otosclerosis

Otosclerosis (Fig. 15–55) is more accurately called *otospongiosis*, which reflects the active phase of the disease.

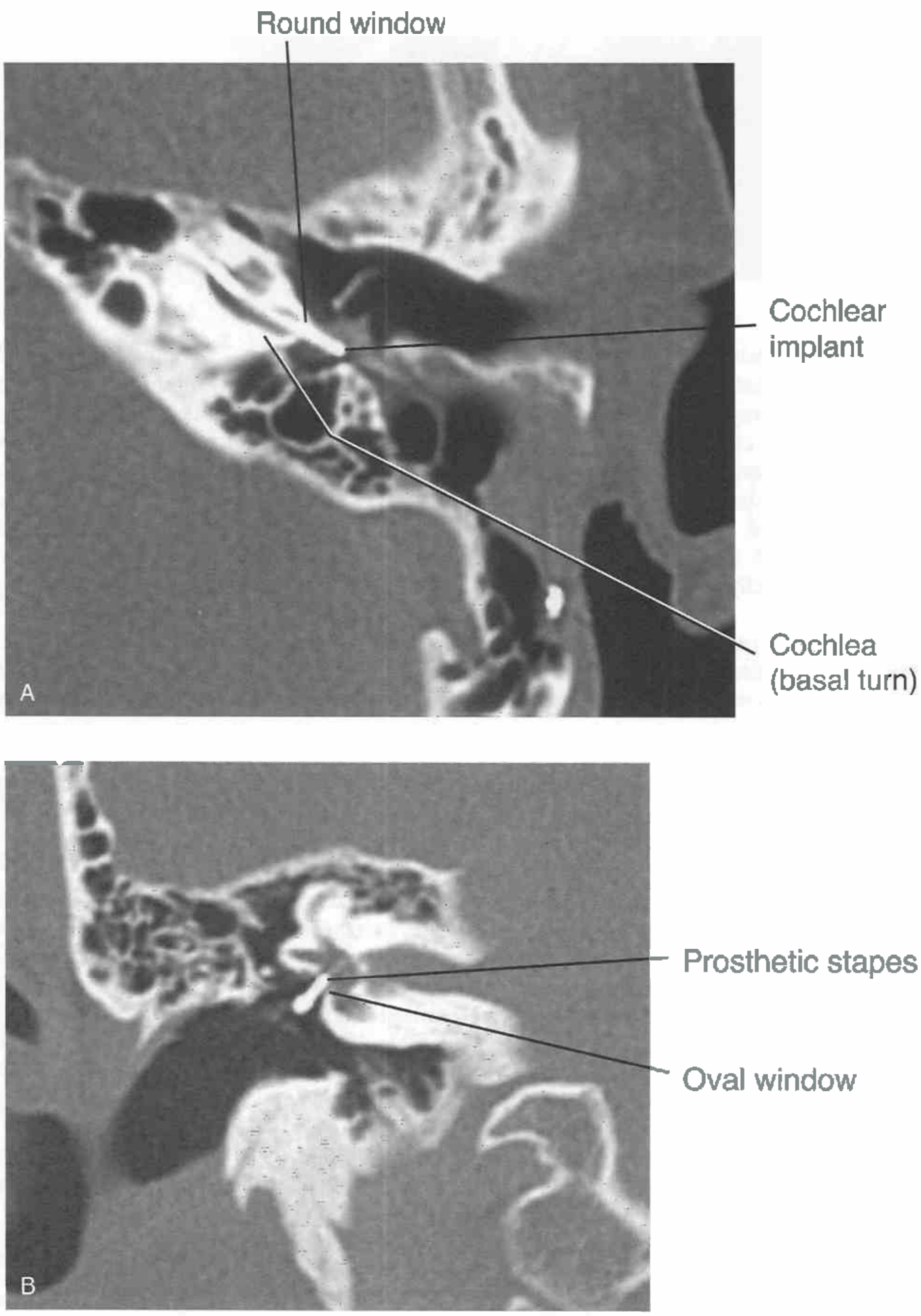

Figure 15–56 Prostheses. *A*, Axial CT section through the round window and cochlea demonstrates a cochlear implant. The wire enters the round window and the basal turn of the cochlea and is seen as a thin, linear density. *B*, Coronal CT scan shows a metallic prosthetic stapes angled from the long process of the incus up into the oval window niche. It ends at the stapes footplate in a normal position.

Illustration continued on following page

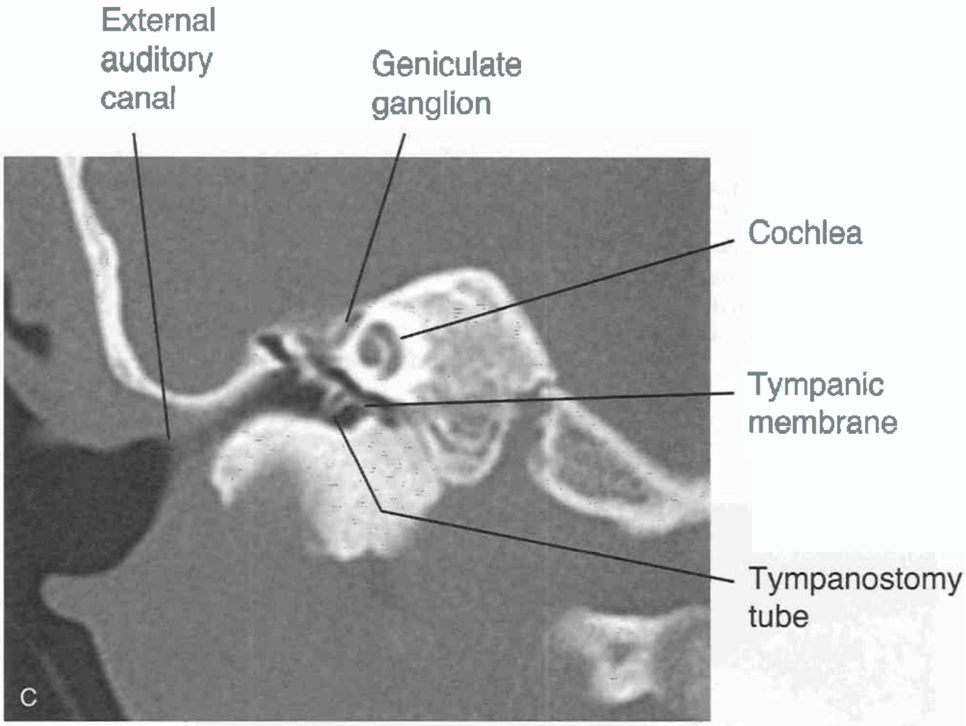

Figure 15–56 *Continued C,* Coronal CT scan shows a small tympanostomy tube as two thin linear densities protruding from the tympanic membrane. The middle ear and the external auditory canal are clear. Other structures depicted include the cochlea and the geniculate ganglion.

This primary bone disease is fairly common; histological studies show that it occurs in up to 10% of the population, but clinical symptoms are present in only 10% of those with histologic changes. If the disease process involves the labyrinthine capsule, there may be progressive neurosensory hearing loss. Involvement of the oval window and stapes footplate causes conductive hearing loss, whereas involvement of the cochlea causes neurosensory hearing loss. Occasionally, there is a combination of both types of deafness.

The human otic capsule is unique because mature bone remains in a state of primary ossification. This enchondral capsule is never replaced by mature haversian osseous tissue. Pathologically, otosclerosis consists of replacement of the primitive and chondral bony capsule by mature haversian bone. The disease begins as scattered foci of bony resorption containing many osteoclasts, osteoblasts, and irregular, loose trabeculae. These so-called spongiotic foci are less dense than normal bone and represent the *active* disease (otospongiosis), which can cause hearing loss. In the *inactive (sclerotic)* phase, a few cells or vessels are contained within sclerotic foci. Otosclerosis usually begins before puberty, is familial, and is bilateral in about 90% of patients. Women are affected twice as often as men.

Cochlear (labyrinthine) otosclerosis (see Fig. 15–55) has a characteristic CT appearance. Crescentic low-density regions parallel the margins of the basal turn of the cochlea, the entire cochlea, or the whole otic capsule. On CT scans, the active or spongiotic phase appears as areas of demineralization involving the enchondral layer of the cochlea or the otic capsule.[37] CT scanning may be able to show a fine enchondral band of decreased density in some patients with normal hearing. Presumably, this represents histologic (incipient) otosclerosis. Other patients may have areas of inactive otosclerotic foci.

Spongiotic changes involving the oval window and stapes footplate are referred to as *fenestral otosclerosis*, a type that is more difficult to identify on CT scans. However, the otosclerotic phase may be readily appreciated.[36] Patients with early stapedial vestibular otosclerosis show small lucencies within the otic capsule with soft tissue swelling predominantly at the anterior margin of the oval window. Later on, dense otosclerotic foci may cover these structures. The round window may also be affected.

Most patients with otosclerosis are treated with stapedectomy and prosthetic implants. State-of-the-art CT scanning may be used in evaluating metallic, plastic, and ceramic prostheses after such procedures (Fig. 15–56).[13] Patients who experience recurring hearing loss after ossiculoplasties may also be examined by CT to determine whether dislocation of the prosthesis has occurred.

Osteogenesis Imperfecta

Osteogenesis imperfecta (Fig. 15–57) produces otic capsule and oval window changes identical to those seen with otosclerosis.[36, 37] Deafness is a common finding, with progressive hearing loss starting in childhood or as late as the third decade of life. When the otosclerotic process extends into the medial aspect of the cochlear capsule, the enchondral band of demineralization produces a characteristic double lucency appearance *(double-ring sign)* of the cochlea. If the process is severe and extensive, the outline of the cochlea becomes totally indistinguishable from the surrounding petrous bone.

Paget's Disease (Osteitis Deformans)

Paget's disease (osteitis deformans) (Fig. 15–58) is a chronic inflammatory disorder that results in the eventual

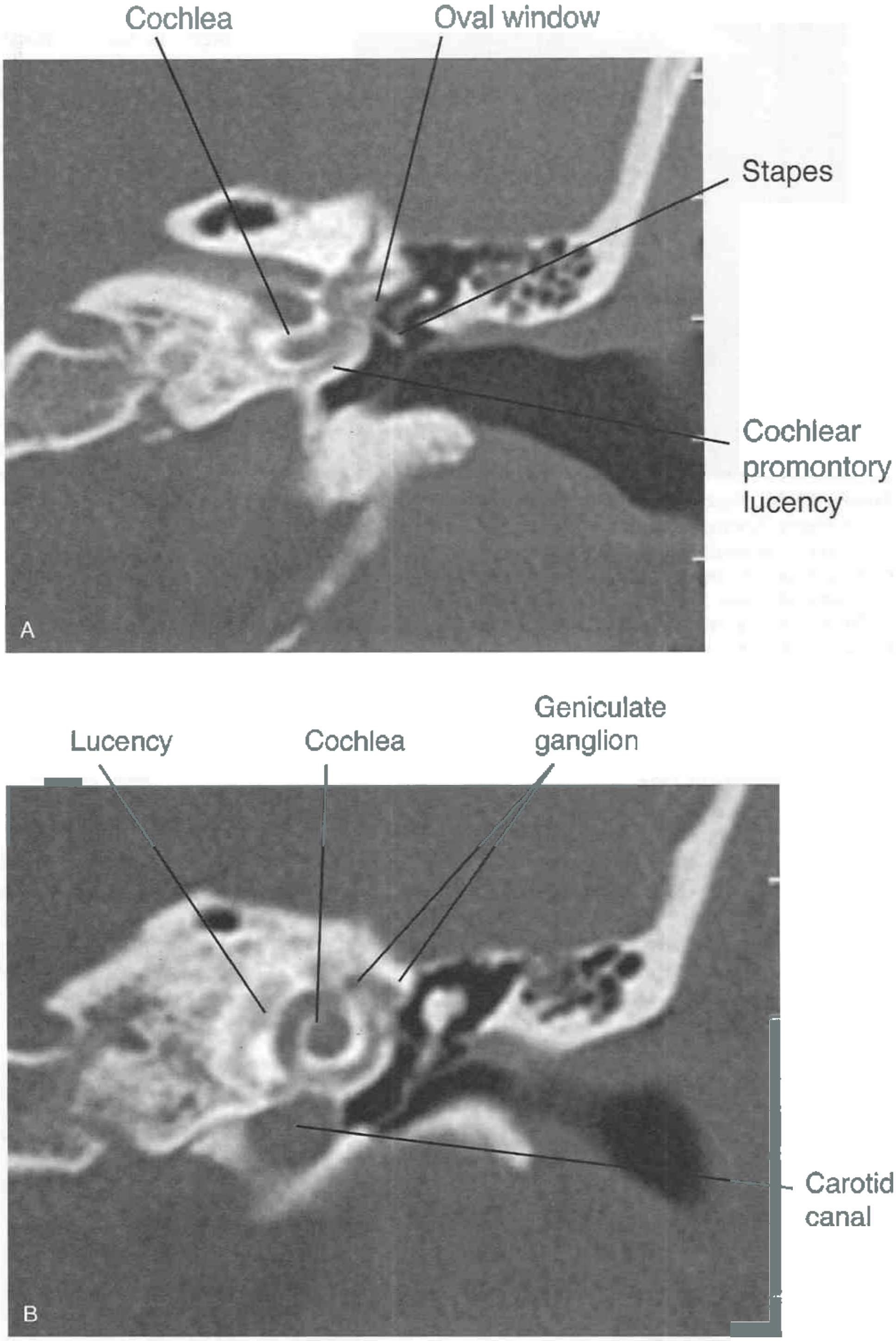

Figure 15–57. Osteogenesis imperfecta in a young patient with hearing loss and facial palsy. *A*, Coronal CT image demonstrates a broad lucency adjacent to the basal turn of the cochlea. There is also thickening of the soft tissues filling the oval window niche, mimicking severe fenestral and cochlear otosclerosis. *B*, Coronal image, anterior in relationship to *A*, shows erosive changes involving the geniculate ganglion region and paralleling the cochlea.

replacement of normal bone by thickened, less dense, weaker bone. The incidence of Paget's disease in patients over 40 years of age is 3%, and the skull is affected in 65% to 70% of patients. When Paget's disease involves the temporal bone, it is most often bilateral, with similar structural changes in a given pair of temporal bones.

Paget's disease can produce narrowing and tortuosity of the external auditory canal. Exostoses and chronic external otitis are fairly common and lead to the secondary development of external canal cholesteatomas. In addition to the overgrowth of bone in the external auditory canal (which may cause conductive hearing loss), there may be concentric overgrowth of the tympanic bone. This bony overgrowth leads to conductive hearing loss because the tympanic annulus and tympanic membrane become relaxed, resulting in inadequate function.

Paget's disease can affect the inner ear, with demineralization of the petrous pyramids and labyrinthine capsule. These areas of demineralization are intermixed with areas of apparent thickening in the skull base.

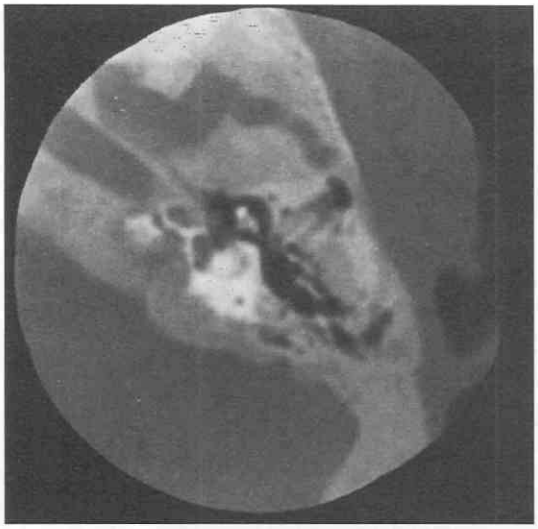

Figure 15–58. Paget's disease in an older man with bilateral neurosensory hearing loss. Axial CT scan of the left ear shows tremendous thickening of the entire temporal bone. The central portion of the otic capsule adjacent to the vestibule and semicircular canals are least affected. The internal auditory canal is not visible because of pagetoid changes in the inner ear. (Courtesy of Dr. Jacqueline Vignaud.)

Fibrous Dysplasia[43]

Fibrous dysplasia (Fig. 15–59) is a disease manifested by aberrant maturation of bone. Histologically, normal spongiotic bone is replaced and the medullary cavities of affected bones are filled by abnormal fibrous tissue. The bony structures have an increased density, in comparison with normal bone and in contrast to Paget's disease, where the thickened bone is less dense than normal bone. Solitary monostotic fibrous dysplasia of the petrous pyramid may occur, but widespread involvement is more common. The changes in the temporal bone are usually proliferative, whereas the changes in the calvaria are usually expansile.

Patients with fibrous dysplasia can show both conductive and neurosensory hearing loss. Conductive hearing loss results from narrowing or occlusion of the external auditory canal. Such stenosis is common and may be responsible for cholesteatoma formation.[23] These external canal cholesteatomas may lead to a condition of external canal stenosis termed *keratosis obturans*. The mastoid portion may show hyperostotic thickening of cell walls, leading to obliteration of mastoid air cells.

Fibrous dysplasia may involve the petrous portion of the temporal bone. Areas of sclerosis may alternate with areas of resorption and expansion. The thickened bone is regular and typically is not fragmented.[27] Frank destruction of the petrous ridge or otic capsule is usually associated with malignant degeneration, which occurs in approximately 1 in 200 patients.

Osteopetrosis

Osteopetrosis is a heredity disorder characterized by excessive calcification of bones and spontaneous fractures. The disease process may be mild, with a benign course and normal life span (autosomal dominant). Alternatively, the disease may follow a malignant course, causing death early in life (autosomal recessive). Patients can have hydrocephalus, subarachnoid hemorrhage, extramedullary hematopoiesis, and severe headaches with progressive visual and hearing loss.

CT scans show extensive sclerosis of the petrous pyramids. There is a normal density difference between the otic capsule and the surrounding bone. Progressive neurosensory hearing loss is caused by obliteration of the labyrinth or narrowing of the internal auditory canals.

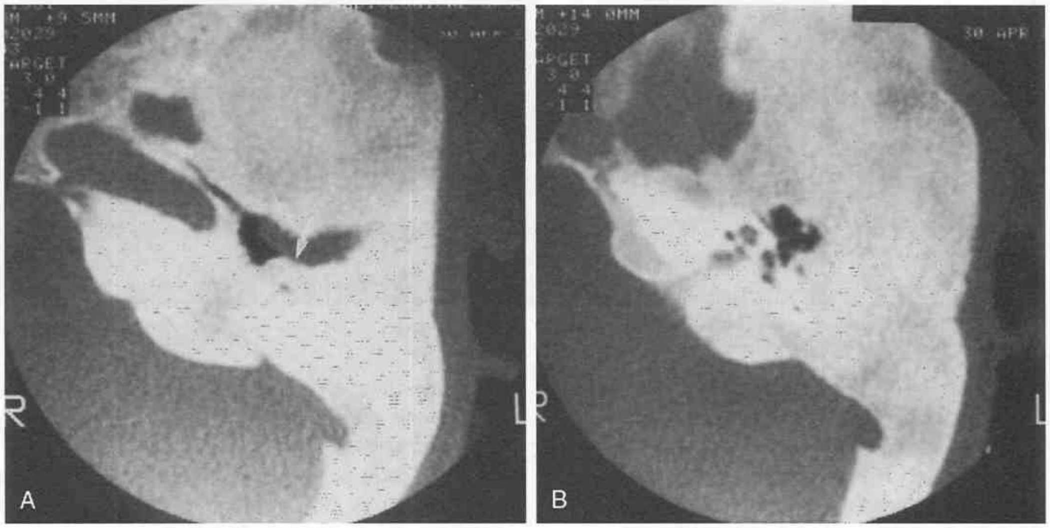

Figure 15–59. Fibrous dysplasia in a young man with a long-standing, left-sided conductive hearing loss and stenosis of the left external auditory canal (EAC). *A* and *B*, Axial CT scans of the left temporal bone show tremendous bony overgrowth, with diffuse sclerosis and thickening of the temporal bone. The labyrinthine capsule is still identifiable despite excessive new bone formation. Note the total obliteration of the mastoid air cells. The tympanic cavity is compressed, and the EAC is severely narrowed. A soft tissue mass *(arrow)* in the EAC represents a secondary cholesteatoma (keratosis obturans) caused by chronic obstruction.

Acknowledgments

We would like to acknowledge Linda Chakeres for editing the complete text and John Croyle for printing most of the images. We would also like to thank Anton Hasso, M.D., C. Roger Bird, Barbara Carter, Charles Lanzieri, Theodore Larson, William Lo, Galdino Valvassori, Jacqueline Vignaud and Jeffrey Jones, M.D., for the use of their figures.

References

1. Alvi A, Bereliani A: Acute intracranial complications of temporal bone trauma. Otolaryngol Head Neck Surg 119:609, 1998.
2. Bergeron RT, Osborn AG, Som PM: Head and Neck Imaging Excluding the Brain. St. Louis, CV Mosby, 1984.
3. Bergeron RT, et al: The temporal bone. In Som PM, Bergeron RT (eds): Head and Neck Imaging, 2nd ed. St. Louis, CV Mosby, 1991.
4. Bird CR, Hasso AN, Stewart CE: Malignant primary neoplasms of the ear and temporal bone studied by high-resolution computed tomography. Radiology 146:171, 1983.
5. Brogan M, Chakeres DW: Computed tomography and magnetic resonance imaging of the normal anatomy of the temporal bone. Semin Ultrasound CT MR 10:178, 1989.
6. Brogan M, Chakeres DW: Gd-DTPA MR imaging of cochlear schwannoma. AJNR AM J Neuroradiol 11:407, 1990.
7. Brogan M, Chakeres DW, Schmalbrock P: Comparison of high-resolution 3DFT and computed tomography in the evaluation of the otic capsule and the vestibular aqueduct. AJNR Am J Neuroradiol 12:1, 1991.
8. Chakeres DW: Clinical significance of partial volume averaging of the temporal bone. Am J Neuroradiol 5:297, 1984.
9. Chakeres DW: Computed tomography of the ear: A tailored approach. Radiol Clin North Am 22:3, 1984.
10. Chakeres DW, Kapila A: The normal CT anatomy of the brainstem and related structures using direct longitudinal scanning with metrizamide cisternography. Radiology 149:709, 1983.
11. Chakeres DW, Kapila A, LaMasters D: Soft tissue abnormalities of the external auditory canal: Subject review of CT findings. Radiology 156:105, 1985.
12. Chakeres DW, LaMasters DL: Paragangliomas of the temporal bone: High-resolution CT studies. Radiology 150:749, 1984.
13. Chakeres DW, Mattox DW: Computed tomographic evaluation of non-metallic middle ear prostheses. Invest Radiol 20:596, 1985.
14. Chakeres DW, Spiegel RK: A systematic technique for comprehensive evaluation of the temporal bone by computed tomography. Radiology 146:97, 1983.
15. Chakeres DW, Schmalbrock P, Brogan M, et al: Normal venous anatomy of the brain: demonstration with gadopentetate dimeglumine in enhanced 3-D MR angiography. AJNR 11:1107, 1990.
16. Chintapalli K, Unger JM, Shaffer K: Otosclerosis: Comparison of complex-motion tomography and computed tomography. Am J Neuroradiol 6:85, 1985.
17. Curtin HD: CT of acoustic neuroma and other tumors of the ear. Radiol Clin North Am 22:77, 1984.
18. Curtin HD, Wolfe R, May M: Malignant external otitis: CT evaluation. Radiology 145:383, 1982.
19. Dahlen RT, Harnsberger HR, Gray SD, et al: Overlapping thin-section fast spin-echo MR of the large vestibular aqueduct syndrome. AJNR Am J Neuroradiol 18:67, 1997.
20. Dailiana T, Chakeres D, Schmalbrock P, et al: High-resolution MR of the intraparotid facial nerve and parotid duct. AJNR Am J Neuroradiol 18:165, 1997.
21. Dalley RW, Robertson WD, Lapointe JS: Computed tomography of a cerebellopontine angle lipoma. J Comput Assist Tomogr 10: 704, 1986.
22. Hasso AN, Vignaud J, DeSmedt E: Pathology of the temporal bone and mastoid. In Newton TH, Hasso AN, Dillon WP (eds): Modern Neuroradiology, vol 3. Computed Tomography of the Head and Neck. New York, Raven Press, 1988.
23. Hasso AN, Vignaud J, DeSmedt E: Normal anatomy of the temporal bone and mastoid. In Newton TH, Hasso AN, Dillon WP (eds): Modern Neuroradiology, vol 3, Computed Tomography of the Head and Neck. New York, Raven Press, 1988.
24. Hermans R, Feenstra L, Marchal G, Baert AL: Three-dimensional CT imaging of the ossicular chain. Clin Otolaryngol 20:475, 1995.
25. Howard JD, Elster AD, May JS: Temporal bone: Three-dimensional CT. Radiology 177:421, 1990.
26. Johnson DW: CT of the post surgical ear. Radiol Clin North Am 22: 67, 1984.
27. Johnson DW, Hasso AN, Stewart CE: Temporal bone trauma: High-resolution computed tomographic evaluation. Radiology 151:411, 1984.
28. Johnson DW, Hinshaw DB, Hasso AN: Computed tomography of local complications of temporal bone cholesteatomas. J Comput Assist Tomogr 9:519, 1985.
29. Johnson DW, Voorhees RL, Lufkin RB: Cholesteatomas of the temporal bone: role of computed tomography. Radiology 148:461, 1983.
30. Koizuka I, Seo R, Kubo T, et al: High-resolution MRI of the human cochlea. Part 2. Acta Otolaryngol Suppl 520:256, 1995.
31. Latack JT, Gabrielsen TO, Knake JE: Facial nerve neuromas: Radiologic evaluation. Radiology 149:731, 1983.
32. Lemmerling MM, Mancuso AA, Antonelli PJ, Kubilis PS: Normal modiolus: CT appearance in patients with a large vestibular aqueduct. Radiology 204:213, 1997.
33. Lo WW, Daniels DL, Chakeres DW, et al: The endolymphatic duct and sac. AJNR Am J Neuroradiol 18:881, 1997.
34. Lo WWM, Solit-Bohman LG: High-resolution CT of the jugular foramen: Anatomy and vascular variants and anomalies. Radiology 150:743, 1984.
35. Lo WWM, Solit-Bohman LG, Lambert PR: High-resolution CT in the evaluation of glomus tumors of the temporal bone. Radiology 150:737, 1984.
36. Mafee MF, Henrikson GC, Deitch RL: Use of CT in the evaluation of stapedial otosclerosis. Radiology 156:709, 1985.
37. Mafee MF, Valvassori GE, Deitch RL: Use of CT in the evaluation of cochlear otosclerosis. Radiology 156:703, 1985.
38. Mafee MF, Lachenauer CS, Kumar A, et al: CT and MR imaging of intralabyrinthine schwannoma: Report of two cases and review of the literature. Radiology 174:395, 1990.
39. Mark AS, Seltzer S, Harnsberger HR: Sensorineural hearing loss: More than meets the eye? AJNR Am J Neuroradiol 14:37, 1993.
40. Martin N, Sterkers O, Nahum H: Chronic inflammatory disease of the middle ear cavities: Gd-DTPA-enhanced MR imaging. Radiology 176:399, 1990.
41. Mayer TE, Brueckmann H, Siegert R, et al: High-resolution CT of the temporal bone in dysplasia of the auricle and external auditory canal. AJNR Am J Neuroradiol 18:53, 1997.
42. Mendelson DS, Som PM, Mendelson MH: Malignant external otitis: The role of computed tomography and radionucleotides in evaluation. Radiology 149:745, 1983.
43. Palacios E, Valvassori G: Fibrous dysplasia of the temporal bone. Ear Nose Throat J 78:415, 1999.
44. Pappas DG, Simpson LC, McKenzie RA, Royal S: High-resolution computed tomography: Determination of the cause of pediatric sensorineural hearing loss. Laryngoscope 100:564, 1990.
45. Phelps PD: Glomus tumors of the ear: An imaging regime. Clin Radiol 41:301, 1990.
46. Phelps PD, Lloyd GAS: The radiology of carcinoma of the ear. Br J Radiol 54:103, 1981.
47. Phelps PD, Lloyd GAS: Radiology of the ear, Boston, Blackwell, 1983.
48. Remley KB, Coit We, Harnsberger HR, et al: Pulsatile tinnitus and the vascular tympanic membrane: CT, MR, and angiographic findings. Radiology 174:383, 1990.
49. Robert Y, Carcasset S, Rocourt N,et al: Congenital cholesteatoma of the temporal bone: MR findings and comparison with CT. AJNR Am J Neuroradiol 16:755, 1995.
50. Schmalbrock P, Chakeres DW, Monroe JW, et al: Assessment of internal auditory canal tumors: A comparison of contrast-enhanced T1-weighted and steady-state T2-weighted gradient-echo MR imaging. AJNR Am J Neuroradiol 20:1207, 1999.
51. Schmalbrock P, Dailiana T, Chakeres DW, et al: Submillimeter-resolution MR of the endolymphatic sac in healthy subjects and patients with Meniere disease. AJNR Am J Neuroradiol 17:1707, 1996.
52. Swartz JD: Cholesteatomas of the middle ear: Diagnosis, etiology and complications. Radiol Clin North Am 22:15, 1984.
53. Swartz JD: The facial nerve canal: CT analysis of the protruding tympanic segment. Radiology 153:443, 1984.
54. Swartz JD, Bazarnic ML, Naidich TP: Aberrant internal carotid artery lying within the middle ear. Neuroradiology 27:322, 1985.

55. Swartz JD, Faerber EN: Congenital malformations of the external and middle ear: High-resolution CT findings of surgical import. Am J Neuroradiol 6:71, 1985.
56. Swartz JD, Goodman RS, Russell KB: High-resolution computed tomography of the middle ear and mastoid. Radiology 148:455, 1983.
57. Tanioka H, Shirawkawa T, Michida T, Sasaki Y: Three-dimensional reconstructed MR imaging of the inner ear. Radiology 178:141, 1991.
58. Taylor S: The petrous temporal bone (including the cerebellopontine angle). Radiol Clin North Am 20:67, 1982.
59. Tsuruda JS, Shimakawa A, Pelc NJ, Saloner D: Dural sinus occlusion: Evaluation with phase-sensitive gradient-echo MR imaging. AJNR Am J Neuroradiol 12:481, 1991.
60. Valavanis A, Kubik S, Oguz M: Exploration of the facial nerve canal by high-resolution computed tomography: Anatomy and pathology. Neuroradiology 24:139, 1983.
61. Valavanis A, Kubik S, Schubiger O: High-resolution CT of the normal and abnormal fallopian canal. Am J Neuroradiol 4:748, 1983.
62. Valavanis A, Schubiger O, Oguz M: High-resolution CT investigation of nonchromaffin paragangliomas of the temporal bone. Am J Neuroradiol 4:516, 1983.
63. Virapongse C, Rothman SLG, Kier EL: Computed tomographic anatomy of the temporal bone. Am J Neuroradiol 3:379, 1982.
64. Virapongse C, Rothman SLG, Sasaki C: The role of high-resolution computed tomography in evaluating disease of the middle ear. J Comput Assist Tomogr 6:711, 1982.
65. Welling DB, Clarkson MW, Miles BA, et al: Submillimeter magnetic resonance imaging of the temporal bone in Meniere's disease. Laryngoscope 106:1359, 1996 [erratum, 107:147, 1997].
66. Welling B, Schmalbrock P, Chakeres D: Submillimeter MRI of the temporal bone in Meniere's disease. Laryngoscope 106:1359, 1996.
67. Wiet RJ, Pyle GM, O'Connor CA, et al: Computed tomography: How accurate a predictor for cochlear implantation? Laryngoscope 100: 687, 1990.
68. Zonneveld FW, et al: Direct multiplanar computed tomography of the petrous bone. Radiographics 3:400, 1983.

16 The Sinonasal Cavity

Charles F. Lanzieri

Embryology[25]

The nasal sac or primitive nasal cavity begins to develop from the stomodeum as early as the 24th fetal day. The stomodeum forms on the ventral and superior aspect of the embryo between the first branchial arches. There is an eventual thinning of the cellular layers to first form a buccopharyngeal membrane. At about the 28th fetal day, the buccopharyngeal membrane disappears, and communication between the amnion and internal cavity is established.

At about the 28th fetal day, the nasal placode first forms just superior to the first branchial arch and just lateral to the stomodeum. At about the 31st day, there is an infolding in the center of the nasal placode, which forms the nasal pit. The nasal sacs grow dorsally from each nasal pit into the ventral portion of the developing brain. At first, the sacs are separated from the oral cavity by the oronasal membrane, but this membrane soon ruptures, bringing the nasal and oral cavities into communication. These regions of continuity are called the *primitive choanae,* which lie posterior to the primary palate. After the secondary palate develops, the choanae are located at the junction of the nasal cavity and the pharynx.

At about the 48th fetal day, the lateral palatine processes fuse with each other and the nasal septum; the oral and nasal cavities are again separated. This fusion also results in separation of the nasal cavities from each other.

While these changes are occurring, the superior, middle, and inferior conchae develop as elevations on the lateral wall of each nasal cavity; in addition, the ectodermal epithelium in the roof of each nasal cavity becomes specialized into the olfactory region. Some cells differentiate into olfactory cells that give origin to fibers that grow into the olfactory bulbs of the brain.

The paranasal sinuses develop during late fetal life and early infancy as small diverticula of the lateral nasal wall. During childhood, these sinuses extend into the maxilla, the ethmoid, and the frontal and sphenoid bones, reaching their maximum size at puberty.

Anatomy and Normal Variants

The nose serves to inspire and expire air and to warm, moisturize, and filter that air. It has been estimated that approximately 2 L of water is produced daily by the serous glands of the sinonasal cavity and is used to humidify the inspired air.[30] A surface film of mucus also traps larger particles, and the action of the associated cilia serves to transport the mucus and particulate matter posteriorly and inferiorly into the nasopharynx at approximately 1 cm/minute.[30]

The nasal mucosa is vascular pseudostratified columnar ciliated epithelium that contains both serous and mucous glands.[11] In the most superior portion of the nasal fossa is a less vascular and nonciliated epthelium, the olfactory mucosa.[11] It contains the efferent axon of the bipolar olfactory nerve fibers that transform the physical stimuli of odors into nerve impulses that are then transmitted through the cribiform plate into the olfactory gyri.[11] A special lipolipid is secreted by this mucosa, which is necessary for the dissolution of odors that are transmitted to the bipolar neurons.[51] Since smells can be perceived only if the substance is in solution, a dried olfactory mucosa has no perception of smell.[18] In addition, there is no ciliary action within the olfactory mucosa, so that sniffing is necessary to bring the fragrance-bearing material to the olfactory recess and to this mucosa.[45]

The medial wall of each nasal cavity is the nasal septum, which is partially bony and made up of the perpendicular plate of the ethmoid and the vomer; the more anteroinferior portion of the nasal septum is cartilaginous. The lateral wall of the nasal fossa, however, is extremely complex.[2–6, 11, 18, 30, 45, 51] The ostia for the paranasal sinuses open into the lateral wall, which is separated into either three or four fossae or meatus by either three or four nasal turbinates or chonchae (Fig. 16–1).

The tubinates are delicate projections of bone that become smaller as they ascend superiorly into the nasal cavity. Because the paranasal sinuses develop predictably from outpouchings of the lateral nasal wall, the drainage pattern is also predictable. The frontal and anterior ethmoid

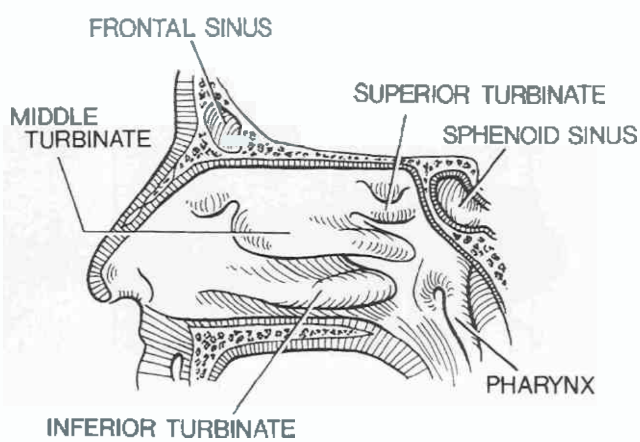

Figure 16–1. Anatomic drawing. The medial aspect of the right nasal cavity is shown. The superior, middle, and inferior turbinates divide each nasal cavity into three fossae or meatus. This anatomy and the anatomic variations are important for understanding disease processes and for surgical planning.

and maxillary sinuses nearly always drain between the middle and inferior nasal turbinates into the middle meatus. The posterior ethmoids nearly always drain between the superior and middle turbinates or middle meatus. The sphenoid sinus may drain between the superior and supreme turbinate or superior meatus or directly into the most superior and posterior recess of the nasal cavity (the *sphenoethmoidal recess*). Functionally, it is useful to think of each of these groupings of sinuses and their respective meatus as a single unit. Clinically, the most important of these is the middle meatus, also called the *ostiomeatal unit*. In the common inflammatory syndromes, the middle meatus and associated anterior ethmoid, frontal, and ipsilateral maxillary sinuses are most often involved as a unit.

The inferior turbinate is covered by a thick mucous membrane that contains a dense venous plexus with large vascular spaces and erectile tissue. In this sense, it is somewhat different from the other turbinates. The nasolacrimal duct is the only consistent opening within the inferior meatus. If one were to remove the middle turbinate and examine the middle meatus, one would find a slightly curved slit, the hiatus semilunaris, on the lateral surface of the middle meatus. Into this slit drain the ethmoid air cells and maxillary sinus. Into the anterior recess of this slit drains the frontonasal duct if this duct exists.

In approximately 50% of patients, the nasofrontal duct drains directly into the ethmoid air cells, which then drain into the frontal recess. This important drainage space is covered medially by the uncinate process of the ethmoid bone. The length and configuration of the uncinate process determine the ease of upward transportation of mucous secretions.

Just superior to the hiatus semilunaris lies the bullosa ethmoidalis, which is an inferiorly placed ethmoid air cell. The size and degree of pneumatization of this ethmoid bulla determine the size of the opening of the ostiomeatal unit into the middle meatus. The relative sizes, shapes, and configurations of these structures determine, to some extent, the frequency of obstruction and the propensity for inflammatory changes within the ostiomeatal unit.

In approximately 80% of the population, there is an alternating pattern of increased production of secretions and shunting of blood into the vascular mucosa of the inferior and middle turbinates, from side to side.[52] The nonfunctioning side retains secretions and becomes vascularly congested and engorged, while the passage of respiratory air is carried almost entirely by the open nasal side. The frequency of the cycle varies from 30 minutes to several hours. It is important to remember the existence of the nasal cycle in a fairly large portion of the human population when interpreting studies of the paranasal sinuses, because normally engorged turbinates may be mistaken for inflammatory or neoplastic processes.

The vascular and lymphatic anatomy of the nasal fossa is highly complex.[29] The arterial supply involves both branches of the internal and external carotid arteries. Of the many arteries that may supply portions of the sinonasal cavity, the sphenopalatine division of the internal maxillary artery is the most important (Fig. 16–2). This artery arises from the sphenopalatine portion of the internal maxillary artery and exits the pterygopalatine fossa. It then enters the nasal fossa posterior and superior to the middle turbinate.

The sphenopalatine artery has two major divisions: a posterolateral nasal branch and a posterior septal branch. The lateral nasal arteries ramify over the turbinates before providing collateral circulations to the paranasal sinuses. The trunk of the sphenopalatine artery extends medially along the roof of the nasal cavity, giving the posterior septal arteries as their terminal branches.

The termination of the posterior septal arteries at the anterior nasal septum continues as the nasopalatine artery, which exits the incisive canal and anastomoses with the greater palatine artery. Lymphatic drainage from the anterior portion of the sinonasal cavity is anteriorly into the face and finally into the submandibular group of lymph nodes. From the posterior half of the sinonasal cavity and

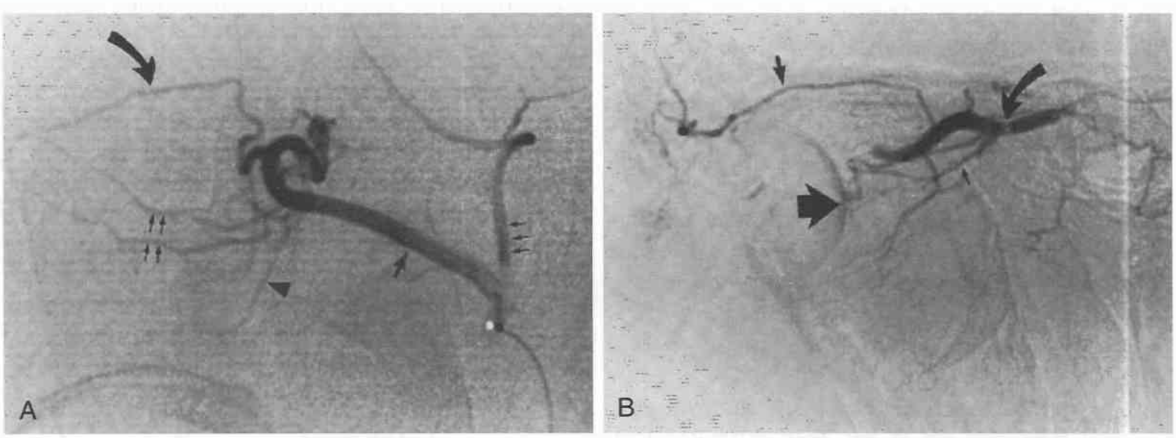

Figure 16–2. Vascular anatomy. *A*, Selective injection into the external carotid artery. The main supply to the nasal cavity and sinuses from the external carotid is via the sphenopalatine artery *(short arrow)*. The terminal branches include the descending palatine artery *(arrowhead)*, the inferior orbital artery *(curved arrow)*, and the septal arteries *(small arrows)*. The middle meningeal artery *(triple arrows)* is also shown. This vessel may be important for supply to the sinuses and orbits. *B*, Selective injection into the ophthalmic artery *(curved arrow)*. The retinal blush *(large arrow)* is supplied by the central retinal artery *(small arrow)*. Proximal to the origin of the central retinal artery, other branches from the ophthalmic artery may supply the soft tissue including the extraocular muscles *(mid-sized arrow)*. The anterior and posterior ethmoidal arteries, which are too small to be seen in the normal patient, also arise from the ophthalmic artery.

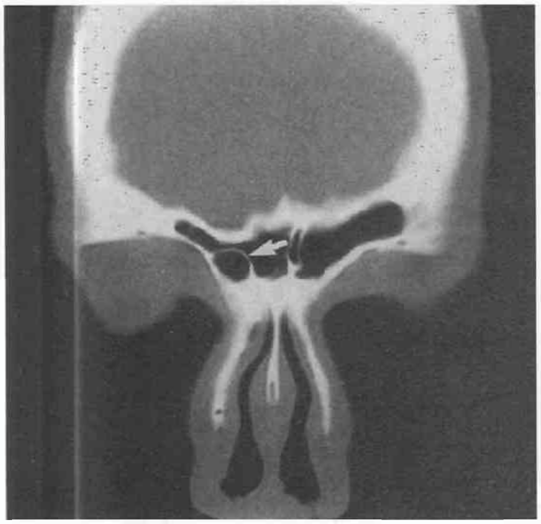

Figure 16–3. Supraorbital ethmoid. Within the right frontal sinus in this coronal CT scan is an isolated air cell *(arrow)* whose drainage pathway could be shown to be into the superior meatus. This air cell is therefore a posterior ethmoid air cell and is located within the right frontal sinus, which is important in understanding disease processes and surgical planning.

nasopharynx, lymphatic drainage is into the retropharyngeal and internal jugular lymph node chains.[45]

The venous drainage of the sinonasal cavity is into the anterior facial vein, which then anastomoses with the common facial vein and drains blood into the internal jugular vein. The anterior facial vein also anastomoses with the ophthalmic veins, which drain directly via the pterygoid venous plexus into the cavernous sinus. Therefore, infection within the sinonasal cavity may gain rapid access to the cavernous sinuses and cranial cavity.[30]

Supply from the internal carotid artery via the ophthalmic artery is through the anterior and posterior ethmoidal arteries, which send numerous small branches through the cribriform plate to anastomose with the nasal branch of the sphenopalatine artery (Fig. 16–3). An important anastomotic region is Little's or Kiesselbach's area, located anteriorly and inferiorly on the nasal septum.[29] This region is supplied by multiple branches of the facial, sphenopalatine, and greater palatine arteries and is often referred to as *Kiesselbach's plexus.* This is the site of the majority of epistaxis episodes.

Anatomic Variations

Frontal Sinuses

Embryologically, the frontal sinuses are anterior ethmoid air cells that grow into the frontal bone. They drain via the nasofrontal duct into the anterior portion of the infundibulum. The frontal sinuses are absent at birth and begin to develop after the second year of life.[8] In approximately 5% of the population, they are absent. The upward growth of the paranasal sinuses carries them to the midportion of the orbit at approximately age 4 years and to the top of the orbits at about age 8 years.[22] At approximately 10 to 12 years of age, the final adult size is reached.[49]

The size of the frontal sinuses depends on mechanical stresses from mastication and the effect of growth hormone. The intrasinus septum lies in the midline at the level of the inferior extent of the frontal sinuses but may extend far to one side, depending on the different growth rates of the two frontal sinuses.

Ethmoid Complex

The ethmoid sinuses begin to develop in the 5th month of fetal life.[8] There is wide variation in the numbers and sizes of cells. The anterior ethmoid air cells are more numerous, with more numerous septa than in the posterior ethmoid air cells. Pneumatization of the ethmoids is widely variable. Far anterior ethmoid air cells (agger nasi) cells are represented in a large portion of the population and may be situated anterior to the frontonasal duct.[45] During endoscopic nasal sinus surgery, the swelling of the agger nasi may be mistaken for the nasolacrimal duct.[16,48] The anterior ethmoid air cells may also extend superiorly into one of the frontal sinuses and into the roof of the orbit where they mimic the frontal sinus. These supraorbital ethmoid air cells should be considered distinct from the frontal sinuses themselves (see Fig. 16–3). The inferiorly located posterior ethmoid air cells may extend laterally in the infraorbital direction and bulge into the maxillary sinuses. This is the second type of "sinus within a sinus" (Fig. 16–4). The ethmoid air cells may pneumatize the middle turbinate; this condition is known as *concha bullosa* and occurs in approximately 10% of the population.[45,48] In rare instances, the superior turbinate or uncinate process may be similarly pneumatized. The concha bullosa may contribute to obstruction and inflammatory changes within the ostiomeatal unit (Fig. 16–5).

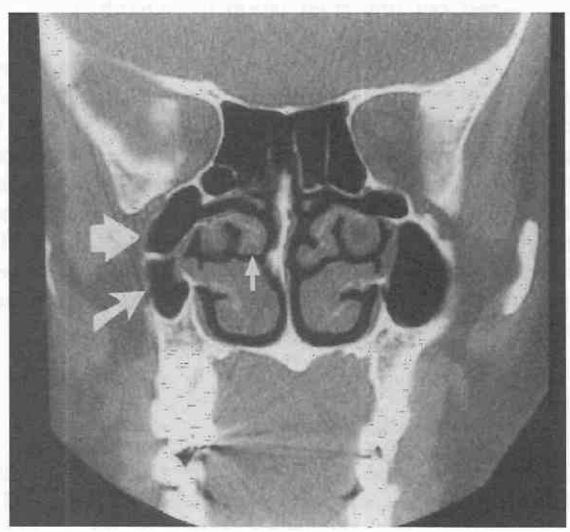

Figure 16–4. Infraorbital ethmoid. The right-sided maxillary sinus appears to have a horizontal septation within it. Closer inspection reveals that the superior portion of the right-sided maxillary sinus is actually a posterior ethmoid air cell *(large arrow)* and drains its contents superior to the middle turbinate *(small arrow)*. This structure therefore represents an ectopic posterior ethmoid air cell within the expected position of the right-sided maxillary sinus, which can also be seen *(angled arrow)*.

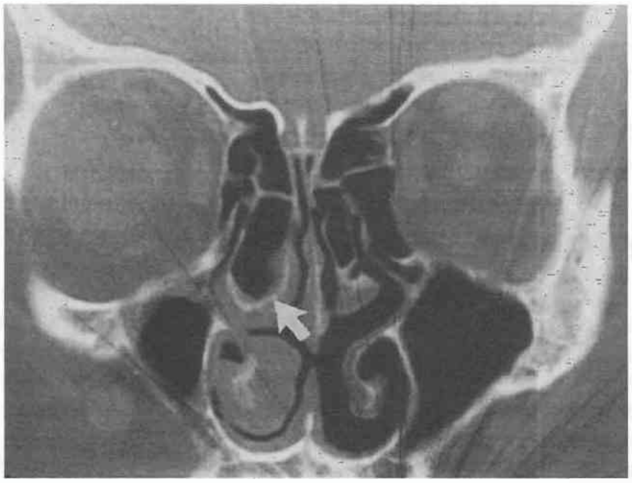

Figure 16–5. Concha bullosa. Pneumatization of the middle turbinate by anterior ethmoid air cells may cause this structure to enlarge. On this coronal CT scan, one can appreciate bilateral pneumatization of the middle turbinates, larger on the right *(arrow)*. The redundant mucosa on the surface of the right middle turbinate further narrows the middle meatus on the right side and may be the source of obstruction and secondary infection.

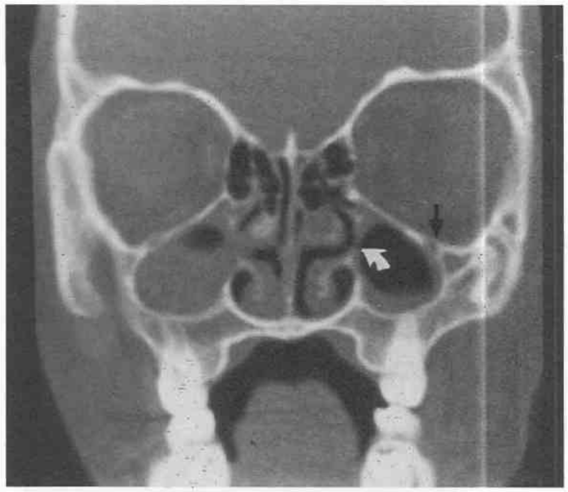

Figure 16–6. Maxillary hiatus. Coronal CT scan from a 9-year-old boy. The maxillary sinuses begin as lateral outpouchings from the lateral nasal wall and are usually present at birth, although they may not be fully pneumatized. There is progressive enlargement of the maxillary antrum in all directions. In the coronal plane, the lateral margin of the maxillary sinus usually reaches the level of the groove for the infraorbital nerve *(small arrow)* at about age 8 years. This patient has acute sinusitis with air-fluid levels present in both maxillary sinuses. Although the natural ostia of both maxillary sinuses are obstructed by a soft tissue mass, there is a small accessory opening for the left maxillary sinus called the maxillary hiatus *(curved arrow)*, which may help to drain the left maxillary sinus secretions.

Sphenoid Sinus

The sphenoid sinuses begin to develop in the 4th or 5th fetal month from a posterior outgrowth of the nasal capsule into the sphenoid bone. The sinus undergoes its major development beginning in about the 3rd year of life and reaches its adult size early in the 2nd decade of life.[49] In most people, the sphenoid sinus extends posterior to the anterior sella wall and beneath the sella floor. In less than half of the population, they extend only to the anterior wall of the sella turcica.[20]

In a small but important group of individuals (<1%), the sphenoid sinus does not reach the anterior wall of the sella turcica. This is important to the neurosurgeon considering a transsphenoidal hypophysectomy. The sphenoid sinus may extend laterally and inferiorly into the pterygoid plates of the sphenoid bone as well as superiorly and laterally into the posterior and anterior clinoid processes. The pterygoid process is described as being extensively pneumatized in nearly 10% of the population. The number of sphenoid air cells ranges from 1 to 3 with approximately one third of the population in each of these categories.

Maxillary Sinus

The maxillary sinus is the first sinus to form, beginning in approximately the 17th day of gestation. By the end of the first year of life, the lateral extent of the maxillary sinus extends into the medial portion of the floor of the orbit and reaches the infraorbital canal by the 2nd year. The adult configuration usually is attained early in the second decade of life.[24] Hypoplasia of the maxillary sinus occurs in between 1% and 7% of the population and may result from trauma, infection, surgical intervention, or irradiation. There are congenital first and second branchial arch anomalies such as Treacher Collins syndrome, in which there is congenital hypoplasia of one of the maxillary sinuses.

The maxillary sinus is unique for its relationship to the upper molar teeth and canine teeth, which may project into the maxillary antrum. Inflammatory, neoplastic, and congenital odontogenic processes uniquely affect the maxillary sinuses. In the medial wall of the maxillary sinus is a bony dehiscence known as the *maxillary hiatus* (Fig. 16–6). This is separated from the nasal cavity by the mucous membranes of both the nasal cavity and the maxillary sinus. This membranous septum is important to the surgeon seeking to irrigate the antrum and to establish a secondary pathway of drainage. It is also important for the radiologist to recognize, because it may appear to be a direct communication between the nasal cavity and maxillary sinus on imaging examinations.

Imaging Technique

Computed Tomography

Computed tomography (CT) of the paranasal sinuses is usually requested when inflammatory or neoplastic processes of the paranasal sinuses are suspected and when suspected inflammatory disease does not respond to conservative therapy.[1] An initial screening examination has been proposed as a substitute for plain film examination (Fig. 16–7).

Several types of protocols are used for this purpose. A

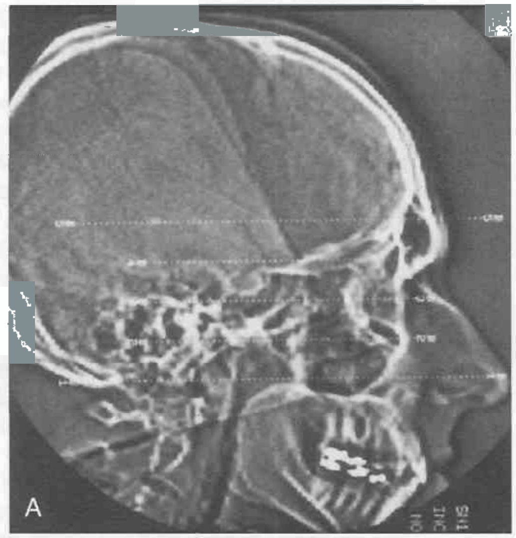

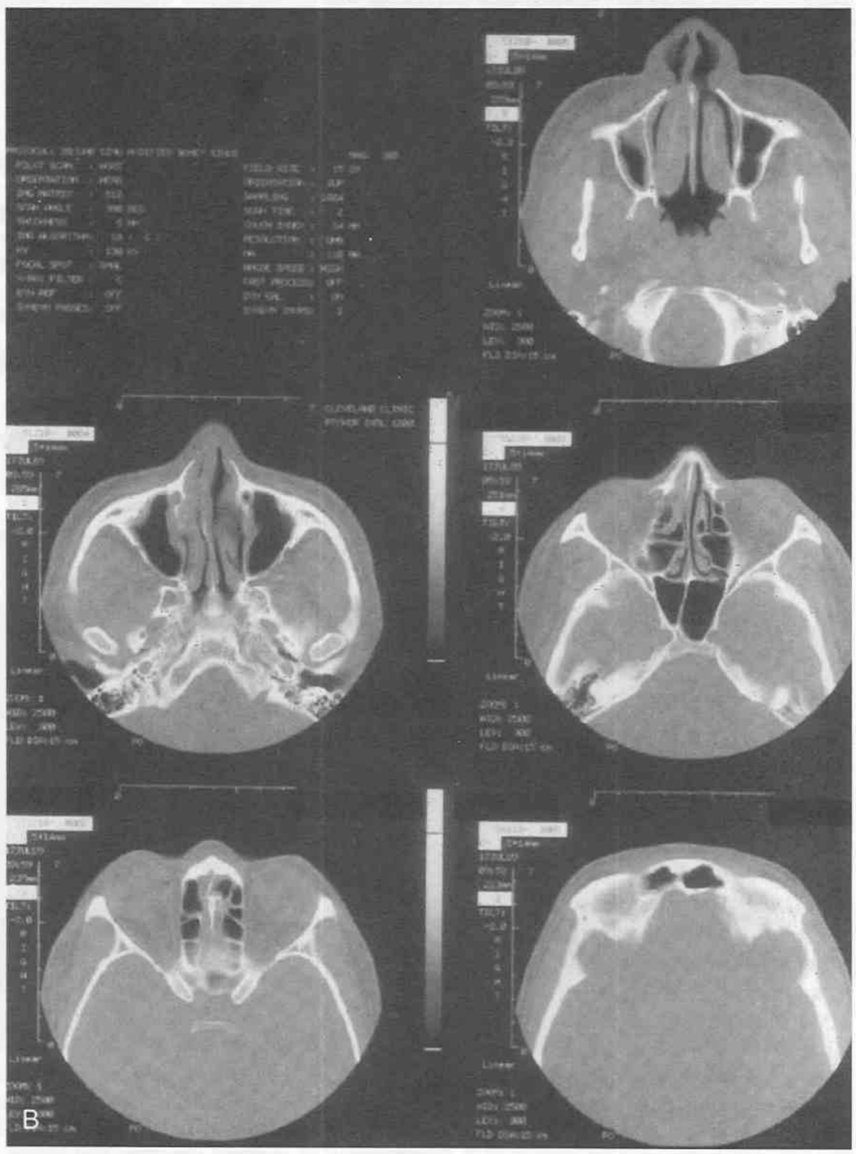

Figure 16–7. Simple CT scan. Because of the difficulty in interpreting plain radiographs of the paranasal sinuses, and because of the difficulty in reliable reproducibility for follow-up examination, a limited examination of the paranasal sinuses can be performed instead as a routine screening procedure. On the lateral topogram *(A)* five slices are chosen in equidistant intervals beginning at the hard palate and ending at the top of the frontal sinus. The images, as shown in *B*, will be identical in the same patient on all subsequent examinations. This facilitates the interpretation of follow-up studies and allows quick and easy comparison. The examination can be performed in 15 minutes at a cost similar to that for plain radiography and at a similar radiation dose.

particularly effective protocol has been a limited number of axial sections through the paranasal sinuses. Approximately five or six axial images, beginning at the alveolar ridge and extending through the top of the frontal sinus, can effectively produce two images through each sinus in the axial plane in approximately 15 minutes of room time and 1 or 2 minutes of scan time. This technique has the advantage over plain film radiography in its ease of performance for both patient and technologist. It is also highly reproducible compared with plain film examinations. There is a low repeat rate of images, and the radiation dose is significantly less than the standard for plain films of the paranasal sinuses. This limited examination can be used to establish the presence of inflammatory disease on a noncontrast CT scan and for follow-up examination during medical therapy.

If surgical intervention is contemplated, especially if endoscopic nasosinus surgery is proposed, a more detailed view of the anatomy within the sinonasal cavity is required.[54] For this purpose, overlapping thin sections through the paranasal sinuses are most useful (Fig. 16–8).

The ideal examination plane is perpendicular to the hard palate; however, the nearly ubiquitous presence of dental amalgam often forces the use of a prodental or retrodental plane. This study is almost always performed without the use of intravenous (IV) contrast injection. Contrast enhancement of paranasal sinus masses has not been shown to aid in the differential diagnosis; rather, the bony architecture and anatomic configuration as well as the anatomic variations are the most important information sought in this examination.

Magnetic Resonance Imaging

Magnetic resonance imaging (MRI) studies currently offer some advantages over CT scans in imaging of the paranasal sinuses. The main purpose of the MRI study is

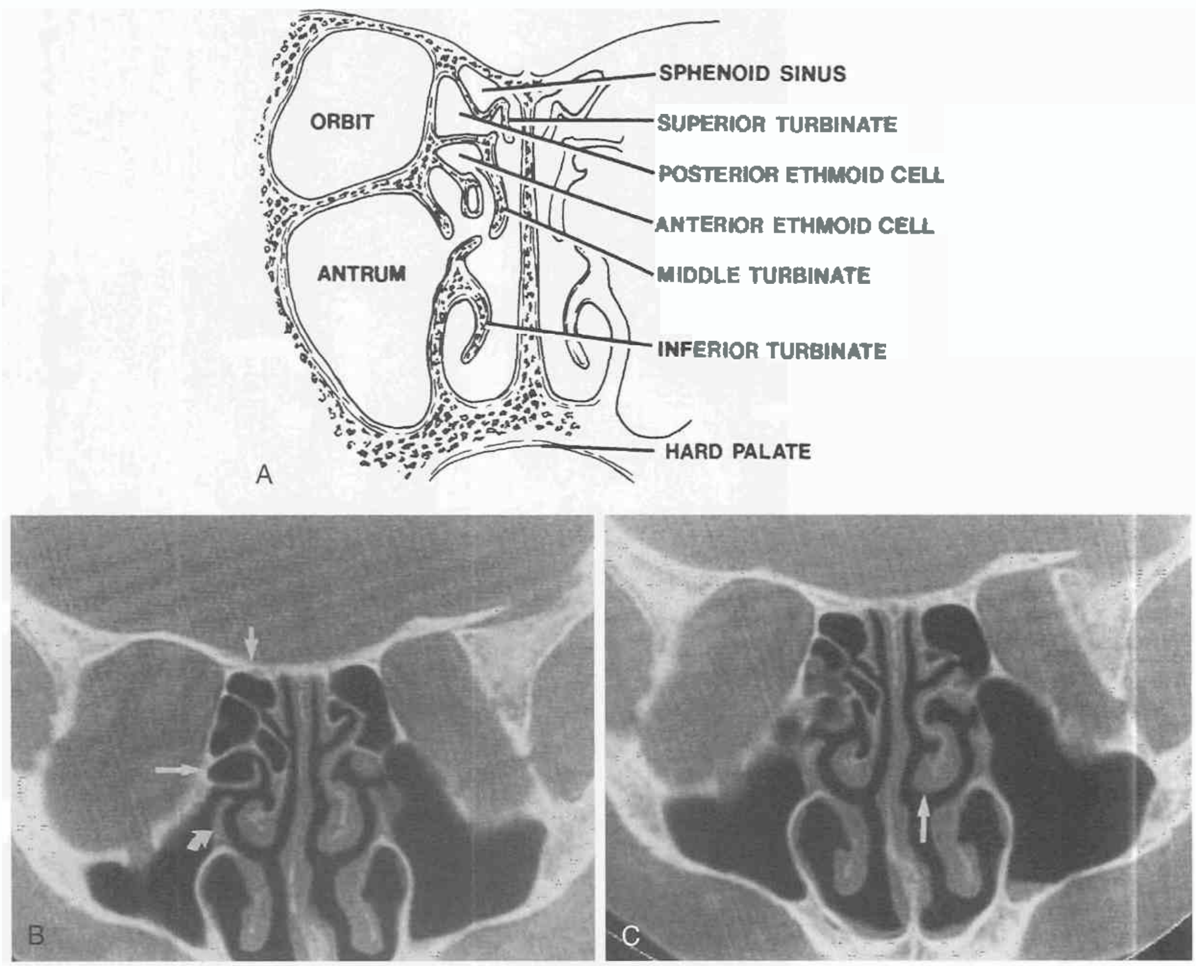

Figure 16–8. Normal coronal anatomy. *A*, The nasal fossa can be divided into three separate meatus based on the relationship of spaces within the nasal cavity to the turbinates. The nasal lacrimal duct drains into the inferior meatus below the inferior turbinate. *B*, The frontal sinuses, anterior ethmoid air cells *(long arrow)*, and maxillary sinus drain into the middle meatus. The uncinate process of the ethmoid bone *(curved arrow)* is a membranous or ossified structure that forms the medial border of the infundibulum of the maxillary sinus. The posterior ethmoid air cells *(short arrow)* and sphenoid sinus drain into the superior meatus, inferior to the superior turbinate. *C*, A common anatomic variation of the middle turbinate, which on the left side curves in the lateral rather than the medial direction *(arrow)*. Like the concha bullosa, this narrows the middle meatus and may lead to obstruction and inflammatory change within the ostiomeatal unit. Note the air-fluid level in the left maxillary sinus.

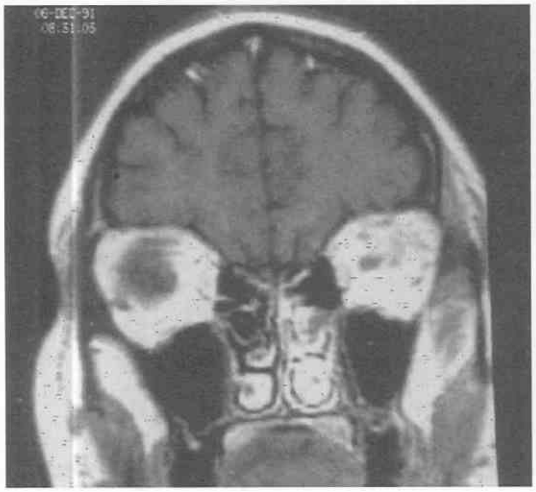

Figure 16–9. Normal MRI study. This T1-weighted image (TR500, TE32) was obtained in the coronal plane following contrast injection. The vascular nature of the turbinates is manifested as intense enhancement following contrast injection. The turbinates and nasal mucosa alternately engorge with blood and then shrink. This patient may be in the left-sided engorgement phase of the nasal cycle. Note the enlarged turbinates and thickened nasal mucosa.

to map the extent of a sinonasal mass or inflammatory process into either the orbit or cranial cavity. For this purpose, the multiplanar capabilities of MRI are unsurpassed. In addition, the signal characteristics of a sinonasal mass may help to distinguish inflammatory from neoplastic sinonasal diseases.[40, 41,44] If the mass is neoplastic, this ability allows for better surgical planning and radiation planning.

The use of gadolinium has been proposed as a method for differentiating sinonasal neoplasms from inflammatory masses.[17] The MRI protocol for examination of the paranasal sinuses should include T1- and T2-weighted images in two planes, *axial* and *coronal.* Sagittal or off-sagittal images parallel to the optic nerve may then be obtained if necessary. Gadolinium (Gd-DTPA) may then be given, and repeated scanning can be performed according to the preference of the radiologist (Fig. 16–9).

Inflammatory Processes

The "common cold" is a viral rhinitis thought to be secondary to rhinoviruses, parainfluenza, and influenza viruses.[33] Clinically, these infections last for 1 to 3 days, and the anatomic changes within the paranasal sinuses are completely reversible. There is usually mucosal thickening within the nasal fossa and turbinates as well as the mucosa of the paranasal sinuses. If a sinus ostium is obstructed, an acute bacterial sinusitis may result in superinfection. The most common bacterial pathogens in these cases are streptococci, *Haemophilus,* and staphylococci as well as *Pseudomonas.* Anaerobic infections may also occur secondary to *Bacteroides.*[10]

As previously noted, because of the unique anatomy of the maxillary sinus, the presence of the roots of the molar teeth, infections secondary to odontogenic causes account for approximately 15% of maxillary sinus infections.[45] The imaging hallmark of acute bacterial sinusitis is an air-fluid level within the affected sinus (see Fig. 16–6). This is most commonly visualized within the maxillary sinus. Repeated episodes of acute and subacute sinusitis may result in a persistent change within the paranasal sinuses (chronic sinusitis). The intrasinus mucosa may then be atrophic or hypertrophic. In any event, there is loss of the normal ciliary function and flow of secretions, resulting in a sinus that is less resistant to infection.[45] Thus, a vicious circle of infection and reinfection occurs.

Although allergic sinusitis and viral sinusitis tend to be symmetrical and involve the nasal fossa as well as the paranasal sinuses, bacterial sinusitis tends to be isolated to a single sinus or a group of contiguous sinuses. Additionally, the presence of nasal polyps is most common in allergic, rather than infected, patients (Fig. 16–10).

In the pediatric population, sinus opacification and mucosal thickening should be reported, but their significance remains in doubt especially in children under the age of 2 years.[47] Tears, normal retained secretions, and normal redundant mucosa may account for apparently abnormal findings in this population (see Fig. 16–9).

Air-fluid levels within the maxillary sinuses are usually the result of acute bacterial sinusitis. Although it has become a much less common procedure in recent years, lavage of the maxillary antrum with saline solution was previously a common cause of an air-fluid level within the maxillary sinus as well. In instances of direct trauma or barotrauma in individuals exposed to high altitude or deep immersion, hemorrhage within one of the paranasal sinuses may mimic acute sinusitis. Hemorrhage may also mimic acute sinusitis in patients with bleeding disorders such as hemophilia, or in cases of epistaxis. Intubated patients (specifically those with nasotracheal intubation) may present with air-fluid levels, especially within the sphenoid sinuses from mechanical changes within the nasopharynx. These are not necessarily acute bacterial infections (Box 16–1).

Ostiomeatal Unit

Recent advances in the understanding of mucociliary function and the pathophysiology of the nasal cavity and paranasal sinuses, along with the concomitant advances in functional endoscopic surgery directed toward restoring normal mucociliary drainage and ventilation of the sinuses, have required a more detailed evaluation of the functional anatomy of the paranasal sinuses in preoperative patients.[14,54] The ostiomeatal unit is the middle meatus of the nasal cavity and the sinuses which that meatus serves to drain: These are the frontal sinus, the anterior ethmoid sinuses, and the maxillary sinus. Radiographic evaluation is therefore directed toward assessing the patency of the maxillary sinus ostium, the ostia of the anterior ethmoid air cells, the hiatus semilunaris, and the middle meatus.

The coronal plane is best for demonstrating the anatomy of the ostiomeatal unit.[21] One should attempt to identify the natural ostium of the maxillary sinus and anterior ethmoid sinuses, establish their patency, and ascertain that

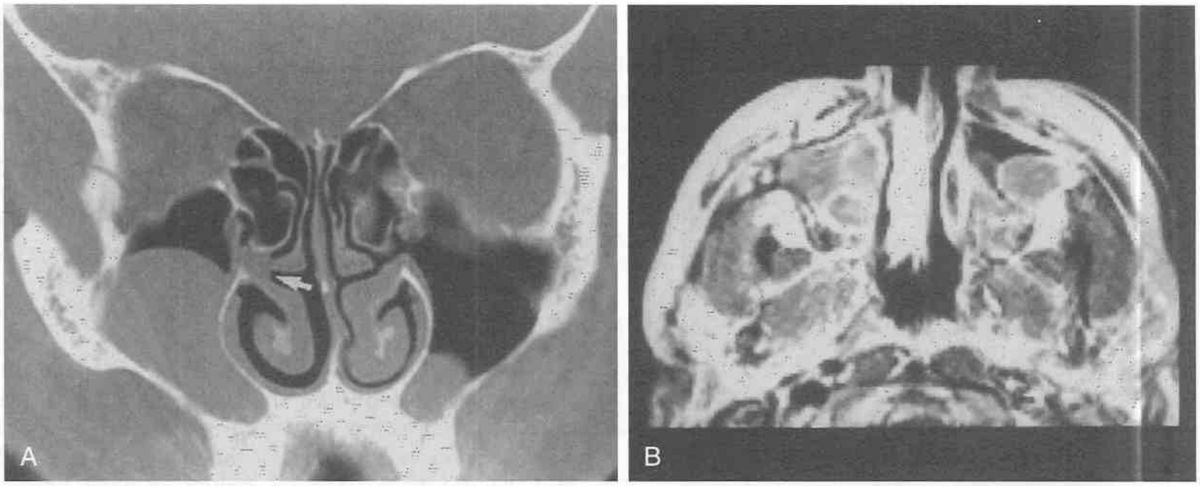

Figure 16–10. Nasal polyps. Retention cysts and nasal polyps are indistinguishable on CT scans and MRI studies. Rounded, soft tissue density structures within the maxillary sinuses on the CT scan *(A)* represent retention cysts or polyps when there is no bone destruction or expansion. These are usually asymptomatic; however, when they occur near the orifices of sinuses such as in the infundibulum *(arrow)*, postobstructive changes in the corresponding ostiomeatal unit may occur. On MRI examination following contrast injection *(B)*, there is linear enhancement on the surface of most polyps and retention cysts. This helps to distinguish them from solid masses.

these spaces are free of mucosal thickening or polypoid masses. In addition, various anatomic variations may predispose to poor mucociliary function.[14, 48,54] The most common of these is concha bullosa, which is an enlarged and pneumatized middle turbinate. This is most often small and without impairment of the function of the middle meatus, but it may become large and compress the uncinate process, obstructing the middle meatus and infundibulum. The middle turbinate may also be curved so that its convexity is directed toward the medial wall of the nasal septum. The concave portion of the middle turbinate then serves to narrow the middle meatus. This anatomic variation is known as a *paradoxical middle turbinate.*

Box 16–1. Unilateral Sinus Opacification

Congenital

Aplasia (e.g., Treacher Collins syndrome, cleidocranial dysostosis)
Normal underdeveloped sinus

Inflammatory

Sinusitis: acute, chronic
Polyp or retention cyst
Mucocele/mucopyocele

Trauma

Fracture
Intrasinus hemorrhage

Neoplastic

Benign: osteoma, antrochoanal polyp, inverted papilloma, juvenile angiofibroma, odontogenic
Malignant: squamous cell carcinoma, adenoid cystic, adenocarcinoma, lymphoma, metastases

There are several variations involving the anterior ethmoid air cells, which may narrow the middle meatus. Ethmoid air cells that extend inferior to the ethmoid bulla and within the roof of the maxillary sinus may narrow the infundibulum from above. These are called *Halle cells.* The anterior ethmoids, which form the superior contour of the middle meatus, are called the *ethmoid bullae.* These may become enlarged and extend into the hiatus semilunaris, blocking the infundibulum. The uncinate process itself may be of varying sizes, shapes, and positions.[16] For example, if it is elongated and directed laterally, obstruction of the infundibulum may result. The nasal septum is deviated to one side or another in more than 90% of people. When the deviation is significant or when a small bone spur forms at the cartilaginous junction with the bony portion of the septum, obstruction of the middle meatus may also result.

Cysts

The most common incidental finding within the maxillary sinuses is a rounded soft tissue density, which is found on routine examinations in about 10% of plain film studies and approximately 30% to 40% of CT studies.[45] Pathologically, this finding may represent a mucous retention cyst, a

Box 16–2. Expansile Sinonasal Mass

Polyp
Mucocele
Odontogenic cyst
Schwannoma
Juvenile angiofibroma
Plasmocytoma
Giant cell tumor
Lymphoma

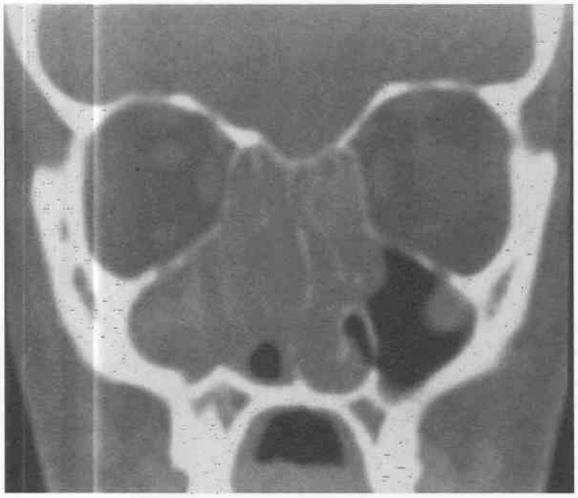

Figure 16–11. Fungal infection. Retention cysts, polyps, and fluid are usually of soft tissue density. When there is increased density within sinus cavities, as seen in this patient, one must entertain the thought of intrasinus hemorrhage, inspissated secretions, or fungal infection.

serous retention cyst, or a polyp. These three entities cannot be clearly differentiated from one another on sectional or plain film imaging modalities. This is of little consequence since all three are regarded as common benign entities (Box 16–2).

Fungal Diseases

Various fungal diseases involve the sinonasal cavities. The most common and most important of these include mucormycosis, histoplasmosis, and candidiasis and diseases caused by *Aspergillus*.[27] The radiographic features of fungal diseases involving the paranasal sinuses are usually nonspecific and include opacification of the sinus as well as a sclerotic bony reaction (Fig. 16–11). Air-fluid levels are uncommon and, when present, suggest a bacterial infection rather than a fungal infection.[45]

Mucormycosis occurs almost exclusively in immunocompromised hosts. Fifty percent to 75% of these patients have poorly controlled or uncontrolled diabetes mellitus. The causative organisms are invasive and tend to spread rapidly from the nasal cavity to the paranasal sinuses.[27] They have a propensity for invading blood vessels. In doing so, they denude the endothelial lining and initiate thrombosis, which leads to venous cerebral infarcts. Invasion of the orbits, cavernous sinuses, and ophthalmic veins is common (Fig. 16–12). Intracranial extension, via emissary vein, may extend to the meninges and eventually lead to cerebral abscess (Fig. 16–13). Progression may be rapid, occurring within a few days. The disease also occurs in immunocompromised patients with hematologic malignancies and those with acquired immunodeficiency syndrome (AIDS). Because fungi tend to bind calcium, manganese, and other heavy metals, a large number of affected paranasal sinuses may appear hyperdense on CT scans and of low signal intensity on MRI studies[53] (Box 16–3). In the latter stages of infection, bony destruction may mimic an aggressive tumor such as squamous cell carcinoma (Box 16–4).

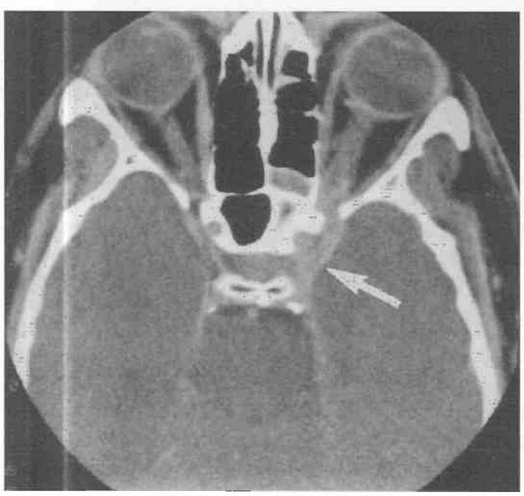

Figure 16–12. Cavernous sinus involvement. Cavernous sinus thrombosis or thrombophlebitis is most often secondary to sinus infection. Note the opacification in this patient's posterior ethmoid and sphenoid sinus on the left side. There is secondary enlargement and enhancement of the left cavernous sinus *(arrow)* and optic nerve.

Box 16–3. Sinus with T2 Signal Void

Air-containing: normal
Hemorrhagic: tumor or trauma
Chronic secretions: mucocele
Fungal infection
Tooth: odontogenic tumor

Box 16–4. Opacified Sinus with Bone Destruction

Inflammatory

Fungal infection:	Mucormycosis
	Aspergillosis
Granulomatous disease:	Wegener's granulomatosis
	Midline destructive granuloma

Neoplastic

Benign:	Inverting papilloma
	Juvenile angiofibroma
Malignant:	Squamous cell carcinoma
	Adenoid cyst
	Adenocarcinoma
	Lymphoma
	Metastasis

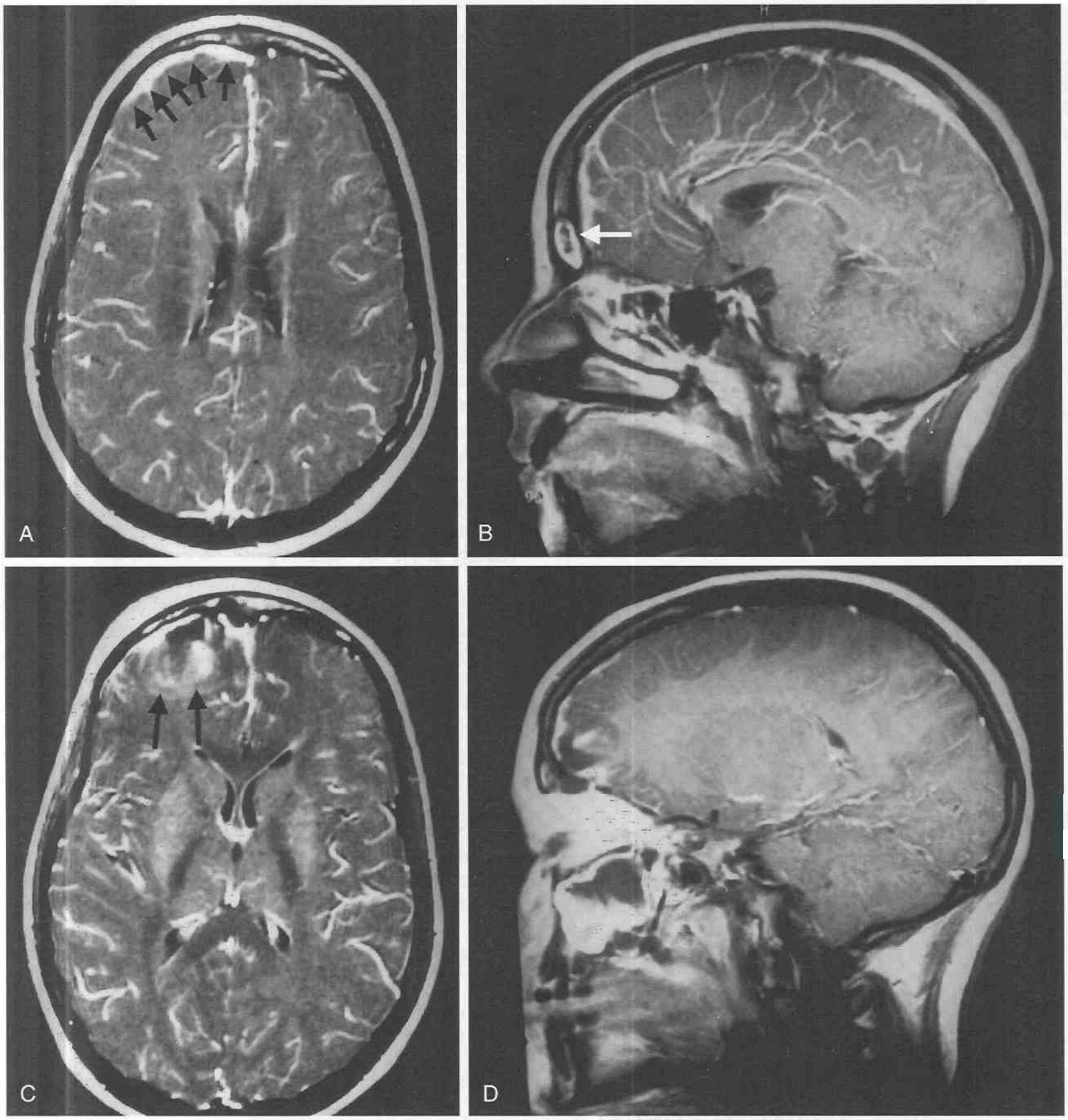

Figure 16–13. Sinusitis with intracranial extension. These contrast-enhanced T1-weighted images were obtained through the head of a patient with sinusitis and neurologic findings. *A* and *B* demonstrate meningeal enhancement *(small arrows)* in the left frontal region just posterior to the infected left frontal sinus *(large arrow)*. *C* and *D*, Adjacent slices reveal the presence of an associated cerebral abscess *(arrows)* in the left frontal lobe. Cerebral abscess has occurred by direct extension, without apparent bone involvement, probably via emissary veins.

On the other hand, *Aspergillus* infection usually occurs in otherwise healthy patients and has no relationship to pulmonary aspergillosis, which is known to occur in debilitated patients. The radiographic appearance, however, is similar to other fungal infections with opacification of a single paranasal sinus, a hyperdense paranasal sinus on CT scans, hypointense signal on T2-weighted MRI studies from heavy metal, and osseous destruction mimicking aggressive tumor in the later stages. Although less aggressive than mucormycosis, *Aspergillus* infection may cause a vasculitis that results in cerebral thrombosis as well.

Granulomatous Diseases

Various granulomas produce diseases that may involve the sinonasal cavities. These include granulomas caused by organisms such as *Nocardia* and infectious diseases such as

aspergillosis,[23] actinomycoses,[34] tuberculosis, and syphilis.[5] Granulomas can be caused by autoimmune or collagen-vascular diseases such as Wegener's granulomatosis,[31] lymphoma or lymphatoid diseases such as midline granuloma, and processes such as sarcoidosis. In addition, granulomas may be the result of exposure to irritants such as beryllium and chromium.

In general, granulomatous diseases affect the paranasal sinuses first by causing a nonspecific inflammatory type of reaction with mucosal thickening and increased secretions.[45] The nasal septum may exhibit focal thickening, or septal erosions may be found. The paranasal sinuses are usually involved secondary to nasal cavity involvement. The maxillary and ethmoid sinuses, as with inflammatory diseases, are most often affected. When the sinuses are involved, a nonspecific inflammatory reaction is seen. Air-fluid levels are usually not present. Bony changes of the nasal cavity and paranasal sinuses may include thickened and sclerotic walls and septa. This is from the chronic inflammatory reaction (Fig. 16–14).

Wegener's granulomatosis is fundamentally a necrotizing granulomatous vasculitis that initially involves the respiratory tract and eventually spreads to include the kidneys as well as other organs. When the sinonasal cavity is involved, the nasal septum is affected initially with diffuse thickening followed by septal perforation. A more aggressive and idiopathic granulomatous process is so-called idiopathic midline granuloma,[13] which is characterized by a necrotizing inflammatory reaction involving the sinonasal cavities and midline of the face as well as the upper respiratory tract. This is a more localized disease with the lungs and kidneys unaffected.

Tuberculosis may involve the paranasal sinuses secondary to pulmonary infection. The sinus disease is again nonspecific. Another granulomatous disease involving the paranasal sinuses is actinomycosis, which only rarely involves the paranasal sinuses and is usually the result of direct extension from the mandible.

Figure 16–14. Wegener's granulomatosis. Granulomatous disease within the paranasal sinuses may be manifested as linear enhancement *(arrow)* or nodule enhancement. Destruction of osseous structures out of proportion to soft tissue thickening should lead one to think of a granulomatous process or lymphoma.

Mucoceles

Mucoceles are the most common expansile lesions of the paranasal sinuses.[45] A mucocele develops from obstruction of a sinus ostium.[50] The continued secretions of the sinus mucosa cause expansion and remodeling of the bony margins. Expansion of the sinus cavity causes erosion of internal septa and displacement of adjacent organs such as the intraorbital structures (Fig. 16–15). The frontal sinuses are most commonly affected, accounting for approximately 60% of all mucoceles.[45] The ethmoid sinuses account for approximately 25% of all mucoceles. The maxillary sinuses account for approximately 10%, and the remaining 1% or 2% are the rare sphenoid sinus mucoceles.[45] The presenting symptoms are those of mass effect with proptosis or cosmetic deformity. Pain is rare unless the mucocele is infected, in which case it is referred to as a mucopyocele.

On CT scans, a mucocele appears as an expanded sinus filled with homogeneous material of fairly low attentuation (~15 HU) (Fig. 16–16). As one would expect, on MRI studies most mucoceles are isointense to soft tissue such as adjacent brain on T1-weighted images and show increased signal on T2-weighted images because of their high water content. However, a mucocele that has been present for many months may be of low signal on T2-weighted images and may even produce a signal void. This may be because of the high concentration of proteinaceous secretions and the slow resorption of water through the mucosa.[7,39,40]

Neoplastic Processes

Papillomas (Fig. 16–17)

The mucosa of the sinonasal cavity is ciliated columnar epithelium containing mucus-secreting glands called *Bowman's glands*. This unique mucosa is of ectodermal origin and gives rise to a distinct class of lesions with a hyperplastic zone of basement membrane enclosing epithelium that in some patients falls inward on itself, forming a polyp with an irregular or verrucose surface. These lesions are known as *papillomas* and are important to differentiate from simple cysts and polyps of the sinonasal cavity because of the possibility of malignant degeneration within the papillomas.[2,45] Fungiform papillomas make up approximately half of all papillomas. These nearly always arise from the nasal septum, are usually solitary and unilateral, and may have an irregular surface much like that of other papillomas but are not considered premaliguant. Fungiform papillomas must therefore be differentiated from inverted papillomas or endophytic papillomas, which make up approximately 50% of all sinonasal papillomas. These tend to occur in middle-aged men, characteristically arise from the lateral nasal wall in the region of the root of the middle turbinate, and may extend laterally into the paranasal sinuses, especially the maxillary sinus.

The most common presenting symptoms are nonspecific, including nasal obstruction, epistaxis, and anosmia. The rate of malignancy associated with inverted papillomas is approximately 15%. Although inverted papillomas most often have degenerated into squamous cell carcinomas, other tumors such as mucoepidermoid and adenocarcinomas have been reported.

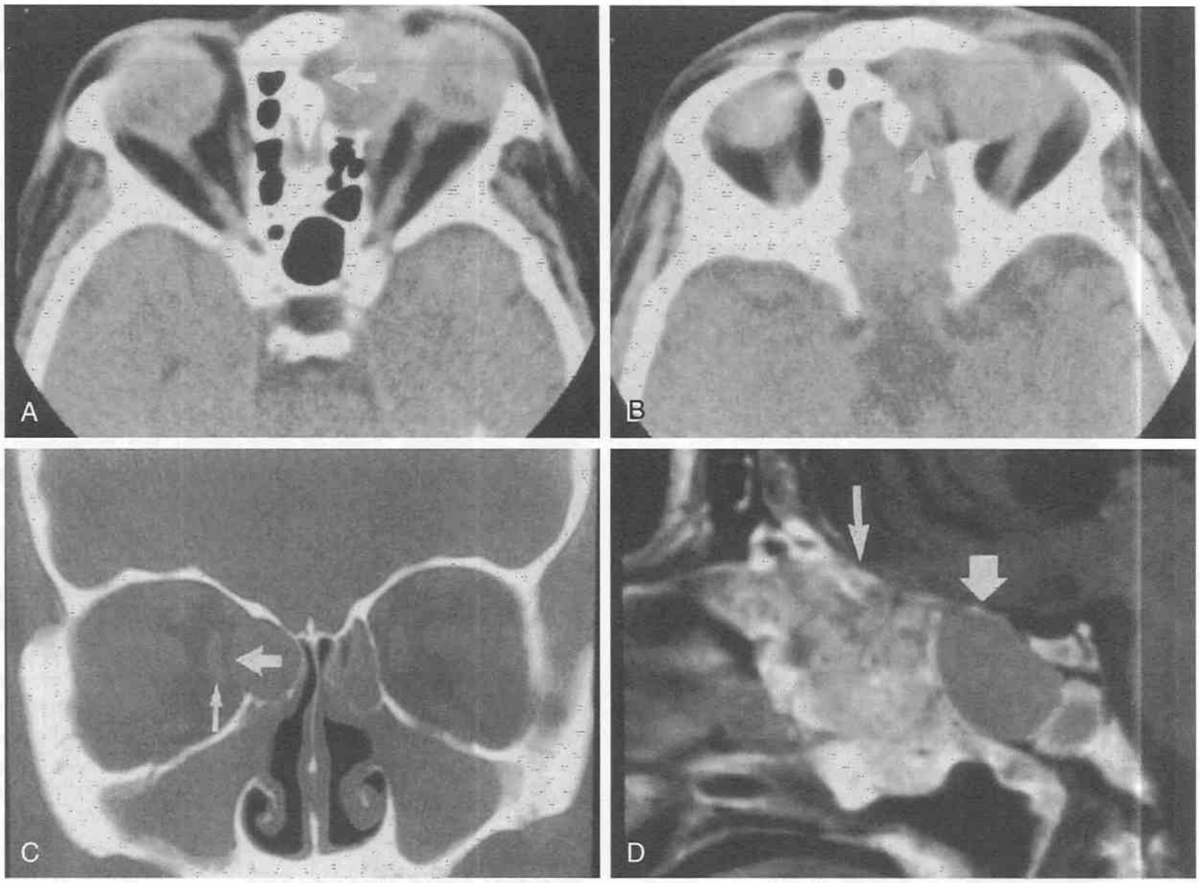

Figure 16–15. Mucocele. Sixty percent of mucoceles occur in the frontal sinus. *A*, An expansile mass is shown arising from the left frontal sinus with destruction of the lateral wall of the left frontal sinus *(arrow)*. *B*, A slightly more superior image in the same patient depicts dehiscence of the posterior wall of the left frontal sinus (*arrow*), which is also the anterior wall of the anterior cranial fossa. *C*, An anterior ethmoid mucocele is shown with lateral expansion into the right orbit and dehiscence of the right medial orbital wall *(large arrow)*. There is medial displacement of orbital contents such as the medial rectus *(small arrow)*, leading to diplopia. Mucoceles may be the result of sinus obstruction from either inflammation or tumor. *D*, Postcontrast sagittal T1-weighted image (TR500, TE32) in the midline. There is solid enhancement in the region of the ethmoid air cells *(long arrow)*, peripheral enhancement with central secretions within the sphenoid sinus *(short arrow)*, and a mucocele with linear peripheral enhancement secondary to sinus obstruction from tumor.

Carcinoma

Squamous cell carcinoma of the sinonasal cavity arises most commonly from the maxillary sinus. This structure is involved in at least 80% of all patients with squamous cell carcinoma at some point in their course.[3] These lesions occur primarily in men in the 6th and 7th decades of life. Most are low-grade tumors that arise from the nasal septum near the mucocutaneous junction. Because of the paucity of symptoms or mild symptoms, these tumors are often misdiagnosed or go undiagnosed with such chronic complaints as sinusitis, polyposis, and lacrimal duct obstruction until a mass in the oral cavity or cheek is noticed. The 5-year survival is approximately 25% to 30%.[3] The main cause of unsuccessful response is local recurrence. When examining post-treatment patients, one may encounter radiation-induced changes. These can be differentiated from local recurrence (Fig. 16–18). The primary pathologic and therefore imaging feature of these lesions is propensity to destroy bone even in the presence of a relatively small demonstrable mass.

Because of the similarity in density of squamous cell carcinoma and other carcinomas to adjacent secretions within obstructed sinuses, a small region of bony abnormality and apparent destruction is important for the early imaging diagnosis of carcinoma, especially squamous cell carcinoma. The use of IV contrast injection for CT scanning is rarely useful for differentiating tumor from inflammatory conditions or masses within the sinuses. The tumors themselves tend to enhance very little, whereas inflammatory mucosa may sometimes enhance brightly. However, the data suggest that enhanced (gadolinium [Gd-DTPA]) MRI examinations may be most useful for differentiating neoplastic from inflammatory masses within the paranasal sinuses when this diagnosis is in doubt[17] (Fig. 16–19).

Approximately 10% of tumors of the sinonasal tract are glandular in origin. These include tumors that arise from minor salivary glands such as adenoid cystic carcinomas and mucoepidermoid carcinomas. They also include adenocarcinomas.[2, 3,45] Adenoid cystic carcinomas are unusual because of their course. Many tend to recur many years following their initial diagnosis and treatment. These lesions also tend to spread along perineural sheaths and to

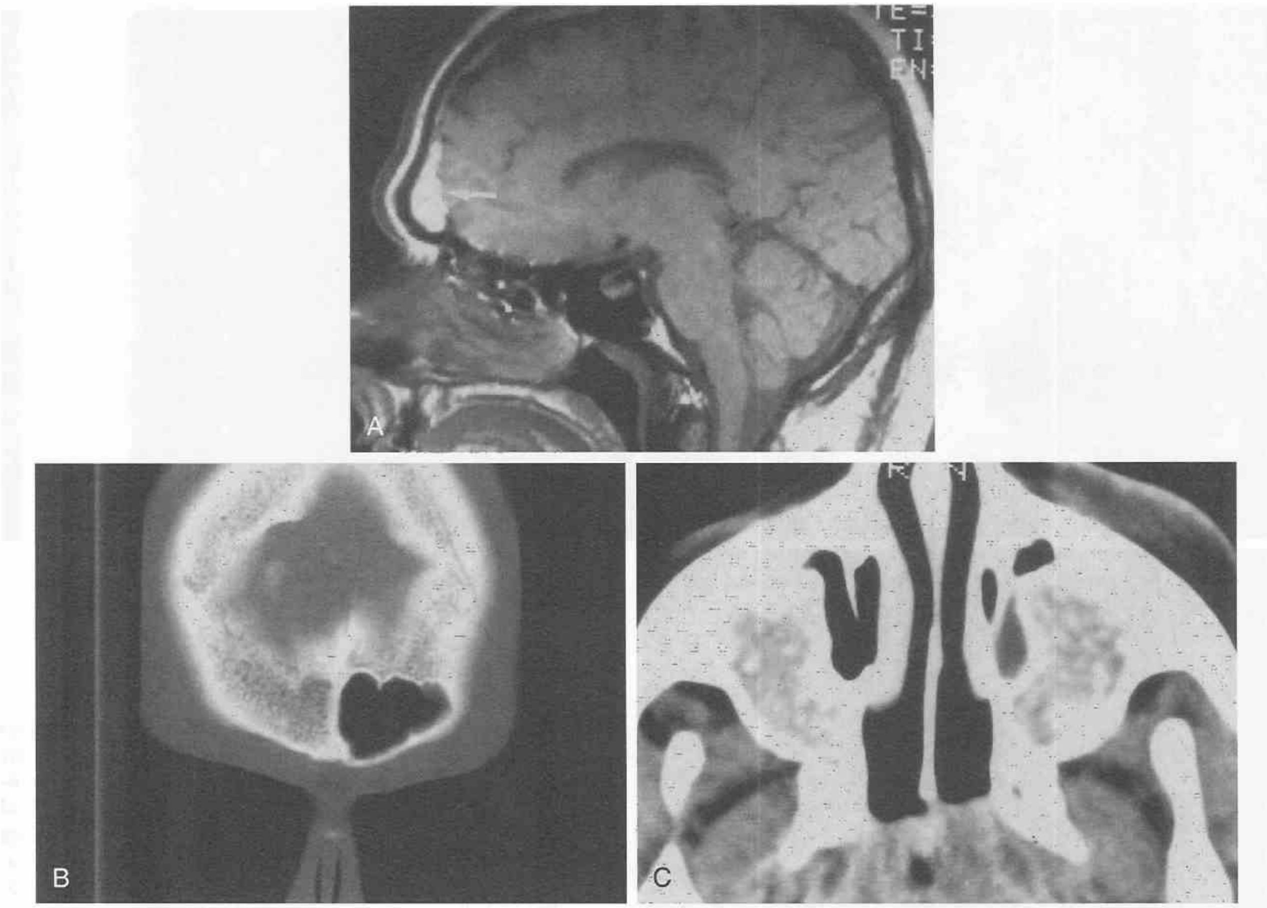

Figure 16–16. Imposters. *A*, Sagittal T1-weighted (TR500, TE32) image in the midline. Increased signal is seen overlying the frontal sinus *(arrow)*. This may represent fat, hemorrhage, or a paramagnetic substance in a metastatic tumor such as a melanoma. The accompanying coronal CT image *(B)* shows a nonpneumatized and nondeveloped right frontal sinus. The marrow signal from this right frontal sinus was thought to produce the abnormal signal on the MRI study in *A*. *C*, Non–contrast-enhanced axial CT scan through the maxillary sinuses in a patient with sickle cell disease. The speckled pattern overlying the maxillary sinuses proved to be hyperactive marrow within the maxillary sinuses.

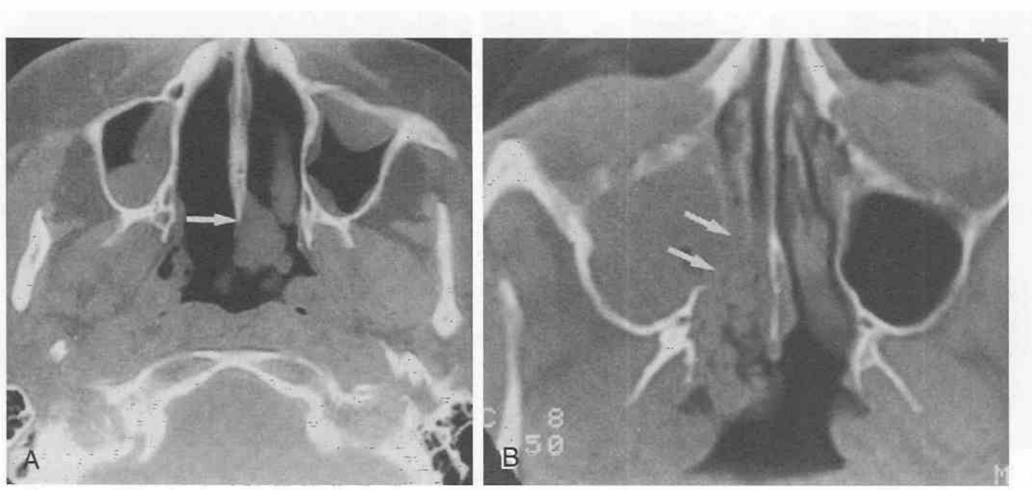

Figure 16–17. Papillomas. *A*, Polypoid soft tissue mass is shown based on the nasal septum (*arrow*), which proved to be a fungiform papilloma on biopsy. *B*, Polypoid soft tissue mass is shown based on the lateral nasal wall *(arrows)*. This is a biopsy-proven inverted papilloma. Distinguishing between these two lesions is important because of the malignant potential of the inverted papilloma.

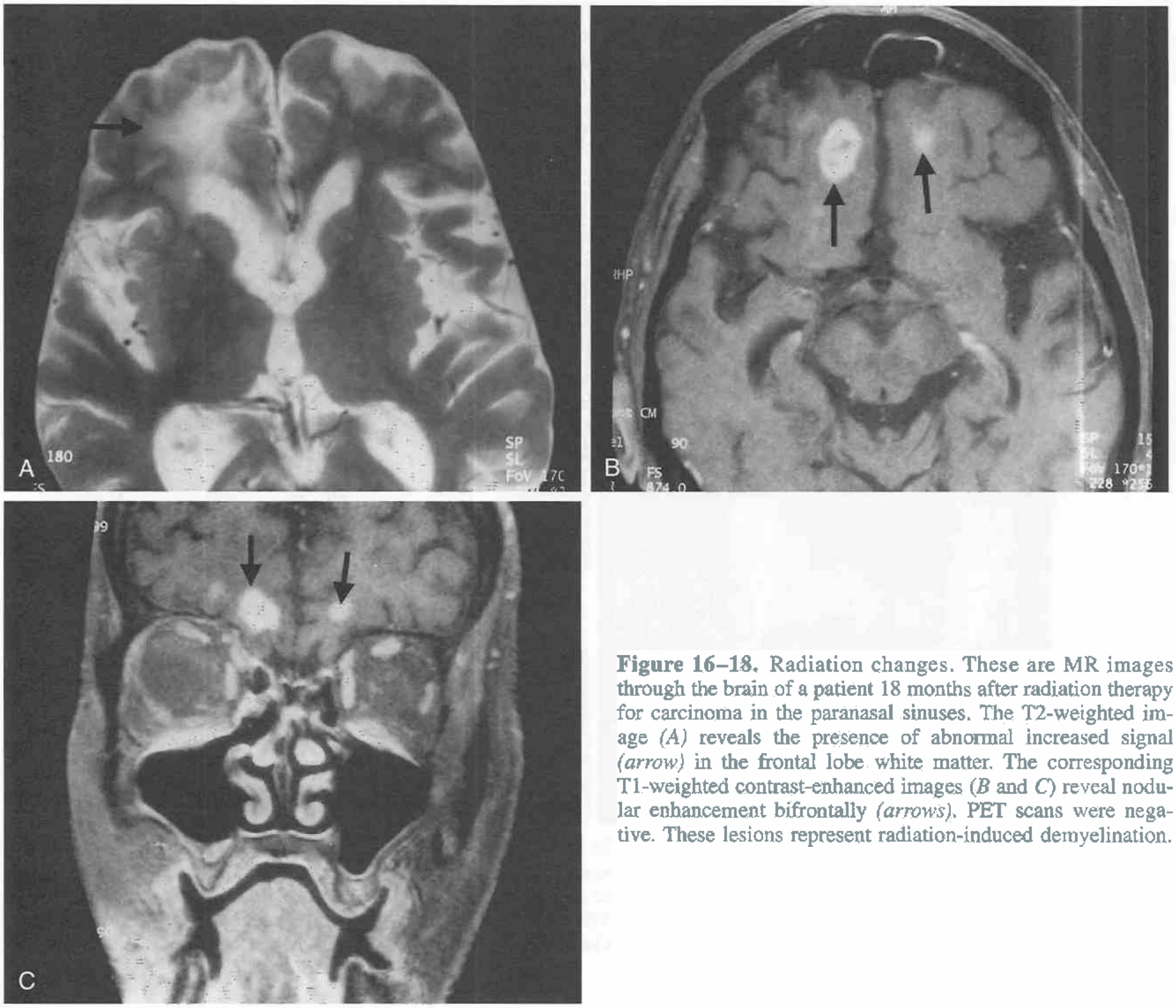

Figure 16–18. Radiation changes. These are MR images through the brain of a patient 18 months after radiation therapy for carcinoma in the paranasal sinuses. The T2-weighted image *(A)* reveals the presence of abnormal increased signal *(arrow)* in the frontal lobe white matter. The corresponding T1-weighted contrast-enhanced images (*B* and *C*) reveal nodular enhancement bifrontally *(arrows)*. PET scans were negative. These lesions represent radiation-induced demyelination.

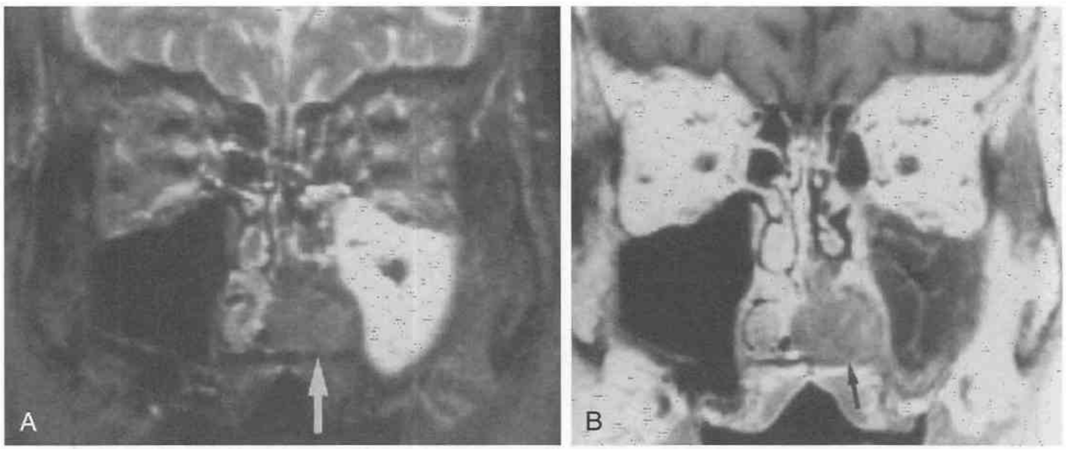

Figure 16–19. Squamous cell carcinoma. *A*, On this coronal T2-weighted image (TR3000, TE60), structures containing water, such as cerebrospinal fluid and inflammatory polyps, in the left maxillary sinus are of increased signal intensity. More cellular masses such as skeletal muscle and the mass within the inferior meatus on the left *(arrow)* are of more intermediate signal intensity. Cellular masses within the nasal cavity and sinonasal tract should be suspected of being neoplasms. *B*, The accompanying post–contrast-enhanced T1-weighted image (TR500, TE32) shows the expected surface linear enhancement on the inflammatory polyps in the left maxillary sinus *(arrow)*. The turbinates and normal nasal mucosa enhance brightly inhomogeneously. The suspected nasal mass enhances somewhat less intensely than the normal turbinates. This is a biopsy-proven squamous cell carcinoma.

leave normal skip areas between the primary lesion and a local metastatic site along a nerve. This is often the case when a tumor arising in the maxillary sinus gains access to the mandibular nerve and extends toward the skull base.

At the time of radical antrectomy, the surgeon may be informed that the frozen sections showed no evidence of tumor. Some studies indicate that in many cases there has already been distant regional metastasis into the cavernous sinus at the time of surgery with an intervening normal segment of the trigeminal nerve. It has become the role of the imaging specialist, therefore, to evaluate the cavernous sinus and the more proximal portions of the trigeminal nerve in such patients to establish proper staging before radical and disfiguring surgery is undertaken.

Most adenocarcinomas arise from the ethmoid air cells and are especially common in hardwood workers and Bantu Indians.

A biopsy specimen revealing adenocarcinoma must be considered to represent a metastasis to the head and neck from kidney, lung, breast, or digestive tract until a metastatic workup is negative.

Olfactory Neuroblastoma[42]

The olfactory neuroblastoma or esthesioneuroblastoma is an uncommon tumor that originates from neural crest cells and arises from the olfactory mucosa. The incidence curve for this disease has a bimodal shape, with the first peak in the 2nd decade and the 2nd peak in the 6th decade. This polypoid tumor may be soft or firm but may be friable and bleed profusely.

A unique feature regarding olfactory neuroblastomas and the importance of these lesions to the imaging physician concerns its unique site of origin and pathway of spread. The mass may be relatively slow-growing for a malignant tumor and may cause some expansion and remodeling of bony structures. It may therefore be mistaken for benign disease. On the other hand, the tumor has a propensity for intracranial extension through the dura in the region of the cribriform plate. A change in surgical philosophy now dictates that a craniofacial resection should be performed as the initial procedure in all patients. With this protocol, cure rates have approached the 90% survival mark. Before this approach, recurrence neared 50%, with metastasis in approximately a third of patients (Fig. 16–20).

Lymphoma

Lymphomas represent the most common sarcomas involving the sinonasal tract.[9] The majority of these are non–Hodgkin's types of lymphomas. Non–Hodgkin's lymphoma is the second most common malignancy of the head and neck following squamous cell carcinoma. It is important to try to recognize lymphoma as distinct from squamous cell carcinoma because of its different clinical course and the marked radiosensitivity of lymphomas relative to squamous cell carcinoma. Grossly, these tend to be bulky soft tissue masses that may enhance following gadolinium injection and tend to remodel bone and occasionally erode bone rather than destroy bone.[19] The nasal cavity and maxillary sinus are the most common sites of origin.

Benign Tumors

One of the most important benign tumors of the sinonasal structures—although by no means the most common benign tumor in this region—is the juvenile angiofibroma or nasopharyngeal angiofibroma (Fig. 16–21). This is a highly vascular and nonencapsulated polypoid mass that is histologically benign but highly aggressive.[4] It occurs almost exclusively in males in the second decade of life, who present with nasal obstruction and severe epistaxis as well as facial deformity and proptosis. The site of origin is thought to be the nasopharyngeal region at the pterygopalatine fossa or sphenopalatine foramen. Involvement of the pterygopalatine fossa is seen in approximately 90% of patients as asymmetry in the size or widening of this structure and an absence of the normal fat plane between

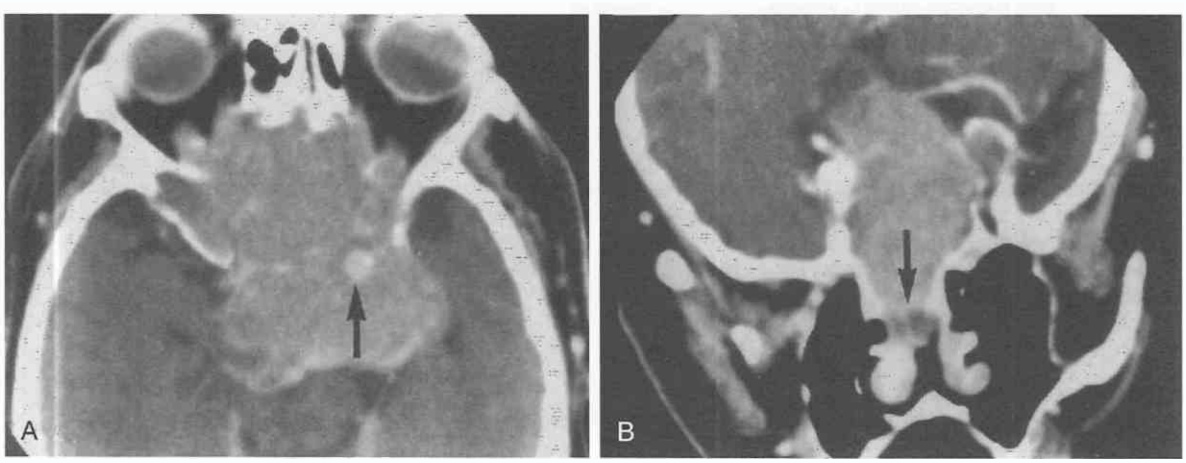

Figure 16–20. Esthesioneuroblastoma. This unique tumor arises from the olfactory mucosa in young adults. It typically spreads anteriorly into the orbital apices and posteriorly into the suprasellar region. The left carotid artery is encased *(A) (arrow)*. There is also inferior extension into the nasal cavity as seen in the post–contrast-enhanced coronal image *(B) (arrow)*.

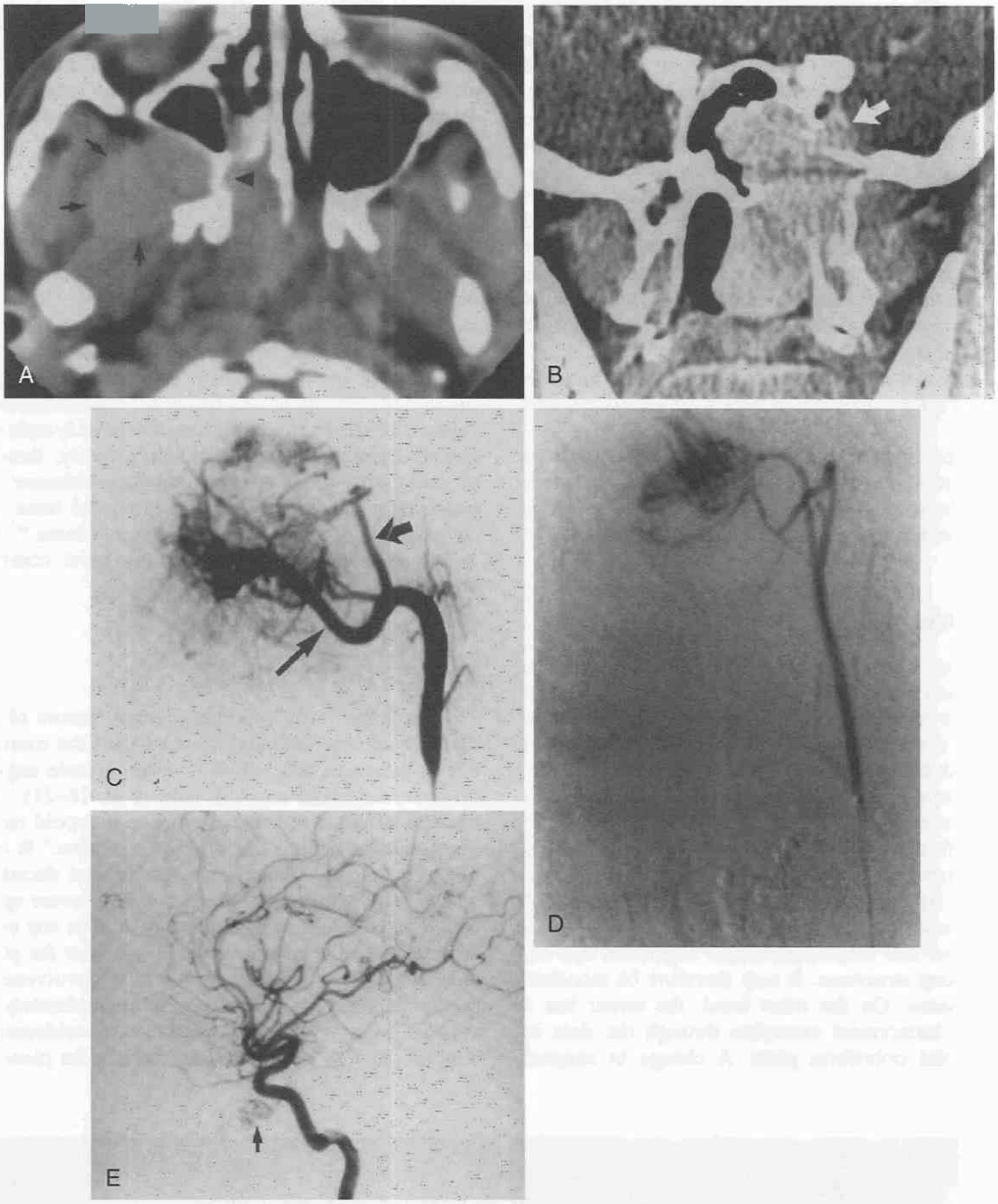

Figure 16–21. Juvenile angiofibroma. Axial post–contrast-enhanced CT scan *(A)* through the paranasal sinuses reveals an enhancing mass within the infratemporal fossa *(arrows)* that extends into and expands the pterygopalatine fissure *(arrowhead)*. In the coronal view *(B)* there is extension into the nasal cavity with destruction of the pterygoid plates and extension into the sphenoid sinus. There is also lateral extension into the region of the cavernous sinus with bone destruction *(arrow)*. These masses are usually supplied by terminal branches of the sphenopalatine artery *(C, long arrow)*. In this particular patient, because of the extension intracranially, there is supply from dural vessels such as the middle meningeal artery *(C, short arrow)*. In addition, there is also supply from other external carotid branches such as the ascending pharyngeal *(D)*. In patients with intracranial extension or with extension into the clivus, there may be supply from branches of the internal carotid artery *(E, arrow)*.

the pterygoid plates and the back of the maxillary sinus.[46] The tumor may extend anteriorly and superiorly into the maxillary and ethmoid sinuses or superiorly into the cranial fossa. There is also the possibility of extension superiorly through the inferior orbital fissure into the orbit and then through the superior orbital fissure into the brain.

Because of the extreme vascularity of the tumor and propensity for profuse hemorrhage, the imaging physician must recognize this entity when it occurs and should strongly discourage biopsy. Ultimately, an arteriogram should be performed to demonstrate the major feeding vessels, which are most often the internal maxillary artery

and ascending pharyngeal artery. Preoperative embolization of these branches of the external carotid artery may greatly reduce blood loss at surgery, allowing for a more careful dissection and, therefore, complete resection in addition to minimizing the risk of multiple transfusions. Contrast-enhanced CT or MRI examination reveals a polypoid and infiltrating enhancing mass that involves the nasopharynx and pterygopalatine fissures and extends anteriorly into the nasal cavity, maxillary sinuses, and ethmoid sinuses.[45] Again, the orbits and cavernous sinuses may be involved.

The treatment of choice is surgical resection. The role of radiation therapy is not clear, although control of tumor growth has been reported. The use of estrogen therapy is also recommended.[2] Many of these tumors begin to involute toward the end of puberty, and the goal of therapy is to minimize facial deformity and bone destruction and to minimize the need for transfusions and the occurrence of fatal epistaxis, until the tumor begins to involute and fibrose as part of its natural history. There is no premalignant potential.

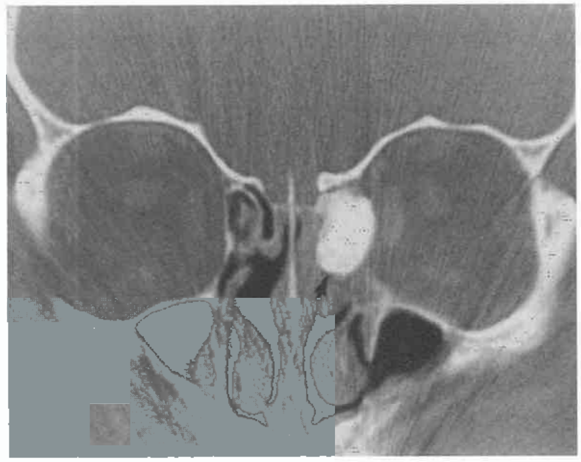

Figure 16–22. Osteoma. The densely calcified nodular structure at the base of the left frontal sinus *(arrow)* is an osteoma. This is a common benign tumor within the anterior ethmoids or inferior frontal sinuses and may cause spontaneous cerebrospinal fluid rhinorrhea.

Neurogenic Tumor[34]

Schwannomas are benign, encapsulated, slowly growing tumors of the nerve sheath that occur in patients from the 4th to 7th decades. Few have been reported within the sinonasal cavity, although a fairly sizable proportion do occur in the head and neck. These are slow-growing expansile lesions that are important for one to recognize as differential diagnostic possibilities when faced with a similar sinonasal mass. Most importantly, they may mimic juvenile angiofibromas by bowing forward the posterior wall of the maxillary sinus. They do not, however, usually involve the pterygopalatine fissure and by that observation may be differentiated from juvenile angiofibromas in younger patients.

Neurofibromas also occur in the head and neck. These are hamartomatous lesions associated with neurofibromatosis I. Some of these may not be differentiable from schwannomas in the head and neck. When plexiform neurofibromas arise from the soft tissues or subcutaneous tissues, they may infiltrate from superficial to deep within the paranasal sinuses. At times these may be aggressive and destructive and mimic malignant tumors.

Fibro-osseous Lesions[45]

Fibro-osseous lesions are probably the most common noninflammatory benign masses of the sinonasal region. Of all the nonepithelial tumors of the paranasal sinuses, approximately 25% are thought to be fibro-osseous in origin.

One of the more common incidental findings, which is a fibro-osseous lesion, is the osteoma (Fig. 16–22). This benign proliferation commonly occurs within the frontal sinus and may cause obstruction or directly erode from the frontal or ethmoid sinus into the cranial cavity, causing a spontaneous cerebrospinal fluid (CSF) leak. These are often described as "ivory" or highly dense bone, which is obvious on both plain film and CT examinations. Osteomas may be small incidental findings on plain film or CT scans but may obstruct the frontal sinuses and again cause CSF rhinorrhea. When multiple osteomas are seen—especially when the skull and mandible are primarily involved—one should entertain the diagnosis of Gardner's syndrome, and investigation of the gastrointestinal tract should be undertaken in a search for intestinal polyps (Box 16–5).

Fibrous dysplasia[6] is an idiopathic disorder in which the medullary bone is replaced by a poorly organized and loosely woven bone that is also expanded compared with normal adjacent bone (Fig. 16–23). The monostotic type is the most common, involving approximately 75% of all patients. In approximately 25% of the patients, bones of the head and neck are involved, with the maxilla and mandible being the most common sites. Polyostotic fibrous dysplasia accounts for approximately one quarter of all cases of fibrous dysplasia. There is a small potential for

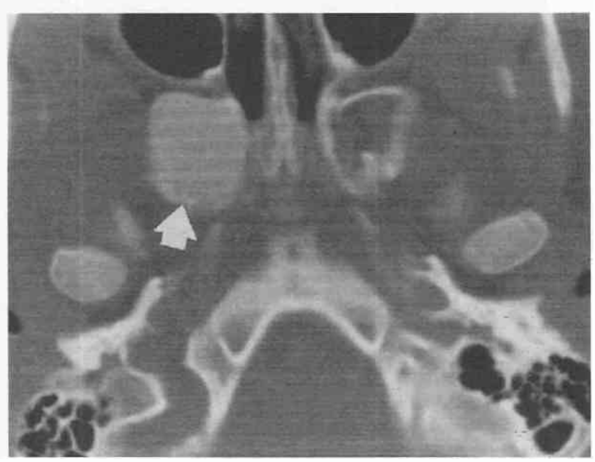

Figure 16–23. Fibrous dysplasia. Polyostotic or monostotic fibrous dysplasia frequently occurs in the facial bones. This axial CT scan through the skull base shows monostotic fibrous dysplasia affecting the pterygoid bones on the right *(arrow)*.

Box 16–5. Syndromes Affecting the Paranasal Sinuses

Gardner's Syndrome

Osteoma (sinus)
Cysts and skin tumors
Intestinal polyposis

Kartagener's Syndrome

Chronic sinusitis
Bronchiectasis
Situs inversus

Basal Cell Nevus Syndrome

Basal cell carcinoma
Dermal pits
Calcification of dural structures
Cysts in mandible and maxilla
Axial skeleton and rib abnormalities

Cystic Fibrosis

Nasal polyposis
Sinusitis
Mucoceles

Louis-Bar Syndrome (Ataxia-Telangiectasia)

Cerebellar ataxia
Pulmonary infection
Sinus infection

Wegener's Granulomatosis

Granulomatous sinuses and respiratory tract
Vasculitis
Glomerulonephritis

Figure 16–24. Osteopetrosis. *A*, A frontal radiograph of the sinuses in a 1-year-old girl reveals the classic sclerotic and chalky appearance of the facial bones and orbits. *B* and *C*, Axial and coronal CT scans also show the typical appearance of this rare disease with thickened sclerotic bone and secondary obstruction of the sinuses.

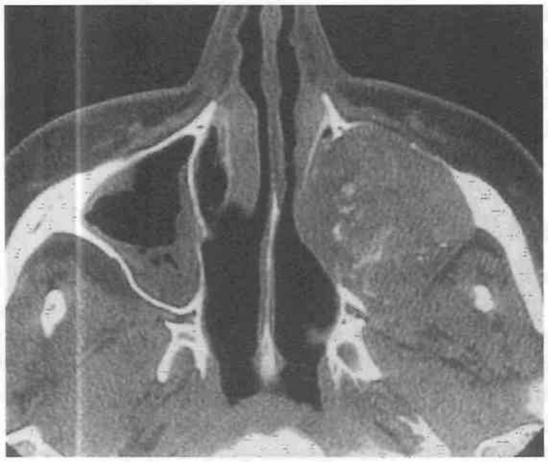

Figure 16–25. Ossifying fibroma. An expansile mass with calcified matrix forming arches or rings is indicative of a benign primary bone tumor. With expansion and destruction, a more aggressive process must always be suspected such as a chondrosarcoma or osteogenic sarcoma.

malignant transformation (~0.5% of patients). This most often occurs in the polyostotic form. Radiographically, the affected bones are noted to be abnormal because of their texture. There is a ground-glass or ivory appearance of the affected bone with expansion of the middle table blending into the inner and outer tables. Osteopetrosis rarely occurs in the paranasal sinuses (Fig. 16–24).

The ossifying fibroma, unlike fibrous dysplasia, contains a lamellar rather than woven pattern of bone and has a normal number of osteoblasts and osteoclasts (Fig. 16–25). Internal regions of disorganization with discrete zones contain either osseous issue or fibrous tissue. Pathologically, the differential diagnosis from fibrous dysplasia is difficult, whereas from an imaging standpoint the differential diagnosis is often much easier.

Giant cell tumors[43] or osteoclastomas make up approximately 5% of all primary bone lesions. Most of these are located in the epiphyseal regions of the long bones, especially around the knee. Approximately 2% of all giant cell tumors, however, occur in the head and neck. These may be located in the region of the sphenoid temporal bone or ethmoid sinuses. Approximately 10% to 15% of giant cell tumors have histologic evidence of malignancy, and these lesions should be irradiated following complete surgical excision. From an imaging point of view, these tumors are lytic lesions with narrow zones of transition. A high index of suspicion is necessary on the part of the imaging physician to raise this diagnosis early so that aggressive surgery and radiation therapy can be undertaken.[38]

Odontogenic tumors that arise from the alveolar ridge may extend to the maxillary sinus.[37] Approximately 10% to 15% of all maxillary sinus inflammatory and neoplastic diseases have an odontogenic origin. A high index of suspicion is required on the part of the imaging physician when confronted with a suspicious mass within the maxillary sinus; coronal examinations should be done to evaluate the possibility of extension of a cyst or mass from the alveolar ridge into the maxillary sinus (Fig. 16–26).

The most common odontogenic lesions involving the maxillary sinus are *odontogenic cysts*.[26] These fall into three broad categories.

Primordial cysts represent approximately 5% of odontogenic cysts and are thought to arise from a supernumerary tooth germ in a patient with an otherwise normal complement of teeth. These are cystic masses that expand from the alveolar ridge superiorly into the maxillary sinus. They are unassociated with either normal or abnormal tooth buds.

Dentigerous cysts represent approximately 95% of follicular cysts and are thought to arise from an unerupted tooth after the crown of the tooth has been developed.[45] The crown of the affected tooth projects into the cystic mass, and the roots of the unerupted tooth project centrifugally from it. These are unilocular and grow slowly, loosening and disrupting the relationship of adjacent teeth. They may also present as cystic masses within the maxillary sinus. These *periodontal* or *radicular cysts* are also known as *periapical abscesses* or *granulomas* and are the result of inflammatory changes at the tooth root associated with dental caries.

Other unusual tumors of the upper molar teeth include

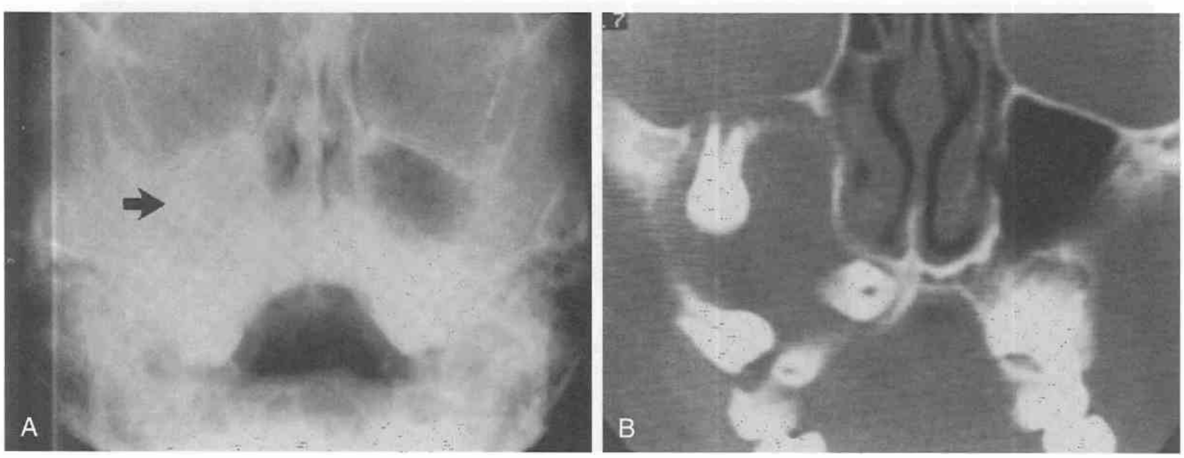

Figure 16–26. Odontogenic mass. On the Waters view of the paranasal sinuses, a teardrop-shaped density was identified in the right maxillary sinus *(A, arrow)*. The accompanying coronal CT image *(B)* revealed an expansile mass containing multiple teeth.

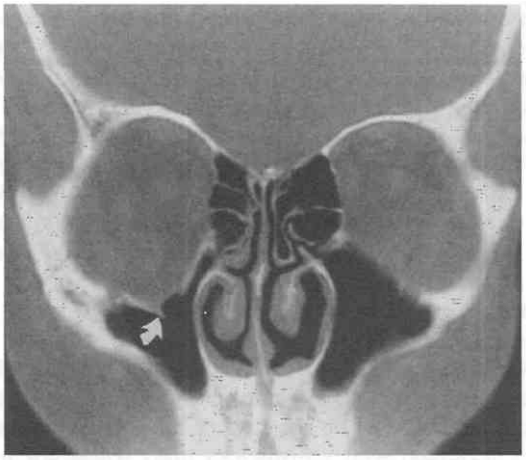

Figure 16–27. Inferior orbital wall fracture. Coronal CT scan reveals a fracture in the inferior wall of the right orbit with downward displacement of the fragment *(curved arrow)* but without herniation of the orbital contents.

multilocular ameloblastoma and the highly dense cementoma. These are beyond the scope of this chapter.

Trauma[45]

Because of extensive overlying edema, hemorrhage, and soft tissue injury, the deformity of the underlying facial skeleton is often concealed at the time of presentation to the emergency department following trauma. There may be subtle clinical signs such as palpable stepoff of the orbital rim, hypertelorism, midface elongation, or CSF rhinorrhea. Radiographic examination is key to the diagnosis of facial and orbital fractures on a timely basis so that these lesions can be treated along with other potentially life-threatening injuries.[15,32]

Before imaging evaluation of the patient with suspected facial fractures, or to rule out such fractures, one should evaluate the cervical spine for fracture and/or instability on both a clinical and imaging protocol. When it has been established that the patient can cooperate for coronal examination and is stable regarding other injuries that may have been sustained, axial and coronal noncontrast CT examination through the paranasal sinuses is recommended in all instances.

Nasal Bone

Fractures of the nasal bone are the most common fracture of the facial skeleton.[36] These may be isolated or associated with other injuries. Plain film examination with oblique cone-down views of the nasal bones is the most sensitive study for identifying and mapping these lesions. In children, when the intranasal suture is not yet ossified, dislocation of the cartilaginous portion of the nose is more common. In adults, when the nose is struck, linear fracture traversing the long axis of the nose is the expected lesion.

Orbit

A blow to the orbit most often strikes the inferior orbital rim. It is now thought that the relatively thick rim of the orbit has elastic properties that allow it to bend posteriorly and rebound anteriorly following trauma. During this posterior excursion of the inferior orbital rims, however, there may be wrinkling and then crumbling of the floor of the orbit.[12] There is a groove within the floor of the orbit (the groove for the infraorbital nerve) that acts as a fault line, allowing orbital floor fractures to occur as the most common isolated fracture of the orbit. With more extensive force, there may be fracture of both the inferior orbital rim and the orbital floor. The former lesion is known as a "pure" blowout fracture, whereas the latter lesion, involving the inferior orbital rim, is known as a "impure" blowout fracture (Fig. 16–27).

Although the medial orbital wall, the lamina papyracea, is the thinnest bone in the body, it is supported by laterally and medially running septa of the ethmoid air cells. These act as struts between free segments of the lamina papyracea to prevent medial orbital blowout. Fractures through the

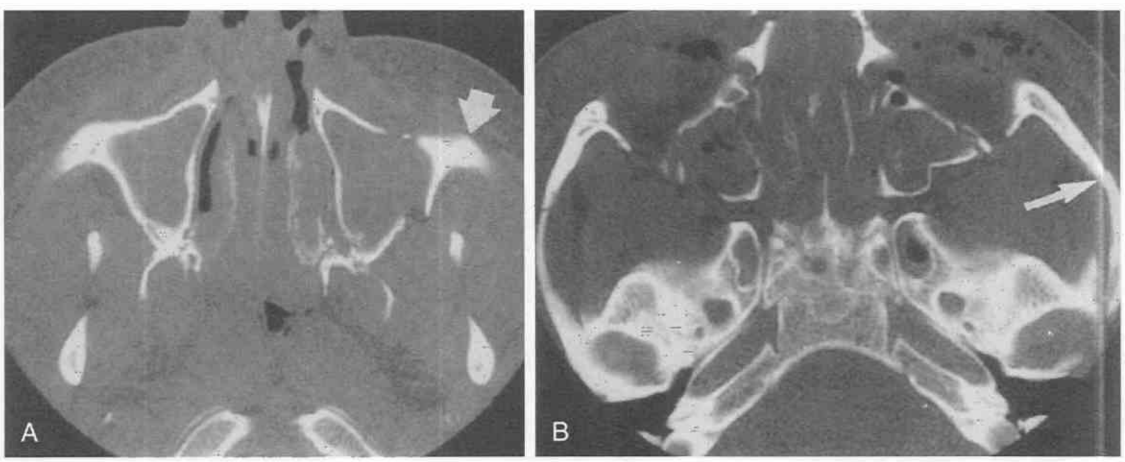

Figure 16–28. Trimalar fracture. On the axial view the trimalar fracture *(A, arrow)* is manifested as fractures of the anterior sinus wall and posterior sinus wall. *B*, Fracture of the ipsilateral zygomatic arch is shown.

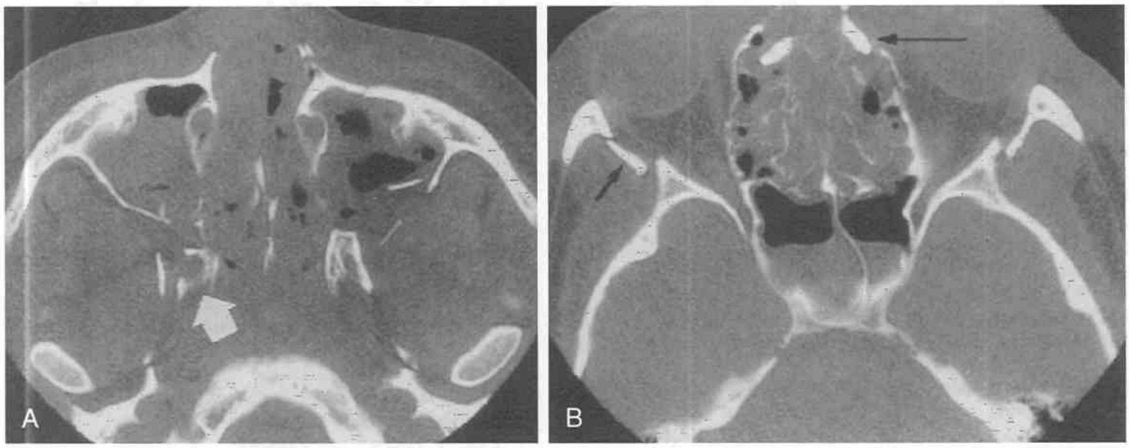

Figure 16–29. Le Fort fractures. The unifying fracture among all types of Le Fort fractures is fracture through the pterygoid plates *(A, arrow)*. Le Fort I fractures are rare. With Le Fort II types, the medial orbital wall *(B, long arrow)* is fractured, with continuation of the fracture line through the floor of the orbit and into the pterygoid plates. A Le Fort III fracture *(B, short arrow)* extends from the medial wall of the orbit to the lateral orbital wall and then inferiorly through the pterygoid plates.

medial orbital wall still occur either through transmission from direct trauma to the nose or from increased intraorbital pressure. Blowout fractures of the orbital roof also occur. Again, these may be caused by transmitted force through the superior orbital rim. More often they are the result of extension of fracture elsewhere in the skull into the superior orbital rim.

Side of the Face

Trauma to the side of the face or lateral orbital rim may result in the familiar tripod or trimalar fracture[28] (Fig. 16–28). This is a complex fracture involving the floor of the orbit, the anterior and posterior walls of the maxillary sinus, the zygomatic arch, the zygomaticofrontal suture, and the posterior wall of the orbit. Although it actually has at least four points, in any single plane it may appear as a three-pointed fracture fragment; thus, the eponyms are tripod and trimalar.

Le Fort Fractures

The unifying feature of Le Fort fractures is disruption of the pterygoid plates.[35] Because of the associated disruption of the pterygoid venous plexus, it is important to recognize these fractures as potentially life-threatening because of the relatively large nasopharyngeal hematoma that sometimes occurs.

There are three types of Le Fort fractures:

The *Le Fort I* fracture is a horizontal fracture above the hard palate with separation of the hard palate and lower portion of the pterygoid plates from the rest of the facial infrastructure.

The *Le Fort II* fracture begins at the bridge of the nose and extends laterally along the medial wall of the orbit and then inferiorly along the inferior wall of the orbit, through the anterior wall of the maxillary sinus, and then posteriorly through the alveolar recess of the maxillary sinus into the pterygoid plates.

The *Le Fort III* fracture also begins as a fracture through the base of the nose or glabella and extends along the medial wall of the orbit, much as the Le Fort II fracture does. Rather than extending into the floor of the orbit, however, there is extension of the fracture line along the lateral wall of the orbit, inferiorly through the maxillary sinus and then posteriorly through the pterygoid plates (Fig. 16–29).

References

1. Babbel R, Harnsberger HR, Nelson B, et al: Optimization of techniques in screening CT of the sinuses. AJNR Am J Neuroradiol 12: 849–854, 1991.
2. Barnes L, Verbin RS, Gnepp DR: Diseases of the nose, paranasal sinuses and nasopharynx. In Barnes L (ed): Surgical Pathology of the Head and Neck, vol 1. New York, Marcel Dekker, 1985, pp 403–451.
3. Batsakis JG: Tumors of the Head and Neck: Clinical and Pathological Considerations. In Baltihouse Z (ed): Baltimore, Williams & Wilkins, 1979, pp 177–178.
4. Bryan N, Sessions RB, Horowitz BL: Radiographic management of juvenile angiofibromas. AJNR Am J Neuroradiol 2:157–166, 1981.
5. Chapnick JS, Bach MC: Bacterial and fungal infections of the maxillary sinus. Otolaryngol Clin North Am 9:43, 1976.
6. Dehner LP: Fibro-osseous lesions of bone. In Ackerman LU, Spjut HJ, Abell MR (eds): Bones and Joints. International Academy of Pathology, Monograph No. 17. Baltimore, Williams & Wilkins, 1976, pp 209–235.
7. Dillon WP, Som PM, Fullerton GD: Hypointense MR signal in chronically inspissated sinonasal secretions. Radiology 174:73078, 1990.
8. Dodd GD, Jing BS: Radiology of the Nose, Paranasal Sinuses and Nasopharynx. Baltimore, Williams & Wilkins, 1977.
9. Duncavage JA, Campbell BH, Hanson GH: Diagnosis of malignant lymphomas of the nasal cavity, paranasal sinuses and nasopharynx. Laryngoscope 93:1276, 1983.
10. Evans FO, Sydnor JB, Moore WEC, et al: Sinusitis of the maxillary antrum. N Engl J Med 293:735, 1976.
11. Goss CM: Gray's Anatomy of the Human Body, 27th ed. Philadelphia, Lea & Febiger, 1963, pp 1167–1176.
12. Hammerschlag SB, Hughes S, O'Reilly GV, et al: Another look at blow out fractures of the orbit. AJNR Am J Neuroradiol 3: 331–335, 1982.
13. Harrison DFN: Midline destructive granuloma: Fact or fiction? Laryngoscope 97:1049, 1987.
14. Kennedy DW, Zinreich SJ, Rosenbaum AE, et al: Functional endoscopic sinus surgery. Arch Otolaryngol 111:576–582, 1985.
15. Kreipke DL, Moss JJ, Franco JM, et al: Computed tomograpy and

thin-section tomography in facial trauma. AJNR Am J Neuroradiol 5:423, 1984.
16. Lanzieri CF, Levin HL, Rosenbloom SA, et al: Three dimensional surface rendering of nasal anatomy for CT data. Arch Otolaryngol 115:1444–1446, 1989.
17. Lanzieri CF, Shah M, Krauss D, et al: Use of Gd-DTPA enhanced MRI for differentiating mucoceles from neoplasms in the paranasal sinuses. Radiology 178:425–428, 1991.
18. Last RJ: Anatomy Regional and Applied, 6th ed., London, Churchill Livingstone, 1978, pp 398–406.
19. Lee YY, et al: Lymphomas of the head and neck: CT findings at initial presentation. AJNR Am J Neuroradiol 8:665, 1987.
20. Levine HL: The sphenoid sinus, the neglected sinus. Arch Otolaryngol 104:585–587, 1978.
21. Maffe MF: Endoscopic sinus surgery: Role of the radiologist. AJNR Am J Neuroradiol 12:855–860, 1991.
22. Maresh MM: Paranasal sinuses from birth to late adolescence. Am J Dis Child 60:58, 1940.
23. McGill TJ, Simpson G, Healy GR: Fulminant aspergillosis of the nose and paranasal sinuses: A new clinical entity. Laryngoscope 90: 748, 1980.
24. Modic MT, Weinstein MA, Berlin J, et al: Maxillary sinus hypoplasia visualized with CT. Radiology 135:383–385, 1980.
25. Moore KL: The special sense organs. In The Developing Human. Philadelphia, WB Saunders, 1973, pp 335–349.
26. Mourshed F: A roentgen study of dentigerous cysts. Oral Surg 18: 47–61, 1964.
27. Myerowitz RL, Guggenheimer J, Barnes L: Infectious diseases of the head and neck. In Barnes L (ed): Surgical Pathology of the Head and Neck, vol 2. New York, Marcel Dekker, 1985, pp 1771–1822.
28. Nalcamura T, Gross CW: Arch Otolaryngol 97:288–290, 1973.
29. Osborn AG: The nasal arteries. AJNR Am J Neuroradiol 130:89, 1978.
30. Paff GH: Anatomy of the Head and Neck. Philadelphia, WB Saunders, 1973, pp 183–203.
31. Paling MR, Roberts HL, Fauci AS: Paranasal sinus obliteration in Wegener's granulomatosis. Radiology 144:539, 1982.
32. Pathria MN, Blaser SI: Diagnostic imaging of craniofacial fractures. Radiol Clin North Am 27:839–853, 1989.
33. Postic WP, Wetmore RF: Pediatric rhinology. In Goldman JL (ed): The Principles and Practice of Rhinology. New York, John Wiley & Sons, 1987, pp 801–845.
34. Richtsmeier WJ, Johns ME: Actinomycosis of the head and neck. In Batsakis J, Savory J (eds): Critical Review in Clinical Laboratory Sciences, vol II. Boca Raton, Fla, CRC Press, 1979, pp 175–202.
35. Rogers LF: Radiology of Skeletal Trauma, vol 1. New York, Churchill Livingstone, 1982.
36. Schultz RC, Oldham RJ: An overview of facial injuries. Surg Clin North Am 57:987–1010, 1977.
37. Shafer WG, Hine WK, Levy BM: A Textbook of Oral Pathology. Philadelphia, WB Saunders, 1974.
38. Smith GA, Ward PH: Giant cell lesions of the facial skeleton. Arch Otolaryngol 104:186, 1978.
39. Som PM, Dillon WP, Curtin HD, et al: Hypointense paranasal sinus foci: Differential diagnosis with MRI in relation to CT findings. Radiology 176:777–781, 1990.
40. Som PM, Dillon WP, Fullerton GD, et al: Chronically obstructed sinonasal secretions observations on T1 and T2 shortening. Radiology 172:515–520, 1989.
41. Som PM, Dillon WP, Sze G, et al: Benign and malignant sinonasal lesions with intracranial extension: Differentiation with MRI. Radiology 172:763–766, 1989.
42. Som PM, Lawson W, Biller H, et al: Ethmoid sinus disease: CT evaluation in 400 cases. Radiology 159:591–597, 1986.
43. Som PM, Lawson W, Cohen BA: Giant cell lesions of the facial bones. Radiology 147:129–183.
44. Som PM, Shapiro MD, Biller HF, et al: Sinonasal tumors and inflammatory tissues: Differentiation with MRI. Radiology 167:803–808, 1988.
45. Som PM: Sinonasal cavity. In Som PM, Burgeron RT (eds): Head and Neck Imaging, 2nd ed. St. Louis, Mosby–Year Book, 1991, pp 51–276.
46. Som PM, Cohen BA, Sacher M, et al: The angiomatous polyp and the angiofibroma: Two different lesions. Radiology 144:324, 1982.
47. Swischuk LE, Hayden CK, Dillard RA: Sinusitis in children. Radiographics 2:241–252, 1982.
48. Terrier F, Weber W, Rue fen acht D, et al: Anatomy of the ethmoid: CT endoscopic and macroscopic. AJNR Am J Neuroradiol 6:77–84, 1985.
49. Towbin R, Dunbar JJ: The paranasal sinuses in children. Radiographics 2:253–280, 1982.
50. Van Tassel P, Lee YY, Jing BS, et al: Mucoceles of the paranasal sinuses. AJNR Am J Neuroradiol 10:607–612, 1989.
51. Williams HG: Nasal physiology. In Paparella MM, Shumrick DA (eds): Otolaryngology: Basic Science and Related Disciplines, vol 1. Philadelphia, WB Saunders, 1973, pp 329–346.
52. Zinreich SJ, Kennedy DW, Kumar AJ, et al: MRI of the nasal cycle. J Comput Assist Tomogr 12:1014, 1988.
53. Zinreich SJ, Kennedy DW, Malat J, et al: Fungal sinusitis: Diagnosis with CT and MRI. Radiology 169:439–444, 1988.
54. Zinreich SJ, Kennedy DW, Rosenbaum AE, et al: Paranasal sinuses: CT imaging. Requirements for endoscopic surgery. Radiology 163: 769–775, 1987.

17

Cervical Adenopathy and Neck Masses

Roy A. Holliday, Deborah L. Reede

High-resolution computed tomography (CT) and magnetic resonance imaging (MRI) have proved to be invaluable tools for evaluating the soft tissue structures of the neck. Although many imaging modalities are available for the evaluation of a neck mass, including radiography, ultrasonography, angiography, and radioisotope imaging, CT and MRI provide anatomical detail that cannot be obtained with these other modalities. CT and MRI demonstrate both the precise location of a neck mass and its relationship to adjacent vascular, muscular, and neural structures. In addition to providing this anatomical detail, CT and MRI frequently are able to characterize the vascularity and internal architecture (solid versus cystic) of a neck mass.

The combination of soft tissue characterization and anatomical localization afforded by CT and MRI allows radiologists to make a substantial contribution to the preoperative assessment of the patient with a neck mass. Although an exact tissue diagnosis is not always possible, careful analysis of the imaging features of a neck mass in combination with clinical history and physical examination produce a reasonably short differential diagnosis in nearly every case.

Imaging Technique

CT imaging of the neck is performed with the patient supine on the scanner gantry. Contiguous 5-mm-thick axial images are usually obtained from the level of the superior orbital rim to the lung apex. Care must always be taken to avoid image degradation by dental amalgam. One common solution is to acquire images from the superior orbital rim to the hard palate with the use of gantry angulation parallel to the central skull base. Images from the alveolar ridge of the mandible to the lung apex are then obtained with a gantry angulation parallel to the body of the mandible. If the patient's chin is fully extended, this latter series may be obtained with a 0-degree gantry angulation.

Intravenous contrast enhancement is essential for CT examinations of the soft tissue of the neck, to facilitate both tissue characterization of neck masses and separation of neck masses from normal vascular structures. Most investigators recommend an initial rapid bolus of approximately 50 mL of contrast material administered over 1 to 2 minutes before image acquisition, followed by a steady rapid drip infusion of the remaining 100 to 150 mL during scanning. Power injectors, commonly used for abdominal or thoracic CT scanning, can be readily adapted for neck CT examinations. Contrast administration should be interrupted during changes in gantry angulation.

Optimal MRI of the neck requires the use of surface coils. Images of the suprahyoid neck may be obtained by placement of the patient well inside many standard head surface coils. Images of the infrahyoid neck require dedicated anterior neck surface coils, because the use of posteriorly placed cervical spine surface coils results in suboptimal images owing to signal drop-off.

Current MRI techniques involve acquisition of T1-weighted images in sagittal, axial, and coronal projections with corresponding T2-weighted images obtained in the projection that best depicts the lesion. Slice thicknesses of 4 to 6 mm with 1- to 2-mm intervals between slices are commonly used. The prolonged scan times of axial T2-weighted images often result in images of diminished diagnostic quality owing to gross patient motion as well as artifacts produced by swallowing, respiratory motion, and cardiac pulsations. To overcome these problems, rapid spin-echo techniques are often used to obtain T2-weighted images in shorter scan times.[49]

Contrast administration is not essential in MRI of neck masses. The use of multiple pulse sequences and multiple projections is usually sufficient to differentiate neck masses from adjacent vascular structures. When contrast enhancement is required for tissue characterization, fat-suppressed T1-weighted images are commonly used, particularly in the assessment of cervical adenopathy.[47]

Choice of Imaging Modality

MRI and CT should be considered complementary, rather than competitive, modalities for imaging neck masses. The advantages MRI offers over CT in imaging other parts of the body (multiplanar capability, lack of ionizing radiation, safer contrast agents) also apply to imaging the soft tissues of the neck. By comparison, CT examinations offer the advantages of superior assessment of osseous integrity, shorter examination time, wider patient access, and lower cost.[12] The authors prefer to use contrast-enhanced CT as the initial study to assess neck masses in adults. In children and in adults whose clinical status precludes the use of iodinated contrast material, MRI is the study of choice, although a limited noncontrast CT study may be required for the evaluation of osseous integrity. The remainder of this chapter reflects this preference and emphasizes the normal and abnormal CT appearance of the soft tissues of the neck.

Normal Gross Anatomy

The neck is composed of the posteriorly located nucha and the anteriorly located cervix. The *nucha*, which consists primarily of the vertebral column and its associated musculature, is discussed in detail in Chapter 19. For practical purposes, the *cervix* (which also means neck) can be thought of as a cylinder of soft tissue whose superior extent is a line connecting the occiput and the tip of the chin and whose inferior extent parallels the course of the first rib at the thoracic inlet.[13]

The most important landmark to identify when one is studying the neck in any plane is the sternocleidomastoid muscle. The sternocleidomastoid muscle takes its origin from the mastoid tip and digastric notch at the skull base and extends anteriorly, inferiorly, and medially, spiraling across the anterior aspect of the neck on each side to insert as two heads on the medial third of the clavicle and the manubrium. The course of the sternocleidomastoid muscle is the basis for the division of the soft tissues of the neck into two paired spaces, the anterior and posterior triangles (Fig. 17–1). The sternocleidomastoid muscle forms the posterior border of the anterior triangle and the anterior border of the posterior triangle. All structures located anterior to the sternocleidomastoid muscle lie within the anterior triangle; those deep as well as posterior to it are in the posterior triangle.[32] It is important to remember that no septum or fascial plane physically separates the anterior from the posterior triangle.

The anterior triangles have a common side, abutting each other in the midline. Their borders are the sternocleidomastoid muscle posteriorly, the mandible superiorly, and the midline medially. The hyoid bone divides this triangle into a suprahyoid portion and an infrahyoid portion, each of which has two subdivisions.

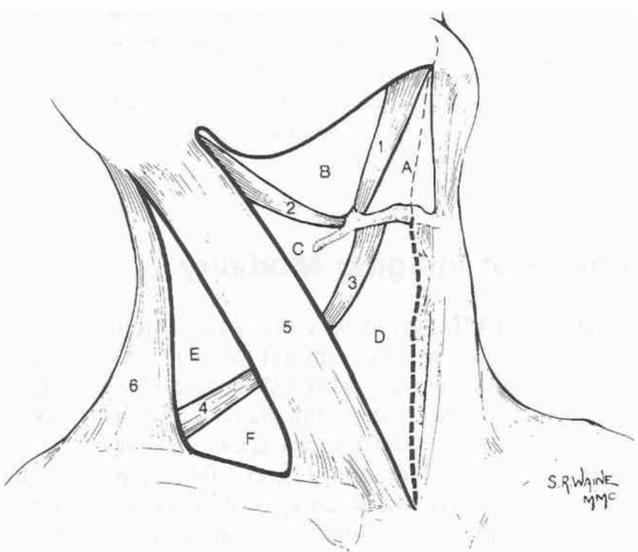

Figure 17–1. Triangles of the neck. 1, Anterior belly of the digastric muscle; 2, posterior belly of the digastric muscle; 3, superior belly of the omohyoid muscle; 4, inferior belly of the omohyoid muscle; 5, sternocleidomastoid muscle; 6, trapezius muscle. A, Submental triangle; B, submandibular triangle; C, carotid triangle; D, muscular triangle; E, occipital triangle; F, subclavian triangle. (From Reede DL, Whelan MA, Bergeron RT: CT of the soft tissue structures of the neck. Radiol Clin North Am 22:239, 1984.)

The suprahyoid division contains the laterally located submandibular triangles and the medially located submental triangles. Superiorly these triangles are separated from the oral cavity by the mylohyoid muscle. This muscle forms a sling connecting the two inner surfaces of the mandible with the hyoid bone. By definition, structures above the mylohyoid muscle are in the oral cavity; those below are in the neck.

The base of each submandibular triangle is formed by the ramus of the mandible. The other two sides of each submandibular triangle are formed by the anterior and posterior bellies of the digastric muscle. The digastric muscle takes its origin from a depression on the skull base between the mastoid tip and the styloid process known as the *digastric notch*. The posterior belly of the digastric muscle extends anteriorly, inferiorly, and medially from the digastric notch to the greater cornu of the hyoid bone. The anterior belly of the digastric muscle extends from the greater cornu anteriorly, superiorly, and medially to insert on the anterior border of the mandible, inferior to the attachment of the mylohyoid muscle.

The major structures contained within the submandibular triangle are numerous small lymph nodes and the submandibular salivary glands. The anterior surface of the submandibular gland abuts the posterior free margin of the mylohyoid muscle, so a small portion of each submandibular gland lies within the posterior oral cavity but the majority of the gland lies within the suprahyoid neck.

The base of the submental triangle is formed by the hyoid bone. The other two sides of the submental triangle are formed by the anterior bellies of the digastric muscles. No major anatomical structures are located in this triangle except for a few small lymph nodes and branches of the facial artery and vein.

The infrahyoid division of the anterior triangle is divided by the superior belly of the omohyoid muscle into two parts, the carotid triangle superolaterally and the muscular triangle inferomedially. The infrahyoid portion of the anterior triangle contains the larynx, hypopharynx, trachea, esophagus, lymph nodes, and thyroid and parathyroid glands.

The two sides of each posterior triangle are the sternocleidomastoid muscle anteriorly and the trapezius muscle posteriorly. The base of each triangle is formed by the clavicle. The inferior belly of the omohyoid muscle crosses the inferior aspect of the posterior triangle and divides it into two unequal parts, the occipital triangle anteriorly and the subclavian triangle inferiorly.

The major structures located within the occipital triangle are the spinal accessory nerve (cranial nerve XI) and its associated chain of lymph nodes. The major structures located within the subclavian triangle are the transverse cervical vessels and their associated chain of lymph nodes. Also present within the posterior triangle are the exiting cervical nerve roots, the cervical components of the brachial plexus, and nutrient vessels.

The internal jugular vein and its associated chain of lymph nodes closely parallel the deep surface of the anterior margin of the sternocleidomastoid muscle, thereby bridging the anterior and posterior triangles. The arterial and neural components of the carotid sheath, the common

carotid artery, the internal carotid artery, and the vagus nerve, also traverse the neck within the anterior triangle.[32]

Normal Sectional Anatomy

The sternocleidomastoid muscle is a constant landmark that can always be identified on axial CT scans or MR images through the neck. As one progresses from superior to inferior, the location of the sternocleidomastoid muscle moves from a far lateral position to a paramedian position. With this change in position of the sternocleidomastoid muscle comes a change in relative sizes of the anterior and posterior triangles. Superiorly the anterior triangle occupies the majority of the cross-sectional area of the neck because there is little space between the sternocleidomastoid and trapezius muscles. Inferiorly the posterior triangle occupies the majority of the cross-sectional area of the neck because there is little space between the anterior surface of the sternocleidomastoid muscle and the midline.

The mylohyoid muscle, the major landmark separating the oral cavity from the suprahyoid neck, is readily identified on both coronal and axial images. On axial images (Fig. 17–2*A* and *B*), the muscle appears in cross-section as

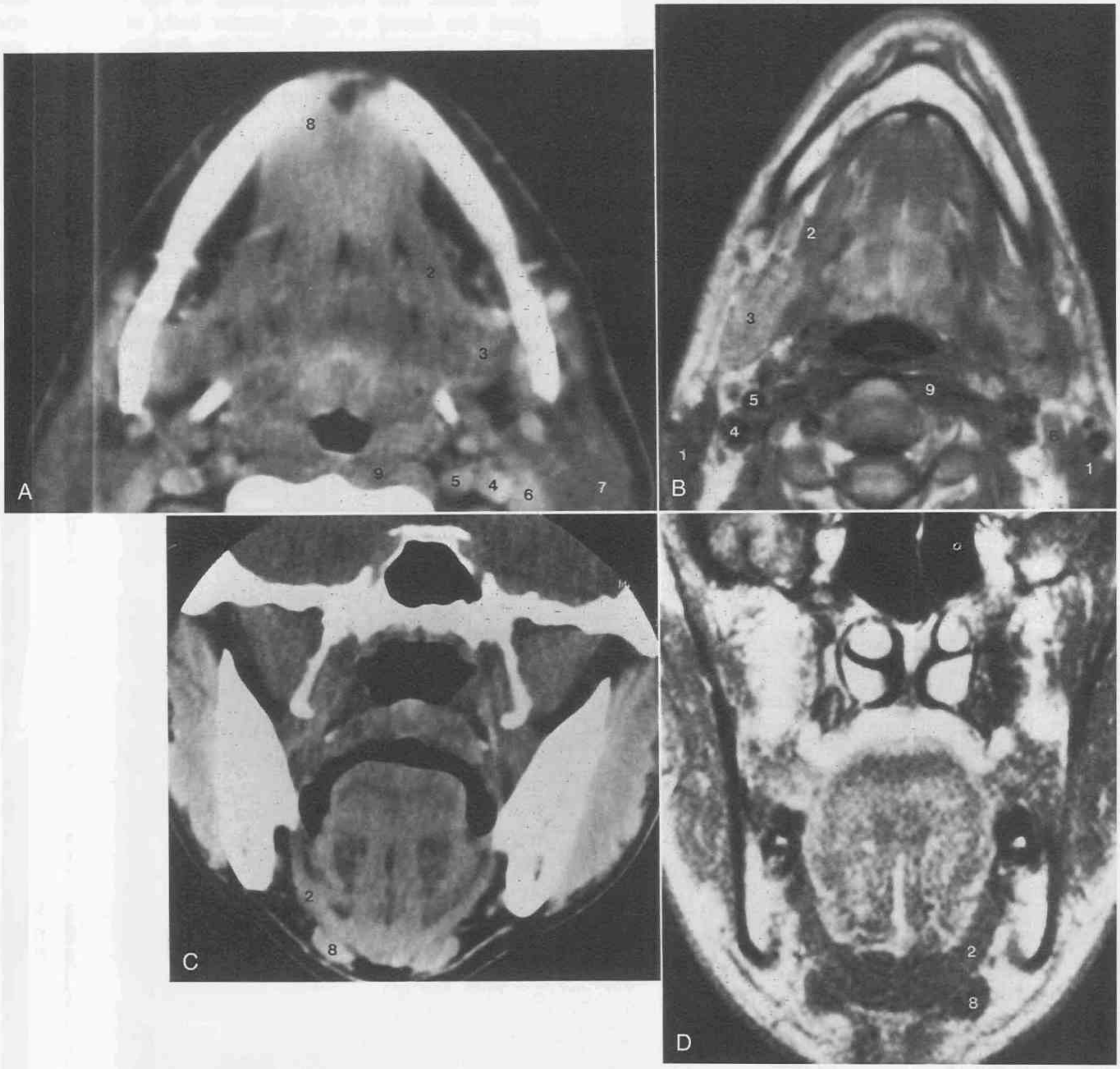

Figure 17–2. Normal sectional anatomy at the junction of the oral cavity and neck. *A*, Contrast-enhanced CT image at the level of the mandible. The sternocleidomastoid muscle is posterior to the parotid gland. *B*, T1-weighted MR image at a similar level in a different patient. Note the greater tissue contrast between the mylohyoid muscle and the submandibular gland on MRI. Coronal CT scan (*C*) and coronal T1-weighted MR image (*D*) demonstrate the anterior belly of the digastric inferior to the sling-shaped mylohyoid muscle. 1, Sternocleidomastoid muscle; 2, mylohyoid muscle; 3, submandibular gland; 4, internal jugular vein; 5, internal carotid artery; 6, posterior belly of digastric muscle; 7, parotid gland; 8, anterior belly of digastric muscle; 9, longus colli muscle.

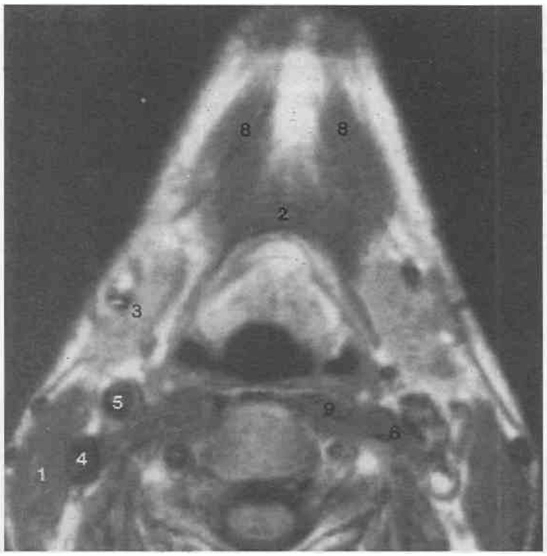

Figure 17–3. Normal axial anatomy of the suprahyoid neck. T1-weighted MR image in same patient as Figure 17–2*B*. The submental triangle is located between the two anterior bellies of the digastric muscle. 1, Sternocleidomastoid muscle; 2, mylohyoid muscle; 3, submandibular gland; 4, internal jugular vein; 5, internal carotid artery; 6, posterior belly of digastric muscle; 8, anterior belly of digastric muscle; 9, longus colli muscle.

two separate muscle bundles medial to the mandible. As axial images are obtained from superior to inferior, the distance between the separate bundles decreases. The superior aspect of the submandibular gland is identified on axial images at the posterior margin of the mylohyoid muscle. On coronal images, the muscle has the configuration of a hammock suspended from the medial (lingual) surface of the mandible (Fig. 17–2*C* and *D*).[12]

Immediately inferior to the mylohyoid muscle, the anterior bellies of the digastric muscle can be identified (Fig. 17–3). Depending on the degree of angulation used on axial imaging, varying amounts of mylohyoid muscle can be seen projecting between the anterior bellies of the digastric muscle. The cervical portion of the submandibular gland lies lateral to each anterior belly of the digastric muscle. The posterior belly of the digastric muscle can usually be identified medial and posterior to the parotid gland, separating the gland from the contents of the carotid sheath.[32]

The hyoid bone is the major bony landmark of the anterior neck (Fig. 17–4). The hyoid is best identified on axial CT images, where its central body and greater horns (cornua) appear in the midline as an "inverted U" approximately at the level of the C3-4 disk space. The carotid bifurcation is typically located at or near the level of the hyoid bone. The thyroid cartilage has an *inverted V* appearance on axial images. The superior third of the cartilage is not fused in the midline at the level of the thyroid notch. Immediately superficial to the two halves of

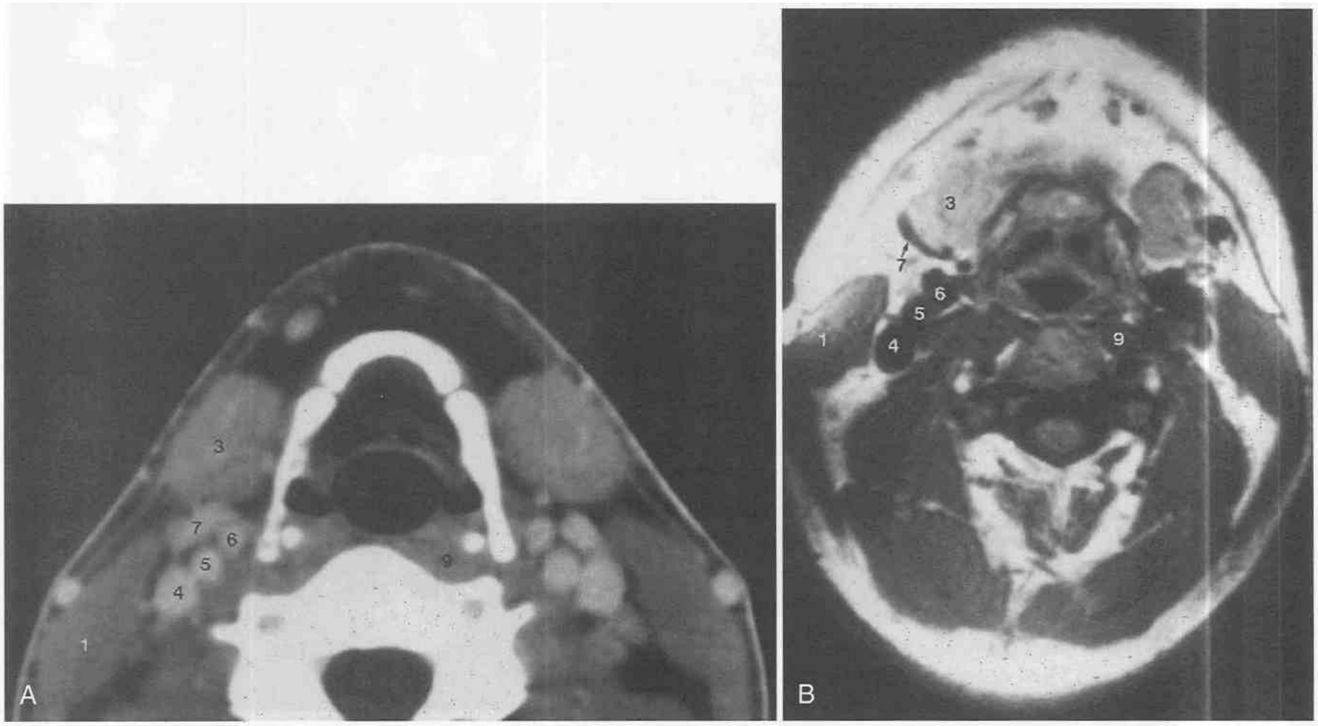

Figure 17–4. Normal axial anatomy at the level of the hyoid bone. *A*, Contrast-enhanced CT scan. Note that the normal retrofacial vein or proximal external carotid artery might be mistaken for a lymph node or other mass on a noncontrast examination. *B*, T1-weighted MR image demonstrates the same soft tissue and vascular anatomy without intravenous contrast. 1, Sternocleidomastoid muscle; 3, submandibular gland; 4, internal jugular vein; 5, internal carotid artery; 6, external carotid artery; 7, retrofacial vein; 9, longus colli muscle.

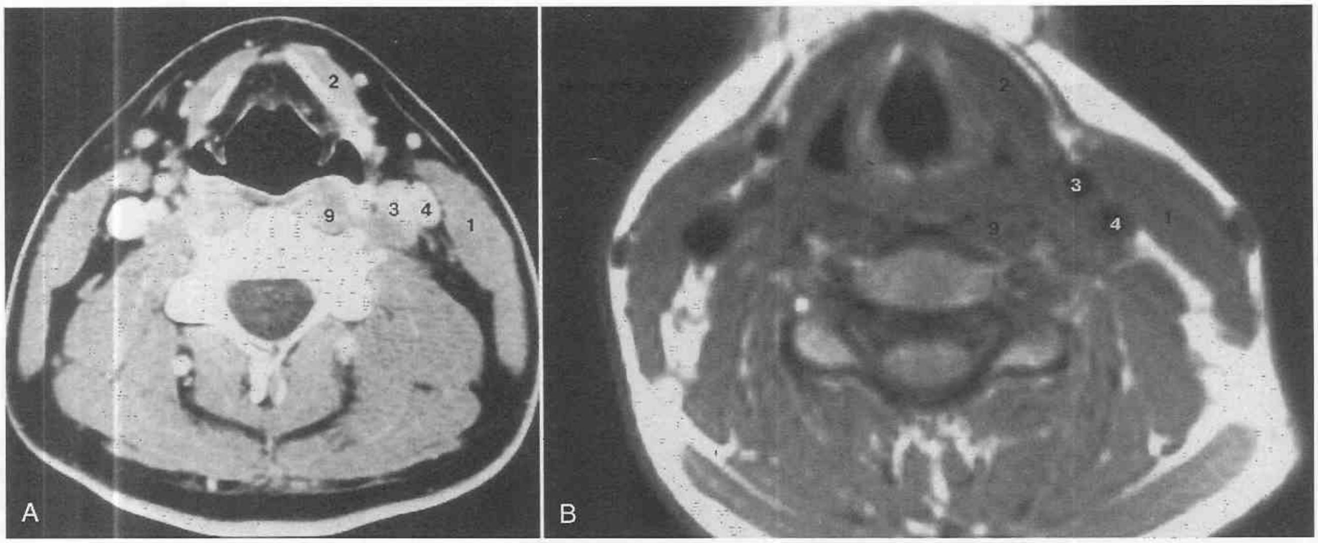

Figure 17–5. Normal axial anatomy at the level of the thyroid cartilages. *A*, CT scan. *B*, T1-weighted MR image. Note how the anterior margin of the sternocleidomastoid muscle is located anterior to the vertebral body. Compare with Figure 17–2*B*. 1, Sternocleidomastoid muscle; 2, strap muscle; 3, internal carotid artery; 4, internal jugular vein; 9, longus colli muscle.

the thyroid cartilage are the strap muscles (sternohyoid, sternothyroid, thyrohyoid, and superior belly of the omohyoid). The degree and pattern of ossification of the cartilages vary with the age and sex of the patient. Separation of nonossified cartilage from the overlying strap muscles is accomplished more easily with MRI than CT.

At the level of the thyroid cartilage (Fig. 17–5), the carotid sheath structures are situated along the anterior surface of the sternocleidomastoid muscle or slightly deep to it, posterior and lateral to the thyroid cartilage.

The superior cornua of the thyroid cartilage are easily identified as paired calcified structures located lateral to two of the extrinsic muscles of the spine, the longus colli muscles. The inferior cornua of the thyroid cartilage articulate with the posterior aspect of the cricoid cartilage.

The cricoid cartilage has a characteristic circular appearance on axial imaging. As with the thyroid cartilage, the degree of ossification of the cricoid varies with age. In adult patients, the cricoid cartilage appears on CT scans as a thin rim of calcification surrounding a lucent medullary center.[32] On T1-weighted MR images, the cricoid appears as a ring of tissue isointense to fat.

At approximately the level of the cricoid cartilage (Fig. 17–6), the superior pole of the thyroid gland appears on axial images as a triangular soft tissue structure situated between the cricoid cartilage medially and the carotid sheath structures laterally. The normal gland enhances uniformly with iodinated intravenous contrast material.[32] On noncontrast T1-weighted images, the gland is homogeneous in appearance and slightly hyperintense to skeletal muscle. The level of the cricoid cartilage also marks the point at which the omohyoid muscle crosses over the internal jugular vein.

Images at the level of the first tracheal ring (Fig. 17–7) demonstrate the lower poles of the thyroid gland and the adjacent carotid sheath structures. The sternocleidomastoid muscles have a paramedian position just superior to their insertions on the sternum and clavicle. The esophagus is usually collapsed, lying posterior to the trachea and usually just to the left of the midline.

The posterior triangle of the normal supracricoid neck appears as a fat-filled cleft containing a few small soft tissue structures representing nutrient vessels, lymph nodes, and nerves.[32] Beginning at the level of the cricoid cartilage, the anterior scalene muscle can be identified in the medial aspect of the posterior triangle, posterior to the carotid sheath structures. The anterior scalene, which arises from the transverse processes of C3 through C6 and inserts on the superior and posterior surfaces of the medial first rib, lies directly anterior to the exiting trunks of the brachial plexus. At the level of the first tracheal ring, the brachial plexus is identified as a heterogeneous low-density or low-signal-intensity focus immedia

tely posterior to the anterior scalene muscle.

Evaluation of Cervical Adenopathy

Enlarged cervical lymph nodes are the most common cause of a neck mass in an adult. In patients older than 40 years, the enlarged nodes are most often secondary to metastatic carcinoma, usually from a primary neoplasm of the aerodigestive tract. In patients between the ages of 21 and 40, the enlarged nodes are most often secondary to lymphoma.[37] The optimal evaluation of cervical lymph nodes requires close attention to radiographic detail as well as an understanding of basic anatomical and pathologic principles of otolaryngology.

Anatomic Principles

Approximately 300 lymph nodes are located in the head and neck. The French anatomist Rouivere[34] divided these nodes into the following 10 principal groups (Fig. 17–8):[34]

1. Occipital nodes.

Figure 17–6. Normal axial anatomy at the level of the cricoid cartilage and inferior cornua of the thyroid cartilage. *A,* CT scan. The asymmetry in the diameters of the internal jugular veins is a normal variant. *B,* T1-weighted MR image. 1, Sternocleidomastoid muscle; 2, thyroid gland; 3, internal carotid artery; 4, internal jugular vein; 8, trapezius muscle; 9, longus colli muscle.

2. Mastoid nodes.
3. Parotid nodes.
4. Facial nodes.
5. Submandibular nodes.
6. Submental nodes.
7. Sublingual nodes.
8. Retropharyngeal nodes.
9. Anterior cervical nodes.
10. Lateral cervical nodes.

The first six groups form a *lymphoid collar* at the junction of the head and neck. Each group is responsible for the primary lymphatic drainage of a different region of the neck, as follows:

Occipital: Scalp and subcutaneous tissues of the occiput and superior neck.
Mastoid: Parietal scalp and auricle.
Parotid: Forehead, temporal scalp, lateral face, posterior cheek, lateral gingiva, buccal mucous membrane, exterior auditory canal, and parotid gland.
Facial: Lateral eyelids, anterior cheek, midface.
Submandibular: Lateral chin, lower and upper lips, lower cheek, anterior nose, medial eyelids, gingiva, anterior tongue, floor of the mouth, and submandibular and sublingual glands.
Submental: Central chin, lower lip, anterior gingiva, anterior floor of mouth, and tip of tongue.

The sublingual nodes also drain the tongue and floor of mouth but are not always identifiable as a separate group. The retropharyngeal nodes are further divided into medial and lateral groups. The medial group lies in the midline of the suprahyoid neck directly posterior to the pharynx. Enlargement of the medial group of retropharyngeal nodes is most commonly seen in neonates and young children. The lateral group is located anterior to the longus colli and longus capitus muscles, medial to the internal carotid artery, in both the suprahyoid and the infrahyoid neck. The retropharyngeal lymph nodes primarily drain the nasopharynx and posterior oropharynx as well as the paranasal sinuses, middle ear, posterior palate, and nasal cavity.

The anterior cervical nodes are toward the midline of the infrahyoid neck, located between the two carotid

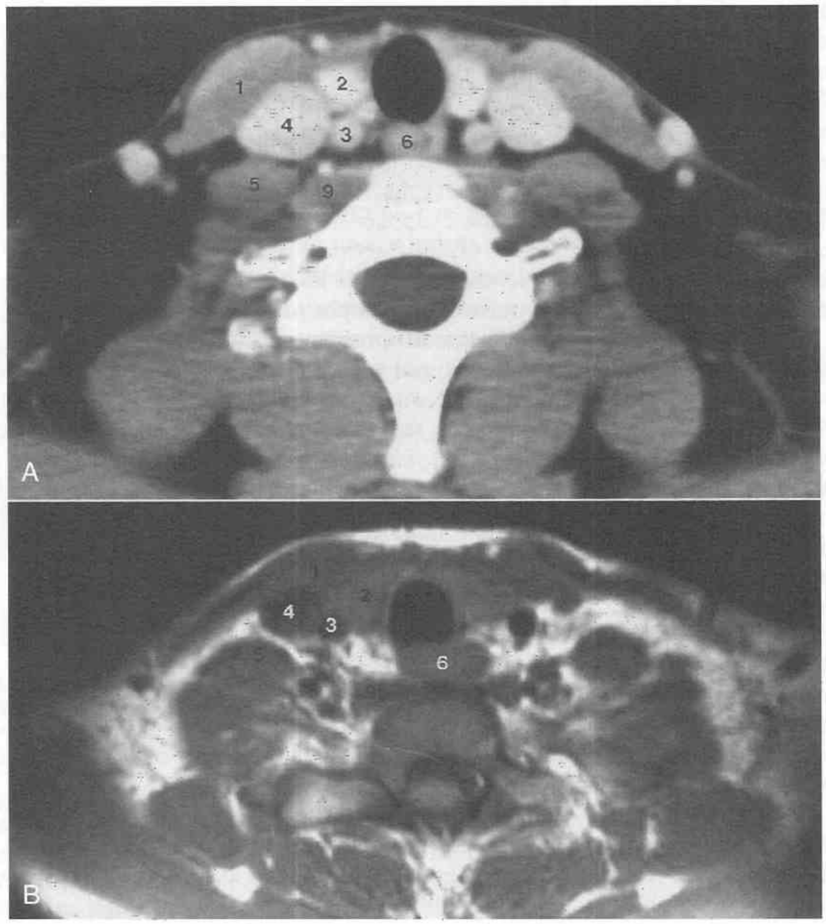

Figure 17–7. Normal axial anatomy at the level of the first tracheal ring. *A*, CT scan. *B*, T1-weighted MR image. Note the relative sizes of the fat-filled posterior triangles and the anterior triangle between the right and left sternocleidomastoid muscles. Compare with Figures 17–2*B* and 17–5*B*. 1, Sternocleidomastoid muscle; 2, thyroid gland; 3, internal carotid artery; 4, internal jugular vein; 5, anterior scalene muscle; 6, esophagus; 9, longus colli muscle.

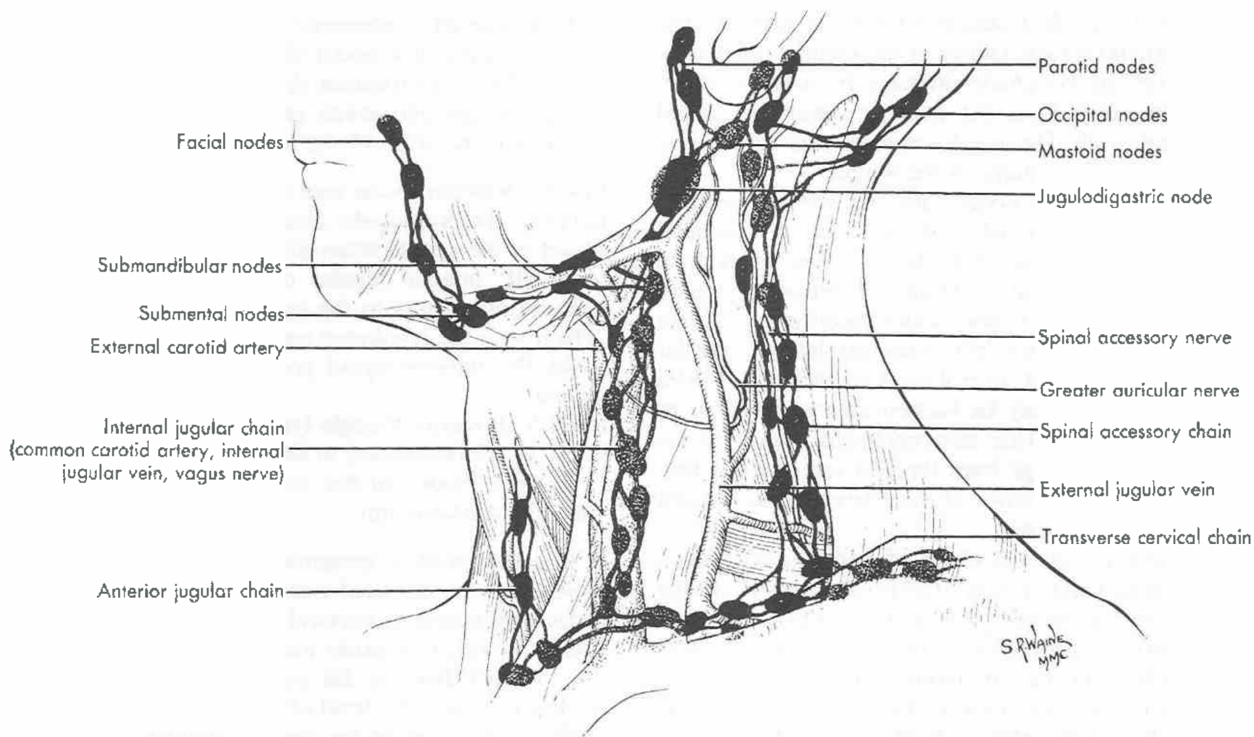

Figure 17–8. Nodal chains of the neck. (From Reede DL, Bergeron RT: CT of cervical lymph nodes. J Otolaryngol 11:411, 1982.)

sheaths. There are two divisions to this nodal group. The superficial division lies on the anterior surface of the strap muscles, following the course of the anterior jugular vein. The deep division of the anterior cervical nodes (also known as the juxtavisceral nodes or anterior compartment nodes) is located anterior to the larynx, thyroid gland, and trachea as well as in the tracheoesophageal groove. Included in the deep division is the Delphian node, located in the cricothyroid membrane of the larynx. The deep division drains the supraglottic and infraglottic larynx, piriform sinuses, thyroid gland, trachea, and esophagus.

The lateral cervical group constitutes the primary nodes of clinical interest in head and neck malignancies because it serves as a common route of drainage for all of the major regional structures. Similar to the anterior cervical nodes, the lateral cervical nodes are divided into superficial and deep divisions. The nodes in the superficial division follow the course of the external jugular vein. The deep division of lateral cervical nodes is further subdivided into the spinal accessory, internal jugular, and transverse cervical chains.

The spinal accessory chain of nodes follows the course of the spinal accessory nerve (cranial nerve XI) in the posterior triangle of the neck, deep to the sternocleidomastoid muscle. The spinal accessory chain receives drainage from the occipital and mastoid nodes as well as the lateral portions of the neck and shoulders.

The internal jugular chain of nodes follows the course of the internal jugular vein. At the superior aspect of this chain under the skull base, it is impossible to separate the internal jugular chain from the superior aspect of the spinal accessory chain. As the internal jugular vein descends in the neck, it is crossed by two muscles, the posterior belly of the digastric muscle superiorly and the omohyoid muscle inferiorly. At each junction of muscle and vein, a single lymph node, larger than adjacent nodes, is present. The jugulodigastric node (also known as the sentinel or tonsillar node) receives the lymphatic drainage from the submandibular nodes as well as the palatine tonsil and lateral oropharyngeal wall. The jugulo-omohyoid node receives all of the lymphatic drainage of the tongue.

The internal jugular nodes (also known as the deep cervical nodes) are arranged either in series or in parallel interconnecting rows adjacent to the vein. The nodes drain the parotid, submandibular, submental, retropharyngeal, and some anterior chain nodes. Nodes superior to the point where the omohyoid muscle crosses the internal jugular vein are usually located anterolateral to the vein. Nodes inferior to this point may be located anterior, medial, or posterior to the vein. This infraomohyoid node also receives lymphatic drainage from the arm and superior thorax. Among the most inferior of the internal jugular nodes are the nodes of Virchow.

The transverse cervical chain of nodes (also known as the supraclavicular nodes) follow the course of the transverse cervical vessels. The nodes in this chain connect the inferior aspects of the spinal accessory, internal jugular, and anterior jugular chains. The transverse cervical chain also receives drainage from the subclavicular nodes, the skin of the anterolateral neck, and the upper chest wall.

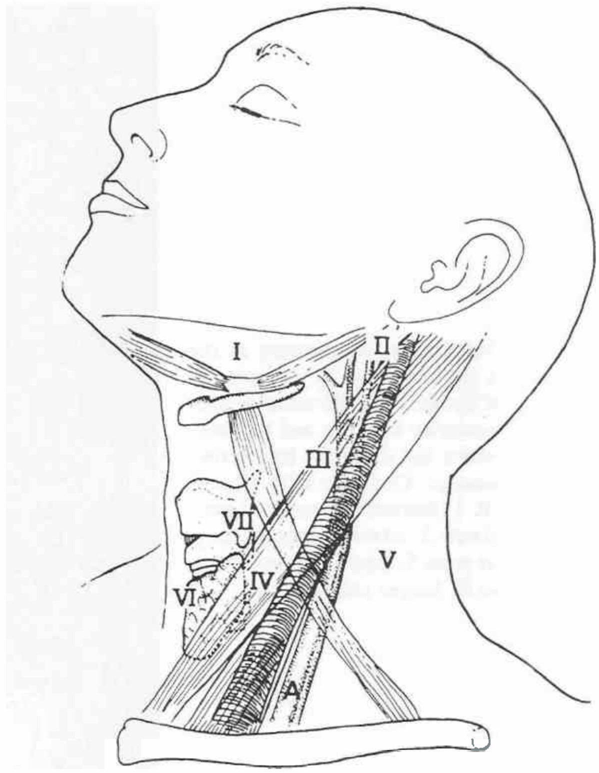

Figure 17–9. Simplified nodal classification. Diagram of the head and neck in left anterior oblique projection. Palpable nodes are indicated with use of a simplified nomenclature of Roman numerals I through VII. See text for explanation. (From Som PM: Lymph nodes of the neck. Radiology 165:596, 1987.)

In an attempt to eliminate the variations in nodal terminology, a simplified nodal classification was proposed in 1981.[36] This classification divides the clinically palpable cervical nodes into seven groups, each designated by a roman numeral (Fig. 17–9), as follows:

Level I: Submandibular and submental lymph nodes.
Level II: Internal jugular chain from the skull base to the level of the carotid bifurcation.
Level III: Internal jugular chain from the level of the carotid bifurcation to the level of the intersection of the chain with the omohyoid muscle.
Level IV: Infraomohyoid portion of the internal jugular chain.
Level V: Posterior triangle lymph nodes.
Level VI: Nodes related to the thyroid gland.
Level VII: Nodes in the tracheoesophageal groove and superior mediastinum.

It is important to remember that this system does not include all the cervical lymph nodes. Retropharyngeal nodes and transverse cervical nodes are not included. The system, however, is easily transferred to sectional imaging (Fig. 17–10). Because the carotid bifurcation is typically located at or near the level of the hyoid bone and the level of the intersection of the internal jugular chain with the omohyoid muscle is at the level of the cricoid cartilage,

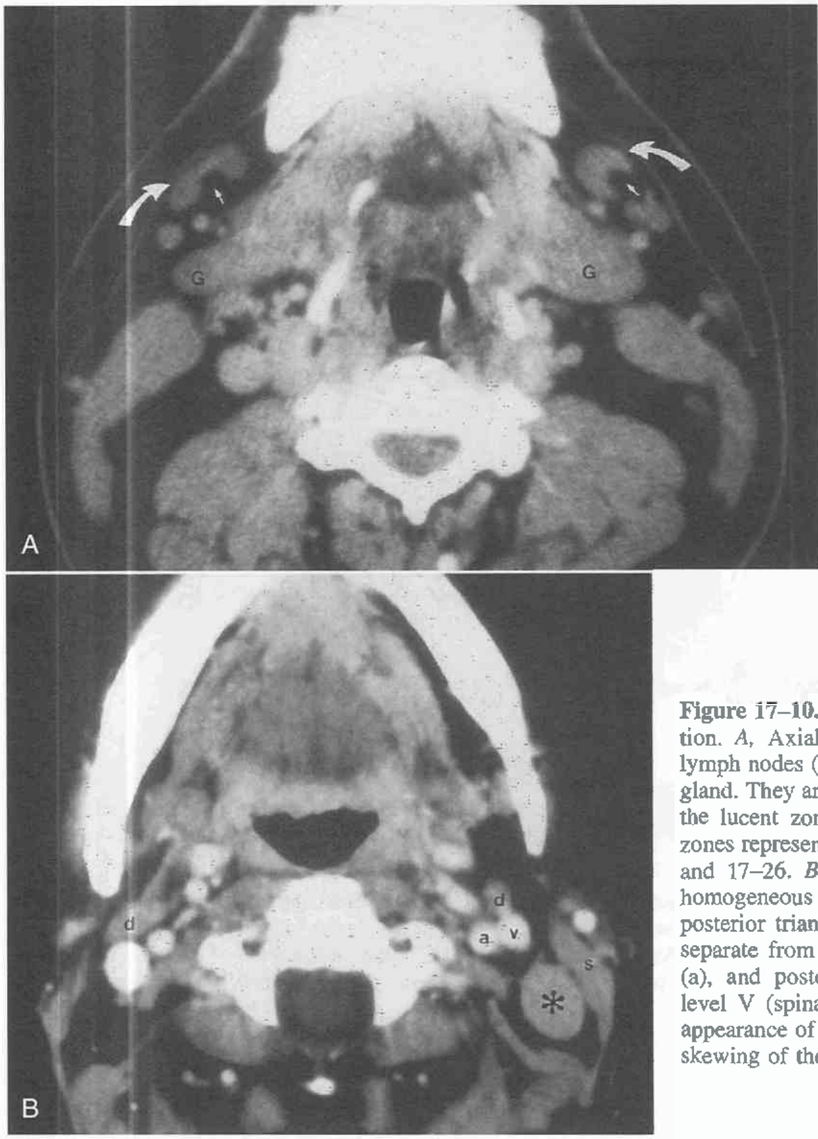

Figure 17–10. Sectional imaging using simplified nodal classification. *A*, Axial contrast-enhanced CT scan demonstrates bilateral lymph nodes (*curved white arrows*) anterior to each submandibular gland. They are level I (submandibular triangle) lymph nodes. Note the lucent zone of fat eccentrically located in each node. These zones represent prominent nodal hila. Compare with Figures 17–12 and 17–26. *B*, Axial contrast-enhanced CT scan demonstrates a homogeneous 2.5-cm diameter lymph node (*asterisk*) in the left posterior triangle deep to the sternocleidomastoid muscle (s) and separate from the internal jugular vein (v), internal carotid artery (a), and posterior belly of the digastric muscle (d). This is a level V (spinal accessory chain) lymph node. Asymmetry in the appearance of right and left digastric muscles is secondary to slight skewing of the patient's head within the scanner gantry.

the following *axial levels* may be used in staging nodal disease at imaging (Fig. 17–11)[42]:

Axial level II: Suprahyoid internal jugular chain.
Axial level III: Infrahyoid internal jugular chain above the cricoid cartilage.
Axial level IV: Infracricoid internal jugular chain.

Patients referred for imaging of cervical lymph nodes typically can be assigned to one of three categories. The first is a patient with a known malignancy of the head and neck in whom nodal staging is required. The second is a patient with a neck mass, already demonstrated by aspiration cytology to be metastatic squamous cell carcinoma, in whom no primary head and neck malignancy is identified. The third is a patient with a neck mass of uncertain origin.

Nodal Staging

CT remains the standard for assessing palpable and nonpalpable nodal metastases in patients with tumors of the head and neck. Based on the work of Mancuso[20,21] and others, the following criteria have been adopted by most centers:

1. Normal lymph nodes are often invisible on CT. When present, these nodes have an ovoid (lima bean) shape and are of homogeneous soft tissue density. Normal lymph nodes typically measure less than 1.0 cm in diameter.
2. Any node measuring more than 1.5 cm in diameter is abnormal. Reactive as well as neoplastic nodes may produce this pattern. Reactive adenopathy is most commonly encountered in submandibular and jugulodigastric nodes.
3. Any node with a central lucency, regardless of size, is abnormal (Fig. 17–12). Nodes with this CT appearance, often referred to as *necrotic*, are focally or completely replaced with tumor (typically, metastatic squamous cell carcinoma). Actual necrosis of nodal tissue is not commonly seen on pathologic examination. Care must be

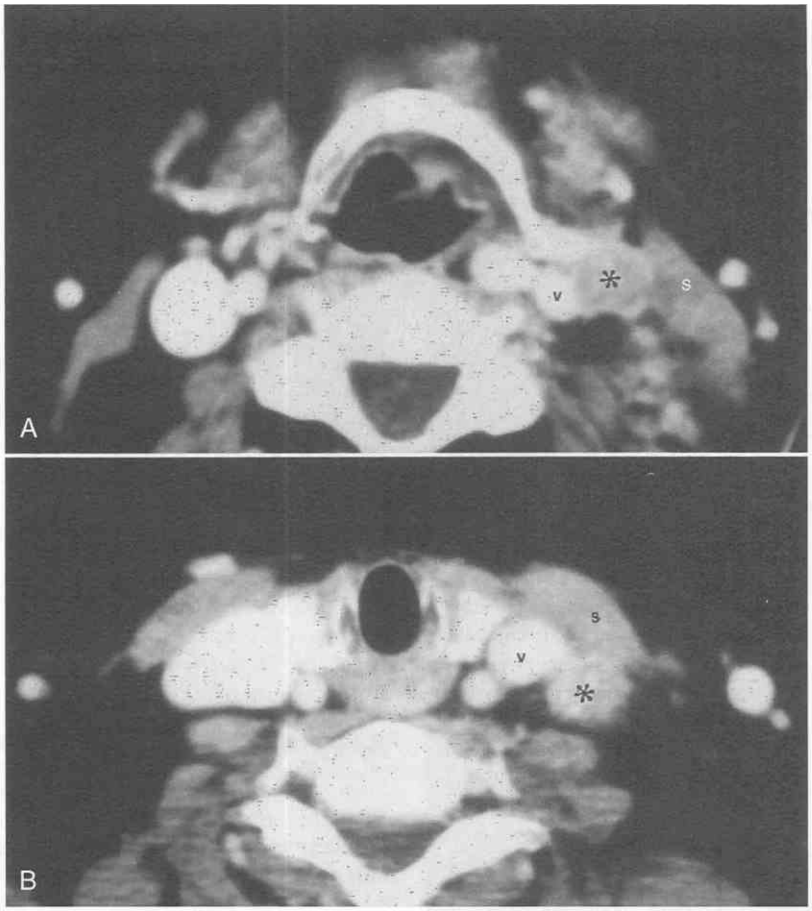

Figure 17–11. Internal jugular chain lymph nodes. *A,* Axial contrast-enhanced CT scan at the level of the hyoid bone demonstrates a 2-cm-diameter lymph node (*asterisk*) medial to the left sternocleidomastoid muscle (s) and lateral to the left internal jugular vein. This lymph node is present at the junction of axial levels II and III. *B,* Axial contrast-enhanced CT scan at the level of the cricoid cartilage demonstrates a 2-cm-diameter lymph node (*asterisk*) immediately posterior to the left internal jugular vein (v). This lymph node is present at the junction of axial levels III and IV.

taken not to mistake the fatty hilum of a normal node for the abnormal lucency. The fatty hilum is located at the periphery of the node (see Fig. 17–10*A*).

4. Obliteration of fascial planes surrounding a node is abnormal. The CT appearance of "dirty fat" surrounding a node may be seen in cases of extranodal spread of tumor or inflammation as well as after surgery or radiation therapy to the neck. In general, extranodal spread of tumor tends to cause a more focal obliteration of fascial planes than the other processes. Correlation with clinical history is essential (see Fig. 17–26).[31]

Many centers with active head and neck tumor services have more stringent criteria for assessing nodal size. Expounding on the pathologic studies of van den Brekel, these centers consider all lymph nodes with a short axis greater than or equal to 1.2 cm significant.[45] An alternative system is to maintain the size criterion of 1.5 cm for submandibular and jugulodigastric nodes but to consider nodes at other levels that measure 1.0 cm or larger to be significant.[42] When these criteria are used, approximately 80% of the enlarged (homogeneous) nodes are secondary to metastatic disease, and 20% are caused by reactive hyperplasia.[31]

When the extranodal changes described here obliterate fascial planes between a lymph node and adjacent structures (muscles, vessels), there may be clinical fixation of the node to these structures. The amount of fixation is subjective, depending on the individual examiner. It is difficult to predict solely on the basis of CT findings whether clinical fixation exists. The only sure sign of nodal fixation is if the structure in question is completely surrounded by a nodal mass. This point is particularly important in evaluation of the internal or common carotid artery.[24] Loss of definition of the vessel wall, with visualization of an otherwise normal lumen, is consistent with infiltration of the vessel wall (Fig. 17–13).

The utility of spin-echo MRI in evaluation of nodal disease remains limited. T1-weighted images usually provide good differentiation between intermediate signal nodes and the surrounding high-intensity fat, allowing for accurate measurement of nodal size. Assessment of central nodal necrosis is more difficult on MRI than on CT. Tumor cells within nodes tend to produce intermediate signal on T1-weighted and T2-weighted images, whereas areas of actual nodal necrosis usually appear as areas of low signal on T1-weighted images and of high signal on T2-weighted

Figure 17–12. Metastases to small lymph nodes. Axial contrast-enhanced CT scan obtained at a level between the hyoid bone and the cricoid cartilage demonstrates two lymph nodes (*white arrows*) in the left internal jugular chain, each measuring 1 cm in diameter with central hypodensity not equal to that of fat. Each of these level III lymph nodes demonstrates a *necrotic center.* Multiple small nodes deep to the left sternocleidomastoid muscle (s) have a homogeneous appearance.

Figure 17–13. Extranodal spread of tumor. Axial contrast-enhanced CT scan demonstrates an irregular interface between the large left necrotic nodal mass and the cervical fat. Anteriorly, the overlying platysma is thickened and irregular (*curved white arrows*). Posterolaterally, there is extension through the platysma into the subcutaneous fat (*straight arrows*). This nodal mass was immobile or "fixed" on physical examination. Note how the mass engulfs the arteriosclerotic left internal carotid artery (*open black arrow*).

images.[47] One practical solution is to consider any lymph node that is heterogeneous in appearance abnormal, but even this alternative can fail if the dynamic gray scale of the images is limited or the signal-to-noise ratio low.[42]

The Unknown Primary

Approximately 5% of all patients with carcinoma and 12% of patients with head and neck carcinoma have nodal metastases as the sole presenting complaint.[40] In cases in which a head and neck malignancy is not appreciated by the otolaryngologist on initial clinical examination, knowledge of the pathways of nodal drainage, in combination with the ability of CT to detect nonpalpable pathologic lymph nodes, allows the radiologist to identify potential sites of neoplasm, particularly when the tumor is predominantly submucosal in nature.

The location of the enlarged lymph node(s) should direct suspicion of the primary site of neoplasm as follows (Fig. 17–14)[31]:

Level I: Oral cavity, submandibular gland.
Level II: Nasopharynx, oropharynx, parotid gland, supraglottic larynx.
Level III: Oropharynx, hypopharynx, supraglottic larynx.
Level IV: Subglottic larynx, hypopharynx, esophagus, thyroid.
Level V: Nasopharynx, oropharynx.
Levels VI and VII: Thyroid, larynx, lung.

Bilateral nodal disease is particularly common in tumors of the soft palate, tongue, epiglottis, and nasopharynx. Isolated nodal disease in the supraclavicular fossa is unlikely to be secondary to a malignancy of the aerodigestive tract; more likely sites are lung, breast, stomach, and thyroid.[42]

Figure 17–14. The unknown primary. Axial contrast-enhanced CT scan demonstrates a clinically palpable pathologic lymph node in level III of the right internal jugular chain (*asterisk*). Flexible nasopharyngoscopy failed to demonstrate a primary neoplasm. CT examination demonstrates asymmetrical soft tissue density in the right paralaryngeal space. Direct laryngoscopy confirmed the diagnosis of squamous cell carcinoma of the laryngeal ventricle.

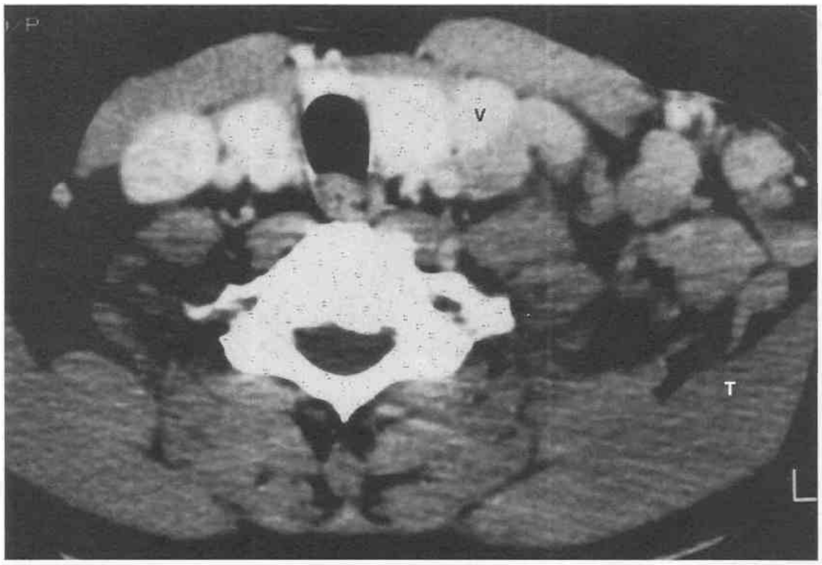

Figure 17–15. Hodgkin's disease. Axial contrast-enhanced CT scan at the level of the first tracheal ring demonstrates multiple enlarged homogeneous lymph nodes filling the left posterior triangle. Lymph nodes adjacent to the internal jugular vein (V) are level IV nodes. Lymph nodes adjacent to the trapezius muscle (T) are level V nodes.

Neck Masses

Isolated nodal masses may mimic a wide variety of lesions in the neck, including masses of congenital, neural, and infectious origins. The key to limiting differential diagnosis is correlation with clinical history. Multiple masses in the neck are most likely secondary to nodal enlargement. Although aspiration cytology or excisional biopsy is necessary to confirm the diagnosis of nodal disease, identification of certain CT patterns of nodal disease facilitates clinical evaluation, as follows:

1. Large homogeneous lymph nodes are most commonly encountered in lymphoma, sarcoid, and infectious mononucleosis. CT cannot reliably differentiate Hodgkin's from non-Hodgkin's lymphoma (Fig. 17–15).[31]
2. Total or relatively uniform enhancement of an enlarged node is usually encountered in inflammatory processes. Exceptions to this rule include nodal involvement by Kaposi's sarcoma, thyroid carcinoma, and renal cell carcinoma (Fig. 17–16).
3. Calcification within lymph nodes is unusual. Most commonly, the calcific deposits are the result of prior granulomatous disease.[28] Metastatic papillary carcinoma of the thyroid is the most common cause of neoplastic nodal calcifications.[42] In rare instances, metastatic or lymphomatous nodes may calcify after irradiation or chemotherapy.[3,5]
4. The presence of multiple nodes with a variety of CT appearances (homogeneous, necrotic, enhancing, and calcified) is most compatible with granulomatous disease of cervical lymph nodes. In urban centers, tuberculosis is the most common cause (Fig. 17–17).[28] Thyroid carcinoma may also produce this spectrum of CT appearances.[42]

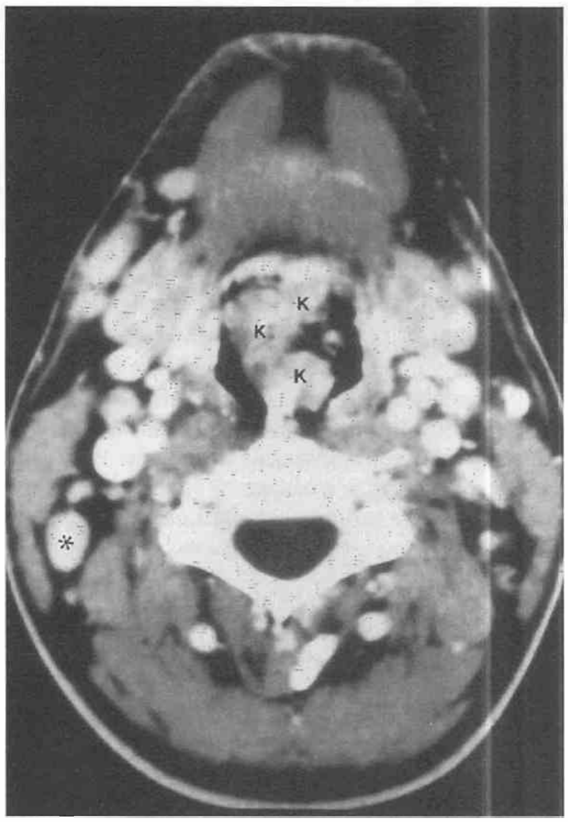

Figure 17–16. Kaposi's sarcoma. Axial contrast-enhanced CT scan at the level of the anterior bellies of the digastric muscles demonstrates multiple, uniformly enhancing masses in the anterior and posterior triangles of the neck bilaterally, the largest identified in the left spinal accessory chain (*asterisk*). Multiple oropharyngeal lesions are also present (K).

Evaluation of Non-Nodal Neck Masses

The CT and MRI appearances of nodal and non-nodal neck masses often overlap. Careful attention to imaging

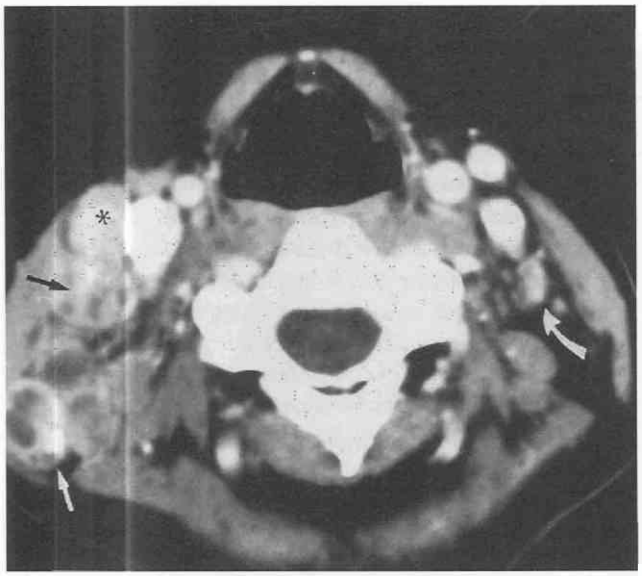

Figure 17–17. Tuberculous adenitis. Axial contrast-enhanced CT scan at the level of the thyroid cartilage demonstrates lymph nodes that are variably homogeneous (*asterisk*), necrotic (*black arrow*), enhancing (*curved white arrow*), and calcified (*straight white arrow*). The patient, who is 12 years old, has little ossification of the thyroid cartilages.

Figure 17–18. Type II second branchial cleft cyst. Axial contrast-enhanced CT scan demonstrates a unilocular cystic mass with minimal rim enhancement along the anterior margin of the left sternocleidomastoid muscle (s) displacing the left submandibular gland (G) anteriorly.

findings and correlation with clinical history are essential to correct diagnosis of a mass of developmental, inflammatory, vascular, neural, or mesenchymal origin.

Masses of Developmental Origin

The most common developmental mass identified on imaging is the branchial cleft cyst. This lesion is the result of incomplete obliteration of the first, second, third, or fourth branchial apparatus. The majority of these lesions arise from the second branchial apparatus, which forms the facial muscles, styloid process, pinna, and portions of the ossicular chain and muscles of the middle ear.[2] The second branchial cleft cyst most commonly identified at imaging is the Bailey type II cyst, which is secondary to persistence of the embryologic cervical sinus.[2] These type II second branchial cleft cysts often manifest as painless fluctuant masses along the course of the anterior margin of the sternocleidomastoid muscle. They most commonly manifest in patients between the ages of 10 and 40 years but may become clinically obvious at any age.[33]

On contrast-enhanced CT (Fig. 17–18), a type II second branchial cleft cyst characteristically appears as a well-circumscribed, unilocular, low-density mass adjacent to the anterior margin of the sternocleidomastoid muscle. CT attenuation measurements of these and other cystic masses range from 10 to 25 HU.[11] On MRI (Fig. 17–19), the contents of the cyst are usually isointense with cerebrospinal fluid on T2-weighted images. On T1-weighted images, the cyst contents are usually hyperintense to cerebrospinal fluid and may even be hyperintense to skeletal muscle.[18]

The extent of rim enhancement of branchial cleft cysts is variable. Thick rim enhancement and indistinctness of fascial margins may occur if the cyst becomes infected. Septations are uncommon and are usually found only in cases of previous infection or needle aspiration. Infected cysts may mimic necrotic jugular chain lymph nodes or cervical abscesses on both CT and MRI.

If sufficiently large, the type II second branchial cleft cyst displaces the carotid artery and jugular vein medially or posteromedially. In contrast, the type III second branchial cleft cyst courses between the external and internal carotid arteries.[2]

Cystic hygroma is the most common form of lymphagiomatous malformation occurring in the neck. Although there are multiple theories of pathogenesis for lymphagiomas, most experts believe that cystic hygromas form because the primordial lymphatic sacs failed to drain into the veins, resulting in hugely dilated cystic lymphatic spaces.[46]

Seventy-five percent of cystic hygromas occur in the neck, and 20% in the axilla. Cystic hygromas are usually isolated malformations in patients in whom the remainder of the lymphatic system is normal. They may occasionally be associated with a more generalized failure of lymphatic system development, as seen in cases of the 45,X chromosome karyotype (Turner's syndrome).[48]

In contrast to branchial cleft cysts, cystic hygromas typically manifest at or shortly after birth. The clinical presentation is often characteristic: a painless, easily compressible mass that may transilluminate on physical examination. Patients are usually asymptomatic, unless there is significant airway obstruction.[33] Cervical cystic hygromas are most commonly found in the posterior triangle but can also occur in the floor of mouth, submental triangle, and submandibular triangles. Because up to 10% of cervical cystic hygromas may extend into the mediastinum, imaging is performed to assess the extent of the lesion and its relationship to adjacent structures before surgical resection.

On contrast-enhanced CT (Fig. 17–20), cystic hygromas are low density in appearance without peripheral rim enhancement. Larger lesions may be multiloculated and are

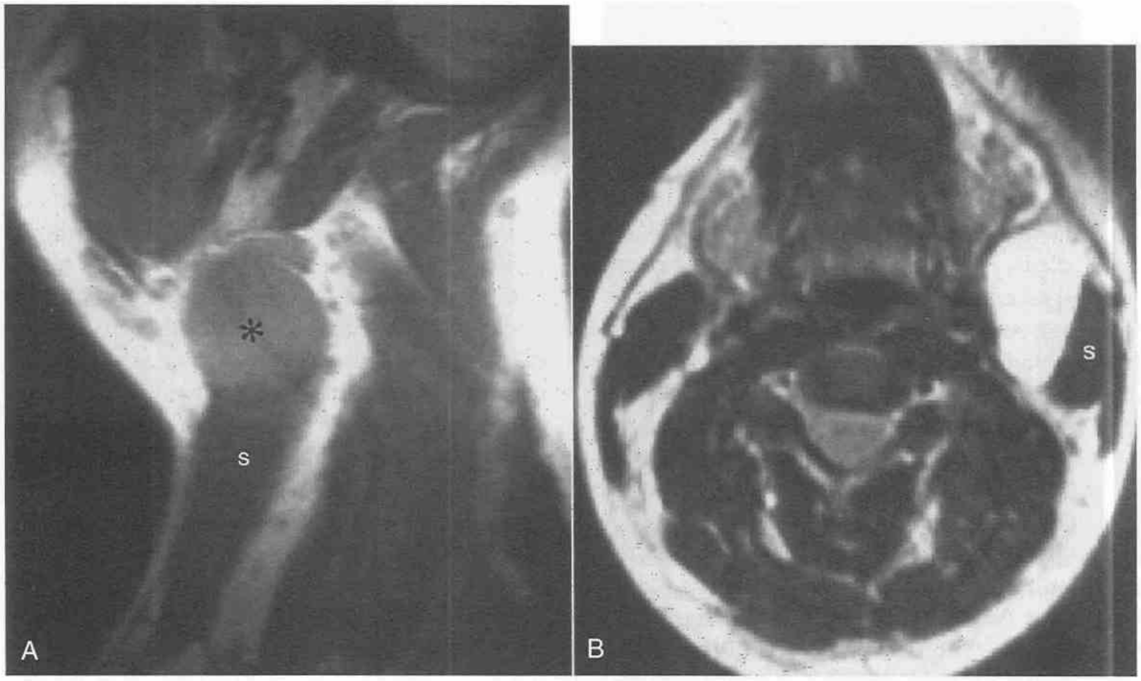

Figure 17–19. Type II second branchial cyst. *A*, Sagittal T1-weighted MR image demonstrates a well-circumscribed anterior triangle mass (*asterisk*) mildly hyperintense to muscle along the anterior margin of the sternocleidomastoid muscle (s). *B*, Axial T2-weighted MR image demonstrates a hyperintense mass along the anterior margin of the left sternocleidomastoid muscle (s). Compare with Figure 17–18.

often poorly circumscribed. In contrast to other cystic-appearing masses in the neck, cystic hygromas typically insinuate themselves between adjacent structures rather than displace vascular or muscular structures.[33]

The multiplanar capability of MRI makes it the ideal imaging modality for evaluating cystic hygromas (Fig. 17–21). On T2-weighted images, the hygromas are isointense with cerebrospinal fluid. Their appearance on T1-weighted images is more variable, either hypointense or hyperintense to skeletal muscle, depending on the relative protein concentration of the lymph fluid and prior episodes of trauma or infection.[18,38]

Thyroglossal duct cysts are the result of incomplete involution of an embryologic tract, the thyroglossal duct. It is through the duct that the thyroid gland passes during its migration from the foramen cecum in the tongue to its final position in front of the trachea. If any portion of this epithelium-lined duct persists after birth, a cyst may develop. The hyoid bone is intimately associated with the thyroglossal duct during its development; a thyroglossal duct cyst may be located anterior to, posterior to, or within the hyoid bone.[30]

Thyroglossal duct cysts account for approximately 70% of all congenital neck masses, with the overwhelming majority occurring in the pediatric age group. Routine sectional imaging of thyroglossal duct cysts is not performed in children because the clinical presentation (a painless midline neck mass that moves on swallowing) is so typi-

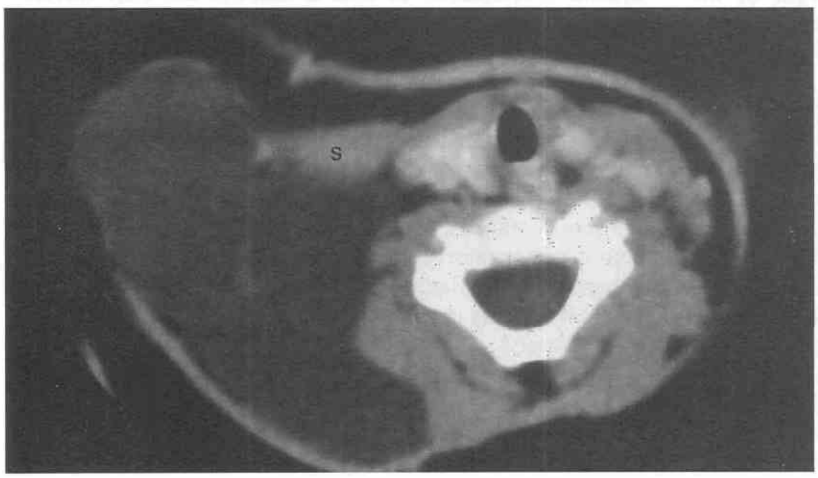

Figure 17–20. Cystic hygroma. Axial contrast-enhanced CT scan at the level of the first tracheal ring demonstrates a multilocular cystic mass without rim enhancement occupying the entire right posterior triangle extending toward the right axilla. S, Sternocleidomastoid muscle.

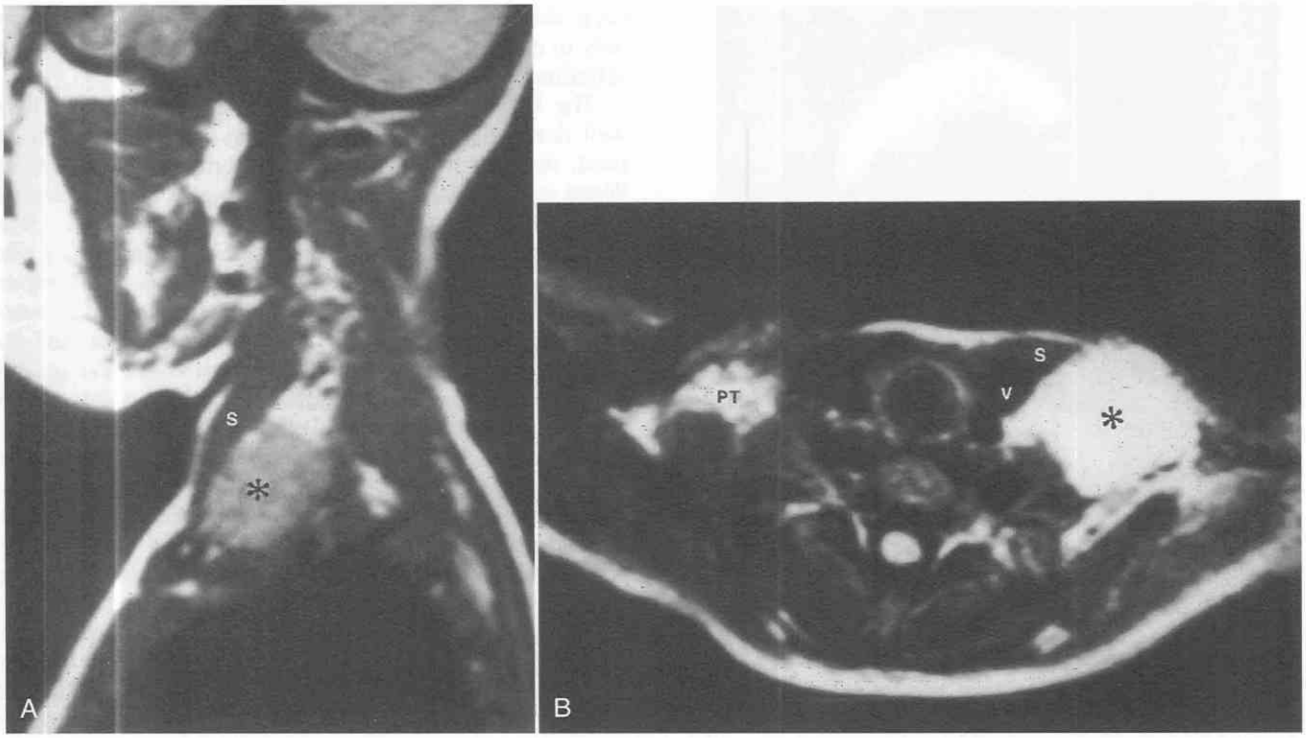

Figure 17–21. Cystic hygroma. *A,* Sagittal T1-weighted MR image demonstrates a lobulated posterior triangle mass (*asterisk*) that is moderately hyperintense to muscle and located deep to the posterior margin of the sternocleidomastoid muscle (s). Note how the hygroma tracks posterior to the internal jugular vein (V). *B,* The hygroma appears virtually isointense to fat in the right posterior triangle (PT), owing to window width and level.

cal.[33] Ultrasonography or radioisotope scanning may be performed to confirm a normal position of the thyroid before surgery.

CT or MRI is usually performed preoperatively in cases of suspected thyroglossal duct cyst in adults to confirm the diagnosis and to exclude other nodal masses. On contrast-enhanced CT, a well-circumscribed, low-density mass is present (Fig. 17–22).[30] Peripheral rim enhancement or internal septations are occasionally seen. The MRI signal characteristics of thyroglossal duct cysts are the same as those of branchial cleft cysts or small cystic hygromas.

Suprahyoid thyroglossal duct cysts are midline in location. The more common infrahyoid thyroglossal duct cysts often have both midline and off-midline components, the latter being embedded in the strap muscles. It is the location of an infrahyoid thyroglossal duct cyst in the strap muscles, not its signal or attenuation characteristics, that allows for a definitive radiographic diagnosis.[30] The presence of a solid mass along the thyroglossal duct should raise suspicion of ectopic thyroid tissue, in which occult malignancy is more likely.

Dermoid cysts are the rarest of the congenital neck

Figure 17–22. Thyroglossal duct cyst. Axial contrast-enhanced CT scan at a level immediately inferior to the hyoid bone demonstrates a cystic anterior triangle mass with peripheral rim enhancement (*asterisk*) embedded within the strap muscles to the right of midline. M, Left strap muscles; S, right sternocleidomastoid muscle.

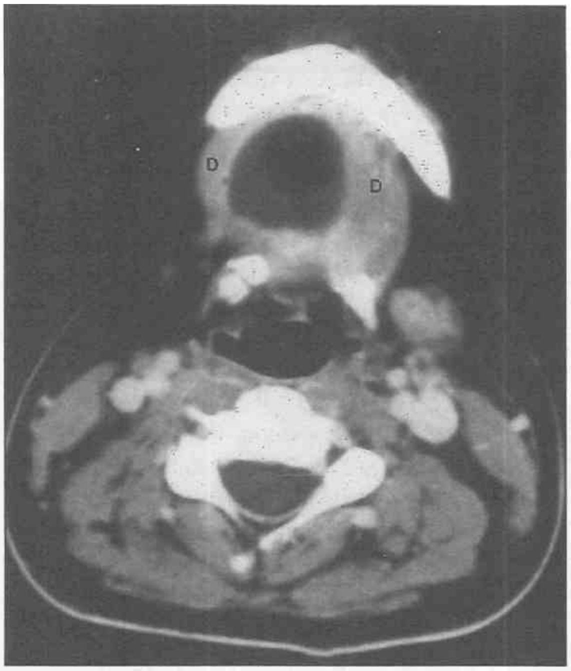

Figure 17–23. Dermoid cyst. Axial contrast-enhanced CT scan demonstrates a mass with peripheral rim enhancement in the submental triangle. The mass contains a fatty component anteriorly and a fluid component posteriorly. D, Anterior bellies of the digastric muscles. The central portion of the hyoid bone is absent because of previous surgery to remove a thyroglossal duct cyst. (From Reede DL, et al: Nonnodal pathologic conditions of the neck. In Som PM, Bergeron RT (eds): Head and Neck Imaging, 2nd ed. St. Louis, CV Mosby, 1991.)

lesions. Only 7% of all dermoid tumors occur in the head and neck. The majority of head and neck dermoids occur in the orbit, nasal cavity, or oral cavity; true cervical dermoids are rare. The term *dermoid cyst* has been used to include the following three types of cysts: (1) epidermoids or epidermal cysts, (2) dermoids, and (3) teratoid cysts.[22,33] These three types of congenital cysts can be differentiated histologically by the presence or absence of an epithelial lining and the cyst contents. Differentiation among the three types of dermoid cysts by sectional imaging is often impossible.

Most cervical dermoid cysts occur in the midline or just off-midline and are usually present at birth. In contrast to thyroglossal duct cysts, dermoid cysts typically do not move with swallowing. On CT, the presence of fat within the mass suggests a diagnosis of dermoid rather than epidermoid (Fig. 17–23. In the absence of demonstrable fat, epidermoids and dermoids cannot be distinguished by CT or MRI.

Masses of Inflammatory Origin

It is often difficult to determine clinically whether a patient with an erythematous, painful, and swollen neck has a simple cellulitis or a potentially life-threatening deep neck abscess. With sectional imaging, it is possible not only to diagnose an abscess but also to differentiate it from cellulitis.[12,33]

The CT characteristics of neck infections have been well described. Abscesses appear as single or multiloculated, low-density masses that conform to fascial spaces. When intravenous iodinated contrast agent is administered, abscesses demonstrate peripheral rim enhancement. Cutaneous and subcutaneous manifestations of infection are also seen. The manifestations include enlargement of adjacent muscles (myositis), thickening of the overlying skin, prominent linear densities within the subcutaneous fat, and enhancement of fascial planes. The presence of these cutaneous and subcutaneous manifestations without a low-density collection is consistent with cellulitis (Fig. 17–24).[12,33]

A "characteristic" appearance of cervical infections on MRI has yet to be defined. In general, abscesses appear as single or multiloculated masses that are hypointense to skeletal muscle on T1-weighted images and markedly hyperintense on T2-weighted images. The use of MRI contrast agents should demonstrate an enhancing rim in a mature abscess. Differentiation of abscesses from other noninfectious masses on MRI requires careful attention to variations in the dynamic gray scale. Particular attention must be paid to window and level settings because subtle changes in cervical fat may be obscured by the hyperintense signal of cervical fat on T1-weighted images (Fig. 17–25).

No studies have yet compared CT and MRI in the evaluation of cervical infection. Several problems have been noted by investigators using MRI to evaluate inflammatory disease: First, the cutaneous manifestations of infection are not obvious on MR images; second, subcutaneous manifestations of infection may be obscured on MR images if imaging parameters are not carefully monitored; third, after intravenous administration of contrast agent, the enhancing rim may become isointense with surrounding fat, limiting detection or delineation of the abscess unless fat-suppression techniques are used; fourth, areas of abscess formation and cellulitis both tend to be hyperintense on T2-weighted images, hampering differentiation between the two processes.[12,33]

The authors prefer the use of contrast-enhanced CT to assess suspected inflammatory disease in adults. In children and in adults whose clinical status precludes the use of iodinated contrast material, MRI is the study of initial choice, although a limited noncontrast CT study may be required for evaluation of osseous integrity. If MRI is not available, ultrasonography is an alternative modality for localizing suspected collections for surgical drainage.

Regardless of the modality used, the following important principles must be remembered:

1. Radiographic changes in the skin, fat, and fascial planes of the neck are not pathognomonic for an infectious process. Inflammatory reactions after radiotherapy or surgery can mimic cervical infections.
2. Radiographically, a necrotic tumor, nodal disease with extension into the adjacent soft tissues, and a thrombosed vessel may all mimic an abscess on sectional images (Fig. 17–26). Clinical correlation is essential.
3. Not every infectious process demonstrates the radio-

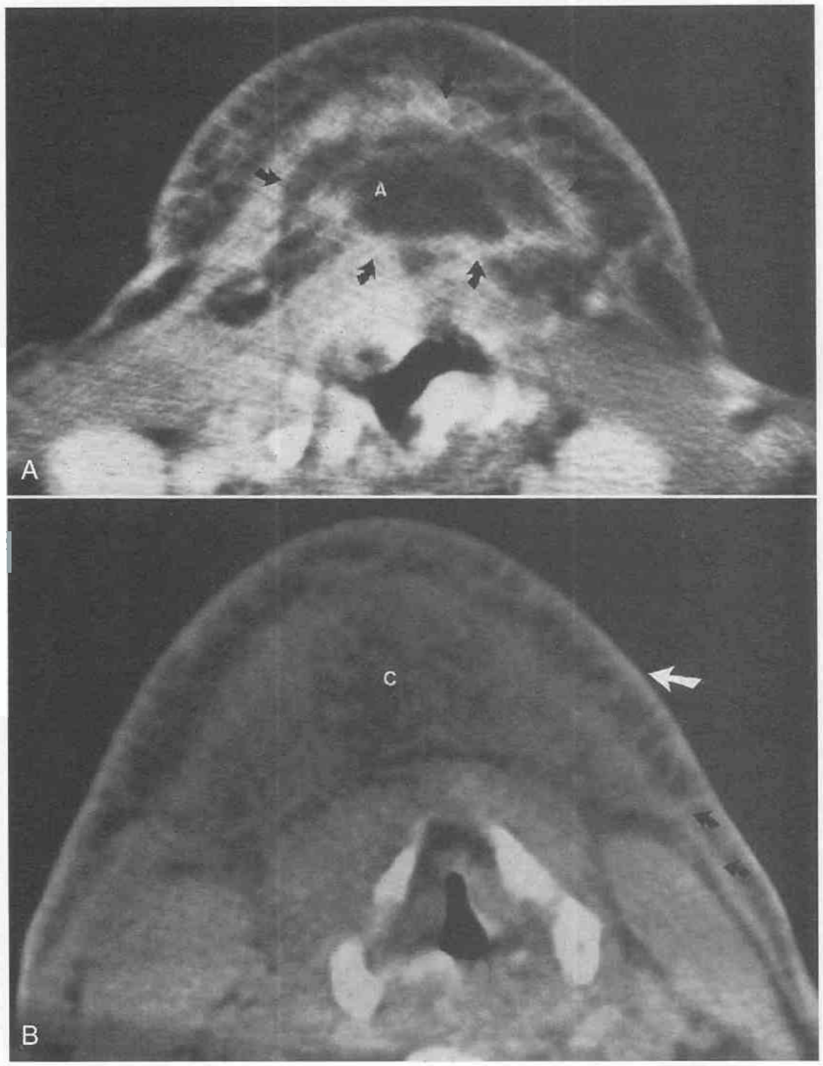

Figure 17–24. Abscess versus cellulitis. *A*, Axial contrast-enhanced CT scan demonstrates a low-density collection (A) in the anterior triangle surrounded by an irregular rim of contrast enhancement (*arrows*) consistent with abscess. *B*, Axial contrast-enhanced CT scan in a different patient demonstrates irregular linear densities in the fat of the anterior triangle (C). There is thickening of the platysma muscle (*black arrows*) and the skin (*white arrow*). No fluid collections are present. This image is compatible with cellulitis. (From Holliday RA, Prendergast NC: Imaging inflammatory processes of the oral cavity and suprahyoid neck. Oral Max Surg Clin North Am 4:215, 1992.)

graphic changes listed here. Granulomatous infections with *Mycobacterium* and occasionally *Actinomycosis* species often appear as "bland" masses, without central necrosis or peripheral cellulitic changes.

4. Inflammatory lesions are always in a state of evolution. It is possible that a patient may be studied before a cellulitis has "ripened" to a frank collection of pus. If a diagnosis of cellulitis is made and the patient shows no response to appropriate antibiotic therapy, a second examination should be performed to ensure that an abscess cavity has not formed.[12,19]

Once a diagnosis of cervical abscess is established, it is important to "map out" the sites of abscess accurately to ensure proper surgical drainage. Cervical infections frequently spread along the fascial planes within the neck. Abscesses are often located within a single compartment or "space" within the neck. The following summary of fascial anatomy is designed to facilitate mapping of cervical infections. It must be acknowledged that any classification of fascial anatomy is somewhat arbitrary because fasciae are simply the more obvious layers of the general connective tissue packing with the body. Nevertheless, the following definitions are stressed in both the anatomical and the surgical literature (Figs. 17–27 and 17–28).

Two cervical fasciae exist, the superficial and the deep.[10, 12, 17, 23, 26,41] The superficial cervical fascia is a layer of connective tissue that surrounds the head and neck, encircling the platysma muscle. The fascia also contains blood vessels, lymphatic channels, cutaneous nerves, and hair follicles. Its primary function is to allow the skin to glide easily over the deeper structures of the neck. Infections that track along the superficial cervical fascia are often secondary to skin infections and rarely track deeper into the neck.

The deep cervical fascia consists of three layers: the superficial layer, known as the investing fascia; the middle layer, known as the visceral fascia; and the deep layer, which has two divisions separated by a potential space—the alar layer anteriorly and the prevertebral layer posteriorly.

The investing fascia surrounds all the important structures of the neck. The visceral fascia surrounds the aerodigestive tract. The deep layer surrounds the vertebral column and paravertebral muscles. All three layers are closely

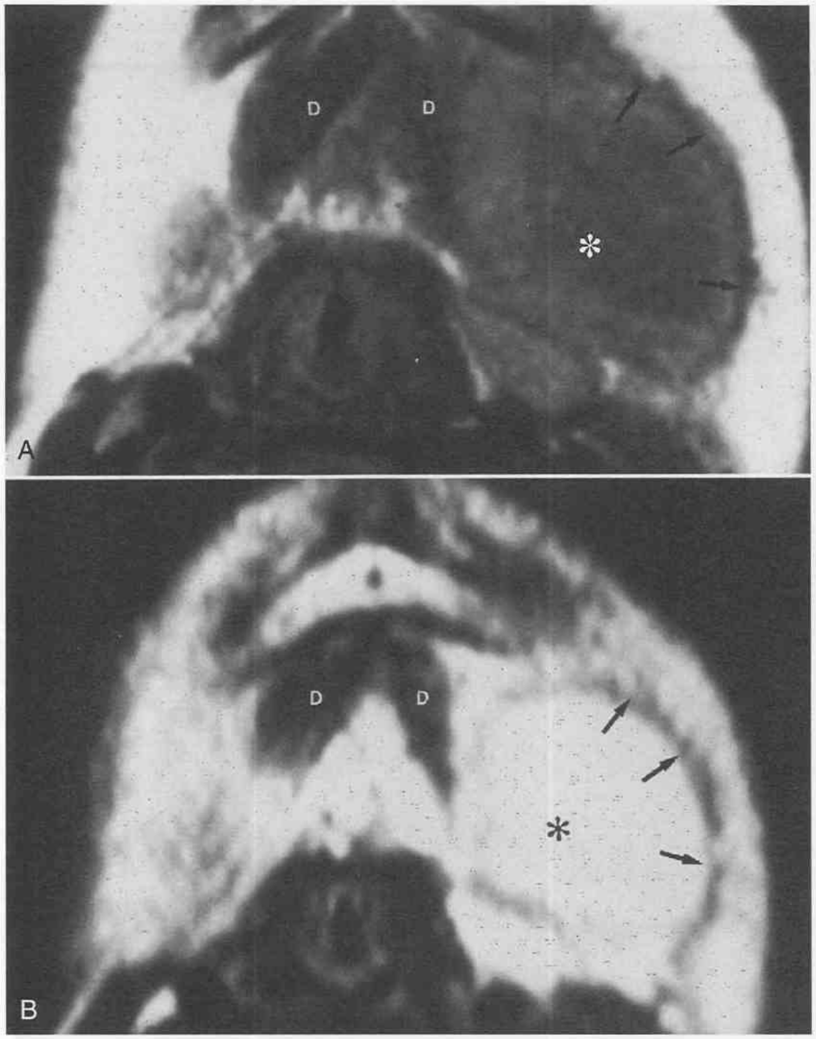

Figure 17–25. Abscess. *A,* Axial T1-weighted MR image demonstrates a mass (*asterisk*) in the right submandibular triangle that is hypointense to the anterior bellies of the digastric muscles. *B,* Corresponding axial T2-weighted MR image demonstrates hyperintense signal within the mass (*asterisk*). Note that inflammatory changes in the fat lateral to the abscess (*arrows*) are not as easily appreciated as on CT scans. (From Holliday RA, Prendergast NC: Imaging inflammatory processes of the oral cavity and suprahyoid neck. Oral Max Surg Clin North Am 4:215, 1992.)

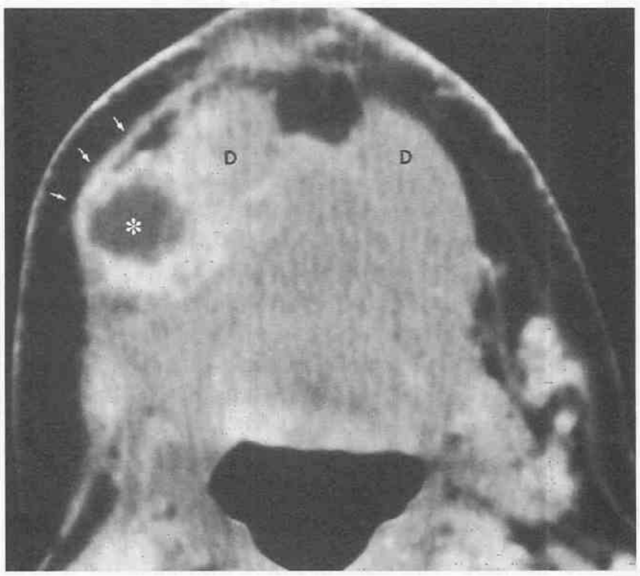

Figure 17–26. Metastatic lymph node mimicking abscess. Axial contrast-enhanced CT scan demonstrates a low-density right submandibular triangle mass (*asterisk*) surrounded by an irregular rim of contrast enhancement. The overlying platysma muscle is thickened. The patient, who was afebrile, had a history of treatment for squamous cell carcinoma of the right oropharynx 2 years before this examination. Needle aspiration of the mass yielded atypical squamous cells.

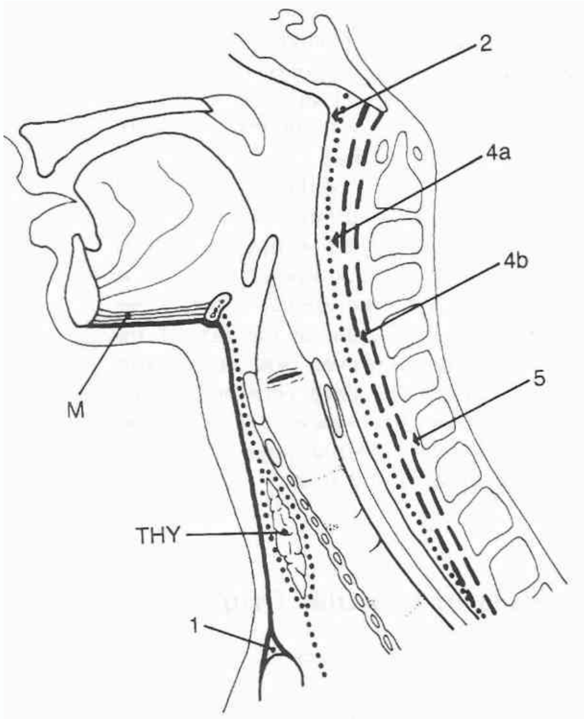

Figure 17–27. The layers of deep cervical fascia and the cervical spaces, sagittal view. *Solid line,* investing fascia; *dotted line,* visceral fascia; *broken line,* prevertebral fascia. 1, Suprasternal space of Burns; 2, visceral space; 4a, retrovisceral component of the retropharyngeal space; 4b, danger space; 5, prevertebral space. M, mylohyoid muscle; THY, thyroid gland. (Adapted from Smoker WRK, Harnsberger HR: Normal anatomy of the neck. In Som PM, Bergeron RT (eds): Head and Neck Imaging, 2nd ed. St. Louis, Mosby Year Book, 1990, pp 498–518.)

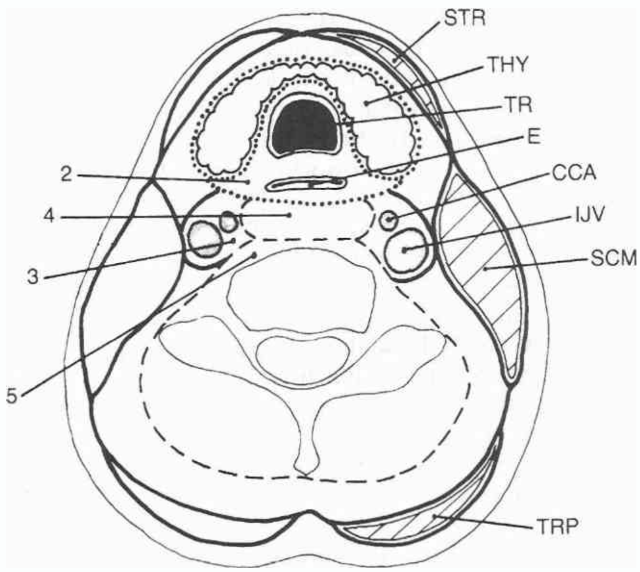

Figure 17–28. The layers of deep cervical fascia and the cervical spaces of the infrahyoid neck, axial view. *Solid line,* investing fascia; *dotted line,* visceral fascia; *broken line,* prevertebral fascia. 2, Visceral space; 3, carotid space; 4, retropharyngeal space; 5, prevertebral space. CCA, common carotid artery; E, esophagus; IJV, internal jugular vein; SCM, sternocleidomastoid muscle; STR, strap muscles; THY, thyroid gland; TR, trachea; TRP, trapezius muscle. (Adapted from Smoker WRK, Harnsberger HR: Normal anatomy of the neck. In Som PM, Bergeron RT (eds): Head and Neck Imaging, 2nd ed. St. Louis, Mosby Year Book, 1990, pp 498–518.)

associated in the anterolateral neck, where they all contribute to the formation of the carotid sheath, which surrounds the carotid artery, internal jugular vein, and vagus nerve.

The investing fascia is attached posteriorly to the ligamentum nuchae and the spinous processes of the cervical vertebral bodies. As it extends anteriorly, the fascia splits to envelope the trapezius and sternocleidomastoid muscles, forming the roof of the posterior triangle. In the suprahyoid neck, the fascia also splits to surround the parotid and submandibular glands before attaching to the body of the hyoid bone and the inferior surface of the mandible.

In the infrahyoid neck, the investing fascia splits to surround the strap muscles anterior to the larynx and trachea. The fascia also invests the omohyoid muscle, holding the muscle close to the clavicle, so contraction of the muscle results in a downward rather than a lateral pull on the hyoid bone. The investing fascia is attached superiorly to the external occipital protuberance, the mastoid process, and the skull base. It is attached inferiorly to the clavicle, the acromion, and the anterior and posterior surfaces of the sternum.

The visceral fascia extends from the central skull base to the mediastinum, encircling the pharynx, esophagus, larynx, and trachea. In the mediastinum, the visceral fascia blends with the pericardium, forming the anterior border of the retropharyngeal space. In the infrahyoid neck, the fascia is attached anteriorly to the cricoid and thyroid cartilages and splits to form the capsule of the thyroid gland.

The deep layer of the deep cervical fascia, like the investing fascia, begins in the posterior midline. The deep layer forms the floor of the posterior triangle, covering the paraspinal and scalene muscles. The deep layer is attached laterally to the transverse processes of the vertebral bodies, where it then splits into the anterior alar and posterior prevertebral layers as they extend anterior to the vertebral body. The alar and prevertebral layers have different craniocaudad extensions; although both attach superiorly at the skull base, the alar layer blends with the visceral layer along the posterior margin of the esophagus at the level of approximately T2, whereas the prevertebral layer extends more inferiorly anterior to the anterior longitudinal ligament.

The three layers of the deep cervical fascia delineate spaces in and through which bacterial infections can spread in the infrahyoid neck. The visceral space includes all structures within the confines of the visceral fascia and is continuous with the anterior mediastinum.

The retropharyngeal space is situated in the midline directly posterior to the pharynx. The anterior boundary of the retropharyngeal space is formed by the visceral fascia, and the posterior boundary is formed by the deep layer of the deep cervical fascia.

The retropharyngeal space can be further divided by the alar layer into the *retrovisceral space* anteriorly and the *danger space* posteriorly. Depending on its location, infection in the retropharyngeal space can extend inferiorly in

the retrovisceral space to the level of approximately T3 (where the alar layer and the visceral layer fuse) or in the danger space inferiorly to the level of the diaphragm. Because it is impossible to separate these two smaller spaces radiographically, the retropharyngeal space may be considered as a single radiographic space, with the recognition that all infections in the retropharyngeal space must be evaluated in full, and scans of either the superior mediastinum or entire chest may be necessary.

Infections of the retropharyngeal space in children are usually secondary to infection of the medial retropharyngeal lymph nodes. In adults, retropharyngeal space infection is most commonly the result of perforation of the posterior wall of the pharynx or esophagus. Infections of the parapharyngeal space or posterior pharyngeal wall, if unchecked, may penetrate the visceral fascia and involve the retropharyngeal space.[12] Regardless of their origin, retropharyngeal space abscesses have a characteristic "bow tie" appearance on axial images that facilitates identification.[7] Sagittal MR images are ideal for definition of the superior and inferior extension of retropharyngeal abscesses before surgical intervention (Fig. 17–29).

The prevertebral space includes those structures (vertebral bodies, paravertebral and scalene muscles, vertebral arteries) that are surrounded by the deep layer of the deep cervical fascia. Lying posterior to the retropharyngeal space, the prevertebral space may be further divided into anterior and posterior compartments by the attachment of the deep layer of deep cervical fascia to the transverse processes. Infections of the prevertebral space are usually secondary to vertebral infection (osteomyelitis) or posterior extension arising in the retropharyngeal space.

The carotid space is a potential space within the carotid sheath. Because little areolar tissue is present within the sheath, actual infection of the carotid space is rare. The carotid sheath, however, with its contributions from all three layers of the deep cervical fascia, is a conduit of infection from one space to another. Septic or reactive thrombosis of the internal jugular vein may produce swelling within the carotid space.[12]

Figure 17–29. Retropharyngeal space abscess. Sagittal T2-weighted MR image demonstrates a hyperintense mass in the retropharyngeal space (*asterisks*) with anterior displacement of the airway. The abscess extends inferiorly to the level of the third thoracic vertebra (T3), implying involvement of the retrovisceral space rather than the danger space. (From Holliday RA, Prendergast NC: Imaging inflammatory processes of the oral cavity and suprahyoid neck. Oral Max Surg Clin North Am 4:215, 1992.)

Masses of Vascular Origin

Asymmetry in the diameter of the internal jugular veins is a normal variant and should not be confused with a mass (see Fig. 17–6). Tortuous arterial vessels may manifest as a pulsatile mass in the supraclavicular fossa or neck. Masses lying in close proximity to the internal or common carotid arteries may transmit normal arterial pulsations. Sectional imaging can differentiate between these "pulsatile" masses and aneurysms of the cervical arterial system.

Internal jugular vein thrombosis, most commonly secondary to central venous catheterization or intravenous drug abuse, is readily diaguosed on sectional imaging. On contrast-enhanced CT, the central portion of the thrombosed vessel is usually less dense than contrast-enhanced blood. Enhancement of the wall of the vein is often present and may extend into surrounding fascial planes.[1] A number of lesions may mimic a thrombosed vein on one or more sequential CT scans. Lesions that may be confused with a thrombosed vessel include necrotic lymph nodes, cervical abscesses, infected branchial cleft cysts, and thrombosed carotid arteries (Fig. 17–30). In most cases, careful analysis of sequential images and correlation with clinical history can distinguish venous thrombosis from other lesions.[33]

In the evaluation of venous patency with MRI, care must be taken not to confuse flow-related enhancement with thrombosis. The MRI diagnosis of venous thrombosis often requires partial flip angle imaging or phase imaging to confirm findings identified on spin-echo sequences.[4]

Paragangliomas, commonly known as glomus tumors, are neoplasms of neural crest cell origin that arise within the adventitial layer of blood vessels at multiple sites in the head and neck, including the middle ear (glomus tympanicum), parapharyngeal space (glomus jugulare), and larynx. The two most common paragangliomas to present as a neck mass arise at the carotid bifurcation (carotid body tumor) and along the nodose ganglion of the vagus nerve (glomus vagale). Such a mass typically manifests as a painless slow-growing mass in the anterior triangle of the suprahyoid neck. The mass is commonly pulsatile, and a bruit may be auscultated over it.[33]

The most constant feature of the glomus vagale or

Figure 17–30. Internal jugular vein thrombosis. *A,* Axial contrast-enhanced CT scan at the level of the cricoid cartilage demonstrates hypodensity with peripheral rim enhancement (*curved white arrow*) lateral to the right common carotid artery (A). 3, Left common carotid artery; IJV, left internal jugular vein. *B,* Axial contrast-enhanced CT scan at the level of the jugular vein (*curved white arrow*) and the necrotic left internal jugular chain lymph node (*white arrow*) metastatic from the left supraglottic carcinoma (*white arrowheads*). Arteriosclerotic change is present in the common carotid arteries bilaterally (A).

carotid body tumor on CT scans is intense enhancement after intravenous contrast administration. Dynamic CT scanning after bolus contrast administration has been reported as a reliable method of differentiating paragangliomas from schwannomas, because the former have a vascular flow curve but the latter do not.[43]

MRI has all but replaced dynamic CT in the imaging evaluation of suspected glomus or carotid body tumors. Paragangliomas more than 1.5 cm in diameter should demonstrate curvilinear areas of signal void representing areas of high vascular flow (Fig. 17–31).[25] Schwannomas, which classically are avascular lesions on angiography, do not demonstrate areas of signal void.[33]

Identifying areas of signal void within a neck mass on MRI allows the confident diagnosis of paraganglioma only if the mass is present in the correct location. Carotid body tumors arise in the juxtahyoid neck and separate the internal and external carotid arteries on sectional imaging. Glomus vagale tumors arise in the suprahyoid neck and displace the internal carotid artery anteromedially and the internal jugular vein posterolaterally. Other neck masses with areas of signal void on MRI, such as nodal metastases from renal cell or thyroid carcinoma,[42] do not demonstrate these vascular displacements. This MRI appearance is not pathognomonic for paraganglioma and may be seen in a variety of high-flow lesions. An imaging diagnosis of paraganglioma should prompt a careful search for additional lesions because multiple glomus tumors occur in up to 10% of the general population and in up to 33% of patients with a family history of paraganglioma.[27]

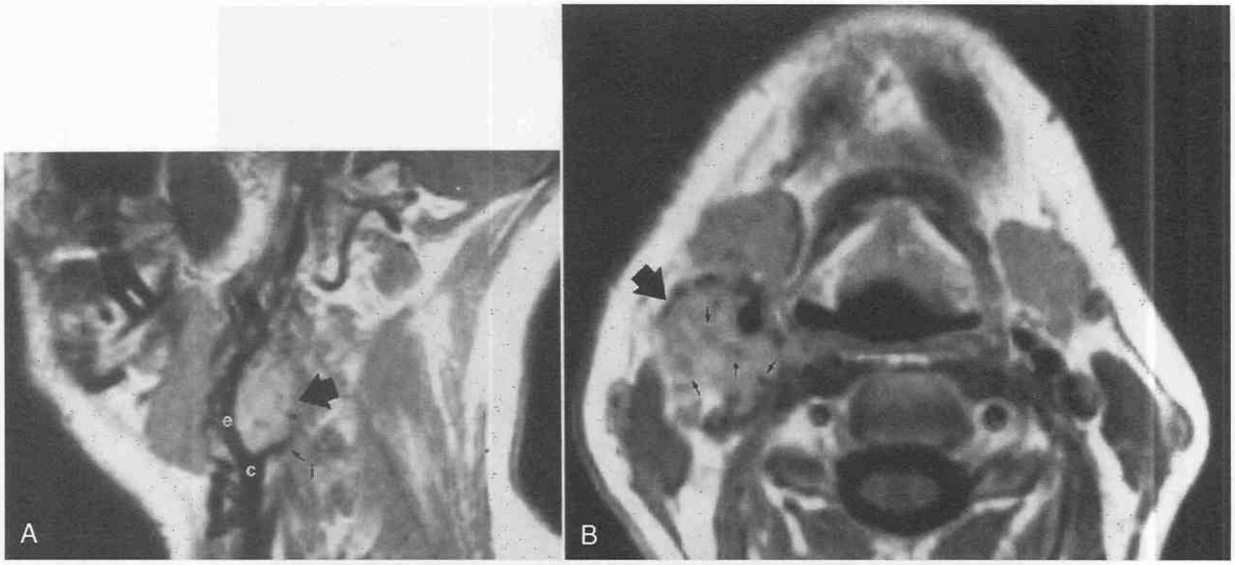

Figure 17–31. Carotid body tumor. *A,* Sagittal T1-weighted MR image demonstrates a heterogeneous mass (*arrow*) at the bifurcation of the common carotid artery (c) splaying the external (e) and internal (i) carotid arteries. *B,* Axial T1-weighted MR image at the level of the hyoid bone in the same patient demonstrates a right anterior triangle mass (*large black arrow*) with multiple internal areas of relative signal void (*small black arrows*).

Masses of Neural Origin

Schwannomas and neurofibromas are the most common types of neurogenic tumors found in the head and neck. Common sites for schwannomas and neurofibromas in the neck are the vagus nerve (cranial nerve X), the ventral and dorsal cervical nerve roots, the cervical sympathetic chain, and the brachial plexus. Associated motor dysfunction and pain in the distribution of a sensory nerve are inconstant clinical findings.[15]

Without a clinical history of neurofibromatosis, it is impossible to distinguish between these two neural masses on sectional imaging. Most neural tumors appear hypodense or isodense to skeletal muscle on noncontrast CT. These tumors tend to be hypointense or isointense to skeletal muscle on T1-weighted MR images and variably hyperintense on T2-weighted images. Variations in the CT or MRI appearance of masses of neural origin are commonly thought to be secondary to variations in cellularity or lipid content. The enhancement pattern of neural tumors is highly variable. Intense, uniform enhancement, inhomogeneous enhancement, and lack of enhancement have all been reported. It is not unusual for an isolated schwannoma to be mistaken for a nodal mass on sectional imaging (Fig. 17–32).[11, 18, 29, 42]

The correct imaging diagnosis of a neural tumor requires a thorough knowledge of the normal anatomy of the major nerves in the neck. A tumor arising from the vagus nerve manifests as a mass in the anterior triangle, displacing the internal or common carotid artery anteromedially and the

Figure 17–32. Schwannoma. Axial contrast-enhanced CT scan at the level of the hyoid bone demonstrates a heterogeneous mass (*curved white arrow*) deep to the right sternocleidomastoid muscle. An initial radiographic diagnosis of nodal metastases was offered because of the location of the mass posterior to the internal jugular vein (v) and the patient's history of prior right facial melanoma.

Figure 17–33. Vagal schwannoma. Axial contrast-enhanced CT scan at the level of the thyroid notch demonstrates a predominantly low-density mass (*curved white arrow*) deep to the anterior margin of the right sternocleidomastoid muscle (s) that is splaying the internal jugular vein (v) and the internal carotid artery (I). e, External carotid artery.

internal jugular vein posterolaterally (Fig. 17–33).[14] Neoplasms of the cervical nerve roots manifest a mass in the posterior triangle, which may extend into one of the neural foramina of the cervical spine (Fig. 17–34). Sympathetic chain tumors demonstrate a constant relationship with the longus colli muscles. Brachial plexus schwannomas and neurofibromas in the infrahyoid neck often displace the anterior scalene muscle anteriorly.[39]

Masses of Mesenchymal Origin

Lipomas are the most common cervical neoplasms of mesenchymal origin. They typically manifest as painless, slow-growing masses, occurring most commonly in the midline of posterior neck or the posterior triangle. Their CT appearance—a homogeneous, nonenhancing mass isodense with subcutaneous fat—is diagnostic (Fig. 17–35).[33,44] The overwhelming majority of lipomas identified on MRI are isointense to subcutaneous fat on all pulse sequences. Lipomas may or may not have a demonstrable capsule on sectional images. Liposarcomas arise from totipotential mesenchymal cells and are rarely encountered in the head and neck. Liposarcomas occur de novo and are not the result of malignant degeneration of preexisting lipomas. Liposarcomas are differentiated from lipomas on the basis of their faster growth rate and the presence of soft tissue and mucoid elements admixed with fat on sectional imaging.

None of the remaining mesenchymal tumors can be confidently diagnosed by sectional imaging alone. These rare lesions tend to appear largely isodense or isointense to skeletal muscle on noncontrast CT or T1-weighted MR images. Inhomogeneous contrast enhancement is usually observed. Rhabdomyosarcoma and other malignant mesenchymal tumors tend to destroy bone and distort soft tissue planes.[16] Desmoids and other benign mesenchymal tumors tend to have sharply circumscribed borders and typically do not infiltrate adjacent soft tissue or destroy bone.[8] The primary role of imaging is one of lesion localization, not lesion characterization.

Masses Arising from the Aerodigestive Tract

Masses may be detected on sectional images of the neck that represent cervical extensions of diseases arising within the oral cavity, larynx, or hypopharynx. A *ranula* is a mucous retention cyst that arises from an obstructed sublingual or minor salivary gland in the floor of the mouth. Simple ranulas are limited to the sublingual space and are seen as intraoral mass lesions. Diving (or plunging) ranulas herniate through or around the mylohyoid muscle and extend into the submandibular triangle. Diving ranulas have been likened to pancreatic pseudoceles because they both contain proteolytic enzymes that allow the mass to infiltrate adjacent tissues.

On CT, ranulas are thin-walled unilocular homogeneous cystic lesions. As with congenital cystic masses, prior infection or surgical intervention results in septations or irregular rim enhancement (Fig. 17–36).[8] On MRI, ranulas are typically hypointense to skeletal muscle on T1-weighted images and isointense to cerebrospinal fluid on T2-weighted images. An imaging diagnosis of diving ranula should be considered only when the lesion abuts or involves the sublingual space. The multiplanar capacity of MRI may facilitate documentation of a *tail of tissue* within the floor of mouth.[18]

A laryngocele is an abnormal dilatation of the saccule (appendix) of the laryngeal ventricle. Although a small proportion of laryngoceles are congenital, the majority are the result of chronic increases in intralaryngeal pressure. Neoplasms or localized inflammation and edema may partially obstruct the ventricle. The resulting ball-valve mechanism traps air within the saccule. Mucus produced by the respiratory epithelium of the ventricle may result in a fluid-filled laryngocele (*laryngeal mucocele*). Internal laryngoceles are limited to the paralaryngeal space. External or combined internal and external laryngoceles extend from the paralaryngeal space into the anterior triangle of the neck via fenestrations in the thyrohyoid membrane.[9] On CT or MRI, the external component of a laryngocele appears as

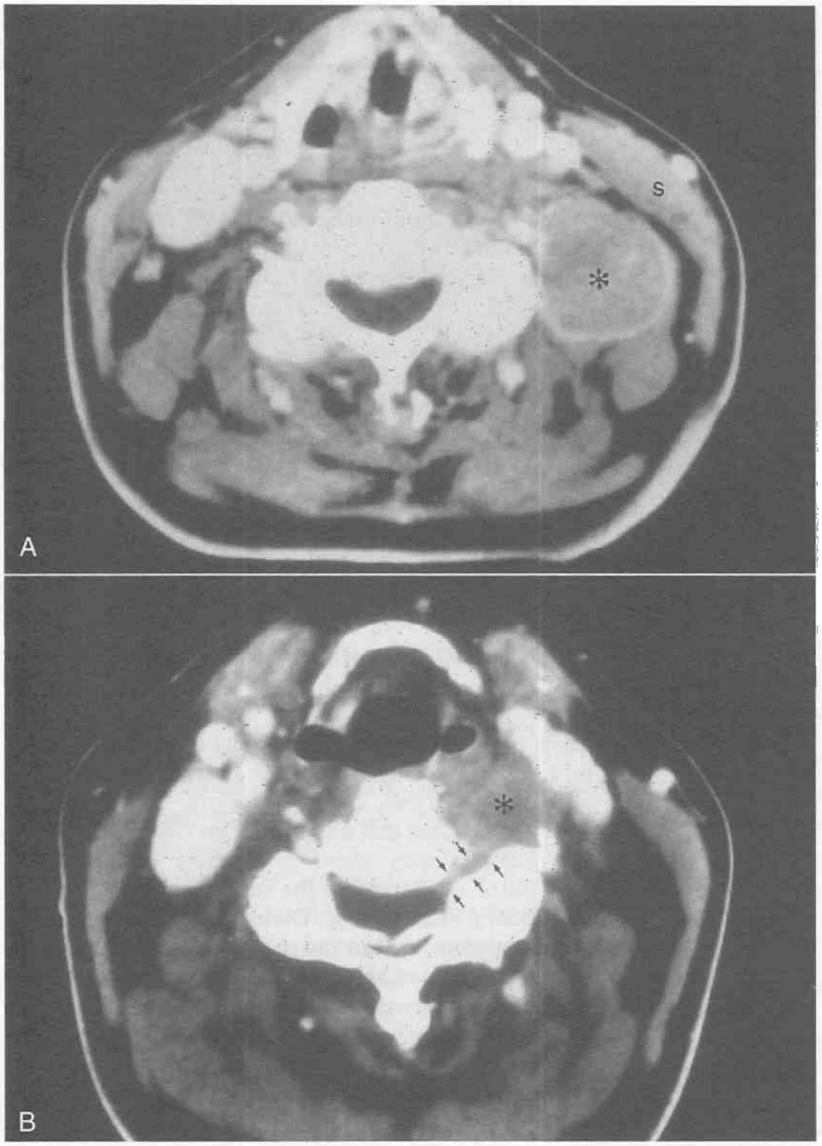

Figure 17–34. Dorsal cervical nerve root schwannoma. *A*, Axial contrast-enhanced CT scan at the level of the thyroid cartilages demonstrates a rim-enhancing solid posterior triangle mass (*asterisk*) deep to the left sternocleidomastoid muscle (S). On this single image, differentiation of neural tumor from enhancing lymph node would be impossible. *B*, Axial contrast-enhanced CT scan at the level of the hyoid bone demonstrates that the mass (*asterisk*) involves the neural foramen (*arrows*), allowing the correct radiologic diagnosis of neural tumor.

Figure 17–35. Lipoma. Axial contrast-enhanced CT image at the level of the thyroid notch in an adolescent patient demonstrates a uniform-fat-density mass in the anterior triangle (L), superficial to the right strap muscles (S). Imaging was performed to exclude the possibility of thyroglossal duct cyst. Compare with Figure 17–22.

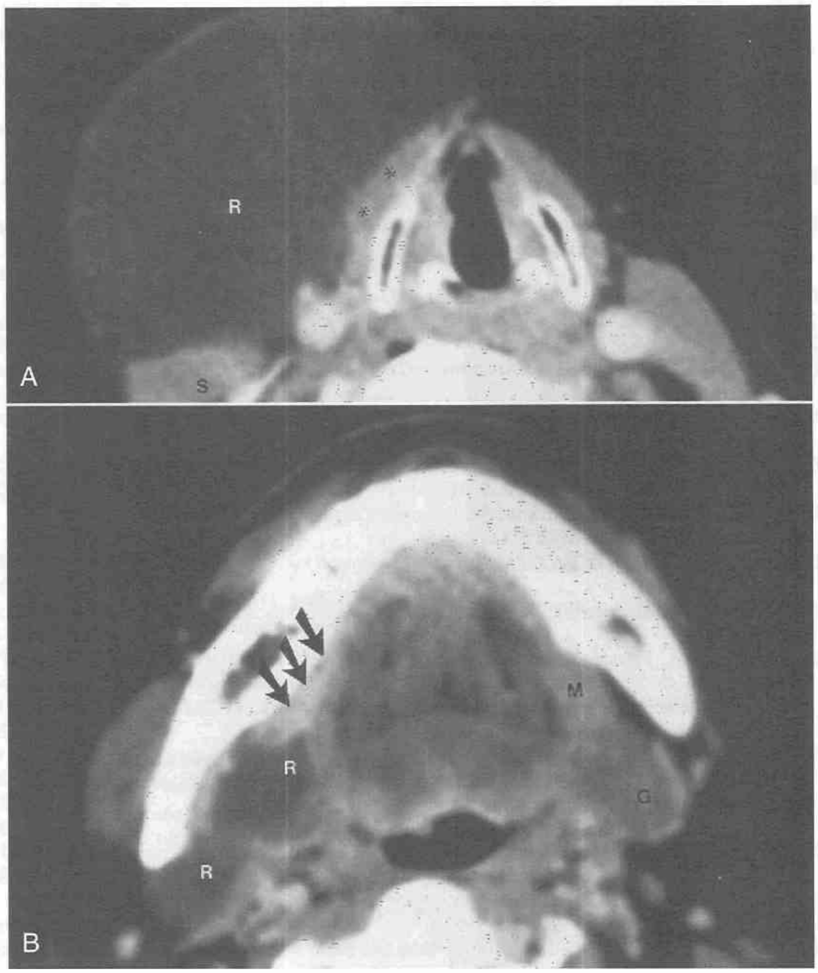

Figure 17–36. Ranula. *A,* Axial contrast-enhanced CT scan at the level of the thyroid cartilage demonstrates a unilocular cystic anterior triangle mass deforming the anterior margin of the right sternocleidomastoid muscle (S). On the basis of this single image, differential diagnosis would include second branchial cleft cyst, lymphangioma, and necrotic lymph node. Thyroglossal duct cyst should be excluded from the differential diagnosis because the mass is extrinsic to the strap muscles (*asterisks*). *B,* Axial contrast-enhanced CT image at the level of the mandible demonstrates the origin of the ranula in the posterior oral cavity, medial to the enhancing mylohyoid muscle (*arrows*). M, Right mylohyoid muscle; G, right submandibular gland.

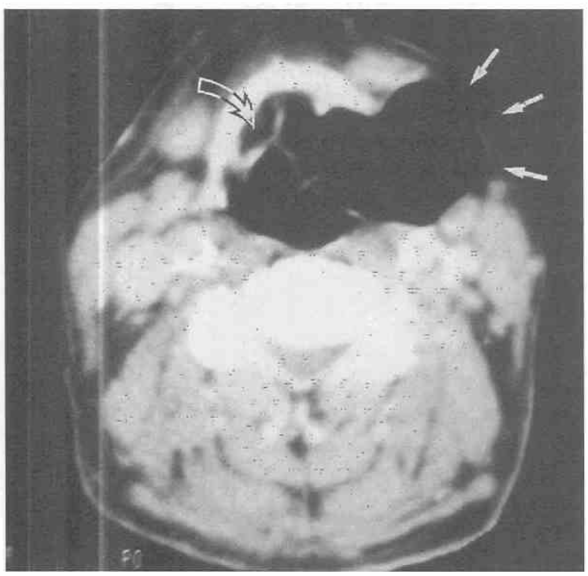

Figure 17–37. Combined laryngocele. Axial contrast-enhanced CT image at the level of the hyoid bone demonstrates a thin-walled, air-filled, right anterior triangle mass (*white arrows*) in direct continuity with the left paralaryngeal space. *Curved arrow,* right paralaryngeal space.

a thin-rimmed, fluid-filled or air-filled mass directly lateral to the thyrohyoid membrane. Continuity with the internal component can be demonstrated on axial or direct coronal images (Fig. 17–37).

A *pharyngocele* is an abnormal dilatation of the piriform sinus, which may also herniate through the thyrohyoid membrane to manifest in the anterior triangle. The less common pharyngocele is differentiated from a laryngocele by the demonstration of continuity with the piriform sinus rather than the laryngeal ventricle. Neoplasms or abscesses involving the apex of the piriform sinus may extend into the anterior triangle of the infrahyoid neck through the cricothyroid membrane.[35]

References

1. Albertyn LE, Alcock MK: Diagnosis of internal jugular vein thrombosis. Radiology 162:502, 1987.
2. Benson MT, Dalen K, Marcuso AA, et al: Congenital anomalies of the branchial apparatus: Embryology and pathologic anatomy. Radiographics 12:943, 1992.
3. Bertrand M, Chen JT, Lipshitz HL: Lymph node calcification in Hodgkin's disease after chemotherapy. AJR 129:1108, 1977.
4. Braun IF, Hoffman JC Jr, Malko JA, et al: Jugular venous thrombosis: MR imaging. Radiology 157:357, 1985.
5. Brereton ND, Johnson RE: Calcification in mediastinal lymph nodes after radiation therapy of Hodgkin's disease. Radiology 112:705, 1973.
6. Coit WE, Harnsgerger HR, Osborn AG, et al: Ranulas and their mimics: CT evaluation. Radiology 163:211, 1987.

7. Davis WL, Harnsberger HR, Smoker WR, et al: Retropharyngeal space: Evaluation of normal anatomy and diseases with CT and MR imaging. Radiology 174:59, 1990.
8. Egund N, Ekeland L, Sako M, Persson B: CT of soft tissue tumors. AJR 137:725, 1981.
9. Glazer HS, Mauro MA, Aronberg DJ, et al: Computed tomography of laryngoceles. AJR 140:549, 1983.
10. Grodinsky M, Holyoke EA: The fasciae and fascial spaces of the head, neck and adjacent regions. Am J Anat 367, 1938.
11. Harnsberger HR, Mancuso AA, Muraki AS, et al: Branchial cleft anomalies and their mimics: computed tomographic evaluation. Radiology 152:739, 1984.
12. Holliday RA, Prendergast NC: Imaging inflammatory processes of the oral cavity and suprahyoid neck. Oral Max Surg Clin North Am 4:215, 1992.
13. Hollinshead WH: Textbook of Anatomy, 3rd ed. New York, Harper & Row, 1974.
14. Jacobs JM, Harnsberger HR, Lufkin RB, et al: Vagal neuropathy: Evaluation with CT and MR imaging. Radiology 164:97, 1987.
15. Katz AD, Passy V, Kaplan L: Neurogenous neoplasms of the major nerves of face and neck. Arch Surg 102:51, 1971.
16. Latack JT, Hutchinson RJ, Heyn RM: Imaging of rhabdomyosarcomas of the head and neck. AJNR 8:353, 1985.
17. Levitt GW: Cervical fascia and deep neck infections. Otol Clin North Am 9:703, 1976.
18. Mancuso AA, Dillon WP: The neck. Radiol Clin North Am 27: 407, 1989.
19. Mancuso AA, Hanafee WN: Oral cavity and oropharynx including tongue base, floor of the mouth and mandible. In Computed Tomography and Magnetic Resonance Imaging of the Head and Neck, 2nd ed. Baltimore, Williams & Wilkins, 1985.
20. Mancuso AA, Harnsberger HR, Muraki AS, et al: Computed tomography of cervical and retropharyngeal lymph nodes: Normal anatomy, variants of normal and applications in staging head and neck cancer. I: Normal anatomy. Radiology 148:709, 1983.
21. Mancuso AA, Harnsberger HR, Muraki AS, et al: Computed tomography of cervical and retropharyngeal lymph nodes: Normal anatomy, variants of normal and applications in staging head and neck cancer. II: Pathology. Radiology 148:715, 1983.
22. New GB, Erich JB: Dermoid cyst of the head and neck. Surg Gynecol Obstet 65:38, 1937.
23. Nyberg DA, Jeffrey RB, Brant-Zawadzki M, et al: Computed tomography of cervical infections. J Comput Assist Tomogr 9:288, 1985.
24. Ogura JH, Biller HF: Head and neck—surgical management. JAMA 221:77, 1972.
25. Olsen WL, Dillon WP, Kelly WM, et al: MR imaging of paragangliomas. AJR 148:201, 1987.
26. Paonessa DF, Goldstein JC: Anatomy and physiology of head and neck infections. Otol Clin North Am 9:561, 1976.
27. Pratt LW: Familial carotid body tumors. Arch Otolaryngol 97:334, 1973.
28. Reede DL, Bergeron RT: Cervical tuberculous adenitis: CT manifestations. Radiology 154:701, 1985.
29. Reede DL, Bergeron RT: CT of cervical lymph nodes. J Otolaryngol 11:411, 1982.
30. Reede DL, Bergeron RT, Som PM: CT of thyroglossal duct cyst. Radiology 157:121, 1985.
31. Reede DL, Som PM: Lymph nodes. In Som PM, Bergeron RT (eds): Head and Neck Imaging, 2nd ed. St. Louis, 1991, CV Mosby.
32. Reede DL, Whelan MA, Bergeron RT: CT of the soft tissue structures of the neck. Radiol Clin North Am 22:239, 1984.
33. Reede DL, et al: Nonnodal pathologic conditions of the neck. In Som PM, Bergeron RT (eds): Head and Neck Imaging, 2nd ed. St. Louis, CV Mosby, 1991.
34. Rouviere H: Lymphatic system of the head and neck. In Anatomy of the Human Lymphatic System (transl. M Tobias). Ann Arbor, MI, Edwards Brothers, 1938.
35. Schwartz JM, Holliday RA, Breda SB: CT diagnosis of piriform sinus perforation. J Comput Assist Tomogr 12:869, 1988.
36. Shah JP, Strong E, Spiro RH, Vikram B: Surgical grand rounds, neck dissection: Current status and future possibilities. Clin Bull 11: 25, 1981.
37. Shumrick DA: Biopsy of head and neck lesions. In Paparella MN, Shumrick DA (eds): Otolaryngology, vol 1. Philadelphia, WB Saunders, 1973.
38. Siegel MJ, Glazer HS, St Amour TE, et al: Lymphangiomas in children: MR imaging. Radiology 170:467, 1989.
39. Silver AJ, Mawad ME, Hilal SK, et al: Computed tomography of the carotid space and related cervical spaces. Part II: Neurogenic tumors. Radiology 150:729, 1984.
40. Simpson GT: The evaluation of neck masses of unknown etiology. Otol Clin North Am 13:489, 1980.
41. Smoker WRK, Harnsberger HR: Normal anatomy of the neck. In Som PM, Bergeron RT (eds): Head and Neck Imaging, 2nd ed. St. Louis, CV Mosby, 1991.
42. Som PM: Review: Detection of metastasis in cervical lymph nodes: CT and MR criteria and differential diagnosis. AJR 158:961, 1992.
43. Som PM, Biller HF, Lawson W, et al: Parapharyngeal space masses: An updated protocol based on 104 cases. Radiology 153:149, 1984.
44. Som PM, Scherl MP, Rao VM, Biller HF, et al: Rare presentations of ordinary lipomas of the head and neck. AJNR 7:657, 1986.
45. van den Brekel MHW, Stel HV, Castelijns JA, et al: Cervical lymph node metastasis: Assessment of radiologic criteria. Radiology 177: 379, 1990.
46. Weingast BR: Congenital lymphangiectasia with fetal cystic hygroma: Report of two cases with coexistent Down's syndrome. J Clin Ultrasound 16:663, 1988.
47. Yousem DM, SOM PM, Hackney DB, et al: Central nodal necrosis and extracapsular neoplastic spread in cervical lymph nodes: MR imaging versus CT. Radiology 182:753, 1992.
48. Zadvinskis DP, Benson MT, Kerr HH, et al: Congenital malformations of the cervicothoracic lymphatic system: Embryology and pathogenesis. Radiographics 12:1175, 1992.
49. Zoarski GH, Mackey JK, Arzai Y, et al: Head and neck: Initial clinical experience with fast spin-echo MR imaging. Radiology 188: 323, 1993.

18

The Larynx

Hugh D. Curtin

Imaging of the larynx can be an extremely difficult endeavor. The anatomy is complex. The target moves with every breath and every swallow. In certain situations, however, imaging addresses questions that the clinician has difficulty in answering and can make a considerable difference in treatment planning.

Imaging must be considered in light of the capabilities of modern endoscopy.[1, 10, 18] As the technology of imaging has progressed, so too has the instrumentation available for direct visualization. The mucosa can be examined thoroughly. To be relevant, imaging must provide information that cannot be obtained by direct visualization. Thus, the usual intent of the radiologist is to evaluate the deeper tissues. In some cases, a bulky lesion of the upper larynx may block the view of the lower larynx, and imaging may assist in defining caudal extent of disease.

The radiologist seeking to assess laryngeal pathology obviously must be familiar with the anatomy. The disease processes and their behavior are important. The radiologist must also be familiar with the available therapeutic options to emphasize the information that will be important in making clinical decisions.

This chapter begins with a discussion of anatomy, including the normal appearance in the various imaging planes. A brief mention of technical considerations in applying magnetic resonance imaging (MRI) and computed tomography (CT) scans to the task of examining the larynx is followed by descriptions of imaging of various pathologic conditions. The important clinical considerations in each disease are stressed.

Anatomy

The larynx is a system of mucosal folds supported by a cartilaginous framework.[15] Tension and movement of the mucosal folds are accomplished by the actions of small muscles pulling against the cartilaginous framework.

The clinical organization of the larynx emphasizes the mucosal anatomy, making the mucosa a good starting point for the present discussion. This concept is particularly important to the radiologist because descriptions of tumors must encompass the relationship to the landmarks on the mucosal surface.

From the superior view (the view of the endoscopist), the first landmark seen is the *epiglottis*. The upper edge of the epiglottis represents the most superior limit of the larynx. The epiglottis is the anterior boundary of the entrance into the larynx. Anteriorly, two small sulci—the *valleculae*—separate the free portion of the epiglottis from the base of the tongue (Fig. 18–1). From the lateral margin of the epiglottis, the aryepiglottic (AE) folds curve around to the small interarytenoid notch. Together these structures complete the boundaries of the airway at the entrance into the larynx.

The inner mucosal surface of the larynx, or *endolarynx*, can be thought of as the working part of the organ. Two prominent parallel folds stretch from front to back along the lateral aspect of each side of the airway (Figs. 18–2 and 18–3; see also Fig. 18–1). These are the true and false vocal cords or folds, and they are in the horizontal plane. The *true cord* (the *glottis*) is the key functional component in the generation of voice and has a fine edge at the medial margin. The more superiorly placed *false vocal fold* has a more blunted medial edge.

Separating these two folds is one of the most important landmarks in the larynx. The *ventricle* is a thin cleft between the *true cord* and the *false cord*, stretching from the most anterior limit of the cord almost to the posterior limit of the larynx.

Above the false cord the mucosa sweeps upward and outward to the *aryepiglottic (AE) folds*. Inferiorly, the mucosa covering of the true cord sweeps outward into the subglottic area, eventually merging smoothly with the mucosa of the trachea.

A final important mucosal landmark is the *anterior commissure*, the point where the true vocal cords converge anteriorly to attach to the inner (posterior) surface of the anterior angle of the thyroid cartilage.

The three parallel structures—the true cord, the false cord, and the ventricle—organize the larynx into three regions: the supraglottis, the glottis, and the subglottis.

The true cord is the glottis. The glottic region of the larynx extends from the upper surface of the true cord to a line somewhat arbitrarily chosen as being 1 cm below the level of the ventricle. The subglottic region is between this arbitrary line and the inferior edge of the cricoid cartilage, the lower margin of the larynx. There is no defined mucosal structure representing the exact boundary or separation of the glottic and subglottic regions.

The supraglottic region is the part of the larynx that is above the ventricle. This region includes the false cords, the epiglottis, and the AE folds.

Laryngeal Skeleton

The laryngeal cartilages are the supporting framework of the larynx. The major cartilages include the cricoid, the thyroid, the arytenoid, and the epiglottic. The smaller cartilages, the corniculate and the cuneiform, reside in the aryepiglottic fold and are not of particular importance to the radiologist.

The *cricoid cartilage* is the foundation of the larynx and

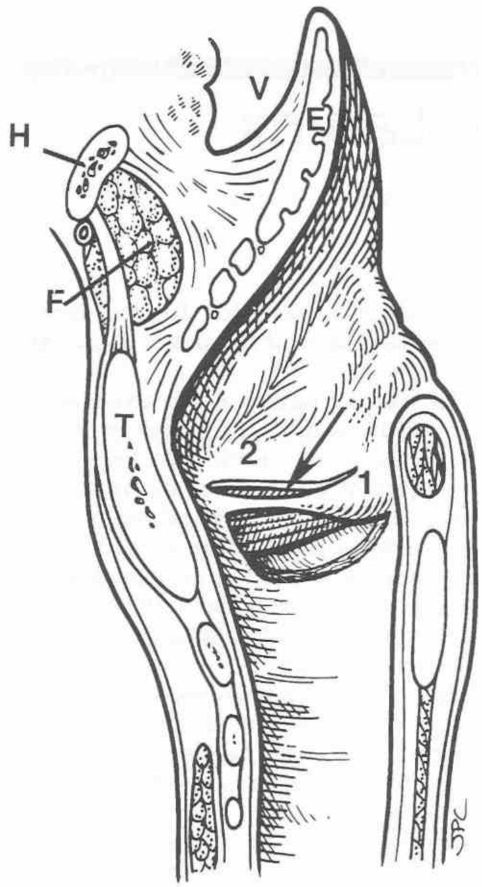

Figure 18–1. The larynx is split sagittally, with a view of the lateral wall of the airway. The mucosa over the true cord (1) has been removed to show the thyroarytenoid muscle (TAM), which extends from the arytenoid to the thyroid cartilage. The upper edge of the muscle *(arrow)* indicates the level of the ventricle. The false cord (2) is just above the ventricle. E, epiglottis; F, preepiglottic fat; H, hyoid; T, thyroid cartilage; V, vallecula. (From Curtin HD: The larynx. In Som PM, Bergeron RT [eds]: Head and Neck Imaging, 2nd ed. St. Louis, Mosby–Year Book, 1991.)

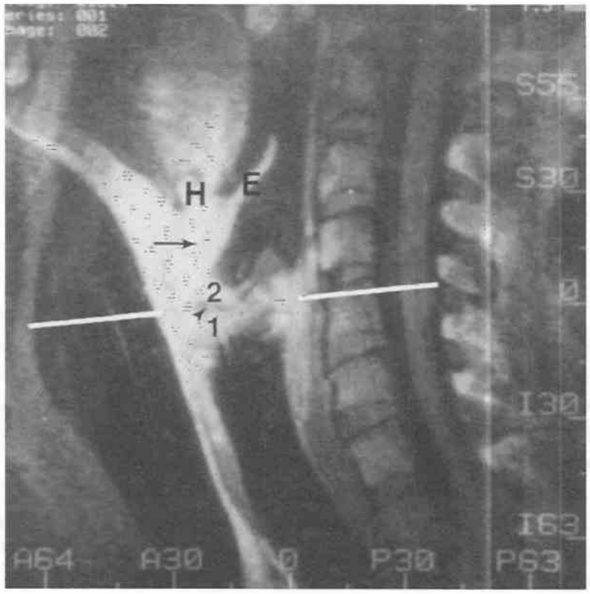

Figure 18–2. Sagittal T1-weighted MRI study. This sagittal slice is just off midline. The slice shows the anterior part of the true cord (1) and false cord (2) separated by the low signal intensity of the laryngeal ventricle *(arrowhead)*. The axial image plane should be along the ventricle, as indicated by the white line. The preepiglottic fat is shown by an *arrow*. E, epiglottis; H, hyoid. (From Curtin HD: MR and CT of the larynx. In Thrall JH [ed]: Current Practice of Radiology, 3rd ed. St. Louis, Mosby–Year Book, 1994.)

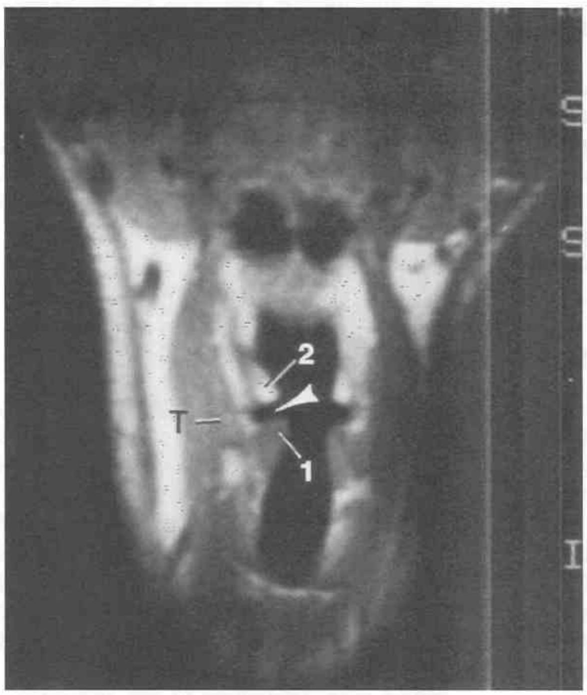

Figure 18–3. Coronal T1-weighted image. This slice would be perpendicular to the white line in Figure 18–2 at the level of 1 and 2. The thyroarytenoid muscle (1) makes up the bulk of the true cord. The paraglottic space at the level of the false cord (2) is filled predominantly with fat. The ventricle is the air-filled slit *(arrowhead)* between the two. T, thyroid cartilage. (From Curtin HD: MR and CT of the larynx. In Thrall JH [ed]: Current Practice of Radiology, 3rd ed. St. Louis, Mosby–Year Book, 1994.)

is the only complete ring. The posterior part is larger than the anterior, giving the cartilage the appearance of a signet ring facing posteriorly. The lower margin of the cricoid cartilage represents the lower margin of the larynx.

The *thyroid* and the *arytenoid cartilages* articulate with the cricoid. The thyroid cartilage is large and can be thought of as forming a shield for most of the inner larynx. The arytenoid cartilages perch on the superior edge of the posterior cricoid.

The arytenoid cartilage spans the ventricle. The upper arytenoid is at the level of the supraglottic larynx. The lower arytenoid has a pointed process anteriorly, called the vocal process. Because of its characteristic shape and position, the arytenoid cartilage can help localize the ventricle on axial scanning. This is most helpful on CT scans, where the vocal process may be directly visualized. The upper margin of the arytenoid is at the level of the lower false cord just above the ventricle. The vocal process is at the level of the true cord just below the ventricle. Indeed,

the vocal ligament, which represents the medial margin of the true cord, attaches to the vocal process.

The epiglottic cartilage, except for its superior tip, is totally contained within the external framework of the larynx. This cartilage is made up of elastic fibrocartilage and does not calcify. Grossly, this cartilage has multiple perforations resembling more a mesh than a solid plate, and the epiglottic cartilage is thus not a major barrier to tumor spread. Inferiorly, the epiglottic cartilage is connected to the inner surface of the anterior part of the thyroid cartilage by the thyroepiglottic ligament.

Muscles and Ligaments

The cartilages are connected by a system of muscles and ligaments. Several muscles are mentioned in the remainder of the chapter. One deserves special attention. The *thyroarytenoid muscle* (TAM) stretches from the arytenoid cartilage to the inner surface of the anterior thyroid cartilage (Fig. 18–4; see Fig. 18–1). This muscle parallels the true cord and makes up the bulk of the true cord.

The cricothyroid and thyrohyoid ligaments span the greater part of the intervals between the cricoid cartilage, the thyroid cartilage, and the hyoid bone and represent, along with the cartilages, the outer limits of the larynx.

Two membranes are found just deep to the mucosa. The conus elasticus (also called the *cricovocal ligament* or *lateral cricothyroid ligament*) stretches from the vocal ligament to the upper margin of the cricoid cartilage. Some descriptions indicate the membrane attaching to the inner surface of the ring as well. This membrane or fascial layer merges with the anterior cricothyroid ligament in the anterior midline.

A similar structure is seen in the supraglottic larynx. A thin ligament called the *ventricular ligament* is found in the lower margin of the false cord and the quadrangular membrane sweeps superiorly from the ventricular ligament terminating in the AE fold.

The fan-shaped hyoepiglottic ligament stretches from the epiglottis to the hyoid bone and divides the supraglottic larynx into a superior (suprahyoepiglottic) and an inferior (infrahyoepiglottic) area.[27]

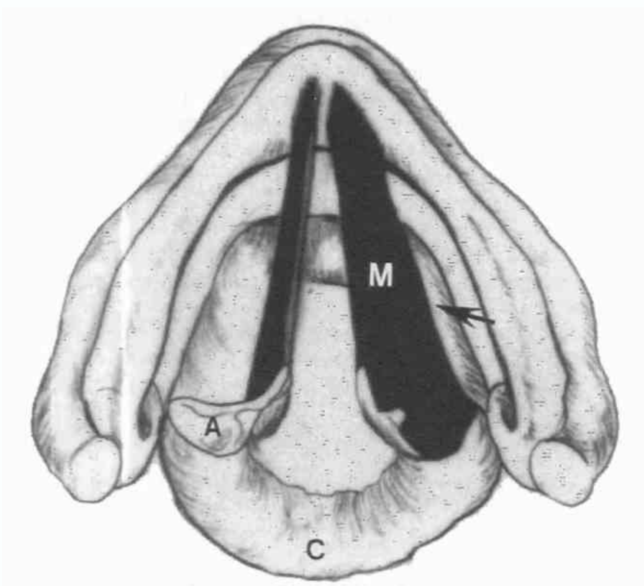

Figure 18–4. View from above, looking down at the skeletonized larynx. The thyroarytenoid muscle (M) is seen stretching from the arytenoid to the thyroid cartilage. *Arrow* indicates the point where paraglottic spread of tumor is expected to intersect the lateral cord. The opposite side shows the vocal ligament stretching from the vocal process of arytenoid to the thyroid cartilage. A, arytenoid; C, cricoid. (From Curtin HD: MR and CT of the larynx. In Thrall JH [ed]: Current Practice of Radiology, 3rd ed. St. Louis, Mosby–Year Book, 1994.)

Spaces

The paraglottic space and the preepiglottic space are situated between the mucosal surface and the cartilaginous outer limit of the larynx.

The paraglottic space is found laterally and represents much of the soft tissue wall of the larynx (Figs. 18–5 and 18–6). Although descriptions of the paraglottic space vary, I am using Tucker and Smith's original descriptions,[25] with the medial boundary represented by the conus elasticus and quadrangular membrane. The lateral boundary is the external skeleton of the larynx, formed predominantly by the inner cortex of the thyroid cartilage. At the level of the supraglottic larynx, the paraglottic space is filled mostly with fat. Below the ventricle, the TAM fills the paraglottic region.

A small recess of the ventricle, called the *laryngeal saccule* or *appendix*, extends upward into the paraglottic space of the supraglottic larynx. This structure is within the paraglottic fat lateral to the quadrangular membrane.

The preepiglottic space is between the epiglottis posteriorly and the thyroid cartilage and thyrohyoid membrane anteriorly.

The hyoepiglottic ligament forms the roof of the preepiglottic and paraglottic spaces.

Imaging Considerations

Although CT scanning is limited to the axial plane, it has the advantage of fast imaging speed. The advent of multidetector CT represents a significant improvement in the application to the larynx.[6] The scan is faster and thus allows the entire larynx to be covered in a single breath-hold. The thinner-slice thickness allows multiplanar reformatted images comparable in quality to direct imaging.

At present, magnetic resonance imaging (MRI) is better at differentiating various soft tissues compared with CT. MRI may allow better analysis of potential cartilage invasion or improved definition of the tumor muscle interface.

Motion artifact is a significant problem in imaging of the larynx. CT scanning tries to avoid the problem by its use of fast imaging. The spiral acquisition may cover the larynx in 10 to 20 seconds. The examination can be performed during slow, shallow respiration, or the scan can be done with the breath held.

More elaborate schemes are required for MRI studies.

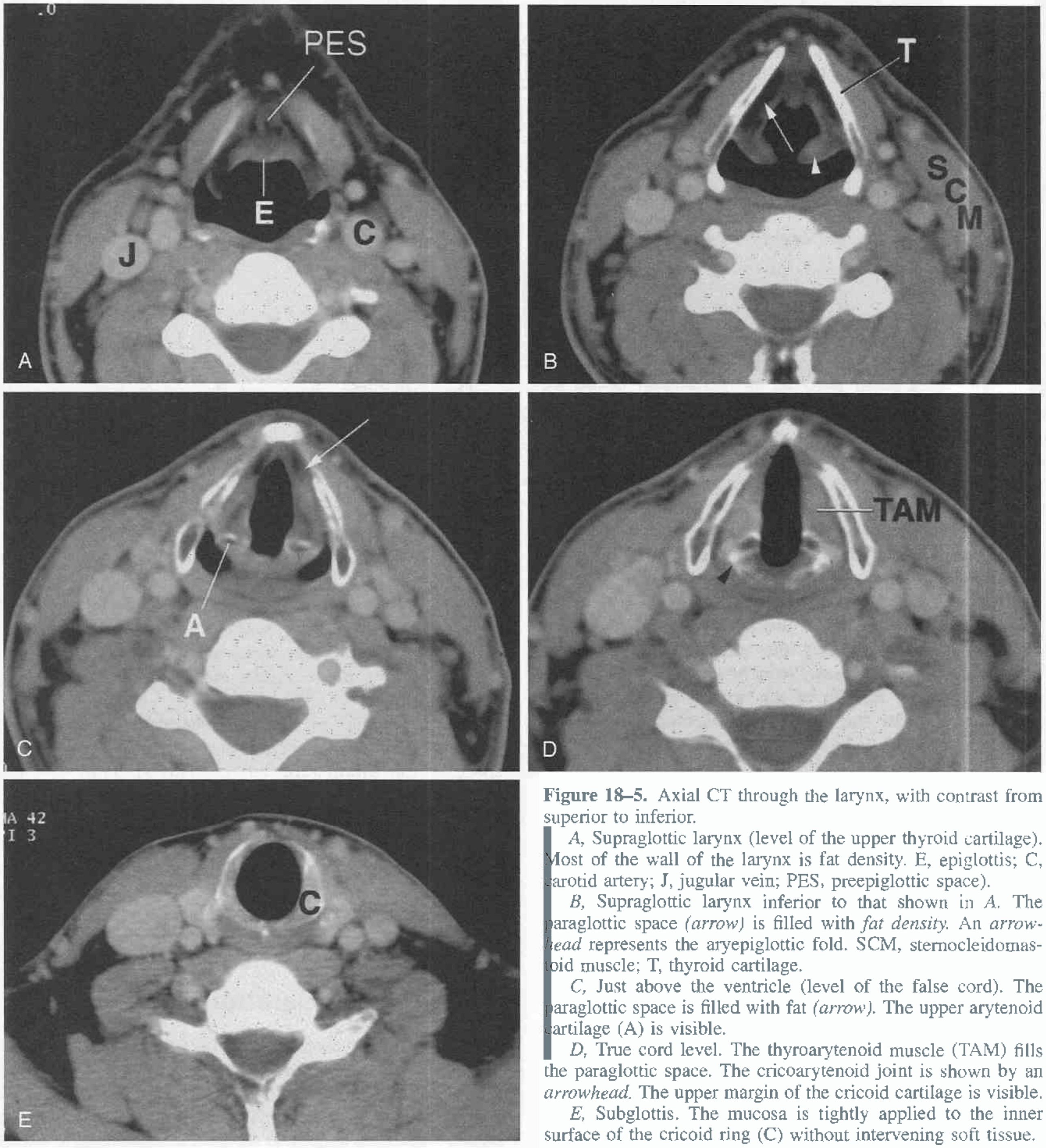

Figure 18–5. Axial CT through the larynx, with contrast from superior to inferior.

A, Supraglottic larynx (level of the upper thyroid cartilage). Most of the wall of the larynx is fat density. E, epiglottis; C, carotid artery; J, jugular vein; PES, preepiglottic space).

B, Supraglottic larynx inferior to that shown in *A.* The paraglottic space *(arrow)* is filled with *fat density.* An *arrowhead* represents the aryepiglottic fold. SCM, sternocleidomastoid muscle; T, thyroid cartilage.

C, Just above the ventricle (level of the false cord). The paraglottic space is filled with fat *(arrow).* The upper arytenoid cartilage (A) is visible.

D, True cord level. The thyroarytenoid muscle (TAM) fills the paraglottic space. The cricoarytenoid joint is shown by an *arrowhead.* The upper margin of the cricoid cartilage is visible.

E, Subglottis. The mucosa is tightly applied to the inner surface of the cricoid ring (C) without intervening soft tissue.

At our institution, before the examination begins, usually before the patient is placed on the table, the patient practices breathing with the abdominal muscles rather than with the chest muscles. Surface coils, a necessity in laryngeal MRI studies, are positioned so that any chest movement does not bump the coil. Although speed of imaging is always an advantage, some have recommended using up to multiple excitations on the T1-weighted sequence. This gives longer imaging times but averages out some of the motion. Fast spin-echo imaging also shortens imaging times.

The use of contrast agents is controversial. At our institution, contrast material is usually used for tumor imaging. Gadolinium, combined with fat suppression, has given good preliminary results.

Imaging emphasizes the importance of the ventricle, and axial images are taken along the plane of the ventricle. The position of the ventricle is estimated in axial images by the

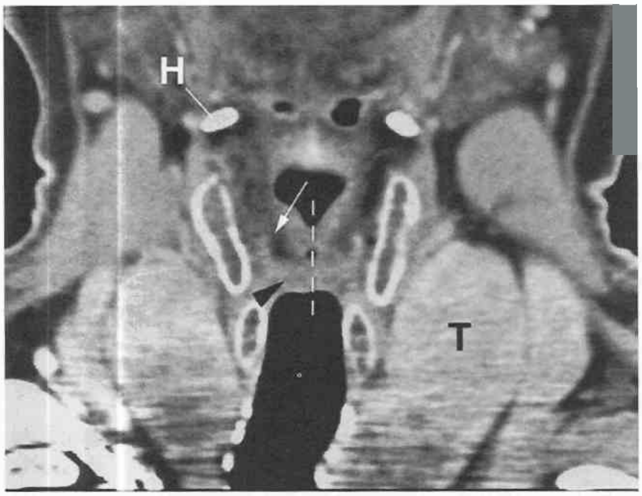

Figure 18–6. Reformatted coronal image through the larynx (multidetector CT). The patient is holding his breath. The position of the closed airway is represented by the *dashed line*. Note the density of fat in the paraglottic space at the supraglottic level *(arrow)*. The thyroarytenoid muscle *(arrowhead)* forms the bulk of the true cord (glottic level). The thyroid cartilage and cricoid cartilage are also visible. H, hyoid bone; T, thyroid gland.

appearance of the cartilages or by the transition from the fat to muscle in the paraglottic region.

In MRI studies, the coronal images are perpendicular to the ventricle. Even if the ventricle is not actually visible, its position can be predicted by the transition from fat to muscle in the paraglottic space.

Pathology

Most laryngeal imaging is performed in order to evaluate patients with tumors of or trauma to the larynx.[11–14, 21, 23, 24] The tumors can be mucosal or submucosal. In most instances, the larynx is visualized directly—if not by endoscopy, at least by mirror—and the radiologist should emphasize information that is not obtainable by direct visualization.

Mucosal Tumors

Most tumors that come to imaging are squamous cell carcinomas arising from the mucosa of the larynx.[2] With the possible exception of rare tumors arising deep within the ventricle, these tumors are detected before imaging. Indeed, imaging currently cannot rule out a small malignancy and thus is not a substitute for direct visualization.

The otolaryngologist can assess smaller lesions completely. The margins of a small tumor may be readily visible, with no further information required. Alternatively, a patient with a large tumor may obviously require a total laryngectomy, and imaging may not add significant information. Imaging is most important for the patients with moderate-sized tumors in whom some sort of voice-sparing procedure is considered. Such treatment options include partial laryngectomies and radiotherapy. The feasibility of these therapies depends on the origin and the extent of the tumor. The following discussion of imaging of carcinoma of the larynx is organized according to the tumor's site of origin.

Supraglottic Tumors

The usual voice-sparing surgical option for supraglottic squamous cell carcinoma is the supraglottic laryngectomy (Fig. 18–7). The resection is made along the ventricle, and the surgeon removes the entire supraglottic larynx, leaving at least one—and usually both—arytenoid cartilages.[1, 10, 18, 26] The patient retains the true cords and can thus generate voice in the usual manner. The protective function of the supraglottic larynx, particularly the epiglottis, is lost, and the patient must learn how to swallow without aspirating.

Tumor crossing the ventricle is the primary contraindication for the supraglottic laryngectomy (Box 18–1). The incision passing along the ventricle would cut through tumor. Tumor growing along the mucosa to reach the true cord may be obvious at direct visualization. In a smaller lesion, the tumor may invade into the deeper tissues and follow the paraglottic space around the ventricle into the lateral edge of the true cord. This type of spread is unusual

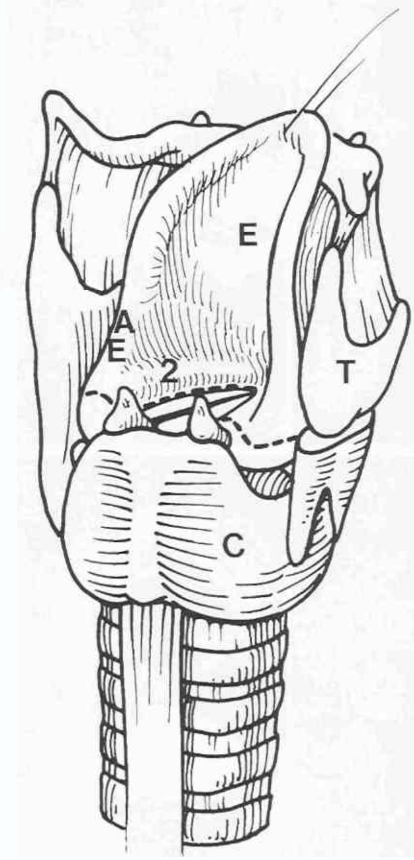

Figure 18–7. Diagram of a supraglottic laryngectomy. The *dotted line* shows the incision of a supraglottic laryngectomy and passes along the ventricle between the true cord and the false cord (2). AE, aryepiglottic fold; C, cricoid cartilage; E, epiglottis; T, thyroid cartilage. (From Curtin HD: Imaging of the larynx: Current concepts. Radiology 173:1–11, 1989.)

as an isolated phenomenon but should be checked during imaging of a supraglottic tumor.

Box 18–1. Contraindications to Supraglottic Laryngectomy

- Tumor extension onto the cricoid cartilage
- Bilateral arytenoid involvement
  Arytenoid fixation
- Extension onto the glottis or impaired vocal cord mobility
- Thyroid cartilage invasion
- Involvement of the apex of the piriform sinus or postcricoid region
- Involvement of the base of the tongue more than 1 cm posteriorly to the circumvallate papillae

From Lawson W, Biller HF, Suen JY: Cancer of the larynx. In Suen JY, Myers E (eds): Cancer of the Head and Neck. New York, Churchill Livingstone, 1989, pp 533–591.

Axial imaging parallels the ventricle and, therefore, is somewhat limited in its ability to identify the level of this key structure. The paraglottic space of the false cord level is predominantly fat, but at the true cord level it is predominantly muscle. The transition between the two represents the approximate level of the ventricle.

If a normal slice can be found below the tumor but still within the supraglottic larynx, the supraglottic laryngectomy is technically possible (Fig. 18–8). If the tumor can be identified at the level of the cord as well as in the supraglottis, the decision is again made and the patient cannot have the usual supraglottic resection. If surgery is chosen as the therapy, the patient must have a total laryngectomy.

On axial images, the lateral edge of the TAM should be carefully examined for the earliest evidence of transglottic spread. A narrow extension of the paraglottic fat is often seen along the outer margin of the muscle. Tumor spreading around the ventricle will grow into this fat and eventu-

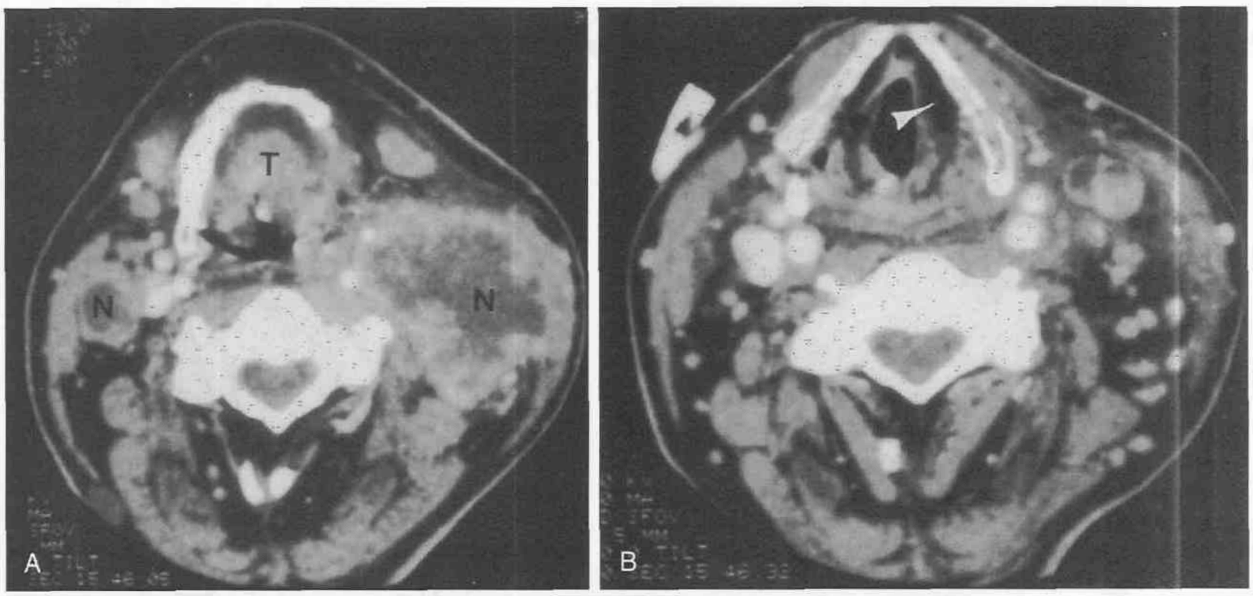

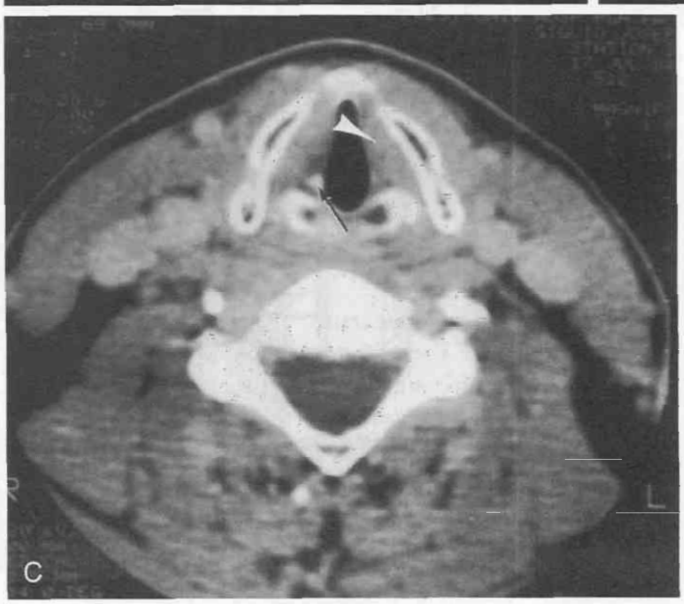

Figure 18–8. CT scan of a supraglottic tumor separated from the ventricle. *A,* Axial slice shows the tumor (T) at the level of the hyoid bone. Note the metastatic nodes (N). The left node shows considerable irregularity, indicating extracapsular tumor spread. *B,* The axial slice, slightly lower than in *A,* is normal. The normal paraglottic fat *(arrowhead)* indicates that the slice is at the supraglottic level and thus between the tumor and the ventricle. *C,* A slice through the true vocal cord would show the normal muscle density *(arrowhead).* The vocal process is represented by an *arrow.*

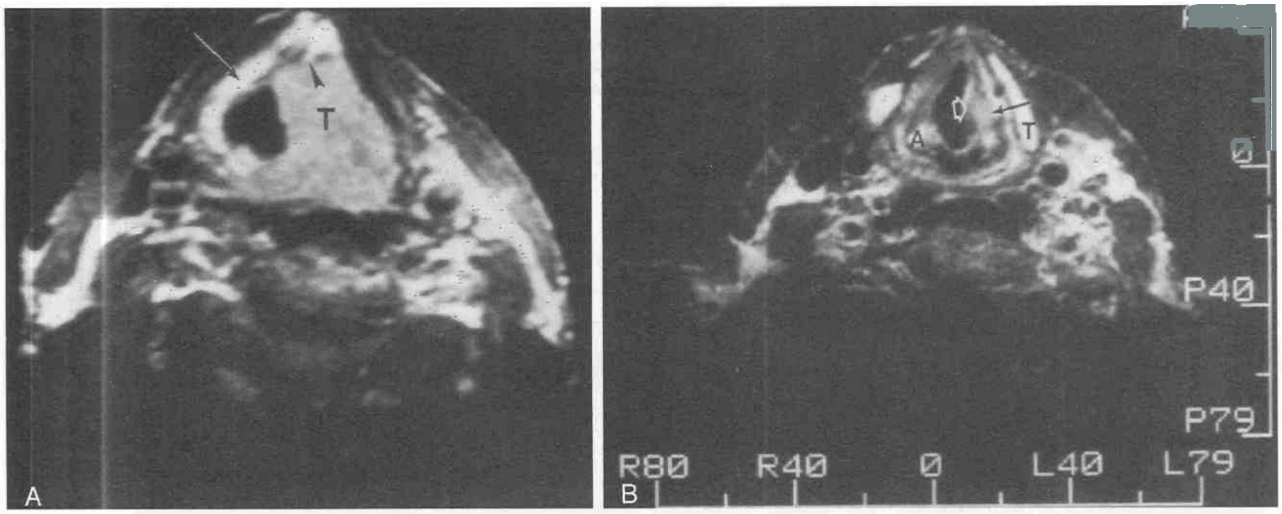

Figure 18–9. Supraglottic tumor with paraglottic spread into the lateral edge of the true cord. *A,* Axial slice through the supraglottic level shows the tumor (T). Note the interface of tumor with fat in the preepiglottic space *(arrowhead)* and the normal paraglottic fat *(arrow)* on the opposite side. *B,* Axial slice at the level of the cord shows a small amount of tumor *(arrow)* prying its way between the thyroid cartilage (T) and the thyroarytenoid muscle (TAM) *(open arrow).* This is at the true cord level below the level of the ventricle. A, arytenoid. (*B,* From Curtin HD: MR and CT of the larynx. In Thrall JH [ed]: Current Practice of Radiology, 3rd ed. St. Louis, Mosby–Year Book, 1994.)

ally will appear to "pry" the muscle away from the thyroid cartilage.

Tumor can be distinguished readily from the fat in the supraglottic paraglottic space. The interface between tumor and muscle at the true cord level is more difficult to visualize. MRI offers the advantage of better tissue differentiation because of its various pulse sequences, but this advantage can be realized only if the patient is able to control motion (Fig. 18–9).

Coronal images are perpendicular to the ventricle and may also be helpful in showing the relationship between tumor and the lateral aspect of the true cord (Figs. 18–10 and 18–11).

Midline tumor can cross the level of the ventricle to involve the anterior commissure. This area can be difficult to evaluate either by direct visualization or by imaging. If there is deep growth from the anterior commissure into the attachment of the cord or through the cricothyroid membrane, imaging may detect tumor that is unappreciated clinically (see "True Cord").

Anterior growth from a supraglottic carcinoma brings the tumor into the preepiglottic space (see Figs. 18–8 and 18–9). The preepiglottic space as well as the paraglottic space has a rich lymphatic drainage, and tumor invasion heightens the concern regarding nodal metastases. Invasion is easily appreciated on axial imaging because the tumor is contrasted against the fat. Such involvement is not a contraindication to a supraglottic laryngectomy.

Thyroid cartilage invasion is usually considered a contraindication to the supraglottic laryngectomy. Such invasion is uncommon unless the tumor is large and has crossed the ventricle.[16] In such a case, the patient would be excluded as a candidate on the basis of ventricular involvement. Involvement of the epiglottic cartilage is not a contraindication. (Cartilage assessment is discussed in the text on true cord lesions.)

The supraglottic partial laryngectomy is the most accepted surgical therapy for tumors limited to the area above the ventricle. More extensive resections have been used for lesions extending beyond the boundaries of supraglottic laryngectomy.[19] Pearson's near-total laryngectomy is done for supraglottic cancer extending to one cord. The resection

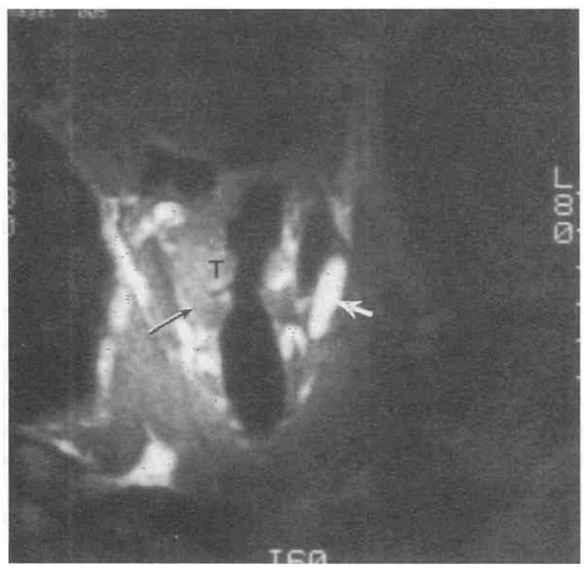

Figure 18–10. Supraglottic carcinoma extending around the ventricle into the lateral cord. The tumor (T) is readily visible to the endoscopist. A small amount of tumor *(arrow)* is seen extending around the lateral aspect of the ventricle into the superolateral margin of the thyroarytenoid muscle (TAM). The mucosa at the true cord level was normal. Thyroid cartilage is represented by a *white arrow.* (From Curtin HD: MR and CT of the larynx. In Thrall JH [ed]: Current Practice of Radiology, 3rd ed. St. Louis, Mosby–Year Book, 1994.)

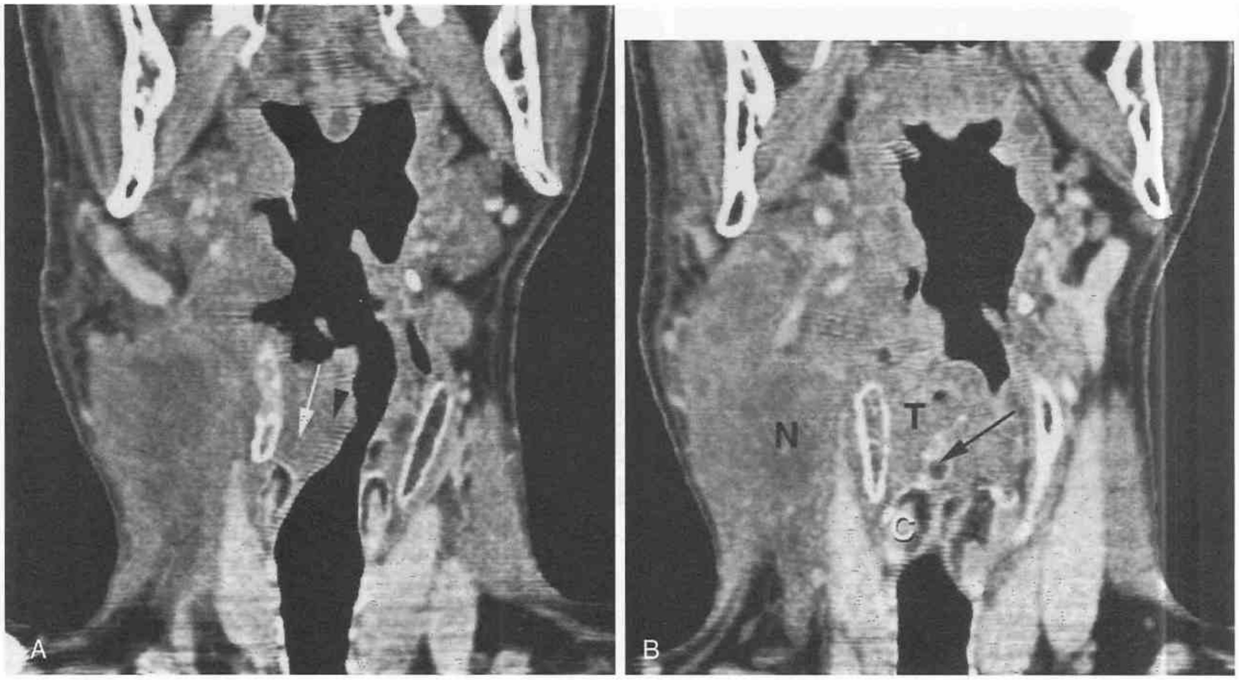

Figure 18–11. Transglottic tumor, reformatted coronal image (multidetector). *A*, The tumor follows *(arrow)* the paraglottic space around the ventricle widening the cord as the tumor infiltrates. An *arrowhead* represents the approximate level of the ventricle. *B*, Note the relationship of the tumor to the arytenoid cartilage *(arrow)*, the thyroid cartilage (T) (immediately lateral), and the cricoid (C). N, metastatic node.

is continued to include the cord and to take the upper margin of the cricoid. The supracricoid partial laryngectomy with cricohyoidopexy takes the anterior cords to the level of cricoid. Minor involvement of the thyroid cartilage is not a contraindication. In either of these approaches, the inferior extent remains the most important assessment at imaging.

An alternative to the partial laryngectomies already mentioned is endoscopic laser surgery.[26] Lesions of the suprahyoid epiglottis, the AE fold, and the false cord are more appropriate for this type of surgery compared with lesions of the laryngeal surface of the epiglottis. The latter tumors are partially hidden by the epiglottis and thus are less accessible to endoscopic resection.

Radiation therapy is also performed for supraglottic cancer. The same landmarks and considerations for supraglottic laryngectomy pertain to assessment for radiation therapy. The bulk of the tumor is also a prognostic factor. Patients with larger tumors fare worse than those with smaller tumors. One study used a 6-mL volume as a separation, with larger tumors carrying a much worse prognosis than smaller ones.[20]

Nodal metastases are very common in supraglottic tumors. Metastases can be bilateral.

True Cord

There are several options for therapy of glottic carcinoma, including simple resection, laser resection, and radiotherapy. Vertical hemilaryngectomy may be considered for a lesion involving the true cord. In this procedure, the surgeon removes the true and false cord on one side of the larynx using a vertical incision through the thyroid cartilage. The lesion can cross the anterior commissure and involve the anterior one third of the opposite cord and still be treatable by vertical hemilaryngectomy. The incision through the thyroid cartilage is moved laterally toward the opposite side.

Contraindications for vertical hemilaryngectomy are listed in Box 18–2. The most important assessments done at imaging concern inferior extension of the tumor, deep invasion at the anterior commissure, and cartilage invasion. Submucosal superior extension crossing the ventricle into the supraglottic larynx is a problem only occasionally.

Box 18–2. Contraindications to Vertical Frontolateral Hemilaryngectomy*

- Tumor extension from the ipsilateral vocal cord across the anterior commissure to involve more than one third of the contralateral vocal cord
- Extension subglottically >10 mm anteriorly and >5 mm posterolaterally
- Extension across the ventricle to the false cord
- Thyroid cartilage invasion
- Impaired vocal cord mobility a relative contraindication

*This technique can still be used if the vocal process and anterior surface of the arytenoid are involved, but involvement of the cricoarytenoid joint, interarytenoid area, opposite arytenoid, or rostrum of the cricoid is a contraindication.

From Lawson W, Biller HF, Suen JY: Cancer of the larynx. In Suen JY, Myers E (eds): Cancer of the Head and Neck. New York, Churchill Livingstone, 1989, pp 533–591.

Inferior extension is quantified relative to the cricoid cartilage. The cricoid cartilage is the foundation of the

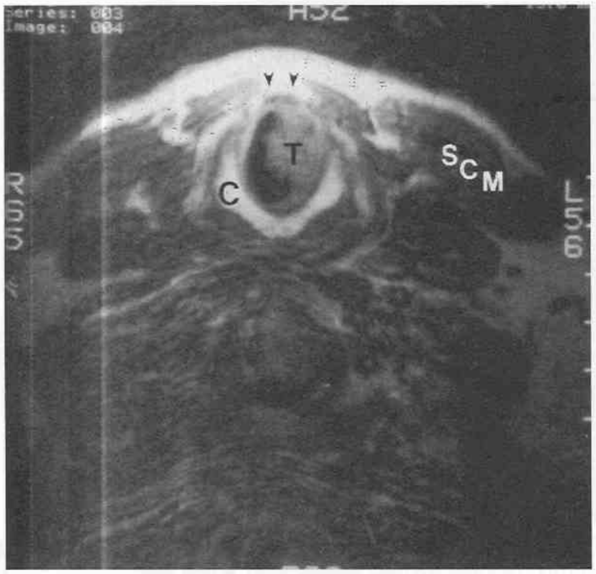

Figure 18–12. Vocal cord lesion with subglottic extension. T1-weighted MRI study. The patient presented with a lesion of the true cord (not shown). The tumor (T) is within the ring of the cricoid cartilage (C). Note the intact fat planes *(arrowheads)* just anterior to the cricothyroid membrane. SCM, sternocleidomastoid. (From Curtin HD: Imaging of the larynx: Current concepts. Radiology 173:1–11, 1989.)

larynx, and most surgeons suggest that even partial resections of this important cartilage are not possible.

At imaging, if the tumor can be identified within the ring of the cricoid cartilage, the standard vertical laryngectomy cannot be done and laryngectomy is usually recommended (Fig. 18–12).

Deep invasion at the anterior commissure may involve the thyroid cartilage or the cricothyroid membrane (Fig. 18–13; see Fig. 18–12).[17] The subtle fat plane anterior to

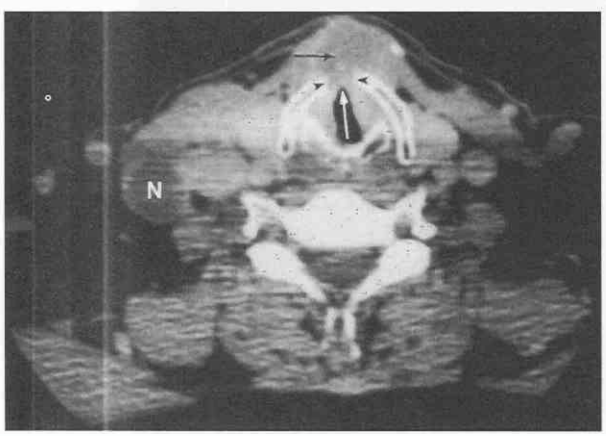

Figure 18–13. Tumor of the anterior commissure extending anteriorly. A small tumor was seen at the anterior commissure *(white arrow)*. Anterior extension carried the tumor through the thyroid cartilage *(arrowheads)* with a prominent nodule in the anterior soft tissues *(black arrow)*. N, metastatic node. (From Curtin HD: The larynx. In Som PM, Bergeron RT [eds]: Head and Neck Imaging, 2nd ed. St. Louis, Mosby–Year Book, 1991.)

the membrane should be examined closely on the axial image.

Cartilage invasion (discussed next) is considered a contraindication for vertical hemilaryngectomy. Minor thyroid cartilage invasion has been treated with supracricoid partial laryngectomy with cricohyoepiglottopexy.[19] In this procedure, more of the supraglottic larynx is removed and the cricoid cartilage is then suspended from the remaining supraglottic tissues and hyoid bone.

Cartilage Invasion

Cartilage invasion is considered a contraindication to both the standard supraglottic and vertical hemilaryngectomies. The subject is discussed here because such invasion is more of a concern in lesions involving the true cord.

With both CT and MRI studies, the most reliable sign of cartilage involvement is identification of tumor on the extralaryngeal or outer surface of the cartilage. Minor degrees of cartilage invasion can be difficult to detect. The variability of ossification of the major cartilages can lead to problems in detecting cartilage invasion.

The nonossified part of the cartilage can have approximately the same appearance as tumor on CT scans. MRI has the advantage of better tissue discrimination, and although there are no large series available, early results suggest that tumor can be differentiated from nonossified cartilage based on the intensity of the signal.[7, 8]

If signal is bright on the T1-weighted image, that part of the cartilage can reliably be considered normal. The high signal represents fat in ossified cartilage, and carcinoma is never that bright. On T1-weighted images, tumor and nonossified cartilage are usually dark. The nonossified cartilage may be slightly darker than tumor. Regions that are dark on T1-weighted images are examined on the long repetition time (TR) sequence. Nonossified cartilage remains relatively dark on long TR sequence images. Tumor tends to be significantly brighter than nonossified cartilage (Figs. 18–14 and 18–15). One cannot rely on the long TR image alone because fat may be fairly bright, even though the sequence is T2-weighted. Indeed, the tumor may have the same signal as the fat on T2-weighted images particularly if fast spin-echo sequences are used.

Tumor, then, is dark or intermediate on T1-weighted images and usually relatively brighter on T2-weighted images. T2-weighted images show tumor as intermediate to bright. This signal pattern does not definitely indicate tumor. Edema, fibrosis, or even red marrow have also been described with this pattern.[5]

Edema is of particular concern because squamous cell carcinoma often has a peritumoral inflammatory response. Edema may be slightly brighter than tumor on T2-weighted images, but more experience is needed before a definite statement can be made regarding separation of tumor and edema. Edema of the cartilage presumably means that tumor is at least very close. In my experience, at least the perichondrium has been invaded if edema is present in the cartilage.

At CT, irregularity of the inner cortex may suggest that tumor is eroding; however, this sign is questionable because of the variability of ossification. The cortex may be interrupted normally. Asymmetric sclerosis, particularly of

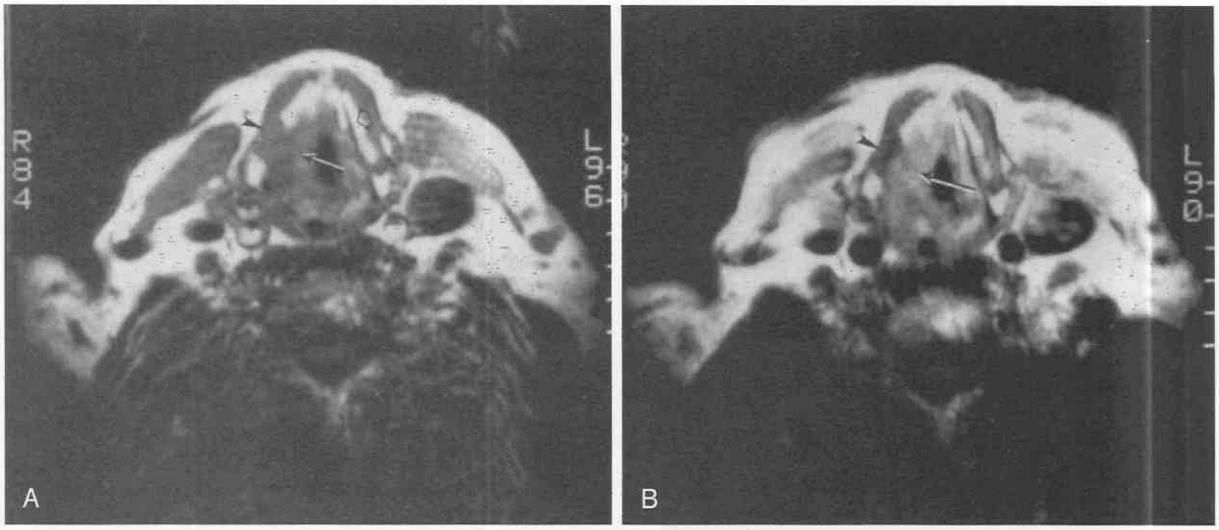

Figure 18–14. Supraglottic tumor without cartilage invasion. *A,* Short TR, short TE. The tumor *(arrow)* abuts an area of the cartilage *(arrowhead)* that has the same signal intensity. On the opposite side, a normal ossified thyroid lamina with bright signal of medullary fat *(open arrow)* is identified. *B,* Long TR, short TE. The tumor *(arrow)* is significantly brighter than the nonossified cartilage *(arrowhead).* (From Curtin HD: MR and CT of the larynx. In Thrall JH [ed]: Current Practice of Radiology, 3rd ed. St. Louis, Mosby–Year Book, 1994.)

the thyroid and cricoid cartilages, may indicate tumor.[4] Tumor may obliterate the medullary fat within the cartilage.

Further study regarding the significance of various signal patterns and CT findings is needed. For instance, the effect of the various imaging findings on prognosis of various therapies, particularly radiotherapy, may potentially change management.[9]

Subglottic Tumors

Subglottic tumors are rare. When they do occur, the only surgical option is almost always a total laryngectomy because of the proximity to the cricoid cartilage.

Hypopharynx

Although the hypopharynx is not actually part of the larynx, it is so intimately associated that discussion is warranted here. Decisions about potential surgical resection usually relate to the proximity of the tumor to landmarks within the larynx, and the assessment is thus quite similar to that of lesions within the larynx itself.

Two regions of the hypopharynx have important relationships to the larynx: the *piriform sinuses* and the *postcricoid region.*

The piriform sinuses indent the posterior wall of the

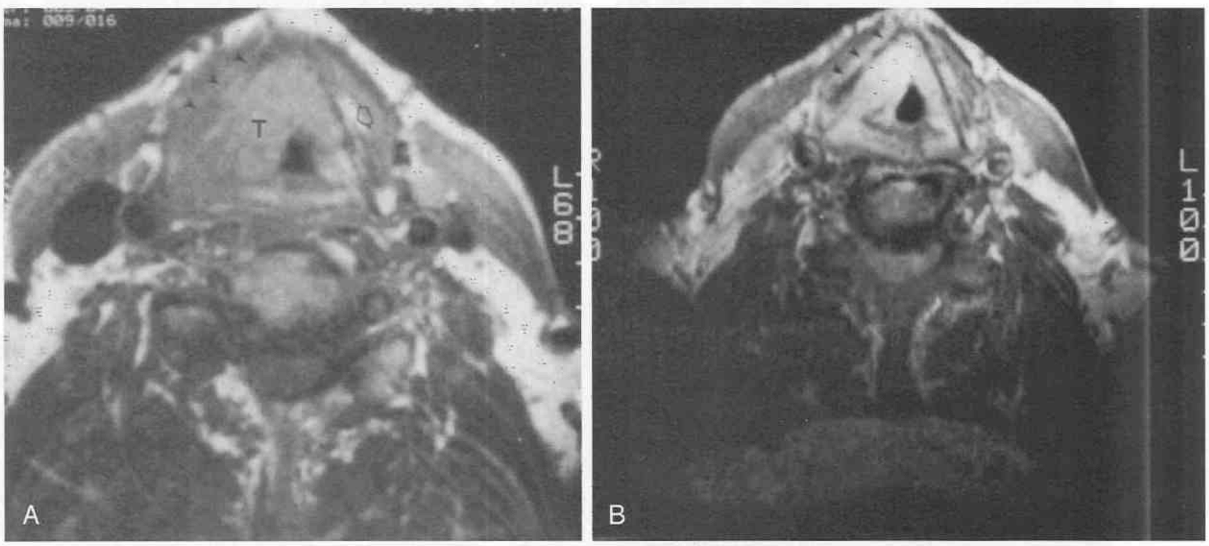

Figure 18–15. Tumor involving cartilage, axial MRI study. *A,* Short TR, short TE T1-weighted image shows tumor (T) against a suspicious area of cartilage *(small arrowheads).* The cartilage has a more intermediate signal rather than the high signal of fat. A normal thyroid lamina is seen on the opposite side *(open arrow). B,* Long TR, long TE T2-weighted image shows significant "brightening" compared with that in *A.* The behavior of this area is the same as that of the tumor. Nonossified cartilage remains as a dark linear structure within the higher-intensity tumor. (From Curtin HD: MR and CT of the larynx. In Thrall JH [ed]: Current Practice of Radiology, 3rd ed. St. Louis, Mosby–Year Book, 1994.)

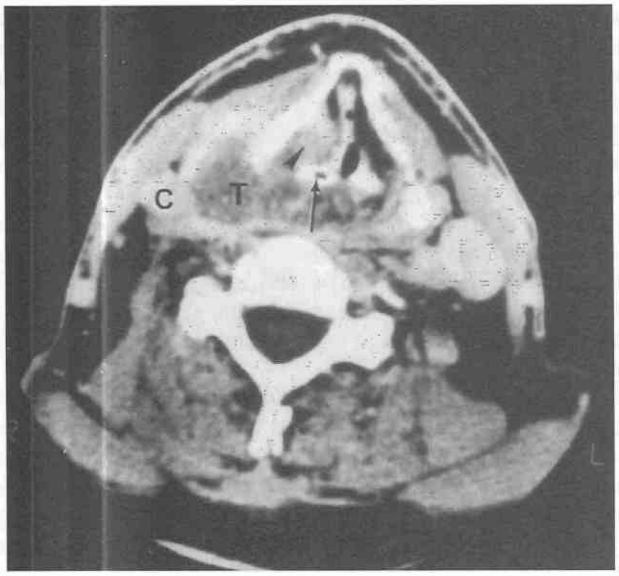

Figure 18–16. Tumor (T) of the piriform sinus. The lesion protrudes through the thyroarytenoid gap between thyroid cartilage and arytenoid *(arrow)*. The tumor thus invades the paraglottic space *(arrowhead)* of the supraglottic larynx. Compare with the fat in the paraglottic space on the normal side. C, carotid artery.

larynx. The anterior wall of the piriform sinuses represents the posterior wall of the paraglottic space. The piriform sinus makes up the lateral aspect of the AE fold.

If a tumor is localized to the upper piriform sinus, a supraglottic resection may be considered along with resection of the tumor. A tumor that invades the paraglottic region of the larynx can follow the paraglottic pathway to reach the level of the cord, and in these patients a total laryngectomy is usually required (Fig. 18–16).

The postcricoid region is that area of the lower hypopharynx that covers the posterior aspect of the cricoid cartilage. To achieve an appropriate margin, the surgeon must usually remove the cricoid and then perform a total laryngectomy. In these patients, the inferior extension within the pharynx should be estimated to help the surgeon decide the appropriate method of reconstructing the food passage.

Lymph Nodes

Metastasis to the lymph nodes is a major consideration in carcinoma of the larynx. The subject of lymph nodes is covered elsewhere in this book, but brief comments about major pathways of spread are appropriate.

Nodal metastases are a major concern with supraglottic tumors. Spread to the jugular nodes occurs very frequently because of the rich lymphatic drainage. The margin of the true cord does not have any lymphatics; therefore, tumors of the true cord do not spread to the lymph nodes unless there is deep invasion or, alternatively, unless the tumor has grown along the mucosa to involve the subglottic region.

Because the subglottic mucosa does have lymphatic drainage, a primary tumor arising in this location or a glottic tumor extending into the area secondarily can metastasize to the nodes. In these patients, the nodes along the esophagus and in the upper mediastinum become a significant concern.

Radiation Therapy

From a surgical perspective, the evaluation of patients uses landmarks that are slightly more precise, but many of the same findings are appropriate when radiotherapy is chosen as the treatment.

The dimensions of the tumor in the axial plane are relevant, since they reflect the bulk of the tumor and relate to the depth of invasion into the soft tissues.

The vertical extent of the tumor should be estimated, although the precision relating to the ventricle is less crucial. Extension into the subglottic area is very important because the treatment portals may be changed to include the paratracheal and upper mediastinum regions.

Formerly, cartilage involvement was considered a contraindication to radiation therapy. Tumor recurrence is more frequent, as is radiation chondritis and chondronecrosis. More recently, however, some have expressed the opinion that relatively subtle involvement is not an absolute contraindication.

Other Mucosal Tumors

Many benign lesions, such as polyps and papillomas, arise from the mucosa of the larynx. These lesions are seldom evaluated by CT or MRI studies. Submucosal tumors can ulcerate through the mucosa (see "Submucosal Tumors" next).

Although almost all malignancies arising from the mucosa of the larynx are squamous cell carcinoma, occasional malignancies arise from the minor salivary glands with histologies such as adenocarcinoma, adenoid cystic carcinoma, and mucoepidermoid carcinoma.

Verrucous carcinoma is an exophytic, slow-growing variant of squamous cell carcinoma. It does not usually metastasize, but it can be locally aggressive. There are no particular imaging features, but the lesion has a typical exophytic "warty" appearance on direct inspection.

Submucosal Tumors

Lesions presenting beneath an intact mucosa usually arise from the nonepithelial elements of the larynx.[2, 3] Such tumors include chondroid lesions, hemangiomas, neurogenic tumors, and rare lesions such as leiomyoma, rhabdomyoma, and lipomas. Sarcomas arising from the same various mesenchymal elements are often submucosal, but with increasing size they can lead to mucosal ulceration.

In rare instances, a squamous cell carcinoma can appear to be entirely submucosal. Such a lesion arises in the ventricle or ventricular saccule (appendix). The tumor expands upward into the paraglottic space and downward into the true cord rather than medially toward the lumen of the larynx.

A submucosal tumor represents a different problem. Unlike the squamous cell carcinoma, in which the actual tumor can be seen and is easily accessible for biopsy, the submucosal tumor presents as a bulge beneath an intact mucosa. In these patients, imaging is used not only to show

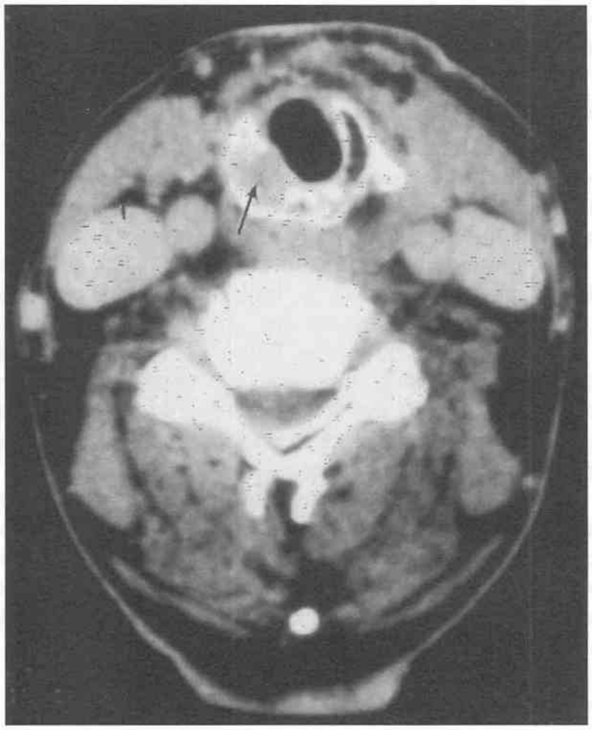

Figure 18–17. Chondroid lesion of the cricoid cartilage. The lesion *(arrow)* expands the cricoid cartilage. The apparent origin in the cartilage suggests the diagnosis. A higher slice showed calcifications.

the extent of the lesion but also to help identify the type of tumor. With certain tumors, the findings are characteristic enough that the diagnosis can be predicted accurately. When the diagnosis is not definitive after imaging, certain findings can still be helpful to the otolaryngologist.

The first question is whether the tumor is a chondroid lesion. Chondrosarcomas and chondromas arise from the cartilaginous framework of the larynx (Figs. 18–17 and 18–18); most arise from the cricoid. The thyroid cartilage is the second most common site of origin. Differentiation between benign and malignant can be difficult even at histopathologic examination. These tumors can compromise the airway, and treatment is usually surgical. A partial laryngectomy can be curative if the entire lesion is resected. If the cricoid cartilage is extensively involved, a total laryngectomy may be considered because of the key role of this cartilage in maintaining a patent airway.

With either CT or MRI, the cricoid origin may be obvious and may give a clue as to the identity of the lesion (see Fig. 18–17). The cartilage may be expanded, indicating a lesion arising within the cricoid rather than eroding into the cartilage from a more superficial mucosal origin.

The cartilaginous matrix is the most characteristic finding at imaging (see Fig. 18–18). CT scans are better than MRI studies at demonstrating the calcifications within the matrix of the tumor. Such calcifications are extremely rare in other lesions. Relapsing polychondritis can have fairly extensive calcification; however, this is extremely rare and should not involve the larynx exclusively.

If the lesion does not have the imaging characteristics of a cartilage lesion, the radiologist tries to determine whether the lesion is vascular. Hemangiomas and paragangliomas enhance intensely on CT scans if a bolus or rapid drip of intravenous contrast material is used. The knowledge that a tumor is vascular has obvious implications if biopsy or resection is planned.

Most of the other tumors mentioned have no specific identifying characteristics. They do not have a cartilaginous matrix and do not enhance brightly. The absence of these two imaging characteristics is useful information in limiting the diagnostic possibilities.

Cysts also present as submucosal masses and are described next.

Cysts

Three types of cysts arise within or in intimate association with the larynx: The *saccular* cyst (laryngocele) and the *mucosal* cyst arise within the larynx, and the *thyroglos-*

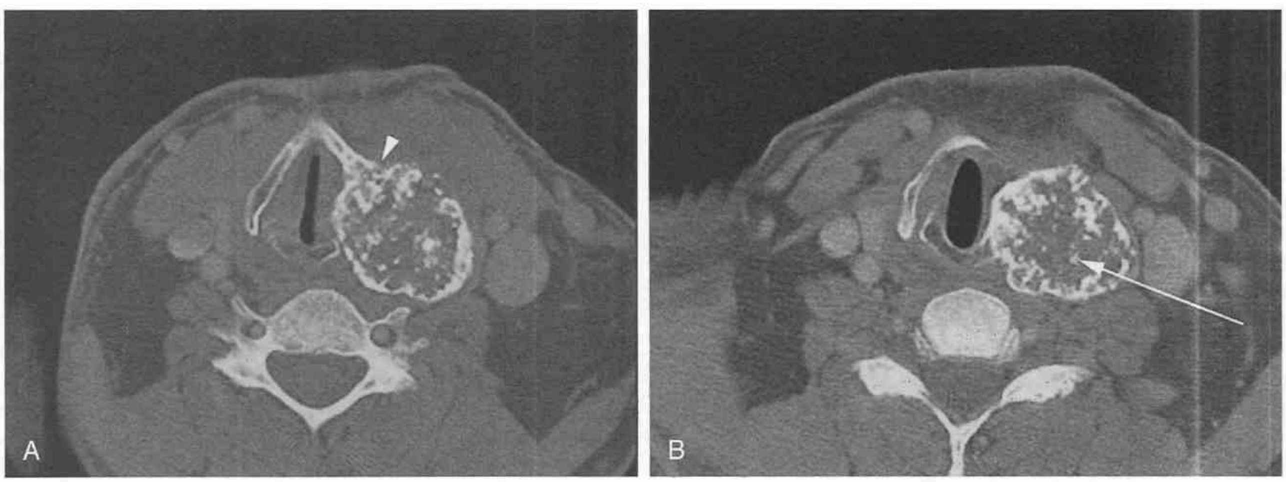

Figure 18–18. Chondrosarcoma, axial CT scan. *A,* The tumor expands *(arrowhead)* the thyroid lamina. *B,* Note the stippled density *(arrow)* within the cartilage representing cartilage formation.

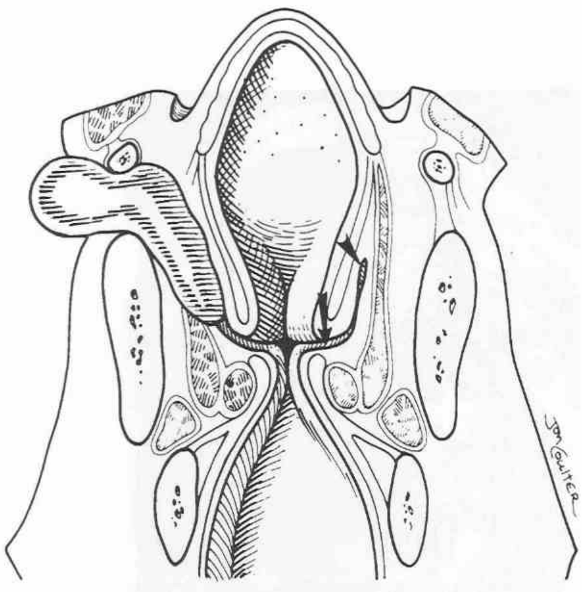

Figure 18–19. Diagram of a laryngocele. Coronal section through the larynx shows the ventricle *(arrow)* and the ventricular appendix *(arrowhead)* on the normal side. When this appendix is obstructed, it dilates (i.e., it fills with either fluid or air) to form a saccular cyst or laryngocele. In the diagram, the lateral extent of the saccular cyst protrudes through the lateral cricothyroid membrane. (From Curtin HD: The larynx. In Som PM, Bergeron RT [eds]: Head and Neck Imaging, 2nd ed. St. Louis, Mosby–Year Book, 1991.)

sal duct cyst arises just outside the larynx in close association with the strap muscles.

Saccular Cyst (Laryngocele)

The saccular cyst, or laryngocele, represents a dilatation of the ventricular saccule or appendix (Fig. 18–19). Strict terminology refers to the abnormality as a saccular cyst if it is fluid-filled and as a laryngocele if it is air-filled. Many simply refer to the lesions as air-filled or fluid-filled laryngoceles. The laryngocele is a supraglottic abnormality, and the true cord is normal.

Either presents as a submucosal mass or bulge in the supraglottic larynx (Figs. 18–20 to 18–22). The air or fluid within is readily identifiable, and the extent can be determined. A small cyst or laryngocele may be confined to the supraglottic paraglottic space and is referred to as "internal." A larger lesion may protrude laterally through the thyrohyoid membrane just anterior to the upper horn of the thyroid cartilage. Any component outside the membrane is referred to as "external" (see Fig. 18–21). A pure external laryngocele is rare. The external component is seen in combination with an internal component. This is called a *mixed laryngocele*. When the external component is large, the laryngocele can present as a neck mass.

Laryngoceles and saccular cysts are benign. However, these abnormalities can occur when tumor in the ventricle causes obstruction of the laryngeal saccule; therefore, both the radiologist and the endoscopist must carefully examine this key area (see Fig. 18–22).

Mucosal Cyst

A mucosal cyst is considered to be an obstructed mucous gland and can present anywhere mucosa is present. The benign nature of this cyst may be suggested by the smooth appearance, and this diagnosis is considered when a cystic-appearing mass is found on a mucosal surface.

Thyroglossal Duct Cyst

The thyroglossal duct cyst arises from the remnant left as the thyroid gland descends to the appropriate position in the lower neck. The cyst can arise above or below the hyoid bone. A cyst that arises below the hyoid bone is usually found just off midline in the region of the strap muscles anterior to the larynx (Fig. 18–23).

The appearance of the thyroglossal duct cyst is characteristic and should not be confused with saccular cyst arising within the larynx itself. A thyroglossal duct cyst in rare circumstances may bulge over the anterior notch of the thyroid cartilage but should not pass through the lateral aspect of the thyrohyoid membrane. The paraglottic space should not be involved.

Post-therapy Appearance of the Larynx

Both surgery and radiotherapy significantly distort the normal appearance of the larynx.

After a total laryngectomy, the food passage may dilate to mimic an airway, but the laryngeal landmarks are no longer seen. Lower CT or MRI slices show the tracheostomy site.

The appearance of the glottic and subglottic levels is unchanged by a supraglottic laryngectomy. With the supraglottic larynx removed, the characteristic landmarks of the paraglottic and preepiglottic spaces are not identified. Usually, the hyoid bone is removed. The major portion of the thyroid cartilage above the level of the cords is also removed.

The vertical hemilaryngectomy can produce a variable appearance. One cord is removed, leading to significant asymmetry at the glottic level. Part of the upper larynx is removed on the ipsilateral side. The position of the original lesion dictates the position of the cuts through the thyroid cartilage, resulting in significant variability in appearance among patients with vertical hemilaryngectomies. At times, the surgeon may attempt to reconstruct the cord using a small slip taken from the strap muscles. This can lead to significant soft tissue that cannot be readily distinguished from tumor.

Radiotherapy can cause characteristic apparent swelling of the soft tissues over the arytenoid cartilage and supraglottic region. Subtle reticulation or stranding of the supraglottic fat is seen. Initially, this represents local inflammation and edema, but small-vessel changes make the appearance more permanent.

Trauma

Direct trauma can result in fractures or dislocations of the cartilages in the larynx. Soft tissue injuries such as

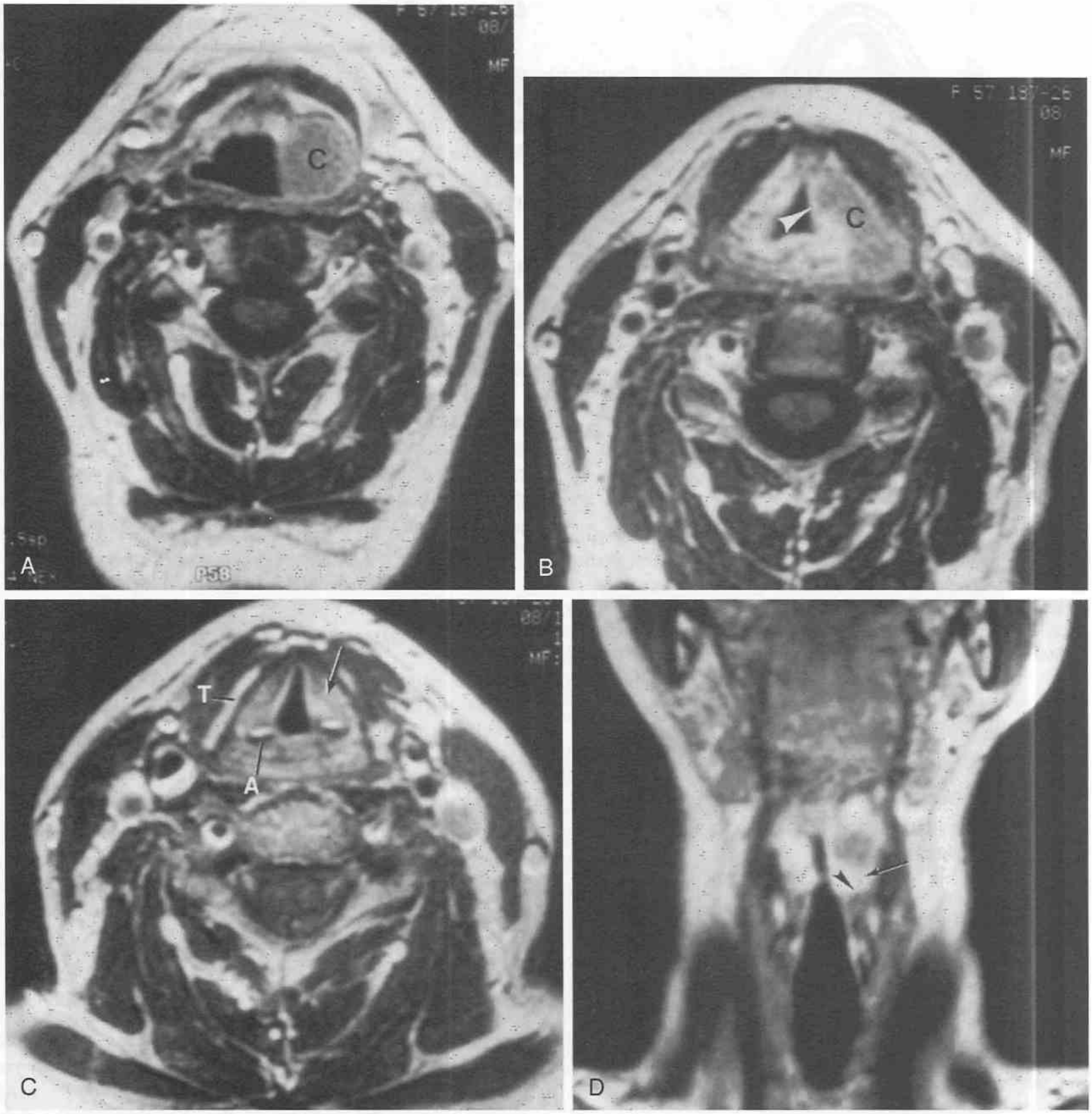

Figure 18–20. Saccular cyst (laryngocele). *A,* Postgadolinium T1-weighted axial image through the upper epiglottis shows the cyst (C). *B,* Slightly lower image shows the cyst (C) in the paraglottic space at the false cord level. The mucosa *(arrowhead)* is intact. *C,* Axial image through the true cord level shows no evidence of tumor. A, arytenoid; T, thyroid. The thyroarytenoid muscle (TAM) is shown by an *arrow. D,* Coronal image shows the lower margin of the lesion *(arrow)* above the upper edge of the TAM *(arrowhead);* thus, the cyst is above the ventricle.

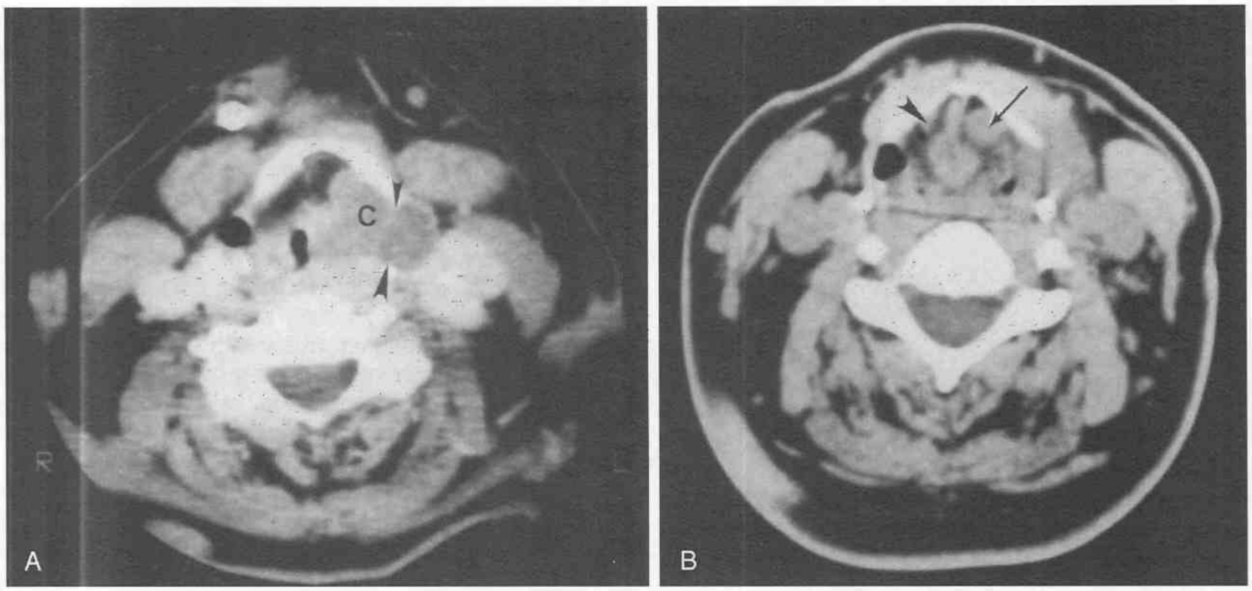

Figure 18–21. Saccular cyst (laryngocele). *A,* The cystic structure has both an internal and external component. The sacc[redacted] cyst (C) protrudes through the thyrohyoid membrane, approximately at the *arrowheads.* Note the sharp margin of the cyst. *B,* Slightly lower slice shows the dilated appendix *(arrow)* just above the ventricle. Again, note the sharp margin. The fat in the paraglottic space indicates that this is still above the ventricle. A normal appendix is on the opposite side *(arrowhead).*

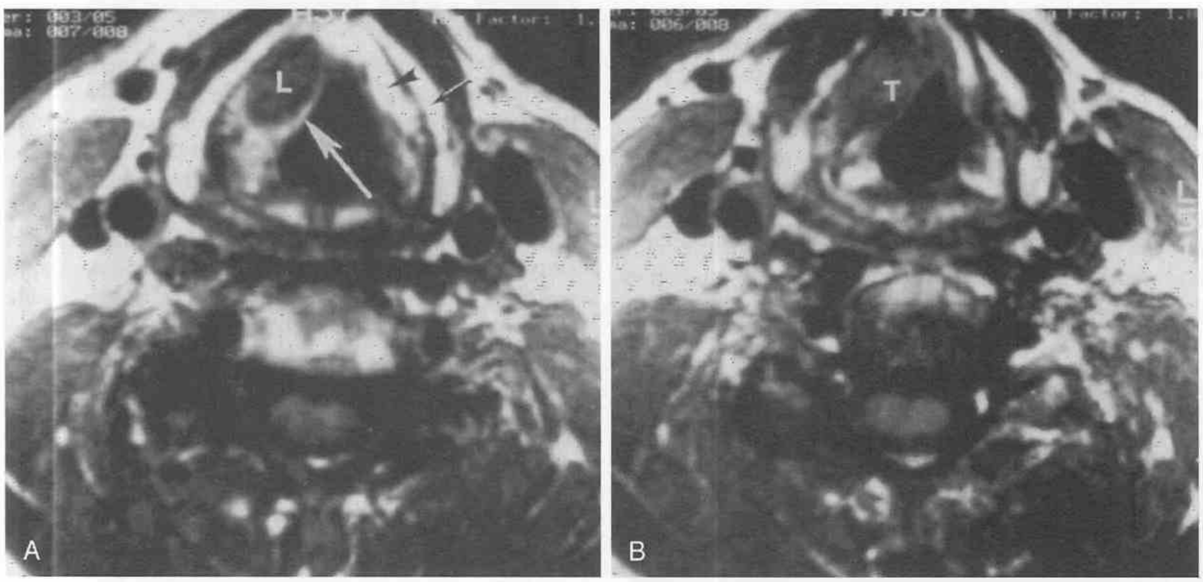

Figure 18–22[redacted]ar cyst [redacted]aryngoce[redacted]he sacc[redacted] (L) is seen [redacted]g the paraglottic space at the level of the false cord. N[redacted]ntact mu[redacted]. T[redacted]aglottic fa[redacted] normal side[redacted] remains of high signal intensity. Fat is shown in the thyroid cartilage *(black arrow). B,* Slightly lower slice shows a tumor (T) filling the ventricle and causing the obstruction of the ventricular appendix, causing the saccular cyst. (From Curtin HD: MR and CT of the larynx. In Thrall JH [ed]: Current Practice of Radiology, 3rd ed. St. Louis, Mosby–Year Book, 1994.)

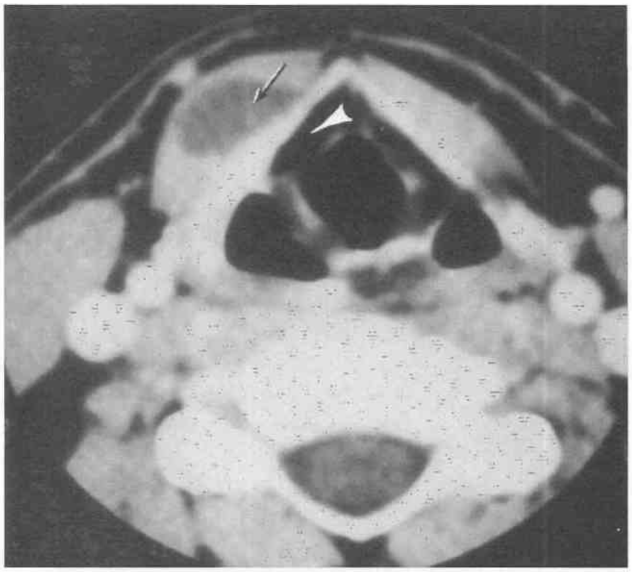

Figure 18–23. Thyroglossal duct cyst. The cystic structure *(arrow)* is seen on the outer surface of the thyroid cartilage intimately associated with the strap muscles. Note that the paraglottic fat *(arrowhead)* remains clear.

mucosal tears and hematomas can occur in isolation but are often seen in conjunction with fractures. CT scanning is usually used because of the ability to visualize the calcified cartilage and because of the speed of imaging. The fragile airway is more easily managed and monitored in the CT scan than in the more confined area of the MRI study.

In young patients, the cartilage may not be calcified but it can often be seen as slightly increased density against the contiguous soft tissues.

Fractures usually affect the thyroid or cricoid cartilage. The thyroid cartilage can have vertical or horizontal fractures (Fig. 18–24). Vertical fractures are easily detected in the axial scan plane, but horizontal fractures may be undetectable unless there is some displacement of the fracture fragments. Reformatted images may help to define horizontal fractures.

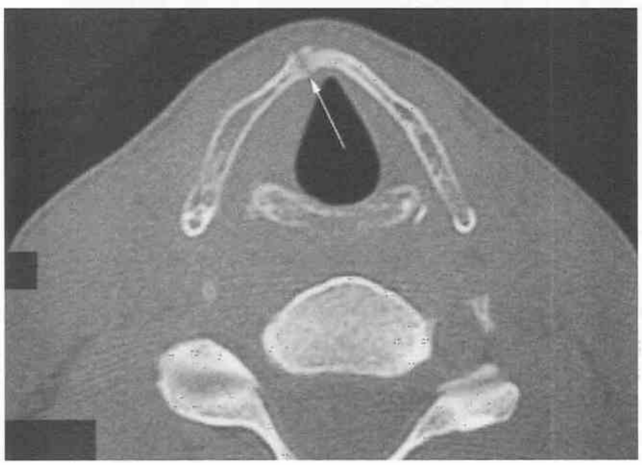

Figure 18–24. Vertical fracture of the larynx; axial CT. The *arrow* indicates a fracture.

The cricoid fracture is, characteristically, a double break (Fig. 18–25). The force of the blow pushes the anterior arch posteriorly, fracturing the ring in two or more places. The ring collapses inward. There is swelling in the subglottic soft tissues, giving apparent soft tissue against the inner surface of the cricoid cartilage, where normally the mucosa is very thin or almost invisible at imaging.

Compromise of the airway is a concern. Any inward displacement reduces the lumen of the airway. Equally of concern is the possibility of a tear of the mucosa. A fracture fragment protruding through the mucosa often results in chondritis and chondronecrosis with further airway restriction. If there is any suspicion of a fragment pushed toward the airway, direct visualization, at endoscopy or at open exploration, is indicated for a thorough assessment of the mucosa.

If there is sufficient force to fracture the thyroid cartilage, the lower epiglottis can be torn or avulsed. This situation can be seen, particularly with horizontal fractures where the fragments are pushed posteriorly, creating a shearing force across the lower epiglottis. Because the epiglottis does not calcify significantly, this abnormality is not detectable by CT scans. The only finding may be hematoma obscuring the fat in the preepiglottic space.

The arytenoid cartilage is not often fractured, but the cricoarytenoid joint can be dislocated (Fig. 18–26). This can occur with fairly minimal trauma to the lateral larynx or may result from more severe insult associated with fractures of the major cartilages. The arytenoid is normally perched just off midline. The radiologist tries to verify that the cartilage is in the normal position or grossly displaced. Currently, a subtle displacement cannot be confidently excluded.

The lower horns of the thyroid cartilage articulate with the lateral cricoid cartilage. This cricothyroid joint can theoretically be dislocated, usually in association with fractures of either the thyroid or cricoid cartilages. Because the attachment of the horn to the cricoid cartilage is fairly strong, a fracture of the lower horn is considered more common. One must be careful in making this diagnosis, since slight obliquity of the slice can cause apparent asymmetry of the space between the two cartilages. Each of the inferior horns must be followed down to the point of articulation.

Miscellaneous Problems

Although tumors and trauma account for most imaging of the larynx, imaging can be useful for several other problems.

Vocal Cord Paralysis

Vocal cord paralysis is most commonly a problem that affects the recurrent laryngeal nerve. All of the muscles in the larynx except the cricothyroid muscle are innervated by this nerve, but the most characteristic finding is the result of atrophy of the TAM. Normally, the TAM makes up the bulk of the true cord. With atrophy, the characteristic CT density or MRI intensity is no longer seen. The ventricle enlarges into the volume vacated by the atrophied muscle so that air can be seen where there should be

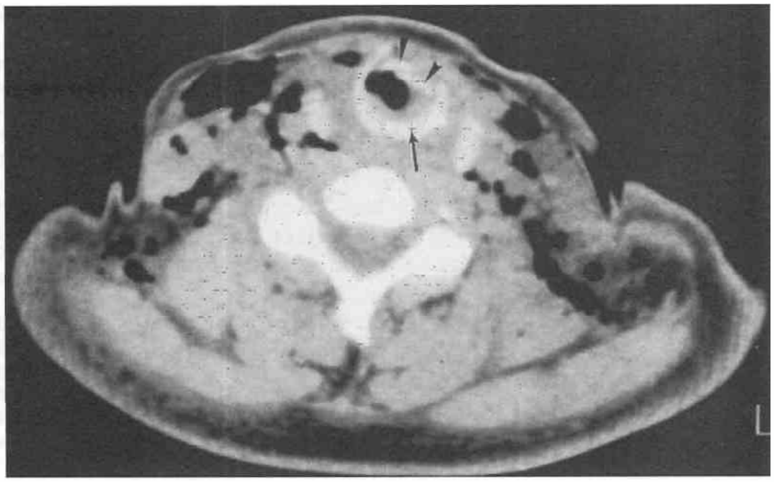

Figure 18–25. Fracture of the cricoid cartilage; the ring has been fractured. Fragments from the anterior ring *(arrowheads)* have been pushed back into the airway. These fragments would be in danger of perforating the mucosa. The lamina of the cricoid *(arrow)* is not fractured. Note the air in the soft tissues and the soft tissue within the ring of the cricoid cartilage. (From Curtin HD: MR and CT of the larynx. In Thrall JH [ed]: Current Practice of Radiology, 3rd ed. St. Louis, Mosby–Year Book, 1994.)

muscle. The vocal ligament remains, and the arytenoid cartilage may be in a fairly normal position or may be tipped slightly. The piriform sinus on the affected side often enlarges as well.

The posterior cricoarytenoid muscle is very thin, but since the axial plane provides a perfect cross-section, atrophy of this muscle may also be appreciated.[22] In this case, fat appears to be closely applied to the posterior surface of the cricoid cartilage instead of the typical muscle density.

In most instances, atrophied muscle is seen in patients with known paralysis. If the cause of the paralysis is not known, the course of the vagus nerve and the recurrent laryngeal nerve is examined. CT scanning is usually performed because of the distance that must be covered and because bone detail is important at the level of the jugular foramen in the temporal bone. The nerve is just posterior to the carotid artery and jugular vein on transit through the neck. Lower in the neck, the nerve moves forward with respect to the carotid artery. The left nerve loops around the aortic arch, and the right nerve loops around the subclavian artery. The nerve on both sides ascends along the tracheoesophageal groove to reach the larynx. A lesion at any level can involve the nerve and cause paralysis.

Superior laryngeal nerve paralysis is much less common, and characteristic radiographic findings have not been described. An extremely rare paralysis is "adductor paralysis." In this form, all muscles innervated by the recurrent laryngeal nerve are affected except the posterior cricoarytenoid. This muscle, unopposed, rotates the arytenoid and the cord laterally. This rare form of paralysis is not as well understood as the other more common paralyses but is thought to be related to an intracranial pathologic process.

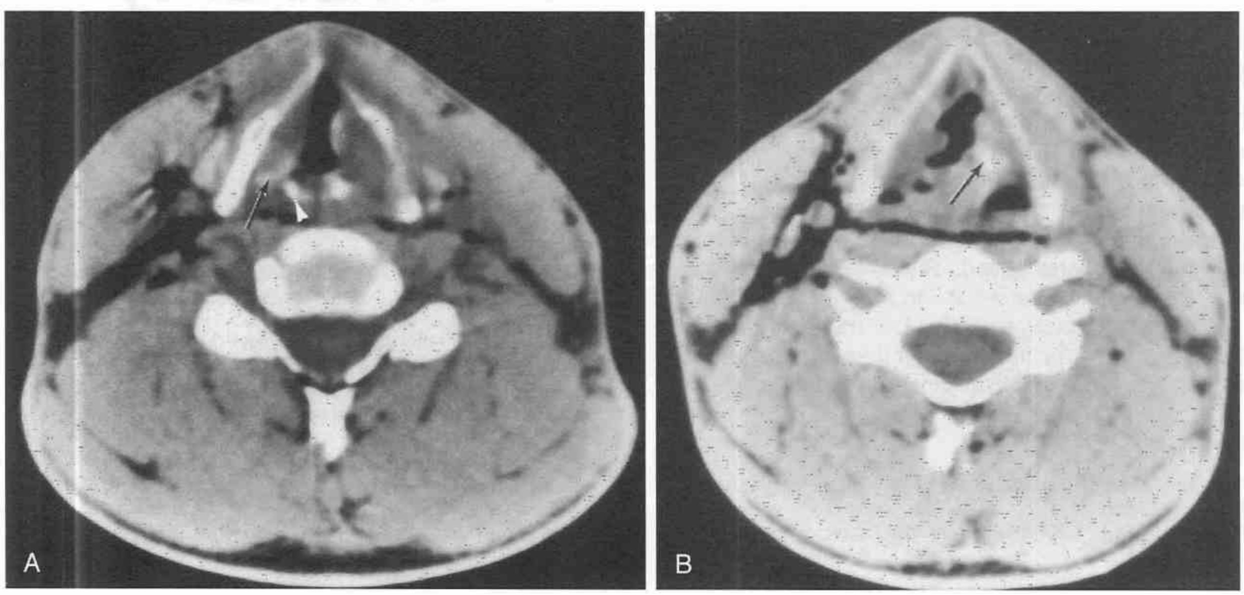

Figure 18–26. Arytenoid dislocation. *A,* CT axial slice through the level of the cricoarytenoid joint. There is a normal configuration on the right. The arytenoid cartilage *(arrow)* articulates normally with the small articular surface of the cricoid *(arrowhead)* on the superior edge of the cricoid cartilage. The arytenoid on the left is not identified in a normal position. *B,* Higher slice shows the dislocated arytenoid *(arrow)* in the supraglottic area.

Stenosis

Subglottic stenosis and tracheal stenosis can be evaluated by plain films, but imaging can give information about the cross-sectional area of the remaining airway. CT can show narrowing or stenosis of anterior and posterior commissures. The position of the cartilage relative to the airway can also be visualized. CT scans can determine whether the cartilage has collapsed into the airway or whether the cartilage remains in the normal position with the stenosis related only to soft tissue.

Such narrowing can be congenital or may be the result of trauma. Granulation tissue can develop after tracheostomy. The length of the narrowing and the relationship to the vocal cords should be estimated. Plain films can be very helpful in estimating the length of the abnormality.

Granulomatous Disease

Granulomatous disease, either of infectious or noninfectious etiology, can involve the larynx. Although rare, it can involve any of the mucosal surfaces and can be mistaken for tumor. The findings at imaging are nonspecific.

Rheumatoid Arthritis

Rheumatoid arthritis can involve the cricoarytenoid joint. This process is not usually evaluated radiologically.

Polychondritis

Relapsing polychondritis is a rare disease of unknown etiology. The cartilages of the larynx and trachea (among others) become inflamed, with edema of surrounding tissues. Calcifications of the abnormal tissue are characteristic and can be highly prominent. If calcifications are particularly prominent, the increased soft tissues and calcifications can mimic chondroid lesions.

Summary

CT or MRI can be done for tumor imaging. One approach is to do CT as a first step, reserving MRI for answering specific questions remaining after CT. MRI is then done in a small fraction of cases. At our institution we begin with MRI in those cases where supraglottic laryngectomy is contemplated. This is because of a preference for MRI when looking at the region of the ventricle and the thyroarytenoid muscle. Contrast-enhanced CT scans are preferred for imaging of submucosal masses. CT scans are done without enhancement in trauma cases.

References

1. Bailey BJ, Biller HF (eds): Surgery of the Larynx. Philadelphia, WB Saunders, 1985.
2. Barnes L, Gnepp DR: Diseases of the larynx, hypopharynx, and esophagus. In Barnes L (ed): Surgical Pathology of the Head and Neck, vol 1. New York, Marcel Dekker, 1985, pp 141–226.
3. Becker M, Moulin G, Kurt AM, et al: Non-squamous cell neoplasms of the larynx: Radiologic-pathologic correlation. Radiographics 18: 1189–1209, 1998.
4. Becker M, Zbaren P, Delavelle J, et al: Neoplastic invasion of the laryngeal cartilage: Reassessment of criteria for diagnosis at CT. Radiology 203:521–532, 1997.
5. Becker M, Abaren P, Laeng H, et al: Neoplastic invasion of the laryngeal cartilage: Comparison of MR imaging and CT with histopathologic correlation. Radiology 194:661–669, 1995.
6. Bruning R Sturm C, Hong C, et al: The diagnosis of stages T1 and T2 in laryngeal carcinoma with multislice spiral CT. Radiologie 39: 939–942, 1999.
7. Castelijns JA, Gerritsen GJ, Kaiser MC, et al: Invasion of laryngeal cartilage by cancer: Comparison of CT and MR imaging. Radiology 166:199–206, 1987.
8. Castelijns JA, Gerritsen GJ, Kaiser MC, et al: MRI of normal or cancerous laryngeal cartilages: Histopathologic correlation. Laryngoscope 97:1085–1093, 1987.
9. Castelijns JA, van den Brekel MW, Smit EM et al: Predictive value of MR imaging-dependent and non-MR imaging-dependent parameters for recurrence of laryngeal cancer after radiation therapy. Radiology 196:735–739, 1995.
10. Cummings CW, Fredrickson JM, Harker LA, et al: Otolaryngology–Head and Neck Surgery, 3rd ed, vol 3. St. Louis, Mosby–Year Book, 1998.
11. Curtin HD: Imaging of the larynx: Current concepts. Radiology 173: 1–11, 1989.
12. Curtin HD: The larynx. In Som PM, Curtin HD (eds): Head and Neck Imaging, 3rd ed, vol 1. St. Louis, Mosby–Year Book, 1996, pp 612–707.
13. Curtin HD: Imaging of the larynx. In Valvassori GE. Mafee MF, Carter BL (eds): Imaging of the Head and Neck. New York, Thieme, 1995, pp 366–389.
14. Giron J, Joffre P, Serres-Cousine O, et al: Magnetic resonance imaging of the larynx: Its contribution compared to x-ray computed tomography in the pre-therapeutic evaluation of cancers of the larynx. Apropos of 90 surgical cases. Ann Radiol (Paris) 33:170–184, 1990.
15. Gray H, Williams PL, Bannister LH: Gray's Anatomy: The Anatomical Basis of Medicine and Surgery, 38th ed. New York, Churchill Livingstone, 1995.
16. Kirchner JA: Two hundred laryngeal cancers: Patterns of growth and spread as seen in serial section. Laryngoscope 87:474–482, 1977.
17. Kolbenstvedt A, Charania B, Natvig, et al: Computed tomography in T1 carcinoma of the larynx. Acta Radiol 30:467–469, 1989.
18. Lawson W, Biller HF, Suen JR: Cancer of the larynx. In Suen JY, Myers EN (eds): Cancer of the Head and Neck. New York, Churchill Livingstone, 1989, pp 533–556.
19. Levine PA, Brasnu DF, Ruparelia A, et al: Management of advanced-stage laryngeal cancer. Otolaryngol Clin North Am 30:101–112, 1997.
20. Mancuso AA, Mukherji SK, Schmalfuss J, et al: Preradiotherapy computed tomography as a predictor of local control in supraglottic carcinoma. J Clin Oncol 17:631–637, 1999.
21. Phelps PD: Review: carcinoma of the larynx: The role of imaging in staging and pre-treatment assessments. Clin Radiol 46:77–83, 1992.
22. Romo LV, Curtin HD: Atrophy of the posterior cricoarytenoid muscle as an indicator of recurrent laryngeal nerve palsy. AJNR Am J Neuroradiol 20:467–471, 1999.
23. Sakai F, Gamsu G, Dillon WP, et al: MR imaging of the larynx at 1.5 T. J Comput Assist Tomogr 14:60–71, 1990.
24. Teresi LM, Lufkin RB, Hanafee WN: Magnetic resonance imaging of the larynx. Radiol Clin North Am 27:393–406, 1989.
25. Tucker GF, Smith HR: A histological demonstration of the development of laryngeal connective tissue compartments. Trans Am Acad Ophthal Otol 66:303–318, 1962.
26. Zeitels SM: Surgical management of early supraglottic cancer. Otolaryngol Clin 30:59–78, 1997.
27. Zeitels SM, Kirchner JA: Hyoepiglottic ligament in supraglottic cancer. Ann Otol Rhinol Laryngol 104 (10 pt 1):770–775, 1995.

19

Nasopharynx and Oropharynx

Sherif Gamal Nour, Jonathan S. Lewin

The pharynx is a fibromuscular tube that forms the upper part of the aerodigestive tract. It extends from the skull base down to the C6 vertebral level, serving as a conduit that conveys both air and food to the respiratory and alimentary tracts, respectively. The nasopharynx, oropharynx, and hypopharynx (laryngopharynx) are the three classic pharyngeal subdivisions that lie directly on the spine behind the nose, oral cavity, and larynx, respectively. The nasopharynx and oropharynx constitute the suprahyoid part of the pharynx. Formed of a thin muscle layer, the pharyngeal wall is lined by a mucous membrane and covered by loose fascia that permits pharyngeal movement during deglutition.[113, 116]

A diverse range of pathologic conditions may involve the nasopharynx and oropharynx. These may occur primarily within the layers of the pharyngeal wall or in the deep suprahyoid neck spaces adjacent to the pharynx, or they may protrude from the nose or skull base to hang in the airway as pharyngeal masses. In addition, pharyngeal disease may be a consequence of functional rather than anatomic derangement.

Prior to the modern imaging era, few tools were available for investigating pharyngeal disease. Having no more than a lateral plain x-ray, a conventional tomogram, or a contrast laryngopharyngogram, the radiologist had to depend on such signs as soft tissue fullness, intraluminal filling defects, and abnormalities in the pharyngeal margins imaged in profile[145]; all of these signs constituted indirect evidence of pathology, yet no means existed to visualize the actual disease process.

Although amenable to clinical inspection, pharyngeal mucosal lesions may be difficult to evaluate because of anatomic variations and patient compliance.[145] A mucosal lesion, as detected by endoscopy, may represent no more than the "tip of an iceberg," with the exact deep extent always remaining uncertain to the endoscopist. Moreover, associated cervical lymph nodes, unless of palpable size, may be overlooked in the clinical setting.

The advent of cross-sectional imaging exemplified in computed tomography (CT), then magnetic resonance imaging (MRI), has revolutionized the diagnosis of pharyngeal and deep neck disease. For the first time, the radiologist was able to gain true insight into the actual pathology, to define its exact site of origin, to map out its extent, and to study its effect on vital neighboring neck structures. With this wealth of information, the radiologist could interact with the clinician in a more effective manner and could make invaluable contributions to treatment decision making.

The improved understanding of the complex suprahyoid neck anatomy offered by these modern imaging modalities has led to the development of a new approach to the diagnosis of pathologic conditions involving this region that utilizes the concept of fascially defined spaces rather than the classic pharyngeal subdivisions. As CT and MRI have become the basic tools for evaluating nasopharyngeal and oropharyngeal pathology, the current classifications of nasopharyngeal and oropharyngeal carcinomas adopted by the International Union Against Cancer (UICC) and the American Joint Committee on Cancer (AJCC) are now based on cross-sectional imaging findings.

The continuing evolution of MRI has gone beyond the mere imaging of anatomic changes to approach near real-time recording of the functional status of the pharynx, and the time is not far before the radiologic focus of interest broadens to include disorders of pharyngeal function, such as obstructive sleep apnea.

Finally, interventional MRI is a rapidly growing part of current radiologic practice and has been successfully applied to the pharynx and adjoining deep neck spaces to guide biopsies and minimally invasive therapeutic procedures.

Anatomy

The topics to be discussed are summarized in Box 19–1.

Traditional Classification

Classically, the suprahyoid head and neck region is divided into the nasopharynx, oropharynx, and oral cavity (Fig. 19–1), with the exact contents of each compartment dependent on how much of the adjoining deep tissues are included.[4, 65, 128]

Nasopharynx

The *nasopharynx* is the uppermost part of the aerodigestive tract. It measures approximately 2 × 4 cm in anteroposterior and craniocaudal diameters, respectively. It is bounded posterosuperiorly by the basisphenoid, basiocciput, and upper two cervical vertebrae as well as by the prevertebral muscles.[65, 108, 113, 128]

Anteriorly, it communicates with the nasal cavity through the choana. Inferiorly, it is in direct continuity with the oropharynx, and the plane of division is a horizontal line drawn along the hard and soft palates and passing

Box 19–1. Anatomy

I. **Traditional Classification**
   A. Nasopharynx
   B. Oropharynx
II. **Spatial Approach**
   A. Superficial fascia
   B. Deep fascia
      1. Superficial layer (investing fascia)
         a. Description
         b. Spaces included
            (1) Masticator space
            (2) Parotid space
            (3) Submandibular and sublingual spaces
            (4) Muscular space
            (5) Suprasternal space (of Burns)
      2. Deep layer (prevertebral fascia)
         a. Description
         b. Spaces included
            (1) Perivertebral space
            (2) Danger space
      3. Middle layer (visceral fascia)
         a. Description
            (1) Buccopharyngeal fascia
            (2) Cloison sagittale
            (3) Fascia of tensor veli palatini
         b. Pharyngobasilar fascia (pharyngeal aponeurosis)
         c. Spaces included
            (1) Pharyngeal mucosal space
            (2) Retropharyngeal space
            (3) Parapharyngeal space
               (a) Prestyloid
               (b) Retrostyloid

posteriorly to the *Passavant's ridge* (a ridge of pharyngeal musculature that opposes the elevated soft palate).[65, 108, 113, 128, 142] The features of the lateral nasopharyngeal walls are discussed later.

Oropharynx

The oropharynx is the part of the aerodigestive tract that lies behind the oral cavity (it can be seen through the open mouth). It is separated from the oral cavity by the circumvallate papillae of the tongue, the anterior tonsillar pillars, and by the soft palate. The posterior third of the tongue and lingual tonsil are therefore considered to be within the oropharynx and not in the oral cavity.[65]

Posteriorly, the superior and middle constrictor muscles separate the oropharynx from the prevertebral muscles overlying the second and third cervical vertebrae.

Superiorly, the oropharynx communicates with the nasopharynx.

Inferiorly, it is separated from the hypopharynx by the pharyngoepiglottic fold and from the larynx by the epiglottis and glossoepiglottic fold.[65, 119, 128]

The features of the lateral oropharyngeal walls include two faucial arches:

1. The anterior (palatoglossus muscle) arch.
2. The posterior (palatopharyngeus muscle) arch.

Between them lies the tonsillar fossa, which contains the palatine tonsil on each side.[119]

Spatial Approach

Although the classic classification of nasopharynx, oropharynx, and hypopharynx is quite effective in regard to superficial mucosal lesions, such as squamous cell carcinoma, this "non-fascially based" classification is much less helpful to the radiologist attempting to accurately localize deeply seated head and neck lesions as evaluated on cross-sectional imaging.[4, 65]

The traditional classification of the suprahyoid head and neck into the nasopharynx, oropharynx, and oral cavity has thus been largely replaced by a somewhat complicated, yet more useful scheme that divides this region into multiple spaces, defined by the layers of cervical fascia. Such a "spatial approach" provides a satisfactory means of localizing the space of origin of a suprahyoid lesion and, consequently, helps to limit the differential diagnosis to a unique set of pathologic processes specific to each anatomic space.[4, 40, 65, 67, 128, 162] Moreover, it utilizes surgically and pathologically defined terminology, thereby creating a "common language" for the radiologist and the referring surgeon.[65]

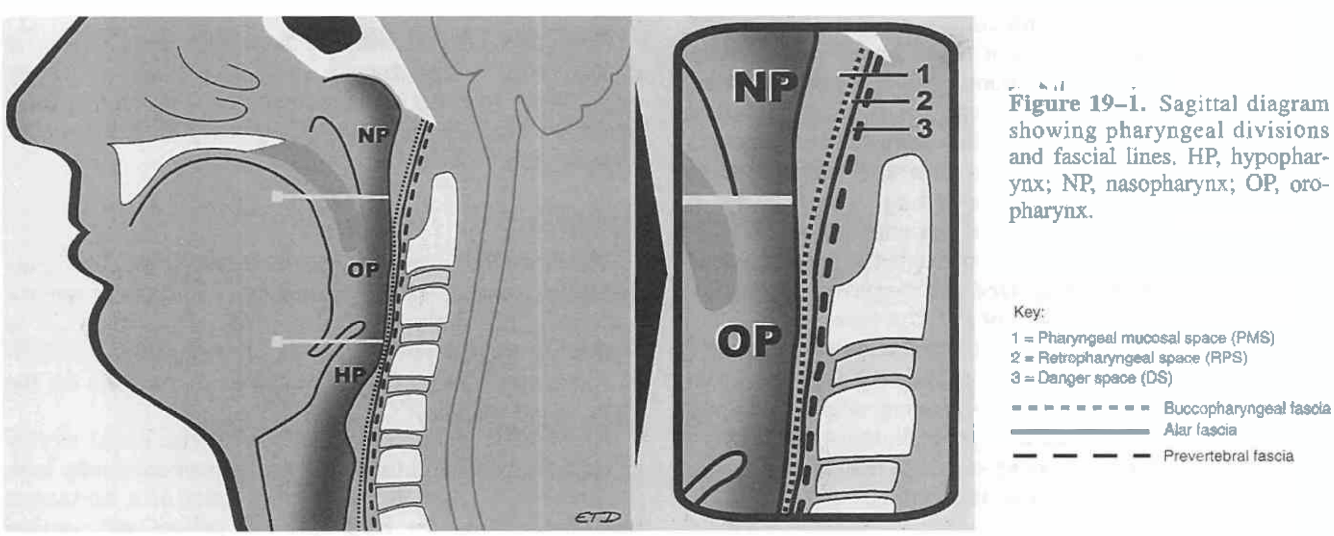

Figure 19–1. Sagittal diagram showing pharyngeal divisions and fascial lines. HP, hypopharynx; NP, nasopharynx; OP, oropharynx.

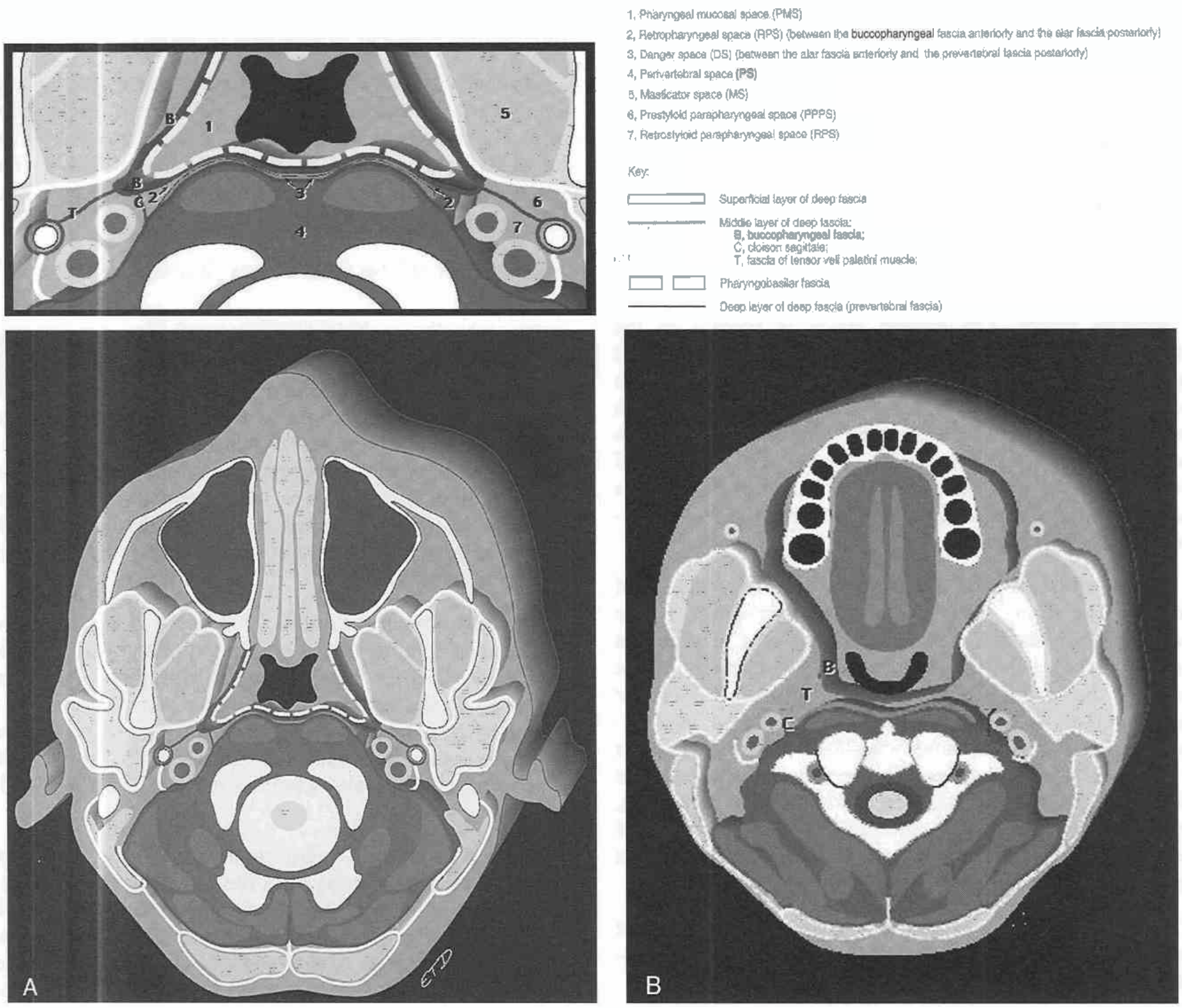

Figure 19–2. Diagrammatic layout of the suprahyoid neck spaces and their fascial boundaries at the level of the nasopharynx *(A)*, detail of the nasopharynx *(inset)*, and the oropharynx *(B)*.

Crucial to an appreciation of suprahyoid neck spaces is a proper understanding of the fascial framework of the head and neck (Fig. 19–2; see Figs. 19–5 and 19–6). For the sake of completeness, each of these spaces is addressed here, with particular emphasis given to those most relevant to the subject of this chapter.

Basically, two major compartments constitute the head and neck fasciae: the superficial and deep layers.

Superficial Fascia

The superficial fascia is a loose fatty layer, with the platysma muscle embedded in its deep portion.[61, 87]

Deep Fascia

The deep fascia is a complex of multiple sheets, which are generally subdivided into three layers:

- A superficial layer (investing fascia)
- A deep layer (prevertebral fascia)
- A middle layer (visceral fascia)

Superficial Layer of the Deep Fascia (Investing Fascia)

Description

The superficial layer forms a complete collar around the neck and is attached *superiorly* to the lower border of the mandibular body back to its angle and more posteriorly to the mastoid processes, the superior nuchal line, and to the external occipital protuberance.

Inferiorly, this layer attaches to the acromion and spine of the scapula, to the clavicle, and to the manubrium sterni. The two halves of the investing fascia attach *posteriorly* to the ligamentum nuchae and cervical spinal processes.

Anteriorly, they are continuous and are attached to the hyoid bone, where they converge with the middle (visceral) layer of the deep fascia, dividing the neck into suprahyoid and infrahyoid portions.[61, 113]

Spaces

The investing fascia splits to enclose number of structures within the neck, thereby forming the following fascial spaces:

Masticator Space. Above the attachment to the lower border of the mandible, a part of the investing fascia continues upward to enclose the muscles of mastication and the mandible (ramus and posterior body) by splitting into a superficial and a deep layer. The superficial layer covers the masseter muscle and then attaches to the zygomatic arch (this is continuous with the fascia covering the parotid gland forming the parotid-masseteric fascia). The deep layer runs deep to both pterygoid muscles to attach to the skull base, separating the masticator from the prestyloid compartment of the *parapharyngeal space* (PPS).[40, 61, 64, 70]

Parotid Space. The parotid space is formed as the investing fascia splits between the mastoid process and the angle of the mandible to enclose the gland, forming its capsule.[14, 16] The medial aspect of the parotid space, which contains the deep lobe of the parotid gland, extends through the stylomandibular tunnel (the gap between the styloid process and the posterior margin of the mandible) for a variable distance before it meets the prestyloid compartment of the PPS.[87]

Submandibular and Sublingual Spaces. A layer of the investing fascia splits to line the undersurface of the submandibular gland before reattaching to the mandible at the mylohyoid line, thereby forming the capsule of the gland. In the radiologic literature, the term *submandibular space* is given to the entire area superficial to the mylohyoid muscle down to the superficial layer of investing fascia as it extends from the hyoid bone to the mandible. The *sublingual space* is the area deep to the mylohyoid muscle, up to the mucosa of the mouth floor. The relevance of these spaces to this chapter is their free communication with the prestyloid compartment of the PPS.[70, 87]

Muscular Spaces. Muscular spaces are formed as the fascia splits to enclose the trapezius, the sternocleidomastoid, and the inferior belly of the omohyoid muscles.[61, 70]

Suprasternal Space (of Burns). This shallow space is formed just above the manubrium sterni as the investing fascia splits to attach to the anterior and posterior borders of the jugular notch.[61, 70]

Deep Layer of the Deep Fascia (Prevertebral Fascia)

Description

The deep layer encircles the vertebral column as well as the paraspinal and prevertebral muscles, with a firm insertion on the spinous and transverse processes of the vertebral column. The prevertebral fascia extends from the skull base down to the third thoracic vertebra, where it fuses with the anterior longitudinal ligament in the posterior mediastinum.[61, 113] Some authors have described a slip of the prevertebral fascia, the alar fascia, which is immediately anterior to it and has a similar coronal plane of orientation.[61, 87]

Spaces

Perivertebral Space. The perivertebral space (PVS) is enclosed by the circumferential prevertebral fascia and is divided by the fascial attachment to the cervical transverse processes into the anterior prevertebral and posterior paraspinal compartments.[65, 67, 128] This space extends from the skull base to the coccyx and is tight enough to resist the superoinferior spread of infection or neoplasms.[132]

Danger Space. This thin potential space lies between the prevertebral fascia posteriorly and the alar fascia anteriorly. The space is named as such because it extends from the skull base to the level of the diaphragm and is filled with loose areolar tissue, which provides a ready conduit for the spread of infection.[132]

Middle Layer of the Deep Fascia (Visceral Fascia)

Description

There has been considerable confusion in the literature concerning the layers composing the visceral fascia, with most of the anatomic references focusing mainly on the pretracheal fascia in regard to the fascial layers between the investing and prevertebral fasciae.[61, 113] However, to give the reader a full understanding of the spatial anatomy of this region, it would be more appropriate in this context to stress the layers relevant to the suprahyoid neck. The following basic fascial planes comprise the visceral fascia above the hyoid bone.

Buccopharyngeal Fascia. This fascia is a thin layer of loose connective tissue that covers the pharyngeal constrictor muscles and permits pharyngeal movement. It attaches superiorly to the skull base, having the same attachment as the pharyngobasilar fascia (see later), and is continuous anteriorly over the buccinator muscle.[65, 70, 113, 119, 128] The buccopharyngeal fascia is not visible on CT scans or MR images.[83]

Cloison Sagittale. These bilateral, small, sagittally oriented fascial slips extend from the buccopharyngeal fascia anteriorly to the prevertebral fascia posteriorly, near its attachment to the transverse processes of the cervical vertebrae. The importance of these tiny fascial slips is that they separate the medially positioned *retropharyngeal space* (RPS) from the laterally positioned retrostyloid compartments of the PPS.[87] These slips are sometimes also called the *alar fascia*, but this term is better avoided to prevent confusion with the alar fascia described earlier.[87]

Fascia of Tensor Veli Palatini. This relatively thick fascial sheet envelops the styloid process and its musculature and extends anteromedially to merge with the fascia associated with the tensor veli palatini muscle. It then continues further anteriorly to fuse with the pterygomandibular raphe and the buccopharyngeal fascia.[40, 158] This fascial layer divides the PPS into anterolateral (prestyloid) and posteromedial (retrostyloid) compartments.[40, 158]

Pharyngobasilar Fascia (Pharyngeal Aponeurosis)

This important fourth fascial sheet lies between the superficial and the deep layers of the deep fascia, but it is usually considered to be separate from the middle layer. As a tough membrane, it forms an almost closed, very resistant chamber that determines the configuration of the nasopharynx.[83, 142] It attaches superiorly to the skull base from the medial pterygoid plates, passing posteriorly to the petrous bones just anterior to the carotid foramina, where it reflects medially on either side to be continuous over the longus capitis and rectus capitis muscles. The fascia de-

scends from the skull base, forming an elongated ring that closes the gaps above the superior constrictor muscle of the pharynx bilaterally.

References on anatomy describe the fascia to then continue lining the inner surface of the pharyngeal musculature, thereby supporting the mucous membrane of most of the nasal portion of the pharynx, then it becomes much thinner below, at about the level of the soft palate.[70, 83, 96, 113, 119, 128] From the functional and imaging perspectives, the most relevant portion of the pharyngobasilar fascia is that above the superior constrictor muscle, hence the name the *pharyngeal aponeurosis* (see Fig. 19–5). Formed of dense fibrous tissue, the pharyngobasilar fascia shows up on MRI images as a low-intensity line extending from the medial pterygoid plate to the carotid foramen medial to the tensor palatini.[83]

Thus, the constrictor muscles of the pharynx are "sandwiched" between the pharyngobasilar fascia (inside) and the buccopharyngeal fascia (outside). Above the upper edge of the superior constrictor muscle (between it and the skull base), the two fascial layers blend to form, along with the lining mucosa, the thin wall of the lateral pharyngeal recesses (fossae of Rosenmüller).[83, 96, 113] Anterior to these recesses, a natural defect in the pharyngobasilar fascia (sinus of Morgagni) exists on each side, transmitting the eustachian tubes and levator veli palatini muscles from the skull base to the *pharyngeal mucosal space* (PMS).[83, 96, 119, 128] The torus tubarius, the most prominent anatomic landmark on the lateral nasopharyngeal walls, is a ridge lying between the orifice of the eustachian tube anteroinferiorly and the fossa of Rosenmüller posterosuperiorly on each side. It is formed by the levator veli palatini muscle together with the cartilaginous eustachian tube and the overlying mucosa.[83, 96, 119]

Spaces

The deep face and neck spaces, defined by the just-described layers of visceral fascia, are presented next.

Pharyngeal Mucosal Space. The PMS is the area of the nasopharynx and oropharynx on the inner (airway) side of the buccopharyngeal fascia. The latter separates the PMS from the PPS laterally and the RPS posteriorly. The PMS is thus composed of the five layers forming the pharyngeal wall. From internal to external, they are as follows[113]:

1. *Mucous membrane*. The upper part of the nasopharynx is lined by respiratory epithelium (pseudostratified ciliated columnar). Inferiorly, where food contact is more of an issue, the epithelium changes to a stratified squamous type.[96]
2. *Submucosa*. The submucosa contains minor salivary glands and prominent lymphoid tissue of Waldeyer's ring (adenoids, palatine tonsils, lingual tonsils, and submucosal lymphatics). Lymphoid tissue may also normally be present in the epithelium (lymphoepithelium).[65, 96, 128]
3. *Dense pharyngobasilar fascia*.
4. *Superior constrictor muscle of the pharynx*. Above this muscle, layers 3 and 5 are adherent and are pierced by the eustachian tube (cartilaginous end) and the levator palatini muscle, which are considered within the PMS.
5. *Thin buccopharyngeal fascia*. This fascia forms the outer confinement of the PMS.

Retropharyngeal Space. The RPS[87, 128] is a small, potential space that is bounded as follows:

1. *Anteriorly* by the buccopharyngeal fascia, separating it from the PMS.
2. *Posteriorly* by the prevertebral fascia, separating it from the perivertebral space.
3. *Laterally* by the cloison sagittale, separating it from the retrostyloid compartment of the PPS on each side.[87]
4. *Superiorly* by the skull base.
5. *Inferiorly* by the fusion of the buccopharyngeal and prevertebral fasciae between the T2 and T6 spinal levels.[45]

The RPS normally contains a small amount of fat and, in the suprahyoid region, the lateral (nodes of Rouviere) and medial retropharyngeal lymph nodes.[45, 65]

The medial retropharyngeal lymph nodes are located near the midline and are seldom seen unless they are pathologically enlarged.[39, 45] The lateral retropharyngeal (LRP) lymph nodes are found immediately medial to the internal carotid artery, adjacent to the longus capitis muscle, and are usually most prominent at the C1-C2 level but can occasionally be visualized down to the level of the palate.[39, 45, 101] The LRP nodes are usually identified on MR images and, to a lesser extent, on CT scans.

In adults, the nodes are usually smaller than 3 to 5 mm, but nodes of up to 1 cm can be considered normal if they are homogeneous.[45, 101] In children, the LRP nodes may be as large as 2 cm in size, particularly if the adenoids are prominent.[39] This lymph node chain provides drainage for the nasopharynx, oropharynx, middle ear, nasal cavities, and paranasal sinuses.[39, 132]

Parapharyngeal Space. The PPS is an anatomic recess, shaped like an inverted pyramid with its base at the base of the skull and its apex at the greater cornu of the hyoid bone. It occupies the space between the muscles of mastication and the deglutitional muscles.[40, 67, 131, 156, 158] It has the following boundaries and relations:

1. *Laterally*
   a. *Anterolaterally;* separated from the masticator space by the layer of investing fascia covering the medial aspect of the medial pterygoid muscle.[28, 96, 119, 158]
   b. *Posterolaterally;* separated from the parotid space by the layer of investing fascia covering the deep lobe of the parotid gland.[119, 158] However, this is a sparse fascial layer that does not present a barrier to the spread of disease.[87]
2. *Medially;* separated from the PMS by the buccopharyngeal fascia, while its extreme posterior part is separated from the RPS by the cloison sagittale.[103, 128, 158]
3. *Posteriorly;* separated from the perivertebral space by the prevertebral fascia.[103, 119, 158]
4. *Anteriorly*
   a. *Anterosuperiorly* (at the level of the pterygomandibular raphe); closed by the convergence of the buccopharyngeal fascia with the fascia covering the medial aspect of the medial pterygoid muscle.[87, 119]
   b. *Anteroinferiorly* (at the level of the mylohyoid muscle); PPS is often continuous with the sublingual and submandibular spaces, thereby allowing lesions to

pass from one space to another without crossing a fascial boundary.[36, 65, 70]

5. *Inferiorly;* PPS is generally described as extending down to the hyoid bone; however, the fusion of multiple fascial layers and muscle sheaths near the angle of the mandible limit the caudal extent of the space,[87] and the styloglossus muscle can be considered the functional inferior boundary of the PPS.[87]

The PPS, as just defined, is a larger area of the deep face than the fatty triangles seen on either side of the pharynx. This definition, which is supported by most authors, implies the division of the PPS by the fascia of tensor veli palatini (see earlier) into the following[87, 131]:

1. *Prestyloid PPS,* anterolateral to the fascia.
2. *Retrostyloid PPS,* posteromedial to the fascia. This is the suprahyoid extension of the carotid space (carotid sheath and its contents).

The contents of the suprahyoid neck spaces along with the common disease processes involving each space are listed in Table 19–1.

Table 19–1. Anatomic Spaces of the Suprahyoid Neck: Their Contents and Common Disease Processes

	Contents	Differential Diagnosis of Lesions
Pharyngeal mucosal space (PMS)	1. Mucosa 2. Submucosa containing a. Minor salivary glands b. Lymphoid tissue (adenoids, palatine, and lingual tonsils) 3. Pharyngobasilar fascia 4. Superior and middle constrictor muscles 5. Buccopharyngeal fascia (enclosing layer) + Cartilaginous eustachian tube } Originate outside PMS + Levator veli palatini muscle	***Pseudomass*** • Asymmetric fossae of Rosenmüller • Pharyngitis • Infectious • Postirradiation ***Congenital*** Thornwaldt's cyst ***Inflammatory*** • *Adenoidal and tonsillar: hypertrophy, inflammation, abscess* • Postinflammatory • Dystrophic calcification • Retention cyst ***Benign tumor*** • *Juvenile angiofibroma* • Pleomorphic adenoma (benign mixed tumor) of minor salivary glands ***Malignant tumor*** • *Squamous cell carcinoma* • *Non-Hodgkin's lymphoma* • Minor salivary gland malignancy • Rhabdomyosarcoma (pediatric)
Prestyloid parapharyngeal space (PPPS)	1. Fat 2. Pterygoid venous plexus 3. Internal maxillary artery 4. Ascending pharyngeal artery 5. Branches of the mandibular division (V3) of trigeminal nerve	***Pseudomass*** • *Asymmetrical pterygoid venous plexus* ***Congenital*** • 2nd branchial cleft cyst ***Inflammatory*** • *Spread of infection* from adjacent spaces • PMS: pharyngitis, adenoiditis, tonsillitis, peritonsillar abscess, retromandibular vein thrombosis • PS: parotid calculus disease, deep lobe parotid abscess • MS: dental infection, 3rd upper molar extraction with violation of pterygomandibular raphe • Infection secondary to penetrating trauma to the lateral pharyngeal wall ***Benign tumor*** • Pleomorphic adenoma (benign mixed tumor) • Extending from deep lobe of parotid gland • Arising from salivary gland rests in PPS • Lipoma ***Malignant tumor*** • Mucoepidermoid carcinoma, Adenoid cystic carcinoma, Malignant mixed tumor } of salivary gland rest in PPS • *Spread of malignancy* from • Adjacent spaces • PMS: squamous cell carcinoma, non-Hodgkin's lymphoma, minor salivary gland malignancy • PS: mucoepidermoid carcinoma, adenoid cystic carcinoma • MS: sarcoma • Skull base tumor

Table continued on following page

RoshanKetab
Medical Publishers
TEHRAN - IRAN
Tel: +98 (21) 66950639
TelFax: +98 (21) 66963783-6

Table 19–1. Anatomic Spaces of the Suprahyoid Neck: Their Contents and Common Disease Processes *Continued*

	Contents	Differential Diagnosis of Lesions

Retrostyloid parapharyngeal space (RPPS)
Carotid space (CS)
	1. Internal carotid artery
	2. Internal jugular vein
	3. Lower 4 cranial nerves (IX–XII)
	4. Sympathetic chain
	5. Lymph nodes (deep cervical chain)
		Pseudomass
		• *Ectatic internal carotid artery*
		• *Asymmetrical internal jugular veins*
		Inflammatory
		• Carotid space cellulitis or abscess
		  • Spread from adjacent spaces
		  • Breakdown of infected internal jugular lymph nodes
		Vascular
		• *Internal jugular vein thrombosis or thrombophlebitis*
		• *Internal carotid artery thrombosis, mural thrombus, aneurysm, pseudoaneurysm, or dissection*
		Benign tumor
		• *Paraganglioma*
		  • Glomus jugulare
		  • Glomus vagale
		  • Carotid body tumor
		• Nerve sheath tumor
		  • *Schwannoma*
		  • Neurofibroma
		• Meningioma (of jugular foramen)
		Malignant tumor
		• *Lymph node metastasis from squamous cell carcinoma*
		• *Direct invasion by primary squamous cell carcinoma*
		• *Non-Hodgkin's lymphoma*

Retropharyngeal space (RPS)	1. Fat
	2. Lymph nodes
	  a. Lateral retropharyngeal (of Rouviere)
	  b. Medial retropharyngeal
		Pseudomass
		• Tortuous internal carotid artery
		• Edema fluid or lymph spilling into RPS secondary to venous or lymphatic obstruction
		Congenital
		• Hemangioma
		• Lymphangioma
		Inflammatory
		• *Reactive adenopathy*
		• *Suppurative adenopathy (intranodal abscess)*
		• *Cellulitis, abscess*
		Benign tumor
		• Lipoma
		Malignant tumor
		• Nodal metastases
		  • *Squamous cell carcinoma of head and neck (most common: nasopharynx)*
		  • Melanoma
		  • Thyroid carcinoma
		• *Nodal non-Hodgkin's lymphoma*
		• *Direct invasion from primary squamous cell carcinoma (especially posterior wall primary lesions)*

Masticator space (MS)	1. Mandible (ramus + posterior body)
	2. Muscles of mastication
	  a. Lateral pterygoid
	  b. Medial pterygoid
	  c. Masseter
	  d. Temporalis
	3. Inferior alveolar and lingual nerves (branches of the mandibular division V3 of trigeminal nerve)
		Pseudomass
		• *Accessory parotid gland*
		• *Benign masseteric hypertrophy (unilateral/bilateral)*
		• Mandibular nerve (cranial nerve V3) denervation atrophy
		Congenital
		• Hemangioma
		• Lymphangioma
		Inflammatory
		• *Odontogenic abscess (especially lower 2nd and 3rd molars)*
		• Mandibular osteomyelitis
		Benign tumor
		• Osteoblastoma
		• Leiomyoma
		• Nerve sheath tumor (schwannoma-neurofibroma)
		Malignant tumor
		• *Sarcoma: chondrosarcoma, osteosarcoma, soft tissue sarcoma*
		• Malignant schwannoma
		• *Non-Hodgkin's lymphoma*
		• *Infiltrating squamous cell carcinoma from oropharynx (retromolar trigone)*
		• *Rhabdomyosarcoma (pediatric)*
		• Mandibular metastases (from cancer of lung, breast, kidney)

Table continued on following page

Table 19–1. Anatomic Spaces of the Suprahyoid Neck: Their Contents and Common Disease Processes *Continued*

	Contents	Differential Diagnosis of Lesions
Parotid space (PS)	1. Parotid gland 2. Facial nerve VII 3. External carotid artery (ECA) (terminating in parotid gland into internal maxillary and superficial temporal arteries) 4. Retromandibular vein 5. Intraparotid and periparotid lymph nodes	***Congenital*** • 1st branchial cleft cyst • Hemangioma (pediatric) • Lymphangioma (pediatric) ***Inflammatory*** • Cellulitis/abscess • Benign lymphoepithelial lesions (AIDS) • Reactive adenopathy ***Benign tumor*** • *Pleomorphic adenoma (benign mixed tumor)* • *Warthin's tumor (papillary cystadenoma lymphomatosum)* • Oncocytoma • Lipoma • Facial nerve schwannoma or neurofibroma ***Malignant tumor*** • *Primary* • Carcinoma • *Mucoepidermoid* • *Adenoid cystic* • Acinous cell • Squamous cell • Non-Hodgkin's lymphoma • Malignant mixed tumor • *Metastatic (within parotid nodes)* • *Squamous cell carcinoma of scalp* • *Melanoma of scalp* Non-Hodgkin's lymphoma
Perivertebral space (PVS)	1. Prevertebral muscles 2. Scalene muscles 3. Vertebral arteries and veins 4. Brachial plexus 5. Phrenic nerve	***Pseudomass*** • *Vertebral body osteophyte* • Anterior disk herniation ***Inflammatory*** • *Vertebral body osteomyelitis (pyogenic/tuberculosis)* • *Cellulitis, abscess* ***Vascular*** • Vertebral artery dissection, aneurysm, or pseudoaneurysm ***Benign tumor*** • Schwannoma/neurofibroma (cervical nerve roots, brachial plexus) • Vertebral body benign bony tumors ***Malignant tumor*** • *Primary* • Chordoma • Non-Hodgkin's lymphoma • Vertebral body primary malignant tumor • *Metastatic* [redacted] • *Direct invasion of squamous cell carcinoma*

Note: Shaded entries indicate the most common lesions.
AIDS, acquired immunodeficiency syndrome.
Data from Barakos, 1991[4]; Curtin, 1987[40]; Harnsberger, 1991[67] and 1995[65]; Lewin, 1995[87]; Norbesh, 1996[128]; and Silver et al, 1984.[156]

Normal Imaging Anatomy

The anatomy of the normal suprahyoid neck, as seen with CT and MRI, is demonstrated in Figures 19–3 to 19–6.

Imaging Rationale and Techniques

CT and MRI are currently the primary modalities for investigating the suprahyoid neck region. This region, which extends from the skull base to the hyoid bone, is surrounded, for the most part, by bones that limit external clinical examination. In addition, while the superficial extent of mucosal lesions can be readily identified by the examining physician, their deep extent as well as lesions confined to the deep spaces are almost totally inaccessible for clinical or endoscopic evaluation.

In many cases of suprahyoid neck masses, MRI offers benefits over CT because of its higher soft tissue contrast resolution, multiplanar capability, and superiority in detecting perineural tumor spread and intracranial invasion.[65]

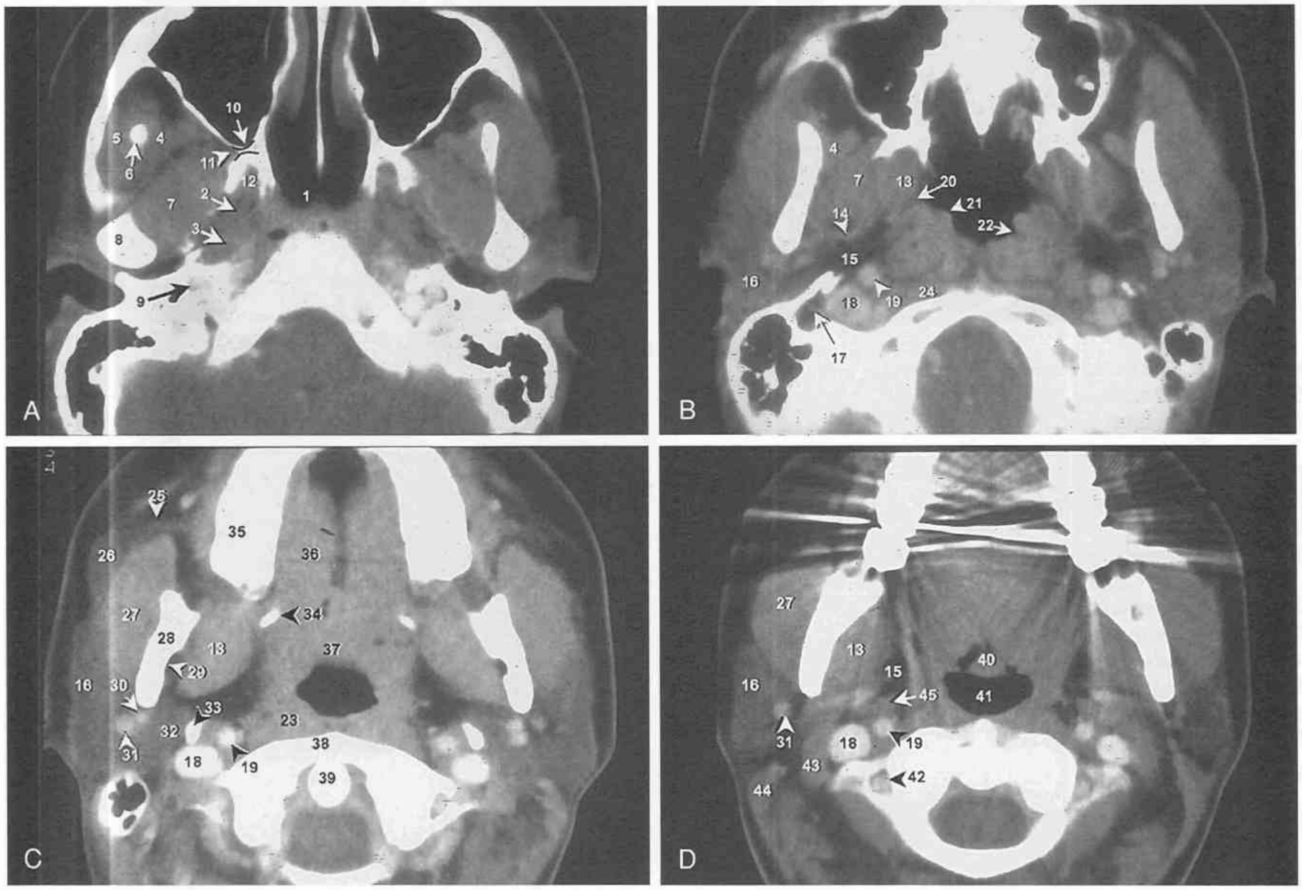

Figure 19–3. *A–G,* Normal imaging anatomy of the nasopharynx and oropharynx on a contrast-enhanced axial CT scan (5-mm slice thickness).

1 Nasopharyngeal airway
2 Tensor veli palatini muscle
3 Levator veli palatini muscle
4 Temporalis muscle (deep = medial head)
5 Temporalis muscle (superficial = lateral head)
6 Coronoid process of mandible
7 Lateral pterygoid muscle
8 Condylar process of mandible
9 Internal carotid artery in vertical segment of petrous canal
10 Pterygopalatine fossa (basal part)
11 Pterygomaxillary fissure
12 Pterygoid fossa between medial and lateral pterygoid plates
13 Medial pterygoid muscle
14 Internal maxillary vessels
15 Fat in prestyloid compartment of parapharyngeal space
16 Parotid gland (superficial lobe)
17 Facial nerve surrounded by fat in stylomastoid foramen
18 Internal jugular vein
19 Internal carotid artery
20 Eustachian tube orifice
21 Torus tubarius overlying levator veli palatini muscle
22 Lateral pharyngeal recess (fossa of Rosenmüller)
23 Longus capitis muscle
24 Rectus capitis anterior muscle
25 Parotid (Stensen's) duct
26 Accessory parotid tissue
27 Masseter muscle
28 Ramus of mandible
29 Mandibular foramen
30 External carotid artery
31 Retromandibular vein (lying superficial to external carotid artery)
32 Deep lobe of parotid gland extending through stylomandibular tunnel
33 Styloid process
34 Pterygoid hamulus (projecting inferiorly from medial pterygoid plate)
35 Alveolar process of maxilla
36 Hard palate
37 Soft palate
38 Anterior arch of atlas (C1 vertebra)
39 Odontoid process (dens)
40 Uvula
41 Oropharyngeal airway
42 Vertebral artery in foramen transversarium
43 Posterior belly of digastric muscle

Illustration continued on following page

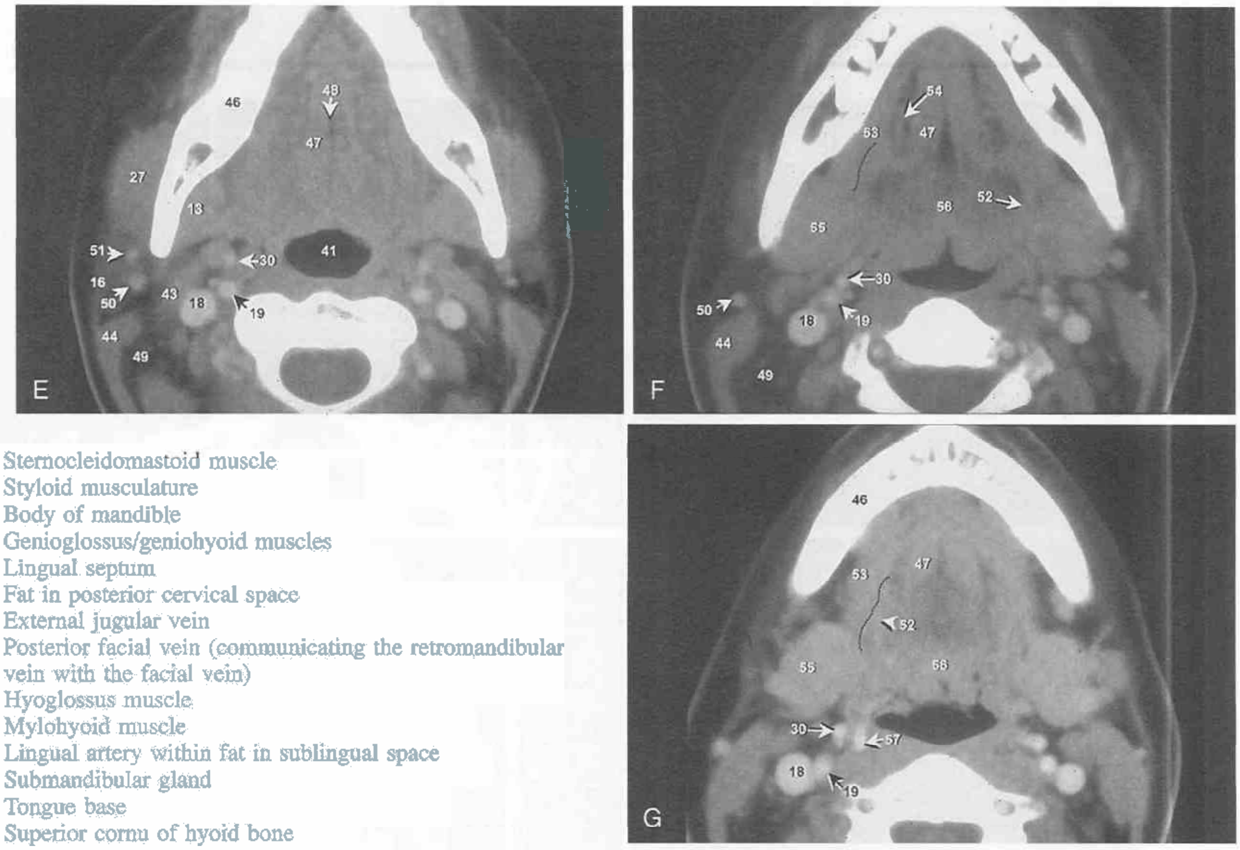

44 Sternocleidomastoid muscle
45 Styloid musculature
46 Body of mandible
47 Genioglossus/geniohyoid muscles
48 Lingual septum
49 Fat in posterior cervical space
50 External jugular vein
51 Posterior facial vein (communicating the retromandibular vein with the facial vein)
52 Hyoglossus muscle
53 Mylohyoid muscle
54 Lingual artery within fat in sublingual space
55 Submandibular gland
56 Tongue base
57 Superior cornu of hyoid bone

Figure 19–3 *Continued.*

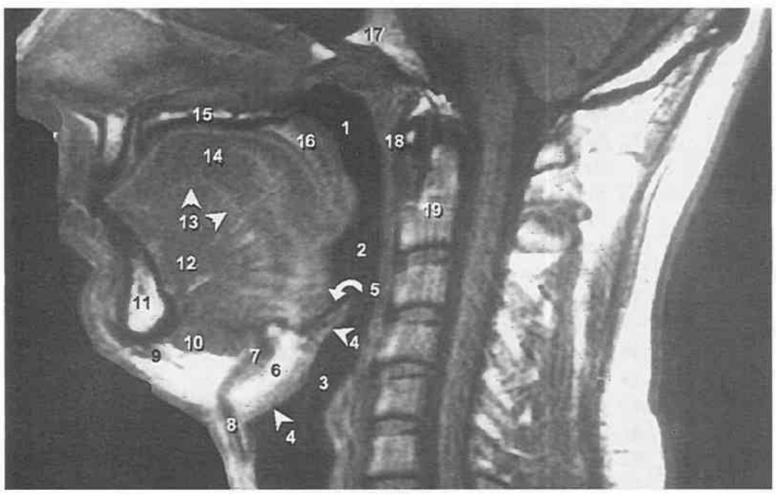

1 Nasopharyngeal airway
2 Oropharyngeal airway
3 Hypopharyngeal airway
4 Epiglottis
5 Vallecula
6 Preepiglottic fat
7 Hyoid bone
8 Thyroid cartilage
9 Mylohyoid muscle
10 Geniohyoid muscle
11 Symphysis menti
12 Genioglossus muscle
13 Lingual septum
14 Body of tongue
15 Hard palate
16 Soft palate/uvula
17 Clivus
18 Anterior arch of atlas (first cervical vertebra)
19 Odontoid process (dens)

Figure 19–4. Normal imaging anatomy of the pharynx and oral cavity on a midsagittal, non–contrast-enhanced, T1-weighted MR image.

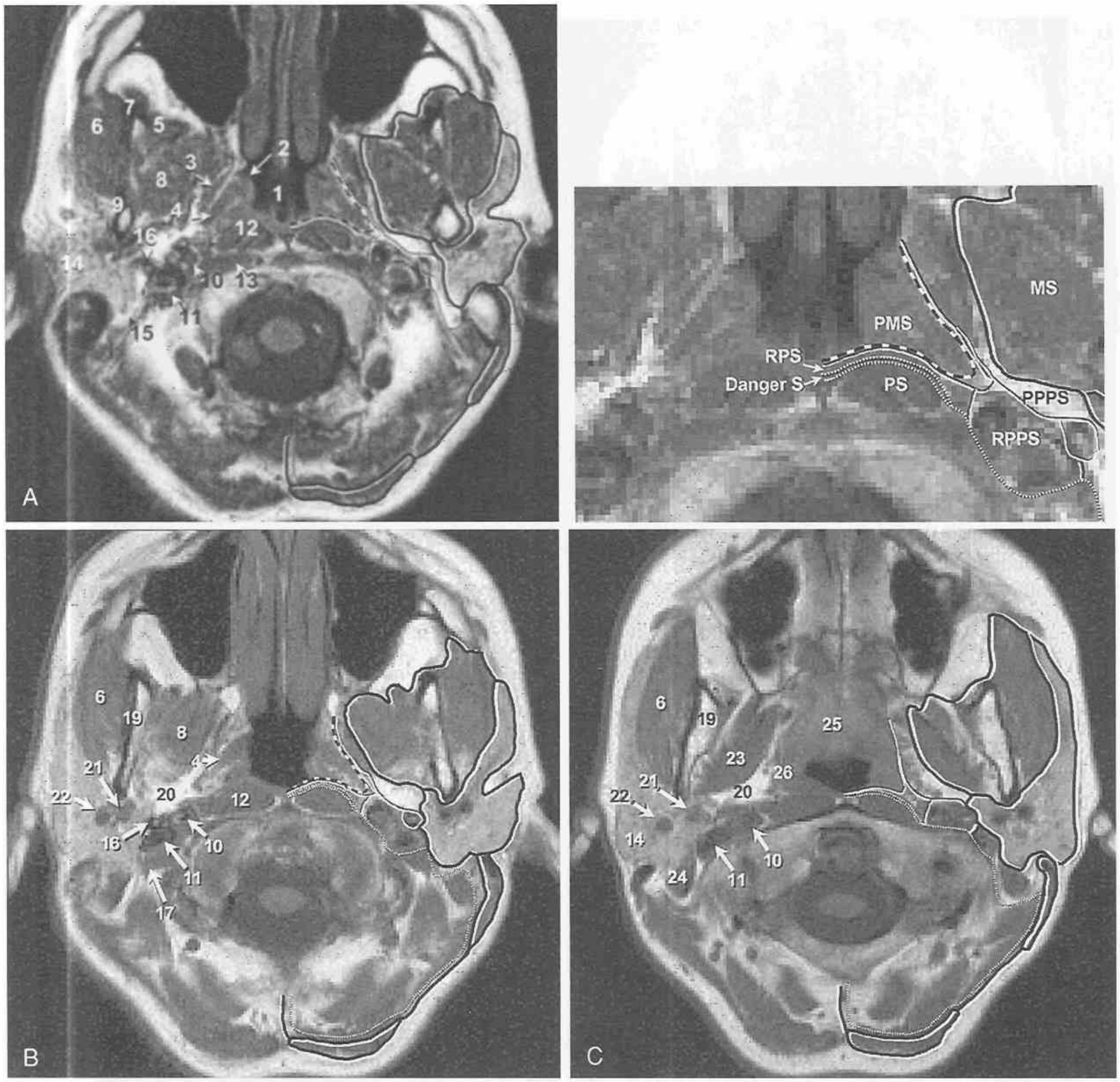

Figure 19–5. *A–I,* Normal imaging anatomy of the nasopharynx, oropharynx, and oral cavity on an axial nonenhanced, T1-weighted MR image. MS, masticator space; PMS, pharyngeal mucosal space; PPPS, prestyloid parapharyngeal space; PS, perivertebral space; RPPS, retrostyloid parapharyngeal space (carotid space); RPS, retropharyngeal space. The central region of *A* is depicted *(inset).*

1 Nasopharyngeal airway
2 Torus tubarius
3 Tensor veli palatini muscle
4 Levator veli palatini muscle
5 Temporalis muscle (deep = medial head)
6 Masseter muscle
7 Coronoid process of mandible
8 Lateral pterygoid muscle
9 Neck of the mandible
10 Internal carotid artery
11 Internal jugular vein
12 Longus capitis muscle
13 Rectus capitis anterior muscle
14 Parotid gland (superficial lobe)
15 Facial nerve emerging from stylomastoid foramen and entering parotid gland
16 Styloid process
17 Rectus capitis lateralis muscle
18 Fat in infratemporal fossa
19 Ramus of mandible
20 Fat in prestyloid compartment of parapharyngeal space
21 External carotid artery
22 Retromandibular vein
23 Medial pterygoid muscle
24 Posterior belly of digastric muscle
25 Soft palate
26 Superior constrictor muscle of pharynx

Illustration continued on following page

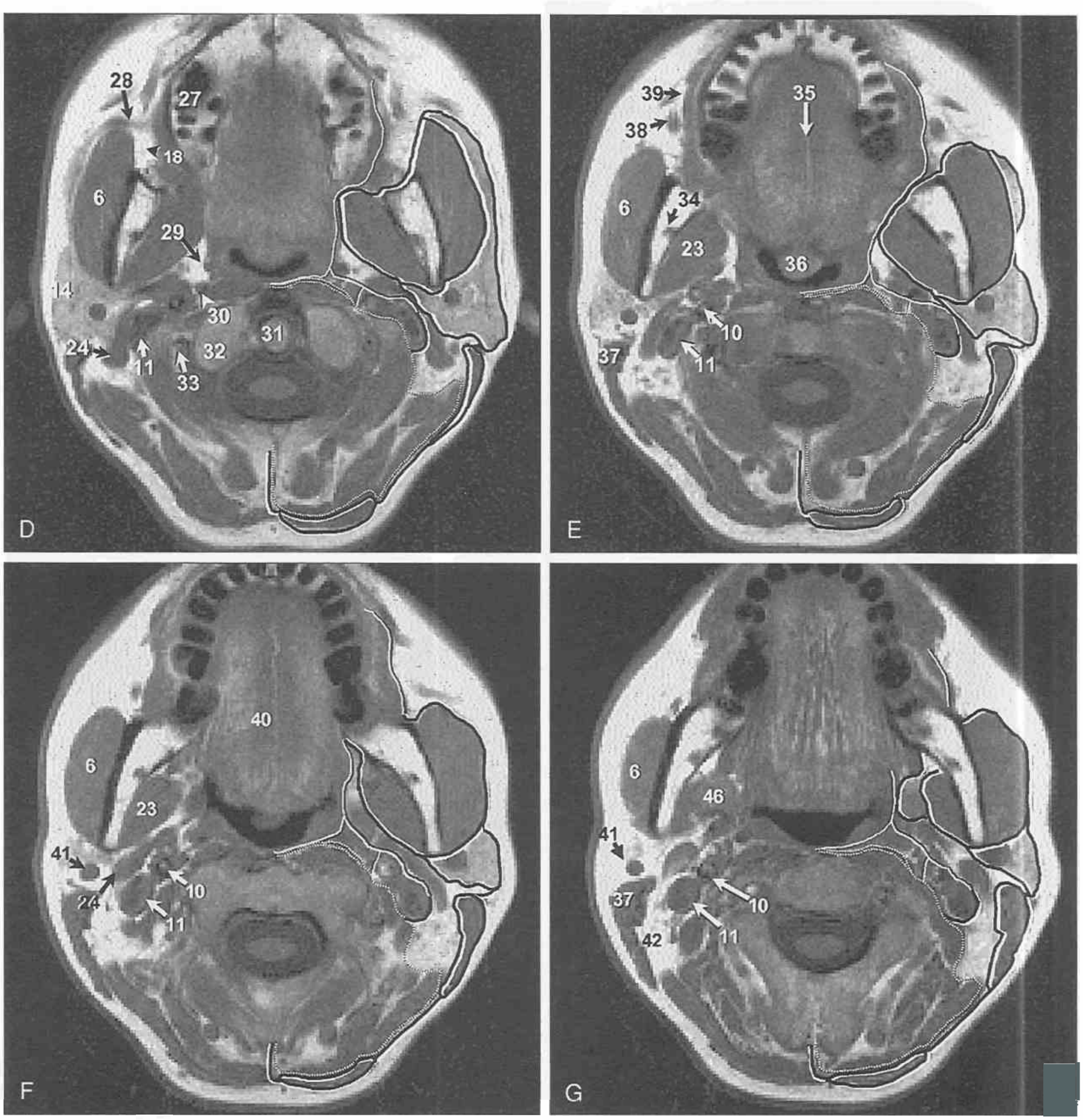

Figure 19–5. *Contin*[redacted].

27 Alveolar process of maxilla
28 Parotid (Stensen's) duct
29 Ascending pharyngeal artery overlying superior constrictor muscle of pharynx
30 Lateral retropharyngeal lymph node (of Rouviere) in retropharyngeal space
31 Odontoid process (dens)
32 Lateral mass of atlas (C1 vertebra)
33 Vertebral artery in foramen transversarium
34 Mandibular foramen transmitting inferior alveolar nerve and vessels
35 Lingual septum
36 Uvula
37 Sternocleidomastoid muscle
38 Anterior facial vein
39 Buccinator muscle
40 Genioglossus/geniohyoid muscles
41 External jugular vein
42 Fat in posterior cervical space
43 Hyoglossus muscle
44 Mylohyoid muscle
45 Fat in sublingual space
46 Submandibular gland
47 Oropharyngeal airway
48 Tongue base
49 Body of mandible

Illustration continued on following page

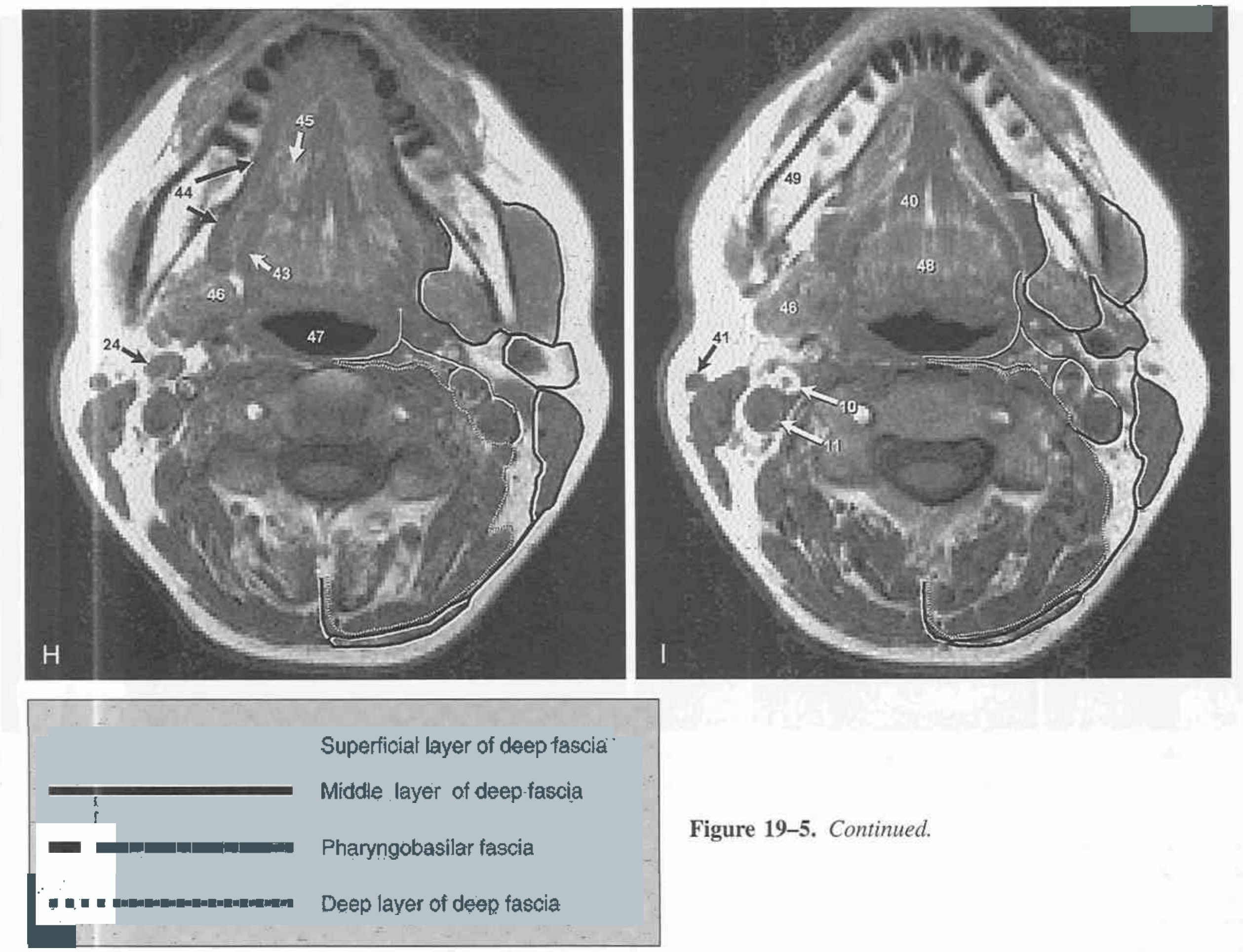

Figure 19–5. *Continued.*

Computed Tomography

Patient Positioning

Patients are examined in the supine position for axial scans and in the prone position for direct coronal scans. The prone position is recommended whenever a nasopharyngeal or palatal mass is suspected and there is a possibility of skull base erosion.[119] Scanning is done during suspended respiration and attention must always be paid to proper head position.[119]

Intravenous Contrast

A confident assessment of the possible cervical lymphadenopathy associated with nasopharyngeal and oropharyngeal pathology requires optimal vascular opacification with an iodinated contrast medium. This is achieved by delivering a loading bolus (50 mL, 2 mL/second) via a power injector, followed by continuous contrast infusion (1 mL/second).[119]

Acquisition Parameters

A preliminary lateral scout view is obtained. Axial scans are planned parallel to the infraorbital-meatal line and should cover the whole region from the external auditory canal to the upper border of the manubrium sterni. Such extended coverage ensures proper evaluation of the pharynx, skull base, and all node-bearing areas. Examination is best performed with 3- to 5-mm-thick contiguous slices and a small field of view (FOV). An additional high-resolution bone reconstruction algorithm should be used to evaluate any pathologic bone involvement.[81, 119]

Magnetic Resonance Imaging

Patient Positioning

Axial, sagittal, and coronal scans are obtainable without the need to reposition the supine patient. A head coil is convenient for scanning the nasopharynx and oropharynx. In patients with malignancies, since the entire neck must be evaluated for nodal disease, a dedicated neck coil must be used in addition in order to cover the area from the mouth floor to the supraclavicular region.[83, 96, 119] Besides head motion, pharyngeal motion (e.g., swallowing and snoring) must also be prevented to ensure optimal image quality.[119]

Intravenous Contrast

Postintravenous gadolinium-DTPA T1-weighted studies are helpful in detection of pathologic lesions. Such images improve the visualization of small lesions; provide excellent evaluation of lesion extension, subtle infiltration, and perineural spread; and aid in the assessment of tumor recurrence after radiotherapy or surgery.[108, 128, 140, 177]

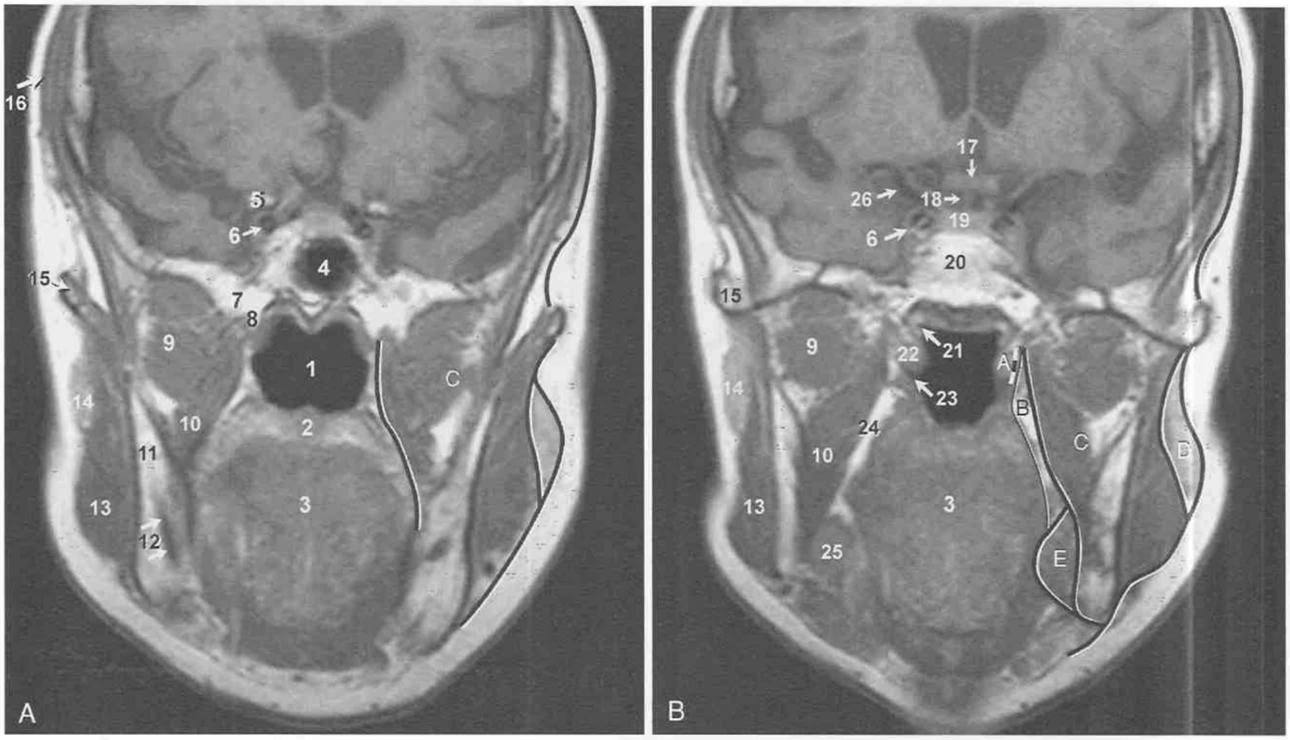

Figure 19–6. *A–D,* Normal imaging anatomy of the nasopharynx and oropharynx on a coronal non–contrast-enhanced, T1-weighted MR image. A, pharyngeal mucosal space (PMS); B, prestyloid parapharyngeal space (PPPS); C, masticator space (MS); D, parotid space (PS); E, submandibular space.

1 Nasopharyngeal airway
2 Soft palate
3 Tongue
4 Sphenoid sinus
5 Anterior clinoid process
6 Internal carotid artery
7 Greater wing of sphenoid bone
8 Root of medial pterygoid plate of sphenoid bone
9 Lateral pterygoid muscle
10 Medial pterygoid muscle
11 Ramus of mandible
12 Mandibular canal
13 Masseter muscle
14 Parotid gland
15 Zygomatic arch
16 Temporalis muscle
17 Optic chiasm
18 Pituitary stalk
19 Pituitary gland
20 Clivus
21 Fossa of Rosenmüller (lateral pharyngeal recess)
22 Torus tubarius overlying levator veli palatini muscle
23 Eustachian tube opening
24 Fat in prestyloid parapharyngeal space
25 Submandibular salivary gland
26 Middle cerebral artery

Pulse Sequences and Acquisition Parameters

In general, T1-weighted images provide the best fat-muscle and fat-tumor contrast, whereas T2-weighted images provide the best muscle–lymphoid tissue contrast.[95, 119, 171]

The axial plane is often most useful, and both axial T1-weighted and T2-weighted images, encompassing at least the region from the palate to the hyoid bone, should be performed in all cases. It is recommended that T2-weighted images, using a fast spin-echo with fat-suppression technique, be acquired because this method yields very high conspicuity of lesions.[89, 128]

Coronal T1-weighted images improve the evaluation of lesions adjacent to the skull base and within the submandibular or sublingual spaces, and sagittal T1-weighted images are helpful in the evaluation of midline lesions.

Contrast-enhanced T1-weighted images are also best obtained with the use of fat-suppression techniques in order to achieve better definition of the enhanced areas, particularly for blocking the marrow signal in the evaluation of the skull base or other involved bone. However, suboptimal fat-suppression techniques may create artifactual bright signals that mimic pathologic processes, particularly in the high nasopharynx and in the low orbit.[2, 128]

As stated, additional neck scanning for nodal metastases using a neck coil is required for patients with malignancies.

Slice thickness should be no more than 3 to 4 mm for T1-weighted images and 5 mm for T2-weighted images, with an interslice gap of 1 mm or less. For T1-weighted images, echo time (TE) should be kept as short as possible

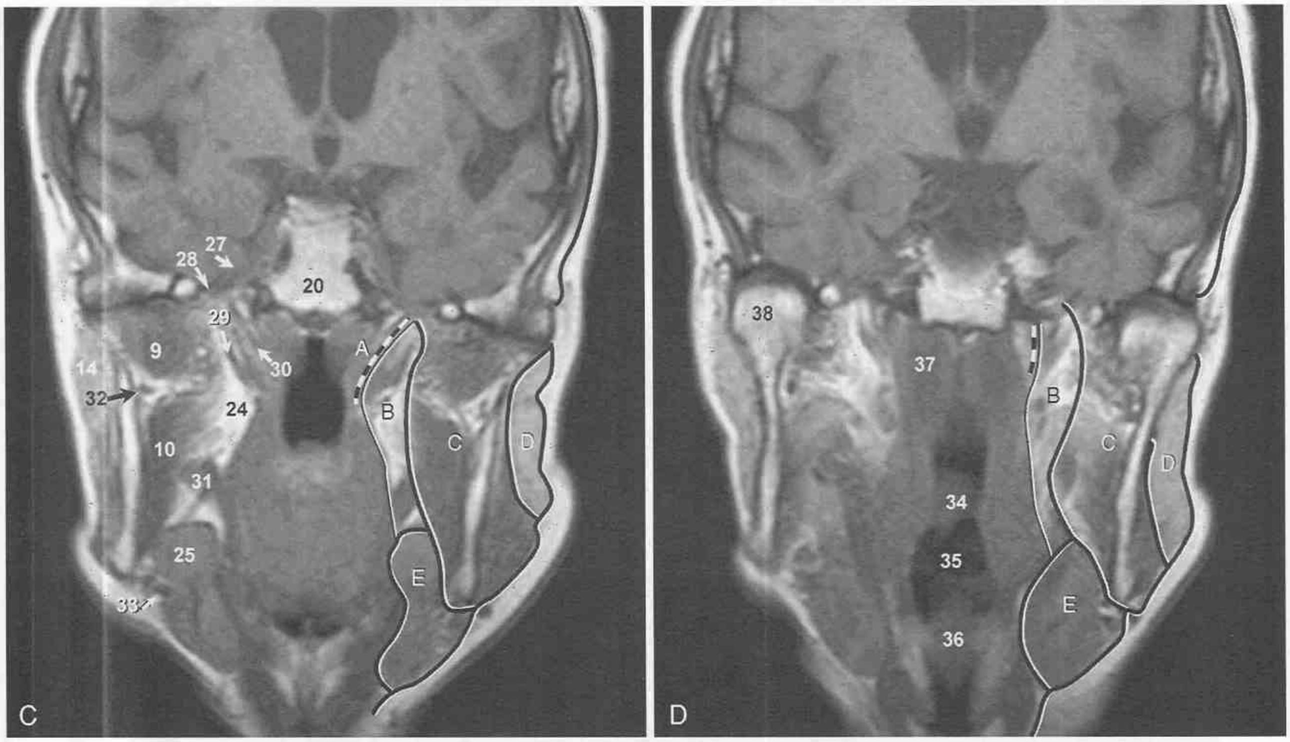

Figure 19–6. *Continued.*

27 Mandibular division of trigeminal nerve
28 Foramen ovale
29 Tensor veli palatini muscle
30 Levator veli palatini muscle
31 Styloglossus muscle
32 Internal maxillary artery
33 Facial vein
34 Uvula
35 Oropharyngeal airway
36 Epiglottis
37 Longus capitis muscle
38 Head of mandible

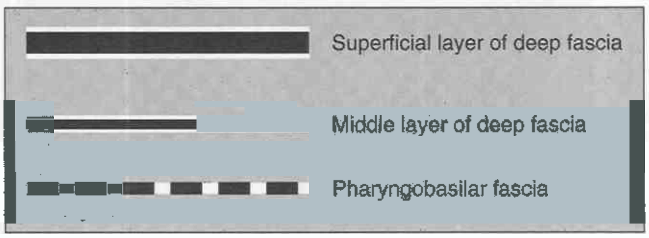

in order to reduce the magnetic susceptibility artifact. Motion compensation gradients and spatial presaturation pulses may also be helpful in reducing flow and other motion artifacts. Phase encoding should be swept in an anteroposterior direction so that the vascular "ghost artifacts" are thrown anteroposteriorly and not across the pharyngeal tissues.[65] The optimal field of view, matrix size, and number of signal averages depend upon the particular imaging system and field strength, but they should reflect a compromise between adequate signal-to-noise, spatial resolution, and total examination length.

Several newer MRI techniques have been applied to nasopharyngeal and oropharyngeal imaging, including:

1. MR angiography for evaluation of vascular occlusion or displacement by a mass.[128, 176]
2. Functional upper airway imaging to study the soft palate function in patients with sleep apnea and cleft palate.[107, 128]
3. Perfusion imaging to assess tumor vascularity and response to treatment.
4. Spectroscopy to determine the primary presentation of malignancy and possible tumor recurrence.[128]

Pathology

Lesions Arising within the Pharyngeal Wall and Adjoining Deep Neck Spaces

Lesions of the Pharyngeal Mucosal Space

Pseudomass

Asymmetric Fossae of Rosenmüller

Asymmetry of the lateral pharyngeal recesses may result from inflammatory debris or asymmetry in the amount of lymphoid tissue, thereby giving the impression of a mass in the PMS.[42, 65, 128] A true tumor is ruled out when[42, 65]:

1. The adjoining soft tissue planes in the PPS and RPS are maintained.
2. The nasopharyngeal mucosa is clinically intact.
3. The collapsed recess opens when rescanning by CT is used during the Valsalva maneuver.

Congenital Lesions

Thornwaldt's Cyst

Thornwaldt's cyst is a congenital midline posterior PMS cyst, lined by pharyngeal mucosa. It results from focal adhesion of pharyngeal mucosa to the notochord, which is then carried up as the notochord ascends to the developing skull base. A resultant nasopharyngeal diverticulum is created (a pharyngeal bursa),[28] whose orifice becomes obliterated after an attack of pharyngitis, thereby forming the cyst. Thornwaldt's cysts are present in 4% of all autopsy specimens (and MR images of the head).[42, 65, 119]

Clinical Presentation. The peak age incidence is 15 to 30 years. Thornwaldt's cyst is usually an asymptomatic, incidental finding in head MRI. The cyst is usually infected with anaerobic bacteria, and when intracystic pressure increases, the orifice opens and the patient presents with persistent or periodic nasopharyngeal drainage, halitosis, and foul taste. Dull occipital headache has also been described.[42, 65, 108, 119]

Imaging Features (Fig. 19–7). Thornwaldt's cyst appears as a well-circumscribed, thin-walled, midline (but may be slightly off-center) posterior nasopharyngeal mucosal space cyst lodged between the prevertebral muscles. It varies in diameter from a few millimeters to several centimeters. On CT scans, a small cyst may be missed whereas a larger one usually is seen as hypodense mucoid attenuation. CT attenuation of the cyst increases as does its protein content, and occasionally it may mimic a soft tissue mass. MRI readily identifies the cyst, whose T1-weighted signal intensity increases from low to high with increasing protein content.

On T2-weighted and fluid-attenuated inversion recovery (FLAIR) images, signal intensity is high.[42, 65, 77, 119] Postcontrast studies show marginal enhancement.[28] Other imaging features may include superimposed cervical adenitis secondary to cyst infection.[6, 11, 128]

Inflammatory Conditions

Adenoidal and Tonsillar Hypertrophy

Hypertrophy of these lymphoid tissues represents immunologic activity and not a disease process per se. It is most commonly seen in the adenoids,[65] which begins to be

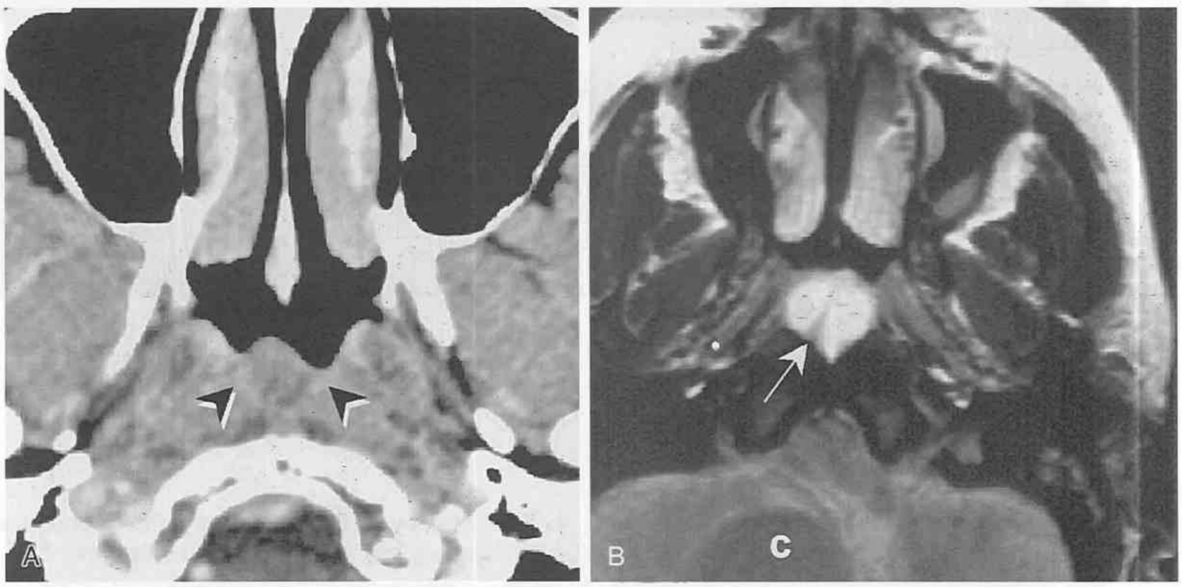

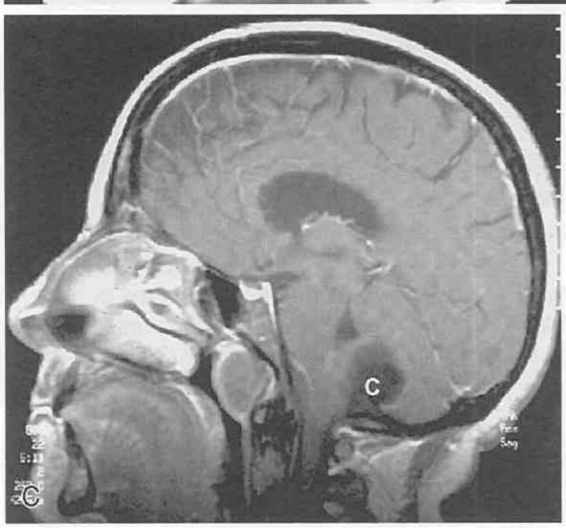

Figure 19–7. Thornwaldt's cyst. *A*, Contrast-enhanced CT scan shows a small Thornwaldt cyst occupying the typical midline posterior nasopharyngeal location. Marginal enhancement delineates the otherwise isodense cyst *(arrowheads)*. Axial T2-weighted *(B)* and sagittal postgadolinium-enhanced, T1-weighted *(C)* MR image of another Thornwaldt cyst. The T2-weighted image demonstrates a sharply defined, hyperintense mass lesion resting on the posterior nasopharyngeal wall and dipping between the longus capitis muscles. An internal septum is noted *(white arrow, B)*. Rim enhancement is apparent on the postgadolinium-enhanced scan. The intermediate T1-weighted signal of the cyst denotes its high protein content. Note the incidental right-sided posterior fossa arachnoid cyst (c in *B* and *C*).

prominent by the age of 2 to 3 years and to regress from adolescence onward. Failure to visualize adenoidal tissue in a young child should raise the possibility of an immune deficiency state.[119] In adults, smoking not uncommonly induces nasopharyngeal lymphoid hyperplasia.[53]

Clinical Presentation. Infants present with difficulty in feeding, whereas older children present with other symptoms of nasal obstruction, such as mouth breathing and snoring. Otitis media may result from encroachment on the orifice of the eustachian tube.[65] Dysphagia may be caused by palatine tonsillar hypertrophy.[13, 134] Adenoidectomy or tonsillectomy is indicated when hypertrophy results in nasopharyngeal airway obstruction, chronic otitis media, or serous middle ear effusion.[13, 58, 59]

Imaging Features (Fig. 19–8). Hypertrophic adenoids appears as a homogenous fullness of the nasopharyngeal mucosal space, which obliterates the fossae of Rosenmüller and encroaches upon the nasopharyngeal airway. On CT scans, the adenoid is isodense to the underlying prevertebral muscles and may contain small cysts and calcifications. On T1-weighted MRI scans, it is isointense to the muscles as well but can be identified by its bright T2-

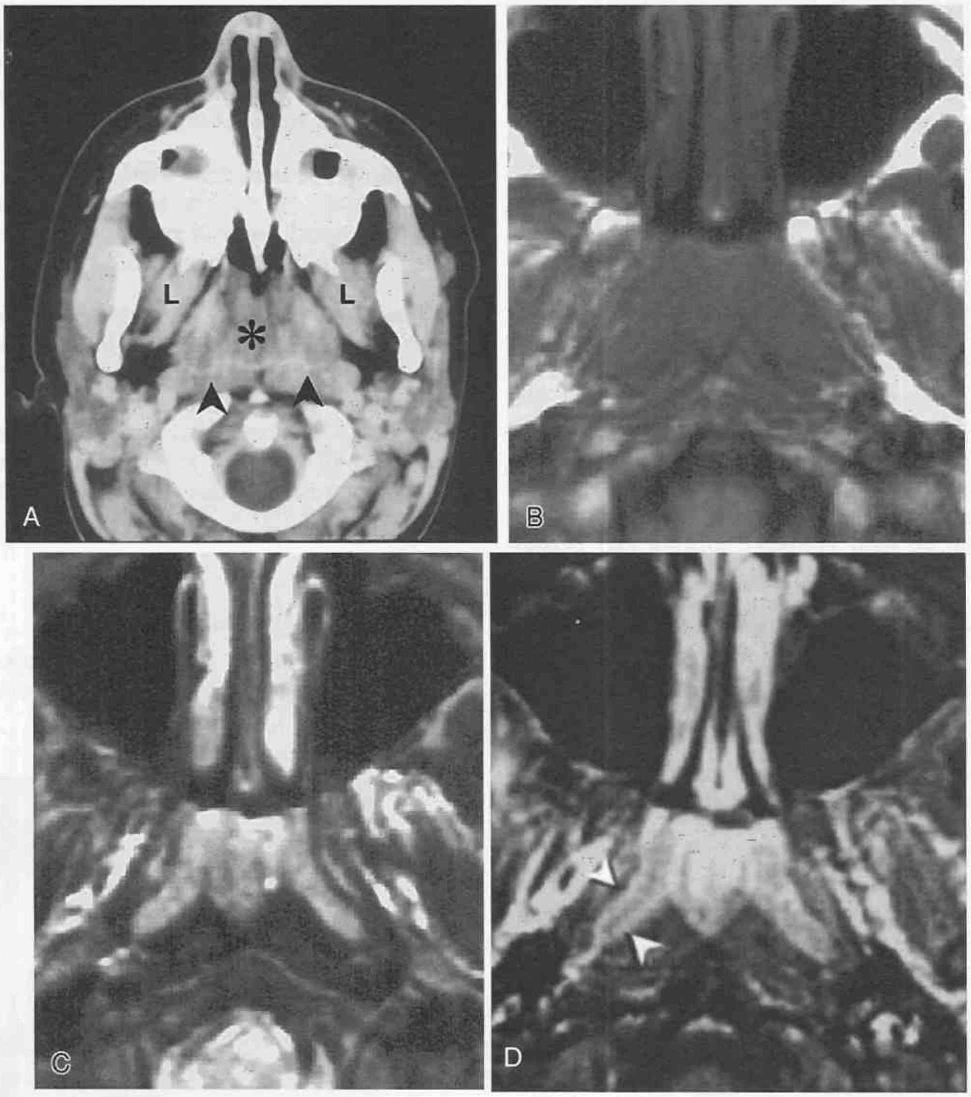

Figure 19–8. Adenoidal hypertrophy.

A, Contrast-enhanced CT scan of the nasopharynx demonstrates enlarged adenoid tissue. The thin, enhancing line separating the adenoids *(asterisk)* from the prevertebral muscles represents the intact pharyngobasilar fascia, indicating that the mass is totally within the confines of the pharyngeal mucosal space. Also note the intact fat planes separating the mass from the lateral pterygoid (L) muscles on either side.

B–D, MR images at the level of the nasopharynx in a 10-year-old girl. *B*, Axial unenhanced, T1-weighted image (TR = 570 msec, TE = 14 msec) shows a homogeneous mass filling the nasopharyngeal airway and displaying an isointense signal to the adjacent muscles. *C*, Axial T2-weighted image (TR = 2500 msec, TE = 90 msec) more accurately identifies the adenoidal tissue as a bright signal casting the shape of the airway and well contrasted against the dark prevertebral muscles. *D*, Axial gadolinium-enhanced, T1-weighted MR image (TR = 594 msec, TE = 14 msec) elegantly demonstrates the pharyngobasilar fascia as a thin, enhancing line *(arrowheads)*, marginating the deep and lateral adenoid surfaces and confirming the noninvasive nature of the lesion.

weighted signal. On postcontrast scans, the pharyngobasilar fascia normally enhances as a thin, continuous line outlining the deep adenoid surface.

Identification of this line is a reliable sign of the noninvasive nature of the mass, although it does not guarantee benign pathology.[65, 119] In fact, it may be impossible to differentiate between hypertrophic adenoids and nasopharyngeal lymphoma on the basis of CT or MRI,[47] and a definitive diagnosis can be made only by biopsy. Other imaging features include reactive cervical adenopathy[119] and eustachian tube dysfunction, which is best detected as bright T2 signals of fluid in the mastoid air cells.[108]

Hypertrophic palatine tonsils are less common and present as bilateral, smooth oval, or rounded soft tissue masses encroaching upon either side of the oropharyngeal air column. Hypertrophic lingual tonsils are the least common. They occur at the tongue base and encroach posteriorly upon the valleculae. CT and MRI appearances of both are similar to those of adenoidal hypertrophy.[73]

Tonsillitis and Peritonsillar Abscess

Acute tonsillitis or adenotonsillitis may be caused by viral or bacterial infection. The disease is usually self-limited, but when severe, infection may suppurate, resulting in a peritonsillar abscess (quinsy) or, rarely, in a tonsillar abscess. A peritonsillar abscess entails accumulation of pus in the tonsillar bed (between the tonsillar capsule and the faucial arches), with medial displacement of the tonsil. The abscess may further extend deeper into the neck to involve the PPS or lateral part of the RPS.[73, 119] Peritonsillar abscesses constitute 49% of head and neck space infections in children.[173] When secondary to infectious mononucleosis, it is associated with cervical lymphadenopathy and hepatosplenomegaly.[96]

Clinical Presentation. The patient is typically a child or a young adult. Patients with simple tonsillitis present with fever and sore throat. In a patient with peritonsillar abscess, initial tonsillitis may be followed by a few days of lucidity before the development of rapidly progressive dysphagia, otalgia, and perhaps trismus if the medial pterygoid muscle is involved. Pharyngeal wall protrusion is seen on clinical examination.[65, 119]

Imaging Features. Imaging is rarely performed in the stage of acute, uncomplicated tonsillitis. When a peritonsillar abscess is clinically suspected, the radiologist's responsibilities are to[65, 73]:

1. Confirm the diagnosis.
2. Determine the degree of airway compromise.
3. Determine whether the abscess is confined to the PMS or has spread into the PPS or the RPS.
4. Comment, in the case of a deeply extending abscess, on the status of internal carotid artery and internal jugular vein.

A peritonsillar abscess confined to the PMS appears as a diffuse, ill-defined thickening of the tonsillar region that bulges medially into the oropharyngeal airway with preserved parapharyngeal fat. On noncontrast CT scans, the inflammatory process appears hypodense to isodense.[42] On MR images, it is also hypointense to isointense to the surrounding muscles on T1-weighted images and hyperintense on T2-weighted images. Postcontrast studies are essential to delineate the enhancing rim of a mature abscess wall that requires drainage.[184]

Imaging features of a deeply extending abscess are discussed later under the appropriate topics.

Postinflammatory Dystrophic Calcification

Clumps of tonsillar calcification (tonsilloliths) may be detected incidentally on CT scans (Fig. 19–9) and indicate previous or chronic tonsillitis. Less commonly, they are seen in the adenoids or the lingual tonsil.[65, 128, 184]

Postinflammatory Retention Cyst

Postpharyngitis sequelae also include the formation of mucous retention cysts in the inflamed obstructed mucous glands. These cysts are similar to those that develop within the paranasal sinuses.[4, 184]

Clinical Presentation. These retention cysts are usually asymptomatic but may be large enough to cause a superficial pharyngeal mass or otitis media secondary to eustachian tube orifice compromise.[65]

Imaging Features. The cyst appears as a well-defined mass in the PMS. It is usually a few centimeters in diameter but can grow to a large size.[65, 128] Both CT and MRI demonstrate the appearance of a typical cyst (i.e., hypodense on CT scans, dark on T1-weighted images, and bright on T2-weighted images). However, a high protein content increases CT density and T1-weighted signal intensity.

Benign Tumors

Juvenile Nasopharyngeal Angiofibroma

This angiofibroma is a highly vascular, benign yet locally invasive, noncapsulated mesenchymal tumor.[108, 180] It

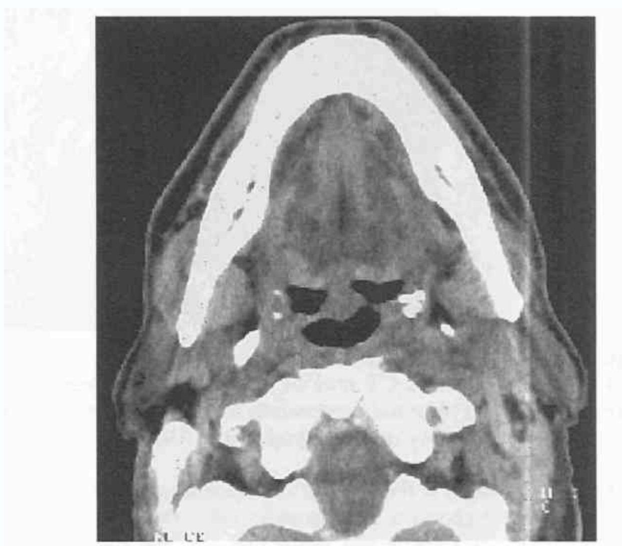

Figure 19–9. Dystrophic calcification of the faucial tonsils. CT scan at the level of the oropharynx shows bilateral clusters of tonsillar calcification (tonsilloliths), more evident on the left side.

is thought to arise near the sphenopalatine foramen[28, 184] at the junction between the nose and the nasopharynx at the root of the medial pterygoid plate. It represents 0.5% of all head and neck neoplasms,[42] and the incidence is higher in the Far East than in the United States.[184]

Clinical Presentation. Juvenile angiofibroma occurs almost exclusively in adolescent boys,[28, 184] with the mean age at presentation 15 years.[42] The most common presenting symptom is nasal speech attributed to nasal obstruction (91%), the next most common is severe recurrent epistaxis (59%), and the least common is facial deformity.[42] On examination, a dark red (probably ulcerating) mass is seen in the nasal fossa and postnasal space.[133]

Imaging Features (Figs. 19–10 and 19–11). Juvenile angiofibroma appears on CT and MRI images as a soft tissue mass varying in size from a small nodule resting on the sphenopalatine foramen and striding the choana to a quite large, locally aggressive growth extending in any or a combination of the following directions:

1. *Posteriorly.* The tumor may protrude into or may totally fill the nasopharyngeal airway.
2. *Anteriorly.* The tumor may block and expand the ipsilateral nasal fossa. Large tumors may also extend directly into the contralateral nasal fossa through the choana.
3. *Medially.* The tumor may push the nasal septum significantly to encroach upon or even to obliterate the contralateral nasal fossa.
4. *Laterally.* In 90% of cases, the tumor extends laterally through the sphenopalatine foramen into the pterygopalatine fossa.[63] The fossa is widened with classic anterior bowing of the posterior maxillary antral wall along with posterior displacement and, possibly, erosion of the pterygoid laminae. Bowing of the posterior antral wall (Holman-Miller sign)[184] is a nonspecific sign that can be produced by any slowly growing mass, whereas erosion of the pterygoid lamina is probably a pathognomonic sign.[133] From the pterygopalatine fossa, the tumor may further extend laterally through the pterygomaxillary fissure into the masticator space (infratemporal fossa).[28]
5. *Superiorly.* In 65% of cases, juvenile angiofibromas erode the floor of the sphenoid sinus to invade the sinus cavity.[180] It is important to differentiate intrasinus tumor invasion from obstructed secretions.[73] This is best done by T2-weighted MRI. The ethmoid air cells may also be invaded.[108] Intraorbital extension, with subsequent proptosis, can occur from the pterygopalatine fossa through the inferior orbital fissure, which becomes widened.[28, 42] Intracranial invasion (into the middle cranial fossa) can then occur from the orbit through the superior orbital fissure[28, 42, 180] or by direct erosion of the roof of the sphenoid sinus.[108] Coronal scans are valuable for precise detection of superior tumor extension.
6. *Inferiorly.* The tumor can grow sufficiently to push the soft palate and bulge into the oropharynx and adjoining oral cavity.

On unenhanced CT scans, the tumor appears isodense; on MR images, it displays intermediate T1-weighted and strongly bright T2-weighted signal intensities. On both T1-weighted and T2-weighted images, characteristic punctate areas of signal void indicate the highly vascular stroma. Postcontrast CT and MRI reveal intense enhancement.[42, 133, 180]

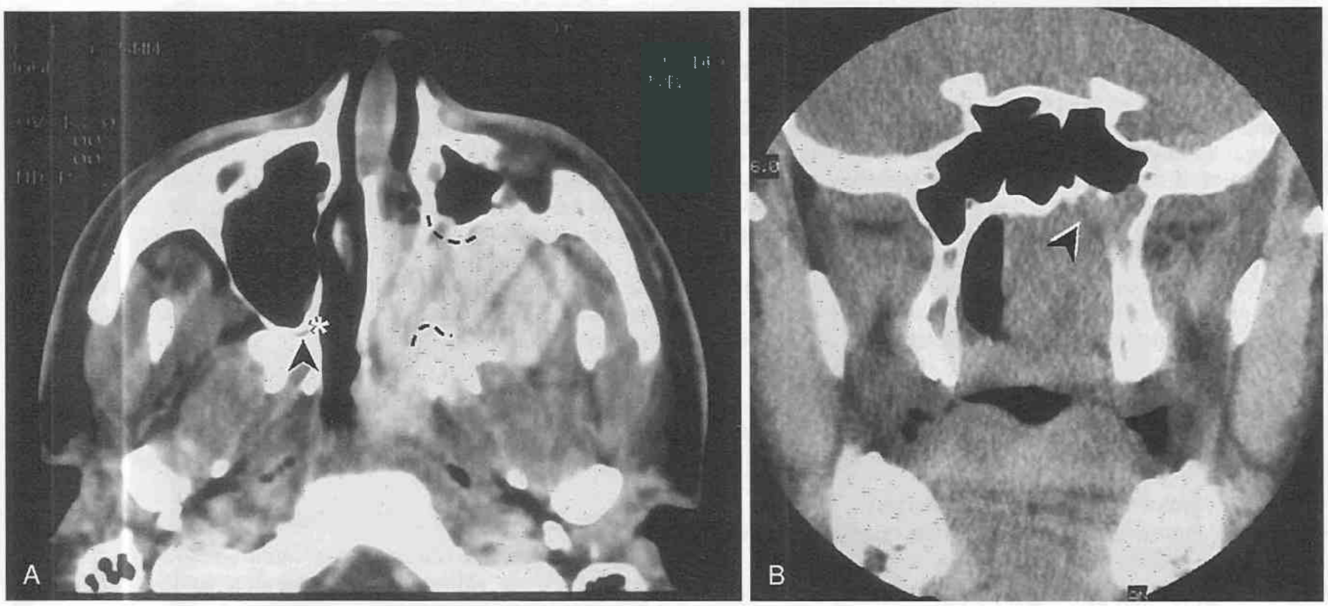

Figure 19–10. Juvenile nasopharyngeal angiofibroma. *A,* Axial contrast-enhanced CT scan demonstrates the typical features of nasopharyngeal angiofibroma (grade 2). A strongly enhancing mass lesion is centered on the markedly widened pterygopalatine fossa and is displacing the yet intact posterior maxillary antral wall forward. (Compare the distance between the *dashed lines* on the left side to the normal-sized basal part of the pterygopalatine fossa on the right side *[black arrowhead].*) The sphenopalatine foramen, where an angiofibroma is believed to arise, is located at a higher level above the *asterisk. B,* Coronal nonenhanced CT scan shows a large, isodense nasopharyngeal soft tissue mass in a 14-year-old boy. The mass occupies most of the airway and is eroding the root of the medial pterygoid plate *(arrowhead)* as well as the floor of the sphenoid sinus, yet without frank intrasinus extension.

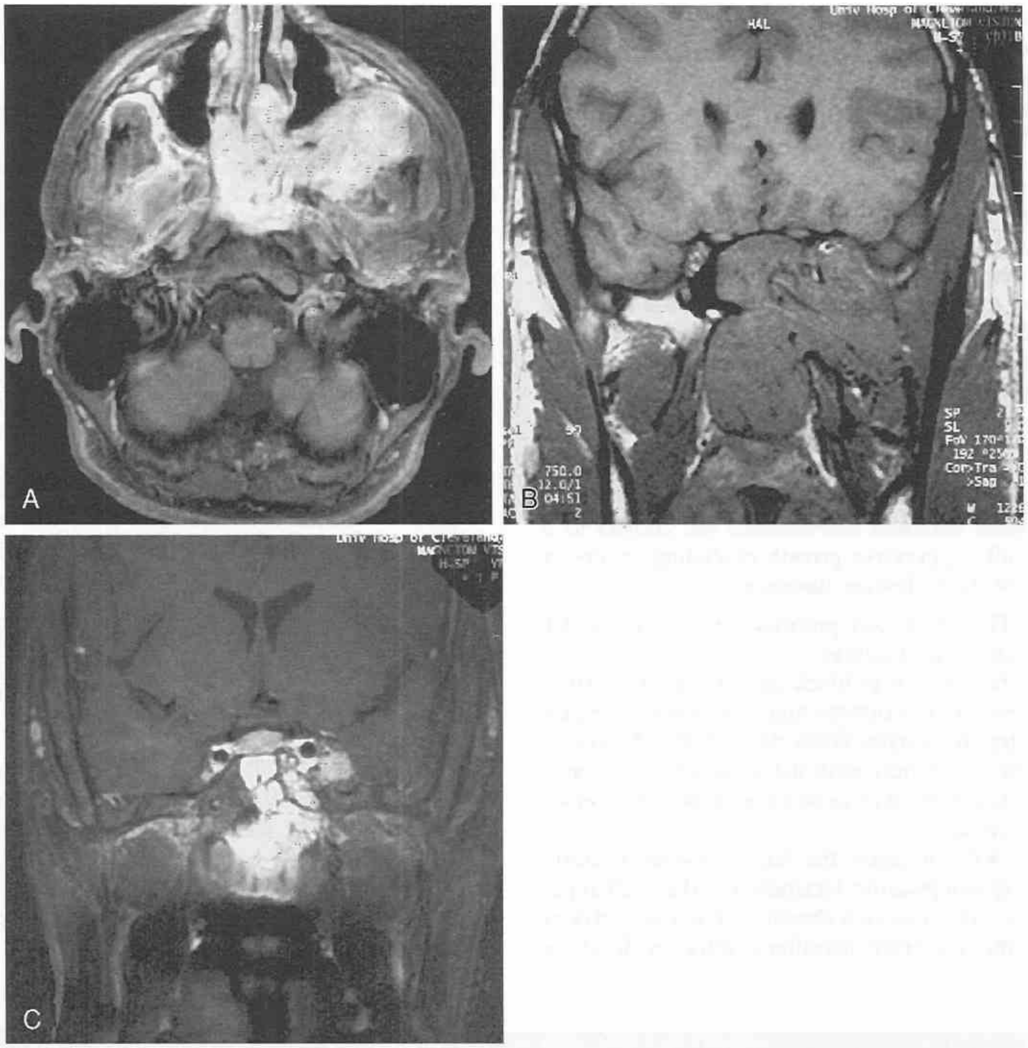

Figure 19–11. Juvenile nasopharyngeal angiofibroma. MRI scan of a grade 3 angiofibroma in a 15-year-old boy.

A, Axial postgadolinium-enhanced, T1-weighted scan (TR = 779 msec, TE = 12 msec) shows a large, intensely enhancing mass centered on the left sphenopalatine foramen region. It totally occupies the nasopharyngeal airway, plugs both choanae, and extends into the nasal fossae, more on the left side. The mass extends laterally to cause marked widening of the pterygopalatine fossa, from which it emerges through the pterygomaxillary fissure into the masticator space (infratemporal fossa). Note the remodeling and anterior displacement of the posterior wall of left maxillary sinus as a result of chronic pressure.

B, Coronal nonenhanced, T1-weighted image of the same patient shows the angiofibroma as an intermediate signal soft tissue mass with multiple linear and punctate signal voids, representing the rich tumor vascularity. The mass is eroding the floor of the sphenoid sinus to fill and expand its left-sided compartment.

C, Coronal postgadolinium-enhanced, T1-weighted image shows the same patient at a different plane. The tumor has extended into the left cavernous sinus, abutting yet incompletely encasing the cavernous segment of the internal carotid artery. Such extension has probably occurred from the pterygopalatine fossa via the foramen rotundum.

The following imaging-based grading system of juvenile angiofibromas has been proposed.[28, 136, 172, 184]

- *Grade 1,* tumor confined to nasopharynx
- *Grade 2,* tumor extending into pterygopalatine fossa or masticator space
- *Grade 3,* tumor extending into orbit or intracranially

This scheme would predict the prognosis and recurrence rate and would indicate the optimal surgical approach.

The high tumor vascularity contraindicates biopsy, and preoperative embolization is necessary. The primary supply is through the maxillary artery. Minor contributors include the ascending pharyngeal and ascending palatine branches of the external carotid artery, and sometimes the tumor may have a supply from the internal carotid artery.[42, 180, 184]

Benign Mixed Tumor of Minor Salivary Glands

Benign mixed tumor *(pleomorphic adenoma)* may arise in the minor salivary glands located in the submucosal layer of the PMS, soft palate (most common site), or tongue base. Extrapharyngeal sites include the mouth, nose, paranasal sinuses, larynx, and trachea.[119]

Clinical Presentation. The presentation varies from a small submucosal nodule to a large pedunculated mass that compromises the pharyngeal airway.[65]

Imaging Features. When the tumor is small, it is best detected by MRI as a sharply demarcated, rounded, homogeneous PMS mass of low to intermediate T1-weighted and very high T2-weighted signal intensities.[105, 184] CT and MRI show a larger tumor as a pedunculated mass encroaching upon the nasopharyngeal or oropharyngeal airway. The appearance is nonspecific, and a biopsy usually enables the diagnosis.[65, 119]

Malignant Tumors

Squamous Cell Carcinoma

Nasopharyngeal Carcinoma. Squamous cell carcinoma (SCC) constitutes 70% of adult nasopharyngeal malignancies.[108, 119, 124] These are further subdivided into[149]:

- *Type 1,* keratinized squamous cell carcinoma (25%)
- *Type 2,* nonkeratinized carcinoma (12%) (sometimes called transitional cell carcinoma)
- *Type 3,* undifferentiated carcinomas (63%)

Several etiologic factors interact to predispose to the development of nasopharyngeal squamous cell carcinoma, such as:

- Genetic susceptibility
- Environmental factors (including chemical carcinogens)
- Exposure to Epstein-Barr virus,[30] which is very highly associated with types 2 and 3 of nasopharyngeal SCC[33, 180, 184]

The highest incidence is found in southern China and southeast Asia[28] and is seven times higher in Americans of Chinese ancestry than in non-Chinese Americans.[46] A higher incidence is also found in African Americans.[49]

Other risk factors include chronic sinonasal infection, nitrosamines (in dry-salted fish), polycyclic hydrocarbons, and poor living conditions.[119, 124]

Most tumors arise in the fossa of Rosenmüller and tend toward submucosal spread to infiltrate the palatal muscles and eustachian tube orifice.[28, 30]

Clinical Presentation. Nasopharyngeal carcinoma is more common in men, and most cases in the United States are diagnosed during the sixth decade of life.[30, 119] Reports from southeast Asia, however, indicate middle age, adolescence, and even childhood presentation.[17]

Patients with early-stage disease may be asymptomatic or may present with nonspecific, commonly overlooked symptoms such as postnasal drip and nasopharyngeal irritation.[108] Middle ear effusion secondary to involvement of the eustachian tube orifice or tensor veli palatini muscle[80] is also an early sign, and older patients with otitis media should always undergo imaging to rule out nasopharyngeal tumors.[4]

Cervical lymphadenopathy prompting initial medical consultation is also a common presenting symptom.[30] Patients with advanced disease may present with nasal obstruction, epistaxis, trismus, proptosis, and various cranial nerve palsies; the trigeminal nerve is the most commonly involved.[23, 28, 108, 119, 166]

Imaging Features

Early Cancer. As stated, most tumors arise in the lateral pharyngeal recess (fossa of Rosenmüller), and their signal intensity is almost similar to that of the adjacent mucosa.[42] The earliest imaging sign is thus asymmetrical superficial nasopharyngeal mucosa. This sign, however, should be cautiously interpreted because physiologic asymmetry of the fossae of Rosenmüller does exist. In addition to the measures listed earlier in this section, careful attention must be given to the following[4, 119, 178, 184]:

1. The fat stripe between the tensor and levator veli palatini muscles. Obliteration of the normally bright T1-weighted signal of this stripe may be one of the earliest indications of nasopharyngeal carcinoma (Fig. 19–12).
2. The ipsilateral middle ear and mastoid air cells. Detection of middle ear effusion or otomastoiditis as a bright

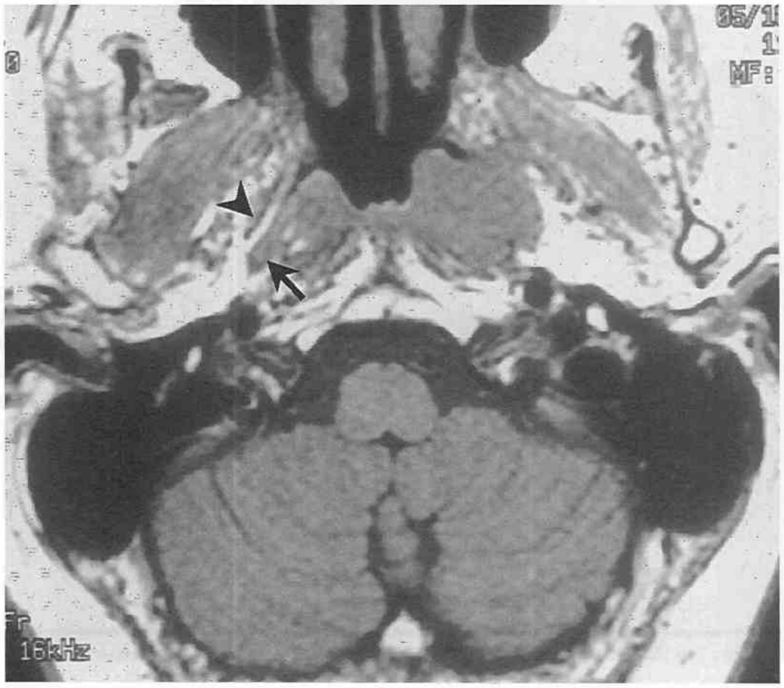

Figure 19–12. Nasopharyngeal carcinoma. Axial non–contrast-enhanced, T1-weighted MRI of the nasopharynx demonstrates a small, left-sided, isointense mass lesion in the pharyngeal mucosal space of the nasopharynx infiltrating the ipsilateral prestyloid parapharyngeal fat and barely touching the adjacent lateral pterygoid muscle. This appearance raises the possibility of masticator space invasion as well. Note the preserved fat stripe between the levator veli palatini muscle *(arrow)* and the tensor veli palatini muscle *(arrowhead)* on the normal right side.

T2-weighted signal is a warning sign of eustachian tube dysfunction.

3. Associated cervical lymphadenopathy. In particular, enlarged ipsilateral LRP lymph nodes (of Rouviere) presenting low to intermediate T1-weighted and high T2-weighted signals (Fig. 19–13).

Imaging of the entire neck with a dedicated neck coil is the essential next step, since up to 90% of these patients have cervical lymphadenopathy at presentation and about 50% have bilateral disease.[108, 110, 119] Although the LRP nodes are considered first-echelon nodes, they are first involved in only 65% of cases and skipped in the remaining 35% of patients, in whom internal jugular nodes are involved without radiographic evidence of retropharyngeal node disease.[30, 31]

Advanced Cancer. The most reliable sign of nasopharyngeal malignancy is the detection of an aggressive mass infiltrating the deep fascia and spaces around the nasopharynx (Fig. 19–14).[100, 119] On CT, it appears as an isodense mass that does not show significant enhancement in the postcontrast study even when it is large.[154]

On plain T1-weighted MR images, the tumor is isointense to the adjacent muscles.[81] This sequence is valuable for detecting replacement of the high-signal fat in the deep fascial spaces with the intermediate-signal tumor. On T2-weighted images, the tumor displays intermediate to high signal intensity.[119, 154, 178]

Considerable enhancement of the solid parts of the tumor occurs in the postgadolinium scans. Fat-saturated, postgadolinium T1-weighted images are particularly valuable for defining the extent of tumor infiltration into the marrow of the skull base or the retrobulbar fat while maintaining good contrast between the enhancing tumor and adjacent muscles.[5, 126, 154] In addition, both fat-saturated, postcontrast T1-weighted and fat-saturated T2-weighted sequences have been shown to improve the detection of lymphadenopathy as well as the presence of nodal necrosis or extracapsular nodal spread.[5, 38, 69, 126]

Although CT is particularly helpful for detecting involvement of thin bony structures, such as the cortical bones of the skull base, paranasal sinuses, and orbits,[30, 119, 154] MRI better delineates infiltration of bone marrow.[30] It is generally agreed that MRI is the modality of choice in the diagnosis of primary as well as recurrent nasopharyngeal carcinoma.[29, 30, 76, 126, 127, 154] The imaging appearance is usually nonspecific for a particular type of malignancy, and CT and MRI images of squamous cell carcinoma may be almost identical to those of nasopharyngeal lymphoma or minor salivary gland malignancies.[65, 119]

Role of Imaging

When evaluating cases of nasopharyngeal carcinoma, the radiologist has the following primary tasks[184]:

- To provide accurate tumor staging
- To define tumor margins for the radiation oncologist
- To evaluate the response to radio/chemotherapy

The most recent (fifth) edition of the Tumor-Node-Metastasis (TNM) classification of nasopharyngeal carcinoma, published in 1997 as a collaborative project of the UICC and the AJCC, is given in Table 19–2.[1, 174]

Nasopharyngeal carcinoma has been described as spreading along well-defined routes,[30, 146] with a tendency to grow along the path of least resistance,[108, 119] as follows:

1. ***Lateral spread*** is the most common direction.[30, 119, 147, 165, 166, 186] The tumor creeps out of the PMS through the only dehiscence in the superolateral part of the tough pharyngobasilar fascia, the sinus of Morgagni, to reach the PPS.[119] This pattern of spread occurs quite early and

Figure 19–13. Enlarged lateral retropharyngeal lymph node (of Rouviere). Nonenhanced, axial T1-weighted MR image at the level of the oropharynx shows the typical appearance of enlarged left-sided node of Rouviere (N) in a patient with nasopharyngeal carcinoma. The enlarged node appears as a well-defined paramedian retropharyngeal small soft tissue mass of intermediate T1-weighted signal intensity. It effaces and displaces the parapharyngeal fat anterolaterally and mildly rotates the oropharyngeal airway in a counterclockwise direction.

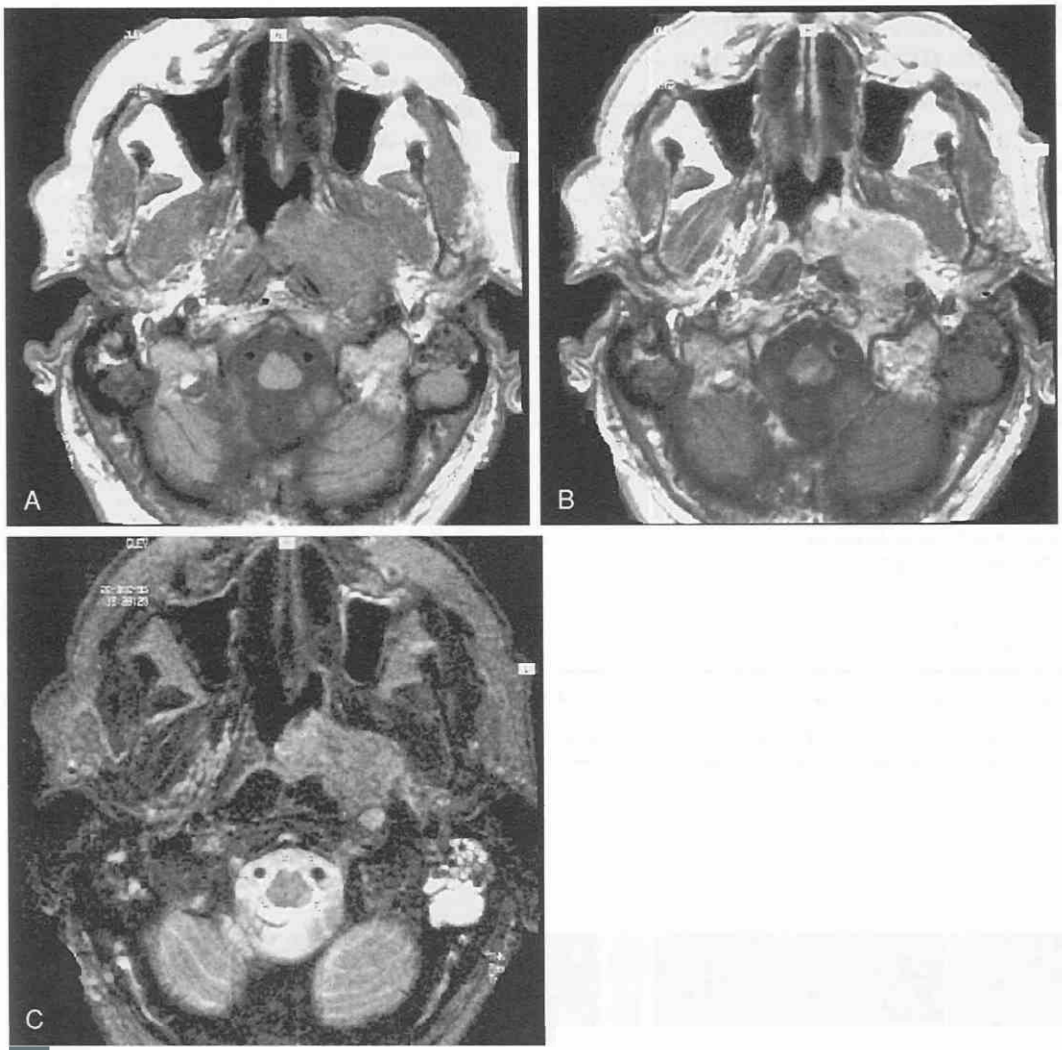

Figure 19–14. Nasopharyngeal carcinoma infiltrating the left parapharyngeal space.

A, Axial nonenhanced, T1-weighted MR image demonstrates a soft tissue mass (~4 × 2.5 cm) involving the left aspect of the pharyngeal mucosal space, bulging into the nasopharyngeal airway, and extending deeply into the ipsilateral prestyloid parapharyngeal space. (Compare the size and shape of parapharyngeal fat on both sides.) The imperceptible fat planes between the tumor and the lateral pterygoid muscle anteriorly and prevertebral muscles posteriorly suggest masticator and perivertebral space involvement.

B, Axial postgadolinium-enhanced, T1-weighted MRI scan shows considerable tumor enhancement and delineates the exact tumor boundaries except in relation to parapharyngeal fat, an issue already observed on the nonenhanced scan.

C, Axial T2-weighted MR image of the same patient shows a tumor of intermediate signal intensity. Note the associated fluid signal within the left mastoid air cells secondary to eustachian tube obstruction.

is seen in 60% of patients at presentation[29, 184] as partial or complete effacement of the parapharyngeal triangle of fat (see Figs. 19–12 and 19–14). From there, the tumor may further extend laterally to break into the masticator space, infiltrating the pterygoid muscles and giving rise to trismus.[19, 21, 30] Once the masticator space is violated, careful scrutiny should be made to detect the highly possible perineural infiltration of the mandibular nerve. The latter acts as a "cable" along which the tumor tracks upward to gain intracranial access through the foramen ovale, invade the gasserian ganglion in Meckel's cave (Fig. 19–15), and follow the preganglionic segment of the trigeminal nerve as far as the pons, often resulting in denervation atrophy of the muscles of mastication (Fig. 19–16).[30, 65] Perineural spread is often clinically silent until the intracranial segment of the nerve has been infiltrated.[166] Such perineural infiltration is best evaluated by precontrast and postcontrast coronal T1-weighted MRI, particularly with fat-suppression techniques.[5, 166] The mandibular nerve, lying between the medial and lateral pterygoid muscles, demonstrates abnormal thickening and enhancement with effacement of the surrounding fat planes.[82, 119] Imaging signs of perineural tumor spread are detailed later (see "Oropharyngeal Carcinoma").

2. *Posterolateral spread* occurs into the retrostyloid compartment of the PPS, thereby putting cranial nerves IX through XII at risk of involvement.[30]
3. With *posterior spread*, the tumor first infiltrates the RPS, obliterating its fat stripe, then invades the periver-

Table 19–2. Tumor-Node-Metastasis (TNM) Classification of Nasopharyngeal Carcinoma

T Staging	
T1	Tumor confined to nasopharynx
T2	Tumor extends to soft tissue of oropharynx and/or nasal fossa:
T2a	Without parapharyngeal extension*
T2b	With parapharyngeal extension*
T3	Tumor invades bony structures and/or paranasal sinuses
T4	Tumor with intracranial extension and/or involvement of cranial nerves, infratemporal fossa, hypopharynx, or orbit
N Staging	
N0	No regional lymph node metastasis
N1	Unilateral node(s): 6 cm or less in greatest dimension above supraclavicular fossa
N2	Bilateral node(s): 6 cm or less in greatest dimension, above supraclavicular fossa
N3	Metastasis in lymph node(s):
N3a	Greater than 6 cm in dimension
N3b	In the supraclavicular fossa
M Staging	
M0	No distant metastases
M1	Distant metastases are present

*Parapharyngeal extension denotes posterolateral infiltration of tumor beyond the pharyngobasilar fascia.

From Fleming I, Cooper J, Henson D, et al (eds): Manual for Staging of Cancer, 5th ed. American Joint Committee on Cancer. Philadelphia, Lippincott-Raven, 1997.

tebral space. Involvement of the prevertebral muscles is not uncommon and is best assessed by T2-weighted or enhanced MRI (see Fig. 19–14*B* and *C*). In late-stage disease, vertebral body destruction and spinal canal invasion occur at times.[30, 130]

4. *Superior spread* results in skull base erosion and/or intracranial tumor extension, most commonly into the middle cranial fossa.[29] Skull base erosion occurs in up to one third of patients,[22] whereas the frequency of detectable intracranial spread varies from 12% on CT scans up to 31% on MR images.[29, 146] The most common route of intracranial spread is through the foramen ovale,[27, 29, 30, 166] either via perineural mandibular nerve infiltration (see earlier) or by direct tumor extension into the foramen.[119] Other less common routes include:

   a. Extension into the foramen lacerum, where the tumor encases the internal carotid artery, which leads it into the cavernous sinus, putting the III, IV, and VI nerves as well as the ophthalmic and maxillary divisions of the trigeminal nerves at risk of involvement.[29, 30, 119]
   b. Direct destruction of the skull base (Fig. 19–17), commonly at the sites of muscular attachments, particularly the levator and tensor veli palatini.[29, 100, 119]
   c. Direct invasion of the sphenoid sinus.[29]

Intracranial extension into the posterior cranial fossa may also occur through the jugular foramen along the neurovascular bundle[23, 108, 112] or through the foramen

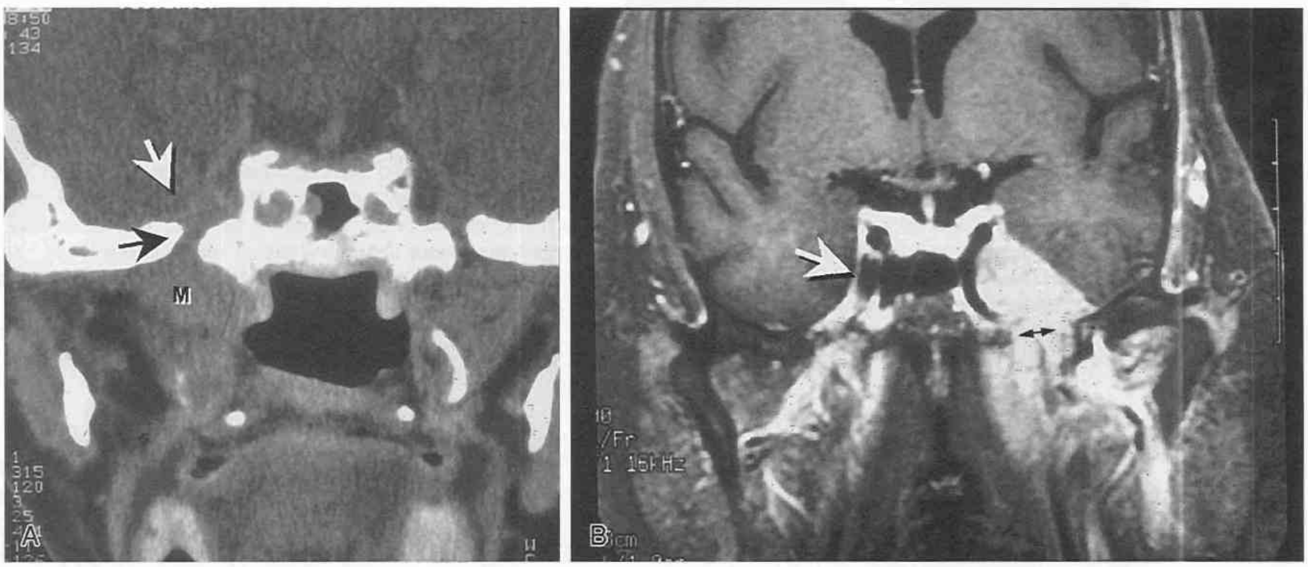

Figure 19–15. Intracranial extension of nasopharyngeal carcinoma through the foramen ovale. The following images demonstrate a common route of intracranial extension of nasopharyngeal carcinoma through the foramina ovale while the skull base is intact. Such tumor extension occurs along the mandibular division of the trigeminal nerve and indicates that the tumor has already violated the masticator space.

A, Postcontrast coronal CT scan shows a mildly enhancing, right-sided soft tissue mass lesion (M), responsible for the asymmetry of the nasopharyngeal airway and extending intracranially, as evidenced by (1) the presence of a small parasellar enhancing soft tissue component *(white arrow)* obliterating the normal cerebrospinal fluid density of Meckel's cave and (2) widening of the right-sided foramen ovale *(black arrow)*.

B, Postgadolinium-enhanced, coronal fat-suppressed, T1-weighted MR image of another patient shows an intensely enhancing, left-sided parapharyngeal and masticator space mass lesion that extends intracranially through the widened ipsilateral foramen ovale *(double arrow)* to attain an extra-axial location within the middle cranial fossa, obliterating Meckel's cave and elevating the left temporal lobe of the brain. The *white arrow* indicates a normal Meckel's cave.

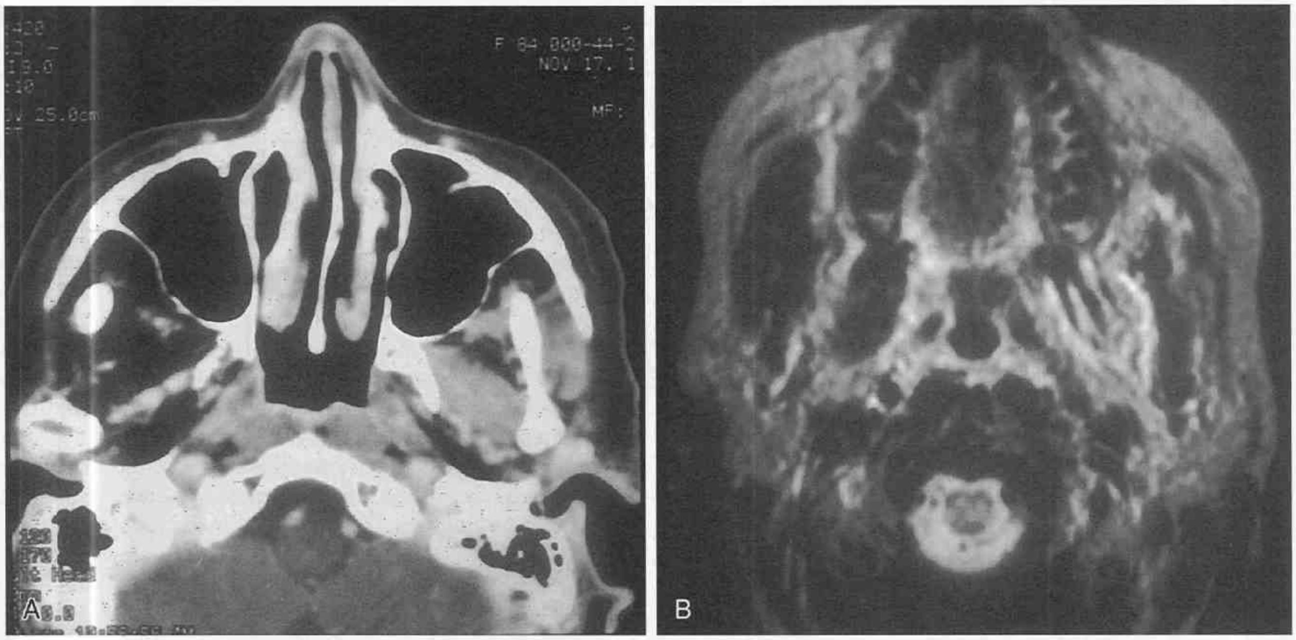

Figure 19–16. Atrophy of muscles of mastication. Enhanced axial CT scan at the level of the nasopharynx *(A)* and axial T2-weighted MRI scan at the level of the oropharynx *(B)* demonstrate atrophy of the right and left masticator spaces, respectively, with consequent abundance of intermuscular fat planes.

magnum, but it is usually associated with gross bone destruction.[27] Indirect intracranial access has also been described through the foramen rotundum[20, 24, 27, 125] and superior orbital fissure (see later).[30] A knowledge of the routes of intracranial spread of nasopharyngeal carcinoma is important in order to understand that bone erosion may not always be present. Indeed, the first sign of intracranial infiltration may be a mere dural thickening, along the floor of the middle cranial fossa,[30] that is best appreciated on contrast-enhanced coronal MR images.

5. *Inferior spread* may occur, often submucosally, and may be clinically occult down to the oropharynx, thereby increasing the T classification from stage T1 to stage T2. The tough pharyngobasilar fascia forms a moderately resistant barrier to tumor outgrowth, and such spread may be indicated by asymmetry of the PMS below the level of the hard palate or at the level of C1-C2.[30, 108, 119]

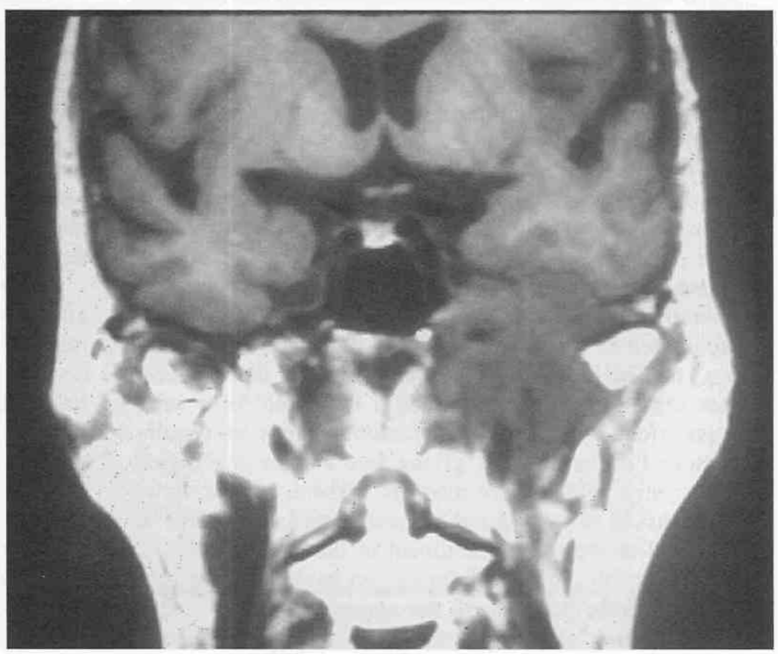

Figure 19–17. Intracranial extension of nasopharyngeal carcinoma through skull base erosion. Coronal nonenhanced, T1-weighted MRI scan demonstrates an intermediate-signal-intensity soft tissue mass infiltrating the skull base on the left side and extending into the epidural space underneath the left temporal lobe of the brain. The ipsilateral Meckel's cave is compressed yet patent (see Fig. 19–15), suggesting that intracranial extension in this case has not occurred through the foramen ovale.

6. *Anterior spread* occurs into the posterior aspect of the nasal cavity from which the tumor may extend through the sphenopalatine foramen into the pterygopalatine fossa.[30] Once within the latter, perineural infiltration of the maxillary division of the trigeminal nerve is a potential route for intracranial extension through the foramen rotundum.[20] Uncommonly, further spread from the pterygopalatine fossa may occur through the inferior orbital fissure into the orbit, then through the superior orbital fissure into the cavernous sinus and middle cranial fossa. Invasion of the maxillary antrum and posterior ethmoids is also uncommon.[30, 119] Obliteration of the normal fat within the pterygopalatine fossa on CT and MRI is a sign of its infiltration.[32, 44]

Evaluation of follow-up scans after radiotherapy is one of the most challenging parts of the radiologic work-up of nasopharyngeal carcinoma. The clinician expects the radiologist to differentiate residual or recurrent tumor from postirradiation granulation tissue, because endoscopy that is already hampered by radiation-induced mucositis is not successful in detecting deep recurrence. Furthermore, biopsy needs to be guided to areas under suspicion and is somewhat limited by the poor capacity of tissues to recover.[125]

Such evaluation is primarily the function of MRI because the CT attenuation of tumor and fibrous tissue are similar.[125] On MR images, mature scar tissue (formed of dehydrated hypocellular collagen) does not enhance with contrast and exhibits dark signal on T2-weighted images, an appearance that is readily distinguishable from tumor tissue.[30, 125, 130] Yet immature scar (formed of well-hydrated hypercellular granulation tissue) cannot be differentiated from recurrent tumor on the basis of MR signal characteristics, because both show contrast enhancement and intermediate to high T2-weighted signal.[30, 99, 125] In the latter case, the following measures may facilitate the diagnosis:

1. Ideally, a postradiotherapy baseline MRI is performed for comparison with future studies. This should be delayed for 3 to 4 months after completion of radiotherapy to allow for total resolution of slowly regressing tumors and acute postirradiation reactive changes (including thickening of the posterior pharyngeal wall and retropharyngeal edema). Progressively growing masses or tissue thickening should be deemed a recurrent tumor. Unchanging lesions do not exclude the possibility of tumor recurrence, whereas a regressive change points to a resolving postirradiation reaction or a contracting scar.[119, 125, 148]
2. When previous scans are unavailable, detection of an obviously positive lymph node is a reliable sign of recurrence.[119] Otherwise, studying the lesion's morphology may be helpful. It has been proposed that a recurrent tumor usually presents as a lobulated lump with mass effect, whereas postirradiation changes are usually a more diffuse process, giving rise to nasopharyngeal asymmetry with straight margins.[25] These criteria, however, should be considered suggestive and should not be regarded as the sole determinant of tumor recurrence.
3. When feasible, some techniques can be used to measure the metabolic activity of the mass in question, thus distinguishing a recurrent tumor by its high metabolic rate from postirradiation scar tissue. These techniques include positron emission tomography (PET) with 18-fluorodeoxyglucose (FDG), thallium 201 scanning, and MR spectroscopy.[54, 79, 117–119]

Finally, it is worth noting that meningeal infiltration, particularly in the posterior cranial fossa, may be the only manifestation of tumor recurrence without a detectable nasopharyngeal mass (due to submucosal spread). This occurs through the jugular foramen or the foramen magnum, each an uncommon route of spread in pretreatment patients. Thus, the basal meninges, the jugular foramen, and the foramen magnum as well as the internal acoustic meatus should always be scrutinized for occult recurrence. The pattern of flow in the jugular bulb, often giving rise to an intermediate to high T1-weighted signal and postcontrast enhancement, may complicate the evaluation of tumor recurrence within the jugular foramen. T2-weighted images and MR angiography are valuable in such cases.[27]

Oropharyngeal Carcinoma. As in the nasopharynx, squamous cell carcinomas constitute the vast majority (90%) of all malignant neoplasms involving the oropharynx.[85, 108] Again, most of these are poorly differentiated carcinomas.[8] Predisposing factors for oropharyngeal squamous cell carcinoma are tobacco, alcohol, and syphilis.[108, 119] Carcinoma arises most commonly from the palatine tonsils and base of the tongue.[184] Less common sites are the faucial arches, soft palate, and the posterior pharyngeal wall. Spread pattern and lymphatic drainage vary according to the site of origin,[119] yet the overall incidence of cervical metastatic lymphadenopathy is 50% to 70%, which renders the prognosis unfavorable in most cases.[8]

Clinical Presentation. Patients often present with a sore throat, localized pain, referred ipsilateral otalgia, dysphagia, trismus, or a neck mass. Examination usually reveals a friable ulcerating mass.[55, 152]

Imaging Features

Carcinoma of the Base of the Tongue (Fig. 19–18). Base of tongue carcinoma often arises on one side behind the circumvallate papillae, and it is more aggressive and infiltrative than that involving the anterior two thirds of the tongue. As a result of the rich lymphatic network in this region, up to 75% of patients have lymph node metastases at initial diagnosis, primarily involving the internal jugular and, to a lesser extent, the spinal accessory nodes. Submandibular nodes are also involved when the tumor infiltrates the mouth floor.[119]

Unfortunately, differentiation between carcinoma and normal lymphoid tissue (lingual tonsil) at the tongue base may be difficult on the basis of tissue morphology, CT density, and MR signal characteristics. Lingual tonsils may be large, lobular, and asymmetrical. Moreover, the T2-weighted MR signal as well as the enhancement patterns on MRI and CT are similar for both carcinoma and lymphoid tissue. The usual infiltrative nature, coupled with the high incidence of metastatic lymphadenopathy associated with carcinoma, confirms the diagnosis. Otherwise, a deep endoscopic biopsy is needed.[8, 56, 62, 81]

Tongue base carcinoma may extend *anteriorly* to infiltrate the mobile portion of the tongue and the floor of

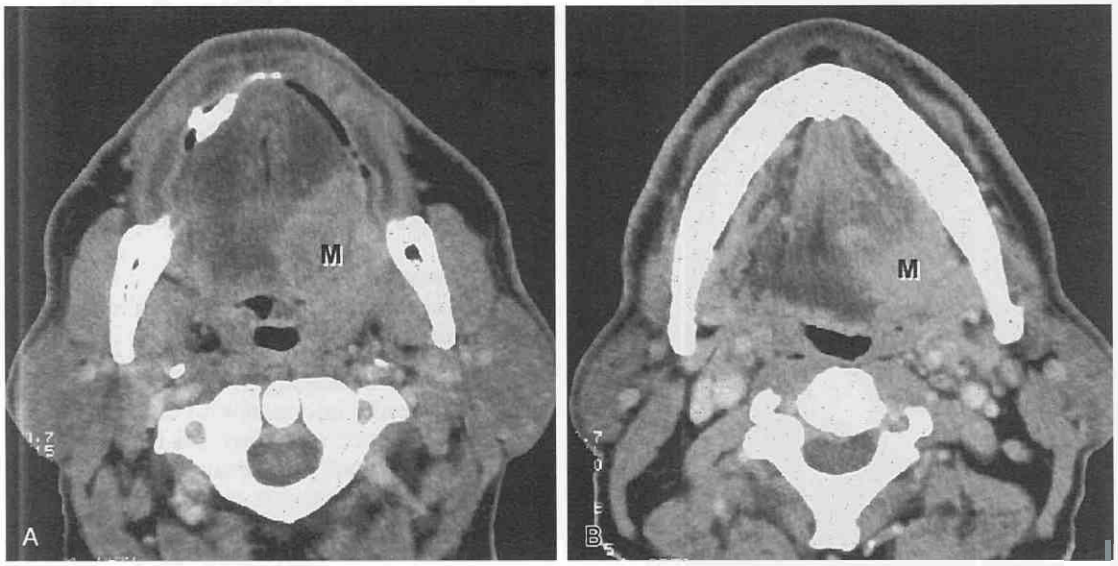

Figure 19–18. Squamous cell carcinoma of the tongue base. *A*, Contrast axial CT scan demonstrates a large, mildly enhanced mass lesion (M) involving the left root of the tongue, obliterating the normal fat plane between the pharynx and the medial pterygoid muscle, and extending posteriorly to infiltrate the anterior tonsillar pillar (palatoglossus muscle). *B*, Section at the level of floor of mouth in the same patient shows the tongue base mass to be violating the left sublingual space (harboring the left neurovascular bundle of the tongue) and infiltrating the ipsilateral genioglossus/geniohyoid muscles, yet stopping short of the midline.

the mouth; *laterally* to involve the pterygoid muscles and mandible; *superiorly* into the tonsillar fossa and soft palate; and *inferiorly* to fill the vallecula and to invade the preepiglottic space, the epiglottis, or the hypopharynx.[8]

Carcinoma of the Palatine Tonsils and Faucial Arches (Figs. 19–19 and 19–20). This carcinoma may arise from the mucosa lining the tonsillar bed, remnants of the palatine tonsils, and the anterior or, rarely, the posterior tonsillar pillar.[119] Of these patients, 76% have clinically positive lymph node metastases occurring primarily in the jugulodigastric group. Spinal accessory as well as submandibular and retropharyngeal nodes may also be involved.[8, 56, 119]

The tumor forms a bulging mass that thickens one side of the oropharynx from the soft palate to the hyoid bone.[108] Spread may occur *laterally* to invade the superior constrictor muscle into the parapharyngeal then the masticator space, with the potential risk of extension to the skull base (see "Nasopharyngeal Carcinoma"). Posterolateral extension into the retrostyloid PPS may lead to encasement of the internal carotid artery.[185] *Inferiorly*, the tumor may spread to the glossotonsillar sulcus, base of the tongue, and mouth floor, while superiorly it may infiltrate the soft palate and nasopharynx.[8] It may be difficult to differentiate oropharyngeal tumors spreading up to the nasopharynx and vice versa. However, oropharyngeal tumors extending upward tend to invade the ipsilateral nasopharynx and masticator space in contrast to nasopharyngeal tumors, which tend to infiltrate the oropharynx in a diffuse fashion.[119]

Although the tonsillar regions may normally appear asymmetrical, they should be regarded with suspicion whenever they are associated with obliteration of the PPS or cervical lymphadenopathy.[56, 123]

Carcinoma of the Soft Palate. The soft palate is associated

Figure 19–19. Squamous cell carcinoma of the left palatine tonsil has spared the parapharyngeal space. Axial CT scan obtained during bolus intravenous contrast administration reveals a rather ill-defined, mildly enhancing soft tissue mass centered on the left tonsillar fossa and extending along the anterior tonsillar pillar (palatoglossus muscle) into the soft palate and tongue base. Extension along the posterior pillar (palatopharyngeus muscle) into the posterior pharyngeal wall is also noted. The lost definition of prevertebral fat plane on the left side suggests perivertebral space invasion yet may be due to mere compression. The parapharyngeal space is intact.

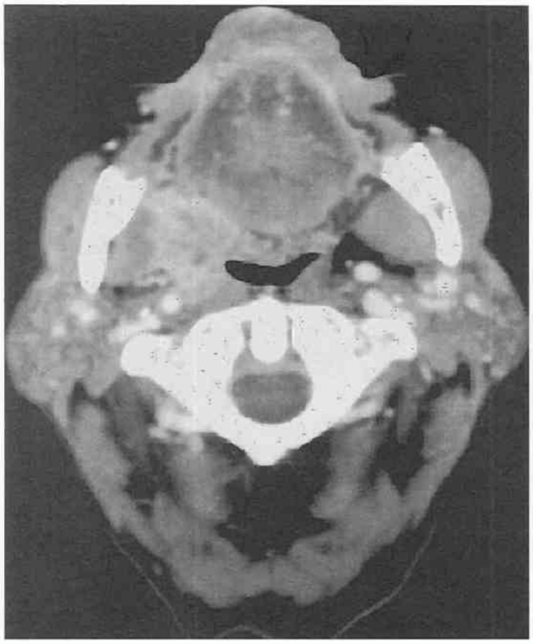

Figure 19–20. Squamous cell carcinoma of the right palatine tonsil has infiltrated the parapharyngeal space. Enhanced axial CT scan at the level of the oropharynx shows a well-defined intensely enhancing mass lesion involving the right tonsillar region, with central nonenhancing areas suggestive of tumor necrosis. The tumor infiltrates (1) the anterior tonsillar pillar into the right tongue base; (2) the posterior tonsillar pillar into the posterior pharyngeal wall, with possible involvement of the perivertebral space; (3) the prestyloid and poststyloid parapharyngeal spaces, where it abuts yet incompletely encases the internal carotid artery; and (4) the masticator space, where the tumor is seen as inseparable from the medial pterygoid muscle. Given such lateral extension, perineural spread along the mandibular nerve (V3) intracranially should be of concern.

with the best prognosis of all oropharyngeal carcinomas. The tumor usually arises on the oral side of the palate. Metastatic cervical lymphadenopathy is seen in 60% of patients at presentation; however, the incidence is far less (8%) for tumors less than 2 cm in diameter (stage T1). The high internal jugular and subdigastric nodes are first involved, followed by the lower internal jugular or retropharyngeal nodes.[119]

The tumor usually spreads first to the tonsillar pillars and hard palate. Other potential pathways include *lateral* infiltration along the tensor and levator veli palatini muscles into the PPS and up the skull base. *Superior* spread occurs to the nasopharynx or through the greater and lesser palatine foramina into the pterygopalatine fossa, then into the cavernous sinus.[119] Palatine tumors are best evaluated by sagittal and coronal T1-weighted MRI. A tumor shows up as low signal in contrast to the normal bright T1-weighted signal of the palate caused by mucous glands and fat.[119]

Carcinoma of the Posterior Oropharyngeal Wall. Fortunately, this carcinoma is rare, as it carries the worst prognosis among all oral and oropharyngeal carcinomas.[8, 56, 108] Arising in a silent area, the tumor is usually advanced at presentation. It tends to creep submucosally to infiltrate the adjacent oropharyngeal sites, the nasopharynx, and the hypopharynx. Thus, the tumor may be relatively superficial yet extensive. Spreading *posterolaterally*, it may encase the carotid artery at an early stage. *Posteriorly*, it infiltrates the RPS, obliterating its fat stripe, but the prevertebral fascia is breached only at a later stage. Sagittal and axial postcontrast T1-weighted MRI best demonstrates this tumor, which may consist merely of subtle mucosal thickening.[56, 108, 152]

Role of Imaging

The primary roles of the radiologist in evaluating oropharyngeal carcinoma are to:

1. Provide tumor staging.
2. Relay specific information to the surgeon regarding the involvement of some key anatomic structures that are crucial to planning the treatment strategy.
3. Assess post-therapeutic tumor recurrence.

The UICC/AJCC TNM classification of oropharyngeal carcinoma is presented in Table 19–3.

A problem-oriented radiologic assessment of oropharyngeal carcinoma should include specific comments on issues having a direct effect on the type and extent of subsequent surgery. These can be detailed as follows.

Invasion of Deep Fascial Spaces, Perineural Infiltration, and Skull Base or Intracranial Extension. As described earlier, oropharyngeal carcinomas can spread to invade the various fascial spaces about the pharynx (see Figs. 19–19 and 19–20). Perineural infiltration occurs primarily along the mandibular and maxillary divisions of the trigeminal nerve up to the skull base and intracranially.

Table 19–3. UICC/AJCC Tumor-Node-Metastasis (TNM) Classification of Oropharyngeal Carcinoma

T Staging	
T1	Tumor 2 cm or less in greatest dimension
T2	Tumor more than 2 cm but not greater than 4 cm in greatest dimension
T3	Tumor more than 4 cm in greatest dimension
T4	Tumor invading adjacent structures (including bone [mandible, maxilla, hard plate], soft tissues of neck, deep muscles of tongue, larynx)
N Staging	
N0	No lymph node involvement
N1	Ipsilateral lymph nodes 3 cm or less
N2	
N2a	Ipsilateral lymph node greater than 3 cm, but not more than 6 cm
N2b	Multiple ipsilateral lymph nodes, but none greater than 6 cm
N2c	Bilateral or contralateral lymph nodes, but none greater than 6 cm
N3	Lymph nodes greater than 6 cm
M Staging	
M0	No distant metastases
M1	Distant metastases are present

AJCC, American Joint Committee on Cancer; UICC, International Union Against Cancer.

Data from Beahrs OH, et al (eds): Manual for Staging of Cancer, 4th ed. Philadelphia, JB Lippincott, 1992[7]; and Leslie A et al: J Comput Assist Tomogr 23: 43–49, 1999.[86]

Direct imaging signs of perineural spread (see Fig. 19–15) include:

1. Thickening and enhancement of the effected nerves (with attention also paid to possible skip lesions).
2. Abnormal enhancement in Meckel's cave.
3. Lateral bulging of the cavernous sinus dural membrane.

Indirect signs include:

1. Foraminal enlargement on CT (see Fig. 19–15*A*).
2. Atrophy of muscles of mastication (in mandibular nerve infiltration) (see Fig. 19–16).
3. Obliteration of the normal fat plane in the pterygopalatine fossa (in maxillary nerve infiltration).[41, 82, 184]

Detection of subtle cortical skull base erosions requires coronal CT scanning, whereas MRI best assesses marrow infiltration. Intracranial extension may be first detected as abnormal meningeal thickening and enhancement. Again, this may be seen without skull base erosion.

Reporting such tumor extension changes the management of tonsillar and soft palate carcinoma from wide local excision through an intraoral approach to a more extensive surgery, depending on the structures infiltrated. At many institutions, imaging evidence of bulky tumor abutting the skull base precludes surgery.[115]

Preepiglottic Fat Infiltration. The preepiglottic space consists of the fat filling the area anterior to the epiglottis and posterior to the hyoid bone and thyrohyoid membrane. The site is best seen on sagittal T1-weighted MR images as a bright stripe (see Fig. 19–4). On axial scans, it appears as a C-shaped area of bright T1-weighted signal on MRI and low attenuation on CT.[8, 65]

The preepiglottic space may be invaded by carcinoma of the tongue base (and, less commonly, by carcinoma of the piriform sinus). Infiltration is seen as soft tissue replacement of the normal fat content on either MRI or CT.[8, 65]

A correct diagnosis is critical because preepiglottic invasion implies extension of surgery to include partial (supraglottic) or even total laryngectomy in combination with tongue base surgery. The consequent high morbidity and impairment of both swallowing and speaking adversely affect the patient's life quality.[9, 184] Peritumoral edema, adjacent inflammation, and partial-volume effect on CT may mimic preepiglottic fat infiltration and should be always excluded.[120]

Bilateral or Deep Tongue Base Invasion. Carcinoma originating primarily from the tongue base or extending to it from other oropharyngeal sites may spread across the midline or invade deeply into the floor of the mouth to involve the neurovascular bundle of the tongue (see Fig. 19–18*B*). The latter, consisting of the lingual artery as well as the lingual, glossopharyngeal (IX), and hypoglossal (XII) nerves, runs along the sublingual space on either side of the hyoglossus muscle to supply the tongue from posterior to anterior.[121, 184]

The precise tumor extent can be depicted on postcontrast and T2-weighted MR images. One may also assess its relationship to the neurovascular bundle on postcontrast CT by locating the enhancing lingual vessels between the hyoglossus and genioglossus muscles on each side of the floor of the mouth.[121]

Accurate detection of such tumor extension has an important impact on the subsequent surgical procedure. That is, if one lingual neurovascular bundle can be preserved, partial glossectomy would be performed and the patient would still be able to function well in regard to both swallowing and speaking. For tumors that cross the midline and violate the contralateral lingual neurovascular bundle, treatment options include either total glossectomy (with lifelong feeding gastrotomy) or radiation therapy and chemotherapy.[115, 184]

Encasement of the Internal Carotid Artery. This situation may occur from extension of oropharyngeal carcinoma into the retrostyloid PPS. Some suggest that when the tumor wraps more than 270 degrees of the arterial circumference on axial scans, it is unlikely to be resected without sacrificing the artery.[110] At many institutions, surgery is precluded when imaging studies confirm the presence of internal carotid artery encasement.[115]

Bone Invasion

Mandibular Invasion. Advanced oropharyngeal carcinoma may extend to invade the mandible. Thin-section CT best depicts subtle cortical erosion, whereas MRI is best suited for detecting marrow invasion. Infiltrated areas of bone marrow appear dark on T1-weighted images, bright on T2-weighted images, and enhanced in postcontrast studies. Before the bone marrow is classified as "infiltrated," it is important to exclude other conditions demonstrating the same MR signal behavior, such as radiation fibrosis, osteoradionecrosis, osteomyelitis, and periodontal disease.[34, 155, 184]

From a management perspective, tumors abutting the periosteum, but not fixed to it, are resected with periosteum for margin control. Tumors invading the periosteum or the cortex are removed with the cortex; for tumors infiltrating the mandibular marrow, resection of that segment of the mandible may be required.[8, 34, 184]

Maxillary Invasion. The maxilla may be invaded *directly*, by carcinoma of the soft palate, or *indirectly*, by tonsillar carcinoma invading the retromolar trigone, then the maxilla.[184] Coronal thin-section CT best demonstrates subtle maxillary erosions. When the maxilla is involved, management reverts from wide local excision to resection through a partial maxillectomy.[8]

Prevertebral Muscle Invasion. Advanced cases of pharyngeal carcinoma, particularly those arising in the posterior pharyngeal wall, may invade the prevertebral muscles. Findings such as obliteration of the retropharyngeal fat stripe, irregular muscle contour, bright T2-weighted muscle signal, or postcontrast muscle enhancement on MRI or CT (see Figs. 19–19 and 19–20) should motivate the radiologist to report possible prevertebral muscle invasion. The definite extent, however, is determined by surgical evaluation, since these imaging findings may also be due to peritumoral edema without actual muscle invasion. When the tumor is proven to be fixed, it is deemed irresectable.[8, 94, 184]

Assessment of post-therapeutic oropharyngeal tumor recurrence is often difficult because of the similar imaging appearance of recurrent tumor and post-treatment changes.[72, 167] Because oropharyngeal cancer is primarily a surgical disease, tumor resection—and sometimes the

application of reconstructive procedures (e.g., myocutaneous or free flaps)—often further complicates interpretation by distorting the local anatomy.

As discussed earlier (see "Nasopharyngeal Carcinoma"), the optimal practice is to compare scans with a baseline post-treatment study. Otherwise, the detection of an obvious mass that is compressing rather than retracting the adjacent tissues or obvious lymphadenopathy will point to tumor recurrence.[119]

Non-Hodgkin's Lymphoma

Pharyngeal non-Hodgkin's lymphoma (NHL) arises from the rich extranodal lymphoid tissue of the PMS, the tongue base, or the palate.[65, 184] Generally, 60% of cases of NHL arises in extranodal lymphoid tissue; of these, 60% occur in the head and neck.[119, 182]

Clinical Presentation. Patients are usually older men presenting when having localized nasopharyngeal or oropharyngeal disease, with symptoms indistinguishable from those of squamous cell carcinoma arising at the same site.[119] However, patients may present with systemic manifestations that point to the diagnosis. These include fever, malaise, weight loss, hepatosplenomegaly, and distant lymphadenopathy.[65] Distant lymphadenopathy is present in 80% of patients with primary extranodal NHL.[119]

Imaging Features. The imaging features of NHL of the PMS may be identical to those of the more common squamous cell carcinoma on both CT and MRI. Although lymphoma tends to grow in a circumferential fashion, forming a diffuse, bulky, non-necrotic, superficial mass without early invasion of the PPS,[133] large lesions may invade the deep neck spaces, spread perineurally, and invade the skull base in a pattern similar to that of squamous cell carcinoma.[119] Superficial lymphomas primarily involving the tongue base or palatine tonsils may be also indistinguishable from benign lymphoid hyperplasia.[184]

The diagnosis of NHL is suggested when the following associations are present:

- Large non-necrotic lymph nodes in atypical drainage areas
- Extranodal, extralymphatic lesions[65]
- Clinical systemic manifestations

Malignancy of the Minor Salivary Glands

The minor salivary glands are the least common site of PMS malignancy. The tumor arises from the minor salivary glands in the submucosa of the nasopharynx and tongue base, yet its most common site is the soft palate. Generally, 50% of minor salivary gland tumors are malignant.[119] A spectrum of histologic types exists, with adenoid cystic carcinoma the most frequent, followed by mucoepidermoid carcinoma and malignant mixed tumors.[26, 28]

Clinical Presentation. Tumors usually occur in adults with no sex predilection.[119] Symptoms are nonspecific[65] and depend on the site of origin of the tumor.

Imaging Features. The tumor appears as a soft tissue mass in the PMS that is indistinguishable on both CT and MRI from squamous cell carcinoma or NHL. Biopsy is required for the definitive diagnosis.

Among all malignant nasopharyngeal and oropharyngeal neoplasms, adenoid cystic carcinoma is associated with the highest incidence of perineural spread.[37, 41, 82, 184] Such spread is diagnosed histologically in about 50% of adenoid cystic carcinomas, and when the diagnosis is missed at initial evaluation, treatment failure may result.[119] The direct and indirect imaging signs of perineural tumor spread have been described earlier (see "Oropharyngeal Carcinoma").

Nasopharyngeal Rhabdomyosarcoma

Rhabdomyosarcoma is a malignant mesenchymal tumor that occurs primarily in children. It can arise anywhere in the body, with the head and neck the most common sites of origin (28% to 36%), followed by the urinary bladder and then the extremities.[42] Within the head and neck, the orbit and the nasopharynx are the most commonly involved areas. The tumor arises from the nasopharyngeal muscles, located within the PMS, and is associated with metastatic lymphadenopathy in 50% of cases. Distant metastases occur in the lung and bone.[42]

Clinical Presentation. The peak age of incidence is 2 to 5 years, and boys are more susceptible than girls (2:1). The usual presenting symptoms are rhinorrhea, sore throat, and serous otitis media. Skull base invasion is common, giving rise to cranial nerve palsies.[42, 119]

Imaging Features. The imaging appearance of rhabdomyosarcoma is basically that of a malignant nasopharyngeal growth in a child. The diagnosis is suggested on basis of the patient's age rather than a characteristic radiological appearance.

The tumor appears as a bulky nasopharyngeal soft tissue mass that commonly extends intracranially through both destruction of the skull base and widening of the basal foramina and fissures. CT shows an isodense mass to the brain, whereas MRI shows the tumor to be isointense on T1-weighted images and hyperintense on T2-weighted images.[42] Postcontrast studies show a variable amount of enhancement. The same imaging features may be seen in children in cases of neuroblastoma and rhabdoid tumor.[119]

Lesions of the Retropharyngeal Space

Pseudotumors

The clinical appearance of an RPS mass may result from:

1. A tortuous internal carotid artery that extends medially and results in a bulge in the posterior pharyngeal wall.
2. Retropharyngeal hematoma.
3. Edema due to jugular vein or lymphatic obstruction. Edema of the RPS most commonly involves both its suprahyoid and infrahyoid portions and demonstrates low-attenuation enlargement of the space.[45]

Congenital Lesions

Hemangioma and Lymphangioma

Hemangioma and lymphangioma are usually infiltrative lesions that do not respect the fascial boundaries (i.e.,

"trans-spatial" diseases) and may extend into the RPS as a part of multiple space involvement.

On CT scans, hemangiomas appear as relatively dense lesions and typically demonstrate intense enhancement.[141] On MR images, they display intermediate signal intensity on T1-weighted and intermediate-weighted images, with heterogeneous increased signal intensity on T2-weighted images.[3, 52] Following gadolinium administration, enhancement is usually intense.[3, 141] Areas of signal void from associated vascular structures may be identified but are much more common with high-flow lesions.[3]

Lymphangiomas typically appear on both CT and MRI as multiloculated, poorly circumscribed lesions.[138] They exhibit fluid attenuation and signal intensity, and they have imperceptible, nonenhancing rims.[138] Hemorrhage may occur into a lymphangioma and may manifest clinically as rapid enlargement of the lesion; this may be identified as an area of high attenuation on CT and bright signal on T1-weighted MRI.[3, 138] Hemorrhage-fluid levels may also be seen.[3]

Congenital vascular anomalies are currently classified as follows[122, 139]:

1. *True hemangiomas*. These often involute with age. Involuting hemangiomas show focal areas of bright T1-weighted signal resulting from fatty replacement.[3] Hemangiomas may look identical to venous malformations unless the venous malformation contains phleboliths.[3]
2. *Vascular malformations* (arterial, capillary, venous, lymphatic, and combined). These anomalies remain stable or slowly grow with the patient. Patients with these lesions typically require some form of therapy when cosmetic disfigurement, bleeding, or functional impairment is present.[91]

From a therapeutic perspective, the most important issue is to classify these lesions as *low-flow* vascular malformations, which are often successfully treated with percutaneous sclerotherapy,[60] and as *high-flow*" vascular malformations, which are often treated with transarterial embolization.[91, 183] T2-weighted MRI elegantly show the difference between these categories; low-flow lesions appear predominantly bright, and high-flow lesions appear predominantly signal void.[60, 91, 183]

Inflammatory Conditions

Retropharyngeal Infections

Infection of the RPS is uncommon in adults, in whom it is most often due to direct posterior pharyngeal wall trauma as may occur during endoscopy or attempted nasogastric tube insertion.[164] This decreased incidence is most likely related to atrophy of the retropharyngeal lymph node chains following puberty.[132, 164] Most commonly affected are patients 4 years of age or younger, in whom pharyngitis or infection of the adenoids or faucial tonsils (generally with streptococci or staphylococci) spreads to the retropharyngeal lymph node chains.

Typically, RPS infections progress in four successive phases and can be stopped at any stage by appropriate treatment:

1. *Reactive lymphadenopathy*. This phase represents the first response of the retropharyngeal lymph nodes to spread of infection. The nodes react by hyperplasia without disruption of their internal architecture.
2. *Suppurative lymphadenitis*. The infected nodes suppurate, with consequent development of an intranodal abscess.[145]
3. *Retropharyngeal cellulitis or abscess*. Early spread of the organism outside an affected lymph node may result in cellulitis, causing the tissues to swell without focal fluid collection.[65] When the enlarged suppurated nodes eventually rupture into the RPS, an abscess is formed. The abscess typically starts at the location of the lateral retropharyngeal lymph node chains lateral to the midline and above the level of the hyoid bone.[179] Infection then spreads to involve the entire RPS from side to side.[45]
4. *Complicated retropharyngeal abscess*. When untreated, a retropharyngeal abscess can further spread locally into adjacent neck spaces, track downward into the superior mediastinum, or penetrate the alar fascia into the danger space, where it may spread down to the level of the diaphragm.[132]

Clinical Presentation. Patients present with swelling adjacent to the soft palate, which may be displaced anteriorly; fever; sore throat; dysphagia; mild to moderate neck stiffness; and occasionally a muffled voice. Breathing may become strained or noisy if the airway becomes compromised.[179]

Imaging Features

Reactive Lymphadenopathy. At this phase, enlarged lateral retropharyngeal lymph nodes (>1 cm in diameter) can be seen, keeping the configuration of normal nodes (oval or kidney-shaped) and usually presenting a homogenous texture.[65]

Suppurative Lymphadenitis. Suppurated lymph nodes appear enlarged and demonstrate central low attenuation on CT or fluid signal intensity on MRI.[45, 179] However, these central changes can also be seen in early liquefying nodes without complete suppuration. Frankly suppurated nodes can be identified by their enhancing rims (Figs. 19–21*A*) and by the associated edema of the RPS.[65]

Retropharyngeal Cellulitis or Abscess. The most common finding in patients with infection of the RPS is that of cellulitis localized to the RPS at the level of the nasopharynx or oropharynx.[45] It is seen as diffuse thickening (>75% of anteroposterior diameter of vertebral body[42]) and as enhancement of the retropharyngeal soft tissues (see Fig. 19–21).

When an abscess forms, it appears as an area of fluid collection marginated by an enhancing rim, with possible air or air-fluid level seen within.[42] As stated, it starts at the region of lateral retropharyngeal nodes (Fig. 19–22) but may spread to involve the entire RPS (see Fig. 19–21*B*), where it may attain a characteristic "bowtie" appearance.[65] Significant mass effect is often present,[119] and the degree of pharyngeal airway compromise should always be sought.

It is also important to distinguish a true retropharyngeal abscess, which necessitates surgical drainage, from both suppurative adenitis (with surrounding edema) and cellulitis, because the latter two conditions may respond to conservative treatment without the need for intervention.[65, 119]

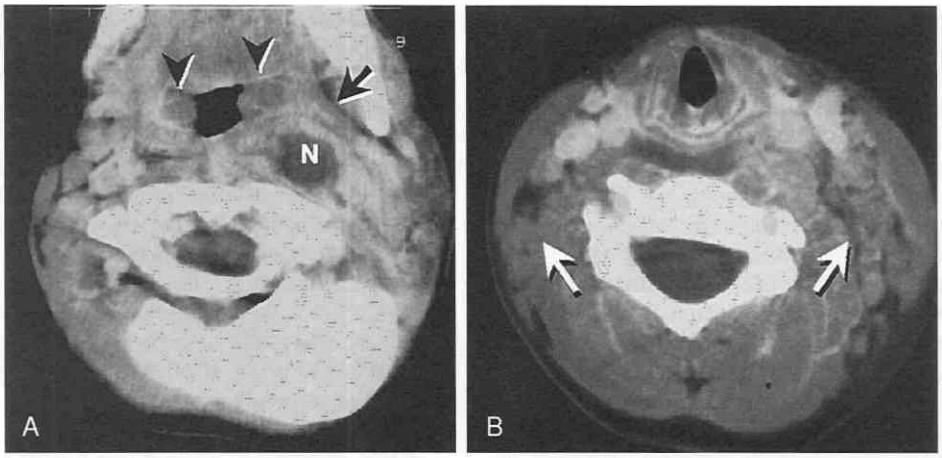

Figure 19–21. Retropharyngeal infection in a 5-year-old boy presenting with left upper neck swelling.

A, Postcontrast CT scan reveals enlarged, left-sided lateral retropharyngeal lymph node (of Rouviere) (N), displaying central low attenuation and thick, enhancing margin, a picture consistent with suppurative lymphadenitis (intranodal abscess). The associated enlargement of palatine tonsils *(arrowheads)* indicates the source of infection. Note the integrity of the ipsilateral prestyloid parapharyngeal space *(arrow)*.

B, Section at a lower level in the same patient shows low fluid attenuation casting the entire retropharyngeal space. The presence of a thin, enhancing rim marginating the collection suggests a retropharyngeal abscess (caused by rupture of another suppurated lymph node), rather than a mere associated edema, and necessitates the establishment of drainage. Note the bilateral posterior cervical space lymphadenopathy *(arrows)*.

Complicated Retropharyngeal Abscess. The parapharyngeal fat may appear dense as a result of associated inflammation (see Fig. 19–21). When suppuration extends into this space, however, external drainage (rather than the transoral approach used with most retropharyngeal abscesses) is indicated.[164]

Although axial CT usually demonstrates the full extent of retropharyngeal infection, sagittal MRI may occasionally be helpful to better define the superoinferior extent of disease and associated displacement or compression of the pharynx, larynx, trachea, or esophagus.[179]

Extension of RPS infection into the danger space cannot be differentiated from an RPS process unless abscess or cellulitis extends below the T2 to T6 vertebral level.

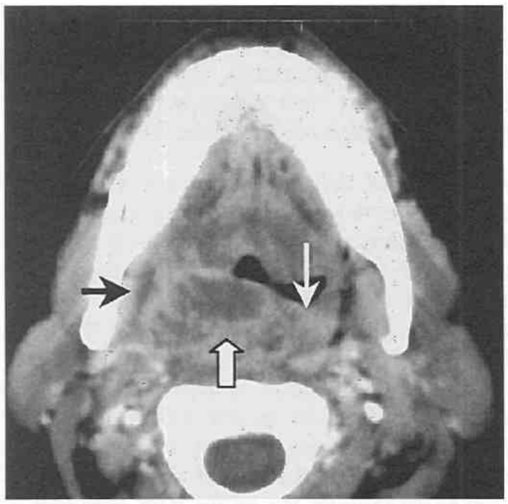

Figure 19–22. Retropharyngeal infection. Axial contrast-enhanced CT scan through the oropharynx demonstrates enhancing, thickened retropharyngeal soft tissue consistent with cellulitis *(thin white arrow)* and a low attenuation collection on the right suggesting abscess formation *(thick white arrow)* that causes significant airway compromise. Note the abscess starting at the region of the lateral retropharyngeal lymph node (of Rouviere). Associated inflammation results in increased attenuation of the prestyloid parapharyngeal fat on the right *(black arrow)*.

Benign Tumors

Retropharyngeal Lipoma

Benign tumors of the RPS are rare, although lipoma has been reported.[45] This tumor is readily identifiable on both CT and MRI as a retropharyngeal soft tissue mass with characteristic low CT density (−50 to −100 HU), bright T1 signal, and diminished signal on T2-weighted images.

Malignant Tumors

Malignant tumors of the RPS are much more common than benign tumors and are usually secondary to the following[45]:

1. Direct extension of primary squamous cell carcinoma of the nasopharynx, posterior oropharyngeal wall, or hypopharynx.
2. Metastatic involvement of retropharyngeal lymph nodes.
   a. Most commonly, from a nasopharyngeal primary squamous cell carcinoma but may also be seen with an oropharyngeal carcinoma.[45] Enlarged nodes may show central necrosis.
   b. Metastases from other areas, such as thyroid carcinoma and malignant melanoma.[45] Involved nodes may present bright T1-weighted signals, in melanotic melanoma resulting from the paramagnetic effect and in thyroid carcinoma resulting from the high protein (thyroglobulin) content.[65]

In addition, the retropharyngeal lymph node chains may

be involved by non-Hodgkin's lymphoma, either as an initial site or as a part of a multiple chain involvement. Involved nodes initially appear unilateral and homogeneous, but later extranodal progression may cause the lymphomatous tissue to fill the entire RPS.[65]

Lesions of the Prestyloid Parapharyngeal Space

Pseudotumor

Asymmetrical Pterygoid Venous Plexuses

Occasionally, the pterygoid venous plexus of one side (overlying the inner surface of the lateral pterygoid muscle) is larger than that of the other side. The vascular nature of this anatomic variant can be depicted by its racemose enhancement on postcontrast CT scans and on contrast-enhanced, fat-suppressed, axial T1-weighted MR images.[65]

Congenital Lesions

Atypical (Parapharyngeal) Second Branchial Cleft Cyst

The lower face and neck are formed from six pairs of branchial arches. Between them lay five endodermal pharyngeal pouches on the inner aspect and five ectodermal clefts on the outer aspect.[10, 16] The second pharyngeal pouch forms the tonsillar fossa and palatine tonsils, whereas the second branchial cleft (together with the third and fourth clefts) forms an ectoderm-lined tract, called the *cervical sinus*,[66] which is obliterated at a later stage of development.

Failure of the cervical sinus to become completely obliterated results in a second branchial cleft sinus, a fistula, or, more commonly, a cyst anywhere along a line from the oropharyngeal tonsillar fossa to the supraclavicular region of the neck.[66] Although the most common location for a second branchial cleft cyst is the submandibular space,[36] the cyst can atypically present in the PPS, arising from the parapharyngeal portion of the embryonal tract.[66]

Clinical Presentation. Although congenital, these cysts most commonly present in young adults and are often precipitated by respiratory tract infection or trauma.[66] Small cysts are asymptomatic. Patients with a large cyst in the parapharyngeal location may present with parotid gland bulge, dysphagia, or vague neck discomfort.[15] On examination, the posterolateral oropharyngeal wall appears to be bulging internally.[65]

Imaging Features. In its atypical (parapharyngeal) location, the cyst appears on CT and MRI as a thin, smooth-walled structure of fluid attenuation or signal intensity extending from the deep margin of the palatine tonsil into the parapharyngeal fat toward the skull base.[65] Occasionally, T1 hyperintensity may result from high protein content or intracystic hemorrhage.[15] When infected, the cyst wall may become thickened and irregular, and the surrounding fat planes may become obscured.[66]

As mentioned, the most common site of a second branchial cleft cyst is within the submandibular space, characteristically displacing the submandibular gland anteriorly, the sternocleidomastoid muscle posterolaterally, and the carotid sheath posteromedially.[36] At this location, it is important to consider cystic metastasis of papillary thyroid carcinoma in the differential diagnosis. An enhancing soft tissue nodule in cystic metastasis may provide a clue to the diagnosis.

Other cystic lesions of the submandibular space (but rarely giving the characteristic pattern of displacement of adjacent structures) include submandibular gland cysts, lymphangiomas, necrotic or cystic nerve sheath tumors, and epidermoid or dermoid cysts.[66]

Inflammatory Conditions

Parapharyngeal Space Infection

Infection of the prestyloid compartment of the PPS most commonly arises from spread of peritonsillar abscesses, retrotonsillar vein thrombopheblitis, third molar extractions with violation of the pterygomandibular raphe, penetrating injury to the lateral pharyngeal wall, or extension of deep lobe parotid abscesses or as a complication of local anesthesia for tonsillectomy or dental surgery.[164, 179] Inflammation may also spread from the submandibular glands, branchial cleft, or thyroglossal duct cysts or from temporal bone infections through petrous apex air cells.[164]

Patterns of spread of inflammatory changes within the PPS and the adjacent spaces depend on individual differences in fascial anatomy that may arise from normal variation, previous trauma, surgery, infection, or radiation therapy.[132] The virulence and antibiotic sensitivity of the invading organism, as well as the general health and immunologic status of the host, may also affect the spread of infection.[132] Once inside the prestyloid PPS, infection can readily extend into the parotid, masticator, submandibular, or retrostyloid compartment of the PPS.[164]

Clinical Presentation. Clinical presentation of the PPS and the adjacent spaces includes the sudden onset of fever and chills. Dysfunction of cranial nerves IX through XII or the sympathetic plexus may also occur with extension into the retrostyloid compartment, and trismus may occur with masticator space involvement. Painful swelling of the gingival tissues of the maxilla and of the cheek on the involved side may also be noted.[179] On clinical examination, a medial bulge of the lateral pharyngeal wall is commonly seen.[164, 179]

Complications of PPS infection include erosion of the adjacent carotid artery with fatal hemorrhage or pseudoaneurysm formation as well as extension to the RPS with possible asphyxia or dysphagia from the resulting mass effect and inflammation.[179] Paranasal sinus and orbital involvement, intracranial extension, and osteomyelitis may also result.[52]

Imaging Features. Imaging of the PPS and the adjacent spaces may be of great assistance in detecting complications of deep neck infections and determining the optimal timing and approach for surgical drainage.[164] Imaging is most useful when infection is complex, widespread, or difficult to assess clinically.[52] On CT, cellulitis may present as a soft tissue mass with obliteration of adjacent fat planes. The mass is often ill defined, enhancing, and extending along fascial planes (Fig. 19–23) and into subcutaneous tissues.[52, 179] Involved muscles may enhance and appear enlarged, and overlying subcutaneous tissues often demon-

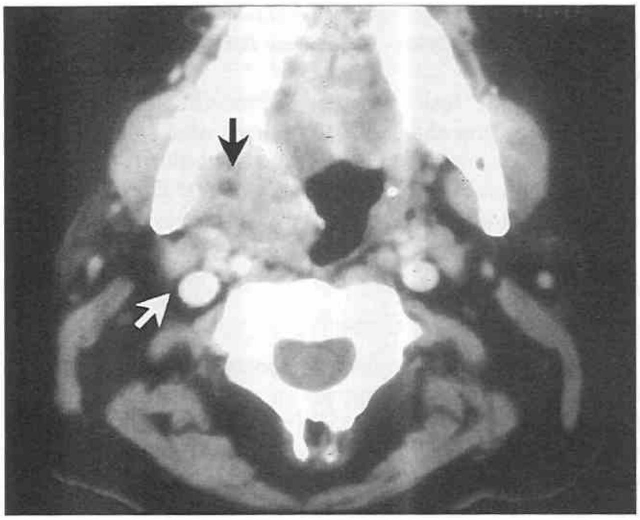

Figure 19–23. Prestyloid compartment parapharyngeal space infection from spread of tonsillitis. Axial contrast-enhanced CT scan at the level of the oropharynx demonstrates enlargement of the right faucial tonsil with obliteration of the prestyloid parapharyngeal fat on the right. One small area of decreased attenuation is noted within the inflammatory process, which may represent a small abscess cavity *(black arrow)*. Fat planes surrounding the contents of the retrostyloid compartment of the parapharyngeal space remain intact *(white arrow)*.

strate linear or mottled increased attenuation beneath thickened skin.[179]

Abscesses of the deep neck spaces, reported to represent up to 9% of masses within the PPS, often appear as unilocated or multiloculated cystic lesions with air or fluid attenuation centers. They may have somewhat irregular, enhancing walls or surrounding tissue edema and may conform to the surrounding fascial boundaries.[103, 164, 179] Occasionally, pus formation is incomplete or may be delayed by antibiotic therapy, and an area of low attenuation on CT, suggesting an abscess cavity, may not yield pus on aspiration or exploration.[179]

Although axial and coronal CT may determine the extent of disease and presence of complications, MRI often provides superior localization because of its multiplanar capabilities and better soft tissue contrast resolution. Inflammatory exudate is of low to intermediate signal intensity on T1-weighted images and is often isointense with adjacent muscle.[179] Both cellulitis and abscess cavities exhibit increased signal intensity on T2-weighted images.

Gadolinium contrast agents may help to differentiate abscess from cellulitis by demonstrating an enhancing abscess wall. Neither MRI nor CT findings can typically differentiate a bacterial from a granulomatous origin of inflammation.[179]

Benign Tumors

Most prestyloid PPS tumors are benign. Of these, the majority are of salivary gland origin, with pleomorphic adenoma representing the most common histology.[84]

Benign Mixed Salivary Gland Tumor (Pleomorphic Adenoma)

Salivary gland tumors in the prestyloid PPS commonly arise from the deep lobe of the parotid gland and extend into the PPS through the stylomandibular tunnel.[84] However, salivary gland tumors can also arise primarily within the prestyloid compartment from congenital rests of salivary gland tissue.[84, 162]

Clinical Presentation. The patient typically presents with a painless mass, since benign salivary gland tumors seldom result in other symptoms.[68]

Imaging Features. The CT appearance of a benign salivary gland tumor is usually that of an ovoid soft tissue mass. When small, the tumor is typically homogeneous; when larger, it may show variable areas of low attenuation that represent sites of cystic degeneration or seromucinous collections. Focal areas of high attenuation representing calcification may also be present.[162]

The MR appearance of a benign salivary gland tumor is that of a well-defined mass with low to intermediate signal intensity on T1-weighted and intermediate-weighted (long TR, short TE) images and intermediate increased signal on T2-weighted images (Fig. 19–24). Smaller lesions are typically homogeneous in appearance, whereas lesions greater than 2.5 cm in diameter are often heterogeneous on all pulse sequences and may have internal foci of low signal or signal void, corresponding to areas of calcification or fibrosis (see Fig. 19–24).[162] Areas of high signal intensity on T1-weighted and intermediate-weighted MR images may also occur in larger tumors and correspond to areas of local hemorrhage.[162] With the prevalence of such findings, mass heterogeneity is not a useful predictor of a benign versus a malignant neoplasm.[162] The best predictors of a benign pleomorphic adenoma are the presence of dystrophic calcifications, best detected with CT, or a well-defined, highly lobulated tumor contour, best seen with MRI.[162]

The site of origin of prestyloid compartment salivary neoplasms is of importance in the surgical management of these patients, because a lesion arising within the deep lobe of the parotid gland is usually treated with operative control of the facial nerve in order to prevent nerve damage, whereas a lesion totally confined to the prestyloid PPS without connection to the parotid gland may be treated with little concern for facial nerve injury.[159] At some institutions, a submandibular approach without control of the facial nerve is also used for deep lobe parotid masses when the tumor does not approach the stylomandibular tunnel.

For an accurate diagnosis of an extraparotid origin of a prestyloid parapharyngeal tumor, an intact fat plane between the posterolateral margin of the tumor and the deep portion of the parotid gland must be clearly demonstrated. Careful attention is necessary because this connection may be a very thin isthmus of tissue that is best detected on high-resolution, thin-section, axial T1-weighted MR images. When lesions are greater than 4 cm in diameter, the intervening fat plane may be obliterated by mass effect alone and distinguishing between intraparotid and extraparotid origin may be impossible (see Fig. 19–24).[162] In such cases, the surgical approach for a tumor of parotid origin is often used in order to minimize the risk of facial nerve damage.[159, 162]

Parapharyngeal Lipoma

Parapharyngeal lipomas are uncommon lesions that are readily identified by their characteristic low attenuation on

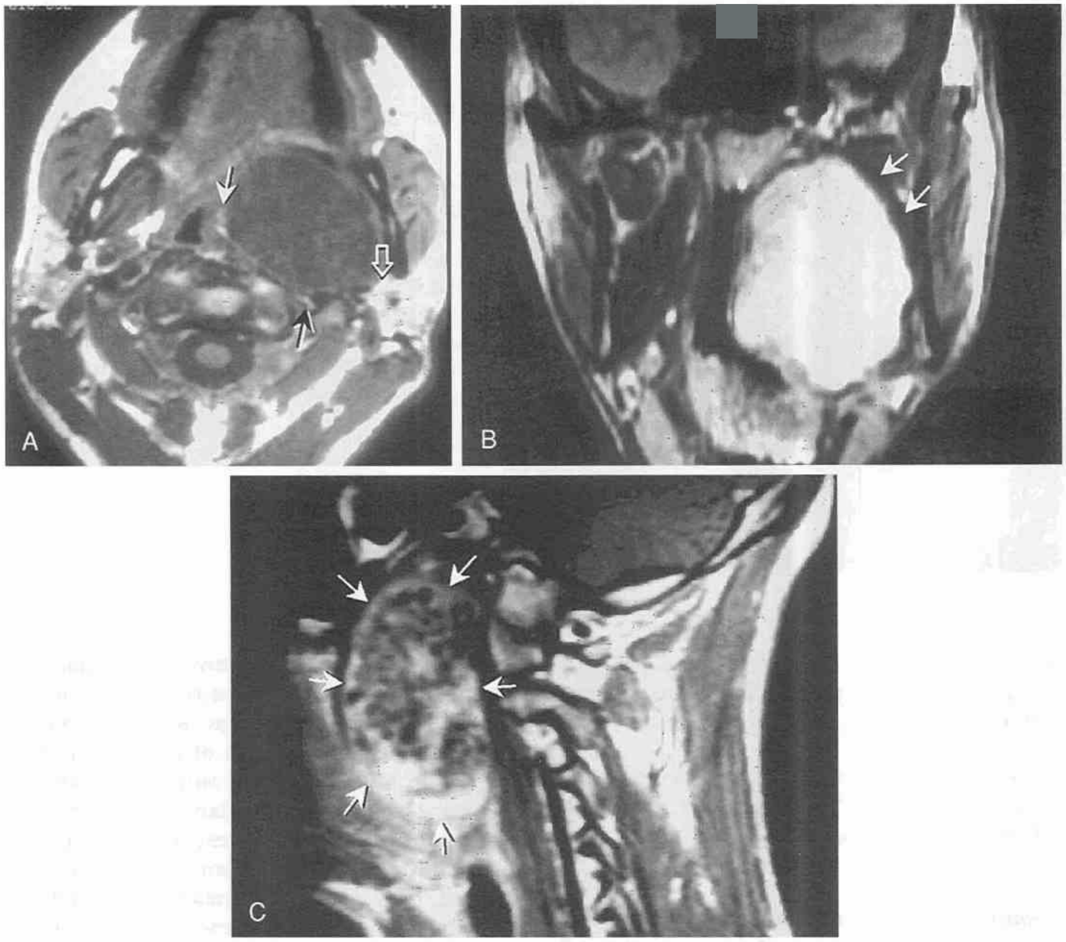

Figure 19–24. Pleomorphic adenoma.

A, Nonenhanced, T1-weighted axial image (TR = 500 msec, TE = 12 msec) demonstrates a well-defined mass of lower signal intensity than adjacent muscle, replacing the prestyloid parapharyngeal fat with minimal residual fat displaced medially *(straight white arrow)* and the internal carotid artery displaced posteriorly *(straight black arrow)*. No intact fat plane can be demonstrated between the lesion and the deep lobe of the parotid gland *(open arrow)*.

B, Intermediate-weighted (TR = 2500 msec, TE = 30 msec) coronal image demonstrates the mass as relatively homogeneous, of increased signal intensity relative to adjacent muscles and lymphoid tissue, and well defined. The oropharyngeal mucosa is displaced medially. The left medial pterygoid muscle is compressed and displaced superolaterally *(arrows)*.

C, Contrast-enhanced, T1-weighted (TR = 500 msec, TE = 15 msec) sagittal image demonstrates marked heterogeneity of the mass, with multiple low-signal-intensity regions that may represent areas of calcification or fibrosis. Both sagittal and coronal images are useful in revealing the craniocaudal extent of the lesion, which fills most of the prestyloid parapharyngeal space *(arrows)*. The mass is inseparable from the deep lobe of the parotid gland and must be considered as arising from the deep lobe for surgical planning. However, the deep lobe of the parotid gland has been compressed and displaced laterally, with no visible connection to the mass at surgery.

CT and by their characteristic signal intensity, which parallels that of fat on all MRI pulse sequences.

Malignant Tumors

Malignant tumors of the prestyloid compartment of the PPS are much less common than benign lesions. These tumors include malignancies of salivary gland origin (e.g., mucoepidermoid, adenoid cystic, and acinic cell carcinomas) along with direct invasion of malignancies of the adjacent spaces.[156, 162] Differentiation from benign tumors may be difficult because approximately two thirds of salivary gland malignant tumors have smooth, well-defined margins.[162] However, the presence of an irregular, ill-defined margin or infiltration of surrounding tissues may be present, suggesting a more aggressive lesion. Unfortunately, an inflammatory reaction surrounding a benign tumor may occasionally result in a similar appearance.[161]

Lesions Arising Outside the Pharynx and Bulging into the Pharyngeal Airway

Antrochoanal Polyps

An antrochoanal polyp is a benign antral polyp that expands, widens the sinus ostium, and prolapses into the nasal cavity. When the polyp is large, it fills the ipsilateral nasal fossa and extends backward through the choana into

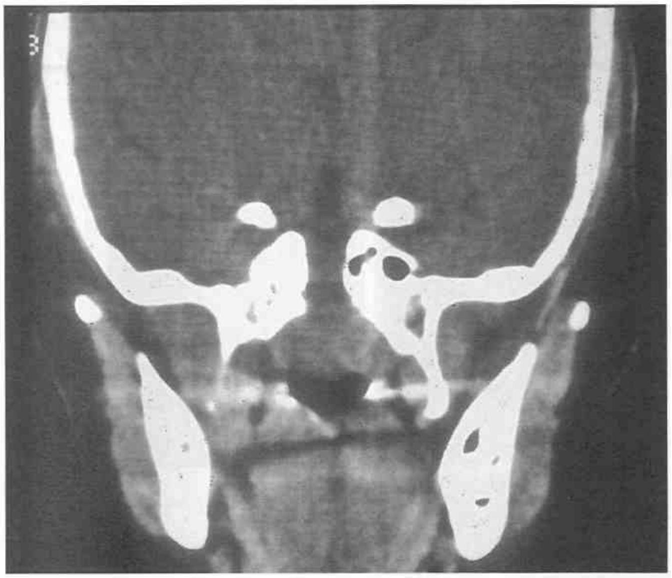

Figure 19–25. Basal cephalocele. Coronal nonenhanced CT scan shows a large midline, isodense nasopharyngeal soft tissue mass that is significantly compromising the airway in a child. The obvious associated midline skull base defect represents the persistent hypophyseal (craniopharyngeal) canal and suggests that the postnasal mass is actually a herniated pituitary gland. Note the consequent downward traction of the suprasellar cistern into the basal defect.

the nasopharynx. Occasionally, it becomes large enough to hang down into the oropharynx. Antrochoanal polyps represent 5% of all nasal polyps.[42, 119]

Clinical Presentation. The patient is typically a teenager or a young adult. A history of allergy is present in 15% to 40% of cases, with an incidence of additional nasal polyps in 8%.[42, 160]

Imaging Features. A large antrochoanal polyp appears as a smoothly outlined mass within the nasopharyngeal airway; it is continuous into the nasal cavity and maxillary antrum on one side. The maxillary ostium is widened, yet the sinus itself is not expanded. There is no bone erosion. Absence of bone erosion is a distinguishing feature from juvenile nasopharyngeal angiofibroma. An antrochoanal polyp typically presents as a homogenous, low-mucoid-attenuation (10 to 18 HU) mass on CT, but older lesions develop fibrous stroma, resulting in a higher attenuation. On MR images, these polyps display low to intermediate T1-weighted and T2-weighted signal intensity. Postcontrast studies show mucosal enhancement on the surface.[42, 97, 133, 160]

Sphenochoanal Polyps

Sphenochoanal polyps are rare, with an etiology similar to that of antrochoanal polyps. They arise in the sphenoid sinus and extend through the sphenoid ostium and sphenoethmoidal recess into the nose, then backward through the choana into the nasopharynx. Identification of the sinus of origin (sphenoid and not maxillary) is important in order to determine the surgical approach.[181]

Persistent Hypophyseal (Craniopharyngeal) Canal

Persistent hypophyseal canal is a rare congenital defect of the skull base that is worthy of mention. The canal connects the pituitary fossa to the nasopharynx, allowing the pituitary gland to herniate downward into the nasopharyngeal airway and to present as a midline nasal polyp that might cause significant airway obstruction in neonates.[74]

Because acquired polyps are almost unknown in children younger than 2 years of age, it is necessary to interpret, with a high index of suspicion, midline nasal polyps in young children, particularly when the polyp is coupled with hypertelorism. In these cases, it is always best to ascertain that the sellar floor is completely intact and that the pituitary gland is normally located within its fossa. Coronal CT or MRI is best suited for such evaluation.[74] Picking up these rare cases is crucial in order to prevent inadvertent hypophysectomy and consequent panhypopituitarism.

Occasionally, a persistent hypophyseal canal may be wide enough to allow a large basal cephalocele to form in the postnasal space (Fig. 19–25).[74]

Nasopharyngeal and Oropharyngeal Trauma

The suprahyoid portions of the pharynx (i.e., nasopharynx and oropharynx) are less vulnerable to trauma than the infrahyoid pharynx (hypopharynx) or the larynx[119]; most radiologically documented nasopharyngeal or oropharyngeal injuries are described in the literature as case reports.*

The clinicopathologic outcome and the imaging findings expected after trauma to this part of the pharynx, to a large extent, are dictated by the mechanisms of trauma. By convention, these are classified into *blunt* (closed) and *penetrating* (open) types.

Blunt Trauma

Blunt head and neck trauma, such as that caused by motor vehicle accidents, may result in the formation of retropharyngeal hematoma, a condition that may progress rapidly into a life-threatening airway obstruction.[18, 45]

*See references 43, 75, 104, 106, 114, 129, 135, 137, 153, 157, 169, 170, and 175.

Once post-traumatic, prevertebral soft tissue fullness is seen on the emergency radiographs, the primary concern should be directed toward securing and maintaining the patient's airway,[43] followed by a CT scan to evaluate for potential cervical spine fractures. CT sections should start as high as the skull base to detect possible occipital condyle fractures[104] and should cover as low as the inferior extent of the hematoma, which may reach down to the mediastinum.

Retropharyngeal hematomas have also been reported following minor blunt trauma,[43] minor hyperextension injuries,[129] and airbag deployment in minor motor vehicle accidents.[170]

Nontraumatic causes of retropharyngeal hematoma include anticoagulant therapy and complications of aneurysms, tumors, and infections.[129]

Penetrating Trauma

Trauma leading to pharyngeal perforation may be accidental or iatrogenic. Accidental perforations usually involve the oropharynx and may be caused by foreign bodies,[45] fish bones,[169] gunshots,[162] and direct injury by intraoral sharp objects, as when, for example, a child falls with a toothbrush in the mouth.[137] Iatrogenic perforations more commonly involve the nasopharynx and may complicate upper gastrointestinal endoscopy,[175] assisted ventilation,[45] neonatal pharyngeal suction catheters, and nasogastric or tracheal intubation during resuscitation of newborns.[135]

Pharyngeal perforation may result in any or a combination of the following problems:

1. *Surgical emphysema*. Emphysema may be caused by air dissecting its way through the torn pharyngeal wall. Retropharyngeal free air is the most common sequela of perforation and is readily identified on CT. Occasionally, large amounts of interstitial air may cast multiple deep fascial spaces and may extend downward, giving rise to pneumomediastinum.[45, 143, 157, 175]
2. *Retropharyngeal abscess*. Abscess occurs less often and is due to the spread of organisms from the oral bacterial flora. Uncontrolled infection may spread into the deep fascial planes, resulting in fascitis or parapharyngeal abscess[119]; may extend downward along the RPS to cause mediastinitis; and may even enter the danger space to reach down to the diaphragm.[157] The imaging features of retropharyngeal abscess have been described earlier.
3. *Vascular injury*. Internal carotid artery thrombosis and cerebral ischemia may complicate posterolateral oropharyngeal injury, particularly when a child falls with a sharp object in the mouth. Typically, the internal carotid artery is injured 1 to 3 cm above the common carotid bifurcation, where it is separated from the oropharyngeal airway only by the tonsil and the superior constrictor muscle. The patient classically presents after a lucid interval of occasionally more than 24 hours, with disturbed consciousness, hemiplegia, and possibly expressive aphasia if ischemia involves the dominant cerebral hemisphere.[137]

Carotid artery thrombosis has also been reported following blunt intraoral[114] and minor pharyngeal injuries.[153]

Obstructive Sleep Apnea Syndrome

Obstructive sleep apnea syndrome is an episodic upper airway obstruction during sleep, most commonly occurring at the pharyngeal level.[102] The condition may be considered, in part, a neuromuscular disorder. Normally, the neural output to the pharyngeal muscles decreases with the onset of sleep, thus reducing their tone. With inspiration, the negative pressure created in the upper airway has the potential to collapse the hypotonic pharyngeal wall if the pharyngeal airway is originally smaller or more compliant than normal.[57]

Clinical Presentation. Obstructive sleep apnea is most common among obese males. The incidence also increases with age, snoring, tobacco and alcohol use, and the use of sedatives as well as with genetic and familial risk factors.[102]

The repetitive episodes of apnea during sleep, lasting from 10 to more than 60 seconds,[102] result in arterial oxygen desaturation and recurrent awakening, leading to the syndrome, which is characterized by daytime somnolence, morning headache, and poor concentration.[57, 78] Other conditions that have been linked to the syndrome include gastroesophageal reflux, impotence, cardiac arrhythmias, hypertension, and increased risk of stroke and myocardial infarction.[78, 102]

Role of Imaging. The diagnosis of obstructive sleep apnea is a clinical one that is supported by (1) overnight *polysomnography* (continuous recording of relevant physiologic changes during sleep) to determine the physiologic severity, and by (2) *transnasal fiberoptic endoscopy* to estimate the actual grade of airway narrowing.[102]

With the emergence of new imaging technology, dynamic imaging of the pharynx in near real-time has become a reality, permitting the noninvasive assessment of functional pharyngeal abnormalities. Many reports have described the use of *ultrafast CT* (electron beam CT)[12, 50, 51, 57, 163] and *MR fluoroscopy*[78, 144 150, 151, 168] for the dynamic evaluation of upper airways in these patients.

Ultrafast CT scanning utilizes an electron gun to produce a fast-moving electron beam that hits multiple detector rings in the gantry, permitting the simultaneous acquisition of multiple image sections. This results in a superior temporal resolution, and images can be obtained in as little as 50 to 100 msec.[71] Other than its use of ionizing radiation, the disadvantage of selecting ultrafast CT in evaluating patients with obstructive sleep apnea is the inability to obtain primary images in the midsagittal plane.[78]

The term *MR fluoroscopy* has been introduced with the development of numerous rapid gradient-echo sequences capable of acquiring MR images as fast as 0.3 to 7 seconds per frame.[88, 93] Fluoroscopic MR imaging has been used for functional imaging of the upper airways utilizing GRASS (gradient-recalled acquisition in the steady state[78, 150, 151] and FLASH (fast low-angle shot) sequences.[78, 168] Images are obtained in the sagittal and axial planes during quiet nasal respiration, simulation of snoring, and performance of the Müller maneuver (inspiratory effort with the mouth and nose closed).[78] Axial scans are obtained at the levels of the oropharynx and velopharynx (the lowest part of nasopharynx opposite the soft palate, which is one of the narrowest sites in patients experiencing obstructive sleep apnea).[14]

Two fundamental imaging abnormalities are sought in evaluation of these patients[57, 78]:

1. Narrowing of the luminal cross-sectional area of the pharynx, as seen on axial images. The length of narrowing is determined on sagittal images.
2. Increased compliance of pharyngeal walls. The mobility of the uvula, tongue base, and posterior pharyngeal wall is assessed on sagittal images, whereas the mobility of the lateral pharyngeal walls is assessed on axial images.

Suprahyoid Neck Biopsy and Interventional MRI

Interventional MRI is the use of MR techniques to guide radiologic interventions, including both diagnostic and minimally invasive therapeutic procedures.

In areas of complex anatomy, the tissue contrast, spatial resolution, and multiplanar capabilities peculiar to MRI provide the obvious advantages for its use to guide interventional procedures. This is particularly true for sampling suprahyoid neck lesions,[88, 92, 109] an endeavor in which CT guidance is limited by several factors, including the following:

1. The inability to maintain a confident localization of the vascular anatomy throughout the procedure.
2. The inability to go beyond a single imaging plane (usually axial).
3. The frequent improper definition of pharyngeal submucosal lesions on CT.
4. The beam-hardening artifacts inherent in CT at the skull base.

On the contrary, the major benefits of using MRI for procedure guidance in this region (Fig. 19–26) are as follows[88, 92, 109]:

1. The ability to continuously visualize the internal carotid, vertebral, and major branches of the external carotid arteries during the entire needle insertion procedure. The high vascular conspicuity is due to flow-related enhancement effects inherent in the gradient-echo sequences used for procedure guidance.
2. The multiplanar imaging capabilities that ensure precise needle centralization along the axial as well as the craniocaudal dimensions of the lesion. In addition, imaging in any arbitrary plane allows the needle trajectory to be tailored according to the individual case.
3. The ability to guide needle insertion with continuous, near real-time imaging so that the needle can be redirected in order to avoid critical structures in a time-efficient manner.
4. The ability to shift between T1-weighted and T2-weighted contrast during the procedure to maximize lesion conspicuity. T2-weighted techniques also allow sampling of the non-necrotic regions of complex masses, thus increasing the diagnostic tissue yield.

An additional use of the interventional MRI techniques that form the basis for biopsy guidance is application of these methods for the monitoring of direct intralesional drug injection, including injection for sclerotherapy of vascular malformations. The same rapid image updates used

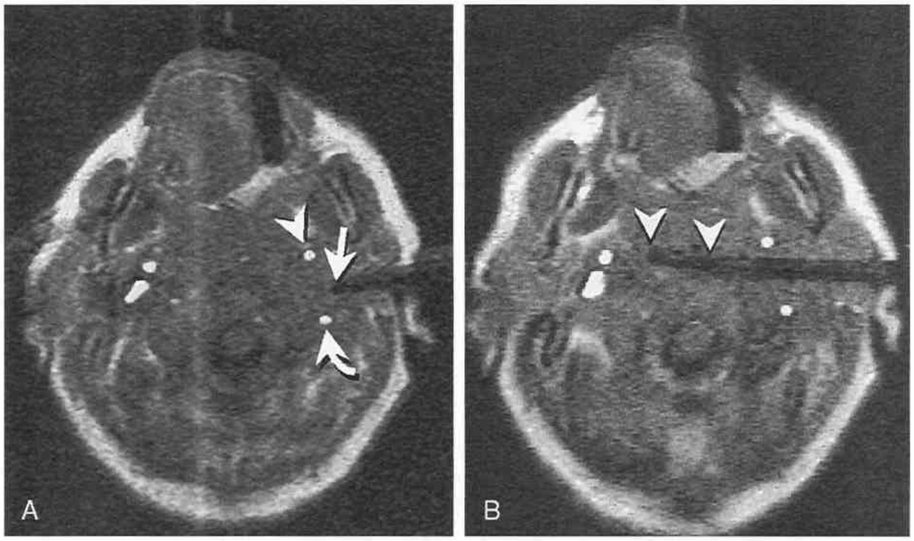

Figure 19–26. Interventional near-real-time, MR-guided suprahyoid neck biopsy. Images from continuous series obtained at 7 seconds per image with fast imaging with steady-state precession (FISP) sequence (TR = 18 msec, TE = 7 msec, 4 signal averages, flip angle = 90 degrees) obtained during guidance of needle insertion in a 68-year-old man with a C1-2 vertebral and prevertebral mass. A previous attempt at surgical transoral biopsy had been unsuccessful.

A, Image obtained early, during needle insertion, demonstrates the needle tip passing through the left parotid space. An ill-defined mass can be seen in the prevertebral space. High vascular conspicuity resulting from 2D Fourier transform technique allows ready visualization of flow-related enhancement within the internal carotid *(arrowhead)* and vertebral *(curved arrow)* arteries. The needle tip *(straight arrow)* can be interactively directed to avoid these major vascular structures.

B, The needle is redirected more anteriorly once it is safely beyond the internal carotid artery (ICA). The location of the needle's side notch is shown as an area of thinning of the distal needle tip (between *arrowheads*). Histologic examination revealed chronic osteomyelitis and cellulitis, and the offending organism was successfully isolated.

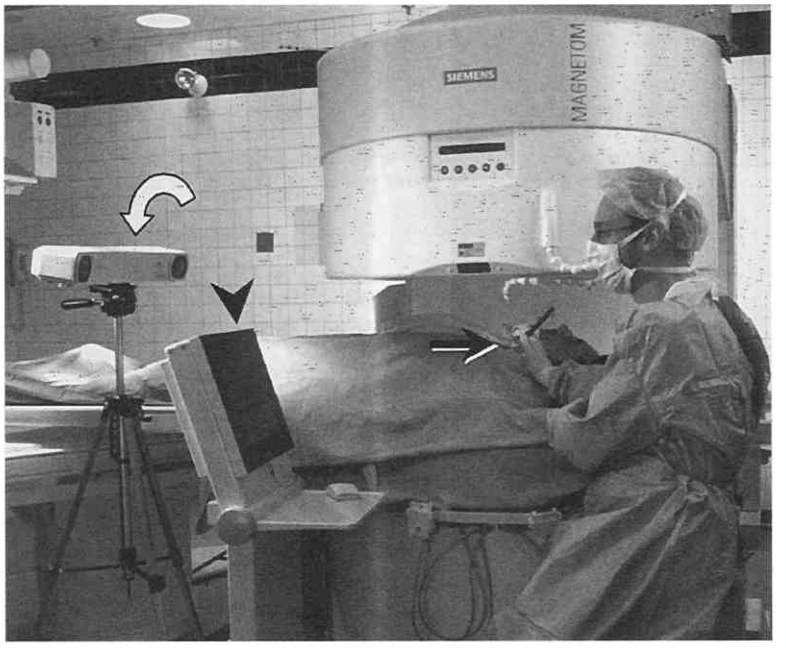

Figure 19–27. Interventional MRI suite setup for radiologic intervention has an open magnet design to provide easy patient access and a video camera sensor array *(curved arrow)* to detect the location and orientation of a hand-held probe *(black arrow)*. The system automatically acquires continuous MR images based on the probe position and automatically updates display of four images on shielded liquid crystal diode monitor adjacent to the scanner *(arrowhead)*. A computer mouse on the LCD console and foot pedals (not shown) allow the scanner to be operated by the radiologist throughout the procedure.

for interactive needle placement can be used to monitor the injection of sclerosing agents for the treatment of low-flow vascular malformations.[91] The multiplanar images obtained with MRI allow the injection of alcohol or other sclerosing agents to be monitored during administration to ensure filling of the entire targeted portion of the malformation and to exclude extravasation or dissipation of the agent through venous egress.[91]

The accuracy and safety of MRI-guided procedures depend on proper needle visualization. Achieving this task requires a sound understanding of a number of user-defined imaging parameters as well as needle trajectory decisions, which are beyond the scope of this chapter.[88, 90, 93, 109]

Three basic components combine to form the foundation of the modern interventional MRI suite:

1. The availability of an "open" magnet imaging system to facilitate the patient access necessary for performing the procedures (Fig. 19–27).
2. The application of new, fast gradient-echo pulse sequences that allow a wide range of tissue contrast in a time frame sufficient for device tracking (between 0.3 and 7 seconds per image), even at the low field strengths of open magnets and with the suboptimal coil position sometimes required to access the puncture site.[35, 48, 93, 98, 109]
3. The ability to view images in near real-time at the scanner side through an in-room high resolution radiofrequency-shielded monitor (see Fig. 19–27).[88, 93, 186]

With these three components, the entire procedure can be performed with the operator sitting next to the patient and without the need to remove the operator's hand from the interventional device at any time. This manner of intervention, analogous to an angiographic or sonographically guided procedure, is well suited to the skill set developed by radiologists during more conventional types of image-guided intervention.

References

1. American Joint Committee on Cancer: In Fleming I, Cooper J, Henson D, et al (eds): Manual for Staging of Cancer, 5th ed. Philadelphia, Lippincott-Raven, 1997.

1a. American Joint Committee on Cancer: In Beahrs OH, Henson DE, Hutter RVP, Kennedy BJ (eds): Manual for Staging of Cancer, 4th ed. Philadelphia, JB Lippincott, 1992.

2. Anzai Y, Lufkin RB, Jabour BA, Hanafee WN: Fat-suppression failure artifacts simulating pathology on frequency-selective fat-suppression MR images of the head and neck. AJNR Am J Neuroradiol 13:879–884, 1992.
3. Baker LL, Dillon WP, Hieshima GB, et al: Hemangiomas and vascular malformations of the head and neck: MR characterization. AJNR Am J Neuroradiol 14:307–314, 1993.
4. Barakos JA, Dillon WP, Chew WM: Orbit, skull base, and pharynx: Contrast-enhanced fat suppression MR imaging. Radiology 179: 191–198, 1991.
5. Barakos JA: Head and neck imaging. In Brant WE, Helms CA (eds): Fundamentals of Diagnostic Radiology, 2nd ed. Philadelphia, Lippincott Williams & Wilkins, 1999, pp 211–232.
6. Battino RA, Khangure MS: Is that another Thornwaldt's cyst on M.R.I.? Australas Radiol 34:19–23, 1990.
7. Beahrs OH, Henson DE, Hutter RVP, Kennedy BJ (eds): Manual for Staging of Cancer, 4th ed. American Joint Committee on Cancer. Philadelphia, JB Lippincott, 1992.
8. Becker M, Hasso AN: Imaging of malignant neoplasms of the pharynx and larynx. In Taveras JM, Ferruci JT (eds): Radiology: Diagnosis, Imaging, Intervention. Philadelphia, JB Lippincott, 1996, pp 1–16.
9. Becker M: Oral cavity, oropharynx, and hypopharynx. Semin Roentgenol 35:21–30, 2000.
10. Benson MT, Dalen K, Mancuso AA, et al: Congenital anomalies of the branchial apparatus: Embryology and pathologic anatomy. Radiographics 12:943–960, 1992.
11. Boucher RM, Hendrix RA, Guttenplan MD: The diagnosis of Thornwaldt's cyst. Trans Pa Acad Ophthalmol Otolaryngol 42:1026–1030, 1990.
12. Brasch RC, Gould RG, Gooding CA, et al: Upper airway obstruction in infants and children: Evaluation with ultrafast CT. Radiology 165: 459–466, 1987.
13. Brodsky L, Koch RJ: Anatomic correlates of normal and diseased adenoids in children. Laryngoscope 102:1268–1274, 1992.
14. Caballero P, Alvarez-Sala R, Garcia-Rio F, et al: CT in the evaluation of the upper airway in healthy subjects and in patients with obstructive sleep apnea syndrome. Chest 113:111–116, 1998.

15. Cerezal L, Morales C, Abascal F, et al: Pharyngeal branchial cyst: Magnetic resonance findings. Eur J Radiol 29:1–3, 1998.
16. Chandler JR, Mitchell B: Branchial cleft cysts, sinuses, and fistulas. Otolaryngol Clin North Am 14:175–186, 1981.
17. Chia KS, Lee HP, Seow A, et al: Trends in Cancer Incidence in Singapore, 1968–1992. Singapore, Singapore Cancer Registry, 1996.
18. Chin KW, Sercarz JA, Wang MB, Andrews R: Spontaneous cervical hemorrhage with near-complete airway obstruction. Head Neck 20: 350–353, 1998.
19. Chong VF: Masticator space in nasopharyngeal carcinoma. Ann Otol Rhinol Laryngol 106:979–982, 1997.
20. Chong VF, Fan YF: Maxillary nerve involvement in nasopharyngeal carcinoma. AJR Am J Roentgenol 167:1309–1312, 1996.
21. Chong VF, Fan YF: Radiology of the masticator space. Clin Radiol 51:457–465, 1996.
22. Chong VF, Fan YF: Skull base erosion in nasopharyngeal carcinoma: Detection by CT and MRI. Clin Radiol 51:625–631, 1996.
23. Chong VF, Fan YF: Jugular foramen involvement in nasopharyngeal carcinoma. J Laryngol Otol 110:987–990, 1996.
24. Chong VF, Fan YF: Pterygopalatine fossa and maxillary nerve infiltration in nasopharyngeal carcinoma. Head Neck 19:121–125, 1997.
25. Chong VF, Fan YF: Detection of recurrent nasopharyngeal carcinoma: MR imaging versus CT. Radiology 202:463–470, 1997.
26. Chong VF, Fan YF: The retropharyngeal space: Route of tumour spread. Clin Radiol 53:64–67, 1998.
27. Chong VF, Fan YF: Meningeal infiltration in recurrent nasopharyngeal carcinoma. Australas Radiol 44:23–27, 2000.
28. Chong VF, Fan YF: Radiology of the nasopharynx: Pictorial essay. Australas Radiol 44:5–13, 2000.
29. Chong VF, Fan YF, Khoo JB: Nasopharyngeal carcinoma with intracranial spread: CT and MR characteristics. J Comput Assist Tomogr 20: 563–569, 1996.
30. Chong VF, Fan YF, Mukherji SK: Carcinoma of the nasopharynx. Semin Ultrasound CT MR 19: 449–462, 1998.
31. Chong VF, Fan YF, Khoo JB: Retropharyngeal lymphadenopathy in nasopharyngeal carcinoma. Eur J Radiol 21:100–105, 1995.
32. Chong VF, Fan YF, Khoo JB, Lim TA: Comparing computed tomographic and magnetic resonance imaging visualisation of the pterygopalatine fossa in nasopharyngeal carcinoma. Ann Acad Med Singapore 24:436–441, 1995.
33. Chong VF, Fan YF, Toh KH, et al: Magnetic resonance imaging and computed tomography features of nasopharyngeal carcinoma with maxillary sinus involvement. Australas Radiol 39:2–9, 1995.
34. Chung TS, Yousem DM, Seigerman HM, et al: MR of mandibular invasion in patients with oral and oropharyngeal malignant neoplasms. AJNR Am J Neuroradiol 15:1949–1955, 1994.
35. Chung YC, Merkle EM, Lewin JS, et al: Fast T(2)-weighted imaging by PSIF at 0.2 T for interventional MRI. Magn Reson Med 42: 335–344, 1999.
36. Coit WE, Harnsberger HR, Osborn AG, et al: Ranulas and their mimics: CT evaluation. Radiology 163:211–216, 1987.
37. Conley J, Dingman DL: Adenoid cystic carcinoma in the head and neck (cylindroma). Arch Otolaryngol 100:81–90, 1974.
38. Crawford SC, Harnsberger HR, Lufkin RB: The role of gadolinium-DTPA in the evaluation of extracranial head and neck lesions. Radiol Clin North Am 27:219–242, 1989.
39. Cross RR, Shapiro MD, Som PM: MRI of the parapharyngeal space. Radiol Clin North Am 27:353–378, 1989.
40. Curtin HD: Separation of the masticator space from the parapharyngeal space. Radiology 16:195–204, 1987.
41. Curtin HD, Williams R, Johnson J: CT of perineural tumor extension: Pterygopalatine fossa. AJR Am J Roentgenol 144:163–169, 1985.
42. Dähnert W. Ear, nose, and throat disorders. In Radiology Review Manual, 4th ed. Baltimore, Williams & Wilkins, 1999, pp 314–35.
43. Daniello NJ, Goldstein SI: Retropharyngeal hematoma secondary to minor blunt head and neck trauma. Ear Nose Throat J 73: 41–43, 1994.
44. Daniels DL, Rauschning W, Lovas J, et al: Pterygopalatine fossa: Computed tomographic studies. Radiology 149:511–516, 1983.
45. Davis WL, Harnsberger HR, Smoker WR, Watanabe AS: Retropharyngeal space: Evaluation of normal anatomy and diseases with CT and MR imaging. Radiology 174:59–64, 1990.
46. Dickson RI: Nasopharyngeal carcinoma: An evaluation of 209 patients. Laryngoscope 91:333–354, 1981.
47. Dillon WP, Mills CM, Kjos B, et al: Magnetic resonance imaging of the nasopharynx. Radiology 152:731–738, 1984.
48. Duerk JL, Lewin JS, Wendt M, Petersilge C: Remember true FISP? A high SNR, near 1-second imaging method for T2-like contrast in interventional MRI at .2 T. J Magn Reson Imaging 8:203–208, 1998.
49. Easton JM, Levine PH, Hyams VJ: Nasopharyngeal carcinoma in the United States: A pathologic study of 177 U.S. and 30 foreign cases. Arch Otolaryngol 106:88–91, 1980.
50. Ell SR, Jolles H, Galvin JR: Cine CT demonstration of nonfixed upper airway obstruction. AJR Am J Roentgenol 146:669–677, 1986.
51. Ergun GA, Kahrilas PJ, Lin S, et al: Shape, volume, and content of the deglutitive pharyngeal chamber imaged by ultrafast computerized tomography. Gastroenterology 105:1396–1403, 1993.
52. Faerber EN, Swartz JD: Imaging of neck masses in infants and children. Crit Rev Diagn Imaging 31:283–314, 1991.
53. Finkelstein Y, Malik Z, Kopolovic J, et al: Characterization of smoking-induced nasopharyngeal lymphoid hyperplasia. Laryngoscope 107:1635–1642, 1997.
54. Fischbein NJ, AAssar OS, Caputo GR, et al: Clinical utility of positron emission tomography with ^{18}F-fluorodeoxyglucose in detecting residual/recurrent squamous cell carcinoma of the head and neck. AJNR Am J Neuroradiol 19:1189–1196, 1998.
54a. Fleming I, Cooper J, Henson D, et al (eds): Manual for Staging of Cancer, 5th ed. American Joint Committee on Cancer. Philadelphia, Lippincott-Raven, 1997.
55. Franco RA, Har-El G: Cancer of the head and neck. In Lucente FE, Har-EL G (eds): Essentials of Otolaryngology, 4th ed. Philadelphia, Lippincott Williams & Wilkins, 1999, pp 326–335.
56. Gale DR: CT and MRI of the oral cavity and oropharynx. In Valvassori GE, Mafee MF, Carter BL (eds): Imaging of the Head and Neck. Stuttgart, Thieme, 1995, pp 445–474.
57. Galvin JR, Rooholamini SA, Stanford W: Obstructive sleep apnea: Diagnosis with ultrafast CT. Radiology 171:775–778, 1989.
58. Gates GA, Avery CA, Prihoda TJ: Effect of adenoidectomy upon children with chronic otitis media with effusion. Laryngoscope 98: 58–63, 1988.
59. Gates GA, Avery CA, Prihoda TJ, Cooper JC Jr: Effectiveness of adenoidectomy and tympanostomy tubes in the treatment of chronic otitis media with effusion. N Engl J Med 317:1444–1451, 1987.
60. Govrin-Yehudain J, Moscona AR, Calderon N, Hirshowitz B: Treatment of hemangiomas by sclerosing agents: An experimental and clinical study. Ann Plast Surg 18:465–469, 1987.
61. Gray H: Muscles and fasciae. In Clemente CD (ed): Gray's Anatomy, 30th American Edition. Philadelphia, Lea & Febiger, 1985, pp 429–605.
62. Gromet M, Homer MJ, Carter BL: Lymphoid hyperplasia at the base of the tongue: Spectrum of a benign entity. Radiology 144: 825–828, 1982.
63. Gullane PJ, Davidson J, O'Dwyer T, Forte V: Juvenile angiofibroma: A review of the literature and a case series report. Laryngoscope 102:928–933, 1992.
64. Hardin CW, Harnsberger HR, Osborn AG, et al: Infection and tumor of the masticator space: CT evaluation. Radiology 157:413–417, 1985.
65. Harnsberger HR: Head and neck imaging. In Osborne AG, Bragg DC (eds): Handbooks in Radiology (series), 2nd ed. St. Louis, Mosby–Year Book, 1995.
66. Harnsberger HR, Mancuso AA, Muraki AS, et al: Branchial cleft anomalies and their mimics: Computed tomographic evaluation. Radiology 152:739–748, 1984.
67. Harnsberger HR, Osborn AG: Differential diagnosis of head and neck lesions based on their space of origin: Part 1. The suprahyoid part of the neck. AJR Am J Roentgenol 157:147–154, 1991.
68. Heeneman H, Maran AG: Parapharyngeal space tumours. Clin Otolaryngol 4:57–66, 1979.
69. Hillsamer PJ, Schuller DE, McGhee RB Jr, et al: Improving diagnostic accuracy of cervical metastases with computed tomography and magnetic resonance imaging. Arch Otolaryngol Head Neck Surg 116:1297–301, 1990.
70. Hollinshead WH, Rosse Cornelius. Pharynx and larynx. In Textbook of Anatomy, 4th ed. Philadelphia, JB Lippincott, 1985, pp 987–1006.
71. Huda W, Slone RM: Computers and computed tomography. In Review of radiologic physics. Philadelphia, JB Lippincott, 1995, pp 93–109.

72. Hudgins PA, Burson JG, Gussack GS, Grist WJ: CT and MR appearance of recurrent malignant head and neck neoplasms after resection and flap reconstruction. AJNR Am J Neuroradiol 15: 1689–1694, 1994.
73. Hudgins PA, Jacobs IN, Castillo M: Pediatric airway disease. In Som PM, Curtin HD (eds): Head and Neck Imaging, 3rd ed. St. Louis, Mosby–Year Book, 1996, pp 545–611.
74. Hughes ML, Carty AT, White FE: Persistent hypophyseal (craniopharyngeal) canal. Br J Radiol 72:204–206, 1999.
75. Hung T, Huchzermeyer P, Hinton AE: Air rifle injury to the oropharynx: The essential role of computed tomography in deciding on surgical exploration. J Accid Emerg Med 17:147–148, 2000.
76. Hunink MG, de Slegte RG, Gerritsen GJ, Speelman H: CT and MR assessment of tumors of the nose and paranasal sinuses, the nasopharynx and the parapharyngeal space using ROC methodology. Neuroradiology 32:220–225, 1990.
77. Ikushima I, Korogi Y, Makita O, et al: MR imaging of Thornwaldt's cysts. AJR Am J Roentgenol 172:1663–1665, 1999.
78. Jager L, Gunther E, Gauger J, Reiser M: Fluoroscopic MR of the pharynx in patients with obstructive sleep apnea. AJNR Am J Neuroradiol 19:1205–1214, 1998.
79. Kao CH, ChangLai SP, Chieng PU, et al: Detection of recurrent or persistent nasopharyngeal carcinomas after radiotherapy with 18-fluoro-2-deoxyglucose positron emission tomography and comparison with computed tomography. J Clin Oncol 16:3550–3555, 1998.
80. King AD, Kew J, Tong M, et al: Magnetic resonance imaging of the eustachian tube in nasopharyngeal carcinoma: Correlation of patterns of spread with middle ear effusion. Am J Otol 20:69–73, 1999.
81. King AD, Lam WW, Leung SF, et al: MRI of local disease in nasopharyngeal carcinoma: Tumour extent vs tumour stage. Br J Radiol 72:734–741, 1999.
82. Laine FJ, Braun IF, Jensen ME, et al: Perineural tumor extension through the foramen ovale: Evaluation with MR imaging. Radiology 174:65–71, 1990.
83. Lanzieri CF, Lewin JS: Oropharynx and nasopharynx. In Stark DD, Bradley WG (eds): Magnetic Resonance Imaging, 3rd ed. St. Louis, Mosby, 1999.
84. Lawson VG, LeLiever WC, Makerewich LA, et al: Unusual parapharyngeal lesions. J Otolaryngol 8:241–249, 1979.
85. Lenz M, Greess H, Baum U, et al: Oropharynx, oral cavity, floor of the mouth: CT and MRI. Eur J Radiol 33:203–215, 2000.
86. Leslie A, Fyfe E, Guest P, et al: Staging of squamous cell carcinoma of the oral cavity and oropharynx: A comparison of MRI and CT in T- and N-staging. J Comput Assist Tomogr 23:43–49, 1999.
87. Lewin JS: Imaging of the suprahyoid neck. In Valvassori GE, Mafee MF, Carter BL (eds): Imaging of the Head and Neck. Stuttgart, Thieme, 1995, pp 390–423.
88. Lewin JS: Interventional MR imaging: Concepts, systems, and applications in neuroradiology. AJNR Am J Neuroradiol 20:735–748, 1999.
89. Lewin JS, Curtin HD, Ross JS, et al: Fast spin-echo imaging of the neck: Comparison with conventional spin-echo, utility of fat suppression, and evaluation of tissue contrast characteristics. AJNR Am J Neuroradiol 15:1351–1357, 1994.
90. Lewin JS, Duerk JL, Jain VR, et al: Needle localization in MR-guided biopsy and aspiration: Effects of field strength, sequence design, and magnetic field orientation. AJR Am J Roentgenol 166: 1337–1345, 1996.
91. Lewin JS, Merkle EM, Duerk JL, Tarr RW: Low-flow vascular malformations in the head and neck: Safety and feasibility of MR imaging-guided percutaneous sclerotherapy—preliminary experience with 14 procedures in three patients. Radiology 211:566–570, 1999.
92. Lewin JS, Nour SG, Duerk JL: Magnetic resonance image-guided biopsy and aspiration. Top Magn Reson Imaging 11:173–183, 2000.
93. Lewin JS, Petersilge CA, Hatem SF, et al: Interactive MR imaging-guided biopsy and aspiration with a modified clinical C-arm system. AJR Am J Roentgenol 170:1593–1601, 1998.
94. Loevner LA, Ott IL, Yousem DM, et al: Neoplastic fixation to the prevertebral compartment by squamous cell carcinoma of the head and neck. AJR Am J Roentgenol 170:1389–1394, 1998.
95. Lufkin RB, Wortham DG, Dietrich RB, et al: Tongue and oropharynx: Findings on MR imaging. Radiology 161:69–75, 1986.
96. Mafee MF: Nasopharynx, parapharyngeal space, and skull base. In Valvassori GE, Mafee MF, Carter BL (eds): Imaging of the Head and Neck. Stuttgart, Thieme, 1995, pp 332–363.
97. Mafee MF, Carter BL: Nasal cavity and paranasal sinuses. In Valvassori GE, Mafee MF, Carter BL (eds): Imaging of the Head and Neck. Stuttgart, Thieme, 1995, pp 248–331.
98. Mahfouz AE, Rahmouni A, Zylbersztejn C, Mathieu D: MR-guided biopsy using ultrafast T1- and T2-weighted reordered turbo fast low-angle shot sequences: Feasibility and preliminary clinical applications. AJR Am J Roentgenol 167:167–169, 1996.
99. Mancuso AA: Imaging in patients with head and neck cancer. In Million RR, Cassisi NJ (eds): Management of Head and Neck Cancer: A Multidisciplinary Approach. Philadelphia, JB Lippincott, 1994; 43–59.
100. Mancuso AA, Hanafee WN: Nasopharynx and parapharyngeal space. In Computed Tomography and Magnetic Resonance Imaging of the Head and Neck, 2nd ed. Baltimore, Williams & Wilkins, 1985, pp 428–498.
101. Mancuso AA, Harnsberger HR, Muraki AS, Stevens MH: Computed tomography of cervical and retropharyngeal lymph nodes: Normal anatomy, variants of normal, and applications in staging head and neck cancer: Part I. Normal anatomy. Radiology 148:709–714, 1983.
102. Maniglia AJ, Davis JA, Maniglia JV: Obstructive sleep apnea syndrome. In Lee KJ (ed): Essential Otolaryngology: Head and Neck Surgery, 7th Edition. Stamford, Conn, Appleton & Lange, 1999, pp 859–874.
103. Maran AG, Mackenzie IJ, Murray JA: The parapharyngeal space. J Laryngol Otol 98:371–380, 1984.
104. Mariani PJ: Occipital condyle fracture presenting as retropharyngeal hematoma. Ann Emerg Med 19:1447–1449, 1990.
105. Maroldi R, Battaglia G, Farina D, et al: Tumours of the oropharynx and oral cavity: Perineural spread and bone invasion. JBR-BTR 82: 294–300, 1999.
106. Mazzon D, Zanatta P, Curtolo S, et al: Upper airway obstruction by retropharyngeal hematoma after cervical spine trauma: Report of a case treated with percutaneous dilational tracheostomy. J Neurosurg Anesthesiol 10:237–240, 1998.
107. McGowan JC 3d, Hatabu H, Yousem DM, et al: Evaluation of soft palate function with MRI: Application to the cleft palate patient. J Comput Assist Tomogr 16:877–882, 1992.
108. Mendenhall WM, Million RR, Mancuso AA, et al: Nasopharynx. In Million RR, Cassisi NJ (eds): Management of Head and Neck Cancer: A Multidisciplinary Approach. Philadelphia, JB Lippincott, 1994, pp 599–626.
109. Merkle EM, Lewin JS, Aschoff AJ, et al: Percutaneous magnetic resonance image-guided biopsy and aspiration in the head and neck. Laryngoscope 110:382–385, 2000.
110. Mesic JB, Fletcher GH, Goepfert H: Megavoltage irradiation of epithelial tumors of the nasopharynx. Int J Radiat Oncol Biol Phys 7:447–453, 1981.
111. Meyer JS, Hoffer FA, Barnes PD, Mulliken JB: Biological classification of soft-tissue vascular anomalies: MR correlation. AJR Am J Roentgenol 157:559–564, 1991.
112. Mineura K, Kowada M, Tomura N: Perineural extension of nasopharyngeal carcinoma into the posterior cranial fossa detected by magnetic resonance imaging. Clin Imaging 15:172–175, 1991.
113. Moore KL: The neck. In Clinically Oriented Anatomy, 3rd ed. Baltimore, Williams & Wilkins, 1992, pp 783–852.
114. Moriarty KP, Harris BH, Benitez-Marchand K: Carotid artery thrombosis and stroke after blunt pharyngeal injury. J Trauma 42:541–543, 1997.
115. Mukherji SK, Castelijns J, Castillo M: Squamous cell carcinoma of the oropharynx and oral cavity: How imaging makes a difference. Semin Ultrasound CT MR 19:463–475, 1998.
116. Mukherji SK, Castillo M: Normal cross-sectional anatomy of the nasopharynx, oropharynx, and oral cavity. Neuroimaging Clin North Am 8:211–218, 1998.
117. Mukherji SK, Drane WE, Tart RP, et al: Comparison of thallium-201 and F-18 FDG SPECT uptake in squamous cell carcinoma of the head and neck. AJNR Am J Neuroradiol 15:1837–1842, 1994.
118. Mukherji SK, Gapany M, Phillips D, et al: Thallium-201 single-photon emission CT versus CT for the detection of recurrent squamous cell carcinoma of the head and neck. AJNR Am J Neuroradiol 20:1215–1220, 1999.
119. Head and Neck Imaging, 3rd ed. St. Louis, Mosby–Year Book, 1996, pp 437–487.
120. Mukherji SK, Mancuso AA, Mendenhall W, et al: Can pretreatment CT predict local control of T2 glottic carcinomas treated with

radiation therapy alone? AJNR Am J Neuroradiol 16: 655–662, 1995.
121. Mukherji SK, Weeks SM, Castillo M, et al: Squamous cell carcinomas that arise in the oral cavity and tongue base: Can CT help predict perineural or vascular invasion? Radiology 198:157–162, 1996.
122. Mulliken JB, Glowacki J: Hemangiomas and vascular malformations in infants and children: A classification based on endothelial characteristics. Plast Reconstr Surg 69:412–422, 1982.
123. Muraki AS, Mancuso AA, Harnsberger HR, et al: CT of the oropharynx, tongue base, and floor of the mouth: Normal anatomy and range of variations, and applications in staging carcinoma. Radiology 148: 725–731, 1983.
124. Neel HB, Slavitt DH: Nasopharyngeal cancer. In Baily BJ (ed): Head and Neck Surgery: Otolaryngology. Philadelphia, JB Lippincott, 1993, pp 1257–1260.
125. Ng SH, Chang JT, Ko SF, et al: MRI in recurrent nasopharyngeal carcinoma. Neuroradiology 41:855–862, 1999.
126. Ng SH, Chang TC, Ko SF, et al: Nasopharyngeal carcinoma: MRI and CT assessment. Neuroradiology 39:741–746, 1997.
127. Ng SH, Chong VF, Ko SF, Mukherji SK: Magnetic resonance imaging of nasopharyngeal carcinoma. Top Magn Reson Imaging 10:290–303, 1999.
128. Norbash AM: Nasopharynx and deep facial spaces. In Eldman RR, Hesselink JR, Zlatkin MB (eds): Clinical Magnetic Resonance Imaging, 2nd ed. Philadelphia: WB Saunders, 1996, pp 1079–1109.
129. O'Donnell JJ, Birkinshaw R, Harte B: Mechanical airway obstruction secondary to retropharyngeal haematoma. Eur J Emerg Med 4: 166–168, 1997.
130. Olmi P, Fallai C, Colagrande S, Giannardi G: Staging and follow-up of nasopharyngeal carcinoma: Magnetic resonance imaging versus computerized tomography. Int J Radiat Oncol Biol Phys 32:795–800, 1995.
131. Olsen KD: Tumors and surgery of the parapharyngeal space. Laryngoscope 104:1–28, 1994.
132. Paonessa DF, Goldstein JC: Anatomy and physiology of head and neck infections (with emphasis on the fascia of the face and neck). Otolaryngol Clin North Am 9:561–580, 1976.
133. Phelps PD: The pharynx and larynx: The neck. In Sutton D (ed): Textbook of Radiology and Imaging, 6th ed. New York, Churchill Livingstone, 1998, pp 1273–1295.
134. Potsic WP: Assessment and treatment of adenotonsillar hypertrophy in children. Am J Otolaryngol 13:259–264, 1992.
135. Pumberger W, Bader T, Golej J, et al: Traumatic pharyngo-oesophageal perforation in the newborn: A condition mimicking oesophageal atresia. Paediatr Anaesth 10:201–205, 2000.
136. Radkowski D, McGill T, Healy GB, et al: Angiofibroma: Changes in staging and treatment. Arch Otolaryngol Head Neck Surg 122: 122–129, 1996.
137. Rayatt SS, Magennis P, Hamlyn PJ: Carotoid artery thrombosis following a penetrating oro-pharyngeal injury of unusual aetiology. Injury 29:320–322, 1998.
138. Reede DL, Holliday RA, Som PM, Bergeron RT: Non-nodal pathologic conditions of the neck. In Som PM, Bergeron RT (eds): Head and Neck Imaging. St. Louis, Mosby–Year Book, 1991.
139. Robertson RL, Robson CD, Barnes PD, Burrows PE: Head and neck vascular anomalies of childhood. Neuroimaging Clin North Am 9: 115–132, 1999.
140. Robinson JD, Crawford SC, Teresi LM, et al: Extracranial lesions of the head and neck: Preliminary experience with Gd-DTPA–enhanced MR imaging. Radiology 172:165–170, 1989.
141. Rossiter JL, Hendrix RA, Tom LW, Potsic WP: Intramuscular hemangioma of the head and neck. Otolaryngol Head Neck Surg 108: 18–26, 1993.
142. Ryan SP, McNicholas MMJ (eds): Head and neck. In Anatomy for Diagnostic Imaging. London, WB Saunders Company, Ltd, 1994, pp 1–44.
143. Schoem SR, Choi SS, Zalzal GH, Grundfast KM: Management of oropharyngeal trauma in children. Arch Otolaryngol Head Neck Surg 123:1267–1270, 1997.
144. Schoenberg SO, Floemer F, Kroeger H, et al: Combined assessment of obstructive sleep apnea syndrome with dynamic MRI and parallel EEG registration: Initial results. Invest Radiol 35:267–276, 2000.
145. Seaman WB: Pharynx: Radiology. In Margulis AR, Burhenne HJ (eds): Alimentary Tract Radiology, 3rd ed. St Louis, CV Mosby, 1983; pp 491–518.
146. Sham JS, Cheung YK, Choy D, et al: Nasopharyngeal carcinoma: CT evaluation of patterns of tumor spread. AJNR Am J Neuroradiol 12:265–270, 1991.
147. Sham JS, Choy D: Prognostic value of paranasopharyngeal extension of nasopharyngeal carcinoma on local control and short-term survival. Head Neck 13:298–310, 1991.
148. Sham JS, Wei WI, Kwan WH, et al: Nasopharyngeal carcinoma: Pattern of tumor regression after radiotherapy. Cancer 65:216–220, 1990.
149. Shanmugaratnam K, Sobin LH: Histologic typing of upper respiratory tract tumors. In International Histologic Classification of Tumors. No. 19. Geneva, World Health Organization, 1978.
150. Shellock FG, Schatz CJ, Julien PM, et al: Dynamic study of the upper airway with ultrafast spoiled GRASS MR imaging. J Magn Reson Imaging 2:103–107, 1992.
151. Shellock FG, Schatz CJ, Julien P, et al: Occlusion and narrowing of the pharyngeal airway in obstructive sleep apnea: Evaluation by ultrafast spoiled GRASS MR imaging. AJR Am J Roentgenol 158: 1019–1024, 1992.
152. Sheman LJ: Diseases of the oropharynx. In Lee KJ (ed): Textbook of Otolaryngology and Head and Neck Surgery. New York, Elsevier, 1989, pp 407–414.
153. Sidhu MK, Shaw DW, Roberts TS: Carotid artery injury and delayed cerebral infarction after minor pharyngeal trauma. AJR Am J Roentgenol 167:1056, 1996.
154. Sievers KW, Greess H, Baum U, et al: Paranasal sinuses and nasopharynx CT and MRI. Eur J Radiol 33:185–202, 2000.
155. Sigal R, Zagdanski AM, Schwaab G, et al: CT and MR imaging of squamous cell carcinoma of the tongue and floor of the mouth. Radiographics 16:787–810, 1996.
156. Silver AJ, Mawad ME, Hilal SK, et al: Computed tomography of the carotid space and related cervical spaces: Part I. Anatomy. Radiology 150:723–728, 1984.
157. Siou G, Yates P: Retropharyngeal abscess as a complication of oropharyngeal trauma in an 18-month-old child. J Laryngol Otol 114:227–228, 2000.
158. Som PM, Biller HF, Lawson W: Tumors of the parapharyngeal space: Preoperative evaluation, diagnosis and surgical approaches. Ann Otol Rhinol Laryngol Suppl 90:3–15, 1981.
159. Som PM, Biller HF, Lawson W, et al: Parapharyngeal space masses: An updated protocol based upon 104 cases. Radiology 153:149–156, 1984.
160. Som PM, Brandwein M: Sinonasal cavities: Inflammatory diseases, tumors, fractures, and postoperative findings. In Som PM, Curtin HD (eds): Head and Neck Imaging, 3rd ed. St. Louis, Mosby–Year Book, 1996, pp 126–315.
161. Som PM, Braun IF, Shapiro MD, et al: Tumors of the parapharyngeal space and upper neck: MR imaging characteristics. Radiology 164:823–829, 1987.
162. Som PM, Sacher M, Stollman AL, et al: Common tumors of the parapharyngeal space: Refined imaging diagnosis. Radiology 169: 81–85, 1988.
163. Stein MG, Gamsu G, de Geer G, et al: Cine CT in obstructive sleep apnea. AJR Am J Roentgenol 148:1069–1074, 1987.
164. Stiernberg CM: Deep-neck space infections: Diagnosis and management. Arch Otolaryngol Head Neck Surg 112:1274–1279, 1986.
165. Su CY, Hsu SP, Chee CY: Electromyographic study of tensor and levator veli palatini muscles in patients with nasopharyngeal carcinoma: Implications for eustachian tube dysfunction. Cancer 71: 1193–1200, 1993.
166. Su CY, Lui CC: Perineural invasion of the trigeminal nerve in patients with nasopharyngeal carcinoma: Imaging and clinical correlations. Cancer 78:2063–2069, 1996.
167. Sugimura K, Kuroda S, Furukawa T, et al: Tongue cancer treated with irradiation: Assessment with MR imaging. Clin Radiol 46: 243–247, 1992.
168. Suto Y, Matsuo T, Kato T, et al: Evaluation of the pharyngeal airway in patients with sleep apnea: Value of ultrafast MR imaging. AJR Am J Roentgenol 160:311–314, 1993.
169. Tenofsky PL, Porter SW, Shaw JW: Fatal airway compromise due to retropharyngeal hematoma after airbag deployment. Am Surg 66: 692–694, 2000.
170. Tsai YS, Lui CC: Retropharyngeal and epidural abscess from a swallowed fish bone. Am J Emerg Med 15:381–382, 1997.
171. Unger JM: The oral cavity and tongue: Magnetic resonance imaging. Radiology 155:151–153, 1985.

172. Ungkanont K, Byers RM, Weber RS, et al: Juvenile nasopharyngeal angiofibroma: An update of therapeutic management. Head Neck 18:60–66, 1996.
173. Ungkanont K, Yellon RF, Weissman JL, et al: Head and neck space infections in infants and children. Otolaryngol Head Neck Surg 112: 375–382, 1995.
174. Union Internationale Contre le Cancer: In Sobin L, Wittekind C (eds): TNM Classification of Malignant Tumors, 5th ed. New York, Wiley-Liss, 1997.
175. Verron P, Grandpierre G, Vergeau B, et al: Nasopharyngeal perforation: An exceptional accident during digestive endoscopy. Ann Otolaryngol Chir Cervicofac 115:27–28, 1998.
176. Vogl TJ, Dresel SH: New developments in magnetic resonance imaging of the nasopharynx and face. Curr Opin Radiol 3:61–66, 1991.
177. Vogl T, Dresel S, Bilaniuk LT, et al: Tumors of the nasopharynx and adjacent areas: MR imaging with Gd-DTPA. AJR Am J Roentgenol 154:585–592, 1990.
178. Wakisaka M, Mori H, Fuwa N, Matsumoto A: MR analysis of nasopharyngeal carcinoma: Correlation of the pattern of tumor extent at the primary site with the distribution of metastasized cervical lymph nodes—preliminary results. Eur Radiol 10:970–977, 2000.
179. Weber AL, Baker AS, Montgomery WW: Inflammatory lesions of the neck, including fascial spaces: Evaluation by computed tomography and magnetic resonance imaging. Isr J Med Sci 28:241–249, 1992.
180. Weissleder R, Rieumont MJ, Wittenberg J (eds): Head and neck imaging. In Primer of Diagnostic Imaging, 2nd ed. St. Louis, Mosby–Year Book, 1997, pp 547–94.
181. Weissman JL, Tabor EK, Curtin HD: Sphenochoanal polyps: Evaluation with CT and MR imaging. Radiology 178:145–148, 1991.
182. Wong DS, Fuller LM, Butler JJ, Shullenberger CC: Extranodal non-Hodgkin's lymphomas of the head and neck. Am J Roentgenol Radium Ther Nucl Med 123:471–481, 1975.
183. Yakes WF, Haas DK, Parker SH, et al: Symptomatic vascular malformations: Ethanol embolotherapy. Radiology 170:1059–1066, 1989.
184. Yousem DM, Chalian AA: Oral cavity and pharynx. Radiol Clin North Am 36:967–981, 1998.
185. Yousem DM, Hatabu H, Hurst RW, et al: Carotid artery invasion by head and neck masses: Prediction with MR imaging. Radiology 195: 715–720, 1995.
186. Yu ZH, Xu GZ, Huang YR, et al: Value of computed tomography in staging the primary lesion (T-staging) of nasopharyngeal carcinoma (NPC): An analysis of 54 patients with special reference to the parapharyngeal space. Int J Radiat Oncol Biol Phys 11:2143–2147, 1985.

20

Thyroid and Parathyroid Glands

Theodore C. Larson III, Michelle M. Smith, Wui K. Chong, William H. Martin

Thyroid Gland

The shield-shaped thyroid gland is normally positioned anterior and lateral to the cricoid cartilage, although its position may be located more superiorly, anterior to the thyroid cartilage, or more inferiorly, anterior to the trachea. The thyroid contains two lobes, each with a superior and inferior pole; an isthmus; and, in 50% to 80% of patients, a pyramidal lobe that originates from the isthmus or the medial aspect of either lobe. The pyramidal lobe develops along the distal embryonic thyroglossal duct, which explains its location. Similarly, thyroid tissue may be ectopically located anywhere along its developmental migration track (i.e., as a lingual thyroid at the base of the tongue, within a vestigial thyroglossal duct cyst, or further caudally within the mediastinum) (Fig. 20–1).

The superficial location of a normally positioned thyroid gland makes imaging easily accomplished with ultrasonography. Using a 7.5- to 10-MHz linear-array transducer provides 2-mm spatial resolution, although penetration depth and range of view are somewhat curtailed. The normal thyroid gland is homogeneous and more echogenic than muscle but less echogenic than fat. The standard examination provides transverse and longitudinal planar images with evaluation of regional cervical lymph nodes.

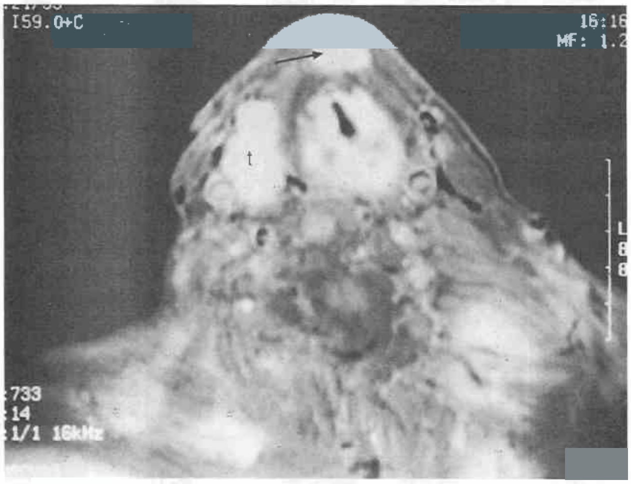

Figure 20–1. Axial T1-weighted MR postgadolinium image with fat suppression shows ovoid enhancing tissue *(arrow)* anterior to the larynx. The tissue, which shows the same signal intensity and enhancement as the enlarged right thyroid lobe (t), represents pyramidal lobe tissue involved by goiter (same patient as in Figure 20–27).

Ultrasonography is often the first modality used to image the thyroid gland because it is convenient, inexpensive, quick, and easy to perform. Ultrasonography readily identifies and distinguishes between cystic and solid lesions without using ionizing radiation, although thyroid disorders and diseases that are purely cystic are uncommon. Ultrasonography typically detects more thyroid masses than does computed tomography (CT), magnetic resonance imaging (MRI), or scintigraphy because of its greater spatial resolution. Limitations of ultrasonography include difficulties in evaluating ectopically located thyroid tissue, predicting the functional status of thyroid nodules, and surveying the neck for metastatic lymphadenopathy.

Radiopharmaceuticals used in evaluating the thyroid include technetium 99m–pertechnetate (^{99m}Tc), iodine 123 (^{123}I), iodine 131 (^{131}I), thallium 201 (^{201}Tl), ^{99m}Tc-sestamibi (MIBI [methyl-isobutyl-isonitrile]), fluoro-18-deoxyglucose (^{18}FDG), gallium 67 (^{67}Ga), indium 111 (^{111}In)–octreotide, and ^{131}I-metaiodobenzylguanidine (mIBG). ^{123}I is the preferred agent for imaging substernal thyroid glands, and ^{131}I is preferred for detecting metastases after thyroid ablation.

CT evaluation of the thyroid is performed in the axial plane, usually after the intravenous (IV) administration of iodinated contrast material. The performance of CT and scintigraphic examinations must be coordinated because the administration of IV contrast material for a CT examination interferes with thyroidal uptake of radioiodine and ^{99}Tc for 4 to 6 weeks. An advantage of CT is that the entire neck as well as the mediastinum can be surveyed for metastatic lymphadenopathy and ectopic thyroid tissue; CT also permits the detection of any unassociated concomitant conditions (Fig. 20–2). CT is excellent at characterizing the density of a thyroid lesion, thus defining the presence of calcification, cysts, or hemorrhage. The borders of a thyroid mass are usually well delineated by CT; thus, invasion of adjacent structures such as the trachea, larynx, and vascular structures of the carotid sheath can be identified.

MRI of the thyroid, like CT, can be used to evaluate the contents of the entire neck. Advantages of MRI over CT include improved soft tissue discrimination and lack of beam-hardening artifacts; however, MRI is not superior in the identification of malignant lymphadenopathy.[160] Differentiation between hemorrhagic lesions and lesions of increased protein content such as colloid-containing masses can be difficult, both being of either bright or dark signal

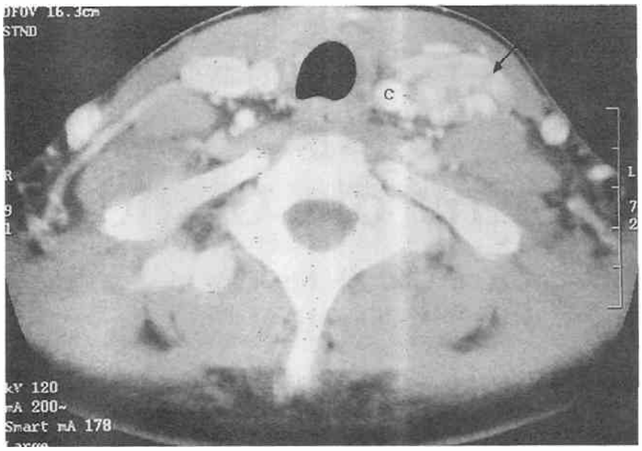

Figure 20–2. Axial postcontrast CT scan performed in a patient after thyroidectomy for papillary carcinoma. The heterogeneously enhancing mass *(arrow)* in the left neck lateral to the left common carotid artery (c) is consistent with a diagnosis of nodal metastasis.

intensity on T1-weighted and T2-weighted images. MRI also demonstrates well the relationship of thyroid lesions to adjacent structures, which assists in determining whether local invasion is present.

In most instances, fine-needle aspiration of palpable suspected thyroid masses can be accomplished freehand without imaging assistance; biopsy of small or nonpalpable lesions can be accomplished with the aid of ultrasonographic, CT, or MRI guidance.[139, 157] Solid, hypoechoic thyroid nodules 8 mm or larger are typically selected for needle aspiration. Smaller nodules can be difficult to aspirate in a precise manner and are more often followed with serial ultrasonographic examinations. A 20- or 22-gauge needle is employed for sampling the solid portion of the mass, with imaging used to guide needle placement and avoid the common carotid artery and internal jugular vein (Fig. 20–3).

Sensitivity and specificity for fine-needle aspirations are reported to be greater than 94%, but results are highly dependent on the expertise of the cytopathologist, and nondiagnostic material may be present in as many as 20% of cases.[7, 28, 31, 40, 43, 66, 139, 157] Fine-needle aspiration, with or without imaging guidance, is the most cost-effective method of diagnosis of primary and recurrent thyroid malignancy.

Pathologic Thyroid Conditions

Thyroid Malignancies

Malignant thyroid neoplasms constitute the most common endocrine cancer. These include the well-differentiated papillary and follicular carcinomas as well as a mixed papillary-follicular variety. Less common but more aggressive malignancies include medullary carcinoma, anaplastic carcinoma, lymphoma, metastatic disease, and other rare neoplasms, such as sarcoma. The most common or these is papillary carcinoma, which accounts for approximately 70% of all thyroid malignancies.[67, 106, 139] Follicular carcinoma comprises about 10%; medullary carcinoma, 5%; anaplastic carcinoma, about 5%, and the remaining malignancies together, about 1%.[17, 67]

Imaging of thyroid neoplasms using any of a number of modalities is typically not specific for malignancy, since benign processes often simulate malignant tumors. Nodules with irregnlar margins or masses that invade normal local structures revealed on any imaging examination suggest a malignant process. Irregular borders are visualized in approximately 60% of thyroid malignancies, yet are also seen in approximately 45% of benign thyroid tumors.[130]

Multiple small, highly echogenic foci (with or without shadowing) on sonography strongly suggest the presence of microcalcifications within malignancies.[109] Coarse or peripheral (eggshell) calcification, visualized on CT or with sonography, suggests a benign nodule (Fig. 20–4).[109] Overall, calcification is found in 13% of thyroid masses, including 17% of malignancies and 11% of benign lesions.[130]

Thyroid masses with hemorrhage; cysts; diminished density, isodensity, or increased density (or signal intensity); contrast enhancement; and well-circumscribed margins examined on ultrasonography, CT, or MRI may be benign or malignant.[90, 159] Cystic elements are found in 38% of thyroid malignancies but also in 62% of benign thyroid entities.[130]

Although most thyroid carcinomas are hypoechoic at sonography, most hypoechoic nodules are benign because benign thyroid nodules are much more common than malignant thyroid nodules. Sonographically, 75% of thyroid

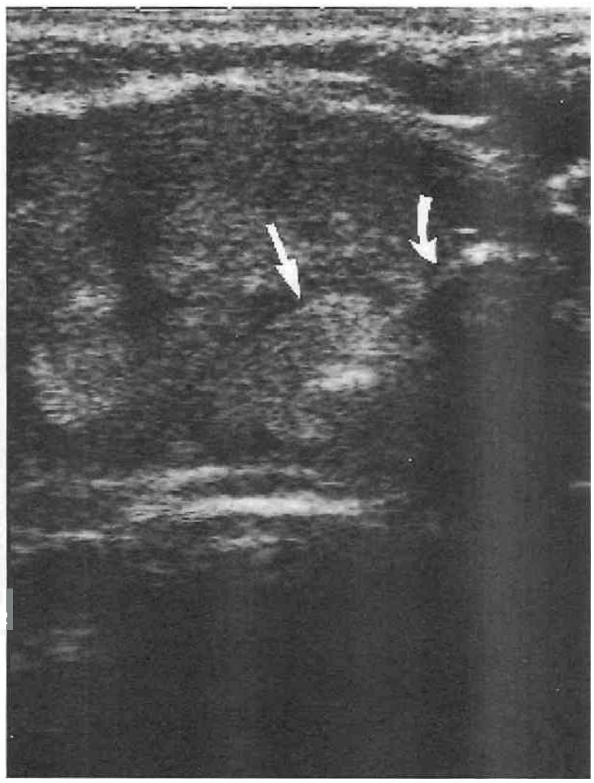

Figure 20–3. Ultrasound-guided, fine-needle aspiration of a thyroid mass. A 22-gauge needle *(curved arrow)* is being inserted into a left thyroid lobe mass *(straight arrow)* under real-time sonographic guidance. Cytologic examination revealed a follicular adenoma.

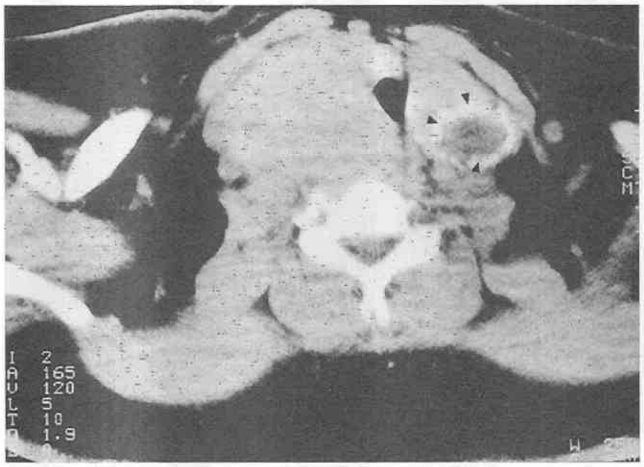

Figure 20–4. Axial CT scan through the lower neck shows peripheral coarse calcifications *(arrowheads)* in an adenoma within an enlarged, goitrous thyroid gland. This peripheral calcification may also be thin and eggshell-like.

carcinomas are hypoechoic, 23% are isoechoic, and only 2% are hyperechoic.[130] Purely cystic or completely hyperechoic nodules are very rarely malignant. Benign nodules may coexist with malignant nodules, however. For instance, 33% of thyroidectomy specimens containing papillary carcinoma also harbor benign nodules.[46]

Color Doppler imaging demonstrates the vascularity of malignant and benign thyroid nodules, with malignant nodules typically showing central intranodular vascularity and benign lesions being characterized by peripheral perinodular vascularity.[124] There is considerable overlap, however, and the distribution of vessels on color Doppler imaging is not a reliable means of differentiating benign from malignant nodules.[124]

More than 99% of "hot" thyroid masses on scintigraphy are benign, typically representing hyperplastic or adenomatous nodules.[28, 50] A "cold" nodule is associated with a 15% to 25% incidence of malignancy, which increases to as great as 50% if the patient has had earlier neck irradiation.[116]

The role of imaging includes the following:

1. Evaluation of thyroid capsule transgression.
2. Detection of neoplastic infiltration into adjacent structures, including prevertebral and local musculature, the carotid sheath, and the aerodigestive tract (Fig. 20–5).
3. Identification of malignant lymphadenopathy.

Enlarged lymph nodes, nodes demonstrating extracapsular spread, and clustered nodes suggest pathologic involvement but are not specific findings of malignant lymphadenopathy.[131, 139] None of the imaging modalities can reliably predict malignant thyroid histology.

Papillary Carcinoma

Papillary carcinoma is characterized histologically by psammoma bodies, "ground-glass" nuclear material, and a fibrovascular papillary stroma.[67] When cyst formation is present, the carcinoma is termed a *cystadenocarcinoma*. Papillary carcinomas are often encapsulated, and they are bilateral or multifocal in 10% to 15% of cases.[152] The incidence of malignant lymphadenopathy is approximately 50%,[67] and 22% of cases of malignant lymphadenopathy arise from occult thyroid tumors.[4] Malignant nodes may be cystic, necrotic, hemorrhagic, or calcified, and they may contain colloid (Fig. 20–6).[131, 132] In approximately 5% of patients, distant metastases occur to lungs, skeleton, or central nervous system.[67] With adequate resection, ^{131}I therapy, and chronic suppressive therapy with thyroxine (T_4), the 20-year survival rate is reported to be 94%.[78] Tumors with both papillary and follicular components behave like purely papillary carcinomas.

Imaging of papillary carcinoma typically demonstrates a solid, hypoechoic (77%) or isoechoic (14%) thyroid mass, often with associated microcalcifications (Fig. 20–7).[130] The lesions most commonly appear to be hypofunctioning (cold) using ^{99m}Tc-pertechnetate and radioiodine (Fig. 20–8) but may demonstrate increased uptake of ^{201}Tl, ^{99m}Tc-MIBI, or ^{18}FDG.

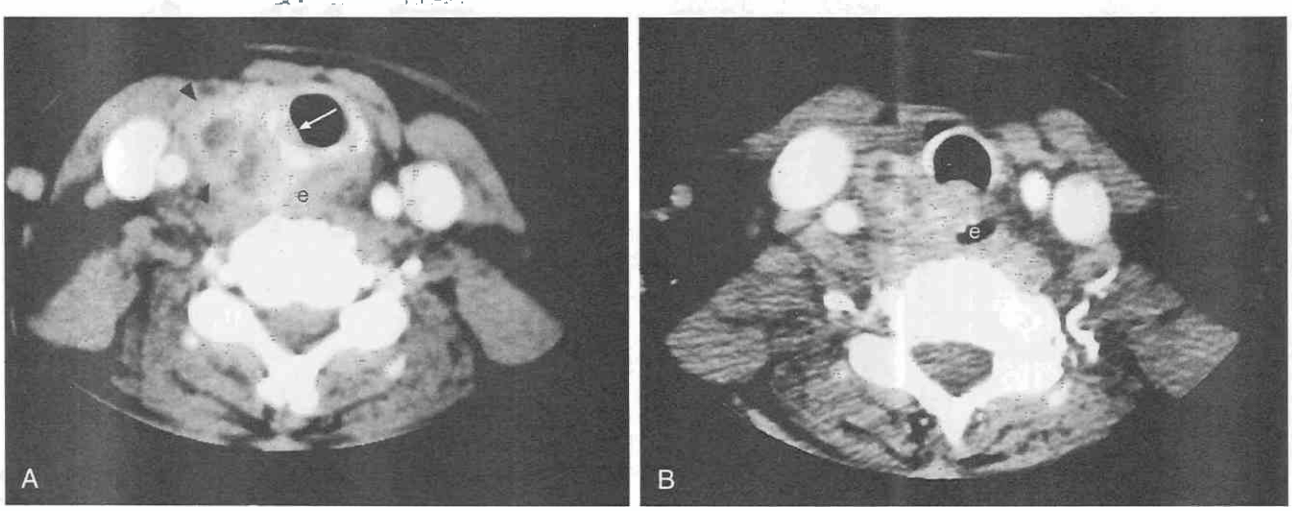

Figure 20–5. *A,* Axial postcontrast CT shows a heterogeneously enhancing mass *(arrowheads)* within the right thyroid lobe, with invasion of the cricoid ring and submucosal extension of tumor *(arrow)*. e, esophagus. *B,* CT image in the same patient at a lower level shows the mass invading the trachea and esophagus (e). Papillary carcinoma was found at surgery.

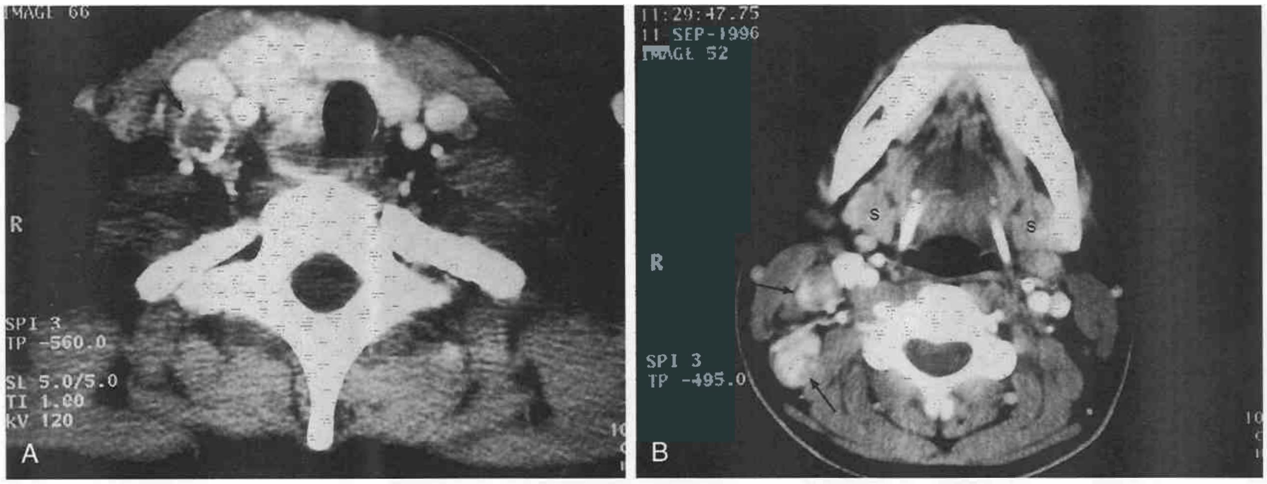

Figure 20–6. Papillary carcinoma with nodal metastases. *A,* Axial postcontrast CT shows a heterogeneous, multilobular mass involving the right thyroid lobe without tracheal invasion. A peripherally calcified lymph node *(arrow)* is seen in the right tracheoesophageal groove. *B,* CT in the same patient at the level of the mandible shows two enlarged, enhancing lymph nodes *(arrows)* within the right posterior triangle and one along the left jugular chain. Normal submandibular glands (s).

Radioiodine uptake by functioning thyroid carcinomas and their metastases is usually less than 10% that of normal thyroid tissue. Therefore, distant and nodal metastases may not be visualized by radioiodine scanning prior to the ablation of any postoperative thyroid remnant.[17] Optimal ^{131}I uptake by neoplastic tissue is also dependent on thyroid-stimulating hormone (TSH). Adequate endogenous TSH levels of greater than 40 μU/mL can be attained 2 weeks after the discontinuance of exogenous liothyronine (T_3) therapy or 4 to 6 weeks after the discontinuance of levothyroxine (T_4) therapy.[33] Preliminary experience indicates that the use of recombinant human TSH as a method of stimulating radioiodine uptake in patients taking exogenous thyroid hormone (TH) replacement yields a detection rate for metastases nearly equal to that seen following thyroid hormone withdrawal.[59]

Thyroglobulin is an iodinated glycoprotein synthesized by both benign and malignant thyroid tissue. Approximately 90% of patients with metastases demonstrate an elevated serum thyroglobulin level.[72] Following surgery and ^{131}I ablation, it should be undetectable (<5 ng/mL) if no functioning thyroid metastases remain. Serum thyroglobulin is a highly sensitive and specific indicator of

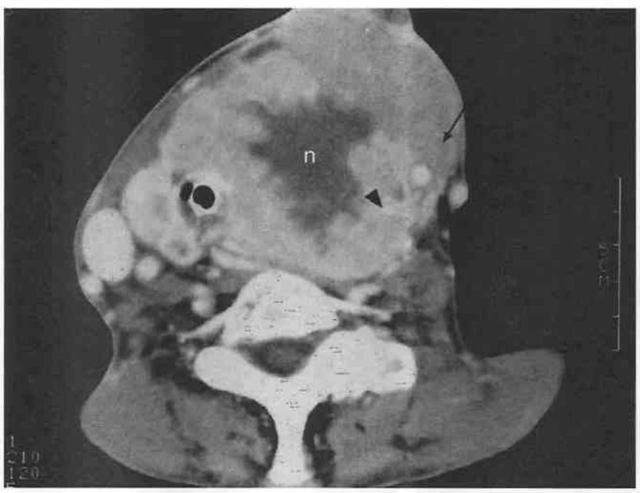

Figure 20–7. Axial postcontrast CT scan shows papillary carcinoma arising from the left thyroid lobe with calcification *(arrowhead)*, central necrosis (n), and deviation of the intubated trachea. The mass encases the left common carotid artery *(arrow)*.

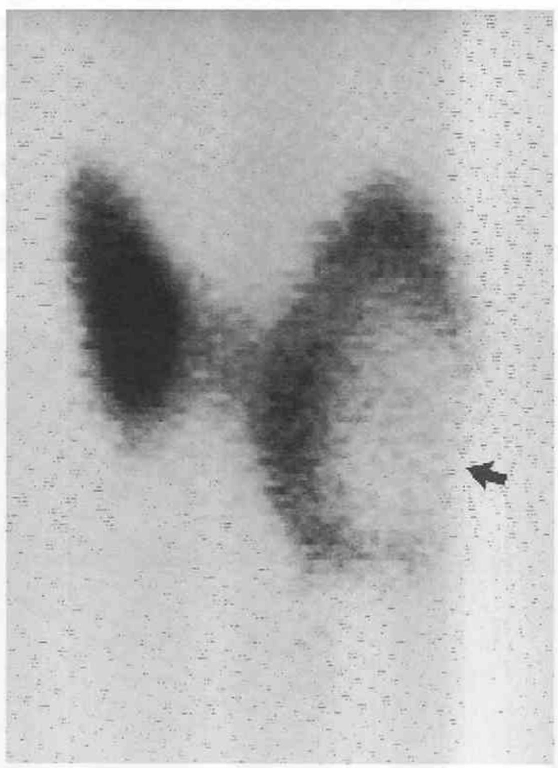

Figure 20–8. An anterior view obtained during technetium 99m–pertechnetate scintigraphy shows a large solitary hypofunctioning nodule *(arrow)* in the lower pole of the left thyroid lobe. The nodule was subsequently resected and found to represent a papillary carcinoma. The right thyroid lobe is normal.

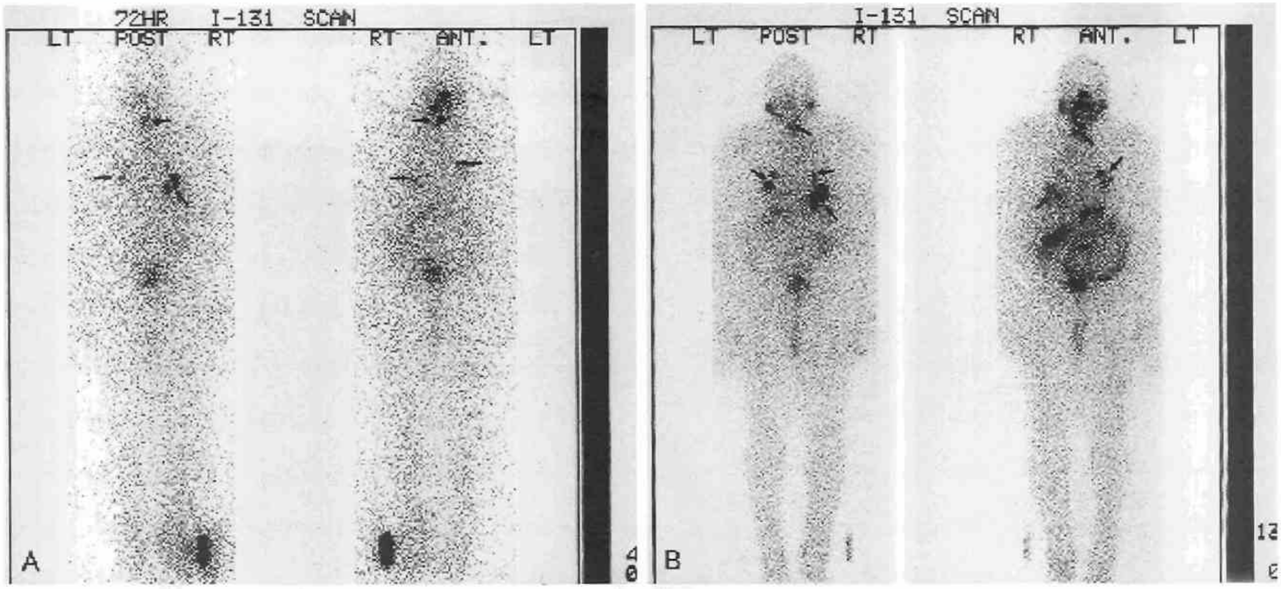

Figure 20–9. *A*, Several definite and a few equivocal metastatic foci *(arrows)* are identified in the neck and thorax 72 hours after the administration of a 3-mCi diagnostic dose of iodine 131. *B*, One week after administration of a 200-mCi therapeutic dose of iodine 131, whole body images more clearly define two metastatic foci in the neck *(arrows)* and at least five lung lesions *(arrows)*.

residual or metastatic thyroid carcinoma in patients after ablation.

After surgery and ^{131}I ablation, patients with well-differentiated thyroid carcinoma (papillary and follicular) are assessed for recurrence annually (or less frequently) using whole body radioiodine scintigraphy and serum thyroglobulin monitoring. The sensitivity of ^{131}I scintigraphy for the detection of persistent or metastatic thyroid carcinoma is 50% to 70% with a diagnostic dose of 2 to 5 mCi.[115] Additional lesions are often detected or more easily defined with scintigraphy following a therapeutic dose of 100 to 200 mCi (Fig. 20–9).[8] The combination of ^{131}I scanning and serum thyroglobulin determination improves the detection of metastatic disease to 85% to 100%.[8]

Although the specificity of ^{131}I scintigraphy is high, false-positive findings related to renal, gastrointestinal (GI), other excretory pathways may be confusing. Because it is not necessary to withdraw thyroid hormone therapy prior to scanning, ^{201}Tl or ^{99m}Tc-MIBI imaging is more convenient for the patient. The sensitivity for either of these two agents is 60% to **90%**.[8] It is not uncommon to see a positive ^{201}Tl or ^{99m}Tc-MIBI scan in a thyroglobulin-positive patient with a negative ^{131}I scan (Fig. 20–10). Thyroid carcinoma metastases that are poorly visualized with ^{131}I and ^{201}Tl have been successfully imaged with ^{18}FDG positron emission tomography (PET) while patients remained on a thyroid hormone–suppressive regimen.[13, 126]

Ultrasonography, CT, and MRI are also effective adjunctive imaging modalities in defining the extent of metastatic disease. Compared with ^{131}I scintigraphy, diphosphonate bone scanning is insensitive in detecting the skeletal metastases of differentiated thyroid carcinoma.

Follicular Carcinoma

Follicular carcinoma is usually well marginated and encapsulated, but it may be locally invasive.[158] Associated lymphadenopathy is seen in approximately 5% of patients, but there is a greater propensity for hematogenous metastasis (Fig. 20–11).[67] Prognosis for follicular carcinoma is poorer than that for papillary carcinoma. Papillary elements may be present in follicular carcinomas, giving a mixed papillary-follicular variety with behavior similar to that of papillary carcinoma. Hürthle cell carcinoma is an unusual variant of follicular carcinoma that frequently demonstrates ^{201}Tl and ^{99m}Tc-MIBI uptake.[1] It is a nonfunctional malignancy with no radioiodine uptake.

Ultrasonography of follicular carcinomas demonstrates a hypoechoic mass in approximately 45% of cases and an isoechoic mass in the remainder (Fig. 20–12).[34, 130] Follicular carcinoma uncommonly develops cystic regions, but compared with papillary carcinoma, it more frequently invades local vasculature, including the carotid sheath.[67] CT and MRI typically demonstrate a solid mass not dissimilar to papillary carcinoma (Fig. 20–13) and are useful for demonstrating local invasion of normal anatomy, extension into the mediastinum, and cervical lymphadenopathy. Nuclear medicine imaging characteristics are similar to those of papillary carcinomas.

Medullary Carcinoma

Medullary carcinoma of the thyroid (MCT) is derived from the parafollicular C cells, which are of neural crest origin. Approximately 80% to 90% of MCTs secrete calcitonin, which is used as a sensitive indicator of tumor presence and volume.[151] MCTs that do not produce calcitonin have a poorer prognosis.[15] Most MCTs also express carcinoembryonic antigen (CEA)[151]; early studies using radiolabeled monoclonal antibodies to CEA indicate a high sensitivity and specificity for the detection of MCT and determination of its extent (Fig. 20–14).[5, 103] This is particularly useful for identifying MCT recurrence.

Although most MCTs express somatostatin receptors, only 40% to 60% are detected using somatostatin receptor scintigraphy (^{111}In-octreotide) (see Fig. 20–14).[21, 58] The

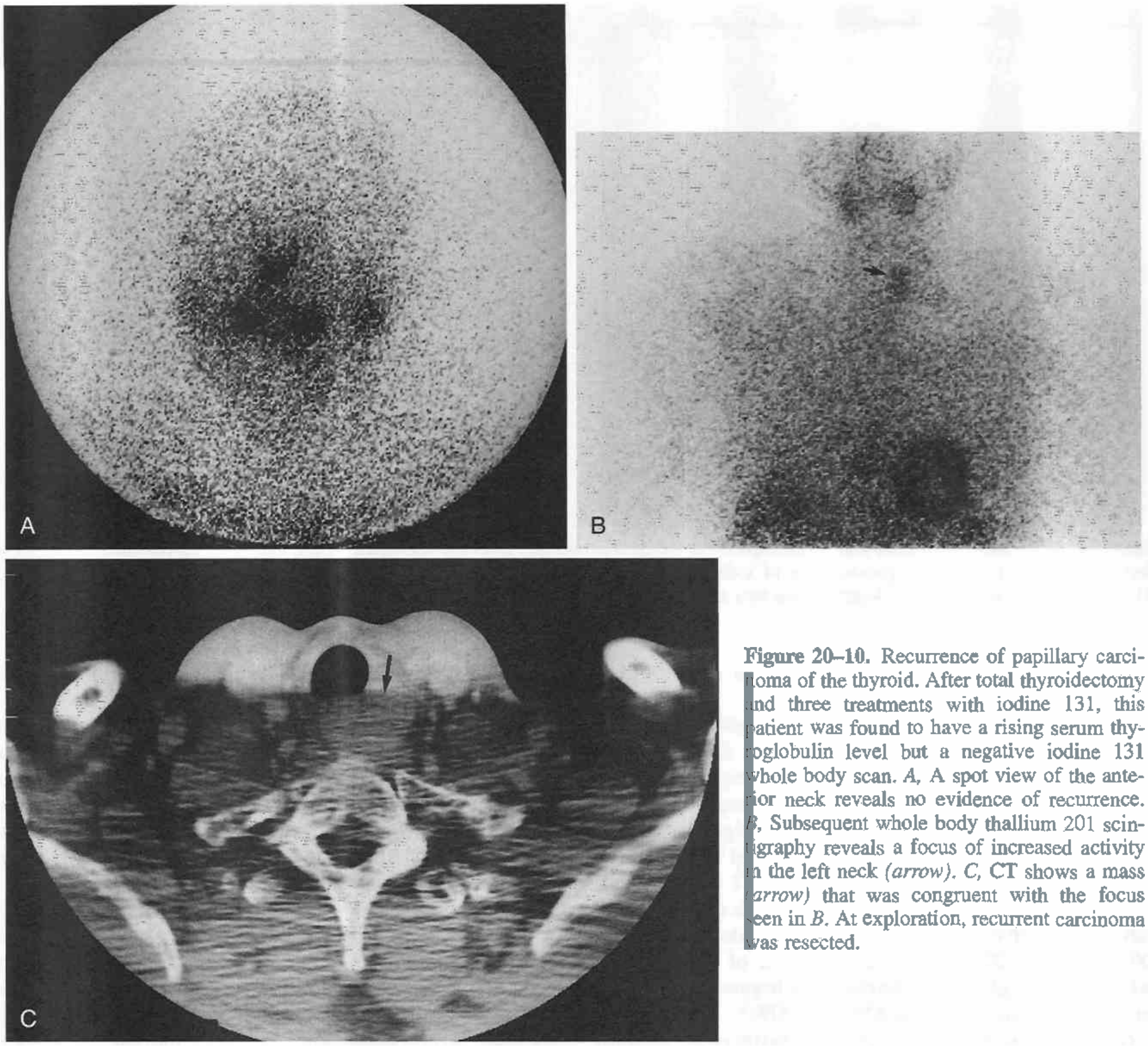

Figure 20–10. Recurrence of papillary carcinoma of the thyroid. After total thyroidectomy and three treatments with iodine 131, this patient was found to have a rising serum thyroglobulin level but a negative iodine 131 whole body scan. *A,* A spot view of the anterior neck reveals no evidence of recurrence. *B,* Subsequent whole body thallium 201 scintigraphy reveals a focus of increased activity in the left neck *(arrow). C,* CT shows a mass *(arrow)* that was congruent with the focus seen in *B.* At exploration, recurrent carcinoma was resected.

higher the serum calcitonin level, the more likely the tumor can be detected using ^{111}In-octreotide imaging. MCT is not radioiodine-avid and cannot be treated effectively with ^{131}I. ^{201}Tl, ^{99m}Tc-dimercaptosuccinic acid (DMSA), and ^{131}I-mIBG have been reported to be highly sensitive and specific for MCT, especially when basal calcitonin levels are greater than 1000 pg/mL.[6, 127] MCT may also take up ^{67}Ga. Evidence is emerging that FDG PET may represent the most effective imaging modality for detection of metastatic MCT.[89]

On ultrasonographic examinations, MCTs are typically hypoechoic, although focal calcium may cause echogenic foci, both at the primary site and within metastatic lymph nodes.[8, 34, 130] CT and MRI demonstrate a solid mass, are helpful for displaying surgical anatomy, and best reveal adjacent lymphadenopathy; malignant lymph nodes are seen in approximately 50% of cases.[158] CT and MRI are often inadequate for identifying MCT recurrences.[21] Selective venous sampling for calcitonin levels using transfemoral catheter techniques is a sensitive and specific method of localizing MCT, but it is invasive, time consuming, and expensive.[88]

MCT is most often sporadic, but a familial link is seen in approximately 15% of adult patients.[158] MCT is a component of multiple endocrine neoplasia type 2A (MEN-2A) and type 2B (MEN-2B) syndromes. MEN-2A is called Sipple's syndrome and MEN-2B (or MEN-3) is termed the *mucosal neuroma syndrome.* In MEN-2A, virtually all patients have MCT, one third have parathyroid hyperplasia, and roughly one third harbor pheochromocytomas. Patients with the MEN-2B syndrome, in addition to having MCT, demonstrate mucocutaneous and alimentary tract ganglioneuromas, café-au-lait spots, and marfanoid facies; in addition, pheochromocytomas develop. A missense mutation of the *ret* oncogene has been identified on chromosome 10 in families with either the MEN-2A or the MEN-2B syndrome.[88]

Anaplastic Carcinoma

Anaplastic carcinoma, typically seen in older patients, is a very aggressive head and neck malignancy that carries

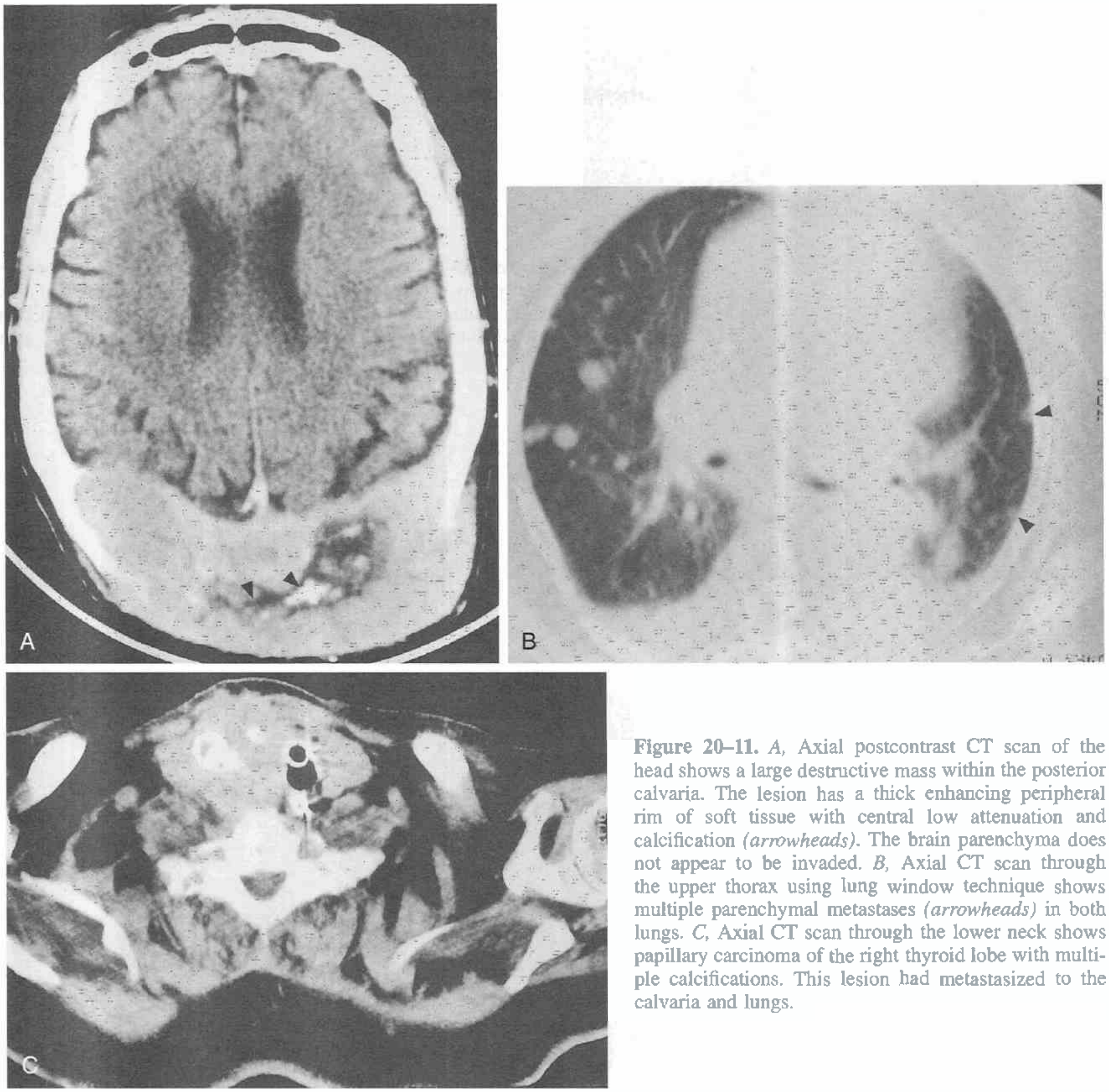

Figure 20–11. *A,* Axial postcontrast CT scan of the head shows a large destructive mass within the posterior calvaria. The lesion has a thick enhancing peripheral rim of soft tissue with central low attenuation and calcification *(arrowheads)*. The brain parenchyma does not appear to be invaded. *B,* Axial CT scan through the upper thorax using lung window technique shows multiple parenchymal metastases *(arrowheads)* in both lungs. *C,* Axial CT scan through the lower neck shows papillary carcinoma of the right thyroid lobe with multiple calcifications. This lesion had metastasized to the calvaria and lungs.

a poor prognosis.[158] Patients typically survive only a few months after the pathologic diagnosis is confirmed. Metastases are often widespread. This type of thyroid malignancy can be present within goiter or may be associated with other thyroid malignancies.[67, 122]

Conventional nuclear medicine techniques using ^{99m}Tc-pertechnetate or radioiodine demonstrate only a nonspecific hypofunctioning mass. ^{201}Tl, ^{99m}Tc-MIBI, and ^{18}FDG reveal increased activity within the primary mass as well as within metastases.[122] Although these tumors are ^{67}Ga-avid, this radionuclide cannot be used to differentiate anaplastic carcinoma from other malignancies, thyroiditis, or thyroid granulomatous infections.

On ultrasonography, anaplastic thyroid carcinoma typically appears as a large hypoechoic mass.[34, 116] CT demonstrates calcification in approximately 60% of cases and necrosis in 75%.[142] Metastatic lymphadenopathy develops in approximately 75% of patients, and in 50% of these the lymph nodes are necrotic.[142] Local invasion of vasculature or the aerodigestive tract is seen in approximately 40% of patients (Figs. 20–15 and 20–16),[15] and in 25% the malignancy extends into the mediastinum (Fig. 20–17).[142] CT, MRI, and ultrasonography can be used to evaluate the extent of local disease, although ultrasonography does not allow visualization of caudal advancement into the mediastinum.[142]

Lymphoma

Primary lymphoma of the thyroid gland is usually a B-cell neoplasm and is most commonly seen in older women with current or prior Hashimoto's thyroiditis.[41, 67] Virtually all patients with primary lymphoma of the thyroid have coexistent autoimmune thyroiditis.[41]

Lymphomas typically appear as solitary (80%) or multifocal hypoechoic nodules (20%) on ultrasonographic

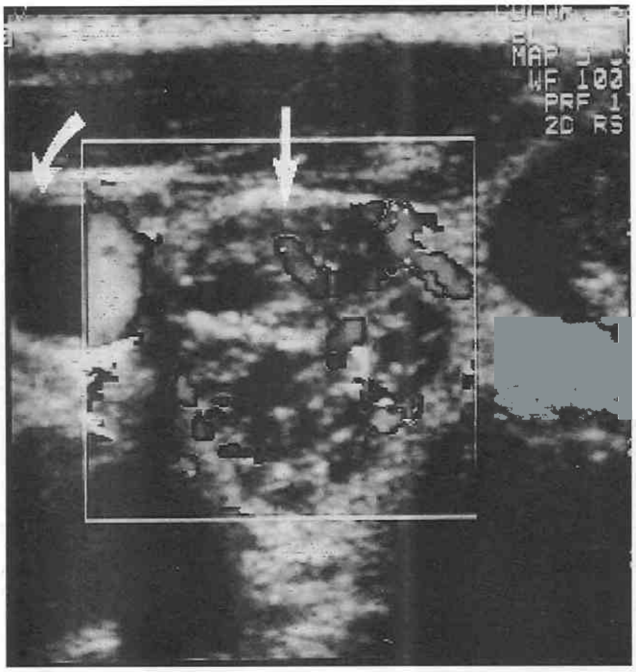

Figure 20–12. Follicular carcinoma of the thyroid. A predominantly hypoechoic heterogeneous mass *(arrow)* with central vascularity (indicated by Doppler enhancement) is seen within the right lobe of the thyroid. *Curved arrow* indicates common carotid artery.

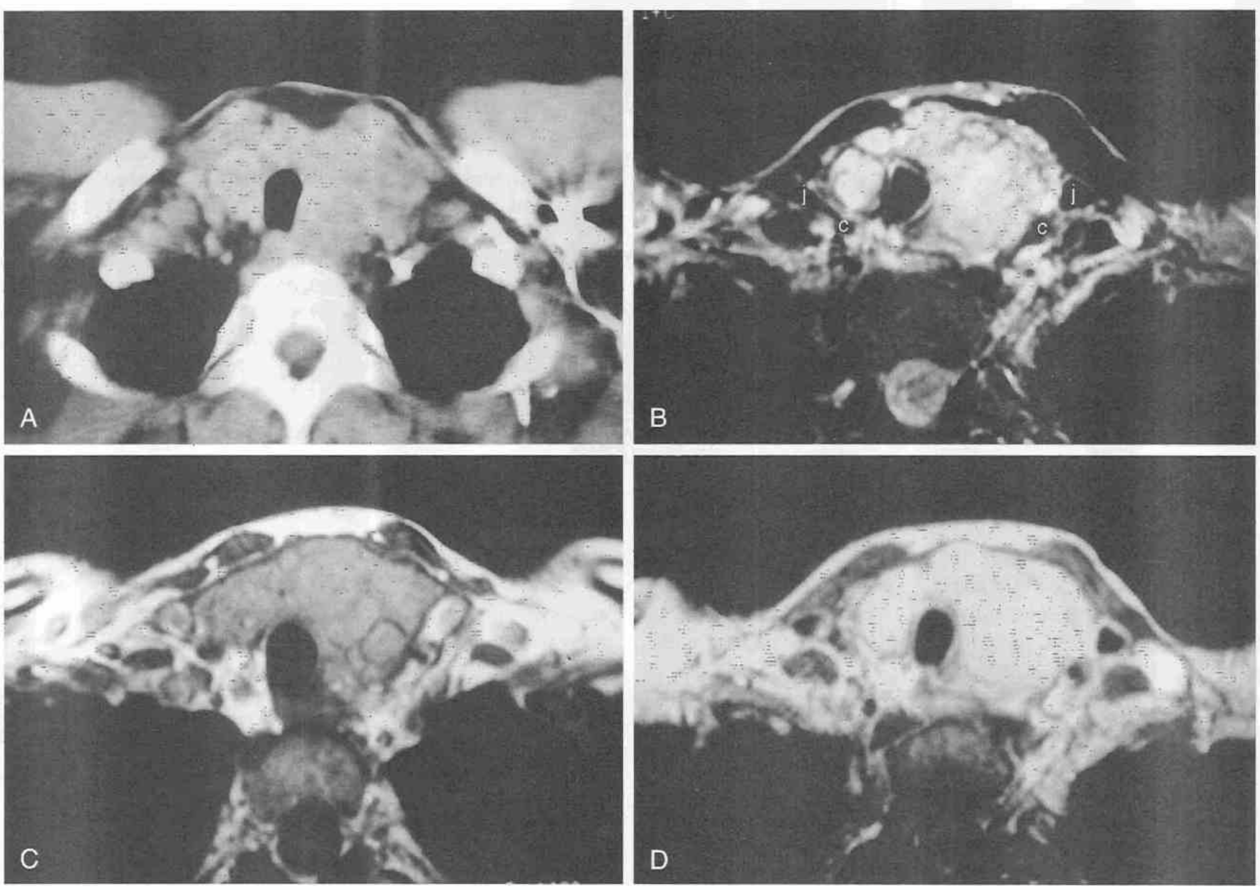

Figure 20–13. *A,* Axial CT image shows a lobular mass arising from the left lobe of the thyroid; it has a slight mass effect on the trachea. *B,* Axial T2-weighted MR image demonstrates a predominantly hyperintense mass splaying the bilateral common carotid arteries (c) and internal jugular veins (j). There is no evidence of tracheal invasion. *C,* Axial T1-weighted MR image demonstrates that the mass is of intermediate signal intensity. *D,* Axial T1-weighted MR image after contrast administration shows diffuse enhancement throughout the mass. Follicular carcinoma without tracheal invasion was seen at surgery.

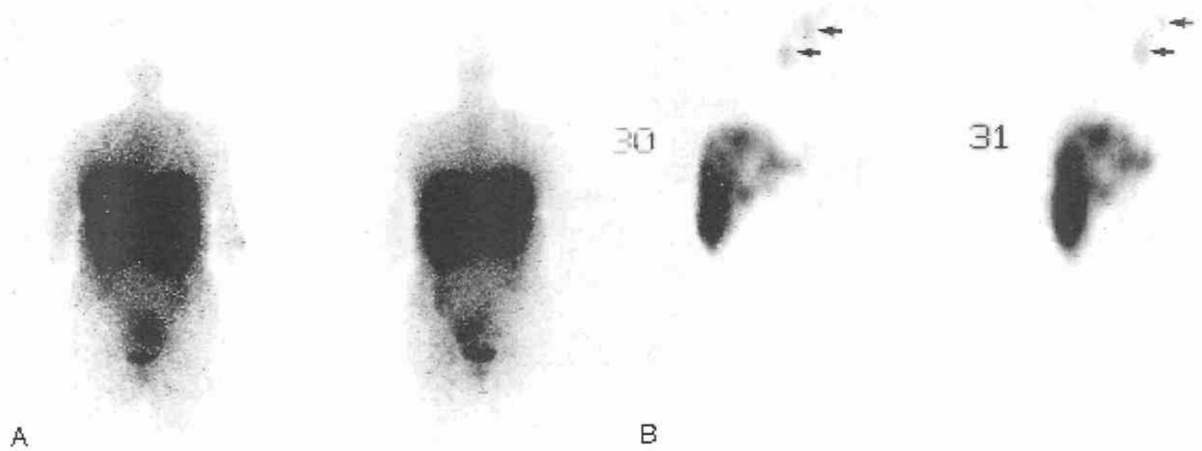

Figure 20–14. *A,* Following total thyroidectomy, a patient with medullary carcinoma of the thyroid and persistent elevation of serum calcitonin and carcinoembryonic antigen (CEA) was found to have a negative indium 111–octreotide scan. *B,* Whole body and SPECT imaging with iodine 131–labeled anti-CEA monoclonal antibody (performed at Garden State Cancer Center, Newark, N.J.) revealed two metastatic foci in the mediastinum *(arrows).* CT scan (not shown) did not demonstrate liver metastases. (From Martin WH, Delbeke D, Habibian MR: Oncologic imaging. In Habibian MR, Delbeke D. Martin WH, Sandler MP [eds]: Nuclear Medicine Imaging: A Teaching File. Philadelphia, Lippincott Williams & Wilkins, 1999, p 700).

studies,[34, 130, 141] and they are photopenic on ^{99m}Tc-pertechnetate or radioiodine scintigraphy. Although lymphomas accumulate both ^{67}Ga and ^{18}FDG, so may the adjacent areas involved by autoimmune thyroiditis. Gallium 67 and ^{18}FDG, however, may demonstrate distant metastases.[52] Most lymphomas accumulate ^{201}Tl and ^{99m}Tc-MIBI, both of which may be used to assess response to therapy.[120] These tumors are isodense or hypodense on CT, without or with IV contrast material, and typically cause homogeneous enlargement of a lobe or of the entire thyroid (Fig. 20–18).[141] Necrosis or calcification is seen in a minority of cases.[141] Local invasion (19% to 51%) or metastasis to regional lymph nodes (14% to 44%)[141] can be demonstrated by ultrasonography, CT, and MRI, each modality having its own advantages and limitations.[143] On MRI, lymphoma often shows increased signal intensity on T2-weighted images[123] and enhances less compared with other thyroid tumors.[90]

Metastases

Approximately 3% of individuals with a primary malignancy outside the thyroid gland have metastatic disease to

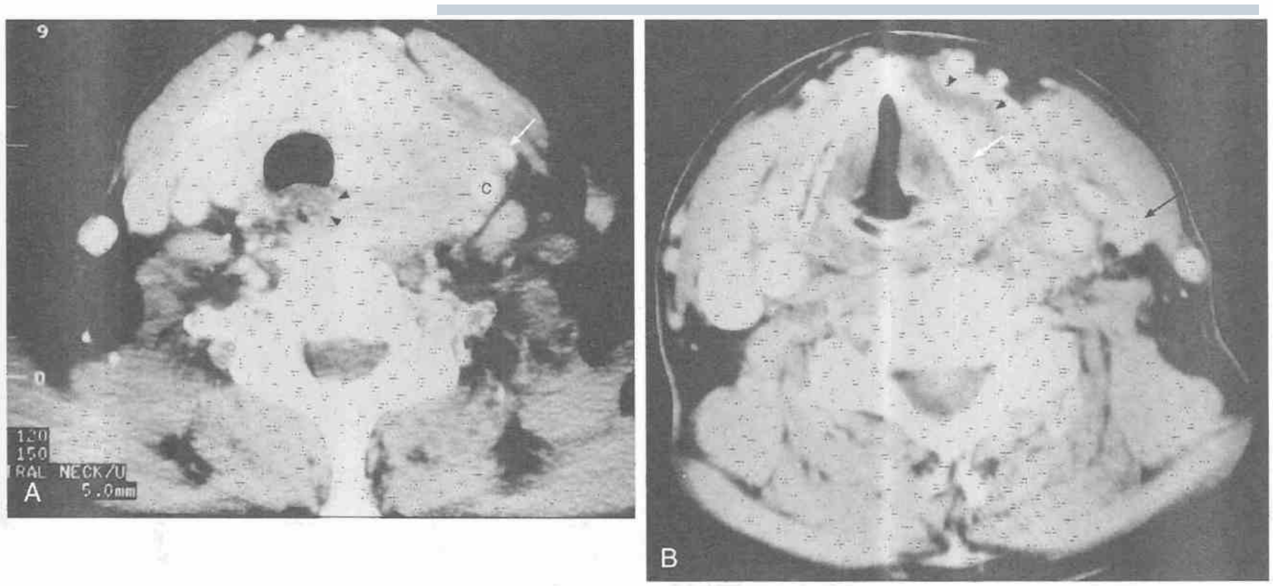

Figure 20–15. Anaplastic carcinoma. *A,* Axial postcontrast CT image shows an enhancing mass arising from the left thyroid lobe with invasion of the esophagus *(arrowheads)* and left carotid sheath. c, left common carotid artery; *arrow* indicates left internal jugular vein. *B,* CT scan of the same patient at the level of the true vocal cords shows the superior extent of the invasive tumor as it insinuates itself between the thyroid cartilage and the strap musculature *(arrowheads).* Invasion of the left thyroid ala has occurred *(white arrow).* An enhancing pathologic lymph node *(black arrow)* can be seen on the left, with spiculated margins indicative of extracapsular spread of tumor.

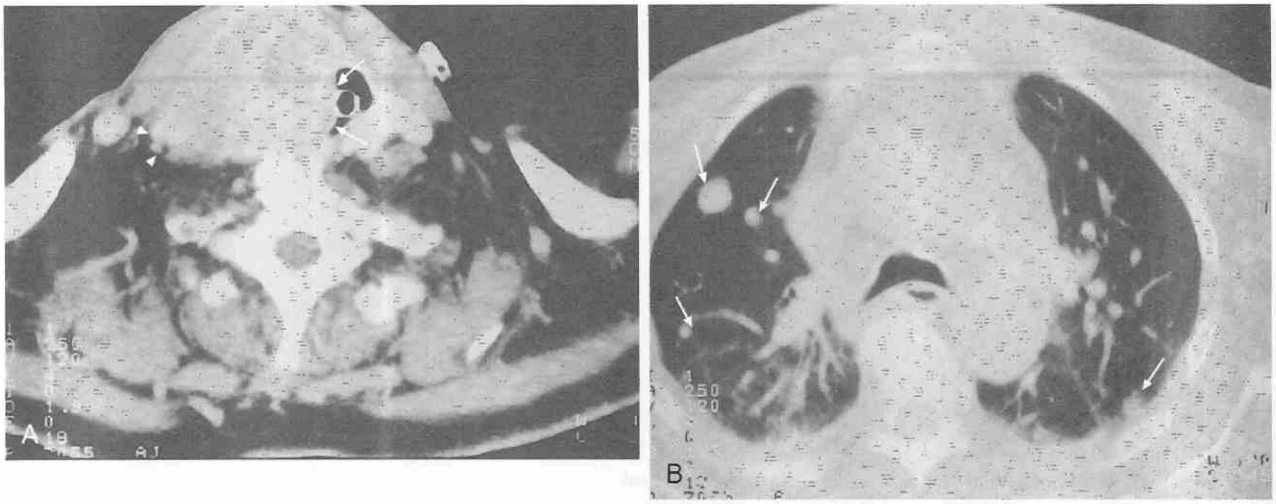

Figure 20–16. Anaplastic thyroid carcinoma. *A,* Axial postcontrast CT scan shows a large right thyroid lobe mass with tracheal invasion *(arrows).* The lesion marginates but does not surround the right common carotid artery *(arrowheads).* An endotracheal tube is in place. *B,* Axial CT scan through the thorax in the same patient shows multiple pulmonary metastases *(arrows).*

the thyroid at autopsy.[119] The two most common malignancies to metastasize to the thyroid are bronchogenic carcinoma and renal cell carcinoma. The appearance of metastatic lesions is nonspecific and may be multifocal. These lesions usually occur in the context of widespread metastases.

Other Malignant Neoplasms and Teratomas

Leukemic infiltration of the thyroid may mimic the imaging appearance of lymphoma. Squamous cell carcinoma, mucoepidermoid carcinoma, and columnar cell carcinoma of the thyroid gland have been reported sporadically. Other rare tumors of the thyroid, such as teratomas and sarcomas, typically present as solid masses. Teratomas are typically midline masses, usually contain fatty as well as soft tissue elements and fluid, frequently calcify, and may have well-developed teeth and osseous elements.[158, 159] As with other neoplasms, ultrasonography, CT, or MRI is helpful for identifying regional lymphadenopathy and local invasion in malignant varieties.

Benign Thyroid Neoplasms

More than 95% of thyroid nodules are benign.[87] Most of these are hyperplastic (colloid) nodules (Fig. 20–19), and the remainder are adenomas. Solitary hyperplastic nodules are common incidental findings at sonography. It is estimated that 40% or more of the general population have thyroid nodules that are detectable with modern high-resolution sonography.[112]

The number of nodules increases with age. Thyroid nodules can be solid, cystic, or mixed, appearing isoechoic

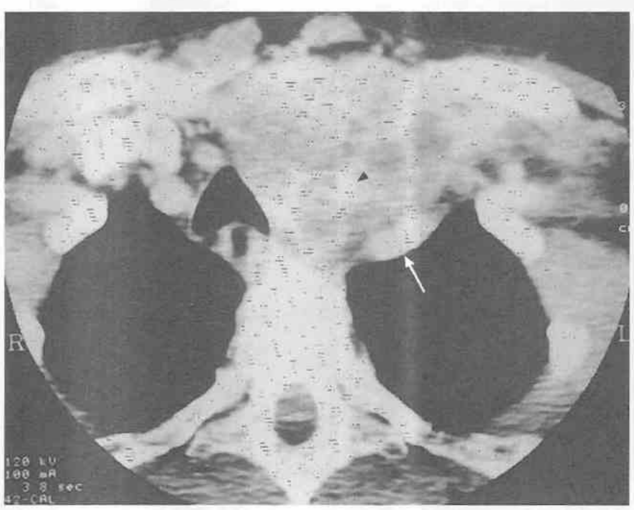

Figure 20–17. Anaplastic carcinoma. Axial postcontrast CT image demonstrates a lobulated, heterogeneously enhancing left thyroid lobe mass surrounding the left common carotid artery *(arrowhead)* and displacing the left subclavian artery *(arrow)* posteriorly. The mass extends into the upper mediastinum.

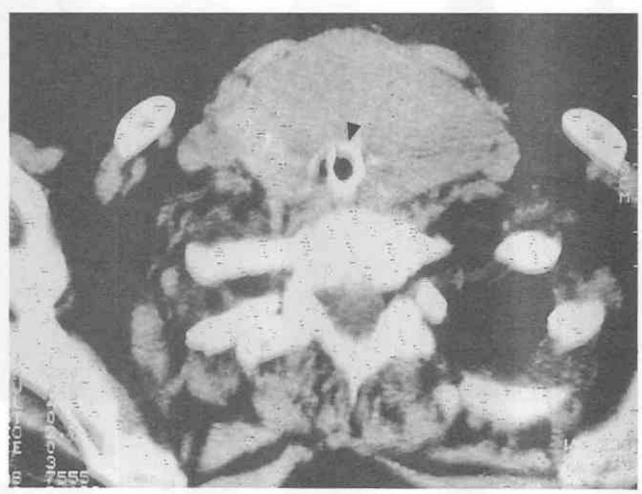

Figure 20–18. Thyroid lymphoma. Axial CT scan at the thoracic inlet shows marked thyroid enlargement involving both lobes and the isthmus. The gland is homogeneous in density, and no calcifications are present. The tracheal airway is compromised and an endotracheal tube *(arrowhead)* is in place.

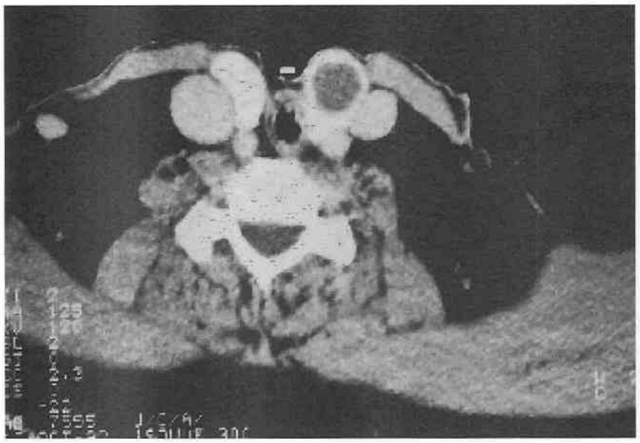

Figure 20–19. Axial postcontrast CT image shows a well-circumscribed, homogeneous, low-density mass within the left thyroid lobe. Despite its low density, the lesion is not cystic. The diagnosis was a hyperplastic thyroid nodule.

with a hypoechoic margin (or halo), hypoechoic, or hyperechoic. The presence of a hypoechoic halo makes the lesion 4 to 12 times more likely to be benign.[130] Cystic, degenerating nodules tend to have thicker walls than simple cysts and often contain solid components.

Thyroid Adenomas

Thyroid adenomas are seen more commonly in women. They are usually less than 3 cm in diameter, have well-delineated margins, and may become cystic, may involute, or may develop internal hemorrhage, necrosis, calcification, or fibrosis.[158] Most thyroid adenomas are hyperechoic or isoechoic at ultrasonography (see Fig. 20–3), whereas most carcinomas are hypoechoic, sometimes with poorly defined borders. Echogenicity alone cannot differentiate between benign and malignant nodules, however (see preceding discussion). Thyroid adenomas are typically of increased signal intensity on T2-weighted MR images but are often heterogeneous (Fig. 20–20).[30] They enhance on both CT and MR images and on CT scans appear solid or cystic when the adenoma has degenerated (see Fig. 20–4).

Thyroid adenomas may be *functioning* or *nonfunctioning*. Functioning thyroid adenomas may be autonomous or hypertrophic, and both types may result in hyperthyroidism with suppressed TSH levels but usually not until the adenoma is larger than 2.5 cm in diameter.[28] Plummer's disease defines a solitary or several autonomous hyperfunctioning (hot) nodules within an enlarged thyroid gland that are unresponsive to administration of exogenous thyroid hormone.

Both hypertrophic and autonomous functioning thyroid adenomas avidly take up ^{99m}Tc-pertechnetate and radioiodine (Fig. 20–21). A hypertrophic functioning adenoma appears cold after the administration of exogenous thyroid hormone, whereas an autonomous functioning nodule remains hot.[116] Other thyroid conditions that demonstrate avid uptake of ^{99m}Tc-pertechnetate include rare malignancies, ectopic thyroid tissue, some normal thyroid variants, and thyroiditis.[106] Radioiodine is more specific than ^{99m}Tc-pertechnetate in identifying a functioning thyroid adenoma.

When ^{99m}Tc-pertechnetate or ^{123}I is used, nonfunctioning thyroid adenomas appear photopenic compared with adjacent uninvolved thyroid tissue, which is identical to findings with papillary carcinoma (see Fig. 20–8). Numerous other benign entities may appear similarly cold, including degenerated follicular adenomas, adenomatous hemorrhage, cysts, nodular goiters, amyloid deposition, and inflammatory disorders.[116] Although most thyroid malignancies are cold, 75% to 85% of solitary cold nodules are benign.[133] Fine-needle aspiration biopsy may be used to characterize solitary cold thyroid nodules with high sensitivity and specificity.[40]

Thyroid Cysts

Thyroid cysts are also nonfunctioning cold thyroid masses. True thyroid cysts are rare, representing fewer than 1% of all thyroid masses. Most cystic masses are degenerating adenomatous nodules.[158] These are anechoic with thin walls and through-transmission on ultrasonography (Fig. 20–22), of low density on CT (Fig. 20–23) and of increased signal intensity on T2-weighted MR images, and they may show decreased or increased signal intensity on T1-weighted MR images. The increased signal intensity on T1-weighted images is related to the presence of hemorrhage, colloid, or increased protein content. Colloid cysts typically demonstrate such increased signal intensity on T1-weighted MR images.[116] CT density also increases with infection or spontaneous or traumatic internal hemorrhage. Any cystic thyroid mass with a solid component must be approached with suspicion for malignancy (especially papillary carcinoma), although a completely cystic nodule with uniformly thin walls is almost always benign.

Goiter and Multinodular Goiter

The enlarged thyroid, termed a *goiter*, may be hypofunctioning, hyperfunctioning, or normally functioning. The enlarged thyroid may present as a neck mass with or without tracheal or esophageal compression. Thyroid enlargement is best determined by measuring the diameter of the isthmus or the anterior-posterior diameter of the thyroid lobes. The normal isthmus is less than 6 mm in thickness, and each thyroid lobe measures less than 20 to 25 mm in the anterior-posterior dimension. The association of thyroid carcinoma with goiter is less than 3%.[83]

With scintigraphy, multinodular goiter most often demonstrates heterogeneous distribution of the radiopharmaceutical, with foci of increased and decreased activity (Fig. 20–24). Ultrasonography well demonstrates individual nodules within a goiter (Fig. 20–25). These nodules may be palpable or nonpalpable, regardless of whether the patient has clinically evident thyroid disease. Doppler imaging often reveals hypervascularity throughout the goiter. Pathologic characterization of each nodule within a goiter by imaging is unreliable unless typical malignant characteristics are demonstrated (see preceding discussion) or unless the nodule is hot and thus benign on nuclear medicine scintigraphy. The rare occurrence of papillary carcinoma representing one or more of the thyroid nodules is a consideration, although it is unlikely. Multiple cold nodules within a goiter may obviate the need for biopsy; however, an enlarging or dominant mass should prompt histologic evaluation.[116,125]

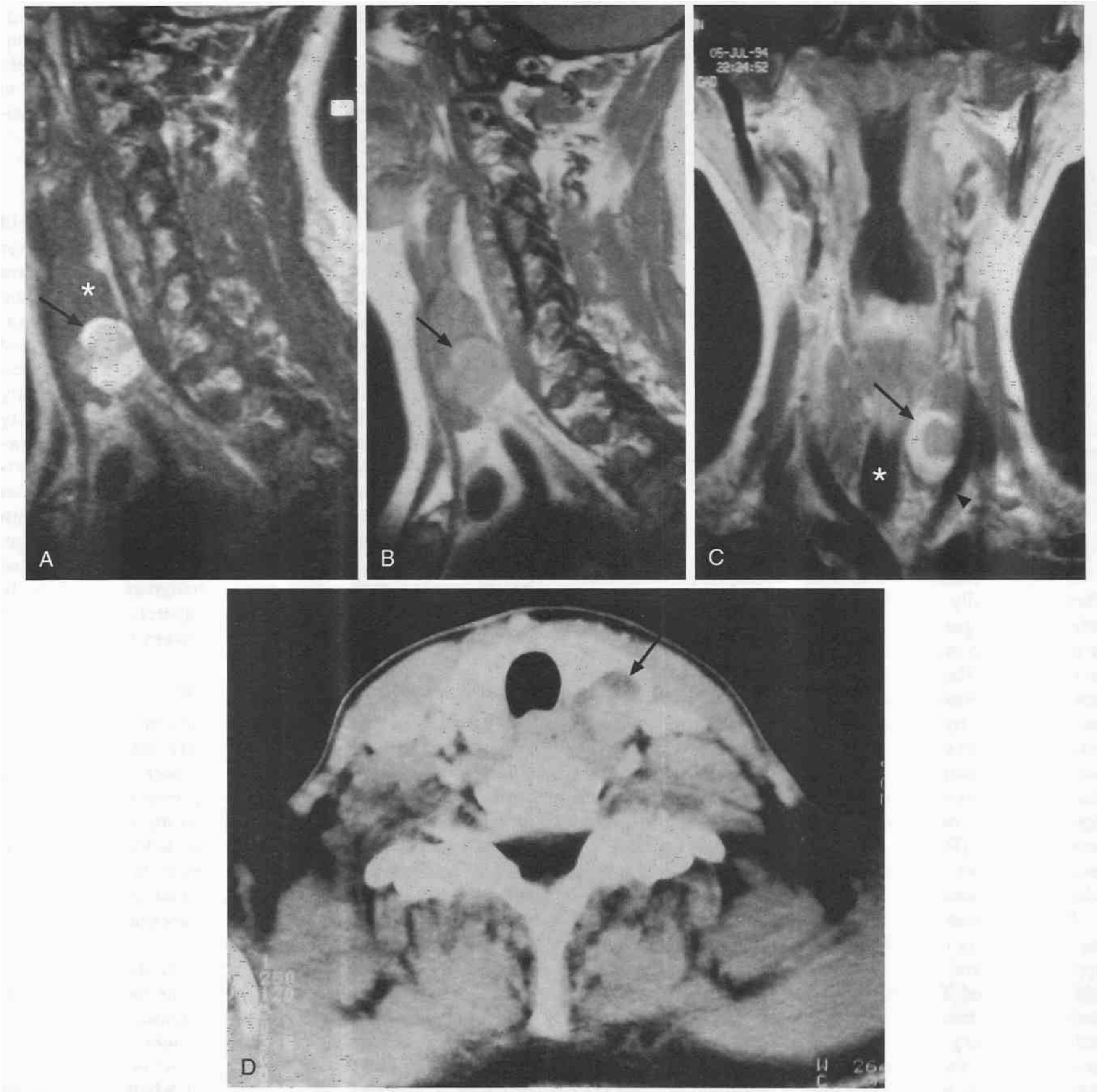

Figure 20–20. Follicular adenoma. *A,* Sagittal T2-weighted MR image demonstrates a mixed-signal-intensity ovoid mass *(arrow)* within the lower pole of the left thyroid gland. The lesion is peripherally hyperintense with a central nodule of intermediate signal. The normal thyroid parenchyma *(asterisk)* is homogeneously hypointense. *B,* Sagittal T1-weighted MR image shows the mass *(arrow)* to be of intermediate signal intensity but distinguishable from normal parenchyma. *C,* Coronal T1-weighted postgadolinium MR image shows enhancement of the peripheral component of the mass *(arrow)* with no appreciable enhancement of the central nodule. Note the relationship of the mass to the trachea *(asterisk)* and left common carotid artery *(arrowhead)*. *D,* Axial postcontrast CT scan shows the well-circumscribed mass *(arrow)* in the posterior left thyroid lobe, with mixed attenuation. The imaging features of the nodule are nonspecific.

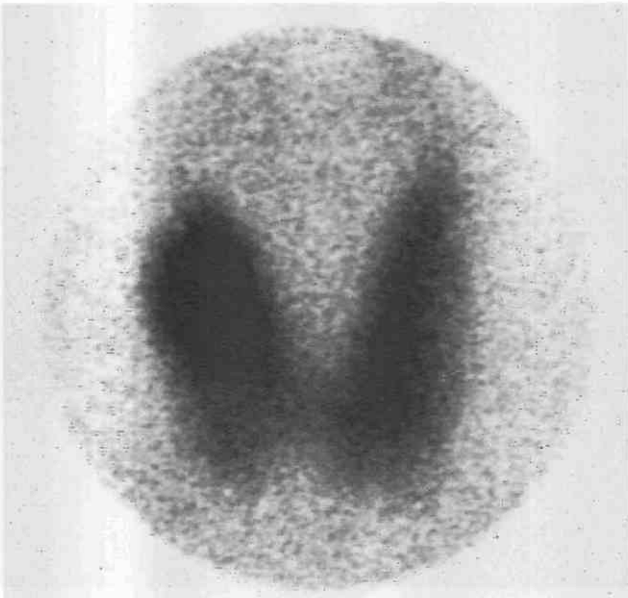

Figure 20–21. With technetium 99m–pertechnetate scintigraphy, an anterior view identifies a solitary hyperfunctioning nodule in the upper pole of the right thyroid lobe. Extranodular thyroid activity is not suppressed, consistent with a diagnosis of euthyroidism.

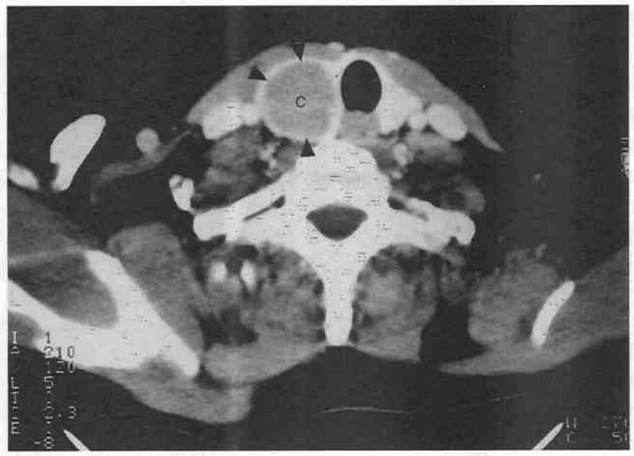

Figure 20–23. Axial postcontrast CT image demonstrates a well-circumscribed, low-density colloid cyst (C) within the right lobe of the thyroid. The nongoitrous thyroid parenchyma at the periphery of the lesion enhances normally *(arrowheads).*

Ultrasonographic and CT imaging typically demonstrate the goitrous thyroid as heterogeneous and display nodular enlargement of one or both lobes with cysts and often calcification (Fig. 20–26). Hemorrhage may be seen in 60% of cases.[95] On an MR image, multinodular goiter is typically heterogeneous; signal intensity is isointense to normal thyroid or increased on T1-weighted images and mixed on T2-weighted images.[30, 95] Contrast enhancement is typically diffuse and mottled on CT and MRI scans (Fig. 20–27). In some instances, all imaging modalities demonstrate a uniform parenchymal appearance in an enlarged thyroid gland.

Ultrasonography is not an imaging option for evaluating the possibility of a substernal goiter because the sternum prevents mediastinal interrogation. CT and MRI, however, demonstrate a substernal goiter well, and both may reveal cervical thyroid tissue contiguous with the mediastinal mass (Fig. 20–28). If a radionuclide scan is contemplated, iodinated contrast media should be withheld during CT scanning because these agents may precipitate thyroid storm in some thyrotoxic patients. Because of the presence of interfering mediastinal blood pool activity with ^{99m}Tc-pertechnetate, ^{123}I should be used to assess mediastinal masses.

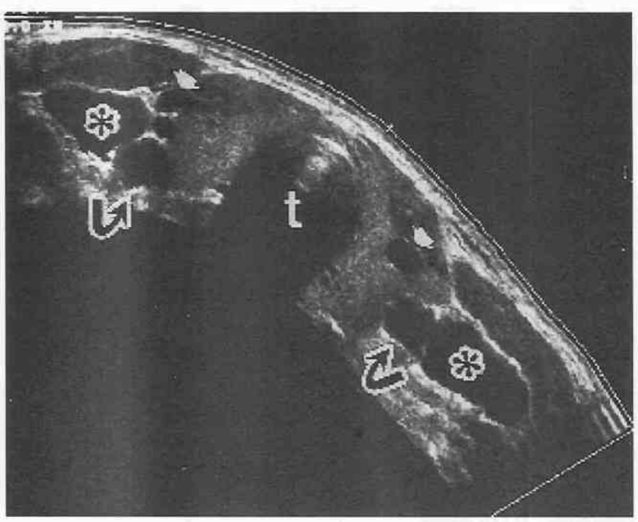

Figure 20–22. Transverse sonogram of the thyroid performed with an extended field of view (Siescape [Siemens]) shows the entire thyroid and adjacent structures. The right and left lobes are separated by the trachea (t). The isthmus lies superficial to the trachea. Simple cysts *(arrows)* are seen in the right and left lobes, which are otherwise normal. *Curved arrows* indicate common carotid arteries; *asterisks* show internal jugular veins.

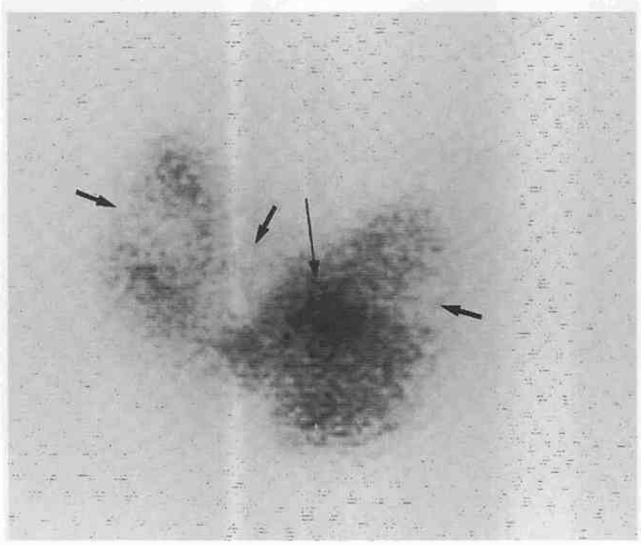

Figure 20–24. An asymmetrical thyroid gland with multiple foci of increased *(long-stemmed arrow)* and decreased *(arrows)* uptake of technetium 99m–pertechnetate is typical of multinodular goiter, but it may also be seen in Hashimoto's thyroiditis.

Hyperthyroidism

Hyperthyroidism may be caused by Graves' disease (diffuse toxic goiter), toxic nodular goiter (Plummer's disease), autonomous toxic adenomas, and, rarely, ectopic thyroid tissue, thyroid inflammation, or bulky differentiated carcinoma. At scintigraphy, uptake of the radiopharmaceutical within the gland or each functioning nodule is increased, and background and salivary gland activity are diminished. In the case of a toxic nodule, activity within the remainder of the gland is suppressed (Fig. 20–29).

Women are 10 times more likely than men to have hyperthyroidism. The diagnosis is made by the detection of elevated circulating levels of thyroid hormones, accompanied by suppressed TSH levels in all cases other than those caused by a TSH-producing pituitary adenoma. Elevated or high-normal radioiodine uptake confirms that the thyroid is hyperfunctional. Suppressed thyroid uptake generally indicates that the hyperthyroidism is caused by exogenous administration of thyroid hormone or that it is the result of thyroid parenchymal destruction due to subacute thyroiditis or postpartum thyroiditis; a rare alternative is struma ovarii (a thyroxine-producing ovarian teratoma).[155]

Patients with elevated serum thyroid hormone levels and increased thyroidal radioactive iodine uptake at 24 hours typically have Graves' disease or toxic nodular goiter. Patients with elevated thyroid function test findings and normal radioactive iodine uptake typically have Plummer's disease or a Graves' disease variant with rapid iodine turnover.

Percutaneous ethanol ablation of autonomous thyroid nodules has been successful in treating hyperthyroidism.[19, 69, 101]

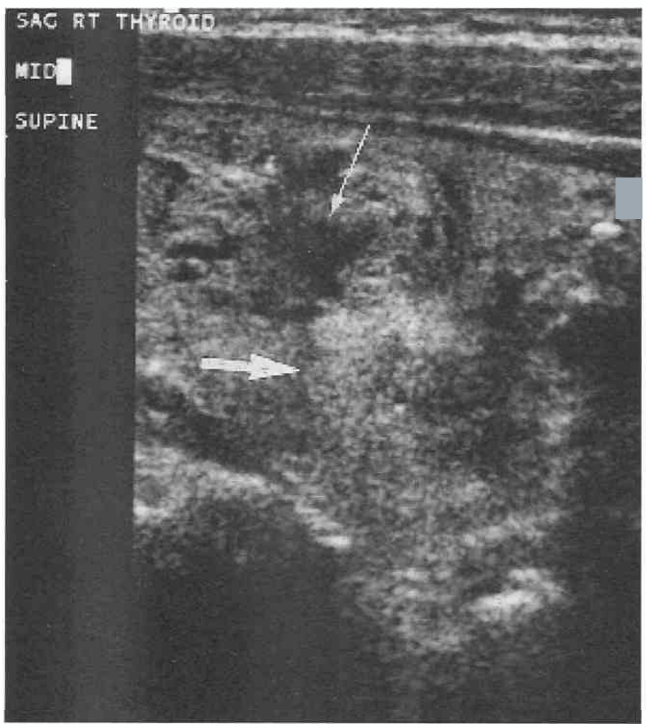

Figure 20–25. Multinodular goiter. Sagittal sonographic image of the right lobe of the thyroid reveals a heterogeneous, enlarged thyroid with predominantly hyperechoic *(large arrow)* but also hypoechoic *(small arrow)* nodules.

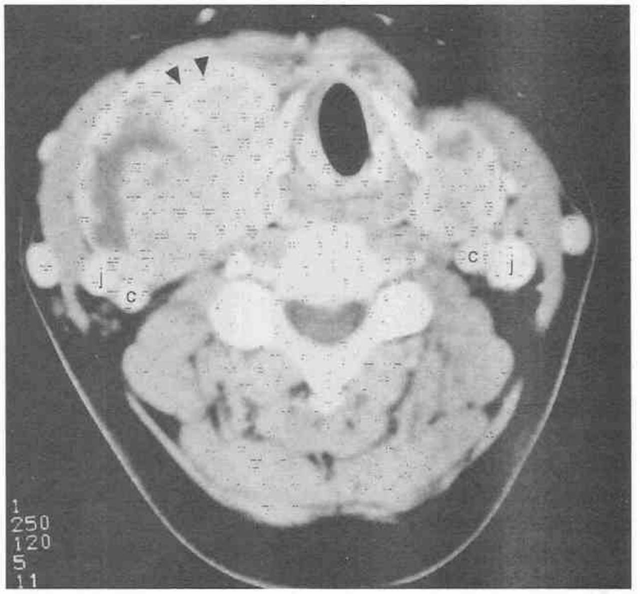

Figure 20–26. Multinodular goiter. CT scan at the level of the cricoid cartilage shows bilaterally enlarged, heterogeneous thyroid lobes. Several foci of calcification *(arrowheads)* are seen within the larger right lobe. The common carotid arteries (c) and internal jugular veins (j) are displaced posterolaterally.

Graves' Disease

Graves' disease is the most common cause of hyperthyroidism. It occurs most often in young women, is related to abnormal production of a thyroid stimulating immunoglobulin, and may be familial.

On CT or MR images, patients with Graves' disease demonstrate a diffusely enlarged, contrast-enhancing thyroid gland.[158] A hypertrophied pyramidal lobe is a common accompaniment.[158] Sonographically, the gland appears diffusely hypoechoic and markedly hypervascular by Doppler flow imaging ("thyroid inferno").[107] Nuclear medicine scintigraphy reveals markedly elevated iodine uptake by a diffusely enlarged thyroid gland (Fig. 20–30). Occasionally, a patient with Graves' disease has an enlarged thyroid gland with one or more nodules. Although a solitary cold solid nodule in a patient with Graves' disease may represent an area of nonfunctioning, TSH-dependent, hyperplastic tissue (Marine-Lenhart disease),[116] the possibility of coexistent malignancy must be entertained. Fine-needle aspiration biopsy is usually recommended and is safe despite the hypervascularity of the gland. Malignant thyroid tumors are seen only rarely in patients with Graves' disease (~0.5% of reported cases).[15, 25]

Orbital findings in patients with Graves' disease include exophthalmos, increased extraocular muscle thickness, and excessive retrobulbar fat.

Hypothyroidism

Hypothyroidism is diagnosed more often in women than in men, and the condition is found in as many as 3% to 5% of people older than age 65.[159] In the Western world, autoimmune Hashimoto's thyroiditis is the most common cause of hypothyroidism; worldwide, however, iodine deficiency is the leading cause of endemic goiter. Other

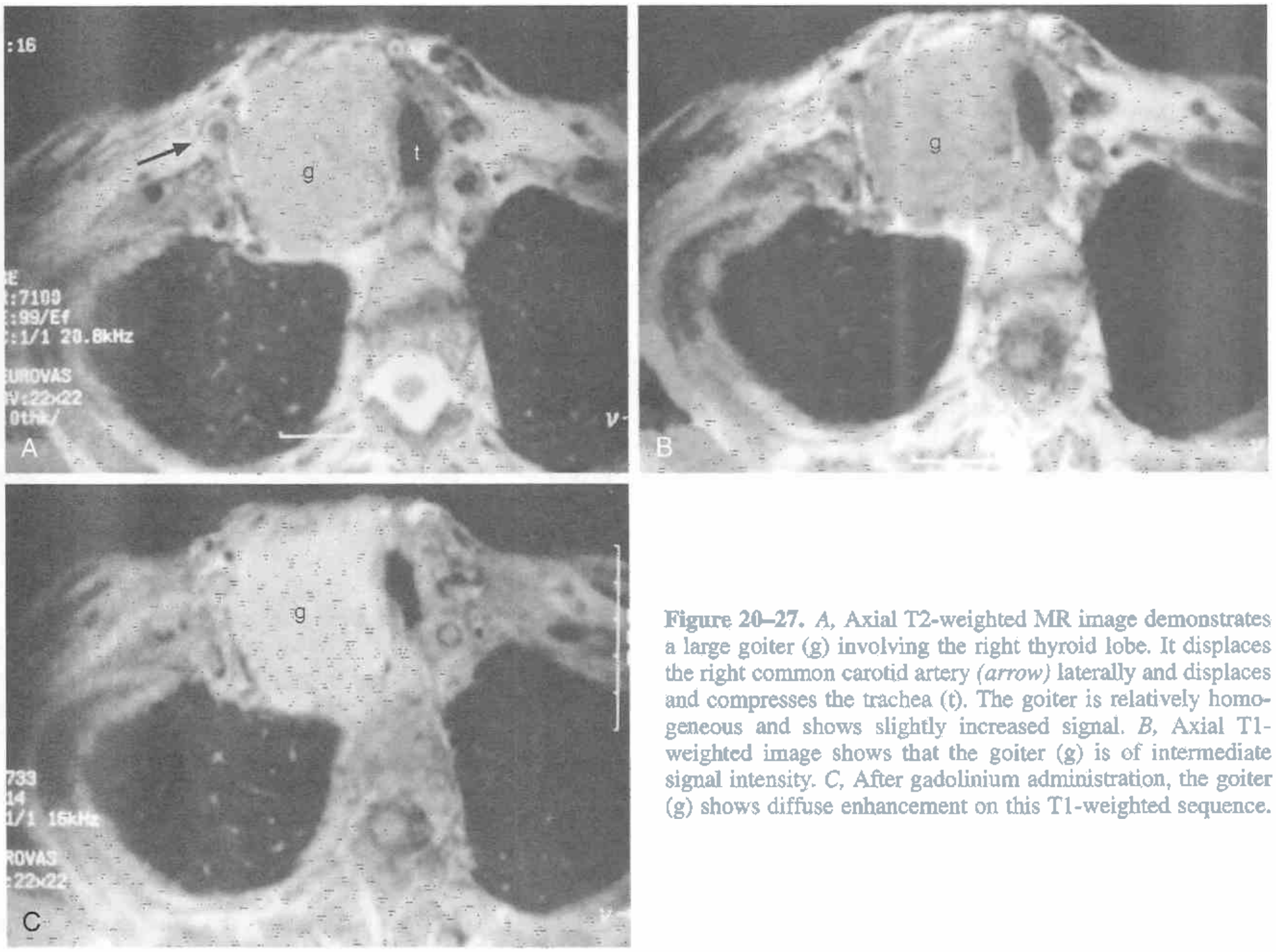

Figure 20–27. *A,* Axial T2-weighted MR image demonstrates a large goiter (g) involving the right thyroid lobe. It displaces the right common carotid artery *(arrow)* laterally and displaces and compresses the trachea (t). The goiter is relatively homogeneous and shows slightly increased signal. *B,* Axial T1-weighted image shows that the goiter (g) is of intermediate signal intensity. *C,* After gadolinium administration, the goiter (g) shows diffuse enhancement on this T1-weighted sequence.

causes include previous thyroidectomy, previous radiation (^{131}I or external beam), congenital organification defects, subacute or chronic thyroiditis, dietary or environmental goitrogens, antithyroid medications such as propylthiouracil (PTU) and methimazole, hypothalamic or pituitary disease, and exogenous iodine (medications, foods, contrast agents). Radioiodine uptake is low or low-normal in patients with hypothyroidism except when caused by iodine deficiency.

Congenital hypothyroidism may be secondary to thyroid aplasia, hypoplasia or hemiaplasia, thyroid ectopia, abnormal thyroxine production, pituitary or hypothalamic disorders, or autoimmune disease. In the infant with congenital hypothyroidism, a ^{99m}Tc-pertechnetate scan is often used to detect the amount of normally located thyroid gland and any ectopic functioning tissue. Scintigraphy and other imaging modalities are usually not necessary in the remainder of patients with hypothyroidism.

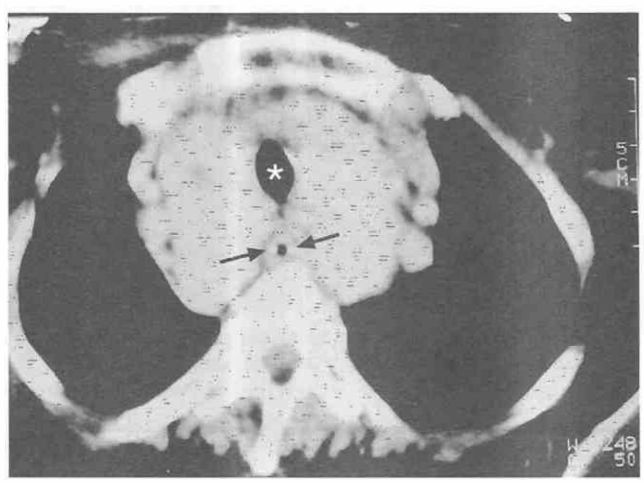

Figure 20–28. Substernal goiter. CT scan through the upper thorax shows an enlarged thyroid gland posterior to the sternum (S). Both lobes are symmetrically enlarged, with slight heterogeneity of the parenchyma. The trachea *(asterisk)* is slightly compressed in the midline, and the great vessels are displaced laterally. Neither tracheal nor esophageal *(arrows)* invasion has occurred.

Thyroid Inflammatory Disorders

Bacterial Thyroiditis

Bacterial thyroiditis may be spontaneous, may arise from hematologic seeding, may occur in an immune-compromised host, may result from a cervical puncture wound, may develop because of an infected third or fourth branchial cleft cyst (usually left-sided),[2, 44] or may arise from an aerodigestive tract or thyroglossal duct fistula.[53] It typically follows a fulminant course. MRI or CT scans of acute bacterial thyroiditis are sometimes used to evaluate airway compromise, associated lymphadenopathy, carotid sheath inflammation (including jugular vein thrombosis), and associated congenital cysts) and to identify fistulous tracts and abscesses.[16]

De Quervain's Thyroiditis

De Quervain's thyroiditis (or subacute granulomatous thyroiditis) is a subacute condition that usually presents with a diffusely tender thyroid in middle-aged women following a viral respiratory tract infection. Coxsackievirus, adenovirus, echovirus (enteric cytopathogenic human orphan virus), influenza virus, and mumps virus have been implicated as causative agents.[67, 149] Approximately 50% of patients present with mild, transient, destruction-induced hyperthyroidism followed by mild hypothyroidism, eventually returning to euthyroidism over a period of 6 to 9 months.[106, 119]

Sonographically, the thyroid gland appears hypoechoic.[34] Uptake of radioiodine (or ^{99m}Tc-pertechnetate) is heterogeneous and initially low (0% to 5%); it later becomes elevated before returning to normal. On ultrasonography, MRI, CT, or nuclear scintigraphy, the end-stage thyroid gland may be atrophic, although this is rare. More than 90% of patients with subacute thyroiditis have a normal thyroid gland with normal function and normal appearance on any imaging test at long-term follow-up.

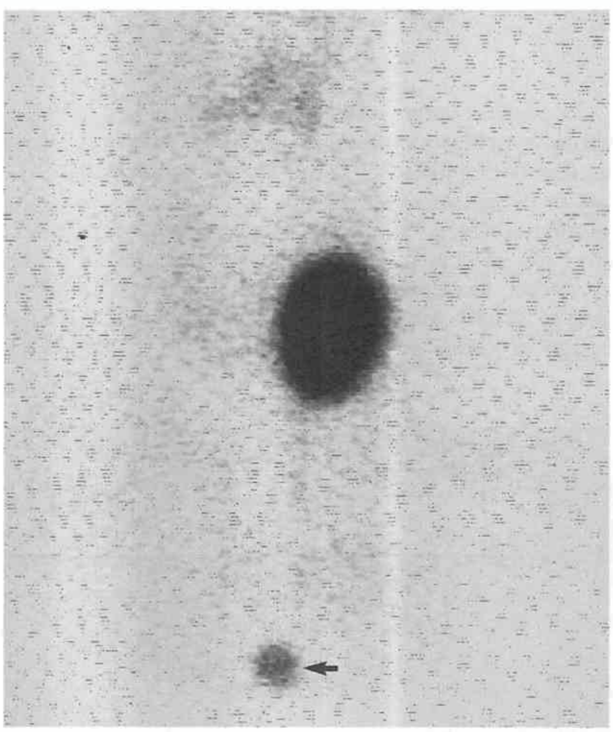

Figure 20–29. With technetium 99m–pertechnetate, a solitary large focus of increased activity is identified in the left neck. The lack of contralateral thyroid activity and the virtual absence of background activity are consistent with a diagnosis of solitary toxic adenoma. The suprasternal notch is identified with a cobalt marker *(arrow)*.

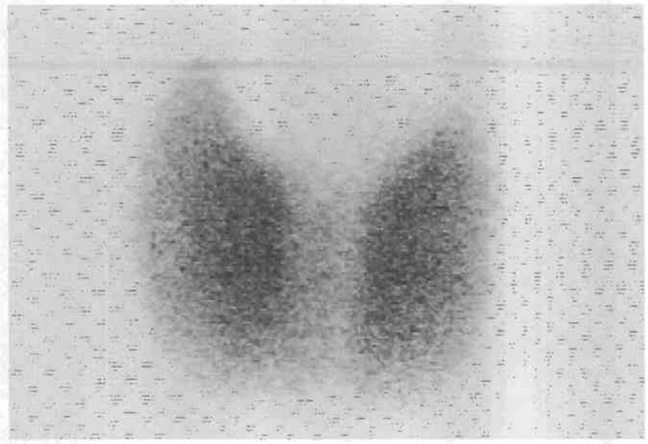

Figure 20–30. Diffusely increased radionuclide uptake in an enlarged gland is typical of Graves' disease. Background activity is absent and the isthmus is thickened.

Hashimoto's Thyroiditis

Hashimoto's thyroiditis is a chronic lymphocytic infiltration of the thyroid. It is the most common of the thyroiditides, it primarily occurs in women between ages 40 and 60 years, and it is the most common thyroiditis in children.[158] The disease is caused by an autoimmune response to thyroglobulin, colloid, or other thyroid antigens. Other autoimmune diseases may be associated, such as adrenal insufficiency, pernicious anemia, and systemic lupus erythematosus. More than 50% of patients with Hashimoto's thyroiditis are hypothyroid.[158] There is also a predisposition for development of non-Hodgkin's lymphoma.[141]

The radionuclide scan may be normal, may reveal a homogeneously enlarged gland, or may demonstrate diffuse heterogeneous activity; in some patients, a solitary region of photopenia may be seen. Radioiodine uptake may be normal, low, or high.[25] The affected gland frequently accumulates ^{18}FDG or ^{67}Ga.[154]

At ultrasonography, the thyroid gland is enlarged and diffusely hypoechoic or multinodular (Fig. 20–31).[156] Calcification may be seen on CT or ultrasonography (Fig. 20–32). On T2-weighted MR images, Hashimoto's thyroiditis typically demonstrates increased signal intensity, sometimes with linear, low-signal-intensity strands, possibly representing fibrosis.[30, 104]

Riedel's Thyroiditis

Riedel's thyroiditis, also termed struma thyroiditis, is a rare chronic inflammatory condition of the thyroid gland. The gland enlarges and may demonstrate regional mass effect with hoarseness and dysphagia caused by the extensive associated neck fibrosis. The condition is more com-

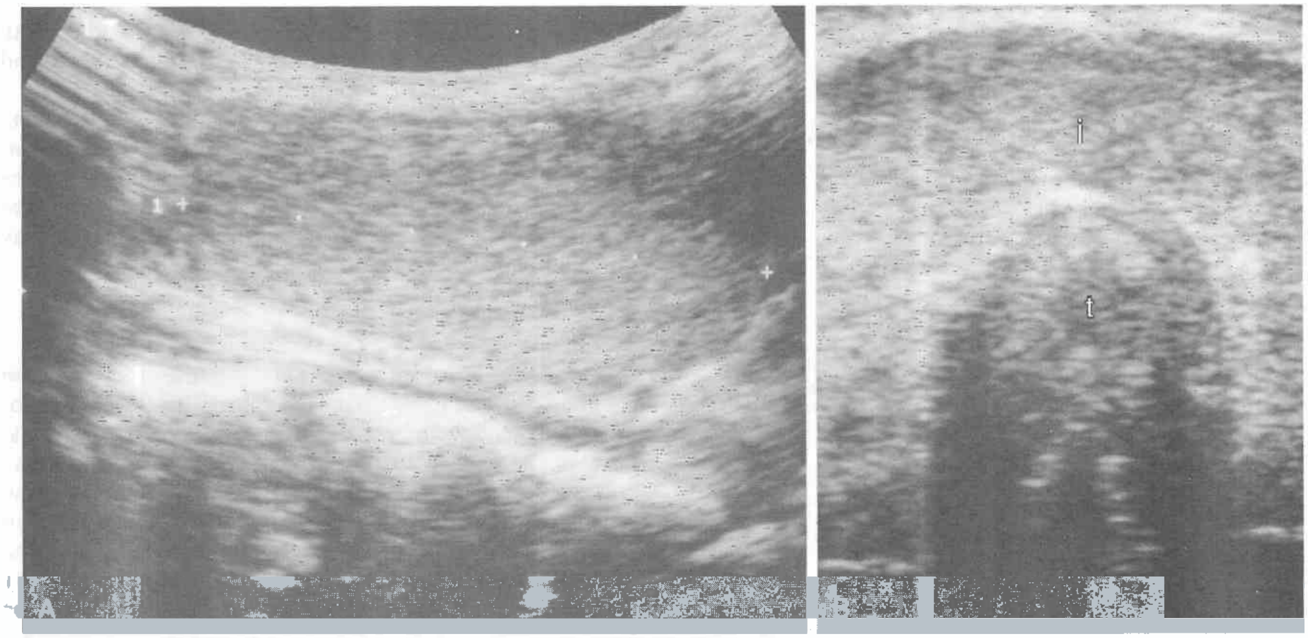

Figure 20–31. *A*, Sagittal ultrasound image of the right thyroid lobe shows an enlarged lobe with homogeneous, slightly hypoechoic echotexture. No focal nodules, cysts, or calcifications are noted in this patient with Hashimoto's thyroiditis. *B*, Transverse ultrasound image shows homogeneous, hypoechoic parenchyma with enlargement of the thyroid isthmus (i) as well as both lobes. The centrally located trachea (t) demonstrates artifact posterior to it generated by internal air.

mon in women. It may affect one or both thyroid lobes and typically causes hypothyroidism.

At imaging, the thyroid appears enlarged and homogeneously hypoechoic on ultrasonography and hypodense to isodense on CT.[34, 104] Riedel's thyroiditis may mimic malignancy with local infiltration, and it often calls for surgery for definitive diagnosis and relief of compressive symptoms.

Diminished signal intensity on T1-weighted and T2-weighted MR images is thought to be caused by chronic fibrosis.[104] Riedel's thyroiditis may be associated with other fibrotic conditions such as retroperitoneal fibrosis, mediastinal fibrosis, sclerosing cholangitis, and orbital pseudotumor.[70]

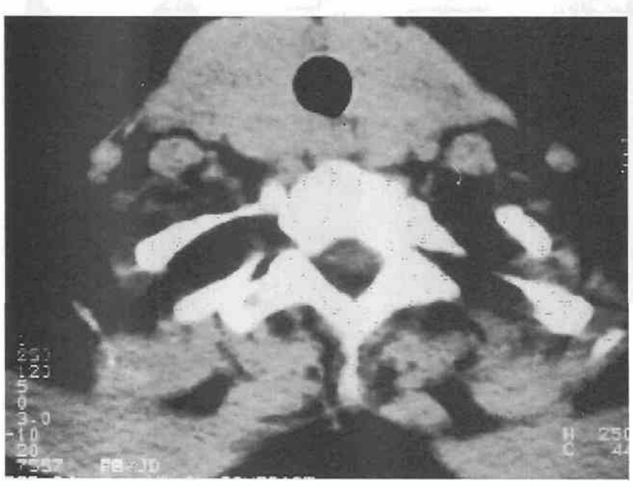

Figure 20–32. Unenhanced CT scan shows a diffusely enlarged, homogeneous thyroid gland in a patient with Hashimoto's thyroiditis. No focal masses or calcifications are noted.

Miscellaneous Thyroid Conditions

Other inflammatory but rare thyroid conditions include tuberculosis, sarcoidosis, fungal diseases, and opportunistic organisms, especially in patients with acquired immunodeficiency syndrome (AIDS). Amyloidosis and hemochromatosis may replace thyroid parenchyma and may cause decreased signal intensity on T2-weighted MR images.[158] Radiation received from external beam or radioactive iodine therapy may lead to fibrosis and atrophy of the thyroid gland.

Developmental Thyroid Anomalies

Lingual Thyroid

Lingual thyroid results from arrest of migration of the thyroid anlage at the foramen cecum in the base of the tongue to its normal location in the anterior neck. The condition occurs in one in 3000 patients with thyroid disease, and it is the most common form of functioning ectopic thyroid tissue (90% of cases).[119] Arrest of migration may be complete or incomplete, typically occurring in the midline of the tongue base between the circumvallate papillae and the epiglottis. Rare cases may involve the entire tongue. Thyroid tissue in its normal location in the neck is absent in 70% to 80% of cases,[38, 119] and most of these patients are hypothyroid.

Ectopic thyroid tissue is more common in women than men (7:1) and may present as an enlarging mass at puberty or during pregnancy secondary to hormonal changes.[158] Malignancy in lingual thyroid tissue occurs in 2.8% of cases.[85]

Radionuclide ^{99m}Tc-pertechnetate, ^{123}I, or ^{131}I scintigraphy demonstrates avid tracer uptake within the midline of

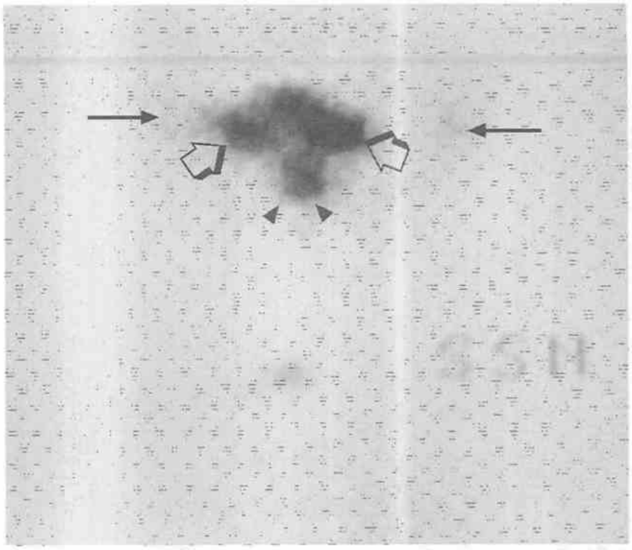

Figure 20–33. Lingual thyroid. Frontal projection of a technetium 99m–pertechnetate thyroid scan shows prominent uptake of radiotracer in the base of the tongue *(arrowheads)*. Tracer uptake is absent where it would be expected in the thyroid tissue in the lower neck. Normal uptake is noted in the parotid *(arrows)* and submandibular *(open arrows)* glands.

the tongue base if a lingual thyroid is present (Fig. 20–33). If surgery is contemplated, radionuclide evaluation with ^{123}I or ^{99m}Tc-pertechnetate is recommended to detect additional functioning thyroid tissue in the neck. Unenhanced CT shows a hyperdense mass in the base of the tongue. With iodinated contrast material, the lingual thyroid densely and homogeneously enhances (Fig. 20–34).

MRI shows lingual thyroid tissue to be isointense to normal thyroid tissue on T1-weighted images and hyperintense on T2-weighted images.[38] The mass enhances strongly after administration of gadolinium-based contrast material. Additional thyroid tissue lower in the neck may be identified with either CT or MRI.

Thyroglossal Duct Cyst

The thyroglossal duct cyst (TDC) is the most common congenital cystic neck mass, accounting for 70% of nonodontogenic congenital neck abnormalities. The thyroglossal duct is the embryologic tract along which the thyroid anlage courses as it descends from the foramen cecum in the tongue base to its normal location in the low anterior neck. TDCs may occur anywhere along the course of the duct but typically occur about the hyoid bone. The majority of cysts (65%) are located within the thyrohyoid membrane and are infrahyoid in location.[3] Fifteen percent of TDCs are at the level of the hyoid, and 20% are suprahyoid.[3] Suprahyoid TDCs are more likely to be at the midline, imbedded between the anterior bellies of the digastric muscles. Infrahyoid lesions are paramedian and tend to be located within the strap musculature. Two percent are completely intralingual.

Most TDCs present in young adulthood, with 50% occurring before age 10 years and 70% before age 30. Rarely, they may present in older adults. There is no known sex

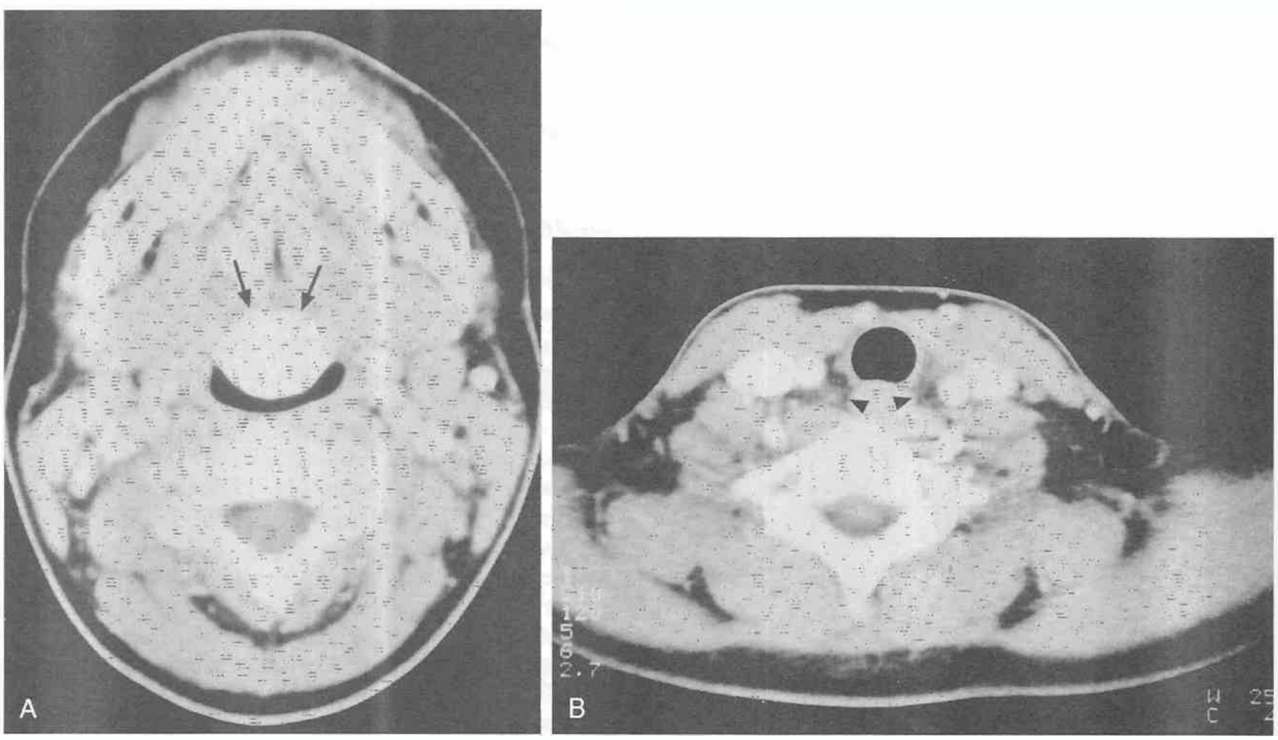

Figure 20–34. *A,* Enhanced CT image at the level of the oropharynx shows a well-circumscribed, homogeneously enhancing mass *(arrows)* in the tongue base, consistent with a diagnosis of ectopic lingual thyroid tissue. *B,* CT scan in the same patient at the expected level of the thyroid gland demonstrates no paratracheal thyroid tissue *(arrowheads)*.

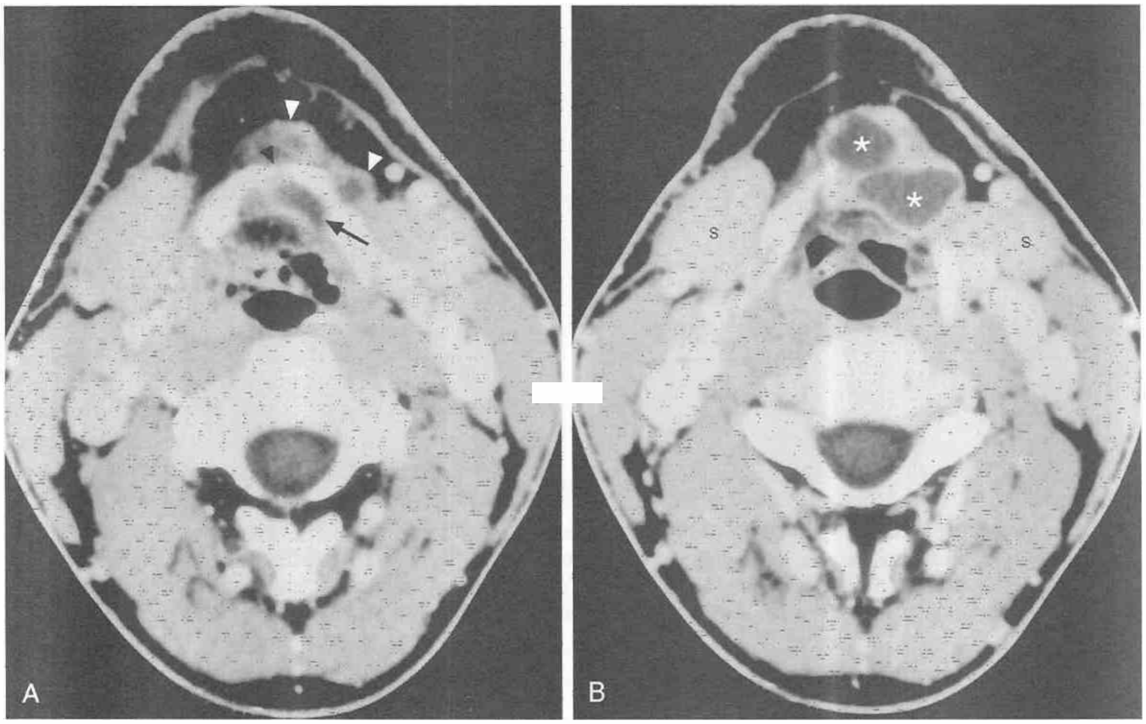

Figure 20–35. Thyroglossal duct cyst. *A,* Axial postcontrast CT scan at the level of the hyoid bone shows a multilobulated low-density mass traversing the hyoid bone. A component of the lesion is deep to the hyoid within the pre-epiglottic fat *(arrow)*, and the remainder is seen anterior to the hyoid *(white arrowheads)*. The bone defect can be seen within the central aspect of the hyoid bone *(black arrowhead)*. Note also the submandibular glands (s). *B,* Axial CT scan in the same patient 5 mm caudal to *A* shows two low-attenuation components of the mass *(asterisks)* and their relationship to the hyoid bone. Submandibular glands are normal.

predilection. Coexisting carcinoma, usually of the papillary type, occurs in 1% of patients with TDC.[3, 45, 47] Follicular carcinoma, adenocarcinoma, and squamous cell carcinoma have been reported. Ectopic thyroid tissue is present within the wall of TDC in fewer than 5% of cases.[3, 97]

CT demonstrates a unilocular or multilocular low-density mass, usually 2 to 4 cm in diameter, present anywhere from the tongue base to the superior margin of the thyroid gland. When located within the hyoid bone, a defect in the bone itself may be apparent on CT (Fig. 20–35). TDC contents may be isodense to hyperdense because of increased protein content or hemorrhage. The capsule of the lesion may uncommonly enhance unless the patient has a history of trauma or current or previous infection. Prior or active superinfection is seen in approximately 60% of patients. Enhancement of the surrounding musculature and obscuration of fascial planes indicate TDC superinfection and overlying cellulitis (Fig. 20–36). Nodules of enhancing tissue within the cyst raise the possibility of concurrent malignancy but may represent only ectopic thyroid tissue.

MRI signal characteristics vary, depending on the protein content of the fluid within the cyst. TDCs most commonly show low to intermediate signal intensity on T1-weighted images, increased signal intensity when proteinaceous, and high signal on T2-weighted images (Fig. 20–37).

With both CT and MRI, enhancing ectopic thyroid tissue may be seen along the course of the thyroglossal duct. Scintigraphy is more sensitive in the detection of these ectopic thyroid rests. Ultrasonography of a TDC displays an anechoic, cystic mass with through-transmission. Internal echoes within the cyst may be caused by increased protein content or hemorrhage. Both ultrasonographic and nuclear medicine imaging can confirm the presence of a normal thyroid gland before TDC resection.[65]

Parathyroid Glands

Typically, four parathyroid glands are present (two superiorly and two inferiorly) along the posterior margins of

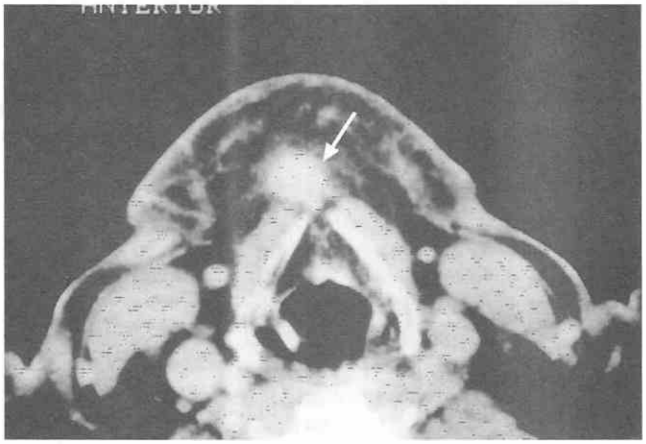

Figure 20–36. Infected thyroglossal duct cyst. Axial postcontrast CT scan at the level of the upper thyroid cartilage demonstrates an enhancing, slightly heterogeneous soft tissue mass *(arrow)* within the anterior cervical space. Stranding within the fat surrounding the lesion suggests infection.

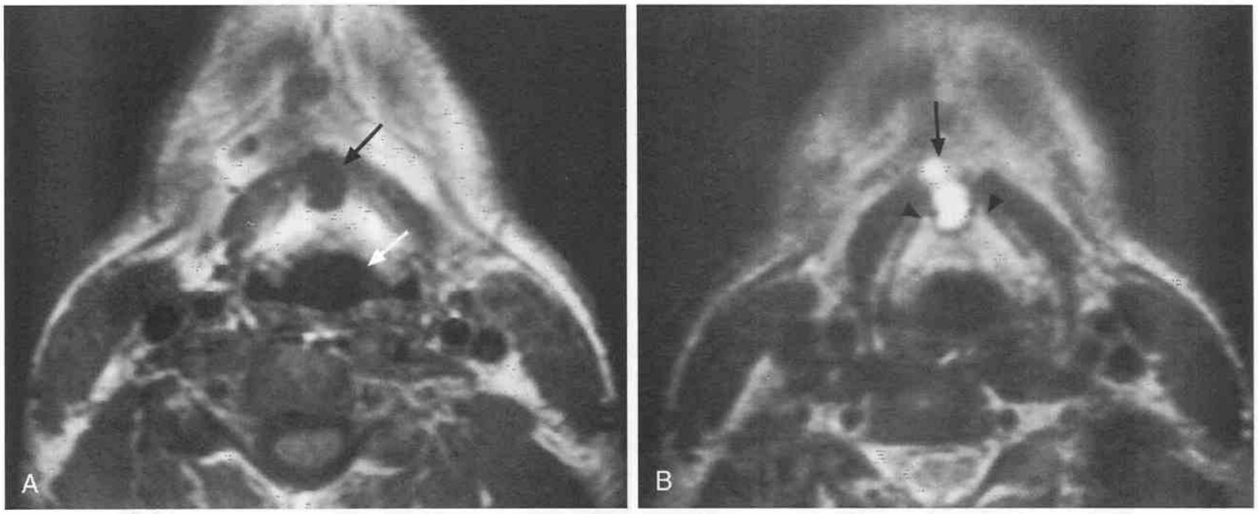

Figure 20–37. Thyroglossal duct cyst. *A,* Axial T1-weighted MR image just inferior to the hyoid bone shows a rounded, low-signal-intensity mass *(black arrow)* in the anterior pre-epiglottic fat at the superior margin of the thyroid cartilage. The normal epiglottis *(white arrow)* is demonstrated. *B,* Axial T2-weighted image slightly inferior to *A* shows the lesion *(arrow)* extending anterior to the thyroid cartilage *(arrowheads)* between the strap muscles. The lesion shows increased signal intensity on the T2-weighted sequence.

both lobes of the thyroid; however, the location of the inferior parathyroid glands may vary. In approximately 20% of patients, they are located anywhere from the carotid bifurcations to the upper mediastinum as well as within the thyroid or behind the trachea or esophagus.[28, 35, 92, 106] Ten percent to 25% of patients have more than four parathyroid glands, with the supernumerary glands most often found in the upper mediastinum.[67, 68]

Parathyroid pathology may be detected by radionuclide scintigraphy, ultrasonography, CT, MRI, angiography, and venous sampling. The success of all of these techniques, except venous sampling, depends, to a varying degree, on the size of the abnormal gland.

The radiopharmaceutical of choice for imaging parathyroid enlargement is ^{99m}Tc-MIBI, employing a double-phase protocol.[36, 62, 77, 84] ^{99m}Tc-MIBI accumulates in both parathyroid and thyroid glands but is retained longer in pathologic parathyroid tissue. Imaging 2 to 3 hours after ^{99m}Tc-MIBI injection allows physiologic washout of thyroid radioactivity but persistent accumulation within the abnormal parathyroid tissue (Fig. 20–38).[140] Increased mitochondrial content in parathyroid adenomas is believed to be responsible for the observed MIBI concentration.[99] Because of the high sensitivity of MIBI scintigraphy (80% to 90%) in detecting parathyroid adenomas,[99, 100, 140] ^{99m}Tc/^{201}Tl subtraction imaging is used only rarely in current clinical practice.[76] Oblique planar views and single photon emission computed tomography (SPECT) have been reported to improve sensitivity and localization of abnormal parathyroid glands.[86, 93, 105, 118] Subtraction of thyroid activity with ^{123}I may be used with MIBI and can be useful when concomitant thyroid disease is suspected.[9]

Ultrasonographic evaluation of the parathyroid gland employs a 7- to 10-MHz transducer and adequately delineates parathyroid gland enlargement when the glands are located in characteristic parathyroid locations. Normal parathyroid glands are not detected. When parathyroid gland enlargement is not found in the region of the thyroid, the entire anterior neck from mandible to suprasternal notch is examined sonographically, including the retrotracheal region via a lateral approach; however, ectopic parathyroid gland location in the neck may escape ultrasonographic detection. Ultrasonography cannot be used to identify mediastinal parathyroid adenomas. Parathyroid masses within a goitrous thyroid or surgical bed are difficult to discern. Thyroid nodules (particularly when posteriorly located) and cervical lymph nodes (especially within the tracheoesophageal groove) may mimic parathyroid pathology.[60]

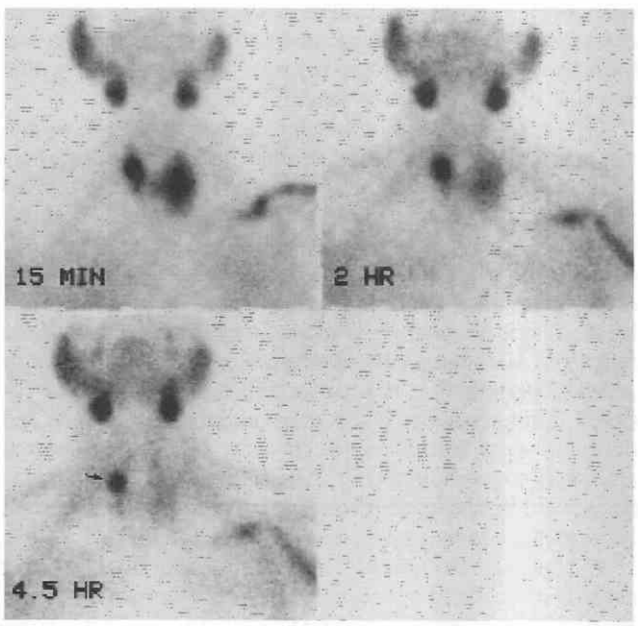

Figure 20–38. With dual-phase technetium 99m–MIBI imaging, an immediate anterior view of the neck reveals a focus of increased activity in the upper pole of the right thyroid lobe. On the 2-hour delayed image, the thyroid activity has washed out to a large degree; the persistent focus of increased activity in the upper right neck *(arrow)* was further confirmed on a 4.5-hour delayed scan, at which point there was additional thyroid washout. At surgery, a solitary parathyroid adenoma was resected.

Lymph nodes can sometimes be distinguished from parathyroid adenomas by a hyperechoic central fatty hilum and absence of the vascularity commonly seen with color Doppler imaging within parathyroid adenomas.[76] Thyroid nodules appear less vascular than parathyroid adenomas and more often demonstrate calcification, cystic changes, and heterogeneous echogenicity. A hyperechoic capsule favors a parathyroid adenoma. These sonographic features are inconsistent, however, and differentiating abnormal parathyroid glands from lymphadenopathy and thyroid masses is not always possible.

An advantage of CT is its ability to evaluate the entire neck and the mediastinum from the skull base to the aortic arch. Distinguishing lymphadenopathy from parathyroid adenomas with CT is problematic, as it is with ultrasonography. The use of CT requires the administration of IV contrast material, but only 25% of parathyroid adenomas enhance (Fig. 20–39).[135]

CT evaluation of parathyroid adenomas may produce false-negative or false-positive results as a result of artifactual obscuration of parathyroid adenomas that may be caused by patient or respiratory motion, shoulder underpenetration or beam-hardening artifact, suboptimal technical factors, or inherently poor soft tissue differentiation. Identifying parathyroid adenomas may be especially challenging in the postoperative neck, where normal tissue planes are distorted and metallic clips generate streak artifact.

MRI evaluation of the neck employs standard T1-weighted, T2-weighted, and postcontrast T1-weighted imaging. Normal parathyroid glands are not visualized by MRI.[60] Parathyroid adenomas and parathyroid hyperplasia are typically bright on T2-weighted images, show soft tissue signal intensity on T1-weighted images, and enhance with contrast material; however, approximately 40% of abnormal glands have atypical MRI signal characteristics.[42, 51, 56, 60, 61, 90, 102, 121, 134]

Pathologic parathyroid glands may contain fat, hemorrhage, sclerosis, or fibrosis, which may alter the expected MRI signal intensity.[60, 61] Contrast-enhanced T1-weighted images should be performed with fat suppression to allow the enhancing adenoma to be differentiated from dark neck fat.[32, 48] MRI features are not specific for parathyroid adenomas, however, and cannot differentiate adenomas from other neck masses and lymphadenopathy.[60, 79, 90, 137]

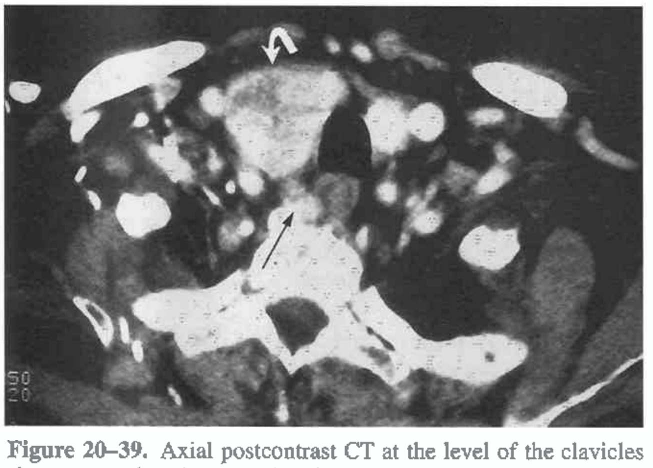

Figure 20–39. Axial postcontrast CT at the level of the clavicles shows an enhancing parathyroid adenoma *(arrow)* in the right tracheoesophageal groove. Goitrous enlargement of the right lobe of the thyroid can be visualized *(curved arrow)*.

High-resolution MRI scanning is currently performed with surface coils, which may have a limited region of coverage. Multiple surface coils may be necessary to evaluate the neck together with the upper mediastinum. MRI is also susceptible to artifact degradation, particularly from patient and respiratory motion, flowing blood, or cerebrospinal fluid pulsation.

Several different imaging modalities may be combined to improve the sensitivity and specificity of parathyroid adenoma and hyperplastic gland identification in the virgin neck, the previously operated neck, and in ectopic locations.[61] MRI is particularly useful for identifying abnormal ectopic parathyroid glands.[51, 60, 61, 79, 137]

Fine-needle biopsy employing ultrasonographic, CT, or MRI guidance may be used to sample parathyroid gland enlargement.[114, 128, 129] Cytology, immunocytochemistry, and radioimmunoassay for parathyroid hormone (PTH) may be conducted to evaluate the aspirated material.

Pathologic Parathyroid Conditions

Hyperparathyroidism

Hyperparathyroidism is a common endocrinopathy manifested by hypercalcemia and elevated circulating levels of PTH, with or without associated urinary, cardiovascular, GI, skeletal, or psychiatric abnormalities.[54] The solitary parathyroid adenoma is most often found along the inferior pole of a thyroid lobe[158] and is responsible for primary hyperparathyroidism in 80% of patients.[34, 35, 106, 144, 145] Hyperplastic parathyroid glands (10%), multiple parathyroid adenomas (2% to 5%), and parathyroid carcinoma (1%) make up the remainder.[34, 35, 106, 144, 145, 147] In 10% to 20% of patients, parathyroid adenomas are ectopic in location.[27, 35, 92, 106]

Therapy for primary hyperparathyroidism is usually surgical resection of the abnormal gland or glands, especially in view of growing evidence of adverse cardiac and skeletal effects of chronic hyperparathyroidism.[39, 74, 136] The use of routine preoperative imaging for patients with uncomplicated primary hyperparathyroidism is controversial.[10, 80, 111, 146] Some surgeons recommend no preoperative imaging of patients with hyperparathyroidism, reporting a 90% to 95% cure rate in previously unoperated patients.[22, 109, 111, 117, 144] The success rate of finding a hyperplastic parathyroid gland or adenoma at surgery, however, is less than 70% if the pathologic parathyroid gland is in an ectopic location.[81, 144, 158]

Some authors have justified routine preoperative imaging with claims of improving operative success rates, decreasing the risk of recurrent laryngeal nerve and normal parathyroid gland injury, and lowering cost, operating time, and blood loss.[11, 18, 36, 64, 75, 113, 117] With the emergence of minimally invasive parathyroidectomy performed using local anesthesia and a hand-held gamma probe intraoperatively, preoperative radionuclide localization is becoming standard practice.[96] In addition, preoperative imaging can identify concomitant thyroid pathology in up to 50% of patients.[29, 63, 108, 153]

Parathyroid Adenomas

The identification of parathyroid adenomas has been evaluated using multiple imaging modalities with a range of specificities and sensitivities. Ultrasonographic identification of parathyroid adenomas is reported to have a sensitivity of 64% and a specificity of 94%.[76, 108] The detection rate significantly improves when the parathyroid adenomas are large.[108] At sonography, parathyroid adenomas are typically homogeneously hypoechoic, sometimes with a hyperechoic capsule (Fig. 20–40).[36, 108, 135] Adenomas may be partially cystic or inhomogeneous with foci of hypoechogenicity or hyperechogenicity.

Color Doppler imaging reveals parathyroid adenomas to be uniformly hypervascular, which may help distinguish them from other neck masses.[76]

CT is reported to have a sensitivity of 70% and a specificity of 90% for parathyroid adenoma detection.[135] MRI has accuracy and sensitivity rates of 74% to 92% for identifying parathyroid adenomas (Fig. 20–41).[61, 79, 134, 137] ^{99m}Tc-MIBI imaging has a reported sensitivity rate of 82% to 100% and is generally considered the standard initial imaging modality to identify a parathyroid adenoma.[18, 36, 61, 77, 84, 99, 100, 140] It can detect not only the typical cervical single adenoma or rare dual adenomas but also ectopic and mediastinal adenomas (Fig. 20–42).

The fusion of metabolic sestamibi SPECT images with CT images offers optimized localization of a mediastinal adenoma for surgical planning and guidance, with or without the use of an intraoperative handheld gamma probe. Concomitant benign or malignant thyroid abnormalities (e.g., thyroid adenomas) may cause increased uptake of ^{99m}Tc-MIBI and lead to a false-positive scan.[81, 87, 99, 100, 140] Many of these false-positive results can be reduced by the use of subtraction techniques with ^{123}I.[49]

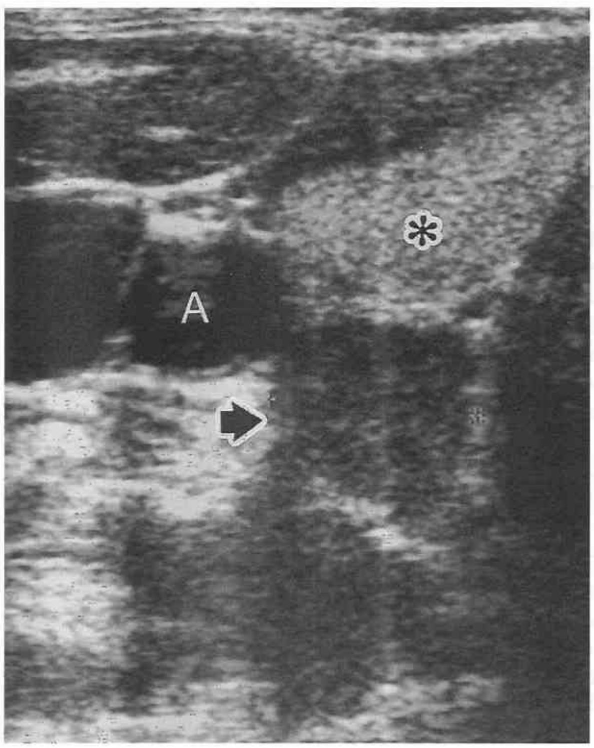

Figure 20–40. Parathyroid adenoma. Transverse sonographic image shows a hypoechoic mass *(arrow)* inferior to the right lobe of the thyroid *(asterisk)*. A, right common carotid artery.

Patients who are not candidates for surgical resection of parathyroid adenomas may be treated with percutaneous alcohol injection using ultrasonographic, CT, or MRI guidance.[148] This is a minimally invasive procedure with few risks if care is taken to avoid vascular structures during needle puncture. With a 22-gauge needle, 0.5 to 1 mL of 98% dehydrated alcohol is injected in multiple locations in the adenoma. Monitoring of serum calcium levels indicates success of the technique, and repeated percutaneous alcohol injections may be performed if necessary.

Parathyroid Hyperplasia

Parathyroid hyperplasia may be primary, secondary, or tertiary. Secondary and tertiary hyperparathyroidism are caused by chronic renal failure and are complicated by a variable degree of associated renal osteodystrophy. ^{99m}Tc-MIBI scanning is the imaging examination of choice to evaluate secondary and tertiary hyperparathyroidism, although only a minority of these patients require preoperative imaging. It is also the preferred imaging study for parathyroid hyperplasia evaluation, with a reported detection rate as high as 75% (Fig. 20–43).[34, 36, 61, 77, 92, 99, 100, 106, 140] False-negative MIBI results therefore occur in at least 25% of cases. Ultrasonography has been reported to have a sensitivity rate of 30% to 69%, CT 45% to 88%, and MRI 40% to 74%.[34, 35, 61, 79, 102, 106, 135, 137] Some hyperplastic parathyroid glands may calcify.[128] Imaging cannot differentiate parathyroid hyperplasia from parathyroid adenomas, and no modality typically identifies all four parathyroid glands.

Patients who are not surgical candidates may be treated by percutaneous alcohol ablation of hyperplastic parathyroid glands with the use of image guidance techniques similar to those used for adenoma reduction.[128, 129]

In approximately 30% of patients, primary parathyroid hyperplasia is familial rather than sporadic, a component of MEN syndrome. MEN-1, also termed *Wermer's syndrome*, is an autosomal dominant disorder with high penetrance. The locus for this genetic syndrome is on chromosome 11. In addition to primary parathyroid hyperplasia, patients with MEN-1 have pancreatic islet cell tumors such as insulinomas, gastrinomas (Zollinger-Ellison syndrome), pancreatic polypeptide-producing tumors, glucagonomas, or vasoactive intestinal peptide tumors (VIPomas), and pituitary adenomas. Thyroid disorders, including goiter, adenomas, or thyroiditis; adrenal adenomas or carcinomas; and carcinoid tumors have also been reported. Parathyroid hyperplasia is also a component of MEN-2A and, occasionally, MEN-2B (or MEN-3) syndrome (see earlier discussion of medullary thyroid carcinoma).

Persistent or Recurrent Hyperparathyroidism

Persistent or recurrent hyperparathyroidism after attempted surgical cure presents a serious challenge. In approximately 50% of cases, reoperation reveals abnormal parathyroid glands in a perithyroidal location that were missed at the initial surgery.[22, 80, 110] Other parathyroid ade-

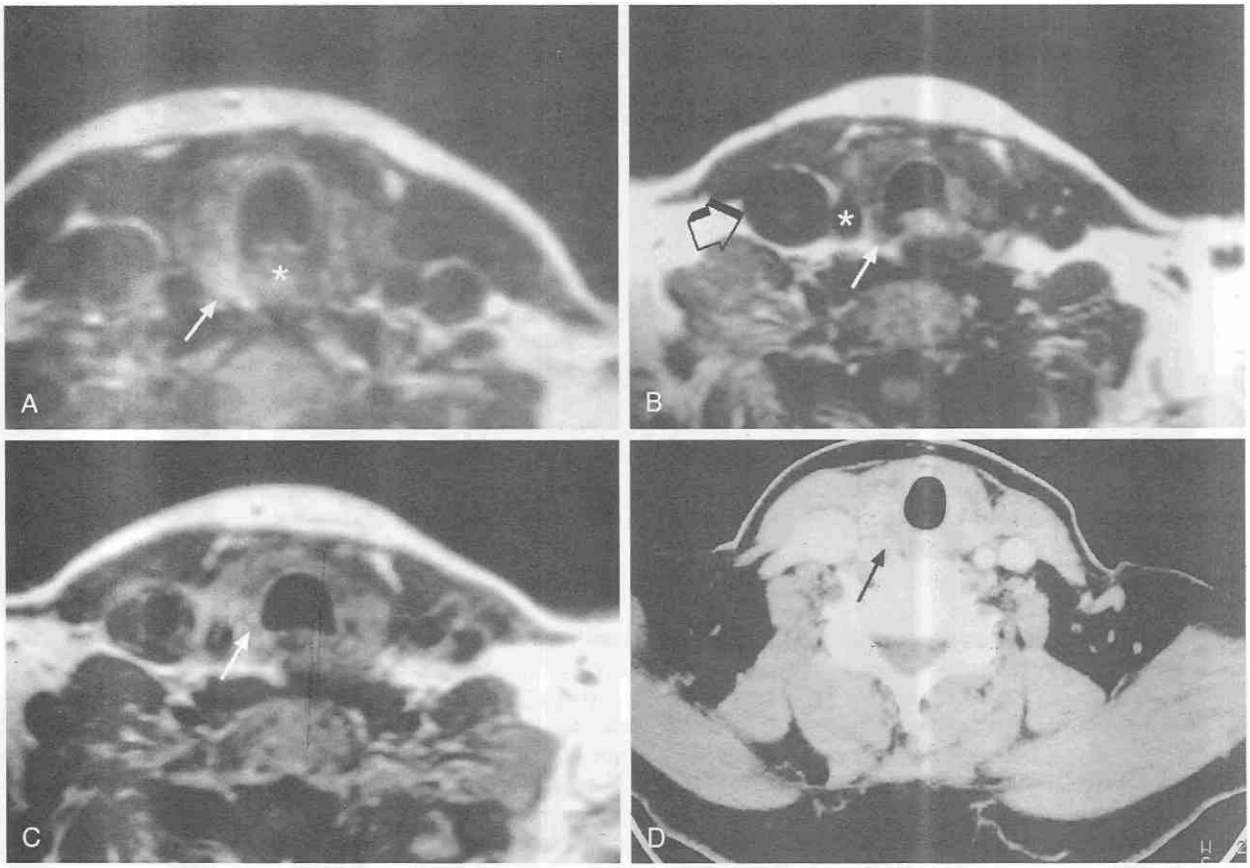

Figure 20–41. Surgically proven parathyroid adenoma. *A,* Axial T2-weighted MR image shows an ovoid mass *(arrow)* of increased T2-weighted signal posterior to the right lobe of the thyroid and adjacent to the esophagus *(asterisk). B,* Axial T1-weighted MR image demonstrates that the mass *(arrow)* is isointense to thyroid parenchyma. Flow voids can be seen in the right common carotid artery *(asterisk)* and right internal jugular vein *(open arrow). C,* Axial T1-weighted MR image after gadolinium contrast administration demonstrates enhancement within the lesion *(arrow). D,* Axial postcontrast CT image shows a homogeneously enhancing ovoid mass *(arrow)* in the right tracheoesophageal groove.

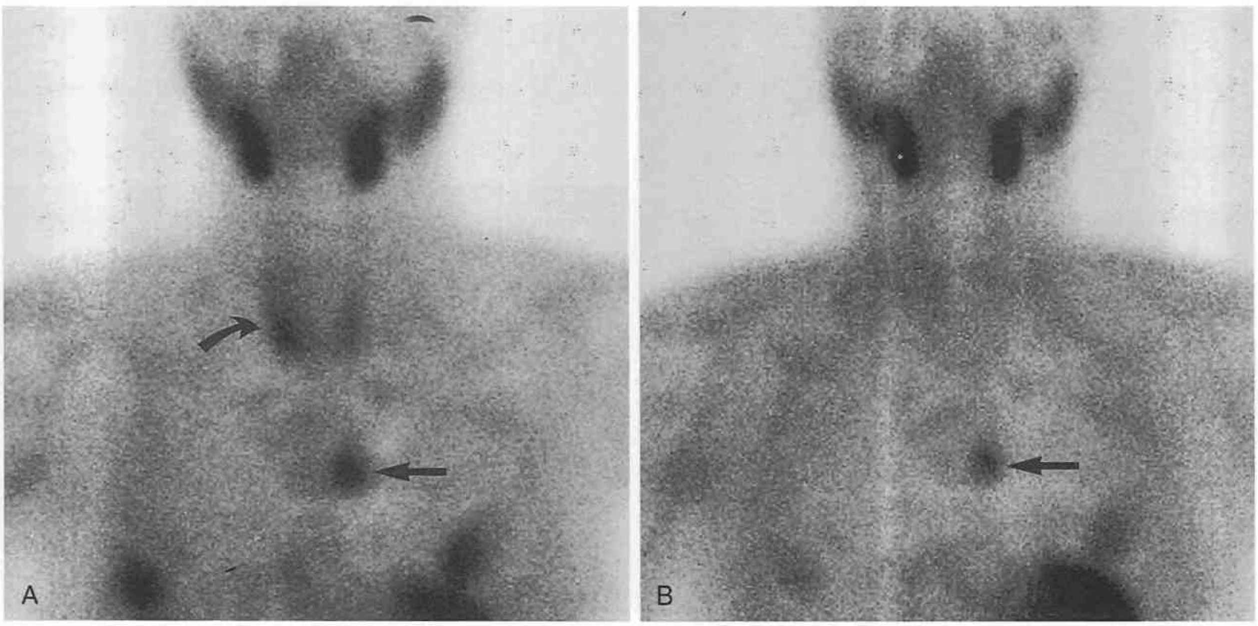

Figure 20–42. *A,* An anterior image of the neck and thorax immediately following technetium 99m–MIBI injection demonstrates physiologic thyroid activity *(curved arrow)* with a single focus of increased activity in the chest to the left of midline *(arrow). B,* Most of the thyroid activity has faded by 2 hours on the delayed images, thus accentuating the persistent mediastinal abnormality *(arrow).* At surgery, a mediastinal parathyroid adenoma was resected, resulting in postoperative eucalcemia.

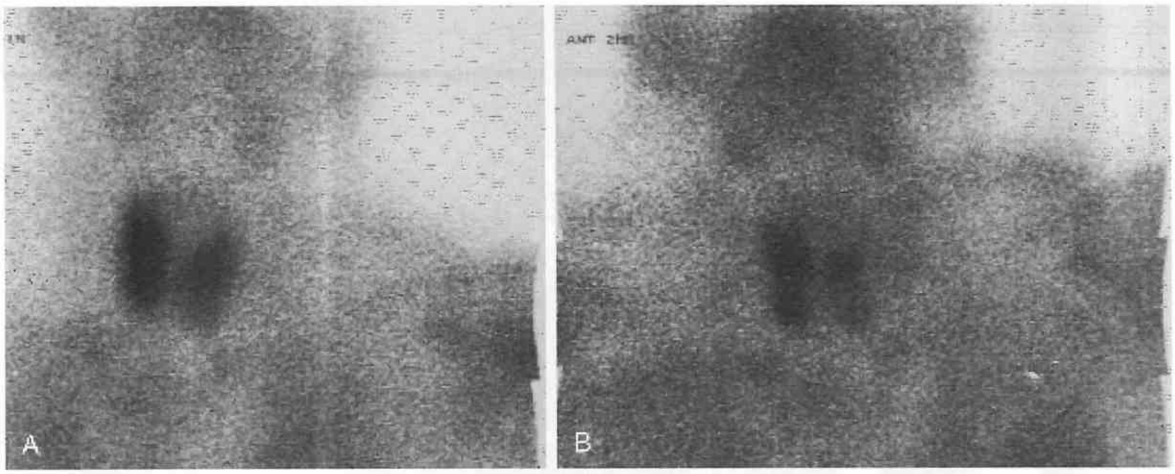

Figure 20–43. Dual-phase technetium-99m–MIBI imaging—immediate *(A)* and 2-hour-delayed *(B)* acquisitions—of a patient with chronic renal failure. Imaging reveals four persistent foci of increased activity on the delayed images *(B)*, consistent with parathyroid hyperplasia.

noma locations, however, include the anterior mediastinum, deep in the tracheoesophageal groove, and deep cervical, intrathyroidal, and parathymic locations.[60, 80, 82, 110] Imaging can assist the surgeon in preoperatively identifying a persistent or ectopic parathyroid adenoma or parathyroid hyperplasia, increasing surgical success from 60% to 90%.[61, 79, 106]

99mTc-MIBI imaging is the mainstay for identifying the source of persistent hyperparathyroidism; it has a sensitivity of 80% to 90% (Fig. 20–44).[61, 62, 73, 77, 150] Persistent postoperative thyroid MIBI uptake due to suspected thyroiditis may obscure residual parathyroid adenoma or hyperplasia.[36] Ultrasonography, CT, and MRI have variable sensitivities of between 25% and 90% for the detection of residual parathyroid tissue.[42, 51, 57, 61, 79, 81, 102, 135] Some authors recommend MRI as a complementary imaging modality to ^{99m}Tc-MIBI scintigraphy.[24, 98]

Although the success of ^{18}FDG PET imaging of parathyroid adenomas has been variable, carbon 11 (^{11}C) methionine PET imaging is reported to be more successful than CT or ultrasonography in patients requiring either primary or reoperative resection.[94, 138] In the patient with persistent or recurrent hyperparathyroidism, most investigators recommend initial functional imaging with ^{99m}Tc-MIBI, complemented by anatomic imaging with MRI or CT; ultrasonography plays a limited role in these patients.[98] ^{18}FDG or ^{11}C-methionine PET may be attempted in patients without localization after ^{99m}Tc-MIBI scintigraphy.

Other approaches include parathyroid venous sampling

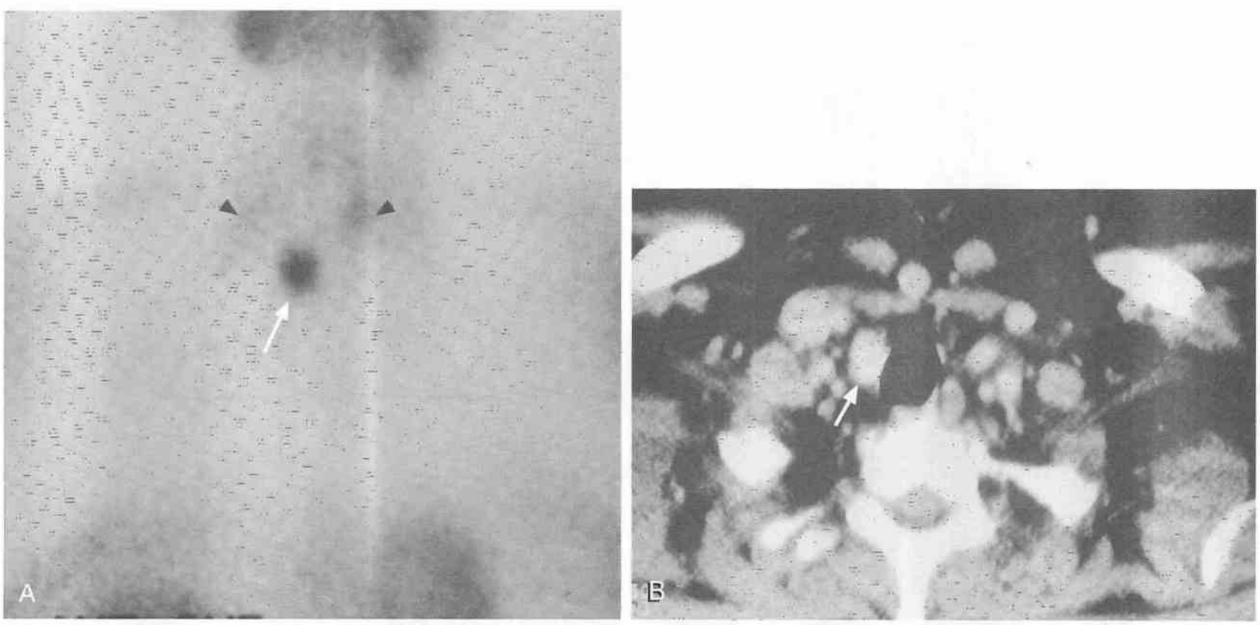

Figure 20–44. *A,* Anterior projection of neck and upper chest from a technetium 99m–MIBI radionuclide scan in a patient with persistent hyperparathyroidism after thyroidectomy demonstrates a prominent focus of tracer uptake within the low right neck *(arrow)*. Uptake within the thyroid parenchyma *(arrowheads)* is mild. *B,* Axial postcontrast CT scan through the lower neck in the same patient demonstrates an enhancing right paratracheal soft tissue mass *(arrow)*, found to be a parathyroid adenoma at reoperation.

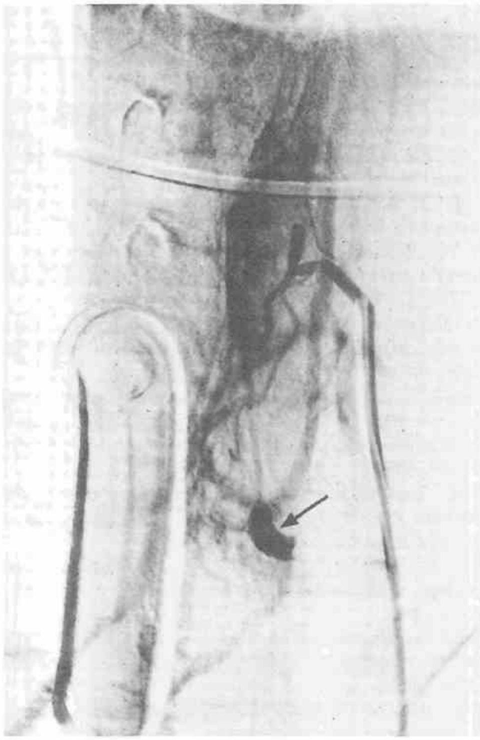

Figure 20–45. Digital subtraction angiographic image in AP projection. Left superior thyroidal artery injection shows a homogeneously enhancing mass consistent with a parathyroid adenoma *(arrow)* within the low left neck. (Courtesy of M. Mazer, M. D.)

and arteriography (Fig. 20–45).[20] These invasive procedures have sensitivities of 50% to 80%[24, 82] but may be valuable in selective cases, particularly in previously operated patients who have fibrotic scar tissue, abnormal tissue planes, postoperative inflammation, or enlarged reactive lymph nodes, which may lead to false-negative or false-positive results with other imaging studies.

Other Parathyroid Masses

Parathyroid Cysts

Parathyroid cysts are rare, comprising only 0.6% of all thyroid and parathyroid lesions,[159] but they may be large at presentation. Most present in middle-aged women.[68] Parathyroid cysts may develop from pharyngeal pouch remnants or may represent degenerated parathyroid adenomas.[158] Almost all are found caudal to the inferior margin of the thyroid, and most are associated with the inferior parathyroid glands.[159] Mimics include thyroid or thymic cysts and necrotic lymph nodes.[71]

Symptoms may be secondary to tracheal, esophageal, or laryngeal nerve compression or from cyst hemorrhage and subsequent pain.[159] Ultrasonography demonstrates an anechoic mass in a typical parathyroid gland location. CT demonstrates a well-circumscribed, low-density parathyroidal mass. MRI may demonstrate bright signal intensity on T1-weighted images if the contents of the cyst have an increased protein content or hemorrhage. ^{99m}Tc-MIBI may demonstrate a photopenic focus. Fine-needle aspiration yields a characteristic clear watery fluid with high PTH and low thyroglobulin content and may be curative if combined with a sclerosing agent.[14]

Parathyroid Carcinoma

Parathyroid carcinoma is a rare cause of hyperparathyroidism, with an incidence of 1% to 2% and no sex preference.[159] Thirty percent of patients present with metastatic lymphadenopathy; distant metastases are seen in approximately 25%.[159] Approximately 90% of parathyroid carcinomas cause hyperparathyroidism.[67, 68] Parathyroid carcinomas are indistinguishable from parathyroid adenomas in all imaging studies except when local invasion of neighboring structures is present.[23] ^{99m}Tc-MIBI and ^{18}FDG PET may be used to detect local and distant metastases.[55, 73, 94]

References

1. Balon HR, Fink-Bennett TD, Stoffer SS: Technetium 99m–sestamibi uptake by recurrent Hürthle cell carcinoma of the thyroid. J Nucl Med 33:1393, 1992.
2. Bar-Ziv J, Slasky BS, Sichel TY, et al: Branchial pouch sinus tract from the piriform fossa causing acute suppurative thyroiditis, neck abscess, or both: CT appearance and the use of air as a contrast agent. AJR Am J Roentgenol 167:1569, 1996.
3. Batsakis JG: Tumors of the Head and Neck: Clinical and Pathological Considerations. Baltimore, Williams & Wilkins, 1979.
4. Beahrs OH, Kiernan PD, Hubert JP Jr: Cancer of the thyroid gland. In Suen JY, Myers E (eds): Cancer of the Head and Neck. New York, Churchill Livingstone, 1981, pp 599–632.
5. Behr TM, Gratz S, Markus PM, et al: Anti-carcinoembryonic antigen antibodies versus somatostatin analogs in the detection of metastatic medullary thyroid carcinoma: Are carcinoembryonic antigen and somatostatin receptor expression prognostic factors? Cancer 80: 2436, 1997.
6. Bigsby RJ, Lepp EK, Litwin DEM, et al: Technetium-99m pentavalent dimercaptosuccinic acid and thallium-201 in detecting recurrent medullary carcinoma of the thyroid. Can J Surg 35:388, 1992.
7. Boland GW, Lee MJ, Mueller PR, et al: Efficacy of sonographically guided biopsy of thyroid masses and cervical lymph nodes. AJR Am J Roentgenol 161:1053, 1993.
8. Briele B, Hotze AL, Kropp J, et al: Comparison of ^{99m}Tc-MIBI and Tl-201–chloride in the follow-up of patients with differentiated thyroid carcinoma. J Nucl Med 33:844, 1992.
9. Burke GJ, Wei JP, Binet EF: Parathyroid scintigraphy with iodine-123 and ^{99m}Tc-sestamibi: Imaging findings. AJR Am J Roentgenol 161:1265–1268, 1993.
10. Carlson GL, Faradon JR, Clayton B, et al: Thallium isotope scintigraphy and ultrasonography: Comparative studies of localization techniques in primary hyperparathyroidism. Am Surg 60:12, 1990.
11. Casas AT, Burke GJ, Mansberger AR Jr, et al: Impact of technetium-99m–sestamibi localization on operative time and success of operations for primary hyperparathyroidism. Am Surg 60:12–16, 1994.
12. Charkes ND: Graves' disease with functioning nodules (Marine-Lenhart syndrome). J Nucl Med 13:885, 1972.
13. Chung JK, So Y, Lee JS, et al: Value of FDG PET in papillary thyroid carcinoma with negative ^{131}I whole-body scan. J Nucl Med 40:984, 1999.
14. Clark OH: Parathyroid cysts. Am J Surg 135:385–402, 1978.
15. Compagno J: Diseases of the thyroid. In Barnes L (ed): Surgical Pathology of the Head and Neck. New York, Marcel Dekker, 1985, pp 1435–1486.
16. Coret A, Heyman Z, Bendet E, et al: Thyroid abscess resulting from transesophageal migration of a fish bone: Ultrasound appearance. J Clin Ultrasound 21:152, 1993.
17. DeGroot LJ, Sridama V: Thyroid neoplasm. In: DeGroot LJ (ed): Endocrinology. Philadelphia, WB Saunders, 1989, pp 758–776.
18. Denham DW, Norman J: Cost-effectiveness of preoperative sestamibi scan for primary hyperparathyroidism is dependent solely upon the surgeon's choice of operative procedure. J Am Coll Surg 186: 293, 1998.
19. DiLelio A, Rivolta M, Casati M, et al: Treatment of autonomous

thyroid nodules: Value of percutaneous ethanol injection. AJR Am J Roentgenol 164:207, 1995.
20. Doppmann JL: Parathyroid localization: Arteriography and venous sampling. Radiol Clin North Am 14:163, 1976.
21. Dorr U, Wurstlin S, Frank-Raue K, et al: Somatostatin receptor scintigraphy and magnetic resonance imaging in recurrent medullary thyroid carcinoma: A comparative study. Horm Metab Res 27(suppl):48, 1993.
22. Edis AJ, Sheedy PF, Beahrs OH, et al: Results of reoperation for hyperparathyroidism, with evaluation of preoperative localization studies. Surgery 84:384, 1978.
23. Edmonson GR, Charboneau JW, James EM, et al: Parathyroid carcinoma: High-frequency sonographic features. Radiology 161:65–67, 1986.
24. Fayet P, Hoeffel C, Fulla Y, et al: Technetium-99m sestamibi scintigraphy, magnetic resonance imaging and venous blood sampling in persistent and recurrent hyperparathyroidism. Br J Radiol 70: 459–464, 1997.
25. Fisher DA, Oddie TH, Johnson DE, Nelson JC: The diagnosis of Hashimoto's thyroiditis. J Clin Endocrinol Metab 40:785, 1975.
26. Frank-Raue K, Raue F, Buh HJ, et al: Localization of occult persisting medullary thyroid carcinoma before microsurgical reoperation: High sensitivity of selective venous catheterization. Thyroid 2: 113, 1992.
27. Freitas JE, Freitas AE: Thyroid and parathyroid imaging [review]. Semin Nucl Med 24:234, 1994.
28. Freitas JE, Gross MD, Ripley S, et al: Radionuclide diagnosis and therapy of thyroid cancer: Current status report. Semin Nucl Med 15:106–131, 1985.
29. Funari M, Campos Z, Gooding GA, et al: MRI and ultrasound detection of asymptomatic thyroid nodules in hyperparathyroidism. J Comput Assist Tomogr 16:615–619, 1992.
30. Gefter WB, Spritzer CE, Livolsi VA, et al: Thyroid imaging with high-field strength surface-coil MR. Radiology 164:483, 1987.
31. Gharib H, Goellner JR, Johnson DA: Fine-needle aspiration cytology of the thyroid: An appraisal. Ann Intern Med 118:282–289, 1993.
32. Goddard PR: Localization of abnormal parathyroid gland: Value of fat suppression. Radiology 190:903, 1994.
33. Goldman JM, Lini BR, Aamodt RL, Robbins J: Influence of triiodothyronine withdrawal time on I-131 uptake post-thyroidectomy for thyroid cancer. J Clin Endocrinol Metab 50:734, 1980.
34. Gooding GA: Sonography of the thyroid and parathyroid. Radiol Clin North Am 31:967–989, 1993.
35. Gooding GAW, Okerlund MD, Stark DD, et al: Parathyroid imaging: Comparison of double-tracer (Tl-201, Tc-99m) scintigraphy and high-resolution ultrasound. Radiology 161:57–64, 1986.
36. Gordon BM, Gordon L, Hoang K, Spicer KM: Parathyroid imaging with ^{99m}Tc-sestamibi. AJR Am J Roentgenol 167:1563–1568, 1996.
37. Gorman B, Charboneau JW, James EM, et al: Ultrasonic evaluation of benign and malignant nodules in echographically multinodualr thyroids. J Clin Ultrasound 22:71, 1994.
38. Guneri A, Ceryan K, Igci E, et al: Lingual thyroid: The diagnostic value of magnetic resonance imaging. J Laryngol Otol 105:493–495, 1991.
39. Guo C-Y, Thomas WEG, Al-Dehaimi AW, et al: Longitudinal changes in bone mineral density and bone turnover in postmenopausal women with primary hyperparathyroidism. J Clin Endocrinol 81:3487, 1996.
40. Hamburger JI, Hamburger SI: Fine-needle biopsy of thyroid nodules: Avoiding the pitfalls. N Y State J Med 86:241–249, 1986.
41. Hamburger JI, Miller JM, Kini SR: Lymphoma of the thyroid. Ann Intern Med 99:685–693, 1983.
42. Hamilton R, Greenburg BM, Gefter W, et al: Successful localization of parathyroid adenomas by magnetic resonance imaging. Am J Surg 155:370–373, 1988.
43. Hanbridge AE, Arenson AM, Shaw PA, et al: Needle size and sample adequacy in ultrasound-guided biopsy of thyroid nodules. Can Assoc Radiol J 46:199, 1995.
44. Hatabu H, Kasagi K, Yamamoto K, et al: Acute suppurative thyroiditis associated with pyriform sinus fistula: Sonographic findings. AJR Am J Roentgenol 155:845–847, 1990.
45. Hawkins DB, Jacobsen BE, Klatt EC: Cysts of the thyroglossal duct. Laryngoscope 92:1254–1258, 1982.
46. Hay ID: Papillary thyroid carcinoma. Endocrinol Metab Clin North Am 19:545, 1990.
47. Hays LL, Marlow SF Jr: Papillary carcinoma arising in a thyroglossal duct cyst. Laryngoscope 78:2189–2193, 1968.
48. Higgins CB: Role of magnetic resonance imaging in hyperparathyroidism. Radiol Clin North Am 31:1017, 1993.
49. Hindie E, Melliere D, Simon D, et al: Primary hyperparathyroidism: Is technetium-99m–sestamibi/iodine-123 subtraction scanning the best procedure to locate enlarged glands before surgery? J Clin Endocrinol Metab 80:302–307, 1995.
50. Hopkins CR, Reading CC: Thyroid and parathyroid imaging. Semin Ultrasound CT MR 16:279, 1995.
51. Kang YS, Rosen K, Clark OH, et al: Localization of abnormal parathyroid glands of the mediastinum with MR imaging. Radiology 189:137–141, 1993.
52. Kasagi K, Hatabu H, Tokuda Y, et al: Lymphoproliferative disorders of the thyroid gland: Radiological appearances. Br J Radiol 64: 569–575, 1991.
53. Kawanaka M, Sugimoto Y, Suehiro M, et al: Thyroid imaging in a typical case of acute suppurative thyroiditis with abscess formation due to infection from a persistent thyroglossal duct. Ann Nucl Med 8:159–162, 1994.
54. Khan A, Samtani S, Varma VM, et al: Preoperative parathyroid localization: Prospective evaluation of technetium 99m sestamibi. Otolaryngol Head Neck Surg 11:467, 1994.
55. Kitapci MT, Tastekin G, Turgut M, et al: Preoperative localization of parathyroid carcinoma using Tc-99m MIBI. Clin Nucl Med 18: 217–219, 1993.
56. Kneeland JB, Kruback AJ, Lawson TL, et al: Enlarged parathyroid glands: High-resolution local coil MR imaging. Radiology 162: 143–146, 1987.
57. Kohri K, Tshikawa Y, Kodama M: Comparison of imaging methods for localization of parathyroid tumors. Am J Surg 164:140, 1992.
58. Kwekkeboom DJ, Reubi JC, Lamberts SW, et al: The potential value of somatostatin receptor scintigraphy in medullary thyroid carcinoma. J Clin Endocrinol Metab 76:1413, 1993.
59. Ladenson PW, Braverman LE, Mazzaferri EL, et al: Comparison of administration of recombinant human thyrotropin with withdrawal of thyroid hormone for radioactive iodine scanning in patients with thyroid carcinoma. N Engl J Med 337:88, 1997.
60. Lee VS, Spritzer CE: MR imaging of abnormal parathyroid glands. AJR Am J Roentgenol 170:1097–1103, 1998.
61. Lee VS, Spritzer CE, Coleman RE, et al: The complementary roles of fast spin-echo MR imaging and double-phase ^{99m}Tc-sestamibi scintigraphy for localization for hyperfunctioning parathyroid glands. AJR Am J Roentgenol 167:1555–1562, 1996.
62. Lee VS, Wilkinson RH Jr, Leight GS, et al: Hyperparathyroidism in high-risk surgical patients: Evaluation with double-phase technetium-99m-sestamibi imaging. Radiology 197:627–633, 1995.
63. Lever EG, Refetoffs S, Strauss FH II, et al: Coexisting thyroid and parathyroid disease: Are they related? Surgery 94:893–900, 1983.
64. Levin KE, Clark AH, Duh QY, et al: Reoperative thyroid surgery. Surgery 111:604, 1992.
65. Lim-Dunham JE, Feinstein KA, Yousefzadeh DK, Ben-Ami T: Sonographic demonstration of a normal thyroid gland excludes ectopic thyroid in patients with thyroglossal duct cyst. AJR Am J Roentgenol 164:1489, 1995.
66. Lin JD, Huang BY, Weng HF, et al: Thyroid ultrasonography with fine-needle aspiration cytology for the diagnosis of thyroid cancers. J Clin Ultrasound 25:111, 1997.
67. Livolsi V: The thyroid and parathyroid. In Sternberg SS (ed): Diagnostic Surgical Pathology, 2nd ed. New York, Raven Press, 1994, pp 523–560.
68. Livolsi VA: Pathology of the parathyroid glands. In Barnes L (ed): Surgical Pathology of the Head and Neck. New York, Marcel Dekker, 1985, pp 1487–1563.
69. Livraghi T, Paracchi A, Ferrari C, et al: Treatment of autonomous thyroid nodules with percutaneous ethanol injection: 4-year experience. Radiology 190:529, 1994.
70. Loevner LA: Imaging of the thyroid gland. Semin Ultrasound CT MR 17:539, 1996.
71. Loevner LA: Imaging of the parathyroid glands. Semin Ultrasound CT MR 17:563, 1996.
72. Lubin E, Mechlis-Frish S, Zatz S, et al: Serum thyroglobulin and iodine-131 whole-body scan in the diagnosis and assessment of treatment for metastatic differentiated thyroid carcinoma. J Nucl Med 35:257, 1994.

73. Majors JD, Burke GJ, Mansberger AR Jr, et al: Technetium Tc-99m sestamibi scan for localizing abnormal parathyroid glands after previous neck operations: Preliminary experience in reoperative cases. South Med J 88:327–330, 1995.
74. Massry SG, Goldstein DA: The search for uremic toxin(s) "X" ("X" = PTH). Clin Nephrol 11:181, 1979.
75. Mattar AG, Wright ES, Chittal SM, et al: Impact on surgery of preoperative localization of parathyroid lesions with dual radionuclide subtraction scanning. Can J Surg 29:57, 1986.
76. Mazzeo S, Caramella D, Lencioni R, et al: Usefulness of echo-color Doppler in differentiating parathyroid lesions from other cervical masses. Eur Radiol 7:90–95, 1997.
77. McBiles M, Lambert AT, Cote MG, et al: Sestamibi parathyroid imaging. Semin Nucl Med 25:221–234, 1995.
78. McConahey WM, Hay ID, Woolner LB, et al: Papillary thyroid cancer treated at the Mayo Clinic 1946 through 1970: Initial manifestations, pathologic findings, therapy, and outcome. Mayo Clin Proc 61:978–996, 1986.
79. McDermott VG, Fernandez RJM, Meakem TJ III, et al: Preoperative MR imaging in hyperparathyroidism: Results and factors affecting parathyroid detection. AJR Am J Roentgenol 166:705–710, 1996.
80. Miller DL: Pre-operative localization and international treatment of parathyroid tumors: When and how? World J Surg 15:706, 1991.
81. Miller DL, Doppman JL, Krudy AG, et al: Localization of parathyroid adenomas in patients who have undergone surgery: Part 1. Noninvasive imaging methods. Radiology 162:133, 1987.
82. Miller DL, Doppman JL, Shawker TH, et al: Localization of parathyroid adenomas in patients who have undergone surgery: Part II. Invasive procedure. Radiology 162:138, 1987.
83. Miller JM: Carcinoma and thyroid nodules: The problem in an endemic goiter area. N Engl J Med 252:247, 1955.
84. Mitchell BK, Kinder BK, Cornelius E, Stewart AF: Primary hyperparathyroidism: Preoperative localization using technetium-sestamibi scanning. J Clin Endocrinol Metab 80:7–10, 1995.
85. Montgomery ML: Lingual thyroid: Comprehensive review. West J Surg 43:661–671, 1935.
86. Morka ET, Kwan WP, Clark OH: Technetium-99m–sestamibi for parathyroid imaging. West J Med 161:413, 1994.
87. Mortensen JD, Woolner LB, Bennett WA: Gross and microscopic findings in clinically normal thyroid glands. J Clin Endocrinol Metab 15:1270, 1955.
88. Mulligan LM, Eng C, Healey CS, et al: Specific mutations of the RET proto-oncogene are related to disease phenotype in MEN 2A and FMTC. Nat Genet 6:70, 1994.
89. Musholt TJ, Musholt PB, Dehdashti F, Moley JF: Evaluation of fluorodeoxyglucose-positron emission tomographic scanning and its association with glucose transporter expression in medullary thyroid carcinoma and pheochromocytoma: A clinical and molecular study. Surgery 122:1049–1061, 1997.
90. Nakahara H, Noguchi S, Murakami N, et al: Gadolinium-enhanced MR imaging of thyroid and parathyroid masses. Radiology 202: 765–772, 1997.
91. Nel CJC, van Heerden JA, Goellner JR, et al: Anaplastic carcinoma of the thyroid: A clinicopathologic study of 82 cases. Mayo Clin Proc 60:51, 1985.
92. Neumann DR, Esselstyn CB, Eastwood J, et al: Localization of mediastinal parathyroid adenoma in recurrent postoperative hyperparathyroidism with Tc-99m sestamibi SPECT. Clin Nucl Med 20: 175, 1995.
93. Neumann DR, Esselstyn CB, Go RT, et al: Comparison of double-phase Tc-99m-sestamibi subtraction SPECT in hyperparathyroidism. AJR Am J Roentgenol 169:1671, 1997.
94. Neumann DR, Esselstyn CB, MacIntyre WJ, et al: Comparison of FDG-PET and sestamibi-SPECT in primary hyperparathyroidism. J Nucl Med 37:1809–1815, 1996.
95. Noma S, Kanaoka M, Minami S, et al: Thyroid masses: MR imaging and pathologic correlation. Radiology 168:759–764, 1988.
96. Norman J, Chheda H, Farrell C: Minimally invasive parathyroidectomy for primary hyperparathyroidism: Decreasing operative time and potential complications while improving cosmetic results. Ann Surg 64:391–396, 1998.
97. Noyek AM, Friedberg J: Thyroglossal duct and ectopic thyroid disorders. Otolaryngol Clin North Am 14:187, 1981.
98. Numerow LM, Morita ET, Clark OH, Higgens CB: Persistent/recurrent hyperparathyroidism: A comparison of sestamibi scintigraphy, MRI and ultrasonography. J Magn Reson Imaging 5:702–708, 1995.
99. Oates E: Improved parathyroid scintigraphy with Tc-99m MIBI, a superior radiotracer. Appl Radiol 37–42, 1994.
100. O'Doherty MJ, Kettle AG, Wells P, et al: Parathyroid imaging with technetium-99m–sestamibi: Preoperative localization and tissue uptake studies. J Nucl Med 33:313–318, 1992.
101. Özdemir H, Ilgit ET, Yucal C, et al: Treatment of autonomous thyroid nodules: Safety and efficacy of sonographically guided percutaneous injection of ethanol. AJR Am J Roentgenol 163:929, 1994.
102. Peck WW, Higgins CB, Fisher MR, et al: Hyperparathyroidism: Comparison of MR imaging with radionuclide scanning. Radiology 163:415–420, 1987.
103. Peltier P, Curtet C, Chatal JF, et al: Radioimmunodetection of medullary thyroid cancer using a bispecific anti-CEA/anti-indium-DTPA antibody and an indium-111–labeled DTPA dimer. J Nucl Med 34:1267–1273, 1993.
104. Perez Fontan FJ, Cordido Carballido F, Pombo Felipe F, et al: Riedel thyroiditis: US, CT, and MR evaluation. J Comput Assist Tomogr 17:324–325, 1993.
105. Perez-Monte JF, Brown ML, Shah AN, et al: Parathyroid adenomas: Accurate detection and localization of abnormal parathyroid glands of the mediastinum with MR imaging. Radiology 189:137–141, 1993.
106. Price DC: Radioisotopic evaluation of the thyroid and the parathyroids. Radiol Clin North Am 31:991–1015, 1993.
107. Ralls PW, Mayekawa DS, Lee KP, et al: Color-flow Doppler sonography in Graves' disease: "Thyroid inferno." AJR Am J Roentgenol 150:781–784, 1988.
108. Reading CC, Charboneau JW, James EM, et al: High-resolution parathyroid sonography. Am J Roentgenol 139:539–546, 1982.
109. Reading CC, Gorman CA: Thyroid imaging techniques. Clin Lab Med 13:711–724, 1993.
110. Rodriguez JM, Tezelman S, Siperstein AE, et al: Localization procedures in patients with persistent or recurrent hyperparathyroidism. Arch Surg 129:870–875, 1994.
111. Roe SM, Burns RP, Graham LD, et al: Cost-effectiveness of preoperative localization studies in primary hyperparathyroidism disease. Ann Surg 219:582, 1994.
112. Rojeski MT, Gharib H: Nodular thyroid disease: Evaluation and management. N Engl J Med 313:428, 1985.
113. Russell CF, Laird JD, Ferguson WR: Scan-directed unilateral cervical exploration for parathyroid adenoma: A legitimate approach? World J Surg 14:406, 1990.
114. Sacks BA, Pallotta JA, Cole A, et al: Diagnosis of parathyroid adenomas: Efficacy of measuring parathormone levels in needle aspirates of cervical masses. AJR Am J Roentgenol 163:1223, 1994.
115. Sandler MP, Martin WH, Powers TA: Thyroid imaging. In Sandler MP, et al (eds): Diagnostic Nuclear Medicine, 3rd ed. Baltimore, Williams & Wilkins, 1996, pp 911–942.
116. Sandler MP, Patton JA, Ossoff RH: Recent advances in thyroid imaging. Otolaryngol Clin North Am 23:251–270, 1990.
117. Satava RM, Beahrs OH, Scholz DA: Success rate of cervical exploration for hyperparathyroidism. Arch Surg 110:625, 1975.
118. Schurrer ME, Seabold JE, Gurll NJ, Simonson TM: Sestamibi SPECT scintigraphy for detection of postoperative hyperfunctional parathyroid glands. AJR Am J Roentgenol 166:1465–1470, 1996.
119. Schwartz SI, Shires GT, Spencer FC, et al: Principles of Surgery, 3rd ed. New York, McGraw Hill, 1979, p 1547.
120. Scott AM, Kostakoglu L, O'Brien JP, et al: Comparison of technetium-99m-MIBI and thallium-201–chloride uptake in primary thyroid lymphoma. J Nucl Med 33:1396–1398, 1991.
121. Seelos KC, DeMarco R, Clark OH, et al: Persistent and recurrent hyperparathyroidism: Assessment with gadopentetate dimeglumine-enhanced MR imaging. Radiology 177:373–378, 1990.
122. Senga O, Miyakawa M, Shirota H, et al: Comparison of Tl-201 and Ga-67-citrate scintigraphy in the diagnosis of thyroid tumors [concise communication]. J Nucl Med 23:225, 1982.
123. Shibata T, Noma S, Nakano Y, Konishi J: Primary thyroid lymphoma: MR appearance. J Comput Assist Tomogr 15:629–633, 1991.
124. Shimamoto K, Endo T, Ishigaki T, et al: Thyroid nodules: Evaluation with color Doppler ultrasonography. J Ultrasound Med 12:673, 1993.
125. Shulkin BL, Shapiro B: The role of imaging tests in the diagnosis of thyroid carcinoma. Endocrinol Metab Clin North Am 19:523–543, 1990.

126. Sisson JC, Ackerman RJ, Meyer MA, Wahl RL: Uptake of 18-fluoro-2-deoxy-D-glucose by thyroid cancer: Implications for diagnosis and therapy. J Clin Endocrinol Metab 77:1090, 1993.
127. Skowsky WR, Wilf LH: Iodine-131 metaiodobenzylguanidine scintigraphy of medullary carcinoma of the thyroid. South Med J 84:636, 1991.
128. Solbiati L, Giangrande A, De Pra L, et al: Percutaneous ethanol injection of parathyroid tumors under ultrasound guidance: Treatment for secondary hyperparathyroidism. Radiology 155:607–610, 1985.
129. Solbiati L, Montali G, Croce F, et al: Parathyroid tumors detected by fine-needle aspiration biopsy under ultrasonic guidance. Radiology 148:793, 1983.
130. Solbiati L, Volterrani L, Rizzatto G, et al: The thyroid gland with low uptake lesions: Evaluation by ultrasound. Radiology 155:187–191, 1985.
131. Som PM: Lymph nodes of the neck. Radiology 165:593–600, 1987.
132. Som PM, Brandwein M, Lidov M, et al: The varied appearance of papillary carcinoma cervical nodal disease: CT and MR findings. AJNR Am J Neuroradiol 15:1129–1138, 1994.
133. Spies WG, Wojtowizc CH, Spies SM, et al: Value of post-therapy whole-body I-131 imaging in the evaluation of patients with thyroid carcinoma having undergone high-dose I-131 therapy. Clin Nucl Med 14:793, 1989.
134. Spritzer CE, Gefter WB, Hamilton R, et al: Abnormal parathyroid glands: High-resolution MR imaging. Radiology 162:487–491, 1987.
135. Stark DD, Gooding GAW, Moss AA: Parathyroid imaging: Comparison of high-resolution CT and high-resolution sonography. Am J Roentgenol 141:633–638, 1983.
136. Stefenelli T, Abela C, Frank H, et al: Cardiac abnormalities in patients with primary hyperparathyroidism: Implications for follow-up. J Clin Endocrinol Metab 82:106, 1997.
137. Stevens SK, Chang JM, Clark OH, et al: Detection of abnormal parathyroid glands in postoperative patients with recurrent hyperparathyroidism: Sensitivity of MR imaging. AJR Am J Roentgenol 160:607, 1993.
138. Sundin A, Johansson C, Hellman P, et al: PET and parathyroid L-[carbon-11] methionine accumulation in hyperparathyroidism. J Nucl Med 37:1766–1770, 1996.
139. Sutton RT, Reading CC, Charboneau JW, et al: US-guided biopsy of neck masses in postoperative management of patients with thyroid cancer. Radiology 168:769, 1988.
140. Taillefer R, Boucher Y, Potvin C, et al: Detection and localization of parathyroid adenomas in patients with hyperparathyroidism using a single radionuclide imaging procedure with technetium-99m–sestamibi (double phase study). J Nucl Med 33:1801–1807, 1992.
141. Takashima S, Morimoto S, Ikezoe J, et al: Primary thyroid lymphoma: Evaluation with CT. Radiology 171:439–443, 1988.
142. Takashima S, Morimoto S, Ikezoe J, et al: CT evaluation of anaplastic thyroid carcinoma. AJR Am J Roentgenol 154:1079, 1990.
143. Takashima S, Nomura N, Noguchi Y, et al: Primary thyroid lymphoma: Evaluation with US, CT, and MRI. J Comput Assist Tomogr 19:282, 1995.
144. Thompson CT: Localization studies in patients with hyperparathyroidism. Br J Surg 75:97, 1988.
145. Thompson NW, Eckhauser FE, Harness JK: The anatomy of primary hyperparathyroidism. Surgery 92:814, 1982.
146. Uden P, Aspelin P, Berglund J, et al: Preoperative localization in unilateral parathyroid surgery. A cost-benefit study on ultrasound, computed tomography and scintigraphy. Acta Chir Scand 150:29, 1990.
147. van Heerden JA, Weiland LH, ReMine WH, et al: Cancer of the parathyroid gland. Arch Surg 114:475, 1979.
148. Verges BL, Cercueil JP, Vaillant G, et al: Results of ultrasonically guided percutaneous ethanol injection into parathyroid adenomas in primary hyperparathyroidism. Acta Endocrinol 129:381–387, 1993.
149. Volpé JR: Subacute (de Quervain's) thyroiditis. J Clin Endocrinol Metab 8:81–95, 1979.
150. Weber CJ, Vansant J, Alazraki N, et al: Value of technetium 99m sestamibi iodine 123 imaging in reoperative parathyroid surgery. Surgery 114:1011–1018, 1993.
151. Williams ED: Medullary carcinoma of the thyroid. In DeGroot LJ (ed): Endocrinology. Philadelphia, WB Saunders, 1989, pp 1132–1150.
152. Woolner LB, Beahrs OH, Black BM, et al: Classification and prognosis of thyroid cancer. Am J Surg 102:354–387, 1961.
153. Yao M, Jamieson C, Blend R: Magnetic resonance imaging in preoperative localization of diseased parathyroid glands: A comparison with isotope scanning and ultrasonography. Can J Surg 36:241–244, 1993.
154. Yasuda S, Shohsu A, Ide M, et al: Diffuse F-18 FDG uptake in chronic thyroiditis. Clin Nucl Med 22:341, 1997.
155. Yeh EL, Meade RC, Reutz PP: Radionuclide study of struma ovarii. J Nucl Med 14:118–121, 1973.
156. Yeh HC, Futterweit W, Gilbert P: Micronodulation: Ultrasonographic sign of Hashimoto thyroiditis. J Ultrasound Med 15:813, 1996.
157. Yokozawa T, Fukata S, Kuma K, et al: Thyroid cancer detected by ultrasound-guided fine-needle aspiration biopsy. World J Surg 20:848, 1996.
158. Yousem DM: Parathyroid and thyroid imaging. Neuroimaging Clin N Am 6:435, 1996.
159. Yousem DM, Scheff AM: Thyroid and parathyroid. In Som PM, Curtin HD (eds): Head and Neck Imaging, 3rd ed. St. Louis, Mosby–Year Book, 1996, p 952.
160. Yousem DM, Som PM, Hackney DB, et al: Central nodal necrosis and extracapsular neoplastic spread in cervical lymph nodes: MR imaging versus CT. Radiology 182:753, 1992.

21 Pediatric Head and Neck Imaging

John C. Egelhoff

Head and neck pathology in children encompasses diseases that are both unique to the pediatric age group as well as processes that occur in adults. The diseases that cross age barriers may have a different biologic behavior pattern or clinical presentation when they occur in children. Fortunately, most pediatric head and neck pathology is composed of benign tumors, congenital masses, and inflammatory lesions. In contrast to the situation with adults, primary malignancies are a less frequent occurrence in children. To approach the imaging algorithms and differential diagnoses in a logical method, imaging specialists should have a basic knowledge and understanding of the pathology that occurs in the head and neck in children.

The topic of the head and neck pathology in children represents a vast spectrum of diseases. This chapter focuses on extracranial disease processes of the head and neck, specifically the most common congenital masses, benign and malignant tumors, neurogenic masses, vasoformative lesions, and masslike conditions, including inflammatory processes related to adenitis. Additional topics in head and neck pathology are presented in other chapters.

Imaging

The imaging modality of choice in children with head and neck pathology depends on the clinical findings, the patient's age, and the location of the mass. Generally, the initial imaging study in the young child is sonography. The ability to perform this examination without giving sedation and the lack of ionizing radiation are primary advantages. Sonography is excellent in differentiating solid from cystic masses and is useful in defining the location and extent of these masses. Ultrasound may be helpful in the differentiation of phlegmon from abscess in cases of suppurative adenitis. Color-flow Doppler imaging can be used to assess vascular patency when masses involve the vascular bundle and to demonstrate the appearance of intralesional and perilesional vascularity.

Computed tomography (CT) enables an accurate diagnosis in most cases of extracranial head and neck pathology in children. In addition to the obvious advantage of evaluating bony involvement, CT can assess the location and extent of masses, the internal attenuation values and enhancement characteristics, and the relationship of masses to critical adjacent structures. The full extent of masses and inflammatory processes is better delineated by CT compared with sonography. With newer scanners, multiplanar reconstruction (MPR) is helpful in further defining pathology. The speed of the new multidetector scanners should significantly decrease the need for sedation in the pediatric patient. In our experience, CT is the mainstay of imaging of pediatric head and neck pathology because of the speed and ease of the study as well as the useful diagnostic information obtained for the clinician.

Magnetic resonance imaging (MRI), with its multiplanar capabilities, is very helpful in the evaluation of skull base masses for the detection of intracranial extension. Flow-sensitive techniques and magnetic resonance angiography (MRA) are useful in assessing involvement of the vascular bundle by tumor, vascular patency, and, in rare cases, intralesional vascularity. In some cases, soft tissue signal characteristics of tumors on MRI give a more definitive diagnosis. In our experience, MRI is usually reserved as a secondary study because of the longer imaging time, necessitating the need for additional sedation; this liability also dictates the need for dedicated nursing support and monitoring equipment, which may not be available at all facilities.

Conventional angiography is used primarily in the evaluation of vascular masses that are potentially amenable to embolization. Embolization can be used as a primary means of therapy in lesions such as vasoformative masses or as an adjunctive treatment before surgery in lesions such as juvenile nasopharyngeal angiofibroma.

Congenital Masses of the Neck

The most common benign congenital masses of the neck in children include thyroglossal duct cysts (72%) and anomalies of the branchial apparatus (24%). Thymic cysts, dermoid and epidermoid cysts, and teratomas are less common congenital masses of the head and neck in the pediatric age group.[191]

Thyroglossal Duct Cyst

Thyroglossal duct cysts (TDCs) are the second most common benign cervical mass in children after reactive lymphadenopathy,[177,242] comprising approximately 70% of congenital neck masses in children.[244] At approximately 3 weeks of gestation, the thyroid gland begins to develop as a midline endodermal diverticulum from the floor of the pharynx, between the tuberculum impar and copula. Over the following 4 weeks of embryonic development, the primitive thyroid gland enlarges to form a bilobed divertic-

ulum that will descend caudally along the epithelial-lined thyroglossal duct. This duct extends from the foramen cecum at the tongue base (at the junction of the anterior two thirds and posterior one third of the tongue) to the lower neck (at the future location of the pyramidal lobe of the thyroid gland).

As the diverticulum descends, it remains ventral to all arch derivatives caudal to the first arch. Thus, the path of the primitive thyroid gland courses over the anterior and inferior aspects of the hyoid bone (with a small posterior loop behind the hyoid), thyroid cartilage, and cricoid cartilage. Caudal migration leaves a connecting tract (thyroglossal duct) between the foramen cecum and pyramidal lobe of the thyroid gland. In the usual course of events, the duct involutes between 8 and 10 weeks of gestation. Thyroglossal duct cysts or fistula form when any part of the duct fails to involute, thus leaving functioning secretory epithelium behind.[97, 191, 244]

Thyroglossal duct cysts usually present in the first 5 years of life, with approximately 66% noted before age 7 years. Males and females are equally affected. The cysts are more commonly found in Caucasians.[5] Unless infection is a complicating factor, patients with thyroglossal duct cysts typically present with a nontender, mobile, 2- to 4-cm, subcutaneous midline neck mass of variable firmness. Occasionally, there is a history of fluctuating size; more commonly, however, the cyst demonstrates an abrupt or gradual increase in size with time. Complications of infection, fistula formation, or rupture of the mass can also lead to clinical presentation.[97, 229] Fistulous openings are almost always secondary to infection associated with spontaneous or surgical drainage.[5] Coexisting carcinoma in the wall of the cyst is reported in fewer than 1% of patients with TDC. This typically occurs in adults and is thyroid in origin.[5, 19, 34, 45]

Microscopically, TDC is lined by simple columnar or squamous epithelium. Infrequently, inflammatory changes can distort the usual mucosal findings with variable amounts of fibrous tissue in the cyst wall. This usually forces the pathologist to make a presumptive diagnosis based on clinical and surgical evidence. Thyroid tissue is uncommonly found in the wall of the cyst, accounting for the rare occurrence of thyroid carcinoma.[97, 177, 242]

Thyroglossal duct cysts are classified by location as follows: infrahyoid (65%), suprahyoid (20%), and at the level of the hyoid (15%).[20, 164, 193, 244] Initial imaging evaluation is often performed with ultrasound, which demonstrates a well-defined, thin-walled, midline, or paramedian mass with increased through transmission and variable internal echogenicity. Infected cysts typically have a thicker wall with variable increased internal echogenicity. Thus, the pattern of internal echogenicity in these cysts may not be helpful in distinguishing infected from noninfected lesions.[141, 253] TDC appears as a mass of relatively decreased attenutation to muscle with variable rim enhancement on CT (Fig. 21–1). Cysts below the level of the hyoid are almost always embedded in the strap muscle.[193] Infection or hemorrhage alters these imaging characteristics[193] (Fig. 21–1). The primary differential considerations by imaging include: dermoid and epidermoid cysts, branchial cleft cysts (if TDC is paramedian in location), or rarely, sebaceous cysts.[177]

Historically, preoperative nuclear medicine imaging of the thyroid was performed to document normal functioning thyroid tissue, because the only functioning tissue was occasionally located within the thyroglossal duct cyst.[186] More recently, reports indicate that preoperative identification of a normal thyroid gland by ultrasound confirms the presence of a source of thyroid hormone separate from the thyroglossal duct cyst, precluding additional imaging studies.[141]

The treatment (the Sistrunk procedure) is surgical, with removal of all tissue along the course of the duct as far as the foramen cecum. Removal of the central portion of the hyoid bone as well as the tract coursing behind the hyoid has led to a decreased rate of recurrence (~3% to 5%).[177, 229]

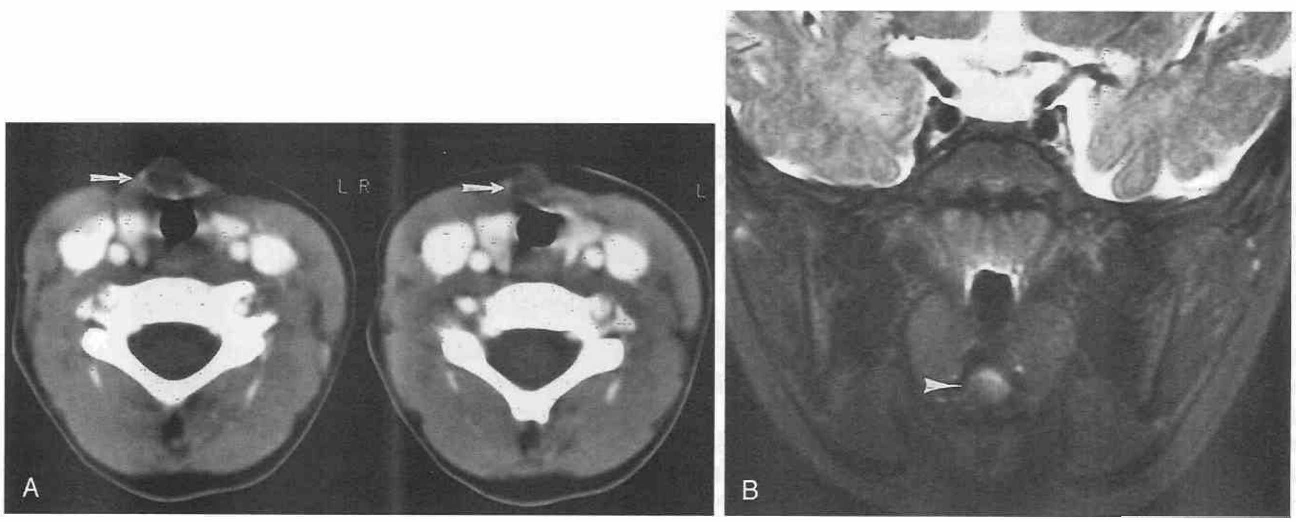

Figure 21–1. Thyroglossal duct cyst. *A*, Axial postcontrast CT scan demonstrates a midline mass of decreased attenuation *(arrows)* at the level of the thyroid gland. Minimal rim enhancement is present. *B*, Coronal fast spin-echo (FSE) MRI scan shows an oval-shaped mass of slightly hyperintense signal at the base of the tongue, in the area of the foramen cecum *(arrowhead)* in this infected cyst.

Anomalies of the Branchial Apparatus

A basic knowledge of the normal embryogenesis of the branchial apparatus and the derivatives is helpful in the understanding the imaging appearance of these anomalies.[142, 148, 191, 223] The branchial apparatus is a complex structure derived from neural crest cells. It develops between the 2nd and 7th weeks of gestation. This embryonic structure can be subdivided into five pairs of mesodermal arches that lie between five paired ectodermal branchial clefts (grooves) externally and four endodermal pharyngeal pouches internally.[148] The fifth arch lies buried near the site of the laryngotracheal outgrowth and by convention is called the sixth arch. These are the primitive structures that give rise to the muscles, bones, and ligaments of the face and neck as well as their nerve and blood supply.[191]

After 4 weeks of gestation, at which time the branchial arches are well defined, the first and second arches begin to thicken and enlarge. This thickening and enlargement of the first and second arches joins with the third and fourth arches and their intervening closing membranes to form a shallow ectodermal pit called the cervical sinus of His. The second and fifth clefts then merge with each other, obliterating the cervical sinus. The first and second pouches merge to form the tubotympanic recess that further develops into the middle ear and eustachian tube. The ventral portion of the second branchial pouch gives rise to the tonsillar fossa. The inferior parathyroid, thymus, and piriform sinus are formed by the third pouch and the superior parathyroid gland and apex of the piriform sinus by the fourth pouch. The first branchial cleft is the only cleft to give rise to an adult structure, the epithelium of the external auditory canal.[165]

Although the cause of branchial anomalies is controversial, current theories include (1) an origin as *vestigial remnants* secondary to incomplete obliteration of the branchial apparatus and (2) structures that arise from "buried" epithelial *cell rests*. In the vestigial remnant theory, incomplete obliteration of any portion of a branchial cleft, pouch, or the cervical sinus of His can lead to formation of a sinus, fistula, or cyst. In the cell rest theory, trapped cells located anywhere in the branchial apparatus are thought to be capable of forming branchial cysts later in life.[24, 148]

Anomalies of the branchial apparatus are classified as fistula, sinus, or cyst. If there is persistence of both a branchial cleft and a corresponding pharyngeal pouch, a communication in the form of a fistula can develop. In this case, an epithelium-lined tract connects the skin to the lumen of the foregut (pharyngeal mucosa). A branchial sinus is an incomplete tract that usually opens externally to the lateral skin surface of the neck. Communication with an associated cyst is variable. Both fistulas and sinuses can be lined by squamous, ciliated, or columnar epithelium. Congenital cysts of branchial origin have no internal or external communication with the skin or pharynx. The cysts are thin-walled and lined with squamous or columnar epithelium.[24, 148]

First Branchial Anomalies

First branchial apparatus anomalies account for 5% to 8% of all branchial anomalies, and are usually in the form of a cyst or sinus.[95] Although both Arnot[9a] and Work[260] attempted to classify first branchial anomalies into two distinct subtypes, Olsen found this scheme difficult in the categorization of all first branchial anomalies.[77, 180] An understanding of these anomalies is not intuitive; thus, a grasp of the regional embryology appears to be more helpful rather than an attempt to subclassify them.

The first branchial apparatus gives rise to portions of the middle ear, external auditory canal, eustachian tube, mandible, and maxilla. The formation of these structures is completed by 6 and 7 weeks of gestation. The parotid gland and facial nerve form and migrate between 6 and 8 weeks of gestation. First branchial apparatus anomalies present in a variable relationship to the parotid gland and facial nerve. They can arise anywhere along the nasopharynx, middle ear cavity, external auditory canal, superficial or deep lobes of the parotid gland, superficial to the parotid gland, angle of the mandible, or anterior or posterior to the pinna.[24]

Although this anomaly occurs in childhood, it is more commonly encountered in middle-aged women who present with recurrent abscesses or inflammatory processes at the angle of the mandible or ear. If the anomaly is related to the parotid gland, the patient often presents with recurrent parotid abscesses, which are unresponsive to therapy. Refractory cases, associated with facial nerve palsy, can mimic a parotid neoplasm clinically.[242] If the cyst drains into the external auditory canal, the initial presentation may be otorrhea.

On ultrasound, CT, and MRI, a first branchial cyst appears as a typical cystic mass that may be located within, superficial, or deep to the parotid gland and near the external canal of the ear or angle of the mandible (Fig. 21–2). Infected cysts have variable wall thickness and enhancement characteristics. When the anomaly is located in the parotid gland, imaging findings are nonspecific and do not allow this mass to be differentiated from other cystic masses of the parotid gland.[127]

Second Branchial Anomalies

Approximately 95% of all branchial anomalies are related to the second branchial apparatus. The most common

Figure 21–2. First branchial apparatus cyst. Axial postcontrast CT scan. A nonenhancing, kidney-shaped mass is seen superficial to, but contiguous with, the parotid gland *(curved arrow)*.

location of this anomaly is the submandibular space; however, occurrence may be anywhere from the oropharyngeal fossa to the supraclavicular region of the neck.[127] Three fourths of these anomalies are cysts.[127] Fistulas or sinuses usually present before age 10 years, whereas cysts are more common between ages 10 and 40 years.[158, 231] There is no gender predilection.[67]

Bailey classified second branchial cysts into four subtypes based on location[12, 162, 175, 215]:

Type I cysts lie deep to the platysma muscle and the overlying cervical fascia, and anterior to the sternocleidomastoid muscle. These cysts are thought to represent a remnant of the tract between the sinus of His and skin.

Type II cysts, thought to be the result of persistence of the sinus of His, are the most common. They are located posterior to the submandibular gland, anterior and medial to the sternocleidomastoid muscle and anterior and lateral to the carotid space.

Type III cysts course medially, between the internal and external carotid arteries, and may extend to the lateral wall of the pharynx or skull base. These cysts are thought to arise from a dilated pharyngeal pouch.

Type IV cysts arise from a remnant of the pharyngeal pouch and lie in the mucosal space of the pharynx, adjacent to the pharyngeal wall.

Second branchial cleft cysts most commonly present as a fluctuant, nontender mass at the lateral aspect of the mandibular angle.[162, 230, 231] If the cyst becomes infected, patients seek medical attention with a clinical history of a slowly enlarging, painful mass.[231] If a fistula is present, an ostium is usually noted at birth at the anterior border of the junction of the middle and inferior third of the sternocleidomastoid muscle. The associated tract courses deep to the platysma muscle, ascends laterally along the carotid sheath, and continues above and lateral to the hypoglossal and glossopharyngeal nerves. It then passes between the internal and external carotid arteries before terminating in the region of the palatine tonsillar fossa.[12, 24]

Because these cysts usually present as a neck mass in the young child, sonography is often the initial imaging study. The cysts range in size from 1 to 10 cm.[58, 243] If the anomaly is uncomplicated, the sonographic appearance is typical for a cyst (i.e., a sharply marginated, anechoic, compressable mass with increased through transmission).[127] A well-circumscribed, thin-walled mass of decreased attenuation is present on CT[230] (Fig. 21–3). On MRI, the fluid within the cyst varies from hypointense to slightly hyperintense to muscle on T1-weighted images and is usually hyperintense to muscle on T2-weighted images.[95] When the cyst is infected, it can demonstrate increased echogenicity on a sonogram, relatively increased attenuation on a CT scan, and relatively hyperintense MRI signal, with variable contrast enhancement and edema of surrounding tissue.[24, 95, 162, 168, 242] Occasionally, the "beak sign," pathognomonic of a Bailey type III second branchial cyst, is present. In this case, the medial aspect of the cyst is compressed and forms a beak as it extends between the internal and external carotid arteries on axial CT or MRI.[93]

Third and Fourth Branchial Anomalies

Both third and fourth branchial anomalies are rare.[49] In spite of the rarity of third branchial cysts, they are the second most common congenital lesion of the posterior cervical space after lymphatic malformation.[183] Anomalies of the fourth branchial apparatus usually appear as a sinus rather than a cyst or fistula. The majority of third and fourth anomalies are found on the left.[49]

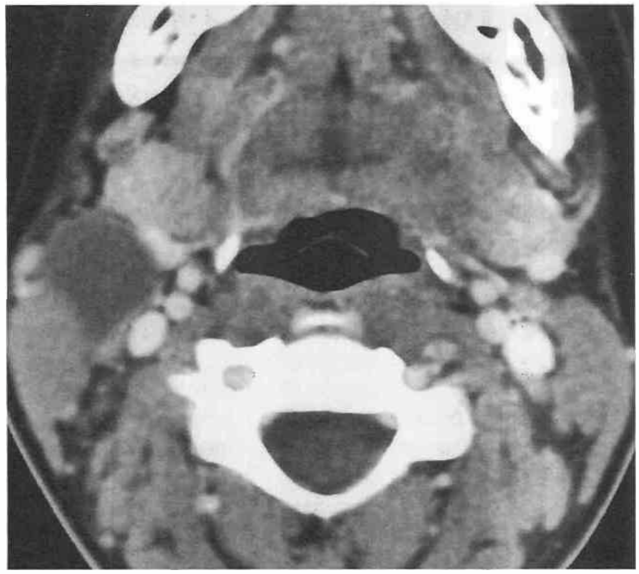

Figure 21–3. Second branchial apparatus cyst. Axial postcontrast CT scan. A rounded, nonenhancing mass is present in the typical position of a Bailey type II cyst. The cyst lies posterior and lateral to the submandibular gland, anterior and medial to the sternocleidomastoid muscle, and lateral to the carotid space.

Because the dorsal aorta between the third and fourth arches involutes, a third branchial apparatus anomaly originates in the posterior cervical space.[24] Third branchial cleft cysts must be located posterior to the common or internal carotid artery, and between the hypoglossal nerve (below) and glossopharyngeal nerve (above). If the anomaly is in the form of a fistula, it will have a cutaneous opening similar to a second branchial fistula (i.e., anterior to the lower sternocleidomastoid muscle). It then courses posterior to the common or internal carotid artery, anterior to the vagus nerve, and between the hypoglossal and glossopharyngeal nerves. The fistula pierces the thyrohyoid membrane and enters the piriform sinus anterior to the internal pharyngeal nerve.

A third branchial cleft cyst often presents as a painless, fluctuant mass in the posterior triangle of the neck after a viral upper respiratory infection. On imaging, the cyst most commonly appears as a unilocular mass with variable wall thickness and enhancement characteristics.[127]

Fistulas of the fourth branchial apparatus have not been reported.[49] Anomalies related to the fourth branchial cleft are in the form of a sinus tract. The tract arises from the piriform sinus and pierces the thyrohyoid membrane. It then descends along the tracheoesophageal groove and continues into the mediastinum, following a course under the aortic arch on the left and ascending into the neck, anterior to the common or internal carotid artery. This is in contrast to third branchial remnants, which course posterior to the carotid artery (Fig. 21–4). Rarely, the tract may descend on the right coursing under the subclavian artery.[24]

Differentiating third from fourth branchial anomalies on

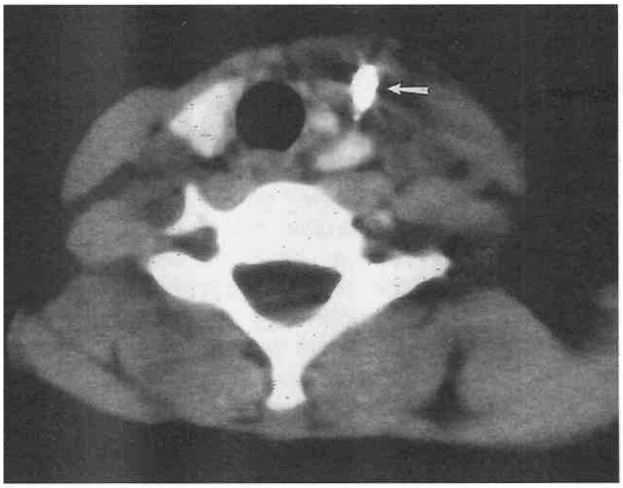

Figure 21–4. Fourth branchial apparatus sinus. Axial noncontrast CT after the patient had ingested oral contrast medium. Barium is present in a sinus tract *(arrow)* that lies anterior to the thyroid gland on the left. The tract arose from the piriform sinus and continued into the mediastinum.

imaging is problematic. Key relationships include the carotid artery and the superior laryngeal nerve. Third branchial anomalies lie posterior to the carotid artery, whereas fourth branchial anomalies are anterior to it. Those anomalies above the superior laryngeal nerve are third branchial origin, whereas those below the nerve are related to the fourth branchial apparatus.[49] On imaging, both third and fourth branchial anomalies related to the piriform sinus may appear similar to external laryngoceles.[24]

Cervical Thymic Remnants

Cervical thymic remnants are rare lesions derived from the third and fourth pharyngeal pouches. During the 6th week of gestation, thymic primordia (endoderm) develops from lateral and ventral diverticula of the third pharyngeal pouch, with a small contribution from the fourth pharyngeal pouch. These hollow outgrowths, which are connected to the pharynx by the thymopharyngeal ducts, begin to elongate in a caudal plane. At the end of the 6th week, the diverticula are obliterated secondary to epithelial proliferation. These two solid masses join in the midline before their final descent into the anterior mediastinum at the 9th week of gestation. In the 10th week of gestation, lymphocytes invade the endodermal structure to form lymphoid tissue in the thymus. The superior thymic primordia usually regresses.[17, 256]

Currently, two main theories have been reported to explain the etiology of thymic remnants. The *congenital theory*, favored by the most authorities, states that these cysts arise secondary to persistence of thymopharyngeal duct remnants. Progressive, cystic degeneration of thymic (Hassall's) corpuscles, primitive endodermal cells, lymphocytes, and the epithelial reticulum of the thymus have been proposed as the origin in the *acquired theory*.[15, 65, 266] As related to the embryologic development, these cysts may be located beneath or medial to the sternocleidomastoid and anywhere from the level of the hyoid to the superior mediastinum.[17]

Because the thymus reaches its greatest relative size at 2 to 4 years of age and its greatest absolute size at puberty, most thymic cysts are detected in childhood.[82] Two thirds of thymic cysts are detected in the first decade of life (most commonly, at 3–8 years of age), with the remaining one third detected in the second and third decades.[33, 93, 231, 256] Seventy-three percent of thymic cysts are found in males.[33, 68, 160]

Most patients are asymptomatic, with 80% to 90% presenting with a slowly enlarging, painless neck mass near the thoracic inlet, anterior or deep to the sternocleidomastoid muscle.[57, 65, 67, 68, 88, 160, 174, 254] Hoarseness, dysphasia, stridor, and dyspnea in the newborn may occasionally be seen as the initial complaint secondary to the mass effect. Infection, hemorrhage, or Valsalva maneuvers can cause rapid enlargement of the cyst.[15, 174, 198, 231, 254] Seventy percent of thymic cysts are left-sided, 23% are right-sided, and the remaining 7% are midline or pharyngeal in location.[15, 51]

Cervical thymic remnants may be found anywhere along the path of the thymopharyngeal duct, which courses along the carotid sheath, from the level of the angle of the mandible to the superior mediastinum. The lesions vary in size (1 to 17 cm) and shape (round to elongated).[15, 26, 33] Most cysts are unilocular and have a smooth lining.[33, 65, 160, 191] A connection between the cervical thymic anomaly and the mediastinal thymic gland may persist in the form of direct extension or a remnant of the thymopharyngeal duct in 50% of cases.[38, 52, 88, 247] A fibrous strand may also remain between the cervical thymic cyst and the thyroid gland.[65] Cervical thymic cysts are often associated with thyroid and parathyroid inclusion cysts.[15]

Grossly, thymic cysts are well defined, thin-walled, uniloculated, or multiloculated masses. They are lined by stratified or pseudostratified, cuboidal, or columnar epithelium with pathognomonic Hassall's corpuscles within the wall.[15, 160] The wall may also contain lymphoid tissue or giant cells with cholesterol clefts and granulomas.[38, 65, 68, 160]

Thymic tissue must be present within the lesion for the pathologic diagnosis. Occasionally, thyroid or parathyroid tissue is also found within the cyst or cyst wall.[48, 247] As derivatives of the third and fourth branchial clefts, thymic cysts can extend through the thyrohyoid membrane and into the piriform sinus.[68] There have been no reports of malignant degeneration of thymic cysts in children or the development of myasthenia gravis or immunologic deficiencies following excision of a thymic cyst. However, malignant degeneration has been documented in ectopic solid thymic tissue.[124, 174]

Because most ectopically located thymic masses are primarily cystic, sonography usually shows a large, well-defined unilocular or multilocular cyst parallel to the sternocleidomastoid muscle with hypoechogenicity and increased through-transmission. A homogeneous, near-water attenuation, uniloculated or multiloculated, nonenhancing mass is seen located along the course of the carotid sheath on CT[26, 33, 114, 140, 161] (Fig. 21–5). MRI of thymic cysts demonstrates a fluid-filled mass with signal characteristics isointense to hyperintense to water.[149] If hemorrhage or infection is present, imaging characteristics vary accordingly.[33, 231]

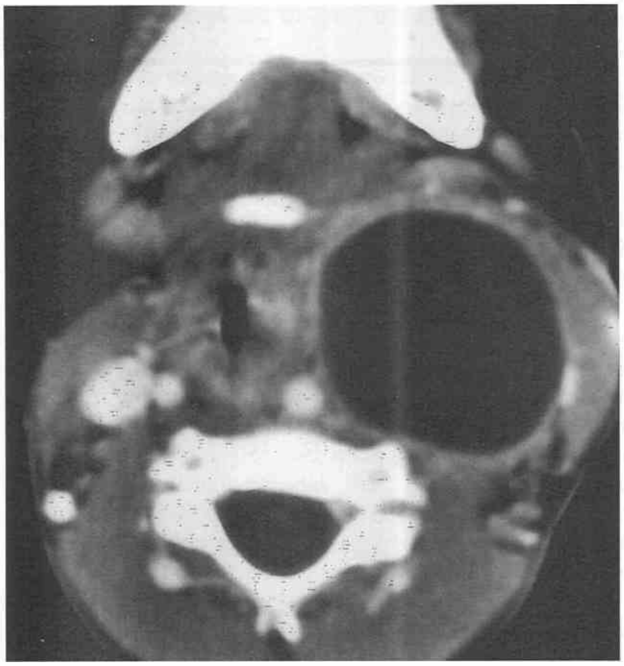

Figure 21–5. Thymic cyst. Axial postcontrast CT scan. A large, round, nonenhancing mass is present in a position similar to a second branchial apparatus cyst; however, the sternocleidomastoid muscle lies in a more lateral position.

The main differential consideration of thymic remnants is a second branchial cleft cyst. A true thymic cyst passes posterior to the carotid bifurcation and terminates in the piriform sinus, whereas a second branchial cleft cyst passes between the internal and external carotid arteries and ends in the superior tonsillar pillar. Fifty percent of cervical thymic cysts extend into the superior mediastinum, whereas mediastinal extension with branchial cleft anomalies does not occur.[15,174] If a mass is located in the area of the inferior pole of the thyroid gland, a thymic origin should be considered.[125] Other differential considerations would include thyroglossal duct cyst, lymphatic malformation, cystic neuroblastoma, lympadenopathy, external laryngocele, and vallecular cysts.[33,114]

Dermoid and Epidermoid Cysts

The terminology and classification of dermoid, epidermoid, and teratoids cysts of the head and neck can lead to confusion because of overlapping features. All of these cysts can be considered in the spectrum of teratomas. The masses share a common feature of containing tissue that is foreign to the body part from which it originates. Dermoids and epidermoids are ectoderm-lined inclusion cysts, with dermoids containing skin appendages, and epidermoids lacking these elements. Teratoid cysts may be composed of tissues of other organ systems.[108]

Dermoid cysts of the neck commonly occur near midline, along lines of embryonic fusion.[119] In the neck, the most common location is the floor of the mouth, accounting for 11.5% of all dermoids.[173] Other locations in the head and neck include the anterior neck, tongue, and palate.[172,173] Epidermoid cysts are rarely found in the head and neck. When they occur, they are usually present in infancy.[230] There is no gender predilection with dermoid or epidermoid cysts.[104,231]

Dermoid cysts typically become clinically apparent in the second or third decades of life.[104,231] They most commonly present as a soft, slowly growing, suprahyoid, midline neck mass. Size is variable, from a few millimeters to 12 cm. A rapid increase in size can be seen secondary to association with a sinus tract, pregnancy, or increasing desquamation of skin appendage products.[182,230] Lesions lying in the floor of the mouth, in the sublingual space, are often clinically inapparent or exhibit minimal mass effect. If located in the submandibular space, the lesion usually presents with a more obvious swelling or mass effect.[104,252] In contrast to thyroglossal duct cysts, which move with protrusion of the tongue because of their association with the hyoid bone, dermoid cysts are nonmobile with this maneuver.[182]

On pathologic examination, dermoid cysts are well-defined, encapsulated masses lined with squamous epithelium. They may contain skin appendages in the form of sweat or sebaceous glands or hair follicles. Inclusion of skin appendages can lead to the formation of keratin and sebaceous material and, occasionally, hair.[225] The incidence of malignant degeneration into squamous cell carcinoma is approximately 5%. Epidermoid cysts lack skin appendages but otherwise are similar in histologic appearance to dermoids.[230]

Because dermoid cysts typically present in older children, CT is often performed as the initial imaging study. Dermoid cysts appear as a thin-walled, unilocular mass with homogeneously decreased attenuation, with CT measurements in the negative numbers (0 to −18 HU)[108] (Fig. 21–6). Occasionally, a "sac of marbles" appearance, representing multiple, small fatty nodules within the fluid, is seen within the cyst. This appearance is virtually pathognomonic of a dermoid cyst. A more heterogeneous appearance can be present secondary to a difference in composition of the various skin appendage components. Fluid-fluid levels are a rare finding. After administration of contrast medium, thin, peripheral enhancement is often present.[230] On MRI, signal changes are variable and dependent on the composition of the cyst. T1-weighted signal can be hyperintense secondary to lipid concentration or isointense to muscle; T2 signal is usually hyperintense to muscle.[104,252]

When dermoids are located in the floor of the mouth, accurate localization by imaging is important for surgical planning. Most commonly, dermoids in the floor of the mouth lie above the mylohyoid muscle, which places them in the sublingual space. These cysts are amenable to an intraoral surgical approach. Cysts that lie below the mylohyoid muscle are localized to the submandibular space, necessitating an external, submandibular approach. Coronal CT or MRI is the optimal imaging plane for localization of these masses into the appropriate space.[230]

Epidermoid cysts most commonly have homogeneously decreased attenuation on CT, with hypointense T1-weighted and hyperintense T2-weighted signal to muscle on MRI closely following water signal. With this imaging appearance, it is difficult to distinguish epidermoid cyst

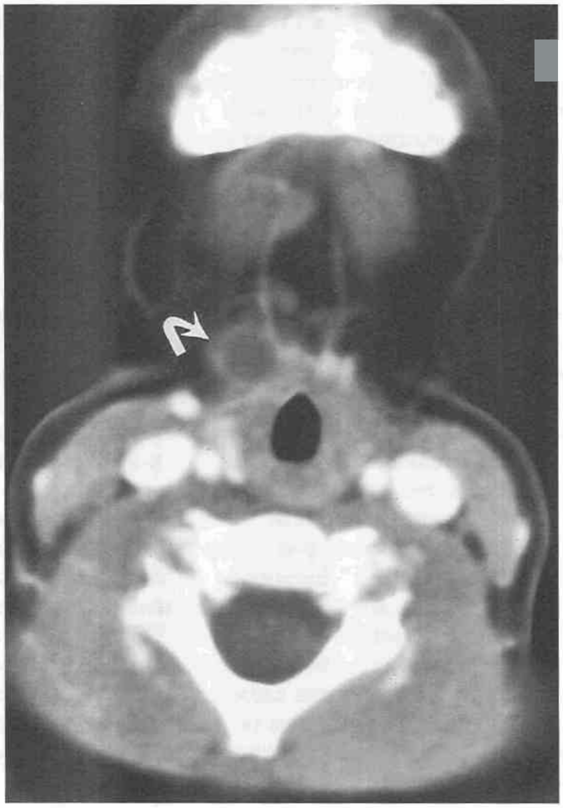

Figure 21–6. Dermoid cyst. Axial postcontrast CT scan. A well-defined mass of decreased attenuation lies in the anterior neck, slightly off midline *(curved arrow)*. Attenuation values were 0 to −5 Hounsfield units (HU).

from uncomplicated cystic lesions in the floor of the mouth, such as a lymphatic malformation or ranula.[48]

Teratoma

Teratomas constitute approximately 9% of all pediatric head and neck neoplasms, with fewer than 5% of all teratomas occurring in the head and neck.[9, 47, 115] In the pediatric population, most teratomas are extragonadal in location, with 82% found in the sacrococcygeal area.[14, 240] Locations in the head and neck include the neck, orbit, nasal cavity, paranasal sinus, oral cavity, oropharynx, nasopharynx, temporal bone, and ear.[1, 60, 97, 132, 239] Teratomas are thought to arise from misplaced, pleuripotential, primordial germ cells. They are classified as "true neoplasms" because of their biologic behavior of progressive and invasive growth patterns.[200]

Teratomas have been subclassified by Ewing and Arnold into four types[66a, 203]:

1. *Dermoids*—masses of ectodermal and mesodermal elements, composed mostly of adipose tissue with fragments of muscle, cartilage, or bone.
2. *Teratoids*—masses containing elements of all three germ layers, differing from true teratomas because of their poor histologic differentiation.
3. *True teratomas*—masses containing elements of all three germ layers, with differentiation to enable recognizable organs by histologic examination.
4. *Epignathi*—masses containing elements of all three germ layers, with differentiation greater than true teratoma, usually incompatible with life.

Cervical Teratoma

Grossly, cervical teratomas are encapsulated, partially cystic masses with a variegated appearance on cut section. These tumors contain diverse histopathologic findings with variable degrees of maturation. Mature elements are derived from ectoderm, mesoderm, and endoderm; immature tissue arises mostly from neuroectoderm. Neuroectodermal elements (both mature and immature) tend to predominate in cervical teratomas. Although cells in this tumor can be found in any stage of differentiation, the degree of histologic maturity should not be equated with malignant potential.[9, 66a]

Clinically, teratomas are divided into (1) those present at birth or in early childhood and (2) those presenting in the first decade of life. The clinical presentation is variable and depends on the size and location of the tumor. Congenital tumors (presenting in the first 60 days of life) tend to have a benign clinical behavior, but they exhibit a high mortality rate secondary to airway compression with pulmonary compromise. Tumors that present later are usually smaller but carry a higher incidence of malignancy.[200] True cervical teratomas are large and can lead to obstetric complications, such as difficult labor with malpresentation, premature labor, stillbirth, and acute respiratory distress.[35] Extensive unilateral or more diffuse cervical swelling is often present.[222, 228] Maternal polyhydramnios has been reported in 18% of patients with cervical teratomas.[99, 197, 201]

Because of the frequent use of ultrasonography in obstetrics, the diagnosis is often made antenatally. On sonograms, teratomas demonstrate heterogeneous echogenicity with multiloculated areas of cystic and solid regions, angulated cyst walls, and acoustic shadowing from calcifications. The mass may appear well defined or, less commonly, infiltrative.[200] After birth, the patients are usually referred for CT.

Imaging characteristics directly reflect the pathologic makeup of the tumor, often demonstrating a heterogeneous attenuation pattern and appearing primarily cystic, solid, or multicystic. Most cervical teratomas are large, measuring up to 12 cm in size, with approximately 50% containing calcification[200, 258] (Fig. 21–7). Both CT and MRI are helpful in delineating the extent of the tumor and the degree of airway compromise.[105] The MRI appearance is a mass of heterogeneous signal on all pulse sequences with the fatty component, hyperintense on T1-weighted sequences, and areas of calcification, hypointense or hyperintense on T1-weighted images. Attenuation values and signal characteristics of fat and bone, in a mass of the head and neck in a young child, is nearly pathognomic of teratoma. Variable enhancement is present on both CT and MRI after contrast administration. Intubation is commonly required in these patients before scanning.[200]

The primary differential consideration of a cervical teratoma is lymphatic malformation, which more closely follows water signal on all pulse sequences on MRI. Other

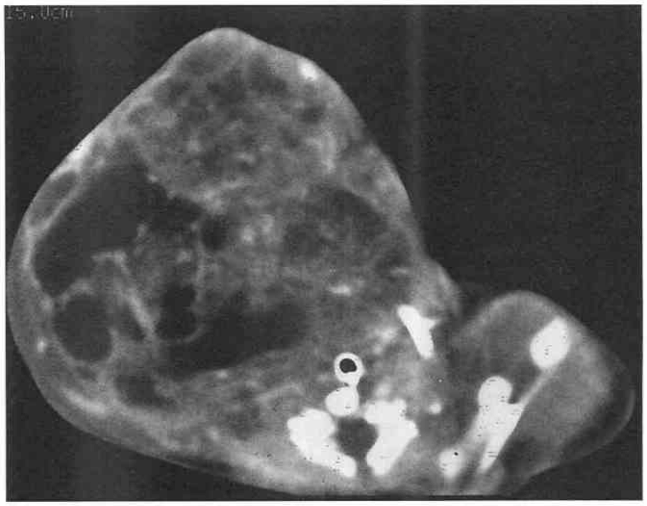

Figure 21–7. Cervical teratoma. Axial postcontrast CT scan. The majority of the anterior neck is involved with an extremely large, heterogeneous mass with mild enhancement. The vascular bundle on the right is not visualized secondary to tumor involvement. The infant required intubation because of mass effect on the airway.

differential considerations include thyroglossal duct cyst, branchial cleft cyst, goiter, hemangioma, and external laryngocele.[57]

Despite the appearance of teratomas on CT and MR, cervical teratomas do not typically infiltrate surrounding tissue; thus, complete surgical resection is usually possible.[200] Surgery is mandatory for congenital cervical teratomas, as the mortality rate is 80% to 100% secondary to airway complications, if the tumor is left untreated. Thus, differentiating this tumor from other congenital space-occupying masses of the neck is crucial. The incidence of true malignancy of congenital teratoma is low (<5%), associated anomalies are uncommon, and the prognosis with surgery is excellent.[90, 187]

Congenital Nasal Masses

Nasopharyngeal Teratoma

Greater than 50% of nasopharyngeal teratomas are seen in the first year of life, with nearly all true tridermal tumors present at birth.[255] They usually arise from the superior or lateral wall of the nasopharynx. For teratomas in the nasal cavity, there is a predilection for girls.[87] The typical clinical presentation involves a neonate with severe respiratory distress, stridor, and dysphagia. These tumors can attain a large size and protrude from the mouth or nostrils.[21, 222, 228]

The imaging appearance is similar to that of the cervical teratoma (Fig. 21–8). In addition to airway evaluation and evidence of vascular involvement, MRI is helpful in excluding intracranial extension.[258] Differential considerations for nasopharyngeal teratoma include dermoid, encephalocele, nasal glioma, rhabdomyosarcoma, hemangioma, lipoma, neurofibroma, and lymphoma.[226]

Nasal Dermoid

Nasal dermoids are thought to result from a lack of regression of a diverticulum of dura that extends through the foramen cecum between the developing nasal cartilage and nasal bone.[16, 184,209] Depending on the patency of the diverticulum and its contents, the resultant lesion can be a dermal sinus, dermoid cyst, nasal glioma, or encephalocele.[184] Nasal dermoid cysts and dermal sinuses make up 3.7 to 12.6% of all dermoids of the head and neck.[179, 209]

Most nasal dermoids are sporadic in nature; however, several familial cases have been reported.[27, 167] Nasal dermoid cysts and dermoid sinuses can present at any age but are most commonly found in younger children, with a mean age of presentation of 3 years.[184] There is no sexual predilection.[86, 184, 209] These lesions may be found at any location between the glabella and the base of the columela.[184] Approximately 56% present as midline cysts, and 44% present as midline sinus ostia.[184] Rarely, multiple sinus ostia or the simultaneous occurrence of a sinus and a cyst at the glabella and nasal bridge can be seen.[209]

The most common clinical presentation is a painless, cystic enlargement of any part of the nose, associated with one or more dimples.[179] Externally, midline pits, fenestra, or discrete masses are present. Associated hair may protrude from the defect (pit or fenestra).[3, 20, 27, 30, 167, 209] Intermittent episodes of inflammation or discharge of sebaceous or inflammatory material can cause a variation in the size of the mass. Signs and symptoms of meningitis or behavioral changes related to life-threatening frontal lobe abscess can be seen when intracranial extension is present.[179, 209]

Extension of both nasal dermoid cysts and dermal sinuses varies. These lesions can end blindly in the superficial tissues, or they may extend both intracranially and extracranially.[209] Reported incidence of intracranial extension varies between 0 and 57%.[155, 179] Intracranial extension of dermoids typically occurs into the epidural space in the region of the crista galli. There may be further extension, between the leaves in the falx; however, it is rare for the lesion to extend beyond the interdural space.[37, 184]

Both CT and MRI are useful in the evaluation of these lesions. The course of a dermal sinus is seen on CT as a well-defined gap between the nasal bones, in the midline or in the frontal bone.[179] The findings of an enlarged foramen cecum and bifid or distorted crista galli are suggestive of, but not pathognomonic of, intracranial extension (Fig. 21–9). These findings can be present with or without intracranial extension or with intracranial extension of a fibrous cord without dermoid elements.[184] The fibrous tract and ostium usually appear as an isodense or hypodense to soft tissue channel with variable extension. Bony canals are well seen on CT and can extend through the nasal bones, nasal septum, and skull base. Noninfected dermoid cysts appear on CT as nonenhancing masses of fat attenuation with an isodense rim to soft tissue. Stranding of the surrounding soft tissues and change in the attenuation value of the cyst suggests secondary infection of the mass. The appearance of an infected dermoid cyst is similar to an abscess with a peripheral rim of enhancement.[113]

MRI is extremely valuable in assessing these lesions. Thin-slice (3-mm), sagittal, coronal, and axial T1-weighted sequences should be obtained. Enlargement of the foramen cecum with intracranial extension is best demonstrated on sagittal T1-weighted images. Dermoid cysts most commonly have isointense to hyperintense T1-weighted signal as compared with brain, with associated chemical shift

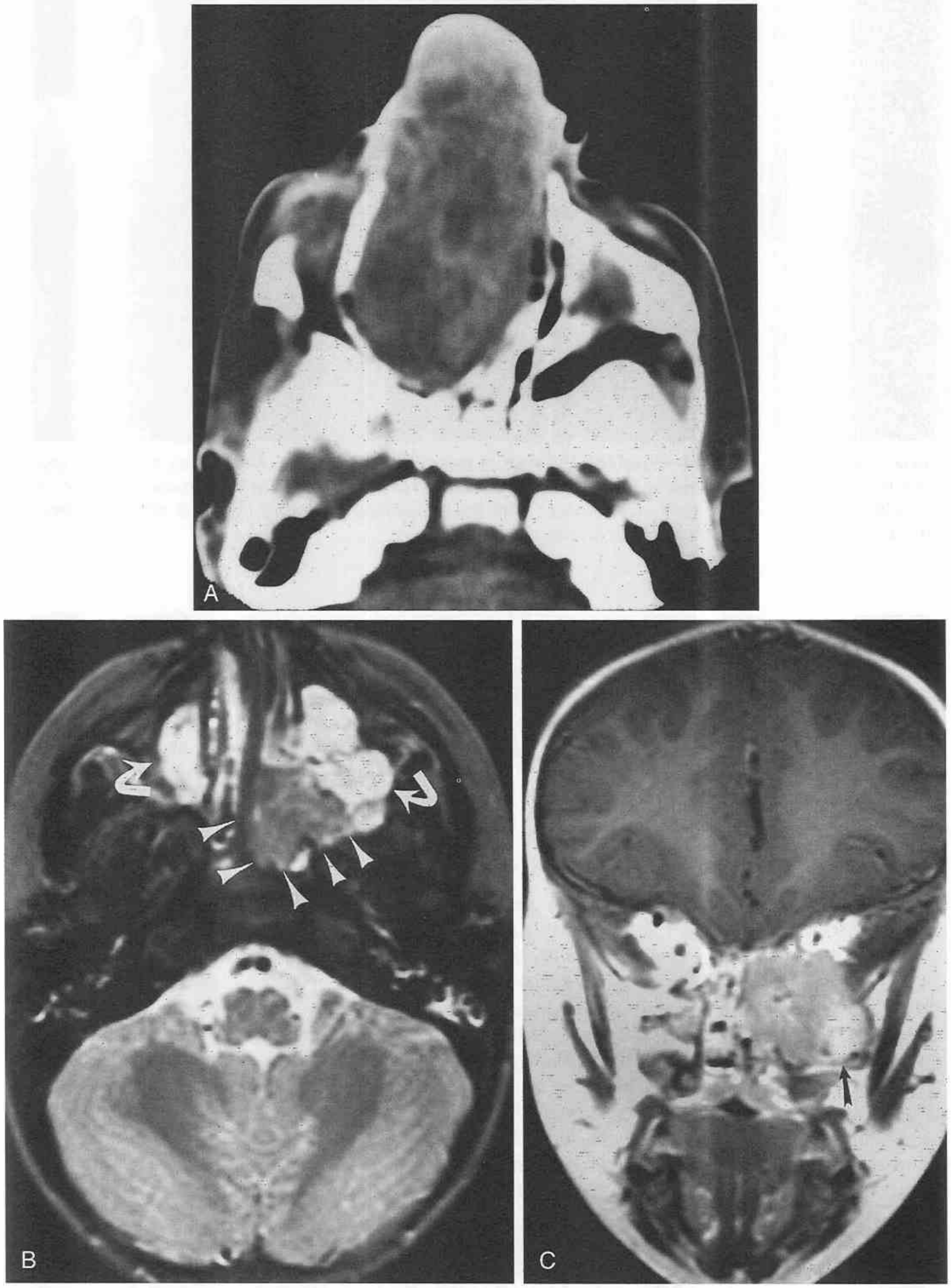

Figure 21–8. Na[redacted]aryn[redacted] tera[redacted]a. *A*, Ax[redacted]oncontra[redacted]T sc[redacted]A he[redacted]gene[redacted]s is filling and causi[redacted]arked expansion of the nasal cavity in an infant. *B*, Axial T2-weighted MRI scan. A mass of the posterior nasal cavity *(arrowheads)* extends into the left maxillary sinus in another patient. The mass shows slightly heterogeneous signal, whereas maxillary sinus disease shows hyperintense signal *(curved arrow)*. *C*, Coronal T1-weighted postcontrast MRI scan. Moderate enhancement of the mass is seen after contrast administration, with the obstructive maxillary sinus disease showing a greater degree of enhancement *(arrow)*.

Figure 21–9. Nasal dermoid. *A*, Sagittal T1-weighted MRI scan. A mass of relative isointensity to gray matter is present in the anterior nasal cavity *(arrowheads)*. It extends through an enlarged foramen cecum *(open arrow)* to the intracranial cavity. *B*, Axial T1-weighted MRI scan shows a bifid appearing crista galli *(arrowheads)*, with the intracranial portion of the nasal dermoid appearing isointense to gray matter in the area of the foramen cecum *(open arrow)*.

artifact. Fibrous tracts are isointense to gray matter on T1-weighted sequences.

The surgical approach with these lesions is dissection of the extracranial portion of the tract to the area of the foramen cecum. If dermal elements are found in the cephalic most portion of the specimen, intracranial dissection is performed.[184, 209]

Nasal Glioma

Nasal gliomas are congenital masses of heterotopic glial tissue with extranasal (60%), intranasal (30%), and mixed (10%) forms. These masses occur sporadically with no familial tendency or sexual predilection. They are rarely associated with other congenital malformations.[234] Extranasal gliomas lie external to the nasal bones and nasal cavity and most commonly occur slightly off midline at the bridge of the nose. The intranasal form is found within the nasal or nasopharyngeal cavity, the oral cavity, or, rarely, the pterygopalatine fossa. A communication between with the extranasal and intranasal components of the mixed form occurs via a defect in the nasal bones or around lateral edges of the nasal bones.[234]

Extranasal gliomas clinically present as a firm, reddish to bluish, skin-covered mass that is found in early infancy or childhood. These masses do not exhibit pulsations or increase in size with a Valsalva maneuver or compression of the ipsilateral jugular vein (Furstenburg sign).[233] They are typically slow-growing; however, they may grow more or less rapidly than the adjacent soft tissue.[234] Intranasal gliomas present as large, firm submucosal masses that extend inferiorly, toward or near the nostril.[234] They may cause obstruction of the nasal passage and respiratory compromise in infants or obstruction of the nasolacrimal duct with resultant epiphora. Cerebrospinal rhinorrhea, meningitis, or epistaxis can also be seen at initial clinical presentation.

On pathologic examination, nasal gliomas resemble reactive gliosis rather than a neoplasm.[146] Metastasis or invasion of surrounding tissue has not been reported.[231] Tiny bits of fibrous or gemistocytic astrocytes, without evidence of mitotic activity, are evident on histologic examination. Fibrous septations and prominent zones of granulation tissue are also found.[231]

Distinguishing a nasal glioma from an encephalocele is difficult on imaging unless a communication between the mass and the intracranial subarachnoid space is documented. If a communication is present, the mass is classified as an encephalocele rather than a nasal glioma. Evaluation is best accomplished with MRI in the sagittal plane. Otherwise, encephaloceles and nasal gliomas appear as masses of soft tissue signal, isointense to gray matter, without a clear distinction between the two on imaging (Fig. 21–10).

Anterior Basal Encephalocele

The reported incidence of encephalocele varies geographically. The incidence of occipital encephaloceles is greater in the United States and Western Europe, whereas anterior basal cephaloceles are more common in the Far East and parts of Asia.[192] Overall, cephaloceles account for 10% to 20% of all craniospinal malformations. Anterior basal cephaloceles make up approximately 10% of cephaloceles, with the occipital form accounting for 75% and the nasal and orbital forms 15%.[133] The incidence of basal cephaloceles is between 1 and every 35,000 to 40,000 live births.[262]

Figure 21–10. Nasal glioma. *A*, Axial noncontrast CT scan. The anterior nasal cavity on the left is filled with a mass of slightly less than soft tissue attenuation. There is bony remodeling of the nasal bone on the left. *B*, Sagittal T1-weighted MRI scan. The anterior nasal mass is isointense to gray matter *(arrowheads)* and shows no evidence of intracranial communication.

The term *cephalocele* refers to an extracranial herniation of intracranial contents through a midline defect in the skull base and dura mater. Anomalies that contain neural elements are termed *encephaloceles*; those that contain meninges and subarachnoid space are termed *meningoceles*.[133]

There is no universal agreement on the etiology of anterior cephalocele; however, the anomaly is thought to be secondary to imperfect closure of the anterior neuropore of the neural tube at approximately the 25th day of gestation. Cephaloceles related to the sphenoid bone may be secondary to persistence of the craniopharyngeal canal or failure of normal union of basilar ossification centers.[189]

On histologic examination, the herniated neural tissue in an encephalocele contains neurons with prominent astrogliosis. The cyst wall is composed of glia and fibrous connective tissue without neurons.[192] Basal cephaloceles are categorized according to location into the following:

- Sphenopharyngeal (through the sphenoid body and into the pharynx)
- Spheno-orbital (through the superior orbital fissure)
- Sphenoethmoidal (through sphenoid and ethmoid bones resulting in a posterior nasal mass)
- Trans(fronto)ethmoidal (through the cribriform plate resulting in an anterior nasal mass);
- Sphenomaxillary (a theoretical type that extends into the maxillary sinus)

A transsphenoidal cephalocele is a subtype of the sphenopharyngeal form, in which the herniated contents extend into the sphenoid sinus.[189]

The most common type of basal cephalocele, the sphenopharyngeal, usually presents as a pharyngeal mass with signs and symptoms related to airway obstruction (snoring, mouth breathing, nasal obstruction) or cerebrospinal fluid leak (runny nose).[170,262]

Frontoethmoidal encephaloceles commonly present in the neonatal or infantile period with a nasal mass or nasal stuffiness; nasopharyngeal cephaloceles present toward the end of the first decade with mouth breathing or nasal stuffiness. Craniofacial anomalies are not uncommon with frontoethmoidal cephaloceles. Pituitary and hypothalamic dysfunction and a decrease in visual acuity can be seen with sphenoethmoidal and sphenopharyngeal cephaloceles secondary to herniation of the pituitary gland, hypothalamus, and optic apparatus into the sac. Agenesis of the corpus callosum is found in approximately 80% of these patients.[16]

Coronal CT of the skull base is useful in evaluating the typically smooth and well-defined bony margins of the defect as well as the soft tissue component of the lesion. CT with intrathecal contrast material may be useful in determining the continuity of the subarachnoid space with this anomaly; however, this is rarely needed with the availability of MRI evaluation. MRI is superior in evaluating the contents of the cephalocele to include (1) the exact position of the pituitary stalk and gland; (2) the position and state of the optic nerves, chiasm, and optic tracts; (3) the state of the limbic system and cingulate gyrus; (4) the degree of bony dehiscence of the skull base; and (5) the presence of other anomalies[190] (Fig. 21–11).

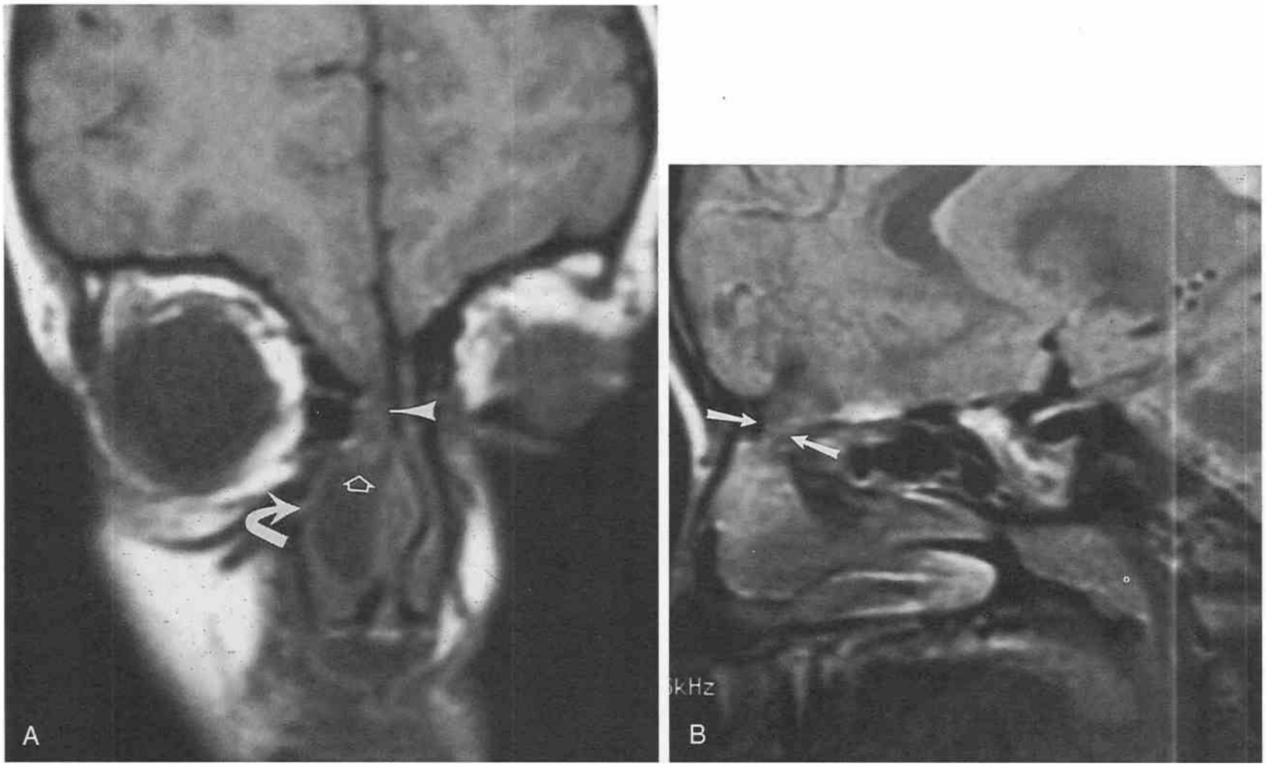

Figure 21–11. Trans(fronto)ethmoidal encephalocele. *A*, Coronal T1-weighted MR image shows inferior displacement of the right gyrus rectus, with continuity of neural tissue extending through the foramen cecum *(arrowhead)* and into the right anterior nasal cavity *(curved arrow)*. The mass contains a small amount of neural tissue *(arrowhead)* in addition to cerebrospinal fluid. *B*, Sagittal intermediate-weighted image demonstrates extension of the neural tissue through the foramen cecum *(arrows)*.

Malignant Neoplasms

Primary malignancies of the head and neck comprise approximately 5% of all malignant neoplasms in the pediatric age group.[111] Lymphoma and rhabdomyosarcoma are the most common tumors in this category; however, primary neuroblastoma, nasopharyngeal carcinoma, thyroid carcinoma, and synovial sarcoma also occur in children.[111]

Lymphoma

Malignant lymphoma represents a heterogeneous group of solid lymphoreticular neoplasms.[139, 217] It is the second most common solid malignant tumor in children and the most common malignancy in the head and neck in this age group.[111] This tumor accounts for approximately 50% of pediatric head and neck malignancies and is equally divided between non-Hodgkin's lymphoma and Hodgkin's lymphoma.[98, 111]

Hodgkin's Disease

Hodgkin's disease has a bimodal age distribution, with the first peak occurring in teenagers and young adults (with a fairly good prognosis) and the second peak in adults over 40 years of age (with a less optimistic prognosis). The disease is rarely encountered in children younger than 5 years of age. There is a male predominance of 3:1 in the preteen years, with the female incidence increasing with age.[146]

Most patients present with painless adenopathy, with 80% to 90% involving cervical lymph nodes. Fever, night sweats, and weight loss are seen as associated systemic symptoms.[248]

Histologically, the tumor consists of polymorphous infiltration of malignant cells (Reed-Sternberg and their mononuclear variants) with morphologically normal reactive cells (lymphocytes, plasma cells, and eosinophils). The diagnostic Reed-Sternberg cell contains multiple nuclei with eosinophilic nucleolus and moderately abundant, slightly eosinophilic cystoplasm. The Rye histologic classification is based on the proportion of lymphocytes and histiocytes in the lymph nodes.[40, 120, 145] Hodgkin's disease has been subclassified into the following forms: (1) lymphocyte predominance, (2) nodular sclerosing (rare in children), (3) mixed cellularity, and (4) lymphocyte depletion.[145]

Non-Hodgkin's Lymphoma

Non-Hodgkin's lymphoma tends to occur in children between the ages of 7 and 11 years, with a male predominance of 3:1. Approximately 15% of cases arise in the head and neck. This disease may involve virtually any structure in the head and neck; however, the majority of children with this form of lymphoma have widespread disease with bone marrow involvement at diagnosis.[92]

The clinical presentation is a neck mass or masses that can cause pressure on vital structures, leading to symptoms related to tracheal compression or superior vena cava syndrome. Primary involvement of Waldeyer's ring may lead to middle ear effusion or nasal obstruction, whereas Burkitt's lymphoma can present as a large mass of the jaw, thyroid, or parotid gland.

The most common histologic types of non-Hodgkin's lymphoma are[36, 53, 126]:

- Malignant lymphoma, lymphoblastic (30% to 35%)
- Malignant lymphoma, undifferentiated (Burkitt's and non-Burkitt's) (40% to 50%)
- Large-cell (15% to 20%)

Histologically, cytologically, and immunologically, the tumor cells in lymphoma and acute lymphoblastic leukemia share some common properties. These two disease processes are better conceptualized as a spectrum of disease rather than separate processes. Leukemia is associated with primary bone marrow involvement; non-Hodgkin's lymphoma, primary lymph node involvement. Arbitrarily, if greater than 25% of bone marrow cells are lymphoblasts, the diagnosis is leukemia.

Imaging is usually not helpful in differentiating Hodgkin's from non-Hodgkin's disease or metastatic lymphadenopathy. The sites of tumor deposition are subdivided as follows[94]:

- Nodal (most common)
- Extranodal, lymphatic (Waldeyer's ring)
- Extranodal, extralymphatic (orbit, paranasal sinuses deep fascial spaces, mandible, salivary glands, skin, and larynx)

Hodgkin's disease shows more predictable biologic behavior. The disease typically spreads from one nodal group to the next contiguous nodal group. Extranodal disease is rare in Hodgkin's disease.[40, 94, 139] In contrast, extranodal disease, with or without associated nodal involvement, occurs frequently in non-Hodgkin's disease. Waldeyer's ring, paranasal sinuses, and nasal cavity are the most common extranodal sites of disease in non-Hodgkin's lymphoma.[139] Widespread disease at presentation is also more common in patients with non-Hodgkin's lymphoma, with cervical adenopathy only part of the clinical picture rather than the major finding.[40, 94, 139] However, both Hodgkin's and non-Hodgkin's lymphomas can present as painless neck masses with unilateral or bilateral cervical adenopathy, involving the mid and lower jugular nodal chains, with relative sparing of the upper jugular chains.[94, 139]

CT demonstrates nodal and extranodal masses of intermediate attenuation (Fig. 21–12); MRI shows homogeneous, intermediate-signal-intensity masses on all pulse sequences.[92] Mild peripheral enhancement can be seen after administration of contrast medium. Calcification of lymph nodes is rare in untreated lymphoma and necrosis of lymph nodes is uncommon.[94] Sonography of cervical adenopathy in patients with lymphoma demonstrates multiple areas of decreased echogenicity, simulating cystic masses. When lymphoma involves the nasopharynx, it usually displays less aggressive imaging characteristics and lacks bone destruction; however, this is not a constant finding. When bony destruction is present, it is typically a permeative pattern rather than the aggressive, lytic pattern found in rhabdomyosarcoma and squamous cell carcinoma.[92, 139]

In addition to imaging the neck, evaluation of patients with head and neck lymphoma should include CT of the chest and abdomen. Gallium 67 scanning is also recommended in the initial staging of the tumor, evaluation of response to treatment, and detection of recurrent and metastatic disease as well as a predictor of clinical outcome in both Hodgkin's and non-Hodgkin's disease.[75]

Infectious causes, such as infectious mononucleosis syndrome and human immunodeficiency virus, as well as phenytoin (Dilantin) hypersensitivity, rheumatoid arthritis, and systemic lupus erythematosis, can produce a pattern of adenopathy similar to lymphoma on imaging.[62]

Rhabdomyosarcoma

Soft tissue sarcomas account for 7% of all malignancies in children younger than 15 years of age in the United States. More than 50% of these tumors are rhabdomyosarcomas, with approximately 38% found in the head and neck.[150] Rhadomyosarcoma is a malignant tumor that arises from primitive pleuripotential mesenchymal cells that are capable of differentiating into skeletal muscle. Thus, these tumors may develop anywhere in the body.[137]

The most common site of primary head and neck rhabdomyosarcoma in children is the orbit and nasopharynx, followed by the paranasal sinuses and middle ear. Other locations in the head and neck include the parapharyngeal soft tissues and nasal cavity.[41, 137, 207] There is a bimodal age distribution occurring at 2 to 5 years of age and in the late teenage years. Most patients are younger than 10 years of age at presentation.[150, 151]

The clinical presentation varies with the anatomic site of the tumor. Those tumors found in the neck present as a painless, enlarging mass. Parameningeal rhabdomyosarcomas usually present with a bloody discharge from the nose or ear, chronic otitis media with or without a facial nerve palsy, or symptoms attributed to an upper respiratory infection. Orbital rhabdomyosarcomas typically present with rapid development of proptosis, decreased vision secondary to optic nerve compression, or a palpable mass leading to an early diagnosis.[137, 207]

Histologically, there are four distinct subtypes of rhabdomyosarcoma:

- Embryonal
- Botryoid (a variant of embryonal)
- Pleomorphic
- Alveolar

The embryonal form is the most common subtype found in the head and neck in children. These densely cellular tumors are composed of lymphocyte-sized cells with hyperchromatic, round to oval nuclei and stellate or bipolar cell processes. Rhabdomyosarcomas tend to have a loose stromal network with a high overall water content. The pleomorphic type is seen only in adults, and the alveolar type occurs the extremities of older children and young adults.[41, 264]

The Intergroup Rhabomyosarcoma Study divided head and neck rhabdomyosarcomas into three categories based

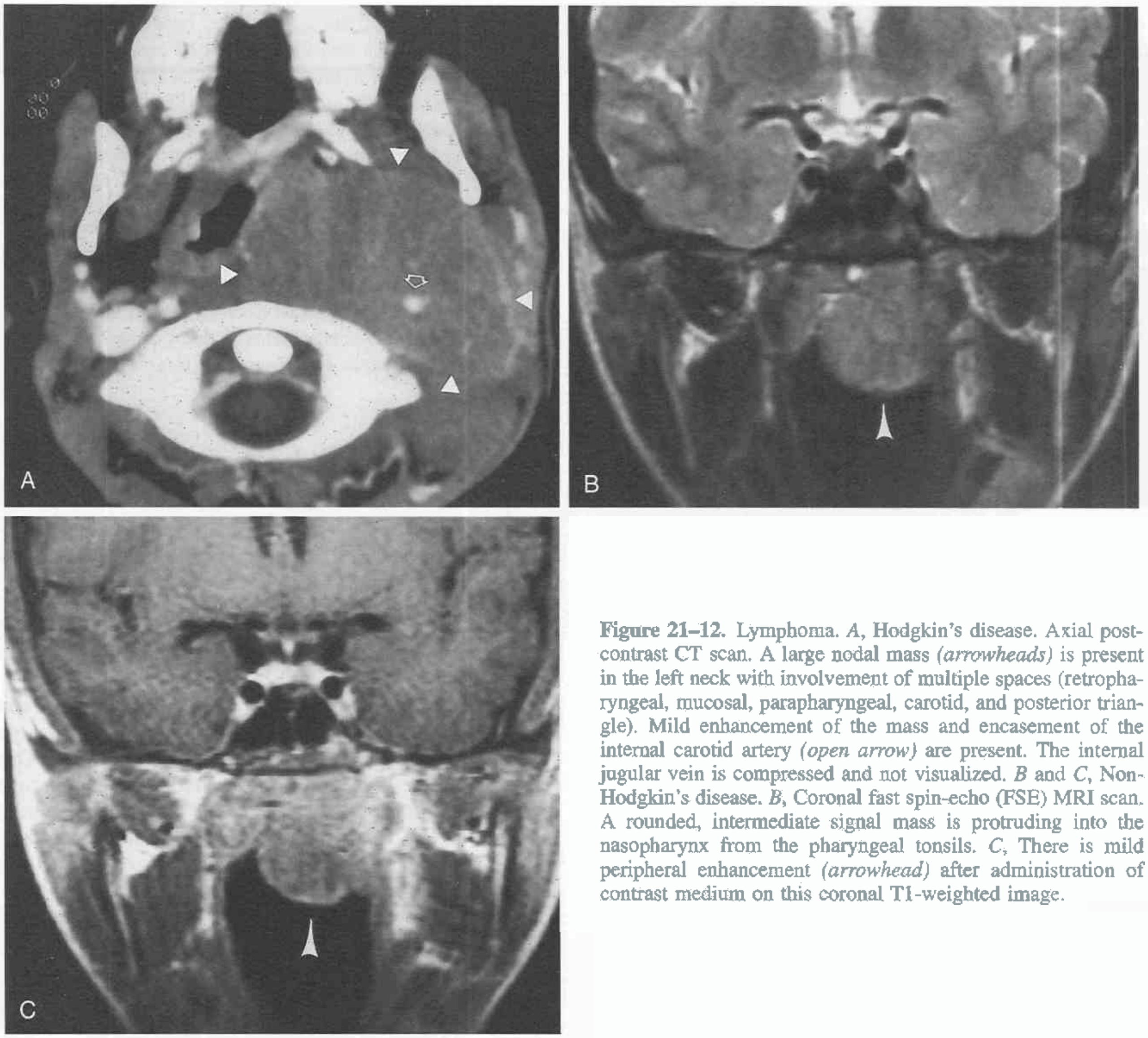

Figure 21–12. Lymphoma. *A*, Hodgkin's disease. Axial postcontrast CT scan. A large nodal mass *(arrowheads)* is present in the left neck with involvement of multiple spaces (retropharyngeal, mucosal, parapharyngeal, carotid, and posterior triangle). Mild enhancement of the mass and encasement of the internal carotid artery *(open arrow)* are present. The internal jugular vein is compressed and not visualized. *B* and *C*, Non-Hodgkin's disease. *B*, Coronal fast spin-echo (FSE) MRI scan. A rounded, intermediate signal mass is protruding into the nasopharynx from the pharyngeal tonsils. *C*, There is mild peripheral enhancement *(arrowhead)* after administration of contrast medium on this coronal T1-weighted image.

on site of origin: (1) orbit, (2) parameningeal (middle ear, paranasal sinuses, nasopharynx), and (3) all other head and neck sites. Those tumors that are paramedian in location (nasopharynx, paranasal sinuses, nasal cavity) have a tendency to extend through the skull base and to invade the meninges. Bony erosion has been reported in 18% of the tumors in this subgroup and 67% of middle ear tumors.[41, 264] The tumor spreads to the lymph nodes of the neck in 12% to 50% of cases. Hematogeneous spread also occurs to lung, bone, brain, bone marrow, and breast.[41, 257, 264]

The usual CT appearance of rhabdomyosarcoma is a poorly-defined, inhomogeneous mass that distorts soft tissue planes and causes bony destruction. After contrast administration, rhabdomyosarcomas usually enhance to the same degree as subjacent muscle on CT.[41, 137] Although MRI findings are not specific, most rhabdomyosarcomas are isointense to minimally hyperintense to muscle on T1-weighted sequences and hyperintense to muscle and fat on T2-weighted sequences. The signal intensity can be homogeneous (most common) or heterogeneous, and there is marked enhancement after contrast administration (Fig. 21–13). Intratumoral hemorrhage can be present.[264]

Because meningeal involvement is the worst prognostic indicator in head and neck rhabdomyosarcoma, sagittal and coronal postcontrast MRI with fat saturation is crucial in evaluating potential dural and meningeal disease and intracranial extension.[25] Coronal CT is the imaging modality of choice for evaluation of bone destruction of the skull base.[41] Thus, all patients with suspected rhabdomyosarcoma should undergo both CT and MRI.

The MRI characteristics of this tumor are similar to those of lymphoma and nasopharyngeal carcinoma. AIDS-related Kaposi's sarcoma may also have similar imaging characteristics; however, generalized adenopathy in the neck is typically present with rhabdomyosarcoma.[265]

Those tumors that are not amenable to a good surgical outcome (middle ear, nasopharynx, paranasal sinuses) are treated with chemotherapy and irradiation. If intracranial extension is detected, additional radiotherapy is given to the base of the brain with whole brain irradiation as well

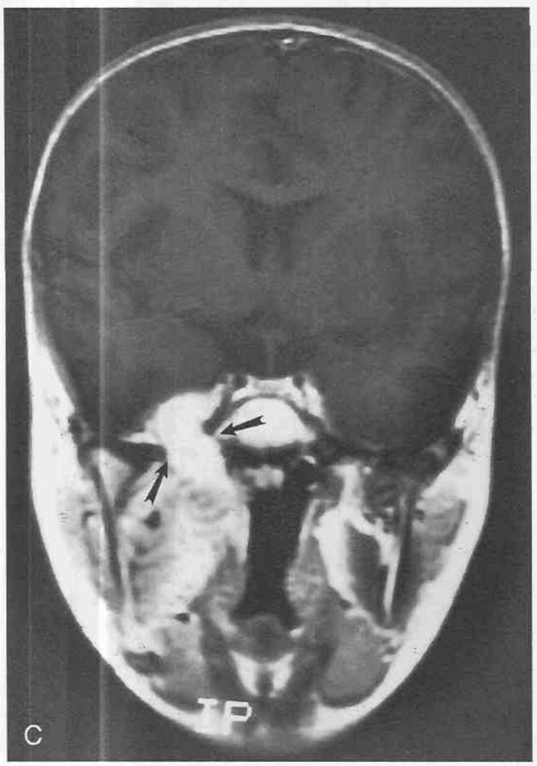

Figure 21–13. Rhabdomyosarcoma. Sagittal *(A)* and axial *(B)* postcontrast T1-weighted MRI scans. There is marked enhancement of the mass filling the nasal cavity and nasopharynx. Extension can be seen intracranially along the floor of the anterior cranial fossa *(A) (arrows)* and the medial aspect of the middle cranial fossa *(B) (arrowheads)* as well as into the left orbit *(B) (arrows)*. *C,* Coronal T1-weighted MRI scan in a second patient demonstrates intracranial extension of an enhancing infratemporal fossa mass through the foramen ovale on the right *(arrows)*.

as intrathecal chemotherapy. With the remainder of the tumors, it is assumed that all patients have systemic disease at presentation; consequently, they are treated locally and regionally with surgery and irradiation, or both, as well as systemically with chemotherapy.[152]

The prognosis is closely related to initial extent of disease.[238] The tumors with associated parameningeal disease commonly present with advanced disease (grade III or IV) and carry a 35% to 64% 2-year disease-free survival rate. This poor survival rate is secondary to the tendency for invasion of the skull base with associated meningeal and intracranial disease. Orbital rhabdomyosarcoma carries the best prognosis, with an 80% to 90% 2-year disease-free survival rate. All other head and neck primary tumors carry an intermediate prognosis, approximately a 78% 2-year disease-free survival rate.[79,137]

Neuroblastoma

Neuroblastoma is a neural crest tumor arising from the sympathetic nervous system. Overall, it represents the most common malignant tumor in children younger than 1 year of age, with the most frequent primary sites the adrenal gland and retroperitoneum.[129] The occurrence of this tumor in infants in a primary cervical location is rare, accounting for less than 5% of all neuroblastomas. Most neuroblastomas located in the neck represent metastatic disease from an abdominal or thoracic primary tumor.[39,224]

Patients present with a painless, smooth, rubbery mass with symptoms of dysphasia, hoarseness, stridor, and respiratory difficulty.[2,224] Horner's syndrome, with accompanying hematochromia of the iris, has also been reported.[2]

Histologic examination reveals a densely cellular tumor composed of small cells, sometimes arranged in whirls or rosette-like structures with intermingled larger primitive ganglion-like cells and intercellular neuronal tissue. A spectrum of maturational changes is seen from the most immature, malignant neuroblastoma to benign ganglioneuroma. Bone marrow involvement is common.[216]

Because patients are young infants presenting with a neck mass, ultrasound is often the initial imaging modality. Sonographic findings are nonspecific, showing a hypoechoic or complex mass with evidence of cervical adenopathy. Small echogenic foci, consistent with calcifications, are sometimes present.[2] CT scans reveal a sharply circumscribed mass in the poststyloid parapharyngeal space. Calcifications may be present on noncontrast images. Because the mass usually originates posterior to the vascular sheath, the carotid artery and jugular vein are displaced anteriorly. After contrast administration, the tumor enhances to the same degree or slightly greater than muscle (Fig. 21–14).

Increased signal intensity to muscle is seen on T1-weighted and T2-weighted MRI. MRI is superior to CT in the evaluation of these tumors. MRI better delineates the mass and demonstrates the interfaces between the mass and surrounding soft tissue structures as well as the exact relationship of the tumor to the surrounding vessels.[61,72]

With cervical neuroblastoma, intracranial extension is rare, and only one case of intraspinal extension has been reported in this location.[54,188] Because cervical neuroblastoma is more commonly a metastatic lesion, chest and abdominal CT, as well as nuclear MIBG whole body imaging, should be performed in the initial evaluation to rule out other sites of involvement.

Differential considerations are limited to those processes that involve the poststyloid parapharyngeal and carotid spaces, including nodal tumors (metastases, lymphoma) and neurogenic tumors (schwannoma, neurofibroma, paraganglioma).

Treatment is based on stage of the disease, age of the patient at diagnosis, and other biologically determined factors.[29] The treatment is complex and may include surgery, radiotherapy, chemotherapy, and bone marrow transplant. Cervical neuroblastoma is frequently localized, at stage I or II. Infants younger than 1 year of age have the best overall survival rate (74% to 82%) with neuroblastoma. This possibly reflects both early presentation as well as spontaneous regression and maturation of the tumor to a benign ganglioneuroma in young infants. Papillary carcinoma of the thyroid has been reported in these patients years after radiotherapy treatment.[54]

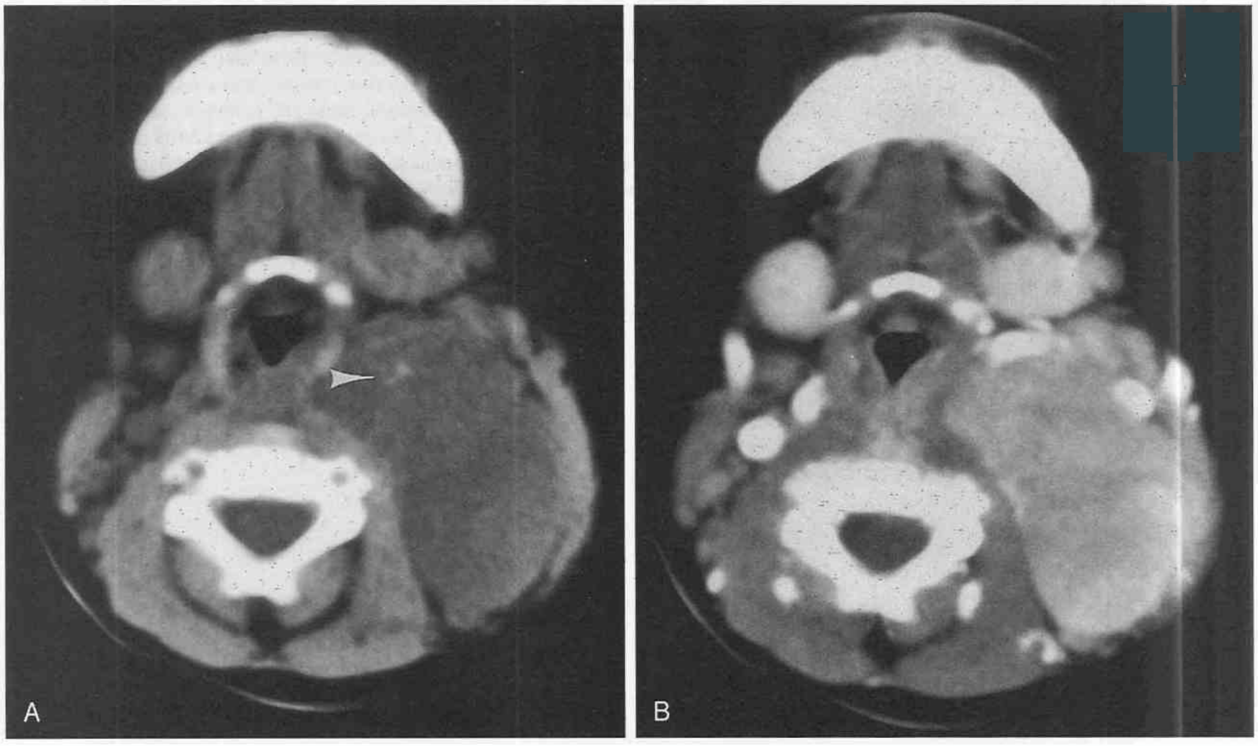

Figure 21–14. Cervical neuroblastoma. Axial precontrast *(A)* and postcontrast *(B)* CT scans. *A*, Small areas of calcification are seen *(arrowhead)* in a large mass of slightly decreased attenuation in the posterior triangle. *B*, There is moderate, homogeneous enhancement after contrast administration.

Nasopharyngeal Carcinoma

Nasopharyngeal carcinoma is rare in children, accounting for fewer than 1% of pediatric malignancies.[4, 18, 43] An increased incidence of this tumor has been noted in certain geographic locations and populations, specifically in southern China and Alaska. In Taiwan, nasopharyngeal carcinoma represents the most common cancer among Chinese males.[106] There also appears to be an increased incidence in the African American population in the United States.[63, 263]

The most common clinical presentation of childhood nasopharyngeal carcinoma is tender cervical adenopathy. This reflects the regional spread of the tumor at initial presentation. Serous otitis media can be seen from eustachian tube obstruction by the tumor or interference of muscular action of the tensor veli palatini muscle. Nasal obstruction; epistaxis; referred pain to the ear, neck, or throat; or cranial nerve paresis can be noted at presentation. Distant metastases are uncommon at initial diagnosis.[213, 237]

Nasopharyngeal carcinoma is an undifferentiated epidermoid-type tumor rather than an adenocarcinoma or a sarcoma. Multiple cell patterns (e.g., squamous cell, transitional cell, spindle cell, clear cell, polyhedral cell) can be seen with these tumors. On the basis of these cell types, a simplified approach to the classification of these tumors has been adopted by the World Health Organization, in which three types are proposed[214]:

- Type I, keratinizing squamous cell carcinoma
- Type II, nonkeratizining squamous cell carcinoma
- Type III, undifferentiated carcinoma

Types I and II have been associated with Epstein-Barr virus, whereas type III has been associated with childhood nasopharyngeal carcinoma. In the pediatric age group, nasopharyngeal carcinoma is usually an undifferentiated, epidermoid carcinoma or lymphoepithelioma (transitional cell).[70, 112, 144]

MRI or CT should be used to evaluate the nasopharyngeal area and skull base. Nasopharyngeal carcinoma usually arises in the posterior lateral wall of the nasopharynx in the region of the fossa of Rosenmueller. It may obstruct the lateral recess and cause asymmetry of the airway secondary to mass effect. The tumor can also originate from the posterior-superior wall, the posterior wall, or the anterior wall of the nasopharynx.[21]

CT is ideal for evaluation of bony erosion of the skull base, which is not uncommon with nasopharyngeal carcinoma.[220] However, MRI has been found superior to CT in the evaluation of primary lesions of the nasopharynx in both adults and children.[261] Undifferentiated carcinomas are invasive tumors with poorly defined margins and associated bony destruction. On CT scans, these tumors tend to be noncalcified with a variable enhancement pattern (Fig. 21–15). The magnetic resonance (MR) signal intensity of the masses is isointense to muscle on T1-weighted images and isointense to hyperintense to muscle on T2-weighted images.[185] Homogeneous, hypointense T1-weighted signal intensity and inhomogeneous, hyperintense T2-weighted signal intensity with inhomogeneous enhancement after contrast administration has been reported with squamous cell carcinoma of the oral cavity. Necrotic cervical adenopathy is common, particularly in the retropharyngeal and high jugular chains.[261]

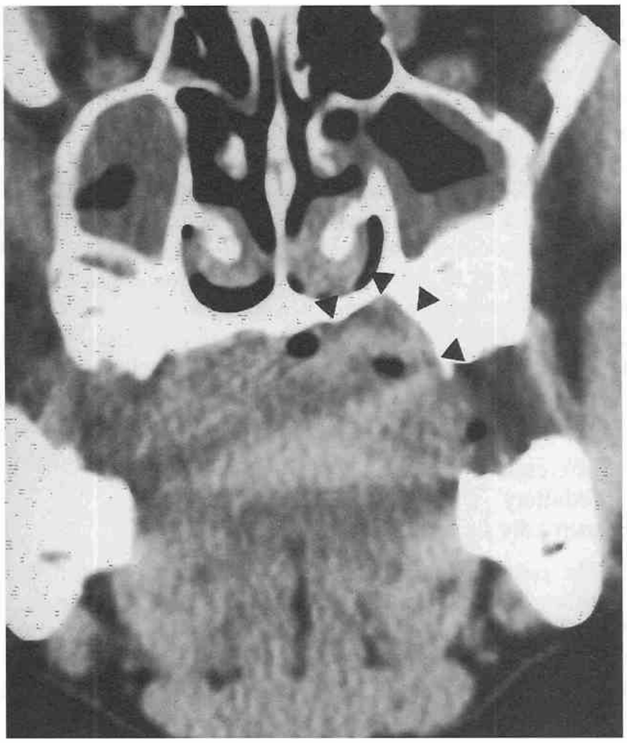

Figure 21–15. Nasopharyngeal carcinoma. Coronal noncontrast CT scan. A soft tissue mass is present in the roof of the oral cavity, causing erosion of the hard palate and maxilla *(arrowheads)*.

In children, differential considerations by imaging primarily include lymphoma, rhabdomyosarcoma, neuroblastoma, and, occasionally, juvenile nasopharyngeal angiofibroma or inflammatory processes that destroy bone.[97] The most common sites of metastatic disease are the cervical lymph nodes, lungs, and bone; as a result, survey CT of the chest and nuclear bone scanning should be included in the imaging workup of these tumors.[220]

Treatment is focused on local control of disease with radiotherapy, with or without chemotherapy, before metastatic spread occurs.[112] The 5-year relapse-free survival rate is 36%, with an overall 5-year survival rate of 51%.[111]

Thyroid Carcinoma

Thyroid carcinoma is uncommon in the pediatric age group, representing 1% to 1.5% of all malignancies in children. This neoplasm primarily occurs in older children and adolescents, particularly females. In contrast to thyroid carcinoma in adults, the tumor in children tends to be more aggressive at diagnosis; however, the prognosis is generally good.[23, 73, 78, 250, 267]

In the past, the relationship between radiotherapy and thyroid carcinoma was well known, with 20% to 50% of children with this neoplasm having a history of radiation exposure.[208, 268] The use of radiotherapy for benign conditions such as thymic enlargement, tonsillar and adenoidal hypertrophy, hemangioma, and lymphatic malformation peaked in the 1940s, with a resultant increase in thyroid carcinoma in the 1960s and 1970s.[69, 251] Although the use

of radiotherapy for such benign conditions in children has declined, a greater number of children are surviving cancer with adjuvant radiotherapy. Thus, delayed thyroid carcinoma may become more of a concern in the future. The period between exposure to radiation and the occurrence of thyroid carcinoma may be as long as 25 years.[268]

The differentiated carcinomas (papillary and follicular) most commonly present with cervical lymphadenopathy or a thyroid nodule. There is a high incidence of cervical metastases (43 to 87%) and pulmonary metastases (up to 15%) at presentation in children with this type of thyroid carcinoma.[78, 202, 250] The clinical course in these children appears to be similar to sporadic thyroid carcinoma.[69, 251]

Thyroid carcinoma is subdivided into the following types:

- Differentiated (papillary or follicular)
- Medullary
- Anaplastic or nondifferentiated

The *papillary* form is the most common type found in children, accounting for approximately 90% of cases.[73, 96, 259] This tumor is well differentiated, with cuboidal epihelium on fibrovascular stalks projecting into cystic spaces. Squamous metaplasia, psammoma bodies, oxyphilic change, and lymphatic invasion are common.[156] Pure *follicular* adenocarcinoma is the second most common type of thyroid carcinoma occurring in children, accounting for 5% to 10% of cases.[73, 96]

Medullary carcinoma accounts for approximately 5% of thyroid neoplasms in children. These tumors originate from parafollicular cells (C cells), which are derived from neural crest tissue that migrate to the thyroid during embryogenesis.

Anaplastic carcinoma rarely occurs in children.[123]

Microscopically, these tumors have a variable pattern of solid and follicular growth with malignant change, demonstrated by evidence of angioinvasion or invasion of the capsule. Pulmonary and osseous metastases and blood vessel invasion are more common with follicular adenocarcinoma than with papillary carcinoma.[6, 259]

On radionuclide scanning, thyroid carcinoma is usually "cold" (nonfunctioning) but rarely may be "hot" (functioning).[78] After a mass has been localized to the thyroid gland by radionuclide scanning or palpation, sonography can determine whether the mass is cystic or solid. Cystic masses in the thyroid gland are almost always benign, representing an adenoma or colloid cyst; however, they may be complicated by hemorrhage and/or debris, simulating a solid or mixed tumor. Occasionally, malignant thyroid lesions are purely cystic.[11, 78] Most thyroid carcinomas have ill-defined margins and variable echogenicity, as compared with the normal thyroid gland.[78, 205, 221] Microcalcifications, irregular margins, and detectable flow in the mass by Doppler imaging raises the suspicion of malignancy.

Ultrasound is also useful in detecting nonpalpable metastatic lymph nodes. Echogenic foci within the mass or lymph nodes, representing calcifications, are characteristic of primary or metastatic medullary carcinoma.[78, 85] In the presence of a known thyroid carcinoma, a survey CT of the neck should be performed to evaluate for metastatic lymphdenopathy (Fig. 21–16).[76, 85, 227]

MRI has been reported to be helpful in differentiating recurrent thyroid carcinoma from fibrosis. On MRI, recurrent carcinoma appears as low to medium T1 signal intensity and medium to high T2 signal intensity, whereas low signal intensity on both T1-weighted and T2-weighted sequences is noted with fibrosis. In this setting, "low" signal is defined as less than muscle; "medium" signal, greater than muscle but less than fat; and "high" signal, greater than or equal to fat.[10] Thyroid masses with partial destruction of the pseudocapsule on MRI may suggest papillary carcinoma.[176]

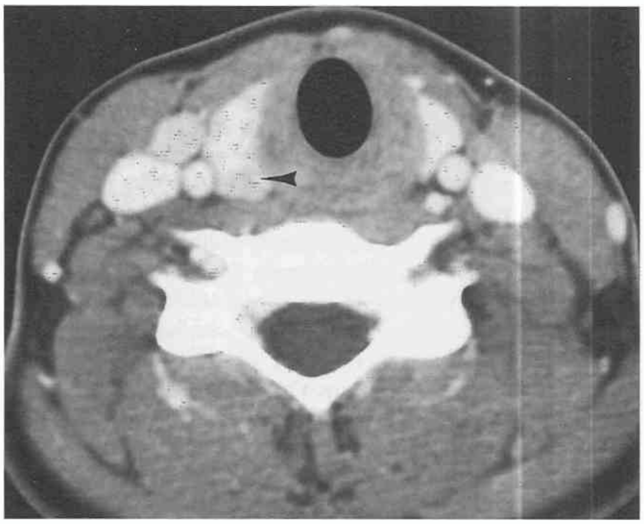

Figure 21–16. Thyroid carcinoma. Axial postcontrast CT scan. A subtle area of relatively decreased attenuation is noted in the posterior aspect of the right lobe of the thyroid gland.

Surgery is the mainstay of treatment for primary thyroid carcinoma.[134, 267] The best survival rates are with papillary carcinoma (86.3%) followed by follicular (85.3%), medullary (44%), and anaplastic (19%) types.[73, 96, 202] The overall mortality rate for children with thyroid carcinoma is 17%, with 75% of patients dying of complications of the tumor rather than the disease.[23, 73, 78, 250, 259, 267]

Synovial Sarcoma

Synovial sarcoma accounts for approximately 8% to 10% of all soft tissue malignancies, with 85% occurring in the extremities.[166, 218] Despite the name, these neoplasms do not arise from synovial tissue but are so named because of their similarity to synovium.[219] Synovial sarcomas usually arise in or near tendon or tendon sheaths rather than joints or bursal surfaces. Synovial tissue is not usually found in head and neck; synovial sarcomas are thought to arise from pleuripotential mesenchymal tissue that can differentiate into synovioblastic cells.[22, 91, 131] The most common sites of synovial sarcoma in the head and neck are the cervical soft tissues and parapharyngeal tissues, with an orofacial location less common.[199, 218]

Patients typically present between 15 and 35 years of age, with a slight male predominance.[165] The most common clinical presentation is a painless mass with symptoms of dysphagia, hoarseness, and headache.[7]

Histologically, synovial sarcomas may be *biphasic* and

monophasic. The biphasic type contains epithelial and spindle cell components; the monophasic type contains only spindle cells.[100] These well-circumscribed tumors contain gland-like spaces or clefts, surrounded by fibrosarcoma-like areas.[66]

CT is useful in demonstrating calcification and evaluating erosive changes of bone associated with synovial sarcomas. Calcification, in the form of round concretions, is present in approximately 30% of soft tissue sarcomas and may be a helpful finding in distinguishing this mass from other head and neck primary tumors in children.[195] MRI, however, is considered the imaging modality of choice for detection and staging of this tumor because of its inherent better soft tissue resolution. Tumor extent, vascular invasion, and intratumoral hemorrhage are better assessed by MRI.[219] Synovial sarcomas of the head and neck have variable, heterogeneous MRI signal on both T1-weighted and T2-weighted sequences, with variable heterogeneous enhancement after contrast administration.[219]

In our experience, we have found the imaging appearance to most commonly be a well-defined mass with an irregular wall, necrotic center, and minimal wall enhancement on CT; however, this tumor may be solid, cystic, or mixed in composition[195,219] (Fig. 21–17). Because 12.5% of patients have metastases to cervical lymph nodes at presentation, CT or MRI of the neck should be included in the initial evaluation. CT of the chest should also be performed, since pulmonary metastases are not uncommon.[9,199]

Treatment is surgical with wide local excision. Radiation and chemotherapy may be used as adjunctive treatment if excision is not complete.[163] The rate of local recurrence is high, with metastases to the lungs usually occurring within 2 years.[91] The survival rate is 40% at 5 years and 25% at 10 years, primarily because of pulmonary metastases.[91,165,199,218]

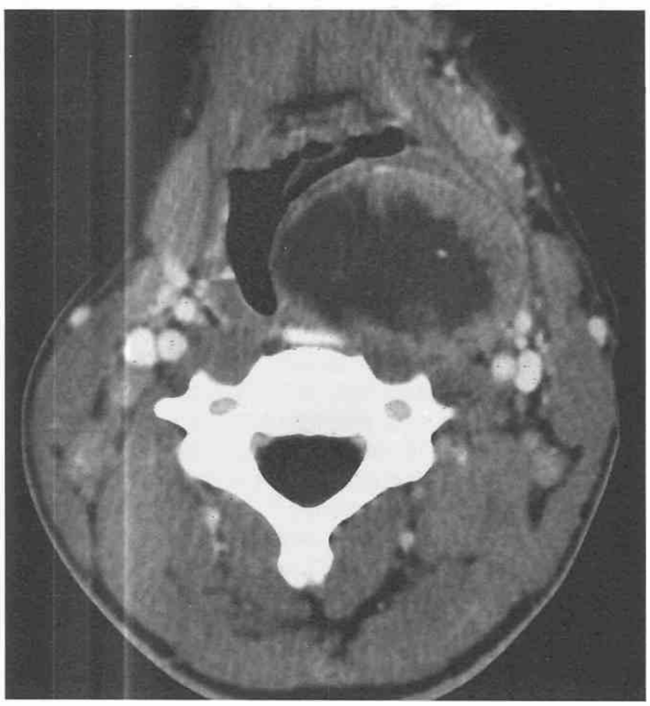

Figure 21–17. Synovial sarcoma. Axial postcontrast CT scan demonstrates a large, well-defined parapharyngeal mass with extension into the hypopharynx. The mass has an irregular wall, a necrotic center, and no evidence of significant enhancement.

Benign Masses

Juvenile Nasopharyngeal Angiofibroma

Juvenile nasopharyngeal angiofibroma (JNA) comprises 0.5% of head and neck tumors in children.[56] This benign but locally invasive tumor of the nasopharynx is the most commonly encountered vascular mass of the nasal cavity in children.[22] The name of the tumor arises from the fact that it is almost exclusively found in adolescent males.[56] Patients with JNA usually present between 7 and 21 years of age, with a peak incidence between 14 and 18 years.[22] Although the etiologic mechanism of this tumor has not been defined, it arises from the fibrovascular stroma normally found in the nasopharynx. Most JNAs arise in the area of the sphenopalatine foramen and pterygopalatine fossa.[22]

Patients most commonly present with complaints of nasal obstruction (91%) or severe, spontaneous epistaxis (59%). Other signs and symptoms include purulent nasal rhinorrhea from associated sinus infection, hyponasal speech, anosmia, facial deformity secondary to the locally invasive nature of the tumor, exophthalmos, hearing loss, or rarely signs of intracranial mass effect from extension of the tumor. Episodes of recurrent epistaxis have been related to the vascular fragility of the tumor, which is thought to be secondary to increased levels of circulating estrogens.[22,136]

Histologically, JNAs are composed of spindle or stellate fibrocytes in a connective tissue stroma with many wide, thin-walled vessels. The myofibroblast represents the principal cell of the tumor. Myofibroblasts interfere with the synthesis of collagen and elastin and are capable of transforming into smooth muscle.[136] Fine vessels invade the fibrovascular stroma, producing pseudolymphatic endothelialized spaces. The final appearance of the tumor represents a spectrum from a cellular or purely fibrous mass, to a cavern-like mass with a fibrovascular stroma. If the fibrous component of the tumor predominates, the incidence of local invasion and the frequency of epistaxis are decreased.[56]

Imaging gives important information for both the diagnosis and management of these tumors. JNAs are slow-growing masses that extend along and through fissures and foramina. They usually remodel bone rather than destroy it.[102] JNAs can extend in multiple planes, including medially into the nasopharynx, laterally through the pterygopalatine fossa and pterygomaxillary fissure and into the infratemporal fossa, and superiorly via foramina at the skull base or the sphenoid sinus into the middle cranial fossa and cavernous sinus. They tend to slowly enlarge over time and may involve the paranasal sinuses (ethmoid, maxillary, and sphenoid), and orbits.[210]

Anterior bowing of the posterior wall of the maxillary sinus on plain film (Holman-Miller sign) was the earliest reported radiographic finding with JNA,[102] although this finding is not specific.[235] This tumor should be evaluated

with CT, MRI, and angiography. CT is useful for the evaluation of bony involvement, whereas MRI is better for determining intracranial extension of tumor and differentiating tumor extension into sinuses from postobstructive sinus disease. CT and MRI should be performed without and with contrast in axial and coronal planes. Fat saturation should be employed with postcontrast MR images.

Findings can include a nasopharyngeal mass, widening of the pterygopalatine fossa, anterior displacement of the posterior maxillary sinus wall with associated widening of the pterygomaxillary fissure, opacification of one or more paranasal sinuses, erosion of the sphenoid bone with a mass in the sphenoid sinus, erosion of the hard palate or medial wall of the maxillary sinus, deviation of the nasal septum, and intracranial extension. On MRI, JNA is isointense to hypointense to muscle on T1-weighted images and isointense to hyperintense to muscle on T2-weighted images.[80, 143] Flow voids are often present on MRI, and homogeneous, intense enhancement is typically seen on both CT and MRI scans after contrast administration (Fig. 21–18).[56, 210, 211]

Angiography is useful to define the vascular supply of the tumor for preoperative embolization. Typically, JNAs are supplied by branches of the external carotid artery, most commonly the internal maxillary or ascending pharyngeal artery. Numerous hypertrophied and tortuous vessels are seen without segmental narrowing, beading, or aneurysm formation. A persistent, dense blush is present throughout the capillary and venous phases. Early draining veins and arteriovenous shunting are usually absent.[135, 196] To fully define the potential vascular supply of the tumor, bilateral internal and external carotid artery injections as well as selective injections of the ipsilateral internal maxillary, ascending pharyngeal, and ascending palatine arteries should be performed.[135, 136]

From an imaging standpoint, the primary differential consideration is an angiomatous polyp. Patients may have similar symptoms; however, angiomatous polyps tend to occur at a slightly older age (in the 3rd decade). Angiomatous polyps are located primarily in the nasal cavity and do not invade the pterygopalatine fossa or intracranial cavity. Only rarely is there extension of angiomatous polyps into the sphenoid sinus, and the mass is hypovascular or avascular on MRA with only a few feeding vessels present. The enhancement pattern is less intense than with JNA, and flow voids are not present on MRI scans.[232] Other considerations of a nasopharyngeal mass in children include lymphoma, rhabdomyosarcoma, nasopharyngeal carcinoma, and esthesioneuroblastoma.[20]

To assist in selecting the best surgical approach, Sessions and colleagues developed a staging calcification based on extent of the lesion.[210] The most common approach to therapy is total resection (as feasible) within 24 hours of embolization. Radiotherapy is reserved for inoperative disease or residual disease, when reoperation is not practical. Intracranial extension of tumor does not always preclude surgery; however, parasellar disease may make en bloc resection impossible. In such a case, patients usually undergo debulking with extensive beam radiotherapy.[28, 89, 121] In addition to embolization, hormonal therapy and cryotherapy are reported to be adjunctive treatments to surgery. The efficacy of testosterone agonist and estrogen therapy (to cause involution of blood vessels) and cryotherapy (to control bleeding from small tumors) have not been widely accepted.[8, 71]

The long-term prognosis of this benign tumor is good. Surgery alone carries a 25%–60% recurrence rate; radiotherapy alone carries a 25% recurrence rate.[117, 136] Recurrence usually occurs within the first 12 months of therapy and is unusual after 24 months. Factors predisposing to recurrence include the multilobulated nature of the tumor, leading to invasion of adjacent sinuses and fascial planes. The natural irregularity of the nasopharynx also makes complete extirpation difficult in some cases.[117, 136]

Neurogenic Tumors

Tumors of neurogenic origin constitute a small but significant group of head and neck masses in children.[46] Neurofibromas and schwannomas represent the most common nerve sheath tumors of the peripheral nerves in the head and neck.[21] Solitary neurofibromas and schwannomas can be seen as sporadic lesions, whereas plexiform and multiple neurofibromas occur in association with neurofibromatosis type 1.[20, 122] Approximately 25% of solitary neurogenic tumors originate along the course of a cervical or cranial nerve, with the exception of the olfactory nerve, which lacks schwann cells, and the optic nerve.[194] Twenty-five percent to 45% of schwannomas occur in the head and neck. The most common locations include the face, scalp, orbit, oral cavity, parapharyngeal space, middle ear, larynx, and neck.[55, 83, 84, 122, 233, 236]

The normal nerve fiber is ensheathed by schwann cells (the neurolemma) which in turn, is surrounded by the endoneurial fibroblasts (the neurilemma). The schwann cell is thought of as the precursor of the neurofibroma, the schwannoma, and, probably, the neurogenic sarcoma.[246]

Neurofibromas are unencapsulated nerve sheath tumors that are composed of schwann cells, with collagen in a mucous matrix. Solitary neurofibromas are typically subcutaneous and well defined, whereas plexiform neurofibromas are more commonly infiltrative with ill-defined margins. Multiple and plexiform neurofibromas are associated with neurofibromatosis type 1. Five percent to 13% of plexiform neurofibromas undergo malignant degeneration.[20]

Schwannomas are encapsulated tumors, usually attached to or surrounded by a nerve. Microscopically, they are composed of two types of tissues: cellular Antoni type A and less cellular Antoni type B. Compact spindle cells in parallel orientation with palisading nuclei oriented around bundles of fiber form Verocay bodies. Schwannomas are almost never associated with neurofibromatosis type 1 and rarely undergo malignant change.[20]

Neurofibromas can arise at any age. Schwannomas most commonly present between 20 and 50 years of age, with occasional occurrences in childhood. Neurofibromas are characteristically asymptomatic, whereas schwannomas are often painful and tender. The pain may be localized or radicular in nature with associated paraesthesias.[20]

On imaging, solitary neurofibromas and schwannomas present as well-defined lobulated masses with a tendency to cross fascial planes. Neurofibromas appear as isointense masses to muscle with rare calcification and variable en-

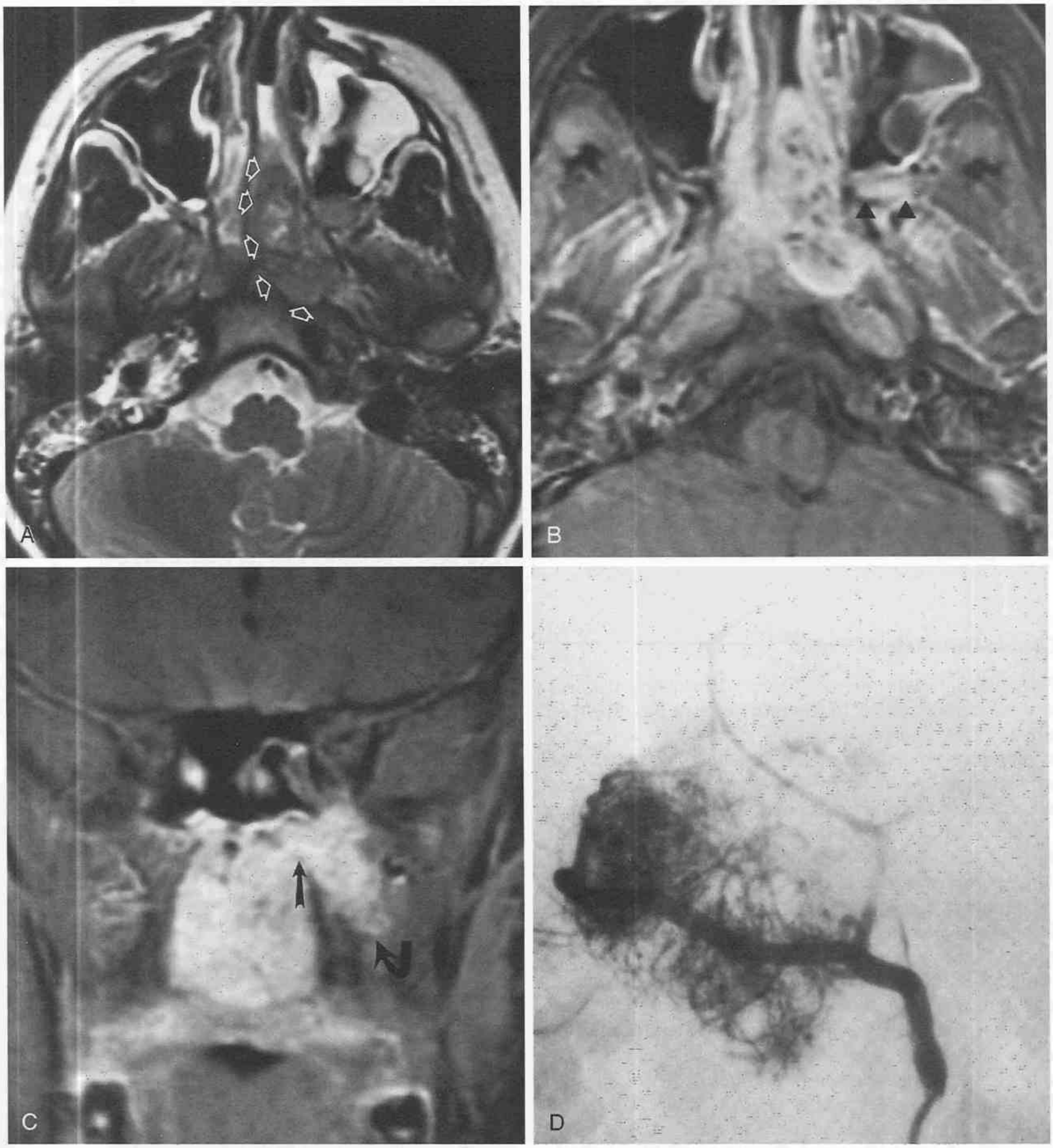

Figure 21–18. Juvenile nasopharyngeal angiofibroma. *A*, Axial T2-weighted MRI scan. The posterior nasal cavity and nasopharynx are expanded by a large mass of mixed-signal intensity *(open arrows)*. *B* and *C*, Postcontrast axial *(B)* and coronal *(C)* MRI scans show flow voids within the mass *(B)*, with extension through the sphenopalatine foramen *(C) (arrow)*, the pterygopalatine fossa, and the pterygomaxillary fissure *(B) (arrowheads)* and into the infratemporal fossa *(C) (curved arrow)*. *D*, Selective internal maxillary artery angiogram demonstrates multiple, tortuous, and hypertrophied branches supplying this nasal mass.

hancement on CT. Schwannomas typically enhance more homogeneously, with either iodinated contrast or gadolinium. On MRI, neurofibromas are hypointense to isointense to muscle on T1-weighted images and hyperintense to muscle on T2-weighted images. Variable enhancement is seen after contrast administration (Fig. 21–19). Schwannomas have intermediate T1-weighted signal and hyperintense T2-weighted signal to muscle, with more uniform enhancement after contrast administration. Heterogeneous signal intensity can be seen centrally in these tumors secondary to cystic degeneration and hemorrhage. This event is more common with schwannomas.[233]

Plexiform neurofibromas are poorly defined, infiltrative masses that can erode bone and expand neural foramina of the cervical spine. They have a more complex appearance on MRI, with wavy cords of signal hypointensity surrounded by areas of mixed isointensity and hyperintensity on T2-weighted images.[233]

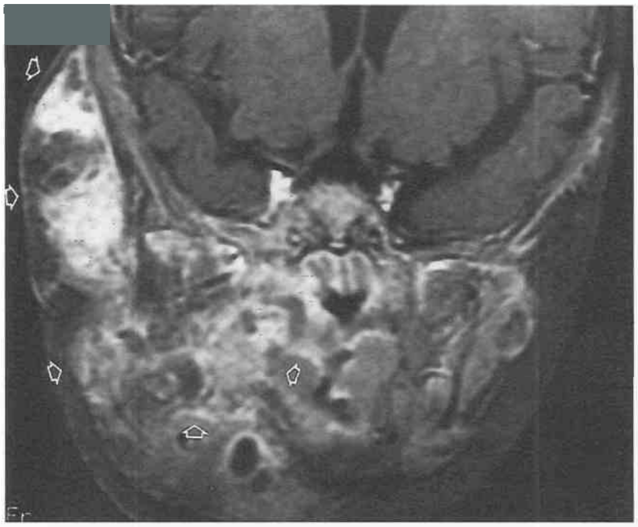

Figure 21–19. Plexiform neurofibroma. Coronal T1-weighted, postcontrast MRI scan with fat saturation. The majority of the right masticator space is involved with an ill-defined, heterogeneously enhancing mass *(open arrowheads)* in this patient with neurofibromatosis.

Esthesioneuroblastoma

Esthesioneuroblastoma, or olfactory neuroblastoma, is a neurogenic tumor related to the primordia of the olfactory apparatus. This uncommon neural crest tumor originates from olfactory epithelium of the superior nasal cavity or cribriform plate region.[159, 171, 212] Olfactory epithelium can also be found in the middle turbinates and adjacent paranasal sinuses, which may explain the occasional unusual location of these tumors.[212] Spread of tumor to the paranasal sinuses, anterior cranial fossa, olfactory bulbs, orbits, and cavernous sinus is common.[64, 118]

Esthesioneuroblastoma occurs in all age groups; however, a bimodal age peak has been noted in the 2nd and 6th decades.[110] There is a slight male predominance. The most common clinical presentations are epistaxis, reflecting the vascular nature of the tumor, and unilateral nasal obstruction.[59, 206] Other less common presenting symptoms include anosmia, sinus pain, and diplopia.[59]

The diagnosis is dependent on the demonstration of neural elements by histochemical or biochemical techniques, with electromicroscopy the most reliable method. Appearance of either an intercellar fibrillary background or Homer-Wright rosettes is diagnostic for esthesioneuroblastoma.[44, 159, 241] This tumor is often considered "the great imposter" by pathologists, as it can be confused with other small cell malignancies, such as undifferentiated squamous cell carcinoma and lymphoma.[249]

Esthesioneuroblastomas are typically superior nasal cavity lesions with both bony remodeling and destructive bony growth properties.[206] These tumors appear on CT as homogeneous, moderately enhancing, soft tissue masses centered in the superior nasal cavity, with frequent extension into the ethmoid and maxillary sinuses.[109, 249] MRI signal characteristics and enhancement patterns of esthesioneuroblastomas are nonspecific. Isointense to hypointense T1-weighted and isointense to hyperintense T2-weighted signals relative to gray matter have been reported. Enhancement patterns on MRI are variable, from mild to marked and homogeneous or heterogeneous (Fig. 21–20).[59, 206] Cysts along the intracranial margin of the sinonasal mass on MRI have been reported as highly suggestive of esthesioneuroblastoma.[234]

Destructive bony changes are usually best evaluated with coronal CT; however, the changes are typically not subtle and MRI can easily detect this finding.[206] Calcification, a finding reported as suggestive of esthesioneuroblastoma, can best be seen on CT; however, it is often difficult to distinguish true calcification from residual bony destruction with this tumor.[59, 234] Coronal, postcontrast MRI images are best for the evaluation of intracranial extension of disease (25% to 30% of cases) and extension of disease into the orbits or paranasal sinuses (40% of cases).[59, 234, 249] Coronal postcontrast, T1-weighted MRI is useful in the differentiation of nonenhancing obstructive sinus disease from enhancing tumor or recurrent disease.[59, 206]

Hematogeneous metastasis to the cervical lymph node occurs in 17% of patients at presentation. Thus, if cervical lymphadenopathy is present clinically, CT or MRI of the neck should be performed for evaluation of metastatic disease.

More widespread disease to lungs, bone, and liver occur in 14 to 20% of patients. This is unusual at presentation and more commonly occurs with relapse of disease.[64, 118, 206, 249]

Treatment is determined by stage of disease at presentation, with most patients undergoing surgical resection and adjuvant radiotherapy.[206] The 2-year survival rate is 88%.[140]

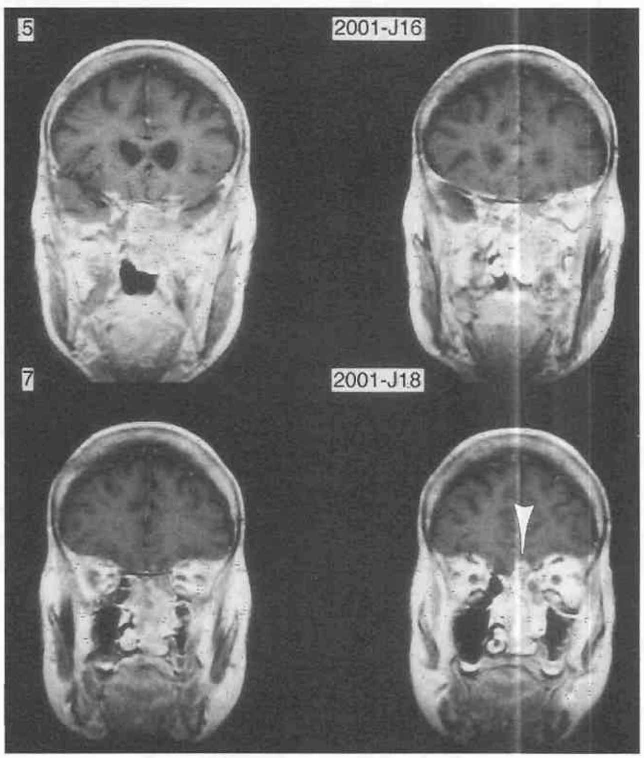

Figure 21–20. Esthesioneuroblastoma. Coronal T1-weighted postcontrast MRI scan. Marked enhancement of the mass is filling most of the nasal cavity. Intracranial extension is noted within the mass as it extends into the floor of the anterior cranial fossa on the left *(arrowhead).*

Vascular Malformations (Vasoformative Lesions)

In the past, there had been widespread use of different terminology regarding vascular and lymphatic malformations of the head and neck in children. In 1982, Mulliken and Glowacki proposed a classification of hemangiomas and vascular malformations based on cellular turnover, histology, natural history, and physical findings. The two major categories in this classification system are (1) hemangioma of infancy and (2) vascular malformation.[169]

Hemangioma of infancy behaves predictably. These masses appear in infancy, increase in size secondary to endothelial cell proliferation, and spontaneously involute by adolescence.[13] Vascular malformations are the result of abnormal development of blood or lymphatic vessels. These lesions increase in size as a child grows, have normal endothelial mitotic activity, and fail to involute.[169] In contrast to hemangiomas of infancy, which are clinically obvious at birth, vascular malformations may not become apparent until late infancy or childhood, even though the lesions are present at birth.[13] Vascular malformations can also be more complex in composition, with multiple vascular elements present. A rapid increase in size may be seen with infection, trauma, or endocrine changes (pregnancy, puberty).[169]

Vascular malformations are categorized according to the dominant component of the malformation: (1) capillary, (2) venous, (3) lymphatic, (4) arterial (with or without fistulas), and (5) combined (capillary venous, lymphaticovenous, arteriovenous [AVM]).[169]

Both hemangioma of infancy and vascular malformation can be further classified according to flow characteristics as follows[13,116]:

- Hemangioma of infancy, venous, and lymphatic malformations—low-flow lesions
- AVMs—high-flow lesions
- Combined malformations—low-flow or high-flow lesions

One report has suggested classifying capillary hemangioma of infancy as a high-flow lesion because of the presence of flow voids within the mass on MRI.[157]

On CT, hemangioma of infancy is a well-defined mass of isodense attenuation to muscle, with isointense T1-weighted and hyperintense T2-weighted signal to muscle on MRI.[13] Flow voids within the lesion on MRI are a helpful secondary to finding to distinguish this mass from other soft tissue lesions in infancy.[157] Postcontrast CT and MRI scans show a diffuse, homogeneous enhancement pattern (Fig. 21–21). These masses progressively enlarge over a period of several months before spontaneously involuting. Areas of hyperintense T1-weighted signal on MRI scans may be seen during the period of involution secondary to fatty replacement.[13,157]

Venous malformations (cavernous hemangiomas) are well-defined, predominantly solid soft tissue masses that can have associated bony remodeling or deformity. These masses tend to cross fascial planes and do not spontaneously involute. On MRI, venous malformations have characteristics of low-flow lesions; thus, they lack intralesional flow voids.[13,157] They demonstrate intermediate T1-weighted signal and heterogeneous, hyperintense T2-weighted signal to muscle with homogeneous or mildly heterogeneous enhancement after contrast administration (Fig. 21–22).[13] Heterogeneous signal secondary to intralesional phleboliths (usually hypointense T1-weighted and T2-weighted signal) and venous lakes (hyperintense T2-weighted signal) may be found within the lesion.[13,157]

AVMs do not typically cause mass effect because of a lack of an underlying supporting stroma within the lesion (Fig. 21–23). Serpiginous flow voids on T1-weighted and T2-weighted sequences and decreased T1-weighted signal secondary to intraosseous extension with marrow involve-

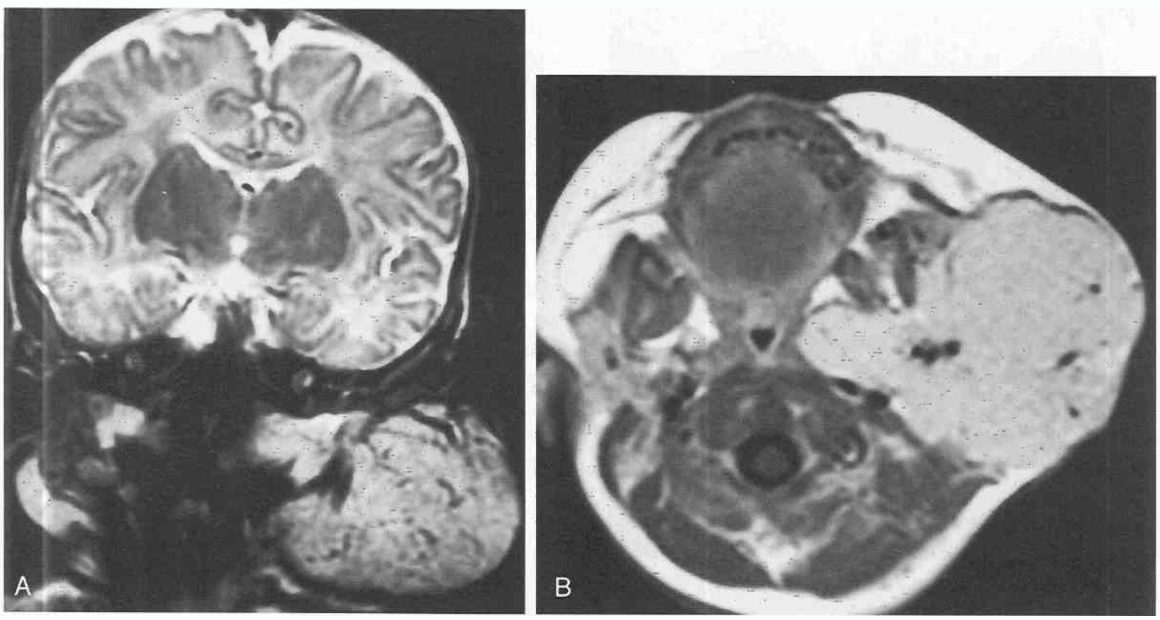

Figure 21–21. Hemangioma of infancy. *A*, Coronal fast spin-echo (FSE) MRI scan shows a large mass involving the superficial and deep components of the parotid space. The mass has multiple intralesional flow voids and diffusely hyperintense signal. *B*, Marked enhancement of the mass with intralesional flow voids is noted on this axial T1-weighted postcontrast MRI scan.

ment may be seen. The signal voids correlate with AV shunting present on angiography. Invasive, combined vascular malformations are seen as infiltrative, solid masses with serpiginous flow voids. Intermediate T1-weighted and hyperintense T2-weighted signals are seen with mixed lesions (see Fig. 21–3).[13]

Lymphatic malformations are classified according to the size of the embryonic lymphatic sacs into three types[22]:

- Lymphangioma simplex
- Cavernous lymphangioma
- Cystic hygroma

Imaging findings are variable and depend on the degree of vascularity of the lesion, the size of the intralesional cystic spaces, and the presence or absence of hemorrhage within the lesion.

Lymphangioma simplex is composed of very small cystic spaces. This subtype thus can appear as a solid mass on ultrasound, CT, or MRI.

Cavernous lymphangioma has moderate-sized cystic spaces; consequently it has a more typical cystic appearance on imaging with anechoic collections and intervening septations on ultrasound and fluid attenuation spaces on CT.[74,128] On MRI, these masses follow water signal with hypointense T1-weighted and hyperintense T2-weighted signal to muscle. Enhancement of the septations can occur after contrast administration, however, most of the lesion does not enhance.[147]

Cystic hygroma is composed of large, nonenhancing fluid-filled spaces with attenuation values and signal characteristics following water in uncomplicated lesions (Fig. 21–24). Secondary infection or hemorrhage into the mass alters the imaging characteristics, with changes dependent on the stage of breakdown of the blood products. With infection or hemorrhage into the mass, echogenicity on ultrasound, attenuation on CT, and signal intensity on MRI typically increase, with variable enhancement of the mass and surrounding soft tissues.[147]

Figure 21–22. Venous malformation. Axial T2-weighted MRI scan. An irregular mass with heterogeneous hyperintense signal is noted *(curved arrow)*, involving the superior compartment of the right masticator space and associated superficial, subcutaneous soft tissues.

Figure 21–23. Arteriovenous malformation. Axial postcontrast CT scan. Multiple areas of vascular enhancement are present in the left masticator space *(curved arrows)* and retromandibular space, with an absence of mass effect.

Angiographically, hemangiomas of infancy are distinguished from vascular malformations by the presence of a well-defined mass demonstrating intense tissue staining in an organized lobular pattern. Angiographic findings of vascular malformations are variable and depend on the predominant vascular channel type. These masses are typically diffuse lesions composed of vessels without intervening tissue stain.[32]

There are two primary options in the management of low-flow lesions of the head and neck. Hemangiomas of infancy spontaneously involute, so that conservative therapy with observation is indicated. Low-flow vascular malformations and rapidly growing hemangiomas associated with hemorrhage or ulceration and lesions posing a threat to the airway or vision, may warrant more aggressive therapy. In this case, additional therapeutic options include steroid administration, laser photocoagulation therapy, sclerotherapy, embolization, and surgical resection.[13]

Selective arteriography is indicated for complicated AVMs of the head and neck, because these patients may be candidates for embolization with or without surgical intervention. They should also be evaluated for coagulopathy if hemorrhage is noted in the lesion.[116,169] Some of the combined vascular malformations, with features of both low and high flow, may be highly invasive and resistant to all forms of therapy.[116]

Mass-Like Conditions

Fibromatosis Colli

Fibromatosis colli, also referred to as muscular or congenital torticollis, is a benign condition in infants related

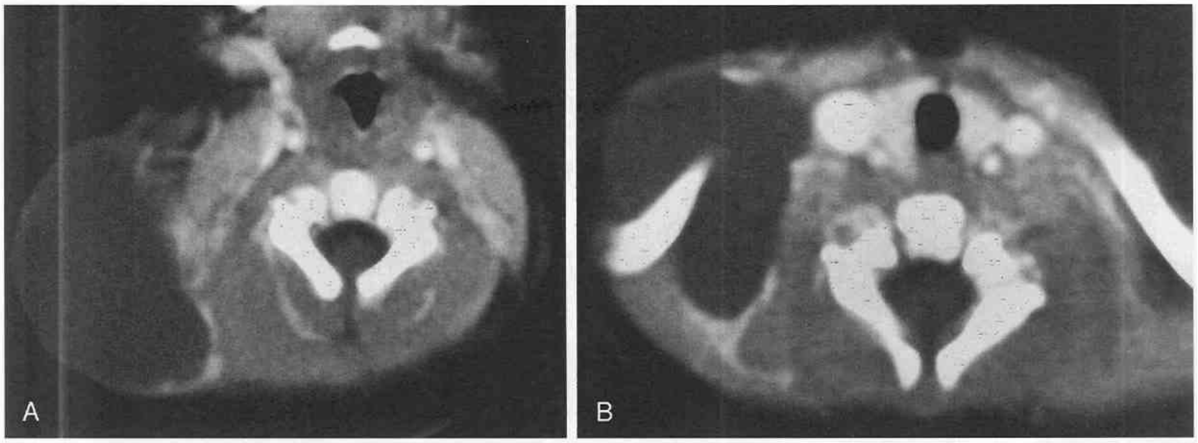

Figure 21–24. Lymphatic malformation (cystic hygroma). Axial postcontrast CT scan. *A* and *B*, A large, nonenhancing mass of decreased attenuation is present off the lateral aspect of the right neck with extension to the area of the thoracic inlet. Minimal peripheral enhancement is present.

to the sternocleidomastoid muscle (SCM). There are two main theories regarding the etiologic mechanism. These infants often have a history of breech presentation with forceps delivery. The first theory postulates birth trauma with subsequent intramuscular hematoma and fibrosis as the cause.[107] The second theory attributes the condition to fetal intrauterine malpositioning, with torticollis causing the pseudotumor. Histologic findings of fibrosis without hemorrhage in this condition favor the second theory.[154,245]

Infants typically present at 2 to 4 weeks of age with torticollis and a firm, nontender palpable neck mass. Parents are often concerned initially, because the mass may increase in size for a few weeks. However, the natural history is regression of the process by 4 to 8 months of age in 80% of infants. There is a right-sided predominance (75%).[154,245]

The goal of imaging is exclusion of other causes of a mass in the muscle, such as a primary tumor. If the patient is referred for imaging, ultrasound is the imaging modality of choice. Sonographic findings include focal or diffuse enlargement of the SCM, with variable internal echogenicity in contrast to normal muscle.[50,128] A peripheral rim of decreased echogenicity may also be present. This is thought to represent compressed subjacent normal muscle.[42] In the appropriate clinical setting, this pattern should allow the imager to make the correct diagnosis. CT and MRI are reserved for cases in which the diagnosis is not confirmed by ultrasound.[42,81] CT findings include a focally or diffusely enlarged SCM with the area of the "mass" isodense to muscle. If contrast material is administered, the mass demonstrates a variable enhancement pattern. On MRI, the enlarged muscle is isointense on T1-weighted and isointense to slightly hyperintense to muscle on T2-weighted images (Fig. 21–25).

Treatment is directed primarily toward physical therapy. In rare cases, when this treatment is unsuccessful, a muscle release may be performed.

Adenopathy or Adenitis of the Neck

Cervical adenopathy is a very common finding in children, usually related to a developing immune system that is responding to exposure to multiple new antigens. In most pediatric patients, imaging is not required, since cervical adenopathy is reactive in nature. When a case is atypical in clinical presentation or is refractory to medical treatment or when suppuration is suspected, imaging may be requested. In the case of an inflammatory process, the child typically presents with a painful and tender neck mass with associated cervical nodal masses. In this scenario, the imager specialist should address these primary questions:

- Is the process cellulitis or a drainable fluid collection?
- Is there evidence of complication in the form of vascular compromise, airway compression, or osteomyelitis?

The distinction between cellulitis and a drainable abscess is important; the former is usually treated medically, but the latter typically necessitates surgical intervention.

Sonography is a quick, noninvasive method of evaluating the presence of an abscess, with a reported sensitivity of 90% to 95%.[130,153] The usual appearance of an abscess is a mass of relatively decreased central echogenicity with variable internal echoes. Peripheral flow around an area of liquefaction on Doppler imaging is present in up to 89% of soft tissue abscesses.[138] Cellulitis has a more homogeneous or striated appearance on sonography.[31] The sonographic appearance of nonsuppurative adenitis is multiple, oval-shaped masses, with decreased or variable echogenicity. Scattered Doppler flow can be seen in the hila of nodes.[128] Although sonography is sensitive in detecting adenopathy and inflammatory masses, it lacks specificity in distinguishing infected congenital cystic masses from suppurative masses.[138]

CT has been used most often in an attempt to make this differentiation. On CT scans, cellulitis appears as an ill-defined area of decreased attenuation with mild, diffuse enhancement and "strandlike" infiltration of surrounding soft tissue. A drainable abscess is seen as a single or multiloculated area of decreased attenuation that conforms to fascial spaces and has surrounding peripheral rim enhancement (Fig. 21–26). Secondary findings of adjacent myositis, infiltration with stranding of surrounding fat, skin thickening, engorgement of veins and lymphatics, and enhancement of fascial planes can also be seen.[103,178]

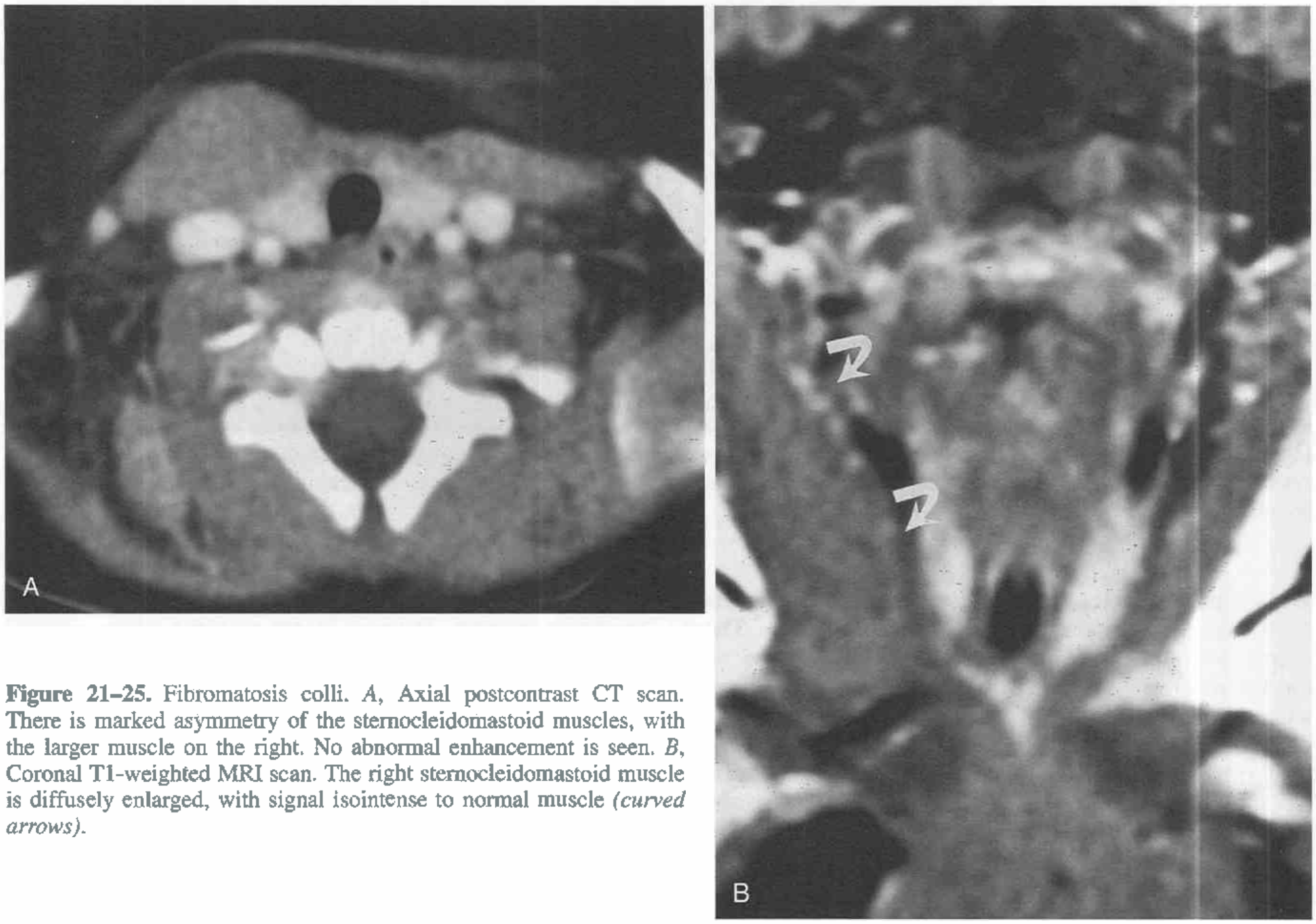

Figure 21–25. Fibromatosis colli. *A*, Axial postcontrast CT scan. There is marked asymmetry of the sternocleidomastoid muscles, with the larger muscle on the right. No abnormal enhancement is seen. *B*, Coronal T1-weighted MRI scan. The right sternocleidomastoid muscle is diffusely enlarged, with signal isointense to normal muscle *(curved arrows)*.

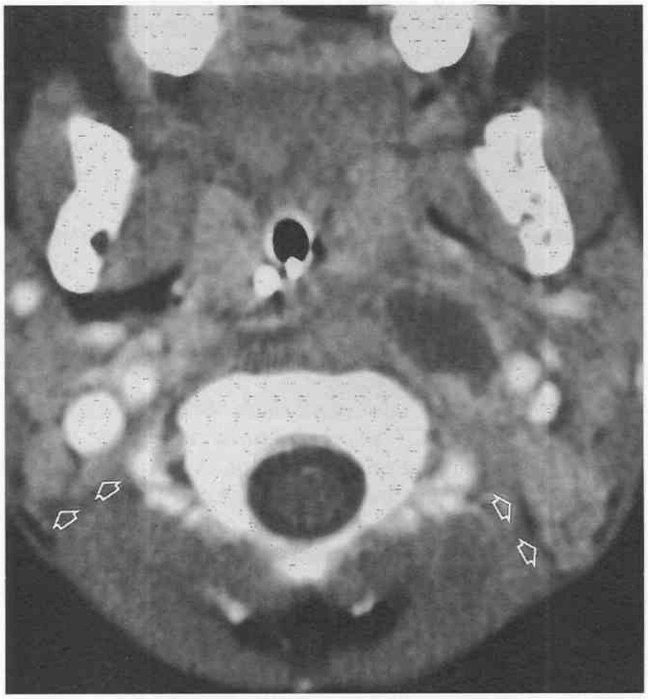

Figure 21–26. Retropharyngeal abscess. Axial postcontrast CT scan. An oval-shaped area of decreased attenuation is noted in the left retropharyngeal space with faint peripheral enhancement. Displacement of the carotid space laterally and effacement of the parapharyngeal fat are present. Bilateral spinal accessory chain adenopathy *(open arrows)* is noted.

Our experience in a CT study of 32 pediatric patients with deep-neck inflammatory processes found a specificity of approximately 75% in distinguishing abscess from cellulitis. A complete, circumferential ring of enhancement was the most sensitive imaging finding. However, this imaging appearance can also be seen with necrotic nodal disease, infected branchial cleft cysts, necrotic neoplasms, and thrombosed vessels. Thus, pertinent clinical history and findings and laboratory data are crucial elements to assist in sorting the imaging findings.

Inflammatory processes in the neck rarely cross into the mediastinum, secondary to constraints of fascial planes. If an infection is present in the visceral space anteriorly or prevertebral space posteriorly, however, the potential exists for extension into the mediastinum. The pretracheal component of the visceral space extends from the hyoid bone to the level of the aortic arch in the anterior mediastinum. The retrovisceral component of the visceral space and prevertebral space extend from the skull base superiorly to the posterior mediastinum inferiorly.[101,181] With antibiotic therapy, this complication is rarely encountered today.

References

1. Abemayor E, Newman A, Bergstrom L, et al: Teratomas of the head and neck in childhood. Laryngoscope 94:1489–1492, 1984.
2. Abramson SJ, Berdon WE, Ruzal-Shapiro C, et al: Cervical neuroblastoma in eleven infants: A tumor with favorable prognosis. Pediatr Radiol 23:253–257, 1993.
3. Ackerman WE, Phero JC: An aid to nasal tracheal intubation. J Oral Maxillofac Surg 47:1341, 1989.
4. Ahern V, Jenkin D, Banerjee D, et al: Nasopharyngeal carcinoma in the young. Clin Oncol (R Coll Radiol) 6:24–30, 1994.
5. Allard RHB: The thyroglossal cyst. Head Neck Surg 5:134–146, 1982.
6. Altman AJ, Schwartz AD: Malignant Diseases of Infancy, Childhood, and Adolescence. Philadelphia, WB Saunders, 1983.
7. Amble FR, Olsen KD, Nascimento AG, Foote RL: Head and neck synovial cell sarcoma. Otolaryngol Head Neck Surg 107:631–637, 1992.
8. Antonelli AR, Cappiello J, DiLorenzo D, et al: Diagnosis, staging and treatment of juvenile nasopharyngeal angiofibroma (JNA). Laryngoscope 97:1319–1325, 1987.
9. Arnold J: Ein fall von congenital em zusammdengesetzen lipom der zungl und des pharynx mit perforation in die schaedelhoehle. Virchows Arch 50:782, 1870.
9a. Arnot RS: Defects of the first branchial cleft. S Afr J Surg 9: 93–98, 1971.
10. Auffermann W, Clark OH, Thurnher S, et al: Recurrent thyroid carcinoma: Characteristics on MR images. Radiology 168:753–757, 1988.
11. Bachrach LK, Daneman D, Daneman A, Martin DJ: Use of ultrasound in childhood thyroid disorders. J Pediatr 103:547–551, 1983.
12. Bailey H: Branchial cysts and other essays on surgical subjects in the faciocervical region. London, Lewis, 1929.
13. Baker LL, Dillon WP, Hieshima GB: Hemangiomas and vascular malformations of the head and neck: MR characterization. AJNR Am J Neuroradiol 14:307–314, 1993.
14. Bale PM, Painter DM, Cohen D: Teratomas in childhood. Pathology 7:209–218, 1975.
15. Barat M, Sciubba JJ, Abramson AL: Cervical thymic cyst: Case report and review of literature. Laryngoscope 95:89–91, 1985.
16. Barkovich AJ, Vandermarck P, Edwards MB, Cogen PH: Congenital nasal masses: CT and MR imaging features in 16 cases. AJNR Am J Neuroradiol 12:105–116, 1991.
17. Barrick B, O'Kell RT: Thymic cysts and remnant cervical thymus. J Pediatr Surg 4:355–357, 1969.
18. Barrios NJ: Childhood nasopharyngeal carcinoma. J La State Med Soc 145:151–155, 1993.
19. Batsakis JG: Teratomas of the head and neck. In Batsakis JG (ed): Tumors of the Head and Neck: Clinical and Pathological Considerations. Baltimore, Williams & Wilkins, 1979.
20. Batsakis JG: Tumors of the Head and Neck: Clinical and Pathological Considerations. Baltimore, Williams & Wilkins, 1979.
21. Batsakis JG, Solomon AR, Rice DH: The pathology of head and neck tumors: Carcinoma of the nasopharynx: Part II. Head Neck Surg 3:511, 1981.
22. Batsakis JG: Vasoformative tumors. In Tumors of the Head and Neck: Clinical and Pathological Considerations. Baltimore, Williams & Wilkins, 1979.
23. Becher SP, Skolnik EM, O'Neill IV: The nodular thyroid. Otolaryngol Clin North Am 13:53–58, 1980.
24. Benson MT, Dalen K, Mancuso AA, et al: Congenital anomalies of the branchial apparatus: Embryology and pathologic anatomy. Radiographics 12:942–960, 1992.
25. Berry MP, Jenkin RDT: Parameningeal rhabdomyosarcomas in the young. Cancer 48:281–288, 1981.
26. Boyd J, Templer J, Harvey J, Decker J: Persistent thymopharyngeal duct cyst. Otolaryngol Head Neck Surg 109:135–139, 1993.
27. Bradley PJ: Nasal dermoids in children. Int J Pediatr Otorhinolaryngol 3:63–70, 1981.
28. Bremer JW, Neel III HB, DeSanto LW, Jones GC: Angiofibroma: Treatment trends in 150 patients during 40 years. Laryngoscope 96: 1321–1329, 1986.
29. Breslow N, McCann B: Statistical estimation of prognosis for children with neuroblastoma. Cancer Res 31:2098, 1971.
30. Brownstein MH, Shapiro L, Slevin R: Fistula of the dorsum of the nose. Arch Dermatol 109:227–229, 1974.
31. Buckley AR, Moss EH, Blokmanis A: Diagnosis of peritonsillar abscess: Value of intraoral sonography. AJR Am J Roentgenol 162: 961–964, 1994.
32. Burrows PE, Mulliken JB, Fellows KE, Strand RD: Childhood hemangiomas and vascular malformations: angiographic differentiation. AJR Am J Roentgenol 141:483–488, 1983.
33. Burton EM, Mercado-Deane MG, Howell CG, et al: Cervical thymic cysts: CT appearance of two cases including a persistent thymopharyngeal duct cyst. Pediatr Radiol 25:363–365, 1995.
34. Butler EC, Dickey JR, Shill OS Jr, Shalak E: Carcinoma of the thyroglossal duct remnant. Laryngoscope 79:264–271, 1969.
35. Byard R, Jimenez C, Carpenter B, Smith C: Congenital teratomas of the neck and nasopharynx: A clinical and pathological study of 18 cases. J Paediatr Child Health 26:12–16, 1989.
36. Callihan TR, Berard CW: Childhood non-Hodgkin's lymphomas in current histologic perspective. In Rosenberg HS, Berstein J (eds): Perspectives in Pediatric Pathology, vol 7. New York, Raven Press, 1982.
37. Card CG: Pathologic quiz. Arch Otolaryngol 104:301, 1978.
38. Carpenter RI: Thymic cyst of the neck with prolongation to the thymus gland. Otolaryngol Head Neck Surg 90:494–496, 1982.
39. Casselman JW, Smet MH, Van Damme B, Lemahieu SF: Primary cervical neuroblastoma: CT and MR findings. J Comput Assist Tomogr 12:684–686, 1988.
40. Castellino RA: Hodgkin's disease: Practical concepts for the diagnostic radiologist. Radiology 159:305, 1986.
41. Castillo M, Pillsbury H: Rhabdomyosarcoma of the middle ear: Imaging features in two children. AJNR Am J Neuroradiol 14: 730–733, 1993.
42. Chan YL, Cheng JC, Metreweli C: Ultrasonography of congenital muscular torticollis. Pediatr Radiol 22:356, 1992.
43. Chang AY, Su SW, Zen SH, Wang WC: Nasopharyngeal carcinoma in young patients. Am J Clin Oncol 14:1–4, 1991.
44. Chaudhry AP, Haar LG, Koul A, Nickerson PA: Olfactory neuroblastoma (esthesioneuroblatoma): A light and ultrastructural study of two cases. Cancer 44:564–579, 1979.
45. Choy FJ, Ward R, Richardson R: Carcinoma of the thyroglossal duct. Am J Surg 108:361–369, 1964.
46. Coffin CM, Dehner LP: Peripheral neurogenic tumors of the soft tissues in children and adolescents: A clinicopathologic study of 139 cases. Pediatr Pathol 9:387–407, 1989.
47. Cohen AF, Mitsudo S, Ruben RJ: Nasopharyngeal teratoma in the neonate. Int J Pediatr Otorhinolaryngol 14:187–195, 1987.
48. Coit W, Harnsberger H, Osborn A, et al: Ranulas and their mimics: CT evaluation. Radiology 163:211–216, 1987.
49. Cote D, Gianoli G: Fourth branchial cleft cysts. Otolaryngol Head Neck Surg 114:95–97, 1996.

50. Crawford SC, Harnsberger HR, Johnson L: Fibromatosis colli of infancy. AJR Am J Roentgenol 151:1183, 1988.
51. Cressman W, Myer C: Clinical and pathologic diagnosis: Pathologic quiz case 1. Arch Otolaryngol Head Neck Surg 118:772–774, 1992.
52. Cressman WR, Myer III CM: Pathologic quiz case 1. Arch Otolaryngol Head Neck Surg 118:772–774, 1992.
53. Crist WM, Kelly DR, Ragab AJ, et al: Predictive ability of Lukes-Collins classification for immunologic phenotypes of childhood non-Hodgkin's lymphoma: An institutional series and literature review. Cancer 48:2070–2075, 1981.
54. Cushing BA, Slovis TL, Philippart AI, et al: A rational approach to cervical neuroblastoma. Cancer 50:785–787, 1982.
55. Das Gupta TK, Brasfield RD, Strong EW, Hajdu SI. Benign solitary schwannomas (neurilemomas). Cancer 24:355, 1969.
56. Davis KR: Embolization of epistaxis and juvenile nasopharyngeal angiofibromas. AJNR Am J Neuroradiol 7:953, 1986.
57. Day LH, Arnold GE: Rare tumors of the ear, nose and throat: Second series: Uncommon benign tumors of the head and neck. Laryngoscope 81:138, 1971.
58. Deane S, Telander R: Surgery for thyroglossal duct and branchial cleft anomalies. Am J Surg 136:348–353, 1978.
59. Derdyn CP, Moran CJ, Wippold FJ II, et al: MRI of ethesioneuroblastoma. J Comput Assist Tomogr 18:16–21, 1994.
60. DeVries SM, Decker TN: Frequency dependence of interear asymmetries and binaural interaction in the human ABR. Ear Hear 9: 275–282, 1988.
61. Dietrich RB, Kangarloo H: Retroperitoneal mass with intradural extension: Value of magnetic resonance imaging in neuroblastoma. AJR Am J Roentgenol 146:251–4, 1986.
62. Dorfman RF, Warnke R: Lymphadenopathy simulating the malignant lymphomas. Hum Pathol 5:519, 1974.
63. Easton JM, Levine PH, Hyams VJ: Nasopharyngeal carcinoma in the United States: A pathologic study of 177 U.S. and 30 foreign cases. Arch Otolaryngol 106:88, 1980.
64. Elkon D, Hightower SI, Lim ML, et al: Esthesioneuroblastoma. Cancer 44:1087–1094, 1979.
65. Ellis H: Cervical thymic cysts. Br J Surg 54:17–20, 1967.
66. Enzinger FM, Weiss SW: Soft Tissue Tumors. St. Louis, CV Mosby, 1983.
66a. Ewing J: Neoplastic Diseases. Philadelphia, WB Saunders, 1942, pp 1057–1060.
67. Faerber E, Swartz J: Imaging of neck masses in infants and children. Crit Rev Diagn Imaging 31:283–314, 1991.
68. Fahmy S: Cervical thymic cysts: Their pathogenesis and relationship to branchial cysts. J Laryngol Otol 86:47–60, 1974.
69. Favus MJ, Schneider AB, Stachura ME, et al: Thyroid cancer occurring as a late consequence of head-and-neck irradiation: Evaluation of 1056 patients. N Engl J Med 294, 1976.
70. Fedder M, Gonzales MF: Nasopharyngeal carcinoma: A brief review. Am J Med 79:365–369, 1985.
71. Fitzpatrick PJ, Briant TD, Berman JM: The nasopharyngeal angiofibroma. Arch Otolaryngol 106:234, 1980.
72. Fletcher BD, Kopiwoda SY, Strandjord SE, et al: Abdominal neuroblastoma: Magnetic resonance imaging and tissue characterization. Radiology 155:699–703, 1985.
73. Frankenthaler RA, Seilin RV, Cangir A, Goepfert H: Lymph node metastases from papillary-follicular thyroid carcinoma in young patients. Am J Surg 160:341–343, 1990.
74. Friedman AP, Haller JO, Goodman JD, Nagar H: Sonographic evaluation of noninflammatory neck masses in children. Radiology 147: 693, 1983.
75. Front D, Ben-Haim S, Israel O, et al: Lymphoma: Predictive value of Ga-67 scintigraphy after treatment. Radiology 182:359–362, 1992.
76. Fuji Y, Wakasugi M, Yamada K, et al: A study of ultrasonic diagnostic criteria for thyroid nodules. Paper presented at Proceedings of the Japanese Society of Ultrasound in Medicine, Tahamatsu, Japan, 1990.
77. Gainsford JC, Anderson US: First branchial cleft cysts and sinuses. Plast Reconstruct Surg 55:299–304, 1975.
78. Garcia CJ, Daneman A, McHugh K, et al: Sonography in thyroid carcinoma in children. Br J Radiol 65:977–982, 1992.
79. Gehan EA, Glover FN, Maurer HM, et al: Prognostic factors in children with rhabdomyosarcoma. Natl Cancer Inst Monogr 83–92, 1981.
80. Ginsberg LE: Neoplastic diseases affecting the central skull base: CT and MR imaging. AJR Am J Roentgenol 159:581–589, 1992.
81. Glasier CM, Seibert JJ, Williamson SI, et al: High resolution ultrasound characterization of soft tissue masses in children. Pediatr Radiol 17:233–237, 1987.
82. Goldstein G, Mackey IR: The Human Thymus. St. Louis, Warren H. Green, 1969.
83. Gooder P, Farrington T: Extracranial neurilemmoma of the head and neck. J Laryngol Otol 94:243, 1980.
84. Gore DO, Rankow R, Hanford JM: Parapharyngeal neurilemmoma. Surg Gynecol Obstet 103:193, 1956.
85. Gorman B, Charboneau JW, James EM, et al: Medullary thyroid carcinoma: Role of high-resolution US. Radiology 162:147–150, 1987.
86. Griffith BH: Frontonasal tumors: Their diagnosis and management. Plast Reconstr Surg 57:692, 1976.
87. Grosfeld JL, Ballantine TVN, Lowe D, Baehner RL: Benign and malignant teratomas in children: Analysis of 160 cases. World J Surg 4:29, 1976.
88. Guba AM Jr, Adam AE, Jaques DA, Chambers RG: Cervical presentation of thymic cysts. Am J Surg 136:430–436, 1978.
89. Guillane PJ, Davidson J, O'Dwyer T, Forte V: Juvenile angiofibroma: A review of the literature and case series report. Laryngoscope 102:928–933, 1992.
90. Gundry SR, Wesley JR, Klein MD, et al: Cervical teratomas in the newborn. J Pediatr Surg 18:382–386, 1983.
91. Hajdu SI, Shiu MH, Fortner JG: Tendosynovial sarcoma: A clinicopathological study of 136 cases. Cancer 39:1201, 1977.
92. Han MH, Chang KH, Kim IO, et al: Non-Hodgkin lymphoma of the central skull base: MR manifestations. J Comput Assist Tomogr 17:567–571, 1993.
93. Harnsberger H: Handbook of Head and Neck Imaging. St. Louis, Mosby–Year Book, 1995.
94. Harnsberger H, Bragg D, Osborn A, et al: Non-Hodgkin's lymphoma of the head and neck: CT evaluation of nodal and extranodal sites. AJNR Am J Neuroradiol 8:673–678, 1987.
95. Harnsberger H, Mancuso A, Muraki A, et al: Branchial cleft anomalies and their mimics: Computed tomographic evaluation. Radiology 152:739–748, 1984.
96. Harness JK, Thompson NW, McLeod MK, Pasieka JL, Fukuuchi A: Differentiated thyroid carcinoma in children and adolescents. World J Surg 16:547–554, 1992.
97. Hawkins DB, Park R: Teratomas of the pharynx and neck. Ann Otol 81:848–853, 1972.
98. Healy GB: Malignant tumors of the head and neck in children: Diagnosis and treatment. Otolaryngol Clin North Am 13:483–488, 1980.
99. Heroman WH, Golden SM, Yudt WM: Nasopharyngeal teratoma in the newborn. Ear Nose Throat J 59:19–27, 1980.
100. Hirsch RJ, Yousem DM, Loevner L, et al: Synovial sarcomas of the head and neck. MR findings. AJR Am J Roentgenol 169: 1185–1188, 1997.
101. Hollinshead WH: Anatomy for Surgeons: The Head and Neck, vol 1. New York, Harper and Row, 1968.
102. Holman CB, Miller WE: Juvenile nasopharyngeal fibroma. Am J Roentgenol 94:292, 1965.
103. Holt GR, McManus K, Newman RK, et al: Computed tomography in the diagnosis of deep-neck infections. Arch Otolaryngol 108: 693–696, 1982.
104. Howell C: The sublingual dermoid cyst. Oral Surg Oral Med Oral Pathol 59:578–580, 1985.
105. Howell CG, Van Tassel P, EL Gammal T: High resolution computed tomography in neonatal nasopharyngeal teratoma. J Comput Assist Tomogr 8:1179, 1984.
106. Hsu MM, Huang SC, Lynn TC, et al: The survival of patients with nasopharyngeal carcinoma. Otolaryngol Head Neck Surg 90: 289–295, 1982.
107. Hulbert KF: Congenital torticollis. J Bone Joint Surg 32B:50, 1950.
108. Hunter T, Paplanus S, Chernin M, Coulthard S: Dermoid cyst of the floor of the mouth: CT appearance. AJR Am J Roentgenol 141: 1239–1240, 1983.
109. Hurst RW, Erickson S, Cail WS, et al: Computed tomographic features of esthesioneuroblastoma. Neuroradiology 31:253–257, 1989.
110. Hyams VJ, Batsakis JG, Michaels L: Tumors of the upper respiratory tract and ear. Fascicle 25, 2nd Series. Atlas of Tumor Pathology. Washington, DC, Armed Forces Institute of Pathology, 1988, pp 180–181.

111. Jaffe BF, Jaffe N: Head and neck tumors in children. Pediatrics 51: 731–740, 1973.
112. Jenkins RD, Anderson JR, Jereb B, et al: Nasopharyngeal carcinoma—a retrospective review of patients less than thirty years of age: A report from Children's Cancer Study Group. Cancer 47: 360–366, 1981.
113. Johnson GF, Weisman PA: Radiological features of dermoid cysts of the nose. Radiology 82:1016, 1964.
114. Jones JE, Hession B: Cervical thymic cysts. Ear Nose Throat J 75: 678–680, 1996.
115. Jordan RB, Gauderer MW. Cervical teratomas: An analysis. Literature review and proposed classification. J Pediatr Surg 23:583–591, 1988.
116. Kaban L, Mulliken JB: Vascular anomalies of the maxillofacial regions. J Oral Maxillofac Surg 44:203, 1986.
117. Kadin MR, Thompson RW, Bentson JR, et al: Angiographic evaluation of the regression of an extensive juvenile nasopharyngeal angiofibroma after radiation therapy: A case report with therapeutic implications. Br J Radiol 47:902–905, 1974.
118. Kadish S, Goodman M, Wang CC: Olfactory neuroblastoma: A clinical analysis of 17 cases. Cancer 37:1571–1576, 1976.
119. Kapadia SB, Popek EJ, Barnes L: Pediatric otorhinolaryngic pathology: Diagnosis of selected lesions. Pathol Annu 29:159–209, 1994.
120. Kaplan HS: Hodgkin's disease: Unfolding concepts concerning its nature, management and prognosis. Cancer 45:2439–2474, 1980.
121. Kasper ME, Parsons JT, Mancuso AA, et al: Radiation therapy for juvenile angiofibroma: Evaluation by CT and MRI, analysis of tumor regression, and selection of patients. Int J Radiat Oncol Biol Phys 25:689–694, 1993.
122. Katz AG, Passy V, Kaplan L: Neurogenous neoplasma of major nerves of the face and neck. Arch Surg 103:51–56, 1971.
123. Kaufman FR, Roe TF, Isaacs H Jr, Weitzman JJ: Metastatic medullary thyroid carcinoma in young children with mucosal neuroma syndrome. Pediatrics 70:263–267, 1982.
124. Kelley DJ, Gerber ME, Willging JP: Cervicomediastinal thymic cysts. Int J Pediatr Otorhinolaryngol 39:139–146, 1997.
125. Kiyosue H, Miyake H, Komatsu E, Mori H: MRI of cervical masses of thymic origin. J Comput Assist Tomogr 18:206–208, 1994.
126. Kjeldsberg CR, Wilson JF, Berard CW: Non-Hodgkin's lymphoma in children. Hum Pathol 14:612, 1983.
127. Koeller KK, Alamo L, Adair CF, Smirniotopoulos JG: Congenital cystic masses of the neck: Radiologic-pathologic correlation. Radiographics 19:121–146, 152–153, 1999.
128. Kraus R, Han BK, Babcock DS, Oestreich AE: Sonography of neck masses in children. AJR Am J Roentgenol 146:609, 1986.
129. Kretschmar CS, Colbach C, Bhan I, Crombleholme TM: Desmoplastic small cell tumor: A report of three cases and a review of the literature. J Pediatr Hematol Oncol 18:293–298, 1996.
130. Kreutzer EW, Jafek BW, Johnson ML, Zunkel DE: Ultrasonography in the preoperative evaluation of neck abscesses. Head Neck Surg 4:290–295, 1982.
131. Krugman ME, Rosin HD, Toker C: Synovial sarcoma of the head and neck. Arch Otolaryngol 98:53, 1973.
132. Lack EE: Extragonadal germ cell tumors of the head and neck region: Review of 16 cases. Hum Pathol 16:56–64, 1985.
133. Laine FJ, Nadel L, Braun IF: CT and MR imaging of the central skull base: Part 2. Pathologic spectrum. Radiographics 10:797–821, 1990.
134. LaQuaglia MP, Corbally MT, Heller G, et al: Recurrence and morbidity in differentiated thyroid cancer in children. Surgery 104: 1149, 1988.
135. Lasjaunias PL: The radioanatomical basis of arterial embolization for epistaxis. J Neuroradiol 6:45–53, 1979.
136. Lasjaunias P, Picard L, Manelfe C, et al: Angiofibroma of the nasopharynx. J Neuroradiol 7:73–79, 1980.
137. Latack J, Hutchinson R, Heyn R: Imaging of rhabdomysarcomas of the head and neck. AJNR Am J Neuroradiol 8:353–359, 1987.
138. Latifi HR, Siegel MJ: Color Doppler flow imaging of pediatric soft tissue masses. J Ultrasound Med 13:165–169, 1994.
139. Lee Y-Y, Van Tassel P, Nauert C, et al: Lymphomas of the head and neck: CT findings at initial presentation. AJNR Am J Neuroradiol 6:665–671, 1987.
140. Levine PA, McClean WC, Cantrell RW: Esthesioneuroblastoma: The University of Virginia Experience 1960–1985. Laryngoscope 96: 742–746, 1986.
141. Lim-Dunham JE, Feinstein KA, Yousefzadeh DK, Ben-Ami T: Sonographic demonstration of a normal thyroid gland excludes ectopic thyroid in patients with thyroglossal duct cyst. AJR Am J Roentgenol 164:1489–1494, 1995.
142. Liston SL, Siegel LG: Branchial cysts, sinuses, and fistulae. Ear Nose Throat J 58:9–17, 1979.
143. Lloyd GA, Phelps PD: Juvenile angiofibroma: Imaging by magnetic resonance, CT and conventional techniques. Clin Otolaryngol 11: 247–259, 1986.
144. Lombardi F, Gasparini M, Gianni C, et al: Nasopharyngeal carcinoma in childhood. Med Pediatr Oncol 10:243–250, 1982.
145. Lukes RJ, Butler J, Hicks EB: The prognosis of Hodgkin's disease according to the histologic type and the clinical stage: Role of the reactions of the host. Nouv Rev Fr Hematol 6:15–22, 1966.
146. MacMahon B: Epidemiology of Hodgkin's disease. Cancer Res 26: 1189–201, 1966.
147. Mancuso AA, Dillon WP: The neck. Radiol Clin North Am 27: 407, 1989.
148. Maran ADG, Buchanan DR: Branchial cysts, sinuses, and fistulae. Clin Otolaryngol 3:77–92, 1978.
149. Marra S, Hotaling AJ, Raslan W: Cervical thymic cyst. Otolaryngol Head Neck Surg 112:338–340, 1995.
150. Maurer HM: The intergroup rhabdomyosarcoma study: Update, November 1978. Natl Cancer Inst Monogr 56:61–68, 1981.
151. Maurer HM, Beltangady M, Gehan EA, et al: The intergroup rhabdomyosarcoma study: I. A final report. Cancer 61:209–220, 1988.
152. Maurer HM, Moon T, Donaldson M, et al: The intergroup rhabdomyosarcoma study: A preliminary report. Cancer 40:2015–2026, 1977.
153. McCurdy JA Jr, Nadalo LA, Yim DW: Evaluation of extrathyroid masses of the head and neck with gray scale ultrasound. Arch Otolaryngol 106:83–87, 1980.
154. McDonald D: Sternomastoid tumour and muscular torticollis. J Bone Joint Surg 51:432–443, 1969.
155. McQuown SA, Smith JD, Gallo AE Jr: Intracranial extension of nasal dermoids. Neurosurgery 12:531, 1983.
156. Meissner WA, Warren S: Tumors of the thyroid gland. Atlas of Tumor Pathology. Washington, DC, Armed Forces Institute of Pathology, 1969.
157. Meyer JS, Hoffer FA, Barnes PD, Mulliken JB: Biological classification of soft-tissue vascular anomalies: MR correlation. AJR Am J Roentgenol 157:559, 1991.
158. Michael A, Mafee M, Valvassori G, Tan W. Dynamic computed tomography of the head and neck: differential diagnosis value. Radiology 1985:413–419, 1985.
159. Micheau C: A new histochemical approach to olfactory esthesioneuroma: A nasal tumor of neural crest origin. Cancer 40:314–318, 1977.
160. Mikal S: Cervical thymic cyst: Case report and review of the literature. Arch Surg 109:558–562, 1974.
161. Miller M, DeVito M: Cervical thymic cyst. Otolaryngol Head Neck Surg 112:586–588, 1995.
162. Miller M, Rao V, Tom B: Cystic masses of the head and neck: Pitfalls in CT and MR interpretation. AJR Am J Roentgenol 159: 601–607, 1992.
163. Miser AW, Miser JS: The treatment of cancer pain in children. Pediatr Clin North Am 36:979–999, 1989.
164. Montgomery WW: Surgery of the Upper Respiratory System. Philadelphia, Lea & Febiger, 1973.
165. Moore DM: Synovial sarcoma of the head and neck. Arch Otolaryngol Head Neck Surg 113:311–313, 1987.
166. Morton MJ, Berquist TH, McLeod RA, et al: MR imaging of synovial sarcoma. AJR Am J Roentgenol 156:337–340, 1991.
167. Muhlbauer WD, Dittmar W: Hereditary median dermoid cysts of the nose. Br J Plast Surg 29:334–340, 1976.
168. Mukherji SM, Tart RP, Slattery WH: Evaluation of first branchial anomalies by CT and MR. J Comput Assist Tomogr 17:576, 1993.
169. Mulliken JB, Glowacki J: Hemangiomas and vascular malformations in infants and children: A classification based on endothelial characteristics. Plast Reconstr Surg 69:412–420, 1982.
170. Nager GT: Cephaloceles. Laryngoscope 97:77–84, 1987.
171. Nakashima T, Kimmelman CP, Snow JB Jr: Structure of human fetal and adult olfactory neuroepithelium. Arch Otolaryngol 110: 641–646, 1984.
172. New G: Congenital cysts of the tongue, the floor of the mouth, the pharynx, and the larynx. Arch Otolaryngol 45:145–158, 1947.

173. New G, Erich J: Dermoid cysts of the head and neck. Surg Gynecol Obstet 65:48–55, 1937.
174. Nguyen Q, deTar M, Wells W, Crockett D: Cervical thymic cyst: Case reports and review of the literature. Laryngoscope 106:247–252, 1996.
175. Nicolai P, Luzzago F, Maroldi R: Nasopharyngeal cysts. Arch Otolaryngol Head Neck Surg 115:860, 1989.
176. Noma S, Kanaoka M, Minami S, et al: Thyroid masses: MR imaging and pathologic correlation. Radiology 168:759–764, 1988.
177. Noyek AM, Friedberg J: Thyroglossal duct and ectopic thyroid disorders. Otolaryngol Clin North Am 14:187–201, 1981.
178. Nyberg DA, Jeffrey RB, Brant-Zawadzki M, et al: Computed tomography of cervical infections. J Comput Assist Tomogr 9:288–296, 1985.
179. Okuda Y, Oi S: Nasal dermal sinus and dermoid cyst with intrafacial extension. Childs Nerv Syst 3:40–43, 1987.
180. Olsen KD, Maragos NE, Weiland LH: First branchial cleft anomalies. Laryngoscope 90:423, 1980.
181. Paonessa DF, Goldstein JC: Anatomy and physiology of head and neck infections (with emphasis on the fascia of the face and neck). Otolaryngol Clin North Am 9:561, 1976.
182. Park Y: Evaluation of neck masses in children. Am Fam Physician 51:1904–1912, 1995.
183. Parker G, Harnsberger H, Smoker W: The anterior and posterior cervical spaces. Semin US CT MR 12:257–273, 1991.
184. Pensler JM, Bauer BS, Naidich TP: Craniofacial dermoids. Plast Reconstr Surg 82:953–958, 1988.
185. Phillips CD, Futterer SF, Lipper MH, Levine PA: Sinonasal undifferentiated carcinoma: CT and MR imaging of an uncommon neoplasm of the nasal cavity. Radiology 202:477–480, 1997.
186. Pinczower E, Crockett DM, Atkinson JB, Kun S: Preoperative thyroid scanning in presumed thyroglossal duct cysts. Arch Otolaryngol Head Neck Surg 118:985, 1992.
187. Pinelli V, Pierro V, Bottero S, et al: Dysontogenetic neoplasms of the thyroid gland in infancy: Two case reports. Int J Pediatr Otorhinolaryngol 10:101–10, 1985.
188. Plantaz D, Hartmann O, Kalifa C, et al: Dumbbell neuroblastoma. Experience at the Gustave Roussy Institute in 38 cases treated from 1982 to 1987. Arch Fr Pediatr 48:529–533, 1991 (erratum, 48: 742, 1991).
189. Pollock JA, Newton TH, Hoyt WF: Transsphenoidal and transethmoidal encephaloceles: A review of clinical and roentgen features in 8 cases. Radiology 90:442–453, 1968.
190. Poncelet V, Dooms G, Mathurin P, Cornelius G: Contributory aspects of MRI in the evaluation of basal encephaloceles. J Neuroradiol 16:214–220, 1989.
191. Pounds LA: Neck masses of congenital origin. Pediatr Clin North Am 28:841–844, 1981.
192. Rapport RL II, Dunn RC Jr, Alhady F: Anterior encephalocele. J Neurosurg 54:213–219, 1981.
193. Reede DL, Bergeron RT, Som PM: CT of thyroglossal duct cysts. Radiology 157:121–125, 1985.
194. Rice DH, Coulthard SW: Neurogenic tumors of the head and neck in children. Ann Plast Surg 2:441, 1978.
195. Robinson DL, Destian S, Hinton DR: Synovial sarcoma of the neck: Radiographic findings with a review of the literature. Am J Otolaryngol 15:46–53, 1994.
196. Rosen L, Hanafee W, Nahum A: Nasopharyngeal angiofibroma: An angiographic evaluation. Radiology 86:103–107, 1966.
197. Rosenfeld CR, Coln CD, Duenhoelter JH: Fetal cervical teratoma as a cause of polyhydramnios. Pediatrics 64:176–179, 1979.
198. Rosevear W, Singer M: Symptomatic cervical thymic duct cyst in a neonate. Otolaryngol Head Neck Surg 89:738–741, 1981.
199. Roth JA, Enzinger FM, Tannenbaum M: Synovial sarcoma of the neck: A follow-up study of 24 cases. Cancer 35:1243–1253, 1975.
200. Rothschild MA, Urken ML, Catalano P: Evaluation and management of congenital cervical teratoma: A case report and review. Arch Otolaryngol Head Neck Surg 120:444, 1994.
201. Rowe LD: Neonatal airway obstruction secondary to nasopharyngeal teratoma. Otolaryngol Head Neck Surg 88:221–226, 1980.
202. Samuel AM, Sharma SM: Differentiated thyroid cancer in children and adolescents. Cancer 67:2186–2190, 1991.
203. Saphir O: Teratoma of the neck. Am J Pathol 5:313–323, 1929.
204. Reference deleted.
205. Scheible W, Leopold GR, Woo VL, Gosink BB: High-resolution real-time ultrasonography of thyroid nodules. Radiology 133:413–417, 1979.
206. Schuster JJ, Phillips CD, Levine PA: MR of esthesioneuroblastoma (olfactory neuroblastoma) and appearance after craniofacial resection. AJNR Am Neuroradiol 15:1169–1177, 1994.
207. Schwartz R, Movassaghi N, Marion E: Rhabdomyosarsoma of the middle ear: A wolf in sheep's clothing. Pediatrics 65:1131–1132, 1980.
208. Segal K, Sidi J, Levy R, Abraham A: Thyroid carcinoma in children and adolescents. Ann Otol Rhinol Laryngol 94:346–349, 1985.
209. Sessions RB: Nasal dermal sinuses—new concepts and explanations: II. Laryngoscope 92(suppl 29), 1982.
210. Sessions RB, Bryan RN, Naclerio, et al: RM. Radiographic staging of juvenile angiofibroma. Head Neck Surg 3:279–283, 1981.
211. Sessions RB, Wills PI, Alford BR, et al: Juvenile nasopharyngeal angiofibroma: Radiographic aspects. Laryngoscope 86:2–18, 1976.
212. Shah JP, Fighali J: Esthesioneuroblastoma. Am J Surg 142:456–458, 1981.
213. Sham JS, Wei WI, Lau SK, et al: Serous otitis media: An opportunity for early recognition of nasopharyngeal carcinoma. Arch Otolaryngol Head Neck Surg 118:794–797, 1992.
214. Shanmugaratnam K, Chan SH, de-The G, et al: Histopathology of nasopharyngeal carcinoma correlations with epidemiology, survival rates, and other biological characteristics. Cancer 44:1029, 1991.
215. Shidara K, Uruma T, Yasuoka Y, Kamei T: Two cases of nasopharyngeal branchial cyst. J Laryngol Otol 107:453, 1993.
216. Shimada H, Chatten J, Newton WA: Histopathologic prognostic factors in neuroblastic tumors: Definition of subtypes of ganglioneuroblastoma and age-linked classification of neuroblastoma. J Natl Cancer Inst 73:405, 1984.
217. Shlansky-Goldberg RD, Rao VM, Choi HY, et al: Hodgkin disease of the maxillary sinus. J Comput Assist Tomogr 12:507–509, 1988.
218. Shmookler BM, Enzinger FM, Brannon RB: Orofacial synovial sarcoma: A clinicopathologic study of 11 new cases and review of the literature. Cancer 50:269, 1982.
219. Sigal R, Chancelier MD, Luboinski B: Synovial sarcomas of the head and neck: CT and MR findings. AJNR Am J Neuroradiol 13: 1459, 1992.
220. Silver AJ, Mawad ME, Hilal SK, et al: Computed tomography of the nasopharynx and related spaces. Radiology 147:725–731, 1983.
221. Simeone JF, Daniels GH, Mueller PR: High-resolution real-time sonography of the thyroid. Radiology 145:431, 1982.
222. Singh RK, Hasan SA, Srivastava RW: Teratoma of the nasopharynx. Ear Nose Throat J 67:692–695, 1988.
223. Smith JF, Kielmovitch I: Branchial cysts anomaly in a newborn. Laryngoscope 100:163–165, 1989.
224. Smith MCF, Smith RJH, Bailey CM: Primary cervical neuroblastoma in infants. J Laryngol Otol 99:209–214, 1985.
225. Smirniotopoulos J, Chiechi M: Teratomas, dermoids, and epidermoids of the head and neck. Radiographics 15:1437–1455, 1995.
226. Snow JB Jr: Neoplasms of the nasopharynx in children. Otolaryngol Clin North Am 10:11–24, 1977.
227. Solbiati L, Cioffi V, Ballarati E: Ultrasonography of the neck. Radiol Clin North Am 30:941–954, 1992.
228. Soller AN: Nasopharyngeal teratoma. Arch Otolaryngol 82:49–52, 1965.
229. Solomon JR, Rangecroft L: Thyroglossal-duct lesions in childhood. J Pediatr Surg 19:555–560, 1984.
230. Som P: Cystic lesions of the neck. Postgrad Radiol 7:211–236, 1987.
231. Som P, Sacher M, Lanzieri C, et al: Parenchymal cysts of the lower neck. Radiology 157:399–406, 1985.
232. Som PM, Cohen FA, Sacher M: The angiomatous polyp and the angiofibroma: Two different lesions. Radiology 144:329–334, 1982.
233. Som PM, Curtin HD: Head and Neck Imaging. St. Louis, Mosby–Year Book, 1996.
234. Som PM, Lidov M, Brandwein M, et al: Sinonasal esthesioneuroblastoma with intracranial extension: Marginal tumor cysts as a diagnostic MR finding. AJNR Am J Neuroradiol 15:1259–1262, 1994.
235. Som PM, Shugal JMA, Cohen BA, Biller HF: The nonspecificity of the antral bowing sign in maxillary sinus pathology. J Comput Assist Tomogr 5:350, 1981.
236. Stout AP: The peripheral manifestations of the specific nerve sheath tumor (neurilemomas). Cancer 24:751, 1935.
237. Su C-Y, Hsu S-P, Lui C-C: Computed tomography, magnetic reso-

nance imaging, and electromyographic studies of tensor veli palatini muscles in patient with nasopharyngeal carcinoma. Laryngoscope 103:673–678, 1993.

238. Sutow WW: Cancer of the head and neck in children. JAMA 190: 414, 1964.
239. Tanimura F, Tachibana M, Dejima K, et al: Teratoma of the soft palate with multifocal cyst formation in the tongue and the brain. Arch Otorhinolaryngol 243:320–323, 1986.
240. Tapper D, Lack EE: Teratomas in infancy and childhood. Ann Surg 198:398–409, 1984.
241. Taxy J, Hidvegi DF: Olfactory neuroblastoma: An ultrastructural study. Cancer 39:131–138, 1977.
242. Telander R, Deane S: Thyroglossal and branchial cleft cysts and sinuses. Surg Clin North Am 57:779–791, 1977.
243. Telander R, Filston H: Review of head and neck lesions in infancy and childhood. Surg Clin North Am 72:1429–1447, 1992.
244. Thomas JR: Thyroglossal-duct cysts. Ear Nose Throat J 58:21–29, 1979.
245. Tom LW, Rossiter JL, Sutton LN, Davidson RS: Torticollis in children. Otolaryngol Head Neck Surg 105:1, 1991.
246. Toriumi DM, Atihal RA, Murad T, Sisson GA Sr: Extracranial neurogenic tumors of the head and neck. Otolaryngol Clin North Am 19:609–617, 1986.
247. Tovi F, Mares A: The aberrant cervical thymus: Embryology, pathology and clinical implications. Am J Surg 136:631–637, 1978.
248. Ultmann JE, Cunningham JK, Gelhorn A: The clinical picture of Hodgkin's disease. Cancer Res 26:1047, 1966.
249. Vanhoenacker P, Hermans R, Sneyers W, et al: Atypical aesthesioneuroblastoma: CT and MRI findings. Neuroradiology 35:466–467, 1993.
250. Vassilopoulou-Sellin R, Klein MJ, Smith TH, et al: Pulmonary metastases in children and young adults with differentiated thyroid cancer. Cancer 71:1348–1352, 1993.
251. Viswanathan K, Gierlowski TC, Schneider AB: Childhood thyroid cancer: Characteristics and long-term outcome in children irradiated for benign conditions of the head and neck. Arch Pediatr Adolesc Med 148:260–265, 1994.
252. Vogl T, Steger W, Ihrier S, et al: Cystic masses in the floor of the mouth: Value of MR imaging in planning surgery. AJR Am J Roentgenol 161:183–186, 1993.
253. Wadsworth DT, Siegel MJ: Thyroglossal duct cysts: Variability of sonographic findings. AJR Am J Roentgenol 163:1475–1477, 1994.
254. Wagner CW, Vinocur CD, Weintraub WH, Golladay ES: Respiratory complications in cervical thymic cysts. J Pediatr Surg 23:657–660, 1988.
255. Walker EA: Teratomas of the pharynx. Am Surg 29:219–226, 1963.
256. Weber PC, Rueger RG, Pickeral J: Thymic cysts. Am J Otolaryngol 17:64–66, 1996.
257. Wexler LH, Lee JH. Pediatric soft tissue sarcomas. Cancer 44: 221, 1994.
258. Wiatrak B, Myer C, Bratcher G: Report of a nasopharyngeal teratoma evaluated with magnetic resonance imaging. Otolaryngology 102:186–190, 1990.
259. Winship T, Rosvoll RF: Thyroid carcinoma in childhood: Final report on a 20-year study. Clin Proc Children's Hosp Wash 26: 327, 1970.
260. Work WP: Newer concepts of first branchial cleft defects. Laryngoscope 82:1581–1593, 1972.
261. Yasumoto M, Shibuya H, Takeda M, Korenaga T: Squamous cell carcinoma of the oral cavity: MR findings and value of T1- versus T2-weighted fast spin-echo images. AJR Am J Roentgenol 164: 981–987, 1994.
262. Yokota A, Matsukado Y, Fuwa I, et al: Anterior basal encephalocele of the neonatal and infantile period. Neurosurgery 19:468–478, 1986.
263. Young JL Jr, Miller RW: Incidence of malignant tumors in the U.S. in children. J Pediatr 86:254, 1975.
264. Yousem D, Lexa F, Bilaniuk L, Simmerman R: Rhabdomyosarcomas in the Head Neck: MR imaging evaluation. Radiology 177:683–686, 1990.
265. Yousem SA, Colby TV, Urich H: Malignant epitheliod schwannomas arising in a benign schwannoma. Cancer 55:2799, 1985.
266. Zarbo R, McClatchey K, Areen R, Baker S: Thymopharyngeal duct cyst: A form of cervical thymus. Ann Otol Rhinol Laryngol 92: 284–289, 1983.
267. Zimmerman D, Hay ID, Gough IR, et al: Papillary thyroid carcinoma in children and adults: Long-term follow up of 1039 patients conservatively treated at one institution during three decades. Surgery 104: 1157–1166, 1988.
268. Zohar Y, Strauss M, Laurian N: Adolescent versus adult thyroid carcinoma. Laryngoscope 96:555, 1986.

Part IV

Imaging of the Spine

Edited by
Jeffrey L. Sunshine

22 Degenerative Diseases of the Spine

David S. Jacobs

Back pain resulting from degenerative disease of the spine is one of the most common causes of disability in adults of working age. Between 60% and 80% of adults suffer from low back pain at some time in their lives. Medical costs resulting from back pain exceed $50 billion per year and may be as high as $100 billion.[23, 24, 38, 83]

Back pain results from many causes, including degenerative and congenital spinal stenosis, neoplasm, infection, trauma, and inflammatory or arthritic processes. Acquired spinal stenosis due to degenerative joint and disk disease accounts for the vast majority of cases.[57]

The following structures may be responsible for the origin of degenerative spinal stenosis:

1. Bone (spondylolisthesis, spondylolysis, osteophytosis).
2. Ligament (hypertrophy of the spinal ligaments, particularly the ligamentum flavum).
3. Facet joint (facet hypertrophy, synovial cyst).
4. Disk (bulging and herniation).

Most often, acquired narrowing of the spinal canal is due to a combination of bone, ligament, joint, and disk disease. The most common location of these changes is the lumbar spine, followed by the cervical spine. Thoracic disk herniation, formerly thought to be rare, is now being recognized with increased frequency with the advent of magnetic resonance imaging (MRI).[75]

Before the emergence of computed tomography (CT), plain films of the spine, spinal tomography, myelography, and diskography were the primary imaging modalities for the diagnosis of spinal stenosis and disk herniation. CT scans provided a noninvasive, nonoperator-dependent method of direct imaging of the spinal canal without injection of intrathecal contrast. CT was superior to myelography in visualizing lateral foraminal stenoses, disk protrusions, and lateral recess stenosis. In addition, it overcame the myelographic limitation of visualizing lower lumbar narrowing. In the latter case, abundant epidural fat in the lower lumbar spine, particularly at L5, may prevent displacement of the myelographic column by a protruding disk.

Finally, and most important, myelography does not delineate the cause of the narrowing (i.e., disk versus ligamentous versus bony hypertrophy). CT scans can reveal the cause of the pathology directly. Postmyelography CT scans offer even more sensitivity because of the increased the contrast between thecal sac, nerve roots, and soft tissues of the spinal column.[19]

With the development of MRI, the debate over CT scanning versus myelography became moot. MRI has become the modality of choice in the evaluation of spinal degenerative disease. MRI is superior even to contrast-enhanced CT scans in distinguishing bone, disk, ligament, nerve, thecal sac, and spinal cord. MRI provides multiplanar imaging capability. Pulse sequences can be adjusted to evaluate specific areas of interest or to more accurately define the disease process.

CT does retain some advantage over MRI with regard to bone detail, such as in the evaluation of osteophytes. CT and myelography will remain important in patients who, for technical reasons, cannot enter the MRI scanner (e.g., those with pacemakers or claustrophobia) or in patients whose MRI findings do not correlate with clinical symptoms. Many surgeons are still more comfortable with the bone detail of CT scans as a superior "road map" for the operating room. Additionally, recent technology allows the construction of a "virtual" spine from high-resolution CT images. Superb three-dimensional (3D) images of the spine can be obtained from high-resolution axial data acquired from helical CT scanners. This provides surgeons with a preoperative and intraoperative road map of the surgical site, thus improving accuracy and safety (Fig. 22–1). CT, therefore, still has a major role in the evaluation and management of degenerative spine disease.

Lumbar Spine

Anatomic Considerations

A more extensive discussion of the anatomy of the spine is presented in Chapter 24; however, a brief review of the lumbar diskovertebral complex as it relates to degenerative disease is warranted here.

The spinal canal is formed by the vertebral body anteriorly, the pedicles laterally, the laminae posterolaterally, and the base of the spinous process posteriorly (Fig. 22–2). This arrangement forms a protective ring for the neural tube. At the inferolateral aspect of each vertebra, a bony tunnel, the neural foramen, is appreciated bilaterally. The walls of the foramina are formed by the vertebral pedicle superiorly, the pedicle of the next vertebral body inferiorly, the facets posteriorly, and the diskovertebral junction anteriorly. When viewed sagittally, the foramina have a keyhole appearance and are 5 to 10 mm deep (Fig. 22–3). All of these relationships are important to understand when evaluating spinal stenosis.

Inferior to the termination of the spinal cord at approximately T12-L1, the lumbosacral nerve roots travel in a bundle within the dural sac. As this bundle travels inferi-

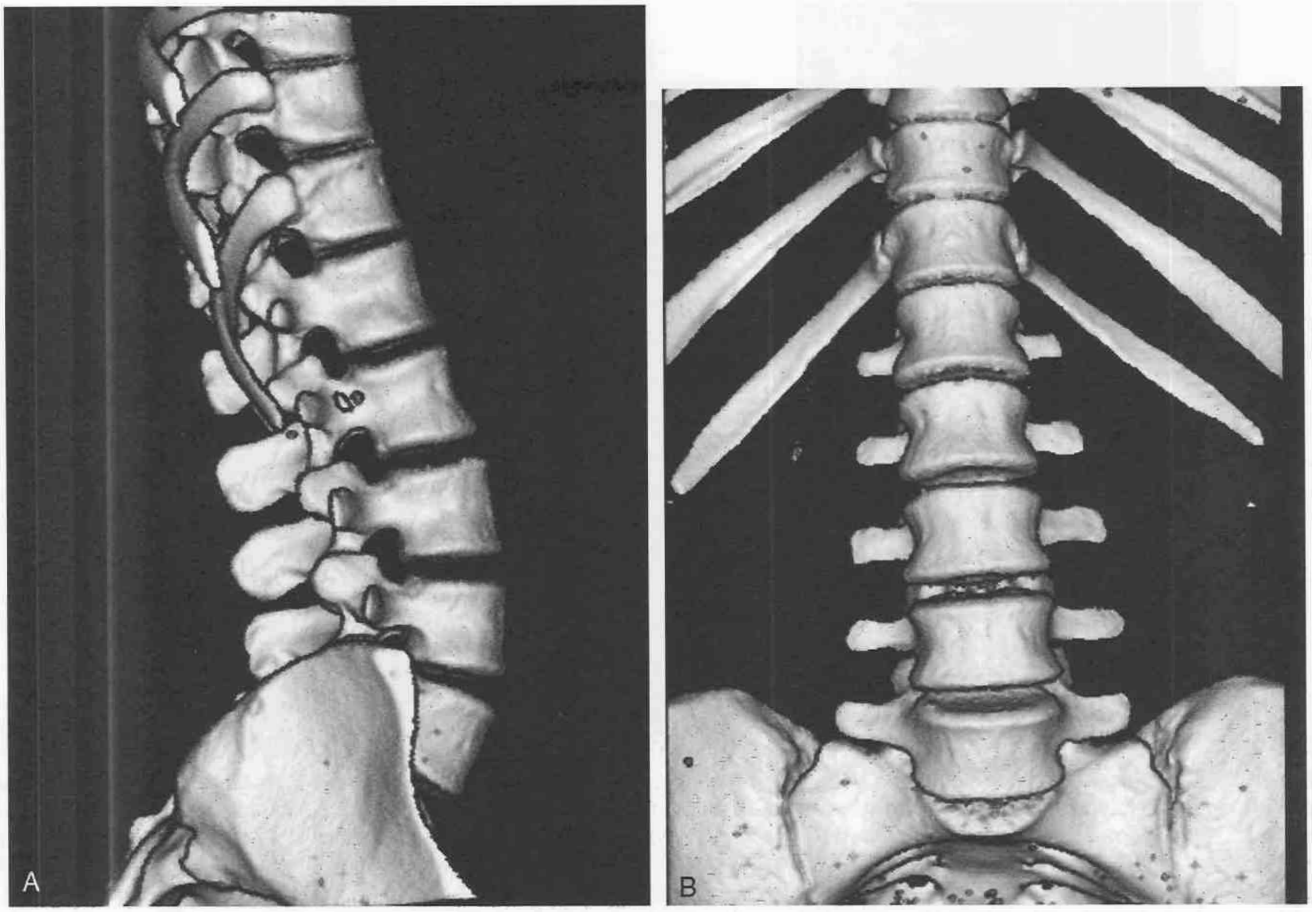

Figure 22–1. Lateral *(A)* and frontal *(B)* 3D images of the lumbar spine reconstructed from 1.5-mm-thick axial data on a helical CT scanner. Images can be rotated in any direction, thus providing a "virtual" surgical field.

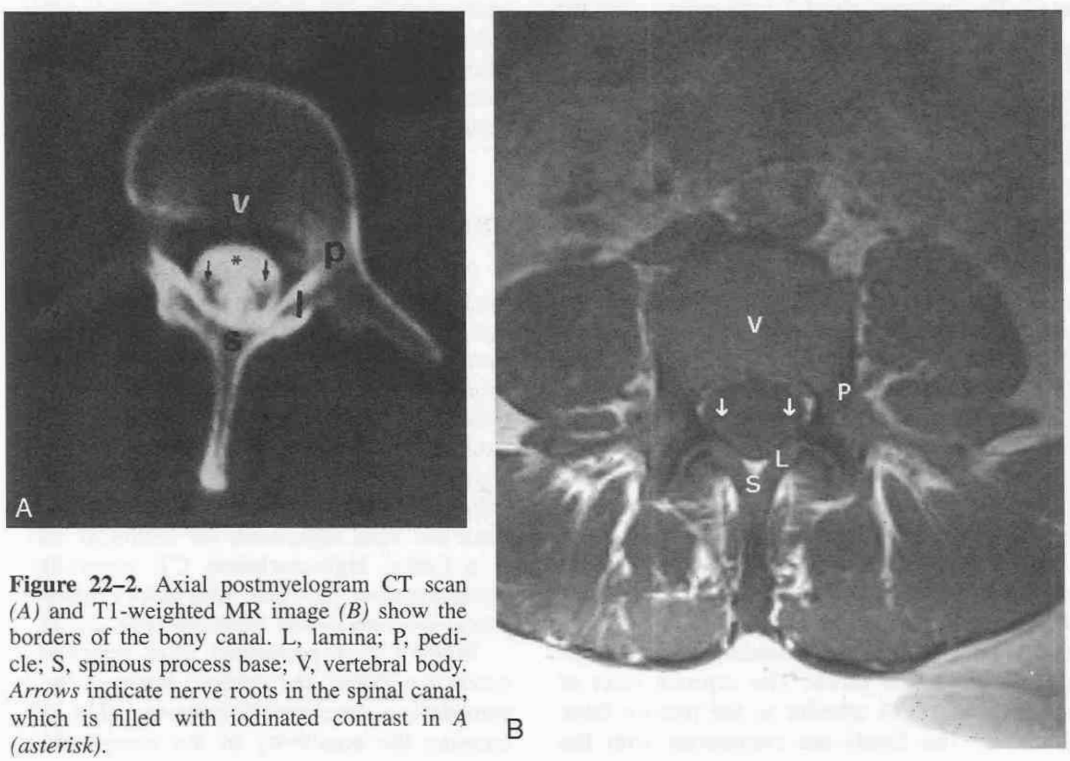

Figure 22–2. Axial postmyelogram CT scan *(A)* and T1-weighted MR image *(B)* show the borders of the bony canal. L, lamina; P, pedicle; S, spinous process base; V, vertebral body. *Arrows* indicate nerve roots in the spinal canal, which is filled with iodinated contrast in *A* (*asterisk*).

Figure 22–3. Parasagittal *(A)* and axial *(B)* T1-weighted MR images illustrate the neural foramina and its borders. D, disk forming the anterior border; I, inferior facet of the superior vertebra; P, superior and inferior pedicles forming the roof and floor; S, superior facet of lower vertebra; V, vertebra forming the anterior border. *Arrows* indicate exiting roots surrounded by bright epidural fat; on the parasagittal view *(A)*, the roots exit at the top of the "keyhole," behind the vertebral portion of the diskovertebral junction. The ligamentum flavum is indicated by *asterisks*.

orly, the most laterally positioned roots leave the group in a wide arc to exit through their respective neural foramina. The roots exit under the pedicle of the vertebra for which they are named. For instance, the L5 root exits under the L5 pedicle. Note that the roots exit through the top of the foraminal "keyhole," just posterior to the diskovertebral junction (see Fig. 22–3). Several small arteries, veins, and nerves accompany the roots through the foramina. The bottom of the keyhole, which is just posterior to the disk itself, contains primarily fat. The exiting roots are surrounded by a sleeve of cerebrospinal fluid (CSF)–containing dura for a very short distance. This sleeve terminates by fusing with the epineurium of the proximal spinal nerve.

After sending off the exiting nerve roots, the cauda equina continues inferiorly within the dural tube. A new set of roots is now positioned laterally. Before reaching the next set of neural foramina, these roots travel separately from the group within the *lateral recesses*. These are small anterolateral niches medial to the vertebral pedicles. As the roots reach the next diskovertebral junction, the process is repeated (Fig. 22–4).

On axial images of the diskovertebral junction, epidural fat lies concentrically around the thecal sac, surrounds exiting nerve roots, and continues into the neural foramina. The vertebral body and disk are seen anteriorly. Posterolateral to the thecal sac are the *facets*. The superior facet of the lower vertebral body lies anterior to the interior facet of the body above. The facets are continuous with the laminae that fuse in the midline to form the base of the spinous process (see Figs. 22–2 to 22–4).

The synovial-lined diarthrodial facet joints lie in an oblique parasagittal plane. This plane is relatively coronally oriented in the upper lumbar spine but more sagittally oriented at lower levels. Flush against the laminae and facets is the V-shaped ligamentum flavum, which can occasionally hypertrophy enough to cause canal narrowing.

Imaging Techniques

Although MRI has largely replaced CT as the imaging modality of choice for evaluation of the degenerative lumbar spine, CT is still used as the initial imaging modality in many institutions. In disk disease and canal stenosis, for example, studies have shown greater than 80% correlation between MRI and surgical findings in type and location of pathology. Correlation between CT and surgical findings were similar.[4, 20, 53, 77] Other studies, however, dispute the validity of many of these analyses.[39] If the patient cannot enter the MRI equipment for technical reasons or if cost is a factor, high-resolution CT, especially with sagittal reconstruction, provides satisfactory images of the disk, thecal sac, and neural foramina (Fig. 22–5).

When CT is performed after injection of intrathecal contrast material, the contrast between the thecal sac and surrounding structures is improved (Fig. 22–2*A*), thus increasing the sensitivity of the examination.[26] This is an

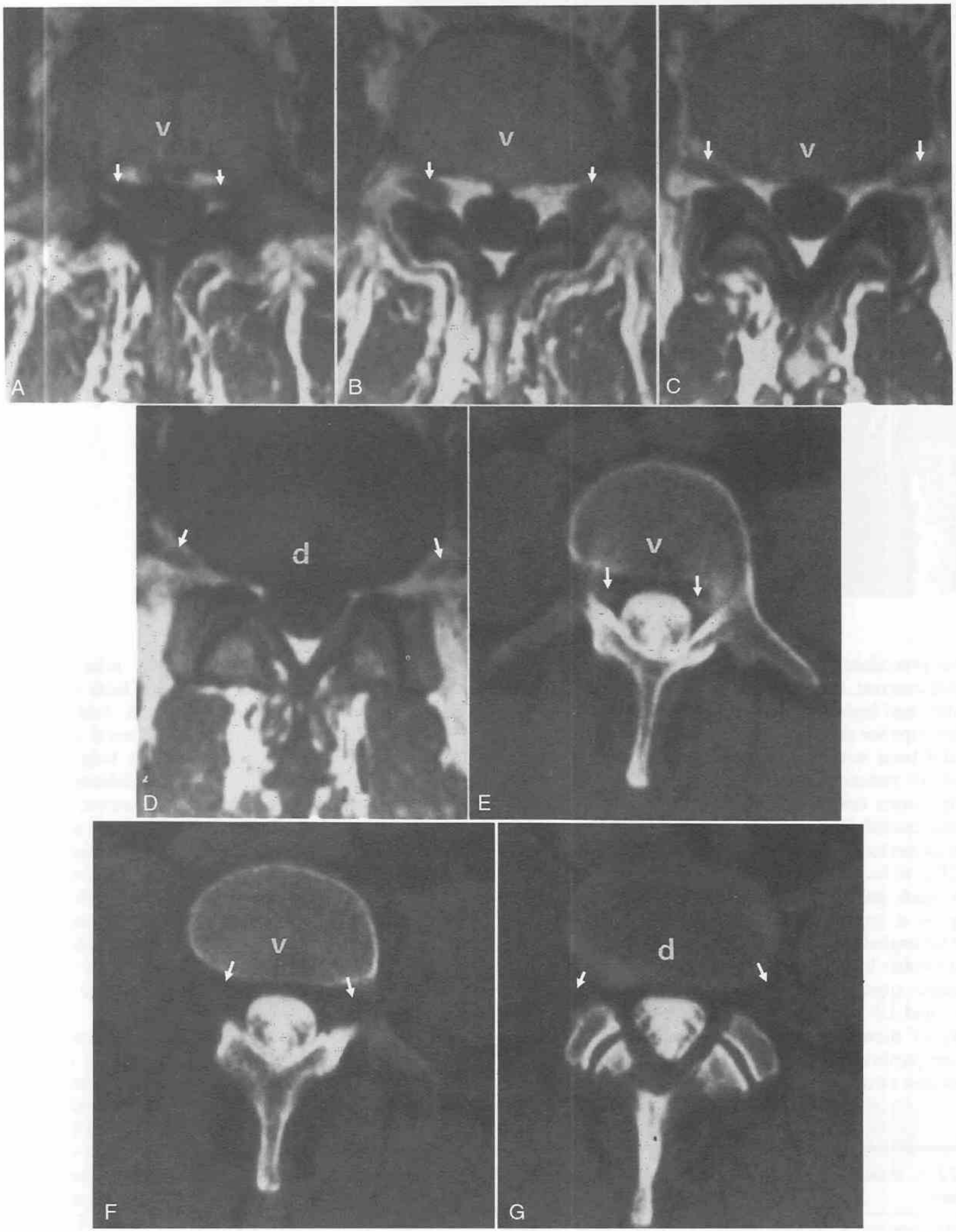

Figure 22–4. Axial T1-weighted MR image depicts the path of lumbar nerve roots through the canal. *A,* At the midbody level, the preexiting roots *(arrows)* are positioned in the lateral recesses. *B* and *C,* Just inferior to *A* at the superior aspect of the diskovertebral junction, the roots lie within the foramina. *D,* At the inferior aspect of the diskovertebral junction, the roots have already exited the foramina. *E–G,* Postmyelogram CT scan showing the same sequence of events. d, disk; v, vertebral body. Note epidural fat, bright on T1-weighted MRI and dark on CT scan, surrounding the sac and roots.

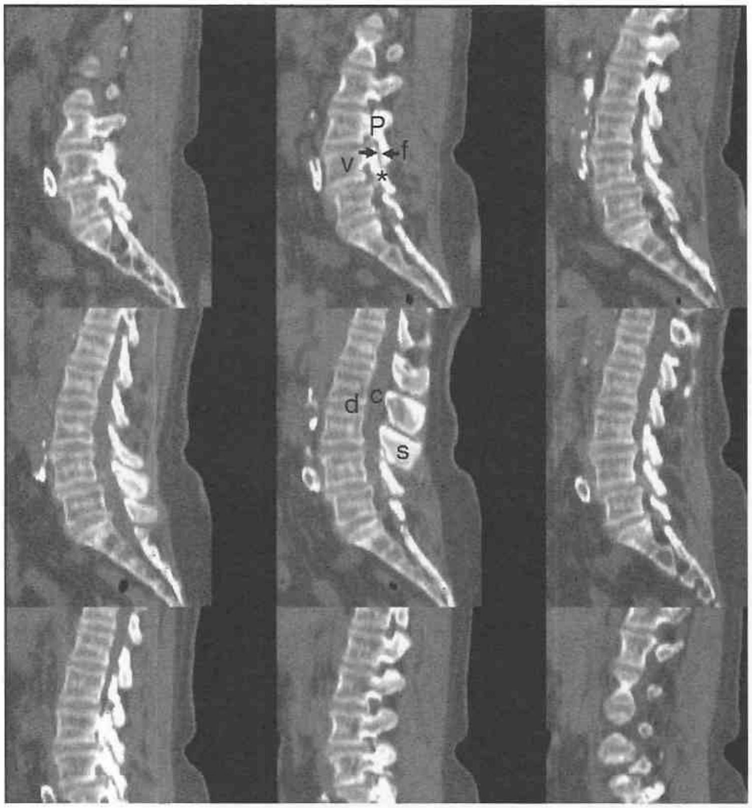

Figure 22–5. Sagittally reconstructed CT scan. Same patient as in Figure 22–1. The spinal canal (c) as well as the disk (d) is appreciated. Note excellent bone detail, particularly of the pedicle (P), pars interarticularis *(asterisk)*, and facets (f). s, spinous process.

invasive procedure, however, with the associated risks of iodinated contrast, bleeding, and infection. The multiplanar capability and high soft tissue contrast resolution of MRI provides superior delineation of disk, fat, nerves, ligaments, CSF, and bone without thecal puncture, intravenous (IV) contrast, or radiation exposure. Furthermore, routine CT imaging covers only a limited number of levels and may miss unexpected disease slightly higher or lower than the area of suspected pathology.

If CT is to be the initial imaging modality for evaluation of low back pain, slices 4 to 5 mm thick with 1 mm overlap is a typical protocol (Box 22–1). These slices should be angled parallel to the disk, compensating for the normal lumbar lordosis.

Because approximately 90% of disk herniations occur at L4-5 and L5-S1, with most of the remainder at L3-4, imaging of these levels is usually sufficient.[25, 32, 33] The slices are preferably contiguous (i.e., not only through the disk but also through the vertebral body). Selective imaging through the disk and end plate may miss lateral recess stenosis and migrated disk fragments. Both soft tissue and bone windows should be photographed. Additional images can be obtained, depending on the clinical circumstances. Sagittal or coronal reconstruction may help in evaluation of suspected spondylolysis or spondylolisthesis (see Fig. 22–5). For useful reconstructions, however, usually thin-section images are required. If CT scans are performed after myelography, the same techniques are used. However, my preference is to image the entire lumbar spine from L1 through S1 after myelography. Although degenerative disease of the upper lumbar spine is less common, there is only "one chance" to image the spine while the contrast material is in the thecal sac. Therefore, after myelography, I am unwilling to risk missing lesions in the upper lumbar region.

The osseous anatomy of the lumbar spine is best seen with wide ("bone") window settings. This is helpful for evaluation of osteophytes, fractures, spondylolysis, and facets. Narrower (soft tissue) window settings help to differentiate disk (80 to 120 Hounsfield units [HU]) from dural sac/nerve roots (0 to 60 HU). Epidural fat (−50 to −100 HU) is also well seen on these settings. The *ligamentum flavum* is seen as a soft-tissue-density structure flush against the anterior rims of the laminae and facets (Fig. 22–6).

MRI provides an abundance of choices for spine imaging. Pulse sequences can vary considerably from institution to institution, depending on the type of scanner, MRI vendor, imaging time available, and the individual preferences of the radiologist. There is no one best way to image the spine.

At our institution, MRI of the lumbar spine is performed

Box 22–1. **Routine CT Scans of Lumbar Degenerative Disease**

- Axial contiguous images from L3 to S1 (begin more superiorly if higher levels are of concern)
- Slice thickness = 4 mm, intersection gap = 3–4 mm
- Intrathecal contrast optional but preferable
- Both wide and narrow window settings
- Sagittal reconstructions if spondylolysis or spondylolisthesis is suspected

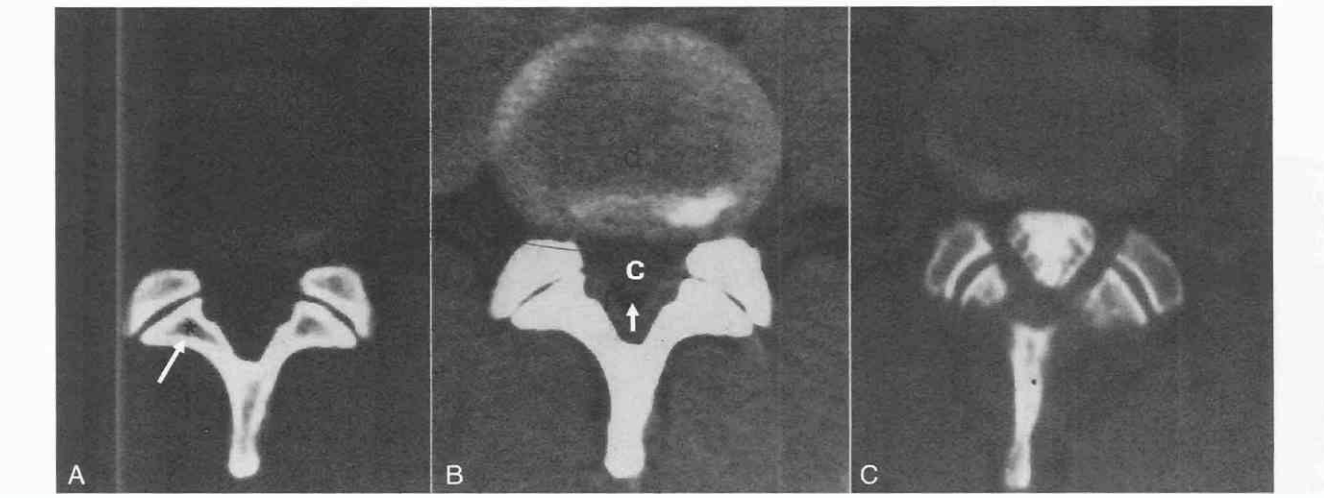

Figure 22–6. Axial CT scan using wide (bone) windows (W, 1450, L, 100) *(A)* and narrow (soft tissue) windows (W, 400; L, 40) *(B)*. Bone detail is better on the wide window settings. The cortex *(black arrow)* and marrow *(asterisk)* can best be distinguished with wide windows. However, contrast between the disk (d), epidural fat *(white arrow)*, ligamentum flavum (l), and canal (c) are best seen with narrow windows. *C*, Iohexol accentuates the contrast between the sac and the surrounding structures.

in both the sagittal and axial planes. The sagittal examination provides information on vertebral alignment and integrity of the vertebral bodies and pars and a general overview of the thecal sac, cauda equina, and nerve roots. The nerve roots within the neural foramina are well visulaized on sagittal images. The overall marrow signal is also best evaluated in this plane. Any abnormality on sagittal views should be confirmed on axial views and vice versa. The sagittal plane should include the conus down to at least the level of S1.

At our institution, we obtain all scans by using *fast spin-echo* (FSE) sequences. FSE is a variant of the *rapid acquisition relaxation–enhanced* (RARE) pulse sequence.[79] This method minimizes imaging time in spine patients, who are often quite uncomfortable lying in one position for any length of time. Additionally, because the FSE sequences take less time, they allow for higher-resolution scans with higher matrices.

Our protocol consists of a set of sagittal and axial FSE T1-weighted images as well as sagittal and axial FSE T2-weighted images (Box 22–2). Sagittal views should cover the entire width of the spine from foramen to foramen. Axial views should be obtained parallel to the plane of the disk space. It is preferable that the axials cover not only the disk space but also as much of the adjacent vertebral body as possible. This is because disk herniations may extend or migrate well beyond the confines of the interspace and may be missed if they are not covered on axial views.

T1-weighted images provide the best anatomic information because the bright epidural fat outlines the normal, darker structures of the spine and spinal canal. T1-weighted images provide optimal contrast between these structures. Moreover, because vertebral marrow has a significant amount of fat, the osseous anatomy is well visualized on T1 sequences (Fig. 22–7*A*; see Fig. 22–4). Any infiltrative pathology of the marrow (e.g., a neoplasm) can be seen as abnormal low signal within the bright vertebral fat. Marrow is also bright on FSE T2-weighted sequences (less so on standard T2-weighted, spin-echo sequences). Most pathologic processes, such as neoplasms, are also bright on these sequences and thus may "blend in" with the normal fat and may be missed on these images.

On T1-weighted images, bone is of intermediate to high signal intensity, depending on the degree of fatty marrow. Low signal intensity in bone suggests pathologic infiltration. Disks reflect intermediate signal intensity. The nerve roots, which also reflect intermediate signal intensity, are surrounded by low-signal-intensity CSF, which in turn is enveloped by high-signal fat. On T1-weighted images, ligamentum flavum reflects intermediate to low-signal intensity (see Figs. 22–2 to 22–4).

Box 22–2. Example of Routine MRI for Lumbar Degenerative Disease

1. Sagittal fast spin-echo, T1-weighted image to include conus to S1
   a. Field of view = 28 cm, slice thickness = 4–5 mm, intersection gap = 1 mm, matrix = 256 × 512
2. Sagittal fast spin-echo, T2-weighted image
   a. Field of view = 28 cm, thickness = 4–5 mm, intersection gap = 1 mm, matrix = 320 × 512
3. Axial fast spin-echo, T1-weighted image to include L2 through S1
   a. Field of view = 20 cm, slice thickness = 4 mm, intersection gap = 1 mm, matrix = 256 × 256
   b. Axial views obtained parallel to the plane of the disk space
   c. Extra-axial views performed through any abnormality seen at any level
4. Axial fast spin-echo, T2-weighted image
   a. Field of view = 20 cm, thickness = 4–5 mm, intersection gap = 1 mm, matrix = 256 × 256
5. If postoperative spine, repeat sagittal and axial fast spin-echo, T1-weighted images after gadolinium administration

Figure 22–7. Spinous anatomy.

A, Sagittal T1-weighted (TR = 700 msec, TE_{eff} = 12 msec, ETL = 4) MR image. Marrow fat is brighter than the water-filled disk. Nerve roots *(black arrows)* are slightly hyperintense to the dark cerebrospinal fluid *(white arrows)*.

B–D, Various T2-like MRI sequences. *B,* Standard proton-density (TR = 2700 msec, TE = 20 msec). *C,* Standard T2 (TR = 2000 msec, TE = 80 msec). *D,* Fast spin-echo, T2-weighted (TR = 4000, TE_{eff} = 108 msec, ETL = 16) MR image.

E, Short tau inversion recovery (STIR) sequence, used for fat suppression.

In general, the water-filled disk is brighter than bone on T2-weighted sequences. However, the contrast between various structures varies, depending on the sequence used. The "internuclear cleft" *(asterisk)*, a normal structure within the disk, is best seen on the T2-like images. Note the darkened fat of the vertebral marrow on the STIR sequence relative to all the other sequences. ETL, echo train length; TE_{eff}, effective echo time; TR, repetition time.

T2-weighted images optimize contrast between disk, bone, and CSF. T2-weighted images and many of the gradient-echo sequences make the CSF "myelographically" bright and the bone darker, which helps reveal the effects of osteophytes and bony hypertrophy on the thecal sac, as noted previously. Unlike standard spin-echo images, fat remains bright on FSE sequences. FSE sequences can therefore decrease contrast. This can sometimes decrease contrast between the bright spinal fluid and epidural fat. If necessary, fat-suppressed images can be used to ameliorate this problem. We do not find this routinely necessary unless bony neoplasm is suspected. The differentiation between

disk and bone is poorer on T2-weighted images and on gradient-echo sequences. Therefore, the imaging specialist should pay careful attention to both T1-weighted and T2-weighted sequences when analyzing the images.

Nondiskogenic Spinal Stenosis

Pathogenesis

Even in the absence of disk herniation, a combination of facet overgrowth and osteophyte formation at the vertebral end plates can lead to spinal stenosis. These changes are generally referred to as *spondylosis*.

The pathogenesis of spondylosis is believed to be due to recurrent rotational forces on the diskovertebral junction during cyclic axial loading. This results in thinning of the cartilaginous end plate, disk resorption, and consequent disk thinning. Stresses are then redistributed to the bone, leading to facet hypertrophy and end-plate osteophyte formation. Facet changes are exacerbated by repeated synovial irritation.[56] As the inferior and superior facets grind one upon another, the vertebral body becomes predisposed to either anterior (anterolisthesis) or posterior (retrolisthesis) slippage on the vertebra inferior to it.

The final result of these degenerative osteoarthritic changes is stenosis of the spinal canal, neural foramina, or lateral recesses or a combination of these.[9, 18, 22, 36, 40, 42] This causes nerve root compression as well as other pathophysiologic events, leading to the pain commonly known as *sciatica*.[60] The specific focus of narrowing depends on the structure involved.

Facet Hypertrophy

With repeated strains on the apophyseal joints, the articular cartilage is gradually stripped away and the underlying bone hypertrophies. Because the facets make up part of the wall of the neural foramen, foraminal narrowing can result, impinging on the exiting nerve roots (Fig. 22–8). These changes predominate in the lower lumbar spine.[64]

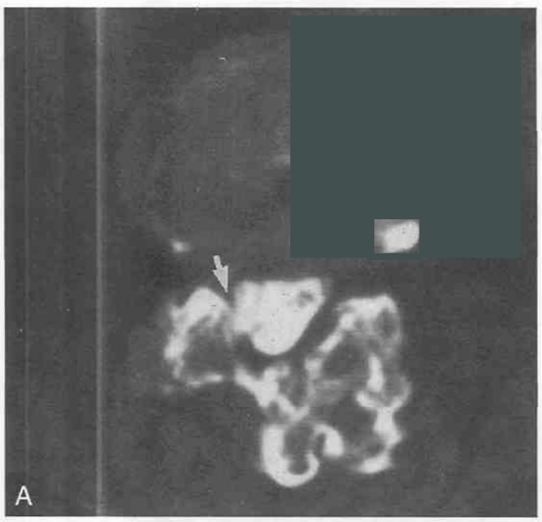

Figure 22–8. *A,* Facet hypertrophy. Postmyelogram CT scans shows massive facet hypertrophy bilaterally. *Arrow* indicates facet encroachment on the thecal sac. Compare with normal facets in Figure 22–4*G*. *B,* T2-weighted MR image shows hypertrophied facets (f) and ligamentum flavum (l) encroaching on the foramina, *(arrows)*, obliterating the foraminal fat and severely narrowing the canal (c). *C,* T2-weighted MR image shows asymmetrical facet hypertrophy. The left facet exerts mass effect on the canal *(black arrow)*. Compare with normal facets in Figures 22–3*B* and 22–4*C* and *D*.

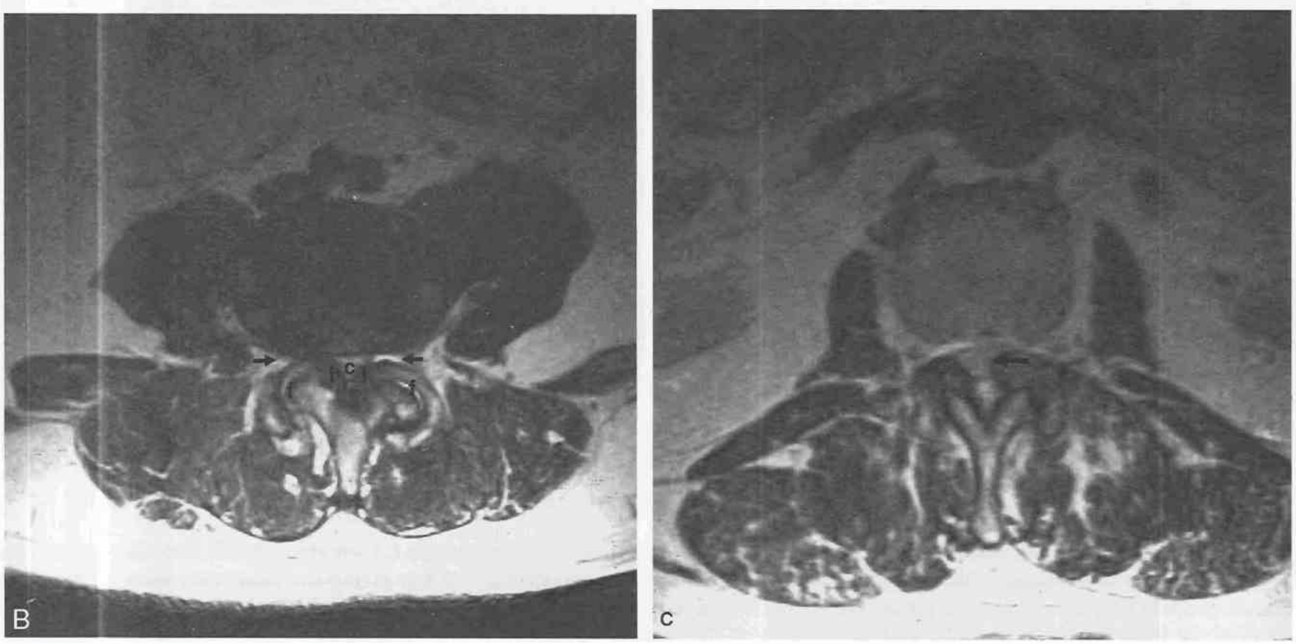

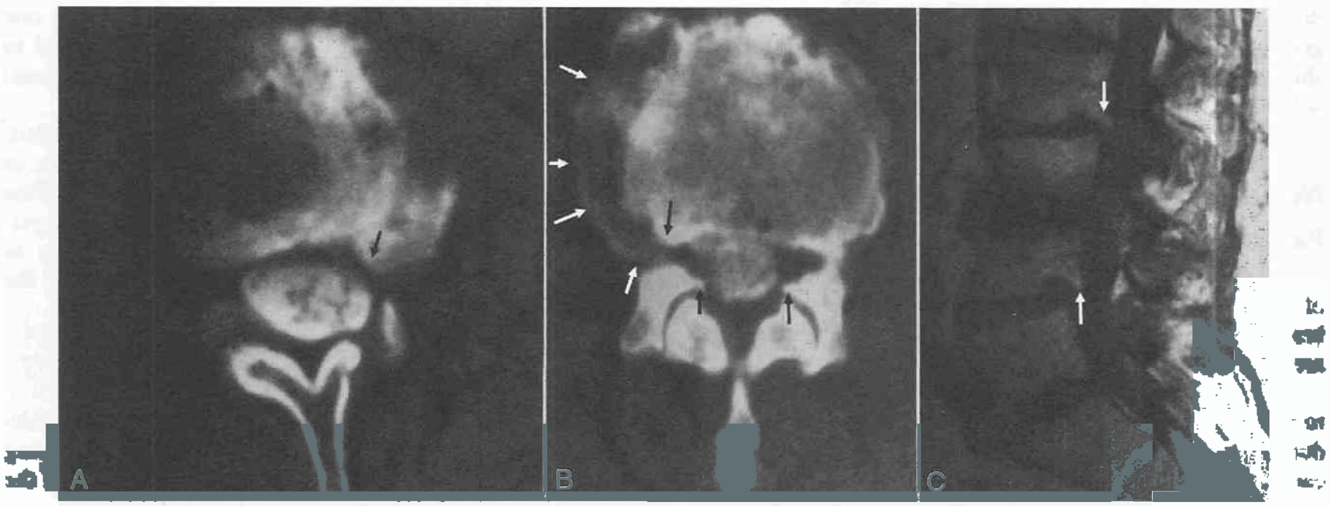

Figure 22–9. Osteophytes. *A* and *B*, Postmyelogram CT scans show osteophytes *(arrows)* encroaching on the canal and foramina. *C*, Sagittal T1-weighted MR image shows osteophytes *(arrows)* encroaching on the canal.

Osteophytes

With advancing age, osteophytosis of the lumbar vertebral end plates becomes increasingly common. The prevalence of osteophytes in patients aged 50 years and older is approximately 60% to 80%. The exact mechanism of osteophyte formation is debated, but it, too, probably results from complex stresses on the spine. Osteophytes are more common in men[64] and in individuals who are engaged in heavy physical labor. Depending on size, shape, and location, osteophytes can narrow or focally impinge on any part of the neural canal (Fig. 22–9).

Spondylolisthesis

As facets constantly grind upon one another they become smooth and "slippery." Thus, the ability of the superior (anterior) facet of a vertebral body to hold in check the inferior (posterior) facet of the vertebral body above becomes deficient. The upper vertebral body gradually slips forward over the lower one (Fig. 22–10). This is most common at L4-5, where the facets are oriented more sagittally than at any other level and are therefore most predisposed to slippage.[64]

Spondylolisthesis is divided into four grades of severity

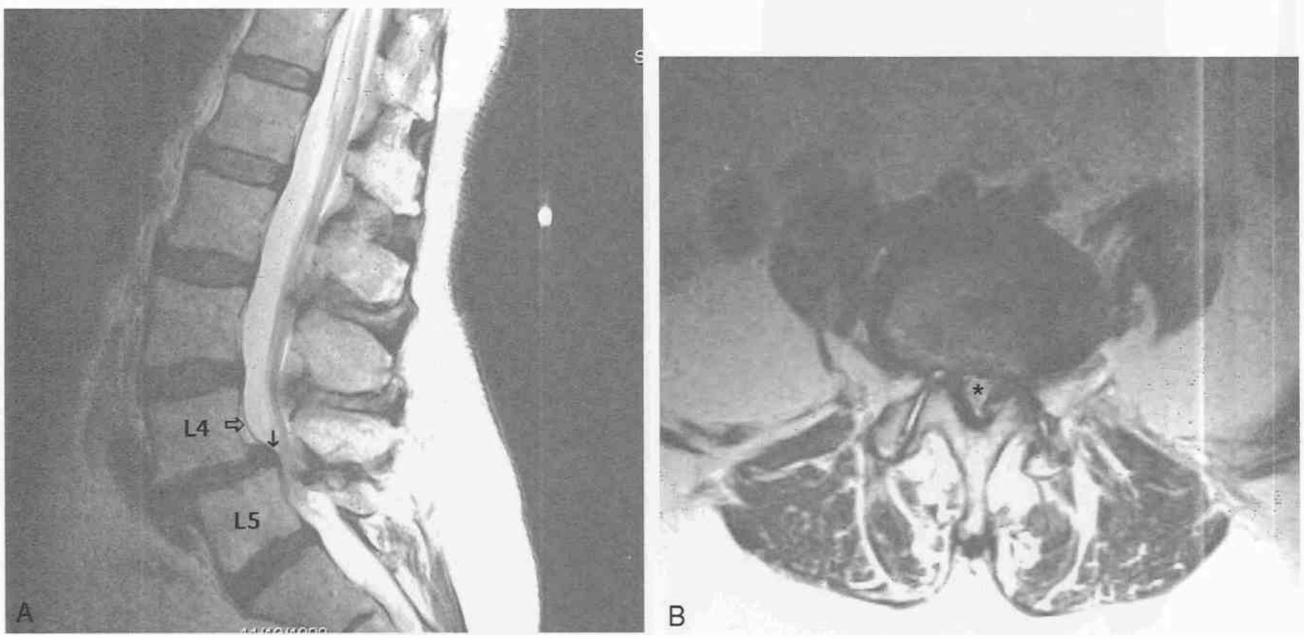

Figure 22–10. *A*, Spondylolisthesis. Sagittal T2-weighted image of spondylolisthesis of the L4 vertebra off L5. Note the severe canal stenosis caused by the slippage. The disk *(closed arrow)* is exposed by the slippage of L4, giving the false impression of herniation ("pseudoherniation"). The posterior longitudinal ligament *(open arrow)* is displaced by the spondylolisthesis. *B*, Axial scan at the L4-5 level of the same patient as in *A*. Note severe stenosis of the canal *(asterisk)*.

according to whether 25%, 50%, 75%, or 100% of a vertebral body has slipped forward upon its neighbor. As slippage becomes more severe, the spinal canal and/or the neural foramina can progressively narrow at that level, producing symptoms.

Fractures of the pars interarticularis (spondylolysis) are not prerequisites for degenerative spondylolisthesis.

Ligamentum Flavum Hypertrophy

The reasons for ligamentum flavum thickening are not completely understood, but they are probably related to mechanical instability and asymmetrical stresses on the facets. Because this structure lies flush against the posterior wall of the bony canal, ligamentum flavum hypertrophy contributes to canal narrowing (Figs. 22–11 and 22–12).[64]

Lateral Recess Stenosis

Bony overgrowth of the lateral recesses can occur as part of the degenerative process, resulting in entrapment of the lateral *(preexiting)* roots. Alternatively, when herniated disk material extrudes up or down into the lateral recesses, the preexiting roots can become compromised. Facet and ligamentum flavum hypertrophy can also contribute to lateral recess stenosis (see Fig. 22–12).

Synovial Cysts

With chronic irritation, tears can develop in the capsule of the facet joint and fluid can migrate through the capsule into the epidural space and form a cyst (Fig. 22–13). The cysts are usually of simple fluid intensity (dark on T1-weighted and bright on T2-weighted images); however,

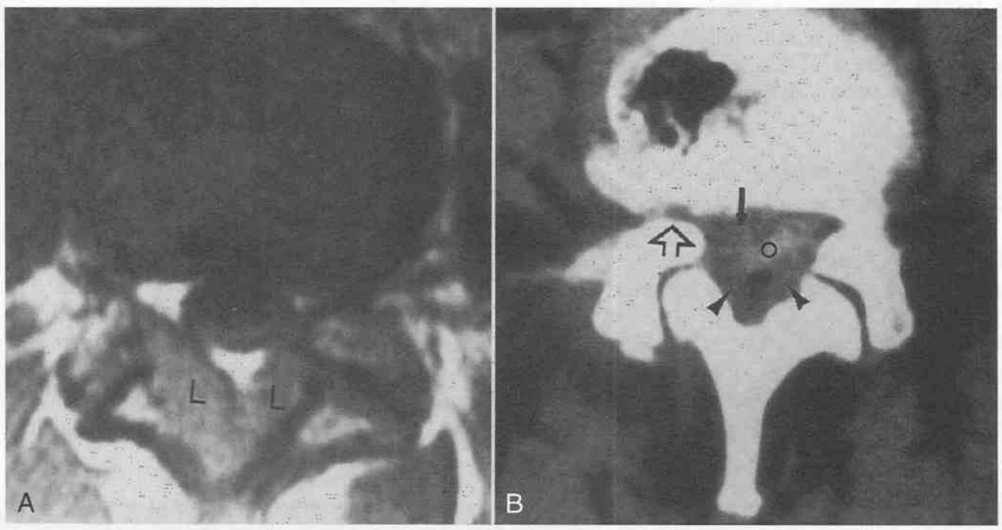

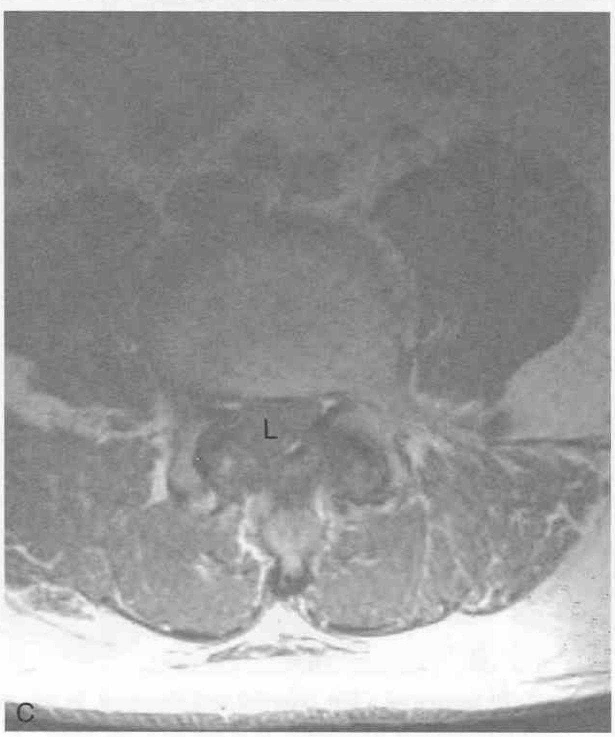

Figure 22–11. Ligamentum flavum hypertrophy. *A,* Axial T1-weighted MR image. The ligament (L) is markedly enlarged, but the capacious canal is not compromised in this case. *B,* Postmyelogram CT scan in another patient. The contrast column *(circle)* is compressed by hypertrophied ligamentum flavum *(arrowheads)* as well as by herniated disk *(arrow)*. Note also lateral recess stenosis, caused by a hypertrophied facet *(open arrow)*. *C,* T1-weighted axial MR image shows unilateral ligamentum flavum hypertrophy in the same patient as in Figure 22–8*B* but at a different level. The hypertrophied right ligamentum flavum (L) impinges on the canal. See also Figures 22–8*B* and 22–12*B*.

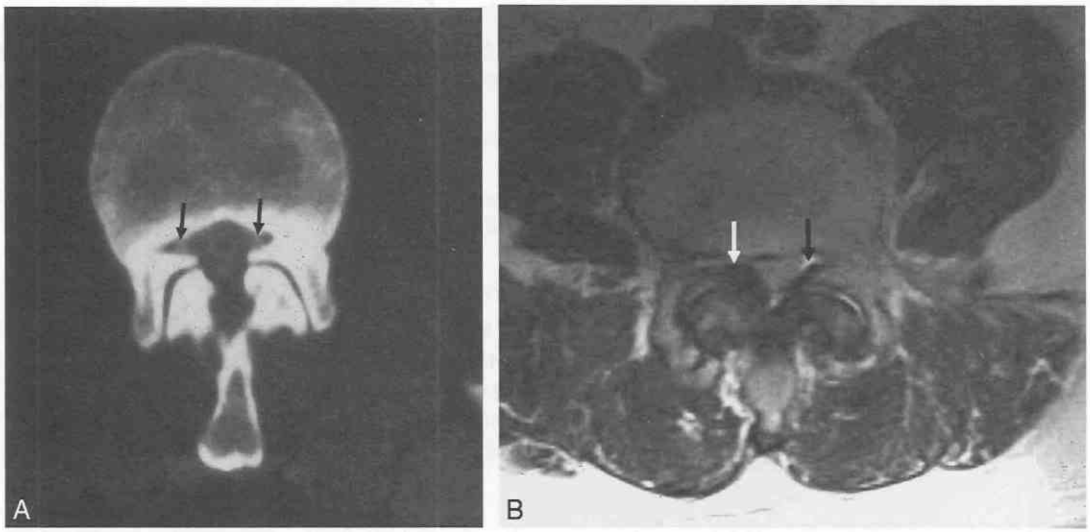

Figure 22–12. *A,* Lateral recess stenosis. CT scan shows preexiting nerve roots *(arrows)* within tiny lateral recesses. This patient with achondroplasia had nondegenerative congenital spinal stenosis. Compare with normal lateral recesses in Figure 22–4*E*. *B,* T2-weighted scan, same patient as in Figure 22–11*C*. The hypertrophied ligamentum flavum has obliterated the right lateral recess *(white arrow).* The left lateral recess *(black arrow)* is also narrowed by the hypertrophied facet, but some epidural fat can still be seen.

they may be brighter on T1-weighted and darker on T2-weighted images if the fluid contains proteins. These cysts can exert mass effect on or can narrow the canal, resulting in nerve-root symptoms. Synovial cysts can be resected surgically or may be aspirated under CT guidance.[46]

Other Causes of Stenosis

Disk bulges or *herniations* (see later, "Bulging and Herniated Disks") can narrow any part of the canal or foramina. Stenosis can be unilateral, bilateral, or diffuse.

Although lumbar degenerative disease typically begins at L4-L5 and L5-S1, the entire lumbar spine can become involved as mechanical stresses gradually shift cephalad.

Accurate assessment of the normal dimensions of the spinal canal can be difficult because of wide variations caused by body habitus and age. On lumbar CT scans, an anteroposterior dimension of less than 11.5 mm (measured from disk-vertebral body edge to the base of spinous process), an interpediculate distance of less than 16 mm, and a

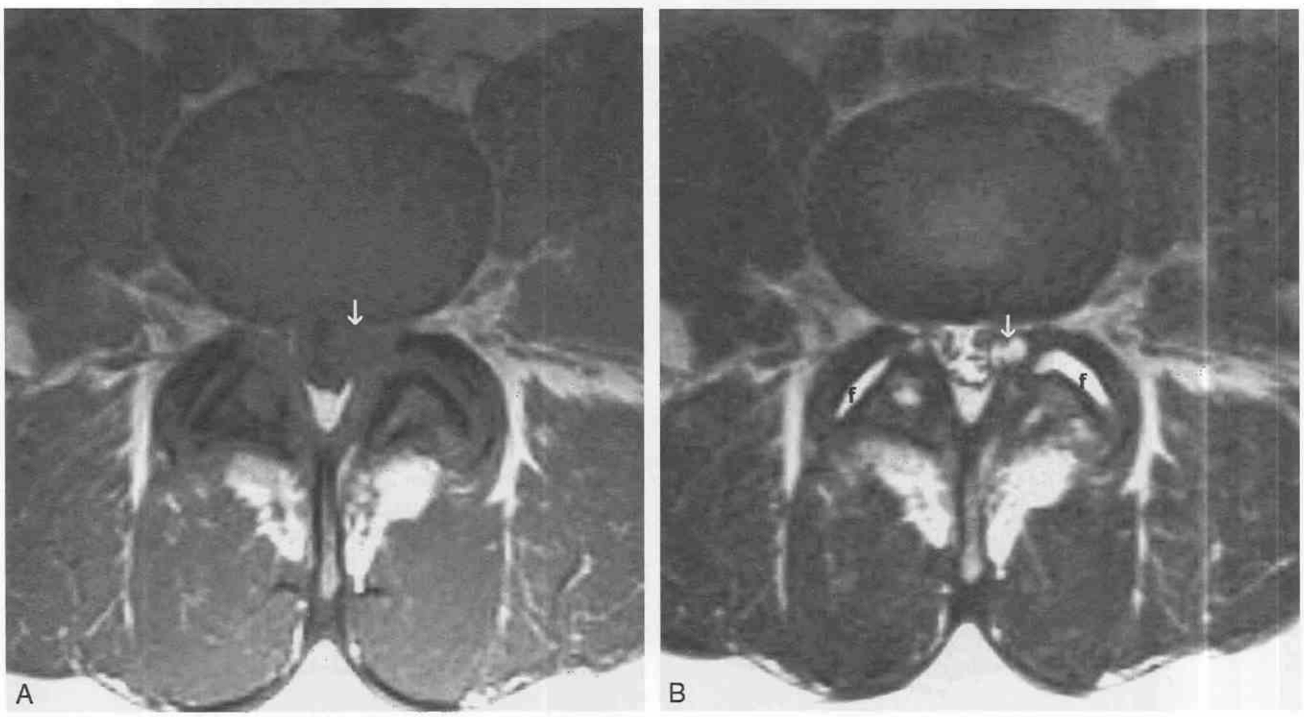

Figure 22–13. Synovial cyst. T1-weighted *(A)* and T2-weighted *(B)* images of a left synovial cyst *(arrows)*. In this case, the synovial fluid is isointense to cerebrospinal fluid on both sequences. The cyst emanates from fluid (f) in the joint capsules.

cross-sectional area smaller than 1.45 mm² are considered

Clinical Considerations

The clinical presentation of lumbar spinal stenosis usually begins with a history of chronic low back, bilateral-buttock, and thigh pain. If nerve-root compression is a feature, the pain may radiate down an extremity. Numbness and weakness, as well as coldness, tingling, and burning, may also occur. Many patients describe transient motor deficits.

The pain is more vague and poorly localized than that associated with a herniated disk. In fact, degenerative spinal stenosis may mimic peripheral vascular disease, simulating the symptoms of vascular claudication. In contrast to vascular claudication, however, the patient with spinal stenosis assumes a chronic stooped, flexed position (simian posture) in order to alleviate the pain. In patients with vascular claudication, pain is alleviated by standing and resting. In patients with spinal stenosis, the pain takes longer to subside, and walking distance before the onset of pain is more variable.

Physical changes resulting from peripheral vascular disease, such as decreased pulses and skin breakdown, are not present.[18, 27, 29, 41, 57, 62] On physical examination, the lumbar lordotic curve becomes straightened or reversed and pain may be reproduced on extension. Decreased lumbosacral motion is noted. It is not common to elicit motor or sensory deficits. In most cases, abnormal reflexes corresponding to L4 and L5 nerve roots are noted. Positive straight leg raising may be found. Objective weakness of the muscles may be supplied by the L5 and S1 nerves.[18, 27, 29, 41, 44, 62]

The pathophysiology of clinical symptoms related to spinal stenosis is complex, controversial, and not well understood. Most investigators believe that direct compression of nerve roots plays a major role in pain production, although arterial and venous obstruction may also be important. Some suggest that pseudoclaudication may be related to true vascular insufficiency of nerve roots.[57] Release of irritating chemicals by surrounding structures, nerve edema, chronic impairment of axonal transport, and intraneural microcirculation insufficiency may also be factors.[60]

Diskogenic Spinal Stenosis

The three major components of the intervertebral disk are the nucleus pulposus, the annulus fibrosus, and the end plate. The nucleus pulposus is the jelly-like core of the disk, containing 90% water mixed with delicate fibrous strands. The nucleus merges with the surrounding capsule, the collaginous annulus fibrosus. The cartilaginous end plate fuses the inferior and superior surfaces of the vertebral body to the disk (Fig. 22–14). The components of the disk complex optimize shock absorption from mechanical stresses on the vertebral column.

The normal intervertebral disk on CT scans are approximately 50 to 100 HU, which is somewhat denser than the surrounding ligaments and much denser than epidural fat and the fluid-filled thecal sac. This makes the disk easily distinguishable from neighboring structures, particularly in the case of disk herniation.

On T1-weighted MR images, the disk is a fairly homogeneous structure, isointense to muscle. On images with a long repetition time (TR), the disk becomes brighter because of its water content. On T2-weighted images, the nucleus pulposus, which is more hydrated than the annulus fibrosus, becomes even brighter than the annulus.

Pathogenesis

The pathogenesis of disk degeneration is complex and not well understood. End-plate and disk degeneration is probably a normal consequence of the aging process. By age 50 years, 85% to 95% of adults show evidence of degenerative disk disease at autopsy.[63] The cartilaginous end plate becomes thinner. The nucleus pulposus and, to a lesser degree, the annulus fibrosus lose up to 70% of their water content. The disk tissue also undergoes biochemical changes with respect to its collagen and proteoglycan content. The entire volume of the disk decreases with aging.[1, 11, 16] Annular fibers become stretched, leading to disk bulging (which is usually not significant unless the canal is already small). These changes occur most frequently in the parts of the lumbar spine most subjected to mechanical stresses (i.e., L4-5 and L5-S1).

Whether normal disk aging plays a predisposing role is unclear, but the sequence of events in disk herniation appears to be as follows. The annulus becomes frayed during repeated flexional and rotational forces, resulting in radial and concentrically oriented fissures in the annulus. This then predisposes the nucleus to further degeneration and subsequent herniation into and then through the annular fibers.[51] Although central disk herniations are by no means rare, disks tend to herniate posterolaterally because the posterior longitudinal ligament and annular fibers are thickest and strongest in the midline and thinner laterally.

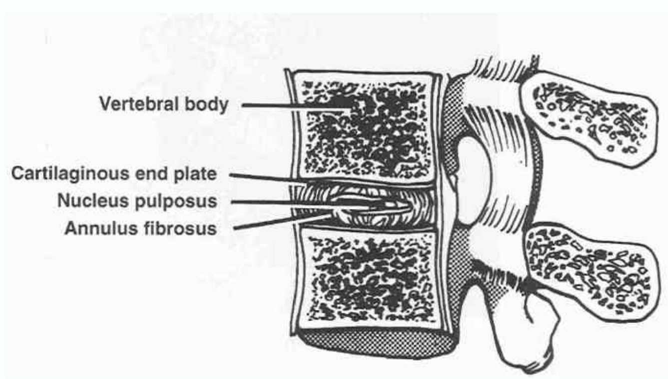

Figure 22–14. Disk anatomy. The jelly-like nucleus pulposus is encircled by the fibers of the annulus fibrosus. The cartilaginous end plate, which fuses with the vertebral body, covers the superior and inferior disk surfaces. (Modified from Modic MT: Magnetic Resonance Imaging of the Spine. St. Louis, Mosby–Year Book, 1989.)

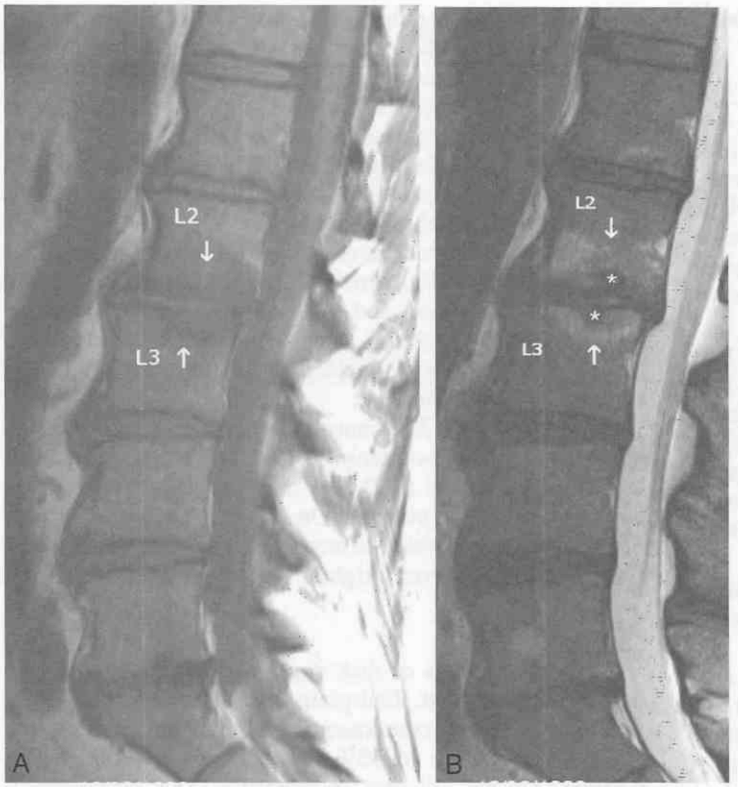

Figure 22–15. Type I end-plate changes. *A*, T1-weighted MR image shows hypointensity of the inferior L2 and superior L3 end plates *(arrows)*. *B*, T2-weighted MR image shows that the end plates have become hyperintense. This is the earliest stage of disk degeneration. The lower lumbar disks are dark on the T2-weighted scan because they have become dehydrated from degeneration. Note small Schmorl's nodes *(asterisks)*.

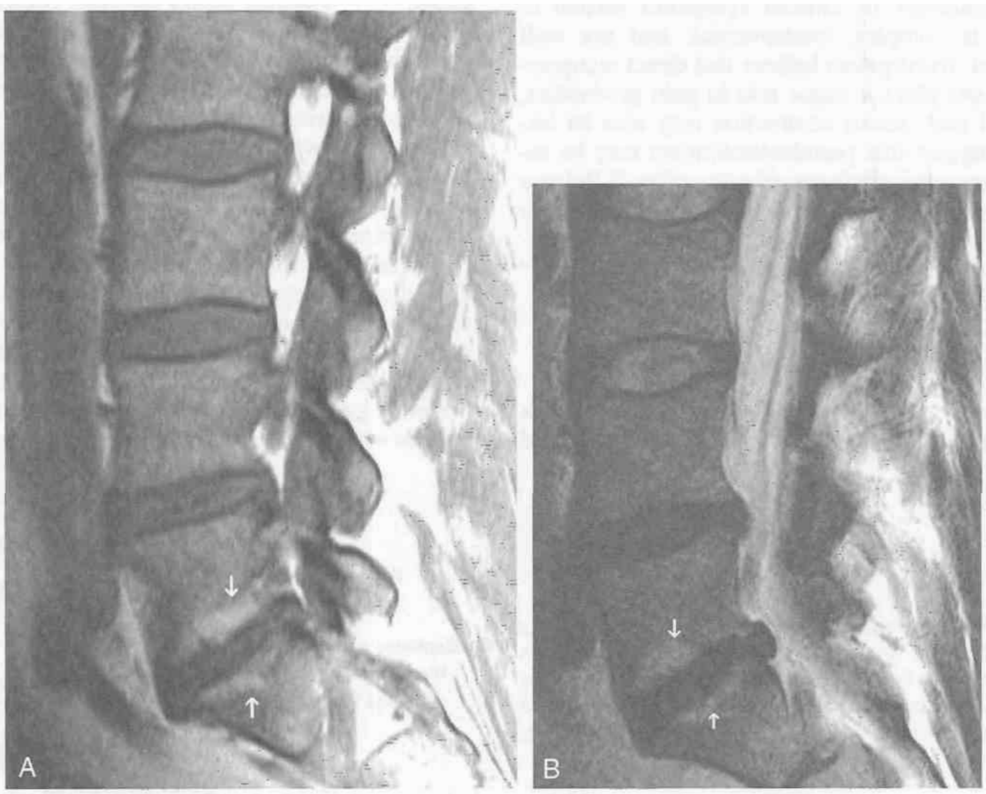

Figure 22–16. Type II end-plate changes. T1-weighted *(A)* and fast spin-echo, T2-weighted *(B)* MR images show fatty end plates *(arrows)*, which are hyperintense on T1-weighted and fast spin-echo, T2-weighted images.

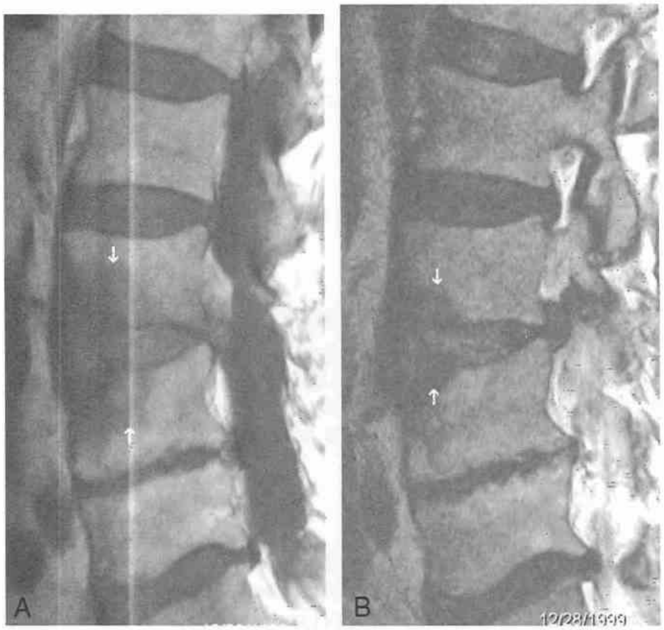

Figure 22–17. Type III end-plate changes. T1-weighted *(A)* and T2-weighted *(B)* MR images show hypointensity of the inferior L3 and superior L4 end plates on both sequences *(arrows)*.

Radiographic Changes

The earliest radiographically visible changes of intervertebral disk degeneration are those that occur at the end plate. These are best seen on MRI. Three types of end-plate changes have been described[17, 56]:

Type I changes demonstrate low signal intensity on T1-weighted images and high signal intensity on T2-weighted images (Fig. 22–15). This stage is believed to reflect replacement of the end-plate marrow with vascular fibrous tissue in response to chronic "injury."

Type II changes, the next stage, show high signal intensity on T1-weighted and on FSE T2-weighted images (Fig. 22–16). This stage represents replacement of the end-plate marrow with fatty tissue. (On standard spin-echo, T2-weighted images, the fatty end plates thus become slightly darker.) Type II changes tend to remain stable with time.

Type III changes, or the final stage if it occurs, are represented by low signal intensity on both T1-weighted and T2-weighted images (Fig. 22–17). This stage correlates with bony sclerosis seen on CT scans and plain films of severely degenerated end plates. This is the only end-plate change visible on CT scans or radiographs. Whether these end-plate changes have any prognostic significance has not been established; however, they are part of the normal aging process and must not be confused with other pathologic processes, such as tumor and infection (Fig. 22–18).

Bulging and Herniated Disks

Classification

The most important step in the analysis of the degenerative lumbar spine—after the vertebrae, end plates, ligaments, and joints—is the disk itself. As mentioned, the intervertebral disk is made up of a jelly-like nucleus pulposus, surrounded by a tough, fibrous annulus fibrosus. Unfortunately, no universally accepted classification of disk herniation exists. The one presented here[51] may differ from those offered by other texts and institutions.[47, 49]

Abnormal disks can be classified as *bulging* or *herniated*. A *herniated disk* can be subclassified as (1) protruded, (2) extruded, or (3) sequestered.

Bulging Disk

An *annular bulge* represents an extension of the disk margin beyond the confines of the adjacent vertebral end plate. The annular fibers are stretched but intact. The disk bulges diffusely around the posterior (and sometimes lateral) aspects of the end plate (Figs. 22–19 and 22–20). This does not usually lead to clinical symptoms unless the spinal canal is already congenitally small or narrow owing to spondylosis.

Protruded Disk

When some of the inner fibers of the annulus tear but the outer layers remain intact, the nucleus can focally

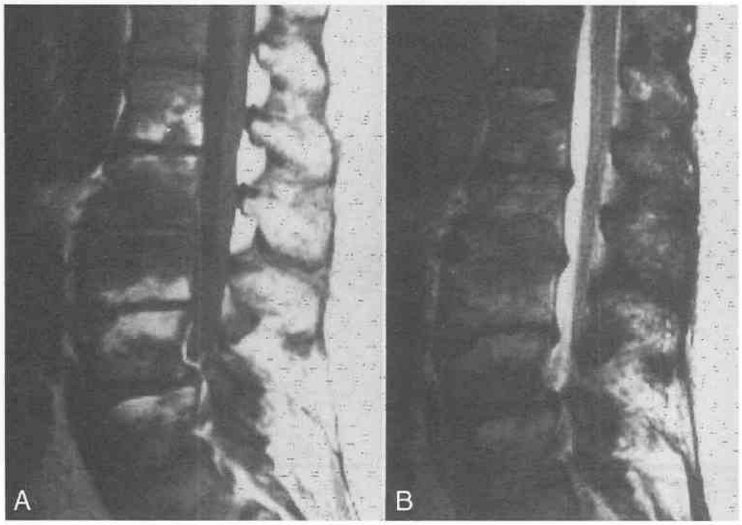

Figure 22–18. T1-weighted *(A)* and T2-weighted *(B)* MR images show end-plate changes of varying stages. The resulting marrow heterogeneity is easily confused with bone metastases.

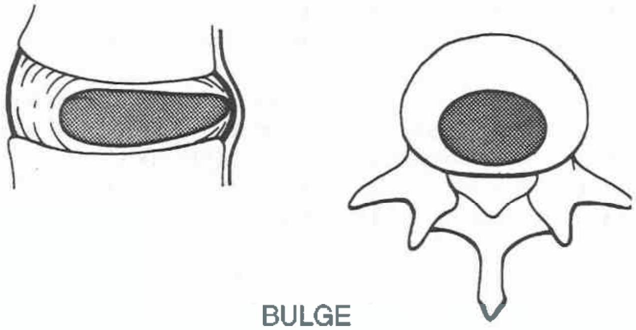

Figure 22–19. Illustration of a bulging disk. The disk bulges diffusely beyond the vertebral body margin. The annular fibers are stretched but completely intact. (Modified from Modic MT: Magnetic Resonance Imaging of the Spine. St. Louis, Mosby–Year Book, 1989.)

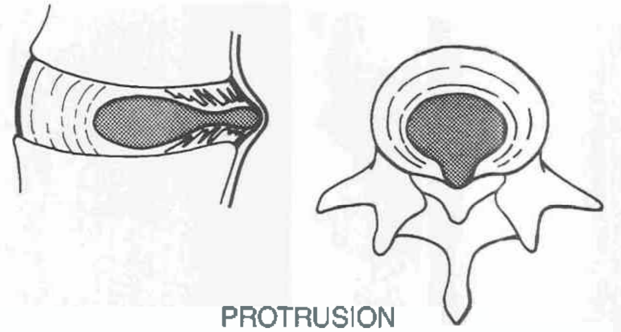

Figure 22–21. Illustration of disk protrusion. A portion of nucleus pulposus herniates focally through a rent in the inner annular fibers. The outer annular fibers are intact. (Modified from Modic MT: Magnetic Resonance Imaging of the Spine. St. Louis, Mosby–Year Book, 1989.)

herniate through the inner tear. This is the simplest (and probably earliest) type of disk herniation and is called a *disk protrusion* (Fig. 22–21).

Disk herniation is distinguished from annular bulge by its focality. Whereas a disk usually bulges fairly uniformly along its margins, a disk herniates through one particular spot—the annular tear. The signal intensity (on MRI) and density (on CT scans) of the protruded segment are generally, but not invariably, the same as those of the nonherniated portion.

Extruded Disk

A *disk extrusion* occurs when the nucleus pulposus herniates through a complete tear of the annulus fibrosus and is contained only by the posterior longitudinal ligament (Fig. 22–22). The herniated segment, however, remains attached to the parent disk but may extend cephalad or caudad. It can be difficult to differentiate between a disk protrusion and extrusion when the amount of herniated disk is small. This distinction, however, is not clinically significant; it is more important to recognize that these are simply different degrees of herniation and that the significance of a herniated disk is its effect on the spinal canal and nerve roots (Figs. 22–23 and 22–24).

Sequestered Disk

Finally, when an extruded nucleus breaks free of the parent disk, it is termed a *sequestered disk* or *free fragment* (Fig. 22–25). The sequestered portion may or may not be confined by the posterior longitudinal ligament. In fact, it may migrate inferiorly or superiorly to a different interspace or, in rare cases, may even penetrate the dura. Free fragments also tend to resemble the parent disk on both CT scans and on short TR MR images (Fig. 22–26).

On long TR or gradient-echo MR images, sequestered disks may be of higher signal intensity than the disk of

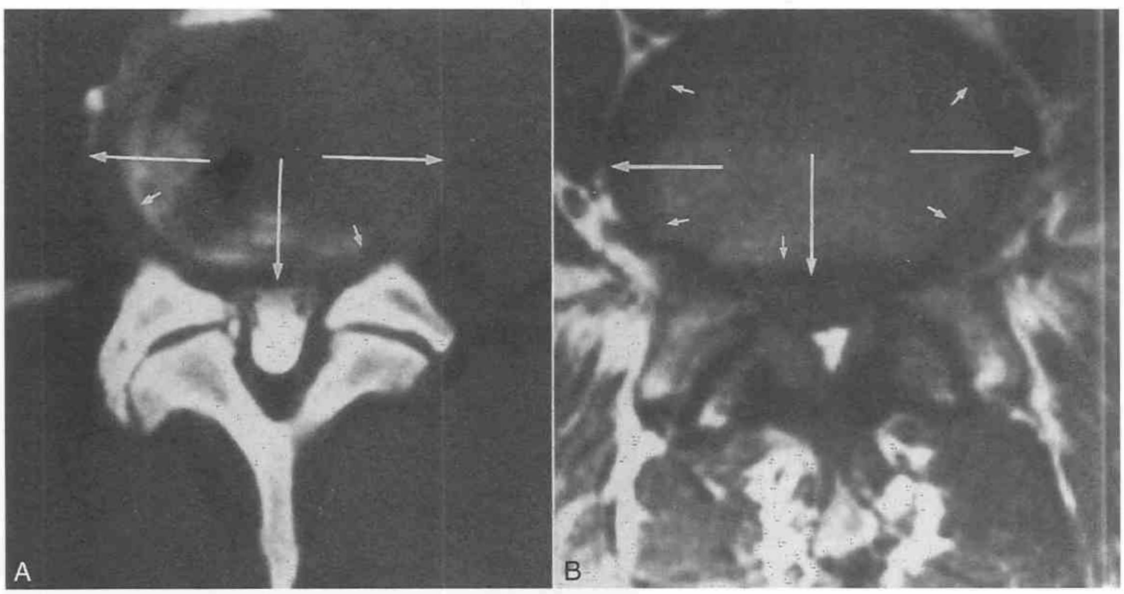

Figure 22–20. Disk bulge. Postmyelogram CT scan *(A)* and T1-weighted *(B)* MR image show disk margins *(long arrows)* diffusely bulging beyond the bone margins *(short arrows)*.

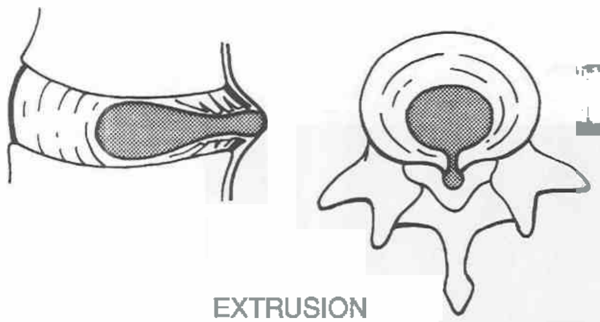

Figure 22–22. Illustration of disk extrusion. The nucleus has herniated through a complete annular tear but remains connected to the parent disk. (Modified from Modic MT: Magnetic Resonance Imaging of the Spine. St. Louis, Mosby–Year Book, 1989.)

origin. The most important distinction, however, is the lack of a connection between the extruded component and the parent disk. This is better appreciated on MR sagittal views than on axial views. On CT scans, sagittal reconstructions are often necessary to confirm the presence of a free fragment. Because there is no connection to the parent disk, free fragments can be confused with neoplasm, abscess, or postoperative epidural fibrosis.

Clinical Considerations

The clinical presentation of disk herniation is different than that of nondiskogenic spinal stenosis, in that it tends to be acute and occurs in younger individuals between ages 30 and 45. The inciting event is usually a fall, sudden lifting, or rotation. Sometimes it occurs spontaneously.

The pain usually begins in the lower back, and the patient flexes anteriorly or laterally to reduce the pain. Pain is exacerbated by standing, sitting, or by increased CSF pressure induced by coughing, sneezing, or bowel movements. Because the most commonly compressed roots are

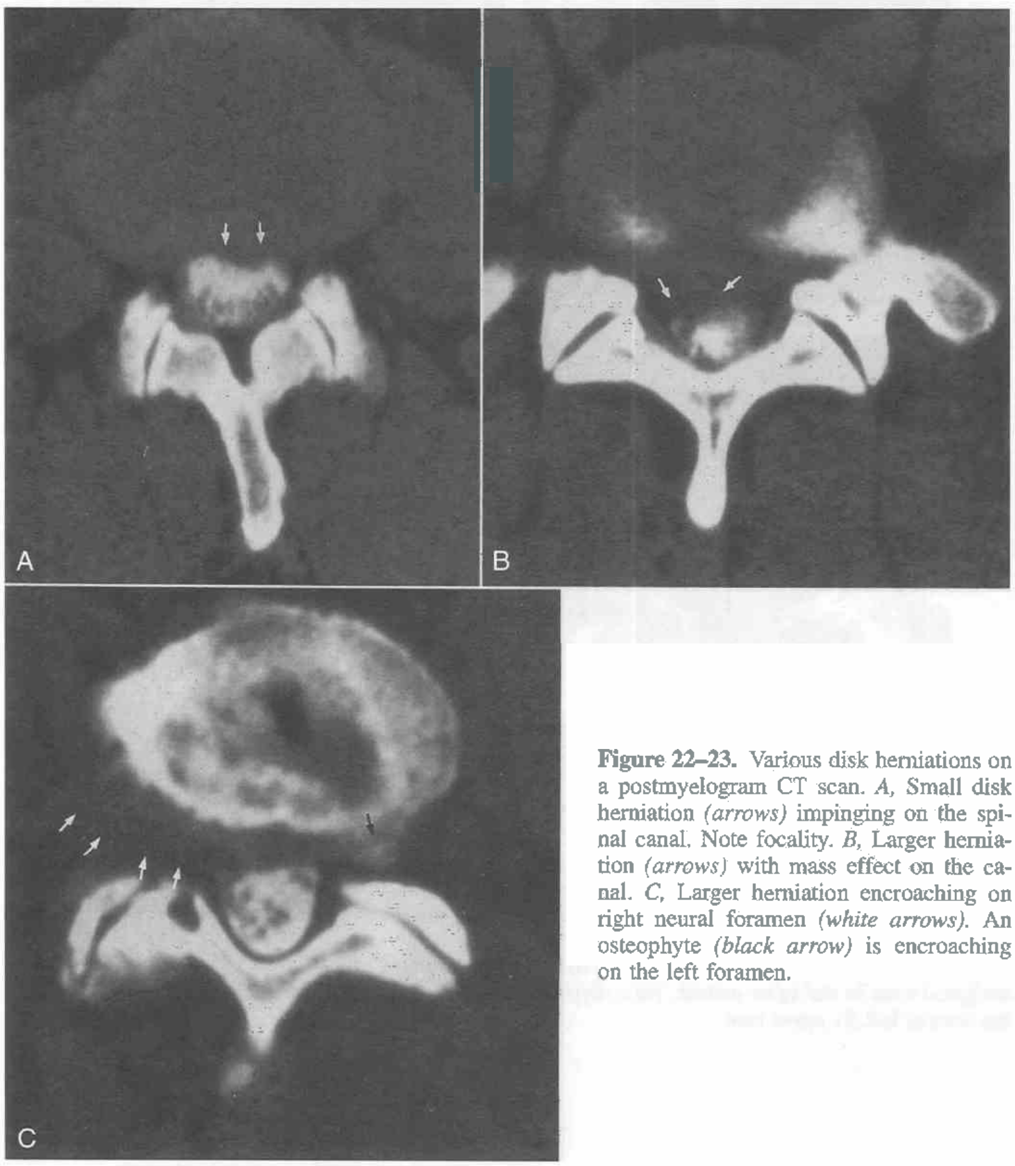

Figure 22–23. Various disk herniations on a postmyelogram CT scan. *A,* Small disk herniation *(arrows)* impinging on the spinal canal. Note focality. *B,* Larger herniation *(arrows)* with mass effect on the canal. *C,* Larger herniation encroaching on right neural foramen *(white arrows).* An osteophyte *(black arrow)* is encroaching on the left foramen.

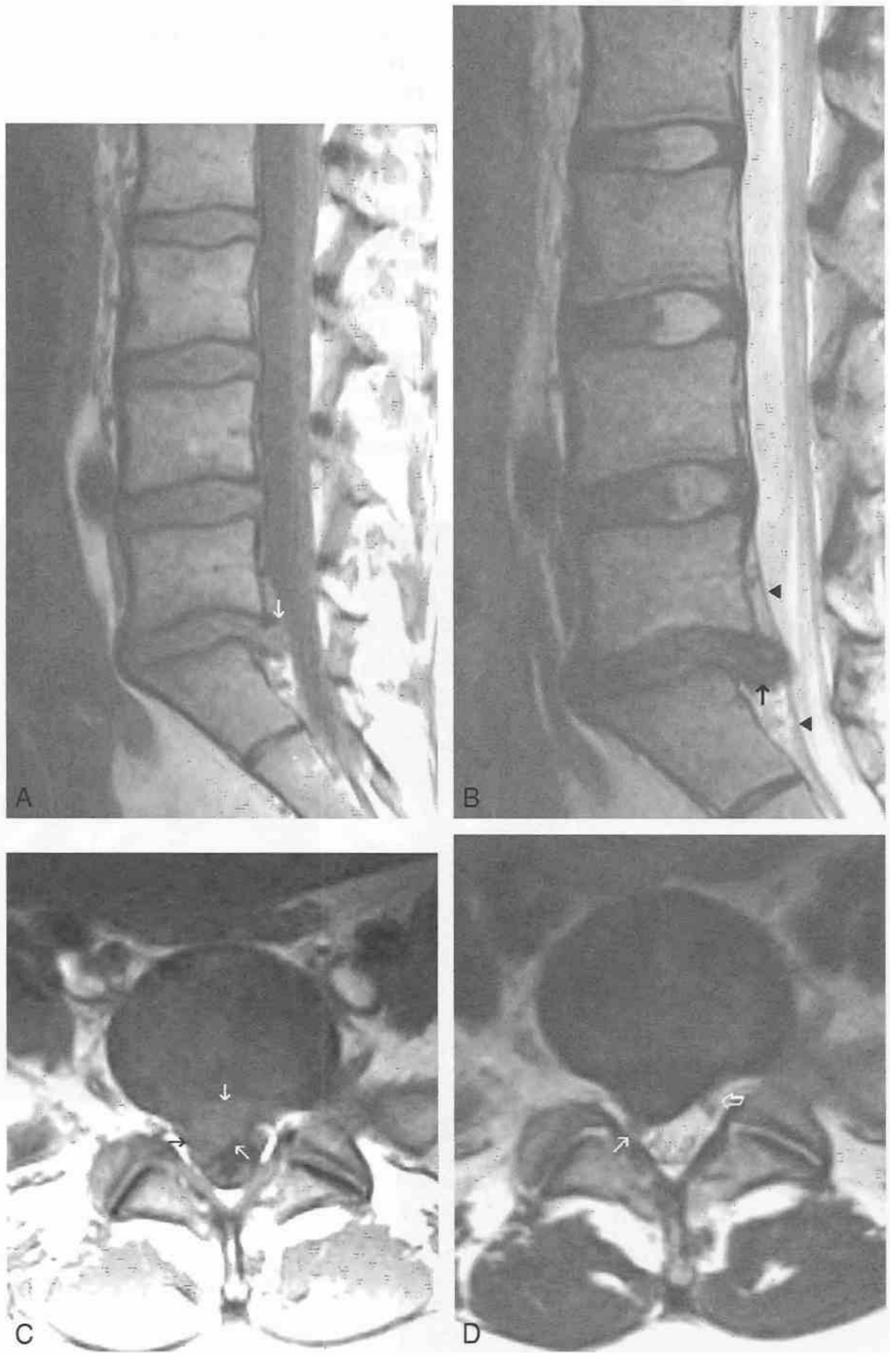

Figure 22–24. Various disk herniations as shown with MRI.

A, Sagittal T1-weighted MRI in a patient with a right paramedian disk herniation *(arrows).*

B, Sagittal T2-weighted MRI of the same patient. Disk herniation *(arrow)* and displacement of the posterior longitudinal ligament *(arrowheads)* by the disk.

C, Axial T1-weighted scan of the same patient. *Arrows* indicate the herniated disk.

D, Axial T2-weighted scan in the same patient. Note displacement of the right S1 nerve root *(closed arrow)* by the disk. The *open arrow* indicates the normal left S1 nerve root.

Figure 22–24 *Continued*

E–G, Multiple disk herniations in a different patient. T2-weighted right parasagittal (*E*) and midline sagittal (*F*) images. The right L4-5 foramen and nerve root (*arrow* in *E*) are crowded by an L4-5 disk herniation. Note how the L1-2 herniation extends superiorly behind the posterior longitudinal ligament (*arrow* in *F*). *G*, Axial T1-weighted view of L4-5 herniation. The disk presses on and displaces the intraforaminal right L4 root. The herniated disk and *G*, displaced root form a large soft tissue mass (*white arrow*). Note the normal left L4 root (*black arrow*) with surrounding fat.

H and *I*, Sagittal (*H*) and axial (*I*) T2-weighted MR images of a huge herniated disk lying behind the L4 vertebral body. The disk is so large that one cannot tell if it emanates from the L3-4 or the L4-5 interspace. The disk is probably *sequestered*, or broken off from the native disk.

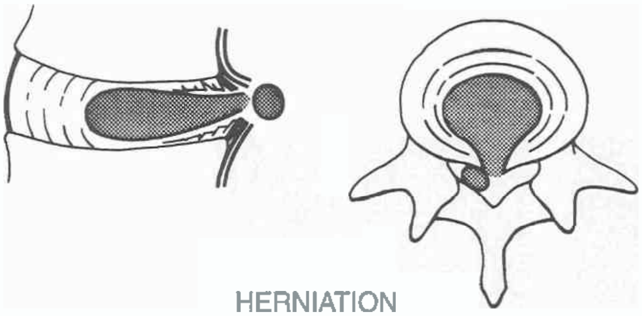

Figure 22–25. Illustration of a sequestered disk. Disk material has herniated through a complete annular tear and has broken off from the parent disk. The disk fragment can migrate freely. (Modified from Modic MT: Magnetic Resonance Imaging of the Spine. St. Louis, Mosby–Year Book, 1989.)

L5 and S1, pain radiates down the lower extremity in these radicular distributions (Fig. 22–27). Paresthesias may also be a feature. The radiculopathy has both a mechanical component, owing to compression by the herniated disk, and an inflammatory component, owing to nerve root edema.

Medical treatment, usually with steroids, anti-inflammatory agents, and a regimen of physical therapy, can reverse the inflammatory component and alleviate symptoms. If pain persists as a result of the mechanical component, surgery may be necessary.[47]

Postoperative Lumbar Spine

Imaging of Complications

Scarring and Recurrent Disk Herniation

A variety of surgical techniques are available for treatment of spinal stenosis and disk disease. The surgeon may remove a variable amount of bone from the posterior elements to expose an area for *diskectomy*, spinal canal *decompression*, or both. In a *laminectomy*, much of the vertebral body lamina is removed (Fig. 22–28). Sometimes the exposure is widened by removal of a variable amount of facet joint for better visualization and decompression. In a *laminotomy*, only a small amount of lamina is removed near a herniated disk for adequate exposure.

On CT and MRI, laminectomy sites are fairly obvious because of the bone removal involved. In a *microdiskectomy*, however, only a tiny bit of lamina is removed and sometimes the operative site is difficult to locate on CT scans or MR images. Before the advent of MRI, contrast-enhanced CT scans were the preferred method of evaluating the postoperative spine.[80] This method has essentially been replaced by MRI because of its superior ability to differentiate postoperative soft tissue changes (e.g., *scarring* versus *recurrent disk herniation*),[67] its multiplanar capability, and the use of relatively safe contrast agents. MRI changes in the postoperative spine are now well described[13, 67, 70, 71] and are summarized here.

In the immediate postlaminectomy period, the signal from normal bone and ligament is replaced by edema at the resection site. This is heterogeneously isointense to muscle on T1-weighted images and increased on T2-weighted images. In a purely decompressive laminectomy without diskectomy, significant mass effect on the thecal sac is unusual unless a hematoma is present. Between 6 weeks and 6 months after surgery, the postoperative edema is replaced by scar tissue posterior to the thecal sac. The scar appearance can range from low to high signal intensity on T2-weighted images (Fig. 22–29).

If a diskectomy is performed with the laminectomy, additional changes related to the diskectomy are appreciated. In the early postoperative period, there is edema in the anterior epidural space in addition to disruption of the posterior annular margin due to disk curettage. On T1-weighted images, this is reflected by anterior epidural intermediate signal intensity that may blend with the remaining native disk. On T2-weighted images, this area may be variably hyperintense. This probably results from edema[67] and possibly even blood.[6]

The imaging specialist must therefore exercise care in

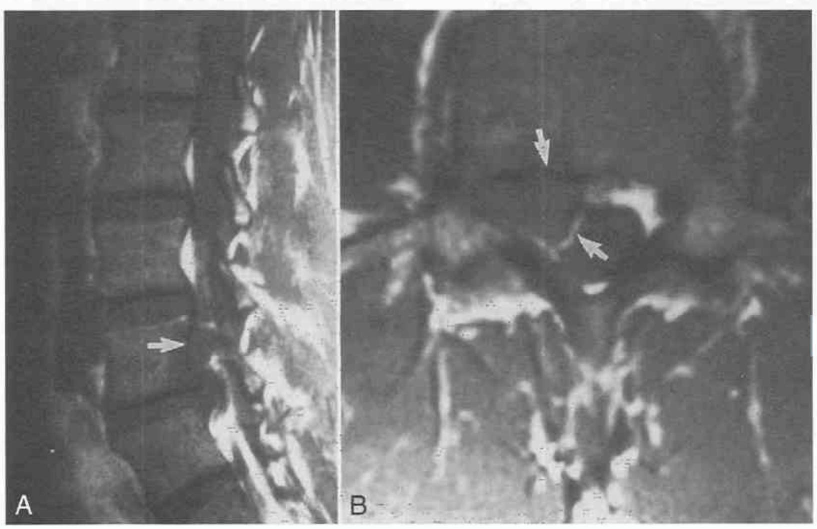

Figure 22–26. Sequestered disk. *A*, Sagittal MR image shows an L4-5 disk fragment *(arrow)* lying posterior to the L4 body. *B*, Axial MR image shows the fragment *(arrows)* obliterating the L4 root in the right lateral recess and pressing on the thecal sac. See also Figure 22–24*H* and *I*.

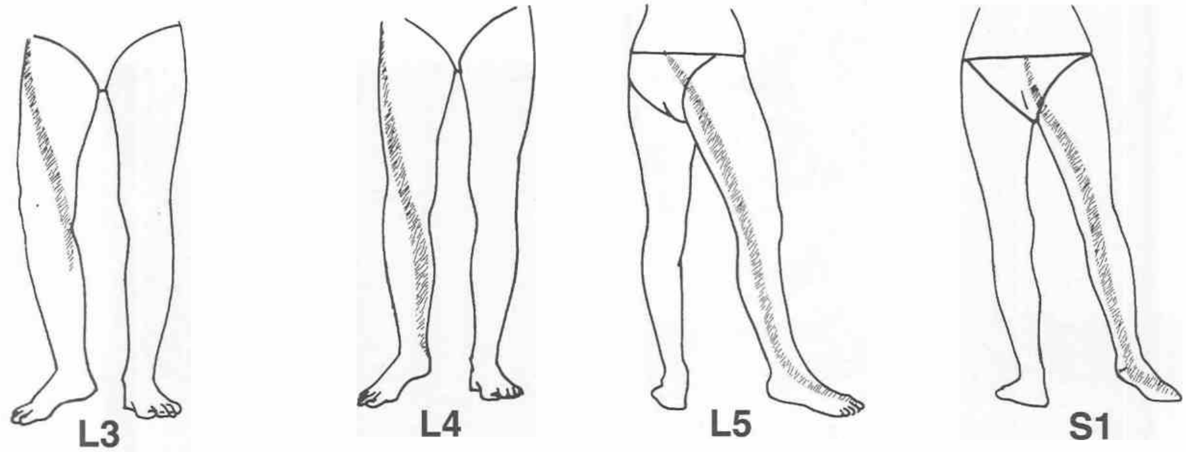

Figure 22–27. Illustration of lower extremity radiculopathies resulting from common disk herniations.

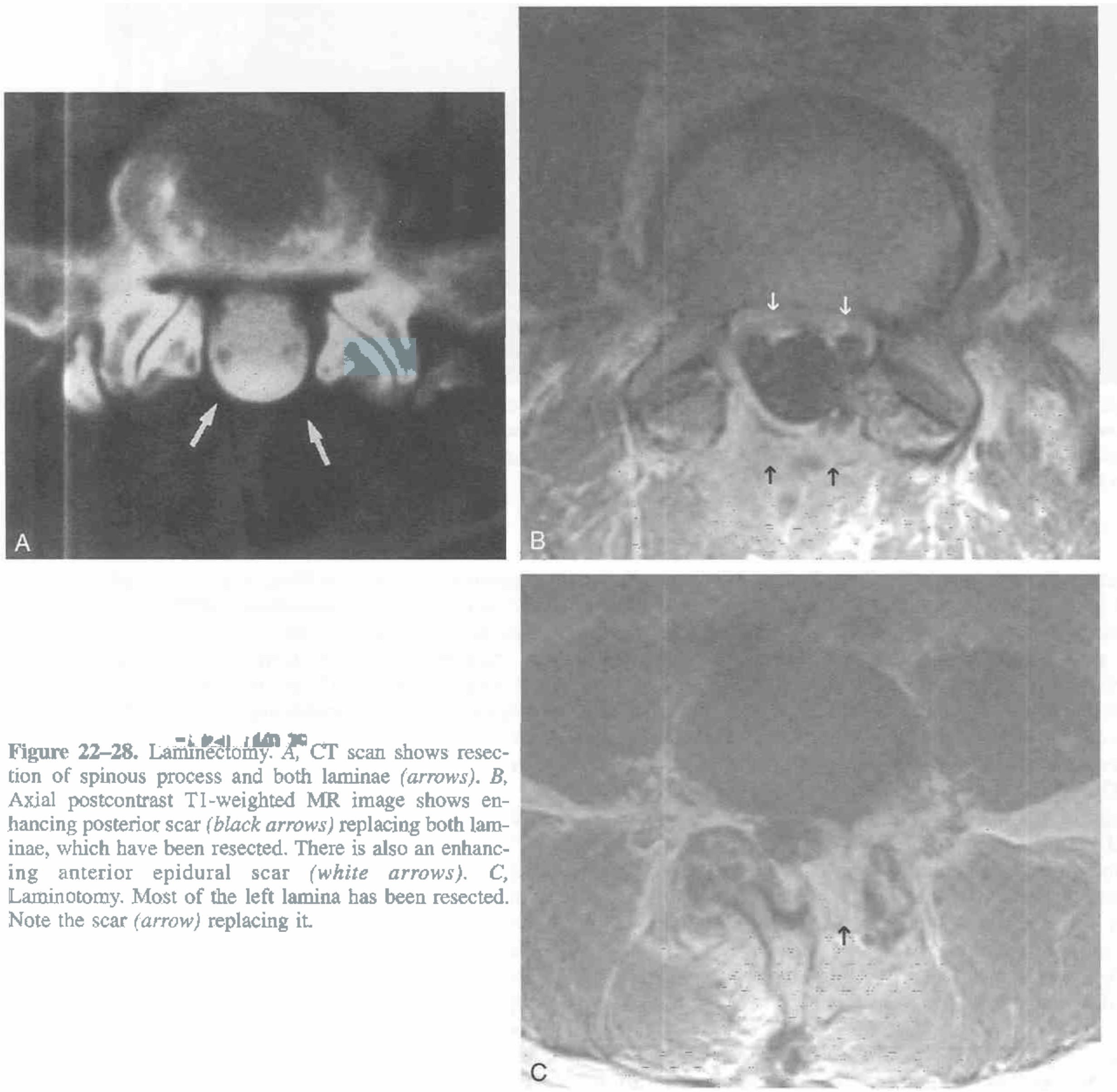

Figure 22–28. Laminectomy. *A*, CT scan shows resection of spinous process and both laminae *(arrows)*. *B*, Axial postcontrast T1-weighted MR image shows enhancing posterior scar *(black arrows)* replacing both laminae, which have been resected. There is also an enhancing anterior epidural scar *(white arrows)*. *C*, Laminotomy. Most of the left lamina has been resected. Note the scar *(arrow)* replacing it.

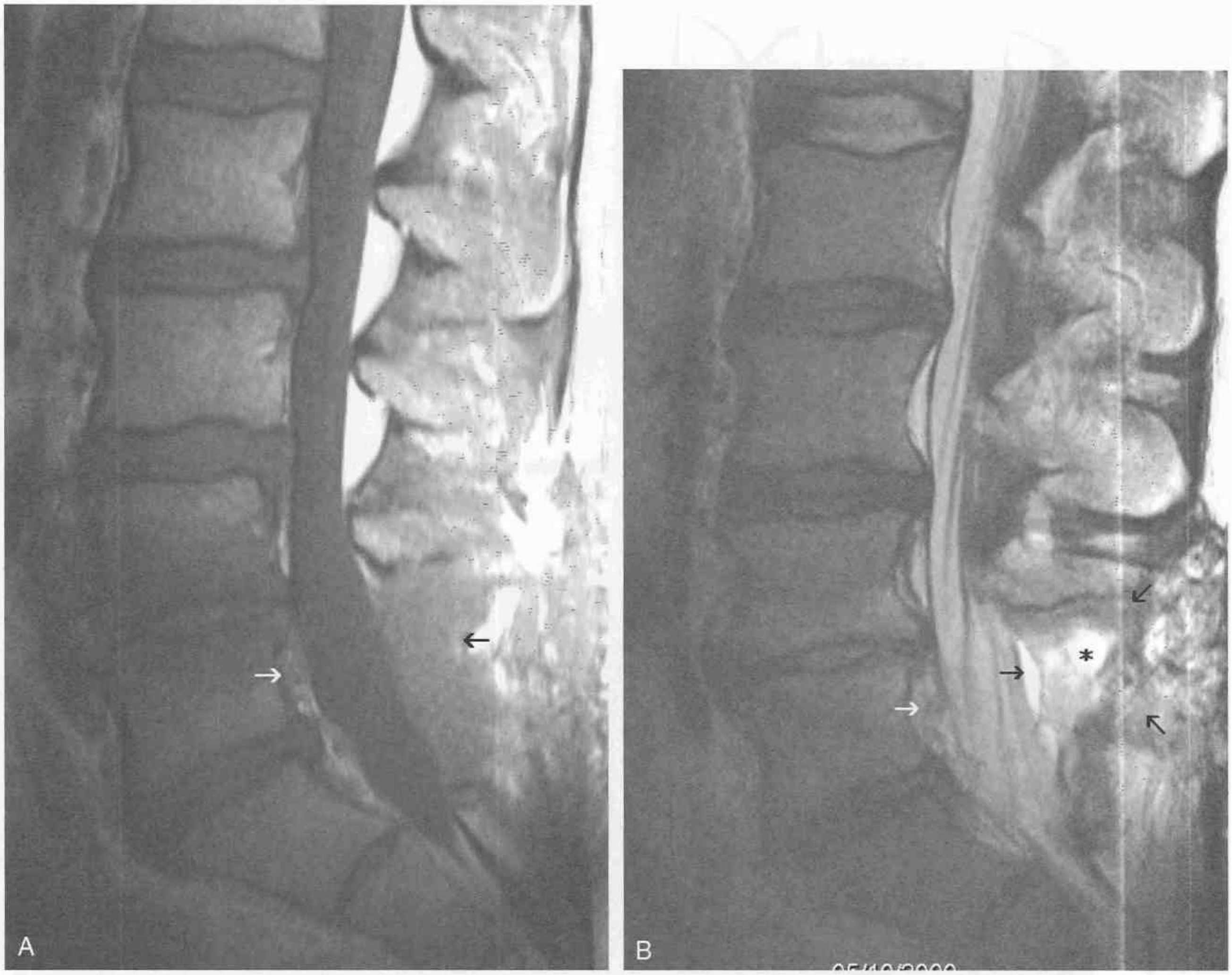

Figure 22–29. Laminectomy. *A,* Sagittal unenhanced, T1-weighted MR image shows an isointense, posterior epidural scar *(black arrow).* The anterior epidural scar from this L4-5 diskectomy is also seen *(white arrow).* Note resection of L5 spinous process. *B,* T2-weighted MR image shows the scar *(arrows)* as hyperintense but heterogeneous. A small, focal fluid collection *(asterisk)* is also visible. This is a normal postoperative finding.

interpreting early postoperative changes because this normal mass effect on the thecal sac may mimic recurrent or residual disk herniation (Fig. 22–30). Furthermore, confusing areas of gadolinium enhancement may be seen in the normal early postoperative spine, including the paraspinal muscles, facet joints, and nerve roots.[6] Therefore, gadolinium cannot be used for the evaluation of scar versus recurrent disk herniation in the early postoperative period.

The reasons for all of these normal early postoperative changes have not been completely worked out. Therefore, MRI should probably not be used in the early postoperative period unless other complications, such as hematoma, pseudomeningocele, and infection, are suspected. By 6 weeks after surgery, the edema and mass effect subside and the thecal sac margin returns to normal.

In a patient with late postsurgical recurrent back pain, the distinction between recurrent disk herniation and scarring must be made because reoperation on a scar may lead to a poor result with the formation of more scar tissue. Noncontrast MRI is at least equivalent to contrast CT scanning in distinguishing scar from disk,[13] with a 79% accuracy rate for noncontrast MRI and a 71% accuracy rate for contrast CT scans in one study.[78]

Scar tissue tends to conform to the shape of, and often to enwrap, the dural sac and exiting nerve roots, and it does not have a definable margin (Fig. 22–31). Mass effect on the thecal sac may or may not be present; however, the dura may actually retract toward the scar.

On non–contrast-enhanced MR images, anterior epidural scar tissue is generally hypointense to isointense to disk on T1-weighted sequences and hyperintense on T2-weighted sequences. Lateral and posterior scar tissue may be somewhat more variable. Herniated disks tend to be contiguous with the native disk space (unless sequestered) and have a definable margin (see Fig. 22–24). Mass effect on the thecal sac is present. Herniated disks tend to be of low signal intensity on all pulse sequences but large, extruded, and sequestered disks can be hyperintense on T2-weighted sequences, making distinction between a disk, a scar, and CSF difficult.[48] Morphology, rather than signal characteris-

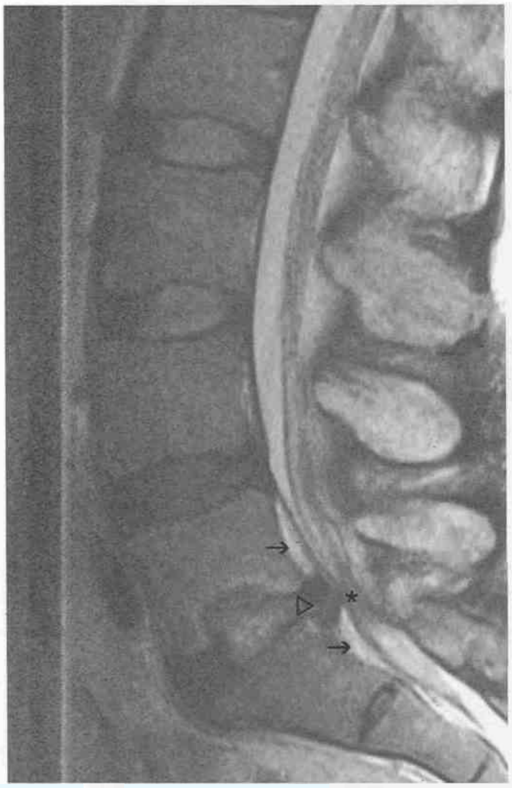

Figure 22–30. Early view of the postoperative spine. T2-weighted image shows apparent severe canal stenosis *(asterisk)* from a soft tissue structure *(arrowhead)*, which probably represents soft tissue swelling and blood, but mimics the appearance of disk herniation. Note subligamentous edema *(arrows)*, also a normal postoperative finding. The patient was asymptomatic at this particular level.

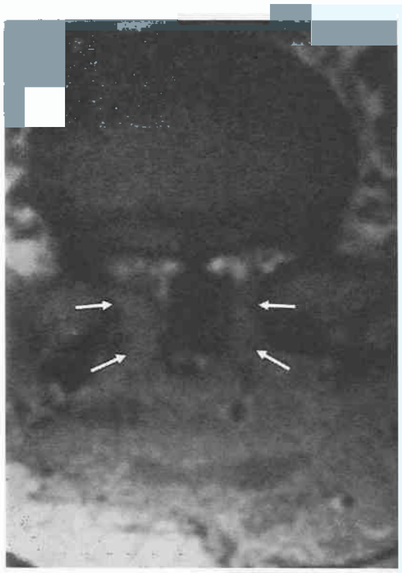

Figure 22–31. Axial T1-weighted MR image shows an epidural scar *(arrows)* partially encircling and compressing the thecal sac. The posterior margins of the scar are ill defined.

Figure 22–32. Sagittal T1-weighted postoperative MR image shows an apparent recurrent disk herniation *(arrow)* at L4-5. With contrast enhancement, this proved to be scar tissue.

tics, is therefore probably a more useful method of distinguishing a scar from a disk on the noncontrast MRI.[30, 67] Even so, well-defined scar tissue can mimic a disk herniation on unenhanced MR images (Fig. 22–32).

Gadolinium-enhanced MRI has met with considerable success in differentiating postoperative scarring from recurrent disk herniation. Accuracy of contrast-enhanced MRI has been reported to be as high as 96%.[31, 74] Scar tissue consistently enhances postoperatively (Fig. 22–33) [illegible] continues to enhance months to years after surgery.[31] A herniated disk should not enhance (Fig. 22–34).

One caveat: Even though anterior epidural scar invariably shows this pattern of consistent enhancement, posterior epidural scar may not. In fact, posterior epidural scar may show a rapid decline in enhancement over a period of months,[31, 68] although the reason for this is not known.

As noted previously, a herniated disk does not enhance in the immediate postinjection period. If delayed images are obtained, contrast medium may diffuse into the herniated disk from adjacent scar tissue, causing disk enhancement as well. Therefore, care must be taken to complete the enhanced portion of the examination no more than 30 minutes after injection. Gadolinium is particularly useful when a mixture of scar and recurrent disk herniation is found; the enhancing scar can be separated from the nonenhancing, low-signal recurrent disk herniation (Fig. 22–35). However, an enhancing, inflammatory reaction around a herniated disk is a common occurrence, even in the absence of prior surgery. This peridiskal reaction may actually be prominent enough to obscure a small herniation that it surrounds, thus masking it and mimicking pure scar tissue.

These enhancement characteristics generally apply to patients in the late postoperative period (>6 weeks after surgery). Scar tissue has been shown to enhance in the early postoperative period.[6] As mentioned, however, differentiation of this enhancement from the myriad normal immediate postoperative changes may be difficult. The enhancement of epidural scar is probably related to "leaky

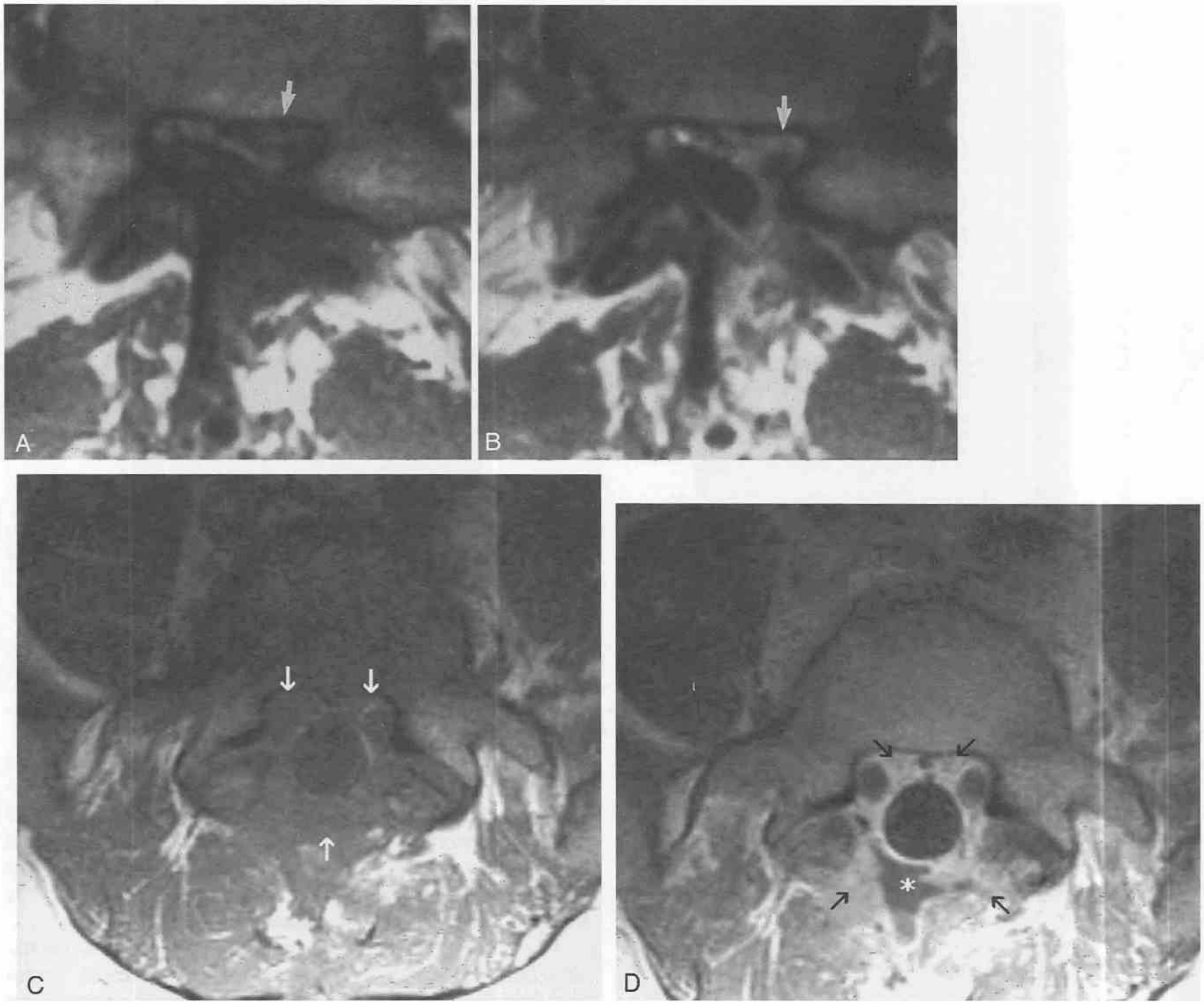

Figure 22–33. Same patient as in Figure 22–32. *A,* Axial unenhanced T1-weighted MR image shows an apparent recurrent disk herniation *(arrow)*. *B,* After gadolinium administration, the scar tissue *(arrow)* enhances intensely, enwraps the left L5 root, and compresses the thecal sac. No evidence of disk herniation is seen. Axial unenhanced *(C)* and enhanced *(D)* T1-weighted MR images demonstrate postoperative scar *(arrows)* in another patient. Note small, nonenhancing postoperative fluid collection *(asterisk)*, which can be seen only after contrast administration. This is a common postoperative finding.

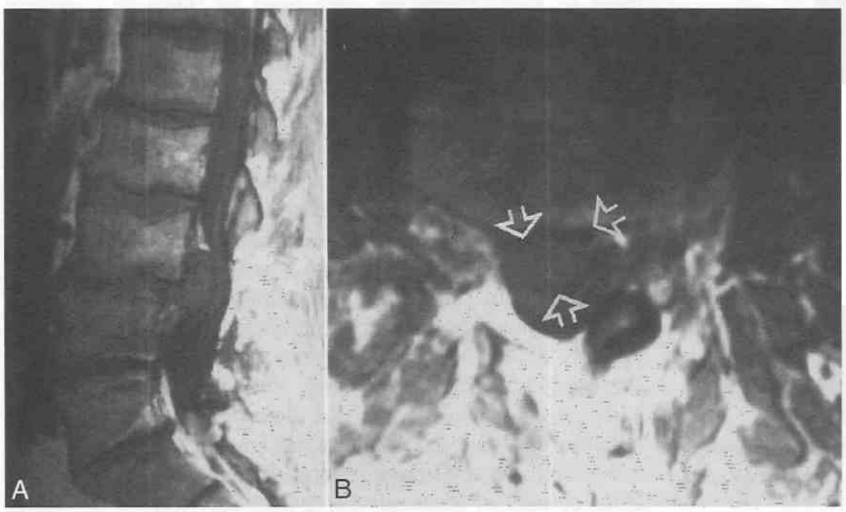

Figure 22–34. Postoperative disk herniation. *A,* Sagittal unenhanced MR image shows major disk herniation. *B,* Axial MR image after gadolinium administration shows no disk enhancement *(arrows)*.

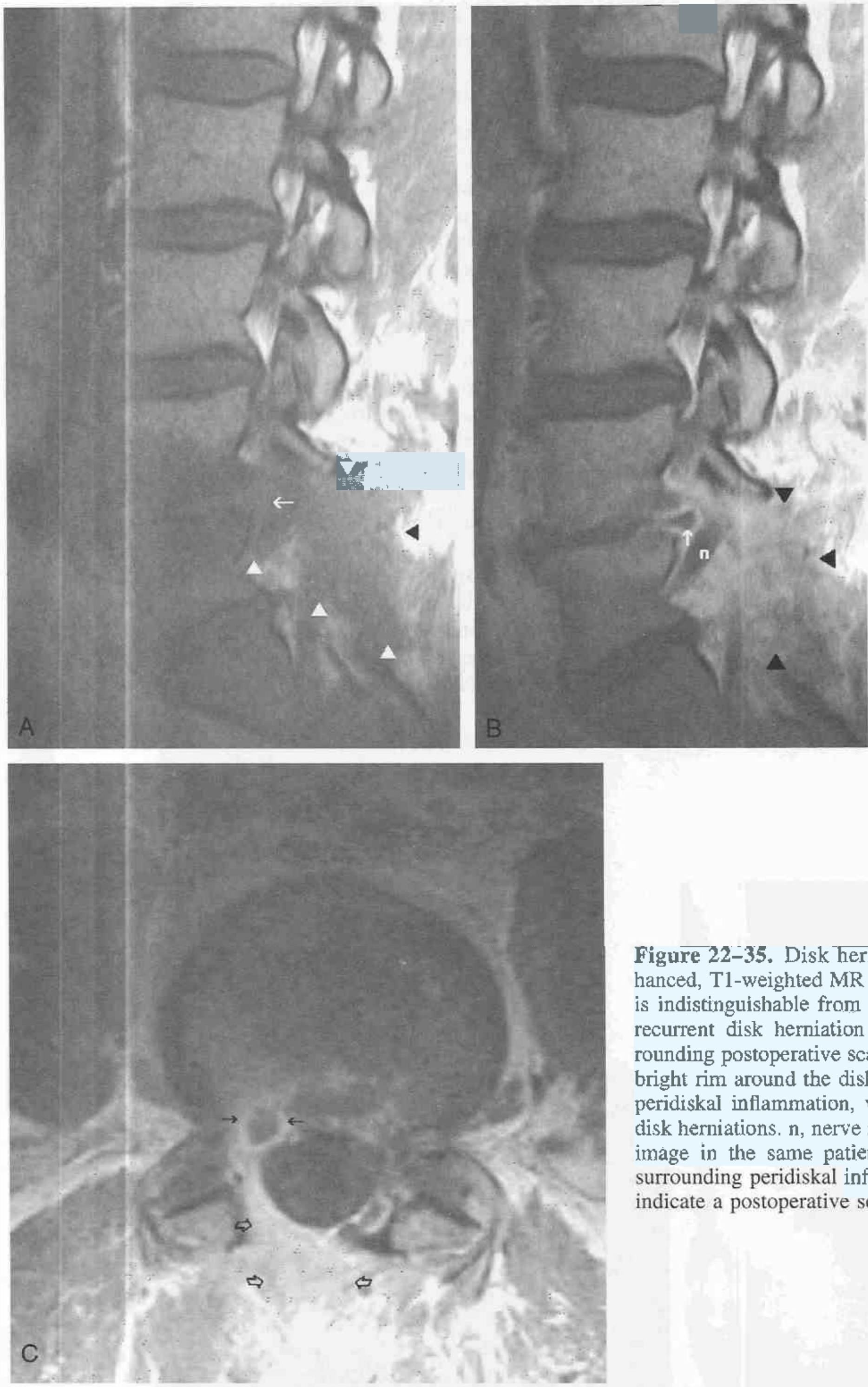

Figure 22–35. Disk herniation. *A,* Postoperative sagittal unenhanced, T1-weighted MR image. Recurrent disk herniation *(arrow)* is indistinguishable from scarring *(arrowheads). B,* Nonenhancing recurrent disk herniation *(arrow)* now stands out from the surrounding postoperative scar *(arrowheads).* The intensely enhancing bright rim around the disk is not a postoperative scar but, instead, peridiskal inflammation, which can be seen even on nonoperated disk herniations. n, nerve root. *C,* Axial enhanced T1-weighted MR image in the same patient shows recurrent disk herniation with surrounding peridiskal inflammation *(closed arrows). Open arrows* indicate a postoperative scar.

vascularity,"[69] which can persist years after surgery; in contrast, the herniated disk is avascular.

In summary, a recurrent herniated disk is an avascular, well-defined, low-intensity mass that does not enhance on early postinjection images. It has a well-defined margin and is usually located in the anterior epidural space contiguous with or near the native disk space. An epidural scar is a vascular structure with ill-defined margins that tends to encircle the thecal sac and roots. Anteriorly, it consistently enhances even years after surgery. Posterior epidural enhancement may decline over time. Whereas morphology and enhancement are quite reliable in differentiating a disk from a scar, signal characteristics and mass effect may overlap and should be used only as secondary signs.

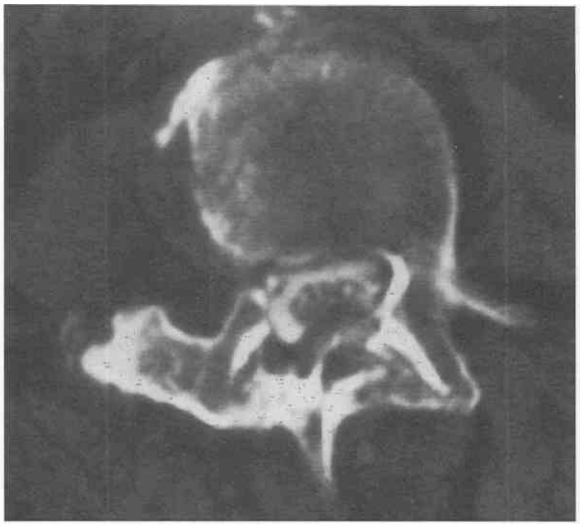

Figure 22–36. Postoperative bone overgrowth. Postmyelogram CT scan shows severe hypertrophy of posterior elements compressing the spinal canal.

Other Complications

Aside from recurrent disk herniation, several postoperative complications may occur, including:

- Bony stenosis
- Pseudomeningocele
- Arachnoiditis
- Disk space infection
- Epidural abscess

Bony Stenosis

Bony stenosis may account for up to 60% of failed back surgery cases.[80] Osteophytes and hypertrophic bone vary in MRI signal appearance, depending on degree of marrow content. CT, particularly with intrathecal contrast material, is especially helpful in evaluating canal narrowing resulting from postoperative bone overgrowth (Fig. 22–36).

Pseudomeningocele

A pseudomeningocele is a localized collection of fluid communicating with the thecal sac. This results from an iatrogenic dural tear during surgery.[81] Whereas small postoperative fluid collections along the soft tissues of the incision site may be a normal finding, a pseudomeningocele is not. MRI and CT scans show a saclike area of fluid intensity adjacent to the dura (Fig. 22–37). Blood or debris may be present within the fluid. Differentiation between abscess, postoperative fluid collection, and pseudomeningocele may be difficult. However, pseudomeningocele is likely if a communication between the thecal sac and the collection can be demonstrated, or if, on CT myelography, contrast medium enters the fluid collection.[67]

Arachnoiditis

Arachnoiditis represents an inflammatory reaction in which nerve roots adhere to the thecal sac and to each

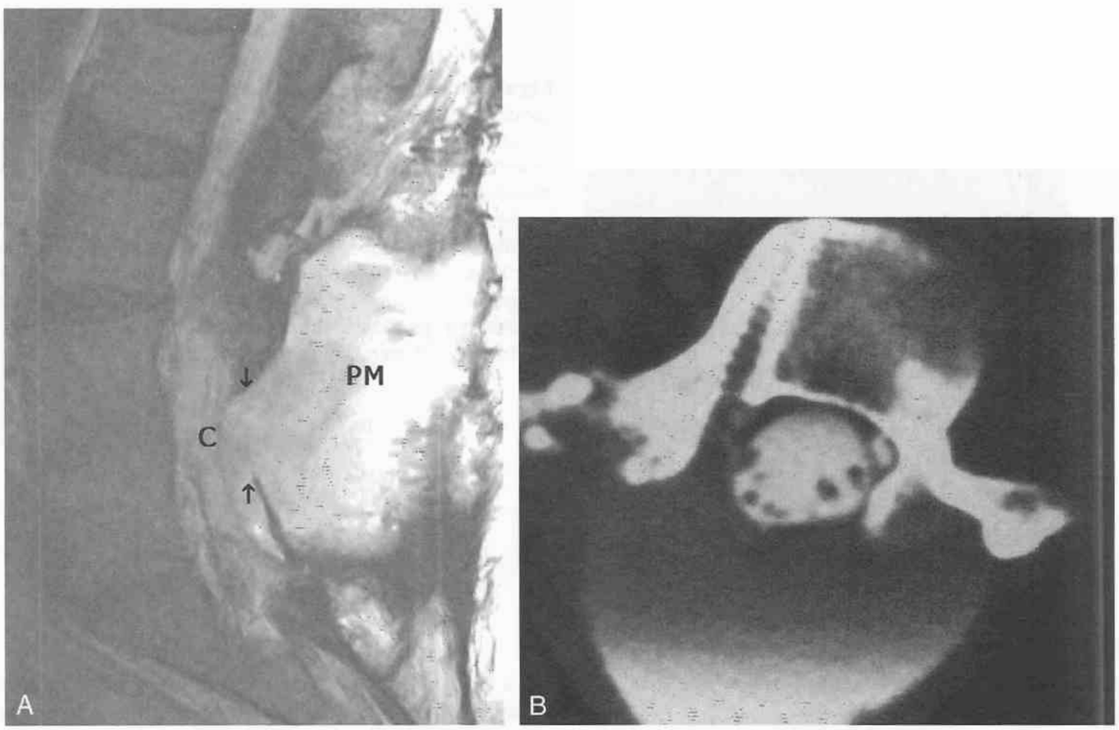

Figure 22–37. Pseudomeningocele. *A*, Postsurgical sagittal T2-weighted MRI shows large pseudomeningocele (PM). The communication (between the *arrows*) between the pseudomeningocele and the canal (C) is quite large. Compare with small, normal postoperative fluid collection shown in Figure 22–27, *B*, Axial postoperative CT scan in a different patient shows a large amount of intrathecally injected contrast pooling in a pseudomeningocele. Demonstrating the actual connection between the pseudomeningocele and the thecal sac can be difficult at times and could not be shown in this figure.

other. This can occur after laminectomy and is one of the causes of failed back surgery.[14] Normally, the nerve roots are symmetrically distributed within the dependent portion of the CSF (see Fig. 22–4G). In arachnoiditis, nerve roots clump together centrally or adhere to the dura peripherally. In advanced stages, the lumbar spinal canal is filled with inflammatory soft tissue. These changes are obvious on both MRI[72] and on CT myelography (Fig. 22–38). Interestingly, enhancement is not a prominent feature.

Disk Space Infection

Postoperative disk space infection and epidural abscess are uncommon but serious postlaminectomy complications. Although diskitis in adults is usually characterized by hematogeneous spread, bacterial contamination from disk manipulation can occur.

Disk space infection typically presents as hypointensity on T1-weighted images and as hyperintensity on T2-weighted images in the disk and adjacent end plates, with poor definition of the end plates themselves. These signal changes reflect reactive edema. On T2-weighted images, the internuclear cleft (the normal horizontal band of low signal intensity in the center of the nucleus pulposus) is lost. In disk space infection, the disk and adjacent end plates usually enhance with gadolinium administration (Fig. 22–39).[7] Despite the myriad early normal postoperative changes in the epidural space, generally no signal intensity or morphologic changes are found in the disk space itself or in the adjacent end plates after uncompli-

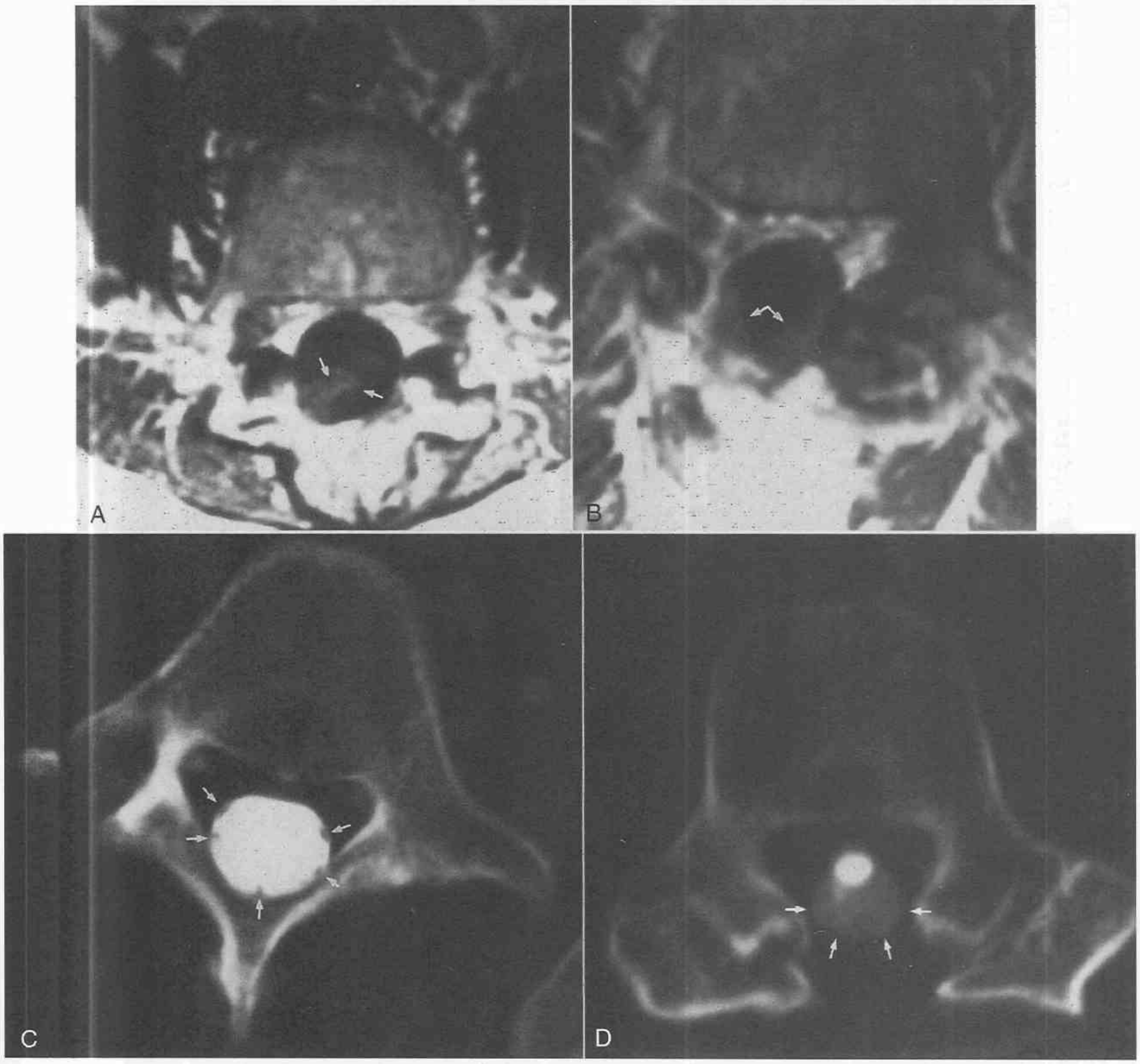

Figure 22–38. Arachnoiditis. *A,* Axial postoperative unenhanced T1-weighted MR image shows clumping of nerve roots *(arrows)* within the spinal canal. *B,* Enhanced scan in another postoperative patient shows the nerve roots adhering peripherally to the dura *(arrows)*. Note that root enhancement is not a feature. *C,* Postmyelogram CT scan shows nerve roots adhering peripherally to the dura *(arrows)*. This gives the appearance of an "empty" thecal sac. *D,* Postmyelogram CT scan shows advanced arachnoiditis. Most of the spinal canal is filled with inflammatory tissue *(arrows)*, with only a small amount of contrast noted anteriorly.

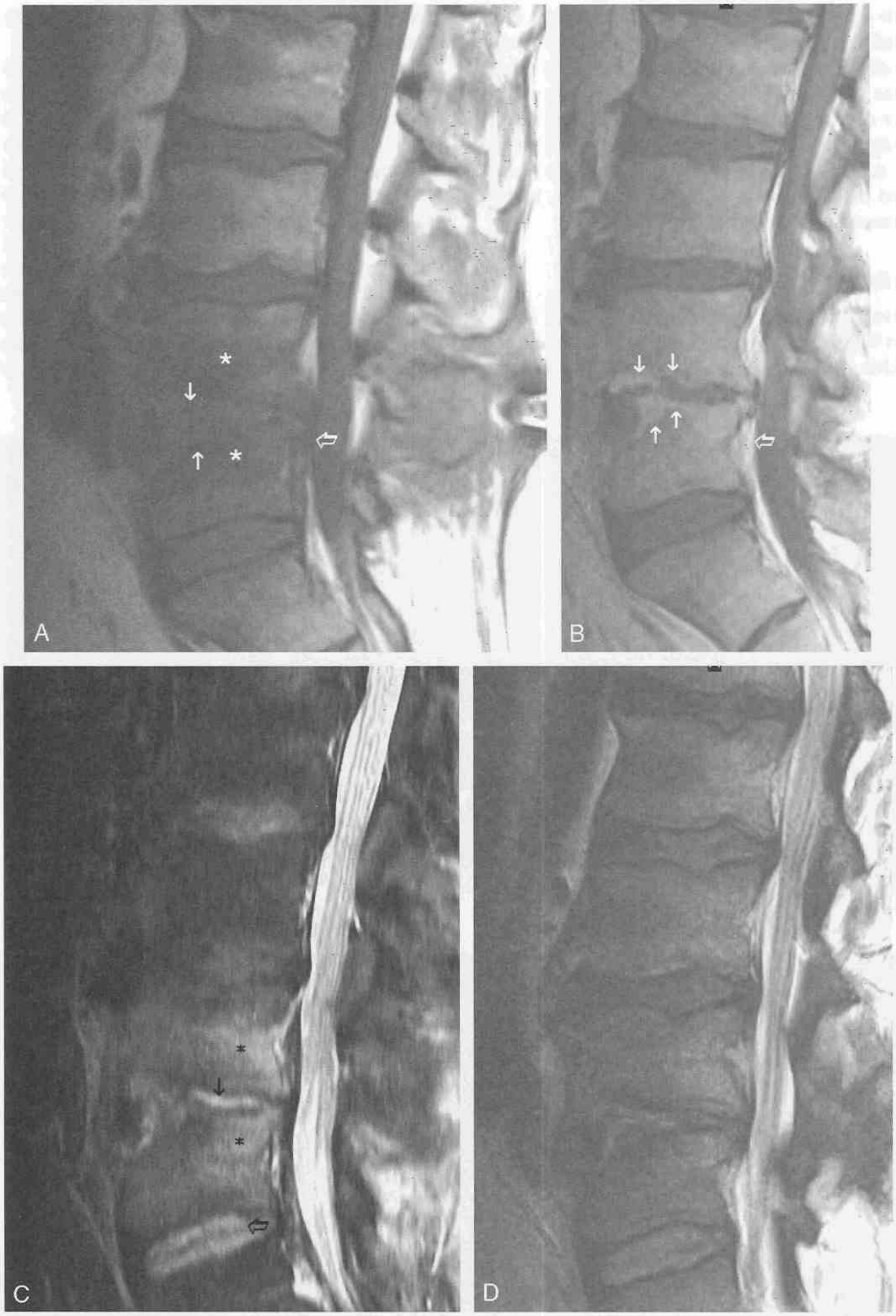

Figure 22–39. Postoperative infection.

A, T1-weighted unenhanced MR image of L4-5 diskitis/osteomyelitis. Dark signal *(asterisks)* denotes edema in the vertebral end plates and marrow. The infected disk is conforming to the shape of eroded end plates *(closed arrows)*. Abnormal soft tissue is seen in the anterior epidural space *(open arrow)*.

B, T1-weighted enhanced MR image in the same patient. The margins of the disk enhance *(closed arrows)* as does the infected anterior epidural soft tissue *(open arrow)*.

C, Short tau inversion recovery (STIR) sequence shows the bone edema *(asterisks)* markedly well. Note loss of the internuclear cleft in the infected disk *(closed arrow)* compared with a normal nondegenerated, noninfected disk *(open arrow)*.

D, Fast spin-echo, T2-weighted MR image does not show the edema nearly as well as the STIR sequence, which is indispensable for evaluation of osteomyelitis.

cated diskectomy.[7] Therefore, any disk space or end-plate abnormality in the postoperative period should be viewed with suspicion.

Several problems occur, however, in differentiating both degenerated disks and normal postoperative disks from disk infection:

1. *Type I* degenerated end plates are also hypointense on T1-weighted images and hyperintense on T2-weighted images and may enhance with gadolinium. However, no change should occur in the appearance of the unenhanced disk after uncomplicated diskectomy. Comparison of preoperative and postoperative scans is thus important. Furthermore, the cortical margins should remain sharp after uncomplicated diskectomy, whereas the margins are indistinct in infection.
2. *Type II* degenerated end plates have high signal intensity on T1-weighted images and high to slightly lower signal intensity on T2-weighted images. This high T1 signal may mask the low T1 signal found in disk space infection. In this case, too, it is important to look for abnormal disk signal, to compare preoperative and postoperative scans, and to evaluate cortical margins.
3. Infected disks and end plates usually enhance with gadolinium; uncommonly, however, the normal postoperative disk can enhance. Boden and colleagues[7] observed that it is unlikely for normal postoperative patients to have all three abnormal findings (i.e., low disk/end-plate signal on T1-weighted images, high disk/end-plate signal on T2-weighted images, and disk/end-plate enhancement with gadolinium). This "triad" suggests disk infection in the symptomatic patient.

MRI using fat suppression has made the diagnosis of postoperative diskitis/osteomyelitis easier. Short tau inversion recovery (STIR) imaging shows disk and bone edema that may be difficult to visualize on T1-weighted and T2-weighted images because of bright, fatty marrow obscuring the edema (Fig. 22–39*C*).

Epidural Abscess

Epidural abscess is also hypointense on T1-weighted images and hyperintense on T2-weighted images and shows mass effect on the thecal sac. Because these changes may be masked by the similar signal of CSF, gadolinium should be given when epidural abscess is suspected (Fig. 22–39).[76]

Cervical Spine

After the lumbar spine, the cervical spine is next most commonly affected by spondylosis and disk herniation.[57] The most frequently involved interspaces are C4-5, C5-6, and C6-7. This may be due to the greater degree of motion at these levels.[21] Although many concepts of nondiskogenic and diskogenic degeneration (osteophyte formation, foraminal stenosis, spondylolisthesis, and disk herniation) are much the same as in the lumbar canal, a couple of important anatomic and clinical differences should be emphasized:

1. Because the cervical spinal cord carries neurons from both the upper and lower extremities, symptoms referable to arms, legs, or both may occur.
2. Because the dimensions of even the normal cervical spinal canal are small relative to the lumbar, small spondylitic or disk changes may cause significant symptoms.

Anatomic Considerations

Although the basic anatomy of the cervical and lumbar vertebrae and diskovertebral junctions are similar, several important differences as they may relate to spondylosis warrant brief review.

Unlike the more rounded configuration of the lumbar sac, the cervical spinal canal is triangular. The cervical spinal cord is oval (Fig. 22–40). The canal decreases in size from C1 to C3 and is uniform from C3 to C7. The normal lower limit anteroposterior diameter of the canal is 16 mm at C1, 15 mm at C2, and 12 mm in the lower cervical spine.[52]

The exiting cervical nerve roots travel in an inferior direction through the foramina at about 45 degrees with respect to the coronal plane (Fig. 22–41). This differs from the lumbar roots, which travel inferiorly but nearly parallel with the coronal plane. This makes sagittal imaging of the cervical nerve roots less optimal than in the lumbar spine.

The cervical nerve roots exit above (not below, as in the lumbar spine) the pedicle of its corresponding vertebral body. Because there are eight cervical roots but only seven vertebrae, the relationship changes at the C8 root, which passes above the T1 pedicle. The T1 root then passes under the T1 pedicle and the pattern is the same as in the lumbar spine the rest of the way down.

In addition to the body, laminae, pedicles, spinous, and transverse processes, the cervical vertebrae have uncinate processes, or joints of Luschka, paired bony ridges projecting superiorly from the posterolateral margins of the vertebral bodies. They fit into notches on the posterolateral surfaces of the inferior end plates of the vertebral bodies above. On axial images, they can be seen indenting the posterolateral disk margin as they bridge the vertebral bodies (Fig. 22–42; see Fig. 22–41). The uncinate processes contribute to the anterior walls of the neural foramina; if hypertrophied, they can cause foraminal stenosis. Whereas the lumbar facet joints are fairly sagittally oriented, the cervical facets are obliquely positioned, their surfaces lying halfway between a coronal and axial plane (see Figs. 22–41 and 22–42).

The vertebral arteries pass through the bony transverse foramina, located on the lateral aspects of vertebrae C1 to C6 (see Fig. 22–40). The arteries can rarely be compressed by foraminal spurs.

Imaging Techniques

At our institution, CT scans of the cervical spine for degenerative disease are usually done following myelography (see Figs. 22–40 and 22–42). Investigators have found that the increased sensitivity of CT myelography over standard CT in the cervical spine is even greater than in the

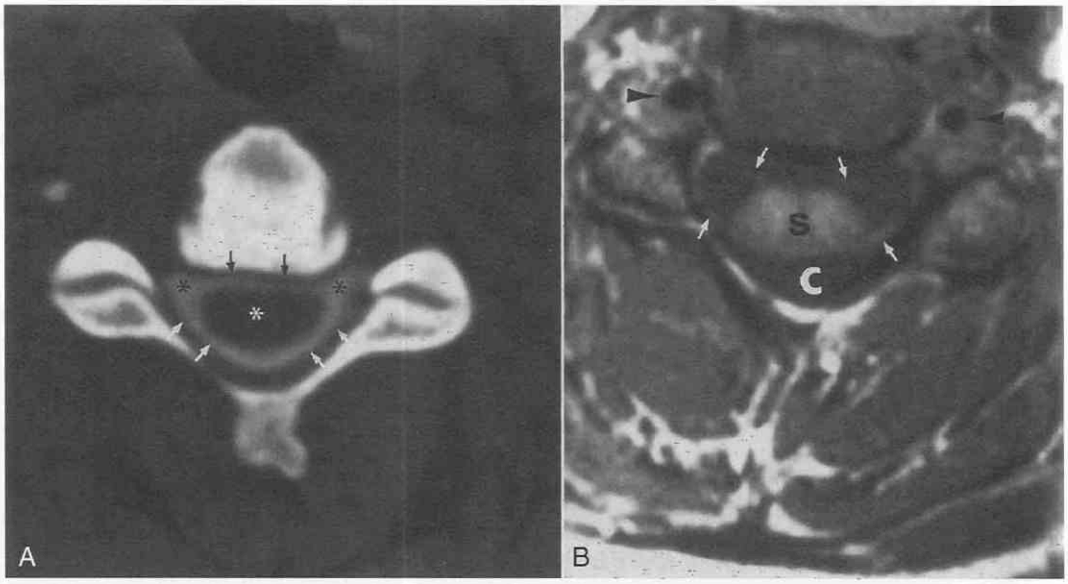

Figure 22–40. Cervical images. *A*, Cervical postmyelogram CT scan. Note the triangular configuration of the spinal canal *(arrows)* and oval shape of the spinal cord *(white asterisk)*. The nerve root sheaths *(black asterisk)* can be seen exiting through the neural foramina. *B*, Axial cervical T1-weighted MR image. c, spinal canal; s, spinal cord. *Arrows* indicate nerve roots; *arrowheads* indicate vertebral arteries in the transverse foramina.

lumbar spine.[12] After myelography, 2-mm contiguous axial images through the levels of concern are obtained. Both bone and soft tissue windows are photographed. Unlike lumbar CT myelography, cervical CT myelography is done soon after the intrathecal injection because contrast material in the cervical canal tends to flow away from the cervical canal more quickly and the injection volume is generally smaller than in the lumbar canal (Box 22–3).

As in the lumbar spine, numerous choices are available for MRI of the cervical spine. We obtain a set of fast spin-echo, T1-weighted and T2-weighted sagittal images of the entire cervical region (Fig. 22–43). These images should include the cerebellar tonsils down to the first thoracic level.

With the development of stronger x-y-z gradient coils,

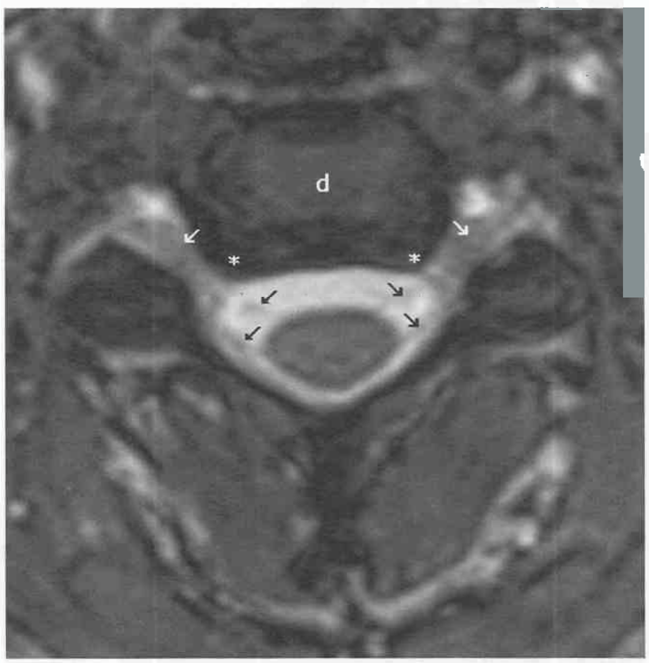

Figure 22–41. Axial cervical gradient-echo MR image. The exiting nerve roots approach the neural foramina at a 45-degree angle. Both the anterior and posterior divisions can be seen *(black arrows)*; they then join to form the dorsal root ganglia in the foramina *(white arrows)*. Note hypointense uncovertebral joints of Luschka *(asterisks)* indenting the posterolateral disk (d) margins.

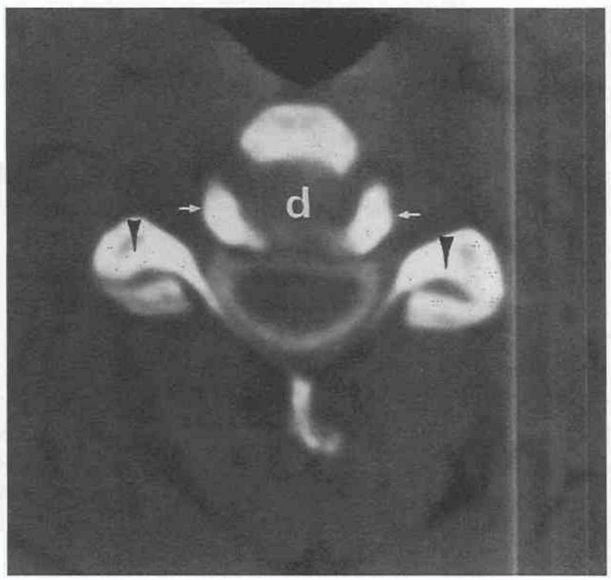

Figure 22–42. Cervical postmyelogram CT scan. The uncovertebral joints of Luschka are indenting the posterolateral disk (d) margins *(arrows)* (see Fig. 22–41). Note also the near-horizontal orientation of the facet joints *(arrowheads)* (see also Fig. 22–41).

Box 22–3. Routine CT of Cervical Degenerative Disease

- Axial contiguous images from C2 to T1
- Slice thickness = 2–3 mm, intersection gap = 2 mm
- Both wide and narrow window settings
- Intrathecal contrast preferable

Box 22–4. Example of Routine MRI of Cervical Degenerative Disease

1. Sagittal fast spin-echo, T1-weighted image to include cerebellar tonsils to T1 level
   a. Field of view = 26–28 cm, thickness = 3–4 mm, intersection gap = 1 mm, matrix = 256 × 512
2. Sagittal fast spin-echo, T2-weighted image to include cerebellar tonsils to T1 level
   a. Field of view = 26–28 cm, thickness = 3–4 mm, intersection gap = 1 mm, matrix = 384 × 512
3. Axial 2D gradient-echo sequence to cover at least C2-3 through C6-7 interspaces
   a. Field of view = 20 cm, thickness = 3 mm, intersection gap = 1 mm, matrix = 384 × 512
4. Axial 3D gradient-echo sequence contiguous to cover at least C2-3 through C6-7
   a. Field of view = 20 cm, reconstructed thickness = 2 mm, matrix = 512 × 512
   b. Apply magnetization transfer pulse
5. If postoperative spine, substitute noncontrast T1-weighted, fast spin-echo axial views for one of the gradient-echo sequences
   a. Field of view = 20 cm, thickness = 3 mm, intersection gap = 1 mm, matrix = 256 × 256

matrices in the range of 300 to 600 can be obtained, greatly increasing image resolution. The stronger gradients also allow for shorter imaging times and larger fields of view (allowing inclusion of the upper thoracic spine in the cervical images—a request often made by referring physicians) with little or no decrease in image resolution. We also obtain a set of 2D gradient-echo as well as 3D (volume) gradient-echo axial images from the C3-4 interspace down to at least the C6-7 interspace. The T1-weighted images are used for evaluation of overall anatomy and marrow abnormalities. The gradient-echo images bring out the "myelographic effect," enhancing contrast between bone-root-cord and CSF (see Fig. 22–41). We use both 2D and 3D gradient-echo axial views because we find that overall image quality tends to be better with 2D sequences, but the thinner slices obtained with 3D sequences often help to detect small lesions. We apply a magnetization transfer pulse to the 3D images to help darken the cord and roots, thus increasing the myelographic contrast effect.

Again, imaging sequences may vary widely among institutions. For instance, some centers routinely obtain T1-weighted axial views, whereas we do not, except in the postoperative cervical spine. All 2D images are 3 to 4 mm thick with a 1- to 1.5-mm gap (Box 22–4). Given the 45-degree angle of the exiting nerve roots, some authors advocate using sagittal oblique images (perpendicular to the foramina) rather than direct sagittal views for optimal foraminal imaging.[55] This, however, requires two separate sets of oblique images, one for each side, and is therefore more time-consuming. We occasionally make use of the

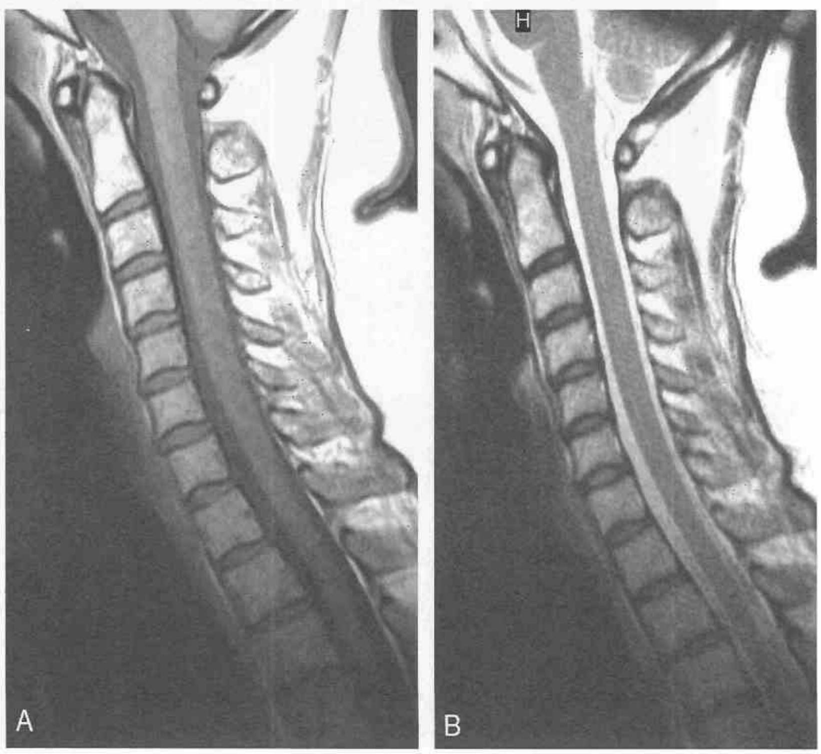

Figure 22–43. Sagittal fast spin-echo, T1-weighted *(A)* and T2-weighted *(B)* cervical MR images. The field of view should include cerebellar tonsils to at least the first thoracic level. A large field of view helps to include the upper thoracic spine.

sagittal oblique when there is obvious clinical radiculopathy without obvious MRI findings. The oblique images occasionally reveal small, but strategically located intraforaminal disk herniations.

Because the cervical spine is small and "crowded," volume averaging, patient motion, flow and pulsation artifacts, and small-structure (e.g., foraminal stenosis) evaluation are more problematic in the cervical than in the lumbar spine. More refined imaging techniques (e.g., volume imaging, fast spin-echo imaging, magnetization transfer, motion compensation) to alleviate these problems are evolving rapidly, and numerous new sequences and techniques emerge constantly.

Nondiskogenic Spinal Stenosis

Degenerative disease of the cervical spine is very common after age 40 and may, in fact, affect 70% of people older than age 70.[37, 43] In older individuals, *facet hypertrophy* and *osteophytosis* become more problematic than disk herniation; whereas osteophytes and facet disease worsen with age, disk material becomes harder, more immobile, and less likely to protrude.[8] As in the lumbar spine, osteophytes can compress any portion of the neural canal and foramina (Fig. 22–44). Ligamentum flavum hypertrophy can contribute to spinal and foraminal stenosis (see Fig. 22–44). Unique to the cervical spine are the uncinate processes, or joints of Luschka, which contribute to the anterior wall of the neural foramina. Uncinate hypertrophy or osteophytosis, therefore, may lead to foraminal stenosis (Fig. 22–45).[45, 58] Facet hypertrophy generally narrows the foramina (see Fig. 22–45).

CT is well suited for visualization of bone and facet disease. On MRI, osteophytes can be of high, intermediate, or low signal intensity on T1-weighted images, depending on their yellow marrow content.[54] Intermediate-signal and low-signal osteophytes may blend in with adjacent liga-

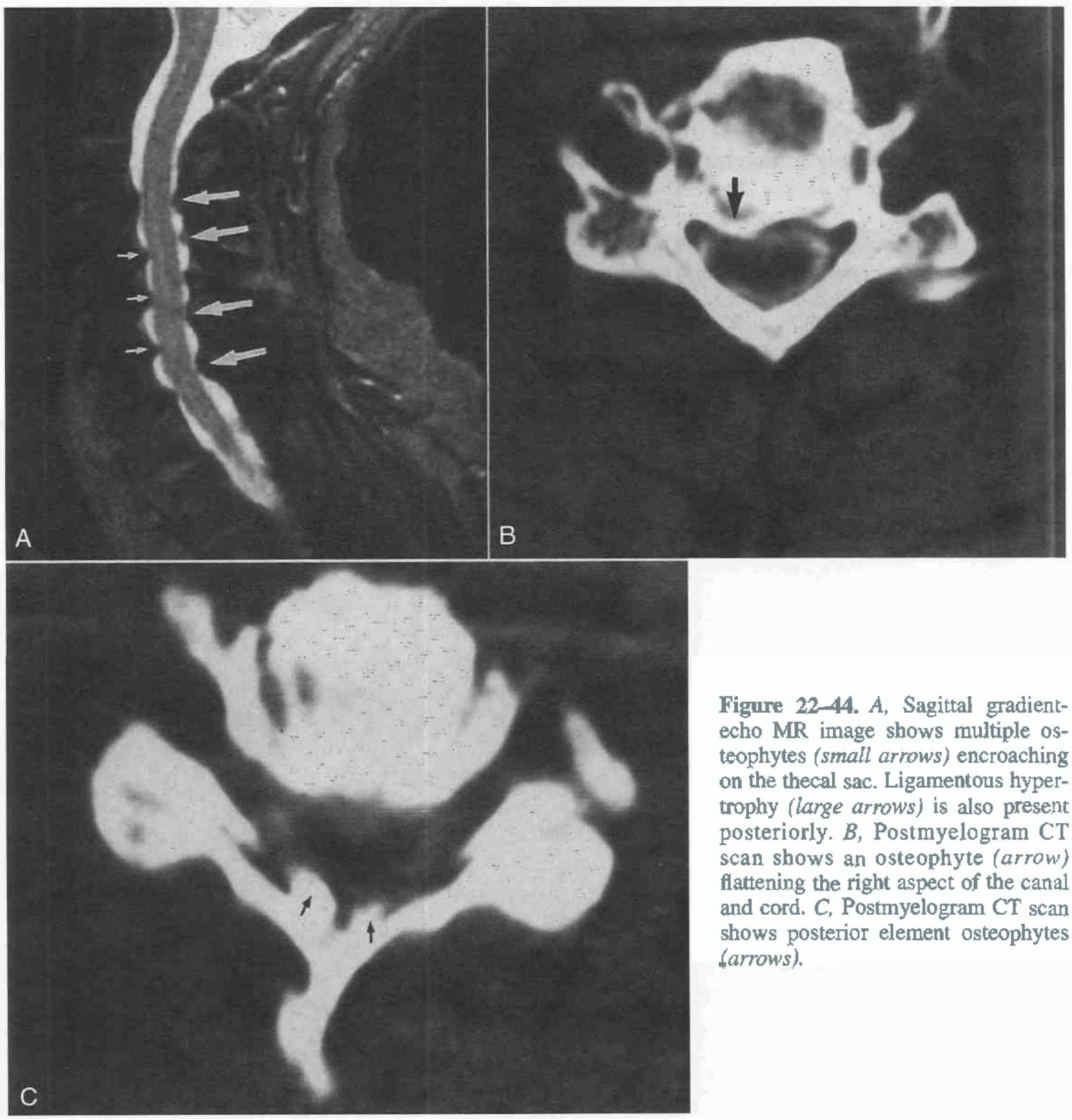

Figure 22–44. *A,* Sagittal gradient-echo MR image shows multiple osteophytes *(small arrows)* encroaching on the thecal sac. Ligamentous hypertrophy *(large arrows)* is also present posteriorly. *B,* Postmyelogram CT scan shows an osteophyte *(arrow)* flattening the right aspect of the canal and cord. *C,* Postmyelogram CT scan shows posterior element osteophytes *(arrows).*

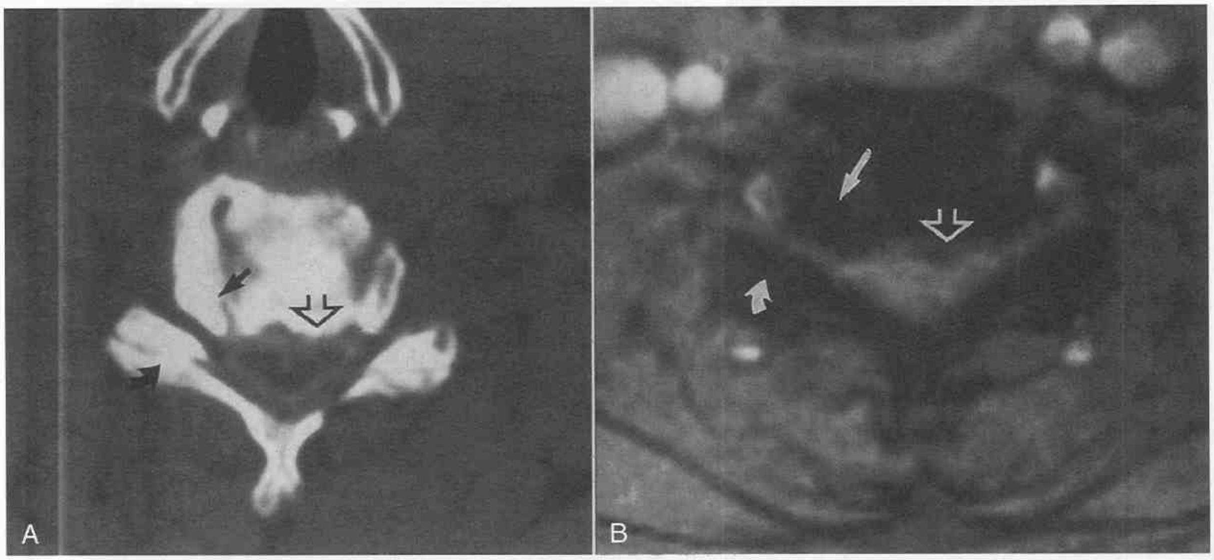

Figure 22–45. Postmyelogram CT scan *(A)* and axial gradient-echo *(B)* MR image show hypertrophied uncovertebral joint *(closed arrows)* narrowing the right neural foramen. Right-sided facet hypertrophy *(curved arrows)* contributes to this narrowing. Note also osteophytes *(open arrows)*.

ments and CSF in the cervical region, where volume averaging is already a problem.

As mentioned, we obtain gradient-echo images in the cervical region, which makes bone very dark regardless of marrow content. This stands out nicely against the myelographically bright CSF. One must beware, however, of the "blooming" effect, in which osteophyte size may be exaggerated on gradient-echo sequences owing to magnetic susceptibility. Thus, spinal stenosis secondary to osteophytes seen on gradient-echo sequences should be confirmed on T1-weighted images, whose magnetic susceptibility effects are not as prominent.

Posterolateral bone, ligament, and facet disease, which impinge on the nerve roots, can lead to upper extremity radiculopathy. Central disease that compresses the cervical cord can produce myelopathy as well,[10, 28, 59] resulting in lower extremity symptoms, including spasticity, weakness, and gait disturbance.[8, 28] Clinically, this syndrome must be differentiated from other forms of myelopathy, such as multiple sclerosis, spinal neoplasm, and various intrinsic spinal cord diseases. In addition, if large spurs compress the vertebral arteries, symptoms of vertebrobasilar insufficiency may occur.[8]

Although common in Japan, *ossification of the posterior longitudinal ligament* (OPLL) is a fairly rare cause of spinal stenosis in the United States. There is no known etiologic mechanism. The ossified posterior longitudinal ligament can impinge on the spinal canal, resulting in nerve root or spinal cord compression. This entity is well visulaized on plain films as a vertical band of ossified tissue along the posterior margin of the vertebral bodies. On CT scans, the involved portion of the ligament is replaced by the high density of calcium. On MR images, the ossification is represented by low signal on short TR, long TR, and gradient-echo sequences (Fig. 22–46). However, fatty marrow within the ossification can yield areas of high signal intensity on T1.[61]

Diskogenic Spinal Stenosis

Early in the course of cervical spinal osteoarthritis, the most common cause of pain is direct nerve-root compression by a laterally herniated cervical disk, which ordinarily occurs without prior trauma. This results in neck and arm pain with paresthesias in a dermatomal distribution. Both sensory and motor abnormalities occur. Cervical disk herniations are most common in the second through fourth decades of life.[8]

These herniations are well seen on both CT myelography (Fig. 22–47) and MRI (Fig. 22–48) as extradural soft tissue masses contiguous with the parent disk and focally protruding posterolaterally into the canal and/or neural foramina. Central disk herniations are less common and can cause spinal cord compression, resulting in myelopathy as well as radiculopathy (Fig. 22–48*E*).[8]

Postoperative Cervical Spine

Postoperative Changes

Most decompressive procedures on the cervical spine are now performed via an anterior approach.[15, 34, 65] With the *Smith-Robinson* technique, the disk and end-plate material are removed and are replaced with an osseous wedge from the iliac bone.[65] During the *Cloward* technique, the surgeon removes posterior and posterolateral osteophytes, drills a hole into the disk space and end plates, and reinserts a prefitted piece of bone.[15] Strut grafts are used for cervical stabilization after multilevel decompressive surgery is performed. The grafted bone bridges the involved vertebral bodies.

Although these techniques are commonly used, many other approaches, both anterior and posterior, are available (Fig. 22–49). In the immediate diskectomy-fusion postoperative period, the signal intensity of the intervertebral bone

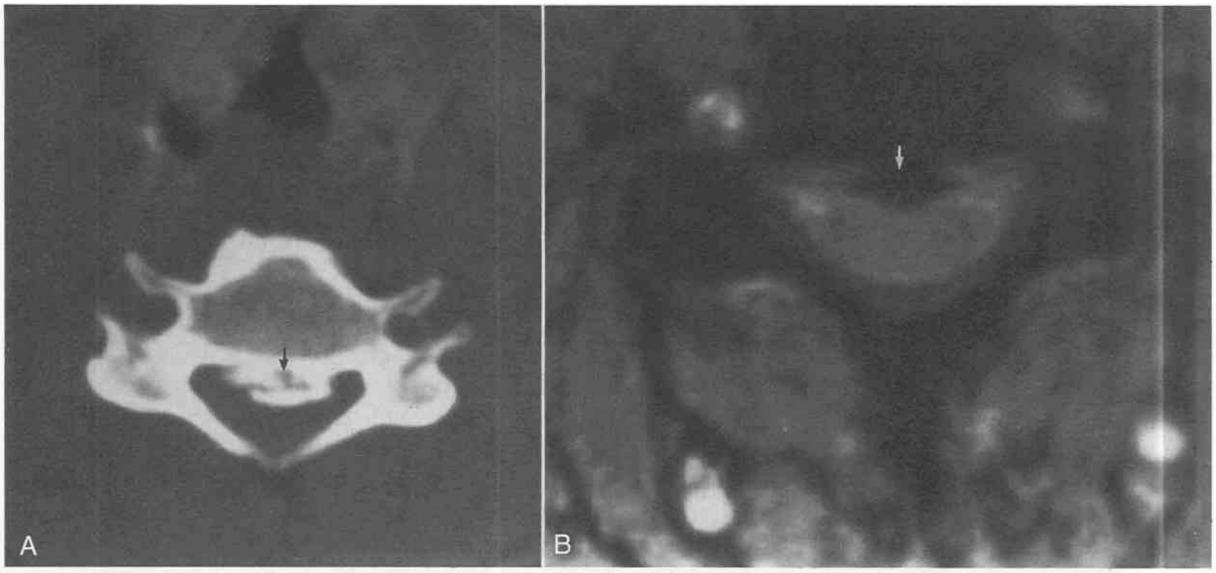

Figure 22–46. Ossified posterior longitudinal ligament. Axial noncontrast CT scan *(A)* and axial gradient-echo MR image *(B)* show the ossified ligament *(arrows)* impinging on the spinal canal.

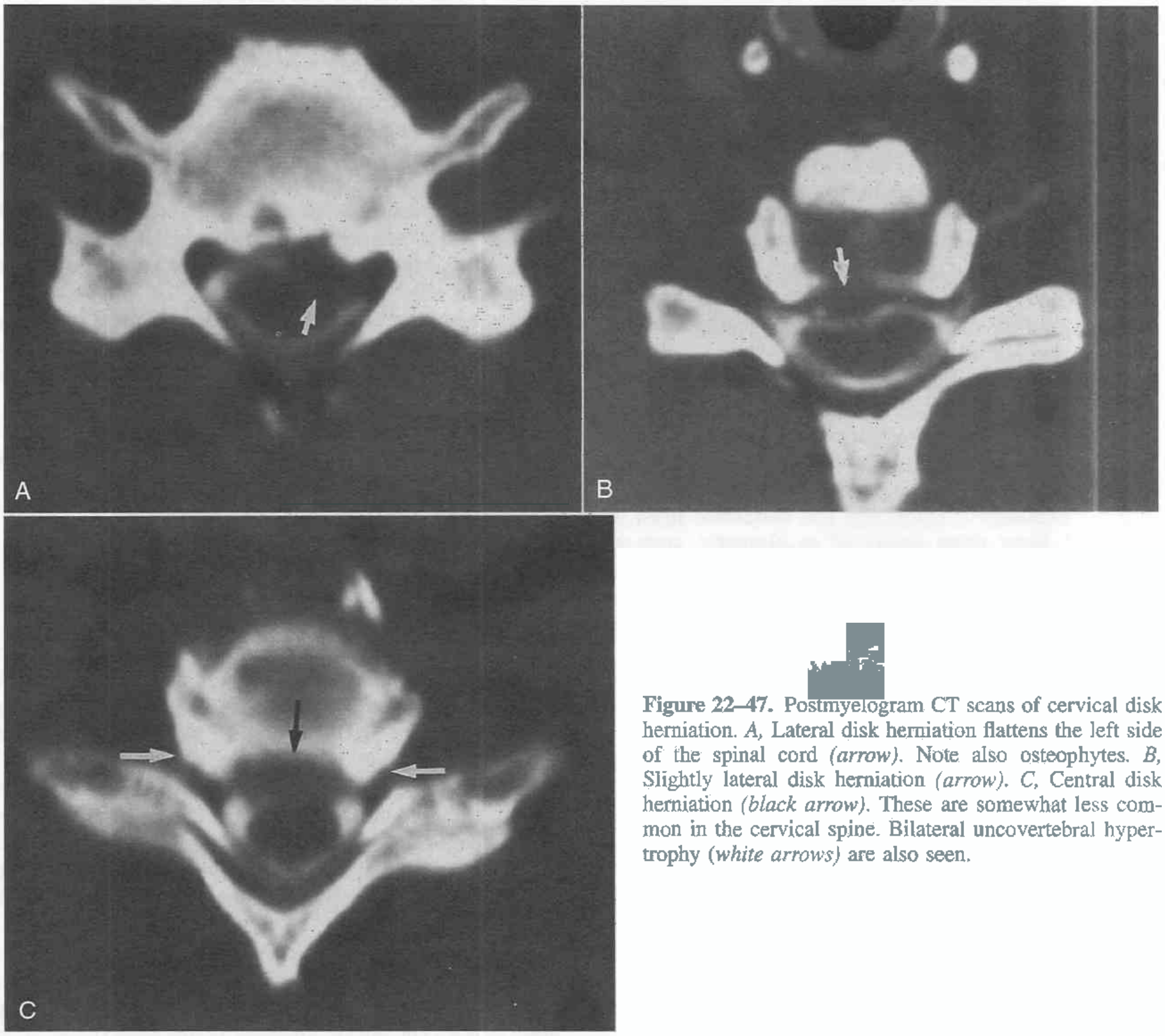

Figure 22–47. Postmyelogram CT scans of cervical disk herniation. *A,* Lateral disk herniation flattens the left side of the spinal cord *(arrow)*. Note also osteophytes. *B,* Slightly lateral disk herniation *(arrow)*. *C,* Central disk herniation *(black arrow)*. These are somewhat less common in the cervical spine. Bilateral uncovertebral hypertrophy *(white arrows)* are also seen.

Figure 22–48. MR images of cervical disk herniation. Sagittal fast spin-echo, T1-weighted *(A)* and axial gradient-echo *(B)* images show a small central disk herniation *(arrows)*. In the cervical spine, herniations can be quite subtle. Sagittal fast spin-echo, T1-weighted *(C)* and T2-weighted *(D)* images of multiple disk herniations *(arrows)* in a single patient.

Illustration continued on following page

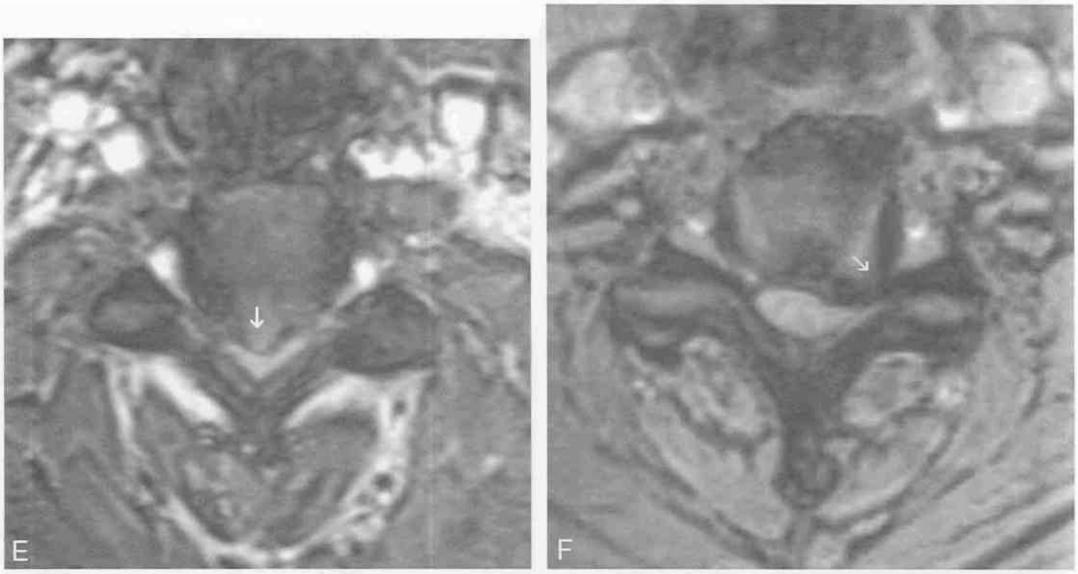

Figure 22–48 *Continued*
E–G, Axial gradient-echo images in a patient with multiple disk herniations. *E,* This centrally herniated disk severely narrows the canal at one level *(arrow)*. *F,* This laterally herniated disk severely narrows the left foramen *(arrow)* at another level. *G,* Osteophytes, which are much darker than disk herniations on gradient-echo imaging, are present as well *(arrow)*.

grafts on MRI may be quite variable, according to whether the marrow is cellular or fatty and whether the bone is cancellous or compact. Adjacent end plates can have normal signal or signal that reflects postoperative Disk and end-plate changes in the late postoperative period are even more variable, reflecting not only the composition of the bone graft but also, possibly, the amount of revascularization, postoperative stresses, and intraoperative trauma received by the end plate and graft.[70, 73]

Strut grafts are easily seen as long wedges of bone bridging the anterior aspects of the vertebral bodies. On MR images, the signal of the bulk of the graft may be variable but low-signal cortex outlines the graft margins (see Fig. 22–49). Solid bony fusions without replacement of disk by graft are seen as continuous marrow signal with no definable interspace (Fig. 22–49*C*). One of the most common types of procedures seen today involves anterior diskectomy, followed by interbody fusion with a piece of bone and placement of an anterior plate-screw device for maximum stability (Fig. 22–49*D–G*).

Complications

Complications of cervical spine decompression are similar to those in the lumbar region, including (1) bony stenosis, (2) disk herniation, (3) pseudomeningocele, and (4) infection. There are, however, some differences.

1. Bony stenosis may be caused not only by osteophyte formation but also by uncovertebral hypertrophy or by overgrowth of the fusion mass itself. These can produce spinal as well as foraminal stenosis. When one is looking at gradient-echo images of the cervical spine, the surgical material used may cause magnetic susceptibility "blooming" artifact and may mimic severe spinal stenosis when in fact no stenosis exists (see Fig. 22–49*D–G*). It is important, therefore to examine all images carefully, especially the T1-weighted and T2-weighted sequences. These sequences (especially FSE) tend not to exaggerate the degree of spinal stenosis. We substitute a set of T1-weighted axial images for one of the gradient-echo axial views to mitigate these artifacts in the postoperative cervical spine (see Fig. 22–49*G*).

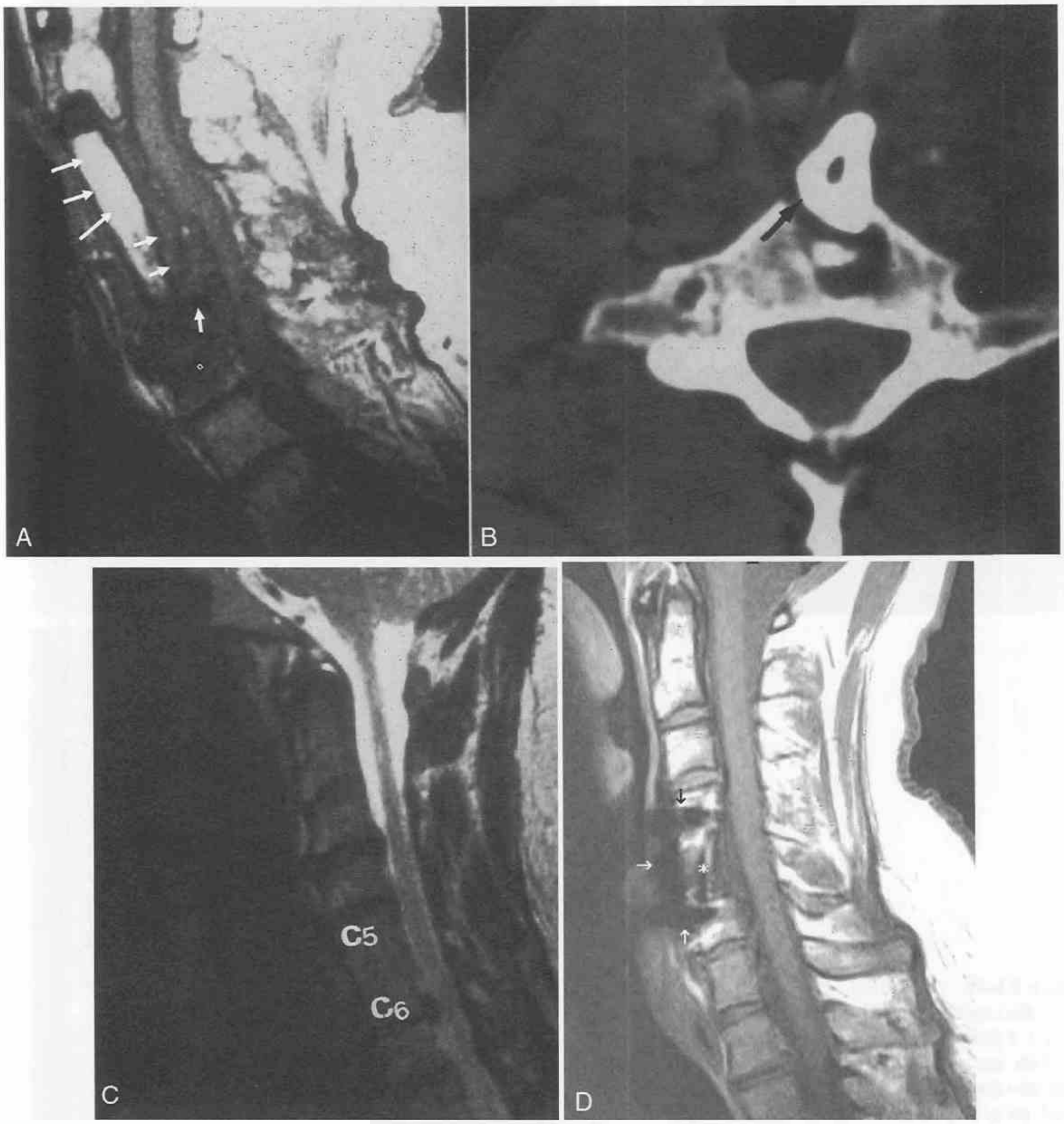

Figure 22–49. Various types of cervical fusions.

A, Large fibular strut graft *(black arrows)* for multilevel fusion. Note early postoperative edema *(white arrows)* causing cord compression.

B, Axial CT scan in a different patient shows a fibular strut graft *(arrow)* fusing C4-5.

C, Solid C5-6 fusion.

D–G, C4-6 fusion by means of plate-screw combination and interbody bone graft. *D,* T1-weighted image. *Arrows* indicate a plate-screw device. *Asterisk* indicates interbody bone graft. No significant spinal stenosis post-grafting.

Illustration continued on following page

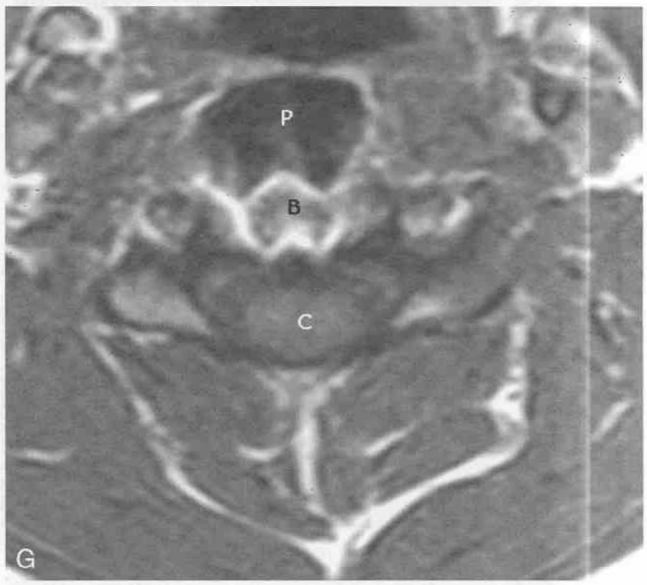

Figure 22–49 *Continued*
E, Fast spin-echo, T2-weighted sequences produces artifact from the metal portion of the graft *(arrows)* but does not show significant spinal stenosis. *F,* Axial gradient-echo image. Artifact falsely suggests severe spinal stenosis. c, cord. *G,* Axial T1-weighted image shows the true, nonstenotic configuration of the canal. B, bone graft; C, cord; P, metal plate.

2. Because most or all of a disk is removed and replaced in a cervical diskectomy and fusion, postoperative recurrent disk herniations tend not to occur unless residual disk material is inadvertently left behind. Graft extrusion, however, is an uncommon complication that can mimic a herniated disk at the operative level. Cervical disk herniations at nearby levels can occur from the altered stresses within the spine.[70]
3. Cervical spine instability can be a significant problem in a patient's status after cervical laminectomy.[67] Both MRI and CT scans with sagittal or coronal reconstructions can demonstrate postoperative scoliotic, kyphotic, and rotational deformities as well as malalignment. These scans can also be performed in flexion and extension to demonstrate abnormal motion. Unfortunately, no effective way of evaluating graft integrity by CT or MRI exists to date.

Thoracic Spine

Both disk herniation and spinal stenosis of the thoracic spine are less common than in the lumbar and cervical spine. The infrequency of thoracic spinal stenosis is proba-

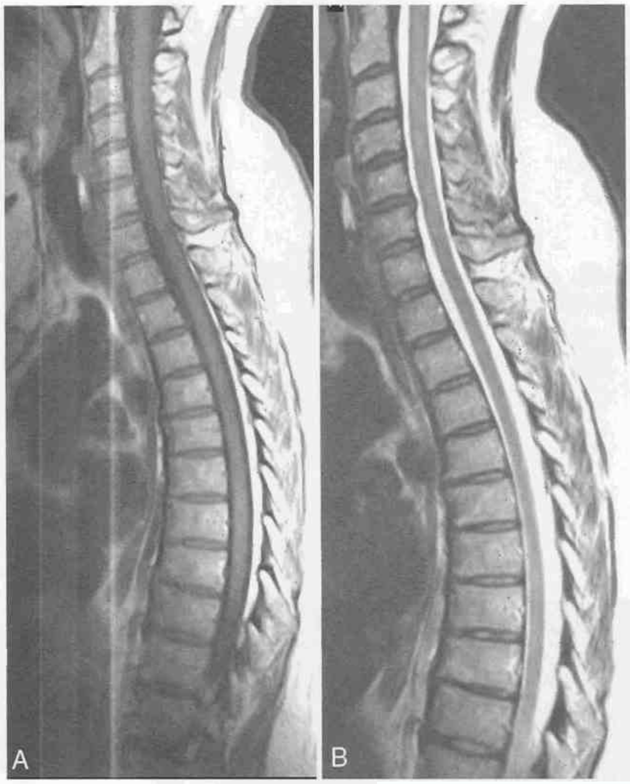

Figure 22–50. Sagittal fast spin-echo, T1-weighted *(A)* and T2-weighted *(B)* thoracic MR images. The entire thoracic spine as well as the cervical spine is easily included in the field of view.

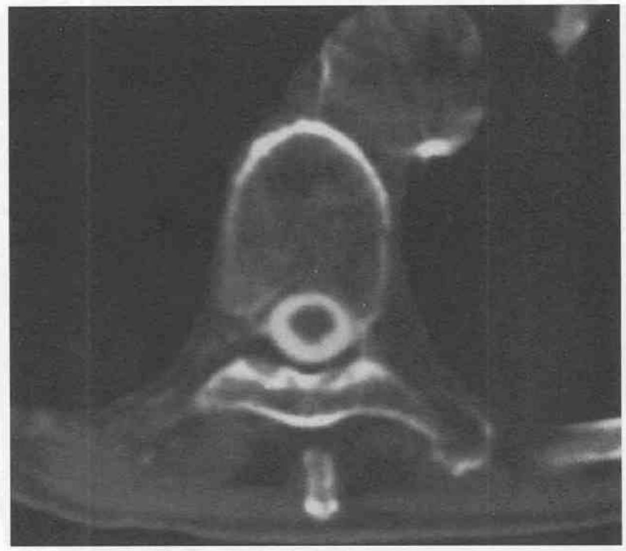

Figure 22–51. Normal postmyelogram thoracic CT scan. Note the round shape of the normal thoracic cord and canal.

bly due to the large size of the thoracic canal relative to the cord.[51] To produce compressive symptomatology, bony or ligamentous hypertrophy must be fairly large. The incidence of thoracic disk herniation is also less than in the remainder of the spine. This is presumably due to the limited mobility of the thoracic spine and because the weight-bearing axis does not intersect the posterior margins of the vertebral bodies.[5, 66] Most patients with operated thoracic disks report an incidence of less than 2%, although autopsy series report an incidence of between 7% and 15%.[2] With the emergence of MRI, these herniations are being recognized with increased frequency.[74]

Imaging Techniques

MRI demonstrates both thoracic canal stenosis and thoracic disk herniations quite well. MRI is also useful for excluding other causes of thoracic disease, such as tumor or infection. At our institution, we obtain T1-weighted sagittal sequences, followed by FSE T2-weighted sagittal sequences (Fig. 22–50). These images are then inspected, and axial images are obtained through the level of concern as needed (Box 22–5).

CT myelography complements MRI in evaluation of spinal stenosis caused by bony hypertrophy or ligamentous ossification owing to its superior ability to image calcium. Because of its length, covering the entire thoracic spine with CT using a reasonable number of slices is difficult. Therefore, if CT scanning is to be performed, it is probably best done after myelography or MRI to define the level of pathology (Fig. 22–51). CT images can then be obtained through the level of concern (Box 22–6). With modern, large field-of-view coils, MRI can be used to depict the entire thoracic spine in one shot (see Fig. 22–50), thus making MRI the preferred imaging modality for thoracic degenerative disease.

Box 22–5. Example of Routine MRI of Thoracic Degenerative Disease

1. Sagittal T1 to include entire thoracic spine
   a. Field of view = 40 cm, slice thickness = 3–4 mm, intersection gap = 1 mm, matrix = 512 × 512
2. Sagittal fast spin-echo, T2-weighted image to include entire thoracic spine
   a. Field of view = 40 cm, slice thickness = 3–4 mm, intersection gap = 1 mm, matrix = 512 × 512
3. Axial fast spin-echo, T1-weighted and T2-weighted images through areas of concern as needed

Nondiskogenic Spinal Stenosis

Acquired thoracic spinal stenosis can result from hypertrophy of the bony posterior elements.[84] Since the advent of CT scanning, hypertrophy or calcification of the posterior longitudinal ligament (Fig. 22–52) and degenerative ligamentum flavum hypertrophy are also being recognized with increased frequency in the thoracic spine.[3, 50]

Box 22–6. Routine CT of Thoracic Degenerative Disease

- Axial contiguous images through areas of concern
- Slice thickness = 4 mm, intersection gap = 4 mm
- Intrathecal contrast medium preferable
- Both wide and narrow window settings

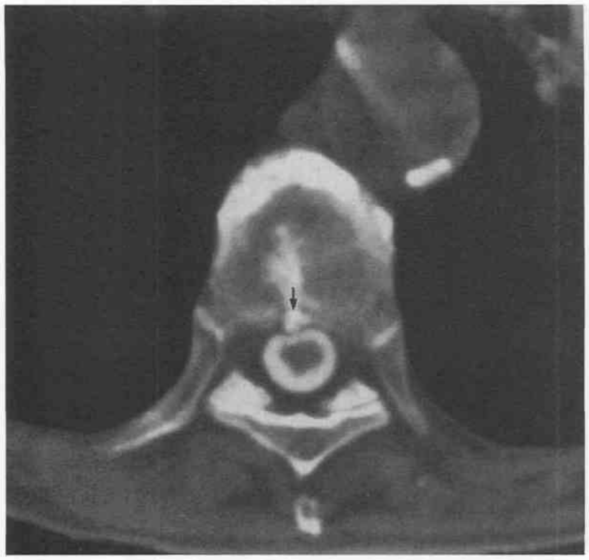

Figure 22–52. An ossified posterior longitudinal ligament *(arrow)* impinges on the thoracic spinal canal.

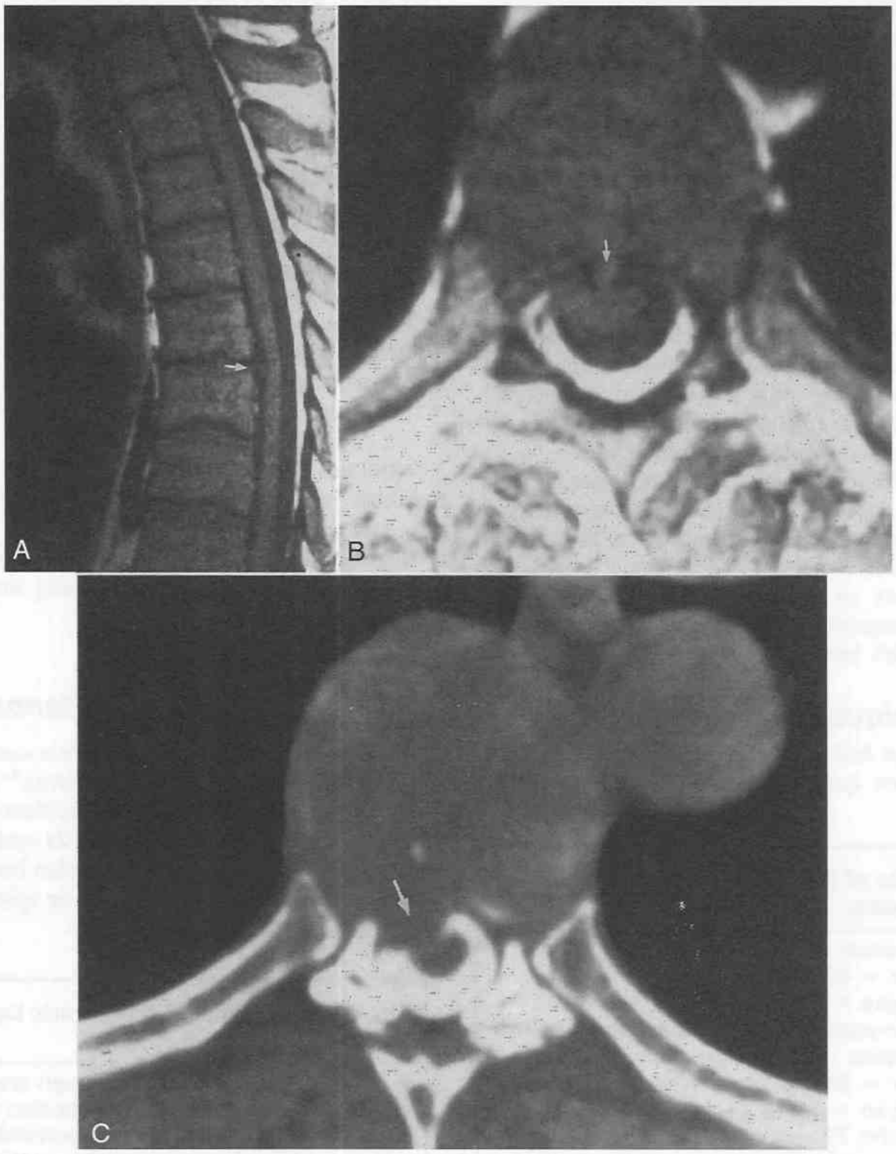

Figure 22–53. Sagittal *(A)* and axial *(B)* T1-weighted MR images of central disk herniation *(arrows)*. *C*, Postmyelogram CT scan of slightly lateral disk herniation *(arrow)*.

Diskogenic Spinal Stenosis

Most thoracic disk herniations occur in the lower thoracic spine. T11 and T12 are the most common locations. Unlike the case with the rest of the spine, most thoracic herniations are centrally, rather than laterally, located (Fig. 22–53). Multilevel thoracic herniation is rare. Most patients with thoracic disk herniations are between 30 and 50 years of age.[66]

Nondegenerative Spinal Stenosis

Nondegenerative spinal stenosis has numerous causes, the most common of which is idiopathic congenital or developmental narrowing of the spinal canal. This is probably due to inadequate development of the canal and foramina. Symptoms usually arise when degenerative changes of disks, facets, and ligaments are superimposed on an already small canal.[25]

Box 22–7 summarizes the nondegenerative causes of spinal stenosis.

Box 22–7. Nondegenerative Causes of Spinal Stenosis

A. Congenital-developmental stenosis
  1. Idiopathic
  2. Achondroplasia/hypochondroplasia
  3. Hypophosphatemic vitamin D–resistant rickets
  4. Morquio's disease
  5. Congenital dysplasias associated with lax atlantoaxial joints
  6. Down's syndrome
  7. Spondylolisthesis
  8. Scoliosis
  9. Spinal dysraphism

B. Acquired stenosis
  1. Degenerative
    a. Spondylosis
    b. Spondylolisthesis
    c. Scoliosis
    d. Ossification of the posterior longitudinal ligament
    e. Ligamentum flavum hypertrophy or ossification
    f. Intraspinal synovial cysts
  2. Postoperative
    a. Postlaminectomy
    b. Postfusion
    c. Postdiskectomy
  3. Post-traumatic
  4. Metabolic
    a. Epidural lipomatosis
    b. Osteoporosis leading to vertebral fractures
    c. Acromegaly
    d. Calcium pyrophosphate deposition disease
    e. Renal osteodystrophy
    f. Hypoparathyroidism
    g. Oxalosis
  5. Miscellaneous
    a. Paget's disease
    b. Ankylosing spondylitis
    c. Diffuse idiopathic skeletal hyperostosis
    d. Rheumatoid arthritis
    e. Fluorosis
    f. Scheurmann's disease
    g. Osteopoikilosis
  6. Combined
    a. Combined lumbar and cervical stenosis
    b. Combined developmental/congenital and degenerative stenosis

Modified from Moreland LW, Lopez-Mendez A, Alarcon GS: Spinal stenosis: A comprehensive review of the literature. Semin Arthritis Rheum 19:127–149, 1989.

References

1. Adams P, Eyre DR, Muir H: Biochemical aspects of development and aging of human lumbar intervertebral disks. Rheumatol Rehabil 16:22–29, 1977.
2. Arseni C, Nash F: Protrusion of thoracic intervertebral discs. Acta Neurochir 11:3–33, 1963.
3. Barnett GH, et al: Thoracic spinal canal stenosis. J Neurosurg 66: 338–344, 1987.
4. Bates DB, Rugierri P: Imaging modalities for evaluation of the spine. Radiol Clin North Am 29:675–690, 1991.
5. Blumenkopf B: Thoracic intervertebral disk herniations: Diagnostic value of magnetic resonance imaging. Neurosurgery 23:36–40, 1988.
6. Boden SD, Davis DO, Dina TS, et al: Contrast-enhanced MR imaging performed after successful lumbar disk surgery: Prospective study. Radiology 182:59–64, 1992.
7. Boden SD, Davis DO, Dina TS, et al: Postoperative diskitis: Distinguishing early MR imaging findings from normal postoperative disk space changes. Radiology 184:765–771, 1992.
8. Bohlman HH: Osteoarthritis of the cervical spine. In Osteoarthritis Diagnosis and Management. Philadelphia, WB Saunders, 1984, pp 443–459.
9. Bowen V, Shannon R, Kirkaldy-Willis WH: Lumbar spinal stenosis: A review article. Child's Brain 4:257–277, 1978.
10. Brain WR, Northfield DW, Wilkinson M: The neurological manifestations of cervical spondylosis. Brain 75:187–225, 1952.
11. Brown MD: The pathophysiology of disc disease: Symposium on disease of the intervertebral disc. Orthop Clin North Am 2:359–370, 1971.
12. Brown BM, Schwartz RH, Frank E, Blank NK: Preoperative evaluation of cervical radiculopathy and myelopathy by surface-coil MR imaging. AJR Am J Roentgenol 151:1205–1212, 1988.
13. Bundschuh CV, et al: Epidural fibrosis and recurrent disk herniation in the lumbar spine: Assessment with magnetic resonance. AJNR Am J Neuroradiol 9:169–178, 1988.
14. Burton CV, Kirkaldy-Willis WH, Yong-Hing K, Heithoff KB: Causes of failure of surgery on the lumbar spine. Clin Orthop 157:191–199, 1981.
15. Cloward RB: The anterior approach for removal of ruptured cervical discs. J Neurosurg 15:602–614, 1958.
16. Coventry MB: Anatomy of the intervertebral disk. Clin Orthop 67: 9–15, 1969.
17. de Roos A, Krossel H, Spritzer C, Dalinka M: MR imaging of marrow changes adjacent to end plates in degenerative lumbar disk disease. Am J Roentgenol 149:531–534, 1987.
18. Dorwart RH, Volger JB III, Helms CA: Spinal stenosis. Radiol Clin North Am 21:301–325, 1983.
19. Dublin AB, McGahan JP, Reid MH: The value of computed tomographic metrizamide myelography in the neuroradiologic evaluation of the spine. Radiology 146:79–86, 1983.
20. Epstein NE, Epstein JA, Carras R, Hyman RA: Far lateral lumbar disc herniations and associated structural abnormalities: An evaluation in 60 patients of the comparative value of CT, MRI, and myelo-CT in diagnosis and management. Spine 15:534–539, 1990.
21. Epstein BS, Epstein JA, Jones MD: Cervical spine stenosis. Radiol Clin North Am 15:215, 1977.
22. Epstein BS, Epstein JA, Jones MD: Lumbar spinal stenosis. Radiol Clin North Am 15:227–239, 1977.
23. Frymoyer JW, Cats-Baril WL: An overview of the incidences and costs of low back pain. Orthop Clin North Am 22, 1991.
24. Frymoyer JW, Pope MH, Clements JH, et al: Ricks factors in low back pain: An epidemiological survey. J Bone Joint Surg Am 65: 213–218, 1983.
25. Gaskill MF, Lukin R, Wiot JG: Lumbar disc disease and stenosis. Radiol Clin North Am 29:753–764, 1991.
26. Goldberg AL, Soo MS, Deeb ZL, Rothfus WE: Degenerative disease

of the lumbar spine: Role of CT-myelography in the MR era. Clin Imaging 15:47–55, 1991.
27. Hall S, Bartleson JD, Onofrio BM, et al: Lumbar spinal stenosis: Clinical features, diagnostic procedures, and results of surgical treatment in 68 patients. Ann Intern Med 103:271–275, 1985.
28. Harris P: Cervical spine stenosis. Paraplegia 15:25–132, 1977–1978.
29. Hawkes CH, Roberts GM: Neurogenic and vascular claudication. J Neurol Sci 38:337, 1978.
30. Hochhauser L, Kieffer SA, Cacayorin ED, et al: Recurrent postdiskectomy low back pain: MR-surgical correlation. AJR Am J Roentgenol 151:755–760, 1988.
31. Hueftle MG, Modic MT, Ross JS, et al: Lumbar spine: Postoperative MR imaging with Gd-DTPA. Radiology 167:817–824, 1988.
32. Jackson RP, Becker GJ, Jacobs RR, et al: The neuroradiographic diagnosis of lumbar herniated nucleus pulposus: I. A comparison of computed tomography, myelography, CT-myelography, discography and CT-discography. Spine 14:1356–1361, 1989.
33. Jackson RP, Cain JE Jr, Jacobs RR, et al: The neuroradiographic diagnosis of lumbar herniated nucleus pulposus: II. A comparison of computed tomography, myelography, CT-myelography and magnetic resonance imaging. Spine 14:1362–1367, 1989.
34. Jacobs B: Anterior cervical spine fusion. Surg Ann 8:413–446, 1976.
35. Reference deleted.
36. Kallina C: Degenerative lumbar stenosis. Clin Geriatr Med 1:391–400, 1985.
37. Kellgren JH, Lawrence JS: Osteoarthritis and disk degeneration in an urban population. Ann Rheum Dis 17:388–397, 1958.
38. Kelsey JL, White AA 3rd, Pastides H, et al: The impact of musculoskeletal disorders on the population of the United States. J Bone Joint Surg [Am] 61:959–964, 1979.
39. Kent DL, Haynor DR, Larson EB, Deyo RA: Diagnosis of lumbar spinal stenosis in adults: A meta-analysis of the accuracy of CT, MR and myelography. AJR Am J Roentgenol 158:1135–1144, 1992.
40. Kirkaldy-Willis WH: The relationship of structural pathology to the nerve root. Spine 9:49–52, 1984.
41. Kirkaldy-Willis WH, Paine KW, Cauchoix J, McIvor G: Lumbar spinal stenosis. Clin Orthop Relat Res 99:30–50, 1974.
42. Kirkaldy-Willis WH, Wedge JH, Yong-Hing K, Reilly J: Pathology and pathogenesis of lumbar spondylosis and stenosis. Spine 3:319–328, 1978.
43. Lawrence JS, Bremner JM, Bier F: Osteoarthrosis: Prevalence in the population and relationship between symptoms and x-ray changes. Ann Rheum Dis 25:1–24, 1966.
44. Lipson SJ: Spinal stenosis. Rheum Dis Clin North Am 14:613–618, 1988.
45. Lipson SJ, Muir H: Vertebral osteophyte formation in experimental disk degeneration: Morphologic and proteoglycan changes over time. Arthritis Rheum 23:319–324, 1980.
46. Liu SS, Williams KD, Drayer BP, et al: Synovial cysts of the lumbosacral spine: Diagnosis by MR imaging. AJNR Am J Neuroradiology 10:1239–1242, 1989.
47. Manelfe C (ed): Imaging of the Spine and Spinal Cord. New York, Raven Press, 1992, pp 269–331.
48. Masaryk TJ, Ross JS, Modic MT, et al: High-resolution imaging of sequestered lumbar intervertebral disks. AJR Am J Roentgenol 150: 1155–1162, 1988.
49. McNab I: Backache. Baltimore, Williams & Wilkins, 1977.
50. Miyasaka K, Kaneda K, Ito T, et al: Ossification of spinal ligaments causing thoracic radiculomyelopathy. Radiology 143:463–468, 1982.
51. Modic MT: Degenerative disorders of the spine. In Magnetic Resonance Imaging of the Spine. St. Louis, Mosby–Year Book, 1989, pp 75–119.
52. Modic MT: Normal anatomy. In Magnetic Resonance Imaging of the Spine. St. Louis, Mosby–Year Book, 1989, pp 35–74.
53. Modic MT, Masaryk T, Boumphrey F, et al: Lumbar herniated disk disease and canal stenosis: Prospective evaluation by surface coil MR, CT, and myelography, Am J Roentgenol 147:757–765, 1986.
54. Modic MT, Masaryk T, Malopulos GP, et al: Cervical radiculopathy: Prospective evaluations with surface coil MR imaging, CT with metrizamide, and metrizamide myelography. Radiology 161:753–759, 1986.
55. Modic MT, Masaryk T, Ross JS, et al: Cervical radiculopathy: Value of oblique MR imaging. Radiology 163:227–231, 1987.
56. Modic MT, Steinberg PM, Ross JS, et al: Degenerative disk disease: Assessment of changes in vertebral body marrow with MR imaging. Radiology 166:193–199, 1988.
57. Moreland LW, Lopez-Mendez A, Alarcon GS: Spinal stenosis: A comprehensive review of the literature. Semin Arthritis Rheum 19: 127–149, 1989.
58. Munrone I: The importance of the sagittal diameters of the cervical spinal canal in relation to spondylosis and myelopathy. J Bone Joint Surg 56B:30–36, 1974.
59. Nurick S: The pathogenesis of the spinal cord disorder associated with cervical spondylosis. Brain 95L87–95L100, 1972.
60. Olmarker K, Rydevik B: Pathophysiology of sciatica. Orthop Clin North Am 22:223–234, 1991.
61. Otake S, Matsuo M, Nishizawa S, et al: Ossification of the posterior longitudinal ligament: MR evaluation, AJNR AM J Neuroradiol 13: 1059–1067, 1992.
62. Paine KWE: Clinical features of lumbar spinal stenosis. Clin Orthop Relat Res 115:77–82, 1976.
63. Quinet RJ, Hadler NM: Diagnosis and treatment of backache. Semin Arthritis and Rheum 8:261–287, 1979.
64. Resnick D: Degenerative diseases of the vertebral column. Radiology 156:3–14, 1985.
65. Robinson RA, Smith GW: Anterolateral cervical disc removal and interbody fusion for cervical disk syndrome. Bull Johns Hopkins Hosp 96:223, 1955.
66. Rosenbloom S: Thoracic disc disease and stenosis. Radiol Clin North Am 29:765–775, 1991.
67. Ross JS: Magnetic resonance assessment of the postoperative spine. Radiol Clin North Am 29:793–808, 1991.
68. Ross JS, Blaser S, Masaryk T, et al: Gd-DTPA enhancement of posterior epidural scar: An experimental model. AJNR Am J Neuroradiol 10:1083–1088, 1989.
69. Ross JS, Delamarter R, Hueftle MG, et al: Gadolinium-DTPA enhanced MR imaging of the postoperative lumbar spine: Time course and mechanism of enhancement. AJR Am J Roentgenol 152:825–834, 1989.
70. Ross JS, Hueftle MG: Postoperative spine. In Magnetic Resonance Imaging of the Spine. St. Louis, Mosby–Year Book, 1989, pp 120–148.
71. Ross JS, Masaryk T, Modic MT, et al: Lumbar spine: Postoperative assessment with surface coil MR imaging. Radiology 164:851–860, 1987.
72. Ross JS, Masaryk T, Modic MT, et al: MR imaging of lumbar arachnoiditis. AJR Am J Roentgenol 149:1025–1032, 1987.
73. Ross JS, Masaryk TJ, Modic MT: Postoperative cervical spine: MR assessment. J Comput Assist Tomogr 11:955–962, 1987.
74. Ross JS, Masaryk T, Schrader M, et al: MR imaging of the postoperative lumbosacral spine: Assessment with gadopentetate dimeglumine. AJR Am J Roentgenol 155:867–872, 1990.
75. Ross JS, Perez-Reges N, Masaryk T, et al: Thoracic disk herniation: MR imaging, Radiology 165:511–515, 1987.
76. Sandhu FS and Dillon WP: Spinal epidural abscess: Evaluation with contrast-enhanced MR imaging. AJNR Am J Neuroradiol 12:1087–1093, 1991.
77. Schnebel B, Kingston S, Watkins R, Dillin W: Comparison of MRI to contrast CT in the diagnosis of spinal stenosis. Spine 14:332–337, 1989.
78. Sotiropoulos S, Chafetz NI, Lang P, et al: Differentiation between postoperative scar and recurrent disk herniation: Prospective comparison of MR, CT, and contrast enhanced CT. AJNR AM J Neuroradiol 10:639–643, 1989.
79. Sze G: Fast spin echo imaging in the evaluation of the spine. Paper presented at 30th Annual Meeting of American Society of Neuroradiology, June 1992, St. Louis.
80. Teplick JG, Haskin ME: Computed tomography of the postoperative lumbar spine. Am J Roentgenol 141:865–884, 1983.
81. Teplick JG, Peyster RG, Teplick SK, et al: CT identification of post laminectomy pseudomeningocele. Am J Roentgenol 140:1203–1206, 1983.
82. Ulrich CG, et al: Quantitative assessment of the lumbar spinal canal by computed tomography. Radiology 134:137–143, 1980.
83. Valkenburg HA, Haanen HCM: The epidemiology of low back pain. In White AA, Gordon SL (eds): American Academy of Orthopedic Surgeons: Symposium on Idiopathic Low Back Pain. St. Louis, CV Mosby, 1982, pp 9–22.
84. Yamamoto I, Matsumae M, Ikeda A, et al: Thoracic spinal stenosis: Experience with seven cases. J Neurosurg 68:37–40, 1988.

23

Extramedullary Spinal Tumors

Donna M. Plecha

Progress continues to be made in the evaluation of extramedullary spinal tumors. Magnetic resonance imaging (MRI) is usually the imaging modality of choice for evaluating the spine if there is clinical concern for tumor. Although MRI is not usually helpful in determining the specific diagnosis or for grading neoplasms, it is excellent for determining the extent of involvement as well as anatomic detail such as spinal cord compression, and it may help to limit the diagnostic possibilities. It has also facilitated the determination of whether a tumor is extradural, intradural/extramedullary, or intramedullary.

Extradural Tumors of the Spine

Extradural tumors of the spine are the most common of all spinal tumors. Most extradural tumors of the spine are metastatic lesions because the vertebral bodies are highly vascularized. The thoracic spine is most commonly involved. Spinal cord compression is seen in 5% of cancer patients with bone metastasis.[4] Metastatic lesions in the epidural space usually result from direct extension of vertebral body metastasis. Otherwise, there can be epidural involvement from hematogenous spread through the epidural and paravertebral venous plexus.[13]

Most metastatic lesions of the spine originate from breast, lung, or prostate cancer.[24] The most common initial symptoms include local pain and radicular pain. With more advanced disease, motor dysfunction and/or sphincter dysfunction may occur. Therapies include surgery and radiation, or both,[3, 4, 41] and preoperative transarterial embolization of the spinal metastasis. The latter is safe and effective; it can limit blood loss during surgery and aid in more complete tumor resection.[39] Outcome is related to the patient's condition at diagnosis, radiosensitivity of the tumor, and tumor biology.[31] Early initiation of therapy is important to preserve motor function.[41] Bach and colleagues[4] found that 79% of patients who could walk at diagnosis were still ambulatory after treatment, but only 18% of nonambulatory patients were able to walk after therapy. Therefore, timely initiation of therapy is critical.

Spin-echo (SE) T1-weighted sequences are excellent for determining the extent of metastatic disease because of their high signal-to-noise ratio. Also, the high fat content of the bone marrow contributes to excellent contrast (Fig. 23–1). The metastatic lesions alter the usual fat content within the vertebral bodies, thereby causing a decrease in signal intensity on T1-weighted SE images. T2-weighted SE sequences are also helpful as abnormal bone marrow usually demonstrates increased signal intensity on T2-weighted images. In addition, fat saturation techniques offer potential advantages for increasing the conspicuousness of bone marrow lesions. T2-weighted fat-saturated fast spin-echo (FSE) and short TI inversion recovery (STIR) sequences have also been used to increase lesion conspicuity.[26, 32]

Abnormal bone marrow signal intensity on any imaging sequence is nonspecific and does not always mean that a patient has metastatic disease. Kim and colleagues attempted to differentiate between hematopoietic malignancies and metastasis.[16] They assessed lymphoma, leukemia, and multiple myeloma lesions in an attempt to distinguish them from metastasis using the following criteria: pattern of involvement, signal change of the vertebral body, location of the paraspinal mass, cortical destruction, contour change, and compression fracture. Although the two categories overlapped, diffuse involvement was more commonly seen in hematopoietic malignancies than in metastasis, and cortical destruction was more commonly seen in metastasis that in hematopoietic malignancies. The other parameters examined failed to show any statistically significant difference between the two groups.[16] The authors found that it was difficult to evaluate young patients because of persistent red marrow.

Patients with metastatic disease often present with compression fractures. When a patient does not have widespread metastatic disease, it is sometimes difficult to differentiate between pathologic and benign compression fractures of the spine, and various MRI sequences have been used in an attempt to differentiate between them. Baker and colleagues[5] examined 53 patients with a total of 34 benign compression fractures and 27 pathologic fractures. The authors used a presaturation technique, suppressing either fat or water signal with a presaturation pulse, to obtain "fat" and "water" images. STIR and SE images were also used.

Most compression fractures more than 1 month old showed marrow signal isointense to that of the surrounding normal vertebral bodies. When the fracture was acute, however, the edema caused signal intensity changes similar to vertebral bodies involved with tumor. Only seven patients had acute benign fractures less than 1 month old. All showed high signal intensity on T2-weighted images and low signal intensity on T1-weighted SE images. In five of the patients, the water images and the T2-weighted images of the problematic vertebral bodies showed heterogeneous patterns. In the other two patients, the involved vertebral bodies showed diffusely homogeneous increased signal intensity throughout.

Another seven patients had pathologic compression fractures, all of which showed homogeneous diffuse decreased

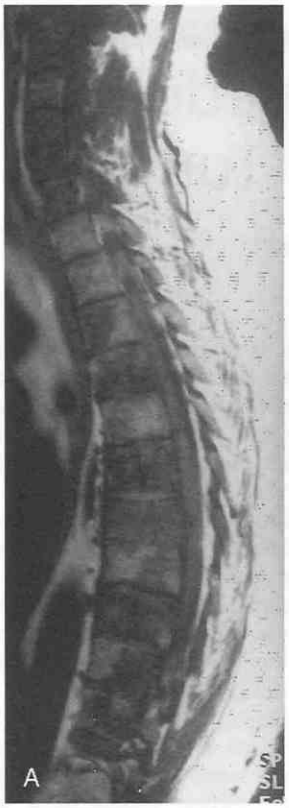

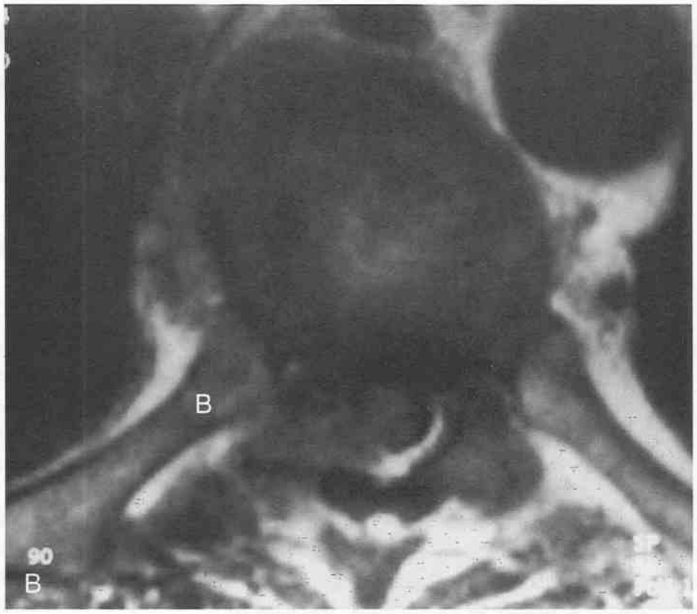

Figure 23–1. *A,* Sagittal T1-weighted image of the thoracic spine demonstrating multiple areas of abnormal bone marrow signal intensity. This patient has diffuse metastatic disease. *B,* T1-weighted axial image shows a right-sided metastatic mass causing mass effect on the spinal cord and thecal sac.

signal intensity on the T1-weighted images and increased signal intensity on the T2-weighted, STIR, and water images. The fat images showed a complete absence of fatty marrow signal intensity. Therefore, the patterns of signal intensity changes between the two groups did overlap.

Because each group was composed of only seven patients, it is difficult to determine whether the findings are statistically significant. Another difference between the benign and malignant acute fractures was that the pathologic fractures tended to have convex outward anterior and posterior margins compared to the more sharply angulated borders of the acute benign fractures.

Baur and colleagues[7] assessed MR diffusion-weighted imaging (DWI) for its ability to distinguish between malignant and benign causes of spinal compression fractures. When they studied DWI of bone marrow, they found that acute benign compression fractures either showed lower signal intensity than normal bone marrow or were isointense with normal bone marrow. They thought that this difference was caused by free extracellular water in the bone marrow edema and/or hemorrhage. When DWI is used, increased signal intensity is seen where diffusion of water is decreased or restricted, such as in vertebral bodies invaded by tumor cells. Baur and coworkers[7] demonstrated that the pathologic fractures showed increased signal intensity within the bone marrow; this corresponded to a decrease in the apparent diffusion coefficient.

MR DWI does have drawbacks, however. For example, it has low spatial resolution and a low signal-to-noise ratio. In an editorial, Le Bihan[20] argued that it is more difficult to separate the effects of T1 and T2 from diffusion effects with the steady-state free precession (SSFP) diffusion sequence than with an SE-based diffusion sequence. SSFP diffusion-weighted imaging needs to be studied further to establish its usefulness in distinguishing pathologic from benign vertebral fractures.

Percutaneous vertebroplasty has been used in patients with compression fractures (Fig. 23–2). This procedure, developed in France, involves injection of polymethylmethacrylate cement into the collapsed vertebra. The stabilization and reinforcement provided by the cement can alleviate pain. Barr and colleagues[6] performed percutaneous vertebroplasty in 47 patients (eight of whom had tumor involvement in the spine) for stabilization of the spine. Only 50% of the patients experienced significant pain relief. Possible complications of this procedure include cement extravasation and asymptomatic epidural venous filling.

Multiple Myeloma

As stated, multiple myeloma can appear similar to metastatic disease on spine images. Usually, compressive lesions involve the spine. When the disease is isolated to a single vertebral body, it is called a plasmacytoma. When multiple bones are involved, the term *multiple myeloma* is used. Multiple myeloma is more common in men and is usually seen in the sixth decade of life.

The tumor is composed of monoclonal B cells within the bone marrow. The lesions show decreased signal intensity on T1-weighted images and increased signal intensity on T2-weighted images (Fig. 23–3). A study examining

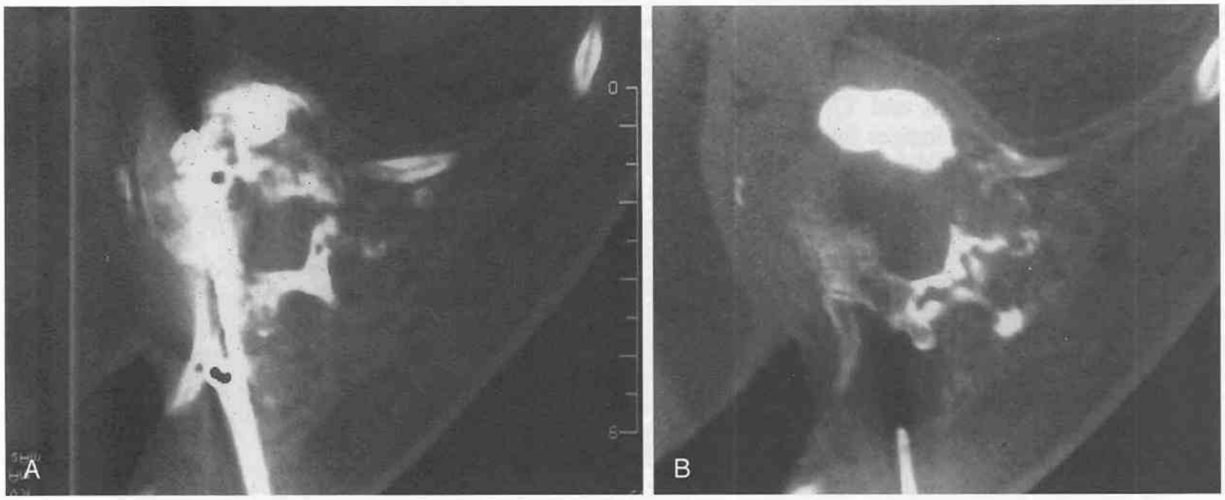

Figure 23–2. *A,* Axial CT image with needle in place through the pedicle of a metastatic vertebral body during percutaneous vertebroplasty. *B,* Axial CT image after injection of polymethylmethacrylate cement.

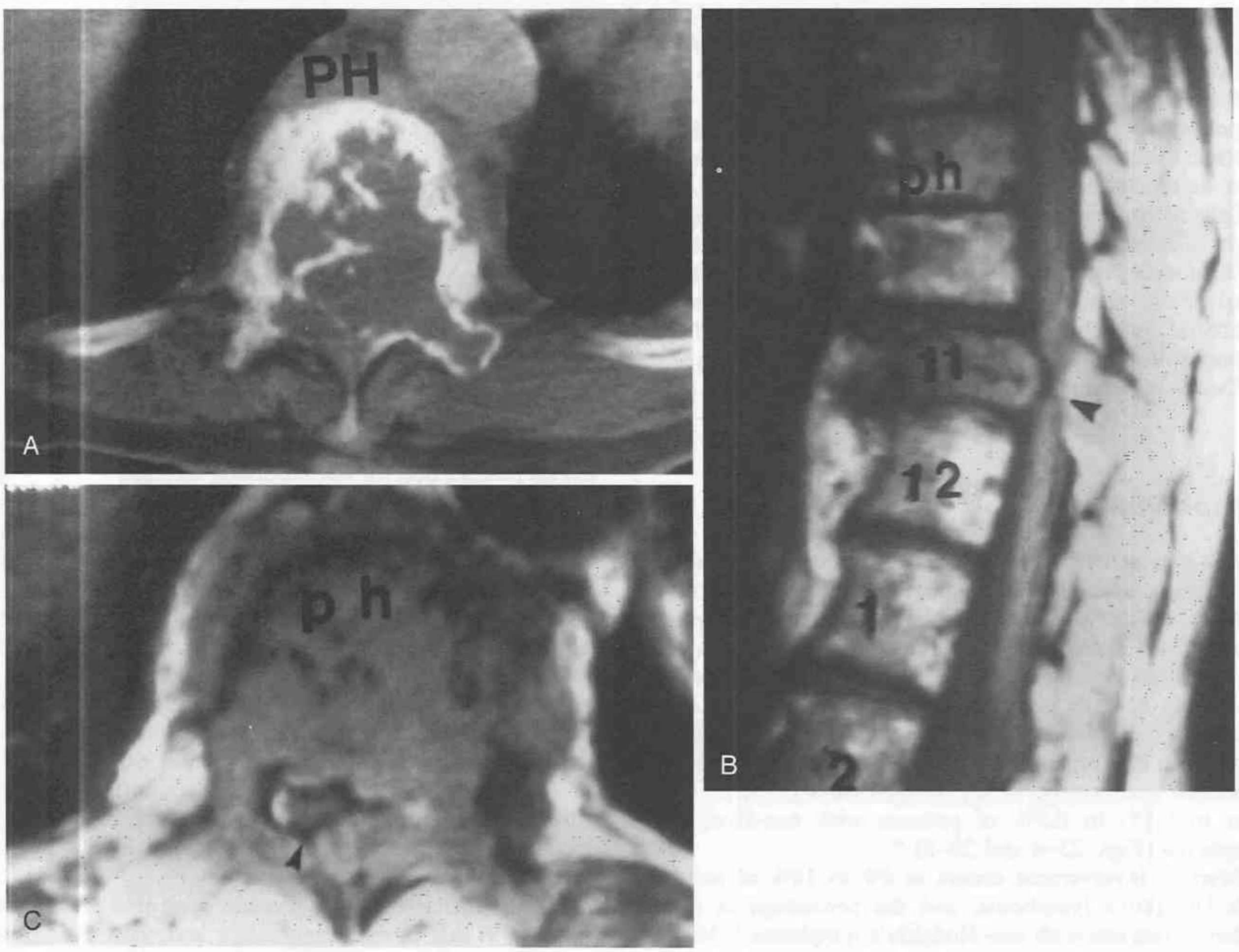

Figure 23–3. *A,* Axial CT image through the T11 vertebral body shows a destructive lesion with a soft tissue component, which proved to be multiple myeloma. *B,* Sagittal T1-weighted image through the lumbar spine shows compression and bone marrow replacement of the T11 vertebral body with associated spinal cord compression. There is also abnormal signal intensity in the surrounding vertebral bodies. *C,* T1-weighted axial image demonstrating significant spinal cord compression secondary to multiple myeloma mass involving T11. The abnormal signal intensity of the mass is isointense to muscle.

the MRI characteristics of multiple myeloma found that these lesions were better identified with T2-weighted images than with T1-weighted images in 65% of patients.[22] Another study found that STIR and T2-weighted images were better than T1-weighted images for detecting lesions and that contrast enhancement did not increase lesion detection.[34]

Various patterns of involvement of spinal multiple myeloma have been described. Focal lesions, diffuse involvement, and a heterogeneous pattern of tiny lesions on a normal marrow background were described in a study of 29 patients.[27] It was noted that diffuse and focal marrow patterns of involvement were associated with more abnormal serum hemoglobin levels and a higher percentage of marrow plasmacytosis. A similar study showed similar results: the diffuse pattern corresponded to patients with higher marrow plasmacytosis, higher cellularity, higher serum calcium, higher β_2-microglobin levels, and lower hemoglobin levels.[21]

Another classification scheme was presented in a study of 61 patients.[19] The MRI patterns noted were described as diffuse, nodular, diffuse and nodular, and normal. More patients showing the normal and nodular MRI patterns of bone marrow signal intensity survived than patients showing the diffuse and the diffuse and nodular patterns.[19]

Even though contrast-enhanced MRI was not found to be helpful in the initial detection of lesions in patients with multiple myeloma, it may be helpful for following their responses to therapy. Patterns of complete response to treatment included resolution of the marrow abnormalities seen before treatment and of persistent abnormality with peripheral rim enhancement. Signs of partial response included conversion of a diffuse pattern of involvement to a variegated or focal pattern, and a decrease of the marrow involvement seen on MRI with persistent enhancement.[28] A similar study of 18 patients demonstrated patterns of response that included rim enhancement, no enhancement, and early enhancement.[35]

Lymphoma

Lymphoma within the spine can present in several different ways. There can be extension from primary involvement in adjacent paravertebral lymph nodes into the neuroforamen and spinal canal. Primary involvement can also occur within the highly vascular vertebral body, and it commonly extends into the epidural space, causing mass effect on the spinal cord and exiting nerve roots. Lymphoma can also arise in the epidural space along the leptomeninges and, rarely, in the intramedullary space, as is seen in 0.1% to 6.5% of patients with non-Hodgkin's lymphoma (Figs. 23–4 and 23–5).[37]

Marrow involvement occurs in 4% to 14% of patients with Hodgkin's lymphoma, and the percentage is much higher in patients with non-Hodgkin's lymphoma.[29] MRI is the imaging modality of choice because it is sensitive in picking up marrow involvement and in detecting mass effect on the spinal cord and spread into the epidural space and paraspinal soft tissue. Moulopoulos and colleagues describe a "wrap-around sign": tumor envelops the cortex of vertebral bodies without altering the shape of these vertebral bodies. This sign was found in patients with lymphoma but not in those with metastatic disease or with multiple myeloma.[29]

Primary Tumors of the Spine

Other extradural tumors include primary tumors of the spine, which occur much less frequently than does metastatic spinal disease. However, when a patient presents with a solitary lesion, a primary tumor of the spine should be considered. Both benign and malignant tumors can be seen in the spine. Patients usually present with nonspecific back pain.

Osteoid Osteoma

The lumbar spine is the most common site of osteoid osteomas, followed by the cervical, thoracic, and sacral spine.[30] Patients present with the classic symptoms of painful scoliosis, focal or radicular pain, gait disturbance, and muscle atrophy. The pain is worse at night, and salicylates usually help.[30] Vertebral posterior elements are usually involved.

Plain films reveal a round to oval area of lucency with surrounding sclerosis. Associated scoliosis may be found, with the lesion located at the concave apex of the curve. CT, the study of choice for evaluating osteoid osteoma,[11] reveals an area of low attenuation with surrounding sclerosis (Fig. 23–6) and sometimes a central calcification. MRI usually shows a nidus reflecting low to intermediate signal intensity on T1-weighted images and intermediate to high signal intensity on T2-weighted images. Any associated sclerosis or calcification shows low signal intensity on all pulse sequences.[30]

Osteoblastoma

Osteoblastoma is another benign tumor of the spine; it has no predilection for any particular location in the spine.[17] Patients usually present with dull pain, paresthesias, paraparesis, and paraplegia. Scoliosis can be associated with osteoblastoma, although less frequently than with osteoid osteomas, and it may be convex toward the side of the lesion.[30] Most commonly, osteoblastomas are expansile with small calcifications and a sclerotic rim.[18]

The second most frequent radiographic appearance of osteoblastoma is that of a central radiolucent area with surrounding sclerosis that can have central calcification. This is similar in appearance to osteoid osteoma, yet the clinical presentation and curve of the scoliosis may help to differentiate between the two. Also, osteoblastomas are usually bigger and they more commonly extend into the vertebral body.

A third possible radiographic appearance of osteoblastoma is that of more aggressive bone destruction, with expansion and extension into adjacent soft tissues.[30] CT commonly shows expansile lesions with associated sclerosis; these lesions may also have a chondroid matrix. MR imaging is usually nonspecific yet it is helpful in determining mass effect on the adjacent spinal cord and thecal sac.

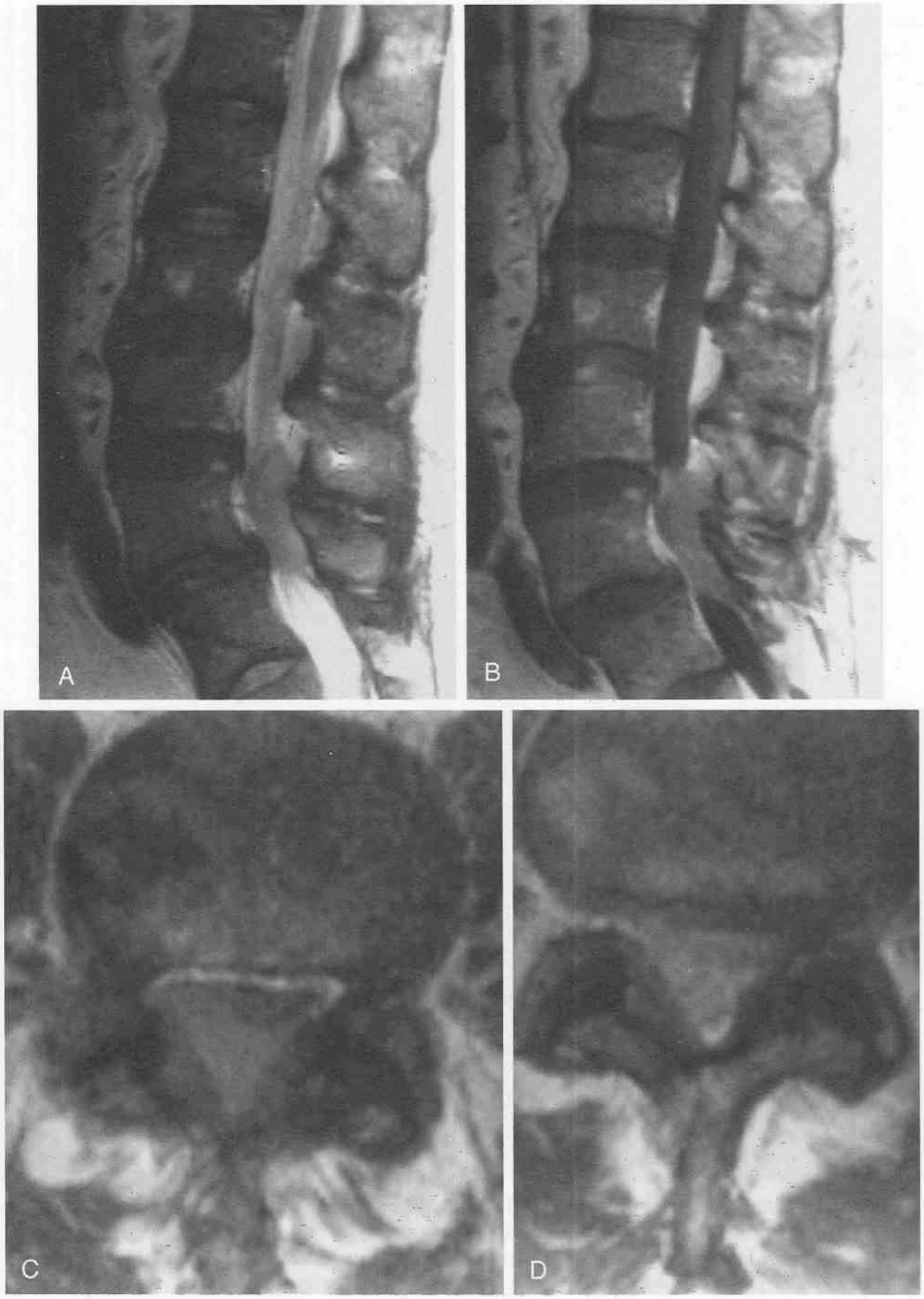

Figure 23–4. *A,* Sagittal MRI fast spin-echo T2-weighted image through the lumbar spine. A mass is seen posterior to the L4 vertebral body. The mass was biopsied and proved to be lymphoma. *B,* MRI sagittal spin-echo T1-weighted image through the lumbar spine following the intravenous administration of Gadoteridol. The mass enhances within the spinal canal. *C,* Axial T1-weighted image through the mass, which is extradural in location, causing mass effect on the adjacent thecal sac. *D,* Axial T1-weighted image through the mass, after the intravenous administration of Gadoteridol.

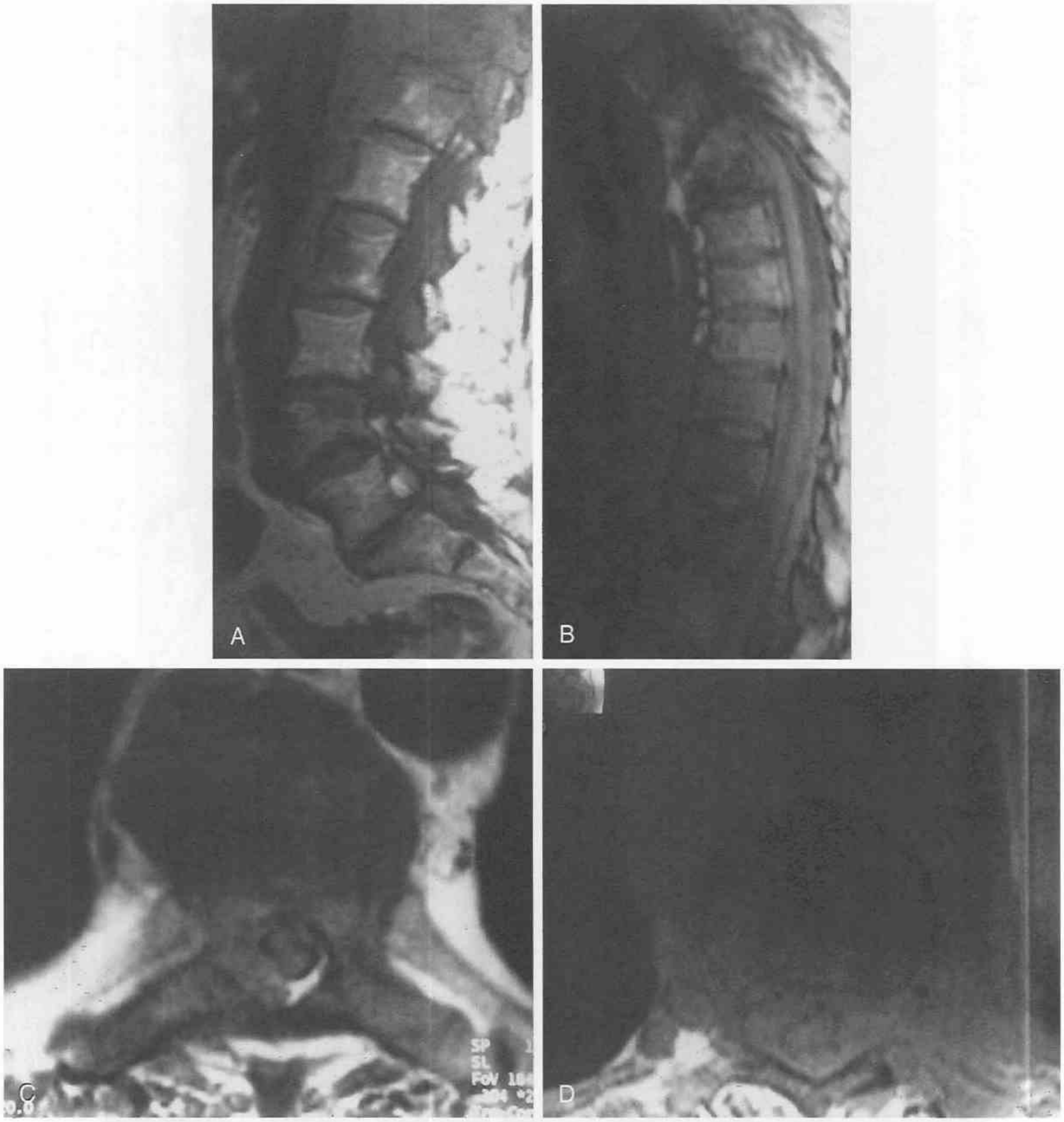

Figure 23–5. *A,* T1-weighted sagittal MRI image through the lumbar spine showing a large mass anterior to the spine from T11 to L4. There is destruction and replacement of the T11 vertebral body. *B,* T1-weighted sagittal image through the thoracic spine showing a large mass anterior to the mid and lower thoracic vertebral bodies, which turned out to be lymphoma. *C,* T1-weighted axial image demonstrating an extradural mass that is causing mass effect on the thecal sac on the right. *D,* T1-weighted axial image showing lymphoma surrounding the vertebral body and extending into the epidural space that surrounds the thecal sac.

Figure 23–6. Axial CT image showing a lucency of the lamina of T1 with surrounding sclerosis, which proved to be an osteoid osteoma.

Signal intensity is usually low to intermediate on T1-weighted and intermediate to high on T2-weighted images (Figs. 23–7 and 23–8).[8, 17]

Giant Cell Tumors

Giant cell tumors (GCT) in the spine usually involve the sacrum, followed by the thoracic, cervical, and lumbar areas.[30] Pain is the most common presenting symptom; however, pain can be accompanied by neurologic deficits.[38] GCT usually presents as a large mass with bone destruction and bony expansion. When the sacrum is involved, the sacroiliac joint can be crossed. Within the spine, vertebral bodies are most commonly involved, although giant cell tumors can cross disk spaces and extend into the posterior elements, and they can be associated with vertebral collapse.[30]

CT reveals a soft tissue attenuation mass, which may have a rim of sclerosis (Fig. 23–9). If hemorrhage is involved, however, a mixed attenuation mass, or possibly fluid-fluid levels, may be seen.

MRI usually shows a mass with mixed signal intensity.[25, 30] Fluid-fluid levels of various signal intensities may be seen if hemorrhage is present. The signal intensity depends on the age and state of the blood: it may be high on both T1-weighted and T2-weighted images if blood is present. In the absence of hemorrhage, GCTs may have low to intermediate signal intensity on both T1-weighted and T2-weighted images; this may help to differentiate them from other tumors, which usually have increased signal intensity on T2-weighted images.[30]

Complete resection is the treatment of choice for GCT, yet it is not always possible. Adjuvant radiotherapy is also used. It has been argued that radiation therapy should be used for patients with incomplete excision or for those with local recurrence.[15, 38]

Aneurysmal Bone Cysts

Aneurysmal bone cysts are seen most commonly in the thoracic spine, followed by the lumbar and cervical spine. Symptoms, including pain and neurologic deficits, are usually associated with mass effect on the spinal cord.

Radiographs, CT, and MRI demonstrate an expansile lesion centered in the posterior elements that commonly extends into the vertebral bodies. This lesion is usually lytic as well as expansive, with eggshell-like peripheral calcification (Fig. 23–10). ABCs can cross disk spaces and extend into adjacent structures. Both CT and MRI can evaluate for fluid-fluid levels. MRI is, however, better at showing both the extent of the mass and the mass effect on the spinal cord and nerve roots. A soft tissue rim is often seen on CT. It appears as a rim of decreased signal intensity on all MRI sequences. This rim is a thickened periosteal membrane, which, together with septations, can enhance with gadolinium.

Complete resection is the treatment of choice, but it is not always possible because of tumor location and size. Radiation and embolotherapy have also been used as treatment.[30]

Osteochondromas

Osteochondromas of the spine are uncommon. They usually occur within the cervical spine, especially at C2, and like most benign spinal lesions they usually occur in the posterior elements. CT imaging with thin slices is the modality of choice to evaluate osteochondromas. Continuity of the cortex and the marrow between the lesion and the vertebra is visible on CT (Fig. 23–11).[30] MRI can also be helpful in identifying mass effect on the spinal canal. Central yellow bone marrow shows high signal intensity on T1-weighted images because of its fat content, and the corresponding signal intensity on T2-weighted images is intermediate (Fig. 23–12).[30] Surgical resection is the treatment of choice.

Chordoma

Chordoma is an uncommon malignant tumor of the spine arising from a remnant of the notochord. It usually occurs at the sacrococcygeal region or at the skull base. Because it is a slow-growing tumor, chordoma usually presents as a large destructive lesion with an associated large soft tissue mass. Calcifications are commonly seen within the mass on radiographs and CT, and they usually occur peripherally. Attenuation in the center of the mass is low, and it may be higher peripherally.[30, 36]

Coronal CT images are optimal for evaluating foramen and sacroiliac joint involvement. Advances in multidetector CT and in three-dimensional reconstructive capabilities may be helpful in evaluating the extent of disease. For determining the extent of disease in surrounding soft tissue, however, MRI is superior.[35] On T1-weighted images, chordoma usually shows low to intermediate signal intensity, and it shows high signal intensity on T2-weighted images because of its high water content (Fig. 23–13).[30]

Complete excision of the chordoma is necessary because of its poor sensitivity to radiotherapy and chemotherapy, but complete resection is not always possible. Preoperative MRI may help to determine the amount of involvement in the adjacent gluteal muscles; this may be important when

Text continued on page 778

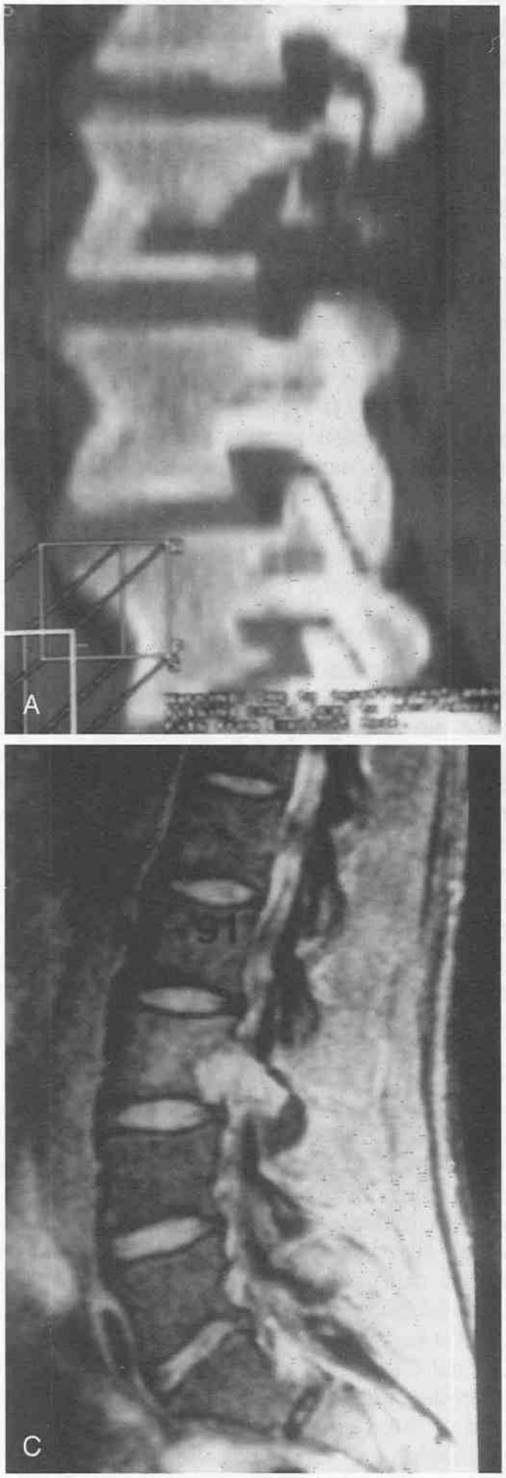

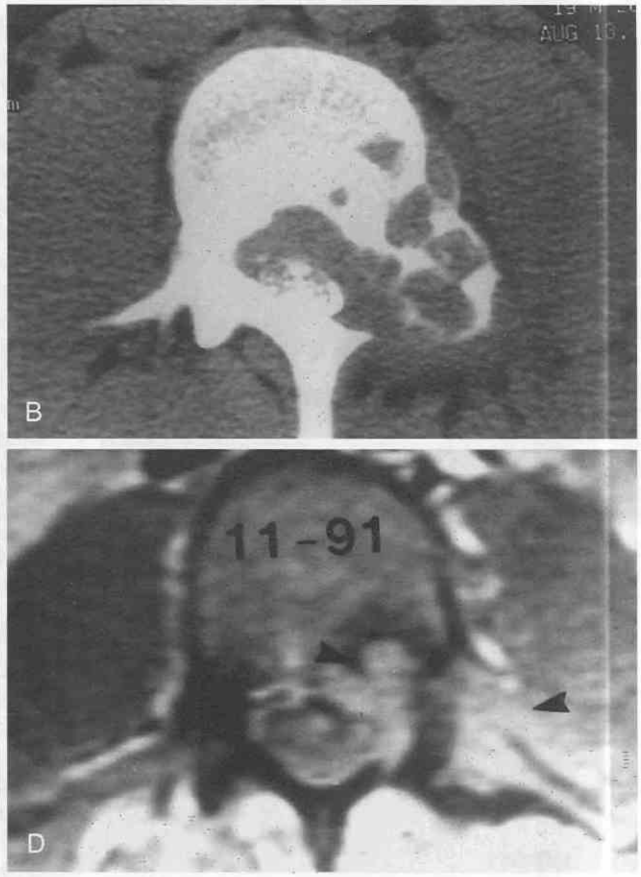

Figure 23–7. *A,* Sagittal CT reconstructed image demonstrates a lytic lesion of the L3 vertebral body. This lesion proved to be an osteoblastoma. *B,* Axial CT postmyelogram image in the same patient, showing an expansile lesion of L3 involving the pedicle, vertebral body, and lamina of L3. There is also associated mass effect on the adjacent thecal sac. *C,* T2-weighted sagittal image demonstrating the osteoblastoma with increased signal intensity involving the L3 vertebra. *D,* T1-weighted axial image demonstrating the mass, which is isointense to muscle. The extension of the osteoblastoma into the canal is clearly demonstrated; the image shows the mass effect on the thecal sac.

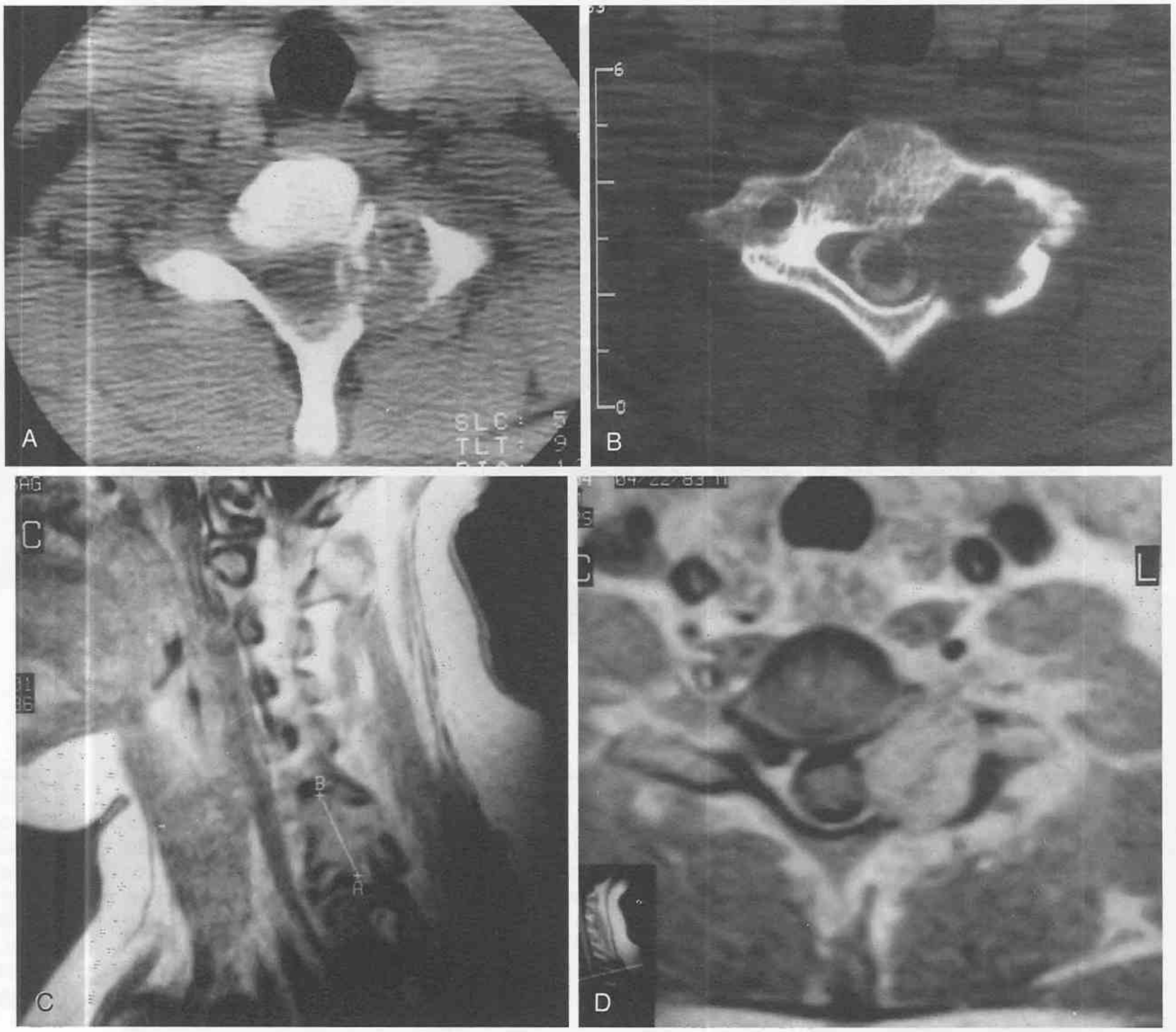

Figure 23–8. *A,* Axial CT image through C7 demonstrating an expansile osteoblastoma of the C7 facet. *B,* Axial CT image after myelogram through C7 showing the mass involving the vertebral artery foramen on the left. *C,* T1-weighted sagittal image after injection of contrast material with the enhancing mass involving the left C7 facet. *D,* T1-weighted axial image through the osteoblastoma involving the C7 facet and lamina.

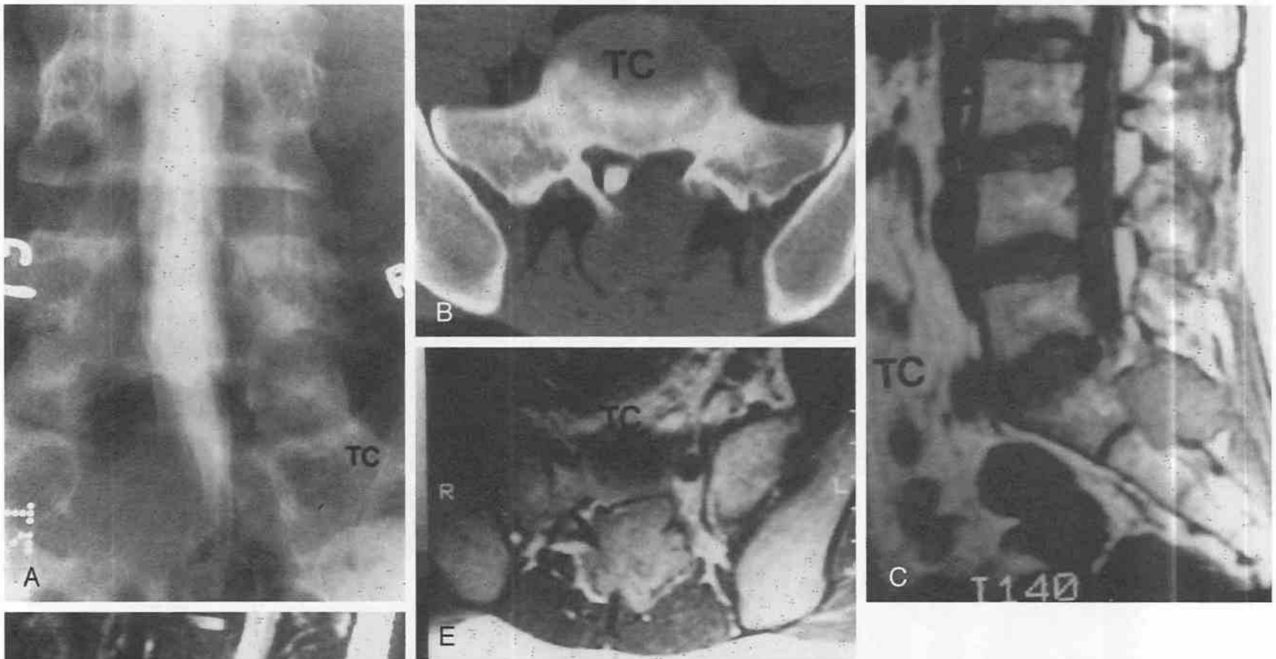

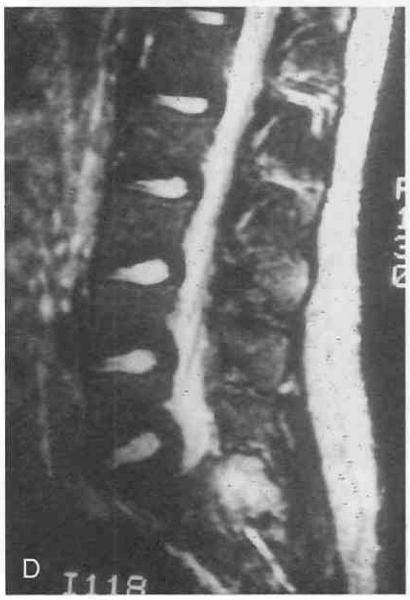

Figure 23–9. *A,* Frontal view of the lumbosacral junction showing giant cell tumor causing bone destruction of the left proximal sacrum and mass effect on the thecal sac, pushing it to the left. *B,* Axial CT image after myelogram, demonstrating a destructive soft tissue mass involving the posterior elements of the sacrum and causing mass effect on the thecal sac. *C,* T1-weighted sagittal image of the lumbar spine clearly demonstrates the giant cell tumor involving the posterior aspect of the sacrum. The mass has mixed signal intensity. Evidence of hemorrhage or fluid-fluid levels is not seen. *D,* T2-weighted sagittal image of the same giant cell tumor, demonstrating mixed signal intensity. Again, evidence of fluid-fluid levels is not seen. *E,* T1-weighted axial image of giant cell tumor of the sacrum demonstrating signal intensity that is mixed but higher than that of muscle.

Figure 23–10. *A,* Axial CT image demonstrating an expansile aneurysmal bone cyst (ABC) of the L5 vertebral body with some rimlike calcification. The extension of the mass into the spinal canal is not well delineated. *B,* T1-weighted sagittal image through the lumbar spine, demonstrating the ABC that involves the L5 vertebral body. The mass is mixed in signal intensity and extends into the spinal canal. *C,* T2-weighted sagittal image of the lumbar spine. The ABC has increased signal intensity, with areas of lower signal intensity within it. *D,* T1-weighted axial image through the L5 vertebral body after administration of contrast material. An enhancing, expansile ABC with pockets of nonenhancing fluid signal intensity extends into the spinal canal and posterior lateral soft tissues. The septations are enhanced, as stated in the text.

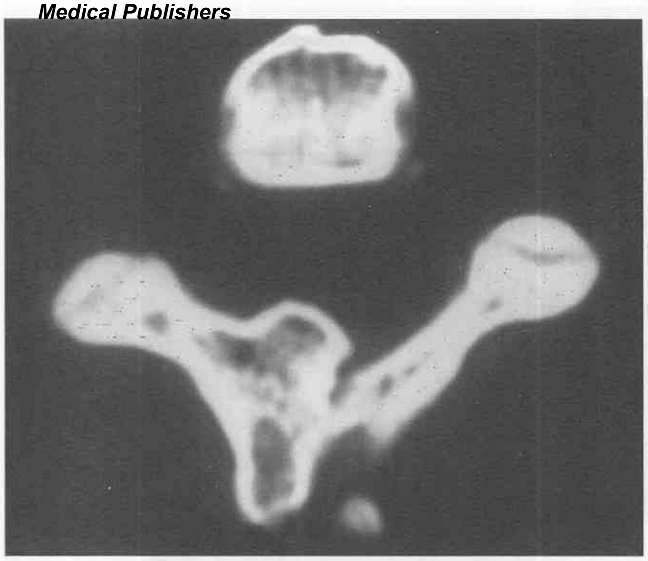

Figure 23–11. Axial CT image through an osteochondroma involving the spinous process and lamina of a vertebral body. This image demonstrates continuity of the cortex and marrow between the lesion and the vertebra.

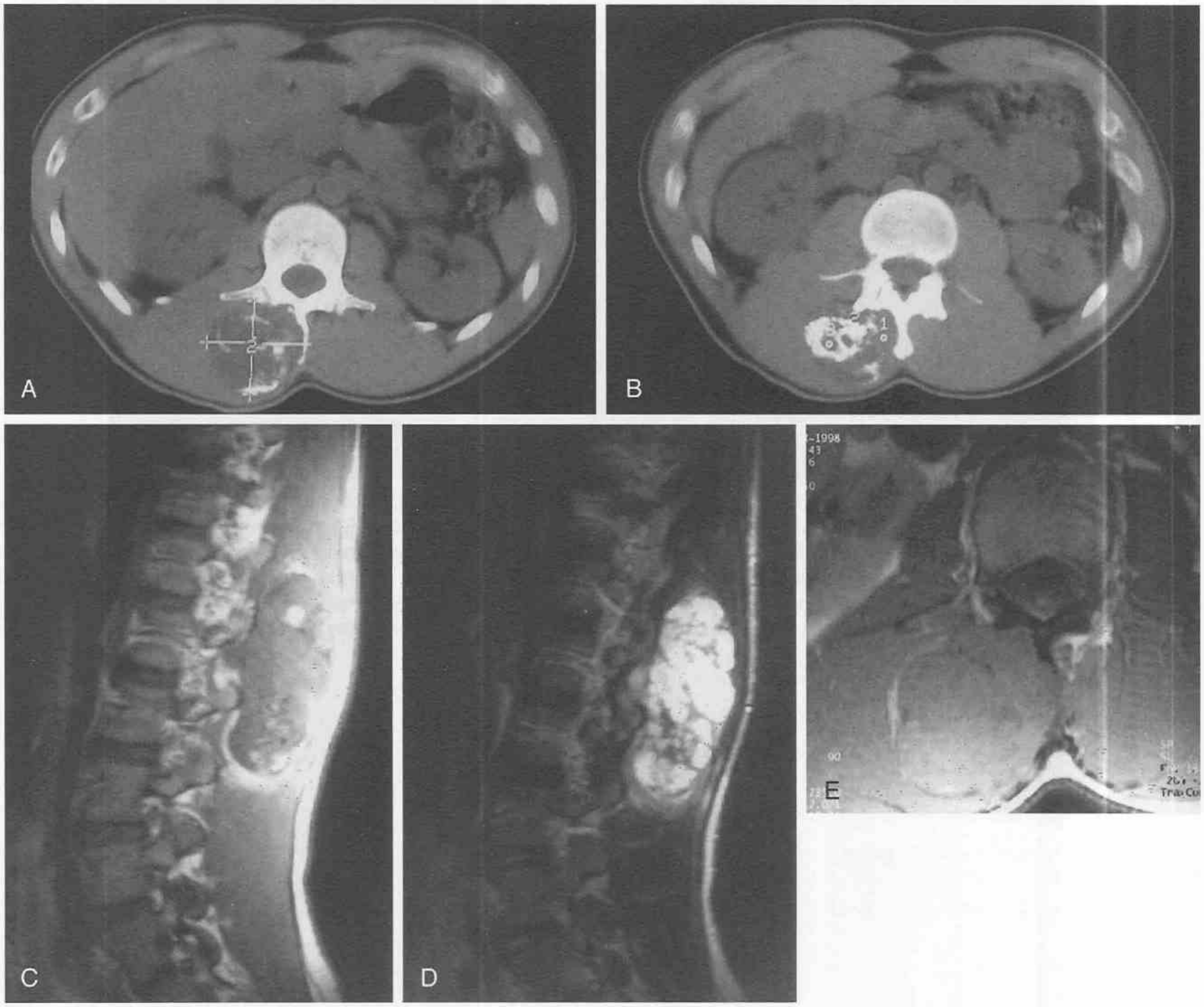

Figure 23–12. *A,* Axial CT image demonstrating an osteochondroma that involves the posterior elements of the L1 vertebral body. This mass is not in the typical C2 location, and it is larger than usually seen. There is no definite continuity of cortex and marrow between the mass and L1. *B,* Axial CT image of L1, showing the same mass with scalloping of the right aspect of the spinous process and calcification within the mass. *C,* T1-weighted sagittal image to the right of midline. The osteochondroma is mixed in signal intensity. *D,* T2-weighted image of the lumbar spine shows the same mass having mixed signal intensity. This is a nonspecific appearance. *E,* T1-weighted axial image of the lumbar spine showing that the mass has mixed signal intensity and does not involve the spinal canal.

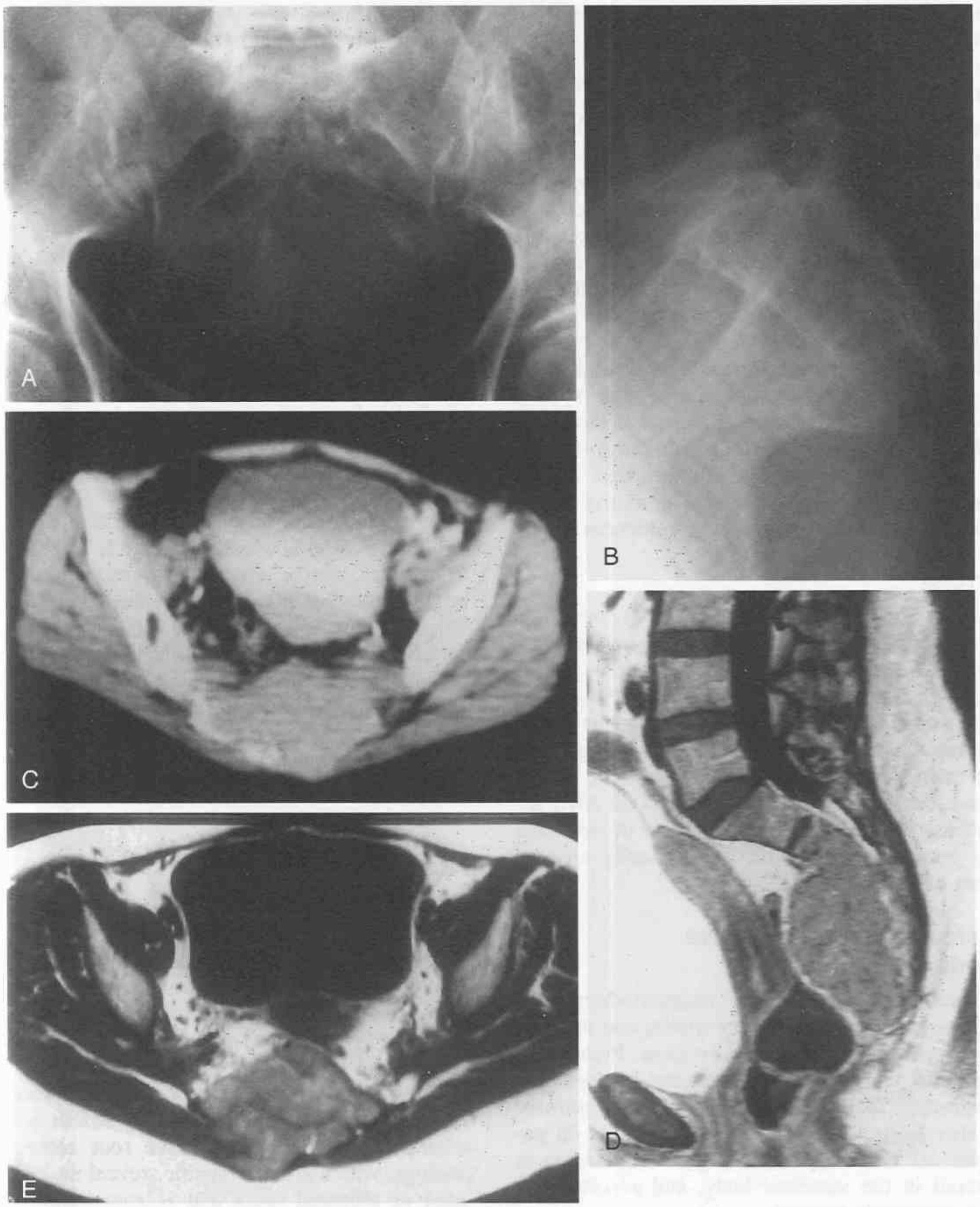

Figure 23–13. *A,* Plain film AP view of the sacrum. There is destruction of the inferior and left aspect of the sacrum. *B,* Lateral plain film of the sacrum demonstrating destruction of the inferior sacrum. *C,* Axial CT image of the sacrum. The soft tissue mass that is destroying the sacrum has proved to be a chordoma. This mass is in the usual sacrococcygeal region of the spine. *D,* T1-weighted sagittal image (with contrast enhancement) of the sacrum nicely demonstrating the extent of the soft tissue tumor, which exhibits mild enhancement. The mass is causing anterior displacement of the rectum. *E,* T1-weighted axial image of the sacrum demonstrating the chordoma and its effects on the surrounding tissues.

chordoma infiltrating the gluteal muscles may account for local recurrences.[46]

Chondrosarcoma

Chondrosarcoma is most commonly seen in the thoracic spine, but it is also found within the posterior elements or the vertebral body. Patients usually have a good prognosis, because spinal chondrosarcoma is usually low grade.[30]

CT is a sensitive modality for revealing the chondroid matrix characteristic of chondrosarcomas, the bone destruction, and the soft tissue component.[40] On CT, the soft tissue component can have decreased attenuation because its water content is higher than that of muscle.

MRI is helpful for evaluating any associated mass effect on the spinal cord and/or extension across disk spaces, which is seen in 35% of cases.[30, 40] Because of the water content of this tumor, signal intensity within the soft tissue component is usually decreased on T1-weighted images and increased on T2-weighted images. The matrix shows decreased signal intensity on all imaging sequences.[30]

Osteosarcoma

Osteosarcoma in the spine is rare; it is most commonly seen in the lumbosacral region and usually involves the vertebral body eccentrically. On plain films, osteosarcoma presents with a dense matrix; an ivory vertebral body can be seen. MRI is helpful in determining the extent of the soft tissue component and its effect on surrounding structures. If the matrix exhibits dense mineralization, it may appear to have decreased signal intensity on all MRI sequences. Patients with primary osteosarcoma of the spine have a very poor prognosis, with death usually ensuing within 2 years of the diagnosis.[30]

Ewing's Sarcoma and Permeative Neuroectodermal Tumor

Ewing's sarcoma and permeative neuroectodermal tumor (PNET) are radiographically very similar and are usually seen within the sacrococcygeal region. Presenting symptoms include pain and often bowel and bladder dysfunction. Metastatic foci are more common, yet primary lesions are also seen. These tumors usually occur in patients between 10 and 30 years of age.[30] The lesion is usually centered in the vertebral body, and a soft tissue component is commonly present.

MRI is the modality of choice to determine both tumor extent and involvement of surrounding tissue. The appearance of the tumor on MRI, however, is nonspecific. Signal intensity is intermediate on T1-weighted images and intermediate to high on T2-weighted images.[2, 14] Immunohistochemical studies are used to distinguish between PNET and Ewing's sarcoma.

Chemotherapy and radiation are the treatments of choice for both entities.[30]

Intradural Extramedullary Tumors

Nerve Sheath Tumors

Nerve sheath tumors make up the majority of extramedullary tumors within the dural space. Patients commonly present with radicular pain, possible gait disturbance, and sphincter dysfunction. The pain experienced results from the fact that the tumors usually arise on the dorsal sensory nerve root. Neurofibromas and schwannomas are both derived from Schwann cells; however, neurofibromas also have collagen and fibroblasts.[9]

Patients with neurofibromatosis type 1 (NF-1) usually have intraforaminal nerve sheath tumors extending into the spinal canal in a dumbbell-shaped configuration. Only about 1.6% of patients with NF-1 have symptomatic spinal tumors.[44] Patients with NF-2 usually have intraspinal intradural tumors, and 30% to 40% of these patients have neurologic deficits and symptoms.[23]

Plain films, which are nonspecific, may show enlargement of the neuroforamen (Fig. 23–14). MRI is the study of choice for evaluation of these tumors associated with the spine. On T1-weighted images, nerve sheath tumors are typically isointense to muscle. Increased signal intensity on T2-weighted images is typical for nerve sheath tumors whether using conventional SE or FSE imaging.[43] Postgadolinium imaging is commonly used to increase conspicuity of lesions. Nerve sheath tumors commonly enhance brightly, thereby increasing detection (Figs. 23–15 and 23–16). Fat-saturation techniques following administration of contrast material are also helpful for lesion detection.[12]

Total resection of nerve sheath tumors is needed to prevent recurrence. Neurofibromas have nerve fibers passing through them and are therefore difficult to remove completely. Schwannomas are usually eccentric in location, making total resection easier.

Paragangliomas

Extra-adrenal paragangliomas are rare, originating from cells of neural crest origin. Usually these tumors are located at the glomus jugulare or near or within the carotid body. Spinal paragangliomas are rare and can be seen in the intradural, extramedullary compartment, usually in the lumbar spine in the area of the cauda equina.[1] Rarely, they are also seen in the cervical and thoracic spine.

Paragangliomas of the spine are predominantly of the sympathetic type. Patients usually present with symptoms related to spinal cord or nerve root compression. MRI findings, which are nonspecific, reveal an enhancing lobulated or ellipsoid mass that is encapsulated and usually found in the intradural extramedullary space. Paragangliomas are usually isointense to the spinal cord on T1-weighted imaging and nonhomogeneous on T2-weighted imaging. Generally, paragangliomas are slow growing and benign.[42]

Intradural Extramedullary Metastases

Various types of intradural extramedullary metastases occur. Drop metastases originate from central nervous system primary neoplasms, such as cerebral glioblastoma, posterior fossa medulloblastoma, anaplastic astrocytoma, and ependymoma. These are seeded through the cerebrospinal fluid (CSF) from the head. They are most commonly seen in the lumbar location in the area of the conus medullaris or the cauda equina.



Figure 23–14. *A,* Lateral plain film of the cervical spine, demonstrating enlargement of a neuroforamen. *B,* Axial CT image through C2–C3, after myelography, showing an extra-axial mass that is causing mass effect on the spinal cord on the left and extending into the neuroforamen on the left. *C,* Gross specimen photograph of a smooth, bilobed schwannoma.

Nonvisceral neoplasms with CSF seeding include melanoma, lymphoma, and leukemia.[47] Systemic malignancies, such as breast and lung cancer, metastasize to the subarachnoid space. When these patients are diagnosed with intradural extramedullary spinal canal metastases, they usually have widespread disease and a very poor prognosis.[10] Most of the metastatic lesions are found on the conus medullaris and the cauda equina.

Whatever their source, the intradural extramedullary metastatic lesions are usually best seen on postcontrast, T1-weighted MR images of the spine. The lesions are not as well seen on either precontrast T1-weighted images or T2-weighted images; however, these sequences are helpful in evaluating for spinal bone metastasis and spinal cord compression. Therefore, a combination of precontrast and postcontrast images is used to evaluate the spine in patients with suspected intradural extramedullary metastatic disease. The metastatic lesions are usually seen as nodular enhancing lesions on the conus medullaris and the cauda equina, yet they can occur anywhere along the intradural space of the spinal canal. Abnormally thin extramedullary areas of enhancement may also indicate metastatic disease.[10]

An intraspinal meningioma can present as an intradural extramedullary mass. As in the head, this mass is isointense to the cord on MRI T1-weighted and T2-weighted images, and it homogeneously enhances after the administration of contrast medium. Enhancement of the adjacent meninges is known as the dural tail sign. Quekel and Versteege[33] argue that to evaluate spinal meningiomas for the dural tail sign, sagittal, axial, and coronal planes should all be obtained following the administration of gadolinium. The dural tail sign is very suggestive of meningioma.

Weil and coworkers[45] reported on a patient who had

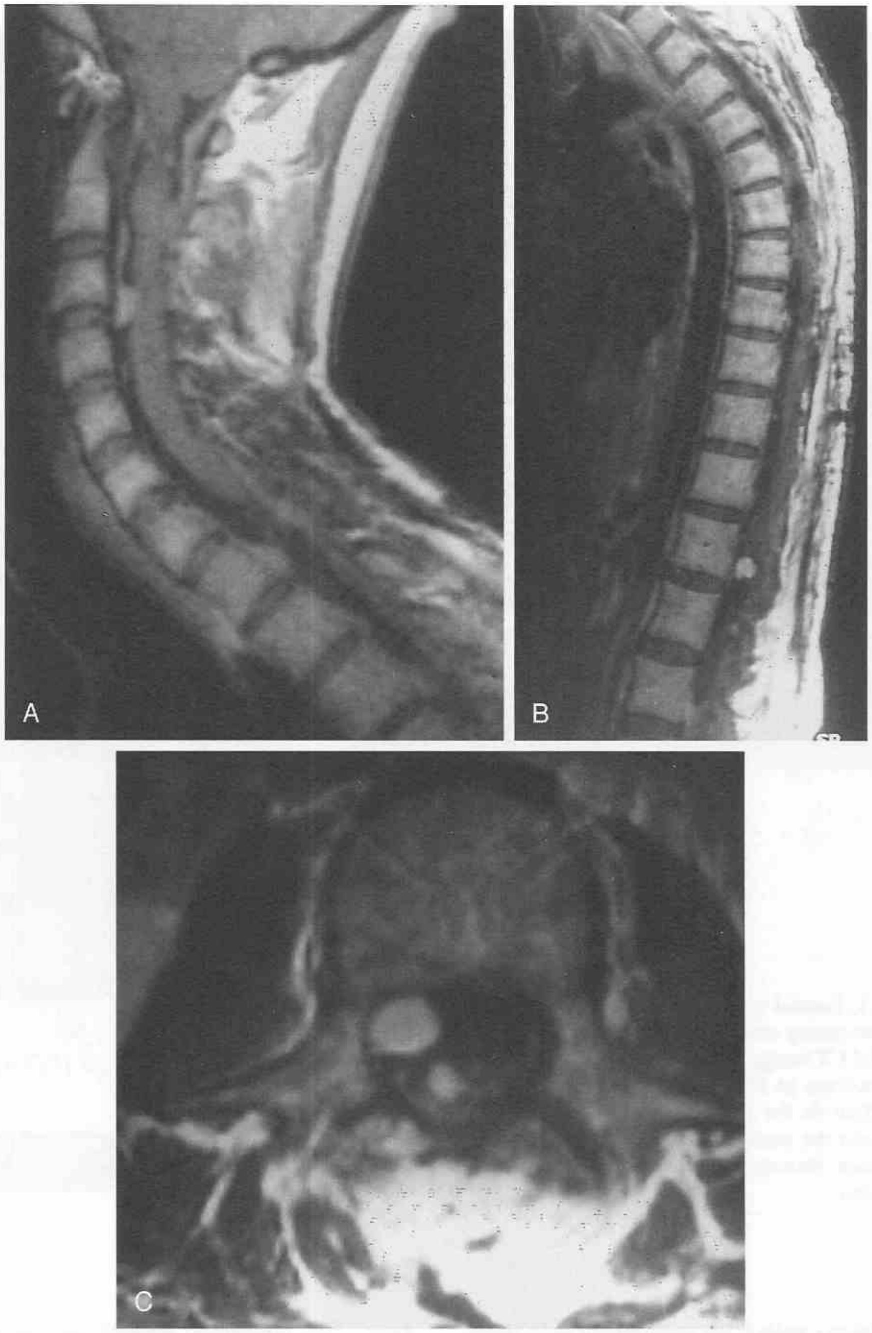

Figure 23–15. *A,* T1-weighted post–contrast-enhanced sagittal image of the cervical spine, demonstrating an enhancing extra-axial mass posterior to C2–C3 in a patient with known neurofibromatosis type 1. *B,* T1-weighted sagittal post–contrast-enhanced image through the thoracic spine, with enhancing neurofibromas in the lower thoracic spine. *C,* T1-weighted axial image showing extra-axial enhancing neurofibromas.

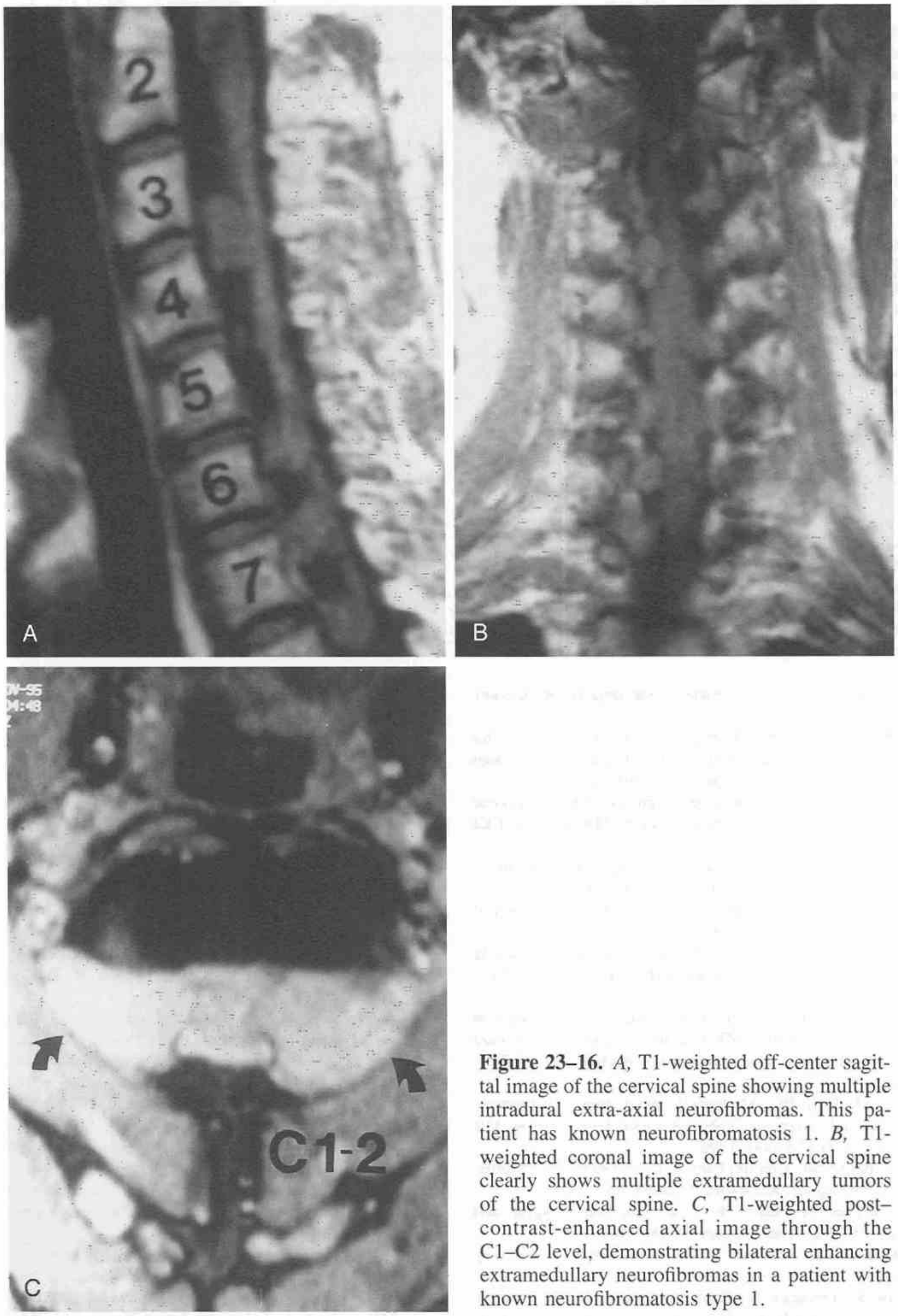

Figure 23–16. *A,* T1-weighted off-center sagittal image of the cervical spine showing multiple intradural extra-axial neurofibromas. This patient has known neurofibromatosis 1. *B,* T1-weighted coronal image of the cervical spine clearly shows multiple extramedullary tumors of the cervical spine. *C,* T1-weighted post–contrast-enhanced axial image through the C1–C2 level, demonstrating bilateral enhancing extramedullary neurofibromas in a patient with known neurofibromatosis type 1.

concurrent intradural and extradural meningiomas in the cervical spine. They recommend that when an epidural meningioma is found on MRI, special attention should be paid to the intradural space to find the high incidence of a concurrent meningioma.

Summary

Extramedullary tumors of the spine are usually best imaged with MRI, although CT can sometimes be helpful. Although the diagnosis is not always apparent, the radiologist can provide vital pretreatment information about the extent of disease and its effects on the spinal cord and nerve roots.

References

1. Aggarwal S, Deck JHN, Kucharczyk W: Neuroendocrine tumor (paraganglioma) of the cauda equina: MR and pathologic findings. AJNR Am J Neuroradiol 14:1003–1007, 1993.

2. Baba Y, Ohkubo K, Seino N, et al: Osseous primitive neuroectodermal tumor: A case report. Radiat Med 16:297–300, 1998.
3. Bach F, Agerlin N, Sorenson JB, et al: Metastatic spinal cord compression secondary to lung cancer. J Clin Oncol 10:1781, 1992.
4. Bach F, Larsen BH, Rhode K, et al: Metastatic spinal cord compression: Occurrence, symptoms, clinical presentations and prognosis in 398 patients with spinal cord compression. Acta Neurochir (Wien) 107:37, 1990.
5. Baker L, Goodman S, Perkash I, et al: Benign versus pathologic compression fractures of vertebral bodies: Assessment with conventional spin-echo, chemical-shift, and STIR MR imaging. Radiology 174:495–502, 1990.
6. Barr J, Barr M, Lemley T, McCann R: Percutaneous vertebroplasty for pain relief and spinal stabilization. Spine 25:923–928, 2000.
7. Baur A, Stabler A, Bruning R, et al: Diffusion-weighted MR imaging of bone marrow: Differentiation of benign versus pathologic compression fractures. Radiology 207:349–356, 1998.
8. Crim JR, Mirra JM, Eckardt JJ, Seeger LL: Widespread inflammatory response to osteoblastoma: The flare phenomenon. Radiology 177: 835–836, 1990.
9. Francel PC: Extrinsic spinal cord mass lesions. Pediatr Rev 19: 389–395, 1998.
10. Frey I, Le Breton C, Lefkopoulos A, et al: Intradural extramedullary spinal canal secondary neoplasms: MR findings in 30 patients. Eur Radiol 8:1187–1192, 1998.
11. Gamba JL, Martinez S, Apple J, et al: Computed tomography of axial skeletal osteoid osteomas. Am J Roentgenol 142:769–772, 1984.
12. Georgy BA, Hesselink JR: MR imaging of the spine: Recent advances in pulse sequences and special techniques. AJR Am J Roentgenol 162:923, 1994.
13. Gilbert RW, Kim JH, Posner JB: Epidural spinal cord compression from metastatic tumor: Diagnosis and treatment. Ann Neurol 3:40, 1978.
14. Hashimoto M, Akabane Y, Tete E: Ewing's sarcoma of the sacrum. Radiat Med 17:451–453, 1999.
15. Khan DC, Malhotra S, Stevens RE, Steinfeld AD: Radiotherapy for the treatment of giant cell tumor of the spine: A report of six cases and review of the literature. Cancer Invest 17:110–113, 1999.
16. Kim J, Ryu K, Choi W, et al: Spinal involvement of hematopoietic malignancies and metastasis: Differentiation using MR imaging. Clin Imaging 23:125–133, 1999.
17. Kroon HM, Schurmans J: Osteoblastoma: Clinical and radiologic findings in 98 new cases. Radiology 175:783–790, 1990.
18. Kumar R, Guinto FC, Madewell JE, et al: Expansile bone lesions of the vertebra. Radiographics 8:749–769, 1988.
19. Kusumoto S, Jinnai I, Itoh K, et al: Magnetic resonance imaging patterns in patients with multiple myeloma. Br J Haematol 99:649–655, 1997.
20. Le Bihan D: Differentiation of benign versus pathologic compression fractures with diffusion-weighted MR imaging: A closer step toward the "Holy Grail" of tissue characterization? Radiology 207:305–307, 1998.
21. Lecouvet FE, Vande Berg BC, Michaux L, et al: Stage III multiple myeloma: Clinical and prognostic value of spinal bone marrow MR imaging. Radiology 209:653–660, 1998.
22. Libshitz HI, Malthouse SR, Cunningham D, et al: Multiple myeloma: Appearance at MR imaging. Radiology 182:833–837, 1992.
23. Mautner VF, Lindenau M, Hazim W, et al: The neuroimaging and clinical spectrum of NF2. Neurosurgery 38:880–886, 1996.
24. McLain RF, Weinstein JN: Tumors of the spine. Semin Spine Surg 2:157, 1990.
25. Meyers SP, Yaw K, Devaney K: Giant cell tumor of the thoracic spine: MR appearance. AJNR Am J Neuroradiol 15:962–964, 1994.
26. Mirowitz S, Apicella P, Reinus W, Hammerman A: MR imaging of bone marrow lesions: Relative conspicuousness on T1-weighted, fat-suppressed T2-weighted, and STIR images. AJR Am J Roentgenol 162:215–221, 1994.
27. Moulopoulos LA, Varma DG, Dimopoulos MA, et al: Multiple myeloma: Spinal MR imaging in patients with untreated newly diagnosed disease. Radiology 185:833–840, 1992.
28. Moulopoulos LA, Dimopoulos MA, Alexanian R, et al: Multiple myeloma: MR patterns of response to treatment. Radiology 193: 441–446, 1994.
29. Moulopoulos LA, Dimopoulos MA, Vourtsi A, et al: Bone lesions with soft-tissue mass: Magnetic resonance imaging diagnosis of lymphomatous involvement of the bone marrow versus multiple myeloma and bone metastases. Leuk Lymphoma 34:179–184, 1999.
30. Murphey M, Andrews C, Flemming D, et al: From the Archives of the AFIP. Primary tumors of the spine: Radiologic-pathologic correlation. Radiographics 16:1131–1158, 1996.
31. O'Connor MI, Currier BL: Metastatic disease of the spine. Orthopedics 15:611, 1992.
32. Pui M, Chang S: Comparison of inversion recovery fast spin-echo (FSE) with T2-weighted fat-saturated FSE and T1-weighted MR imaging in bone marrow lesion detection. Skeletal Radiol 25:149–152, 1996.
33. Quekel LG, Versteege CW: The "dural tail sign" in MRI of spinal meningiomas. J Comput Assist Tomogr 19:890–892, 1995.
34. Rahmouni A, Divine M, Mathieu D, et al: Detection of multiple myeloma involving the spine: Efficacy of fat-suppression and contrast-enhanced MR imaging. AJR Am J Roentgenol 160:1049–1052, 1993.
35. Rahmouni A, Divine M, Mathieu D, et al: MR appearance of multiple myeloma of the spine before and after treatment. AJR Am J Roentgenol 160:1053–1057, 1993.
36. Rosenthal DI, Scott JA, Mankin HJ, et al: Sacrococcygeal chordoma: Magnetic resonance imaging and computed tomography. Am J Roentgenol 145:143–147, 1985.
37. Salvati M, Cervoni L, Artico M, et al: Primary spinal epidural non-Hodgkin's lymphoma: A clinical study. Surg Neurol 46:339–343, 1996.
38. Sanjay BK, Sim FH, Unni KK, et al: Giant-cell tumours of the spine. J Bone Joint Surg Br 75:148–154, 1993.
39. Shi HB, Suh DC, Lee HK, et al: Preoperative transarterial embolization of spinal tumor: Embolization techniques and results. AJNR Am J Neuroradiol 20:2009–2015, 1999.
40. Shives TC, McLeod RA, Unni KK, Schray MF: Chondrosarcoma of the spine. J Bone Joint Surg Am 71:1158–1165, 1989.
41. Simeone FA: Spinal cord tumors in adults. In Youmans JR (ed): Neurological Surgery, 3rd ed, vol 5. Philadelphia, WB Saunders, 1990, p 3531.
42. Sundgren P, Annertz M, Englund E, et al: Paragangliomas of the spinal canal. Neuroradiology 41:788–794, 1999.
43. Sze G, Merriam M, Oshio K, et al: Fast spin echo imaging in the evaluation of intradural disease of the spine. AJNR Am J Neuroradiol 13:1383, 1992.
44. Thakkar SD, Feigen U, Mautner VF: Spinal tumours in neurofibromatosis type 1: An MRI study of frequency, multiplicity and variety. Neuroradiology 41:625–629, 1999.
45. Weil SM, Gewirtz RJ, Tew JM Jr: Concurrent intradural and extradural meningiomas of the cervical spine. Neurosurgery 27:629–631, 1990.
46. Yonemoto T, Tatezaki S, Takenouchi T, et al: The surgical management of sacrococcygeal chordoma. Cancer 85:878–883, 1999.
47. Yousem DM, Patrone PM, Grossman RI: Leptomeningeal metastases: MR evaluation. J Comput Assist Tomogr 14:255–261, 1990.

24 The Spinal Cord

Jeffrey L. Sunshine, Scott Kolodny

Classically, evaluation of lesions within the spinal neural axis has been made on the basis of anatomic location. Lesions can be divided into *extradural, intradural-extramedullary,* and *intramedullary.* Intramedullary lesions of the spinal cord, in turn, can be subdivided according to their etiology into (1) ischemic disease; (2) vascular malformations; (3) neoplastic processes; and (4) infectious, inflammatory, and demyelinating diseases. After a brief review of spinal cord anatomy, this chapter focuses on the intramedullary lesions of the spinal cord and their appearances on magnetic resonance imaging (MRI) and, to a lesser extent, on computed tomography (CT) scans.

Anatomy

The spinal cord represents a caudal extension of the medulla oblongata; it terminates in the conus medullaris, typically at or just below the thoracolumbar junction in adults. The cord is slightly flattened along its anterior and posterior surfaces and is enlarged in two regions. The cord widens first for the brachial plexus at C3 to T2, then for the lumbar plexus at T9 to T12. The filum terminale represents extension from the conus to the coccyx, and the cauda equina refers to the extension of spinal nerve roots caudally from the conus within the lumbar subarachnoid space.

The three-layered meningeal covering of the central nervous system (CNS) is contiguous with the spinal cord, and all lie within the bony spinal canal. The innermost layer, the pia mater, is adherent to the surface of the cord and extends from the lateral surface of the cord to a dural arachnoid membrane, forming the dentate ligaments. The arachnoid membrane remains closely adherent to the outer layer, the dura mater, allowing for a potential subdural space between the two layers. The subarachnoid space remains filled with cerebrospinal fluid (CSF) and is contiguous with the intracranial subarachnoid space. The dura extends to the S2 level, forming the dural (thecal) sac, which is surrounded externally by epidural fat to fill the remainder of the volume of the spinal canal.

The gray matter of the spinal cord is located internally, in contradistinction to the gray matter of the brain, and is surrounded by white matter tracts; the proportion of gray matter increases in the cervical and lumbar regions. Both dorsal (sensory) and ventral (motor) roots arise along the entire length of the cord and these unite to form a total of 31 paired spinal nerves. There are 8 cervical, 12 thoracic, 5 lumbar, and 5 sacral roots.

The arterial supply to the spinal cord, although variable, can be divided into three major regions.[74] Branches of the intracranial vertebral artery, cervical vertebral arteries, and cervical trunks produce radicular arteries that form the predominant blood supply to the cervicothoracic region, generally ending after the first several thoracic vertebral segments.

A single radicular artery, usually located at approximately the T7 level, supplies the midthoracic cord. This represents the smallest territorial division and typically extends from T4 through T8.

The artery of Adamkiewicz, which arises from a low thoracic or upper lumbar artery, supplies the final thoracolumbar region. This important artery usually arises from an intercostal branch in the region of T9 to T12. In a few people, it may arise from a branch at a higher level but then the conus medullaris can be additionally supplied from a lower and smaller radicular artery. Least often, the artery of Adamkiewicz arises from the upper lumbar arteries.

At the levels of the spinal cord, radicular branches enter the spinal canal through the neural foramina and lead to the anterior as well as to the paired posterior spinal arteries on the cord surface. These spinal arteries in turn generate a rich anastomotic arcade, with the anterior artery supplying the central gray matter and the posterior arteries feeding the dorsal columns and posterior peripheral white matter. Modern MRI machines and the newer gradient sequences allow excellent anatomic depiction of the arteries and veins of the spinal cord without the need to rely solely on catheter-based conventional angiograms.[11]

Ischemia

Spinal cord ischemia can arise and lead to infarction for a variety of reasons, including trauma to or dissection of the arterial supply, atherosclerotic and embolic disease, hypotension (e.g., cardiac arrest), complications of thoracoabdominal surgery or spinal angiography, vasculitis, hypercoagulation diseases, and spontaneous idiopathic incidence. More rarely, cord ischemia and infarcts arise secondary to vascular malformations[102,108] or to hypercoagulation diseases as in patients harboring antiphospholipid antibodies.[47] Spinal cord infarction can be iatrogenic, resulting from neurosurgical procedures performed with the patient in a sitting position[90] or as a result of wayward migration of embolic materials during endovascular interventions.[73] In addition to dissection of direct arterial supply to the cord, dissection or high-grade stenoses involving larger proximal vessels, such as the vertebral artery, have also caused cord infarction.[4,115] In patients who have undergone trauma, the presence of intramedullary hemorrhage (Fig. 24–1) portends less chance of recovering motor activation and a good functional outcome.[35,36]

Spinal cord ischemia has been described in four progres-

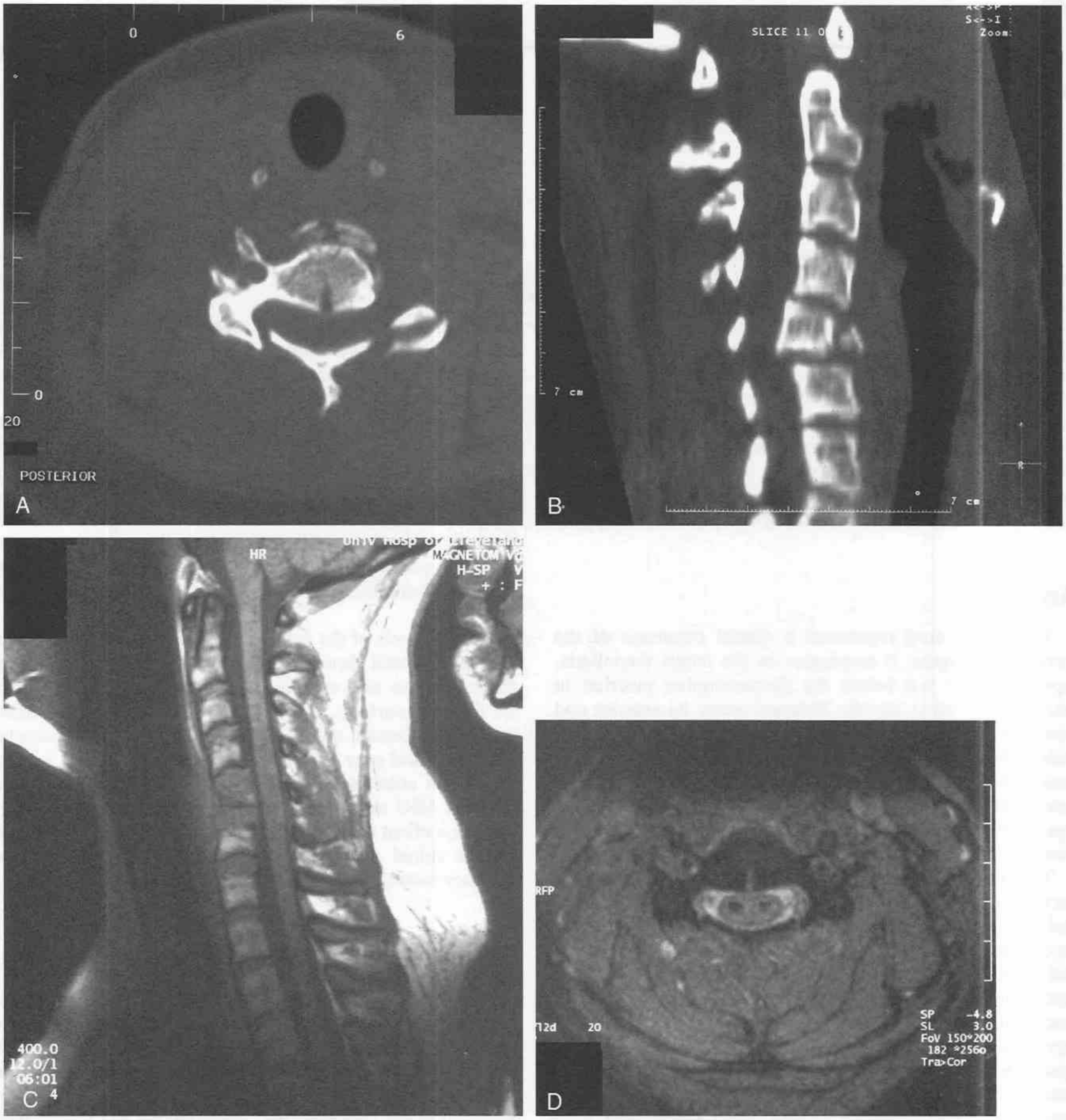

Figure 24–1. Spinal cord trauma with intramedullary hemorrhage. *A,* Axial CT section reveals the comminuted fracture of the vertebra and posterior elements with compression of the spinal canal. *B,* Sagittal CT reconstruction shows the anterior fracture of C5 and the posterior displacement of bone into the spinal canal. *C,* T1-weighted sagittal MR demonstrates the abnormal hypointense marrow signal in C5 from edema as well as the mild loss of height and again the posterior extension. No definite cord abnormality is seen. *D,* This axial FLASH (fast low-angle shot) T2-weighted section reveals two foci of abnormal hypointense regions within the cord from acute blood products.

sive patterns, best seen on T2-weighted axial MR images. The most descriptive and smallest insult produces hyperintensity limited to the paired anterior horns of the central gray matter in a pattern that has been descriptively labeled "owl's eyes."[74] Next, the paired posterior horns of the gray matter are involved in a pattern reminiscent of a butterfly (Fig. 24–2). When the insult becomes more severe, the damage extends laterally to involve the corticospinal tracts. Finally, in the worst situations, the entire area of the cord can be homogeneously affected (Fig. 24–3). Insults that cause a change of signal intensity limited to the anterior horns most often have a better functional outcome, and

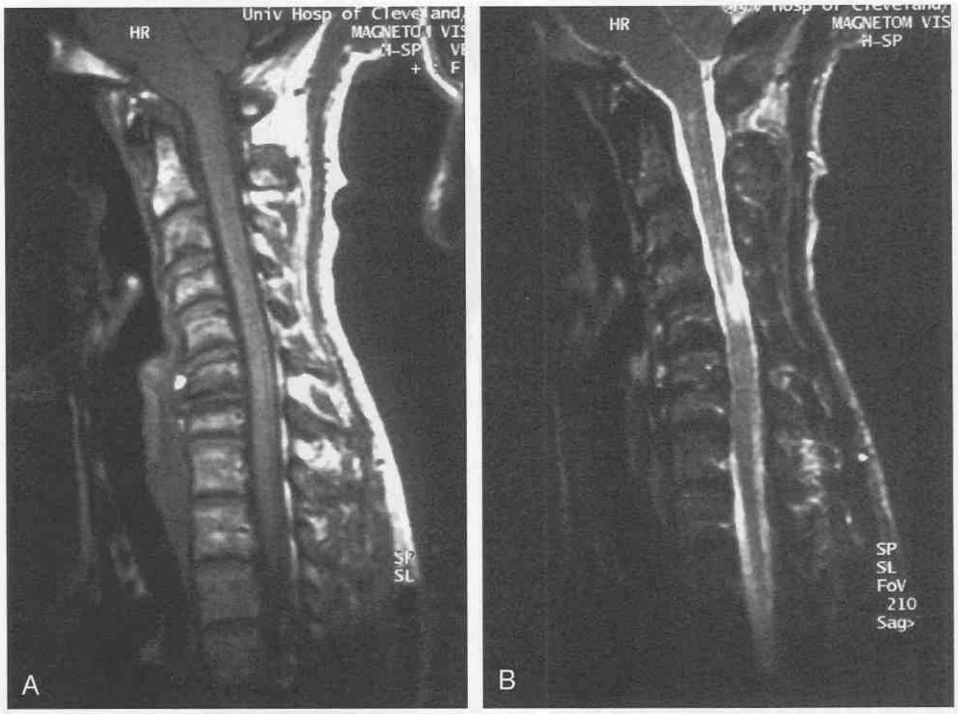

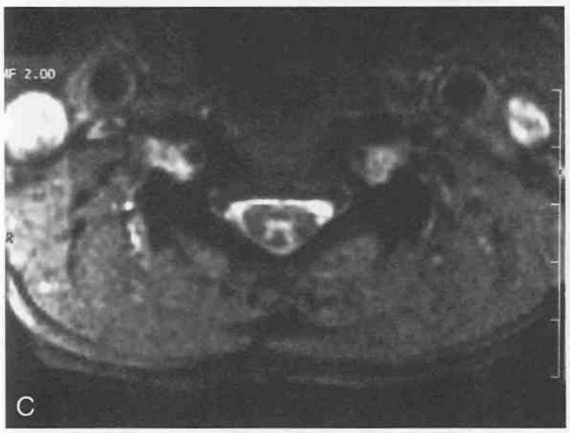

Figure 24–2. Cord infarction. *A,* T1-weighted sagittal MR image shows no definite intramedullary abnormality. *B,* T2-weighted sagittal MR image reveals marked focal hyperintensity along the central and posterior cord centered at C5. *C,* A gradient-echo, FLASH (fast low-angle shot), T2-weighted axial section demonstrates the butterfly pattern of cord infarction involving the bilateral anterior and posterior horns of the gray matter.

indeed embolic events to spinal arteries arising during catheter angiography have been reported to resolve spontaneously.[37]

T1-weighted images best demonstrate associated swelling, particularly the associated enlargement of the cord.[47] Gadolinium-enhanced T1-weighted images show disruption of the blood-brain barrier in the late acute and subacute phases of infarction. This disruption tends to involve the peripheral margins of the central gray matter, whereas in anterior cord syndrome the ventral margins tend to be involved more than the peripheral, probably as a result of the posterior collateral supply.[31,39] MRI, especially T2-weighted images, demonstrates associated abnormalities of the aorta and of adjacent vertebral bodies.[34,131]

Vascular Malformations

Vascular malformations of and around the spinal cord have been variously classified as (1) dural arteriovenous fistulas (AVFs), (2) perimedullary intradural or cord AVFs, (3) cavernous angiomas, and (4) spinal cord arteriovenous malformations (AVMs). Diagnosis of these malformations has been improved tremendously with the application of MRI techniques that enable the reliable demonstration of the primary vascular lesion and the secondary cord edema and myelopathy. Until very recently, diagnosis required confirmation by demonstration of the primary vasculopathy with conventional spinal angiograms, but the advent of contrast-enhanced MR angiography has allowed direct noninvasive demonstration of the lesions.[5, 9, 10, 71, 72]

Spinal Cord Arteriovenous Malformations

Cord AVMs are congenital in origin and are composed of the typical nidus of abnormal vessels arising from arterial feeders that then lead directly to hypertensive "arterialized" venous drainage. Those with a typically compact, wholly intramedullary nidus have been termed *glomus*

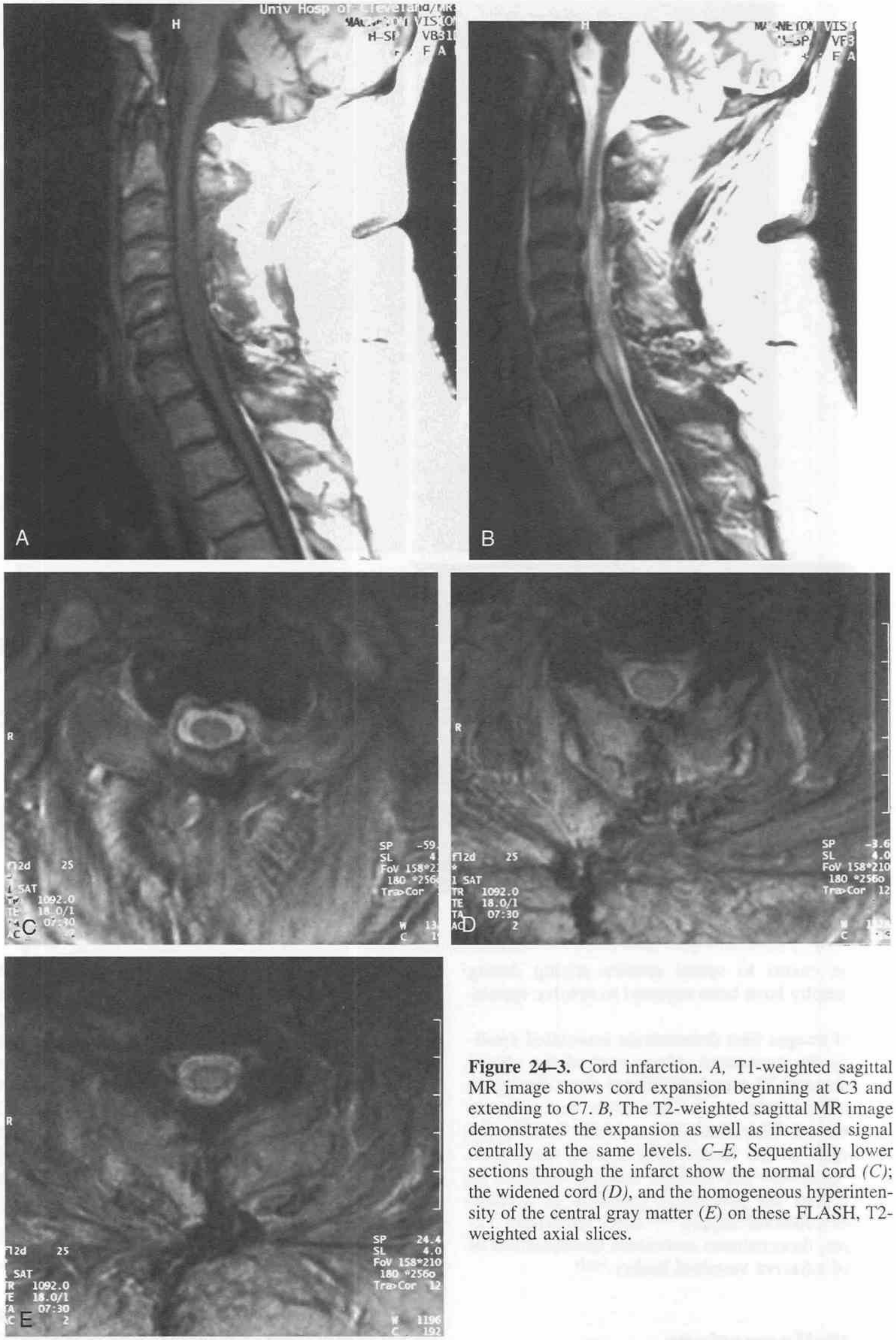

Figure 24–3. Cord infarction. *A,* T1-weighted sagittal MR image shows cord expansion beginning at C3 and extending to C7. *B,* The T2-weighted sagittal MR image demonstrates the expansion as well as increased signal centrally at the same levels. *C–E,* Sequentially lower sections through the infarct show the normal cord *(C)*; the widened cord *(D)*, and the homogeneous hyperintensity of the central gray matter *(E)* on these FLASH, T2-weighted axial slices.

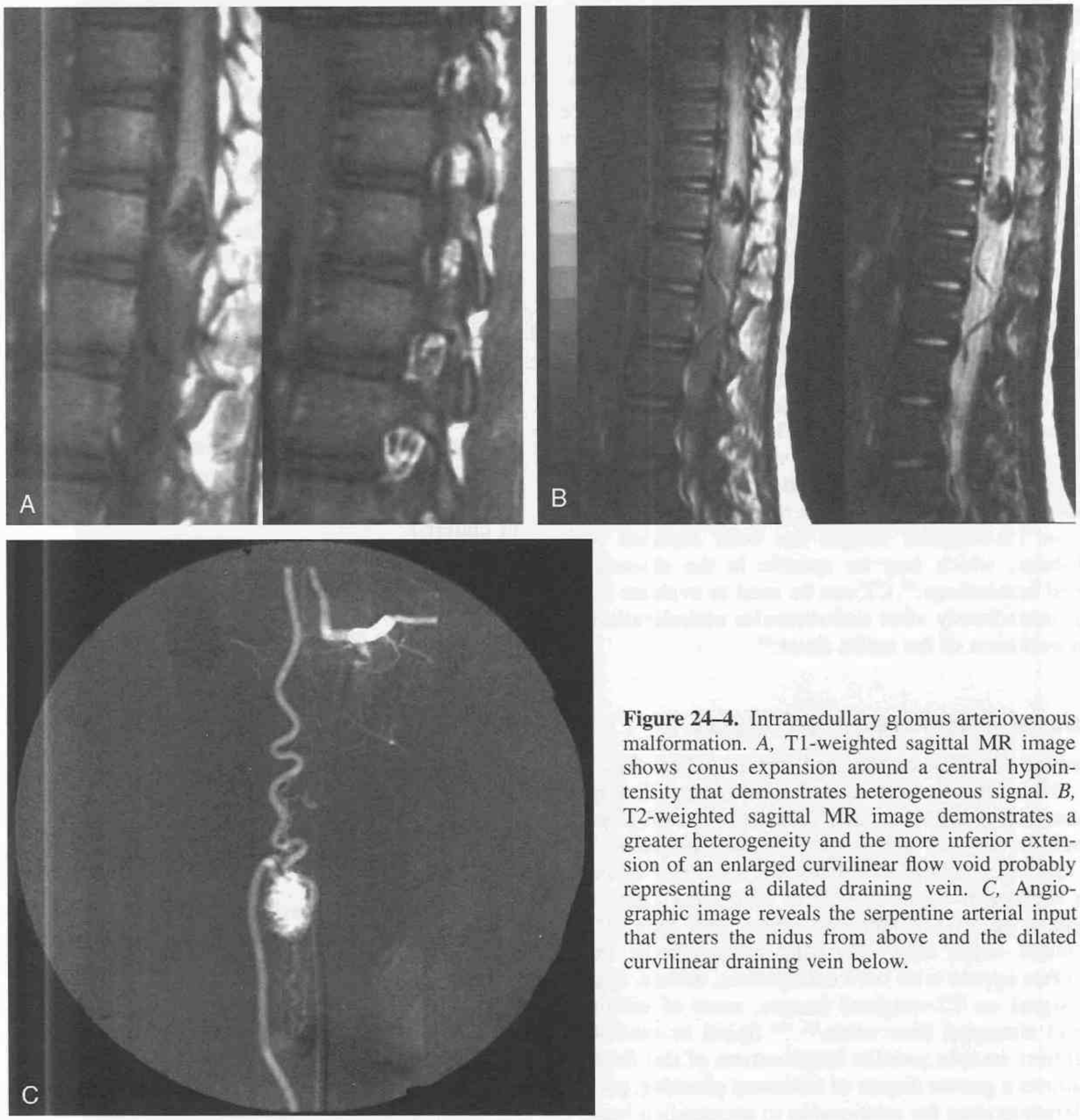

Figure 24–4. Intramedullary glomus arteriovenous malformation. *A,* T1-weighted sagittal MR image shows conus expansion around a central hypointensity that demonstrates heterogeneous signal. *B,* T2-weighted sagittal MR image demonstrates a greater heterogeneity and the more inferior extension of an enlarged curvilinear flow void probably representing a dilated draining vein. *C,* Angiographic image reveals the serpentine arterial input that enters the nidus from above and the dilated curvilinear draining vein below.

AVMs (Fig. 24–4), and those with a looser configuration that often extends into the extramedullary spaces have been labeled *juvenile-type AVMs.*[2] In rare instances, these malformations occur in conjunction with vertebral angiomas and skin nevi, all at the same metameric level; this is called the *Cobb syndrome.*[80]

AVMs present a risk of hemorrhage and ensuing complications as well as effects of venous hypertension, which may include spinal cord edema, ischemia, or infarct. Indeed, this is the only subset of vascular malformations that show associated spinal artery aneurysm formation, most likely the result of long-standing high flow. When such aneurysms occur, they frequently hemorrhage.[6]

MRI can often be used to detect spinal AVMs when the effects of high flow, signal changes about the nidus, hemorrhage, and edema are readily apparent.[61] In addition, the telltale curvilinear filling defects can be seen on CT myelography.[60] Spinal AVMs that occur within the cord substance can be complicated by associated infarct that appears bright on T2-weighted images and enhances with gadolinium.[108] If spinal AVMs spontaneously thrombose (*Foix-Alajouanine syndrome*), an associated cord ischemia can occur, leading to cord infarct.[102] Even greater sensitivity for the lesions, and in particular for the shunt, is gained through application of dynamic MRI using a T2-weighted sequence and tracking of a gadolinium bolus.[123]

Spinal AVFs are the more common spinal cord vascular malformations; they are subdivided into malformations involving only the dural branches of a radicular artery (*dural AVFs*) and those arising directly from the spinal arteries (*intradural AVFs*). Dural AVFs are probably acquired, whereas intradural AVFs are thought to be congenital. The larger congenital lesions often present in childhood with hemorrhage of focal neurologic deficits.[104]

Dural Arteriovenous Fistulas

Dural AVFs, whose point of shunt is within the dural surface, comprise the majority of all spinal vascular malformations.[93] The resultant venous engorgement can produce venous hypertensive changes in the spinal cord, often in the midthoracic to upper lumbar region, that in turn induce cord myelopathy. The myelopathic changes, both clinically and on MR images, can occur distal to the level of the fistula; this can become particularly disorienting near the cervicomedullary junction, where the fistula can be intracranial but the myelopathy cervical to thoracic or vice versa.[8, 18, 33, 92] Disruption of such a fistula can produce subarachnoid hemorrhage at a distance from the lesion.[49]

MRI typically shows hyperintensity on T2-weighted images, possible cord enlargement, and, at times, cord enhancement secondary to infarct.[65] The high vascular flow usually produces the expected flow voids in the vicinity of the fistula on MR images or dilated vessels on myelography.[41] Of interest, a surrounding peripheral rim of hypointensity on T2-weighted images has been reported with these fistulas, which may be specific in the absence of associated hemorrhage.[53] CT can be used to evaluate these fistulas immediately after endovascular embolization to confirm occlusion of the entire shunt.[20]

Intradural Arteriovenous Fistulas

Intradural AVFs lie on the cord surface, where they are further subdivided by size: type I, small; type II, larger, with dilatation of the artery and vein; and type III, largest, with multiple feeders and marked venous dilatation.[2] A variant on this classification defines type I as those draining only to meningeal veins, type II to meningeal veins and then retrograde to subarachnoid veins, and type III to subarachnoid veins only.[7] On MRI examinations, these lesions often appear with cord enlargement, edema, hyperintense signal on T2-weighted images, areas of enhancement, and abnormal flow voids.[65, 122] Spiral or multislice CT scanners enable precise localization of the fistula, which allows a greater degree of treatment planning, particularly demonstrating the relationship to surrounding bone.[48]

Cavernous Angiomas

Cavernous angiomas are most often intramedullary, and the risk to the patient is of hemorrhage into functioning tissues. Cavernous angiomas can be found at any cord level, and they are multiple in a significant minority of cases.[22, 127] These angiomas show a typical reticulated pattern of heterogeneous signal intensity on all MR sequences, producing the classic "popcorn" appearance best demonstrated on T2-weighted sequences.[15] This pattern, in association with a family history, other lesions in the neural axis, and a tendency toward diminished signal intensity over time, can confirm the diagnosis.[125]

Neoplasms

Intramedullary neoplasms consist of (1) primary cord neoplasms (e.g., ependymomas and astrocytomas) and, to a lesser extent, (2) hemangioblastomas, (3) intramedullary metastases, and (4) other even less common entities (e.g., intramedullary lipomas). In adults, intramedullary neoplasms comprise 7% to 22% of all spinal neoplasms and include, in decreasing order of frequency, ependymomas (65%); astrocytomas (25%); glioblastoma (7.5%); and rare hemangioblastomas, oligodendrogliomas, and metastases.[91, 105, 109, 113] Intramedullary metastases are usually not neural in origin; lung cancer is the most common primary tumor to metastasize to the cord, followed by breast cancer. Lymphoma, colon and renal tumors, head and neck carcinoma, and melanoma also metastasize to the cord but less commonly.[12, 23, 43] In children, intramedullary lesions account for one third of spinal neoplasms and include astrocytomas (58%), ependymomas (28.5%), teratomas, and dermoid or epidermoid tumors (5.8%).

Hemangioblastomas and intramedullary metastases, such as glioblastoma, primitive neuroectodermal tumor, and Wilms' tumor, occur infrequently in the spinal cords of children.[17, 26, 32, 81]

Diffuse fusiform or focal expansion of the cord with loss of the normal cord contour and resultant distortion of the surrounding subarachnoid space is the hallmark of intramedullary tumors on MR images as they are on CT myelograms. Differentiation between the white matter tracts and the butterfly or H-shaped central gray matter may often be obtained with high-resolution MRI.[112] MRI can also be used to demonstrate the longitudinal extent of abnormal signal and enhancement as well as the internal derangement of spinal parenchymal architecture. These abilities have established the superiority of MRI over other neuroimaging techniques in the evaluation of intramedullary processes.

Traditionally, CT myelography demonstrated intramedullary masses as expansile lesions of the spinal cord, displacing the intrathecal contrast material within the subarachnoid space peripherally; occasionally, however, intramedullary lesions are not shown to expand the cord. One series noted a normal myelographic appearance in 42% of patients with intramedullary neoplasms.[43] Abnormal signal on standard or fast spin-echo T2-weighted images and abnormal contrast enhancement confirm the presence of intramedullary neoplasms on MRI despite lack of cord expansion.[118] Exophytic growth of intramedullary lesions, most commonly in the region of the conus medullaris, may result in both focal cord expansion and cord displacement by the exophytic process. Exophytic growth of intramedullary lesions has been described in astrocytomas, mixed gliomas, ependymomas, and hemangioblastomas.

With early imaging and contrast enhancement, it is possible to locate intramedullary parenchymal lesions within specific quadrants of the spinal cord or within the central canal of the cord. Intramedullary neoplasms, however, are usually relatively large when initially imaged, and they distort the parenchyma of the cord over the length of several segments. Signal intensity changes of most intramedullary processes are nonspecific, and it is often impossible on unenhanced MRI to differentiate neoplasm from associated edema or postoperative gliosis because of similar nonspecific T1 and T2 lengthening.[27, 94, 110, 129] Tumor

and edema have similar MRI characteristics, whereas associated cysts may become more hyperintense on T2-weighted sequences than the adjacent abnormal cord. Features that help distinguish tumor-related cysts from syringes include abrupt changes in diameter and position of the cyst, uneven thickness of the surrounding cord, increased T2-weighted signal of tumor cysts, and pathologic enhancement.[106, 126] Cystic lesions associated with tumor, however, may not be well defined without contrast administration.[16, 42]

After administration of contrast, there is striking and immediate enhancement of most intramedullary neoplasms on both CT scans and MR images. The focus of enhancement is usually smaller than the region of abnormal signal and spinal cord enlargement defined on the unenhanced views, helping to localize the actual neoplastic focus.[64, 79, 117] Occasionally, lesions fail to enhance and may be identified by abnormal signal intensity only.

Unfortunately, enhancement patterns are nonspecific, although astrocytomas tend to enhance in a more irregular manner compared with ependymomas or hemangioblastomas and are often eccentrically located. Cystic degeneration tends to indicate astrocytoma, whereas signal changes consistent with pigment or fat/calcium tend to indicate melanoma or teratoma, respectively.[69] Ependymomas and hemangioblastomas both enhance homogeneously and are more likely to be associated with cysts and syringes. Up to 75% of hemangioblastomas are cystic, and draining veins and cord edema, probably secondary to vascular shunt-related congestion, may also be seen in hemangioblastomas.[21, 44, 89, 111] Heterogeneous signal on T1-weighted and T2-weighted images, hypointensity at the tumor margins resulting from firm pseudocapsule formation, and intratumoral hypointensity from hemorrhage suggest ependymoma.[69, 86]

Ependymomas

Ependymomas represent 65% of spinal cord neoplasms. They are found more commonly in men and usually present between 20 and 60 years of age. They represent the most common glial tumor of the lower cord. Three quarters are myxopapillary subtypes and arise within the conus or filum terminale, and the remainder are found in the cervical and thoracic cords. Ependymomas within the cervical and thoracic cords are generally indistinguishable from astrocytomas; however, astrocytomas are far more common in the cervical cord and slightly more common in the thoracic cord than ependymomas.[78]

Ependymomas are usually histologically benign and slowly growing, which generally allows them to reach a large size by the time they manifest clinically. They may span one to five vertebral body segments and are highly vascular, often resulting in intratumoral hemorrhage that can be visualized on imaging.[132] They may be large enough to produce marked expansion of the spinal canal, and the vertebral bodies on either side of the disk may be excavated, with the pedicles and neural arches eroded. Smaller ependymomas tend to displace nerve roots, whereas larger tumors tend to engulf adjacent nerve roots and may become indistinguishable from them.

Ependymomas appear isodense to hypodense on nonenhanced spinal CT and enhance after the intravenous (IV) administration of contrast material. Although calcification has been reported to be common in posterior fossa and supratentorial ependymomas, it has not been commonly observed in spinal cord ependymomas. Ependymomas of the cauda equina are reasonably characteristic, usually appearing as a spherical mass centrally within the spinal canal. After administration of a water-soluble contrast agent, myelographic and postmyelographic CT scans demonstrate the nerve roots of the cauda equina above and below the tumor mass, thus delineating the conus as separate from the mass.

The MRI appearance of spinal ependymomas is variable, depending on the location within the spinal cord. In the cervical and thoracic regions, they appear as expansile lesions of the cord in the sagittal and axial planes and are slightly hypointense on T1-weighted images and hyperintense on T2-weighted images. In addition, intratumoral cyst cavities have occasionally been reported in these locations.[132] In the cauda equina region, the tumors are typically spherical masses with signal intensities similar to those found elsewhere (Fig. 24–5). Because of possible episodes of rebleeding from the fibrovascular stroma, however, repeated episodes of subarachnoid hemorrhage may lead to hemosiderin deposition within the subarachnoid space. This appears as areas of marked hypointensity on T2-weighted images.[132] Gadolinium enhancement is generally in a homogeneous, well-circumscribed pattern, rendering the lesion more conspicuous.

Astrocytomas

Astrocytomas represent one third of intramedullary gliomas and may occur at any location along the cord. They are most common between 20 and 50 years of age and are slightly more common in men. Seventy-five percent of these tumors are low-grade (grade I or II). Astrocytomas tend to occur in the cervical and thoracic segments, where they have an incidence equal to or greater than that of ependymomas. In children, the proportional incidence of astrocytomas to ependymomas is higher than that in adults.[132]

Intratumoral cysts within astrocytomas, as well as syringomyelia at one or both ends of the cord associated with astrocytomas, occur with variable incidences. Most astrocytomas are solitary tumors, but they can be multiple in the case of neurofibromatosis. Histologically, the low-grade tumors are fibrillary astrocytomas with pilocytic features. On noncontrast CT scans, astrocytomas of the spinal cord appear as hypointense to isointense lesions.[85] After administration of IV contrast material, these lesions often enhance heterogeneously, with nonenhancing portions of tumor representing intratumoral cyst cavities.[45] Water-soluble myelographic scans demonstrate fusiform enlargement of the spinal cord, with focal nodules or abrupt changes in size indicating the likelihood that the cord mass represents a tumor and not a syrinx. Syringes at either end of the tumor generally have a sausage-like appearance, being uniformly expanded and lacking any focal nodules. Calcification within astrocytic tumors of the spinal cord is not common.[132]

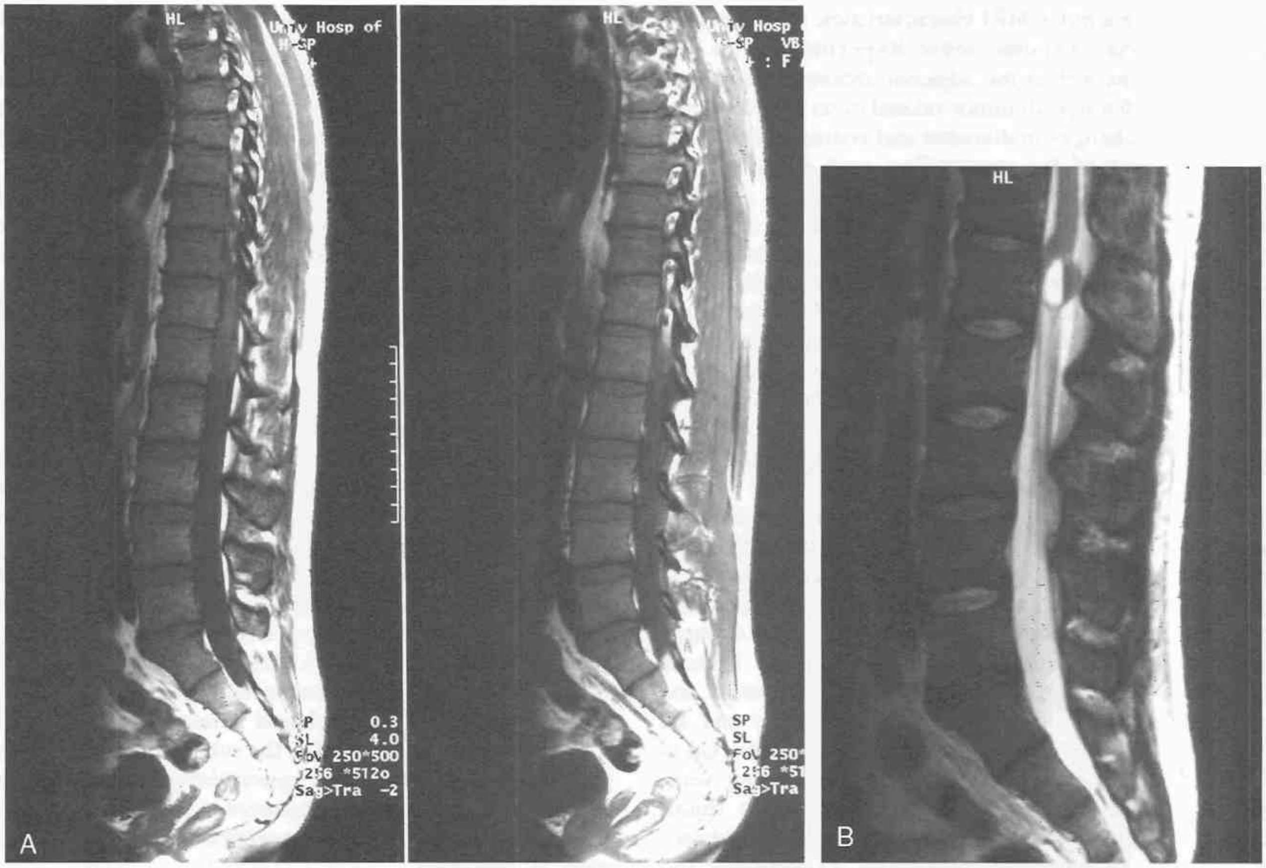

Figure 24–5. Conus myxopapillary ependymoma. *A,* T1-weighted sagittal MR image shows a hypointense expansion of the conus. *B,* T2-weighted sagittal MR image demonstrates an exophytic cystic lesion of the conus that contains a fluid-fluid level.

MRI is the best way to demonstrate enlargement of the spinal cord by an astrocytoma (Fig. 24–6). Sagittal and axial plane images demonstrate expansion of the cord. T1-weighted images demonstrate astrocytomas to be low in signal intensity whereas proton-density–weighted and T2-weighted images show them to be high in signal intensity.[107,129] Intratumoral cysts are irregular areas; their contents reflect a signal intensity similar to that of CSF. Syrinxes at either end of the tumor demonstrate parallel walls, and their contents also demonstrate signal intensity similar to that of CSF. Axial images demonstrate the asymmetrical expansion of the cord by tumor tissue. Astrocytomas tend to enhance more heterogeneously than ependymomas, partly because of the high incidence of intratumoral cysts, and IV gadolinium administration aids in the detection and characterization of astrocytomas.[94]

Hemangioblastomas

Hemangioblastomas are uncommon tumors of the spinal cord, representing 1.6% to 3.6% of spinal cord tumors; they are most often found in association with von Hippel–Lindau disease.[132] They are usually found in middle-aged adults, demonstrate no sexual predilection, and are solitary in 80% of cases. Although they are usually solitary, hemangioblastomas may be multiple in von Hippel–Lindau disease. Approximately 50% of hemangioblastomas are cystic with a mural tumor nodule. The cysts are often high in protein content and are suggestive of prior episodes of hemorrhage.[132] The tumors may arise in the cervical or thoracic cord, usually causing diffuse focal widening of the cord.

On nonenhanced CT scans, the tumor nidus appears isodense to slightly hyperdense in attenuation, and after administration of IV contrast material, the tumor markedly enhances; the enhancing tumor nodule appears distinct from the associated cyst. On contrast myelographic scans, the spinal cord appears enlarged with multiple serpentine filling defects from arteries and veins that result from this relatively vascular tumor.[132]

MR images demonstrate an enlarged, infiltrated spinal cord, and in half the cases a cyst containing a mural nodule can be identified. A large syrinx may also accompany the tumor, helping to support the diagnosis.[94] Gadolinium enhancement (Fig. 24–7) is the most useful technique to differentiate the mural tumor nidus from the associated reactive, cystic changes.[94, 116, 117]

Intramedullary Metastases

Hematogenous metastases to the spinal cord from a primary site outside the CNS (lung, breast, melanoma) are

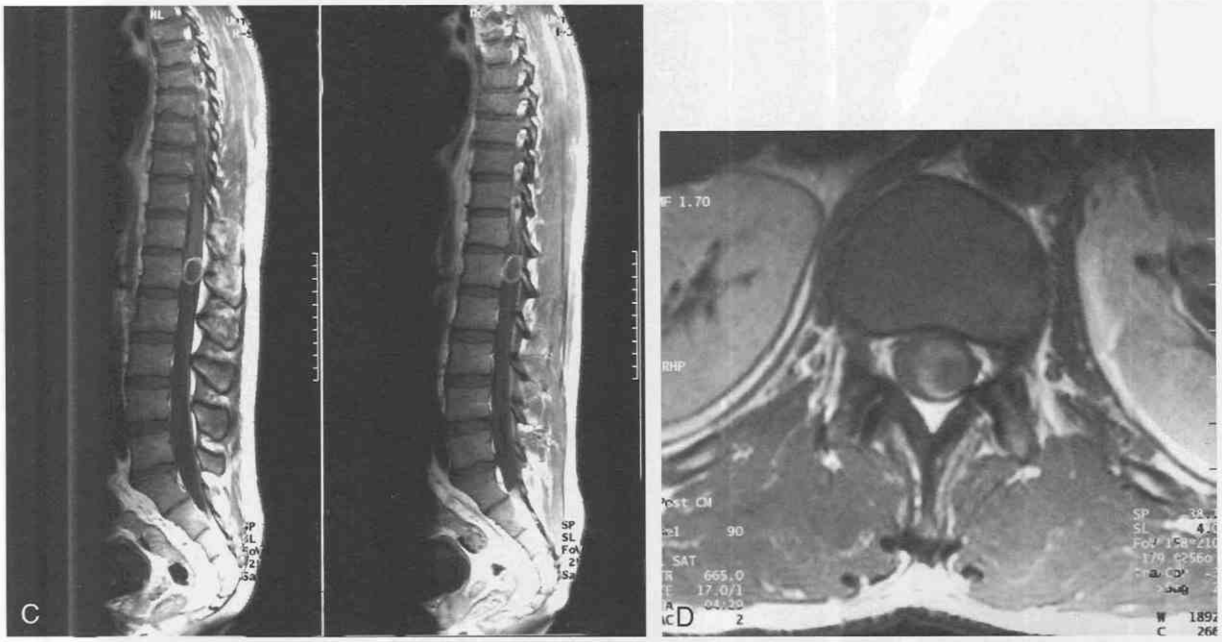

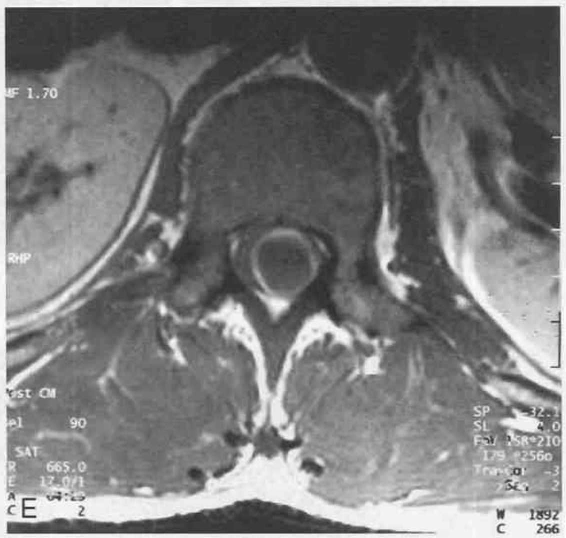

Figure 24–5. *Continued, C.* A postcontrast T1-weighted sagittal MR image shows the sharp rim enhancement of the tumor. *D* and *E,* A postcontrast T1-weighted axial section demonstrates compression of the conus by the enhancing cystic mass.

rare, even when there are metastatic lesions to other spinal structures, such as the vertebral bodies and the epidural space.[30] Of the tumors of non-neurogenic origin metastasizing to the cord, lung carcinoma is the most common (Fig. 24–8), and breast carcinoma is the second most common. Other reported primary tumors are much less common; they include lymphoma, melanoma, colorectal carcinoma, Hodgkin's disease, head and neck carcinoma, and leukemia.[99]

Drop metastases from primary brain tumors can seed down the central canal of the spinal cord and produce an appearance similar to that of an intramedullary metastasis. These metastases are usually from malignant gliomas, ependymomas, medulloblastomas, and pineal tumors. Although apparent on CT myelograms, these, like other lesions, are best detected by MRI with contrast enhancement.[50]

In most instances, the intramedullary metastatic lesion is small and does not produce significant mass effect. Therefore, a discernible change in the size of the spinal cord cannot be noticed on either contrast-enhanced myelographic or postmyelogram CT scans.[130] In a few instances, focal enlargement of the cord may be sufficient to be seen by either modality.

MRI is the best technique for evaluating intramedullary spinal cord metastatic lesions. Enlargement of the spinal cord, even when subtle, is best seen on T1-weighted images in the sagittal plane and is the first indication of an intramedullary lesion. Lesions are hyperintense on T2-weighted images and generally enhance heterogeneously after IV gadolinium administration (Fig. 24–9). T2-weighted signal intensity changes and abnormal enhancement can be seen in the absence of cord enlargement.[99] Subsequent to the intramedullary metastasis, a blockage and then dilatation of the central canal can occur, producing a typical syrinx in association with the mass.[56,97]

Text continued on page 796

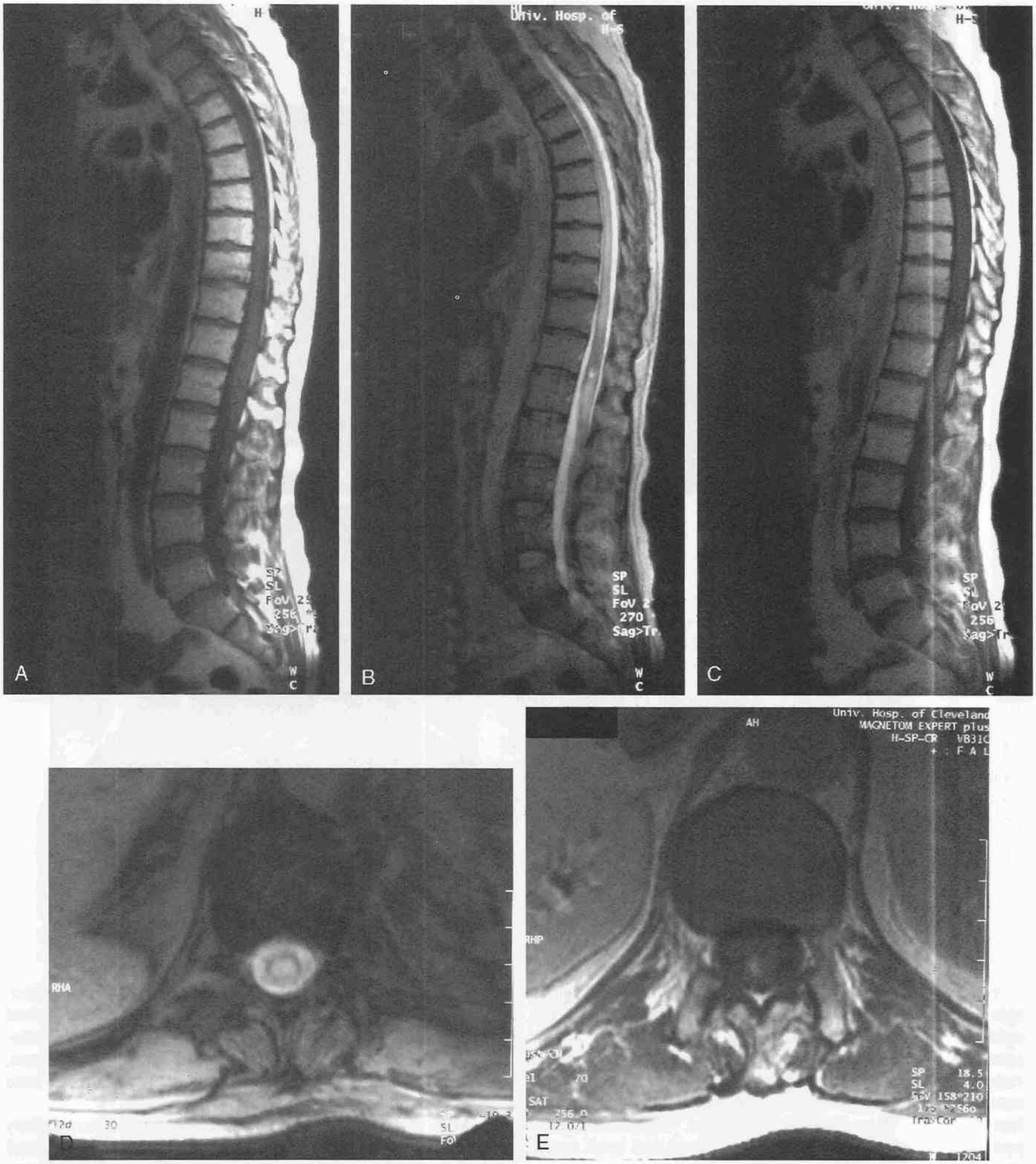

Figure 24–6. Cord astrocytoma. *A,* T1-weighted sagittal MR image shows marked expansion of the cervical cord by a large cystic lesion. *B,* T2-weighted, fast spin-echo, sagittal MR image confirms the cystic nature of the mass and better demonstrates the long inferior extent of the associated cystic syrinx. *C,* Postcontrast T1-weighted sagittal MR image reveals the heterogeneous nodular enhancement within the larger cervical cyst. *D,* Postcontrast T1-weighted axial section demonstrates the homogeneous enhancement of the solid component. *E,* T1-weighted axial section lower in the cord confirms the central syrinx.

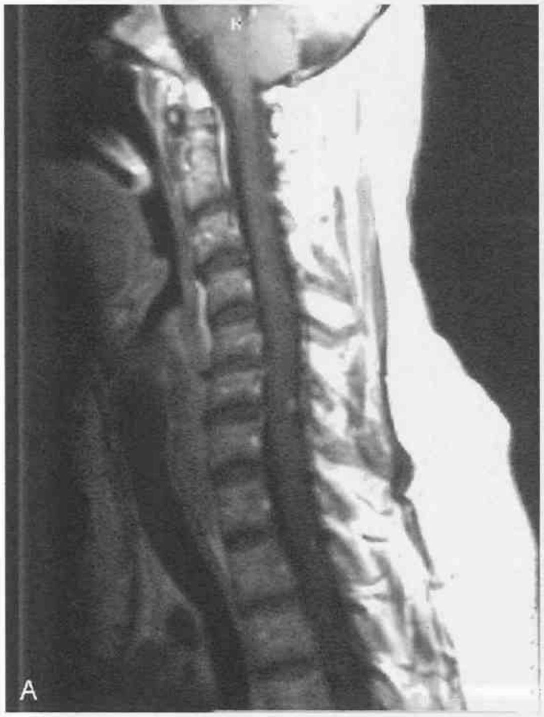

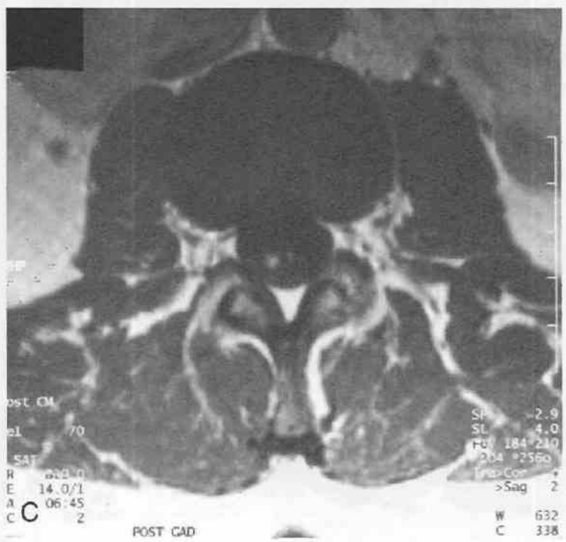

Figure 24–7. Multiple hemangioblastomas in a patient with von Hippel–Lindau syndrome. *A,* Postcontrast T1-weighted sagittal MR image of the cervical spine shows a posterior peripheral enhancing nodule at the C6–7 level. *B,* Postcontrast T1-weighted sagittal MR image of the lumbar spine demonstrates an enhancing nodule at the tip of the conus. *C,* Postcontrast T1-weighted axial section reveals the solid enhancing nodule within the peripheral substance of the conus medullaris.

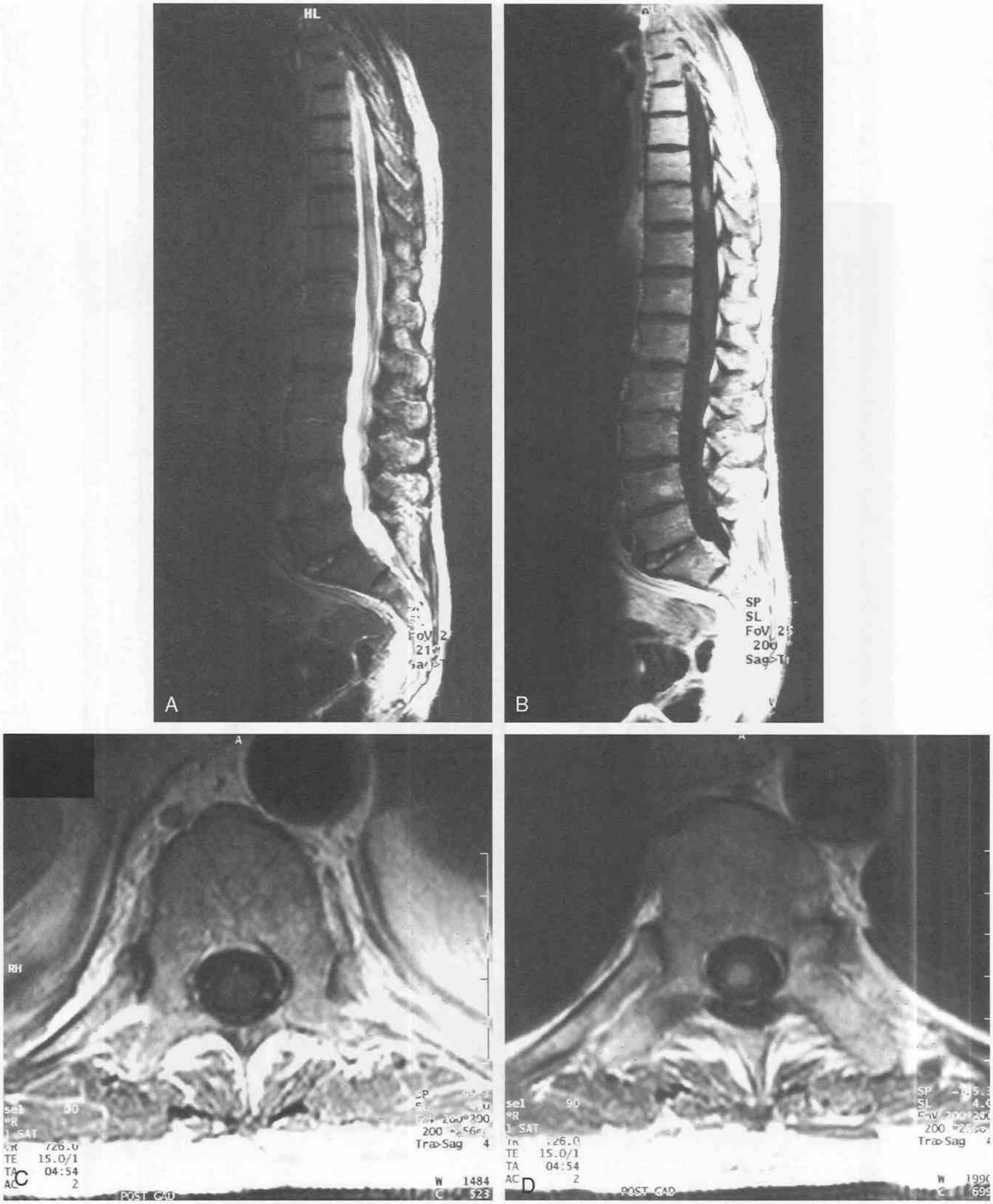

Figure 24–8. Intramedullary drop metastases to the cord from lung brain metastasis. *A,* T2-weighted, fast spin-echo, sagittal MR image shows a band of hyperintensity along the posterior cord. *B,* Postcontrast T1-weighted sagittal MR image demonstrates a heterogeneously enhancing ovoid mass in the lower thoracic cord. *C,* This T1-weighted axial section shows an eccentric hypointensity without definite distortion of the cord surface. *D,* This T1-weighted postcontrast axial section confirms the homogeneous enhancement of the mass.

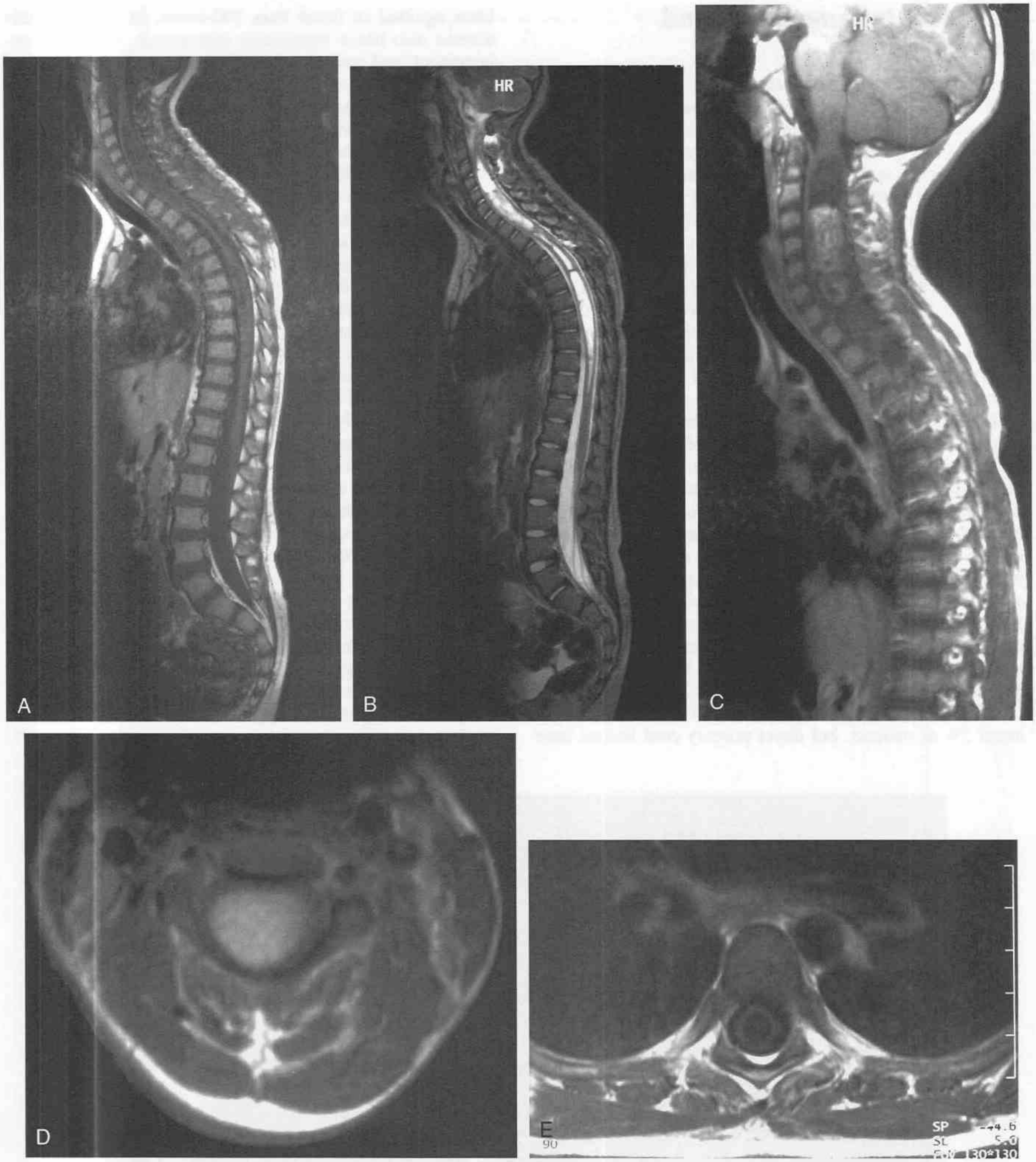

Figure 24–9. Hematogenous metastasis to the conus medullaris from lung carcinoma. *A,* T1-weighted sagittal MR image shows expansion of the inferior cord. *B,* T2-weighted sagittal MR image demonstrates abnormal hyperintense signal in the conus and a more focal area of greater signal intensity. *C,* Postcontrast T1-weighted sagittal MR image shows heterogeneous enhancement extending over the length of more than one vertebral body of the lower cord. *D,* A gradient-echo, FLASH (fast low-angle shot), T2-weighted axial section confirms cord expansion and the central signal intensity abnormality. *E,* Postcontrast T1-weighted axial section highlights a focal area of greater enhancement.

Infection, Inflammation, and Demyelination

Infectious diseases typically occur around the spinal cord, as in osteomyelitis, diskitis, and epidural abscesses, but more rarely they can involve the intramedullary substance. Cord infection can be expected to produce decreased signal with T1 weighting, increased intensity on T2-weighted images, and early variable enhancement with gadolinium, representing myelitis or abscess.[83] These lesions occur as a result of hematogenous dissemination and can arise, for example, from typical pyogenic bacteria, in syphilis or in tuberculosis.[40, 84] The myelitis can have associated enhancement that may resolve after successful antimicrobial therapy, whereas frank abscesses can show typical rim enhancement.[57, 84] A congenital lesion, such as a dermal sinus, can allow formation of an unusually high number of intramedullary abscesses.[25]

Intramedullary involvement in the prototypical granulomatous diseases, tuberculosis and sarcoidosis, is rare. When the cord is involved in tuberculosis, an enhancing intramedullary tuberculoma is expected, but fewer than 150 examples have been reported among patients with normal immune systems.[101] In patients with acquired immunodeficiency syndrome (AIDS), this entity may arise slightly more often, but the tuberculoma has a nonspecific appearance, its signal intensity is decreased on T1-weighted images and increased on T2-weighted images, and peripheral or nodular enhancement is seen.[76] Very rarely, a frank abscess within the cord arises, at times in association with meningitis of tuberculosis.[119]

CNS involvement in systemic sarcoidosis occurs in about 5% of patients, but direct primary cord lesions have been reported in fewer than 100 cases. In the cord, this disease also has a nonspecific appearance, with cord enlargement and multifocal patchy areas of enhancement, again frequently in association with meningitis.[87] These lesions should resolve, however, after appropriate steroid therapy, perhaps with the exception of infrequently reported central calcifications.[95, 128]

Parasitic myelitis can produce a similar appearance in association with a CSF eosinophilia.[63] Although rare, typical parasitic diseases have been reported to involve the spinal cord: schistosomiasis,[29] toxoplasmosis in patients with AIDS,[98, 103] and cysticercosis. When schistosomiasis invades the cord, it can cause a nonspecific myelitis, or the ova can induce formation of granulomas that can be identified on CT myelograms.[46] In patients with cysticercosis, syringomyelia or cystic intramedullary lesions can be present and are associated with brain parenchymal lesions.[68]

Involvement of the spinal cord as a direct result of fungal disease occurs only rarely and typically only in those with significant immune compromise. Aspergillosis is the most common fungal disease of the cord, typically presenting as a myelopathy but also reported as occluding principally the anterior spinal artery.[59, 96] Cord abscesses caused by *Candida, Coccidioides,* and *Nocardia* have been reported.[1, 70, 82] Similarly, cord granulomas caused by *Cryptococcus* and *Histoplasma* have been described in isolated reports.[55, 114]

Viral infections of the spinal cord are encountered most often among patients with immune compromise. In patients with AIDS, intramedullary infection with human immunodeficiency virus type I (HIV-1) causes a vacuolar myelopathy that shows nonspecific hyperintensity on T2-weighted images.[3, 124] Herpes zoster typically affects the skin but can produce a myelitis that shows cord enlargement, hyperin-

Figure 24–10. Degenerative changes of the spine with cord effect. *A,* T2-weighted FLASH (fast low-angle shot) axial section demonstrates a posterior disk-osteophyte complex impressing upon the thecal sac and the central cord. *B,* T2-weighted fast spin-echo sagittal MR image confirms the degenerative changes along the posterior vertebral line and demonstrates nonspecific abnormal hyperintensity within the substance of the cord at the C6 level.

tensity on T2-weighted images, and variable enhancement.[38,51] Cord involvement by the Epstein-Barr virus has been reported as either encephalomyelitis or isolated myelitis, demonstrating the same nonspecific findings as the preceding viral disorders.[13,28]

Degenerative and demyelinating disorders can cause an acute transverse myelitis, or myelopathy. When the spinal canal narrows because of degenerative changes in the bones, joints, and disks, pressure to the cord can occur that will cause myelopathic changes visible on MR images (Fig. 24–10). The causes are uncertain and may include edema, inflammation, ischemia, or gliosis.[75]

The lesions of multiple sclerosis, the prototypical demyelinating disease, tend to be located at the cervical level, although they can be found throughout the medullary substance, whereas the lesions of idiopathic myelitis tend to appear at the thoracic levels.[19,66] The lesions of multiple sclerosis often demonstrate multiplicity within the CNS, underscoring the need for separation in time and space to diagnose this multiphasic disease.

In contrast, acute disseminated encephalomyelitis arises as a monophasic illness after exposure to a viral vaccine; multifocal plaques may appear, but they do not recur after improvement, which is slow.[24] In the rare instances when these plaques do recur in the absence of a diagnosis of multiple sclerosis, other autoimmune disorders, perhaps involving the presence of anti-cardiolipin antibodies, may be considered.[14] A delayed postradiation myelopathy can occur, but the diagnosis remains one of exclusion, with nonspecificity of the signal changes and enhancement on MR images.[58] Collagen vascular diseases, in particular in 1% to 2% of patients with systemic lupus erythematosus, can also cause a transverse myelitis that rarely affects the entire cord.[62,88]

Unfortunately, the lesions of all these disorders have a similar appearance: hyperintense plaques within the cord substance on T2-weighted images, possible cord enlargement, and possible enhancement. Only the spinal cord enlargement can be well seen on CT scans; thus, the modality of choice is MRI, in which the absence of cord expansion has become the best predictor of a non-neoplastic cause to an unknown cord lesion.[67,77] These lesions are best depicted with fast STIR (short tau inversion recovery) sequences, and in contrast to similar lesions in the brain, they are not well demonstrated by FLAIR (fluid-attenuated inversion recovery) sequences (Fig. 24–11).[52,54]

In multiple sclerosis, the most common source of myelitis seen in the United States, lesions tend to occur in multiples (Fig. 24–12), to be eccentrically located (Fig. 24–13), to involve less than half the cross-sectional area of the cord, and to extend less than two vertebral bodies in length.[120]

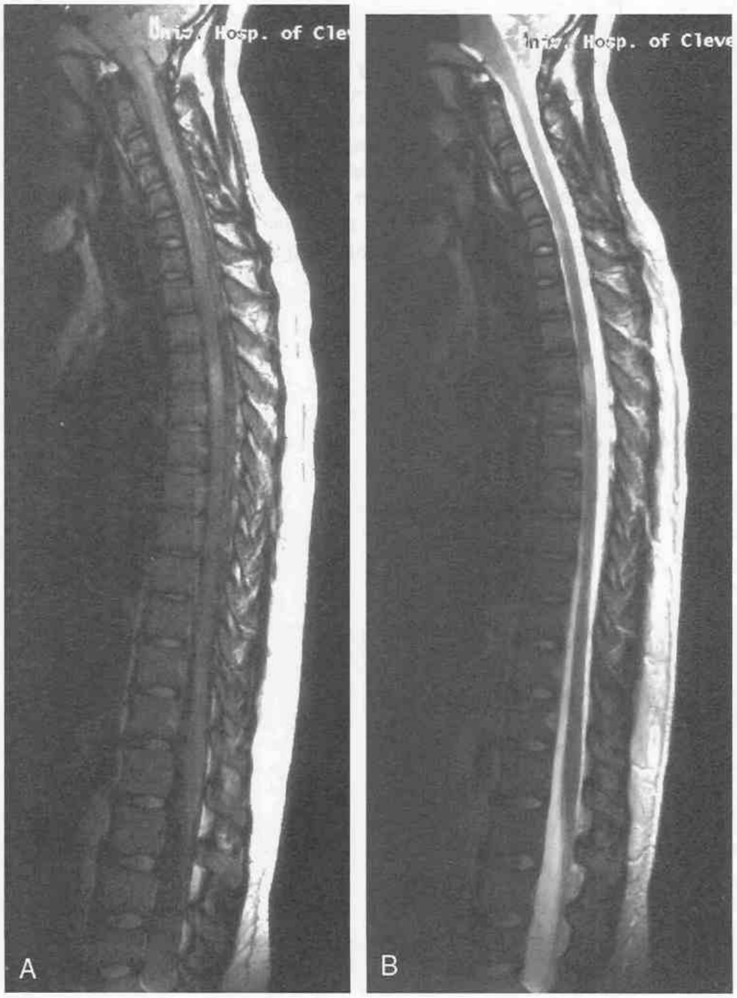

Figure 24–11. Multiple sclerosis plaque. *A,* A FLAIR (fluid-attenuated inversion recovery) sagittal MR image shows the lesion within the anterior cord centered at the third thoracic vertebra. *B,* The same lesion is even better demonstrated by the fast spin-echo T2-weighted sequence, and its appearance is not significantly diminished because of the high signal from the surrounding cerebrospinal fluid.

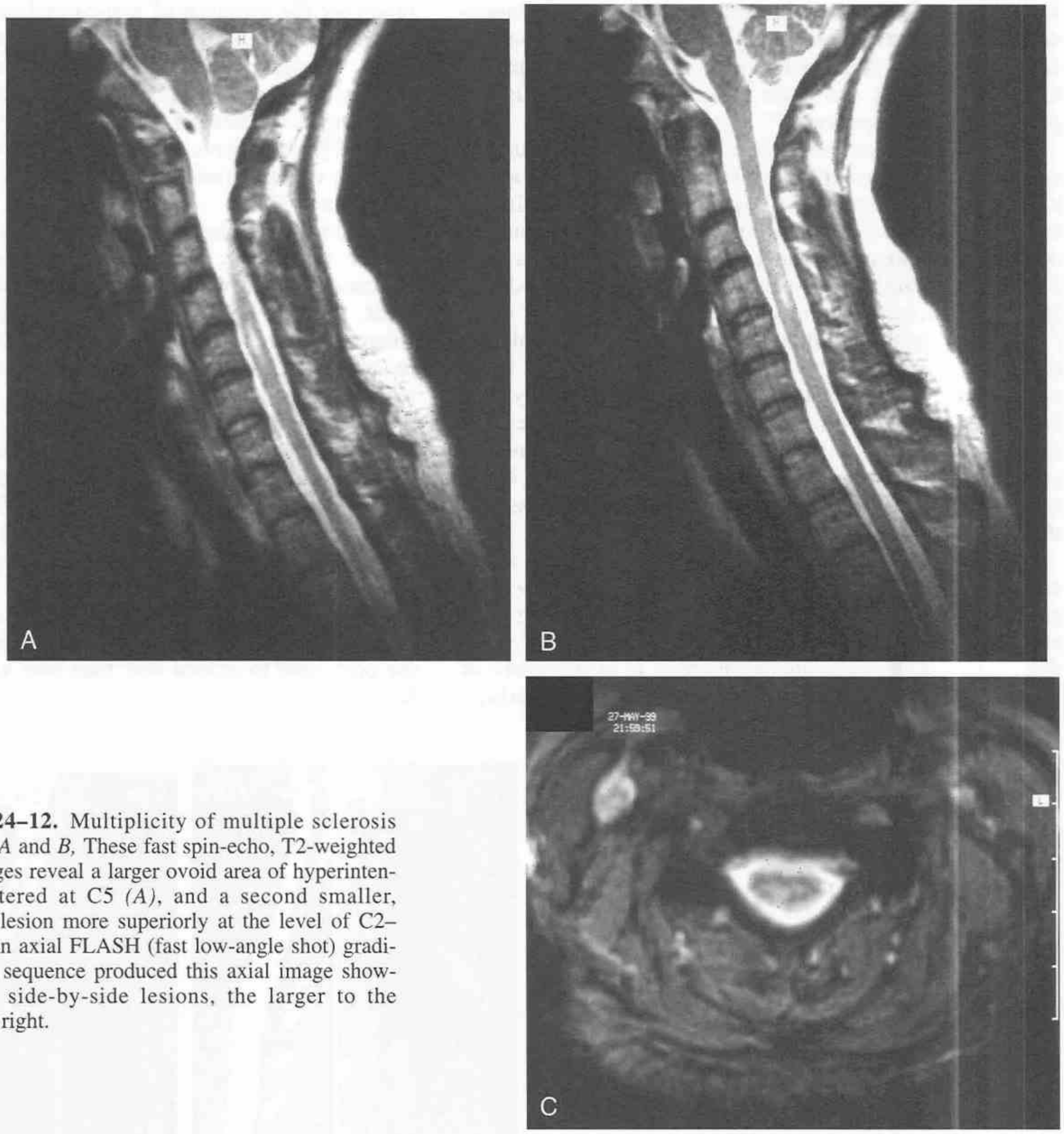

Figure 24–12. Multiplicity of multiple sclerosis plaques. *A* and *B,* These fast spin-echo, T2-weighted MR images reveal a larger ovoid area of hyperintensity centered at C5 *(A)*, and a second smaller, rounded lesion more superiorly at the level of C2–C3. *C,* An axial FLASH (fast low-angle shot) gradient-echo sequence produced this axial image showing two side-by-side lesions, the larger to the patient's right.

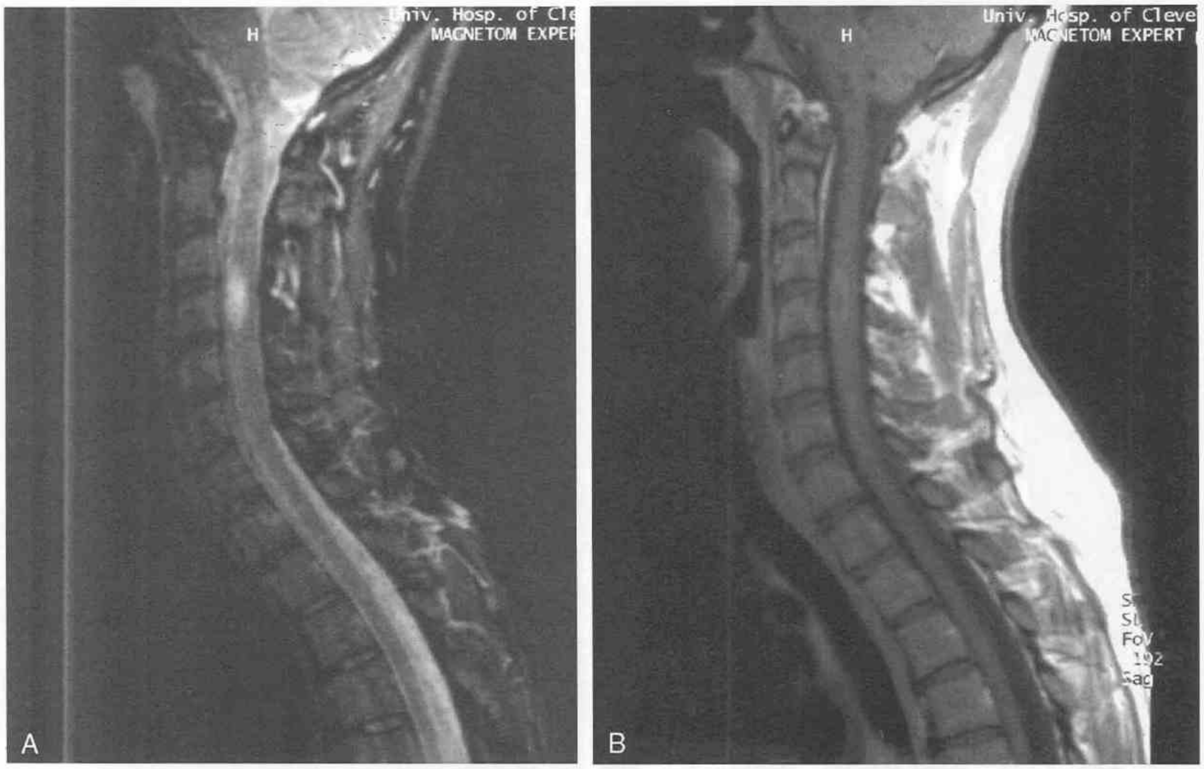

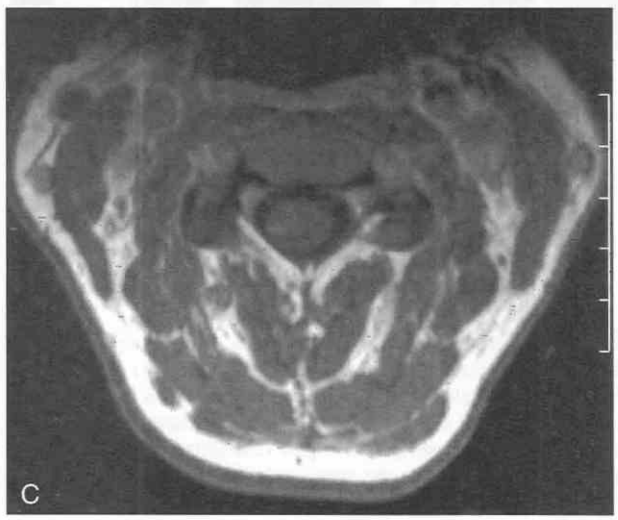

Figure 24–13. Eccentricity of multiple sclerosis plaques. *A,* A STIR (short tau inversion recovery) sagittal MR image shows a broad ovoid hyperintensity along the anterior cord at C4. *B,* The postcontrast T1-weighted sagittal MR image reveals eccentric anterior rim enhancement. *C,* The postcontrast T1-weighted axial section demonstrates a low level of rim enhancement eccentrically positioned in the right anterior quarter of the cord.

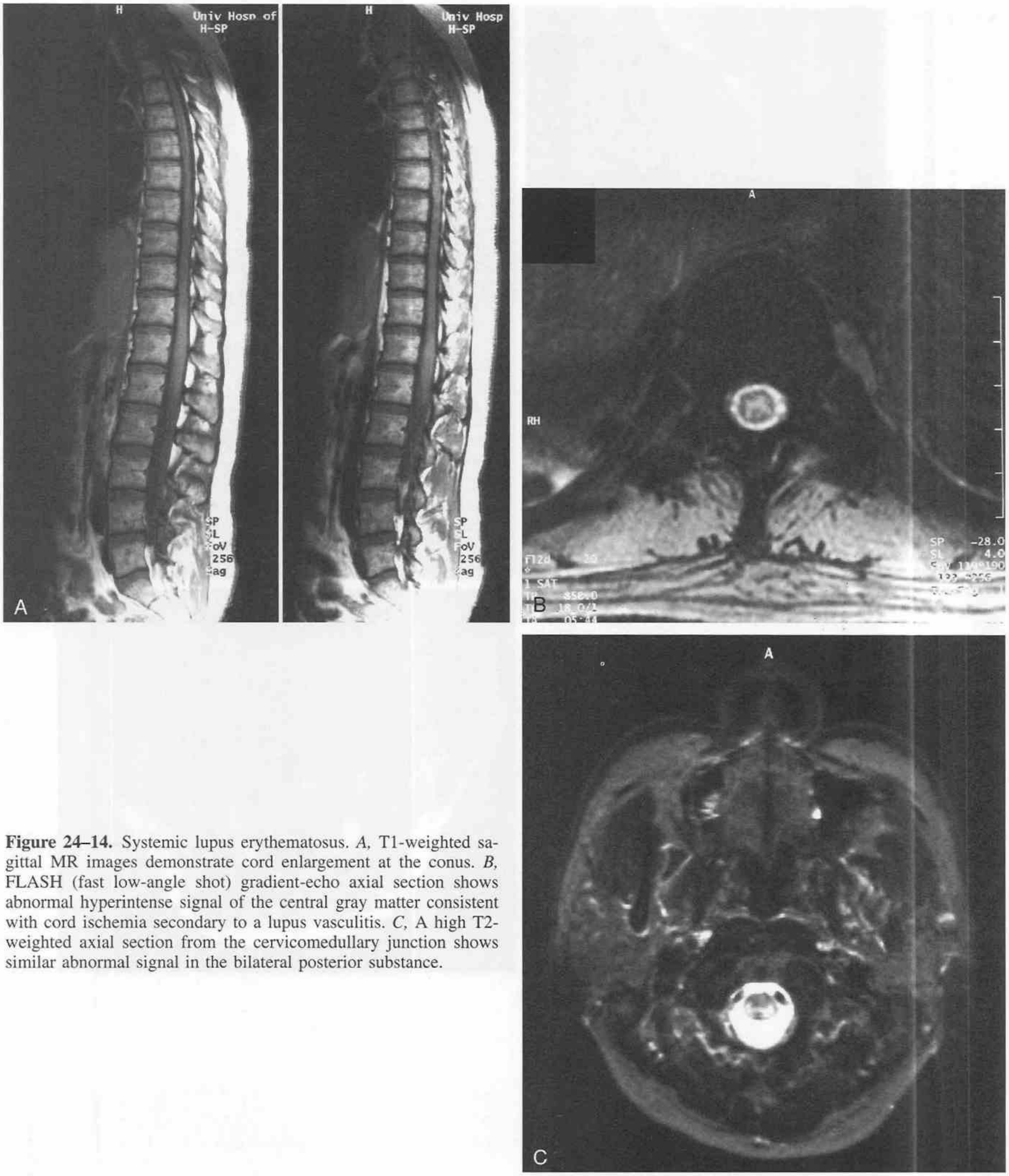

Figure 24–14. Systemic lupus erythematosus. *A,* T1-weighted sagittal MR images demonstrate cord enlargement at the conus. *B,* FLASH (fast low-angle shot) gradient-echo axial section shows abnormal hyperintense signal of the central gray matter consistent with cord ischemia secondary to a lupus vasculitis. *C,* A high T2-weighted axial section from the cervicomedullary junction shows similar abnormal signal in the bilateral posterior substance.

The relevance of enhancement depends on the underlying cause. In infection, it represents a more mature myelitis moving toward abscess; in demyelination, it represents acuity of the process with concurrent active destruction of myelin.[66] Some have reported an increased specificity when diagnosing lesions after gadolinium enhancement in multiple sclerosis.[121] Yet, any or all of these findings, including abnormal signal, cord thickening, and enhancement, can be seen in each of these disorders, even the more rare manifestations such as lupus[100]; indeed, some, as in lupus, may even appear indistinct from other causes of spinal cord infarct on MR images (Fig. 24–14).

References

1. Banuelos AF, Williams PL, Johnson RH, et al: Central nervous system abscesses due to *Coccidioides* species. Clin Infect Dis 22: 240–250, 1996.

Bao YH, Ling F: Classification and therapeutic modalities of spinal vascular malformations in 80 patients. Neurosurgery 40:75–81, 1997.

3. Barakos JA, Mark AS, Dillon WP, Norman D: MR imaging of acute transverse myelitis and AIDS myelopathy. J Comput Assist Tomogr 14:45–50, 1990.
4. Bergqvist CA, Goldberg HI, Thorarensen O, Bird SJ: Posterior cervical spinal cord infarction following vertebral artery dissection. Neurology 48:1112–1115, 1997.

Binkert CA, Kollias SS, Valavanis A: Spinal cord vascular disease: Characterization with fast three-dimensional contrast-enhanced MR angiography. AJNR Am J Neuroradiol 20:1785–1793, 1999.

Biondi A, Merland JJ, Hodes JE, et al: Aneurysms of spinal arteries associated with intramedullary arteriovenous malformations: I. Angiographic and clinical aspects. AJNR Am J Neuroradiol 13:913–922, 1992.

Borden JA, Wu JK, Shucart WA: A proposed classification for spinal and cranial dural arteriovenous fistulous malformations and implications for treatment [published erratum appears in J Neurosurg 82:705–706, 1995]. J Neurosurg 82:166–179, 1995.

Bousson V: Intracranial dural fistula as a cause of diffuse MR enhancement of the cervical spinal cord. J Neurol Neurosurg Psychiatry 67:227–230, 1999.

9. Bowen BC: Spinal dural arteriovenous fistulas: Evaluation with MR angiography. AJNR Am J Neuroradiol 16:2029–2043, 1995.
10. Bowen BC: MR angiography of the spine. Magn Reson Imaging Clin North Am 6:165–178, 1998.
11. Bowen BC: Vascular anatomy and disorders of the lumbar spine and spinal cord. Magn Reson Imaging Clin North Am 7:555–571, 1999.
12. Brunberg JA, DiPietro MA, Venes JL, et al: Intramedullary lesions of the pediatric spinal cord: Correlation of findings from MR imaging, intraoperative sonography, surgery, and histologic study. Radiology 181:573–579, 1991.
13. Caldas C: Case report: Transverse myelitis associated with Epstein-Barr virus infection. Am J Med Sci 307:45–48, 1994.
14. Campi A, Filippi M, Comi G, Scotti G: Recurrent acute transverse myelopathy associated with anticardiolipin antibodies. AJNR Am J Neuroradiol 19:781–786, 1998.
15. Chabert E: Intramedullary cavernous malformations. J Neuroradiol 26:262–268, 1999.
16. Chamberlain MC, Sandy AD, Press GA: Spinal cord tumors: Gadolinium-DTPA–enhanced MR imaging. Neuroradiology 33:469–474, 1991.
17. Chang WT, Chen HC, Peng HC: Solitary spinal cord metastasis of Wilms' tumor. J Pediatr Surg 25:550–552, 1990.
18. Chen CJ, Chen CM, Lin TK: Enhanced cervical MRI in identifying intracranial dural arteriovenous fistulae with spinal perimedullary venous drainage. Neuroradiology 40:393–397, 1998.
19. Choi KH, Lee KS, Chung SO, et al: Idiopathic transverse myelitis: MR characteristics [see comments]. AJNR Am J Neuroradiol 17: 1151–1160, 1996.
20. Cognard C: The role of CT in evaluation of the effectiveness of embolisation of spinal dural arteriovenous fistulae with *N*-butyl cyanoacrylate. Neuroradiology 38:603–608, 1996.

Colombo N, Kucharczyk W, Brant-Zawadzki M, et al: Magnetic resonance imaging of spinal cord hemangioblastoma. Acta Radiol Suppl 369:734–737, 1986.

22. Cosgrove GR, Bertrand G, Fontaine S, et al: Cavernous angiomas of the spinal cord. J Neurosurg 68:31–36, 1988.
23. Costigan DA, Winkelman MD: Intramedullary spinal cord metastasis: A clinicopathological study of 13 cases. J Neurosurg 62:227–233, 1985.
24. David P: MRI of acute disseminated encephalomyelitis after coxsackie B infection. J Neuroradiol 20:258–265, 1993.
25. Dev R, Husain M, Gupta A, Gupta RK: MR of multiple intraspinal abscesses associated with congenital dermal sinus. AJNR Am J Neuroradiol 18:742–743, 1997.
26. Di Lorenzo N: Primary spinal neoplasms in childhood: Analysis of 1234 published cases (including 56 personal cases) by pathology, sex, age and site—differences from the situation in adults. Neurochirurgia (Stuttg) 25:153–164, 1982.
27. Dillon WP, Norman D, Newton TH, et al: Intradural spinal cord lesions: Gd-DTPA-enhanced MR imaging. Radiology 170:229–237, 1989.
28. Donovan WD: Case report: MRI findings of severe Epstein-Barr virus encephalomyelitis. J Comput Assist Tomogr 20:1027–1029, 1996.
29. Dupuis MJ, Atrouni S, Dooms GC, Gonsette RE: MR imaging of schistosomal myelitis. AJNR Am J Neuroradiol 11:782–783, 1990.
30. Edelson RN, Deck MD, Posner JB: Intramedullary spinal cord metastases: Clinical and radiographic findings in nine cases. Neurology 22:1222–1231, 1972.
31. Elksnis SM, Hogg JP, Cunningham ME: MR imaging of spontaneous spinal cord infarction. J Comput Assist Tomogr 15:228–232, 1991.
32. Epstein F, et al: Intramedullary tumors of the spinal cord. In McLaurin RL (ed): Pediatric Neurosurgery: Surgery of the Developing Nervous System, 2nd ed. Philadelphia, Grune & Stratton, 1989, pp 428–442.
33. Ernst RJ: Cervical myelopathy associated with intracranial dural arteriovenous fistula: MR findings before and after treatment. AJNR Am J Neuroradiol 18:1330–1334, 1997.
34. Faig J: Vertebral body infarction as a confirmatory sign of spinal cord ischemic stroke: Report of three cases and review of the literature. Stroke 29:239–243, 1998.
35. Flanders AE, Spettell CM, Friedman DP, et al: The relationship between the functional abilities of patients with cervical spinal cord injury and the severity of damage revealed by MR imaging. AJNR Am J Neuroradiol 20:926–934, 1999.
36. Flanders AE, Spettell CM, Tartaglino LM, et al: Forecasting motor recovery after cervical spinal cord injury: Value of MR imaging. Radiology 201:649–655, 1996.
37. Forbes G, Nichols DA, Jack CR Jr, et al: Complications of spinal cord arteriography: Prospective assessment of risk for diagnostic procedures. Radiology 169:479–484, 1988.
38. Friedman DP: Herpes zoster myelitis: MR appearance. AJNR Am J Neuroradiol 13:1404–1406, 1992.
39. Friedman DP, Flanders AE: Enhancement of gray matter in anterior spinal infarction. AJNR Am J Neuroradiol 13:983–985, 1992.
40. Friess HM, Wasenko JJ: MR of staphylococcal myelitis of the cervical spinal cord. AJNR Am J Neuroradiol 18:455–458, 1997.
41. Gilbertson JR, Miller GM, Goldman MS, Marsh WR: Spinal dural arteriovenous fistulas: MR and myelographic findings. AJNR Am J Neuroradiol 16:2049–2057, 1995.
42. Goy AM, Pinto RS, Raghavendra BN, et al: Intramedullary spinal cord tumors: MR imaging, with emphasis on associated cysts. Radiology 161:381–386, 1986.
43. Grem JL, Burgess J, Trump DL: Clinical features and natural history of intramedullary spinal cord metastasis. Cancer 56:2305–2314, 1985.
44. Hackney DB: Neoplasms and related disorders. Top Magn Reson Imaging 4:37–61, 1992.
45. Handel S, Grossman R, Sarwar M: Case report: Computed tomography in the diagnosis of spinal cord astrocytoma. J Comput Assist Tomogr 2:226–228, 1978.
46. Haribhai HC, Bhigjee AI, Bill PL, et al: Spinal cord schistosomiasis: A clinical, laboratory and radiological study, with a note on therapeutic aspects. Brain 114:709–726, 1991.
47. Hasegawa M: Spinal cord infarction associated with primary antiphospholipid syndrome in a young child: Case report. J Neurosurg 79:446–450, 1993.
48. Hasegawa M: The efficacy of CT arteriography for spinal arteriovenous fistula surgery: Technical note. Neuroradiology 41:915–919, 1999.
49. Hashimoto H: Spinal dural arteriovenous fistula with perimesencephalic subarachnoid haemorrhage. J Clin Neurosci 7:64–66, 2000.
50. Heinz R: Detection of cerebrospinal fluid metastasis: CT myelography or MR? AJNR Am J Neuroradiol 16:1147–1151, 1995.
51. Hirai T: Case report: Varicella-zoster virus myelitis—serial MR findings. Br J Radiol 69:1187–1190, 1996.
52. Hittmair K: Spinal cord lesions in patients with multiple sclerosis: Comparison of MR pulse sequences. AJNR Am J Neuroradiol 17: 1555–1565, 1996.
53. Hurst RW: Peripheral spinal cord hypointensity on T2-weighted MR images: A reliable imaging sign of venous hypertensive myelopathy. AJNR Am J Neuroradiol 21:781–786, 2000.

54. Keiper MD, Grossman RI, Brunson JC, Schnall MD: The low sensitivity of fluid-attenuated inversion-recovery MR in the detection of multiple sclerosis of the spinal cord. AJNR Am J Neuroradiol 18:1035–1039, 1997.
55. Kelly DR, Smith CD, McQuillen MP: Successful medical treatment of a spinal histoplasmoma. J Neuroimaging 4:237–239, 1994.
56. Keung YK: Secondary syringomyelia due to intramedullary spinal cord metastasis: Case report and review of literature. Am J Clin Oncol 20:577–579, 1997.
57. King SJ, Jeffree MA: MRI of an abscess of the cervical spinal cord in a case of *Listeria* meningoencephalomyelitis. Neuroradiology 35: 495–496, 1993.
58. Koehler PJ: Delayed radiation myelopathy: Serial MR-imaging and pathology. Clin Neurol Neurosurg 98:197–201, 1996.
59. Koh S: Myelopathy resulting from invasive aspergillosis. Pediatr Neurol 19:135–138, 1998.
60. Kohno M: Postmyelographic computerized tomographic scan in the differential diagnosis of radiculomeningeal arteriovenous malformation: Technical note. Surg Neurol 47:68–71, 1997.
61. Kohno M: Preoperative and postoperative magnetic resonance imaging (MRI) findings of radiculomeningeal arteriovenous malformations: Important role of gravity in the symptoms and MRI. Surg Neurol 48:352–356, 1997.
62. Kovacs B: Transverse myelopathy in systemic lupus erythematosus: An analysis of 14 cases and review of the literature. Ann Rheum Dis 59:120–124, 2000.
63. Kumar J, Kimm J: MR in *Toxocara canis* myelopathy. AJNR Am J Neuroradiol 15:1918–1920, 1994.
64. Lapointe JS, Graeb DA, Nugent RA, Robertson WD: Value of intravenous contrast enhancement in the CT evaluation of intraspinal tumors. AJR Am J Roentgenol 146:103–107, 1986.
65. Larsson EM, Desai P, Hardin CW, et al: Venous infarction of the spinal cord resulting from dural arteriovenous fistula: MR imaging findings. AJNR Am J Neuroradiol 12:739–743, 1991.
66. Larsson EM, Holtas S, Nilsson O: Gd-DTPA–enhanced MR of suspected spinal multiple sclerosis. AJNR Am J Neuroradiol 10: 1071–1076, 1989.
67. Lee M: Nonneoplastic intramedullary spinal cord lesions mimicking tumors. Neurosurgery 43:788–794, 1998.
68. Leite CC, Jinkins JR, Escobar BE, et al: MR imaging of intramedullary and intradural-extramedullary spinal cysticercosis. AJR Am J Roentgenol 169:1713–1717, 1997.
69. Li MH, Holtas S: MR imaging of spinal intramedullary tumors. Acta Radiol 32:505–513, 1991.
70. Lindner A: Magnetic resonance image findings of spinal intramedullary abscess caused by *Candida albicans:* Case report. Neurosurgery 36:411–412, 1995.
71. Mascalchi M: MR angiography of spinal vascular malformations. AJNR Am J Neuroradiol 16:289–297, 1995.
72. Mascalchi M: Identification of the feeding arteries of spinal vascular lesions via phase-contrast MR angiography with three-dimensional acquisition and phase display. AJNR Am J Neuroradiol 18:351–358, 1997.
73. Mascalchi M: Posterior spinal artery infarct. AJNR Am J Neuroradiol 19:361–363, 1998.
74. Mawad ME, Rivera V, Crawford S, et al: Spinal cord ischemia after resection of thoracoabdominal aortic aneurysms: MR findings in 24 patients. AJNR Am J Neuroradiol 11:987–991, 1990.
75. Mehalic TF, Pezzuti RT, Applebaum BI: Magnetic resonance imaging and cervical spondylotic myelopathy. Neurosurgery 26:217–226, 1990.
76. Melhem ER, Wang H: Intramedullary spinal cord tuberculoma in a patient with AIDS. AJNR Am J Neuroradiol 13:986–988, 1992.
77. Merine D, Wang H, Kumar AJ, et al: CT myelography and MR imaging of acute transverse myelitis. J Comput Assist Tomogr 11: 606–608, 1987.
78. Miller GM, Forbes GS, Onofrio BM: Magnetic resonance imaging of the spine. Mayo Clin Proc 64:986–1004, 1989.
79. Miyasaka K: Computed tomography and magnetic resonance imaging of intramedullary spinal cord tumors. Acta Radiol Suppl 369: 738–740, 1986.
80. Miyatake S, Kikuchi H, Koide T, et al: Cobb's syndrome and its treatment with embolization: Case report. J Neurosurg 72:497–499, 1990.
81. Mock A, Levi A, Drake JM: Spinal hemangioblastoma, syrinx, and hydrocephalus in a two-year-old child. Neurosurgery 27:799–802, 1990.
82. Mukunda BN: Solitary spinal intramedullary abscess caused by *Nocardia asteroides*. South Med J 92:1223–1224, 1999.
83. Murphy KJ, Brunberg JA, Quint DJ, Kazanjian PH: Spinal cord infection: Myelitis and abscess formation [see comments]. AJNR Am J Neuroradiol 19:341–348, 1998.
84. Nabatame H, Nakamura K, Matuda M, et al: MRI of syphilitic myelitis. Neuroradiology 34:105–106, 1992.
85. Nagakawa H, et al: Computed tomography of soft tissue masses related to the spinal column. In Post MJ (ed): Radiographic Evaluation of the Spine: Current Advances with Emphasis on Computed Tomography. New York, Masson, 1980, pp 320–352.
86. Nemoto Y, Inoue Y, Tashiro T, et al: Intramedullary spinal cord tumors: Significance of associated hemorrhage at MR imaging. Radiology 182:793–796, 1992.
87. Nesbit GM, Miller GM, Baker HL Jr, et al: Spinal cord sarcoidosis: A new finding at MR imaging with Gd-DTPA enhancement. Radiology 173:839–843, 1989.
88. Neumann-Andersen G: Involvement of the entire spinal cord and medulla oblongata in acute catastrophic-onset transverse myelitis in SLE. Clin Rheumatol 19:156–160, 2000.
89. Neumann HP, Eggert HR, Scheremet R, et al: Central nervous system lesions in von Hippel-Lindau syndrome. J Neurol Neurosurg Psychiatry 55:898–901, 1992.
90. Nitta H: Cervical spinal cord infarction after surgery for a pineal region choriocarcinoma in the sitting position: Case report. Neurosurgery 40:1082–1085, 1997.
91. Nittner K: Spinal meningiomas, neurinomas, and neurofibromas, and hourglass tumors. In Vinken PJ, Bruyn GW (eds): Handbook of Clinical Neurology. New York, Elsevier North-Holland, 1976, pp 177–322.
92. Oishi H: Successful surgical treatment of a dural arteriovenous fistula at the craniocervical junction with reference to pre- and postoperative MRI. Neuroradiology 41:463–467, 1999.
93. Oldfield EH, Di Chiro G, Quindlen EA, et al: Successful treatment of a group of spinal cord arteriovenous malformations by interruption of dural fistula. J Neurosurg 59:1019–1030, 1983.
94. Parizel PM: Gd-DTPA-enhanced MR imaging of spinal tumors. AJR Am J Roentgenol 152:1087–1096, 1989.
95. Pascuzzi RM, Shapiro SA, Rau AN, et al: Sarcoid myelopathy. J Neuroimaging 6:61–62, 1996.
96. Pfausler B: Syndrome of the anterior spinal artery as the primary manifestation of aspergillosis. Infection 23:240–242, 1995.
97. Phuphanich S: Magnetic resonance imaging of syrinx associated with intramedullary metastases and leptomeningeal disease. J Neuroimaging 6:115–117, 1996.
98. Poon TP, Tchertkoff V, Pares GF, et al: Spinal cord *Toxoplasma* lesion in AIDS: MR findings. J Comput Assist Tomogr 16:817–819, 1992.
99. Post MJ, Quencer RM, Green BA, et al: Intramedullary spinal cord metastases, mainly of nonneurogenic origin. AJR Am J Roentgenol 148:1015–1022, 1987.
100. Provenzale JM, Barboriak DP, Gaensler EH, et al: Lupus-related myelitis: Serial MR findings. AJNR Am J Neuroradiol 15:1911–1917, 1994.
101. Ratliff JK: Intramedullary tuberculoma of the spinal cord: Case report and review of the literature. J Neurosurg 90:125–128, 1999.
102. Renowden SA: Case report: Spontaneous thrombosis of a spinal dural AVM (Foix-Alajouanine syndrome)—magnetic resonance appearance. Clin Radiol 47:134–136, 1993.
103. Resnick DK, Comey CH, Welch WC, et al: Isolated toxoplasmosis of the thoracic spinal cord in a patient with acquired immunodeficiency syndrome: Case report. J Neurosurg 82:493–496, 1995.
104. Ricolfi F: Giant perimedullary arteriovenous fistulas of the spine: Clinical and radiologic features and endovascular treatment. AJNR Am J Neuroradiol 18:677–687, 1997.
105. Russell DS, Rubenstein LJ: Pathology of Tumors of the Nervous System. Baltimore, Williams & Wilkins, 1989.
106. Schubeus P, Schorner W, Hosten N, Felix R: Spinal cord cavities: Differential-diagnostic criteria in magnetic resonance imaging. Eur J Radiol 12:219–225, 1991.
107. Scotti G, Scialfa G, Colombo N, Landoni L: Magnetic resonance diagnosis of intramedullary tumors of the spinal cord. Neuroradiology 29:130–135, 1987.

108. Sener RN, Larsson EM, Backer R, Jinkins JR: MRI of intradural spinal arteriovenous fistula associated with ischemia and infarction of the cord. Clin Imaging 17:73–76, 1993.
109. Shapiro R (ed): Tumors. In Myelography. Chicago, Year Book Medical Publishers, 1984, pp 345–421.
110. Slasky BS, Bydder GM, Niendorf HP, Young IR: MR imaging with gadolinium-DTPA in the differentiation of tumor, syrinx, and cyst of the spinal cord. J Comput Assist Tomogr 11:845–850, 1987.
111. Solomon RA, Stein BM: Unusual spinal cord enlargement related to intramedullary hemangioblastoma. J Neurosurg 68:550–553, 1988.
112. Solsberg MD, Lemaire C, Resch L, Potts DG: High-resolution MR imaging of the cadaveric human spinal cord: Normal anatomy. AJNR Am J Neuroradiol 11:3–7, 1990.
113. Steinbok P: Intramedullary spinal cord tumors in children. Neurosurg Clin North Am 3:931–945, 1992.
114. Su MC, Ho WL, Chen JH. Intramedullary cryptococcal granuloma of spinal cord: A case report. Chung Hua I Hsueh Tsa Chih (Taipei) 53:58–61, 1994.
115. Suzuki K: Anterior spinal artery syndrome associated with severe stenosis of the vertebral artery. AJNR Am J Neuroradiol 19:1353–1355, 1998.
116. Sze G: Gadolinium-DTPA in spinal disease. Radiol Clin North Am 26:1009–1024, 1988.
117. Sze G: Intramedullary disease of the spine: Diagnosis using gadolinium-DTPA–enhanced MR imaging. AJR Am J Roentgenol 151: 1193–1204, 1988.
118. Sze G, Merriam M, Oshio K, Jolesz FA: Fast spin-echo imaging in the evaluation of intradural disease of the spine. AJNR Am J Neuroradiol 13:1383–1392, 1992.
119. Tacconi L: Intramedullary spinal cord abscess: Case report. Neurosurgery 37:817–819, 1995.
120. Tartaglino LM, Friedman DP, Flanders AE, et al: Multiple sclerosis in the spinal cord: MR appearance and correlation with clinical parameters. Radiology 195:725–732, 1995.
121. Tas MW, Barkhol F, van Walderveen MA, et al. The effect of gadolinium on the sensitivity and specificity of MR in the initial diagnosis of multiple sclerosis. AJNR Am J Neuroradiol 16:259–264, 1995.
122. Terwey B, Becker H, Thron AK, Vahldiek G: Gadolinium-DTPA enhanced MR imaging of spinal dural arteriovenous fistulas. J Comput Assist Tomogr 13:30–37, 1989.
123. Thorpe JW, Kendall BE, MacManus DG, et al: Dynamic gadolinium-enhanced MRI in the detection of spinal arteriovenous malformations. Neuroradiology 36:522–529, 1994.
124. Thurnher MM, Post MJ, Jinkins JR: MRI of infections and neoplasms of the spine and spinal cord in 55 patients with AIDS. Neuroradiology 42:551–563, 2000.
125. Turjman F, Joly D, Monnet O, et al: MRI of intramedullary cavernous haemangiomas. Neuroradiology 37:297–302, 1995.
126. Valk J: Magnetic resonance imaging in the differentiation of spinal cord tumours and hydromyelia. Acta Radiol Suppl 369:242–244, 1986.
127. Vishteh AG, Zabramski JM, Spetzler RF: Patients with spinal cord cavernous malformations are at an increased risk for multiple neuraxis cavernous malformations. Neurosurgery 45:30–32, 1999.
128. Waubant E: MRI of intramedullary sarcoidosis: Follow-up of a case. Neuroradiology 39:357–360, 1997.
129. Williams AL, Haughton VM, Pojunas KW, et al: Differentiation of intramedullary neoplasms and cysts by MR. AJR Am J Roentgenol 149:159–164, 1987.
130. Winkelman MD, Adelstein DJ, Karlins NL: Intramedullary spinal cord metastasis: Diagnostic and therapeutic considerations. Arch Neurol 44:526–531, 1987.
131. Yuh WT, Marsh EE, Wang AK, et al: MR imaging of spinal cord and vertebral body infarction [see comments]. AJNR Am J Neuroradiol 13:145–154, 1992.
132. Zimmerman RA: Imaging of tumors of the spinal canal and cord. Radiol Clin North Am 26:965–1007, 1988.

25 Magnetic Resonance Imaging of Infections of the Spine

Charles F. Lanzieri

Because infections of the spine present with subtle and nonspecific symptoms, they represent a diagnostic problem, and imaging plays a key role in the initial diagnosis and subsequent management. Clinical symptoms, which commonly include fever, malaise, back pain, and focal tenderness, are often insidious in onset and can be attributed to a variety of common conditions. By the time focal neurologic findings such as extremity weakness or meningismus appear, the stage is set for rapid progression to permanent neurologic deficits at worst and a chronic state of osteomyelitis at best. The infection can rapidly spread to the epidural space with concomitant paraplegia. Delayed diagnosis increases the morbidity and mortality of spinal infections; diagnostic imaging is therefore critical.

Infection of the spine initially involves either the disk space or the vertebral body, and spread occurs via the arterial or venous system or by direct inoculation during diagnostic procedures. Pyogenic infections evolve more rapidly than nonpyogenic infections, which have a more indolent course. Pyogenic infections are commonly caused by *Staphylococcus aureus*, which accounts for about 60% of this category of infection.[2, 5, 12] The most common cause of the nonpyogenic infections is *Mycobacterium tuberculosis*. Specific pathogens are more common in patients with predisposing conditions. For example, *Salmonella* is a common cause of osteomyelitis in patients with sickle cell disease, and *Serratia* and *Candida* are commonly seen in patients using intravenous drugs. The course of nonpyogenic infections is even more insidious and has a slower evolution than that of pyogenic infections. Infections caused by the tubercle bacillus or fungus are very difficult to diagnose.

Before cross-sectional imaging in the 1980s, radiologic diagnosis of disk space infections and vertebral osteomyelitis depended on interpretation of plain radiographs and radionuclide studies. Radiographs are usually unrevealing for the first 2 to 8 weeks of the disease process. Radionuclide studies have demonstrated incorporation of technetium 99m in 80% of infected bone sites by the 10th day of the infection.[15] These examinations, however, have significant limitations, most notably false-positive results. Radionuclide bone scans cannot reliably differentiate cellulitis from osteomyelitis. False negatives also occur when the blood supply to the infected bone or disk space is impaired.

The use of high-resolution computed tomography (CT) was found to be very useful because of its ability to demonstrate bone destruction or focal osteopenia early in the course of the infection. Its ability to demonstrate prevertebral soft tissue swelling and cellulitis, however, was disappointing.

Magnetic resonance imaging (MRI) quickly became the study of choice for evaluating patients with spinal complaints. Its advantages include multiplanar capability, superior soft tissue contrast resolution, and a unique ability to detect end-plate, disk space, and marrow changes. In addition, MRI can demonstrate subtle changes far earlier in the course of the disease than previously employed techniques. Finally, MRI is extremely useful for following patients with proven spinal infection and for planning aspirations or other interventions. This has a direct impact on patient management. MRI has dramatically changed the outcome of patients with spinal infections over the last 10 years.

Pathophysiology

Infectious processes can extend to the spine by several mechanisms. Direct extension occurs secondary to trauma or surgical intervention for reasons other than infection. Diagnostic lumbar punctures or epidural injections as well as surgery for herniated disks are common causes. Contiguous spread can occur from adjacent infected structures. Hematogenous spread can come from distant sites. A source of hematogenous dissemination can be found in up to half of the patients with spinal osteomyelitis.[4] The most common sources are the genitourinary tract, the skin, and the respiratory tract.[18] The arterial system is thought to be a much more common route of spread to the spine, although extension via the epidural venous plexus occurs via the pelvic plexus of veins.[19]

A number of events occur during the first few weeks of infectious spondylitis. The organism commonly settles in the anterior portion of the subchondral bone marrow. The infection then spreads within the marrow space or into the adjacent intervertebral disk, causing osteomyelitis and/or diskitis. Nonpyogenic infection may spread into the subligamentous space, and from there it may penetrate the ligament and the adjacent soft tissues. Disk-sparing infections of adjacent vertebral bodies are a common sign of tubercle bacillus infection.[5] Both pyogenic and nonpyo-

genic infections tend to remain within the vertebral body and disk spaces and do not usually involve the posterior elements and adjacent ligaments and soft tissues. This type of involvement is more typical of metastatic disease.

Although pyogenic infections rarely involve the posterior elements, tuberculosis (TB) sometimes does. The level most often involved in TB spondylitis is L1, but the thoracolumbar junction is most affected in general. The cervical and lumbar levels are less frequently involved.

Following successful therapy for infection, the reparative process can include partial or complete bony ankylosis of the disk space. Without adequate or proper therapy, bony lysis occurs, with subsequent collapse of the vertebral body. In nonpyogenic infections such as TB, anterior wedging with secondary kyphotic deformity occurs.

Pyogenic Disk Space Infections

Pyogenic infections, which have a peak incidence in the sixth and seventh decades of life, are caused by both gram-positive and gram-negative bacteria. The dominant inflammatory cell is the polymorphonuclear leukocyte. Both the vertebral body and the adjacent disk space become involved. The cancellous bone adjacent to the cartilaginous end plate is richly vascular throughout adulthood, which makes it a common site for visitation from hematogenously borne pathogens. The infection then spreads across the disk to involve the adjacent vertebral body. Most of the time, the infection is limited to the disk space and the two adjacent vertebral bodies. In about 25% of cases, multiple levels are involved.[8] Infectious agents settle in the most vascular spaces in the spine.

In children, who have a rich vascular supply in and around the disk spaces, infections can spread directly to the disk.[5] In adults, the disk space is nearly avascular; therefore, infections begin in the subchondral bone adjacent to the end plate, which is very vascular throughout adulthood. Pyogenic infections are often self-limited in children and may be cured with bed rest and antibiotics.

The population most commonly affected by vertebral osteomyelitis consists of adults in the sixth to seventh decade of life. The lumbar spine is the site most commonly affected, followed by the thoracic and cervical spine. Men are affected more often than women, at a ratio of two to one. Treatment with parenteral antibiotics for about 6 weeks is usually required for cure. Surgical intervention is necessary when there are neurologic findings and an epidural mass is identified, or when there is secondary instability and fusion needs to be performed.

Radiographic findings are usually subtle and may not appear until relatively late in the process (Fig. 25–1). The hallmark of disk space infection on plain radiographic examination is disk space narrowing. This is followed by erosion of the adjacent end plates. It may be several days or weeks before these findings are evident. The characteristic findings of disk space narrowing and end-plate irregularity may not be seen until the fourth week of the infection. Prominence of the retropharyngeal soft tissues is a variable finding. Plain films cannot demonstrate the important intraspinal complications of infection that are ultimately responsible for neurologic symptoms. CT is very useful in

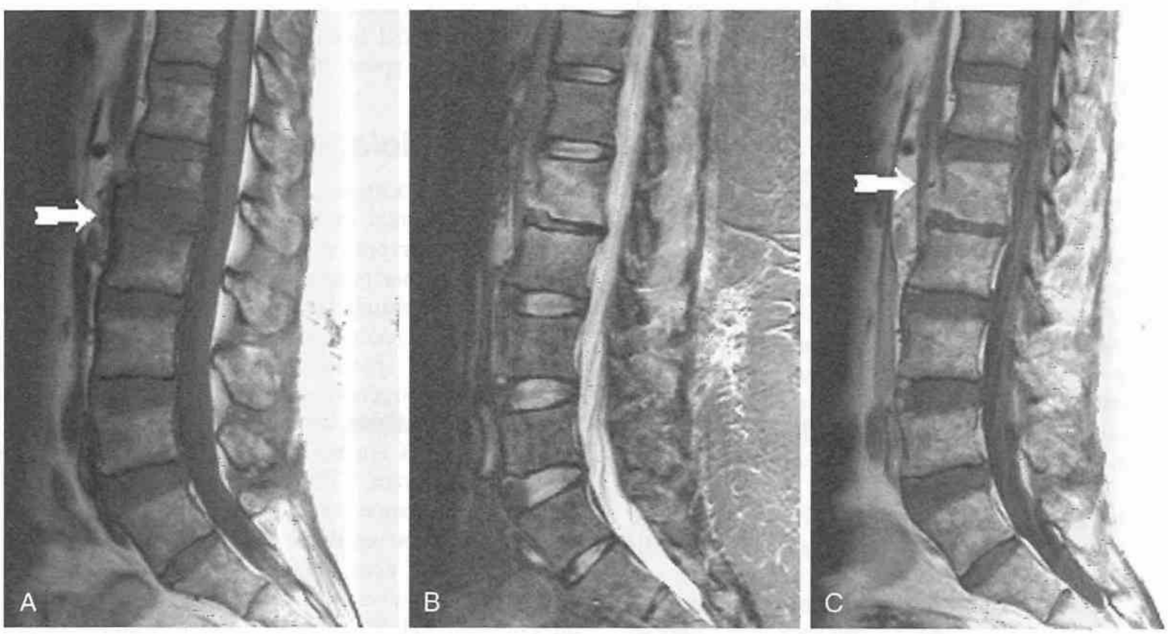

Figure 25–1. Lumbar disk space infection with osteomyelitis.

A, T1-weighted sagittal MR image through the lumbar spine. The *arrow* indicates a disk space infection at the L1-2 level. The normal cortical dark line along both articular surfaces, especially along the inferior surface of L1, is not visible. A decrease in the signal coming from the marrow fat in both vertebrae indicates the presence of marrow edema.

B, T2-weighted image in the same location shows edema in the marrow and slightly increased signal in the interspace. Although the disk space at L1-2 is not brighter than the adjacent disk spaces, the normal internuclear cleft is lost. In addition, a much lower signal would be expected in a partially collapsed and degenerated disk.

C, Post–contrast-enhanced image in the same location. Although the disk space itself does not show enhancement, the vertebral bodies do. The *arrow* indicates loss of the anterior cortical margin of L1, a sign of upward spread of infection.

these patients because it is more sensitive than plain film. In addition, the soft tissue changes begin to become evident.

MRI offers the best opportunity to image and confirm vertebral infections early in their course. The first MR findings reflect the replacement of normal bone marrow by inflammatory tissue and edema in association with structural changes such as disk space narrowing.[10] The sensitivity of MRI for disk space infections is the same as that of radionuclide studies and the specificity is much higher. Even early studies using nonenhanced MRI showed a sensitivity of 96%, a specificity of 92%, and an accuracy of 92%.[10] Evidence of vertebral osteomyelitis appears at about the same time on MRI as it does on gallium or technetium 99m radionuclide studies.[10]

Marrow replacement first appears as decreased signal on T1-weighted images because of edema or infiltration of fat in the bone marrow. On T2-weighted images, marrow edema is reflected as increased signal because of the additional water content in the marrow. A band of increased signal in the subchondral bone marrow is highly suggestive of pathologic change in the adjacent disk space. Unfortunately, this change is somewhat nonspecific and can be seen in a variety of conditions including recent trauma and early degenerative disease. Changes in the disk space are seen on both T1-weighted and T2-weighted images. On the T1-weighted images, narrowing of the interspace with slight loss of signal can usually be visualized.

The most dramatic, recognizable, and reliable sign of disk space infection on MRI is the increased signal seen on T2-weighted images. In adults, this is accompanied by loss of the normal band of decreased signal that represents what is referred to as the intranuclear cleft. These findings may be supported by the observation of swelling and edema in the adjacent soft tissues (Fig. 25–2). When the

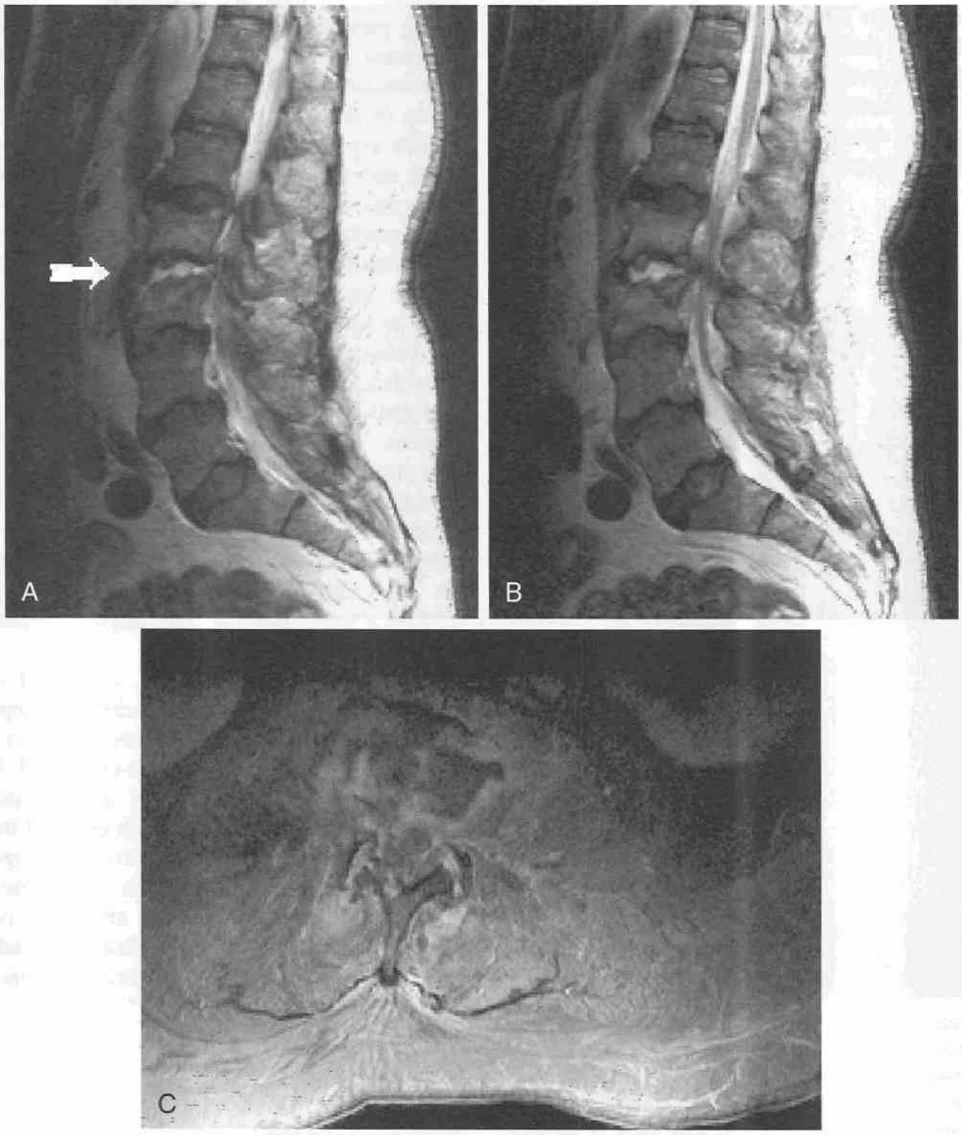

Figure 25–2. Lumbar disk space infection with osteomyelitis and paraspinal cellulitides. *A* and *B,* Sagittal T2-weighted images through the lumbar spine. Bright signal is associated with the L2-3 intervertebral disk. This is the hallmark of diskitis on an MRI scan *(arrow). C,* Post–contrast-enhanced axial T1-weighted image. Enhancement can be visualized in and around the L2-3 interspace, as well as in the paraspinal soft tissues and within the spinal canal. These represent paraspinal and epidural cellulitides. If left untreated, they could progress to abscess formation.

bony cortex of the vertebral body becomes involved, the normally dark cortical margin on all MRI sequences can no longer be visualized. This implies osteomyelitis. If intravenous contrast material is given, enhancement within the disk space and in the adjacent vertebral bodies usually increases diagnostic confidence.[13]

Some pitfalls exist in diagnosing disk space infections using MRI. The intermediate changes seen in degenerative disk disease may mask the early changes of a disk space infection. Both processes produce low signal on T1-weighted images. In the case of degenerative disease, the infiltration of fat into the subchondral portion of the vertebra is an intermediate change that increases the T1 signal intensity. Since infection lowers the degree of T1 signal, a canceling effect occurs that potentially masks the edema. The T2-weighted images should be reviewed carefully to search for edema in suspected infections. Occasionally, a degenerated disk transiently contains cystic areas. This causes increased signal on T2-weighted images and mimics one of the hallmarks of diskitis, a bright interspace.

Although many disk space infections represent hematogenous seeding, a significant number are secondary to surgery involving the disk space. Disk space infections follow up to 3% of surgical procedures on the spine.[5] Clinical suspicion is raised when, in the first few postoperative weeks, patients present with back pain radiating to the extremities and signs of infection such as elevated white blood cell count, an elevated sedimentation rate, and fever. Because signal changes in the vertebral bodies, disk spaces, and adjacent soft tissues occur following surgery, the diagnosis of postoperative infection is difficult.

Cervical vertebral osteomyelitis and diskitis are usually diseases of older people, but they occur frequently in younger patients who are intravenous drug abusers (Fig. 25–3).[16]

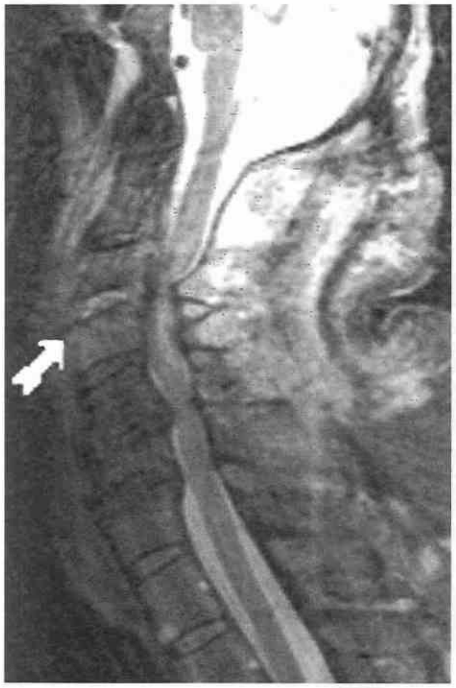

Figure 25–3. Cervical disk space infection. Disk space infections and diskitis are unusual occurrences in the cervical spine. T2-weighted sagittal image shows increased signal in the C3-4 intervertebral disk space and edema in the adjacent bone marrow fat *(arrow)*. The cortical margins remain intact and there is no evidence of a paraspinal abscess. Increased signal in the adjacent spinal cord represents the presence of myelomalacia from chronic cord compression. Although this patient had not had previous surgery, the same appearance is seen following cervical diskectomy.

Epidural Abscesses

Epidural abscesses can occur either spontaneously or secondary to disk space infection and osteomyelitis. Imaging greatly improves patient outcome because a specific diagnosis based only on clinical signs and symptoms is impossible and early treatment is important. MRI is the study of choice when an epidural abscess is suspected and results are positive before radionuclide scanning.[1] Clinical signs and symptoms include back and radicular pain, stiffness, and cramping. Rapid expansion can result in permanent neurologic deficits, the result of direct cord or root compression in most cases, with secondary white matter injury. Vascular thrombosis and direct infiltration of the cord or roots are less common.

Although MRI and myelographic CT are similar in sensitivity for identifying epidural abscesses,[10] MRI offers the ability to distinguish between causes of epidural masses. Thus MRI can differentiate epidural abscess from hematoma, tumor, or disk fragment (Fig. 25–4). Because it is noninvasive, it is the obvious first choice for imaging. Epidural abscesses appear as isointense masses on T1-weighted images, and the intensity is frequently increased on T2-weighted images.[12] Patients with epidural abscess almost always have accompanying meningeal thickening and enhancement.

Without contrast injection, any fluid collection in, or necrotic portion of, the subarachnoid or epidural space can be overlooked. Although not necessary for the diagnosis of disk space infections, contrast-enhanced MRI is essential for the accurate diagnosis of abscess collections in the epidural space (Fig. 25–5). With contrast injection, epidural abscesses are easily demonstrated. Homogeneous enhancement of the mass is seen, with central necrosis indicating a focal fluid collection. Most abscesses occur adjacent to an infected interspace and generally spread to between two and four vertebral levels. Rarely, extension may involve the entire length of the spine.[14]

Tuberculosis

Tubercle bacillus infections are more insidious than pyogenic infections of the spine. As in pyogenic infections, the initial symptoms are nonspecific and early diagnosis is

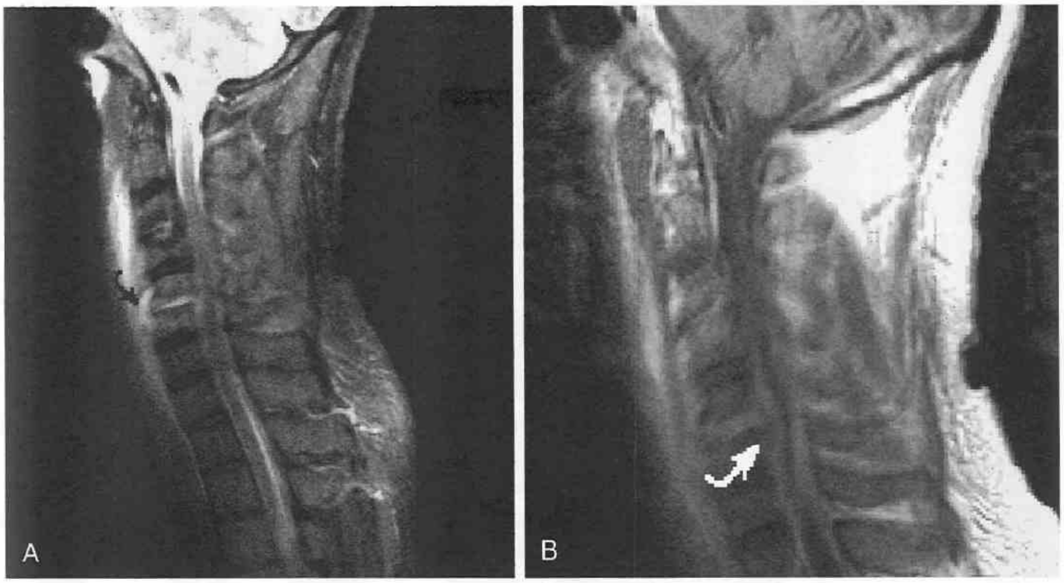

Figure 25–4. Cervical disk space infection with epidural abscess. *A*, T2-weighted sagittal image through the cervical spine. The C5-5 intervertebral disk space has increased signal, indicating the presence of diskitis. Although there is no evidence of adjacent marrow edema and the cortical margins are intact, a region of increased signal in the paraspinal soft tissues anterior to the interspace *(arrow)* indicates the presence of paraspinal cellulitis. *B*, T1-weighted sagittal image reveals contrast enhancement of the interspace, which confirms disk space infection. Thickening and enhancement of the meninges in the cervical spine and a small epidural fluid collection in the epidural space *(arrow)* indicate the presence of an epidural abscess.

difficult. In the case of TB, the symptoms may last for months or years prior to diagnosis. Tuberculous vertebral osteomyelitis remains a significant medical problem in developing countries.

The skeleton is the most common extrapulmonary site of involvement, and spinal TB occurs in 50% of the cases of skeletal TB. Vertebral osteomyelitis is estimated to occur in 0.03% of all TB cases.[7] The TB bacillus spreads to the vertebral body hematogenously and, like pyogenic organisms, lodges in the anterior and subchondral portion of the vertebral body. The granulomatous inflammatory response to the bacillus results in a tubercle, which then invades the surrounding soft tissues and forms a tuberculous abscess. As the abscess grows, the periosteum and the longitudinal ligaments of the spine are elevated and the abscess extends up and down the spine to involve adjacent vertebra. The thoracolumbar junction is most frequently involved; involvement of the cervical and thoracic spine is unusual. Classically, spinal tuberculosis initially involves the anterior and inferior portion of the vertebral body (Fig. 25–6). Extension to other vertebral bodies occurs beneath the anterior and posterior longitudinal ligaments and is referred to as subligamentous spread. The disk spaces usually remain relatively spared.

Involvement of the posterior elements of vertebral bodies is more common in TB than in other forms of infection. Infection of multiple vertebral bodies and posterior elements is involved, with sparing of the disk spaces. This makes differentiation of TB from metastatic neoplasm difficult.[17]

Nontuberculous Granulomatous Spondylitis

The granulomatous response is a nonspecific response to an antigenic stimulus, and it is observed in a variety of pathologic conditions, including infections, neoplasms, and autoimmune diseases. The pathologic hallmark is the presence of mononuclear phagocytic cells and multinucleated giant cells. Organisms that infect the spine and cause a granulomatous reaction include the tubercle bacillus, *Brucella*, and fungi. In endemic areas of the Middle East and Asia, granulomatous spondylitis is still quite common.

Brucella is a small gram-negative coccobacillus common in cattle and swine. In the United States, the most common species are *B. abortus* and *B. suis*. When infecting humans, the organism often affects the lumbar spine. The disk space is usually spared and vertebral osteomyelitis may be accompanied by soft tissue fibrosis. The morphology of the vertebral body is preserved despite evidence of infection. The posterior elements are typically spared and the disk space is slightly reduced despite being involved with infection.

Fungal infections of the spine include coccidioidomycosis (most frequently encountered in the southwestern United States), blastomycosis (found in the central and southeastern states), and actinomycosis. The findings in fungal infections are not specific to the infecting agent. Multiple vertebral bodies are involved but the disk spaces are spared. On plain radiographs, lytic lesions with sclerotic margins are seen. Lytic bony lesions with sclerotic margins are frequently seen with sparing of the interspace. Epidural

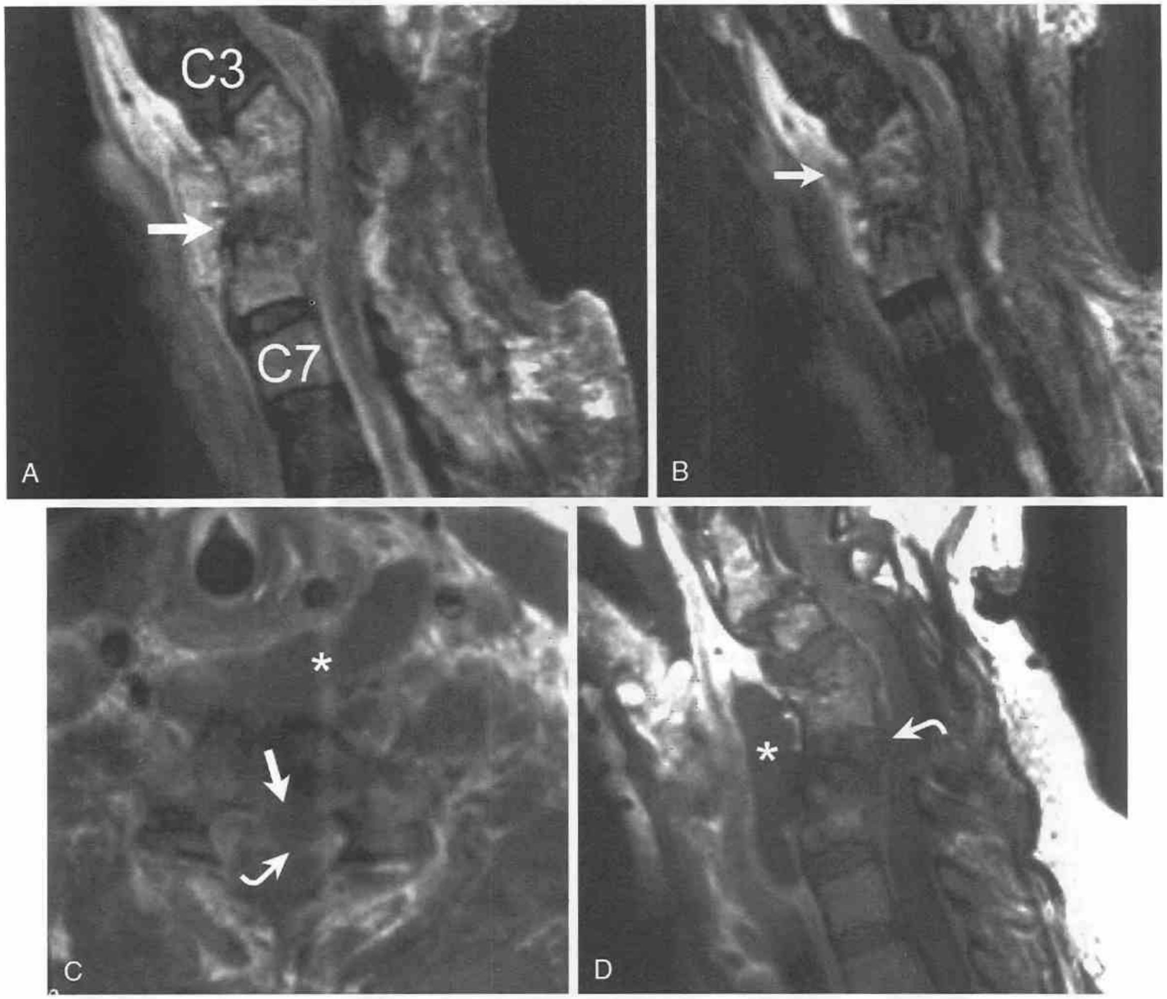

Figure 25–5. Retropharyngeal abscess with extension to the spine. Although retropharyngeal abscesses can progress to involve the adjacent spine, the opposite can also happen.

A, T2-weighted sagittal image reveals the presence of multilevel diskitis and osteomyelitis. Vertebral bodies C4 through T1 have increased signal, and the cortical margins are lost. There has been collapse of C4 and C6 and the C4-5 and C6-7 interspaces are obliterated from previous surgery and ongoing infection. A multilevel laminectomy has been performed as part of this patient's cervical decompression.

B, Post–contrast-enhanced and fat-suppressed T1-weighted image shows enhancement within the vertebral bodies and paraspinal soft tissues anterior to the spine. A focal region of nonenhancement just anterior to C5 *(arrow)* represents the presence of a small abscess in the paraspinal soft tissues. Images *C* and *D* were obtained several days later when the patient had failed to improve on antibiotic therapy.

C, Post–contrast-enhanced T1-weighted image through C6. The *asterisk* lies within a large retropharyngeal abscess that is contiguous with the C6 vertebral body. The *curved arrow* points to the thickened and enhancing meninges. The *straight arrow* indicates the presence of a fluid collection within the epidural space. This is an epidural abscess.

D, Sagittal image also shows the retropharyngeal and paraspinal abscess *(asterisk)* and the epidural abscess *(curved arrow).*

and meningeal involvement is seen with all of these types of infections, but the *degree* of involvement is usually somewhat less than that seen with TB abscess of a similar size.

Sarcoidosis

Sarcoidosis is a noncaseating granulomatous condition that affects multiple organs in adults in the third through fifth decades. About 5% of patients have central nervous system involvement. Involvement of the vertebral bodies is rare.[6] In the spine, where it is most often seen in the thoracolumbar region, it usually manifests as leptomeningeal thickening, and enhancement is seen after injection of contrast material. Mixed lytic and sclerotic changes have been seen in single or adjacent vertebrae. The intervertebral disks are spared.

Intramedullary Cord Infections

The human immunodeficiency virus (HIV) causes a vacuolar degeneration of the central nervous system. In

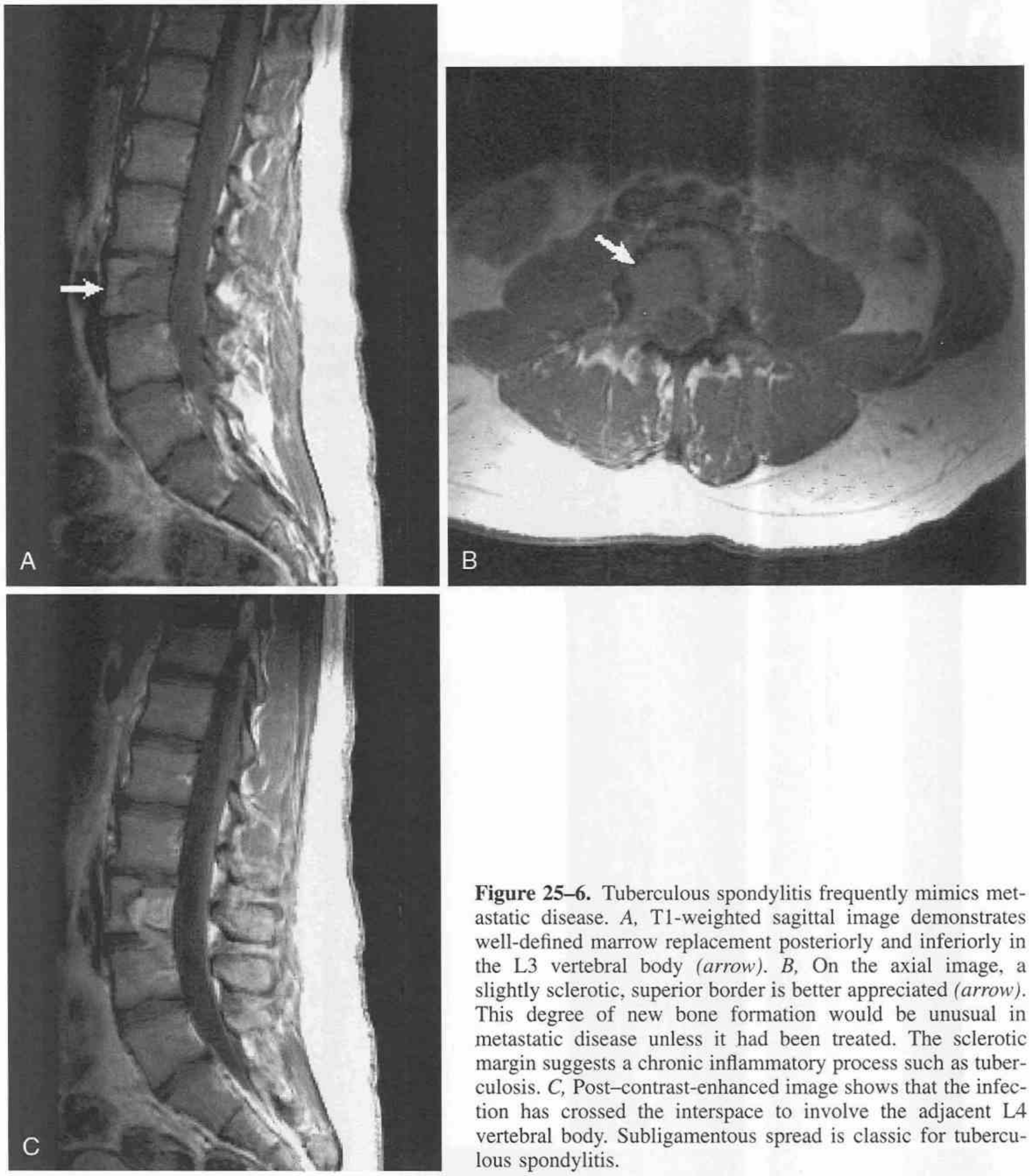

Figure 25–6. Tuberculous spondylitis frequently mimics metastatic disease. *A,* T1-weighted sagittal image demonstrates well-defined marrow replacement posteriorly and inferiorly in the L3 vertebral body *(arrow)*. *B,* On the axial image, a slightly sclerotic, superior border is better appreciated *(arrow)*. This degree of new bone formation would be unusual in metastatic disease unless it had been treated. The sclerotic margin suggests a chronic inflammatory process such as tuberculosis. *C,* Post–contrast-enhanced image shows that the infection has crossed the interspace to involve the adjacent L4 vertebral body. Subligamentous spread is classic for tuberculous spondylitis.

the brain, this feature of the acquired immunodeficiency syndrome (AIDS) is recognized as focal frontal lobe atrophy or volume loss. In the spinal cord, increased signal can be seen within a short segment of the cord. This carries the general name of transverse myelitis (Fig. 25–7), and it is caused by other infectious agents as well.

In patients who have transverse myelitis but are negative for HIV, other viral infections such as herpes zoster should be considered. A variety of noninfectious causes also exist, including nutritional deficiencies, toxins, and drugs.[3, 9] Common autoimmune and demyelinating diseases, such as multiple sclerosis and lupus erythematosus, also cause transverse myelitis.

The spinal cord itself can sometimes become infected, and a cord abscess may form.[11] The symptoms of cord infection are indistinguishable from those of an epidural abscess. Sources of cord infection include hematogenous spread, which is known to be a complication of congenital dermal sinuses, and bacterial endocarditis.

It has been suggested that the pathophysiology of cord infection is similar to that of cerebral infection. In the initial myelitis phase, cord edema and enlargement are observed. At approximately 1 week, a poorly defined ring of enhancement begins to appear. This results in the formation of an abscess cavity, which is relatively isointense on T1-weighted images and hyperintense on T2-weighted images. Cord abscesses are less well defined and less intensely enhancing than brain abscesses. This may be

Figure 25–7. Transverse myelitis. T2-weighted sagittal image through the cervical spine demonstrates the presence of increased signal in the dorsal columns of the spinal cord. This appearance is nonspecific and can be caused by a demyelinating process or infarction. In this instance, it was associated with a transient myelitis.

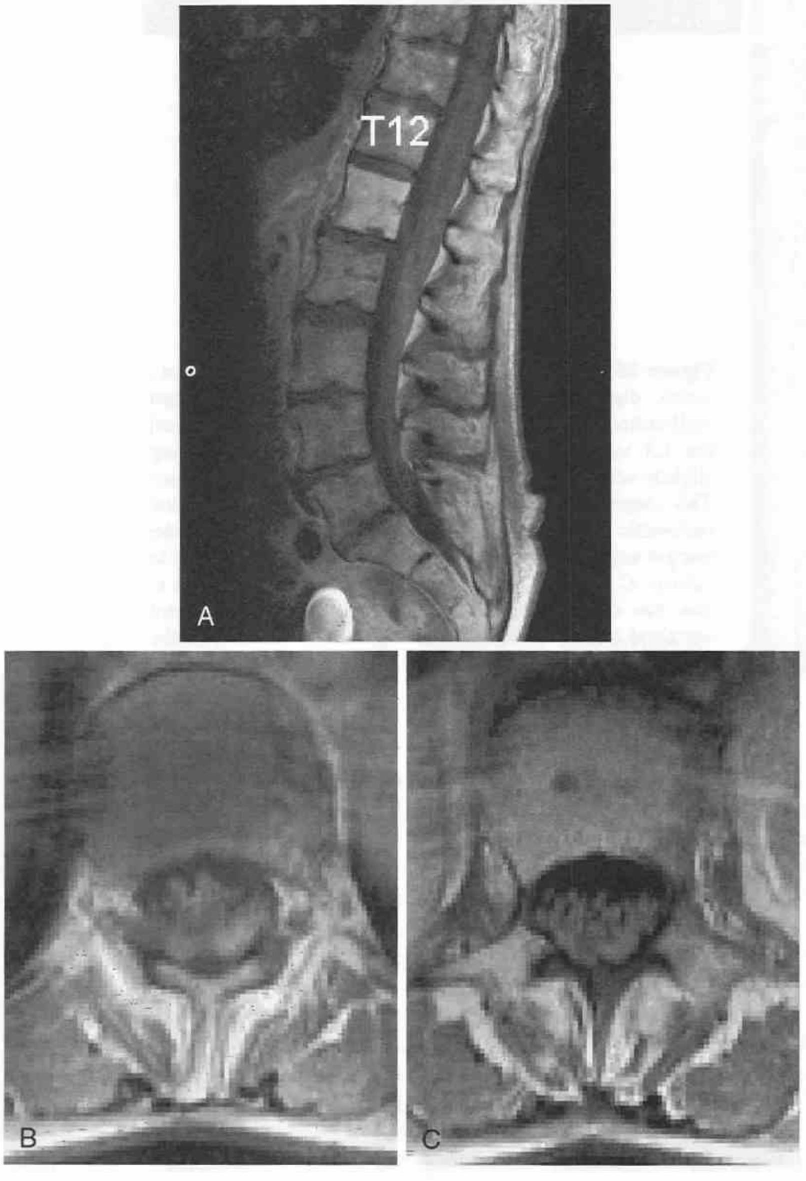

Figure 25–8. Meningeal infection, with subtle enhancement of the meninges covering the lumbar nerve roots. *A,* Post–contrast-enhanced T1-weighted image. The end of the conus medullaris at T12 is a flame-shaped structure that is slightly hypointense relative to the enhancing meninges and nerve roots. *B* and *C,* Axial contrast-enhanced images below the conus show that the nerve roots are thickened and enhancing. This nonspecific finding is compatible with meningitis and other disease processes.

because the cord is relatively hypovascular compared with the brain.

Bacterial abscess of the spinal cord has been thought to occur as a result of bacteremia.[2] Recently, cord abscesses have been reported in patients in whom the source of infection was not found.[11]

Meningeal Infection

Many infectious agents gain access to the central nervous system by first infecting the meninges. When encountered on MR images, meningeal infections produce a vague and subtle enhancement of both the dura and the leptomeninges (Fig. 25–8). Like transverse myelitis, this is a nonspecific finding; it can be caused by trauma, recent lumbar puncture, and various vascular malformations. For detecting meningeal infection, analysis of the cerebrospinal fluid is much more sensitive and specific, and much cheaper to perform, than any imaging procedure.

References

1. Angtuaco EJ, McConnell JR, Chadduck WM, Flanigan S: MR imaging of spinal epidural sepsis. AJR AM J Roentgenol 149:1249–1253, 1987.
2. Baby R, Jafer JJ, Hray PP, et al: Intramedullary abscess associated with spinal cord ependymoma. Neurosurgery 30:121–124, 1992.
3. Barakos JA, Mark AS, Dillon WP, et al: MR imaging of acute transverse myelitis and AIDS myelopathy. J Comput Assist Tomogr Comput 14:45, 1990.
4. Brant-Zawadole M: Infection. In Newton TH, Potts DG (eds): Computed Tomography of the Spine and Spinal Cord. San Anselmo, Calif, Clavadel Press, 1983, p 205.
5. Enzmann DR: Infection/inflammation. In Enzmann DR, De La Paz RL, Rubin J (eds): Magnetic Resonance of the Spine. St. Louis, Mosby–Year Book, 1990, p 260.
6. Kenney CM 3rd, Goldstein SJ: MRI of sarcoid spondylodiskitis. J Comput Assist Tomogr 16:660–662, 1992.
7. Lin-Greenberg A, Cholankeril J: Vertebral arch destruction in tuberculosis: CT features. J Comput Assist Tomogr 14:300–302, 1990.
8. Malawski SK: Pyogenic infection of the spine. Int Orthop 1:125, 1977.
9. Merine D, Way H, Kumer AJ, et al: CT myelography and MRI of acute transverse myelitis. J Comput Assist Tomogr 11:606, 1987.
10. Modic MT, Feiglin DH, Piraino DW, et al: Vertebral osteomyelitis: Assessment using MR. Radiology 157:157–166, 1985.
11. Murphy KJ, Brunberg JA, Quint DJ, et al: Spinal cord infection: Myelitis and abscess formation. AJNR Am J Neuroradiol 19:341–348, 1998.
12. Post MJD, Quencer RM, Montalvo BM, et al: Spinal infection: Evaluations with MR imaging and intraoperative ultrasound. Radiology 169:765, 1988.
13. Post MJD, Sze G, Quencer RM, et al: Gadolinium-enhanced MR in spinal infection. J Comput Assist Tomogr 14:721, 1990.
14. Post MJD, Bowen BC, Sze G: Magnetic resonance imaging of spinal infection. Rheum Dis Clin North Am 17:773–794, 1991.
15. Rinsley L, Gonis ML, Shurman DJ, et al: Technetium bone scanning in experimental osteomyelitis. Clin Orthop 128:361, 1977.
16. Ross PM, Fleming JL: Vertebral body osteomyelitis: Spectrum and natural history: A retrospective analysis of 37 cases. Clin Orthop 118: 190–198, 1976.
17. Smith AS, Weinstein MA, Lanzieri CF, et al: Tuberculous spondylitis: A contradiction of the MR characteristics of vertebral osteomyelitis. AJNR Am J Neuroradiol 10:619–625, 1989.
18. Waldvogel FA, Papageorgiou PS: Osteomyelitis: The past decade. N Engl J Med 303:360, 1980.
19. Wiley AM, Trueter J: The vascular anatomy of the spine and its relationship to pyogenic vertebral osteomyelitis. J Bone Joint Surg 413:796, 1959.

26 Image-Guided Spinal Interventions

Wade H. Wong, Huy M. Do, Barton Lane

Spine Biopsies

Biopsies of the spine can play an important role in determining the correct diagnosis because imaging, although sensitive, is often nonspecific. When the patient may have an infection, a prompt biopsy can help the clinician define the organism and determine the optimal antibiotic sensitivity for early treatment. A spinal biopsy can provide a pathologic diagnosis that is critical to staging and treatment planning of neoplasms.

Image guidance for biopsies of the spine is commonly provided with fluoroscopy or computed tomography (CT) scanning. In unique situations, image guidance with magnetic resonance imaging (MRI) might be provided.

Fluoroscopy

Biopsies of the lumbar spine are readily and efficiently performed with fluoroscopic guidance. C-arm fluoroscopy is preferable to single-plane fluoroscopy because it allows the patient to remain in a stationary position while multiplanar relationships of the biopsy needle relative to the target are rapidly determined. The technique of fluoroscopic needle biopsy of the lower lumbar spine begins as follows. The patient is positioned *isocentrically* within the C-arm fluoroscope in such a way that the target area within the patient is centered in the rotational axis of the C-arm fluoroscope. This can be rapidly accomplished by first positioning the target in the lateral view and then adjusting its location so that it is centered on the anteroposterior view.

Most biopsies of the spine can be performed with local anesthesia, although conscious sedation is sometimes helpful. After the patient is prepared and draped, an anesthetic needle is used to anesthetize the skin with a rather generous wheal, so that if the point of entry must be moved, it can be done so without having to reanesthetize the skin. Leaving the anesthetic needle in the skin by detaching the syringe from the needle with the needle along the intended trajectory course saves time in subsequent needle placements. With the initial anesthetic needle serving as a relative directional marker both on images and on the skin, longer needles can subsequently be placed with positional readjustments as necessary, so that the final needle can be placed in tandem (or coaxial) fashion relative to the target zone.

Most biopsies of the lumbar spine (from about L2 to L5) can be performed from a posterior-lateral starting point, usually about 10 cm lateral to the spinous processes on an average-sized adult. The view taken from this *posterior-lateral approach* is similar to that for a facet injection or for a diskogram (Fig. 26–1). Use of this approach permits a favorable trajectory to the center of the spine while avoiding the thecal sac if the operator should direct the needle too far posteriorly or avoiding the bowel or other internal abdominal viscera if the operator should direct the needle too far laterally.

Final needle placement is confirmed through visualization of the needle position on the anterior-posterior plane as well as on the lateral plane. This helps to confirm the needle position and depth.

An alternative to the posterior-lateral approach is the

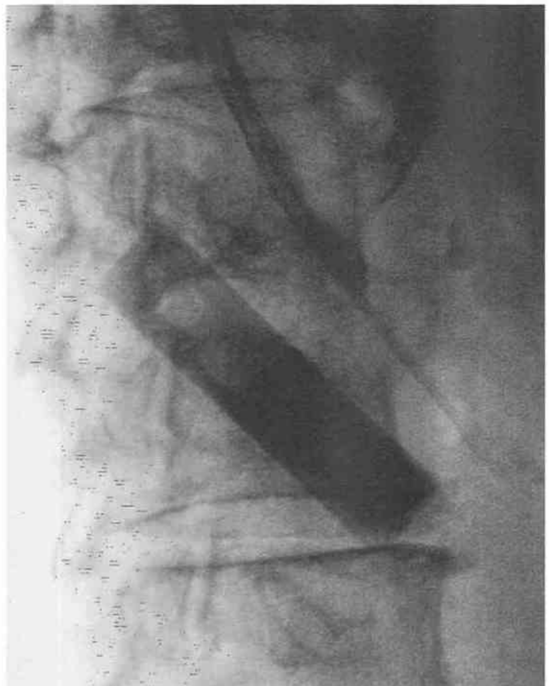

Figure 26–1. Fluoroscopically guided biopsy of L3 vertebra from a posterior-lateral approach starting about 10 cm lateral to the spinous processes in an average-size patient. This approach provides a clear view of the articular facet joints and would be the same for a facet injection or for a lumbar diskogram. When the bone is entered, anterior and lateral views should be obtained to determine the correct depth of placement in the vertebra. An 11-gauge core biopsy needle was used, and the diagnosis was staphylococcal osteomyelitis.

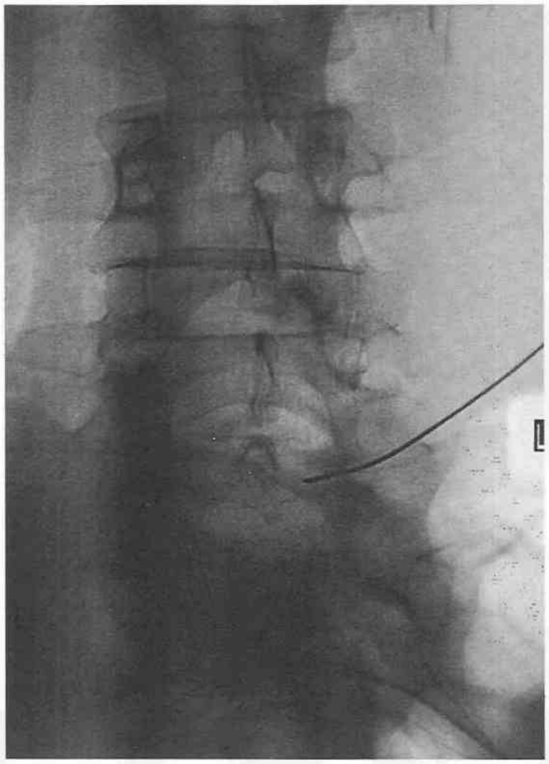

Figure 26–2. Fluoroscopically guided needle biopsy of the L5-S1 disk using a curved needle from a posterior-lateral starting point. The needle was passed over the iliac crest and then down to the level of the L5-S1 disk, at which point the needle was rotated medially to enter the disk. This is the same technique that would be used for a diskogram at the L5-S1 level. The diagnosis was diskitis due to *Streptococcus viridans*.

transpedicular approach, in which the needle is passed through the pedicle. With this approach, the needle can be angled slightly superiorly or inferiorly but movement medially or laterally is somewhat limited. For the transpedicular approach, the operator should avoid entering too far medially or inferiorly on the pedicle as this runs the risk of injury to the nerve root either in the lateral recess or at the neural foramen.

Fluoroscopically guided biopsies of the inferior margin of L5, the L5-S1 intervertebral disk, and the superior margin of S1 may be difficult from a posterior-lateral approach unless a curved needle is used to pass the needle over the intervening iliac crest and then down into the target area (Fig. 26–2). This technique is similar to performing an L5-S1 diskogram from the posterior-lateral approach.[59]

In all other areas of the spine, CT may be the preferred method of biopsy unless a transpedicular approach is taken with fluoroscopy.[4, 44] In the upper lumbar and thoracic regions, CT provides a means of visualizing the adjacent lung and other posteriorly located visceral organs, such as the kidneys, in the case of a high lumbar target.

In the cervical region, CT may also be the preferred method of image guidance for biopsies because it can be used to define the positions of the jugular vein, carotid artery, vertebral artery, and pharyngeal and esophageal structures more accurately than fluoroscopy can (Fig. 26–3). Furthermore, to perform cervical biopsies with fluoroscopy, the operator may have to place his or her fingers in such a way as to deviate the carotid sheath laterally and the pharyngeal structures medially. This still poses the risk of inadvertent perforation of the esophagus, pharynx, or one of the major blood vessels that have been fixed in position. In addition, fluoroscopically guided needle biopsies of the cervical spine may subject the operator's hands to radiation while the fingers are pressing between the carotid sheath and the pharynx/esophagus.

For paraspinous soft tissue biopsies, fluoroscopy is at a great disadvantage, compared with CT, in that it is difficult to visualize a paraspinous soft tissue target under fluoroscopy, whereas these areas become apparent under CT (Fig. 26–4).

If CT is chosen for image guidance for spine biopsy, the area of concern should first be localized with a scout film. We often place a V-shaped reference marker over the area of concern (see Fig. 26–3*A*). This marker consists of a polyethylene catheter that is bent at an acute angle and taped over the target zone. The marker helps to localize the level at which the optimal target will be found by providing a measurement of the distance between the limbs of the V, and we can confirm the location through localization with the laser light. From one of the limbs of the V marker on the patient, a starting point can be measured on the CT scanner and duplicated on the patient's skin surface.

We then prepare the patient. We use progressively longer anesthetic needles and deliver local anesthetic agent with a very large skin wheal. We leave the anesthetic needles in place, after they are disconnected from the syringe, along the anticipated trajectory for the biopsy needles. We scan and then readjust the trajectory of the anesthetic needles accordingly and place progressively longer anesthetic needles to the target, correcting the course trajectory as necessary. When we finally reach the periosteum along the optimal trajectory, we direct a bone biopsy needle into the bone and into the target zone, usually from a tandem technique. If a smaller bone biopsy needle is used (e.g., a 17-gauge needle), a larger coaxial guiding needle can be used for multiple passes.

The advantage of using a coaxial system is that the operator can easily perform multiple biopsies along an intended trajectory. The disadvantage is that most bone biopsy needles are quite large, often 13 and 11 gauge, and a considerably larger guiding needle is necessary for coaxial passage.

The advances of slip ring technology with a continuously rotating x-ray tube, x-ray tubes with improved heat capacity, more sensitive semiconductor detectors, new imaging reconstruction algorithms, and high-speed parallel-array processor systems for real-time raw data reconstruction and display allowed the eventual development of real-time CT fluoroscopy.[11] Helical CT scanners with CT fluoroscopy are widely available. Depending on the vendor, frame rates vary from two to eight frames per second, and the continuous CT fluoroscopy time varies from 40 to 100 seconds.

The main advantage of CT fluoroscopy guidance, compared with conventional CT guidance, is the decreased time needed for the procedure; the operator can see in real

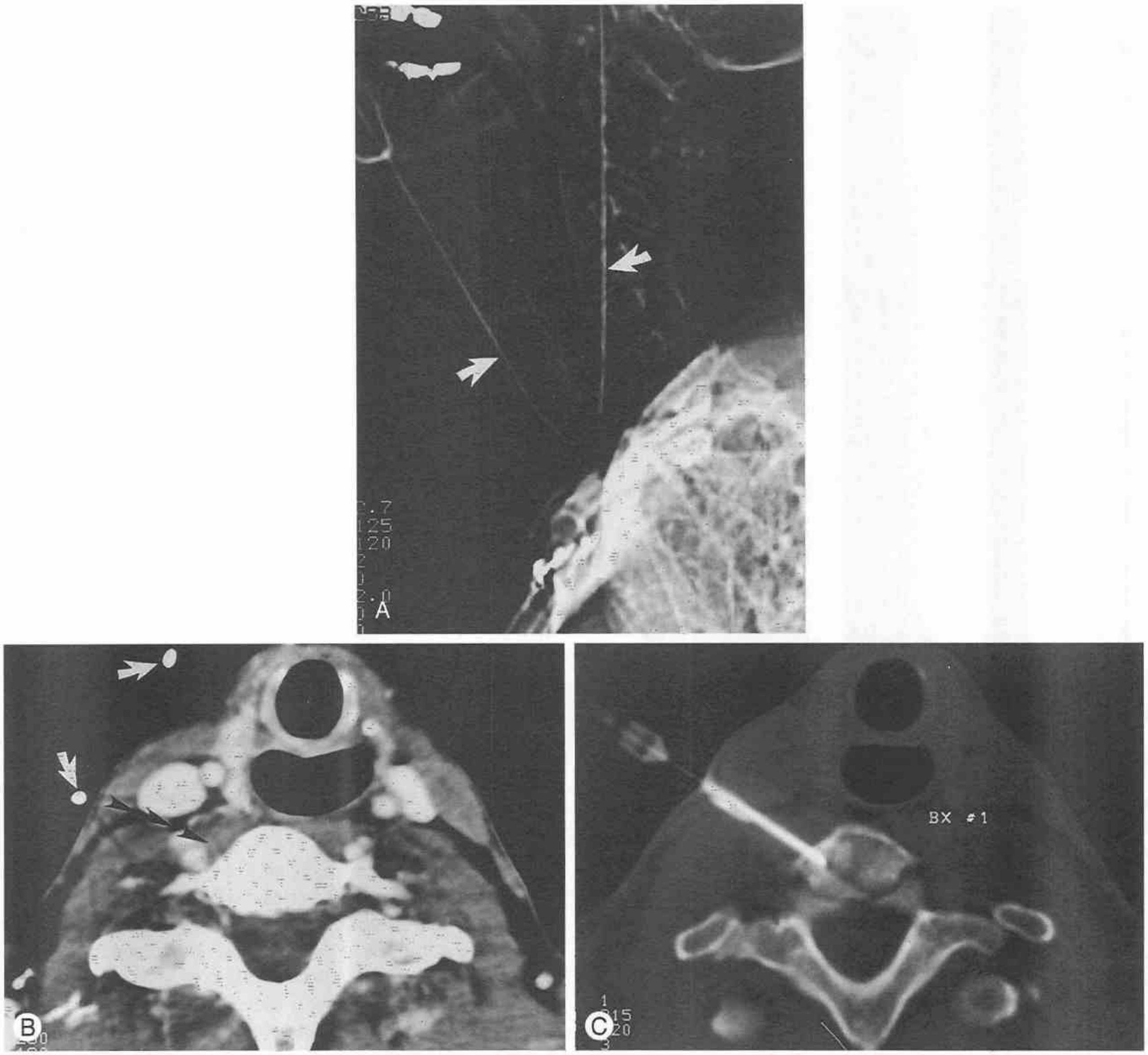

Figure 26–3. CT-guided biopsy of the cervical spine.

A, Lateral scout view of the cervical spine with an overlying V-shaped polyethylene marker for reference *(white arrows).* Measurement of the distance between the V can help to confirm the location from which biopsy samples are to be taken and can provide a reference mark for measurement to the starting point.

B, The V-shaped catheter on this patient's skin surface is outlined *(white arrows),* and the level to be targeted is confirmed by matching the distance between the V-shaped catheter at this level with what is seen on the scout view. *Black arrowheads* denote the needle course taken posterior to the jugular vein and anterior to the vertebral artery.

C, Biopsy is performed with a lightweight 17-gauge EZEM bone biopsy needle under CT guidance along the intended trajectory course. This needle has no heavy handles to throw it off course if it is unsupported when directed under CT guidance.

time the movements of the biopsy needle (Figs. 26–5 and 26–6). The disadvantage is increased radiation exposure to the operator,[11, 32, 33, 36] which should improve with the developments of special needle holders and even more sensitive semiconductor detectors, permitting improved image quality with lower milliampere doses.[11, 32, 33]

For CT needle guidance in the thoracic region, the usual trajectory is between the rib head and vertebral body *(costovertebral approach).* This approach avoids placement of the needle through the lung or through the exiting nerve root at the neural foramen. This technique usually allows good angulation when other various zones of the vertebral body are targeted. The alternative approach to thoracic biopsies is a transpedicular approach, which provides limited medial or lateral angulation for targets throughout the vertebral body. A transpedicular approach can be used under either CT or fluoroscopic guidance (Fig. 26–7).

For cervical biopsies, most patients tolerate being on a side (lateral) position for longer periods of time than they would in a prone position, which often results in claustrophobia. The trajectory chosen should avoid the carotid sheath, pharynx, esophagus, vertebral artery, and spinal

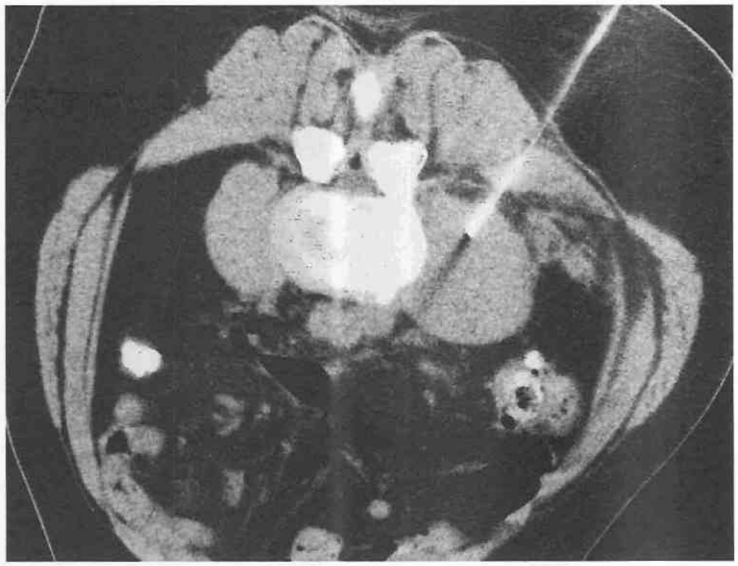

Figure 26–4. CT-guided needle biopsy of a painful paraspinous muscle mass. This lesion could not be seen fluoroscopically, and CT guidance was therefore necessary. A 25-gauge needle easily yielded cytologic samples to make the diagnosis of a metastatic transitional cell carcinoma to the psoas muscle before the primary malignancy site was discovered.

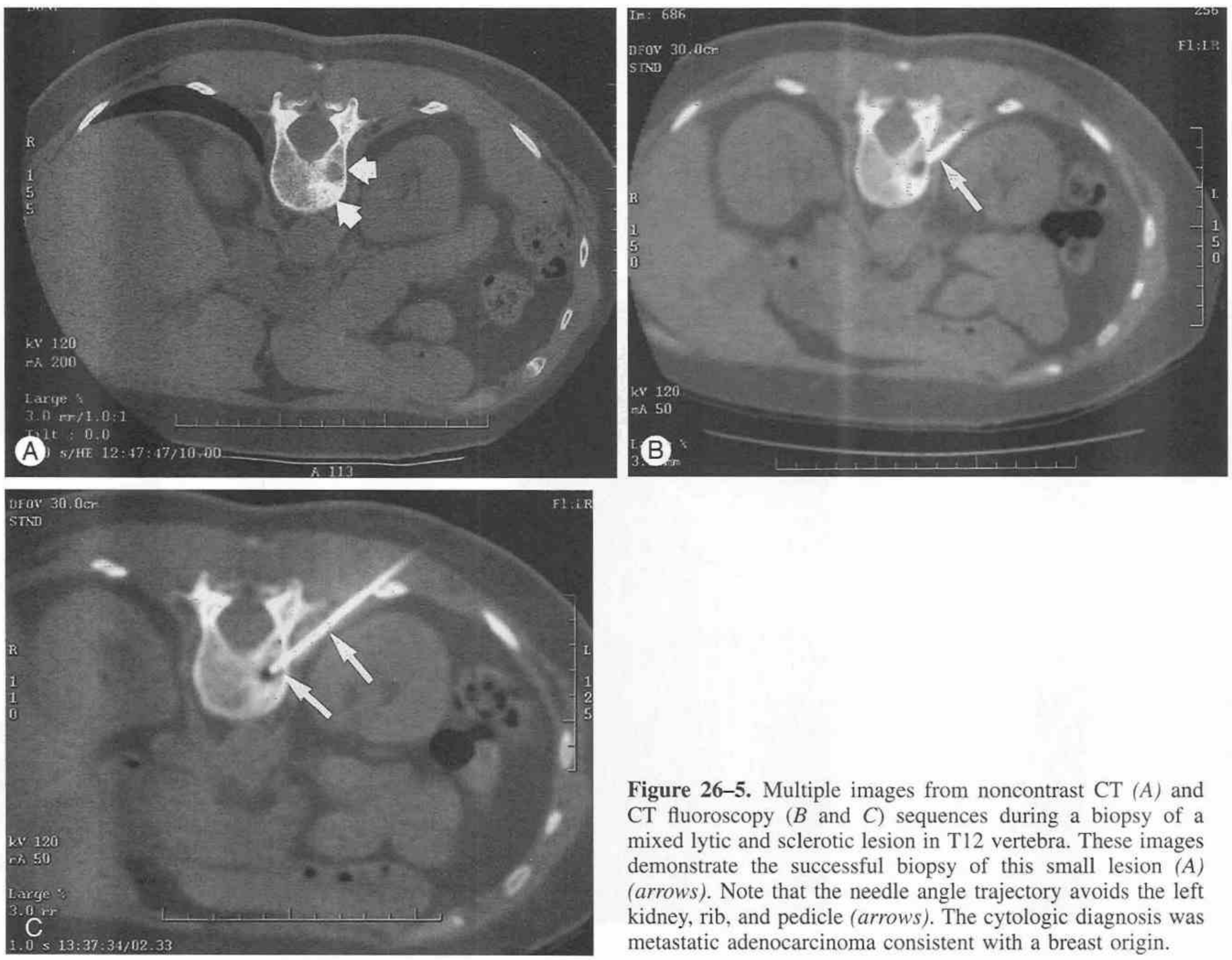

Figure 26–5. Multiple images from noncontrast CT *(A)* and CT fluoroscopy (*B* and *C*) sequences during a biopsy of a mixed lytic and sclerotic lesion in T12 vertebra. These images demonstrate the successful biopsy of this small lesion *(A)* *(arrows)*. Note that the needle angle trajectory avoids the left kidney, rib, and pedicle *(arrows)*. The cytologic diagnosis was metastatic adenocarcinoma consistent with a breast origin.

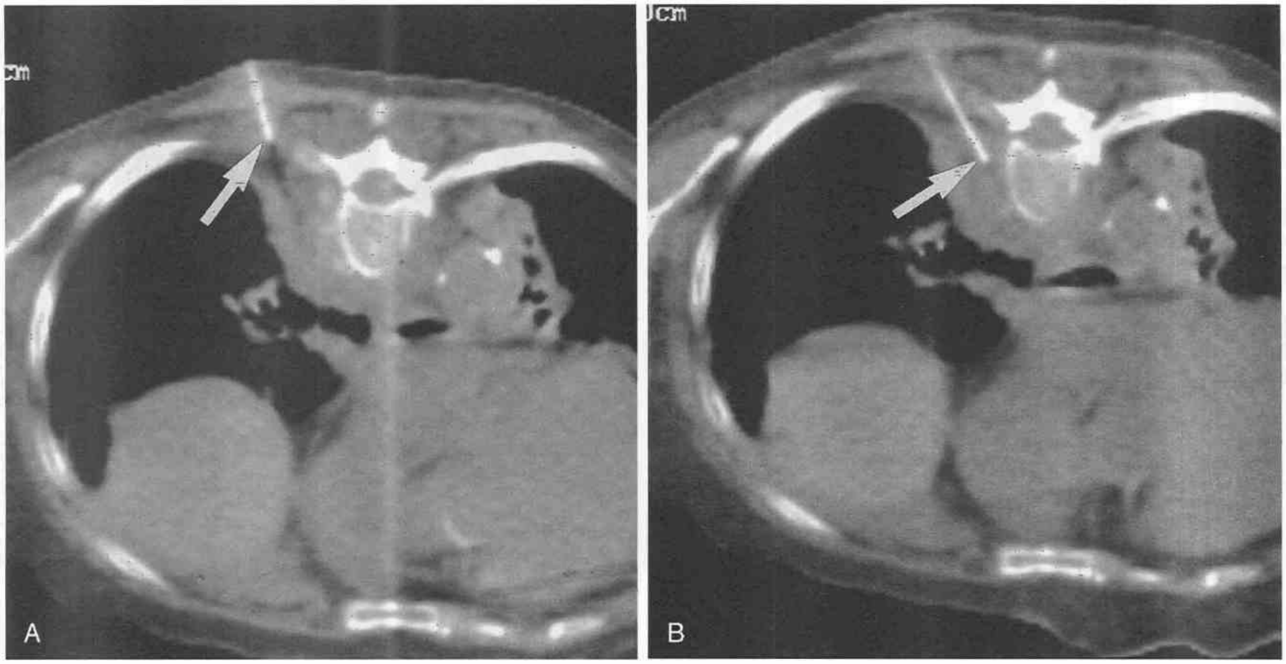

Figure 26–6. Biopsy of a left paraspinal soft tissue mass. CT fluoroscopy images demonstrate advancement of biopsy needle with changes in needle orientation and depth from *A* to *B (arrows)*. CT fluoroscopy allows the changes to be made in real time. The pathologic process was bacterial osteomyelitis.

Figure 26–7. CT-guided thoracic spine biopsy; two approaches are shown. One follows the posterior aspect of the rib down to the costovertebral junction *(white arrow)*. If this approach cannot be easily made, an alternative approach is transpedicular *(black arrow)*. The diagnosis was metastatic mucinous carcinoma of the colon.

contents. Sometimes it is very difficult to select a trajectory to avoid any of these structures. In some cases, a transpedicular trajectory may have to be taken. At other times, a stiff, large-bore needle can be placed behind the carotid sheath to shove the carotid sheath anteriorly, with the needle then redirected more posteriorly toward the target. From that point, coaxial biopsy needles can be passed through the larger guiding needle into the spinal target area.

Aspiration may be necessary for biopsy of soft tissue masses or abnormal fluid accumulations, whether present in soft tissues or bone. Aspiration techniques are often best performed with two operators using two sets of hands. One set of hands directs the needle into the target and performs the biopsy with forward and back rotary motions in the area of abnormality, usually with excursions of about 1 cm or less; the other set of hands provides suction via extension tubing from the needle to a large syringe (30 to 50 mL) with about 10 to 15 mL of suction pressure. The operator should be careful not to withdraw excessive amounts of blood because this action may interfere with the pathologist's diagnosis.

Biopsy of fluid-filled necrotic masses should also include the rim of the necrotic zone because the actual abnormal histology may be around the periphery, whereas the center may contain only necrotic debris. If the operator encounters a large paraspinous abscess, percutaneous drainage of the abscess at the time of biopsy by additionally placing a large-bore (10 French) catheter either with the Seldinger technique or with a single-pass trocar system (e.g., Cope). This can provide a large-volume specimen as well as a way to initiate therapy by draining the abscess.

Before performing a biopsy on lesions that are suspected to be caused by infection, the operator should ask the referring physician whether the patient has been taking antibiotics, which can interfere with organ growth and yield false-negative results. Ideally, any lesion that is thought to be due to infection should immediately undergo biopsy well before antibiotics are started. If antibiotics have already been started, they may have to be discontinued for 1 week to 10 days before the biopsy to ensure adequate growth of the organisms for positive results.

We generally request that a pathologist be available at the time of the biopsy to confirm whether an adequate sample has been taken. If the pathologist cannot make an initial diagnosis, further specimens may be necessary. Sometimes excessive blood in the specimen interferes with the pathologist's ability to make a clear diagnosis. If a specimen of paraspinous soft tissue lesions is obtained for biopsy and considerable blood is found in the specimen, sometimes a very thin (e.g., 25-gauge) needle without aspiration (instead of a larger-bore needle) may yield positive cytology. On the other hand, a spring-loaded cutting core biopsy needle (e.g., Cook, Temno) might be considered to slice free a portion of the target without the aspiration of a great deal of blood.

If the operator suspects that the lesion is an extremely vascular mass, such as a renal cell carcinoma with metastasis to the spine, a spinal angiogram may have to be obtained. If the angiogram confirms the vascular nature of the lesion, spinal embolization, via either arterial access or direct puncture of the lesion with the injection of either absorbable gelatin powder (Gelfoam, Gel-O-Foam) or polyvinyl alcohol particles, may be necessary before samples of the lesion are taken. This measure may help to prevent serious hemorrhage.

Needles

A variety of needles can be used for biopsy of the spine and paraspinous soft tissues.

Thin-Walled Needles

20- and 22-Gauge Needles

Straight, thin-walled needles (e.g., 20- and 22-gauge Chiba-type) can be used to aspirate abscesses, disks, soft tissues, or abnormally lytic bone lesions. Because 20-gauge needles are somewhat stouter than 22-gauge needles, directional control is more easily accomplished with 20-gauge needles, particularly if a complex curved trajectory must be used. The 20-gauge needle does not produce quite as much trauma as that from the 18-gauge needle and is usually sufficiently stout to penetrate a thin shell of bone in the presence of a lytic bone lesion.

25-Gauge Needles

The 25-gauge needle is often used in biopsies of very vascular soft tissue masses in the paraspinous areas and have the advantage of limiting the blood loss.

Core Biopsy Needles

Spring-loaded core biopsy needles (e.g., Temno or Cook) may be necessary for paraspinous soft tissue masses that are quite fibrous or reluctant to give up cells during fine-needle aspiration. Because lymphomas, schwannomas, and certain other fibrous tumors are often resistant to fine-needle aspiration, the use of a cutting type of needle (e.g., a spring-loaded core biopsy needle) may be necessary to obtain an adequate sample. With core biopsy needles, it can be difficult to maintain direction because of the weight of the handle when they are used under CT guidance. It may be best to direct the cutting needle through a coaxial guiding needle, which can be placed precisely under CT guidance, and avoid the problem of handle weight of the core biopsy needle.

Bone Biopsy Needles

A variety of bone biopsy needles are available, ranging from sharp-threaded, drilling-type 17-gauge needles (e.g., EZEM) to large-bore 11-gauge needles (e.g., Mannon, Cook). For sclerotic or blastic bone lesions of the spine, the more specimen that is collected, usually the better it is for the pathologist, because these lesions are often difficult to adequately decalcify for diagnosis. Therefore, for sclerotic bone lesions, bone biopsy needles of 11 gauge or larger are usually best.

When a spinal lesion is in a place that is difficult to access (e.g., a tight passage between the carotid sheath and vertebral artery in the upper cervical spine), lightweight short drilling needles, such as the 17-gauge EZEM, may be advantageous in setting and keeping trajectories in shallow soft tissues, in contrast to larger 11-gauge needles with heavy handles, which often throw the trajectory of the needle off course when used under CT guidance. Because

the small 17-gauge EZEM needles are short and very lightweight, they can be set in shallow soft tissues during targeting and still hold their trajectory without hand support. Because they are also very sharp and are threaded, they can thus be drilled deeply into the bone to obtain core samples very effectively in most cases.

General Precautions

Before biopsy, the operator should check for coagulopathies (bleeding time, prothrombin time, partial thromboplastin time, platelets). For coagulopathic patients or patients receiving anticoagulants, the procedure may have to be postponed.

When biopsies are performed on thoracic lesions, the operator should always be cautious of a possible pneumothorax; at termination of the procedure, either a follow-up set of CT scans through the lungs with lung windows or an expiratory chest x-ray film should be obtained to rule out a pneumothorax. A chest tube kit should be obtained or arrangements for the placement of a chest tube made before biopsy of the thoracic spine.

When pushing or drilling a needle through very dense bone, and when vital structures such as the aorta, the carotid artery, or the vertebral artery are located just beyond the target zone along the trajectory path, the operator may want to use a détente technique with one hand pushing the needle toward the target and the other hand grasping the needle shaft to provide a counteraction force, if necessary, to prevent piercing beyond the target area into vital structures if resistance to the needle should suddenly give way.

The operator should also be cautious when delivering the sample to the pathologist. It is wise to have a pathology team available to accept the specimens to avoid embarrassing misplacement. When delivering a bone core that may be impacted within the bone biopsy needle, it is prudent to avoid pushing the core out of the needle with such force that it suddenly flies off the slide and becomes lost. To remove a bone core from the biopsy needle, the operator should use the appropriate trocar design that is intended for such removal.

MRI-Guided Spinal Biopsies

Increasingly, MRI is being used for guidance and control of minimally invasive percutaneous and surgical procedures. Technologic advances such as the introduction of open and short-bore magnet designs, the proliferation of fast imaging sequences, and the availability of MRI-compatible instruments have aided the growth of this field.[36] We discuss the role of interventional MRI as it pertains to percutaneous spinal biopsies. For readers interested in MRI guidance related to neurosurgical procedures, potential percutaneous vascular applications, laser therapy, radiofrequency ablation, and biopsy of other parts of the body, more detailed works are recommended.*

The best design of an MRI system with regard to high-quality images and low field inhomogeneity would be a spherical magnet.[23] However, this design presents a suboptimal environment for MRI-guided intervention, which requires free access to the patient. Early reports of MRI-guided biopsies and aspirations were made with conventional cylindric superconducting systems.[42] This technique is similar to CT-guided procedures, in which access to the patient is limited and the patient must be withdrawn from the magnet for the manipulation of biopsy equipment, resulting in relatively long procedure times.

Three types of magnets are used clinically for MRI-guided therapy:

1. Closed, short-bore cylindrical superconducting systems operating at between 1.0 and 1.5 tesla (T).
2. Open, midfield ("double-donut") systems operating at 0.5 T.
3. Open, low-field (biplanar) systems operating at between 0.064 and 0.3 T.

The improvement in access to the patient that is afforded by the open magnets is traded for decreased field strength and image quality.[36, 54]

The main advantage of closed magnets, operating at high field strengths, is superior image quality relative to static magnetic field strengths and homogeneity. Also, the excellent signal-to-noise ratio achieved with these systems is well suited for temperature monitoring and mapping during ablative therapy with laser or radiofrequency.[1, 2, 23, 24, 36, 42] The disadvantages of this type of magnet design are the limited access to the patient and the relatively longer procedure times.

MRI-compatible accessories are available from several manufacturers. As with other cross-sectional imaging–guided modalities, such as CT and ultrasonography, the correct needle choice depends on whether tissue is required for cytologic or histologic analysis. Fine-aspiration, side-cutting, and bone biopsy needles are available in sizes ranging from 14 to 24 gauge. To achieve minimal artifact and no torque in the magnetic field, needles are composed of nonferromagnetic metals such as titanium, tantalum, and tungsten with aluminum or vanadium alloy.[43]

The main disadvantage of these needles is their relative bluntness and softness compared with stainless steel needles. Thus, in the case of intact cortical bone or sclerotic bony lesions, the biopsy procedure may be technically difficult and time-consuming and the patient may experience some discomfort. MRI-compatible bone drill systems are being developed to overcome this somewhat vexing problem.[43]

Factors such as lesion conspicuousness, needle passive image artifacts, and image contrast between the lesion and the instruments must be considered in an MRI-guided procedure. The instrumentation-based image artifacts depend mainly on the following[1, 37, 57]:

- Needle size
- Orientation of the needle to B_0
- The field strength B_0
- The imaging sequence parameters used for the procedure

The greater the angle of the needle to B_0, the more conspicuous is the artifact size, with maximum visibility at 90 degrees. The artifact becomes larger with increasing MRI field strength. Put simply, gradient-echo sequences are more sensitive to local field inhomogeneities and intravoxel

*See references 1, 2, 7, 24, 30, 31, 34, 39, 48, and 51 to 54.

dephasing than spin-echo sequences are. Therefore, techniques such as T2-weighted fast spin-echo sequences produce smaller artifacts than those noted with gradient-echo scans. The physical basis of these phenomena is beyond the scope of this discussion and has been well described in the literature.[1, 16, 36–38] Effective clinical application of MRI-guided procedures requires consideration of these different factors and appropriate adaptation.

Indications for percutaneous biopsy of the spine include cytologic or histologic analysis and diagnosis of soft tissue or bone lesions of unknown etiology. MRI is an alternative to CT and ultrasound in imaging guidance; MRI's multiplanar imaging capability probably is the most advantageous feature of this modality when compared with the other two modalities. This feature is important in planning needle trajectories in which the operator would want to avoid vascular structures (e.g., in head and neck biopsies) or in other important tissue planes (e.g., interposed bowel or the diaphragm). Occasionally, MRI can be used to visualize lesions that are either invisible or poorly seen on CT scans or sonograms. The superior soft tissue contrast and spatial resolution that MRI affords are most dramatic in the setting of bone marrow changes of unknown etiology, which are often invisible with CT (Fig. 26–8). An MRI-guided proce-

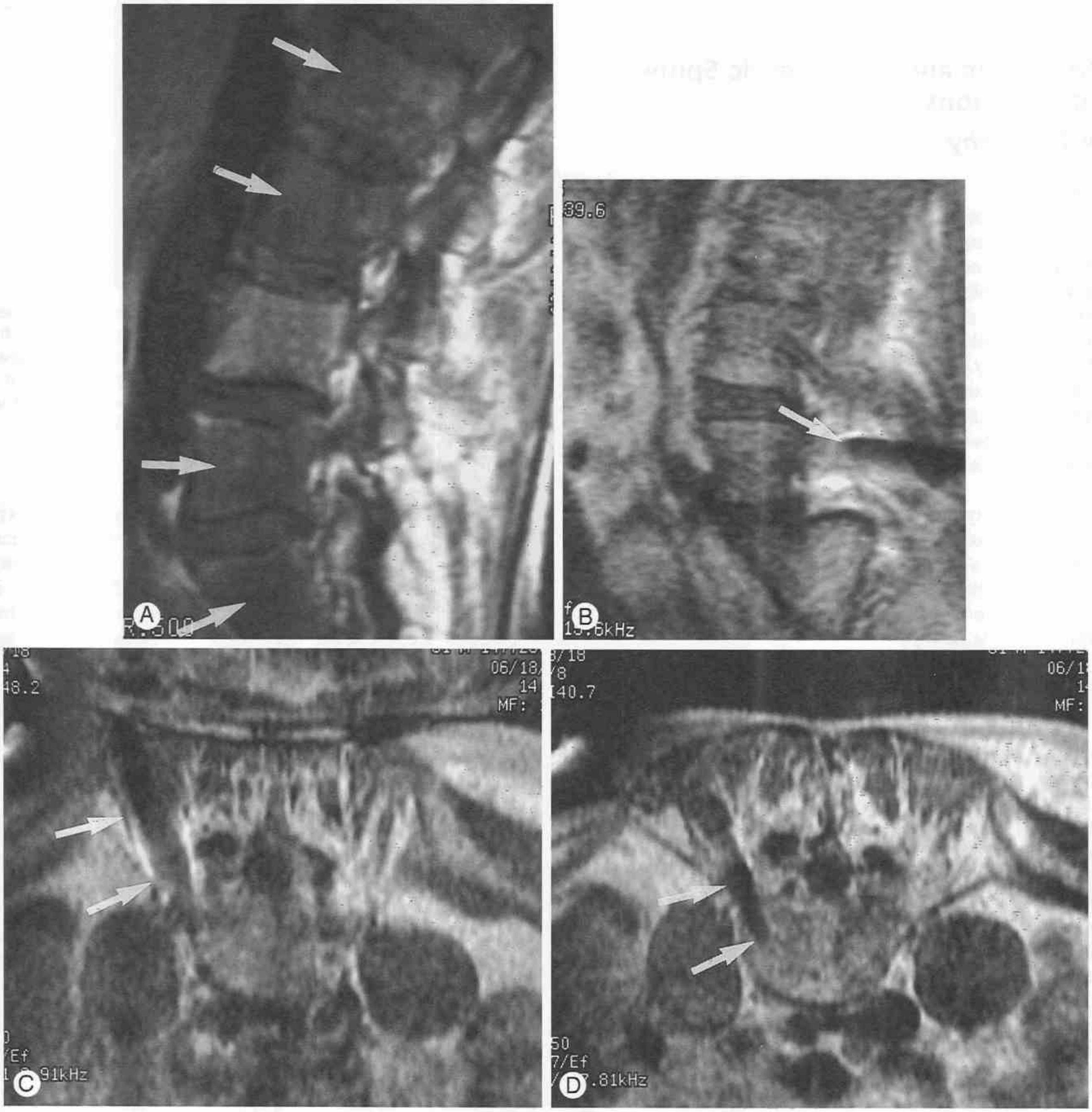

Figure 26–8. Bone marrow changes of unknown etiology. This potential abnormality was not visible on CT. *A,* Sagittal T1-weighted localizer image demonstrates patchy infiltration of the bone marrow in multiple lumbar vertebral bodies *(arrows). B–D,* Real-time axial images during left L5 transpediculate biopsy. Note susceptibility artifacts from needle. Cytologic diagnosis was negative for malignancy.

dure is also advantageous when radiation exposure is a consideration, as in younger patients, or when a patient has a history of allergy to an iodinated contrast agent.

MRI-guided biopsies of soft tissue and bony lesions of the spine appear to be safe and effective. There are obvious limitations to this technique, such as smaller lesions, which may be obscured by needle artifacts. Patient size and weight may also be limiting factors. Early results of MRI-guided biopsies seem to be as accurate as those of CT-guided techniques.[28, 43] MRI-guided techniques (not only biopsy and aspiration but also intraoperative monitoring and therapeutic procedures) are under constant evaluation and evolution and will probably become important tools in the armamentarium of radiology.

Diagnostic and Therapeutic Spine Interventions

Diskography

Indications

Diskography is commonly performed when imaging results are confusing or inconclusive. Sometimes the images may reveal more levels of abnormality than would be suspected on the basis of the clinical examination. At other times, images may fail to reveal any apparent abnormalities when the clinical examination strongly suggests a diskogenic etiology.[50] Shellhas and colleagues[49] reported that diskography could be extremely beneficial when MRI findings were negative. Colhoun and associates[8] noted that of 137 patients with positive diskographic findings, 89% derived significant sustained clinical benefit from subsequent surgery.

Diskography may also be used in the evaluation of postsurgical diskogenic pain and of presurgical fusion when disk disease is suspected in relation to underlying spinal instability.[22] Diskography is also indicated for the diagnosis of disk disease before percutaneous diskectomy or intradiskal electrolytic therapy.

Technique

The diskogram is a provocative test that is based on reproduction of the patient's original pain as a result of an increase in intradiskal pressure caused by the injection of fluid into the disk. This fluid is usually intrathecally compatible iodine contrast medium (e.g., Omnipaque 180), and the pressure increase is usually accomplished by injecting 1 to 1.5 mL into a lumbar disk or about 0.5 mL into a cervical disk. Because of the risk of infection, many operators add a broad-spectrum antibiotic to the iodine contrast mixture (e.g., cefazolin at about 50 mg per 1 mL of iodinated contrast medium).[49]

For lumbar diskography, a posterior-lateral approach is usually taken under fluoroscopic guidance. The most common disks to be injected in the lumbar region are L3-4, L4-5, and L5-S1.

Straight needle trajectories can usually be taken for the L3-4 and L4-5 disks (Fig. 26–9); however, because the iliac crest blocks a direct trajectory to the L5-S1 disk, a curved trajectory of the needle must be taken for the L5-S1 disk. The operator passes a curved needle superiorly over the iliac crest from a posterior-lateral starting point, then inferiorly to the level of the disk, and then medially into the disk (see Fig. 26–2). A C-arm fluoroscope is definitely advantageous for this complex trajectory. Some operators use CT scanning, which may be appropriate for L3-4 and L4-5 diskography, but the orientation of the L5-S1 disk makes access with CT guidance difficult unless a transthecal approach is used. For thoracic and cervical diskography, CT guidance may be preferred to fluoroscopic guidance, similar to image-guided biopsies (Fig. 26–10). Some operators prefer to perform cervical diskography with fluoroscopic guidance, in which case they deviate the carotid sheath laterally and then deviate the pharynx/esophagus medially with the fingers of one hand and then with the other hand pass a very thin (25-gauge) needle into the disk.

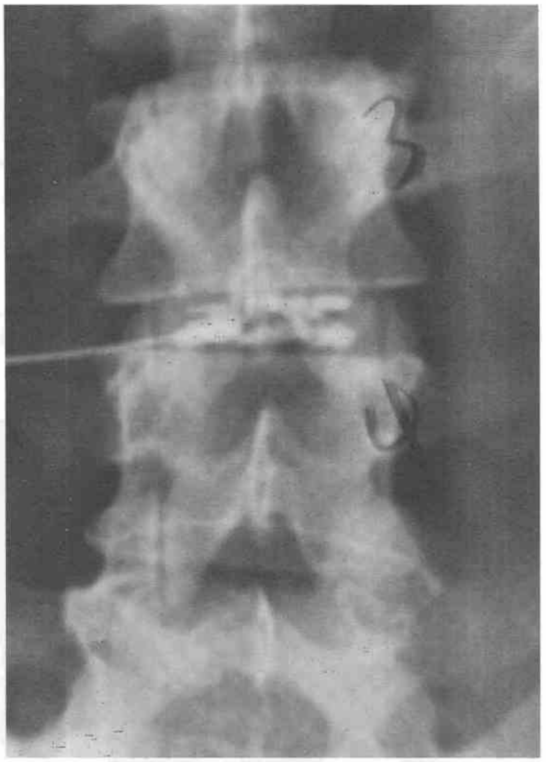

Figure 26–9. Anteroposterior view of contrast medium injected into the L3-4 disk following a posterior-lateral approach for needle placement under fluoroscopic guidance. Injection of contrast medium demonstrates a bifid configuration of medium in a normal-appearing disk. However, the patient complained of marked pain reproduction on injection into this disk.

After diskography, a CT scan of the disk containing injected contrast medium can be performed to obtain additional information. Sometimes this secondary information reveals other corroborative evidence of disk disease, such as an annular tear (Fig. 26–11).

Complications

The frequency of complications following diskography has been reported to be as high as 3% by Fraser and associates,[17] but the general overall rate is less than

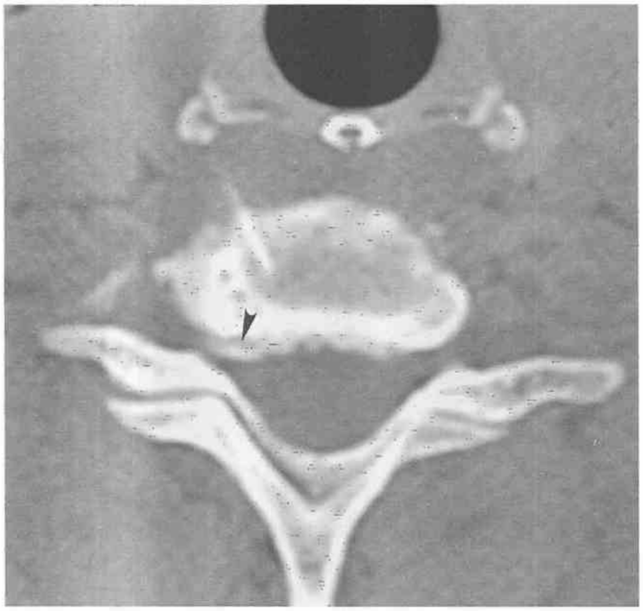

Figure 26–10. Cervical diskography at the C5-6 level performed with CT guidance using a 25-gauge needle via an anterior-lateral approach. The patient's right arm pain was reproduced exactly on injection of 0.5 mL of iodine contrast medium. After injection, the CT scan also demonstrates a small amount of contrast medium filling a right posterior-lateral disk protrusion *(arrowhead).*

0.15%.[22] Complications can include infection, bleeding, nerve injury, chemical diskitis,[50] hypotension (vagal), pneumothorax, and cerebrospinal fluid leak leading to spinal headaches.

Initial Spine Interventions: Epidural Steroid Injections versus Joint Injections

The most common spinal interventional procedures that may be both diagnostic and therapeutic include epidural steroid injections and joint injections (facet and sacroiliac joint injections). Often, these injections represent the initial diagnostic spine interventions that lead to more definitive therapy.

The evaluation of back pain starts with a history and physical examination, and findings are correlated with the imaging study. If the pain is *radicular* in nature, the operator may start with an epidural steroid injection. If the patient benefits from this injection, a subsequent epidural steroid injection can be administered about 4 weeks later, leading to another epidural steroid injection in about 4 weeks if there is continued positive benefit. At that point, maintenance epidural steroid injections at about 2- to 3-month intervals can be administered for continued pain relief.

If at any time the patient does not experience a positive benefit, he or she should be reevaluated. If the pain instead seems to be more focal, a joint injection may be considered.

If relief does not result after the epidural steroid injections, the patient should be considered for a surgical evaluation or referred for treatment with oral medications (narcotics, nonsteroidal anti-inflammatory drugs).

If on initial evaluation the patient's pain seems to be more *focal* (i.e., over a facet or sacroiliac joint), a joint injection might be given first. If there is positive benefit, another joint injection can be administered in 4 weeks; again, if there is positive benefit, a subsequent joint injection can be administered in 4 weeks.

If there continues to be positive benefit, maintenance joint injections can be considered for long-term therapy at 2- to 3-month intervals. If the patient does not receive positive benefit from the initial three joint injections, he or she should be reevaluated.

If the pain pattern seems to be more *radicular* than *focal*, epidural steroid injections should be considered. Otherwise, the patient may be a candidate for either surgical or medical referral.

Epidural Steroid Injections

Epidural steroid injections are commonly administered when the patient is experiencing radicular symptoms, often

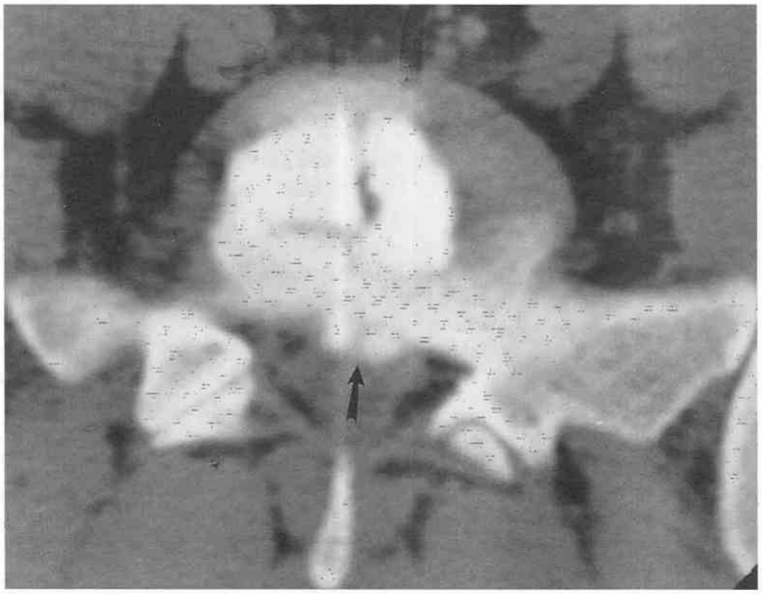

Figure 26–11. Postdiskography CT scan reveals contrast medium in the L5-S1 disk filling a small central disk protrusion. Although the CT scan appears to be abnormal, indicating an annular tear, the patient was totally asymptomatic. Thus, disk protrusion would be considered only an incidental finding at diskography.

due to spinal stenosis, which may be a result of generalized degenerative changes, disk disease, or facet arthrosis. Postsurgical scarring may also be an indication for epidural steroid injections. If an exact cause of pain is not clearly discerned, an epidural steroid injection may sometimes be the first injection procedure attempted to alleviate pain.[5, 14]

Injection at Lumbar Sites

For low lumbar disease, the operator can administer a caudal injection.[45] The operator palpates an indentation along the lowest portion of the sacrum and, under fluoroscopic guidance, inserts a needle into the sacral hiatus. Caution is needed to prevent inadvertent placement of the needle anterior to the sacrum (into the rectum) or posterior to the sacrum (into the posterior sacral soft tissues). The needle should not be directed superiorly to S3 because a low-lying thecal sac might be encountered.

Iodine contrast medium is injected (~2 mL iohexol [46.36% iodine; Omnipaque 180]) to confirm optimal placement in the sacral epidural space and not into the thecal sac. A long-acting steroid (18 mg betamethasone [Celestone]) is then usually injected.

For other sites of the lumbar spine, from about L3 superior into the cervical region, the operator places an epidural needle such as a Tuohy, which has a somewhat curved blunted tip, into the epidural space, as with a myelographic approach (either midline between the spinous processes or paramedian). C-arm fluoroscopy is usually the preferred imaging modality.

Needle Placement

Two techniques are commonly deployed for placing the epidural needle in the correct location.

1. *Direct saline pressure method.* A glass syringe with saline is connected to the end of the epidural needle, and intermittent pressure is applied as the needle is directed to the epidural space under fluoroscopic guidance. On reaching the epidural space, there typically is a remarkable loss of resistance such that the plunger is easily pushed forward with very little resistance.
2. *Hanging drop method.* A drop of saline is placed over the posterior hole of the Tuohy needle, which is then guided by fluoroscopy down to the epidural space. The blunt tip of the Tuohy needle tends to depress the rather tough dura, creating a vacuum effect, and this sucks the drop of saline inward to signify that the needle has reached the epidural space. The operator confirms needle tip location by performing an epidurogram. This is easily accomplished with an injection of about 2 mL of intrathecally compatible iodine contrast (Omnipaque 180).

At fluoroscopic examination, the anteroposterior view should reveal a streaky contrast medium collection that may extend out through the nerve root sleeves; the lateral view may show a linear collection of contrast medium adjacent to the expected location of the thecal sac (Figs. 26–12 and 26–13). If the needle penetrates the thecal sac, the injection of steroids, and especially a local anesthetic agent, should be avoided. The injection procedure can be postponed for 1 week to allow the hole in the thecal sac to heal, or the epidural steroid injection can be administered at a different but adjacent level.

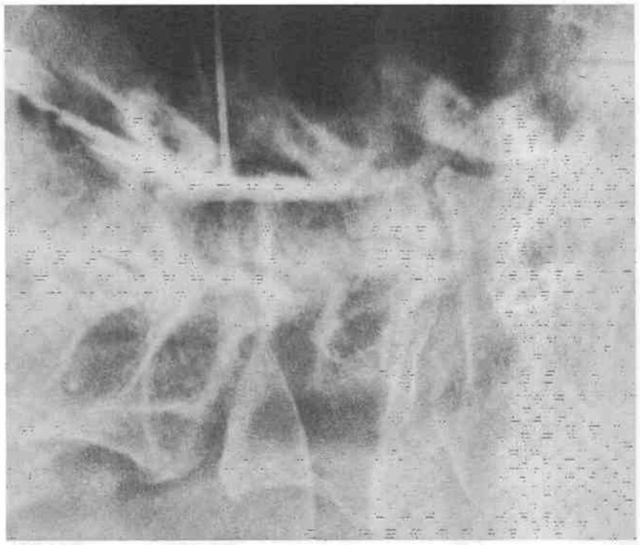

Figure 26–12. Lumbar epidural steroid injection. The lateral view demonstrating the linear accumulation of contrast medium along the posterior aspect of the lumbar epidural space. There is no intrathecal contrast filling. This epidurogram confirms optimal needle placement.

A study by Johnson and colleagues[27] that involved 5334 patients showed that the efficacy of epidural steroid injections with fluoroscopically guided needle placement and confirmatory epidurography was extremely high (97%) and the complication rate was very low (0.07%). This is in contrast to *blind* epidural steroid injections, as commonly performed by anesthesiologists, who experience up to a 30% rate of inaccurate needle placement.

Facet Injections

Facet disease can cause focal pain or referred local pain.[3, 18, 41] Median branch nerves from the nerve roots above and below the facet joints supply the innervation to the facet joints.[6] The injection into a facet joint under fluoroscopic guidance is not usually difficult unless there is considerable hypertrophic degenerative spurring, which may alter the choice of entry point into the facet joint. In those cases, targeting by CT guidance may be preferred.

On the needle's entry into a facet joint, the operator injects a very small amount of iodinated contrast agent (0.1 to 0.2 mL of Omnipaque 180) to confirm needle tip location within the facet joint. The operator should visualize a linear contrast medium accumulation in the facet joint or filling of the recesses (or both) that appears as bulbous collections of contrast medium along the superior and inferior margins of the facet joint (Fig. 26–14). A local anesthetic agent (lidocaine) can be injected for diagnostic purposes, whereas an injection of a long-acting anesthetic agent and a long-acting steroid (0.5 mL of a 50:50 mixture of 0.25% bupivacaine [0.25% Marcaine] and 6 mg/mL betamethasone) is administered. In the cervical region, a fluoroscopically guided lateral approach is usually taken (Fig. 26–15) except for the C1-2 facet joint, which is composed of the lateral masses of C1 and C2. CT guidance

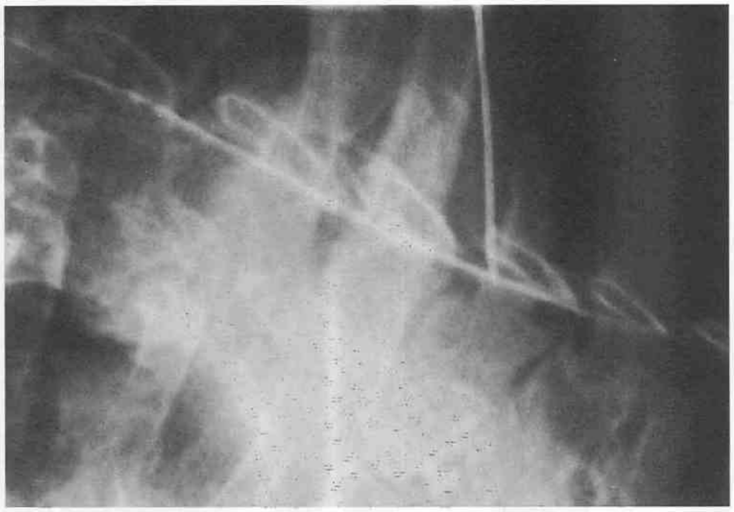

Figure 26–13. Cervical epidural steroid injection showing a linear contrast accumulation in the posterior cervical epidural space. No intrathecal contrast medium accumulation is seen. This epidurogram confirms optimal needle placement.

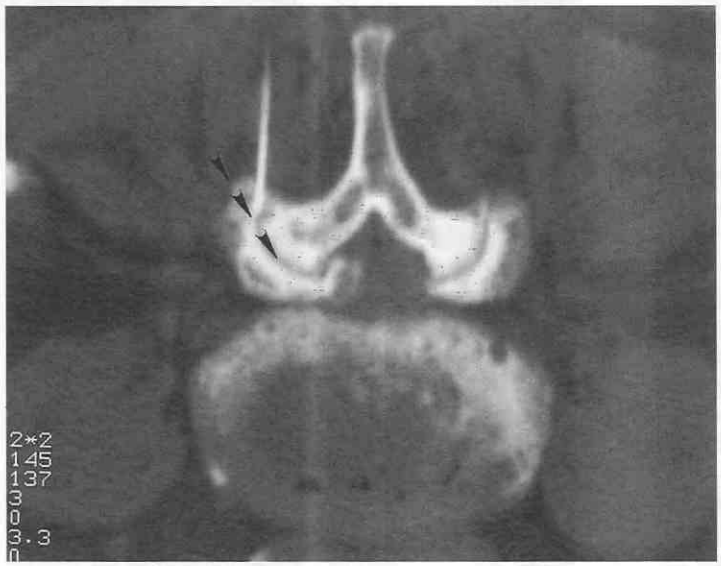

Figure 26–14. Lumbar facet injection under CT guidance. Initial attempts were performed under fluoroscopic guidance, but the visualized trajectory to the facet joint *(arrowheads)* was blocked by the posterior-superior articular facet osteophyte. Therefore, CT guidance was used to reveal the true posterior entry point into the joint. Most facet injections can be performed rapidly with fluoroscopic guidance, but the more difficult ones, such as this one, should be reserved for CT guidance.

Figure 26–15. Lateral view of the cervical spine showing correct needle placement for C3-4 articular facet joint injection. The operator should not approach the joint too far anteriorly to avoid puncture of the vertebral artery. Contrast medium in the joint shows a normal linear accumulation along the joint margins, which confirms correct needle placement.

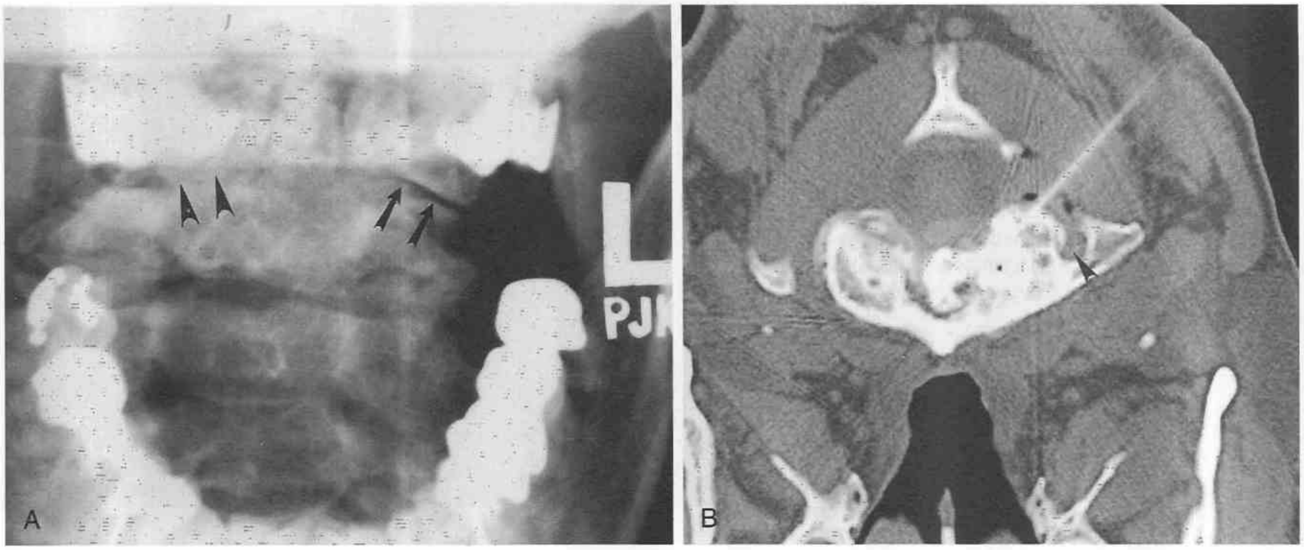

Figure 26–16. C1-2 articular facet joint injection. *A,* Anteroposterior view. Plain film of the C1-2 facet joints demonstrates that the normal facet joint *(arrows)* is made up of the lateral masses, whereas the abnormal right-sided facet joint *(arrowheads)* is extremely sclerosed. *B,* Injection of the right C1-2 facet joint with CT guidance from a posterior-lateral approach that avoids the vertebral artery *(arrowhead),* with the needle well positioned in the C1-2 facet joint.

may be preferred to fluoroscopic guidance to avoid injury to the vertebral artery or the C1 and C2 nerve roots during injection into the C1-2 facet joint (Fig. 26–16).

An alternative to injection into the facet joints may be achieved by blocking the median branch nerves, which pass over the superior medial boundaries of the transverse processes arising above and below the level of the facet joint. This is known as a *median branch block.* If this procedure is effective in relieving pain, radiofrequency ablation of the median branch nerves may be considered for longer pain relief.[13]

As in the facet joints, pain emanating from the sacroiliac joints is typically focal, locally referred, or both. The sacroiliac joint injection is commonly made under fluoroscopic guidance. Placing the fluoroscope or the patient at an oblique angle until the joint margins are optimally seen may reveal the correct trajectory for the needle. However, overlap of the ilium and sacrum often presents problems for straight needle passage into the joint. Therefore, in some cases injection with CT guidance may be preferred (Fig. 26–17).

The sacroiliac joint is a diarthrodial joint in which the lower half is the synovial portion and thus the target area. When fluoroscopy is chosen, the optimal site for placement of a needle into the synovial portion of the sacroiliac joint is usually along the most inferior margin, which tends to have less bony overlap of the ilium on the sacrum (Fig. 26–18). Injection of iodinated contrast medium (~1 mL of Omnipaque 180) confirms correct needle placement, as defined by a linear streak of contrast medium in the joint. The operator can then inject about 3 mL of 1% lidocaine for diagnostic purposes or the same amount of a 50:50 mixture of a long-acting anesthetic agent (0.25% bupivacaine) and steroid (6 mg/mL betamethasone) for therapeutic purposes.

The complication rate following joint injection (facet and sacroiliac joints) with the use of thin 22- or 25-gauge

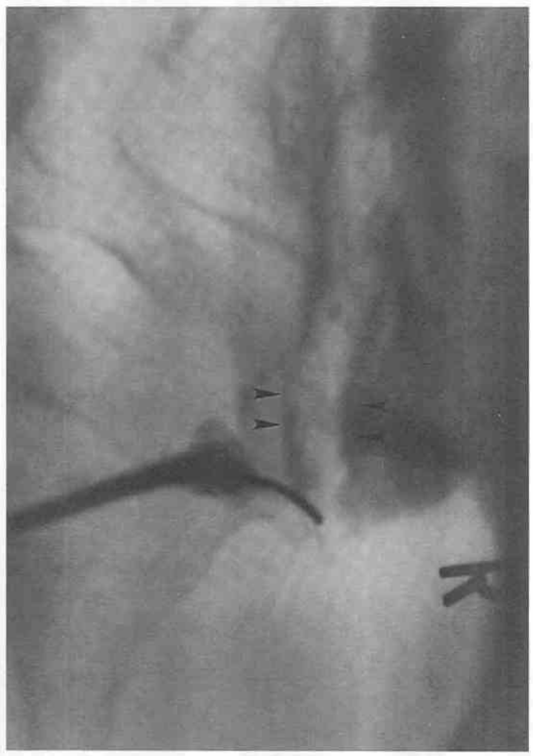

Figure 26–17. Bilateral sacroiliac joint injections with CT guidance. The left side of the sacroiliac joint was difficult to approach fluoroscopically. *Arrowheads* indicate the apparent approach to the left sacroiliac joint under fluoroscopy, but the iliac bone blocks access to this joint, which is somewhat curved. The right joint has a straighter trajectory and was able to be accessed with fluoroscopy. Nevertheless, CT provides the most accurate way of defining the opening to the sacroiliac joints. In this case, the true opening to the right side of joint was situated much more medially than was apparent under fluoroscopy.

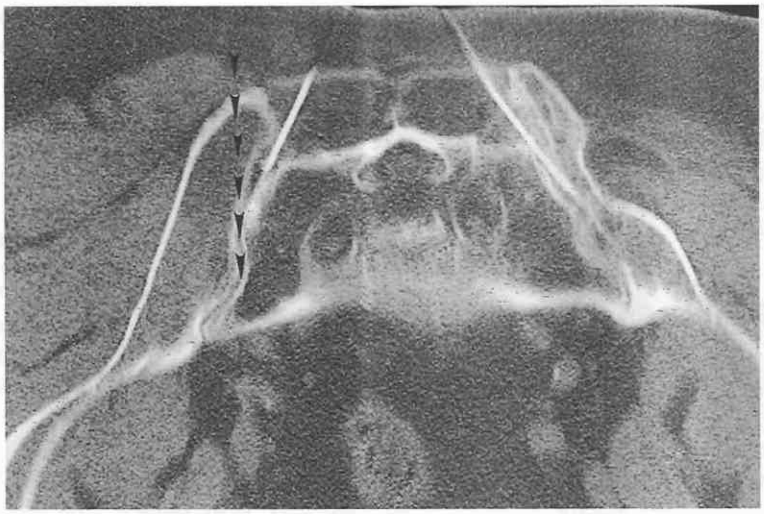

Figure 26–18. Fluoroscopically guided sacroiliac joint injection. A 25-gauge needle was placed along the most inferior margin of the right sacroiliac joint. This inferior position tends to have less bony overlap of the ilium on the sacrum than when the joint is approached from a more superior position. Iodine contrast medium has been injected and is collecting along the joint margins *(arrowheads),* confirming correct needle placement.

needles is extremely low. Nevertheless, general precautions regarding coagulopathies, infections, allergic reactions, and hypotensive (vagal) events should always be considered.

Nerve Root Blocks

Nerve root blocks can be helpful diagnostically when the imaging findings are rather confusing. When multiple abnormalities are seen on an image, the blockade of pain related to a specific nerve root may specify the clinically relevant abnormality. Nerve root blocks may also be helpful therapeutically when there is irritation of a nerve root or when a patient is having radicular pain but is not a reasonable surgical candidate. Nerve root blocks can be achieved through injection into the ganglion at the neuroforamen,[61] but the operator must be cautious to avoid communication with the subarachnoid space if a particularly long nerve root sleeve is present.

Careful scrutiny during injection of iodine contrast medium is necessary to rule out intrathecal communication. Alternatively, the operator can inject into the nerve roots along the postganglionic segment.

Lumbar Nerve Root Injections

In the lumbar region, the operator would insert a needle just over the superior margin of the midsection of the subjacent (lower) transverse process and probe gently with a 25-gauge needle until there is a paresthesia to the lower extremity. The operator then backs the needle off very slightly and injects iodine contrast medium, which should outline the nerve root sheath, with the nerve root being seen as a linear filling defect (Fig. 26–19). At that point, the operator can inject 1 to 2 mL of 1% lidocaine for diagnostic purposes or, for more permanent therapeutic pain relief, 1 to 2 mL of a 50:50 mixture of 0.25% bupivacaine and a long-acting steroid (6 mg/mL betamethasone).

Thoracic Nerve Root Injections

In the thoracic region, the postganglionic nerve roots can be located just under the inferior margin of the rib. For thoracic nerve root blocks, the operator should be extremely cautious of needle depth to avoid a pneumothorax. Nerve root blocks can readily be accomplished under fluoroscopy.

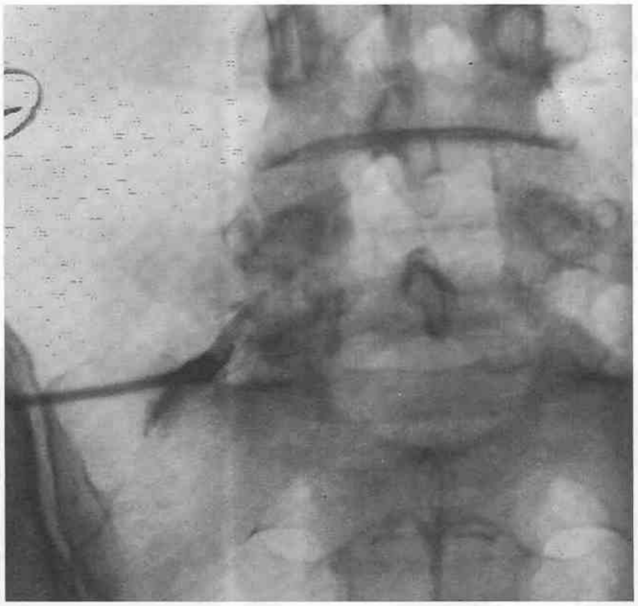

Figure 26–19. Left L5 nerve root block, postganglionic segment. A needle is directed into the ganglionic portion of the nerve root at the neural foramen or along the postganglionic portion of the nerve root. To find the postganglionic portion of a lumbar nerve root, the operator passes a needle deeply from approximately the midsection of the lower transverse process or, in this case, the equivalent midsection of the sacral wing. Gentle probing is performed until the patient acknowledges an electric shock down the lower extremity. The needle is withdrawn just slightly, and iodine contrast medium is injected along the nerve sheath. Contrast medium can be seen tracking along the nerve sheath back toward the neural foramen. Injection of lidocaine can be administered for diagnostic purposes, and injection of bupivacaine and long-acting steroid can be administered for more therapeutic measures.

Cervical Nerve Root Injections

In the cervical region, the operator may prefer CT guidance to avoid the pharynx/esophagus and carotid sheath or vertebral artery, although some operators prefer to use fluoroscopic guidance for cervical nerve root blocks, similar to the technique of cervical diskography. To avoid the vertebral artery, the operator should place the needle in the posterior neuroforamen.

Trigger-Point Injections

Local soft tissue injections of an anesthetic agent, steroids, or both may be helpful when the patient has myofascial pain, perhaps due to scarring, myofascial strain, or strain related to ununited bone fusion. Targeted areas to be injected are based on subjective responses of the patient to soft tissue tenderness. These injections may help bring about relief and allow time for healing to occur (Fig. 26–20). For diagnostic pain relief in the soft tissues, 1 to 4 mL of 1% lidocaine may be injected, whereas a similar amount of long-acting anesthetic agent and steroid can be injected for longer therapeutic relief (e.g., bupivacaine, 0.25%, and betamethasone, 6 mg/mL).

Sympathetic Ganglion Blockade

Deep visceral pain may cause considerable referred pain from visceral somatic reflex arcs, which may worsen pain cycles. Sympathetic nerve blocks may help to decrease pain by breaking up reflex arcs. The common sympathetic ganglion blocks include:

1. *Stellate ganglion block* for upper extremity and lower facial and neck pain.
2. *Celiac ganglion block* for pain of the upper abdomen.
3. *Lumbar sympathetic block* for pain related to the lower extremities.
4. *Impar ganglion block* for pain in the lower pelvis and perineal regions.

Stellate Ganglion Block

Indications for blockade of the stellate ganglion include pain in the upper arm due to arterial insufficiency, Raynaud's phenomenon, reflex sympathetic dystrophy, posttraumatic syndrome with swelling, hyperhidrosis, and cyanosis, Pancoast tumors of the upper thorax, and herpes zoster of the neck and head.

Stellate ganglion blockade is accomplished under either fluoroscopic or CT guidance by directing a thin (25-gauge) needle to the stellate ganglion located at the anterior-lateral aspect of the C7 vertebral body and the junction with its transverse process (Fig. 26–21).[15] The syringe attached to the end of the needle should be aspirated to be sure that the tip of the needle is not in a blood vessel—especially the vertebral artery. Injection of iodinated contrast medium further substantiates the location of the stellate ganglion and the absence of any intravascular filling.

For temporary pain relief, 0.25% bupivacaine (8 mL) can be injected on a weekly basis (usually up to 8 weeks). For pain ablation, 8 mL of absolute alcohol or 6% phenol can be used for neurolysis, preferably with the patient under general anesthesia, because the injection of absolute alcohol can be extremely painful. When effective stellate ganglion blockade is achieved, Horner syndrome develops and there may be venous engorgement and paresis of the ipsilateral face and arm.

The risks and complications of stellate ganglion blockade include the following:

- Intraspinal extension of the medication (particularly if a long nerve root sleeve is encountered, which may lead to paralysis or even seizures)
- Intravascular injection

Figure 26–20. Trigger-point local soft tissue injections. The patient complained of considerable soft tissue tenderness in an area that was related to soft tissue strain adjacent to an ununited bone fusion. Weekly injections of 0.25% bupivacaine (6 mL) provided enormous pain relief for the patient until soft tissue healing was adequate.

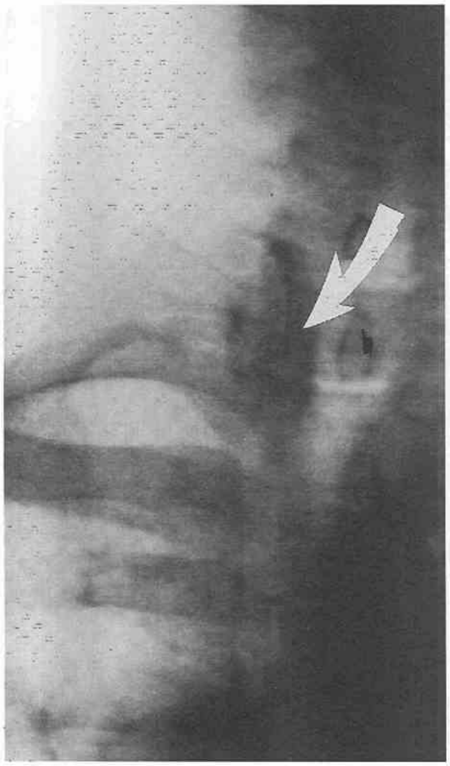

Figure 26–21. Stellate ganglion blockade. Fluoroscopic guidance was used to place a 25-gauge needle along the lateral margin of the C7 vertebra and junction with the transverse process. Iodine contrast medium was injected *(arrow)* and revealed no evidence of intravascular contrast accumulation. Next, 8 mL of 0.25% bupivacaine was injected slowly.

- Paralysis of an adjacent phrenic nerve or a recurrent laryngeal nerve (which may lead to hoarseness or even diaphragmatic paralysis)
- Pneumothorax
- Hypotension with brachycardia (accelerator nerves through the heart also pass through the stellate ganglion)

Relative contraindications include:

- Recent myocardial infarction, because the patient may not be able to elevate the heart rate in cases of stress due to blockage of the accelerator nerves to the heart
- Coagulopathy
- Contralateral pneumothorax
- Glaucoma

Celiac Ganglion Block

Celiac sympathetic plexus blockades can be extremely helpful when the patient has deep visceral pain, as commonly occurs from terminal pancreatic cancer, chronic pancreatitis, or visceral arterial insufficiency. The operator places a thin needle from either a posterior or an anterior approach into the celiac, which is located just anterior to the aorta and surrounding the celiac artery.[55] CT guidance is often preferred, although ultrasound guidance with an anterior approach through the liver has been favored by some operators.[26]

For a posterior approach with CT guidance, the operator starts by locating the celiac artery by scanning it at approximately the T12 level. A needle is directed from a posterior paraspinous location through the crura of the diaphragms in order to pass the needle anterior to the aorta at the level of the celiac artery (Fig. 26–22). The operator may need to pass a needle directly through the aorta to reach the target zone. Iodine contrast medium is injected to confirm location and the absence of intravascular communication. Temporary blockade is achieved when the operator injects bupivacaine; for permanent ablation, neurolysis can be obtained by an injection of absolute alcohol or 6% phenol.

Successful celiac blockade is usually accompanied by hypotension because blood tends to pool in the visceral circulation. This is usually treated effectively with additional intravenous fluids.

Relative contraindications to celiac ganglion blockade include bowel obstruction (because there may be an increase in motility resulting from obliteration of sympathetic input) and coagulopathy.

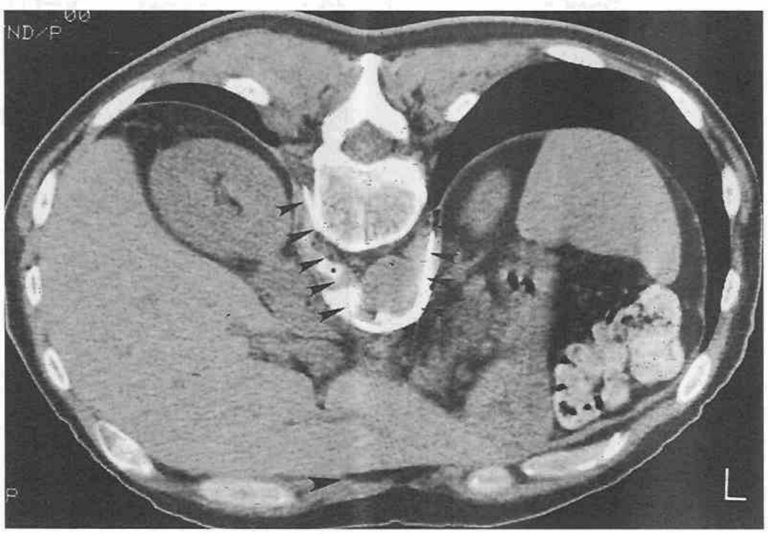

Figure 26–22. Celiac sympathetic plexus blockade from a posterior approach with CT guidance. Needles have been placed just posterior to the crura of the diaphragms at the T12 level. The needles are placed very close to the T12 vertebra and are directed in such a manner that the tips of the needles pass just anterior to the aorta. The celiac plexus is located at either side of the celiac artery. Iodine contrast medium confirms needle tip locations before the injection of absolute alcohol for celiac plexus ablation in a patient with severe upper abdominal pain from terminal pancreatic malignancy.

Lumbar Sympathetic Block

Blockade of the lumbar sympathetic plexus may be helpful in cases of lower extremity reflex sympathetic dystrophy, ischemia from chronic arterial emboli or Raynaud's phenomenon, phantom limb pain resulting from amputation, frostbite of the lower extremities, and hyperhidrosis of the lower extremities. The lumbar sympathetic plexus extends from approximately L5 to L2. Blockade is most effectively achieved when the operator directs a needle under either fluoroscopic or CT guidance to the anterior-lateral aspect of the L2 vertebra.[20] A posterior-anterior approach slightly off midline is usually taken.

Injection of iodine contrast medium confirms the absence of intravascular communication in either the aorta or inferior vena cava and that the needle is positioned retroperitoneally (Fig. 26–23). Temporary relief can be obtained by injection of about 10 mL of 0.5% bupivacaine on a weekly basis during a period of up to 6 to 8 weeks to break visceral somatic reflex pain cycles.

Complications may include inadvertent injections, neuralgia to the genital femoral nerve, urethral injury, hypotension, impotence, and bleeding.

Impar Ganglion Block

Blockade of the impar ganglion may be helpful when the patient has deep lower pelvic pain, pain from the perineum, or presacral pain. The operator places a thin, 22-gauge needle from a starting point between the sacrum and coccyx through the sacral coccygeal ligament and then directs it superiorly and posteriorly to the anterior surface of the sacrum. Iodine contrast medium is injected to ensure that the rectum has not been violated (Fig. 26–24).

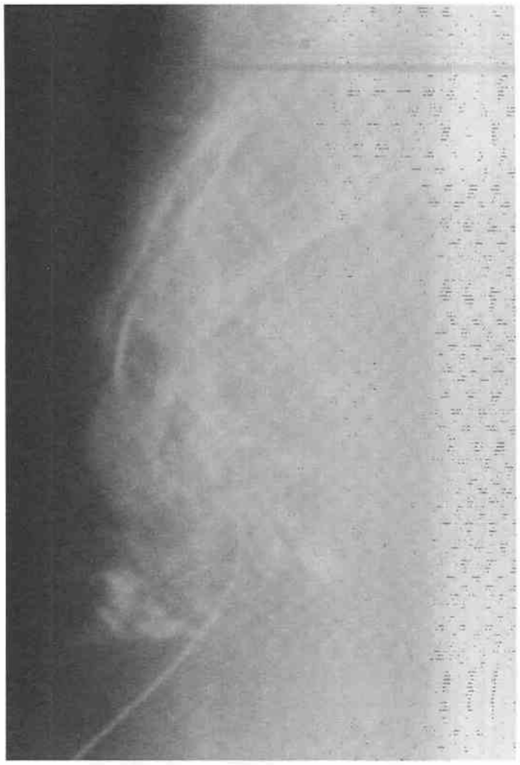

Figure 26–24. Fluoroscopic guidance of a double-curved needle in which the tip is placed just anterior to the sacrum. Iodine contrast medium reveals good dispersion without filling of the rectum. Absolute alcohol was injected for ablation of the impar ganglion in a patient with severe perineal pain from a malignancy.

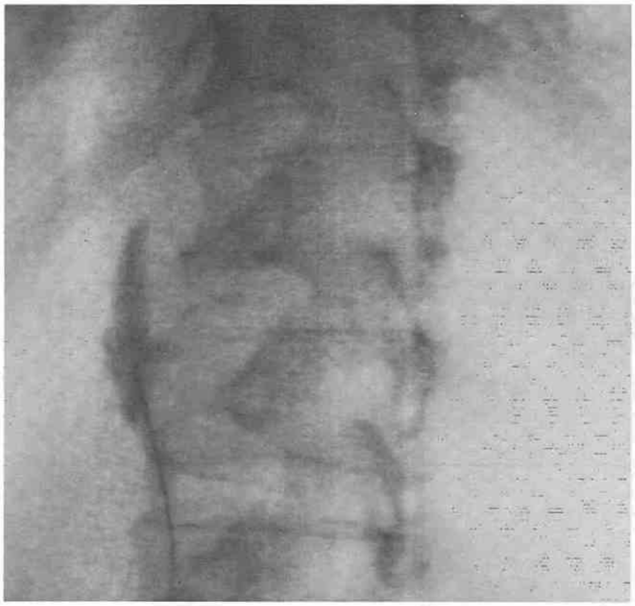

Figure 26–23. Lumbar sympathetic blockade. Fluoroscopic guidance of a 22-gauge needle from a slightly posterior-lateral approach to the anterior-lateral aspect of the L2 vertebra. Contrast medium is injected, showing retroperitoneal dispersion and the lack of intravascular communication. Then 10 mL of 0.25% bupivacaine was injected at weekly intervals for 6 weeks to ameliorate the patient's pain from reflex sympathetic dystrophy.

For temporary pain relief, a long-acting anesthetic agent such as bupivacaine can be injected. For more permanent pain relief, absolute alcohol or 6% phenol can be injected, preferably with the patient under local anesthesia.

Vertebroplasty and Balloon Kyphoplasty: Novel Treatments of Painful Osteoporotic and Other Vertebral Compression Fractures

In the United States, there are more than 35 million cases of osteoporosis, of which 1.5 million result in fragility fractures. Seven hundred thousand of these fragility fractures affect the spine, and 200,000 of these fragility fractures of the spine are refractory to nonoperative care, resulting in frustratingly continued debilitating pain.[46, 56]

The primary cause of osteoporosis is related to aging, and this is becoming more problematic as people continue to live longer. However, secondary causes of osteoporosis may also lead to fragility fractures of the spine and include steroids, alcoholism, low calcium intake, hormonal imbalances, and metabolic problems, including malabsorption of calcium through the gastrointestinal tract and renal disease.

Conventional medical management consists primarily of bed rest, narcotics, and braces. Pain from a vertebral compression fracture may take more than 1 year to resolve with this treatment. Surgical management may involve anterior and posterior approaches with instrumentation, for which outcomes are typically poor because the bone is inherently weak. This may lead to collapse and even neurologic deficits.

Vertebroplasty

Background

The technique of vertebroplasty was begun in the mid-1980s by a French neuroradiologist, Dr. Herve Deramond, who performed this procedure to treat a painful hemangioma of the cervical spine in a desperate patient.[19] This procedure was based on the principle of treating benign tumors of bone in other parts of the body by injection of polymethylmethacrylate (bone cement). For this painful hemangioma, Deramond injected bone cement and completely ameliorated the patient's pain. He subsequently used the vertebroplasty technique to treat painful metastatic vertebral compression fractures with excellent results.

Vertebroplasty has been used to treat painful osteoporotic compression fractures with excellent results. The first vertebroplasties performed in the United States occurred in the mid-1990s.[21, 25] In 1998, a modification of the vertebroplasty technique *(balloon kyphoplasty)* was designed to reestablish vertebral body height with the use of an inflatable balloon before fixation of the vertebra through the injection of bone cement.

In a review of the literature from France and the United States, more than 336 patients have received this treatment, and 90% of these patients experienced a dramatic reduction in or disappearance of pain, usually within 48 hours.[10, 12, 21, 25, 35, 40] Average follow-ups were 1 to 3 years, but some have been for as long as 10 years. These patients continue to be free of their original fracture pain.

Complications rates have ranged from 1% to 6% and have included radiculopathies, rib fractures, bleeding, pulmonary embolus, and canal compromise.

Indications

In the United States, most vertebroplasties and balloon kyphoplasties are performed for osteoporotic vertebral compression fractures. However, vertebroplasty can also be performed for destructive osteolytic metastases, particularly when the patient is not a candidate for chemotherapy and radiation therapy (Box 26–1). Most vertebral hemangiomas are asymptomatic, but for the few that cause considerable pain, vertebroplasty may be an effective treatment.

Box 26–1. **Indications for Vertebroplasty**

- Osteoporotic painful vertebral compression fractures
- Compression fractures of the vertebra due to metastatic disease
- Multiple myeloma
- Painful vertebral hemangioma

Figure 26–25. T1-weighted MR image demonstrating edema of a painful compression fracture of T7.

Technique

The selection of patients for vertebroplasty or balloon kyphoplasty should be based on correlation of findings on careful physical history and physical examination, plain films, MRI, and/or bone scanning (Fig. 26–25). We perform our physical examinations with fluoroscopy in an effort to correlate the focus of pain found on percussion directly over the spinous processes (Fig. 26–26). Vertebroplasty involves the placement of a large-bore (11- or 13-gauge) needle, with the tip positioned in the anterior third of the vertebral body. Percutaneous entry is used under multidirectional fluoroscopy or combined portable fluoroscopy and CT guidance.[38] A transpedicular approach is usually taken (Fig. 26–27), but a single posterior-lateral approach can be taken on the lower lumbar vertebrae.

For the smaller upper thoracic vertebrae, a costovertebral approach can be used if the pedicles are too small. Conscious sedation and a local anesthetic agent are appropriate for most patients.

Injection of the vertebra with iodine contrast medium (see Fig. 26–27*C*) can provide a vertebral venogram and a means of predicting unwanted runoff of the bone cement into the epidural veins or into the inferior vena cava. If exuberant filling of either epidural veins or the inferior vena cava is seen during contrast injection, unwanted embolization of bone cement to the lungs or the epidural veins can be avoided by injecting bone cement after it reaches a very doughy, viscous state.

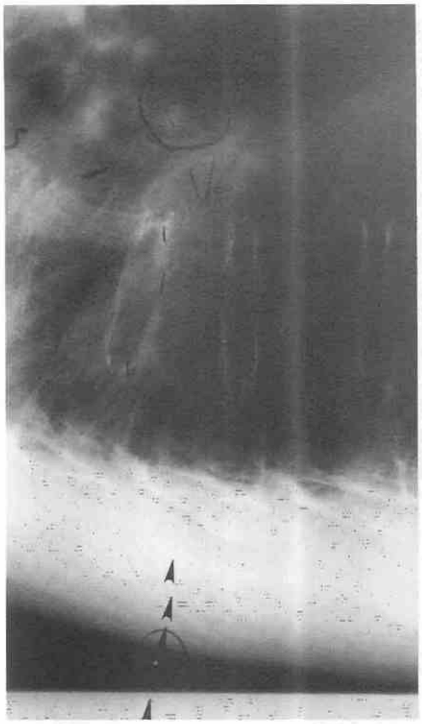

Figure 26–26. Physical examination reveals point of tenderness by percussion, which was demarcated by a lead shot marker *(arrowheads)*. This confirms that the patient's tenderness is emanating from the T7 compression fracture and correlates well with the MRI findings of marrow edema (see Fig. 26–25).

Because of the risk of infection, most operators administer prophylactic antibiotics either in the form of a broad-spectrum antibiotic such as cefazolin (Ancef) administered (2 g) intravenously or by mixing tobramycin powder (1.2 g) into the bone cement.[10, 25]

To avoid unwanted embolization of the bone cement to either the epidural veins or the inferior vena cava and lungs, optimal visualization of the bone cement during the time of injection is extremely important. Therefore, maximum opacification of the bone cement is desired and is usually obtained by mixing in 6 g of sterile USP barium.

For vertebroplasty, filling of at least the anterior two thirds of the vertebra is desired. This is done under high pressure via 1-mL Luer-Lok syringes or a high-pressure injection device (Parallax Technology). The patient should not be moved until the remaining sample of bone cement in the mixing bowl has adequately hardened (usually 20 to 30 minutes).

Generally, most patients can be treated on an outpatient basis if they are carefully observed in a recovery area for 4 to 6 hours after the procedure.

Technique Notes

The patient should be left in the prone position until the sample methacrylate in the mixing bowl is completely hardened (20 to 30 minutes). The patient is then taken to the recovery area for 4 to 6 hours, after which discharge occurs. Follow-up patient visits are made within 24 hours, at 1 week, at 4 weeks, and then at 4-month intervals or as necessary (Box 26–2).

Box 26–2. **Vertebroplasty Procedure**

- *Informed consent*
- *Sterile set-up*
- *Needle placement*

For placement of large-bore needles under multidirectional fluoroscopic or combined CT portable fluoroscopic technique, the choice of entry depends upon size and configuration of the vertebra. Transpedicular approaches are most common. In the lumbar region, the orientation of the pedicle in relation to the vertebra is relatively horizontal; in the thoracic region, there is a posterior-anterior downward orientation of the pedicles relative to the vertebra. This means that in the thoracic area the operator should begin somewhat higher than normally anticipated. If the pedicles are too small in the upper thoracic region, a costovertebral approach can be used.

- *Vertebral venography*

Nonionic, intrathecally compatible iodine contrast medium is used. (If the patient is allergic to iodine contrast medium, gadolinium can be used.) Usually, the injection of 3 to 4 mL of contrast medium is adequate. If the contrast medium does not wash out of the vertebra before bone cement injection, injection of a small amount of saline into the vertebra usually eliminates any residual opacity.

- If there is overly exuberant flow of contrast medium into the inferior vena cava or into the epidural veins, the bone cement should be allowed to reach a highly viscous, doughy state before it is injected.
- *Mixing the bone cement*

There are various brands. Some provide more of a doughy consistency (Zimmer). Refrigeration of the bone cement overnight increases the working time. For opacification, 6 g of USP sterile barium per level is excellent.

We usually mix the bone cement and barium for about 1 minute and load the methacrylate into 1-mL syringes. We do not inject the bone cement until it becomes somewhat doughy in consistency (~3 to 4 minutes). The 1-mL syringes provide a high-pressure injection.

- *Injection of bone cement into the vertebra*

Injection is administered under direct fluoroscopic visualization, with the needles placed in the anterior third of the vertebra. The needle is initially filled, and the methacrylate is then injected slowly and progressively in a retrograde manner to fill the more posterior portions of the vertebra. Usually, injection of approximately 2 to 3 mL of bone cement on a side is adequate. If the methacrylate clogs in the needle, the stylet of the needle can be reinserted to push the methacrylate out from the needle tip and to clear the needle for further injection of bone cement.

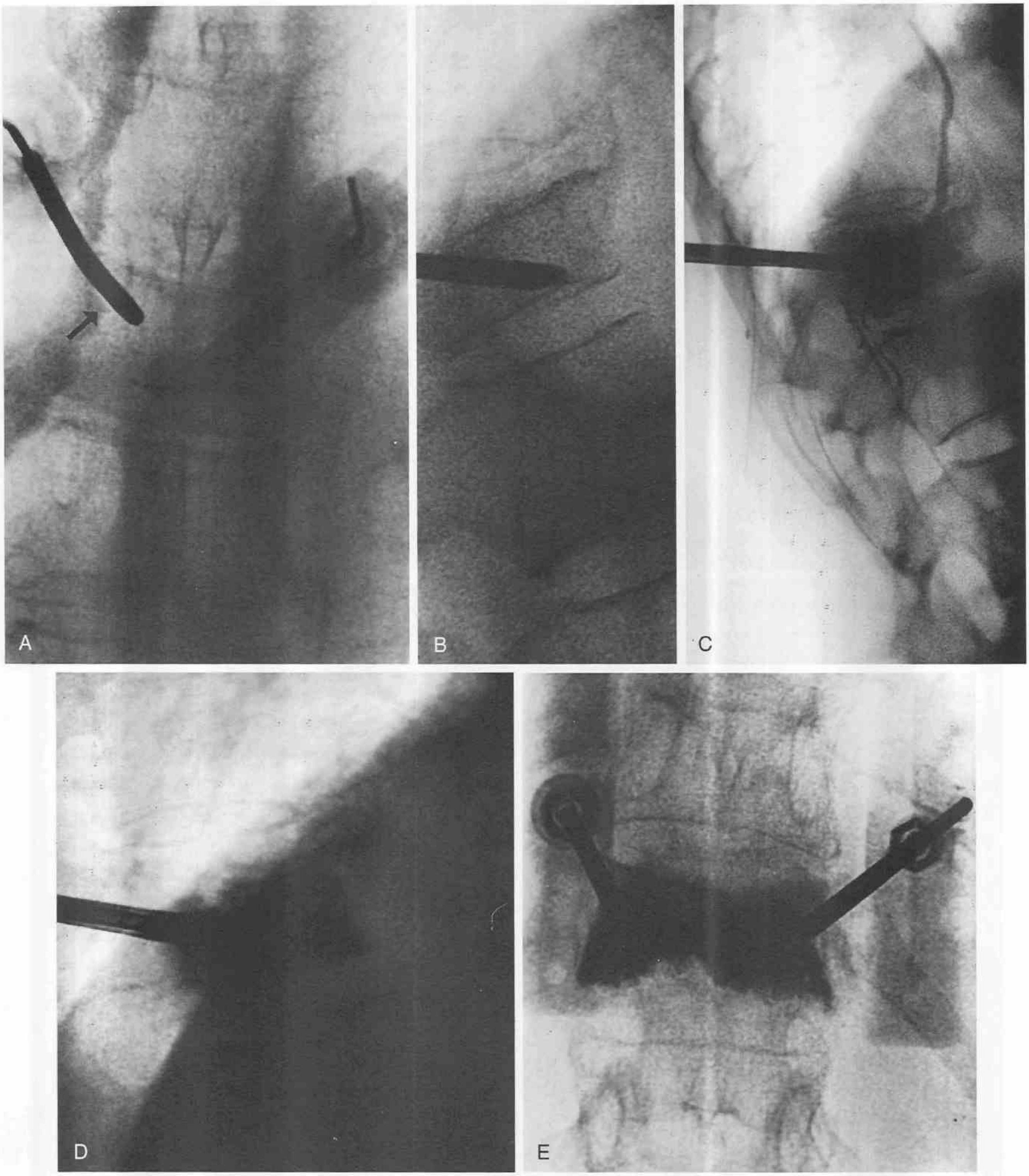

Figure 26–27. Vertebroplasty.

A, At the T7 vertebra, 11-gauge needles have been directed through the T7 pedicles *(arrow)*. In the thoracic region, the pedicles run posterior-anterior in a slightly superior-inferior direction, and thus the needle passage should be made to accommodate this configuration.

B, Lateral view demonstrating needle placement via a transpedicular approach. The needles have been extended to the anterior margins of the vertebra.

C, Vertebral venography showing runoff to the inferior vena cava. Caution should be exercised during injection of bone cement (polymethylmethacrylate). If the cement is too "runny," it may embolize to the lungs.

D and *E,* Final distribution of bone cement throughout the T7 vertebra. The patient's back pain disappeared within 1 hour of the procedure.

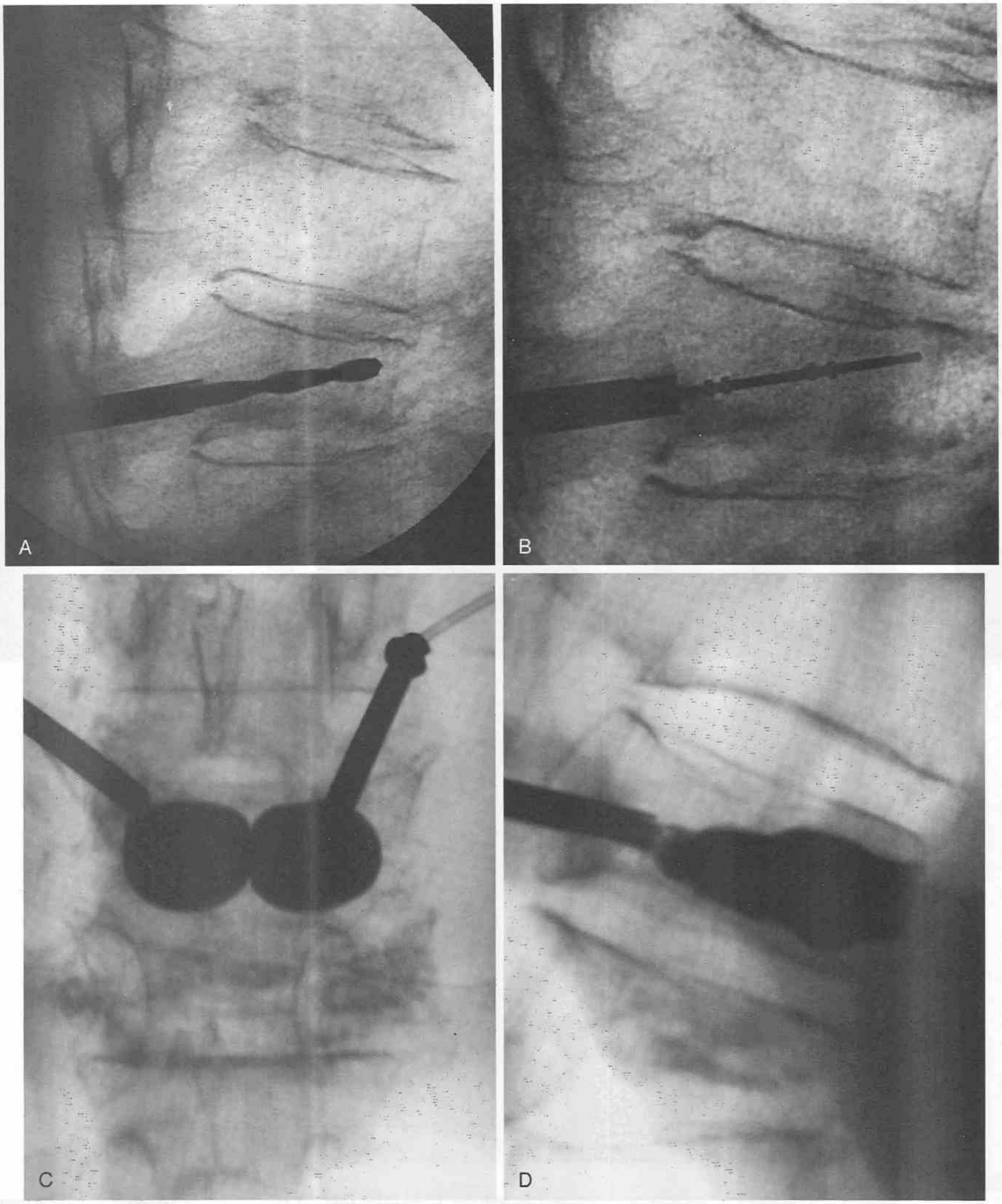

Figure 26–28. Balloon kyphoplasty, T12 vertebra. *A,* A 3-mm drill is directed through the anterior extent of the vertebral body after initial placement of 11-gauge needles and subsequent placement of a working cannula. *B,* Insertion of the inflatable balloon tamp before inflation. *C,* Inflation of the inflatable balloon tamp, anteroposterior view. *D,* Application of bone cement after height restoration. Note the rectangular, rather than previously wedge-shaped, configuration of the vertebral body.

Balloon Kyphoplasty

Although vertebroplasty is effective in ameliorating the pain of a vertebral compression fracture, it usually leaves a deformity of the vertebra (*kyphosis*). Prospective and retrospective studies have demonstrated decreased longevity of people with kyphotic vertebral compression fractures versus those without the fractures.[29] In addition, people with kyphosis who have underlying chronic obstructive lung disease continue to have exacerbating problems with their breathing as a result of decreased lung capacity.[47]

Patients with severe kyphotic curvatures often complain of gastrointestinal problems of bloating and the feeling of partial bowel obstruction along with diminished appetite because the ribs and sternum press on the lower abdomen. Patients who have a severe kyphosis have a center of gravity that has shifted anteriorly, and they may move about in an unbalanced manner.[9, 58] This may result in an increased risk of falls because of their incorrect balance position.

Balloon kyphoplasty is an attempt to reduce the unwanted effects of a kyphosis before the stability of the fracture is restored and the pain is removed. It is performed in a manner similar to that of vertebroplasty, but it also incorporates the addition of an inflatable bone tamp, which can help to reestablish vertebral body height before fixation with bone cement (Fig. 26–28). An added advantage of the use of the inflatable bone tamp may be that it creates a cavity within the fractured vertebra for which the injection of bone cement can be performed under low pressure, reducing the chances of unwanted leakage of methacrylate into adjacent venous or other structures (Box 26–3).

Box 26–3. **Balloon Kyphoplasty Procedure**

- *Informed consent*
- *Sterile set-up*
- *Percutaneous access to the vertebra similar to vertebroplasty with large-bore needles*
- *Insertion of guide pin through the large-bore needle*

Remove the large-bore needle. Insert the stiffening obturator over the guide pin. Place the working cannula over the guide pin and obturator with the tip of the cannula along the posterior margin of the vertebral body.

Remove the guide pin and obturator. Place a 3-mL drill through the working cannula, and through hand rotation advance the drill to the anterior third of the vertebra (see Fig. 26–28*A*). This creates a cavity for insertion of the inflatable bone tamp.

Remove the drill. Insert the bone tamp, and inflate under direct visualization with specified pressures. Maximum expansion of the bone tamp occurs when pressure dropoffs cease, the edge of the bone tamp reaches one of the end plates, or the bone tamp reaches its maximum volume.

- *Deflation and removal of bone tamp*

Mix the cement, as for vertebroplasty, with opacifying agents. Place bone cement in filler tube, and inject the same amount of bone cement to match the volume of the maximum balloon inflation of the bone tamp.

Results

Analysis of the first 24 kyphoplasties performed at the University of California, San Diego, revealed average vertebral body height restorations of 52% at the anterior vertebral body, 66% at the midvertebral body, and 53% at the posterior vertebral body. All patients in this group experienced dramatic pain relief, usually within hours of the procedure. There were no complications in this group.

At the time of the writing of this chapter, there are about a dozen centers at which kyphoplasties are performed. According to the Kyphon Corporation, 462 fractures have been treated in 291 procedures in 261 patients throughout these centers. Pain relief has been obtained in 90% of the cases, as confirmed by return to active daily living questionnaires. There have been no failures. The longest follow-up is 18 months. The procedure is well tolerated, and patients who require subsequent procedures look forward to undergoing the kyphoplasty.

The complication rate has been less than 2% (similar to that of vertebroplasty). No complication has been balloon-related.

Clinical trials for kyphoplasty are starting, with one randomized study comparing kyphoplasty with medical therapy. Other studies to evaluate height restoration, improved respiratory function, and improved quality of life are expected to follow.

Summary

Vertebroplasty is a procedure that can help stabilize a painful vertebral compression fracture and eradicate the pain. The balloon kyphoplasty is a modification of the vertebroplasty that provides an opportunity to restore vertebral body height before stabilization and pain ablation.

The vertebroplasty, kyphoplasty, and a variety of other image-guided spine interventions provide the radiologist with an opportunity to do much more than simply image. Using the knowledge of imaging anatomy, a radiologist can effectively intervene as both a diagnosing and a treating physician. To do so, however, requires that the radiologist also be willing to examine the patient, counsel the patient, and monitor the patient over time.

References

1. Adam G, Bucker A, Nolte-Ernsting C, et al: Interventional MR imaging: Percutaneous abdominal and skeletal biopsies and drainages of the abdomen. Eur Radiol 9:1471–1478, 1999.
2. Anzai Y, Lufkin R, DeSalles A, et al: Preliminary experience with MR-guided thermal ablation of brain tumors. AJNR Am J Neuroradiol 16:39–48; discussion, 49–52, 1995.
3. Aprill C, Dwyer A, Bogduk N: Cervical zygoapophyseal joint pain patterns: II. A clinical evaluation. Spine 15:458–461, 1990.
4. Babu NV, Titus VT, Chittaranjan S, et al: Computed tomographically guided biopsy of the spine. Spine 19:2436–2442, 1994.
5. Benzon H: Epidural steroid injections. Pain Digest 1:271–280, 1992.
6. Bogduk N, Narsland A: The cervical zygoapophyseal joint as a source of neck pain. Spine 13:610–617, 1988.
7. Castro DJ, Lufkin RB, Saxton RE, et al: Metastatic head and neck malignancy treated using MRI guided interstitial laser phototherapy: An initial case report. Laryngoscope 102:26–32, 1992.
8. Colhoun E, McCall IW, Williams L, et al: Provocation discography as a guide to planning operations of the spine. J Bone Joint Surg Br 70:267–271, 1988.
9. Cortet B, Houvenagel E, Puisisux F, et al: Spinal curvatures and quality of life in women with vertebral fractures secondary to osteoporosis. Spine 24:1921–1925, 1999.

10. Cotton A, Boutry N, Cortet B, et al: Vertebroplasty: State of the art. Radiographics 18:311–320, 1998.
11. Daly B, Templeton PA: Real-time CT fluoroscopy: Evolution of an interventional tool. Radiology 211:309–315, 1999.
12. Do H, Jensen M, et al: Percutaneous vertebroplasty in treatment of patients with vertebral osteonecrosis (Kummel's disease). Article 2. Neurosurg Forum 7:1999.
13. Dreyfus P: Low back pain and the zygoapophyseal joints. Arch Phys Med Rehabil 77:290–300, 1996.
14. El-Khoury G, Renfrew D: Percutaneous procedures for the diagnosis and treatment of lower back pain: Diskography, facet joint injection, and epidural injection. AJR Am J Radiol 157:685–691, 1991.
15. Erickson SJ, Hogan QH: CT-guided injection of stellate ganglion: Description of technique and efficacy of sympathetic blockage. Radiology 188:707–709, 1993.
16. Frahm C, Gehl HB, Melchert UH, et al: Visualization of magnetic resonance-compatible needles at 1.5 and 0.2 Tesla. Cardiovasc Intervent Radiol 19:335–340, 1996.
17. Fraser RD, Osti OL, Vernon-Roberts B: Discitis after discography. J Bone Joint Surg Br 69:31–35, 1987.
18. Fukui S, Ohseto K, Shiotani M, et al: Referred pain distribution of the cervical zygoapophyseal joints and cervical dorsal rami. Pain 68: 79–83, 1996.
19. Gaibert P, Deramond H, Rosat P, Le Gars D: Preliminary note on the treatment of vertebral hemangioma by percutaneous acrylic vertebroplasty. Neurochirurgie 33:166–168, 1987.
20. Gangi A, Dietemann J, Schultz A, et al: Interventional radiologic procedures with CT guidance for cancer pain management. Radiographics 16:1289–1304, 1996.
21. Ganj A, Kastler BA, Dietemann JL: Percutaneous vertebroplasty guided by a combination of CT and fluoroscopy. AJNR Am J Neuroradiol 15:83–86, 1994.
22. Guyer RD, Ohnmeiss DD: Contemporary concepts in spine care lumbar discography. Spine 20:2048–2059, 1995.
23. Hinks RS, Bronskill MJ, Kucharczyk W, et al: MR systems for image-guided therapy. J Magn Reson Imaging 8:19–25, 1998.
24. Jager L, Muller-Lisse GU, Gutmann R, et al: Initial results with MRI-controlled laser-induced interstitial thermotherapy of head and neck tumors. Radiologe 36:236–244, 1996.
25. Jensen M, Evans A, Mathis JM, et al: Percutaneous polymethyl methacrylate vertebroplasty in the treatment of osteoporotic vertebral body compression fractures: Technical aspects. AJNR Am J Neuroradiol 18:1897–1904, 1997.
26. Jimenez A, Martinez-Nogura A, et al: Percutaneous neurolysis of celiac plexus via anterior approach with sonographic guidance. AJR Am J Radiol 161:1061–1063, 1993.
27. Johnson B, Schellhas K, Pollei SR: Epidurography and therapeutic epidural injections: Technical considerations and experience with 5334 cases. AJNR Am J Neuroradiol 20:697–705, 1999.
28. Jolesz FA, Blumenfeld SM: Interventional use of magnetic resonance imaging. Magn Reson Q 10:85, 1994.
29. Kado D, Browner W, Palerno L, et al: Vertebral fractures and mortality in older women: A prospective study. Arch Intern Med 159: 1215–1220, 1999.
30. Kahn T, Bettag M, Ulrich F, et al: MRI-guided laser-induced interstitial thermotherapy of cerebral neoplasms. J Comput Assist Tomogr 18:519–532, 1994.
31. Kahn T, Harth T, Bettag M, et al: Preliminary experience with the application of gadolinium-DTPA before MR imaging-guided laser-induced interstitial thermotherapy of brain tumors. J Magn Reson Imaging 7:226–229, 1997.
32. Katada K, Kato R, Anno H, et al: Guidance with real-time CT fluoroscopy. Nippon Acta Radiol 200:851–856, 1994.
33. Kato R, Katada K, Anno H, et al: Radiation dosimetry at CT fluoroscopy: Physicians hand dose and development of needle holders. Radiology 201:576–578, 1996.
34. Knauth M, Wirtz CR, Tronnier VM, et al: Intraoperative MR imaging increases the extent of tumor resection in patients with high-grade gliomas. AJNR Am J Neuroradiol 20:1642–1646, 1999.
35. Lemley T, Barr M, et al: Percutaneous vertebroplasty: A new technique for treatment of benign and malignant vertebral body compression fractures. Surg Physician Assist 3:24–27, 1997.
36. Lewin JS: Interventional MR imaging: Concepts, systems, and application in neuroradiology. AJNR Am J Neuroradiol 20:735–748, 1999.
37. Lewin JS, Duerck JL, Jain JR, et al: Needle localization in MR-guided biopsy and aspiration: Effect of field strength, sequence design, and magnetic field orientation. AJR Am J Radiol 166:1337–1345, 1996.
38. Lewin JS, Petersilge CA, Hatem SF, et al: Interactive MR imaging-guided biopsy and aspiration with a modified clinical C-arm system. AJR Am J Radiol 170:1593–1601, 1998.
39. Martin AJ, Hall WA, Liu H, et al: Brain tumor resection: Intraoperative monitoring with high-field-strength MR imaging: Initial results. Radiology 215:221–228, 2000.
40. Mathis J, Petric M, Naff N: Percutaneous vertebroplasty treatment of steroid induced osteoporotic compression fractures. Arthritis Rheum 4:171–175, 1998.
41. Mooney V, Robertson J: Facet joint syndrome. Clin Orthop 115: 149–156, 1976.
42. Mueller PR, Stark DD, Simeone JF, et al: MR-guided aspiration biopsy: Needle design and clinical trials. Radiology 161:605–609, 1986.
43. Neuerburg JM: MR-guided bone biopsy. In Lufkin RB (ed): Interventional MRI. St. Louis, Mosby, 1999, pp 381–386.
44. Parker SH, Stavros AT, Dennis MA: Needle biopsy techniques. Radiol Clin North Am 33:1171, 1995.
45. Renfrew DL, Moore TE, Kathol MH, et al: Correct placement of epidural steroid injections: Fluoroscopic guidance and contrast administration. AJNR Am J Neuroradiol 12:1003–1007, 1991.
46. Riggs BL, Melton LJ: The worldwide problem of osteoporosis: Insights afforded by epidemiology. Bone 17:5055–5115, 1995.
47. Schlaich C, Minnie H, et al: Reduced pulmonary function in patients with spinal osteoporotic fractures. Osteoporosis Int 8:261–267, 1998.
48. Schwartz RB, Hsu L, Wong TZ, et al: Intraoperative MR imaging guidance for intracranial surgery: Experience with the first 200 cases. Radiology 211:477–488, 1999.
49. Schellhas KP, Garvey TA, Johnson BA, et al: Cervical diskography: Analysis of provoked responses at C2-C3, C3-C4, and C4-C5. AJNR Am J Neuroradiol 21:269–275, 2000.
50. Schellhas KP, Smith MD, Gundry CR, et al: Cervical discogenic pain prospective correlation of magnetic resonance imaging and discography in asymptomatic subjects and pain sufferers. Spine 21:300–312, 1996.
51. Smits HFM, Bos C, van der Weide R, et al: Interventional MR: Vascular applications. Eur Radiol 9:1488–1495, 1999.
52. Strother CM, Unal O, Frayne R, et al: Endovascular treatment of experimental canine aneurysms: Feasibility with MR imaging guidance. Radiology 215:516–519, 2000.
53. Vogl TJ, Mack MG, Muller PK, et al: Interventional MR: Interstitial therapy. Eur Radiol 9:1479–1487, 1999.
54. Vogl TJ, Mack MG, Muller P, et al: Recurrent nasopharyngeal tumors: Preliminary clinical results with interventional MR imaging–controlled laser-induced thermotherapy. Radiology 196:725–33, 1995.
55. Waldman SD, Winnie AP: Interventional Pain Management. Philadelphia, WB Saunders, 1996, pp 269–271.
56. Wasnich U: Vertebral fracture epidemiology. Bone 18:1795–1835, 1996.
57. Wesbey G, Edelman RR, Harris R: Artifacts in MR-imaging: Description, causes, and solutions. In Edelman RR, Hesselink JR (eds): Clinical Magnetic Resonance Imaging. Philadelphia, WB Saunders, 1990, pp 74–80.
58. White A, Panjabi M: Clinical Biomechanics of the Spine, 2nd ed. Philadelphia, JB Lippincott, 1990, pp 155–163.
59. Wong W. Common spine interventions: Percutaneous biopsies. Proc Am Soc Neuroradiol 36:107–109, 1998.
60. Wong W, Kerber C, et al: Unusual nonpyogenic disk inflammation following discography: A report of 3 cases. Paper presented at 28th Annual Meeting of Western Neuroradiological Society, Syllabus 84, 1996.
61. Zenaro H, Douset V, Viaud B, et al: Periganglionic foraminal injections performed under CT control. AJNR Am J Neuroradiol 19: 349–352, 1998.

Part V

Imaging of the Chest

Edited by
John R. Haaga

27 Non-neoplastic Parenchymal Lung Disease

Janet E. Kuhlman

Evaluation of non-neoplastic parenchymal lung disease begins with careful examination of the posteroanterior (PA) and lateral chest films, together an invaluable source of information about the nature and extent of pulmonary diseases. Increasingly, however, conventional computed tomography (CT) and more advanced imaging techniques, such as high-resolution CT (HRCT, or thin-section CT), spiral and multidetector CT, ultrafast electron beam CT, and magnetic resonance imaging (MRI), have become integral parts of the evaluation process, serving as important adjuncts to the plain film for the purposes of detection, diagnosis, and characterization of parenchymal lung disease.

CT as an imaging modality has distinct advantages over conventional radiography in displaying the anatomy and pathology of the lung. The cross-sectional format of CT permits visual examination of the lung that is unencumbered by superimposed structures, such as the chest wall, heart, and pulmonary vessels. With the advent of HRCT, delineation of the lung parenchyma down to the level of the secondary pulmonary lobule, the basic building block of the lung, is possible. This additional information provided by HRCT allows a more detailed analysis of pathologic processes affecting the lung. Increasingly, HRCT is being used as the technique of choice to evaluate diffuse and focal lung diseases.[142, 146, 168, 229, 230]

Spiral (or helical) CT takes advantage of new slip-ring technology and has revolutionized the way we look at the lung.[40, 84, 112, 171, 200, 223] A continuously rotating detector combined with continuous table feed allows rapid data acquisition through the chest during a single breath-hold.[84] Spiral CT results in a gapless, volumetric acquisition that eliminates problems of slice misregistration caused by variations in the depth of inspiration.[40, 84, 112, 171, 200, 223] The resulting data set is more accurate, more reproducible from one study to the next, and more quickly acquired. In the lung, spiral CT facilitates the process of evaluating small pulmonary nodules and allows the generation of three-dimensional (3D) images of the lung that are not degraded by respiratory motion (Fig. 27–1).[40, 84, 112, 171, 200, 223] The faster acquisition times ensure evaluation of the lung during maximum vascular enhancement and may decrease the total volume of intravenous (IV) contrast material required for adequate enhancement.

Multidetector CT takes the advantages of spiral CT several steps further by combining rows of detectors and by interleaving or interspacing multiple helical data sets that are simultaneously acquired. Multidetector scanners can cover greater distances, at faster speeds, with thinner slice thicknesses.

Ultrafast electron beam CT replaces the rotating detector gantry of conventional CT scanners with a deflectable electron beam and generates CT images in 0.1 to 0.05 second. Electron beam CT adds another dimension of speed to the data acquisition process and is fast enough to stop cardiac motion on displayed images, allowing detailed depiction of coronary artery calcifications. It has also been used to capture dynamic processes, such as air trapping resulting from small airway disease or changes in the caliber of the trachea and bronchi during various phases of the respiratory cycle.[213]

Although MRI has a clear advantage over other imaging modalities in evaluating cardiac and vascular disorders of the chest, its role in the evaluation of parenchymal lung disease has been limited. Obstacles to lung imaging include respiratory motion and magnetic susceptibility effects caused by air-tissue interfaces. Rapid evolution of MRI technology suggests that some of these problems may be overcome in the near future. Promising areas under current investigation include MRI evaluation of the pulmonary circulation, arteriovenous malformations (AVMs), and other vessel-related disorders of the lung. Assessment of chest wall disease and peridiaphragmatic processes, which do not suffer as much from respiratory or magnetic susceptibility artifacts, already benefits from the multiplanar capabilities of MRI and its improved soft tissue contrast.

Techniques

Several approaches to examining parenchymal lung disease with CT exist, and no one method is optimal for all indications.[142] Many authors advocate the use of standard conventional CT as the initial screening test, followed by a few select HRCT slices through areas of interest. In cases of occult pulmonary disease or a lung process that may affect the lung diffusely, surveying the entire chest at 1-cm intervals using HRCT techniques may be preferable. This multilevel HRCT examination is more likely to detect early or subtle manifestations of lung disease and is more accurate in determining the full extent of lung damage.

Multidetector and spiral CT are ideal for detecting and evaluating small pulmonary nodules and pulmonary emboli and for 3D imaging of the lung.[40, 112, 200] Spiral CT can

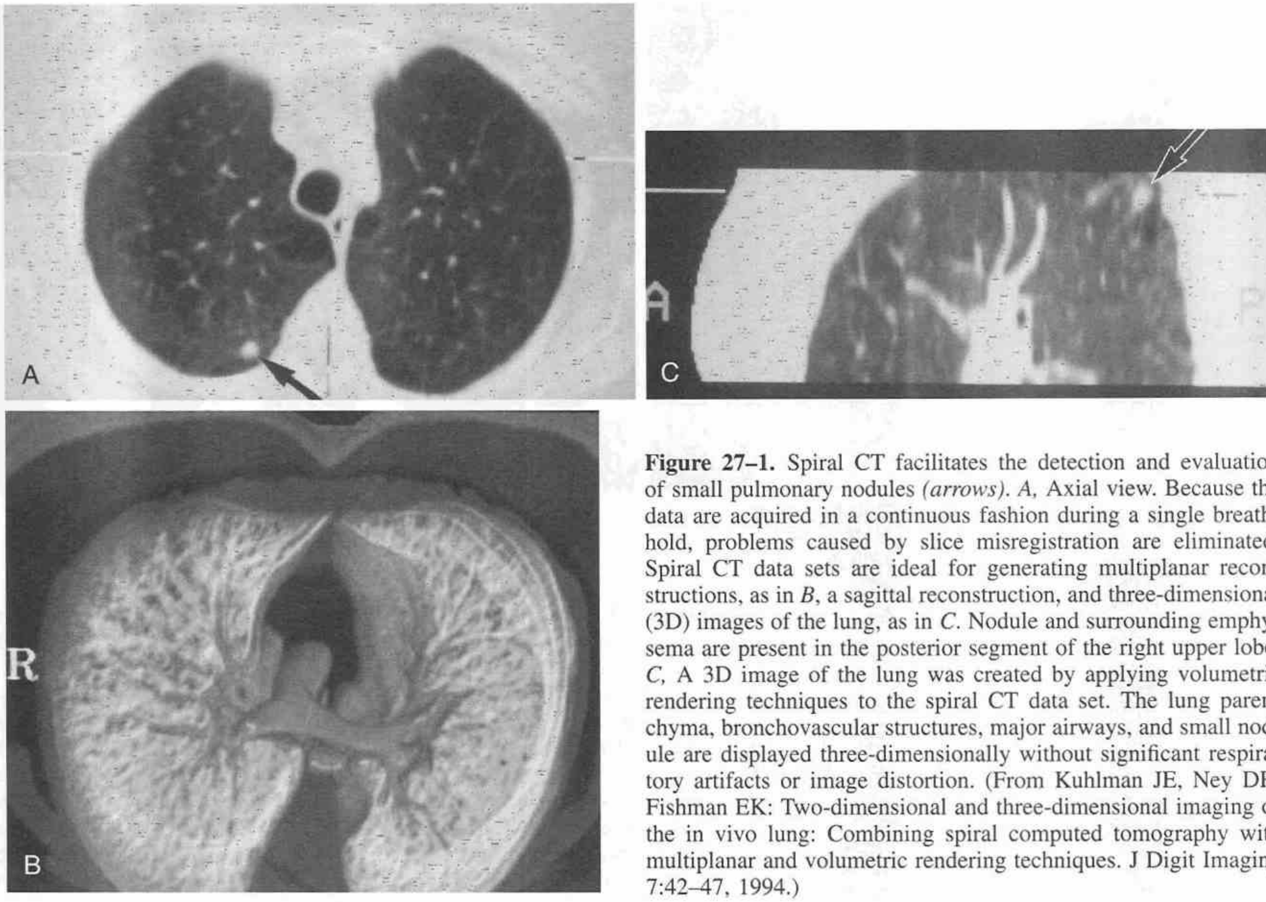

Figure 27–1. Spiral CT facilitates the detection and evaluation of small pulmonary nodules *(arrows)*. *A,* Axial view. Because the data are acquired in a continuous fashion during a single breath-hold, problems caused by slice misregistration are eliminated. Spiral CT data sets are ideal for generating multiplanar reconstructions, as in *B*, a sagittal reconstruction, and three-dimensional (3D) images of the lung, as in *C*. Nodule and surrounding emphysema are present in the posterior segment of the right upper lobe. *C,* A 3D image of the lung was created by applying volumetric rendering techniques to the spiral CT data set. The lung parenchyma, bronchovascular structures, major airways, and small nodule are displayed three-dimensionally without significant respiratory artifacts or image distortion. (From Kuhlman JE, Ney DR, Fishman EK: Two-dimensional and three-dimensional imaging of the in vivo lung: Combining spiral computed tomography with multiplanar and volumetric rendering techniques. J Digit Imaging 7:42–47, 1994.)

also be combined with high-resolution algorithms and thin-section techniques. Ultrafast CT, or cine-CT, is a prerequisite for evaluating airway physiology in real time, for example, capturing differences in lung attenuation and airway caliber that result from reversible or irreversible airway disease.[213]

High-Resolution CT (Thin-Section CT)

HRCT combines the use of thinly collimated CT slices that are 1 to 1.5 to 2 mm in thickness, with a high-spatial-frequency algorithm that enhances edge detection.[142] On many older CT models, the high-resolution algorithm is a bone reconstruction algorithm. On many newer CT models, a special high-resolution lung algorithm is available. Thin collimation decreases partial volume averaging and improves the ability of CT to demonstrate small pulmonary lesions. High-spatial-frequency algorithms, by decreasing the amount of smoothing of the image data, enhance edge detection and make lung structures look sharper. HRCT technical features increase spatial resolution but also increase the amount of noise visible in the image.

Although not essential, increases in kilovolt peak (kVp) and milliampere (mA) settings may be used to improve signal-to-noise ratio in HRCT images.[142] Field of view should be reduced to cover the lung parenchyma only, thus maximizing the fine detail of the lungs (Fig. 27–2). IV contrast is not used for high-resolution CT examinations that are limited to evaluating the lung parenchyma.

To optimize an HRCT examination, additional considerations are important.[141, 142, 227, 228] Retrospective targeting of the reconstructed image to a particular area of interest can further enhance depiction of abnormal lung parenchyma (see Fig. 27–2). Confusion caused by crowded pulmonary vessels and dependent lung edema or microatelectasis is minimized if HRCT scans are obtained at suspended end-inspiratory volume. If necessary, prone views can be taken to differentiate focal dependent edema or microatelectasis, commonly seen in the lung bases of normal patients, from early pulmonary fibrosis.

Although the best HRCT results are obtained with breath-holding techniques, this is not always possible in an acutely ill patient with respiratory compromise or in a pediatric patient.[126] Faster scan times, on the order of 1 second or less, are now available on many state-of-the-art scanners and greatly reduce respiratory motion artifacts, allowing for good-quality, high-resolution examinations to be performed even in these patients.

Image processing is also important. HRCT images are viewed at lung window settings. Exact settings vary depending on the scanner make and model, but typical window settings are in the range of 1650 (window width) and −600 (window center). Images of the mediastinum can be reconstructed using a standard soft tissue algorithm and viewed using mediastinal window settings of 410 (window

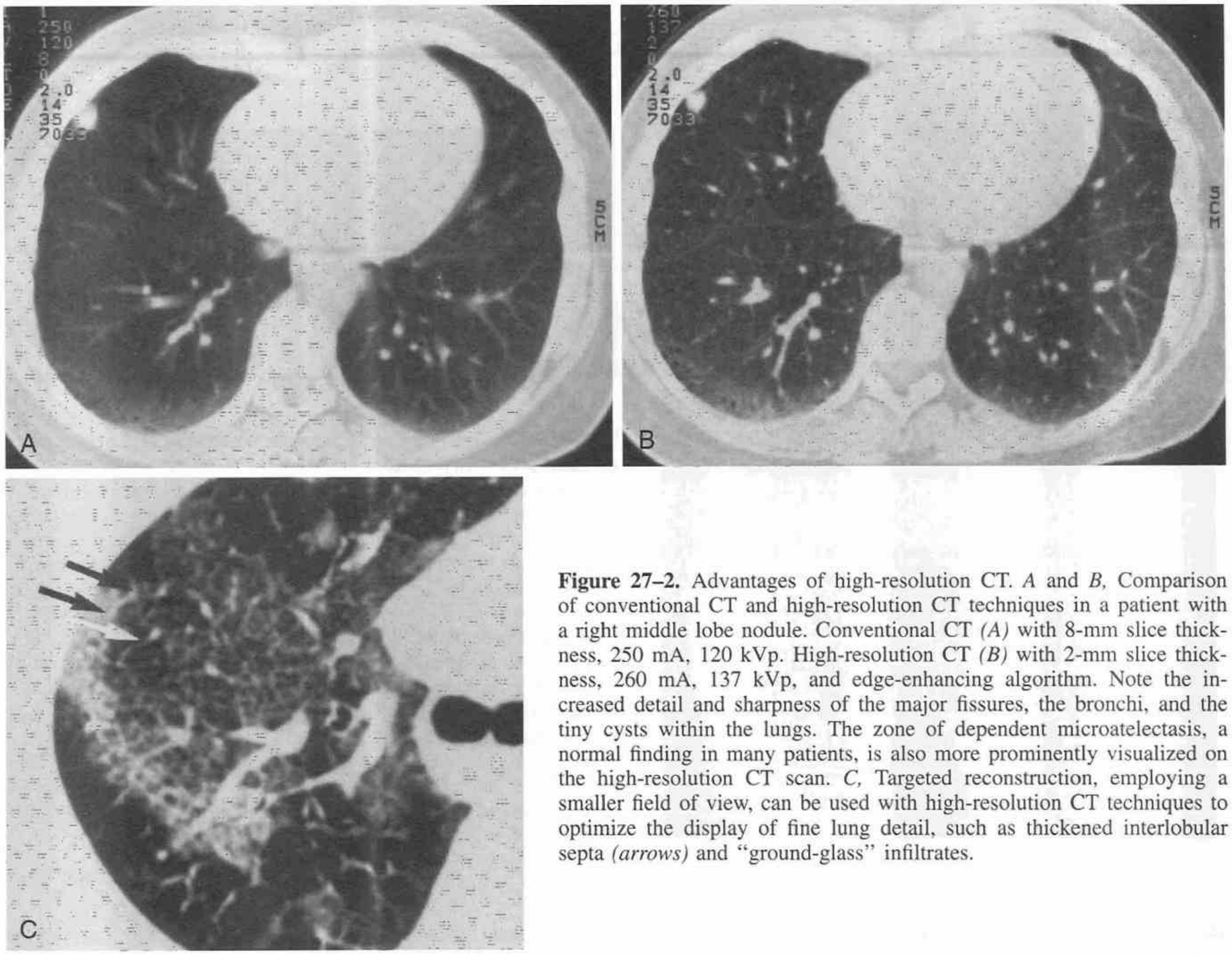

Figure 27–2. Advantages of high-resolution CT. *A* and *B*, Comparison of conventional CT and high-resolution CT techniques in a patient with a right middle lobe nodule. Conventional CT *(A)* with 8-mm slice thickness, 250 mA, 120 kVp. High-resolution CT *(B)* with 2-mm slice thickness, 260 mA, 137 kVp, and edge-enhancing algorithm. Note the increased detail and sharpness of the major fissures, the bronchi, and the tiny cysts within the lungs. The zone of dependent microatelectasis, a normal finding in many patients, is also more prominently visualized on the high-resolution CT scan. *C*, Targeted reconstruction, employing a smaller field of view, can be used with high-resolution CT techniques to optimize the display of fine lung detail, such as thickened interlobular septa *(arrows)* and "ground-glass" infiltrates.

width) and 3 (window center). Additional window settings are adjusted manually at the time of imaging to enhance depiction of subtle "ground-glass" opacities that are best appreciated on wider window settings.

Although HRCT algorithms are excellent for delineating diseases of the lung parenchyma, they are less appropriate for examining abnormalities of the mediastinum or the abdomen. The reconstruction algorithm used in HRCT makes detection of mediastinal adenopathy and focal liver lesions more difficult. High-resolution algorithms also tend to accentuate pleural thickness, an important factor to keep in mind during evaluation of patients with asbestos exposure for pleural disease. For assessment of a small pulmonary nodule for the presence of calcification, a standard lung algorithm should be used because the edge-enhancement properties of many HRCT algorithms make small nodules appear denser than they really are and can falsely simulate calcification.

Spiral or Helical CT

Spiral CT techniques can be easily adapted for evaluation of the lung.[40, 84, 112, 171, 200, 223] Most helical scanners are capable of generating a series of consecutive scans lasting 1 second or less, obtained in a continuous fashion during a single breath-hold maneuver. The operator chooses the thickness of the slice collimation with a range of 1 to 10 mm. Table speed is set to between 1 and 10 mm/second. Pitch (table speed divided by slice thickness) is usually best kept between 1 and 2. The reconstruction algorithm and interval between reconstructed images (the degree of slice overlap) are chosen to suit the clinical problems at hand.

Numerous protocol variations exist. Two examples for lung evaluation are as follows:

1. A survey examination of the chest might use a slice acquisition thickness of 7 mm, a pitch of 1.4, a reconstruction interval of 5 mm, and a lung algorithm for lung images and a standard algorithm for soft tissue images.
2. A focused study with greater detail that will cover a shorter distance might use a slice acquisition thickness of 3 mm, a pitch of 1 to 1.7, and a reconstruction interval of 1 mm employing a high-resolution lung algorithm.

Total acquisition times and recommended mA and kVp vary by manufacturer. Once axial images are reconstructed, the spiral CT data set can be transferred to a free-standing workstation where multiplanar reconstructions and 3D image analysis can be performed (see Fig. 27–1).[112]

Whether or not IV contrast is required for the chest spiral CT examination depends on the clinical question to be answered and the type of disease process anticipated.

Multidetector CT

The possible protocol variations multiply rapidly with the additional capabilities of multidetector scanners. One example of a protocol in use for evaluating pulmonary emboli uses the following multidetector CT parameters:

- Slice thickness, 1.25 mm
- Reconstruction interval, 0.6 mm
- Table speed, 7.5 mm/rotation
- Time per rotation, 0.8 second

IV contrast (150 mL) is injected at 4 mL/second, with a scan delay time of 25 seconds. Scanning begins at the diaphragm and proceeds to the top of the chest. All images are reviewed on an independent workstation using a paging mode, and selected images are also viewed from hard-copy film.

CT Patterns and Signs of Non-neoplastic Lung Disease

As experience with CT accumulates, patterns and signs of non-neoplastic lung disease have emerged. Many of the HRCT patterns and signs are refinements of those first recognized on conventional CT of the lung. In an attempt to arrive at a differential diagnosis for focal or diffuse lung disease, it is helpful first to characterize the parenchymal CT abnormalities into one of three categories[98]:

- Air space disease
- Interstitial disease
- Cystic lung disease

Once the predominant category has been established, the lung disease can be further characterized on the basis of patterns of distribution and by recognizing a few specific CT signs.

Categories of Lung Disease

Air Space Disease

One of the earliest manifestations of focal air space disease on CT scans is the presence of small 4- to 10-mm opacities called *acinar nodules*.[146] These are not true nodules when examined pathologically but, rather, represent clusters of alveoli that are filled with fluid, inflammatory cells, or blood, depending on the disease process. As air space disease becomes more severe and extensive, acinar densities coalesce to form larger opacities and eventually progress to lobular, subsegmental, segmental, lobar, and multilobar involvement (Fig. 27–3). Air-bronchograms on CT scans are hallmarks of air space consolidation, just as they are on conventional chest radiographs (Fig. 27–4).

Interstitial Disease

Features of interstitial disease on conventional CT and HRCT include nodules, reticulation, and thickening of the pulmonary septa (Fig. 27–5).[20, 177, 197, 240] Interfaces that exist between the lung and the pleural surfaces, or between the lung and the bronchovascular bundles, become irregular and shaggy (see Fig. 27–5).[240] HRCT supplements and enhances conventional CT in the detection of early interstitial lung disease by providing greater detail of the smaller, more peripheral lung elements and interlobular septa.

Cystic Lung Disease and Abnormal Air Spaces

Cystic disease of the lung encompasses a wide variety of pathologic processes that are characterized by "holes" or abnormal air-containing spaces within the lung parenchyma.[114] Cystic structures identified on CT scans include blebs, bullae, cavities, pneumatoceles, "honeycombing," (see "Subpleural Distributions" later), dilated bronchi, and dilated terminal airways and alveolar sacs. Lung diseases that produce abnormal air spaces in the lung include cavitating pulmonary infections, vascular-embolic disorders, bronchiectasis, emphysema, pulmonary fibrosis, adult respiratory distress syndrome (ARDS), and unusual disorders such as Langerhans' histiocytosis, lymphangiomyomatosis, and tracheolaryngeal papillomatosis. The mechanisms by which abnormal air spaces are produced include focal ischemic necrosis of the lung, as seen with septic emboli; disruption of elastic-fiber networks, as found in emphysema; and retractile fibrosis with remodeling of the lung architecture, as seen in the honeycomb lung (Fig. 27–6).

Characterization of Lung Disease

Once lung disease has been characterized as air space, interstitial, or cystic in nature, it can be further analyzed as to its pattern and distribution. *Focal* lung disease may demonstrate specific CT signs that aid in narrowing the differential diagnosis. *Diffuse* lung disease may be evenly or unevenly distributed throughout the lung. It may affect primarily the central regions, the subpleural zones, or the tissues surrounding the bronchovascular structures. Different lung diseases tend to exhibit different patterns of distribution, and recognizing the patterns increases diagnostic accuracy and confidence.

CT Signs of Focal Lung Disease

Non-neoplastic Pulmonary Nodules

Etiology

CT evaluation of a known or suspected solitary pulmonary nodule makes up a significant part of any chest CT schedule. According to CT criteria,[80, 90, 204, 205, 216, 217, 217a, 241] at least three benign causes of a solitary pulmonary nodule can be reliably identified:

- Calcified granulomas
- Hamartomas
- Pulmonary AVMs

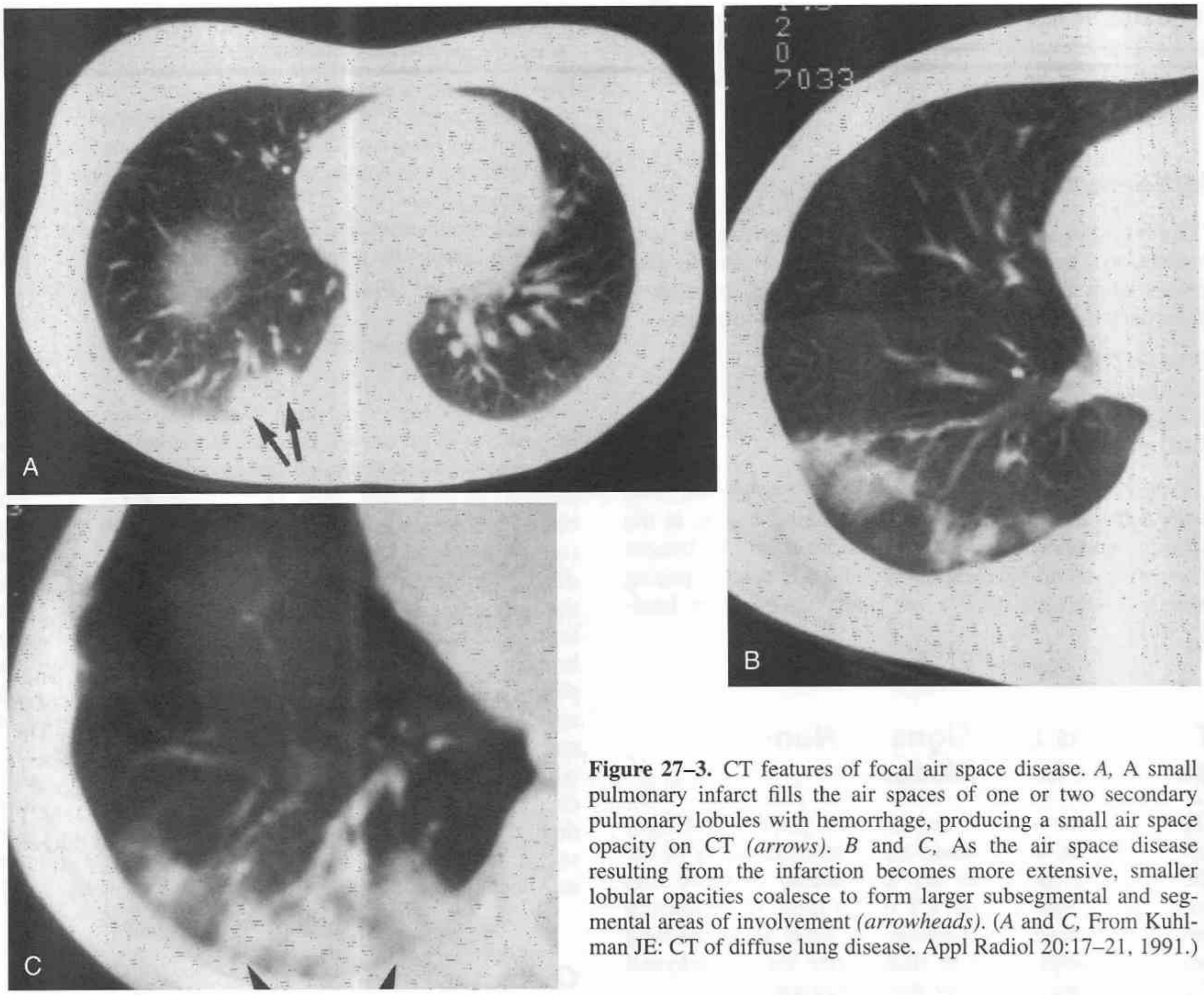

Figure 27–3. CT features of focal air space disease. *A,* A small pulmonary infarct fills the air spaces of one or two secondary pulmonary lobules with hemorrhage, producing a small air space opacity on CT *(arrows). B* and *C,* As the air space disease resulting from the infarction becomes more extensive, smaller lobular opacities coalesce to form larger subsegmental and segmental areas of involvement *(arrowheads).* (*A* and *C,* From Kuhlman JE: CT of diffuse lung disease. Appl Radiol 20:17–21, 1991.)

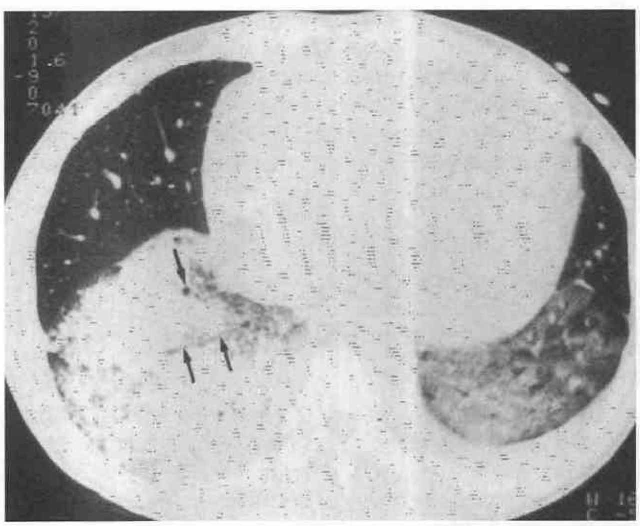

Figure 27–4. Multilobar pneumonia. Air-bronchograms are a hallmark of air space disease on CT scans, as they are on plain films. (From Kuhlman JE: CT of diffuse lung disease. Appl Radiol 20:17–21, 1991.)

Granulomas. A well-circumscribed pulmonary nodule measuring 2 cm or less in diameter that demonstrates CT attenuation in the range of calcium on a phantom-calibrated, unenhanced CT scan of the chest is usually a *benign calcified granuloma* (Fig. 27–7).[80, 90, 204, 205, 216, 217, 241] The absolute threshold value in Hounsfield units (HU) for designating calcification varies from one CT scanner and manufacturer to another, but it can be calibrated for any individual scanner using a phantom. When a solitary pulmonary nodule is not obviously calcified on CT scans but appears to be of higher CT density than soft tissue, the nodule's CT attenuation can be compared with a CT reference phantom for more accurate assessment.[80, 90, 216, 217, 240] Nodules demonstrating CT attenuations greater than the CT reference phantom were benign in 90% of cases reported in one series.[216]

In addition to the density of the nodule, the pattern of calcification is also important and must be either homogeneous throughout the nodule, in a pattern of concentric rings, or in a "popcorn" distribution to fit the CT criteria for benign calcification. The one exception is in the setting of metastatic osteogenic sarcoma. Lung metastases from osteogenic sarcoma are typically calcified in a homogeneous pattern. Although lung cancers and other malignan-

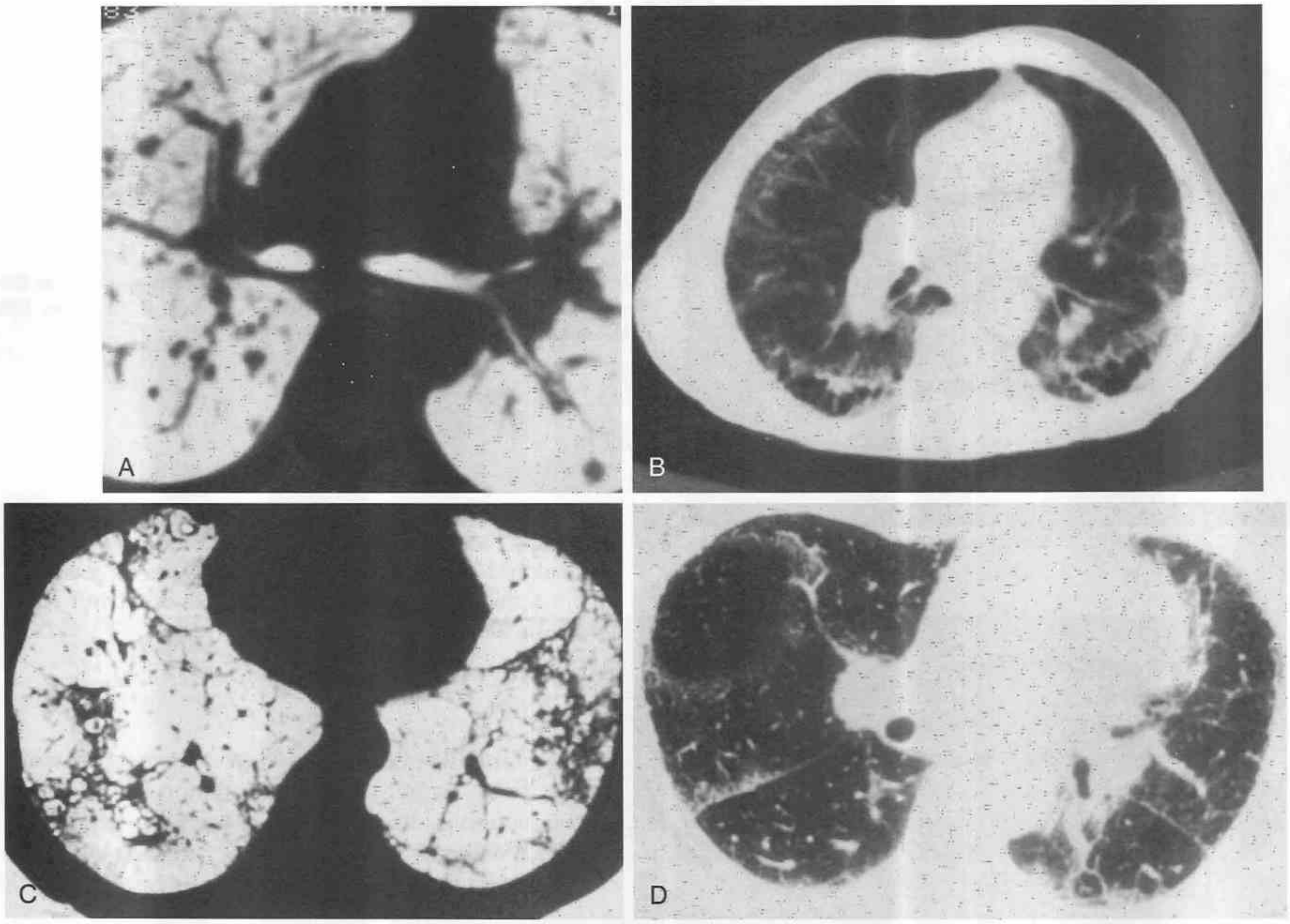

Figure 27–5. CT features of interstitial disease. *A,* Small interstitial nodules in a patient with sarcoidosis. Reticulation *(B)* and thickening of the pulmonary septa *(C)* in two patients with idiopathic pulmonary fibrosis. *D,* Irregular and shaggy interfaces between the lung and the fissures, pleural surfaces, and mediastinum are CT features characteristic of interstitial disease. Idiopathic pulmonary fibrosis. (*A, B,* and *D,* From Kuhlman JE: CT of diffuse lung disease. Appl Radiol 20:17–21, 1991.)

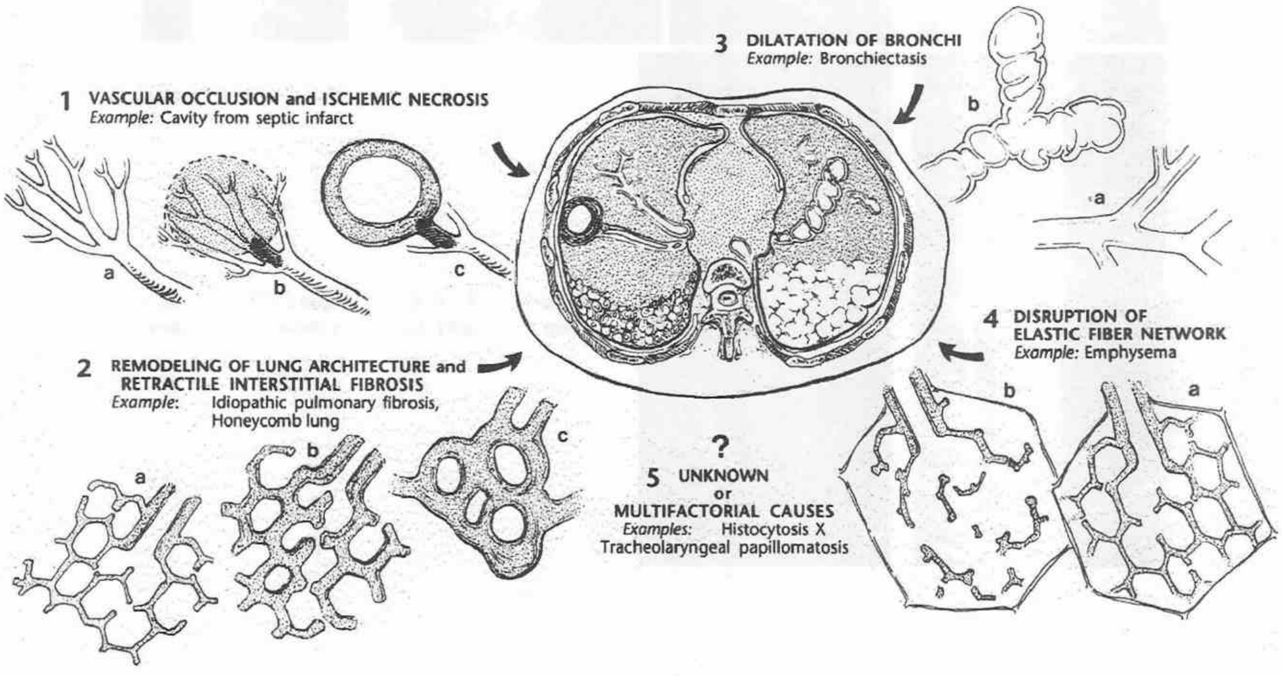

Figure 27–6. Mechanisms by which cystic or abnormal air spaces are created in the lung. (From Kuhlman JE: Abnormal air-filled spaces in the lung. Radiographics 13:47–75, 1993.)

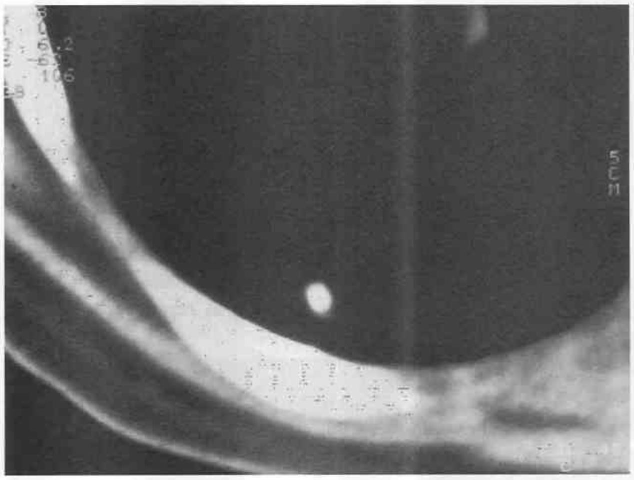

Figure 27–7. Benign calcified granuloma. Nodule is as dense as the ribs on soft tissue window settings and measures greater than 160 Hounsfield units on a calibrated, noncontrast CT scan.

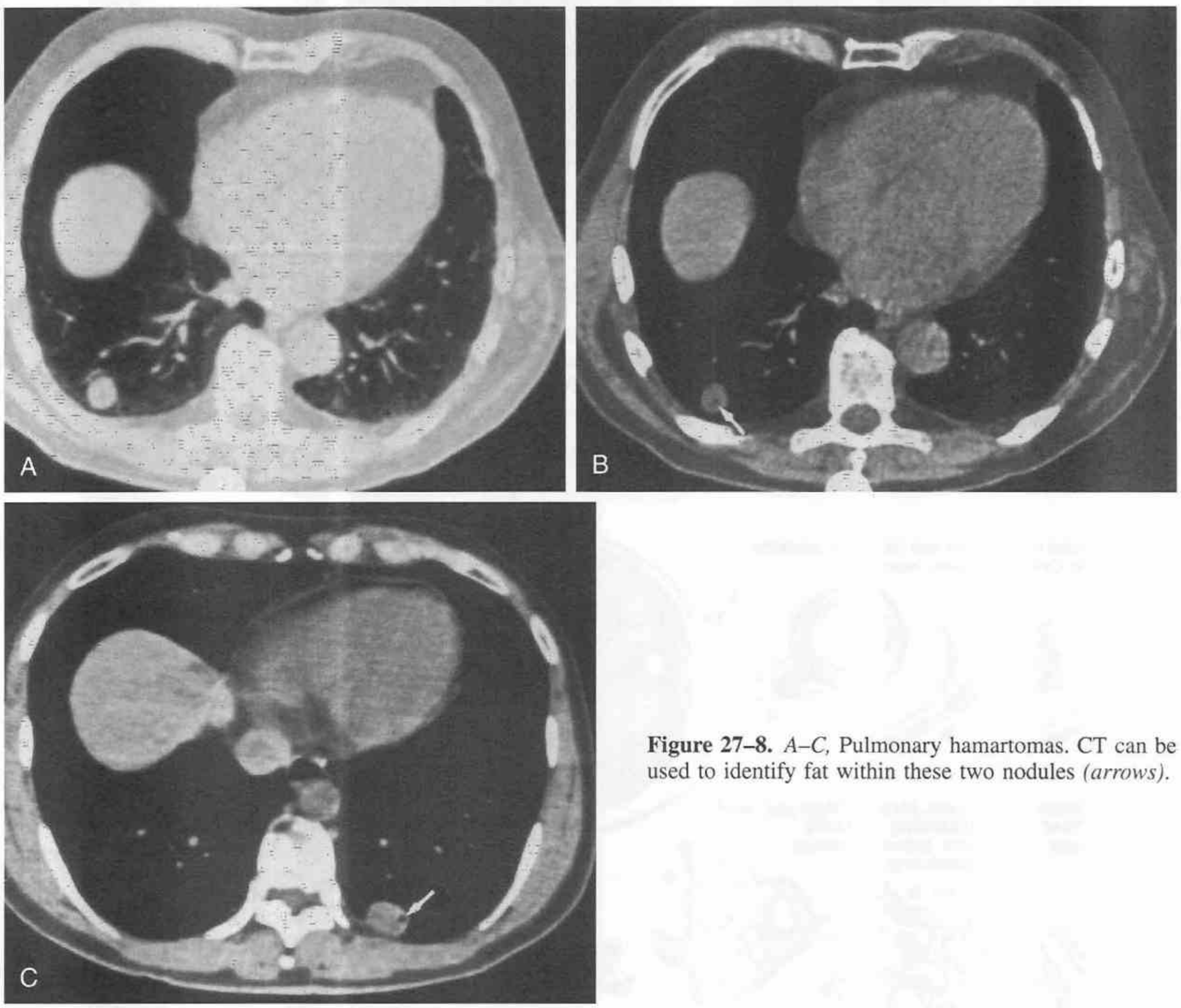

Figure 27–8. *A–C,* Pulmonary hamartomas. CT can be used to identify fat within these two nodules *(arrows).*

cies may contain small areas of calcification, they rarely demonstrate calcification in one of the benign patterns described previously.

Finally, the morphology and edge of the nodule must also be considered. The presence of spiculation or irregularity of the margins of a nodule should greatly raise a concern for malignancy, even in the presence of calcification, because many such lesions are cancerous.[241]

Hamartomas. The pulmonary hamartoma, a benign growth of multiple tissue components, may also be identified on the basis of CT attenuation properties.[205] Hamartomas are composed of a number of tissues, including soft tissue, muscle elements, and fat. About 30% of hamartomas contain enough fat to be detected by CT, and CT identification of fat within a solitary pulmonary nodule is diagnostic of hamartoma (Fig. 27–8). The CT attenuation of fat is in the range of −20 to −160 HU or less and can be reliably measured by a region-of-interest (ROI) cursor.

Hamartomas are typically well-circumscribed, smooth, round, or lobulated nodules; 20% contain calcification, often in a popcorn distribution. When fat is identified within an area of air space consolidation rather than in a nodule on CT scans, this should suggest the diagnosis of *lipoid pneumonia.* Lipoid pneumonia is usually caused by the chronic use of mineral oil nasal drops.

Pulmonary Arteriovenous Malformations. The third cause of a benign solitary pulmonary nodule that can be recognized on CT scans is a pulmonary AVM. An enlarged feeding artery leading to a pulmonary nodule and an enlarged draining vein are characteristic features of a pulmonary AVM (Fig. 27–9). Dynamic CT scanning, performed after a bolus injection of contrast material, can be used to confirm the vascular nature of the lesion by following the enhancement pattern and time-density curves of the lesion, which parallel those of the heart and pulmonary arteries.

Enhancement of Benign and Neoplastic Nodules

After administration of IV contrast material, nodules that are not calcified on CT scans may show some enhancement but do not show the degree and rapidity of enhancement seen with AVMs. Malignant nodules tend to enhance more than benign, inactive granulomas, which show very little or no enhancement. Studies by Swenson and others suggest that noncalcified nodules that show contrast enhancement above a certain threshold during the first 3 to 5 minutes after IV contrast injection are more likely to be neoplastic.[217, 217a, 217b, 239a, 242] However, nodules caused by active inflammatory disease, such as active granulomas resulting from fungal infection or tuberculosis (TB), may also show significant contrast enhancement.[242] Additionally, false-negative results have been reported, including a few lung cancers that did not show enhancement above the target threshold value.[242]

By preprogramming a series of short helical or dynamic scans sequentially through a nodule under investigation, one can monitor nodule enhancement during a bolus IV injection of contrast material. The characteristics of malignant nodules are discussed further elsewhere in this text.

Vessel-Related Disorders

A number of vessel-related disorders of the lung produce focal lung disease, including *pulmonary infarcts, septic emboli, hematogenous metastases,* and *pulmonary vasculitis.*[11, 33, 65, 78, 106, 109, 152, 186, 207] All of these disorders may show similar CT features, such as multiple peripheral nodules or wedged-shaped opacities that abut the pleura, that cavitate, or that demonstrate a feeding vessel.

The *feeding vessel sign* consists of a nodule or focal opacity that demonstrates a pulmonary vessel leading to it. The presence of a feeding vessel indicates either that the lesion has a hematogenous origin or that the disease process occurs in close proximity to small pulmonary vessels. The feeding vessel sign can be used to characterize lung disease that results from a disseminated neoplastic or infectious process that seeds the lung via the bloodstream, such as hematogenous metastases, septic emboli, and multiple pulmonary infarcts (Figs. 27–10 and 27–11).[33, 65, 78, 106, 142, 150, 186, 207] This sign is also visible when vasculitis affects

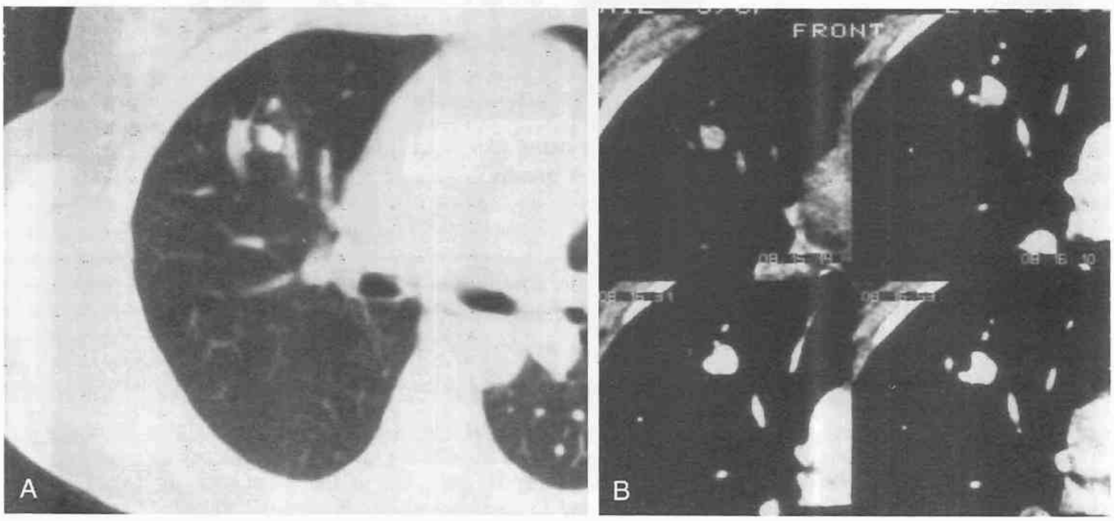

Figure 27–9. Pulmonary arteriovenous malformations. *A,* CT shows a nodule with a feeding artery and draining vein. *B,* The vascular nature of the lesion can be confirmed by dynamic CT scanning after a bolus injection of contrast material and by noting that the nodule enhances and fades as rapidly as the heart and pulmonary arteries.

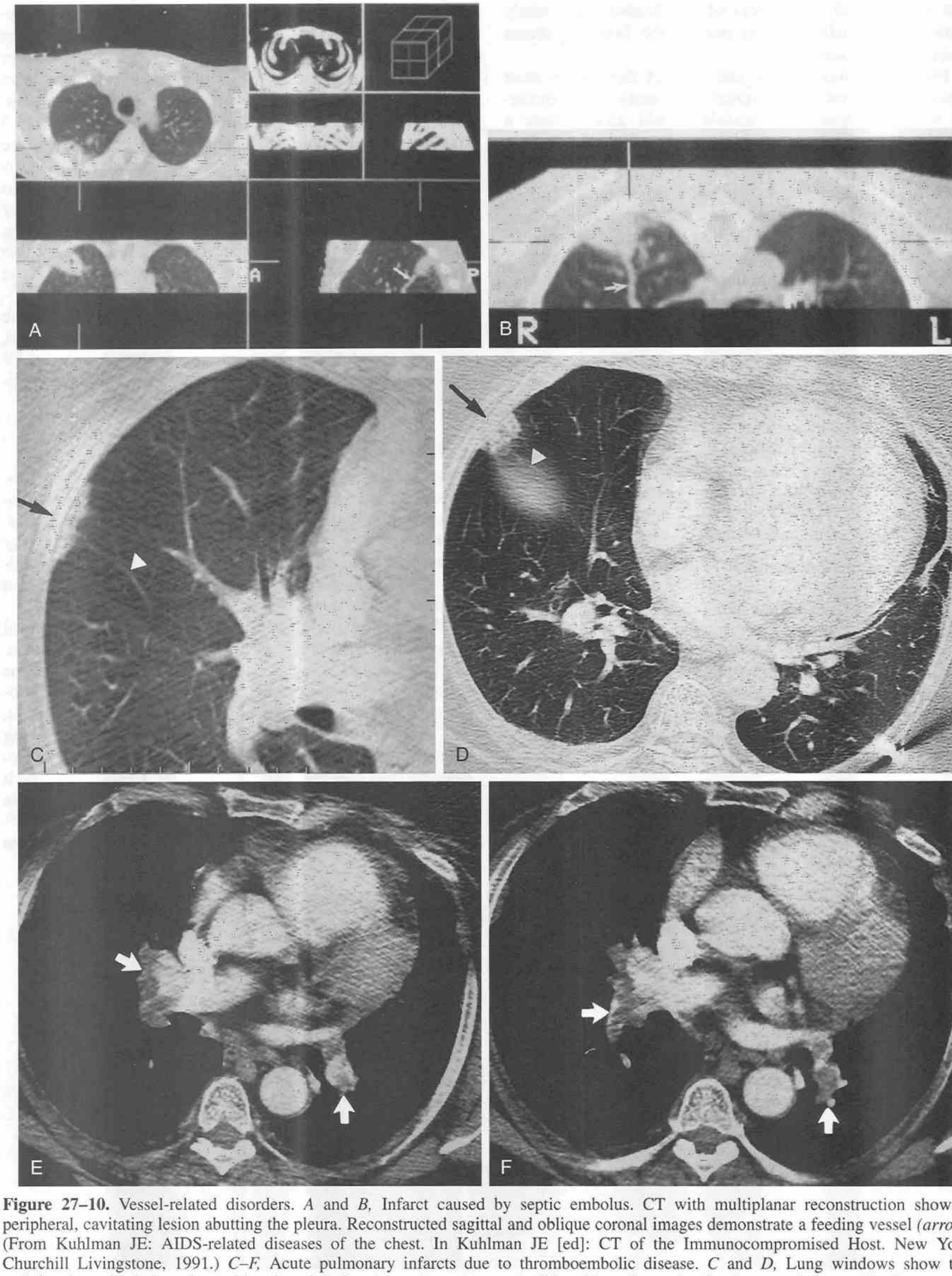

Figure 27–10. Vessel-related disorders. *A* and *B*, Infarct caused by septic embolus. CT with multiplanar reconstruction shows a peripheral, cavitating lesion abutting the pleura. Reconstructed sagittal and oblique coronal images demonstrate a feeding vessel *(arrow)*. (From Kuhlman JE: AIDS-related diseases of the chest. In Kuhlman JE [ed]: CT of the Immunocompromised Host. New York, Churchill Livingstone, 1991.) *C–F*, Acute pulmonary infarcts due to thromboembolic disease. *C* and *D*, Lung windows show two peripheral, wedged-shaped opacities that abut the pleura *(arrows)*, compatible with a diagnosis of pulmonary infarcts. Feeding vessels lead toward the infarcts *(arrowhead)*. *E* and *F*, In the same patient, spiral CT with IV contrast enhancement demonstrates filling defects *(arrows)* within the right and left pulmonary arteries caused by multiple pulmonary emboli.

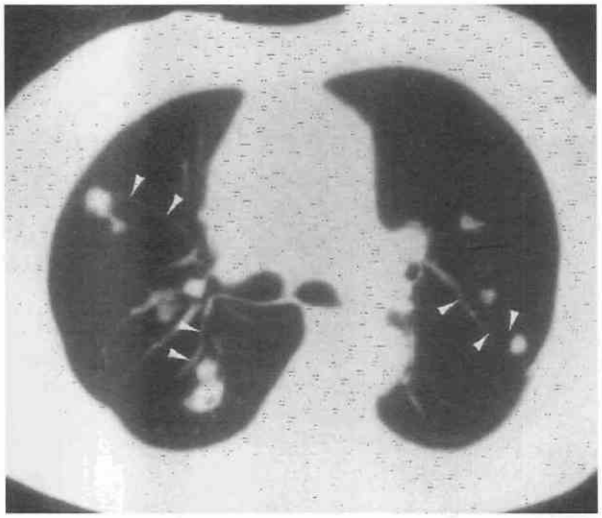

Figure 27–11. Hematogenous metastases. CT shows multiple pulmonary nodules, each with a discrete feeding vessel leading to it *(arrowheads)*. (From Kuhlman JE: CT of diffuse lung disease. Appl Radiol 20:17–21, 1991.)

the pulmonary vessels, as in Wegener's granulomatosis and lymphomatoid granulomatosis.[109]

Wegener's Granulomatosis

Wegener's granulomatosis is a necrotizing granulomatous vasculitis that affects pulmonary vessels, most commonly the small and medium-sized arteries and veins.[24, 34, 52, 236] Nodules and cavities are typical chest film findings.[2, 117, 130] On CT scans, these cavities and nodules are often peripheral and pleura-based and demonstrate a prominent adjacent vessel to the lesions (Figs. 27–12 and 27–13).[109]

In tissue studies, Wegener's lesions show central necrosis surrounded by a granulomatous reaction.[74, 135, 136, 143, 198, 225] Frequently, a thrombosed vessel demonstrating active vasculitis is identified in close proximity to the necrotic lesion, and the resulting ischemia is believed to contribute to cavity formation within the granulomatous nodule (see Fig. 27–12).[74, 135, 136, 143, 198, 225]

Wegener's granulomatosis may also present as patchy or diffuse pulmonary hemorrhage on a CT scan. This occurs when pulmonary capillaries are primarily involved by the vasculitic process (Fig. 27–14).[136]

Thromboembolism

The role of multidetector and spiral CT in the evaluation of suspected *pulmonary thromboembolic disease* is evolving rapidly but remains controversial.[14a, 183a] Large, prospective, properly designed accuracy trials are needed to provide reliable estimates of the sensitivity and specificity of spiral and multidetector CT in diagnosis of pulmonary emboli.[14a, 183a, 239b] Remy-Jardin and colleagues demonstrated that spiral CT achieved a high degree of accuracy in identifying central pulmonary emboli down to the second-order to fourth-order pulmonary arteries.[184a, 184b] In other studies, reported sensitivities of spiral CT vary from 53% to 100%, and specificities vary from 81% to 100%.[14a, 67a, 183a, 184a, 184b, 239b]

An important limitation of spiral CT is the lower sensitivity for detecting smaller peripheral emboli in subsegmental arteries, the importance of which remains uncertain.[67a] Detecting clots in obliquely oriented segmental vessels in the right middle lobe and lingula may be particularly difficult as well.[184a] False-positive results also occur when hilar and intersegmental lymph nodes, unopacified pulmonary veins, or mucous plugs are misinterpreted on spiral CT as emboli.[15a, 68a, 184a, 184b] Remy-Jardin and coworkers have shown that multiplanar images may provide additional, complementary information in difficult cases.[184b]

Findings of acute pulmonary emboli include filling defects that wholly or partially occlude the contrast-opacified pulmonary arteries, or a "tail" of clot within an opacified vessel.[116a, 184a, 184b, 239b] Chronic thrombi often appear as crescentic or laminar filling defects adherent to the walls of the pulmonary artery.[90a, 184a, 239b] Calcification may be identified in chronic clots in patients with long-standing pulmonary hypertension.[90a] Associated parenchymal lung findings in thromboembolic disease include the CT findings of acute or chronic pulmonary infarcts, and wedged-shaped, focal air space opacities that abut the pleura.[34a] Other nonspecific findings in acute pulmonary embolus include pleural effusions. In chronic thromboembolic disease, the lung parenchyma may demonstrate mosaic attenuation, with areas of decreased attenuation associated with "pruned" or attenuated vessels.[90a]

Bronchiolitis Obliterans Organizing Pneumonia

The clinical diagnosis of bronchiolitis obliterans organizing pneumonia (BOOP) is often a difficult and elusive one.[14, 18, 32, 37, 49–51, 68, 145] Patients present with a subacute onset of nonspecific symptoms, including cough, dyspnea, fever, and flulike illness. BOOP may be associated with autoimmune disorders, such as Sjögren's syndrome and polymyalgia rheumatica, or with collagen vascular and rheumatologic diseases; frequently, however, it is idiopathic. Although a definitive diagnosis of BOOP is usually made only by open lung biopsy, in the appropriate clinical setting certain CT features should suggest BOOP as a diagnostic possibility.

BOOP may have many CT appearances, but most cases demonstrate one of four patterns on CT scans: (1) a focal nodular form, (2) a form resembling pneumonia, (3) a pattern characterized by subpleural opacities, or (4) a pattern of ground-glass infiltrates (Figs. 27–15 to 27–19).[22, 32, 147, 158, 173, 228]

When BOOP is more focal in nature, it appears on CT scans as multiple nodular or masslike areas of focal consolidation that occur primarily in the periphery of the lung (see Figs. 27–15 and 27–16).[22, 147, 158, 173, 228] The opacities frequently conform in size and configuration to one or more secondary pulmonary lobules.[173] Often a small pulmonary artery or a small bronchiole can be traced into the center of the nodular area of consolidation, and a small air-bronchogram can be seen surrounded by the focal area of air space consolidation.[22] This is a common pattern of BOOP identified on CT scans, and the pathologic features of the disease help to explain the CT appearance.

In BOOP, fibrovascular plugs of granulation tissue form

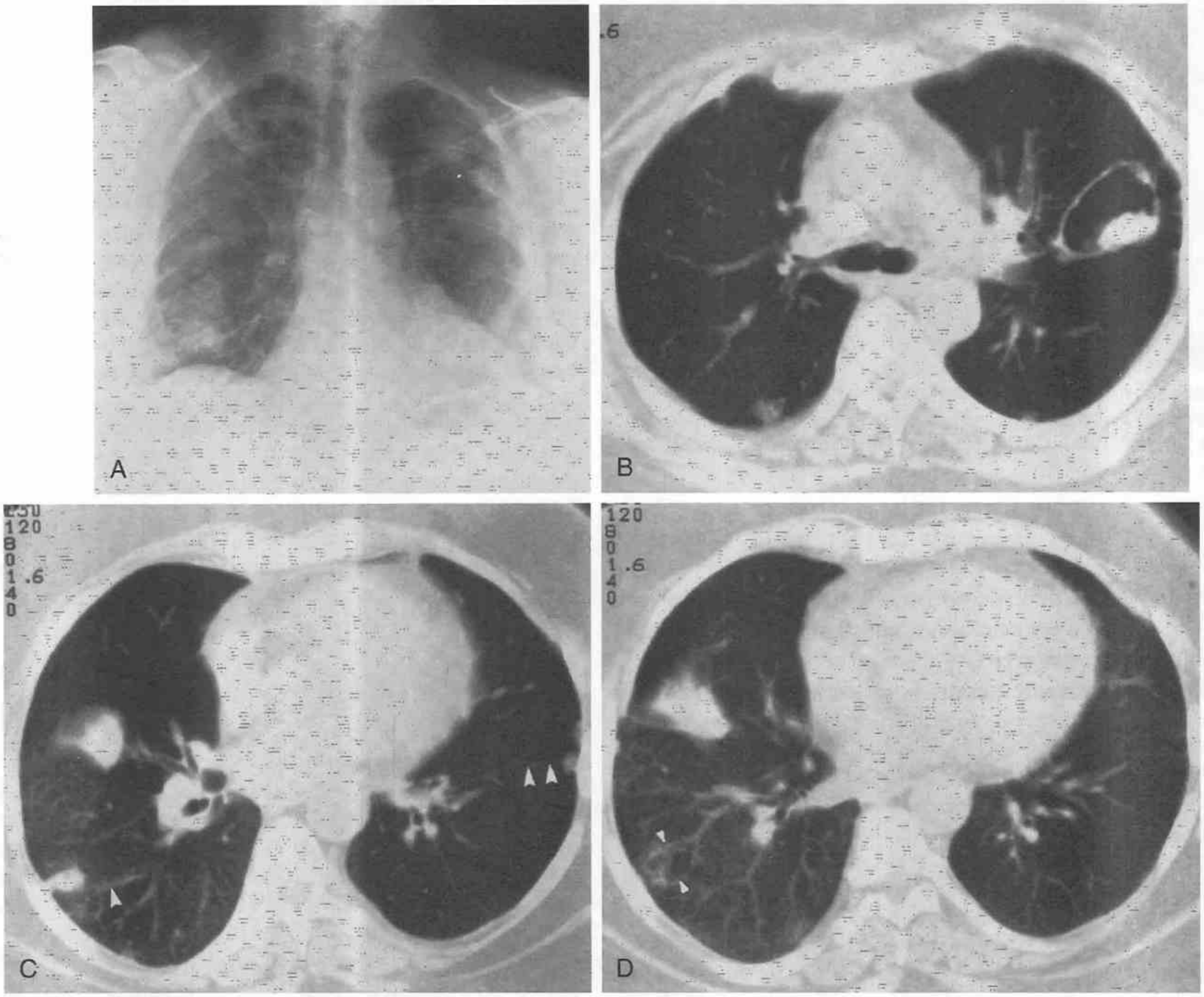

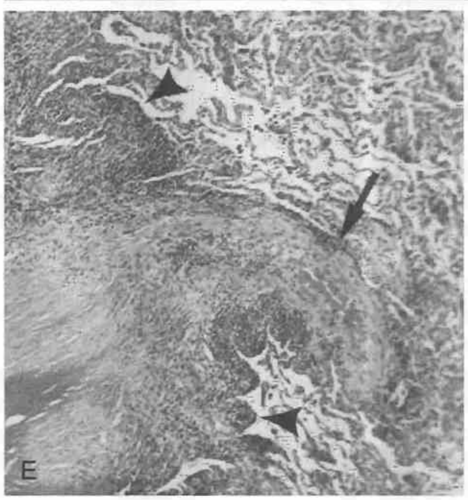

Figure 27–12. Wegener's granulomatosis. *A,* Chest film shows multiple ill-defined opacities and probable cavities. *B,* On this CT scan, a cavitating mass abutting the fissure and several tiny nodules abutting the pleura are identified. *C* and *D,* Several of the smaller lesions demonstrate a feeding vessel *(arrowheads). E,* Lung biopsy specimen shows one necrotic nodule with a surrounding granulomatous reaction *(arrowheads)* and an adjacent thrombosed arterial vessel resulting from vasculitis *(arrow).* (*B, C,* and *E,* From Kuhlman JE, Hruban RH, Fishman EK: Wegener granulomatosis: CT features of parenchymal lung disease. J Comput Assist Tomogr 15: 948–952, 1991.)

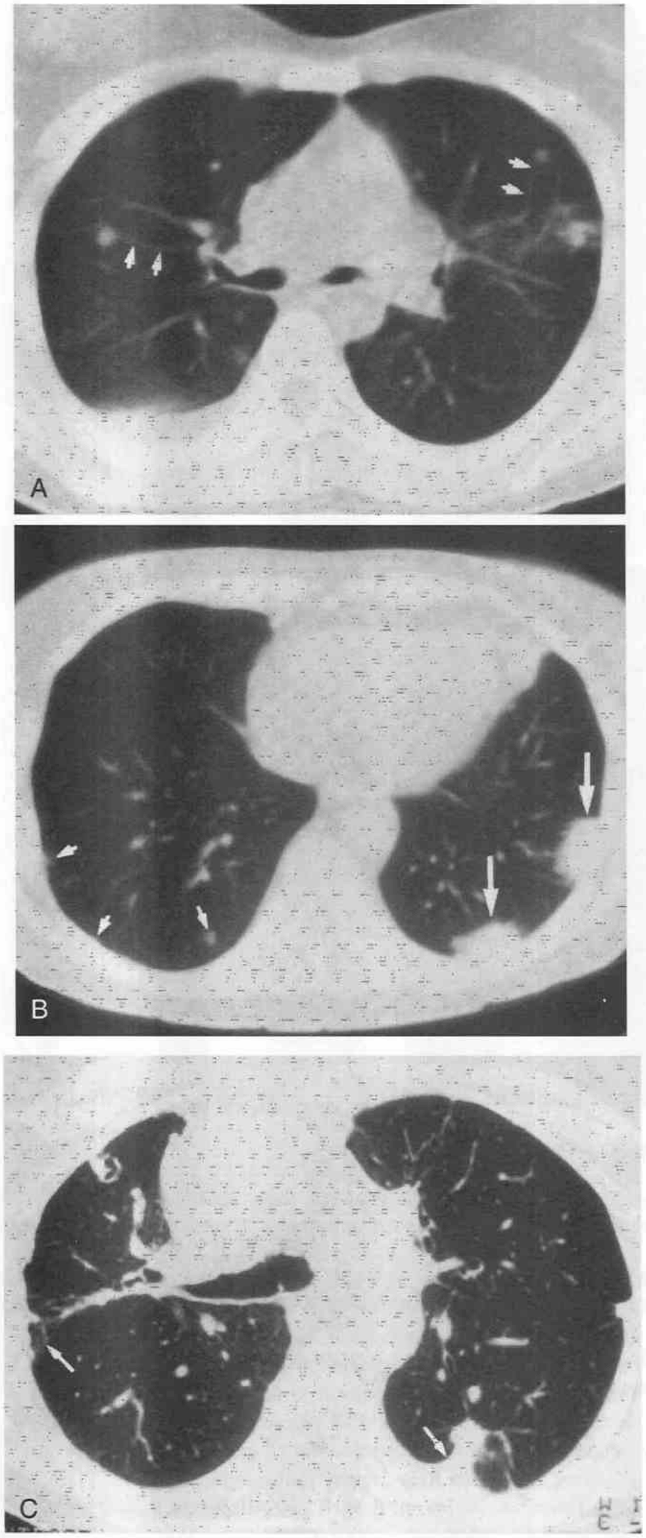

Figure 27–13. CT findings of Wegener's granulomatosis. *A,* Multiple nodules with feeding vessels *(arrows).* (From Kuhlman JE, Hruban RH, Fishman EK: Wegener granulomatosis: CT features of parenchymal lung disease. J Comput Assist Tomog 15:948–952, 1991.) *B,* Two pleura-based lesions *(large arrows)* resembling infarcts, and several smaller peripheral nodules *(small arrows). C,* Patient with long-standing Wegener's granulomatosis under treatment. Scarring, spiculation, and pleural reaction can be seen around peripheral pulmonary nodules *(arrows).*

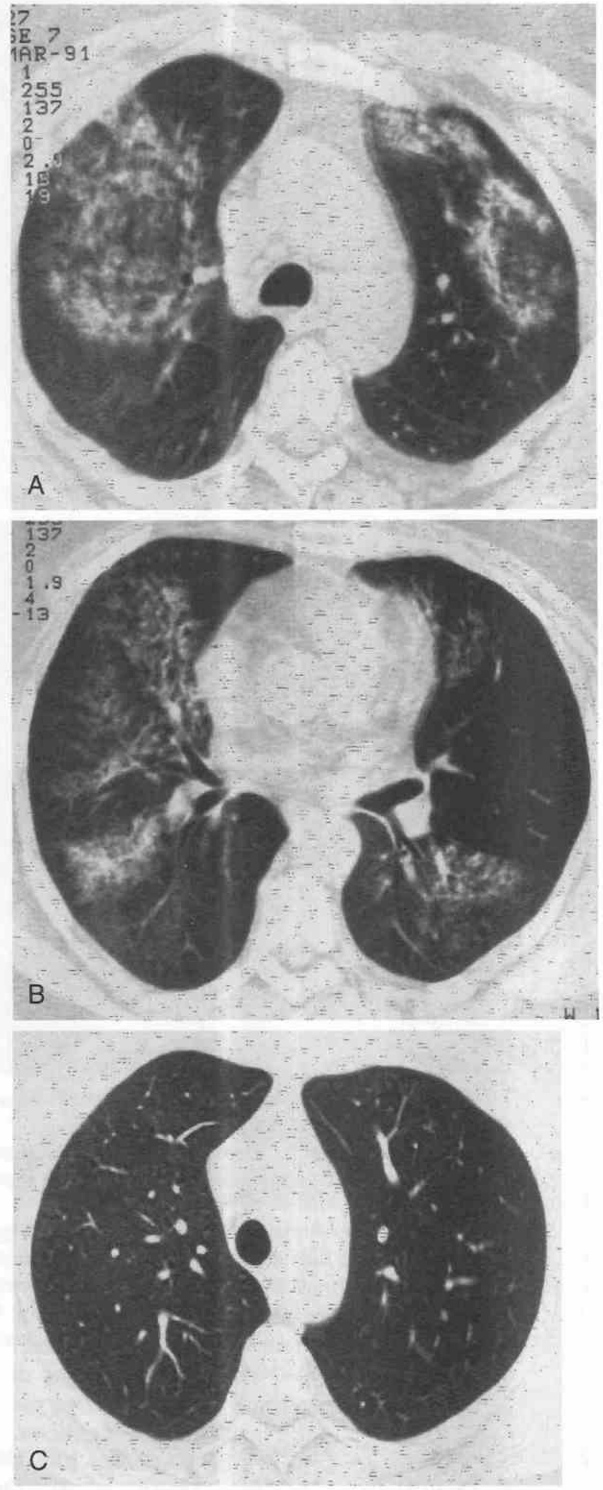

Figure 27–14. This patient presented with hemoptysis caused by Wegener's vasculitis affecting primarily the capillaries of the lung. *A* and *B,* On CT scans, patchy air space filling is seen as a result of pulmonary hemorrhage. *C,* A few weeks later, a CT scan shows nearly complete clearing of the air space disease.

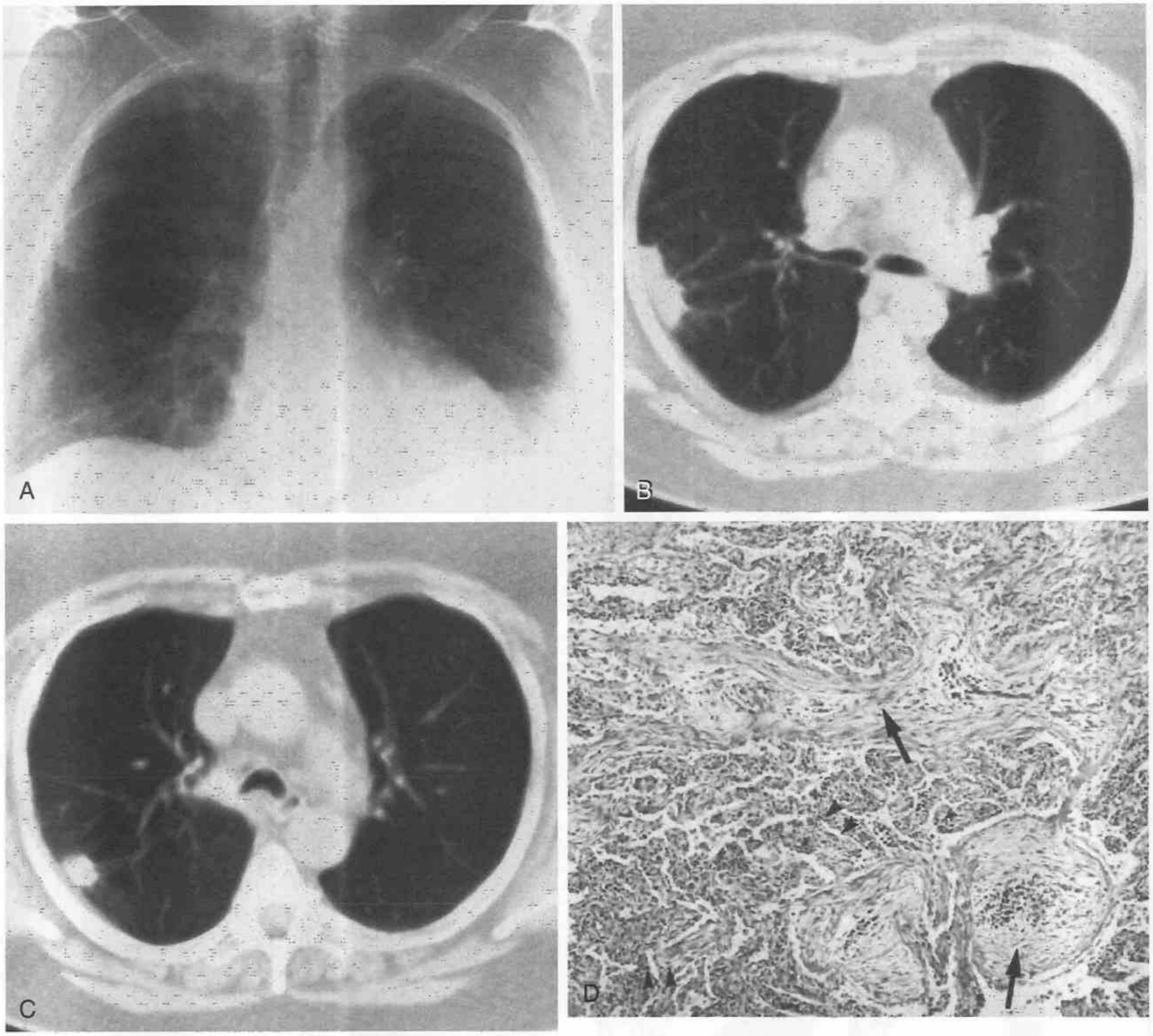

Figure 27–15. CT features of bronchiolitis obliterans with organizing pneumonia (BOOP).

A, Chest film shows ill-defined peripheral opacities.

B and *C,* On CT scans, nodular areas of focal consolidation are identified in the periphery of the lung, abutting the pleura. The opacities conform in size and configuration to one or more secondary pulmonary lobules. Small pulmonary vessels can be traced into the lesions.

D, Open lung biopsy demonstrates the classic histopathology of BOOP. The distal small airways are obliterated with fibrovascular plugs *(arrows)*, and the inflammatory process has extended out from the obliterated bronchioles in a centrifugal fashion, filling the surrounding air spaces with organizing pneumonia *(arrowheads)*.

(B–D, From Bouchardy LM, Kuhlman JE, Ball WC, et al: CT findings in bronchiolitis obliterans organizing pneumonia (BOOP) with x-ray, clinical, and histologic correlations. J Comput Assist Tomogr 17:352–357, 1993.)

in distal bronchioles and alveolar ducts.[35, 88, 91, 239] The inflammatory or fibrotic process then extends out from the obliterated small airway in a centripetal or radial fashion into the surrounding alveolar spaces, producing organizing pneumonia (see Fig. 27–15). Nishimura and Itoh[173] have stressed the panlobular nature of BOOP and that its distribution on CT scans and pathologic examination frequently conforms to the margins of the secondary pulmonary lobule. Review of the anatomy of the secondary pulmonary lobule is illustrative.

The secondary pulmonary lobule is a polyhedral structure that can be thought of as the basic building block of the lung. Interlobular septa containing connective tissue, pulmonary veins, and lymphatics define the margins of the secondary pulmonary lobule, whose sides measure approximately 1 to 2.5 cm in length.[73, 230] The secondary pulmonary lobule is made up of 3 to 12 acini and is supplied by several terminal bronchioles. A lobular core supplies the central portion of the secondary lobule and consists of a pulmonary artery and its accompanying bronchiolar branches. This lobular core or centrilobular complex can often be seen on HRCT as a small dot or centrilobular

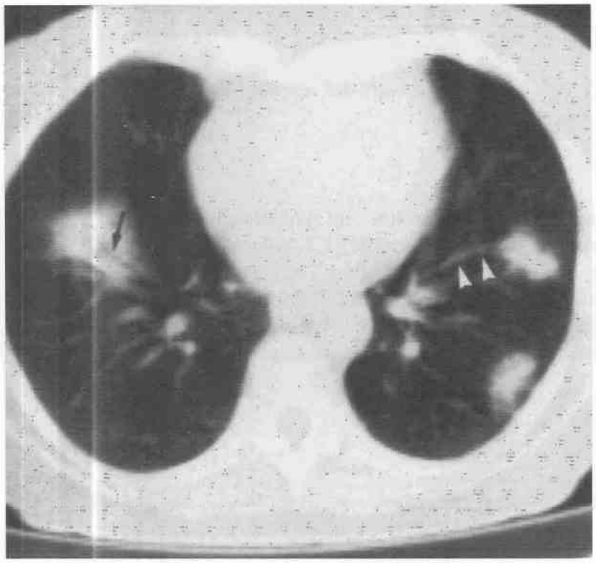

Figure 27–16. CT features of bronchiolitis obliterans organizing pneumonia (BOOP), nodular form. CT shows multiple nodular opacities with air-bronchogram *(arrow)* and associated vessel *(arrowheads)*. (From Bouchardy LM, Kuhlman JE, Ball WC, et al: CT findings in bronchiolitis obliterans organizing pneumonia (BOOP) with x-ray, clinical, and histologic correlations. J Comput Assist Tomogr 17:352–357, 1993.)

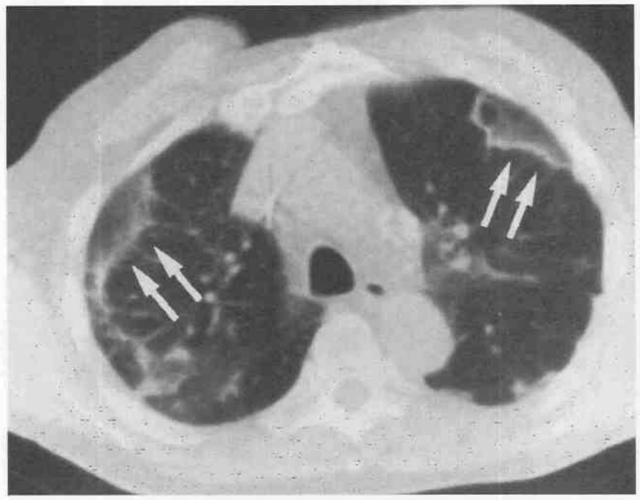

Figure 27–18. CT features of bronchiolitis obliterans organizing pneumonia (BOOP), subpleural form. Irregular peripheral bands of increased CT attenuation parallel the pleural surfaces *(arrows)*. An intervening zone of relatively spared lung can be seen between the pleural surface and the band. (From Bouchardy LM, Kuhlman JE, Ball WC, et al: CT findings in bronchiolitis obliterans organizing pneumonia (BOOP) with x-ray, clinical, and histologic correlations. J Comput Assist Tomogr 17:352–357, 1993.)

density within the center of the secondary pulmonary lobule.[73, 230] Primarily, the pulmonary artery of the lobular core is seen on HRCT because visualization of the accompanying bronchiole depends on its wall thickness, not its diameter, which is below the resolution of HRCT. Normal intralobular bronchioles and interlobular septa usually are not detected on HRCT.[230] Their presence usually indicates abnormal thickening of the bronchiolar walls or septal interstitium.

Because BOOP begins as an inflammatory process that obliterates small distal bronchiolar airways and secondarily spreads into the surrounding air spaces to fill secondary pulmonary lobules, it is easy to understand why areas of consolidation secondary to BOOP appear to be centered on small pulmonary arteries and small bronchi on CT examination.

As the organizing pneumonia of BOOP becomes more extensive, larger areas of consolidation are seen on the CT scan, and the CT appearance becomes indistinguishable from that of a bacterial pneumonia (see Fig. 27–17).

BOOP may also show other patterns on CT scans. Irregular bandlike areas of variable attenuation in the periphery of the lung are typical of some cases of BOOP (see Fig. 27–18), and subpleural reticulations can be seen in up to 23% of patients.[14, 22] Patchy ground-glass infiltrates have also been reported in this disease (see Fig. 27–19).[22, 173]

Figure 27–17. CT features of bronchiolitis obliterans organizing pneumonia (BOOP), pneumonic form. A large area of consolidation caused by BOOP is demonstrated on CT and is indistinguishable by appearance from a bacterial pneumonia. Air-bronchograms can be visualized. (From Bouchardy LM, Kuhlman JE, Ball WC, et al: CT findings in bronchiolitis obliterans organizing pneumonia (BOOP) with x-ray, clinical, and histologic correlations. J Comput Assist Tomogr 17:352–357, 1993.)

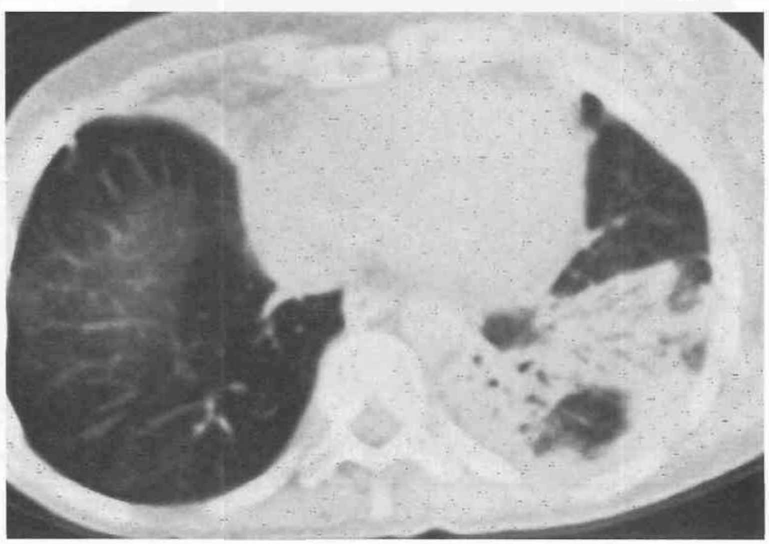

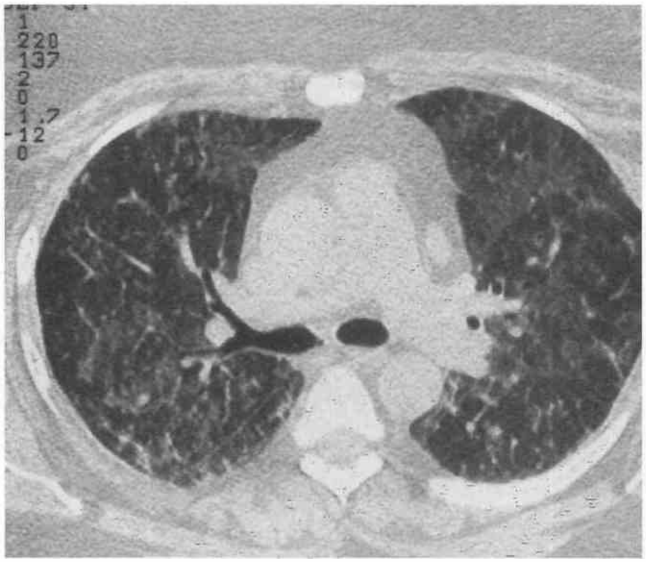

Figure 27–19. CT features of bronchiolitis obliterans organizing pneumonia (BOOP). Another CT presentation of BOOP is as diffuse, but patchy, "ground-glass" infiltrates. (From Bouchardy LM, Kuhlman JE, Ball WC, et al: CT findings in bronchiolitis obliterans organizing pneumonia (BOOP) with x-ray, clinical, and histologic correlations. J Comput Assist Tomogr 17:352–357, 1993.)

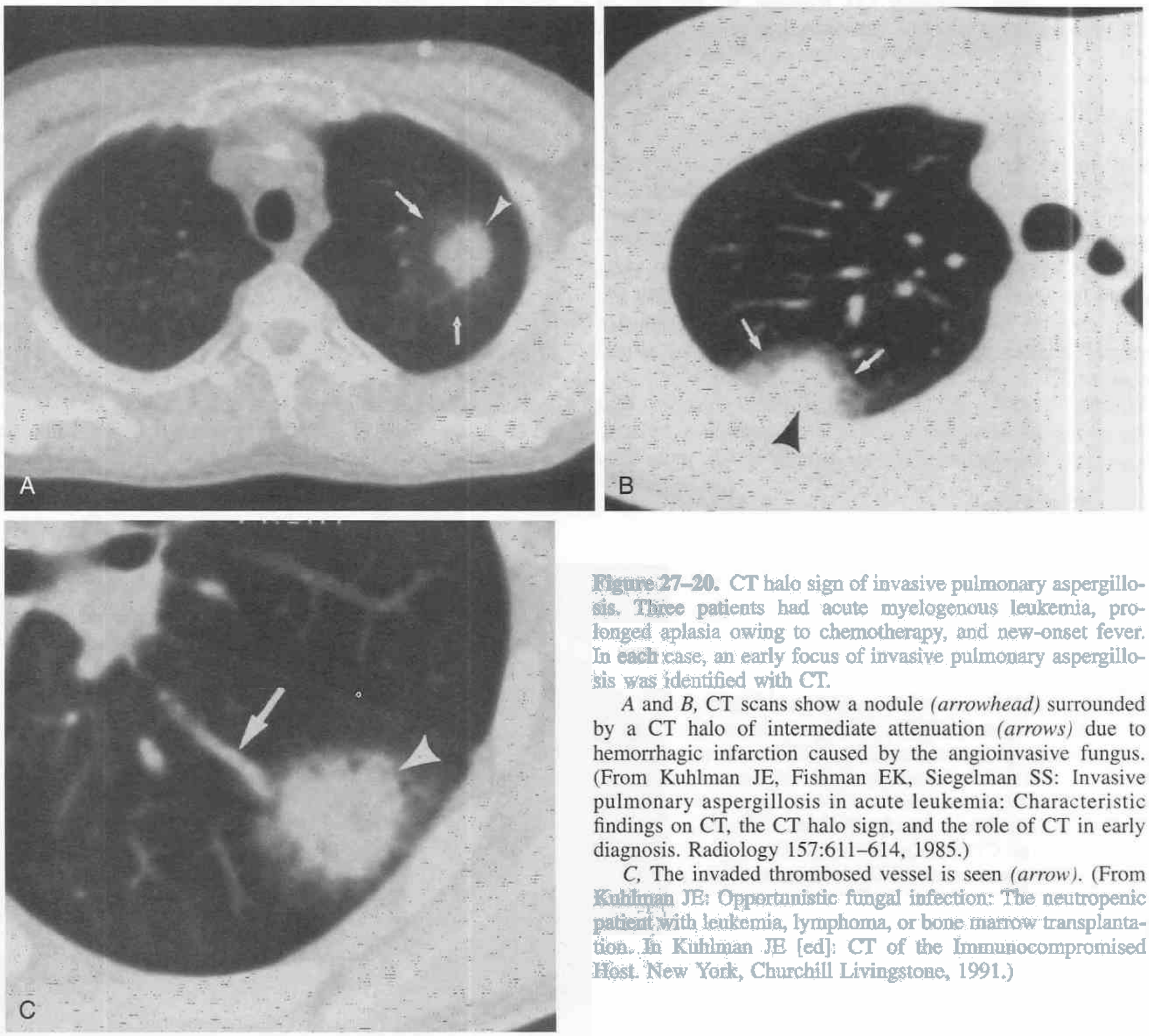

Figure 27–20. CT halo sign of invasive pulmonary aspergillosis. Three patients had acute myelogenous leukemia, prolonged aplasia owing to chemotherapy, and new-onset fever. In each case, an early focus of invasive pulmonary aspergillosis was identified with CT.

A and *B*, CT scans show a nodule *(arrowhead)* surrounded by a CT halo of intermediate attenuation *(arrows)* due to hemorrhagic infarction caused by the angioinvasive fungus. (From Kuhlman JE, Fishman EK, Siegelman SS: Invasive pulmonary aspergillosis in acute leukemia: Characteristic findings on CT, the CT halo sign, and the role of CT in early diagnosis. Radiology 157:611–614, 1985.)

C, The invaded thrombosed vessel is seen *(arrow)*. (From Kuhlman JE: Opportunistic fungal infection: The neutropenic patient with leukemia, lymphoma, or bone marrow transplantation. In Kuhlman JE [ed]: CT of the Immunocompromised Host. New York, Churchill Livingstone, 1991.)

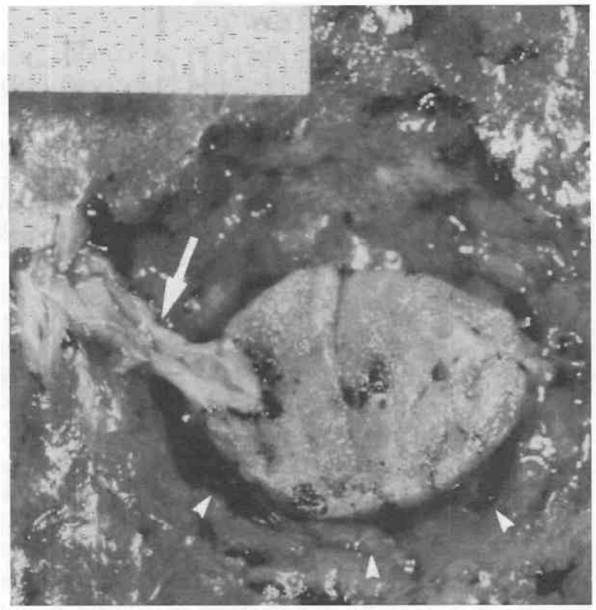

Figure 27–21. Gross pathologic specimen of invasive pulmonary aspergillosis shows an early focus of infection with surrounding hemorrhage *(arrowheads)* and invaded thrombosed vessel adjacent to nodule *(arrow)*. (From Kuhlman JE, Fishman EK, Burch PA, et al: CT of invasive pulmonary aspergillosis. AJR Am J Roentgenol 150:1015–1020, 1988.)

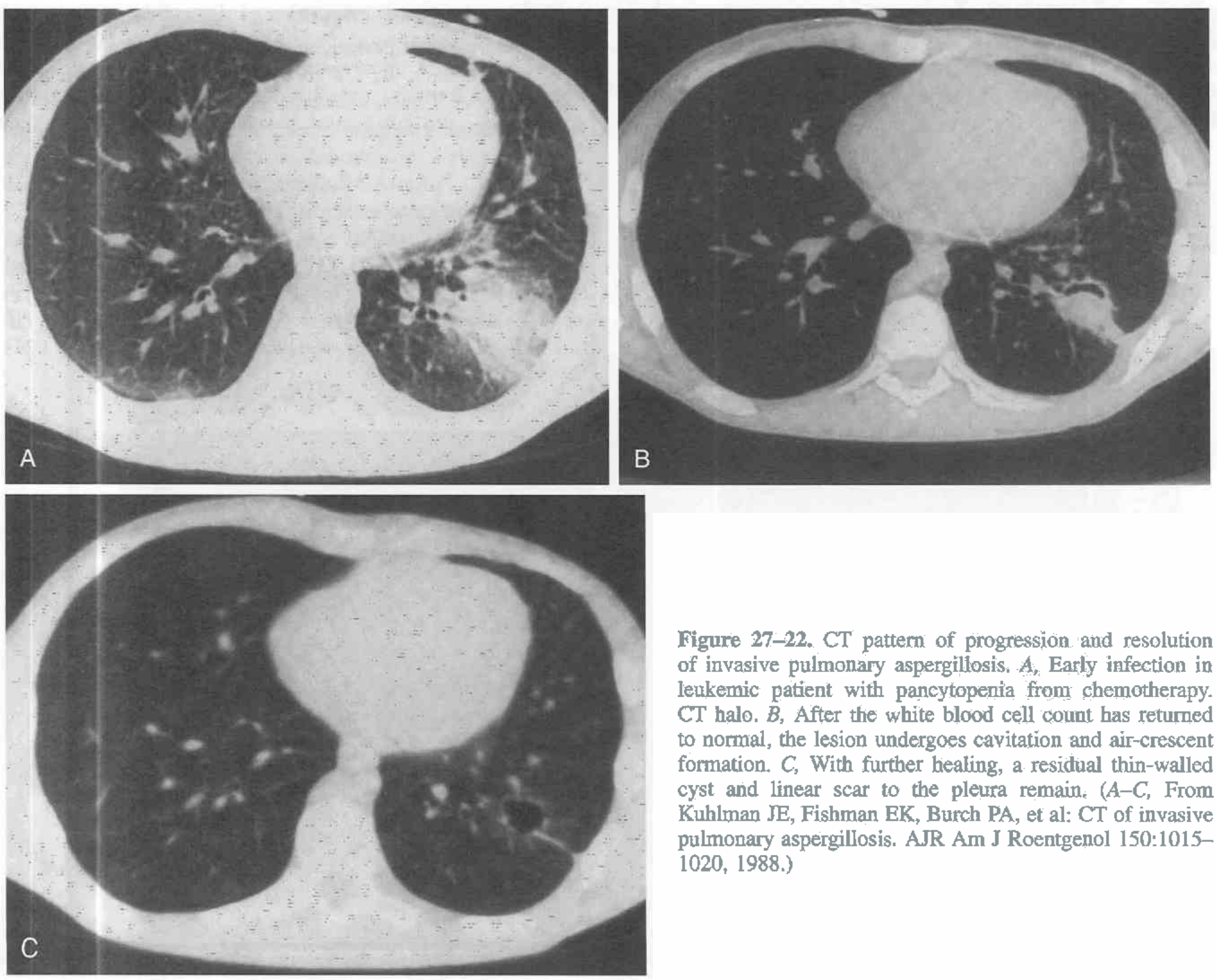

Figure 27–22. CT pattern of progression and resolution of invasive pulmonary aspergillosis. *A*, Early infection in leukemic patient with pancytopenia from chemotherapy. CT halo. *B*, After the white blood cell count has returned to normal, the lesion undergoes cavitation and air-crescent formation. *C*, With further healing, a residual thin-walled cyst and linear scar to the pleura remain. (*A–C*, From Kuhlman JE, Fishman EK, Burch PA, et al: CT of invasive pulmonary aspergillosis. AJR Am J Roentgenol 150:1015–1020, 1988.)

Invasive Pulmonary Aspergillosis

The CT *halo sign* can be used to identify invasive pulmonary aspergillosis in the patient with acute leukemia who is undergoing aplasia-producing chemotherapy.[27, 61, 97, 100, 103, 104, 107] This sign consists of a round pulmonary mass or nodule with a surrounding halo of intermediate CT attenuation (Fig. 27–20). The halo represents hemorrhage around a focal area of lung infarction caused by the *Aspergillus* organism that invades pulmonary vessels (Fig. 27–21).[76, 176] Other angioinvasive infections (mucormycosis, *Candida*, *Torulopsis*, and angioinvasive *Pseudomonas*) may produce similar CT findings, but *Aspergillus* is by far the most common organism to produce this CT finding in the specific clinical setting of a leukemic patient with prolonged bone marrow aplasia following chemotherapy.

In patients with acute leukemia undergoing chemotherapy, lung infection by invasive pulmonary aspergillosis follows a typical pattern of progression and resolution (Fig. 27–22).[27, 61, 97, 100, 103, 104, 107] As the bone marrow recovers from aplasia and the white blood cell count returns to normal, the pulmonary lesions begin to cavitate, producing the familiar air crescent sign. With further healing, the lesions tend to shrink and fade from the periphery, leaving behind thin-walled cysts or linear scars to the pleura.

In the nonleukemic, non-neutropenic patient, the CT halo sign is less specific. It may represent something other than invasive pulmonary aspergillosis, such as other types of angioinvasive infections, hemorrhagic metastases, or any process that produces a nodule with surrounding hemorrhage or edema.

Rounded Atelectasis

Rounded atelectasis is another cause of benign focal lung disease that can be differentiated from malignancy using CT criteria (Fig. 27–23).[48, 127, 128, 144] CT features of rounded atelectasis include a pleura-based mass found adjacent to an area of pleural thickening and associated with volume loss of the involved lobe. Sweeping or curling into the mass are adjacent vessels and small bronchi forming a *comet's tail* or *vacuum cleaner sign* that course down to the mass from the pulmonary hilum.[48, 127, 128, 144]

On pathologic examination, rounded atelectasis represents a focal area of atelectatic lung that rolls or curls up on itself, taking the nearby bronchi and blood vessels along with the infolding lung in the process. Rounded atelectasis is always found adjacent to an area of pleural thickening, and the process is thought to begin with an adhesive pleural effusion or pleural reaction, which entraps the adjacent atelectatic lung. Although many cases of rounded atelectasis are the result of asbestos-related pleural disease, other causes of pleural reaction may produce similar findings.

Bronchiectasis

Dilatation of one or more bronchi results in bronchiectasis.[179] Most causes of bronchiectasis are irreversible and include such diverse categories of disease as immunologic defects (X-linked agammaglobulinemia), ciliary dysmotility syndromes (Kartagener's syndrome), genetic disorders (cystic fibrosis), childhood or repeated infections (pertussis, TB), and congenital abnormalities of the bronchial

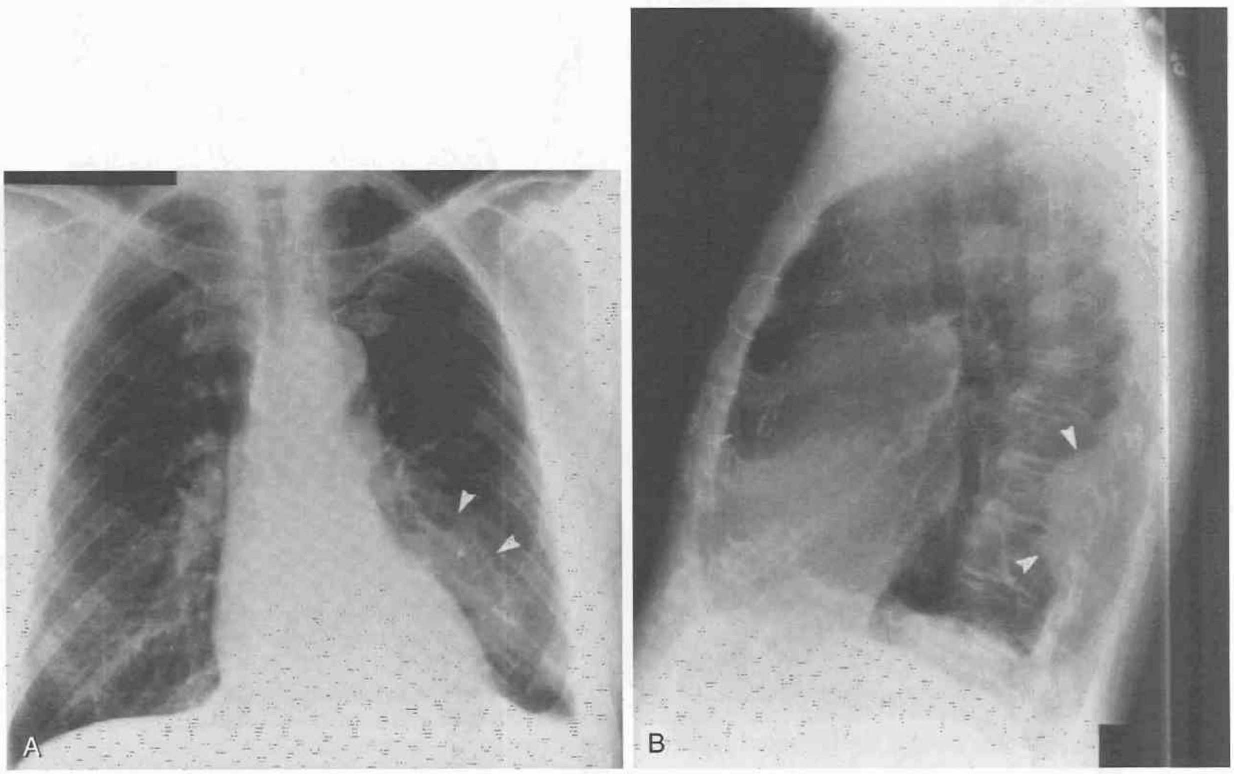

Figure 27–23. CT features of rounded atelectasis. *A* and *B*, Chest film shows ill-defined mass in the posterior left lower lobe *(arrowheads)*. The patient underwent coronary bypass surgery, and now evidence of pleural thickening with blunting of the left costophrenic angle can be seen.

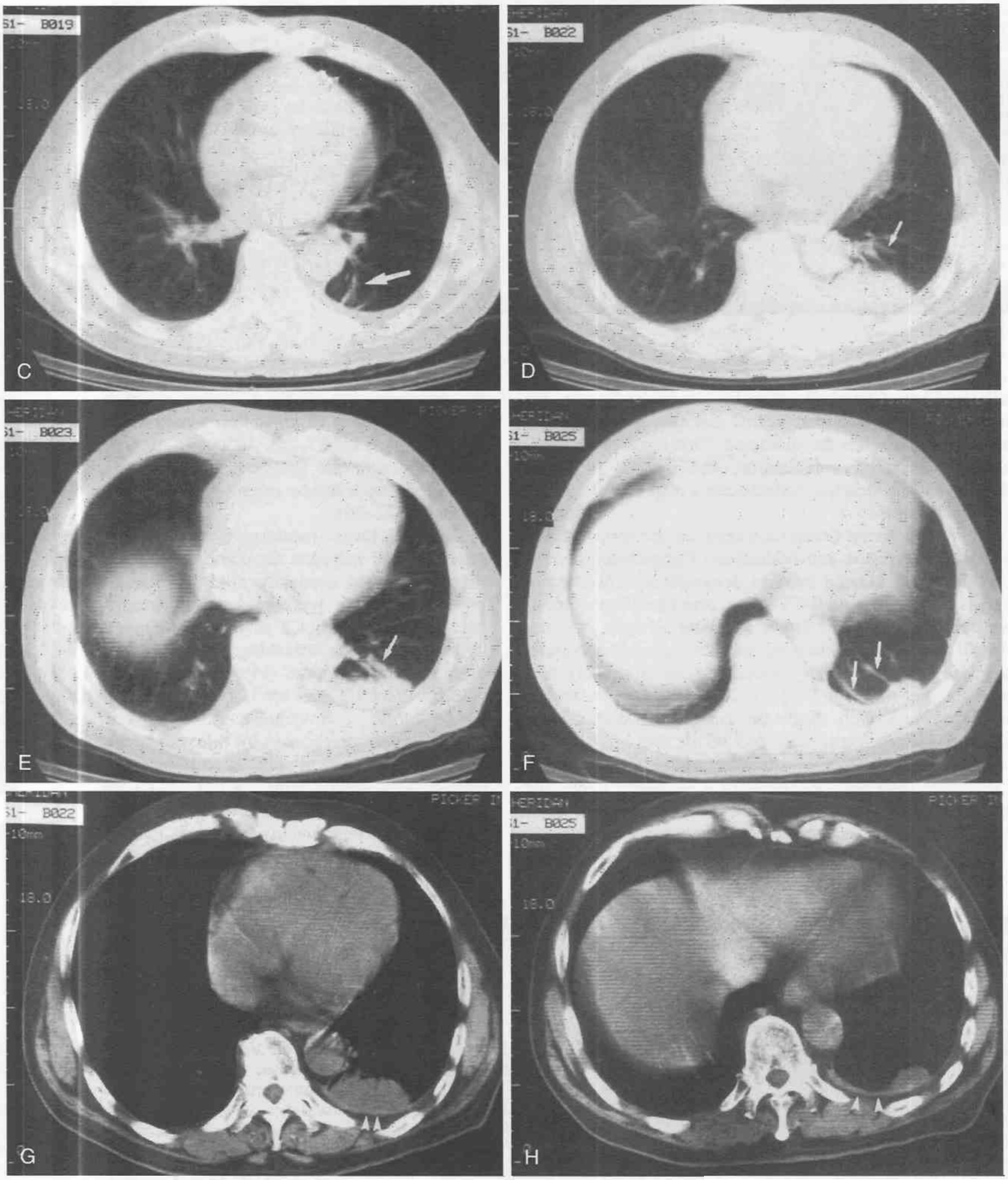

Figure 27–23. *Continued.* *C–H,* Typical features of round atelectasis are visualized by CT. A rounded pleura-based mass is present, with adjacent pleural thickening *(arrowheads).* Vessels and lung markings curl into the lesion, producing the comet's tail or vacuum cleaner sign *(arrows).* The predisposing cause in this patient was not asbestos exposure but previous thoracic surgery.

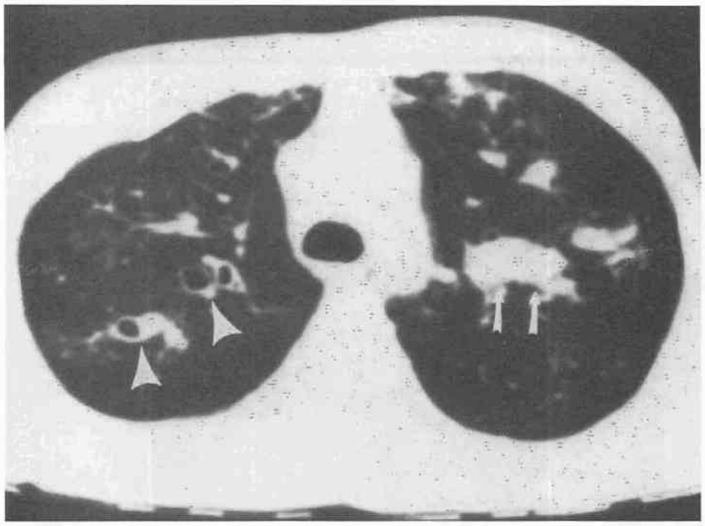

Figure 27–24. CT signs of bronchiectasis. The signet ring sign *(arrowheads)* consists of the dilated bronchus (the ring) and its accompanying pulmonary artery (the signet). A large mucous plug fills one of the dilated bronchi *(arrows)*. (From Kuhlman JE, Reyes BL, Hruban RH, et al: Abnormal air spaces in the lung. Radiographics 13:47–75, 1993.)

wall (Williams-Campbell syndrome).[214] In each case, the protective airway mechanisms that maintain airway sterility and airway clearance are disrupted. This leads to repeated bacterial infections, colonization, and mucous plugging, followed by a destructive inflammatory response and resultant bronchiectasis.

CT has replaced bronchography as the noninvasive method for diagnosis and evaluation of bronchiectasis.[45, 82, 166, 169, 202, 210, 226] Dilated bronchi demonstrate a number of characteristic features on CT scans, and when bronchiectasis affects primarily the larger proximal airways, it is not difficult to recognize. Because each bronchus is accompanied by a pulmonary artery, bronchiectasis commonly produces a *signet ring sign* (Fig. 27–24). The dilated bronchus seen in cross-section forms the ring; the accompanying pulmonary artery forms the signet of the ring.

In cylindrical bronchiectasis, when the dilated bronchus is sectioned longitudinally by the CT scanning plane, the parallel thickened airway walls resemble a *railroad track* or *tram track*. If the bronchiectasis is varicose in nature, the structure seen on the CT scan resembles a *string of pearls* with areas of dilatation alternating with areas of constriction (Fig. 27–25). In cystic bronchiectasis, when dilated bronchi are grouped together and cut in cross-section, an appearance resembling a *cluster of grapes* is seen (Fig. 27–26).

Air-fluid levels resulting from retained secretions or superimposed infection are commonly identified in dependent portions of cystically dilated bronchi. When dilated bronchi are filled with inspissated material, mucoid impaction results. On a CT scan, *mucous plugs* are identified by recognizing the branching tubular nature of the opacity on multiple CT sections (Fig. 27–27 and see Fig. 27–24).

Bronchiectatic cysts are larger air spaces that develop in severe forms of bronchiectasis, such as cystic fibrosis. Such cysts are recognized by their connection to a dilated proximal bronchus. In contrast to blebs or bullae, bronchiectatic cysts demonstrate discrete, often thickened walls and may be multiloculated (Fig. 27–28).[70, 221]

In *central bronchiectasis*, there is marked dilatation of

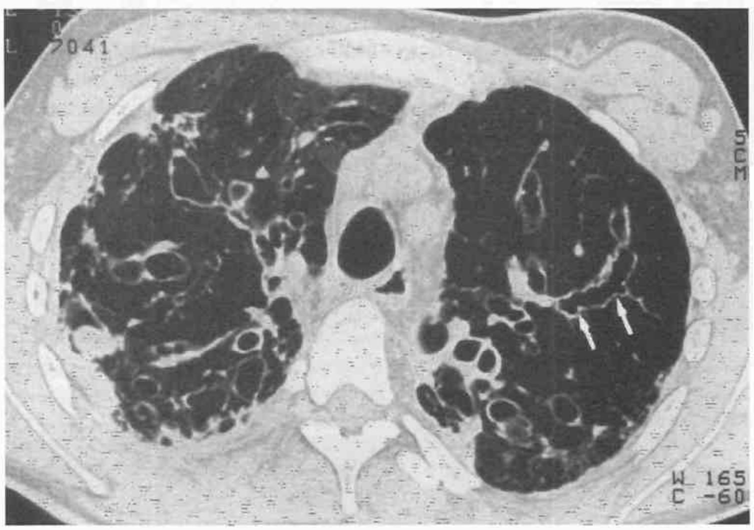

Figure 27–25. CT signs of bronchiectasis in a patient with advanced cystic fibrosis. When a dilated bronchus is sectioned longitudinally by the CT scanning plane, it often demonstrates a *string of pearls* configuration with alternating areas of dilatation and constriction *(arrows)*. (From Kuhlman JE, Reyes BL, Hruban RH, et al: Abnormal air spaces in the lung. Radiographics 13:47–75, 1993.)

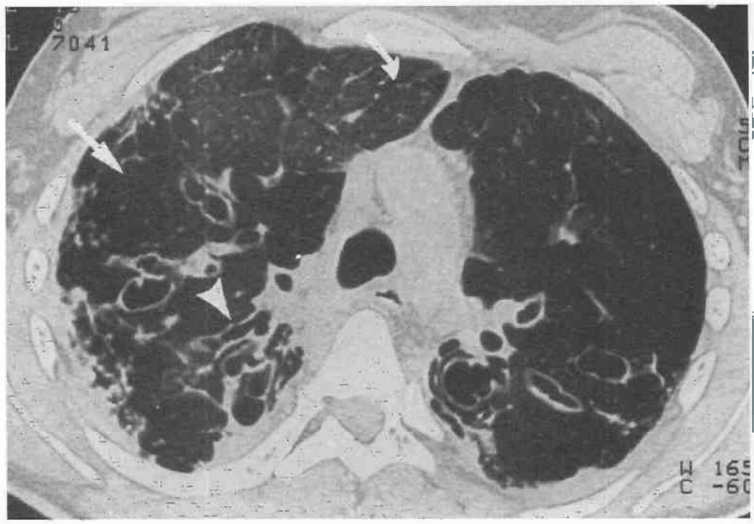

Figure 27–26. CT signs of bronchiectasis. Cystically dilated bronchi when grouped closely together may demonstrate a cluster-of-grapes appearance on CT *(arrowheads)*. The relative oligemia *(large arrow)* of some of the pulmonary segments can be compared with more normal lung *(curved arrow)* in this patient with advanced bronchiectasis. This is an example of mosaic attenuation. The subtle differences in CT attenuation of the lung parenchyma reflect both the degree of vascular perfusion and the air space inflation of each segment. Relative underperfusion, resulting from reflex shunting of blood away from hypoxic segments, and hyperinflation of affected segments caused by air trapping contribute to decreased lung density on CT. (From Kuhlman JE, Reyes BL, Hruban RH, et al: Abnormal air spaces in the lung. Radiographics 13:47–75, 1993.)

the proximal bronchi with relative sparing of more distal segments. Central bronchiectasis is a hallmark of *allergic bronchopulmonary aspergillosis* (Fig. 27–29).[42]

Allergic bronchopulmonary aspergillosis is characterized on plain films and CT by central bronchiectasis and abundant mucous plugging. This disease typically produces fleeting opacities, which come and go on plain films, and some of the more dramatic examples of the finger-in-glove sign of mucous plugging. A history of refractory asthma is the clue to the diagnosis, which can be confirmed by a set of clinical and laboratory criteria that include elevated IgE levels, precipitating antibodies against *Aspergillus*, peripheral blood eosinophilia, immediate and late skin reactions to *Aspergillus* antigen, and *Aspergillus* mycelia in sputum or mucous plugs.[225a]

Recognizing *bronchiolectases*, or disease affecting the smaller peripheral airways, is more difficult (Fig. 27–30). This is particularly true in cases of *panbronchiolitis* caused

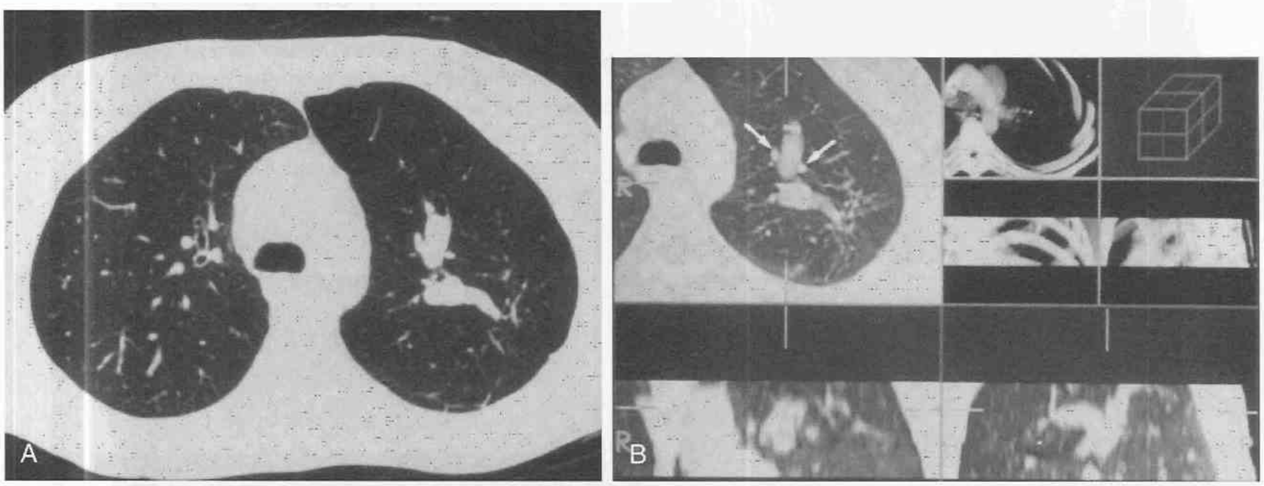

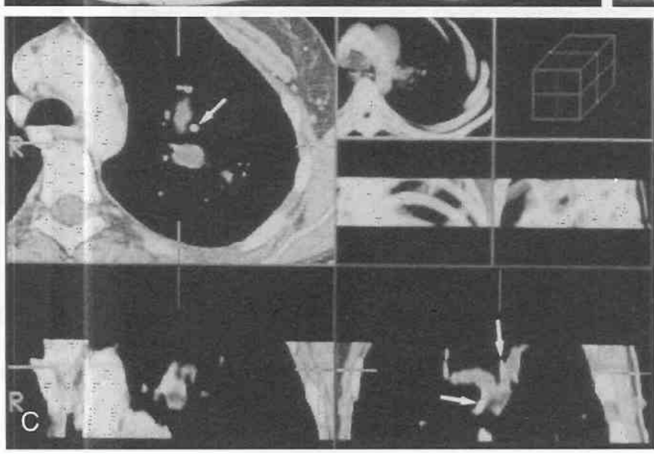

Figure 27–27. *A–C,* A new focal lung opacity was seen on chest films after fever developed in a patient with cancer who was receiving chemotherapy. With a spiral CT data set, multiplanar reconstructions of the lung identify the opacity as a branching, tubular structure compatible with a diagnosis of mucous plug. Distinct small pulmonary arteries *(arrows)* accompany the dilated, mucus-filled bronchi.

Figure 27–28. Bronchiectatic cysts are recognized on CT by identifying their connection to a dilated bronchus *(arrows)*. Histologically, the walls of bronchiectatic cysts are lined with collagenous fibrous tissue.

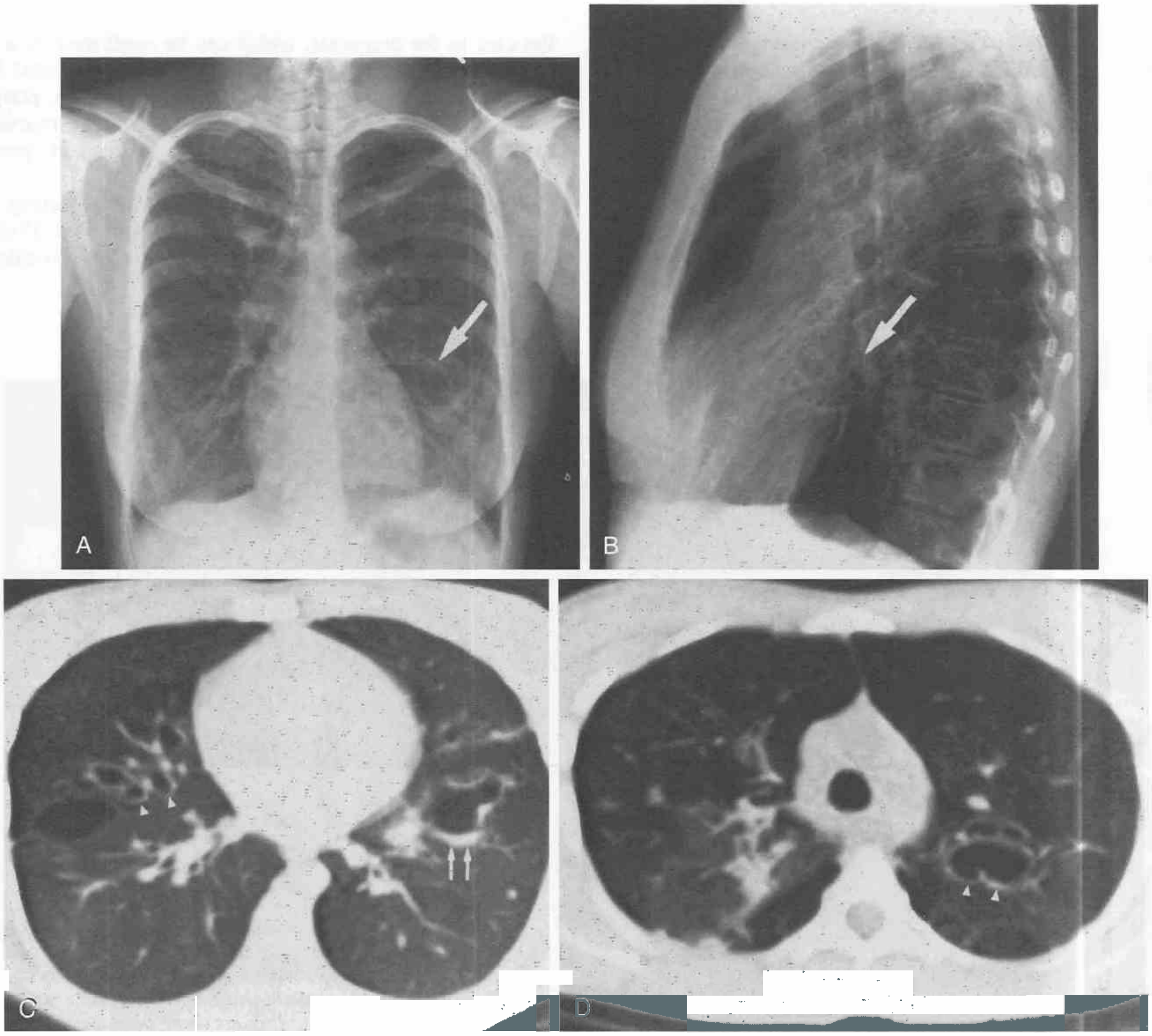

Figure 27–29. Central bronchiectasis is a characteristic feature of allergic bronchopulmonary aspergillosis. *A* and *B*, Posteroanterior and lateral chest films show central thin-walled cystic lesions *(arrows)*. *C* and *D*, CT more clearly identifies the abnormalities as dilated, tubular bronchi *(arrowheads)* and areas of cystic bronchiectasis. An air-fluid level can be visualized *(arrows)*. (From Kuhlman JE, Reyes BL, Hruban RH, et al: Abnormal air spaces in the lung. Radiographics 13:47–75, 1993.)

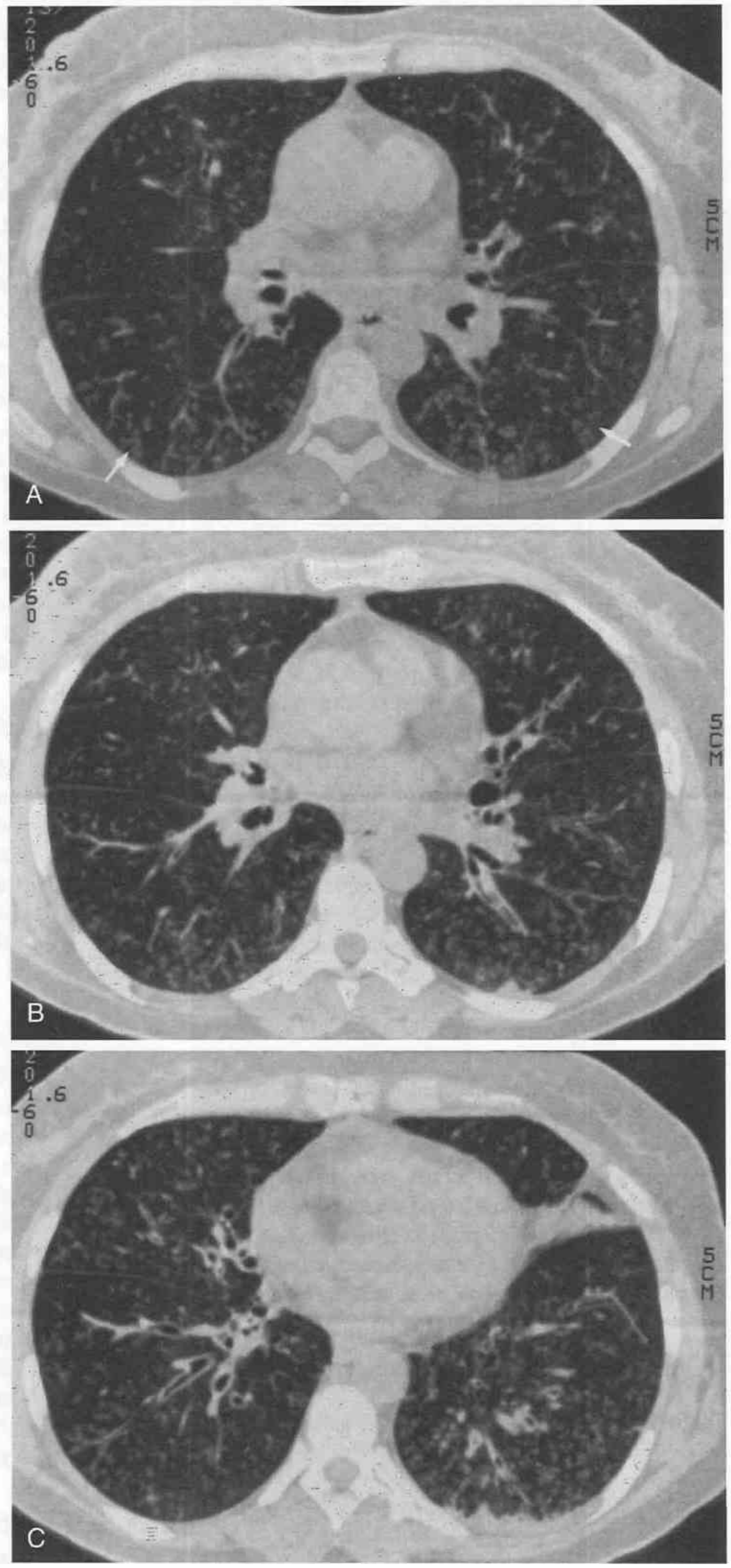

Figure 27–30. *A–C,* Panbronchiolitis. Bronchiolectases or bronchiectatic disease of the smaller peripheral airways may have an appearance on CT that mimics multiple tiny nodules. CT shows peribronchial thickening and mild dilatation of the proximal bronchi. In addition, multiple tiny dots in a centrilobular location are noted; they result from bronchiolectases of the smaller, peripheral airways. The CT appearance has been described as "tree-in-bud" opacities *(arrows).*

by viral or bacterial infections or other inflammations. Thickened peripheral bronchioles, because of their small size and short length, do not demonstrate the same longitudinal features seen in larger airways and may be mistaken for small nodules. If dilated, these distal small airways may mimic small cavitating nodules. The appearance of inflamed distal bronchioles often resembles small buds on a tree branch and has been described with the phrase *tree-in-bud opacities.*[80a]

CT Features of Diffuse Lung Disease

Diffuse lung disease demonstrates many patterns of distribution on CT scans. These patterns are often helpful in characterizing the nature of the lung disease and arriving at a limited differential diagnosis for the pulmonary process.[155]

Diffuse air space disease may be distributed primarily centrally or peripherally, or it may affect both the central and the peripheral zones of the lung. A few diffuse diseases of the lung produce an abnormality of the lung parenchyma referred to as ground-glass opacities (Fig. 27–31).[146, 157] These opacities may be distributed homogeneously or in a patchy or mosaic pattern, or they may be limited to the centrilobular region of the secondary pulmonary lobule.[4a]

Diffuse interstitial disease and diffuse cystic lung disease may also have several patterns of distribution, including peribronchial and subpleural locations. Examples of cystic lung disease that produce diffuse patterns of distribution include panlobular emphysema and lymphangiomyomatosis.

Ground-Glass Opacities

The ground-glass opacity is characterized by a subtle increase in CT attenuation of the lung parenchyma that does not obliterate the outlines of the bronchi or pulmonary vessels (see Fig. 27–31).[4a, 155, 157] It may be homogeneous and diffuse or more uneven in its distribution, producing a patchwork pattern often described by the term *mosaic attenuation*. Diseases that typically produce ground-glass opacities on CT scans include *Pneumocystis carinii* pneumonia (PCP), cytomegalovirus (CMV) pneumonia, alveolar proteinosis, acute pulmonary edema, extrinsic allergic alveolitis, and the acute alveolitis stage of desquamative interstitial pneumonitis (DIP) and usual interstitial pneumonitis (UIP) (see Fig. 27–31).[64, 110, 206] HRCT enhances detection of subtle ground-glass opacities, particularly in cases in which the chest film or the conventional CT scan are normal or show equivocal findings (Fig. 27–32).

Patchwork or Mosaic Attenuation Patterns

Sometimes the parenchymal abnormality is less uniform and distinctly patchy in its distribution, with areas of normal lung interspersed with abnormal zones. This pattern may be thought of as a "patchwork" pattern because of the striking, sometimes bizarre and mosaic appearance of the lung on CT scans (see Figs. 27–31 and 27–32). Patchy differences in lung CT attenuation are seen in a number of diffuse pulmonary processes, such as *obliterative bronchiolitis (bronchiolitis obliterans), bronchopulmonary dysplasia, asthma, hypersensitivity pneumonitis, PCP, DIP, pulmonary hemorrhage, and chronic thromboembolic disease.*[98, 110, 126, 213a]

Diseases that produce mosaic attenuation on CT scans fall into three basic categories:

- Airway disease
- Vascular disease
- Infiltrative disease

The causes of the underlying differences in CT attenuation vary, depending on the disease category.[213a, 238b]

In some lung diseases, abnormal areas of lung are those that demonstrate increased CT attenuation either because the alveolar spaces are filled with edema fluid or cells (see Figs. 27–14 and 27–32) or because the relative amount of air in the alveolar space is decreased as a result of encroaching, thickened interstitium. In other diseases, such as advanced cystic fibrosis (see Fig. 27–26), obliterative bronchiolitis, and bronchopulmonary dysplasia (Fig. 27–33), the abnormal areas of lung are those that demonstrate decreased CT attenuation relative to the surrounding normal lung, as a result of focal air-trapping and reflex oligemia caused by vasoconstriction. In chronic thromboembolic disease, the lung pattern has been described by some authors as "mosaic perfusion" to reflect the belief that differences in pulmonary vascular perfusion contribute in large part to the differences in lung attenuation visualized on CT scans.[114, 126, 138]

Obliterative Bronchiolitis (Bronchiolitis Obliterans)

Also known as *constrictive bronchiolitis*, obliterative bronchiolitis has many causes: past infection, Swyer-James syndrome, inhalational injury, and drug use. It is also seen in association with collagen vascular diseases (rheumatoid arthritis, lupus, and scleroderma); in bone marrow transplant recipients with chronic graft-versus-host disease; and as the primary manifestation of chronic rejection in lung and heart-and-lung transplant recipients.[119a]

Swyer-James Syndrome

Swyer-James syndrome is a form of obliterative bronchiolitis that results from a childhood viral infection that goes on to produce postinfectious bronchiolitis obliterans (see Fig. 27–33*B–D*).[137a, 152a] Typical findings include a small, hyperlucent lung that demonstrates air-trapping on expiratory films or CT. A small pulmonary artery on the affected side is characteristic. On CT scans, one can better appreciate not only the small main pulmonary artery but also diminution and pruning of all the pulmonary artery branches on the affected side.

Bronchiectasis is a CT feature of Swyer-James syndrome that is not widely recognized but is often present.[137a, 152a] CT studies have shown that lung changes in Swyer-James syndrome are not exclusively unilateral.[152a]

Centrilobular and Peribronchiolar Patterns

A few lung diseases produce CT abnormalities that are confined, at least initially, to the region immediately surrounding the central core bronchioles of the secondary pulmonary lobule. On first examination, these CT abnormalities may be mistaken for tiny nodules, but closer in-

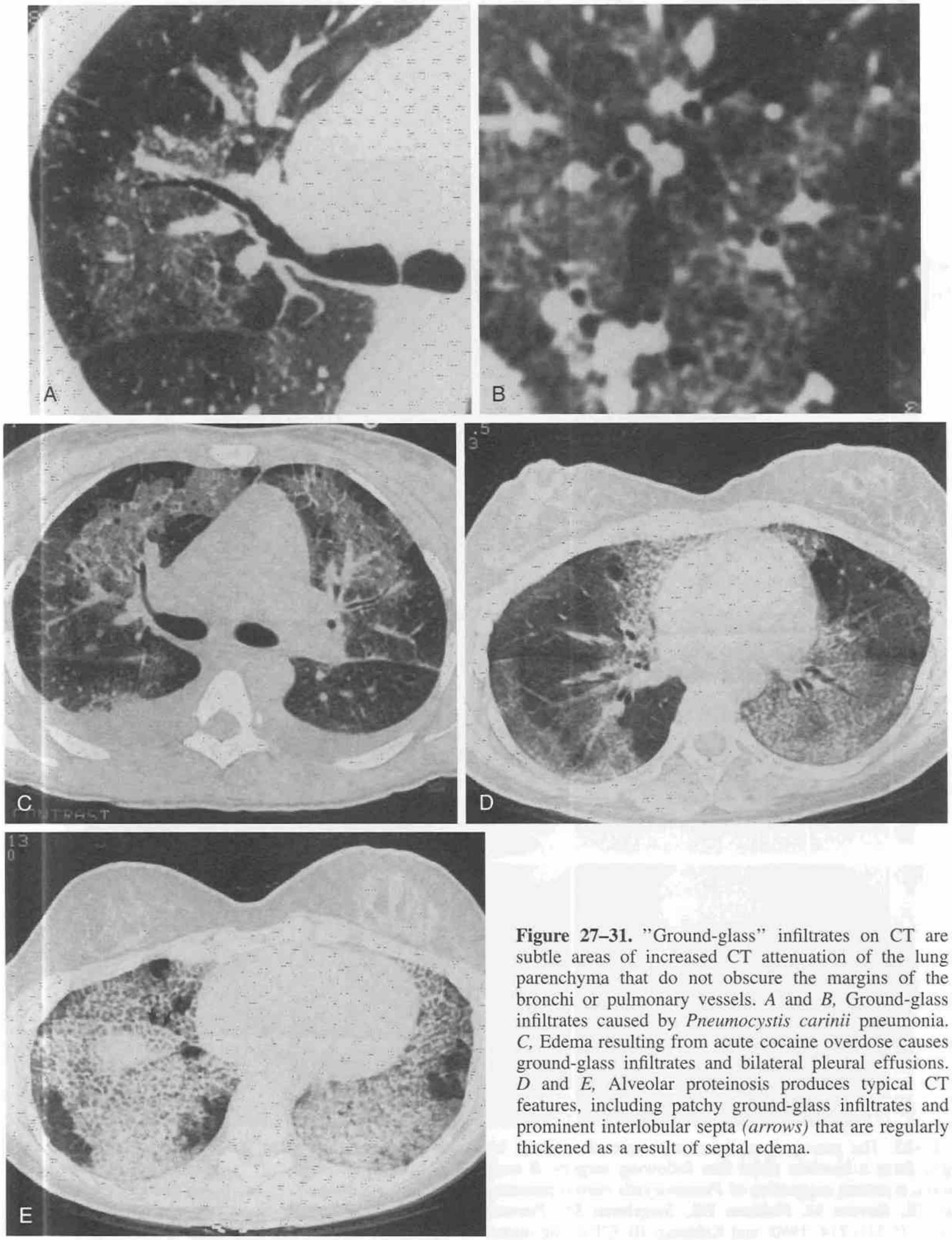

Figure 27–31. "Ground-glass" infiltrates on CT are subtle areas of increased CT attenuation of the lung parenchyma that do not obscure the margins of the bronchi or pulmonary vessels. *A* and *B*, Ground-glass infiltrates caused by *Pneumocystis carinii* pneumonia. *C*, Edema resulting from acute cocaine overdose causes ground-glass infiltrates and bilateral pleural effusions. *D* and *E*, Alveolar proteinosis produces typical CT features, including patchy ground-glass infiltrates and prominent interlobular septa *(arrows)* that are regularly thickened as a result of septal edema.

spection reveals that each represents a nodular opacity centered around the centrilobular complex of the secondary pulmonary lobule and its small bronchiolar branches.

Diseases that cause this type of CT abnormality are often characterized histologically by peribronchiolar infiltration with inflammatory cells or lymphocytes or with granulomatous reaction. Early graft-versus-host disease affecting the lung in the bone marrow transplant recipient produces such a CT appearance because of infiltration of lymphocytes around the small bronchioles. Panbronchiolitis, whether caused by infection or exposure to an irritant, may produce a similar CT appearance.[4, 4a]

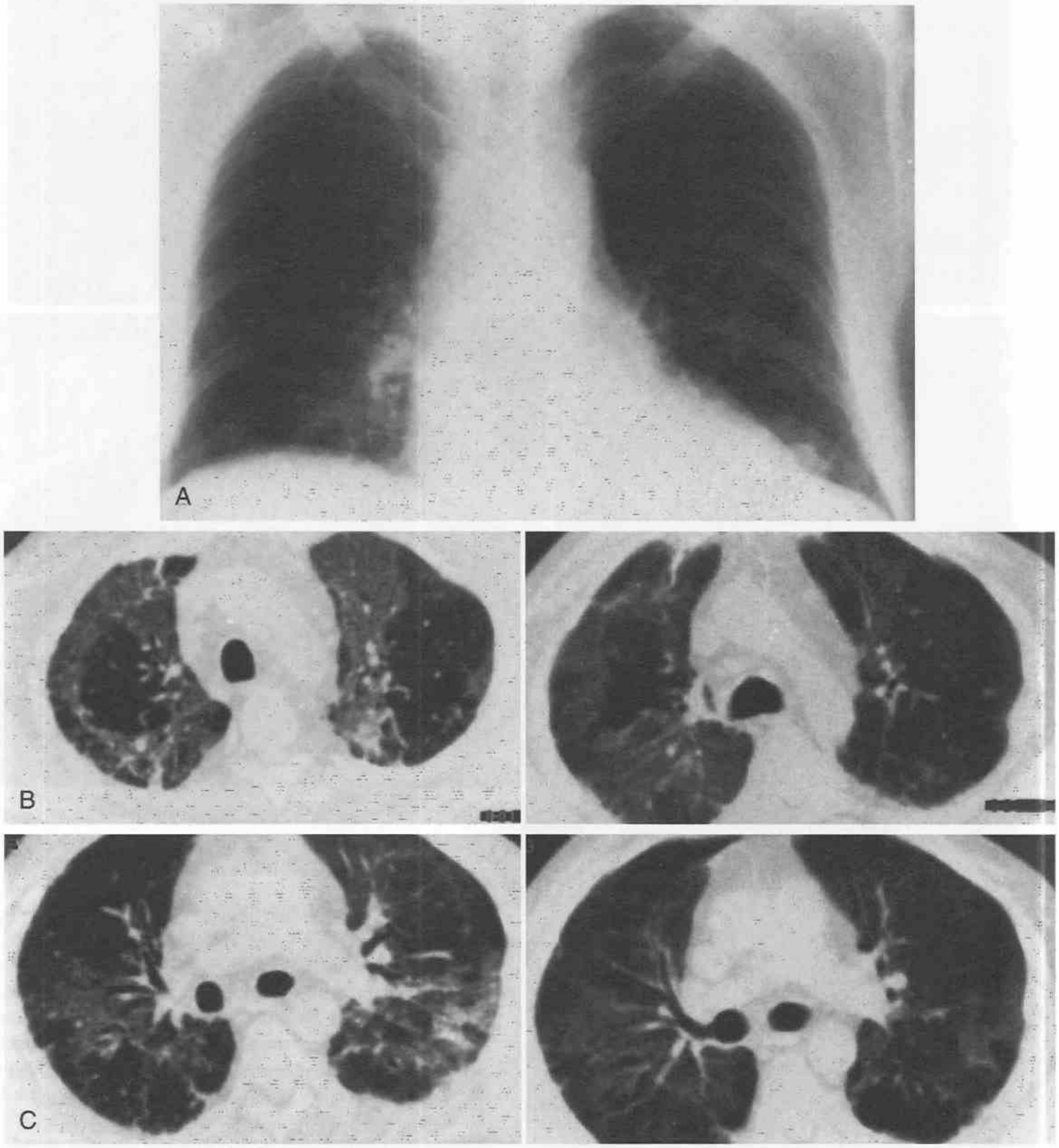

Figure 27–32. The patient is an immunocompromised heart transplant recipient with fever. *A,* The chest film was interpreted as unchanged from a baseline chest film following surgery. *B* and *C,* CT scan shows dramatic "ground-glass" infiltrates in a patchy distribution, a pattern suggestive of *Pneumocystis carinii* pneumonia, which was subsequently confirmed at bronchoscopy. (*A–C,* From Kuhlman JE, Kavaru M, Fishman EK, Siegelman SS: *Pneumocystis carinii* pneumonia: Spectrum of parenchymal CT findings. Radiology 175:711–714, 1990; and Kuhlman JE: CT of the immunocompromised and acutely ill patient. In Zerhouni EA [ed]: CT and MRI of the Thorax. New York, Churchill Livingstone, 1990.)

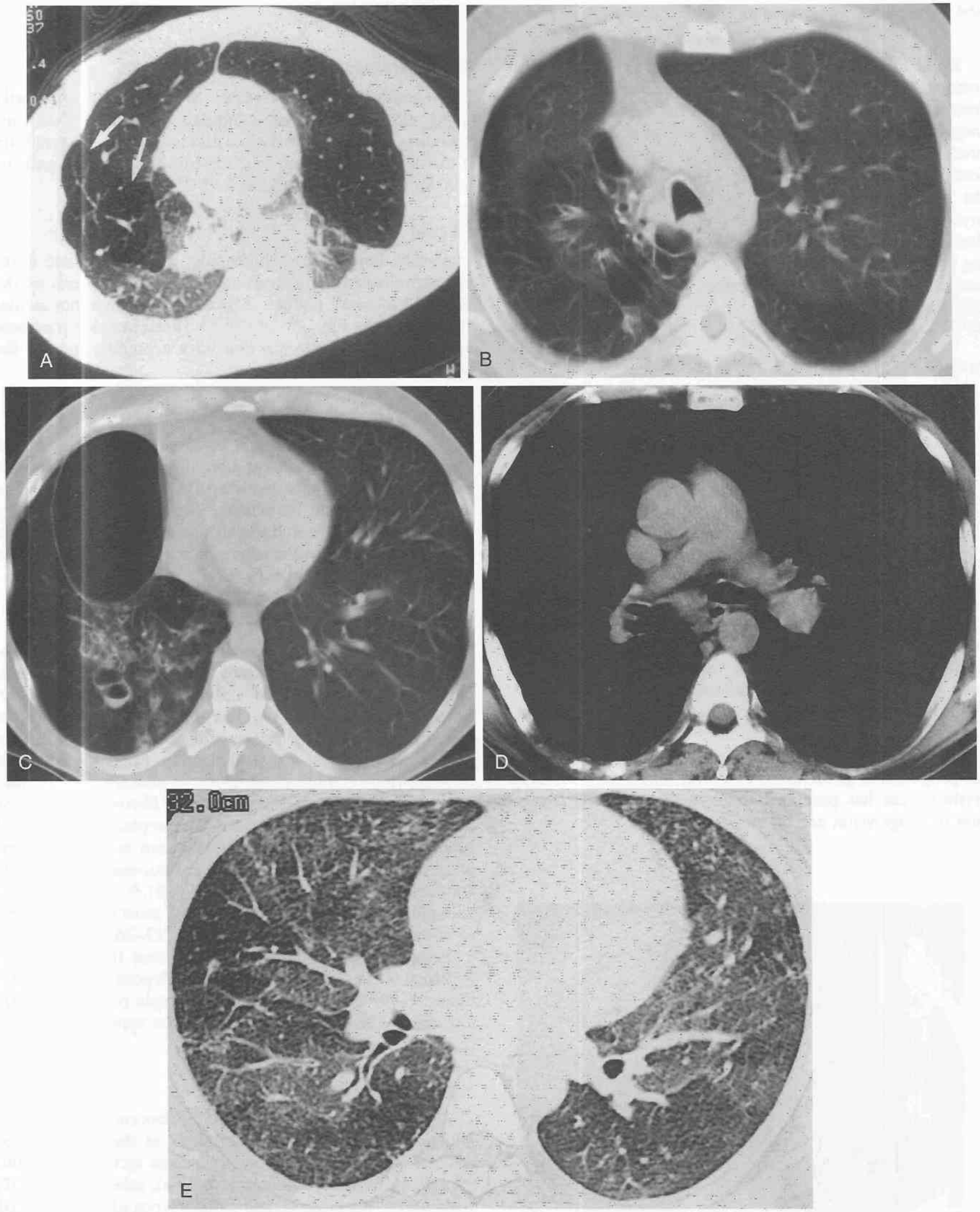

Figure 27–33. Mosaic attenuation, three cases.

A, Case 1. CT scan of bronchopulmonary dysplasia and bronchiolitis obliterans in a child demonstrates a pattern of mosaic attenuation. Segments of the lung *(arrows)* show decreased CT attenuation. Within these segments, the pulmonary vessels are small and attenuated as well. A combination of reflex vasoconstriction and hyperinflation due to air trapping probably accounts for the lower CT attenuation in these areas. (From Kuhlman JE: CT of diffuse lung disease. Appl Radiol 20:17–21, 1991.)

B–D, Case 2. Swyer-James syndrome. CT shows a small, hyperlucent right hemithorax with bronchiectasis and mosaic attenuation on the right side. Perfusion is decreased, and the caliber of the pulmonary artery branches is markedly decreased on the right. *D,* The main pulmonary artery on the right is also small, compared to the artery on the left.

E, Case 3. Mosaic attenuation accentuated on expiratory high-resolution CT views indicates air trapping. The patient is a 32-year-old woman with a history of asthma who uses an inhaler.

Bronchogenic spread of TB may also produce a focal form of this pattern when expectorated caseous material from a TB cavity is spread through the airways, becomes inspissated in small bronchioles, and secondarily causes bronchiolar dilatation, thickening, and peribronchiolar infection and inflammation (Fig. 27–34).[161] This produces the tree-in-bud appearance on CT scans. TB and other mycobacterial infections often produce some of the most dramatic examples of tree-in-bud opacities,[80a] but this finding is not necessarily specific for mycobacterial infections and can be seen in other causes of bronchiolitis, both infectious and inflammatory.

Diffuse Panbronchiolitis

Diffuse panbronchiolitis, the disease entity, is a chronic inflammatory disease of unknown cause found most commonly in Asians but occasionally in Americans and Europeans.[4, 4a] Clinically, patients present with chronic cough, dyspnea, wheezing, and sputum production. Associated chronic paranasal sinusitis is common.

CT findings include bronchiolectasis and milder bronchiectasis, peribronchiolar thickening, tree-in-bud opacities, and peripheral areas of mosaic attenuation. Bronchiolar changes are the dominant finding on CT scans and these changes are strikingly diffuse, involving all lobes.[4, 4a] Tissue studies show infiltration of the walls and tissues, centering on the respiratory bronchioles, with lymphocytes, plasma cells, and histiocytes. This inflammatory process causes secondary dilatation of the more proximal airways, beginning with the terminal bronchioles.[4, 4a]

Progression to respiratory failure is often rapid and the prognosis is poor. Treatment with long-term, low-dose erythromycin has produced some success; disease regression or progression can be monitored with CT.[4, 4a]

Figure 27–34. Peribronchiolar densities of "ground-glass" opacity and consolidation, resulting from spread of tuberculosis, look like tiny, "fuzzy" nodules on CT scans (called "tree-in-bud" opacities). The apparent nodules actually represent inspissated caseous material in small bronchioles, with surrounding peribronchiolar inflammation and infection.

Bronchovascular Distributions

A number of lung diseases are distributed primarily along the bronchovascular bundles and within their surrounding lymphatic interstitial tissues. Lung diseases with a distinct bronchovascular distribution include *sarcoidosis* and *Kaposi's sarcoma* (KS).[105, 108, 165, 208, 235]

Sarcoid

In addition to septal thickening, reticulation, and fibrosis, pulmonary sarcoid is characterized on CT scans by the presence of small nodules adjacent to the bronchovascular structures (see Fig. 27–5*A*).[108, 208] These nodules represent aggregates of granulomas that have a predilection for the peribronchovascular lymphatics.

Kaposi's Sarcoma

Kaposi's sarcoma, when it involves the lung, is another example of peribronchovascular disease.[165] The sarcoma infiltrates along and around the bronchovascular bundles and the surrounding lymphatics. On CT scans, pulmonary lesions resulting from Kaposi's sarcoma radiate from the pulmonary hila in a distinctive pattern, often appearing to encase and coat the bronchi (Fig. 27–35).[105, 165, 235]

Beaded Septum Sign

Thickening of the interlobular septa and bronchovascular interstitium is a CT feature of many diffuse interstitial lung diseases and may be smooth, irregular, or nodular. Smooth thickening of the interlobular septa is seen in diseases such as *interstitial pulmonary edema* and *alveolar proteinosis*. Irregular septal thickening, often accompanied by distortion of lung architecture, is characteristic of diseases causing interstitial pulmonary fibrosis. Prominent nodular thickening of the interlobular septa, reminiscent of beads on a string, is an appearance seen in cases of lymphangitic carcinomatosis, some granulomatous diseases, and occasionally silicosis (Fig. 27–36).[20, 146, 160, 240] Lymphangitic carcinomatosis produces the most dramatic cases of nodular septal thickening (see Fig. 27–36).

Pathologic correlation has shown that the beaded appearance is caused by endolymphatic deposits of metastatic tumor.[146, 160, 185] Sarcoidosis is an example of a granulomatous disease that may produce a similar appearance on CT scans (see Fig. 27–36).

Subpleural Distributions

A few lung diseases produce CT abnormalities that are initially most severe in the periphery of the lung, the so-called "subpleural zone." Such diseases include idiopathic pulmonary fibrosis (fibrosing alveolitis), asbestosis, BOOP, eosinophilic pneumonia, and certain types of drug-induced lung disease (Fig. 27–37). The subpleural CT abnormalities may consist of ground-glass opacities, arcades of reticulation, or a meshwork of small cystic spaces known as *honeycombing* (see Fig. 27–37).[240]

Honeycombing is a distinct form of pulmonary damage and lung remodeling that consists of multiple small cystic air spaces ranging in size from 1 to 10 mm. Histologically, the walls of the cystic spaces are composed of granulomatous or fibrous tissue, and the process has a distinct predi-

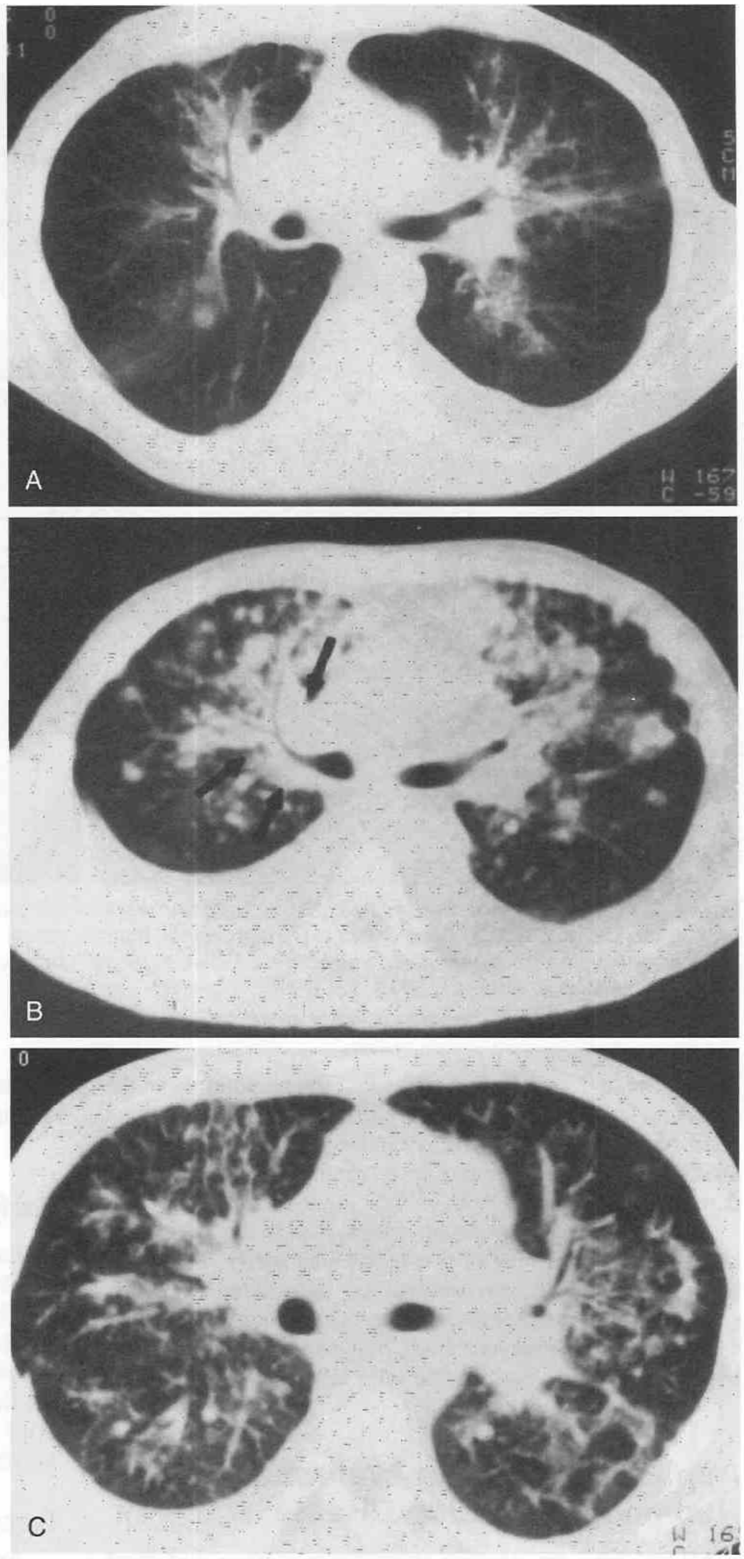

Figure 27–35. *A–C,* Bronchovascular distributions. In three patients with Kaposi's sarcoma (KS) involving the lung, the distinct tendency of KS to spread along the peribronchovascular interstitium is shown. On CT, pulmonary lesions caused by KS radiate out from the pulmonary hila and often appear to encase or coat the bronchi *(arrows).* (*A,* From Kuhlman JE: AIDS-related diseases of the chest. In Kuhlman JE [ed]: CT of the Immunocompromised Host. New York, Churchill Livingstone, 1991. *B,* From Kuhlman JE, Fishman EK, Burch PA, et al: Diseases of the chest in AIDS: CT diagnosis. Radiographics 9:827–857, 1989. *C,* From Kuhlman JE: CT of diffuse lung disease. Appl Radiol 20:17–21, 1991.)

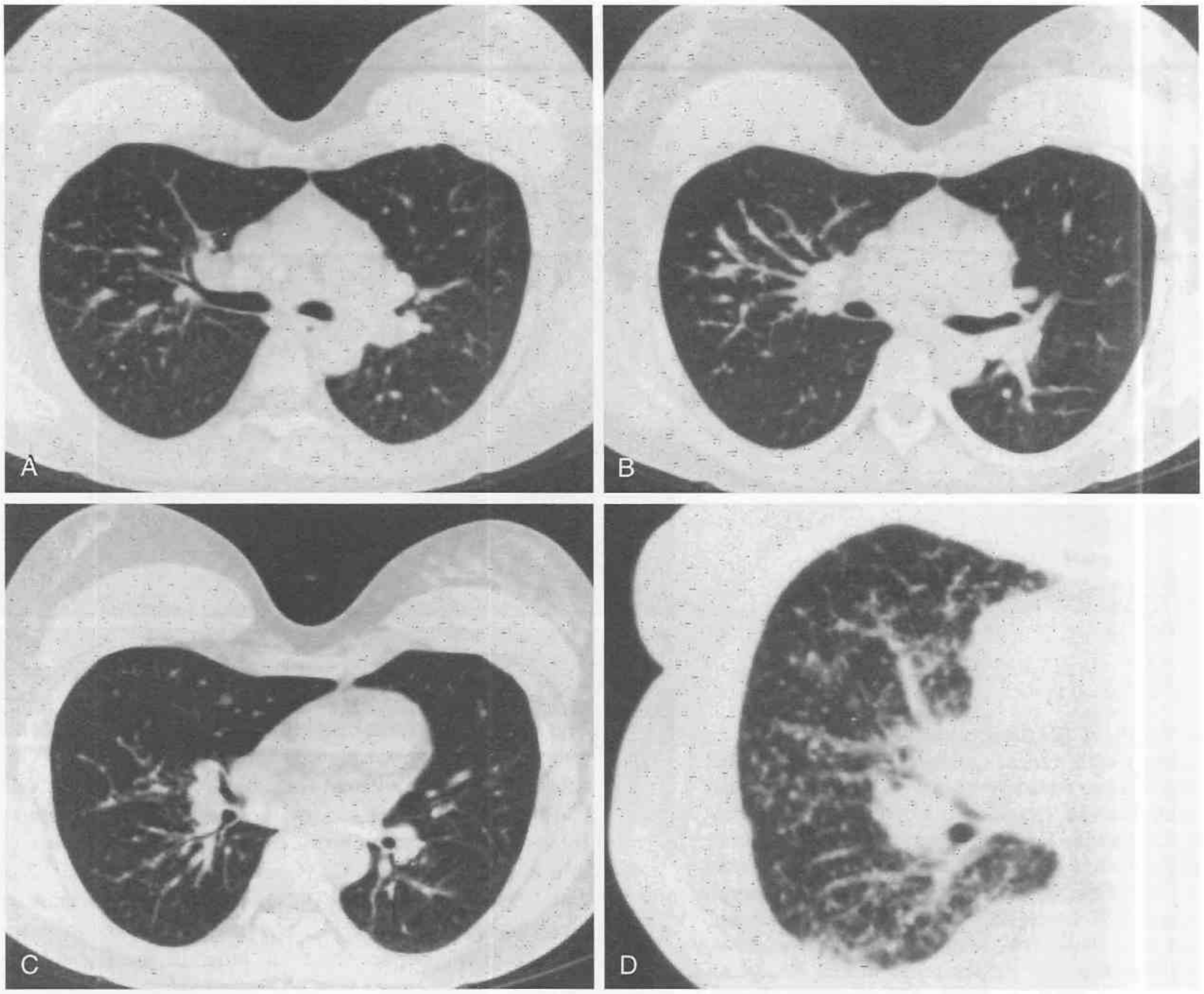

Figure 27–36. The beaded-septum sign. *A–C,* Prominent nodular thickening of the interlobular septa and the peribronchovascular interstitium due to sarcoidosis results in a CT appearance reminiscent of beads on a string. *D,* The most dramatic examples of the beaded septum sign are the result of lymphangitic spread of tumor, in this case lung cancer. (*D,* From Kuhlman JE: CT of diffuse lung disease. Appl Radiol 20:17–21, 1991.)

lection for the subpleural zones.[181] Honeycombing is the common final pathway for many diffuse lung diseases that produce interstitial fibrosis, including fibrosing alveolitis, DIP, pneumoconiosis, sarcoidosis, rheumatoid lung, scleroderma, and others.[120, 181, 211, 215, 232]

The presence of ground-glass opacities in the subpleural zone is often indicative of reversible lung injury. Treatment with corticosteroids or removal of the offending agent, such as a toxic drug, may reverse the pulmonary damage. The presence of honeycombing, however, is usually indicative of permanent, irreversible lung injury.[211]

Application of CT in Evaluation of Non-neoplastic Lung Disease

CT features are used to characterize diffuse and focal lung diseases for diagnosis, and HRCT improves both diagnostic accuracy and specificity.[19, 20] In addition to its diagnostic role, however, CT has other important clinical applications, including early detection of lung disease, quantification of lung damage, monitoring lung response to therapy, and detection of complications.

Early Detection and Diagnosis

Early detection of pulmonary disease is crucial in a number of clinical settings. Detection of occult lung infection in the immunocompromised patient may improve survival.[27] Early documentation of lung damage caused by pneumoconiosis has important environmental health and medicolegal implications. Early identification of pulmonary drug toxicity may lead to interventions that prevent irreversible lung injury.[101]

Opportunistic Lung Infection

An immunocompromised patient with unexplained fever or respiratory symptoms presents a common and difficult clinical problem. CT has been used successfully to detect and characterize opportunistic infections in patients with leukemia, acquired immunodeficiency syndrome (AIDS),

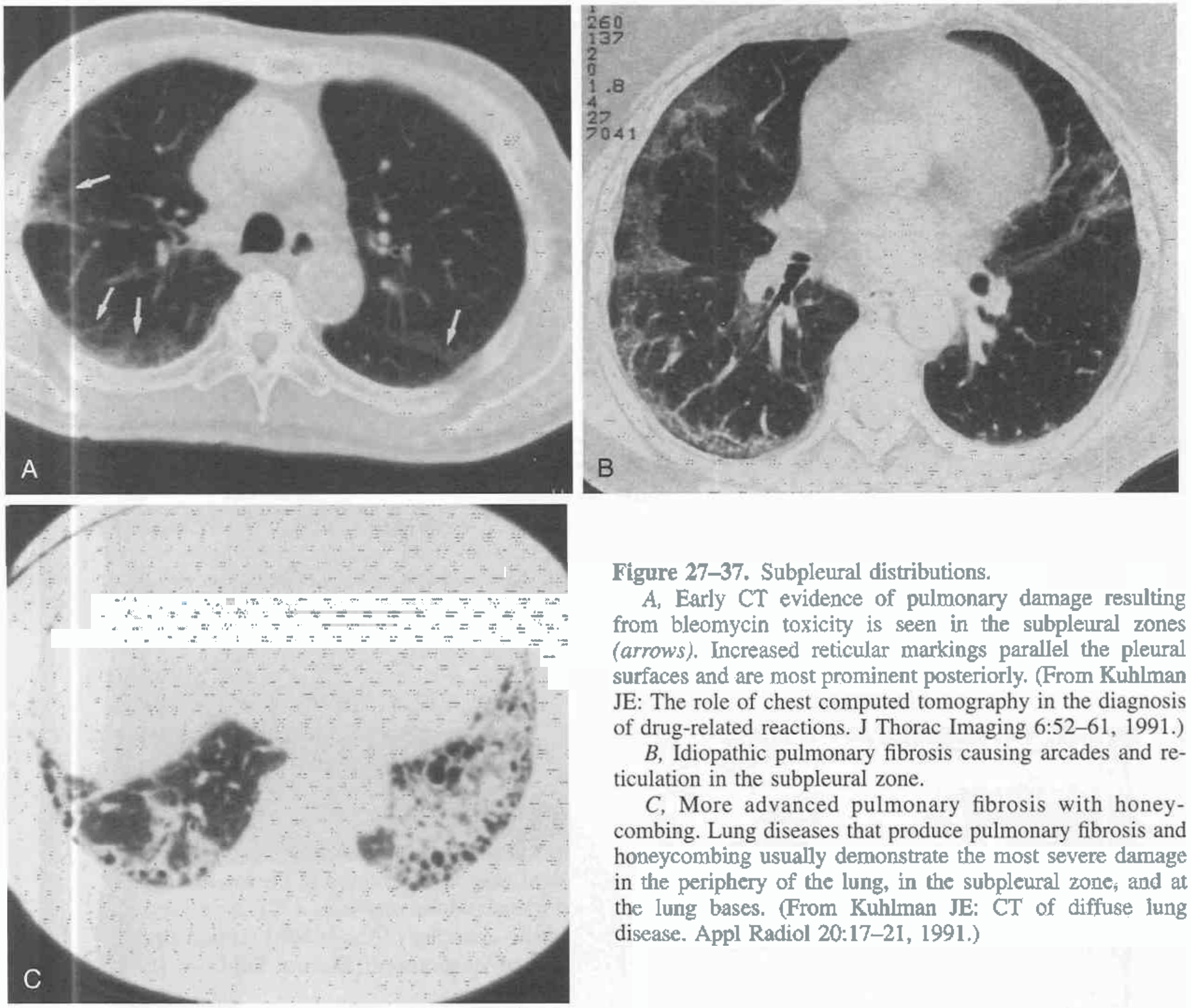

Figure 27–37. Subpleural distributions.

A, Early CT evidence of pulmonary damage resulting from bleomycin toxicity is seen in the subpleural zones *(arrows).* Increased reticular markings parallel the pleural surfaces and are most prominent posteriorly. (From Kuhlman JE: The role of chest computed tomography in the diagnosis of drug-related reactions. J Thorac Imaging 6:52–61, 1991.)

B, Idiopathic pulmonary fibrosis causing arcades and reticulation in the subpleural zone.

C, More advanced pulmonary fibrosis with honeycombing. Lung diseases that produce pulmonary fibrosis and honeycombing usually demonstrate the most severe damage in the periphery of the lung, in the subpleural zone, and at the lung bases. (From Kuhlman JE: CT of diffuse lung disease. Appl Radiol 20:17–21, 1991.)

and disorders treated with bone marrow transplantation (Fig. 27–38) (see Figs. 27–20, 27–22, 27–32).[27, 97, 100, 103, 104, 107, 110] HRCT aids in the early detection of lung infection in these patients. CT patterns and signs help to characterize the nature of the infection and direct invasive biopsy procedures to areas of the lung most affected. CT is also helpful in monitoring response of lung infection to appropriate therapy and in detecting relapse of infection.

Acquired Immunodeficiency Syndrome

When routine chest films fail to reveal a cause of unexplained fever or respiratory symptoms in a patient with AIDS, CT plays an important diagnostic and management role (see Fig. 27–38). CT can detect early or subtle lung infection when chest films remain negative or equivocal. In the patient with AIDS who may have many reasons to have fever or symptoms, the ability of CT to confirm the presence or absence of significant lung infection is critical in expediting the diagnostic workup. CT patterns of parenchymal lung involvement may suggest the most likely diagnosis, and CT can be used to select the diagnostic approach most likely to yield a positive culture specimen.

P. carinii *Pneumoniae Infection*

PCP is still one of the most common life-threatening lung infections to occur in patients with AIDS in industrialized countries.[1, 30, 31, 46, 93, 99, 105, 164] PCP can have a variety of presentations, from acute fulminant respiratory failure to a more insidious onset with nonspecific symptoms of nonproductive cough, malaise, and low-grade fever.[93] In a patient with AIDS, this more insidious presentation is more common.

The classic chest film findings of PCP are well known and include bilateral ground-glass infiltrates in a perihilar or sometimes upper lobe distribution.[1, 31, 46] The diagnosis is straightforward in patients who demonstrate these findings. Early in the course of infection, however, the chest film may appear normal or show only minimal increased lung markings, and a reported 10% of patients with documented PCP have normal or equivocal chest films.[46] In this setting, CT can be used to confirm or exclude the presence of parenchymal lung infiltrates.

CT patterns of PCP are varied, but the most common pattern is of diffuse or patchy, ground-glass infiltrates that do not obscure bronchovascular margins (Fig. 27–39).[110] Increased interstitial markings can also be seen, particularly

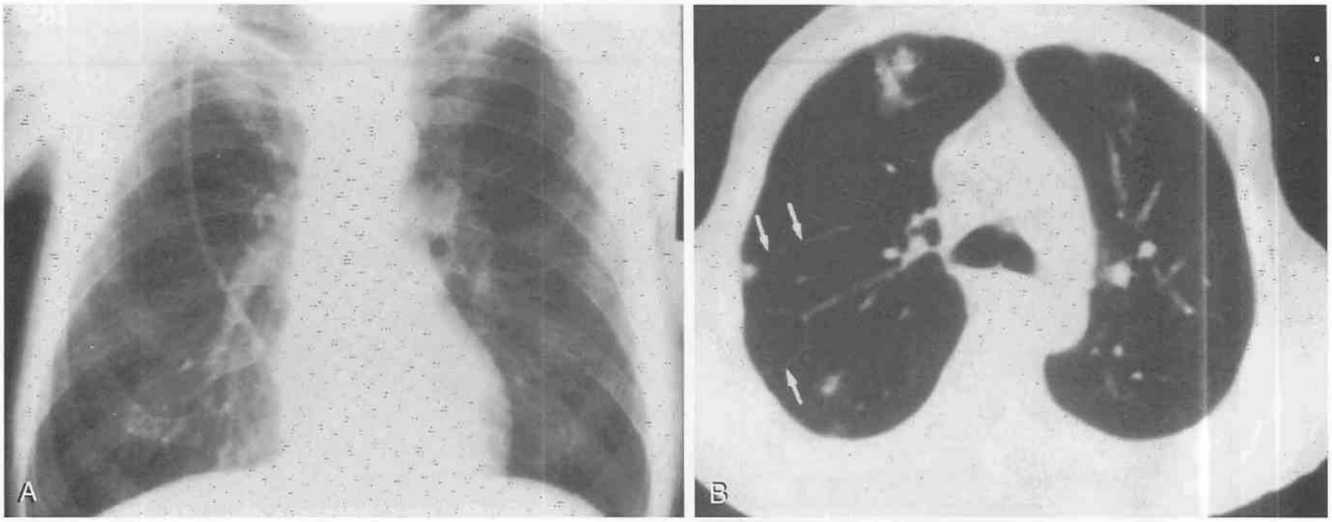

Figure 27–38. Unexplained fever in a patient with acquired immunodeficiency syndrome (AIDS). *A,* Chest film shows central venous line but no obvious infiltrates. *B,* CT identifies multiple inflammatory nodules with feeding vessels *(arrows),* compatible with a diagnosis of septic emboli. The source of the septic emboli was found to be the central venous catheter that had become infected. (*B,* From Kuhlman JE, Fishman EK, Burch PA, et al: Diseases of the chest in AIDS: CT diagnosis. Radiographics 9:827–857, 1989.)

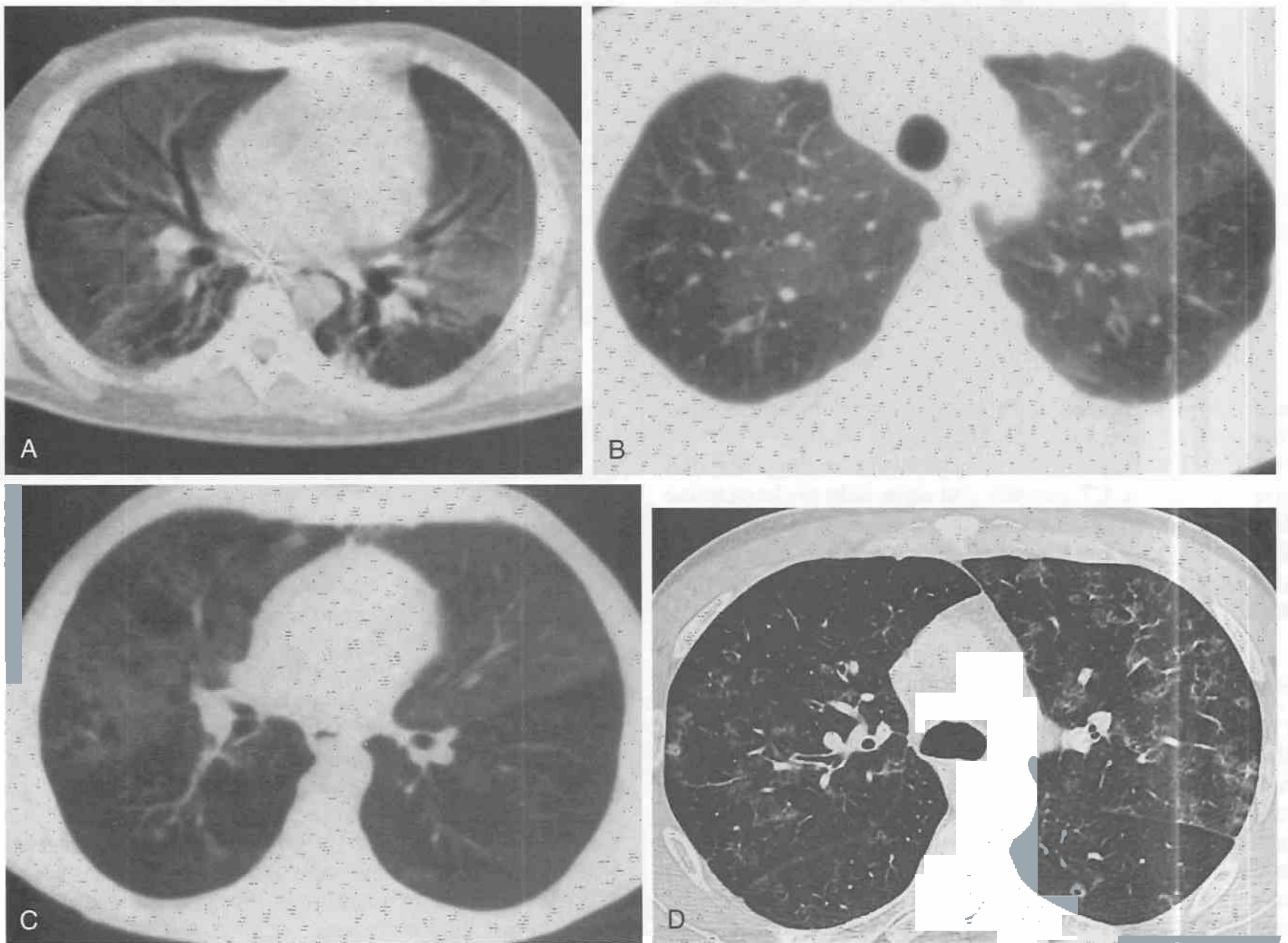

Figure 27–39. *Pneumocystis carinii* pneumonia (PCP): CT patterns of involvement.

A, Diffuse "ground-glass" infiltrates. (From Kuhlman JE, Kavuru M, Fishman EK, Siegelman SS: *Pneumocystis carinii* pneumonia: Spectrum of parenchymal CT findings. Radiology 175:711–714, 1990.)

B–D, Patchy ground-glass infiltrates.

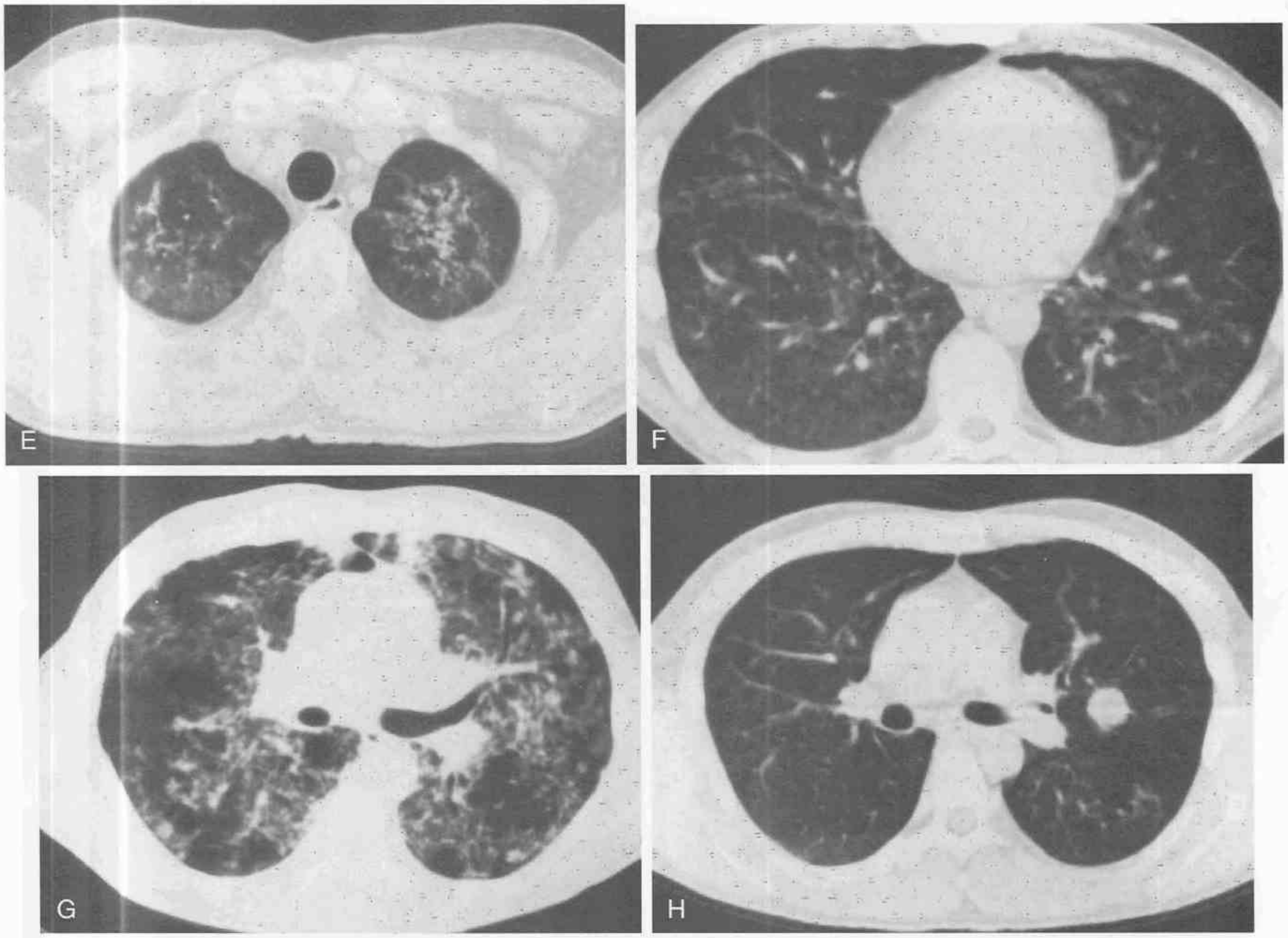

Figure 27–39. *Continued. E–G,* Mixed infiltrates with ground-glass and interstitial components.

E, From Kuhlman JE: CT of the immunocompromised and acutely ill patient. In Zerhouni EA [ed]: CT and MRI of the Thorax. New York, Churchill Livingstone, 1990; *F,* From Kuhlman JE, Fishman EK, Burch PA, et al: Diseases of the chest in AIDS: CT diagnosis. Radiographics 9:827–857, 1989; *G,* From Kuhlman JE: AIDS-related diseases of the chest. In Kuhlman JE [ed]: CT of the Immunocompromised Host. New York, Churchill Livingstone, 1991.)

H, Solitary pulmonary nodule, an unusual manifestation of PCP seen in a few patients with AIDS.

in patients who have had repeated *Pneumocystis* infections (20% to 40% of patients), because of the interstitial fibrosis that develops as the infection heals.

Another CT pattern of PCP, which is quite different in appearance, occurs with the cystic form (Fig. 27–40).* On CT scans, the cystic form of PCP is characterized by one or more thin-walled cysts or cavities that are somewhat irregular in shape and may be coarse or delicate in appearance. Surrounding ground-glass infiltrates are often present. This form of PCP may also be associated with CT manifestations of disseminated infection, including enlarged lymph nodes with calcifications found in the mediastinum and abdomen, and other calcifications in the liver, spleen, and kidneys (Fig. 27–41).[99, 183]

Many patients with cystic PCP or lymph node and visceral calcifications caused by *Pneumocystis* infection were reported to be receiving aerosolized pentamidine for prophylaxis against PCP. The aerosolized drug may partially clear or partially suppress the pulmonary infection, but it may not attain high-enough concentrations in the blood to prevent dissemination of the *Pneumocystis* organism. The chronic infection that remains in the lung may predispose to cystic cavity formation. More recently, aerosolized pentamidine has been less often used as a prophylactic agent, having been replaced by other, more effective drugs. Despite this change, the cystic form of PCP continues to be seen and some report an increasing frequency of this pattern of presentation.[20a]

A rare CT presentation of PCP is the *solitary pulmonary nodule*.[13, 110] A nodule may form in those individuals positive for the human immunodeficiency virus (HIV) who have less severe immunosuppression and can still mount a granulomatous response to the infection (see Fig. 27–39*D*). Pleural effusions are an uncommon finding in uncomplicated PCP. Rare cases of pleural effusions caused by disseminated *Pneumocystis* infection have been reported, and pleural calcifications may be demonstrated.[20a] More often in the patient with AIDS, the cause of a pleural effusion is a bacterial, fungal, or mycobacterial infection; lymphoma;

*See References 13, 30, 41, 53, 83, 92, 105, 125, 149, 193, 203, and 222.

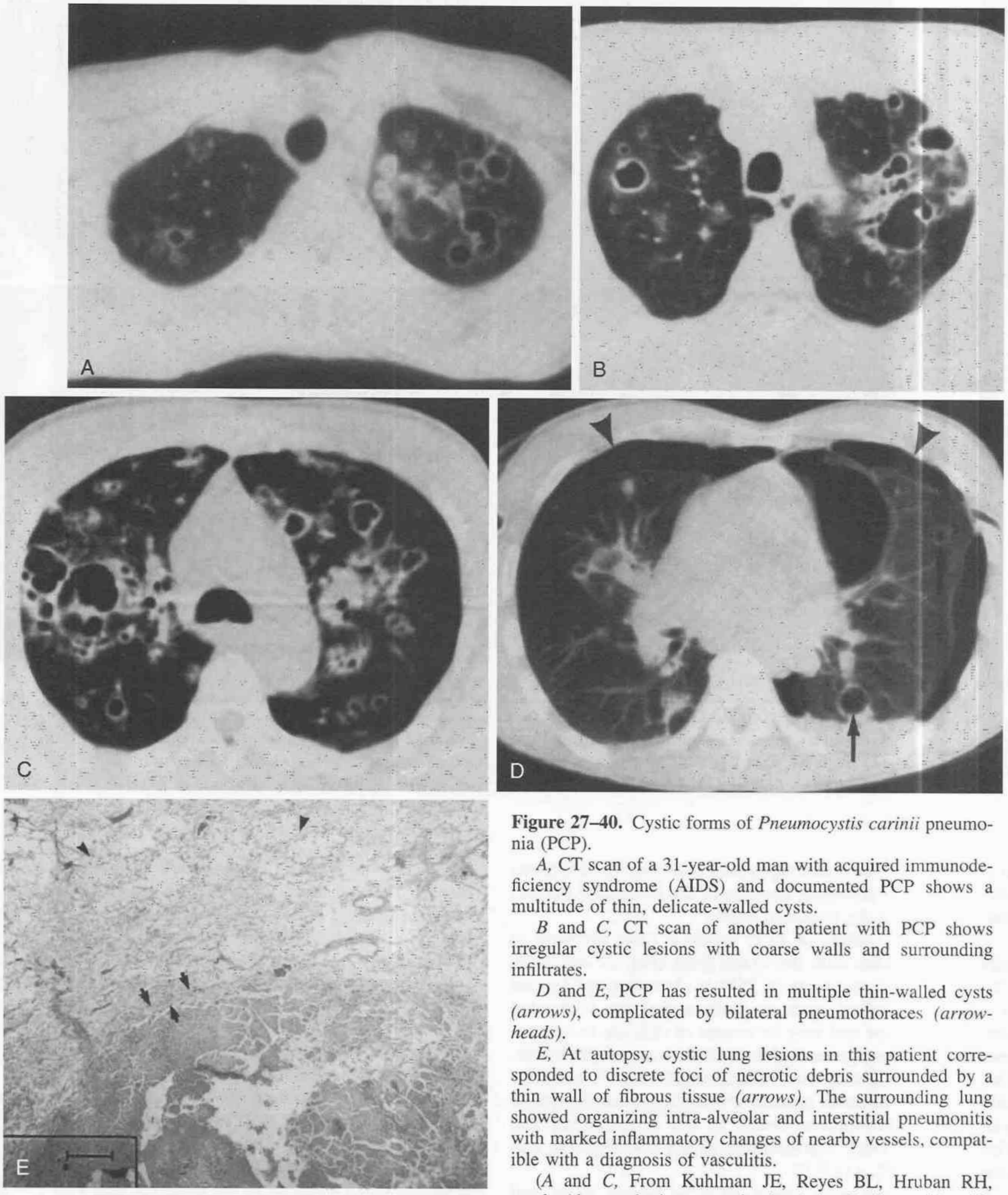

Figure 27–40. Cystic forms of *Pneumocystis carinii* pneumonia (PCP).

A, CT scan of a 31-year-old man with acquired immunodeficiency syndrome (AIDS) and documented PCP shows a multitude of thin, delicate-walled cysts.

B and *C,* CT scan of another patient with PCP shows irregular cystic lesions with coarse walls and surrounding infiltrates.

D and *E,* PCP has resulted in multiple thin-walled cysts *(arrows),* complicated by bilateral pneumothoraces *(arrowheads).*

E, At autopsy, cystic lung lesions in this patient corresponded to discrete foci of necrotic debris surrounded by a thin wall of fibrous tissue *(arrows).* The surrounding lung showed organizing intra-alveolar and interstitial pneumonitis with marked inflammatory changes of nearby vessels, compatible with a diagnosis of vasculitis.

(*A* and *C,* From Kuhlman JE, Reyes BL, Hruban RH, et al: Abnormal air spaces in the lung. Radiographics 13: 47–75, 1993.)

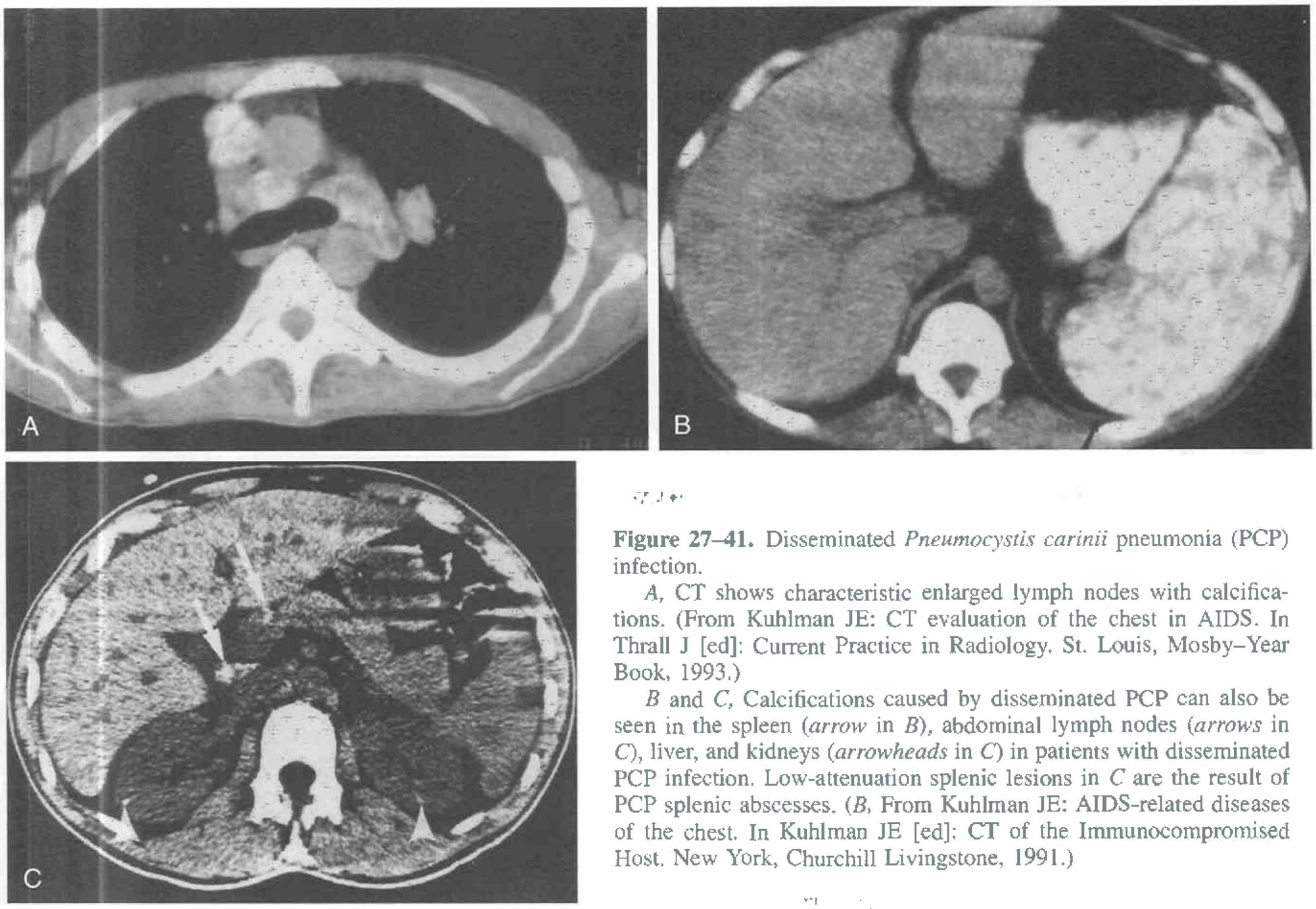

Figure 27–41. Disseminated *Pneumocystis carinii* pneumonia (PCP) infection.

A, CT shows characteristic enlarged lymph nodes with calcifications. (From Kuhlman JE: CT evaluation of the chest in AIDS. In Thrall J [ed]: Current Practice in Radiology. St. Louis, Mosby–Year Book, 1993.)

B and *C,* Calcifications caused by disseminated PCP can also be seen in the spleen (*arrow* in *B*), abdominal lymph nodes (*arrows* in *C*), liver, and kidneys (*arrowheads* in *C*) in patients with disseminated PCP infection. Low-attenuation splenic lesions in *C* are the result of PCP splenic abscesses. (*B,* From Kuhlman JE: AIDS-related diseases of the chest. In Kuhlman JE [ed]: CT of the Immunocompromised Host. New York, Churchill Livingstone, 1991.)

or Kaposi's sarcoma. Although less well recognized, PCP infection can also cause airway abnormalities, including bronchiolitis and bronchiolitis obliterans.[20a]

Several ancillary CT findings may be identified in patients with PCP or HIV disease. Apical and paraseptal bullae and spontaneous pneumothoraces are often noted in these relatively young patients (Fig. 27–42 and see Fig. 27–40).[15, 111, 139, 170, 195] In a patient with AIDS, pneumothoraces are often difficult to resolve because of persistent air leaks. They may require more invasive procedures than simple chest tube placement, including pleurodesis, lung stapling, or pleurectomy to reexpand the lung.

Fungal Infection

In patients with AIDS, fungal infections involving the lungs usually present as multiple nodules or cavities (Fig. 27–43).[96, 99, 105, 164] When present, fungal lung infection usually suggests disseminated disease. Other nonpulmonary manifestations of fungal disease, such as CT findings of esophagitis with esophageal wall thickening or focal lesions in the liver, may be the first indication of a disseminated fungal infection both in patients with AIDS and in other immunocompromised hosts (Figs. 27–44 and 27–45).

Any number of fungal species may cause pulmonary infection in the AIDS patient, including *Candida albicans*, *Coccidioides immitis*, *Histoplasma capsulatum*, and *Cryptococcus neoformans*. Infections caused by *Aspergillus* occur in patients with AIDS but much less frequently than they occur in other immunocompromised patients such as those with leukemia and prolonged neutropenia. This is because the body's immune response to *Aspergillus* infection requires only intact neutrophils and macrophages rather than healthy T cells or antibodies.

Neutrophil function is relatively preserved in AIDS patients until end stages of the disease. *Aspergillus* infections are seen, however, in AIDS patients who are taking corticosteroids or multidrug regimens that suppress neutrophil counts. *Cryptococcus* is the most common fungal pathogen to affect the lungs in patients with AIDS, almost always (>90% of cases) in conjunction with infection of the central nervous system.

Nocardial Infection

Nocardia is yet another opportunistic organism that is increasingly being recognized in the patient with AIDS.[96, 99, 105] On CT scans, *Nocardia* infection may start out as a small inflammatory nodule but eventually develops into a cavitary mass or more extensive cavitary pneumonia involving one or more segments or lobes of the lung (Fig. 27–46).

Although the unusual opportunistic infections are usually emphasized in regard to pulmonary infections in AIDS, it is important to keep in mind that bacterial infections, often severe, aggressive, and recurrent ones, occur fre-

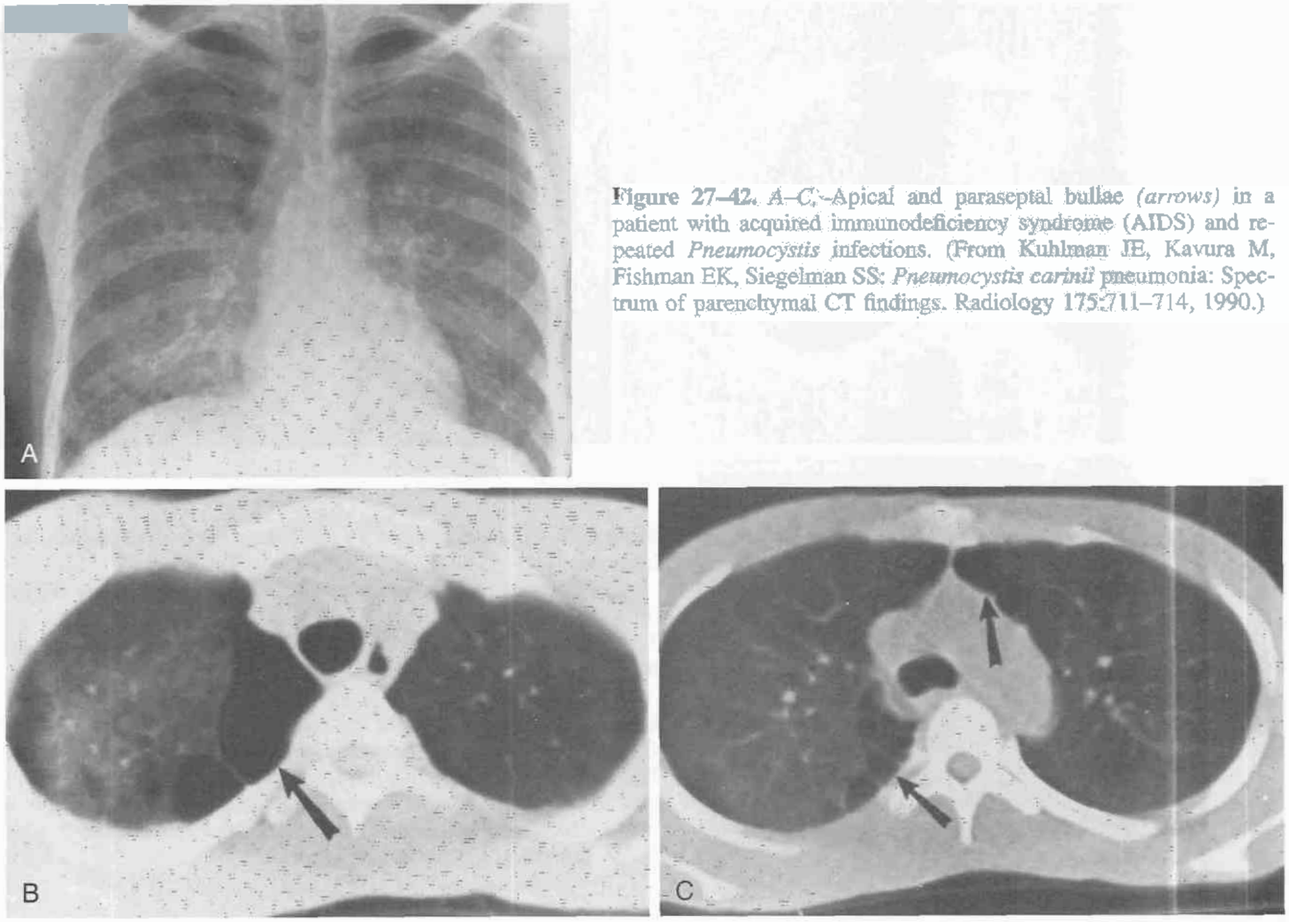

Figure 27–42. *A–C,* Apical and paraseptal bullae *(arrows)* in a patient with acquired immunodeficiency syndrome (AIDS) and repeated *Pneumocystis* infections. (From Kuhlman JE, Kavuru M, Fishman EK, Siegelman SS: *Pneumocystis carinii* pneumonia: Spectrum of parenchymal CT findings. Radiology 175:711–714, 1990.)

quently in patients with AIDS, including those caused by *Streptococcus pneumoniae*, *Staphylococcus pneumoniae*, and *Haemophilus influenzae*.

Tuberculosis

Of increasing concern is the resurgence of TB as a significant communicable pulmonary infection in the United States, resulting in part from the AIDS epidemic.[224] Emergence of multiresistant strains poses an ever-growing threat to public health on a global scale.

CT manifestations of pulmonary TB depend to a large extent on the health of the individual's immune system (Figs. 27–47 to 27–55). In the immunocompetent host, cavitation is one of the hallmarks of reactivation TB.[56, 167] Cavities develop when centers of granulomatous reaction to the TB bacillus undergo caseation necrosis. On CT scans, cavities owing to TB can be thick-walled or thin-walled and are indistinguishable from those caused by other atypical mycobacterial species.[6, 36, 56, 134, 167, 238]

Often with the development of tuberculous cavitation, the necrotizing process erodes into the tracheobronchial tree and the expelled tuberculous material spreads by the endobronchial route to other parts of the lung.

Typical CT features of bronchogenic spread include patchy areas of air space disease consisting of poorly defined nodular opacities measuring from 3 to 10 mm in diameter.[56, 59, 80a, 167] Compared with the smaller discrete nodules found in miliary TB,[8, 71] the nodular opacities seen in bronchogenic spread are nonuniform in size and unevenly distributed.

Various terms have been used to describe these nodular opacities, including acinar nodules, acinose lesions, acinar shadows, and tree-in-bud opacities.[80a] Pathologically, the lesions seen on CT scans correspond to peribronchiolar foci of infection and granulomatous reaction that are centered around the terminal respiratory bronchioles and their surrounding alveoli.[10, 56, 80a, 167, 182] In cases of suspected TB, CT can be used to identify a small or occult cavity that is the source of the bronchogenic spread and to demonstrate the full extent of the infection, which is often widely scattered in both lungs.

If the host's immune system and the ability to mount a granulomatous response are intact, the reactivated infection is often contained and healing begins with the deposition of collagen and scar tissue around areas of caseous necrosis.[8] Eventually, dystrophic calcifications form within granulomatous nodules, lymph nodes, and fibrotic strands, and the lung assumes the characteristic appearance of chronic fibrocalcific TB. Further scarring leads to lung distortion, bronchiectasis, volume loss, and cicatrization atelectasis and compensatory emphysema. Fibrotic, masslike lesions may form in the lung apices and may be difficult to distinguish from apical lung cancers or scar carcinomas on the basis of CT appearances alone.[238]

Text continued on page 878

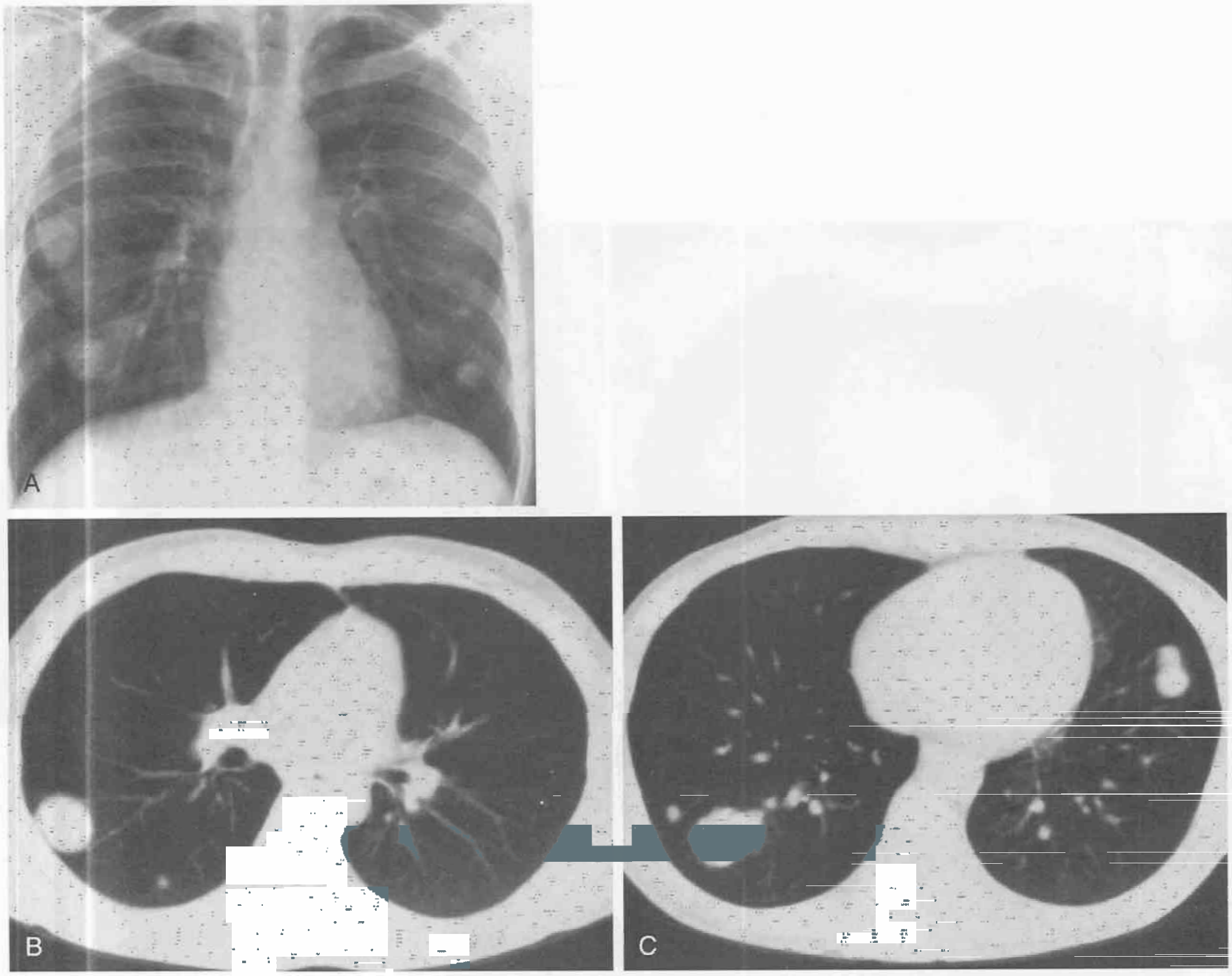

Figure 27–43. Disseminated cryptococcal infection. Chest film (*A*) and CT (*B*, *C*) show multiple pulmonary nodules.

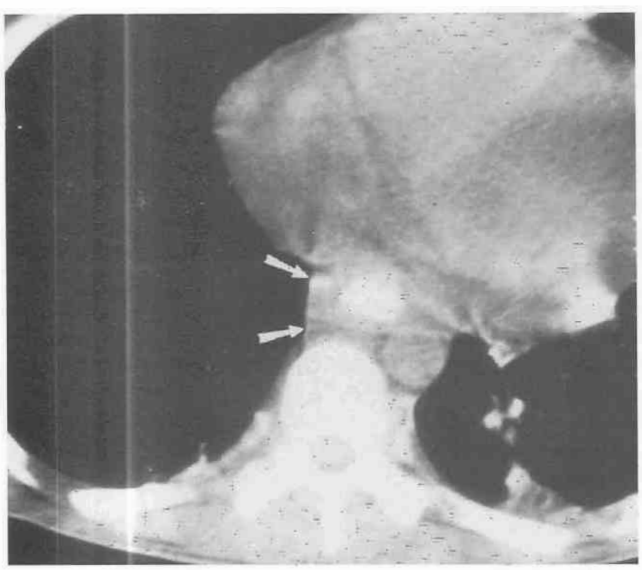

Figure 27–44. Cytomegaloviral esophagitis. Marked thickening of the esophageal wall is evident on the CT scan. Oral contrast material is retained within the dilated, inflamed esophagus. (From Kuhlman JE: AIDS-related diseases of the chest. In Kuhlman JE [ed]: CT of the Immunocompromised Host. New York, Churchill Livingstone, 1991.)

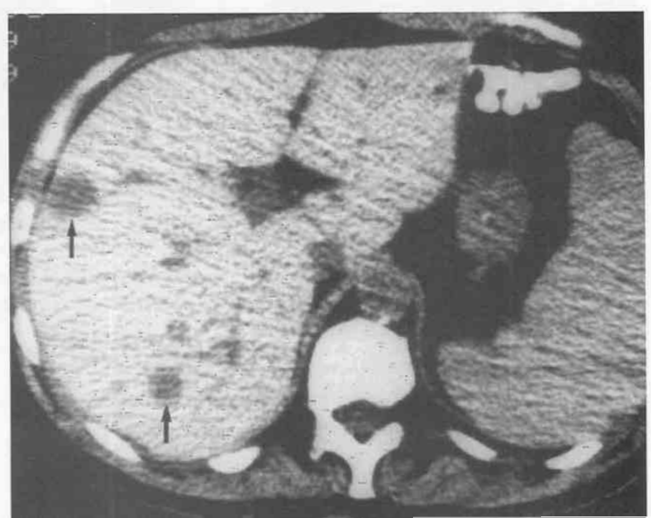

Figure 27–45. Disseminated candidiasis. CT shows multiple filling defects in the liver caused by fungal abscesses *(arrows)*. (From Kuhlman JE: CT of the immunocompromised and acutely ill patient. In Zerhouni EA [ed]: CT and MRI of the Thorax. New York, Churchill Livingstone, 1990.)

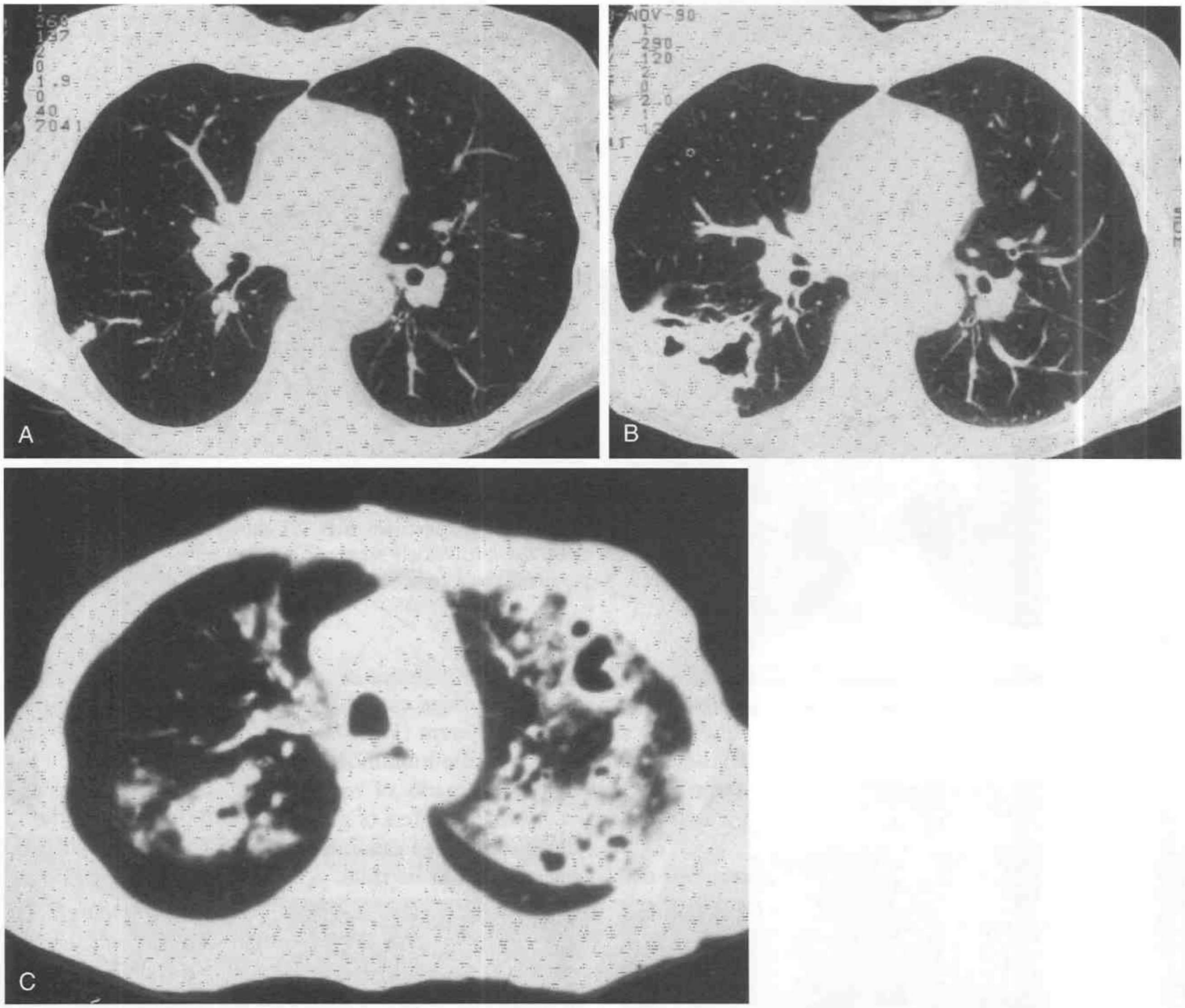

Figure 27–46. Nocardiosis in a patient with acquired immunodeficiency syndrome (AIDS). *A*, Initial CT scan on a patient with positive status for human immunodeficiency virus (HIV) infection shows a small inflammatory nodule in the right lower lobe. *B*, *Nocardia* infection has progressed to a large necrotic cavity. *C*, *Nocardia* infection in another patient with AIDS presented as a multilobar cavitary pneumonia. (*C*, From Kuhlman JE: AIDS-related diseases of the chest. In Kuhlman JE [ed]: CT of the Immunocompromised Host. New York, Churchill Livingstone, 1991.)

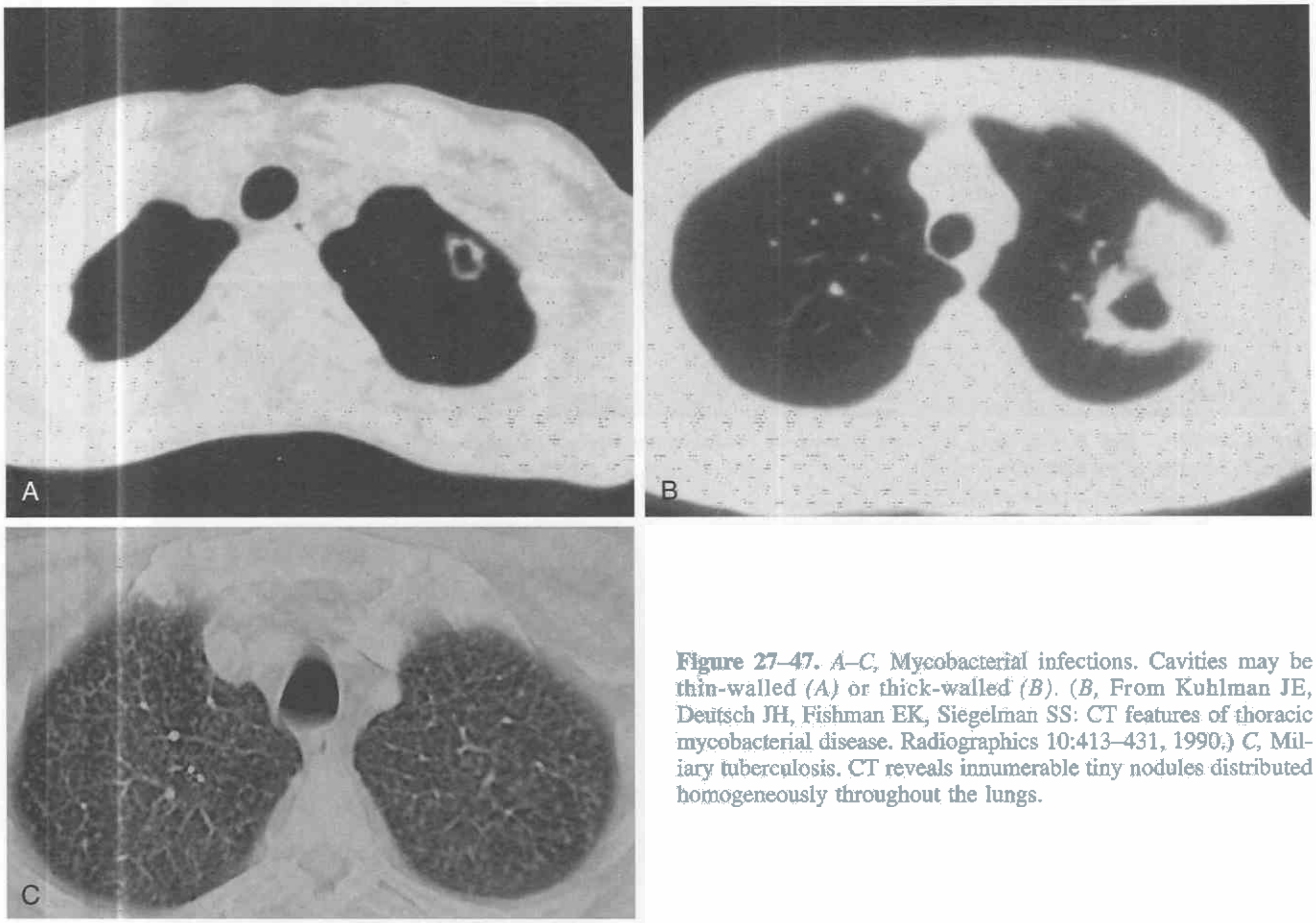

Figure 27–47. *A–C*, Mycobacterial infections. Cavities may be thin-walled *(A)* or thick-walled *(B)*. (*B*, From Kuhlman JE, Deutsch JH, Fishman EK, Siegelman SS: CT features of thoracic mycobacterial disease. Radiographics 10:413–431, 1990.) *C*, Miliary tuberculosis. CT reveals innumerable tiny nodules distributed homogeneously throughout the lungs.

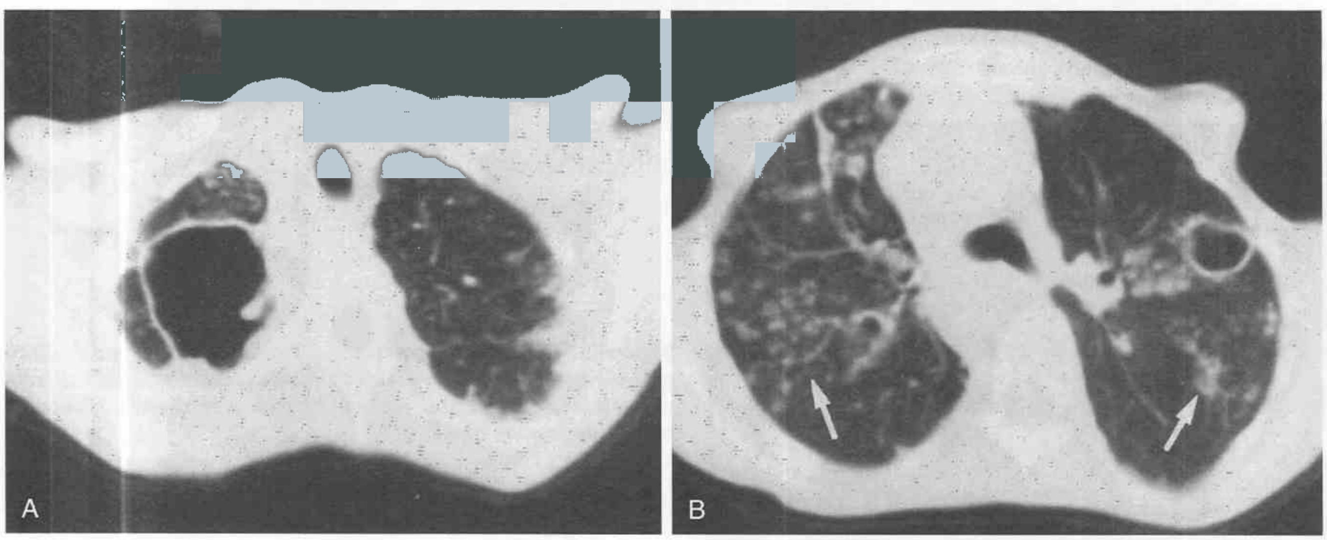

Figure 27–48. CT features of bronchogenic spread of mycobacterial disease. *A* and *B*, CT scan shows a large cavity in the right upper lobe and a smaller ca[redacted] on the left. Widely scattered areas of bronchogenic spread *(arrows)* are identified, demonstrating a "tree-in-bud" pattern. The patient has a right-sided aortic arch.

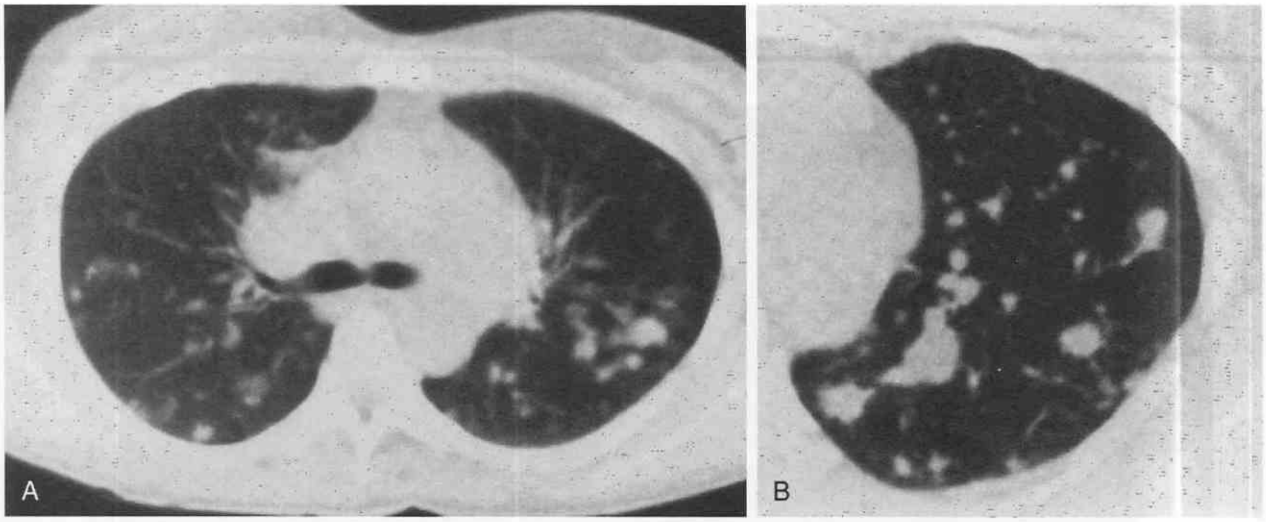

Figure 27–49. *A* and *B,* On these CT scans, areas of bronchogenic spread of tuberculosis appear as poorly marginated, "fluffy" nodular densities of variable size.

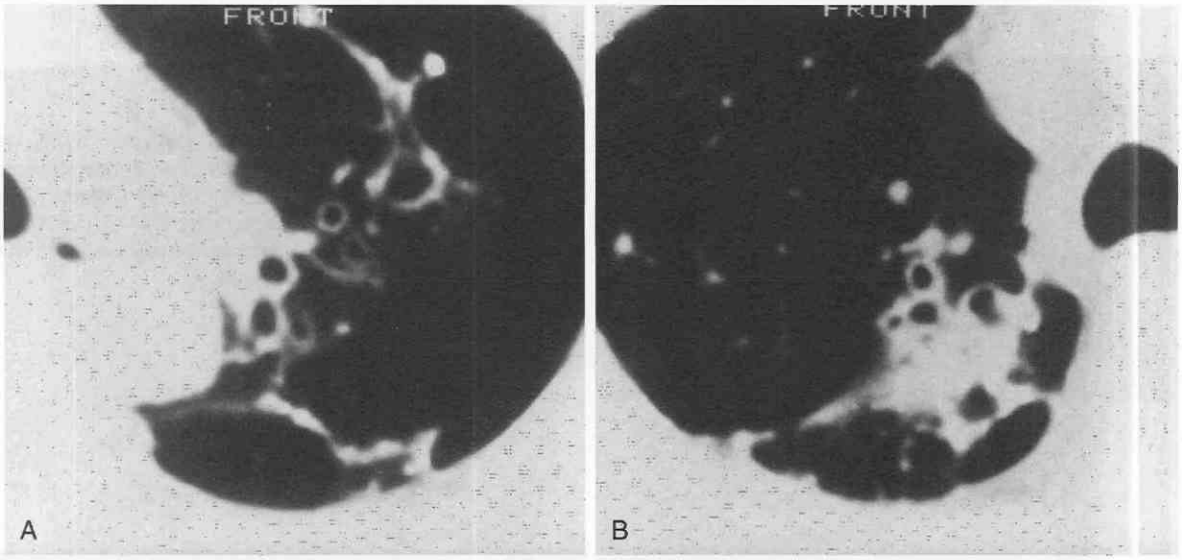

Figure 27–50. *A* and *B,* CT features of chronic fibrocalcific tuberculosis (TB) include scarring, calcified granulomata, bronchiectasis, architectural distortion, and fibrotic masses.

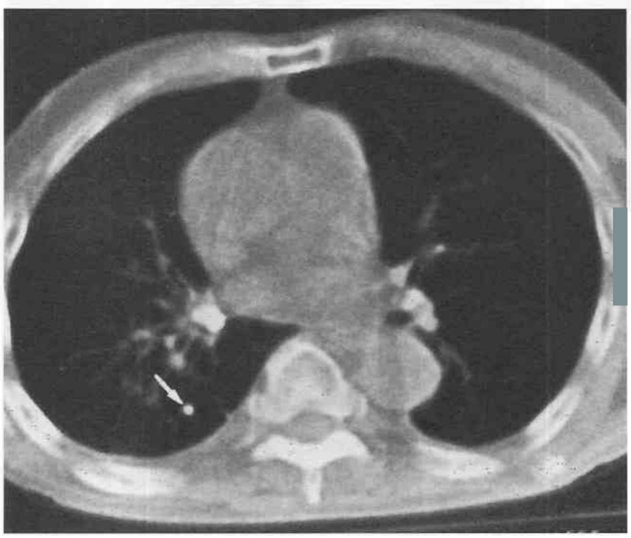

Figure 27–51. Ranke's complex. CT image shows the calcified parenchymal scar (Ghon's lesion) *(arrow)* and the calcified hilar nodes representing healed regional lymphatic involvement from the initial tuberculosis infection.

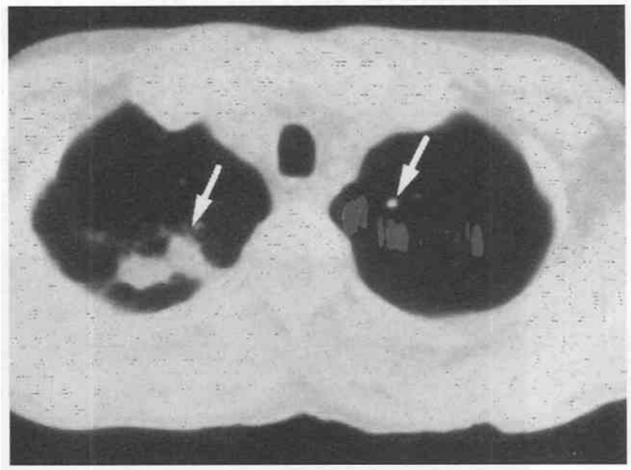

Figure 27–52. Simon's foci, an example of healed sites of tuberculosis (TB) seeded to the lung apices at the time of the primary TB infection. The masslike opacity seen in the right apex was the result of healed TB in this case, but on the basis of the CT appearance alone, it is indistinguishable from that of lung cancer. Such opacities require close, serial follow-up to ensure stability in size over time or biopsy, in some cases, to exclude neoplasm. (From Kuhlman JE, Deutsch JH, Fishman EK, Siegelman SS: CT features of thoracic mycobacterial disease. Radiographics 10:413–431, 1990.)

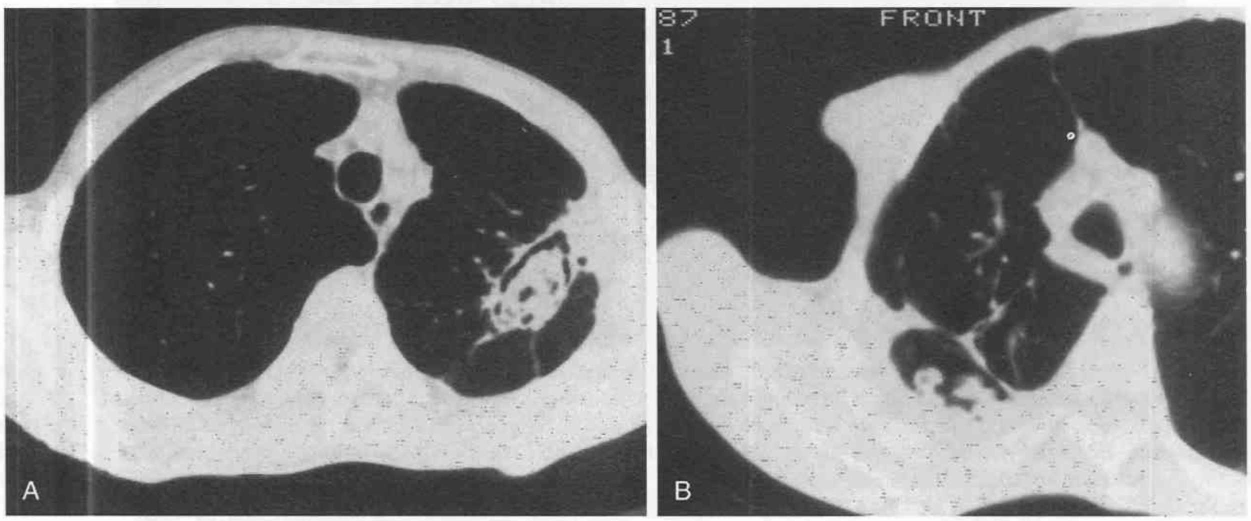

Figure 27–53. *A* and *B,* Aspergillomas, growing in old tuberculous cavities, are identified on CT.

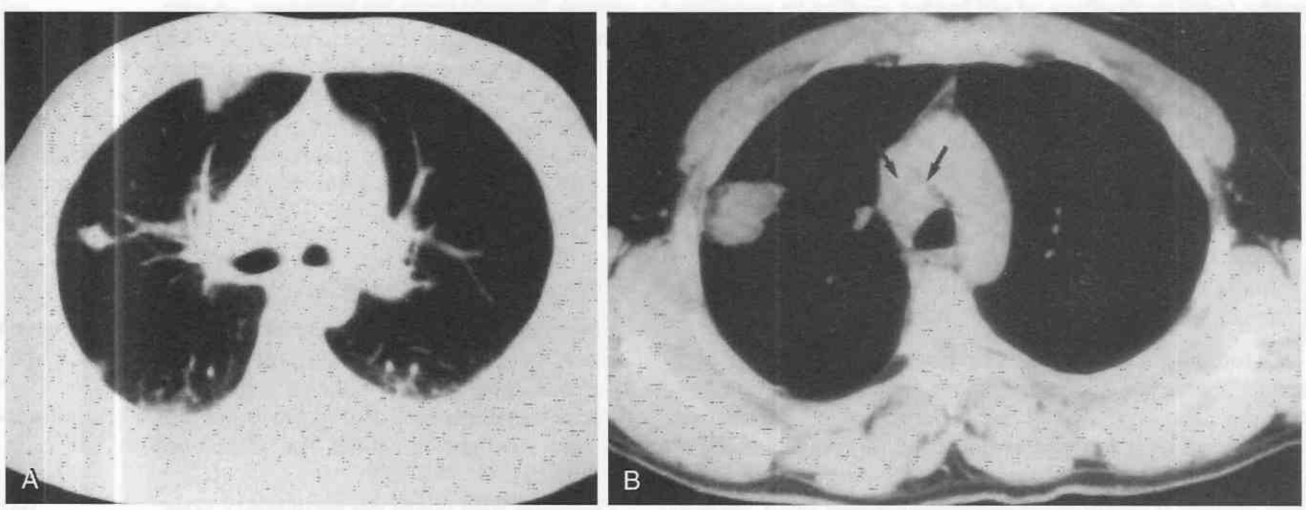

Figure 27–54. *A* and *B,* Tuberculosis in a patient with acquired immunodeficiency syndrome (AIDS). CT shows multiple inflammatory lung masses and bulky mediastinal nodes *(arrows)* resulting from tuberculosis (TB). Lymphadenopathy is the rule rather than the exception in patients with AIDS and TB. (From Kuhlman JE: CT evaluation of the chest in AIDS. In Thrall J [ed]: Current Practice in Radiology. St. Louis, Mosby–Year Book, 1993.)

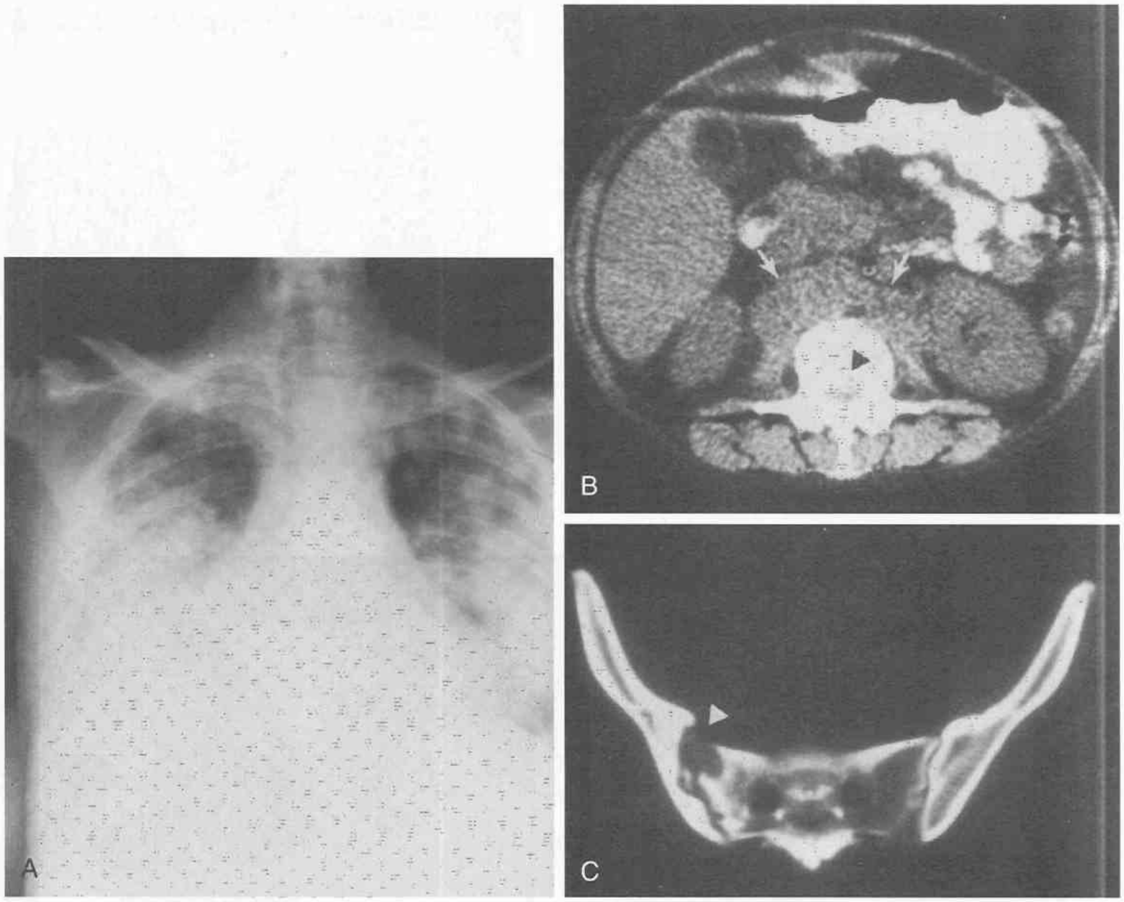

Figure 27–55. Tuberculosis in a patient with advanced acquired immunodeficiency syndrome (AIDS). A woman with status positive for human immunodeficiency virus (HIV) infection was shown at autopsy to have bilateral pulmonary infiltrates (*A*), extensive lymphadenopathy (*B, arrows*), and multiple lytic bone lesions (*B* and *C, arrowheads*) caused by widely disseminated tuberculosis. (From Kuhlman JE: AIDS-related diseases of the chest. In Kuhlman JE [ed]: CT of the Immunocompromised Host. New York, Churchill Livingstone, 1991.)

Frequently on CT scans, evidence of earlier TB infection can be found in the form of old healed cavities or sequelae, such as[56, 102]:

1. *Ghon's lesion,* the parenchymal scar or granuloma that occurs at the site of initial TB infection. This lesion is often calcified.
2. *Ranke's complex,* consisting of a parenchymal scar and the associated calcified lymph nodes in the pulmonary hilum or mediastinum. The presence of this complex suggests regional lymphatic spread.
3. *Simon's foci,* or healed residua of TB seeded to the lung apices at the time of primary infection.

Chronic TB cavities may permanently scar the lung and remain open even after sterilization. These chronic cavities may become complicated by superimposed infection or colonization with *Aspergillus* fungi that form mycetomas.[190]

Although TB produces many chronic lung changes, disease activity cannot be determined on the basis of CT appearances alone. Fibrotic areas of lung and cavities that look inactive on chest radiographs or CT may in fact harbor viable organisms.[56, 238] The radiologic stability of TB-induced lung changes, however, can be assessed with serial chest films or serial CT scans. Follow-up CT examinations have become an important adjunct to sputum cultures in assessing response to treatment in infected patients.

In part because of the declining exposure rate of children to TB, a larger number of first-time exposures are occurring in adulthood, making cases of primary rather than reactivation TB in the adult more common than before. Mediastinal and hilar adenopathy is often an indication of primary TB infection.[81, 123]

Tuberculosis in Special Patient Populations

A number of individuals are at increased risk for development of active TB, including older, debilitated, and malnourished patients and patients with AIDS.[56, 81, 154, 167, 194] Special considerations also apply to patients with sarcoidosis and silicosis, in whom the prevalence of TB is increased.[56, 81, 154, 167, 194, 238]

Patients with AIDS are particularly susceptible to mycobacterial infections both from *Mycobacterium tuberculosis* and from other atypical organisms, such as *M. avium–intracellulare* (MAI), *M. avium complex* (MAC), and *M. kansasii.*[56, 134] In 10% to 20% of patients with AIDS, *M.*

avium–intracellulare infections are detected sometime during their life from blood, sputum, or bone marrow cultures. At autopsy, more than 50% of these patients are found to be infected. Despite these statistics, pulmonary infiltrates caused by *M. avium–intracellulare* are considerably less common than those caused by TB.[134]

The most common CT manifestation of *M. avium–intracellulare* infection is diffuse adenopathy. Regardless of mycobacterial species, however, the normal granulomatous response to mycobacterial infection is poor or absent in the patient with AIDS, and disseminated disease is more common than in the immunologically competent host.[6, 56, 134]

The AIDS population is particularly vulnerable to the spread of TB. In some parts of Africa, the combination of AIDS and TB has become epidemic. Manifestations of TB in the patient with AIDS depend on the degree of immunosuppression. In a patient with early HIV infection and milder immunosuppression, TB presents in a more classic fashion with cavitary disease and bronchogenic spread. TB that occurs in the setting of more severe immunosuppression or full-blown AIDS is more often atypical and aggressive in its manifestations, presenting in a manner more reminiscent of primary TB, primary progressive TB, or miliary TB.[96, 102]

In the patient with advanced AIDS, widely disseminated and extrapulmonary disease and multiple pulmonary masses with significant adenopathy are not uncommon presentations of TB. Mediastinal and hilar adenopathy as a manifestation of TB in an AIDS patient is the rule rather than the exception. After administration of contrast material, tuberculous lymph nodes demonstrate characteristic low-attenuation necrotic centers and rim enhancement on CT scans.[12, 81, 123, 154] In addition, traditional tests for TB exposure (e.g., the tuberculin skin test) are unreliable in patients with AIDS because most patients are anergic.

M. avium–intracellulare *in Older Women*

M. avium–intracellulare infection can also strike otherwise healthy, immunocompetent hosts. A distinct subtype has been reported in women between ages 50 and 90 years who have no underlying illness but present with a chronic, persistent cough. This subtype has a fairly characteristic CT appearance, with scattered areas of mild tubular bronchiectasis associated with nodular opacities and tree-in-bud forms. Cavitation is less common than in TB.[70a, 153a]

Pulmonary Drug Toxicity

Early detection of drug-induced lung toxicity is another application of HRCT that is under current investigation.* Patients with respiratory symptoms who are receiving bleomycin, methotrexate, amiodarone, or other potentially toxic agents to the lung benefit from CT evaluation (Figs. 27–56 to 27–61). Early detection of drug-induced pulmonary damage increases the likelihood that lung damage will be reversible when the drug is withdrawn.

*See References 16, 17, 26, 28, 115, 116, 163, 172, 187, 188, and 209.

Bleomycin

In cases of *bleomycin lung,* HRCT has been more sensitive than chest radiographs in detecting early pulmonary toxicity, more accurate in quantifying the extent of pulmonary damage, and more helpful in monitoring disease progression or resolution.[16, 17] The extent of pulmonary damage, as seen on CT scans, correlates well with measurements of impaired gas transfer and pulmonary function.[16, 17]

CT features of bleomycin lung toxicity include linear reticulations, fibrotic bands, and nodular opacities that may mimic pulmonary metastases or recurrent tumor (see Fig. 27–58).[16, 163, 188] These changes often appear first in the periphery of the lung and at the lung bases, paralleling the pleural surfaces (see Fig. 27–37).[16, 163, 188] As the pulmonary toxicity becomes more severe, the reticular and nodular opacities coalesce to form large confluent opacities. Diffuse air space disease can also be seen with acute bleomycin

Regardless of the offending agent, early CT findings of drug-induced pulmonary toxicity are often confined to the subpleural zone. The apparent susceptibility of this region to lung toxicity may be related to the limited collateral airflow within the region or to the increased pressure and friction the zone experiences from the overlying pleura.[54]

Amiodarone

Amiodarone is an antiarrhythmic agent that can cause significant and potentially irreversible pulmonary toxicity.[62, 132, 175, 237] The drug is used primarily to treat refractory life-threatening arrhythmias. Early recognition of pulmonary toxicity is important because prompt discontinuation of the drug often results in resolution of toxicity.[62, 175]

Unfortunately, few radiographic or laboratory findings are specific for amiodarone toxicity. Symptoms are also nonspecific, making early diagnosis of pulmonary toxicity on the basis of clinical evidence difficult. Onset of symptoms may be insidious, and symptoms caused by amiodarone toxicity, such as pleuritic chest pain, shortness of breath, malaise, and low-grade fever, may be similarly produced by cardiac decompensation, pneumonia, or pulmonary infarction, all common concurrent problems in heart disease patients.[62, 175] Fortunately, because of its unique chemical composition (which contains three iodine moieties), amiodarone—when deposited in sufficient quantities within the lung—can be recognized by its high CT attenuation, which aids in diagnosis (see Figs. 27–59 to 27–61).[28, 115, 116, 172, 187, 209]

On unenhanced scans, CT features of amiodarone lung toxicity include areas of consolidation or focal atelectasis showing high CT attenuation in the range of 80 to 110 HU.[28, 115, 116, 172, 187, 209] The high-attenuation areas frequently abut the pleura, show adjacent pleural reaction, and may be wedge-shaped. Increased attenuation is also frequently demonstrated in the liver, spleen, thyroid gland, and occasionally in the heart muscle. Nonspecific pulmonary infiltrates, interstitial infiltrates, mixed alveolar and interstitial disease, and conglomerate masses may also be seen.[28, 115, 116, 172, 187, 209]

Nonenhanced CT findings of high-attenuation parenchymal abnormalities are thought to be related to the iodinated

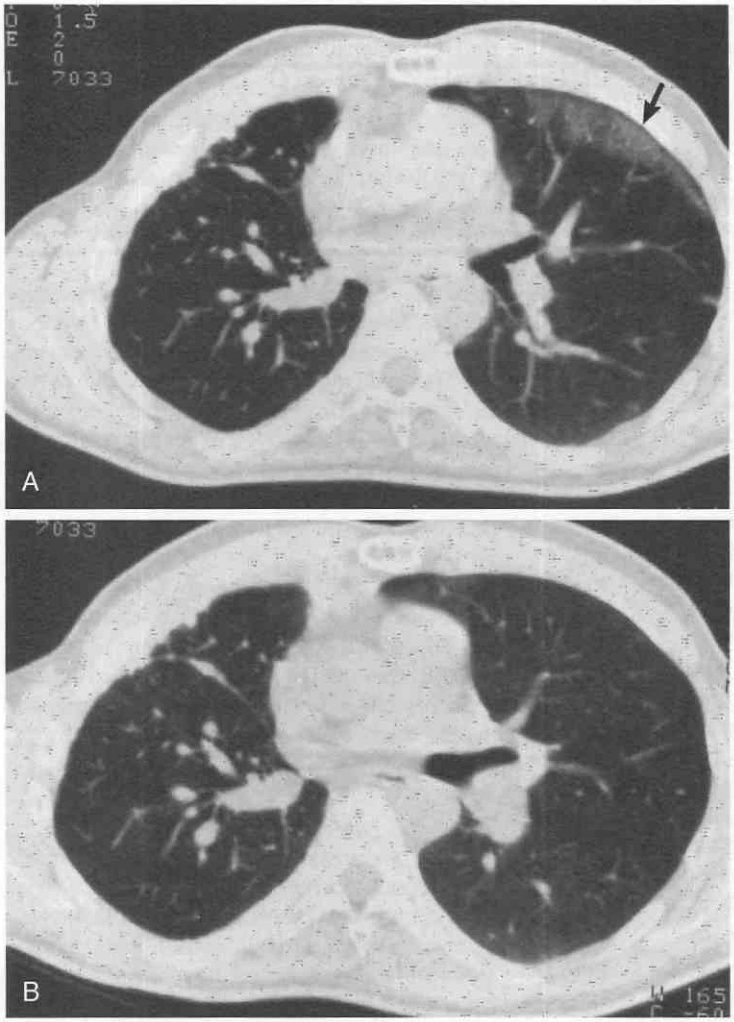

Figure 27–56. CT detection of drug-induced lung toxicity. Patient with recurrent lung cancer receiving ipomeanol, an investigational chemotherapeutic agent known to cause potential lung toxicity. *A,* CT shows development of a band of increased attenuation in the subpleural region, not detected on plain films *(arrow)*. *B,* After discontinuation of the drug, the abnormality resolved.

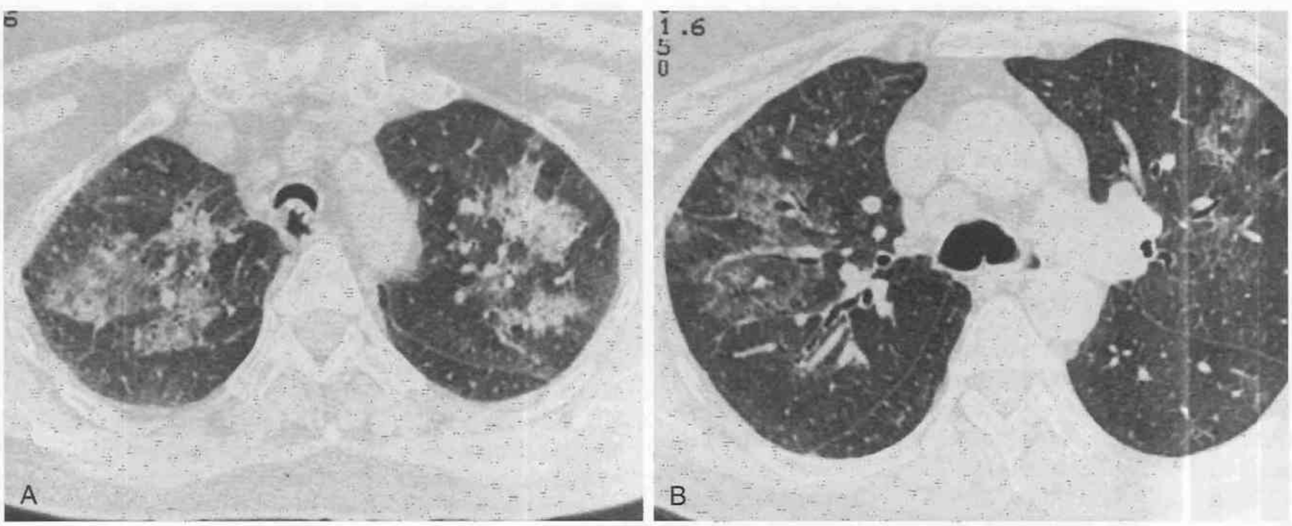

Figure 27–57. *A* and *B,* Methotrexate pulmonary toxicity. The patient, a 59-year-old woman who was taking methotrexate for treatment of severe psoriasis, experienced subacute onset of fatigue, shortness of breath, and a nonproductive cough. CT shows patchy "ground-glass" infiltrates that were difficult to appreciate on chest radiographs. Cultures were negative for infection, and a lung biopsy specimen showed changes consistent with a diagnosis of methotrexate lung toxicity.

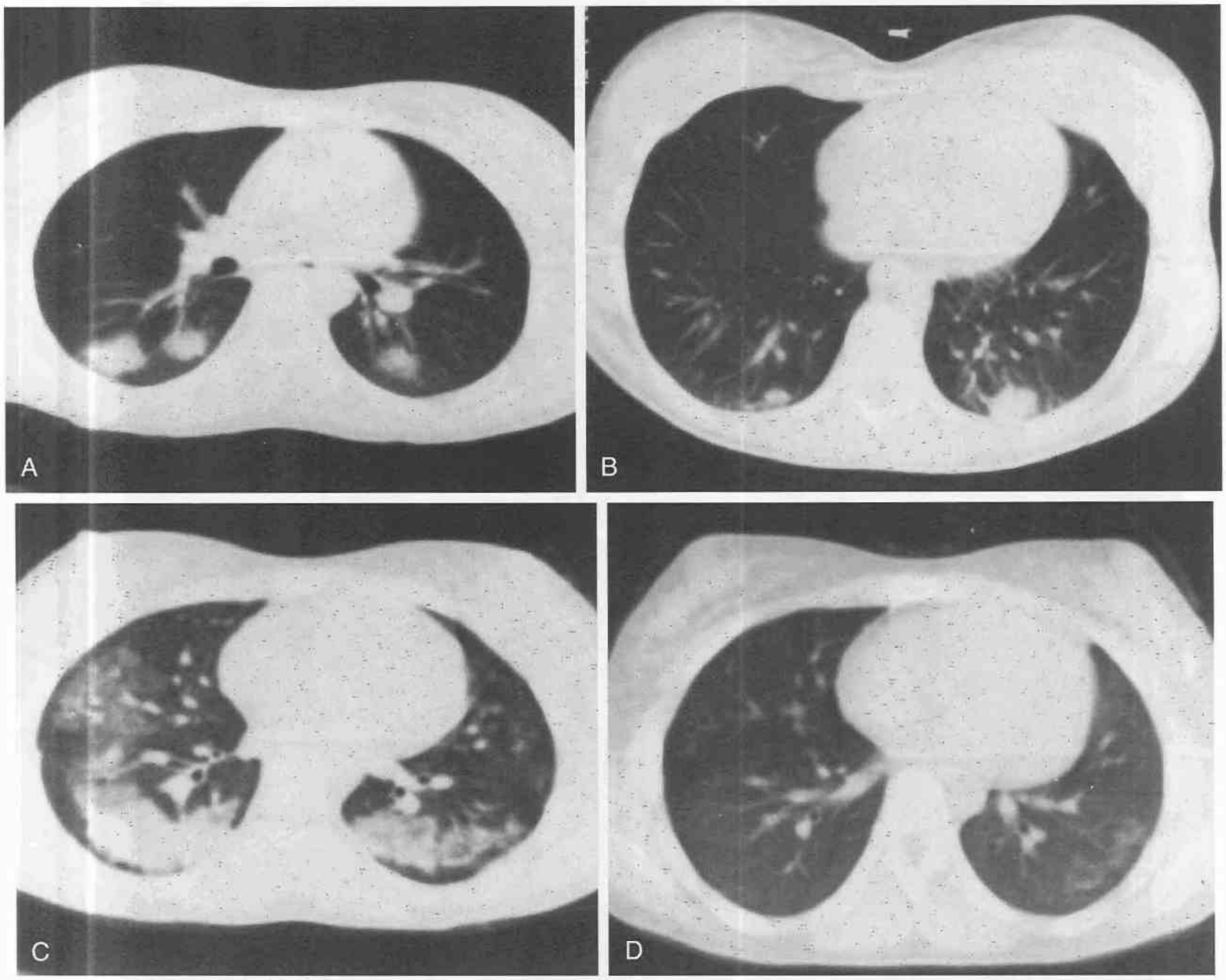

Figure 27–58. Bleomycin lung toxicity, CT features. *A* and *B*, CT shows nodular opacities, which may be mistaken for tumor recurrence or metastases but are actually caused by bleomycin toxicity, proven by biopsy. *C*, CT can be used to follow the progression or resolution of pulmonary toxicity. In this case, the nodular opacities progressed to larger areas of confluence. *D*, After discontinuation of the drug, a follow-up CT scan shows nearly complete resolution of the pulmonary lesions.

chemistry of the drug and its prolonged half-life within the lung.* Amiodarone is known to accumulate in high concentrations within the lung and the liver, where its half-life is 15 to 60 days.[137, 201] Trapped by foamy macrophages, the drug becomes incorporated within lysosomes, where the cationic, amphophilic drug interacts with phospholipids to form a drug-lipid complex that resists biodegradation.† Characteristic lamellar inclusion bodies form within the lysosomes and interfere with lipid degradation and surfactant turnover, ultimately inducing a fibrotic reaction within the lung. These unique properties of amiodarone and the use of CT to discriminate attenuation levels provide a means of identifying those patients with significant pulmonary accumulation of the drug.

Recognizing amiodarone-induced lung changes in nonenhanced CT scans is particularly important in those patients who present with pleuritic chest pain. At least three cases of acute pulmonary decompensation have been reported that occurred after pulmonary arteriography was attempted in patients who presented with pleuritic chest pain caused by amiodarone lung toxicity. Performing pulmonary arteriography in these patients to exclude pulmonary infarction should be avoided if possible.[237]

High-Attenuation Parenchymal Abnormalities

A few other disease processes can produce high-attenuation parenchymal abnormalities on CT scans, as follows:

1. *Metastatic pulmonary calcifications* occurring as the result of hyperparathyroidism from renal failure or from the infusion of large amounts of calcium salts in children with congenital heart disease can cause high-attenuation consolidations on CT scans.[115, 131]
2. Focal and multifocal, high-density lung opacities have been reported in cases of *amyloid*, probably resulting from dystrophic calcification within areas of amyloid accumulation.
3. *Pulmonary ossification* in patients with long-standing

*See References 9, 29, 39, 44, 67, 77, 85, 115, 116, 124, 137, 162, 187, 189, and 201.

†See references 9, 29, 39, 44, 62, 67, 77, 85, 124, 137, 162, and 189.

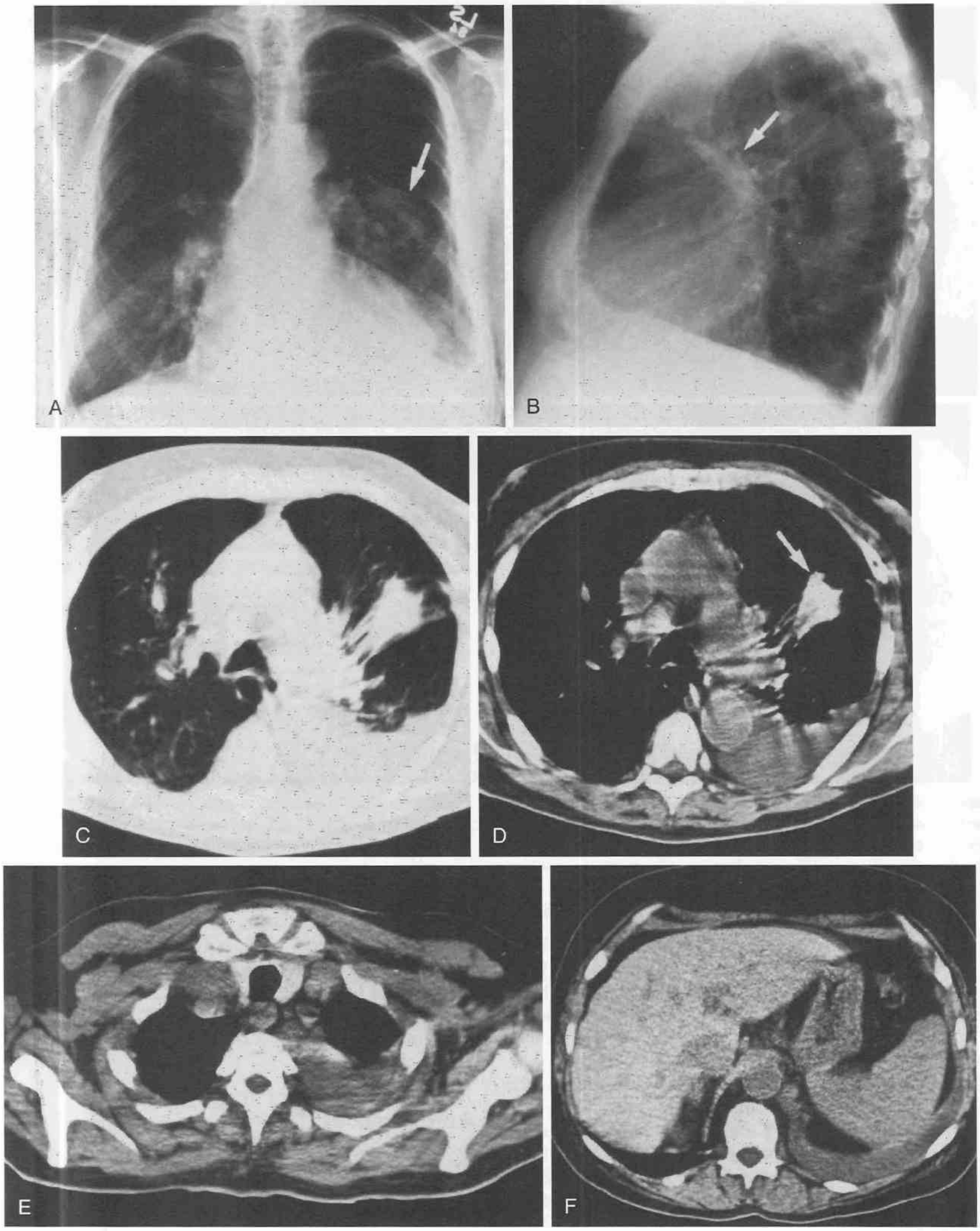

Figure 27–59. Amiodarone toxicity. A 69-year-old man with chronic obstructive pulmonary disease, ischemic cardiomyopathy, and ventricular arrhythmias required antiarrhythmic medication. He presented with a 2-week history of increasing shortness of breath and pleuritic chest pain.

A and *B*, Chest film shows ill-defined opacity or area of focal atelectasis *(arrows)* and left pleural effusion.

C and *D*. Nonenhanced CT scan shows the focal lung opacity demonstrating high attenuation on soft tissue window settings *(arrow)* compatible with a diagnosis of amiodarone toxicity. Bronchoscopy was negative for tumor and for infection and yielded abundant foamy macrophages.

E and *F*, Other CT evidence of amiodarone exposure includes dense thyroid and dense liver resulting from the iodine content of the drug, which accumulates in these organs.

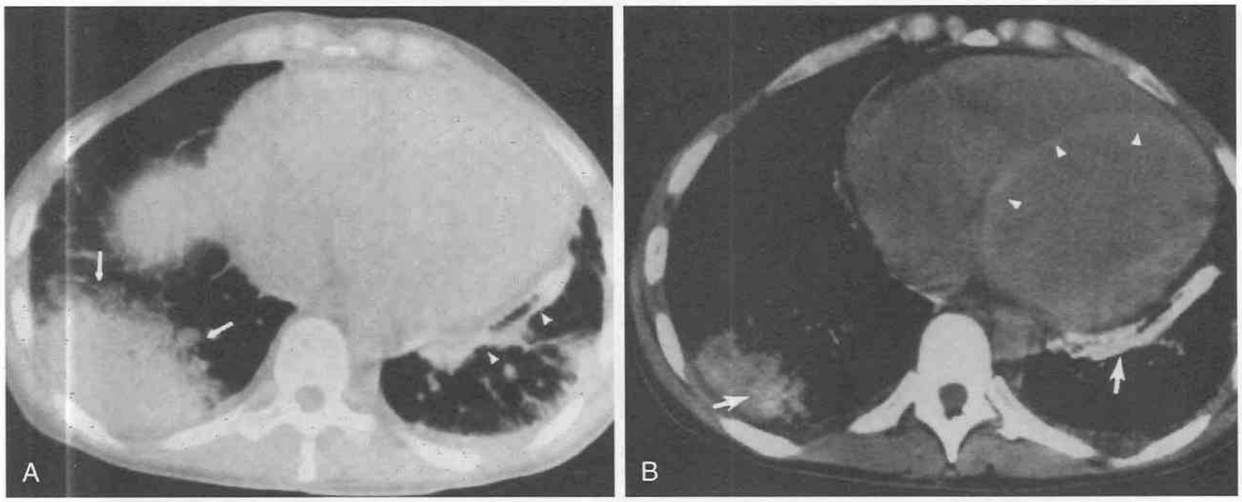

Figure 27–60. Amiodarone toxicity. *A* and *B*, The patient, a 40-year-old-woman with arrhythmias who had been taking amiodarone for 32 months, presented with pleuritic chest pain and shortness of breath. *A*, Noncontrast CT shows a large, wedge-shaped area of consolidation in the right lung base *(arrows)*. A band of atelectasis is noted adjacent to the left heart border *(arrowheads)*. *B*, Both areas demonstrate high attenuation on soft tissue window settings *(arrows)*. The increased attenuation of the heart muscle is a result of amiodarone deposition *(arrowheads)*. (From Kuhlman JE, Tergen C, Ren H, et al: Amiodarone pulmonary toxicity: CT findings in symptomatic patients. Radiology 177:121–125, 1990.)

mitral stenosis can produce high-density air space opacities in the lung parenchyma.[238a]

Occupational Lung Disease

The use of CT, especially HRCT, in the evaluation of occupational lung diseases is rapidly expanding.[3, 5, 86, 184] A number of reports suggest that HRCT is superior to conventional radiographs and standard CT in the detection of pulmonary damage resulting from asbestosis and pneumoconiosis. HRCT is being used to detect evidence of occupational lung disease, to determine the extent of the damage, and to follow the disease progression.

CT features of different types of pneumoconiosis are beginning to be recognized and characterized. HRCT findings that have been described in *silicosis* include micronodules, subpleural nodules, conglomerate masses, and focal emphysema (Fig. 27–62).[184]

CT has become an important adjunct to conventional radiographs in the evaluation of *asbestos-related diseases*.[3, 5, 86] CT is more sensitive and specific than plain films for identifying and documenting the presence of *pleural*

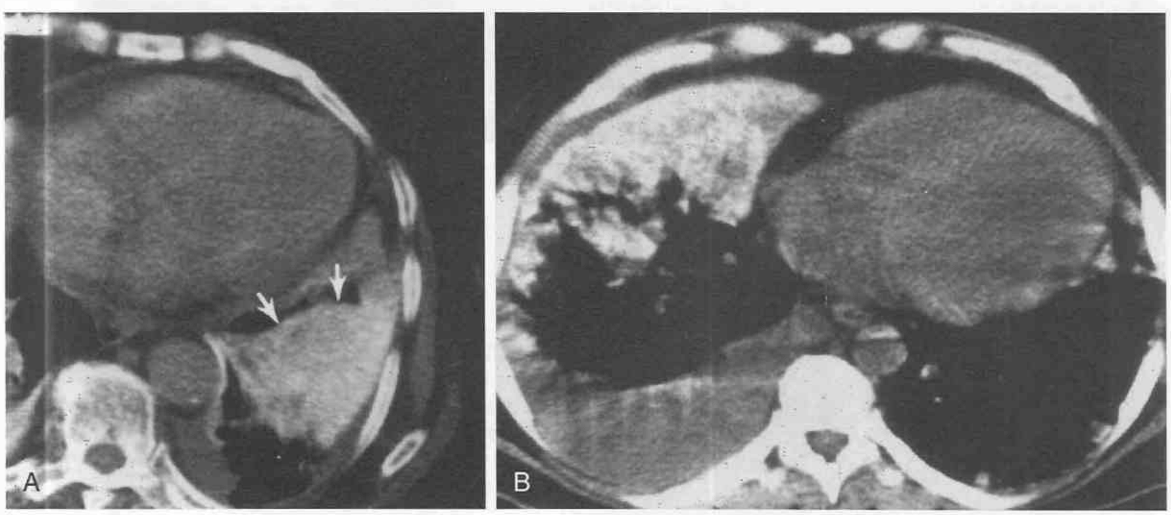

Figure 27–61. High-density infiltrates on noncontrast CT, differential diagnosis. *A*, High-density atelectatic lung measuring 105 Hounsfield units because of amiodarone toxicity. (From Kuhlman JE, Teigen C, Ken H, et al: Amiodarone pulmonary toxicity: CT findings in symptomatic patients. Radiology 177:121–125, 1990.) *B*, High-density consolidation in the right middle lobe in this patient was the result of metastatic pulmonary calcification of chronic renal failure in an area of pneumonia. (From Kuhlman JE, Ren H, Hutchins GM, Fishman EK: Fulminant pulmonary calcification complicating renal transplantation: CT demonstration. Radiology 173: 459–460, 1989.)

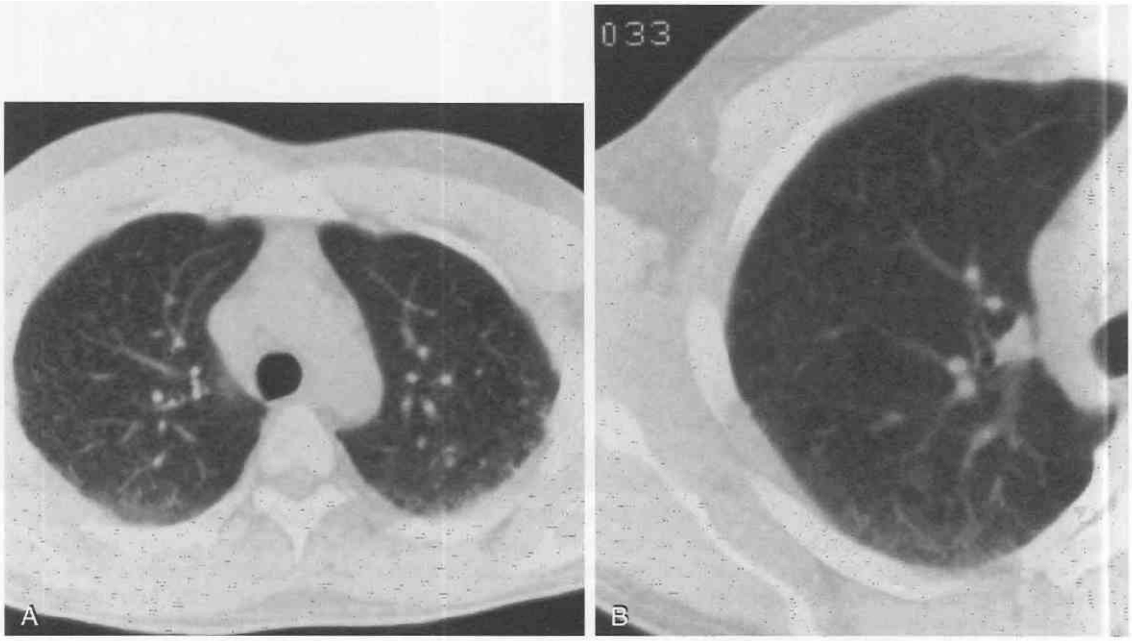

Figure 27–62. *A* and *B*, CT findings in a patient with silicosis. The diffuse profusion of micronodules is caused by silicosis. (From Kuhlman JE: CT of diffuse lung disease. Appl Radiol 20:17–21, 1991.)

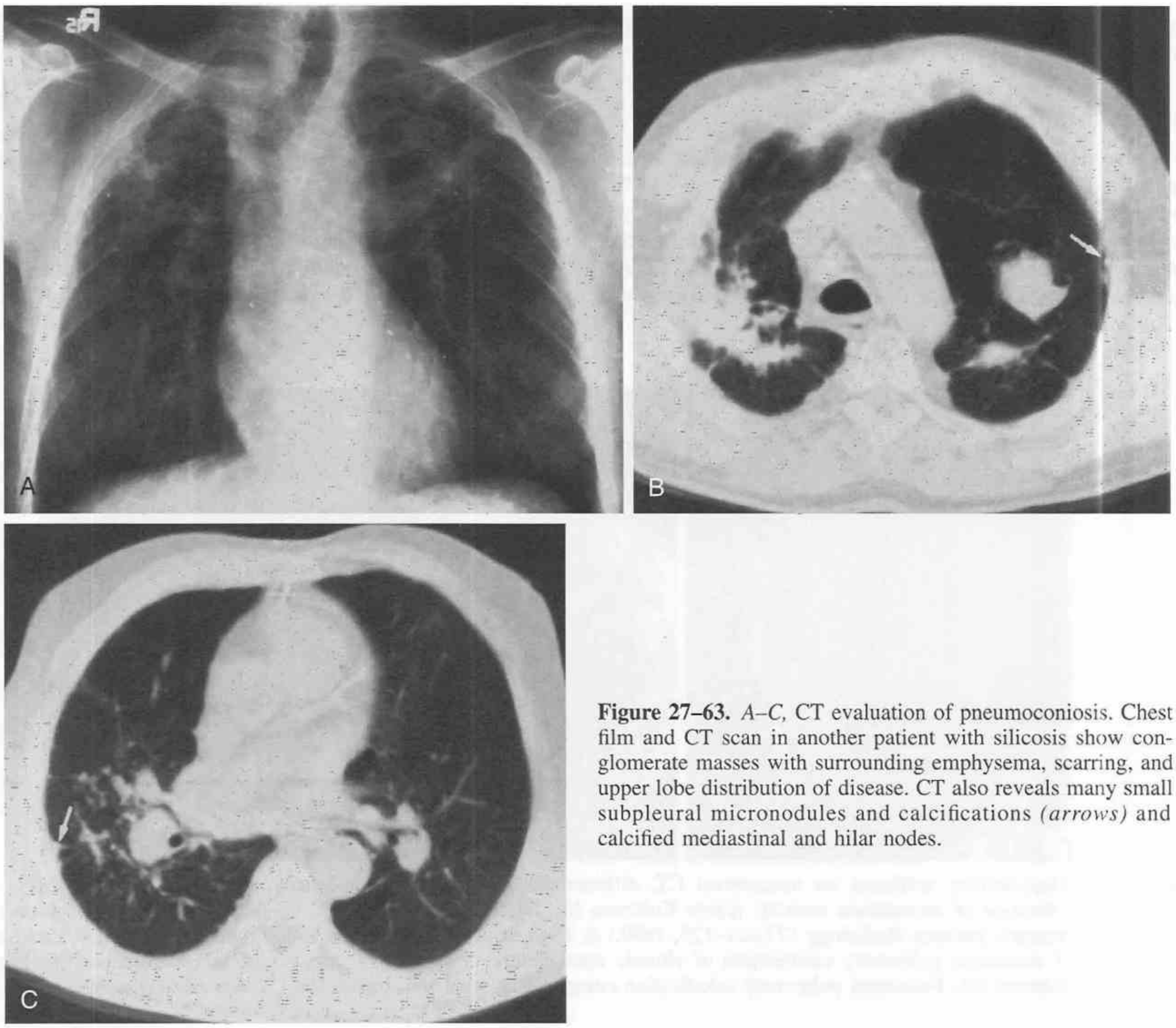

Figure 27–63. *A–C*, CT evaluation of pneumoconiosis. Chest film and CT scan in another patient with silicosis show conglomerate masses with surrounding emphysema, scarring, and upper lobe distribution of disease. CT also reveals many small subpleural micronodules and calcifications *(arrows)* and calcified mediastinal and hilar nodes.

plaques, *pleural thickening*, and *pleural calcifications*, all of which are important markers of asbestos exposure (Fig. 27–63). Mimics of pleural plaques on plain films, such as rib companion shadows, extrapleural fat, and prominent intercostal muscles, are readily distinguished from pleural plaques by CT examination.

CT is also helpful in evaluating other asbestos-related pleural changes, such as *rounded atelectasis*. Rounded atelectasis has a typical CT appearance that distinguishes it from an asbestos-related malignancy, such as *lung cancer* or *mesothelioma* (see "CT Signs of Focal Lung Disease" earlier and Fig. 27–23). HRCT is also used to search for evidence of interstitial fibrosis, which may indicate the presence of *asbestosis*. Findings such as thickened interlobular septa, honeycombing, and subpleural septal lines, although not specific for asbestosis, do indicate the presence of interstitial fibrosis and, when found in association with pleural plaques, are compatible with asbestos-induced parenchymal lung damage.[3, 5, 86]

Quantification of Lung Damage

Emphysema

Quantification of lung damage is another potential application for HRCT in the management of diffuse lung disease. One such application is the assessment of the severity and extent of pulmonary **emphysema**.[43, 63, 148]

In emphysema, destruction of the alveolar walls and the underlying elastic fiber network of the lung results in permanent enlargement of the air spaces distal to the terminal bronchiole.[7] Involvement of the proximal portions of the acinus (the respiratory bronchioles) results in centrilobular emphysema (CLE) (Fig. 27–64), whereas enlargement of all elements, from the respiratory bronchioles to the terminal blind alveoli, results in panlobular emphysema (Fig. 27–65).[75]

Emphysema is thought to result from an imbalance in the elastase/antielastase activities within the lung. Alveolar wall destruction results from proteolytic destruction by elastin whenever there is a relative increase in elastase activity in comparison to antielastase forces, such as alpha$_1$-antitrypsin activity.[58, 75, 79, 119, 121, 196, 199, 233, 234]

CT features of emphysema include intraparenchymal low-attenuation areas, pulmonary vascular pruning, pulmonary vascular distortion, and abnormal lung density gradients (see Figs. 27–64 and 27–65).[55] Visual grading systems as well as more sophisticated computer-generated attenuation maps of the lung can be used to grade pulmonary emphysema in both a qualitative and a quantitative fash-

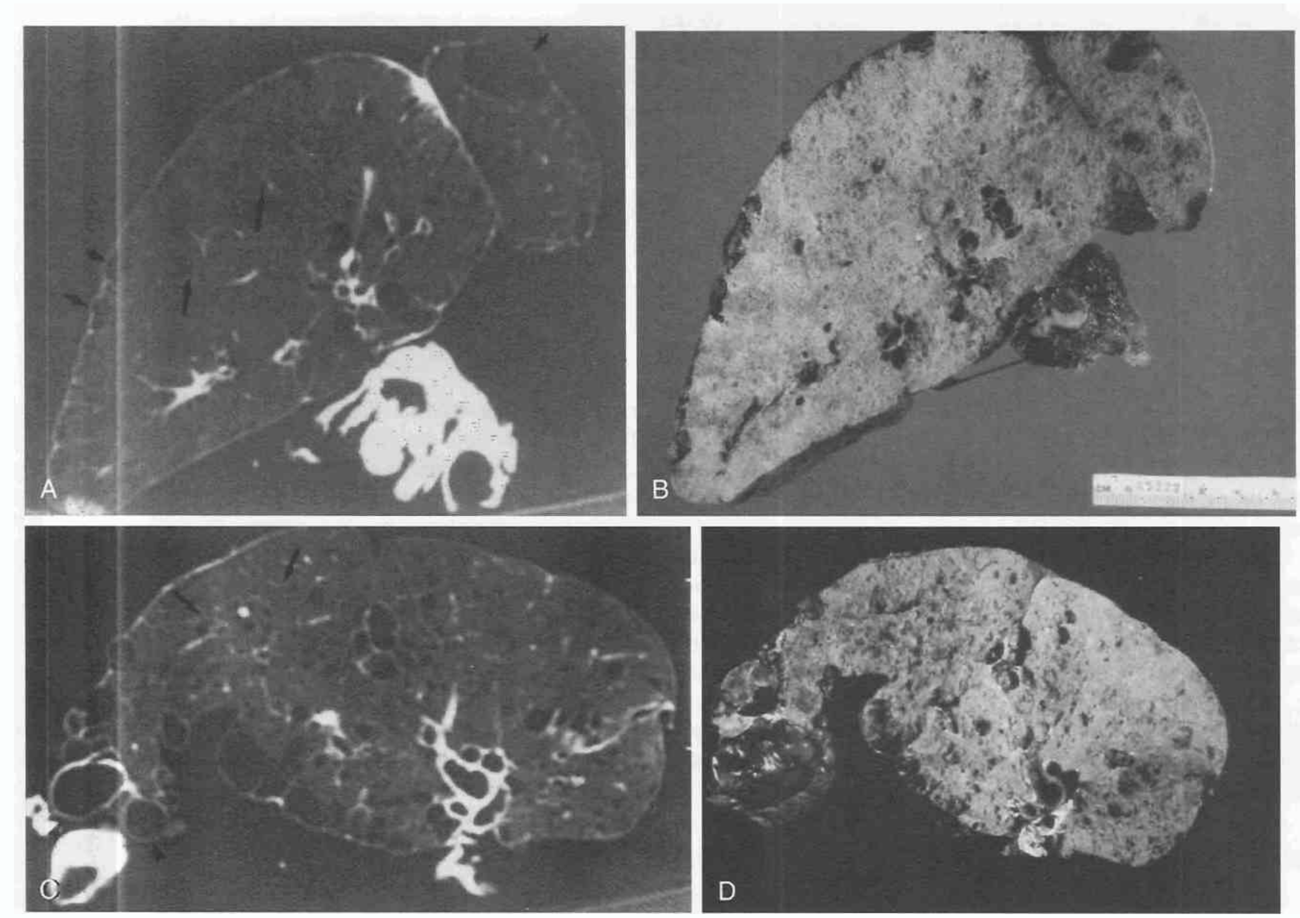

Figure 27–64. Centrilobular emphysema: correlation between CT and pathology studies. *A*, CT scan of an inflated-fixed lung specimen demonstrates focal areas of nonperipheral low attenuation *(long arrows)* and small peripheral bullae *(short arrows)*. *B*, Corresponding gross pathologic specimen. *C*, More severe centrilobular emphysema. CT of lung specimen shows more marked dilatation of the centrilobular air spaces *(arrows)* and large peripheral bullae *(arrowheads)*. *D*, Matching gross specimen. (*A–D*, From Hruban RH, Meziane MA, Zerhouni EA, et al: High-resolution computed tomography of fixed-inflated lungs: Pathologic-radiologic correlation of centrilobular emphysema. Am Rev Respir Dis 136:935–940, 1987.)

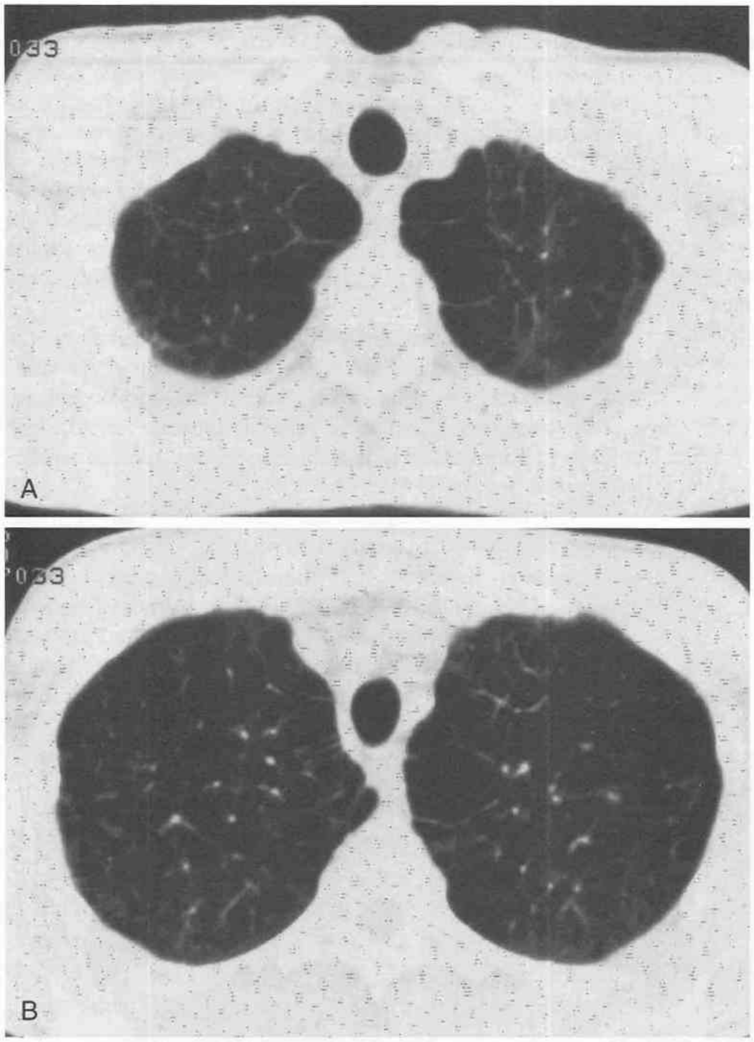

Figure 27–65. *A* and *B*, Panacinar emphysema. High-resolution CT findings of panacinar bullous emphysema include intraparenchymal low-attenuation areas (lung dropout), pulmonary vascular pruning and distortion, abnormally low CT attenuation of the lung, and enlarged air spaces.

ion.[11a] These attempts to assess the extent and severity of emphysema using HRCT criteria have achieved a high degree of success, with emphysema scores correlating well with pulmonary function tests and measurements of impaired diffusing capacity.[43, 63]

CT provides more accurate assessments of emphysema than conventional radiographs, and CT scores of centrilobular emphysema correlate well with the severity of disease demonstrated on pathologic examinations of inflated-fixed lung specimens.[43, 75, 148, 168] HRCT has also been found to be accurate in evaluating experimentally induced emphysema in pig lungs exposed to elastase.[174] Increasingly, HRCT is being used to assess the extent and severity of emphysema in clinical practice as well.[11a, 55]

Lymphangiomyomatosis

Another pulmonary disease whose severity is more accurately depicted with HRCT than with conventional radiography is lymphangiomyomatosis (LAM).[118, 156] Patients with LAM present with symptoms of shortness of breath and dyspnea on exertion that resemble those of emphysema, but the disease occurs exclusively in women of child-bearing age. The symptoms are typically out of proportion to the abnormalities seen on conventional chest films, which may be remarkably normal. In more severe cases, chest radiographs may demonstrate hyperinflation, honeycombing, irregular opacities, coarse reticulations, chylous pleural effusions, and pneumothoraces.[38, 57, 95, 118, 156]

The HRCT appearance of LAM is usually dramatic and characterized by bilateral, diffuse involvement of the lung with thin-walled, cystic air spaces (Fig. 27–66).[118, 156] The cystic spaces generally measure less than 0.5 cm in mild disease but can be greater than 1 cm in diameter when more than 80% of the parenchyma is involved.[156] Most of the spaces have identifiable walls ranging from faintly perceptible to 2 mm thick. Typically, the lung is involved uniformly, with no predilection for upper or lower lobes.

Pathologically, LAM is characterized by widespread proliferation of atypical smooth muscle cells in the bronchial tree, alveolar septa, and pulmonary and lymphatic vessels (Fig. 27–67).[38, 57, 95] The pathogenesis of the cystic spaces seen on HRCT is not known. One theory suggests that obstruction of small airways by the proliferating smooth muscle cells causes distal air trapping and air cyst formation. Other evidence has shown there is an increased number of disrupted elastic fibers within the lungs of patients affected by LAM. Fukuda and colleagues[57] postulate

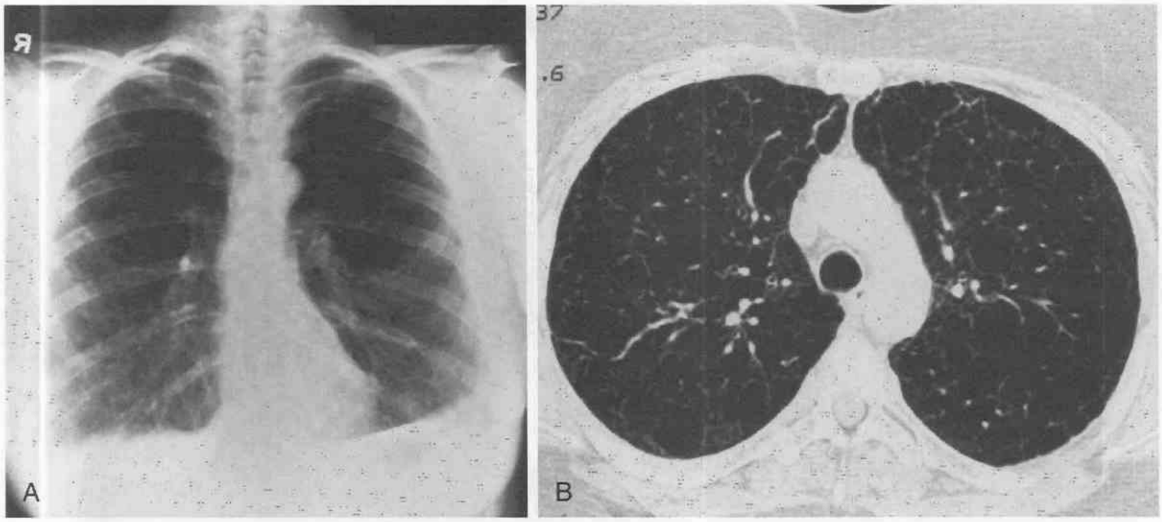

Figure 27–66. The patient is a 43-year-old woman with shortness of breath and recurrent pneumothoraces. *A*, Chest film shows hyperinflation and coarse reticulations. The severity of the symptoms was out of proportion to the chest film abnormalities. (From Kuhlman JE, Reyes BL, Hruban RH, et al: Abnormal air-filled spaces in the lung. Radiographics 13:47–75, 1993.) *B*, High-resolution CT shows extensive replacement of normal lung architecture with innumerable thin-walled, dilated, cystic air spaces that resemble severe panacinar emphysema. In fact, this patient has diffuse lymphangiomyomatosis.

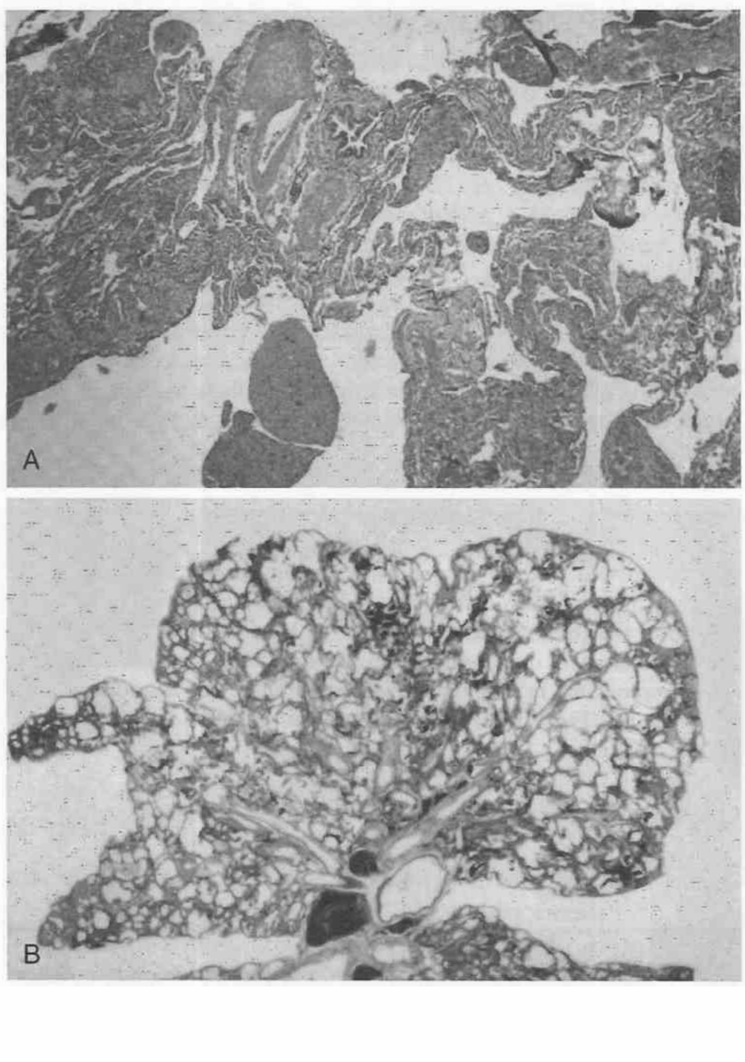

Figure 27–67. Pathology of lymphangiomyomatosis. *A*, Histologic specimen shows proliferation of smooth muscle fibers in the interstitium, and alveolar septa of the lung with remodeling of normal lung architecture. *B*, Low-power view of the lung shows replacement of the lung by cystic, dilated air spaces. (From Kuhlman JE, Reyes BL, Hruban RH, et al: Abnormal air-filled spaces in the lung. Radiographics 13:47–75, 1993.)

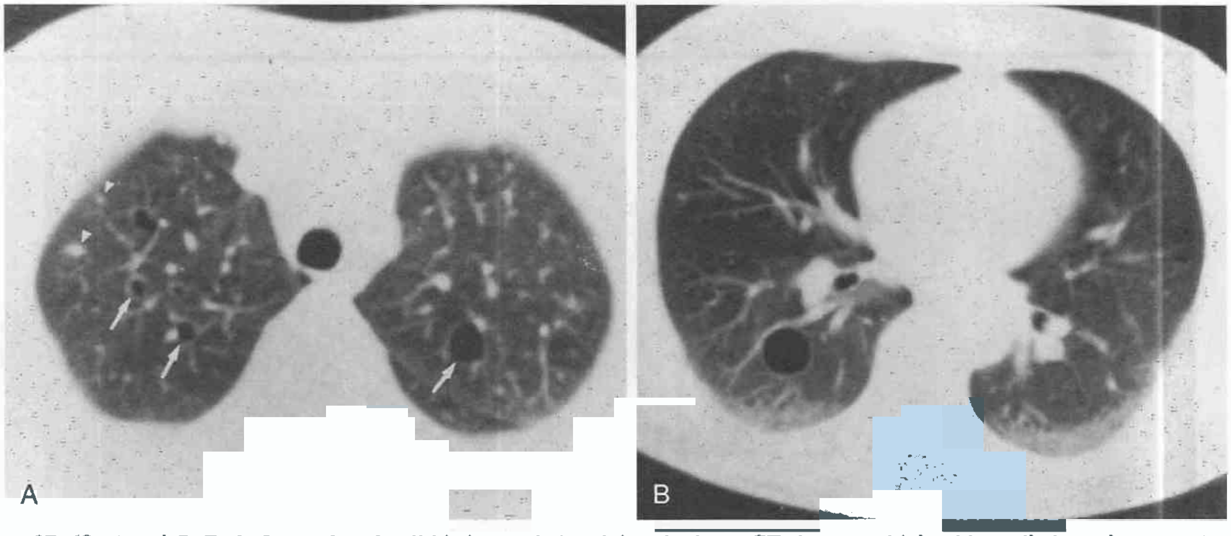

Figure 27–68. *A* and *B*, Early Langerhans' cell histiocytosis involving the lung. CT shows multiple, thin-walled regular cysts *(arrows)* and tiny nodules *(arrowheads)*. (From Kuhlman JE, Reyes BL, Hruban RH, et al: Abnormal air-filled spaces in the lung. Radiographics 13:47–75, 1993.)

that the emphysema-like lesions seen in LAM on pathologic examination result from increased elastic fiber degradation caused by an upset of the elastase/antielastase balance within the lung.

Pulmonary Langerhans' Cell Histiocytosis (Histiocytosis X, Eosinophilic Granuloma)

A lung disease whose radiographic and CT appearance resembles lymphangiomyomatosis is pulmonary Langerhans' cell histiocytosis (formerly, histiocytosis X and eosinophilic granuloma) (Figs. 27–68 to 27–71).[70b] Langerhans' cell histiocytosis is a granulomatous disease of unknown origin that may affect the lung exclusively or may affect multiple organ systems.[133] It is in the spectrum of disseminated disorders, including Letterer-Siwe disease, Hand-Schüller-Christian syndrome, and eosinophilic granuloma.[133] Granulomas, in each case, are formed by eosinophils and cells of the monocyte-macrophage system, which are Langerhans' cells. Langerhans' cell histiocytosis affects mostly young and middle-aged adults, who present with complaints of cough, dyspnea on exertion, and sometimes chest pain from pneumothorax (20%) or bone involvement.[70b, 133] These patients are almost invariably (>90%) smokers.[70b]

Findings on plain chest films include any combination of reticulation, nodules (2 to 5 mm), cysts (<1 cm), honeycombing, and emphysematous changes.[133, 153] The upper lung zones tend to be more involved and the costophrenic angles spared. Lung volumes are usually normal but sometimes increased. This has been attributed to the opposing effects of emphysema and the cicatricial fibrosis that occurs in this disease.

HRCT demonstrates the extent and distribution of parenchymal lung damage in Langerhans' cell histiocytosis more accurately than conventional radiography.[25, 153] HRCT findings of pulmonary Langerhans' histiocytosis include small nodules (2 to 5 mm or less), cystic air spaces (usually <1 cm), honeycombing, and changes compatible with emphysema (see Figs. 27–68 and 27–70).[25, 153] Much of what

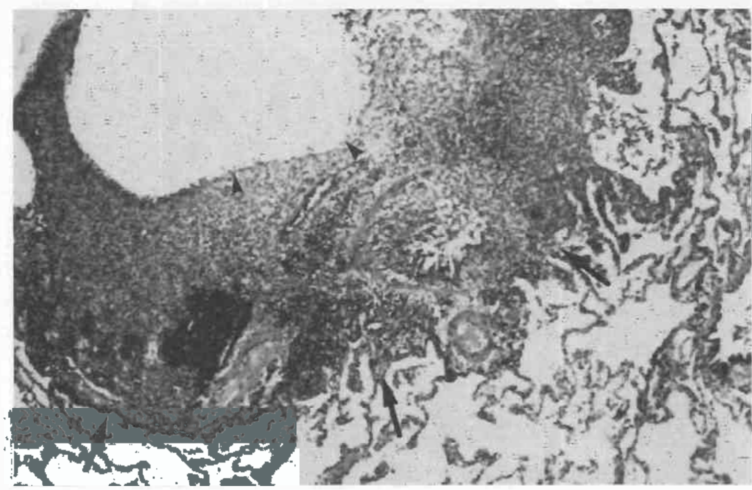

Figure 27–69. Histologic specimen of lung tissue affected by Langerhans' cell histiocytosis. A focus of granulomatous reaction *(arrows)* has created a cystic space *(arrowheads)* through retraction and remodeling of the lung architecture. (From Kuhlman JE, Reyes BL, Hruban KH, et al: Abnormal air-filled spaces in the lung. Radiographics 13:47–75, 1993.)

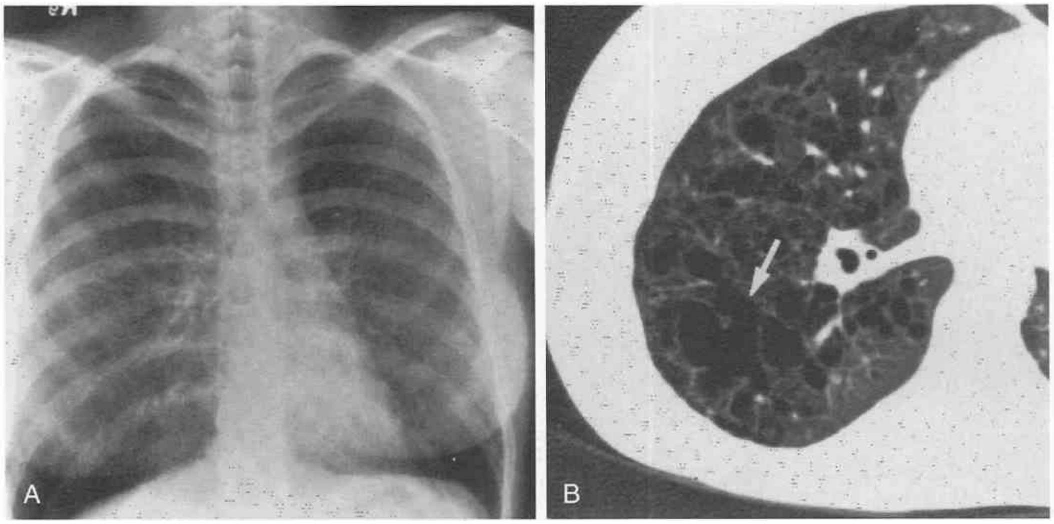

Figure 27–70. Advanced Langerhans' cell histiocytosis. *A,* Chest film in a 19-year-old woman with diabetes insipidus and dyspnea. A right pneumothorax and increased reticulations are present. *B,* High-resolution CT more clearly shows that the lung has been replaced by cystic spaces of varying sizes, some of which have coalesced into bizarre shapes *(arrow).* (From Kuhlman JE, Reyes BL, Hruban RH, et al: Abnormal air-filled spaces in the lung. Radiographics 13:47–75, 1993.)

appears to be reticulation and emphysema on plain films can be shown to be discrete cystic air spaces with definable walls on HRCT.[25] Sometimes several cystic spaces coalesce to form bizarrely shaped air spaces on CT scans. CT also demonstrates more of the smaller (<2 mm) nodules that are frequently not visible on plain radiographs (see Fig. 27–68).[25] These small nodules are more common in the early stages of the disease and tend to spare the lung bases and predominate in the upper lung zones.[70b] With progression, cystic changes take over the lung. Bullae, cavitating nodules, and traction bronchiectasis are also features of Langerhans' cell histiocytosis that can be appreciated on CT examination.[25, 153]

The mechanism by which cystic spaces form in pulmonary Langerhans' cell histiocytosis is uncertain.[87] Central necrosis of granulomatous nodules may produce the thin-walled cavities seen in early pulmonary Langerhans' histiocytosis (see Fig. 27–69). Others have postulated a check-valve obstruction of bronchioles leading to dilatation of distal airspaces. Another theory suggests that progressive fibrosis occurs around areas of bronchiolar inflammation and granuloma formation. This leads to retractile, paracicatricial emphysema in these peribronchiolar areas with disruption and remodeling of the elastic fiber network that eventually produces a honeycomb lung (see Fig. 27–71).[70b, 87]

Tracheolaryngeal Papillomatosis

Tracheolaryngeal papillomatosis is another rare disease whose lung dissemination is best documented and assessed with CT evaluation. Laryngeal papillomatosis results from an infection by the human papillomavirus that is transmitted from mother to child during birth. Papillomas grow in the upper airways of the child and consist of cauliflower-like lesions with fibrovascular cores or stalks covered by a stratified squamous epithelium.[47]

In the juvenile tracheolaryngeal form of papillomatosis,

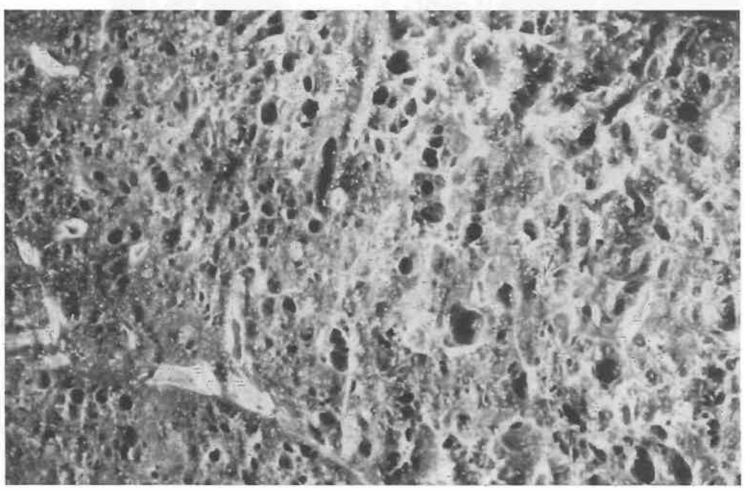

Figure 27–71. Advanced Langerhans' cell histiocytosis. Gross lung specimen shows diffuse replacement of the lung by cystic spaces.

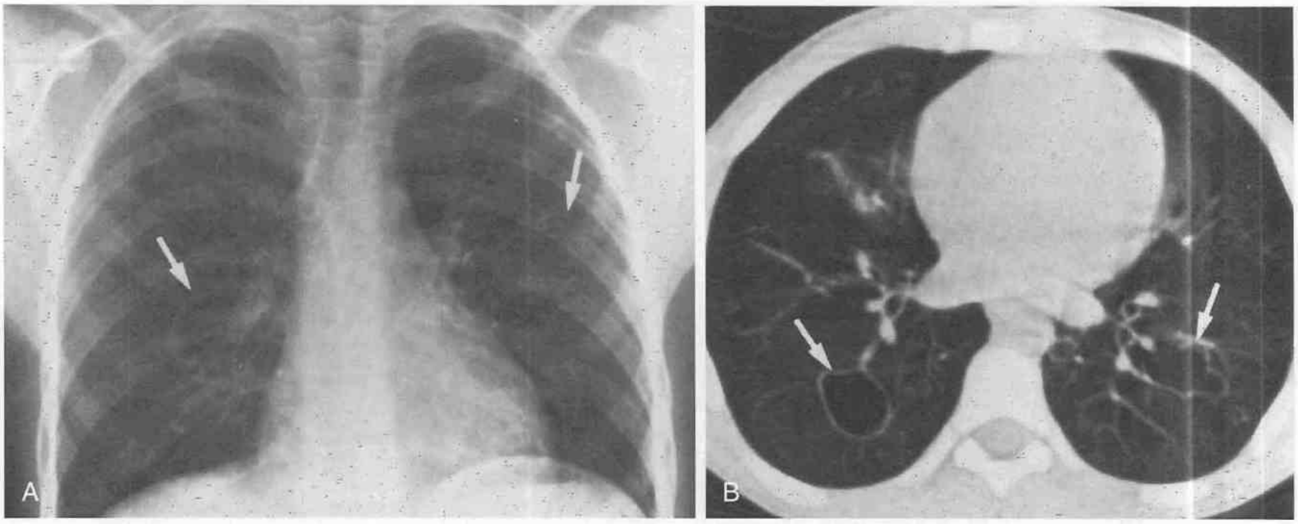

Figure 27–72. CT features of juvenile tracheolaryngeal papillomatosis. Several thin, delicate-walled cystic air spaces are seen *(arrows)* on the chest film (*A*) and the CT scan (*B*) in this 12-year-old boy with upper airway papillomas. (From Kuhlman JE, Reyes BL, Hruban RH, et al: Abnormal air-filled spaces in the lung. Radiographics 13:47–75, 1993.)

the disease extends inferiorly into the tracheobronchial tree (5% of cases) and into the lung parenchyma (1% of cases) (Figs. 27–72 to 27–74).[94] When the lung parenchyma is involved, round nodules, either solid or cystic, may be seen on chest radiographs or CT (see Fig. 27–72). The small cystic lesions eventually enlarge to several centimeters in diameter, with varying wall thickness (see Fig. 27–73).[89, 94] On CT scans, the lesions are widely distributed but with a predilection for the lower lobe and the posterior.

The pathogenesis of lung involvement in tracheolaryngeal papillomatosis is believed to be via aerial dissemination. Small fragments of papillomatous tissue break off from the upper airways (secondary to bronchoscopy, surgery, tracheostomy) and travel through the major bronchi, where they lodge in the distal small airways causing obstruction and distal air trapping. There, the papilloma fragments enlarge centrifugally and grow along the expanded air spaces. Eventually the papillomatous masses undergo cavitation to form larger cavitary air spaces that are lined by stratified squamous epithelium (see Fig. 27–74).[89, 94]

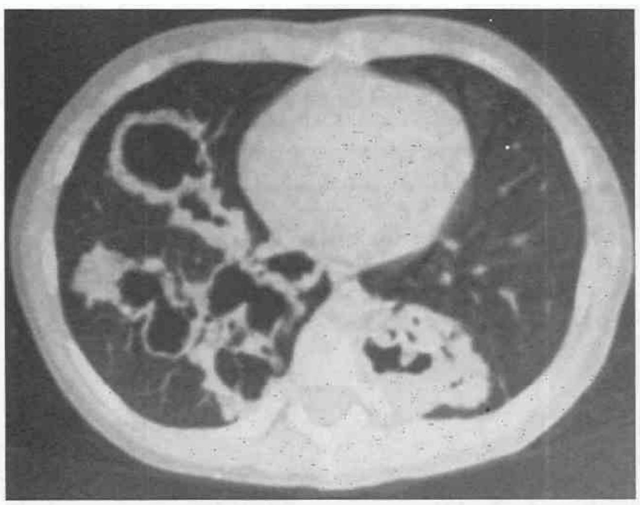

Figure 27–73. Advanced tracheolaryngeal papillomatosis. CT shows extensive cavitary spaces that have a branching and clustered appearance reminiscent of cystic bronchiectasis. The walls are thick and irregular. (From Kuhlman JE, Reyes BL, Hruban RH, et al: Abnormal air-filled spaces in the lung. Radiographics 13:47–75, 1993.)

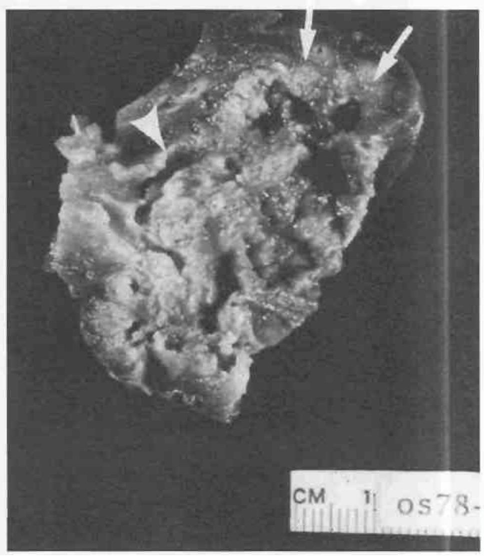

Figure 27–74. Pathology of tracheolaryngeal papillomatosis. A large cavitary space *(arrows)* is lined with verrucous papillomatous tissue. The adjacent bronchus is also involved *(arrowhead)*. Papilloma fragments lodge in distal airways, where they grow along the terminal air spaces. Cavitary spaces form when papillomatous tissues cause bronchiolar obstruction or when papillomatous tumor masses necrose. (From Kuhlman JE, Reyes BL, Hruban RH, et al: Abnormal air-filled spaces in the lung. Radiographics 13:47–75, 1993.)

Monitoring Disease Activity, Complications, and Response to Therapy

Interstitial Pulmonary Fibrosis

Interstitial pulmonary fibrosis may be idiopathic (idiopathic pulmonary fibrosis [IPF], fibrosing alveolitis, and UIP) or may be associated with a number of other disease entities, including collagen vascular disorders (rheumatoid arthritis, polymyositis, lupus, scleroderma, and mixed connective tissue–overlap syndromes), asbestosis, drug toxicity, sarcoidosis, end-stage Farmer's lung, and Langerhans' cell histiocytosis, among others.

CT is useful in diagnosis of IPF in symptomatic patients with nonspecific abnormalities on chest radiographs and in monitoring the disease status in these patients.[155, 159, 211, 215, 227–230] CT visual scoring systems of IPF correlate better than plain film findings with clinical and functional assessments of disease severity.[155, 159, 211, 215, 227–230]

In the early stages of IPF, subpleural ground-glass infiltrates and crescentic densities are identified in the peripheral aspects of the lungs and posterior segments of the lower lobes bilaterally. Later, these subpleural crescentic densities evolve into reticulation and subpleural honeycombing (Figs. 27–75 and 27–76). As honeycombing and fibrosis progress, traction bronchiectasis develops.[155, 159, 211, 215, 227–230] Some honeycomb cysts enlarge to great size as the lung parenchyma is gradually replaced and remodeled by progressive fibrosis.

CT can be used quite effectively to monitor the progression of IPF and its response to treatments such as corticosteroids. The significance of ground-glass opacities in IPF remains controversial. Some authors believe that the presence of such opacities on CT scans in cases of IPF indicates the presence of active alveolitis that may respond to treatment. Other authors have challenged this notion with pathologic correlation studies showing that ground-glass opacities can correspond to areas of alveolitis or to areas of fine fibrosis. The presence of honeycombing on CT scans, however, is a fairly reliable indication of irreversible lung damage.[155, 159]

Adult Respiratory Distress Syndrome

The patient with ARDS generally requires high positive-pressure mechanical ventilation and is at high risk for development of barotrauma in the form of interstitial emphysema, subpleural air cyst formation, pneumothorax, and pneumomediastinum (see Figs. 27–23 and 27–24).[231] Although CT has not been used extensively in patients with ARDS, it may play a role in the evaluation of acute and long-term complications in this setting.[45a, 148a] CT assessments of disease severity and their prognostic implications are currently under investigation by several authors (Fig. 27–77).[21, 45a, 66, 140, 151, 180, 212, 220]

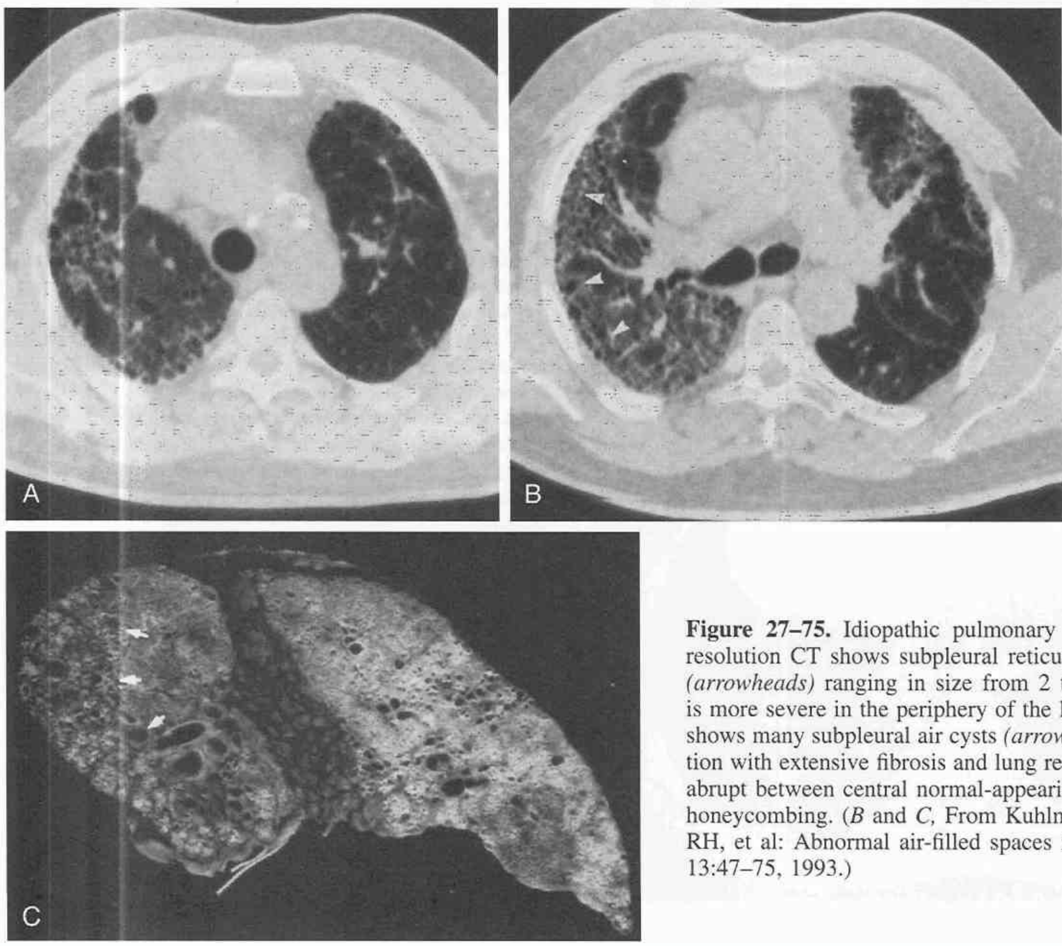

Figure 27–75. Idiopathic pulmonary fibrosis. *A* and *B*, High-resolution CT shows subpleural reticulations and small air cysts *(arrowheads)* ranging in size from 2 to 10 mm. Honeycombing is more severe in the periphery of the lung. *C*, Autopsy specimen shows many subpleural air cysts *(arrows)* in a subpleural distribution with extensive fibrosis and lung remodeling. The transition is abrupt between central normal-appearing lung and the peripheral honeycombing. (*B* and *C*, From Kuhlman JE, Reyes BL, Hruban RH, et al: Abnormal air-filled spaces in the lung. Radiographics 13:47–75, 1993.)

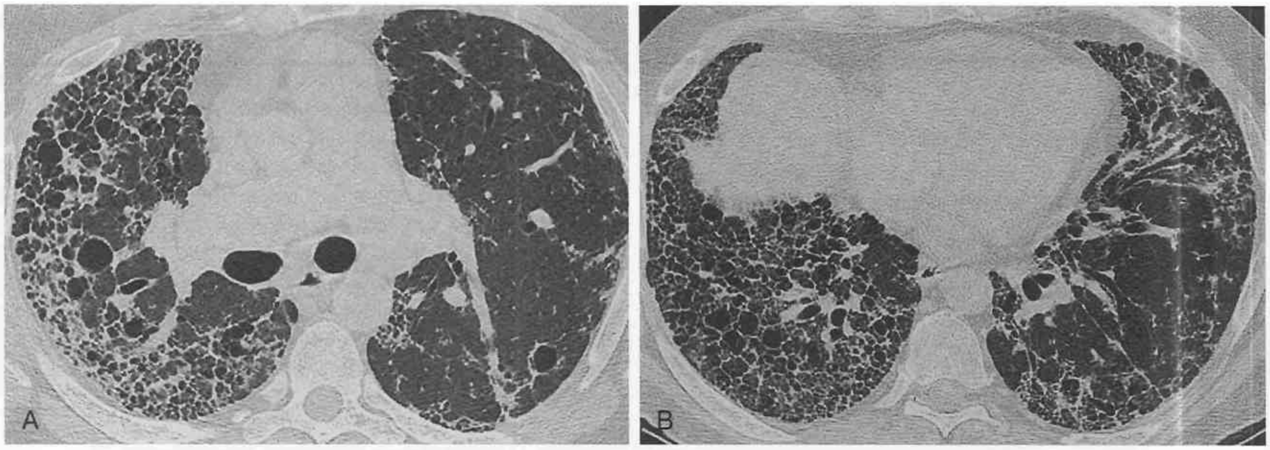

Figure 27–76. *A* and *B*, Interstitial pulmonary fibrosis associated with polymyositis. High-resolution CT shows reticulation and honeycombing in the periphery of the lung and in the lung bases, more severe on the right than on the left. Note "traction" bronchiectasis due to interstitial fibrosis.

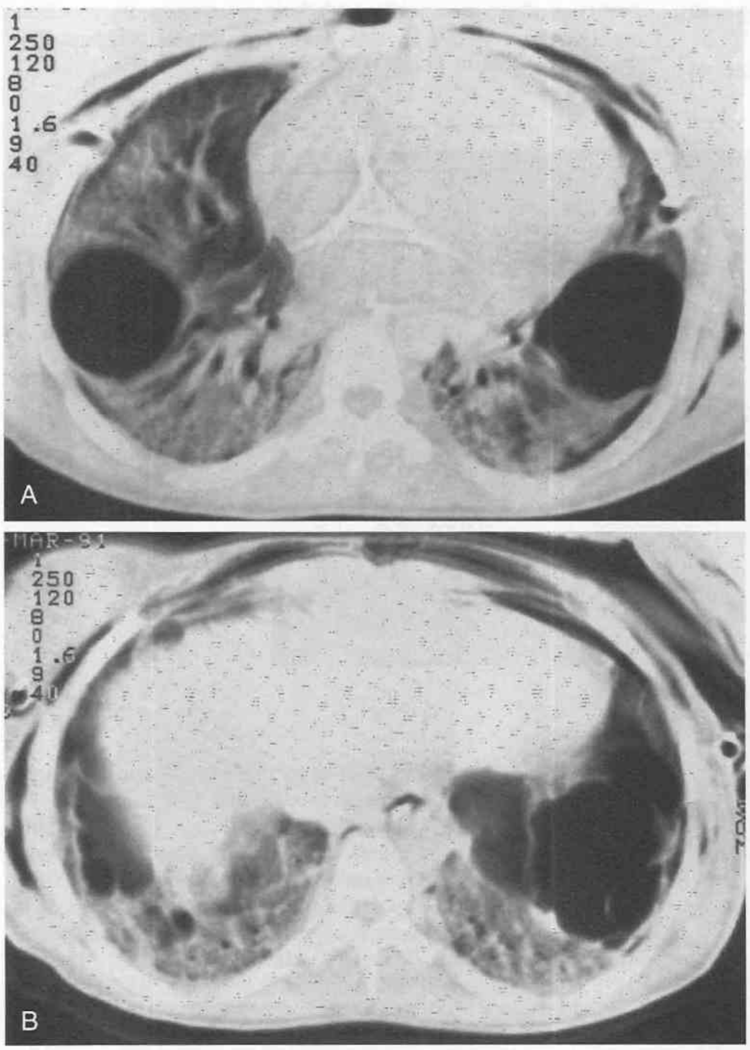

Figure 27–77. *A* and *B*, High-resolution CT of adult respiratory distress syndrome (ARDS) and its complications. Postpartum pneumonia and ARDS developed in a 17-year-old girl. Bilateral "ground-glass" infiltrates compatible with a diagnosis of ARDS are evident on CT scanning. Large extra-alveolar air cysts have developed. CT shows that these air cysts have no discernible walls and are located in the subpleural and basal regions of the lung. Bilateral chest tubes are in place for complicating pneumothoraces. Subcutaneous emphysema is present.

The pathophysiology of barotrauma-related complications in ARDS was first examined by Macklin and Macklin[129] and then further elucidated by Westcott and Cole.[231] The process begins with rupture of weaker alveoli along the margins of the interlobular septa and bronchovascular structures as a result of increased airway pressures. Air then dissects along the interlobular septa and along the perivascular spaces, producing interstitial emphysema. Interstitial air may then rupture into the pleural space causing pneumothorax or into the mediastinum causing pneumomediastinum. Or air may collect in extra-alveolar spaces within the interstitium, forming large air cysts. These air cysts typically are found in the lung bases and subpleural zones adjacent to the diaphragm or mediastinum. They may enlarge to great size, causing respiratory and circulatory compromise, and they may be mistaken for loculated pneumothoraces.[129, 231]

On CT scans, subpleural air cysts associated with ARDS appear as air spaces with no definable walls (see Fig. 27–77).[212] They typically expand into the fissures or subpulmonic zones and compress adjacent lung parenchyma as they enlarge. Although a CT scan is not as easy to obtain as a portable chest film in critically ill, ventilator-dependent patients, CT is more accurate in identifying and localizing complications of barotrauma, such as pneumothoraces, pneumomediastinum, and subpleural air cysts. This may become important in those select patients who are not responding to treatment or who deteriorate suddenly for unclear reasons. For example, what may appear to be an appropriately placed chest tube on a portable supine chest radiograph may be found to be inadequate in location on CT scans.

In addition, a few investigators have begun to correlate patient outcome in ARDS with the extent and severity of pulmonary infiltrates and complications as graded by CT.[21, 66, 140, 151, 180, 212, 220] Further study is necessary to determine whether CT findings of ARDS are reliable prognostic indicators.

Sarcoidosis

CT is used extensively to identify, stage, and monitor patients with pulmonary sarcoidosis, a disease of unknown origin that is characterized pathologically by the presence of noncaseating granuloma.[219] The lung and the intrathoracic lymph nodes are the most commonly affected organs of the body, and thoracic complications account for most of the morbidity and mortality caused by this disease.[178] Although only 60% of patients with sarcoidosis demonstrate chest film abnormalities, histologic evidence of granulomatous disease is almost always present on biopsy specimens taken from the lung.[178]

CT is more accurate than conventional radiography in detecting subtle areas of parenchymal involvement and in delineating the full extent of lung disease caused by sarcoidosis.[69, 108, 191, 208] CT features of pulmonary sarcoidosis include thickening of the interlobular septa, reticulonodular disease, multinodular disease, mixed infiltrates, and masslike consolidations. In pulmonary sarcoidosis, the noncaseating granulomas have a propensity for forming in association with the lymphatics of the interstitial tissues in the peribronchial, perivascular, and subpleural spaces as well as in the interlobular septa. These granulomas produce the reticulonodular infiltrates seen on CT scans, which may appear predominantly linear or nodular depending on the size of the granulomas and the amount of fibrosis that is present (Fig. 27–78). Granulomas that form along the interlobular septa can produce an appearance resembling the beaded septum sign seen in lymphangitic carcinomatosis.[108, 178]

Pulmonary involvement in sarcoidosis is usually bilateral, although it may be asymmetrical. Multinodular disease may have several distributions; for example, tiny nodules, 1 to 3 mm in size, distributed evenly throughout the lung in a miliary pattern, or large, coarser nodules that are more varied in size and more unevenly scattered. Subpleural nodules, septal nodules, and perihilar peribronchovascular nodules are typical of sarcoidosis. Mixed patterns with reticulation, thickening of the interlobular markings, fibrosis, and pleural thickening may also be seen.[69, 108, 191, 208]

Occasionally, sarcoidosis presents as multiple, round, masslike consolidations on chest films and CT. The masses often demonstrate air-bronchograms, and this form of sarcoidosis has been called *alveolar* or *acinar* sarcoid (Fig. 27–79).[60, 108, 122, 191, 218] These masses, however, do not represent true air space filling in the sense that a pneumonia would; rather, the masses represent numerous granulomas that have coalesced within the interstitium, forming massive conglomerates that compress the surrounding air spaces.

Pathologically, pulmonary sarcoidosis begins as an acute alveolitis followed by a phase of granuloma formation within the lung interstitium.[219] In most cases, the disease stabilizes at this stage, leaving the patient with persistent granulomas in the lung, or the lung disease resolves completely. In 20% of patients, however, the disease progresses.[178] With more advanced disease, findings of pulmonary fibrosis dominate the CT picture. Progressive fibrosis and architectural distortion lead to honeycombing, fibrocystic changes, bullae, traction bronchiectasis, and retraction of the pulmonary hila (Fig. 27–80). The upper lung zones are more severely affected, and evidence of secondary pulmonary hypertension and cor pulmonale is frequently seen. Fibrotic conglomerate masses reminiscent of those seen in silicosis may also develop in advanced disease.[69, 108]

True cavities lined by noncaseating granulomas are extremely rare (<0.6%) in sarcoidosis.[178, 191] Most apparent cavities are the result of fibrocystic disease and bullae that develop in advanced disease, and they are lined by fibrous tissue, not granulomas. Superimposed infection of fibrocystic spaces, particularly with *Aspergillus*, is a frequent complication of sarcoidosis and accounts for significant morbidity and mortality.

In the patient with advanced sarcoidosis and hemoptysis, CT is useful in detecting or confirming the presence of complicating aspergillomas, particularly when the chest radiograph is difficult to interpret because of extensive disease and fibrosis (Fig. 27–81).[69, 108, 208] CT scans obtained in the supine and prone positions usually demonstrate movement of mycetomas within cystic spaces. Superimposed bacterial infections may also complicate fibrocystic spaces in sarcoidosis, and there is a higher incidence of TB in sarcoid patients than in the population as a whole.[178]

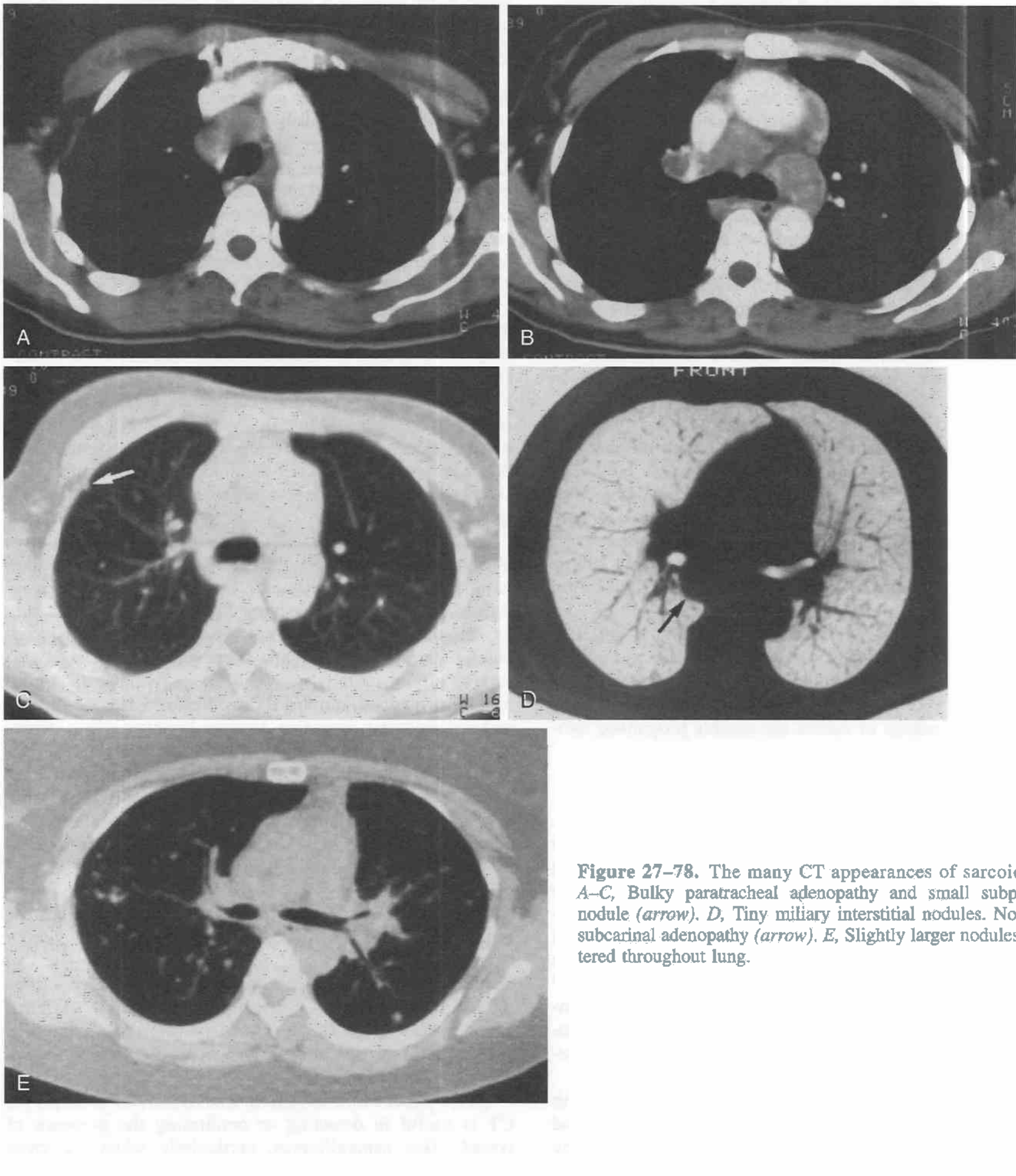

Figure 27–78. The many CT appearances of sarcoidosis. *A–C,* Bulky paratracheal adenopathy and small subpleural nodule *(arrow)*. *D,* Tiny miliary interstitial nodules. Note the subcarinal adenopathy *(arrow)*. *E,* Slightly larger nodules scattered throughout lung.

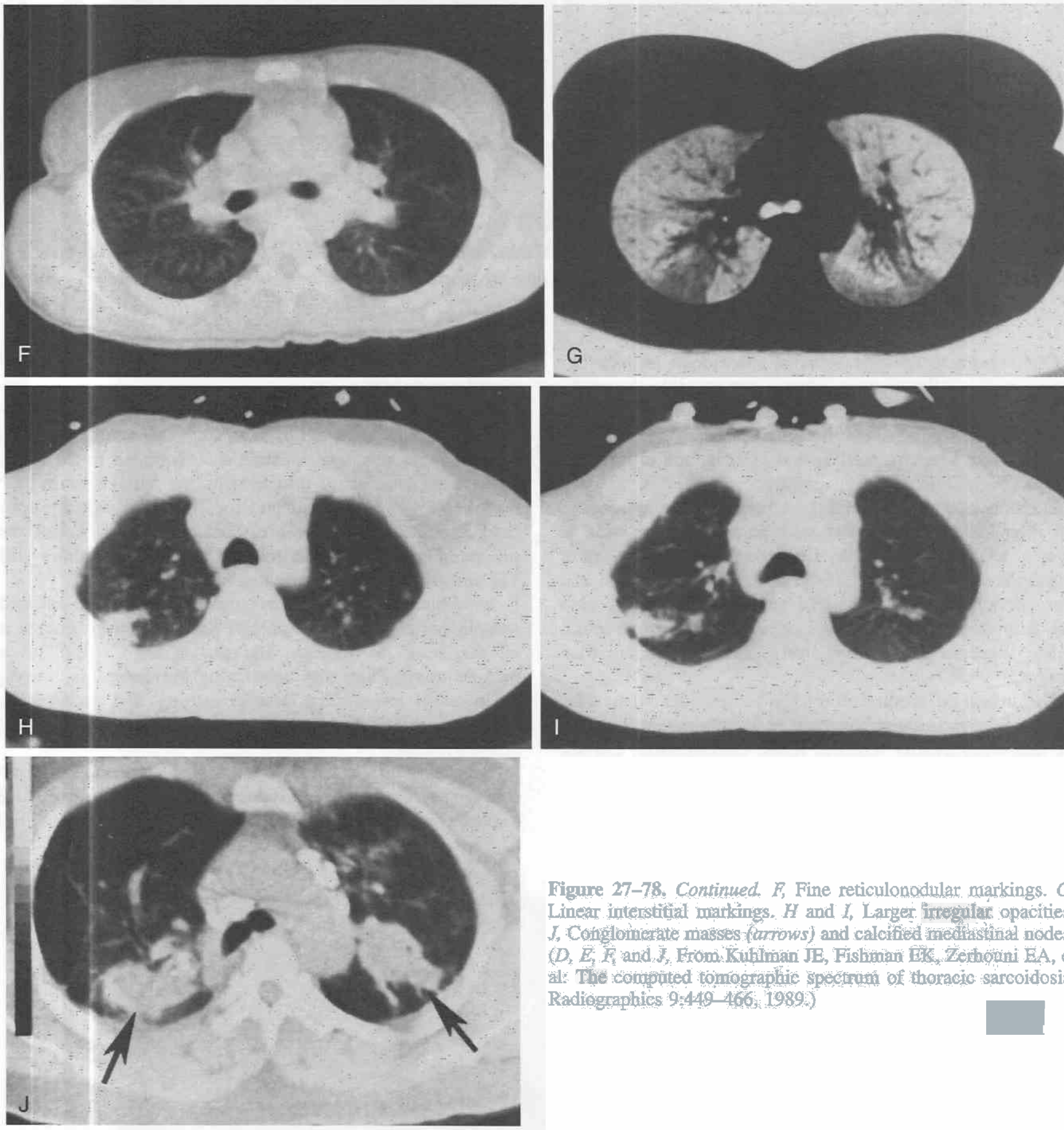

Figure 27–78. *Continued. F,* Fine reticulonodular markings. *G,* Linear interstitial markings. *H* and *I,* Larger irregular opacities. *J,* Conglomerate masses *(arrows)* and calcified mediastinal nodes. (*D, E, F,* and *J,* From Kuhlman JE, Fishman EK, Zerhouni EA, et al: The computed tomographic spectrum of thoracic sarcoidosis. Radiographics 9:449–466, 1989.)

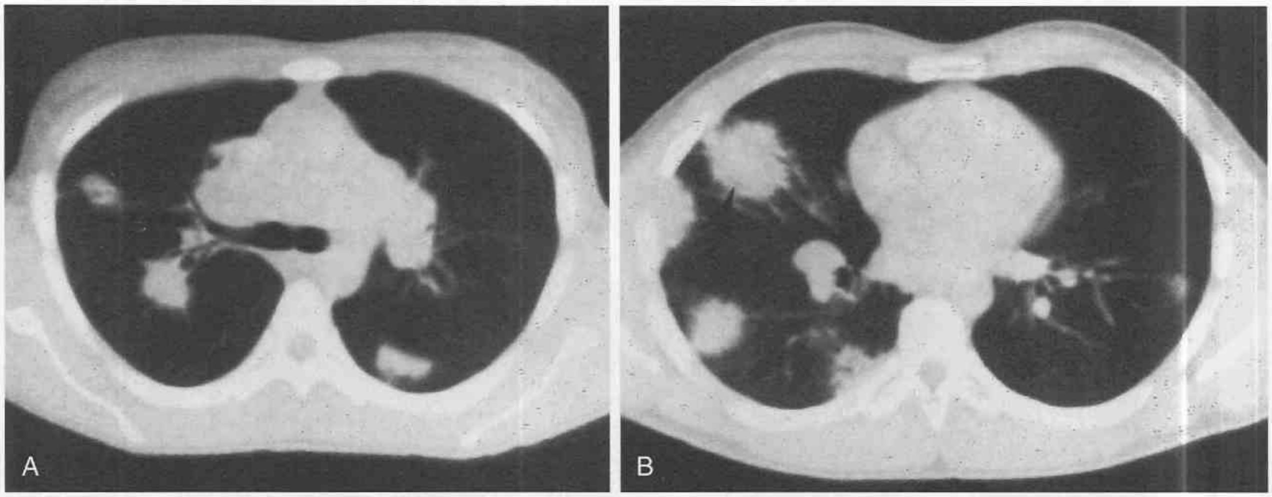

Figure 27–79. *A* and *B*, Alveolar sarcoid. CT shows round masslike consolidations with air-bronchograms. Note hilar adenopathy.

Other thoracic complications of sarcoidosis include extension of the inflammatory, fibrotic process into the mediastinum, resulting in fibrosing mediastinitis. On CT scans, abnormal fibrotic tissue can be seen to narrow and obstruct the mainstem bronchi, mediastinal vessels, and pulmonary vessels (Fig. 27–82).[69, 108]

Lymphadenopathy is even more common than parenchymal lung disease in patients with sarcoidosis, and CT is superior to chest radiography for delineating the full extent of lymphadenopathy (Fig. 27–83).[69, 178, 191] Paratracheal and hilar adenopathy are typical of sarcoidosis, but CT also may demonstrate adenopathy in the anterior mediastinum, axilla, internal mammary chain, and below the diaphragm.[69, 191, 192]

The major differential diagnosis to consider when adenopathy is seen in these locations is lymphoma, and definitive diagnosis usually requires tissue confirmation. Certain CT patterns of nodal involvement, however, favor a diagnosis of sarcoidosis. Symmetrical paratracheal and hilar adenopathy, especially when accompanied by reticulonodular infiltrates, is suggestive of sarcoidosis in the non–HIV-positive patient.[69]

In contrast to adenopathy caused by neoplastic disorders, enlarged lymph nodes resulting from sarcoidosis tend to remain discrete and maintain their rounded nodal shape, rather than coalescing into amorphous nodal masses.[69, 108] Calcifications within hilar and mediastinal nodes are common in sarcoid, which is one of the diseases that can produce eggshell calcifications in lymph nodes along with TB, fungal infections, and silicosis.

In clinical practice, CT examination of the patient with sarcoidosis is an integral part of the evaluation process at all stages of the disease. Indications for CT evaluation include establishing and confirming the diagnosis, staging the disease, monitoring disease activity and progression, assessing treatment response, and detecting and evaluating complications.[108]

Patients with chest film abnormalities and possible sarcoidosis may benefit from further characterization of their pulmonary disease by CT. CT also serves as a road map

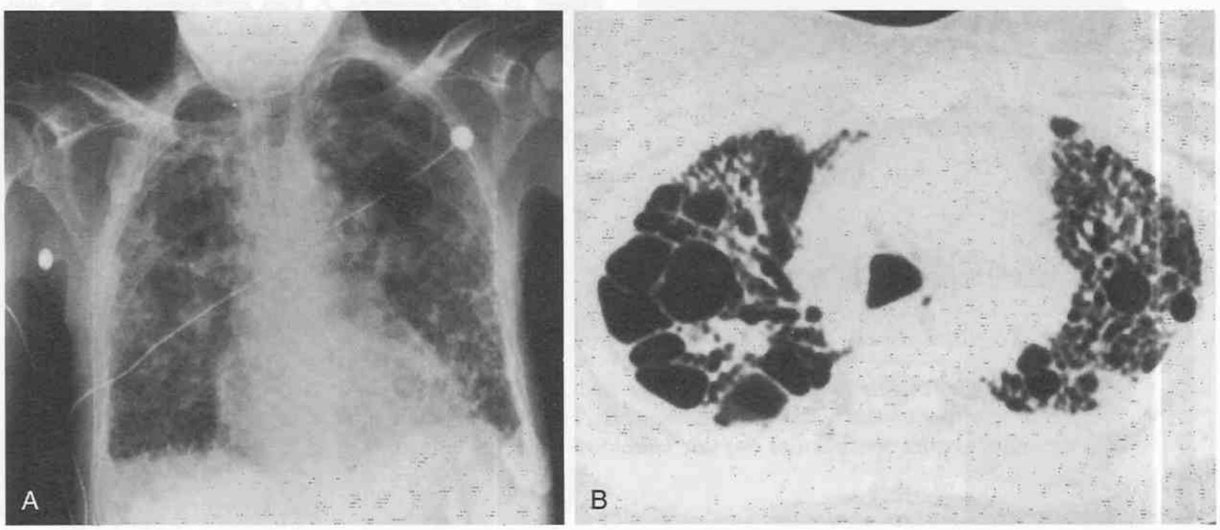

Figure 27–80. *A* and *B*, Advanced sarcoid with lung fibrosis, honeycombing, and extensive fibrocystic changes.

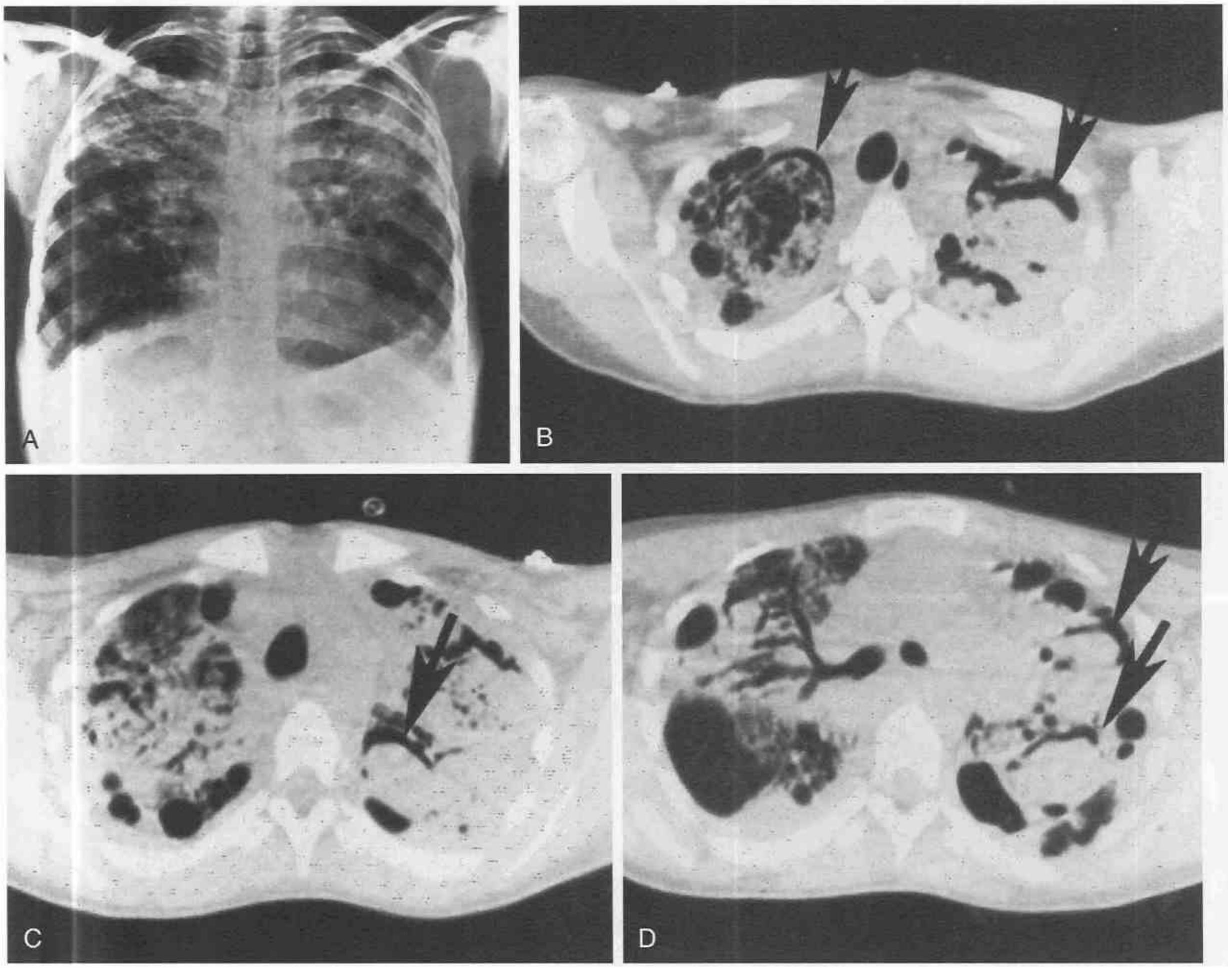

Figure 27–81. Complication of sarcoidosis—mycetoma formation. *A,* Chest film shows extensive upper lobe disease and fibrosis resulting from sarcoidosis. *B–D,* CT reveals that at least five mycetomas are present *(arrows). (A* and *B,* From Kuhlman JE, Fishman EK, Zerhouni EA, et al: The computed tomographic spectrum of thoracic sarcoidosis. Radiographics 9:449–466, 1989.)

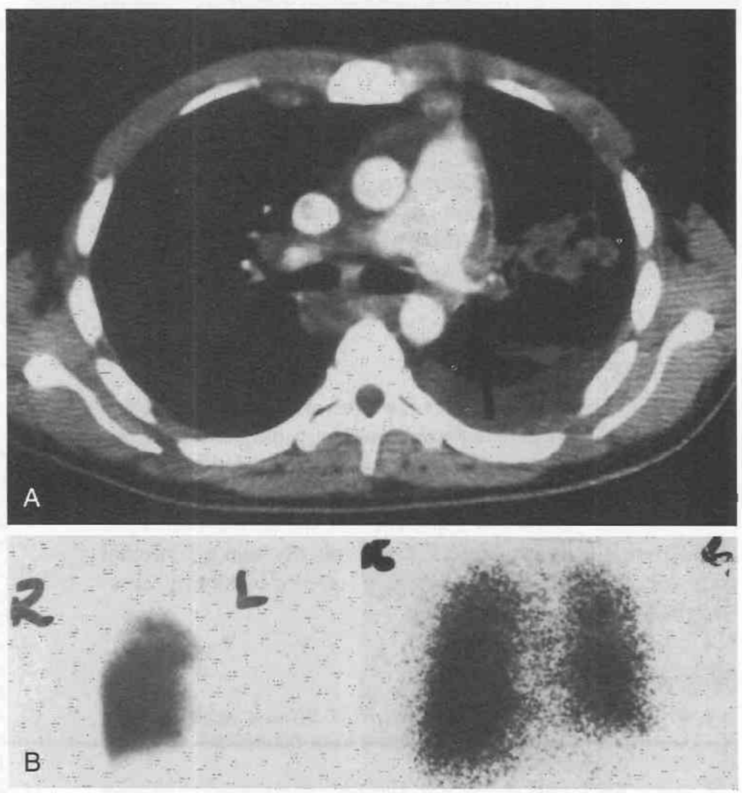

Figure 27–82. Fibrosing mediastinitis resulting from sarcoidosis. *A,* CT shows abnormal soft tissue infiltration of the mediastinal fat with amputation of the left pulmonary artery *(arrow).* Enlarged internal mammary nodes as well as lung disease and a left pleural effusion are present. *B,* A ventilation-perfusion scan shows ventilation but no perfusion to the left lung. (From Kuhlman JE, Fishman EK, Zerhouni EA, et al: The computed tomographic spectrum of thoracic sarcoidosis. Radiographics 9:449–466, 1989.)

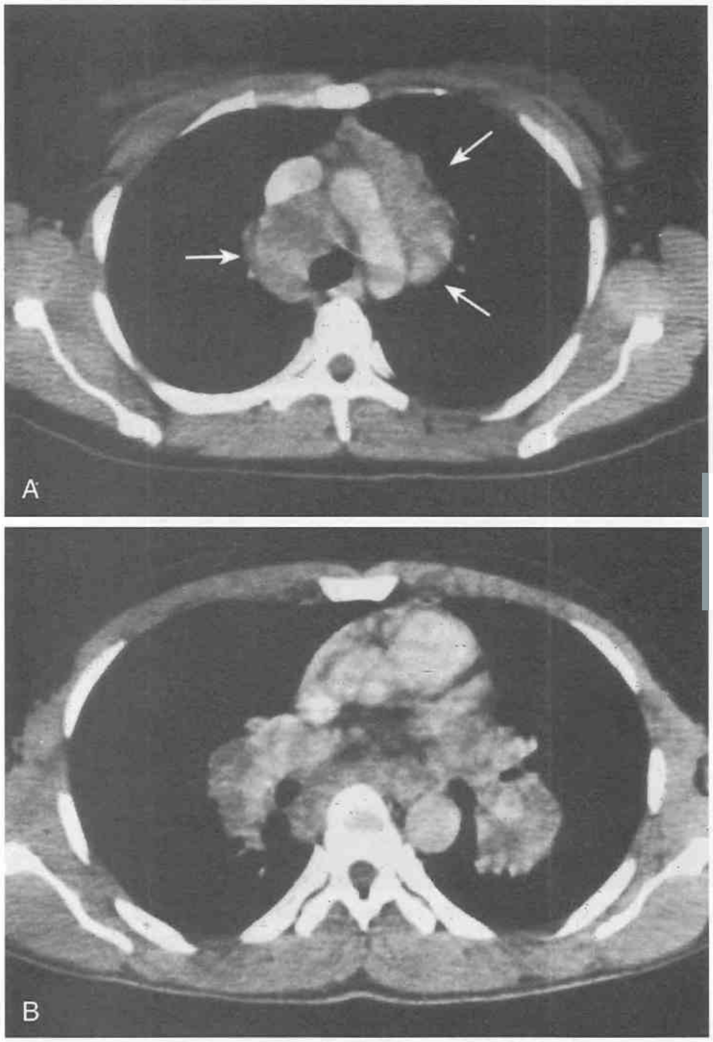

Figure 27–83. CT evaluation of sarcoidosis to determine the extent of adenopathy. *A,* Bulky anterior mediastinal and right paratracheal adenopathy *(arrows)*. *B,* Bilateral hilar and subcarinal adenopathy. (From Kuhlman JE, Fishman EK, Zerhouni EA, et al: The computed tomographic spectrum of thoracic sarcoidosis. Radiographics 9:449–466, 1989.)

for planning biopsy procedures, localizing the best sites for transbronchial lung biopsy, percutaneous biopsy, and nodal sampling. Patients with known sarcoidosis also benefit from CT evaluation when atypical radiographic findings require further explanation or when complications are suspected but have not been detected by conventional radiography.[69, 108]

Summary

CT remains an adjunct to the conventional chest radiograph in the evaluation of non-neoplastic lung diseases. As an adjunct, however, CT is an important, indispensable asset. When combined with HRCT techniques and the emerging fast scanning capabilities of spiral, multidetector, and ultrafast electron beam CT, CT has become a powerful tool for detecting, characterizing, and quantifying non-neoplastic diseases of the lung.

References

1. Abd AG, Nierman DM, Ilowite JS, et al: Bilateral upper lobe PCP in a patient receiving inhaled pentamidine prophylaxis. Chest 94: 329–331, 1988.
2. Aberle DR, Gamsu G, Lynch D: Thoracic manifestations of Wegener granulomatosis: Diagnosis and course. Radiology 174:703–709, 1990.
3. Aberle DR, Gamsu G, Ray CS, Feuerstein IM: Asbestos-related pleural and parenchymal fibrosis: Detection with high-resolution CT. Radiology 166:729–734, 1988.
4. Akira M, Higashihara T, Sakatani M, Hara H: Diffuse panbronchiolitis: Follow-up CT examination. Radiology 189:559–562, 1993.
4a. Akira M, Kitatani F, Yong-Sik L, et al: Diffuse panbronchiolitis: Evaluation with high-resolution CT. Radiology 168:433–438, 1988.
5. Akira M, Yamamoto S, Yokoyama K, et al: Asbestosis: High-resolution CT: Pathologic correlation. Radiology 176:389–394, 1990.
6. Albelda SM, Kern JA, Marinelli DL, Miller WT: Expanding spectrum of pulmonary disease caused by nontuberculous mycobacteria. Radiology 157:289–296, 1985.
7. American Thoracic Society: Chronic bronchitis, asthma, and pulmonary emphysema. Statement by the Committee on Standards for Nontuberculous Respiratory Diseases. Am Rev Respir Dis 85:762–768, 1962.
8. Amos A, Denning D, Katz D, Smith H: Computed tomography of chest in diagnosis of miliary tuberculosis. Lancet 1:1269–1270, 1987.
9. Andreason F, Agerbaek H, Bjerregaard P, Gotzsche H: Pharmacokinetics of amiodarone after intravenous and oral administration. Eur J Clin Pharmacol 19:293–299, 1981.
10. Auerbach O, Dail DH: Mycobacterial infections. In Dail DH, Hammar SP (eds): Pulmonary Pathology. New York, Springer-Verlag, 1988, pp 173–188.
11. Balakrishnan J, Meziane MA, Siegelman SS, Fishman EK: Pulmo-

nary infarction: CT appearance with pathologic correlation. J Comput Assist Tomogr 13:941–945, 1989.
11a. Bankier AA, De Maertelaer V, Keyzer C, Gevenois PA: Pulmonary emphysema subjective visual grading versus objective quantification with macroscopic morphometry and thin-section CT densitometry. Radiology 211:851–858, 1999.
12. Barnett SM: CT findings in tuberculous mediastinitis. J Comput Assist Tomogr 10:165–166, 1986.
13. Barrio JL, Suarez M, Rodriguez JL, et al: PCP presenting as cavitating and noncavitating solitary pulmonary nodules in patients with AIDS. Am Rev Respir Dis 134:1094–1096, 1986.
14. Bartter T, Irwin RS, Nash G, et al: Idiopathic bronchiolitis obliterans organizing pneumonia with peripheral infiltrates on chest roentgenogram. Arch Intern Med 149:273–279, 1989.
14a. Bates SM, Ginsberg JS: Helical computed tomography and the diagnosis of pulmonary embolism. Ann Intern Med 132:240–242, 2000.
15. Beers MF, Sohn M, Swartz M: Recurrent pneumothorax in AIDS patients with PCP: A clinicopathologic report of three cases and review of the literature. Chest 98:266–270, 1990.
15a. Beigelman C, Chartrand-Lefebvre C, Howarth N, Grenier P: Pitfalls in diagnosis of pulmonary embolism with helical CT angiography. AJR Am J Roentgenol 171:579–585, 1998.
16. Bellamy EA, Husband JE, Blaquiere RM, Law MR: Bleomycin-related lung damage: CT evidence. Radiology 156:155–158, 1985.
17. Bellamy EA, Nicholas D, Husband JE: Quantitative assessment of lung damage due to bleomycin using computed tomography. Br J Radiol 60:1205–1209, 1987.
18. Bellomo R, Finlay M, McLaughlin P, Tai E: Clinical spectrum of cryptogenic organizing pneumonitis. Thorax 46:554–558, 1991.
19. Bergin CJ, Muller NL: CT in the diagnosis of interstitial lung disease. Am J Roentgenol 145:505–510, 1985.
20. Bergin CJ, Muller NL: CT of interstitial lung disease: A diagnostic approach. AJR Am J Roentgenol 148:8–15, 1987.
20a. Boiselle PM, Crans CA, Kaplan MA: The changing face of *Pneumocystis carinii* pneumonia in AIDS patients. AJR Am J Roentgenol 172:1301–1309, 1999.
21. Bombino M, Gattinoni L, Pesenti A, et al: The value of portable chest roentgenography in adult respiratory distress syndrome: Comparison with computed tomography. Chest 100:762–769, 1991.
22. Bouchardy LM, Kuhlman JE, Ball WC, et al: CT findings in bronchiolitis obliterans organizing pneumonia (BOOP) with x-ray, clinical, and histologic correlations. J Comput Assist Tomogr 17:352–357, 1993.
23. Reference deleted.
24. Boudes P: Purely granulomatous Wegener's granulomatosis: A new concept for an old disease. Semin Arthritis Rheum 19:365–370, 1990.
25. Brauner MW, Grenier P, Mouelhi MM, et al: Pulmonary histiocytosis X: Evaluation with high-resolution CT. Radiology 172:255–258, 1989.
26. Brown WG, Hasa FM, Barbee RA: Reversibility of severe bleomycin induced pulmonary pneumonitis. JAMA 239:2012–2014, 1978.
27. Burch PA, Karp JE, Merz WG, et al: Favorable outcome of invasive aspergillosis in patients with adult acute leukemia. J Clin Oncol 5: 1985–1993, 1987.
28. Butler S, Smathers RL: Case report. Computed tomography of amiodarone pulmonary toxicity. J Comput Assist Tomogr 9:375–376, 1985.
29. Camus P, Jeannin LRE: Speculation on the mechanism for amiodarone-induced pneumonitis (Letter). Radiology 150:279–280, 1984.
30. Case Records of the Massachusetts General Hospital. Case 9–1989. N Engl J Med 320:582–587, 1989.
31. Chaffey MH, Klein JS, Gamsu G, et al: Radiographic distribution of PCP in patients with AIDS treated with prophylactic inhaled pentamidine. Radiology 175:715–719, 1990.
32. Chandler PW, Myung SS, Friedman SE, et al: Radiographic manifestations of bronchiolitis obliterans with organizing pneumonia vs usual interstitial pneumonia. Am J Roentgenol 157:899–906, 1986.
33. Chintapalli D, Thorsen MK, Olson DL, et al: Computed tomography of pulmonary thromboembolism and infarction. J Comput Assist Tomogr 12:553–559, 1988.
34. Churg A: Pulmonary angiitis and granulomatosis revisited. Hum Pathol 14:868–883, 1983.
34a. Coche EE, Muller NL, Kim K, et al: Acute pulmonary embolism: Ancillary findings at spiral CT. Radiology 207:753–758, 1998.
35. Colby TV: Pathologic aspects of bronchiolitis obliterans organizing pneumonia. Chest 102:38s–43s, 1992.
36. Contreras MA, Cheung OT, Sanders DE, Goldstein RS: Pulmonary infection with nontuberculous mycobacteria. Am Rev Respir Dis 137:149–152, 1988.
37. Cordier JF, Loire R, Brune J: Idiopathic bronchiolitis obliterans organizing pneumonia: Definition of characteristic clinical profiles in a series of 16 patients. Chest 96:999–1004, 1989.
38. Corrin B, Liebow AA, Friedman PJ: Pulmonary lymphangiomyomatosis: A review. Am J Pathol 79:348–367, 1975.
39. Costa-Jussa FR, Corrin B, Jacobs JM: Amiodarone lung toxicity: A human and experimental study. J Pathol 143:73–79, 1984.
40. Costello P, Anderson W, Blume D: Pulmonary nodule: Evaluation with spiral volumetric CT. Radiology 179:875–876, 1991.
41. Cupples JB, Blackie SP, Road JD: Granulomatous PCP mimicking tuberculosis. Arch Pathol Lab Med 113:1281–1284, 1989.
42. Currie DC, Goldman JM, Cole PJ, Strickland B: Comparison of narrow section CT and plain chest radiography in chronic ABPA. Clin Radiol 38:593–596, 1987.
43. Dakai F, Gamsu G, Im JG, Ray CS: Pulmonary function abnormalities in patients with CT-determined emphysema. J Comput Assist Tomogr 11:936–938, 1987.
44. Dake MD, Madison JM, Montgomery CK, et al: Electron microscopic demonstration of lysosomal inclusion bodies in lung, liver, lymph nodes, and blood leukocytes of patients with amiodarone pulmonary toxicity. Am J Med 78:506–512, 1985.
45. Davis SD, Berkmen YM, King T: Peripheral bronchial involvement in relapsing polychondritis: Demonstration by thin-section CT. AJR Am J Roentgenol 153:953–954, 1989.
45a. Desai SR, Wells AU, Rubens MB, et al: Acute respiratory distress syndrome: CT abnormalities at long-term follow-up. Radiology 210: 29–35, 1999.
46. DeLorenzo LJ, Huang C, Maguire G, Stone G: Roentgenographic patterns of PCP in 104 patients with AIDS. Chest 91:323–327, 1987.
47. DiMarco AF, Montenegro H, Payne CB, Kwon KH: Papillomas of the tracheobronchial tree with malignant degeneration. Chest 74: 4–5, 1978.
48. Doyle TC, Lawler GA: CT features of rounded atelectasis of the lung. Am J Roentgenol 143:225–228, 1984.
49. Epler GR: Bronchiolitis obliterans organizing pneumonia: Definition and clinical features. Chest 102:2s–6s, 1992.
50. Epler GR, Colby TV: The spectrum of bronchiolitis obliterans. Chest 83:161–162, 1983.
51. Epler GR, Colby TV, McLoud TC, et al: Bronchiolitis obliterans organizing pneumonia. N Engl J Med 312:152–158, 1985.
52. Fauci AS, Haynes BF, Katz P, Wolffe SM: Wegener's granulomatosis: Prospective clinical and therapeutic experience with 85 patients for 21 years. Ann Intern Med 98:76–85, 1983.
53. Feuerstein IM, Archer A, Pluda JM, et al: Thin-walled cavities, cysts, and pneumothorax in PCP: Further observation with histopathologic correlation. Radiology 174:697–702, 1990.
54. Fleischman RW, Baker JR, Thompson GR, et al: Bleomycin induced interstitial pneumonia in dogs. Thorax 26:675–681, 1971.
55. Foster WI, Pratt PC, Roggli VL, et al: Centrilobular emphysema: CT-pathologic correlation. Radiology 159:27–32, 1986.
56. Fraser RG, Pare JAP: Diagnosis of Diseases of the Chest, vol 2, 3rd ed. Philadelphia, WB Saunders, 1989.
57. Fukuda Y, Kawamoto M, Yamamoto A, et al: Role of elastic fiber degradation in emphysema-like lesions of pulmonary lymphangiomyomatosis. Hum Pathol 21:1252–1261, 1990.
58. Fukuda Y, Masuda Y, Ishizaki M, et al: Morphogenesis of abnormal elastic fibers in lungs of patients with panacinar and centriacinar emphysema. Hum Pathol 20:652–659, 1989.
59. Gale ME, Karlinsky JB: Computed Tomography of the Chest: A Teaching File. Chicago, Year Book Medical, 1988.
60. Galzer HS, Levitt RG, Shackelford GD: Peripheral pulmonary infiltrates in sarcoidosis. Chest 86:741–744, 1984.
61. Gefter WB, Albelda SM, Talbot GH, et al: Invasive pulmonary aspergillosis and acute leukemia. Radiology 157:605, 1985.
62. Gefter WB, Epstein DM, Pietra GG, Miller WT: Lung disease caused by amiodarone: A new antiarrhythmic agent. Radiology 147: 339–344, 1983.
63. Goddard PR, Nicholson EM, Laszlo G, Watt I: Computed tomography in pulmonary emphysema. Clin Radiol 33:379–387, 1982.
64. Godwin JD, Muller NL, Takasugi JE: Pulmonary alveolar proteinosis: CT findings. Radiology 169:609–613, 1988.

65. Godwin JD, Webb WR, Gamsu G, Ovenfors C: Computed tomography of pulmonary embolism. Am J Roentgenol 135:691–695, 1980.
66. Golding RP, Knape P, Strack Van Schinjndel RJM, et al: Computed tomography as an adjunct to chest x-rays of intensive care unit patients. Crit Care Med 16:211–216, 1988.
67. Goldman IS, Winkler HL, Raper SE, et al: Increased hepatic density and phospholipidosis due to amiodarone. Am J Roentgenol 144: 541–546, 1985.
67a. Goodman LR, Curtin JJ, Mewissen MW, et al. Detection of pulmonary embolism in patients with unresolved clinical and scintigraphic diagnosis: Helical CT versus angiography. AJR Am J Roentgenol 164:1369–1374, 1995.
68. Gosink BB, Friedman PJ, Liebow AA: Bronchiolitis: Roentgenologic-pathologic correlation. Am J Roentgenol 117:816–832, 1973.
68a. Greaves SM, Hart EM, Brown K, et al: Pulmonary thromboembolism. Spectrum of findings on CT. AJR Am J Roentgenol 165: 1359–1363, 1995.
69. Hamper UM, Fishman EK, Khouri NF, et al: Typical and atypical CT manifestations of pulmonary sarcoidosis. J Comput Assist Tomogr 10:928–936, 1986.
70. Hansell D, Strickland B: HRCT in pulmonary cystic fibrosis. Br J Radiol 62:1–5, 1989.
70a. Hartman TE, Swenson SJ, Williams DE: *Mycobacterium avium–intracellulare* complex: Evaluation with CT. Radiology 187:23–26, 1993.
70b. Hartman TE, Tazelaar HD, Swensen SJ, Muller NL: Cigarette smoking: CT and pathologic findings of associated pulmonary diseases. Radiographics 17:377–390, 1997.
71. Hauser H, Gurret JP: Miliary tuberculosis associated with adrenal enlargement: CT appearance. J Comput Assist Tomogr 10:254–256, 1986.
72. Heger JJ, Prystowshky EN, Jackman WM, et al: Clinical efficacy and electrophysiology during long-term therapy for recurrent ventricular tachycardia or ventricular fibrillation. N Engl J Med 305: 539–545, 1981.
73. Heitzman ER, Markarian B, Berger I, Dailey E: The secondary pulmonary lobule: A practical concept for interpretation of radiographs. 1. Roentgen anatomy of the normal secondary pulmonary lobule. Radiology 93:508–513, 1969.
74. Hensley MJ, Feldman NT, Lazarus JM, Galvanek EG: Diffuse pulmonary hemorrhage and rapidly progressive renal failure. Am J Med 66:894–898, 1979.
75. Hruban RH, Meziane MA, Zerhouni EA, et al: High-resolution computed tomography of fixed-inflated lungs: Pathologic-radiologic correlation of centrilobular emphysema. Am Rev Respir Dis 136: 935–940, 1987.
76. Hruban RH, Ren H, Kuhlman JE, et al: Inflation-fixed lungs: Pathologic-radiologic (CT) correlation of lung transplantation. J Comput Assist Tomogr 14:329–335, 1990.
77. Hruban Z: Pulmonary and generalized lysosomal storage induced by amphophilic drugs. Environ Health Perspect 55:53–76, 1984.
78. Huang RM, Naidich DP, Lubat E, et al: Septic pulmonary emboli: CT-radiologic correlation. AJR Am J Roentgenol 153:41–45, 1989.
79. Hunninghake GW, Gadek JE, Fales HM, Crystal RG: Human alveolar macrophage derived chemotactic factors for neutrophils. J Clin Invest 66:473–483, 1980.
80. Huston J III, Muhm JR: Solitary pulmonary nodules: Evaluation with a CT reference phantom. Radiology 170:653–656, 1989.
80a. Im JG, Itoh H, Shim YS, et al: Pulmonary tuberculosis: CT Findings—early active disease and sequential change with antituberculous therapy. Radiology 186:653–660, 1993.
81. Im JG, Song KS, Kang HS, et al: Mediastinal tuberculous lymphadenitis: CT manifestations. Radiology 164:115–119, 1987.
82. Joharjy I, Bashi SA, Adbullah AK: Value of medium-thickness CT in the diagnosis of bronchiectasis. AJR Am J Roentgenol 149: 1133–1137, 1987.
83. Judson MA, Postic B, Weiman DS: PCP manifested as a hilar mass and cavitary lesion: Presentation in a patient receiving aerosolized pentamidine prophylaxis. South Med J 83:1309–1312, 1990.
84. Kalender WA, Seissler W, Klotz E, Vock P: Spiral volumetric CT with single-breath-hold technique, continuous transport, and continuous scanner rotation. Radiology 176:181–183, 1990.
85. Kannan R, Nademanee K, Hendrickson JA, et al: Amiodarone kinetics after oral doses. Clin Pharmacol Ther 31:438–444, 1982.
86. Katz D, Dreel L: Computed tomography in pulmonary asbestosis. Clin Radiol 30:207–213, 1979.
87. Katzenstein ALA, Askin FB: Surgical Pathology of Non-neoplastic Lung Disease, 2nd ed. Philadelphia, WB Saunders, 1990, pp 511–520.
88. Katzenstein ALA, Myers JL, Prophet WD, et al: Bronchiolitis obliterans and usual interstitial pneumonia. A comparative clinicopathologic study. Am J Surg Pathol 10:373–381, 1986.
89. Kawanami T, Bowen A: Juvenile laryngeal papillomatosis with pulmonary parenchymal spread. Pediatr Radiol 15:102–104, 1985.
90. Khan A, Herman PG, Vorwerk P, et al: Solitary pulmonary nodules: Comparison of classification with standard, thin-section, and reference phantom CT. Radiology 179:477–481, 1991.
90a. King MA, Ysrael M, Bergin CJ: Chronic thromboembolic pulmonary hypertension: CT findings. AJR Am J Roentgenol 170;955–960, 1998.
91. King TE: Bronchiolitis obliterans. Lung 167:69–93, 1989.
92. Klein JS, Warnock M, Webb RW, Gamsu G: Cavitating and noncavitating granulomas in AIDS patients with PCP. AJR Am J Roentgenol 152:753–754, 1989.
93. Kovacs JA, Heimenz JW, Macher AM, et al: *Pneumocystis carinii* pneumonia: A comparison between patients with acquired immunodeficiency syndrome and patients with other immunodeficiencies. Ann Intern Med 100:633–671, 1984.
94. Kramer SS, Wehunt WD, Stocker JT, Kashima H: Pulmonary manifestations of juvenile laryngotracheal papillomatosis. Am J Roentgenol 144:687–694, 1985.
95. Kruglik GD, Reed JC, Daroca PJ: RPC from the AFIP. Diagn Radiol 120:583–587, 1976.
96. Kuhlman JE: AIDS-related diseases of the chest. In Kuhlman JE (ed): CT of the Immunocompromised Host: Contemporary Issues in Computed Tomography, vol 14. New York, Churchill Livingstone, 1991, pp 27–69.
97. Kuhlman JE: CT of the immunocompromised and acutely ill patient. In Zerhouni EA (ed): CT and MRI of the Thorax: Contemporary Issues in Computed Tomography. New York, Churchill Livingstone, 1990, pp 1–22.
98. Kuhlman JE: CT of diffuse lung disease. Appl Radiol 20:17–22, 1991.
99. Kuhlman JE: CT evaluation of the chest in AIDS. In Thrall JH (ed): Current Practice in Radiology, 3rd ed. St. Louis, Mosby–Year Book, 1993.
100. Kuhlman JE: Opportunistic fungal infection: The neutropenic patient with leukemia, lymphoma, or bone marrow transplantation. In Kuhlman JE (ed): CT of the Immunocompromised Host: Contemporary Issues in Computed Tomography. New York, Churchill Livingston, 1991, pp 5–25.
101. Kuhlman JE: The role of chest computed tomography in the diagnosis of drug-related reactions. J Thorac Imaging 6:52–61, 1991.
102. Kuhlman JE, Deutsch JH, Fishman EK, Siegelman SS: CT features of thoracic mycobacterial disease. Radiographics 10:413–431, 1990.
103. Kuhlman JE, Fishman EK, Burch PA, et al: Invasive pulmonary aspergillosis in acute leukemia: The contribution of CT to early diagnosis and aggressive management. Chest 92:95–99, 1987.
104. Kuhlman JE, Fishman EK, Burch PA, et al: CT of invasive pulmonary aspergillosis. AJR Am J Roentgenol 150:1015–1020, 1988.
105. Kuhlman JE, Fishman EK, Knowles MG, et al: Diseases in the chest in AIDS: CT diagnosis. Radiographics 9:827–857, 1989.
106. Kuhlman JE, Fishman EK, Siegelman SS: CT diagnosis of pulmonary septic emboli. Radiology 174:211–213, 1990.
107. Kuhlman JE, Fishman EK, Siegelman SS: Invasive pulmonary aspergillosis in acute leukemia: Characteristic findings on CT, the CT halo sign, and the role of CT in early diagnosis. Radiology 157: 611–614, 1985.
108. Kuhlman JE, Fishman EK, Zerhouni EA, et al: The CT spectrum of thoracic sarcoidosis. Radiographics 9:449–466, 1989.
109. Kuhlman JE, Hruban RH, Fishman EK: Wegener granulomatosis: CT features of parenchymal lung disease. J Comput Assist Tomogr 15:948–952, 1991.
110. Kuhlman JE, Kavuru M, Fishman EK, Siegelman SS: *Pneumocystis carinii* pneumonia: Spectrum of parenchymal CT findings. Radiology 175:711–714, 1990.
111. Kuhlman JE, Knowles MC, Fishman EK, Siegelman SS: Premature bullous pulmonary damage in AIDS: CT diagnosis. Radiology 173: 23–26, 1989.
112. Kuhlman JE, Ney DR, Fishman EK: 2D and 3D imaging of the in vivo lung: Combining spiral CT with multiplanar and volumetric rendering techniques. Radiology 181(suppl):274, 1991.

113. Kuhlman JE, Ren H, Hutchins GM, Fishman EK: Fulminant pulmonary calcification complicating renal transplantation: CT demonstration. Radiology 173:459–460, 1989.
114. Kuhlman JE, Reyes BL, Hruban RH, et al: Abnormal air-filled spaces in the lung. Radiographics 13:47–75, 1993.
115. Kuhlman JE, Scatarige JC, Fishman EK, et al: CT demonstration of high attenuation pleural-parenchymal lesions due to amiodarone therapy. J Comput Assist Tomogr 11:160–162, 1987.
116. Kuhlman JE, Teigen C, Ren H, et al: Amiodarone lung: CT findings in symptomatic patients. Radiology 177:121–125, 1990.
116a. Kuzo RS, Goodman LR: CT evaluation of pulmonary embolism: Techniques and interpretation. AJR Am J Roentgenol 169:959–965, 1997.
117. Landman S, Burgener F: Pulmonary manifestations in Wegener's granulomatosis. Am J Roentgenol 122:750–757, 1974.
118. Lenoir S, Grenier P, Brauner MW, et al: Pulmonary lymphangiomyomatosis and tuberous sclerosis: Comparison of radiographic and thin-section CT findings. Radiology 175:329–334, 1990.
119. Leopold TG, Gough J: The centrilobular form of emphysema and its relation to chronic bronchitis. Thorax 12:219–235, 1957.
119a. Leung AN, Fisher K, Valentine V, et al: Bronchiolitis obliterans after lung transplantation: Detection using expiratory HRCT. Chest 113:365–370, 1998.
120. Lillington GA, Siefkin AM: Fibrosing alveolitis: Causes, characteristics and consequences. Postgrad Med 71:128–137, 1982.
121. Linhartova A: Lesions in resected lung parenchyma with regard to possible initial phase of pulmonary emphysema. Pathol Res Pract 181:71–76, 1986.
122. Littner MR, Schachter EN, Putman CE, et al: The clinical assessment of roentgenographically atypical pulmonary sarcoidosis. Am J Med 62:361–368, 1977.
123. Liu CI, Fields WR, Chung IS: Tuberculous mediastinal lymphadenopathy in adults. Diagn Radiol 126:369–371, 1978.
124. Liu FL, Cohen RD, Downar E, et al: Amiodarone pulmonary toxicity: Functional and ultrastructural evaluation. Thorax 41:100–105, 1986.
125. Liu YC, Tomashefski JF, Tomford W, Green H: Necrotizing PCP vasculitis associated with lung necrosis and cavitation in a patient with AIDS. Arch Pathol Lab Med 113:494–497, 1989.
126. Lynch DA, Brasch RC, Hardy KA, Webb WR: Pediatric pulmonary disease: Assessment with high-resolution ultrafast CT. Radiology 176:243–248, 1990.
127. Lynch DA, Gamsu G, Aberle DR: Conventional and high resolution computed tomography in the diagnosis of asbestos-related diseases. Radiographics 9:523–551, 1989.
128. Lynch DA, Gamsu G, Ray CS, Aberle DR: Asbestos-related focal lung masses: Manifestations on conventional and high-resolution CT scans. Radiology 169:603–607, 1988.
129. Macklin MT, Macklin CC: Malignant interstitial emphysema of the lungs and mediastinum as an important occult complication in many respiratory diseases and other conditions. Medicine 23:281–358, 1944.
130. Maguire R, Fauci AS, Doppman JL, Wolff SM: Unusual radiographic features of Wegener's granulomatosis. AJR Am J Roentgenol 130:233–238, 1987.
131. Mani TM, Lalleland D, Corone S, Mauriat D: Metastatic pulmonary calcifications after cardiac surgery in children. Radiology 174:463–467, 1990.
132. Marchlinski FE, Gansler TS, Waxman HL, Josephson ME: Amiodarone pulmonary toxicity. Ann Intern Med 97:839–845, 1982.
133. Marcy TW, Reynolds HY: Pulmonary histiocytosis X. Lung 163: 129–150, 1985.
134. Marinelli DL, Albelda SM, Williams TM, et al: Nontuberculous mycobacterial infection in AIDS: Clinical, pathologic, and radiographic features. Radiology 160:77–82, 1986.
135. Mark EJ, Matsubara O, Tan-Liu NS, Fienberg R: The pulmonary biopsy in the early diagnosis of Wegener's (pathergic) granulomatosis: A study based on 35 open lung biopsies. Hum Pathol 19: 1065–1071, 1988.
136. Mark EJ, Ramirez JF: Pulmonary capillaritis and hemorrhage in patients with systemic vasculitis. Arch Pathol Lab Med 109:413–418, 1985.
137. Markos J, Veronese ME, Nicholson MR, et al: Value of hepatic computerized tomographic scanning during amiodarone therapy. Am J Cardiol 56:89–92, 1985.
137a. Marti-Bonmati L, Perales FR, Catala F, et al: CT findings of Swyer-James Syndrome. Radiology 172:477–480, 1989.
138. Martin KW, Sagel SS, Siegel BA: Mosaic oligemia simulating pulmonary infiltrates on CT. Am J Roentgenol 147:670–673, 1986.
139. Martinez C, Romanelli A, Mullen MP, Lee M: Spontaneous pneumothoraces in AIDS patients receiving aerosolized pentamidine (Letter). Chest 94:1317–1318, 1988.
140. Maunder RJ, Shuman WP, McHugh JW, et al: Preservation of normal lung regions in the adult respiratory distress syndrome: Analysis by computed tomography. JAMA 255:2463–2465, 1986.
141. Mayo JR: High-resolution computed tomography: Technical aspects. Radiol Clin North Am 29:1043–1049, 1991.
142. Mayo JR, Webb WR, Gould R, et al: High-resolution CT of the lungs: An optimal approach. Radiology 163:507–510, 1987.
143. McDonald TJ, DeRemee RA: Wegener's granulomatosis. Laryngoscope 93:220–231, 1983.
144. McHugh K, Blaquiere RM: CT features of rounded atelectasis. AJR Am J Roentgenol 153:257–260, 1989.
145. McLoud TC, Epler GR, Colby TV, et al: Bronchiolitis obliterans. Radiology 159:1–8, 1986.
146. Meziane MA, Hruban RH, Zerhouni EA, et al: High-resolution CT of the lung parenchyma with pathologic correlation. Radiographics 8:27–54, 1988.
147. Miki Y, Hatabu H, Takahashi M, et al: Computed tomography of bronchiolitis obliterans. J Comput Assist Tomogr 12:512–514, 1988.
148. Miller RR, Muller NL, Vedal S, et al: Limitations of computed tomography in the assessment of emphysema. Am Rev Respir Dis 139:980–983, 1989.
148a. Miller WT, Tino G, Friedberg JS: Thoracic CT in the intensive care unit: Assessment of clinical usefulness. Radiology 209:491–498, 1998.
149. Milligan SA, Stulbarg MS, Gamsu G, Golden JA: PCP radiographically simulating tuberculosis. Am Rev Respir Dis 132:1124–1126, 1985.
150. Milne EN, Zerhouni EA: Blood supply of pulmonary metastases. J Thorac Imaging 2:15–23, 1987.
151. Mirvis SE, Tobin K, Kostrubiak I, Belzberg H: Thoracic CT in detecting occult disease in critically ill patients. AJR Am J Roentgenol 148:685–689, 1987.
152. Miyagawa Y, Nagata N, Shigematsu N: Clinicopathological study of migratory lung infiltrates. Thorax 46:233–238, 1991.
152a. Moore ADA, Godwin JD, Dietrich PA, et al: Swyer-James syndrome: CT findings in eight patients. AJR Am J Roentgenol 158: 1211–1215, 1992.
153. Moore ADA, Godwin JD, Muller NL, et al: Pulmonary histiocytosis X: Comparison of radiographic and CT findings. Radiology 172: 249–254, 1989.
153a. Moore EH: Atypical mycobacterial infection in the lung: CT appearance. Radiology 187:777–782, 1993.
154. Morgan EJ: Silicosis and tuberculosis. Chest 75:202–203, 1979.
155. Muller NL: Clinical value of high-resolution CT in chronic diffuse lung disease. AJR Am J Roentgenol 157:1163–1170, 1991.
156. Muller NL, Chiles C, Kullnig P: Pulmonary lymphangiomyomatosis: Correlation of CT and radiographic and functional findings. Radiology 175:335–339, 1990.
157. Muller NL, Guerry-Force ML, Staples CA, et al: Differential diagnosis of bronchiolitis obliterans with organizing pneumonia: Clinical, functional and radiologic findings. Radiology 162:151–156, 1987.
158. Muller NL, Staples CA, Miller RR: Bronchiolitis obliterans organizing pneumonia: CT features in 14 patients. AJR Am J Roentgenol 154:983–987, 1990.
159. Muller NL, Staples CA, Miller RR, et al: Idiopathic pulmonary fibrosis: CT and pathologic correlation. Radiology 165:731–734, 1987.
160. Munk PI, Muller NL, Miller RR, Ostrow DN: Pulmonary lymphangitic carcinomatosis: CT and pathologic findings. Radiology 166: 705–709, 1988.
161. Murata K, Itoh H, Todo G, et al: Centrilobular lesions of the lung: Demonstration by high-resolution CT and pathologic correlation. Radiology 161:641–645, 1986.
162. Myers JL, Kennedy JI, Plumb VJ: Amiodarone lung: Pathologic findings in clinically toxic patients. Hum Pathol 18:349–354, 1987.
163. Nachman JB, Baum ES, White H, Cruissi FG: Bleomycin-induced pulmonary fibrosis mimicking recurrent metastatic disease in a patient with testicular carcinoma: Case report of the CT scan appearance. Cancer 47:236–239, 1981.

164. Naidich DP, Garay SM, Goodman PC: Pulmonary manifestations of AIDS. In Federle MD, Megibow AJ, Naidich DP (eds): Radiology of AIDS. New York, Raven Press, 1988, pp 47–76.
165. Naidich DP, Garay S, Rybak BJ: Kaposi's sarcoma CT: Radiographic correlation. Chest 96:723–728, 1989.
166. Naidich D, McCauley DI, Khouri NF, et al: Computed tomography of bronchiectasis. J Comput Assist Tomogr 6:437–444, 1982.
167. Naidich DP, McCauley DI, Leitman BS, et al: CT of pulmonary tuberculosis. In Siegelman SS (ed): Computed Tomography of the Chest. New York, Churchill Livingstone, 1984, pp 175–217.
168. Nakata H, Kimoto T, Nakayama T, et al: Diffuse peripheral lung disease: Evaluation by high-resolution computed tomography. Radiology 157:181–185, 1985.
169. Newmark H, Willis G, Ablemayor E, Chakmakian V: Kartagener's syndrome seen on CT. Comput Radiol 9:279–281, 1985.
170. Newsome GS, Ward DJ, Pierce PF: Spontaneous pneumothorax in patients with AIDS treated with prophylactic aerosolized pentamidine. Arch Intern Med 150:2167–2168, 1990.
171. Ney DR, Kuhlman JE, Hruban RH, et al: Three-dimensional CT: Volumetric reconstruction and display of the bronchial tree. Invest Radiol 25:736–742, 1990.
172. Nicholson AA, Hayward C: The value of computed tomography in the diagnosis of amiodarone-induced pulmonary toxicity. Clin Radiol 40:564–567, 1989.
173. Nishimura K, Itoh H: High-resolution computed tomographic features of bronchiolitis obliterans organizing pneumonia. Chest 102: 26s–31s, 1992.
174. Noma S, Herman PG, Kan A, et al: Sequential morphologic changes of elastase-induced pulmonary emphysema in pig lungs. Invest Radiol 26:446–453, 1991.
175. Olson LK, Forrest JV, Friedman PJ, et al: Pneumonitis after amiodarone therapy. Radiology 150:327–330, 1984.
176. Orr DP, Myerowitz RL, Dubois PJ: Pathoradiologic correlation of invasive pulmonary aspergillosis in the compromised host. Cancer 41:2028–2039, 1978.
177. Paltiel HJ, Azouz EM, Elleltine DW, Bernstein M: Computed tomography in interstitial lung disease. J Comput Tomogr 10:349–355, 1986.
178. Pare JAP, Fraser RG: Diseases of the chest of unknown origin. In Pare JAP, Fraser R (eds): Synopsis of Diseases of the Chest. Philadelphia, WB Saunders, 1983, pp 604–651.
179. Pare JAP, Fraser RG: In Pare JAP, Fraser RG (eds): Synopsis of Diseases of the Chest. Diseases of the Airways. Philadelphia, WB Saunders, 1983, p 558.
180. Peruzzi W, Garner W, Bools J, et al: Portable chest roentgenography and computed tomography in critically ill patients. Chest 93:728–726, 1988.
181. Pimentel JC: Tridimensional photographic reconstruction in a study of the pathogenesis of honeycomb lung. Thorax 22:444–452, 1967.
182. Pratt PC: Pathology of tuberculosis. Semin Roentgenol 14:196–203, 1979.
183. Radin DR, Baker EL, Klatt EC, et al: Visceral and nodal calcification in patients with AIDS-related *Pneumocystis carinii* infection. AJR Am J Roentgenol 154:27, 1990.
183a. Rathbun SW, Raskob GE, Whitsett TL: Sensitivity and specificity of helical computed tomography in the diagnosis of pulmonary embolism: A systematic review. Ann Intern Med 132:227–232, 2000.
184. Remy-Jardin M, Beuscart R, Sault MC, et al: Subpleural micronodules in diffuse infiltrative lung disease: Evaluation with thin-section CT scans. Radiology 177:133–139, 1990.
184a. Remy-Jardin M, Remy J, Wattinne L, Giraud F: Central pulmonary thromboembolism: Diagnosis with spiral volumetric CT with the single breath-hold technique—comparison with pulmonary angiography. Radiology 1992; 185:381–387.
184b. Remy-Jardin M, Remy J, Cauvain O, et al: Diagnosis of central pulmonary embolism with helical CT: Role of two-dimensional multiplanar reformations. AJR Am J Roentgenol 165:1131–1138, 1995.
185. Ren H, Hruban RH, Kuhlman JE, et al: High resolution computed tomography of inflation-fixed lungs: The beaded-septum sign of pulmonary metastases. J Comput Assist Tomogr 13:411–416, 1989.
186. Ren H, Kuhlman JE, Hurban RH, et al: High resolution computed tomography of inflation-fixed lungs: A wedge-shaped density and associated vascular sign in the diagnosis of pulmonary infarction. J Comput Assist Tomogr 14:82–86, 1990.
187. Ren H, Kuhlman JE, Hruban RH, et al: Computed tomography–pathology correlation of amiodarone lung. J Comput Assist Tomogr 14:760–765, 1990.
188. Rimmer MJ, Dixon AK, Flower CDR, Sikora K: Bleomycin lung: Computed tomographic observations. Br J Radiol 58:1041–1045, 1985.
189. Riva E, Gerna M, Neyroz P, et al: Pharmacokinetics of amiodarone in rats. J Cardiovasc Pharmacol 4:270–275, 1982.
190. Roberts CMR, Citron KM, Strickland B: Intrathoracic aspergilloma: Role of CT in diagnosis and treatment. Radiology 165:123–128, 1987.
191. Rockoff SD, Rohatgi PK: Unusual manifestations of thoracic sarcoidosis. Am J Roentgenol 144:513–528, 1985.
192. Saksouk FA, Haddad MC: Detection of mesenteric involvement in sarcoidosis using computed tomography. Br J Radiol 60:1135–1136, 1987.
193. Sandhu J, Goodman PC: Pulmonary cysts associated with PCP in patients with AIDS. Radiology 173:33–35, 1989.
194. Scadding JG: *Mycobacterium* tuberculosis in the aetiology of sarcoidosis. Br Med J 2:1617, 1960.
195. Scannell DA: Pneumothoraces and PCP in two AIDS patients receiving aerosolized pentamidine. Chest 97:479–480, 1990.
196. Schmidt RA, Glenny RW, Godwin JD, et al: Panlobular emphysema in young intravenous Ritalin abusers. Am Rev Respir Dis 143: 649–656, 1991.
197. Schurwitzki H, Stiglbauer R, Graninger W, et al: Interstitial lung disease in progressive systemic sclerosis: High-resolution CT versus radiography. Radiology 176:755–759, 1990.
198. Scully RE, Mark EJ, McNeely BU: Case records of the Massachusetts General Hospital. Weekly clinicopathological exercises. Case 12–1986. N Engl J Med 314:834–844, 1986.
199. Senior R, Connolly NL, Cury JD, et al: Elastin degradation by human alveolar macrophages. Am Rev Respir Dis 139:1251–1256, 1989.
200. Shaffer K, Pugatch RD: Small pulmonary nodules: Dynamic CT with a single-breath technique. Radiology 173:567–568, 1989.
201. Shenasa M, Vaisman U, Wojciechowski M, et al: Abnormal abdominal computerized tomography with amiodarone therapy and clinical significance. Am Heart J 107:929–933, 1984.
202. Shin MS, Ho K-J: CT of bronchiectasis in association with tuberculosis. Clin Imaging 13:36–43, 1989.
203. Shin MS, Liendo C, Ho KJ: *Pneumocystis carinii* pneumonia in an AIDS patient: Unusual manifestation as multiple cavitary and noncavitary peripheral nodules and spontaneous pneumothorax. Clin Imaging 13:225–227, 1989.
204. Siegelman SS, Khouri NF, Leo FP, et al: Solitary pulmonary nodules: CT assessment. Radiology 160:307–312, 1986.
205. Siegelman SS, Khouri NF, Scott WW Jr, et al: Pulmonary hamartoma: CT findings. Radiology 160:313–317, 1986.
206. Silver SF, Muller NL, Miller RR, Lefcoe MS: Hypersensitivity pneumonitis: Evaluation with CT. Radiology 173:441–445, 1989.
207. Sinner WN: Computed tomographic patterns of pulmonary thromboembolism and infarction. J Comput Assist Tomogr 2:395–399, 1978.
208. Solomon A, Kreel L, McNicol M, Johnson N: Computed tomography in pulmonary sarcoidosis. J Comput Assist Tomogr 3:754–758, 1979.
209. Standertskjold-Nordenstam CG, Wandtke JC, Hood WB Jr, et al: Amiodarone pulmonary toxicity: Chest radiography and CT in asymptomatic patients. Chest 88:143–145, 1985.
210. Stanford DW, Galvin J: The diagnosis of bronchiectasis. Clin Chest Med 9:691–699, 1988.
211. Staples CA, Muller NL, Vedal S, et al: Usual interstitial pneumonia: Correlation of CT with clinical, functional and radiologic findings. Radiology 162:377–381, 1987.
212. Stark P, Greene R, Kott MM, et al: CT findings in ARDS. Radiologie 27:367–369, 1987.
213. Stern EJ, Webb WR, Golden JA, Gamsu G: Cystic lung disease associated with eosinophilic granuloma and tuberous sclerosis: Air trapping at dynamic ultrafast high-resolution CT. Radiology 182: 325–329, 1992.
213a. Stern EJ, Swensen SJ, Hartman TE, Frank MS. CT mosaic pattern of lung attenuation: Distinguishing different causes. AJR Am J Roentgenol 165:813–816, 1995.
214. Stockley RA: Bronchiectasis: New therapeutic approaches based on pathogenesis. Clin Chest Med 8:481–494, 1987.

215. Strickland B, Strickland NH: The value of high definition, narrow section computed tomography in fibrosing alveolitis. Clin Radiol 39:589–594, 1988.
216. Swensen SJ, Harms GF, Morin RL, Myers JL: CT evaluation of solitary pulmonary nodules: Value of 185-H reference phantom. AJR Am J Roentgenol 156:925–929, 1991.
217. Swensen SJ, Morin RL, Schueler BA, et al: Solitary pulmonary nodule: CT evaluation of enhancement with iodinated contrast material—a preliminary report. Radiology 182:343–347, 1991.
217a. Swenson SJ, Brown LR, Colby TV, Weaver AL: Pulmonary nodules: CT evaluation of enhancement with iodinated contrast material. Radiology 1995; 194:393–398.
217b. Swenson SJ, Brown LR, Colby TV, et al: Lung nodule enhancement at CT: Prospective findings. Radiology 201:447–455, 1996.
218. Tellis CJ, Putnam JS: Cavitation in large multinodular pulmonary disease: A rare manifestation of sarcoidosis. Chest 71:792–793, 1977.
219. Thomas PD, Hunninghake GW: Current concepts of the pathogenesis of sarcoidosis. Am Rev Respir Dis 135:747–760, 1987.
220. Tocino IM, Miller MH, Fairfax WR: Distribution of pneumothorax in the supine and semirecumbent critically ill adult. Am J Roentgenol 144:901–905, 1985.
221. Tomashefski U, Bruce M, Stern RC, et al: Pulmonary air cysts in cystic fibrosis. Hum Pathol 16:253–261, 1985.
222. Travis WD, Lipschik GY, Suffredini AF, et al: Atypical pathologic manifestations of PCP in AIDS. Am J Surg Pathol 14:615–625, 1990.
223. Vock P, Soucek M, Daepp M, Kalender WA: Lung: Spiral volumetric CT with single-breath-hold technique. Radiology 176:864–867, 1990
224. Wally OR: Centers for Disease Control. Tuberculosis, final data—United States, 1986. MMWR Morb Mortal Wkly Rep 36: 817–820, 1988.
225. Walton EW: Giant-cell granuloma of the respiratory tract (Wegener's granulomatosis). Br Med J pp 265–270, 1958.
225a. Ward S, Heyneman L, Lee MJ, et al: Accuracy of CT in the diagnosis of allergic bronchopulmonary aspergillosis in asthmatic patients. AJR Am J Roentgenol 173:937–942, 1999.
226. Watanabe Y, Nishiyama Y, Kanayama H, et al: Congenital bronchiectasis due to cartilage deficiency: CT demonstration. J Comput Assist Tomogr 11:701–703, 1987.
227. Webb WR: High-resolution CT of the lung parenchyma. Radiol Clin North Am 27:1085–1097, 1989.
228. Webb WR, Muller NL, Naidich DP (eds): High-Resolution CT of the Lung. New York, Raven Press, 1992.
229. Webb WR, Muller NL, Zerhouni EA: High-resolution CT of the lung: Current clinical uses. Perspect Radiol 2:61–69, 1989.
230. Webb WR, Stein MG, Finkbeiner WE, et al: Normal and diseased isolated lungs: High-resolution CT. Radiology 166:81–87, 1988.
231. Westcott JL, Cole S: Barotrauma. In Herman PG (ed): Radiology of Iatrogenic Disorders: Iatrogenic Thoracic Complications. New York, Springer-Verlag, 1983, pp 79–109.
232. Westcott JL, Cole SR: Traction bronchiectasis in end-stage pulmonary fibrosis. Radiology 161:665–669, 1986.
233. Werb Z, Gordon S: Elastase secretion by stimulated macrophages. J Exp Med 142:361–377, 1975.
234. White R, Kuhn C: Effects of phagocytosis of mineral dusts on elastase secretion by alveolar and peritoneal exudative macrophages. Arch Environ Health 35:106–109, 1980.
235. Wolff SD, Kuhlman JE, Fishman EK: Thoracic Kaposi's sarcoma in AIDS: CT findings. J Comput Assist Tomogr 17:60–62, 1993.
236. Wolff SM, Fauci AS, Horn RG, Dale DC: Wegener's granulomatosis. Ann Intern Med 81:513–525, 1974.
237. Wood DW, Osborn MJ, Rooke J, Holmes DR: Amiodarone pulmonary toxicity: Report of two cases associated with rapidly progressive fatal adult respiratory distress syndrome after pulmonary angiography. Mayo Clin Proc 60:601–603, 1985.
238. Woodring JH, Vandiviere HM, Fried AM, et al: Update: The radiographic features of pulmonary tuberculosis. Am J Roentgenol 146: 497–506, 1986.
238a. Woolley K, Stark P: Pulmonary parenchymal manifestations of mitral valve disease. Radiographics 19:965–972, 1999.
238b. Worthy SA, Muller NL, Hartman TE, et al: Mosaic attenuation pattern on thin-section CT scans of the lung: Differentiation among infiltrative lung, airway, and vascular diseases as a cause. Radiology 205:465–470, 1997.
239. Wright JL, Cagle P, Churg A, et al: Diseases of the small airways. Am Rev Respir Dis 146:240–262, 1992.
239a. Yamashita K, Matsunobe S, Tsuda T, et al: Solitary pulmonary nodules: Preliminary study of evaluation with incremental dynamic CT. Radiology 194:399–405, 1995.
239b. Zeman RK, Silverman PM, Vieco PT, Costello P: CT angiography. AJR Am J Roentgenol 165:1079–1088, 1995.
240. Zerhouni EA, Naidich DP, Stitik FP, et al: CT of the pulmonary parenchyma: Interstitial disease. J Thorac Imaging 1:54–64, 1985.
241. Zerhouni EA, Stitik FP, Siegelman SS, et al: CT of the pulmonary nodule: A cooperative study. Radiology 160:319–327, 1986.
242. Zhang M, Kono M: Solitary pulmonary nodules: Evaluation of blood flow patterns with dynamic CT. Radiology 205:471–478, 1997.

28 Primary Pulmonary Neoplasms

Jeremy J. Erasmus, H. Page McAdams, Santiago E. Rossi

Although most primary pulmonary tumors are carcinomas, a large histologic spectrum of benign and malignant tumors of the lung exists. This chapter reviews the more common neoplasms according to the classification proposed by the World Health Organization (WHO) (Table 28–1) and emphasizes the radiologic manifestations of these neoplasms and the use of imaging in diagnosis and management.

Malignant Neoplasms of the Lung

Epithelial Tumors

Lung Cancer

Epidemiology

Lung cancer is a common malignancy. The American Cancer Society (ACS) estimated that 169,500 new cases would be diagnosed in the United States in the year 2001.[4,4a] The number of new cases in men, however, decreased from a high of 86.5 per 100,000 in 1984 to 69.1 in 1997.[257] The incidence of lung cancer in women has continued to increase since the 1960s, and in 1997 although the rate of increase slowed in the 1990s, 43.1 per 100,000 new cases occurred in 1997. The annual mortality rate in men decreased during the 1990s, whereas the rate in women continues to increase.[257] Lung cancer remains the leading cause of cancer-related deaths in both men and women in the United States, and the ACS estimated that it would account for 28% of all cancer deaths in the year 2001.[4a]

Etiology

The strongest risk factor for the development of lung cancer is cigarette smoking; an estimated 85% to 90% of lung cancers in men and 80% in women have been attributable to smoking.[4, 9, 58, 234, 237] The length of time and the number and type of cigarettes smoked are directly related to the risk of lung cancer.[61, 196, 235] Squamous cell and small-cell carcinomas have the highest association with smoking, whereas adenocarcinomas are the predominant cell type in nonsmokers.[61] The change in smoking habits (use of filter tips, decrease in tar yield), however, has been postulated to account for the recent increase in incidence of adenocarcinomas in cigarette smokers.[61, 228, 262]

Involuntary smoke exposure (passive smoking) is generally considered to be associated with an increased risk of lung cancer, although the numerous variables in the epidemiologic data make this difficult to conclude with certainty.[4, 185, 196, 230, 237] Spousal smoking has, however, been estimated to increase the lung cancer risk by 20% in women who have never smoked.[23]

Environmental and occupational exposures to particulate and chemical substances are additional risk factors.[212, 243] Exposure to the naturally occurring radioactive gas radon, both in homes and in mines, is the most important risk factor after cigarette smoking.[152, 196, 212, 245] It is estimated that 7000 to 30,000 lung cancer deaths occur annually in the United States as a result of residential exposure to radon.[245]

Asbestos is a carcinogen, and although there is an unequivocal association between lung cancer and asbestos exposure, the magnitude of the risk is frequently overestimated (most cohort studies show less than a twofold increase in risk).[74] Although the risk of lung cancer in workers exposed to asbestos may depend on individual occupational exposure characteristics (i.e., duration, concentration, and fiber type), the increased risk may be largely limited to those with radiologic evidence of asbestosis or to cigarette smokers.[74, 188, 236, 252] It has been estimated that as many as 33% of lung cancers that occur in smokers exposed to asbestos are the result of the synergistic effect of the two carcinogens.[53]

Additional risk factors for development of lung cancer include exposure to arsenic, chloromethyl ethers, chromium, isopropyl oil, mustard gas, nickel, beryllium, chloroprene, vinyl chloride, and various smelting by-products such as lead and copper.[212] Other factors, such as focal or diffuse pulmonary fibrosis and ionizing radiation, have been reported to increase the risk of lung cancer. Epidemiologic data, however, do not clearly establish a cause-and-effect relationship, except in some patients with Hodgkin's disease treated with radiation.[120] Finally, although not clearly understood, genetic susceptibility to lung cancer may be involved in a small number of cases.[10, 54, 177, 196]

Histologic Classification

Lung cancer is divided by the WHO Classification into two major histologic categories: *non–small-cell* lung carcinoma (NSCLC) and *small-cell* lung carcinoma (SCLC) (see Table 28–1).[227] NSCLC is further subdivided into histologic variants such as squamous cell carcinoma, adenocarcinoma, and large-cell carcinoma, according to the most differentiated portion of the tumor. Many tumors,

Table 28–1. Histologic Classification of Lung Tumors

- I. **Epithelial Tumors**
  - A. Benign
    - Papillomas
    - Adenomas
  - B. Malignant
    - Squamous cell carcinoma
      - Variants: papillary, clear cell, small-cell, basaloid
    - Adenocarcinoma
      - Acinar adenocarcinoma
      - Papillary adenocarcinoma
      - Bronchioloalveolar carcinoma
      - Solid adenocarcinoma with mucin
      - Adenocarcinoma with mixed subtypes
      - Variants: fetal, clear cell, signet-ring, colloid
    - Large cell carcinoma
      - Variants: clear cell, large-cell neuroendocrine, combined large-cell neuroendocrine, basaloid, lymphoepithelioma-like carcinomas
    - Adenosquamous carcinoma
    - Small-cell carcinoma
      - Variant: combined small-cell carcinoma
    - Carcinomas with pleomorphic sarcomatoid or sarcomatous elements
      - Carcinomas with spindle and/or giant cells (pleomorphic carcinoma, spindle cell carcinoma, giant cell carcinoma)
      - Carcinosarcomas
      - Pulmonary blastoma
    - Carcinoid tumor
      - Typical carcinoid
      - Atypical carcinoid
    - Carcinomas of salivary-gland type
      - Mucoepidermoid carcinoma
      - Adenoid cystic carcinoma
- II. **Mesenchymal Tumors**
  - Primary pulmonary sarcomas
    - Vascular sarcomas (angiosarcoma, epithelioid, emangioendothelioma)
    - Spindle cell sarcomas (malignant fibrous histiocytoma, hemangiopericytoma, fibrosarcoma, leiomyosarcoma, synovial sarcoma)
- III. **Lympoproliferative Disorders**
  - Lymphoid interstitial pneumonia
  - Nodular lymphoid hyperplasia
  - Low-grade marginal-zone B-cell lymphoma of the mucosa-associated lymphoid tissue (MALT)
  - Lymphomatoid granulomatosis
- IV. **Miscellaneous Tumors**
  - Hamartoma
  - Granular cell tumors
  - Sclerosing hemangioma
  - Clear cell tumor
- V. **Tumor-like Lesions**
  - Hyalinizing granuloma
  - Amyloid tumor

Modified from Travis WD, Colby TV, Corrin B, et al: Histological Typing of Lung and Pleural Tumors, 3rd ed. Berlin, Springer-Verlag, 1999.

however, are composed of more than one histologic type and are classified as *combined tumors*. Additionally, NSCLC are graded as *well-differentiated*, *moderately differentiated*, or *poorly differentiated* according to the least differentiated feature.[227] Exceptions to this grading classification are pleomorphic carcinoma, carcinosarcoma, and SCLC, all of which are poorly differentiated tumors.[227]

Squamous Cell Carcinoma. Squamous cell carcinomas have been decreasing in relative incidence and now constitute 25% of all lung cancers. They typically occur in central bronchi and frequently manifest as postobstructive pneumonia or atelectasis (Fig. 28–1).[189, 202, 225] Mucoid impaction, bronchiectasis, and hyperinflation are uncommon radiologic manifestations (Fig. 28–2).[202, 225, 258]

Approximately one third of squamous cell carcinomas occur beyond the segmental bronchi and usually range in size from 1 to 10 cm (Fig. 28–3).[202, 225] Squamous cell carcinomas are more likely to cavitate than the other histologic cell types of lung cancer.[202] Cavitation occurs in 10% to 30% and is more common in large peripheral masses and poorly differentiated tumors.[225] Cavitation is typically eccentric with thick, irregular walls, although thin walls may occur in rare circumstances.[202] Most squamous cell carcinomas grow slowly, and extrathoracic metastases tend to occur late.[202]

Adenocarcinoma. Adenocarcinomas have increased in incidence and are now the most common cell type, compos-

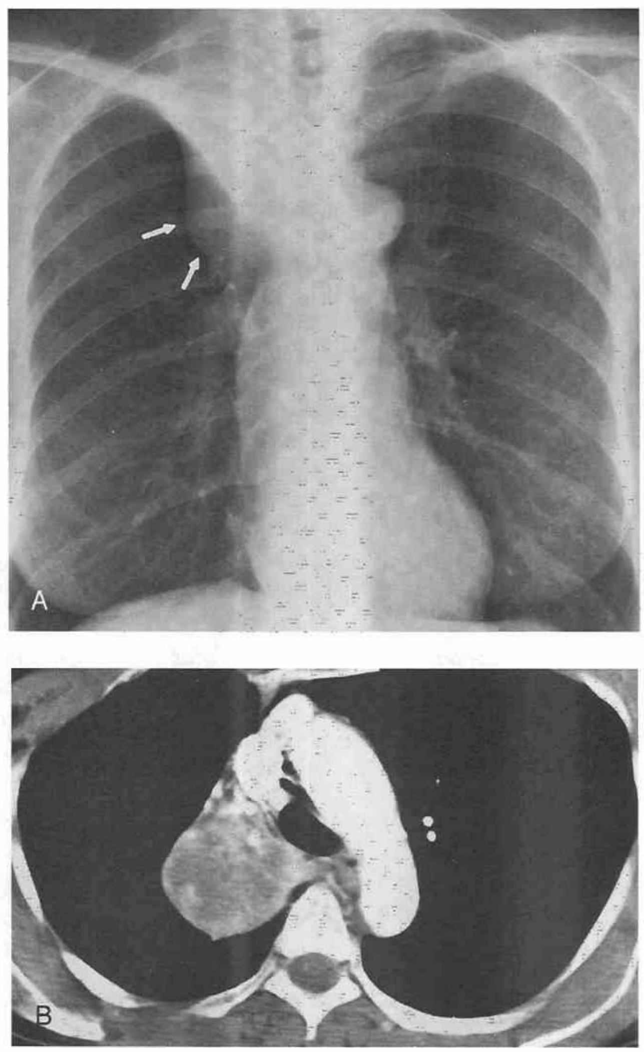

Figure 28–1. Squamous cell lung cancer seen as a central endobronchial mass. *A*, Posteroanterior chest radiograph shows complete atelectasis of the right upper lobe. Convexity in the lower portion of the atelectatic lung *(arrows)* is the result of a large central mass. *B*, CT confirms the large central mass in the region of the right upper lobe bronchus.

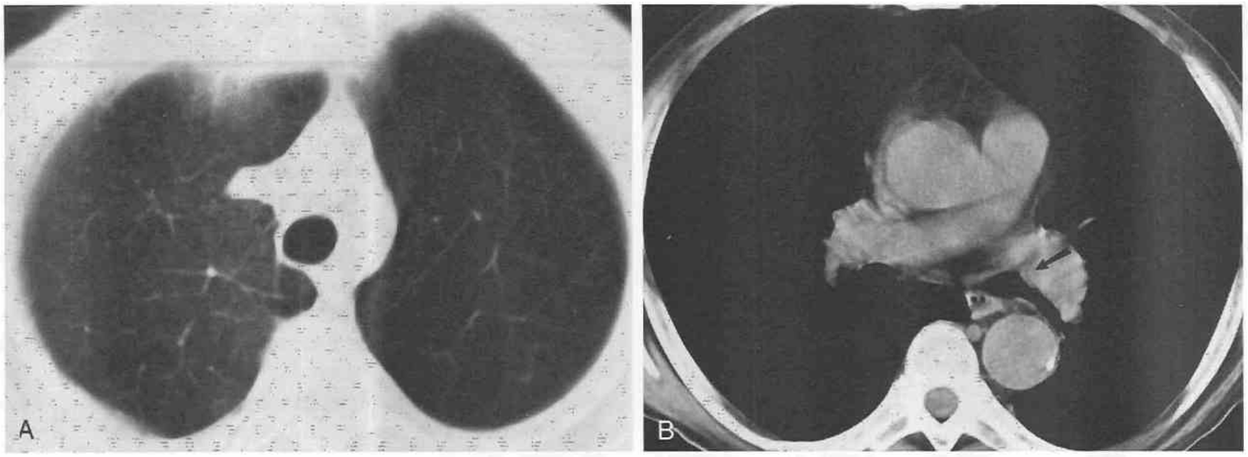

Figure 28–2. Squamous cell lung cancer with obstructive hyperinflation of the left upper lobe. *A* and *B*, CT scan shows hyperlucency of the left upper lobe and an endobronchial mass that completely occludes the left upper lobe bronchus (*arrow* in *B*).

ing 25% to 30% of all lung cancers.[189] Adenocarcinomas typically manifest as peripheral, solitary pulmonary nodules. Nodules can have an irregular or spiculated margin as a result of parenchymal invasion and an associated fibrotic response (Fig. 28–4).[202, 225] Lymphangitic carcinomatosis, although uncommon at presentation, occurs more frequently with adenocarcinomas and typically manifests radiologically as thickening of interlobular septa or multiple small pulmonary nodules (Fig. 28–5).[125] Intrathoracic metastases to hilar and mediastinal nodes are present in 18% to 40% and in 2% to 27% of patients, respectively, and tend to occur more often with more centrally located adenocarcinomas.[189, 225, 261]

Bronchioloalveolar cell carcinoma (BAC), a subset of adenocarcinoma, constitutes 0.5% to 10% of all lung cancers.[49] BAC can be either solitary or multifocal at the time of initial presentation. To explain this difference, it has been proposed that the origin of BAC is either *monoclonal* (with multifocality due to dissemination by aerosolization, intrapulmonary lymphatics, and intra-alveolar growth) or *polyclonal* (with multifocality due to de novo tumor growth at multiple sites).[11, 88, 128, 138, 202]

The most common radiologic manifestation is a peripheral, solitary nodule that can remain stable in size for many years (Fig. 28–6).[42, 87, 108, 225] Although cavitation in these nodules is uncommon, the occurrence of multiple small, focal, low-attenuation regions (pseudocavitation) or air-bronchograms within the nodule can occasionally be useful in suggesting the diagnosis.[108, 162, 251, 273] The diffuse form may present as multiple nodules (usually small, occasion-

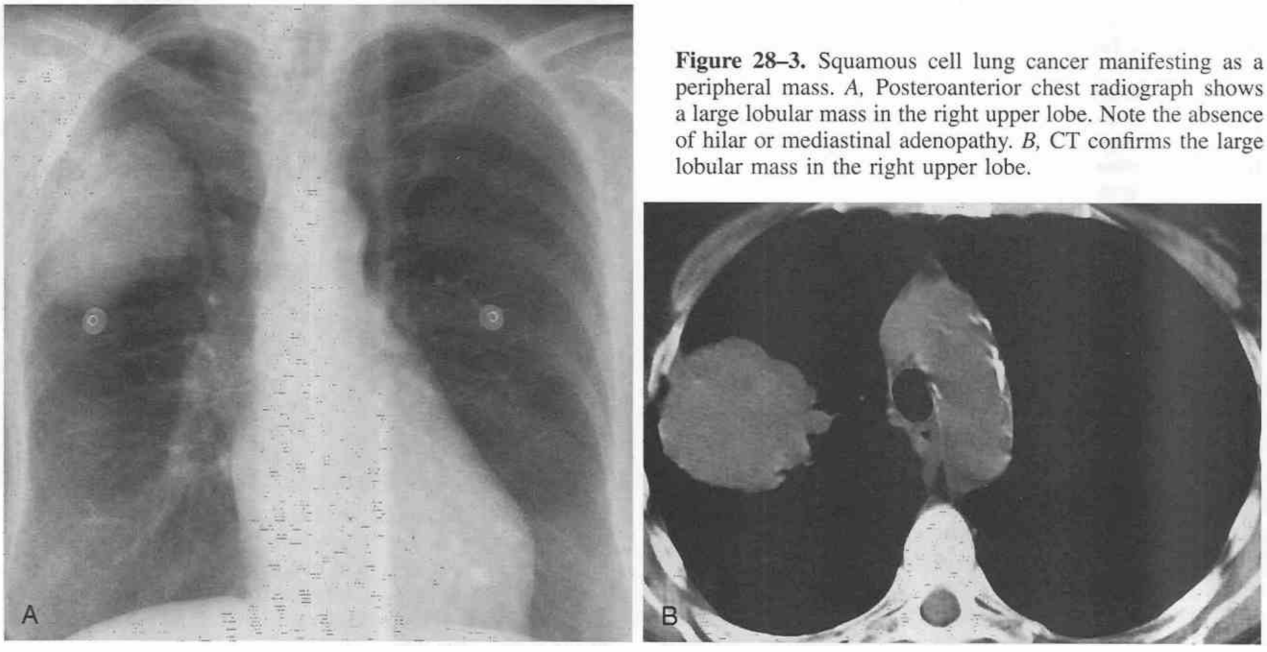

Figure 28–3. Squamous cell lung cancer manifesting as a peripheral mass. *A*, Posteroanterior chest radiograph shows a large lobular mass in the right upper lobe. Note the absence of hilar or mediastinal adenopathy. *B*, CT confirms the large lobular mass in the right upper lobe.

Figure 28–4. Adenocarcinoma manifesting as a pulmonary nodule. CT scan shows a nodule in the apical segment of the right upper lobe. The spiculated margin is typical of lung cancer.

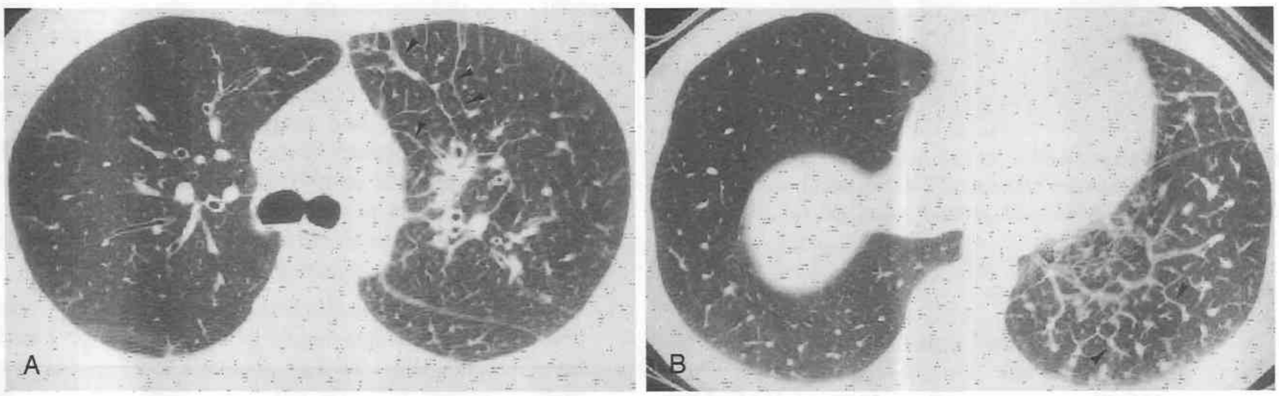

Figure 28–5. Adenocarcinoma of the lung appearing as lymphangitic carcinomatosis. *A* and *B*, Thin-section CT scan shows thickening of bronchial walls and interlobular septa *(arrowheads)* in the left lung. Nodularity of the septa is suggestive of malignancy.

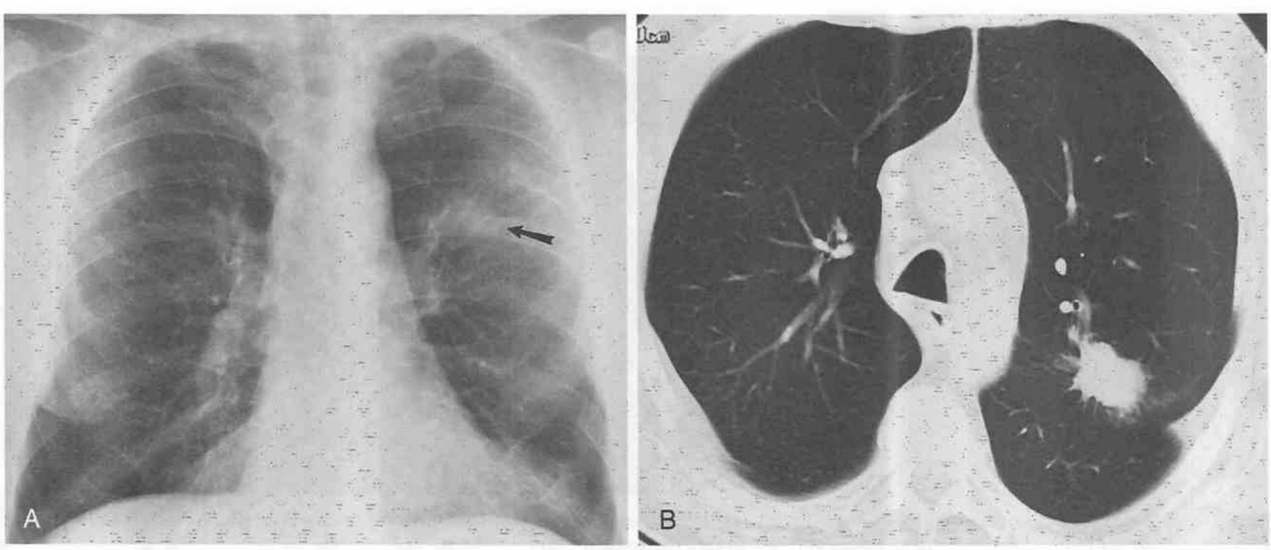

Figure 28–6. Bronchioloalveolar cell carcinoma seen as a solitary pulmonary nodule. *A*, Posteroanterior chest radiograph shows a nodule *(arrow)* in left upper lobe. *B*, CT scan reveals a spiculated margin suggestive of malignancy.

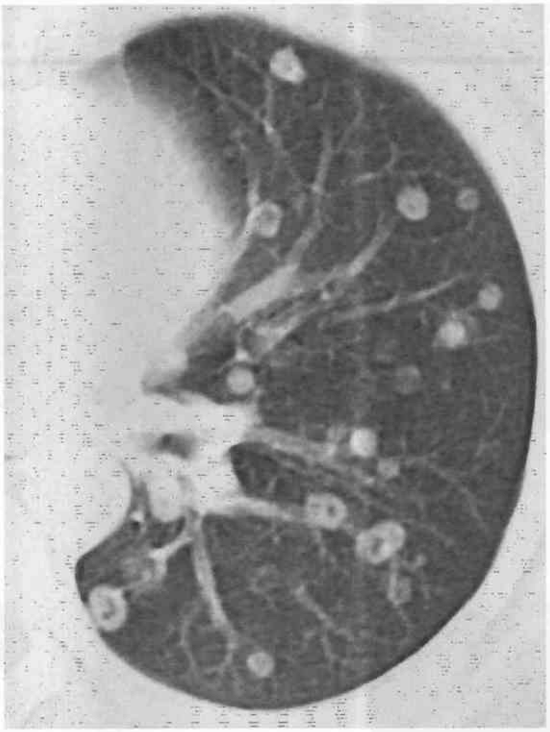

Figure 28–7. Bronchioloalveolar cell carcinoma (BAC) manifesting as multiple pulmonary nodules. CT shows small, well-marginated pulmonary nodules with central areas of cavitation (the "Cheerio" sign of BAC).

ally cavitary), "ground-glass" opacities, and opacities resembling pneumonia (Figs. 28–7 and 28–8).[2, 11, 42, 50, 87, 138, 202] Most patients with the diffuse form of BAC have a combination of these findings (Fig. 28–9).[2] Hilar and mediastinal adenopathy and pleural effusions are uncommon.[42, 87, 162, 202]

Large-Cell Carcinoma. These lesions make up 10% to 20% of all lung cancers.[58, 202] Most are peripheral, poorly marginated masses greater than 7 cm in diameter (Fig. 28–10).[21, 58, 189, 201, 202, 225] Although growth is typically rapid, cavitation is uncommon.[201] Hilar and mediastinal adenopathy occurs in up to one third of patients at presentation, and early extrathoracic metastases are common.[58, 201, 202, 225]

Small-Cell Lung Cancer. SCLCs compose 20% to 25% of all lung cancers.[58] The primary tumor is typically small, is central in location, and is associated with marked hilar and mediastinal adenopathy and distant metastases to liver, bone marrow, adrenals, and brain (Figs. 28–11 and 28–12).[58, 189, 225, 233] Pleural effusions occur in 5% to 40% of patients.[176, 202, 253] Approximately 5% of SCLCs manifest as small, peripheral, solitary pulmonary nodules without intrathoracic adenopathy, disseminated extrathoracic disease, or pleural effusions.[75, 233]

Clinical Manifestations

Most patients are in their fifth and sixth decades of life and are symptomatic at presentation.[5, 58, 196] Symptoms are variable and depend on the local effects of the primary mass, the presence of regional or distant metastases, and the coexistence of paraneoplastic syndromes.

Central endobronchial carcinomas can manifest as fever, dyspnea, hemoptysis, and cough.[5] Cough productive of copious amounts of watery sputum (bronchorrhea) typically also occurs in patients with BAC and extensive parenchymal disease, but this is rarely seen.[50] Symptoms that can occur as a result of local growth and invasion of adjacent nerves, vessels, and mediastinal structures include:

1. Chest pain (peribronchial nerve involvement); vocal cord paralysis and hoarseness (recurrent laryngeal nerve involvement) (Fig. 28–13); dyspnea due to diaphragmatic paralysis (phrenic nerve involvement) (Fig. 28–14); Horner's syndrome—ptosis, mycosis, anhidrosis (sympathetic chain and stellate ganglion involvement by superior sulcus tumors) (Fig. 28–15).[172]
2. Facial swelling, headaches, enlarged collateral chest wall vessels (superior vena cava obstruction).[172]
3. Dysphagia (esophageal invasion).

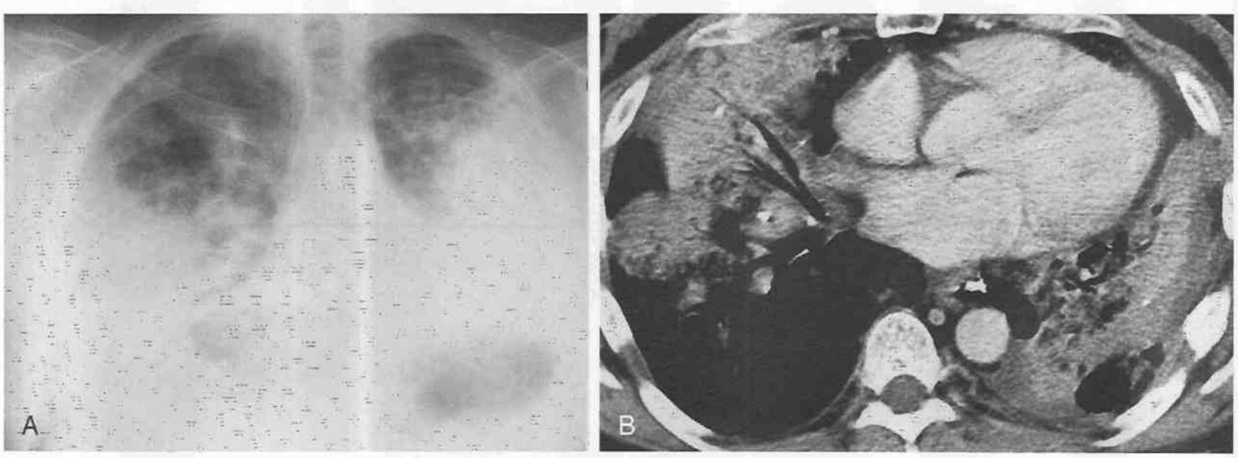

Figure 28–8. Bronchioloalveolar cell carcinoma appearing as homogeneous opacities mimicking pneumonia. *A,* Posteroanterior chest radiograph shows diffuse, bilateral, homogeneous pulmonary opacities. Surgical clips are present in the medial aspect of the left hemithorax because of prior partial pulmonary resection. *B,* CT confirms the diffuse bilateral pulmonary consolidation and reveals a small left pleural effusion.

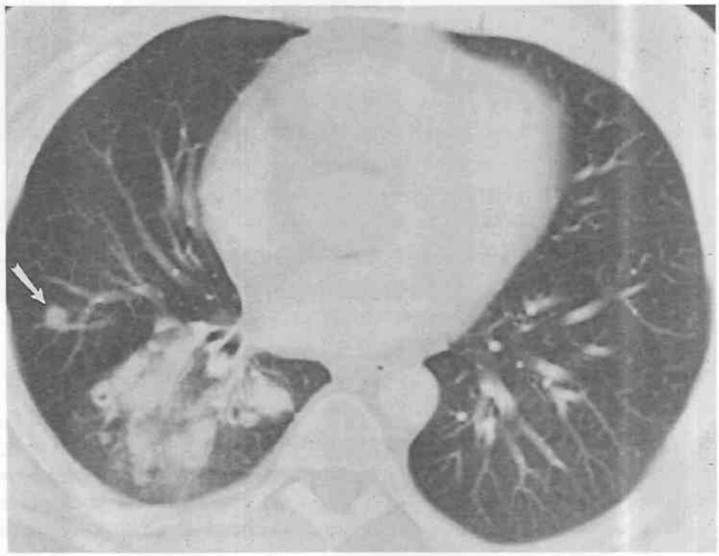

Figure 28–9. Bronchioloalveolar cell carcinoma seen as nodules and consolidation. CT scan shows an opacity in the right lower lobe resembling pneumonia and a small nodule *(arrow)*. Numerous small, well-circumscribed nodules were scattered throughout both lungs (not shown).

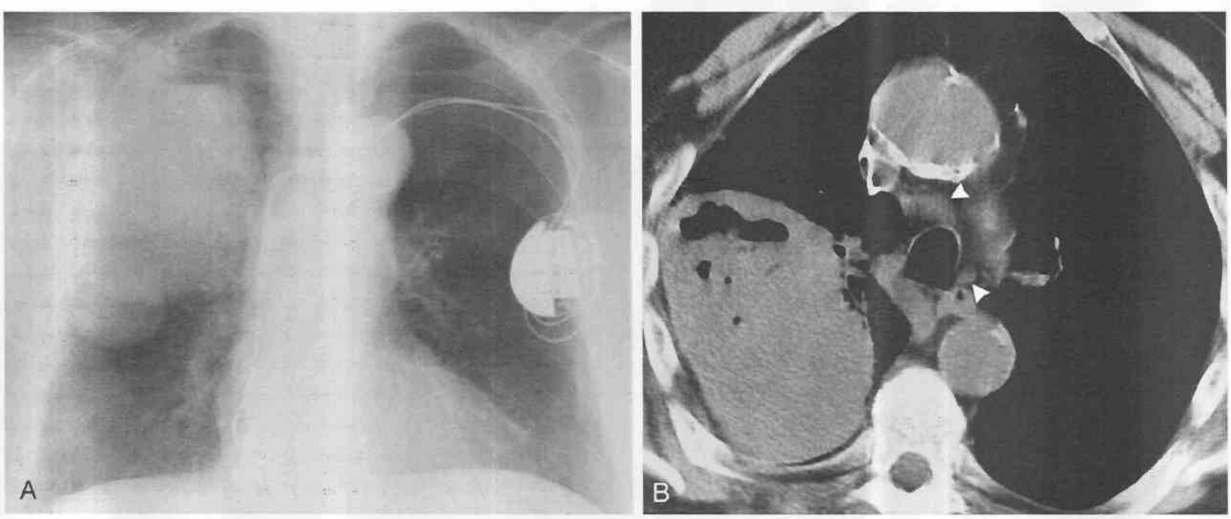

Figure 28–10. Large-cell lung cancer manifesting as a large cavitary mass. *A*, Posteroanterior chest radiograph shows a large, lobular mass in the right upper lobe. Cavitation is present with an air-fluid level in the upper aspect of mass. *B*, CT shows a well-circumscribed mass with eccentric cavitation and thick walls. Note the nonenlarged, paratracheal and low left paratracheal lymph nodes *(arrowheads)*.

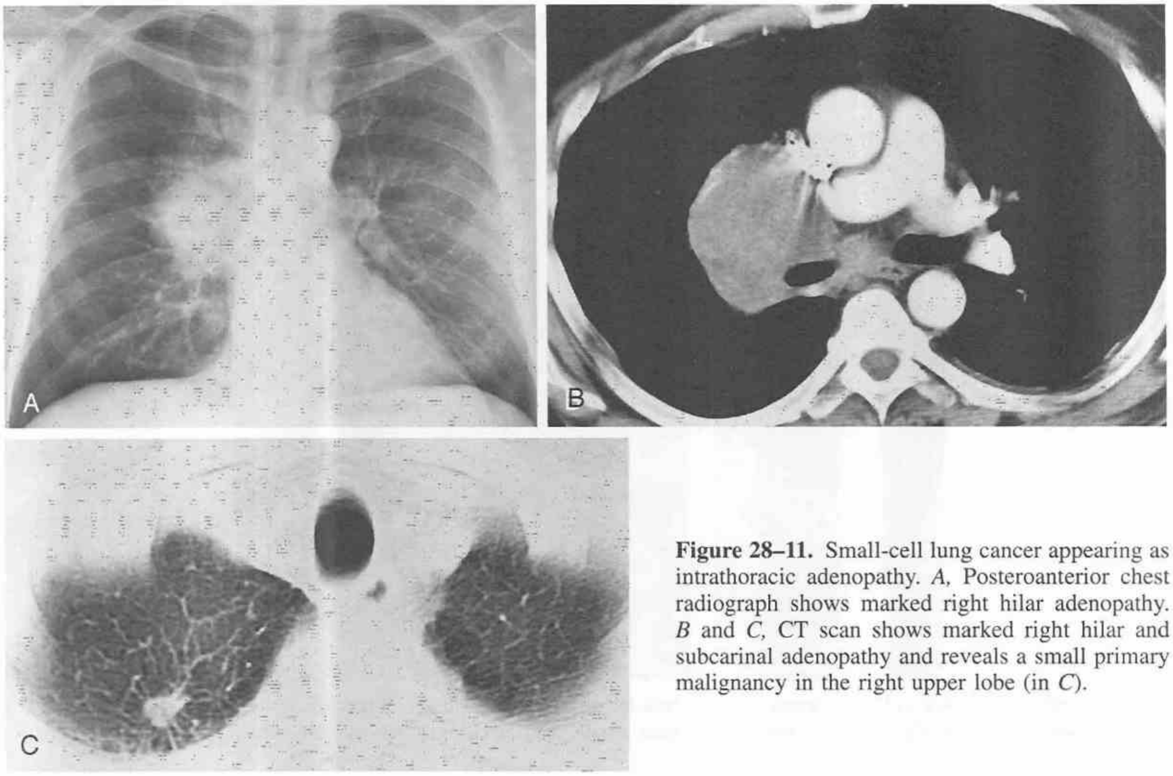

Figure 28–11. Small-cell lung cancer appearing as intrathoracic adenopathy. *A*, Posteroanterior chest radiograph shows marked right hilar adenopathy. *B* and *C*, CT scan shows marked right hilar and subcarinal adenopathy and reveals a small primary malignancy in the right upper lobe (in *C*).

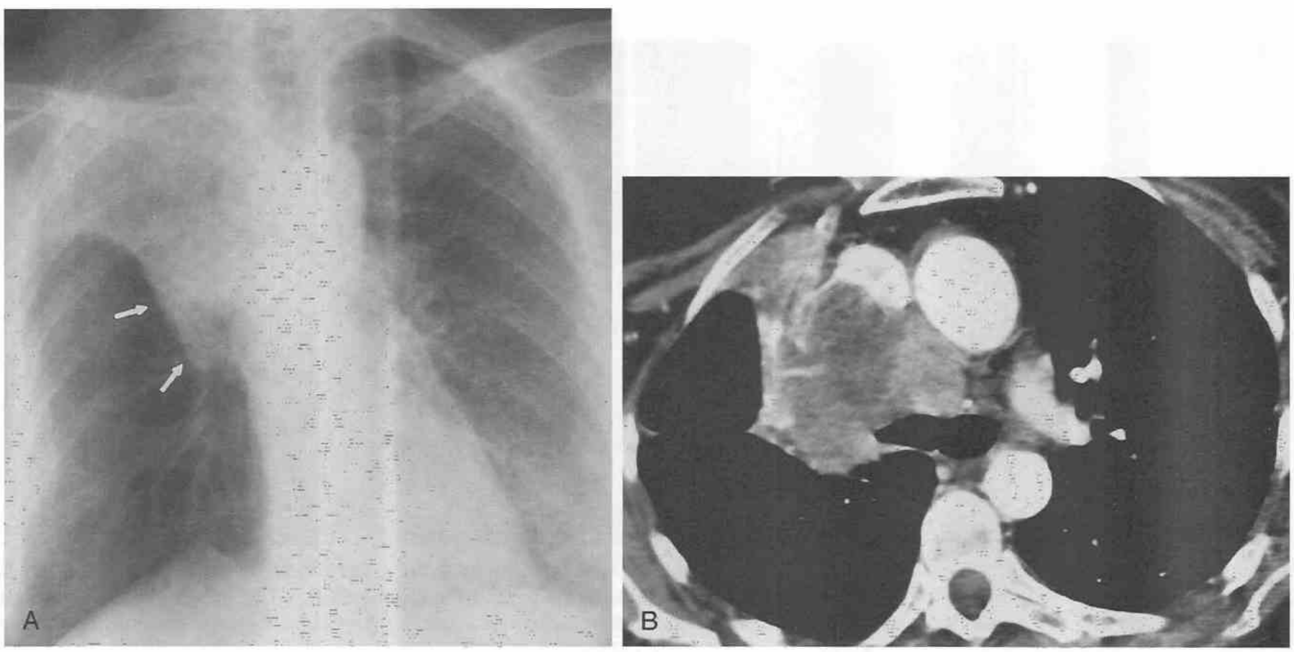

Figure 28–12. Small-cell lung cancer seen as intrathoracic adenopathy and atelectasis. *A*, Posteroanterior chest radiograph shows complete atelectasis of the right upper lobe with mild convexity of the distal aspect of the minor fissure *(arrows)* caused by an underlying right hilar mass. *B*, CT scan confirms marked hilar and mediastinal adenopathy and reveals occlusion of the right upper lobe bronchus.

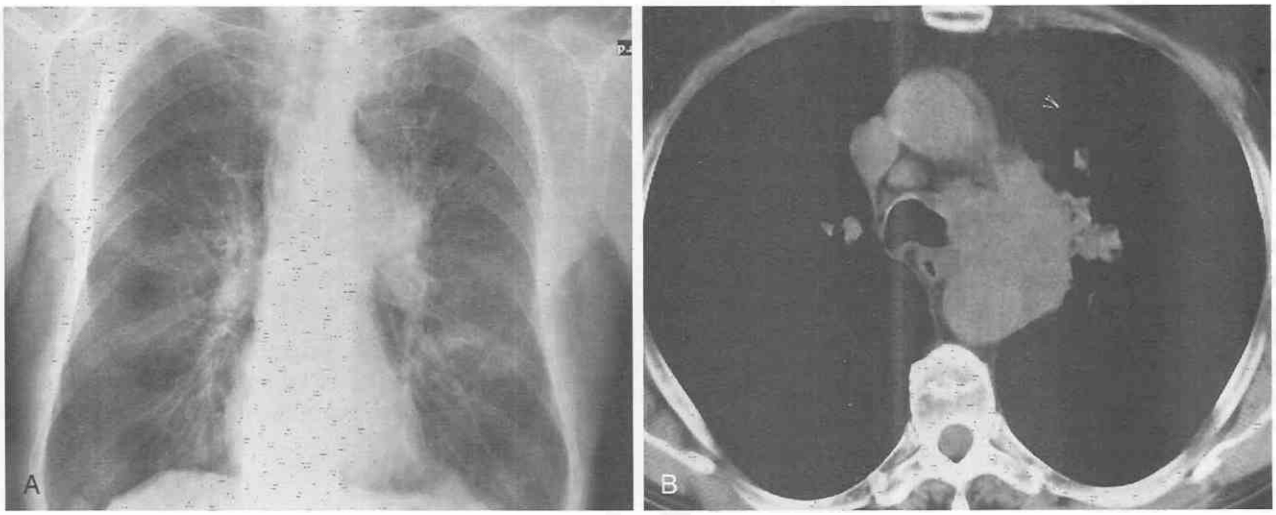

Figure 28–13. Small-cell lung cancer in a 76-year-old man pres[redacted]th hoarseness caused by involvement of the recurrent laryngeal nerve. *A,* Posteroanterior chest radiograph shows an aortopulmon[redacted]dow mass. *B,* CT reveals mediastinal invasion with an extension of the mass into the aortopulmonary window (the anatomic location of recurrent laryngeal nerve).

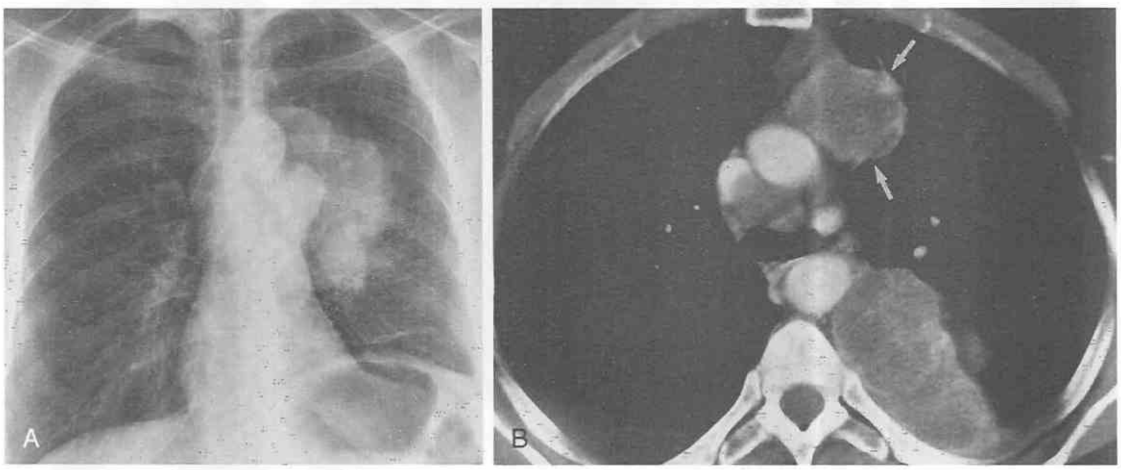

Figure 28–14. Small-cell lung cancer in a 50-year-old woman with diaphragmatic paralysis resulting from phrenic nerve involvement. *A,* Posteroanterior chest radiograph shows a large lobular mass in the left lower lobe and elevation of the left hemidiaphragm. *B,* CT reveals a necrotic mass in the left lower lobe and mediastinum *(arrows)* in the anatomic location of the phrenic nerve.

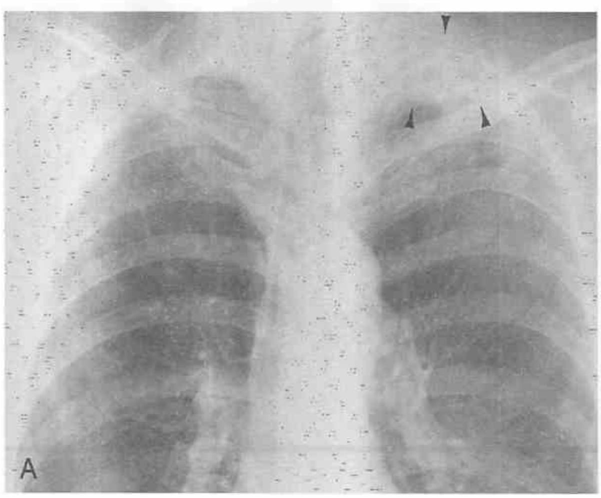

Figure 28–15. Non–small-cell lung cancer in a 54-year-old man with Pancoast's tumor and with a 2-month history of neck pain. *A,* Posteroanterior chest radiograph shows a left apical mass with destruction of the first rib *(arrowheads)*. *B,* CT confirms the left superior sulcus tumor and destruction of the left first rib.

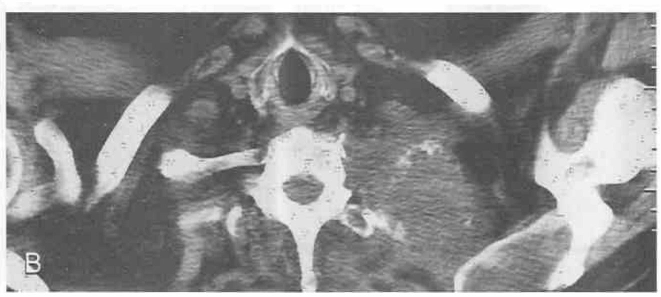

Many patients present with symptoms related to extrathoracic metastases, most commonly bone pain or central nervous system (CNS) abnormalities.[5, 100] Clinical signs and symptoms can also be caused by tumor excretion of a bioactive substance, or hormone, or as a result of an autoimmune phenomenon.[5, 171] These paraneoplastic syndromes occur in 10% to 20% of lung cancer patients and are usually associated with SCLC.[5, 22, 124, 220] Antidiuretic and adrenocorticotropin hormones are the more frequently excreted hormones and can result in hyponatremia and serum hypo-osmolarity and in Cushing's syndrome (central obesity, hypertension, glucose intolerance, plethora, hirsutism), respectively.[27, 40, 121, 157, 199, 202] Other hormones that can be elevated are calcitonin; growth hormone; human chorionic gonadotropin; and, rarely, prolactin and serotonin.[124]

Neurologic paraneoplastic syndromes (Lambert-Eaton myasthenic syndrome, paraneoplastic cerebellar degeneration, paraneoplastic encephalomyelitis, paraneoplastic sensory neuropathy) are rare and are usually associated with SCLC.[25, 26, 28, 33, 113, 179] The neurologic symptoms typically precede the diagnosis of lung cancer by up to 2 years, are incapacitating, and progress rapidly, although improvement can occur after treatment of the lung cancer.[33, 113]

Miscellaneous paraneoplastic syndromes associated with lung cancer include acanthosis nigricans, dermatomyositis, disseminated intravascular coagulation, and hypertrophic pulmonary osteoarthropathy (HPO). Of these, HPO is the most common, occurring in up to 17% of patients with adenocarcinoma (Fig. 28–16).[143]

Radiologic Evaluation

Although imaging has an important role in the diagnosis, staging, and monitoring of patients with lung cancer, the role of imaging in screening for malignancy is not clearly defined.

Screening

Because diagnosis of lung cancer at an early stage is associated with an improved prognosis, screening has been

Figure 28–16. Non–small-cell lung cancer in an asymptomatic 64-year-old woman. *A*, CT scan shows a large right upper lobe mass. *B*, Technetium 99m (^{99m}Tc)–labeled methylene diphosphonate (MDP) bone scintigraphy shows linear areas of increased radiotracer uptake in the femurs and tibias. This appearance is characteristic of hypertrophic pulmonary osteoarthropathy.

advocated to detect lung cancer before clinical presentation. The ACS does not, however, recommend routine radiologic evaluation for the detection of lung cancer but instead advocates primary prevention.[59] This recommendation is based on the results of four large randomized trials undertaken in the 1970s, which evaluated the utility of chest radiographs and sputum cytology in lung cancer screening. These trials showed that screening improved long-term survival rates without reducing mortality (considered the best evidence that screening is effective, as it is not affectedby lead-time bias, length bias, and overdiagnosis bias).[12, 60, 105, 151, 218]

A reanalysis of the data from these trials has suggested some justification for the use of chest radiography in lung cancer screening.[216, 217] Additionally, because of the concerns about design and methodology of the previous trials, together with improved detection of small lung cancers using computed tomography (CT), there has been a renewed interest in reevaluating screening. Consequently, new multi-institutional screening studies in the United States, supported by the National Cancer Institute as well as by other smaller trials in Japan and Germany, are being performed to reexamine the role of screening in lung cancer management.[83, 93, 161, 207]

Diagnosis

Because most patients with lung cancer have advanced disease at presentation, diagnosis is usually not difficult. Nevertheless, 20% to 30% of patients with lung cancer present with a solitary pulmonary nodule, which may be difficult to differentiate from a benign nodule.[242] Certain morphologic and physiologic features, however, may suggest a diagnosis of lung cancer:

1. *Size.* The larger the nodule, the more likely it is to be malignant.[76, 86, 273] Small size, however, cannot be used to reliably exclude lung cancer, since up to 42% ofresected lung cancers are less than 2 cm in diameter.[203, 242, 269]
2. *Margins.* Lung cancers typically have irregular or spiculated margins.[76, 202, 225, 269, 273] Although suggestive of lung cancer, these findings can occasionally be seen with benign nodules.[76, 273] Furthermore, a smooth margin, a feature typical of benign nodules, cannot be used to exclude lung cancer, because 20% of malignant nodules have this appearance.[205]
3. *Internal morphology.* Except for fat (attenuation, −40 to −120 Hounsfield units [HU]) and calcification within a nodule, internal morphology is unreliable in distinguishing lung cancer from a benign nodule.[76, 160, 204, 273] Calcification occurs histologically in up to 14% of lung cancers and may be detected by CT.[123, 159] The calcification is typically amorphous in appearance (Fig. 28–17), unlike the diffuse solid, central punctate, laminated, or popcorn-like calcifications that are diagnostic of benign nodules. Amorphous calcification, however, is not diagnostic of lung cancer, because similar calcifications are occasionally detected in benign lesions. Cavitation occurs in benign nodules and lung cancer. Malignant nodules typically have thick, irregular walls, whereas benign nodules have smooth, thin walls.[259, 260, 273] These findings, however, are not specific, and wall thickness cannot be used to confidently differentiate benign nodules from lung cancer.
4. *Growth.* Lung cancers typically double in volume (an increase of 26% in diameter) between 30 and 400 days (average, 240 days).[119] Although absence of growth over a 2-year period is usually reliable for confirming that a nodule is benign,[72, 73, 118] it is difficult to reliably detect growth in small nodules because the small change in diameter associated with a doubling of volume may not be visible on radiographs. The use of CT can improve the accuracy of growth assessment. It has been reported that growth can be detected in lung cancers as small as 5 mm when CT imaging is repeated within 30 days.[264] Furthermore, the measurement of serial volumes of small nodules (which increase proportionally faster than diameters), may be an accurate and potentially useful method for assessing the rate of growth.[265] At present, the determination of when and how to observe and image small nodules in the assessment of tumor growth rate has not been resolved.
5. *Blood supply.* Blood supply to malignant pulmonary nodules is qualitatively and quantitatively different from the blood supply to benign nodules. Contrast-enhanced CT can be used to image this difference by determining nodule enhancement. Typically, malignant nodules enhance more than 20 HU, whereas benign nodules enhance less than 15 HU (Fig. 28–18).[223]
6. *Metabolism.* Metabolism of glucose is typically increased in lung cancer cells. Positron emission tomography (PET), using a D-glucose analog, ^{18}F-2-deoxy-D-glucose (FDG), can be used in imaging this increase and in differentiating malignant from benign nodules.[197]

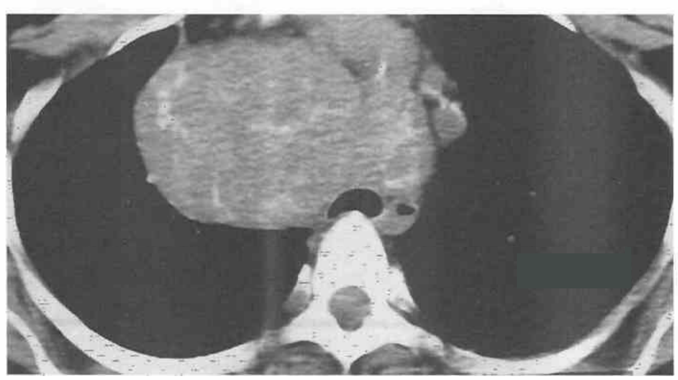

Figure 28–17. Non–small-cell lung cancer manifesting as a calcified mass. CT shows a large, right upper lobe mass with mediastinal invasion. Scattered areas of amorphous calcification in the mass are typical of, but not diagnostic for, malignancy.

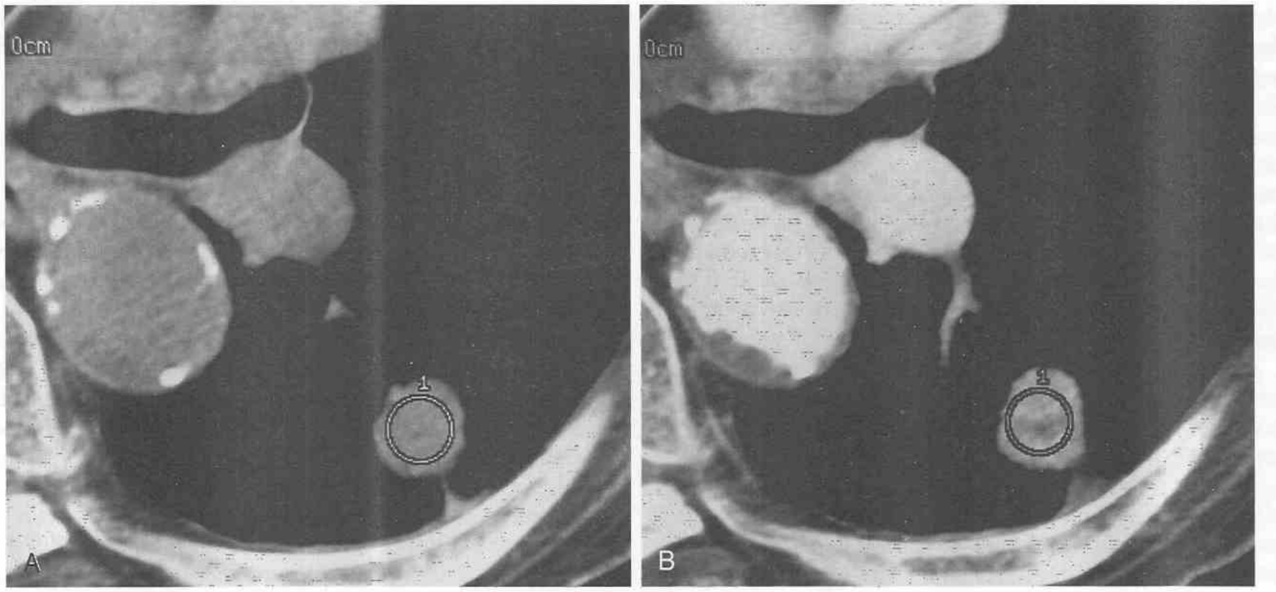

Figure 28–18. Non–small-cell cancer appearing as an enhancing nodule after administration [redacted]ontrast material. *A*, Non-contrast-enhanced CT scan shows a left lung nodule with an attenuation value of 24 Hounsfield units (HU). *B*, Contrast-enhanced CT scan shows nodule enhancement of 70 HU and central necrosis. Enhancement of more than 20 HU suggests malignancy. Resection revealed non–small-cell cancer. (Courtesy of Tom Hartman, M.D., Mayo Clinic, Rochester, Minn.)

Nodules as small as 1 cm can be imaged; if FDG uptake is low, the nodules are almost certainly benign.[41, 101, 114, 173, 174] Nodules with increased FDG uptake are generally considered malignant (Fig. 28–19), although inflammatory and infectious processes (e.g., rheumatoid nodules, tuberculosis, histoplasmosis) may result in increased FDG uptake.[101, 173, 174, 238]

Staging

Non–Small-Cell Lung Cancer. Because treatment and prognosis depend on the anatomic extent of NSCLC at initial presentation, accurate assessment is important.[145, 150] The International Staging System for Lung Cancer is used to describe the extent of NSCLC in terms of the primary tumor (T status), lymph nodes (N status), and metastases (M status) (Table 28–2).[145] The TNM descriptors can be determined clinically (history, physical examination, radiologic imaging) or by pathologic analysis of samples obtained by biopsy or surgery. In general, the clinical stage underestimates the extent of disease when compared with the pathologic stage.[145]

Primary Tumor (T Status). The T status defines the size, location, and extent of the primary tumor. Because the extent of the primary tumor determines therapeutic management (surgical resection or palliative radiotherapy or chemotherapy), imaging is often performed to assess the degree of pleural, chest wall, and mediastinal invasion.

CT is useful in confirming gross chest wall invasion

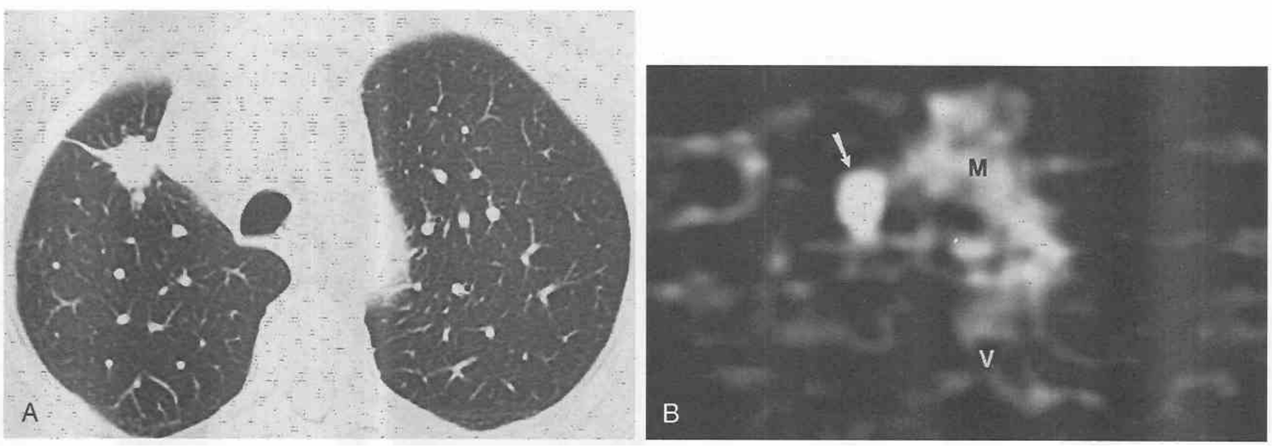

Figure 28–19. Non–small-cell lung cancer seen as hypermetabolic nodule on a PET scan with ^{18}F-fluorodeoxyglucose (FDG-PET). *A*, CT scan shows a nodule in the right upper lobe. The irregular margin suggests malignancy. *B*, Axial PET image with FDG shows increased uptake within the nodule *(arrow)* when compared to adjacent mediastinum. Findings suggest malignancy. Resection revealed squamous cell cancer. M, mediastinum; V, vertebral body.

Table 28–2. International Staging System for Lung Cancer

Primary Tumor (T)	
TX	Primary tumor cannot be assessed, or tumor proven by the presence of malignant cells in sputum or bronchial washings but not visualized by imaging or bronchoscopy
T0	No evidence of primary tumor
Tis	Carcinoma *in situ*
T1	Tumor ≤3 cm in greatest dimension, surrounded by lung or visceral pleura, without bronchoscopic evidence of invasion more proximal than the lobar bronchus* (i.e., not in the main bronchus)
T2	Tumor with any of the following features of size or extent: >3 cm in greatest dimension; Involves main bronchus, ≥2 cm distal to the carina; Invades the visceral pleura; Associated with atelectasis or obstructive pneumonitis that extends to the hilar region but does not involve the entire lung
T3	Tumor of any size that directly invades any of the following: chest wall (including superior sulcus tumors), diaphragm, mediastinal pleura, parietal pericardium; or tumor in the main bronchus <2 cm distal to the carina, but without involvement of the carina; or associated atelectasis or obstructive pneumonitis of the entire lung
T4	Tumor of any size that invades any of the following: mediastinum, heart, great vessels, trachea, esophagus, vertebral body, carina; or tumor with a malignant pleural or pericardial effusion,† or with satellite tumor nodule(s) within the ipsilateral primary-tumor lobe of the lung
Regional Lymph Nodes (N)	
NX	Regional lymph nodes cannot be assessed
N0	No regional lymph node metastasis
N1	Metastasis to ipsilateral peribronchial and/or ipsilateral hilar lymph nodes, and intrapulmonary nodes involved by direct extension of the primary tumor
N2	Metastasis to ipsilateral mediastinal and/or subcarinal lymph node(s)
N3	Metastasis to contralateral mediastinal, contralateral hilar, ipsilateral or contralateral scalene, or supraclavicular lymph node(s)
Distant Metastasis (M)	
MX	Presence of distant metastasis cannot be assessed
M0	No distant metastasis
M1	Distant metastasis present‡

*The uncommon superficial tumor of any size with its invasive component limited to the bronchial wall, which may extend proximal to the main bronchus, is also classified T1.

†Most pleural effusions associated with lung cancer are due to tumor. However, there are a few patients in whom multiple cytopathologic examinations of pleural fluid show no tumor. In these cases, the fluid is nonbloody and is not an exudate. When these elements and clinical judgment dictate that the effusion is not related to the tumor, the effusion should be excluded as a staging element and the patient's disease should be staged T1, T2, or T3. Pericardial effusion is classified according to the same rules.

‡Separate metastatic tumor nodule(s) in the ipsilateral nonprimary-tumor lobe(s) of the lung also are classified M1.

From Mountain CF: Revisions in the international system for staging lung cancer. Chest 111:1710–1717, 1997.

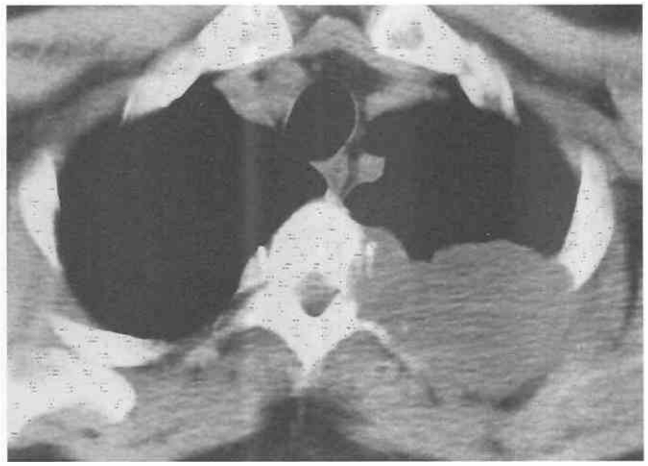

Figure 28–20. Non–small-cell lung cancer and chest wall invasion. CT scan shows a left upper lobe lung mass with destruction of the adjacent rib and the vertebral body.

(Fig. 28–20) but is inaccurate in differentiating between anatomic contiguity and subtle invasion.[100, 182, 184, 266] Findings suggestive of chest wall invasion include[100, 184]:

- Tumor-pleura contact extending over more than 3 cm
- An obtuse angle at the tumor-pleura interface
- Thickening of the pleura or increased attenuation of the extrapleural fat adjacent to the tumor

Although magnetic resonance imaging (MRI) offers superior soft tissue contrast resolution, the sensitivity (63% to 90%) and specificity (84% to 86%) of MRI in identifying chest wall invasion is similar to that of CT (Fig. 28–21).[100, 166, 182, 247] MRI is, however, particularly useful in the evaluation of superior sulcus tumors and can be used to assess invasion of the brachial plexus, subclavian vessels, and vertebral bodies (Fig. 28–22).[100, 247, 248]

Imaging with CT or MR is useful in confirming gross invasion of the mediastinum (Figs. 28–23 and 28–24), but these modalities are inaccurate in determining subtle invasion (56% to 89% and 50% to 93%, respectively).[100, 126, 134, 148, 247] CT and MRI findings that can be useful in suggesting subtle mediastinal invasion include[71, 84, 100, 134]:

- Tumor-mediastinal contact extending over more than 3 cm
- Obliteration of the fat plane between the mediastinum and tumor
- Tumor contacting more than 90 degrees of the aortic circumference

Primary lesions associated with malignant pleural effusions or pleural metastases are classified as T4 lesions. Up to 33% of patients with NSCLC have pleural metastases at presentation.[5, 145] The diagnosis of pleural metastases or malignant effusion, however, can be difficult to confirm. Pleural thickening and nodularity on CT scans suggests metastatic pleural disease (Fig. 28–25), but these abnormalities may not be present in association with a malignant effusion.[182] Furthermore, cytologic evaluation is positive in only approximately 66% of patients with a malignant pleural effusion at presentation.[5] In the absence of fluid with positive findings in cytologic studies, a T4 classification is still assigned if the effusion appears to be from the underlying malignancy.[144, 145]

Regional Lymph Nodes (N Status). The presence and location of nodal metastasis are of major importance in determining management and prognosis in patients with NSCLC.[146] To enable a consistent and standardized description of N status, nodal stations are defined by the American Thoracic Society in relation to anatomic structures or

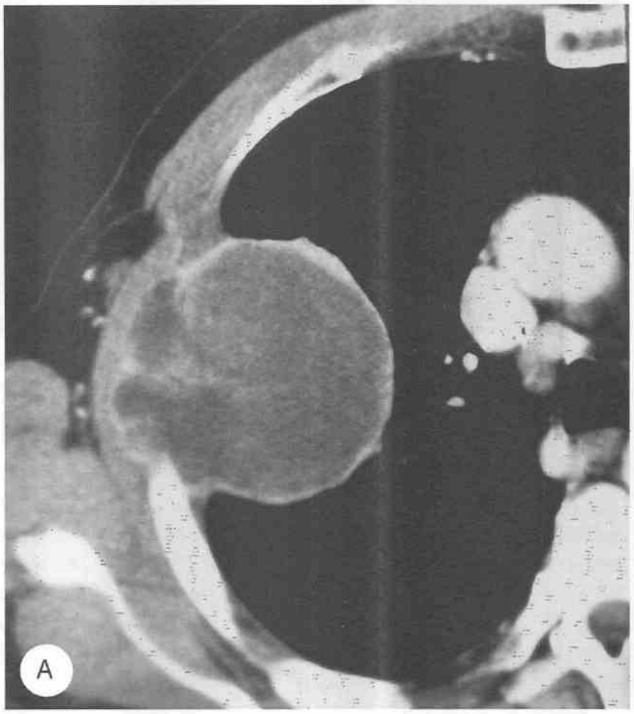

Figure 28–21. Small-cell lung cancer and chest wall invasion. *A,* CT shows a large, well-circumscribed peripheral lung mass with invasion of the chest wall. *B,* Coronal fast spin-echo MRI shows mass abutting the chest wall and the surrounding ribs *(asterisks)* and extending through the intercostal space into the soft tissues of the chest wall *(arrow).*

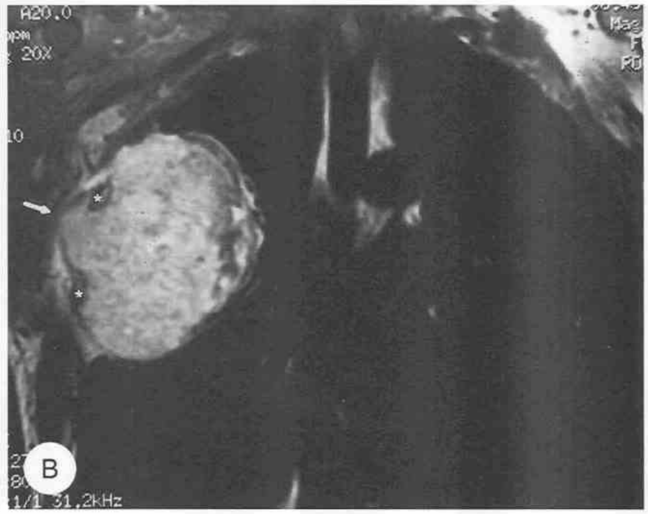

Figure 28–22. Pancoast's tumor with local chest wall invasion. *A* and *B,* Coronal T1-weighted MR images show a mass (M) in the apex of the left hemithorax, with loss of the adjacent soft tissue plane consistent with local invasion *(arrowheads).* *Asterisks* in *A* indicate rib.

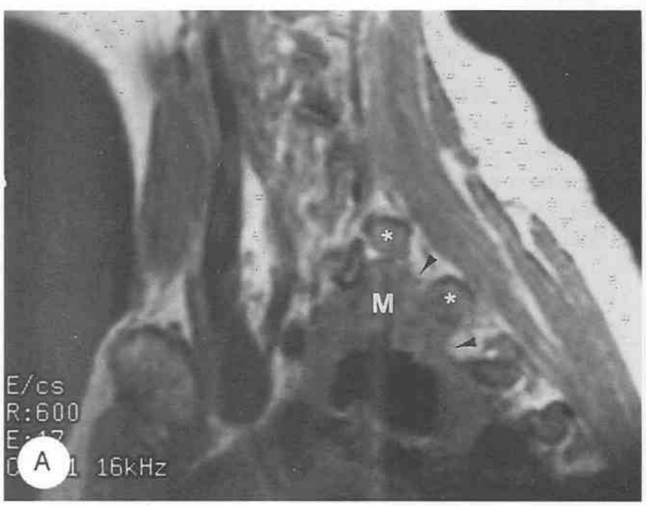

Figure 28–23. Non–small-cell cancer with mediastinal invasion. CT scan shows a large, left upper lobe mass with invasion of the anterior mediastinum. Broad abutment and loss of soft tissue plane between the mass and the transverse aorta suggest vascular invasion.

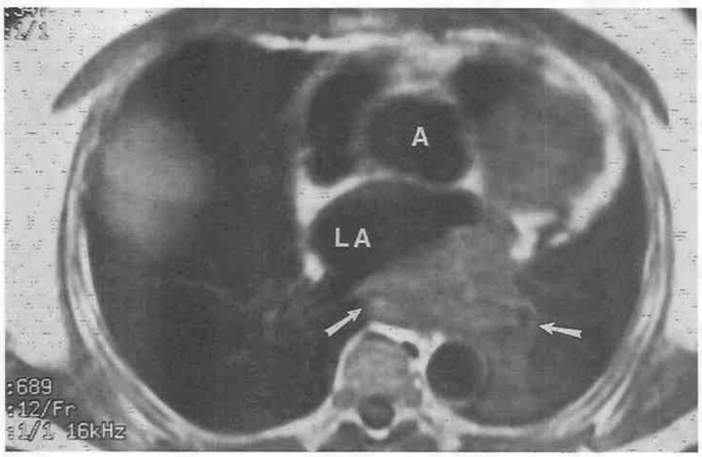

Figure 28–24. Non–small-cell lung cancer invading the left atrium. Axial T1-weighted MR image shows a left lower lobe mass that has an intermediate signal intensity extending into the left atrium *(arrows)*. A, aorta; LA, left atrium. (From Erasmus JJ, McAdams HP, Donnelly LF, Spritzer CE: MR imaging of mediastinal masses. MRI Clin North Am 8: 59–89, 2000.)

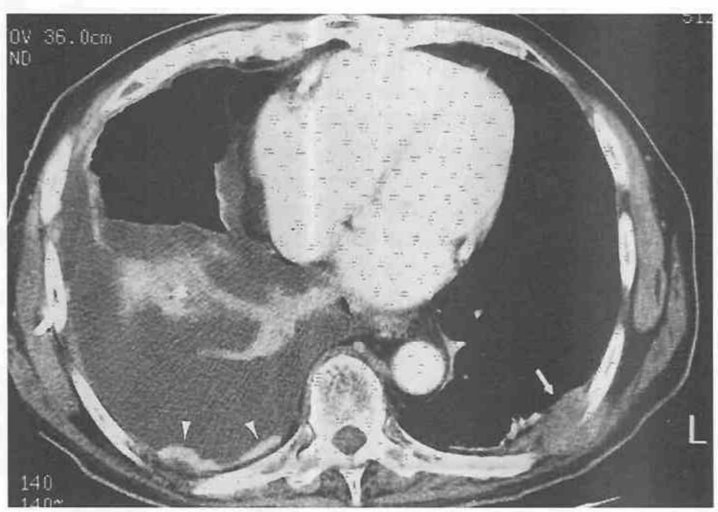

Figure 28–25. Non–small-cell lung cancer and pleural metastases. Contrast-enhanced CT shows a large right pleural effusion and enhancing nodular pleural metastases *(arrowheads)*. *Arrow* indicates compressive atelectasis of the right lower lobe and a metastatic left rib lesion.

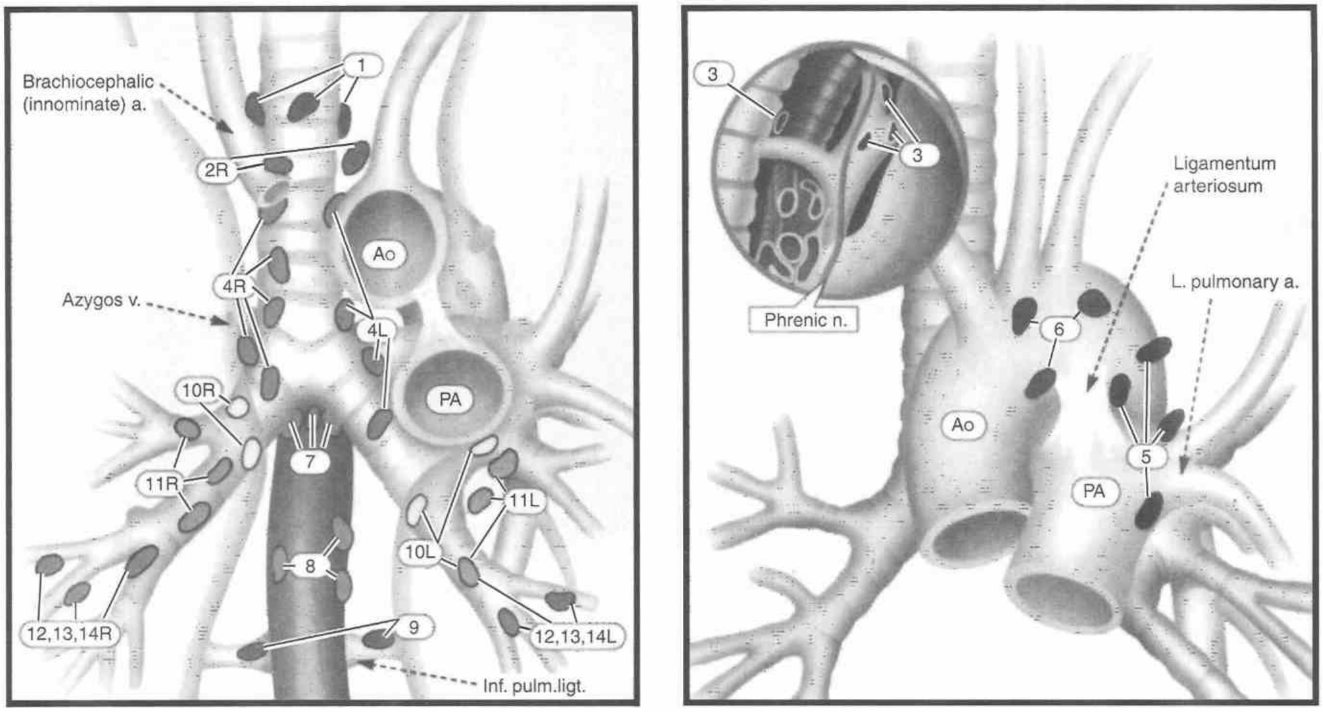

Figure 28–26. Nodal stations defined in relation to anatomic structures or boundaries. Superior mediastinal nodes: 1, highest mediastinal; 2, upper paratracheal; 3, prevascular and retrotracheal; 4, lower paratracheal (including azygos nodes); Aortic nodes: 5, subaortic (anteroposterior window); 6, para-aortic (ascending aorta or phrenic). Inferior mediastinal nodes: 7, subcarinal; 8, paraesophageal (below carina); 9, pulmonary ligament. N_1 nodes: 10, hilar; 11, interlobar; 12, lobar; 13, segmental; 14, subsegmental. (From Mountain CF: Revisions in the international system for staging lung cancer. Chest 111:1710–1717, 1997.)

boundaries that can be identified before and during thoracotomy (Fig. 28–26 and Table 28–3).[145, 146]

Size is the only criterion used to diagnose nodal metastases, with nodes greater than 10 mm in short-axis diameter considered abnormal.[69, 70] Because enlarged nodes can be hyperplastic or reactive and small nodes can harbor metastases, the accuracies of CT and MRI in detecting ipsilateral metastases to hilar nodes (N1 disease) are only 62% to 88% and 68% to 74%, respectively.[68, 126, 135, 200, 246] Fortunately, accuracy in determining N1 disease is usually not essential, because in most cases this does not prevent surgical resection.[135, 182] The accuracies of CT (56% to 82%) and MRI (50% to 82%) in detecting mediastinal nodal metastases (N2, N3 disease) are also not optimal.[7, 100, 126, 148, 211, 246, 247]

FDG-PET is more accurate (range, 81% to 96%) than CT and MRI in determining N status.[44, 175, 213, 244] FDG-PET is particularly useful in detecting metastatic disease in normal-sized nodes and in differentiating hyperplastic nodes from enlarged nodal metastases (Fig. 28–27).[213, 241, 244] It has been advocated that a normal FDG-PET scan and normal-sized nodes on CT can obviate the need for mediastinoscopy in some patients with potentially resectable lung cancer.[213, 241, 244]

Metastatic Disease (M status). Patients with NSCLC commonly have extrathoracic metastases to the adrenal glands, liver, brain, bones, and lymph nodes at presentation.[100, 145, 181] The role of imaging in detecting these metastases, however, is not clearly defined. Because a normal clinical examination result, combined with normal routine laboratory tests, such as hematocrit, alkaline phosphatase, gamma-glutamyl transferase (GGT), and serum glutamic-oxaloacetic transaminase (SGOT), has a negative predictive value greater than 95%, radiologic evaluation for occult metastases may not be required.[206, 224] In fact, considering the high cost and low incidence (0.5% to 0.9%) of detecting metastases in patients with T1 N0 to T2 N0 disease and no clinical findings of metastases, it has been suggested that extrathoracic imaging should not be performed in the staging evaluation of these patients.[224] Routine imaging of the abdomen is still performed by many clinicians, however, because of the poor reliability of clinical and laboratory findings in the detection of intra-abdominal metastases.

Metastases to the adrenal glands are common and are detected in up to 20% of patients at presentation (Fig. 28–28).[100, 155, 164, 167, 168] A small (<3 cm) adrenal mass, however, is more likely to be benign in the absence of other extrathoracic metastases.[100] CT and MRI can be useful in the evaluation of adrenal masses.

CT and MRI features favoring malignancy include[43, 136, 140]:

- Size greater than 3 cm
- Poorly defined margins
- Irregularly enhancing rim
- Invasion of adjacent structures
- High signal intensity on T2-weighted sequences

A confident diagnosis of benignity can be made if an

Table 28–3. Classification of Regional Lymph Nodes in Lung Cancer

Nodal Station	Anatomic Landmarks
N2 nodes—All N2 nodes lie within the mediastinal pleural envelope	
1 Highest mediastinal nodes	Nodes lying above a horizontal line at the upper rim of the bracheocephalic (left innominate) vein where it ascends to the left, crossing in front of the trachea at its midline
2 Upper paratracheal nodes	Nodes lying above a horizontal line drawn tangential to the upper margin of the aortic arch and below the inferior boundary of No. 1 nodes
3 Prevascular and retrotracheal nodes	Prevascular and retrotracheal nodes may be designated 3A and 3P; midline nodes are considered to be ipsilateral
4 Lower paratracheal nodes	The lower paratracheal nodes on the right lie to the right of the midline of the trachea between a horizontal line drawn tangential to the upper margin of the aortic arch and a line extending across the right main bronchus at the upper margin of the upper lobe bronchus, and contained within the mediastinal pleural envelope; the lower paratracheal nodes on the left lie to the left of the midline of the trachea between a horizontal line drawn tangenital to the upper margin of the aortic arch and a line extending across the left main bronchus at the level of the upper margin of the left upper lobe bronchus, medial to the ligamentum arteriosum and contained within the mediastinal pleural envelope
	Researchers may wish to designate the lower paratracheal nodes as No. 4s (superior) and No. 4i (inferior) subsets for study purposes; the No. 4s nodes may be defined by a horizontal line extending across the trachea and drawn tangential to the cephalic border of the azygos vein; the No. 4i nodes may be defined by the lower boundary of No. 4s and the lower boundary of No. 4, as described above
5 Subaortic (aortopulmonary window)	Subaortic nodes are lateral to the ligamentum arteriosum or the aorta or left pulmonary artery and proximal to the first branch of the left pulmonary artery and lie within the mediastinal pleural envelope
6 Para-aortic nodes (ascending aorta or phrenic)	Nodes lying anterior and lateral to the ascending aorta and the aortic arch or the innominate artery, beneath a line tangential to the upper margin of the aortic arch
7 Subcarinal nodes	Nodes lying caudal to the carina of the trachea, but not associated with the lower lobe bronchi or arteries within the lung
8 Paraesophageal nodes (below carina)	Nodes lying adjacent to the wall of the esophagus and to the right or left of the midline, excluding subcarinal nodes
9 Pulmonary ligament nodes	Nodes lying within the pulmonary ligament, including those in the posterior wall and lower part of the inferior pulmonary vein
N1 nodes—All N1 nodes lie distal to the mediastinal pleural reflection and within the visceral pleura	
10 Hilar nodes	The proximal lobar nodes, distal to the mediastinal pleural reflection and the nodes adjacent to the bronchus intermedius on the right; radiographically, the hilar shadow may be created by enlargement of both hilar and interlobar nodes
11 Interlobar nodes	Nodes lying between the lobar bronchi
12 Lobar nodes	Nodes adjacent to the distal lobar bronchi
13 Segmental nodes	Nodes adjacent to the segmental bronchi
14 Subsegmental nodes	Nodes around the subsegmental bronchi

From Mountain CF, Dresler CM: Regional lymph node classification for lung cancer staging. Chest 111:1718–1723, 1997.

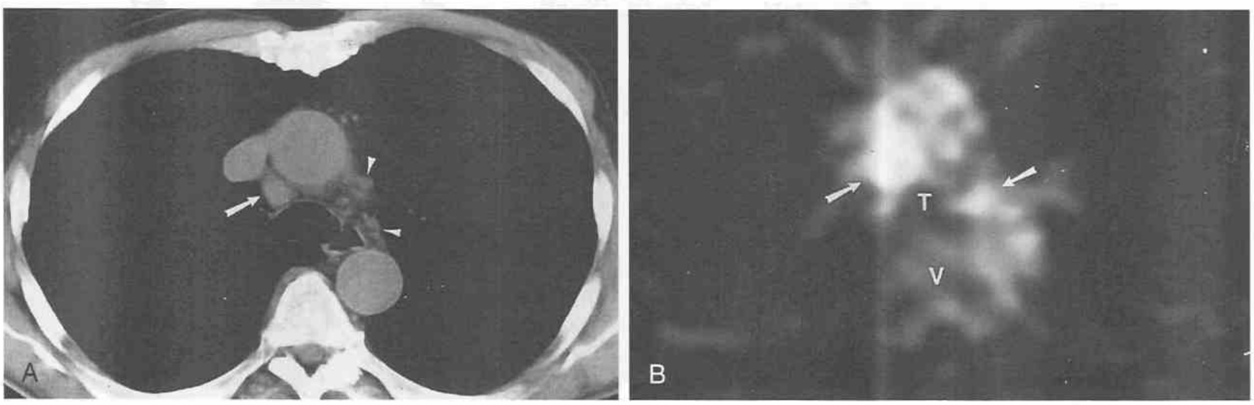

Figure 28–27. Non–small-cell lung cancer and intrathoracic nodal metastasis. *A,* CT shows an 11-mm right paratracheal node *(arrow)* and smaller, normal-sized aortopulmonary window lymph nodes *(arrowheads). B,* Axial PET image with ^{18}F-fluorodeoxyglucose (FDG-PET) shows markedly increased uptake in mediastinal nodes. Mediastinoscopy confirmed metastatic disease *(arrows).* T, trachea; V, vertebral body.

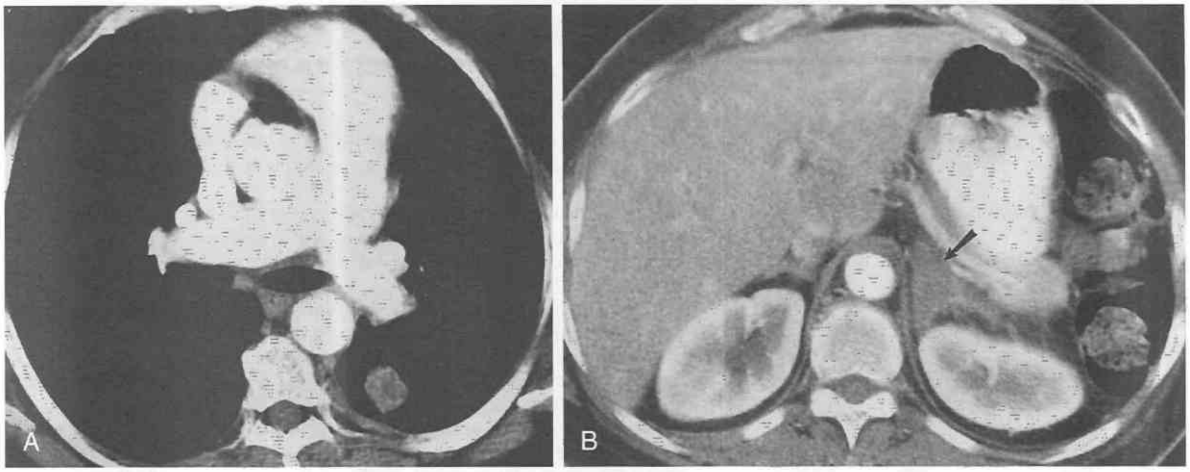

Figure 28–28. Non–smal[redacted]l lung cancer and adrenal metastasis. *A,* [redacted]shows a [redacted]ule in the left lower lobe. There is no hilar or mediastinal adenopathy. *B,* CT of the abdomen reveals a left adrenal mass *(arrow).* Biopsy confirmed metastasis.

adrenal mass has an attenuation value less than 10 HU on a non–contrast-enhanced CT scan.[14] MRI, using chemical shift analysis and dynamic gadolinium enhancement, can also be used to determine whether an adrenal mass is benign (Fig. 28–29).[13, 165, 198] Unfortunately, the status of some adrenal lesions remains indeterminate after radiologic evaluation, and biopsy is required.[178]

CNS metastases are common and are detected in up to 18% of patients at presentation (Fig. 28–30).[89, 139] Up to 10% of these patients (usually with large-cell carcinomas and adenocarcinomas) are asymptomatic.[89, 139, 154, 195] Consequently, it has been suggested that routine CT of the brain should be performed in the initial staging evaluation of all patients with NSCLC.[56] Because CNS metastases are usually associated with neurologic signs and symptoms, however, imaging for CNS metastases in asymptomatic patients with NSCLC is not considered cost-effective and is not generally recommended.[30, 206]

Patients with skeletal metastases are usually symptomatic or have laboratory abnormalities indicating bone metastases.[195] Because occult skeletal metastases are only occasionally detected in asymptomatic patients by imaging, it is recommended that bone radiographs, technetium 99m-methylene diphosphonate (^{99m}Tc-MDP) bone scintigraphy, and MRI be performed only to evaluate a history of focal bone pain or elevated alkaline phosphatase.[122, 137, 195, 206, 214]

Because staging performed on the basis of symptomatology, abnormal laboratory indices, and conventional radiologic imaging incorrectly assigns some patients with NSCLC, FDG-PET is being used as an additional imaging modality to improve staging accuracy. FDG-PET has a higher sensitivity and specificity than CT in detecting metastases to the adrenals, bones, and extrathoracic lymph nodes.[20, 52, 114, 129, 195, 238, 249] Whole body PET imaging allows the physician to stage intrathoracic and extrathoracic disease in a single study, to detect occult extrathoracic metas-

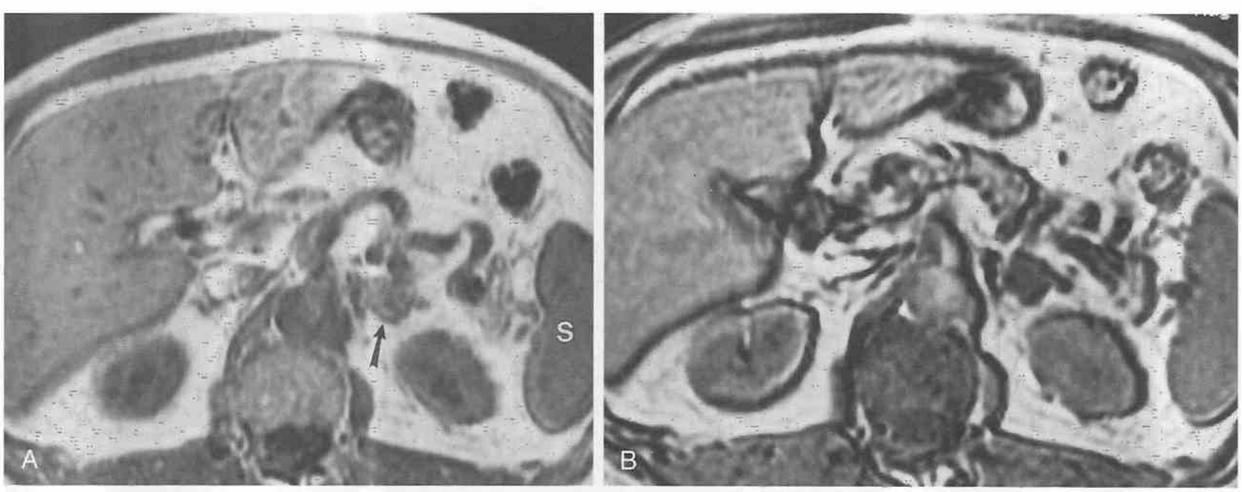

Figure 28–29. Non–small-cell lung cancer and incidental adrenal aden[redacted] evaluate[redacted] chemical shift MRI. *A,* In-phase (TR = 200 msec, TE = 4.2 msec) spoiled gradient-recalled echo MR image shows a left adrenal mass *(arrow)* that is slightly hyperintense compared with the spleen (S). *B,* Opposed-phase (TR = 200 msec, TE = 1.8 msec) spoiled gradient-recalled echo MR image shows that the left adrenal mass is now markedly hypointense. The findings are typical of those for adenoma. The patient underwent resection of primary lung malignancy.

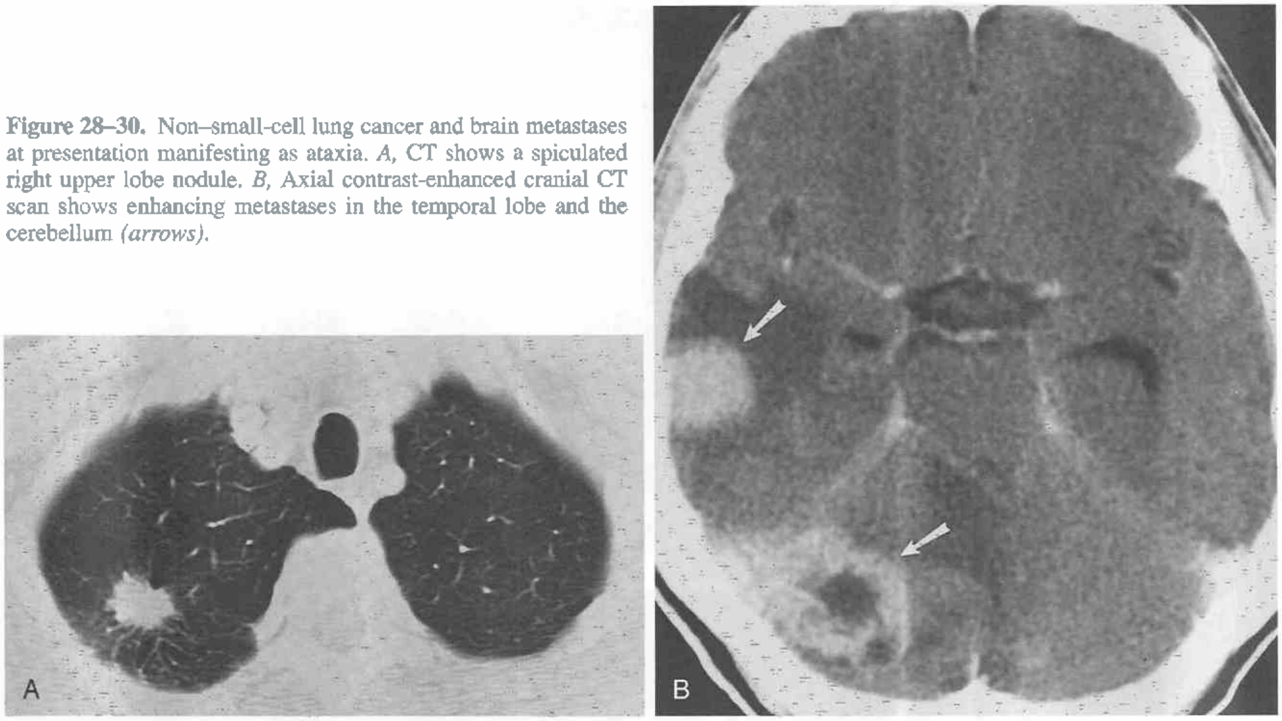

Figure 28–30. Non–small-cell lung cancer and brain metastases at presentation manifesting as ataxia. *A,* CT shows a spiculated right upper lobe nodule. *B,* Axial contrast-enhanced cranial CT scan shows enhancing metastases in the temporal lobe and the cerebellum *(arrows).*

tases in 11% to 14% of patients selected for curative resection, and to alter management in up to 40% of cases (Fig. 28–31).[114, 238, 249]

Staging Classification. The International Staging System for Lung Cancer combines the TNM subsets into categories, or stages, that have similar treatment options and prognosis (Table 28–4).[17, 145]

Stages I and II. Patients with *stage I* disease are typically optimal candidates for surgical resection with survival rates of 57% to 85%.[145] The prognostic implications of larger tumor size and location and the involvement of intrapulmonary and hilar lymph nodes are reflected in the decreased 5-year survival rates of 34% and 22% to 24% in patients with stage IIA (T1 N1 M0) and *stage IIB* (T2 N1 M0, T3 N0 M0) disease, respectively.[145]

Table 28–4. Stage Grouping: Tumor-Node-Metastases (TNM) Subsets

Stage	TNM Subset		
IA	T1	N0	M0
IB	T2	N0	M0
IIA	T1–2	N1	M0
IIB	T3	N0	M0
IIIA	T1–2	N2	M0
	T3	N1–2	M0
IIIB	T4	N0–2	M0
	T1–4	N3	M0
IV	Any T	Any N	M1

Stage III. Stage IIIA (T3 N1 M0, T1–T3 N2 M0) identifies patients with locally advanced disease (extrapulmonary extension of the primary tumor) and ipsilateral hilar or mediastinal nodes. These patients are potential surgical candidates, although extracapsular extension of metastasis or involvement of high paratracheal nodes is a contraindication to curative resection.[144] Increasing tumor size and extent of local invasion appear to be directly related to the extent of lymph node involvement and the decrease in survival rates.[145] The 5-year survival rate is 9% to 13% in clinically staged patients and 23% to 25% in surgical-pathologic staged patients.[145]

Stage IIIB (T4 N0–2 M0, T1–T4 N3 M0) identifies patients with nonresectable NSCLC (i.e., satellite nodules in the lobe with the primary tumor, malignant effusion, invasion of nonresectable structures, contralateral hila, or mediastinal nodal disease).[145] Most stage IIIB patients receive radiation therapy and adjuvant chemotherapy, and the 5-year survival is 3% to 8%.[145] The classification of satellite nodules as T4 disease, however, may imply a worse prognosis than is warranted. It has been advocated that these patients undergo definitive resection if there are no other contraindications to surgery (Fig. 28–32).[19, 112]

Stage IV. Stage IV patients have distant metastatic disease, including metastatic nodules in the ipsilateral nonprimary tumor lobes.[145] With the uncommon exception of a resectable intrathoracic NSCLC and a resectable solitary brain metastasis, stage IV carries the worst prognosis, with only 1% of patients alive at 5 years.[145, 194]

Small-Cell Lung Cancer. SCLC is generally staged according to the Veteran's Administration Lung Cancer

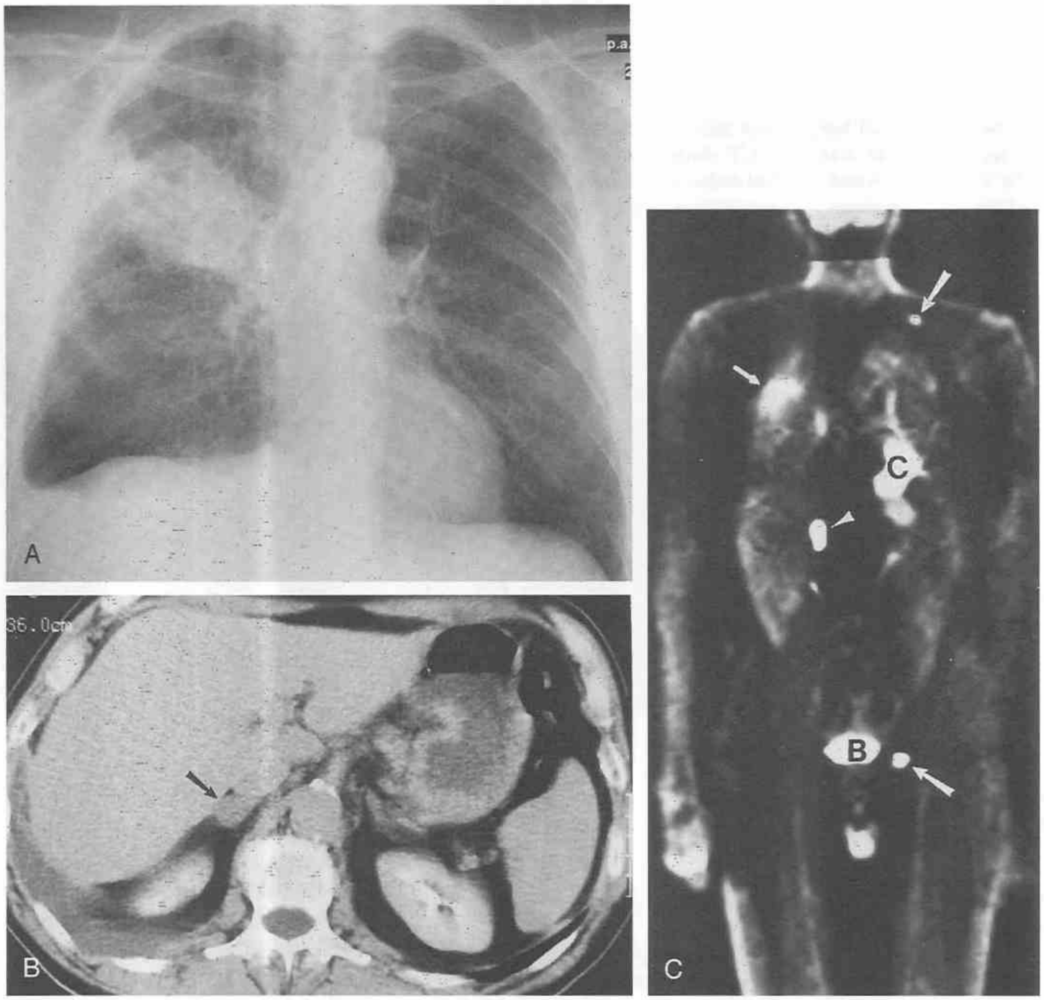

Figure 28–31. Non–small-cell lung cancer and extrathoracic metastases. *A,* Posteroanterior chest radiograph shows a right upper lobe mass. A small, right pleural effusion can be seen. *B,* CT reveals a small, right adrenal mass *(arrow)* and confirms a small right pleural effusion. *C,* Whole body PET image with ^{18}F-fluorodeoxyglucose (FDG-PET) shows increased uptake in the primary lung mass *(small arrow)* and in the adrenal metastasis *(arrowhead).* Focal areas of increased uptake in the upper aspect of the left hemithorax and pelvis *(large arrows)* were unsuspected bone metastases. B, bladder activity; C, cardiac activity.

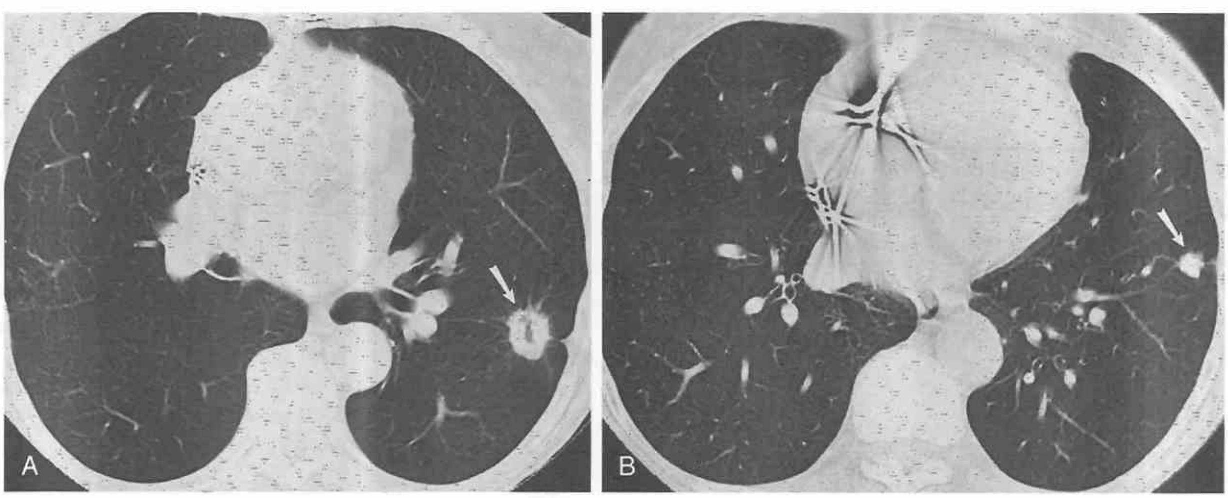

Figure 28–32. Non–small-cell lung cancer appearing as two lung nodules. *A* and *B,* CT scan shows two nodules in the left lower lobe, one of which is cavitary (*arrow* in *A* and in *B*). A satellite nodule in the ipsilateral lobe is classified as T4, not M1, disease.

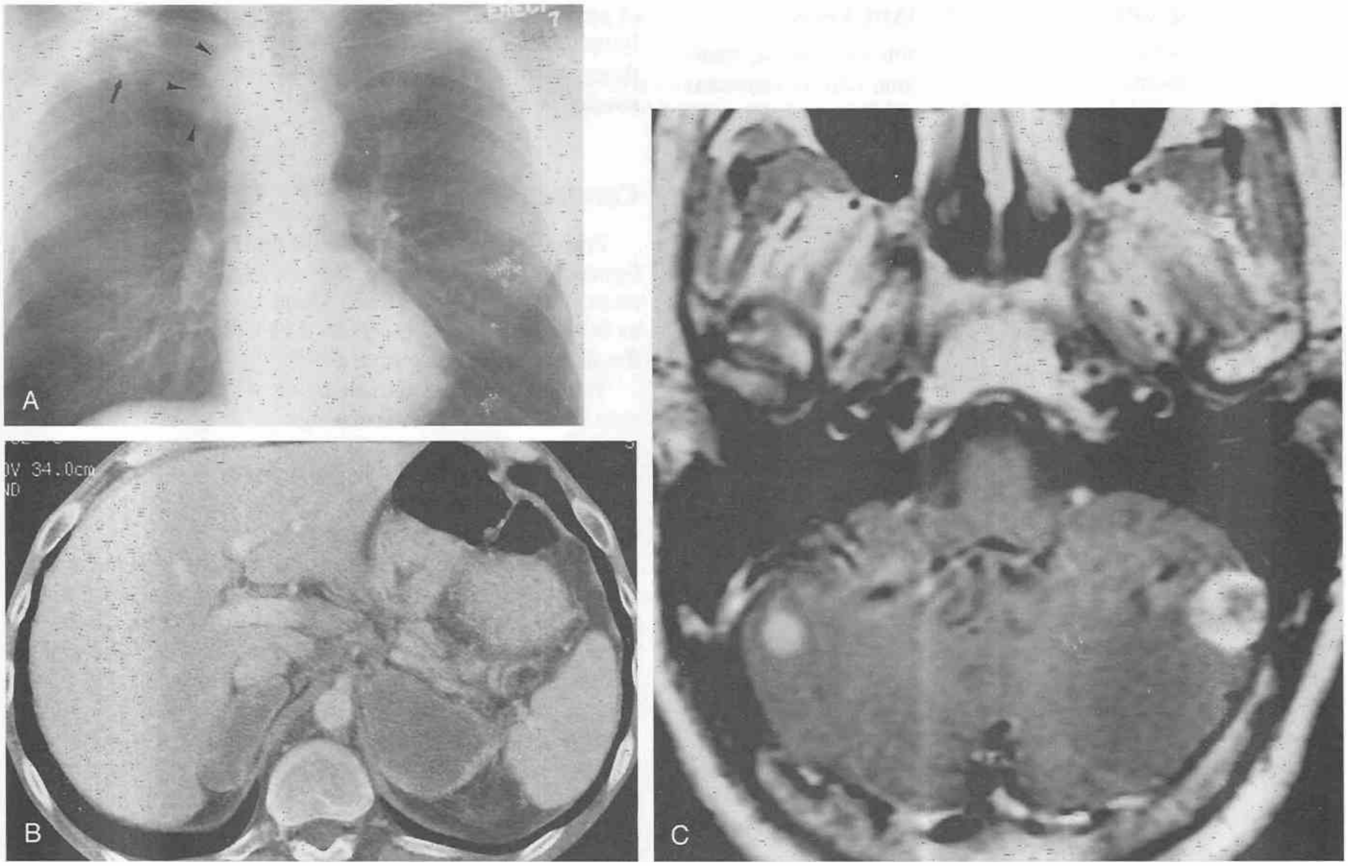

Figure 28–33. Small-cell lung cancer with disseminated metastases at presentation. *A*, Posteroanterior chest radiograph shows a poorly marginated mass in the right upper lobe *(arrowheads)* and a smaller right upper lobe nodule *(arrow)*. *B*, CT shows large, bilateral necrotic adrenal metastases. *C*, Axial contrast-enhanced cranial MR image shows enhancing cerebellar metastases.

Study Group (VALG) recommendations as *limited disease* (LD) or *extensive disease* (ED).[37] LD defines tumor confined to a hemithorax and the regional lymph nodes. Unlike the TNM classification for NSCLC, metastases to the ipsilateral supraclavicular, contralateral supraclavicular, and mediastinal lymph nodes are considered local disease. Additionally, an ipsilateral malignant pleural effusion is often treated as limited disease.[37] ED includes tumor with noncontiguous metastases to the contralateral lung and distant metastases.[37, 215]

Most patients with SCLC have ED at presentation (Fig. 28–33).[92, 100] Common sites of metastatic disease include the liver, bone, bone marrow, brain, and retroperitoneal lymph nodes.[92] Although there is no consensus regarding the imaging and invasive procedures that should be performed in the staging evaluation of patients with SCLC, MRI has been advocated to assess the liver, adrenals, brain, and axial skeleton in a single study.[92] Evaluation of extrathoracic metastatic disease usually includes the following:

1. *Bone marrow aspiration, ^{99m}Tc-MDP bone scintigraphy, and MRI.* Patients with bone (30%) and bone marrow (17% to 34%) metastases are often asymptomatic, and blood alkaline phosphatase levels are frequently normal.[1, 37, 209, 210] Because isolated bone and bone marrow metastases are uncommon, however, routine bone marrow aspiration and radiologic imaging for occult metastases are usually performed only if there are other findings of ED.
2. *Brain MRI.* CNS metastases are common (10% to 27%) at presentation, and approximately 5% of patients are asymptomatic.[1, 18, 37] Because therapeutic CNS radiation and chemotherapy can decrease morbidity and improve prognosis, routine MRI of the brain is recommended in patients with SCLC.[37, 46, 240]
3. *CT or MRI of the abdomen.* Metastases to the liver (30%) and retroperitoneal nodes (11%) are common at presentation.[1, 37] Because patients are often asymptomatic and liver function tests can be normal, staging evaluation routinely includes CT or MRI of the abdomen.

Carcinomas with Pleomorphic Sarcomatoid or Sarcomatous Elements

Sarcomatoid carcinomas are lung malignancies containing carcinomatous and sarcomatous components.[149, 254] They represent a clinicopathologic continuum that includes pulmonary blastoma, carcinosarcoma, and carcinomas with spindle or giant cells.[149, 254]

Carcinomas with Spindle or Giant Cells

Sarcomatoid carcinomas (pleomorphic carcinoma, spindle cell carcinoma, giant cell carcinoma, carcinosarcoma) are rare, composing 0.3% to 1% of malignant lung neoplasms.[48, 149] Most patients are men, and mean age at presentation is 65 years (range, 44 to 78 years).[90, 149] Most patients present with cough, dyspnea, hemoptysis, chest pain, or weight loss.[48, 90, 149] Although sarcomatoid carcinomas are usually localized at presentation, distant metastases occur frequently and the prognosis is poor.[90, 149, 254]

Radiologically, these neoplasms can manifest either as large peripheral masses or as polypoid endobronchial lesions with atelectasis or postobstructive pneumonia.[90, 98, 149, 254] Calcification and cavitation are uncommon, but necrosis and hemorrhage can manifest as heterogeneous attenuation on CT.[98, 149, 254] Hilar or mediastinal adenopathy is uncommon.[149] Pleural effusion can occur as a result of local invasion.[98] Metastases involve sites similar to those of lung cancer (lung, liver, bones, adrenals, brain).[254]

Pulmonary Blastoma

Pulmonary blastoma is a rare malignancy that makes up an estimated 0.25% to 0.5% of primary lung tumors.[62, 104, 106, 111] The tumor derives its name from its histologic resemblance to fetal lung tissue. Pulmonary blastomas, however, are thought to arise from primitive pluripotential stem cells and may represent a variant of carcinosarcoma.[255] Although the age range at presentation is wide (0 to 80 years), these tumors typically occur in adults, with a peak incidence between 40 and 60 years of age.[62, 104, 106, 111] Patients are often symptomatic at presentation; cough, hemoptysis, and chest pain are frequent manifestations.[104] Pulmonary blastoma is an aggressive malignancy and the overall 5-year survival rate is poor.[34, 62]

Radiologically, pulmonary blastomas typically manifest as large (range, 2.5 to 26 cm), well-marginated masses located peripherally in the lung (Fig. 28–34).[62, 250] Multiple masses, cavitation, and calcification are rare.[250] Local invasion of the mediastinum and pleura occurs in 8% and 25% of cases, respectively.[62] Metastases to hilar and mediastinal lymph nodes are present in 30% of resected cases.[62] Extrathoracic metastases are common and have a distribution similar to that of lung cancer.[62, 111]

Carcinoid Tumor

Primary pulmonary carcinoid tumors are low-grade malignancies that constitute 1% to 2% of primary lung tumors.[133] They are classified histologically as typical (80% to 90%) or atypical (10% to 20%) tumors, depending on the degree of cellular atypia.[38, 96, 219]

Typical carcinoid tumors occur with equal frequency in men and women; the mean age at diagnosis is 35 to 50 years.[38, 219] Tumors usually arise in lobar, segmental, or proximal subsegmental bronchi (80% to 85%) and are generally 1 to 4 cm in size. They rarely metastasize to regional nodes or beyond the thorax.[38]

Atypical carcinoid tumors are usually discovered at a slightly older age (mean, 55 to 60 years), are often larger, and have equal central and peripheral distributions.[96, 219] They behave more aggressively than do typical carcinoid tumors and frequently metastasize to regional nodes, lung, liver, and bone.[29, 96]

Clinical manifestations depend on the histologic type and the location of the carcinoid tumor.[219] Peripheral tumors are usually asymptomatic, whereas central neoplasms can manifest as cough, hemoptysis, or recurrent infection (Fig. 28–35).[38] Paraneoplastic manifestations, such as carcinoid syndrome (cutaneous flushing, bronchospasm, chronic diarrhea, and valvular heart disease) and Cushing's syndrome, are rare and more common with atypical carcinoid tumors.[38, 133]

Radiologically, carcinoid tumors manifest most commonly as central endobronchial masses, with or without atelectasis or consolidation (Fig. 28–36).[272] A peripheral, well-marginated pulmonary nodule is a less common manifestation (Fig. 28–37). The tumors are usually less than 3 cm in size, although occasionally they may be as large as

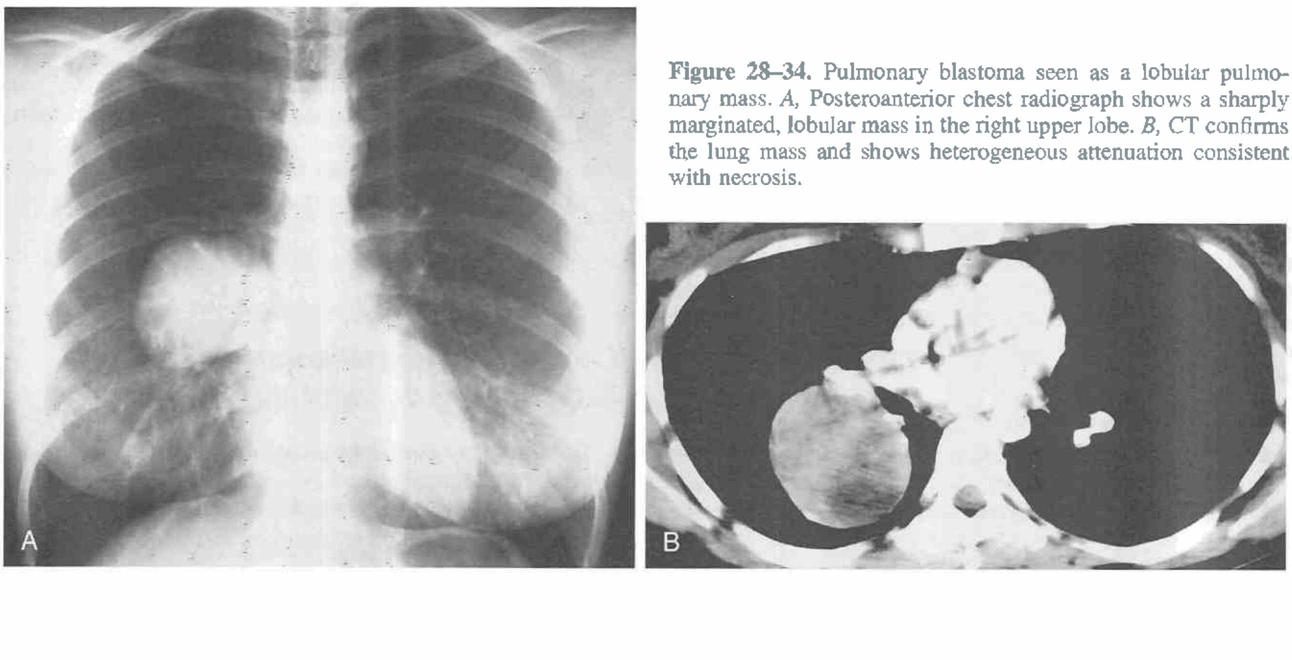

Figure 28–34. Pulmonary blastoma seen as a lobular pulmonary mass. *A,* Posteroanterior chest radiograph shows a sharply marginated, lobular mass in the right upper lobe. *B,* CT confirms the lung mass and shows heterogeneous attenuation consistent with necrosis.

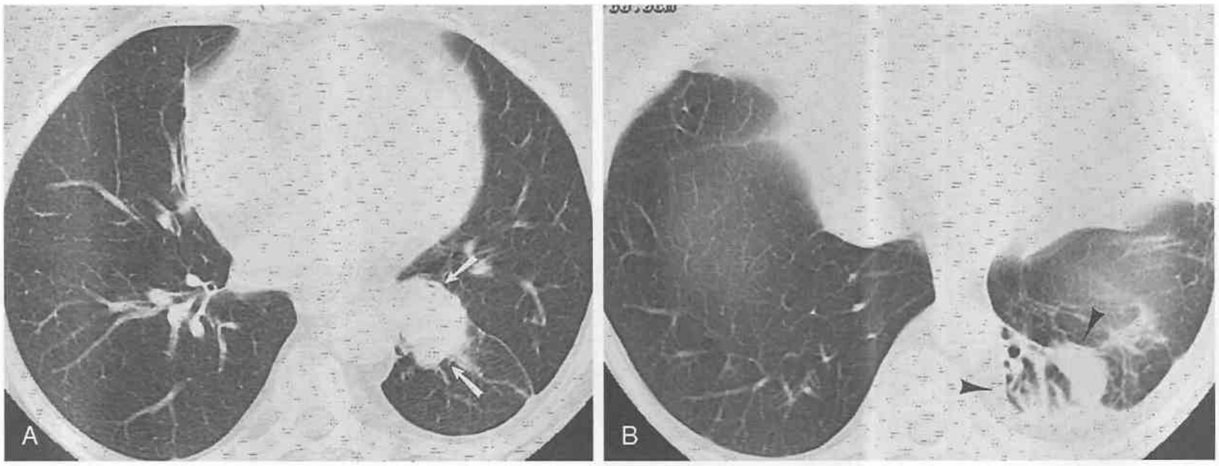

Figure 28–35. Typical carcinoid tumor manifesting as recurrent pulmonary infections. *A* and *B*, CT shows a mass in the segmental bronchus of the left lower lobe (*arrows* in *A*), left lower lobe volume loss, and distal bronchiectasis in the atelectatic lung (*arrowheads* in *B*).

10 cm in diameter.[133, 147, 239] Calcification is detected by CT in approximately 25% of carcinoid tumors (Fig. 28–38).[272] Hilar and mediastinal adenopathy and extrathoracic metastases are uncommon at presentation and occur more frequently in patients with atypical carcinoid tumors.[127, 147, 153]

Carcinomas of the Salivary Gland Type

Mucoepidermoid Carcinoma

Mucoepidermoid carcinoma (formerly categorized as a bronchial adenoma) is a rare tracheobronchial tumor composed of distinct areas of epidermoid cells and mucus-secreting cells. Although patients vary widely in age at presentation, the tumors are more common in adults, with a peak incidence between 35 and 45 years.[267] They typically occur in the main or lobar bronchi but, in rare instances, may be located in the trachea and periphery of the lung.[229, 232, 267] They are usually slow-growing, low-grade neoplasms with a benign clinical course. Although occasionally they exhibit aggressive local behavior, metastases are uncommon.[82, 267]

Radiologically, the tumor usually manifests as a central endobronchial mass and less commonly as a polypoid intraluminal tracheal or peripheral lung nodule or a mass.

Adenoid Cystic Carcinoma (Cylindroma)

Adenoid cystic carcinoma (formerly categorized as a bronchial adenoma) is an uncommon primary tumor of the lung. It occurs most often in the trachea (Fig. 28–39) and

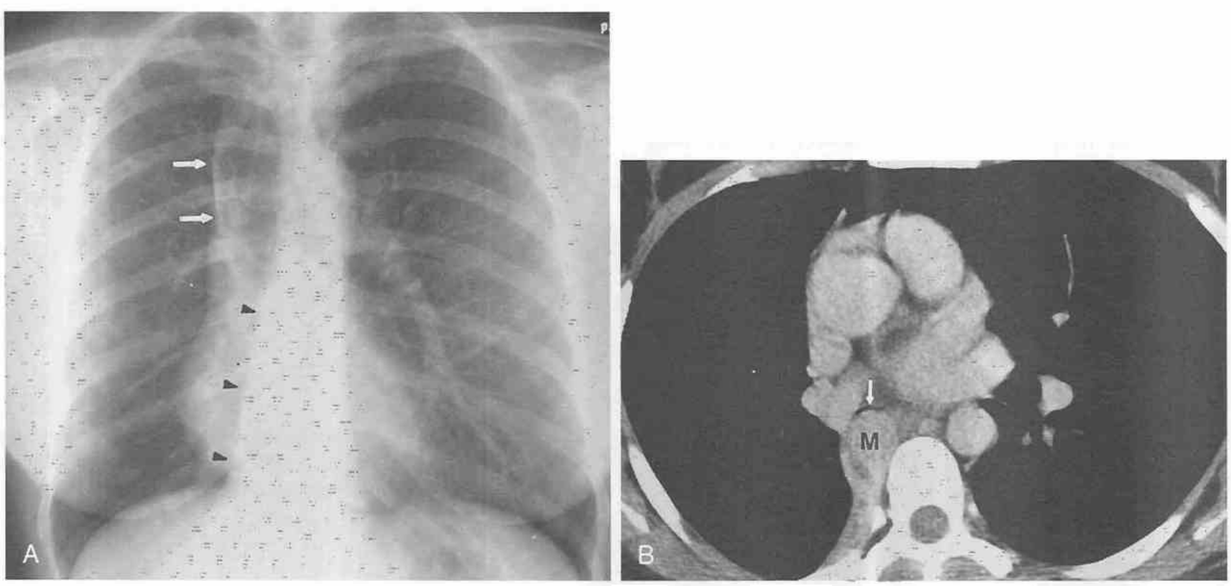

Figure 28–36. Typical carcinoid appearing as a central endobronchial lesion. *A*, Posteroanterior chest radiograph shows complete atelectasis of right lower lobe (*arrowheads*) with compensatory hyperinflation of the left lung. Note the displacement of the anterior junction line (*arrows*). *B*, CT confirms atelectasis of the right lower lobe and reveals an endobronchial mass (M) with marked narrowing of the bronchus intermedius (*arrow*).

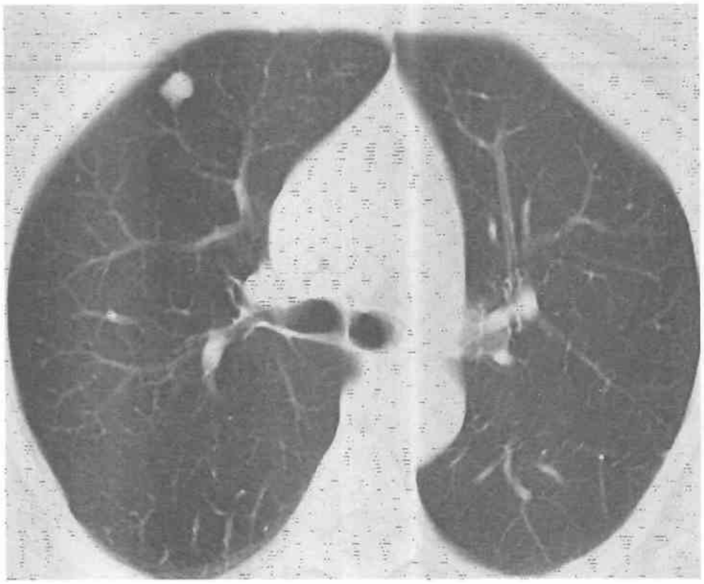

Figure 28–37. Typical carcinoid seen as a solitary peripheral nodule. CT shows a well-circumscribed small nodule in the right upper lobe.

main bronchi, although 10% to 15% are located peripherally in the lung.[3, 31, 36, 66] Adenoid cystic carcinomas occur with equal frequency in men and women; the mean age at diagnosis is 45 to 51 years.[130, 142] They typically exhibit slow, progressive growth.[31] Metastases to regional lymph nodes, lung, bone, liver, and brain are common but tend to occur late in the disease.[66]

Radiologically, the tumor usually manifests as an endotracheal or endobronchial mass that is typically lobulated or polypoid and encroaches on the airway lumen. Masses can be circumferential and may manifest as diffuse stenosis.[132] A less common manifestation is a peripheral lung nodule or mass.[31, 66]

Mesenchymal Tumors

Primary Pulmonary Sarcomas

Primary lung sarcomas with a vascular origin (angiosarcomas, epithelioid hemangioendotheliomas) are rare primary tumors of lung.[222, 256] Most angiosarcomas are lung metastases, and the existence of primary pulmonary angiosarcoma has been questioned.[208] The tumor usually occurs in young adults, and the most frequent radiologic finding is multiple, bilateral nodules.[222]

Epithelioid hemangioendothelioma is typically seen in women younger than 40 years of age (range, 7 to 76 years).[24, 187, 190, 256] Most patients are asymptomatic at presentation; complaints include weight loss, dyspnea, chest pain, cough, and hemoptysis.[24, 35, 256] Behavior is typically indolent, with survival reported up to 24 years following resection.[35]

Pulmonary epithelioid hemangioendothelioma usually manifests radiologically as multiple, 1- to 2-cm pulmonary nodules (Fig. 28–40).[35, 190, 256] Calcification is rarely detected but is common histologically.[35, 190] Hilar adenopathy and pleural effusions occur in 9% of patients.[190] Multiorgan involvement, most commonly the liver, occurs occasionally and may represent metastatic disease or multicentric origin of the tumor.[15, 45, 47, 191]

Primary lung sarcomas with a spindle origin are rare, accounting for fewer than 0.5% of primary lung malignan-

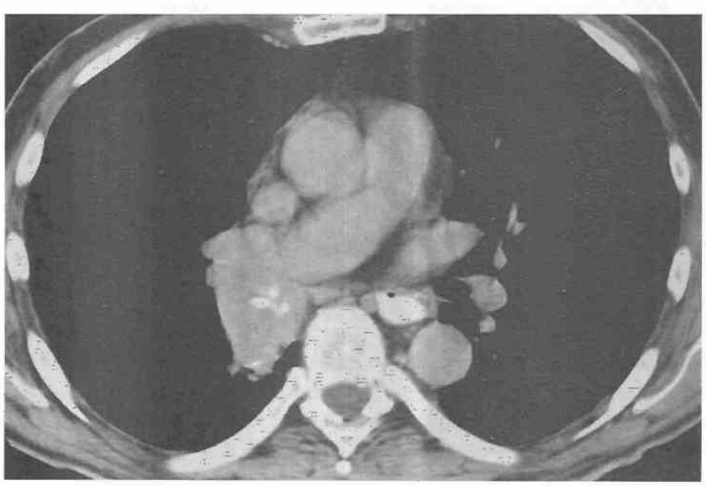

Figure 28–38. Atypical carcinoid tumor with rib and hepatic metastases at presentation. CT shows a large endobronchial mass with dense punctate calcification.

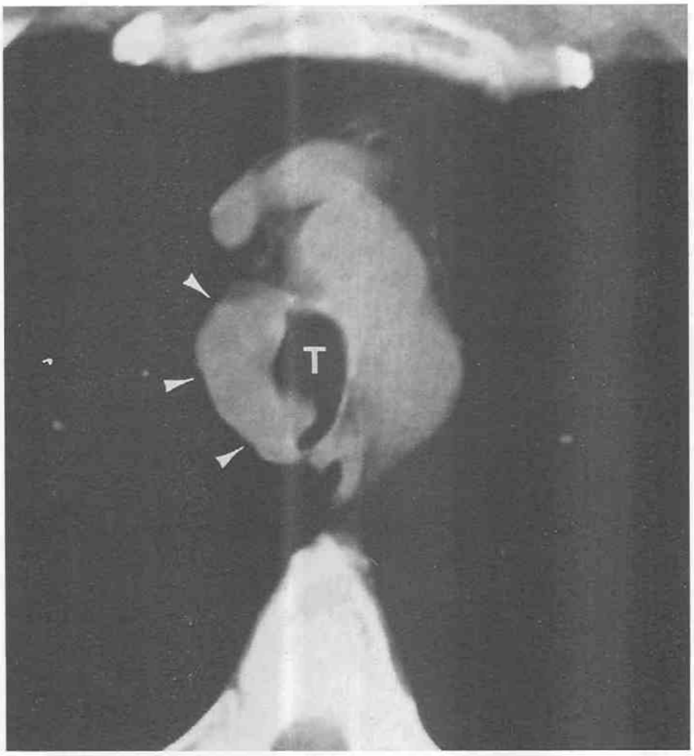

Figure 28–39. Adenoid cystic carcinoma manifesting as a tracheal mass. CT shows a soft tissue mass *(arrowheads)* arising from the lateral wall of the trachea (T). A polypoid endoluminal component can be seen.

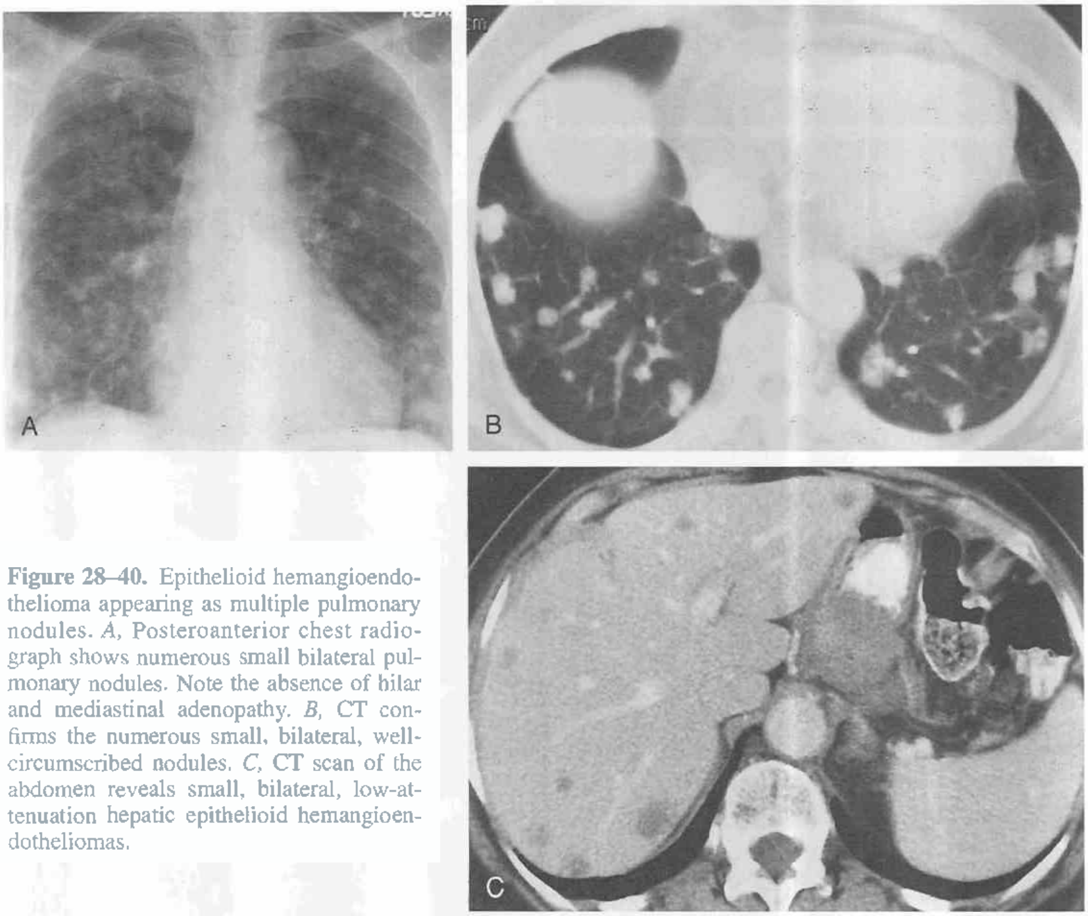

Figure 28–40. Epithelioid hemangioendothelioma appearing as multiple pulmonary nodules. *A,* Posteroanterior chest radiograph shows numerous small bilateral pulmonary nodules. Note the absence of hilar and mediastinal adenopathy. *B,* CT confirms the numerous small, bilateral, well-circumscribed nodules. *C,* CT scan of the abdomen reveals small, bilateral, low-attenuation hepatic epithelioid hemangioendotheliomas.

cies.[8, 222] Spindle cell sarcomas (malignant fibrous histiocytoma, hemangiopericytoma, fibrosarcoma, leiomyosarcoma, synovial sarcoma) are the most common primary pulmonary sarcomas.[94, 141, 222, 270] They are a heterogeneous group of tumors with morphologic similarities to their extrathoracic counterparts.[8] The diagnosis is established only after metastatic disease and sarcoma-like primary lung malignancies (sarcomatoid carcinomas) have been excluded.[8, 62, 90, 149] Pulmonary sarcomas have a peak incidence in the fifth and sixth decades.[91, 141, 222, 268, 270] The tumors are usually slowly growing with late metastases, and the prognosis is generally better than that with lung cancer.[222]

Radiologically, pulmonary sarcomas are more commonly located peripherally, although central and endobronchial masses are reported.[8, 91, 141, 222, 268] Lesions range in size from 0.6 to 25 cm; they are typically sharply marginated and occasionally calcified (Figs. 28–41 and 28–42).[8, 78, 94, 141, 222] Cavitation is uncommon, although CT can show heterogeneous attenuation resulting from necrosis within the mass.[78, 94] Diagnostic angiographic features have been reported for hemangiopericytomas in the soft tissues and bone.[78, 263] The pathognomonic hypervascularity that occurs as a result of the numerous vascular spaces within the tumor, however, are seldom seen on CT scans or MR images of primary pulmonary hemangiopericytomas (Fig. 28–43).

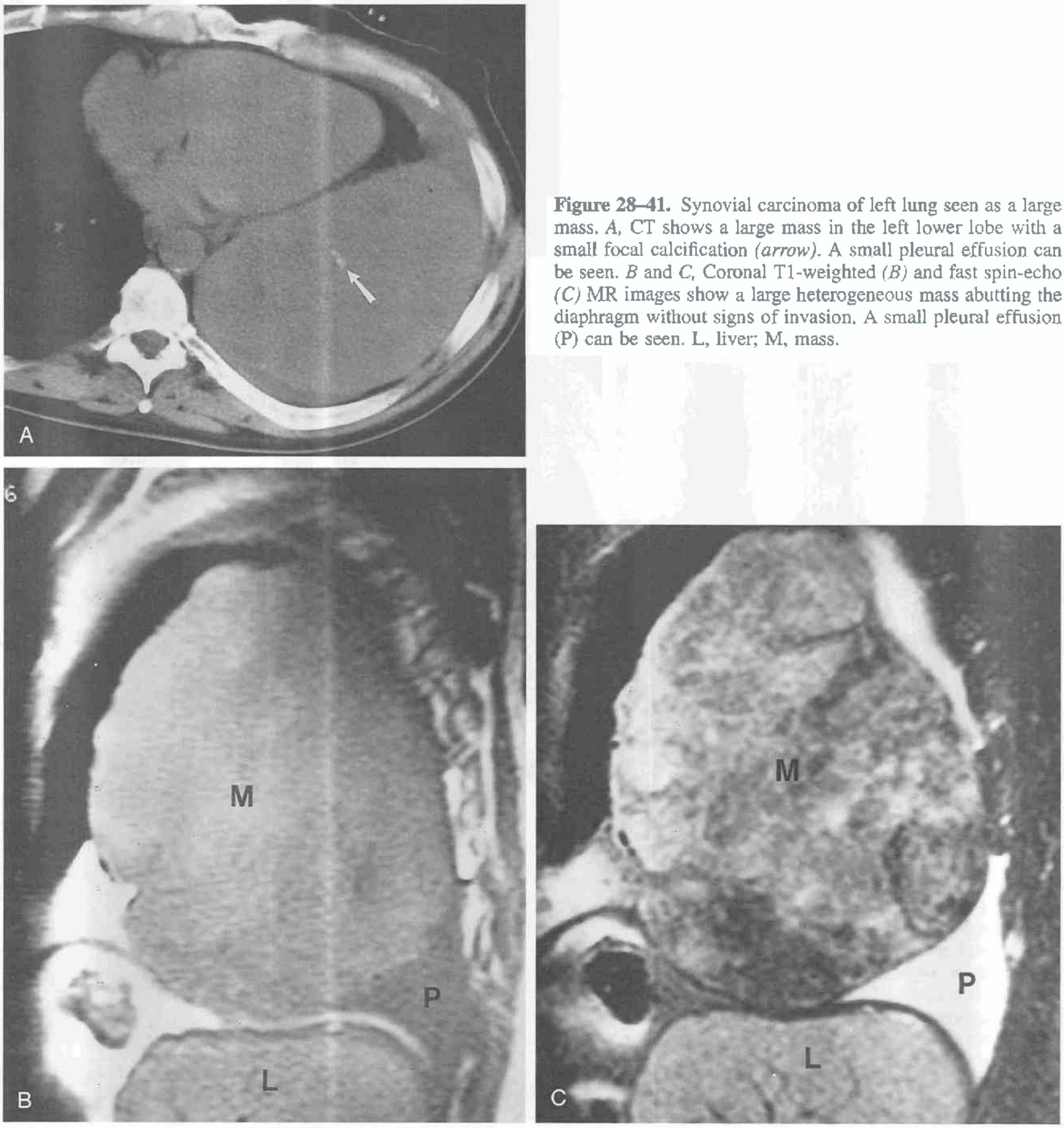

Figure 28–41. Synovial carcinoma of left lung seen as a large mass. *A*, CT shows a large mass in the left lower lobe with a small focal calcification *(arrow)*. A small pleural effusion can be seen. *B* and *C*, Coronal T1-weighted *(B)* and fast spin-echo *(C)* MR images show a large heterogeneous mass abutting the diaphragm without signs of invasion. A small pleural effusion (P) can be seen. L, liver; M, mass.

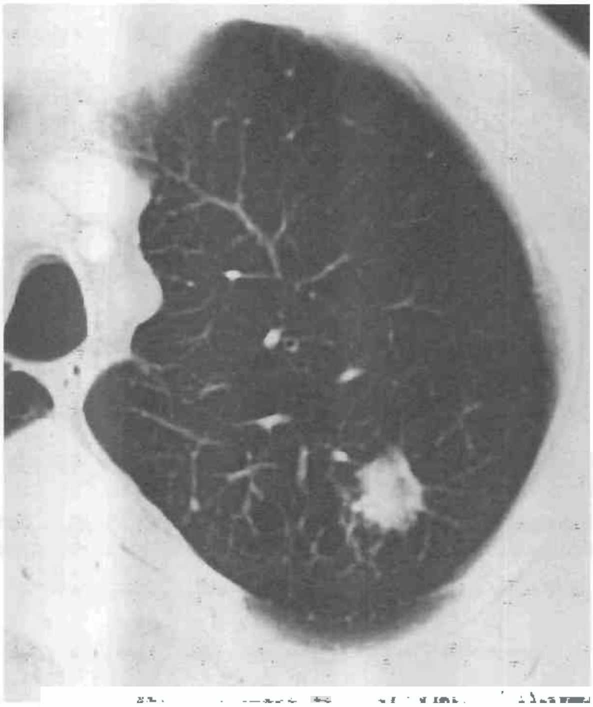

Figure 28–42. Malignant fibrous histiocytoma manifesting as a solitary pulmonary nodule. CT shows a left upper lobe nodule with irregular margins.

Lymphoproliferative Disorders

Primary Lymphomas

Primary pulmonary lymphomas account for fewer than 1% of all lymphomas.[32, 57, 103, 226] The diagnosis is generally considered if (1) the lymphoid proliferation is monoclonal and (2) there are no sites of extrathoracic lymphoma at presentation or for at least 3 months after diagnosis.[16, 32, 57, 183, 226] Criteria used to define primary pulmonary lymphomas are variable, however; some authors restrict the diagnosis to pulmonary parenchymal disease only, but others include hilar adenopathy with or without mediastinal adenopathy.

Primary pulmonary lymphomas encompass a histologic spectrum of malignant lymphomas including non-Hodgkin's lymphoma, Hodgkin's lymphoma, and lymphoproliferative disorders associated with immunodeficiency states (e.g., post-transplant lymphoproliferative disorders, acquired immunodeficiency syndrome).[77] Most primary extranodal lymphomas arise from mucosa-associated lymphoid tissue (MALT) and are sometimes referred to as *maltomas*.[32, 55, 77, 80, 103] In the lung, primary lymphomas are thought to arise from bronchus-associated lymphoid tissue (BALT) that occurs in the airway as a response to chronic stimulation.[231] These tumors are typically non-Hodgkin's lymphomas of B-cell immunophenotype composed of monoclonal lymphocytic cells with low histologic grade, and they have now been classified as extranodal marginal zone lymphomas.[57, 80, 103, 115]

Primary pulmonary lymphomas tend to remain localized

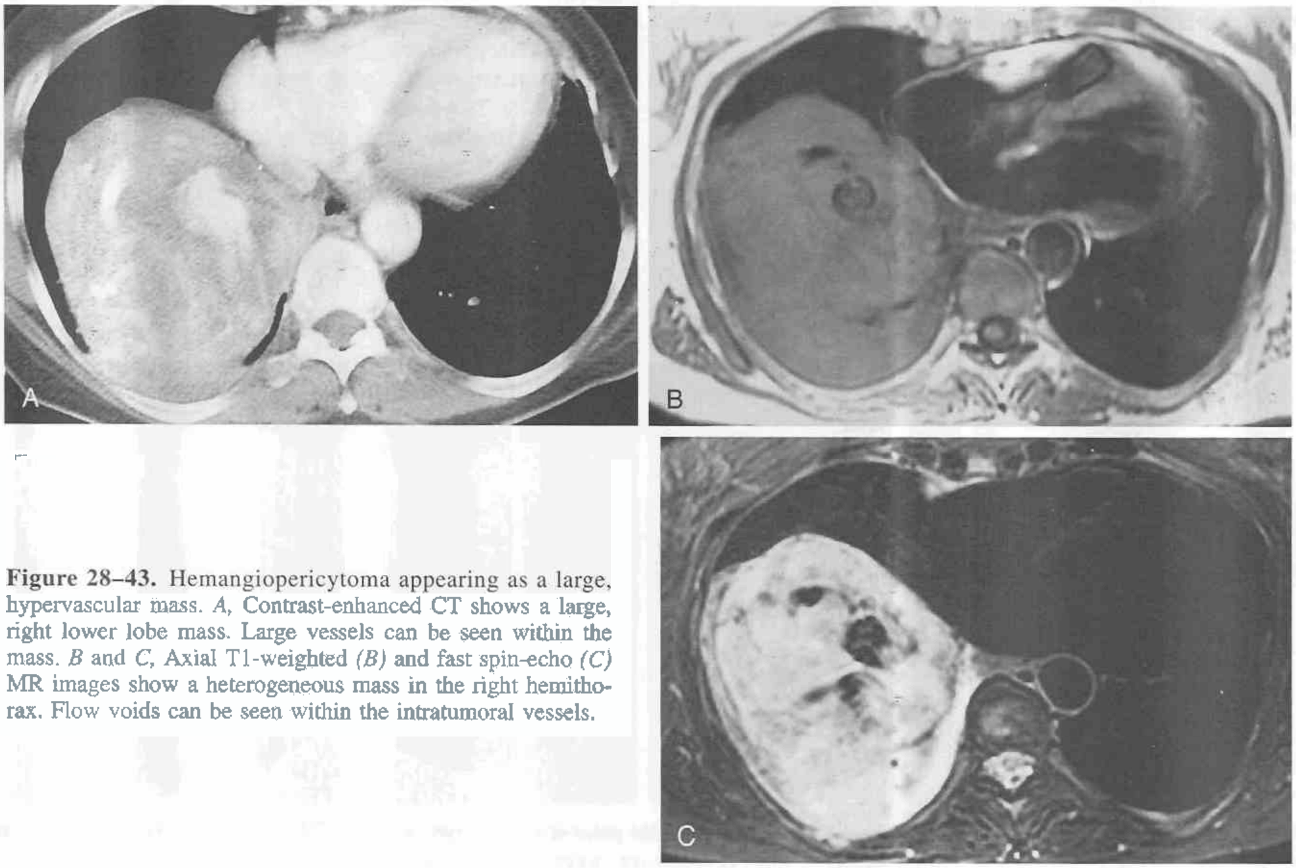

Figure 28–43. Hemangiopericytoma appearing as a large, hypervascular mass. *A*, Contrast-enhanced CT shows a large, right lower lobe mass. Large vessels can be seen within the mass. *B* and *C*, Axial T1-weighted *(B)* and fast spin-echo *(C)* MR images show a heterogeneous mass in the right hemithorax. Flow voids can be seen within the intratumoral vessels.

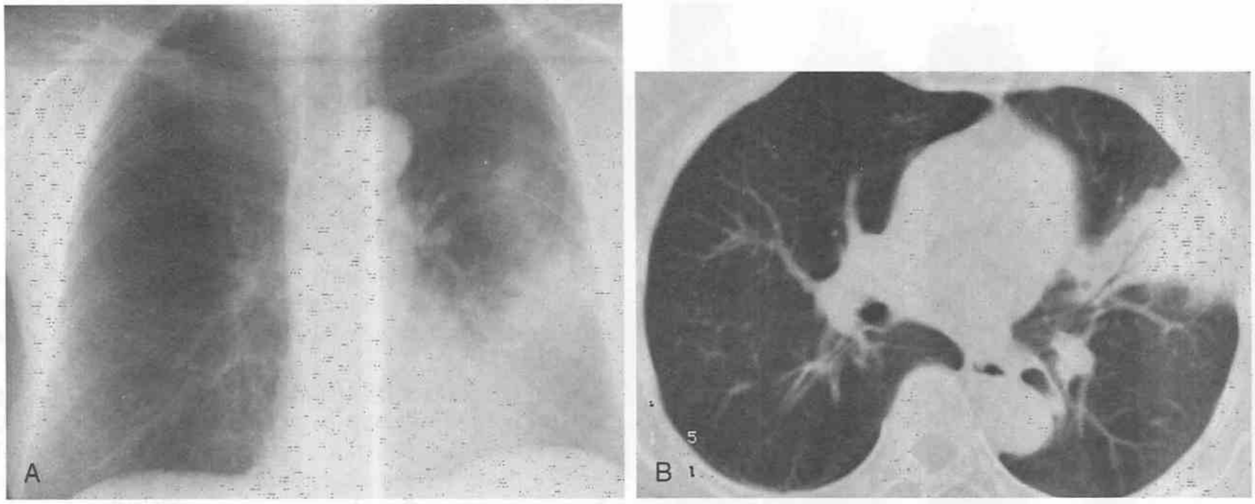

Figure 28–44. Primary pulmonary lymphoma seen as chronic consolidation. *A*, Posteroanterior chest radiograph shows a poorly marginated opacity in the left lung. Note the absence of hilar and mediastinal adenopathy. *B*, CT shows a homogeneous opacity containing air-bronchograms in the left upper lobe.

to the lung, although recurrence after treatment, often at extrapulmonary sites, occurs in up to 50%.[32, 57, 103, 115] High-grade non-Hodgkin's lymphomas, which constitute approximately 13% of primary pulmonary lymphomas, are usually B-cell tumors with aggressive behavior and a poor 5-year survival rate.[32, 57, 103, 115]

Most patients are 55 to 60 years old, although the age range is wide.[97, 115] Patients with low-grade lymphomas are usually asymptomatic at presentation, whereas patients with high-grade tumors usually present with cough, fever, or weight loss.[32]

The most common radiologic manifestations are a solitary nodule or mass and focal consolidation (Fig. 28–44).[32, 57, 109, 115, 158] Less common manifestations include multiple nodules or masses, multifocal consolidation, reticulonodular opacities, and atelectasis (Fig. 28–45).[32, 57, 115, 158] Hilar adenopathy is rare, and pleural effusions occur in 7% to 25% of patients.[32, 97, 103]

Benign Neoplasms of the Lung

Hamartoma

Hamartomas constitute 0.25% of all primary lung tumors and, although uncommon, are the most common benign tumor of lung.[193] The term *hamartoma* was initially used to describe lesions with an abnormal composition or disorganized arrangement of normal lung tissue. Now, however, hamartomas are considered true neoplasms containing a mixture of epithelial and mesenchymal tissues.[204]

Pulmonary hamartomas typically occur in patients older than 30 years, with a peak incidence in the sixth decade (range, 0 to 76 years).[79, 163, 180, 193] Most patients are asymptomatic; symptoms are typically present with central endobronchial lesions and include hemoptysis, recurrent pneumonia, and dyspnea.[63, 67, 193]

Hamartomas are typically solitary, well-marginated, slightly lobular nodules or masses that are less than 4 cm

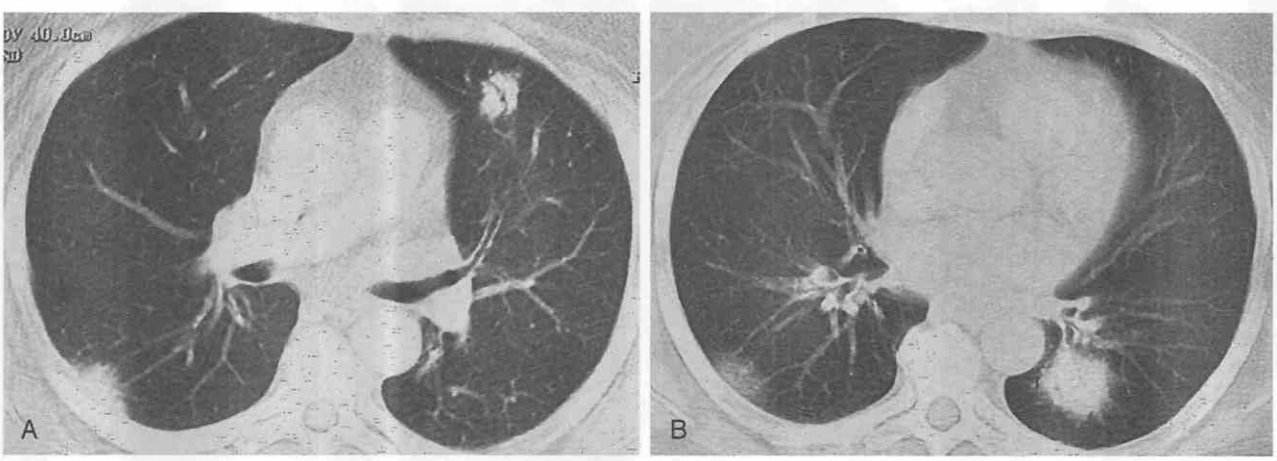

Figure 28–45. Primary pulmonary lymphoma manifesting as bilateral pulmonary opacities. *A* and *B*, CT shows focal, poorly marginated nodular opacities in both lungs. Air-bronchograms within opacities are suggestive of the diagnosis.

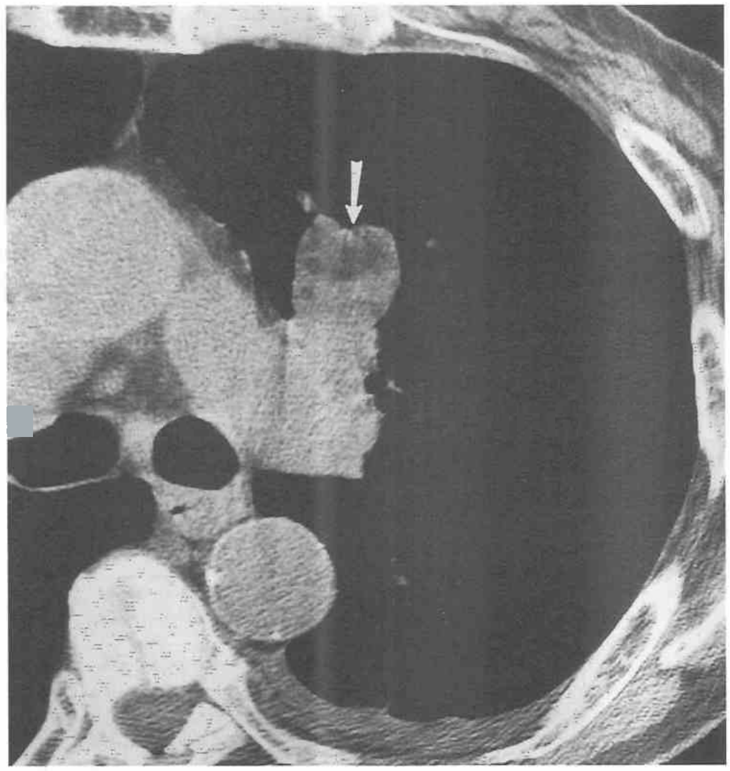

Figure 28–46. Hamartoma appearing as a solitary pulmonary nodule. CT shows a left upper lobe nodule *(arrow)* anterior to the left pulmonary artery. The diagnosis is suggested by small areas of fat (attenuation, −41 Hounsfield units) within the nodule.

in size (range, 1 to 30 cm).[63, 67, 180, 193] Most are located peripherally within the lung. Endobronchial hamartomas are less common (up to 20% of cases).[63, 79, 193] Calcification has been reported in up to 50% but is probably present in fewer than 5% of hamartomas.[107, 204] The presence of "popcorn" calcification, however, is almost pathognomonic of hamartomas. Fat (CT attenuation, −40 to −120 HU) occurs in up to 50% of cases and is a diagnostic feature (Fig. 28–46).[204] Rare radiographic manifestations include cavitation and multiple pulmonary hamartomas.[99]

Granular Cell Tumor

Granular cell tumors (formerly, *granular cell myeloblastomas*) are rare pulmonary neoplasms that are thought to arise from Schwann cells.[39, 131] Patients are usually adults (peak incidence, 30 to 50 years of age; range, 0 to 59 years), and there is a higher incidence in African Americans.[39, 102, 169, 170, 186]

Most pulmonary granular cell tumors manifest as small, central endobronchial masses (range, 0.3 to 6.5 cm in diameter).[39, 85] Multiple lesions, typically in the larger bronchi, are found in up to 25% of cases.[39, 85] Common radiologic findings include atelectasis and obstructive pneumonia, although slow-growing, solitary pulmonary nodules or masses occur in 12% of cases.[39, 85]

Sclerosing Hemangioma

Primary pulmonary sclerosing hemangioma is a benign tumor consisting of thin-walled vessels and connective tissue.[117, 156] Originally thought to represent a vascular tumor, it is now considered to arise from alveolar or bronchiolar epithelium.[81] Most patients are asymptomatic women between 30 and 50 years of age (range, 15 to 77 years).[95, 221]

Radiologically, pulmonary hemangiomas usually manifest as peripheral, well-marginated solitary pulmonary nodules or masses 0.4 to 8.0 cm in diameter (average, 3.0 cm). Multiple pulmonary nodules and calcification are rare.[95, 110]

Clear Cell Tumor

Clear cell tumor is a rare neoplasm of the lung.[65, 116] Most patients are asymptomatic and between 50 and 60 years of age (range, 8 to 70 years).[64, 65] Almost all the tumors behave in a benign nature, although extrathoracic metastases have been reported.[192] Clear cell tumors typically manifest radiologically as well-marginated solitary pulmonary nodules usually less than 3 cm in diameter (range, 0.7 to 6.5 cm).[6, 64, 65, 192, 271]

References

1. Abrams J, Doyle LA, Aisner J: Staging prognostic factors, and special considerations in small cell lung cancer. Semin Oncol 15: 261–277, 1988.
2. Akira M, Atagi S, Kawahra M, et al: High-resolution CT findings of diffuse bronchioloalveolar carcinoma in 38 patients. AJR Am J Roentgenol 173:1623–1629, 1999.
3. Allen MS: Malignant tracheal tumors. Mayo Clin Proc 68:680–684, 1993.
4. American Cancer Society: Cancer Facts and Figures—1997. Racial and Ethnic Patterns. Atlanta, American Cancer Society, 1997.

4a. American Cancer Society on line: Available at *http://www.cancer.org*

5. American Thoracic Society/European Respiratory Society: Pretreatment evaluation of non–small-cell lung cancer. Am J Respir Crit Care Med 156:320–332, 1997.

6. Andrion A, Mazzucco G, Gugliotta P, Monga G: Benign clear cell (sugar tumor) of the lung: A light microscopic, histochemical, and ultrastructural study with review of the literature. Cancer 56:2657–2663, 1985.
7. Arita T, Kuramitsu T, Kawamura M, et al: Bronchogenic carcinoma: Incidence of metastases to normal sized lymph nodes. Thorax 50: 1267–1269, 1995.
8. Attanoos RL, Appleton MAC, Gibbs AR: Primary sarcomas of the lung: A clinicopathological and immunohistochemical study of 14 cases. Histopathology 29:29–36, 1996.
9. Barbone F, Bovenzi M, Cavallieri F, Stanta G: Cigarette smoking and histologic type of lung cancer in men. Chest 112:1474–1479, 1997.
10. Bepler G: Lung cancer epidemiology and genetics. J Thorac Imaging 14:228–234, 1999.
11. Berkmen YM: The many faces of bronchiolo-alveolar carcinoma. Semin Roentgenol 12:207–214, 1977.
12. Berlin NI, Buncher CR, Fontana RS, et al: Early lung detection. Am Rev Respir Dis 103:545–549, 1984.
13. Boland GW, Lee MJ: Magnetic resonance imaging of the adrenal gland. Crit Rev Diagn Imaging 36:115–174, 1995.
14. Boland GW, Lee MJ, Gazelle GS, et al: Characterization of adrenal masses using unenhanced CT: An analysis of the CT literature. AJR Am J Roentgenol 171:201–204, 1998.
15. Bollinger BK, Laskin WB, Knight CB: Epithelioid hemangioendothelioma with multiple site involvement: Literature review and observations. Cancer 73:610–615, 1994.
16. Bragg DG, Chor PJ, Murray KA, Kjeldsberg CR: Lymphoproliferative disorders of the lung: Histopathology, clinical manifestations, and imaging features. AJR Am J Roentgenol 163:273–281, 1994.
17. Buccheri G, Ferrigno D: Prognostic value of stage grouping and TNM descriptors in lung cancer. Chest 117:1247–1255, 2000.
18. Bunn Jr PA, Rosen ST: Central nervous system manifestations of small cell lung cancer. In Aisner J (ed): Contemporary Issues in Clinical Oncology: Lung Cancer. New York, Churchill Livingstone, 1985, pp 287–305.
19. Burnett RJ, Wood DE: The new lung cancer staging system: What does it mean? Surg Oncol Clin North Am 8:231–244, 1999.
20. Bury T, Barreto A, Daenen F, et al: Fluorine-18 deoxyglucose positron emission tomography for the detection of bone metastases in patients with non-small cell lung cancer. Eur J Nucl Med 25: 1244–1247, 1998.
21. Byrd RB, Carr DT, Miller WE, et al: Radiographic abnormalities in carcinoma of the lung as related to histological cell. Thorax 24: 573–575, 1969.
22. Campanella N, Moraca A, Pergolini M, et al: Paraneoplastic syndromes in 68 cases of resectable non-small cell lung carcinoma: Can they help in early detection? Med Oncol 16:129–133, 1999.
23. Cardenas VM, Thun MJ, Austin H, et al: Environmental tobacco smoke and lung cancer mortality in the American Cancer Society's Cancer Prevention Study: II. Cancer Causes Control 8:57–64, 1997.
24. Carter EJ, Bradburne RM, Jhung JW, et al: Alveolar hemorrhage with epithelioid hemangioendothelioma: A previously unreported manifestation of a rare tumor. Am Rev Respir Dis 142:700–701, 1990.
25. Chalk CH, Windebank AJ, Kimmel DW: The distinctive clinical features of paraneoplastic sensory neuronopathy. Can J Neurol Sci 19:346, 1992.
26. Chartrand-Lefebvre C, Howarth N, Grenier P, et al: Association of small cell lung cancer and the anti-Hu paraneoplastic syndrome: Radiographic and CT findings. AJR Am J Roentgenol 170:1513–1517, 1998.
27. Chartrand-Lefebvre D, Howarth N, Grenier P, et al: Association of small cell lung cancer and the anti-Hu paraneoplastic syndrome: Radiographic and CT findings. AJR Am J Roentgenol 170:1513–1517, 1998.
28. Clouston PD, Saper CB, Arbizu T, et al: Paraneoplastic cerebellar degeneration: III. Cerebellar degeneration, cancer and the Lambert-Eaton myasthenic syndrome. Neurology 42:1944, 1992.
29. Colby TV, Koss MN, Travis WD: Tumors of the lower respiratory tract. In Atlas of Tumor Pathology. Washington, DC, Armed Forces Institute of Pathology, 1995.
30. Colice GL, Birkmeyer JD, Black WC, Littenberg B, Silvestri G: Cost-effectiveness of head CT in patients with lung cancer without clinical evidence of metastases. Chest 108:1264–1271, 1995.
31. Conlan AA, Payne WS, Woolner LB, Sanderson DR: Adenoid cystic carcinoma (cylindroma) and mucoepidermoid carcinoma of the bronchus. J Thorac Cardiovasc Surg 76:369–377, 1978.
32. Cordier JF, Chailleux E, Lauque D, et al: Primary pulmonary lymphomas: A clinical study of 70 cases of nonimmunocompromised patients. Chest 103:201–208, 1994.
33. Croft PB, Wilkinson M: The course and prognosis in some types of carcinomatous neuromyopathy. Brain 1:1969, 1992.
34. Cutler CS, Michel RP, Yassa M, Langleben A: Pulmonary blastoma. Cancer 82:462–467, 1998.
35. Dail DH, Liebow AA, Gmelich JT, et al: Intravascular, bronchiolar, and alveolar tumor of the lung (IVBAT): An analysis of twenty cases of a peculiar sclerosing endothelial tumor. Cancer 51:452–464, 1983.
36. Dalton ML, Gatling RR: Peripheral adenoid cystic carcinoma of the lung. South Med J 83:577–579, 1990.
37. Darling GE: Staging of the patient with small cell lung cancer. Chest Surg Clin North Am 7:81–94, 1997.
38. Davila DG, Dunn WF, Tazelaar HD, Pairolero PC: Bronchial carcinoid tumors. Mayo Clin Proc 68:795–803, 1993.
39. Deavers M, Guinee D, Koss MN, Travis WD: Granular cell tumors of the lung. Am J Surg Pathol 19:627–635, 1995.
40. Delisle L, Boyer MJ, Warr D, et al: Ectopic corticotropin syndrome and small cell carcinoma of the lung: Clinical features, outcome, and complications. Arch Intern Med 153:746–752, 1993.
41. Dewan NA, Gupta NC, Redepenning LS, et al: Diagnostic efficacy of PET-FDG imaging in solitary pulmonary nodules. Chest 104: 997–1002, 1993.
42. Dumont P, Gasser B, Rouge C, et al: Bronchoalveolar carcinoma: Histopathologic study of evolution in a series of 105 surgically treated patients. Chest 113:391–395, 1998.
43. Dunnick NR: Adrenal imaging: Current status. AJR Am J Roentgenol 154:927–936, 1990.
44. Dwamena BA, Sonnad SS, Angobaldo JO, Wahl RL: Metastases from non-small cell lung cancer: Mediastinal staging in the 1990s: Meta-analytic comparison of PET and CT. Radiology 213:530–536, 1999.
45. Echevarria RA: Angiogenic nature of "intravascular bronchioloalveolar tumor." Arch Pathol Lab Med 105:627–628, 1981.
46. Elias AD: Small cell lung cancer. State-of-the-art therapy in 1996. Chest 112:251S–258S, 1997.
47. Emery RW, Fox AL, Raab DE: Intravascular bronchioloalveolar tumor. Thorax 37:472–473, 1982.
48. Engle AF, Groot G, Bellot S: Carcinosarcoma of the lung: A case-history of disseminated disease and review of the literature. Eur J Surg Oncol 17:94–96, 1991.
49. Epstein DM: Bronchioloalveolar carcinoma. Semin Roentgenol 25: 105–111, 1990.
50. Epstein DM, Gefter WB, Miller WT: Lobar bronchioloalveolar cell carcinoma. Am J Roentgenol 139:463–468, 1982.
51. Erasmus JJ, McAdams HP, Donnelly LF, Spritzer CE: MR imaging of mediastinal masses. MRI Clin North Am 8:59–89, 2000.
52. Erasmus JJ, Patz EF, McAdams HP, et al: Evaluation of adrenal masses in patients with bronchogenic carcinoma by using ^{18}F-fluorodeoxyglucose positron emission tomography. AJR Am J Roentgenol 168:1357–1360, 1997.
53. Erren TC: Synergy between asbestos and smoking on lung cancer risks. Epidemiology 10:405–411, 1999.
54. Fearon ER: Human cancer syndromes: Clues to the origin and nature of cancer. Science 278:1043–1050, 1997.
55. Ferraro P, Trastek VF, Adlakha H, et al: Primary non-Hodgkin's lymphoma of the lung. Ann Thorac Surg 69:993–997, 2000.
56. Ferrigno D, Buccheri G: Cranial computed tomography as a part of the initial staging procedures for patients with non–small-cell lung cancer. Chest 106:1025–1029, 1994.
57. Fiche M, Caprons F, Berger F, et al: Primary pulmonary non-Hodgkin's lymphomas. Histopathology 26:529–537, 1995.
58. Filderman AE, Shaw C, Matthay RA: Lung cancer: Part I. Etiology, pathology, natural history, manifestations, and diagnostic techniques. Invest Radiol 21:80–90, 1986.
59. Fink D: Guidelines for the cancer related checkup: Recommendations and rationale. In Textbook of Clinical Oncology. Atlanta, American Cancer Society, 1991, pp 153–176.
60. Flehinger BJ, Kimmel M, Melamed MR: National history of adenocarcinoma—large cell carcinoma of the lung: Conclusions from screening programs in New York and Baltimore. J Natl Cancer Inst 80:337–344, 1988.

61. Franceschi S, Bidoli E: The epidemiology of lung cancer. Ann Oncol 10(Suppl 5):S3–S6, 1999.
62. Francis D, Jacobsen M: Pulmonary blastoma. Curr Top Pathol 73: 165–294, 1998.
63. Fudge TL, Ochsner JL, Mills NL: Clinical spectrum of pulmonary hamartomas. Ann Thorac Surg 30:36–39, 1980.
64. Gaffey MJ, Mills SE, Askin FB, et al: Clear cell tumor of the lung: A clinicopathologic, immunohistochemical, and ultrastructural study of eight cases. Am J Surg Pathol 14:248–259, 1990.
65. Gaffey MJ, Mills SE, Ritter JH: Clear cell tumors of the lower respiratory tract. Semin Diagn Pathol 14:222–232, 1997.
66. Gallagher CG, Teskey SR, Kryger M: Atypical manifestations of pulmonary adenoid cystic carcinoma. Br J Dis Chest 80:396–399, 1986.
67. Gjevre JA, Myers JL, Prakash UB: Pulmonary hamartomas. Mayo Clin Proc 71:14–20, 1996.
68. Glazer GM, Gross BH, Aisen AM, et al: Imaging of the pulmonary hilum: A prospective comparative study in patients with lung cancer. Am J Roentgenol 145:245–248, 1985.
69. Glazer GM, Gross BH, Quint LE, et al: Normal mediastinal lymph nodes: Number and size according to American Thoracic Society Mapping. Am J Roentgenol 144:261–265, 1985.
70. Glazer GM, Orringer MB, Chenevert TL, et al: Mediastinal lymph nodes: Relaxation time/pathologic correlation and implications in staging of lung cancer with MR imaging. Radiology 168:429–431, 1988.
71. Glazer HS, Kaiser LR, Anderson DJ, et al: Indeterminate mediastinal invasion in bronchogenic carcinoma: CT evaluation. Radiology 173: 37–42, 1989.
72. Good CA: Management of patient with solitary mass in lung. Chic Med Soc Bull 55:893–896, 1953.
73. Good CA, Wilson TW: The solitary circumscribed pulmonary nodule. JAMA 166:210–215, 1958.
74. Goodman M, Morgan RW, Ray R, et al: Cancer in asbestos-exposed occupational cohorts: A meta-analysis. Cancer Causes Control 10: 453–465, 1999.
75. Govindan R, Ihde DC: Practical issues in the management of the patient with small cell lung cancer. Chest Surg Clin North Am 7: 167–181, 1997.
76. Gurney JW: Determining the likelihood of malignancy in solitary pulmonary nodules with Bayesian analysis. Radiology 186:405–413, 1993.
77. Habermann TM, Ryu JH, Inwards DJ, Kurtin PJ: Primary pulmonary lymphoma. Semin Oncol 26:307–315, 1999.
78. Halle M, Blum U, Dinkel E, Brugger W: CT and MR features of primary pulmonary hemangiopericytomas. J Comput Assist Tomogr 17:51–55, 1993.
79. Hansen CP, Holtveg H, Francis D, et al: Pulmonary hamartoma. J Thorac Cardiovasc Surg 104:674–678, 1992.
80. Harris L, Jaffe ES, Stein H, et al: A revised European-American classification of lymphoid neoplasms: A proposal from the International Lymphoma Study Group. Blood 84:1361–1392, 1994.
81. Heikkila P, Salminen US: Papillary pneumocytoma of the lung: An immunohistochemical and electron microscopic study. Pathol Res Pract 190:194, 1993.
82. Heitmiller RF, Mathisen DJ, Ferry JA, et al: Mucoepidermoid lung tumors. Ann Thorac Surg 47:394–399, 1989.
83. Henschke CI, McCauley DI, Yankelevitz DF, et al: Early lung cancer action project: Overall design and findings from baseline screening. Lancet 354:99–105, 1999.
84. Herman SJ, Winton TL, Weisbrod GL, et al: Mediastinal invasion by bronchogenic carcinoma: CT signs. Radiology 190:841–846, 1994.
85. Hernandez OGT, Haponik EF, Summer WR: Granular cell tumour of the bronchus: Bronchoscopic and clinical features. Thorax 41: 927–931, 1986.
86. Higgins GA, Shields TW, Keehn RJ: The solitary pulmonary nodule. Arch Surg 110:570–575, 1975.
87. Hill CA: Bronchioloalveolar carcinoma: A review. Radiology 150: 15–20, 1984.
88. Holst VA, Finkelstein S, Yousem SA: Bronchioloalveolar adenocarcinoma of lung: Monoclonal origin for multifocal disease. Am J Surg Pathol 22:1343–1350, 1998.
89. Hooper RG, Tenholder MF, Underwood GH, et al: Computed tomographic scanning of the brain in initial staging of bronchogenic carcinoma. Chest 85:774–776, 1984.
90. Ishida T, Tateishi M, Kaneko S, et al: Carcinosarcoma and spindle cell carcinoma of the lung. J Thorac Cardiovasc Surg 100:844–852, 1990.
91. Janssen JP, Mulder JJS, Wagenaar SS, et al: Primary sarcoma of the lung: A clinical study with long-term follow-up. Ann Thorac Surg 58:1151–1155, 1994.
92. Jelinek JS, Redmond J, Perry JJ, et al: Small cell lung cancer: Staging with MR imaging. Radiology 177:837–842, 1990.
93. Kaneko M, Eguchi K, Ohmatsu H, et al: Peripheral lung cancer: Screening and detection with low-dose spiral CT versus radiography. Radiology 201:798–802, 1996.
94. Katz DS, Lane M, Leung AN, et al: Primary malignant pulmonary hemangiopericytoma. Clin Imaging 22:192–195, 1998.
95. Katzenstein AA, Gmelich JT, Carrington CB: Sclerosing hemangioma of the lung: A clinicopathologic study of 51 cases. Am J Surg Pathol 4:343–356, 1980.
96. Kayser K, Kayser C, Rahn W, et al: Carcinoid tumors of the lung: Immuno- and ligandohistochemistry, analysis of integrated optical density, syntactic structure analysis, clinical data, and prognosis of patients treated surgically. J Surg Oncol 63:99–106, 1996.
97. Kennedy JL, Nathwani BN, Berke J, et al: Pulmonary lymphomas and lymphoid lesions. Cancer 56:539–552, 1985.
98. Kim K, Flint JDA, Müller NL: Pulmonary carcinosarcoma: Radiologic and pathologic findings in three patients. AJR Am J Roentgenol 169:691–694, 1997.
99. King TE, Christopher KL, Schwarz MI: Multiple pulmonary chondromatous hamartomas. Hum Pathol 13:496, 1982.
100. Klein JS, Webb WR: The radiologic staging of lung cancer. J Thorac Imaging 7:29–47, 1991.
101. Knight SB, Delbeke D, Stewart JR, Sandler MP: Evaluation of pulmonary lesions with FDG-PET. Chest 109:982–988, 1996.
102. Korompai FL, Awe RJ, Beall AC, Greenberg SD: Granular cell myoblastoma of the bronchus: A new case, 12-year follow-up report, and review of the literature. Chest 66:578–580, 1974.
103. Koss MN: Pulmonary lymphoid disorders. Semin Diagn Pathol 12: 158–171, 1995.
104. Koss MN, Hochholzer L, O'Leary T: Pulmonary blastomas. Cancer 67:2368–2381, 1991.
105. Kubik A, Parkin DM, Khlat M, et al: Lack of benefit from semi-annual screening for cancer of the lung: Follow-up report of a randomized controlled trial on population of high-risk males in Czechoslovakia. Int J Cancer 45:26–33, 1990.
106. Larsen H, Sorensen JB: Pulmonary blastoma: A review with special emphasis on prognosis and treatment. Cancer Treat Rev 22:145–160, 1996.
107. Ledor K, Fish B, Chaise L, Ledor S: CT diagnosis of pulmonary hamartomas. J Comput Assist Tomogr 5:343–344, 1981.
108. Lee KS, Kim Y, Han J, et al: Bronchioloalveolar carcinoma: Clinical, histopathologic, and radiologic findings. Radiographics 17: 1345–1357, 1997.
109. Lee KS, Kim Y, Primack SL: Imaging of pulmonary lymphomas. AJR Am J Roentgenol 168:339–345, 1997.
110. Lee S, Lee Y, Hsu C, Lin C: Bilateral multiple sclerosing hemangiomas of the lung. Chest 101:572–573, 1992.
111. LeMense GP, Reed CE, Silvestri GA: Pulmonary blastoma: A rare lung malignancy. Lung Cancer 15:233–237, 1996.
112. Leong SS, Lima CMR, Sherman CA, Green MR: The 1997 international staging system for non-small cell lung cancer. Have all the issues been addressed? Chest 115:242–248, 1999.
113. Levin KH: Paraneoplastic neuromuscular syndromes. Neurol Clin 15:597–614, 1997.
114. Lewis P, Griffin S, Marsden P, et al: Whole-body ^{18}F-fluorodeoxyglucose positron emission tomography in preoperative evaluation of lung cancer. Lancet 344:1265–1266, 1994.
115. Li G, Hansmann M-L, Zwingers T, et al: Primary lymphoma of the lung: Morphological, immunohistochemical and clinical features. Histopathology 16:519–531, 1990.
116. Liebow AA, Castleman B: Benign clear cell (sugar) tumors of the lung. Yale J Biol Med 43:213–222, 1971.
117. Liebow AA, Hubbell DF: Sclerosing hemangioma (histiocytoma, xanthoma) of the lung. Cancer 9:53, 1956.
118. Lillington GA: Disease-a-Month, 37th ed. St. Louis, Mosby–Year Book, 1991.
119. Lillington GA, Caskey CI: Evaluation and management of solitary multiple pulmonary nodules. Clin Chest Med 14:111–119, 1993.

120. List AF, Doll DC, Greco FA: Lung cancer in Hodgkin's disease: Association with previous radiotherapy. J Clin Oncol 3:215–221, 1985.
121. List AF, Hainsworth JD, Davis BW, et al: The syndrome of inappropriate secretion of antidiuretic hormone (SIADH) in small cell lung cancer. J Clin Oncol 4:1191–1198, 1986.
122. Little AG, Stitik FP: Clinical staging of patients with non-small cell lung cancer. Chest 97:1431–1438, 1990.
123. Mahoney MC, Shipley RT, Corcoran HL, Dickson BA: CT demonstration of calcification in carcinoma of the lung. AJR Am J Roentgenol 154:255–258, 1990.
124. Marchioli CC, Graziano SL: Paraneoplastic syndromes associated with small cell lung cancer. Chest Surg Clin North Am 7:65–79, 1997.
125. Marom EM, Patz EF Jr, Swensen SJ: Radiologic findings of bronchogenic carcinoma with pulmonary metastases at presentation. Clin Radiol 54:665–668, 1999.
126. Martini N, Heelan R, Westcott J, et al: Comparative merits of conventional, computed tomographic, and magnetic resonance imaging in assessing mediastinal involvement in surgically confirmed lung carcinoma. J Thorac Cardiovasc Surg 90:639–648, 1985.
127. Marty-Ané C, Costes V, Pujol J, et al: Carcinoid tumors of the lung: Do atypical features require aggressive management? Ann Thorac Surg 59:78–83, 1995.
128. Matthews MJ: Morphology of lung cancer. Semin Oncol 1:175–182, 1974.
129. Maurea S, Mainolfi C, Bazzicalupo L, et al: Imaging of adrenal tumors using FDG PET: Comparison of benign and malignant lesions. AJR Am J Roentgenol 173:25–29, 1999.
130. Maziak DE, Todd TR, Keshavjee SH, et al: Adenoid cystic carcinoma of the airway: Thirty-two-year experience. J Thorac Cardiovasc Surg 112:1522, 1996.
131. Mazur MT, Shultz JJ, Myers JL: Granular cell tumor: Immunohistochemical analysis of 21 benign tumors and one malignant tumor. Arch Pathol Lab Med 114:692–696, 1990.
132. McCarthy MJ, Rosado-de-Christenson ML: Tumors of the trachea. J Thorac Imaging 10:180, 1995.
133. McCaughan BC, Martini N, Bains MS: Bronchial carcinoids. J Thorac Cardiovasc Surg 89:8–17, 1985.
134. McLoud TC: CT of bronchogenic carcinoma: Indeterminate mediastinal invasion. Radiology 173:15–16, 1989.
135. McLoud TC, Bourgouin PM, Greenberg RW, et al: Bronchogenic carcinoma: Analysis of staging in the mediastinum with CT by correlative lymph node mapping and sampling. Radiology 182: 319–323, 1992.
136. McNicholas MM, Lee MJ, Mayo-Smith WW, et al: An imaging algorithm for the differential diagnosis of adrenal adenomas and metastases. AJR Am J Roentgenol 165:1453–1459, 1995.
137. Michel F, Soler M, Imhof E, Perruchoud AP: Initial staging of non-small cell lung cancer: Value of routine radioisotope bone scanning. Thorax 46:469–473, 1991.
138. Miller WT, Husted J, Frieman D, et al: Bronchioloalveolar carcinoma: Two clinical entities with one pathologic diagnosis. Am J Roentgenol 130:905–912, 1978.
139. Mintz BJ, Tuhrim S, Alexander S, et al: Intracranial metastases in the initial staging of bronchogenic carcinoma. Chest 86:850–853, 1984.
140. Mitchell DG, Crovello M, Matteucci T, et al: Benign adrenocortical masses: Diagnosis with chemical shift MR imaging. Radiology 185: 345–351, 1992.
141. Moran CA, Suster S, Abbondanzo SL, Koss MN: Primary leiomyosarcomas of the lung: A clinicopathologic and immunohistochemical study of 18 cases. Mod Pathol 10:121–128, 1997.
142. Moran CA, Suster S, Koss MN: Primary adenoid cystic carcinoma of the lung: A clinicopathologic and immunohistochemical study of 16 cases. Cancer 73:1390, 1994.
143. Morgan B, Coaldey F, Finlay DB, Belton I: Hypertrophic osteoarthropathy in staging skeletal scintigraphy for lung cancer. Clin Radiol 51:494–497, 1996.
144. Mountain CF: Prognostic implications of international staging system for lung cancer. Semin Oncol 15:236–245, 1988.
145. Mountain CF: Revisions in the international system for staging lung cancer. Chest 111:1710–1717, 1997.
146. Mountain CF, Dresler CM: Regional lymph node classification for lung cancer staging. Chest 111:1718–1723, 1997.
147. Müller NL, Miller RR: Neuroendocrine carcinomas of the lung. Semin Roentgenol 25:96–104, 1990.
148. Musset D, Grenier P, Carette MF, et al: Primary lung cancer staging: Prospective comparative study of MR imaging with CT. Radiology 160:607–611, 1986.
149. Nappi O, Glasner SD, Swanson PE, Wick MR: Biphasic and monophasic sarcomatoid carcinomas of the lung. Am J Clin Pathol 102: 331–340, 1994.
150. Naruke T, Tsuchiya R, Kondo H, et al: Implications of staging in lung cancer. Chest 112:242S–248S, 1997.
151. National Cancer Institute Cooperative Early Lung Cancer Group: Manual of Procedures (NIH Pub No. 79-1972). Bethesda, Md, National Institutes of Health, 1979.
152. National Research Council, Committee on the Biological Effects of Ionizing Radiation: Health Risks of Radon and Other Internally Deposited Alpha-Emitters: BEIR IV. Washington, DC, National Academy Press, 1988.
153. Nessi R, Ricci PB, Ricci SB, et al: Bronchial carcinoid tumors: Radiologic observations in 49 cases. J Thorac Imaging 6:47–53, 1991.
154. Newman SJ, Hansen HH: Frequency, diagnosis, and treatment of brain metastases in 247 consecutive patients with bronchogenic carcinoma. Cancer 33:492–496, 1974.
155. Nielsen ME Jr, Heaston DK, Dunnick NR, Korobkin M: Preoperative CT evaluation of adrenal glands in non-small cell bronchogenic carcinoma. Am J Roentgenol 139:317–320, 1982.
156. Niho S, Suzuki K, Yokose T, et al: Monoclonality of both pale cells and cuboidal cells of sclerosing hemangioma of the lung. Am J Pathol 152:1065–1069, 1998.
157. North WG: Neuropeptide production by small cell carcinoma: Vasopressin and oxytocin as plasma markers of disease. J Clin Endocrinol Metab 73:1316–1320, 1991.
158. O'Donnell PG, Jackson SA, Tung KT, et al: Radiological appearances of lymphomas arising from mucosa-associated lymphoid tissue (MALT) in the lung. Clin Radiol 53:258–263, 1998.
159. O'Keefe ME, Good CA, McDonald JR: Calcification in solitary nodules of the lung. Am J Roentgenol 77:1023–1033, 1957.
160. O'Keefe ME Jr, Good CA, McDonald JR: Calcification in solitary nodules of the lungs. Am J Roentgenol 77:1023–1033, 1957.
161. Ohmatsu H, Kakinuma R, Nishiwaki Y, et al: Lung cancer screening with low-dose spiral CT: Proc Am Soc Clin Oncol 18:463a, 1999.
162. Okubo K, Mark EJ, Flieder D, et al: Bronchoalveolar carcinoma: Clinical, radiologic, and pathologic factors and survival. J Thorac Cardiovasc Surg 118:702–709, 1999.
163. Oldham HN Jr, Young WG Jr, Sealy WC: Hamartoma of the lung. J Thorac Cardiovasc Surg 53:735–742, 1967.
164. Oliver TW Jr, Bernardino ME, Miller JI, et al: Isolated adrenal masses in nonsmall-cell bronchogenic carcinoma. Radiology 153: 217–218, 1984.
165. Outwater EK, Siegelman ES, Huang AB, Birnbaum BA: Adrenal masses: Correlation between CT attenuation value and chemical shift ratio at MR imaging with in-phase and opposed-phase sequences. Radiology 200:749–752, 1996.
166. Padovani B, Mouroux J, Seksik L, et al: Chest wall invasion by bronchogenic carcinoma: Evaluation with MR imaging. Radiology 187:33–38, 1993.
167. Pagani JJ: Normal adrenal glands in small cell lung carcinoma: CT-guided biopsy. Am J Roentgenol 140:949–951, 1983.
168. Pagani JJ: Non-small cell lung carcinoma adrenal metastases. Cancer 53:1058–1060, 1984.
169. Park SH, Kim TJ, Chi JG: Congenital granular cell tumor with systemic involvement: Immunohistochemical and ultrastructural study. Arch Pathol Lab Med 115:934–938, 1991.
170. Paskin DL, Hull JD, Cookson PJ: Granular cell myoblastoma: A comprehensive review of 15 years' experience. Ann Surg 175: 501–503, 1972.
171. Patel AM, Davila DG, Peters SG: Paraneoplastic syndromes associated with lung cancer. Mayo Clin Proc 68:278–287, 1993.
172. Patel AM, Peters SG: Clinical manifestations of lung cancer. Mayo Clin Proc 68:273–277, 1993.
173. Patz EF, Lowe VJ, Hoffman JM, et al: Focal pulmonary abnormalities: Evaluation with F-18 fluorodeoxyglucose PET scanning. Radiology 188:487–490, 1993.
174. Patz EF Jr, Goodman PC: Positron emission tomography imaging of the thorax. Radiol Clin North Am 32:811–823, 1994.

175. Patz EF Jr, Lowe VJ, Goodman PC, Herndon J: Thoracic nodal staging with positron emission tomography (PET) and ^{18}F-2-fluoro-2-deoxy-D-glucose in patients with bronchogenic carcinoma. Chest 108:1617–1621, 1995.
176. Pearlberg JL, Sandler MA, Lewis JW Jr, et al: Small-cell bronchogenic carcinoma: CT evaluation. AJR Am J Roentgenol 150:265–268, 1988.
177. Ponder B: Genetic testing for cancer risk. Science 278:1050–1054, 1997.
178. Porte HL, Ernst OJ, Delebecq T, et al: Is computed tomography guided biopsy still necessary for the diagnosis of adrenal masses in patients with resectable non–small-cell lung cancer? Eur J Cardiothorac Surg 15:597–601, 1999.
179. Posner JB: Paraneoplastic syndromes. Neurol Clin 9:919, 1991.
180. Prohm P, Winter J, Schmücker P: Pulmonary hamartoma. Thorac Cardiovasc Surg 30:302–305, 1982.
181. Quint LE, Francis IR: Radiologic staging of lung cancer. J Thorac Imaging 14:235–246, 1999.
182. Quint LE, Francis IR, Wahl RL, et al: Preoperative staging of non–small-cell carcinoma of the lung: Imaging methods. AJR Am J Roentgenol 164:1349–1359, 1995.
183. Ramani S, Karnad AB: Primary pulmonary non-Hodgkin's lymphoma. N Engl J Med 88:243–245, 1995.
184. Ratto GB, Piacenza G, Frola C, et al: Chest wall involvement by lung cancer: Computed tomographic detection and results of operation. Ann Thorac Surg 51:182–188, 1991.
185. Repace JL, Lowrey AH: Risk assessment methodologies for passive smoking-induced lung cancer. Risk Anal 10:27–37, 1990.
186. Robinson JM, Knoll R, Henry DA: Intrathoracic granular cell myoblastoma. South Med J 81:1453–1457, 1988.
187. Rock MJ, Kaufman RA, Lobe TE, et al: Epithelioid hemangioendothelioma of the lung (intravascular bronchioloalveolar tumor) in a young girl. Pediatr Pulmonol 11:181–186, 1991.
188. Roggli VL, Hammar SP, Pratt PC, et al: Does asbestos or asbestosis cause carcinoma of the lung? Am J Ind Med 26:835–838, 1994.
189. Rosado-de-Christenson ML, Templeton PA, Moran CA: Bronchogenic carcinoma: Radiologic-pathologic correlation. Radiographics 14:429–446, 1994.
190. Ross GJ, Violi L, Friedman AC, et al: Intravascular bronchioloalveolar tumors: CT and pathologic correlation. J Comput Assist Tomogr 13:240–243, 1989.
191. Ruebner BH, Eggleston JC: What is new in epithelioid haemangioendothelioma of the liver? Pathol Res Pract 182:110–112, 1987.
192. Sale GE, Kulander BG: Benign clear-cell tumor (sugar tumor) of the lung with hepatic metastases ten years after resection of pulmonary primary tumor. Arch Pathol Lab Med 112:1177–1178, 1988.
193. Salminen U-S: Pulmonary hamartoma: A clinical study of 77 cases in a 21-year period and review of literature. Eur J Cardiothorac Surg 4:15–18, 1990.
194. Salvati M, Cervoni L, Delfini R: Solitary brain metastases from non-oat cell lung cancer: Clinical and prognostic features. Neurosurg Rev 19:221–225, 1996.
195. Salvatierra A, Baamonde C, Llamas JM, et al: Extrathoracic staging of bronchogenic carcinoma. Chest 97:1052–1058, 1990.
196. Samet JM: The epidemiology of lung cancer. Chest 103:20S–29S, 1993.
197. Schiepers C: Role of positron emission tomography in the staging of lung cancer. Lung Cancer 17:S29–S35, 1997.
198. Schwartz LH, Ginsberg MS, Burt ME, et al: MRI as an alternative to CT-guided biopsy of adrenal masses in patients with lung cancer. Ann Thorac Surg 65:193–197, 1998.
199. Shepherd FA, Laskey J, Evans WK, et al: Cushing's syndrome associated with ectopic corticotropin production and small-cell lung cancer. J Clin Oncol 10:21–27, 1992.
200. Shimoyama K, Murata K, Takahashi M, Morita R: Pulmonary hilar lymph node metastases from lung cancer: Evaluation based on morphology at thin-section, incremental, dynamic CT. Radiology 203:187–195, 1997.
201. Shin MS, Jackson LK, Shelton RW, Greene RE: Giant cell carcinoma of the lung. Chest 89:366–369, 1986.
202. Sider L: Radiographic manifestations of primary bronchogenic carcinoma. Radiol Clin North Am 28:583–597, 1990.
203. Siegelman SS, Khouri MF, Leo FP, et al: Solitary pulmonary nodules: CT assessment. Radiology 160:307–312, 1986.
204. Siegelman SS, Khouri NF, Scott WW Jr, et al: Pulmonary hamartoma: CT findings. Radiology 160:313–317, 1986.
205. Siegelman SS, Zerhouni EA, Leo FP, et al: CT of the solitary pulmonary nodule. Am J Roentgenol 135:1–13, 1980.
206. Silvestri GA, Littenberg B, Colice GL: The clinical evaluation for detecting metastatic lung cancer: A meta-analysis. Am J Respir Crit Care Med 152:225–230, 1995.
207. Sone S, Takashima S, Li F, et al: Mass screening for lung cancer with mobile spiral computed tomography scanning. Lancet 351:1242–1245, 1998.
208. Spencer H: Pathology of the Lung, 4th ed. Oxford, Pergamon Press, 1985.
209. Stahel RA, Babry M, Skarin AT, et al: Detection of bone marrow metastases in small cell lung cancer by monoclonal antibody. J Clin Oncol 3:455–461, 1985.
210. Stahel RA, Ginsberg R, Havemann K, et al: Staging and prognostic factors in small cell lung cancer: A consensus report. Lung Cancer 5:119–126, 1989.
211. Staples CA, Müller NL, Miller RR, et al: Mediastinal nodes in bronchogenic carcinoma: Comparison between CT and mediastinoscopy. Radiology 167:367–372, 1988.
212. Steenland K, Loomis D, Shy C, Simonsen N: Review of occupational lung carcinogens. Am J Ind Med 29:474–490, 1996.
213. Steinert H, Hauser M, Allenman F, et al: Non-small cell lung cancer: Nodal staging with FDG PET versus CT with correlative lymph node mapping and sampling. Radiology 202:441–446, 1997.
214. Stitik FP: Staging of lung cancer. Radiol Clin North Am 28:619–630, 1990.
215. Stitik FP: The new staging of lung cancer. Radiol Clin North Am 32:635–647, 1994.
216. Strauss GM: Screening for lung cancer: An evidence-based synthesis. Surg Oncol Clin North Am 8:747–774, 1999.
217. Strauss GM, Dominioni L: Lung cancer screening and the surgical oncologist: The controversy. Surg Oncol Clin North Am 8:371–387, 1999.
218. Strauss GM, Gleason RE, Sugarbaker DJ: Screening for lung cancer: Another look, a different view. Chest 111:754–768, 1997.
219. Struyf NJA, Van Meerbeeck JPA, Ramael MRL, et al: Atypical bronchial carcinoid tumours. Respir Med 89:133–138, 1995.
220. Stuart-Harris R, Ahern V, Danks JA, et al: Hypercalcemia in small cell lung cancer: Report of a case associated with parathyroid hormone-related protein (PTHrP). Eur J Cancer 29A:1601–1604, 1993.
221. Sugio K, Yokoyama H, Kaneko S, et al: Sclerosing hemangioma of the lung: Radiographic and pathological study. Ann Thorac Surg 53:295–300, 1992.
222. Suster S: Primary sarcomas of the lung. Semin Diagn Pathol 12:140–157, 1995.
223. Swensen SJ, Viggiano RW, Midthun DE, et al: Lung nodule enhancement at CT: Multicenter study. Radiology 214:73–80, 2000.
224. Tanaka K, Kubota K, Kodama T, et al: Extrathoracic staging is not necessary for non–small-cell lung cancer with clinical stage T1–2 N0. Ann Thorac Surg 68:1039–1042, 1999.
225. Theros EG: Varying manifestations of peripheral pulmonary neoplasms: A radiologic-pathologic correlative study. Am J Roentgenol 128:893–914, 1977.
226. Toh HC, Ang PT: Primary pulmonary lymphoma: Clinical review from a single institution in Singapore. Leuk Lymphoma 27:153–163, 1997.
227. Travis WD, Colby TV, Corrin B, et al: Histological Typing of Lung and Pleural Tumours, 3rd ed. Berlin, Springer-Verlag, 1999.
228. Travis WD, Lubin J, Ries L, Devesa SS: United States lung carcinoma incidence trends: Declining for most histologic types among males, increasing among females. Cancer 77:2464–2470, 1996.
229. Trentini GP, Palmieri B: Mucoepidermoid tumor of the trachea. Chest 62:336, 1972.
230. Trichopoulos D, Mollo F, Tomatis L, et al: Active and passive smoking and pathological indicators of lung cancer risk in an autopsy study. JAMA 268:1697–1701, 1992.
231. Tschernig T, Pabst R: Bronchus-associated lymphoid tissue (BALT) is not present in the normal adult lung but in different diseases. Pathobiology 68:1–8, 2000.
232. Turnbull AD, Huvos AG, Goodner JT, et al: Mucoepidermoid tumors of bronchial glands. Cancer 28:539, 1971.
233. Urschel JD: Surgical treatment of peripheral small cell lung cancer. Chest Surg Clin North Am 7:95–103, 1997.
234. U.S. Department of Health and Human Services: Reducing the Health Consequences of Smoking—25 Years of Progress: A Report

of the Surgeon General. Washington, DC, U.S. Government Printing Office, 1989.
235. U.S. Department of Health and Human Services: The Health Benefits of Smoking Cessation: A Report of the Surgeon General. Washington, DC, U.S. Government Printing Office, 1990.
236. Vainio H, Boffetta P: Mechanisms of the combined effect of asbestos and smoking in the etiology of lung cancer. Scand J Work Environ Health 20:235–242, 1994.
237. Valanis BG: Epidemiology of lung cancer: A worldwide epidemic. Semin Oncol Nurs 12:251–259, 1996.
238. Valk PE, Pounds TR, Hopkins DM, et al: Staging non-small cell lung cancer by whole-body positron emission tomographic imaging. Ann Thorac Surg 60:1573–1582, 1995.
239. Valli M, Fabris GA, Dewar AHD, Sheppard MN: Atypical carcinoid tumour of the lung: A study of 33 cases with prognostic features. Histopathology 24:363–369, 1994.
240. van de Pol M, van Oosterhout AGM, Wilmink JT, et al: MRI in detection of brain metastases at initial staging of small-cell lung cancer. Neuroradiology 38:207–210, 1996.
241. Vansteenkiste JF, Stroobants SG, De Leyn PR, et al: Lymph node staging in non–small-cell lung cancer with FDG-PET scan: A prospective study on 690 lymph node stations from 68 patients. J Clin Oncol 16:2142–2149, 1998.
242. Viggiano RW, Swensen SJ, Rosenow EC III: Evaluation and management of solitary and multiple pulmonary nodules. Clin Chest Med 13:83–95, 1992.
243. Vineis P, Thomas T, Hayes R, et al: Proportion of lung cancers in males due to occupation in different areas of the U.S. Int J Cancer 42:851–856, 1988.
244. Wahl RL, Quint LE, Greenough RL, et al: Staging of mediastinal non-small cell lung cancer with FDG PET, CT, and fusion images: Preliminary prospective evaluation. Radiology 191:371–377, 1994.
245. Wang Y, Ju C, Stark AD, Teresi N: Radon mitigation survey among New York State residents living in high radon homes. Health Phys 77:403–409, 1999.
246. Webb WR: MR imaging in the evaluation and staging of lung cancer. Semin Ultrasound CT MR 9:53–66, 1988.
247. Webb WR, Gatsonis C, Zerhouni EA, et al: CT and MR imaging in staging non-small cell bronchogenic carcinoma: Report of the Radiologic Diagnostic Oncology Group. Radiology 178:705–713, 1991.
248. Webb WR, Sostman HD: MR imaging of thoracic disease: Clinical uses. Radiology 182:621–630, 1992.
249. Weder W, Schmid RA, Bruchhaus H, et al: Detection of extrathoracic metastases by positron emission tomography in lung cancer. Ann Thorac Surg 66:886–893, 1998.
250. Weisbrod GL, Chamberlain DW, Tao LC: Pulmonary blastoma: Report of three cases and a review of the literature. J Can Assoc Radiol 39:130, 1988.
251. Weisbrod GL, Towers MJ, Chamberlain DW, et al: Thin-walled cystic lesions in bronchioalveolar carcinoma. Radiology 185:401–405, 1992.
252. Weiss W: Asbestosis: A marker for the increased risk of lung cancer among workers exposed to asbestos. Chest 115:536–549, 1999.
253. Whitley NO, Fuks JZ, McCrea ES, et al: Computed tomography of the chest in small cell lung cancer: Potential new prognostic signs. Am J Roentgenol 141:885–892, 1984.
254. Wick MR, Ritter JH, Humphrey PA: Sarcomatoid carcinomas of the lung. Am J Clin Pathol 108:40–53, 1997.
255. Wick MR, Ritter JH, Humphrey PA: Sarcomatoid carcinomas of the lung: A clinicopathologic review. Am J Clin Pathol 108:40, 1997.
256. Wiess SW, Ishak KG, Dailo DH, et al: Epithelioid hemangioendothelioma and related lesions. Semin Diagn Pathol 3:259–287, 1986.
257. Wingo PA, Ries LA, Giovino GA, et al: Annual report to the nation on the status of cancer, 1973–1996, with a special section on lung cancer and tobacco smoking. J Natl Cancer Inst 91:675–690, 1999.
258. Woodring JH: Unusual radiographic manifestations of lung cancer. Radiol Clin North Am 28:599–618, 1990.
259. Woodring JH, Fried AM: Significance of wall thickness in solitary cavities of the lung: A follow-up study. Am J Roentgenol 140: 473–474, 1983.
260. Woodring JH, Fried AM, Chuang VP: Solitary cavities of the lung: Diagnostic implications of cavity wall thickness. Am J Roentgenol 135:1269–1271, 1980.
261. Woodring JH, Stelling CB: Adenocarcinoma of the lung: A tumor with a changing pleomorphic character. Am J Roentgenol 140: 657–664, 1983.
262. Wynder EL, Hoffmann D: Smoking and lung cancer: Scientific challenges and opportunities. Cancer Res 54:5284–5295, 1994.
263. Yahmai I: Angiographic manifestations of soft-tissue and osseous hemangiopericytomas. Radiology 126:653–659, 1978.
264. Yankelevitz DF, Gupta R, Zhao B, Henschke CI: Small pulmonary nodules: Evaluation with repeat CT: Preliminary experience. Radiology 212:561–566, 1999.
265. Yankelevitz DF, Reeves AP, Kostis WJ, et al: Determination of malignancy in small pulmonary nodules based on volumetrically determined growth rates. Radiology 209(Suppl):375, 1998.
266. Yokoi K, Mori K, Miyazawa N, et al: Tumor invasion of the chest wall and mediastinum in lung cancer: Evaluation with pneumothorax. Radiology 181:147–152, 1991.
267. Yousem SA, Hochholzer L: Mucoepidermoid tumors of the lung. Cancer 60:1346–1352, 1987.
268. Yousem SA, Hochholzer L: Primary pulmonary hemangiopericytoma. Cancer 59:549–555, 1987.
269. Zerhouni EA, Stitik FP, Siegelman SS, et al: CT of the pulmonary nodule: A cooperative study. Radiology 160:319–327, 1986.
270. Zern H, Moran CA, Suster S, et al: Primary pulmonary sarcomas with features of monophasic synovial sarcoma: A clinicopathological, immunohistochemical, and ultrastructural study of 25 cases. Hum Pathol 26:474–480, 1995.
271. Zolliker A, Jacques J, Goldstein AS: Benign clear cell tumor of the lung. Arch Pathol Lab Med 103:526–530, 1979.
272. Zwiebel BR, Austin JHM, Grimes MM: Bronchial carcinoid tumors: Assessment with CT of location and intratumoral calcification in 31 patients. Radiology 179:483–486, 1991.
273. Zwirewich CV, Vedal S, Miller RR, Müller NL: Solitary pulmonary nodule: High-resolution CT and radiologic-pathologic correlation. Radiology 179:469–476, 1991.

29

Mediastinum

H. Page McAdams, Jeremy J. Erasmus, Robert D. Tarver, Charles E. Spritzer

Many excellent textbooks and articles have been written about the mediastinum.[61, 65, 71, 101, 103, 181] This chapter refers to these articles and reviews the recent literature in regard to the anatomy, pathology, and radiologic manifestations of mediastinal diseases.

Imaging the Mediastinum

Although the chest radiograph is usually the initial study that detects a mediastinal abnormality, computed tomography (CT) is primarily used to assess the location and extent of mediastinal disease; because of its superior contrast resolution, it is also used to characterize the tissue components of masses (Fig. 29–1). CT is also useful for distinguishing vascular variants or benign processes of the mediastinum, such as lipomatosis, from true pathologic conditions.

Although CT is usually used to further evaluate an abnormality detected on the chest radiograph, it may be performed in certain clinical situations when the chest radiograph is normal. For example, because of the strong association between myasthenia gravis and thymoma, CT is often performed in patients with myasthenia gravis even when chest radiographic findings are normal (Fig. 29–2). Also, certain malignancies, such as lung cancer, have a marked predilection for metastasis to mediastinal lymph nodes. These lymph node metastases may not be visible on chest radiographs; consequently, CT is used by most thoracic surgeons and oncologists to assess the mediastinal nodes in patients with lung cancer.

Recent advances in CT imaging (i.e., spiral CT and multidetector-row spiral CT) have further improved the ability of CT to image the mediastinum. By significantly shortening scan time, respiratory motion artifacts are limited and, in some instances, the total dose of iodinated contrast medium can be reduced. Spiral CT data sets can also be effectively reconstructed in a variety of nonaxial planes, often facilitating interpretation of mediastinal abnormalities. The application of nonaxial two-dimensional (2D) and three-dimensional (3D) reconstruction techniques has proved most useful for imaging abnormalities of the central airways and great vessels (Figs. 29–3 and 29–4). For example, in the evaluation of stenoses in obliquely oriented bronchi, these reconstruction techniques can improve diagnostic accuracy and confidence of interpretation, although axial CT images usually provide all the information required for diagnosis. Nevertheless, 2D and 3D images, by presenting anatomic information in a context more familiar to referring clinicians, may demonstrate the location and extent of an abnormality in a way that radiologic reports and axial CT images often do not.

Although CT imaging usually provides the requisite information in most patients with mediastinal abnormalities, magnetic resonance imaging (MRI), because of its multiplanar capability and high contrast resolution, is occasionally used to further evaluate the location and extent of disease. MRI is the modality of choice for imaging neurogenic tumors because not only does it demonstrate the number and nature of the lesions but also it optimally depicts intraspinal extension.

Additionally, MRI is useful (1) in confirming the cystic nature of mediastinal lesions that appear solid on CT (Fig. 29–5) and (2) in demonstrating vascular structures in patients in whom iodinated intravenous (IV) contrast medium is contraindicated (Fig. 29–6). Compared with CT, MRI has two potential disadvantages for imaging mediastinal abnormalities: its ability to demonstrate calcification and its spatial resolution are relatively poor.

CT Scanning Techniques

Techniques for CT scanning of the chest vary from institution to institution. Although standard protocols are frequently used without modification, they are occasionally altered to address specific clinical concerns.

Patient Considerations

Most patients are scanned in the supine position with their arms above their head. The prone position can be useful for patients who are claustrophobic or who find the supine position uncomfortable. Occasionally, the prone or decubitus position can be used to more accurately define pathology. CT images obtained from the decubitus position are often useful for evaluating air-fluid or fluid collections. The prone position can be used to evaluate or facilitate biopsy of abnormalities in the retrocardiac area, such as esophageal masses and azygoesophageal lymphadenopathy (Fig. 29–7).

CT scans are performed, if possible, during a single breath-hold. When scanning is performed using narrow collimation on a single-detector-row spiral CT scanner, however, it may not be possible to complete the scan in a single breath-hold. Hyperventilation prior to scanning can improve breath-holding and thus image quality. The mediastinum, however, can be scanned in less than 10 seconds when multidetector-row spiral CT scanners are used. If the patient cannot accomplish a breath-hold for this short length of time, the scan can be performed during quiet breathing, often with good results.

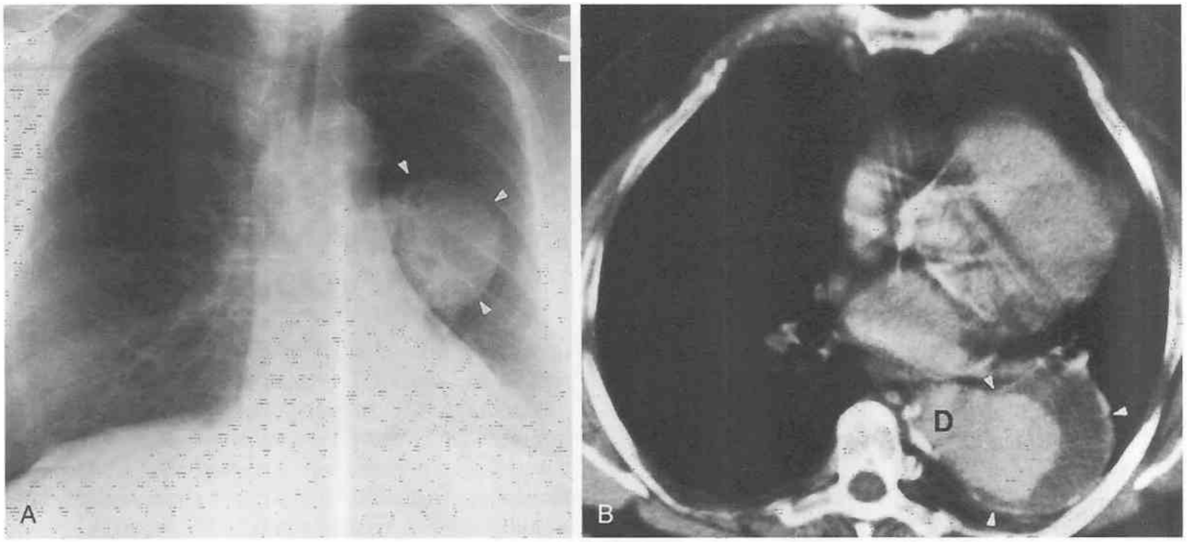

Figure 29–1. Saccular aneurysm of descending aorta. *A,* Posteroanterior chest radiograph shows homogeneous soft tissue mass *(arrowheads)* in the left hemithorax. Acute margins at interface with mediastinum suggest intrapulmonary mass. *B,* Contrast-enhanced CT shows saccular aneurysm *(arrowheads)* of descending aorta (D) with peripheral thrombus.

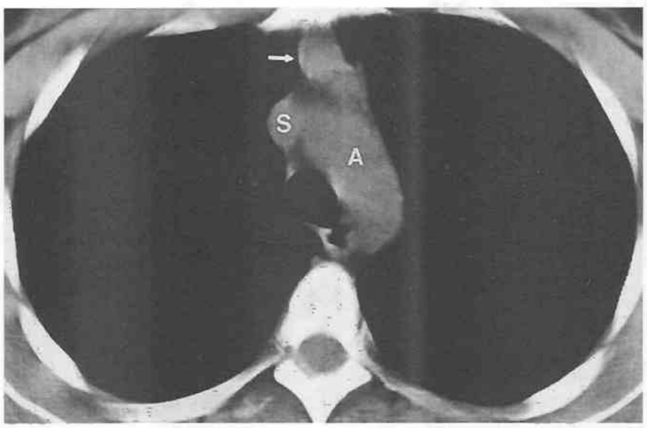

Figure 29–2. Thymoma in woman with myasthenia gravis. Chest radiograph (not shown) was normal. Because of association between myasthenia gravis and thymoma, chest CT was performed and revealed small soft tissue mass in anterior mediastinum *(arrow).* Resection confirmed thymoma. A, aorta; S, superior vena cava.

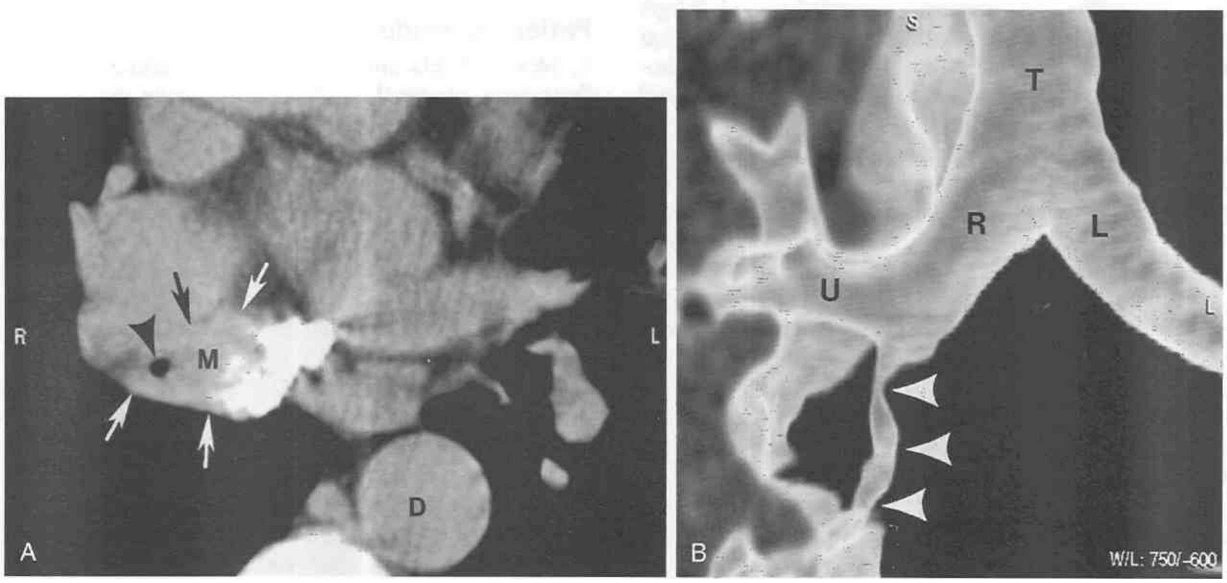

Figure 29–3. Fibrosing mediastinitis. *A,* Axial CT shows marked narrowing of bronchus intermedius *(arrowhead)* by soft tissue attenuation mass (M) *(arrows).* Note extensive subcarinal calcification. D, descending aorta. *B,* Volume-rendered shaded-surface display shows long-segment irregular narrowing of bronchus intermedius *(arrowheads).* Three-dimensional reconstructions can facilitate assessment and treatment of airway stenoses. L, left main bronchus; R, right main bronchus; T, trachea; U, right upper lobe bronchus.

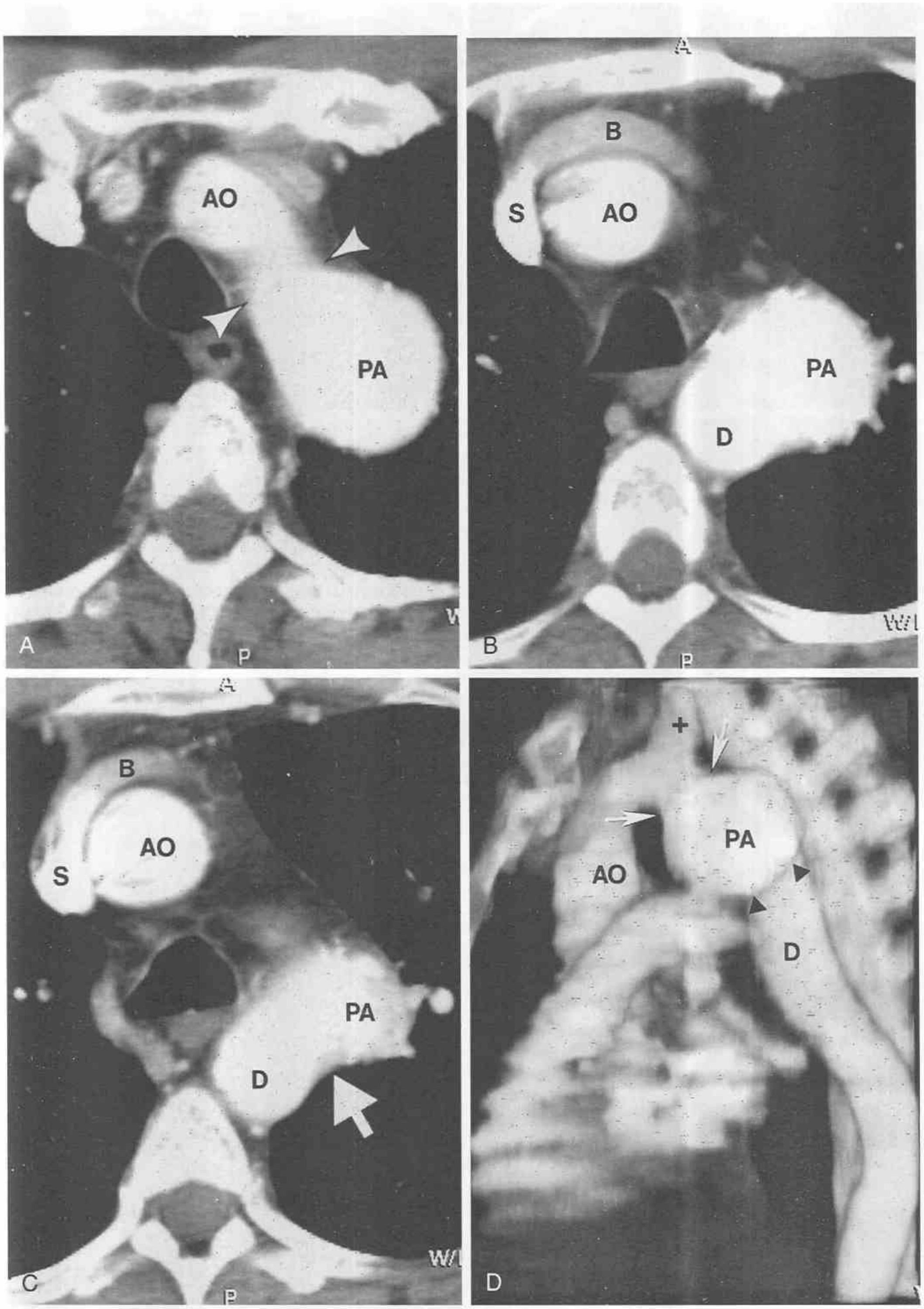

Figure 29–4. Pseudoaneurysm after repair of aortic coarctation. *A–C,* Contrast-enhanced CT shows pseudoaneurysm (P) at site of coarctation repair. A narrow isthmus (*arrowheads* in *A*) can be seen between the pseudoaneurysm and the transverse aorta, and a wide connection (*arrow* in *C*) can be seen between the pseudoaneurysm and the descending aorta. *D,* Oblique volume-rendered maximal intensity projection image clearly shows relationship of pseudoaneurysm to proximal *(arrows)* and distal *(arrowheads)* aorta as well as the brachiocephalic artery (+). Three-dimensional reconstructions of CT angiograms display anatomy in a more familiar perspective to clinicians than axial CT images. A, ascending aorta; B, brachiocephalic vein; D, descending aorta; S, superior vena cava.

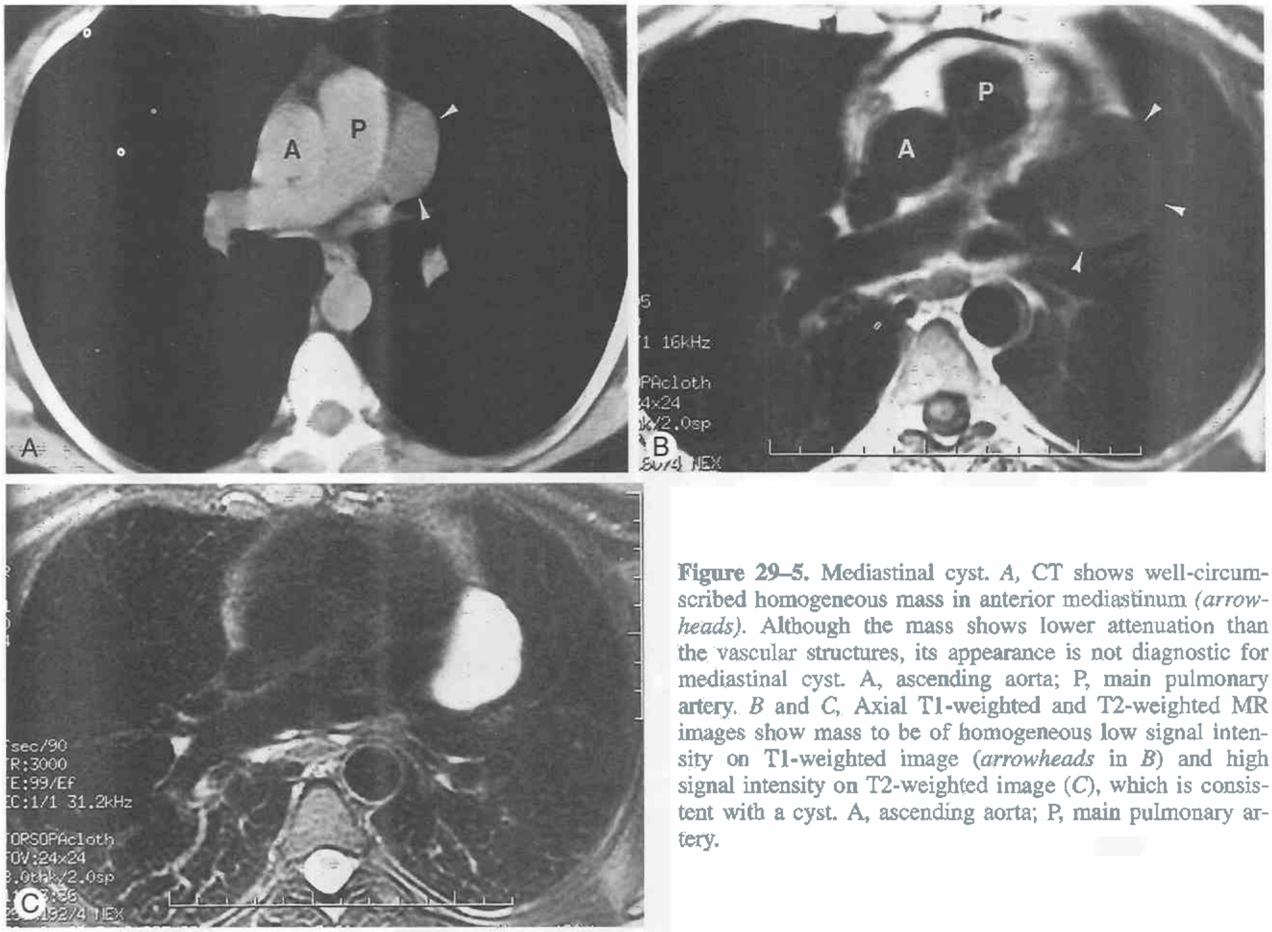

Figure 29–5. Mediastinal cyst. *A,* CT shows well-circumscribed homogeneous mass in anterior mediastinum *(arrowheads).* Although the mass shows lower attenuation than the vascular structures, its appearance is not diagnostic for mediastinal cyst. A, ascending aorta; P, main pulmonary artery. *B* and *C,* Axial T1-weighted and T2-weighted MR images show mass to be of homogeneous low signal intensity on T1-weighted image *(arrowheads* in *B)* and high signal intensity on T2-weighted image (*C*), which is consistent with a cyst. A, ascending aorta; P, main pulmonary artery.

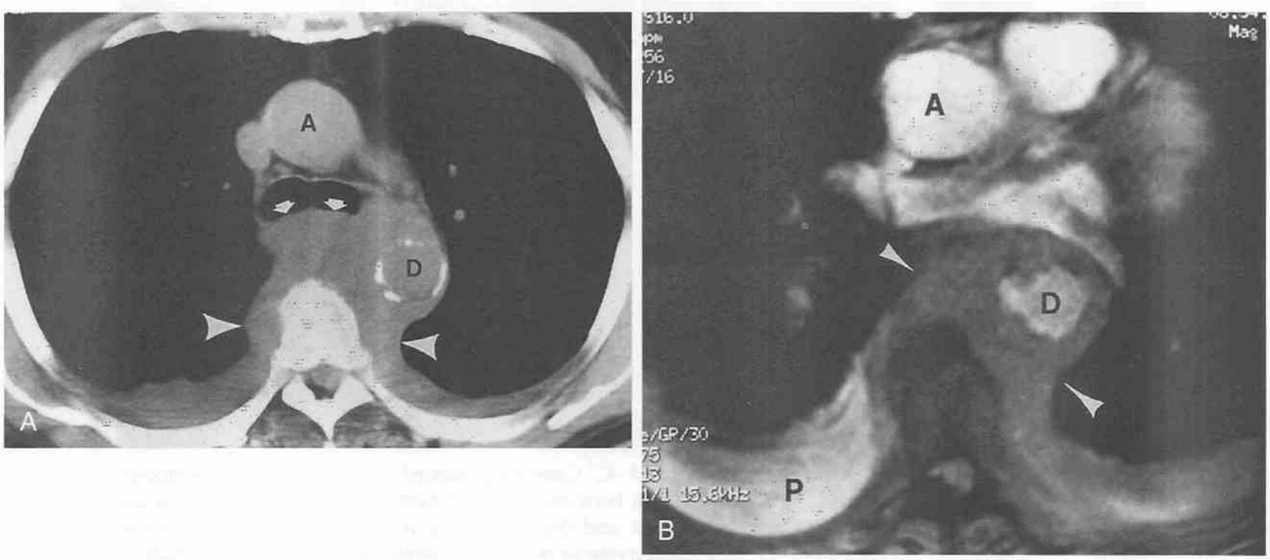

Figure 29–6. Non-Hodgkin's lymphoma in a patient with renal insufficiency. *A,* CT shows homogeneous middle and posterior mediastinal mass encasing descending aorta, anteriorly displacing the tracheal carina *(arrows)* and extending into the paravertebral region bilaterally *(arrowheads).* Small bilateral pleural effusions can be visualized. *B,* Cine gradient-recalled echo MR image performed to evaluate possible vascular invasion confirms flow within descending aorta. A low-signal-intensity mass *(arrowheads)* and a high-signal-intensity pleural effusion (P) can be seen. A, ascending aorta; D, descending aorta.

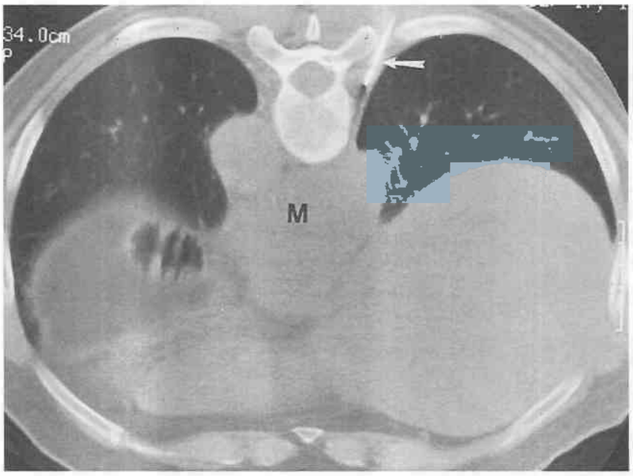

Figure 29–7. CT (extended window) performed with the patient in the prone position to improve access for biopsy of middle mediastinal mass (M). Diagnostic specimen was obtained and confirmed non-Hodgkin's lymphoma. *Arrow* indicates the biopsy needle.

CT Acquisition Parameters

The choice of CT acquisition parameters depends on the clinical situation and the CT scanner. Typically, CT of the mediastinum is performed at 120 to 130 kV and 200 to 300 mA. Most single-detector-row spiral CT machines use a 180-degree linear interpolation algorithm to reconstruct the individual axial slices. Any of a number of possible postprocessing reconstruction algorithms can then be applied to generate the final images. A smoothing or "soft tissue" reconstruction algorithm is used to decrease artifacts caused by abrupt changes between tissues of different density.

The field of view is usually between 34 and 50 cm and, combined with an image matrix of 512 × 512, yields a pixel size of about 1 mm. Smaller fields of view (15 cm) can be used to decrease the pixel size to 0.3 mm. These techniques are usually unnecessary for routine mediastinal imaging but can be useful for imaging the central airways.

With single-detector-row spiral CT, the user must choose three parameters: (1) slice collimation, (2) pitch ratio, and (3) reconstruction interval. For routine mediastinal CT, *slice collimation* is usually set between 7 and 10 mm. For evaluation of small lesions, suspected hilar pathology, or central airway lesions, slice collimation may be decreased to 3 or 5 mm.

Pitch is defined as the ratio between table speed and slice collimation. On a single-detector-row scanner using a 180-degree linear interpolation algorithm, pitch can be increased to 2.0 without significant loss of image quality. Increasing pitch is desirable whenever possible, because increasing pitch decreases scan time proportionately. Increasing pitch beyond 2.0, however, results in unacceptable loss of longitudinal resolution. For routine mediastinal CT, the pitch selected is usually between 1.3 and 2.0.

The image *reconstruction interval* is usually chosen to be the same as, or slightly less than, slice collimation for routine axial imaging. Thus, for a routine 7-mm slice collimation scan, the reconstruction interval is usually either 5 or 7 mm. If nonaxial 2D or 3D reconstructions are to be generated from the axial images, a minimum of 20% to 30% reconstruction overlap is needed to minimize stair-step artifacts between slices. Thus, for a 5-mm slice collimation scan, axial reconstructions should be performed at least every 2 or 3 mm.

With multidetector-row scanners, the user typically has much less flexibility in protocol selection because of the complex physics involved in the reconstruction of individual axial slices from multiple overlapping helices. User-specified parameters are typically slice collimation, table speed, and operation mode. The user does not usually specify pitch per se. Most manufacturers supply information regarding acceptable choices of slice collimation and table speed to optimize image resolution. The General Electric QXi scanner, for example, allows the user to choose one of two modes of operation: *high quality* (HQ—effective pitch = 3.0) or *high speed* (HS—effective pitch = 6.0).

When an imaging protocol is prescribed for a multidetector-row CT scanner, it is best to initially select the slice collimation. The operation mode and maximum allowable table speed are then selected. For routine mediastinal imaging, 7.5-mm collimation in HQ mode with a table speed of 11.75 mm per rotation allows evaluation of most mediastinal abnormalities. Imaging of vascular structures or airways requires narrower collimation (2.5 or 5 mm) and more rapid table speed (15 to 30 mm per rotation table speed) in high-speed mode.

Use of Contrast Medium

Most routine CT scans of the mediastinum can be performed without IV contrast enhancement unless the primary indication is a suspected vascular abnormality (Fig. 29–8). Interpretation of non–contrast-enhanced CT scans, however, can be more difficult and time-consuming than interpretation of contrast-enhanced scans and requires thorough knowledge of mediastinal anatomy and normal variants. There are, however, several advantages to non–contrast-enhanced CT scanning:

1. Scan time is decreased because there is no need to establish IV access, set up the contrast-medium injector, or delay the scan as the bolus is administered.
2. There is no risk of a reaction to contrast medium.
3. The cost is lower.

When needed, IV contrast material is given through a large forearm or antecubital vein by a power injector. Contrast injection rate and total injection volume depends on the indication. For routine purposes, a rate of 2 mL/second for a total volume of 150 mL is sufficient. For vascular imaging (aorta and pulmonary artery), higher injection rates (3 to 4 mL/second) are often necessary. In such cases, it is mandatory that injection be through a relatively large-bore IV catheter (18 or 20 gauge) into a large antecubital vein. The timing of the bolus in relationship to the scan also varies and depends on both the indication (routine versus arterial imaging) and the time required to complete the scan.

Thoracic CT is usually performed without esophageal contrast medium. Oral contrast medium can, however, be helpful in identifying the relationship between the esopha-

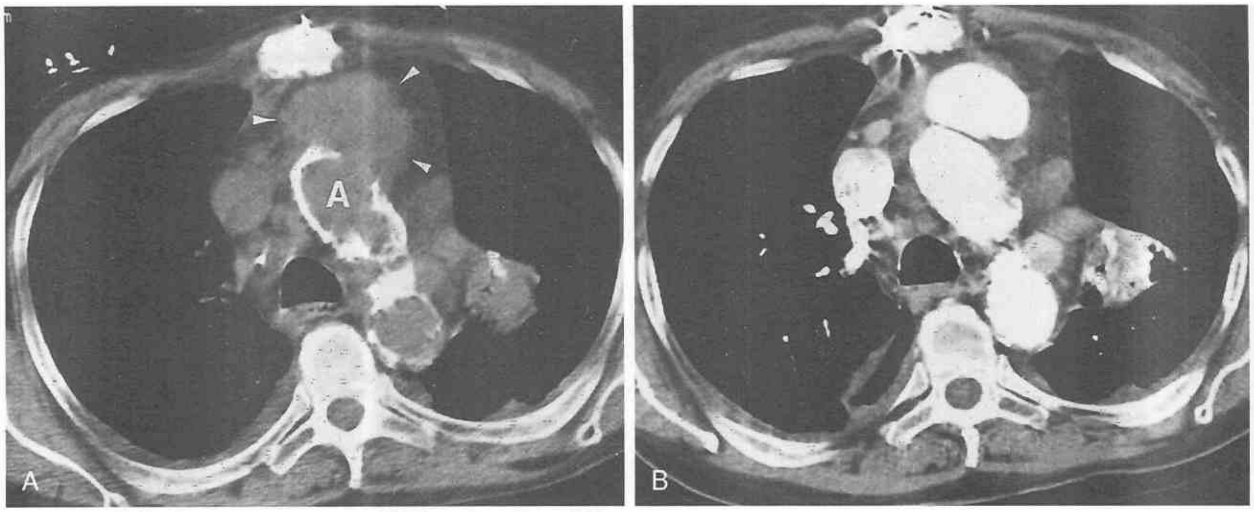

Figure 29–8. Aortic pseudoaneurysm after coronary artery bypass graft surgery. *A,* Non–contrast-enhanced CT performed 4 weeks after surgery to exclude mediastinitis shows heterogeneous low-attenuation mass in anterior mediastinum *(arrowheads)*, suggestive of abscess. A, aorta. *B,* Because of the proximity of the mass to the aorta, the patient was rescanned using intravenous contrast, and the mass was shown to be a pseudoaneurysm arising from the aortic cannulation site.

gus and other mediastinal structures and occasionally, in depicting intrinsic esophageal abnormalities (Fig. 29–9). Commercial preparations of esophageal paste, made of a dilute barium mixture, are available for use. The patient must swallow several teaspoons of the paste and refrain from further swallowing during the examination.

CT Reconstruction and Image Display

CT scans of the mediastinum are usually reconstructed, filmed, and interpreted in axial format. Until recently, sagittal, coronal, and off-axis reconstructions of the thorax were not used because of slice misregistration and respiratory motion artifacts. With the advent of spiral scanning, however, continuous volume data sets can be acquired during a single breath-hold and excellent nonaxial 2D and 3D reconstructed images of mediastinal vascular structures and airways can be generated (see Figs. 29–3 and 29–4). Different reconstruction methods, such as multiplanar reformat imaging, multiplanar volume reformat imaging, and external and internal 3D renderings, vary significantly in computational complexity and time required to generate the images.

Mediastinal CT images may be interpreted in either hard-copy (film) or soft-copy (workstation/display) format. Most axial scans are still printed and interpreted on film. When CT studies of the chest are being filmed, two different window settings are needed because of the wide range in the CT attenuation numbers of the tissues to be displayed: -800 Hounsfield units (HU) for lung and 600 HU for bone. Lung settings should have a wide width to encompass air-filled lung and soft tissue and are usually viewed at a level of -600 and a width of 1200. Because of the smaller density range between fat, soft tissue, bone, and contrast-enhanced vessels, mediastinal settings are usually viewed at a level of 50 and a width of 350.

These levels and widths can be varied to aid in the

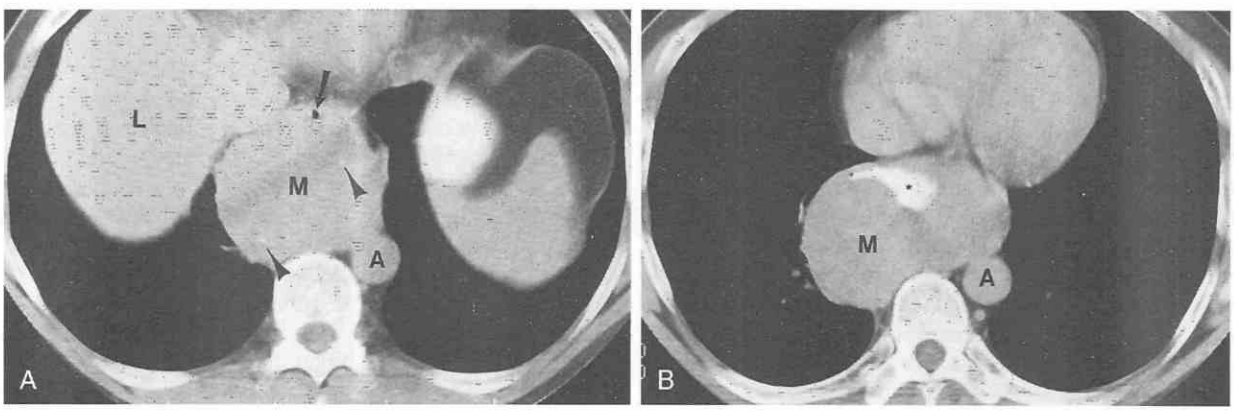

Figure 29–9. Esophageal leiomyoma. *A,* CT shows large middle-mediastinal mass with focal punctate calcifications *(arrowheads)*. The esophagus is displaced anteriorly *(arrow)*. The CT appearance is nonspecific and the origin of mass is uncertain. A, aorta; L, liver; M, mass. *B,* CT following ingestion of oral barium reveals distortion of esophageal lumen *(asterisk)*, consistent with a mass arising within the wall of the esophagus. Resection confirmed leiomyoma. A, aorta; M, mass.

evaluation of any lesion that is not adequately differentiated on the standard settings. For example, during evaluation of a mediastinal mass for subtle calcification, setting the window width on 1 and moving the level between 50 and 300 HU while one views the monitor can often aid detection. Bone windows with a wide width and a level of near 400 HU are often needed to evaluate for possible bone metastases.

Soft-copy interpretation of mediastinal CT is increasing because of the increasing use of (1) picture archiving and communications systems and (2) cine or nonaxial modes for interpretation of complex CT data sets.

MRI Techniques

Spin-Echo Imaging

In the thorax, both T1-weighted and T2-weighted spin-echo images are usually desirable when assessing soft tissue abnormalities.* Although such simple techniques are efficacious for imaging the superior aspect of the mediastinum, cardiac pulsation and respiratory motion degrade images of the lower mediastinum. Many techniques have been developed to correct or eliminate image degradation caused by motion, including:

1. Reducing apparent motion by averaging.
2. Utilizing motion correction techniques.
3. Rapidly acquiring data such that breath-holding is possible.

The simplest method for motion correction is to average the MR signal with many acquisitions. The advantage of multiple acquisitions, however, is offset by an increase in data collection times. Furthermore, for echo times of more than 10 msec, motion artifacts persist in the hilum and adjacent to the heart. Alternatively, breath-held T1-weighted spin-echo imaging using one excitation (NEX), conjugation (half NEX imaging), and short repetition times (TRs), can be used. This technique has a poor signal-to-noise ratio and, although rapid, is still too long to prevent artifacts due to cardiac contraction.

Images can be acquired in fractions of a second using echo-planar sequences. This enables motion to be "frozen" during data acquisition. Such sequences, however, require special hardware and software. More important, because of the large chemical shift between fat and water, echo-planar imaging requires suppression or excitation of either fat or water, reducing the overall contrast available.

Between these extremes of data acquisition resides cardiosynchronous spin-echo imaging using either plethysmography or electrocardiographic (ECG) gating. Image acquisition timed to the cardiac cycle improves delineation of abnormalities within the lower mediastinum and around the heart compared with noncardiosynchronous imaging. For complete assessment of cardiac function, ECG gating is preferred because the precise temporal relationship between each image and the QRS complex is known. If only anatomic information is required, however, plethysmography is generally used because of the simplicity of patient preparation.

*See References 3, 13, 58, 61, 64, 92, 100, 102, 106, 139, and 152.

One consequence of cardiosynchronous acquisitions is that the TR is dependent on the patient's heart rate. Consequently, the acquired images may not be as T1-weighted or T2-weighted as those obtained elsewhere in the body. For example, in a patient with a heart rate of 60 beats/minute, the effective TR is 1000 msec, resulting in images that are neither T1-weighted nor T2-weighted. With a selected echo time (TE) of 20 msec, the image is somewhat proton-density–weighted. Even if the TE is lengthened to 70, images obtained are not truly T2-weighted. To obtain such an image, the TR must be lengthened by multiples of the patient's heart rate. For example, acquiring data over every two heartbeats would increase the TR to 2000 msec. One positive consequence of lengthening the TR is the capability of acquiring images at more anatomic locations. A disadvantage, however, is the doubling of acquisition time and the potentially increased image blur.

Cardiosynchronous acquisitions reduce the effect of cardiac motion but do not compensate for respiratory motion. Respiratory gating, in which MR data are acquired only during periods of apnea, when combined with cardiosynchronous data acquisitions, can be used to improve image quality. This technique, however, is more time-consuming. Using respiratory motion correction algorithms, such as respiratory compensation, can improve image quality by displacing ghost artifacts either outside the imaged field of view or by returning them to their site of origin. These techniques are easily combined with cardiosynchronous data collection and do not significantly increase data acquisition time.

Gated RARE (fast spin-echo, turbo spin-echo) techniques can be used to provide T2-weighted contrast in a fraction of the time when compared with conventional spin-echo acquisitions.

Gradient-Recalled Echo Acquisitions

White blood techniques can be used to assess mediastinal vessels. These gradient-recalled echo (GRE) techniques, such as FLASH (fast low-angle shot) and GRASS (gradient-recalled acquisition in the steady state), render fluid as high signal because of the inflow of unsaturated protons. The stationary tissues appear dark because of their repeated excitation by multiple RF pulses. Within the soft tissues, the contrast available is dependent on the particulars of the acquisition. Either a T1-weighted acquisition (e.g., FLASH) or a more T2-weighted acquisition (e.g., GRASS) can be obtained.[7, 28, 68, 91, 192, 253]

As with spin-echo imaging, the pulsatility of aortic flow and the respiratory motion of most patients results in unsatisfactory images in the lower mediastinum and adjacent to the heart. *Gradient moment nulling* (flow compensation) is routinely employed with such techniques but is generally insufficient to correct all motion artifacts. For complete motion correction, a cardiosynchronous GRE acquisition with respiratory compensation is usually obtained. These sequences have been dubbed *cine MRI.*

With a short TR, GRE data are acquired in 20- to 40-msec segments during the cardiac cycle. The temporal relationship of the data acquisition to the cardiac cycle is recorded and after sufficient data are obtained, a series of images with a frame rate of 10 to 40 frames per minute is

produced and may be viewed as a continuous loop of images through the cardiac cycle. As typically performed, two to four anatomic locations are imaged in a 3- to 5-minute acquisition, depending on the patient's heart rate. The true temporal resolution of the sequence depends on the number of anatomic locations imaged per acquisition and the patient's heart rate. The slower the patient's heart rate and the smaller the number of anatomic locations imaged per acquisition, the higher the temporal resolution. Although high temporal resolution is required for cardiac analysis, a lower frame rate is sufficient to visualize mediastinal structures, allowing more anatomic locations to be acquired per acquisition. As such, 16 anatomic locations can be acquired in 12 to 15 minutes, allowing the entire mediastinum to be covered.

The main limitation of these retrospective cine techniques is their relatively long acquisition times and their sensitivity to arrhythmias. More recently, cardiac-gated, segmented k-space acquisitions have become available. These acquisitions acquire data in a single breath-hold using prospective cardiac gating. The pulse sequence consists of a fast GRE acquisition, such as turbo-FLASH or fast GRASS. TRs are on the order of 5 to 10 msec with echo times of 1 to 3 msec. Flip angles are small, typically 15 to 30 degrees.

As with retrospective techniques, the R-to-R interval in each cardiac cycle is divided into multiple frames of 20 to 80 msec in duration. During each frame, in a fashion analogous to fast spin-echo data acquisition, a number of lines of k-space are acquired. This is referred to as the number of views per segment or the number of views per phase, and it is equivalent to *echo train length* (ETL) or TURBO factor in fast spin-echo or turbo spin-echo imaging. The more views sampled per segment, the smaller the number of R-to-R intervals required and the faster the acquisition.

For example, using eight views per segment, 128 lines of k-space can be acquired over 16 R-to-R intervals, which for most patients is a 15- to 25-second breath-hold. Assuming a TR of 10 msec, view sharing of eight frames, and a heart rate of 60 beats/minute, approximately 12 frames per cardiac cycle can be produced. If the number of frames per segment is increased, the total acquisition time is reduced; however, the number of frames per cardiac cycle is also decreased. In addition, since the data acquisition time for each frame of the cardiac cycle is increased, the amount of image blur is increased.

Although much faster than retrospective cine imaging, these segmented k-space techniques have a shorter acquisition time that is associated with a reduced signal-to-noise ratio. In our experience, a dedicated surface coil is necessary to compensate for this lower signal-to-noise ratio. A final disadvantage of these techniques is the reduced intraluminal signal that results from the slow flow seen during diastole.

Contrast-Enhanced Magnetic Resonance Angiography and Venography

Both arterial and venous anatomy can be visualized with the administration of gadolinium during the acquisition of a fast GRE volume data set. Such techniques have been well described for visualizing the aorta, renal arteries, carotids, and portal vein. These techniques have a rapid acquisition time (10 to 30 seconds) and, as such, a complete MR angiography or MR venography can be acquired in a single breath-hold.

The clear disadvantages of such techniques are the expense of the contrast agent and the small risk of a contrast reaction. In addition, timing arrival of the contrast bolus to the structure of interest is required for optimal visualization.

Summary

Spin-echo imaging, although superb for visualizing the soft tissues, is less specific for assessing vascular patency. White blood or contrast-dependent techniques optimize the signal intensity of flowing blood. A consequence of this, however, is a reduced conspicuity of soft tissue abnormalities within the mediastinum. Consequently, it may be necessary to acquire sequences with both techniques for accurate interpretation of the study.

Normal Mediastinal Anatomy

Comprehensive knowledge of cross-sectional anatomy is required to accurately evaluate mediastinal abnormalities. Interpretation of mediastinal anatomy, however, can be assisted by analyzing CT images at specific levels within the chest that are easily identifiable because of their characteristic anatomic landmarks and appearance.

Thoracic Inlet Level

At the junction of the neck and the thorax, most of the mediastinal structures are vascular (Fig. 29–10). The two brachiocephalic veins are formed as the internal jugular veins join the subclavian veins and are located posterior to

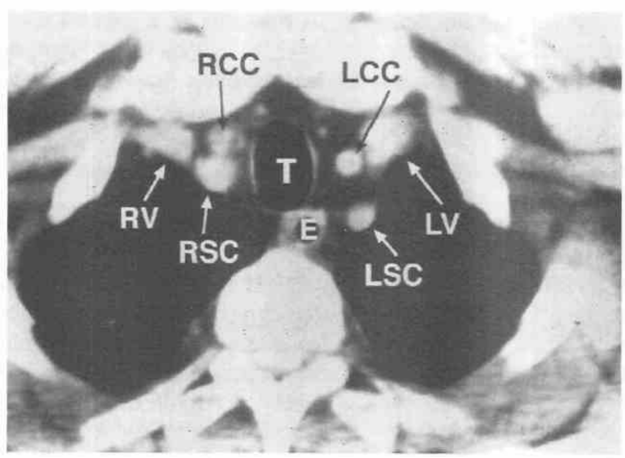

Figure 29–10. Thoracic inlet level. The trachea (T) and esophagus (E) are midline, and they separate the right and left vascular structures. LCC, left common carotid artery; LSC, left subclavian artery; LV, left brachiocephalic vein; RCC, right common carotid artery; RSC, right subclavian artery; RV, right brachiocephalic vein.

the clavicular heads. These veins are the most anterior and lateral of the six vessels. More medially are the two common carotid arteries, and just posterior to these are the subclavian arteries. The subclavian arteries and veins exit the mediastinum to enter the axilla after crossing over the first rib. The esophagus is posterior or posterolateral to the trachea. There are six major vessels at this level.

Left Brachiocephalic Vein Level

The left brachiocephalic vein crosses the midline anterior to the arterial branches of the aorta and joins the more vertically orientated right brachiocephalic vein to form the superior vena cava (SVC). (Fig. 29–11). The internal mammary veins can often be identified coursing posteriorly from a parasternal location to join the brachiocephalic veins.

The right brachiocephalic, left common carotid, and left subclavian arteries are located posterior to the left brachiocephalic vein and anterior to the trachea. The right brachiocephalic artery is the more centrally located artery, whereas the left common carotid artery (the smallest of the three arteries) and the left subclavian artery are located to the left of the midline in a more lateral and posterior position.

The esophagus is posterior or posterolateral to the trachea and anterior to the spine.

Aortic Arch Level

The transverse arch crosses the mediastinum anterior to the trachea coursing obliquely from right to left and from anterior to posterior (Fig. 29–12). The SVC is located adjacent to the anterior aspect of the transverse aorta to the right of the trachea. The fat-filled region posterior to the SVC, anterior to the trachea, and lateral to the aorta is the pretracheal space. Anterior to the transverse aorta is the fat-filled prevascular space, a compartment of the anterior mediastinum that extends cephalad anterior to the great vessels of the aorta and the brachiocephalic veins. If present, the thymus gland is located in this space. Both of these spaces often contain a few small lymph nodes.

The esophagus is posterior or posterolateral to the trachea and anterior to the spine.

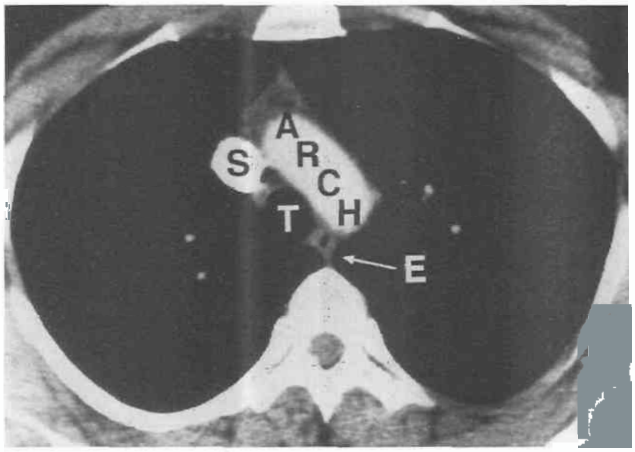

Figure 29–12. Aortic arch level. Superior vena cava (S) and aortic arch (ARCH) lie anterior to the trachea (T) and esophagus (E). The thymus, which has undergone fatty infiltration, is anterior to the arch.

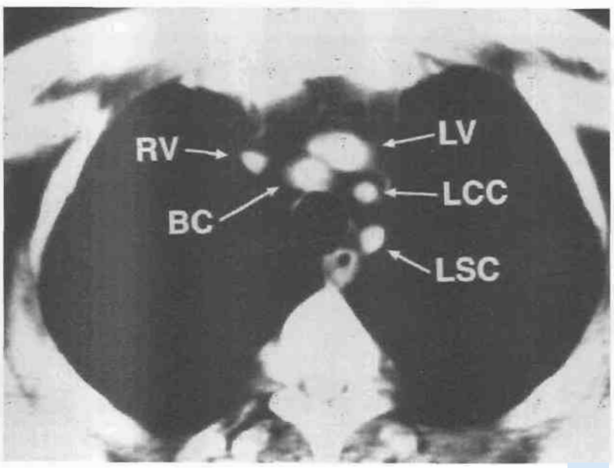

Figure 29–11. Left brachiocephalic vein level. Right (RV) and left (LV) brachiocephalic veins are anterior to right brachiocephalic artery (BC), left common carotid artery (LCC), and left subclavian artery (LSC).

Azygos Arch and Aortopulmonary Window Level

The azygos vein, located anterior and slightly to the right of the spine, arches anteriorly and joins the SVC at this level (Figs. 29–13 and 29–14). The azygos arch may not be seen in its entirety on one slice and may be confused with lymphadenopathy. The ascending and descending aorta are visible as separate structures at this level. The

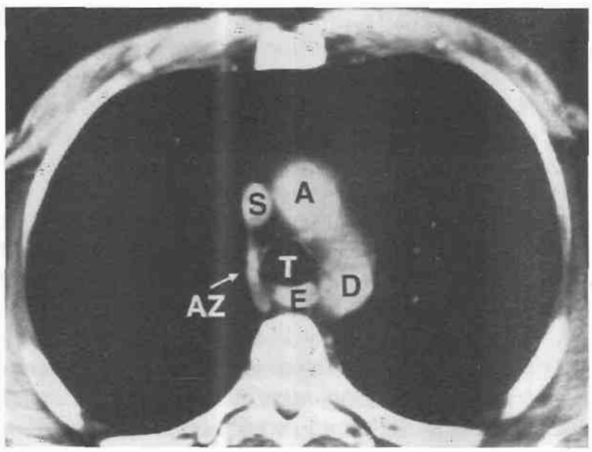

Figure 29–13. Arch of the azygos vein or the aortopulmonary (AP) window level. Azygos vein (AZ) arches from a posterior position along the midesophagus to join the superior vena cava (S), crossing over the right upper lobe bronchus. Between the ascending (A) and descending (D) aorta is the AP window region. E, esophagus; T, trachea.

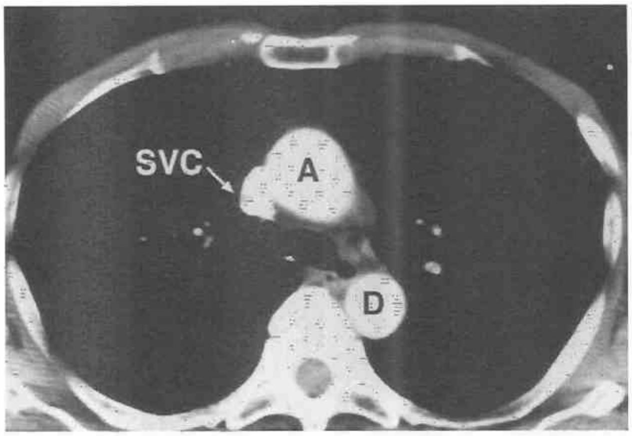

Figure 29–14. Aortopulmonary (AP) window level. AP window is between ascending (A) and descending (D) aorta. SVC, superior vena cava.

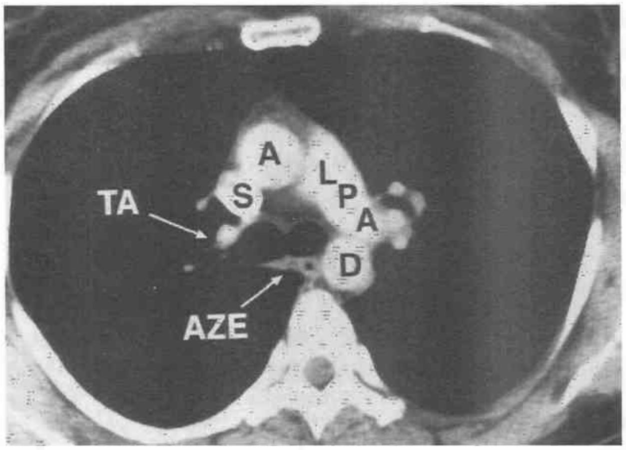

Figure 29–15. Left pulmonary artery level. To the left of the left pulmonary artery (LPA) lie the left superior pulmonary veins. The ascending (A) and descending (D) aorta and superior vena cava (S) maintain their relative positions from the level above. The truncus anterior (TA), or right upper lobe pulmonary artery, is anterior to the right upper lobe bronchus. The azygoesophageal recess (AZE) is a concavity anterior to the spine.

ascending aorta is anterior to the trachea, and the descending aorta is posterolateral to the trachea on the left. Typically, the ascending aorta (mean diameter, 3.5 cm) is larger than the descending aorta (mean diameter, 2.5 cm).

The aortopulmonary window is a space located between the inferior aspect of the aortic arch and the superior aspect of the left main pulmonary artery. In some patients, the close anatomic contiguity of these two structures prevents visualization of this space. The space is otherwise fat-filled and contains a few small lymph nodes, the left recurrent laryngeal nerve, and the ligamentum arteriosum.

The esophagus is posterior to the trachea, anterior to the spine, and medial to the descending aorta.

Left Pulmonary Artery Level

The main pulmonary artery is anterior and to the left of the ascending aorta. The left pulmonary artery curves posteriorly from its origin from the main pulmonary artery and is located anterolateral to the left main bronchus at the level of the carina (Figs. 29–15 and 29–16). The left superior pulmonary veins are located lateral to the posterior portion of the left pulmonary artery.

On the right, at the level of the carina, is the origin of the right upper lobe bronchus. Anterior to the right upper lobe bronchus lies the right upper lobe pulmonary artery or the truncus anterior. The right superior pulmonary veins are located anterior and lateral to the truncus anterior. The azygos vein is located posterior and to the right of the esophagus. The hemiazygos vein parallels the course of the azygos but is to the left of the spine.

The superior pericardial recess, a crescent-shaped extension of the pericardial space, is contiguous with the posterior aspect of the ascending aorta. The space often contains a small amount of fluid and can occasionally be confused with a lymph node. Its characteristic location, shape, and low attenuation, however, allow confident identification.

The concave extension of right lung into the mediastinum anterior to the spine is the azygoesophageal recess, which extends inferiorly from the subcarinal region to the level of the diaphragm.

Right Pulmonary Artery Level

The main pulmonary artery is anterior and to the left of the ascending aorta (Figs. 29–17 and 29–18). The right pulmonary artery extends posteriorly and to the right from the main pulmonary artery, passing anterior to the bronchus intermedius and posterior to the SVC. The right superior pulmonary vein is to the right and lateral to the intrapulmonary portion of the right pulmonary artery. Anterior to the left main and upper lobe bronchi is the left superior pulmonary vein, and posterior to the left upper lobe bronchus is the left lower lobe pulmonary artery.

Left Atrial Level

The anatomy of the mediastinum is complex at this level (Figs. 29–19 and 29–20). Anterior to the SVC is the

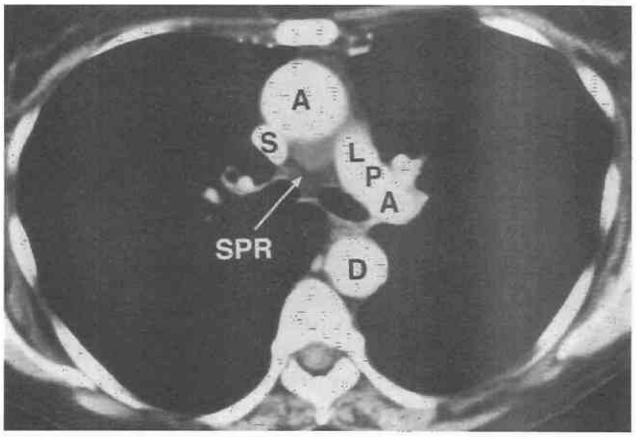

Figure 29–16. Left pulmonary artery level. The superior pericardial recess (SPR) is an extension of the pericardium. A, ascending aorta; D, descending aorta; LPA, left pulmonary artery; S, superior vena cava.

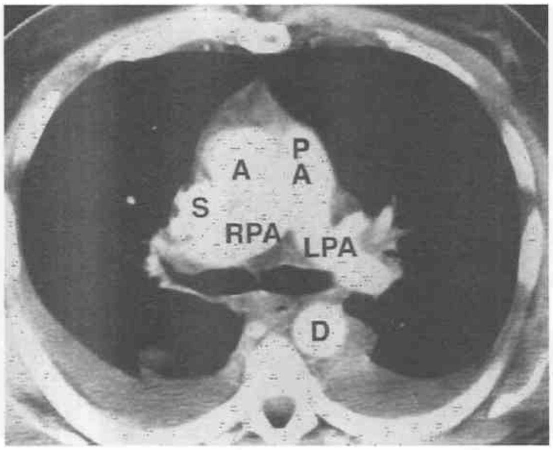

Figure 29–17. Right pulmonary artery level. The main pulmonary artery (PA) divides into the left (LPA) and right (RPA) pulmonary arteries. The right pulmonary artery passes anterior to the right main bronchus, and the left pulmonary artery passes over the left main bronchus. A, ascending aorta; D, descending aorta; S, superior vena cava.

right atrial appendage curving around the ascending aorta. The aorta is located centrally within the mediastinum, and anterior and to the left of the aorta is the pulmonary outflow tract. Posterolateral and to the left of the pulmonary outflow tract is the left atrial appendage. Within the fat, between the left atrial appendage and the aortic root, is the left main coronary artery. The left superior pulmonary vein enters the left atrium immediately posterior to the left atrial appendage. The right superior pulmonary veins enter the left atrium just posterior to the SVC.

Four-Chamber Level

All four chambers of the heart are identified at this level (Figs. 29–21 and 29–22). The posteriorly located left atrium is the most cranial of all the chambers. The right and left inferior pulmonary veins enter the posterolateral aspect of the left atrium. Anterior and to the right is the right atrium. To the left and anterior to the right atrium is the right ventricle located behind the sternum. The left ventricle is to the left and posterior to the right ventricle.

The coronary arteries can be detected if they are calcified or if fat surrounds the heart. The right coronary artery lies in the right atrioventricular groove. The circumflex coronary artery lies in the left atrioventricular groove, and the left anterior descending coronary artery lies in the intraventricular groove between the left and right ventricles.

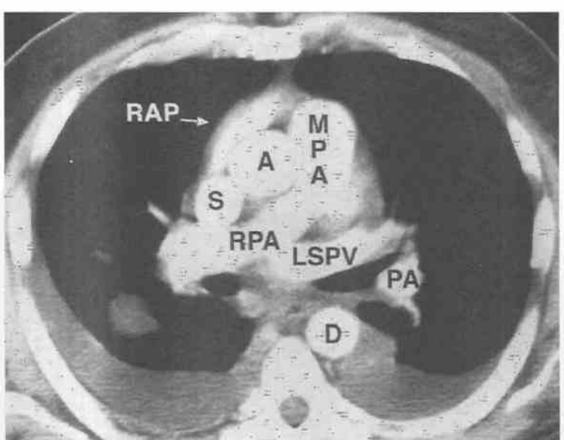

Figure 29–18. Right pulmonary artery level. The main pulmonary artery (MPA) divides into the right pulmonary artery (RPA) and the left pulmonary artery, which is more superior and not visible. The left superior pulmonary vein (LSPV) is anterior to the left main bronchus, and the left pulmonary artery (PA) is posterior. The superior aspect of the right atrial appendage (RAP) is anterior to the superior vena cava (S). A, ascending aorta; D, descending aorta.

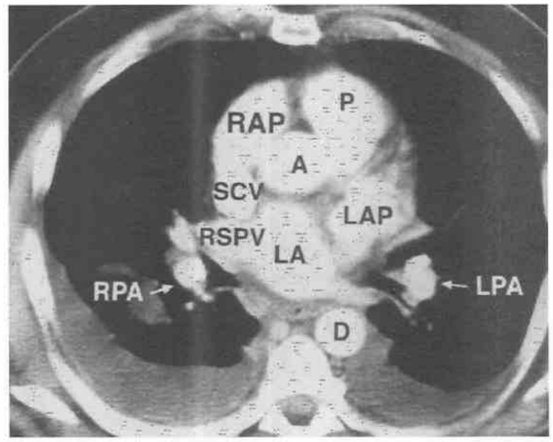

Figure 29–19. Left atrial level. The left atrium (LA) is the most superior and posterior chamber of the heart. Superior pulmonary veins enter the anterosuperior portion of the left atrium. The left atrial appendage (LAP) is situated anterior and to left of the left atrium, adjacent to main pulmonary artery (P). The right atrial appendage (RAP) is anterior to superior vena cava (SVC) and adjacent to ascending aorta (A). D, descending aorta; LPA, left pulmonary artery; RPA, right pulmonary artery; RSPV, right superior pulmonary vein.

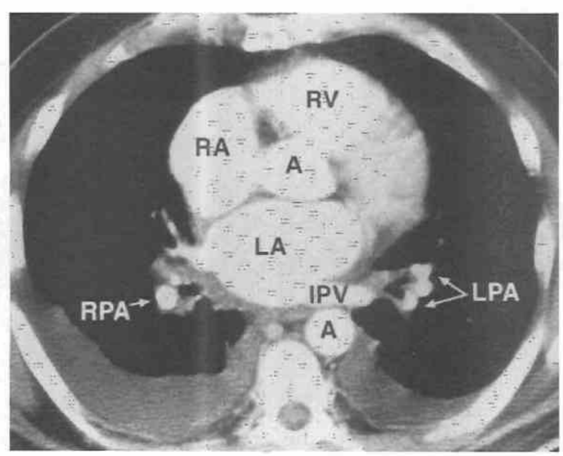

Figure 29–20. Left atrial level. A, aortic root; IPV, left inferior pulmonary vein; LA, left atrium; LPA, left lower lobe pulmonary arteries; RA, right atrium; RPA, right lower lobe pulmonary artery; RV, right ventricle.

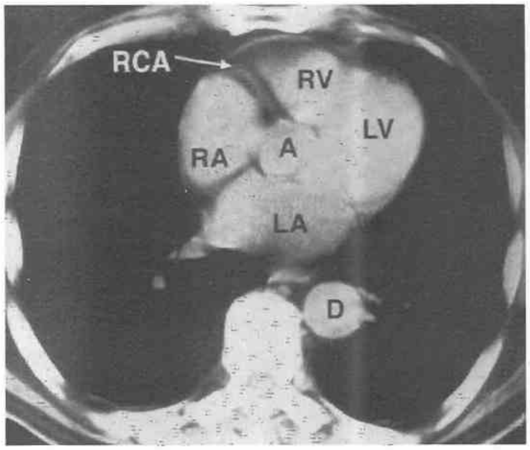

Figure 29–21. Four-chamber level. The right coronary artery (RCA) is visible in the right atrioventricular groove. A, aortic root; D, descending aorta; LA, left atrium; LV, left ventricle; RA, right atrium; RV, right ventricle.

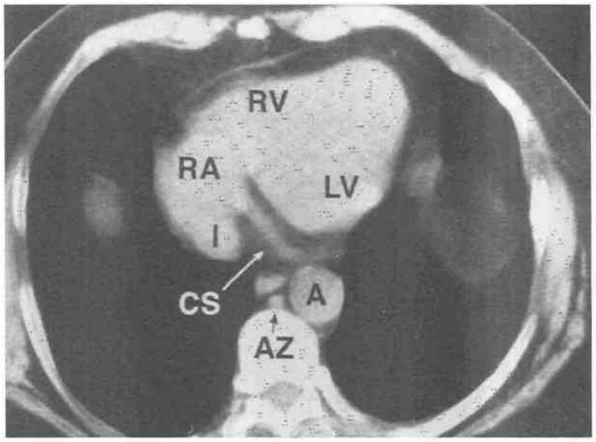

Figure 29–23. Three-chamber level. The left atrium is more cranial to this level and is not visible. The three visualized chambers are right atrium (RA), the right ventricle (RV), and the left ventricle (LV). The coronary sinus (CS) is between the inferior vena cava (I) and the left ventricle. A, descending aorta; AZ, azygos vein.

Three-Chamber Level

The ventricles and the right atrium are identified at this level (the left atrium, because of its more cranial position, is not visible) (Figs. 29–23 and 29–24). The right atrium is located to the right. To the left and anteriorly, the right ventricle with its thin wall is located just beneath the sternum. The thick-walled left ventricle makes up the posterolateral left portion of the mediastinum. Between the left ventricle and the inferior vena cava's opening into the right atrium is the coronary sinus.

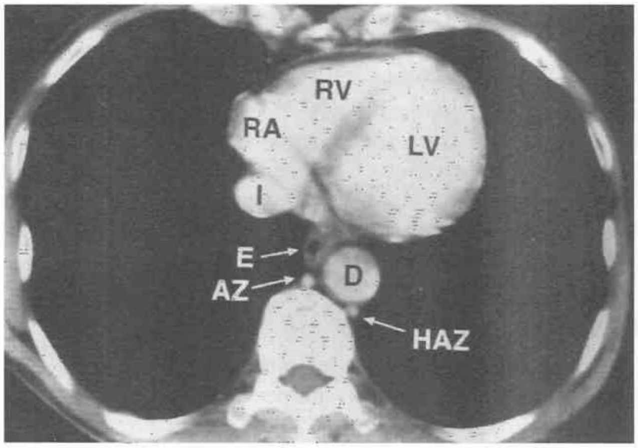

Figure 29–24. Three-chamber level. Esophagus (E) and azygos vein (AZ) form the medial border of the azygoesophageal recess. D, descending aorta; HAZ, hemiazygos vein; I, inferior vena cava; LV, left ventricle; RA, right atrium; RV, right ventricle.

MR Images of the Mediastinum

The standard spin-echo, T1-weighted axial images of the mediastinum are similar in appearance to CT images (Figs. 29–25 to 29–29). However, signal void of the airways can occasionally be confused with the lack of signal in vessels. Coronal and sagittal MR images are helpful in depicting the anatomic relationships of normal mediastinal

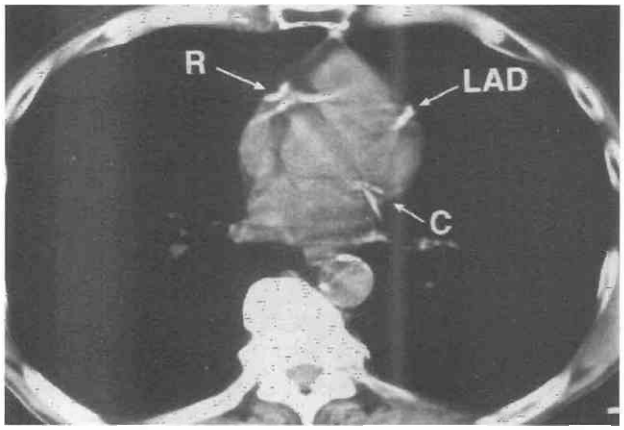

Figure 29–22. Calcified coronary arteries at the four-chamber level. C, circumflex coronary artery; LAD, left anterior descending coronary artery; R, right coronary artery.

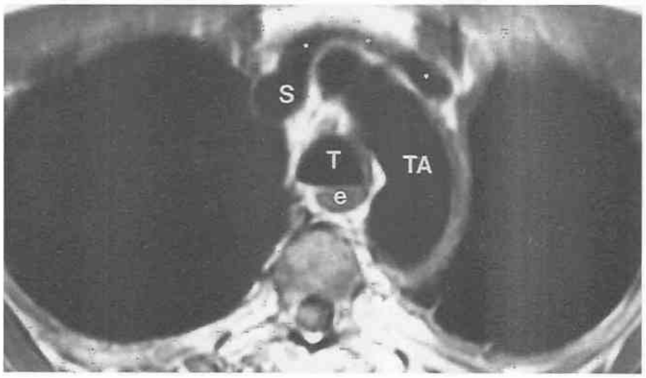

Figure 29–25. Axial MR image of the aortic arch in a patient with mesothelioma of the left hemithorax. e, esophagus; S, superior vena cava; T, trachea; TA, transverse aortic arch. The *asterisks* indicate the left brachiocephalic vein.

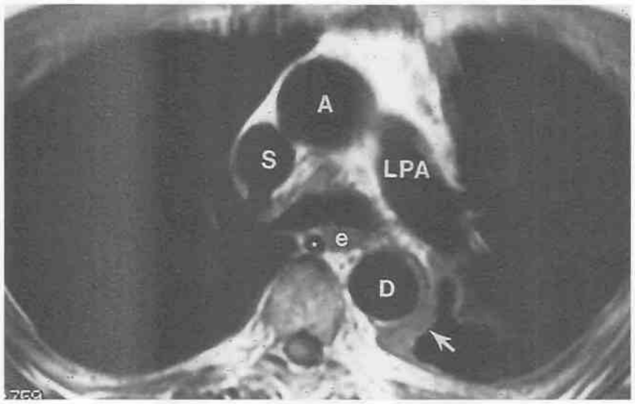

Figure 29–26. Axial MR image of the left pulmonary artery in a patient with mesothelioma of the left hemithorax. Note soft tissue mass *(arrow)* encasing the descending aorta. A, ascending aorta; D, descending aorta; e, esophagus; LPA, left pulmonary artery; S, superior vena cava. The *asterisk* indicates the azygos vein.

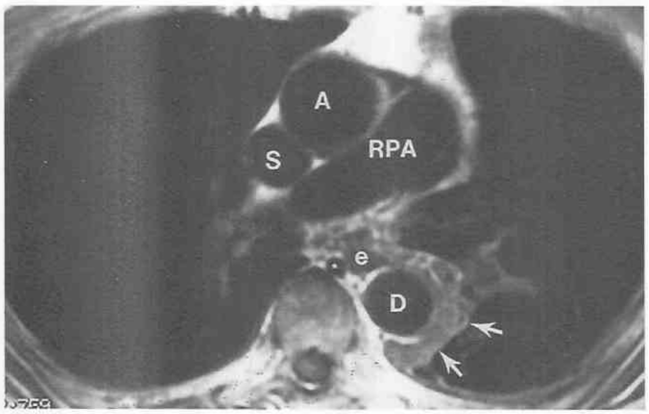

Figure 29–27. Axial MR image of the right pulmonary artery in a patient with mesothelioma of the left hemithorax. A soft tissue mass *(arrows)* encases the descending aorta. A, ascending aorta; D, descending aorta; e, esophagus; RPA, right pulmonary artery; S, superior vena cava. The *asterisk* indicates the azygos vein.

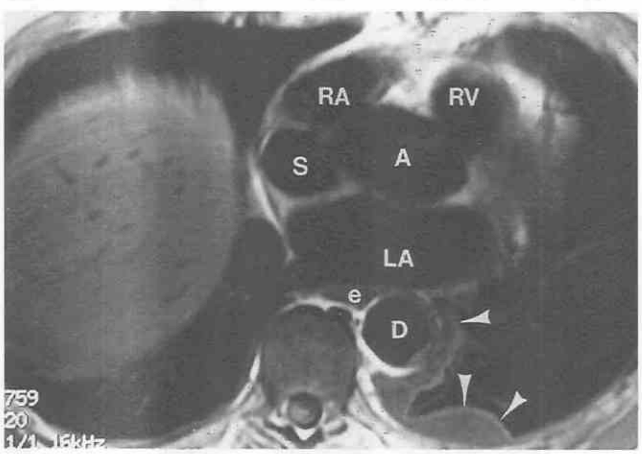

Figure 29–28. Axial MR image at the left atrial level in a patient with mesothelioma of the left hemithorax. Loculated pleural fluid *(arrowheads)* can be seen in the left posterior hemithorax. A, ascending aorta; D, descending aorta; e, esophagus; LA, left atrium; RA, right atrium; RV, right ventricle; S, superior vena cava.

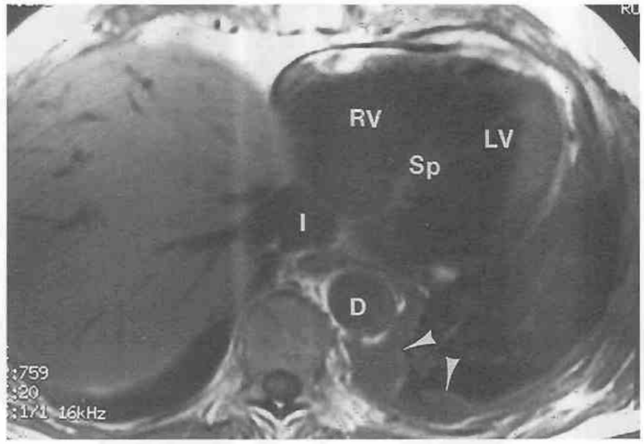

Figure 29–29. Axial MR image at the three-chamber level in a patient with mesothelioma of the left hemithorax. Loculated pleural fluid *(arrowheads)* can be seen in the left posterior hemithorax. D, descending aorta; I, inferior vena cava; LV, left ventricle; RV, right ventricle; Sp, intraventricular septum.

structures as well as in identifying and locating pathology (Figs. 29–30 to 29–34).

Mediastinal Divisions

The mediastinum extends craniocaudally from the thoracic inlet to the diaphragm and, historically, has been divided into compartments (on the chest radiograph) to facilitate lesion localization and aid in diagnosis. This division of the mediastinum into anatomic regions or compartments is still important but not essential because CT and MRI can accurately localize and, in many instances, characterize masses. Despite these advances, however, mediastinal masses are still discussed, classified, and grouped by their position on chest radiographs.

In this chapter, we use the widely accepted division of the mediastinum into superior, anterior, middle, and posterior compartments.

The *superior mediastinum* is the space between the

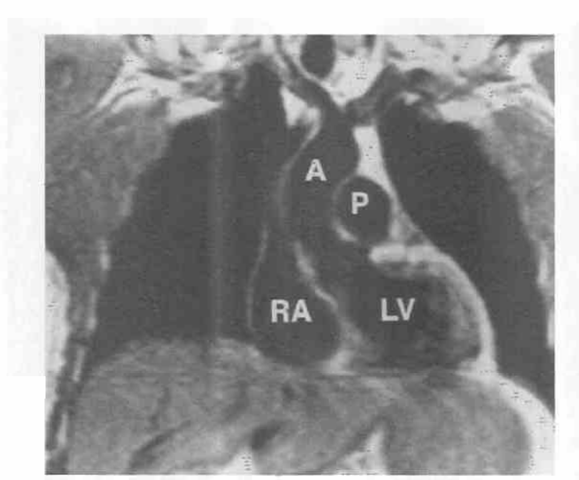

Figure 29–30. Anterior coronal MR image. A, ascending aorta; LV, left ventricle; P, main pulmonary artery; RA, right atrium.

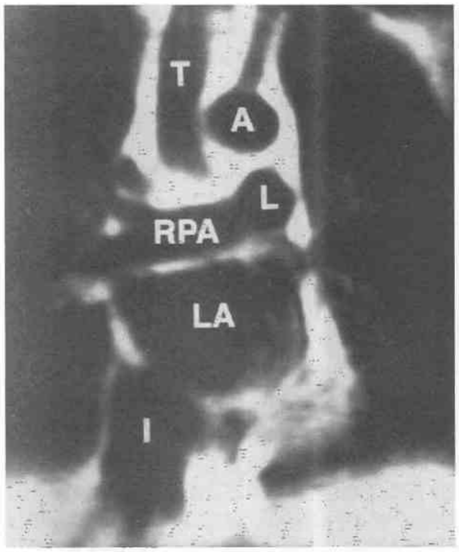

Figure 29–31. Coronal MR image at the right pulmonary artery level. A, aorta; I, inferior vena cava–right atrial junction; L, left pulmonary artery; LA, left atrium; RPA, right pulmonary artery; T, trachea.

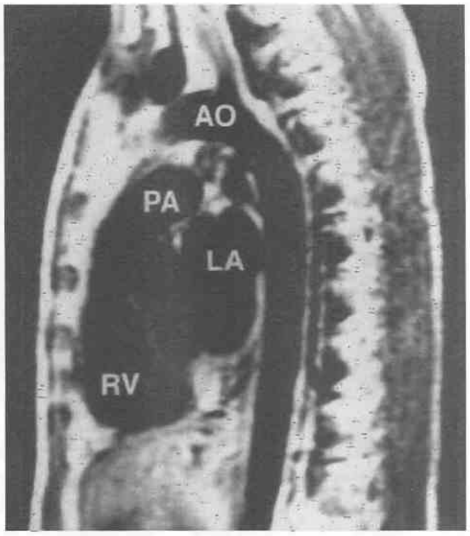

Figure 29–33. Sagittal MR image of the main pulmonary artery. AO, aorta; LA, left atrium; PA, main pulmonary artery; RV, right ventricle.

thoracic inlet and the superior aspect of the aortic arch (i.e., all mediastinal structures above an imaginary line drawn between the sternal angle and the fourth intervertebral disk on the lateral chest radiograph).

The *anterior mediastinum* is the space anterior to the heart and great vessels on the lateral chest radiograph. It is bordered anteriorly by the sternum and posteriorly by the pericardium. Using this designation, normal anterior mediastinal structures include the thymus, the branches of the internal mammary artery and vein, lymph nodes, and fat.

Controversy exists concerning the division between the middle and the posterior mediastinum. Some authors suggest that the division should be the posterior aspect of the pericardium, but others would divide the two by an imaginary line drawn 1 cm posterior to the anterior border of the vertebral bodies. The latter method places most aortic and esophageal lesions in the middle mediastinum and reserves the posterior mediastinum for neurogenic or other paraspinal lesions. Other methods involve dividing the middle and posterior mediastinum on the basis of the azygos arch and the aorta.

For purposes of this discussion, we define the *middle mediastinum* as the space between the anterior border of the pericardium and an imaginary line drawn 1 cm posterior to the anterior border of the vertebral bodies on the lateral radiograph. As such, it contains the heart, the aorta, the superior and inferior venae cavae, the brachiocephalic arteries and veins, the pulmonary arteries and veins, the thoracic duct, the azygos and hemiazygos veins, the phrenic and vagus nerves, the trachea and proximal bronchi, mediastinal fat, and lymph nodes.

The *posterior mediastinum* is defined as the space be-

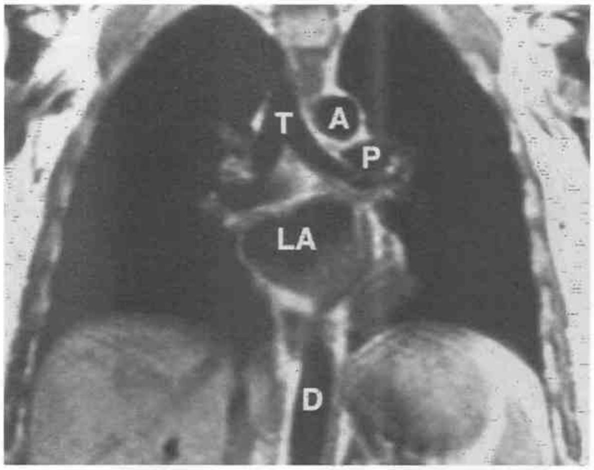

Figure 29–32. Coronal MR image at the carina. A, transverse aortic arch; D, descending aorta; LA, left atrium; P, left pulmonary artery; T, trachea.

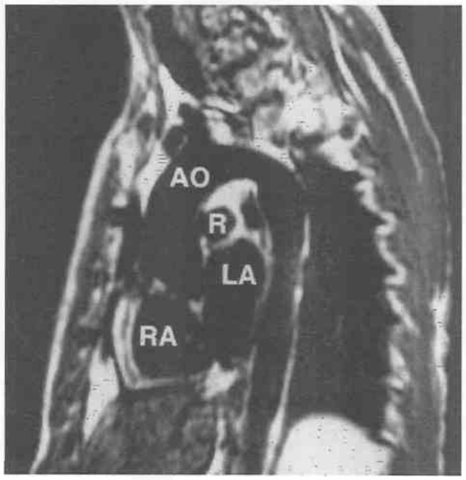

Figure 29–34. Sagittal MR image of the aorta. AO, aorta; LA, left atrium; R, right pulmonary artery; RA, right atrium.

Table 29–1. Classification of Mediastinal Abnormalities by Compartment Affected

Location	Lesion
Superior mediastinum	Thyroid goiter, tortuous great vessels
Anterior mediastinum	Thymic lesions, germ cell tumors, parathyroid adenoma, lymphatic malformations, hemangioma
Middle mediastinum	Esophageal lesions, airway lesions, foregut cysts, pericardial cysts
Posterior mediastinum	Neurogenic tumors, paraspinal abscess, extramedullary hematopoiesis
Multiple compartments	Mediastinitis, lipomatosis, lymphadenopathy (lymphoma, metastases, Castleman's disease, infection), mesenchymal tumors, vascular abnormalities and anomalies, diaphragmatic hernias

Table 29–2. Classification of Mediastinal Abnormalities Based on CT Attenuation Characteristics

CT Attenuation	Lesion
Fat	Lipoma, lipomatosis, thymolipoma, liposarcoma, teratoma, epicardial fat pad, hernia
Water	Thymic cyst, teratoma, pericardial cyst, bronchogenic cyst, esophageal duplication cyst, meningocele, neurenteric cyst
Soft tissue	Thymoma, thymic carcinoma, germ cell tumor, esophageal neoplasm, neurogenic tumor, lymphoma, lymphadenopathy
High attenuation	Calcified nodes (histoplasmosis, tuberculosis, sarcoidosis, silicosis), calcified neoplasm (thymoma, teratoma, treated lymphoma, metastases), fibrosing mediastinitis, hemorrhage, goiter, vascular
Contrast-enhancing	Vascular, goiter, Castleman's disease, hemangioma, paraganglioma

tween the imaginary line drawn 1 cm posterior to the anterior border of the vertebral bodies and the posterior paravertebral gutters. Structures in the posterior mediastinum include nerves, fat, the vertebral column, and lymph nodes.

Mediastinal Abnormalities

A useful approach for discussing mediastinal abnormalities is to divide them into those processes that predominantly affect *specific* compartments (superior, anterior, middle, and posterior mediastinum) and those processes that can affect *multiple* compartments (Table 29–1). An alternative method of classifying mediastinal masses is on the basis of their predominant attenuation characteristics on CT rather than by their location (Table 29–2).[86, 87] We will use the *former* approach in this discussion.

Superior Mediastinal Abnormalities

Common superior mediastinal abnormalities include intrathoracic extension of thyroid goiters or masses and tortuous great vessels.

Thyroid Goiter

On CT, the normal thyroid gland is typically visible at or just below the level of the cricoid cartilage (Fig. 29–35). It appears on a non–contrast-enhanced CT scan as two wedge-shaped structures of homogeneous attenuation on either side of the trachea, separated by a narrow anterior isthmus. Its attenuation is usually increased, compared with that of muscle, because of the iodine content of the gland. It typically enhances homogeneously following administration of IV contrast material. On MR images, the normal thyroid gland usually has intermediate signal intensity, slightly greater than the adjacent muscle, on T1-weighted

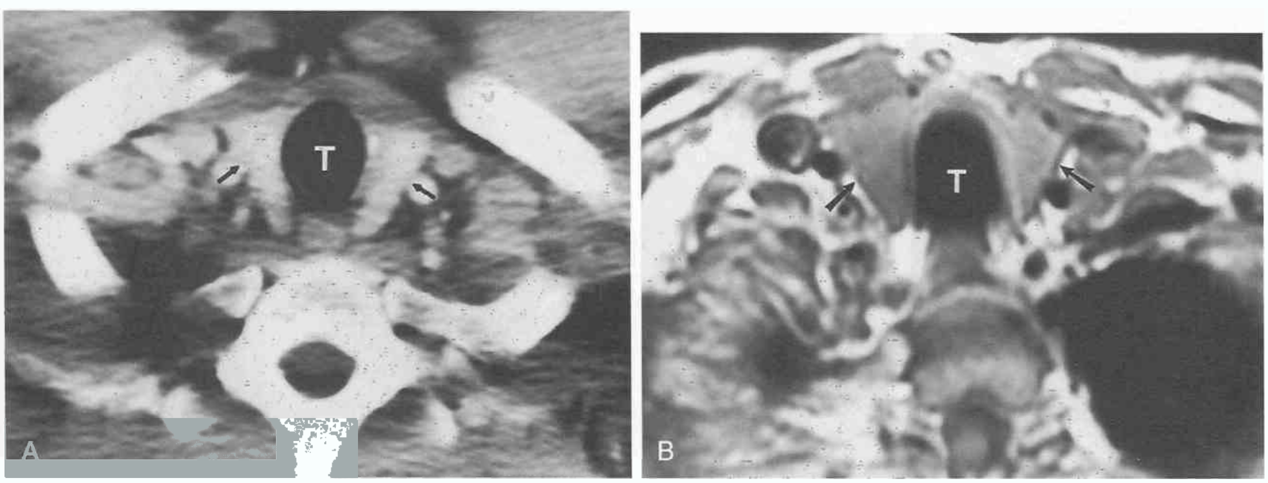

Figure 29–35. Normal thyroid gland. *A*, Contrast-enhanced CT shows typical appearance of thyroid gland *(arrows)*. Enhancement is homogeneous. T, trachea. *B*, T1-weighted axial MR image shows homogeneous intermediate signal intensity typical of normal thyroid gland *(arrows)*. T, trachea.

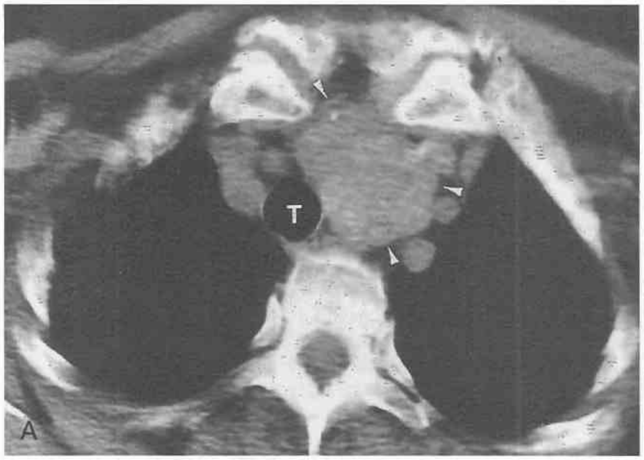

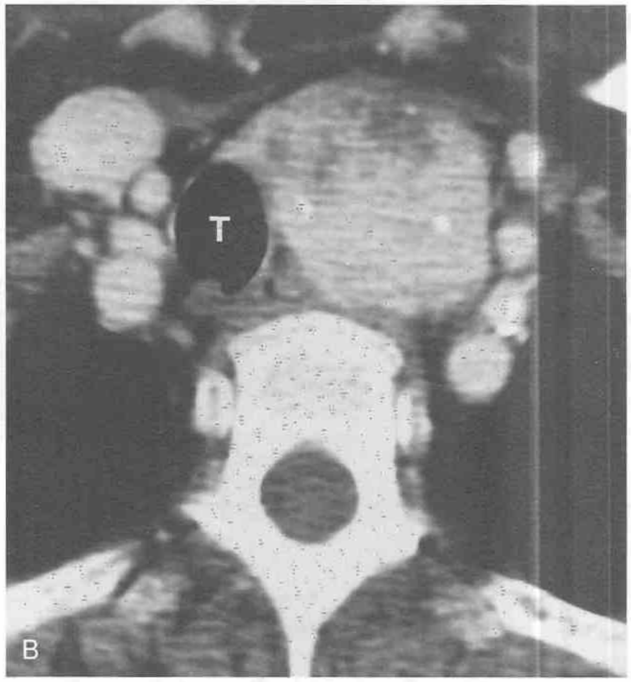

Figure 29–36. Thyroid goiter. *A*, CT shows heterogeneous superior mediastinal mass *(arrowheads)* with punctate calcification. Images at thoracic inlet (not shown) confirmed contiguity of mass with the left thyroid lobe, consistent with intrathoracic extension of goiter. *B*, Contrast-enhanced CT shows heterogeneous enhancement of mass. T, trachea.

images and higher signal intensity on T2-weighted images (see Fig. 29–35).

Most thyroid masses in the mediastinum are caused by intrathoracic extension of thyroid goiters, which can account for up to 10% of mediastinal masses resected at thoracotomy. True ectopic thyroid masses in the mediastinum are rare. Typically, a thyroid goiter extends into the thyropericardiac space anterior to the recurrent laryngeal nerve and brachiocephalic vessels, although posterior extension adjacent to the trachea occurs in 20%. Rarely, thyroid masses may extend behind the esophagus and present as a posterior mediastinal mass.

A mediastinal goiter is usually detected on chest radiographs as a thoracic inlet or superior mediastinal mass that deviates and occasionally narrows the trachea.[20, 78, 84, 105, 107, 182, 227] Although scintigraphy can detect mediastinal goiters, the uptake of technetium or iodine is variable. The CT appearance of a mediastinal goiter is variable, but the goiter can be confidently diagnosed when continuity of the mass with the thyroid gland is visible. Additional features useful in establishing the diagnosis include the following:

1. Heterogeneous attenuation with areas of both high and low attenuation on non–contrast-enhanced scans.
2. Marked enhancement following administration of IV contrast material.
3. Focal punctate or curvilinear calcifications (Figs. 29–36 and 29–37).

The cystic and adenomatoid composition of goiters results in a heterogeneous appearance on both T1-weighted and T2-weighted MR images (Fig. 29–38). On T1-weighted images, goiters may show lower signal intensity than normal thyroid, but high signal intensity can be seen in areas of subacute hemorrhage, colloid cysts, and adenomas. Goiters show high signal intensity on T2-weighted images.

Tortuous Great Vessels

Tortuosity of the great vessels is a common cause of a superior mediastinal abnormality on a chest radiograph. The most common location of the radiographic abnormality is in the right paratracheal region because the right brachiocephalic artery in older patients often has a tortuous course before giving rise to the right subclavian and common carotid arteries. CT without contrast enhancement can often determine that the tortuous vessels are the cause of the apparent mass. Calcification within the vessel walls allows confident identification of tortuous arteries. If any doubt exists as to the vascular nature of the mass, IV contrast enhancement easily identifies the vessels (Fig. 29–39).

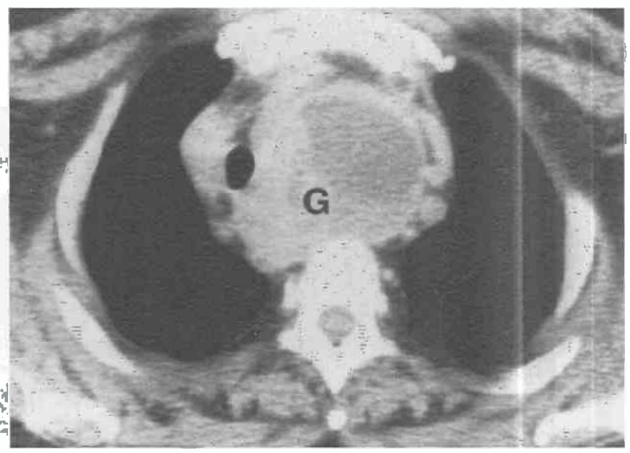

Figure 29–37. Mediastinal goiter. Contrast-enhanced CT shows large goiter *(G)* displacing the trachea to the right, and the left common carotid and subclavian arteries to the left. Enhancement is heterogeneous.

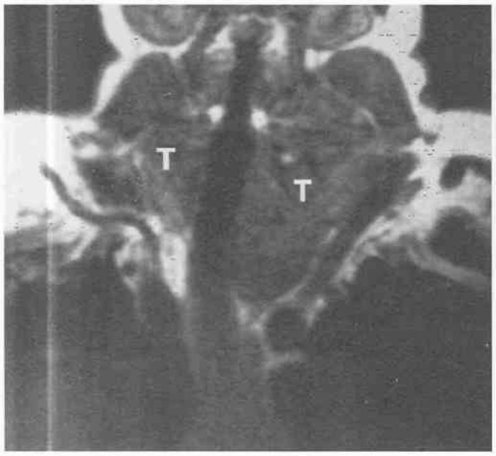

Figure 29–38. Mediastinal goiter. Coronal MR image shows mediastinal thyroid tissue (T) on both sides of trachea, which is deviated to the right at the thoracic inlet.

Anterior Mediastinal Abnormalities

Approximately half of all mediastinal masses occur in the anterior mediastinum. Lesions that occur preferentially in the anterior mediastinum include thymic lesions (cysts, thymolipoma, thymoma, thymic carcinoma), parathyroid adenoma, germ cell tumors, hemangioma, and lymphatic malformations.[34, 243] Lymphoma is another common cause of an anterior mediastinal mass, but it will be considered in the section on diffuse mediastinal diseas

Thymic Lesions

Normal Thymus

The thymus is a bilobed, triangular gland that occupies the thyropericardiac space of the anterior mediastinum and extends inferiorly to the heart.[17, 49, 70, 182, 238] The normal morphology and size of the thymus change markedly with age.[172] Wide variation exists in the normal size of the thymus, particularly in children and young adults. In the newborn, the thymus gland is often larger than the heart. Thymic size decreases with age as the gland undergoes fatty infiltration. The atrophied thymus is often visualized on CT in patients in their fourth decade of life, but it is seen in fewer than 50% of patients over 40 years of age (Fig. 29–40).

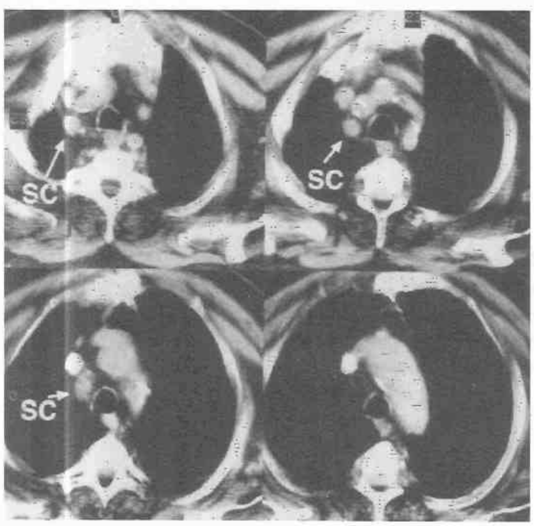

Figu[redacted]**9–39.** Tortu[redacted] great vessels. Contrast-enh[redacted]d CT shows tortuous right brachiocephalic and subclavian artery (SC) causing a right paratracheal "mass." Calcifications can be seen within the arterial wall.

The most useful measurement is the thickness of the lobes measured perpendicular to the long axis of the gland. The normal maximal thickness is 18 mm before age 20 years and 13 mm in older patients. Although these measurements are useful indicators of thymic abnormality, thymic shape is also important; focal contour abnormality of the thymus gland is a finding suggestive of an underlying abnormality.

On CT scans, the normal thymus manifests as a homogeneous, bilobed structure of soft tissue attenuation in the anterior mediastinum (Fig. 29–41). It is usually seen at the level of the aortic arch and the origin of the great vessels. The left lobe is usually slightly larger than the right. Rarely, a lobe is congenitally absent. The normal thymus is easily demonstrated on MRI (Fig. 29–42).

Characteristically, the thymus is homogeneous with intermediate signal intensity (less than that of fat) on T1-weighted images. Because the thymus begins to involute at puberty and is replaced by fat in older patients, the T1-weighted signal intensity of the thyroid increases with age. On T2-weighted images, the thymus shows high signal intensity similar to fat in all age groups and this can make its identification difficult in patients with abundant mediastinal fat.

Thymic masses, on occasion, can be difficult to distinguish from normal thymus.[244] Two important rules should be remembered:

1. Thymic masses usually manifest on CT or MRI as round masses and do not conform to the shape of the normal thymus.
2. Thymic masses usually show heterogeneous attenuation on CT with areas of decreased attenuation and possibly calcification.

Thymic Hyperplasia

Thymic hyperplasia can occur in association with hyperthyroidism, acromegaly, Addison's disease, and stress and in patients receiving chemotherapy or radiation therapy.[22, 79, 94, 153] Differentiating between hyperplasia and other causes of thymic enlargement can be difficult as there are no specific CT attenuation or MR signal intensity characteristics associated with hyperplasia. Thymic rebound or hyperplasia occurs in patients after chemotherapy or radiation therapy and it can be difficult to distinguish this enlargement from recurrent tumor. Generally, with rebound hyperplasia, the thymus has a normal shape and shows homogeneous attenuation on CT or homogeneous signal intensity on MR images (Fig. 29–43; see Fig. 29-40*B*). Asymmetry of the lobes, focal contour abnormalities, and heterogeneous signal intensity on MR or CT are suggestive of tumor.

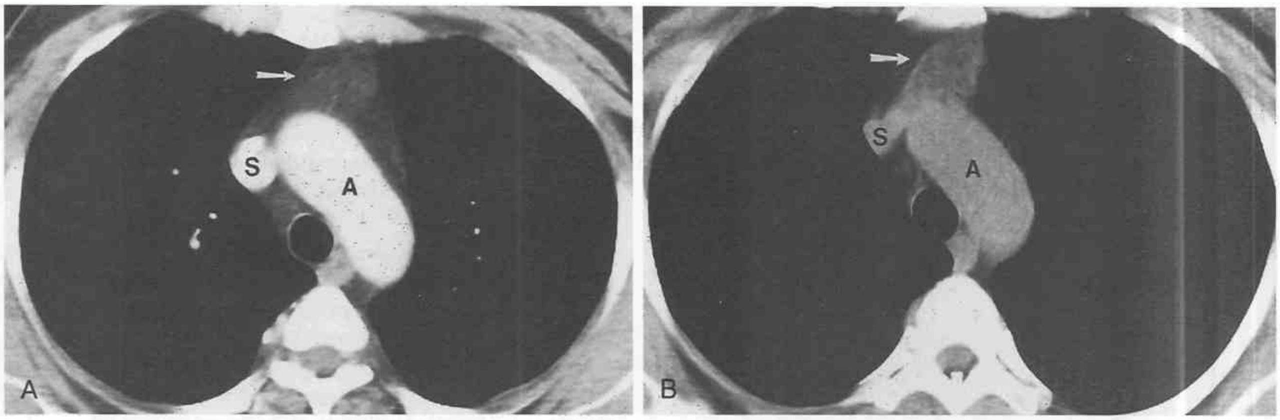

Figure 29–40. Thymus gland in a 42-year-old woman with breast carcinoma. *A,* Contrast-enhanced CT shows fatty replacement of thymus gland. Residual thymic tissue manifests as linear areas of soft tissue in anterior mediastinal fat *(arrow)*. *B,* Non–contrast-enhanced CT 6 months after bone marrow transplantation shows increased soft tissue in anterior mediastinum, consistent with thymic hyperplasia *(arrow)*. A, aorta; S, superior vena cava.

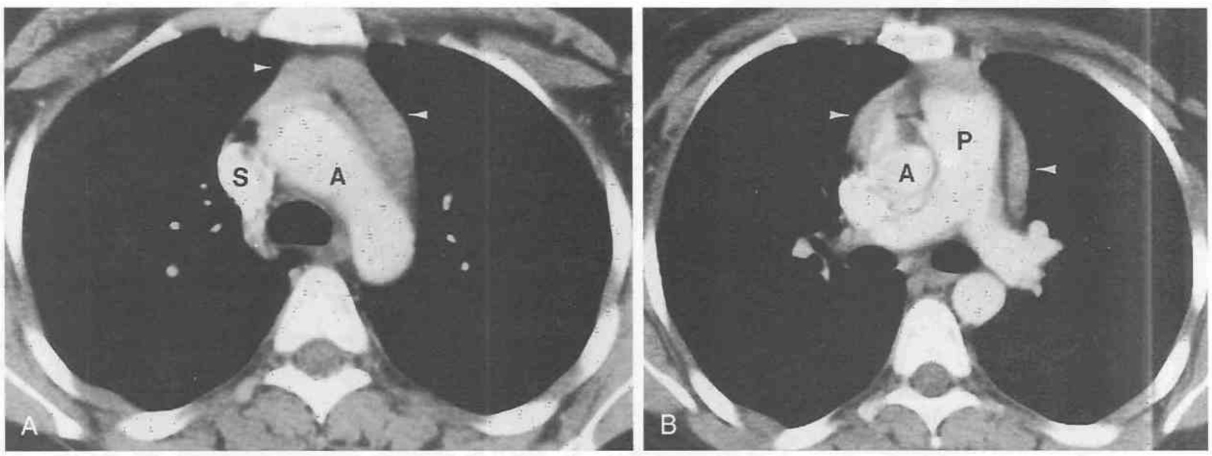

Figure 29–41. Normal thymus gland in a 17-year-old girl. *A* and *B,* Contrast-enhanced CT shows normal thymus gland in anterior mediastinum *(arrowheads)*. Homogeneous attenuation, smooth contours, and close association of lobes to vascular structures in the anterior mediastinum can be seen. A, aorta; P, main pulmonary artery; S, superior vena cava.

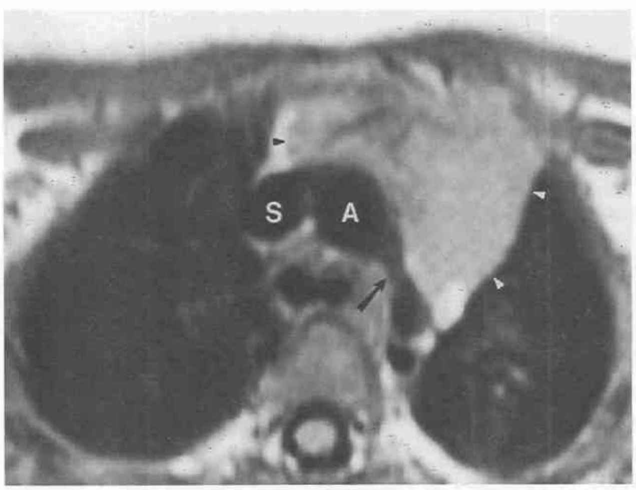

Figure 29–42. Normal thymus in 9-month-old child with coarctation of the aorta. Axial T1-weighted MR image shows thymus gland *(arrowheads)* in the mediastinum anterior to the aorta with homogeneous, intermediate signal intensity less than that of fat. The *arrow* indicates aortic coarctation. A, aorta; S, superior vena cava. (Case courtesy of Donald Frush, M.D., Duke University Medical Center, Durham, NC.)

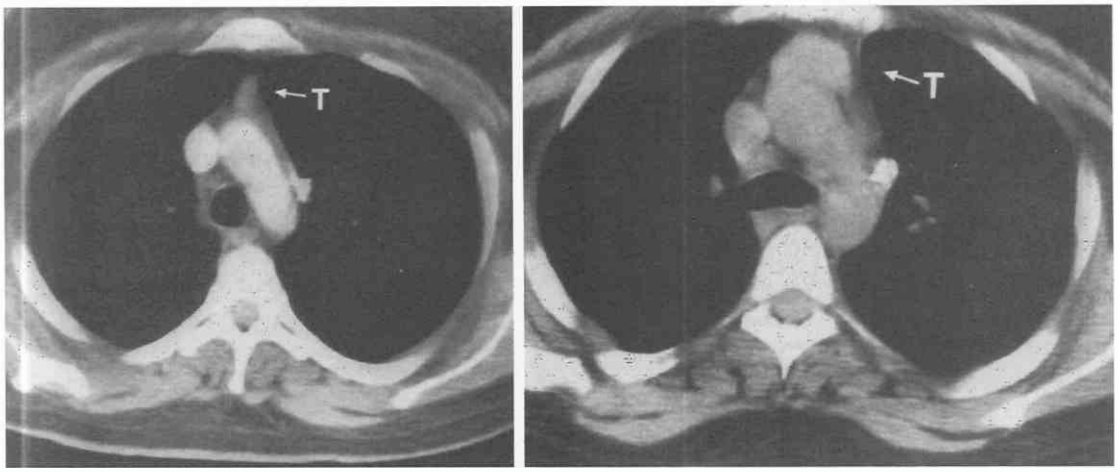

Figure 29–43. Thymic rebound. *A,* CT at the time of chemotherapy. The thymus (T) is small. *B,* CT after cessation of chemotherapy shows that the thymus (T) has increased in size.

Thymic Cysts

Thymic cysts comprise approximately 3% of all anterior mediastinal masses and are either congenital or secondary to inflammation or malignancy (Hodgkin's lymphoma, seminoma, thymic carcinoma).[18, 47, 89, 112, 118, 153, 168, 243, 246]

Congenital thymic cysts most likely arise from remnants of the thymopharyngeal duct and are usually thin-walled, unilocular lesions less than 6 cm in diameter. On CT, they are homogeneous, show the attenuation of water, and have very thin or imperceptible walls. On MRI, they manifest as well-circumscribed, anterior mediastinal masses of high signal intensity on T2-weighted images. Signal intensity usually increases with increasing TR. Occasionally, thymic cysts appear as solid masses on CT because they are filled with proteinaceous fluid. In these cases, MRI can be useful for confirming the cystic nature of the lesion (Fig. 29–44).

Acquired thymic cysts occur in the setting of inflammation or malignancy. Associated malignancies include Hodgkin's lymphoma, seminoma, thymoma, and thymic carcinoma (Fig. 29–45). These cysts usually have walls of variable thickness, are multilocular, and range in size from 3 to 17 cm in diameter. These cysts can contain hemorrhage or calcification. As such, the CT and MR features of acquired thymic cysts are more variable than those of congenital thymic cysts.

Because of their association with thymic neoplasia, care must be taken in the interpretation of cystic lesions of the anterior mediastinum (see Fig. 29–45). A thymic cyst must be evaluated further (by biopsy or resection) to exclude malignancy if it fits any of the following descriptions:

- Multilocular
- Heterogeneous
- Thick-walled
- Associated with a soft tissue component

Thymolipoma

Thymolipomas are rare, benign, slowly growing neoplasms of the anterior mediastinum.[153, 213, 232, 267] They occur with equal incidence in men and women and, although the age range of presentation is wide, most are diagnosed in young adults. On CT, these masses are typically large, show the attenuation of homogeneous fat, and conform to adjacent structures. They are not locally invasive although compression of adjacent structures occurs in approximately 50% of patients. Because they consist of fat and residual thymic tissue, thymolipomas usually show high signal intensity (similar to fat) with interspersed areas of intermediate signal intensity on both T1-weighted and T2-weighted MR images.

Thymoma

Thymomas account for approximately 20% of all mediastinal tumors and are the most common primary tumor of the anterior mediastinum.* Seventy-five percent of thymomas occur in the anterior mediastinum, 15% occur in both the anterior and superior mediastinum, and 6% occur in the superior mediastinum. Another 4% occur ectopically, with the posterior mediastinum being the least common location.

Although thymomas can occur in children, most patients are older than 40 years at presentation. Seventy percent of affected patients present in the fifth and sixth decades of life. The incidence in men and women is the same. Most affected patients are asymptomatic at presentation, and the lesion is detected on routine chest radiographs. Chest pain, cough, and symptoms related to compression of adjacent structures occur in approximately 33% of patients.

Paraneoplastic syndromes are common and include myasthenia gravis (50%), hypogammaglobulinemia (10%), and pure red blood cell aplasia (5%). Although up to 50% of patients with thymoma have myasthenia gravis, only 10% to 20% of patients with myasthenia gravis have a thymoma; however, 65% of these patients have lymphoid hyperplasia of the thymus. Because of the strong association between myasthenia gravis and thymoma, CT is commonly performed in patients with symptoms of myasthenia gravis even if the chest radiograph is normal.

Thymomas are usually 5 to 10 cm in diameter and are

*See References 60, 150, 153, 173, 178, 212, 217, 243, 250, 254, and 264.

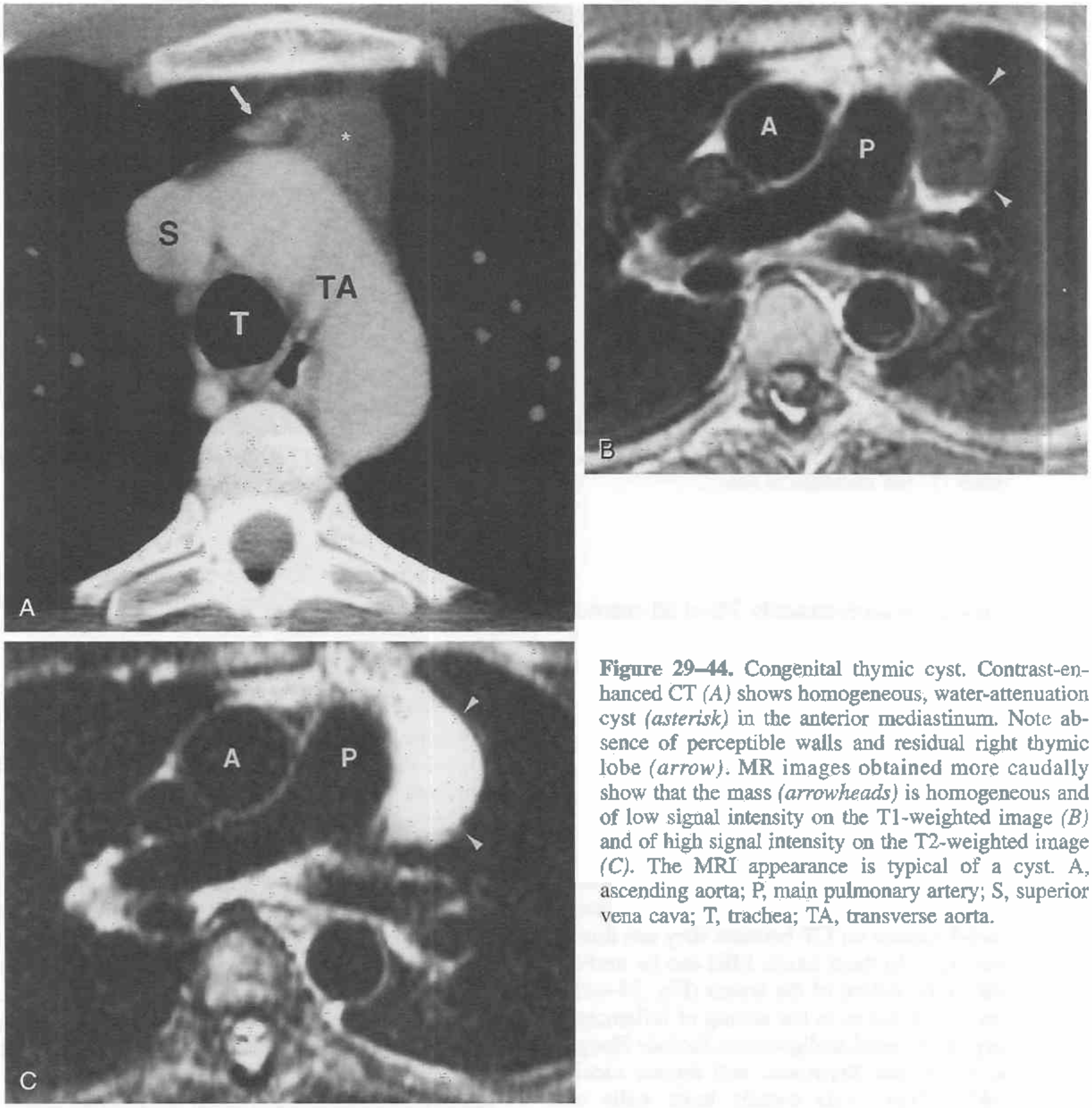

Figure 29–44. Congenital thymic cyst. Contrast-enhanced CT *(A)* shows homogeneous, water-attenuation cyst *(asterisk)* in the anterior mediastinum. Note absence of perceptible walls and residual right thymic lobe *(arrow)*. MR images obtained more caudally show that the mass *(arrowheads)* is homogeneous and of low signal intensity on the T1-weighted image *(B)* and of high signal intensity on the T2-weighted image *(C)*. The MRI appearance is typical of a cyst. A, ascending aorta; P, main pulmonary artery; S, superior vena cava; T, trachea; TA, transverse aorta.

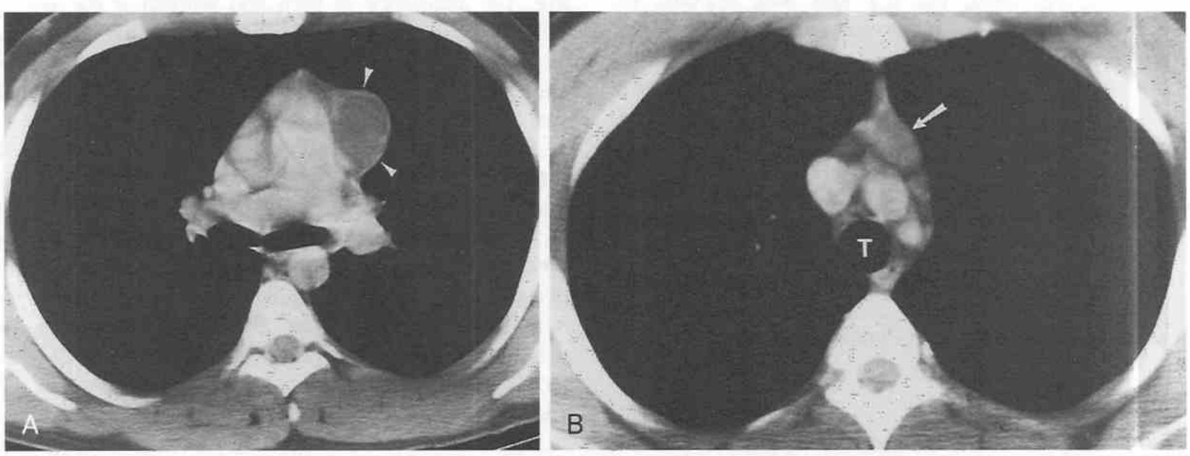

Figure 29–45. Seminoma associated with a thymic cyst. *A*, Contrast-enhanced CT shows well-circumscribed water-attenuation mass in anterior mediastinum. The wall *(arrowheads)* is thin but perceptible. *B*, A more cephalic image reveals a soft tissue component of the mass *(arrow)*. Resection revealed the seminoma. T, trachea.

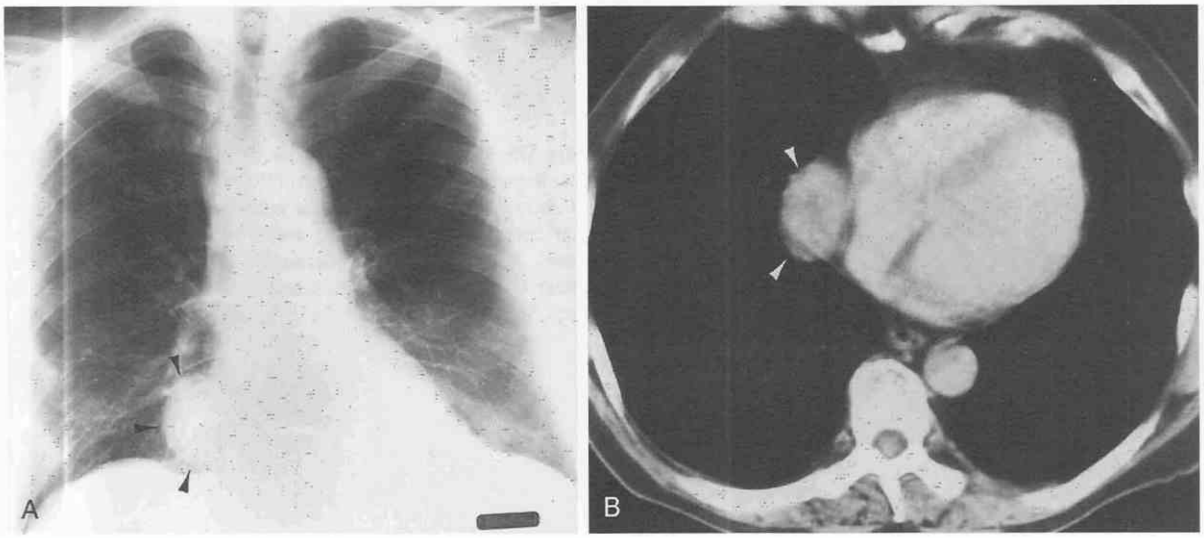

Figure 29–46. Thymoma in a patient with myasthenia gravis. *A*, Posteroanterior chest radiograph shows mass in the right cardiophrenic angle *(arrowheads)*. *B*, Contrast-enhanced CT confirms well-circumscribed heterogeneous cardiophrenic-angle mass *(arrowheads)*. Resection revealed the thymoma.

well marginated, smooth or lobulated mediastinal masses that characteristically arise from one lobe of the thymus. They are usually located anterior to the aortic arch but can occur in the cardiophrenic angle (Fig. 29–46). Most lesions are homogeneous, but necrosis and hemorrhage occur in up to one third.

On CT or MRI scans, thymomas typically manifest as smooth or lobulated masses that distort the normal contour of the thymus (Fig. 29–47). They are typically unilateral masses, although bilateral mediastinal involvement can occur. On CT they can manifest as homogeneous or heterogeneous soft tissue–attenuation masses. Intratumoral cysts or areas of necrosis may be seen. Enhancement following IV administration of contrast material is variable. Calcification, seen in up to 7% of cases, is usually thin, linear, and located in the capsule. On MR images, thymomas manifest with low to intermediate signal intensity (similar to skeletal muscle) on T1-weighted images and high signal intensity on T2-weighted images. Because up to 33% of thymomas have focal areas of necrosis, hemorrhage, and cystic change, the masses can have heterogeneous signal intensity. MRI can occasionally reveal fibrous septa within the masses.

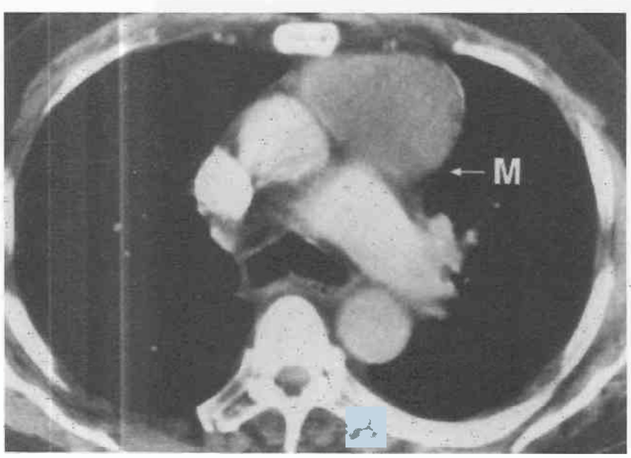

Figure 29–47. Thymoma. Contrast-enhanced CT shows large anterior mediastinal mass (M) anterior to aorta and pulmonary artery. Main pulmonary artery is displaced posteriorly.

Up to 34% of thymomas show local invasion. Such lesions are best termed invasive thymomas rather than malignant thymomas. Histologic features and size do not seem to affect the propensity for invasive behavior. Furthermore, it can be quite difficult to predict biologic behavior of thymomas on the basis of CT or MRI findings alone. Surgical exploration is the most reliable means of determining invasion. Findings that suggest invasive thymoma on CT or MRI include the following (Figs. 29–48 to 29–50):

1. Poorly defined or infiltrative margins.
2. Definite vascular or chest wall invasion.
3. Irregular interface with adjacent lung.
4. Evidence of spread to ipsilateral pleura.

Pleural spread manifests either as isolated pleural nodules ("drop metastases") or as a contiguous pleural mass, often mimicking mesothelioma. Transdiaphragmatic spread may occur; hence, staging MR or CT studies should include the upper abdomen. Pleural effusion is uncommon despite the frequent occurrence of pleural metastases.

Thymic Carcinoma

Thymic carcinomas account for 20% of thymic tumors.[51, 60, 97, 142, 182, 201, 243, 263] They are aggressive malignancies that often exhibit marked local invasion and early dissemination to regional lymph nodes and distant sites. Distant metastases (to lung, liver, brain, and bone) are detected in 50% to 65% of patients at presentation. Tissue studies typically reveal squamous cell carcinoma and lymphoepithelioma-like carcinoma. Symptoms (chest pain, dyspnea, cough, SVC syndrome) are usually the result of

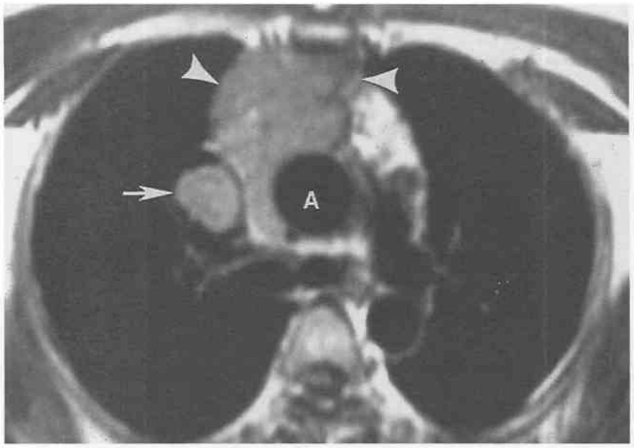

Figure 29–48. Invasive thymoma in a patient with symptoms of superior vena cava (SVC) obstruction. Axial T1-weighted MR images show infiltrative soft tissue mass *(arrowheads)* of intermediate signal intensity encasing the aorta and extending into the SVC *(arrow)*. A, aorta. (From Erasmus JJ, McAdams HP, Donnelly LF, Spritzer CE: MR imaging of mediastinal masses. Magn Reson Imaging Clin North Am 8:59–89, 2000.)

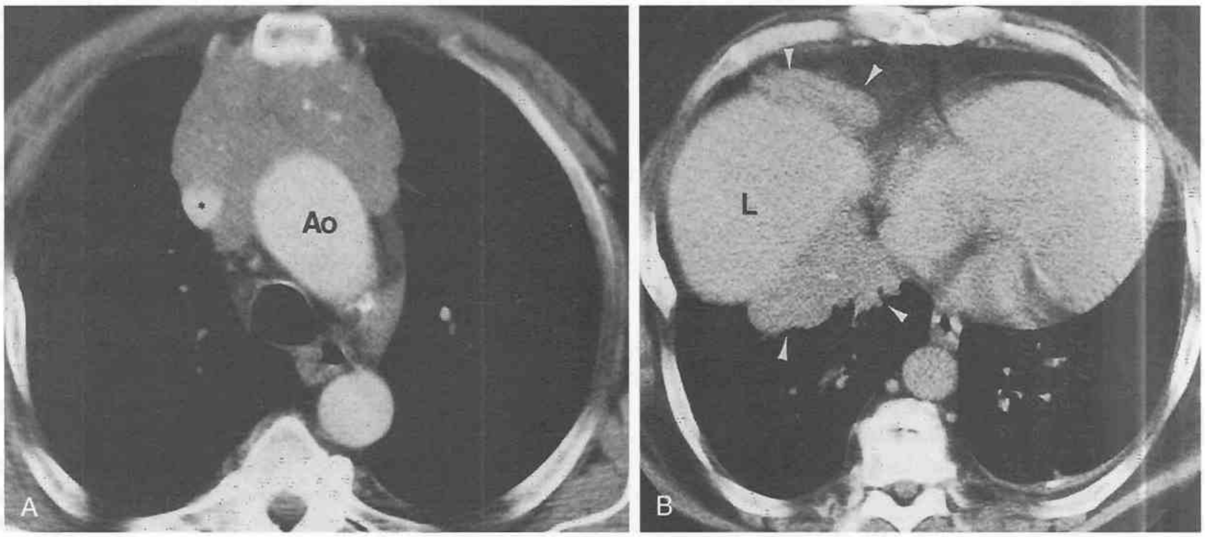

Figure 29–49. Invasive thymoma. *A* and *B,* Contrast-enhanced CT shows heterogeneous anterior mediastinal mass with focal areas of calcification. Note mass extension between superior vena cava *(asterisk)* and ascending aorta (Ao in *A*) and contiguous extension to hemidiaphragm (*arrowheads* in *B*). L, liver.

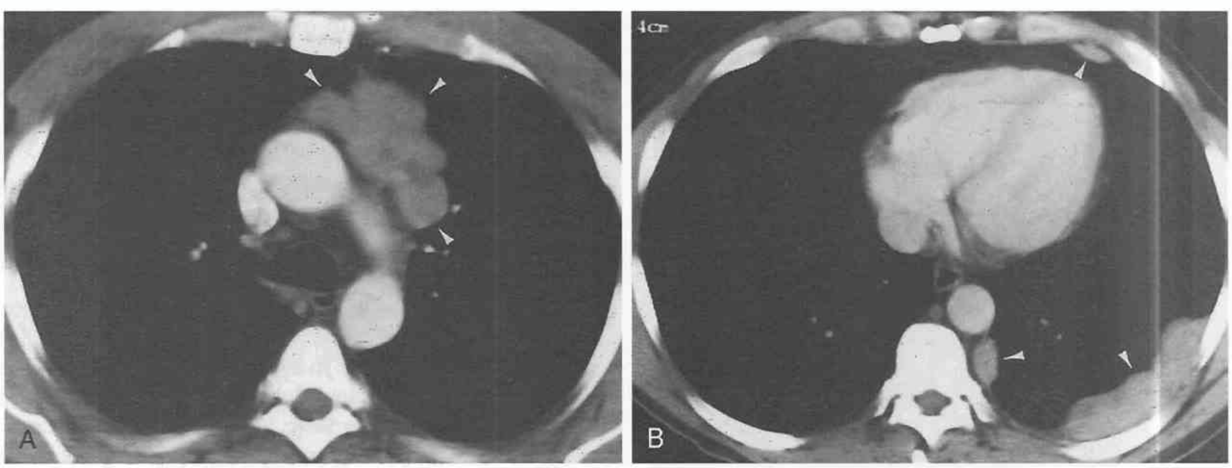

Figure 29–50. Invasive thymoma with pleural metastases. *A* and *B,* Contrast-enhanced CT shows lobular heterogeneous mass (*arrowheads* in *A*) in anterior mediastinum. Noncontiguous pleural metastases ("drop metastases") (*arrowheads* in *B*) are present in the left hemithorax.

compression or invasion of adjacent structures and, unlike thymomas, paraneoplastic syndromes are rare.

Radiologically, thymic carcinomas usually manifest as large, poorly marginated anterior mediastinal masses and are frequently associated with intrathoracic lymphadenopathy and pleural and pericardial effusions. Focal pleural implants are uncommon. On CT, they usually show heterogeneous attenuation and have poorly defined, infiltrative margins (Fig. 29–51). On MRI, they typically show intermediate signal intensity (slightly higher than skeletal muscle) on T1-weighted images and high signal intensity on T2-weighted images. Signal intensity can be heterogeneous because of hemorrhage and necrosis within the masses. MRI can be helpful for revealing local soft tissue and vascular invasion.

Neuroendocrine Tumors of the Thymus

Neuroendocrine tumors are uncommon lesions of the anterior mediastinum.[34, 35, 131, 132, 211] These tumors have varying malignant potential that ranges from relatively benign (thymic carcinoid) to highly malignant (small cell carcinoma of the thymus). Thymic carcinoid tumor is the most common of this group of tumors. Affected patients are typically in the fourth and fifth decades of life; there is a male predominance. Up to 50% of affected patients have hormonal abnormalities and up to 35% have Cushing's syndrome because of tumoral production of adrenocorticotropic hormone (ACTH). Nonfunctioning thymic carcinoids may be seen in association with the multiple endocrine neoplasia syndrome, type 1.

Radiologically, these tumors typically manifest as large masses with a propensity for local invasion. Focal areas of necrosis and punctate calcification may be present. On CT or MRI, the masses usually show heterogeneous attenuation or signal intensity, respectively (Fig. 29–52).

Germ Cell Tumors

Germ cell tumors (teratomas, seminomas, embryonal carcinomas, endodermal sinus tumors, and choriocarcinomas) are thought to arise from mediastinal remnants of embryonal cell migration.[50, 143, 148, 149, 187, 188, 214, 243, 258] They comprise 10% to 15% of anterior mediastinal tumors. The mediastinum is the most common extragonadal primary site of these lesions, and mediastinal lesions account for 60% of all germ cell tumors in adults. Germ cell tumors usually occur in young adults (mean age, 27 years). Most malignant germ cell tumors (>90%) occur in men, whereas benign lesions (mature teratomas) occur with equal incidence in men and women.

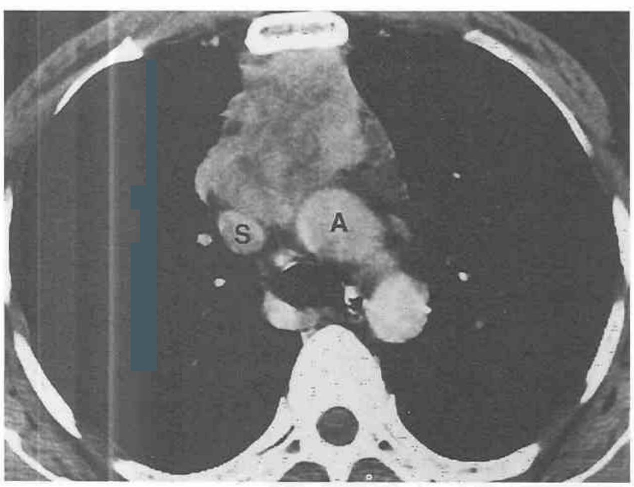

Figure 29–51. Thymic carcinoma. Contrast-enhanced CT shows heterogeneous mass in anterior mediastinum. Low-attenuation regions are consistent with necrosis. A, aorta; S, superior vena cava.

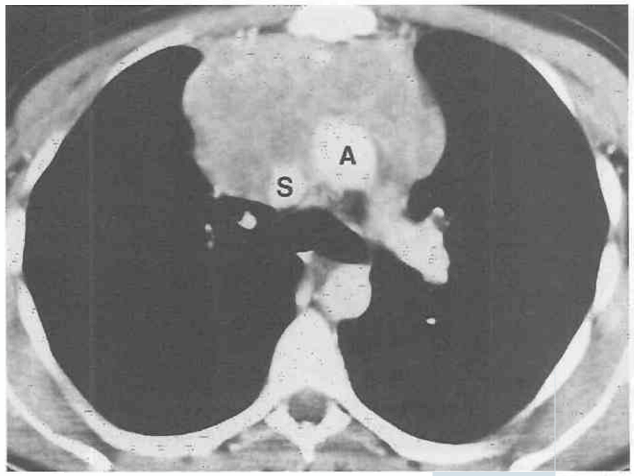

Figure 29–52. Thymic carcinoid. Contrast-enhanced CT shows large anterior mediastinal mass. The mass appears heterogeneous, and infiltration of mediastinum can be seen, with extension of the mass between vascular structures. A, aorta; S, superior vena cava.

Mediastinal Teratoma

Teratomas, the most common mediastinal germ cell tumors, are composed of elements that arise from more than one of the three primitive germ cell layers.[46, 72, 108, 149, 170, 187, 216, 220, 243] These tumors are classified as (1) mature, (2) immature, or (3) malignant.

Mature or benign teratomas are composed of different tissue types (ectoderm, endoderm, mesoderm), with ectodermal derivatives predominating. The term *dermoid cyst* is commonly applied to the tumors in which the ectodermal components predominate. Mature teratomas are common, accounting for 70% of germ cell tumors in childhood and 60% of mediastinal germ cell tumors in adults. Mature teratomas occur most frequently in children and young adults. Patients can be asymptomatic, but chest pain, dyspnea and cough, caused by compression of adjacent structures, are common symptoms. By definition, patients with mature teratoma have normal serum levels of β-human chorionic gonadotropin hormone (β-hCG) and alpha-fetoprotein (AFP); elevation of either of these markers implies a malignant component. Complete resection is the treatment for teratomas and results in a complete cure. Although they are benign, these tumors may be difficult to remove because they are adherent to local structures.

Teratomas typically occur in the anterior mediastinum, although occurrence at other sites, including the middle and posterior mediastinum, accounts for up to 20% of cases. Mature teratomas manifest on CT or MRI as smooth

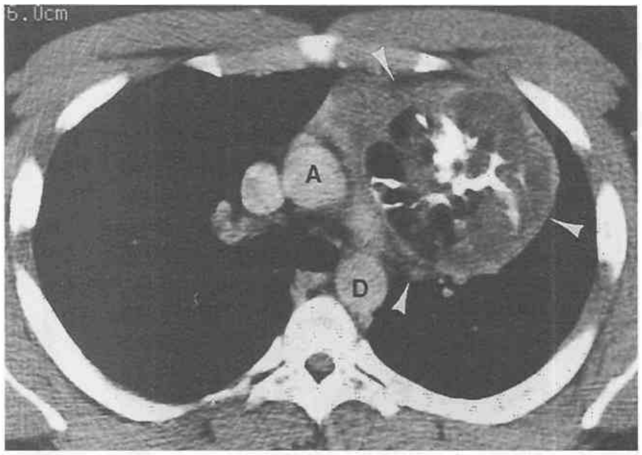

Figure 29–53. Mature teratoma. Contrast-enhanced CT shows large anterior mediastinal mass *(arrowheads)*. The mass, which is composed of fat, calcium, and fluid, is heterogeneous in attenuation. The CT appearance is typical of a mature teratoma. A, ascending aorta; D, descending aorta.

or lobulated mediastinal masses that typically have cystic and solid components, whereas malignant teratomas are usually poorly marginated masses containing areas of necrosis.

The combination of fluid, soft tissue, calcium, or fat is diagnostic of a teratoma (Fig. 29–53); the finding of a fat-fluid level within a mass on CT or MRI is also diagnostic. Fat occurs in up to 75% of mature teratomas and up to 40% of malignant teratomas; however, only 17% to 39% of mature teratomas have all the tissue components, and approximately 15% of mature teratomas manifest only a unilocular or multilocular cystic component (Fig. 29–54). Because of the varying composition of soft tissue, fat, calcium, and hemorrhage, MRI typically demonstrates heterogeneous signal intensity and this finding can be useful in differentiating teratomas from thymomas and lymphomas.

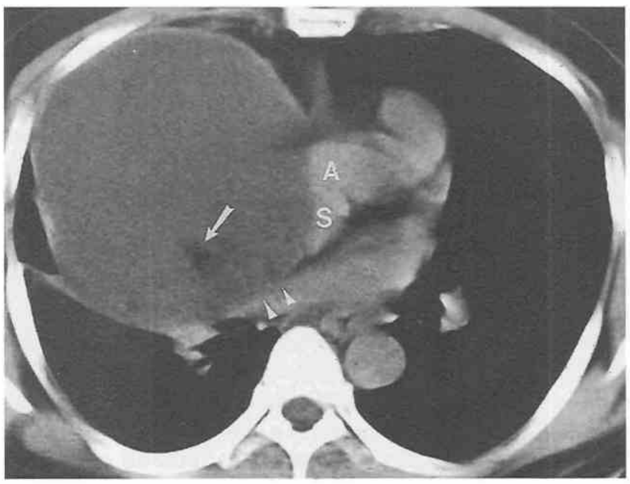

Figure 29–54. Mature teratoma. CT shows a large, predominantly water-attenuation, anterior mediastinal mass with a small focal area of fat *(arrow)*. Mass effect can be visualized on the superior vena cava (S) and the superior pulmonary vein *(arrowheads)*. A, ascending aorta.

Mature teratomas have been reported to rupture into lung, pleural space, and pericardium in up to 33% of patients, and CT or MRI can be useful in detecting fat within these regions.

Seminoma

Seminoma is the most common pure histologic type of malignant mediastinal germ cell tumor in men and accounts for 40% of such tumors.[10, 143, 175, 177, 231, 243] Affected patients are usually in the third and fourth decades of life and are symptomatic at presentation. β-hCG and AFP levels are normal; elevation of AFP indicates a nonseminomatous component of the tumor. On CT or MRI, seminomas manifest as large lobulated masses showing homogeneous attenuation or signal intensity in the anterior mediastinum (Fig. 29–55). Cysts or areas of necrosis may also be seen in association with mediastinal seminoma (see Fig. 29–45). Invasion of adjacent structures is uncommon and calcification is rare. Metastases to regional nodes may occur.

Nonseminomatous Germ Cell Malignancies

The nonseminomatous germ cell tumors of the mediastinum include embryonal cell carcinoma, endodermal sinus tumor, choriocarcinoma, and mixed germ cell tumors.[133, 148, 175] Teratoma with embryonal cell carcinoma (teratocarcinoma) is the next most common subtype, with pure endodermal sinus tumor, choriocarcinoma, and embryonal carcinoma being much less common. Most patients with malignant nonseminomatous germ cell tumors are symptomatic at presentation, with chest pain, cough, dyspnea, weight loss, and fever. Up to 80% of affected patients have elevated levels of AFP and 54% have elevated levels of β-hCG. An association exists between malignant nonseminomatous germ cell tumors of the mediastinum and hematologic malignancies. Up to 20% of affected patients have Klinefelter's syndrome.

On CT or MRI, these tumors manifest as large, poorly marginated masses showing heterogeneous attenuation or signal intensity (Figs. 29–56 and 29–57). Invasion of the adjacent mediastinal structures, chest wall, and lung, as

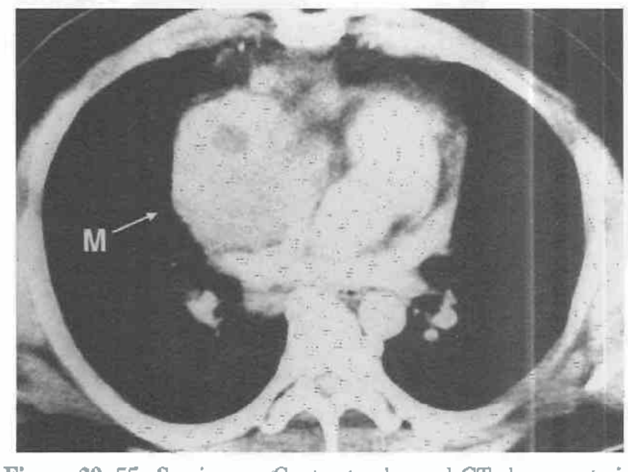

Figure 29–55. Seminoma. Contrast-enhanced CT shows anterior mediastinal mass (M) with a central area of low attenuation consistent with necrosis.

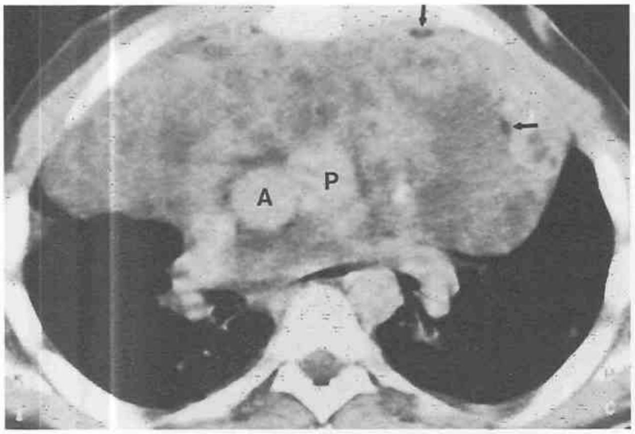

Figure 29–56. Malignant teratoma. Contrast-enhanced CT shows a large anterior mediastinal mass. The mass is heterogeneous in attenuation with components of soft tissue, fluid, calcium, and fat *(arrows)*. The mediastinal invasion is diffuse. A, aorta; P, pulmonary artery.

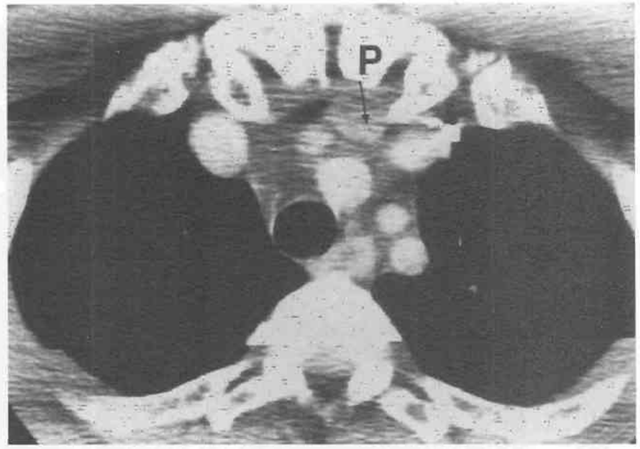

Figure 29–58. Ectopic parathyroid adenoma. CT shows a soft tissue mass in a patient who had undergone neck dissection for hyperparathyroidism with persistently elevated serum calcium. The parathyroid gland (P) is ectopic, located posterior to manubrium.

well as metastases to the regional lymph nodes and distant sites, is common.

Parathyroid Adenoma

Because neck exploration for parathyroid gland removal is curative in over 90% of patients with primary hyperparathyroidism, surgeons often do not obtain preoperative imaging studies to localize the parathyroid glands; however, 10% of parathyroid adenomas are ectopic in location and the majority of ectopic adenomas are located either in the region of the tracheoesophageal groove or in the anterior mediastinum.* Such ectopic adenomas can be missed at surgical exploration. Preoperative localization of ectopic parathyroid adenomas can reduce operative time, postoperative morbidity, and the need for a subsequent surgical procedure.

*See References 1, 8, 114–116, 120, 127, 135, 145, 146, 189, 221, 239, and 241.

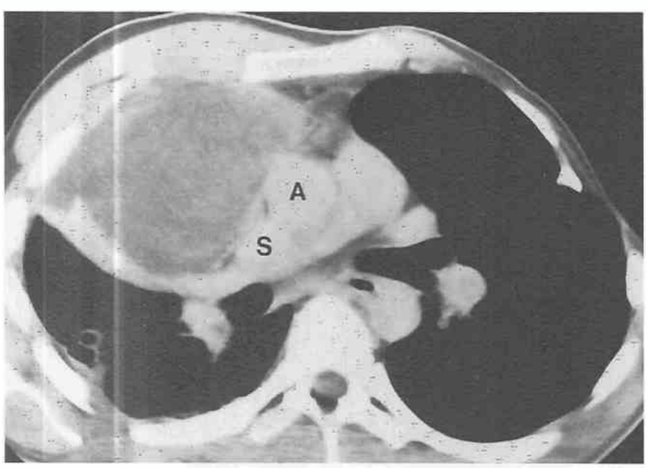

Figure 29–57. Nonseminomatous germ cell malignancy. CT shows large mixed-attenuation anterior mediastinal mass. Transthoracic needle aspiration biopsy revealed endodermal sinus tumor. The left pectoralis major muscle is absent, consistent with Poland syndrome. A, aorta; S, superior vena cava.

Imaging techniques for localizing abnormal parathyroid glands include sonography, radionuclide imaging (technetium-99m–sestamibi [^{99m}Tc-MIBI], ^{99m}Tc-tetrofosmin), CT, and MRI. On CT, ectopic mediastinal parathyroid glands manifest as 1- to 2-cm rounded masses that may resemble lymph nodes (Fig. 29–58). CT or MRI can detect these glands, but careful evaluation is required so that small lesions are not overlooked.

MRI is accurate in identifying abnormal parathyroid glands in ectopic locations. Functioning parathyroid adenomas show intermediate signal intensity on T1-weighted images and usually show marked increased signal intensity on T2-weighted images (Fig. 29–59). Similar findings are seen in cases of parathyroid hyperplasia and carcinoma. Up to 13% of abnormal glands, however, do not show high signal intensity on T2-weighted images because of fibrosis or hemorrhage. Although MR is comparable or superior to other imaging modalities for detecting parathyroid disease (sensitivity, 78%; specificity, 90%; accuracy, 90%), the most appropriate role of MRI is as an adjunct to ^{99m}Tc-MIBI radionuclide imaging. In this setting MRI provides accurate anatomic location of the adenoma and can be useful in predicting the need for mediastinotomy or lateral cervical incision.

Although the precise role of imaging in the evaluation of a virgin neck for hyperparathyroidism may be debated, imaging is useful in second-look procedures and in those patients considered to be at high risk for surgery. In this population, the success rate for surgery is reduced, ranging from 64% to 90%, and the combined use of ^{99m}Tc-MIBI and MRI has been shown to be 89% sensitive and 95% specific for preoperative localization.

Lymphatic Malformations

Lymphatic malformations (previously called lymphangiomas) are rare benign lesions that comprise 0.7% to 4.5% of all mediastinal tumors.[123, 185, 197, 225, 230, 233, 268] Approxi-

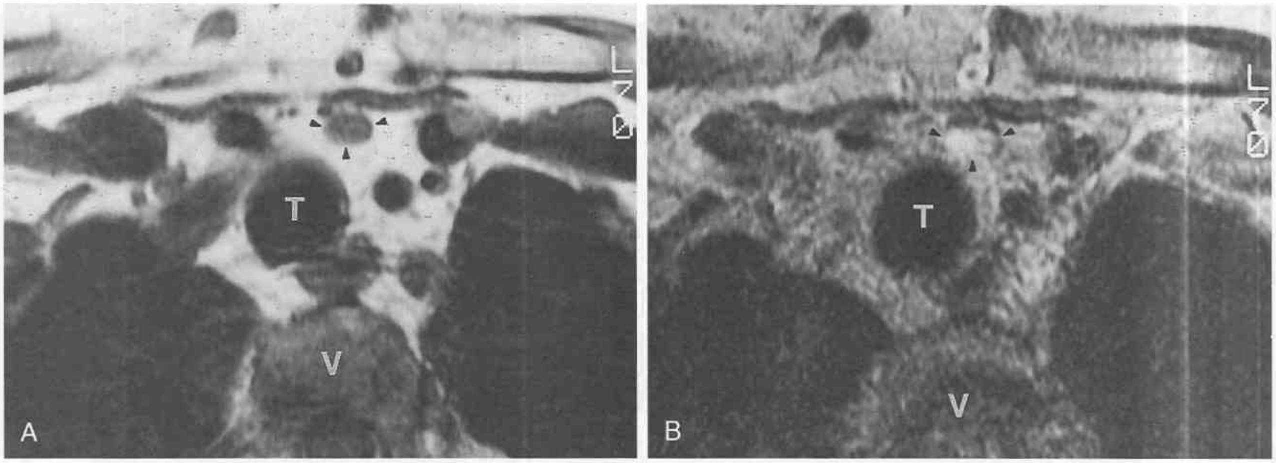

Figure 29–5[redacted]thyroid adenoma in a woman with persistent hyperparathyroidism after surgical neck exploration. MR images show 1-cm mass *(arrowheads)* in anterior mediastinum with intermediate signal intensity (similar to muscle) on T1-weighted image (*A*) and high signal intensity on T2-weighted image (*B*). MR appearance is typical of parathyroid adenoma. T, trachea; V, vertebral body. (Reprinted with permission from Erasmus JJ, McAdams HP, Donnelly LF, Spritzer CE: MR imaging of mediastinal masses. Magn Reson Imaging Clin North Am 8:59–89, 2000.)

mately 75% occur in the neck, 20% in the axillary region, and 5% in the mediastinum. Primary mediastinal lymphatic malformations are rare and most mediastinal lesions are the result of tumor extension from the neck. Lymphatic malformations are usually located in the superior and anterior mediastinum, although they can occur in any mediastinal compartment. They usually occur in patients less than 2 years old and there is a male predominance. In adults, lymphatic malformations are usually located in the mediastinum and are often the result of recurrence of an incompletely resected childhood tumor.

On CT, these lesions manifest as lobular, multicystic tumors that surround and infiltrate adjacent mediastinal structures (Fig. 29–60). They can appear solid on CT because of protein or hemorrhage within the cysts. The cysts are typically 1 to 2 cm in diameter, and the septa may enhance following administration of IV contrast material.

MRI can be useful in confirming the cystic nature of these lesions; lymphatic malformations usually show markedly increased signal intensity on T2-weighted images. Their appearance on T1-weighted sequences is more variable, although most show low to intermediate signal intensity (similar to skeletal muscle) and can contain focal areas of signal intensity higher than that of muscle. Occasionally, lymphatic malformations show high signal intensity similar to that of fat on T1-weighted images.

Because surgical resection is the treatment of choice, multiplanar MRI can be useful in preoperative evaluation of local invasion and determination of anatomic extent of tumor.

Hemangiomas

Hemangiomas are rare mediastinal tumors that account for less than 0.5% of all mediastinal masses.[117, 121, 163, 223, 224]

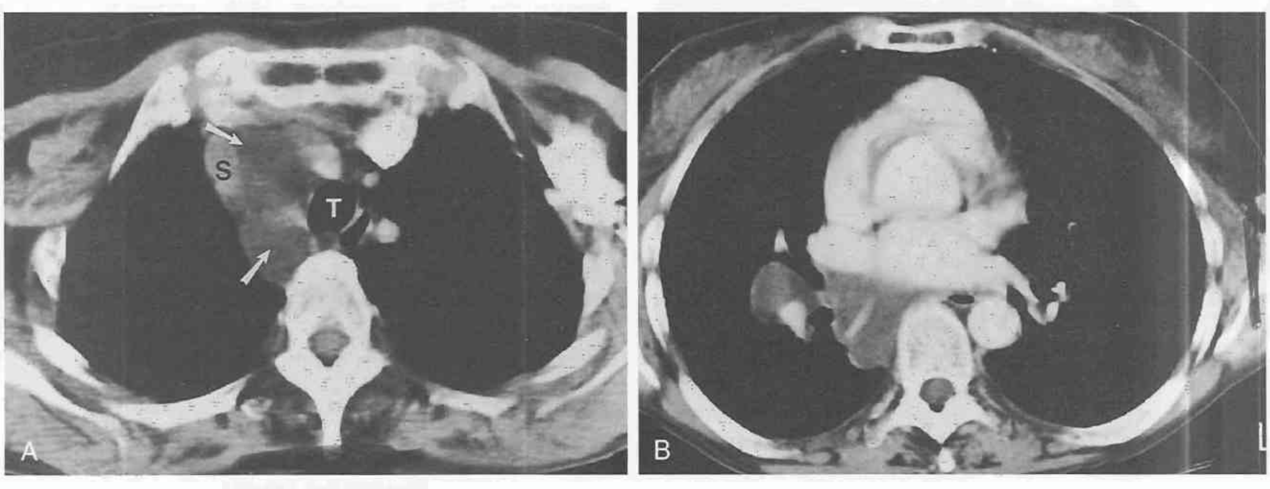

Figure 29–60. Lymphan[redacted]nhanced CT shows homogeneous, water-attenuation mass *(arrows)* in superior mediastinum, which arose in the [redacted]na cava; T, trachea. *B*, The mass diffusely infiltrates mediastinum and extends into the right hilum.

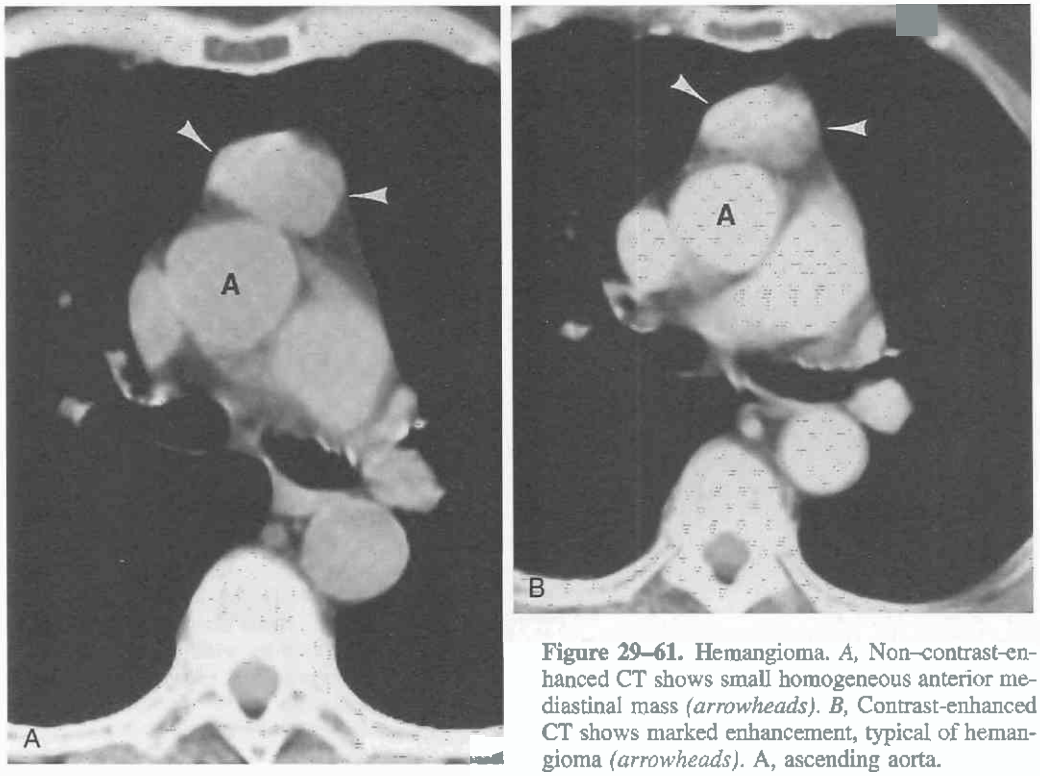

Figure 29–61. Hemangioma. *A,* Non–contrast-enhanced CT shows small homogeneous anterior mediastinal mass *(arrowheads). B,* Contrast-enhanced CT shows marked enhancement, typical of hemangioma *(arrowheads).* A, ascending aorta.

Mediastinal hemangiomas usually occur in the anterior (68%) or posterior mediastinum (22%), although multicompartment involvement occurs in up to 14% of cases. Most mediastinal lesions are cavernous hemangiomas and are composed of large interconnecting vascular spaces with varying amounts of interposed stromal elements such as fat and fibrous tissue. Focal areas of organized thrombus can calcify as phleboliths.

On radiographs, hemangiomas manifest as sharp, smoothly marginated mediastinal masses. Phleboliths are seen in less than 10% of cases. CT typically reveals a heterogeneous mass with intense central or peripheral rimlike enhancement after administration of IV contrast material (Fig. 29–61). Hemangiomas typically show heterogeneous signal intensity on T1-weighted images. In lesions with significant stromal fat, linear areas of increased signal intensity on T1-weighted images can occasionally be identified. The central vascular lakes typically become markedly hyperintense on T2-weighted images, a suggestive feature (Fig. 29–62).

Middle Mediastinal Abnormalities

Lesions that occur primarily in the middle mediastinum include esophageal lesions, airway lesions, foregut duplication cysts, and pericardial cysts.

Esophagus

Esophageal Cancer

CT is used to help stage esophageal carcinoma by demonstrating the following (Fig. 29–63):*

- Thickness of the esophageal wall
- Length of the lesion
- Involvement of adjacent structures such as airway, aorta, pericardium, and spine
- Nodal spread to regional mediastinal, celiac, and gastrohepatic ligament nodes

Endoscopy, endoscopic ultrasound, and esophagography are also helpful in staging esophageal carcinoma. Invasion of local structures is common because the esophagus lacks a serosa. CT and MRI can both overestimate or underestimate the degree of local invasion because the lack of normal fat planes between the esophagus and adjacent structures makes invasion difficult to determine.

Anterior displacement of the carina or left main bronchus suggests airway invasion; contact with the aorta that exceeds one quarter of the aortic circumference suggests the possibility of aortic invasion. All imaging findings must be interpreted in conjunction with the patient's clinical status when planning treatment. CT is also useful in planning radiation treatment ports and for imaging complications resulting from esophagectomy.

The normal esophagus is not optimally demonstrated on MRI because of peristaltic motion and relatively poor spatial resolution. Distinguishing small mucosal tumors from normal esophagus is difficult because both show intermediate signal intensity on T1-weighted images and high signal intensity on T2-weighted images. The role of MRI for intrathoracic staging of esophageal neoplasms is limited. Although some authors have reported high intrathoracic staging accuracy for MRI, most reports suggest that MRI is no better than CT in this regard. MRI can be useful as a problem-solving modality, however, when invasion of pericardium or heart is suspected on CT or if the patient is allergic to iodinated contrast material.

---

*See References 73, 93, 109, 144, 147, 153, 179, 196, 202, 207, and 248.

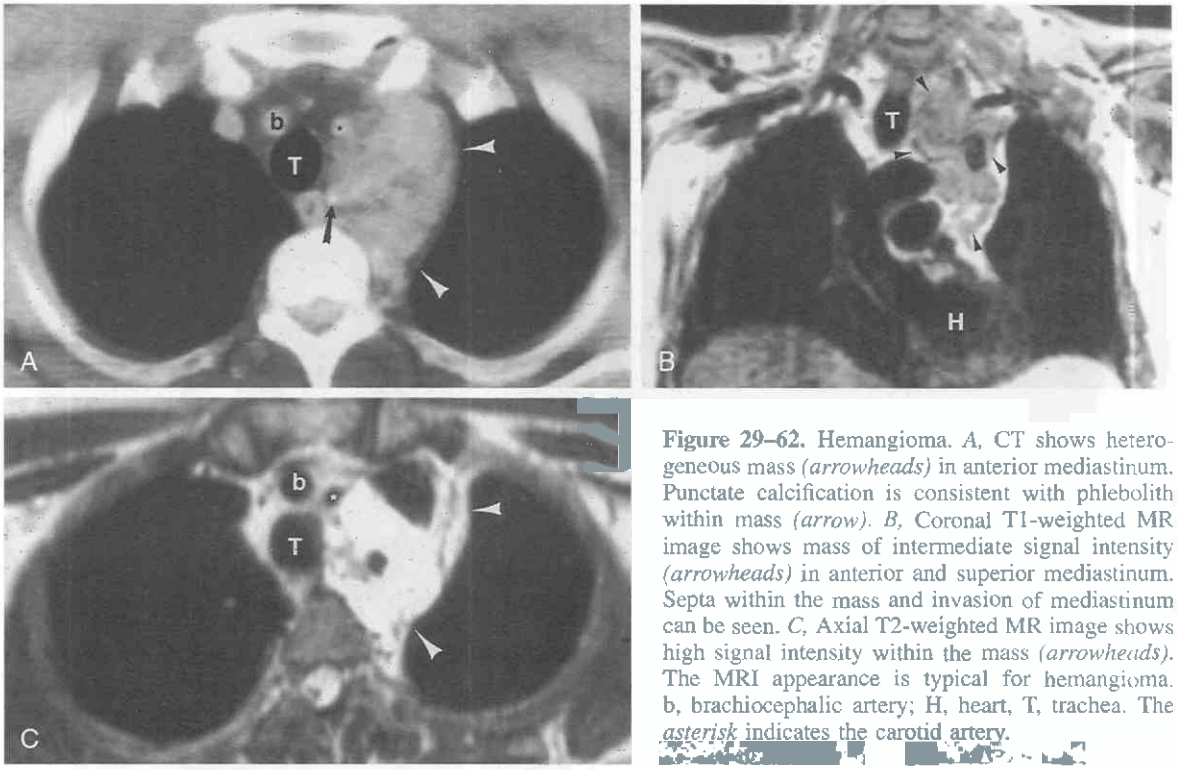

Figure 29–62. Hemangioma. *A,* CT shows heterogeneous mass *(arrowheads)* in anterior mediastinum. Punctate calcification is consistent with phlebolith within mass *(arrow). B,* Coronal T1-weighted MR image shows mass of intermediate signal intensity *(arrowheads)* in anterior and superior mediastinum. Septa within the mass and invasion of mediastinum can be seen. *C,* Axial T2-weighted MR image shows high signal intensity within the mass *(arrowheads).* The MRI appearance is typical for hemangioma. b, brachiocephalic artery; H, heart, T, trachea. The *asterisk* indicates the carotid artery.

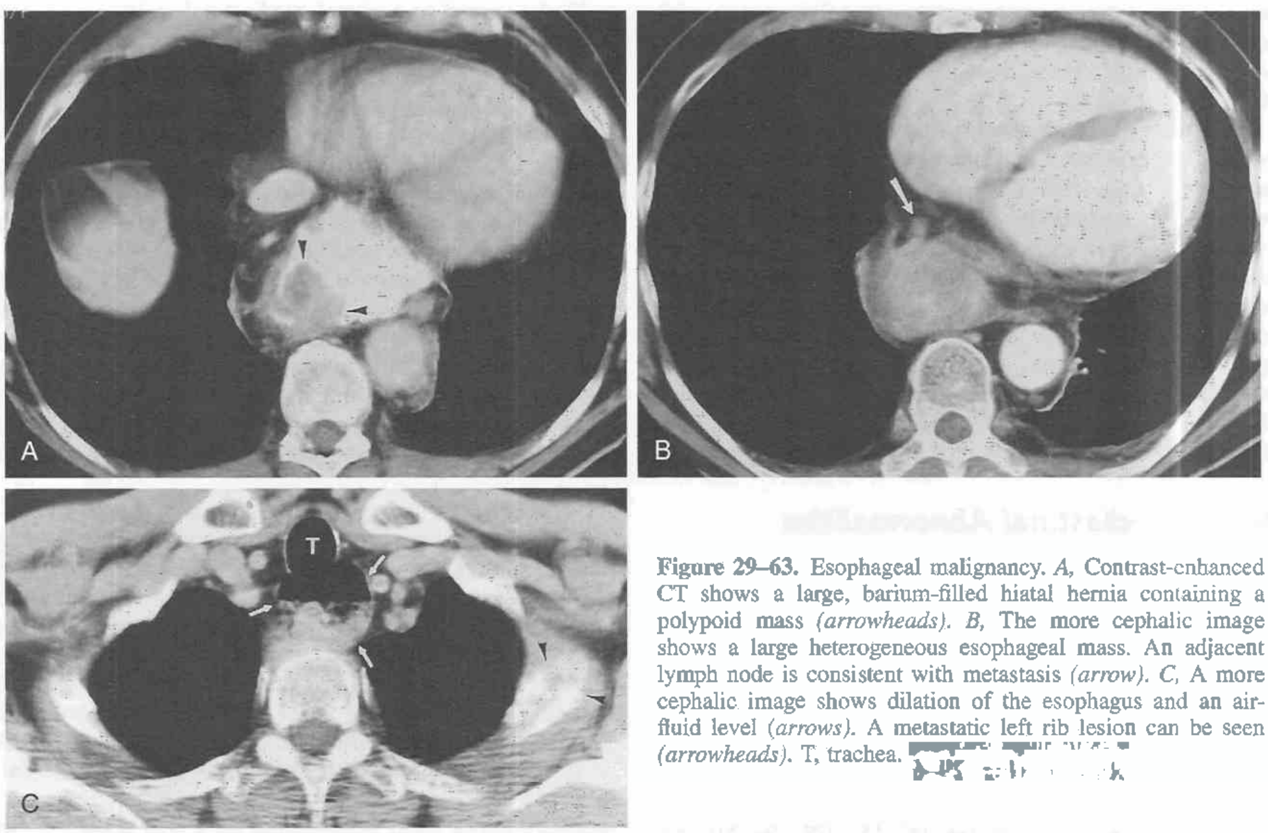

Figure 29–63. Esophageal malignancy. *A,* Contrast-enhanced CT shows a large, barium-filled hiatal hernia containing a polypoid mass *(arrowheads). B,* The more cephalic image shows a large heterogeneous esophageal mass. An adjacent lymph node is consistent with metastasis *(arrow). C,* A more cephalic image shows dilation of the esophagus and an air-fluid level *(arrows).* A metastatic left rib lesion can be seen *(arrowheads).* T, trachea.

Esophageal Dilatation

Esophageal dilatation can be easily demonstrated on CT.[52, 203] Focal dilatation occurs in Zenker's diverticulum (upper esophagus), traction diverticula resulting from granulomatous disease (middle esophagus), and epiphrenic diverticula (lower and on the right). These focal dilatations or diverticula are clearly demonstrated on CT and can be a source of confusion unless oral contrast material is administered.

Diffuse dilatation of the esophagus can occur as a result of motility disorders (achalasia, postvagotomy syndrome, Chagas' disease, scleroderma, systemic lupus erythematosus, presbyesophagus, diabetic neuropathy, esophagitis) or as a result of distal obstruction (carcinoma, stricture, extrinsic compression) (Fig. 29–64).

Airway Lesions

Tumors of the trachea or proximal bronchi can manifest as middle mediastinal masses on chest radiographs or CT.[41, 138, 164] Malignant neoplasms account for 90% of primary tracheal tumors. The most common primary malignancies of the trachea are squamous cell and adenoid cystic carcinomas.[11, 158, 159, 194] Benign neoplasms such as papilloma, adenoma, hamartoma, chondroma, leiomyoma, and granular cell myoblastoma account for less than 10% of primary tracheal tumors. The most common primary malignancy of the major bronchi is non–small cell lung cancer. Carcinoid tumors and mucoepidermoid carcinoma are less common bronchial malignancies that occur in younger patients.[129, 166, 211] These lesions are described in Chapter 28.

Foregut Cysts

Foregut cysts, which account for approximately 20% of all mediastinal masses, probably arise as a result of maldevelopment of the primitive foregut.[234, 235] Bronchogenic cysts are the most common mediastinal foregut cysts; esophageal duplication and neurenteric cysts are less common.

It is important not to confuse these cystic masses with fluid-filled structures within the mediastinum such as fluid-filled pericardial recesses, loculated pleural fluid, extension of ascites through the esophageal hiatus, mediastinal extension of pancreatic pseudocyst, or a fluid-filled and dilated esophagus (Figs. 29–65 and 29–66).

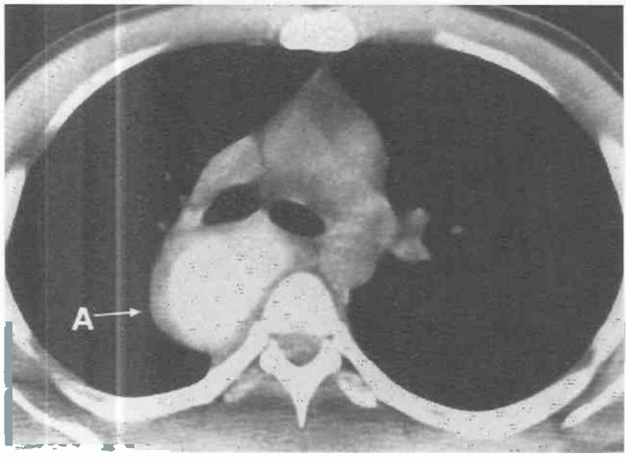

Figure 29–64. Achalasia. CT shows dilated esophagus (A) in a patient with achalasia. The esophagus displaces the azygos vein to the right.

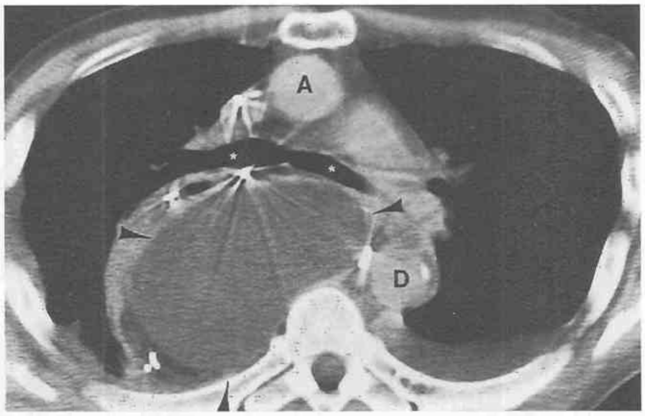

Figure 29–65. Thoracic lymphocele after esophageal resection and gastric pull-through. Contrast-enhanced CT shows large homogeneous fluid collection *(arrowheads)* in middle/posterior mediastinum displacing tracheal carina *(asterisks)* anteriorly and gastric pull-through anterolaterally. A, ascending aorta; D, descending aorta.

Bronchogenic Cyst

Bronchogenic cysts are thought to arise from abnormal budding of the ventral foregut.* Histopathologically, they are lined with ciliated respiratory epithelium, cartilage, smooth muscle, fibrous tissue, and mucous glands. Most bronchogenic cysts occur in the middle mediastinum, typically in the subcarinal or right paratracheal region. In up to 15% of cases, bronchogenic cysts are found in unusual locations including the pleural space, diaphragm, pericardium, lung, and abdomen.

On CT, bronchogenic cysts typically manifest as round or spherical, sharply marginated, homogeneous masses. Approximately half of bronchogenic cysts show water attenuation on CT (Fig. 29–67). The remainder show increased attenuation, most likely secondary to proteinaceous debris or hemorrhage within the lesions (Fig. 29–68). A small percentage have calcified walls or contain calcium suspended within the fluid.

On MR images, lesions typically show low to intermediate signal intensity on T1-weighted images and markedly increased signal intensity on T2-weighted images. The lesions can be heterogeneous on T1-weighted images but are typically homogeneous on T2-weighted images. These MRI characteristics can be useful for differentiating cysts that appear solid on CT from solid neoplasms or lymphadenopathy. Gadolinium administration can also be helpful for distinguishing mediastinal cysts from solid neoplasms by demonstrating a lack of central enhancement and, occasionally, rim enhancement.

Because many ECG-gated T1-weighted pulse sequences have a relatively long TR, fluid-filled lesions can show

*See References 14, 47, 122, 141, 153, 154, 156, 162, 180, 184, and 245.

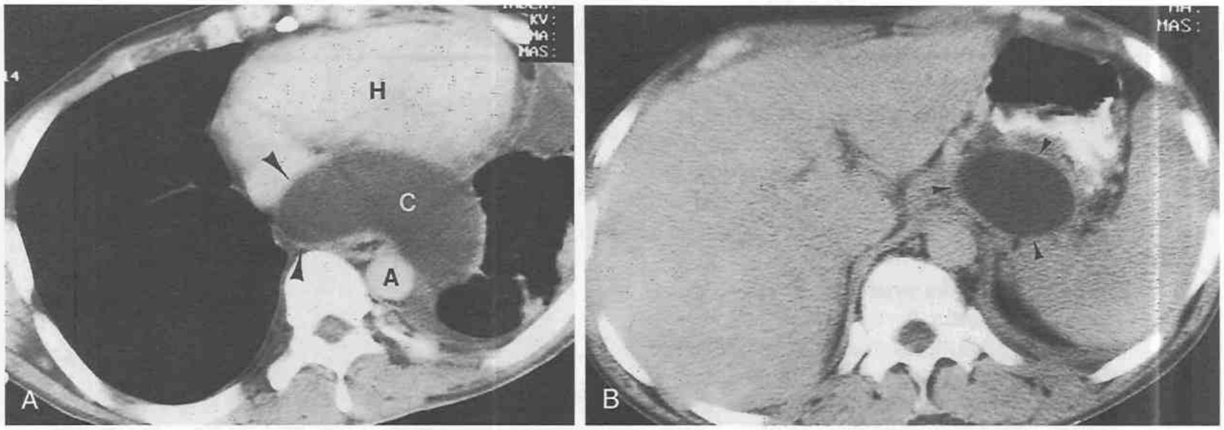

Figure 29–66. Mediasti[redacted]pseudocyst in a patient with chronic pancreatitis. *A,* Contrast-enhanced CT shows homogeneous water-attenuation mass (C) in the middle mediastinum with a thin enhancing rim *(arrowheads)*. A small left pleural effusion can be seen. A, aorta; H, heart. *B,* A more caudal CT image confirms origination of mass *(arrowheads)* from the tail of the pancreas. (Case is courtesy of May Lesar, Bethesda, Md.)

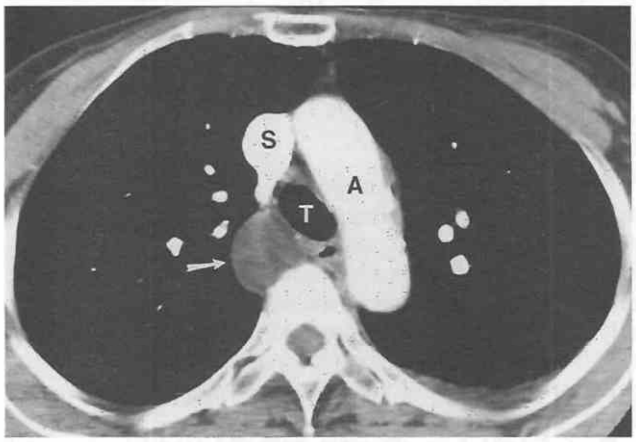

Figure 29–67. Bronchogenic cyst. Contrast-enhanced CT shows well-circumscribed, water-attenuation middle mediastinal mass *(arrow)* with imperceptible wall. The CT appearance is typical for bronchogenic cyst. A, transverse aorta; S, superior vena cava; T, trachea.

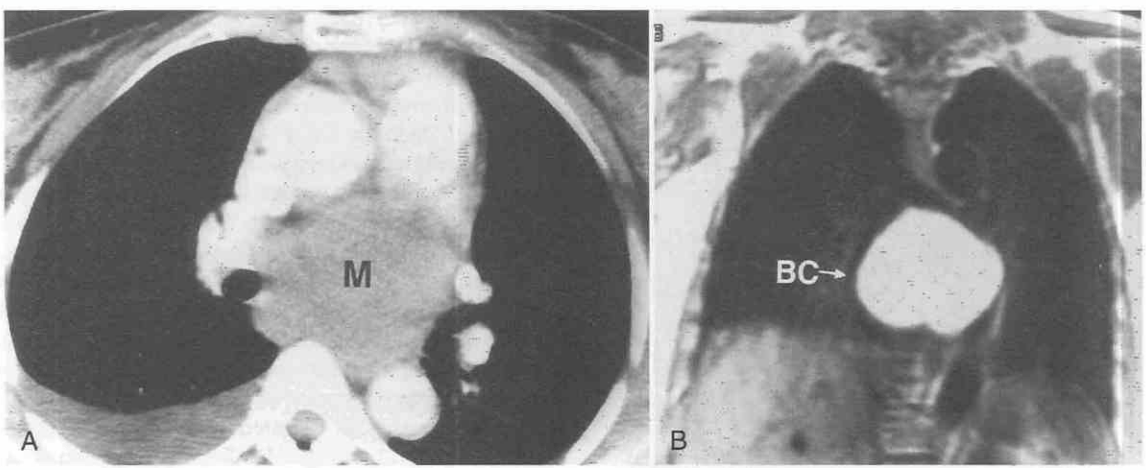

Figure 29–68. Bronchogenic cyst. *A,* CT shows a large homogeneous mass (M) of soft tissue attenuation in subcarinal region. *B,* Coronal T1-weighted MR image shows high signal intensity within the mass (BC), caused by viscous cyst fluid.

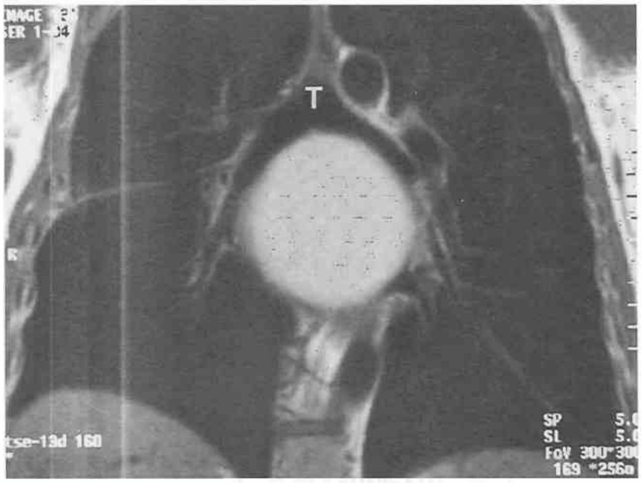

Figure 29–69. Bronchogenic cyst. Coronal T1-weighted MRI shows a subcarinal mass with high signal intensity. Both main bronchi are displaced. The subcarinal location is typical for a bronchogenic cyst. T, trachea.

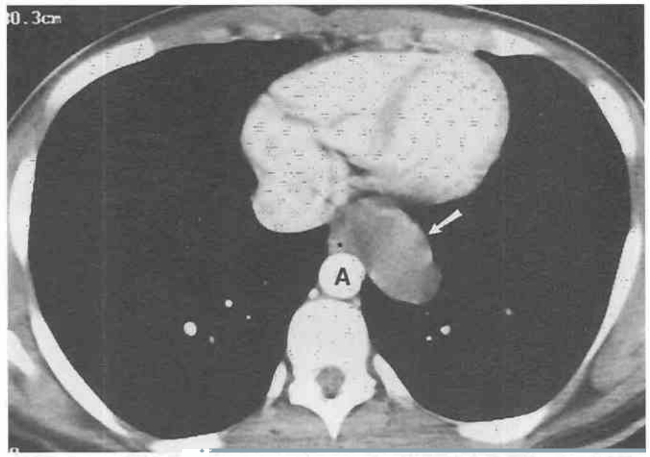

Figure 29–70. Esophageal duplication cyst. Contrast-enhanced CT shows a well-marginated, low-attenuation middle mediastinal mass *(arrow)* adjacent to the left lateral wall of the esophagus *(asterisk)*. Note the lack of enhancement. A, aorta.

intermediate signal intensity. Cysts with proteinaceous, mucinous, or hemorrhagic contents can show a further increase in signal intensity on these sequences (Fig. 29–69). These lesions usually have markedly increased signal intensity on T2-weighted images, however, suggesting their true cystic nature.

Esophageal Duplication and Neurenteric Cysts

Duplication of the esophagus[66, 130, 141, 180, 234, 245] is thought to represent a diverticulum of the primitive foregut or an aberrant recanalization of the gut in embryogenesis. These cysts are located in the middle or posterior mediastinum and may be indistinguishable from a bronchogenic cyst. They are composed of a muscular coat and mucosa that may resemble the esophagus, stomach, or small intestine, although it is usually ciliated. Esophageal duplication cysts usually occur within the wall, or are adherent to the wall, of the esophagus. They are either spherical or tubular and are usually located distally along the lateral aspect of the esophagus.

On CT, the cysts typically manifest as spherical or tubular masses in close proximity to the esophageal wall. They are usually homogeneous and demonstrate water attenuation (Fig. 29–70). Like bronchogenic cysts, however, they may be of soft tissue attenuation because of intracystic hemorrhage or proteinaceous debris. On MRI, they show signal intensity characteristics similar to those of bronchogenic cysts, with variable signal intensity on T1-weighted images, depending on intracystic content, and markedly increased signal intensity on T2-weighted images (Fig. 29–71).

Neurenteric cysts result from incomplete separation of the endoderm and notochord, resulting in a diverticulum of the endoderm. Neurenteric cysts, which are pathologically identical to esophageal duplication cysts, may have either a fibrous connection to the spine or an intraspinal component. These cysts are typically associated with vertebral body anomalies, most commonly a sagittal cleft, that occur at or above the level of the cyst. Most neurenteric cysts occur in the posterior rather than the middle mediastinum, usually above the level of the carina.

The CT and MR appearances of these lesions are similar to those of other foregut cysts. MRI is useful for optimally demonstrating extent of spinal abnormality and degree of intraspinal involvement.

Pericardial Cysts

Pericardial cysts are unilocular, mesothelium-lined cysts that arise from congenital defects related to the ventral and parietal pericardial recesses.[15, 63, 180, 219, 245] True pericardial cysts contain all layers of the pericardium and do not

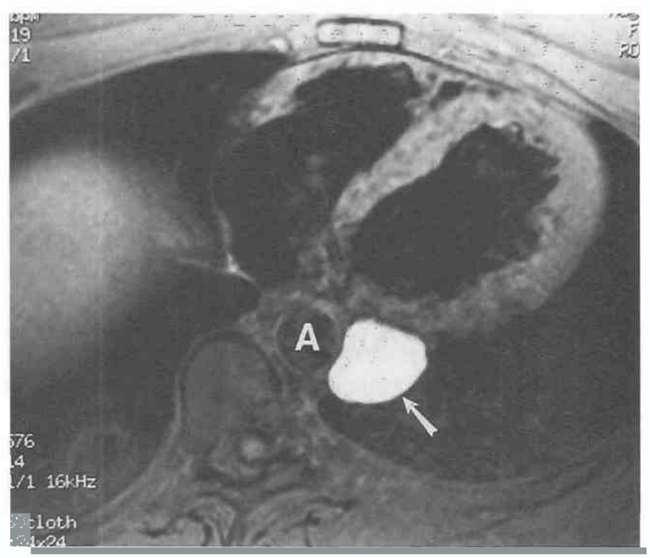

Figure 29–71. Esophageal duplication cyst. Axial T1-weighted MR image shows a well-circumscribed mass *(arrow)* with high signal intensity adjacent to the descending aorta (A). The MRI appearance, which is atypical for a simple cyst, is caused by proteinaceous fluid within the cyst.

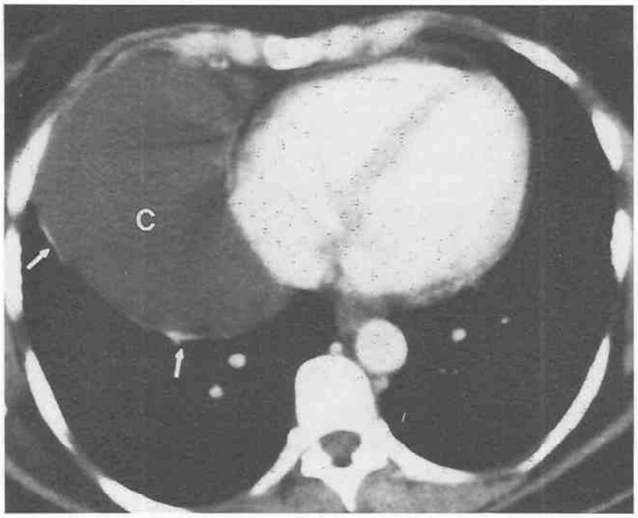

Figure 29–72. Pericardial cyst. Contrast-enhanced CT shows a large, homogeneous, water-attenuation mass (C) in the right cardiophrenic angle. The wall is imperceptible; enhancement at the periphery *(arrows)* is caused by atelectatic lung. The location and appearance are typical for pericardial cyst.

communicate with the pericardial space. They are usually found in asymptomatic adults, often as an incidental finding on chest radiographs. They are typically unilocular cystic lesions with clear fluid contents and thin walls. Pericardial cysts are variable in size and shape and most commonly occur in the right (70%) or left (22%) cardiophrenic angles.

CT shows a homogeneous, nonenhancing, water-attenuation, rounded mass adjacent to the pericardium (Fig. 29–72). The cyst wall may calcify. Pericardial cysts are usually homogeneous on MRI, showing low signal intensity on T1-weighted images and markedly increased signal intensity on T2-weighted images (Fig. 29–73).

Posterior Mediastinal Lesions

Neurogenic Tumors

Twenty percent of all adult and 35% of all pediatric mediastinal neoplasms are neurogenic tumors.[12, 47, 153, 245, 265] Neurogenic tumors account for the majority of posterior mediastinal neoplasms.[124] These lesions can be classified as tumors of peripheral nerves (neurofibromas, schwannomas, malignant tumors of nerve sheath origin), of sympathetic ganglia (ganglioneuromas, ganglioneuroblastomas, neuroblastomas), or of parasympathetic ganglia (paragangliomas, pheochromocytomas). Peripheral nerve tumors are more common in adults and sympathetic ganglia tumors are more common in children.

CT is usually performed in the initial evaluation of a suspected neurogenic tumor and is helpful for identifying intratumoral calcification and for assessing associated bone erosion or destruction. Because neurogenic tumors usually arise in a paravertebral location, intraspinal extension is common.

MRI is the preferred imaging modality for evaluating neurogenic tumors because it allows simultaneous assessment of the following:

- Intraspinal extension
- Spinal cord abnormalities
- Longitudinal extent of tumor

Although the various types of neurogenic tumor can have similar radiologic appearances, certain features aid in the diagnosis. Peripheral nerve tumors typically manifest in adults as round masses oriented along the axis of a peripheral nerve, and they may have an intraspinal component (the "dumbbell" lesion). Tumors of sympathetic ganglia typically manifest in children as oval masses that are elongated along the spine and may contain calcifications on CT.

Benign Peripheral Nerve Tumors

The benign peripheral nerve tumors (schwannomas, neurofibromas) are slow-growing neoplasms and the most common neurogenic tumors of the mediastinum.* Schwannomas are encapsulated neoplasms that arise from the nerve sheath and typically have areas of cystic degeneration and hemorrhage and small focal areas of calcification. Schwannomas grow laterally along the parent nerve and cause symptoms by compressing the nerve.

Neurofibromas differ from schwannomas in that they are unencapsulated and result from proliferation of all nerve elements, including Schwann cells, nerve fibers, and fibroblasts. They grow by diffusely expanding the parent nerve. This type of neural tumor is found in neurofibromatosis-1 (von Recklinghausen's disease). Plexiform neurofibromas are variants of neurofibromas that infiltrate along nerve trunks or plexuses.

Schwannomas and neurofibromas typically occur with equal frequency in men and women, most commonly in the third and fourth decades of life. Thirty percent to 45% of neurofibromas occur in patients with neurofibromatosis. Multiple neurogenic tumors or a single plexiform neurofibroma is pathognomonic of the disease.

On CT, schwannomas and neurofibromas manifest as sharply marginated, unilateral, spherical or lobular posterior mediastinal masses (Fig. 29–74). Pressure erosion of adjacent ribs, or vertebral body or neural foramen enlargement occurs in up to 50% of cases. Punctate intralesional calcification occurs occasionally. On non–contrast-enhanced CT, schwannomas often demonstrate lower attenuation than skeletal muscle because of their high lipid content, interstitial fluid, and areas of cystic degeneration. Neurofibromas are often more homogeneous and show higher attenuation than schwannomas because they have fewer of these histologic features. These lesions may heterogeneously enhance following administration of IV contrast material.

On MRI, schwannomas and neurofibromas show variable signal intensity on T1-weighted images but typically their signal intensity is similar to that of the spinal cord. On T2-weighted images, these neoplasms characteristically show high signal intensity peripherally and low signal intensity centrally (the target sign) as a result of collagen deposition. This feature, when present, helps distinguish neurofibromas from other mediastinal tumors. Also, areas

*See References 9, 26, 36, 74, 95, 136, 153, 155, 206, 245, 247, and 265.

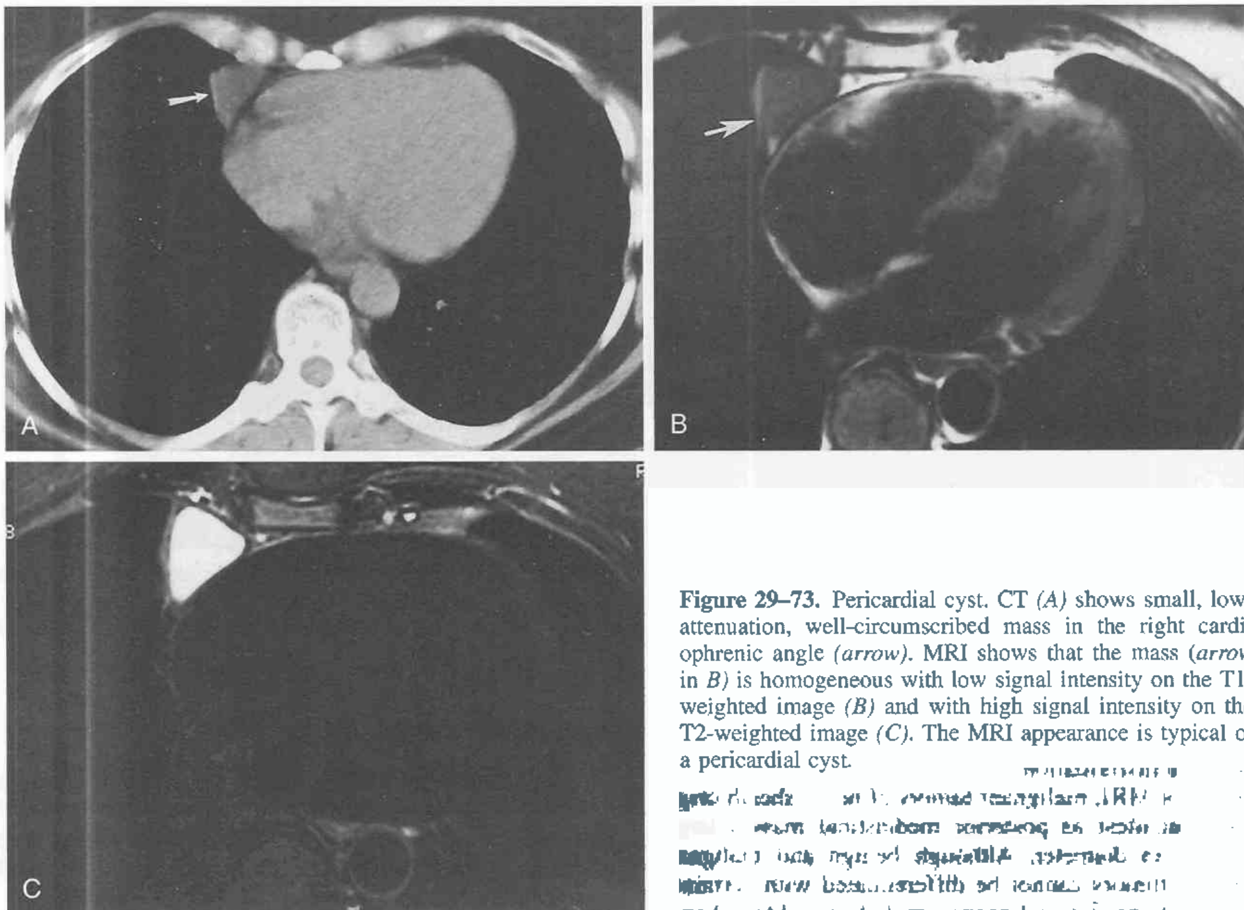

Figure 29–73. Pericardial cyst. CT *(A)* shows small, low-attenuation, well-circumscribed mass in the right cardiophrenic angle *(arrow)*. MRI shows that the mass *(arrow in B)* is homogeneous with low signal intensity on the T1-weighted image *(B)* and with high signal intensity on the T2-weighted image *(C)*. The MRI appearance is typical of a pericardial cyst.

of cystic degeneration within the lesions may result in foci of increased signal intensity on T2-weighted images.

Although the high signal intensity shown by schwannomas and neurofibromas on T2-weighted images can facilitate differentiation of tumors from spinal cord, the tumors can be obscured by the high signal intensity of cerebrospinal fluid. Schwannomas and neurofibromas, however, enhance with gadolinium and this feature can be useful in detecting and determining their intradural extension (Fig. 29–75). Ten percent of paravertebral neurofibromas and schwannomas extend into the spinal canal and appear as dumbbell-shaped masses with widening of the affected neural foramen.

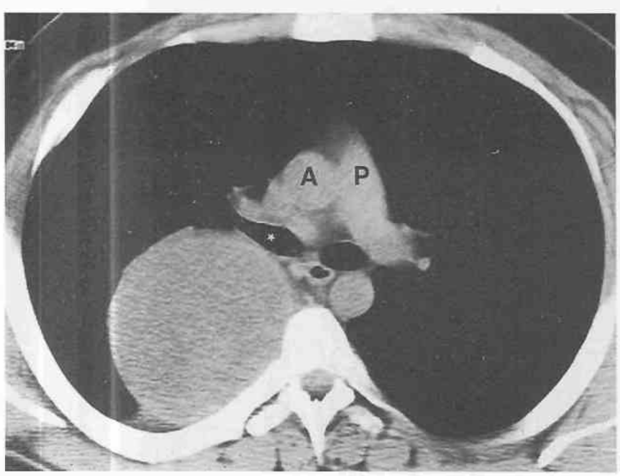

Figure 29–74. Schwannoma. CT shows a large, homogeneous, paraspinal mass. The round shape is typical of a peripheral nerve tumor. A, aorta; P, pulmonary artery. The *asterisk* indicates the right main bronchus.

CT of plexiform neurofibromas demonstrates low-attenuation infiltrative masses along the mediastinal nerves and sympathetic chains, which may occur in any mediastinal compartment. MRI of plexiform neurofibromatosis also demonstrates the infiltrative nature of the tumors, and the masses can show low signal on both T1-weighted and T2-weighted images because of the fibrous nature of the tumors (Fig. 29–76).

Malignant Tumor of Nerve Sheath Origin

Malignant tumors of nerve sheath origin (also called malignant neurofibromas, malignant schwannomas, or neurofibrosarcomas) are rare neoplasms that typically develop from solitary or plexiform neurofibromas in the third to fifth decades of life.* Up to 50% occur in patients with neurofibromatosis-1. In patients with neurofibromatosis-1, these tumors occur at an earlier age (typically in adolescence) and with a higher incidence than in the general population. Because most benign neurogenic tumors are

*See References 9, 26, 55, 80, 110, 136, 155, 157, 245, and 247.

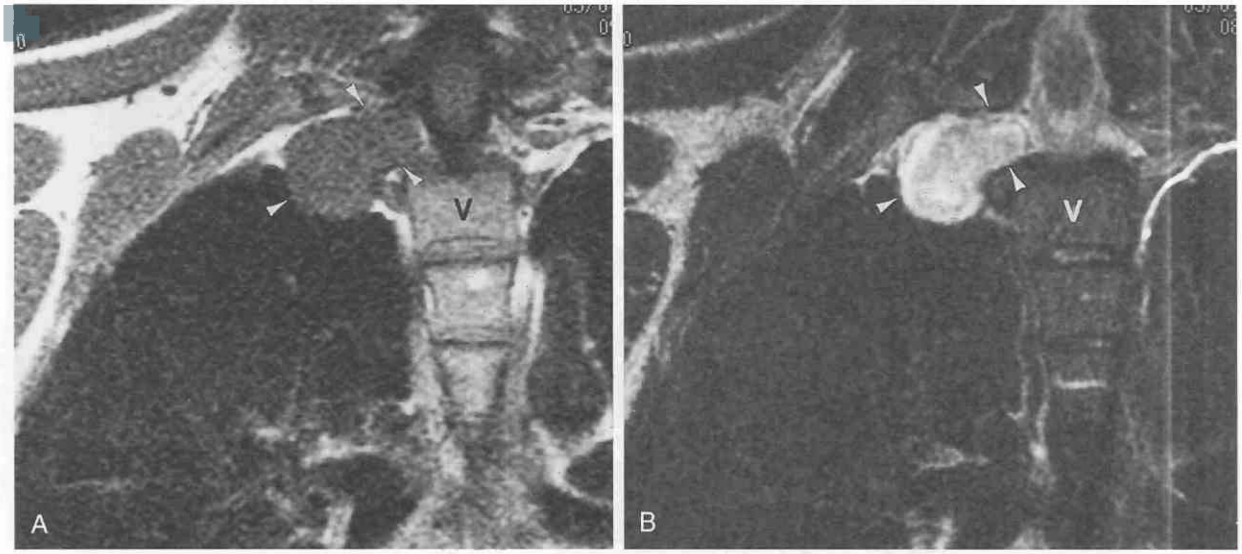

Figure 29–75. Neurofibroma. *A,* Coronal T1-weighted MR image shows a lobular mass extending into the intervertebral foramina *(arrowheads). B,* Coronal gadolinium-enhanced MR image shows heterogeneous enhancement within the mass *(arrowheads).* V, vertebral body. (From Rossi SE, Erasmus JJ, McAdams HP, Donnelly LF: Thoracic manifestations of neurofibromatosis-I. AJR Am J Roentgenol 173:1631–1638, 1999.)

asymptomatic, the development of pain often indicates malignant transformation.

On CT or MRI, malignant tumors of nerve sheath origin typically manifest as posterior mediastinal masses larger than 5 cm in diameter. Although benign and malignant neurogenic tumors cannot be differentiated with certainty, findings that suggest malignancy include a sudden change in size of a preexisting mass or development of heterogeneous signal intensity on MR images (caused by necrosis and hemorrhage). The presence of multiple target signs throughout the lesion on MRI favors the diagnosis of a plexiform neurofibroma rather than a malignant tumor of nerve sheath origin.

Sympathetic Ganglia Tumors

The sympathetic ganglia tumors (ganglioneuromas, ganglioneuroblastomas, neuroblastomas) are rare neoplasms that originate from nerve cells.* Ganglioneuromas and ganglioneuroblastomas usually arise from the sympathetic ganglia in the posterior mediastinum.

Ganglioneuromas are benign neoplasms that usually occur in children and young adults. Ganglioneuroblastomas, which exhibit varying degrees of malignancy, usually occur in patients younger than 10 years. The posterior mediasti-

*See References 2, 19, 40, 48, 74, 218, 229, 240, 245, 247, and 255.

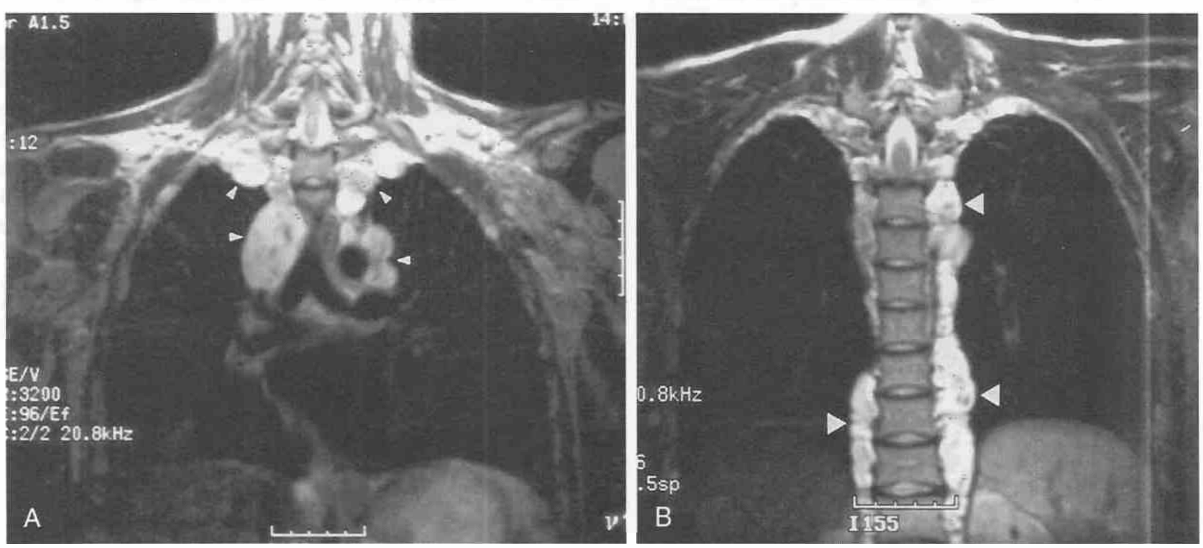

Figure 29–76. Plexiform neurofibromas in a woman with neurofibromatosis. Coronal T1-weighted (*A*) and T2-weighted (*B*) MR images show plexiform neurofibromas along the course of nerves in the superior, middle, and posterior mediastinum *(arrowheads).* Focal central hypointense regions within masses (target sign) are typical of neurofibromas. (From Rossi SE, Erasmus JJ, McAdams HP, Donnelly LF: Thoracic manifestations of neurofibromatosis-I. AJR Am J Roentgenol 173:1631–1638, 1999.)

num is also the most common extra-abdominal location of neuroblastomas: up to 30% of these tumors occur in this region. Neuroblastomas are highly malignant tumors that typically occur in children younger than 5 years. A posterior mediastinal mass in this age group should be considered a neuroblastoma until proven otherwise.

Radiologically, ganglioneuromas and ganglioneuroblastomas usually manifest as well-marginated, elliptical, posterior mediastinal masses that vertically extend over three to five vertebral bodies. They are usually located lateral to the spine and may cause pressure erosion on adjacent vertebral bodies. On CT, they are typically heterogeneous and may contain stippled or punctate calcifications (Fig. 29–77). On T1-weighted and T2-weighted MR images, they usually show homogeneous and intermediate signal intensity (Fig. 29–78). Occasionally, these lesions show heterogeneous and high signal intensity on T2-weighted images. Ganglioneuroblastomas are typically larger and more aggressive than ganglioneuromas, with evidence of local and intraspinal invasion.

On CT, neuroblastomas manifest as a paraspinal mass showing heterogeneous, predominantly soft tissue attenuation. The lesions usually contain areas of hemorrhage, necrosis, cystic degeneration, and calcium (30%). On MRI, the lesions typically demonstrate heterogeneous signal intensity on all pulse sequences and show heterogeneous enhancement following gadolinium administration. Neuroblastomas often show widespread local invasion and have irregular margins, although lesions can be well marginated on CT or MR images. Neuroblastomas also have a tendency to cross the midline.

Parasympathetic Ganglion Tumors

Paragangliomas (chemodectomas) are rare neural tumors of the extra-adrenal parasympathetic system.[71, 174] These tumors are histologically identical to pheochromocytomas and can be functional or nonfunctional. Mediastinal paragangliomas occur in one of two locations:

- In the middle mediastinum, in close association with the origins of the aorta and pulmonary artery (aorticopulmonary paraganglioma)

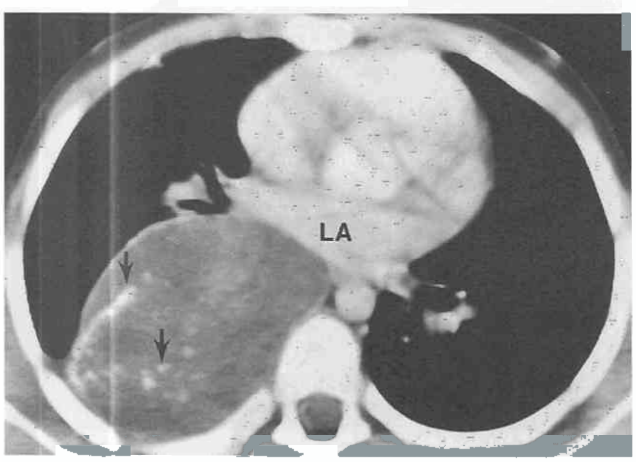

Figure 29–77. Ganglioneuroma. Contrast-enhanced CT shows well-circumscribed low-attenuation paraspinal mass containing punctate calcification *(arrows)*. LA, left atrium.

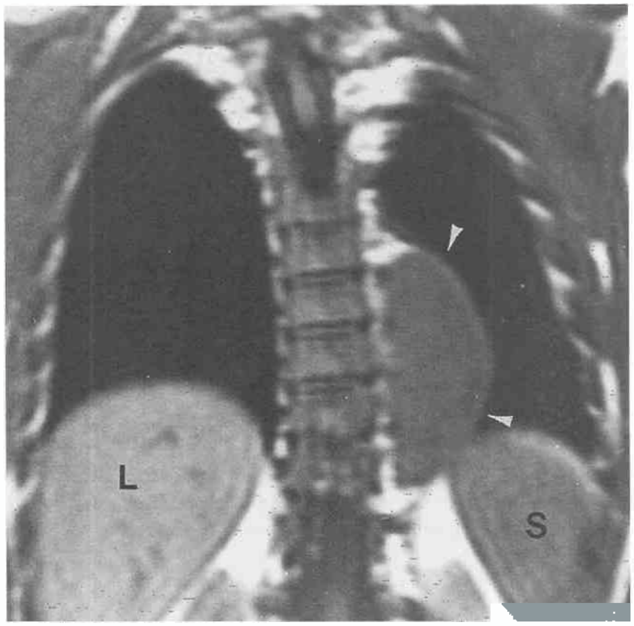

Figure 29–78. Ganglioneuroma. Coronal T1-weighted MR image shows an elliptical paraspinal mass *(arrowheads)* of intermediate signal intensity. Vertical orientation and signal characteristics are typical of a sympathetic ganglion tumor. L, liver; S, spleen.

- In the posterior mediastinum (paravertebral paraganglioma)

On non–contrast-enhanced CT, the lesions are typically heterogeneous and enhance intensely after administration of IV contrast material. On MRI, the lesions are usually hypointense on T1-weighted images and hyperintense on T2-weighted images (Fig. 29–79). Flow voids in the lesion are sometimes seen, indicating their hypervascular nature. The lesions may be well circumscribed or show invasion of surrounding mediastinal structures.

Lateral Thoracic Meningocele

Because of the pressure difference between the thorax and the subarachnoid space, pulsion diverticula, called lateral meningoceles, can develop and protrude through the adjacent neural foramina.[9, 113, 183, 205, 236] They occur most commonly in patients with neurofibromatosis-1. Lateral meningoceles manifest radiographically as well-circumscribed, paravertebral masses that usually occur on the convex side of a scoliosis. On CT, meningoceles manifest as well-circumscribed paraspinal masses that demonstrate water attenuation. The adjacent neural foramen is typically enlarged. These lesions can be confused with low-attenuation neurofibromas. Diagnosis is established by demonstration of communication with the subarachnoid space by CT myelography. MRI can also be helpful in differentiating meningoceles from neurofibromas because meningoceles typically show low signal intensity on T1-weighted images and high signal intensity on T2-weighted images, and they do not enhance after gadolinium administration. Cardiac-gated MR cine images of meningoceles can reveal pulsatile motion that results from communication with the subarachnoid space.

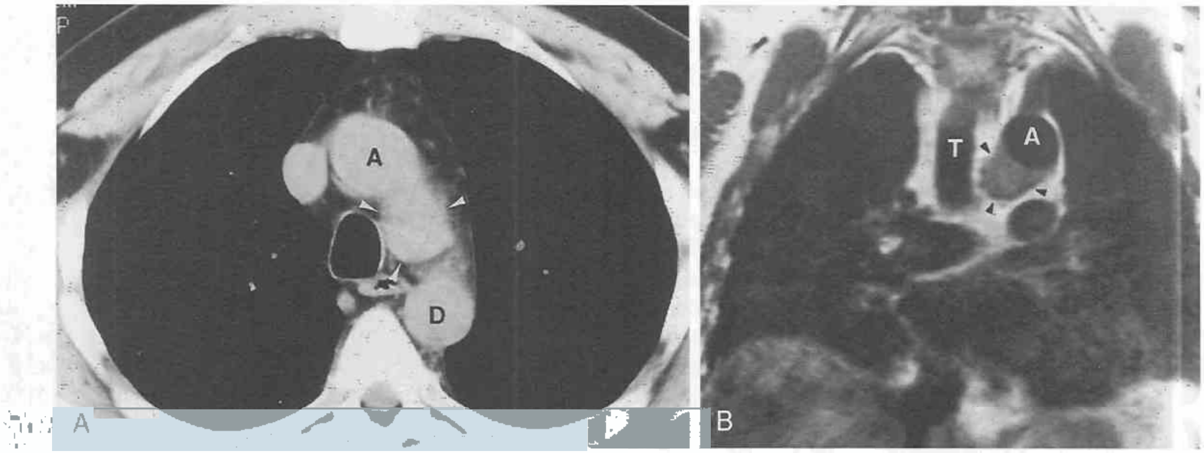

Figure 29–79. Paraganglioma. *A*, CT shows homogeneous soft tissue mass in aortopulmonary window *(arrowheads)*. The mass is difficult to distinguish from the aorta. A, ascending aorta; D, descending aorta. *B*, Coronal T1-weighted MR image shows intermediate-signal-intensity aortopulmonary window mass *(arrowheads)*. Biopsy revealed paraganglioma. A, aorta; T, trachea.

Extramedullary Hematopoiesis

Extramedullary hematopoiesis is a compensatory phenomenon that occurs when erythrocyte production is diminished or destruction is accelerated.[30, 81, 90, 123, 222] Extramedullary hematopoiesis is usually seen in patients with chronic hemolytic disorders such as thalassemia, hereditary spherocytosis, sickle cell disease, or extensive bone marrow replacement resulting from myelofibrosis. Extramedullary hematopoiesis usually is microscopic and commonly involves the liver, spleen, and lymph nodes. Thoracic manifestations are less common and consist of paravertebral soft tissue masses. The masses represent extrusion of the marrow through the thinned cortex of the posterior ribs. Histologically, the masses resemble splenic tissue with hematopoietic elements mixed with fat. They are usually bilateral, contain no calcification, and show no rib destruction. Additional masses can be found along the lateral margins of the ribs.

On CT, extramedullary hematopoiesis manifests as a heterogeneous mass or masses, often with focal areas of fat within the lesion (Fig. 29–80). Extramedullary hematopoiesis typically manifests on MRI as well-marginated, smooth or lobulated, unilateral or bilateral paravertebral masses. T1-weighted and T2-weighted MR images typically show bilateral heterogeneous masses with increased signal intensity on T1-weighted images because of fat within the masses.

Paraspinal Inflammation

Vertebral osteomyelitis can result in a paraspinal abscess. Causative organisms include *Mycobacterium tuberculosis*, *Staphylococcus aureus*, and anaerobic organisms. On CT, a paraspinal abscess manifests as a mass showing heterogeneous attenuation. Rim enhancement following administration of IV contrast material is characteristic (Fig. 29–81). Imaging features that suggest paraspinal abscess include (1) narrowing of adjacent intervertebral disk and (2) destruction of two or more contiguous vertebral bodies.

MRI is especially suited for identifying and demonstrating the extent of paraspinal infections. Spondylitis and vertebral osteomyelitis are often accompanied by epidural or paraspinal inflammatory masses or abscesses. MRI is better than CT for evaluating these infections because of its ability to depict the disk space, the spinal canal and its contents, and the paraspinal regions. T1-weighted images show inflammation as low signal intensity, and T2-weighted images show high signal intensity. The addition of gadolinium diethylenetriamine-penta-acetic acid (Gd-DTPA) is helpful in demonstrating the extent of the inflammatory process.[4, 5, 45, 191]

Diffuse Mediastinal Abnormalities

Numerous lesions, including lymphadenopathy, mediastinitis, mediastinal sarcoma, and metastatic disease, can

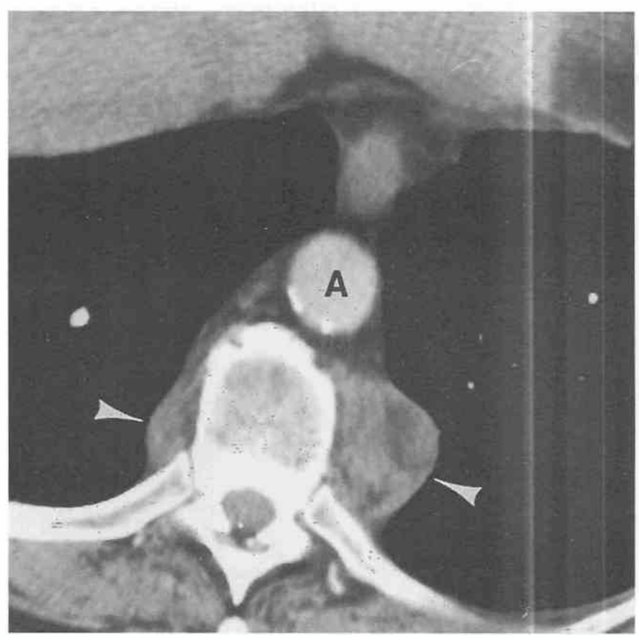

Figure 29–80. Extramedullary hematopoiesis. CT shows well-circumscribed bilateral paravertebral masses *(arrowheads)*. The left mass is heterogeneous and contains focal areas of fat, typical for extramedullary hematopoiesis. A, descending aorta.

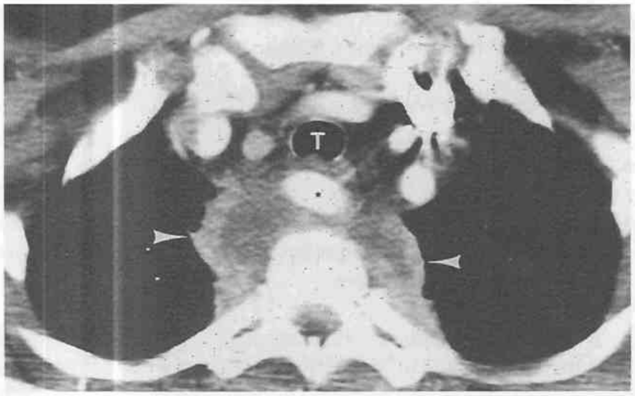

Figure 29–81. Paraspinal abscess caused by vertebral osteomyelitis. Contrast-enhanced CT shows bilateral heterogeneous low-attenuation paraspinal masses *(arrowheads). Staphylococcus aureus* was cultured from the needle aspirate. An anomalous right subclavian artery *(asterisk)* is posterior to the trachea (T).

manifest as diffuse or multicompartment mediastinal disease.

Lymphadenopathy

Lymph nodes are common in all regions of the mediastinum but they are most numerous around the tracheobronchial tree and hence in the middle mediastinum (Fig. 29–82).* Although it is still a subject of some controversy, the generally accepted upper limit of normal for short-axis lymph node diameter is 1 cm.

Enlargement is the primary CT or MRI criterion for establishing the presence of lymph node disease, but attenuation is also important. For instance, diffuse calcification is typical of prior granulomatous infection (tuberculosis, histoplasmosis), sarcoidosis, silicosis, calcifying or ossifying metastases, and treated lymphoma (Figs. 29–83 and 29–84). Nodes with low attenuation centers and rim enhancement are often seen in patients with active infection (tuberculosis, nontuberculous mycobacterial disease) and in patients with metastatic disease to the lymph nodes (lung cancer, testicular germ cell malignancy). Diffuse, intense nodal enhancement after administration of IV contrast material is typical of Castleman's disease and some metastatic processes (renal cell carcinoma). Causes of mediastinal lymph node enlargement may be classified as follows:

- Primary neoplasms of lymph nodes (lymphoma, leukemia)
- Metastases from intrathoracic or extrathoracic primary malignancies
- Nonlymphomatous lymphoid disorders such as Castleman's disease
- Infection (e.g., tuberculosis, fungal infection)

---

*See References 21, 29, 53, 75, 77, 85, 153, 193, 198, and 257.

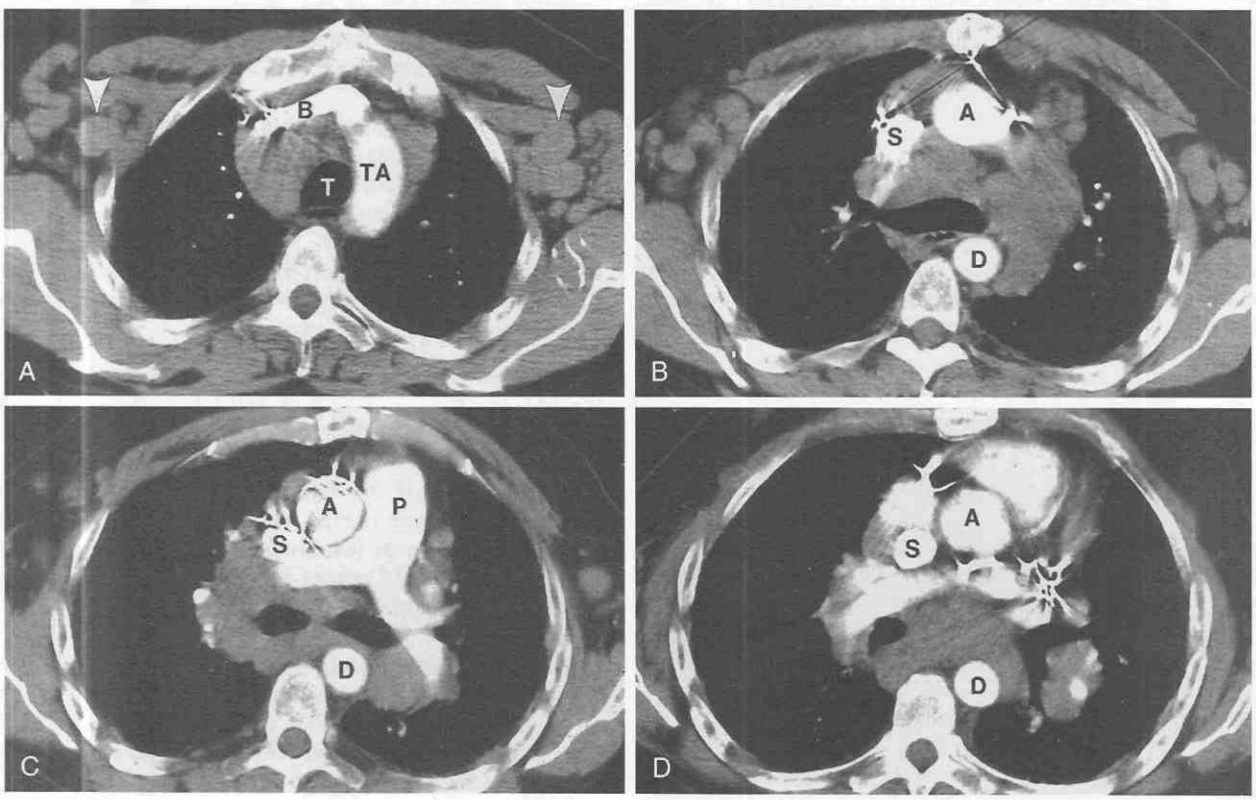

Figure 29–82. Diffuse mediastinal adenopathy in a patient with chronic lymphocytic leukemia. Contrast-enhanced CT shows marked intrathoracic adenopathy in the paratracheal and prevascular mediastinum *(A)*, precarinal region and aortopulmonary window *(B)*, left and right hilum *(C)*, and subcarinal region *(D)*. Axillary adenopathy can be seen (*arrowheads* in *A*). A, ascending aorta; B, brachiocephalic vein; D, descending aorta; P, main pulmonary artery; S, superior vena cava; T, trachea; TA, transverse aorta.

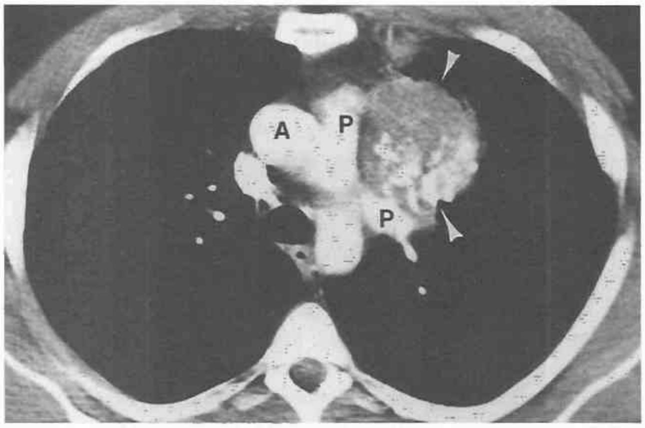

Figure 29–83. Osteosarcoma metastasis to the anterior mediastinum. Contrast-enhanced CT shows a soft-tissue-attenuation mass with extensive osteoid *(arrowheads)* in the anterior mediastinum. A, aorta; P, pulmonary artery.

CT and MRI are generally considered to be equivalent in their ability to detect mediastinal lymph node enlargement (Fig. 29–85). MRI is limited in its ability to detect calcification within nodes, a finding useful for distinguishing benign from malignant lymphadenopathy. Overlap occurs in signal intensity characteristics of benign and malignant lymphadenopathy on both T1-weighted and T2-weighted images. Thus, CT remains the primary modality for diagnosis and characterization of mediastinal lymphadenopathy. MRI can be useful, however, as a problem-solving modality in some cases and for distinguishing enlarged nodes from vascular structures when administration of iodinated contrast material is contraindicated.

Lymphoma

Lymphomas are common mediastinal neoplasms that can be either focal or diffuse.[67, 96, 125, 140, 151, 226, 242] Lymphomas are classified as *Hodgkin's disease* (HD) and *non-Hodgkin's lymphoma* (NHL). HD is the most common mediastinal lymphoma. Of the four types of HD, nodular sclerosing HD is the most common and has a unique predilection for the anterior mediastinum. Other types of HD typically manifest with diffuse mediastinal lymphadenopathy.

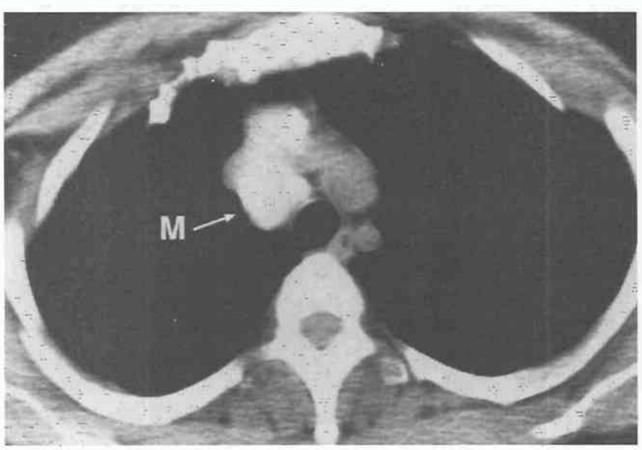

Figure 29–84. Calcified nodes. CT shows calcified right paratracheal lymph nodes (M) caused by histoplasmosis.

NHL that involves the mediastinum usually manifests with diffuse lymphadenopathy involving anterior, middle, and occasionally posterior mediastinal nodal groups. However, large B-cell or lymphoblastic lymphoma can manifest as an isolated anterior mediastinal mass. These large tumors can obstruct the SVC, compress the airway, or invade chest wall and adjacent structures.

Hodgkin's Disease. HD accounts for 0.75% of all cancers diagnosed in the United States each year. The median age at diagnosis is 26 years, and there is a slight male predominance. The incidence of HD has a bimodal distribution, with peaks between 25 and 30 years and 75 and 80 years. The characteristic Reed-Sternberg cell is the diagnostic hallmark of HD. There are four histologic subtypes of HD:

- Lymphocyte predominance (5%), with the best prognosis
- Nodular sclerosing, the most common type (78%), with the second most favorable prognosis
- Mixed cellularity (17%), with the third most favorable prognosis
- Lymphocyte depletion (1%), with the worst prognosis

HD is staged using the Ann Arbor staging system as follows:

Stage I: Involvement of a single lymph node region
Stage II: Involvement of two or more lymph node regions on the same side of the diaphragm (II), or localized involvement of an extralymphatic organ or site and of one or more lymph node regions on the same side of the diaphragm (IIE)
Stage III: Involvement of lymph node regions on both sides of the diaphragm (III), which may also be accompanied by involvement on the spleen (IIIS) or by localized involvement of an extralymphatic organ or site (IIIE), or both (IIIES)
Stage IV: Diffuse or disseminated involvement of one or more extralymphatic organs or tissues, with or without associated lymph node involvement

The absence or presence of fever, night sweats, or unexplained weight loss of 10% or more body weight 6 months before diagnosis are denoted by the suffix letter A or B, respectively.

Stages I and II are treated with radiation alone, and stages III and IV are treated with a combination of radiation and chemotherapy or just chemotherapy alone. Survival is greater than 90% in stages I, II, and IIIA; 80% in stage IIIB; and 75% in stage IV.

Non-Hodgkin's Lymphoma. The NHLs are a heterogeneous group of diseases with differing histology, treatment, and prognosis but with enough similarities that they are considered collectively. Although NHL has no known cause, patients with impaired immune systems are at higher risk for development of this malignancy. NHL makes up 3% of all newly diagnosed cancers in the United States and is four times more common than HD. NHL is the third most common childhood cancer, although the median age

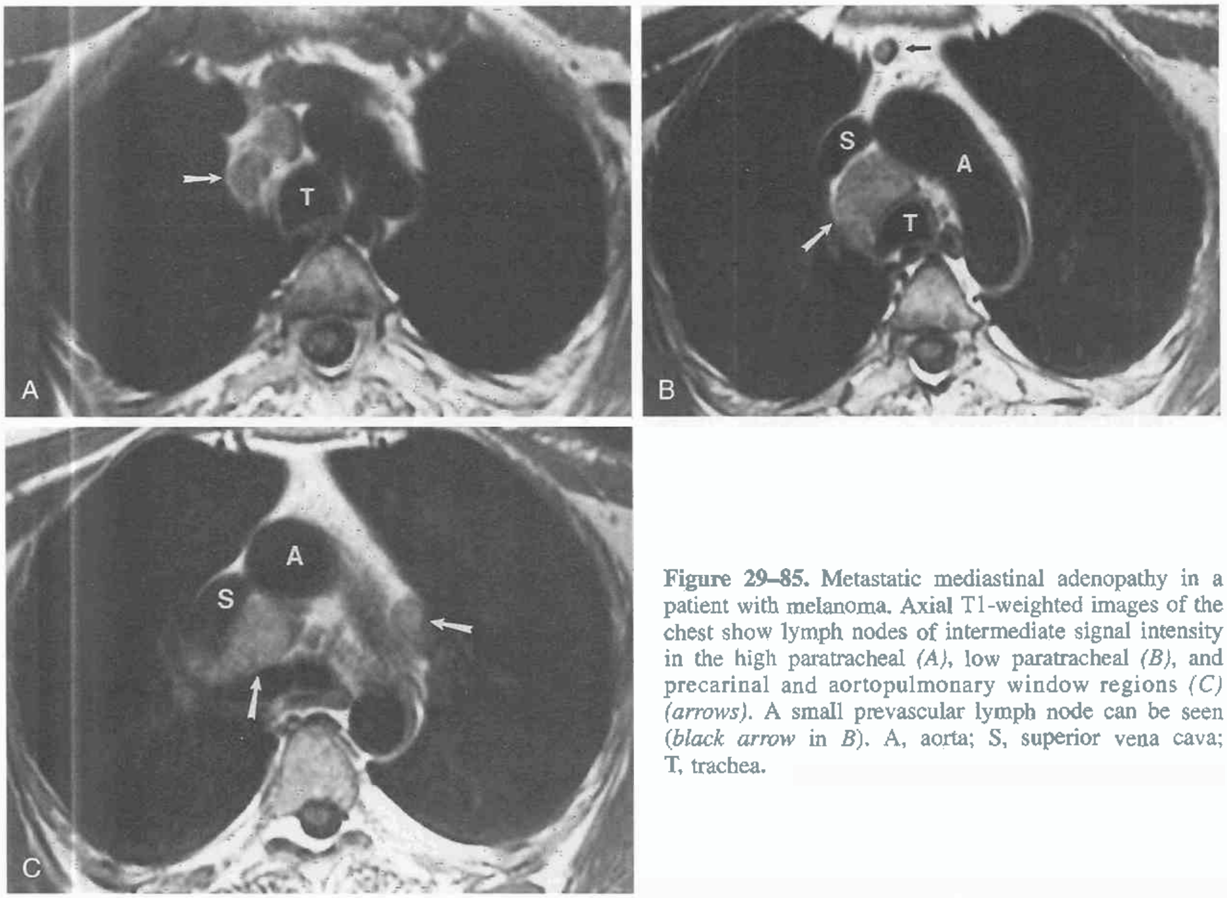

Figure 29–85. Metastatic mediastinal adenopathy in a patient with melanoma. Axial T1-weighted images of the chest show lymph nodes of intermediate signal intensity in the high paratracheal *(A)*, low paratracheal *(B)*, and precarinal and aortopulmonary window regions *(C)* *(arrows)*. A small prevascular lymph node can be seen (*black arrow* in *B*). A, aorta; S, superior vena cava; T, trachea.

at the time of diagnosis is 55 years. There is a male predominance (1.4:1). The histologic classification of NHL is complex, with 10 different cell descriptions divided into three grades of tumors:

- *Low grade* (small lymphocytic; follicular with predominantly small cleaved cells; and follicular with mixed small and large cells)
- *Intermediate grade* (follicular with predominantly large cells; diffuse with small cleaved cells; diffuse with mixed small and large cells; and diffuse with large cells, cleaved or noncleaved)
- *High grade* (diffuse large cells; immunoblastic, small noncleaved cells; and lymphoblastic)

Treatment is complex and involves radiation for lower-grade and chemotherapy for higher-grade tumors. Survival is 50% to 70% in low-grade NHL, 35% to 45% in intermediate-grade NHL, and 20% to 30% in high-grade NHL. Several unique observations are seen in NHL. Low-grade tumors may spontaneously regress, recur, or transform into higher-grade tumors. The incidence of NHL is higher in patients with severe immunologic compromise, including congenital immune disorders, transplant immunosuppression, and human immunodeficiency virus. NHL in these patients is often more aggressive and involves extranodal sites, such as the central nervous system, lung parenchyma, and gastrointestinal tract.

Imaging of Lymphoma. CT is the method of choice for identifying and staging HD and NHL.* CT provides accurate measurement of initial tumor size and extent, and it provides a means to follow response to therapy (Figs. 29–86 to 29–93). Chest CT alters initial treatment plans in approximately 10% of patients with HD by detecting more extensive disease. The anterior mediastinal, pretracheal, and hilar nodes are the nodes most commonly involved with HD. Paracardiac, subcarinal, superior diaphragmatic, internal mammary, and axillary nodes are less frequently involved. Calcification within nodes is usually a consequence of radiation therapy but occasionally is detected before treatment. Central areas of low density represent areas of necrosis; the presence of necrosis does not appear to alter treatment response or survival.

Lymphadenopathy varies in size and extent and can manifest as a solitary large mass or as discrete nodes within masses of matted nodes. It is important to recognize bulky mediastinal lymphadenopathy, identified when the diameter of the nodal mass is greater than one third of the thoracic diameter, because its presence may alter therapy.

Intrathoracic disease is noted in only 40% to 50% of patients with NHL at presentation, compared with 85% of patients with HD. In NHL, the most common nodal sites of involvement are not those of HD (anterior, superior

*See References 1, 6, 24, 33, 37, 39, 76, 119, 153, 182, 186, 190, 204, 237, 252, and 269.

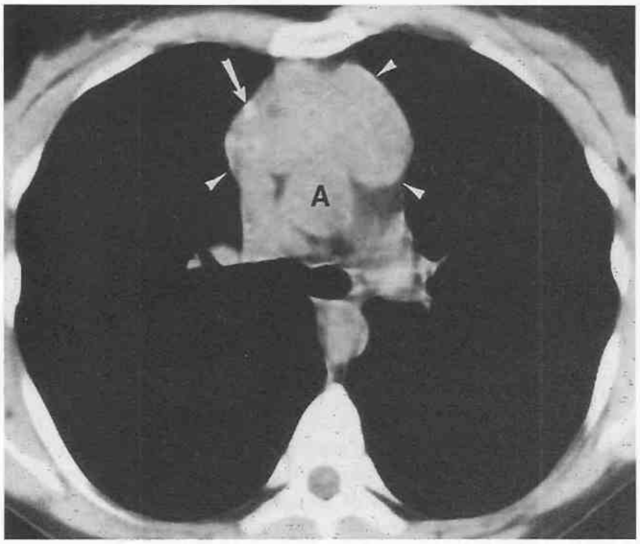

Figure 29–86. Hodgkin[redacted]lymphoma in a [redacted]g woman. CT shows a homogeneous, anterior mediastinal mass *(arrowheads)*. A punctate calcification *(arrow)* can be seen within the mass. A, ascending aorta.

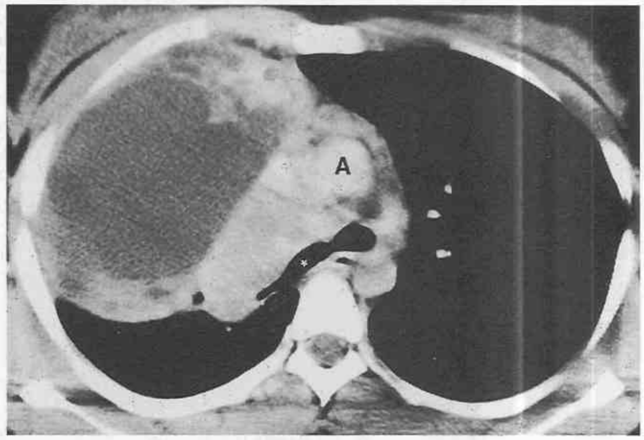

Figure 29–87. Hodgkin's lymphoma. Contrast-[redacted]anced CT shows an anterior mediastinal mass with a large cystic component. The *asterisk* indicates posterior displacement of the right main bronchus. A, ascending aorta.

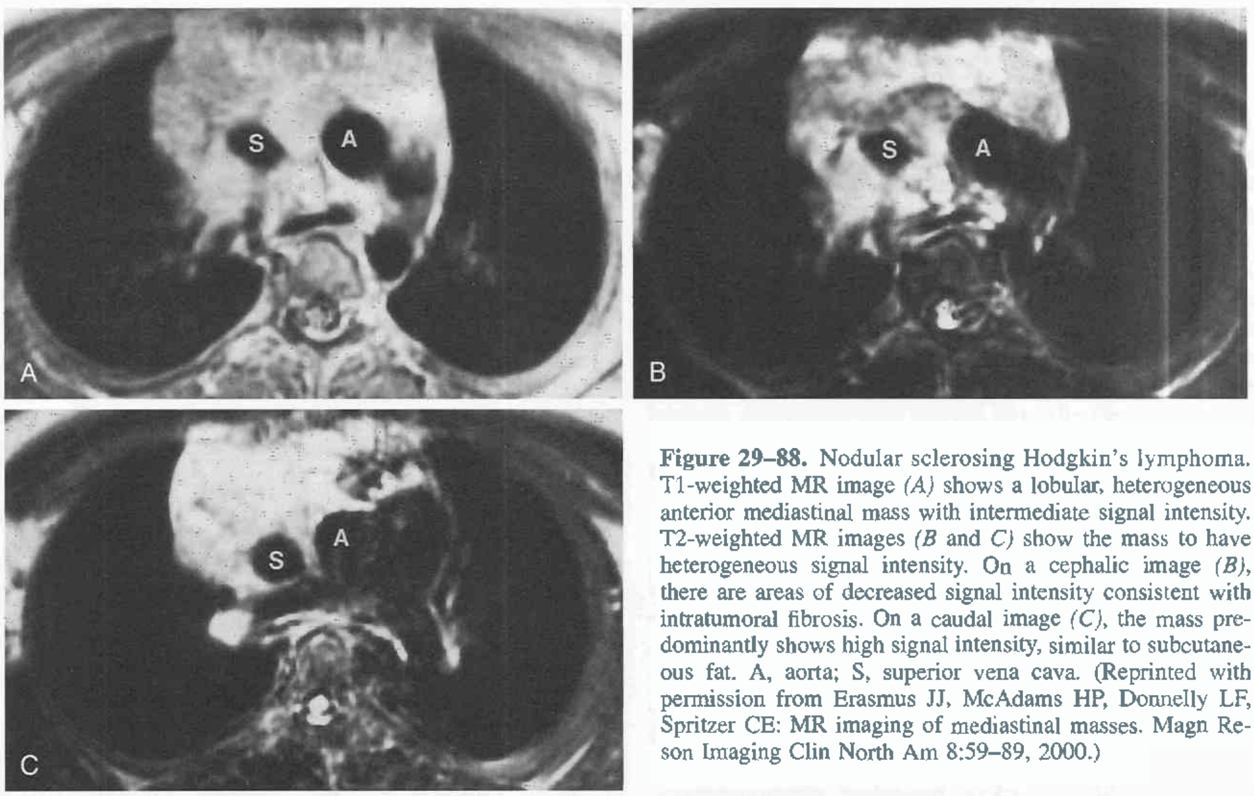

Figure 29–88. Nodular sclerosing Hodgkin's lymphoma. T1-weighted MR image *(A)* shows a lobular, heterogeneous anterior mediastinal mass with intermediate signal intensity. T2-weighted MR images *(B* and *C)* show the mass to have heterogeneous signal intensity. On a cephalic image *(B)*, there are areas of decreased signal intensity consistent with intratumoral fibrosis. On a caudal image *(C)*, the mass predominantly shows high signal intensity, similar to subcutaneous fat. A, aorta; S, superior vena cava. (Reprinted with permission from Erasmus JJ, McAdams HP, Donnelly LF, Spritzer CE: MR imaging of mediastinal masses. Magn Reson Imaging Clin North Am 8:59–89, 2000.)

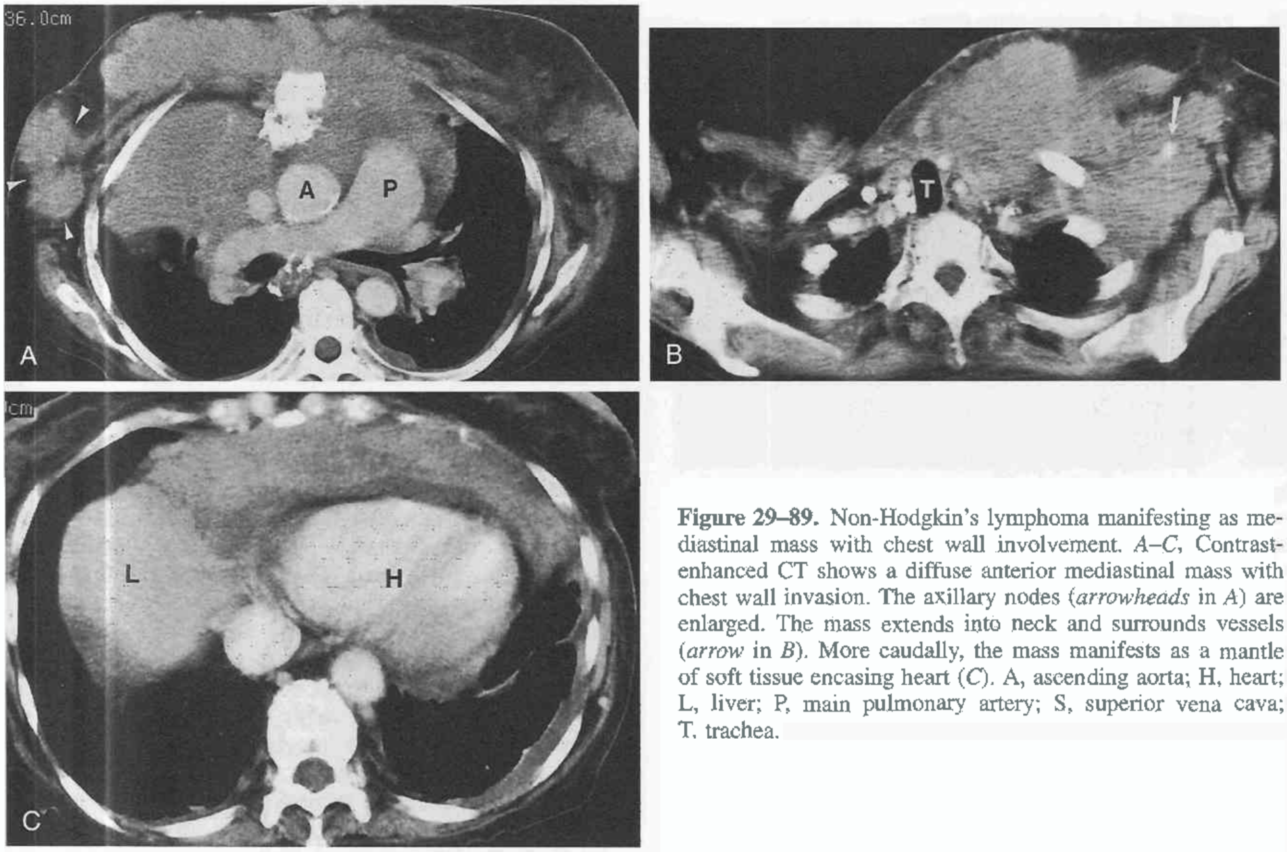

Figure 29–89. Non-Hodgkin's lymphoma manifesting as mediastinal mass with chest wall involvement. *A–C*, Contrast-enhanced CT shows a diffuse anterior mediastinal mass with chest wall invasion. The axillary nodes (*arrowheads* in *A*) are enlarged. The mass extends into neck and surrounds vessels (*arrow* in *B*). More caudally, the mass manifests as a mantle of soft tissue encasing heart (*C*). A, ascending aorta; H, heart; L, liver; P, main pulmonary artery; S, superior vena cava; T, trachea.

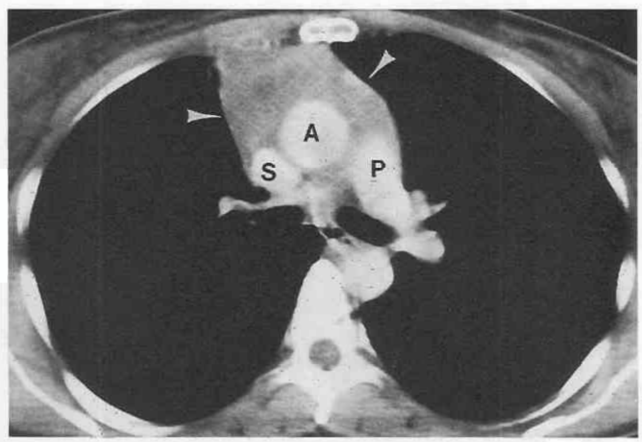

Figure 29–90. Non-Hodgkin's lymphoma manifesting as an anterior mediastinal mass. CT shows a heterogeneous mass *(arrowheads)* with diffuse infiltration of the mediastinum. A, aorta; P, left main pulmonary artery; S, superior vena cava.

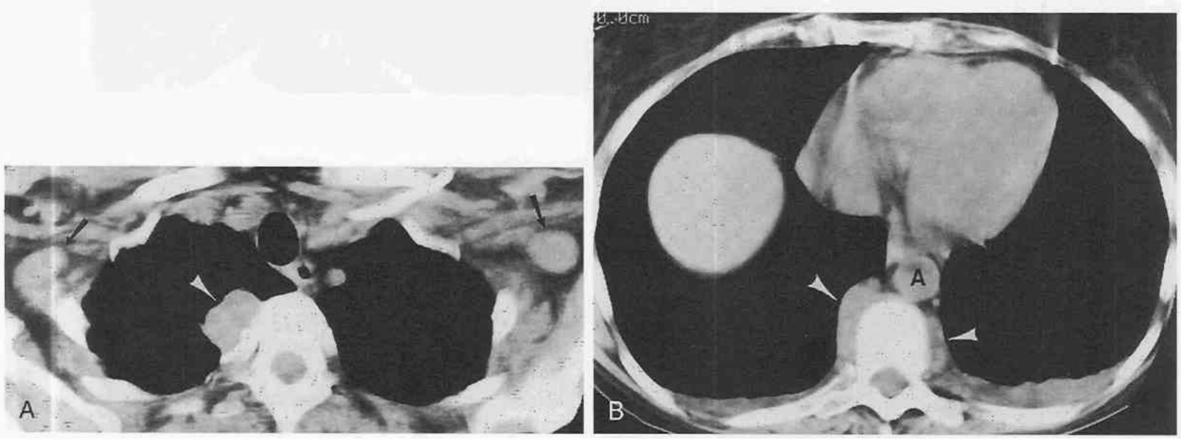

Figure 29–91. Non-Hodgkin's lymphoma manifesting as multifocal disease. *A*, CT shows right paravertebral soft tissue mass *(arrowhead)*. Axillary adenopathy can be seen *(arrows)*. *B*, CT at a more caudal level shows bilateral paravertebral masses *(arrowheads)*. Small pleural effusions can be visualized bilaterally. A, aorta. [redacted]

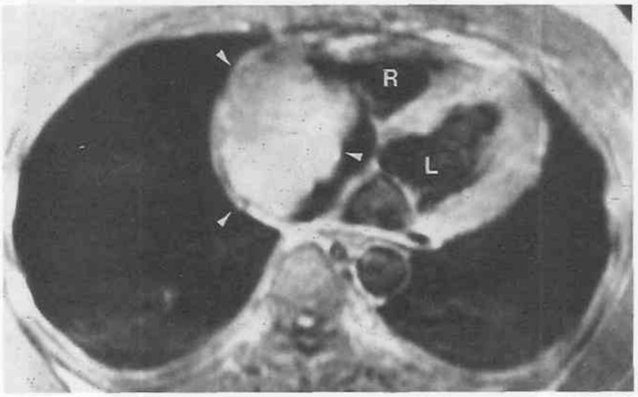

Figure 29–92. Non-Hodgkin's lymphoma with intracardiac involvement. Axial T1-weighted MR image shows a mass of heterogeneous signal intensity extending into right atrium *(arrowheads)*. MRI allows assessment of intravascular and intracardiac tumor extension without administration of intravenous contrast material. L, left ventricle; R, right ventricle. (Reprinted with permission from Erasmus JJ, McAdams HP, Donnelly LF, Spritzer CE: MR imaging of mediastinal masses. Magn Reson Imaging Clin North Am 8:59–89, 2000.)

mediastinal nodes), but rather other nodal sites, lung parenchyma, pleura, and pericardium.

CT and scintigraphy using gallium 67 (^{67}Ga) are usually the primary staging modalities in patients with suspected mediastinal lymphoma. Although MRI can reveal additional information in as many as 15% of cases, it is more often used for assessing suspected SVC obstruction, vascular invasion, and chest wall or mediastinal invasion. MRI has also been used to monitor and evaluate response to therapy, to differentiate fibrosis from residual tumor, and to detect recurrent lymphoma.

Residual masses are seen in the immediate follow-up period in up to 88% of patients with HD and in up to 40% of patients with NHL. These residual masses typically resolve over 12 to 18 months. The presence of residual mediastinal abnormalities is of concern because lymphoma eventually recurs in half of these patients, usually at the site of the original mass. Differentiating residual fibrotic mass from persistent or recurrent tumor can be difficult by conventional imaging. MRI can be a useful adjunct to ^{67}Ga scintigraphy for this assessment.

Because of its high water content, untreated lymphoma is typically homogeneous with low to intermediate signal intensity on T1-weighted images and increased signal intensity on T2-weighted images. Patients with nodular sclerosing HD occasionally have focal regions of low signal intensity within the mass on pretreatment T2-weighted images because of intralesional fibrosis.

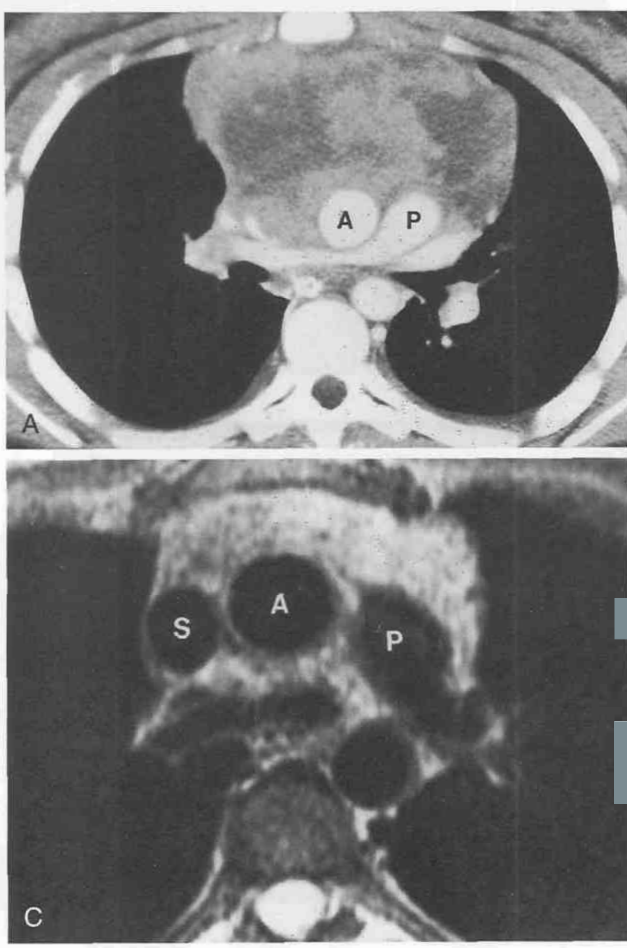

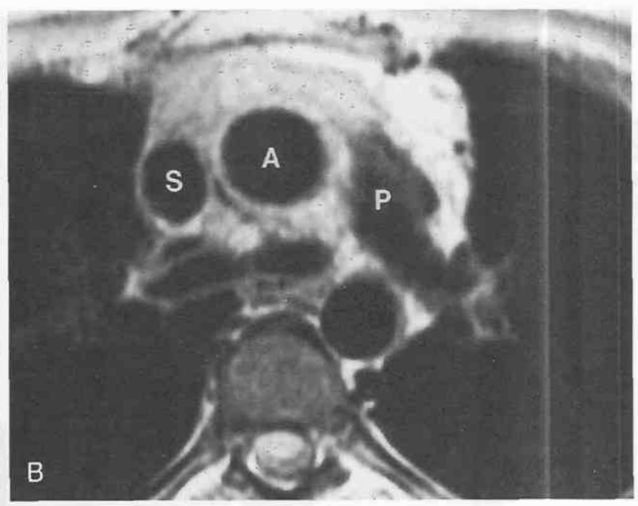

Figure 29–93. Non-Hodgkin's lymphoma. Contrast-enhanced CT *(A)* shows a large heterogeneous anterior mediastinal mass. T1-weighted image *(B)* following therapy shows an intermediate-signal-intensity mass that has decreased in size. The corresponding T2-weighted image *(C)* shows mass to have lower signal intensity than *B*. The decrease in signal intensity suggests that the residual mass is fibrotic. Biopsy confirmed fibrosis and absence of residual tumor. A, ascending aorta; P, main pulmonary artery; S, superior vena cava.

During and immediately after completion of therapy, the lesions typically become heterogeneous on MRI and signal intensity on T2-weighted images becomes more variable. Over the subsequent 4 to 6 months, the residual mass has a tendency to decrease in size and signal intensity on T2-weighted images. Six months after therapy, residual masses resulting from fibrosis should be homogeneous with low signal intensity on both T1-weighted and T2-weighted images. This homogeneous low signal intensity is typical of treated inactive lymphoma. If the mass remains heterogeneous with focal regions of high signal intensity on T2-weighted images, recurrent or residual lymphoma is suggested. Using these findings, MRI can detect persistent or recurrent tumor in treated patients as much as 8 to 12 weeks before the onset of clinical symptoms.

The presence of fat mixed with residual fibrotic tissue is, however, a pitfall on MRI. This potential misinterpretation can be avoided by realizing that regions of high signal intensity detected on T2-weighted images correlate with high signal intensity fat on T1-weighted images (rather than low signal intensity of recurrent tumor). Fat-suppression pulse sequences may also be helpful for distinguishing interspersed fat from areas of residual tumor.

Castleman's Disease

Castleman's disease is also known as angiofollicular or **giant lymph node hyperplasia.**[126, 134, 161, 165, 171, 195] Castleman's disease is not a distinct disease entity but rather a diverse group of rare lymphoproliferative disorders of different tissue types and biologic behaviors. It is currently classified into two major subgroups: localized and disseminated Castleman's disease. There are two major histologic variants: *hyaline vascular* (HV-CD) and *plasma cell* (PC-CD). Although Castleman's disease most often affects the mediastinum, it can occur in any location (mediastinum, 67%; neck, 14%; pelvis, 4%; axilla, 2%).

Localized Castleman's Disease. Most patients with localized thoracic Castleman's disease have HV-CD; localized PC-CD is rare. Localized HV-CD affects all age groups, with a peak incidence in the fourth decade of life. Affected patients are usually asymptomatic at presentation, although symptoms caused by compression or invasion of adjacent structures occur occasionally. Women are more commonly affected than men. Systemic signs and symptoms such as fever, weight loss, and anemia are uncommon.

Histologically, localized HV-CD manifests with massive lymph node hyperplasia, involuted germinal centers, and marked capillary proliferation with endothelial hyperplasia. These masses are typically hypervascular with large feeding vessels. Localized HV-CD can affect any thoracic compartment, but the middle mediastinum and hila are most commonly involved.

Imaging studies show one of three morphologic patterns:

- Solitary mass (50%)
- Dominant infiltrative mass with associated lymphadenopathy (40%)
- Diffuse lymphadenopathy confined to a single mediastinal compartment (10%)

Identification of the first pattern suggests that complete surgical resection is likely. Identification of the second or third pattern suggests that complete excision may be difficult or impossible.

On non–contrast-enhanced CT, localized HV-CD manifests as a homogeneous or heterogeneous mass of soft tissue attenuation. Calcification is uncommon (5% to 10%) and is typically coarse and central in location. HV-CD typically enhances intensely following IV administration of iodinated contrast material (Fig. 29–94). On MRI, the lesions are typically heterogeneous and show increased signal intensity (compared to skeletal muscle) on T1-weighted sequences. They become markedly hyperintense on T2-weighted sequences. Low signal intensity septa are occasionally visible. In larger lesions, flow voids in and around the mass may be identified and are important clues to the hypervascular nature of the lesions. Because the lesions are hypervascular, diffuse enhancement following administration of IV gadolinium is common (Fig. 29–95).

Disseminated Castleman's Disease. Disseminated Castleman's disease is currently regarded as a potentially malignant lymphoproliferative disorder that has been associated with the *POEMS syndrome* (*p*olyneuropathy, *o*rganomegaly, *e*ndocrinopathy, *m*onoclonal proteinemia, and

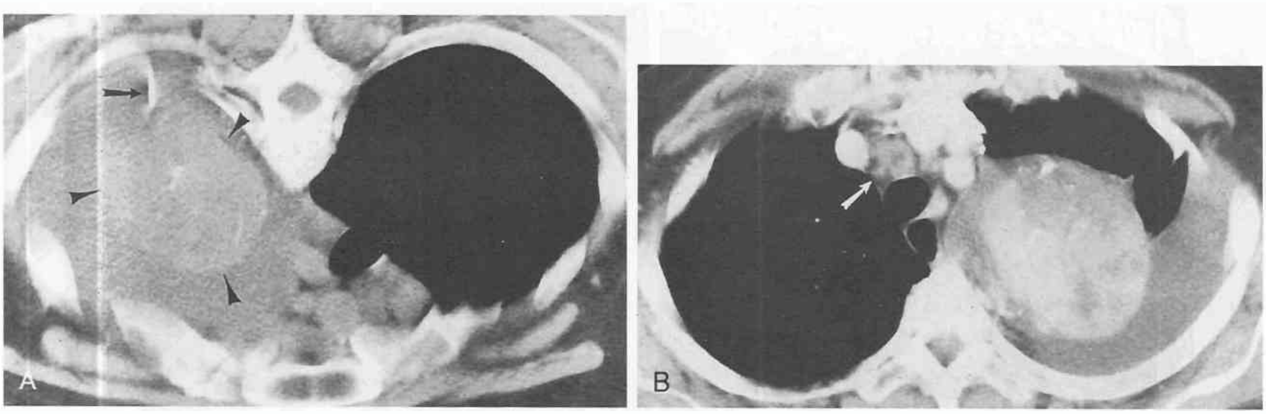

Figure 29–94. Hyaline-vascular Castleman's disease. *A,* CT performed to direct a biopsy on a patient in the prone position shows heterogeneous soft-tissue-attenuation mass in the left posterior mediastinum *(arrowheads).* The biopsy needle *(arrow),* central linear calcification, and left pleural effusion can be seen. *B,* Contrast-enhanced CT with the patient supine shows intense enhancement within the mass as well as a small associated pretracheal node *(arrow).*

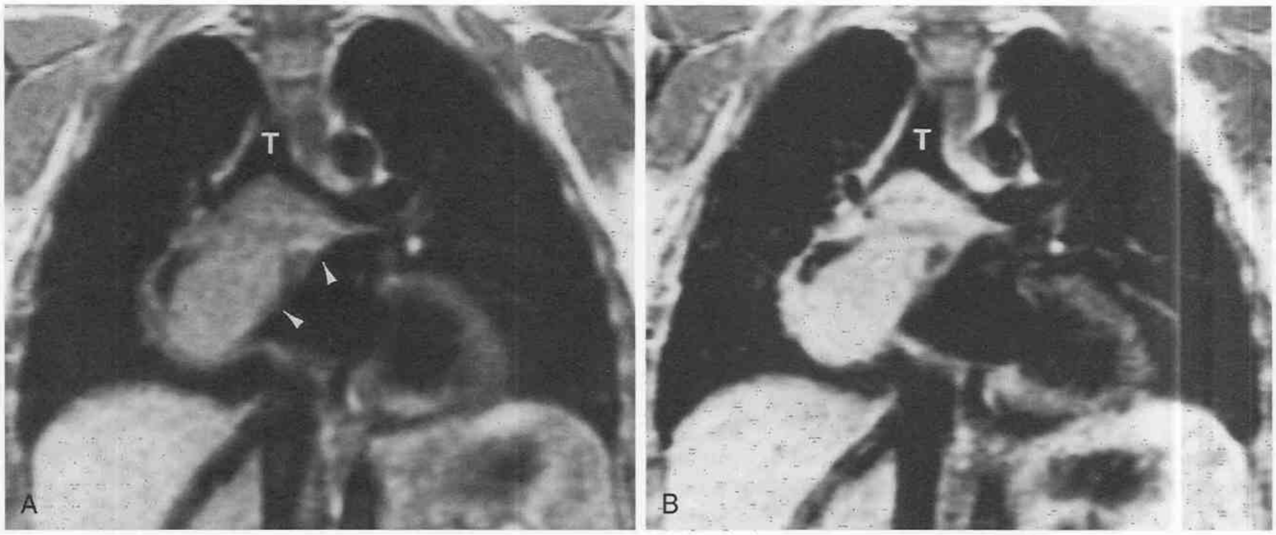

Figure 29–95. Hyaline-vascular Castleman's disease. *A*, Coronal T1-weighted MR image shows large, homogeneous mass *(arrowheads)* in subcarinal region of intermediate signal intensity. Note mass effect on the carina. *B*, Coronal T1-weighted MR image following administration of gadolinium-based contrast material demonstrates diffuse enhancement within the mass, typical of hyaline vascular Castleman's disease. T, trachea.

skin changes), osteosclerotic myeloma, Kaposi's sarcoma, and acquired immunodeficiency syndrome (AIDS). Most patients with disseminated thoracic Castleman's disease have the plasma cell form of the disease. It affects all age groups but the peak incidence is in the fifth decade of life. Women are more commonly affected than men by a ratio of 2:1. Most patients present with systemic complaints of fever, weight loss, and anemia.

Disseminated thoracic Castleman's disease usually manifests on chest radiographs as bilateral mediastinal widening. Focal mediastinal masses are rare. The anterior mediastinum is most commonly affected. On CT, diffuse lymphadenopathy involving multiple mediastinal compartments is noted (Fig. 29–96). The nodes typically range in size from 1 to 6 cm in diameter and demonstrate homogeneous attenuation on non–contrast-enhanced CT scans. Associated findings such as splenomegaly or ascites are common.

Mediastinitis

Acute Mediastinitis

Acute bacterial mediastinitis is a life-threatening condition that requires prompt diagnosis and treatment. Spontaneous or iatrogenic esophageal rupture is the most common cause, accounting for up to 90% of cases. Other causes include direct spread from retropharyngeal or pleural infection and mediastinitis after cardiac surgery.[27, 32, 88, 128, 137, 169, 209, 251, 262]

Findings of esophageal perforation on CT include periesophageal fluid collections (100%), extraluminal mediastinal air (100%), esophageal wall thickening (82%), and

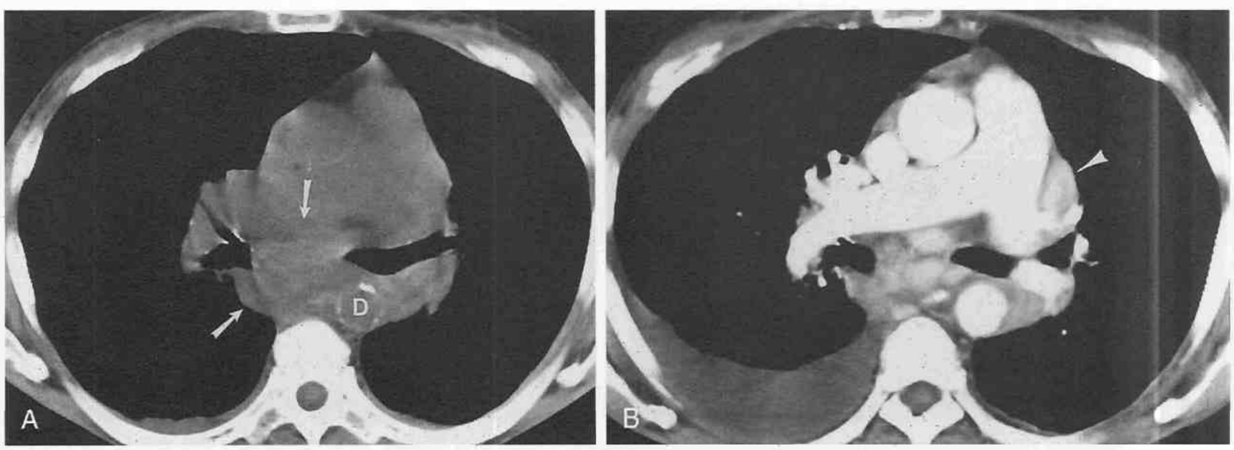

Figure 29–96. Disseminated Castleman's disease. *A*, CT shows marked subcarinal adenopathy *(arrows)*. Paratracheal and prevascular adenopathy was extensive (not shown). D, descending aorta. *B*, Contrast-enhanced CT shows marked enhancement of subcarinal and aortopulmonary window *(arrowhead)* lymph nodes. A right pleural effusion can be seen.

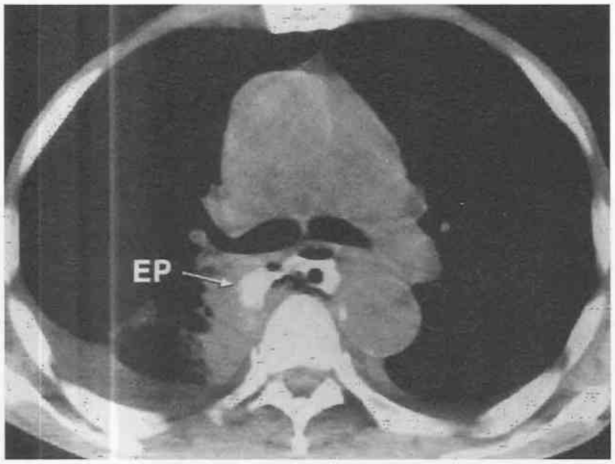

Figure 29–97. Acute mediastinitis after perforation of esophageal carcinoma. CT shows extravasation of esophageal contrast (EP) and air into mediastinum after perforation. A small right pleural effusion can be seen.

pleural effusion (82%) (Fig. 29–97). Pleural effusion tends to be right sided in patients with iatrogenic, midesophageal perforation and left sided in patients with spontaneous, distal esophageal perforation (Boerhaave's syndrome). The site of perforation is uncommonly visualized on CT (18%).

Descending cervical mediastinitis (DCM) is an uncommon but life-threatening cause of mediastinitis. Such infections begin in the head and neck region and spread via fascial planes into the mediastinum, usually in the prevertebral space; from there, the infection spreads into the middle and posterior mediastinum. Typical causes include odontogenic infection as well as suppurative tonsillitis and adenitis and retropharyngeal abscess. CT performed in patients with DCM shows fluid collections in the mediastinum that may be contiguous with fluid collections in the cervical region (Fig. 29–98). CT is essential for confirming the diagnosis; it assists in fluid aspiration to confirm infection and in monitoring the patient's response to therapy.

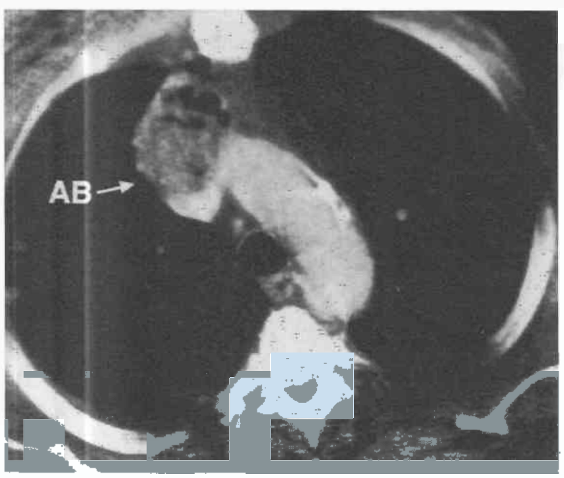

Figure 29–98. Descending cervical mediastinitis. CT shows air-containing mediastinal abscess (AB) that extended from an abscess in the neck.

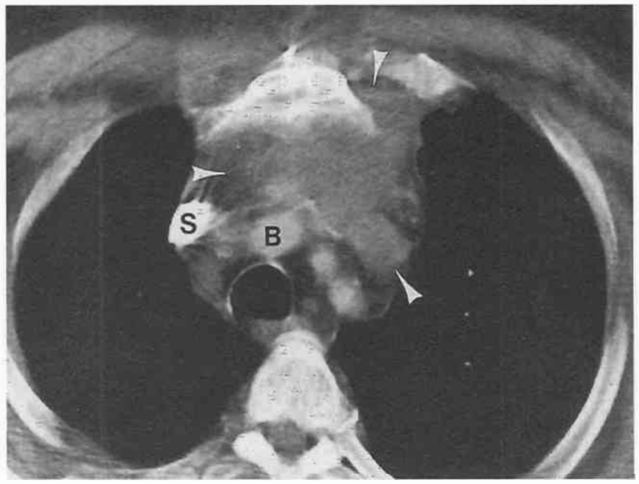

Figure 29–99. Mediastinal hematoma mimicking mediastinal abscess after coronary artery bypass procedure. Contrast-enhanced CT shows well-circumscribed soft tissue abnormality in the fat of the anterior mediastinum *(arrowheads)*. Small focal adjacent air collections *(arrow)* and surgical clips anterior to the ascending aorta can be seen. The needle aspirate confirmed hematoma and the culture was negative for organisms. A, ascending aorta; P, main pulmonary

Mediastinitis after cardiac surgery is uncommon, occurring in only 0.5% to 1% of patients.[25, 69, 208] CT is frequently performed in patients with clinically suspected mediastinitis, but it can be difficult to interpret because fluid and air collections, hematomas, pleural effusions, and increased attenuation of anterior mediastinal fat, all potential findings of mediastinitis, are common and expected findings in the immediate postoperative period. These findings generally resolve, however, in the first days and weeks after median sternotomy.

Needle aspiration of fluid collections may be necessary to rule out infection when mediastinitis is suspected (Fig. 29–99). CT is most useful for distinguishing patients with significant retrosternal fluid collections that require open drainage from those who have only superficial wound infections (Fig. 29–100). CT, however, has limited ability for detecting early changes of sternal osteomyelitis.

Histoplasmosis and tuberculosis can cause acute pericarditis and mediastinitis. As in mediastinitis of any cause, the CT appearance is that of increased attenuation of mediastinal fat, focal fluid collections, or abscesses (Fig. 29–101). Infected lymph nodes can show low attenuation centers and peripherally enhancing rims.

Fibrosing Mediastinitis

Mediastinal fibrosis (sclerosing or fibrosing mediastinitis) is a rare benign disorder caused by proliferation of acellular collagen and fibrous tissue within the mediastinum.[62, 160, 208, 210, 228, 259] An abnormal immunologic response to antigens of *Histoplasma capsulatum* is thought to be the most common cause in the United States. Other causes include *M. tuberculosis* infection, autoimmune disease, radiation therapy, trauma, and drugs such as methysergide. A rare familial form associated with retroperitoneal fibrosis,

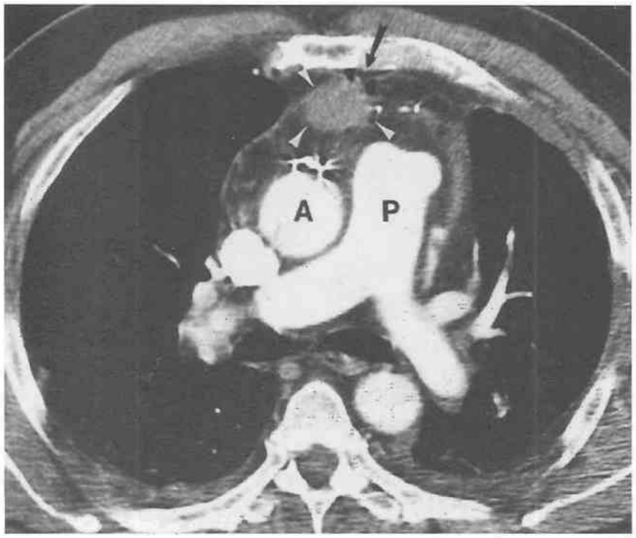

Figure 29–100. Mediastinitis manifesting as mediastinal abscess. CT shows a poorly marginated heterogeneous soft tissue mass *(arrowheads)* in the anterior mediastinum. Note the absence of air within the abscess. The needle was positive for *Staphylococcus aureus* infection. B, brachiocephalic artery; S, superior vena cava.

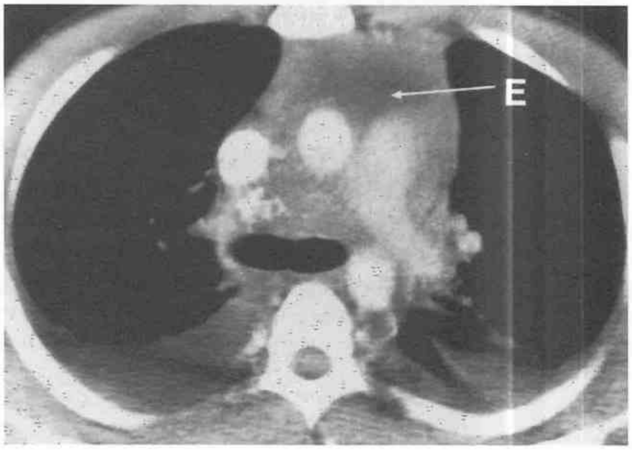

Figure 29–101. Acute mediastinitis caused by histoplasmosis. CT shows diffuse increased attenuation of mediastinal fat and pericardial effusion (E).

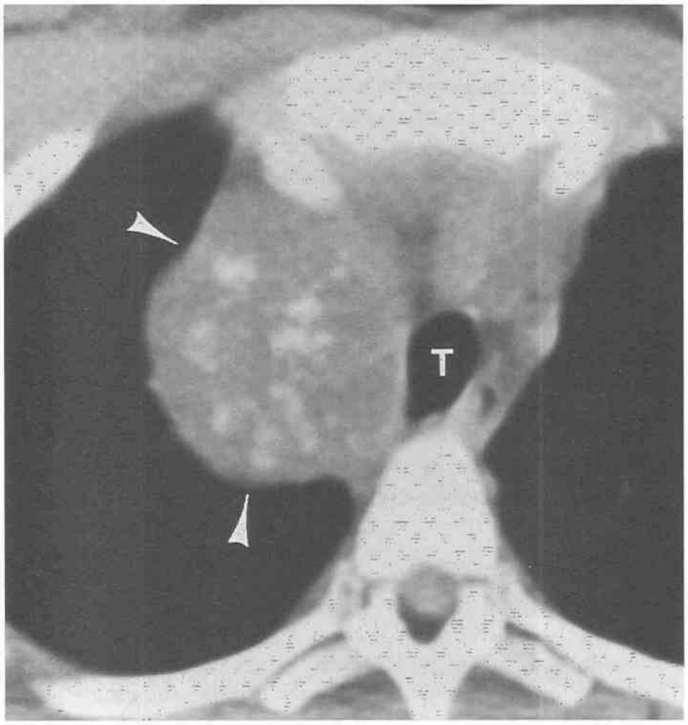

Figure 29–102. Mediastinal granuloma caused by histoplasmosis. CT shows soft-tissue-attenuation mass with punctate calcification *(arrowheads)* in the superior mediastinum. Biopsy confirmed histoplasmosis. T, trachea.

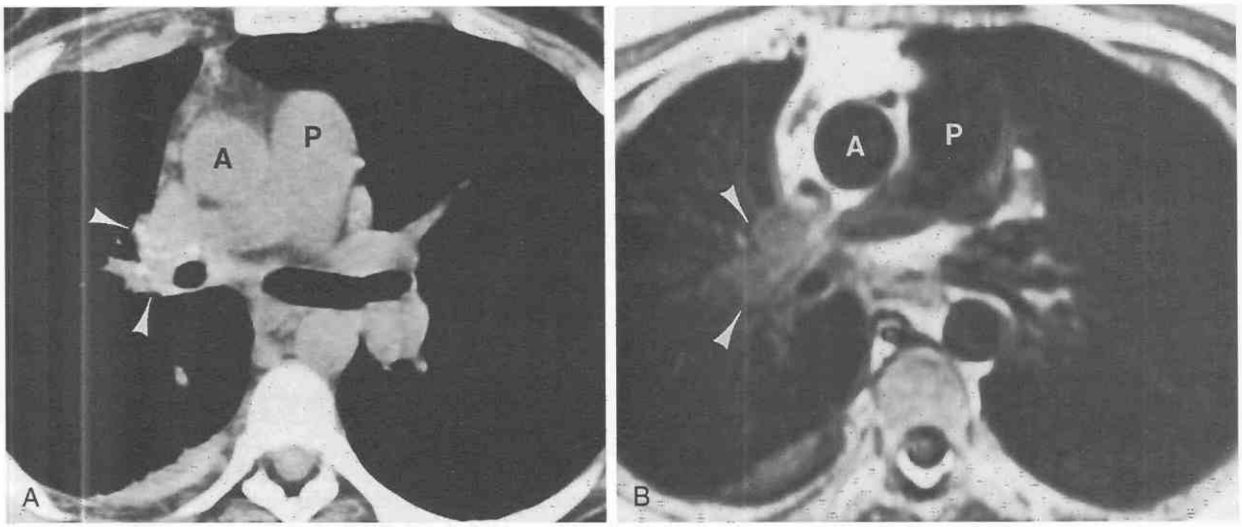

Figure 29–103. Fibrosing mediastinitis in a 45-year-old woman with chest pain. *A,* CT of the chest demonstrates an infiltrating right hilar mass *(arrowheads)* with punctate calcification and right posterior pleural thickening. *B,* Axial T1-weighted MR image shows intermediate-signal-intensity mass *(arrowheads)* and obstruction of the right pulmonary artery. The MRI appearance is nonspecific; the presence of extensive calcification on the CT scan suggests the diagnosis. A, ascending aorta; P, pulmonary artery. (Reprinted with permission from Erasmus JJ, McAdams HP, Donnelly LF, Spritzer CE: MR imaging of mediastinal masses. Magn Reson Imaging Clin North Am 8:59–89, 2000.)

sclerosing cholangitis, Riedel's thyroiditis, and pseudotumor of the orbit is also reported.

Affected patients usually present in the second through fifth decades of life with signs and symptoms caused by obstruction and compression of the SVC, pulmonary veins or arteries, central airways, or esophagus. Patients most commonly present with cough, recurrent pulmonary infection, hemoptysis, or chest pain. Pulmonary venous obstruction may result in symptoms that mimic those of mitral stenosis.

The chest radiographic findings of fibrosing mediastinitis are nonspecific and often underestimate the extent of mediastinal disease. CT and MRI are consequently useful in the evaluation of this disorder (Figs. 29–102 to 29–104). On CT, fibrosing mediastinitis typically manifests as an infiltrative, often calcified hilar or mediastinal process. CT is useful for demonstrating airway, pulmonary arterial and venous involvement.

On MRI scans, the process typically shows heterogeneous signal intensity on T1-weighted and T2-weighted images. Markedly decreased signal intensity on T2-weighted images is occasionally seen and is suggestive of the fibrotic nature of the process. MRI may be superior to CT for defining the full extent of the disease, which is of importance in preoperative planning; however, CT is better for demonstrating calcification within the lesion, a finding that is critical for differentiating fibrosing mediastinitis from other infiltrative disorders of the mediastinum such as metastatic carcinoma or lymphoma.

Hemorrhage

Bleeding can occur within the mediastinum as a result of trauma, surgery, or line placement; after endoscopy; or as a result of abnormal clotting factors. Hemorrhage may extend from the neck or retroperitoneum into the mediastinum. Hemorrhage can manifest as diffuse areas of increased density or as focal areas of increased density within the mediastinal fat.

Mediastinal Lipomatosis

Mediastinal lipomatosis is a benign accumulation of fat within the mediastinum that can manifest as widening of the mediastinum on chest radiographs.[124] Mediastinal

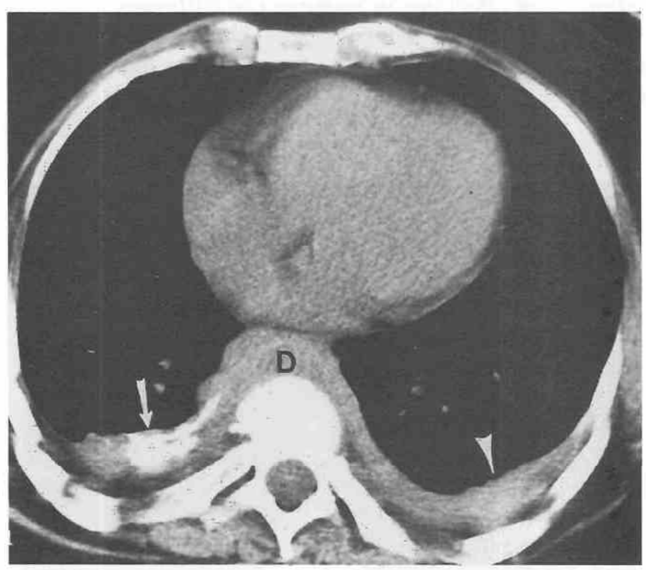

Figure 29–104. Posterior mediastinal fibrosis. CT shows diffuse soft-tissue-attenuation mass encasing the distal aorta (D) and extending into the pleural space *(arrowhead)* bilaterally. Extensive calcification *(arrow)* can be visualized in the right pleural space.

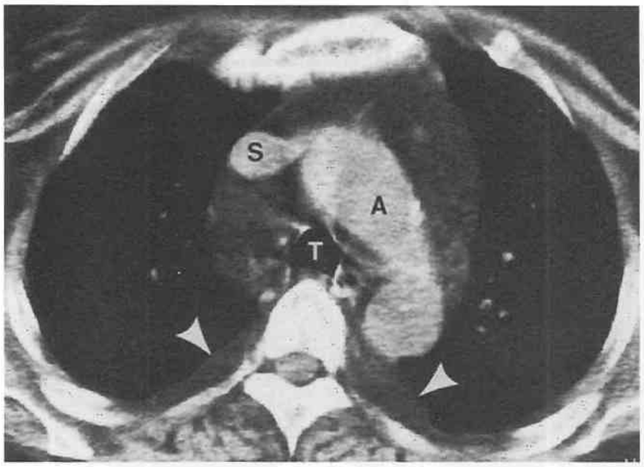

Figure 29–105. Mediastinal lipomatosis. CT shows bilateral mediastinal widening caused by mediastinal fat deposition. Fat deposition is also visible in the paraspinal and posterior pleural regions bilaterally *(arrowheads)*. The distribution is typical of mediastinal lipomatosis. A, aorta; S, superior vena cava; T, trachea.

lipomatosis may be associated with obesity, steroid use, or Cushing's syndrome, but often no predisposing factor is recognized. The accumulation of fat is more pronounced in the upper mediastinum. Mediastinal lipomatosis demonstrates a uniform fat density of −100 HU on CT (Fig. 29–105). If the fat has a higher density or strands of soft tissue density within it, other diagnoses, such as liposarcoma, hemorrhage, tumor infiltration, or mediastinitis, should be considered.

Occasionally, a prominent epicardial fat pad can result in a mediastinal mass (Fig. 29–106).

Mesenchymal Tumors

A variety of mesenchymal tumors can arise in the mediastinum and affect one or multiple compartments.[38, 54, 59, 111, 176, 249] These include malignancies such as leiomyosarcoma and liposarcoma as well as benign desmoid tumors of the mediastinum.

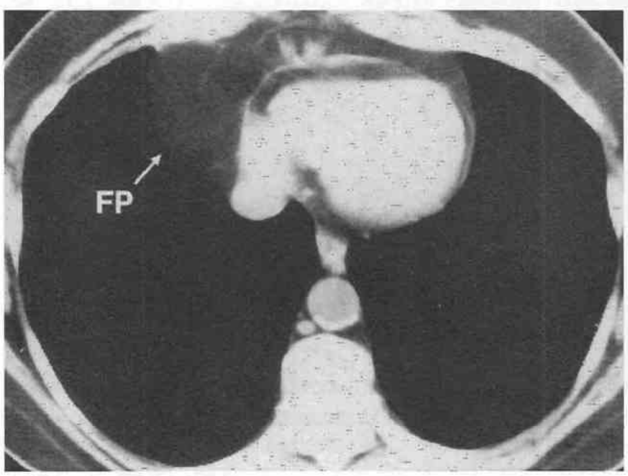

Figure 29–106. Cardiophrenic angle mass. CT shows that this mass is caused by a prominent epicardial fat pad (FP).

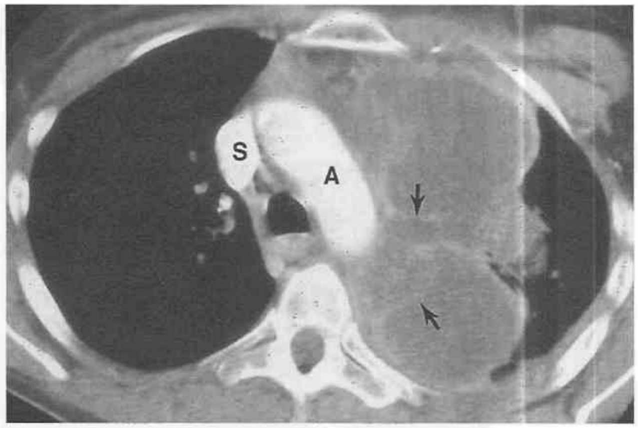

Figure 29–107. Mediastinal liposarcoma. Contrast-enhanced CT shows a large heterogeneous mediastinal mass involving multiple compartments. Note enhancing septa *(arrows)* and absence of adipose tissue within mass. A, aorta; S, superior vena cava.

Liposarcomas typically arise in the anterior mediastinum, occur in middle-aged adults, and present with symptoms of chest pain and dyspnea. Masses are typically large and diffusely infiltrate the mediastinum. Low-grade tumors can have large amounts of fat demonstrable on CT or MR images; high-grade tumors typically manifest as heterogeneous soft tissue masses on CT or MR images (Fig. 29–107).

Leiomyomas and leiomyosarcomas usually arise from the esophagus, although rarely they can arise in the mediastinum independent of the esophagus. They manifest as large middle-mediastinal masses of soft tissue attenuation or signal intensity on CT or MR images. Affected patients typically present with dysphagia.

Other less common mesenchymal sarcomas that may

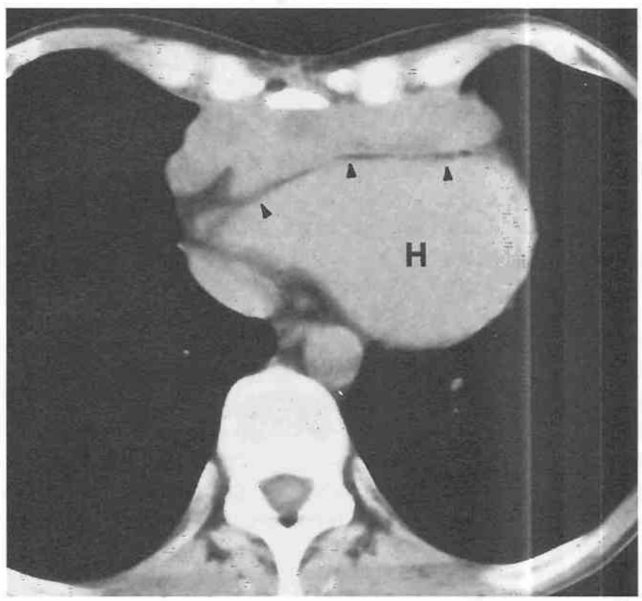

Figure 29–108. Primary mediastinal sarcoma. CT shows large, lobular, heterogeneous anterior mediastinal mass. The fat plane *(arrowheads)* between the mass and the adjacent compressed heart (H) is preserved.

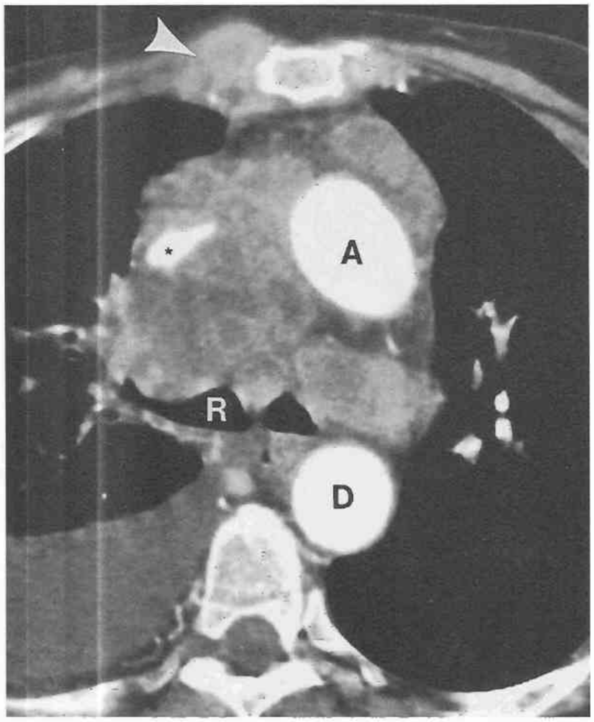

Figure 29–109. Diffuse mediastinal metastases. Contrast-enhanced CT shows diffuse infiltrating mediastinal mass caused by metastatic breast carcinoma. Narrowing of the superior vena cava *(asterisk)*, chest wall metastasis *(arrowhead)*, and large right pleural effusion can be seen. A, ascending aorta; D, descending aorta; R, right main bronchus.

arise within the mediastinum include rhabdomyosarcoma, fibrosarcoma, chondrosarcoma, and osteosarcoma (Fig. 29–108).

Desmoid tumors are uncommon proliferations of fibroblastic cells that typically arise from muscular fascia. Although histologically benign, they can exhibit aggressive behavior with a propensity for local invasion and recurrence after resection. They uncommonly arise within the mediastinum. Most tumors that affect the mediastinum do so by extension from chest wall or head and neck lesions. On CT, desmoid tumors are usually homogeneous and show slightly increased attenuation relative to skeletal muscle. On T1-weighted MR images, they show low signal intensity; on T2-weighted images, they show variable signal intensity. Although the tumors are usually localized, extensive invasion of mediastinal structures is occasionally detected.

Metastatic Malignancy

Metastatic malignancy can occasionally result in a diffuse mediastinal abnormality. This most likely results from extranodal extension in patients with metastatic disease to the mediastinal lymph nodes. Metastatic mucinous tumors to the mediastinum (ovarian, colon) can occur in young patients, and occasionally this occurs prior to the diagnosis of the primary malignancy. Metastatic malignancy appears on CT or MR images as an infiltrating, heterogeneous mass that invades and occasionally obliterates adjacent mediastinal structures (Fig. 29–109). It can be difficult to differentiate metastatic malignancy from fibrosing mediastinitis. Features that suggest fibrosing mediastinitis rather than metastatic malignancy include the following:

- Diffuse calcification within the lesion
- Young age of patient
- No history of extrathoracic primary malignancy

Vascular Abnormalities and Anomalies

A variety of vascular anomalies can simulate a mediastinal mass.[42, 43, 98, 99, 260, 261] These include, but are not limited to, dilation of the pulmonary arteries, dilation of the vena cava, persistence of a left SVC, a persistent vertical vein, the SVC syndrome, dilation of the azygos or hemiazygos veins, mediastinal varices, aneurysms and pseudoaneurysms of the aorta, right-sided and double aortic arches, aberrant subclavian arteries, and tortuous great vessels. In all cases, CT (usually with IV contrast material) or MRI is essential for confirming the diagnosis (Fig. 29–110).

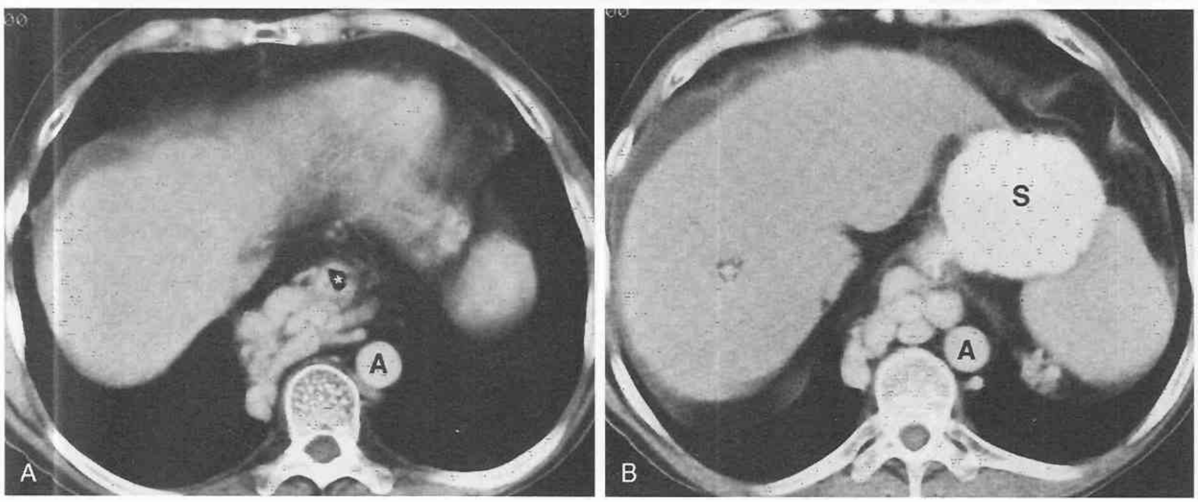

Figure 29–110. Esophageal varices. *A* and *B*, Contrast-enhanced CT shows multiple tubular contrast-enhancing structures surrounding the distal esophagus (*asterisk* on *A*), compatible with esophageal varices. Note moderate ascites. A, aorta; S, stomach.

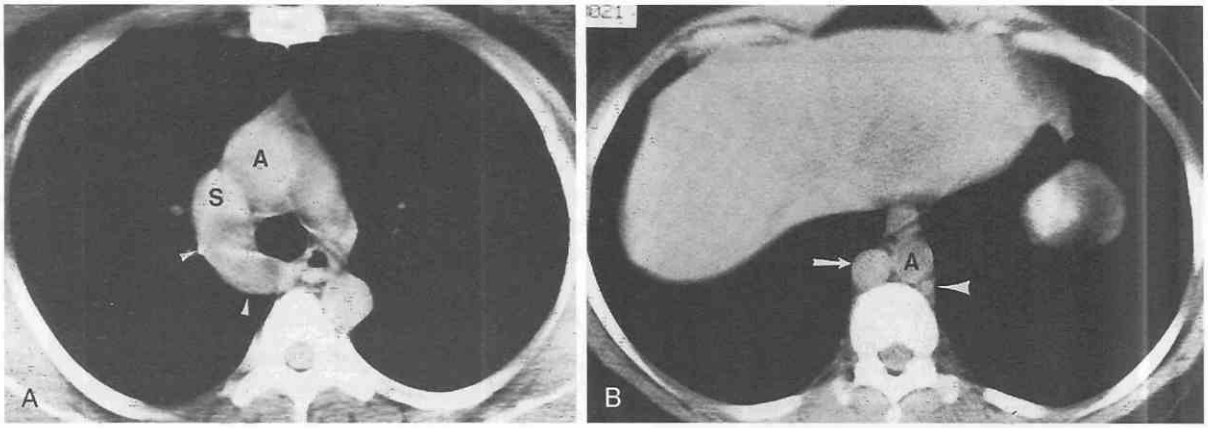

Figure 29–111. Azygous continuation of interrupted inferior vena cava. *A,* CT shows the dilated azygos vein *(arrowheads)* as it enters the posterior aspect of the superior vena cava (S). *B,* Caudal CT shows the dilated azygos vein *(arrow)* near the diaphragmatic hiatus. The hemiazygos vein *(arrowhead)* is normal. A, aorta.

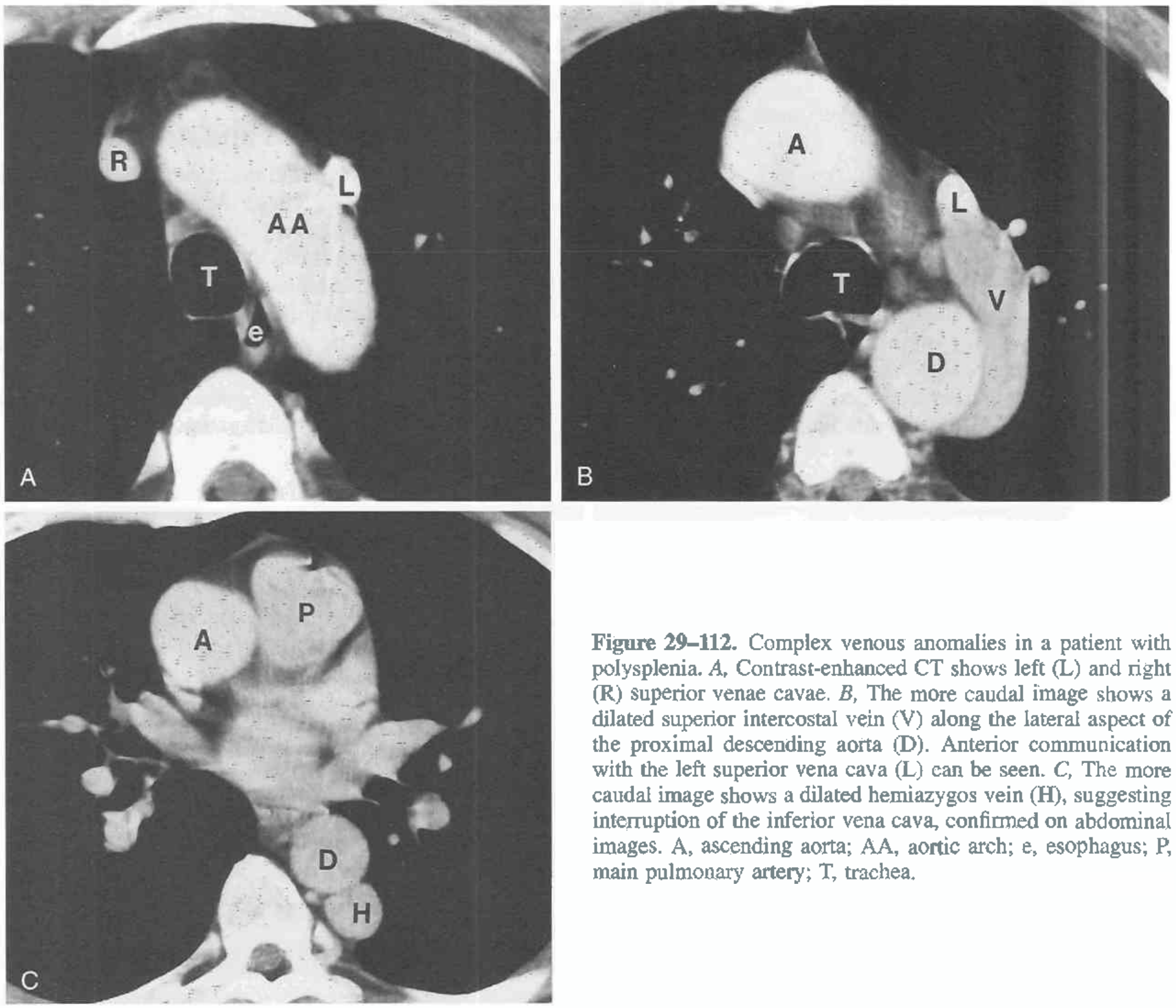

Figure 29–112. Complex venous anomalies in a patient with polysplenia. *A,* Contrast-enhanced CT shows left (L) and right (R) superior venae cavae. *B,* The more caudal image shows a dilated superior intercostal vein (V) along the lateral aspect of the proximal descending aorta (D). Anterior communication with the left superior vena cava (L) can be seen. *C,* The more caudal image shows a dilated hemiazygos vein (H), suggesting interruption of the inferior vena cava, confirmed on abdominal images. A, ascending aorta; AA, aortic arch; e, esophagus; P, main pulmonary artery; T, trachea.

Azygous Continuation of Inferior Vena Cava

Interruption of the inferior vena cava is a congenital abnormality that can be associated with polysplenia.[56, 57, 256] In this anomaly, the infrahepatic, suprarenal segment of the inferior vena cava is absent. Venous blood from the lower extremity and abdomen is diverted into the azygos, or less commonly, the hemiazygos system, resulting in dilation of these veins. Chest radiographs usually show an enlarged azygos vein and a widened paraspinal reflection, and the inferior vena cava is usually not visualized on the lateral radiograph. CT or MRI shows enlargement of the azygos or hemiazygos veins and marked dilation of the azygos arch or the left superior intercostal vein (Figs. 29–111 and 29–112).

Persistent Left Superior Vena Cava

A persistent left SVC[44] occurs in about 1 in 200 adults with normal hearts and in up to 5% of children with congenital heart disease. Most patients with this anomaly have both a right and a left SVC. Occasionally, a persistent brachiocephalic vein connects the two superior venae cavae. On CT, the left SVC is seen as a round density just to the left of the aortic arch. If contrast material is administered via the left arm, the vein enhances (see Fig. 29–112). The left SVC extends inferiorly to the region of the left superior pulmonary veins and then connects into the coronary sinus (Fig. 29–113). Rarely, the vein may connect into the left atrium, giving rise to a small right-to-left shunt.

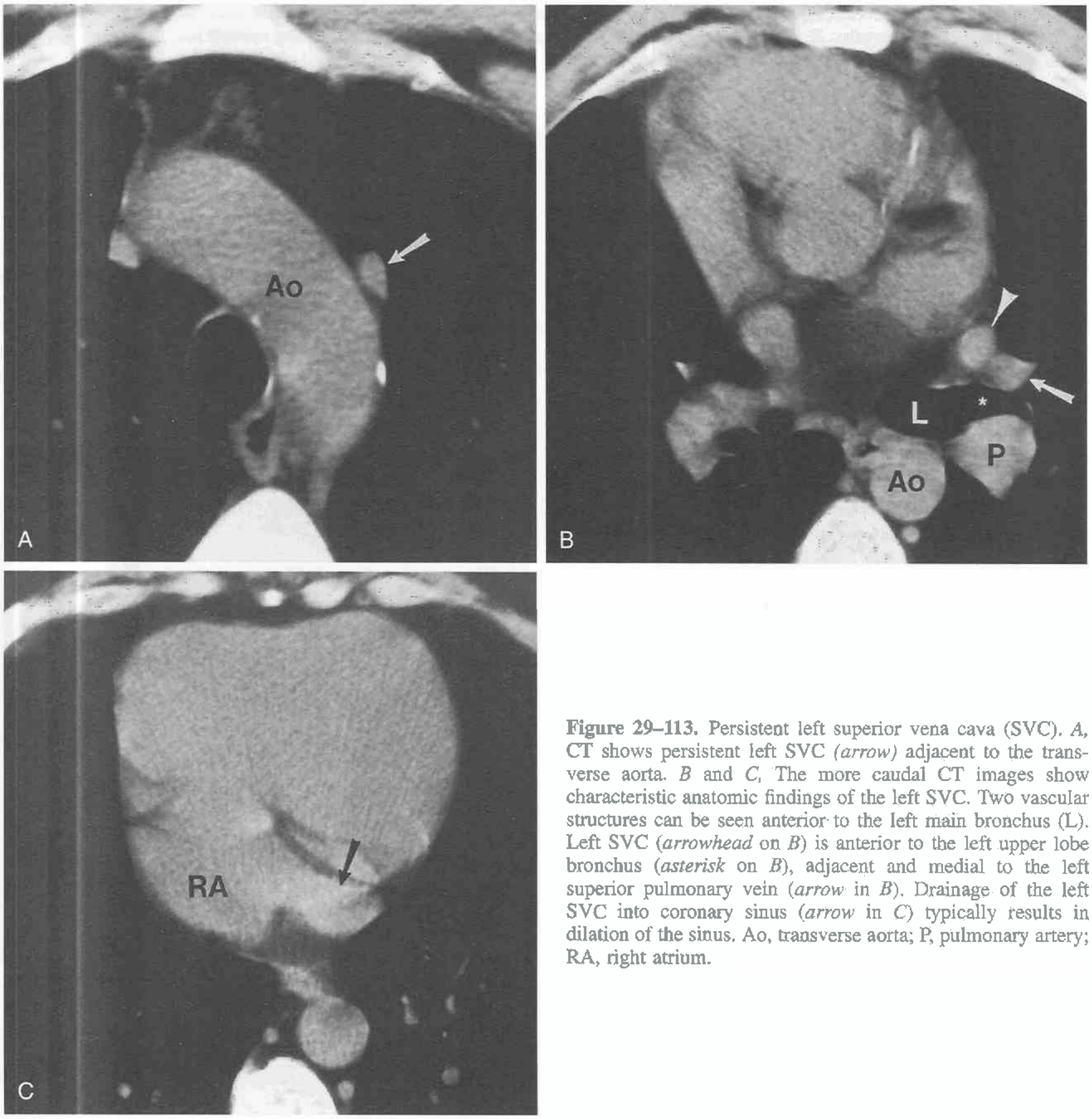

Figure 29–113. Persistent left superior vena cava (SVC). *A*, CT shows persistent left SVC *(arrow)* adjacent to the transverse aorta. *B* and *C*, The more caudal CT images show characteristic anatomic findings of the left SVC. Two vascular structures can be seen anterior to the left main bronchus (L). Left SVC (*arrowhead* on *B*) is anterior to the left upper lobe bronchus (*asterisk* on *B*), adjacent and medial to the left superior pulmonary vein (*arrow* in *B*). Drainage of the left SVC into coronary sinus (*arrow* in *C*) typically results in dilation of the sinus. Ao, transverse aorta; P, pulmonary artery; RA, right atrium.

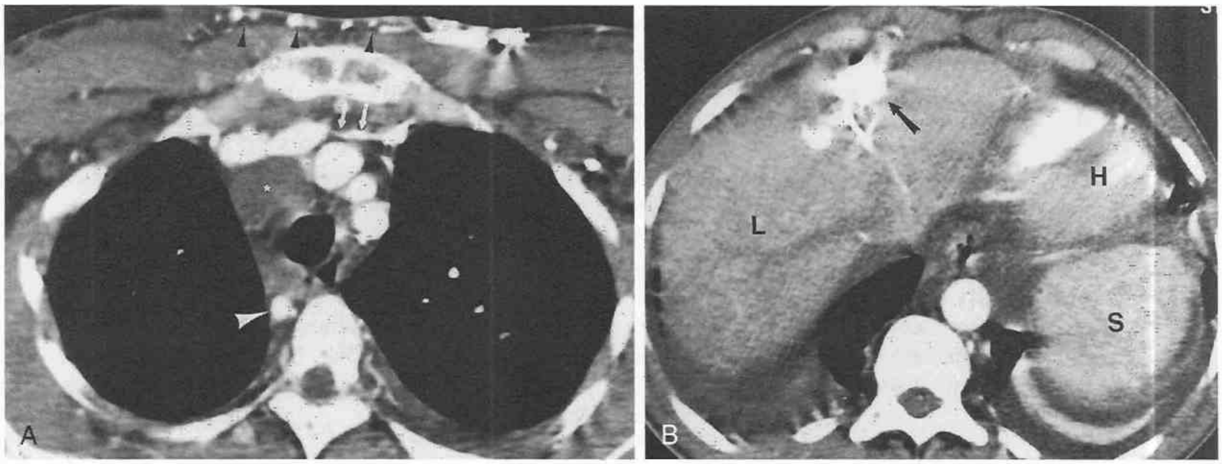

Figure 29–114. Collateral venous channels in a patient with thrombosis of the left subclavian vein caused by an indwelling catheter. *A,* Contrast-enhanced CT shows narrowing of the left subclavian vein *(arrows)*, numerous enlarged veins in soft tissues of the chest *(small arrowheads)* and paravertebral region. The *large arrowhead* indicates an enlarged right superior intercostal vein, and the *asterisk* indicates paratracheal adenopathy. *B,* Contrast-enhanced CT shows collateral venous drainage in the recanalized umbilical vein *(arrow)*. Bilateral pleural effusions can be seen. L, liver; H, heart; S, spleen.

The persistent left SVC should not be confused with the left superior intercostal vein. The superior intercostal vein connects the left brachiocephalic vein with the hemiazygos system. It runs parallel to the aortic arch, is often seen in the fat adjacent to the arch, and normally measures no more than 4 mm in diameter. It can become enlarged as a result of collateral flow in patients with congenital or acquired obstruction of the vena cava (see Fig. 29–112).

Superior Vena Cava or Brachiocephalic Vein Obstruction

Obstruction of the SVC or brachiocephalic veins can result from malignancy, infection, or iatrogenic causes.[23, 266] Lung carcinoma is the most common malignant cause; histoplasmosis-induced fibrosing mediastinitis is the most common infectious cause (in the Midwestern United States); and central venous catheters are the most common iatrogenic cause. In the past, upper extremity venography was the method of diagnosing SVC or brachiocephalic venous obstruction. Contrast CT is the now the most common imaging modality used (Fig. 29–114). MRI can also be useful in patients with contraindications to administration of iodinated contrast material, but it occasionally fails to differentiate complete obstruction from marked narrowing with very slow flow.

Aberrant Right Subclavian Artery

An **aberrant right subclavian artery**[31, 199, 200] is a common vascular abnormality that occurs in about 1 in 200 patients. In younger patients, it is usually not obvious on a chest radiograph; in older patients, however, it can manifest as a right paratracheal mass or, on the lateral radiograph, as a retrotracheal mass—like opacity. On CT, the aberrant right subclavian artery arises as the last and most posterior vessel off the aortic arch, crosses the mediastinum behind the trachea and esophagus, and continues into the neck and axilla along the right of the trachea (Figs. 29–115 and 29–116). Frequently, a diverticulum (Kommerell's) is seen at the origin of the aberrant right subclavian artery from the aorta.

Right Aortic Arch

A right aortic arch[16, 167, 199] is commonly mistaken for a mediastinal mass on chest radiographs, and patients are often referred for CT evaluation of a right paratracheal mass. Most asymptomatic adults with a right-sided aortic arch have an aberrant left subclavian artery. Other anatomic configurations, such as mirror-image branching of the great vessels, are less common and more often associated with severe congenital heart disease. CT or MRI easily identifies

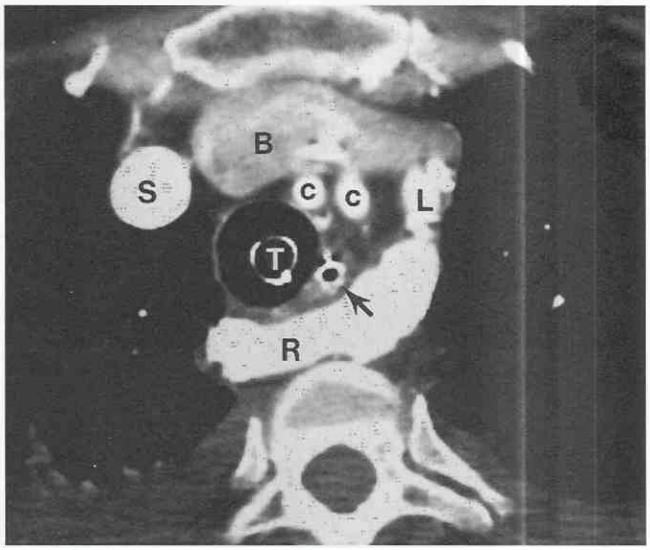

Figure 29–115. Aberrant right subclavian artery. Contrast-enhanced CT shows enhancement of retrotracheal right subclavian artery (R). A nasogastric tube can be seen in the esophagus *(arrow)*. B, brachiocephalic vein; c, left and right common carotid arteries; L, left subclavian artery; S, superior vena cava; T, trachea with endotracheal tube.

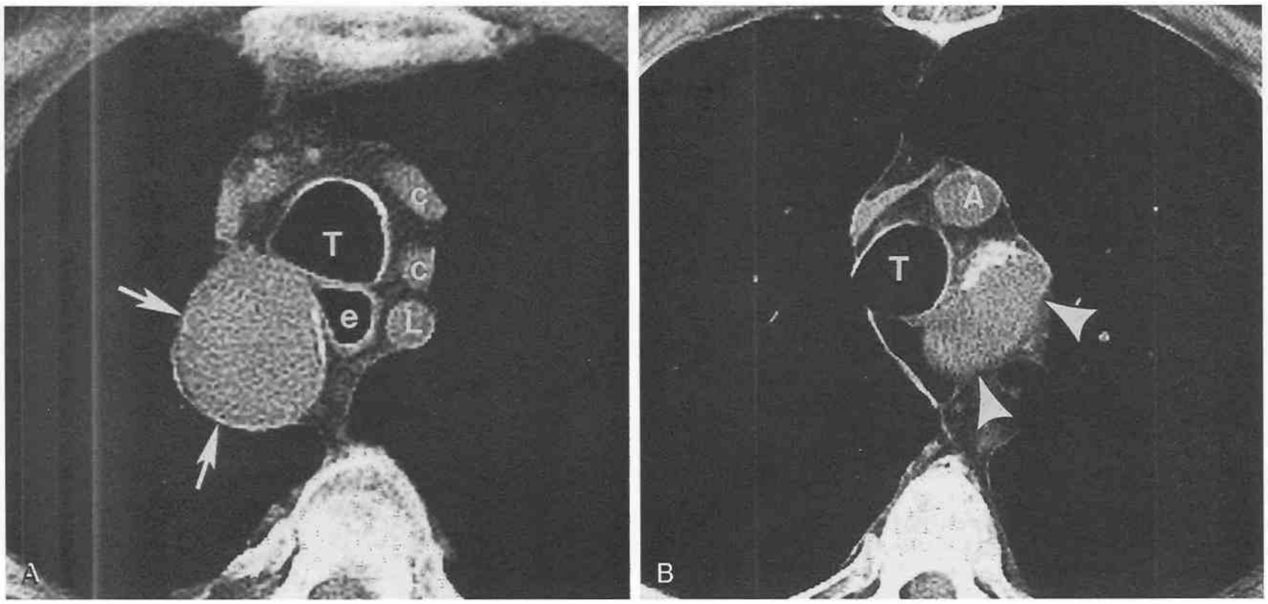

Figure 29–116. Aneurysm of aberrant right subclavian artery. *A,* CT shows homogeneous soft tissue mass *(arrows)* with rim calcification posterior to the trachea (T). *B,* A more caudal CT image confirmed that the mass is an aneurysm of the aberrant right subclavian artery, originating from the proximal descending aorta *(arrowheads).* A, common origin of carotid arteries from aorta; c, left and right common carotid arteries; e, esophagus; L, left subclavian artery.

the aortic arch to the right of the trachea. The aberrant right subclavian artery arises as the last and most posterior vessel off the right-sided aortic arch, crosses the mediastinum behind the trachea and esophagus, and continues into the neck and axilla along the left side of the trachea (Fig. 29–117). Frequently, a diverticulum is seen at the origin of the aberrant left subclavian artery from the aorta.

Double Aortic Arch

Double aortic arches typically manifest in childhood with stridor.[167, 199] Rarely, the lesion manifests in adulthood as an asymptomatic mediastinal mass. On CT or MRI, the double aortic arch is obvious as two large vascular structures encircling the trachea. Each arch gives rise to a subclavian and a carotid artery. The descending aorta is

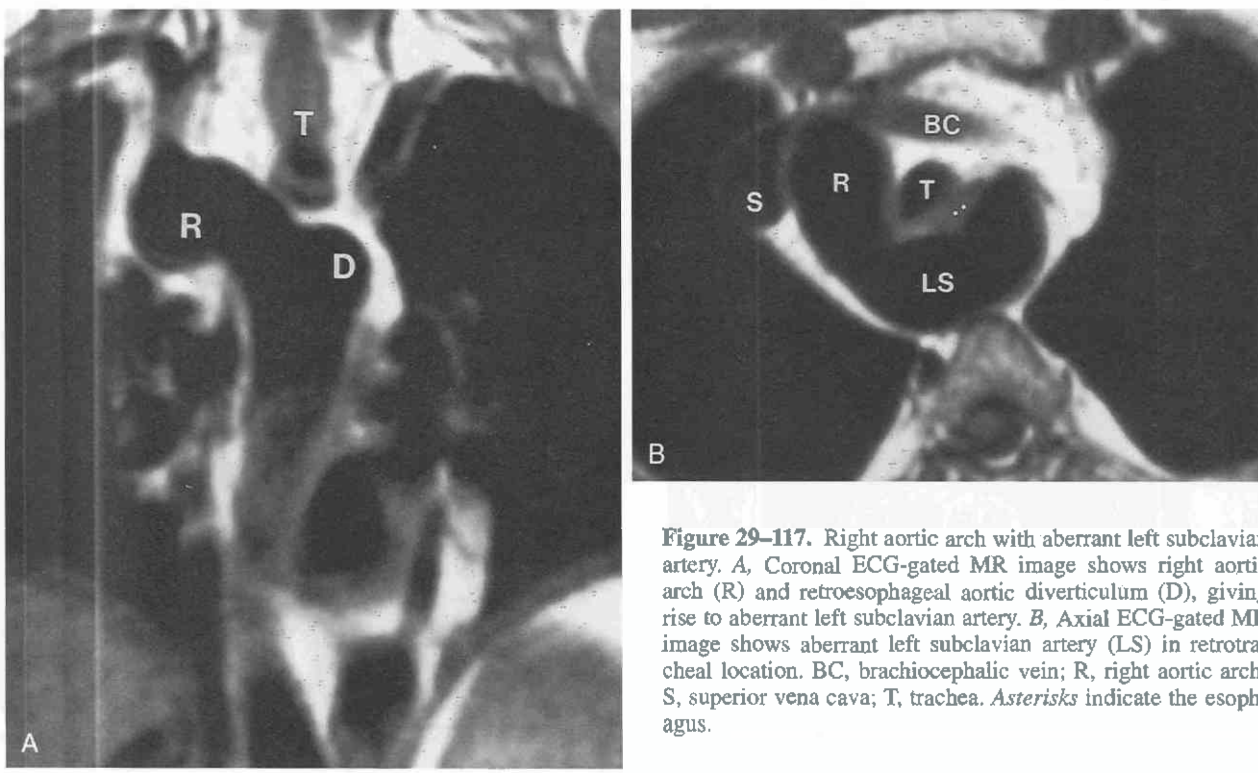

Figure 29–117. Right aortic arch with aberrant left subclavian artery. *A,* Coronal ECG-gated MR image shows right aortic arch (R) and retroesophageal aortic diverticulum (D), giving rise to aberrant left subclavian artery. *B,* Axial ECG-gated MR image shows aberrant left subclavian artery (LS) in retrotracheal location. BC, brachiocephalic vein; R, right aortic arch; S, superior vena cava; T, trachea. *Asterisks* indicate the esophagus.

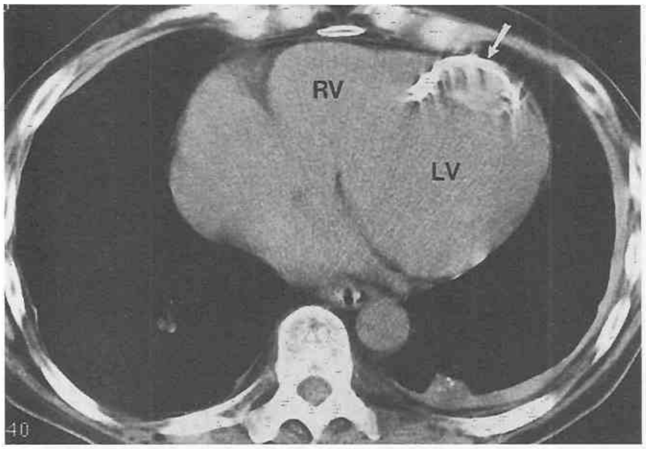

Figure 29–118. Calcified left ventricular aneurysm. CT shows a thin, curvilinear calcification *(arrow)* in the left ventricular apex, consistent with left ventricular aneurysm resulting from a prior infarction. LV, left ventricle; RV, right ventricle.

usually on the left, and the right arch is often higher and slightly larger than the left arch.

Left Ventricular Aneurysm and Pseudoaneurysm

Aneurysms and pseudoaneurysms of the left ventricle[104] often present as mediastinal masses. True left ventricular aneurysms are caused by myocardial ischemia and infarction resulting in focal thinning, dilation, and paradoxical motion of the affected portion of the ventricle. True aneurysms usually occur in the distribution of the left anterior descending coronary artery (along the anterior and apical walls of the left ventricle) and frequently calcify. On CT, they manifest as broad-based areas of thinning of the anterior or apical walls of the left ventricle, often with associated calcification (Figs. 29–118 and 29–119). Mural thrombus may be identified adjacent to the aneurysm. Cine MRI can be useful for demonstrating paradoxical wall motion in the region of the aneurysm.

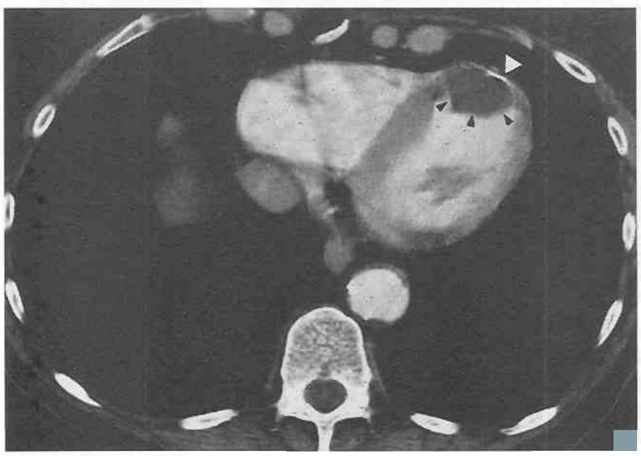

Figure 29–119. Calcified left ventricular aneurysm with apical thrombus. Contrast-enhanced CT shows a thin curvilinear calcification *(white arrowhead)* in the left ventricular apex, consistent with left ventricular aneurysm. Focal wall thinning and adjacent apical thrombus *(black arrowheads)* can be seen.

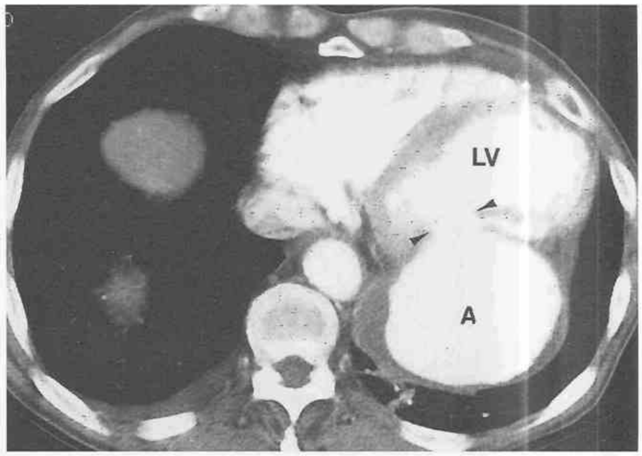

Figure 29–120. Left ventricular pseudoaneurysm. Contrast-enhanced CT shows a large pseudoaneurysm arising from the posterior wall of the left ventricle. A narrow neck *(arrowheads)* between the pseudoaneurysm (A) and the left ventricular cavity (LV) is seen.

Left ventricular pseudoaneurysms result from perforation of the ventricular wall after myocardial infarction. The perforation is contained by pericardium, resulting in pseudoaneurysm formation. Pseudoaneurysms more commonly occur along the posterior and inferior surfaces of the heart and infrequently calcify. On contrast-enhanced CT, they manifest as focal enhancing masses along the posterior or inferior surface of the ventricle, with a narrow communication with the left ventricular chamber (Fig. 29–120). It is important to differentiate pseudoaneurysms from true aneurysms, as the former are prone to delayed rupture whereas the latter are not.

Diaphragmatic Hernia

Abdominal organs or retroperitoneal fat can herniate through areas of congenital or acquired diaphragmatic weakness or tears and manifest as a mediastinal mass on chest radiographs.[71, 82, 83] Common nontraumatic sites of

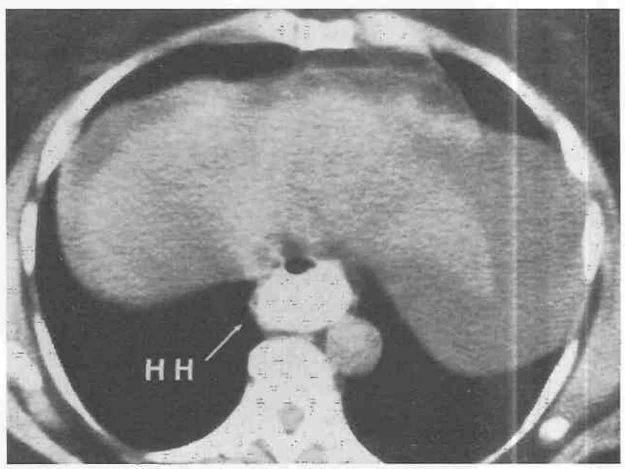

Figure 29–121. Hiatal hernia. CT shows herniation of a portion of the stomach (HH) through the esophageal hiatus.

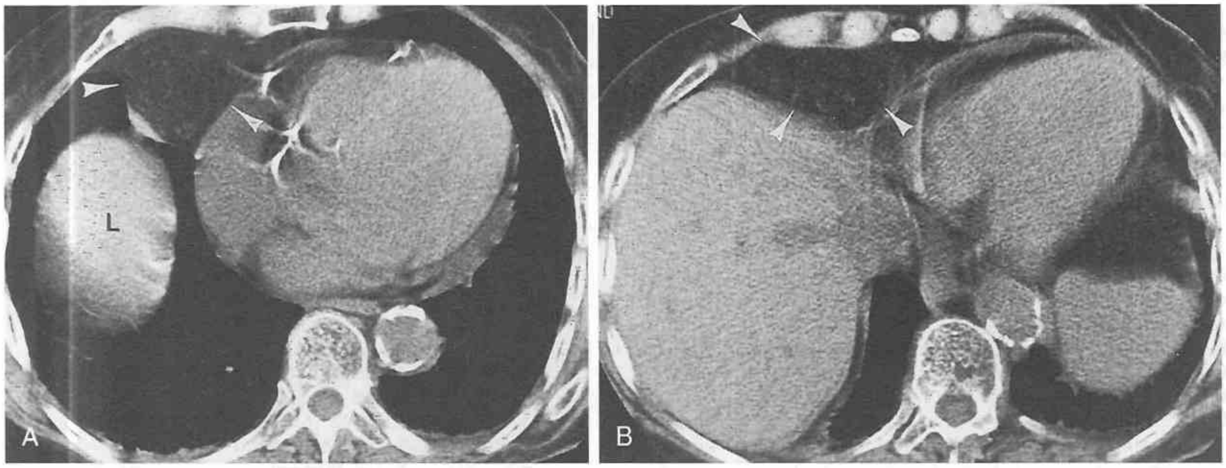

Figure 29–122. Morgagni's hernia. *A* and *B,* CT shows herniation of omental fat *(arrowheads)* into the right cardiophrenic angle. Omental vessels are seen within the fat. L, liver.

herniation include the anterior parasternal hiatus, the esophageal hiatus, and the posterior pleuroperitoneal hiatus. Hiatal hernias are a common cause of a middle mediastinal mass in the lower thorax. The diagnosis is easily made if air or contrast material is seen within the hernia (Fig. 29–121).

Herniation through the anterior parasternal hiatus (foramen of Morgagni) is uncommon and usually manifests as a right-sided mediastinal or cardiophrenic angle mass (Fig. 29–122). These defects are more commonly identified in middle-aged to older adults and are typically asymptomatic. Rarely, defects occur on the left or into the pericardium.

Herniation through the posterior pleuroperitoneal hiatus (foramen of Bochdalek) is the most common cause of congenital diaphragmatic hernia in infants. In adults, the lesions are usually small and asymptomatic and occur more commonly on the left (65%) than on the right (35%). The incidence of small, posterior, fat-containing defects increases with age and degree of emphysema (Fig. 29–123).

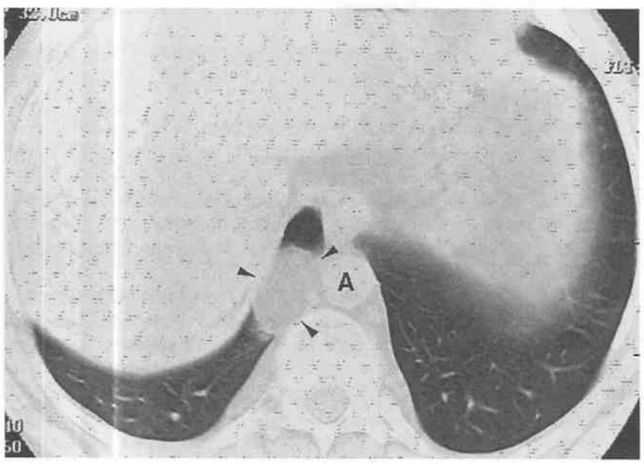

Figure 29–123. Bochdalek's hernia. CT shows homogeneous fat-attenuation mass *(arrowheads)* in the right paraspinal location. Location and CT appearance are consistent with a diagnosis of Bochdalek's hernia. A, aorta.

References

1. Abrahamsen AF, Lien HH, Aas M, et al: Magnetic resonance imaging and ^{67}gallium scan in mediastinal malignant lymphoma: A prospective pilot study. Ann Oncol 5:433–436, 1994.
2. Adam A, Hochholzer L: Ganglioneuroblastoma of the posterior mediastinum: A clinicopathologic review of 80 cases. Cancer 47: 373–381, 1981.
3. Alfidi RJ, Haaga JR, El-Yousef SJ, et al: Preliminary experimental results in humans and animals with a superconducting, whole-body, nuclear magnetic resonance scanner. Radiology 143:175–181, 1982.
4. al-Mulhim FA, Ibrahim EM, el-Hassan AY, Moharram HM: Magnetic resonance imaging of tuberculous spondylitis. Spine 20:2287–2292, 1995.
5. Arizono T, Oga M, Shiota E, et al: Differentiation of vertebral osteomyelitis and tuberculous spondylitis by magnetic resonance imaging. Int Orthop 19:319–322, 1995.
6. Aronberg DJ, Glazer HS, Sagel SS: MRI and CT of the mediastinum: Comparisons, controversies, and pitfalls. Radiol Clin North Am 23:439–448, 1985.
7. Atkinson DJ, Edelman RR: Cineangiography of the heart in a single breath hold with a segmented turboFLASH sequence. Radiology 178:357–360, 1991.
8. Auffermann W, Gooding GA, Okerlund MD, et al: Diagnosis of recurrent hyperparathyroidism: Comparison of MR imaging and other imaging techniques. AJR Am J Roentgenol 150:1027–1033, 1988.
9. Aughenbaugh GL: Thoracic manifestations of neurocutaneous diseases. Radiol Clin North Am 22:741–756, 1984.
10. Aygun C, Slawson RG, Bajaj K, Salazar OM: Primary mediastinal seminoma. Urology 23:109–117, 1984.
11. Azar T, Abdul-Karim FW, Tucker HM: Adenoid cystic carcinoma of the trachea. Laryngoscope 108:1297–1300, 1998.
12. Azarow KS, Pearl RH, Zurcher R, et al: Primary mediastinal masses: A comparison of adult and pediatric populations. J Thorac Cardiovasc Surg 106:67–72, 1993.
13. Bailes DR, Gilderdale DJ, Bydder GM, et al: Respiratory ordered phase encoding (ROPE): A method for reducing respiratory motion artefacts in MR imaging. J Comput Assist Tomogr 9:835–838, 1985.
14. Barakos JA, Brown JJ, Brescia RJ, Higgins CB: High signal intensity lesions of the chest in MR imaging. J Comput Assist Tomogr 13:797–802, 1989.
15. Barakos JA, Brown JJ, Higgins CB: MR imaging of secondary cardiac and paracardiac lesions. AJR Am J Roentgenol 153:47–50, 1989.
16. Baron RL, Gutierrez FR, Sagel SS, et al: CT of anomalies of the mediastinal vessels. Am J Roentgenol 137:571–576, 1981.
17. Baron RL, Lee JK, Sagel SS, Peterson RR: Computed tomography of the normal thymus. Radiology 142:121–125, 1982.

18. Baron RL, Sagel SS, Baglan RJ: Thymic cysts following radiation therapy for Hodgkin disease. Radiology 141:593–597, 1981.
19. Bar-Ziv J, Nogrady MB: Mediastinal neuroblastoma and ganglioneuroma: The differentiation between primary and secondary involvement on the chest roentgenogram. Am J Roentgenol Radium Ther Nucl Med 125:380–390, 1975.
20. Bashist B, Ellis K, Gold RP: Computed tomography of intrathoracic goiters. Am J Roentgenol 140:455–460, 1983.
21. Batra P, Brown K, Steckel RJ, et al: MR imaging of the thorax: A comparison of axial, coronal, and sagittal imaging planes. J Comput Assist Tomogr 12:75–81, 1988.
22. Batra P, Herrmann C Jr, Mulder D: Mediastinal imaging in myasthenia gravis: Correlation of chest radiography, CT, MR, and surgical findings. AJR Am J Roentgenol 148:515–519, 1987.
23. Bechtold RE, Wolfman NT, Karstaedt N, Choplin RH: Superior vena caval obstruction: Detection using CT. Radiology 157:485–487, 1985.
24. Bendini M, Zuiani C, Bazzocchi M, et al: Magnetic resonance imaging and ^{67}Ga scan versus computed tomography in the staging and in the monitoring of mediastinal malignant lymphoma: A prospective pilot study. MAGMA 4:213–224, 1996.
25. Berry DF, Buccigrossi D, Peabody J, et al: Pulmonary vascular occlusion and fibrosing mediastinitis. Chest 89:296–301, 1986.
26. Bhargava R, Parham DM, Lasater OE, et al: MR imaging differentiation of benign and malignant peripheral nerve sheath tumors: use of the target sign. Pediatr Radiol 27:124–129, 1997.
27. Bitkover CY, Cederlund K, Aberg B, Vaage J: Computed tomography of the sternum and mediastinum after median sternotomy. Ann Thorac Surg 68:858–863, 1999.
28. Bluemke DA, Boxerman JL, Atalar E, McVeigh ER: Segmented K-space cine breath-hold cardiovascular MR imaging: Part 1. Principles and technique. AJR Am J Roentgenol 169:395–400, 1997.
29. Boiselle PM, Patz EF Jr, Vining DJ, et al: Imaging of mediastinal lymph nodes: CT, MR, and FDG PET. Radiographics 18:1061–1069, 1998.
30. Boyacigil S, Ardic S, Tokoglu F, et al: Intrathoracic extramedullary haemopoiesis. Australas Radiol 40:179–181, 1996.
31. Branscom JJ, Austin JH: Aberrant right subclavian artery: Findings seen on plain chest roentgenograms. Am J Roentgenol Radium Ther Nucl Med 119:539–542, 1973.
32. Breatnach E, Nath PH, Delany DJ: The role of computed tomography in acute and subacute mediastinitis. Clin Radiol 37:139–145, 1986.
33. Brice P, Rain JD, Frija J, et al: Residual mediastinal mass in malignant lymphoma: Value of magnetic resonance imaging and gallium scan. Nouv Rev Fr Hematol 35:457–461, 1993.
34. Brown LR, Aughenbaugh GL: Masses of the anterior mediastinum: CT and MR imaging. AJR Am J Roentgenol 157:1171–1180, 1991.
35. Brown LR, Aughenbaugh GL, Wick MR, et al: Roentgenologic diagnosis of primary corticotropin-producing carcinoid tumors of the mediastinum. Radiology 142:143–148, 1982.
36. Burk DL Jr, Brunberg JA, Kanal E, et al: Spinal and paraspinal neurofibromatosis: Surface coil MR imaging at 1.5 T1. Radiology 162:797–801, 1987.
37. Canini R, Battista G, Monetti N, et al: Bulky mediastinal lymphomas: Role of magnetic resonance and SPECT-Ga-67 in the evaluation of residual masses. Radiol Med (Torino) 90:448–456, 1995.
38. Casillas J, Sais GJ, Greve JL, et al: Imaging of intra- and extraabdominal desmoid tumors. Radiographics 11:959–968, 1991.
39. Castellino RA: Diagnostic imaging studies in patients with newly diagnosed Hodgkin's disease. Ann Oncol 3(suppl 4):45–47, 1992.
40. Caty MG, Shamberger RC: Abdominal tumors in infancy and childhood. Pediatr Clin North Am 40:1253–1271, 1993.
41. Chao MW, Smith JG, Laidlaw C, et al: Results of treating primary tumors of the trachea with radiotherapy. Int J Radiat Oncol Biol Phys 41:779–785, 1998.
42. Cohen MC, Hartnell GG, Finn JP: Magnetic resonance angiography of congenital pulmonary vein anomalies. Am Heart J 127:954–955, 1994.
43. Cole TJ, Henry DA, Jolles H, Proto AV: Normal and abnormal vascular structures that simulate neoplasms on chest radiographs: Clues to the diagnosis. Radiographics 15:867–891, 1995.
44. Cormier MG, Yedlicka JW, Gray RJ, Moncada R: Congenital anomalies of the superior vena cava: A CT study. Semin Roentgenol 24: 77–83, 1989.
45. Dagirmanjian A, Schils J, McHenry M, Modic MT: MR imaging of vertebral osteomyelitis revisited. AJR Am J Roentgenol 167: 1539–1543, 1996.
46. Davidson AJ, Hartman DS, Goldman SM: Mature teratoma of the retroperitoneum: Radiologic, pathologic, and clinical correlation. Radiology 172:421–425, 1989.
47. Davis RD Jr, Oldham HN Jr, Sabiston DC Jr: Primary cysts and neoplasms of the mediastinum: Recent changes in clinical presentation, methods of diagnosis, management, and results. Ann Thorac Surg 44:229–237, 1987.
48. Davis S, Rogers MA, Pendergrass TW: The incidence and epidemiologic characteristics of neuroblastoma in the United States. Am J Epidemiol 126:1063–1074, 1987.
49. de Geer G, Webb WR, Gamsu G: Normal thymus: Assessment with MR and CT. Radiology 158:313–317, 1986.
50. Dexeus FH, Logothetis CJ, Chong C, et al: Genetic abnormalities in men with germ cell tumors. J Urol 140:80–84, 1988.
51. Do YS, Im JG, Lee BH, et al: CT findings in malignant tumors of thymic epithelium. J Comput Assist Tomogr 19:192–197, 1995.
52. Donner MW, Saba GP, Martinez CR: Diffuse diseases of the esophagus: A practical approach. Semin Roentgenol 16:198–213, 1981.
53. Dooms GC, Hricak H, Moseley ME, et al: Characterization of lymphadenopathy by magnetic resonance relaxation times: Preliminary results. Radiology 155:691–697, 1985.
54. Dosios TJ, Angouras DC, Floros DG: Primary desmoid tumor of the posterior mediastinum. Ann Thorac Surg 66:2098–2099, 1998.
55. Ducatman BS, Scheithauer BW, Piepgras DG, et al: Malignant peripheral nerve sheath tumors: A clinicopathologic study of 120 cases. Cancer 57:2006–2021, 1986.
56. Dudiak CM, Olson MC, Posniak HV: Abnormalities of the azygos system: CT evaluation. Semin Roentgenol 24:47–55, 1989.
57. Dudiak CM, Olson MC, Posniak HV: CT evaluation of congenital and acquired abnormalities of the azygos system. Radiographics 11: 233–246, 1991.
58. Ehman RL, McNamara MT, Pallack M, et al: Magnetic resonance imaging with respiratory gating: Techniques and advantages. Am J Roentgenol 143:1175–1182, 1984.
59. Eisenstat R, Bruce D, Williams LE, Katz DS: Primary liposarcoma of the mediastinum with coexistent mediastinal lipomatosis. AJR Am J Roentgenol 174:572–573, 2000.
60. Endo M, Adachi S, Kusumoto M, et al: A study of the utility of the MR image for the diagnosis of thymic tumors—imaging and pathologic correlation. Nippon Igaku Hoshasen Gakkai Zasshi 53:1–10, 1993.
61. Erasmus JJ, McAdams HP, Donnelly LF, Spritzer CE: MR imaging of mediastinal masses. Magn Reson Imaging Clin North Am 8: 59–89, 2000.
62. Farmer DW, Moore E, Amparo E, et al: Calcific fibrosing mediastinitis: Demonstration of pulmonary vascular obstruction by magnetic resonance imaging. Am J Roentgenol 143:1189–1191, 1984.
63. Feigin DS, Fenoglio JJ, McAllister HA. Madewell JE: Pericardial cysts: A radiologic-pathologic correlation and review. Radiology 125:15–20, 1977.
64. Feinberg DA, Hale JD, Watts JC, et al: Halving MR imaging time by conjugation: Demonstration at 3.5 kG. Radiology 161: 527–531, 1986.
65. Felson B: Chest Roentgenology. Philadelphia, WB Saunders, 1973.
66. Fernandes ET, Custer MD, Burton EM, et al: Neurenteric cyst: Surgery and diagnostic imaging. J Pediatr Surg 26:108–110, 1991.
67. Filly R, Bland N, Castellino RA: Radiographic distribution of intrathoracic disease in previously untreated patients with Hodgkin's disease and non-Hodgkin's lymphoma. Radiology 120:277–281, 1976.
68. Foo TK, Bernstein MA, Aisen AM, et al: Improved ejection fraction and flow velocity estimates with use of view sharing and uniform repetition time excitation with fast cardiac techniques. Radiology 195:471–478, 1995.
69. Francis IR, Dorovini-Zis K, Glazer GM, et al: The fibromatoses: CT-pathologic correlation. Am J Roentgenol 147:1063–1066, 1986.
70. Francis IR, Glazer GM, Bookstein FL, Gross BH: The thymus: Reexamination of age-related changes in size and shape. Am J Roentgenol 145:249–254, 1985.
71. Fraser RS, Muller NL, Colman N, Pare PD: Fraser and Pare's Diagnosis of Diseases of the Chest. 4th ed. Philadelphia, WB Saunders, 1999.

72. Fulcher AS, Proto AV, Jolles H: Cystic teratoma of the mediastinum: Demonstration of fat/fluid level. AJR Am J Roentgenol 154:259–260, 1990.
73. Furukawa H: Magnetic resonance (MR) imaging for the detection of the invasion into neighboring structures in esophageal cancers. Nippon Geka Gakkai Zasshi 92:636–644, 1991.
74. Gale AW, Jelihovsky T, Grant AF, et al: Neurogenic tumors of the mediastinum. Ann Thorac Surg 17:434–443, 1974.
75. Gamsu G, Stark DD, Webb WR, et al: Magnetic resonance imaging of benign mediastinal masses. Radiology 151:709–713, 1984.
76. Gasparini MD, Balzarini L, Castellani MR, et al: Current role of gallium scan and magnetic resonance imaging in the management of mediastinal Hodgkin lymphoma. Cancer 72:577–582, 1993.
77. Gefter WB: Magnetic resonance imaging in the evaluation of lung cancer. Semin Roentgenol 25:73–84, 1990.
78. Gefter WB, Spritzer CE, Eisenberg B, et al: Thyroid imaging with high-field-strength surface-coil MR. Radiology 164:483–490, 1987.
79. Gelfand DW, Goldman AS, Law EJ, et al: Thymic hyperplasia in children recovering from thermal burns. J Trauma 12:813–817, 1972.
80. Ghosh BC, Ghosh L, Huvos AG, Fortner JG: Malignant schwannoma: A clinicopathologic study. Cancer 31:184–190, 1973.
81. Gilkeson RC, Basile V, Sands MJ, Hsu JT: Chest case of the day: Extramedullary hematopoiesis (EMH). AJR Am J Roentgenol 169: 267, 270–263, 1997.
82. Gilkeson RC, Basile V, Sands MJ, Hsu JT: Chest case of the day: Morgagni's hernia. AJR Am J Roentgenol 169:266, 268–270, 1997.
83. Glasser DL, Shanmuganathan K, Mirvis SE: General case of the day: Acute intrapericardial diaphragmatic hernia. Radiographics 18: 799–801, 1998.
84. Glazer GM, Axel L, Moss AA: CT diagnosis of mediastinal thyroid. Am J Roentgenol 138:495–498, 1982.
85. Glazer GM, Orringer MB, Chenevert TL, et al: Mediastinal lymph nodes: Relaxation time/pathologic correlation and implications in staging of lung cancer with MR imaging. Radiology 168:429–431, 1988.
86. Glazer HS, Molina PL, Siegel MJ, Sagel SS: High-attenuation mediastinal masses on unenhanced CT. AJR Am J Roentgenol 156: 45–50, 1991.
87. Glazer HS, Wick MR, Anderson DJ, et al: CT of fatty thoracic masses. AJR Am J Roentgenol 159:1181–1187, 1992.
88. Goodman LR, Kay HR, Teplick SK, Mundth ED: Complications of median sternotomy: Computed tomographic evaluation. Am J Roentgenol 141:225–230, 1983.
89. Graeber GM, Thompson LD, Cohen DJ, et al: Cystic lesion of the thymus: An occasionally malignant cervical and/or anterior mediastinal mass. J Thorac Cardiovasc Surg 87:295–300, 1984.
90. Gumbs RV, Higginbotham-Ford EA, Teal JS, et al: Thoracic extramedullary hematopoiesis in sickle-cell disease. AJR Am J Roentgenol 149:889–893, 1987.
91. Haacke EM, Lenz GW: Improving MR image quality in the presence of motion by using rephasing gradients. AJR Am J Roentgenol 148: 1251–1258 ,1987.
92. Haacke EM, Patrick JL: Reducing motion artifacts in two-dimensional Fourier transform imaging. Magn Reson Imaging 4:359–376, 1986.
93. Halvorsen RA Jr, Thompson WM: CT of esophageal neoplasms. Radiol Clin North Am 1989 27:667–685.
94. Hara M, McAdams HP, Vredenburgh JJ, et al: Thymic hyperplasia after high-dose chemotherapy and autologous stem cell transplantation: Incidence and significance in patients with breast cancer. AJR Am J Roentgenol 173:1341–1344, 1999.
95. Harkin JC, Reed RJ: Atlas of Tumor Pathology: Tumors of the Peripheral Nervous System. Washington, D.C., Armed Forces Institute of Pathology, 1982, pp 25–150.
96. Harris NL, Jaffe ES, Stein H, et al: A revised European-American classification of lymphoid neoplasms: A proposal from the International Lymphoma Study Group. Blood 84:1361–1392, 1994.
97. Hartmann CA, Roth C, Minck C, Niedobitek G: Thymic carcinoma: Report of five cases and review of the literature. J Cancer Res Clin Oncol 116:69–82, 1990.
98. Hartnell GG: Magnetic resonance angiography of systemic thoracic and abdominal veins. Magn Reson Imaging Clin North Am 1: 281–294, 1993.
99. Hartnell GG, Hughes LA, Finn JP, Longmaid HE 3rd: Magnetic resonance angiography of the central chest veins: A new gold standard? Chest 107:1053–1057, 1995.
100. Hawkes RC, Patz S: Rapid Fourier imaging using steady-state free precession. Magn Reson Med 4:9–23, 1987.
101. Heitzman ER: The Mediastinum. Berlin, Springer-Verlag, 1988.
102. Herfkens RJ, Higgins CB, Hricak H, et al: Nuclear magnetic resonance imaging of the cardiovascular system: Normal and pathologic findings. Radiology 147:749–759, 1983.
103. Herold C, Zerhouni E: The mediastinum and lungs. In Higgins CB, Hricak H, Helms CA (eds): Magnetic Resonance Imaging of the Body, 3rd ed. New York, Lippincott-Raven, 1997.
104. Higgins C, Caputo G: Acquired heart disease. In Higgins CB Hricak H, Helms CA (eds): Magnetic Resonance Imaging of the Body, 3rd ed. New York, Lippincott-Raven, 1997.
105. Higgins CB, Auffermann W: MR imaging of thyroid and parathyroid glands: A review of current status. AJR Am J Roentgenol 151: 1095–1106, 1988.
106. Higgins CB, Byrd BF 2nd, McNamara MT, et al: Magnetic resonance imaging of the heart: A review of the experience in 172 subjects. Radiology 155:671–679, 1985.
107. Higgins CB, McNamara MT, Fisher MR, Clark OH: MR imaging of the thyroid. Am J Roentgenol 147:1255–1261, 1986.
108. Hoffman OA, Gillespie DJ, Aughenbaugh GL, Brown LR: Primary mediastinal neoplasms (other than thymoma). Mayo Clin Proc 68: 880–891, 1993.
109. Holscher AH, Dittler HJ, Siewert JR: Staging of squamous esophageal cancer: Accuracy and value. World J Surg 18:312–320, 1994.
110. Hope DG, Mulvihill JJ: Malignancy in neurofibromatosis. Adv Neurol 29:33–56, 1981.
111. Inase N, Ichioka M, Akamatsu H, et al: Mediastinal fibromatosis presenting with superior vena cava syndrome. Respiration 66:464–466, 1999.
112. Indeglia RA, Shea MA, Grage TB: Congenital cysts of the thymus gland. Arch Surg 94:149–152, 1967.
113. Ishaque MA, Crockard HA, Stevens JM: Ossified pseudomeningocoele following laminectomy: Case reports and review of the literature. Eur Spine J 6:430–432, 1997.
114. Ishibashi M, Nishida H, Hiromatsu Y, et al: Comparison of technetium-99m–MIBI, technetium-99m–tetrofosmin, ultrasound and MRI for localization of abnormal parathyroid glands. J Nucl Med 39: 320–324, 1998.
115. Ishibashi M, Nishida H, Hiromatsu Y, et al: Localization of ectopic parathyroid glands using technetium-99m sestamibi imaging: Comparison with magnetic resonance and computed tomographic imaging. Eur J Nucl Med 24:197–201, 1997.
116. Ishibashi M, Nishida H, Kumabe T, et al: Tc-99m tetrofosmin: A new diagnostic tracer for parathyroid imaging. Clin Nucl Med 20: 902–905, 1995.
117. Ishii K, Maeda K, Hashihira M, et al: MRI of mediastinal cavernous hemangioma. Pediatr Radiol 20:556–557, 1990.
118. Jaramillo D, Perez-Atayde A, Griscom NT: Apparent association between thymic cysts and prior thoracotomy. Radiology 172:207–209, 1989.
119. Jochelson M, Mauch P, Balikian J, et al: The significance of the residual mediastinal mass in treated Hodgkin's disease. J Clin Oncol 3:637–640, 1985.
120. Kang YS, Rosen K, Clark OH, Higgins CB: Localization of abnormal parathyroid glands of the mediastinum with MR imaging. Radiology 189:137–141, 1993.
121. Kaplan PA, Williams SM: Mucocutaneous and peripheral soft-tissue hemangiomas: MR imaging. Radiology 163:163–166, 1987.
122. Kataoka K, Matsuura M, Seno N: Study of cystic mediastinal lesions—diagnostic usefulness of magnetic resonance imaging. Nippon Kyobu Geka Gakkai Zasshi 43:438–445, 1995.
123. Kawashima A, Fishman EK, Kuhlman JE: CT and MR evaluation of posterior mediastinal masses. Crit Rev Diagn Imaging 33:311–367, 1992.
124. Kawashima A, Fishman EK, Kuhlman JE, Nixon MS: CT of posterior mediastinal masses. Radiographics 11:1045–1067, 1991.
125. Keller AR, Castleman B: Hodgkin's disease of the thymus gland. Cancer 33:1615–1623, 1974.
126. Keller AR, Hochholzer L, Castleman B: Hyaline-vascular and plasma-cell types of giant lymph node hyperplasia of the mediastinum and other locations. Cancer 29:670–683, 1972.
127. Kelly JD, Forster AM, Higley B, et al: Technetium-99m–tetrofosmin as a new radiopharmaceutical for myocardial perfusion imaging. J Nucl Med 34:222–227, 1993.

128. Kiernan PD, Hernandez A, Byrne WD, et al: Descending cervical mediastinitis. Ann Thorac Surg 65:1483–1488, 1998.
129. Kim TS, Lee KS, Han J, et al: Mucoepidermoid carcinoma of the tracheobronchial tree: Radiographic and CT findings in 12 patients. Radiology 212:643–648, 1999.
130. Kirwan WO, Walbaum PR, McCormack RJ: Cystic intrathoracic derivatives of the foregut and their complications. Thorax 28:424–428, 1973.
131. Klemm KM, Moran CA: Primary neuroendocrine carcinomas of the thymus. Semin Diagn Pathol 16:32–41, 1999.
132. Klemm KM, Moran CA, Suster S: Pigmented thymic carcinoids: A clinicopathological and immunohistochemical study of two cases. Mod Pathol 12:946–948, 1999.
133. Knapp RH, Hurt RD, Payne WS, et al: Malignant germ cell tumors of the mediastinum. J Thorac Cardiovasc Surg 89:82–89, 1985.
134. Krishnan J, Danon AD, Frizzera G: Reactive lymphadenopathies and atypical lymphoproliferative disorders. Am J Clin Pathol 99: 385–396, 1993.
135. Krubsack AJ, Wilson SD, Lawson TL, et al: Prospective comparison of radionuclide, computed tomographic, sonographic, and magnetic resonance localization of parathyroid tumors. Surgery 106:639–644 (discussion, pp 644–636), 1989.
136. Kumar AJ, Kuhajda FP, Martinez CR, et al: Computed tomography of extracranial nerve sheath tumors with pathological correlation. J Comput Assist Tomogr 7:857–865, 1983.
137. Kushihashi T, Munechika H, Motoya H, et al: CT and MR findings in tuberculous mediastinitis. J Comput Assist Tomogr 19:379–382, 1995.
138. Kwong JS, Muller NL, Miller RR: Diseases of the trachea and main-stem bronchi: Correlation of CT with pathologic findings. Radiographics 12:645–657, 1992.
139. Lanzer P, Botvinick EH, Schiller NB, et al: Cardiac imaging using gated magnetic resonance. Radiology 150:121–127, 1984.
140. Lazzarino M, Orlandi E, Paulli M, et al: Primary mediastinal B-cell lymphoma with sclerosis: An aggressive tumor with distinctive clinical and pathologic features. J Clin Oncol 11:2306–2313, 1993.
141. LeBlanc J, Guttentag AR, Shepard JA, McLoud TC: Imaging of mediastinal foregut cysts. Can Assoc Radiol J 45:381–386, 1994.
142. Lee JD, Choe KO, Kim SJ, et al: CT findings in primary thymic carcinoma. J Comput Assist Tomogr 15:429–433, 1991.
143. Lee KS, Im JG, Han CH, et al: Malignant primary germ cell tumors of the mediastinum: CT features. AJR Am J Roentgenol 153:947–951, 1989.
144. Lee T, Lee SK, Chen CL, Chen CY: Role of MR imaging of middle third esophageal carcinoma in determining resectability. Chung Hua I Hsueh Tsa Chih (Taipei) 52:363–367, 1993.
145. Lee VS, Spritzer CE: MR imaging of abnormal parathyroid glands. AJR Am J Roentgenol 170:1097–1103, 1998.
146. Lee VS, Spritzer CE, Coleman RE, et al: The complementary roles of fast spin-echo MR imaging and double-phase ^{99m}Tc-sestamibi scintigraphy for localization of hyperfunctioning parathyroid glands. AJR Am J Roentgenol 167:1555–1562, 1996.
147. Lehr L, Rupp N, Siewert JR: Assessment of resectability of esophageal cancer by computed tomography and magnetic resonance imaging. Surgery 103:344–350, 1988.
148. Levitt RG, Husband JE, Glazer HS: CT of primary germ-cell tumors of the mediastinum. Am J Roentgenol 142:73–78, 1984.
149. Lewis BD, Hurt RD, Payne WS, et al: Benign teratomas of the mediastinum. J Thorac Cardiovasc Surg 86:727–731, 1983.
150. Lewis JE, Wick MR, Scheithauer BW, et al: Thymoma. A clinicopathologic review. Cancer 60:2727–2743, 1987.
151. Lichtenstein AK, Levine A, Taylor CR, et al: Primary mediastinal lymphoma in adults. Am J Med 68:509–514, 1980.
152. Lieberman JM, Alfidi RJ, Nelson AD, et al: Gated magnetic resonance imaging of the normal and diseased heart. Radiology 152: 465–470, 1984.
153. Link KM, Samuels LJ, Reed JC, et al: Magnetic resonance imaging of the mediastinum. J Thorac Imaging 8:34–53, 1993.
154. Lyon RD, McAdams HP: Mediastinal bronchogenic cyst: Demonstration of a fluid-fluid level at MR imaging. Radiology 186:427–428, 1993.
155. Marchevsky AM: Mediastinal tumors of peripheral nervous system origin. Semin Diagn Pathol 16:65–78, 1999.
156. Marin ML, Romney BM, Franco K, et al: Bronchogenic cyst: A case report emphasizing the role of magnetic resonance imaging. J Thorac Imaging 6:43–46, 1991.
157. Martin G, Kleinsasser O: Neurogenic sarcomas of the neck in neurofibromatosis. Arch Otorhinolaryngol 232:273–283, 1981.
158. Mathisen DJ: Tracheal tumors. Chest Surg Clin North Am 6:875–898, 1996.
159. Mathisen DJ: Primary tracheal tumor management. Surg Oncol Clin North Am 8:307, 1999.
160. McAdams HP: Chest case of the day: Fibrosing mediastinitis. AJR Am J Roentgenol 165:189–190, 1995.
161. McAdams HP, Rosado-de-Christenson M, Fishback NF, Templeton PA: Castleman disease of the thorax: Radiologic features with clinical and histopathologic correlation. Radiology 209:221–228, 1998.
162. McAdams HP, Kirejczyk WM, Rosado-de-Christenson ML, Matsumoto S: Bronchogenic cyst: Imaging features with histopathologic correlation. Radiology 217:441–446, 2000.
163. McAdams HP, Rosado-de-Christenson ML, Moran CA: Mediastinal hemangioma: Radiographic and CT features in 14 patients. Radiology 193:399–402, 1994.
164. McCarthy MJ, Rosado-de-Christenson ML: Tumors of the trachea. J Thorac Imaging 10:180–198, 1995.
165. McCarty MJ, Vukelja SJ, Banks PM, Weiss RB: Angiofollicular lymph node hyperplasia (Castleman's disease). Cancer Treat Rev 21:291–310, 1995.
166. McElaney B, McAdams HP: Chest case of the day: Metastatic bronchial carcinoid. AJR Am J Roentgenol 165:186–187, 1995.
167. McLoughlin MJ, Weisbrod G, Wise DJ, Yeung HP: Computed tomography in congenital anomalies of the aortic arch and great vessels. Radiology 138:399–403, 1981.
168. Merine DS, Fishman EK, Zerhouni EA: Computed tomography and magnetic resonance imaging diagnosis of thymic cyst. J Comput Tomogr 12:220–222, 1988.
169. Misawa Y, Fuse K, Hasegawa T: Infectious mediastinitis after cardiac operations: Computed tomographic findings. Ann Thorac Surg 65:622–624, 1998.
170. Moeller KH, Rosado-de-Christenson ML, Templeton PA: Mediastinal mature teratoma: Imaging features. AJR Am J Roentgenol 169: 985–990, 1997.
171. Moon WK, Im JG, Han MC: Castleman's disease of the mediastinum: MR imaging features. Clin Radiol 49:466–468, 1994.
172. Moore AV, Korobkin M, Olanow W, et al: Age-related changes in the thymus gland: CT-pathologic correlation. Am J Roentgenol 141: 241–246, 1983.
173. Moore AV, Korobkin M, Powers B, et al: Thymoma detection by mediastinal CT: Patient with myasthenia gravis. Am J Roentgenol 138:217–222, 1982.
174. Moran CA, Suster S, Fishback N, Koss MN: Mediastinal paragangliomas: A clinicopathologic and immunohistochemical study of 16 cases. Cancer 72:2358–2364, 1993.
175. Moran CA, Suster S, Koss MN: Primary germ cell tumors of the mediastinum: III. Yolk sac tumor, embryonal carcinoma, choriocarcinoma, and combined nonteratomatous germ cell tumors of the mediastinum—a clinicopathologic and immunohistochemical study of 64 cases. Cancer 80:699–707, 1997.
176. Moran CA, Suster S, Perino G, et al: Malignant smooth muscle tumors presenting as mediastinal soft tissue masses: A clinicopathologic study of 10 cases. Cancer 74:2251–2260, 1994.
177. Moran CA, Suster S, Przygodzki RM, Koss MN: Primary germ cell tumors of the mediastinum: II. Mediastinal seminomas—a clinicopathologic and immunohistochemical study of 120 cases. Cancer 80:691–698, 1997.
178. Morgenthaler TI, Brown LR, Colby TV, et al: Thymoma. Mayo Clin Proc 68:1110–1123, 1993.
179. Moss AA, Schnyder P, Thoeni RF, Margulis AR: Esophageal carcinoma: Pretherapy staging by computed tomography. Am J Roentgenol 136:1051–1056, 1981.
180. Murayama S, Murakami J, Watanabe H, et al: Signal intensity characteristics of mediastinal cystic masses on T1-weighted MRI. J Comput Assist Tomogr 19:188–191, 1995.
181. Naidich DP, Webb WR, Muller NL: The mediastinum. In Computed Tomography and Magnetic Resonance of the Thorax. 3rd ed. New York, Lippincott-Raven, 1999, pp 37–160.
182. Naidich DP, Webb WR, Muller NL, et al: Aorta, arch vessels, and great veins. In Computed Tomography and Magnetic Resonance of the Thorax. 3rd ed. Philadelphia, Lippincott-Raven, 1999, pp 505–602.
183. Nakasu Y, Minouchi K, Hatsuda N, et al: Thoracic meningocele in

neurofibromatosis: CT and MR findings. J Comput Assist Tomogr 15:1062–1064, 1991.
184. Nakata H, Egashira K, Watanabe H, et al: MRI of bronchogenic cysts. J Comput Assist Tomogr 17:267–270, 1993.
185. Nanson EM: Lymphangioma (cystic hygroma) of the mediastinum. J Cardiovasc Surg (Torino) 9:447–452, 1968.
186. Negendank WG, al-Katib AM, Karanes C, Smith MR: Lymphomas: MR imaging contrast characteristics with clinical-pathologic correlations. Radiology 177:209–216, 1990.
187. Nichols CR: Mediastinal germ cell tumors: Clinical features and biologic correlates. Chest 99:472–479, 1991.
188. Nichols CR: Mediastinal germ cell tumors. Semin Thorac Cardiovasc Surg 4:45–50, 1992.
189. Norris EH: The parathyroid adenoma: A study of 322 cases. Int Abst Surg 84:1–41, 1947.
190. Nyman R, Forsgren G, Glimelius B: Long-term follow-up of residual mediastinal masses in treated Hodgkin's disease using MR imaging. Acta Radiol 37:323–326, 1996.
191. O'Sullivan R, McKenzie A, Hennessy O: Value of CT scanning in assessing location and extent of epidural and paraspinal inflammatory conditions. Australas Radiol 32:203–206, 1988.
192. Pattany PM, Phillips JJ, Chiu LC, et al: Motion artifact suppression technique (MAST) for MR imaging. J Comput Assist Tomogr 11: 369–377, 1987.
193. Patterson GA, Ginsberg RJ, Poon PY, et al: A prospective evaluation of magnetic resonance imaging, computed tomography, and mediastinoscopy in the preoperative assessment of mediastinal node status in bronchogenic carcinoma. J Thorac Cardiovasc Surg 94:679–684, 1987.
194. Perelman MI, Koroleva N, Birjukov J, Goudovsky L: Primary tracheal tumors. Semin Thorac Cardiovasc Surg 8:400–402, 1996.
195. Peterson BA, Frizzera G: Multicentric Castleman's disease. Semin Oncol 20:636–647, 1993.
196. Picus D, Balfe DM, Koehler RE, et al: Computed tomography in the staging of esophageal carcinoma. Radiology 146:433–438, 1983.
197. Pilla TJ, Wolverson MK, Sundaram M, et al: CT evaluation of cystic lymphangiomas of the mediastinum. Radiology 144:841–842, 1982.
198. Poon PY, Bronskill MJ, Henkelman RM, et al: Mediastinal lymph node metastases from bronchogenic carcinoma: Detection with MR imaging and CT. Radiology 162:651–656, 1987.
199. Predey TA, McDonald V, Demos TC, Moncada R: CT of congenital anomalies of the aortic arch. Semin Roentgenol 24:96–113, 1989.
200. Proto AV, Cuthbert NW, Raider L: Aberrant right subclavian artery: Further observations. AJR Am J Roentgenol 148:253–257, 1987.
201. Quagliano PV: Thymic carcinoma: Case reports and review. J Thorac Imaging 11:66–74, 1996.
202. Quint LE, Glazer GM, Orringer MB: Esophageal imaging by MR and CT: Study of normal anatomy and neoplasms. Radiology 156: 727–731, 1985.
203. Rabushka LS, Fishman EK, Kuhlman JE: CT evaluation of achalasia. J Comput Assist Tomogr 15:434–439, 1991.
204. Radford JA, Cowan RA, Flanagan M, et al: The significance of residual mediastinal abnormality on the chest radiograph following treatment for Hodgkin's disease. J Clin Oncol 6:940–946, 1988.
205. Rainov NG, Heidecke V, Burkert W: Thoracic and lumbar meningocele in neurofibromatosis type 1: Report of two cases and review of the literature. Neurosurg Rev 18:127–134, 1995.
206. Reed JC, Hallet KK, Feigin DS: Neural tumors of the thorax: Subject review from the AFIP. Radiology 126:9–17, 1978.
207. Reinig JW, Stanley JH, Schabel SI: CT evaluation of thickened esophageal walls. Am J Roentgenol 140:931–934, 1983.
208. Rholl KS, Levitt RG, Glazer HS: Magnetic resonance imaging of fibrosing mediastinitis. Am J Roentgenol 145:255–259, 1985.
209. Robicsek F: Postoperative sterno-mediastinitis. Am Surg 66:184–192, 2000.
210. Rodriguez E, Soler R, Pombo F, et al: Fibrosing mediastinitis: CT and MR findings. Clin Radiol 53:907–910, 1998.
211. Rosado de Christenson ML, Abbott GF, Kirejczyk WM, et al: Thoracic carcinoids: Radiologic-pathologic correlation. Radiographics 19:707–736, 1999.
212. Rosado-de-Christenson ML, Galobardes J, Moran CA: Thymoma: Radiologic-pathologic correlation. Radiographics 12:151–168, 1992.
213. Rosado-de-Christenson ML, Pugatch RD, Moran CA, Galobardes J: Thymolipoma: Analysis of 27 cases. Radiology 193:121–126, 1994.
214. Rosado-de-Christenson ML, Templeton PA, Moran CA: From the archives of the AFIP: Mediastinal germ cell tumors—radiologic and pathologic correlation. Radiographics 12:1013–1030, 1992.
215. Rossi SE, Erasmus JJ, McAdams HP, Donnelly LF: Thoracic manifestations of neurofibromatosis-I. AJR Am J Roentgenol 173:1631–1638, 1999.
216. Ruzal-Shapiro C, Abramson SJ, Berdon WE: Posterior mediastinal cystic teratoma surrounded by fat in a 13 month old boy: Value of magnetic resonance imaging. Pediatr Radiol 20:107–109, 1989.
217. Sakai F, Sone S, Kiyono K, et al: MR imaging of thymoma: Radiologic-pathologic correlation. AJR Am J Roentgenol 158:751–756, 1992.
218. Sakai F, Sone S, Kiyono K, et al: Intrathoracic neurogenic tumors: MR-pathologic correlation. AJR Am J Roentgenol 159:279–283, 1992.
219. Salyer DC, Salyer WR, Eggleston JC: Benign developmental cysts of the mediastinum. Arch Pathol Lab Med 101:136–139, 1977.
220. Sasaka K, Kurihara Y, Nakajima Y, et al: Spontaneous rupture: A complication of benign mature teratomas of the mediastinum. AJR Am J Roentgenol 170:323–328, 1998.
221. Satava RM Jr, Beahrs OH, Scholz DA: Success rate of cervical exploration for hyperparathyroidism. Arch Surg 110:625–628, 1975.
222. Savader SJ, Otero RR, Savader BL: MR imaging of intrathoracic extramedullary hematopoiesis. J Comput Assist Tomogr 12:878–880, 1988.
223. Schurawitzki H, Stiglbauer R, Klepetko W, Eckersberger F: CT and MRI in benign mediastinal haemangioma. Clin Radiol 43: 91–94, 1991.
224. Seline TH, Gross BH, Francis IR: CT and MR imaging of mediastinal hemangiomas. J Comput Assist Tomogr 14:766–768, 1990.
225. Shaffer K, Rosado-de-Christenson ML, Patz EF Jr, et al: Thoracic lymphangioma in adults: CT and MR imaging features. AJR Am J Roentgenol 162:283–289, 1994.
226. Shaffer K, Smith D, Kirn D, et al: Primary mediastinal large-B-cell lymphoma: Radiologic findings at presentation. AJR Am J Roentgenol 167:425–430, 1996.
227. Shahian DM, Rossi RL: Posterior mediastinal goiter. Chest 94: 599–602, 1988.
228. Sherrick AD, Brown LR, Harms GF, Myers JL: The radiographic findings of fibrosing mediastinitis. Chest 106:484–489, 1994.
229. Shields TW, Reynolds M: Neurogenic tumors of the thorax. Surg Clin North Am 68:645–668, 1988.
230. Shin MS, Berland LL, Ho KJ: Mediastinal cystic hygromas: CT characteristics and pathogenetic consideration. J Comput Assist Tomogr 9:297–301, 1985.
231. Shin MS, Ho KJ: Computed tomography of primary mediastinal seminomas. J Comput Assist Tomogr 7:990–994, 1983.
232. Shirkhoda A, Chasen MH, Eftekhari F, et al: MR imaging of mediastinal thymolipoma. J Comput Assist Tomogr 11:364–365, 1987.
233. Silverman PM, Korobkin M, Moore AV: CT diagnosis of cystic hygroma of the neck. J Comput Assist Tomogr 7:519–520, 1983.
234. Sirivella S, Ford WB, Zikria EA, et al: Foregut cysts of the mediastinum: Results in 20 consecutive surgically treated cases. J Thorac Cardiovasc Surg 90:776–782, 1985.
235. Snyder ME, Luck SR, Hernandez R, et al: Diagnostic dilemmas of mediastinal cysts. J Pediatr Surg 20:810–815, 1985.
236. So CB, Li DK: Anterolateral cervical meningocele in association with neurofibromatosis: MR and CT studies. J Comput Assist Tomogr 13:692–695, 1989.
237. Spiers AS, Husband JE, MacVicar AD: Treated thymic lymphoma: Comparison of MR imaging with CT. Radiology 203:369–376, 1997.
238. Spritzer C, Gamsu G, Sostman HD: Magnetic resonance imaging of the thorax: Techniques, current applications, and future directions. J Thorac Imaging 4:1–18, 1989.
239. Spritzer CE, Gefter WB, Hamilton R, et al: Abnormal parathyroid glands: High-resolution MR imaging. Radiology 162:487–491, 1987.
240. Stark DD, Moss AA, Brasch RC, et al: Neuroblastoma: Diagnostic imaging and staging. Radiology 148:101–105, 1983.
241. Stevens SK, Chang JM, Clark OH, et al: Detection of abnormal parathyroid glands in postoperative patients with recurrent hyperparathyroidism: Sensitivity of MR imaging. AJR Am J Roentgenol 160:607–612, 1993.
242. Strickler JG, Kurtin PJ: Mediastinal lymphoma. Semin Diagn Pathol 8:2–13, 1991.
243. Strollo DC, Rosado de Christenson ML, Jett JR: Primary mediastinal tumors: Part 1. Tumors of the anterior mediastinum. Chest 112: 511–522, 1997.

244. Strollo DC, Rosado-de-Christenson ML: Tumors of the thymus. J Thorac Imaging 14:152–171, 1999.
245. Strollo DC, Rosado-de-Christenson ML, Jett JR: Primary mediastinal tumors: Part II. Tumors of the middle and posterior mediastinum. Chest 112:1344–1357, 1997.
246. Suster S, Rosai J: Multilocular thymic cyst: An acquired reactive process—study of 18 cases. Am J Surg Pathol 15:388–398, 1991.
247. Swanson PE: Soft tissue neoplasm of the mediastinum. Semin Diagn Pathol 8:14–34, 1991.
248. Takashima S, Takeuchi N, Shiozaki H, et al: Carcinoma of the esophagus: CT vs MR imaging in determining resectability. AJR Am J Roentgenol 156:297–302, 1991.
249. Tam CG, Broome DR, Shannon RL: Desmoid tumor of the anterior mediastinum: CT and radiologic features. J Comput Assist Tomogr 18:499–501, 1994.
250. Tan A, Holdener GP, Hecht A, et al: Malignant thymoma in an ectopic thymus: CT appearance. J Comput Assist Tomogr 15:842–844, 1991.
251. Templeton PA, Fishman EK: CT evaluation of poststernotomy complications. AJR Am J Roentgenol 159:45–50, 1992.
252. Tesoro-Tess JD, Balzarini L, Ceglia E, et al: Magnetic resonance imaging in the initial staging of Hodgkin's disease and non-Hodgkin lymphoma. Eur J Radiol 12:81–90, 1991.
253. Utz JA, Herfkens RJ, Glover G, et al: Rapid Dynamic NMR Imaging of the Heart. Montreal, Canada, Society of Magnetic Resonance in Medicine, 1986.
254. Verstandig AG, Epstein DM, Miller WT Jr, et al: Thymoma—report of 71 cases and a review. Crit Rev Diagn Imaging 33:201–230, 1992.
255. Wang YM, Li YW, Sheih CP, Hsu JC: Magnetic resonance imaging of neuroblastoma, ganglioneuroblastoma, and ganglioneuroma. Chung Hua Min Kuo Hsiao Erh Ko I Hsueh Hui Tsa Chih 36:420–424, 1995.
256. Webb WR, Gamsu G, Speckman JM, et al: Computed tomographic demonstration of mediastinal venous anomalies. Am J Roentgenol 139:157–161, 1982.
257. Webb WR, Gamsu G, Stark DD, Moore EH: Magnetic resonance imaging of the normal and abnormal pulmonary hila. Radiology 152:89–94, 1984.
258. Weidner N: Germ-cell tumors of the mediastinum. Semin Diagn Pathol 16:42–50, 1999.
259. Weinstein JB, Aronberg DJ, Sagel SS: CT of fibrosing mediastinitis: Findings and their utility. Am J Roentgenol 141:247–251, 1983.
260. White CS: MR imaging of thoracic veins. Magn Reson Imaging Clin North Am 8:17–32, 2000.
261. White CS, Baffa JM, Haney PJ, et al: MR imaging of congenital anomalies of the thoracic veins. Radiographics 17:595–608, 1997.
262. White CS, Templeton PA, Attar S: Esophageal perforation: CT findings. AJR Am J Roentgenol 160:767–770, 1993.
263. Wick MR, Scheithauer BW, Weiland LH, Bernatz PE: Primary thymic carcinomas. Am J Surg Pathol 6:613–630, 1982.
264. Wilkins EW Jr, Edmunds LH Jr, Castleman B: Cases of thymoma at the Massachusetts General Hospital. J Thorac Cardiovasc Surg 52:322–330, 1966.
265. Wychulis AR, Payne WS, Clagett OT, Woolner LB: Surgical treatment of mediastinal tumors: A 40 year experience. J Thorac Cardiovasc Surg 62:379–392, 1971.
266. Yedlicka JW, Schultz K, Moncada R, Flisak M: CT findings in superior vena cava obstruction. Semin Roentgenol 24:84–90, 1989.
267. Yeh HC, Gordon A, Kirschner PA, Cohen BA: Computed tomography and sonography of thymolipoma. Am J Roentgenol 140:1131–1133, 1983.
268. Zadvinskis DP, Benson MT, Kerr HH, et al: Congenital malformations of the cervicothoracic lymphatic system: Embryology and pathogenesis. Radiographics 12:1175–1189, 1992.
269. Zinzani PL, Zompatori M, Bendandi M, et al: Monitoring bulky mediastinal disease with gallium-67, CT-scan and magnetic resonance imaging in Hodgkin's disease and high-grade non-Hodgkin's lymphoma. Leuk Lymphoma 22:131–135, 1996.

30 Pleura and Chest Wall

Barbara L. Knisely

After the initial chest radiograph, computed tomography (CT) is the standard imaging modality for the evaluation of chest wall disorders and pleural disease. CT characterizes the type of pleural disease by tissue density, evaluates the extent of pleural and chest wall disease, and differentiates between pleural and parenchymal disease.[35] Magnetic resonance imaging (MRI), with its superior soft tissue contrast, complements CT in patients with pleural disorders. The role of MRI in the chest is limited to specific problem solving, such as select cases of pleural effusions, tumors, infections, and masses.[37, 41] The ability of MRI to obtain images in the coronal and sagittal planes helps in the evaluation of chest wall and pleural abnormalities, particularly the apical regions.[15, 34, 48, 70]

This chapter discusses the CT and MRI findings of pleural and chest wall diseases.

CT Technique

Standard CT examination of the chest includes 10-mm collimation with 10-mm slices obtained from the thoracic inlet through the adrenal glands. Images are obtained with the patient supine in the scanner and with respiration suspended. Helical CT scanners can image the entire chest in a single breath-hold, diminishing respiratory artifact. Coronal and sagittal planes may be reconstructed from the helical CT data for improved evaluation of the pleura and chest wall.

The use of intravenous (IV) contrast is tailored to the individual examination. Contrast may add information in differentiating empyemas from lung abscesses, in distinguishing among solid and cystic lesions, and in identifying areas of necrosis. Images are reviewed in both lung and mediastinal window settings. High-resolution CT (HRCT) images are obtained using 1-mm slices and a high spatial algorithm to evaluate for such diseases as asbestosis in the setting of asbestos exposure.

MRI Technique

There is no standard technique used for the MRI evaluation of chest wall and pleural disease. Common sequences may be as follows:

1. T1-weighted spin-echo (SE) sequences, with a repetition time (TR) of 400 to 600 msec and an echo time (TE) of 15 to 20 msec.
2. Proton-density–weighted and T2-weighted spin-echo sequences (2200–2700/20–30, 80).
3. Fast spin-echo techniques (4000–5600/80–104; 8–12 echo train).

Fat saturation, flow compensation, and presaturation inferiorly and superiorly are added to these sequences. Sequences employed in vascular assessment are as follows:

1. Short tau inversion recovery (STIR) sequences (TR/TE/TI, 2200/43/160 msec).
2. Gradient-recalled acquisition in the steady state (GRASS) sequences (33/13, 30 degrees flip angle).

The slice thickness and intersection gap vary for each examination, depending on the region of interest. The imaging planes (sagittal, axial, coronal, and oblique) are chosen to best depict the anatomy and the abnormality.

Chest MR images are obtained with a large field-of-view scout, usually in the coronal plane, with the patient in either a torso or a body coil. Cardiac gating techniques and respiratory compensation are routinely used. Pulse sequences, imaging planes, and section thickness are designed for the individual patient.

Generally, T1-weighted images provide good anatomic resolution and superb contrast between abnormalities in the extrapleural and pleural fat.[27, 42] T2-weighted images offer good tumor-to-muscle contrast and are helpful in evaluating pleural diseases that invade the chest wall. Additional images with a smaller field of view may be obtained after the initial views with the use of specialized surface coils.

Pleura

Routine CT and MRI cannot perform imaging of the pleura. HRCT depicts the intercostal stripe as a 1- to 2-mm soft tissue line running along the inner aspect of the ribs. This stripe is composed of the visceral and parietal pleura, endothoracic fascia, and the innermost intercostal muscle.[33] The extrapleural fat is seen on HRCT internal to the ribs and is more prominent in obese patients.

Pleural Processes

The features of pleural processes often overlap with parenchymal or extrapleural processes on radiographs. Rib destruction and soft tissue involvement characterize an extrapleural process. Parenchymal lesions typically result in an acute angle with the mediastinum or chest wall.[42] In contrast, pleural processes usually result in an obtuse angle with the chest wall. Despite these general rules, differenti-

ating pleural, extrapleural, and parenchymal processes on CT and MRI may be difficult because more than one compartment may be involved.

Pleural Effusions

A pleural effusion produces a crescent-shaped opacity in the posterior dependent thorax. Loculated pleural effusions appear as fixed lenticula-shaped opacities. Free-flowing pleural fluid in the posterior costophrenic angle may be difficult to differentiate from ascites.

A number of CT signs have been reported to help differentiate pleural from ascitic fluid, namely (1) the diaphragm,[4] (2) the interface,[75] (3) a displaced crus,[19] and (4) a "bare area" sign.[53] The interface and bare area signs are the most accurate.[29]

The interface sign describes a hazy interface with a pleural effusion and a sharp interface with ascites adjacent to the liver or spleen (Figs. 30–1 and 30–2).[75]

The bare area sign describes the restriction of ascites from contacting the posterior liver by the coronary ligaments in the right hemithorax; however, pleural effusion can freely flow in that location.[53]

The diaphragm sign describes the anatomic location of pleural effusion relative to the diaphragm. Pleural effusion is outside the diaphragm, and ascites is inside the diaphragm (see Fig. 30–2).[4]

The displaced crus sign describes the anterolateral displacement of the crus by the pleural effusion, which is located between the crus and the spine (Fig. 30–3).[19] Ascites would cause the opposite displacement of the diaphragmatic crus. On an axial image, ascites is contained within the confines of the diaphragm, whereas effusion lies outside the confines of the diaphragm.

Pleural fluid commonly is heterogeneous on MRI scans because flow artifacts are created by motion within the effusion. Simple pleural effusions show low signal intensity on T1-weighted images and high signal intensity on T2-weighted images because of their water content.[2] CT is currently the study of choice for the evaluation of pleural fluid. However, one study showed that MRI may be slightly superior to CT in the characterization of pleural fluid.[17] The MRI signal intensity of pleural effusions differentiates *transudates* from *exudates*, with exudates producing a higher signal intensity, particularly on T2-weighted images.[17]

Acutely, hemothorax shows high attenuation within the pleural fluid on a nonenhanced CT scan (Fig. 30–4). A fibrothorax may develop if a hemothorax is not drained and is allowed to organize, resulting in pleural thickening. A subacute or chronic hemothorax (Fig. 30–5) demonstrates high signal intensity on both T1-weighted and T2-weighted images.[77] The "concentric ring" sign present in a subacute or chronic hemorrhagic pleural effusion is caused by the dark outer ring (hemosiderin) and the bright

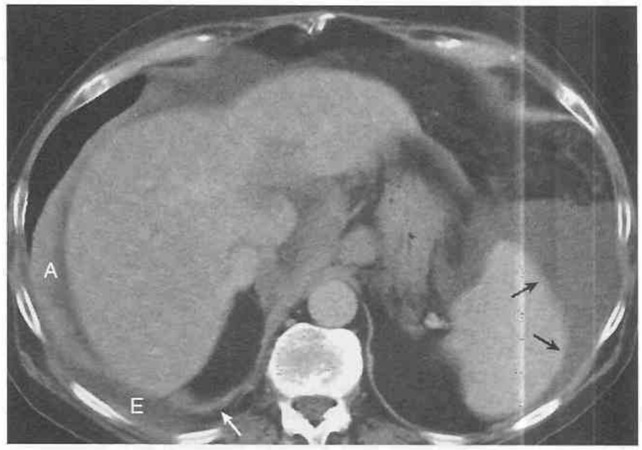

Figure 30–2. CT of "diaphragm" and "interface" signs. Ascites (A) is medial to the diaphragm *(arrow)*, and a pleural effusion (E) is identified lateral to the diaphragm. A sharp interface can be seen between the ascites and the spleen *(arrows)*.

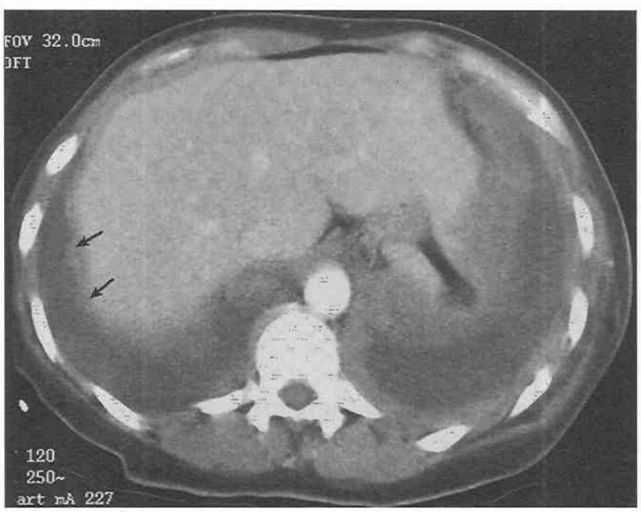

Figure 30–1. CT scan of the "interface" sign. The interface between the pleural effusion and liver laterally is hazy *(arrows)*. A sharp interface would exist between ascites and the liver.

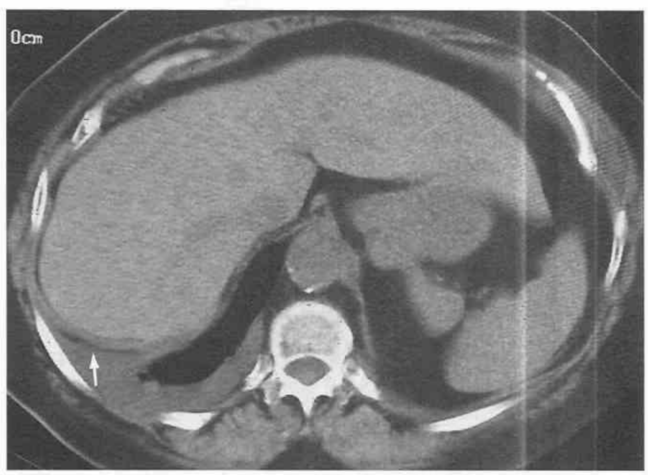

Figure 30–3. CT of "displaced crus" sign. Right pleural effusion forms a crescent-shaped opacity in the dependent portion of the thorax. Lateral displacement of the diaphragmatic crus *(arrow)* describes the displaced crus sign of a pleural effusion.

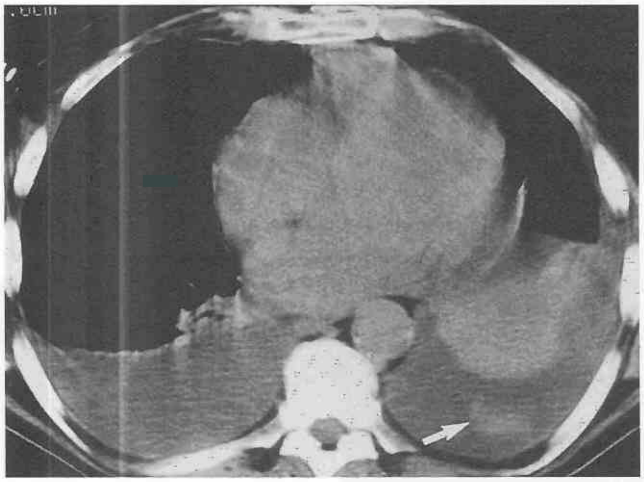

Figure 30–4. Hemothorax following endomyocardial biopsy in a 59-year-old man who developed mild shortness of breath after the biopsy. Nonenhanced CT scan shows a high-attenuation left pleural effusion consistent with hemothorax *(arrow)*. The patient recovered without intervention. (From Knisely BL, Mastey LA, Collins J, Kuhlman JE: Imaging of cardiac transplantation and complications. Radiographics 19:321, 1999.)

central signal intensity (methemoglobin) related to the T1 shortening effects.[28, 42]

On CT scans, chylothorax usually cannot be differentiated from other types of pleural effusions, although one report did show low-attenuation fluid in a chylothorax related to its fat content.[2] Occasionally, a chylothorax may show high signal intensity on T1-weighted and on proton-density–weighted images and lower signal intensity on T2-weighted images related to fat content.[2] On MRI, however, chylothoraces usually cannot be differentiated from simple pleural effusions.

Pleural effusions may be transudates or exudates. The visceral and parietal pleura enhance in exudative effusions, coined the *split-pleura sign*. Transudates do not usually demonstrate pleural enhancement.

Empyemas are characterized on CT by the split-pleura sign, pleural thickening, and air within the pleural space (Fig. 30–6).[72] Empyemas are often associated with parenchymal disease. It may be difficult to differentiate between the two processes. Differentiation is important; patients with empyemas require chest tube drainage, whereas patients with lung abscesses need antibiotics and postural drainage. CT findings that indicate abscess are a spherical shape, thick walls, and abrupt cut-off of vessels and bronchi in adjacent lung at the interface with the abscess.[72] Empyemas are lenticular, usually with thin walls and with compression of adjacent lung bronchi and vessels.[7, 42] Thickened and increased attenuation of the extrapleural fat can be seen in patients with empyemas and is thought to be related to edema.[80]

Malignant neoplasms that arise in the walls of chronic empyemas (most commonly tuberculous empyemas) may be detected by MRI.[44] Neoplasms associated with empyemas include non-Hodgkin's lymphoma, squamous cell carcinoma, mesothelioma, and sarcoma.[44] MRI reveals signal intensities that differ in mature fibrous tissue and in neoplastic tissue, yet the diagnostic value of this potential has not been determined.[44]

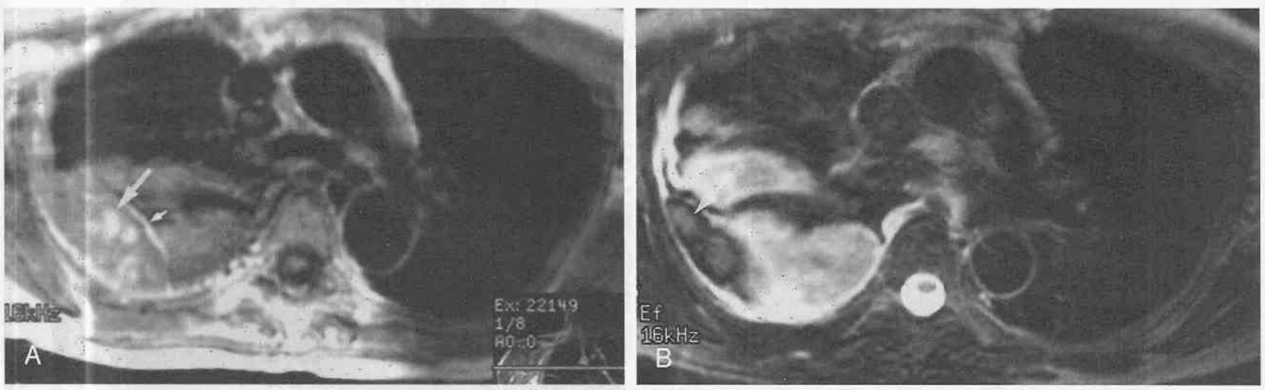

Figure 30–5. Extrapleural hematoma in a 54-year-old woman. Axial T1-weighted (TR = 810 msec, TE = 14 msec) *(A)* and T2-weighted (TR = 4225 msec, TE = 105 msec) *(B)* images show old extrapleural hematoma as a focal ovoid mass with focal areas of increased signal intensity on T1-weighted images and a low-signal-intensity rim on T2-weighted images. The extrapleural location is identified by the displaced subpleural fat line on T1-weighted images *(small arrow* in *A)*. A pleural effusion, with heterogeneous signal intensity on T1-weighted and T2-weighted images, is medial to the extrapleural hematoma *(large arrow* in *A* and *B)*. (*A* and *B*, From Knisely BL, Broderick LS, Kuhlman JE: MR imaging of the pleura and chest wall. MRI Clin North Am 8:125, 2000.) *C*, Noncontrast CT scan shows a high-attenuation right extrapleural hematoma *(small arrows)* and a medial simple pleural effusion *(large arrow)*. [redacted]

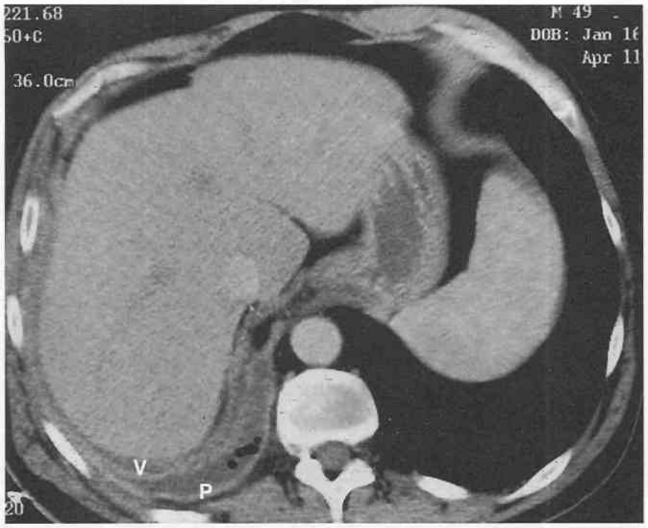

Figure 30–6. Empyema in a 49-year-old man. Contrast-enhanced CT scan shows the split-pleura sign with enhancement of the visceral (V) and parietal (P) pleura. Air bubbles are present in the empyema.

Pleural Air

Standard chest radiographs are the most commonly used radiologic examination for detection of pneumothoraces. In the supine, ventilated, or acutely traumatized patient, CT may detect pneumothoraces not visible on chest radiographs.[76]

A bronchopleural fistula is a communication between the pleura and bronchial tree that results in a persistent air leak (Fig. 30–7). Common causes include necrotizing pulmonary infections and surgical lung resections. CT, particularly thin-section CT, is the imaging modality of choice to show the communication between the airway and the pleura.[82] CT can demonstrate the location, number, size, and underlying cause of bronchopleural fistulas.[73]

Therapeutic options include surgical resection and surgical or image-guided occlusion of the bronchopleural fistula with endobronchial vascular coils or glue. Antibiotics are given to patients with an underlying infection.[56]

Pleural Masses

Benign Pleural Masses

Benign pleural processes include lipoma, asbestos-related disease, localized pleural fibroma, and rounded atelectasis.[40, 83] The most common benign chest wall neoplasms are lipoma and localized pleural fibroma.

On CT scans, lipomas have a homogeneous fat attenuation, occasionally with a few septa or calcifications in areas of fat necrosis. Lipomas are usually located in the lateral pleura, with signal intensity characteristics of subcutaneous fat on all MRI sequences. Benign fibrous tumors of the pleura (previously termed *benign mesotheliomas*) are not asbestos-related and occur in the sixth and seventh decades of life.[20] Most patients with benign pleural fibromas are asymptomatic. Large pleural fibromas may produce symp-

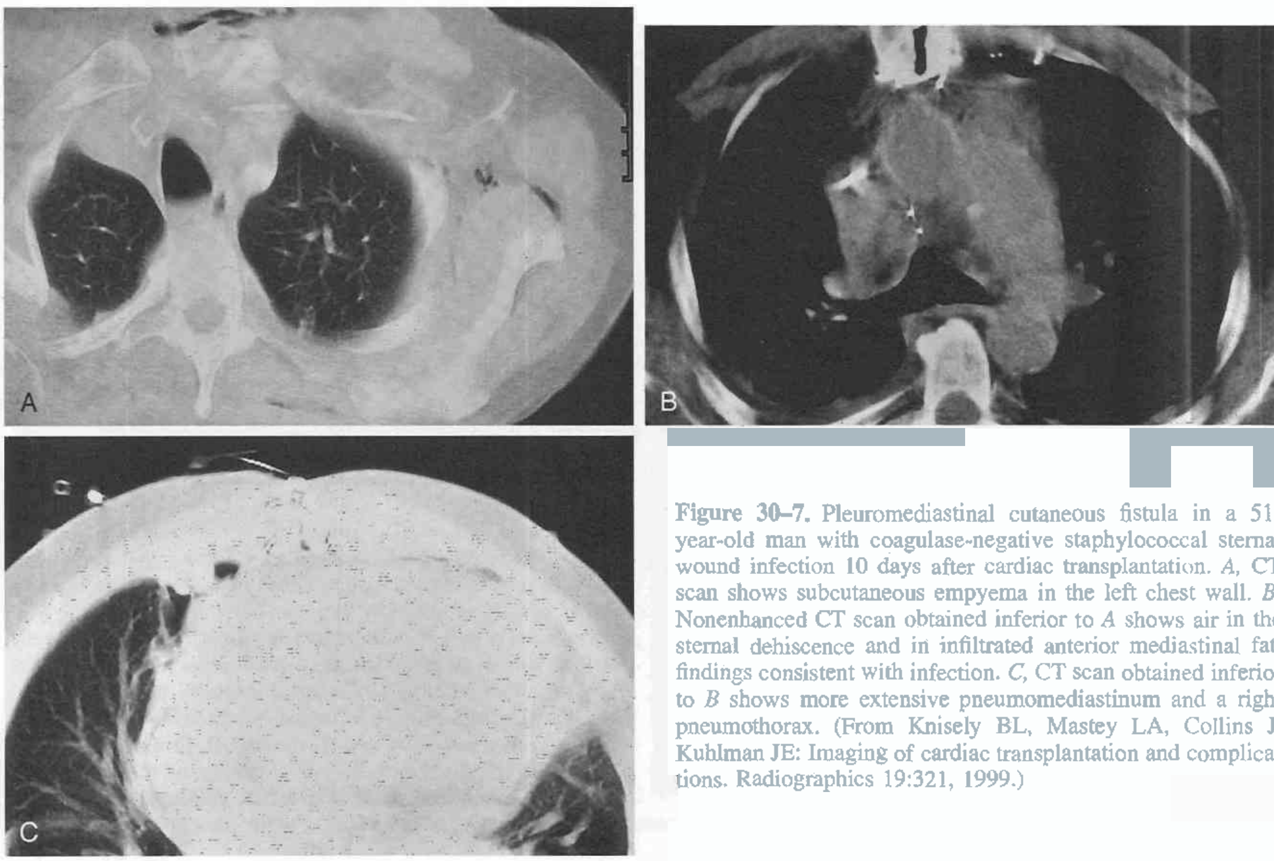

Figure 30–7. Pleuromediastinal cutaneous fistula in a 51-year-old man with coagulase-negative staphylococcal sternal wound infection 10 days after cardiac transplantation. *A*, CT scan shows subcutaneous empyema in the left chest wall. *B*, Nonenhanced CT scan obtained inferior to *A* shows air in the sternal dehiscence and in infiltrated anterior mediastinal fat, findings consistent with infection. *C*, CT scan obtained inferior to *B* shows more extensive pneumomediastinum and a right pneumothorax. (From Knisely BL, Mastey LA, Collins J, Kuhlman JE: Imaging of cardiac transplantation and complications. Radiographics 19:321, 1999.)

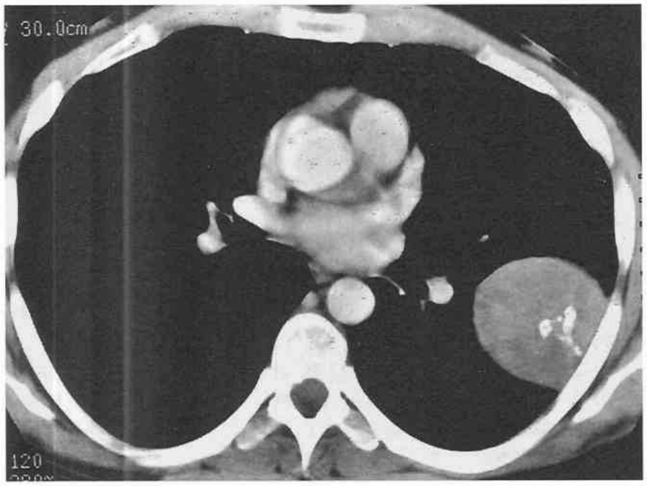

Figure 30–8. Benign pleural fibroma. Enhanced CT scan reveals a soft tissue intrafissural mass with coarse calcifications, pathologically consistent with a benign pleural fibroma. (From Knisely BL, Kuhlman JE: Radiographic and CT imaging of complex pleural disease. Crit Rev Diagn Imaging 38:1, 1997.)

toms of cough, chest pain, and dyspnea. These tumors are associated with an increased incidence of episodic hypoglycemia and hypertrophic pulmonary osteoarthropathy.[9, 20]

On microscopic examination, 60% of pleural fibromas are found to be benign with 40% malignant.[20] A malignant pleural fibroma may have an associated pleural effusion and may grow to more than 10 cm in diameter.[20] Chest wall invasion and local recurrence following surgery can occur with malignant pleural fibromas. The cure rate with surgical excision is 40% for malignant fibromas and 100% for benign fibromas.[20, 50]

The CT appearance is a homogeneous, enhancing soft tissue mass with occasional calcification and associated pleural effusion (Fig. 30–8).[63] On MR images, pleural fibromas are isointense to muscle on T1-weighted images and isointense to hyperintense to muscle on T2-weighted images, and they demonstrate enhancement with IV gadolinium.[23, 39]

Rounded atelectasis (Fig. 30–9) refers to masslike atelectasis abutting the pleura. It has most commonly been described as being related to asbestos exposure.[64, 71] Rounded atelectasis is most commonly seen in the posterior or posteromedial lower lobe, followed by the lingula and right middle lobe.[13] The "comet-tail sign" of vessels and bronchi curving into the mass is seen in both CT and MRI. Displacement of the fissures can confirm the presence of volume loss. On MRI, the signal intensity is comparable to that of liver on T1-weighted images (see Fig. 30–9).[78] The findings of rounded atelectasis on CT and MRI are vital to recognize because this condition may be similar to a pleural or parenchymal neoplasm.[45] Biopsy of rounded atelectasis may be mistaken for malignancy if findings of fibrosis are not seen on histologic examination.[18]

Asbestos-related disease includes simple pleural effusions, pleural plaques and thickening, rounded atelectasis, pleural or parenchymal neoplasms, and asbestosis (interstitial lung disease).[1] Pleural plaques, the most common and specific finding, are located along the diaphragmatic and chest wall parietal pleura.[65] Calcification of pleural plaques may occur; calcifications range in thickness from 1 to 10 mm (Fig. 30–10). Diffuse pleural thickening, which may also be seen in asbestos exposure, frequently follows an asbestos-related benign pleural effusion. On CT scans, pleural plaques are recognized as focal soft tissue masses located inferiorly along the paravertebral pleura. A fibrothorax related to previous hemorrhage or infection should be the primary differential diagnosis if unilateral, thicker, more irregular calcified pleural plaques are present in a patient without a history of asbestos exposure.

Malignant Pleural Masses

Malignant mesothelioma (Fig. 30–11) is a highly lethal tumor whose increased incidence is related to the industrial use of asbestos.[31] CT imaging of mesothelioma shows

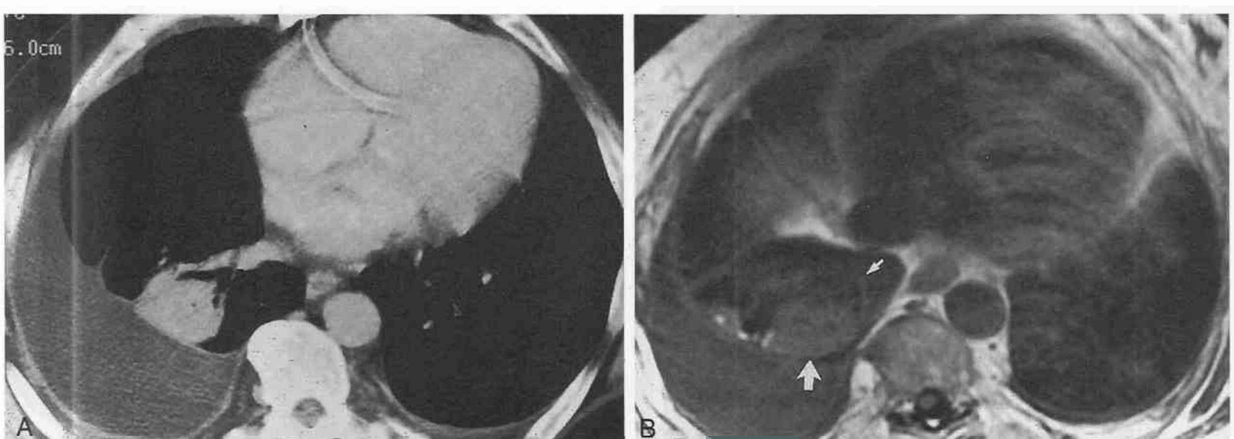

Figure 30–9. Rounded atelectasis in a 65-year-old man. *A,* Contrast-enhanced CT scan reveals right pleural effusion and right lower lobe mass of atelectatic lung with incurving bronchi and vessels. *B,* Axial T1-weighted (TR = 400msec, TE = 14 msec) image shows an ovoid mass *(large arrow)* with an inwardly curving bronchovascular structure *(small arrow)* in the right lower lobe. The mass demonstrates isointense signal intensity relative to liver. A large right pleural effusion can be seen posteriorly. (*B,* From Knisely BL, Broderick LS, Kuhlman JE: MR imaging of the pleura and chest wall. MRI Clin North Am 8:125, 2000.)

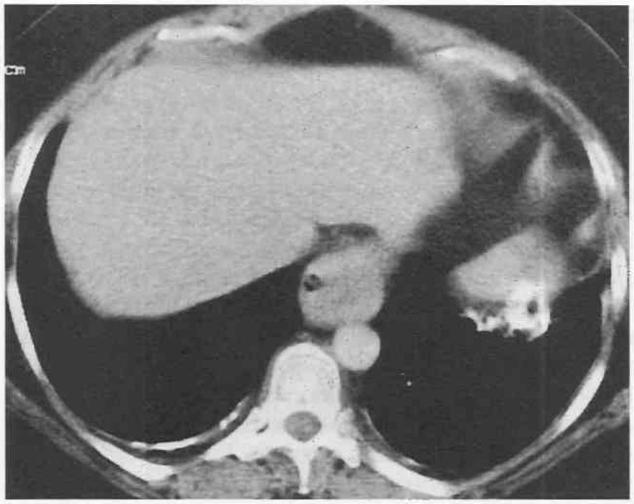

Figure 30–10. Asbestos exposure. Contrast-enhanced CT scan shows bilateral calcified pleural plaques posteriorly with involvement of the left diaphragm.

unilateral, diffuse, nodular pleural thickening, usually with associated pleural effusion. The tumor sometimes encases the lung, extends into the fissures, and causes unilateral volume loss. MRI reveals minimal increased signal intensity on T1-weighted sequences and moderate increased signal intensity on T2-weighted sequences. Mesothelioma (Fig. 30–12) occasionally presents as an effusion without soft tissue thickening or as a discrete pleural mass.[3, 36, 42]

MRI is superior to CT in demonstrating a solitary focus of invasion of the chest wall or endothoracic fascia and in showing invasion of the diaphragm.[31] MRI staging of mesothelioma does not change operative planning, and CT is the standard diagnostic examination because of its cost-effectiveness.[31] For patients who are surgical candidates, extrapleural pneumonectomy is the procedure of choice, although the prognosis is extremely poor.

Metastatic disease is the most common neoplasm of the pleura (Fig. 30–13).[40, 42] Lung, breast, stomach, and ovarian carcinomas are the most common sources of metastatic pleural disease.[62] Lymphoma and thymoma may also involve the pleural surface.[68] Metastatic pleural adenocarcinoma can mimic the radiographic appearance of mesothelioma with diffuse nodular pleural thickening. Metastatic adenocarcinoma and mesothelioma may be differentiated by immunochemistry, histochemistry, and electron micros-

Pleural effusion is the most common manifestation of pleural metastases. Diffuse pleural thickening and solid pleural masses or nodules may also be seen in metastatic pleural disease. [redacted]

Chest Wall

Knowledge of the cross-sectional anatomy of the chest wall allows adequate evaluation of soft tissue abnormalities (Fig. 30–14). Normal chest wall musculature, vasculature, and bony structures are well visualized on CT scans. A simple method for counting ribs on CT scans is based on identification of the *sternal angle*,[38] an oval high-attenuation structure lacking bone marrow. The second costal cartilages connect to the second ribs laterally and the sternal angle medially. The third to sixth ribs are counted numerically, from anterior to posterior, on the same slice.

Benign Chest Wall Lesions

Lipoma is the most common benign soft tissue mass to involve the chest wall (Fig. 30–15).[52] On CT images, lipomas show the attenuation coefficient of fat and are well

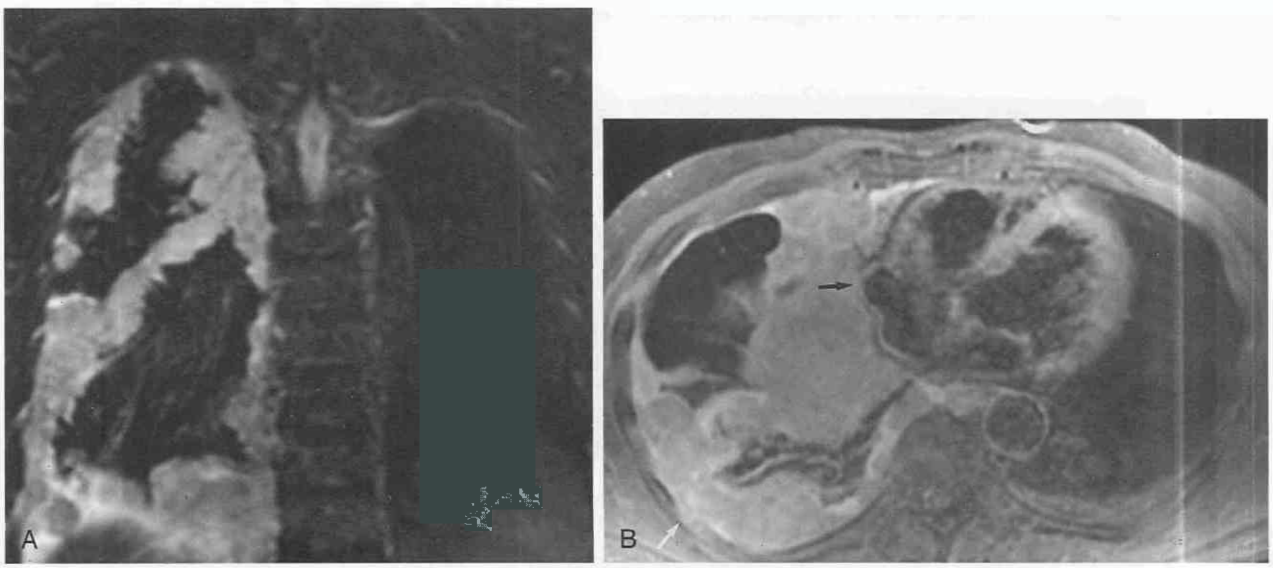

Figure 30–11. Malignant mesothelioma in a 57-year-old man. Coronal T2-weighted (TR = 4500 msec, TE = 105msec) with fat saturation *(A)* and axial T1-weighted (TR = 821 msec, TE = 14 msec) with fat saturation *(B)* gadolinium-enhanced images reveal nodular pleural tumor encasing the right lung, involving the pericardium *(black arrow)*, and extending into endothoracic fascia *(white arrow)*. (From Knisely BL, Broderick LS, Kuhlman JE: MR imaging of the pleura and chest wall. MRI Clin North Am 8:125, 2000.)

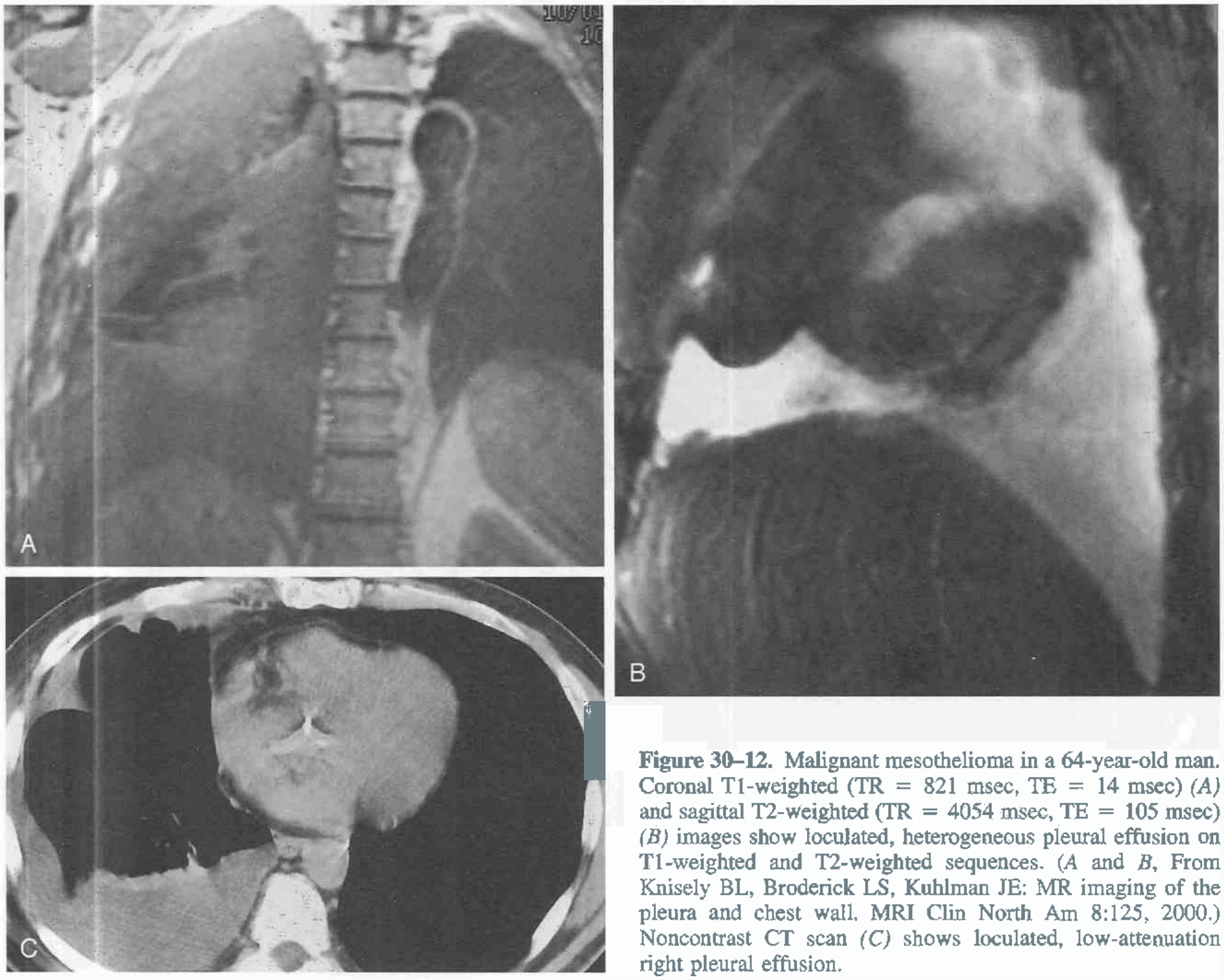

Figure 30–12. Malignant mesothelioma in a 64-year-old man. Coronal T1-weighted (TR = 821 msec, TE = 14 msec) *(A)* and sagittal T2-weighted (TR = 4054 msec, TE = 105 msec) *(B)* images show loculated, heterogeneous pleural effusion on T1-weighted and T2-weighted sequences. (*A* and *B*, From Knisely BL, Broderick LS, Kuhlman JE: MR imaging of the pleura and chest wall. MRI Clin North Am 8:125, 2000.) Noncontrast CT scan *(C)* shows loculated, low-attenuation right pleural effusion.

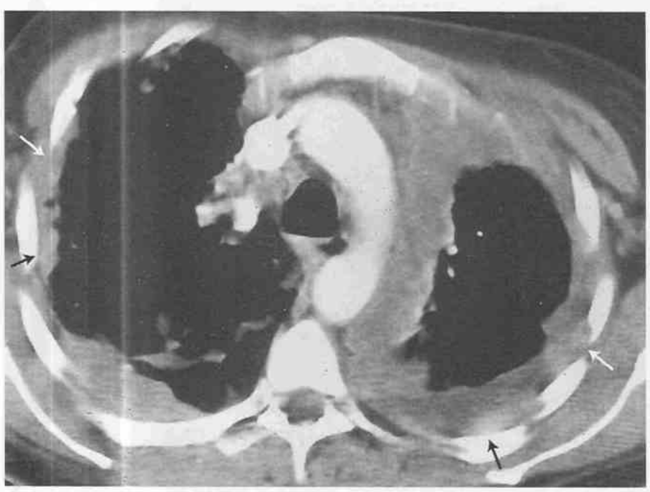

Figure 30–13. CT of metastatic pleural disease from adenoid cystic carcinoma of the parotid gland. A large loculated left pleural effusion and a smaller right effusion can be seen. Pleural soft-tissue attenuation deposits are identified bilaterally *(arrows)*.

circumscribed. On MRI scans, lipomas exhibit fat signal intensities, with high signal intensity on T1-weighted and proton-density–weighted images and slightly lower signal intensity on heavily T2-weighted images. STIR and fat-saturation images depict the low signal intensity of fat. Chemical shift artifact can be seen at the interface of the lipoma with the surrounding soft tissues of higher water content. A few thin, low-signal-intensity, fibrous septations may be seen within the lipoma.[74]

A diagnosis of liposarcoma should be considered if there is heterogeneous signal intensity or if there are islands of soft tissue attenuation within the fatty tumor. MRI plays a role in surgical planning, allowing adequate evaluation of fatty masses that may infiltrate the chest wall or that lie near neurovascular structures.

Chest wall masses may result from anomalies of connective tissues and the lymphatic, vascular, and musculoskeletal systems.[32] Hemangioma (Fig. 30–16) is a broad category of lesions composed of cavernous, venous, arteriovenous, capillary, and mixed vascular malformations.[25, 43] Extraskeletal hemangiomas are uncommon benign lesions located superficially in the skin or subcutaneous tissues or deep within the synovium or musculature.[25, 43] Superficial hemangiomas have curvilinear low-signal-intensity structures on T1-weighted images and show high signal intensity on

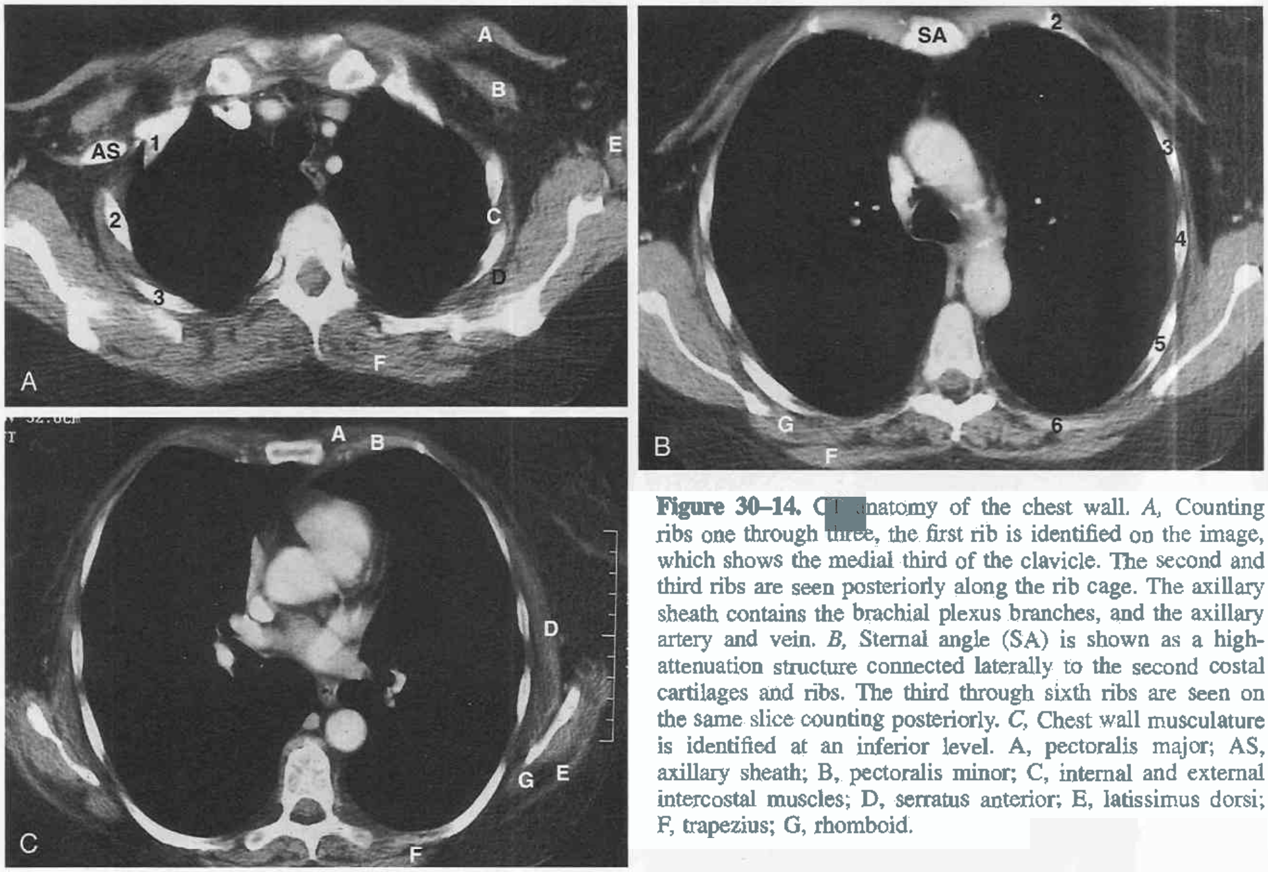

Figure 30–14. CT anatomy of the chest wall. *A,* Counting ribs one through three, the first rib is identified on the image, which shows the medial third of the clavicle. The second and third ribs are seen posteriorly along the rib cage. The axillary sheath contains the brachial plexus branches, and the axillary artery and vein. *B,* Sternal angle (SA) is shown as a high-attenuation structure connected laterally to the second costal cartilages and ribs. The third through sixth ribs are seen on the same slice counting posteriorly. *C,* Chest wall musculature is identified at an inferior level. A, pectoralis major; AS, axillary sheath; B, pectoralis minor; C, internal and external intercostal muscles; D, serratus anterior; E, latissimus dorsi; F, trapezius; G, rhomboid.

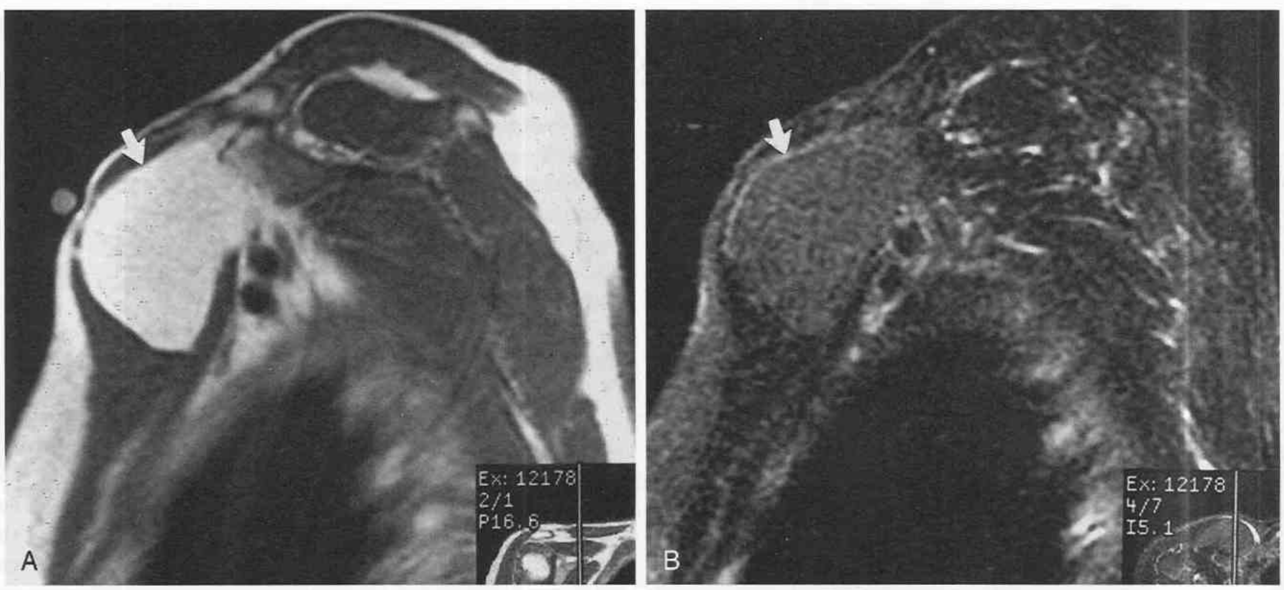

Figure 30–15. Lipoma in a 79-year-old woman. Sagittal T1-weighted (TR = 500 msec, TE = 8 msec) *(A)* and T2-weighted with fat saturation (TR = 4000 msec, TE = 105 msec) *(B)* images show a sharply defined mass *(arrow)* with signal intensity identical to that of subcutaneous fat on all pulse sequences. Fat suppression is demonstrated on T2-weighted images. (From Knisely BL, Broderick LS, Kuhlman JE: MR imaging of the pleura and chest wall. MRI Clin North Am 8:125, 2000.)

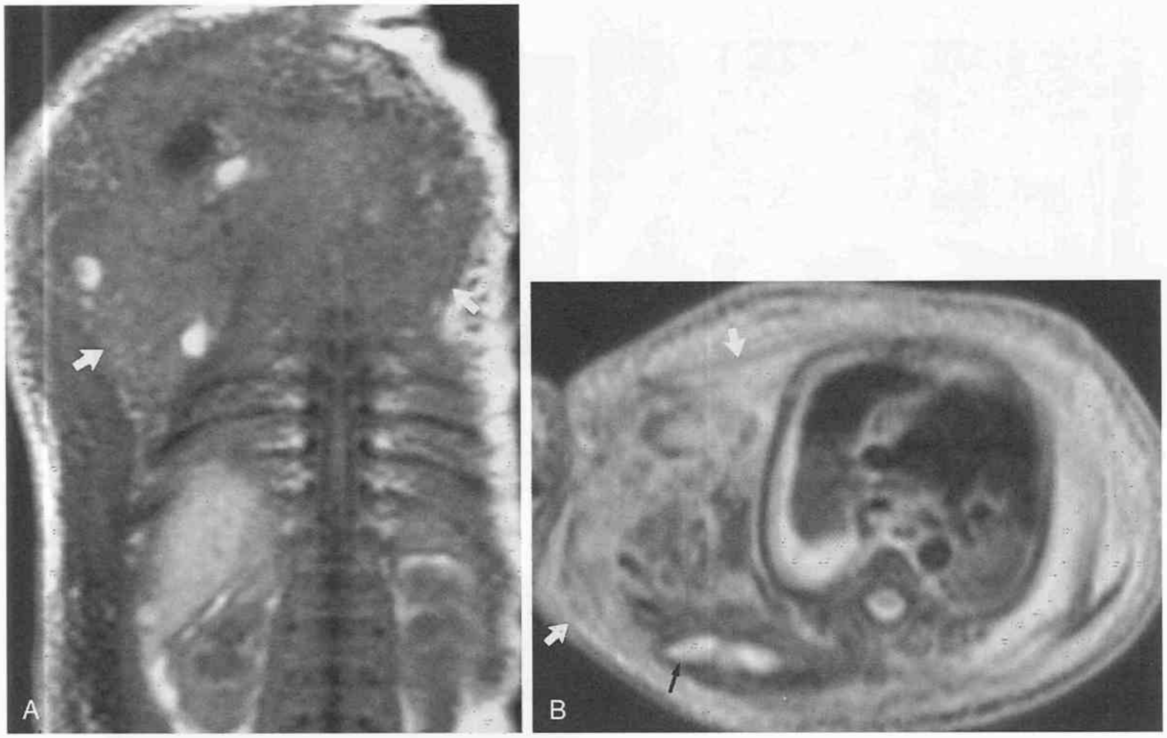

Figure 30–16. Chest wall hemangioma in a 2-day-old girl. Coronal T1-weighted (TR = 450 msec, TE = 12 msec) *(A)* and axial T2-weighted (TR = 3000 msec, TE = 102 msec) *(B)* images show heterogenous soft tissue mass *(white arrows)* involving the lateral and posterior right chest wall. High signal intensity *(black arrow)* on T2-weighted images is hemorrhage, as corresponding T1-weighted images (not shown) show high signal intensity. Multiple foci of high signal on T1-weighted image represent hemorrhage. (From Knisely BL, Broderick LS, Kuhlman JE: MR imaging of the pleura and chest wall. MRI Clin North Am 8:125, 2000.)

T2-weighted images.[25] Muscle atrophy may be a feature of the deep intramuscular hemangiomas.[25]

The MRI appearance of hemangiomas depends on the subtype and components of vascular elements (old blood, thrombus, hemosiderin), fat, and connective tissue.[25] Hemangiomas typically exhibit intermediate signal intensity on T1-weighted images and high signal intensity on T2-weighted images.[25, 32] The hyperintensity on T2-weighted images is thought to be related to stagnant or slow-flowing blood in dilated vascular beds. Arteriovenous malformations (AVMs) are characterized by tubular flow voids on T1-weighted and proton-density–weighted spin-echo sequences and by high signal intensity on gradient-recalled echo sequences.[22] The MRI finding of flowing blood allows the confident diagnosis of an AVM. MRI offers superior soft tissue contrast, which is helpful in evaluating the extension of hemangiomas into muscles, subcutaneous tissues, and the chest wall.[37]

Lymphangiomas are congenital lesions that are usually seen as a neck mass but may extend into the chest wall, axilla, extremities, and mediastinum.[69, 85] Histologically, lymphangiomas are a sequestered collection of lymphatics separated from the remainder of the lymphatic system.[85] Lymphangiomas are locally infiltrating and often recur locally, thus making surgery difficult.[69] Operative planning requires detailed identification of the lymphangioma and its relationship to adjacent neurovascular structures and muscles.

On MRI, lymphangiomas show the signal intensity of water on all pulse sequences, reflecting the fluid content of the dilated lymphatics.[37] The signal intensity of lymphangiomas is comparable to that of cerebrospinal fluid, lower than that of muscle on T1-weighted images, and higher than that of muscle or fat on T2-weighted images.[69] MRI may reveal internal septations within lymphangiomas.[69] STIR images and T2-weighted images with fat suppression show the extension and accentuate the water content of lymphangiomas.

MRI is the preferred imaging modality for evaluating lymphangiomas, especially if the administration of IV contrast medium is contraindicated.

Malignant Chest Wall Lesions

Breast carcinoma is the most common malignant soft tissue chest wall tumor.[79] Mammography is the examination of choice in the detection of breast cancer, with MRI reserved for cases of local chest wall recurrence.[79] Sarcomas (Figs. 30–17 and 30–18) are less common soft tissue tumors of the chest wall, and desmoid tumors are reported as being one of the most common chest wall sarcomas.[10, 79] Patients with soft tissue sarcomas have a 60% 5-year survival rate, a rate that is better than that of other primary chest wall malignancies.[5]

Patients with chest wall sarcomas do not typically present with pain. Pain associated with chest wall sarcoma is a poor prognostic sign.[5]

Desmoid tumors (see Fig. 30–18), previously termed *fibromatosis*, are infiltrative, poorly circumscribed, and ill

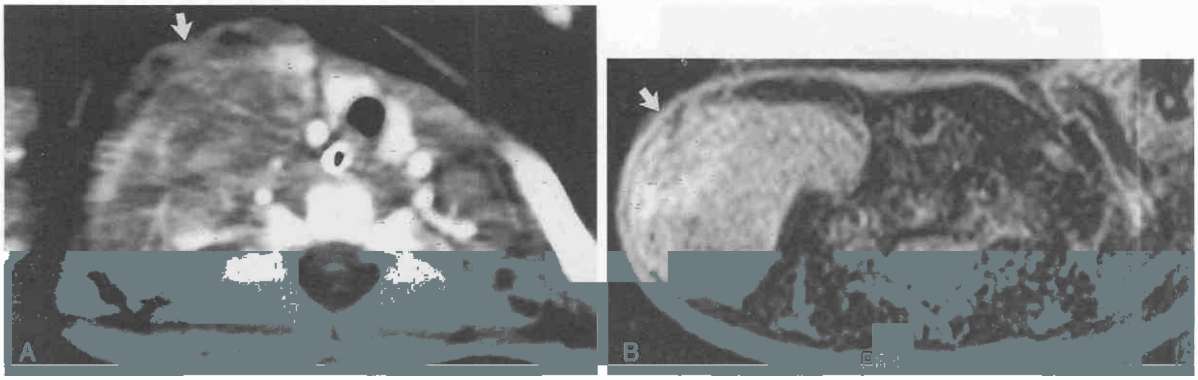

Figure 30–17. Undifferentiated sarcoma of the right neck and superior chest wall in a 4-month-old boy. *A,* Contrast-enhanced axial CT scan shows low-attenuation mass *(arrow)* in the right supraclavicular fossa, causing displacement of midline structures to the left. *B,* Axial T2-weighted (TR = 3200 msec, TE = 105 msec) image shows a tumor mass *(arrow)* demonstrating high signal intensity relative to muscle and involving the right axilla and chest wall. (From Knisely BL, Broderick LS, Kuhlman JE: MR imaging of the pleura and chest wall. MRI Clin North Am 8:125, 2000.)

Figure 30–18. Desmoid tumor in a 60-year-old man. Coronal T1-weighted (TR = 650 msec, TE = 14 msec) *(A)* and sagittal T2-weighted (TR = 2400 msec, TE = 104 msec) *(B)* images show a tumor *(white arrow)* in the right supraclavicular fossa, deviating the brachial plexus anteriorly *(black arrow)*. The tumor shows slightly high signal intensity on T1-weighted and T2-weighted images relative to muscle. (From Knisely BL, Broderick LS, Kuhlman JE: MR imaging of the pleura and chest wall. MRI Clin North Am 8: 125, 2000.)

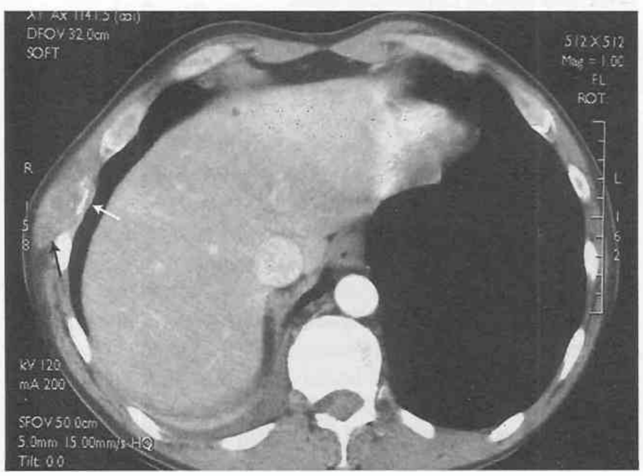

Figure 30–19. CT of right chest wall adenocarcinoma of unknown primary. Ovoid, soft tissue mass *(arrows)* has destroyed the right lateral rib and distorts the normal musculature.

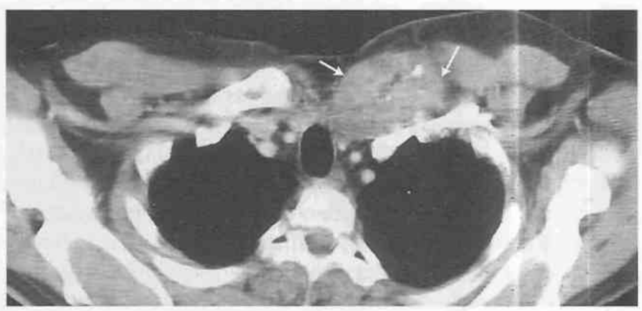

Figure 30–20. CT of metastatic melanoma to the left sternoclavicular joint. Ovoid, heterogeneous soft tissue mass *(arrows)* destroys medial left clavicle and causes posterior compression of left bronchiocephalic vein.

defined.[51] Although these tumors were once considered benign, because metastatic disease is rare, desmoids are now classified as low-grade fibrosarcomas as a result of their locally aggressive behavior.[57] The cause of desmoids is speculative; associations have been reported with estrogen therapy, pregnancy, trauma, and Gardner's syndrome.[21] Interesting to note, spontaneous cures of desmoid tumors have been reported during menopause and menarche.[59]

CT is more helpful in evaluating the extent of soft tissue chest wall tumors than in enabling a specific diagnosis.[35] MRI of desmoids shows a signal intensity isointense to muscle on T1-weighted, and variable on T2-weighted, sequences.[14] MRI of most malignant chest wall lesions shows heterogenous signal intensity, with mainly hypointensity on T1-weighted images and isointensity or hyperintensity on T2-weighted images, relative to subcutaneous fat.[22] Irregular margins and bone or vascular invasion are common findings in malignant lesions.

Current therapy includes wide local excision, with the role of adjuvant radiation therapy undefined.[10] High recurrence rates (18% to 54%) of surgically resected desmoids are seen in young patients and patients with large tumors.[10]

Chest Wall Masses with Rib Destruction

The differential diagnosis for a mass arising within a rib and causing a chest wall mass with rib destruction is limited.[58] Metastasis and multiple myeloma, respectively, are the first and second most common causes of a chest wall mass with associated rib destruction.[58] Metastases to the red marrow of ribs and sternum can occur from primary tumors of the lung, breast, kidney, and thyroid in adults (Figs. 30–19 and 30–20).[79] In children, the most common causes of lytic rib lesions are metastatic neuroblastoma and primary Ewing's sarcoma (Fig. 30–21).[58]

Ewing's Sarcoma

Ewing's sarcoma most frequently affects adolescent boys who present with a painful and rapidly enlarging chest wall mass.[5] Ewing's sarcoma is sometimes called a "medical tumor" because its prognosis is related to the extent of systemic rather than local disease. The overall 5-year survival of 48% is not affected by local recurrence after chest wall resection.[5] Five-year survival decreases to 28% with distant metastases, which occur in 75% of Ew-

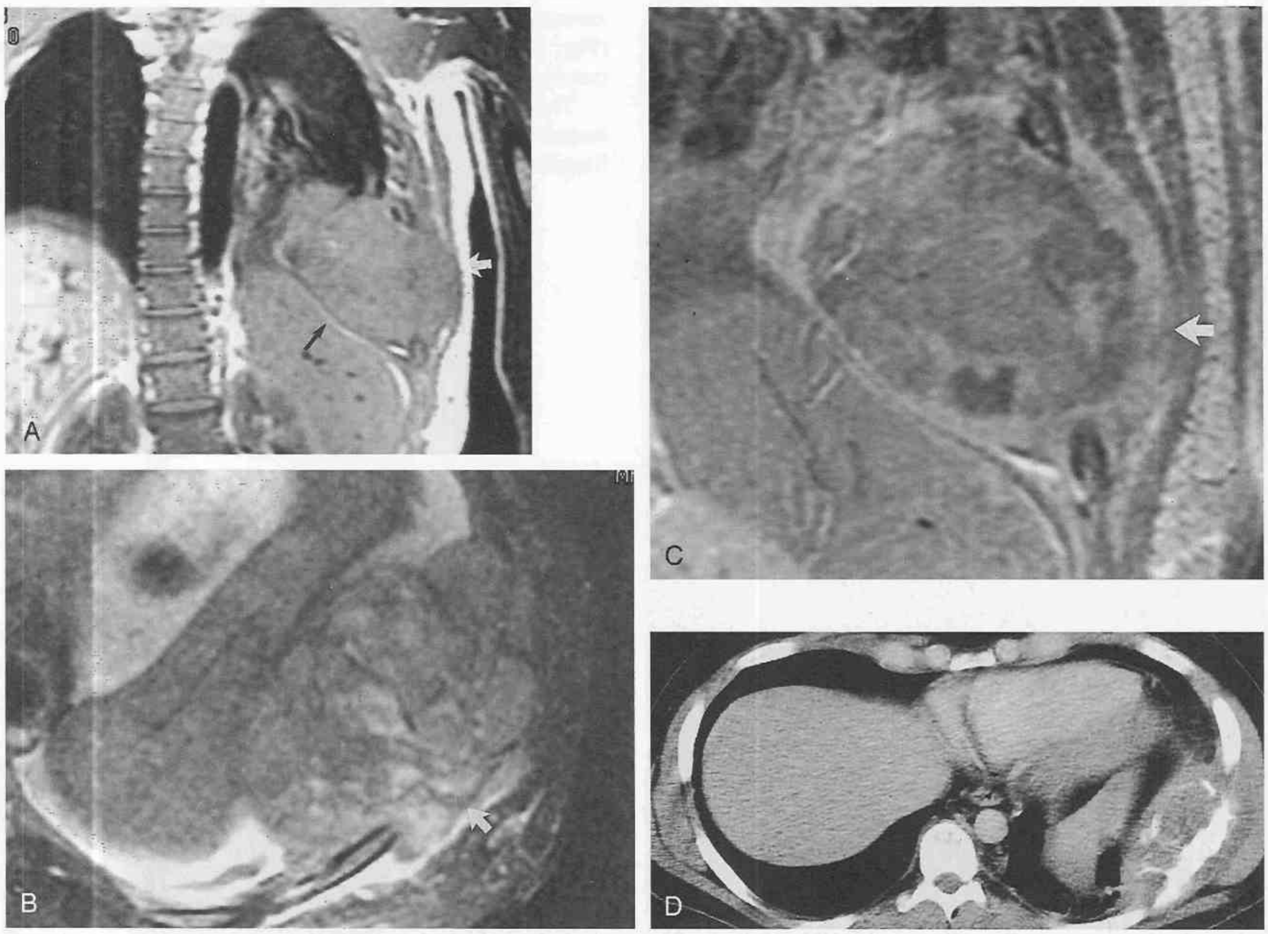

Figure 30–21. Ewing's sarcoma of the left chest wall in a 21-year-old man. *A,* Coronal T1-weighted (TR = 789 msec, TE = 14 msec) sequence shows the tumor mass as isointense to muscle. *B,* Axial T2-weighted (TR = 5217 msec, TE = 80 msec) sequence shows increased signal intensity. *C,* Coronal gadolinium-enhanced T1-weighted with fat saturation (TR = 714 msec, TE = 8 msec) sequence shows heterogeneous enhancement. A fat plane (*black arrow* in *A*) is present between the tumor and the spleen. Tumor has destroyed the left eighth rib and extends into the extrathoracic muscles (*white arrows* in *A–C*). *D,* Contrast-enhanced CT scan reveals the left chest wall mass, with low attenuation relative to muscle, destroying the rib. (*A–C,* From Knisely BL, Broderick LS, Kuhlman JE: MR imaging of the pleura and chest wall. MRI Clin North Am 8:125, 2000.)

ing's sarcoma patients.[11] Treatment includes systemic therapy and autologous bone marrow transplantation if metastatic disease is present.[46]

Askin's Tumor

Askin's tumor (Fig. 30–22) is an uncommon primitive neuroectodermal neoplasm that typically presents as a chest wall or paravertebral mass in young adults.[61] The tumor shares the histologic characteristics of rhabdomyosarcoma, neuroblastoma, Ewing's sarcoma, lymphoma, and small-cell osteosarcoma. It may be distinguished as a distinct pathologic entity on the basis of characteristic immunohistochemical and electron microscopic features.[6, 61]

CT and MRI demonstrate the mass as well as erosions of the ribs or vertebral bodies. Radionuclide technetium Tc 99m bone scans often reveal other occult bony involvement. On MRI scans, an Askin's tumor is seen as a heterogeneous soft tissue mass, representing areas of focal hemorrhage and tumor necrosis. The tumor exhibits a signal intensity greater than that of skeletal muscle on T1-weighted sequences and a high signal intensity on T2-weighted sequences.[61]

Treatment includes combinations of surgery, radiation, and chemotherapy. The overall poor prognosis is poor, however, because of the high rate of local recurrence and the development of distant metastases.[6, 47]

Primary Tumors of the Rib

Primary malignant and benign tumors of the cartilage or bone of the rib may also present as a chest wall mass with rib destruction. These chest wall tumors include osteosarcoma, fibrosarcoma, chondrosarcoma, osteochondroma (Fig. 30–23), giant cell tumor, enchondroma, round cell tumor, hemangioma, and aneurysmal bone cyst.[79]

Traumatic rib fractures (Fig. 30–24) and chest wall hematomas may have the appearance of a chest wall mass. Surgical excision of the involved rib may be necessary at

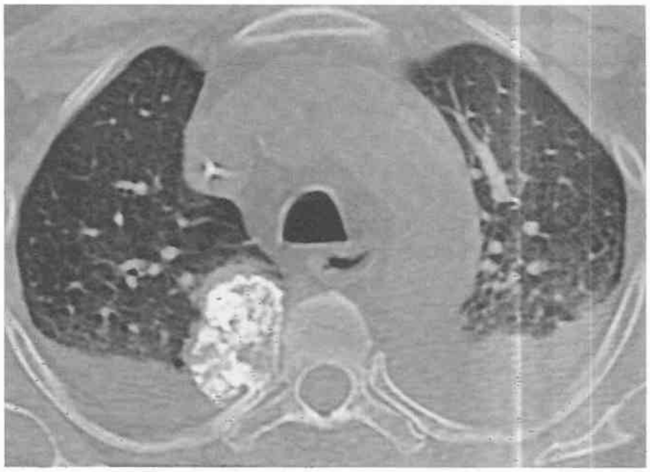

Figure 30–23. CT scan of osteochondroma. Noncontrast CT scan reveals a heterogeneous, lobulated, calcified mass with a cartilaginous cap arising from the right third rib, consistent with an osteochondroma.

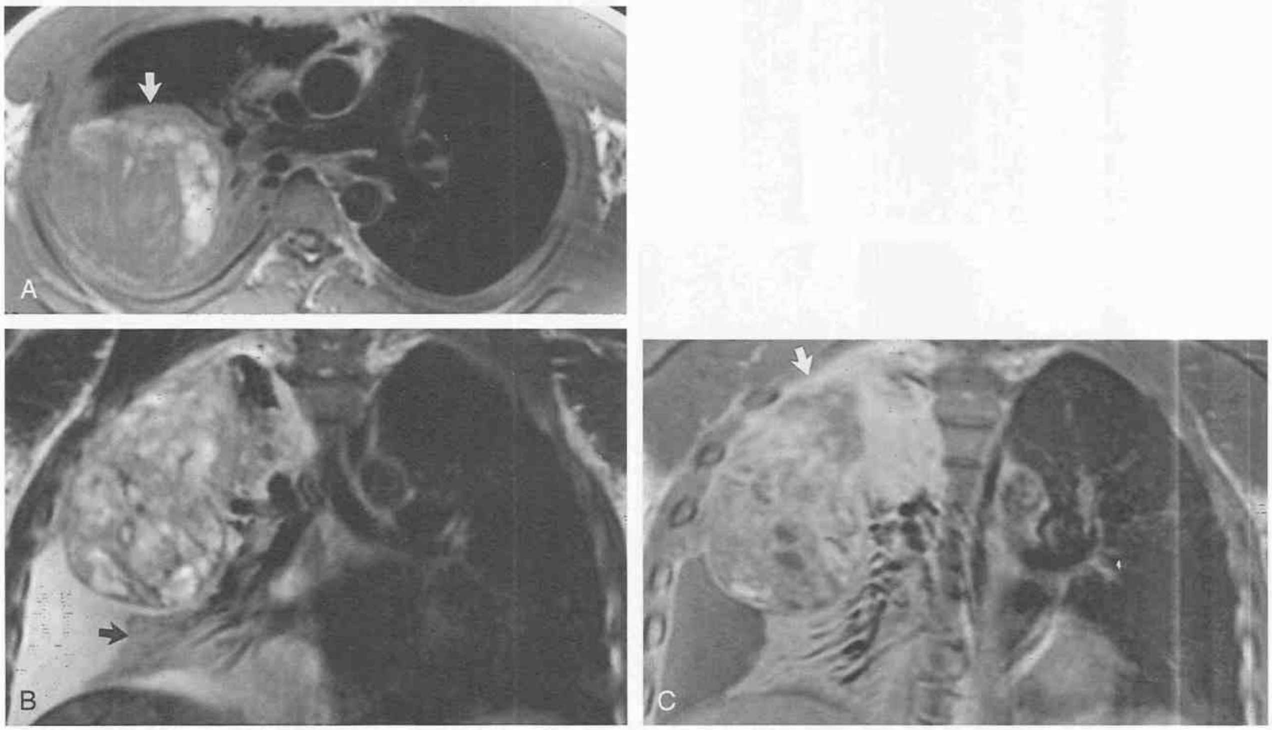

Figure 30–22. Askin's tumor of the pleura in an 18-year-old man. Axial T1-weighted (TR = 731 msec, TE = 12 msec) *(A)* and coronal T2-weighted (TR = 3500 msec, TE = 102 msec) *(B)* images show a heterogenous soft tissue mass *(white arrow)* and effusion causing compressive atelectasis of the adjacent lung *(black arrow)*. High-signal foci on T1-weighted images correspond to high-signal foci on T2-weighted axial images (not shown), consistent with hemorrhage. Coronal T1-weighted (TR = 740 msec, TE = 11 msec) contrast-enhanced image *(C)* shows enhancement of the pleural mass and lack of chest wall invasion *(white arrow)*. (From Knisely BL, Broderick LS, Kuhlman JE: MR imaging of the pleura and chest wall. MRI Clin North Am 8:125, 2000.)

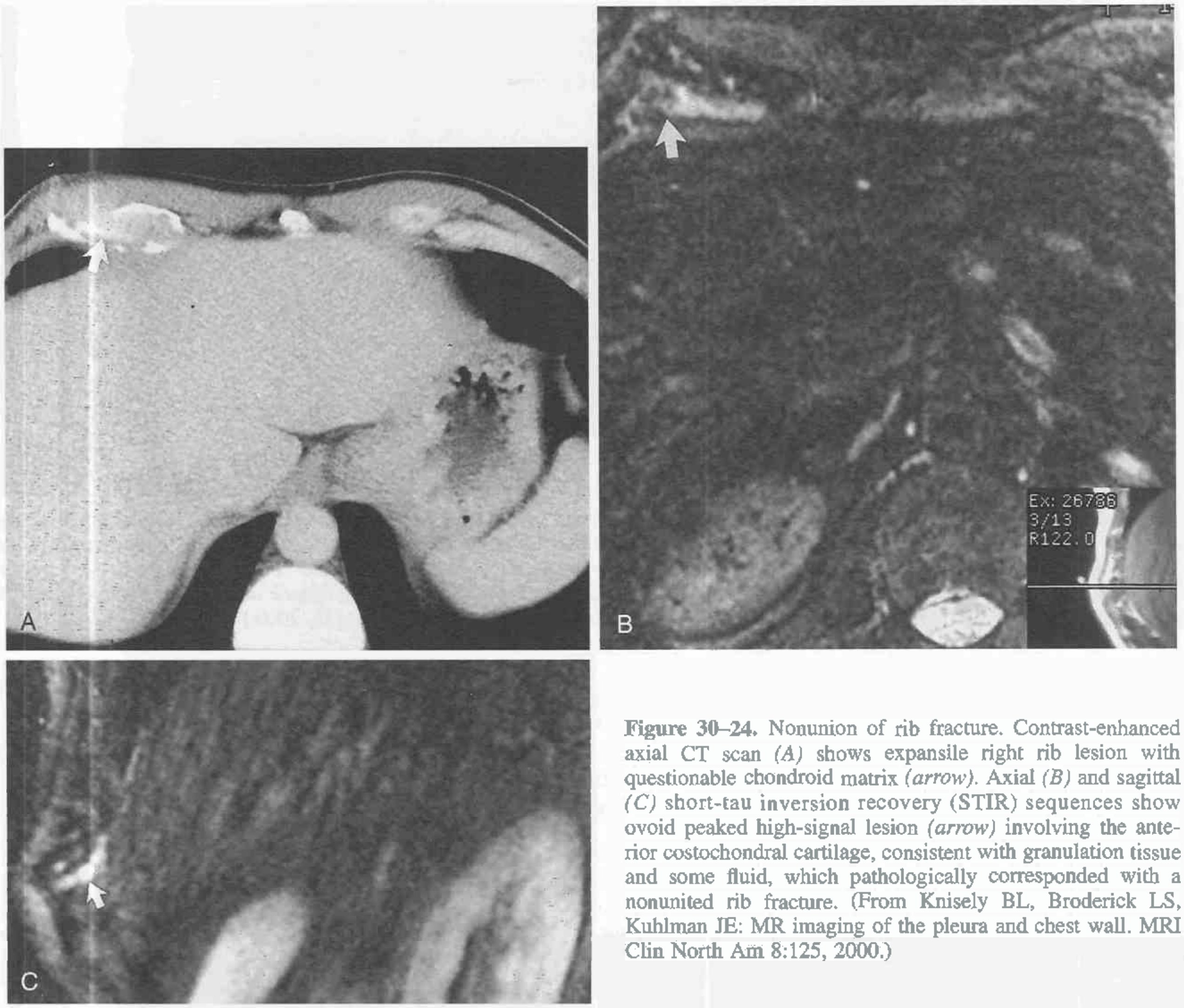

Figure 30–24. Nonunion of rib fracture. Contrast-enhanced axial CT scan *(A)* shows expansile right rib lesion with questionable chondroid matrix *(arrow)*. Axial *(B)* and sagittal *(C)* short-tau inversion recovery (STIR) sequences show ovoid peaked high-signal lesion *(arrow)* involving the anterior costochondral cartilage, consistent with granulation tissue and some fluid, which pathologically corresponded with a nonunited rib fracture. (From Knisely BL, Broderick LS, Kuhlman JE: MR imaging of the pleura and chest wall. MRI Clin North Am 8:125, 2000.)

times because differentiating the nonunion of a rib fracture from a chondroid tumor of the rib on imaging studies may be impossible. The reparative process related to a healing rib fracture may mimic an expanding neoplasm both radiologically and histologically. Rib erosion and chest wall masses may result from an expanding thoracic aneurysm, radiation osteitis, fibrous dysplasia, and eosinophilic granuloma.[66]

MRI is superior to CT in determining the extent of chest wall masses and the infiltration of the bone marrow.[37] However, CT more accurately displays the extent of cortical bone destruction. CT is helpful in evaluating post-traumatic abnormalities (Fig. 30–25) and sternal fractures not seen on standard films.

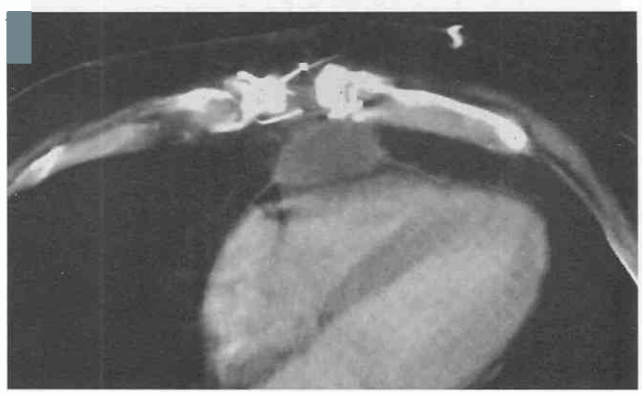

Figure 30–25. Sternal dehiscence in a 52-year-old man who sustained blunt chest trauma 17 months after cardiac transplantation. CT scan shows anterior mediastinal fluid collection consistent with resolving hematoma. (From Knisely BL, Mastey LA, Collins J, Kuhlman JE: Imaging of cardiac transplantation and complications. Radiographics 19:321, 1999.)

Pancoast Tumors

A Pancoast lesion (Figs. 30–26 and 30–27) is a superior sulcus mass that involves the brachial plexus and sympathetic ganglion of the lower neck and upper mediastinum.[30] Lung cancer is the most common cause of Pancoast tu-

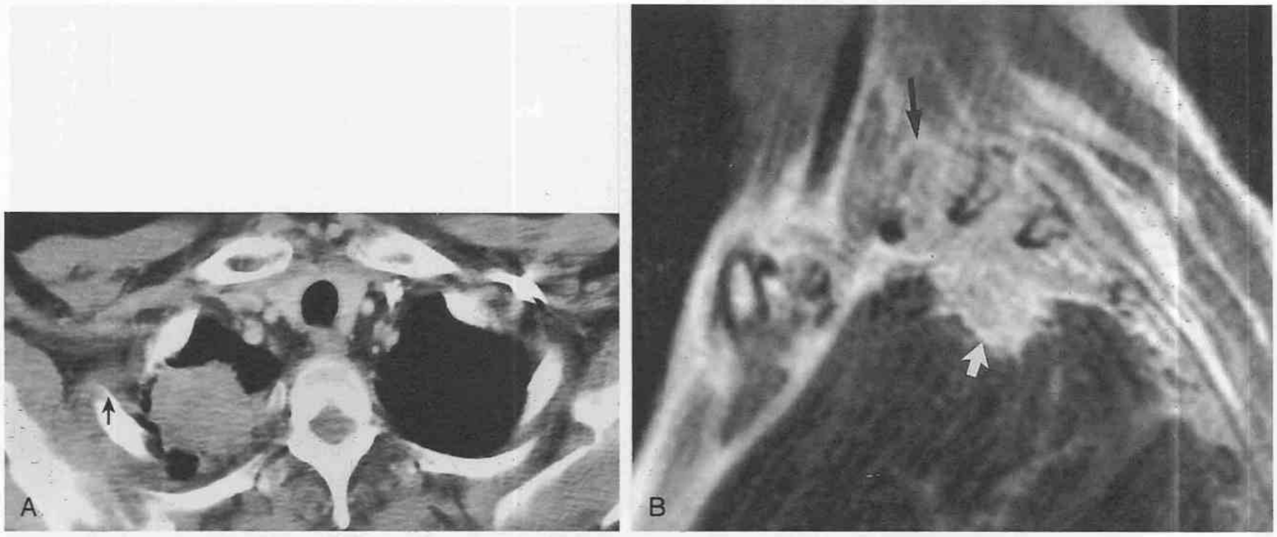

Figure 30–26. Pancoast tumor invading the brachial plexus in a 57-year-old woman. *A,* Contrast-enhanced CT scan shows large right apical mass with central low attenuation suggestive of necrosis. Abnormal soft tissue mass extends into the axilla *(arrow)*, consistent with chest wall involvement. *B,* Sagittal gadolinium-enhanced T1-weighted (TR = 769 msec, TE = 14 msec) image shows enhancing bronchogenic carcinoma *(white arrow)* invading the posterior fat plane of the brachial plexus *(black arrow)*. (*B,* From Knisely BL, Broderick LS, Kuhlman JE: MR imaging of the pleura and chest wall. MRI Clin North Am 8:125, 2000.)

Figure 30–27. Pancoast tumor in a 46-year-old man. Sagittal T1-weighted (TR/TE, 8958/145) *(A)* and sagittal T1-weighted (TR = 869 msec, TE = 14 msec) gadolinium-enhanced with fat saturation *(B)* sequences show left apical bronchogenic carcinoma *(white arrow)* invading the supraclavicular fossa, involving the brachial plexus, and encasing the subclavian artery *(black arrow)*. (From Knisely BL, Broderick LS, Kuhlman JE: MR imaging of the pleura and chest wall. MRI Clin North Am 8:125, 2000.)

mors,[32, 79] but they are also caused by metastatic disease, multiple myeloma, mesothelioma, lymphoma, and breast cancer. Pancoast syndrome is a clinical triad consisting of (1) Horner's syndrome (ptosis, miosis, anhidrosis, and enophthalmos), (2) ipsilateral arm pain, and (3) muscular wasting of the hand, which results from involvement of the nerves.[55]

The superior extension of Pancoast tumors is best depicted on the coronal and sagittal MR images. MRI has an overall accuracy rate of 94% (63% for CT) for demonstrating tumoral chest wall invasion.[30] Streak artifact from the shoulders and the axial plane limits the evaluation of superior sulcus tumors by CT. MRI can also evaluate the tumor's relationship to the supraclavicular fossa, apical fat, subclavian artery and vein, brachial plexus, and costovertebral bony structures. Lung cancer patients with tumors invading the apex on preoperative imaging studies often receive radiation therapy to shrink the tumor prior to surgical resection.[32, 79]

The survival rate in patients with Pancoast lung cancer has increased as a result of the combination of radiation therapy and surgery (with or without chemotherapy).[37]

Chest Wall Invasion by Bronchogenic Carcinoma

The treatment modality of choice for lung cancer depends on the stage and histology of the tumor. Peripheral bronchogenic carcinomas invade the chest wall in only 8% of cases.[8] Limited local invasion is resectable by either an en bloc resection of lung and chest wall or an extrapleural dissection (when tumor is limited to the parietal pleura). The soft tissue contrast resolution and multiplanar capability of MRI are superior to those of CT, making MRI slightly more accurate in the detection of tumor invasion of the chest wall.[30] MRI depicts tumor infiltration of the extrapleural fat and muscles of the chest wall better than CT does (Fig. 30–28). The sensitivity and specificity of MRI in the diagnosis of chest wall invasion range from 63% to 90% and 84% to 86%, respectively.[54, 81]

T1-weighted and T2-weighted spin-echo sequences depict direct chest wall tumor extension, with improved yield on gadolinium-contrast–enhanced sequences (Fig. 30–29).[26] MRI is the examination of choice for the local staging of superior sulcus carcinomas, providing good anatomic detail

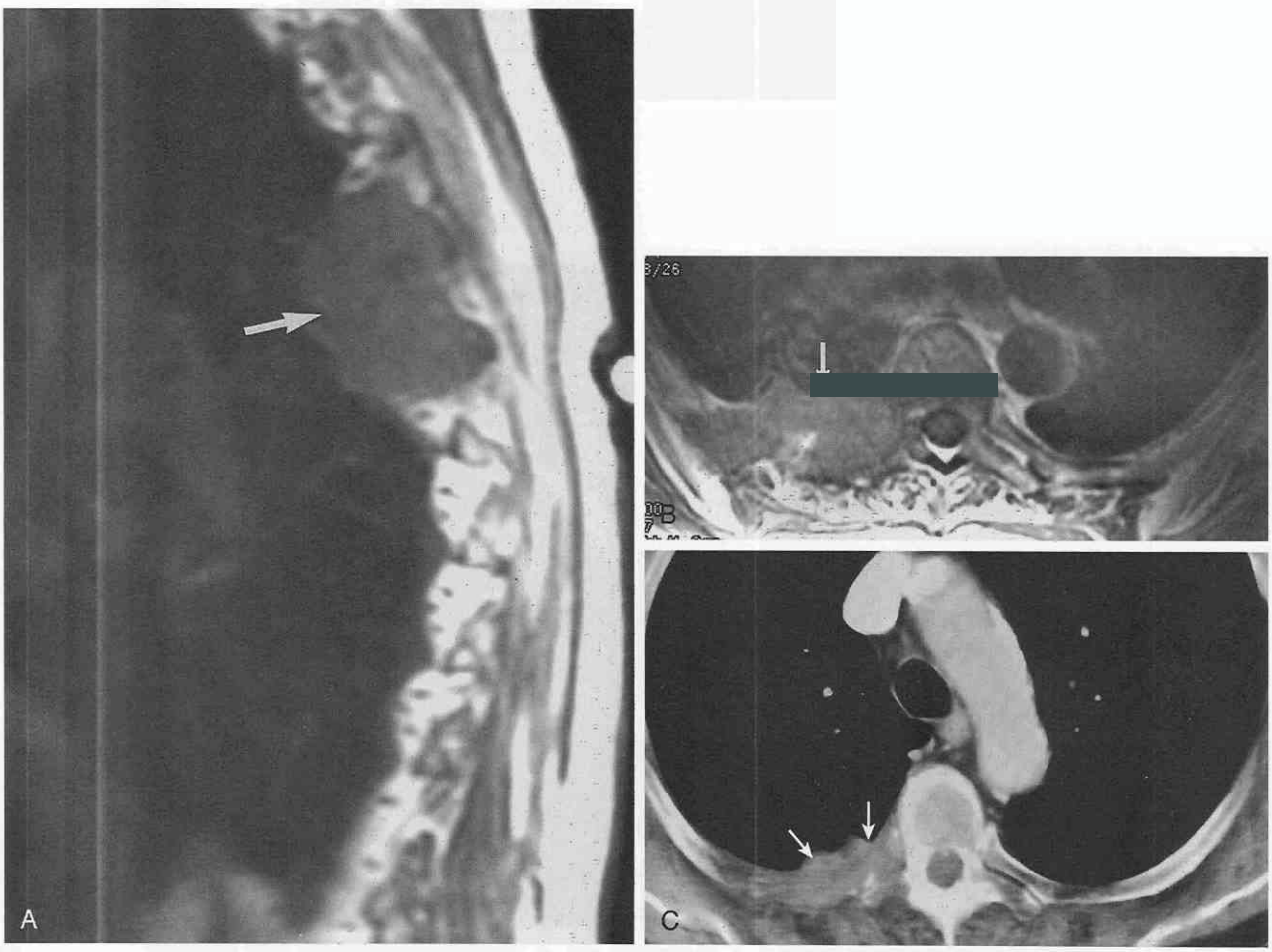

Figure 30–28. Bronchogenic carcinoma invading the posterior chest wall in a 94-year-old woman. T1-weighted sagittal (TR = 550 msec, TE = 16 msec) *(A)* and axial T1-weighted (TR = 700 msec, TE = 17 msec) *(B)* images show a mass *(arrow)* that demonstrates low signal intensity (relative to muscle) in the superior segment of the right lower lobe, invading the posterior right sixth rib and pedicle of the sixth thoracic vertebral body. (*A* and *B*, From Knisely BL, Broderick LS, Kuhlman JE: MR imaging of the pleura and chest wall. MRI Clin North Am 8:125, 2000.) Contrast-enhanced CT scan *(C)* reveals right posterior soft tissue pedicle mass *(arrows)* replacing posterior right rib and thoracic body.

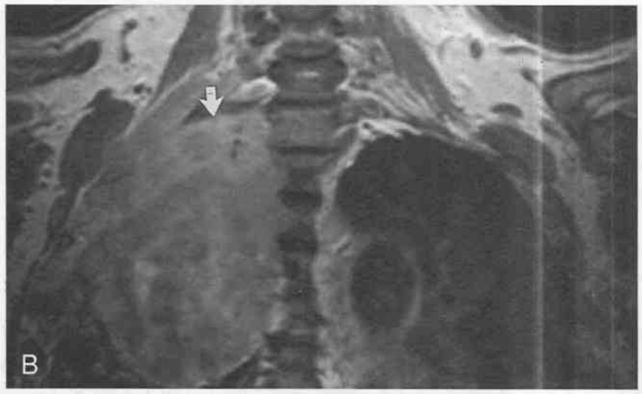

Figure 30–29. Bronchogenic carcinoma in a 60-year-old man. Coronal T1-weighted (TR = 600 msec, TE = 12 msec) *(A)* and coronal T1-weighted (TR = 800 msec, TE = 12 msec) gadolinium-enhanced *(B)* images show a large tumor. Signal intensity of abnormal bone marrow is seen within the thoracic vertebral bodies, consistent with tumor invasion (*arrow* in *A*) and enhancing tumor invading the apex (*arrow* in *B*) of the right chest wall. (From Knisely BL, Broderick LS, Kuhlman JE: MR imaging of the pleura and chest wall. MRI Clin North Am 8:125, 2000.)

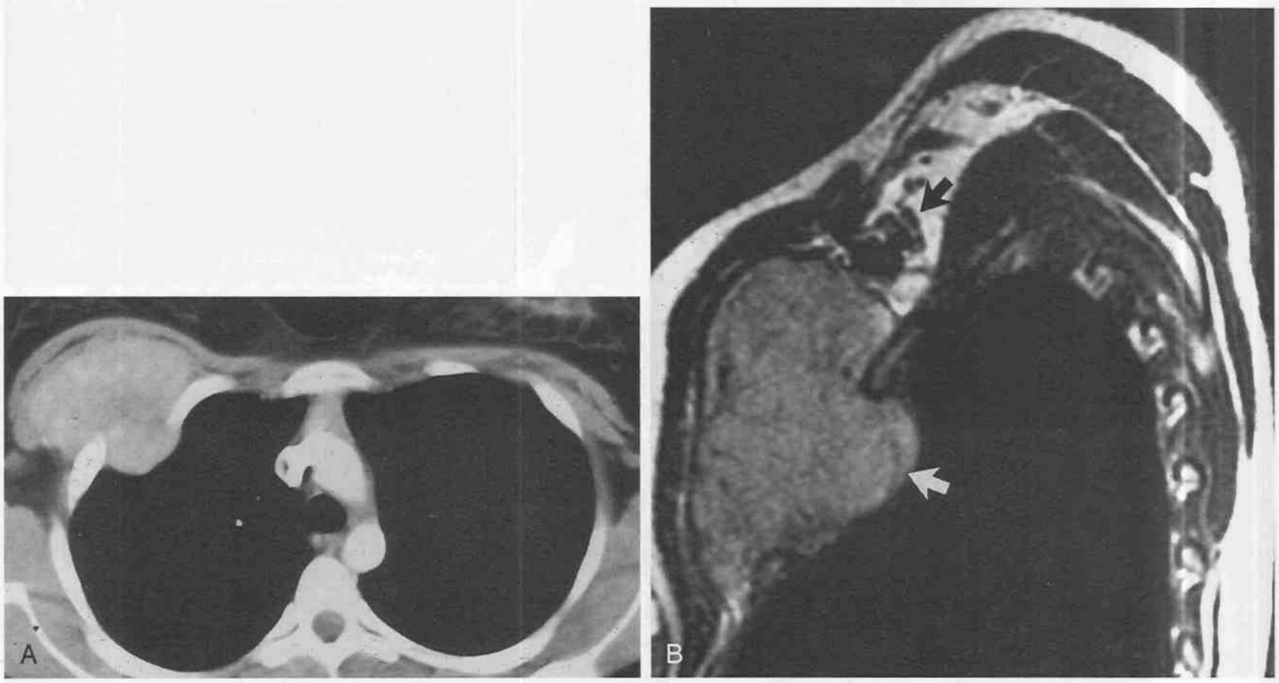

Figure 30–30. Inflammatory myofibroblastic tumor in a 15-year-old girl. *A,* Contrast-enhanced CT scan reveals a high-attenuation mass infiltrating the anterior chest, posterior to the right pectoralis major muscle. *B,* Sagittal T2-weighted (TR = 2066 msec, TE = 104 msec) image shows a mass *(white arrow)* that demonstrates high signal intensity (relative to muscle). It is beneath the pectoralis major muscle and infiltrates the anterior chest between the ribs, sparing the brachial plexus *(black arrow)*. (*B,* From Knisely BL, Broderick LS, Kuhlman JE: MR imaging of the pleura and chest wall. MRI Clin North Am 8:125, 2000.)

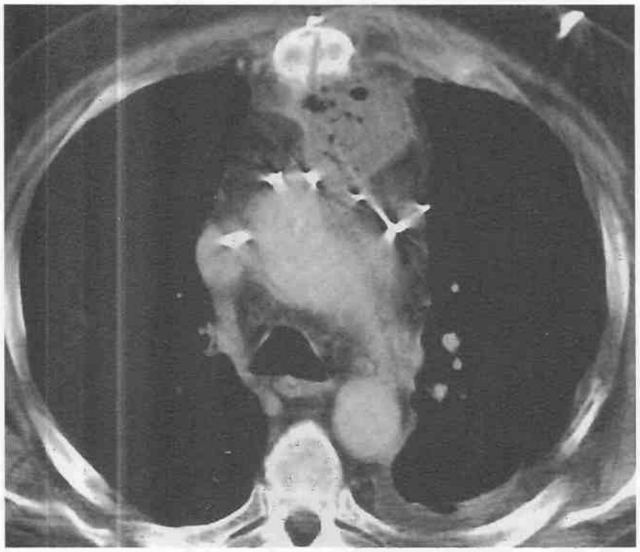

Figure 30–31. Mediastinal abscess in a 62-year-old man who developed a substernal fluid collection 6 weeks after cardiac transplantation. Contrast-enhanced CT scan shows the anterior mediastinal loculated fluid collection with air pockets. Specimen obtained from CT-guided drainage revealed gram-positive cocci, and the patient responded to antibiotic therapy and drainage. (From Knisely BL, Mastey LA, Collins J, Kuhlman JE: Imaging of cardiac transplantation and complications. Radiographics 19: 321, 1999.)

of the apices. The MRI findings of chest wall invasion include loss of the high-signal-intensity extrapleural fat on T1-weighted images and disruption of the soft tissue planes.[32] High signal intensity on T2-weighted images in the muscles suggests tumor involvement, but inflammation and edema may cause similar findings.[32]

Chest Wall Inflammatory and Infectious Diseases

Inflammatory myofibroblastic tumor (Fig. 30–30) is a rare pseudosarcomatous lesion that often involves the lungs of children and young adults.[16] It has been reported in diverse extrapulmonary locations, specifically the trunk, and is characterized by a benign, nonmetastasizing proliferation of myofibroblasts with a potential for recurrence.[16] MRI shows a lesion of intermediate signal intensity on T1-weighted sequences and increased heterogeneous signal intensity on T2-weighted sequences.[24]

Chest wall infections are rare, yet are potentially fatal.[67] Diabetes mellitus, previous surgery or trauma, and immunocompromised states are risk factors associated with infection of the thoracic wall.[67] The prognosis is variable, depending on the length of time to make the diagnosis, the organism type, the severity of immunosuppression, and the extent of infection.[67] Physical findings of fever, focal tenderness, warmth, induration, skin discoloration, redness, or necrosis often underestimate the severity and extent of the chest wall infection, particularly in the immunocompromised patient.[67]

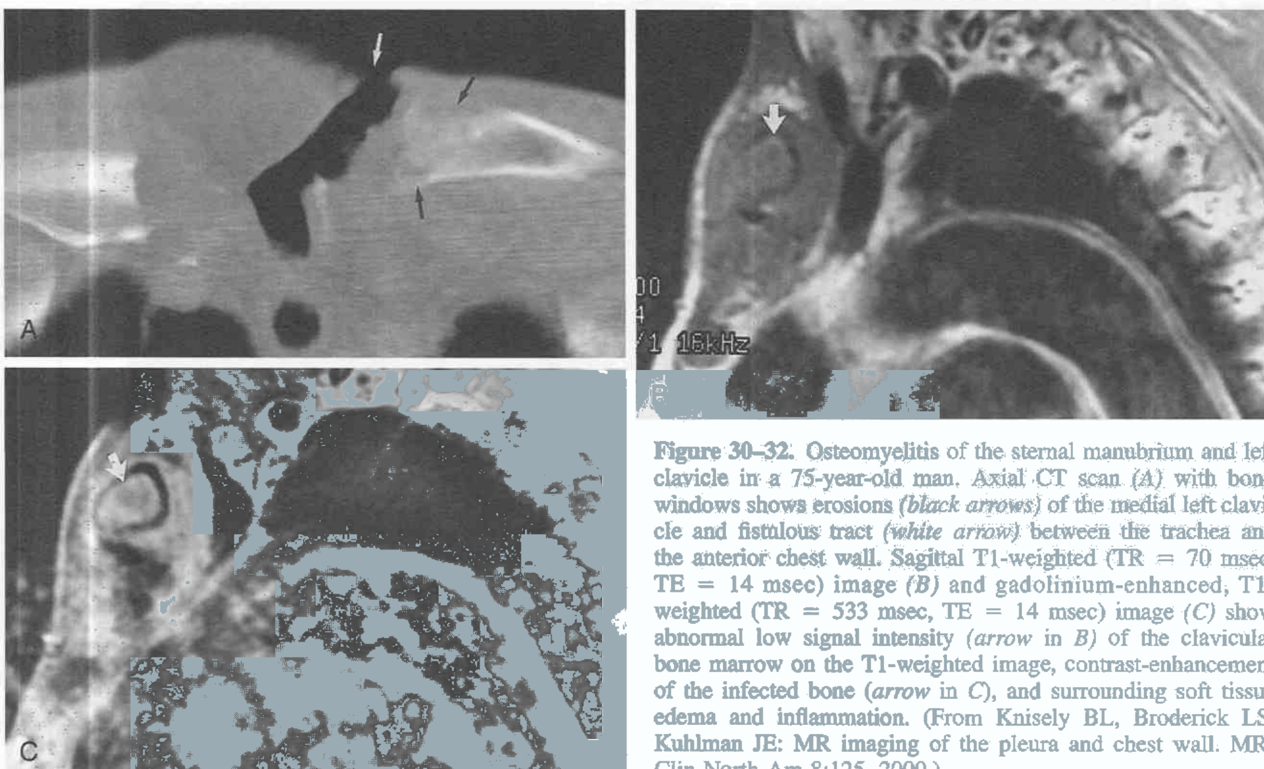

Figure 30–32. Osteomyelitis of the sternal manubrium and left clavicle in a 75-year-old man. Axial CT scan *(A)* with bony windows shows erosions *(black arrows)* of the medial left clavicle and fistulous tract *(white arrow)* between the trachea and the anterior chest wall. Sagittal T1-weighted (TR = 70 msec, TE = 14 msec) image *(B)* and gadolinium-enhanced, T1-weighted (TR = 533 msec, TE = 14 msec) image *(C)* show abnormal low signal intensity *(arrow* in *B)* of the clavicular bone marrow on the T1-weighted image, contrast-enhancement of the infected bone *(arrow* in *C)*, and surrounding soft tissue edema and inflammation. (From Knisely BL, Broderick LS, Kuhlman JE: MR imaging of the pleura and chest wall. MRI Clin North Am 8:125, 2000.)

Chest wall infections are categorized as cellulitis, pyomyositis, abscess, and the more life-threatening necrotizing fasciitis.[67] *Klebsiella* and *Staphylococcus* species are common and severe offending organisms in chest wall infections.[67] *Nocardia* and *Aspergillus* species, actinomycetes, *Blastomyces*, and *Mycobacterium tuberculosis* are less common pathogens affecting the chest wall.[67] CT may identify parasternal fluid collections in febrile postsurgical patients with air collections suggestive of mediastinitis and mediastinal abscess (Fig. 30–31). After surgery, fluid and the thickening of the presternal and poststernal soft tissues are seen for 2 to 3 weeks, with air resolving after 1 week.

MRI delineates the extent of soft tissue involvement and inflammation of the chest wall without requiring IV contrast agents.[37] Coronal and sagittal MR images are key for operative planning, identifying communications between separate, loculated abscesses and outlining the extent of the chest wall infection. On MRI, abscesses show low signal intensity on T1-weighted sequences and high signal intensity on STIR and T2-weighted sequences.[37] T1-weighted images yield superior spatial resolution; STIR and T2-weighted images, because of their superior contrast, are best for determining the degree of abscess extension and for defining the location of the abscess.[67] CT is much more sensitive than MRI for detecting gas in chest wall infections.[37]

Osteomyelitis (Fig. 30–32) of the sternum, manubrium, and clavicles is optimally imaged with MRI because of its multiplanar imaging capability and superior soft tissue contrast.[67] MR images yield a sensitivity and specificity of 88% and 93%, respectively, with focal enhancement on T1-weighted fat-suppressed enhanced images indicative of osteomyelitis.[49] Infection is identified as an area of decreased signal intensity on T1-weighted sequences, compared with the high signal intensity of fatty marrow, and high signal intensity on T2-weighted sequences.

Figure 30–33. Sternoclavicular joint infection and osteomyelitis in a 48-year-old man with an infected subclavian venous catheter. Sagittal T1-weighted (TR = 400 msec, TE = 12 msec) image shows abnormal areas of low signal intensity *(arrows)* in the sternal marrow, consistent with osteomyelitis. Surrounding low signal intensity *(arrow)* in the soft tissues is consistent with abscess. (From Knisely BL, Broderick LS, Kuhlman JE: MR imaging of the pleura and chest wall. MRI Clin North Am 8: 125, 2000.)

IV drug abuse, diabetes mellitus, chronic renal failure, and immunosuppression predispose patients to sternoclavicular joint infections.[84] Subclavian venous catheter sequelae often lead to sternoclavicular joint infections (Fig. 30–33), with *Staphylococcus aureus* the most frequently isolated bacterium in this setting.[12]

Early cases of sternoclavicular joint infections are treated with conservative measures, including catheter removal and peripheral IV antibiotics, with a good response rate. En bloc resection is reserved for a sternoclavicular joint infection that extends beyond the joint on imaging studies.[12]

Summary

CT is the standard imaging modality in the evaluation of pleural and chest wall lesions. CT characterizes pleural effusions, differentiates parenchymal from pleural and chest wall lesions, and demonstrates areas of fatty attenuation or calcification. MRI plays a role in specific cases of tumors, infections, pleural effusions, and masses. MRI provides superior soft tissue contrast, which is helpful in determining the extent of infections and tumors involving the pleura and chest wall. MRI's multiplanar capability helps in the evaluation of chest wall and pleural abnormalities, particularly in the apical regions.

References

1. Aberle DR, Balmes JR: Computed tomography of asbestos-related pulmonary parenchymal and pleural diseases. Clin Chest Med 12: 115, 1991.
2. Aberle DR, Gamsu G, Ray CS: High resolution CT of benign asbestos-related diseases: Clinical and radiographic correlation. AJR Am J Roentgenol 151:883, 1988.
3. Alexander E, Clark RA, Colley DP: CT of malignant pleural mesothelioma. Am J Roentgenol 137:287, 1981.
4. Alexander S, Proto AV, Clark RA: CT differentiation of subphrenic abscess and pleural effusion. Am J Roentgenol 140:47, 1983.
5. Anderson BO, Burt ME: Chest wall neoplasms and their management. Ann Thorac Surg 58:1774, 1994.
6. Askin FF, Rosai J, Sibley RK, et al: Malignant small cell tumor of the thoracopulmonary region in childhood: A distinctive clinicopathologic entity of uncertain histogenesis. Cancer 43:2438, 1979.
7. Barber CE, Hedlund LW, Oddson TA, et al: Differentiating empyemas and peripheral pulmonary abscesses: The value of computed tomography. Radiology 135:755, 1980.
8. Bone RE, Balk R: Staging of bronchogenic carcinoma. Chest 82: 473, 1982.
9. Briselli M, Mark EJ, Dickersin GR: Solitary fibrous timors of the pleura: Eight new cases and review of 360 cases in the literature. Cancer 47:2678, 1981.
10. Brodsky JT, Gordon MS, Hajdu SI, et al: Desmoid tumors of the chest wall: Local recurrent problem. J Thorac Cardiovasc Surg 104: 900, 1992.
11. Burt M, Karpeh M, Ukoha O, et al: Medical tumors of the chest wall: Solitary plasmacytoma and Ewing's sarcoma. J Thorac Cardiovasc Surg 105:89, 1993.
12. Carlos GN, Kesler KA, Coleman JJ, et al: Aggressive surgical management of sternoclavicular joint infections. J Thorac Cardiovasc Surg 113:242, 1997.
13. Carvalho PM, Carr DH: Computed tomography of folded lung. Clin Radiol 41:86, 1990.
14. Casillas J, Sais GJ, Greve JL, et al: Imaging of intra- and extra-abdominal desmoid tumors. Radiographics 11:959, 1991.
15. Castagno AA, Shuman WP: MR imaging in clinically suspected brachial plexus tumor. AJR Am J Roentgenol 149:1219, 1987.
16. Coffin CM, Watterson J, Priest JR, et al: Extrapulmonary inflamma-

tory myofibroblastic tumor (inflammatory pseudotumor): A clinicopathologic and immunohistochemical study of 84 cases. Am J Surg Pathol 19:895, 1995.
17. Davis SD, Henschke CI, Yankelevitz DF, et al: MR imaging of pleural effusions. J Comput Assist Tomogr 14:192, 1990.
18. Doyle TC, Lawler GA: CT features of rounded atelectasis of the lung. Am J Roentgenol 143:225, 1984.
19. Dwyer RA. The displaced crus: A sign for distinguishing between pleural fluid and ascites on computed tomography. J Comput Assist Tomogr 2:598, 1978.
20. England DM, Hochholzer L, McCarthy MJ: Localized benign and malignant fibrous tumors of the pleura: A clinicopathologic review of 223 cases. Am J Surg 13:640, 1989.
21. Enzinger FM, Weiss SW: Soft Tissue Tumors, 3rd ed. St. Louis, Mosby–Year Book, 1995, p 210.
22. Fortier M, Mayo JR, Swenson SJ, et al: MR imaging of chest wall lesions. Radiographics 14:597, 1994.
23. George JC: Benign fibrous mesothelioma of the pleura: MR findings. AJR Am J Roentgenol 106:204, 1993.
24. Georgia JD, Lawrence DP, De Nobile JW: Inflammatory pseudotumor in the retrorectal space: CT and MR appearance. J Comput Assist Tomogr 20:410, 1996.
25. Greenspan A, McGahan JP, Vogelsang P, et al: Imaging strategies in the evaluation of soft-tissue hemangiomas of the extremities: Correlation of the findings of plain radiography, angiography, CT, MRI and ultrasonography in 12 histologically proven cases. Skeletal Radiol 21:11, 1992.
26. Haggar AM, Pearlberg JL, Froelich JW, et al: Chest wall invasion by carcinoma of the lung: Detection by MR imaging. AJR Am J Roentgenol 148:1075, 1987.
27. Hahn D: Mediastinum and lung. In Stark DD, Bradley WE (eds): Magnetic Resonance Imaging. St. Louis, CV Mosby, 1988.
28. Hahn PF, Stark DD, Vici GG, et al: Duodenal hematoma: The ring sign in MR imaging. Radiology 159:379, 1986.
29. Halvorsen RA, Fedyshin PJ, Korobkin M, et al: CT differentiation of pleural effusion from ascites: An evaluation of four signs using blinded analysis of 52 cases. Invest Radiol 21:391, 1986.
30. Heelan RT, Demas BE, Caravelli JF, et al: Superior sulcus tumors: CT and MR imaging. Radiology 170:637, 1989.
31. Heelan RT, Rusch VW, Begg CB, et al: Staging of malignant pleural mesothelioma: Comparison of CT and MR imaging. AJR Am J Roentgenol 172:1039, 1999.
32. Herold CJ, Zerhouni EA: The mediastinum and lungs. In Higgins CB, Hricak H, Helms CA (eds): Magnetic Resonance Imaging of the Body, 2nd ed. New York, Raven Press, 1992, p 461.
33. Im JG, Webb WR, Rosen A, et al: Costal pleura: Appearances of high resolution CT. Radiology 171:125, 1989.
34. Knisely BL, Broderick LS, Kuhlman JE. MR imaging of the pleura and chest wall. MRI Clin North Am 8:125, 2000.
35. Knisely BL, Kuhlman JE. Radiographic and CT imaging of complex pleural disease. Crit Rev Diagn Imaging 38:1, 1997.
36. Kreel L: Computed tomography in mesotheliomas. Semin Oncol 8: 302, 1981.
37. Kuhlman JE, Bouchardy L, Fishman EK, et al: CT and MR findings [letter]. AJR Am J Roentgenol 106:205, 1993.
38. Kurihara Y, Nakajima Y, Ishikawa T, Galvin JR: Counting ribs on chest CT scans: The easiest way. AJR Am J Roentgenol 165:487, 1995.
39. Lee KS, Im JG: Benign fibrous mesothelioma of the pleura: MR findings [letter]. AJR Am J Roentgenol 106:205, 1993.
40. Leung AN, Müller NL, Miller RR: CT in differential diagnosis of diffuse pleural disease. AJR Am J Roentgenol 154:487, 1990.
41. McCloud TC: CT and MR in pleural disease. Clin Chest Med 19: 261, 1998.
42. McCloud TC, Flower CDR: Imaging the pleura: Sonography, CT, and MR imaging. AJR Am J Roentgenol 156:1145, 1991.
43. Meyer JS, Hoffer FA, Barnes PD, et al: Biological classification of soft-tissue vascular anomalies: MR correlation. AJR Am J Roentgenol 157:559, 1991.
44. Minami M, Kawauchi N, Yoshikawa K, et al: Malignancy associated with chronic empyema: Radiologic assessment. Radiology 178:417, 1991.
45. Mintzer RA, Gore RM, Vogelzang RL, et al: Rounded atelectasis and its association with asbestos-induced pleural disease. Radiology 139: 567, 1981.
46. Miser JS, Kinsella TJ, Triche TJ, et al: Preliminary results of treatment of Ewing's sarcoma of bone in children and young adults: Six months of intensive continued modality therapy without maintenance. J Clin Oncol 6:484, 1988.
47. Miser JS, Kinsella TJ, Triche TJ, et al: Treatment of peripheral neuroepithelioma in children and young adults. J Clin Oncol 5: 1752, 1987.
48. Montalvo BM, Morillo G, Sridhar K, et al: MR imaging of malignant pleural mesotheliomas. Radiology 181:109, 1991.
49. Morrison WB, Schweitzer ME, Bock GW, et al: Diagnosis of osteomyelitis: Utility of fat-suppressed contrast-enhanced MR imaging. Radiology 189:251, 1993.
50. Müller NL: Imaging the pleura. Radiology 186:297, 1993.
51. Munden RF, Kemp BL: Desmoid tumor of the chest wall. AJR Am J Roentgenol 172:1149, 1999.
52. Munk PL, Lee MJ, Janzen DL, et al: Lipoma and liposarcoma: Evaluation using CT and MR imaging. AJR Am J Roentgenol 169: 589, 1997.
53. Naidich DP, Megibow AJ, Hilton S, et al: Computed tomography of the diaphragm: Peridiaphragmatic fluid localization. J Comput Assist Tomogr 7:641, 1983.
54. Padovani B, Mouroux J, Seksik L, et al: Chest wall invasion by bronchogenic carcinoma: Evaluation with MR imaging. Radiology 187:33, 1993.
55. Pancoast HK: Superior sulcus tumor: Tumor characterized by pain, Horner's syndrome, destruction of bone and atrophy of hand muscles. JAMA 99:1391, 1932.
56. Ponn RB, D'Agnostino RS, Stern H, Wescott JL: Treatment of peripheral bronchopleural fistulas with endobronchial occlusion coils. Ann Thorac Surg 56:1343, 1993.
57. Posner MC, Shiu MH, Newsome JL, et al: The desmoid tumor: Not a benign disease. Arch Surg 124:191, 1989.
58. Reed JC: Chest wall lesions. In Reed JC (ed): Chest Radiology: Plain Film Patterns and Differential Diagnoses. St. Louis, Mosby–Year Book, 1991, p 8.
59. Reitamo JJ, Scheinin TM, Hayry R: The desmoid syndrome: New aspects in the cause, pathogenesis and treatment of the desmoid tumor. Am J Surg 151:230, 1986.
60. Roggli VL, Kolbeck J, Sanfilippo F, et al: Pathology of human mesothelioma. Pathol Annu 22:91, 1987.
61. Sabate JM, Franquet T, Parellada JA, et al: Malignant neuroectodermal tumour of the chest wall (Askin tumour): CT and MR findings in eight patients. Clin Radiol 49:634, 1994.
62. Sahn SA: Malignant pleural effusion. In Fishman AP (ed): Pulmonary Diseases and Disorders, 2nd ed. New York, McGraw-Hill, 1988, p 1640.
63. Schmutz GR, Fisch-Ponsot C, Regent D, et al: Computed tomography and magnetic resonance imaging of pleural masses. Crit Rev Diagn Imaging 34:309, 1993.
64. Schneider HJ, Felson B, Gonzales LL: Rounded atelectasis. Am J Roentgenol 184:225, 1980.
65. Schwartz DA: New developments in asbestos-related pleural disease. Chest 99:191, 1991.
66. Scott WW, Scott PP, Trerotola SO: Radiology of the Thoracic Skeleton. Philadelphia, BC Decker, 1991.
67. Sharif HS, Clark DC, Aabed MY, et al: MR imaging of thoracic and abdominal wall infections: Comparison with other imaging procedures. AJR Am J Roentgenol 154:989, 1990.
68. Shuman LS, Libshitz HI: Solid pleural manifestations of lymphoma. Am J Roentgenol 142:269, 1984.
69. Siegel MJ, Glazer HS, St. Amour TE, et al: Lymphangiomas in children: MR imaging. Radiology 170:467, 1989.
70. Springer BI, Schiebler ML: Normal anatomy of the thoracic inlet as seen on transaxial MR images. AJR Am J Roentgenol 157:707, 1991.
71. Staples CA: Computed tomography in the evaluation of benign asbestos-related disorders. Radiol Clin North Am 30:1191, 1992.
72. Stark DD, Federle MP, Goodman PC, et al: Differentiating lung abscess and empyema: Radiography and computed tomography. Am J Roentgenol 141:163, 1983.
73. Stern EJ, Sun H, Haramati LB: Peripheral bronchopleural fistulas: CT imaging features. AJR Am J Roentgenol 167:117, 1996.
74. Storey TF, Narla LD: Pleural lipoma in a child: CT evaluation. Pediatr Radiol 21:141, 1991.
75. Teplick JG, Teplick SK, Goodman L, Haskin ME: The interface sign: A computed tomographic sign for distinguishing pleural and intra-abdominal fluid. Radiology 144:359, 1982.

76. Tocino I, Miller MH, Frederick PR, et al: CT detection of acute pneumothorax in head trauma. Am J Roentgenol 143:989, 1984.
77. Tscholakoff D, Sechtem U, deGeer G, et al: Evaluation of pleural and pericardial effusions by magnetic resonance imaging. Eur J Radiol 7: 169, 1987.
78. Verschakelen JA, Demaerel P, Coolen J, et al: Rounded atelectasis of the lung: MR appearance. AJR Am J Roentgenol 152:965, 1989.
79. Vock P: Magnetic resonance imaging and computed tomography of the chest wall. In Higgins C, Pettersson H (eds): Chest and Cardiac Radiology (Nycomed Intercontinental Continuing Education in Radiology Series on Diagnostic Imaging, vol 1). London, Merit Communications, 1991, p 162.
80. Waite RJ, Carbonneau RJ, Balikian JP, et al: Parietal pleural changes in empyema: Appearances at CT. Radiology 175:145, 1990.
81. Webb WR, Gatsonis C, Zerhouni EA, et al: CT and MR imaging in staging non–small cell bronchogenic carcinoma: Report of the Radiologic Diagnostic Oncology Group. Radiology 178:705, 1991.
82. Wescott JL, Volpe JP: Peripheral bronchopleural fistula: CT evaluation in 20 patients with pneumonia, empyema, or postoperative air leak. Radiology 196:175, 1995.
83. Williford ME, Hidalgo H, Putman CE, et al: Computed tomography of pleural disease. Am J Roentgenol 140:909, 1983.
84. Yood YA, Goldenberg DL: Sternoclavicular joint arthritis. Arthritis Rheum 23:232, 1980.
85. Zadvinskis DP, Benson MT, Kerr HH, et al: Congenital malformations of the cervicothoracic lymphatic system: Embryology and pathogenesis. Radiographics 12:1175, 1992.

31

Computed Tomography and Magnetic Resonance Imaging of the Thoracic Aorta

Robert C. Gilkeson, Scott Kolodny

Imaging Techniques

As in so much of radiology, advances in cross-sectional imaging have revolutionized our ability to image the thoracic aorta. Historically, aortic imaging has been performed with contrast angiography. The technique is clearly effective in the evaluation of a variety of aortic diseases. Nevertheless, because of its invasive nature, catheter angiography is not without complications, including arrhythmia, stroke, and hemorrhage. In the modern-day radiology department, delays in the performance of conventional angiography are often longer than those for magnetic resonance imaging (MRI) and computed tomography (CT) scanning, delays that can be particularly detrimental in the trauma setting. Now, with increasingly effective MRI and CT, these techniques have largely replaced conventional angiography in the evaluation of aortic disease.

Since its inception in the late 1970s, CT has become an increasingly important modality for evaluation of disease of the thoracic aorta. Early scanners were limited by their slow acquisition times, but they quickly found a role in the evaluation of mediastinal widening, aortic trauma, and aortic disease.[8, 40] CT evaluation of the thoracic aorta offered additional information about aortic wall thickness, surrounding mediastinal and parenchymal tissues, and disease that was not available from conventional aortography. The use of intravenous (IV) contrast agents and dynamic imaging at preselected sites in the thoracic aorta facilitated the diagnosis of aneurysmal disease and dissection.[39] Later in the 1980s, improvements in scanner technology and contrast delivery systems made 1- to 2-minute scanning of the thoracic aorta possible and further advanced the clinical applications of CT scanning in the thoracic aorta.[131]

The advent of spiral CT technology has represented the greatest advance in the rapid and accurate imaging of thoracic aortic disease.[59] With slip-ring CT technology, the patient moves continuously through the gantry while data are acquired. This technique has enabled more rapid acquisition of data, optimizing contrast enhancement of the aorta and its branch vessels. Equally important, spiral CT technology has allowed volumetric data acquisition.[139] Before spiral CT, the display of imaging data was largely limited to the axial plane, but the spiral CT volumetric data set enables the generation of images in a variety of planes, with the capacity for three-dimensional (3D) and endoscopic images.[56, 116] The development of spiral CT and CT angiography has been a major factor in the replacement by CT of conventional aortography for the evaluation of thoracic aortic disease.

The development of multislice CT has now allowed another quantum advance in our understanding of aortic disease. The single-detector system in traditional CT has been replaced, in multislice CT, by multidetector systems capable of acquiring multiple images in the time traditionally taken to generate one image. With most new multislice systems, imaging of the aorta can be performed four times faster than with conventional single-slice scanners. Scanning with multislice scanners that use subsecond imaging times is often eight times faster than scanning with conventional single-slice CT. The latest advances in detector technology have created eight- and 16-detector systems with rotation times of 400 to 500 msec, further decreasing imaging time and enhancing the quality of these volumetric, angiographic images of the thoracic aorta.

CT Protocols

The following three paramaters are considered important in the development of protocols for CT angiography of the thoracic aorta: (1) sensitivity to intraluminal and extraluminal aortic disease, (2) maximal contrast opacification of the thoracic aorta, and (3) optimal coverage of the pertinent anatomic structures. Maximizing sensitivity to intraluminal abnormalities like atheroembolic disease and aortic dissection requires section thicknesses of 3 to 5 mm. To optimize volumetric reconstruction, reconstruction intervals between 1.5 and 2.5 mm should be used to ensure 50% overlap and optimize spatial reconstruction algorithms. Although a significant amount of research has been aimed at optimization of pitch parameters, full width at half maximum (FWHM) profiles show little degradation of image quality with pitch values up to 2.[93] The range of the scan should be determined by the clinical problem: If

there are suspicions about short segment narrowing, focal aneurysms, or branch vessel abnormalities, a range of 12 to 15 cm can be performed. A survey of the thoracic aorta, evaluating for the full extent of a dissection, aneurysm, or aortitis, generally requires coverage of 25 to 30 cm. Scan parameters, including pitch slice thickness and collimation, vary according to the range value and the ability of the patient to suspend respiration.

Optimal contrast enhancement of the thoracic aorta is crucial to the successful display of aortic disease. In most cases in which single-slice spiral CT is used, injection volumes of 125 to 150 mL are needed for optimal enhancement of the selected scan volume. Nonionic contrast media are preferable at these injection rates and volumes, because they minimize the motion[121] as well as the nausea and vomiting more common with ionic agents. Although earlier reports suggested injection rates of 1.5 to 2.0 mL/sec,[24] current literature supports injection rates of 3 to 4 mL/sec. Biphasic contrast injection protocols have been supported for consistent contrast opacification of the aortic lumen; in

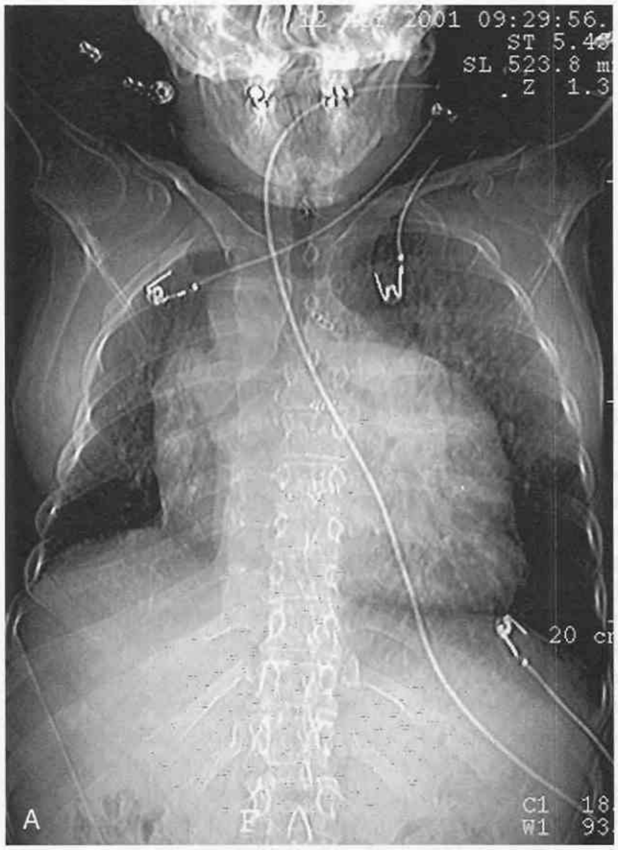

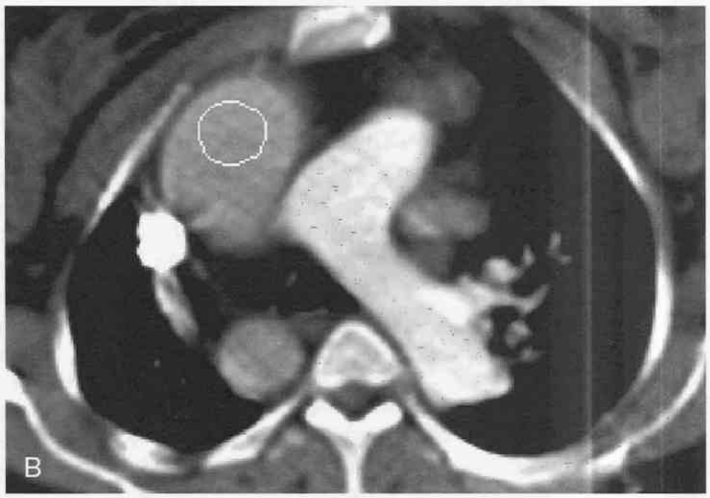

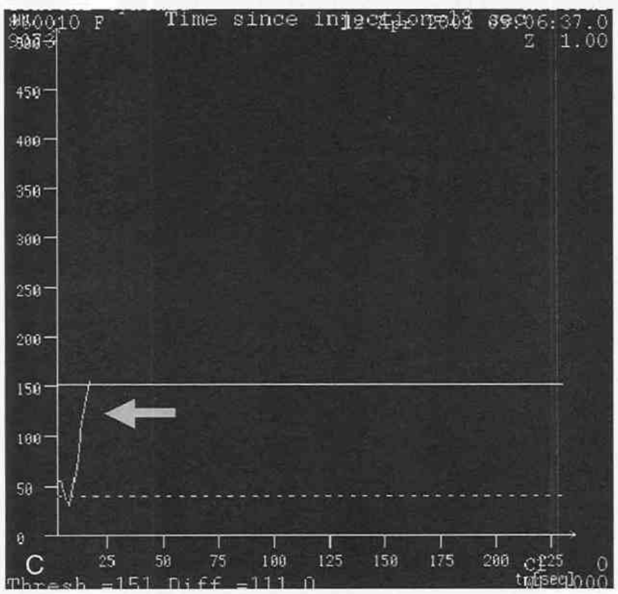

Figure 31–1. *A*, CT tomogram of a young patient with complex congenital heart disease. There is significant cardiomegaly and a right aortic arch. Using an empiric delay for contrast injection would be inappropriate in this clinical setting. *B*, Axial scan demonstrating an automated bolus tracking technique shows the region of interest drawn in the ascending aorta to optimize contrast visualization. *C*, Automated bolus tracking technique for optimizing intravenous injection of contrast material. *Arrow* denotes the time to optimal contrast enhancement of the ascending aorta.

these protocols, IV contrast is injected at 4.0 mL/sec for 50 sec, and then for 2.5 mL/sec for the remainder of the scan. Some research shows this protocol to give a more uniform delivery of contrast agent for the duration of the scan. Power injectors are therefore mandatory for CT evaluation of the aorta.

A variety of researchers have studied the effect of iodine concentration on the quality of aortic opacification.[103, 110] This work shows that there is little difference in the quality of the scans when iodine concentrations ranging from 150 to 300 mg/mL are used. Lower iodine concentrations tend to minimize venous artifacts, although the lower dilutions are often not commercially available in the United States. In our practice, we generally use an iodine concentration of 300 mg/mL; if the evaluation is being performed for suspicion of intra-aortic thrombus or atheroembolic disease, we decrease the iodine concentration to 240 mg/mL to optimize the evaluation of intraluminal disease.

There has been controversy about iodine concentration, and a variety of approaches can be used to optimize the contrast bolus. Some authors support the use of a 20- to 30-mL timing bolus to optimize contrast enhancement in the aorta. In this technique, a slice position in the aorta is preselected, and a test bolus of contrast agent is administered. Images are obtained every 2 to 3 seconds after the start of injection. A time-density curve is generated, and the time to peak opacification is determined.[105] Several commercially available techniques are now available that allow automated triggering of the scan without a test bolus (Fig. 31–1).[113] Despite these techniques, many centers still determine injection delay times empirically. In general, a scan delay of 25 to 30 seconds in patients with normal cardiac output enables optimal contrast opacification. In patients with compromised ventricular function, a scan delay of 35 to 40 seconds is used.[131]

Because of significantly faster imaging times, multislice CT techniques allow for greater flexibility in determining scanning protocols for the thoracic aorta. In general, the entire thoracic aorta can be covered in 10 to 15 seconds with the multislice scanner. At our institution, we favor a 2.5-mm slice thickness, a 1.25-mm reconstruction interval, and a pitch of 1 to 1.5 cm. With a rotation time of 500 msec and slice acquisition of 2.5 mm, the thoracic aorta is evaluated in less than 15 seconds. With standard injection rates and delays, the faster imaging time enables reduction of the volume of IV contrast agent to 100 to 125 mL. When there is a concern about specific valve abnormalities or atheroembolic disease, we often decrease slice thickness to 1.25 mm but maintain a pitch of 1 to 1.5. With the advent of prospective and retrospective electrocardiographic (ECG) gating software, we can also evaluate the thoracic aorta at specific phases of the cardiac cycle, minimizing motion and valvular artifacts.

Postprocessing Techniques

With the advent of spiral CT, volumetric data sets allowed the reformatting of axial data into a variety of imaging options. These options include multiplanar reconstruction (MPR), maximal intensity projection (MIP), volume rendering, and virtual endoscopic techniques. The clinical utility of these reconstruction techniques was initially limited because of the long computer reprocessing time. Now that computer software has become faster and more sophisticated, however, these 3D techniques have become easily accessible to the general radiologist.

Multiplanar reconstructions are one-voxel-thick sections that can be processed in any obliquity (Fig. 31–2). The use of curved MPRs allows for rapid reconstructions of the

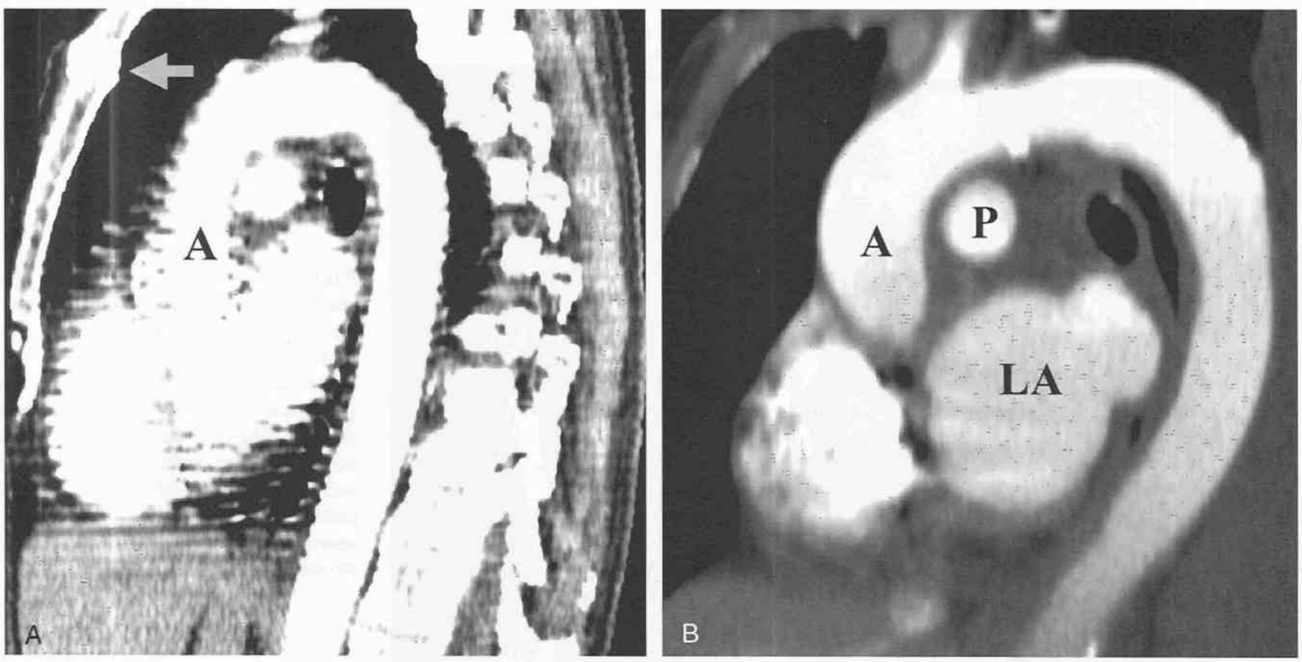

Figure 31–2. *A*, Sagittal multiplanar reconstruction (MPR) CT scan of the thoracic aorta. *Arrow* denotes the position of the sternum. Note the prominent cardiac pulsations with this conventional single-slice CT scan. *B*, Sagittal MPR CT scan of the thoracic aorta obtained with a multislice CT scanner. Note the lack of reconstruction artifacts in comparison with *A*. A = aorta; LA = left atrium; P = pulmonary artery.

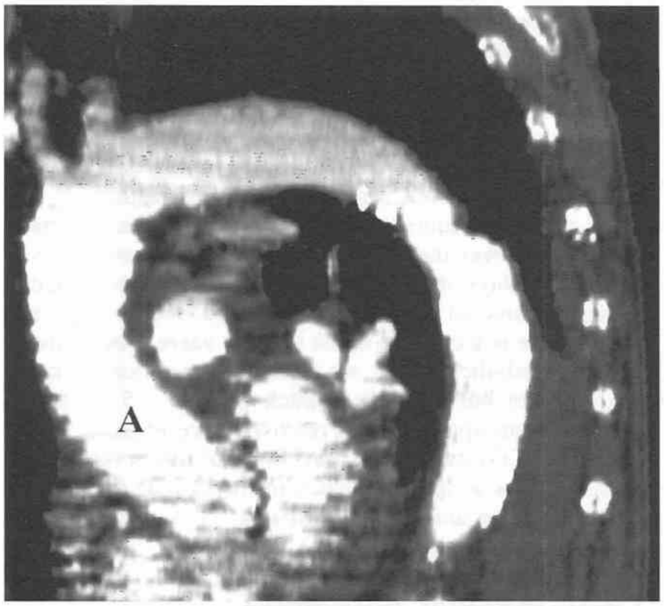

Figure 31–3. Sagittal multiplanar reconstruction CT scan of the thoracic aorta in a patient with suspected pulmonary embolism. Note the prominent cardiac pulsation artifacts. A = aorta.

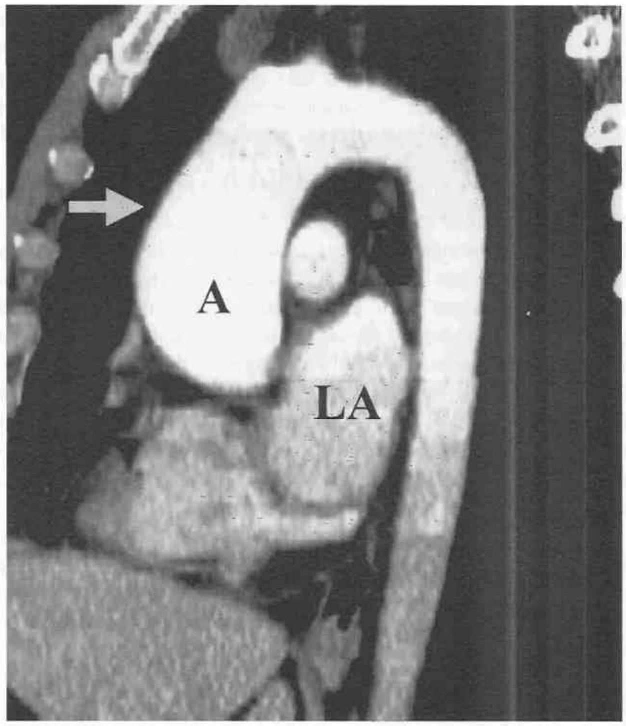

Figure 31–4. ECG-gated sagittal multiplanar reconstruction CT scan of the thoracic aorta in a patient with ascending aortic aneurysm. Note the absence of cardiac pulsation artifacts. *Arrow* denotes the ascending aorta. A = aorta; LA = left atrium.

aorta and selected branch vessels. Although MPR is the most rapid of the postprocessing algorithms, it is limited because of both partial volume effects and stair-stepping artifact due to cardiac pulsation (Fig. 31–3). This artifact can be minimized with a short reconstruction interval, and in the case of multislice scanners, retrospective cardiac gating (Fig. 31–4).

Shaded surface displays (SSDs) and MIP algorithms each have specific advantages and disadvantages in aortic imaging. SSDs allow relatively rapid depiction of anatomic structures (Fig. 31–5), but the aortic lumen is not displayed—clearly a disadvantage in the depiction of aortic dissection and atheroembolic disease. MIP algorithms are

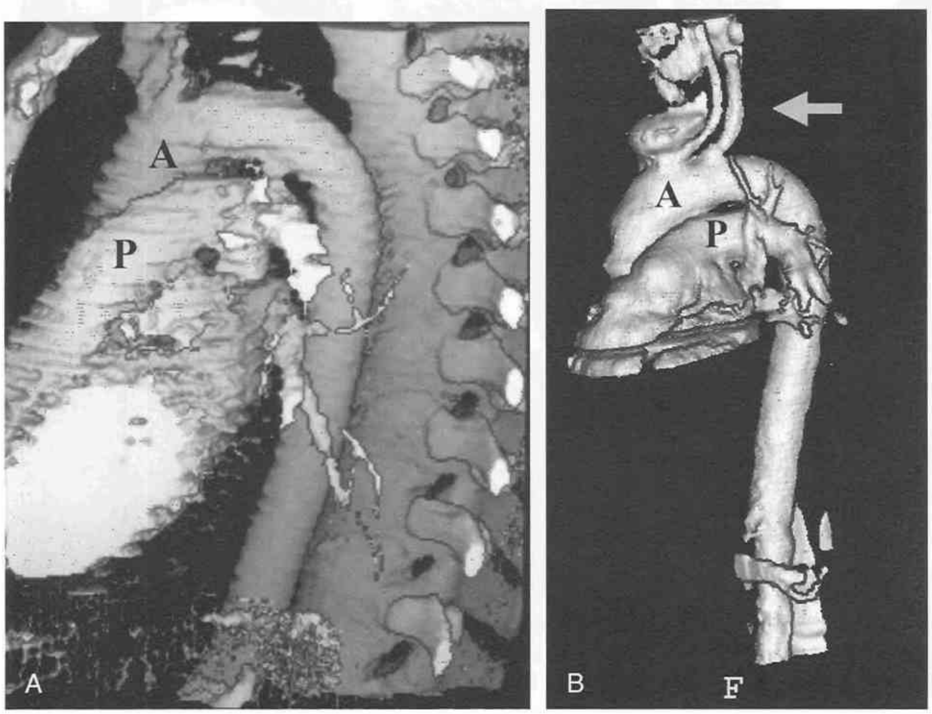

Figure 31–5. *A*, Sagittal oblique shaded surface display (SSD) shows the normal caliber of the thoracic aorta. Note the prominent cardiac pulsation artifacts in the aorta (A) and pulmonary artery (P). *B*, Sagittal oblique SSD of the normal thoracic aorta obtained with a multislice CT scanner. Note the absence of cardiac pulsation artifacts. Arrow denotes absence of pulsation artifacts in branch vessels.

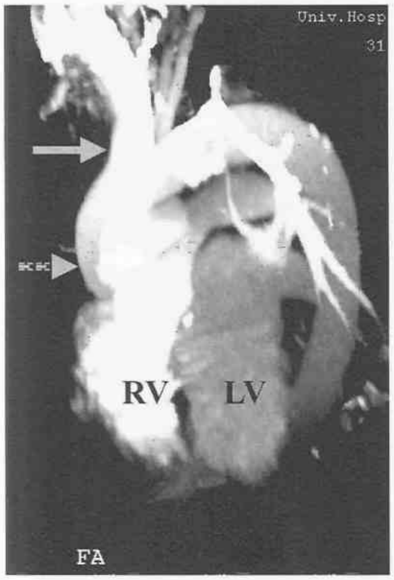

Figure 31–6. Maximum intensity projection (MIP) of the thoracic aorta with intense enhancement of the superior vena cava (*arrows*), which limits evaluation of the aorta. LV = left ventricle; RV = right ventricle.

very effective at evaluating anatomy and areas of stenoses. Their utility in the thoracic aorta is somewhat limited, however, because of the close proximity of a number of high-attenuation structures, particularly mediastinal venous structures, ribs, and spine (Fig. 31–6). Postprocessing of MIP images of the thoracic aorta requires more time and may be less useful in a busy clinical practice.

Volume-rendering techniques have proved to be of greater clinical utility than other 3D techniques.[102] These techniques allow accurate depictions of both the aortic lumen and surrounding structures (Fig. 31–7). Virtual endoscopic techniques have proved to be of great value in our practice, particularly in the setting of atheroembolic disease and for evaluation of the postoperative aorta. The use of virtual endoscopy with SSD offers rapid visualization of the aortic lumen (Fig. 31–8), whereas volume-rendered virtual endoscopy allows closer anatomic depiction along with visualization of the aortic lumen and surrounding extraluminal structures (Fig. 31–9).[55] Although volume-rendering techniques have been historically more time-consuming than SSD techniques, improved computing time have made volume rendering more viable for clinical use.

MRI

From its earliest clinical application, MRI has been an important imaging modality in the evaluation of congenital and acquired aortic disease. MRI has traditionally been a more time intensive modality compared with CT, but improvements in software, faster gradients, new breath-hold techniques, and the use of gadolinium angiography have significantly improved the efficiency of MRI in aortic imaging.

Historically, MRI has utilized "black blood" techniques for the depiction of aortic anatomy, and "white blood" techniques for the depiction of blood flow. Black blood techniques require use of ECG-gated T1-weighted spin-echo (SE) sequences. In black blood sequences, presaturation pulses are used outside the volume of interest to saturate signal from flowing blood in the aorta.[99] Axial slices are obtained at a 7- to 8-mm slice thickness from the origin of the aortic arch vessels to the diaphragm (Fig. 31–10). Sagittal oblique images are obtained as clinically indicated. In patients in whom ECG gating and breath-holding techniques may not be possible, new half-Fourier single-shot turbo spin-echo (HASTE) imaging can be performed (Fig. 31–11).[113] HASTE images can be obtained in

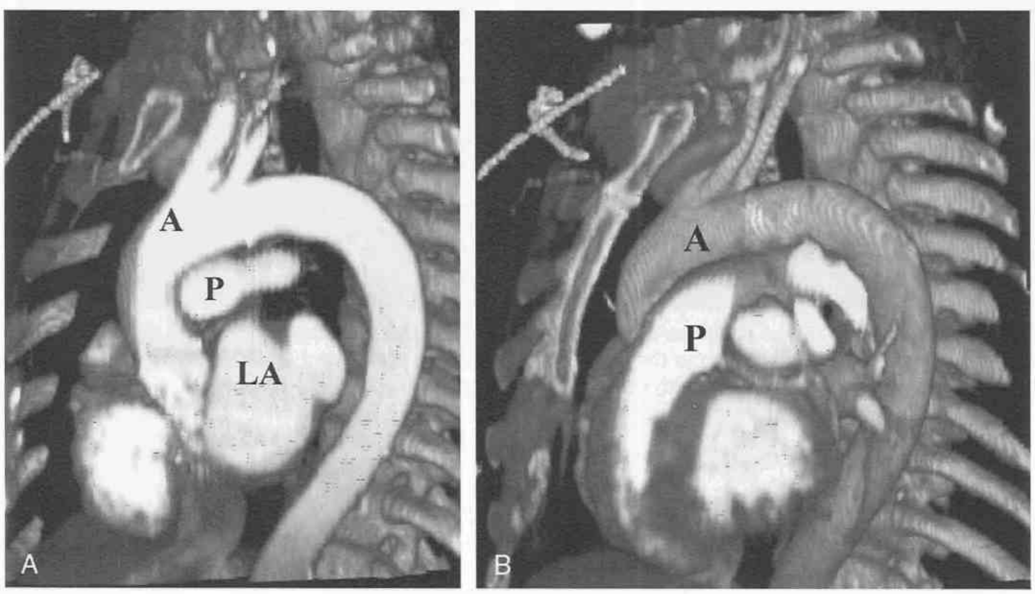

Figure 31–7. *A*, Thin-slab volumetric reconstruction (VR) of the thoracic aorta. Note the superior anatomic display of the thoracic aorta and surrounding anatomic structures. *B*, Thick-slab VR of the thoracic aorta. A = aorta; LA = left atrium; P = pulmonary artery.

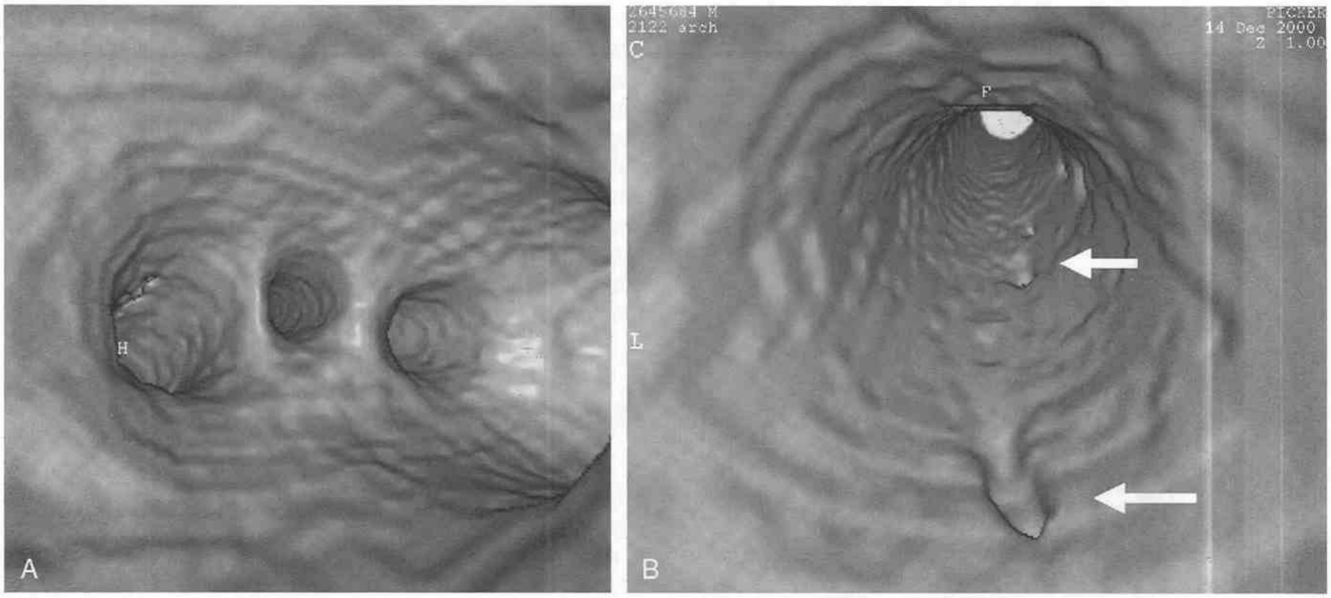

Figure 31–8. *A*, Virtual endoscopic image of the aortic arch obtained with a shaded surface display (SSD) algorithm shows the origins of the great vessels. *B*, Virtual endoscopic image of the aortic arch using an SSD algorithm demonstrates the descending thoracic aorta. Note the origins of the intercostal arteries (*arrows*).

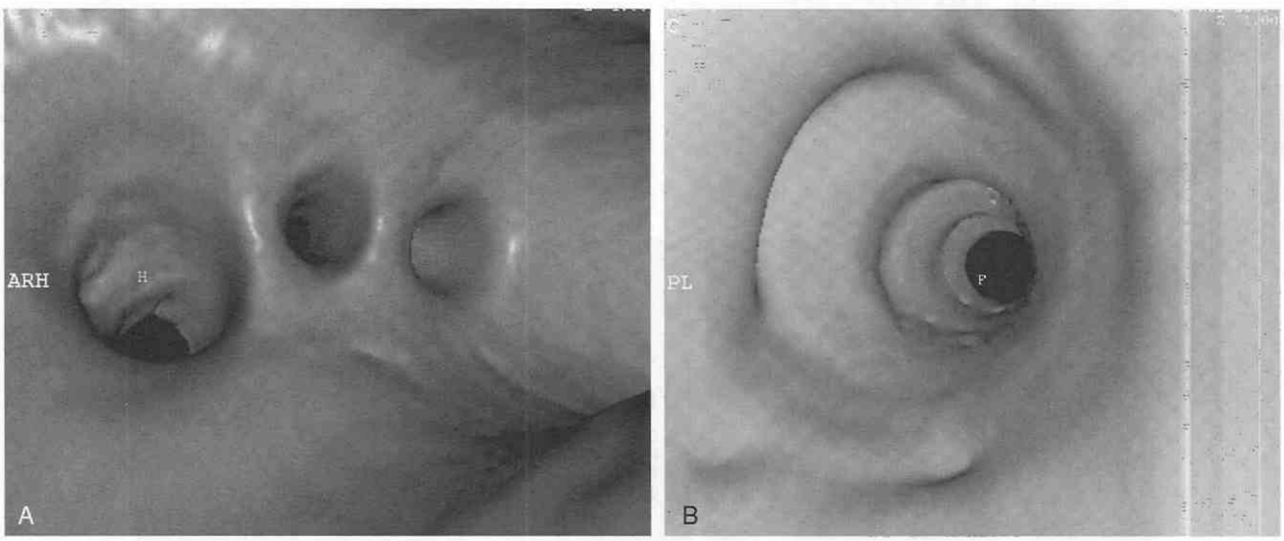

Figure 31–9. *A*, Virtual endoscopic image of the aortic arch using a volume-rendered algorithm shows the origin of the great vessels. The walls of the thoracic aorta are smoother than in the SSD algorithm images shown in Fig. 31–8. *B*, Virtual endoscopic image of the aortic arch using a volume-rendered algorithm displays the normal descending aorta.

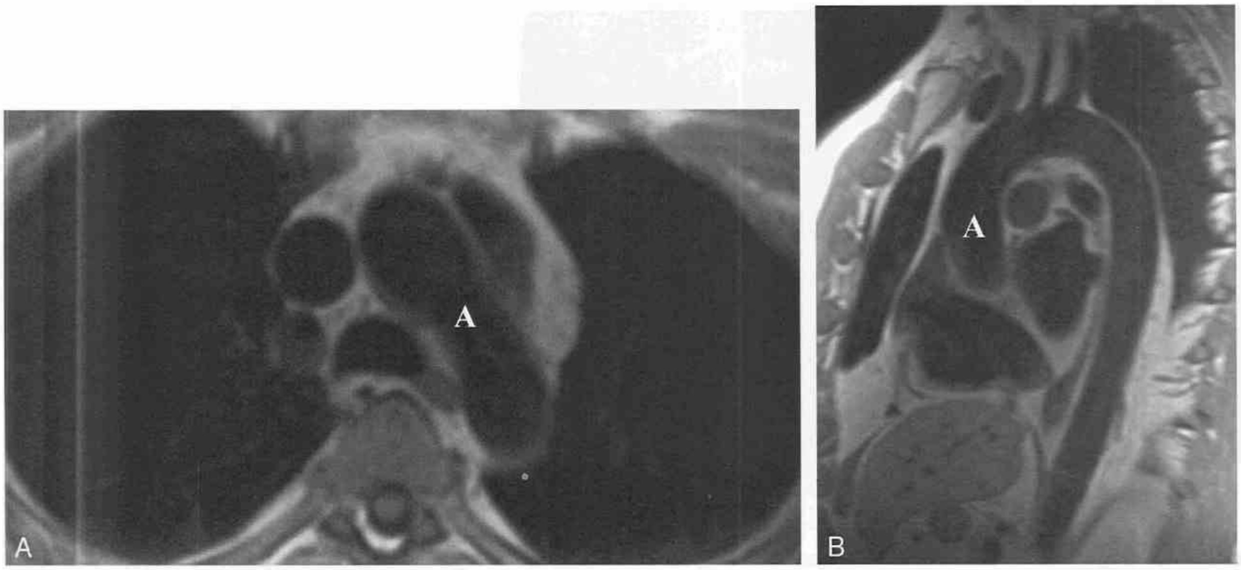

Figure 31–10. *A*, ECG-gated axial T1-weighted image of the aortic arch (A) shows the characteristic signal void ("black blood" technique) within the transverse arch. *B*, ECG-gated sagittal oblique T1-weighted image of the aorta (A) shows signal void ("black blood") within the thoracic aorta.

less than a minute with minimal loss of image quality and spatial resolution.

The standard white blood technique for evaluation of the thoracic aorta has been cine gradient-echo imaging.[6] These sequences have been used effectively in the evaluation of the thoracic aorta and have given radiologists important information about velocity, turbulent, and slow-flow states (Fig. 31–12). Further evaluation with phase-contrast angiography has allowed accurate assessment of aortic flow velocities, valvular function, and collateral blood flow[58] in cases of aortic dissection and coarctation (Fig. 31–13). However, the long imaging times needed for these evaluations can be limiting, and a comprehensive evaluation of the entire thoracic aorta is impractical. As with black blood techniques, effective ECG gating is still important to the success of cine GRE images.

With the advent of gadolinium-enhanced aortic imaging, a new, powerful imaging technique was established.[96] Unlike cine GRE techniques, which rely on the intrinsic signal of flowing blood, gadolinium-enhanced MR angiography takes advantage of the T1-shortening effect of gadolinium within the vascular system.[69] With the introduction of stronger and faster gradients, TR and TE values can be sufficiently shortened to maximize the signal of the gado-

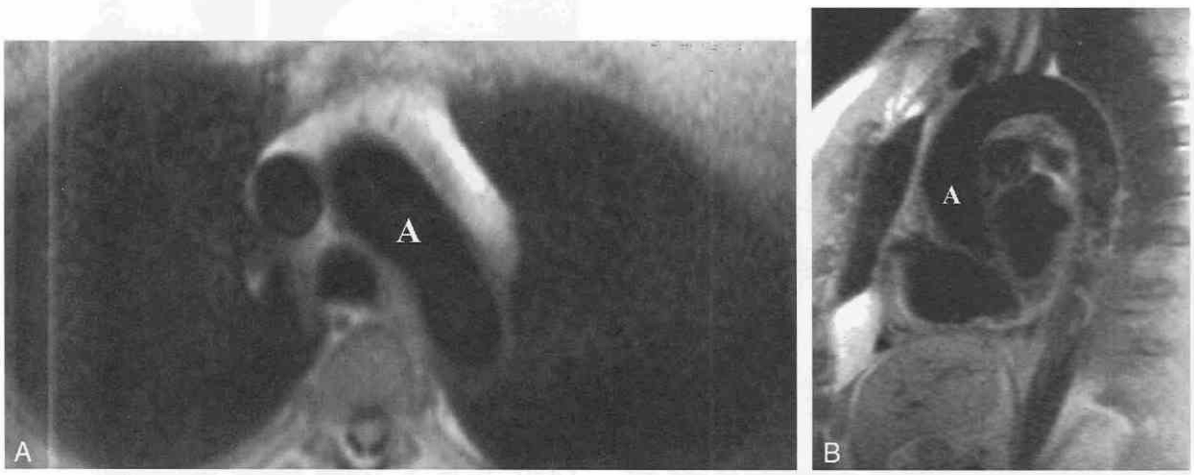

Figure 31–11. *A*, Axial half-Fourier acquisition single-shot turbo spin echo (HASTE) MR image of the thoracic aorta shows a signal void within the aortic arch, similar to that shown in Fig. 31-10*A*. Compared with standard T1-weighted MR imaging, evaluation of the surrounding anatomic structures on this HASTE image is limited. *B*, Sagittal HASTE MR image of the thoracic aorta displays anatomic information comparable to that shown in the standard T1-weighted MR images of the aorta, as shown in Fig. 31–10*B*. As in *A*, rendering of the surrounding anatomy is limited with the HASTE sequence. A = aorta.

Figure 31–12. Axial cine gradient-recalled echo (GRE) MR image of the aortic arch shows the normal appearance of the transverse aorta. A = aorta.

linium-containing aorta in relation to the surrounding stationary tissues (Fig. 31–14).

The success of gadolinium-enhanced angiography depends on close attention to timing of the gadolinium bolus, because of significant variability in individual cardiac outputs and time to peak aortic enhancement. A number of techniques are available to maximize contrast enhancement in the ascending aorta. They include empiric timing based on the estimated cardiac output, use of a timing bolus, and automatic triggering.[95] Though beyond the scope of this chapter, newer techniques available in some centers include true fast imaging with steady-state precession (FISP) of the aorta (Fig. 31–15), which allows almost real-time imaging of the aorta. Such techniques promise to further enhance our accuracy and speed in the diagnosis of aortic disease.

Advanced CT and MRI techniques have similarly improved our evaluation of the aortic valve. ECG-gated multislice CT allows evaluation of the aortic valve in systole and diastole (Fig. 31–16), and virtual endoscopic imaging with multislice CT has enabled 3D imaging of the aortic valve, which is not possible with single-slice CT scanners (Fig. 31–17). The superior time resolution made possible with cine MRI has also enhanced visualization of the normal aortic valve (Fig. 31–18).

Imaging Artifacts

The accurate assessment of aortic disease is complicated by a large number of imaging artifacts that can mimic important and potentially life-threatening aortic disease. With the growing use of multislice CT scanners and ECG gating, these artifacts will be significantly reduced. However, in any discussion of the role of imaging in thoracic

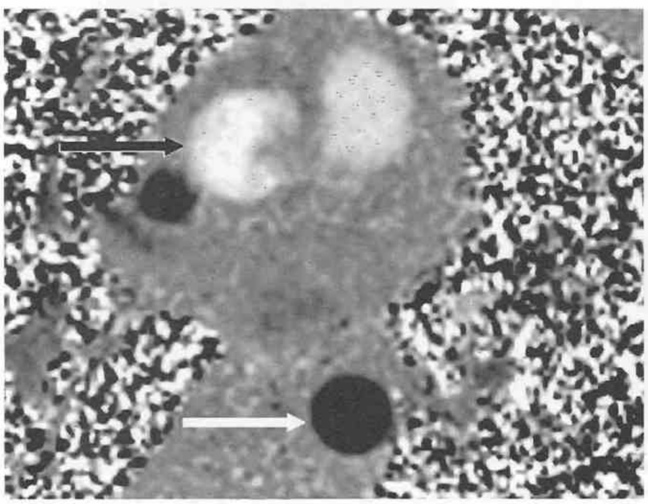

Figure 31–13. Phase-contrast MR image at the level of the midthoracic aorta shows cephalad blood flow displayed in white (*black arrow*), and caudad blood flow in black (*white arrow*).

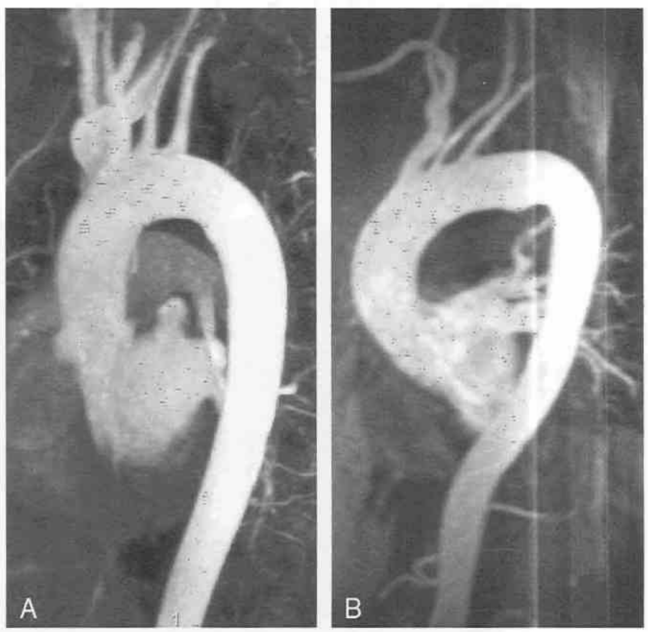

Figure 31–14. *A*, Sagittal oblique gadolinium-enhanced maximum intensity projection (MIP) of the thoracic aorta in a young adult. *B*, Sagittal oblique gadolinium-enhanced MIP of the thoracic aorta in an elderly patient shows marked unfolding of the thoracic aortic arch. Note the smooth appearance of the ductus diverticulum.

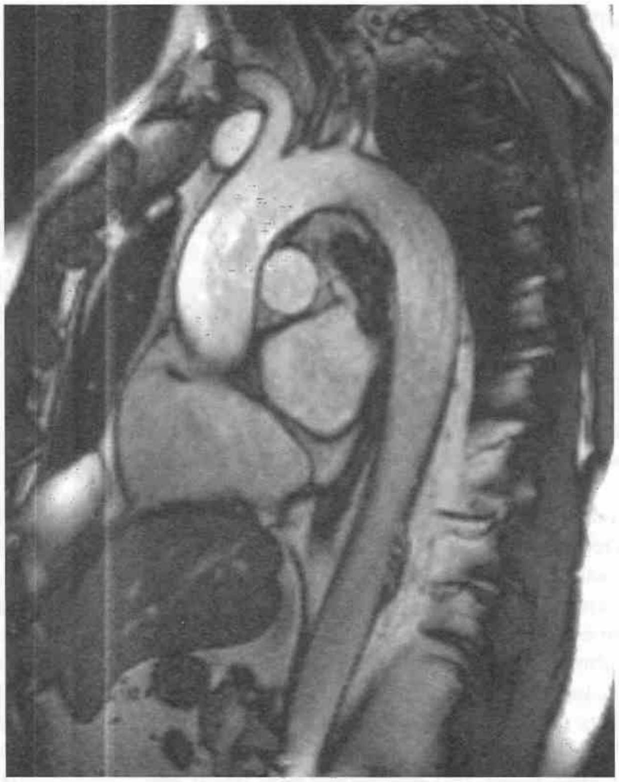

Figure 31–15. True fast imaging with steady-state precession (FISP) cine image of the thoracic aorta. Such images provide information similar to those shown by conventional cine gradient-recalled echo images but with markedly shorter imaging times.

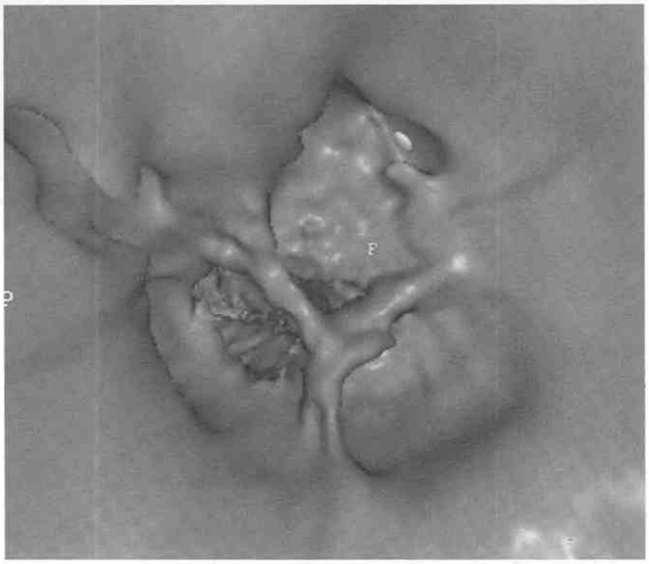

Figure 31–17. ECG-gated virtual endoscopic view of the aortic valve displays the sinuses of Valsalva captured in diastole.

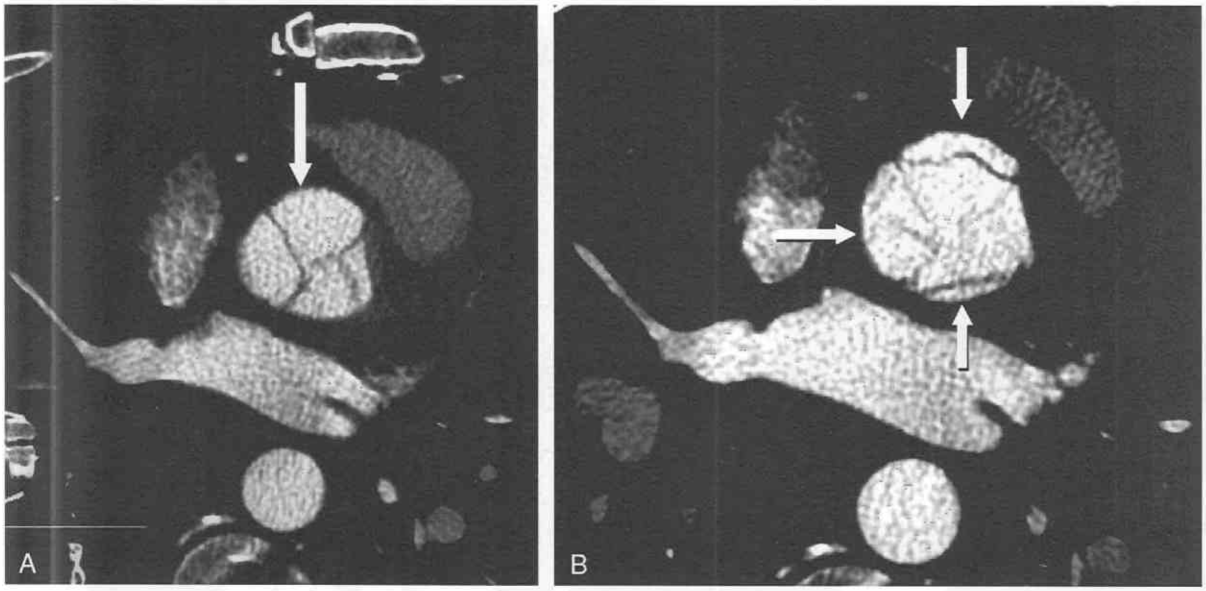

Figure 31–16. *A*, ECG-gated CT scan of the aortic root clearly delineates the three aortic cusps closed in diastole (*arrow*). *B*, ECG-gated CT image of the aortic root in systole captures the opened valve cusps (*arrows*).

Figure 31–18. Coronal oblique image of the aortic root using a cine gradient-recalled echo (GRE) sequence delineates the three aortic cusps in diastole. Arrow denotes valve in diastole.

aortic disease, it is important to consider the wide variety of these artifacts and pitfalls.

Optimal contrast opacification is of great importance in the evaluation of aortic disease. Inadequate contrast opacification limits our evaluation of a variety of aortic diseases, particularly aortic dissection (Fig. 31–19). These limitations can be overcome with a timing bolus or the use of automated bolus-tracking techniques to optimize contrast opacification in the aorta. Even with adequate contrast opacification, there can be imaging difficulty in patients with aortic dissection, in whom there may be significant differences in flow dynamics in the true lumen and false lumen (Fig. 31–20).[9]

Streak artifacts from adjacent vascular structures can cause artifacts that mimic aortic dissection. This appearance, most commonly seen in the ascending aorta and arch vessels, results from the high-attenuation contrast seen in the crossing brachiocephalic veins or superior vena cava (Fig. 31–21). A streak artifact can generally be distinguished from aortic dissection if one follows the artifact beyond the expected course of the aorta. Although streak artifacts can be minimized by pedal injection of the contrast agent, this route is technically more difficult and usually less acceptable to the patient. Some researchers suggest that the use of saline or diluted contrast material at the end of the contrast bolus also minimizes the streak artifacts seen from high attenuation in the brachiocephalic veins.

Adjacent anatomic structures can also mimic aortic dissections or hematoma. They include the right atrial appendage, the superior pericardial recess, and the superior intercostal vein (Figs. 31–22 and 31–23). The atelectatic lung commonly seen adjacent to the descending aorta can sometimes mimic dissection or leak (Fig. 31–24). Close examination of images superior and inferior to these images excludes dissection or hematoma.[111] Aortic pulsation artifacts (Fig. 31–25) are classic mimics of dissection flaps. Pulsation artifacts usually occur in the ascending aorta. Studies using ECG-gated electron beam computed tomography (EBCT) demonstrated significant aortic motion during the cardiac cycle and further classified their common locations. Most commonly, pulsation artifacts are seen at the 7 o'clock and 12 o'clock positions.

Aortic Arch Anomalies

It is important to recognize that the standard branching pattern of the thoracic aorta is seen in only 75% of pa-

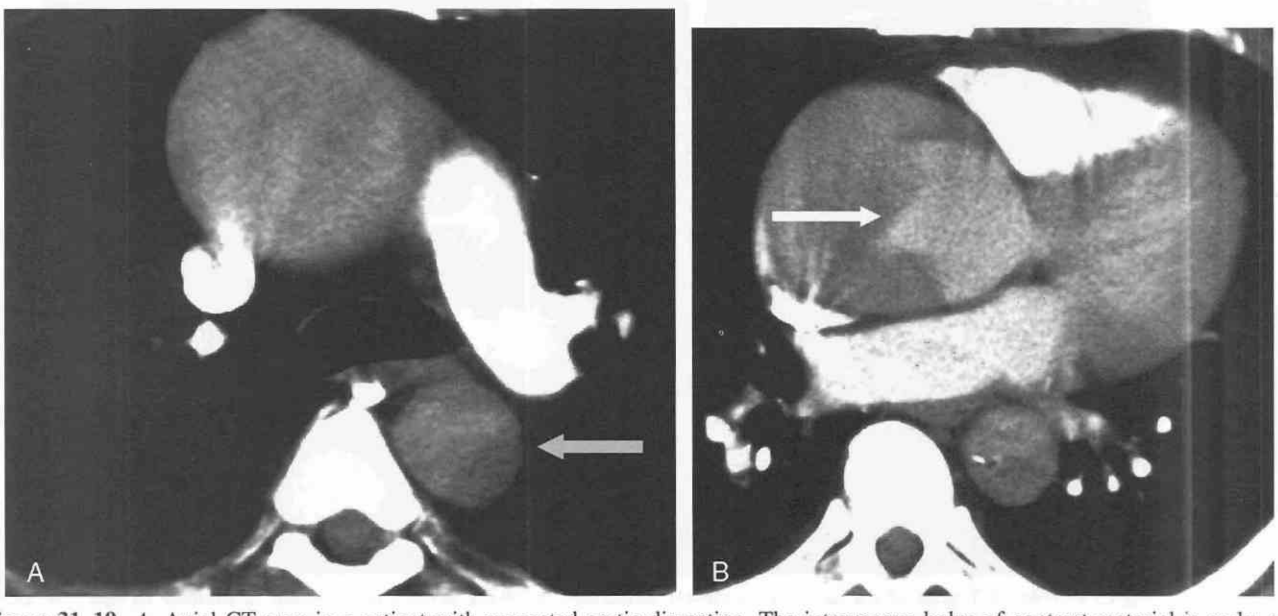

Figure 31–19. *A*, Axial CT scan in a patient with suspected aortic dissection. The intravenous bolus of contrast material is early, and visualization of the thoracic aorta is inadequate. *Arrow* shows descending aorta. *B*, Axial CT scan at the level of the aortic root shows faint opacification of the aortic root with subtle delineation of ascending aortic dissection (*arrow*).

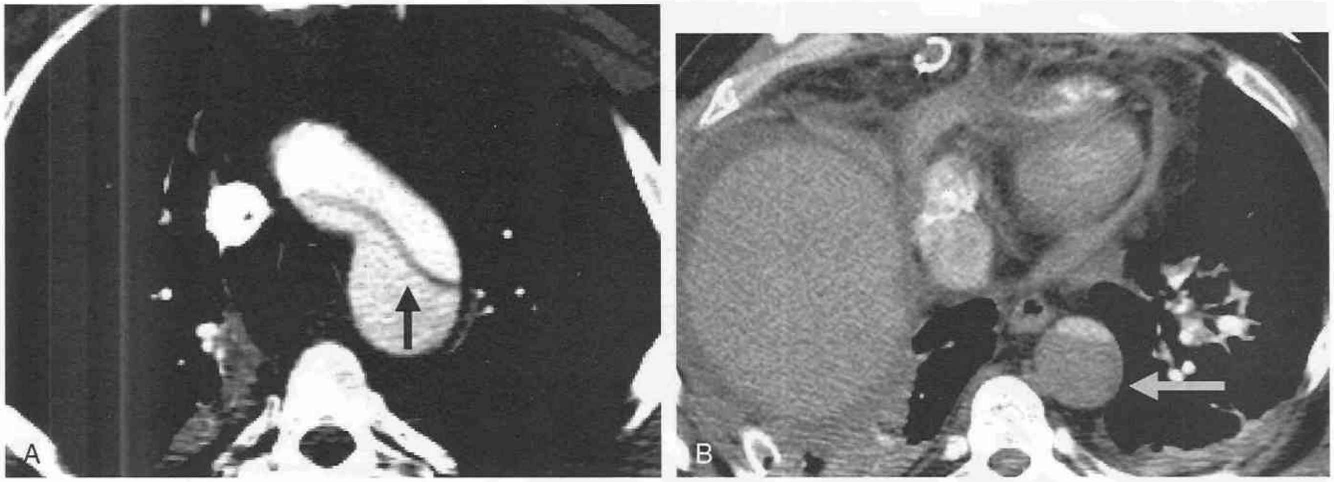

Figure 31–20. *A*, Axial multislice CT scan shows an aortic dissection flap involving the aortic arch (*arrow*). *B*, Axial scan at the level of the descending aorta shows faint opacification of the anteriorly compressed true lumen. The early injection results in inadequate visualization of the false lumen.

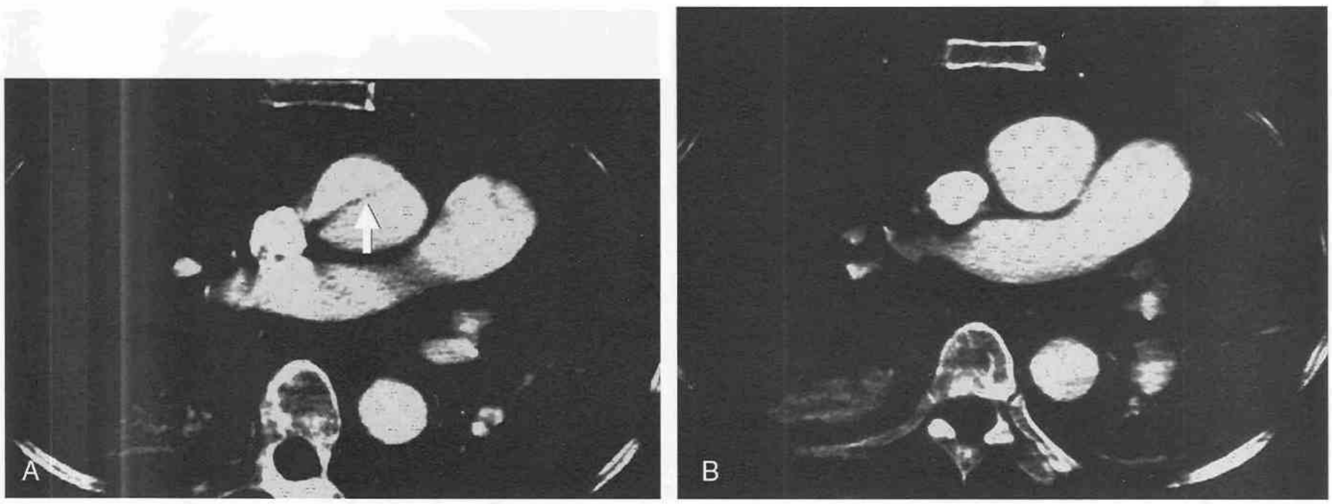

Figure 31–21. *A*, Axial CT scan above the aortic valve shows an apparent linear density mimicking dissection in the ascending aorta, secondary to a beam-hardening artifact from the presence of contrast agent in the superior vena cava (*arrow*). *B*, Axial CT scan superior to scan in *A* shows a normal ascending aorta with no evidence of dissection.

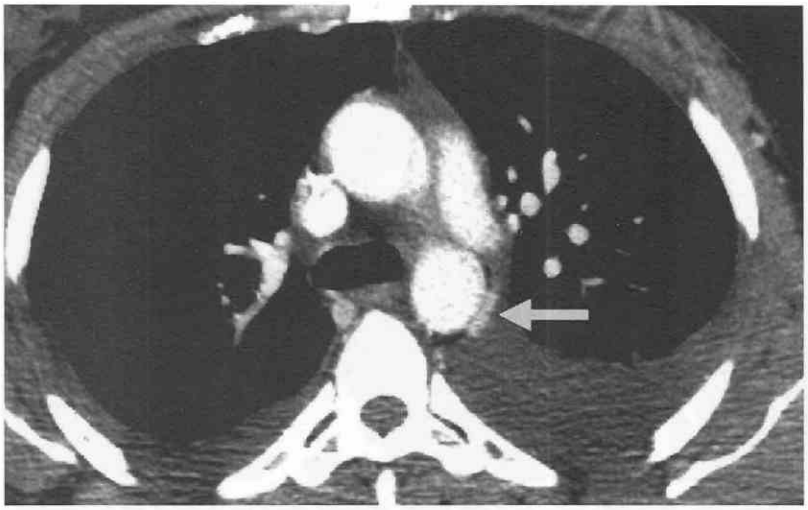

Figure 31–22. Axial CT scan demonstrates a suspicious soft tissue density (*arrow*) adjacent to the descending aorta.

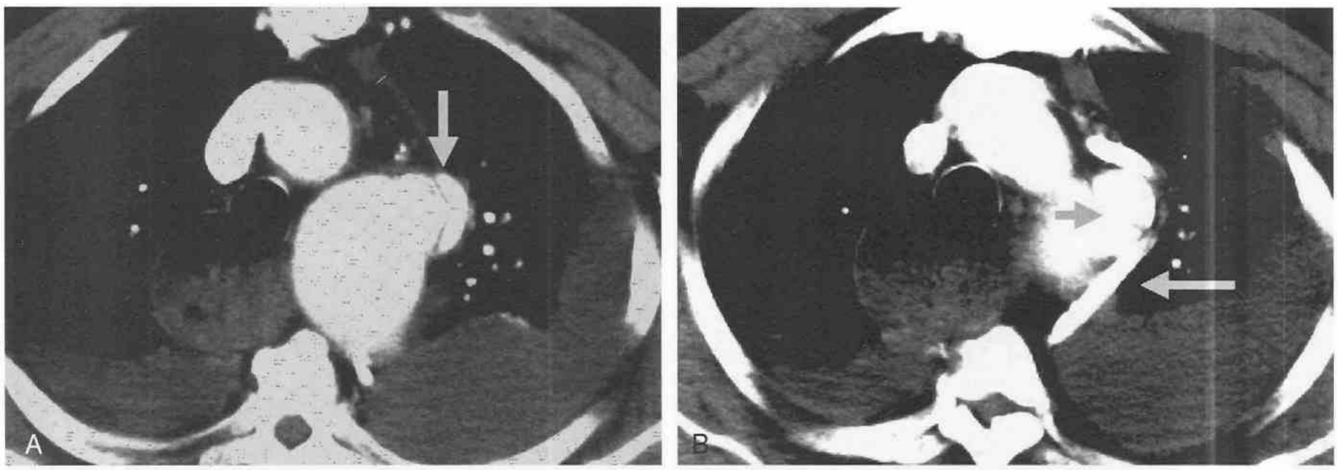

Figure 31–23. *A*, Axial CT scan in a patient with known aortic aneurysm and findings suspicious for possible dissection flap involving the descending aorta (*arrow*). *B*, Axial CT scan superior to *A* shows the full course of the superior intercostal vein (*white arrow*). Note the separate medial dissection flap (*black arrow*).

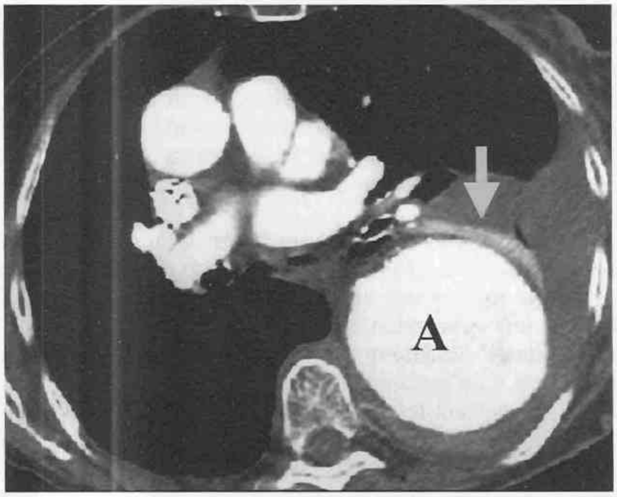

Figure 31–24. Axial CT scan in a patient with a large aortic aneurysm shows abnormal, enhancing soft tissue anterior to the aneurysm (*arrow*). This soft tissue represents atelectatic lung anterior to the aneurysm.

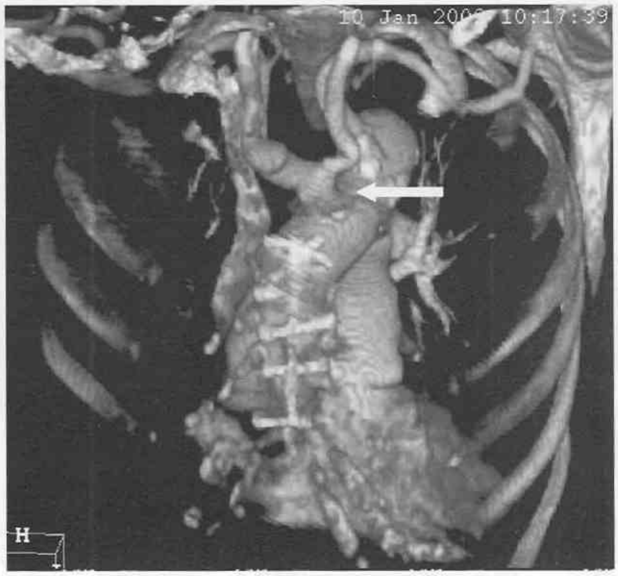

Figure 31–26. Coronal volumetric reconstruction demonstrates the common origin of the right brachiocephalic artery and the left carotid artery (*arrow*).

tients.[12] The most common aortic variant is the so-called bovine arch, in which the right brachiocephalic artery and left common carotid artery have a common origin (Fig. 31–26). Although the left vertebral artery originates from the subclavian artery in most patients, it arises directly from the aortic arch in 5% to 6% of patients (Fig. 31–27); this can be an important variant in patients undergoing cerebral angiography.[123]

Understanding congenital aortic arch anomalies requires comprehension of the embryologic double arch theory. In the standard left arch, the embryologic double arch fuses posteriorly to form the descending aorta. If the right arch is interrupted between the right subclavian artery and the descending aorta, the right subclavian and carotid arteries fuse to form the right brachiocephalic artery, resulting in the standard arch anatomy.[118]

The most common aortic arch anomaly is the left aortic arch with aberrant right subclavian artery. This anomaly occurs when the right arch is interrupted between the right common carotid artery and the right subclavian artery. The right subclavian artery arises from the diverticulum of Kommerell, a persistence of the embryologic right aortic arch. In most cases, the aberrant right subclavian artery crosses posterior to the esophagus (Fig. 31–28), but it courses between the trachea and esophagus in 18% of cases, and in front of the trachea in 4%.[60] The common left aortic arch with aberrant right subclavian artery occurs in 1 in 200 patients. On a lateral radiograph, a posterior impression on the trachea can be seen. Symptoms occur at the two extremes of life in patients with this anomaly. In children, tracheal obstruction or dysphagia can occur,[11] whereas in adults, aneurysms of the aberrant subclavian

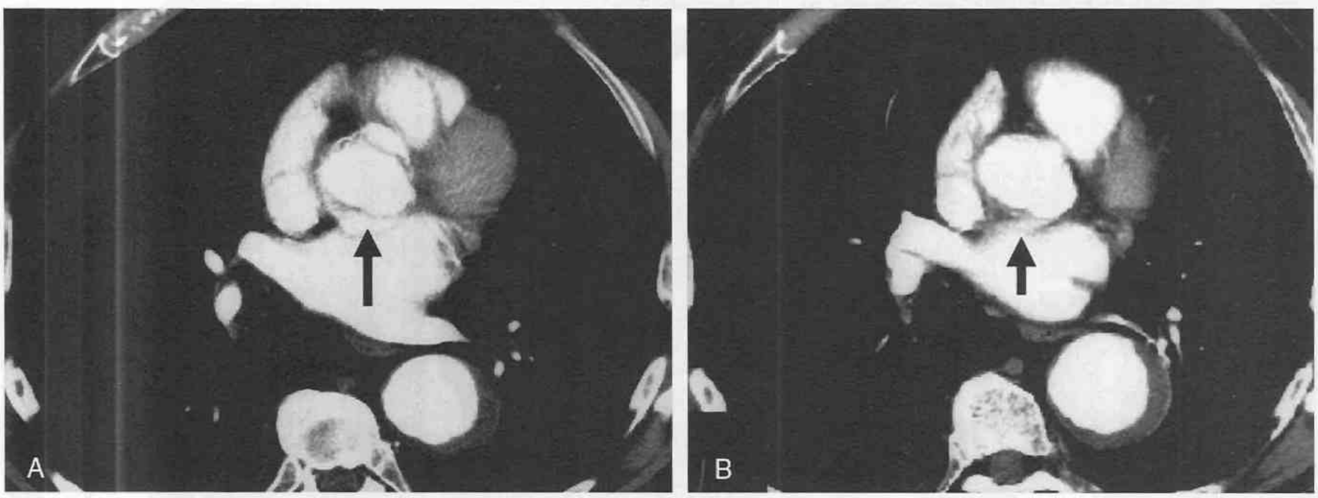

Figure 31–25. *A*, Axial CT scan shows linear pulsation artifacts in the ascending aorta that mimic aortic dissection (*arrow*). *B*, Axial ECG-gated CT scan obtained during diastole demonstrates resolution of these filling defects.

Figure 31–27. Axial CT shows direct origin of the vertebral artery (*arrow*) from the aortic arch.

artery or a prominent diverticulum of Kommerell can occur, resulting in dysphagia classically known as *dysphagia lusoria* (Figs. 31–29 through 31–31).[7] Less common descriptions of the aberrant right subclavian artery have included superior vena cava obstruction and gastrointestinal bleeding. There are isolated case reports of thrombosis with distal embolization in patients with aberrant right subclavian artery.[1]

The right aortic arch is a much less common anomaly, occurring in 0.5% of patients.[63] The three common anomalies of the right aortic arch are (1) right aortic arch with aberrant left subclavian artery, (2) right aortic arch with mirror image branching (see Fig. 31–22), and (3) right aortic arch with isolated left subclavian artery.[36] The right arch with aberrant left subclavian artery occurs in 0.6% to 0.1% (Fig. 31–32). A minority of these anomalies are associated with significant congenital heart disease, although right aortic arch is the second most common cause of vascular ring, after double aortic arch.[132] Right aortic arch with mirror image branching is commonly associated with congenital heart disease, most often seen in patients with tetralogy of Fallot, ventricular septal defects, and truncus arteriosus. We have seen a large variety of unusual

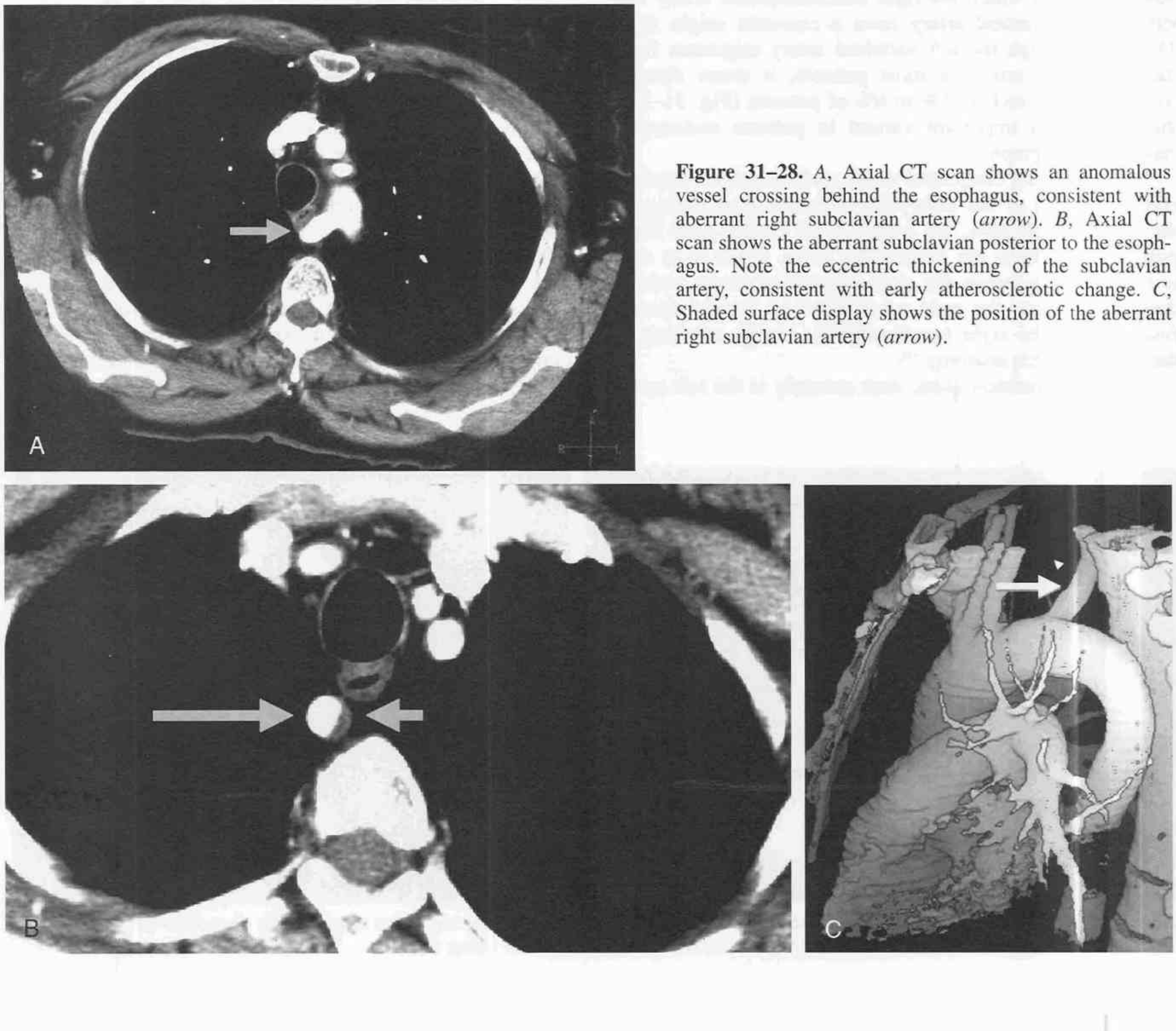

Figure 31–28. *A*, Axial CT scan shows an anomalous vessel crossing behind the esophagus, consistent with aberrant right subclavian artery (*arrow*). *B*, Axial CT scan shows the aberrant subclavian posterior to the esophagus. Note the eccentric thickening of the subclavian artery, consistent with early atherosclerotic change. *C*, Shaded surface display shows the position of the aberrant right subclavian artery (*arrow*).

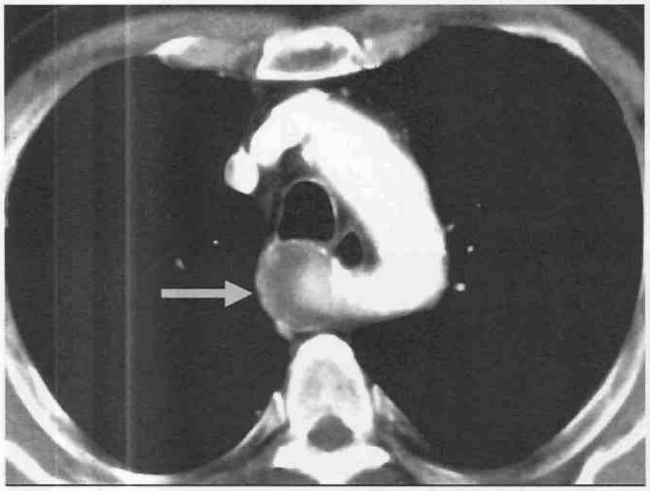

Figure 31–29. Axial CT scan shows aneurysmal dilatation of the aberrant right subclavian artery (*arrow*).

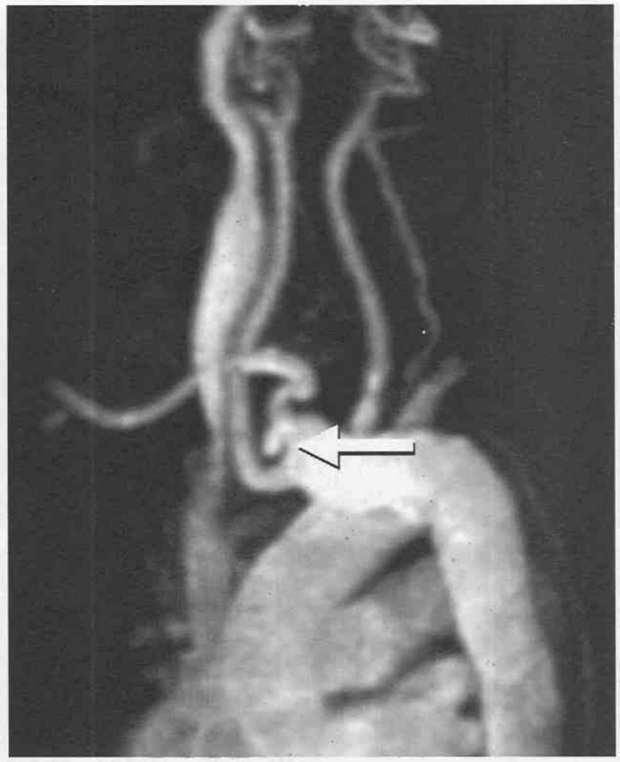

Figure 31–31. Gadolinium MR angiogram of the aortic arch demonstrates a penetrating atherosclerotic ulcer arising from the aberrant right subclavian artery (*arrow*).

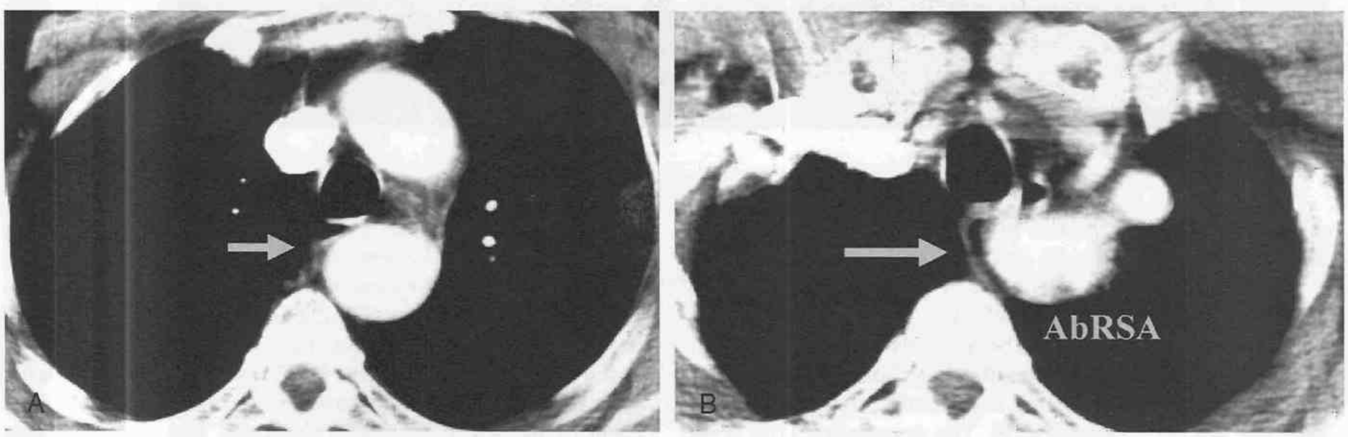

Figure 31–30. *A*, Axial CT scan shows the origin of the right subclavian artery from a diverticulum of Kommerell (*arrow*). *B*, Axial CT scan shows compression of the esophagus by the aberrant right subclavian artery (AbRSA).

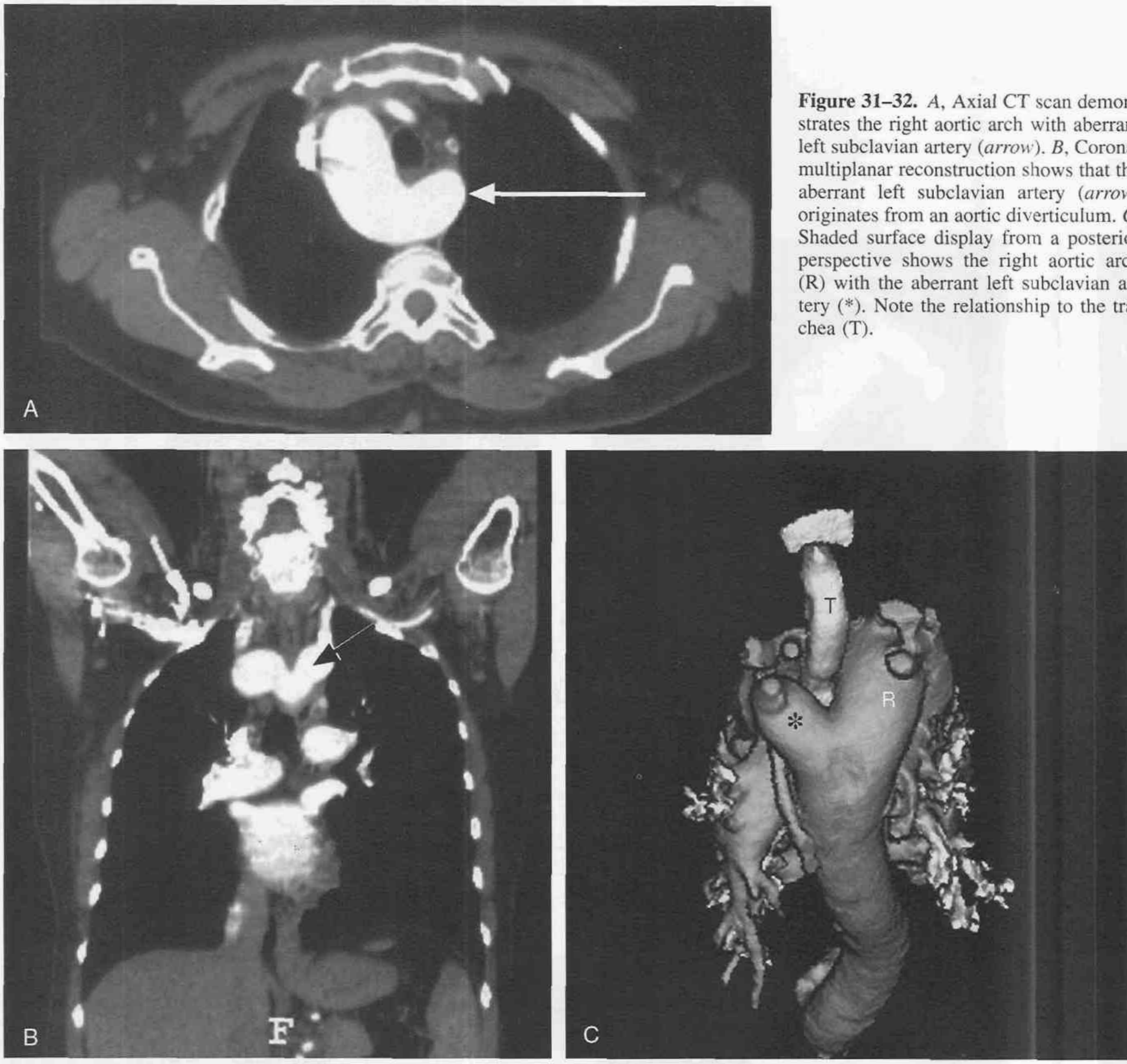

Figure 31–32. *A*, Axial CT scan demonstrates the right aortic arch with aberrant left subclavian artery (*arrow*). *B*, Coronal multiplanar reconstruction shows that the aberrant left subclavian artery (*arrow*) originates from an aortic diverticulum. *C*, Shaded surface display from a posterior perspective shows the right aortic arch (R) with the aberrant left subclavian artery (*). Note the relationship to the trachea (T).

right aortic arch anomalies not associated with congenital heart disease (Figs. 31–33 and 31–34).

Double aortic arch, the result of persistence of the embryologic double arch, is the most common cause of a symptomatic vascular ring. The anomaly is much less commonly associated with congenital heart anomalies. In double aortic arch, the right arch is generally higher and larger than the left arch (Fig. 31–35). The descending arch is on the left side in most patients. Although this anomaly is clearly seen in asymptomatic adult patients, the size of the left aortic arch is quite variable, and the effect of a relatively atretic left arch on tracheal diameter often determines the symptoms (Fig. 31–36). Multislice CT scanning has enabled enhanced visualization of the double aortic arch in infants and neonates (Fig. 31–37).

The cervical aortic arch is an uncommon anomaly of the aorta in which the aortic arch extends into the soft tissues of the neck. Patients with this anomaly are generally asymptomatic, but they can present with dysphagia, stridor, or a pulsatile neck mass (Fig. 31–38). Aneurysms involving a cervical aortic arch have been reported, with several cases of aneurysmal rupture. It is postulated that in patients with the anomaly and an aneurysm, embryologic development of the aortic arch was abnormal, and many patients exhibit cystic medial necrosis.[51]

Coarctation of the Aorta

Coarctation of the aorta is an abnormal narrowing of the descending aorta. It most commonly manifests as a focal area of narrowing distal to the left subclavian artery

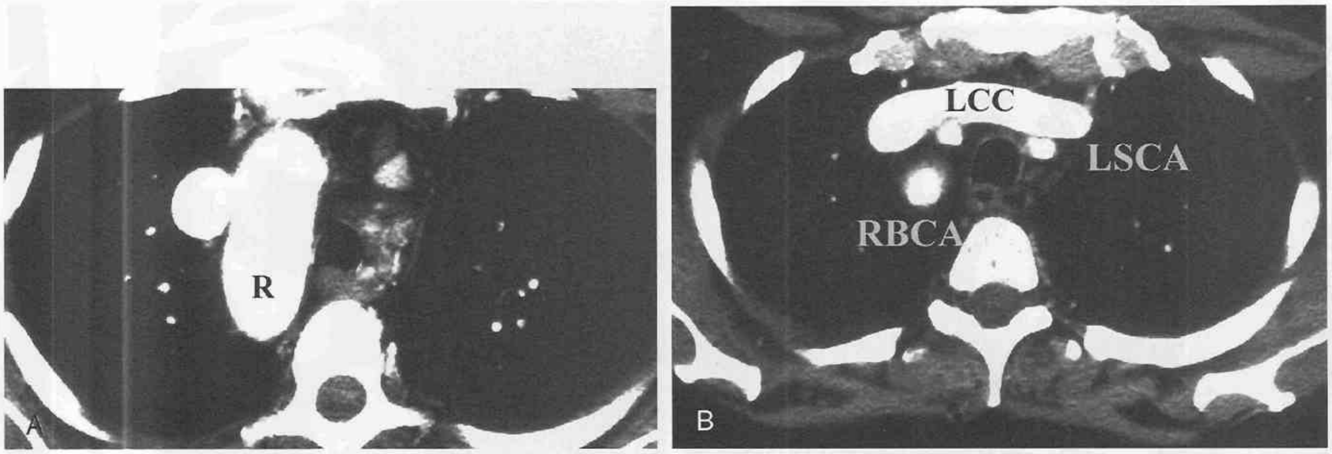

Figure 31–33. *A*, Axial CT scan shows the right aortic arch (R). There is no evidence of an aberrant subclavian artery. *B*, In the same patient, an axial CT scan superior to *A* shows the right brachiocephalic artery (RBCA), the left common carotid artery (LCC), and the left subclavian artery (LSCA), consistent with a normal left aortic arch branching pattern.

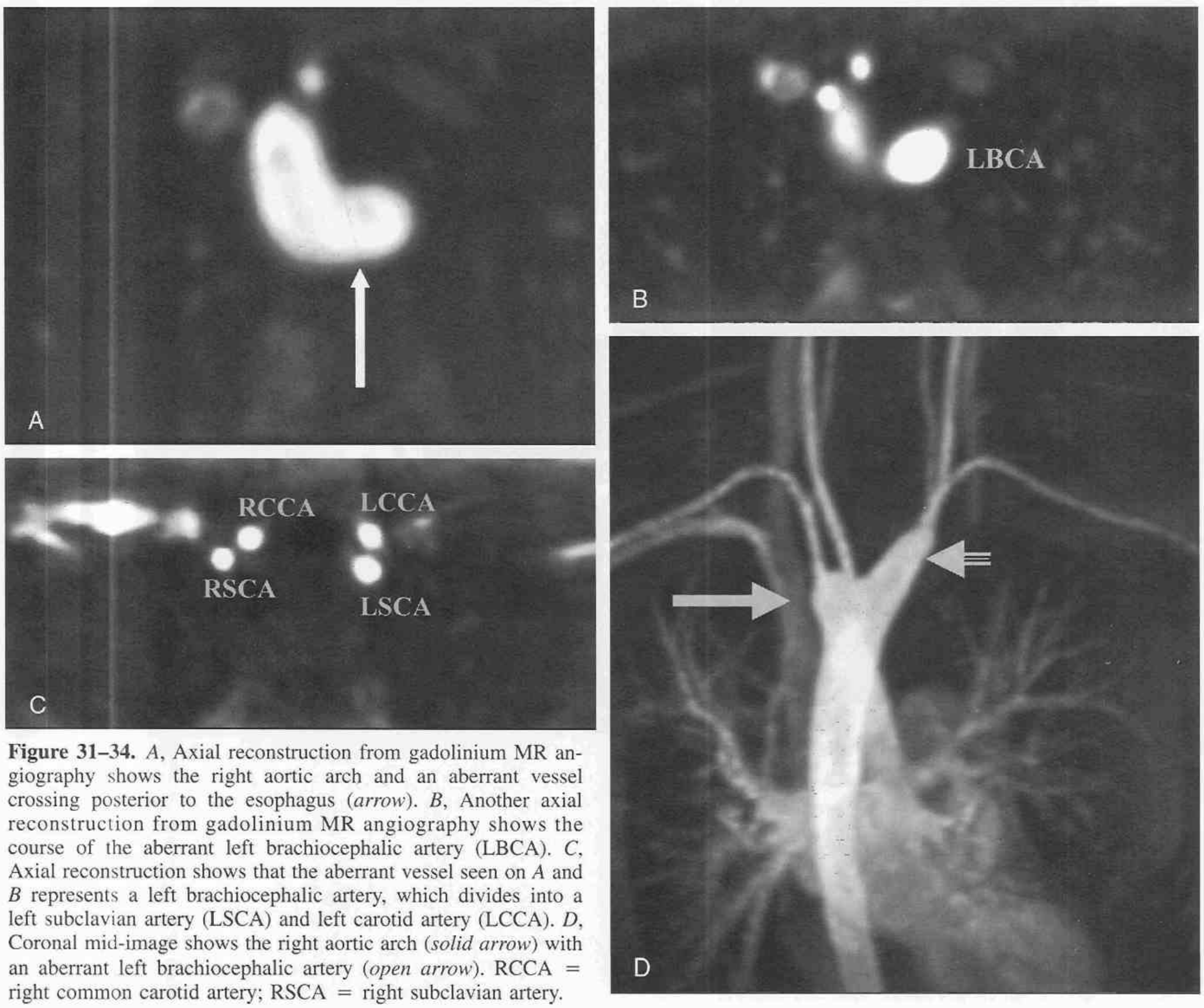

Figure 31–34. *A*, Axial reconstruction from gadolinium MR angiography shows the right aortic arch and an aberrant vessel crossing posterior to the esophagus (*arrow*). *B*, Another axial reconstruction from gadolinium MR angiography shows the course of the aberrant left brachiocephalic artery (LBCA). *C*, Axial reconstruction shows that the aberrant vessel seen on *A* and *B* represents a left brachiocephalic artery, which divides into a left subclavian artery (LSCA) and left carotid artery (LCCA). *D*, Coronal mid-image shows the right aortic arch (*solid arrow*) with an aberrant left brachiocephalic artery (*open arrow*). RCCA = right common carotid artery; RSCA = right subclavian artery.

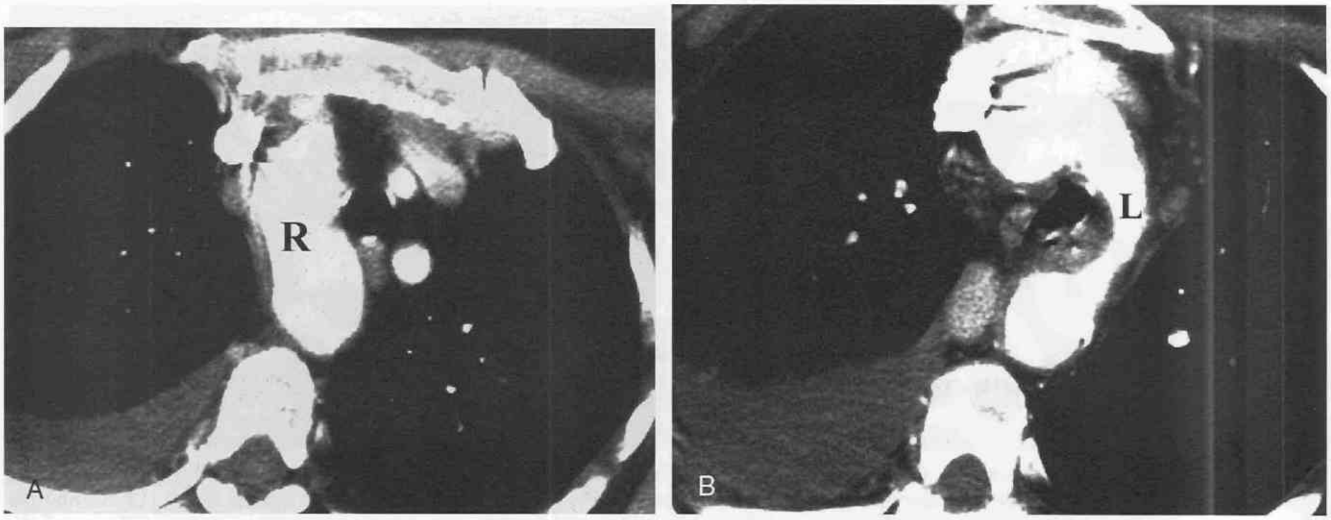

Figure 31–35. *A*, Axial CT scan shows a right-sided aortic arch (R). *B*, An axial CT scan at a level inferior to that of *A* shows a smaller left-sided aortic arch (L).

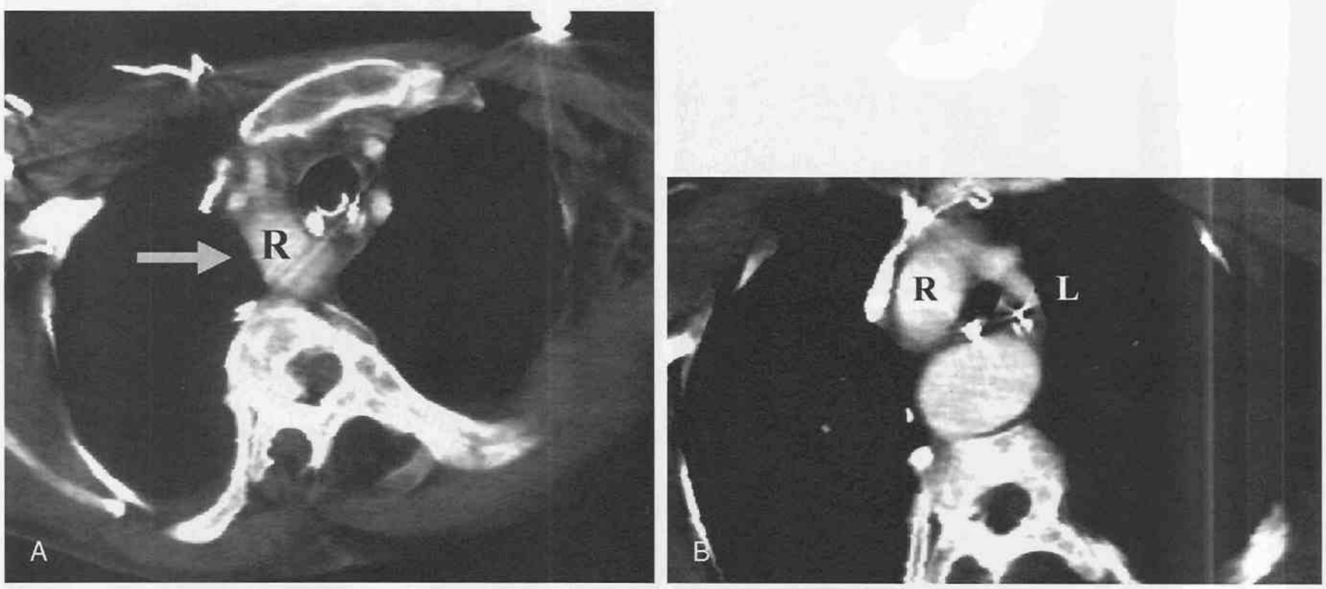

Figure 31–36. *A*, Axial CT scan in a patient with stridor shows the right aortic arch (R). *B*, Another axial CT scan demonstrates a small left aortic arch (L) and a small trachea in the same patient.

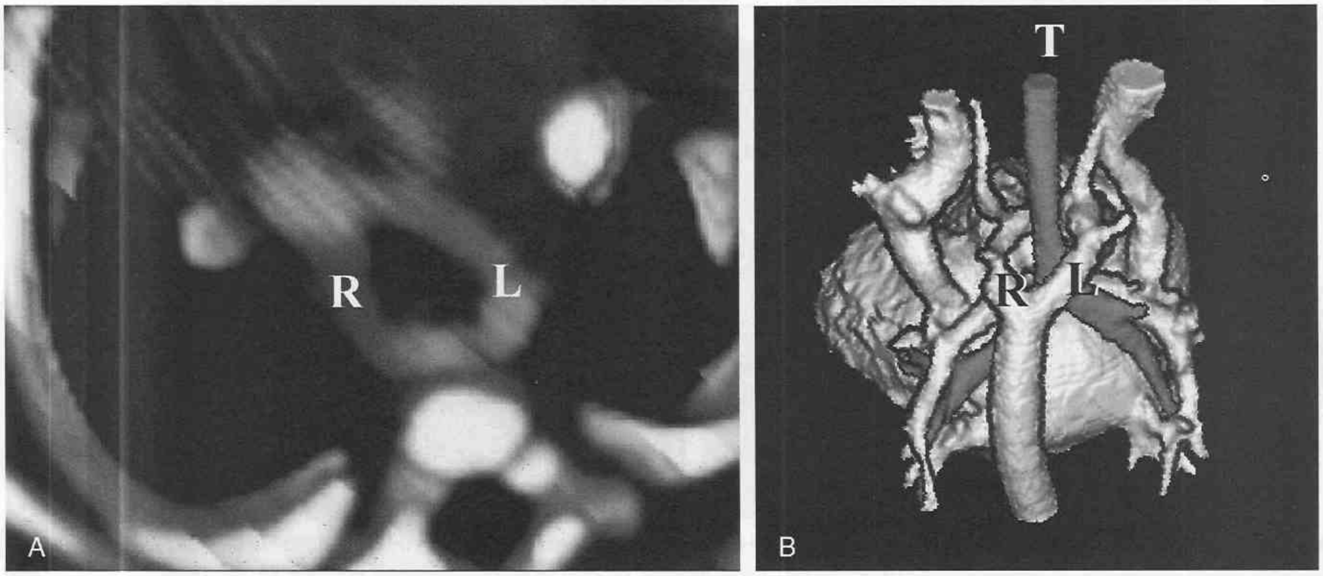

Figure 31–37. *A*, Axial volumetric reconstruction in a newborn with respiratory difficulty shows a double aortic arch. *B*, Shaded surface display in the same patient shows a double aortic arch surrounding the trachea (T). R = right aortic arch; L = left aortic arch.

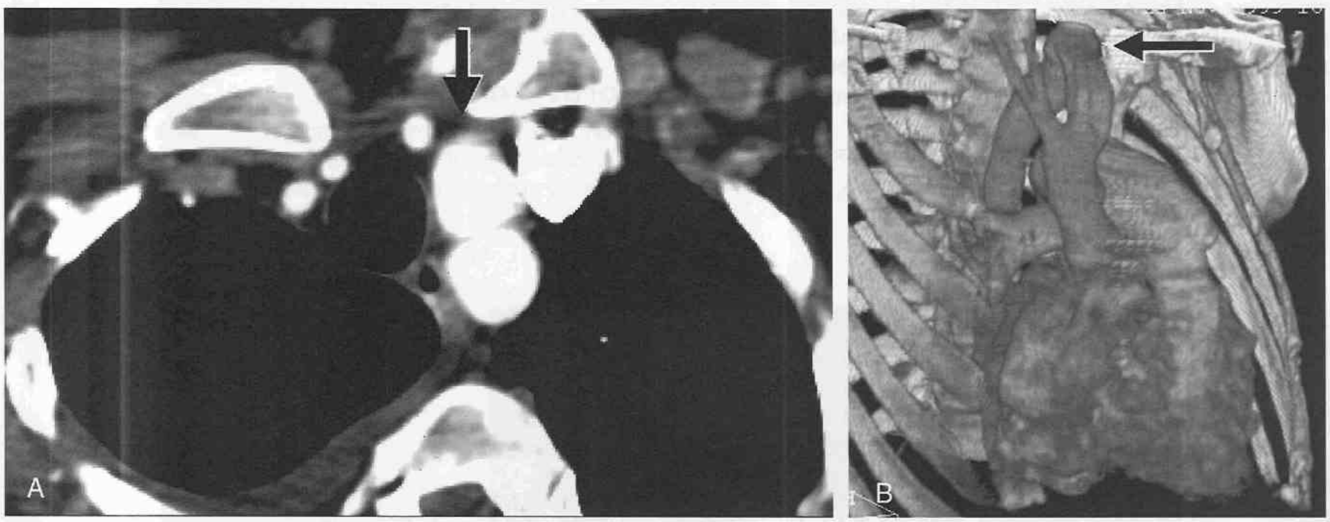

Figure 31–38. *A*, Axial CT scan in a patient with a pulsatile neck mass shows aortic arch at the level of the clavicles (*arrow*). *B*, Volumetric reconstruction demonstrates the position of the thoracic aortic arch at the level of the clavicle (*arrow*).

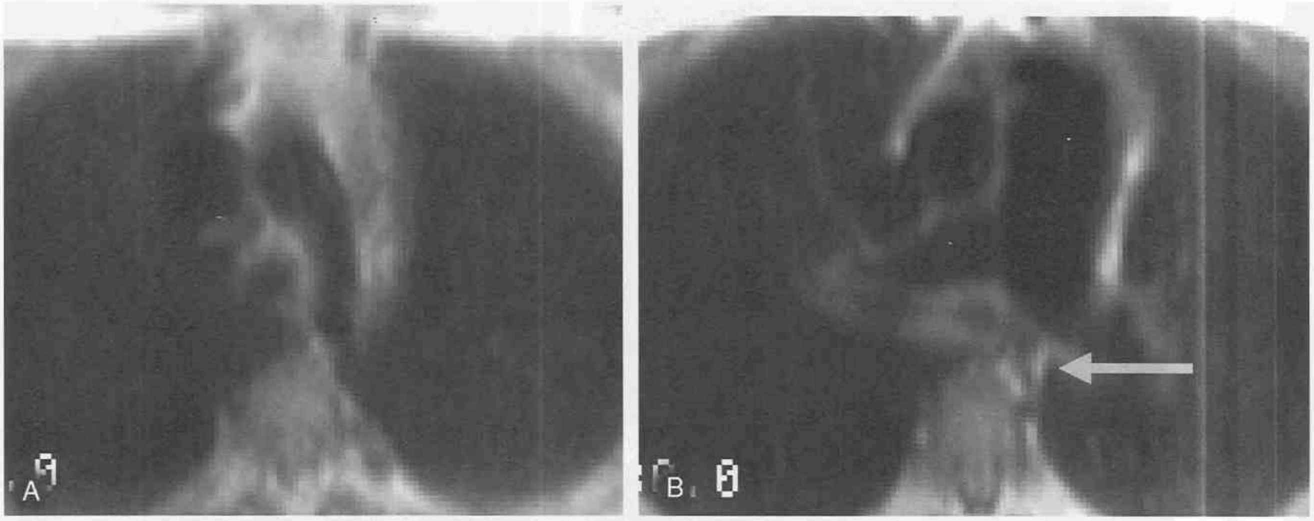

Figure 31–39. *A*, Axial ECG-gated, T1-weighted MR image of the aortic arch shows narrowing of the distal aortic arch. *B*, Axial ECG-gated, T1-weighted image of the aortic arch at a level inferior to that of *A* demonstrates absence of the proximal descending aorta (*arrow*).

(Fig. 31–39). In the infantile form, tubular hypoplasia can affect a longer segment of the descending aorta. This anomaly is associated with bicuspid aortic valve in 75% to 85% of patients (Fig. 31–40).[39, 126] Although coarctation of the aorta classically manifests in infants, 20% of patients are diagnosed in adolescence or adulthood. Presenting symptoms include a murmur, systemic hypertension, and differences in blood pressure between the upper and lower extremities. The incidence of cerebral aneurysms and accelerated atherosclerosis is higher in patients with coarctation of the aorta; these disorders are believed to represent sequelae of the systemic hypertension commonly seen in coarctation.

Imaging of aortic coarctation has been well characterized, and the disorder has been successfully imaged with echocardiography, CT, and MRI (Fig. 31–41). Echocardiography and CT have been effective in evaluation of aortic coarctation, but MRI is currently regarded as the most effective method to comprehensively assess the physiologic significance of aortic narrowing (Fig. 31–42).[115] MRI studies have shown excellent correlation with conventional angiography, whereas cine MRI and phase-contrast techniques have identified physiologically significant coarctation. Newer multislice techniques have improved the CT evaluation of aortic coarctation (Figs. 31–43 and 31–44).

Aortic Aneurysms

By definition, a true thoracic aortic aneurysm involves all components of the vessel wall. The morphologic subtypes of aneurysm are saccular (Fig. 31–45), fusiform

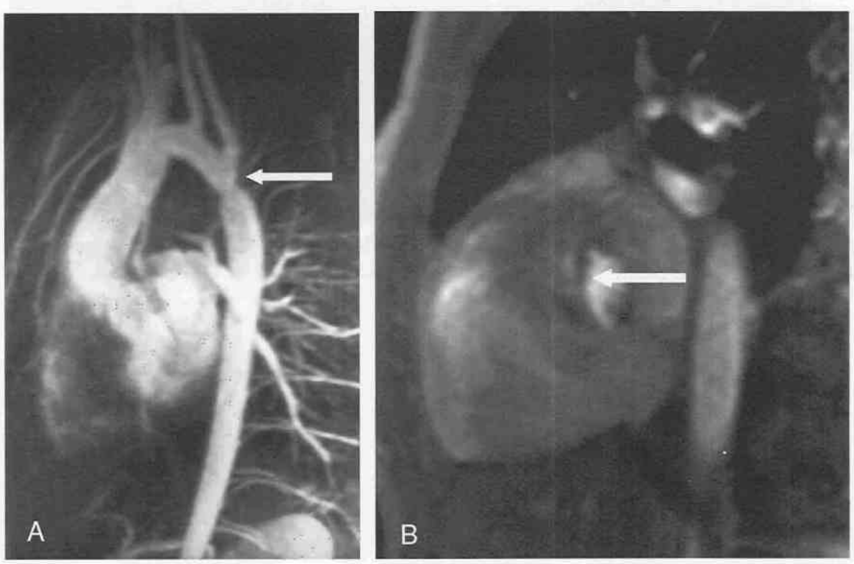

Figure 31–40. *A*, Sagittal oblique gadolinium MR angiogram of a patient with a thoracic aorta shows discrete postductal coarctation (*arrow*). *B*, Oblique cine gradient-recalled echo image demonstrates a bicuspid aortic valve (*arrow*).

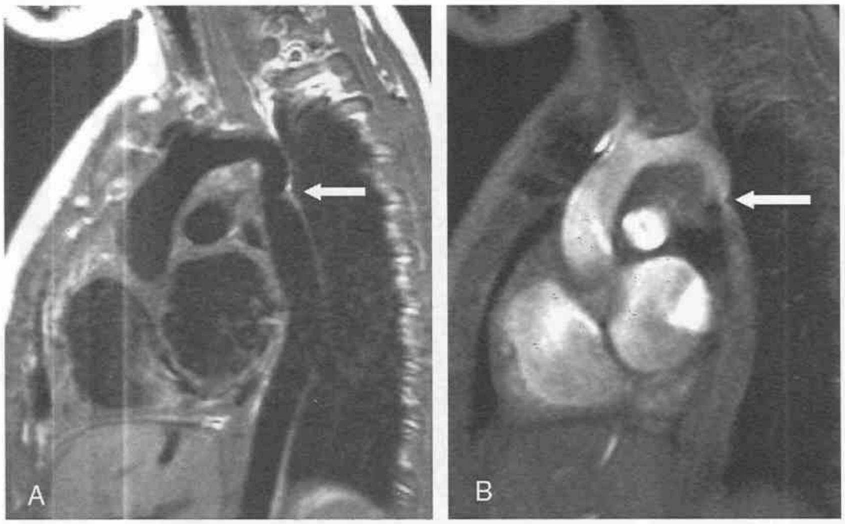

Figure 31–41. *A*, Sagittal oblique ECG-gated T1-weighted MR image (*A*) and sagittal oblique cine gradient-recalled echo image (*B*) of the thoracic aorta show discrete postductal coarctation (*arrow*).

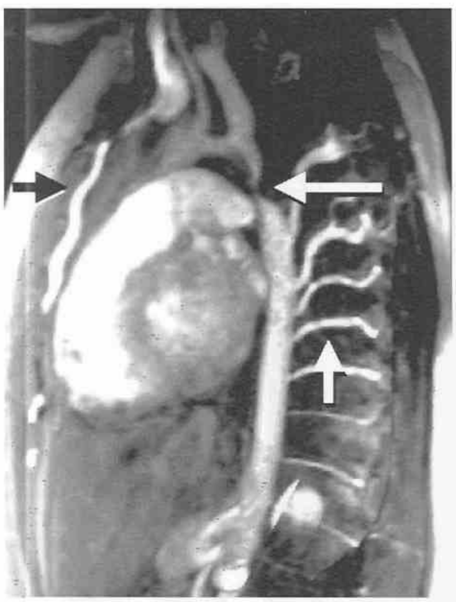

Figure 31–42. Sagittal oblique gadolinium-enhanced MR image demonstrates severe postductal coarctation (*long arrow*) with prominent intercostal aorta (*short arrow*). Note the prominent internal mammary artery (*black arrow*).

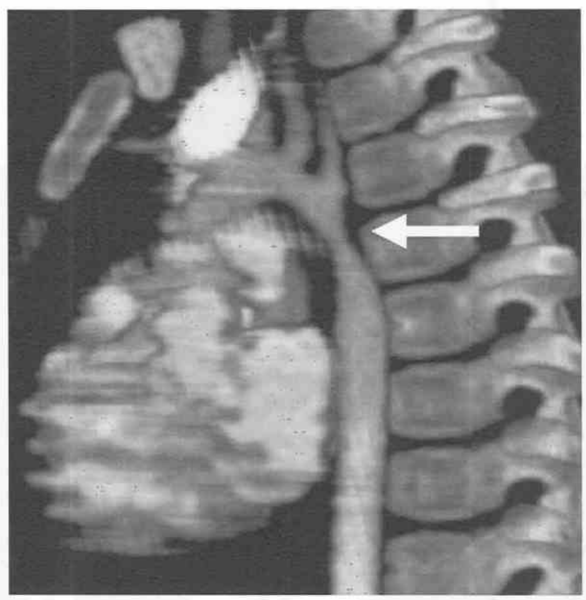

Figure 31–43. Sagittal oblique volume-rendered multislice CT scan of postductal coarctation (*arrow*).

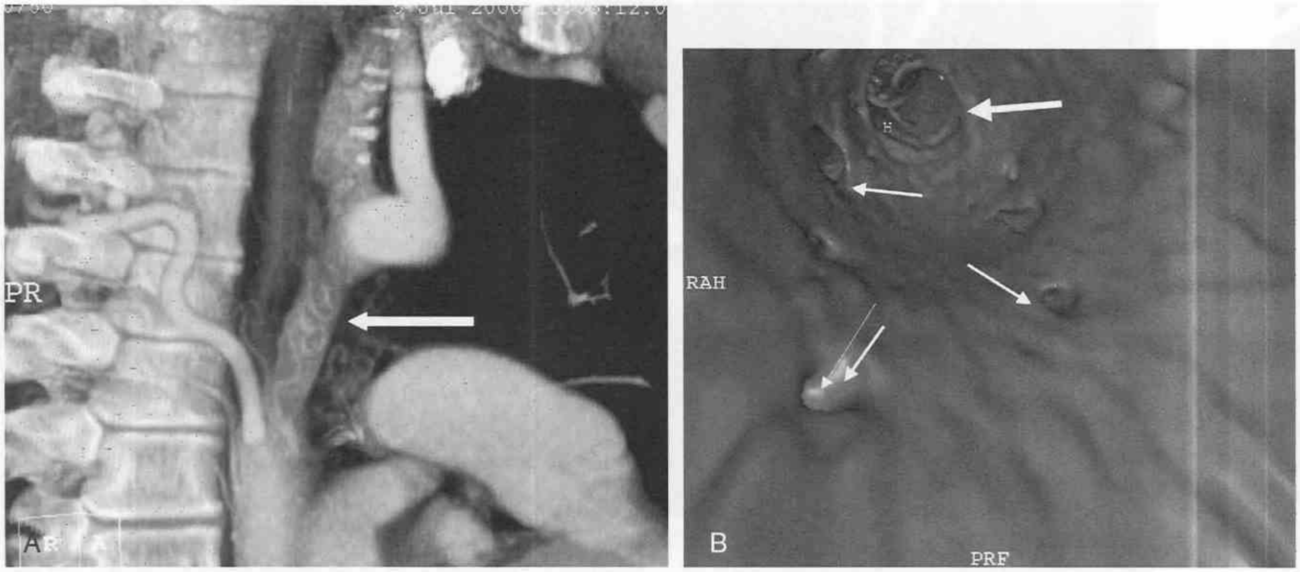

Figure 31–44. *A*, Sagittal oblique volume-rendered CT scan shows persistent coarctation (*arrow*) after surgical repair. Note the markedly enlarged third intercostal artery. *B*, *Large arrow* shows the coarctation. *Small white arrows* show prominent intercostal artery origins.

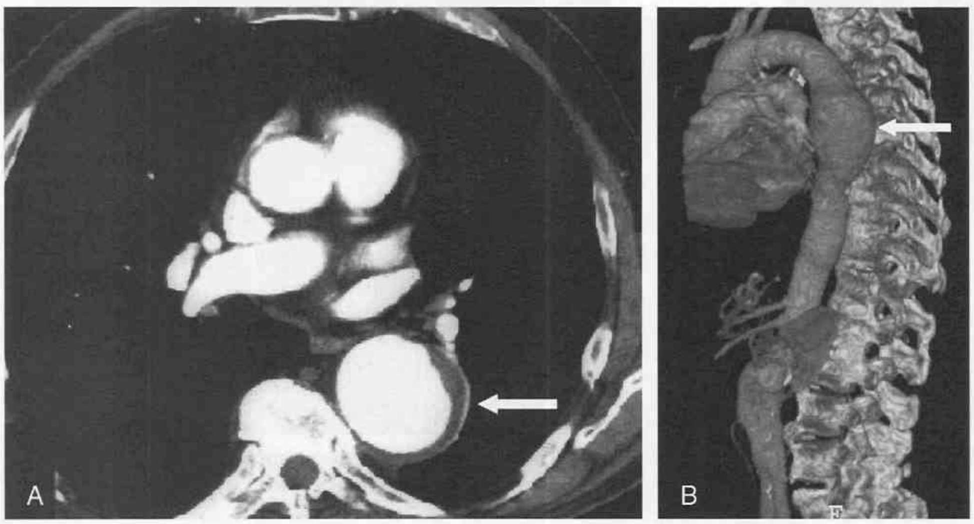

Figure 31–45. *A*, Axial CT scan shows dilatation of the descending aorta with surrounding thrombus (*arrow*). *B*, Sagittal oblique volume-rendered CT scan demonstrates fusiform aneurysm of the descending aorta (*arrow*).

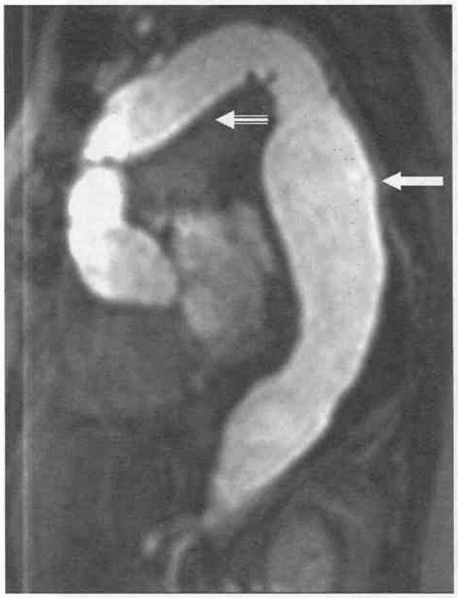

Figure 31–46. Sagittal oblique multiplanar reconstruction of gadolinium-enhanced MR angiography shows a diffuse aneurysm of descending aorta (*thick arrow*). Note the prior transverse arch repair (*thin arrow*).

(Fig. 31–46), dissecting, and false. In addition, acquired aneurysms can be atherosclerotic, mycotic, post-traumatic (Fig. 31–47), or secondary to cystic medial necrosis (Fig. 31–48). Although aneurysms are more common than dissections within the thoracic aorta, acute aneurysmal rupture is an infrequent occurrence (Figs. 31–49 and 31–50).[33, 94] Initial identification of thoracic aortic aneurysms can be suspected from chest radiographs.[50, 57] Most commonly, a mediastinal mass or enlarged segment of the aorta, often containing mural calcification, is visualized. Other findings, such as displacement and compression of the esophagus or trachea and bronchi, may be visible on chest radiographs. Uncommon findings are erosion of the thoracic vertebrae and posterior ribs.

Contrast-enhanced CT can show that a mediastinal mass seen on chest radiographs represents an aneurysm, characterize it, and reveal its exact location. CT can also be used to ascertain whether the aneurysm affects the takeoff of the arch vessels (Fig. 31–51). In addition, CT can demonstrate the following characteristics of the aneurysm: dilatation of the aorta, calcification, intraluminal thrombi, displacement or erosion of adjacent structures, and perianeurysmal thickening and hemorrhage.[38, 39, 133, 134] Identification of mural thrombus and calcification are common with contrast-enhanced CT, because most aortic aneurysms are secondary to arteriosclerosis. Mural thrombus, reported in up to 86% of patients, is typically crescent-shaped and circular in appearance, with the residual aortic lumen appearing smooth.[48, 74, 129] Calcification within the wall of aortic aneurysm has been reported in 83% of patients and typically appears as discontinuous plaques and curvilinear segments.[39, 74] Calcification within the mural thrombus can be seen in up to 17% of aortic aneurysms and can be mistaken for the displaced intimal calcification seen in aortic dissections.[39, 47, 129]

Thoracic aortic aneurysms are most commonly located within the descending aorta at the level of the ligamentum arteriosum, just distal to the origin of the subclavian artery. They are less commonly found within the descending aorta at the level of the aortic hiatus of the diaphragm. The aortic arch is the next most common site, followed by the ascending aorta (Figs. 31–52 and 31–53).[47, 57] In a patient with an aneurysm involving the descending aorta, the esophagus is displaced to the right, and the trachea and bronchi are displaced anteriorly. Aneurysms of the aortic arch and ascending aorta produce compression rather than displacement of adjacent mediastinal structures.[57]

The presence of a thoracic aortic aneurysm should not

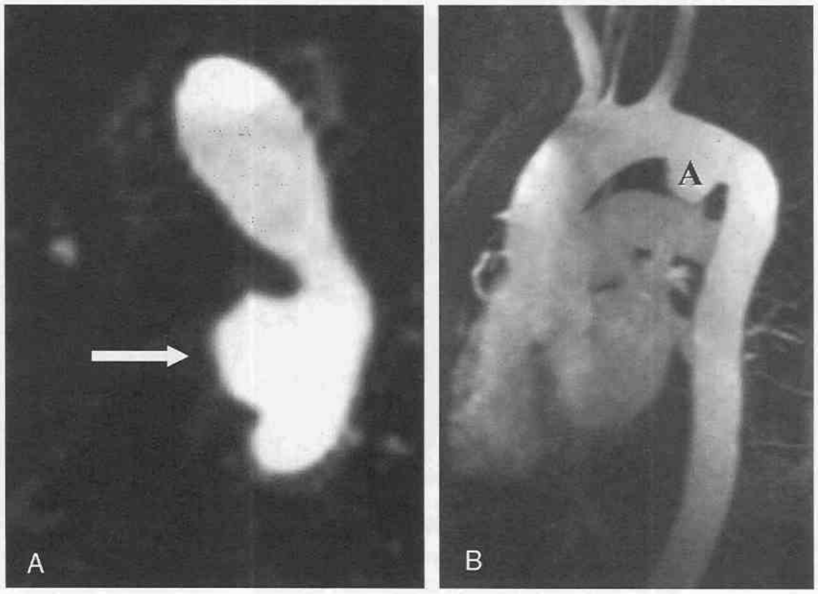

Figure 31–47. *A*, Axial gadolinium-enhanced MR image shows focal outpouching from proximal descending aorta. *B*, Sagittal oblique MR image with gadolinium enhancement of the aorta shows a chronic pseudoaneurysm at the level of the ductus arteriosus. A = aneurysm.

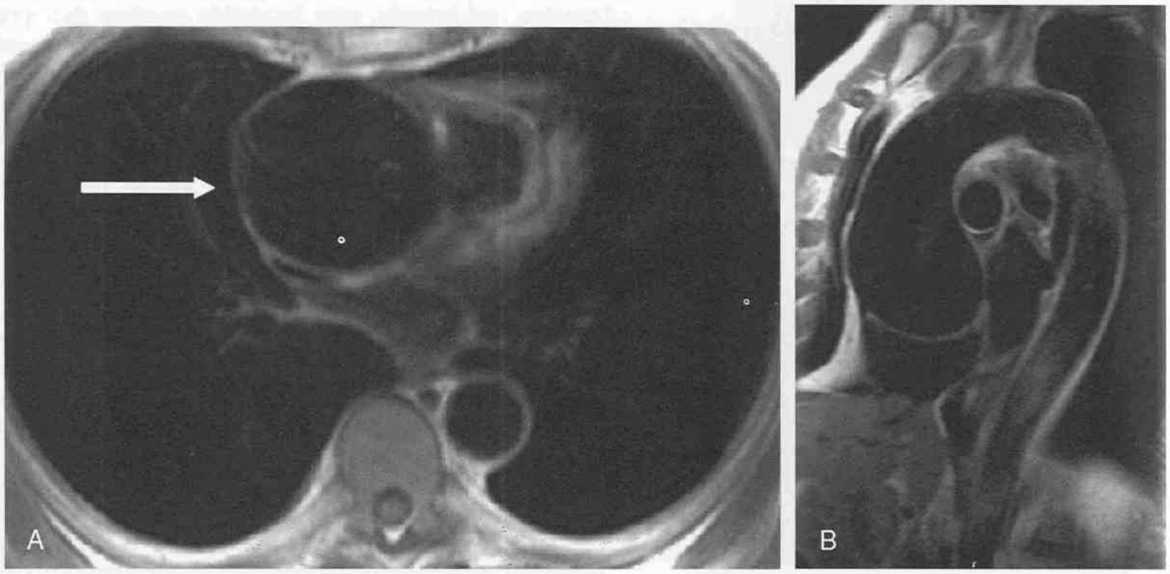

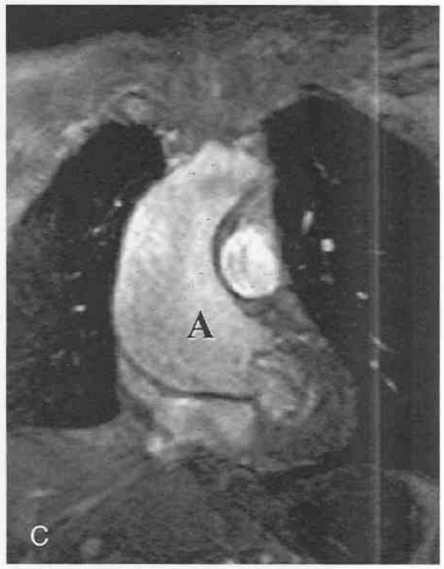

Figure 31–48. *A*, Axial T1-weighted MR image shows marked dilatation of the ascending aorta (*arrow*). *B*, Sagittal oblique T1-weighted MR image of the thoracic aorta shows dilatation of the ascending aorta with effacement of the sinuses of Valsalva. *C*, Coronal cine gradient-recalled echo MR image of the ascending aorta shows dilatation of the ascending aorta without significant valvular insufficiency.

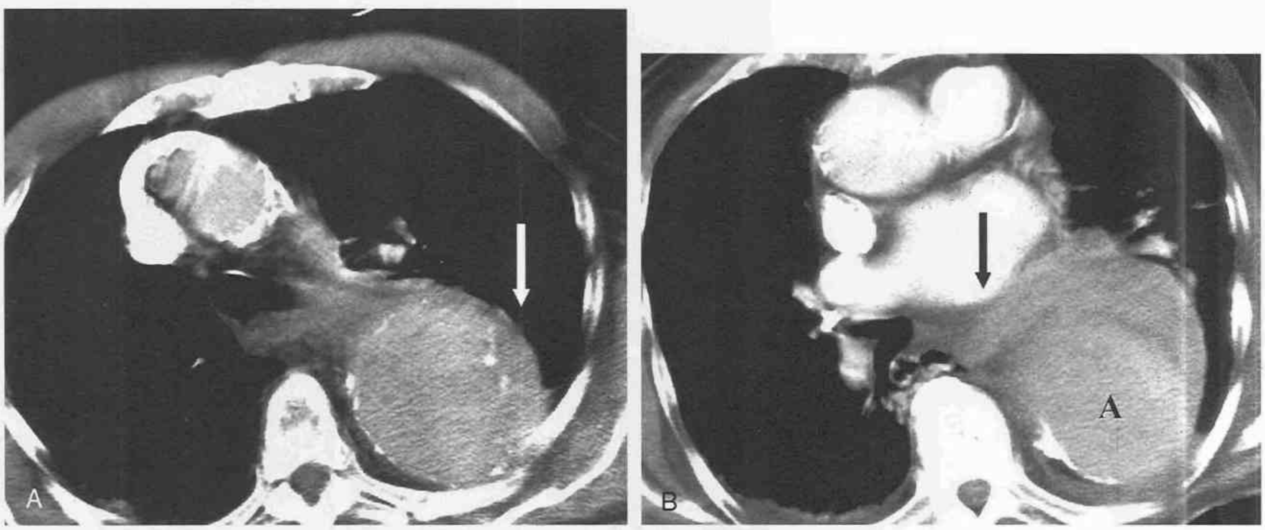

Figure 31–49. *A*, Axial CT scan shows leaking descending aortic aneurysm, with soft tissue extending beyond the mural calcification (*arrow*). *B*, Axial CT scan at a level inferior to that in *A* shows extension of the leak into the mediastinum (*arrow*).

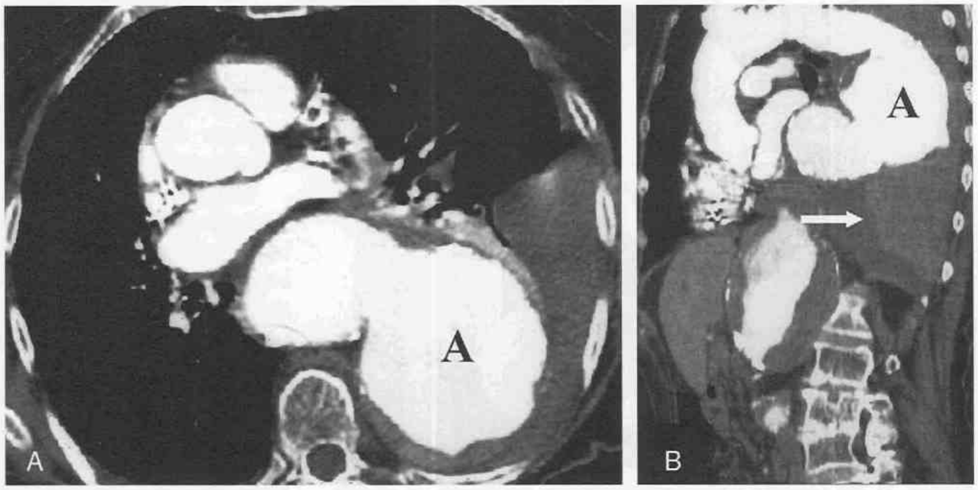

Figure 31–50. *A*, Axial multislice CT scan in a patient with a leaking aortic aneurysm (A). *B*, Sagiittal oblique multislice CT scan shows a large aneurysm (A) and dependent high-density pleural fluid consistent with acute hemorrhage (*arrow*).

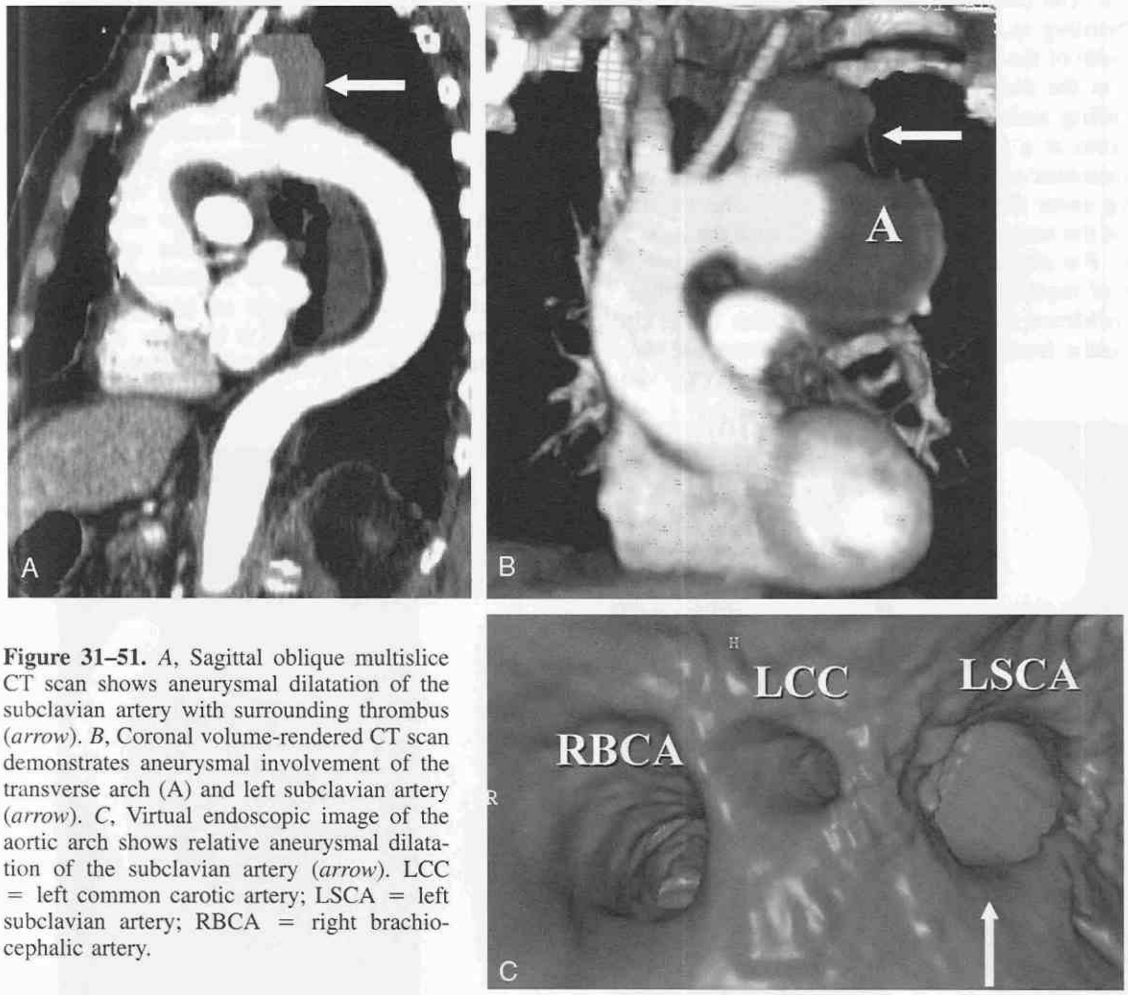

Figure 31–51. *A*, Sagittal oblique multislice CT scan shows aneurysmal dilatation of the subclavian artery with surrounding thrombus (*arrow*). *B*, Coronal volume-rendered CT scan demonstrates aneurysmal involvement of the transverse arch (A) and left subclavian artery (*arrow*). *C*, Virtual endoscopic image of the aortic arch shows relative aneurysmal dilatation of the subclavian artery (*arrow*). LCC = left common carotid artery; LSCA = left subclavian artery; RBCA = right brachiocephalic artery.

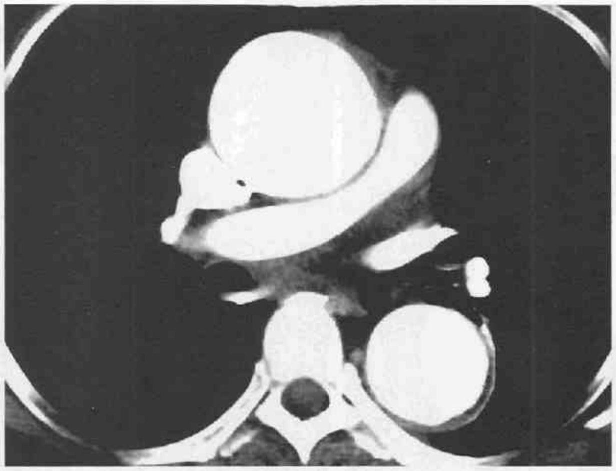

Figure 31–52. Axial CT scan demonstrates an aneurysm of the ascending aorta in a patient presenting with acute chest pain.

be concluded solely from the measurement of aortic circumference. The circumference of the aorta varies significantly according to the size, sex, and age of the patient and the width of the thoracic vertebral body.[49] For practical purposes, in the diagnosis of a thoracic aortic aneurysm, the descending aorta should never be larger than the ascending aorta at a given scan level, and the ratio of the coronal diameter of the ascending aorta to that of the descending aorta should be about 1.5:1.[49] The maximum diameter of the aneurysm correlates well with the incidence of rupture. For aneurysms less than 5 cm in diameter, the incidence of rupture is 2%; for aneurysms larger than 10 cm, the incidence of rupture is greater than 50%. Up to 50% of deaths from thoracic aortic aneurysms are caused by rupture.[33, 94] A leaking or ruptured thoracic aortic aneurysm creates extensive tissue density from mediastinal hematoma and, occasionally, a left pleural effusion (see Fig. 31–50). Rarely, contrast material can be seen beyond the confines of the aortic wall on bolus-injected, contrast-enhanced CT scans.

The advent of helical CT scanners and the use of CT angiography have made diagnosis and characterization of aortic aneurysms easier and more accurate and have also enabled highly accurate differentiation of other diseases of the aorta.[13, 97] In contrast to conventional CT, CT angiography provides an overall picture of the aneurysm; the use of MPR, MIP, and true 3D SSD images permits very precise measurement of the maximum diameter of the aneurysm.[13] In addition, the use of thin beam collimation and maximum vascular enhancement during a single breath-hold sequence allows the extent of the aneurysm to be delineated accurately with respect to the major aortic branches.[140] CT angiography also preserves the advantages of conventional CT—demonstrating extraluminal disease and the relationship of the aneurysm to adjacent organs.

Thoracic aortic aneurysms are also easily identified with MRI.[25, 37, 72, 83, 138] MRI can identify aneurysms involving the ascending aorta, aortic arch, and the descending aorta (Fig. 31–54).[37, 138] The technique readily depicts vascular structures because of a naturally occurring contrast between the low signal intensity of flowing blood and the higher signal intensity of the vessel walls. MRI has several advantages over CT. The first is MRI's multiplanar capability, which makes characterization of the aneurysm and determination of arch vessel involvement easier. The second is that CT requires injection of iodinated contrast medium but MRI does not; this is an important consideration in patients who either have a baseline impairment in renal function or are at risk for contrast medium–induced renal

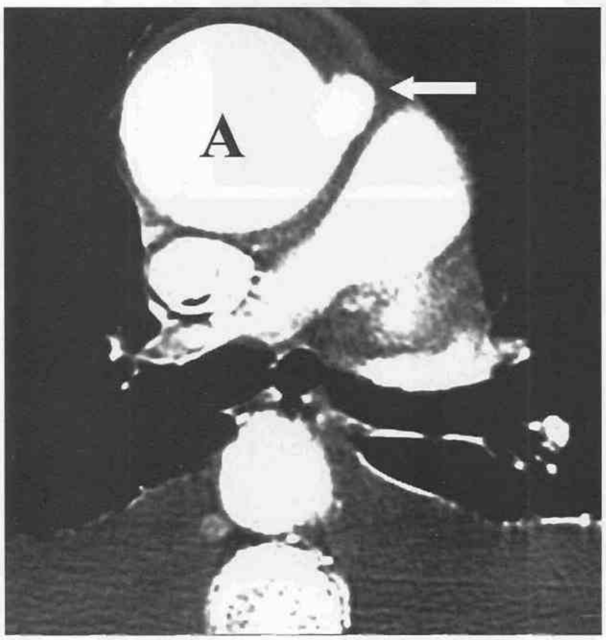

Figure 31–53. Axial CT scan shows an aneurysm in the ascending aorta with an active leak (*arrow*). The patient presented with hemorrhagic pleural effusion and died the next day. A = ascending aorta.

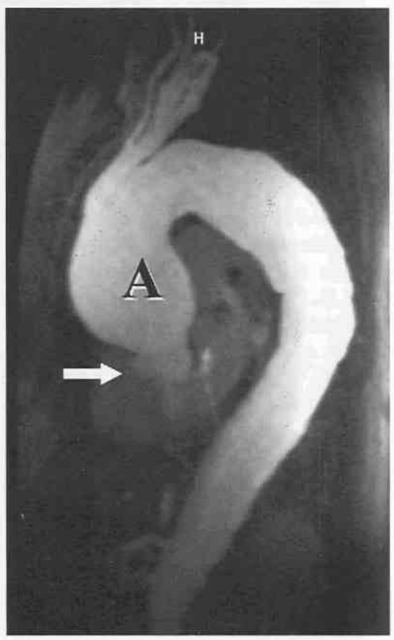

Figure 31–54. Sagittal oblique gadolinium-enhanced MR image shows aneurysmal dilatation of the ascending aorta (A) with sparing of the sinuses of Valsalva (*arrow*).

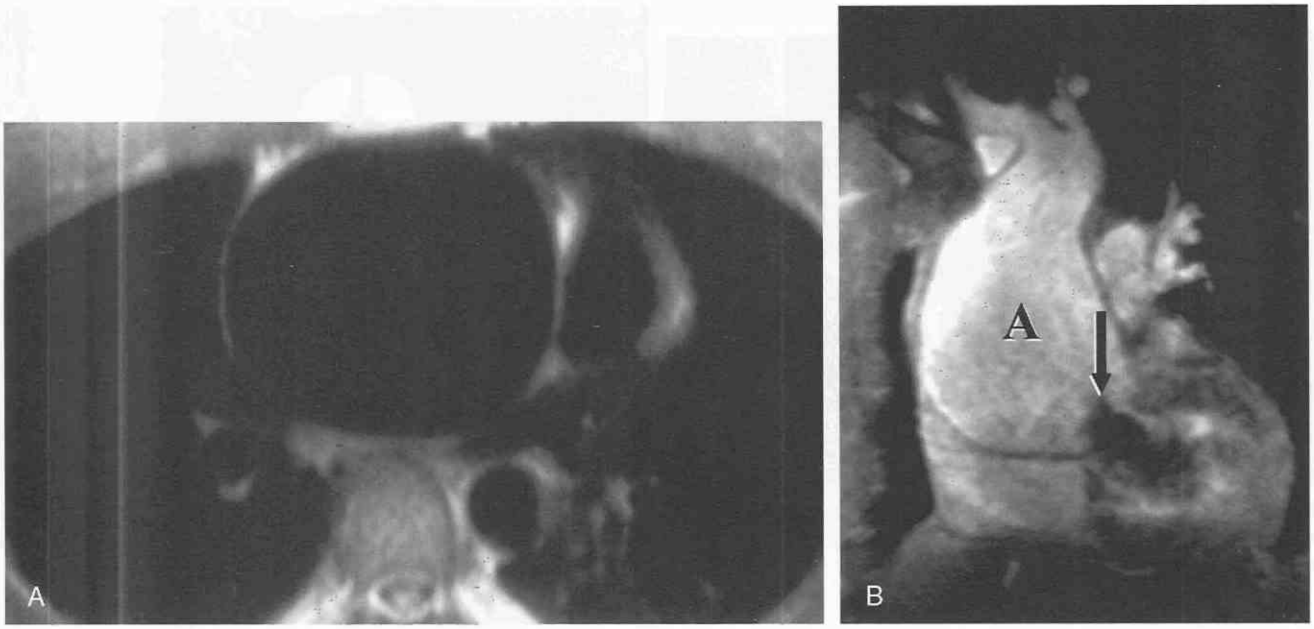

Figure 31–55. *A*, Axial ECG-gated, T1-weighted MR image of the ascending aorta shows marked dilatation of the ascending aorta in a patient with Marfan's syndrome. *B*, Coronal cine gradient-recalled echo MR image of the aorta of the same patient demonstrates a prominent ascending aorta (A) with effacement of the sinuses of Valsalva. There is significant aortic insufficiency, demonstrated by the large area of signal loss/dephasing at the level of the aortic valve (*arrow*).

failure. MRI also provides information on relative blood flow that CT cannot (Fig. 31–55).[35] The limitations of MRI compared with CT include inferior spatial resolution, the inability to ensure that the entire region of interest is imaged in one section, a failure to detect calcifications, and difficulty monitoring critically ill patients.[35] In addition, patients with cardiac pacemakers and some prosthetic cardiac valves and angiographic stents are precluded from undergoing MRI examinations because of the high field strength of the MRI magnet.

Rapidly flowing blood appears on MRI as a signal void on first-echo images, emitting little or no signal, but demonstrates a relative increase in signal intensity on second-echo images. In contradistinction, thrombus within the aortic lumen, when present, demonstrates a relative decrease in signal intensity on second-echo images.[4, 27, 133] These characteristics allow precise measurements of the diameter of thoracic aortic aneurysms and nearly exact correlation with the same measurements obtained on CT.[37] As stated previously, the ability to image in multiple planes with MRI allows accurate characterization of the extent of an aneurysm to determine whether it involves the origins of the arch vessels. Finally, MRI, like CT, is useful in providing information concerning the relationship between aneurysms and the surrounding mediastinal structures, and MRI has been reported to be ideal for detecting mediastinal hematoma, a secondary sign suggesting rupture of the aneurysm.[7]

Thoracic Aortic Dissection

Acute aortic dissection is a true medical emergency that must be recognized promptly and diagnosed accurately. The mortality rate in untreated patients is reported to be approximately 25% during the first 24 hours, 70% during the first 2 weeks, and 90% after 2 weeks.[21, 52] Dissection occurs from a tear in the wall of the aorta with subsequent hemorrhage of blood into the media, creating a second or false lumen. This false lumen is usually located between the inner one third and outer two thirds of the media, rarely involving more than half the circumference of the aorta.[101] By far the condition most commonly predisposing to aortic dissection is systemic hypertension. Other, less common conditions are Marfan's syndrome, Ehlers-Danlos syndrome, pregnancy, syphilis and other causes of aortitis, and coarctation.[101]

The Stanford classification of aortic dissections into two types directly related to prognosis and therapy has become generally accepted.[101] Type A dissections involve the ascending aorta, account for 60% to 70% of dissections, and usually arise within a few centimeters of the aortic valve. Without treatment, type A dissections are virtually always fatal, and death usually results from extension to and involvement of the aortic valve ring and ostia of the coronary arteries, which produces aortic valvular incompetence and left heart failure.[101] Type B dissections involve the descending thoracic aorta, most commonly arising just distal to the origin of the left subclavian artery near the insertion of the ligamentum arteriosum. Classically, type B dissections do not carry the risk of proximal extension and are, therefore, best treated medically with blood pressure reduction. If the dissected segment of the aortic becomes aneurysmally dilated with time, however, surgical intervention may be needed.[101]

The 3-year mortality rates for both surgically and medically treated thoracic aortic dissections are approximately 21% for Stanford type A dissections and 29% for type B

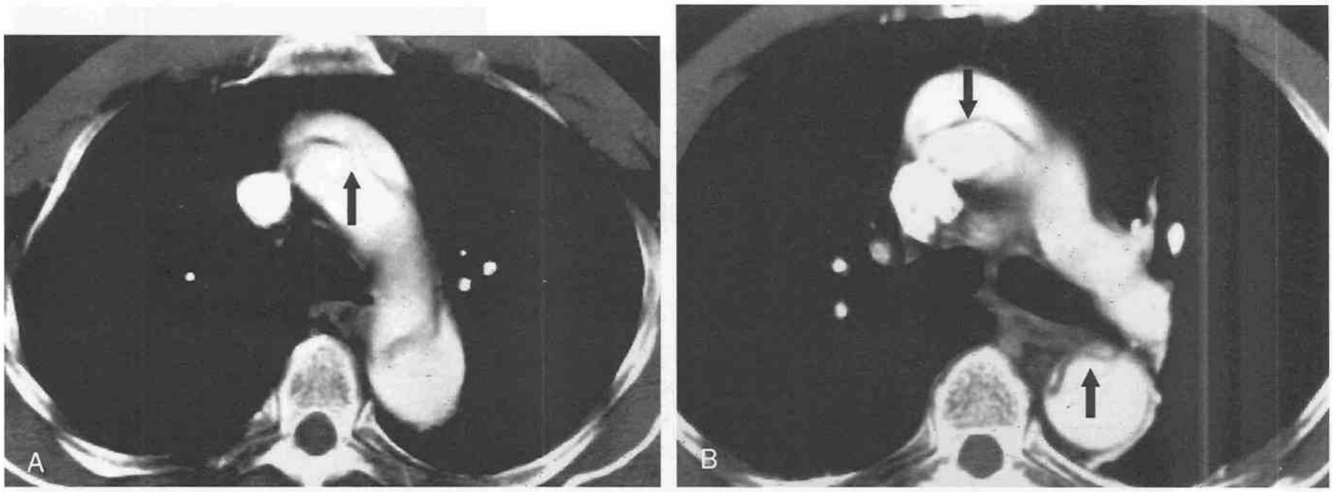

Figure 31–56. *A*, Axial CT scan shows type A aortic dissection with the dissection flap in the aortic arch (*arrow*). *B*, Axial CT scan at a level inferior to that of *A* reveals that the dissection flap involves the ascending aorta (*top arrow*). The true lumen is compressed anteriorly (*bottom arrow*).

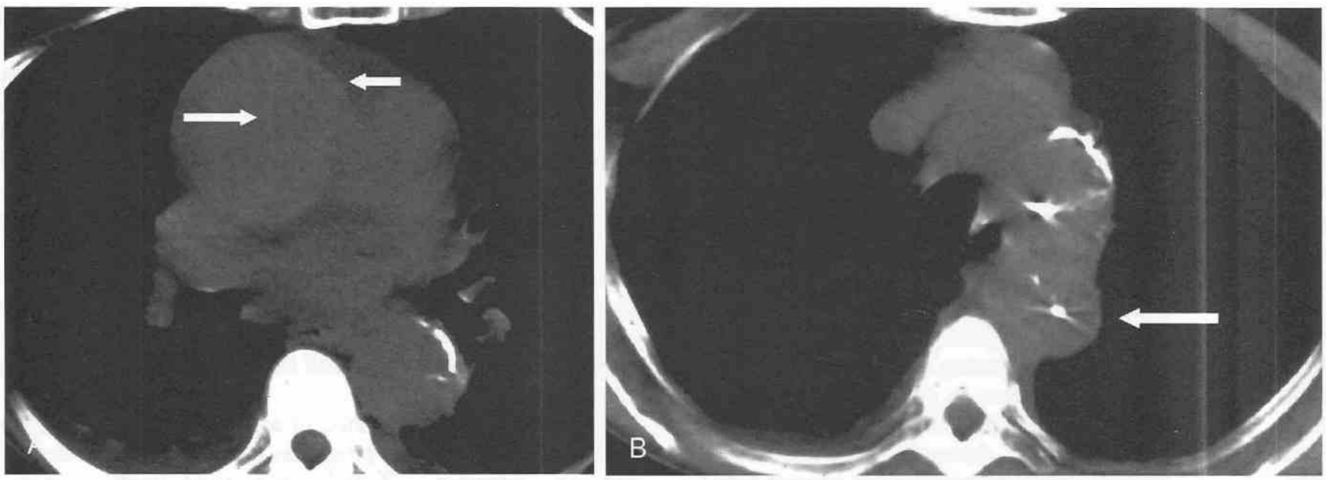

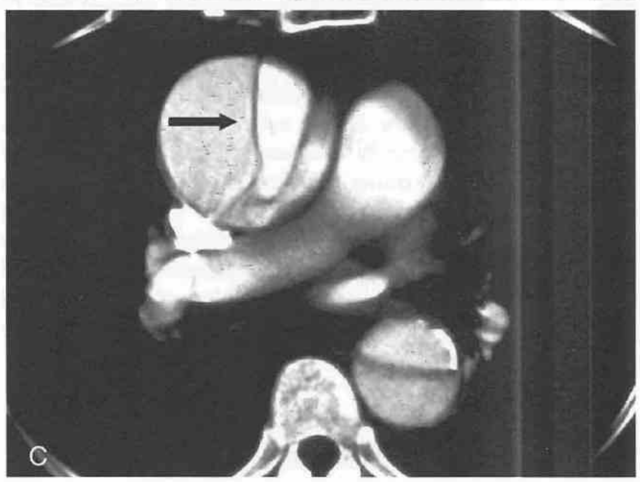

Figure 31–57. *A*, Axial noncontrast CT scan of the aorta shows the line of height attenuation (*long arrow*) in an aneurysmal ascending aorta. There is also a rim of high attenuation along the lateral aortic wall (*short arrow*). *B*, Axial CT scan at a level superior to that of *A* demonstrates medial displacement of aortic calcification (*arrow*). *C*, Contrast-enhanced axial CT scan shows the dissection flap of type A dissection of the thoracic aorta (*arrow*).

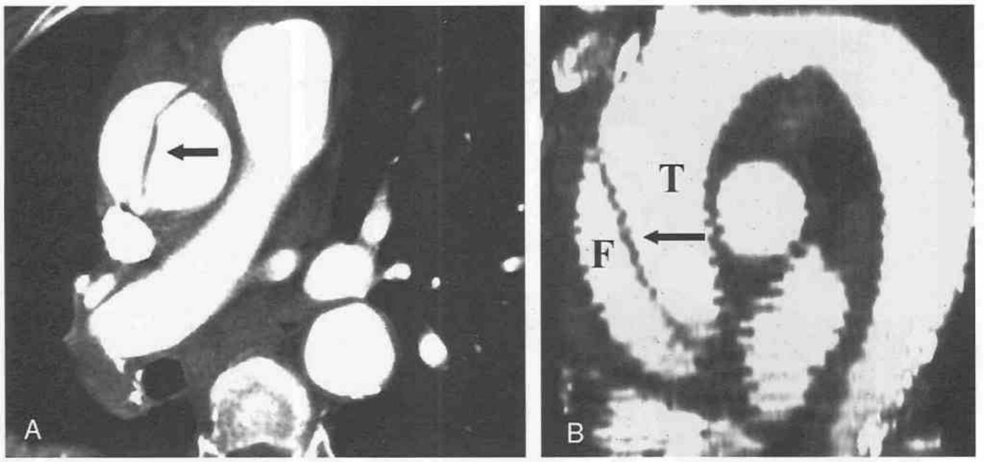

Figure 31–58. *A*, Axial CT scan shows type A dissection flap (*arrow*). *B*, Sagittal oblique multiplanar reconstruction demonstrates the dissection flap (*arrow*) demarcating the false lumen (F) from the posterior true lumen (T).

dissections.[124] Long-term prognosis depends on the development of complications, which mainly consist of new or progressive dissection and dilatation and subsequent rupture of the false lumen.[22]

Although the findings are nonspecific, chest radiographs are frequently abnormal in patients with thoracic aortic dissections.[54] Progressive widening of or progressive changes in the configuration of the aorta on sequential radiographs are highly suspicious for dissection. Unexplained differences in sizes between the ascending and descending portions of the aorta are also suspicious. As with aortic aneurysms, the trachea and esophagus may be displaced. Signs of a left pleural effusion, an apical pleural cap, and paraspinal widening may indicate leakage from a dissection. In addition, enlargement of the cardiac silhouette or plain film evidence of acute left heart failure may be secondary to aortic insufficiency from a type A thoracic aortic dissection. Although found in only a minority of patients, the most specific plain film finding in aortic dissection is displacement of intimal calcification from the outer margin of the aorta by at least 4 to 5 mm.[54]

CT has proved to be a highly reliable modality for diagnosing or excluding aortic dissection (Fig. 31–56).[48, 57, 128] Unlike for aortic aneurysms, however, diagnosis and characterization of thoracic aortic dissection requires both noncontrast and contrast-enhanced scanning.

The diagnosis of aortic dissection can be made from noncontrast scans that demonstrate a crescentic area of increased attenuation within the wall of the aorta, a sign that has been reported to be present in 44% of cases.[47, 137] This finding is believed to represent intramural hemorrhage from rupture of the vasa vasorum without an intimal tear.[137] Other findings have also been described on noncontrast scans. Displaced intimal calcifications are frequently encountered; however, this finding can create a problem if one is trying to differentiate between chronic thrombosed dissections and displaced intimal calcifications from aortic aneurysms with calcifications within thrombi (Fig. 31–57).[47, 74, 129] Rarely, in severely anemic patients, the intimal flap itself can be visualized within the aortic lumen.[23]

After administration of a contrast medium, diagnosis of aortic dissection is made on CT scans that demonstrate two opacified channels separated by an intimal flap.[39, 44, 48, 70] The two lumens are reported to be visible in at least 75% of symptomatic patients with acute aortic dissection. Within the ascending aorta, the false lumen is usually anterior (Fig. 31–58), whereas in the descending aorta, it is usually posterolateral.[70] Other, ancillary findings are less sensitive but have been reported; they include differential flow through the two lumens (Fig. 31–59), an increase in the size of the aorta, and the presence of hemopericardium.[76]

The standard for diagnosis of aortic dissections has long been angiography. However, numerous reports comparing the efficacy of CT with angiography in diagnosing aortic dissections have shown CT to be highly accurate. In most reports, the accuracy of CT compares favorably with that of angiography, including documented cases in which the diagnosis was made only with CT.[87, 104, 128] However, in a small percentage of patients with acute aortic dissection, false-negative CT findings do occur.[88, 66, 19] In addition, in a small percentage of patients with acute aortic dissection, the false channel is thrombosed and does not opacify with administration of contrast medium. This thrombosis of the false channel may represent bleeding into the wall of the aorta from rupture of the vasa vasorum without an intimal

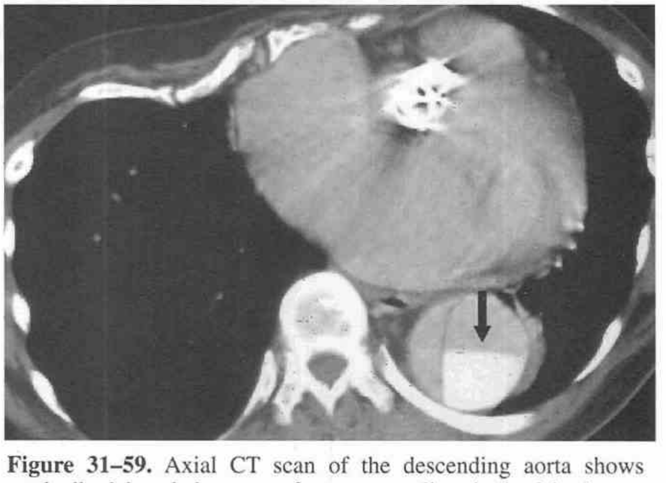

Figure 31–59. Axial CT scan of the descending aorta shows markedly delayed clearance of contrast medium in the false lumen (*arrow*) in a patient with Marfan's syndrome and type B dissection.

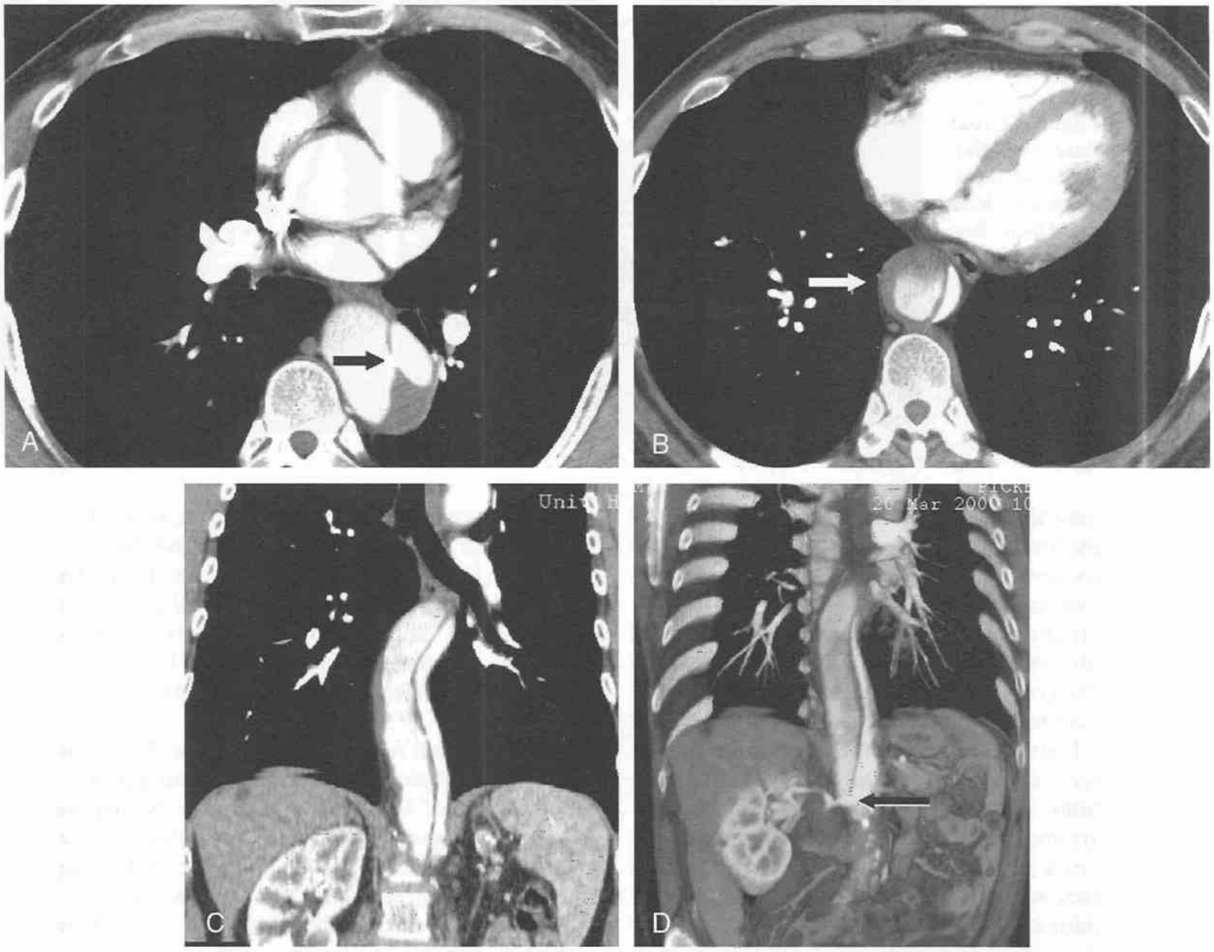

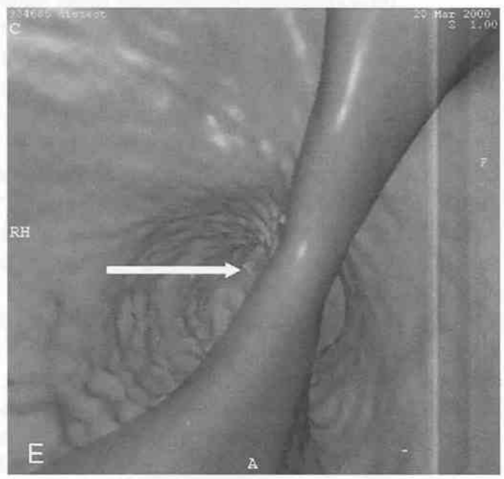

Figure 31–60. *A*, Axial multislice CT scan shows type B dissection. The entry point of the dissection is clearly delineated (*arrow*). *B*, Axial multislice CT scan at a level inferior to that of *A* shows slower flow in the larger false lumen (*arrow*). *C*, Coronal multiplanar reconstruction clearly demonstrates the extent of dissection. Note the lack of pulsation artifact in this multislice CT scan. *D*, Coronal multislice CT scan with volume rendering shows that the dissection flap extends just superior to the takeoff of the right renal artery (*arrow*). *E*, Virtual endoscopic image of the descending aorta shows the dissection flap (*arrow*) separating the true and false lumens.

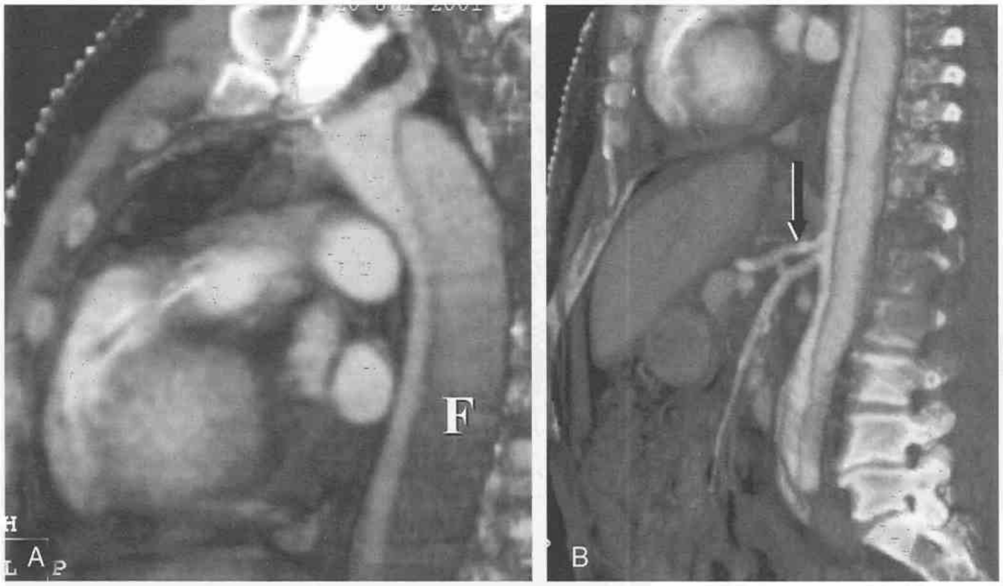

Figure 31–61. *A*, Sagittal oblique volume-rendered, multislice CT scan demonstrates a compressed true lumen with slow flow through the posterior false lumen (F). *B*, Sagittal oblique multislice CT scan shows the smaller true lumen giving rise to the celiac axis (*arrow*) and superior mesenteric artery.

tear. The false lumen is thrombosed more frequently, however, in subacute and chronic dissections. The overall accuracy of CT in diagnosing or excluding aortic dissection exceeds 90%, thereby ensuring its role as a primary modality in the assessment of thoracic aortic dissection.

The advent of helical CT scanners and CT angiography in particular further enhances the role of CT in the diagnosis or exclusion of thoracic aortic dissection. CT angiography can demonstrate the dissection flap more clearly than conventional CT, because scans are obtained during maximal arterial enhancement of the aorta and image reconstructions are thinner in section thickness. Therefore, the origin of the dissection flap as well as major aortic branch involvement can be evaluated in a larger proportion of patients by means of CT angiography (Figs. 31–60 and 31–61).[13] Also, multiplanar and 3D images allow an overall view of the dissection and clarify the anatomic relationship between the dissection flap and the adjacent great vessels, similar to the multiplanar capability of MRI. These advantages were demonstrated in a report by Chung and colleagues,[13] in which no false-positive or false-negative CT angiography findings were obtained in a series of 49 patients with suspected aortic dissection. However, unlike MRI, CT angiography has limitations in the evaluation of coronary artery involvement and aortic regurgitation.[13] Another limitation of CT angiography is that an unopacified false lumen from a short scanning delay time with slow filling of contrast medium can be confused with a thrombosed false lumen.

MRI can generally provide a definitive diagnosis of aortic dissection by demonstrating the two lumens and the intimal flap between them, similar to the criteria for CT.[3, 26, 35, 37] The intimal flap appears as a linear structure of intermediate signal intensity separating the true lumen from the false lumen (Figs. 31–62 and 31–63). Flow characteristics within the two lumens can generally be demonstrated by MRI (Fig. 31–64). Characteristically, significant bright signal within what is presumed to be the false lumen is seen on second-echo sequences because of the presence of slow flow within the false lumen.[26, 27, 37, 133] In reality, however, accurate differentiation between the true and false lumens may not be possible, because flow within the anatomic false lumen may exceed flow within the compressed residual true lumen. In addition, identification of the site of the intimal tear is most often not possible.[37, 133] Blood within the mediastinum is readily visible on MRI, demonstrating the presence of periaortic hematoma. Also, blood within the pericardial sac can be recognized, indicating leakage from the false lumen.[3, 26]

The accuracy of MRI for the diagnosis of aortic dissection has been well established. Radiologists with experience reading MRI sequences have approximately a 95% sensitivity and 90% specificity for detecting aortic dissection.[63] In addition, CT and MRI have proved comparable in the ability to identify or exclude aortic dissection; the sensitivity of MRI has been found to range from 84% to 96%, depending on the series.[3, 35, 37, 63] Several pitfalls in interpretation of MR images of the thoracic aorta for dissection are known.[119, 136] Fluid within the superior pericardial recess can mimic aortic dissection. Less commonly, unusual origins of the arch vessels, an unusual position of the left brachiocephalic vein, motion artifacts, and aortic plaques can all mimic dissection.

MRI also has proved value in evaluating the results of aortic repair.[92, 135] After surgery for aortic dissection, MRI can detect either anastomatic leaks or aneurysmal dilatation distal to the graft site. The modality can also provide useful information about the status of the residual false lumen, which often remains patent after repair.

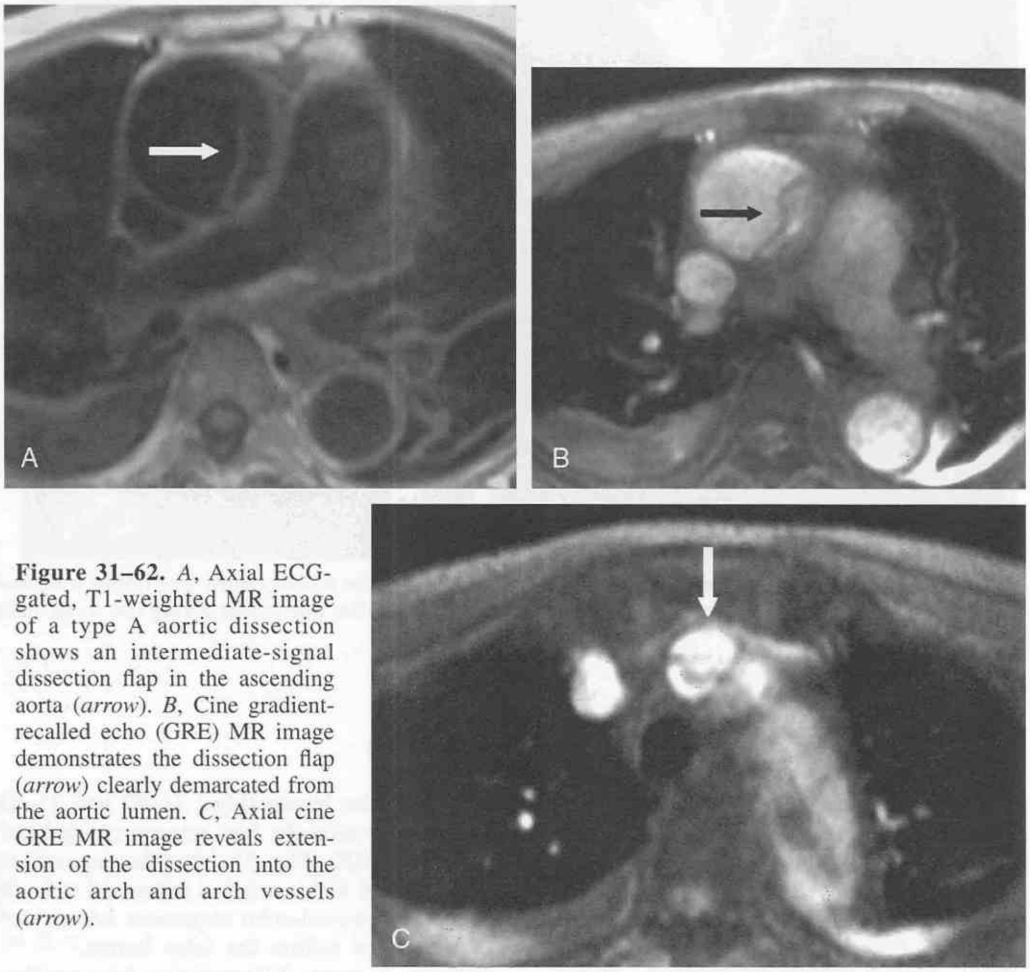

Figure 31–62. *A*, Axial ECG-gated, T1-weighted MR image of a type A aortic dissection shows an intermediate-signal dissection flap in the ascending aorta (*arrow*). *B*, Cine gradient-recalled echo (GRE) MR image demonstrates the dissection flap (*arrow*) clearly demarcated from the aortic lumen. *C*, Axial cine GRE MR image reveals extension of the dissection into the aortic arch and arch vessels (*arrow*).

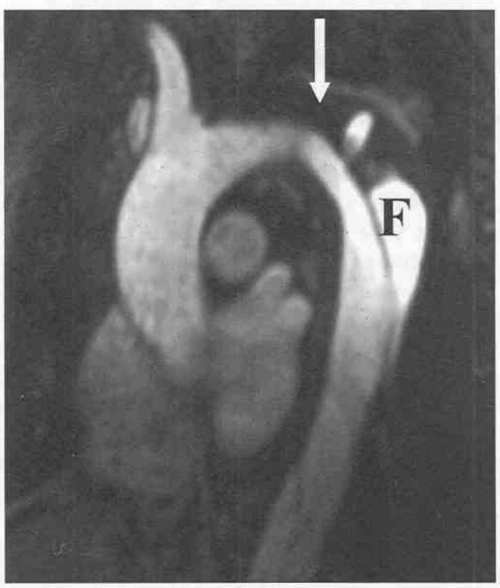

Figure 31–63. Gadolinium-enhanced sagittal oblique multiplanar reconstruction shows the dissection flap and clear demarcation of the true lumen and false lumen (F). Thrombus associated with the false lumen is well delineated (*arrow*).

Thoracic Aortic Trauma

Acute traumatic aortic injury is responsible for 10% to 20% of fatalities resulting from high-speed deceleration trauma (passengers or pedestrians involved in motor vehicle, airplane, and boat accidents and in high falls) and crush injuries to the chest.[20, 41, 65, 66, 90, 117, 122] Eighty percent to 90% of patients involved in high-speed deceleration accidents die before reaching the hospital. Of patients with untreated aortic injury, 30% die within 6 hours, 40% to 50% die within 24 hours, and 90% die within 4 months.[90] Chronic post-traumatic false aneurysms, or pseudoaneurysms, develop in 2% to 5% of patients with undiagnosed acute traumatic aortic injury (Figs. 31–65 and 31–66).[30, 90, 108] Of the patients with thoracic aortic injury who reach the hospital alive, 60% to 70% survive; therefore, prompt and accurate diagnosis and surgical management are critical.[90]

Signs and symptoms of traumatic deceleration injury of the thoracic aorta include chest and midscapular back pain, dyspnea, external signs of chest trauma, hypotension, upper extremity hypertension, bilateral femoral pulse deficits, and a systolic ejection murmur.[67] In general, the injury is a transverse laceration through the aortic intima, ranging in size from less than 1 mm to a completely circumferential tear; however, the adventitia is intact in roughly 60% of

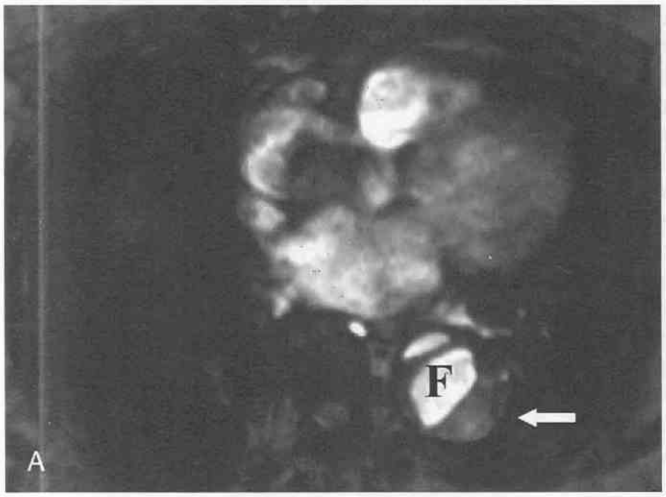

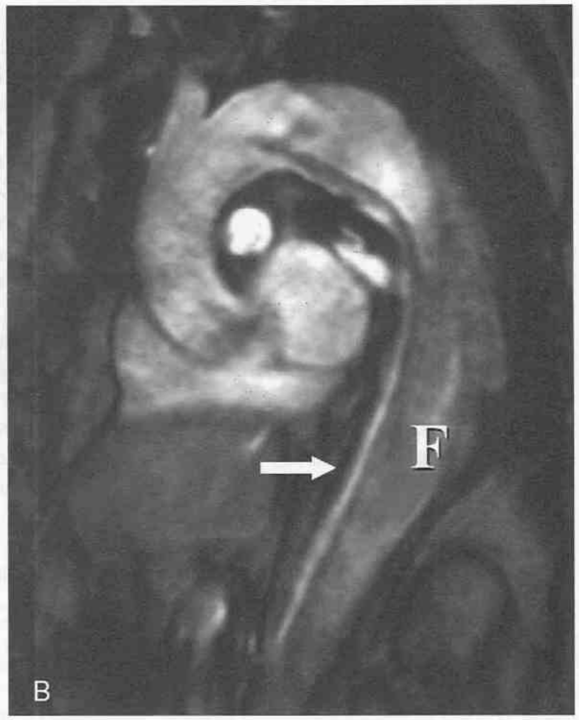

Figure 31–64. *A*, Axial cine gradient-recalled echo (GRE) MR image shows type B dissection, with a smaller, compressed true lumen and a posterior false lumen (F). *B*, Sagittal oblique cine GRE image in a patient with dissection shows bright signal in anterior true lumen, consistent with faster flow (*arrow*). F = false lumen. *Arrow* denotes thrombus surrounding the false lumen.

cases, a feature that aids the development of pseudoaneurysms that delay complete rupture.[90] No portion of the circumference of the aorta is known to be more at risk to injury than any other, but noncircumferential tears are more commonly posterior in the aorta.[90]

Ninety percent of thoracic aortic injuries occur within the proximal descending aorta at the level of the aortic isthmus, immediately distal to the origin of the left subclavian artery and just proximal to the site of attachment of the ligamentum arteriosum.[43] Thoracic aortic injury involving the ascending aorta is identified clinically in only 5% of cases; however, at autopsy, the ascending aorta is found to be the site of injury in 20% to 25% of cases.[43]

The mechanisms of injury, as stated before, involve high-speed deceleration and crushing forces to the chest, most commonly seen in motor vehicle and boat accidents, airplane crashes, and falls from great heights. The forces involved depend on the segment of the aorta affected. Shearing and bending forces affect the aortic isthmus.

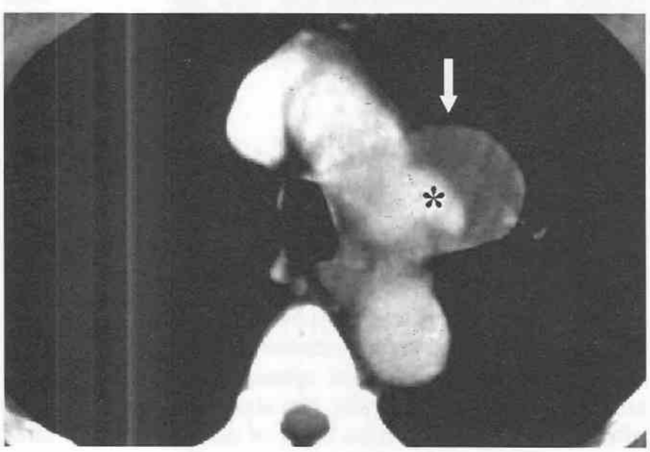

Figure 31–65. Axial CT scan in a patient with remote history of being kicked by a horse shows a large aortic pseudoaneurysm (*) and large amount of surrounding thrombus (*arrow*).

Figure 31–66. Axial CT scan shows a large calcified (*arrow*) aortic pseudoaneurysm (F) in a patient with a remote history of a high-speed motor vehicle accident.

somewhat mobile aortic arch differs from that of the relatively fixed descending aorta. Bending stress occurs as the aorta is flexed off the left pulmonary artery and mainstem bronchus.[10, 73, 112] One mechanism of injury within the ascending aorta is torsion, which occurs by displacement of the heart during impact and affects a region just above the aortic valve. The other mechanism involves the water-hammer effect, in which a sudden increase in intra-aortic pressure may lead to rupture of the ascending aorta into the pericardium and cardiac tamponade. Fractures of thoracic vertebral bodies are often associated with injuries involving the more distal descending aorta.[10, 73, 112]

Chest radiography is the front-line screening test for aortic injury, and abnormal findings on chest radiographs are the most common indication for further evaluation.[43] The anteroposterior projection with the patient in the supine position is most commonly performed and evaluated for signs of mediastinal hematoma, an indication of significant aortic injury. However, aortic trauma is the cause of mediastinal hematoma in only 12.5% of cases.[109] The most sensitive findings are widening of the mediastinum (>8 cm at the arch) and irregularity or obscuring of the aortic arch margin. However, although the sensitivity of these findings for aortic injury is high (around 80%), their specificity is no more than 50%.[91] The more specific signs (with specificities around 80%) include widening of the left paraspinal stripe and right-sided deviation of the trachea, esophagus, or both; however, the sensitivity for these signs is much lower.[91] Chest radiographs with a normal-appearing mediastinum have been documented in patients with known aortic injury.[14, 125] Therefore, chest radiographs are relatively insensitive in patients who have acute traumatic injury of the aorta but little or no mediastinal hemorrhage.

The low positive predictive value of chest radiography has dictated the performance of a large number of thoracic aortograms in the past. Aortograms have long been the reference standard in imaging the post-traumatic thoracic aorta, because of sensitivities approaching 100% and specificities of approximately 98%.[32] The positive predictive value of chest radiographs is low in the setting of aortic trauma. When chest radiography alone is used to screen for thoracic aortic injury, only 10% to 20% of thoracic aortograms are positive for aortic or aortic branch vessel injury.[78, 79] A more accurate and noninvasive screening test for thoracic aortic injury after blunt chest trauma is desirable.

Since its inception, CT has been investigated as a complementary examination for evaluation of traumatic aortic injury to reduce the number of negative aortograms.[17, 31, 34, 47, 75, 80, 81, 84, 100] Mirvis and associates[81] reported the clinical outcomes in 677 patients whose treatment was guided by findings on contrast-enhanced CT scans performed on a nonhelical, fourth-generation scanner. Aortography was performed when CT demonstrated either mediastinal hematoma or direct signs of vessel injury. This study reported a 90% sensitivity for CT, a 99% specificity, and a 90% positive predictive value, with no false-negative CT results. In addition, Gavant and colleagues[34] reported the clinical outcomes in 1518 patients who underwent CT for blunt chest trauma regardless of chest radiograph findings and whose treatment was based on the findings of contrast-enhanced helical CT scanning. Aortography was performed if CT demonstrated either mediastinal hematoma or direct vessel injury. In this study, CT had a 100% sensitivity, an 82% specificity, and a 47% positive predictive value for direct depiction of vessel injury, and no false-negative results were obtained. These findings support the inclusion of CT in the screening for traumatic aortic injury after blunt chest trauma.

Contrast-enhanced CT can be used to evaluate both indirect (mediastinal hemorrhage) and direct signs of aortic injuries. Mediastinal hemorrhage appears as either diffuse or focal soft tissue attenuation surrounding mediastinal structures, and the location of the blood has diagnostic significance. Hemorrhage in the vicinity of and surrounding the aorta and other vascular structures is more suggestive of vascular injury.[18] Direct signs of aortic injury are polypoid (clot) or linear (intimal flap) intraluminal areas of low attenuation, pseudoaneurysm, irregularity of the aortic wall, pseudocoarctation, intramural hematoma, dissection, and frank extravasation of contrast material (Fig. 31–67).[49, 80, 84]

Certain pitfalls make interpretation of CT scans difficult for thoracic aortic injury.[31, 45, 98] They include motion artifacts, partial volume averaging, and support devices. In addition, atelectatic lung (especially in the apical-posterior segment of the left upper lobe and superior segment of the left lower lobe) can mimic hemorrhage adjacent to the aorta. The thymus, pericardial recess, and unopacified vessels can also mimic blood. Knowledge of these common artifacts and mimics of mediastinal blood makes interpretation of scans more accurate.

MRI is a valuable tool for evaluation of the aorta in most trauma patients. Imaging time, incompatibility of MRI equipment with monitoring devices, and inaccessibility of the patient during the examination preclude the routine use and widespread acceptance of MRI in the evaluation of acute thoracic aortic injury.[15, 43, 77] Despite these limitations, several case reports have described MRI's ability to demonstrate acute thoracic aortic injury in awake, alert, and stable patients with no other injuries (Fig. 31–68).[15, 53] A study by Fattori and colleagues[28] concluded that MRI was accurate and reproducible for acute thoracic aortic injury compared with CT, angiography, or both in 24 patients with acute blunt chest trauma who did not undergo surgery. They also concluded that MRI provided complete anatomic data for assessing the severity of the aortic injury. It is the ideal modality for monitoring acute thoracic aortic injury prior to surgical repair.

Intramural Hematoma

The concept of the intramural hematoma was first described by Krukenberg. It describes blood within the wall of the aorta without identifiable intimal tear. Pathologically, intramural hemorrhage is defined as rupture of the vasa vasorum and propagation of subintimal hemorrhage, often secondary to a penetrating atherosclerotic ulcer. Isolated case reports have described spontaneous progression to aortic dissection.[68] Clinically, the signs and symptoms are often indistinguishable from those of dissection. Intramural hematoma progresses either by outward rupture of the aortic wall or by inward extension and formation of an intimal flap.[102]

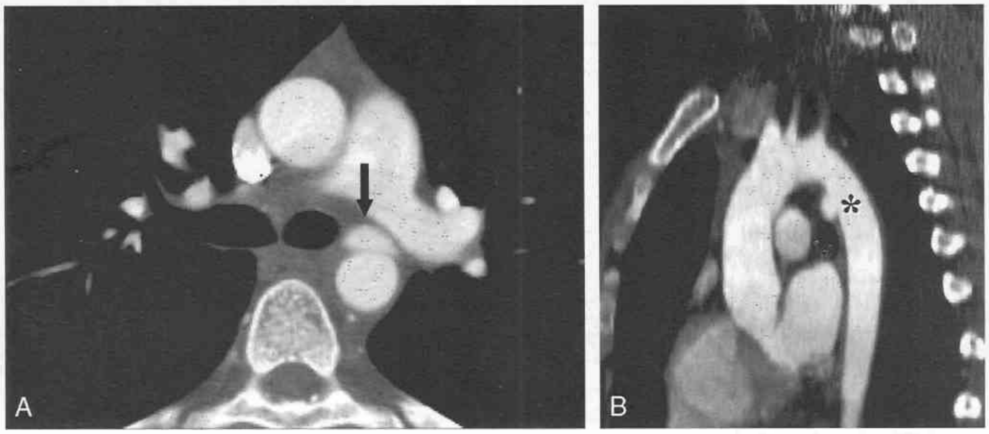

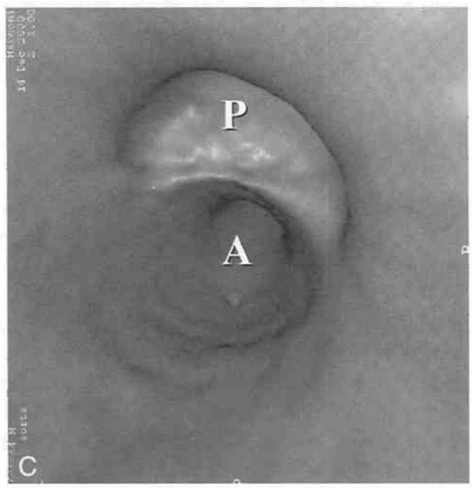

Figure 31–67. *A*, Axial CT scan in a patient who experienced a high-speed motor vehicle accident shows evidence of acute post-traumatic pseudoaneurysm (*arrow*). *B*, Sagittal multiplanar reconstruction demonstrates a focal pseudoaneurysm in the proximal descending aorta (*asterisk*). Note the acute angle of the pseudoaneurysm with the adjacent aorta, a feature that distinguishes it from a ductus diverticulum. *C*, Virtual endoscopic image demonstrates the focal nature of the post-traumatic pseudoaneurysm. P = pseudoaneurysm; A = native aortic lumen.

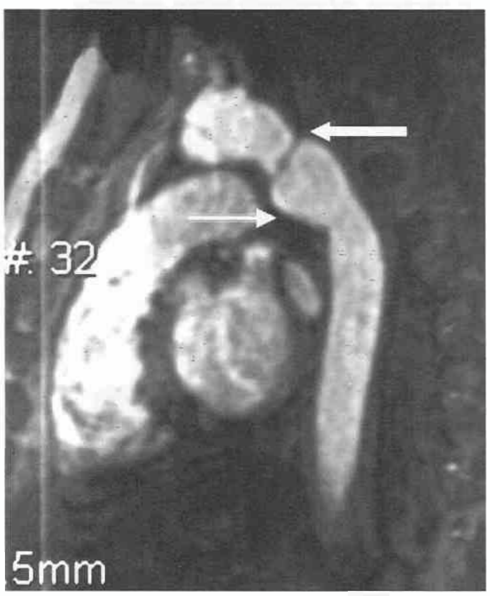

Figure 31–68. Gadolinium MR angiograph shows discrete post-traumatic pseudoaneurysm (*thin arrow*) with associated intimal flap (*thick arrow*) in a young man several months after a high-speed motor vehicle accident.

Distribution of intramural hematomas is equally divided between the ascending and descending portions of the aorta, with a small number occurring in the transverse arch. Studies have shown that the prognosis for patients with such hematomas is very similar to that for patients with aortic dissection. Intramural hematomas of the ascending aorta often progress to dissection, whereas those of the descending aorta progress less often to dissection or aneurysm formation (Fig. 31–69).[85] Our experience suggests that progression to aneurysm formation is more common in patients with descending intramural hematomas and that such patients should be followed more closely than patients with aneurysms of the descending aorta (Fig. 31–70).

The majority of intramural hematomas are the result of penetrating atherosclerotic ulcers (Fig. 31–71). First described as a distinct entity in the literature in 1986 by Stanson and associates,[120] atherosclerotic ulcers are defined by an abnormal outpouching of the contrast medium beyond the expected course of the aortic lumen.[71] Patients present clinically with chest or back pain, and the symptoms commonly mimic aortic dissection. Like dissection, intimal calcifications are displaced medially by the penetrating ulcer. There is an associated subintimal hematoma, and the spiraling flap seen in aortic dissection is absent. Penetrating atherosclerotic ulcers are generally located in the distal two thirds of the descending aorta. The penetrating ulcer can usually be distinguished from aortic dissec-

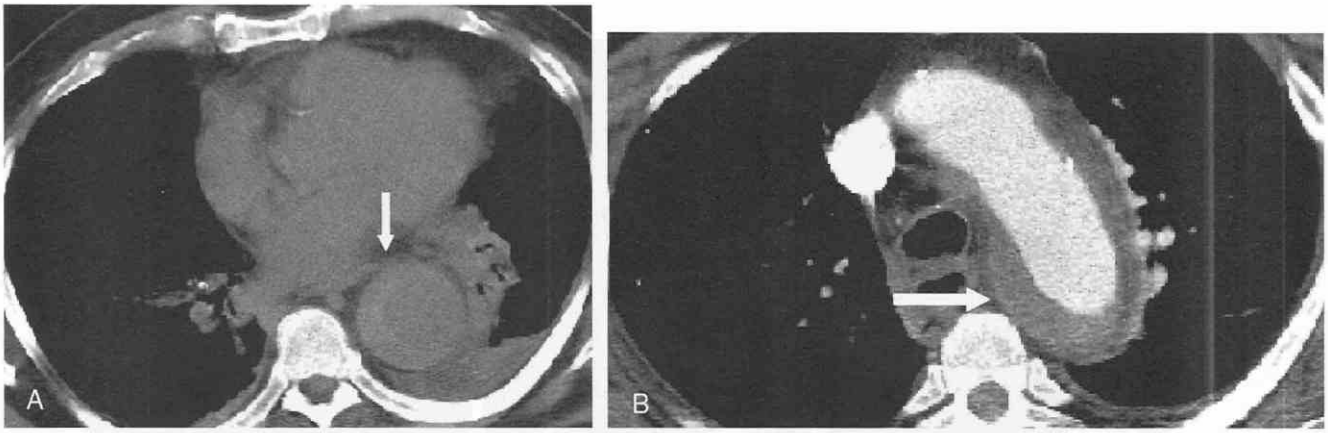

Figure 31–69. *A*, Axial noncontrast CT scan shows a rim of high attenuation of the aortic wall (*arrow*) in a patient with acute chest pain. *B*, Axial CT scan after administration of a contrast agent demonstrates diffuse periaortic soft tissue with high attenuation (*arrow*), a feature consistent with acute intramural hematoma.

tion because of the more focal, irregular nature of the defect, and the dissection flap is often smooth and well defined (Fig. 31–72).

There is controversy about the appropriate treatment of patients with penetrating ulcers. Many patients are first treated medically with antihypertensive medications. Patients for whom such treatment relieves pain and in whom the ulcer has a stable appearance on follow-up imaging can continue to be treated nonsurgically. In patients with continued pain or enlargement of the ulcerated area on follow-up imaging, surgical intervention is warranted (Fig. 31–73). Surgical treatment can be quite different; patients with atherosclerotic ulcers often require a longer interposition graft, whereas those with dissections need a shorter graft at the site of the intimal tear.[16]

Atheroembolic Disease of the Aorta

Appreciation of the importance of aortic atherosclerosis has grown with our increasingly aggressive treatment of cerebrovascular disease. Until the 1990s, close to 40% of cerebrovascular events were classified as "cryptogenic." With the advent of transesophageal echocardiography, the importance of atheroembolic disease of the aorta has become more recognized. Retrospective studies showed that in patients with cerebrovascular accidents, the incidence of aortic atheromas was 20% to 27%,[130] compared with 5% in control subjects. Research showed that aortic plaque size determined risk, with plaques larger than 4 mm resulting in an odds ratio of 13.8 for the incidence of cerebrovascular events (Figs. 31–74 and 31–75). The absence of calcification was a poor prognostic feature, indicating those plaques most likely to embolize. Reports now suggest that CT and MRI may be complementary modalities in the detection of these atheroemboli, particularly in areas of the aortic arch where the tracheal air column limits evaluation with transesophageal echocardiography.[127] Multislice CT will continue to improve the sensitivity of CT scanning for the diagnosis of atheroembolic disease. Newer imaging techniques will prove to be of added benefit in the diagnosis and characterization of these vulnerable plaques.

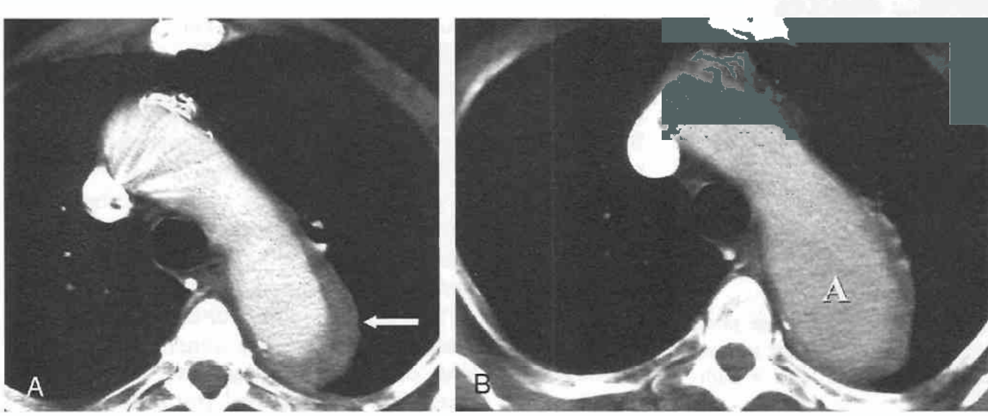

Figure 31–70. *A*, Axial CT scan in a patient with acute back pain. There is a large amount of high-attenuation periaortic soft tissue (*arrow*), a feature consistent with intramural hematoma. *B*, Axial CT scan taken 2 months later shows a rapid increase in the diameter of the descending aorta (A).

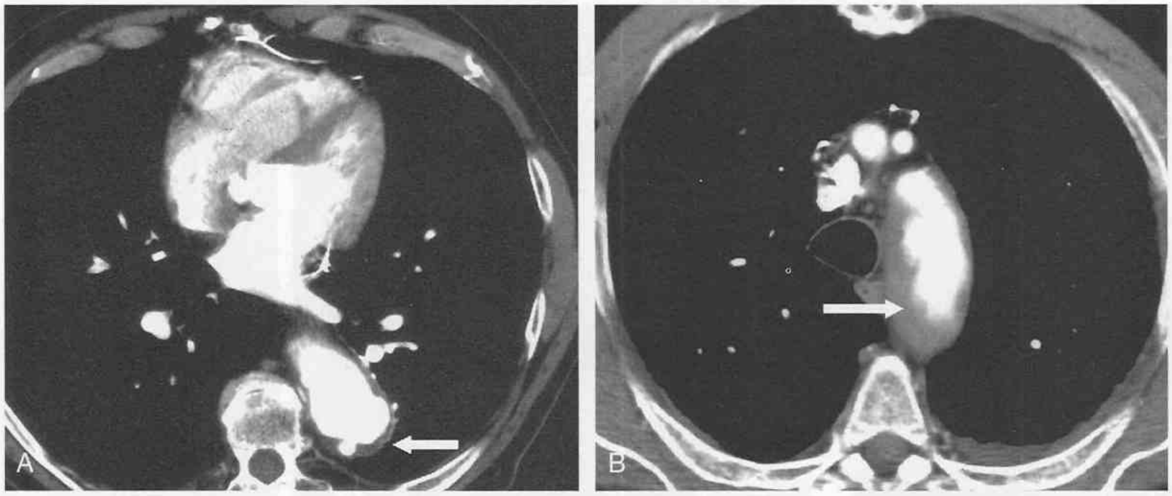

Figure 31–71. *A*, Axial CT scan in a patient with acute back pain and suspected aortic dissection. Note the focal ulceration in the descending aorta (*arrow*). *B*, Axial CT scan at the level of the aortic arch shows high-attenuation periaortic soft tissue (*arrow*), a finding consistent with intramural hematoma. *C*, Axial CT scan obtained 2 months later demonstrates a marked increase in the diameter of the descending aorta.

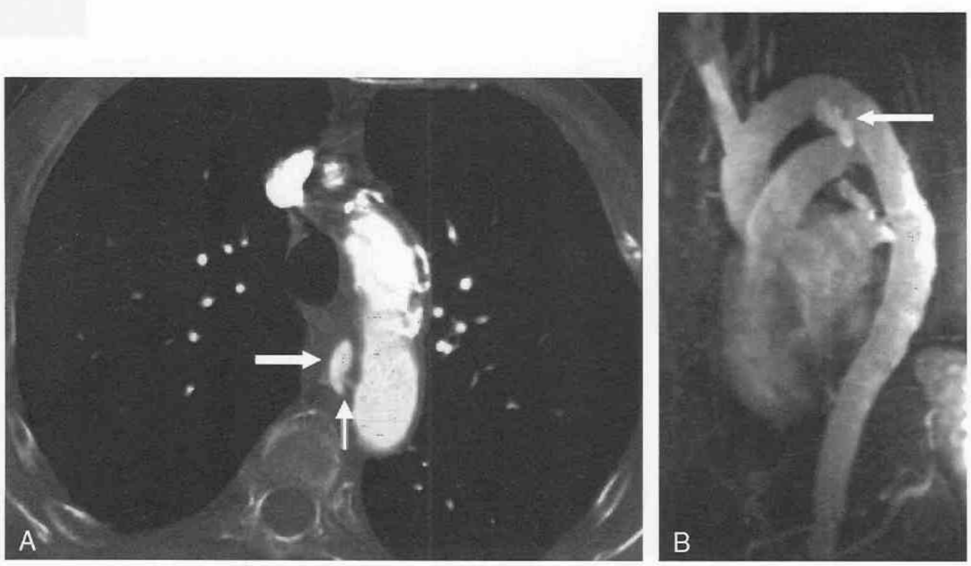

Figure 31–72. *A*, Axial CT scan in an elderly woman with acute back pain. There is a collection of contrast material medial to the descending aorta (*thick arrow*) that has a narrow but discrete communication with the aortic lumen (*thin arrow*). *B*, Sagittal oblique maximum intensity projection from gadolinium MR angiography delineates the focal atherosclerotic ulcer and its relationship with the aortic lumen (*arrow*).

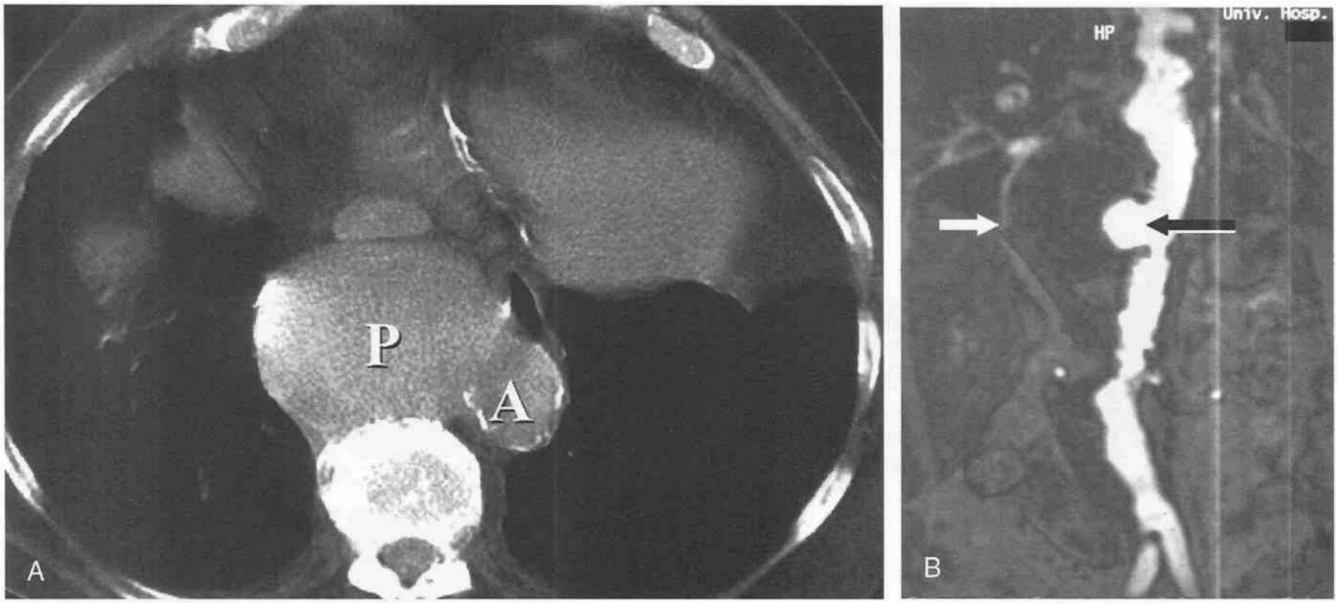

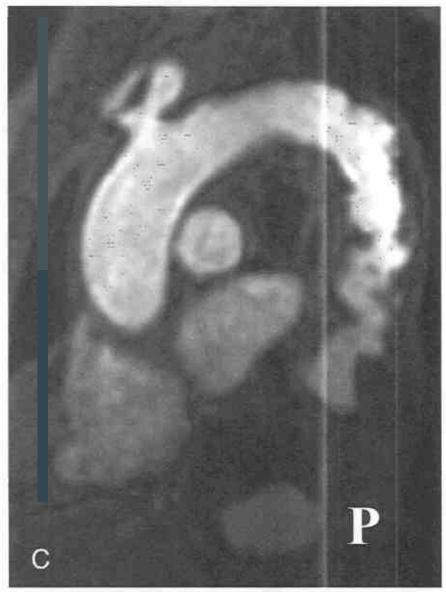

Figure 31–73. *A*, Axial noncontrast CT scan in an elderly patient who presented with a mediastinal mass contiguous with the descending aorta (P). Note the discontinuity of aortic calcification at this level. A = native aortic lumen. *B*, Sagittal maximum intensity projection from gadolinium MR angiography demonstrates an eccentric contrast collection (*black arrow*) with a large amount of surrounding thrombus (*white arrow*). *C*, Sagittal MPR image shows severe atherosclerotic ulceration of the descending aorta. P = pseudoaneurysm.

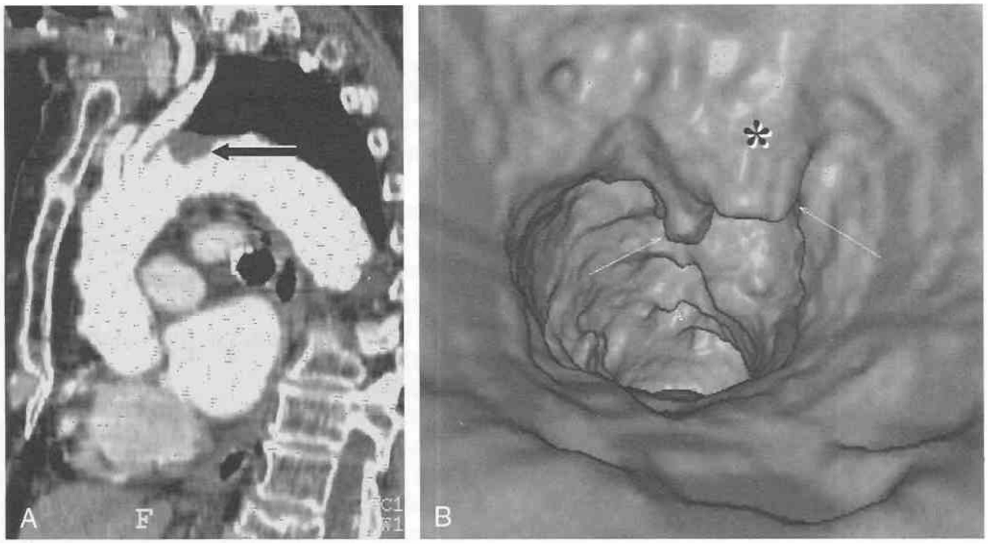

Figure 31–74. *A*, Sagittal oblique multiplanar reconstruction from multislice CT scan in an elderly woman with a history of embolic strokes. Note the large atheroma protruding into the aortic lumen (*arrow*). *B*, Virtual endoscopic image shows large protruding atheroma (*) within the transverse arch.

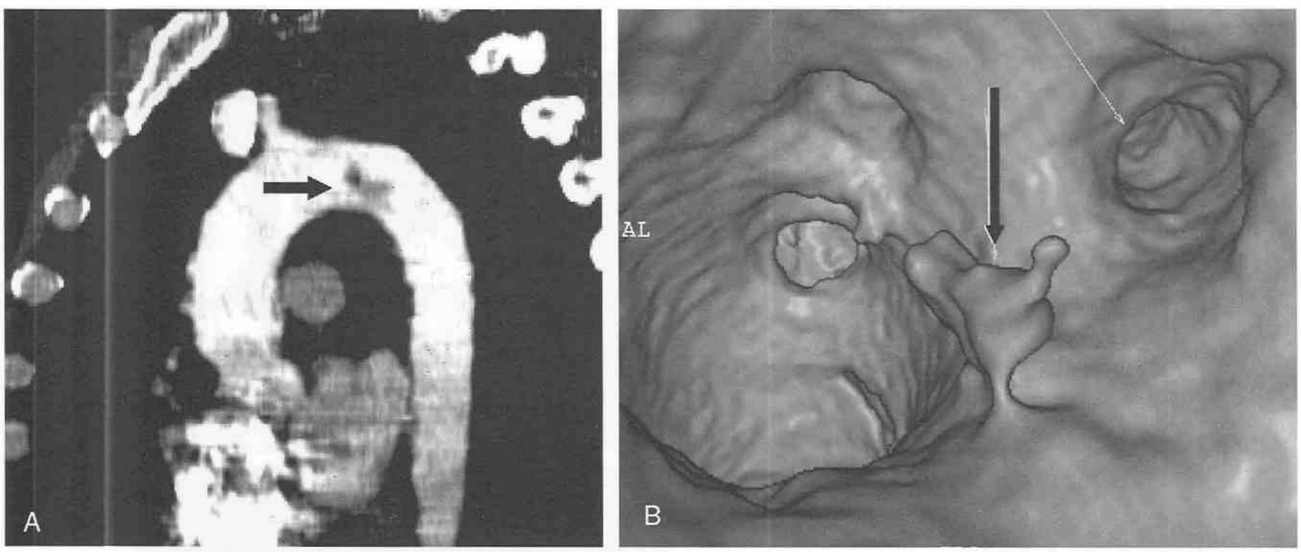

Figure 31–75. *A*, **Sagittal** oblique multiplanar reconstruction from multislice CT scan in a patient with a splenic infarct and arm weakness. There is a polypoid atheroma within the transverse arch (*arrow*). *B*, Virtual endoscopic image of the aortic arch shows a pedunculated atheroma (*arrow*) within the arch.

Aortitis

Inflammatory diseases of the aorta, though rare, have been well characterized in the imaging literature. Takayasu's arteritis is the best described of these disease processes. It is generally classified into four types on the basis of its anatomic location. Type 1 describes disease in the aortic arch, type 2 involves the abdominal aorta, type 3 the entire aorta, and type 4 the pulmonary arteries. In Takayasu's arteritis of the thoracic aorta, disease usually manifests as stenosis, occlusion, and aneurysm formation (Fig. 31–76). Some reports have described the superiority of CT over aortography. Although stenoses and aneurysmal changes are evaluated equivalently by the two modalities, mural changes are better evaluated with CT. In patients with suspected Takayasu's arteritis, initial noncontrast studies will show a high-attenuation aortic wall. Both aortic wall enhancement with contrast agent and delayed enhancement have been described.[89] These findings are important to define, as they may predate clinical symptoms and laboratory data. Documentation of improvement in aortic wall thickening after steroid therapy has been described.[46]

Giant cell arteritis is a vasculitis that often affects the thoracic aorta. On pathologic examination, active granulomatous inflammation with multinucleated giant cells are found in the aortic wall. Although the aortic arch vessels can be involved with stenoses, involvement of the aorta results in aneurysm formation. In a population-based study, 10% of patients with giant cell arteritis experienced aortic aneurysms (Fig. 31–77). These patients may also have aortic valve insufficiency.

Other forms of aortitis affecting the thoracic aorta are granulomatous aortitis (Fig. 31–78), lymphoplasmacytic aortitis (Fig. 31–79),[29] and aortitis associated with antineutrophil cytoplasmic antibody (ANCA).[86] These unusual forms of aortitis are often associated with aneurysm formation, but dissection has also been reported.

The Postoperative Aorta

With the increasing age of the population and the greater prevalence of atherosclerotic disease, larger numbers of aging patients are undergoing cardiothoracic surgery. Postoperative complications in the aorta are an uncommon cause of postoperative morbidity and mortality but they should be considered in patients who present with pain or in whom imaging studies show mediastinal widening. Importantly, many of these changes can occur years after the original operation. During surgery of the heart and

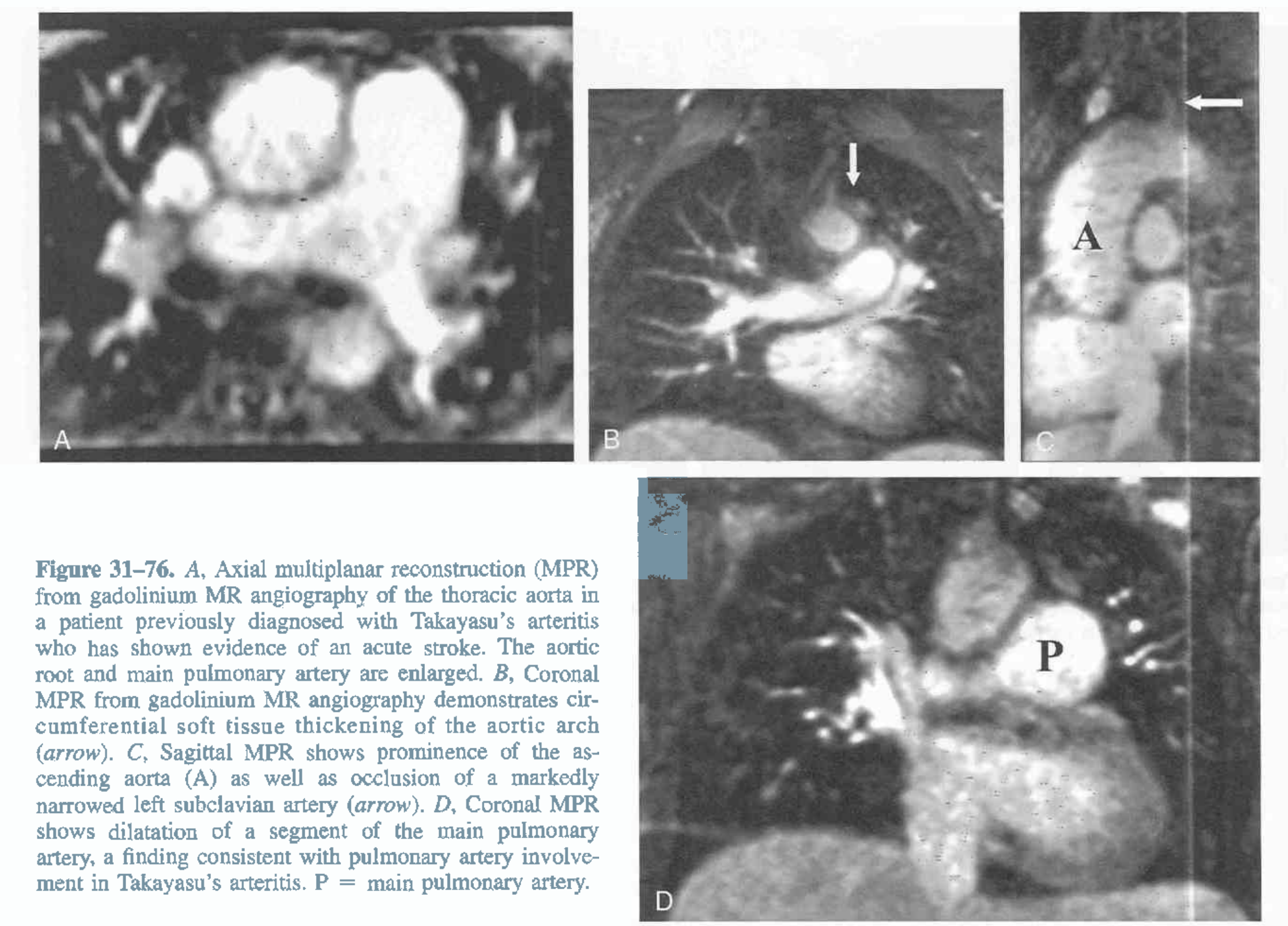

Figure 31–76. *A*, Axial multiplanar reconstruction (MPR) from gadolinium MR angiography of the thoracic aorta in a patient previously diagnosed with Takayasu's arteritis who has shown evidence of an acute stroke. The aortic root and main pulmonary artery are enlarged. *B*, Coronal MPR from gadolinium MR angiography demonstrates circumferential soft tissue thickening of the aortic arch (*arrow*). *C*, Sagittal MPR shows prominence of the ascending aorta (A) as well as occlusion of a markedly narrowed left subclavian artery (*arrow*). *D*, Coronal MPR shows dilatation of a segment of the main pulmonary artery, a finding consistent with pulmonary artery involvement in Takayasu's arteritis. P = main pulmonary artery.

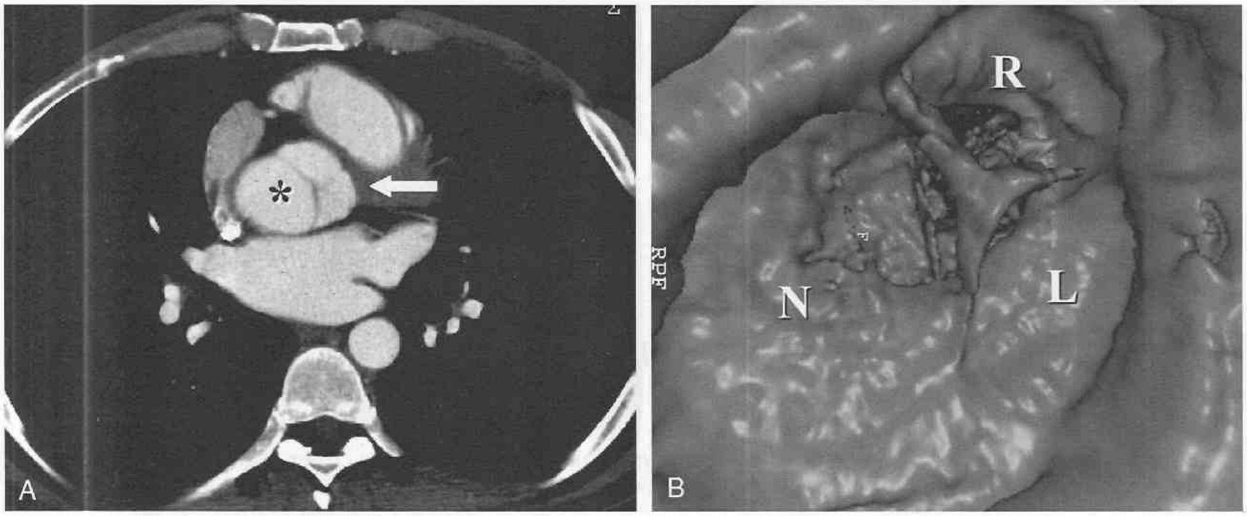

Figure 31–77. *A*, Axial CT scan in a young man in whom a chest radiograph showed an aortic prominence. Note the enlarged aortic root (*arrow*) with asymmetrical enlargement of the noncoronary cusp (*). *B*, Virtual endoscopic image shows normal appearance of the left (L) and right (R) coronary cusps and asymmetrical enlargement of the noncoronary cusp (N).

Figure 31–78. *A*, Axial half-Fourier acquisition single-shot turbo spin echo (HASTE) MR image in a young man in whom a chest radiograph showed mediastinal widening. This image reveals enlargement of the aortic root (A). *B*, Coronal cine gradient-recalled echo MR image at the level of the aortic valve during early diastole shows a linear focus of signal dephasing, a finding consistent with aortic insufficiency (*arrow*).

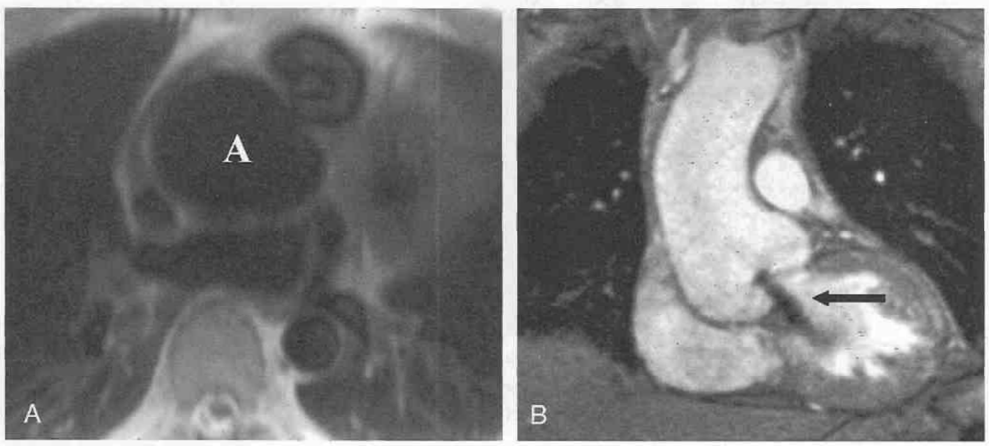

Figure 31–79. *A*, Sagittal oblique multiplanar reconstruction from CT scanning in an older woman who presented with chest pain. There is aneurysmal dilatation of the descending thoracic aorta (A) with marked irregularity or ulceration (*arrow*). *B*, Virtual endoscopic image of the descending aorta shows extensive ulceration (*arrows*).

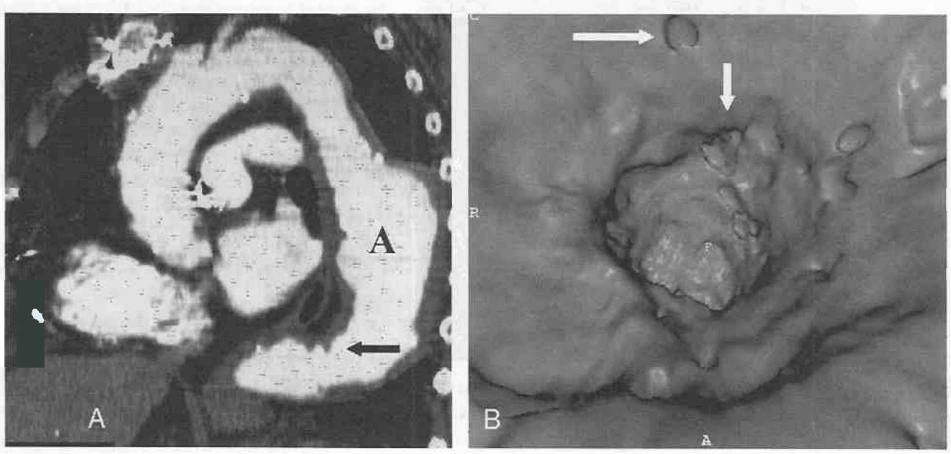

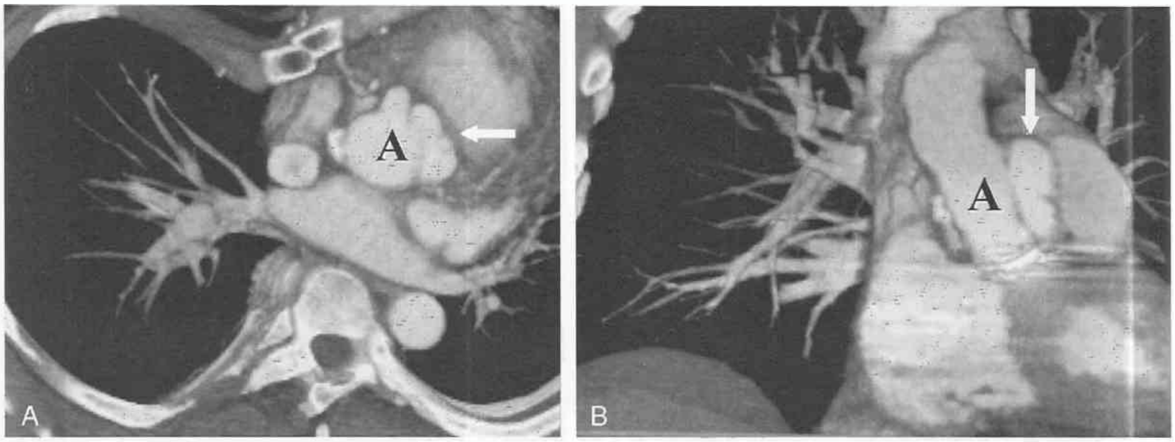

Figure 31–80. A, Axial CT scan with volumetric rendering shows lobulated soft tissue (*arrow*) extending from the aortic root (A). *B*, Coronal volume-rendering image shows pseudoaneurysm (A) arising from the aortic root (*arrow*).

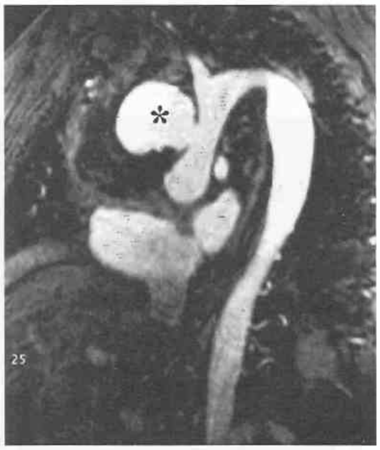

Figure 31–81. Sagittal multiplanar reconstruction from gadolinium MR angiography shows a large pseudoaneurysm (*) arising from the ascending aorta at the site of prior aortic cannulation.

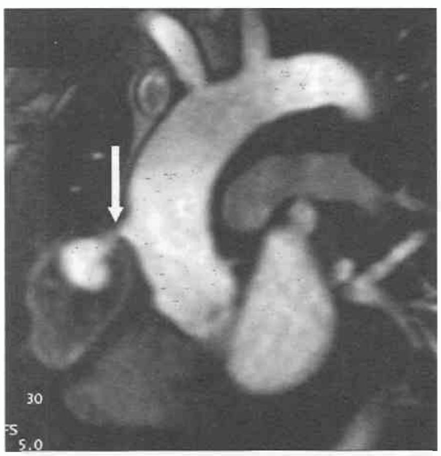

Figure 31–82. Sagittal oblique multiplanar reconstruction from gadolinium MR angiography demonstrates a lobulated aneurysm (*arrow*) arising from the ascending aorta.

great vessels, the aorta is cannulated, coronary artery grafts are placed, and, in aortic valve repair, an aortotomy is performed above the valve. These areas are all sites of potential aneurysm formation (Figs. 31–80 through 31–82).[62] Postoperative pseudoaneurysms and leaks are not uncommon after repair of aortic dissection or aneurysm and should always be considered in any postoperative patient presenting with new symptoms or a mass in the chest or mediastinum. In a large series of patients followed after aortic transposition grafts, 20% of patients required reoperation for periprosthetic pseudoaneurysms. All of the patients with pseudoaneurysms were asymptomatic. The authors of the study proposed serial evaluations in these high-risk patients to better evaluate postoperative complications.

References

1. Akers DL Jr, Fowl RJ, Plettner J, Kempczinski RF: Complications of anomalous origin of the right subclavian artery: Case report and review of the literature. Ann Vasc Surg. 5:385–388, 1991.
2. Amarenco P, Cohen A, Tzourio C, et al: Atherosclerotic disease of the aortic arch and the risk of ischemic stroke. N Engl J Med 33: 1474–1479, 1994.
3. Amparo EG, Higgins CB, Hricak H, et al: Aortic dissection: Magnetic resonance imaging. Radiology 155:399–406, 1985.
4. Amparo EG, Hoddick WK, Hricak H, et al: Comparison of magnetic resonance imaging and ultrasonography in the evaluation of abdominal aortic aneurysms. Radiology 154:451–456, 1985.
5. Aronberg DJ, Glazer HS, Maden K, et al: Normal thoracic aorta diameters by computed tomography. J Comput Assist Tomogr 8: 247–250, 1984.
6. Atkinson DJ, Edelman RR: Cineangiography of the heart in a single breath hold with a segmented turboFLASH sequence. Radiology 178:357–360, 1991.
7. Austin EH, Wolfe WG: Aneurysm of aberrant subclavian artery with a review of the literature. J Vasc Surg 2:571–577, 1985.
8. Axelbaum SP, Schellinger D, Gomes MN, et al: Computed tomographic evaluation of aortic aneurysms. Am J Roentgenol 127: 75–78, 1976.
9. Batra P, Bigoni B, Manning J, et al: Pitfalls in the diagnosis of thoracic aortic dissection at CT angiography. Radiographics 20: 309–320, 2000.
10. Beel T, Harwood AL: Traumatic rupture of the thoracic aorta. Ann Emerg Med 9:483–486, 1980.
11. Bertolini A, Pelizza A, Panizzon G, et al: Vascular rings and slings: Diagnosis and surgical treatment of 49 patients. J Cardiovasc Surg (Torino) 28:301–312, 1987.
12. Bosniak MA: An analysis of some anatomic-roentgenologic aspects

of the brachiocephalic vessels. Am J Roentgenol 91:1222–1231, 1964.
13. Chung JW, Park JH, Im J, et al: Spiral CT angiography of the thoracic aorta. Radiographics 16:811–824, 1996.
14. Cohen AM, Crass JR: Traumatic lacerations of the aorta and great vessels with a normal mediastinum at radiography. J Vasc Interv Radiol 3:541–544, 1992.
15. Cohn SM, Pollak JS, McCarthy S, et al: Detection of aortic tear in the acute trauma patient using MRI. J Magn Reson Imaging 12: 963–967, 1994.
16. Cooke JP, Kazmier FJ, Orszulak TA: The penetrating aortic ulcer: Pathologic manifestations, diagnosis, and management. Mayo Clin Proc 63:718–725, 1988.
17. Costello P, Ecker CP, Tello R, et al: Assessment of the thoracic aorta by spiral CT. AJR Am J Roentgenol 158:1127–1130, 1992.
18. Creasy JD, Chiles C, Routh WD, et al: Overview of traumatic injury of the thoracic aorta. Radiographics 17:27–45, 1997.
19. Danza FM, Fusco A, Falappa P: The role of computed tomography in the evaluation of dissecting aortic aneurysms (letter). Radiology 152:827–829, 1984.
20. Dart CHJ, Braitman HE: Traumatic rupture of the thoracic aorta: Diagnosis and management. Arch Surg 111:697–702, 1976.
21. De Santis RW, Doroghaz RM, Anisten WG, et al: Aortic dissection. N Engl J Med 317:1060–1067, 1987.
22. DeBakey ME, McCollum II, Crawford ES: Dissection and dissecting aneurysms of the aorta: Twenty-year follow-up of five hundred twenty-seven patients treated surgically. Surgery 92:1118–1134, 1982.
23. Demos TC, Posniak HV, Churchill RJ: Detection of the intimal flap of aortic dissection on unenhanced CT images. Am J Roentgenol 146:601–603, 1986.
24. Dillon EH, van Leeuwen MS, Fernandez MA, et al: Spiral CT angiography. AJR Am J Roentgenol 160:1273–1278, 1993.
25. Dinsmore RE, Liberthson RR, Wismer GL, et al: Magnetic resonance imaging of thoracic aortic aneurysms: Comparison with other imaging modalities. Am J Roentgenol 146:309–314, 1986.
26. Dinsmore RE, Wedeen VJ, Miller SW, et al: MRI of dissection of the aorta: Recognition of the intimal tear and differential flow velocities. Am J Roentgenol 146:1286, 1986.
27. Dooms GC, Higgins CB: The potential of magnetic resonance imaging for the evaluation of thoracic arterial disease. J Thorac Cardiovasc Surg 92:1088–1095, 1986.
28. Fattori R, Celletti F, Bertaccini P, et al: Delayed surgery of traumatic aortic rupture: Role of magnetic resonance imaging. Circulation 94: 2865–2870, 1996.
29. Faye-Petersen OM, Arnold MM, Grizzle WE, et al: Lymphoplasmacytic aortitis and acute aortic dissection: An uncommon association. Arch Pathol Lab Med 120:402–404, 1996.
30. Fishbone G, Robbins DI, Osborn DJ, et al: Trauma to the thoracic aorta and great vessels. Radiol Clin North Am 11:543–554, 1973.
31. Fisher RG, Chasen MH, Lamki N: Diagnosis of injuries of the aorta and brachiocephalic arteries caused by blunt chest trauma: CT vs aortography. AJR Am J Roentgenol 162:1047–1052, 1994.
32. Fishman JE: Imaging of blunt aortic and great vessel trauma. J Thorac Imaging 15:97–103, 2000.
33. Fomon JJ, Kurzweg FT, Broadaway RK: Aneurysms of the aorta: A review. Ann Surg 165:557–563, 1967.
34. Gavant ML, Menke PG, Fabian T, et al: Blunt traumatic aortic rupture: Detection with helical CT of the chest. Radiology 197: 125–133, 1995.
35. Geisinger MA, Risius B, O'Donell JA, et al: Thoracic aorta dissections: Magnetic resonance imaging. Radiology 155:407–412, 1985.
36. Glanz S, Gordon DH: Right aortic arch with left descent. J Comput Assist Tomogr 5:256–268, 1981.
37. Glazer HS, Gutierrez FR, Levitt RG, et al: The thoracic aorta studies by MR imaging. Radiology 157:149, 1985.
38. Godwin JD: Examination of the thoracic aorta by computed tomography. Chest 85:564–567, 1984.
39. Godwin JD, Herfkens RL, Skioldebrand CG, et al: Evaluation of dissections and aneurysms of the thoracic aorta by conventional and dynamic scanning. Radiology 136:125–133, 1980.
40. Gomes ML, Macedo AM, Pena SD, et al: Genetic relationships between *Trypanosoma cruzi* strains isolated from chronic chagasic patients in southern Brazil as revealed by RAPD and SSR-PCR analysis. Acta Trop 69:99–109, 1998.
41. Greendyke RM: Traumatic rupture of the aorta: Special reference to automobile accidents. JAMA 195:527–530, 1966.
42. Groskin S, Maresca M, Heitzman ER: Thoracic trauma. In McCort JJ, Mindelzun RE (eds): Trauma Radiology. New York, Churchill Livingstone, 1990, pp 75–127.
43. Groskin SA: Selected topics in chest trauma. Radiology 183:605–617, 1992.
44. Gross SC, Barr I, Eyeler WR, et al: Computed tomography in dissection of the thoracic aorta. Radiology 136:135, 1980.
45. Harris JH Jr, Horowitz DR, Zelitt DL: Unenhanced dynamic mediastinal computed tomography in the selection of patients requiring thoracic aortography for the detection of acute traumatic aortic injury. Emerg Radiol 2:67–76, 1995.
46. Hayashi K, Fukushima T, Matsunaga N, et al: Takayasu's arteritis: Decrease in aortic wall thickening following steroid therapy, documented by CT. Br J Radiol 59:281–283, 1986.
47. Heiberg E, Wolverson MK, Sundaram M, et al: CT characteristics of aortic atherosclerotic aneurysm versus aortic dissection. J Comput Assist Tomogr 9:78–83, 1985.
48. Heiberg E, Wolverson M, Sundaram M, et al: CT findings in thoracic aortic dissection. Am J Roentgenol 136:13–17, 1981.
49. Heiberg E, Wolverson MK, Sundaram M, et al: CT in aortic trauma. Am J Roentgenol 140:1119–1124, 1983.
50. Higgins CB, Silverman NR, Harris RD, et al: Localized aneurysms of the descending thoracic aorta. Clin Radiol 26:474, 1975.
51. Hirao K, Miyazaki A, Noguchi M, et al: The cervical aortic arch with aneurysm formation. J Comput Assist Tomogr 23:959–962, 1999.
52. Hirst AE, John VJ, Kime SW: Dissection aneurysm of the aorta: A review of 505 cases. Medicine 37:217–279, 1958.
53. Hughes JP, Ruttley MS, Musumeci F: Case report: Traumatic aortic rupture—demonstration by magnetic resonance imaging. Br J Radiol 67:1264–1267, 1994.
54. Itzchak Y, Rosenthal T, Adal R, et al: Dissecting aneurysm of the thoracic aorta: Reappraisal of radiologic diagnosis. Am J Roentgenol 125:559, 1975.
55. Johnson PT, Fishman EK, Duckwall JR, et al: Interactive three-dimensional volume rendering of spiral CT data: Current applications in the thorax. Radiographics 18:165–187, 1998.
56. Johnson PT, Heath DG, Bliss DF, et al: Three-dimensional CT: Real-time interactive volume rendering. AJR Am J Roentgenol 167: 581–583, 1996.
57. Joyce JW, Fairbairn JF II, Kincaid OW, et al: Aneurysms of the thoracic aorta: A clinical study with special reference to prognosis. Circulation 29:176, 1964.
58. Julsrud PR, Breen JF, Felmlee JP, et al: Coarctation of the aorta: Collateral flow assessment with phase-contrast MR angiography. AJR Am J Roentgenol 169:1735–1742, 1997.
59. Kalender WA, Seissler W, Klotz E, et al: Spiral volumetric CT with single-breath-hold technique, continuous transport, and continuous scanner rotation. Radiology 176:181–183, 1990.
60. Kalke BR, Magotra R, Doshi SM: A new surgical approach to the management of symptomatic aberrant right subclavian artery. Ann Thorac Surg 44:86–89, 1987.
61. Kastan DJ, Sharma RP, Keith F, et al: Case report: Intimo-intimal intussusception: An unusual presentation of aortic dissection. AJR Am J Roentgenol 151:603–604, 1988.
62. Katsumata T, Moorjani N, Vaccari G, et al: Mediastinal false aneurysm after thoracic aortic surgery. Ann Thorac Surg 70:547–552, 2000.
63. Kersting-Sommerhoff BA, Higgins CB, White RD, et al: Aortic dissection: Magnetic resonance imaging—sensitivity and specificity of MR imaging. Radiology 166:651, 1988.
64. Kersting-Sommerhoff BA, Seelos KC, Hardy C, et al: Evaluation of surgical procedures for cyanotic congenital heart disease by using MR imaging. AJR Am J Roentgenol 155:259–266, 1990.
65. Kirsh MM, Behrendt DM, Orringer MB, et al: The treatment of acute traumatic rupture of the aorta: a ten year experience. Ann Surg 184:308–316, 1976.
66. Kodali S, Jamieson WR, Leia SM, et al: Traumatic rupture of the thoracic aorta: A 20-year review—1969–1989. Circulation 84: 140–146, 1991.
67. Kram HB, Appel PL, Wohlmuth DA, et al: Diagnosis of traumatic thoracic aortic rupture: A 10-year retrospective analysis. Ann Thorac Surg 47:282–286, 1989.

68. Krinsky GA, Ribakove GH: Spontaneous progression of ascending aortic intramural hematoma to Stanford type A dissection fortuitously witnessed during an MR examination. J Comput Assist Tomogr 23:966–968, 1999.
69. Krinsky GA, Rofsky NM, DeCorato DR, et al: Thoracic aorta: Comparison of gadolinium-enhanced three-dimensional MR angiography with conventional MR imaging. Radiology 202:183–193, 1997.
70. Larde D, Belloir C, Vasile N, et al: Computed tomography of aortic dissection. Radiology 136:147, 1980.
71. Levy JR, Heiken JP, Gutierrez FR: Imaging of penetrating atherosclerotic ulcers of the aorta. AJR Am J Roentgenol 173:151–154, 1999.
72. Lois JF, Gomes AS, Brown K, et al: Magnetic resonance imaging of the thoracic aorta. Am J Cardiol 60:358–362, 1987.
73. Lundevall J: The mechanisms of traumatic rupture of the thoracic aorta. Acta Pathol Microbiol Scand 62:34–36, 1964.
74. Machida K, Tasaka A: CT patterns of mural thrombus in aortic aneurysms. J Comput Assist Tomogr 4:840–842, 1980.
75. Mayadag MA, Kirshenbaum KJ, Nadimpalli SR, et al: Thoracic aortic trauma: Role of dynamic CT. Radiology 179:853–855, 1991.
76. Meziane MA, Fishman EK, Siegelman SS: CT diagnosis of hemopericardium in acute dissecting aneurysm of the thoracic aorta. J Comput Assist Tomogr 8:10–14, 1984.
77. Mirvis SE: Applications of magnetic resonance imaging and three-dimensional computed tomography in emergency medicine. Ann Emerg Med 18:1315–1321, 1989.
78. Mirvis SE, Bidwell JK, Buddemeyer EU, et al: Imaging diagnosis of traumatic aortic rupture: A review and experience at a major trauma center. Invest Radiol 22:187–196, 1987.
79. Mirvis SE, Bidwell JK, Buddemeyer EU, et al: Value of chest radiography in excluding traumatic aortic rupture. Radiology 163: 487–493, 1987.
80. Mirvis SE, Kostrubiak I, Whitley NO, et al: Role of CT in excluding major arterial injury following blunt thoracic trauma. AJR Am J Roentgenol 149:601–605, 1987.
81. Mirvis SE, Shanmuganathan K, Miller BH, et al: Traumatic aortic injury: Diagnosis with contrast-enhanced thoracic CT. Radiology 200:413–422, 1996.
82. Moncada R, Churchill R, Reynes C, et al: Diagnosis of dissecting aortic aneurysm by CT. Lancet 1:238–241, 1981.
83. Moore EH, Webb WR, Verrier ED, et al: MRI of chronic posttraumatic false aneurysm of the thoracic aorta. Am Roentgenol 143: 1195–1196, 1984.
84. Morgan PW, Goodman LR, Aprahamian C, et al: Evaluation of traumatic aortic injury: Does dynamic contrast-enhanced CT play a role? Radiology 182:661–666, 1992.
85. Murray JG, Manisali M, Flamm SD, et al: Intramural hematoma of the thoracic aorta: MR image findings and their prognostic implications. Radiology 204:349–355, 1997.
86. Nakabayashi K, Kamiya Y, Nagasawa T: Aortitis syndrome associated with positive perinuclear antineutrophil cytoplasmic antibody: Report of three cases. Int J Cardiol 75(Suppl 1):S89–S94, 2000.
87. Oudkerk M, Overbosch E, Dee P: CT recognition of acute aortic dissection. Am J Roentgenol 141:671, 1983.
88. Paiery RA, Couffinhal JC, Wellers M, et al: Computed tomography versus aortography in diagnosis of aortic dissection. Cardiovasc Intervent Radiol 5:285–291, 1982.
89. Park JH, Chung JW, Im JG, et al: Takayasu arteritis: Evaluation of mural changes in the aorta and pulmonary artery with CT angiography. Radiology 196:89–93, 1995.
90. Parmley LF, Mattingly TW, Manion WC, et al: Nonpenetrating traumatic injury of the aorta. Circulation 17:1086–1101, 1958.
91. Patel N, Stevens KJ Jr, Mirvis S, et al: Imaging in acute thoracic aortic injury due to blunt trauma: A review. Radiology 209:335–338, 1998.
92. Pernes JM, Grenier P, Desbleds MT, et al: MR evaluation of chronic aortic dissection. J Comput Assist Tomogr 975–981, 1987.
93. Polacin A, Kalender WA, Marchal G: Evaluation of section sensitivity profiles and image noise in spiral CT. Radiology 185:29–35, 1992.
94. Pressler V, McNamara J: Thoracic aortic aneurysm: Natural history and treatment. J Thorac Cardiovasc Surg 79:489–498, 1980.
95. Prince MR, Chenevert TL, Foo TK, et al: Contrast-enhanced abdominal MR angiography: Optimization of imaging delay time by automating the detection of contrast material arrival in the aorta. Radiology 203:109–114, 1997.
96. Prince MR, Narasimham DL, Jacoby WT, et al: Three-dimensional gadolinium-enhanced MR angiography of the thoracic aorta. AJR Am J Roentgenol 166:1387–1397, 1996.
97. Quint LE, Francis IR, Williams DM, et al: Evaluation of thoracic aortic disease with the use of helical CT and multiplanar reconstructions: Comparison with surgical findings. Radiology 201:37–41, 1996.
98. Raptopoulos V: Chest CT for aortic injury: Maybe not for everyone (commentary). AJR Am J Roentgenol 162:1053–1055, 1994.
99. Reddy GP, Higgins CB: MR imaging of the thoracic aorta. Magn Reson Imaging Clin North Am 8:1–15, 2000.
100. Rigants H, Marchal G, Baert AL, et al: Initial experience with volume CT scanning. J Comput Assist Tomogr 14:675–682, 1990.
101. Roberts WC: Aortic dissection: anatomy, consequences, and causes. Am Heart J 101:195–214, 1981.
102. Rubin GD: Helical CT angiography of the thoracic aorta. J Thorac Imaging 12:128–149, 1997.
103. Rubin GD, Beaulieu CF, Argiro V, et al: Perspective volume rendering of CT and MR images: Applications for endoscopic imaging. Radiology 199:321–330, 1996.
104. Rubin GD, Dake MD, Napel SA, et al: Abdominal spiral CT angiography: Initial clinical experience. Radiology 186:147–152, 1993.
105. Rubin GD, Dake MD, Semba CP: Current status of three-dimensional spiral CT scanning for imaging the vasculature. Radiol Clin North Am 33:51–70, 1995.
106. Rubin GD, Lane MJ, Bloch DA, et al: Optimization of thoracic spiral CT: Effects of iodinated contrast medium concentration. Radiology 201:785–791, 1996.
107. St. Amour TE, Gutierrez FR, Levitt RG, McKnight RC: CT diagnosis of type A aortic dissections not demonstrated by aortography. J Comput Assist Tomogr 12:963–967, 1988.
108. Sanborn JC, Heitzman ER, Markarian B: Traumatic rupture of the thoracic aorta: Roentgen-pathological correlations. Radiology 95: 293–298, 1970.
109. Sandor F: Incidence and significance of traumatic mediastinal hematoma. Thorax 22:43–62, 1967.
110. Schnyder P, Meuli R, Wicky S: Injection techniques. In Remy Jardin M, Remy J (eds): Spiral CT of the Chest. Berlin, Springer, 1996, pp 41–44.
111. Sebastia C, Pallisa E, Quiroga S, et al: Aortic dissection: Diagnosis and follow-up with helical CT. Radiographics 19:45–60, 1999.
112. Sevitt S: The mechanisms of traumatic rupture of the thoracic aorta. Br J Surg 64:166–173, 1977.
113. Silverman PM, Roberts S, Tefft MC, et al: Helical CT of the liver: Clinical application of an automated computer technique, SmartPrep, for obtaining images with optimal contrast enhancement. AJR Am J Roentgenol 165:73–78, 1995.
114. Simonetti OP, Finn JP, White RD, et al: "Black blood" T2-weighted inversion-recovery MR imaging of the heart. Radiology 199:49–57, 1996.
115. Simpson IA, Chung KJ, Glass RF, et al: Cine magnetic resonance imaging for evaluation of anatomy and flow relations in infants and children with coarctation of the aorta. Circulation 78:142–148, 1988.
116. Smith PA: Virtual angioscopy using spiral CT and real-time interactive volume-rendering techniques. J Comput Assist Tomogr 22: 212–214, 1998.
117. Smith RS, Chang FC: Traumatic rupture of the aorta: Still a lethal injury. Am J Surg 152:660–663, 1986.
118. Soler R, Rodriguez E, Requejo I, et al: Magnetic resonance imaging of congenital abnormalities of the thoracic aorta. Eur Radiol 8: 540–546, 1998.
119. Solomon SL, Brown JJ, Glazer HS, et al: Thoracic aortic dissection: Pitfalls and artifacts in MR imaging. Radiology 177:223, 1990.
120. Stanson AW, Kazmier FJ, Hollier LH, et al: Penetrating atherosclerotic ulcers of the thoracic aorta: Natural history and clinicopathologic correlations. Ann Vasc Surg 1:15–23, 1986.
121. Stockberger SM Jr, Liang Y, Hicklin JA, et al: Objective measurement of motion in patients undergoing spiral CT examinations. Radiology 206:625–629, 1998.
122. Sutorius DJ, Schreiber JT, Helmsworth JA: Traumatic disruption of the thoracic aorta. J Trauma 13:583–590, 1973.
123. Sutton D, Davies ER: Arch aortography and cerebrovascular insufficiency. Clin Radiol 17:330–345, 1966.

124. Svenson LG, Crawford ES, Hess KR, et al: Dissection of the aorta and dissecting aortic aneurysm. Circulation 82(Suppl 4):24–38, 1990.
125. Symbas RJ, Horsley WS, Symbas PN: Rupture of the ascending aorta caused by blunt trauma. Ann Thorac Surg 66:113–117, 1998.
126. Tawes RL Jr, Berry CL, Aberdeen E: Congenital bicuspid aortic valves associated with coarctation of the aorta in children. Br Heart J 31:127–128, 1969.
127. Tenenbaum A, Garniek A, Shemesh J, et al: Dual-helical CT for detecting aortic atheromas as a source of stroke: Comparison with transesophageal echocardiography. Radiology 208:153–158, 1998.
128. Thorsen MK, San Dretto MA, Lawson TL, et al: Dissecting aortic aneurysms: Accuracy of computed tomographic diagnosis. Radiology 148:773–777, 1983.
129. Torres WE, Maurer DE, Steinberg HV, et al: CT of aortic aneurysms: The distinction between mural and thrombus calcification. AJR Am J Roentgenol 150:1317–1319, 1988.
130. Tunick PA, Perez JL, Kronzon I: Protruding atheromas in the thoracic aorta and systemic embolization. Ann Intern Med 115:423–427, 1991.
131. Urban BA, Bluemke DA, Johnson KM, Fishman EK: Imaging of thoracic aortic disease. Cardiol Clin 17:659–682, 1999.
132. VanDyke CW, White RD: Congenital abnormalities of the thoracic aorta presenting in the adult. J Thorac Imaging 9:230–245, 1994.
133. White RD, Dooms GC, Higgins CB: Advances in imaging thoracic aorta disease. Invest Radiol 21:761–778, 1986.
134. White RD, Lipton MJ, Higgins CB, et al: Noninvasive evaluation of suspected thoracic aorta disease by contrast-enhanced CT. Am J Cardiol 57:282–290, 1986.
135. White RD, Ullyot DJ, Higgins CB: MR imaging of the aorta after surgery for aortic dissection. AJR Am J Roentgenol 150:87–92, 1988.
136. Winer-Muram HT, Gold RE: Effusion in the superior pericardial recess simulating a mediastinal mass. AJR Am J Roentgenol 154: 69, 1990.
137. Yamada T, Tada S, Harada J: Aortic dissection without intimal rupture: Diagnosis with MR imaging and CT. Radiology 168:347–352, 1988.
138. Zeitler E, Kaiser W, Schuierer G, et al: Magnetic resonance imaging of clots in the heart and vascular system. Ann Radiol (Paris) 28: 105, 1985.
139. Zeman RK, Berman PM, Silverman PM, et al: Diagnosis of aortic dissection: Value of helical CT with multiplanar reformation and three-dimensional rendering. AJR Am J Roentgenol 164:1375–1380, 1995.
140. Zeman RK, Silverman PM, Berman PM, et al: Abdominal aortic aneurysms: Evaluation with variable collimation helical CT and overlapping reconstruction. Radiology 193:555–560, 1994.

32 Computed Tomography of the Heart and Pericardium

Lynn S. Broderick

Echocardiography is usually the first choice for imaging the heart, although computed tomography (CT) scanning is a preferred method of evaluating the pericardium. In the past, CT was not routinely used for evaluation of the heart. This is primarily because, with the exception of electron beam CT scanners, the scan times were not fast enough to image the heart without cardiac motion. The development of multidetector scanners, coupled with the ability to scan with prospective or retrospective electrocardiography (ECG) gating, will very likely result in increased interest in cardiac imaging by CT.

Mochizuki and associates have reported the use of ECG-gated spiral CT to create two-dimensional (2D) and three-dimensional (3D) CT ventriculography, allowing assessment of left ventricular volumes.[68] Studies are currently under way to determine the usefulness of CT angiography in evaluating the coronary arteries.[52] Even when CT scanning is performed to evaluate other structures, much information can be obtained by careful assessment of the heart and pericardium.

Anatomy

The anatomy of the heart is often well displayed on CT scans of the chest, even in the presence of motion artifact. The most important motion artifact affecting the heart is one that can simulate aortic dissection.[22, 36, 69] Cardiac motion is responsible for the movement of the aortic root, resulting in curvilinear artifacts that may mimic an intimal flap. The curvilinear artifacts are typically located in a left anterior and right posterior location (Fig. 32–1).[36, 92] Multiplanar reformatted images may show a serrated appearance of the aortic wall, confirming that the curvilinear density is artifactual.[92] Knowledge of the typical appearance and location prevents misdiagnosis.

Basic cardiac anatomy can be displayed even with conventional CT scanners. The cardiac chambers, great vessels, and veins are readily identified. With faster scanning times, other finer structures, such as papillary muscles, chordae tendineae, and valve leaflets, can also be identified (Fig. 32–2).

The coronary arteries are easily visualized. The main coronary artery arises from the left aortic cusp and courses approximately 1 cm before giving off the left anterior descending and circumflex arteries. The right coronary artery arises from the right aortic cusp and is more caudally located than the left main coronary artery. Some structures, such as the pericardiacophrenic vein, are not routinely visualized. However, knowledge of their location is useful when they enlarge as a route of collateral circulation (Figs. 32–3 and 32–4).

Evaluation of the Cardiac Chambers

Knowledge of chest radiographic findings of valvular heart disease can be extrapolated to use in interpreting

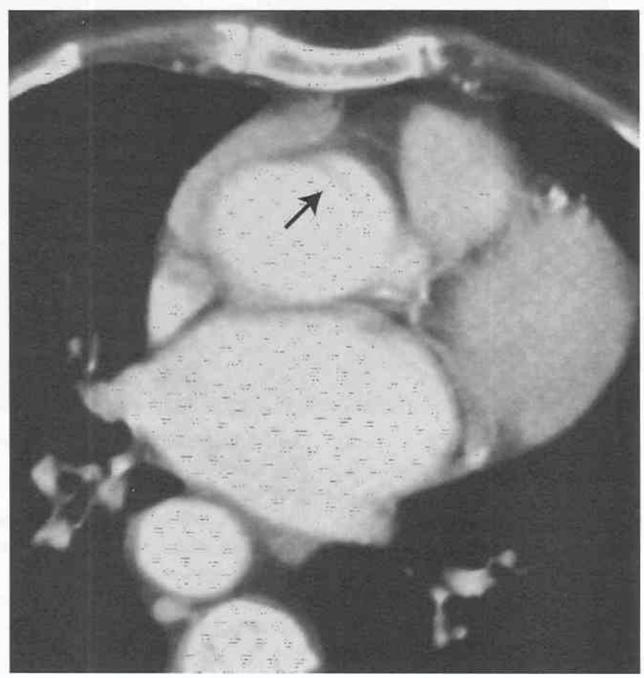

Figure 32–1. Motion artifact. Contrast-enhanced axial CT image shows apparent intimal flap *(arrow)* at the level of the aortic root. This appearance is caused by cardiac motion during scan acquisition. It can be recognized by its characteristic location at the aortic root. It is usually found in a left anterior or right posterior location.

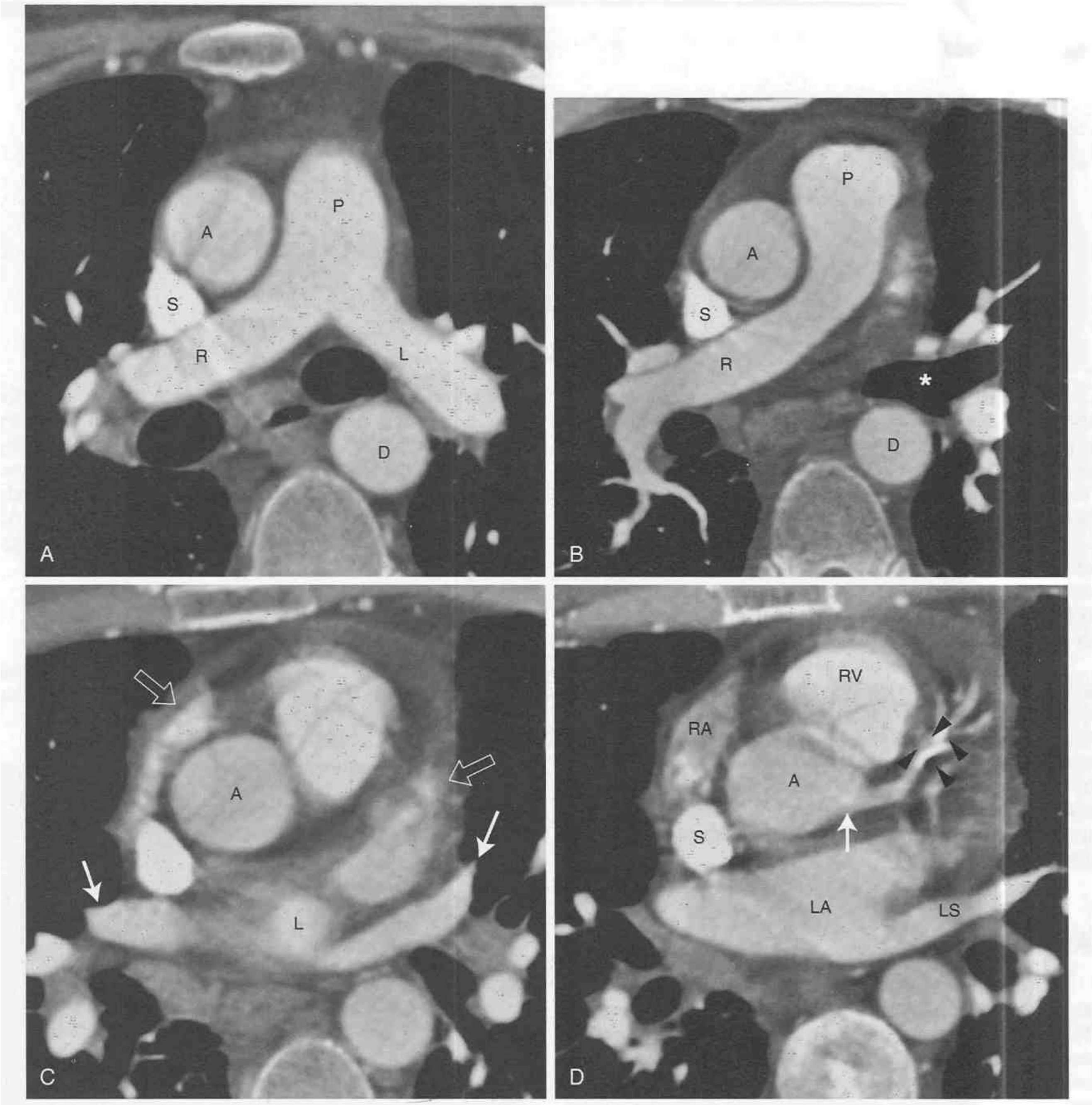

Figure 32–2. N[redacted]l anatomy. Axial contrast-enhanced [redacted] *mages* from the level of the pulmonary arteries (*A*) to the level of the inferior aspect of [redacted] heart (*J*) display normal cardiac anat[redacted].

A, CT image obtained at the level of the pulmonary arteries. A, ascending aorta; D, descending aorta; L, left pulmonary artery; P, main pulmonary artery; R, right pulmonary artery; S, superior vena cava.

B, More inferior CT image demonstrates the hyparterial left mainstem bronchus *(asterisk).* A, ascending aorta; D, descending aorta; P, main pulmonary artery; R, right pulmonary artery; S, superior vena cava.

C, CT image at level of the right and left superior pulmonary veins *(arrows)* and right and left atrial appendages *(open arrows).* Linear densities within the right ventricular/pulmonary artery outflow tract probably represent the valve leaflets *(arrowheads).* L, superior aspect of left atrium; A, ascending aorta.

D, CT image at level of origin of left main coronary artery *(arrow).* Calcification is present within the left anterior descending artery *(arrowheads).* A, ascending aorta; LA, left atrium; LS, left superior pulmonary vein; RA, right atrium; RV, right ventricular outflow tract, also known as the infundibulum; S, superior vena cava.

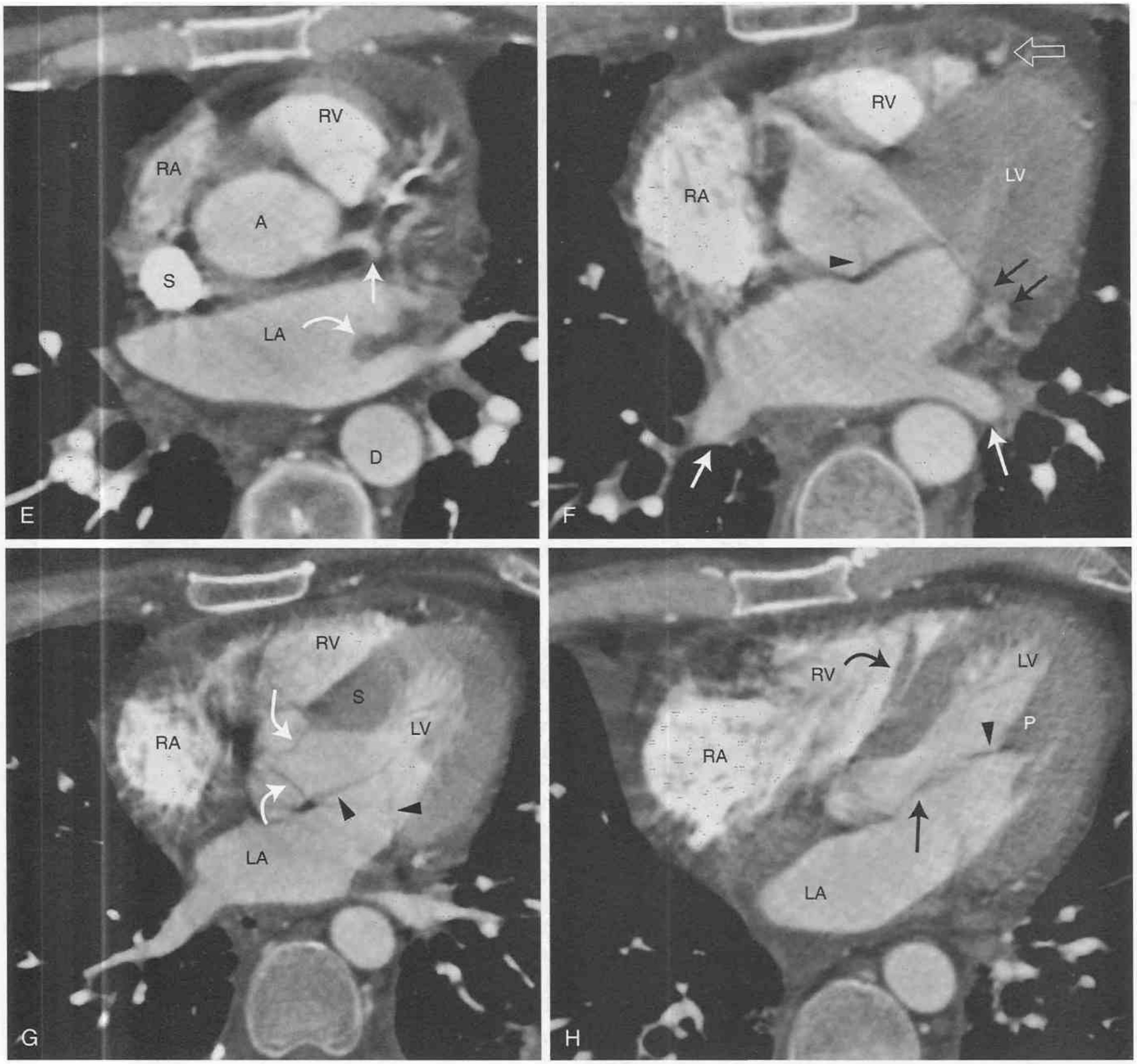

Figure 32–2 *(Continued).*

E, CT image at level of origin of circumflex artery *(arrow)* arising from the left main coronary artery. The normal prominence of the muscle can be visualized between the left superior pulmonary vein posteriorly and the left atrial appendage anteriorly *(curved arrow).* A, ascending aorta; D, descending aorta; LA, left atrium; RA, right atrium; RV, right ventricular outflow tract; S, superior vena cava.

F, CT image at the level of the right and left inferior pulmonary veins *(arrows)* and origin of the right coronary artery *(curved arrow).* The left anterior descending *(open arrow)* and circumflex *(double arrow)* arteries are also visible. LV, left ventricular myocardium; RA, right atrium; RV, right ventricular outflow tract. Portions of the aortic valve are visible *(arrowhead).*

G, CT image at the level of the mitral valve *(arrowheads).* The aortic valve leaflets are also visible *(curved arrows).* The mitral and aortic valves are not separated by myocardium, an indicator that this is the morphologic left ventricle. LA, left atrium; LV, left ventricle; RA, right atrium; RV, right ventricle; S, interventricular septum.

H, More inferior CT image shows the moderator band extending from the interventricular septum to the anterior free wall of the right ventricle *(curved arrow).* In the left ventricle, the chordae tendineae *(arrowhead)* can be seen extending from the papillary muscle (P) to the mitral valve leaflet *(arrow).* LA, left atrium; LV, left ventricle; RA, right atrium; RV, right ventricle.

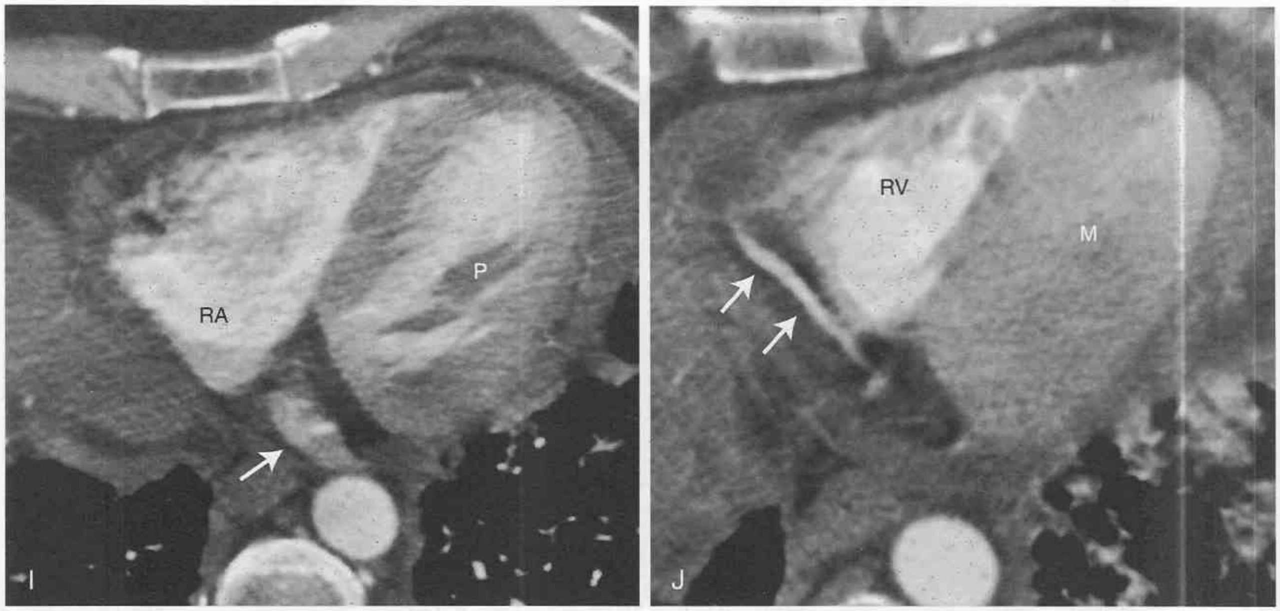

Figure 32–2. *(Continued).*

I, CT image at level of the coronary sinus *(arrow)*, just before it enters the right atrium (RA). Note the papillary muscle (P) within the left ventricle.

J, CT image showing the posterior course of the right coronary artery *(arrows)* in the atrioventricular groove. M, inferior myocardium of the left ventricle; RV, right ventricle.

chest CT scans. The actual valvular structures are often not visualized. This is particularly true for the tricuspid and pulmonic valves. However, portions of the mitral and aortic valves can be identified on routine contrast-enhanced CT scans (see Fig. 32–2). Evidence of chamber enlargement and hypertrophy can also be identified on CT images. The

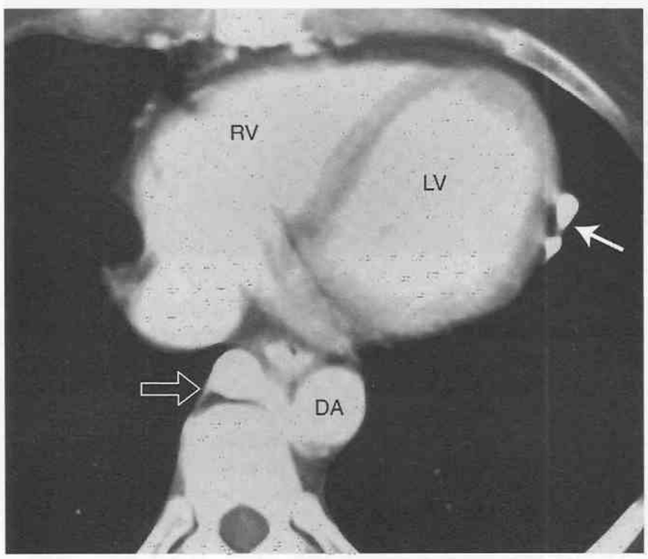

Figure 32–3. Enlarged pericardiacophrenic vein. Axial CT with intravenous contrast medium shows marked distention of the pericardiacophrenic vein *(arrow)*, which is acting as a collateral in this patient with SVC obstruction secondary to fibrosing mediastinitis. The distended azygos vein *(open arrow)* is also providing collateral circulation. DA, descending aorta; LV, left ventricle; RV, right ventricle.

diseased valve can be stenotic or regurgitant, or there may be combined stenosis and regurgitation.

The cardiac chamber, which is proximal to a stenotic valve, must work against an increased pressure load. This results in hypertrophy and dilatation of the chamber. The chamber distal to the stenotic valve is unaffected. When the valve is regurgitant, the proximal chamber experiences an increased volume load because it receives additional blood through the regurgitant valve. This results in dilatation of the chamber. Because this increased blood volume is then pumped through the valve, the receiving chamber also experiences an increased volume load, resulting in dilatation.

Aortic Valve Disease

Aortic stenosis can occur secondary to the presence of a congenital bicuspid aortic valve, rheumatic heart disease, or age-related degeneration of the aortic valve. The bicuspid valve is the most common congenital heart defect and has a prevalence of 4 in 1000 live births. There is a 4:1 male-to-female ratio.[58] Patients with bicuspid aortic valve are at risk for development of aortic stenosis, bacterial endocarditis, and aortic regurgitation.

In the adult form of aortic stenosis secondary to a bicuspid aortic valve, the valve initially functions normally. The valve leaflets are continually traumatized by turbulent blood flow through the bicuspid valve and eventually become fibrotic and calcified, leading to stenosis.[86] Patients with bicuspid aortic valve tend to present with symptoms of aortic stenosis at an earlier age than do patients with degenerative aortic stenosis.

Degenerative aortic stenosis is a slowly progressive dis-

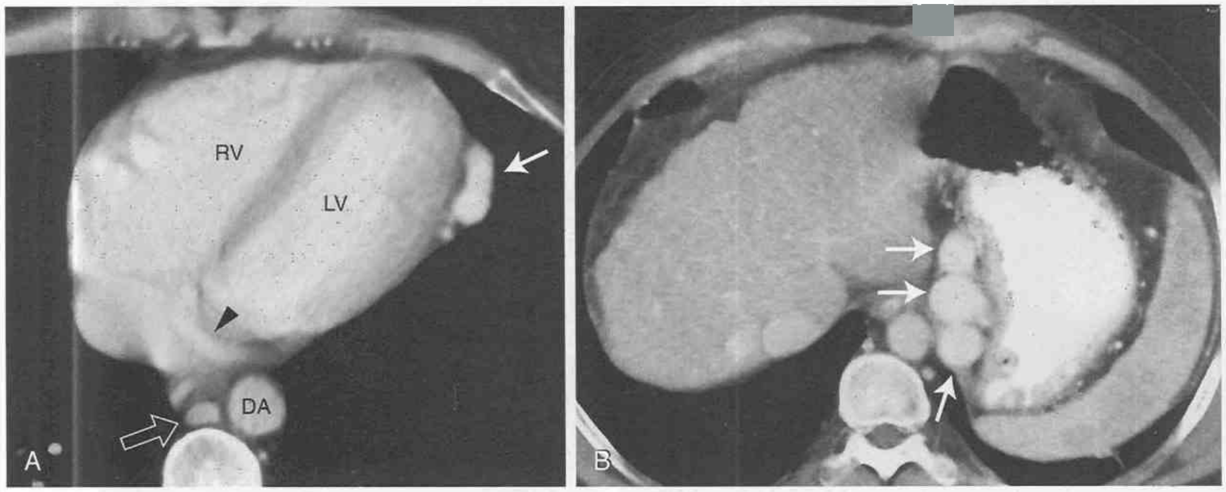

Figure 32–4. **Enlarged pericardiacophrenic vein.** *A,* Axial CT with intravenous contrast medium shows marked distention of the pericardiacophrenic vein *(arrow).* DA, descending aorta; LV, left ventricle; RV, right ventricle. The *open arrow* points to the azygos vein, and the *arrowhead* to the coronary sinus. *B,* More caudal image demonstrates gastric varices *(arrows)* as the cause of the distention of the pericardiacophrenic vein.

order that affects patients 65 years of age or older. It is more common in women, and it is the most common cause of aortic stenosis in older adults. Aortic stenosis may also occur as a manifestation of rheumatic heart disease. However, patients with rheumatic aortic valvular disease usually have a combination of aortic stenosis and regurgitation and the mitral valve is also usually involved. Aortic stenosis secondary to rheumatic heart disease is more common in men than in women.

Calcification of the aortic valve can be detected on CT images. In younger patients, calcification of the aortic valve should raise the question of aortic stenosis.[114] Calcification of the aortic valve in patients older than 65 years of age may be degenerative, and the patient may have no detectable aortic stenosis or may have only mild or moderate aortic stenosis.[57] In this older patient group, the greater the amount of calcification within the valve, the more likely the patient has aortic stenosis (Fig. 32–5).

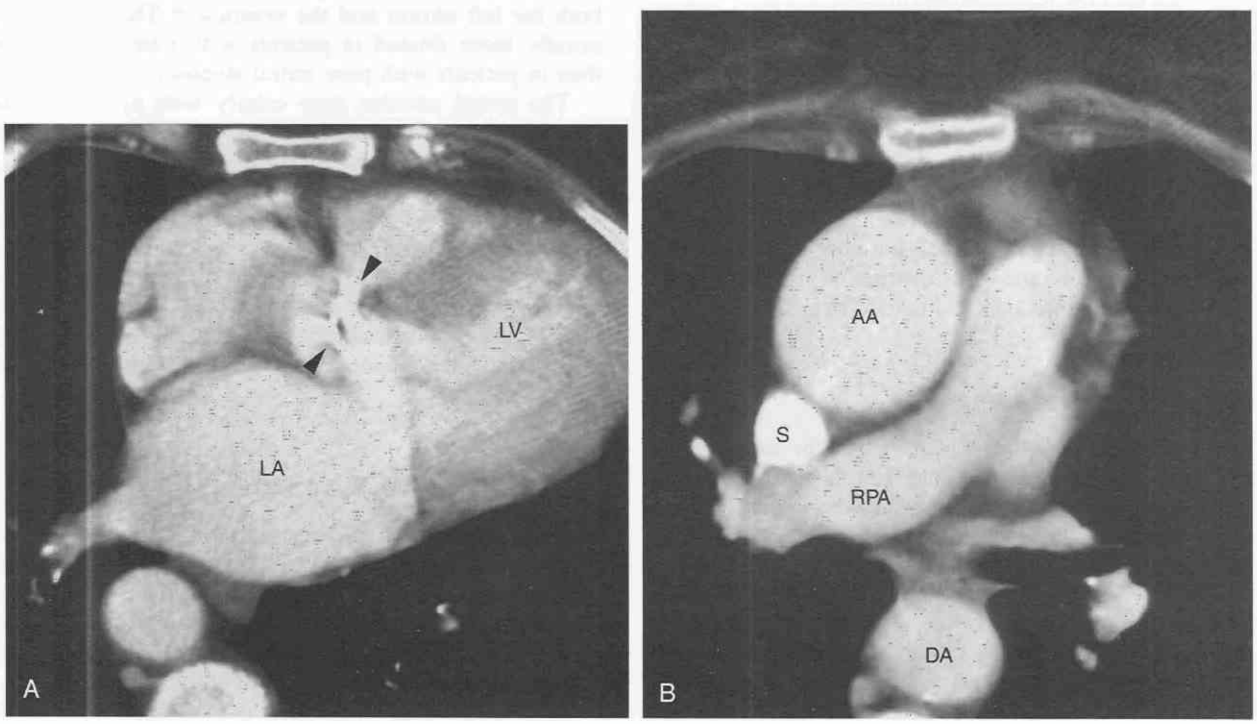

Figure 32–5. Degenerative aortic stenosis in a 73-year-old woman. Axial contrast-enhanced CT images show *(A)* calcification of the aortic valve *(arrowheads)* and *(B)* dilatation of the ascending aorta. Note the thickened myocardium of the left ventricle. AA, ascending aorta; DA, descending aorta; LA, left atrium; LV, left ventricle; RPA, right pulmonary artery; S, superior vena cava.

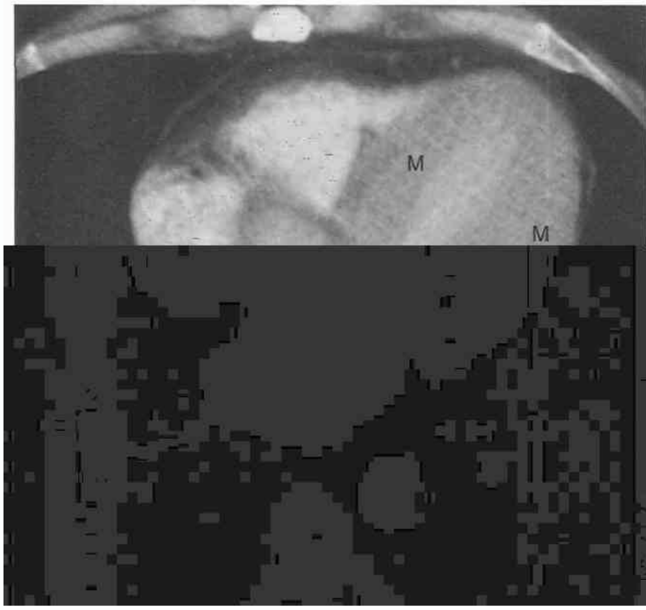

Figure 32–6. Left ventricular hypertrophy in a patient with systemic hypertension, aortic stenosis, and aortic regurgitation. Axial contrast-enhanced CT image shows the markedly thickened left ventricular myocardium (M). The aortic valve is not calcified.

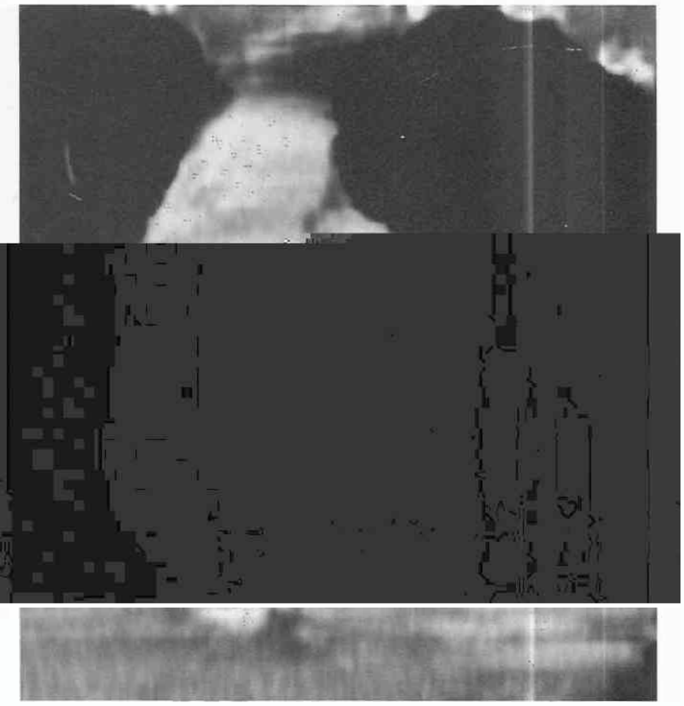

Figure 32–7. Aortic regurgitation. Coronal multiplanar reformatted image from spiral CT following intravenous contrast medium. There is dilatation of the left ventricle (LV) and aneurysmal dilatation of the ascending aorta (AA), typical findings in patients with aortic regurgitation.

CT is also useful in depicting sequelae of aortic stenosis. Hypertrophy of the left ventricular myocardium can be detected (Fig. 32–6).[86] Poststenotic dilatation of the ascending aorta is thought to result from the increased turbulence caused by the jet of blood coursing through the stenotic valve. Cystic medial degeneration has been described as occurring in 11% of patients with aortic stenosis secondary to bicuspid aortic valve, which may also play a role in aortic dilatation.[88] Other conditions associated with bicuspid aortic valve include mitral valve prolapse, aortic coarctation, and aortic dissection.[85, 88]

Aortic regurgitation results in volume overload of the left ventricle, which responds by dilating. Because the ascending aorta also receives an increased volume of blood with each left ventricular contraction, it also dilates.[86] In patients with aortic regurgitation, this combination of left ventricular dilatation and enlargement of the ascending aorta can be recognized on CT images (Fig. 32–7).

Mitral Valve Disease

Rheumatic heart disease, which causes the mitral valve leaflets to become thickened and calcified, is the most common cause of mitral stenosis.[58, 86] Because involvement of the chordae tendineae causes tethering, the mitral valve is often regurgitant as well as stenotic. Pure mitral stenosis results in left atrial enlargement (Fig. 32–8).[86] The left ventricle is not enlarged unless there is also mitral regurgitation. Calcification of the mitral valve can be seen in patients with rheumatic mitral valve disease; however, it may also be seen in elderly patients in conjunction with mitral annulus calcification.[114]

Rheumatic heart disease is also the most common cause of mitral regurgitation. Other causes include abnormal papillary muscle function and endocarditis.[58] Mitral regurgitation causes volume overload of the left atrium and ventricle. When chronic, the regurgitation results in dilatation of both the left atrium and the ventricle.[86] The left atrium is usually more dilated in patients with mitral regurgitation than in patients with pure mitral stenosis.

The mitral annulus may calcify with age. It is easily recognized on chest radiographs as a C-shaped calcific density at the expected location of the mitral valve. Although it has been thought to be a clinically insignificant finding, some believe it to be related to atherosclerotic disease.[103] CT readily depicts calcification of the mitral annulus (Fig. 32–9). It may be difficult to distinguish between calcification of the valve itself and calcification of the mitral annulus. Calcification of the mitral annulus may also hamper detection of calcification within the circumflex artery.

Tricuspid Valve Disease

Tricuspid stenosis may result as a manifestation of rheumatic heart disease, in which case the mitral valve is usually affected as well.[58] Less common causes of tricuspid stenosis include lupus erythematosus and carcinoid syndrome. Tricuspid stenosis results in dilatation of the right atrium with a normal-sized right ventricle.

Tricuspid regurgitation may occur as a result of right ventricular enlargement stretching the tricuspid annulus. Carcinoid syndrome, papillary muscle dysfunction, and bacterial endocarditis may also cause tricuspid regurgita-

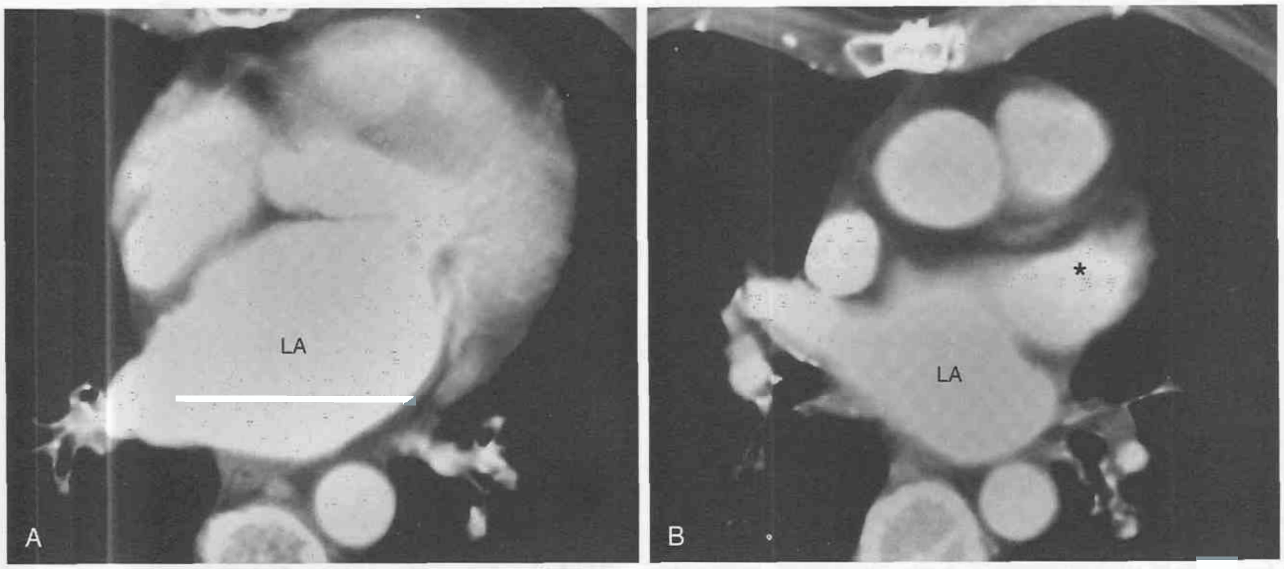

Figure 32–8. Mitral stenosis secondary to rheumatic heart disease. Axial CT with intravenous contrast medium shows *(A)* enlargement of the left atrium (LA) with *(B)* enlargement of the left atrial appendage *(asterisk)*.

tion. The increased volume of blood through the regurgitant valve results in dilatation of both the right atrium and the right ventricle (Fig. 32–10). When intravenous (IV) contrast medium is used, the more densely contrasted blood within the right atrium may reflux into the hepatic veins. Reflux of contrast material into the hepatic veins may also be seen in patients with right heart failure.

Pulmonary Valve Disease

Pulmonary valve stenosis can be recognized on CT scans when there is dilatation of the main and left pulmonary arteries, which results from the poststenotic turbulent jet of blood.

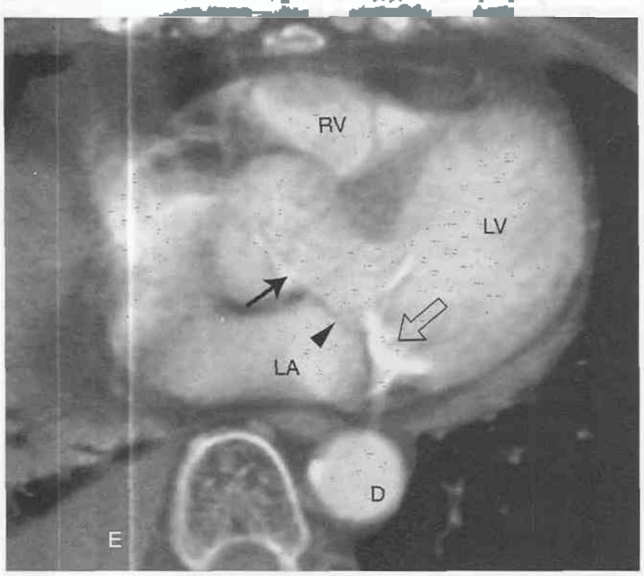

Figure 32–9. Mitral annulus calcification. Axial contrast-enhanced CT image shows calcification of the mitral annulus *(open arrow)*, which was also identified on chest radiograph. Calcification within the mitral annulus may be difficult to differentiate from calcium in the circumflex coronary artery. A small amount of calcification can be visualized within the aortic valve *(arrow)*. The patient did not have evidence of aortic stenosis. D, descending aorta; E, right pleural effusion; LA, left atrium; LV, left ventricle; RV, right ventricle. The *arrowhead* points to the mitral valve leaflet.

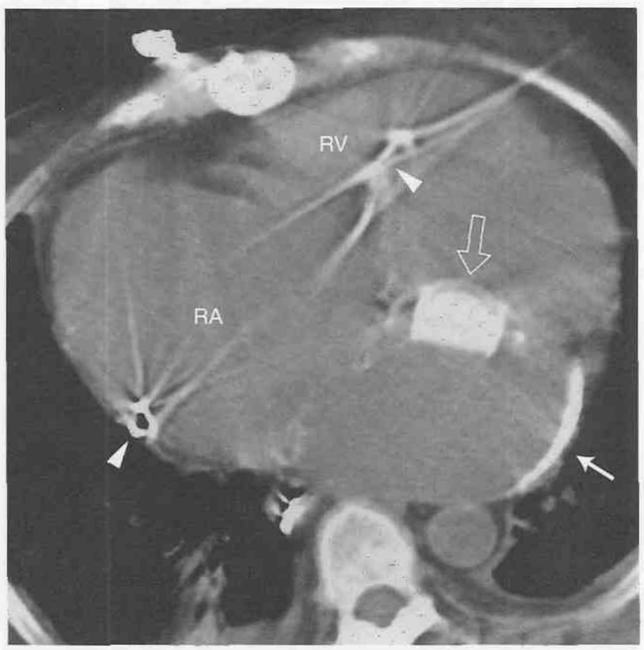

Figure 32–10. Mitral stenosis and tricuspid regurgitation. There is dystrophic calcification of the wall of the left atrium *(arrow)* in this patient with long-standing mitral stenosis who has undergone mitral valve replacement *(open arrow)*. The patient also had tricuspid regurgitation resulting in marked enlargement of the right atrium (RA) and right ventricle (RV). A pacemaker is also present *(arrowheads)*.

Other Causes of Hypertrophy and Chamber Enlargement

The left ventricle may be dilated as a result of ischemic heart disease or cardiomyopathy. Dilatation of cardiac chambers can also be seen in patients with cardiac shunts (Fig. 32–11).

Left ventricular hypertrophy may be seen in patients with aortic stenosis, systemic hypertension (see Figs. 32–5 and 32–6), or hypertrophic cardiomyopathy. Right ventricular hypertrophy may be seen in patients with pulmonary arterial hypertension or outflow obstruction (Fig. 32–12).

Coronary Artery Disease

Postmortem examinations have demonstrated the presence of atheroma whenever coronary artery calcification is present.[14, 83] Accordingly, several methods have been used to screen patients for calcified coronary arteries. Although calcified arteries can be detected on chest radiographs and on fluoroscopy, these methods are limited in their sensitivity because of the superimposition of overlying structures. Guthaner and coworkers reported the detection of coronary artery calcification by CT in 1979, but it was not until the last decade that CT has been evaluated as a possible screening test.[44]

Several studies have compared the calcification of coronary arteries detected by conventional CT with angiographically detected atheromatous disease.[62, 83] Masuda and coauthors[62] performed conventional CT scans (10-mm slice thickness) on 161 patients and identified coronary artery calcification in 108 patients, 90% of whom showed significant vessel narrowing on an angiogram. In addition, 80% of patients with significant lesions on angiography demonstrated calcification on CT scan.

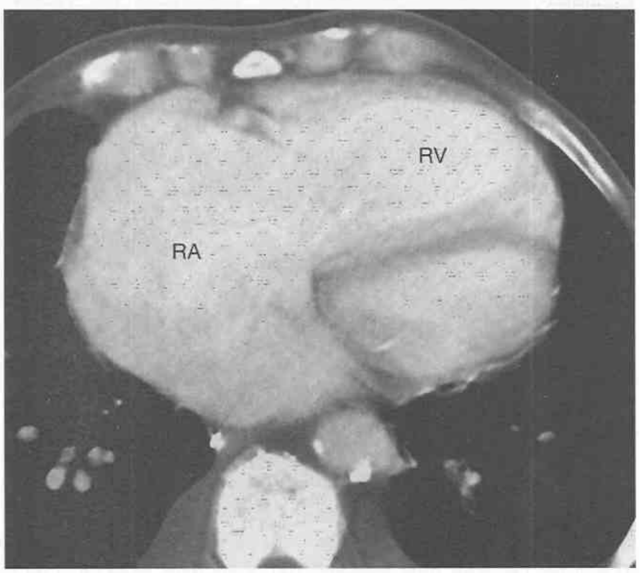

Figure 32–11. Atrial septal defect. Axial CT with intravenous contrast medium shows marked enlargement of both the right atrium (RA) and the right ventricle (RV) in this patient with atrial septal defect documented by echocardiography.

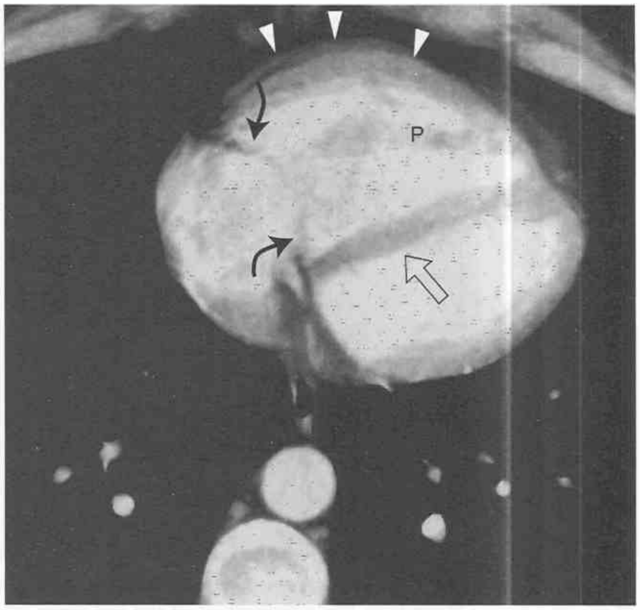

Figure 32–12. Right ventricular hypertrophy in a patient with pulmonary arterial hypertension secondary to chronic obstructive pulmonary disease. Axial contrast-enhanced CT image shows marked thickening of the free wall of the right ventricle *(arrowheads)*, which is as thick as the interventricular septum *(open arrow)*. P, right ventricular papillary muscle. *Curved arrows* point to the tricuspid valve.

Tamiya and coworkers studied 143 patients with 10-mm-thick conventional CT scans and correlated them with angiography. They found that a positive CT scan detecting coronary artery calcification had a 79% sensitivity and an 80% specificity when compared with significant coronary artery stenosis on angiograms.[102]

Agatson and associates[3] evaluated 584 patients with electron beam CT scans for detecting and quantifying coronary artery calcifications using a 3-mm-slice thickness. They defined calcification as densities in the anatomic location of the coronary arteries greater than or equal to 130 Hounsfield units (HU) and with an area of greater than or equal to 1 square millimeter. They scored each lesion based on the maximum density, as follows:

1 = 130–199 HU
2 = 200–299 HU
3 = 300–399 HU
4 = >400 HU

A total score was obtained by adding the scores from all of the slices. Of the 584 patients, 109 had coronary artery disease documented either by angiogram or by a positive history of myocardial infarction. For the other patients, exercise tests or angiographic findings were negative, or these patients were clinically asymptomatic. In the groups with documented coronary artery disease, 96% had coronary artery calcification scores greater than 0. The majority of patients with positive CT scans had calcifications involving the proximal arteries.

Breen's group[15] studied 100 patients undergoing elective angiography with electron beam CT scanning. A scoring system identical to that used in Agatson's study[3] was used,

and calcification was identified as two or more adjacent pixels measuring 130 HU or more. The area and peak CT numbers were also measured. Individual scores were summed for each major vessel. Angiographically depicted stenoses were visually assessed and considered to be "mild" if the narrowing was less than 50% and "significant" if it was greater than or equal to 50% in one or more major branches. Seventy-one patients had positive angiograms, and 75 patients demonstrated calcifications. Of the 47 patients with significant stenoses, all had coronary artery calcifications. The sensitivity of the electron beam CT for detecting patients with a positive angiogram was 95%, and the specificity was 72%. No patients with negative CT scans had significant disease on angiography.

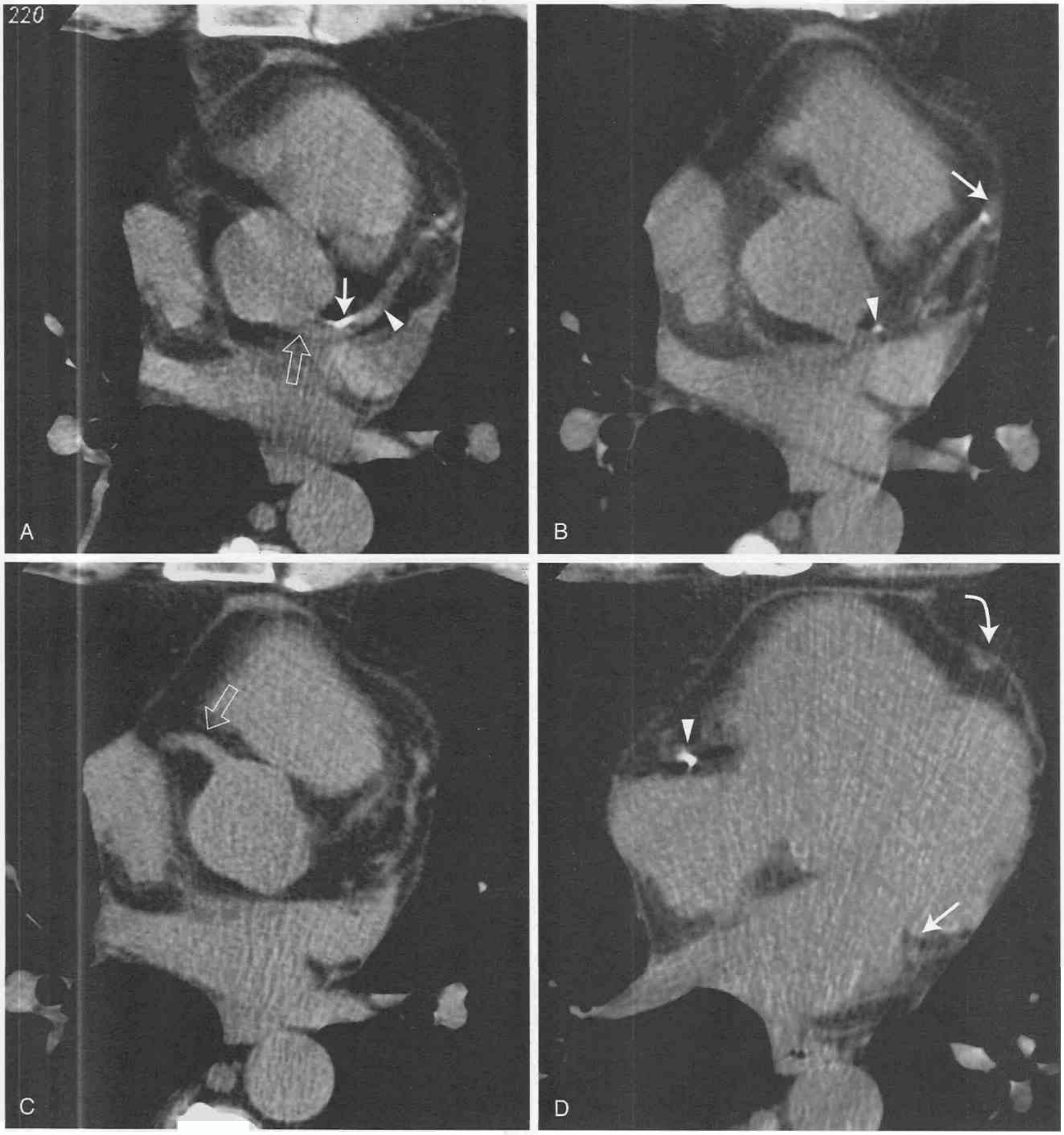

Figure 32–13. Axial CT images using retrospective electrocard[redacted]aphic gating for calcium scoring. *A*, Calcification *(arrow)* is noted at the junction of the left main *(open arrow)* and left anterior descending (LAD) *(arrowhead)* coronary arteries. *B*, More caudal image shows further calcification of the LAD *(arrow)* and calcification in the inferior aspect of the left main artery *(arrowhead)*. *C*, More caudal image shows the origin of the right coronary artery *(open arrow)* without calcification. *D*, More caudal image shows calcification *(arrowhead)* of the right coronary artery as it courses through the atrioventricular groove. The LAD *(curved arrow)* and circumflex artery *(arrow)* are not calcified at this level.

Helical CT can depict coronary artery calcification. Because of the longer acquisition time, some motion degradation of the images occurs, particularly if cardiac gating is not used. This may result in "blurring" of the calcification. Two studies were performed to quantify coronary artery calcification, with dual-slice spiral CT comparing the results with angiography. The sensitivity and specificity of these two studies were 88% to 92% and 52% to 72%, respectively.[16, 94] Note that ECG gating was not used in either study.

Since the publication of these two studies, retrospective cardiac gating has been applied to spiral CT and found to reduce cardiac motion artifact.[113] The major manufacturers of CT equipment have now added cardiac gating to their scanners. Carr and colleagues found that calcium scores obtained with retrospective cardiac gating and a subsecond helical CT scanner correlate well with calcium scores obtained from electron beam CT scanners.[26] Becker and coworkers found that calcium scores using a single-slice CT with prospective ECG gating also correlated well with electron beam CT calcium scores.[11]

Most studies evaluating coronary artery calcium have used the Agatston method of scoring, although other methods of scoring exist. Several authors have found improved reproducibility with alternate scoring methods, including volume-based and mass-based methods as well as use of the Agatston method with average instead of peak density values.[24, 95, 117]

Detection of coronary artery calcium indicates that atherosclerotic disease is present, and the more calcium found, the greater the amount of atherosclerosis (Fig. 32–13). However, the amount of calcium underestimates the true extent of atherosclerotic disease and it does not predict the site of areas of stenosis. Rumberger and colleagues published their criteria for patient selection and guidelines for intervention based on calcium scores.[87] Controversy still exists over which patients should undergo the test. Further studies evaluating clinical outcomes with calcium scores need to be performed.

CT may also detect the sequelae of coronary atherosclerotic disease. Evidence of previous myocardial infarction can be visualized on CT images of the heart, either as an area of thinned myocardium (Fig. 32–14) or as an area of dystrophic calcification (Fig. 32–15) in the infarcted area.

True ventricular aneurysms occur in approximately 10% of patients with a history of myocardial infarction.[1] Bulging of the thinned or calcified myocardium may be seen, consistent with a true aneurysm (see Fig. 32–14). The wall of a true aneurysm is made up of the myocardial scar and the overlying epicardium. It typically has a broad neck, since it is a continuation of the left ventricular cavity. A true aneurysm can gradually expand over time; however, rupture is rare.[100] Rupture of the myocardium usually results in hemopericardium and cardiac tamponade. When the rupture is contained by the pericardium, a pseudoaneurysm results.

Ventricular pseudoaneurysms are thought to occur in the presence of pericardial adhesions,[48] due either to a previous myocardial infarction with associated pericardial inflammation[104, 111] or to pericarditis.[99] Although a rare entity, left ventricular pseudoaneurysm most commonly occurs as a sequela of myocardial infarction or following cardiac sur-

Figure 32–14. True ventricular aneurysm in a patient with history of myocardial infarction. Axial CT image of the heart after administration of intravenous contrast medium shows marked thinning of the cardiac apex *(arrowheads)* compared with the thickness of the lateral wall *(arrow)*. There is slight bulging of the apex. Dyskinesis was present on the echocardiogram.

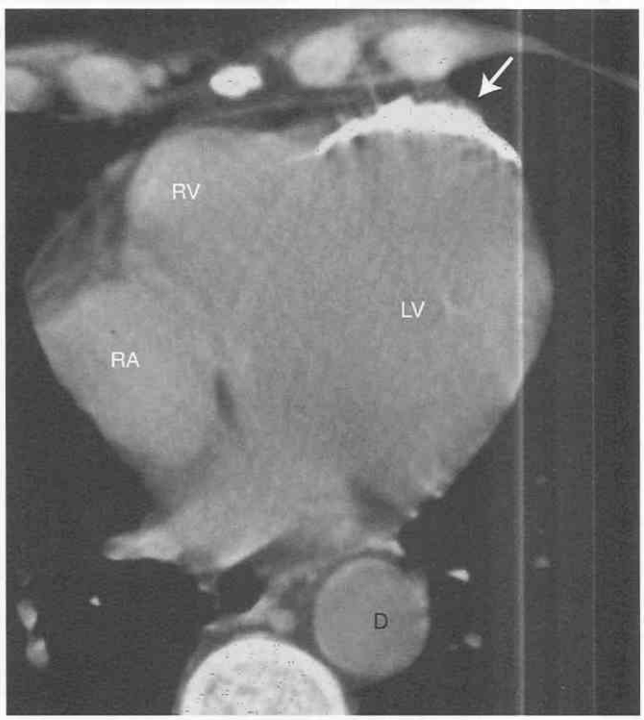

Figure 32–15. Calcified myocardial infarct. Noncontrast-enhanced CT shows dense calcification of the left ventricular apex *(arrow)* in this patient known to have a history of myocardial infarction. D, descending aorta; LV, left ventricle; RA, right atrium; RV, right ventricle.

gery.[60, 74, 84, 89] Less common causes include trauma, myocardial abscess,[60] and endocarditis.[42, 77] Pseudoaneurysms resulting from myocardial infarction occur most commonly in the inferior or posterolateral wall and typically have a narrow neck (Fig. 32–16).[51, 70, 100] The location of postsurgical pseudoaneurysms depends on the type of surgery. Unlike the more common true aneurysms of the left ventricle, pseudoaneurysms of the left ventricle are more prone to rupture, resulting in death.[39, 51, 100, 109, 116]

Coronary artery bypass grafts can be identified on CT

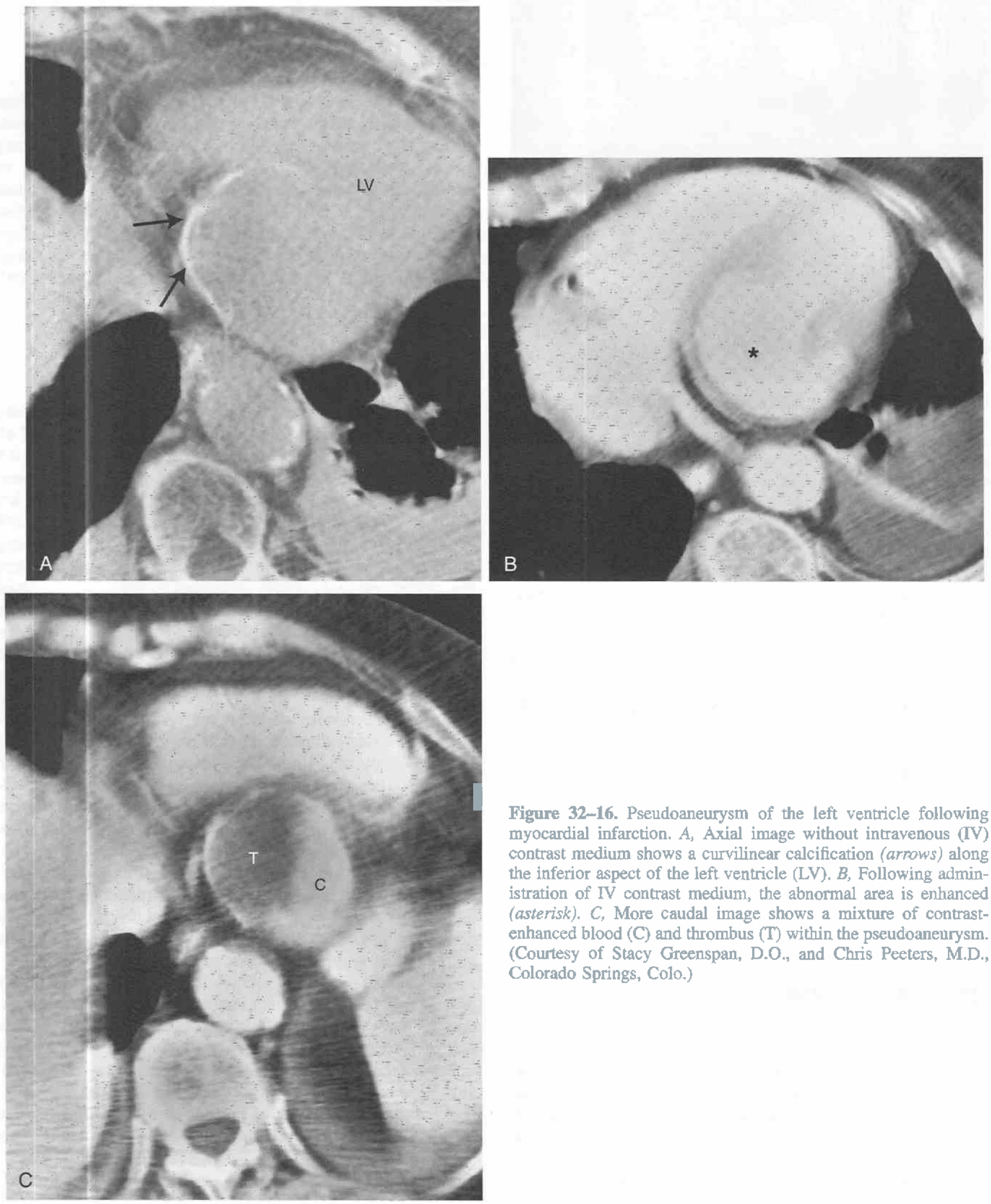

Figure 32–16. Pseudoaneurysm of the left ventricle following myocardial infarction. *A,* Axial image without intravenous (IV) contrast medium shows a curvilinear calcification *(arrows)* along the inferior aspect of the left ventricle (LV). *B,* Following administration of IV contrast medium, the abnormal area is enhanced *(asterisk)*. *C,* More caudal image shows a mixture of contrast-enhanced blood (C) and thrombus (T) within the pseudoaneurysm. (Courtesy of Stacy Greenspan, D.O., and Chris Peeters, M.D., Colorado Springs, Colo.)

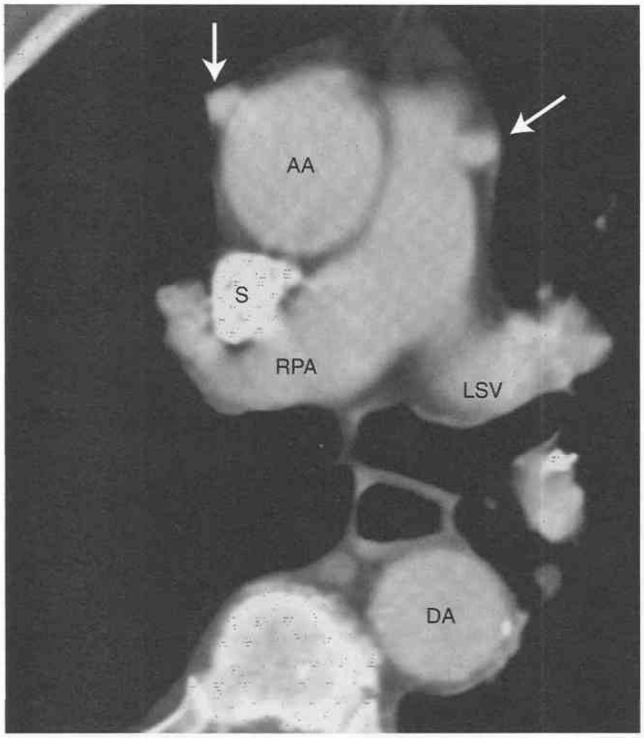

Figure 32–17. Coronary artery bypass grafts. Contrast-enhanced axial CT image shows enhancement of right and left coronary artery bypass grafts *(arrows)*. AA, ascending aorta; DA, descending aorta; LSV, left superior pulmonary vein; RPA, right pulmonary artery; S, superior vena cava.

scans (Fig. 32–17). With faster scanning times, their patency can often be determined. Although it happens rarely, a pseudoaneurysm may develop at the site of the anastomosis, usually the proximal anastomosis. These pseudoaneurysms tend to be identified within weeks to months following bypass surgery and can be associated with mediastinal infection.

True aneurysms are less common and occur in the body of the saphenous graft. They are thought to be related to graft atherosclerosis and are usually identified years after bypass surgery.[79] They are less likely to rupture than pseudoaneurysms of saphenous vein grafts.[105] Saphenous vein graft aneurysms can be detected on a chest radiograph, where it may have the appearance of a mass.[35] CT or magnetic resonance imaging (MRI) demonstrates that the mass is related to a vascular structure, and each modality can depict the amount of associated thrombus within the lumen (Fig. 32–18).

Systemic Disease

The diagnosis of anemia can be suggested on CT scans if an IV contrast agent is not used. In the anemic patient, the blood in the chambers of the heart is less dense than the myocardium because of the reduced protein content in the blood. This difference in density is best appreciated at the level of the interventricular septum (Fig. 32–19). In general, the lower the hemoglobin, the more likely that the myocardium appears denser than the blood. An increase in density of the myocardium may also be seen in patients with hemochromatosis, because of increased iron deposition within the myocardium. In hemochromatosis, the liver is also increased in density.[34, 112] Amiodarone is known to concentrate in the heart,[61] and in patients with amiodarone pulmonary toxicity, it has been described as causing increased density of the myocardium on unenhanced CT scans.[54]

Cardiac Tumors

Metastatic involvement of the heart is more common than primary cardiac tumors, which are very rare. Patients with cardiac tumors may be asymptomatic, or they may present with arrhythmias or hemodynamic, embolic, or constitutional symptoms. The reported incidence of cardiac tumors ranges from 0.001% to 0.03%.[19, 63] Most cardiac tumors have benign histologic features (75%). Although primary cardiac tumors are often evaluated by echocardiography, CT, MRI, or both can be useful in their assessment.

Benign Cardiac Tumors

Myxoma

The most common cardiac tumor, the myxoma, accounts for about 50% of all benign cardiac tumors and 25% of all cardiac tumors. The incidence of cardiac myxoma is 0.5 per million population per year,[12] with a female predominance.[12, 81] The most common anatomic location is the left atrium (75% to 80%), followed by the right atrium (10% to 20%).[7, 12, 19, 55, 63] Less common are myxomas involving either ventricle or involving both atria (5% to 10%), and the mitral valve is rarely involved.[12, 19, 27, 81] Left atrial myxomas are typically pedunculated and arise from the interatrial septum, near the fossa ovalis. Right atrial myxomas tend to be sessile and may arise from areas of the atrium other than the septum.

Patients with myxoma may present with hemodynamic symptoms, embolic disease, or constitutional symptoms.[12, 55, 81] Hemodynamic symptoms are related to outflow obstruction by the tumor. The symptoms may be related to posture and include dyspnea, syncope, and sudden death. Myxomas are known to embolize, and patients may present with stroke or with symptoms related to peripheral or pulmonary emoblization.[12, 55, 81] Embolization of the myxomatous tissue may result in myxomatous pseudoaneurysm.[32] Myxoma may also cause constitutional symptoms, including fever, weight loss, myalgia, and arthralgia.[55] Patients may also have an elevated erythrocyte sedimentation rate, anemia, and leukocytosis.

Myxomas tend to be solitary and to occur sporadically in middle-aged individuals, although they have been reported in all age groups.[19, 63, 81] These tumors carry a low risk of recurrence after resections. Familial myxomas tend to occur at an earlier age, can be multiple (a third of cases), and have a 10% risk of recurrence following resection.[63, 64, 81] Patients tend to present at a younger age than patients with sporadic myxoma. The left atrium is the most common location of familial myxomas (61%).[107]

A third subset of myxomas was described by Carney.[25]

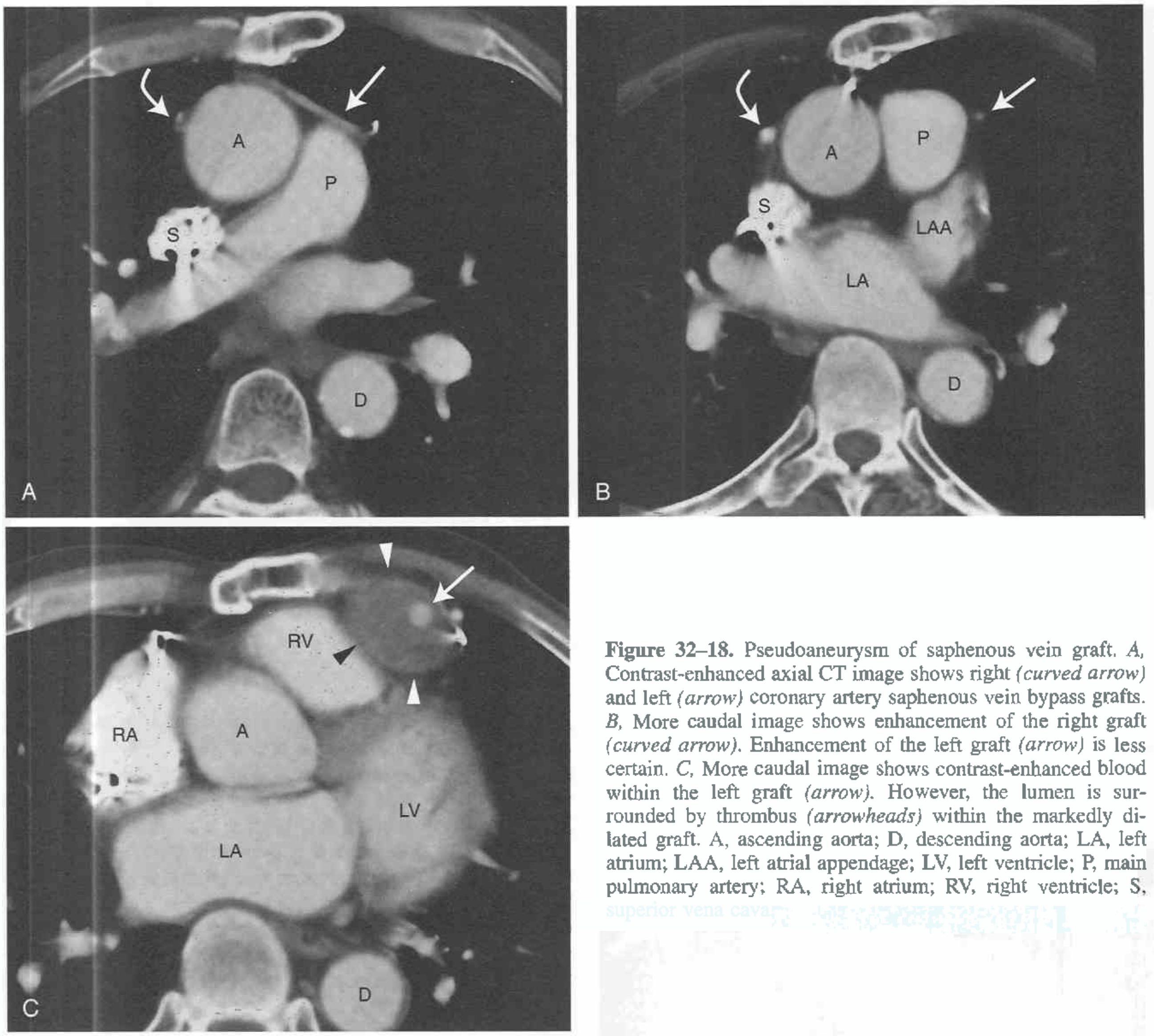

Figure 32–18. Pseudoaneurysm of saphenous vein graft. *A,* Contrast-enhanced axial CT image shows right *(curved arrow)* and left *(arrow)* coronary artery saphenous vein bypass grafts. *B,* More caudal image shows enhancement of the right graft *(curved arrow).* Enhancement of the left graft *(arrow)* is less certain. *C,* More caudal image shows contrast-enhanced blood within the left graft *(arrow).* However, the lumen is surrounded by thrombus *(arrowheads)* within the markedly dilated graft. A, ascending aorta; D, descending aorta; LA, left atrium; LAA, left atrial appendage; LV, left ventricle; P, main pulmonary artery; RA, right atrium; RV, right ventricle; S, superior vena cava.

These myxomas occur in association with pigmented skin lesions and endocrine lesions. Patients tend to present in the third decade of life and tend to have multiple, multicentric, and metachronous myxomas. Only 50% of myxomas involve the left atrium in patients with the Carney complex. Patients with the Carney complex have an increased risk of recurrence of myxoma following resection.[64] Because the Carney complex is inherited as an autosomal dominant trait, family members should be screened for the disease.[25, 78]

On CT, a myxoma has the appearance of a filling defect in the chamber of origin (Fig. 32–20). The mass is usually heterogeneous and may have areas of calcification.[7, 78]

Rhabdomyoma

Rhabdomyomas are the most common pediatric cardiac tumor, typically occurring in children younger than 1 year of age.[63] They are usually multiple and occur most commonly in either ventricle, although the atria may also be involved. They do not occur in association with the heart valves.

Patients are usually asymptomatic. However, the tumors may cause arrhythmias or obstruction, resulting in acute heart failure and sudden death. The incidence of cardiac rhabdomyoma in patients with tuberous sclerosis is 30% to 50%.[97, 110]

Rhabdomyomas are thought to be hamartomatous lesions. They do not show a significant increase in size and may regress over time[2, 37, 110]; thus, they may be monitored in asymptomatic individuals. Echocardiography is usually used for evaluation of these tumors.

Other Benign Cardiac Tumors

Cardiac lipomas are usually solitary and may occur in the myocardial tissue or in a subendocardial or subepicardial location. Because affected patients are usually asymptomatic, the lesions are usually found incidentally. Cardiac lipomas can be associated with rhabdomyomas or tuberous

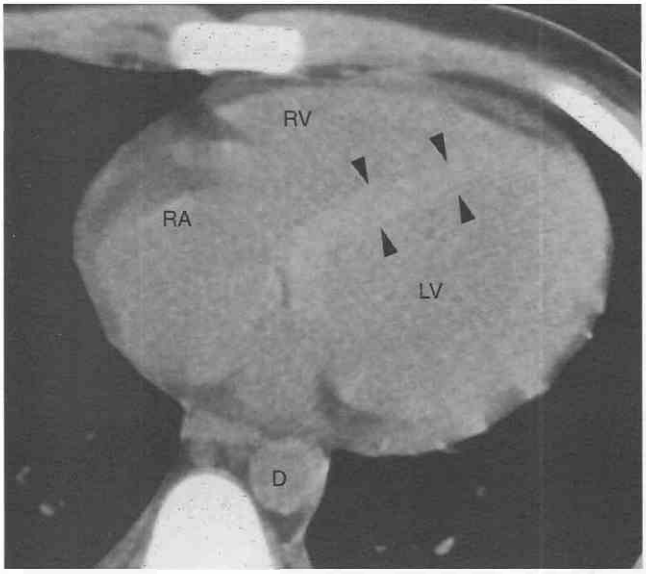

Figure 32–19. Anemia. Axial CT scan without contrast medium in an 18-year-old patient with a hematocrit of 23 mL/dL (normal range, 36 to 47 mL/dL). The interventricular septum *(arrowheads)* is visible because of the reduced density of the blood in the ventricles. D, descending aorta; LV, left ventricle; RA, right atrium; RV, right ventricle.

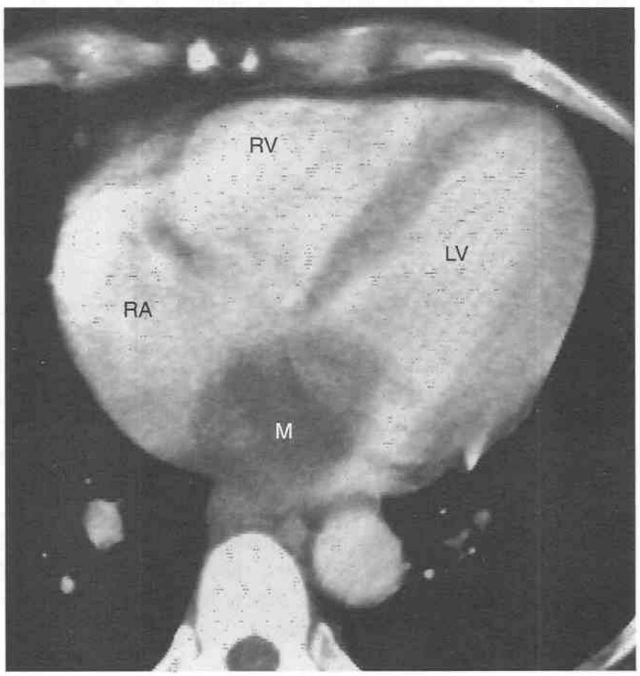

Figure 32–20. Myxoma. This patient presented with symptoms thought to be secondary to mitral stenosis. Axial CT with intravenous contrast medium shows a large mass (M) nearly filling the left atrium. At surgery, the tumor was found to arise from the interatrial septum. LV, left ventricle; RA, right atrium; RV, right ventricle. (Courtesy of Robert D. Tarver, M.D., Indiana University Medical Center.)

sclerosis. These lesions may be first detected by echocardiography. CT or MRI can document their fatty nature, establishing the diagnosis.[106, 118]

Papillary fibroelastoma is a rare lesion, usually affecting older adults (range, 25 to 86 years of age). The tumor occurs most frequently on the valves, but it can occur anywhere in the heart.[19, 63] The tumor is composed of multiple papillary fronds, which predispose it to form thrombi. Because of the risk of lethal embolization of the coronary or cerebral circulation, surgical resection is the treatment of choice.[19, 63] These tumors are usually evaluated with echocardiography. They are not usually seen on CT because of their small size and relation to moving valves.[7]

Cardiac fibromas are the second most common benign pediatric cardiac tumor, although they may also occur in adults. They tend to be solitary lesions that arise in the ventricular myocardium. They may cause lethal arrhythmias and heart failure. On CT, these tumors appear as soft tissue homogeneous masses, often with areas of calcification.[7] They are often fairly large when detected, and surgical resection may require chamber reconstruction.[63]

Malignant Cardiac Tumors

Angiosarcoma

Angiosarcoma is the most common primary malignant cardiac tumor.[19] These tumors usually occur in adults, although they have been reported in a wide age range.[6, 19, 23, 63] Men are affected more often than women.[19, 47, 63] Angiosarcomas usually arise from the free wall of the right atrium (Fig. 32–21) or from the pericardium.[8, 19, 23, 47, 63] Thus, patients tend to present with symptoms of right heart failure, vena cava obstruction, or pericardial disease. Most patients have metastatic disease at the time of diagnosis, most commonly involving the lung.[23] The prognosis is generally poor, although some patients survive longer than 1 year.[6, 19, 23, 47, 63, 98]

Other Malignant Cardiac Tumors

Rhabdomyosarcomas have a slight male predominance and tend to occur in adults. They can arise anywhere within the heart, including the valves, and are frequently multiple. Patients may present with symptoms of pericardial disease, chest pain, dyspnea, or embolic events. Rhabdomyosarcomas are also associated with hypertrophic pulmonary osteoarthropathy, polyarthritis, neurofibromatosis, and eosinophilia.

Fibrosarcomas are rare lesions. They occur in the right and left sides of the heart with equal frequency and are often multiple. Approximately 50% of these tumors involve a cardiac valve.

Primary cardiac osteosarcomas usually arise from the posterior wall of the left atrium near the pulmonary veins.[6, 19, 21, 63] This is in contradistinction to metastatic osteosarcomas, which usually involve the right atrium. These lesions may calcify and may be confused with calcified myxoma. They can be distinguished from calcified myxomas by their location in the posterior wall of the left atrium instead of the usual septal location of myxomas.

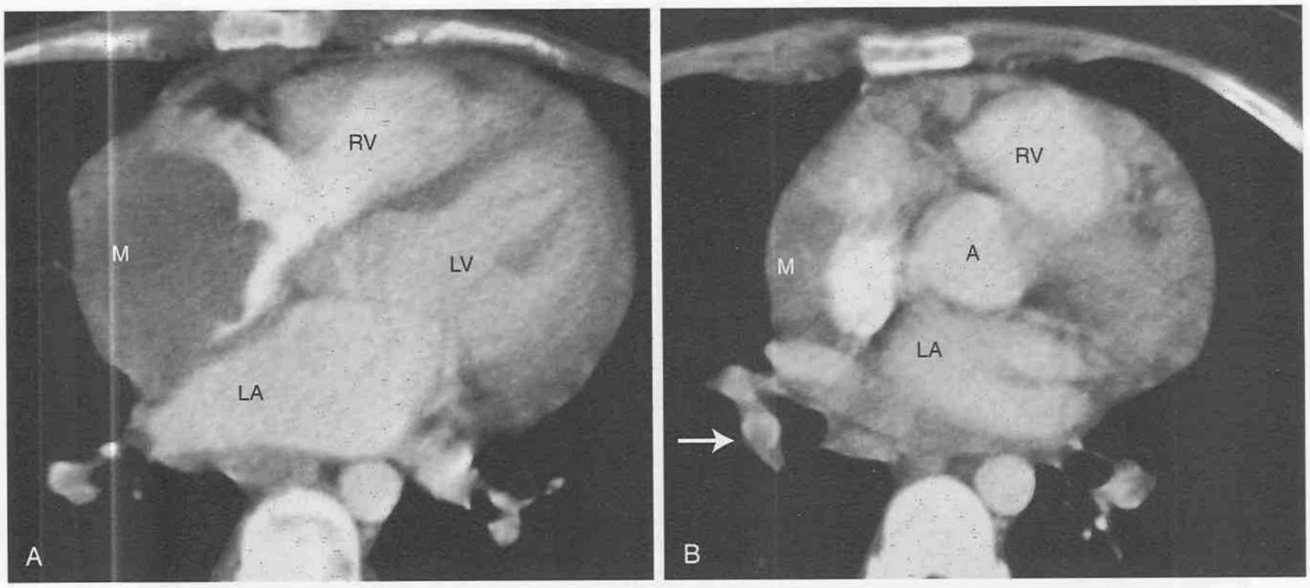

Figure 32–21. Angiosarcoma in a 23-year-old man. Contrast-enhanced axial CT images. *A,* A large mass [redacted]upyi[redacted]ost of the right atrium. LA, left atrium; LV, left ventricle; M, mass; RV, right ventricle. *B,* Image more cephalad shows a filling defect in the right lower lobe pulmonary artery, consistent with tumor thrombus *(arrow)*. The patient had pulmonary and bony metastases as well (not shown). A, ascending aorta; M, mass.

Leiomyosarcomas tend to arise from the posterior wall of the left atrium, typically in the fourth decade of life. They frequently involve the pulmonary veins or the mitral valve, causing symptoms of heart failure.

Liposarcomas are extremely rare lesions, with only 18 reported cases in the literature. Despite their name, histologically little or no fat is detectable. They can occur in the atria, ventricles, or pericardium.

Although up to 25% of patients with *lymphoma* have cardiac involvement at autopsy, primary cardiac lymphoma (lymphoma limited to the heart and/or pericardium) is very rare.[19] Primary cardiac lymphoma is usually a B-cell lymphoma. The most common location is a right-sided lesion, usually arising from the right atrium. Associated pericardial effusion is common (Fig. 32–22).

Secondary Cardiac Tumors

Metastatic cardiac involvement is much more common than primary cardiac neoplasms, but it may be undetected before death. Autopsy studies have found cardiac metastases to be present in up to 20% of patients with neoplasm. They occur most frequently in patients with lymphoma, leukemia, or melanoma (40% to 50%) and in patients with lung or breast cancer (10% to 33%). Direct extension of tumor is the most common route and typically occurs in lung and breast cancers. Symptoms tend to be related to associated pericardial involvement.

Renal cell carcinoma, adrenal carcinoma, hepatocellular carcinoma, and uterine leiomyosarcoma may involve the heart through extension into the inferior vena cava. Thyroid carcinoma may extend through the superior vena cava. Lung cancer may also spread along the pulmonary veins to involve the left atrium.

Finally, lymphangitic metastases may occur as well as hematogenous metastases. Leukemia and lymphoma are the most common tumors to cause cardiac metastases by the lymphangitic route, in which case mediastinal nodes are invariably involved.

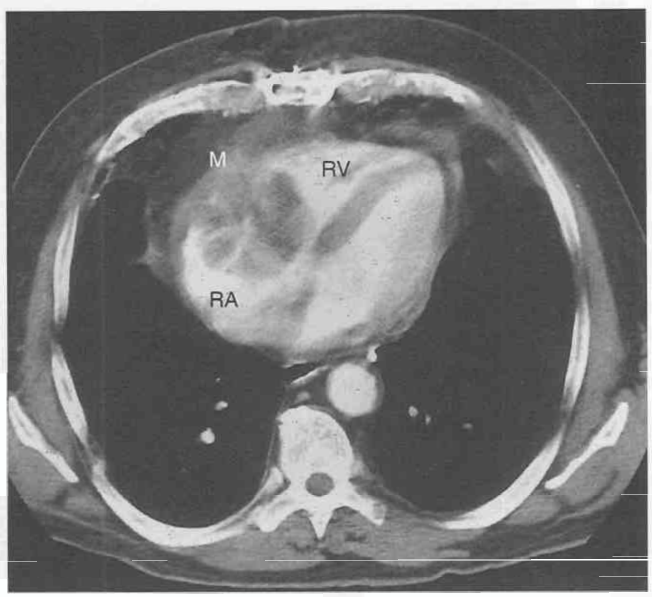

Figure 32–22. Primary cardiac [redacted]phoma in a 42-year-old [redacted]. Contrast-enhanced CT following open biopsy shows a lobulated mass (M) within the right heart at the level of the tricuspid valve. The mass extends into the right atrial and right ventricular cavities. Open surgical biopsy confirmed the tumor involvement of the tricuspid valve, right atrium, and right ventricle. RA, right atrium; RV, right ventricle.

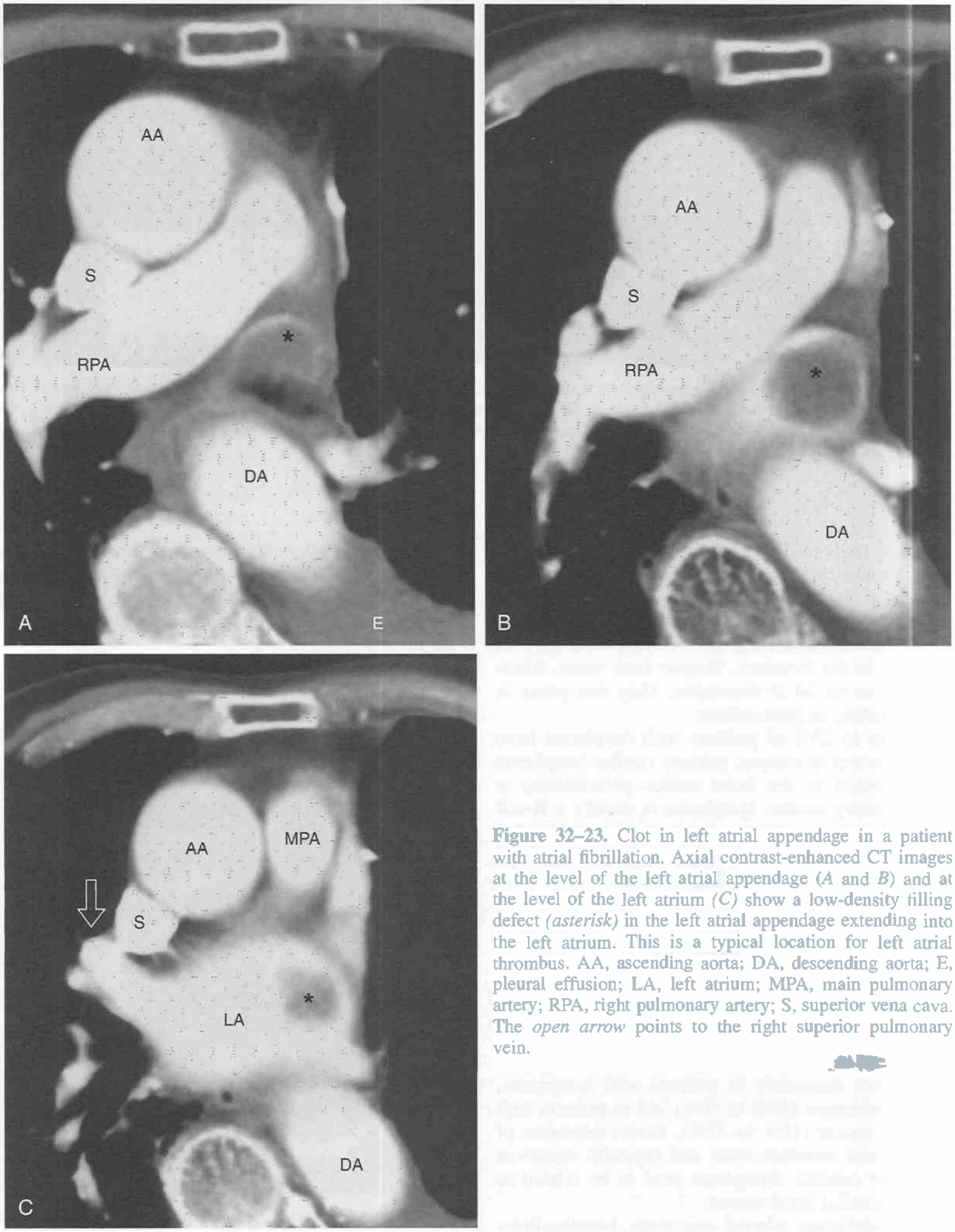

Figure 32–23. Clot in left atrial appendage in a patient with atrial fibrillation. Axial contrast-enhanced CT images at the level of the left atrial appendage (*A* and *B*) and at the level of the left atrium *(C)* show a low-density filling defect *(asterisk)* in the left atrial appendage extending into the left atrium. This is a typical location for left atrial thrombus. AA, ascending aorta; DA, descending aorta; E, pleural effusion; LA, left atrium; MPA, main pulmonary artery; RPA, right pulmonary artery; S, superior vena cava. The *open arrow* points to the right superior pulmonary vein.

Lesions That Mimic Cardiac Tumors

Thrombus

Thrombus within the heart may mimic a cardiac mass. In the atria, thrombus usually involves the appendages (Figs. 32–23 and 32–24).[90] Laminated thrombus may also occur in the left atrium between the pulmonary veins.[90] In the ventricle, thrombus usually occurs over an area of hypokinesis such as a myocardial infarction.[5, 90] If the diagnosis of clot is uncertain on CT images, MRI can be used for further evaluation.[93]

Lipomatous Hypertrophy of the Interatrial Septum

Fat may be detected in the atrioventricular grooves and the interatrial septum. Normally, fat in the interatrial septum measures less than 1 cm anterior and posterior to the fossa ovalis.[17] Lipomatous hypertrophy of the interatrial septum (LHIS), first described by Prior in 1964, results in increased fat deposition in the interatrial septum.[75] This may mimic an atrial tumor on an echocardiogram (Fig. 32–25).[5, 20] Typically, the lesion 34is dumbbell-shaped because of the sparing of the region of the fossa ovalis (Fig. 32–26).[65, 80] Both CT and MRI are able to accurately depict the fatty nature of the lesion and establish the diagnosis.[33]

Pathologically, the lesion is not a true encapsulated lipoma. The fatty tissue resembles fetal or brown fat and is intermixed with myocardial cells. This lesion is most often found incidentally, but it can be associated with atrial arrhythmias.[49, 72, 80] Treatment is directed at controlling the arrhythmia if present.

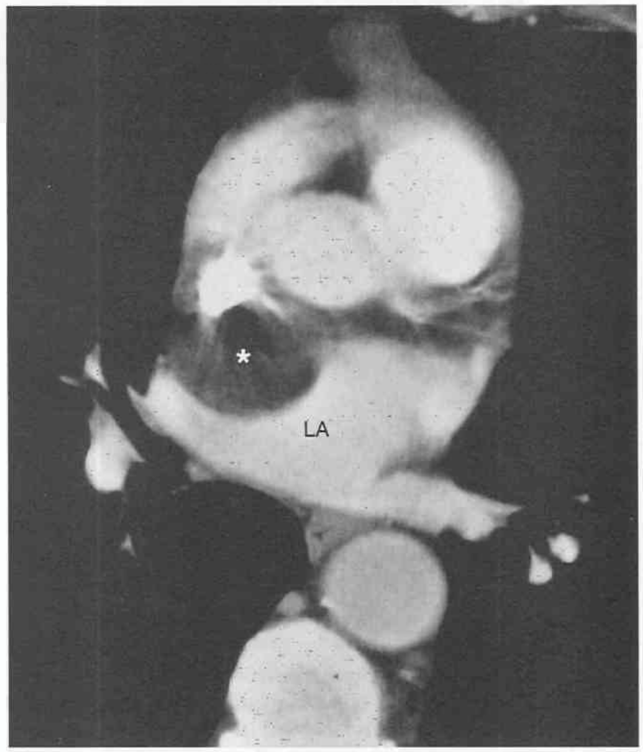

Figure 32–25. Lipomatous hypertrophy of the interatrial septum. Contrast-enhanced axial image shows fatty enlargement of the interatrial septum *(asterisk)*. The fat bulges into the left atrium (LA).

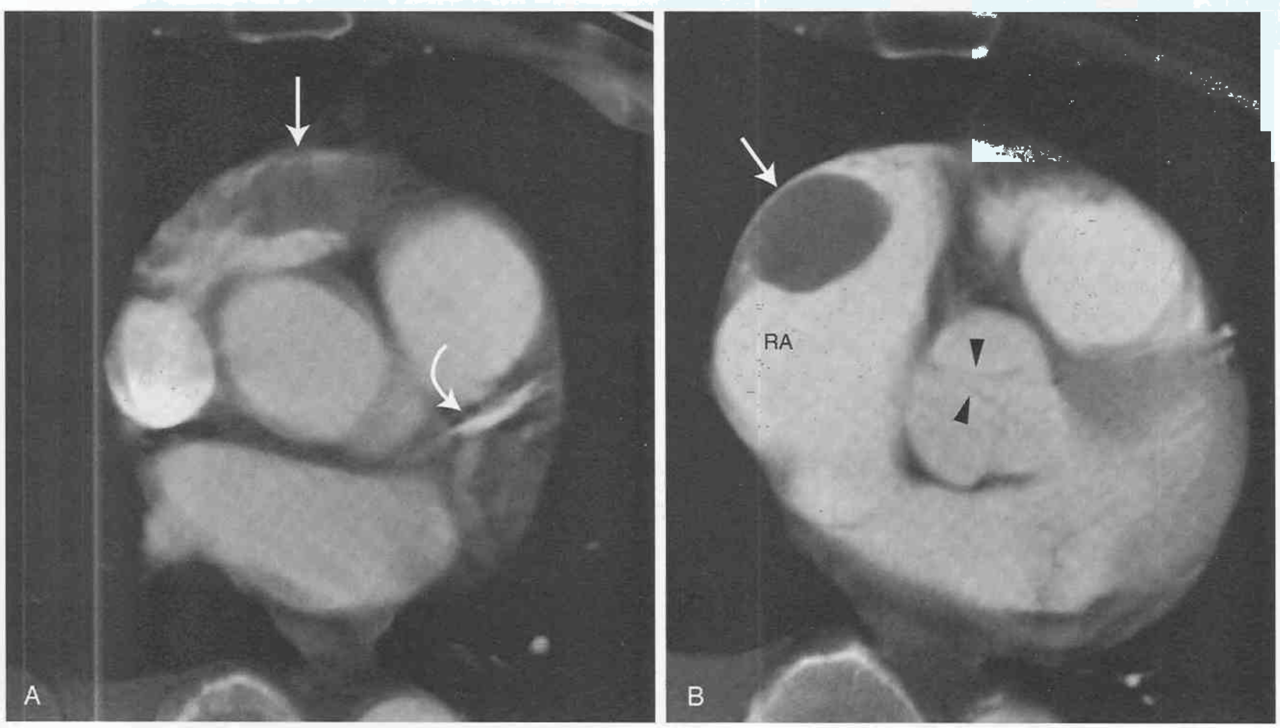

Figure 32–24. Clot in right atrial appendage. Contrast-enhanced axial CT images show *(A)* a large filling defect in the right atrial appendage *(arrow)* and *(B)* extension into the right atrium. The right atrium is enlarged. Thrombus was also found in the pulmonary arterial tree (not shown). There is calcification of the left anterior descending artery *(curved arrow)*. RA, right atrium. The *arrowheads* point to cusps of aortic valve.

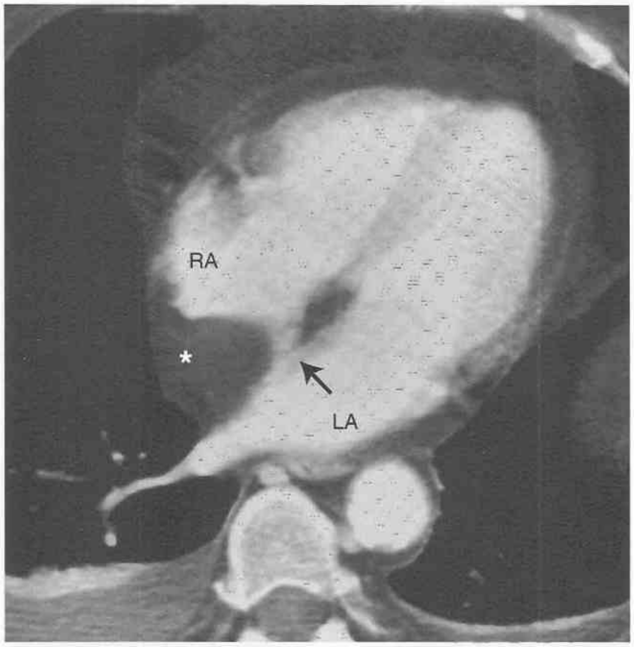

Figure 32–26. Lipomatous hypertrophy of the interatrial septum. Axial CT with intravenous contrast medium shows increased fat deposition within the interatrial septum *(asterisk)*. A characteristic bilobed shape is caused by sparing of the fossa ovale *(arrow)*. LA, left atrium; RA, right atrium.

Normal Anatomic Structures

Normal anatomic structures that may be mistaken for a mass include a prominent moderator band in the right ventricle, prominence of the muscle between the left superior pulmonary vein and the left atrial appendage in the left atrium (see Fig. 32–2*E*), prominent papillary muscles, and a prominent eustachian valve in the right atrium (Fig. 32–27).[5]

Pericardium

The pericardium has two layers: (1) a serous visceral layer (the epicardium), that is adherent to the heart, and (2) a fibrous parietal layer that is attached to the great vessels and the central tendon of the diaphragm. The pericardial space normally contains 20 to 25 mL of pericardial fluid. On CT, the pericardium can be identified when outlined by mediastinal and subepicardial fat. It normally measures only 1 to 2 mm thick.[18, 31] It is best visualized in the caudal and ventral areas. A focal area of increased thickness can usually be seen just anterior to the right ventricle and near the insertion onto the diaphragm.

Pericardial Defect

Congenital pericardial defects are thought to occur when there is premature atrophy of the left duct of Cuvier, resulting in decreased circulation to the left pleuropericardial membrane. Congenital pericardial defect is reported to occur in 1 in 7000 to 1 in 13,000 in autopsy studies. There is a 3:1 male-to-female ratio.

The defect is usually left-sided and may be partial or complete. Patients are usually asymptomatic; however, herniation of the heart or its appendage into a partial defect may result in chest pain or syncope. Also, sudden death due to herniation of the heart through the defect has been reported.[108] Associated congenital anomalies occur in 20% to 50% of patients with pericardial defect, most commonly atrial septal defect, patent ductus arteriosus, tetralogy of Fallot, bronchogenic cyst, or pulmonary sequestration.[66, 108] Most patients with pericardial defects have partial left-sided absence.[66] Much less common are right-sided absence and complete absence of the pericardium.

With a partial left pericardial defect, the typical finding is lack of pericardium covering the main pulmonary artery and the left atrial appendage.[66] In 75% of patients, there is also a large defect in the adjacent parietal pleura.[108] Chest radiographs of patients with a partial left pericardial defect show a discrete bulge in the cardiomediastinal silhouette at the level of the main pulmonary artery and left atrial appendage. Patients with complete absence of the pericardium show a shift of the heart to the left, a long prominent pulmonary artery, a flattened left heart border, and separation of the cardiac apex and diaphragm by lung. CT may demonstrate absence of the pericardium or an abrupt termination of the pericardium if the defect is partial.[50] When the left pericardium is absent, lung is interposed between the main pulmonary artery and the ascending aorta. When placed in the left lateral decubitus position, the heart migrates against the left chest wall. Absence of the sternopericardial ligaments may cause the heart to lie in a more posterior position when the patient is supine.[101]

Acquired pericardial defects also occur and usually follow surgery, although they may be secondary to trauma or to erosion of peptic ulcer disease.[101] Coronary artery bypass

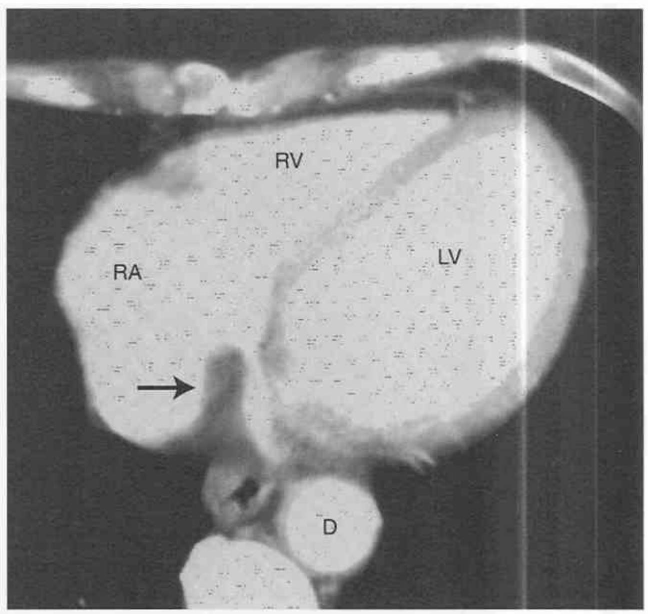

Figure 32–27. Prominent eustachian valve. Axial contrast-enhanced CT image shows a finger-like soft tissue projection within the right atrium *(arrow)*. A prominent eustachian vein was detected by echocardiography. D, descending aorta; LV, left ventricle; RA, right atrium; RV, right ventricle.

graft surgery is the most common cause of a surgical pericardial defect. When a linear midline incision is made, however, it heals readily and herniation does not usually occur.[101] Large or small defects in the pericardium may result from creation of a pericardial window, treatment of pericardial constriction, and surgery for lung cancer and mesothelioma. Radiographic detection of a pericardial defect is possible if there is herniation of the heart or demonstration of continuity of gas or fluid within the pleural and pericardial spaces. As with congenital pericardial defects, CT can demonstrate the discontinuity of surgical pericardial defects.[101] Acute cardiac herniation through a surgical pericardial defect usually occurs within the first 24 hours of surgery and is often triggered by a change in body position, suctioning, or coughing.[101]

Pneumopericardium most commonly occurs secondary to trauma, either barotrauma or blunt or penetrating trauma. It may also occur secondary to erosion of the pericardium by tumor, infection, or a stomach or duodenal ulcer.

Pericardial Cyst

Most pericardial cysts are actually pleuropericardial cysts. True pericardial cysts are rare. Pericardial cysts occur in a 3:2 male-to-female ratio. Most patients are asymptomatic. The cysts are most commonly located in the right cardiophrenic angle but can occur at the left cardiophrenic angle or higher in the mediastinum, and they often have a peripherally pointed contour.[71, 115]

On chest radiographs, the appearance is that of an area of increased soft tissue density at the cardiophrenic angle. CT can demonstrate a sharply demarcated mass whose density is that of water, with very thin or imperceptible walls (Fig. 32–28). Occasionally, the attenuation in a pericardial cyst may be higher than that of water. CT can also document whether there is increased mediastinal fat, which can have a similar appearance on a chest radiograph[73] (Fig. 32–29).

Pericardial Effusion

There are many causes of pericardial effusion[4, 30, 59] (Table 32–1). On CT scans, pericardial effusion is easily detected as an increase in fluid density within the pericardial space. Fluid commonly collects in a location anterior to the right ventricle or lateral to the left ventricle.[40] Pericardial fluid may collect in one of the pericardial sinuses and may be mistaken for other pathologic processes.

Knowledge of the anatomy of the pericardial sinuses helps one to make the correct diagnosis (Fig. 32–30).[29, 43, 56, 66] The superior pericardial recess is located anteriorly and extends anterior to the aortic root to the level of the innominate artery.[29, 43, 56, 66] The superior pericardial recess also extends between the ascending aorta and the main pulmonary artery in a triangular shape. It is continuous with the transverse sinus, which lies posterior to the ascending aorta and the main pulmonary artery.[29, 43, 56, 66]

Pericardial fluid in the superior pericardial recess may mimic aortic dissection, adenopathy, or an anterior mediastinal mass.[28, 71, 91, 96] The transverse sinus often has a lenticu-

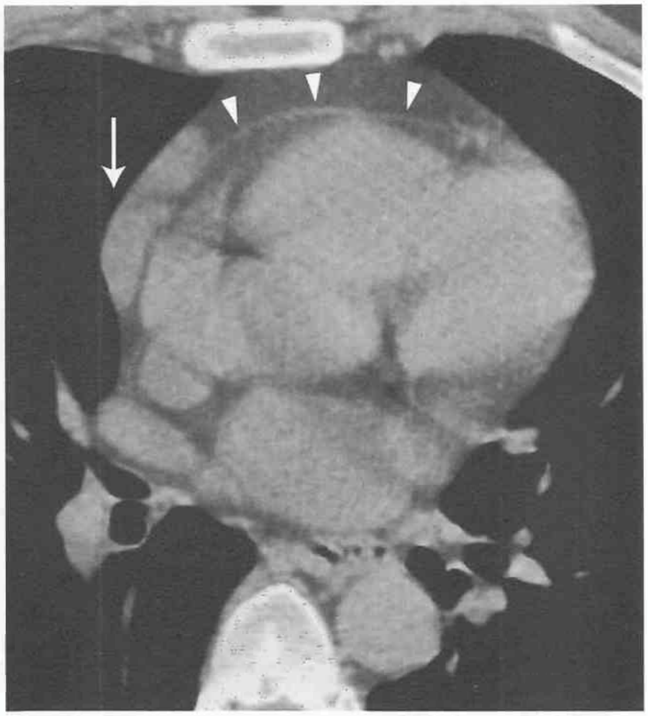

Figure 32–28. Pericardial cyst. Axial CT scan without contrast medium shows an elongated mass *(arrow)* arising from the pericardium *(arrowheads)*. The mass, whose density was similar to that of water, was resected and found to be a pericardial cyst.

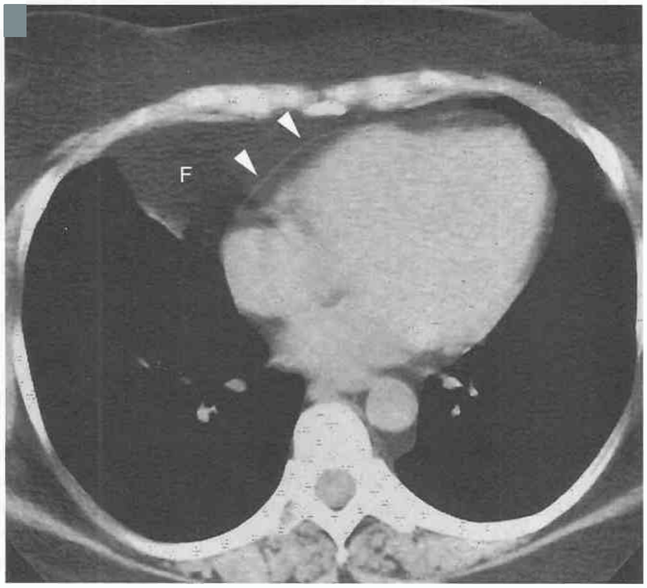

Figure 32–29. Prominent paracardiac mediastinal fat. This patient was evaluated by CT for a masslike density at the right cardiophrenic angle. Axial CT scan without contrast medium shows a collection of fat (F) at the right cardiophrenic angle, consistent with a prominent fat pad. The thin pericardium is outlined by subepicardial and mediastinal fat *(arrowheads)*.

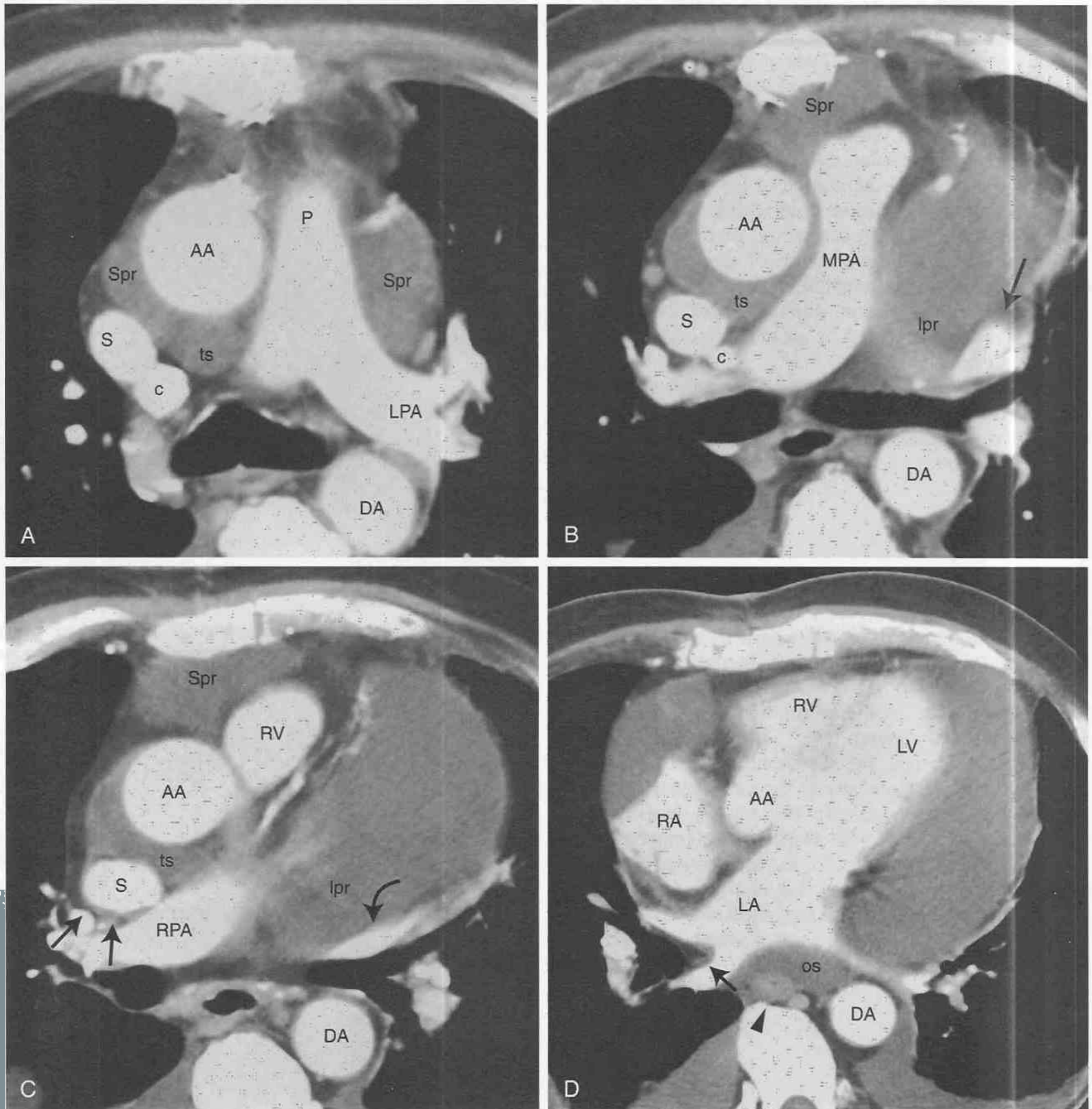

Figure 32–30. Pericardial effusion. Axial CT images following administration of intravenous contrast medium demonstrate the location of the pericardial recesses.

A, CT image at the level of the ascending aorta and main pulmonary artery. Note fluid collecting in the superior pericardial recess (spr) and the continuity of the superior pericardial recess with the transverse sinus (ts). Although fluid is not detectable in this patient, the superior pericardial recess continues along the anterior aspect of the aorta and the main pulmonary artery superiorly to the level of the aortic arch. AA, ascending aorta; C, calcified lymph node; DA, descending aorta; LPA, left pulmonary artery; P, main pulmonary artery; S, superior vena cava.

B, More caudal CT image shows fluid within the superior pericardial recess (spr), anterior to the ascending aorta (AA) and the main pulmonary artery (MPA). Fluid is also present in the transverse sinus (ts) posterior to the ascending aorta and within the left pulmonic recess (lpr). The left pulmonic recess lies anterior to the left superior pulmonary vein *(arrow)* and the left mainstem bronchus. C, calcified lymph node; DA, descending aorta; S, superior vena cava.

C, More caudal CT image shows fluid in the superior pericardial recess (spr), the left pulmonic recess (lpr) anterior to the left superior pulmonary vein *(curved arrow)*, and the transverse sinus (ts). There is a tiny amount of fluid posterior to the superior vena cava (S) within the postcaval recess *(arrows)*. AA, ascending aorta; DA, descending aorta; RPA, right pulmonary artery; RV, right ventricular outflow tract.

D, More caudal CT image shows a small amount of fluid within the right pulmonic vein recess *(arrow)*. The right and left pulmonic vein recesses lie between the superior and inferior pulmonic veins on their respective sides. Fluid also lies within the oblique sinus (os) posterior to the left atrium (LA) and anterior to the esophagus *(arrowhead)*. AA, aortic root; DA, descending aorta; LV, left ventricle; RA, right atrium; RV, right ventricle.

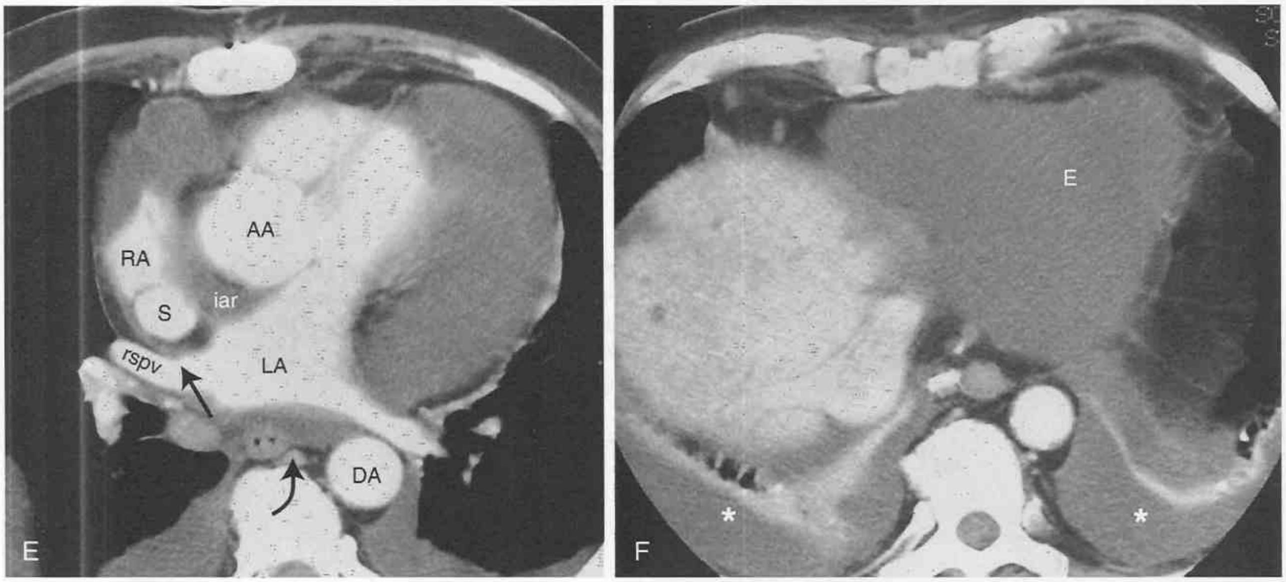

Figure 32–30. *Continued.*
E, More caudal CT image shows fluid within the inferior aortic recess (iar). This recess is located between the ascending aorta (AA) and the inferior aspect of the superior vena cava (S) or the superior aspect of the right atrium (RA). Fluid is also present in the oblique sinus *(curved arrow)* and the postcaval recess *(arrow)*, which is posterolateral to the superior vena cava between the right pulmonary artery and the right superior pulmonary vein (rspv).
F, More caudal CT image shows a significant amount of fluid (E) within the inferior aspect of the pericardium. Bilateral pleural effusions are also present *(asterisks).*

lar shape, which is helpful in distinguishing it from adenopathy.[9, 10, 13] The oblique pericardial sinus lies behind the left atrium, between the pulmonary veins.[43, 56] Less commonly identified recesses include the left pulmonic recess located between the left pulmonary artery and the left superior pulmonary vein, the postcaval recess located between the superior vena cava and the right pulmonary artery and right superior pulmonary vein, and the pulmonary venous recess located between the superior and inferior pulmonary veins.[43, 56, 76]

Thickening of the pericardium, which may show enhancement following administration of IV contrast medium, may be seen in patients with pericarditis.[71] CT can document hemopericardium by showing the increased attenuation of blood within the pericardial space (Fig. 32–31).[71]

Table 32–1. Etiology of Pericardial Effusion

1. Infection (viral, bacterial, fungal, parasitic)
2. Inflammatory (sarcoid, amyloid, inflammatory bowel disease, Whipple's disease, temporal arteritis, Behçet's syndrome)
3. Immunologic (postinfectious, postcardiac injury, postcardiotomy, postinfarction, rheumatic fever, systemic lupus erythematosus, rheumatoid arthritis, Still's disease, ankylosing spondylitis, Reiter's syndrome, scleroderma, mixed connective tissue disease, Wegener's granulomatosis, Churg-Strauss syndrome)
4. Traumatic (hemopericardium, pneumopericardium, radiation)
5. Uremic
6. Neoplastic
7. Hypothyroidism
8. Chylopericarditis
9. Congestive heart failure

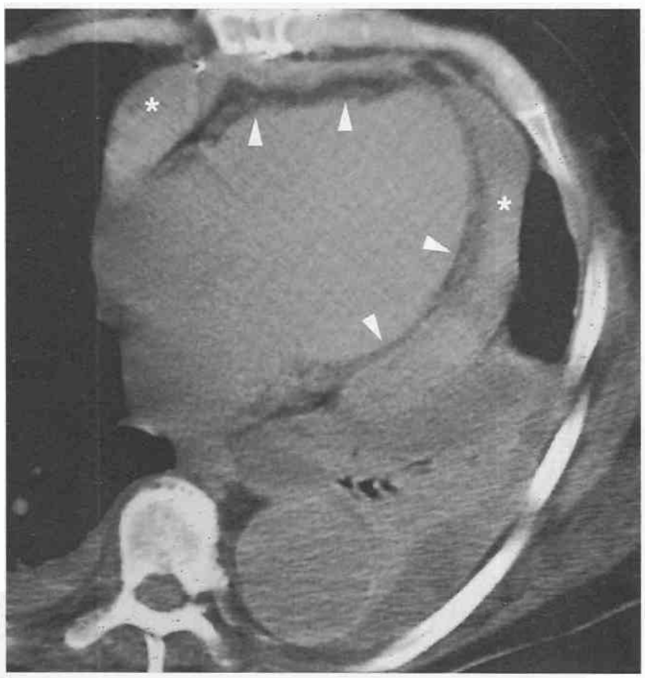

Figure 32–31. Hemopericardium in patient after coronary artery bypass graft surgery. Axial CT scan without contrast medium shows filling of the pericardial space *(asterisks)*, which measured 59 HU, consistent with blood. The pericardial space is separated from the heart by a thin layer of subepicardial fat *(arrowheads).*

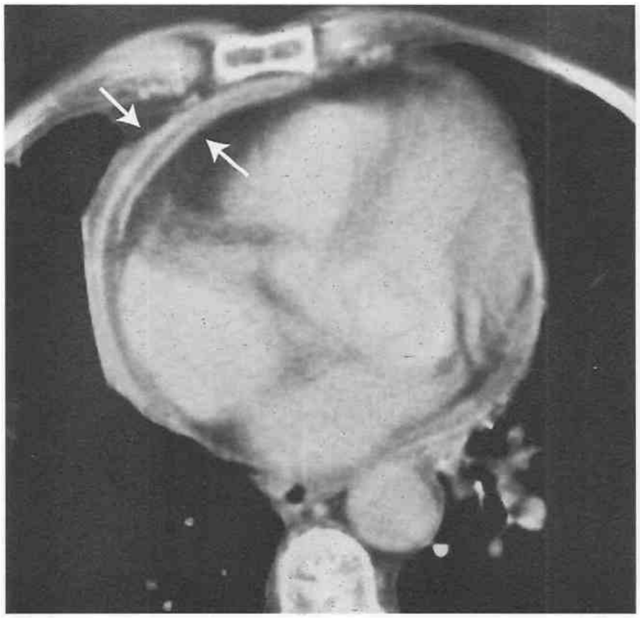

Figure 32–32. Postradiation pericardial thickening. Axial contrast-enhanced CT image shows marked thickening of the visceral and parietal pericardium *(arrows)*. The patient had received radiation for lung carcinoma.

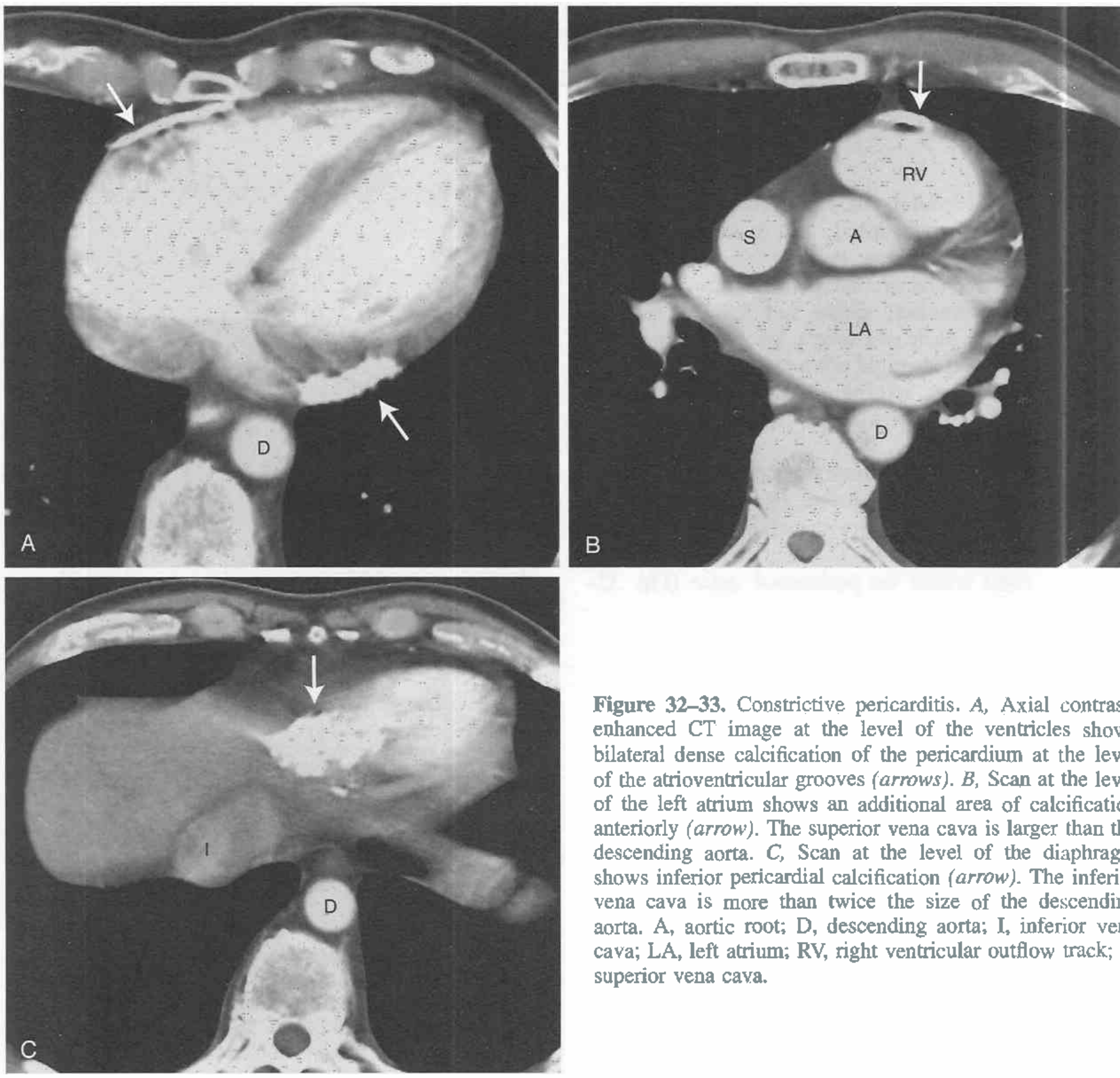

Figure 32–33. Constrictive pericarditis. *A,* Axial contrast-enhanced CT image at the level of the ventricles shows bilateral dense calcification of the pericardium at the level of the atrioventricular grooves *(arrows)*. *B,* Scan at the level of the left atrium shows an additional area of calcification anteriorly *(arrow)*. The superior vena cava is larger than the descending aorta. *C,* Scan at the level of the diaphragm shows inferior pericardial calcification *(arrow)*. The inferior vena cava is more than twice the size of the descending aorta. A, aortic root; D, descending aorta; I, inferior vena cava; LA, left atrium; RV, right ventricular outflow track; S, superior vena cava.

Constrictive Pericarditis

Constrictive pericarditis is a possible sequela in patients with previous pericardial disease, including idiopathic pericarditis, infectious pericarditis, connective tissue disease, neoplastic involvement of the pericardium, postsurgical inflammation, post-radiation therapy pericarditis (Fig. 32–32), uremic pericarditis, and drug-related pericarditis.[38] However, some patients have no known antecedent event. Patients usually present with dyspnea, peripheral edema, and ascites.

Echocardiography demonstrates elevated diastolic filling pressures because the constricting pericardium prevents normal diastolic filling of the heart. Because it is often difficult for echocardiography to distinguish between constrictive pericarditis and restrictive cardiomyopathy, patients may be further evaluated with CT or MRI to determine whether the pericardium is thickened.[38] CT has the advantage of better depicting calcium within the pericardium.

The CT signs of constrictive pericarditis include (1) diffuse, focal, or annular pericardial thickening or calcification; (2) enlargement of the atria or atrium; (3) dilatation of the superior or inferior vena cava; (4) tubelike configuration of the ventricles and narrowing of the atrioventricular groove; and (5) alteration of the normally straight interventricular septum (Fig. 32–33).[82] The constriction can be global or unilateral, or it may affect the atrioventricular groove.

Pericardial Tumors

Metastatic disease, the most common cause of neoplastic involvement of the pericardium, has been reported in up to 20% of autopsy studies. Most patients with pericardial metastases have metastatic disease elsewhere in the body.[53, 115] The most common primary tumors that involve the pericardium secondarily include lung (33%) and breast cancer (25%) and lymphoma/leukemia (15%).[46, 53, 115] Metastatic routes include hematogenous and lymphangitic spread as well as direct extension.

In many cases, the metastases are not radiographically detectable. Pericardial effusion in a patient with a known malignancy should arouse suspicion of metastatic involvement of the pericardium, although nonmalignant causes of pericardial effusion, such as radiation or drug-induced pericarditis, must also be considered. Occasionally, soft tissue nodules or masses may be demonstrated on CT (Fig. 32–34).

CT is often better than echocardiography in detecting pericardial masses. Subepicardial fat may mimic a pericardial mass on echocardiography, and in some cases a mass within the pericardium cannot be distinguished from pericardial effusion.[41, 67]

Primary tumors of the pericardium include mesothelioma, sarcoma, lymphoma, teratoma, and pheochromocytoma.[45, 53] Intrathoracic paragangliomas account for only 1% to 2% of all pheochromocytomas. The most common intrathoracic location of paragangliomas is the posterior mediastinum. Intrapericardial location is very rare.[45] Tumors tend to be large and are most commonly located adjacent to or involving the left atrium.[6, 45] Typically, pericardial mesothelioma presents with diffuse involvement of the pericardium (Fig. 32–35). Any cardiac involvement is usually superficial, and this finding is helpful in distinguishing mesothelioma from pericardial angiosarcoma, which typically has more extensive involvement of the heart.[19, 63]

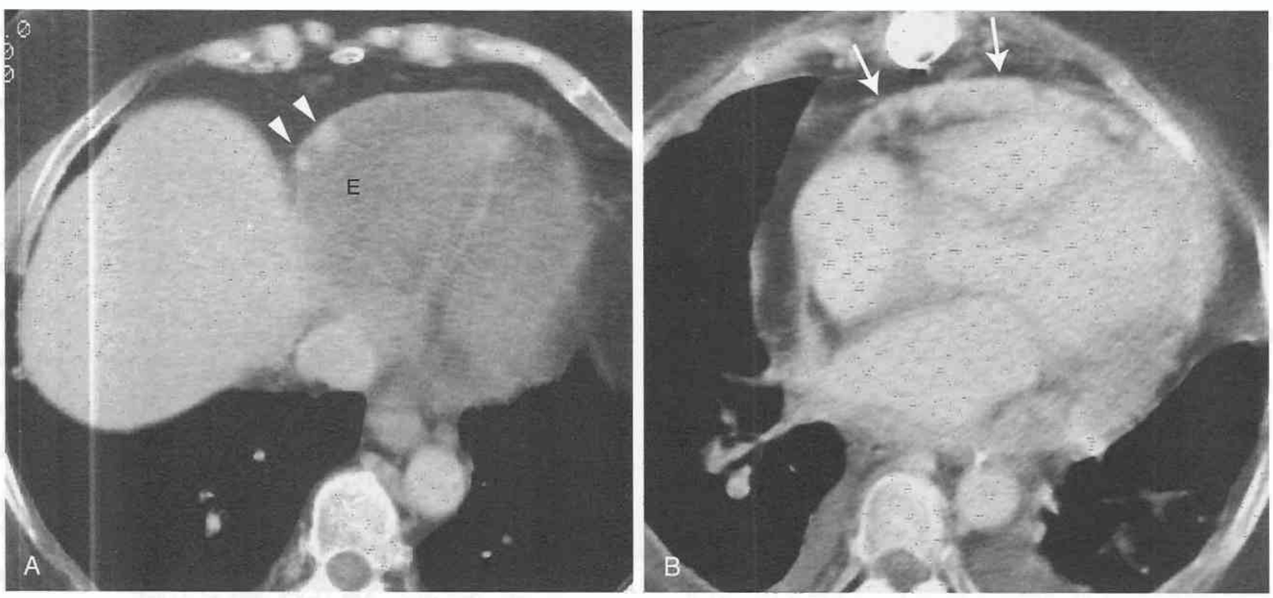

Figure 32–34. Pericardial metastases from renal cell carcinoma. *A,* Axial contrast-enhanced CT at a level just inferior to the heart shows a large pericardial effusion (E). Two soft tissue nodules are identified arising from the parietal pericardium *(arrowheads). B,* Scan performed 6 months later shows filling of the pericardial space with enhancing soft tissue *(arrows).*

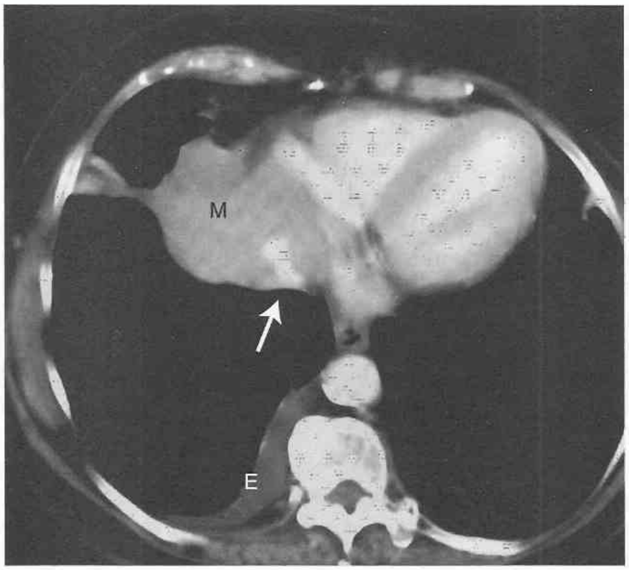

Figure 32–35. Pericardial mesothelioma. Axial contrast-enhanced CT scan shows a large mass (M) arising from the right pericardium, invading the right atrium, and encasing the inferior vena cava *(arrow)*. The patient was initially seen at an outside hospital, where the mass was thought to be arising from the lung. Bronchoscopic findings were negative. The patient was referred for biopsy. E, effusion.

References

1. Abrams DL, Edlelist A, Luria MD, Miller AJ: Ventricular aneurysm. Circulation 27:164–169, 1963.
2. Abushaban L, Denham B, Duff D: Ten-year review of cardiac tumours in childhood. Br Heart J 70:166–169, 1993.
3. Agatson AS, Janowitz WR, Hildner FJ, et al: Quantification of coronary artery calcium using ultrafast computed tomography. J Am Coll Cardiol 15:827–832, 1990.
4. Agner RC, Gallis HA: Pericarditis: Differential diagnostic considerations. Arch Intern Med 139:407–412, 1979.
5. Alam M: Pitfalls in the echocardiographic diagnosis of intracardiac and extracardiac masses. Echocardiography 10:181–191, 1993.
6. Araoz PA, Eklund HE, Welch TJ, Breen JF: CT and MR imaging of primary cardiac malignancies. Radiographics 19:1421–1434, 1999.
7. Araoz PA, Mulvagh SL, Tazelaar HD, et al: CT and MR imaging of benign primary cardiac neoplasms with echocardiographic correlation. Radiographics 20:1303–1319, 2000.
8. Aravot DJ, Banner NR, Cantor AM, et al: Location, localization and surgical treatment of cardiac pheochromocytoma. Am J Cardiol 69:283–285, 1992.
9. Aronberg DJ, Glazer HS, Sagel SS: MRI and CT of the mediastinum: Comparisons, controversies and pitfalls. Radiol Clin North Am 23:439–448, 1985.
10. Aronberg DJ, Peterson RR, Glazer HS, Sagel SS: The superior sinus of the pericardium: CT appearance. Radiology 153:489–492, 1984.
11. Becker CR, Jakobs TF, Aydemir S, et al: Helical and single-slice conventional CT versus electron beam CT for the quantification of coronary artery calcification. AJR Am J Roentgenol 174:543–547, 2000.
12. Bjessmo S, Ivert T: Cardiac myxoma: 40 years' experience in 63 patients. Ann Thorac Surg 63:697–700, 1997.
13. Black CM, Hedges LK, Javitt MC: The superior pericardial sinus: Normal appearance on gradient-echo MR images. AJR Am J Roentgenol 160:749–751, 1993.
14. Blankenhorn DH, Stern D: Calcification of the coronary arteries. Am J Roentgenol 81:772–777, 1959.
15. Breen JF, Sheedy PF, Schwartz RS, et al: Coronary artery calcification detected with ultrafast CT as an indication of coronary artery disease. Radiology 185:435–439, 1992.
16. Broderick LS, Shemesh J, Wilensky RL, et al: Measurement of coronary artery calcium with dual-slice helical CT compared with coronary angiography: Evaluation of CT scoring methods, interobserver variations, and reproducibility. AJR Am J Roentgenol 167: 439–444, 1996.
17. Broderick LS, Conces DJ Jr, Tarver RD: CT evaluation of normal interatrial fat thickness. J Comput Assist Tomogr 20:950–953, 1996.
18. Bull RK, Edwards PD, Dixon AK: CT dimensions of the normal pericardium. Br J Radiol 71:923–925, 1998.
19. Burke A, Virmani R: Tumors of the heart and great vessels. In Atlas of Tumor Pathology. Fascicle 16, Series 3. Washington, DC, Armed Forces Institute of Pathology, 1996.
20. Burke AP, Litovsky S, Virmani R: Lipomatous hypertrophy of the atrial septum presenting as a right atrial mass. Am J Surg Pathol 20:678–685, 1996.
21. Burke AP, Virmani R: Osteosarcomas of the heart. Am J Surg Pathol 15:289–295, 1991.
22. Burns MA, Molina PL, Gutiarrez FR, Sagel SS: Motion artifact simulating aortic dissection on CT. AJR Am J Roentgenol 157: 465–467, 1991.
23. Butany J, Yu W: Cardiac angiosarcoma: Two cases and a review of the literature. Can J Cardiol 16:197–205, 2000.
24. Callister TQ, Cooil B, Raya SP, et al: Coronary artery disease: Improved reproducibility of calcium scoring with an electron-beam CT volumetric method. Radiology 208:807–814, 1998.
25. Carney JA: The Carney complex (myxomas, spotty pigmentation, endocrine overactivity and schwannomas). Dermatol Clin 13:19–26, 1995.
26. Carr JJ, Crouse JR III, Goff DC Jr, et al: Evaluation of subsecond gated helical CT for quantification of coronary artery calcium and comparison with electron beam CT. AJR Am J Roentgenol 174: 915–921, 2000.
27. Chafke N, Kretz JG, Valentin P, et al: Clinical presentation and treatment options for mitral valve myxoma. Ann Thorac Surg 64: 872–877, 1997.
28. Chiles C, Baker ME, Silverman PM: Superior pericardial recess simulating aortic dissection on computed tomography. J Comput Assist Tomogr 10:421–423, 1986.
29. Choe YH, Im JG, Park JH, et al: The anatomy of the pericardial space: A study in cadavers and patients. AJR Am J Roentgenol 149: 693–697, 1987.
30. Corey GR, Campbell PT, van Trigt P, et al: Etiology of large pericardial effusions. Am J Med 95:209–213, 1993.
31. Delille JP, Hernigou A, Sene V, et al. Maximal thickness of the normal human pericardium assessed by electron-beam computed tomography. Eur Radiol 9:1183–1189, 2000.
32. Diflo T, Cantelmo NL, Haudenschild CC, Watkins MT: Atrial myxoma with remote metastasis: Case report and review of the literature. Surgery 111:352–356, 1992.
33. Dooms GC, Hricak H, Sollito RA, Higgins CB: Lipomatous tumors and tumors with fatty components: MR imaging potential and comparison of MR and CT results. Radiology 157:479–483, 1985.
34. Doppman JL, Rienmuller R, Lissner J: The visualized interventricular septum on cardiac computed tomography: A clue to the presence of severe anemia. J Comput Assist Tomogr 5:157–160, 1981.
35. Doyle MT, Spizarny DL, Baker DE: Saphenous vein graft aneurysm after coronary artery bypass surgery. AJR Am J Roentgenol 168: 747–749, 1997.
36. Duvernoy O, Coulden R, Ytterberg C: Aortic motion: A potential pitfall in CT imaging of dissection in the ascending aorta. J Comput Assist Tomogr 19:569–572, 1995.
37. Farooki ZQ, Ross RD, Paridon SM, et al: Spontaneous regression of cardiac rhabdomyoma. Am J Cardiol 67:897–899, 1991.
38. Fowler NO: Constrictive pericarditis: Its history and current status. Clin Cardiol 18:341–350, 1995.
39. Frances C, Romero, A, Grady D: Left ventricular pseudoaneurysm. J Am Coll Cardiol 32:557–561, 1998.
40. Gale ME, Kiewak MG, Hale DR: Pericardial fluid distribution: CT analysis. Radiology 162:171–174, 1987.
41. Glazer GM, Gross BH, Orringer MB, et al: Computed tomography of pericardial masses: Further observations and comparison with echocardiography. J Comput Assist Tomogr 8:895–899, 1984.
42. Grieco JG, Montoya A, Sullivan HJ, et al: Ventricular aneurysm due to blunt chest injury. Ann Thorac Surg 47:322–329, 1989.
43. Groell R, Schaffler GJ, Reinmueller R: Pericardial sinuses and recesses: Findings at elctrocardiographically triggered electron-beam CT. Radiology 212:69–73, 1999.

44. Guthaner DF, Wexler L, Harrell G: CT demonstration of cardiac structures. Am J Roentgenol 113:75, 1979.
45. Hamilton BH, Francis IR, Gross BH, et al: Intrapericardial paragangliomas (pheochromocytomas): Imaging features. AJR Am J Roentgenol 168:109–113, 1997.
46. Hancock EW, Disease of the pericardium. Cardiol Clin 8:673–682, 1990.
47. Herrmann MA, Shanderman RA, Edwards WD, et al: Primary cardiac angiosarcoma: A clinicopathologic study of six cases. J Thorac Cardiovasc Surg 103:655–664, 1992.
48. Hurst CO, Fine G, Keyes JW: Pseudoaneurysm of the heart: Report of a case and review of literature. Circulation 28:47–436, 1963.
49. Hutter AM, Page DL: Atrial arrhythmias and lipomatous hypertrophy of the cardiac interatrial septum. Am Heart J 82:16–21, 1971.
50. Jacob JLB, Souza AS Jr, Parro A: Absence of the left pericardium diagnosed by computed tomography. Int J Cardiol 47:293–296, 1995.
51. Kahn J. Risher MR: MRI of cardiac pseudoaneurysm and other complications of myocardial infarction. Magn Reson Imaging 9: 159–164, 1991.
52. Klingenbeck-Regn K, Schaller S, Flohr T, et al: Subsecond multislice computed tomography: Basics and applications. Eur J Radiol 31:110–124, 1999.
53. Kralstein J, Frishman W: Malignant pericardial diseases: Diagnosis and treatment. Am Heart J 113:785–790, 1987.
54. Kuhlman JE, Teigen C, Ren H, et al: Amiodarone pulmonary toxicity: CT findings in symptomatic patients. Radiology 177:121–125, 1990.
55. Larsson S, Lepore V, Kennergren C: Atrial myxomas: Results of 25 years' experience and review of the literature. Surgery 105: 695–698, 1989.
56. Levy-Ravetch M, Auh YH, Rubenstein WA, et al: CT of the pericardial recesses. Am J Roentgenol 144:707–714, 1985.
57. Lippert JA, White CS, Mason AC, Plotnick GD: Calcification of aortic valve detected incidentally on CT scans: Prevalence and clinical significance. AJR Am J Roentgenol 164:73–77, 1995.
58. Lipton MJ, Coulden R: Valvular heart disease. Radiol Clin North Am 37:319–339, 1999.
59. Maisch B: Pericardial diseases, with a focus on etiology, pathogenesis, pathophysiology, new diagnostic imaging methods, and treatment. Curr Opin Cardiol 9:379–388, 1994.
60. March KL, Sawada SG, Tarver RD, et al: Current concepts of left ventricular pseudoaneurysm: Pathophysiology, therapy and diagnostic imaging methods. Clin Cardiol 12:531–540, 1989.
61. Mason JW, Oates JA, Wood AJ: Drug therapy: Amiodarone. N Engl J Med 316:455–466, 1987.
62. Masuda Y, Naito S, Aoyagi Y, et al: Coronary artery calcification detected by CT: Clinical significance and angiographic correlates. Angiology 41:1037–1047, 1990.
63. McAllister HA, Fenoglio JJ: Tumors of the cardiovascular system. In Hartmann WH, Cowan WR (eds): Fascicles of the Armed Forces Institute of Pathology. Washington, DC, Armed Forces Institute of Pathology, 1977, pp 81–108.
64. McCarthy PM, Piehler JM, Schaff HV, et al: The significance of multiple recurrent and "complex" cardiac myxomas. J Thorac Cardiovasc Surg 91:389–396, 1986.
65. Meaney JF, Kazerooni EA, Jamadar DA, Korobkin M: CT appearance of lipomatous hypertrophy of the interatrial septum. AJR Am J Roentgenol 168:1081–1084, 1997.
66. Miller SW: Imaging pericardial disease. Radiol Clin North Am 27: 1113–1125, 1989.
67. Millman A, Meller J, Motro M, et al: Pericardial tumor or fibrosis mimicking pericardial effusion by echocardiography. Ann Intern Med 86:434–436, 1977.
68. Mochizuki T, Murase K, Higashino H, et al: Two- and three-dimensional CT ventriculography: A new application of helical CT. AJR Am J Roentgenol 174:203–208, 2000.
69. Mukher JI, Varma P, Stark P: Motion artifact simulating aortic dissection on CT. AJR Am J Roentgenol 159:674, 1992.
70. Oliva PB, Hammill SC, Edwards WD: Cardiac rupture, a clinically predictable complication of acute myocardial infarction: Report of 70 cases with clinicopathologic correlations. J Am Coll Cardiol 22: 720–726, 1993.
71. Olson MC, Posniak HV, McDonald V, et al: Computed tomography and magnetic resonance imaging of the pericardium. Radiographics 9:633–649, 1989.
72. Page DL: Lipomatous hypertrophy of the cardiac interatrial septum: Its development and probable clinical significance. Hum Pathol 1: 151–163, 1970.
73. Paling MR, Williamson BR: Epipericardial fat pad: CT findings. Radiology 165:335–339, 1987.
74. Pappas G, Paton B, Davies H: Nonmycotic subvalvular aneurysms after aortic valve replacement. J Cardiovasc Surg 63:925–929, 1972.
75. Prior JR: Lipomatous hypertrophy of the cardiac interatrial septum. Arch Pathol 78:11–15, 1964.
76. Protopapas Z, Westcott JL: Left pulmonic recess of the pericardium: Findings at CT and MR imaging. Radiology 196:85–88, 1995.
77. Qizilbash AH, Schwartz CJ: False aneurysm of left ventricle due to perforation of mitral-aortic intervalvular fibrosa with rupture and cardiac tamponade. Am J Cardiol 32:110–113, 1973.
78. Radin R, Kempf RA: Carney complex: Report of three cases. Radiology 196:383–386, 1995.
79. Reddy GP, Steiner RM: Aneurysm of saphenous vein coronary bypass graft: Diagnosis by computed tomography. 14:147–149, 1999.
80. Reyes CV, Jablokow VR: Lipomatous hypertrophy of the cardiac interatrial septum: A report of 38 cases and review of the literature. Am J Clin Pathol 72:785–788, 1979.
81. Reynen K: Cardiac myxomas. N Engl J Med 333:1610–1617, 1995.
82. Rienmuller R, Gurgan M, Erdmann E, et al: CT and MR evaluation of pericardial constriction: A new diagnostic and therapeutic concept. J Thorac Imaging 8:108–121, 1993.
83. Rifkin RD, Parisi AF, Folland E: Coronary calcification in the diagnosis of coronary artery disease. Am J Cardiol 44:141–147, 1979.
84. Ritoo D, Sutherland GR: Posterior left ventricular pseudoaneurysm after aortic valve replacement in a patient with rheumatoid arthritis: Diagnosis by transesophageal echocardiography. J Am Soc Echocardiogr 7:429–433, 1994.
85. Roberts CS, Roberts WC: Dissection of the aorta associated with congenital malformation of the aortic valve. J Am Coll Cardiol 17: 712–716, 1991.
86. Rozenshtein A, Boxt LM: Computed tomography and magnetic resonance imaging of patients with valvular heart disease. J Thorac Imaging 15:252–264, 2000.
87. Rumberger JA, Brundage BH, Rader DJ, Kondos G: Electron beam computed tomographic coronary calcium scanning: A review and guidelines for use in asymptomatic persons. Mayo Clin Proc 74: 243–252, 1999.
88. Sabet HY, Edwards WD, Tazelaar HD, Daly RC: Congenitally bicuspid aortic valves: A surgical pathology study of 542 cases (1991 through 1996) and a literature review of 2,715 additional cases. Mayo Clin Proc 74:14–26, 1999.
89. Sakai K, Nakamura K, Ishizuka N, et al: Echocardiographic findings and clinical features of left ventricular pseudoaneurysm after mitral valve replacement. Am Heart J 124:975–982, 1992.
90. Salcedo EE, Cohen GI, White RD, Davison MB: Cardiac tumors: Diagnosis and management. Curr Probl Cardiol 17:73–137, 1992.
91. Schlesinger E, Fernbach SK: Pericardial effusion presenting as an anterior mediastinal mass. Pediatr Radiol 16:65–66, 1986.
92. Sebastia C, Pallisa E, Quiroga S, et al: Aortic dissection: Diagnosis and follow-up with helical CT. RadioGraphics 19:45–60, 1999.
93. Seelos KC, Caputo GR, Carrol CL, et al: Cine gradient refocused echo (GRE) imaging of intravascular masses: differentiation between tumor and nontumor thrombus. J Comput Assist Tomogr 16:169–172, 1992.
94. Shemesh J, Apter S, Rozenman J, et al: Calcification of coronary arteries: Detection and quantification with double-helix CT. Radiology 197:779–783, 1995.
95. Shemesh J, Tenenbaum A, Kopecky KK, et al: Coronary calcium measurements by double helical computed tomography: Using the average instead of peak density algorithm improves reproducibility. Invest Radiol 32:503–506, 1997.
96. Shin MS, Jolles PR, Ho KJ: CT evaluation of distended pericardial recess presenting as a mediastinal mass. J Comput Assist Tomogr 10:860–862, 1986.
97. Smith HC, Watson GH, Patel RG, Super M: Cardiac rhabdomyomata in tuberous sclerosis: Their course and diagnostic value. Arch Dis Child 64:196–200, 1989.
98. Sorlie D, Myhre ESP, Stalsberg H: Angiosarcoma of the heart: Unusual presentation and survival after treatment. Br Heart J 51: 94–97, 1984.

99. Spindola-Franco H, Kronacher N: Pseudoaneurysm of the left ventricle. Radiology 127:29–34, 1978.
100. Stewart S, Huddle R, Stueard I, et al: False aneurysm and pseudofalse aneurysm of the left ventricle: Etiology, pathology, diagnosis, and operative management. Ann Thorac Surg 31:259–265, 1981.
101. Tagasuki JE, Godwin JD: Surgical defects of the pericardium: Radiographic findings. AJR Am J Roentgenol 152:951–954, 1989.
102. Tamiya E, Matsui H, Nakajima T, et al: Detection of coronary artery calcification by x-ray computed tomography and its significance: A new CT scoring technique. Angiology 43:22–31, 1992.
103. Tenebaum A, Shemesh J, Fisman EZ, Motro M: Advanced mitral annular calcification is associated with severe coronary calcification on fast dual spiral computed tomography. Invest Radiol 35:193–198, 2000.
104. Tofler GH, Muller JE, Stone PH, et al: Pericarditis in acute myocardial infarction: Characterization and clinical significance. Am Heart J 117:86–90, 1989.
105. Trop I, Samson L, Cordeau MP, et al: Anterior mediastinal mass in a patient with prior saphenous vein coronary artery bypass grafting. Chest 115:572–576, 1999.
106. Tuna IC, Julsrud PR, Click RL, et al: Tissue characterization of an unusual right atrial mass by magnetic resonance imaging. Mayo Clin Proc 66:498–501, 1991.
107. van Gelder HM, O'Brien DJ, Staples ED, Alexander JA: Familial cardiac myxoma. Ann Thorac Surg 53:419–424, 1992.
108. van Son JAM, Danielson GK, Schaff HV, et al: Congenital partial and complete absence of the pericardium. Mayo Clin Proc 68: 743–747, 1993.
109. van Tassel RA, Edwards JE: Rupture of heart complicating myocardial infarction: Analysis of 40 cases including nine examples of left ventricular false aneurysm. Chest 61:104–116, 1972.
110. Webb DW, Thomas RD, Osborne JP: Cardiac rhabdomyomas and their association with tuberous sclerosis. Arch Dis Child 68:367–370, 1993.
111. Widimsky P, Gregor P: Pericardial involvement during the course of myocardial infarction. 1995 108:89–93, Chest.
112. Wojtowicz J, Rzymski K, Czarnecki R: Severe anaemia: Its CT findings in the cardiovascular system. Eur J Radiol 3:108–111, 1983.
113. Woodhouse CE, Janowitz WR, Viamonte M Jr: Coronary arteries: Retrospective cardiac gating technique to reduce cardiac motion artifact at spiral CT. Radiology 204:566–9, 1997.
114. Woodring JH, West JW: CT of aortic and mitral valve calcification. J Ky Med Assoc 87:177–180, 1989.
115. Wychulis AR, Connolly DC, McGoon DC: Pericardial cysts, tumors and fat necrosis. J Thorac Cardiovasc Surg 62:294–300, 1971.
116. Yeo TC, Malouf JF, Oh JK, Seward JB: Clinical profile and outcome in 52 patients with cardiac pseudoaneurysm. Ann Intern Med 128: 299–305, 1998.
117. Yoon HC, Greaser LE, Mather R, et al: Coronary artery calcium: Alternate methods for accurate and reproducible quantitation. Acad Radiol 4:666–673, 1997.
118. Zingas AP, Carrera JD, Murray CA, Kling GA: Lipoma of the myocardium. J Comput Assist Tomogr 7:1098–1100, 1983.

33

Magnetic Resonance Imaging of the Heart

Anna Rozenshtein, Lawrence M. Boxt

Magnetic resonance imaging (MRI) provides diagnostic morphologic and functional information for the evaluation and management of patients with congenital and acquired cardiovascular disease. The usefulness of cardiac MRI lies in adaptation of motion-suppression techniques to cancel out complex cardiac contractile motion. Thus, the most important difference between cardiac and other-organ MRI is the application of electrocardiographic (ECG) gating to the acquisition pulse sequence to suppress contraction-motion artifacts. ECG gating acts by applying a timing signal coincident with cardiac motion to image acquisition.[160, 161, 168, 322] That is, by timing each phase-encoding step in an MRI acquisition to a particular point in the ECG cycle of the heart, reconstructed images are temporally coherent. By convention, the R-wave is chosen as the gating signal because it has the greatest voltage and is therefore easily identified from the ECG (Fig. 33–1). In addition, because the peak of the R-wave indicates the commencement of electromechanical ventricular contraction, images immediately following the R-wave are obtained at ventricular end-diastole, a time when the ventricles are most dilated.

For an image containing N-phase encoding steps, N cardiac cycles, or heartbeats, are needed to acquire an image at one particular phase of the cardiac cycle. Improved acquisition software provides more efficient use of the cardiac cycle. That is, by pulsing several anatomic levels, each at different delays after the R-wave, we can perform multisection spin-echo acquisition.

Short, flip-angle, gradient-echo cine *(cine) imaging*[226, 272] allows acquisition of images of the heart with greater temporal resolution, permitting evaluation of ventricular function, valvular regurgitation or stenosis, and abnormal hemodynamics in congenital heart lesions. When this pulse sequence is used, the same anatomic section is excited with radiofrequency (RF) pulses using a short repetition time (TR) of 5 to 15 msec. The temporal resolution of the examination depends on the repetition time and heart rate. That is, a faster heart rate results in a shorter ECG RR interval (the time between R-waves) and, for any given number of discrete phases of the cardiac cycle, less time between phases. After a fixed number of excitations, the imaging system waits for the next R-wave to advance to the next phase-encoding step.

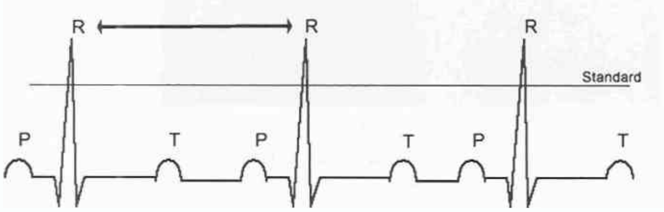

Figure 33–1. Diagram of three beats from a stereotypic electrocardiographic (ECG) strip. The P-, R-, and T-waves are labeled. The RR interval is defined as the time between cardiac cycles and is chosen for the repetition time (TR) in ECG-gated acquisitions. The standard is an arbitrary voltage used for comparison with the ECG voltage. Any signal whose voltage is greater than the standard is chosen as the R-wave for gating purposes.

In some circumstances, an adequate ECG tracing may not be obtained before the examination is begun. This may occur in patients with low cardiac voltage, such as in pericardial effusion. In these individuals, an adequate gating signal may be obtained by application of a peripheral pulse sensor. Peripheral pulse gating (PPG) produces images of diagnostic quality, but one must take care to visually inspect imagery prior to functional analysis. That is, the peak of the peripheral pulse, the timing signal for image acquisition, is delayed in time from the ECG R-wave. Therefore, series of gradient-reversal images do not begin with the end-diastolic image and run through the cardiac cycle toward end-systole. Rather, the first image in each acquisition is obtained at a variable delay after end-diastole. Thus, the series of images acquired at each anatomic level begins somewhere in the cardiac cycle and passes through end-diastole and end-systole, out of phase with a conventionally acquired ECG-gated acquisition. The delay between the ECG R-wave and the peak of the peripheral pulse is a function of the distance between the heart and the monitored extremity artery as well as the biomechanical properties of the aorta and its branches. Series of images obtained using PPG may be of diagnostic quality for morphologic analysis, but cine examinations obtained with PPG should be analyzed with caution.

Recent advances in image-acquisition software have greatly reduced imaging time and allowed acquisition of images during a single breath-hold, thus eliminating motion artifacts and the need for respiratory gating. This is true for the gradient-echo cine acquisitions, as well as the relatively new sequences ideally adapted for morphologic imaging, such as double-inversion recovery techniques.

The high-contrast resolution of spin-echo acquisition (see appendices at the end of this chapter) allows confident differentiation between intraventricular blood and myocardium, necessary for detailed analysis of the epicardial and endocardial borders.[137] Acquisition of gradient-echo cine imagery in the axial plane displays the character of ventricular contraction, including the orientation of the interven-

tricular septum, and the status of the cardiac valves. The high temporal resolution of cine gradient-echo acquisition allows acquisition of ventricular imagery at both end-diastole and end-systole. From these acquisitions, ventricular cavitary volume[29, 86, 180, 205, 271, 292] and myocardial mass[141, 142] may be calculated.

Because MRI requires no assumptions about the shape of the ventricular chamber, end-diastolic and end-systolic ventricular chamber volume is obtained directly by calculating the sum of planimetered ventricular cavity areas times slice thickness through the entire chamber. Left and right ventricular end-diastolic and end-systolic volumes may be calculated, and from these data, stroke volume (the difference between end-diastolic and end-systolic volume),

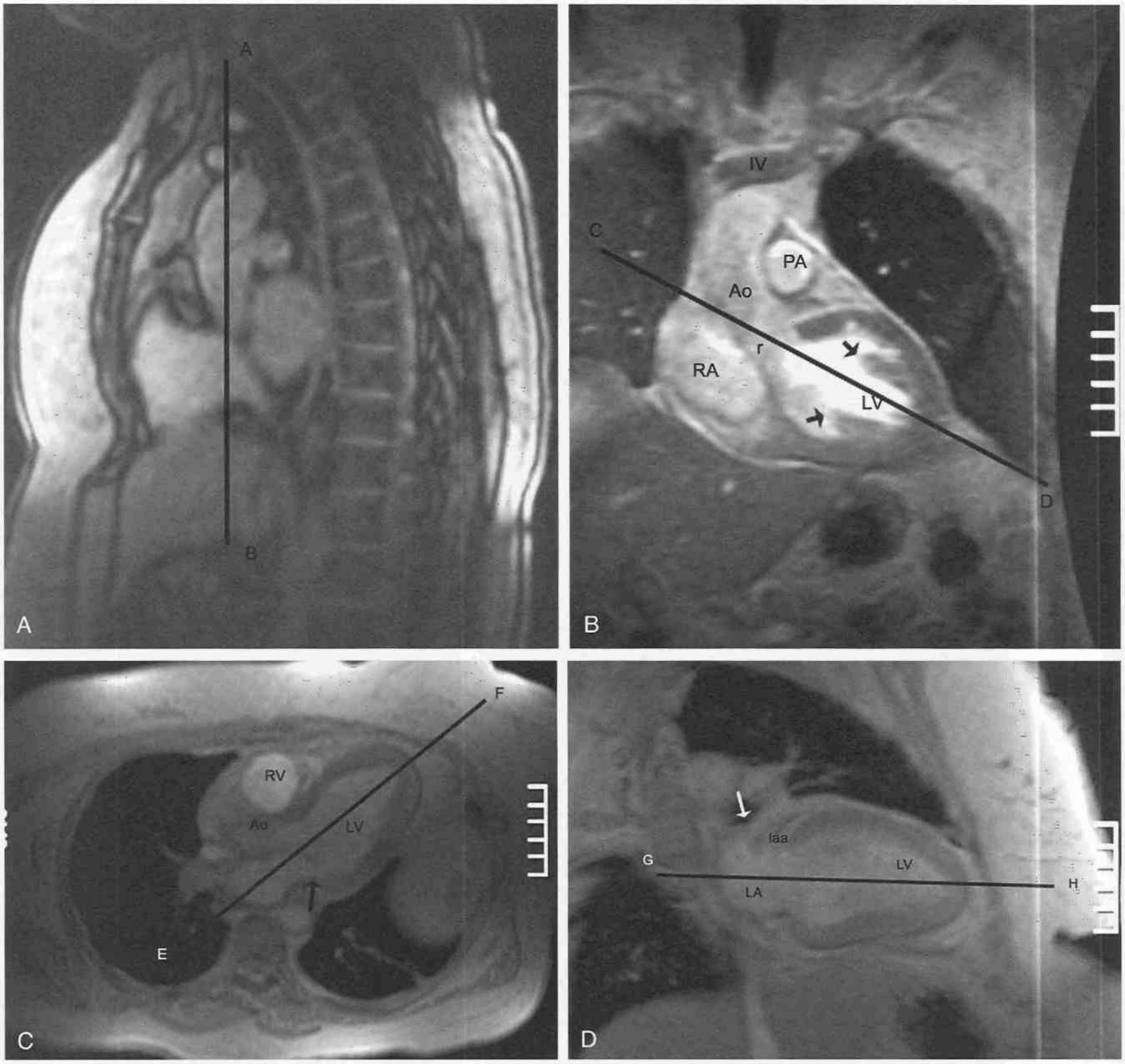

Figure 33–2. Construction of the cardiac short axis and analysis of cavity volume and myocardial mass.

A, Sagittal scout image obtained through the posterior right sinus of Valsalva. From this image, an acquisition is obtained in the coronal plane AB.

B, Coronal scout image through the posterior right sinus of Valsalva (r). The two papillary muscles *(arrows)* are well demonstrated. The innominate vein (IV), main pulmonary artery (PA), ascending aorta (Ao), and right atrium (RA) are labeled. From this image, an oblique axial image is prescribed in plane CD through the aortic valve and left ventricular (LV) apex.

C, The anteroposterior rotation of the heart is compensated for by prescribing a plane (EF) through the mitral valve *(arrow)* and the left ventricular (LV) apex. The right ventricle (RV) and the aortic root (Ao) are labeled.

D, In this section, the line (GH) drawn between the middle of the mitral valve and the apex of the left ventricle (LV) defines the long axis of the LV, its axis of rotation. Images obtained at right angles to this line are in the cardiac short axis. The left atrium (LA), the left upper lobe pulmonary artery *(long arrow)*, and the ostium of the left atrial appendage (laa) are labeled.

ejection fraction (stroke volume divided by end-diastolic volume), and cardiac output (stroke volume × heart rate) may be computed (Fig. 33–2).

In a similar manner, ventricular mass is obtained by summing the volume of myocardium in each image slice over the entire heart. For each tomographic slice, the myocardial volume is the difference between the areas of the epicardial and the endocardial borders times the slice thickness. The sum of the volumes of myocardium times the specific gravity of myocardium (1.05 g/mL) is the myocardial mass.

In principle, these computations can be performed using images obtained in any anatomic section. In practice, however, images obtained in the cardiac short axis are usually used for this purpose. Thus, MRI not only reliably demonstrates morphologic ventricular abnormalities but also allows quantitation of ventricular function (Table 33–1) under pathologic conditions.

In this chapter, we review the use of ECG-gated spin-echo and cine gradient-echo MRI techniques for the diagnosis and evaluation of patients with congenital and acquired heart disease. The clinical role of MRI in the management of these patients differs from medical institution to institution. Availability of MRI scanners configured for cardiac imaging, availability of trained personnel to scan and interpret examinations, and patient referral patterns all affect the volume of clinical cardiac MRI performed at any institution. Nevertheless, the volume of

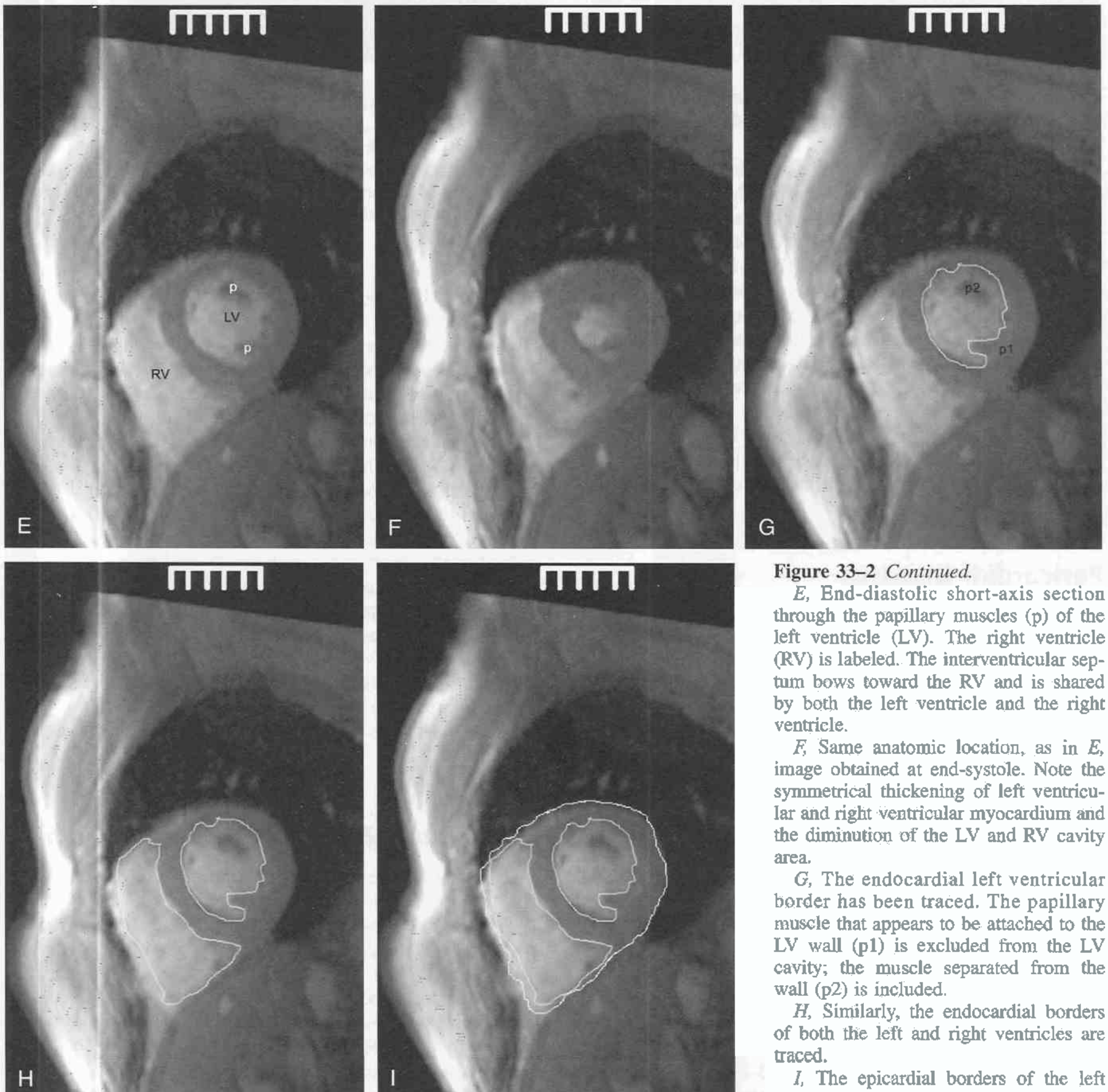

Figure 33–2 *Continued.*

E, End-diastolic short-axis section through the papillary muscles (p) of the left ventricle (LV). The right ventricle (RV) is labeled. The interventricular septum bows toward the RV and is shared by both the left ventricle and the right ventricle.

F, Same anatomic location, as in *E,* image obtained at end-systole. Note the symmetrical thickening of left ventricular and right ventricular myocardium and the diminution of the LV and RV cavity area.

G, The endocardial left ventricular border has been traced. The papillary muscle that appears to be attached to the LV wall (p1) is excluded from the LV cavity; the muscle separated from the wall (p2) is included.

H, Similarly, the endocardial borders of both the left and right ventricles are traced.

I, The epicardial borders of the left and right ventricles are traced.

TABLE 33–1. Left and Right Ventricular Cavity (Volume, Mass, and Derived Values Indexed for Body Surface Area)

Index	Value
Right Ventricle	
End diastolic volume index (RVEDVI)	67.9 ± 13.4 mL/M²
End systolic volume index (RVESVI)	27.9 ± 7.5 mL/M²
Stroke volume index (RVSVI)	40.1 ± 9.7 mL/M²
Ejection fraction (RVEF)	0.59 ± 0.09
Mass index	23.3 ± 1.4 g/M²
Left Ventricle	
End diastolic volume index (LVEDVI)	68.9 ± 13.1 mL/M²
End systolic volume index (LVESVI)	27.1 ± 7.8 mL/M²
Stroke volume index (LVSVI)	41.8 ± 10.9 mL/M²
Ejection fraction (LVEF)	0.60 ± 0.11 g/M²
Mass index	91.6 ± 3.2 g/M²

Data from Boxt LM, Katz J, Kolb T, et al: J Am Coll Cardiol 19: 1508–1515, 1992; and Katz J, Whang J, Boxt LM, Barst RJ: J Am Coll Cardiol 21: 1475–1481, 1993.

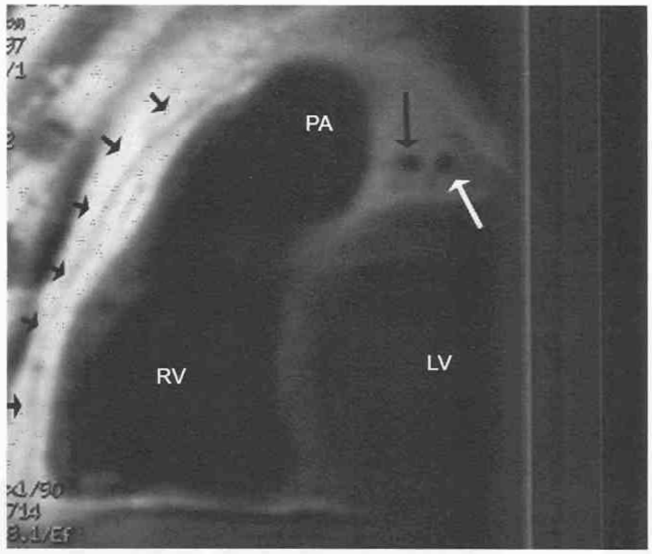

Figure 33–3. Short-axis section from a [redacted] without cardiac disease. The right ventricle (RV), main pulmonary artery (PA), and left ventricular cavity (LV) are labeled. The signal voids of the anterior descending *(long black arrow)* and circumflex *(long white arrow)* coronary arteries are identified. The pencil-thin signal void of the anterior aspect of the pericardial space *(short black arrows)* extends to the top of the pulmonary artery.

cardiac MRI cases performed is increasing, and examinations are performed and interpreted at more and more institutions.

This chapter is best used as a handbook for planning, performing, and interpreting a cardiac MRI study. As the reader will find, although much has indeed been said, much has also been left out. We have made few comments about pulse-sequence parameters. These are set at each site during installation and applications training on the scanner. On the other hand, we pay much attention to pathophysiologic mechanisms and their effect on cardiac morphology and function as displayed in MR images. Our decided emphasis on the medical aspects of the cardiac diseases studied by MRI is intended not only to point out the usefulness of MRI in evaluating the heart but also to help radiologists in planning, performing, and interpreting cardiac MR images with a basic collection of medical data to engage in this practice.

Pericardial Diseases

The pericardium consists of the visceral pericardium (epicardium), the parietal pericardium, and the 20- to 60-mL cavity contained between them. The epicardium is a monolayer of mesothelial cells that covers the external surface of the heart. Beneath the epicardium is either myocardium or epicardial fat. This layer extends for short distances along the pulmonary veins, the superior vena cava below the azygos vein, the inferior vena cava, the ascending aorta to a point 20 to 30 mm above the root, and the main pulmonary artery as far as its bifurcation. It then reflects on itself to become the parietal pericardium, which is a 1-mm-thick outer fibrous layer composed of dense collagen lined on the inside by a monolayer of mesothelial cells.

The visceral pericardium is normally thin and is therefore not visualized separately by any imaging modality. The combination of the visceral pericardium and the small volume of physiologic pericardial fluid constitutes the normal pericardium routinely visualized on MR images as a 1- to 2-mm-thick layer[274, 290] (Fig. 33–3) that can appear focally thicker at the sites of its major attachments. On spin-echo MRI scans, the normal pericardium appears as a pencil-thin line of low signal intensity between the epicardial and pericardial fat. The low signal intensity is attributed to the fibrous nature of the parietal pericardium, the low protein content of pericardial fluid,[317] and the nonlaminar flow patterns caused by cardiac pulsation.[309]

The reflection of pericardium around the great arteries and veins forms the two pericardial "appendages." Anterior to the aorta this contiguous pericardial space is called the *preaortic recess*; posteriorly, it is called the *retroaortic* or *superior pericardial recess* (Fig. 33–4). Posterior and lateral to the heart, the extraparenchymal pulmonary veins and the superior and inferior venae cavae are enveloped by the venous mesocardium, which has the shape of an inverted U. The intrapericardial space between the pulmonary veins is called the *oblique sinus.* It is essential to appreciate the anatomic extent and location of these pericardial sinuses because they are normally seen on MRI[134, 194] and may be confused with adenopathy[5, 165] or aortic dissection.[55, 165]

Congenital Absence of the Pericardium

Congenital absence of the pericardium is a malformation that is thought to be due to compromise of the vascular supply to the pleuropericardial membrane that surrounds the ventral cardiac tube during embryologic development. Pericardial defects may vary in size from small communications between the pleural and pericardial cavities to complete (bilateral) absence of the pericardium. The most common form is complete absence of the left pericardium, with preservation of the pericardium on the right.

Noninvasive modalities, such as contrast-enhanced CT

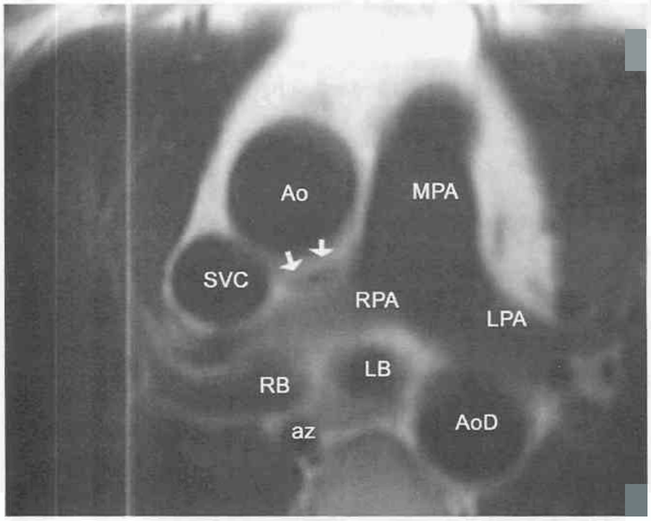

Figure 33–4. Axial spin-echo image. The ascending aorta (Ao), descending aorta (AoD), main pulmonary artery (MPA), left pulmonary artery (LPA), superior vena cava (SVC), left bronchi (LB), right bronchi (RB), and azygos vein (az) are labeled. The superior pericardial recess is seen as a signal void *(arrows)* behind the ascending aorta and anterior to the right pulmonary artery (RPA).

and MRI, have replaced diagnostic pneumothorax and cardiac angiography as the methods of choice[18, 118, 266] for definitive diagnosis of this abnormality. In particular, the multiplanar capabilities of MRI allow direct identification of the absent segment of the parietal pericardium, demonstration of contact between the heart and lung,[118] or recognition of profound leftward displacement and rotation of the heart in the chest (Fig. 33–5).

Pericardial Cysts and Diverticula

If a portion of the pericardium pinches off from pleuropericardial membrane during embryologic development, a cyst forms, containing the same mesothelial lining as the normal pericardium. Similarly, a pericardial diverticulum is a failed cyst; communication with the pleural space persists (Fig. 33–6). Both lesions appear on spin-echo MRI acquisition as fluid-filled[273] paracardiac masses whose signal intensity increases in subsequent multiecho spin-echo images.[273] Gradient-echo acquisition reveals isointensity with rapidly moving blood.

Acquired Pericardial Disease

Normal pericardium most commonly responds to insult by cellular proliferation or the production of fluid or fibrin;

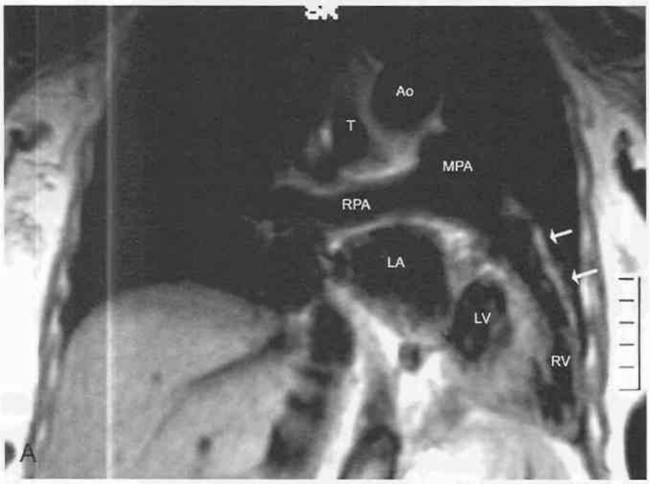

Figure 33–5. Congenital absence of the pericardium. *A,* Coronal spin-echo acquisition. The aortic arch (Ao) displaces the trachea (T) to the right. The aortic arch, the main pulmonary artery (MPA), and, in fact, the entire heart, are displaced into the left chest. Despite the apparent size of the MPA, the right ventricular (RV) cavity appears normal and the RV free wall myocardium *(arrows)* is of normal thickness. LV, left ventricle; RPA, right pulmonary artery. *B,* Axial spin-echo acquisition through the main pulmonary artery (MPA) and right pulmonary artery (RPA). The ascending aorta (Ao) and the main pulmonary artery are displaced toward the left. The MPA is smaller in caliber than the ascending aorta, indicating no increase in pulmonary blood flow. AoD, descending aorta; SV, superior vena cava. *C,* Axial spin-echo image through the cavities of the right ventricle (RV) and left ventricle (LV). Not only is the heart displaced into the left chest; it is rotated in a clockwise manner. AoD, descending aorta; IVC, inferior vena cava; RA, right atrium.

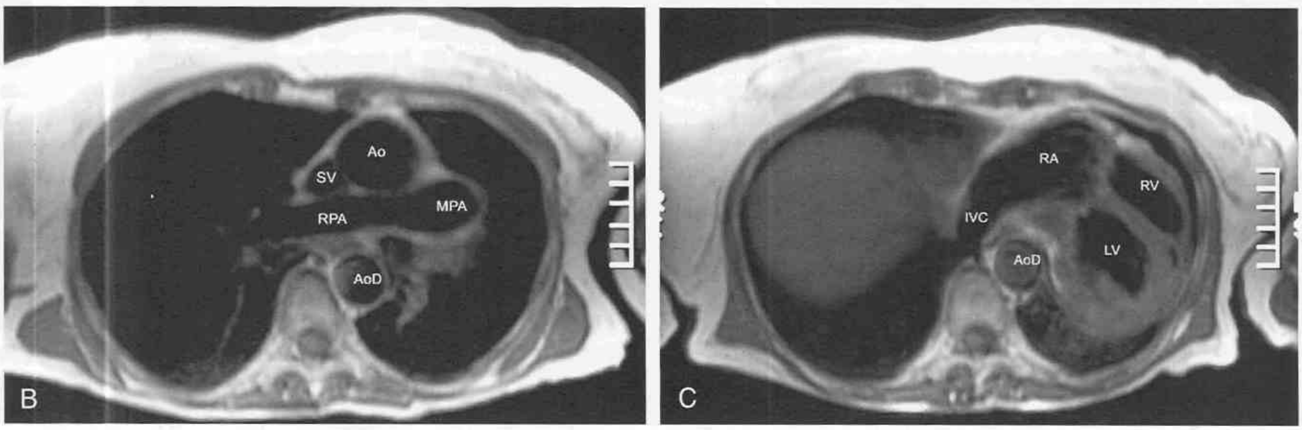

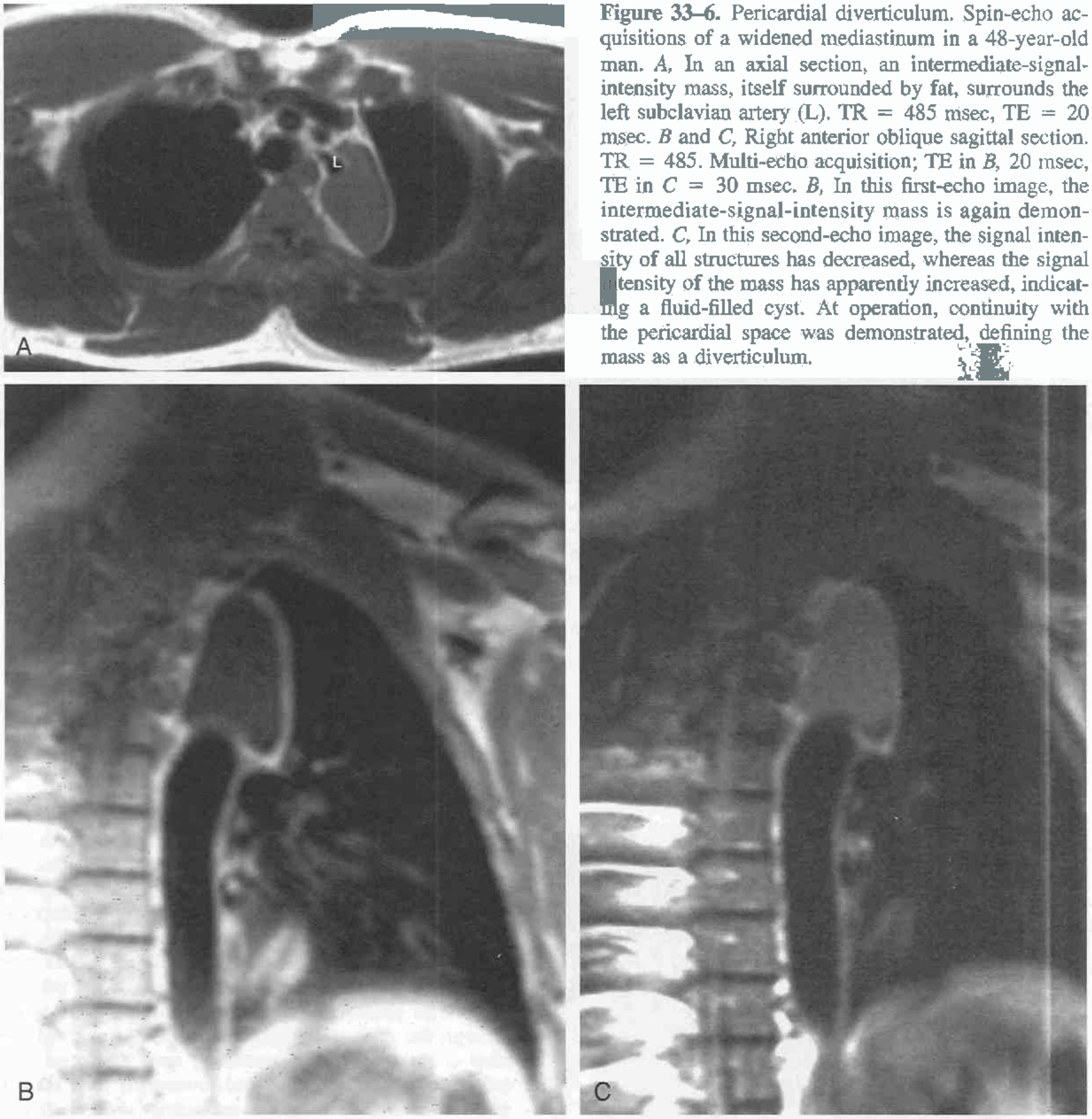

Figure 33–6. Pericardial diverticulum. Spin-echo acquisitions of a widened mediastinum in a 48-year-old man. *A,* In an axial section, an intermediate-signal-intensity mass, itself surrounded by fat, surrounds the left subclavian artery (L). TR = 485 msec, TE = 20 msec. *B* and *C,* Right anterior oblique sagittal section. TR = 485. Multi-echo acquisition; TE in *B,* 20 msec, TE in *C* = 30 msec. *B,* In this first-echo image, the intermediate-signal-intensity mass is again demonstrated. *C,* In this second-echo image, the signal intensity of all structures has decreased, whereas the signal intensity of the mass has apparently increased, indicating a fluid-filled cyst. At operation, continuity with the pericardial space was demonstrated, defining the mass as a diverticulum.

these responses can happen independently or in combination.[251] The most common manifestation of acute pericarditis is an effusion. The fluid may be serous with a clear transudate, or exudate, varying in nature with the underlying cause. Transudative pericardial effusion may develop after cardiac surgery[319] or in congestive heart failure, uremia, postpericardiectomy syndrome,[140] myxedema, and collagen vascular diseases. Hemopericardium may be found in trauma, aortic dissection, aortic rupture,[196] or neoplasm (especially primary pericardial mesothelioma).[3] Chylopericardium resulting from injury or obstruction of the thoracic duct is rare.

MRI is helpful for characterizing pericardial effusions. On spin-echo examination hemorrhagic effusion presents as areas of mixed low, intermediate, and high signal intensity, depending on the age of blood products (Fig. 33–7). Nonhemorrhagic effusions on spin-echo MRI have predominantly low signal intensity (Fig. 33–8),[273] as a result of spin phase change[309] of the pericardial fluid. Gradient-echo MRI sequences display freely mobile pericardial fluid that has high signal intensity. Inflammatory effusion, as seen in uremia, tuberculosis, or trauma, may have medium-signal-intensity components[142, 273] on spin-echo MRI, especially in dependent areas.[142] It has been suggested[273] that the latter may be due to high-protein content of inflammatory pericardial fluid.[251] Furthermore, because adhesions are common in pericardial inflammation, inflammatory effusions may not have the normal free-flow patterns of pericardial fluid that may lead to loci of increased signal intensity on spin-echo MRI, similar in appearance to loculated pericardial effusions (Fig. 33–9). Despite these complex signal characteristics, MRI helps in distinguishing inflammatory pericardial thickening and adhesions from fluid accumulation (intermediate versus predominantly low signal intensity).[142, 273] Fibrous pericardial thickening appears as a low-signal-intensity band surrounding the heart. Pericardial inflammation, as seen in

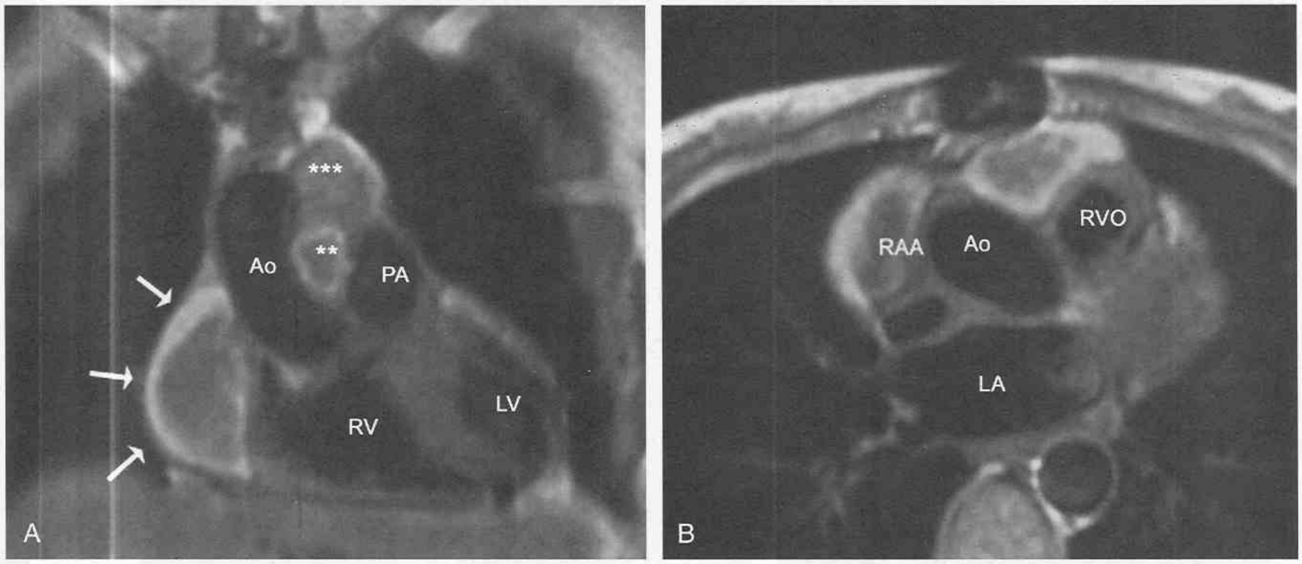

Figure 33–7. MR images obtained from a 53-year-old man who received a heart transplant 36 hours earlier, now with a widened mediastinum and cardiac silhouette. *A,* Coronal spin-echo acquisition shows a rim of increased signal intensity *(arrows)* surrounding the lateral border of the right atrium, above the top (**) of the main pulmonary artery (PA), and in the space between the ascending aorta (Ao) and pulmonary artery (***). LV, left ventricle; RV, right ventricle. *B,* Axial section through the right ventricular outflow tract (RVO). Increased signal intensity surrounds the right atrial appendage (RAA) and is insinuated between the ascending aorta (Ao) and RVO. LA, left atrium.

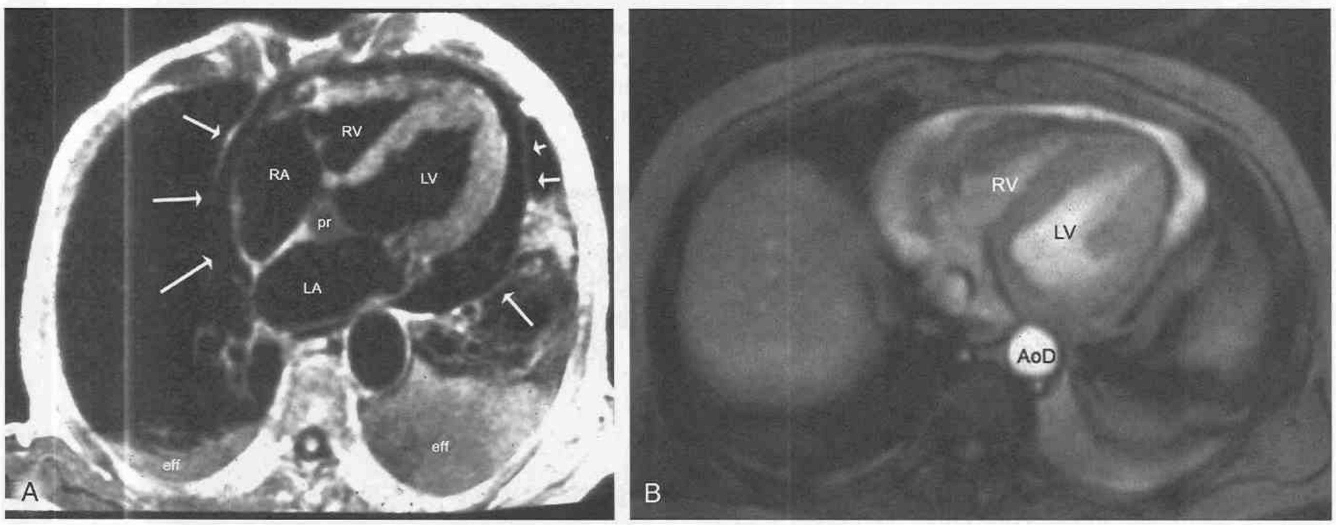

Figure 33–8. MR image obtained from two patients with simple pericardial effusions. *A,* The patient is a 64-year-o[redacted]an with progressive shortness of breath. In this oblique axial section through the posterior right aortic sinus of Valsalva (pr), the parietal pericardium *(arrows)* is separated from the epicardial surfaces of the heart. The left ventricle (LV), right ventricle (RV), left atrium (LA), and right atrium (RA) are labeled. Note the bilateral pericardial effusions (eff) as well. *B,* In this axial gradient-echo acquisition (in another patient), the high-signal-intensity serous pericardial fluid surrounds the heart. AoD, descending aorta; LV, left ventricle; RV, right ventricle.

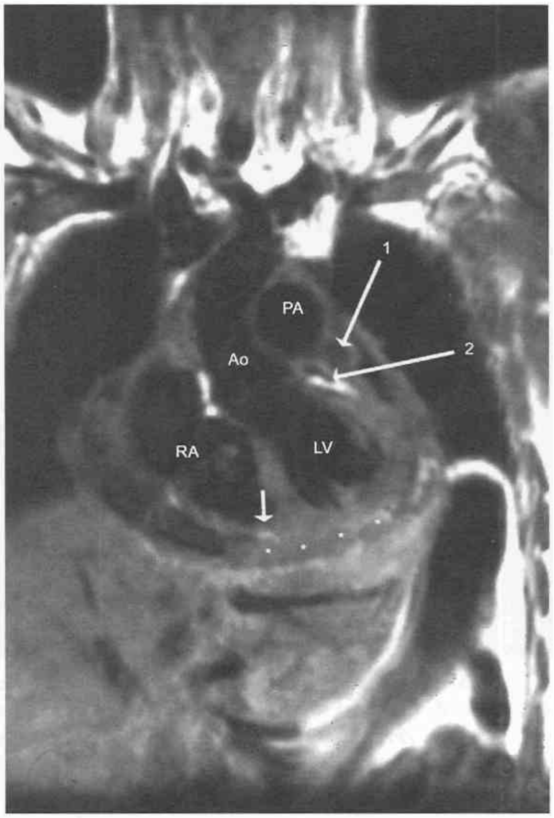

Figure 33–9. Complex pericardial thickening and loculated effusion in pericarditis. Coronal spin-echo acquisition demonstrates increased signal intensity within the pericardial space *(* * * *)* external to the epicardial fat along the inferior aspect *(arrow)* of the right atrium (RA) and left ventricle (LV). In addition, note how thick the pericardium is as it reflects on the main pulmonary artery segment (PA) and ascending aorta (Ao). The left atrial appendage *(arrow 1)* is contained within the pericardium. The proximal left anterior descending coronary artery *(arrow 2)* is identified.

uremic or tuberculous pericarditis or trauma following resuscitation, appears as increased signal intensity compared with myocardium on spin-echo MRI acquisition (Fig. 33–10).[273]

Pericardial Tamponade

Gradual accumulation of pericardial fluid may not produce clinical signs or symptoms. However, rapid accumulation of as little as 100 to 200 mL of fluid can impede diastolic ventricular filling. Pericardial tamponade is a condition in which reduced stroke volume limits maintenance of cardiac output. MRI is often instrumental in suggesting the cause of the effusion (i.e., hemorrhage, neoplastic involvement, inflammation due to tuberculosis or other infectious processes) in this acutely emergent situation.

Pericardial Constriction

The hallmarks of pericardial constriction are pericardial thickening and calcification and abnormal diastolic ventricular function. In most cases, constrictive pericarditis involves the entire pericardium, compromising filling of all cardiac chambers. Occasionally, however, local chronic pericardial thickening has been reported.[54, 214] Focal pericardial thickening is more commonly seen in the postoperative patient and is frequently located anterior to the right ventricle.[184] The clinical findings of constrictive pericarditis overlap with those of restrictive cardiomyopathy, a primary disorder of the myocardium. Differentiation between these two entities is imperative because patients with pericardial constriction may benefit from pericardiectomy[231]; myocardial restriction may be rapidly progressive and necessitate cardiac transplantation.

Symptomatic pericardial constriction can be seen in the absence of conventional radiographically detectable pericardial thickening, however. Masui and associates[184] found pericardial thickening on MR images in 88% of cases of proven constrictive pericarditis. Pericardial thickening is not diagnostic of pericardial constriction[273]; demonstration of pericardial thickening greater than 4 mm (Figs. 33–11 and 33–12) in the face of characteristic hemodynamic findings distinguishes constrictive pericarditis from restrictive cardiomyopathy.[184, 273] Normal pericardium on MR[290] is less than 4 mm in thickness.

ECG-gated spin-echo MRI is an ideal method of investigating the pericardium.[134, 142, 194, 273, 290] It is exquisitely sensitive to changes in pericardial thickness as well as to morphologic and functional changes in the atria and ventricles resulting from focal or diffuse pericardial disease. In pericardial constriction, the right ventricle may appear tubular (see Fig. 33–12).[287] Gradient-echo acquisition demonstrates decreased right ventricular contractile function and limited diastolic excursion, common to both restriction and constriction. Dilatation of the right atrium, venae cavae, coronary sinus, and hepatic veins, reflecting right heart failure, may be seen in patients with constrictive pericarditis as well as in patients with restrictive cardiomyopathy.

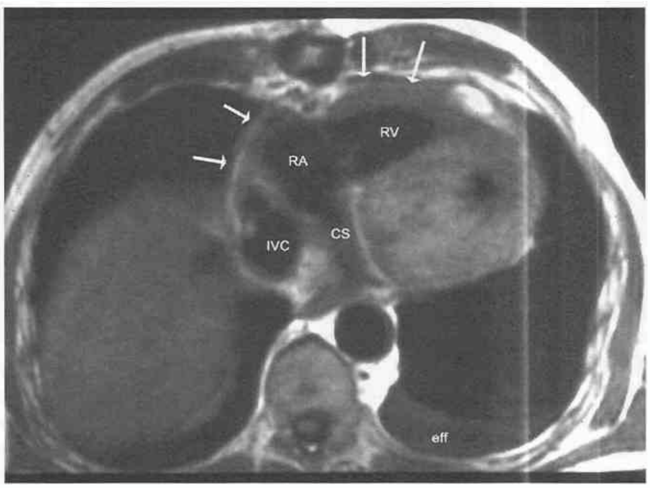

Figure 33–10. MR image obtained from a 68-year-old man, 8 years after coronary artery bypass surgery, who is now complaining of shortness of breath. There is a left pleural effusion (eff). Thickened pericardium *(arrows)* surrounds the lateral aspects of the right atrium (RA) and the anterior aspect of the tubular right ventricle (RV). The coronary sinus (CS) is mildly dilated. IVC, inferior vena cava.

Calcium does not produce an MRI signal. Therefore, on spin-echo MRI, calcification appears as loci of irregular signal voids separating the epicardial and pericardial fat. In constrictive pericarditis, the circumcardiac signal void of the pericardial space is irregular and can be identified in more images and different sections.[287]

Spin-echo and gradient-echo MRI also can accurately evaluate the thickness of the posterior left ventricular wall in patients with constrictive pericarditis. The latter has prognostic significance, because the most common cause of myocardial dysfunction after pericardiectomy is myocardial atrophy.[76] Radiographic demonstration of thinning of the free wall of the left ventricle due to myocardial atrophy was associated with markedly increased mortality after pericardiectomy.[240, 241]

Pericardial Neoplasms

The wide field of view, excellent contrast resolution, and multiplanar capability of MRI make it a method of choice for the diagnosis and evaluation of pericardial neoplasms.[2, 19, 173, 247] Primary pericardial neoplasms are rare. Malignant mesothelioma is the most common primary pericardial malignancy. Primary pericardial lymphoma has also been reported.[267] Teratomas of the pericardium may also be malignant and are most commonly seen in children.

Whether from lymphangitic or hematogenous spread or by direct invasion, pericardial metastases are uncommon[58, 318] and, when found, are usually associated with widespread malignant disease.[69] Metastatic breast carcinoma is the most common pericardial malignancy in women; metastatic lung carcinoma is the most common in men. These lesions are followed in incidence by lymphoproliferative malignancies and melanoma.[69]

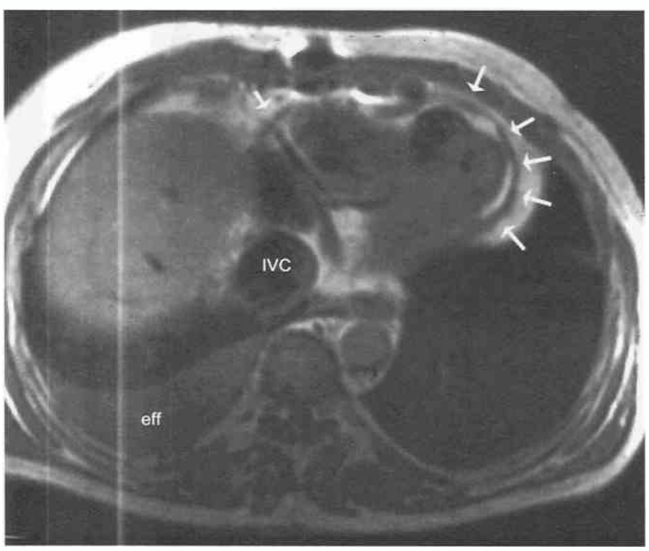

Figure 33–11. Pericardial constriction. Axial spin-echo image obtained at the dome of the right hemidiaphragm in a 59-year-old man with previous coronary artery bypass surgery reveals irregular thickening of the pericardium *(arrows)* extending from the atrioventricular ring to the posterior left ventricular wall. Note the right pericardial effusion (eff) and dilated inferior vena cava (IVC).

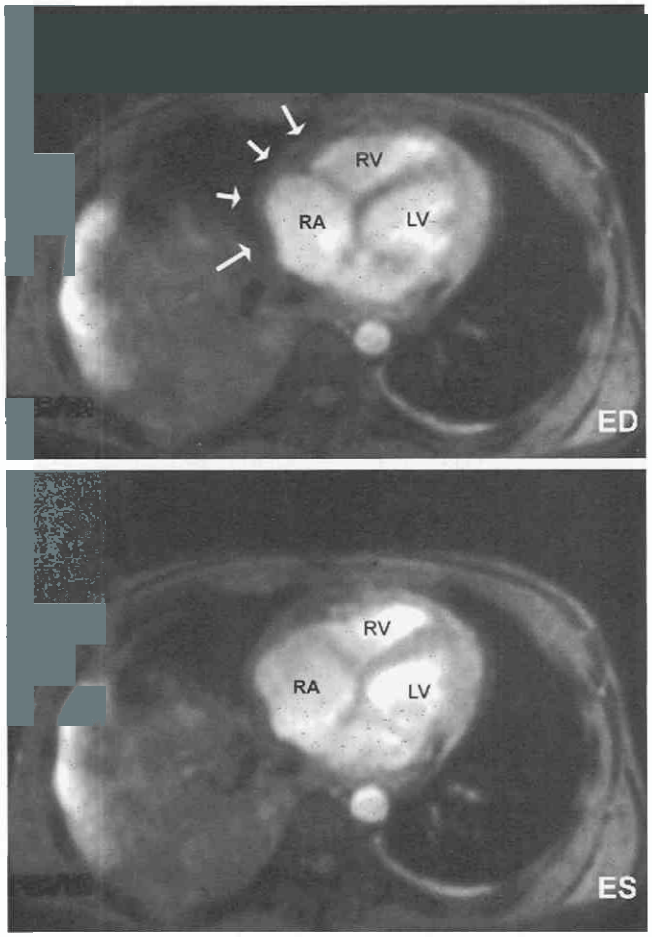

Figure 33–12. MR images obtained from a 23-year-old college student with shortness of breath. The upper gradient-echo acquisition obtained at ventricular end-diastole (ED) shows pericardial thickening increasing the distance between the cavity of the right atrium and the lateral aspect of the heart *(arrows)*. The lower figure obtained at end-systole (ES) shows little change in the volume of the ventricles and a characteristic tubular appearance of the right ventricle (RV). Bilateral pleural effusion is evident. LV, left ventricle.

Pericardial effusion is the most common finding in patients with pericardial malignancy. Uncomplicated free-flowing pericardial fluid demonstrates low signal intensity on T1-weighted spin-echo MRI sequences (see Figs. 33–7 to 33–9).[273, 297] Hemorrhagic effusion, frequently associated with primary malignant mesotheliomas,[3] may present as areas of high, low, or medium signal intensity, depending on the age of hemorrhage.[273]

Focal or generalized pericardial thickening may also be found in patients with malignant pericardial involvement. Direct invasion can be inferred if the normally pencil-thin pericardium appears thickened or interrupted in close proximity to a neoplasm (Fig. 33–13). MRI is useful in suggesting the origin of the neoplasm. Intrapericardial neoplasms compress and deform the normal intrapericardial structures, whereas extrapericardial masses tend to displace the intrapericardial structures without compression or distortion.[106, 162]

Malignant pericardial neoplasms tend to be bulky, often

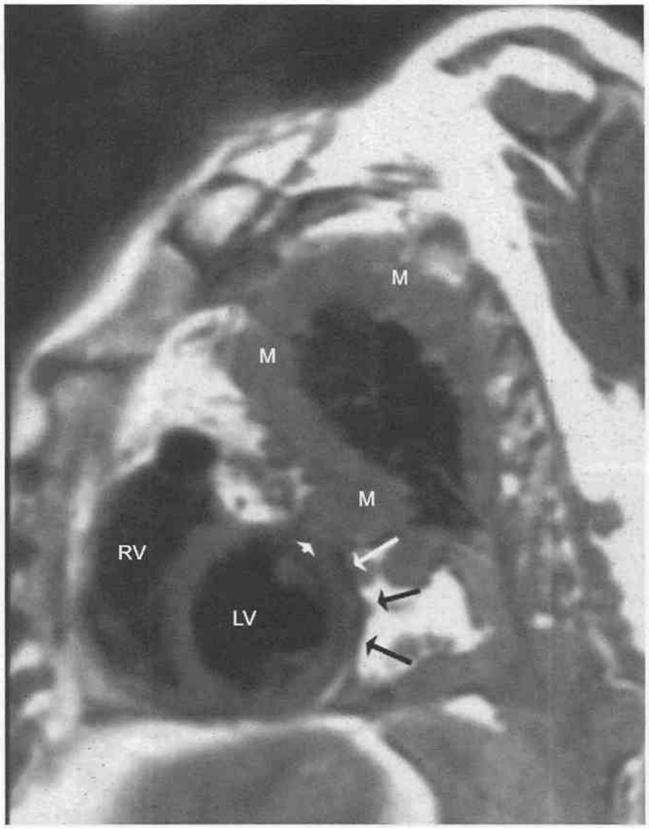

Figure 33–13. MR image of a left pleural mesothelioma in a 66-year-old man. Oblique sagittal spin-echo acquisition shows the markedly thickened pleural mass (M), with thickening of the pericardium *(arrows)* surrounding the posterior left ventricle (LV). There is a break in the pericardium *(arrowhead)* where the mass has penetrated to the left ventricular myocardium. RV, right ventricle.

septated, inhomogeneous in signal intensity, and confined to or immediately contiguous with the pericardium and pericardial space (Fig. 33–14). MRI is excellent at providing information regarding the size, location, and extent of pericardial involvement but is not tissue specific. The fatty tumors (lipomas, fat-containing teratomas) are the exception because of their increased signal intensity on spin-echo T1-weighted MR images. Fatty tumors must be differentiated from focal deposits of subepicardial fat and non-neoplastic lesions (such as mesenteric fat in a hiatal hernia) and focal hemorrhage.

Left-Sided Heart Disease

Pathophysiology of Myocardial Infarction

Myocardial infarction is usually caused by thrombotic occlusion of an epicardial coronary artery.[32] Lack of oxygen supply to the myocardium downstream from the occlusion leads to anaerobic glycolysis with resultant accumulation of lactic acid and other by-products. Within an hour of the initial ischemic insult, subendocardial infarction ensues, subsequently progressing outward toward the subepicardium. The transmural pattern of progression is related to the greater systolic wall stress and oxygen consumption in the subendocardial zone, as well as limited subendocardial collateral flow, which is preferentially shunted to the subepicardial region. This pattern of transmural progression of myocardial infarction is otherwise known as the wavefront of myocardial necrosis.[238, 239]

The infarction is usually completed by 6 hours after occlusion. If reperfusion occurs within this period, potentially viable cells may recover. The reduction of the infarct

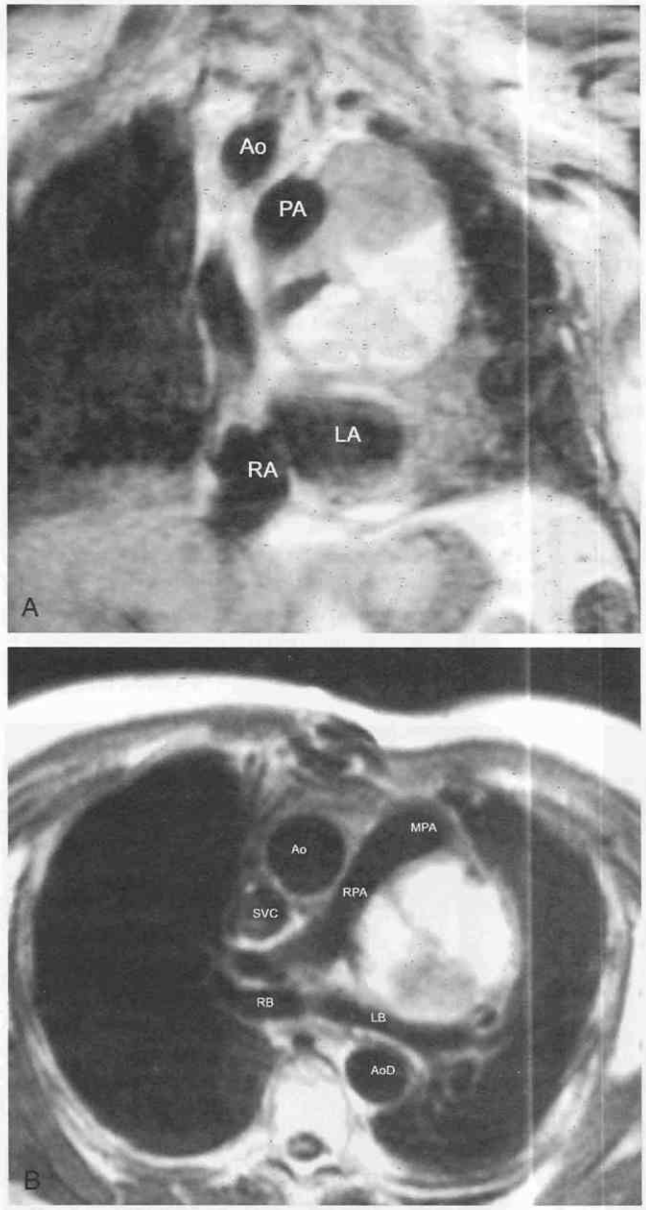

Figure 33–14. MR images of recurrent pericardial sarcoma in a 58-year-old man. *A,* Coronal spin-echo acquisition shows this 15 × 20 cm inhomogeneous mass elevating and displacing the main pulmonary artery (PA), the right pulmonary artery (RA), and the ascending aorta (Ao). LA, left atrium. *B,* Axial section through the displaced right pulmonary artery (RPA) again shows the mass sitting on the roof of the left bronchus (LB). Ao, ascending aorta; AoD, descending aorta; MPA, main pulmonary artery; RB, right bronchus; SVC, superior vena cava.

size achieved by timely reperfusion is predominantly due to the salvage of ischemic but viable subepicardial myocardium. Viable cells also exist in the "border zone" on the lateral margins of the infarct. However, the border zone is narrow and not quantitatively significant.[83, 339]

MRI Examination of Ischemic Heart Disease

Analysis of changes in regional signal intensity after bolus injection and first-pass transit of MRI contrast medium is gaining acceptance for evaluation of myocardial perfusion. Alternative techniques include the use of endogenous tracers, such as deoxyhemoglobin (blood oxygenation level–dependent pulse sequences), spin tagging of arterial water,[6, 330] and the use of intravascular rather than extracellular contrast agents.[41, 154, 242] Intravascular contrast agents, such as ultra-small superparamagnetic iron oxide (USPIO) particles and gadolinium (Gd) chelates (Gd bound to large molecules, such as albumin) remain for a considerable time in the vascular space and thus do not require first-pass imaging.[80]

Assessment of first-pass myocardial perfusion can be obtained by means of fast gradient-echo and echo-planar imaging techniques. Perfusion studies for detection of regional ischemia are accomplished using low doses of MRI contrast media and multislice measurements in the cardiac short axis or along different axes of the heart.[320, 321] With inversion recovery and gradient-echo planar imaging, an ischemic area is identified as a zone of either *low cold-spot* or *high hot-spot signal*, respectively (Fig. 33–15).[320, 321, 341]

Signal intensity versus time curves is generally used for analysis of first-pass imaging studies. Different parameters can be calculated, including, for example[186]:

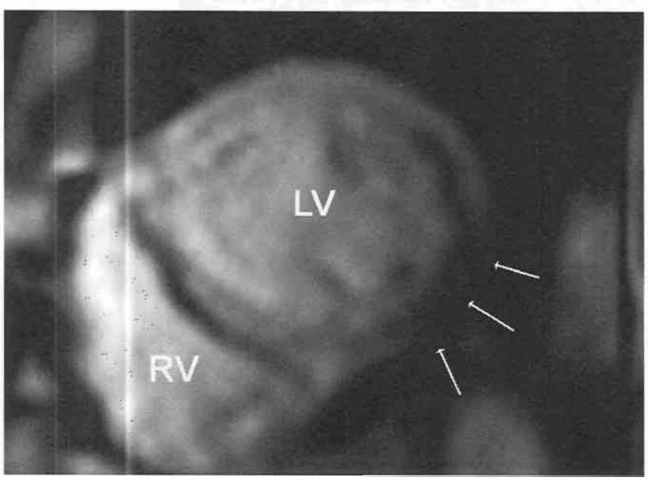

Figure 33–15. Short-axis echo-planar acquisition from a 67-year-old man with a history of acute myocardial infarction. After intravenous administration of gadolinium (Gd-DTPA), the cavity blood of the right ventricle (RV) and the left ventricle (LV) has been opacified, as has the LV myocardium. Note the region of decreased contrast agent uptake *(arrows)*, indicating previous infarction.

1. The rate of signal intensity increase after bolus injection of contrast agent using a linear fit.
2. The maximum signal intensity increase.
3. The time from T_{null} to the maximum signal intensity value.
4. The signal intensity decrease after the peak signal intensity using an exponential fit.

Studies comparing the ability of MRI myocardial perfusion techniques to detect hypoperfused myocardial regions with thallium 201 (^{201}Tl) and technetium 99m (^{99m}Tc) radionuclide imaging and coronary angiography have shown sensitivity rates ranging between 64% and 92% and specificity rates between 75% and 100%.[82, 120, 152, 333] Hartnell and colleagues showed an improved accuracy (similar to scintigraphy) when combining MR myocardial perfusion with cine MRI to detect associated wall motion abnormalities.[120] Wintersperger and coworkers compared myocardial perfusion with myocardial wall thickening in patients with chronic myocardial infarction.[333] Wall thickening was significantly less in hypoperfused areas than in normally perfused areas. The location of hypoperfusion and restricted myocardial wall thickening correlated well. The combination of MR perfusion and cine MRI improved the sensitivity from 72% (using only MRI perfusion) to 100%, whereas the specificity decreased slightly (98% to 93%).

Several studies have stressed the advantages of MRI myocardial perfusion compared with radionuclide imaging to obtain information concerning heterogeneous (subepiendocardial, midendocardial, and subendocardial) transmural enhancement, which may reflect variability in myocardial perfusion across the wall.[81, 328] Cherryman and colleagues studied 103 patients after their first acute myocardial infarction with ECG, echocardiography, ^{201}Tl single photon emission computed tomography (SPECT), and MRI perfusion.[53] They found that dynamic contrast-enhanced MRI was consistently better than Tl-SPECT for detecting anterior septal and inferior posterior infarctions.

Several groups have used the myocardial perfusion reserve or myocardial perfusion reserve index to assess patients with coronary artery disease.[1, 65, 327] The reserve index may be more reliable than determination of coronary flow reserve because the effect of (protective) myocardial collateral flow supply is taken into account. Al-Saadi and associates found a significant difference in myocardial perfusion reserve between ischemic and nonischemic myocardial segments (1.08 ± 0.23 and 2.33 ± 0.41; $P < .001$).[1] Using a cut-off value of 1.5, the diagnostic sensitivity, specificity, and accuracy for the detection of coronary artery stenosis (≥75%) were 90%, 83%, and 87%, respectively. In a similar study by Cullen and colleagues, a negative correlation was found between the myocardial perfusion reserve index and percent coronary artery stenosis ($r = -.81$; $P < .01$).[65]

Functional Imaging in Ischemic Heart Disease

A major strength of MRI is its accurate assessment of ventricular function. Fast gradient-echo techniques provide high-contrast images with high temporal and spatial resolu-

tion that can be obtained within the time of a single breath-hold.[7] This allows evaluation of regional myocardial contraction, ventricular filling and ejection, valve motion, and vascular flow patterns. Excellent visualization of the endocardial and epicardial surfaces of ventricular myocardium on cine MRI displays changes in wall thickening and wall motion throughout the cardiac cycle. The accuracy of measurements and reproducibility make cine MRI appealing as the preferred imaging modality for follow-up of patients.[27] Cine MRI can be used to accomplish the following[6, 16, 128, 130, 225, 278, 324, 325]:

1. Determine regional and global sequelae of past myocardial infarction.
2. Detect ischemic myocardium in patients with coronary artery disease.
3. Differentiate between viable and nonviable myocardium in patients with chronic myocardial ischemia.
4. Measure myocardial mass.

These studies can be performed with the patient at rest or under stress.

Another unique capability of MRI is the use of myocardial tagging. A grid of tag lines is created noninvasively on the myocardium.[9, 342] These tag lines track deformation of underlying myocardium through the cardiac cycle. Myocardial tagging can be used to perform, noninvasively, a myocardial strain analysis and to decompose gross wall deformation into more fundamental units of deformation, such as principal strains or fiber strains.[26, 233] This technique has been used to depict functional recovery after thrombolytic therapy in infarcted myocardium,[25] to elucidate the mechanism of remote myocardial dysfunction,[24, 27, 156, 158] to discriminate between viable and nonviable myocardium using stress myocardial tagging,[63] and to measure the efficacy of medication on left ventricular dysfunction (Fig. 33–16).[155] As a result of the need for computer-intensive postprocessing, the clinical use of MRI tagging is still limited.

Assessment of Myocardial Ischemia, Infarction, and Viability

Demonstrating the benefit of acute reperfusion intervention (i.e., thrombolysis, transluminal angioplasty, or immediate surgical revascularization) necessitates a technique for identification and quantification of infarct size and myocardium at risk at an early stage.[227] In patients with chronic coronary artery disease and ventricular dysfunction, viable myocardium may persist in regions of chronic ischemic injury. Such myocardium may recover after revascularization and improve left ventricular function.

Proton Relaxation Times

The free water content of infarcted myocardium is related to the duration of the ischemic insult,[138, 329] prolonging T1 and T2 relaxation times.[95, 124] Regional differences in T1 and T2 relaxation times may be useful for differentiating normal myocardium from areas of necrosis.[124, 323, 329] Differences in T1 relaxation are not clinically useful for infarct detection unless paramagnetic contrast agents are administered.

Wesbey and colleagues[323] found a linear correlation between T2 relaxation time and the percentage of water content. Furthermore, infarcted tissues were visible as areas of increased signal intensity[124, 253] on T2-weighted MRI sequences (Fig. 33–17). Many groups have used this approach to detect and quantitate myocardial infarctions.[10, 46, 124, 129, 187, 195, 227, 253, 323] However, the relation between changes in relaxation times and the size and stage of myocardial infarction is complex[40, 56, 213, 228, 265, 332, 334] and not completely understood.

Stress Imaging

Pharmacologic stress MRI using the β agonist dobutamine or the vasodilator dipyridamole[17] offers an advantage in differentiating ischemic, stunned, or hibernating myocardium. Dobutamine is preferred because it offers the possibility of both low- and high-dose examinations needed for the differentiation of stunning versus ischemia.[50, 304, 305] In general, analysis of regional endocardial motion, wall thickening, or absolute increase in wall thickness as parameters of regional systolic performance provides a sensitivity and specificity of 70% to 90%.[1, 11, 14, 15, 153, 223, 224, 304, 305] These stress test results could be enhanced by the simultaneous evaluation of regional perfusion.[82, 120] High-dose dobutamine MRI has been found superior to high-dose dobutamine stress echocardiography in detecting patients with significant coronary heart disease (>50% diameter stenosis).[131, 210, 229]

Myocardial Wall Thickness and Dobutamine-Induced Wall Thickening

It is important to differentiate between left ventricular dysfunction caused by irreversible scar from that caused by viable but akinetic ventricular myocardium.[112] Chronic myocardial infarction is associated with myocardium less than 6 mm thick or the presence of focal aneurysm formation (Fig. 33–18). Moderate inotropic stimulation can transiently reverse postischemic myocardial dysfunction; these changes may be demonstrated by echocardiography or MRI. The high-contrast and spatial resolution of MRI resolves the epicardial and endocardial surfaces of the myocardium, thus allowing precise measurement of wall thickness. Baer and coworkers showed that viable myocardium is characterized by preserved end-diastolic wall thickness (>5.5 mm) and a dobutamine-inducible contractile reserve.[12, 16] Both viability parameters reliably predict improvement in regional left ventricular function and ejection fraction after revascularization.[16] Functional studies using cine MRI, performed at rest and during pharmacologic stress, can be performed during repetitive breath-holds and be completed with a contrast-enhanced study to evaluate delayed hyperenhancement in akinetic regions.[262]

Left Ventricular Failure

Left ventricular failure reflects the inability of the ventricle to pump blood and its ability to do so only from an abnormally elevated left atrial filling pressure.[33] It is frequently, but not always, caused by a systolic, contractile abnormality that results in a defect in the ejection of

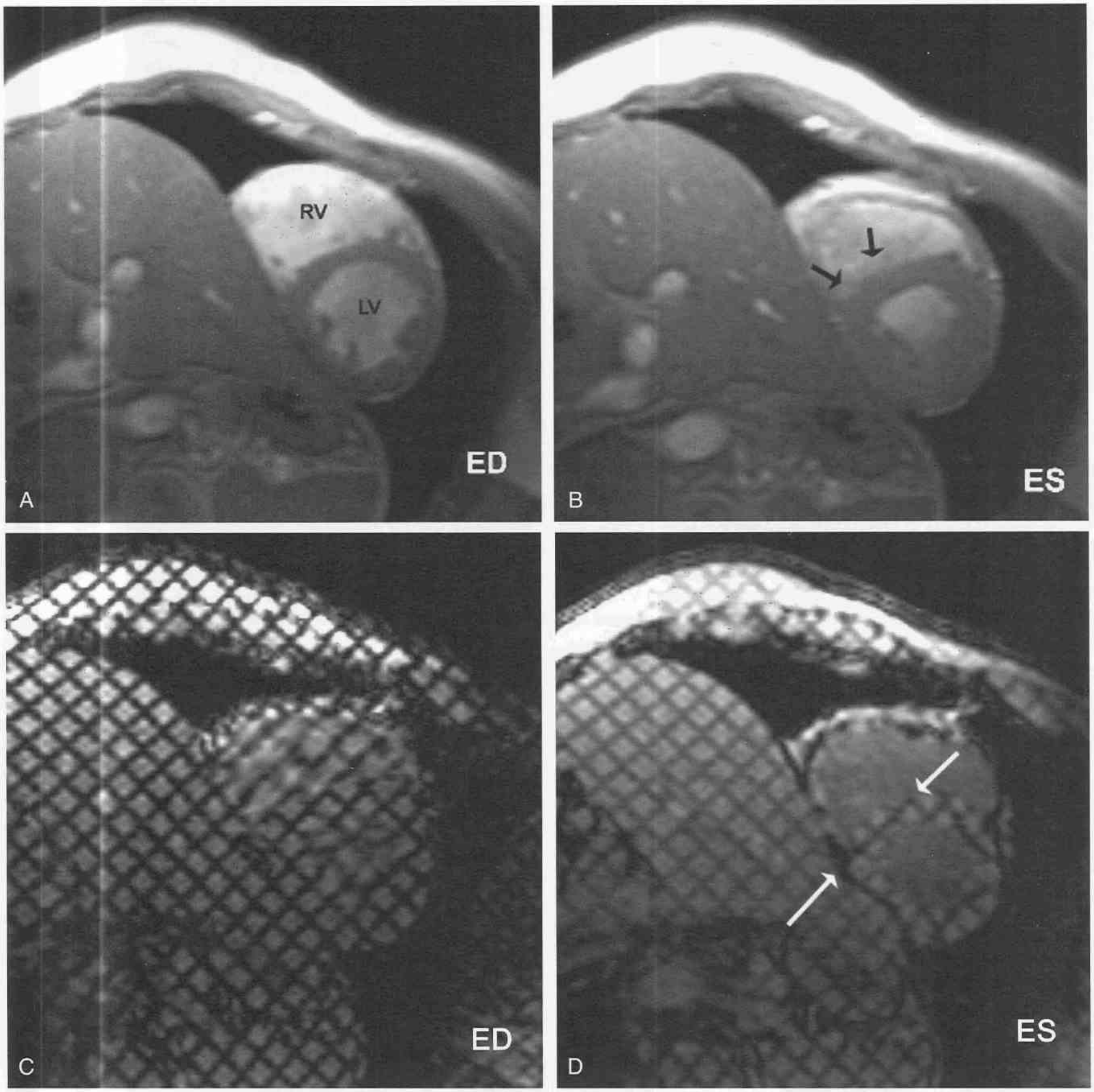

Figure 33–16. Sh[redacted]myocard[redacted] inferos[redacted]lic (ED) short-axis image at the midventricular level, demonstrating normal-appearing left ventricle (LV) and right ventricle (RV). *B,* End-systolic (ES) image obtained at the same anatomic level. There is thickening of both the right and the left ventricular myocardium, but there is diminished thickening of the inferior interventricular septum *(arrows). C,* End-diastolic image obtained at the same anatomic level using myocardial tagging. *D,* End-systolic tagged image. The tag line *(between arrows)* running through the inferior interventricular septum remains straight, indicating a lack of intramyocardial motion.

blood from the heart. However, an abnormality in diastolic function may lead to abnormal ventricular filling, elevated left ventricular end-diastolic pressure, and elevated left atrial pressure. Rapid-onset diastolic failure may be caused by the decrease in compliance seen in acute myocardial ischemia.[123] More insidious onset may occur if chronically ischemic myocardium has been replaced by fibrous scar tissue.

Irrespective of the etiology of the left ventricular failure, MRI is increasingly used in clinical trials to monitor the effects of pharmaceutical therapy on ventricular mass, volume, and ejection fraction. Because MRI techniques do not depend on geometric assumptions about the shape of either ventricle and are less operator dependent than echocardiography, they may be used for accurate and reproducible quantitation of ventricular volume and myocardial mass. The goal of medical therapy in heart failure is to reverse the inexorable dilatation and hypertrophy of the diseased

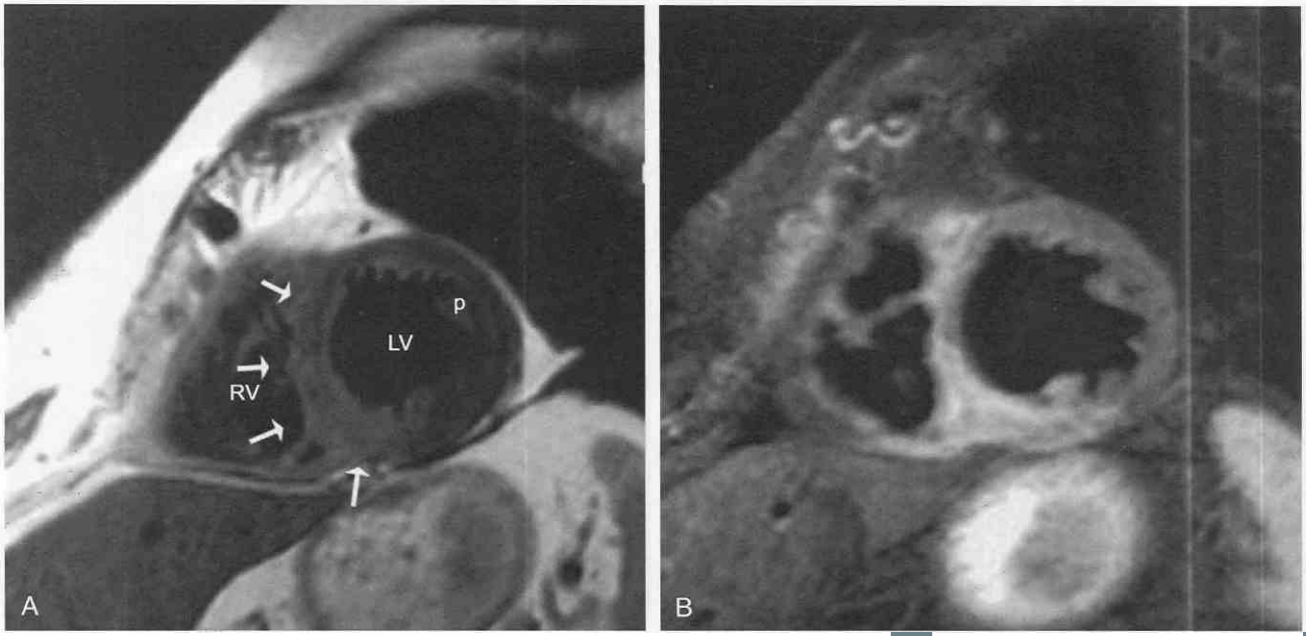

Figure 33–17. Short-axis images obtained from a 58-year-old man with an acute anterior myocardial infarction. *A,* T1-weighted image shows the normal appearance of the left ventricular (LV) and right ventricular (RV) chambers but a relative increase in signal intensity *(arrows)* of the interventricular septum and inferior LV myocardium. The papillary muscle (p) is labeled. *B,* T2-weighted image obtained at the same anatomic level exaggerates the increased signal intensity of the regional myocardial edema.

cardiac muscle. Serial calculations of the ventricular volume and myocardial mass, as well as the stroke volume and ejection fraction, provide an objective measure of the effectiveness of a medical therapeutic regimen.

Cardiomyopathy

MRI techniques allow direct demonstration of the ventricular myocardium. This provides a reproducible means of identifying the distribution of abnormal muscle and characterizing the nature of the abnormality. Cine acquisition displays the epicardial and endocardial borders of the ventricular myocardium, providing temporally resolved imagery from which myocardial mass and ventricular chamber volumes and stroke volume can be computed. This provides a means of estimating ventricular function and allows monitoring the therapeutic response of medical or surgical intervention. Advanced tagging and phase-contrast acquisition techniques provide a means of investigating regional functional disturbance as well as myocardial blood flow.

Cine MRI is an excellent noninvasive technique used to diagnose cardiomyopathy and to distinguish between the three distinct forms of this disease. The clinical usefulness of MRI in patients with cardiomyopathy is reviewed in

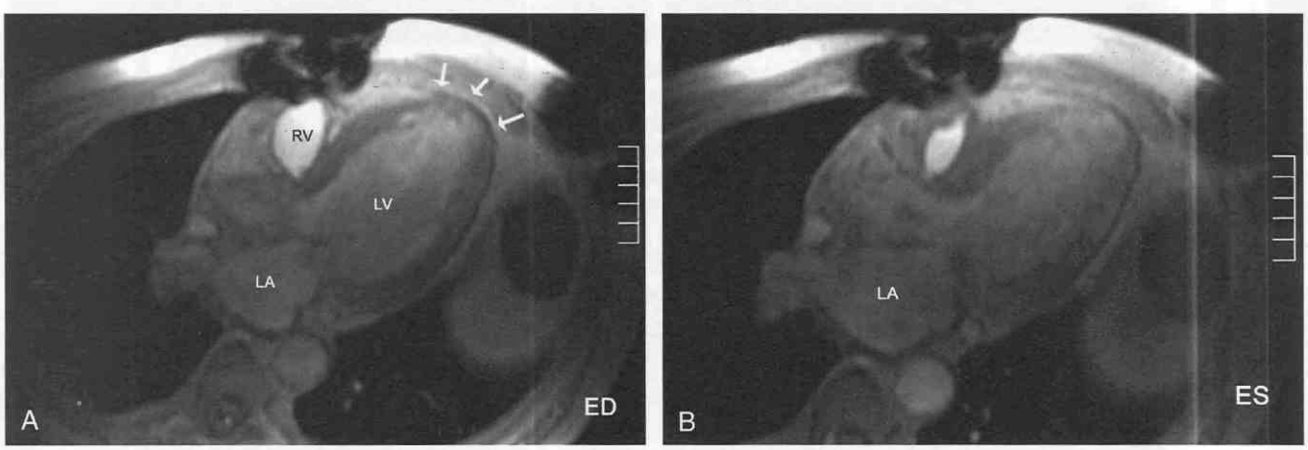

Figure 33–18. *A,* End-diastolic (ED) horizontal long-axis gradient-reversal acquisition from a 64-year-old man with previous myocardial infarction. Poor definition and probable thinning of the distal anteroapical left ventricular (LV) myocardium *(arrows)* are demonstrated. LA, left atrium; RV, right ventricle. *B,* End-systolic (ES) image reveals increased left atrial (LA) size. The anteroapical myocardium is thin and also does not thicken.

terms of information obtained in each of the major categories: dilated, hypertrophic, and restrictive cardiomyopathy.

Dilated Cardiomyopathy

Dilated cardiomyopathy is characterized by ventricular dilatation, decreased contractility, as well as alterations in ventricular diastolic function.[116] Cine MRI reliably quantifies ventricular volume and mass, ejection fraction, and wall stress in patients with dilated cardiomyopathy[99, 276, 313] and may be used to monitor the functional status of the ventricle over time. The high reproducibility of cine MRI (with the variability in volume and mass measurements of $< 5\%$)[276] makes it an invaluable tool in the assessment of effects of medications. MRI was used to evaluate the response of patients with dilated cardiomyopathy to angiotensin-converting inhibitor therapy.[77]

Analysis of cine acquisitions has revealed regional functional abnormalities in these patients not found in normal control subjects. The normal gradient in wall thickening, with gradual increase from base to apex, is absent in dilated cardiomyopathy, as demonstrated on short-axis cine MRI[276, 277] (Fig. 33–19). Myocardial tagging techniques provide a means of quantitating regional changes in myocardial function, reflecting both regional stress-strain relationships, as well as the fibrous anatomy of the heart. Depressed strain values correlate with depressed chamber function. Both of these parameters were shown to be markedly decreased[192] in patients with dilated cardiomyopathy, with preservation of fiber orientation throughout the cardiac cycle. These findings suggest that myocardial tagging may also be a useful tool for testing therapeutic regimens[85] in these patients.

Hypertrophic Cardiomyopathy

Hypertrophic cardiomyopathy presents clinically with both diastolic and systolic dysfunction.[268] The dramatically thickened ventricular myocardium in this family of diseases has a distinctive appearance on MRI. In these patients MRI allows a significantly more comprehensive evaluation of the diseased myocardium than does echocardiography.[102, 230] In patients with hypertrophic cardiomyopathy, MRI allows improved visualization of wall segments (97% of segments) as compared with the use of echocardiography (67% of segments).[230] Regional hypertrophy found on MRI correlated with Q-wave abnormalities demonstrated by ECG, whereas the configuration of the T-wave reflected the distribution of hypertrophy between the basal and apical segments.[264] Use of MRI allows accurate characterization of the distribution of apical hypertrophy; distribution can be described as symmetrical, asymmetrical, or only involving the cardiac apex[281] (Fig. 33–20). In a longitudinal study, MRI was used to demonstrate that the characteristic "spadelike" configuration of the left ventricular chamber may begin with a "nonspade" configuration.[293]

In patients with hypertrophic cardiomyopathy, cine MRI has been used to quantitate left ventricular mass, volumes, and ejection fraction as well as right ventricular function. Suzuki and colleagues[292] found increased right ventricular mass, reduced peak filling rate, and decreased right ventricular filling fractions in these patients. Velocity-encoded cine MRI has been used to study coronary sinus blood flow in patients with hypertrophic cardiomyopathy.[143] Resting coronary blood flow was not significantly different from that found in normal individuals. However, after dipyridamole administration, coronary sinus blood flow in patients with hypertrophic cardiomyopathy increased to a much lower level than that seen in the healthy volunteers, indicating decreased coronary flow reserve. Impaired diastolic function due to nonuniform hypertrophy with subsequent loss of myocardial contractile elements, myocardial perfusion abnormalities, and change in left ventricular geometry has been demonstrated.[338]

Using myocardial tagging, significant reduction in the wall motion of the hypertrophied interventricular septum has been shown.[174] Depressed circumferential segment shortening in the anterior and inferior regions of the interventricular septum[157] and impaired systolic wall thickening (related inversely to wall thickness)[78] have been demonstrated as well.

Restrictive Cardiomyopathy

Restrictive cardiomyopathy is a family of diseases that is characterized by primary diastolic dysfunction with com-

Figure 33–19. MR image of dilated cardiomyopathy in a 59-year-old woman. *A,* End-diastolic (ED) short-axis image through the papillary muscles *(arrows)* shows mild dilatation of the left ventricle (LV) with relative preservation of the right ventricle (RV). *B,* End-systolic (ES) image reveals no regional wall motion abnormality but diminished contraction and relatively increased end-systolic cavity volume.

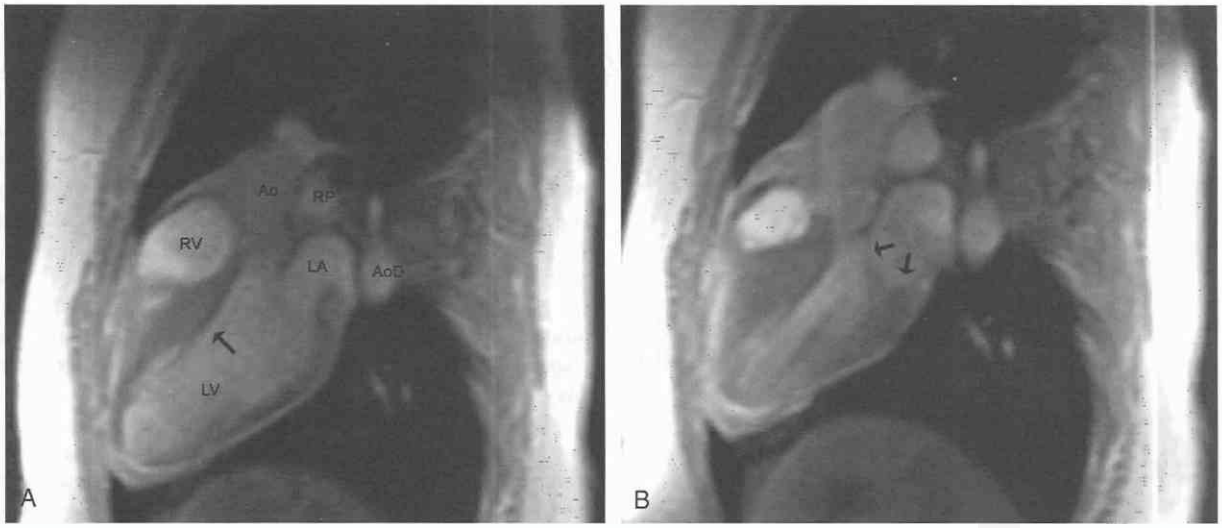

Figure 33–20. MR image obtained from a 17-year-old girl with hypertrophic obstructive cardiomyopathy. *A,* End-diastolic (ED) oblique axial-gradient reversal acquisition shows near-normal left ventricular (LV) size. The superior interventricular septum *(arrow)* is slightly asymmetrical with respect to the remainder of the LV myocardium. The right ventricle (RV), ascending (Ao) and descending (AoD) aorta, left atrium (LA), and right pulmonary artery (RP) are labeled. *B,* End-systolic (ES) image shows a dramatic difference in septal thickening, causing narrowing of the subvalvular left ventricular region. The mitral leaflets *(arrows)* are closed, and there is no mitral regurgitation.

plete or partial preservation of systolic ventricular function; it must be differentiated from pericardial constriction.[231] MRI is the study of choice in this circumstance, allowing both the characterization of the ventricular functional abnormality and demonstration of the pericardial abnormality.[184, 273] Pericardial thickening greater than 4 mm indicates pericarditis underlying the restrictive symptoms and hemodynamic measurements.[184]

Amyloidosis frequently causes restrictive cardiomyopathy. It may be recognized by widespread thickening of all chamber walls and atrioventricular valve leaflets in the face of decreased ejection fraction and abnormal segmental wall motion. When compared with patients with hypertrophic cardiomyopathy, patients with cardiac amyloidosis had enlarged right atria and increased right atrial and ventricular wall thickness.[84] Restrictive cardiomyopathy can be differentiated from hypertrophic cardiomyopathy on cine MRI, because the systolic function (ejection fraction and wall motion) is usually normal to increased in hypertrophic cardiomyopathy but reduced in amyloid heart.

Comparison of MRI findings in patients with amyloid infiltration, patients with hypertrophic cardiomyopathy, and normal volunteers demonstrated a significant decrease in myocardial signal intensity in patients with amyloid heart as opposed to the other two groups, possibly because of magnetic field heterogeneity and decreased proton concentration inherent in amyloid deposition. In addition, mitral and tricuspid regurgitation frequently associated with restrictive cardiomyopathy can be demonstrated and quantified on MRI.[75] In patients with cardiomyopathy due to cardiac sarcoidosis, loci of high myocardial signal intensity were found on T1-weighted images after administration of intravenous Gd.[51, 246]

Myocarditis

Myocarditis is an inflammation of the myocardium associated with myocyte damage or necrosis. In the United States viral etiology accounts for most cases, although it may also be due to chemical agents, local toxin production, as well as immune-mediated diseases. The symptoms are nonspecific, because patients frequently present with palpitations, malaise, shortness of breath, and chest pain or discomfort, and they can be mistaken for cardiomyopathy or coronary artery disease. Most patients recover, but a fraction will develop cardiomyopathy.[38] Some cases of sudden death after a viral illness are thought to represent sequelae of viral myocarditis.[70, 98]

Myocarditis is often a clinical diagnosis, because the definitive diagnosis requires an endomyocardial biopsy. However, a myocardial biopsy is invasive and can be associated with severe complications. In addition, the focal nature of the disease leads to frequent nondiagnostic or false-negative results. Scintigraphy with indium 111 monoclonal antimyosin antibody[22] and gallium 67[307] used noninvasively to assess myocardial inflammation are limited by a high false-positive rate and frequent overestimation of the extent of myocardial damage.[30, 207]

The early experience with MRI for evaluation of myocarditis suggested that T2-weighted and Tl-weighted, Gd-DTPA–enhanced spin-echo sequences were useful.[22, 52, 100, 188, 189] T2-weighted sequences showed increased signal in the affected muscle, probably due to myocardial edema, whereas Gd-DTPA T1-weighted sequences demonstrated enhancement of the damaged myocardial muscle. In a study of 19 patients with viral myocarditis,[97] Gd-DTPA–enhanced MRI was used to follow the course of the disease and to estimate the extent and distribution of myocardial involvement. Early in the course of the disease, myocardial enhancement tended to be localized, reflecting the focal nature of the myocardial inflammation. However, as the disease progressed, the enhancement was seen throughout the muscle, depicting an evolution of myocarditis into a diffuse process.

In a more recent study[252] a group of 20 patients was studied with Gd-DTPA–enhanced spin-echo and cine MRI; 12 had myocarditis, and 8 did not. In the group with myocarditis, wall motion abnormalities as seen on cine MRI matched exactly the regions of abnormal enhancement on Gd-DTPA spin-echo examinations. These authors concluded that in a correct clinical setting, focal myocardial enhancement strongly supports the diagnosis of myocarditis, especially when associated with regional wall motion abnormalities.

Arrhythmogenic Right Ventricular Dysplasia

Arrhythmogenic right ventricular dysplasia is a cardiomyopathy of unknown etiology that is characterized by ventricular tachycardia originating in the right ventricle, ST changes in the right-sided precordial leads of the surface ECG, regional and global right ventricular contractile abnormalities, as well as thinning and fibrofatty replacement of the right ventricular myocardium.[178] Although severe right ventricular dilatation, reduced right ventricular ejection fraction, and right ventricular failure as well as left ventricular dysfunction have been reported,[177a, 316] most individuals have localized or patchy areas of segmental right ventricular thinning and akinesia or dyskinesia and are minimally symptomatic. Differentiation between right ventricular dysplasia and pathologic fatty infiltration can be made on clinical and histologic grounds. Fatty infiltration usually does not cause clinical symptoms,[31] whereas right ventricular dysplasia does. In addition, in right ventricular dysplasia, abnormal foci of fat extend from the epicardial surface through the interstitium, displacing myocardial fibers.[169]

Right ventricular dysplasia appears to be inherited, with a strong familial tendency suggesting an autosomal dominant disorder with variable expression and penetrance.[211] It is usually diagnosed in individuals between 20 and 50 years of age,[68] but it may be diagnosed in young persons[221, 295] as well. The disease is found predominantly in men, and symptoms frequently occur with exercise. This condition must be differentiated from right ventricular outflow tract tachycardia,[37, 139] which carries a significantly lower risk of sudden death. Pathologic changes of right ventricular dysplasia are similar to those found in Uhl's anomaly.

ECG-gated cine cardiac MRI is considered a useful means of assessing right ventricular free wall myocardial thinning and fatty infiltration, as well as global and regional wall motion abnormalities.[8, 31, 243] In axial and short-axis section, the free wall of the normal right ventricle should appear as a relatively homogeneous, intermediate signal intensity extending from the fat of the anterior atrioventricular ring toward the anterior extension of the interventricular septum. There is usually a thin and tapering deposit of epicardial fat extending from the atrioventricular ring along its proximal surface, immediately subjacent to the pencil-thin line of the pericardial space.[159] The myocardium of the free wall is not always demonstrated in all sections because it is relatively thin and sometimes cannot be resolved spatially. The diaphragmatic right ventricular wall is best viewed in short-axis section and should appear slightly thicker than the free wall but thinner than the interventricular septum.

In patients with right ventricular dysplasia, the shape and volume of the right ventricular chamber may appear normal or "dilated" to the eye. The right ventricular free wall myocardium may appear diffusely thinned or have loci of "absent" myocardium, representing local areas of marked thinning (Fig. 33–21). Furthermore, on T1-weighted images, loci of increased intramyocardial signal intensity, representing fatty infiltration, are observed in both the diaphragmatic and free wall. Although these changes may be identified with conventional body coil acquisitions, use of a dedicated cardiac or general purpose chest coil provides the most reliable demonstration of free wall myocardial changes. Care must be exercised to place the coil over the anterior aspect of the heart. The center of the coil should be applied about 5 cm to the left of midline, just medial to the nipple.

Use of gradient-echo acquisition for cine examination of the right ventricle in this condition may be helpful in identifying focal areas of free wall dyskinesia. In a similar but benign syndrome, right ventricular outflow tract tachycardia, focal right ventricular myocardial wall thinning or excavation, or wall motion abnormalities may be identified. However, they are restricted to right ventricular outflow tract, differentiating them from the findings in arrhythmogenic right ventricular dysplasia.[49]

Magnetic Resonance Coronary Arteriography

All forms of MRI are exquisitely sensitive to motion and turbulent blood flow artifacts. Cardiac MRI is especially sensitive to cardiac and respiratory motion and arterial pulsation. MR coronary arteriography attempts to demonstrate vessels smaller than 5 mm in caliber running along the epicardial surface of the contracting heart. Clinical success has been mixed.

Conventional ECG-gated spin-echo (Fig. 33–22) and gradient-echo (Fig. 33–23) MRI usually demonstrate portions of the epicardial coronary arterial tree but cannot be relied on for precise morphologic diagnosis. Recent advances in fast MRI have nearly eliminated respiratory and cardiac motion artifacts; MRI may provide a noninvasive means of visualizing the epicardial coronary arteries. ECG-gated two-dimensional gradient-echo acquisition sequences depict laminar blood flow as bright signal and turbulence or absent blood flow as signal voids. Use of fat-suppression techniques increases the contrast of the epicardial coronary arteries by decreasing the relative signal produced by the epicardial fat surrounding the arteries (Fig. 33–24). In addition, rapid-acquisition sequences allow image acquisition during a single breath-hold with and without the use of k-space segmentation to provide rapid visualization of the epicardial coronary tree.[79, 167, 176, 222, 331]

In a preliminary evaluation of k-space–segmented, fat-suppressed, single–breath-hold MR arteriography[176] in 25 subjects (including 19 healthy volunteers and 6 patients undergoing diagnostic coronary arteriography), the left main coronary artery (LMCA) was identified in 24 (96%)

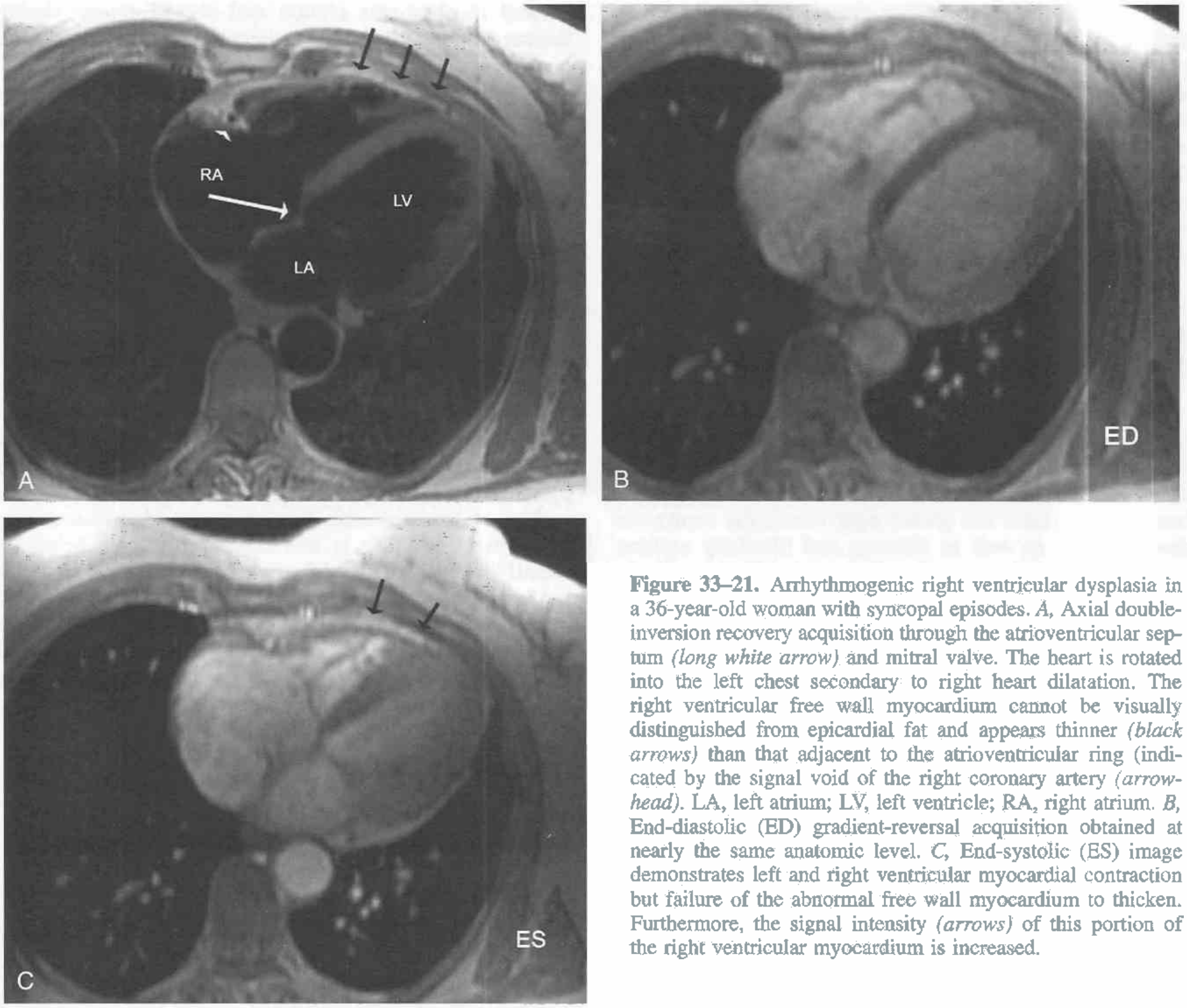

Figure 33–21. Arrhythmogenic right ventricular dysplasia in a 36-year-old woman with syncopal episodes. *A,* Axial double-inversion recovery acquisition through the atrioventricular septum *(long white arrow)* and mitral valve. The heart is rotated into the left chest secondary to right heart dilatation. The right ventricular free wall myocardium cannot be visually distinguished from epicardial fat and appears thinner *(black arrows)* than that adjacent to the atrioventricular ring (indicated by the signal void of the right coronary artery *(arrowhead)*. LA, left atrium; LV, left ventricle; RA, right atrium. *B,* End-diastolic (ED) gradient-reversal acquisition obtained at nearly the same anatomic level. *C,* End-systolic (ES) image demonstrates left and right ventricular myocardial contraction but failure of the abnormal free wall myocardium to thicken. Furthermore, the signal intensity *(arrows)* of this portion of the right ventricular myocardium is increased.

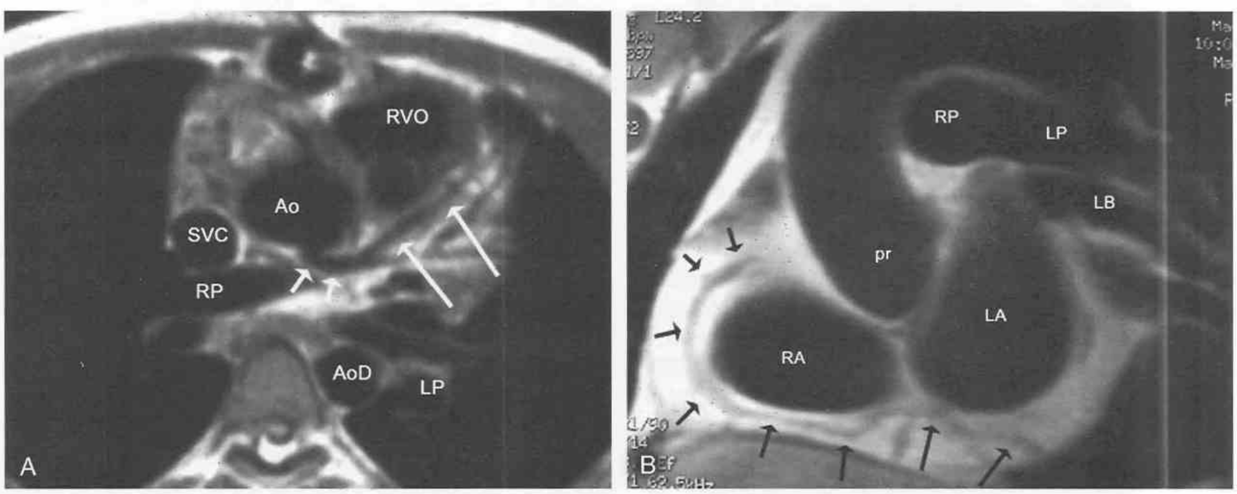

Figure 33–22. Incidental demonstration of the coronary arteries. *A,* Axial spin-echo acquisition obtained from a 52-year-old man with a history of a mediastinal mass. The origin and course of the left main coronary artery *(short arrows)* from the aortic root (Ao) as well as the proximal course of the anterior descending coronary artery *(long arrows)* are clearly seen. The right ventricular outflow tract (RVO), superior vena cava (SVC), right (RP) and descending left (LP) pulmonary arteries, and descending aorta (AoD) are marked. *B,* In this short-axis section, obtained for evaluation of pericardial thickening, almost the entire course of the right coronary artery *(arrows)* can be visualized by its contrast with surrounding fat. The left atrium (LA), the right atrium (RA), the posterior right aortic sinus of Valsalva (pr), the confluence of the right pulmonary artery (RP) and the left pulmonary artery (LP), and the left bronchus (LB) are identified.

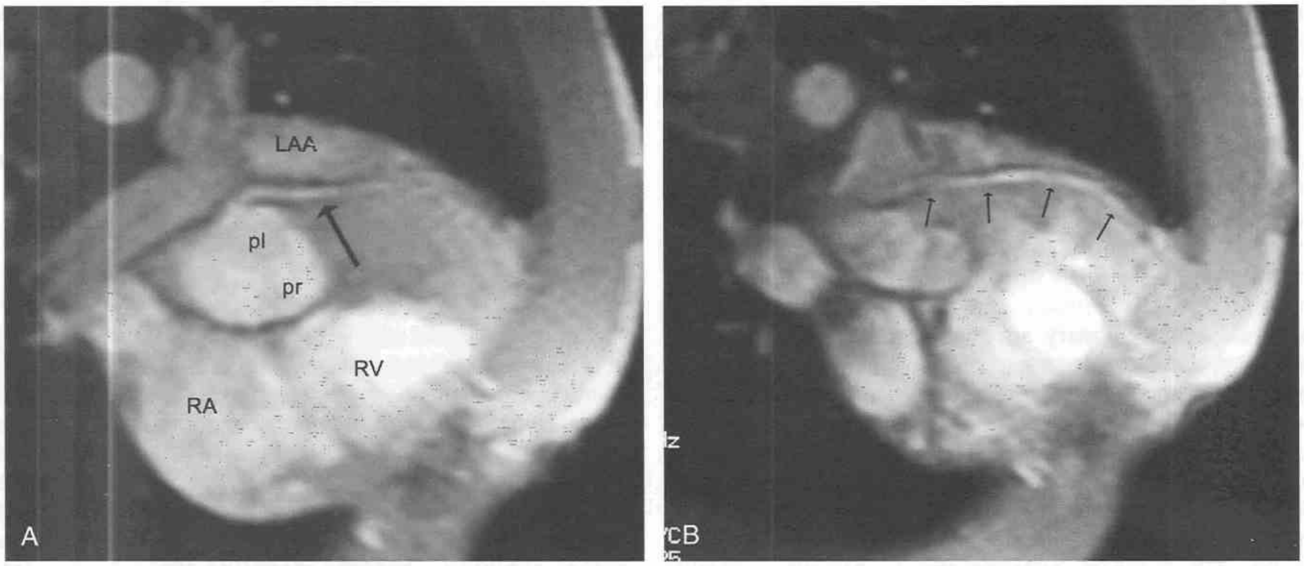

Figure 33–23. Adjacent gradient-echo four-chamber views obtained from a 39-year-old man evaluated for heart failure. *A,* The origin of the left main coronary artery from the posterior left aortic sinus of Valsalva (pl) is clearly seen. As the artery *(arrow)* dips beneath the left atrial appendage (LAA), it moves out of plane and is cut off. The right atrium (RA), the right ventricle (RV), and the posterior right aortic sinus (pr) are labeled. *B,* Gradient-echo acquisition obtained 5 mm caudad to *A.* The circumflex coronary artery *(arrows)* is seen coursing along the posterior aspect of the left ventricle.

subjects. The left anterior descending coronary artery (LAD) and right coronary artery (RCA) were visualized in all 25 individuals. The left circumflex artery (LCx) was seen in 19 (76%). Diagonal branches of the LAD were identified in 20 (80%) subjects. In the 6 patients in this series with angiographically proven coronary artery occlusion, absence of signal distal to the area of occlusion was identified by MR coronary arteriography. In a similar

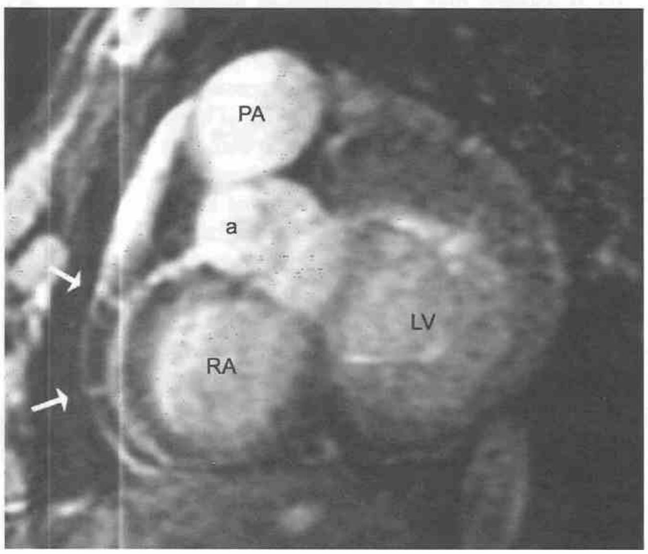

Figure 33–24. K-space–segmented, breath-hold, fat-saturated, short-axis, gradient-echo acquisition. The course of the right coronary artery from the anterior aortic sinus of Valsalva (a) is clearly visible as a result of the fat-suppressed anterior atrioventricular ring. The proximal segments of marginal branches of the right coronary artery *(arrows)* are visible. LV, left ventricle; PA, pulmonary artery; RA, right atrium.

series,[331] 39 adults referred for diagnostic coronary arteriography also underwent single–breath-hold, gradient-echo MR coronary arteriography within 1 week of their conventional arteriograms. Conventional coronary arteriography demonstrated moderate to severe proximal coronary artery narrowing in 74% of patients. Overall sensitivity and specificity of MRI for correct identification of hemodynamically significant (>50%) stenosis was 90% and 92%, respectively. Sensitivity and specificity of the technique for the LMCA were both 100%, 71% and 90% for the LCx, and 100% and 78% for the RCA, respectively.

Duerinckx and Urman[79] reported a series of 20 patients undergoing both conventional and MR coronary arteriography. They found 50% sensitivity for stenosis of the LMCA, 73% sensitivity for stenosis of the LAD, 0% for the LCx, and 62% sensitivity for significant stenosis of the RCA (overall sensitivity, 63%). Specificity in this series was 84% for the LMCA, 37% for the LAD, 82% for the LCx, and 56% for the RCA. Similarly, Pennell and coworkers[222] reviewed this technique of MR coronary arteriography in a group of 21 healthy controls and 5 patients with angiographically proved coronary artery disease. Twenty-two (85%) of the 26 subjects were successfully imaged. The LMCA was identified in 95%, the LAD in 91%, the LCx in 76%, and the RCA in 95% of studies. All five coronary occlusions in their series were identified by MR coronary arteriography. Although most missed vessels occurred early in their series, imaging the circumflex artery was problematic throughout their experience.

Preliminary experience with three-dimensional gradient-echo MRI acquisition[167] provided similar findings. The proximal coronary tree was not identified in all subjects. The LMCA was identified in 4 (57%) of 7 healthy volunteers. In this same group of volunteers, the LAD was identified in 4 (57%) of 7, the LCx in 2 (29%), and the RCA in all 7 (100%). Seven patients studied by conven-

tional coronary arteriography and MR coronary arteriography had 17 diseased arterial segments. MR coronary arteriography demonstrated altered signal intensity in 13 (76%) of these segments.

Administration of intravenous contrast material increases contrast between blood and the surrounding arterial wall. This improves the low signal-to-noise ratios inherent to k-space–sampled breath-hold acquisitions.[108, 126, 149, 166, 237, 310, 343] In a report of the comparison of conventional x-ray angiography with intravenous contrast–enhanced breath-hold MR coronary angiography[177] in 50 patients with suspected coronary artery disease, 76.6% of arterial segments could be adequately analyzed. MR coronary angiography detected the presence of significant (>50%) stenoses and occlusions in 34 of 36 patients and excluded significant stenosis or occlusion in 8 of 14 patients. These workers found a sensitivity of 94.4%, a specificity of 57.1%, a positive predictive value of 85%, and a negative predictive value of 80% for this technique.

For MR coronary arteriography to become a useful modality in the evaluation and management planning of patients with coronary heart disease, it must first be able to reliably demonstrate the entire epicardial coronary tree. (Can one imagine the growth in use of coronary arteriography if it allowed visualization of only the proximal epicardial arteries in only 80% of cases?) MR coronary arteriography cannot as yet provide complete and reliable noninvasive demonstration of the epicardial coronary arteries and their branches. Needless to say, advances in pulse-sequence design, as well as hardware considerations (such as dedicated chest surface coils and higher RF gradients) will undoubtedly improve our ability to demonstrate the coronary arteries using MRI. We must ask whether our ability to demonstrate the coronary arteries per se improves our ability to diagnose coronary artery disease and identify patients at risk for future cardiac events. Then we must improve the sensitivity and specificity for the detection of less severe (<50%) luminal narrowing. Otherwise, the usefulness of MRI for detecting non–flow-limiting plaques, the major source of acute coronary occlusion and sudden cardiac events, will be limited. Furthermore, if MR coronary arteriography is to become a noninvasive replacement for conventional catheter coronary arteriography, then the sensitivity and specificity for detection of significant vessel stenosis must increase. Claims of MRI eventually providing combined morphologic and functional analysis of the heart do not obviate limited spatial resolution, difficulties in the sensitive and specific imaging of the posterior circulation and arterial side branches, as well as differentiation between coronary arteries and cardiac veins.

Magnetic Resonance of Valvular Heart Disease

It is unusual for MRI to be employed as the first imaging technique in the work-up of cardiac murmurs. Nevertheless, MRI yields important information concerning cardiac chamber size, myocardial mass, pulmonary blood flow, and pulmonary venous pressure in these patients. MRI may be useful for demonstration of the jets of valvular dysfunction, as well as the means of quantitating the dysfunction and its sequelae. The response of the heart to valvular dysfunction leads to characteristic changes in chamber volume and myocardial mass to maintain myocardial wall stress and systemic cardiac output. Recognition of the morphologic changes as well as understanding the homeostatic mechanisms that lead to these changes forms the basis of cardiac diagnosis.

Mitral Stenosis

Congenital mitral stenosis is rare and is observed mainly in infants and children.[250] Rheumatic mitral stenosis results from the chronic and progressive fibrotic process instigated by the initial rheumatic inflammatory reaction. The slowly progressive process of reactive fibrosis may take 20 to 40 years before a patient with a history of acute rheumatic fever develops signs or symptoms of rheumatic mitral stenosis. Once symptoms occur, another decade may pass before symptoms become disabling.[255, 336] The mitral leaflets thicken, calcify, and fuse. The chordae tendineae become thickened, fused, and nonpliable. All of these changes cause decreased diastolic leaflet excursion and functional narrowing of the mitral orifice.[250, 336] Isolated mitral stenosis occurs in about 40% of all patients presenting with rheumatic heart disease. Nearly 60% of patients with pure mitral stenosis give a history of previous rheumatic fever.[256, 336]

In the early phases of mitral stenosis, elevated pulmonary venous pressure is transmitted across the capillary bed, resulting in "passive" pulmonary arterial hypertension. This may be identified as an increase in the caliber of the central pulmonary artery segments. However, pulmonary arteriolar resistance subsequently rises in these patients,[110, 337] causing precapillary pulmonary hypertension. On spin-echo MR images (Fig. 33–25), increased pulmonary resistance may be reflected in slowing of pulmonary blood flow, resulting in increased signal within the pulmonary arteries. Chronic elevation in pulmonary resistance results in right ventricular hypertension and myocardial hypertrophy. On gradient-echo MRI (Fig. 33–26) acquisition, thickening of the right ventricular free wall or interventricular septum is evident. Furthermore, the hypertrophic response changes the geometry of the right ventricular cavity, changing the curvature of the interventricular septum. This is first reflected as straightening and subsequently as reversal of the systolic bowing of the septum toward the right ventricle. In addition, change in the geometry of the interventricular septum affects the function of the tricuspid valve papillary muscles, inducing tricuspid regurgitation. Therefore, mitral stenosis frequently presents as a complex lesion, affecting both atria and atrioventricular valves, as well as the right ventricle. Throughout the course of mitral stenosis, until late in the disease, the left ventricular volume, mass, and function remain normal.

Mitral Regurgitation

Acute, severe mitral regurgitation imposes a sudden volume load on an unprepared left ventricle. Although this acts to increase left ventricular stroke volume, forward

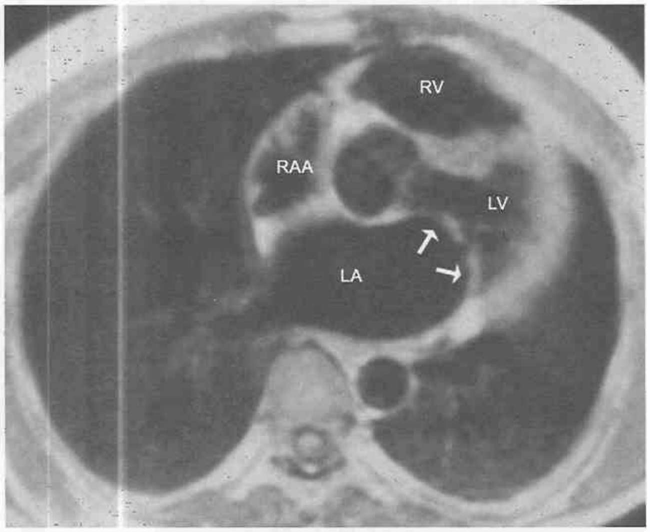

Figure 33–25. Axial spin-echo image of chronic rheumatic mitral stenosis in a 60-year-old man. Left atrial (LA) enlargement is associated with thickening and doming of the mitral leaflets *(arrows)*, increased signal in the gravity-dependent posterior lung parenchyma (indicating interstitial edema), and a normal left ventricle (LV). The right atrial appendage (RAA) and the right ventricle (RV) are both mildly dilated.

stroke volume and total cardiac output are reduced; adequate time for development of compensatory eccentric left ventricular hypertrophy does not transpire. Similarly, the left atrium cannot accommodate the rapid increase in volume, so early systolic left ventricular ejection into the left atrium results in left atrial hypertension and pulmonary vascular congestion. Patients with acute mitral regurgitation commonly present with both low cardiac output and pulmonary congestion. Acute mitral regurgitation results from sudden changes in the chordae tendineae anchoring the valvular leaflets or damage of the leaflets themselves. A good example is infectious endocarditis, which may present with both chordae tendineae rupture and leaflet perforation. Acute papillary muscle dysfunction or rupture of the head of a papillary muscle compromises the apposition of the valve leaflets. Myocardial infarction is a frequent cause of papillary muscle rupture, commonly resulting in severe congestive heart failure and, unless treated emergently, death. Acute myocardial infarction in muscle adjacent to a papillary muscle insertion may result in papillary muscle dysfunction and mitral regurgitation. Other causes of mitral regurgitation include mitral valve prolapse syndrome, acute and/or chronic rheumatic heart disease, and collagen vascular disease. An uncommon cause of mitral regurgitation is ingestion of anorectic agents.[60]

When examined in the acute phase of mitral regurgitation, the most prominent findings are those of severe pulmonary congestion with nearly normal heart size. MRI often reveals the signal-void jet of mitral regurgitation, which appears as an early systolic fan-shaped signal void extending from the mitral annulus into the left atrium (Fig. 33–27). Left ventricular volume is not increased. Spin-echo examination may show normal left atrial size.

In cases of chronic mitral regurgitation, the initial insult may be minor and not sufficient to produce the signs and symptoms of low cardiac output and pulmonary congestion. Adequate time transpires for the ventricular myocardium to hypertrophy as well as for individual myocardial fibers to lengthen.[47,115] This compensatory increase in left ventricular end-diastolic volume permits increased total stroke volume and restoration of forward cardiac output.[344] In an analogous manner, left atrial dilatation allows accommodation of the additional regurgitant volume at a lower left atrial pressure.

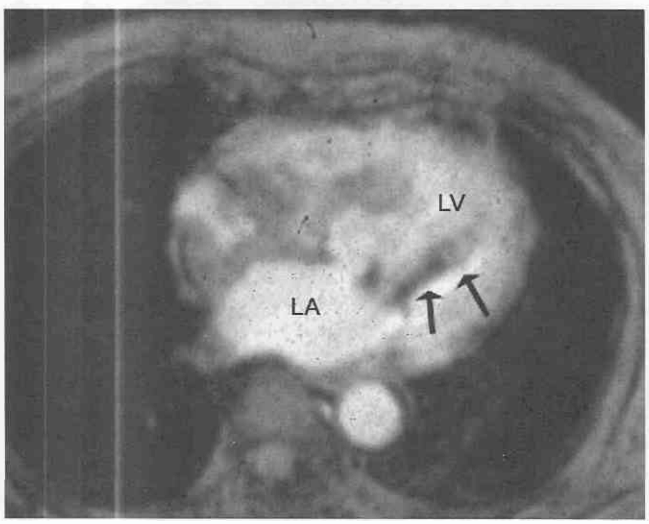

Figure 33–26. Diastolic axial gradient-echo acquisition from a 62-year-old man with chronic rheumatic mitral stenosis. Left atrial (LA) enlargement is seen in the presence of a normal left ventricle (LV). The jet of accelerating flow across the narrow valve orifice *(arrows)* is shown.

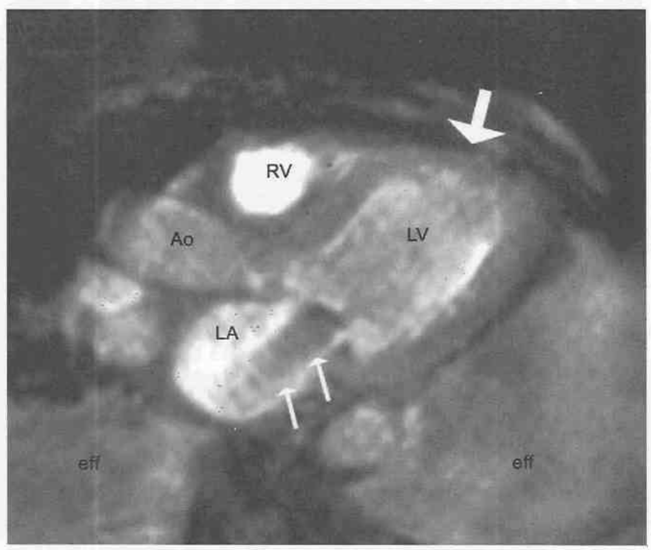

Figure 33–27. MR image demonstrating acute mitral regurgitation in a 52-year-old man suffering an acute myocardial infarction. Systolic oblique axial gradient-echo acquisition. A signal void jet *(small arrows)* extends from the mitral annulus into the normal-appearing left atrium (LA). Although left ventricular (LV) size is normal, the anteroseptal wall *(large arrow)* is akinetic. Ao, aorta; eff, pleural effusion; RV, right ventricle.

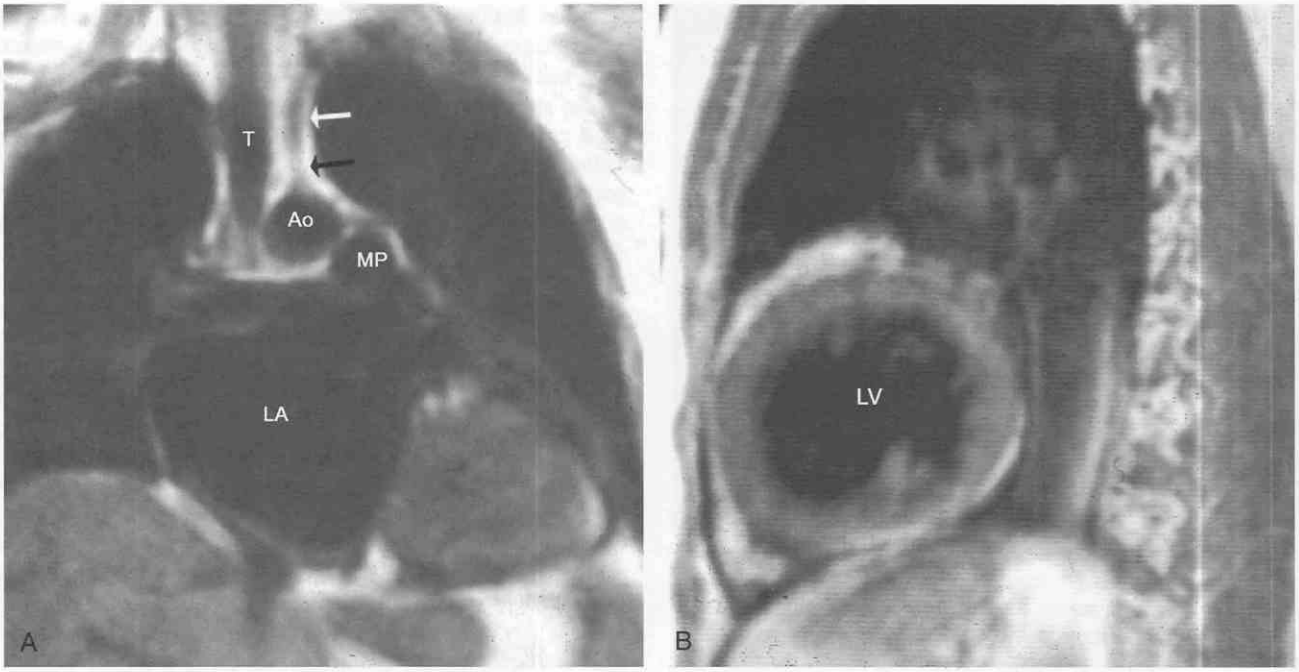

Figure 33–28. Spin-echo acquisition obtained from a 46-year-old woman with chronic mitral regurgitation. *A*, Coronal acquisition at the level of the origin of the left subclavian artery *(arrows)* from the aortic arch (Ao). The left atrium (LA) is markedly enlarged. The main pulmonary artery (MP) is no larger than the Ao, indicating normal pulmonary artery pressure. *B*, Sagittal section through the body of the dilated left ventricle (LV). T, trachea.

Chronic mitral regurgitation may result from the leaflet pathology, such as seen in myxomatous degeneration of the mitral leaflets (Fig. 33–28). In addition, secondary dilatation of the mitral orifice and loss of opposition of the mitral cusp edges due to alteration in the left ventricular geometry may also result in mitral regurgitation, as not uncommonly seen in dilated cardiomyopathy due to ischemic or hypertensive heart disease (Fig. 33–29). MRI evaluation of chronic mitral regurgitation does not demonstrate alveolar edema found in the acute phase. Rather, the dominant findings are those of left atrial and ventricular dilatation. As opposed to mitral stenosis, chronic mitral regurgitation is usually not associated with pulmonary hypertension. Right ventricular hypertrophy and right atrial and ventricular dilatation are not seen. MRI demonstrates left heart and pulmonary vein dilatation with normal or nearly normal left ventricular contractile function and the characteristic jet of mitral regurgitation (Fig. 33–30).

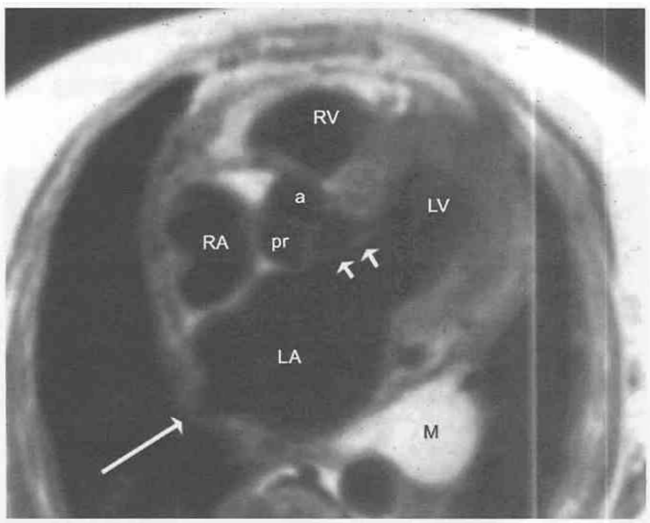

Figure 33–29. Axial spin-echo acquisition obtained from a 30-year-old man with hypertrophic obstructive cardiomyopathy being evaluated for a left atrial mass. Notice the thickened left ventricular (LV) myocardium, the dilatation of the left atrium (LA), and the entrance of the right lower lobe pulmonary vein *(long arrow)*. The anterior mitral leaflet *(short arrows)* is displaced anteriorly from its posterior partner, resulting in mitral regurgitation. Incidentally, the questionable mass (M) is mesenteric fat in a sliding hiatus hernia immediately behind the left atrium. a, anterior aortic sinus of Valsalva; pr, posterior right aortic sinus of Valsalva; RA, right atrium; RV, right ventricle.

Aortic Stenosis

Aortic stenosis (see also the discussion on the bicuspid aortic valve in the section on congenital heart disease) can occur at, below, or above the aortic valve, that is, valvular, subvalvular, or supravalvular stenosis. Regardless of the level of left ventricular outflow obstruction, all such lesions share the physiologic common denominator of increasing left ventricular myocardial strain, with the resultant formation of myocardial hypertrophy. The most common causes of aortic stenosis are congenital, calcific degenerative, and rheumatic disease.[35, 206, 220] Subvalvular and supravalvular aortic stenoses are usually congenital in origin.[249]

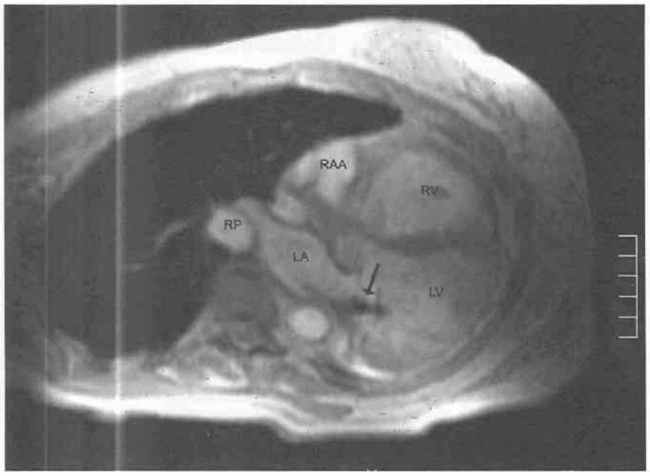

Figure 33–30. Axial gradient-echo acquisition from a 40-year-old woman with exercise intolerance and a history of previous left pneumonectomy for trauma. The heart is rotated and displaced into the left chest. The fan-shaped signal void *(arrow)* extends from the mitral valve into the left atrium (LA). The left ventricle (LV) is dilated. RAA, right atrial appendage; RP, right pulmonary artery; RV, right ventricle.

In congenital aortic stenosis, the aortic valve may be unicuspid or bicuspid. A unicuspid valve usually presents in the newborn period[206] with critical left ventricular outflow obstruction and acute heart failure. MRI is rarely indicated in these patients. If performed, the major findings would be those of interstitial and alveolar pulmonary edema secondary to left heart failure. Calcification is rarely if ever evident this early in the course of any variant of aortic stenosis.

Although a congenitally bicuspid aortic valve is malformed at birth, it rarely causes a significant pressure gradient in infancy. In the early occult stages of the disease, the distorted leaflet architecture causes turbulent blood flow across the valve that traumatizes the leaflet edges, resulting in collagenous generation, lipid deposition, fibrosis, and calcification, similar to that found much later in life in individuals with stenosis of tricuspid aortic valves. Gradually, the leaflets become more rigid and the valve orifice narrows, resulting in a pressure gradient. The congenital malformation makes the valve more susceptible to infectious endocarditis, and this may result in aortic regurgitation.

Patients who present with signs and symptoms of aortic stenosis in middle age or later life usually have tricuspid aortic valves. Their valvular disease is the result of slow, progressive degeneration, calcification of the valve annulus and leaflets, and consequent narrowing of the effective valve area. This abnormality is thought to be the result of normal wear on the valve over a period of years. Hypercholesterolemia and diabetes are important predisposing factors for degenerative aortic stenosis. Commissural fusion is not usually seen in these patients.

Rheumatic aortic stenosis results in commissural adhesion and fusion, the hallmarks of the chronic rheumatic cycle of injury and healing. These aortic valves are frequently both regurgitant and stenotic, fixed in an open configuration. In long-standing cases of rheumatic aortic stenosis, aortic valvular calcification may be found. This further narrows the valvular orifice. Concomitant mitral valvular disease is often present but may not be recognized clinically.

Other than in cases of congenital unicuspid aortic valve, the left ventricular obstruction develops gradually, resulting in increased left ventricular mass that increases wall thickness while maintaining normal chamber volume,[263, 288] allowing the left ventricle to adapt to the systolic pressure overload. MRI reveals the thickened left ventricular myocardium in the absence of left ventricular dilatation. Furthermore, it is useful to demonstrate the abnormal architecture of a congenitally malformed valve.

In cases of valvular aortic stenosis, MRI demonstrates the poststenotic dilatation of the ascending aorta (Fig. 33–31). The aortic caliber is normal at the level of the annulus and increases to its maximum by the level of the transverse right pulmonary artery. The aorta then returns to normal diameter proximal to the arch. The aortic arch and descending aorta are usually normal in caliber. The shape and size of the signal-void jet, as well as its variable extension into the ascending aorta, depend on the shape of the orifice and the degree of its narrowing. The severity of the valvular gradient correlates with the size of the stenotic jet[71] and its extension into the aorta.

If left ventricular outflow obstruction is subvalvular, such as in hypertrophic obstructive cardiomyopathy, then there is no poststenotic dilatation of the aorta. In these patients, however, systolic anterior motion of their anterior mitral leaflet results in mitral regurgitation. Membrane-like subvalvular aortic stenosis does not result in systolic anterior motion and mitral regurgitation. The association of left atrial enlargement (volume loading) with severe left ventricular hypertrophy (pressure loading) is characteristic of subvalvular aortic stenosis. MRI examination in these patients has an additional advantage of demonstrating the

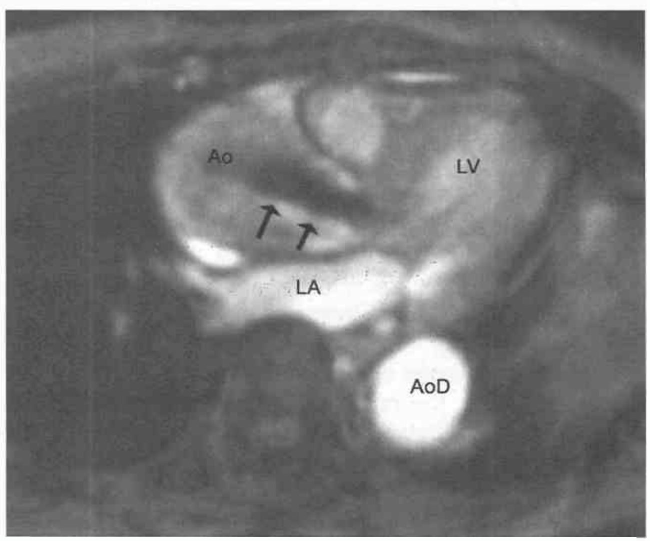

Figure 33–31. Systolic axial gradient-echo acquisition from a 67-year-old man with chronic aortic stenosis. The signal void of accelerating left ventricular (LV) flow is seen as a fan-shaped jet extending from the aortic valve into the dilated ascending aorta (Ao). AoD, descending aorta; LA, left atrium.

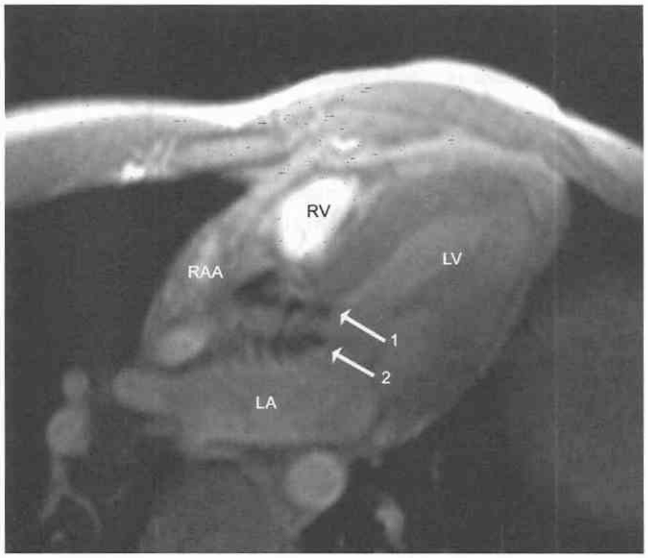

Figure 33–32. Systolic oblique axial gradient-echo acquisition from a 26-year-old man with subvalvular aortic stenosis. Fan-shaped signal voids extend from the crest of the muscular interventricular septum *(arrow 1)* and the attachment of the anterior mitral leaflet *(arrow 2)* into the ascending aorta. The left atrium (LA) is normal, and the left ventricular (LV) myocardium is hypertrophied. RAA, right atrial appendage; RV, right ventricle.

predominately septal (or other asymmetrical) variant of myocardial hypertrophy (Fig. 33–32).

Aortic Regurgitation

Aortic regurgitation may be caused by disease of the aortic valve or of the aorta, which affects the valve. Valvular etiologies include rheumatic heart disease, infectious endocarditis, congenital bicuspid aortic valve, and Marfan's syndrome. Diseases of the aorta include trauma, aortic dissection, and idiopathic dilatation of the aortic annulus. Less commonly, inflammatory and connective tissue disease involving the aorta may result in aortic regurgitation.

Infectious endocarditis, acute aortic dissection, and thoracic trauma produce acute severe aortic regurgitation. This rapidly increases left ventricular filling pressure and reduces cardiac output. These patients often present in shock. Chronic aortic regurgitation causes slow, insidious left ventricular and aortic dilatation. Although dilatation may be pronounced, the function remains normal, and these individuals experience a prolonged asymptomatic phase of their disease.

The left ventricular response to aortic insufficiency depends largely on the rate at which the volume overload develops. Acute dilatation does not allow for ventricular adaptation, resulting in decreased forward cardiac output, elevated left atrial pressure, pulmonary edema, and shock. The value of MRI in patients with acute aortic regurgitation is in noninvasive demonstration of the underlying etiology for the acute left ventricular volume load (i.e., rib fractures and periaortic hematoma in acute aortic injury or the flap of an aortic dissection extending to the aortic valve).

Chronic aortic regurgitation is characterized by increased left ventricular and aortic volume without increase in left ventricular pressure. Concentric and eccentric ventricular myocardial hypertrophy compensates for the increased wall stress induced by the regurgitant volume load. MRI quantitation of left ventricular mass showed that although left ventricular wall thickness may appear normal, myocardial mass does in fact increase in these patients. Thus, left ventricular performance (as reflected in normal ejection fraction) remains normal. With time, left ventricular dilatation is progressive and may become pronounced.[48] MRI demonstrates left ventricular and aortic dilatation (Fig. 33–33). The extent of the aortic dilatation varies with the severity and chronicity of the valvular dysfunction. MRI studies of these patients have the added advantage of direct demonstration of the jet of aortic regurgitation. Typically, this appears as an early diastolic signal void, seen along the anterior mitral leaflet, extending from the aortic valve to the back wall of the left ventricle but, depending on the shape of aortic valvular orifice, may be directed elsewhere in the left ventricle.

Most patients remain asymptomatic during this compensated phase, which may last for decades. Eventually, chronic left ventricular volume loading exceeds the increased contraction of the Frank-Starling mechanism, and the left ventricle begins to fail. MR examination in these patients exhibits the dilated left ventricle and aorta, with increased signal in the lungs resulting from interstitial edema. MRI may be useful for quantifying left ventricular diastolic volume and ejection fraction and for assessing ventricular function. In addition, long-standing aortic regurgitation may cause sufficient left ventricular dilatation to stretch the mitral annulus and induce mitral regurgitation, which in turn leads to left atrial dilatation (Fig. 33–34).

Tricuspid Regurgitation

Tricuspid regurgitation may be acquired or congenital, acute or chronic. This lesion may also be seen in individu-

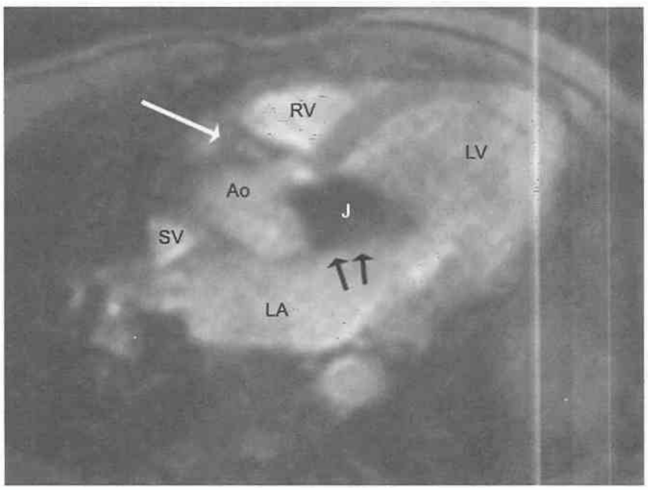

Figure 33–33. Diastolic oblique axial gradient-reversal acquisition from a 38-year-old man with congenital aortic regurgitation. A broad signal void jet (J) extends from the aortic valve into the left ventricle (LV) along the anterior leaflet of the mitral valve *(black arrows)*. The left atrium (LA) is normal. The right ventricle (RV), superior vena cava (SV), and proximal right coronary artery *(white arrow)* are identified. Ao, aorta.

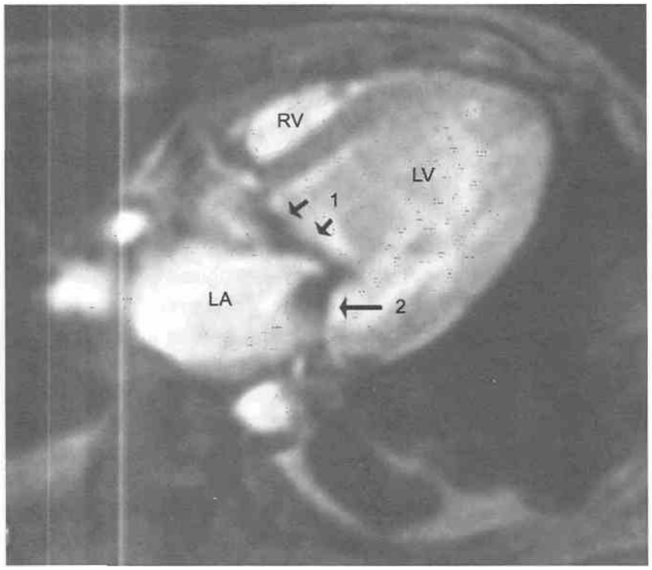

Figure 33–34. Late diastolic oblique axial gradient-echo acquisition from a 70-year-old man with mixed rheumatic aortic and mitral regurgitation. Left ventricular (LV) and left atrial (LA) dilatation in the absence of apparent LV hypertrophy is seen. The signal void jets extend from the aortic valve into the LV *(arrows 1)* and from the mitral valve into the LA *(arrow 2)*. RV, right ventricle.

als with a structurally normal valve. The most common cause of tricuspid regurgitation is pulmonary hypertension. Elevated right ventricular pressure, as seen in pulmonary hypertension of various causes, leads to right ventricular hypertrophy and alteration of shape of the interventricular septum. This distorts the function of papillary muscles originating from the septum, alters right ventricular geometry, and causes tricuspid annular dilatation,[314, 315] all of which results in valvular incompetence.

Infectious endocarditis, carcinoid disease, rheumatoid arthritis, and trauma all may cause acute valvular (including tricuspid) regurgitation. Acute pancarditis of rheumatic heart disease leads to ventricular dilatation, whereas associated valvulitis results in laxity of the mitral and tricuspid annuli. Both lead to tricuspid regurgitation. The tricuspid valve leaflets in patients with Marfan's syndrome are floppy and redundant, which results in valvular regurgitation, often involving the tricuspid valve. Ebstein's anomaly[164, 345] includes congenital malformation of the tricuspid valve, which causes varying and often severe tricuspid regurgitation.

No matter what the inciting event, initial tricuspid regurgitation volume loads the right atrium and right ventricle, resulting in their dilatation, which in turn alters right ventricular geometry, resulting in the vicious cycle of progressive valvular regurgitation.

Spin-echo and gradient-echo MRI sequences demonstrate the morphologic stigmata of tricuspid regurgitation. The right ventricle is normally found immediately behind the sternum. In patients with tricuspid regurgitation and other forms of right heart dilatation, the heart is rotated, displacing the right ventricle toward the left, and moving the right atrium to a position behind the sternum. There is displacement of the superior vena cava medially, as well as clockwise rotation of the cardiac apex with horizontal (coronal) orientation and straightening of the interventricular septum. In severe cases, the interventricular septum bows to the left and may even extrinsically compress the left ventricle.

MRI demonstrates and accurately quantifies right ventricular myocardial hypertrophy. Furthermore, gradient-echo MRI demonstrates the signal void of the regurgitant jet (Fig. 33–35) directed toward the right atrium. Although the direction of the jet depends on the geometry of the valve and its deformity of the leaflets, it is always seen early in systole.

Differential diagnosis of tricuspid regurgitation depends on observation of coexisting findings. Tricuspid regurgitation caused by pulmonary hypertension is associated with dilatation of the right heart, the main pulmonary artery segment, and central hilar pulmonary arteries. Spin-echo MRI demonstrates increased signal in the pulmonary artery segments caused by the slow blood flow in patients with high pulmonary resistance. Left atrial enlargement and evidence of pulmonary hypertension in the face of a normal left ventricle point to mitral stenosis as a cause of the pulmonary hypertension and subsequent tricuspid dysfunction. Increased lung volumes and a normal left atrium suggest chronic obstructive pulmonary disease as the cause of the pulmonary hypertension. Patients with primary right heart failure exhibit right heart dilatation, pleural and pericardial effusion, and evidence of right atrial hypertension, including dilatation of the inferior and superior venae cavae, coronary sinus, hepatic veins, and azygos vein. Finally, right-sided heart eulargement with a small pulmonary artery indicates the decreased right ventricular output found

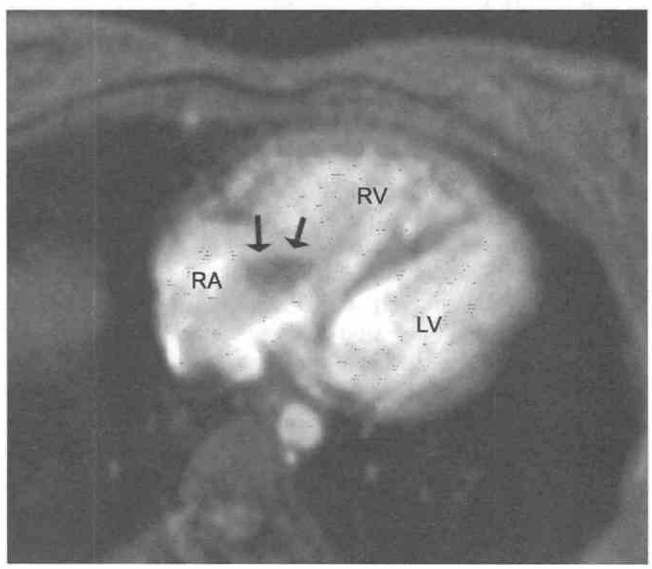

Figure 33–35. Systolic axial gradient-echo acquisition from a 24-year-old woman with primary pulmonary hypertension. The right ventricle (RV) is dilated, and the RV free wall myocardium is as thick as the interventricular septum. The signal void jet *(arrows)* of tricuspid regurgitation extends from the tricuspid valve into the dilated right atrium (RA). The right heart dilatation has rotated in a clockwise manner into the left chest. LV, left ventricle.

in patients with Ebstein's anomaly. All these findings are accurately demonstrated on MRI.

Multivalvular Heart Disease

In combined valvular heart disease, the dominant physiologic alteration, and thus, the clinical and radiologic picture, is determined by the proximal lesion. However, the radiologic appearance varies, depending on the relative severity as well as the physiologic sequelae of each particular valve lesion. The most common cause of multivalvular heart disease is rheumatic. The most common combinations are mitral stenosis with aortic regurgitation, mitral stenosis with tricuspid regurgitation, combined mitral and aortic regurgitation (see Fig. 33–34), combined mitral and aortic stenosis, and combined aortic stenosis and mitral regurgitation.

Quantitative Magnetic Resonance Imaging of Valvular Disease

Accurate estimation of the severity of a valvular lesion is crucial for timing surgical intervention. MRI provides an accurate, reproducible, noninvasive approach to quantification of valvular stenosis and regurgitation, cardiac chamber size, and myocardial mass and function. At present, valvular lesions suspected clinically or suggested on chest radiography are initially evaluated by Doppler echocardiography, followed by cardiac catheterization. Both these methods are semiquantitative and dependent on hemodynamic and technical factors.[62, 258] Valvular regurgitation can be determined by nuclear ventriculography.[144, 245] However, in addition to the drawback of radiation, this technique is influenced by multiple variables, such as the risk of superimposition of the cardiac chambers, the uncertainty of the chamber depth, and the difficulty of quantitation in the face of multiple regurgitant valvular lesions.

The pressure gradient across a valve can be indirectly quantitated using the modified Bernoulli equation.[127] In the early phase of valve disease this may be useful. However, later in the course of the disease, when cardiac output decreases, the technique becomes less accurate.[114] Valve area and cardiac output can be assessed by planimetric analysis of conventional angiocardiography and Doppler echocardiography,[182, 280] and cardiac catheterization,[111] although these techniques also have many limitations.[20, 42]

Cardiac chamber volume can be estimated from spin-echo images. However, accurate measurement of end-systolic and end-diastolic volumes is required for calculation of cardiac output and stroke volume. These values can be reliably obtained only with MRI sequences capable of high-spatial-frequency resolution, such as cine gradient-echo imaging.[119] Furthermore, breath-hold sequences allow a substantial reduction in both imaging time and motion artifacts.[133, 259]

Imaging the ventricles in short-axis section minimizes volume-averaging artifacts. Subsequently, end-diastolic and end-systolic images are selected at each anatomic level. To calculate the end-systolic volume, the areas of the ventricular cavity are measured at end-systole for each level, summed over the entire ventricular mass and multiplied by the slice thickness. The same procedure is repeated for the end-diastolic images, giving the end-diastolic volume. Similarly, the ventricular myocardial volume (which allows estimation of the myocardial mass) is calculated as the sum of the differences between epicardial minus endocardial areas times slice thickness, summed over the entire ventricle.

The prognostically relevant parameters such as stroke volume and ejection fraction, are calculated from the end-systolic and end-diastolic volumes. Extensive research culminated in validation of MRI as an accurate and reproducible method for determining ventricular dimensions and function.[64, 141, 180, 181, 201–205, 298] At present, MRI is considered the clinical gold standard for determination of stroke volume, ejection fraction, myocardial volume (or mass), as well as ventricular volumes.

The reproducibility of ventricular volume measurements is further underscored by the small difference in the right and left ventricular volumes ($<5\%$)[170, 172, 270] in the absence of valvular regurgitation. Therefore, in patients with a solitary insufficient valve, the regurgitant volume and fraction can be calculated as a difference between and the ratio of the right and left stroke volumes.[269, 298]

Direct measurement of chamber stroke volume, regurgitant volume, and regurgitant fraction can be performed using a velocity mapping technique, based on the linear relationship between the velocity of the spins along the magnetic field gradient and their phase shift. This promising technique provides accurate results in the presence of laminar flow patterns but is detrimentally affected by the complex, turbulent flow patterns[88, 335] inherent in valvular heart disease. Recent advances have been made in reducing the influence of the complex flow patterns on the overall accuracy of this technique by decreasing the duration of the magnetic gradient field used for velocity encoding.[150, 282, 284] These pulse sequences were validated in vivo.

In patients with aortic regurgitation, velocity encoding MRI acquisitions may be used for calculating left ventricular stroke volume, as well as regurgitant volume and regurgitant fraction. In these patients, positioning of the imaging plane close to the aortic valve is crucial for accuracy, because the results are heavily influenced by the coronary blood flow and aortic compliance. When these pitfalls are kept in mind, the accuracy rate of this technique is higher than 90%.[283] Clinical relevance of these data is reflected in the usefulness of MRI evaluation of vasodilator therapy in patients with aortic regurgitation.[107] The transvalvular pressure gradient in aortic stenosis may be calculated from the peak velocity across the stenotic valve with accuracy that is higher than 85%.[283] The valve area may be demonstrated by velocity encoding with an accuracy rate that is higher than 81%. The accuracy rate of quantifying the regurgitant volume and fraction in mitral regurgitation was reported as 91% and 94%, respectively, whereas in mitral stenosis the transmural peak velocity across the valve was calculated with an accuracy rate higher than 87%.[283]

Right Ventricular Disorders

Right ventricular disease may be difficult to evaluate by conventional echocardiographic and angiographic means.

Patients with chronic pulmonary disease commonly present with hyperaerated lungs and chest wall deformities, which limit the use ultrasonographic methods. The high association of chronic heart disease, pulmonary disease, and pulmonary hypertension increases the risk of contrast right ventriculography or pulmonary arteriography in this population. MR image acquisition is not limited by pulmonary or chest wall disorders, and contrast administration for MRI evaluation of the right heart has always been interesting but may simply not be necessary.

Right ventricular function is commonly affected by disorders of the left-sided cardiac structures and the lungs. The most common cardiac causes for right ventricular dysfunction are chronic left ventricular ischemia and rheumatic mitral valve disease. Pulmonary diseases causing right ventricular dysfunction include chronic obstructive pulmonary disease and chronic interstitial diseases (i.e., idiopathic pulmonary fibrosis and cystic fibrosis). Chronic pulmonary vascular pathology, including chronic thromboembolism and primary pulmonary hypertension, also have a significant effect on right ventricular performance.

Common to all of these diseases is elevation of pulmonary vascular resistance with a commensurate increase in right ventricular pressure, resulting in right ventricular hypertrophy. Eventually right ventricular dilatation, tricuspid regurgitation, and right ventricular failure supervene. MRI provides direct, noninvasive visualization of the right ventricular chamber as well as the myocardium itself, allowing reliable demonstration of morphologic changes in the size and shape of the ventricle, thickness of the myocardium, and presence of abnormal infiltration by fat or edema. Furthermore, MRI is well suited for accurate and reproducible quantitation of right ventricular volume and myocardial mass.

Both the left and right ventricles share the interventricular septum. Thus, the septum acts as an "interface" between the left and right hearts. Right-sided heart disease impacts on left ventricular function, and vice versa, via the septum. Normally, the septum acts as if a part of the left ventricle. Viewed in short axis (see Fig. 33–19*A* and *B*), the wall segments of the left ventricle, including the interventricular septum, appear to contract radially and symmetrically during systole. The curvature of the interventricular septum is convex toward the right ventricular cavity during both ventricular diastole and systole. Changes in right ventricular shape bow the interventricular septum at the expense of left ventricular shape. That is, right ventricular dilatation may straighten, or even reverse, the contour of the interventricular septum toward the left ventricle (see Fig. 33–3). In such cases, left ventricular filling and thus end-diastolic volume may be impaired, limiting left ventricular output.

The most common cause of right-sided heart failure is chronic left-sided heart failure.[296] The common denominator of this and other left-sided heart problems causing right ventricular dysfunction is chronic left atrial hypertension. That is, the left and right hearts also "communicate" across the pulmonary vascular bed. Pulmonary hypertension and right ventricular failure in patients with mitral stenosis are caused by back-transmission of elevated left atrial pressure and pulmonary arteriolar constriction. Pulmonary arteriolar constriction leads to more severe pulmonary hypertension and right ventricular failure.[275, 336] Chronic mitral stenosis results in severe pulmonary hypertension and right ventricular hypertrophy and, ultimately, right ventricular dilatation and failure. With time, severe pulmonary hypertension results in tricuspid as well as pulmonary insufficiency, further exacerbating the right ventricular failure. The pulmonary hypertension found in chronic mitral stenosis is more commonly found and is generally more severe than that found in chronic left ventricular ischemia. Treatment of the underlying mitral valve disease by mitral valve replacement results in a marked decline in pulmonary vascular resistance and pulmonary artery and right ventricular pressure.[34]

Other, less common causes of chronic left atrial outflow obstruction and pulmonary venous hypertension include left atrial myxoma[122] or thrombus,[294] congenital mitral stenosis,[59] and cor triatriatum.[216] In the latter condition, there is a congenital membrane interposed between the pulmonary veins and the body of the left atrium. Depending on the caliber of the membrane orifice, a pressure gradient exists between the pulmonary veins and mitral valve. Thus, one finds elevated pulmonary venous pressure in the face of normal left atrial pressure. Acquired pulmonary veno-occlusive disease is an uncommon condition that usually presents in children and young adults.[311] Pulmonary venous obstruction causes elevated pulmonary vein pressure and pulmonary resistance in the face of normal left atrial pressure, resulting in pulmonary hypertension with varying degrees of right ventricular failure.

Similar cardiac changes may be found in cor pulmonale, the syndrome of right ventricular hypertrophy, dilatation, and failure resulting from pulmonary hypertension secondary to lung disease.[57] Although this condition may be acute, as seen in sudden, massive pulmonary thromboembolism,[67, 193] it most often develops chronically, resulting from hypoxia-induced pulmonary arteriolar vasoconstriction or fibrosis of the pulmonary vascular bed.[90, 91] The basic components of cor pulmonale are increased pulmonary vascular resistance, pulmonary hypertension, and right ventricular hypertension.

Pericardial disorders, namely cardiac tamponade and pericardial constriction,[163] commonly result in acute and chronic diastolic right ventricular dysfunction, respectively. Although restrictive cardiomyopathy may initially present with right ventricular failure, it generally involves both left and right ventricles. These conditions are discussed in detail earlier in the chapter.

Not only does MR examination allow direct demonstration of the appearance and intraluminal flow characteristics of the pulmonary arteries,[43, 89, 109, 190, 232, 308] it also allows detailed visualization of the shape and internal morphology of the right ventricle.[23, 94, 180] Patients with cor pulmonale typically present with a massively dilated and hypertrophied right ventricle. Both the chamber volume and the myocardial mass are increased. Morphologic examination of the heart in these patients demonstrates thickening of the right ventricular myocardium, bowing of the interventricular septum toward the left ventricular chamber, and clockwise rotation of the cardiac apex on axial MR images (Fig. 33–36). Spin-echo images reveal morphologic changes of underlying disease, such as narrowed valve orifices, or thickened valve leaflets. Functional gradient-echo cine images may reveal the characteristic signal voids

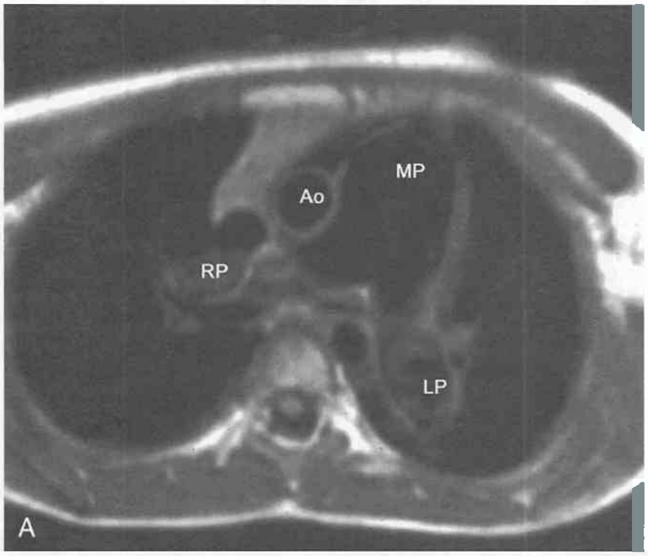

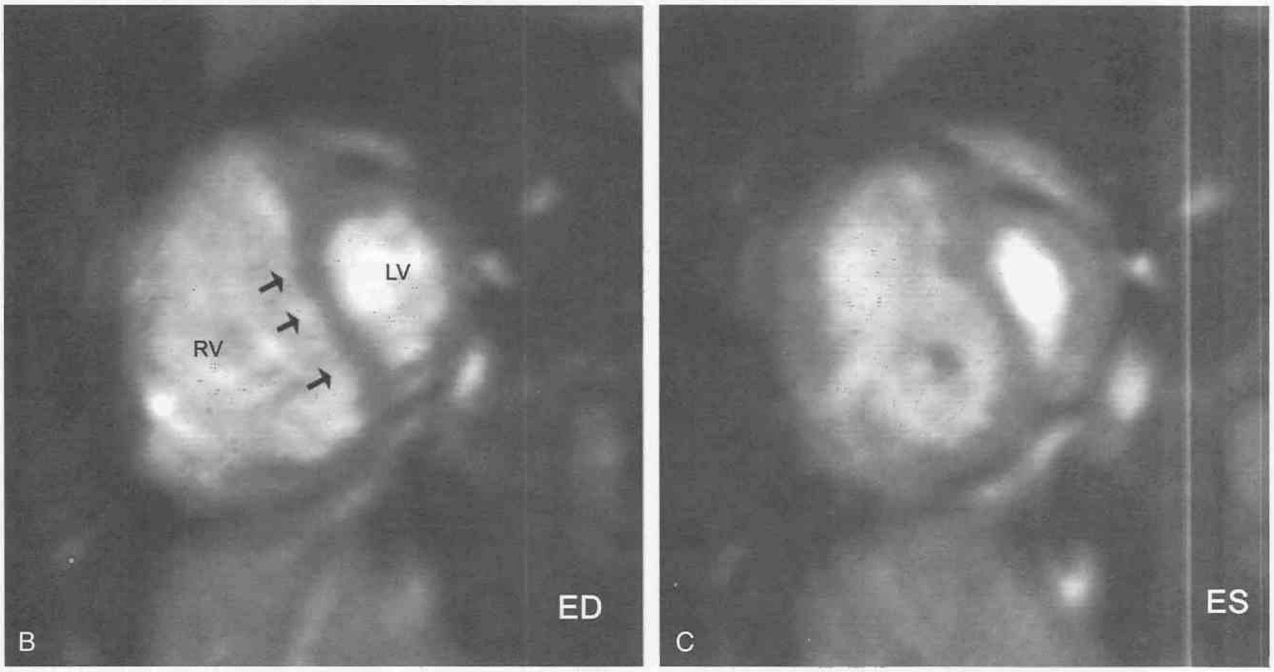

Figure 33–36. MR image obtained from a 6-year-old girl with primary pulmonary hypertension and right ventricular dysfunction.

A, Axial spin-echo acquisition through the pulmonary arteries. The main pulmonary artery (MP) and both left (LP) and right (RP) pulmonary arteries are dilated and show increased signal intensity distally. Note how these mediastinal structures have been displaced toward the left chest by right heart dilatation. Ao, aorta.

B, End-diastolic (ED) short-axis section through the mid-interventricular septum. Note how the dilated right ventricle (RV) causes straightening of the interventricular septum *(arrows)*, indicating diastolic RV volume loading (secondary to associated tricuspid regurgitation). LV, left ventricle.

C, In this end-systolic (ES) frame obtained at the same anatomic level as in *B*, there is reverse bowing of the interventricular septum, indicating systolic dysfunction. Although the right ventricular free wall myocardium is not clearly seen in *B*, it appears thicker than the interventricular septum and posterior left ventricular wall.

caused by mitral stenosis or tricuspid or pulmonary insufficiency.

Pulmonary Disease

Cor pulmonale results from chronic hypoxia or pulmonary vascular occlusion or both. Chronic obstructive and restrictive lung diseases lead to cor pulmonale due to chronic hypoxia. The most common parenchymal lung disease resulting in cor pulmonale is chronic obstructive airway disease.[90] Small airway obstruction results in decreased vital capacity and nonuniform distribution of inspired oxygen. Pulmonary arteriolar vasoconstriction leads to local hypoxemia, which initiates a vicious cycle of increased pulmonary arterial resistance and right ventricular failure. In patients with pure emphysema, parenchymal destruction leads to reduction in the cross-sectional area of the vascular bed, resulting in further increase in pulmonary resistance. Typically, patients with emphysema develop cor pulmonale late in their clinical course.[39] There is a loose correlation between increased right ventricular mass[66, 200] and emphysema symptoms. In one study, all individuals with clinical evidence of cor pulmonale had depressed right ventricular ejection fraction.[21] A similar clinical picture is found in patients with asthma, chronic bronchitis, and cystic fibrosis. Right ventricular failure is a common complication of cystic fibrosis.[145] Nearly one third of patients who die with this diagnosis exhibit overt signs of right-sided heart failure within the last 2 weeks of life.[289]

Interstitial lung disease impairs oxygen diffusion. Progressive interstitial lung disease causes thrombosis and fibrous organization and a decrease in the cross-sectional area of the pulmonary vascular bed.[90, 91] Pulmonary arterial

hypertension is commonly seen in patients with chronic interstitial pneumonia; advanced sarcoidosis and hemosiderosis[215]; and pulmonary fibrosis secondary to collagen vascular diseases, such as rheumatoid arthritis,[96] dermatomyositis,[132] and progressive systemic sclerosis.[257, 260, 291, 299]

Pulmonary vascular occlusive diseases result in a reduction in the cross-sectional area of the pulmonary vascular bed, which causes increased pulmonary resistance, pulmonary hypertension, and right ventricular hypertrophy. Clinical pulmonary thromboembolism is a complication of lower extremity or pelvic deep vein thrombosis.[61, 78a, 121] Silent pulmonary emboli are a relatively common phenomenon.[171] These pulmonary emboli are usually small and occlude only a small portion of the pulmonary arterial bed without eliciting symptoms. These minute thromboemboli lodge in the peripheral branches of the pulmonary arterial tree over a period of many years, resulting in increased pulmonary resistance and arterial pressure. The multiple pulmonary vascular obstructions found in chronic pulmonary thromboembolism[209] are different than the obstructing thrombi found in acute pulmonary embolism. A massive, acute pulmonary embolus must occlude more than half the pulmonary arterial bed before hemodynamic changes and clinical symptoms develop. However, in patients with recurrent thromboembolism, there frequently is underlying pulmonary hypertension. In this population, additional occlusion of a smaller portion of the pulmonary arterial tree has a hemodynamically significant effect. If pulmonary hypertension has existed for some time, the right ventricle undergoes compensatory hypertrophy to maintain adequate cardiac output in the face of the elevated pulmonary vascular resistance. Faced with sudden increase in arterial resistance due to an additional, large pulmonary embolus, the hypertrophied right ventricle cannot maintain adequate cardiac output. In chronic, recurrent pulmonary thromboembolism, emboli lodge repeatedly in the pulmonary arterial tree over a period of years. These patients experience neither pulmonary infarction nor sufficient acute occlusion of the pulmonary vascular bed to cause acute right ventricular failure. Rather, they experience a gradual occlusion of the pulmonary arterial bed accompanied by a progressive increase in pulmonary vascular resistance. Thus, time is available for right ventricular adaptation.

Primary pulmonary hypertension is a rare, progressive disease of unknown etiology[244, 312] characterized by obstructive changes at the level of the precapillary pulmonary arterioles or pulmonary veins and venules. Progression of the disease and clinical deterioration are associated with decreasing right ventricular function.

Right ventricular enlargement of any etiology causing tricuspid annular dilatation results in tricuspid regurgitation. Pulmonary hypertension is the most common cause of tricuspid regurgitation, which increases the preload as well as the afterload on the right ventricle. Tricuspid regurgitation not only results in further right ventricular and right atrial dilatation but also increased right atrial pressure. This has a deleterious effect on right ventricular function by limiting right ventricular myocardial perfusion. Elevated right atrial pressure is transmitted into the coronary sinus. Thus, the difference between aortic diastolic pressure and coronary sinus pressure (the right ventricular myocardial perfusion gradient) is decreased, causing right (and left) ventricular myocardial ischemia and systolic dysfunction.

Cardiac Tumors

Cardiac tumors are rare. They tend to grow slowly, and patients present with signs and symptoms caused by the tumor's distortion of adjacent structures or organs. Although it may be difficult to characterize a particular tissue origin from MRI, these examinations are extremely helpful for characterization of tumor morphology, evaluation of adjacent and distal structure involvement, and the effects of the tumor on cardiac function. The most common cardiac tumors are metastatic malignancies. These lesions reach the heart by direct extension from the lungs and breast. In autopsy studies, metastatic foci of melanoma is commonly found in the heart but is frequently not clinically important. MR examination is helpful for demonstrating extension of such masses through the pericardium to involve ventricular myocardium. Such information is important for evaluation of surgical resectability[173] of such masses.

Three fourths of all primary tumors of the heart are benign and of soft tissue origin,[191] including rhabdomyoma, fibroma, lipoma (Fig. 33–37), angioma, and myxoma. These tumors generally appear as infiltrating masses with signal intensity characteristic of the tissue of origin, that is, high-signal lipoma and intermediate-signal-intensity rhabdomyoma. Differentiation of these benign masses from their sarcomatous counterparts can be inferred by identification of a high-signal-intensity necrotic core, or other evidence of hemorrhage, distant metastasis, or extensive pericardial and pleural effusion. Myxoma (Fig. 33–38) is the most common benign cardiac mass found in all age groups. It can occur at any time, but more than half of the patients are in their 4th, 5th, and 6th decades. Twelve

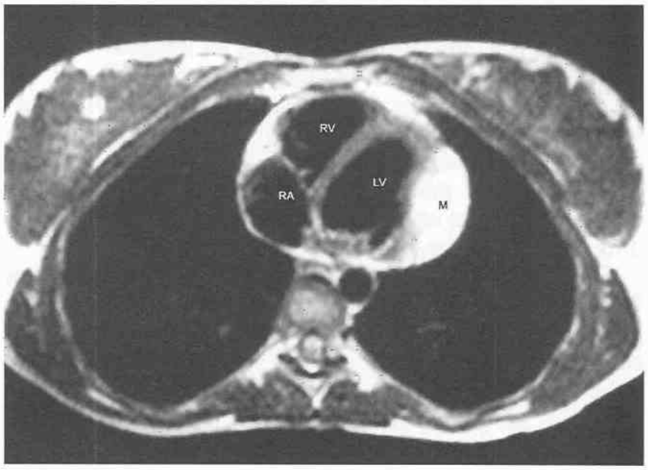

Figure 33–37. Axial spin-echo acquisition from a 35-year-old woman with a myocardial lipoma presenting as an unusual contour on the left heart border of a plain chest film. The high-signal-intensity mass (M) is isointense with subcutaneous and breast fat and infiltrates the posterior left ventricular (LV) wall. No pericardial or pleural effusion is seen. RA, right atrium; RV, right ventricle.

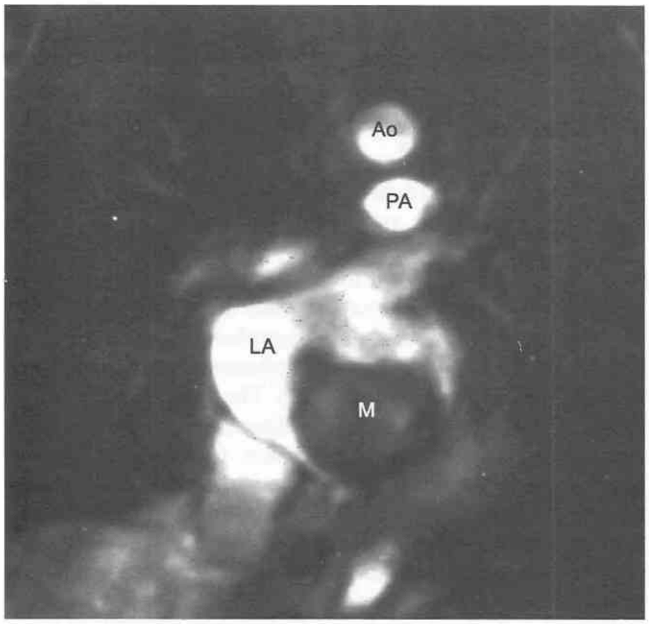

Figure 33–38. Coronal contrast-enhanced gradient-echo image obtained from a 54-year-old man admitted with a cold left lower extremity. The large filling defect of the atrial myxoma (M) is seen within the mildly dilated left atrial (LA) cavity. The normal appearance of the pulmonary artery (PA) indicates that there is no pulmonary hypertension. Ao, aorta.

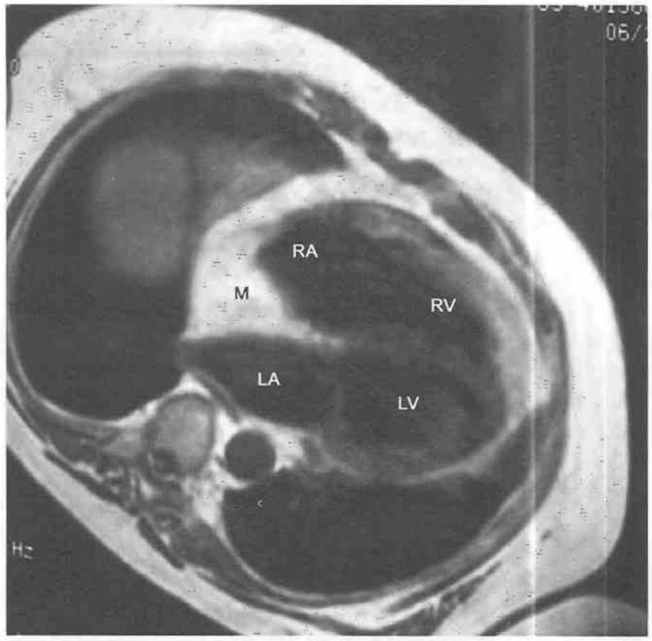

Figure 33–39. Axial spin-echo acquisition from a 59-year-old man with shortness of breath. There is marked deposition of material (M) isointense with the pericardial and subcutaneous fat. The mass extends from the interatrial septum into the right atrium (RA). LA, left atrium; LV, left ventricle; RV, right ventricle.

percent of the Armed Forces Institute of Pathology series[191] were older than 70 years of age. Three fourths of all myxomas originate in the left atrium, mostly attached to the interatrial septum in the region of the limbus of the fossa ovalis. Myxomas may be highly vascular and enhance with intravenous contrast agent administration.

Benign cardiac tumors are usually of intermediate, but homogeneous, signal intensity. Areas of increased signal intensity may represent areas of focal hemorrhage, indicating tumor necrosis, or deposits of fat, reflecting tissue inhomogeneity. Most benign tumors may be "peeled away" from the heart at operation. However, both benign and malignant lesions usually appear to infiltrate adjacent ventricular myocardium. Lipomatous hypertrophy of the interatrial septum (Fig. 33–39) is not truly a malignancy, but rather it is a collection of large fat deposits. It may be isolated to the interatrial septum or may extend along the lateral aspect of the right atrium into the right ventricle. Application of fat saturation during image acquisition may directly characterize the lesion.[4]

Malignant cardiac tumors are usually metastatic. About 10% of patients with malignant neoplasms have cardiac metastases. Clinical dysfunction is usually caused by pericardial involvement. This may be visualized as pericardial effusion, pericardial thickening, or both. Pericardial effusion may be serous or hemorrhagic. The most common metastasis in men is from lung; the most common in women is from breast (Fig. 33–40). These are followed by leukemia and lymphoma (Fig. 33–41). Cardiac involvement is often accompanied by involvement of other organs. Primary cardiac malignant tumors are mostly angiosarcoma, rhabdomyosarcoma, mesothelioma, and fibrosarcoma. Malignant tumors in children are rare. Pericardial involvement is usually found.

Magnetic Resonance Imaging of Congenital Heart Disease

Although gradient-echo (cine) technique is invaluable for evaluation of cardiac function, the increased contrast resolution of spin-echo techniques makes them the work-

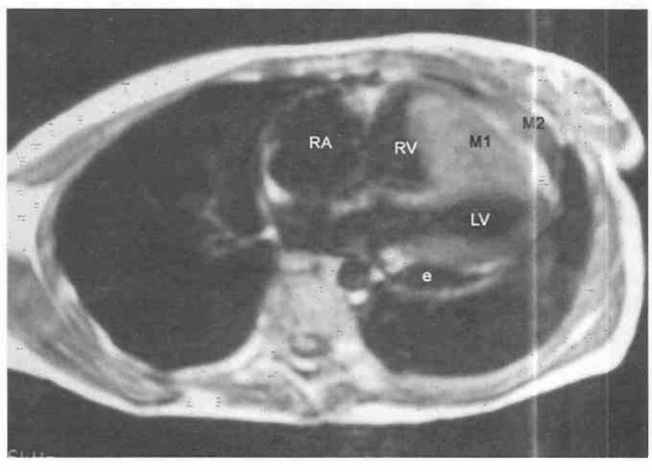

Figure 33–40. MR image obtained from a 32-year-old woman 3 years after mastectomy for adenocarcinoma of the right breast, now complaining of shortness of breath. Nearly the entire right ventricle (RV) is filled with a homogeneous intermediate-signal-intensity mass (M1). The left ventricle (LV) is extrinsically compressed by the mass. In addition, there appears to be a locus of similar material (M2) contained within the pericardial space anterior to the heart. A small posterior pericardial effusion (e) is seen as well. RA, right atrium.

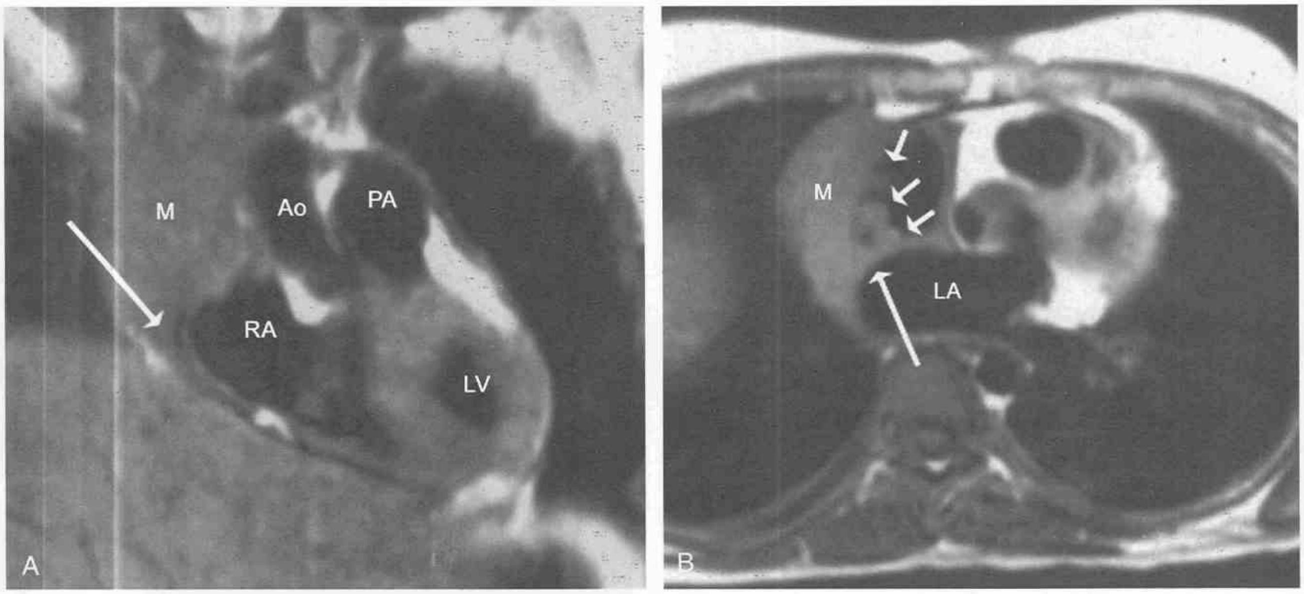

Figure 33–41. MR image obtained from a 16-year-old child with lymphoma. *A*, Coronal spin-echo image obtained through the ascending aorta (Ao) and main pulmonary artery (PA). A bulky, homogeneous, intermediate signal intensity mass is seen along the superior right cardiac border that involves the pericardial space *(arrow)* but seems to spare the right atrium. LV, left ventricle; M, mass; RA, right atrium. *B*, Axial spin-echo acquisition through the superior aspect of the right atrium and aortic valve. The paracardiac and pericardial components of the mass (M) are again seen. In this image, however, there is nodular involvement *(short arrows)* within the right atrium as well as infiltration of the interatrial septum *(long arrow)*.

horse for morphologic evaluation by MR. In cases of congenital heart disease, cine acquisition supplements the anatomic and morphologic information obtained from spin-echo acquisitions. Increased spatial resolution is obtained by decreasing the field of view. Infants and small children may be examined from within a head-imaging coil; this allows thinner slice selection as well as a smaller field of view.

The difference in appearance between pediatric and adult patients with congenital heart disease reflects the hemodynamic alterations of the underlying malformation, the duration of the lesion, and the effects of superimposed acquired cardiovascular disease. Depending on the stage in the natural or "unnatural" (i.e., surgically palliated) history of the disease in which examination is performed, the sequelae and complications of the underlying disease may be different. For example, in an atrial septal defect in a child or adolescent, changes of right ventricular hypertrophy and pulmonary hypertension are usually absent. By the age of 45 years, pulmonary hypertension and right ventricular hypertrophy are to be expected. Furthermore, in the older population, altered left ventricular function and its effect on right ventricular function become issues for examination.

Atrial Morphology and Situs

The segmental approach to diagnosis[300, 302] accurately describes congenital heart lesions and is readily applied to interpretation of static and cine tomographic images obtained from cardiac MRI examination. The premise of the segmental approach is that the three cardiac segments (atria, ventricles, and great arteries) develop independently. By localization and characterization of each of the three cardiac segments and evaluation of the atrioventricular and ventriculoarterial connections and associated anomalies (such as shunts and valve atresia), congenital heart lesions may be diagnosed in a consistent and coherent manner. The usefulness of MRI[117] lies in its ability to demonstrate characteristic morphologic findings needed to name the cardiac chambers, allowing characterization of atrial situs and atrioventricular and ventriculoarterial connections.

The morphologic right atrium (Fig. 33–42) is characterized as the atrial chamber that receives the hepatic venous drainage and the inferior vena cava. It possesses the right atrial appendage and the crista terminalis. The right atrial appendage is a broad-based, triangular-shaped extension of the atrial cavity (a trabeculated "pita pocket"). It is contained within the pericardium and lies anteriorly, medial to the right heart border. The crista terminalis is a fibrous remnant of the valve of the embryologic sinus venosus.[197] It divides the right atrial chamber into a smooth posterior portion and a moderately trabeculated anterior portion (including the appendage). The morphologic left atrium contains the left atrial appendage, which is long and narrower than the right atrial appendage (Fig. 33–43). It passes just inferior to the main pulmonary artery along the left of the heart to reach the radiographic left heart border. The walls of the left atrium are quite smooth; there is no crista terminalis. The left atrium usually receives the pulmonary veins (except in partial or total anomalous pulmonary venous return).

Atrial situs may be directly determined by analysis of the appearance (morphology) of the atria.[105] Alternatively, situs may be deduced from the situs of the lungs (Fig. 33–44). In the normal individual in situs solitus, the mor-

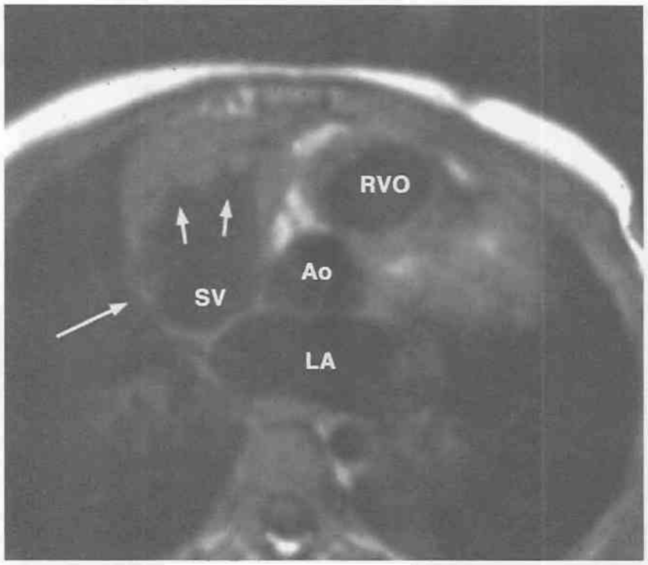

Figure 33–42. Axial spin-echo acquisition from a 6-year-old boy at the level of the aortic root (Ao) and the right ventricular outflow tract (RVO). The characteristic trabeculations of the right atrial appendage *(arrows)* and the wide orifice adjacent to the entry of the superior vena cava (SV) are shown. The high-signal-intensity crista terminalis *(long arrow)* is viewed in cross-section. LA, left atrium.

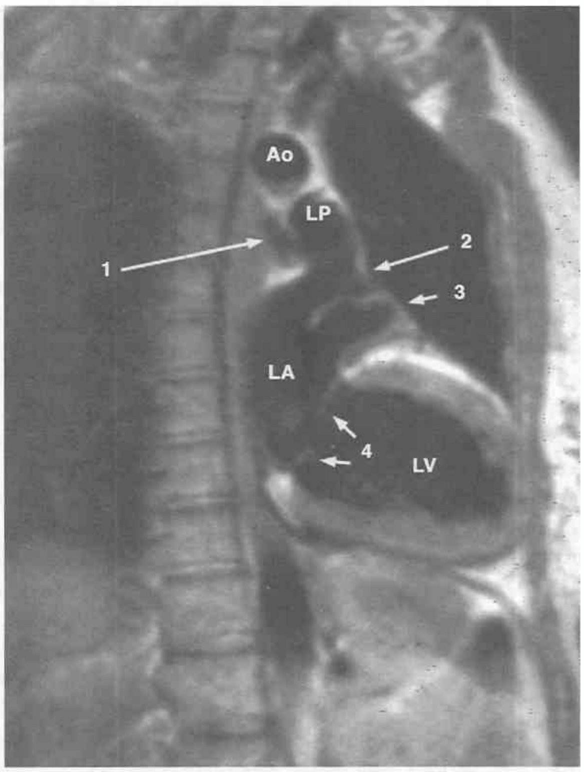

Figure 33–43. Right anterior oblique sagittal spin-echo image obtained from a 38-year-old man. The aortic arch (Ao) and the left pulmonary artery (LP), just after it crosses the left bronchus *(arrow 1)*, are seen. The left upper lobe pulmonary vein *(arrow 2)* enters the left atrium (LA) just superior and posterior to the orifice of the left atrial appendage *(arrow 3)*. The left atrium and the left ventricle (LV) are separated by the mitral valve *(arrows 4)*.

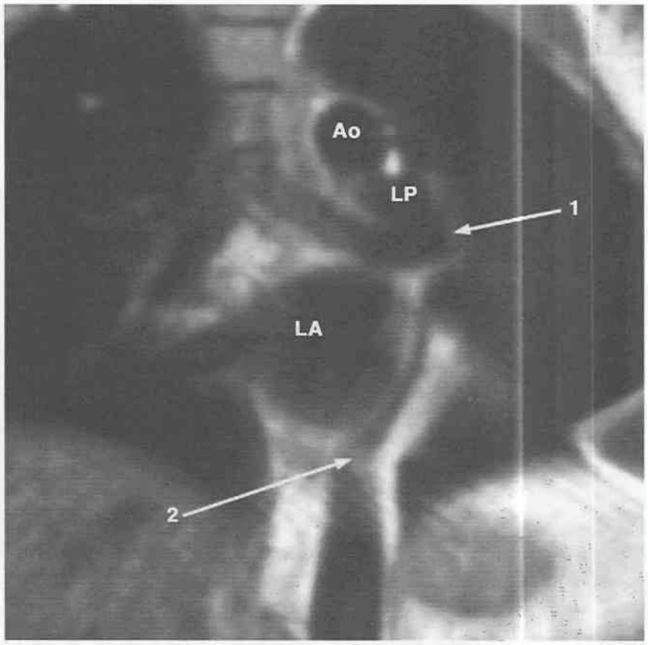

Figure 33–44. Coronal spin-echo acquisition through the tracheal bifurcation in a 40-year-old man with situs solitus. The left pulmonary artery (LP) has just crossed the left main bronchus *(arrow 1)*. The aortic arch (Ao) is superior and medial to the left pulmonary artery. The coronary sinus *(arrow 2)* courses to the right of the fat of the posterior atrioventricular ring, beneath the left atrium (LA).

phologic left bronchus is the bronchus that takes a long course from the tracheal bifurcation before giving origin to the left upper lobe bronchus; the right bronchus is the bronchus that travels for a short distance prior to the origin of the right upper lobe bronchus. The left pulmonary artery courses over the left bronchus; the right pulmonary artery runs anterior and slightly inferior to the right bronchus. Atrial situs inversus is the mirror-image analogue of situs solitus (Fig. 33–45). The morphologic right atrium lies on the left, and the morphologic left atrium is on the right.

Situs ambiguous may be indicated by the presence of symmetrical left-sided and right-sided bronchi. Two left-sided bronchi indicate left isomerism (Fig. 33–46); two right-sided bronchi indicate right isomerism. In atrial situs solitus, the upper abdominal aorta lies to the left of midline and the inferior vena cava to the right; in atrial situs inversus, the abdominal aorta lies to the right. In situs ambiguous, both the aorta and inferior vena cava lie on one side of the midline; on the left side in left isomerism, and on the right in right isomerism. Furthermore, the inferior vena cava in patients with situs ambiguous lies anterior to the aorta.

Ventricular Morphology

The right and left ventricles may be confidently differentiated by their shape, trabecular appearance, and relationship between atrioventricular and semilunar valves. The endocardial surface of the morphologic left ventricle appears smoother than that of the morphologic right ventricle.

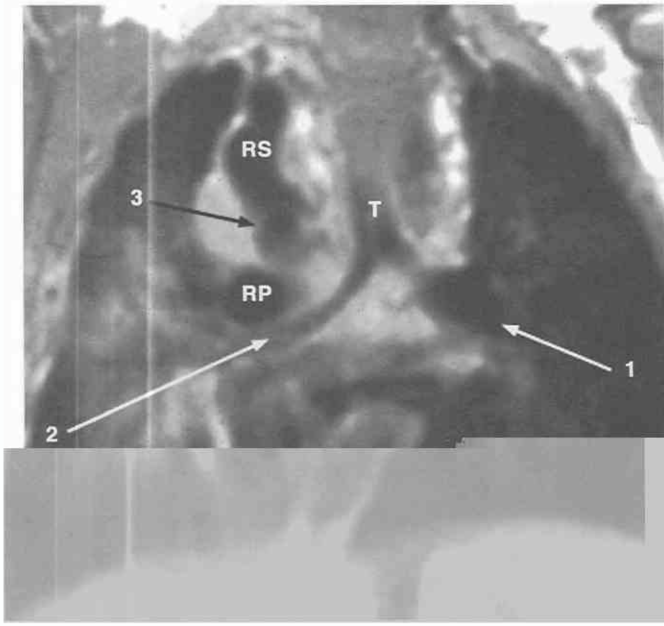

Figure 33–45. Coronal spin-echo acquisition through the tracheal (T) bifurcation in a 6-year-old boy with coarctation of the aorta in complete situs inversus. The left-sided (morphologic right) pulmonary artery *(arrow 1)* is volume-averaged with the left-sided bronchus. The right-sided (morphologic left) pulmonary artery (RP) runs over the top of the right-sided bronchus *(arrow 2)* and lies inferior and lateral to the aortic arch *(arrow 3)*. The aortic arch is diminished in caliber, and the right subclavian artery (RS) is dilated.

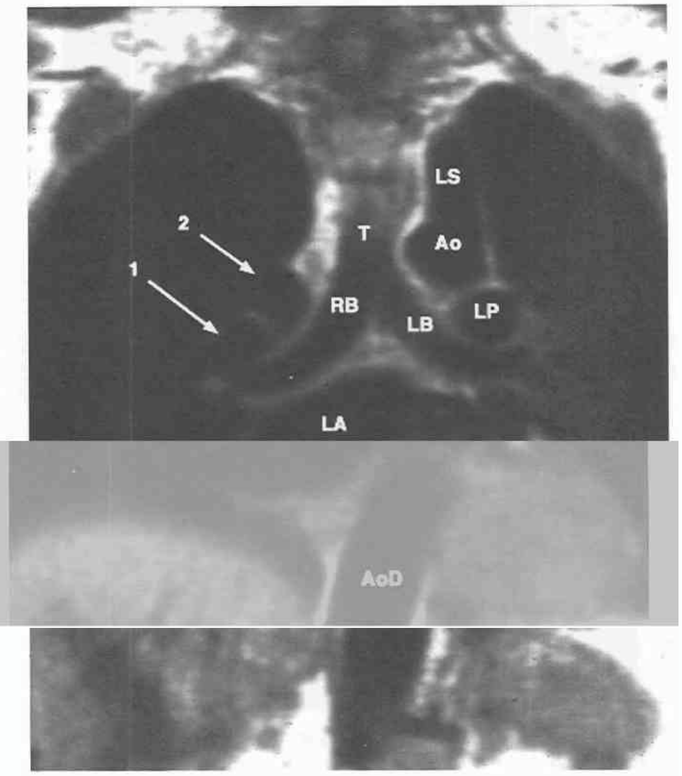

Figure 33–46. Coronal spin-echo acquisition obtained through the tracheal (T) bifurcation and left atrium (LA) from a 76-year-old woman with breast carcinoma. The left-sided bronchus (LB) and the right-sided bronchus (RB) appear symmetrical. The left-sided pulmonary artery (LP) runs over the left bronchus, and the right-sided pulmonary artery *(arrow 1)* runs over the right bronchus. Note that the inferior vena cava is not shown passing through the liver; a dilated azygos vein *(arrow 2)* indicates interruption of the IVC azygos continuation. Incidentally, note the dilated left subclavian artery (LS) originating from the distal aortic arch (Ao); the patient also had an unsuspected mild aortic coarctation. AoD, descending aorta.

The muscular trabeculations of the morphologic right ventricle are thicker and straighter than those of the relatively smooth-appearing left ventricle. These trabeculations are most apparent along the right ventricular side of the interventricular septum. The left ventricle has large papillary muscles that only originate from the free wall. Tricuspid valve papillary muscles originate from both the interventricular septum as well as the free wall of the right ventricle. These are visualized as soft tissue within the right ventricular cavity on spin-echo examination and as filling defects, which increase in size in systolic images, using gradient-echo acquisition. The most reliable means of differentiating the right ventricle from the left ventricle is by demonstration of the right ventricular infundibulum. This circumferential band of myocardium separates the tricuspid valve from the semilunar valve. MR examination is useful for demonstrating the right ventricular infundibulum (Fig. 33–47). The left ventricle has no infundibulum. There is fibrous continuity between the mitral and semilunar valves (Fig. 33–48).

Cardiac Looping

During the third week after fertilization, the ventral cardiac tube loops toward the embryonic right (D [dexter]-looping). As a result of this, the inflow to the ventricle derived from the bulbus cordis subsequently lies to the right of the inflow to the ventricle formed from the true ventricle. By the sixth week after fertilization, the D-looped heart swings around an external axis to come to lie in the left chest, retaining the right-to-left relationship between right and left ventricular inflows. If the heart loops to the left (L [levo]-looping), the inflow to the morphologic right ventricle comes to lie to the left of that of the morphologic left ventricle. Thus, the direction of looping can be ascertained by analysis of the relationships of the inflows of the ventricular chambers.

Atrioventricular and Ventriculoarterial Connection

Atrioventricular concordance exists when blood flows from the morphologic right atrium to the morphologic right ventricle and from the morphologic left atrium to the morphologic left ventricle; this is the result of D-looping of the ventricles (Fig. 33–49). Atrioventricular concordance may exist in either situs solitus (right atrium to the right) or situs inversus (right atrium to the left). An L-looped heart exhibits atrioventricular discordance; right atrial blood flows to the morphologic left ventricle and left atrial

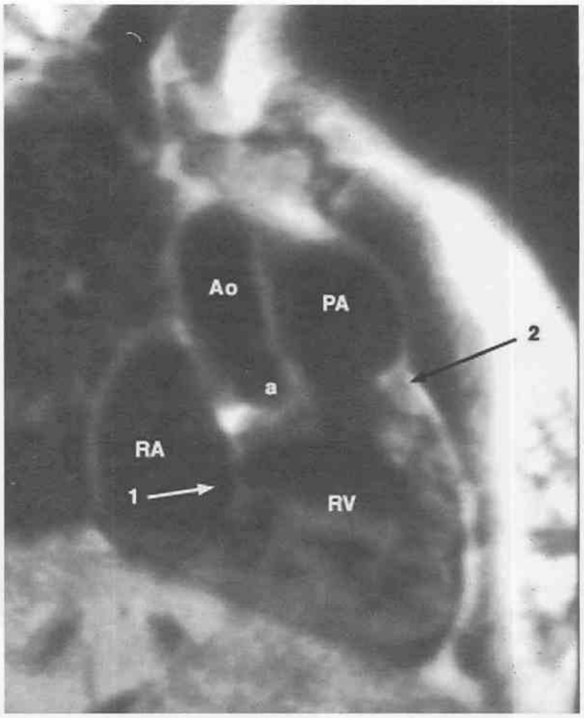

Figure 33–47. Right anterior oblique sagittal spin-echo acquisition through the anterior aortic sinus of Valsalva (a) in a 24-year-old woman with an atrial septal defect. The main pulmonary artery (PA) is dilated, as compared with the ascending aorta (Ao). The tricuspid valve *(arrow 1)* separating the right atrium (RA) from right ventricle (RV) itself is separated from the pulmonary artery by the right ventricular infundibulum *(arrow 2)*.

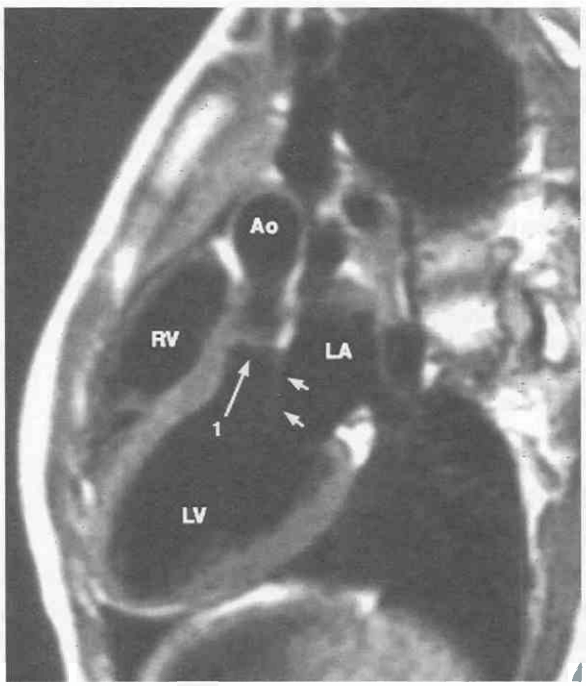

Figure 33–48. Oblique sagittal spin-echo acquisition through the aortic valve *(arrow 1)* in a 9-year-old boy with a bicuspid aortic valve. The valve is thickened, and its caliber is diminished. The anterior mitral leaflet *(short arrows)* attaches to the aortic valve. Ao, aorta; LA, left atrium; LV, left ventricle; RV, right ventricle.

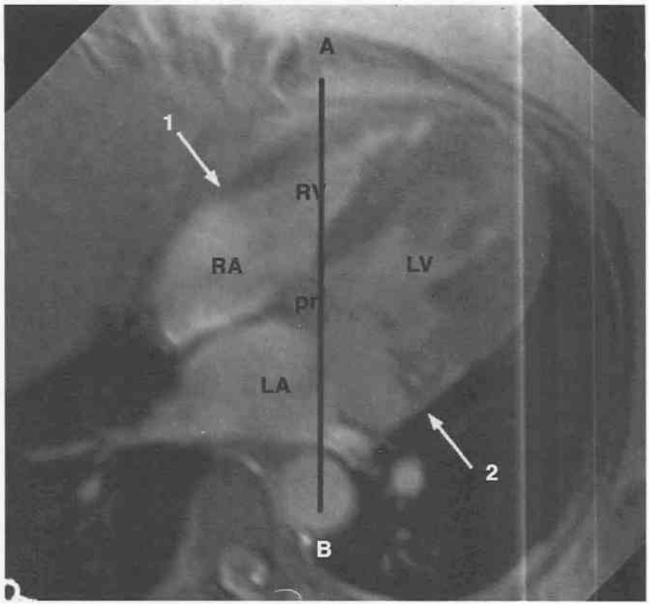

Figure 33–49. Axial early systolic gradient-echo image obtained from a 15-year-old boy with coarctation of the aorta. The line AB is drawn through the center of the heart, just to the left of the posterior right aortic sinus of Valsalva (pr). In a D-loop, the inflow *(arrow 1)* to the right ventricle (RV) lies to the right of the inflow *(arrow 2)* to the left ventricle (LV). LA, left atrium; RA, right atrium.

blood flows to the morphologic right ventricle (Fig. 33–50). Note that D-looping in atrial situs inversus results in L-loop atrioventricular relations and that L-looping in situs inversus results in D-loop relations.

Ventriculoarterial concordance exists when the morphologic right ventricle supports the pulmonary valve and pulmonary artery (see Fig. 33–47) and when the morphologic left ventricle supports the aortic valve and aorta (see Fig. 33–48). Thus, the normal great artery relationship is for the aorta to be to the right with respect to the pulmonary artery (see Fig. 33–3). Ventriculoarterial discordance therefore exists when the right ventricle supports the aorta or the left ventricle supports the pulmonary artery. Generally, ventriculoarterial discordance occurs in two important lesions: (1) D-transposition of the great arteries (D-TGA) and (2) congenitally corrected TGA (CC-TGA or L-TGA). In the former, there is ventriculoarterial discordance in the presence of atrioventricular concordance (Fig. 33–51). In CC-TGA, the association of both atrioventricular and ventriculoarterial discordance results in a double-switched circulation (Fig. 33–52). MR examination may be useful in diagnosing CC-TGA either by explicit demonstration of discordant connections or simply by demonstration of the left-sided upper heart border forming the aorta and the medially located main pulmonary artery segment.[117, 218]

Bicuspid Aortic Valve

Congenital bicuspid aortic valve is the most frequent malformation of the aortic valve, occurring in 0.9% to 2% of all individuals in autopsy series.[248] Although the valve may be stenotic with commissural fusion at birth, it is

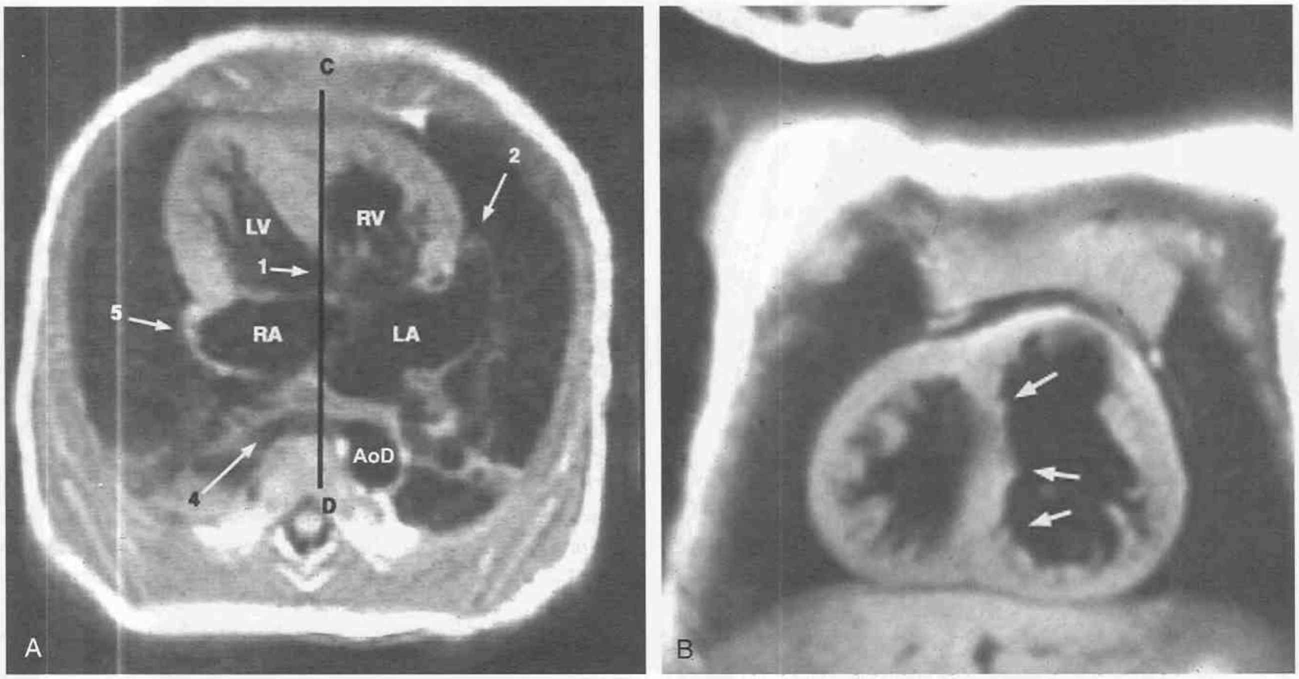

Figure 33–50. MR image obtained from a 7-month-old boy with situs solitus, corrected transposition of the great arteries, ventricular septal defect (VSD), and pulmonary atresia.

A, Axial section through the VSD *(arrow 1).* The line CD is drawn through the center of the heart. In an L-loop, the inflow to the right ventricle (RV) is to the left of the inflow to the left ventricle (LV). The identity of the morphologic left atrium is determined by the characteristic long left atrial appendage *(arrow 2)*; the right atrial appendage *(arrow 5)* is short and broad-based. Notice the large collateral vessel *(arrow 4)* arising from the descending aorta. LA, left atrium; RA, right atrium.

B, Coronal spin-echo section through the ventricles. The right-sided ventricle gives papillary muscles only from the free wall; this is the morphologic left ventricle. The left-sided ventricle gives papillary muscles from the interventricular septum *(arrows)* as well as the free wall; this is the morphologic right ventricle.

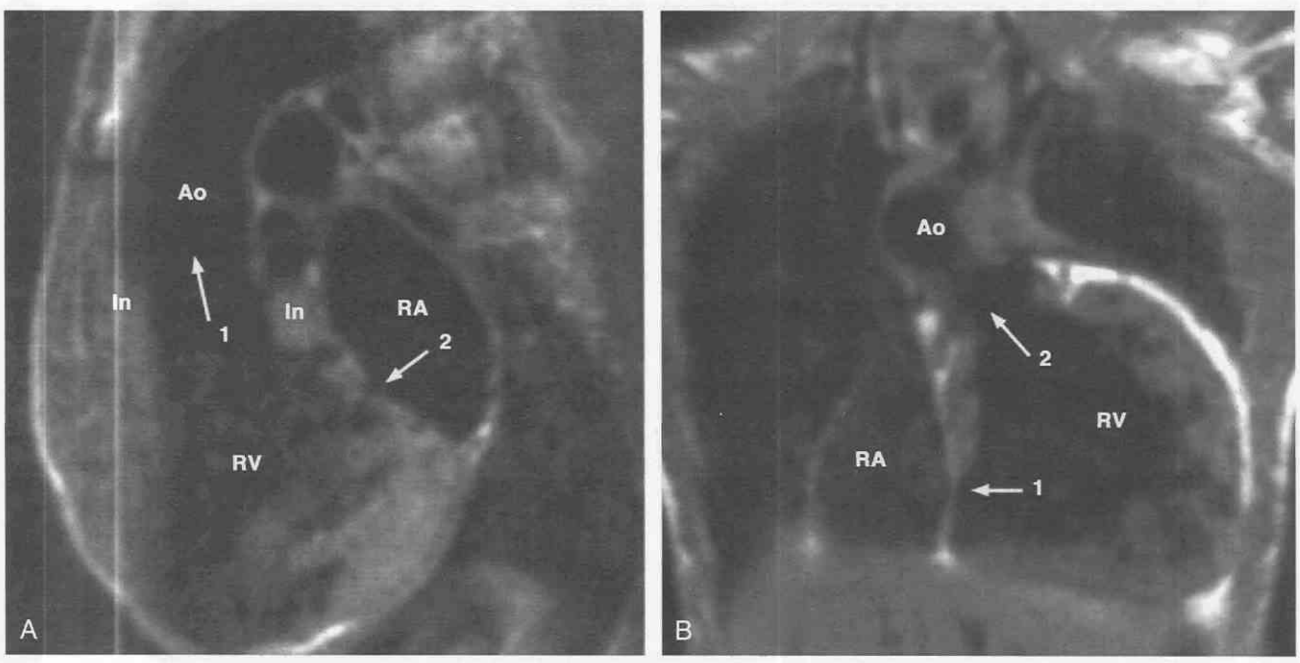

Figure 33–51. D-Transposition of the great arteries in a 4-year-old child. *A,* Sagittal section through the aortic valve. The anterior aorta (Ao) and aortic valve *(arrow 1)* are separated from the tricuspid valve *(arrow 2)* and right atrium (RA) by the circumferential muscular right ventricular (RV) infundibulum (In). *B,* Coronal section through the aortic valve *(arrow 2).* The aorta (Ao) is toward the right. The tricuspid valve *(arrow 1)* that connects the right atrium (RA) and right ventricle (RV) is separated from the aortic valve.

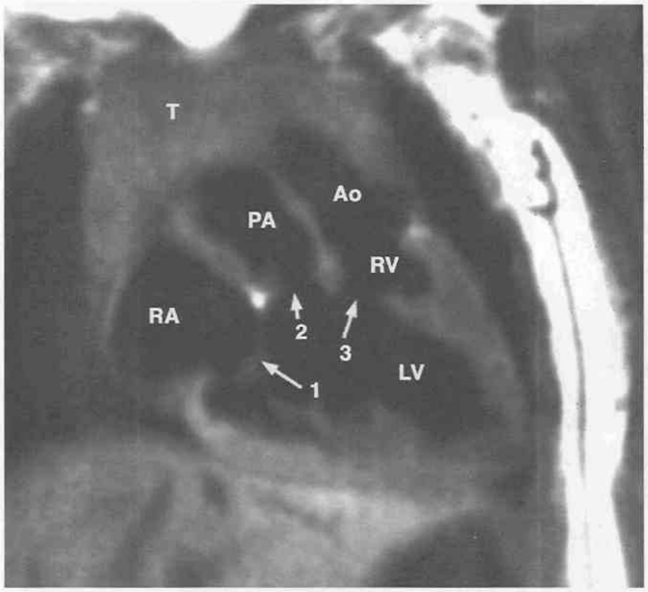

Figure 33–52. Coronal spin-echo acquisitio[redacted]rom a 2-year-old boy with double-inlet left ventricle, congenitally corrected transposition of the great arteries, and tricuspid atresia. The thymus (T) has not yet regressed. The morphologic right atrium (RA) is connected to a ventricular chamber whose atrioventicular valve *(arrow 1)* is continuous with the pulmonary valve *(arrow 2)*; this is the morphologic left ventricle (LV) (atrioventricular discordance). The hypoplastic right ventricle (RV) is filled across a ventricular septal defect *(arrow 3)* (also known as a *bulboventricular foramen*) and supports a left-sided aorta (Ao) (ventriculoarterial discordance). PA, pulmonary artery.

more commonly not responsible for severe stenosis in childhood. However, these valves tend to present later in life, usually by late adolescence. Fibrosis, increasing rigidity and calcification of the leaflets, and subsequent narrowing of the aortic orifice[35] develop as a result of turbulence associated with the abnormal valvular architecture. Stenotic changes resemble those found in cases of degenerative calcific stenosis of a tricuspid aortic valve, but these changes occur several decades earlier in the congenitally malformed valve. About one third of patients born with congenital bicuspid aortic valve remain free of any hemodynamically significant problem. Valvular stenosis develops in about one third of patients. An additional one third of patients develop aortic regurgitation[87] on the basis of organic structural abnormality or after a bout of acute bacterial endocarditis.

The aortic annulus in these patients may be normal, but in more severe cases it is decreased in caliber. The three aortic sinuses of Valsalva may be maldistributed by the unseparated valvular commissures; the valve leaflets themselves may be thickened (Fig. 33–53). Calcium is transparent on MR examination; valvular calcification may have the appearance of thickened loci of signal void relating to the valve annulus or where one expects to find valve leaflets. Aortic valve doming may be demonstrated in off-coronal or sagittal section (Fig. 33–54). Often, dilatation of the ascending aorta and left ventricle is identified in cases of valves with mixed stenosis and regurgitation. In both instances, there is left ventricular hypertrophy; in mixed regurgitant bicuspid aortic valves, left ventricular hypertrophy is less apparent because the left ventricle is dilated as well. Gradient-echo imaging of the abnormal valve produces typical systolic signal-void jets of aortic

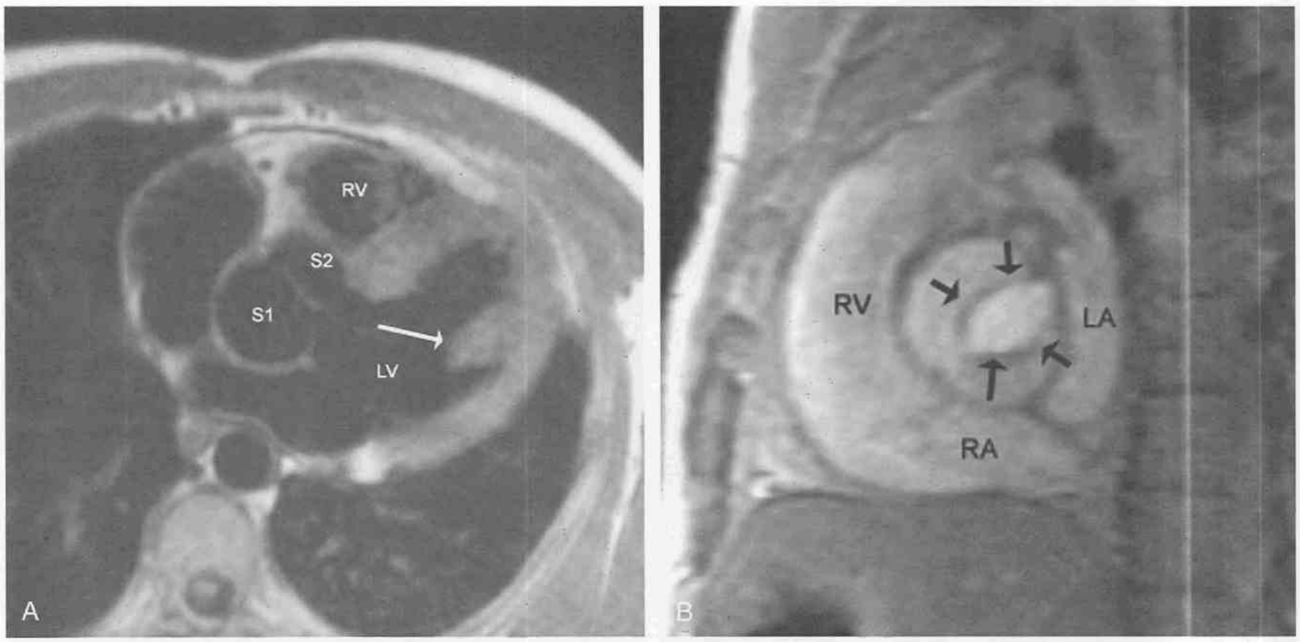

Figure 33–53. MR images obtained from two adult patients with congenital bicuspid aortic valve disease. *A,* Axial spin-echo acquisition from a 23-year-old man. Notice the asymmetry of the two aortic sinuses of Valsalva (S1 and S2). The left ventricular (LV) myocardium is thickened; note the severe hypertrophy of the papillary muscle *(arrow)*. RV, right ventricle. *B,* Systolic short-axis gradient-echo acquisition from a 27-year-old man. There is mild dilatation of the aortic root. The limited valve orifice appears as increased signal intensity sandwiched between the two aortic valve leaflets *(arrows)*. LA, left atrium; RA, right atrium; RV, right ventricle.

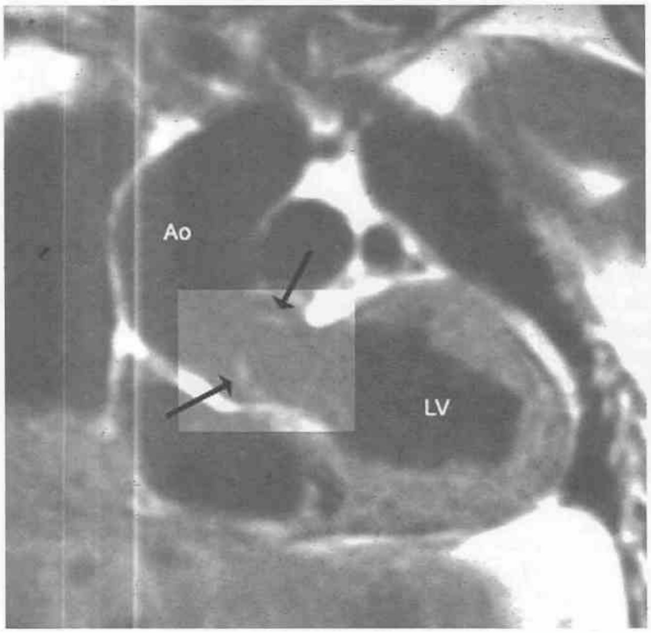

Figure 33–54. Midsystolic oblique coronal spin-echo acquisition from a 19-year-old man with congenital bicuspid aortic stenosis. The center of the image has been image-processed to bring out the appearance of the aortic leaflets *(arrows)*. Notice that the leaflets are thickened and leave a limited valvular orifice. The left ventricular (LV) myocardium is thickened, and there is mild dilatation of the ascending aorta (Ao).

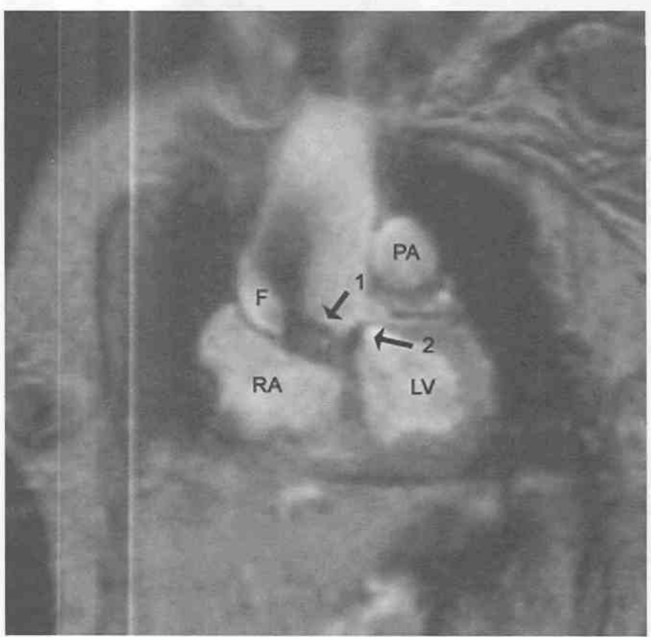

Figure 33–55. Systolic oblique coronal gradient-echo acquisition through the main pulmonary artery (PA) from a 24-year-old woman with bicuspid aortic valve stenosis and an acute aortic dissection. The left ventricular (LV) myocardium is hypertrophied. A signal void jet *(arrow 1)* originates from the signal void of the calcified aortic valve *(arrow 2)* and ricochets off the intimal flap, which separates the true aortic lumen from the false lumen (F). RA, right atrium.

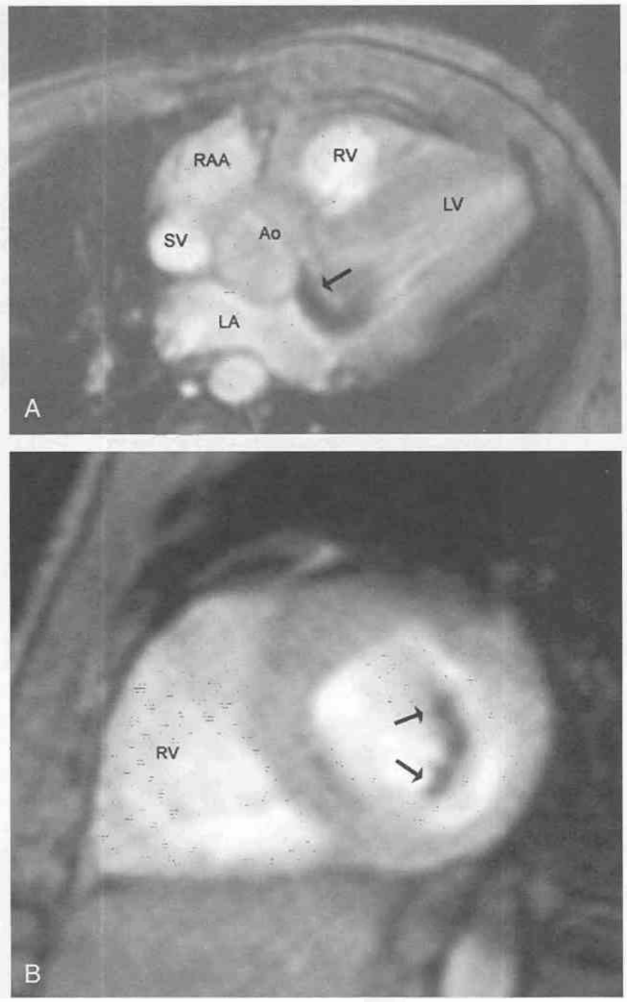

Figure 33–56. MR image obtained from a 30-year-old man with bicuspid aortic valve and aortic regurgitation. *A,* Diastolic oblique axial acquisition through the aortic valve (Ao) at the entry of the superior vena cava (SV) into the right atrium and the right atrial appendage (RAA). The signal void jet of aortic regurgitation *(arrow)* passes along the anterior mitral leaflet and strikes the posterior left ventricular (LV) wall. LA, left atrium; RV, right ventricle. *B,* In this diastolic short-axis image, the signal void jet is seen in cross-section *(arrows)*. RV, right ventricle.

stenosis (Fig. 33–55) and diastolic jets of regurgitation (Fig. 33–56). Correlation between length of signal loss into the aorta and gradient across the valve[199] has been demonstrated in adult patients with aortic stenosis. Direct quantitation of valvular gradients may be obtained by use of phase-velocity mapping.[150, 151] By acquiring images with a sufficiently short echo time (<5 msec), signal loss from all but the most turbulent regions of poststenotic blood flow is eliminated. Signal intensity measurements across the face of a poststenotic jet are proportional to the flow-velocity profile across the valve. Thus, application of a modified Bernoulli equation to flow-velocity measurements provides a noninvasive estimate of valve pressure gradient.

Coarctation of the Aorta

The most common symptomatic congenital lesion of the aortic arch studied by magnetic resonance is coarctation of

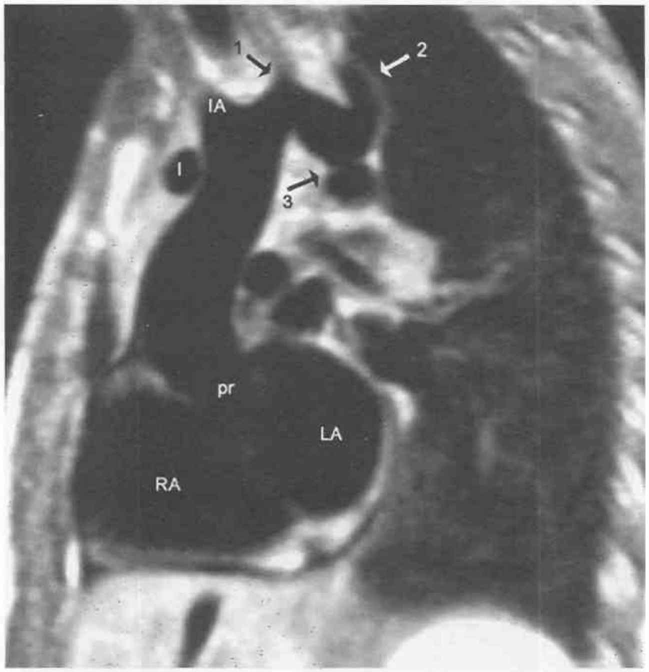

Figure 33–57. Oblique sagittal spin-echo acquisition through the posterior right aortic sinus of Valsalva (pr) from an 11-year-old boy with a 35-mm gradient between upper and lower extremities. The left atrium (LA) and the right atrium (RA) are labeled. Notice the long and undulating course of the ascending aorta and aortic arch. The dilated innominate artery (IA) origin immediately behind the innominate vein (I), the origins of the left common carotid artery *(arrow 1)* and the left subclavian artery *(arrow 2)* are seen. The left subclavian artery appears to run nearly parallel to the distal aortic arch immediately above the coarctation *(arrow 3)* itself.

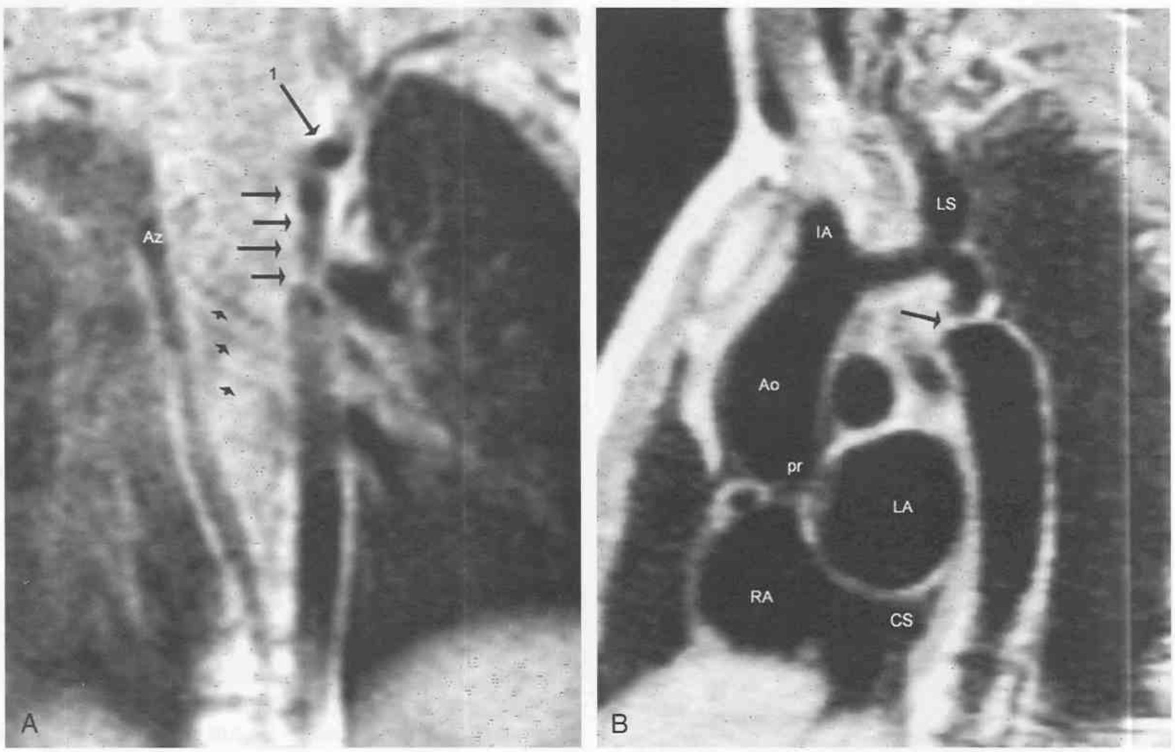

Figure 33–58. MR image obtained from two children with coarctation of the aorta. *A,* Coronal spin-echo acquisition from a 6-month-old girl with a 50-mm aortic gradient. The proximal descending aorta *(parallel long arrows)* distal to the origin of the dilated left subclavian artery *(arrow 1)* tapers to the point of maximal stenosis. Aortic collateral vessels *(arrowheads)* are seen entering the aorta distal to the coarctation. The azygos vein (Az) is labeled. *B,* The patient is a 4-year-old boy with a 60-mm gradient. Left anterior oblique sagittal spin-echo acquisition through the posterior right (pr) aortic sinus of Valsalva. The left (LA) and right (RA) atria are marked. The ascending aorta (Ao) is mildly dilated, and there is hypoplasia of the arch extending from the origin of the innominate artery (IA), beyond the origin of the left subclavian artery (LS) to the actual coarctation itself *(arrow)*. Beyond the coarctation, there is mild poststenotic dilatation. CS, coronary sinus.

the aorta.[146, 306] Coarctation of the aorta is a congenital maldevelopment of the aorta (Fig. 33–57), which presents with hypoplasia of the distal aortic arch and focal narrowing of the proximal descending aorta, almost invariably at the junction of the ductus arteriosus and aorta.

Collateral circulation to the postcoarctation segment usually originates from branches of the proximal subclavian arteries (the internal mammary arteries and thyrocervical trunk). Blood flow is around the shoulder or anterior chest wall and retrograde through the intercostal arteries to the postcoarctation segment of the proximal descending aorta. Occasionally, coarctation of the aorta may be associated with an aberrant subclavian artery. In such circumstances, the aberrant artery is downstream from the coarctation (at low pressure with respect to the ascending aorta) and thus unable to provide collateral flow to the postcoarctation aorta. Plain film examination in these cases may reveal unilateral rib notching.

MR examination of patients with coarctation of the aorta is directed toward demonstration of the location and length of the coarctation segment (Fig. 33–58), the status of the aortic isthmus, and the degree of arterial collateralization present.[28, 146, 279, 306] Furthermore, the relationship of the coarctation to the origins of the left and right subclavian arteries (especially in cases with an aberrant subclavian artery) must be demonstrated. These changes are usually best appreciated in oblique sagittal or coronal sections, parallel to the axis of the ascending and descending aortas. However, in smaller children or older adults, the small caliber of the aorta or aortic tortuosity may necessitate acquisition in additional oblique sections. The origin of the left subclavian artery in many of these patients appears to be "pulled" inferiorly from the distal aortic arch toward the hourglass deformity of the coarctation itself, the so-called capture of the left subclavian artery (see Fig. 33–57). In oblique sagittal sections from the posterior chest, dilated intercostal arteries may be identified traveling along the underside of the posterior upper ribs (Fig. 33–59). The internal mammary arteries run along the inner aspect of the anterior chest wall, on either side of the lateral border of the sternum, and are best identified in axial or coronal section as dilated signal voids (Fig. 33–60). MR examination is a useful means of following the results of balloon dilatation and surgical repair of coarctation.[236, 286] Serial examination allows close follow-up and assessment of residual stenosis and early demonstration of aneurysmal dilatation.

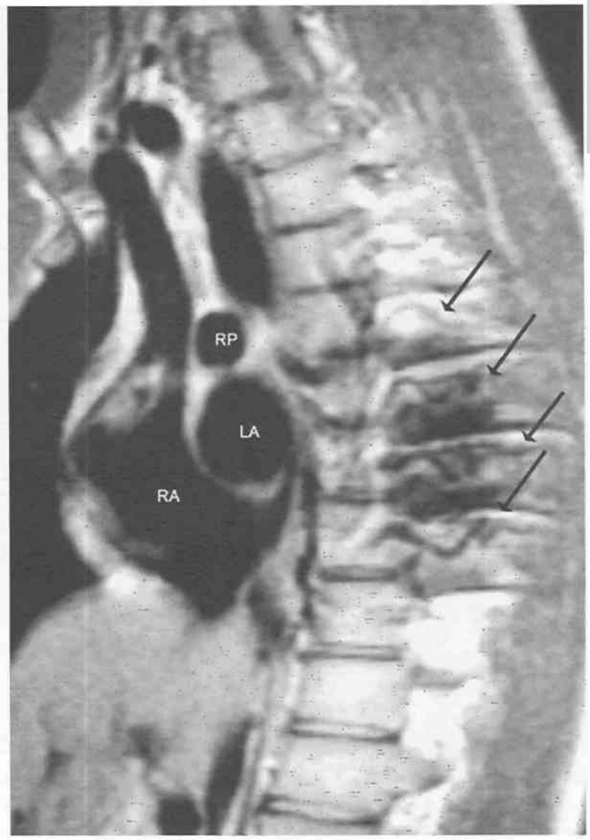

Figure 33–59. Left anterior oblique sagittal spin-echo acquisition through the interatrial septum from a 14-year-old boy with a 50-mm gradient across the coarctation. The left atrium (LA) and right atrium (RA) and the right pulmonary artery (RP) are labeled. Intercostal collateral vessels appear as serpiginous signal voids along the undersides of the ribs *(arrows)*.

Patent Ductus Arteriosus

The ductus arteriosus is the persistent distal left sixth aortic arch. It extends from the underside of the aortic arch just distal to the origin of the left subclavian artery to the left pulmonary artery near its origin. Usually the ductus is left sided, but, in cases of right aortic arch, it may be right sided. Bilateral patent ductus arteriosus is rarely found. This abnormality has a variable morphology. The most common shape of a patent ductus arteriosus is long and cylindrical (Fig. 33–61). An hourglass-like narrowing may be found in its midportion. Frequently, the patent duct has a funnel shape. In this variety there is a broad base on the aortic side and a narrow attachment to the pulmonary artery. Aneurysmal ducti are less common but may appear saccular or spindle shaped. The variable length and orientation of the duct between the aorta and pulmonary artery make its demonstration often difficult. In the coronal section, communication between the underside of the distal aortic arch or proximal aorta with the superior aspect of the left pulmonary artery may be easily demonstrated. Right anterior oblique sagittal section through the arch or proximal descending aorta may demonstrate ductal communication. MR examination for patent ductus arteriosus in infants may be limited by the size of the ductus and spatial resolution of the scanner (Fig. 33–62). There are no data concerning the sensitivity and specificity of MR examination in the diagnosis of patent ductus arteriosus.

Pulmonary Arteries

Echocardiographic examination of the pulmonary arteries may be limited.[125, 208] MRI complements echocardiographic examination for the assessment of the size, patency, confluence, and character of the extraparenchymal pulmonary arteries (Fig. 33–63).[44, 73, 103] Pulmonary arterial anomalies, including pulmonary artery sling and origin of the

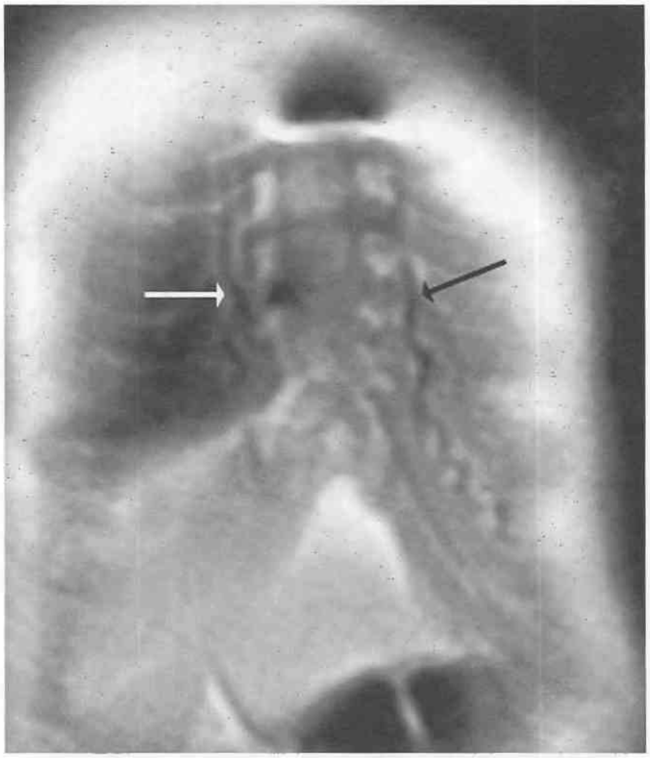

Figure 33–60. Coronal spin-echo acquisition through the posterior aspect of the sternum in a 16-year-old boy with coarctation of the aorta. Both the left and right *(arrows)* internal mammary arteries are dilated and serpiginous.

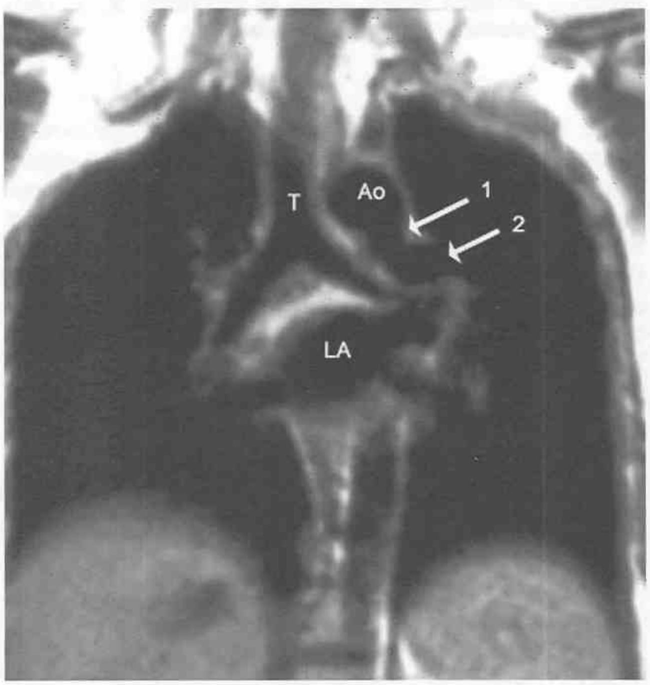

Figure 33–61. Coronal spin-echo acquisition through the trachea (T) and tracheal bifurcation and posterior left atrium (LA) from a 24-year-old woman with pulmonary hypertension. The tubular communication *(arrow 1)* between the underside of the distal aortic arch (Ao) and the top of the left pulmonary artery *(arrow 2)* is the patent ductus.

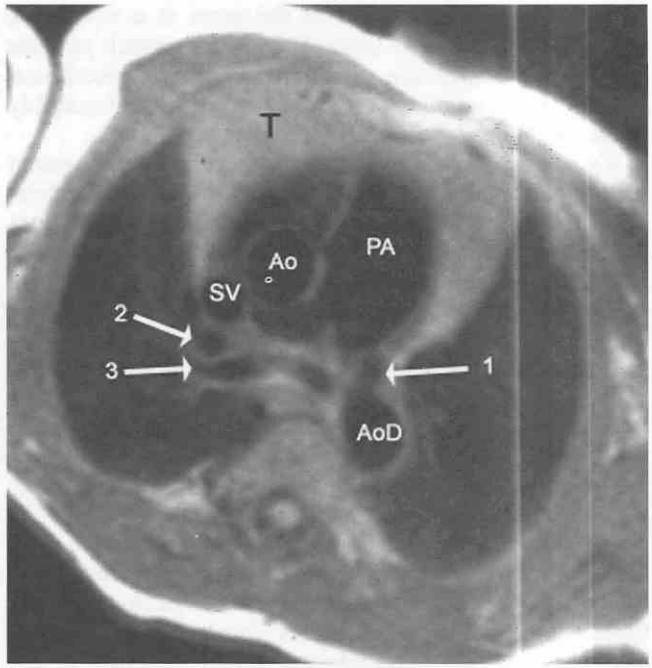

Figure 33–62. Off-axial spin-echo image obtained from a 5-week-old girl with heart failure. The thymus (T) has not regressed. The main pulmonary artery (PA) is dilated and greater in caliber than the ascending aorta (Ao). The right pulmonary artery *(arrow 2)* lies behind the superior vena cava (SV) and in front of the right bronchus *(arrow 3)*. The patent ductus is the signal void communication *(arrow 1)* between the top of the pulmonary artery and the descending aorta (AoD).

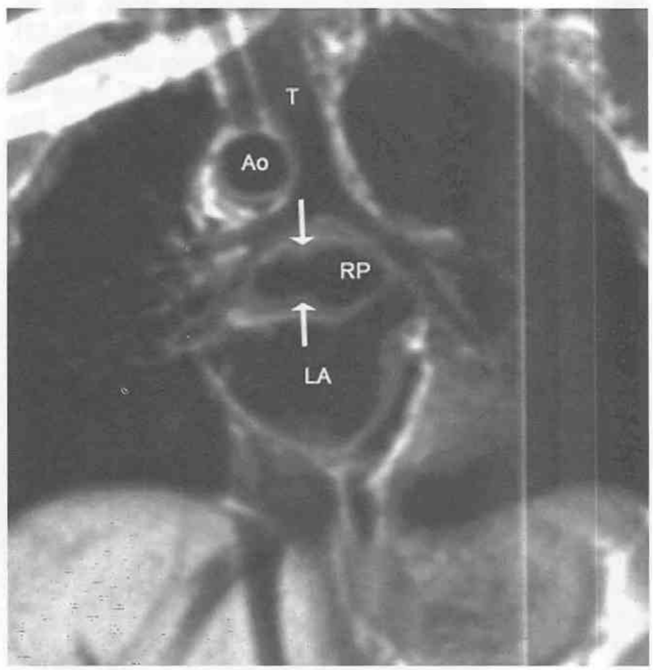

Figure 33–63. Coronal spin-echo acquisition through the trachea (T) and the tracheal bifurcation from a 16-month-old boy with tetralogy of Fallot with pulmonary atresia and right branch pulmonary artery stenosis. The aortic arch (Ao) is right-sided. There is focal narrowing of the transverse right pulmonary artery (RP) *(arrows)* as the artery crosses over the left atrium (LA).

pulmonary artery from the ductus arteriosus, may be characterized directly. Increased pulmonary blood flow, increased pulmonary artery pressure, and poststenotic dilatation of the pulmonary artery can be differentiated based on the character of flow within the dilated pulmonary artery segments. Dilated central pulmonary artery segments without increased signal indicates increased flow (see Figs. 33–36A, 33–45, and 33–62); if increased signal is present, pulmonary artery pressure is elevated. Dilatation of the main pulmonary artery, with or without associated left or right pulmonary arterial enlargement, may be seen in patients with valvular pulmonic stenosis. Aneurysmal dilatation of the pulmonary arterial tree may be found in patients with chronic, mild valvular pulmonic stenosis or pulmonary insufficiency. In patients with pulmonary hypertension and long-standing left-to-right shunts, the pulmonary arterial wall is thickened and increased in signal intensity. The central pulmonary arteries in cases of right ventricular outflow obstruction (including pulmonary atresia or tetralogy of Fallot with pulmonary atresia) may be diminutive or, if atretic, not identifiable. Focal branch stenosis proximal to the pulmonary hila may be identified directly. The main and central pulmonary arteries in cases of supravalvular pulmonic stenosis (as an isolated lesion, or in association with Williams or Noonan's syndromes), reveal diffuse or focal wall thickening (Fig. 33–64). Similarly, pulmonary arterial banding results in focal pulmonary artery narrowing.

Congenital Pulmonary Stenosis

The most common form of congenital pulmonic stenosis is valvular. So-called supravalvular pulmonic stenosis is actually pulmonary arteritis with segmental stenosis and is commonly a component of Noonan's syndrome, Williams syndrome, and congenital rubella syndrome. Subvalvular stenosis is the result of local right ventricular infundibular hypertrophy; the valve is usually normal in these individuals.

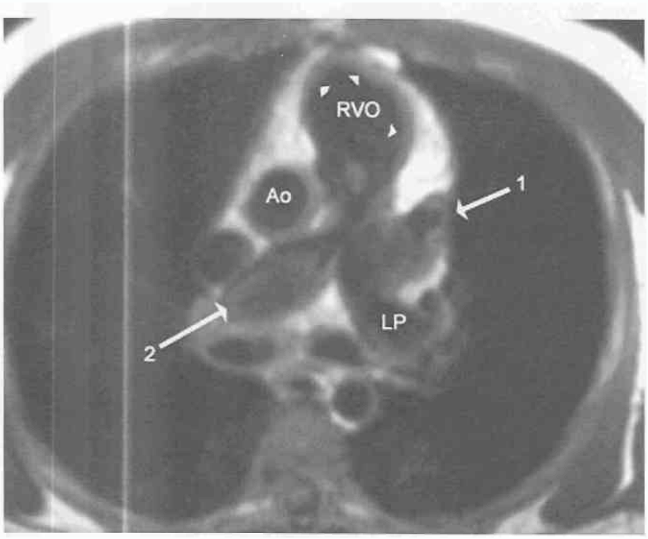

Figure 33–64. Axial spin-echo acquisition through the right ventricular outflow tract (RVO) and left atrial appendage *(arrow 1)* from a 37-year-old man with Williams syndrome. Note the infundibular right ventricular hypertrophy *(arrowheads)*. Turbulence in the right pulmonary artery *(arrow 2)* extends from beyond stenosis at its origin. Ao, aorta; LP, left pulmonary artery.

In patients with noncritical pulmonic stenosis, the pulmonary valve leaflets thicken and fibrose with age, but calcification is rarely found. Right ventricular hypertrophy reflects the severity and duration of the valvular obstruction. Right-sided heart failure is uncommon in infancy and before the 5th decade. Prolonged right ventricular hypertension distorts chamber geometry, causing right ventricular papillary muscle dysfunction and tricuspid regurgitation. Some patients with moderate stenosis progress to more severe obstruction owing to late fibrosis and deformity of the valve leaflets, or superimposed infundibular hypertrophy. Survival into the 7th decade in patients with valvular pulmonary stenosis has been reported.[104, 113]

MR examination in these patients is directed toward differentiating valvular disease from diseases resulting in dilatation of the main pulmonary artery. In patients with valvular pulmonic stenosis, the main and either left or both left and right proximal pulmonary arteries are dilated. Pulmonary blood flow in these patients is normal, so a signal void is expected when examined using spin-echo technique. Gradient-echo acquisition through the right ventricular outflow and proximal main pulmonary artery shows a systolic jet of signal void owing to turbulence extending into the main or left pulmonary artery. Right ventricular hypertrophy is the rule in these individuals but, depending on the severity of the myocardial hypertrophy, the amount of tricuspid regurgitation is variable. Therefore, right ventricular dilatation is unusual, and clockwise cardiac rotation is not usually seen (Fig. 33–65).

Intracardiac Shunts

MR examination is useful for the diagnosis of intracardiac shunt by explicit demonstration of the defect. Alternatively, it may be used to define the constellation of specific chamber dilatation and hypertrophy that may be used to characterize a particular lesion, confirming questionable cases and excluding false-positive cases.

Atrial Septal Defect

Atrial septal defects (ASDs) may be classified on the basis of the location of the defect. *Primum defects*, whether or not they are associated with other atrioventricular septal defects, are medially located, immediately superior to the atrioventricular valves (Fig. 33–66). *Secundum defects* are centrally located in the septum and are usually large. These may be differentiated from a patent foramen ovale by their size (Fig. 33–67). *Sinus venosus defects* are laterally located, appearing as defects between the posterioinferior border of the inferior vena cava and the left atrium, immediately inferior and posterior to the entry of the right upper lobe pulmonary vein (Fig. 33–68).

The interatrial septum is best visualized in axial and left anterior oblique sagittal or short-axis section (Fig. 33–69; see also Fig. 33–67A). It is often infiltrated with fat, in-

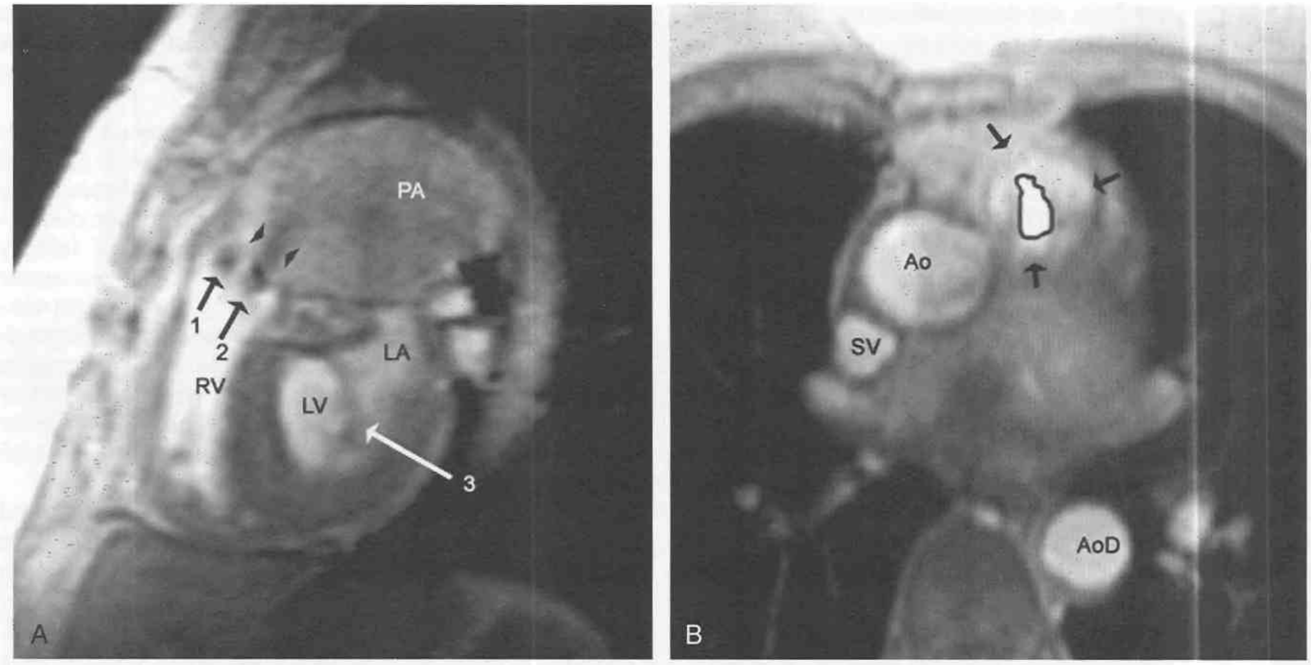

Figure 33–65. MR image obtained from a 74-year-old woman with congenital valvular pulmonic stenosis. *A,* Systolic sagittal gradient-echo acquisition obtained through the pulmonary valve. Two signal voids on the cusps of the pulmonary valve *(arrows 1* and *2)* represent calcific leaflet deposits. A fan-shaped jet of pulmonic stenosis *(arrowheads)* into the dilated main pulmonary artery (PA) can be seen. In this anatomic section, the anterior mitral leaflet *(arrow 3)* can be seen separating the left atrium (LA) from left ventricle (LV). RV, right ventricle. *B,* Systolic oblique axial section through the stenotic pulmonary valve *(arrows).* The valve orifice has been outlined in black. One can see how valve area can be directly quantitated by this technique. Ao, aorta; AoD, descending aorta; SV, superior vena cava.

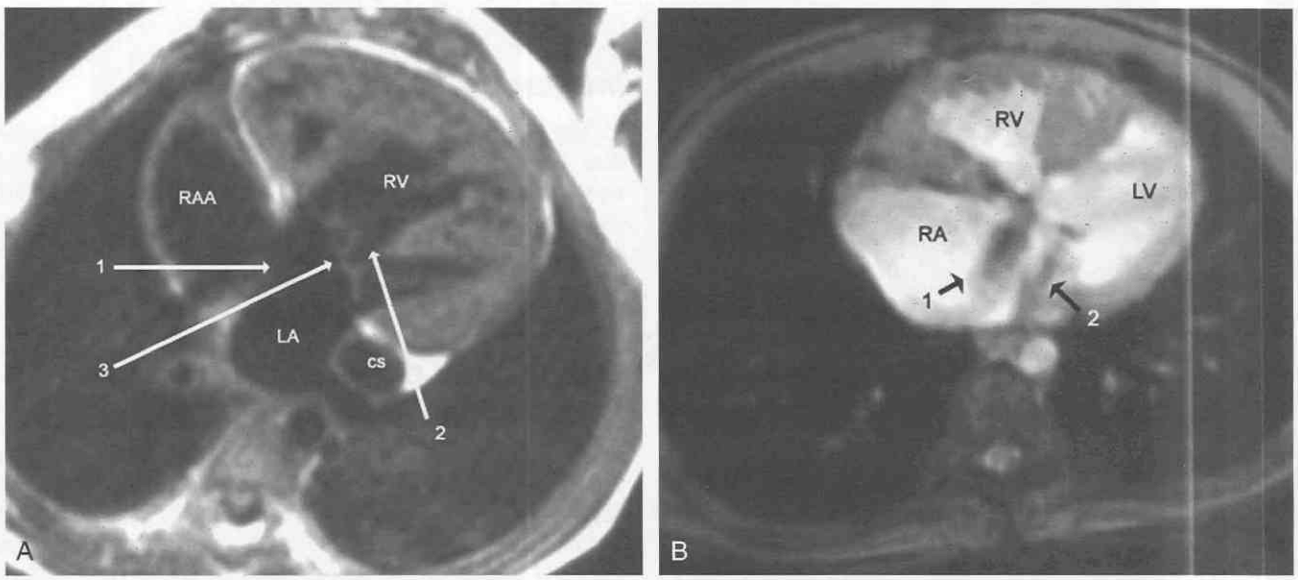

Figure 33–66. MR image obtained from two children with an atrioventricular septal defect (ASD) and a primum ASD. *A,* Axial spin-echo acquisition from a 21-month-old girl. Both the right atrial appendage (RAA) and the left atrium (LA) are dilated. There is a break in the medial aspect of the interatrial septum *(arrow 1)*, indicating a primum ASD. In addition, there is a break in the posterior interventricular septum *(arrow 2)* and a solitary bridging atrioventricular valve *(arrow 3)*. The right ventricular (RV) myocardium is severely hypertrophied. Incidentally, in this child with duplication of the superior vena cava, the left vena cava drains to the dilated coronary sinus (cs).

B, Systolic axial gradient-echo acquisition from a 15-month-old boy with ASD. Note the severe hypertrophy of the right ventricular (RV) and the septal myocardium. The signal void jet *(arrow 1)* extending from just beneath the posterior right aortic sinus of Valsalva into the right atrium (RA) is the shunt through the atrioventricular septal defect. In addition, the signal void jet *(arrow 2)* extending from the mitral valve into the left atrium represents mitral regurgitation through a cleft mitral leaflet. LV, left ventricle.

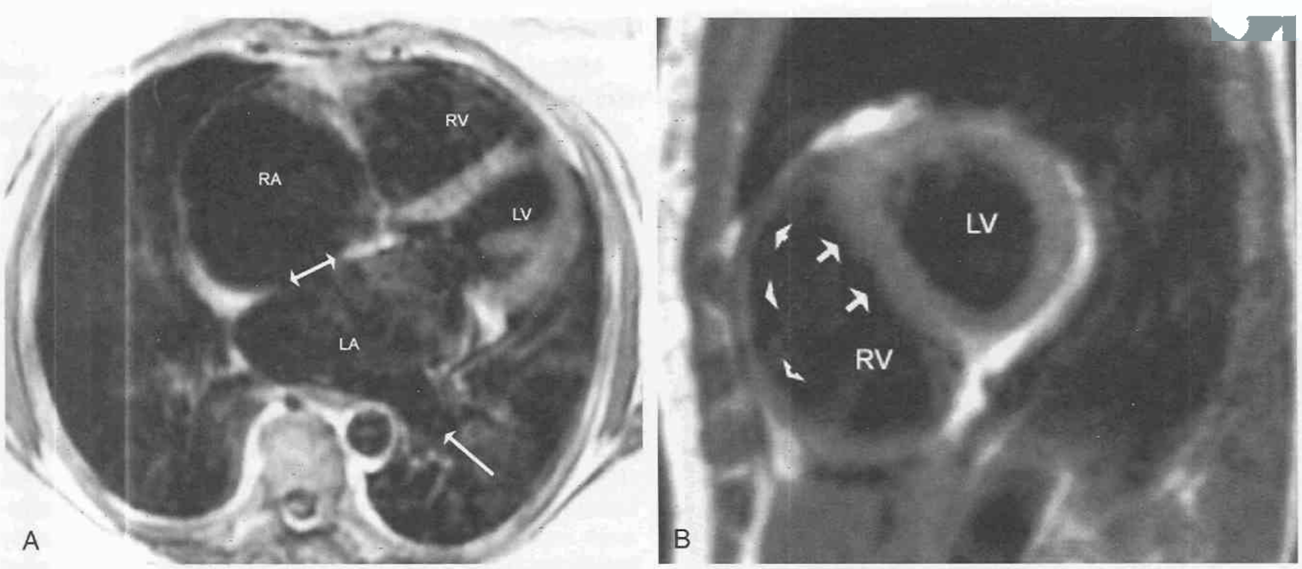

Figure 33–67. MR image obtained from two adult patients with secundum atrial septal defects. *A,* Axial spin-echo acquisition from an asymptomatic 57-year-old woman. The heart has rotated in a clockwise manner into the left chest; the right atrium (RA), the right ventricle (RV), and the left lower-lobe pulmonary vein *(single-headed arrow)* are dilated. The interventricular septum is flat. However, the left atrium (LA) and left ventricle (LV) are normal. The atrial septal defect *(double-headed arrow)* is in the center in the interatrial septum. *B,* Short-axis section from a 43-year-old asymptomatic woman. The dilated right ventricle (RV) has extended below the normal-appearing left ventricle (LV). Despite the RV dilatation, the right ventricular free wall myocardium *(arrowheads)* is not hypertrophied, but the interventricular septum *(short arrows)* is flattened.

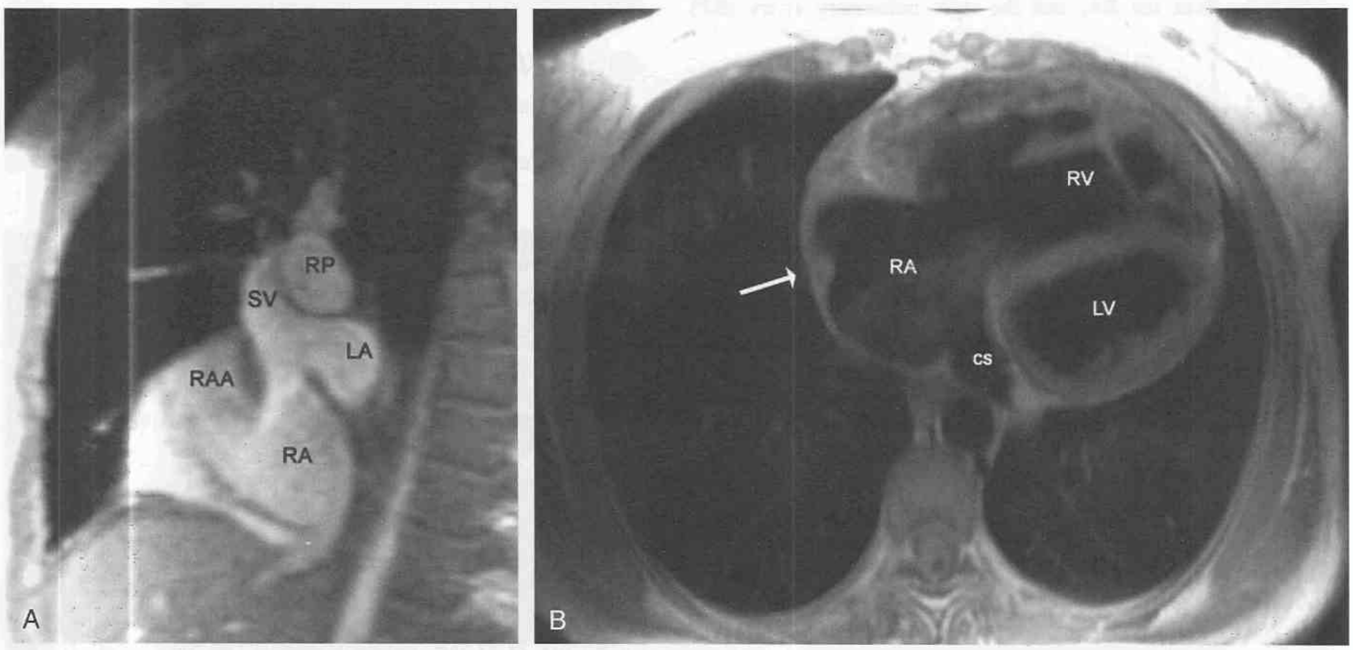

Figure 33–68. MR image obtained from a 28-year-old woman with sinus venosus atrial septal defect. *A,* Right parasagittal gradient-echo acquisition through the entrance of the superior vena cava (SV) into the right atrium (RA). The defect results in continuity among the lower SV, the left atrium (LA), and the right atrium. RAA, right atrial appendage; RP, right pulmonary artery. *B,* Axial spin-echo acquisition through the right atrium (RA) and right ventricle (RV). The right atrium, right ventricle, and coronary sinus (cs) are each dilated, and the heart is rotated into the left chest. The interventricular septum is flat, and RV myocardial trabeculae in this patient are more prominent than in the patient in Figure 33–67*B*. Note the high-signal-intensity crista terminalis *(arrow)* along the lateral aspect of the RA wall. LV, left ventricle.

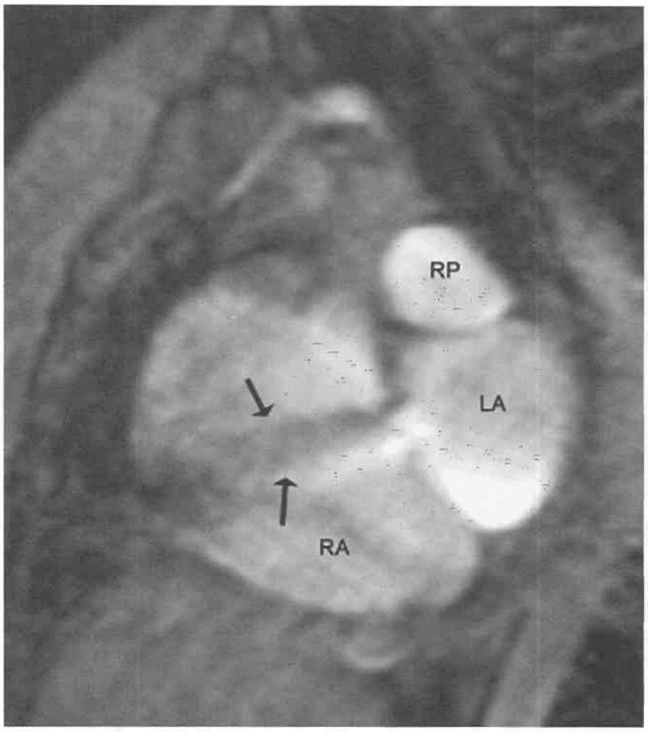

Figure 33–69. Diastolic short-axis acquisition through the interatrial septum in a 30-year-old woman with a secundum atrial septal defect. The interatrial septum is bowed toward the right atrium (RA). The signal void jet of the shunt *(arrows)* extends from the septum into the dilated RA. The left atrium (LA) is smaller than the RA, and the right pulmonary artery (RP) is dilated.

creasing its conspicuity against the signal void of the two atria, and normally bows toward the right atrium. The septum is thinner in the region of the foramen ovale. Care must be taken to avoid making the misdiagnosis of an atrial septal defect based solely on the isolated observation of a break in the septal contour. The diagnosis of a shunt is ensured if the associated morphologic and anatomic changes resulting from the altered flow of blood are identified. In particular, in an atrial septal defect, blood shunts across the atrial septum to volume-load the right atrium and ventricle and pulmonary arteries. Volume loading the right heart results in clockwise (looking from below) cardiac rotation. The plane of the interventricular septum is nearly parallel to the coronal plane. In patients with atrial septal defect, the left atrium decompresses during diastole and is therefore not enlarged. Right ventricular myocardium in simple atrial septal defect is not hypertrophied. The direction of the shunt (left-to-right or right-to-left) can be assessed using gradient-echo technique. Of course, such characterization is dependent on finding the anatomic level of the shunt itself and imaging the defect in a plane to the flow of blood. Administration of intravenous Gd-DTPA may help characterize smaller or less apparent shunts.[175] Atrial-level shunts may be quantitated by means of analysis of velocity-encoded cine MR images.[36] Imaging in the axial plane, MR has an overall 97% sensitivity and 90% specificity for the detection of atrial septal defects.[72]

Ventricular Septal Defect

MRI is a valuable means of diagnosing the presence and size of ventricular septal defects.[74, 135, 340] Large subaortic ventricular septal defects are readily demonstrated on axial spin-echo images as signal voids to the left of the atrioventricular rings and to the right of the crest of the muscular interventricular septum (Fig. 33–70). Separation of the actual defect from the caudal extension of an aortic sinus of Valsalva is best appreciated by obtaining images in oblique sagittal section through the base of the heart. Smaller, and more distal, defects are more difficult to demonstrate directly using spin-echo technique and often necessitate construction of compound angulated sections. GRE cine acquisition portrays the turbulent blood flowing across the defect as a signal-void jet within the cavity of the right ventricle (Fig. 33–71). Membranous ventricular septal defects are identified by the absence of signal in the posterior, superior-most aspect of the interventricular septum, immediately below the aortic valve, and adjacent to the septal leaflet of the tricuspid valve. Supracristal defects may be identified in right anterior oblique sagittal section, or in axial section, immediately below the semilunar valves. Anterior extension into the muscular septum can be identified in axial or right anterior oblique sagittal sections through the interventricular septum. Muscular ventricular septal defects are more difficult to identify directly by spin-echo technique but may be identified by detection of the signal-void jet of the shunted blood using gradient-echo methods (Fig. 33–72). Careful evaluation of cine imagery allows differentiation among left-to-right, right-to-left, and bidirectional shunts.

Other Shunts

Atrioventricular septal defects (endocardial cushion defects) may involve the anterior mitral and septal tricuspid valve leaflets, the membranous interventricular septum, as

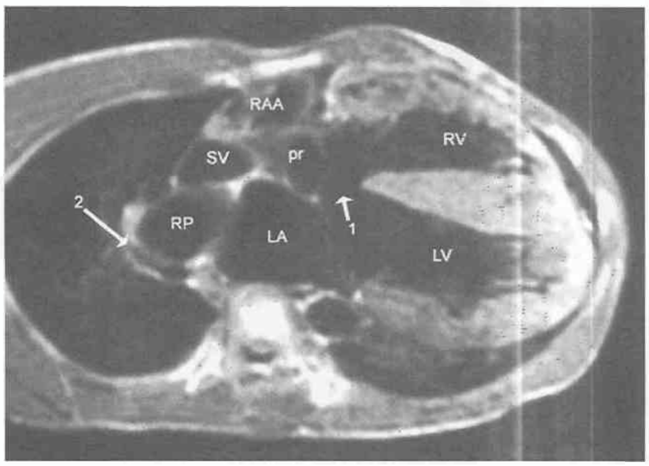

Figure 33–70. Oblique axial spin-echo acquisition through the posterior right aortic sinus of Valsalva (pr). The large membranous ventricular septal defect *(arrow 1)* communicates between the dilated and hypertrophied right ventricle (RV) and the left (LV) ventricle. The visualized right pulmonary artery (RP) lies anterior to the right bronchus *(arrow 2)*. Notice how the unsupported aortic sinus overrides the septum toward the right ventricle. LA, left atrium; RAA, right atrial appendage; SV, superior vena cava.

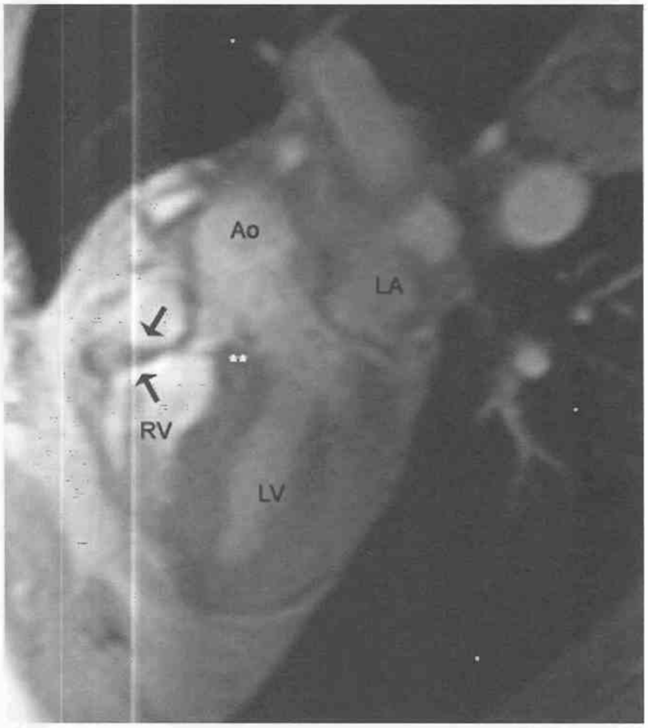

Figure 33–71. Systolic horizontal long-axis section through the posterior interventricular septum in a 50-year-old man with a pinhole ventricular septal defect. At the apex *(arrows)* of a ventricular septal aneurysm that extends between the crest of the muscular interventricular septum *(**)* and the annulus of the aortic valve is the fan-shaped signal void shunt jet into the right ventricle (RV). Ao, aorta; LA, left atrium; LV, left ventricle.

well as the atrioventricular septum and primum portion of the interatrial septum (see Fig. 33–66). Precise classification based on the morphology of the common atrioventricular valve is difficult with MR, but such defects may be characterized by the extent of endocardial cushion abnormality.[135, 219] MRI is useful in determining the size of the ventricular component of the defect as well as the presence of ventricular hypoplasia. Gradient-echo acquisition may be helpful in confirming primum atrial septal defects and demonstrating atrioventricular shunting.

Anomalous pulmonary veins may return to systemic veins above the level of the heart, including the innominate and subclavian veins, or superior vena cava. Veins may drain directly to the right atrium or coronary sinus or below the level of the heart, to the inferior vena cava or portal vein. Axial spin-echo acquisition almost always demonstrates the four pulmonary veins. In a series of 56 patients with various types of congenital heart disease but normal pulmonary venous connection, axial spin-echo MRI showed the sites of connection of all four pulmonary veins in 88% of cases; in a parallel series of 22 patients with partial or total anomalous pulmonary venous return, pulmonary venous anomalies were identified in 95% of cases[185] (Fig. 33–73).

Anomalies of individual pulmonary veins are rare but may be identified using MRI. Pulmonary vein stenosis may be identified by the increased intraluminal signal intensity of obstructed venous inflow to the heart.[254] Pulmonary venous varix may be identified as a dilated tubular structure confluent with the left atrium.[326]

Tetralogy of Fallot

The underlying malformation in patients with tetralogy of Fallot is the malalignment of the ventricular septal

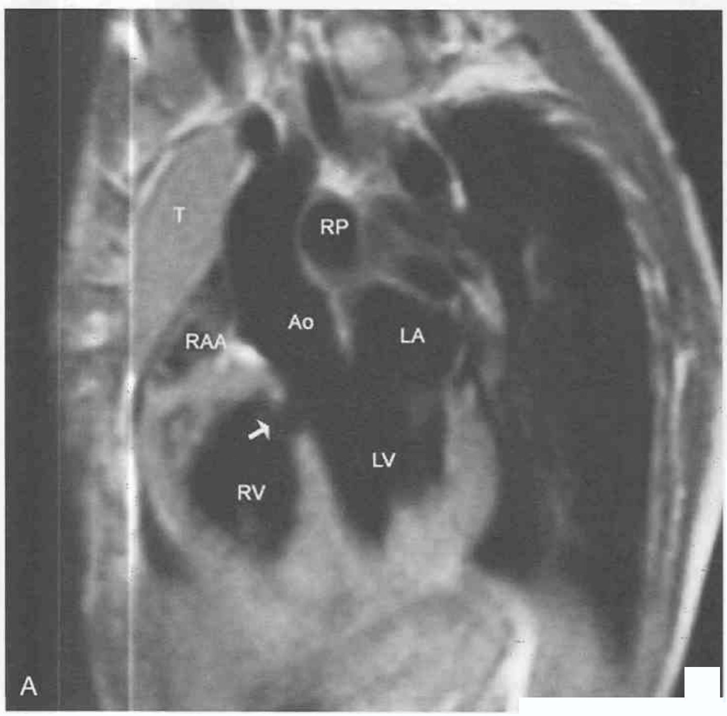

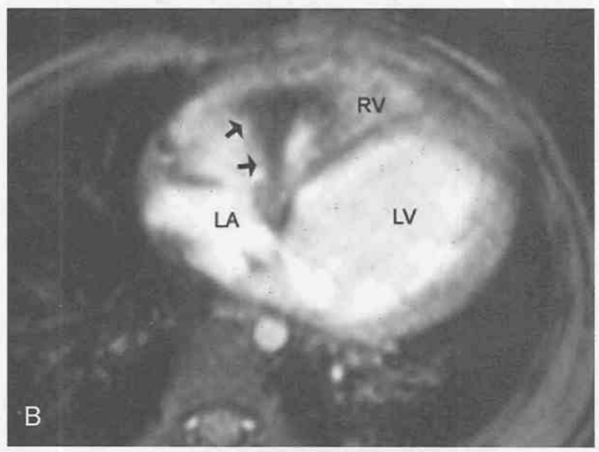

Figure 33–72. MR images obtained from a 5-year-old boy with a muscular ventricular septal defect. *A,* Oblique sagittal spin-echo acquisition through the aortic root (Ao). The defect *(arrow)* is well away from the membranous interventricular septum and the aortic annulus. LA, left atrium; RAA, right atrial appendage; RP, right pulmonary artery; RV, right ventricle; T, thymus. *B,* Systolic axial gradient-reversal acquisition through the defect shows the fan-shaped signal void jet *(arrows)* extending from the dilated left ventricle (LV), through the septum, and into the right ventricle (RV). LA, left atrium.

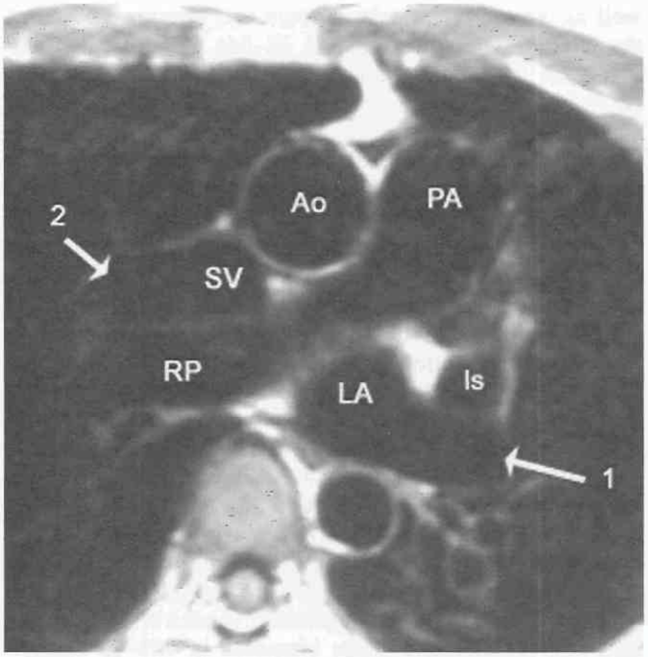

Figure 33–73. Axial spin-echo acquisition from a 23-year-old woman with a sinus venosus atrial septal defect, partial anomalous pulmonary venous return, and bilateral superior venae cavae. The main pulmonary artery (PA) and the right pulmonary artery (RP) are dilated, as is the left lower lobe pulmonary vein *(arrow 1)*. The lateral aspect of the right-sided superior vena cava (SV) is incomplete at the site of entry of the anomalous right upper lobe pulmonary vein *(arrow 2)*. Note the signal void of the left-sided superior vena cava (ls) as it enters the lateral horn of the coronary sinus. Ao, aorta; LA, left atrium.

defect. The degree to which the crista supraventricularis is malaligned determines the severity of right ventricular outflow obstruction as well as the size of the aortic root and the incidence of aortic regurgitation.[179] Aortic regurgitation is found in more than three fourths of adult patients with tetralogy of Fallot with pulmonary atresia.[45] This volume-loads both left and right ventricles but has a more significant effect on the already pressure-loaded right ventricle.

Evaluation of a patient with tetralogy of Fallot requires a series of acquisitions in different planes to characterize the severity of right ventricular outflow obstruction, the ventricular septal defect, and pulmonary morphology. Furthermore, one must assess the status of systemic-to–pulmonary artery collateral vessels and palliative surgical shunts, if present. The typically large perimembranous ventricular septal defect is usually well demonstrated in axial[198] or sagittal section (Fig. 33–74*A*). Aortic caliber and position of the aortic valve with respect to the interventricular septum are explicitly demonstrated in sagittal section (see Fig. 33–33). Slightly cephalad to the ventricular septal defect, the narrowed right ventricular outflow tract and hypertrophied infundibulum may be evaluated (Fig. 33–74*B*). Off-coronal section aids in demonstrating confluence of the pulmonary arteries as well as focal pulmonary artery stenosis (see Fig. 33–63). Addition of coronal imaging is helpful in demonstrating the presence and extent of systemic to pulmonary artery collaterals. Use of either spin-echo or gradient-echo images allows measurement of the size of the main pulmonary artery and each major branch, as well as the adequacy of the central pulmonary confluence. The most commonly used surgical shunt in these patients is a modified Blalock-Taussig shunt. MRI is effective in demonstrating the potency and defining the severity of stenosis within the shunt. Velocity-encoded cine MRI

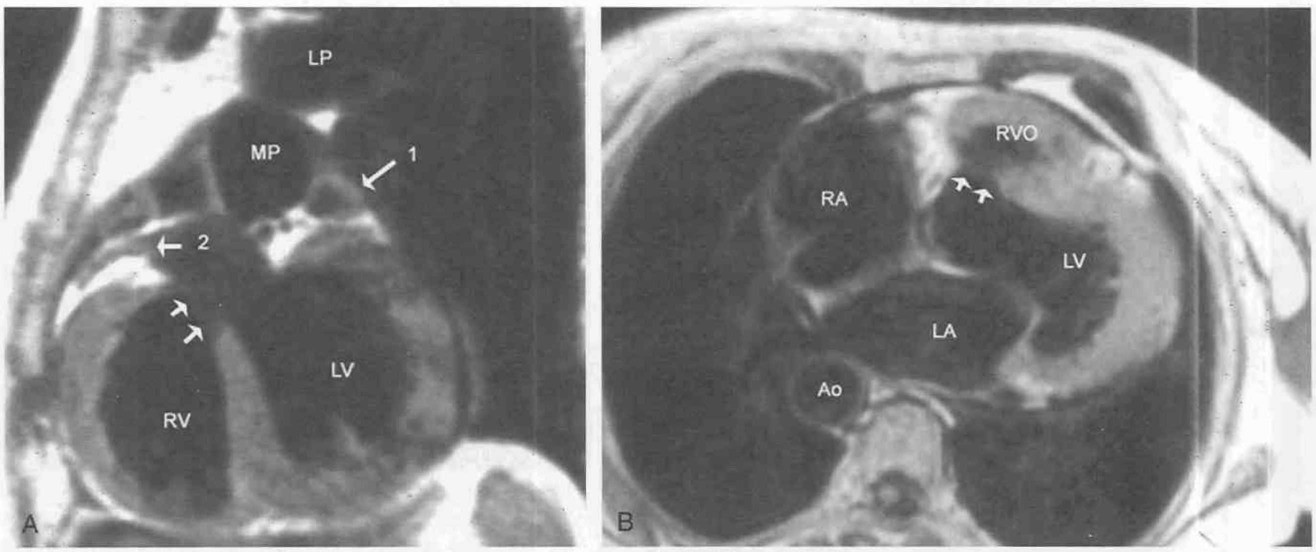

Figure 33–74. MR images obtained from a 53-year-old woman with tetralogy of Fallot. She had received palliative treatment 45 years earlier with a Blalock-Taussig shunt. *A,* Left anterior oblique sagittal spin-echo acquisition through the aortic root shows how the large subaortic ventricular septal defect (VSD) *(paired arrows)* affords communication between the hypertrophied right ventricle (RV) and the mildly dilated left ventricle (LV). The aortic root overrides the VSD. The origin of the right coronary artery *(arrow 2)* is seen. Arrow 1, left atrial appendage. *B,* Axial spin-echo acquisition obtained through the aortic valve. The anteriorly malaligned crista supraventricularis *(arrows)* causes posterior impingement on the hypertrophied right ventricular outflow (RVO) and leaves the VSD behind. Notice the right-sided descending aorta (Ao) in this patient with a mirror-image right aortic arch. LA, left atrium; LV, left ventricle; RA, right atrium.

can be used to measure flow and estimate gradients in these structures. Imaging palliative Blalock-Taussig shunts is best performed in plane with the long axis of the grafts, that is, in oblique sagittal or coronal section.

In cases of pulmonary atresia, there is increased fat deposition in the region of the atretic valve ring.[147] The main pulmonary artery may be identified (and even enlarged) if a surgical shunt procedure was performed prior to examination. More commonly, however, the pulmonary arteries are hypoplastic (Fig. 33–75). Determination of pulmonary artery continuity and exclusion of focal pulmonary artery stenosis are goals of MR examination. The right ventricular myocardium in pulmonary atresia with intact septum is markedly hypertrophied, more so than found in tetralogy of Fallot. The right ventricular cavity is small, the actual size being dependent on the size and competence of the tricuspid valve. The aorta in pulmonary atresia with ventricular septal defect as well as in tetralogy of Fallot is dilated. MR examination provides detailed anatomic information concerning the morphology of the right ventricular outflow tract, the size and course of the central pulmonary arteries, and the sources of collateral blood flow to the lungs[93, 147, 235] in these patients. Systemic-to-pulmonary artery collaterals are usually found posterior to the trachea and main bronchi. MR examination tends to underestimate their number[235] but is useful in demonstrating their origin. The site of connection with the pulmonary arterial tree is often not seen. Patency of palliative shunts may be assumed when no intraluminal signal is identified on spin-echo examination.[147, 235]

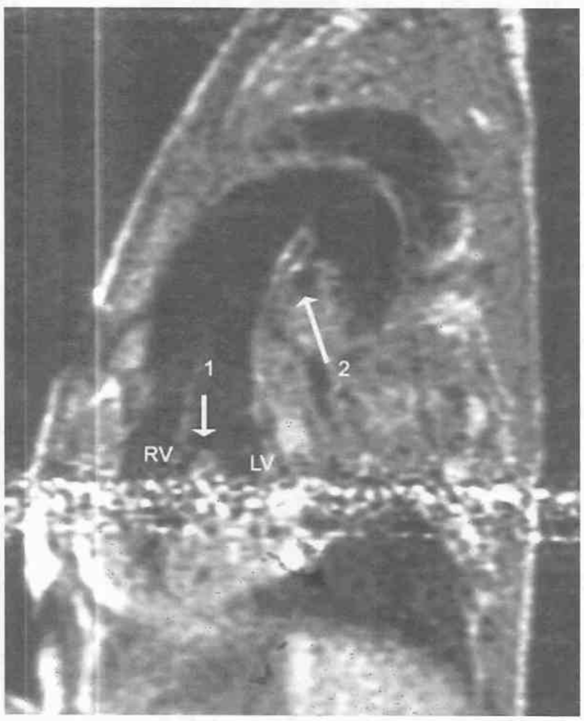

Figure 33–75. Sagittal spin-echo acquisition from a 14-month-old girl with pulmonary atresia and a ventricular septal defect (VSD). The dilated ascending aorta overrides the VSD *(arrow 1)* between the left ventricle (LV) and the hypertrophied right (RV) ventricle. The transverse right pulmonary artery *(arrow 2)* is severely hypoplastic.

In patients with tricuspid atresia, the anterior atrioventricular ring is replaced by fat,[92] and no continuity between the right atrium and right ventricle is found (Fig. 33–76). The right atrium is usually enlarged, and the right ventricle is usually smaller than normal. A large interatrial communication can usually be demonstrated. The shunt itself can be characterized using gradient-echo technique. Axial and sagittal acquisition demonstrates commonly associated lesions, including ventricular septal defect, pulmonary atresia, the relationship between the great arteries, as well as complications of elevated systemic venous pressure, such as mediastinal and pericardial venous collaterals. The results of surgical palliation by the Fontan operation may be demonstrated directly.[136, 148, 212, 217, 261, 285] In addition, application of velocity mapping techniques allows accurate assessment of conduit obstruction.[183, 234]

Univentricular Hearts

Univentricular heart is a compromise term, adopted to avoid the controversy concerning naming hearts with rudimentary ventricular chambers and unusual atrioventricular connections.[301] Generally, a double-inlet ventricle is a ventricle that fills from flow across two atrioventricular valves, or through a single ("common") atrioventricular valve.[303]

When the main chamber is morphologically left ventricular in character, the heart is labeled *double-inlet left ventricle* (the most common type); when the morphology is right ventricular in character, then the heart is named *double-inlet right ventricle.* If the main ventricular chamber cannot be characterized as either left or right ventricular, the chamber is referred to as a *common ventricle* or *ventricular chamber.*

MRI is helpful in the evaluation of patients with univentricular hearts and other complex congenital heart lesions. Direct demonstration of right or left ventricular morphology, the relationship between atrioventricular and semilunar valves, and the origins of papillary muscles all are helpful for characterizing the nature of such a ventricle. In these patients, the axial section provides the greatest amount and most reliable information about systemic and pulmonary venous return and great artery relationships. Axial and off-sagittal section provides image data for determination of atrioventricular and ventriculoarterial connections. The interventricular septum in these patients frequently takes an unusual orientation. This and the common association of atrioventricular valvular atresia often necessitate acquisition of coronal as well as off-sagittal sections.

In patients with double-inlet ventricle, both left and right atrioventricular valves empty into a dominant ventricle (Fig. 33–77). Although a rudimentary opposite chamber is usually present, it may appear only as a slit within the posterior or anterior ventricular myocardium. Isolation of the rudimentary (outflow) chamber from atrial inflow is helpful for full characterization of these lesions. In these cases, communication between dominant ventricle and rudimentary ventricular chamber is via a bulboventricular foramen, generally demonstrated in coronal or even axial section (see Fig. 33–52).

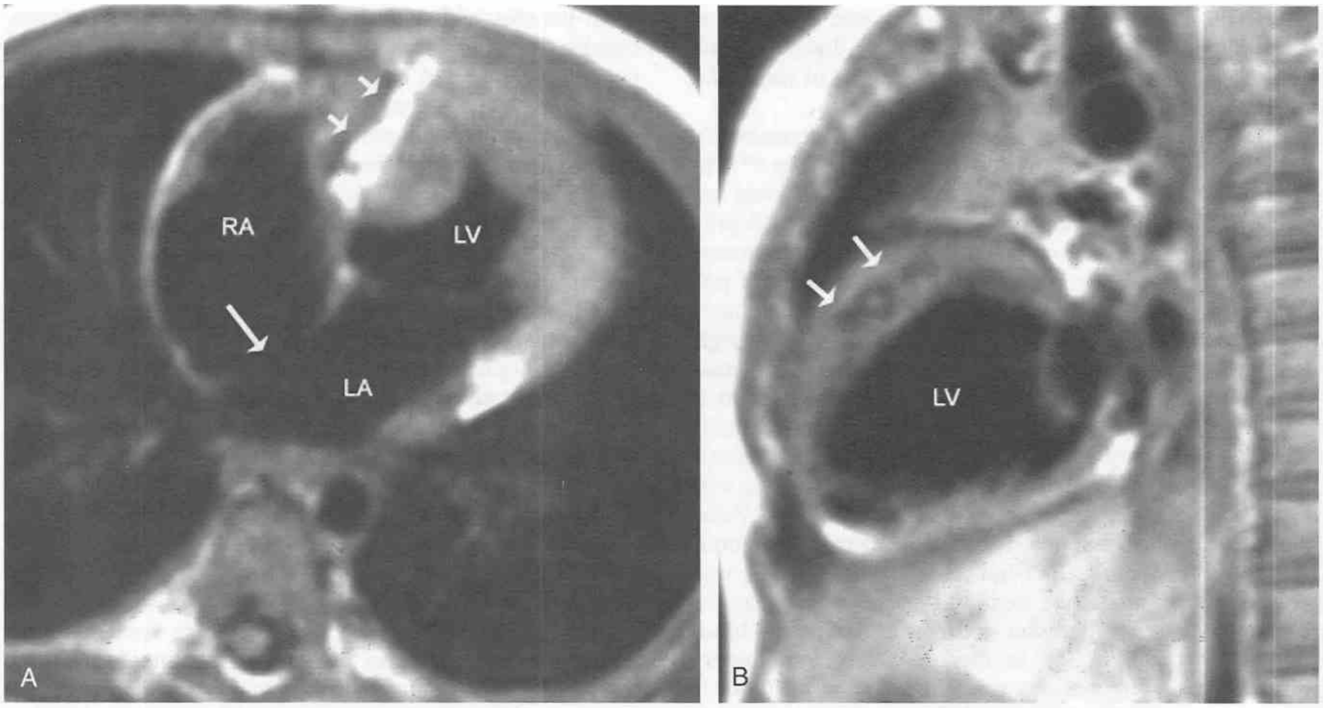

Figure 33–76. MR image obtained from a 4-year-old boy with tricuspid atresia. *A,* Axial spin-echo acquisition through the anterior atrioventricular ring *(short arrows)* shows fatty replacement in the atretic valve ring. The interatrial communication *(long arrow)* between right atrium (RA) and the left atrium (LA) is broad. Note the severe hypertrophy of the left ventricle (LV). *B,* Sagittal spin-echo acquisition through the interventricular septum. The severely hypoplastic right ventricle *(arrows)* is no more than a slit in the septum. LV, left ventricle.

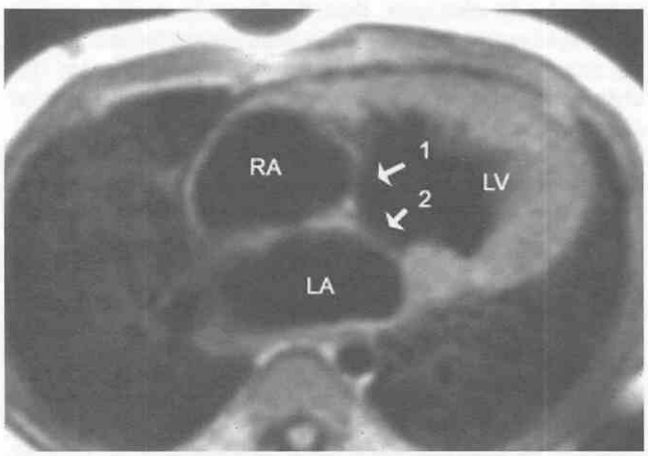

Figure 33–77. MR image obtained from a 2-year-old boy with a double-inlet left ventricle (see Fig. 33–52). Blood drains from the right atrium (RA) through the anterior atrioventricular valve *(arrow 1)* and from the left atrium (LA) through the posterior atrioventricular valve *(arrow 2)* into a dominant left ventricle (LV).

References

1. Al-Saadi N, Nagel E, Gross M, et al: Noninvasive detection of myocardial ischemia from perfusion reserve based on cardiovascular magnetic resonance. Circulation 101:1379–1383, 2000.
2. Amparo EG, Higgins CB, Farmer D, et al: Gated MRI of cardiac and paracardiac lesions. Am J Roentgenol 143:1151–1156, 1984.
3. Anderson JA, Hansen BF: Primary pericardial mesothelioma. Danish Med Bull 21:195, 1974.
4. Applegate PM, Tajik AJ, Ehman RL, et al: Two-dimensional echocardiographic and MRI observations in massive lipomatous hypertrophy of the atrial septum. Am J Cardiol 59:1151–1156, 1987.
5. Aronberg DJ, Peterson RR, Glazer HS, et al: The superior sinus of the pericardium: CT appearance. Radiology 153:489–492, 1984.
6. Atalay MK, Forder JR, Chacko VP, et al: Oxygenation in the rabbit myocardium: Assessment with susceptibility-dependent MR imaging. Radiology 189:759–764, 1993.
7. Atkinson DJ, Edelman RR: Cineangiography of the heart in a single breath hold with a segmented turboflash sequence. Radiology 178: 357–360, 1991.
8. Aufferman W, Wichter T, Breithardt G, et al: Arrhythmogenic right ventricular disease: MR imaging versus angiography. AJR Am J Roentgenol 161:549–555, 1993.
9. Axel L, Dougherty L: Heart wall motion: Improved method for spatial modulation of magnetization for MR imaging. Radiology 172:349–350, 1989.
10. Azhari H, Sideman S, Weiss JL, et al: Three-dimensional mapping of acute ischemic regions using MRI: Wall thickening versus motion analysis. Am J Physiol Heart Circ Physiol 259:28–25. 1990.
11. Baer FM, Smolarz R, Jungehulsing M, et al: Feasibility of high-dose dipyridamole MRI for detection of coronary artery disease and comparison with coronary angiography. Am J Cardiol 69:51–56, 1992.
12. Baer FM, Voth E, Schneider CA, et al: Comparison of low-dose dobutamine-gradient-echo magnetic resonance imaging and positron emission tomography with [18F]fluorodeoxyglucose in patients with chronic coronary artery disease: A functional and morphological approach to the detection of residual myocardial viability. Circulation 91:1006–1015, 1995.
13. Baer FM, Voth E, Schneider CA, et al: Comparison of low-dose dobutamine-gradient-echo magnetic resonance imaging and positron emission tomography with [18F]fluorodeoxyglucose in patients with chronic coronary artery disease: A functional and morphological approach to the detection of residual myocardial viability. Circulation 91:1006–1015, 1995.
14. Baer FM, Voth E, Theissen P, et al: Gradient-echo magnetic reso-

nance imaging during incremental dobutamine infusion for the localization of coronary artery stenoses. Eur Heart J 15:218–225, 1994.
15. Baer FM, Voth E, Theissen P, et al: Coronary artery disease: Findings with GRE MR imaging and Tc-99m-methoxyisobutyl-isonitrile SPECT during simultaneous dobutamine stress. Radiology 193:203–209, 1994.
16. Baer FM, Theissen P, Schneider CA, et al: Dobutamine magnetic resonance imaging predicts contractile recovery of chronically dysfunctional myocardium after successful revascularization. J Am Coll Cardiol 31:1040–1048, 1998.
17. Baer FM, Theissen P, Smolarz K, et al: Dobutamine versus dipyridamole-magnetic resonance imaging: Safety and sensitivity for the diagnosis of coronary artery stenosis. Z Kardiol 82:494–503, 1993.
18. Baim RS, MacDonald IL, Wise DJ, et al: Computed tomography of the absent left pericardium. Radiology 135:127–128, 1980.
19. Barakos JA, Brown JJ, Higgins CB: MR imaging of secondary cardiac and paracardiac lesions. AJR Am J Roentgenol 153:47–50, 1989.
20. Baumgartner H, Kratzer H, Helmreich G, et al: Determination of aortic valve area by Doppler echocardiography using the continuity equation: A critical evaluation. Cardiology 77:101–111, 1990.
21. Berger H, Matthay R, Loke J, et al: Assessment of cardiac performance with quantitative radionuclide angiocardiography right ventricular ejection fraction with reference to finding in chronic obstructive pulmonary disease. Am J Cardiol 41:897–905, 1978.
22. Berger-Klein J, Sochor H, Stanek G, et al: Indium-111 monoclonal antimyosin antibody and magnetic resonance imaging in the diagnosis of acute Lyme myopericarditis. Arch Intern Med 153:2692–2700, 1993.
23. Bouchard A, Higgins CB, Byrd BF III, et al: Magnetic resonance imaging in pulmonary arterial hypertension. Am J Cardiol 56:938–942, 1985.
24. Bogaert J, Bosmans H, Maes A, et al: Remote myocardial dysfunction after acute anterior myocardial infarction: Impact of left ventricular shape on regional function—a magnetic resonance myocardial tagging study. J Am Coll Cardiol 35:1525–1534, 2000.
25. Bogaert J, Maes A, Van de Werf F, et al: Functional recovery of subepicardial myocardial tissue in transmural myocardial infarction after successful reperfusion. Circulation 99:36–43, 1999.
26. Bogaert J, Rademakers FE: Regional nonuniformity of normal adult human left ventricle. Am J Physiol Heart Circ Physiol 280:H610–H620, 2001.
27. Bogaert JG, Bosmans H, Rademakers F, et al: Left ventricular quantification with breath-hold MR imaging: Comparison with echocardiography. MAGMA 3:5–12, 1995.
28. Boxer RA, Singh S, LaCorta MA, et al: Cardiac magnetic resonance imaging in children with congenital heart disease. J Pediatr 109:460–464, 1988.
29. Boxt LM, Katz J, Kolb T, et al: Direct quantitation of right and left ventricular volumes using nuclear magnetic resonance imaging in patients with primary pulmonary hypertension. J Am Coll Cardiol 19:1508–1515, 1992.
30. Bhattacharya S, Lahir A: Clinical role of indium-111 antimyosin imaging. Eur J Nucl Med 18:889–895, 1991.
31. Blake LM, Scheinman MM, Higgins CB: MR features of arrhythmogenic right ventricular dysplasia. AJR Am J Roentgenol 162:809–812, 1994.
32. Braunwald E: Myocardial reperfusion, limitation of the infarct size, reduction of left ventricular dysfunction, and improved survival: Should the paradigm be expanded? Circulation 79:441–444, 1989.
33. Braunwald E: Pathophysiology of heart failure. In Heart Disease, 4th ed. Philadelphia, WB Saunders, 1992, p 393.
34. Braunwald E, Braunwald NS, Ross J Jr, Morrow AG: Effects of mitral-valve replacement on the pulmonary vascular dynamics of patients with pulmonary hypertension. N Engl J Med 273:509–514, 1965.
35. Braunwald E, Goldblatt A, Aygen MM, et al: Congenital aortic stenosis: I. Clinical and hemodynamic findings in 100 patients. II. Surgical treatment and results of operation. Circulation 27:426–462, 1963.
36. Brenner LD, Caputo GR, Mostbeck G, et al: Quantification of left to right atrial shunts with velocity-encoded cine nuclear magnetic resonance imaging. J Am Coll Cardiol 20:1246–1250, 1992.
37. Brooks R, Burgess JH: Idiopathic ventricular tachycardia: A review. Medicine 67:271–294, 1988.
38. Brown CA, O'Connel JB: Myocarditis and idiopathic dilated cardiomyopathy. Am J Med 99:309–314, 1995.
39. Burrows B, Kettel LJ, Niden AH, et al: Patterns of cardiovascular dysfunction in chronic obstructive lung disease. N Engl J Med 286:912–918, 1972.
40. Canby RC, Reeves RC, Evanochko WT, et al: Proton nuclear magnetic resonance relaxation times in severe myocardial ischemia. J Am Coll Cardiol 10:412–420, 1987.
41. Canet E, Revel D, Forrat R, et al: Superparamagnetic iron oxide particles and positive enhancement for myocardial perfusion studies assessed by subsecond T1-weighted MRI. Magn Reson Imaging 11:1139–1145, 1993.
42. Cannon SJ, Richards KL, Crawford M: Hydraulic estimation of the stenotic orifice area: A correction of the Gorlin formula. Circulation 71:1170–1178, 1985.
43. Canter CE, Gutierrez FR, Mirowitz SA, et al: Evaluation of pulmonary arterial morphology in cyanotic congenital heart disease by magnetic resonance imaging. Am Heart J 118:347–354, 1989.
44. Canter CE, Gutierrez FR, Molina P, et al: Noninvasive diagnosis of right-sided extracardiac conduit obstruction by combined magnetic resonance imaging and continuous-wave Doppler echocardiography. J Thorac Cardiovasc Surg 101:724–731, 1991.
45. Capelli H, Ross D, Somerville J: Aortic regurgitation in tetralogy of Fallot and pulmonary atresia. Am J Cardiol 49:1979–1983, 1982.
46. Caputo GR, Sechtem U, Tscholakoff D, Higgins CB: Measurement of myocardial infarct size at early and late time intervals using MR imaging: An experimental study in dogs. AJR Am J Roentgenol 149:237–243, 1987.
47. Carabello BA: Mitral regurgitation: Basic pathophysiologic principles: I. Mod Concepts Cardiovasc Dis 57:53–58, 1988.
48. Carlsson E, Gross R, Hold RG: The radiologic diagnosis of cardiac valvular insufficiencies. Circulation 55:921–933, 1977.
49. Carlson MD, White RD, Trohman RG, et al: Right ventricular outflow tract tachycardia: Detection of previously unrecognized anatomic abnormalities using cine magnetic resonance imaging. J Am Coll Cardiol 24:720–727, 1994.
50. Cigarroa CG, de Filippi C, Brickner ME, et al: Dobutamine stress echocardiography identifies hibernating myocardium and predicts recovery of left ventricular function after coronary revascularization. Circulation 88:430–436, 1993.
51. Chandra M, Silverman ME, Oshinski J, Pettigrew R: Diagnosis of cardiac sarcoid aided by MRI. Chest 110:524–526, 1996.
52. Chandrarama PA, Bradley WG, Kortman KE, et al: Detection of acute myocarditis using nuclear magnetic resonance imaging. Am J Med 83:1144–1146, 1987.
53. Cherryman GR, Tranter J, Keal R, et al: Prospective comparison of contrast-enhanced MRI with thallium 201 SPECT and 2D echocardiography in the localization of acute myocardial infarction. In: Proceedings of International Society for Magnetic Resonance in Medicine. Sixth Scientific Meeting and Exhibition. Sydney, Australia, April 18–24, 1998, p 923.
54. Chesler E, Matha AS, Matisonn RE, Rogers MNA: Subpulmonic stenosis as a result of noncalcific pericarditis. Chest 69:425–427, 1976.
55. Chiles C, Baker ME, Silverman PM: Superior pericardial recess simulating aortic dissection on computed tomography. J Comput Assisr Tomogr 10:421–423, 1986.
56. Choi SH, Choi SH, Kim ST, et al: Irreversibly damaged myocardium at MR imaging with a necrotic tissue–specific contrast agent in a cat model. Radiology 215:863–868, 2000.
57. Chronic cor pulmonale: Report of an expert committee. World Health Organiz Tech Rep Serv 213:1, 1961.
58. Cohen JL: Neoplastic pericarditis. Cardiovasc Clin North Am 7:257–269, 1976.
59. Collins-Nakai RL, Rosenthal A, Casteneda AR, et al: Congenital mitral stenosis: A review of twenty years' experience. Circulation 56:1039–1047, 1977.
60. Connolly HM, Crary JL, McGoon MD, et al: Valvular heart disease associated with fenfluramine-phenteramine. N Engl J Med 337:581–588, 1997.
61. Corrigan TP, Fossard DP, Spindler P, et al: Phlebography in the management of pulmonary embolism. Br J Surg 61:484–488, 1974.
62. Croft CH, Lipscomb K, Mathis K, et al: Limitations of qualitative angiographic grading in aortic or mitral regurgitation. Am J Cardiol 53:1593–1598, 1984.

63. Croisille P, Moore CC, Judd RM, et al: Differentiation of viable and nonviable myocardium by the use of three-dimensional tagged MRI in 2-day-old reperfused canine infarcts. Circulation 99:284–291, 1999.
64. Culham JAG, Vince DJ: Cardiac output by MR imaging: An experimental study comparing right ventricle and left ventricle with thermodilution. Can Assoc Radiol J 39:247–249, 1988.
65. Cullen JH, Horsfield MA, Reek CR, et al: A myocardial perfusion reserve index in humans using first-pass contrast-enhanced magnetic resonance imaging. J Am Coll Cardiol 33:1386–1394, 1999.
66. Cullen JH, Kaemmerlen JT, Daoud A, Katz HL: A prospective clinical pathologic study of the lungs and heart in chronic obstructive lung disease. Am Rev Respir Dis 102:190–204, 1970.
67. Dalen JE, Banas JS Jr, Brooks HL, et al: Resolution rate of acute pulmonary embolism in man. N Engl J Med 280:1194–1199, 1969.
68. Daliento L, Turrini P, Nava A, et al: Arrhythmogenic right ventricular cardiomyopathy in young versus adult patients: Similarities and differences. J Am Coll Cardiol 25:655–664, 1995.
69. Deloran L, Thurber MD, Jesse E, et al: Secondary malignant tumors of the pericardium. Circulation 26:228–241, 1962.
70. Denfield SW, Garson A Jr: Sudden death in children and young adults. Pediatr Clin North Am 37:215–231, 1990.
71. deRoos A, Reichek N, Axel L, Kressel HW: Cine MR imaging in aortic stenosis. J Comp Asst Tomog 13:421–425, 1989.
72. Diethelm L, Dery R, Lipton MJ, Higgins CB: Atrial level shunts: Sensitivity and specificity of MR in diagnosis. Radiology 162: 181–186, 1987.
73. Didier D, Higgins CB: Estimation of pulmonary vascular resistance by MRI in patients with congenital cardiovascular shunt lesions. Am J Roentgenol 147:1127–1131, 1986.
74. Didier D, Higgins CB: Identification and localization of ventricular septal defect by gated magnetic resonance imaging. Am J Cardiol 57:1363–1368, 1986.
75. Didier D, Ratib O, Lerch R, Friedli B: Detection and quantification of valvular heart disease with dynamic cardiac MR imaging. Radiographics 20:1279–1299, 2000.
76. Dines DE, Edwards JE, Burchell WB: Myocardial atrophy in constrictive pericarditis. Mayo Clinic Proc 33:93–99, 1958.
77. Doherty NE, Seelos KC, Suzuki JI, et al: Application of cine NMR imaging for sequential evaluation of response to angiotensin-converting enzyme inhibitor therapy in dilated cardiomyopathy. J Am Coll Cardiol 19:1294–1302, 1992.
78. Dong SJ, MacGregor JH, Crawley AP, et al: Left ventricular wall thickness and regional function in patients with hypertrophic cardiomyopathy: A three-dimensional tagged magnetic resonance imaging study. Circulation 90:1200–1209, 1994.
78a. Dorfman DF, Cronan JJ, Tupper TB, et al: Occult pulmonary embolism: A common occurrence in deep venous thrombosis. Am J Roentgenol 148:263–266, 1987.
79. Duerinckx AJ, Urman MK: Two-dimensional coronary MR angiography: Analysis of initial clinical results. Radiology 193:731–738, 1994.
80. Dulce MC, Duerinckx AJ, Hartiala J, et al: MR imaging of the myocardium using nonionic contrast medium: Signal-intensity changes in patients with subacute myocardial infarction. AJR Am J Roentgenol 160:963–970, 1993.
81. Edelman RR, Li W: Contrast-enhanced echo-planar MR imaging of myocardial perfusion: Preliminary study in humans. Radiology 190: 771–777, 1994.
82. Eichenberger AC, Schuiki E, Kochli VD, et al: Ischemic heart disease: Assessment with gadolinium-enhanced ultrafast MR imaging and dipyridamole stress [see comments]. J Magn Reson Imaging 4:425–431, 1994.
83. Factor SM, Okun EM, Kirk ES: The histological lateral border of the acute canine myocardial infarction. Circ Res 46:640–649, 1981.
84. Fattori R, Rocchi G, Celetti F, et al: Contribution of magnetic resonance imaging in the differential diagnosis of cardiac amyloidosis and symmetric hypertrophic cardiomyopathy. Am Heart J 136:824–830, 1998.
85. Fazio S, Sabatini D, Capaldo B, et al: A preliminary study of growth hormone in the treatment of dilated cardiomyopathy. N Engl J Med 334:809–814, 1996.
86. Feiglin DH, George CR, MacIntyre WJ, et al: Gated cardiac magnetic resonance structural imaging: Optimization by electronic axial rotation. Radiology 154:129–132, 1985.
87. Fenoglio JJ, McAlister HA Jr, DeCastro CM, et al: Congenital bicuspid aortic valve after age 20. Am J Cardiol 39:164–169, 1977.
88. Firmin DN, Nayler GL, Kilner PJ, et al: The application of phase shifts in NMR for flow measurements. Magn Reson Med 14:230–241, 1990.
89. Fisher MR, Higgins CB: Central thrombi in pulmonary arterial hypertension detected by MR imaging. Radiology 158:223–226, 1986.
90. Fishman A: Chronic cor pulmonale. Am Rev Respir Dis 114:775–794, 1976.
91. Fishman A: Pulmonary hypertension and cor pulmonale. In Fishman A (ed): Pulmonary Diseases and Disorders, 2nd ed. New York, McGraw-Hill, 1988, pp 999–1048.
92. Fletcher BD, Jacobstein MD, Abramowsky CR, Anderson RH: Right atrioventricular valve atresia: Anatomic evaluation with MR imaging. AJR Am J Roentgenol 148:671–674, 1987.
93. Formanek AG, Witcofski RL, D'Souza VJ, et al: MR imaging of the central pulmonary arterial tree in conotruncal malformation. Am J Roentgenol 147:1127–1131, 1986.
94. Frank H, Globits S, Glogar D, et al: Detection and quantification of pulmonary hypertension with MR imaging: Results in 23 patients. AJR Am J Roentgenol 161:27–31, 1993.
95. Frank JA, Feller MA, House WV, et al: Measurement of proton nuclear magnetic longitudinal relaxation times and water content in infarcted canine myocardium and induced pulmonary injury. Clin Res 24:217A–223A, 1976.
96. Frank S, Weg J, Harkleroad L, et al: Pulmonary dysfunction in rheumatoid disease. Chest 63:27–33, 1973.
97. Freidrich MG, Strom O, Schultz-Menger J, et al: Contrast media–enhanced magnetic resonance imaging of viral myocarditis. Circulation 97:1802–1809, 1998.
98. Frustaci A, Bellocci F, Olsen EG: Results of biventricular endomyocardial biopsy in survivors of cardiac arrest with apparently normal hearts. Am J Cardiol 74:890–895, 1994.
99. Fudjita N, Hartiala J, O'Sullivan M, et al: Assessment of left ventricular diastolic function in dilated cardiomyopathy with cine MRI: Effect on an angiotensin-converting enzyme inhibitor, benazepril. Am Heart J 125:171–177, 1993.
100. Gagliardi MG, Bevilaqua M, DiRienzi P, et al: Usefulness of magnetic resonance imaging for the diagnosis of acute myocarditis in infants and children and in comparison with endomyocardial biopsy. Am J Cardiol 68:1089–1091, 1991.
101. Manyari D, Klein G, Gulamhusein S: Arrhythmogenic right ventricular dysplasia: A generalized cardiomyopathy? Circulation 68:251–257, 1983.
102. Gaudio C, Pellicula F, Tanzilli G, et al: Magnetic resonance imaging for assessment of apical hypertrophy in hypertrophic cardiomyopathy. Clin Cardiol 15:164–168, 1992.
103. Gefter WB, Hatabu H, Dinsmore BJ, et al: Pulmonary vascular cine MR imaging: A noninvasive approach to dynamic imaging of the pulmonary circulation. Radiology 176:761–770, 1990.
104. Genovese PD, Rosenbaum D: Pulmonary stenosis with survival to the age of 78 years. Am Heart J 41:755–761, 1951.
105. Geva T, Vick GW III, Wendt RE, Rokey R: Role of spin-echo and cine magnetic resonance imaging in the presurgical planning of heterotaxy syndrome. Circulation 90:348–356, 1994.
106. Glazer GM, Gross BH, Orringer MB, et al: Computed tomography on pericardial masses: Further observations and comparison with echocardiography. J Comput Assist Tomogr 8:895–899, 1984.
107. Globits S, Blake L, Bourne M, et al: Assessment of hemodynamic effects on angiotensin-converting enzyme inhibitor therapy in chronic aortic regurgitation by using velocity-encoded cine magnetic resonance imaging. Am Heart J 131:289–293, 1996.
108. Goldfarb JW, Edelman RR: Coronary arteries: Breath-hold, gadolinium-enhanced, three-dimensional MR angiography. Radiology 206: 830–834, 1998.
109. Gomes AS, Lois JF Jr, Williams RG: Pulmonary arteries: MR imaging in patients with congenital obstruction of the right ventricular outflow tract. Radiology 174:51–57, 1990.
110. Gorlin R: The mechanism of the signs and symptoms of mitral valve disease. Br Heart J 16:375–380, 1954.
111. Gorlin R, Gorlin SG: Hydraulic formula for calculation of the area of the stenotic mitral valve, other cardiac valves, and the central circulatory shunts. Am Heart J 41:1–29, 1951.
112. Gould KL: Myocardial viability: What does it mean and how to measure it? Circulation 83:333–335, 1991.

113. Greene DG, Baldwin ED, Baldwin JS, et al: Pure congenital pulmonary stenosis and idiopathic dilation of the pulmonary artery. Am J Med 6:24–40, 1949.
114. Griffith MJ, Carey C, Coltard DJ, et al: Inaccuracies in using aortic valve gradients alone to grade severity of aortic stenosis. Br Heart J 62:372–378, 1989.
115. Grossman W, Jones D, McLaurin LP: Wall stress and patterns of hypertrophy in the human left ventricle. J Clin Invest 56:56–64, 1975.
116. Grossman W, McLaurin LP, Rolett EL: Alterations in left ventricular relaxation and diastolic compliance in dilated cardiomyopathy. Cardiovasc Res 13:514–522, 1979.
117. Guit GL, Bluemm R, Rohmer J, et al: Levotransposition of the aorta: Identification of segmental cardiac anatomy using MR imaging. Radiology 161:673–679, 1986.
118. Guttierez RF, Shackelford GD, McKnight RC, et al: Diagnosis of congenital absence of left pericardium by MR imaging. J Comput Assist Tomogr 9:551–553, 1985.
119. Haase A, Frahm J, Matthaei D, et al: FLASH imaging: Rapid NMR imaging using low flip-angle pulses. J Magn Reson 67:258–266, 1986.
120. Hartnell G, Cerel A, Kamalesh M, et al: Detection of myocardial ischemia: Value of combined myocardial perfusion and cineangiographic MR imaging. AJR Am J Roentgenol 163:1061–1067, 1994.
121. Havig O: Source of pulmonary emboli. Acta Chir Scand 478(suppl): 42–47, 1977.
122. Heath D: Pathology of cardiac tumors. Am J Cardiol 21:315–327, 1968.
123. Hess OM, Osakada G, Lavelle JF, et al: Diastolic myocardial wall stiffness and ventricular relaxation during partial and complete coronary occlusions in the conscious dog. Circ Res 52:387–400, 1983.
124. Higgins CB, Herfkens R, Lipton MJ, et al: Nuclear magnetic resonance imaging of acute myocardial infarction in dogs: Alterations in magnetic relaxation times. Am J Cardiol 52:184–190, 1983.
125. Hirschfel SS, Fleming DG, Doershuk C, et al: Echocardiographic abnormalities in patients with cystic fibrosis. Chest 75:351–355, 1979.
126. Hofman MBM, Henson RE, Kovacs SJ, et al: Blood pool agent strongly improves magnetic resonance coronary angiography using an inversion pre-pulse. Magn Res Med 41:360–367, 1999.
127. Holen J, Aaslid R, Ladmark K, et al: Determination of pressure gradient in mitral stenosis with a noninvasive ultrasound Doppler technique. Acta Med Scand 199:455–460, 1976.
128. Holman ER, Buller VGM, de Roos A, et al: Detection and quantification of dysfunctional myocardium by magnetic resonance imaging: A new three-dimensional method for quantitative wall-thickening analysis. Circulation 95:924–931, 1997.
129. Holman ER, van Rossum AC, Doesburg T, et al: Assessment of acute myocardial infarction in man with magnetic resonance imaging and the use of new paramagnetic contrast-agent gadolinium-BOPTA. Mag Reson Imaging 14:21–29, 1996.
130. Holman ER, Vliegen HW, van der Geest RJ, et al: Quantitative analysis of regional left ventricular function after myocardial infarction in the pig assessed with cine magnetic resonance imaging. Magn Reson Med 34:161–169, 1995.
131. Hundley WG, Hamilton CA, Thomas MS, et al: Utility of fast cine magnetic resonance imaging and display for the detection of myocardial ischemia in patients not well suited for second harmonic stress echocardiography. Circulation 100:1697–1702, 1999.
132. Hunninghake G, Fauci A: Pulmonary involvement in the collagen vascular diseases. Am Rev Respir Dis 119:471–503, 1979.
133. Hunter GJ, Hamberg LM, Weisskoff RM, et al: Measurement of stroke volume and cardiac output with a single breath-hold with echo-planar MR imaging. J Magn Reson Imaging 4:51–58, 1994.
134. Im J-G, Rosen A, Webb WR, Gamsu G: MR imaging of the transverse sinus of the pericardium. AJR Am J Roentgenol 150: 79–84, 1988.
135. Jacobstein MD, Fletcher BD, Goldstein S, Riemender TA: Evaluation of atrioventricular septal defect by magnetic resonance imaging Am J Cardiol 55:1158–1161, 1985.
136. Jacobstein MD, Fletcher BD, Nelson AD, et al: Magnetic resonance imaging: Evaluation of palliative systemic-pulmonary artery shunts. Circulation 70:650–656, 1984.
137. Johnson DE, Vacek J, Gollub SB, et al: Comparison of gated cardiac magnetic resonance imaging and two-dimensional echocardiography for the evaluation of right ventricular thrombi: A case report with autopsy correlation. Cathet Cardiovasc Diagn 14:266–268, 1988.
138. Johnston DL, Brady TJ, Ratner AV, et al: Assessment of myocardial ischemia with magnetic resonance: Effects of a three-hour coronary occlusion with and without reperfusion. Circulation 71:595–560, 1985.
139. Josephson ME, Horowitz LN, Waxman HL, et al: Sustained ventricular tachycardia: Role of the 1-lead electrocardiogram in localizing site of origin. Circulation 64:257–272, 1981.
140. Kaminsky MF, Rodan BA, Osborne DR, et al: Post-pericardiectomy syndrome. Am J Roentgenol 138:503–508, 1982.
141. Katz J, Milliken MC, Stray-Grundersen J, et al: Estimation of human myocardial mass with MR imaging. Radiology 169:495–498, 1988.
142. Katz J, Whang J, Boxt LM, Barst RJ: Estimation of right ventricular mass in normal subjects and patients with primary pulmonary hypertension by nuclear magnetic resonance imaging. J Am Coll Cardiol 21:1475–1481, 1993.
143. Kawada N, Sakuma H, Yamakado T, et al: Hypertrophic cardiomyopathy: MR measurement of coronary blood flow and vasodilator flow reserve in patients and healthy subjects. Radiology 211:129–135, 1999.
144. Kelbaek H, Aldershvile J, Svendsen JH, et al: Combined first-pass and equilibrium radionuclide cardiographic determination of stroke volume for quantification of valvular regurgitation. J Am Coll Cardiol 11:769–773, 1988.
145. Kelminson LL, Cotton EK, Vogel JHK: The reversibility of pulmonary hypertension in patients with cystic fibrosis. Pediatrics 39: 24–35, 1967.
146. Kersting-Sommerhoff BA, Sechtem U, Fisher MR, et al: MR imaging of congenital anomalies of the aortic arch. Am J Roentgenol 143:1192–1194, 1984.
147. Kersting-Sommerhoff BA, Sechtem UP, Higgins CB: Evaluation of pulmonary blood supply by nuclear magnetic resonance imaging in patients with pulmonary atresia. J Am Coll Cardiol 11:166–171, 1988.
148. Kersting-Sommerhoff BA, Seelos KC, Hardy C, et al: Evaluation of surgical procedures for cyanotic congenital heart disease by using MR imaging. AJR Am J Roentgenol 155:259–266, 1990.
149. Kessler W, Laub G, Achenbach S, et al: Coronary arteries: MR angiography with fast contrast-enhanced three-dimensional breath-hold imaging: Initial experience. Radiology 210:566–572, 1999.
150. Kilner PJ, Firmin DN, Reese RSO, et al: Valve and great vessel stenosis: Assessment with MR jet velocity mapping. Radiology 178: 229–235, 1991.
151. Kilner PJ, Manzara CC, Mohiaddin RH, et al: Magnetic resonance jet velocity mapping in mitral and aortic valve stenosis. Circulation 87:1239–1248, 1993.
152. Klein MA, Collier BD, Hellman RS, Bamrah VS: Detection of chronic coronary artery disease: Value of pharmacologically stressed, dynamically enhanced turbo-fast low-angle shot MR images. AJR Am J Roentgenol 161:257–263, 1993.
153. Kleinhans E, Altehoefer C, Arnold C, et al: MRI measurements of left ventricular systolic wall thickening compared to regional myocardial perfusion as determined by 201Tl SPECT in patients with coronary artery disease. Nuklearmedizin 30:61–66, 1991.
154. Kraitchman DL, Wilke N, Hexeberg E, et al: Myocardial perfusion and function in dogs with moderate coronary stenosis. Magn Reson Med 35:771–780, 1996.
155. Kramer CM, Ferrari VA, Rogers WJ, et al: Angiotensin-converting enzyme inhibition limits dysfunction in adjacent noninfarcted regions during left ventricular remodeling. J Am Coll Cardiol 27: 211–217, 1996.
156. Kramer CM, Lima JA, Reichek N, et al: Regional differences in function within noninfarcted myocardium during left ventricular remodeling. Circulation 88:1279–1288, 1993.
157. Kramer CM, Reichek N, Ferrari VA, et al: Regional heterogeneity of function in hypertrophic cardiomyopathy. Circulation 90:186–194, 1994.
158. Kramer CM, Rogers WJ, Theobald TM, et al: Remote noninfarcted region dysfunction soon after first anterior myocardial infarction: A magnetic resonance tagging study. Circulation 94:660–666, 1996.
159. Kriegshauser JS, Julsrud PR, Lund JT: MR imaging of fat in and around the heart. AJR Am J Roentgenol 155:271–274, 1990.
160. Lanzer P, Barta C, Botvinick EH, et al: ECG-synchronized cardiac MR imaging: Method and evaluation. Radiology 155:681–686, 1985.

161. Lanzer P, Botvinick EH, Schiller NB, et al: Cardiac imaging using gated magnetic resonance. Radiology 150:121–127, 1984.
162. Leagus CS, Gregorski RF, Grittenden JJ, et al: Giant intrapericardial bronchogenic cyst: A case report. J Thorac Cardiovas Surg 52: 581–587, 1966.
163. Lee WH, Fisher J: Right ventricular diastolic disorders. Arch Intern Med 143:332–337, 1983.
164. Lev M, Liberthson RR, Joseph RH, et al: The pathologic anatomy of Ebstein's disease. Arch Pathol 90:334–343, 1970.
165. Levy-Ravetch M, Auh YH, Rubenstein WA, et al: CT of the pericardial recesses. Am J Roentgenol 144:707–714, 1985.
166. Li D, Dolan RP, Walovitch RC, Lauffer RB: Three-dimensional MRI of coronary arteries using an intravascular contrast agent. Magn Res Med 39:1014–1018, 1998.
167. Li D, Paschal CB, Haacke EM, Adler LP: Coronary arteries: Three-dimensional MR imaging with fat saturation and magnetization transfer contrast. Radiology 187:401–406, 1993.
168. Lieberman JM, Alfidi RJ, Nelson AD, et al: Gated magnetic resonance imaging of the normal and diseased heart. Radiology 152: 465–470, 1984.
169. Lobo FV, Heggtveit HA, Butany J, et al: Right ventricular dysplasia: Morphological findings in 13 cases. Can J Cardiol 8:261–268, 1992.
170. Longmore DB, Klipstein RH, Underwood SR, et al: Dimensional accuracy of magnetic resonance in studies of the heart. Lancet 1: 1360–1362, 1985.
171. Lopez-Beret P, Pinto JM, Romero A, et al: Systematic study of occult pulmonary thromboembolism in patients with deep venous thrombosis. J Vasc Surg 33:515–521, 2001.
172. Lorenz CH, Walker ES, Morgan VL, et al: Normal human right and left ventricular mass, systolic function, and gender differences by cine magnetic resonance imaging. J Cardiovasc Magn Reson 1: 7–21, 1999.
173. Lund JT, Ehman RL, Julsrud PR, et al: Cardiac masses: Assessment by MR imaging. AJR Am J Roentgenol 152:469–473, 1989.
174. Maier SE, Fischer SE, McKinnon GC, et al: Evaluation of left ventricular segmental wall motion in hypertrophic cardiomyopathy with myocardial tagging. Circulation 86:1918–1926, 1992.
175. Manning WJ, Atkinson DJ, Parker JA, Edelman RR: Assessment of intracardiac shunts with gadolinium-enhanced ultrafast MR imaging. Radiology 184:357–361, 1992.
176. Manning WJ, Li W, Boyle NG, Edelman RR: Fat-suppressed breath-hold magnetic resonance coronary arteriography. Circulation 87: 94–104, 1993.
177. Manning WJ, Li W, Edelman RR: A preliminary report comparing magnetic resonance coronary angiography with conventional angiography. N Engl J Med 328:828–832, 1993.
177a. Manyari D, Klein G, Gulamhusein S: Arrhythmogenic right ventricular dysplasia: A generalized cardiomyopathy? Circulation 68: 251–275, 1983.
178. Marcus FI, Fontaine GH, Guiraudon G, et al: Right ventricular dysplasia: A report of 24 adult cases. Circulation 65:384–398, 1982.
179. Marelli AJ, Perloff JK, Child JS, Laks H: Pulmonary atresia with ventricular septal defect in adults. Circulation 89:243–251, 1994.
180. Markiewicz W, Sechtem U, Higgins CB: Evaluation of the right ventricle by magnetic resonance imaging. Am Heart J 113:8–15, 1987.
181. Markiewicz W, Sechtem U, Kirby R, et al: Measurement of ventricular volumes in the dog by nuclear magnetic resonance imaging. J Am Coll Cardiol 10:170–177, 1987.
182. Martin RP, Rakowski H, Kleiman JH, et al: Reliability and reproducibility of two-dimensional echocardiographic measurement of the stenotic mitral valve orifice area. Am J Cardiol 43:560–568, 1979.
183. Martinez JE, Mohiaddin RH, Kilner PJ, et al: Obstruction in extracardiac ventriculopulmonary conduits: Value of nuclear magnetic resonance imaging with velocity mapping and Doppler echocardiography. J Am Coll Cardiol 20:338–344, 1992.
184. Masui T, Finck S, Higgins CB: Constrictive pericarditis and restrictive cardiomyopathy: Evaluation with MR imaging. Radiology 182: 369–373, 1992.
185. Masui T, Seelos KC, Kersting-Sommerhoff BA, Higgins CB: Abnormalities of the pulmonary veins: Evaluation with MR imaging and comparison with cardiac angiography and echocardiography. Radiology 181:645–649, 1991.
186. Matheijssen NA, Louwerenburg HW, van Rugge FP, et al: Comparison of ultrafast dipyridamole magnetic resonance imaging with dipyridamole SestaMIBI SPECT for detection of perfusion abnormalities in patients with one-vessel coronary artery disease: Assessment by quantitative model fitting. Magn Reson Med 35:221–228, 1996.
187. Matheijssen NAA, De Roos A, Van der Wall EE, et al: Acute myocardial infarction: Comparison of T2-weighted and T1-weighted gadolinium-DTPA–enhanced MR imaging. Magn Reson Med 17: 460–469, 1991.
188. Matsouka H, Hamada M, Honda T, et al: Precise assessment of myocardial damage associated with secondary cardiomyopathies by use of Gd-DTPA enhanced magnetic resonance imaging. Angiology 44:945–950, 1993.
189. Matsouka H, Hamada M, Honda T, et al: Evaluation of acute myocarditis and pericarditis by Gd-DTPA enhanced magnetic resonance imaging. Eur Heart J 15:283–284, 1994.
190. Mazer MJ, Carroll FE, Falke THM: Practical aspects of gated magnetic resonance imaging of the pulmonary artery. J Thorac Imaging 3:73–84, 1988.
191. McAllister A, Fenoglio JJ: Tumors of the cardiovascular system. In Atlas of Tumor Pathology, fascicle 15, series 2. Washington, DC, Armed Forces Institute of Pathology, 1978.
192. McGowan GA, Sapiro EP, Azhari H, et al: Noninvasive measurement of shortening in the fiber and cross-fiber direction in the normal human left ventricle and idiopathic dilated cardiomyopathy. Circulation 96:535–541, 1997.
193. McIntyre KM, Sasahara AA: The hemodynamic response to pulmonary embolism in patients without prior cardiopulmonary disease. Am J Cardiol 28:288–294, 1971.
194. McMurdo KK, Webb WR, von Schulthess GK, Gamsu G: Magnetic resonance imaging of the superior pericardial recesses. Am J Roentgenol 145:985–988, 1985.
195. McNamara MT, Higgins CB, Schechtmann N, et al: Detection and characterization of acute myocardial infarction in man with use of gated magnetic resonance. Circulation 71:717–724, 1985.
196. Meziane MA, Fishman EK, Siegelman SS: CT diagnosis of hemopericardium in acute dissecting aneurysm of the thoracic aorta. J Comput Assist Tomogr 8:10–14, 1984.
197. Mirowitz SA, Gutierrez FR: Fibromuscular elements of the right atrium: Pseudomass at MR imaging. Radiology 182:231–233, 1992.
198. Mirowitz SA, Gutierrez FR, Canter CE, Vannier MW: Tetralogy of Fallot: MR findings. Radiology 171:207–212, 1989.
199. Mitchell L, Jenkins JPR, Watson Y, et al: Diagnosis and assessment of mitral and aortic valve disease by cine-flow magnetic resonance imaging. Magn Reson Med 12:181–197, 1989.
200. Mitchell RS, Stanford RE, Silvers GW, Dart G: The right ventricle in chronic airway obstruction: A clinicopathologic study. Am Rev Respir Dis 114:147–154, 1976.
201. Modelvang J, Stockholm KH, Saunamaki K, et al: Assessment of left ventricular volumes by magnetic resonance in comparison with radionuclide angiography, contrast angiography, and echocardiography. Eur Heart J 13:1677–1683, 1992.
202. Mogelvang J, Stubgaard M, Thomsen C, et al: Evaluation of right ventricular volumes measured by magnetic resonance imaging. Eur Heart J 9:529–533, 1988.
203. Mogelvang J, Thomsen C, Horn T, et al: Determination of left ventricular myocardial volume (mass) by magnetic resonance imaging. Am J Noninvas Cardiol 1:231–236, 1987.
204. Mogelvang J, Thomsen C, Mehlsen J, et al: Evaluation of left ventricular volumes measured by magnetic resonance imaging. Eur Hear J 7:1016–1021, 1986.
205. Mogelvang J, Thomsen C, Mehlsen J, et al: Left ventricular ejection fraction determined by magnetic resonance imaging and gated radionuclide ventriculography. Am J Noninvas Cardiol 1:278–283, 1987.
206. Moller JH, Nakib A, Elliot RS, Edwards JE: Symptomatic congenital aortic stenosis in the first year of life. J Pediatr 69:728–734, 1966.
207. Morguet AJ, Munz DL, Kreuzer H, et al: Scintigraphic detection of inflammatory heart disease. Eur J Nucl Med 21:666–674, 1994.
208. Morin DP, Cottrill CM, Johnson GL, et al: Effect of respiration on the echocardiogram in children with cystic fibrosis. Pediatrics 65: 44–49, 1980.
209. Moser KM, Spragg RG, Utley J, et al: Chronic thrombotic obstruction of major pulmonary arteries: results of thromboendarterectomy in 15 patients. Ann Intern Med 99:299–305, 1983.
210. Nagel E, Lehmkuhl HB, Bocksch W, et al: Noninvasive diagnosis of ischemia-induced wall motion abnormalities with the use of high-

dose dobutamine stress MRI: Comparison with dobutamine stress echocardiography Circulation 99: 763–770, 1999.
211. Nava A, Thiene G, Canciani B, et al: Familial occurrence of right ventricular dysplasia: A study involving nine families. J Am Coll Cardiol 12:1222–1228, 1988.
212. Nawa S, Yamada M, Irie H, Teramoto S: Magnetic resonance evaluation of patency of stented polytetrafluoroethylene graft connecting right atrium to pulmonary artery. Chest 94:1105–1110, 1988.
213. Ni Y, Pislaru C, Bosmans H, et al: Validation of intracoronary delivery of metalloporphyrin as an in vivo "histochemical staining" for myocardial infarction with MR imaging. Acad Radiol 5:S37–S41, 1998.
214. Nishimura RA, Kazmier FJ, Smith HC, Danielson GK: Right ventricular outflow obstruction caused by constrictive pericardial disease. Am J Cardiol 55:1447–1448, 1985.
215. Noonan JA: Pulmonary heart disease. Pediatr Clin North Am 18: 1255–1272, 1971.
216. Ostman-Smith I, Silverman NH, Oldershaw P, et al: Cor triatriatum sinistrum: Diagnostic features on cross-sectional echocardiography. Br Heart J 51:211–219, 1984.
217. Park JH, Han MC, Kim C-W: MR imaging of congenitally corrected transposition of the great vessels in adults. AJR Am J Roentgenol 153:491–494, 1989.
218. Park JH, Han MC, Kim C-W: MR imaging of congenitally corrected transposition in adults. AJR Am J Roentgenol 153:491–494, 1989.
219. Parsons JM, Baker EJ, Anderson RH, et al: Morphological evaluation of atrioventricular septal defects by magnetic resonance imaging. Br Heart J 64:138–145, 1990.
220. Passik CS, Ackerman DM, Pluth JR, Edwards WD: Temporal changes in the causes of aortic stenosis: A surgical pathological study of 646 cases. Mayo Clin Proc 62:119–123, 1987.
221. Pawel BR, de Chadarevian J-P, Wolk JH, et al: Sudden death in childhood due to right ventricular dysplasia. Pediatr Pathol 14: 987–995, 1994.
222. Pennell DJ, Keegan J, Firmin DN, et al: Magnetic resonance imaging of coronary arteries: Technique and preliminary results. Br Heart J 70:315–326, 1993.
223. Pennell DJ, Underwood SR, Longmore DB: Detection of coronary artery disease using MR imaging with dipyridamole infusion. J Comput Assisted Tomography 14:167–170, 1990.
224. Pennell DJ, Underwood SR, Manzara CC, et al: Magnetic resonance imaging during dobutamine stress in coronary artery disease. Am J Cardiol 70:34–40, 1992.
225. Peshock RM, Rokey R, Malloy CM, et al: Assessment of myocardial systolic wall thickening using nuclear magnetic resonance imaging. J Am Coll Cardiol 14:653–659, 1989.
226. Pflugfelder PW, Sechtem U, White RD, Higgins CB: Quantification of regional myocardial function by rapid cine MR imaging. AJR Am J Roentgenol 150:523–529, 1988.
227. Pflugfelder PW, Wisenberg G, Prato FS, et al: Early detection of canine myocardial infarction by magnetic resonance imaging in vivo. Circulation 71:587–594, 1985.
228. Pislaru SV, Ni Y, Pislaru C, et al: Noninvasive measurements of infarct size after thrombolysis with a necrosis-avid MRI contrast agent. Circulation 99:690–696, 1999.
229. Pohost GM, Biederman RWW: The role of cardiac MRI stress testing. Circulation 100:1676–1679, 1999.
230. Pons-Ladio G, Carreras F, Borras X: Comparison of morphologic assessment of hypertrophic cardiomyopathy by magnetic resonance versus echocardiographic imaging. Am J Cardiol 79:1651–1656, 1997.
231. Portal RW, Besterman EMM, Chambers RJ, et al: Prognosis after operation for constrictive pericarditis. Br Med J 1:593–597, 1966.
232. Posteraro RH, Sostman HD, Spritzer CE, Herfkens RJ: Cine-gradient-refocused MR imaging of central pulmonary emboli. AJR Am J Roentgenol 152:465–468, 1989.
233. Rademakers FE, Rogers WJ, Guier WH, et al: Relation of regional cross-fiber shortening to wall thickening in the intact heart: Three-dimensional strain analysis by NMR tagging. Circulation 89:1174–1182, 1994.
234. Rebergen SA, Ottenkamp J, Doornbos J, et al: Postoperative pulmonary flow dynamics after Fontan surgery: Assessment with nuclear magnetic resonance velocity mapping. J Am Coll Cardiol 21:123–131, 1993.
235. Rees RSO, Somerville J, Underwood SR, et al: Magnetic resonance imaging of the pulmonary arteries and their systemic connections in pulmonary atresia: Comparison with angiographic and surgical findings. Br Heart J 58:621–626, 1987.
236. Rees S, Somerville J, Ward C, et al: Coarctation of the aorta: MR imaging in late postoperative assessment. Radiology 173:499–502, 1989.
237. Regenfus M, Ropers D, Achenbach S, et al: Noninvasive detection of coronary artery stenosis using contrast-enhanced three-dimensional breath-hold magnetic resonance coronary angiography. J Am Coll Cardiol 36:44–50, 2000.
238. Reimer KA, Jennings RB: The "wavefront phenomenon" of myocardial ischemic cell death: II. Transmural progression of necrosis within the framework of ischemic bed size (myocardium at risk) and collateral flow. Lab Invest 40:634–644, 1979.
239. Reimer KA, Lowe JE, Rasmussen MM, et al: The "wavefront phenomenon" of ischemic cell death: I. Myocardial infarct size versus duration of coronary blood occlusion in dogs. Circulation 56: 786–794, 1977.
240. Reinmuller R, Doppman JL, Lissner J, et al: Constrictive pericardial disease: Prognostic significance of a nonvisualized left ventricular wall. Radiology 156:753–755, 1985.
241. Reinmuller R, Mahmut G, Erdmann E, et al: CT and MR evaluation of pericardial constriction: A new diagnostic and therapeutic concept. J Thorac Imaging 8:108–121, 1993.
242. Revel D, Canet E, Sebbag L, et al: First-pass and delayed magnetic resonance imaging studies of reperfused myocardial infarction with iron oxide particles. Acad Radiol 3:S398–S401, 1996.
243. Ricci C, Longo R, Pagnan L, et al: Magnetic resonance imaging in right ventricular dysplasia. Am J Cardiol 70:1589–1595, 1992.
244. Rich S: Primary pulmonary hypertension. Prog Cardiovasc Dis 31: 205–238, 1988.
245. Rigo P, Alderson PO, Robertson RM, et al: Measurement of aortic and mitral regurgitation by gated cardiac blood pool scans. Circulation 60:306–312, 1979.
246. Riedy K, Fisher MS, Belic N, Koenigsberg DI: MR imaging of myocardial sarcoidosis. AJR Am J Roentgenol 15:915–916, 1988.
247. Rienmuller R, Lloret JL, Tiling R: MR imaging of pediatric cardiac tumors previously diagnosed by echocardiography. J Comput Assist Tomogr 13:621–626, 1989.
248. Roberts WC: The congenitally bicuspid aortic valve: A study of 85 autopsy cases. Am J Cardiol 26:72–83, 1970.
249. Roberts WC: Valvular, subvalvular, and supravalvular aortic stenosis: Morphologic features. Cardiovasc Clin North Am 5:97–124, 1973.
250. Roberts WC, Perloff JK: Mitral valvular disease: A clinicopathologic survey of the conditions causing the mitral valve to function abnormally. Ann Intern Med 77:939–975, 1972.
251. Roberts WC, Spray TL: Pericardial heart disease: A study of its causes, consequences, and morphologic features. Cardiovasc Clin North Am 7:11–65, 1976.
252. Roditi GH, Hartnell GG, Conhen MC: MRI changes in myocarditis—evaluation with spin-echo cine MR angiography and contrast-enhanced spin-echo imaging. Clin Radiol 55:752–758, 2000.
253. Rokey R, Verani MS, Bolli R, et al: Myocardial infarct size quantification by MR imaging early after coronary artery occlusion in dogs. Radiology 158:771–774, 1986.
254. Ross RD, Bisset GS III, Meyer RA, et al: Magnetic resonance imaging for diagnosis of pulmonary vein stenosis after correction of total anomalous pulmonary venous connection. Am J Cardiol 60: 1199–1201, 1987.
255. Rowe JC, Bland EF, Sprague HB: The course of mitral stenosis without surgery: Ten- and twenty-year perspectives. Ann Intern Med 62:741–749, 1960.
256. Rusted IE, Schiefley CH, Edwards JE: Studies of the mitral valve: II. Certain anatomic features of the mitral valve and associated structures in mitral stenosis. Circulation 14:398–406, 1956.
257. Sackner M, Akgun N, Kimbel P, et al: The pathophysiology of scleroderma involving the heart and respiratory system. Ann Intern Med 60:611–627, 1964.
258. Sahn DJ: Instrumentation and physical factors related to visualization of stenotic and regurgitant jets by Doppler color flow mapping. J Am Coll Cardiol 12:1354–1356, 1988.
259. Sakuma H, Fujita N, Foo TK, et al: Evaluation of left ventricular volume and mass with breath-hold cine MR imaging. Radiology 188:377–380, 1993.

260. Salerni R, Rodnan G, Leon D: Pulmonary hypertension in the CREST variant of progressive systemic sclerosis (scleroderma). Ann Intern Med 86:394–399, 1977.
261. Sampson C, Martinez J, Rees S, et al: Evaluation of Fontan's operation by magnetic resonance imaging. Am J Cardiol 65:819–821, 1990.
262. Sandstede JJW, Lipke C, Beer M, et al: Analysis of first-pass and delayed contrast-enhancement patterns of dysfunctional myocardium on MR imaging: Use in the prediction of myocardial viability. AJR Am J Roentgenol 174:1737–1740, 2000.
263. Sasayama S, Ross J Jr, Franklin D, et al: Adaptations of the left ventricle to chronic pressure overload. Circ Res 38:172–178, 1976.
264. Sato T, Nakamura K, Yamanari H, et al: Relationship between the electrocardiographic features and distribution of hypertrophy in patients with hypertrophic cardiomyopathy. Jpn Circ J 62:483–488, 1998.
265. Schaefer S, Malloy CR, Katz J, et al: Gadolinium-DTPA–enhanced nuclear magnetic resonance imaging of reperfused myocardium: Identification of the myocardial bed at risk. J Am Coll Cardiol 12: 1064–1072, 1988.
266. Schiavone WA, O'Donnell JK: Congenital absence of the left portion of parietal pericardium demonstrated by nuclear magnetic resonance imaging. Am J Cardiol 55:1439–1440, 1985.
267. Scully RE, et al: Case records of the Massachusetts General Hospital: Malignant lymphoma, B-cell immunoblastic type, arising in the pericardium. N Engl J Med 316:1394–1404, 1987.
268. Sechtem U, Higgins CB, Sommerhoff BA, et al: Magnetic resonance imaging of restrictive cardiomyopathy. Am J Cardiol 59:480–482, 1985.
269. Sechtem U, Pflugfelder PW, Cassidy MM, et al: Mitral and aortic regurgitation: Quantification of regurgitant volumes with cine MR imaging. Radiology 167:425–430, 1988.
270. Sechtem U, Pflugfelder PW, Gould RG: Measurement of right and ventricular volumes in healthy individuals with cine MR imaging. Radiology 163:697–702, 1987.
271. Sechtem U, Pflugfelder PW, Gould RG, et al: Measurement of right and left ventricular volumes in healthy individuals with cine MR imaging. Radiology 163:697–702, 1987.
272. Sechtem U, Pflugfelder PW, White RD, et al: Cine MR imaging: Potential for the evaluation of cardiovascular function. AJR Am J Roentgenol 148:239–246, 1987.
273. Sechtem U, Tscholakoff D, Higgins CB: MRI of the abnormal pericardium. Am J Roentgenol 147:245–252, 1986.
274. Sechtem U, Tscholakoff D, Higgins CB: MRI of the normal pericardium. Am J Roentgenol 147:239–244, 1986.
275. Selzer A, Malmborg RO: Some factors influencing changes in pulmonary vascular resistance in mitral valve disease. Am J Med 32: 532–544, 1962.
276. Semelka RC, Tomei E, Wagner S, et al: Interstudy reproducibility of dimensional and functional measurements between cine magnetic resonance studies in the morphologically abnormal left ventricle. Am Heart J 119:1367–1373, 1990.
277. Semelka RC, Tomei E, Wagner S, et al: Normal left ventricular dimensions and function: Interstudy reproducibility of measurement with cine MR imaging. Radiology 174:763–768, 1990.
278. Shapiro EP, Rogers WJ, Beyar R, et al: Determination of LV mass by magnetic resonance in hearts deformed by acute infarction. Circulation 79:706–711, 1989.
279. Simpson IA, Chung KJ, Glass RF, et al: Cine magnetic resonance imaging for evaluation of anatomy and flow relations in infants and children with coarctation of the aorta. Circulation 78:142–148, 1988.
280. Skjaerpe T, Hegrenaes L, Hatle L: Noninvasive estimation of valve area in patients with aortic stenosis by Doppler ultrasound and two-dimensional echocardiography. Circulation 72:810–818, 1985.
281. Soler R, Rodriguez E, Rodriguez JA, et al: Magnetic resonance imaging of apical hypertrophic cardiomyopathy. Thorac Imaging 12: 221–225, 1997.
282. Sondergaard L, Thomsen C, Stalhlber F, et al: Mitral and aortic valvular flow: Quantification with MR phase mapping. J Magn reson Imaging 2:295–302, 1992.
283. Sondergaard L, Stalberg F, Thomsen C: Magnetic resonance imaging valvular heart disease: Review. J Magn Reson Imaging 10:627–638, 1999.
284. Sondergaard L, Stahlberg F, Thomsen C, et al: Accuracy and precision of MR velocity mapping in measurement of stenotic cross-sectional area, flow rate, and pressure gradient. J Magn Reson Imaging 3:433–437, 1993.
285. Soulen RL, Donner RM, Capitanio M: Postoperative evaluation of complex congenital heart disease by magnetic resonance imaging. Radiographics 7:975–1000, 1987.
286. Soulen RL, Kan J, Mitchell S, White RI Jr: Evaluation of balloon angioplasty of coarctation restenosis by magnetic resonance imaging. Am J Cardiol 60:343–345, 1987.
287. Soulen RL, Stark DD, Higgins CB: Magnetic resonance imaging of constrictive pericardial disease. Am J Cardiol 55:480–484, 1985.
288. Spann JF, Bove AA, Natarajan G, Kreulen T: Ventricular performance, pump function, and compensatory mechanisms in patients with aortic stenosis. Circulation 62:576–582, 1980.
289. Stern RC, Borkat G, Hirschfeld SS, et al: Heart failure in cystic fibrosis. Am J Dis Child 134:267–272, 1980.
290. Stark DD, Higgins CB, Lanzer P, et al: Magnetic resonance imaging of the pericardium: Normal and pathologic findings. Radiology 150: 469–474, 1984.
291. Stupi A, Steen V, Owens G, et al: Pulmonary hypertension in the CREST syndrome variant of systemic sclerosis. Arthritis Rheum 29: 515–523, 1986.
292. Suzuki JI, Chang JM, Caputo GR, Higgins CB: Evaluation of right ventricular early diastolic filling by cine nuclear magnetic resonance imaging in patients with hypertrophic cardiomyopathy. J Am Coll Cardiol 18:120–126, 1991.
293. Suzuki J, Shimaomoto R, Nishikawa J, et al: Morphologic onset and early diagnosis in apical hypertrophic cardiomyopathy: A long-term analysis with nuclear magnetic resonance imaging. J Am Coll Cardiol 33:146–151, 1999.
294. Tabak SW, Maurer G: Echocardiographic detection of free-floating left atrial thrombus. Am J Cardiol 53:374–375, 1984.
295. Thiene G, Nava A, Corrado D, et al: Right ventricular cardiomyopathy and sudden death in young people. N Engl J Med 318:129–133, 1988.
296. Thompson WP, White PD: The commonest cause of hypertrophy of the right ventricle: Left ventricular strain and failure. Am Heart J 12:641–649, 1936.
297. Tomoda H, Hoshiai M, Furuya H, et al: Evaluation of pericardial effusion with computed tomography. Am Heart J 99:701–706, 1980.
298. Underwood SR, Klipstein RH, Firmin DM, et al: Magnetic resonance assessment of aortic and mitral regurgitation. Br Heart J 56: 455–462, 1986.
299. Ungerer R, Tashkin D, Furst D, et al: Prevalence and clinical correlates of pulmonary arterial hypertension in progressive systemic sclerosis. Am J Med 75:65–73, 1983.
300. Van Praagh R: The segmental approach to diagnosis in congenital heart disease: The cardiovascular system. Birth Defects 8:4–23, 1972.
301. Van Praagh R, David H, Van Praagh S: What is a ventricle? The single ventricle trap. Pediatr Cardiol 2:74–79, 1982.
302. Van Praagh R: The importance of segmental situs in the diagnosis of congenital heart disease. Semin Roentgenol 20:254–271, 1985.
303. Van Praagh R, Ongley PA, Swan HJC: Anatomic types of single or common ventricle in man. Am J Cardiol 13:367–386, 1964.
304. van Rugge FP, van der Wall EE, Spanjersberg SJ, et al: Magnetic resonance imaging during dobutamine stress for detection and localization of coronary artery disease: Quantitative wall motion analysis using a modification of the centerline method. Circulation 90:127–138, 1994.
305. van Rugge FP, van der Wall EE, de Roos A, Bruschke AV: Dobutamine stress magnetic resonance imaging for detection of coronary artery disease. J Am Coll Cardiol 22:431–439, 1993.
306. von Schulthess GK, Higashino SM, Higgins SS, et al: Coarctation of the aorta: MR imaging. Radiology 158:469–474, 1986.
307. Veluvolu P, Balian AA, Goldsmith R, et al: Lyme carditis: Evaluation by Ga-67 and MRI. Clin Nucl Med 17:823–827, 1992.
308. Vick GW III, Rokey R, Huhta JC, et al: Nuclear magnetic resonance imaging of the pulmonary arteries, subpulmonary region, and aorticopulmonary shunts: A comparative study with two-dimensional echocardiography and angiography. Am Heart J 119:1103–1110, 1990.
309. von Schulthess GK, Higgins CB: Blood flow imaging with MR: Spin-phase phenomena. Radiology 157:687–699, 1985.
310. Vrachliotis TG, Bis KG, Aliabadi D, et al: Contrast-enhanced breath-hold MR angiography for evaluating patency of coronary artery bypass grafts. AJR Am J Roentgenol 168:1073–1080, 1997.

311. Wagenvoort CA: Pulmonary veno-occlusive disease: Entity or syndrome? Chest 69:82–86, 1976.
312. Wagenvoort CA, Wagenvoort N: Primary pulmonary hypertension: A pathologic study of the lung vessels in 156 clinically diagnosed cases. Circulation 42:1163–1184, 1970.
313. Wagner S, Aufferman W, Buser P, et al: Functional description of the left ventricle in patients with volume overload, pressure overload, and myocardial disease using cine nuclear magnetic resonance imaging (NMR). Am J Cardiol Imaging 5:87–97, 1991.
314. Waller BF, Howard J, Fess S: Pathology of tricuspid valve stenosis and pure tricuspid regurgitation: III. Clin Cardiol 18:225–230, 1995.
315. Waller BF, Moriarty AT, Eble JN, et al: Etiology of pure tricuspid regurgitation based on annular circumference and leaflet area: Analysis of 45 necropsy patients with clinical and morphologic evidence of pure tricuspid regurgitation. J Am Coll Cardiol 18:97–102, 1986.
316. Webb J, Kerr C, Huckell V, et al: Left ventricular abnormalities in arrhythmogenic right ventricular dysplasia. Am Heart J 58:568–570, 1986.
317. Webb WR: MR of hila and mediastinum. Cardiovasc Intervent Radiol 6:793–832, 1986.
318. Weinberg BA, Conces DJ Jr, Waller BF: Cardiac manifestations of noncardiac tumors: I. Direct effects. Clin Cardiol 12:289–296, 1989.
319. Weitzman LB, Tinker WP, Kronzon T, et al: The incidence and natural history of pericardial effusion after cardiac surgery—an echocardiographic study. Circulation 69:506–511, 1984.
320. Wendland MF, Saeed M, Masui T, et al: First pass of an MR susceptibility contrast agent through normal and ischemic heart: Gradient-recalled echo-planar imaging. J Magn Reson Imaging 3: 755–760, 1993.
321. Wendland MF, Saeed M, Masui T, et al: Echo-planar MR imaging of normal and ischemic myocardium with gadodiamide injection. Radiology 186:535–542, 1993.
322. Wendt RE III, Rokey R, Vick GW III, Johnston DL: Electrocardiographic gating and monitoring in NMR imaging. Magn Reson Imaging 6:89–95, 1988.
323. Wesbey G, Higgins CB, Lanzer P, et al: Imaging and characterization of acute myocardial infarction in vivo by gated nuclear magnetic resonance. Circulation 69:125–130, 1984.
324. White RD, Cassidy MM, Cheitlin MD, et al: Segmental evaluation of left ventricular wall motion after myocardial infarction: Magnetic resonance imaging versus echocardiography. Am Heart J 115:166–175, 1988.
325. White RD, Holt WW, Cheitlin MD, et al: Estimation of the functional and anatomic extent of myocardial infarction using magnetic resonance imaging. Am Heart J 115:740–748, 1988.
326. Wildenhain PM, Bourekas EC: Pulmonary varix: Magnetic resonance findings. Cathet Cardiovasc Diagn 24:268–270, 1991.
327. Wilke N, Jerosch-Herold M, Wang Y, et al: Quantitative first-pass MR imaging: Assessment of myocardial perfusion reserve. Radiology 204:373–384, 1997.
328. Wilke N, Simm C, Zhang J, et al: Contrast-enhanced first-pass myocardial perfusion imaging: Correlation between myocardial blood flow in dogs at rest and during hyperemia. Magn Reson Med 29:485–497, 1993.
329. Williams ES, Kaplan JI, Thatcher F, et al: Prolongation of proton spin lattice relaxation times in regionally ischemic tissue from dog hearts. J Nucl Med 21:449–453, 1980.
330. Williams DS, Grandis DJ, Zhang W, Koretsky AP: Magnetic resonance imaging of perfusion in the isolated rat heart using spin inversion of arterial water. Magn Reson Med 30:361–365, 1993.
331. Wintersberger BJ, Engelmann MG, von Smekal A, et al: Patency of coronary artery bypass grafts: Assessment with breath-hold contrast-enhanced MR angiography—value of a non-electrocardiographically triggered technique. Radiology 208:345–351, 1998.
332. Wisenberg G, Pflugfelder PW, Kostuk WJ, et al: Diagnostic applicability of magnetic resonance imaging in assessing human cardiac allograft rejection. Am J Cardiol 60:130–136, 1987.
333. Wintersperger BJ, Penzkofer HV, Knez A, et al: Multislice MR perfusion imaging and regional myocardial function analysis: Complimentary findings in chronic myocardial ischemia. Int J Card Imaging 15:425–434, 1999.
334. Wisenberg G, Prato FS, Carroll SE, et al: Serial nuclear magnetic resonance imaging of acute myocardial infarction with and without reperfusion. Am Heart J 115:510–518, 1988.
335. Wolf RL, Ehman RL, Riederer SJ, et al: Analysis of systemic and random error in MR volumetric flow measurements. Magn Reson Med 30:82–91, 1993.
336. Wood P: An appreciation of mitral stenosis: I. Br Med J 1:1051–1063, 1954.
337. Wood P: An appreciation of mitral stenosis: II. Br Med J 1:1113–1124, 1954.
338. Yamanari H, Kakishita M, Fujimoto Y, et al: Regional myocardial perfusion abnormalities and regional myocardial early diastolic function in patients with hypertrophic cardiomyopathy. Heart Vessels 12: 192–198, 1997.
339. Yellon DM, Hearse DJ, Crone R, et al: Characterization of the lateral interface between normal and ischemic tissue in the canine heart during evolving myocardial infarction. Am J Cardiol 47:1233–1239, 1981.
340. Yoo S-J, Lim T-H, Park I-S, et al: Defects of the interventricular septum of the heart: En face MR imaging in the oblique coronal plane. AJR Am J Roentgenol 157:943–946, 1991.
341. Yu K, Saeed M, Wendland M, et al: Real-time dynamics of an extravascular magnetic resonance contrast medium in acutely infarcted myocardium using inversion recovery and gradient-recalled echo-planar imaging. Invest Radiol 27:927–934, 1992.
342. Zerhouni EA, Parish DM, Rogers WJ, et al: Human heart: Tagging with MR imaging—a new method for noninvasive assessment of myocardial motion. Radiology 169:59–63, 1988.
343. Zheng J, Li D, Kyongtae T, et al: Three-dimensional gadolinium-enhanced coronary magnetic resonance angiography: Initial experience. J Cardiovasc Magn Res 1:33–41, 1999.
344. Zile MR, Gaasch WH, Carroll JD, Levine HJ: Chronic mitral regurgitation: Predictive value of preoperative echocardiographic indexes of left ventricular function and wall stress. J Am Coll Cardiol 3: 235–242, 1984.
345. Zuberbuhler JR, Allwork SP, Anderson RH: The spectrum of Ebstein's anomaly of the tricuspid valve. J Thorac Cardiovasc Surg 77:202–211, 1979.

Appendices
Normal Spin-Echo Images of the Heart

Abbreviations

a	Anterior aortic sinus of Valsalva
AAVR	Anterior atrioventricular ring
AbAo	Abdominal aorta
Ao	Aortic arch
AoA	Ascending aorta
AoD	Descending aorta
AoR	Aortic root
APR	Anterior pericardial reflection
AS1	Primum interatrial septum
AS2	Secundum interatrial septum
AS3	Sinus venosus interatrial septum
Az	Azygos vein
CrS	Crista supraventricularis
CS, cs	Coronary sinus
E	Esophagus
HV	Hepatic vein
IA	Innominate artery
IV	Innominate vein
IVC	Inferior vena cava
IVS	Interventricular septum
LA	Left atrium
LAA	Left atrial appendage
LADCA	Left anterior descending coronary artery
LB	Left bronchus
LCC	Left common carotid artery
LLLPV	Left lower lobe pulmonary vein
LMCA	Left main coronary artery
LP	Left pulmonary artery
LSA	Left subclavian artery
LULPV	Left upper lobe pulmonary vein
LV	Left ventricle
MP	Main pulmonary artery
MV	Mitral valve
PAVR	Posterior atrioventricular ring
pl	Posterior left aortic sinus of Valsalva
PM1	Superior papillary muscle
PM2	inferior papillary muscle
pr	Posterior right aortic sinus of Valsalva
RA	Right atrium
RAA	Right atrial appendage
RB	Right bronchus
RCA	Right coronary artery
RP	Right pulmonary artery
RULPA	Right upper lobe pulmonary artery
RULPV	Right upper lobe pulmonary vein
RV	Right ventricle
RVO	Right ventricular outflow tract
SV	Superior vena cava
T	Trachea

Appendix A Axial Sections (Figs. A1 to A10)

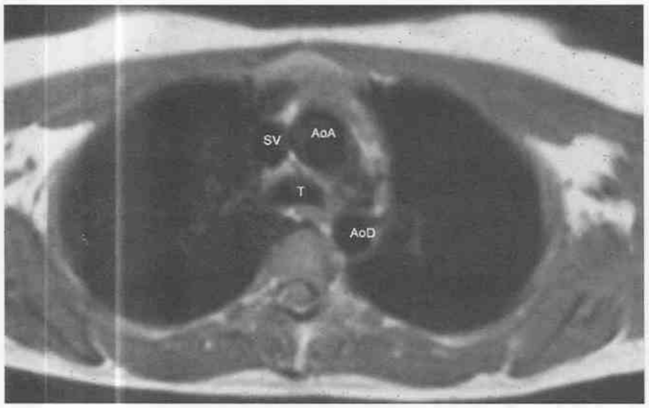

Figure A1

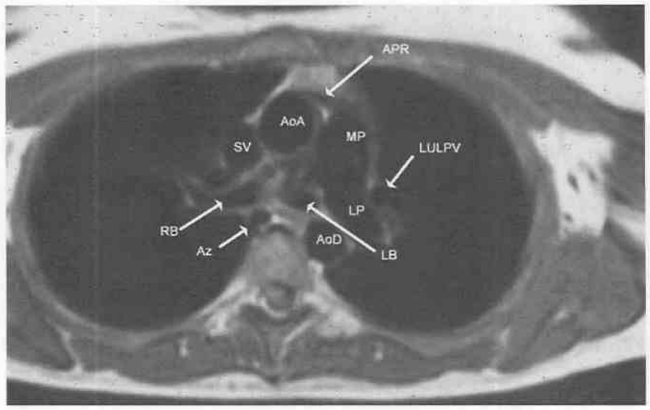

Figure A2

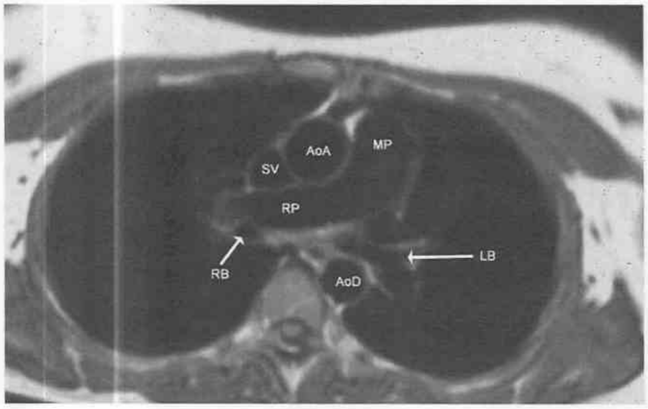

Figure A3

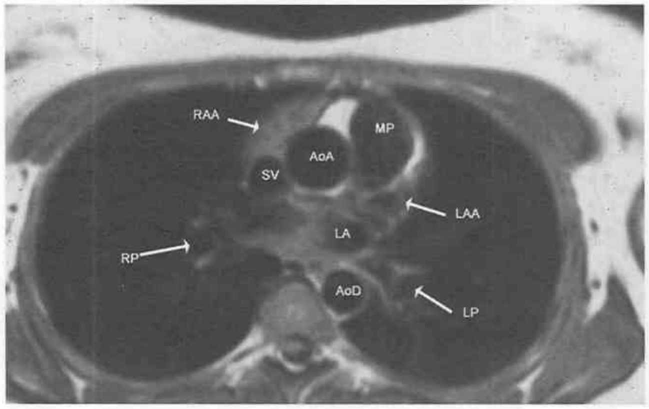

Figure A4

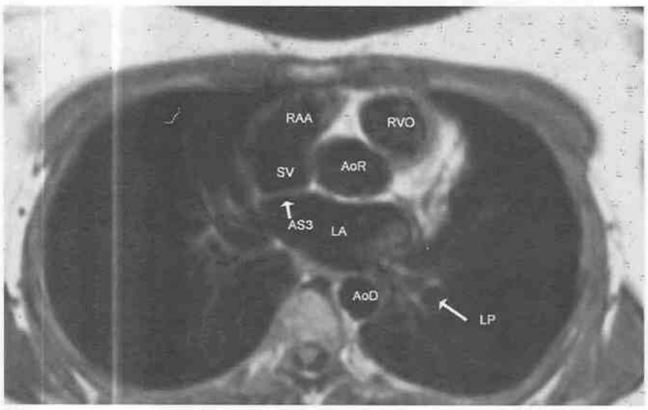

Figure A5

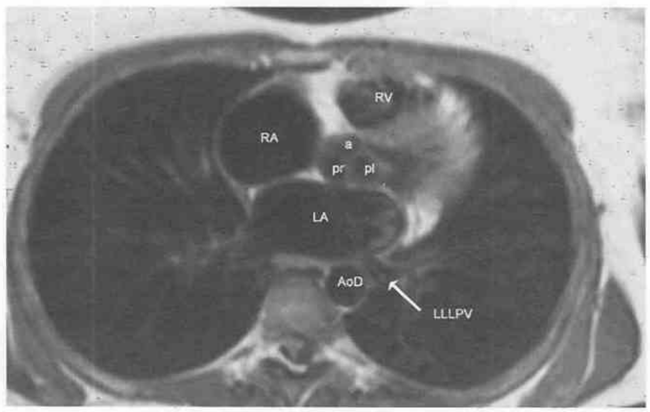

Figure A6

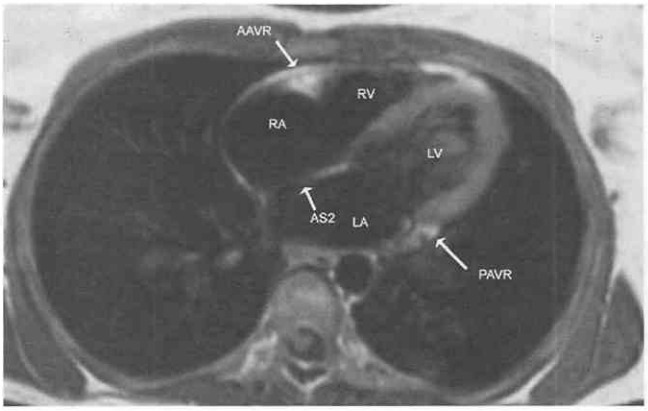

Figure A7

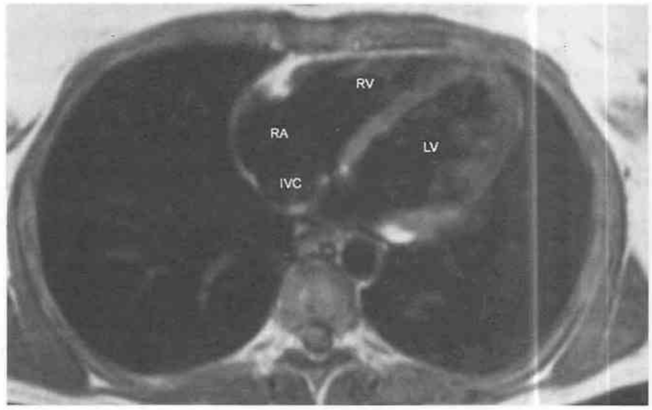

Figure A8

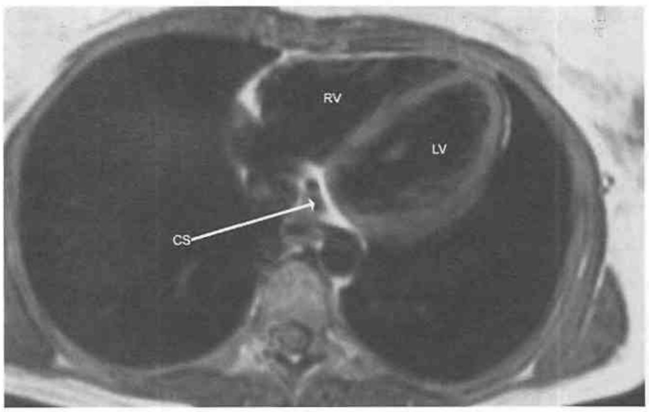

Figure A9

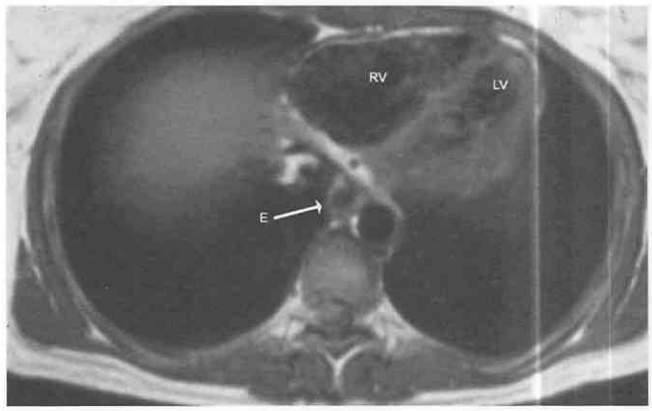

Figure A10

Appendix B Left Anterior Oblique Sagittal Sections (Figs. B1 to B6)

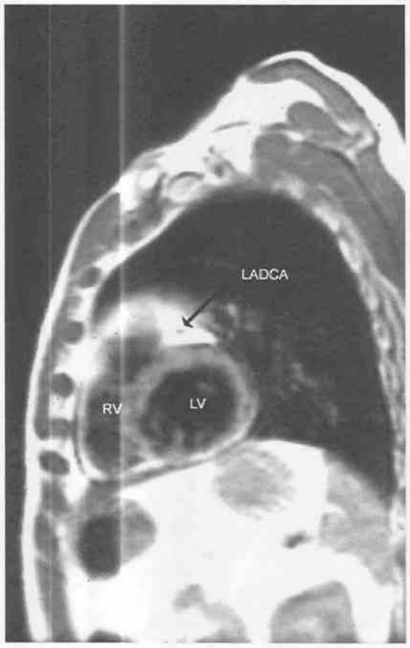

Figure B1

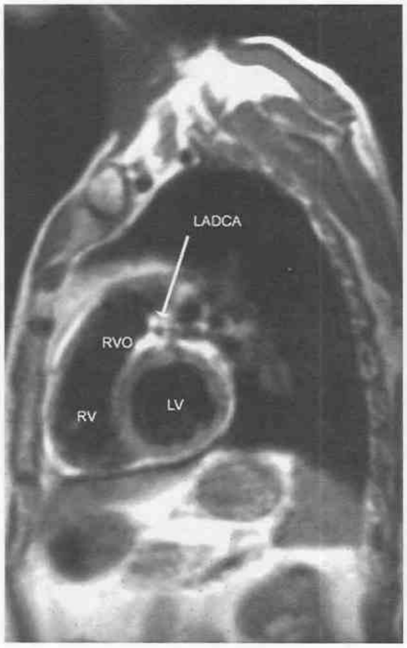

Figure B2

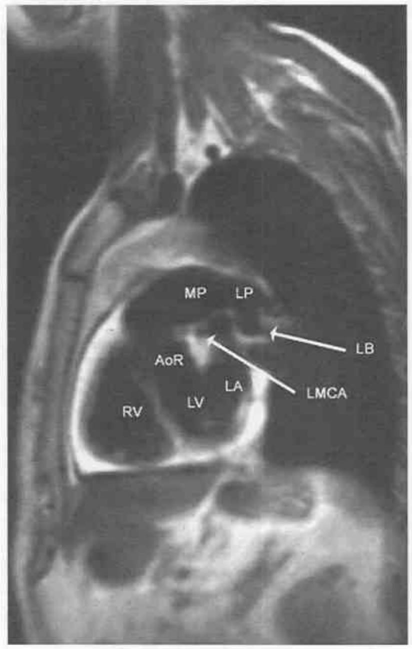

Figure B3

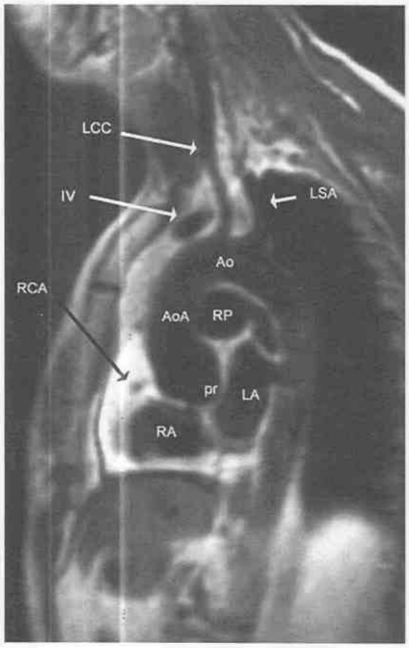

Figure B4

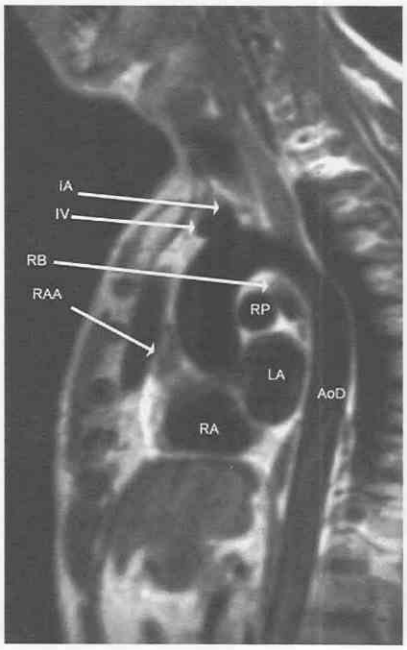

Figure B5

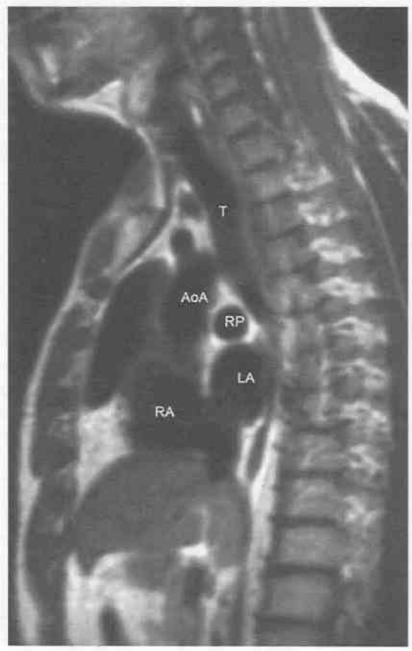

Figure B6

Appendix C Right Anterior Oblique Sections (Figs. C1 to C11)

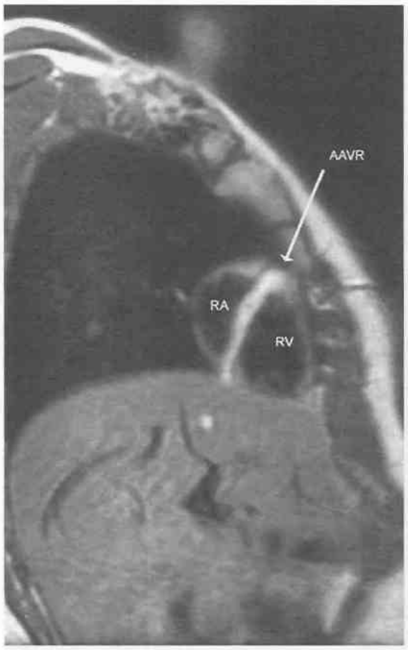

Figure C1

Figure C2

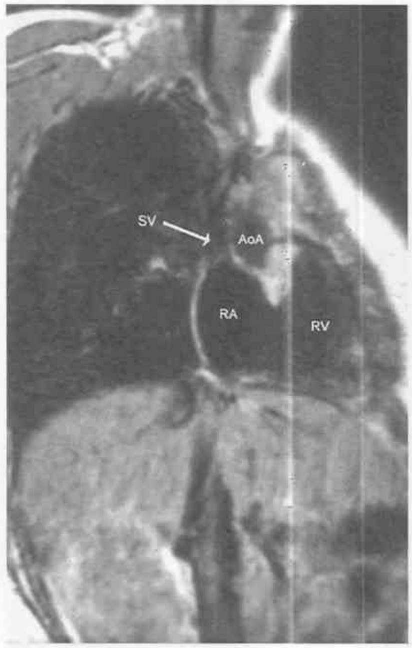

Figure C3

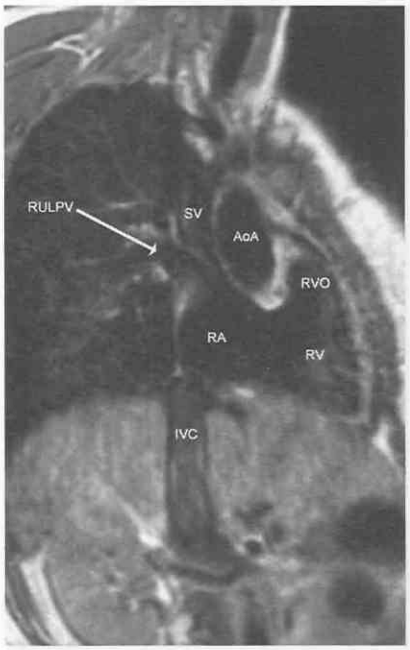

Figure C4

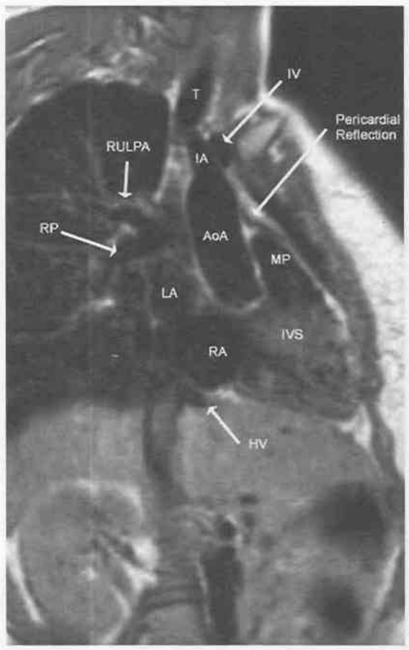

Figure C5

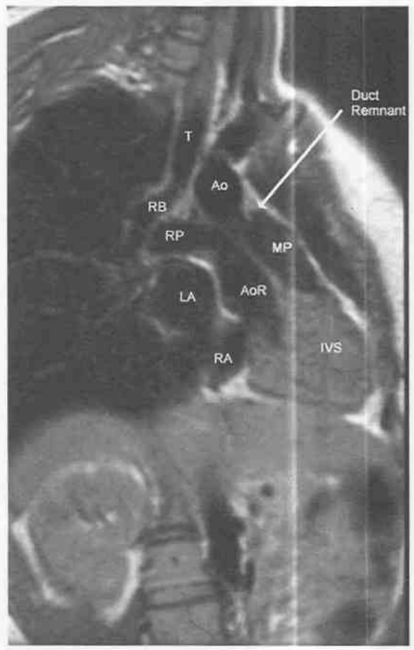

Figure C6

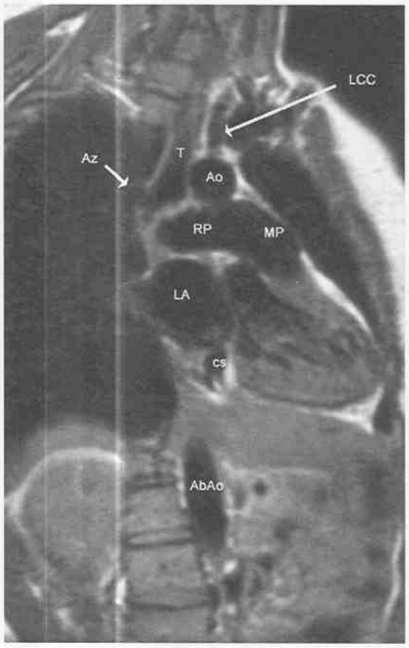

Figure C7

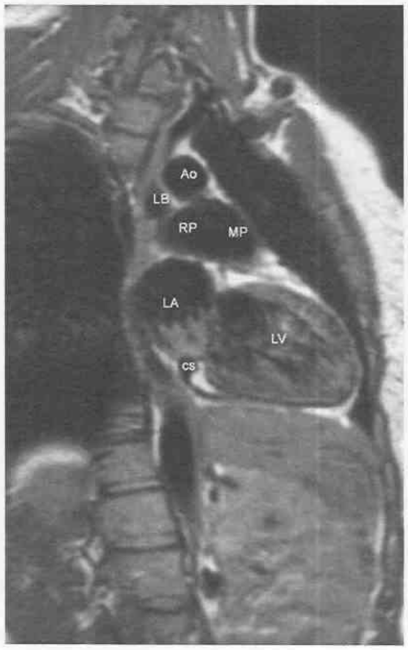

Figure C8

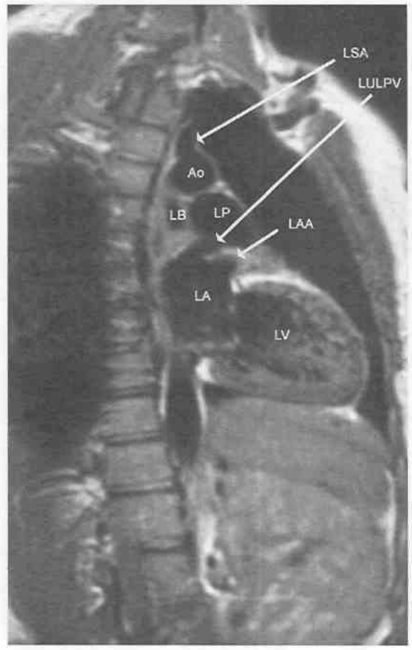

Figure C9

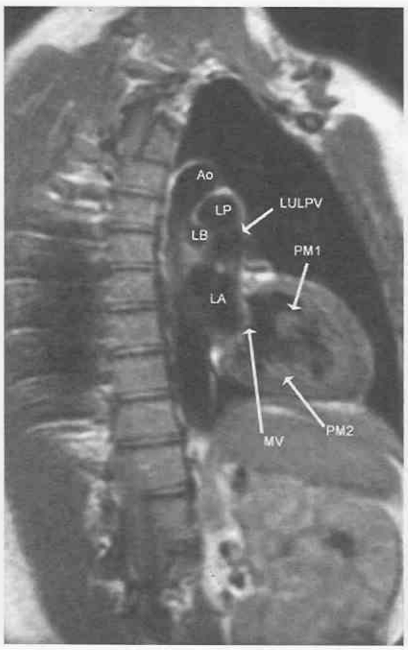

Figure C10

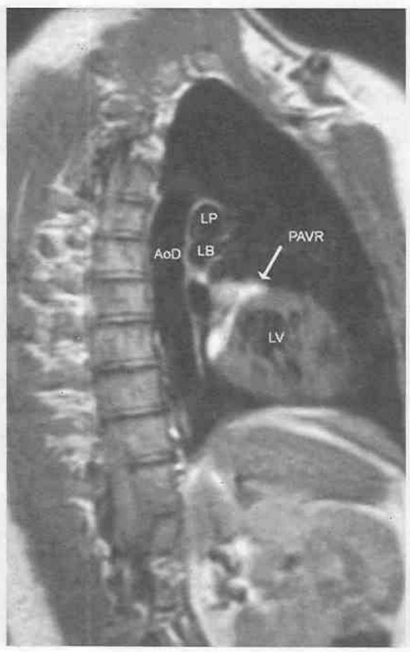

Figure C11

Appendix D Short-Axis Sections (Figs. D1 to D13)

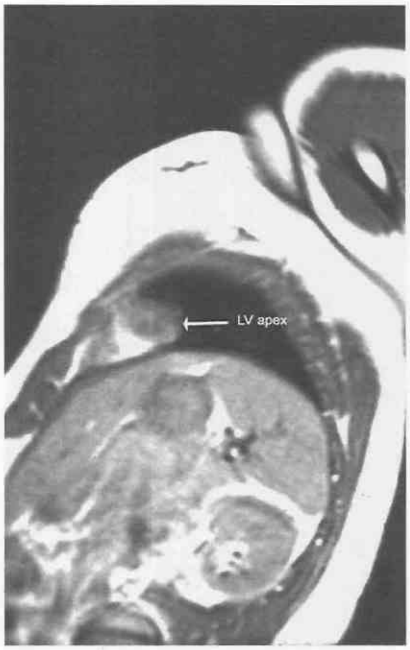

Figure D1

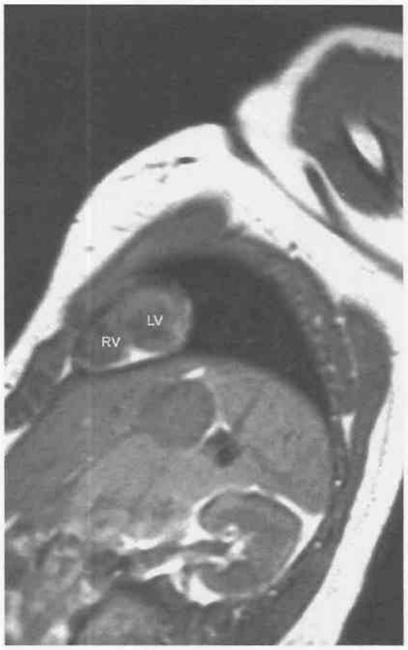

Figure D2

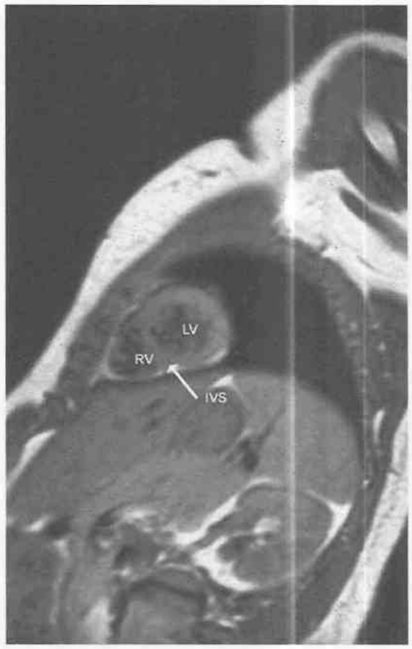

Figure D3

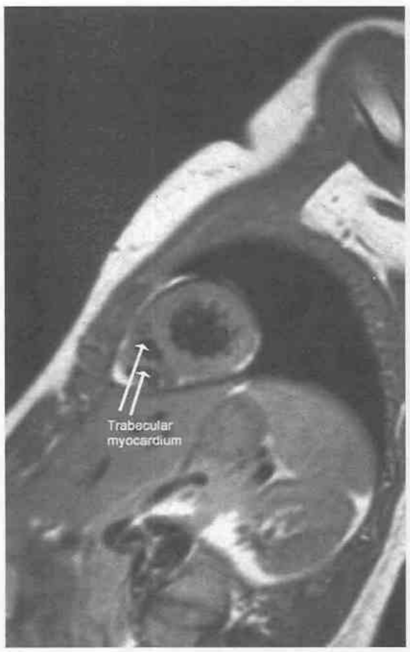

Figure D4


Figure D5

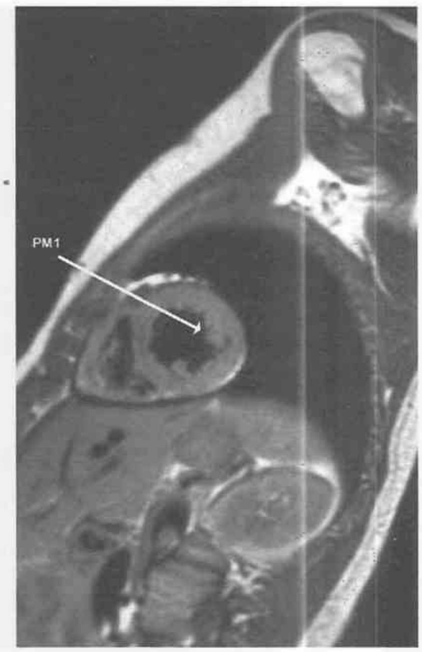

Figure D6

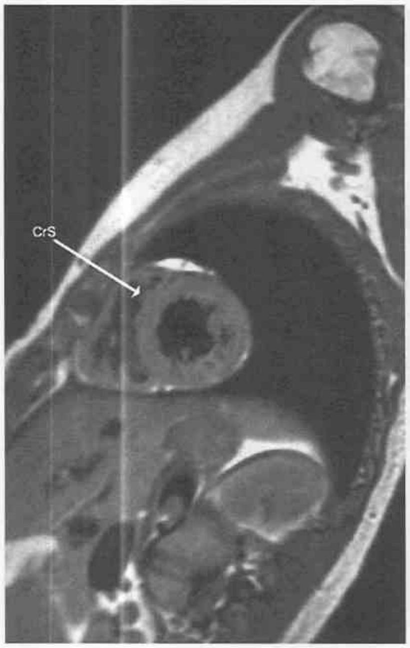

Figure D7

Figure D8

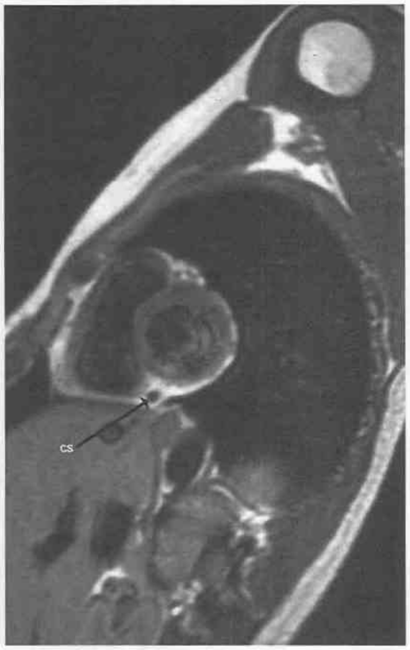

Figure D9

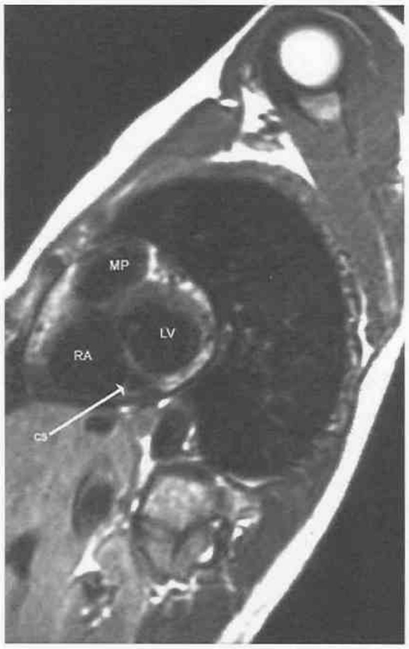

Figure D10

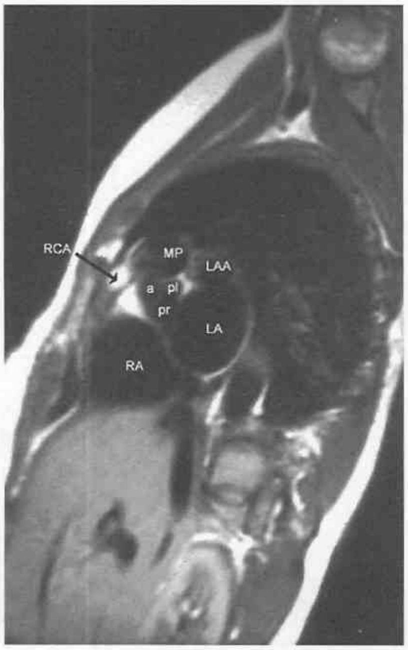

Figure D11

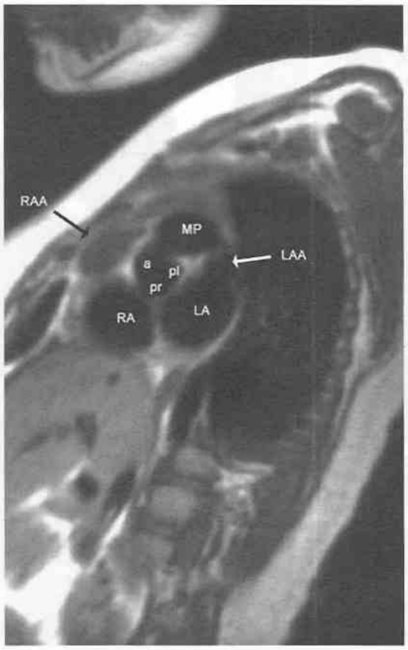

Figure D12

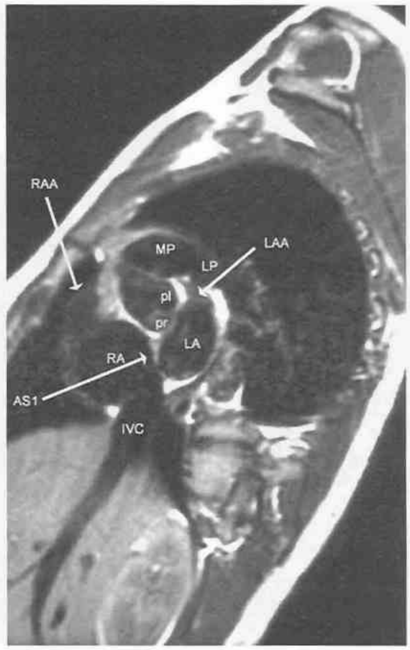

Figure D13

Part VI

Imaging of the Abdomen and Pelvis

Edited by
John R. Haaga

34 The Gastrointestinal Tract

Hyun Kwon Ha, Jeong Kon Kim

General Considerations

Computed tomography (CT) has been increasingly used for patients thought to have a variety of gastrointestinal (GI) tract diseases. Such advances may result from the ability of CT to assess intraluminal, intramural, and extraluminal pathologic processes as well as the development of high-resolution scanners and technical refinements that provide better quality studies. However, it should be stressed that CT is not superior to conventional barium examinations for evaluating mucosal diseases. Therefore, both CT and barium examinations have complementary roles in the diagnosis of GI tract diseases, although both studies are not always required.

Regardless of their primary causes, most inflammatory, neoplastic, and vascular disorders may be recognized on CT by bowel wall thickening or a mass. As our experience has increased in performing and interpreting CT scans, however, we have found considerable overlap of findings in various GI tract diseases. Therefore, to increase the diagnostic accuracy of CT, it is necessary to further investigate bowel wall involvement patterns, such as the degree, length, symmetry, and contrast enhancement in each disease entity. Moreover, observing changes in the perienteric or pericolonic spaces, mesentery, omentum, and peritoneal cavity can narrow the differential diagnosis because this information sometimes provides clues for making a specific diagnosis. In addition, CT is renowned for the common occurrence of false-positive findings because nonopacified or poorly distended bowel may simulate masses, tumors, or infection. Thus, adequate CT examination with optimal opacification of the GI tract in an appropriate amount of contrast agent is essential before we can interpret CT scans.

Optimal Techniques for Abdominal CT

Because bowel wall thickening is the single most important indicator of GI abnormality on CT, adequate CT examination of the GI tract requires bowel discrimination and distention, best achieved by administration of both oral and intravenous (IV) contrast material. IV contrast infusion helps to detect the abnormal bowel if the involved bowel shows abnormal contrast enhancement or a *target sign* or *double-halo sign*. Because the cases in which such findings are demonstrated are limited, however, the role of oral contrast material is stressed more than that of IV contrast material for assessment of GI abnormalities. Optimal opacification of the GI tract with an appropriate amount of contrast agent is essential so as not to overlook those patients with subtle or minimal bowel changes. Furthermore, nonopacified or poorly distended bowel may simulate masses, tumors, or infection.

For the purpose of optimal opacification, the following aspects should be taken into consideration:

1. Type of oral contrast agent.
2. Total volume of oral contrast agent
3. Timing of contrast agent administration.
4. Intestinal transit time.
5. Positioning of the patient.

Although there are no extensive data to support a clear superiority of any particular contrast agent, most institutions have used basically two kinds of oral contrast material: high density or low density. Diluted, 2% to 3% iodine solutions or barium suspensions, which increase the attenuation of the bowel lumen, are most widely used as high-density agents (Fig. 34–1). In contrast, air-density and fat-density contrast agents, which decrease the attenuation of the lumen, can also be used as negative-density agents. Among various agents, 1.5% to 2% barium suspension is the agent that most radiologists prefer.

Barium suspension offers several advantages over water-soluble iodine agents:

1. Barium is relatively palatable.
2. Barium is stable in the pH of the stomach.

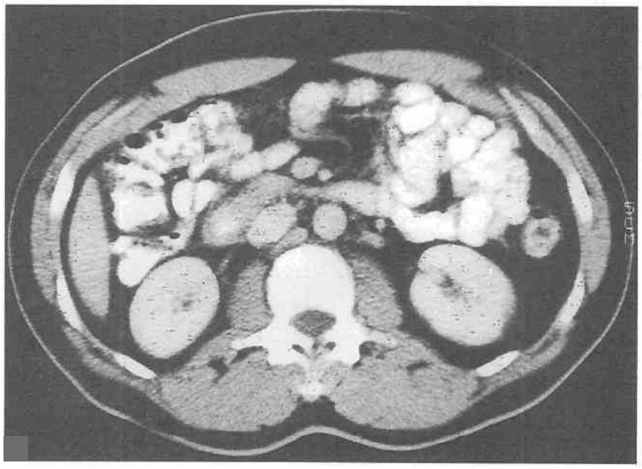

Figure 34–1. Diluted barium solution favorably opacifies the lumen of the gastrointestinal tract.

3. There is no cathartic action.
4. Barium is not absorbed by the GI tract.
5. Barium is relatively safe if aspirated, but it should not be used for the patients who are suspected of having peritoneal spillage.

Diluted iodine solutions are water-soluble agents. Therefore, they may be indicated specifically for:

1. Trauma or suspected GI perforation.
2. Use as a bowel marker when percutaneous CT-guided interventional procedures are performed.
3. Patients with inflammatory bowel disease with suspected abscess, fistulas, or sinus tract formation.

Although controversial, iodine agents also help in speeding up the intestinal transit time because they produce transfer of water into the lumen owing to their hyperosmolarity.[394] However, these agents should be used with caution in patients at high risk for vomiting and aspiration because they have an added toxic and hyperosmotic effect on the pulmonary lining.

Air-density contrast agents can be used alone or as an adjunct to high-density or fat-density contrast agents. In the stomach, carbon dioxide gas is delivered by effervescent granules that have been used during the upper GI series. In the colon, air is insufflated via a rectal tube. These techniques with the use of air or gas not only produce reliable distention and discrimination of the viscus from adjacent structures but also help in assessing the true thickness of the bowel wall (Fig. 34–2).[394, 623]

Wide window settings are required for accurate assessment of the bowel wall thickness. The normal width of the bowel wall is thinner when air-contrast techniques are used, and this feature may therefore increase the sensitivity of CT in detecting GI disease.[623] However, several drawbacks are noted in the air technique; changes in patient positioning, glucagon for bowel relaxation, and fast scanning to avoid artifact are required.[623] In addition, this technique has the potential for obscuring the discrimination between intraluminal and extraluminal air collections.

Although not commonly used, fat-density agents can be applied for local staging and follow-up study of rectal tumors and assessment of diverticulitis.[494] However, caution should be exercised in patients with severe, symptomatic gallbladder disease or acute pancreatitis; fulminant or complicated inflammatory bowel disease; and suspected cysts, pseudocysts, abscess formation, and cystic masses.[494]

In addition to air-density and fat-density agents, the administration of water is used as a negative agent in some institutions, especially for demonstrating pathology in the stomach and rectum. Water has some advantages: it may be the most tolerable agent to the patients, and it produces excellent mural visualization without beam-hardening, motion, or other streak artifacts.

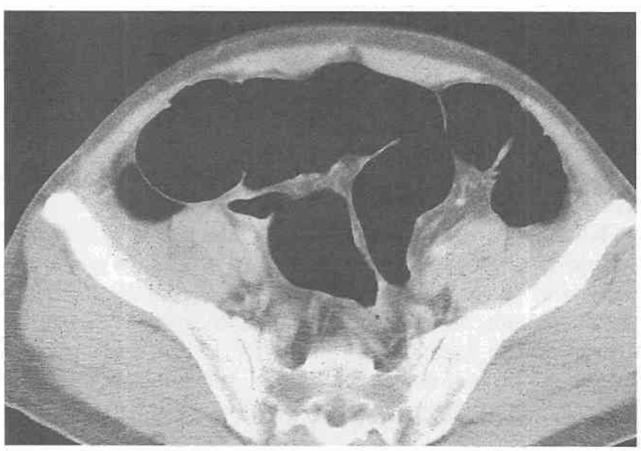

Figure 34–2. CT scan after air insufflation into the rectum.

Bowel Wall Patterns

Inflammatory Diseases

The hallmark of most inflammatory bowel diseases on CT scans is symmetrical and circumferential bowel wall thickening, usually not exceeding 1.5 cm.[263] However, an asymmetrical pattern of bowel wall thickening is also commonly seen in chronic forms of inflammatory bowel diseases (e.g., Crohn's disease, intestinal tuberculosis [TB]) because cicatricial and fibrotic changes do not always occur circumferentially. The degree of bowel wall thickening depends primarily on which intestinal layers—mucosa, submucosa, muscularis propria, or serosa—are predominantly affected by the inflammatory process. Inflammatory processes confined to the mucosa or to the superficial layers of the bowel wall may not be displayed reliably on CT scans unless the full thickness of the bowel wall is involved. Bowel wall thickening results from a variety of pathologic processes occurring in several layers of the intestinal wall, including the following:

1. Transmural granulomatous infiltration with edema, fibrosis, inflammation, and lymphangiectasis in Crohn's disease.
2. A combination of infiltration of the lamina propria by round cells, hypertrophy of the muscularis mucosa, and deposition of submucosal fat in ulcerative colitis.[192]
3. Muscle hypertrophy, fibrosis, edema, intramural inflammation, or organized intramural inflammatory mass in diverticulitis.[24]
4. Edema and necrosis in neutropenic colitis.[171]

Except for certain cases in which the predominant pathologic processes in the intestinal wall result from hematoma or fat accumulation, CT may not clearly determine their primary pathologic process. The stages of the inflammatory process may also affect the degree of thickening, which is more severe in the acute stage than in the chronic stage, because an acute process frequently accompanies the edematous components associated with mucosal ulcerations.

Although some differences are noted in the degree of bowel wall thickness in various inflammatory bowel diseases, bowel wall thickness alone cannot be used as an absolute indicator to establish a specific diagnosis. In certain instances, contrast enhancement patterns of the involved bowel wall, rather than bowel wall thickness, are more helpful for determining the diagnosis. Abnormally thickened bowel wall may enhance homogeneously or

show heterogeneous enhancement with a double-halo sign (two rings) or target sign (three rings). The double-halo or target sign is mainly caused by accumulation of edematous fluid, hemorrhage, lymph, or fat predominantly in the submucosa. If these signs are demonstrated, there is a greater chance of a chronic rather than an acute inflammatory process.[19]

Although these signs are helpful in detecting GI tract abnormalities, they are, unfortunately, not specific for a particular type of disease process. Until recently, it has been generally agreed that the presence of these signs indicates non-neoplastic disease because the signs occur in various inflammatory and vascular disorders (Crohn's disease, ulcerative colitis, pseudomembranous colitis, radiation enterocolitis, eosinophilic gastroenteritis, ischemic bowel diseases, amyloidosis, portal hypertensive colopathy). However, one series has shown that these signs can be seen in a neoplastic process in which abundant fibrosis accumulates in the submucosal layer of the GI tract, especially in patients with metastasis to the GI tract from gastric cancer[205] or *signet ring* cell type of colorectal cancer.[290] In addition, the thickness and enhancing degree of each layer in the double-halo or target sign appear to differ from case to case or even in patients with the same disease entity. Further morphologic investigation of the target appearance on CT scanning would help discriminate inflammatory, ischemic, and neoplastic diseases.

Another characteristic pattern of bowel wall thickening—the *accordion sign*—represents alternating edematous haustral folds separated by transverse mucosal ridges filled with oral contrast material. This sign has been described in the literature as a highly suggestive finding for pseudomembranous colitis[156] and is demonstrated in 4% to 19% of patients with documented pseudomembranous colitis.[432] However, some reports suggest that this sign is also nonspecific and occurs in other conditions such as portal hypertensive colopathy,[252] ischemic colitis, and cytomegalovirus (CMV) colitis.[420] Therefore, the accordion sign should be viewed as indicative of severe colonic edema of uncertain cause.

In addition to bowel wall thickening patterns, observing the length and multiplicity of the involved segment helps to differentiate inflammatory from neoplastic and vascular diseases as well as narrow the range of differential diagnoses among inflammatory bowel diseases. Generally, in the acute stage of inflammatory bowel disease, the length of the involved segment is longer than in neoplastic diseases (<10 cm) but is shorter than in vascular diseases. In the chronic stage, when strictures and fibrosis develop, the involved bowel length becomes much shorter than in the acute stage, thereby simulating neoplastic conditions. Although multiplicity is also more commonly seen in inflammatory bowel diseases, it occurs in some neoplastic diseases, such as lymphoma of the Mediterranean type involving the small intestine and metastatic neoplasm as well as in vascular diseases such as vasculitis.[213]

It is well known that the appearance of a transition zone between the involved and normal segments is important in distinguishing inflammatory from neoplastic conditions on barium study. This finding can also apply to CT interpretation and is useful in differentiating diverticulitis from colonic carcinoma. Although abrupt transition is characteristic of neoplastic diseases, a tapered appearance is a common manifestation of inflammatory diseases.

Neoplastic Diseases

Benign tumors of the small and large intestine include adenomas, lipomas, stromal tumors, hamartomas, fibromas, and hemangiomas. Malignant tumors include adenocarcinomas, lymphomas, sarcomas, and carcinoids. The hallmark of a GI neoplasm on CT is eccentric or asymmetrical wall thickening or mass formation in the bowel; bowel wall thickening usually exceeds 1.5 cm.[263] However, a circumferential pattern of bowel wall thickening can also be seen in neoplastic processes, such as lymphoma, as well as primary and metastatic neoplasms. In certain instances, a mass with a large central cavitation is thought to be a lesion having circumferentially thickened bowel wall owing to misinterpretation of large central cavitation as bowel lumen.

The length of intestine involved in the neoplastic process is usually short (<10 cm), except for cases of infiltrative type of lymphoma, signet ring cell colorectal carcinoma, and linitis plastica type of metastatic neoplasm.[205] Multifocal involvement of the bowel is a common manifestation of lymphoma, lipoma, and metastatic neoplasm. As mentioned earlier, the transition zone to the normal segment is abrupt.

When neoplasms form a mass, the tumor margins are usually smooth in benign neoplasms and lobulated, irregular, or spiculated in a malignancy. Although masses with a diameter smaller than 2 cm may be missed by CT scanning,[315] most polypoid or pedunculated mucosal or submucosal masses are detected incidentally by intussusception with small-bowel obstruction. Exophytic tumor growth is favored by some GI neoplasms, including GI stromal tumors, lymphomas, and metastatic melanomas. However, gastric or colonic adenocarcinomas rarely show such behavior. In a series by Lee and associates,[317] the presence of gastric wall thickening adjacent to an exophytic mass favors the diagnosis of exophytic adenocarcinoma rather than GI stromal tumor.

Analyzing the internal constituents of a mass is helpful in establishing a specific diagnosis. The presence of fat within a mass on a CT scan is a pathognomonic finding for lipoma or liposarcoma. When tumors show internal hemorrhage within a mass that is easily detectable on unenhanced CT, the differential diagnosis includes GI stromal tumor and metastatic melanoma. CT is also useful for detecting internal calcification of a mass. This is most commonly seen in mucinous adenocarcinoma and in GI stromal tumors,[93] but other possibilities include neurogenic tumors, carcinoid and adenocarcinoma, or lymphoma treated with chemotherapy or radiation.

Knowing a lesion site is also useful in the differential diagnosis when neoplasm is suspected on CT. In adenocarcinoma of the small intestine, 42% of the locations are in the duodenum, whereas more than 35% involve the proximal jejunum. Lymphomas primarily affect the ileocecal region in children and young adults, but lymphomas complicating celiac disease usually involve the proximal jejunum.

Ninety percent of carcinoid tumors are located in the

ileum.[64] The malignant form of GI stromal tumors occurs with equal frequency in the jejunum or ileum, whereas the jejunum is more common in the benign form. The colon is a rare site of GI stromal tumors, but when these tumors develop in the colorectum, the most common site is the rectum.[287] Most lipomas are located in the ileum or the ileocecal valve.

A contrast enhancement study not only helps to characterize the tumor but also determines the extent of tumor in the GI tract. Contrast enhancement of the soft tissue mass may depend on the desmoplastic response, its vascularity, and the degree of tumor necrosis. One of the typical tumors eliciting a desmoplastic response is scirrhous gastric cancer[28] or signet ring cell carcinoma of the stomach or colorectum. Because these tumors produce abundant fibrosis in the submucosal layer of the GI tract, they are well enhanced after contrast agent infusion. In contrast, lymphomas that do not elicit a desmoplastic response enhance poorly.[343] The accumulation of intracellular or extracellular mucin also affects the degree of contrast enhancement. Thus, mucinous adenocarcinomas are also poorly enhanced.[413]

Vascular Diseases

Mesenteric ischemia occurs in a variety of conditions, including thromboembolism, bowel obstruction, neoplasm, vasculitis, inflammatory bowel diseases, and trauma and as a result of drug or radiation therapy.[501] Hypoperfusion (low-flow state) of the blood flow is also one of the most common causes of bowel ischemia.

The hallmark of a vascular disorder on CT is concentric bowel wall thickening; the thickness usually does not exceed 1.5 cm. The bowel wall becomes much more thicker in mesenteric ischemia caused by mesenteric venous occlusion than in ischemia of arterial origin. However, intestinal ischemia is not always seen with bowel wall thickening. This is partially the result of the inherent limitation of CT for detecting subtle bowel wall thickening. Moreover, bowel wall is thinned or occasionally invisible when the involved segments become gangrenous. A delayed diagnosis of intestinal ischemia is occasionally encountered in cases having normal-appearing or thinned bowel wall.

A thickened bowel wall is commonly associated with target or double-halo signs owing to the accumulation of edematous fluid or hemorrhage in the submucosal layer of the intestine. Although these signs are nonspecific, close observation of these signs in patients with mesenteric ischemia may help to determine the presence or absence of irreversible changes in the GI tract. For example, diffuse disruption of these signs or discontinuity of the outer (serosal) layer may suggest the presence of irreversible bowel changes.

Target or double-halo signs are also helpful in distinguishing whether bowel ischemia originates from thromboembolism or vasculitis.[28] Although the cause is unclear, the target signs in patients with vasculitis are much more clearly layered than in those with thromboembolism.[70]

Intramural or superior mesenteric or portal vein gas is also occasionally demonstrated in the ischemic segments. However, the presence of intramural gas does not always indicate mesenteric ischemia because it can be seen in patients with pulmonary disease, peptic ulcer disease, collagen vascular disease, steroid administration, and intestinal obstruction.[97, 403]

In contrast to cases of mesenteric ischemia, Behçet's syndrome (a nonspecific necrotizing vasculitis involving multiorgan systems) shows concentric bowel wall thickening or polypoid mass formation on CT[212]; the masslike lesion develops because of marked thickening of the intestinal wall surrounding the large ulceration.

When cases of inflammatory and neoplastic bowel disease are compared, one of the most characteristic CT features of intestinal ischemia caused by frequently encountered thromboembolism is the continuity and segmental distribution of involved segments; ischemic bowel is generally confined to the mesenteric vascular territory. In contrast, nonsegmental distribution and multifocal involvement are characteristics of mesenteric ischemia associated with multiple thromboemboli, vasculitis, and drug or radiation therapy.[501] In addition, ischemia proximal to obstructing colonic carcinoma also causes nonsegmental type of distribution, thus helping detect small, hidden malignancy on CT.

Although the length of the involved segment is usually long in mesenteric ischemia caused by thromboembolism, length depends on the levels of vascular occlusion in the mesenteric vessels; the segment is very short when the vasa recta or intramural vessels are occluded and is very long when the proximal main branches are involved. The end result of mesenteric ischemia may be normalization of the intestinal wall, bowel perforation, or stricture formation. In cases of intestinal stricture formation, the involved bowel is very short, simulating adenocarcinoma or stricture caused by chronic inflammatory bowel disease such as Crohn's disease or intestinal TB.

There are preferential sites for certain types of intestinal ischemia. For example, the duodenum and rectum, which are supplied by abundant blood flow, tend not to develop ischemia caused by thromboembolism. However, these sites are a common location of vasculitis; we presume that immune complex deposition occurs more commonly at sites of increased blood flow.[292]

In radiation enterocolitis, the involved site is confined to the radiation port. Post-traumatic stricture resulting from focal deprivation of mesenteric blood supply resulting from a tear in the mesenteric attachment commonly occurs near the proximal or distal extreme of the small intestine where mesenteric mobility commences.[373] Intestinal ischemia proximal to a colonic carcinoma develops at sites that are vulnerable to increased intraluminal pressure caused by bowel distention.[51, 248] According to the application of *Laplace's law*, tension in the bowel wall increases with both increasing intraluminal pressure and increasing diameter of the obstructed bowel.

Contrast enhancement patterns of vascular disorder, especially mesenteric ischemia, are characteristic. The ischemic segments are not enhanced or are poorly enhanced in the early phase[208] but demonstrate prolonged enhancement in the late phase.[620] These enhancement patterns result from perfusion problems associated with the ischemic segment (i.e., delayed return of the venous blood, with subsequent slowing of the arterial supply in mesenteric venous occlusion and arteriospasm in arterial occlusion). Poor contrast

enhancement or an absence of contrast is reported to be one of the most valuable findings in differentiating simple from strangulated intestinal obstruction, although its sensitivity is not high (34%).[208]

Perigastric, Perienteric, or Pericolonic Changes

Inflammatory Diseases

CT is useful for defining various mesenteric, perienteric and pericolonic abnormalities that commonly occur in inflammatory diseases. Bowel separation is a common finding in Crohn's disease on barium study regardless of the primary cause. CT clearly determines the causes of bowel separation, such as fibrofatty proliferation, abscess formation, phlegmonous changes, and lymphadenopathy. In patients with ulcerative colitis, CT helps to define the causes of widening of the presacral space, such as increased fat deposition, inflammatory infiltration of perirectal fat, or rectal wall thickening.

Although observing mucosal changes is important in identifying GI diseases, differentiating Crohn's disease from intestinal TB is not always easy with barium study, which is the only reliable radiologic tool for assessing mucosal detail. However, observing perienteric or peritoneal changes on CT scans may occasionally yield clues for resolving the difficulty. The presence of partially calcified, enlarged lymph nodes with low-attenuation centers caused by central caseation necrosis is the most diagnostic finding in intestinal TB. Other findings favoring a diagnosis of intestinal TB include diffuse infiltrations in the omentum and mesentery and multiple enlarged nodes larger than 1 cm; the latter finding is unusual in cases of Crohn's disease (usually 3 to 8 mm) if lymphoma or adenocarcinoma is not a complication.[188] In contrast, the incidence of fibrofatty proliferation is much higher in Crohn's disease.

There are several GI diseases in which the presence of inflammatory infiltrates in the perienteric or pericolonic fat adjacent to the bowel is crucial for making a specific diagnosis. The most typical cases in such circumstances include acute appendicitis, primary epiploic appendagitis, and diverticulitis. The definitive diagnosis of *acute appendicitis* is made on CT images by identifying a combination of abnormal-appearing appendix (>6 mm in diameter or nonopacified), periappendiceal inflammatory infiltrates, and a calcified appendicolith.[487, 490] In the absence of abnormal thickening of the appendiceal wall or periappendiceal inflammation, the presence of calcific appendicoliths or air is not clinically significant. Periappendiceal inflammatory changes without evidence of abnormal appendix or appendicolith is a suggestive but nonspecific finding because such conditions can occur in a variety of pathologic conditions (Crohn's disease, typhlitis, diverticulitis, pelvic inflammatory disease, and perforated carcinoma).

Primary epiploic appendagitis is a rare inflammatory intra-abdominal process attributable to either torsion or spontaneous venous thrombosis of an epiploic appendage with subsequent ischemic infarction and inflammation.[575] CT findings are virtually pathognomonic for establishing the diagnosis, and they include a pericolonic, oval-shaped lesion with fat attenuation, thickened visceral peritoneal lining, and pericolic fat stranding.[489, 504]

Diverticulitis results from diverticular perforation with resultant intramural, pericolic, or peritoneal inflammation. On CT, diagnostic findings include the presence of pericolic inflammation and edema, appearing as regions of linear stranding or hazy increased density in the pericolonic fat adjacent to the site of diverticular perforation. In more severe cases, pericolonic phlegmon or abscess may be present.

In the clinical setting, the differentiation of diverticulitis from colonic cancer is crucial for appropriate clinical management. Balthazar and colleagues[24] reported that the imaging appearances overlapped in about 10% of cases. Some researchers have stressed the importance of observing pericolonic or perienteric and mesenteric changes.[86, 87] The incidence of pericolonic lymphadenopathy is much higher in patients with colonic cancer than in patients with diverticulitis, whereas CT findings of fluid at the root of the mesentery and vascular engorgement are much more common in patients with diverticulitis.[446]

Neoplastic Diseases

In a patient with neoplastic disease, distinguishing the depth of tumor invasion in the bowel wall cannot be made with CT. Therefore, observing perigastric or pericolonic or perigastric changes may be essential for staging gastric or colorectal cancers; the margin of the stranding in neoplastic diseases generally appears sharper than that of inflammatory bowel diseases.

Extension of tumor beyond the bowel wall is suggested when the outer borders of involved bowel wall are irregular along with soft tissue or linear strandings in the pericolonic or perigastric fat plane. However, use of these CT signs in staging the tumors has been limited. It is because CT is not sensitive enough to detect microscopic invasion of the adjacent fat. Therefore, a sharp outer border of the bowel wall without strands in the adjacent fat cannot exclude the possibility of tumor extension beyond the bowel wall. Moreover, vascular or lymphatic congestion, coexisting inflammatory changes, acute and chronic radiation changes, or paucity of fat caused by cachexia may produce extraluminal changes similar to those of tumor infiltration.

In addition, *carcinoid tumor* is one of the neoplastic diseases in which CT features provide a reliable and specific diagnosis by revealing the mesenteric change. On CT, these tumors show linear or curvilinear soft tissue strands in the mesenteric fat, radiating from the primary mass to the displaced and angular bowel loops.[465]

Vascular Diseases

In patients with suspected mesenteric ischemia, perienteric or pericolonic changes appear to be somewhat different from those in inflammatory and neoplastic diseases. The presence of both diffuse mesenteric haziness and vascular engorgement is the hallmark of vascular diseases that have outflow disturbance of mesenteric blood flow caused either by mesenteric or portal venous occlusion or by increased mesenteric or portal venous pressure. In contrast, cases of *mesenteric arterial occlusion*, a disorder with inflow disturbance of the mesenteric vessels, do not show mesen-

teric engorgement. In most patients with mesenteric inflow disturbance, however, collateral circulations develop in the mesentery, retroperitoneum, or both. Unfortunately, CT does not clearly discriminate whether increased mesenteric vessels indicate mesenteric engorgement or abundant collateral circulation. Therefore, it is important to scrutinize the presence of thromboembolism in mesenteric vessels if the mesenteric vessels are increased in number, if the diameter or mesenteric haziness is seen, and if advanced liver cirrhosis, which causes increased mesenteric and portal venous pressure, is excluded.

In patients thought to have small-bowel obstruction due to bowel adhesions and bands, volvulus, and hernia, observing mesenteric vascular changes is important to distinguish simple from strangulated intestinal obstruction. Although the presence of severe mesenteric haziness and vascular engorgement favors the diagnosis of strangulated obstruction,[208] a mild degree of such vascular changes is also demonstrated in simple obstruction. However, one may have difficulty in determining the degree of these vascular changes with CT. Accordingly, the signs of mesenteric vascular engorgement and haziness should be interpreted cautiously on CT scans in patients for whom the decision of simple from strangulated intestinal obstruction is critical.

An unusual mesenteric vascular course, such as mesenteric vascular twisting *(whirl sign)*, is also known to be highly specific for the diagnosis of strangulated obstruction.[208] This sign was originally reported in patients with intestinal malrotation associated with volvulus.[154] The whirl sign can also be seen in asymptomatic patients who have undergone gastrectomy with surgical maneuver of the small intestine.

Although mesenteric vascular changes are more commonly seen in patients with vascular disorders, a small group of patients with inflammatory bowel disease, such as Crohn's disease, shows hypervascularity in the perienteric or pericolonic spaces or in the mesentery. This hypervascularity is found in the earlier or active stages of Crohn's disease rather than in the chronic stages.[358] Even though the cause of this finding is not well understood, some researchers hypothesize that hypervascularity is the result of vasculitis with hypercoagulability leading to ischemia,[591] and more recent studies have demonstrated an increased expression of somatostatin receptors in the veins of inflamed intestine.[498] In addition, because bowel ischemia can develop in the colon proximal to cancers, a small tumor can be missed if pericolonic vascular engorgement and haziness due to coexisting colonic ischemia are prominent.

Esophagus

Techniques and Anatomy

The esophagus extends from the pharynx to the cardia of the stomach. It is 20 to 25 cm in length and distends up to 30 mm in breadth but is collapsed at rest.[441] It may be divided into three parts:

1. The *cervical* segment is located near the midline and is posterior to the trachea.

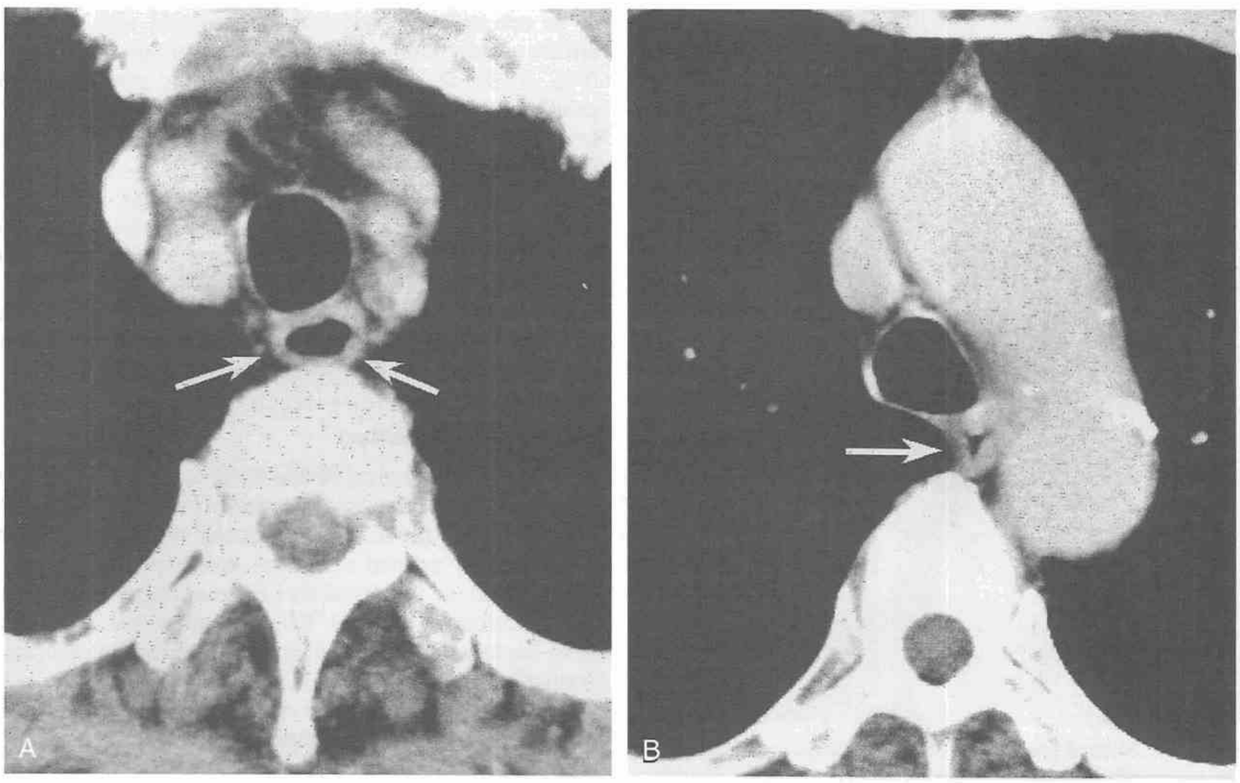

Figure 34–3. Normal esophagus. The cervical *(A)* and thoracic *(B)* segments *(arrows)* of normal esophagus appear as well-defined circular structures of soft tissue on this CT scan.

2. The *thoracic* segment is the longest and lies behind the trachea until the trachea bifurcates.
3. The *abdominal* segment is the shortest segment; it is only a few centimeters in length, escapes the diaphragmatic hiatus, and runs to the cardia of the stomach.

On CT, the esophagus appears as a well-delineated circle of soft tissue (Fig. 34–3). Although the wall thickness of the collapsed esophagus has no absolute normal size, a well-distended esophagus should not exceed 3 mm in wall thickness,[495, 525] and eccentric thickening of the wall should suggest a pathologic condition.[218] An anteroposterior diameter of the esophagus larger than 16 mm and a lateral diameter larger than 24 mm are considered abnormal, although they may increase with advancing age (Fig. 34–4). A small amount of air in the esophagus is visible in approximately 65% of normal individuals, but an air-fluid level, fluid-filled lumen, or lumen caliber higher than 10 mm usually indicates obstruction or severe esophageal dysmotility.[380, 395, 417]

With magnetic resonance imaging (MRI), the normal esophagus is routinely well visualized in the upper thoracic and gastroesophageal regions (Fig. 34–5), whereas the middle portion of the esophagus is flattened behind the left atrium, sometimes making its visualization difficult.[395] The MRI appearance of normal esophageal wall is a low-signal-intensity structure, well defined by high signal intensity of periesophageal fat on T1-weighted images. The normal esophagus also appears with low signal intensity contrasted with high signal intensity of internal contents on T2-weighted image. After administration of IV gadolinium diethylene triaminepentaacetic acid (Gd-DTPA), the muscle layer of the esophagus shows moderate enhancement.[475, 528]

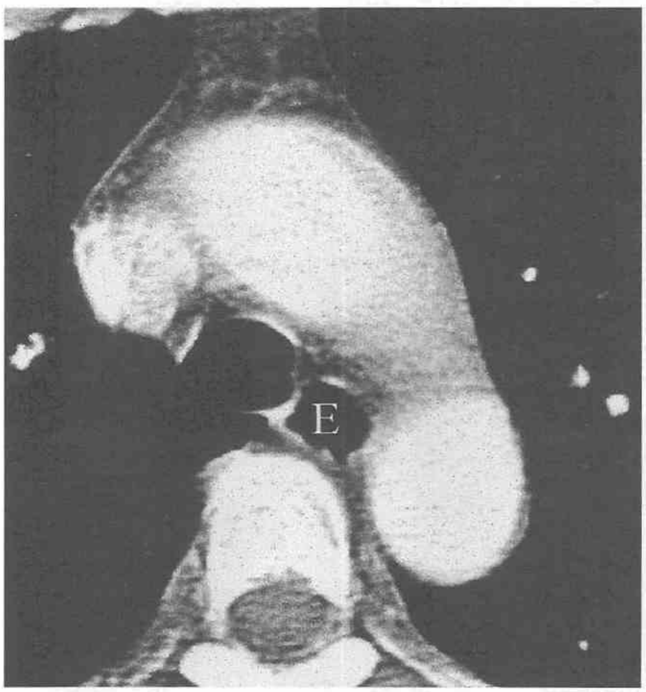

Figure 34–4. Normal esophagus of a 77-year-old man. The lumen of the esophagus (E) is somewhat dilated; however, in older people, mild air-filled dilatation of the esophagus is regarded as a normal condition.

Benign Tumors

Benign tumors of the esophagus are not a common condition, and they contribute about 20% of esophageal neoplasms.[350] Depending on the site of origin, benign esophageal tumors comprise mucosal and submucosal lesions. On CT or MRI, small lesions cannot be demonstrated, so that barium study appears to be superior to cross-sectional image in providing information about small lesions.

Leiomyoma (Stromal Tumor)

The stromal tumor of the esophagus is the most common benign esophageal tumor, accounting for more than 50% of all benign esophageal tumors.[446] Histologically, it is characterized by proliferation of smooth muscle and is most frequently located in the distal third of the esophagus (60%), followed by the middle third (30%) and the proximal third (10%).[533] Most patients are asymptomatic, but some may present with dysphagia, depending on the size of the lesion and how much it encroaches on the lumen. Although most esophageal stromal tumors occur as a solitary lesion, multiple lesions are present in 3% to 4% of patients; the lesion is often associated with Alport's syndrome in children.[185, 477]

Occasionally, stromal tumors arising near the gastroesophageal junction may involve not only the distal esophagus but also the gastric cardia and fundus.[530] In this location, these tumors may cause severe dysphagia due to obstruction of the distal esophagus, and it may be difficult to distinguish them from carcinoma of the cardia involving the distal esophagus.

On CT, a stromal tumor appears as an intraluminal mass or as eccentric or concentric esophageal wall thickening, which usually shows homogeneous soft tissue attenuation (Fig. 34–6) and in rare instances may contain irregular calcifications (Fig. 34–7). The peripheral margins of the lesion are usually smooth, and the surrounding mediastinal fat planes are intact.[380, 399] Sometimes CT appearances of stromal tumor are nonspecific and indistinguishable from those of a localized malignant tumor. In leiomyomatosis, CT reveals marked circumferential or eccentric wall thickening of the distal esophageal wall with soft tissue attenuation. In addition, CT may occasionally show a mass bulging into the gastric fundus or uncharacteristic achalasia associated with distal esophageal wall thickening.[337, 477]

Fibrovascular Polyp

Fibrovascular polyp of the esophagus is a rare, benign intramural tumor that is composed of loose or dense fibrous tissue, adipose tissue, and a vascular structure. The polyp is covered by normal squamous epithelium. It usually develops from the upper third of the esophagus near the level of the cricopharyngeus. This lesion probably originates from the loose submucosal tissue of the cervical esophagus, gradually elongating over a period of years as the polyps are dragged into the middle or distal third of the esophagus by esophageal peristalsis until the intraluminal portion of the lesion becomes massive.[11, 30, 78, 339, 600]

These polyps usually occur in elderly men. Common symptoms include long-standing dysphagia, vomiting,

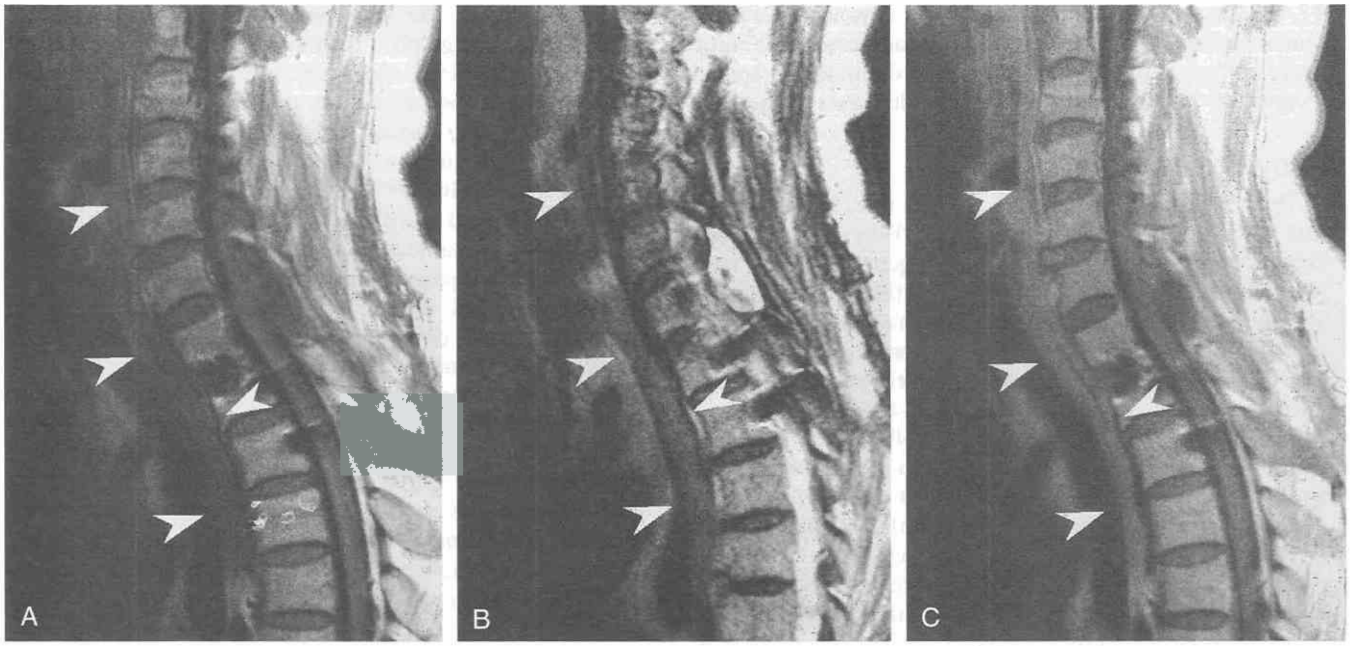

Figure 34–5. MR images of normal esophagus. *A,* On the T1-weighted image, the signal intensity of normal esophageal wall *(arrowheads)* is low. *B,* On the T2-weighted image, the signal intensity of the esophageal wall *(arrowheads)* is also low, contrasted with internal contents of high signal intensity. *C,* After administration of gadolinium-DTPA, esophageal wall *(arrowheads)* shows moderate enhancement.

weight loss, and respiratory difficulty. Occasionally, fibrovascular polyps with a long stalk can be regurgitated into the pharynx or mouth, resulting in sudden death from laryngeal occlusion.[11, 78] Small lesions can be removed endoscopically, but larger masses should be excised surgically because of the potential for hemorrhage.

CT shows a wide spectrum of attenuation from fat to soft tissue, depending on the amount of adipose and fibrovascular tissue in the polyp.[339] If adipose tissue content predominates, intraluminal esophageal mass with fat attenuation is considered as a typical CT sign of a fibrovascular polyp.[11] In addition, CT may help to determine the intraluminal location of the lesion, particularly when oral contrast material surrounds a mass.

MRI demonstrates a lipid-containing substance, mucoid secretion, and nonacute blood within the tumor; on T1-weighted images, high signal intensity is present, and on

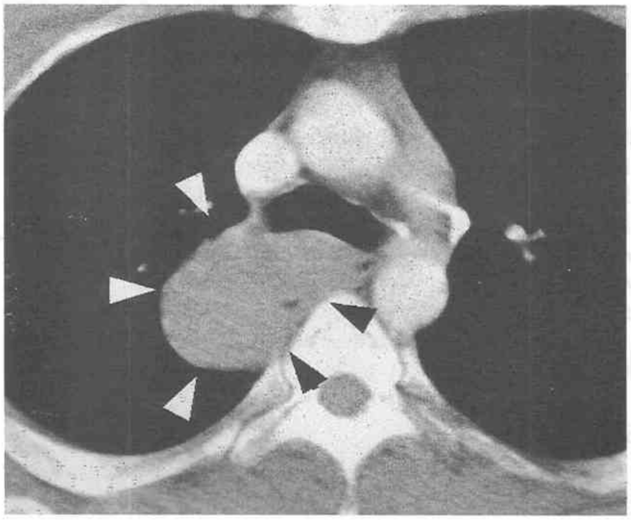

Figure 34–6. Leiomyoma of the esophagus. CT scan shows an eccentric mass *(arrowheads)* of the esophagus at the level of the carina. The lesion shows a smooth margin and homogeneous soft tissue attenuation.

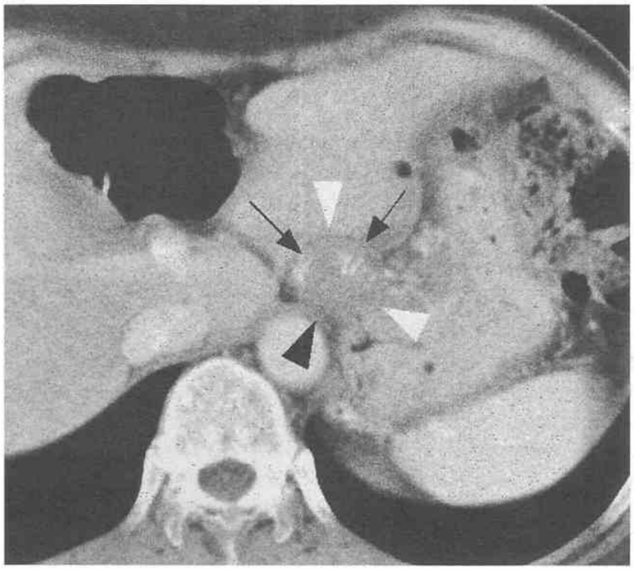

Figure 34–7. Calcified leiomyoma of the esophagus. CT scan demonstrates concentric wall thickening *(arrowheads)* of the gastroesophageal junction. This lesion contains multifocal calcifications *(arrows)*.

T2-weighted images, soft tissue and muscle within the tumor display low signal intensity. In addition to defining tissue composition, MRI is helpful in defining the spatial location of the mass with the use of multiplanar images.[11, 78]

Hemangioma

Hemangioma of the esophagus is a rare, benign tumor that has been reported in fewer than 5% of all esophageal benign tumors.[414] Although the pathogenesis of this neoplasm is still controversial, most agree that hemangioma is a vascular hamartoma or tumor-like malformation.[193] The most common symptoms include hemorrhage and dysphagia. Other minor symptoms are epigastric pain, chest pain, retrosternal pain, weight loss, choking, and melena.[193]

On CT, hemangioma shows a well-defined homogeneous mass with soft tissue attenuation, occasionally containing a small calcification regarded as a phlebolith. After administration of a contrast agent, significant enhancement is usually present, indicating high vascularity; in atypical cases, however, enhancement may be poor.[447, 581] With MRI, hemangioma of the esophagus is manifested as an isointense mass on T1-weighted images and as a hyperintense mass on T2-weighted images. Both fibrosis and reduction of blood flow in the hemangioma may raise the signal intensity on T1-weighted images.[581]

Esophageal Carcinoma

Most malignant neoplasms of the esophagus are squamous cell carcinoma and/or adenocarcinoma. Other rare malignant tumors include spindle cell carcinoma, small-cell carcinoma, malignant stromal tumor, Kaposi's sarcoma, and malignant melanoma. Although squamous cell carcinoma contributes to most cases of esophageal cancer, adenocarcinoma has recently been found to be the predominant type in patients with newly diagnosed esophageal carcinoma, and Barrett's esophagus is seen in many of these patients.[299, 335, 341]

Various terms have been used to describe the status of esophageal carcinoma,[372] for example:

Early esophageal cancer, limited to the mucosa or submucosa without lymph node metastasis
Superficial spreading cancer, limited to mucosa or submucosa with or without lymph node metastasis
Small esophageal cancer, in which the tumor size is less than 3.5 cm, regardless of the depth of invasion and the presence or absence of lymph node metastasis

CT and MRI have been used to stage esophageal carcinoma, because these techniques can reveal extraesophageal extension into adjacent mediastinal structures, including the trachea, bronchi, aorta, and pericardium, and can detect lymphadenopathy in the mediastinum. The main goal of staging is to identify nonresectable lesions and thereby avoid the morbidity of major surgery in patients who would not benefit from such intervention.[221, 417]

Squamous Cell Carcinoma

Squamous cell carcinoma of the esophagus has been thought to occupy about 90% of cases of primary esophageal malignancy. The incidence of this tumor is variable according to geographic location, with the highest incidences in China, Iran, and South Africa.[148, 428] In the United States, tobacco and alcohol are the two major risk factors; other predisposing factors include achalasia, lye strictures, head and neck tumors, celiac disease, Plummer-Vinson syndrome, and tylosis.[609]

Dysphagia and weight loss are the classic presenting symptoms of squamous cell carcinoma. When dysphagia develops, the esophageal lumen has been already reduced by more than 50% of its normal caliber and approximately two thirds of the circumference of the esophageal wall is invaded by the tumor.[189, 335, 609] Ulceration in the tumor may produce odynophagia, and patients may have chest pain unrelated to swallowing if the tumor has invaded the mediastinum.

Squamous cell carcinoma may directly invade the adjacent structures involving the trachea, bronchi, lungs, pericardium, aorta, and diaphragm and may spread to lymph nodes in the mediastinum, neck, and upper abdomen. This tumor can also readily metastasize to the lungs, liver, adrenal glands, and other structures through the bloodstream.[341]

Adenocarcinoma

The most important predisposing factor in development of adenocarcinoma of the esophagus is Barrett's esophagus, of which 40% of cases progress to esophageal adenocarcinoma, called *Barrett's carcinoma*.[84, 144, 299, 335, 341, 342, 372, 417] In patients with Barrett's esophagus, the normal squamous epithelium in the distal esophagus is transformed to columnar epithelium, presumably as a result of chronic reflux disease, with the columnar epithelium extending more than 2 cm above the esophagogastric junction. Unlike squamous cell carcinomas, which tend to occur in the upper mid-esophagus, two thirds of adenocarcinomas arising in Barrett's esophagus are located in the distal esophagus and tend to invade the gastric cardia and fundus.[341] At present, 50% of the tumors at the gastroesophageal junction are thought to be Barrett's carcinoma that is invading the stomach.[417]

Patients with esophageal adenocarcinomas typically present with recent onset of dysphagia and weight loss. Like squamous cell carcinoma, unfortunately, by the time dysphagia has occurred, tumors are usually advanced, so that the prognosis is poor. Moreover, the adenocarcinoma does not respond to chemotherapy and radiation therapy, as does the squamous cell carcinoma.[335, 372] Many investigators advocate endoscopic surveillance of asymptomatic patients with known Barrett's esophagus to detect the dysplastic changes prior to the development of overt carcinoma. Occasionally, early adenocarcinomas can also be detected fortuitously in patients with underlying reflux disease.

Staging

The accurate pretreatment staging of esophageal cancer is important because it determines the operability and the goal of operation, that is, whether treatment will be curative or palliative. The *Tumor-Node-Metastasis (TNM) classification*, in which esophageal tumors are specified according to extent of tumor spread, nodal involvement, and distant

Table 34–1. TNM Staging System for Esophageal Cancer

T—Primary Tumor		N—Regional Lymph Nodes		M—Distant Metastasis	
Tis	Carcinoma in situ	N0	No regional nodes	M0	No distant metastasis
T1	Tumor invades mucosa or submucosa	N1	Regional nodal metastasis*	M1	Distant metastasis†
T2	Tumor invades muscularis propria				
T3	Tumor invades adventitia				
T4	Tumor invades adjacent structures				

* Regional lymph nodes include cervical, mediastinal, and perigastric nodes.
† Celiac lymph node metastasis is regarded as N1 in adenocarcinoma; however, it is regarded as M1 in squamous cell carcinoma.

metastasis, is the most widely accepted system of staging for esophageal cancer (Tables 34–1 and 34–2).[189, 521] TNM staging for both squamous cell carcinoma and adenocarcinoma is similar with minor exceptions in staging related to regional and distant nodal metastases. The criterion for N1 regional nodal metastases for squamous carcinoma includes involvement of cervical, mediastinal, and perigastric nodes. The presence of celiac lymph node metastases in squamous cell carcinoma, however, is classified as M1 (i.e., distant metastasis) versus N1 (i.e., regional nodal disease) for esophageal adenocarcinoma.[521, 580]

Although many investigators have evaluated and compared the usefulness of CT and MRI in staging esophageal carcinoma, controversies remain about which imaging modality is superior. In clinical situations, CT is usually recommended as a routine examination before treatment planning, and CT staging criteria correspondent to the TNM staging system have been proposed by some investigators.[464, 576] Whichever modality is used to stage esophageal carcinoma, the extent of involvement of the esophageal wall by tumor, invasion of adjacent structures, and metastasis of disease to regional nodes or distant organs is the major issue for the radiologist.

Tumor Staging

On CT scans, esophageal carcinoma appears as a mass or wall thickening with soft tissue attenuation. With MRI, esophageal carcinoma is seen as an area of isointensity relative to residual esophageal wall on T1-weighted images and as an area of high signal intensity on T2-weighted images.[563] The depth of tumor infiltration into the esophageal wall, one of the most important prognostic factors, can best be evaluated by endoscopic ultrasonography, which can directly visualize all layers of the esophageal wall.[240]

Compared with endoscopic ultrasonography, CT and MRI are not reliable tools for evaluation of the extent of the tumor in the esophageal wall because they cannot definitively demonstrate the individual layers of the wall. Therefore, CT and MRI cannot differentiate T1 from T2 tumor.[459] In one series in which specimens of esophageal carcinoma were examined with 4.7 T, MRI demonstrated all layers of the esophageal wall, which correlated with pathologic examination.[610] In the future, technical development in imaging modality may improve the ability of CT or MRI to delineate these layers.

Macroscopic periesophageal fat invasion by the tumor can be demonstrated with high accuracy on CT and MR images, although microscopic invasion to periesophageal fat is not revealed.[102, 459] On CT scans, periesophageal fat invasion is shown as strandlike areas of soft tissue attenuation that generate a feathery appearance within the periesophageal fat plane (Fig. 34–8).[417] MRI shows periesophageal fat invasion as having an ill-defined, irregular margin, regional absence of a bright fat signal, and tumor mass into the adjacent mediastinal fat.[240, 610] The overall accuracy of periesophageal fat invasion of esophageal carcinoma

Table 34–2. Stage Grouping of Tumor-Node-Metastasis (TNM) Classification

Stage Grouping	T	N	M
0	Tis	N0	M0
I	T1	N0	M0
IIA	T2	N0	M0
	T3	N0	M0
IIB	T1	N1	M0
	T2	N1	M0
III	T3	N1	M0
	T4	N0–1	M0
IV	T1–4	N0–1	M1

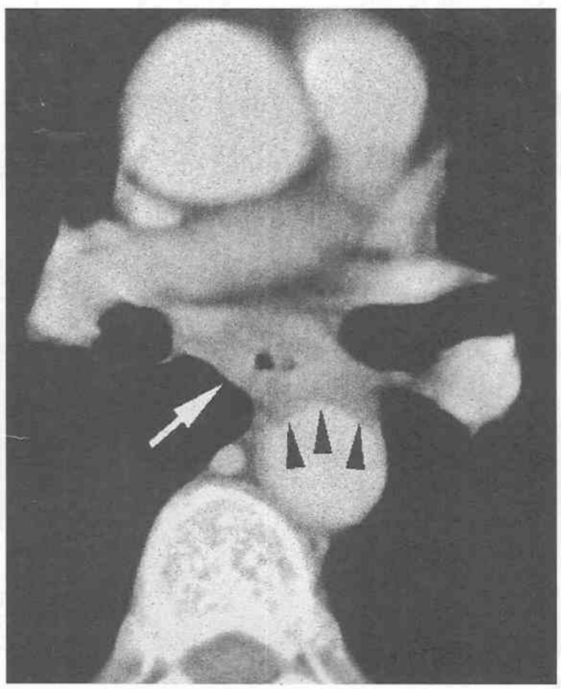

Figure 34–8. Esophageal cancer invading mediastinal fat. CT scan demonstrates circumferential wall thickening of the distal esophagus *(arrow)*. The periesophageal fat is replaced by soft tissue attenuation *(arrowheads)*.

on CT or MRI ranges from 88% to 100%.[240] Although periesophageal fat infiltration adversely affects prognosis, it is not a contraindication to en bloc resection of tumor as a curative treatment.[417]

Accurate evaluation of tracheobronchial, aortic, and bone invasion is important because these are contraindications to surgical resection. The most frequent sites of tracheobronchial involvement are the distal trachea and the left mainstem bronchus.[108] CT or MRI appearances of tracheobronchial invasion are displacement or indentation of the posterior wall of the trachea or the bronchus by tumor mass as well as evidence of direct extension of the tumor into the lumen of the airway (Fig. 34–9). Reported data indicate that the overall accuracy of tracheobronchial invasion of esophageal carcinoma ranges from 88% to 97%.[240] The absence of an intervening fat plane alone, however, does not always suggest tumor invasion because this finding can be seen in normal patients.[380] Moreover, an adjacent mass behind the trachea or main bronchus can produce concavity of the posterior portion of them without invasion (Fig. 34–10) because the cartilage rings are incomplete in the posterior portion of the trachea and main bronchi.[175]

According to Picus and coworkers,[464] aortic invasion can be diagnosed by CT if the area of contact between the esophageal cancer and the aorta creates an arc of more than 90 degrees (Fig. 34–11). The accuracy of this *90-degree criterion* is more than 90% when mediastinal fat planes are preserved above and below the tumor.[36, 464, 576] If the arc is less than 45 degrees, aortic invasion is considered to be absent; an arc of 45 to 90 degrees is considered indeterminate.[464] The overall accuracy of MRI in evaluating aortic invasion is similar to that of CT.[175, 459, 563] Although the presence of the fat plane rules out invasion, absence of the fat plane between the aorta and tumor does not always indicate invasion, such as in tracheobronchial invasion.

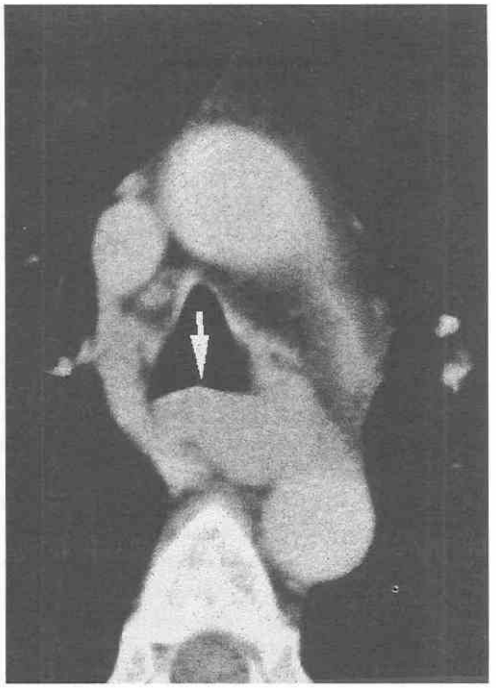

Figure 34–10. Concavity of the posterior tracheal wall mimicking invasion. Although the posterior tracheal wall is concave *(arrow)*, the surface of the posterior wall is smooth. Note that only the concavity of the trachea without surface irregularity or apparent intraluminal protrusion does not suggest the tumor invasion.

This major pitfall occurs in cachectic patients in whom the fat planes are absent throughout the mediastinum. Without clear evidence of displacement of the aorta and direct contact between the aorta and tumor, aortic invasion cannot be diagnosed.[380]

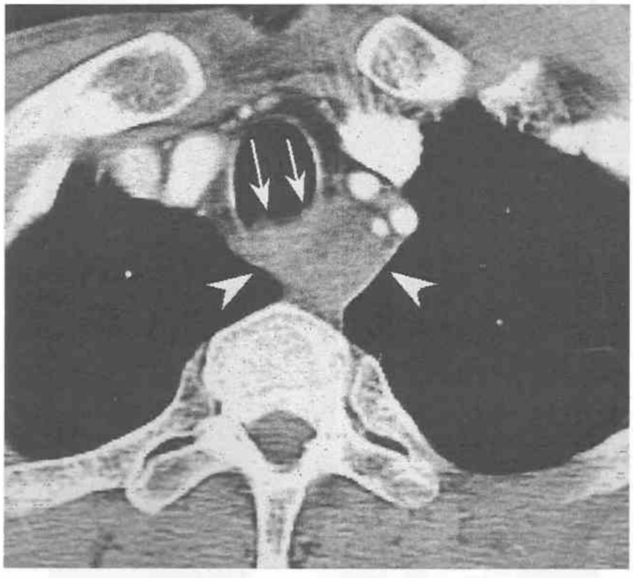

Figure 34–9. Esophageal cancer with tracheal invasion. CT scan shows circumferential wall thickening of the proximal esophagus *(arrowheads)*, which shows irregular interface with the posterior wall of the trachea *(arrows)*, indicating direct extension into the lumen.

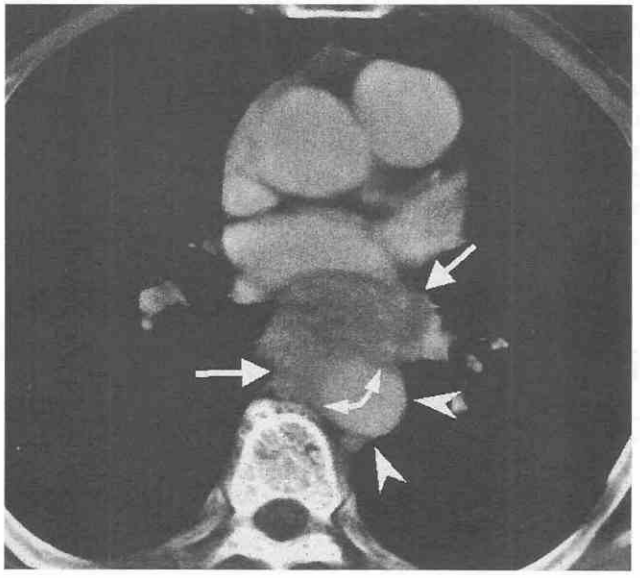

Figure 34–11. Esophageal cancer with aortic invasion. An arc *(curved arrow)* of the contact between the esophageal cancer *(arrows)* and the aorta *(arrowheads)* is more than 90 degrees, indicating aortic invasion.

Bone invasion can be easily identified on CT or MRI with the findings of bone destruction and replacement of bone by soft tissue that are continuous with the main tumor mass.[380, 563] Pleural, pericardial, diaphragmatic, and gastric invasion are not contraindications to surgery because the involved areas can be removed together with the tumor mass at the time of operation. Therefore, the misdiagnosis with CT in identifying tumor involvement in these areas is less critical.[36, 576] Pericardial invasion can be readily diagnosed with high accuracy, ranging from 88% to 97%.[474, 578]

CT or MRI appearances of pericardial invasion[474, 563] are as follows:

1. Pericardial thickening adjacent to the tumor.
2. Pericardial effusion.
3. Inward deformity of the heart with loss of the intervening fat plane at the level of the tumor, with intact fat above and below the tumor.

Although the patient may be cachectic or may have undergone radiation, which can obliterate normal fat planes, tumor invasion should be suggested when a localized obliteration of the fat plane is noted with preserved fat planes above and below the lesion.[222, 417, 580] The CT feature of gastric invasion is a soft tissue mass extending from the esophageal tumor into the proximal stomach under adequate distention.[464] On MR images, gastric tumor extension is diagnosed when a T2-weighted image depicts a mass of high signal intensity to the gastric wall extending from the esophageal tumor into the gastric fundus.[563]

The overall accuracy of gastric invasion on CT and MRI ranges from 79% to 97%.[240, 563] Gastric invasion frequently occurs when the tumor locates in the distal esophagus, especially in adenocarcinoma. Pleural and diaphragmatic invasion cannot be clearly demonstrated on CT[464, 474] because adhesion to these structures by tumor can easily occur without invasion.

Lymph Node Metastasis

Metastatic spread of esophageal cancer occurs commonly in regional or distant lymph nodes because a rich network of lymphatic channels along the esophagus and lack of serosa allows early extraesophageal tumor invasion.[521] Cross-sectional images, including endoscopic ultrasonography, CT, and MRI, have shown a wide range of accuracy in detecting lymph node metastasis.[240, 419, 459] However, most concur that endoscopic ultrasonography shows the highest accuracy (73% to 88%) among them.[240, 419]

With regard to the accuracy of CT and MRI, one prospective series showed only 56% accuracy for mediastinal lymph nodes and 45% for abdominal lymph nodes.[240] Although controversial, MRI may provide accuracy similar to that of CT in detecting a metastatic mediastinal lymph node.[328] It has been widely accepted that lymph nodes with a short axis greater than 1 cm in diameter should be considered to be a metastasized node in the periesophageal region, other mediastinal regions, and the abdomen.[606] However, this criterion still poses a problem because of the high frequency of false-positive and false-negative results.[578]

In some instances, concomitant presence of inflammation associated with tumor may produce large lymph nodes, which limits the accurate predictions of lymph node metastasis on CT. The size criteria for lymph node metastasis typically used for CT are not applicable to esophageal tumors because of microscopic invasion of normal sized nodes. Application of different size criteria to some lymph node chains may improve the capability of cross-sectional imaging for determining metastatic node; according to Balfe and associates,[16] the upper limit of normal lymph node in gastrohepatic ligament was 8 mm.

Distant Metastasis

The liver (32%) and the lung (21%) are the target organs most frequently affected by esophageal carcinoma metastasis. CT clearly demonstrates the metastatic lesions in solid upper abdominal organs and the lung. On CT scans, pulmonary metastasis is shown as one or multiple nodules, and pleural effusion may coexist. Often a single pulmonary nodule produces the dilemma in predicting metastasis. In this situation, biopsy of the solitary pulmonary nodule is usually recommended. Liver metastasis manifests as single or multiple nodules with variable size and ill-defined margins, which are not enhanced as much as normal parenchyma after administration of an IV contrast agent. Although the frequency is low, central necrosis in the metastatic nodule may mimic hepatic cyst.[380]

Adrenal gland enlargement may be another pitfall in the evaluation of metastasis. Adrenal enlargement in patients with esophageal cancer does not always indicate metastasis, because adrenal adenoma is the most common cause of adrenal enlargement. Therefore, radiologic differentiation of adrenal metastasis from adenoma is important in the management of patients with esophageal cancer. Findings that lead to radiologic diagnosis of adenoma include a homogeneous mass, a diameter less than 5 cm, and an attenuation value between −5 and 10 Hounsfield units (HU) on CT.[279] Compared with adenoma, adrenal metastasis usually shows an enlarged heterogeneous gland with loss of normal adrenal shape.[606]

Resectability, Postoperative Findings, and Recurrence

The actual goal of pretreatment staging in esophageal carcinoma is to evaluate tumor resectability. The major criteria for nonresectability include (1) aortic invasion, (2) tracheal invasion, and (3) distant metastasis. According to Takashima and colleagues,[563] sensitivity, specificity, and accuracy for resectability are 100%, 84%, and 87%, respectively, for MRI and 100%, 80%, and 84%, respectively, for CT.

In evaluating patients with esophagogastrectomy, the radiologist must be aware of postoperative appearance. Normal postoperative CT features have been described by Heiken and coworkers.[229] In patients who have undergone a high anastomosis with gastric conduit, both the esophagogastric junction and the stomach are located in the right paravertebral area, and the proximal esophagus above the anastomosis can be dilated (Fig. 34–12). In the lower retrocardiac area, the stomach passes from right to left directly anterior to the descending aorta and then begins to narrow as it enters the diaphragmatic hiatus anterior to the aorta. In patients who have undergone low esophagogastric anastomosis, the esophagogastric junction and the stomach

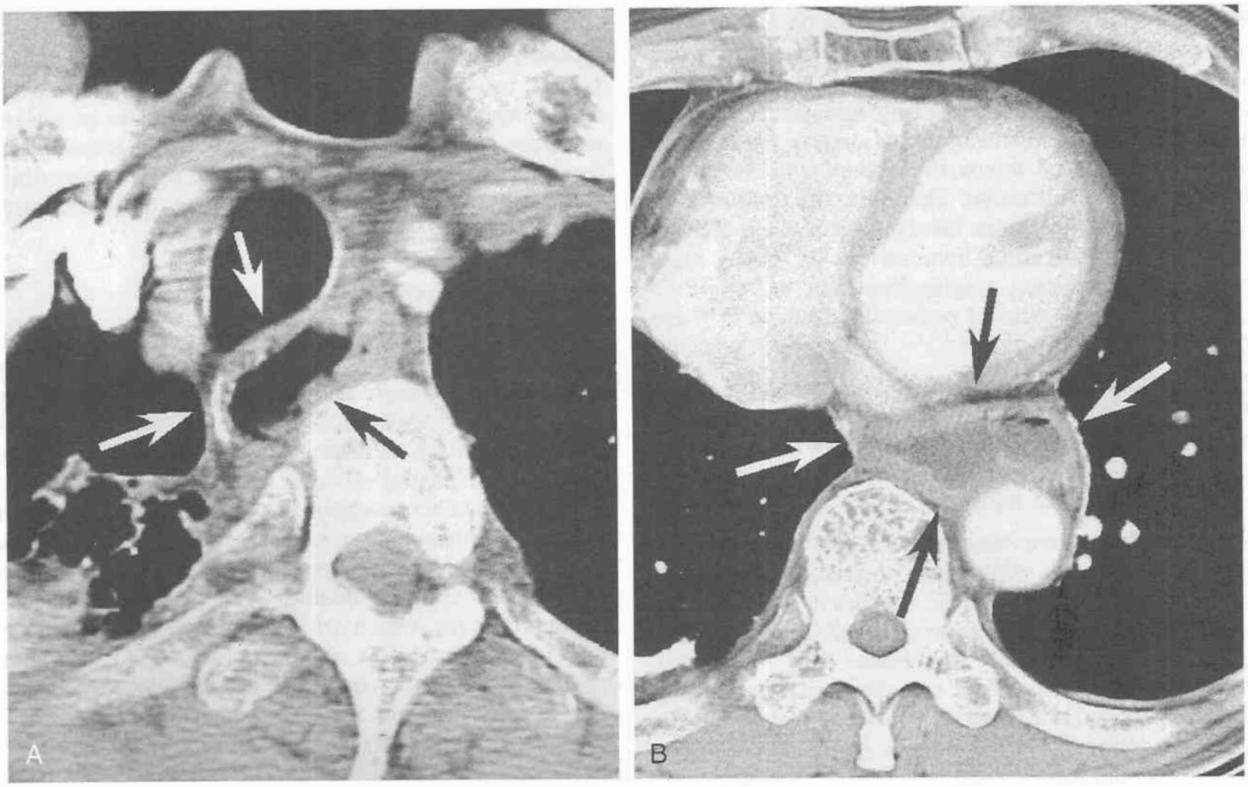

Figure 34–12. Postoperative status of esophageal cancer (high esophagogastric anastomosis). *A,* Proximal anastomosis (esophagogastric junction) *(arrows)* is located posterior to the trachea and right to the vertebra. *B,* In the distal portion, the stomach *(arrows)* passes from right to left in front of the descending aorta.

lie in the left paravertebral region adjacent to the lower thoracic descending aorta.

CT and MRI can play a role in postoperative evaluation because they aid in the diagnosis of early postoperative complications, including mediastinitis or abscess caused by anastomotic leak, lung parenchymal consolidation, pleural effusion or empyema, and subphrenic abscesses.[200, 229, 515] Among these complications, mediastinitis related with anastomotic leak is fatal. When patients who have undergone esophagectomy present with cervical, thoracic, or epigastric pain, fever, dysphagia, or respiratory distress, complications related to anastomotic leak should be considered.[515]

CT findings with postoperative recurrence include soft tissue mass, impression and displacement of normal structures, metastasis to distant organs, abdominal lymph node enlargement, pericardial effusion, and pleural effusion.[75]

Other Malignant Tumors

Small-Cell Carcinoma

Small-cell carcinoma of the esophagus is a rare but aggressive malignant tumor. It occurs in older adults and shows a slight male predominance.[44] Clinical manifestations include rapidly progressive dysphagia, odynophagia, weight loss, and symptoms and signs related to hormone production from small-cell–like carcinoma of the lung.[44, 426] It is notorious for its tendency for early metastasis and rapid fatal course and is indistinguishable from pulmonary small-cell carcinoma.[237, 436]

Only a few radiologic features of esophageal small-cell carcinoma have been reported. Barium study reveals a smoothly marginated, polypoid or fungating mass with a relatively flat central ulcer in the midesophagus.[338] Usually the tumor does not narrow the lumen of the esophagus but expands the lumen. On CT, the tumor shows irregular, eccentric esophageal wall thickening and extensive lymph node metastasis to the mediastinum, supraclavicular region, and abdomen (Fig. 34–13).[147, 586] Because extensive and distant lymph node metastases appear to be a prominent feature of this tumor at presentation, CT examination should cover the abdomen as well as the whole thorax.[147]

Malignant Stromal Tumor (Leiomyosarcoma)

Malignant stromal tumor of the esophagus has been recognized as a rare lesion, accounting for fewer than 1% of all esophageal malignant neoplasms. It usually is found in middle-aged or older adults. Because there is no smooth muscle in the esophagus above the aortic arch, a malignant stromal tumor usually occurs in the middle and distal third of the esophagus.[605] It carries a better prognosis than squamous cell carcinoma owing to its tendency for slow growth, low grade, and late metastasis.[73, 340, 480] The growth pattern can be classified as *polypoid* or *infiltrating.*

CT features include thickening of the esophageal wall and soft tissue mass containing areas of low attenuation

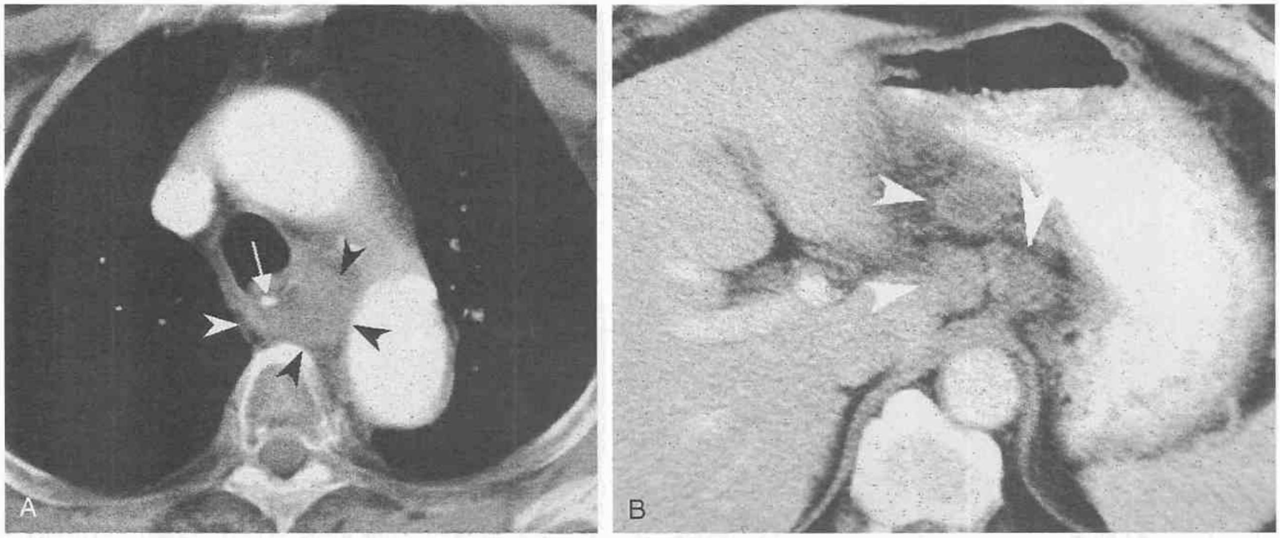

Figure 34–13. Small cell carcinoma of the esophagus. *A,* CT scan at the level of aortic arch demonstrates eccentric wall thickening with soft tissue attenuation in the proximal esophagus. The esophageal lumen *(arrow)* is filled with contrast medium. *B,* CT scan of the upper abdomen demonstrates multiple enlarged lymph nodes *(arrowheads)* in the perigastric area.

associated with necrosis, large exophytic components, and extraluminal gas or orally administered contrast material within the tumor (Fig. 34–14).[340]

In the polypoid type of the lesion, even if the tumor is large, it does not usually cause obstruction. Therefore, a bulky, nonobstructing intraluminal mass with a large exophytic component should be considered a malignant stromal tumor. In contrast, an infiltrating tumor is indistinguishable from infiltrative esophageal cancer.[333] On MR images, this tumor may show a mass with similar signal intensity, with skeletal muscle on T1-weighted images and higher signal intensity on T2-weighted images. There may be an area of signal void owing to extraluminal gas within the tumor.[340]

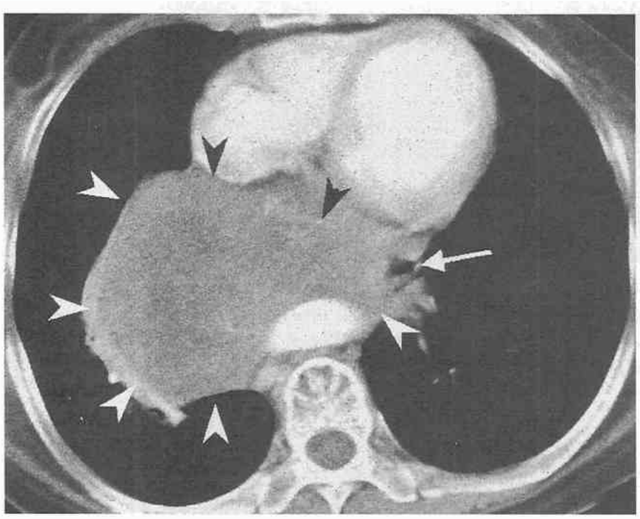

Figure 34–14. Leiomyosarcoma of the esophagus. CT scan shows a large mass *(arrowheads)* with heterogeneous enhancement. Despite the large size of the tumor, the esophageal lumen *(arrow)* is merely displaced but not collapsed.

Malignant Spindle Cell Tumor

Malignant spindle cell tumor is an unusual malignant tumor of the esophagus that contains both carcinomatous and sarcomatous elements with spindle cell metaplasia of the carcinomatous portion of the tumor, hence, the name *spindle cell carcinoma.*[5, 34] On pathologic examination, these tumors consist of innumerable tumor-like spindle cells with islands or nests of carcinomatous cells interspersed throughout the lesion. Affected individuals usually present with recent onset of dysphagia and weight loss. Unfortunately, they carry the same poor prognosis as squamous cell carcinoma of the esophagus.[335]

No reports have demonstrated CT features of malignant spindle cell tumor. In our experience, this disease appears as a large intraluminal mass without obstruction. The lesion shows homogeneous soft tissue attenuation similar to that of stromal tumors on CT scans and more intense enhancement than the adjacent esophageal wall on MR images (Fig. 34–15). On esophagography, malignant spindle cell tumor is shown as a giant polypoid intraluminal mass that characteristically expands the esophagus without obstruction.[436]

The differential diagnosis for these expansile intraluminal masses includes other rare malignant tumors of the esophagus, such as malignant stromal tumor and malignant melanoma.[335]

Lymphoma

The incidence of esophageal lymphoma is lowest among all GI tract tumors, accounting for only 1% to 2% of all cases of GI lymphoma.[53, 435, 511] This tumor usually occurs secondary to generalized non-Hodgkin's lymphoma with direct invasion of the esophagus by lymphomatous nodes in the mediastinum, contiguous spread of lymphoma from the gastric fundus, or synchronous development of lymphoma in the wall of the esophagus.[511]

In rare instances, primary esophageal lymphoma may occur in patients without extraesophageal disease. Primary

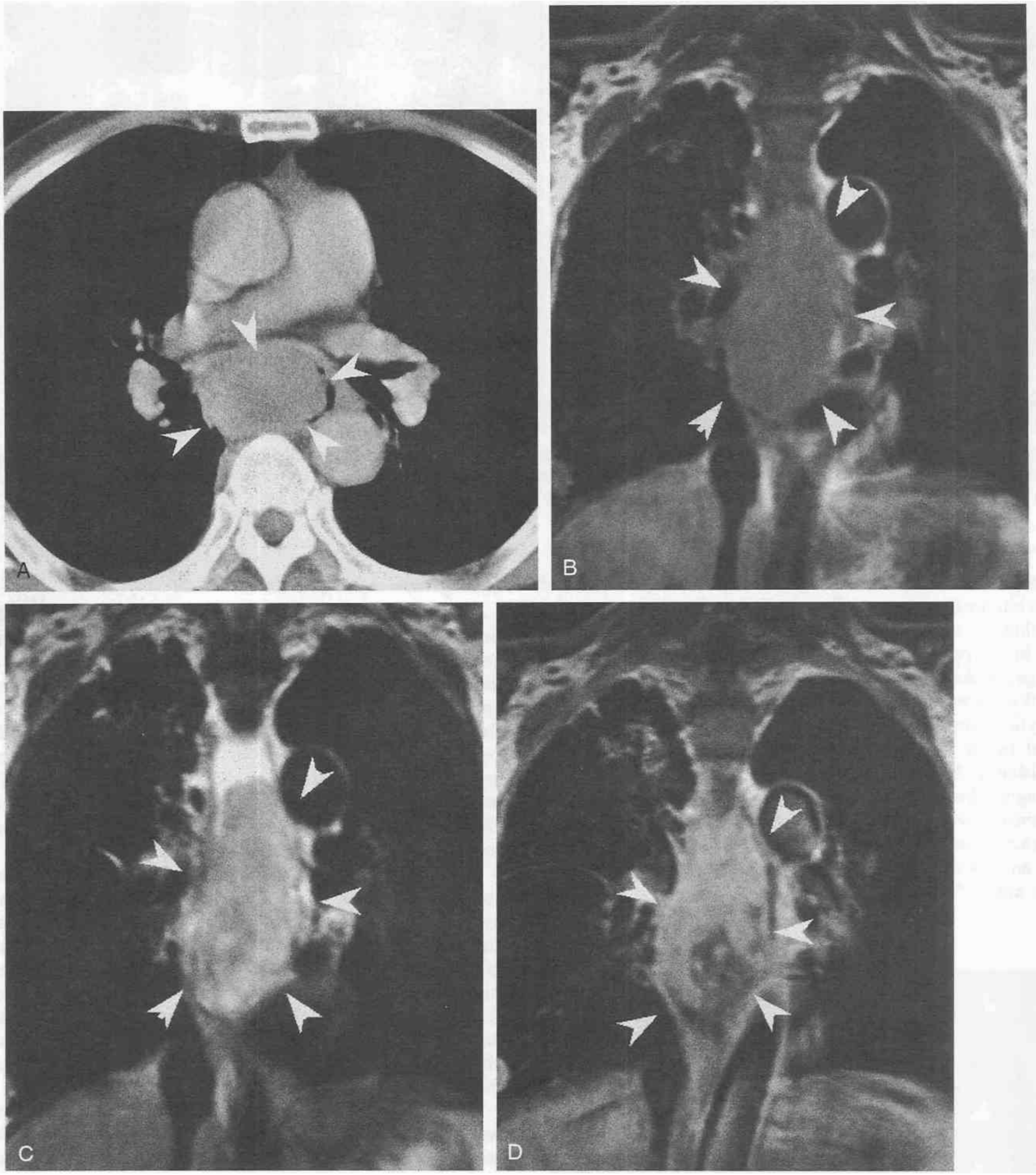

Figure 34–15. Malignant spindle cell tumor of the esophagus. *A*, CT scan shows a giant polypoid intraluminal mass *(arrowheads)* with homogeneous soft tissue attenuation. This lesion is hypointense on T1-weighted image *(B)* and heterogeneously hyperintense on T2-weighted image *(C)*. After administration of gadolinium-DTPA *(D)*, the lesion *(arrowheads)* shows heterogeneous considerable enhancement. The lesion does not cause esophageal obstruction despite its large size.

esophageal lymphomas in patients with acquired immunodeficiency syndrome (AIDS) have been reported.[479, 519] Most cases of esophageal lymphoma have been discovered at autopsy and in patients with widespread disease because esophageal lymphoma does not usually produce symptoms. Occasionally, esophageal lymphoma may cause dysphagia, bleeding, and fistulas.[333, 479, 519] Radiographically, esophageal lymphoma shows irregular narrowing of the distal esophagus owing to contiguous spread of the tumor from the gastric fundus. However, this finding cannot be used to differentiate esophageal lymphoma from carcinoma extending from the gastric fundus to the esophagus.[76, 80, 135, 333]

On CT, esophageal lymphoma is manifested as irregular thickening of the esophageal wall with or without large ulceration.[479, 519] In addition, CT is useful in the evaluation of mediastinal involvement of the lymphoma. Although esophageal lymphoma is rare, the diagnosis should be considered in patients at risk for AIDS when the radiologic findings are not typical for infectious esophagitis or Kaposi's sarcoma. Occasionally, these tumors can produce enlarged, tortuous folds, mimicking the appearance of varices. When multiple nodules are present in the esophagus, the differential diagnosis includes leukemic infiltrates, hematogenous metastases, Kaposi's sarcoma, and multiple stromal tumors.[479]

Primary Malignant Melanoma

Primary malignant melanoma of the esophagus is extremely rare. It originates from the small numbers of melanocytes and their precursors in the esophageal mucosa. As in skin melanoma, esophageal melanoma presumably develops because of malignant degeneration of these preexisting melanocytes.[116, 549] According to Yoo and coworkers,[613] primary malignant melanomas of the esophagus produce characteristic radiographic findings; tumors appear on barium studies as bulky, polypoid intraluminal masses that focally expanded the esophagus without causing obstruction. They tend to grow intraluminally along the longitudinal axis of the esophagus, which leads to the development of a polypoid mass that widens the lumen as it enlarges.

On CT scans, malignant melanomas are shown as large masses involving the esophagus, which may infrequently be associated with lymphadenopathy. Spindle cell carcinoma of the esophagus is the major consideration in the differential diagnosis of a larger, polypoid intraluminal mass in the esophagus.

Other Diseases

Inflammation

Most inflammations of the esophagus are caused by gastroesophageal reflux or infection. Gastroesophageal reflux disease (GERD) is the most common inflammatory disease involving the esophagus. Esophageal infection occurs frequently in immunosuppressed patients with malignancy, organ transplantation, and AIDS and includes *Candida albicans*, herpes simplex, and CMV.[380, 428] Candidiasis is the most common cause of infectious esophagitis and is thought to result from downward spread of the fungus from the oropharynx to the esophagus. In patients with AIDS, a deep esophageal ulcer, an intramural dissection, or fistula formation should suggest the diagnosis of esophageal TB.

On CT scans, esophagitis appears as a long-segmental, uniform, circumferential esophageal wall thickening, often combined with a target sign (Fig. 34–16).[43, 107, 495] According to Berkovich and associates,[43] 55% of patients with esophagitis show a thickened esophageal wall more than 5 mm thick and 17% of patients exhibit the target sign. The thickening is caused by edema, infiltration with inflammatory cells, and muscular spasm. Compared with esophageal carcinoma, which usually shows asymmetrical wall thickening and radial extension into the mediastinum, the mediastinal fat plane is preserved in esophagitis.[380]

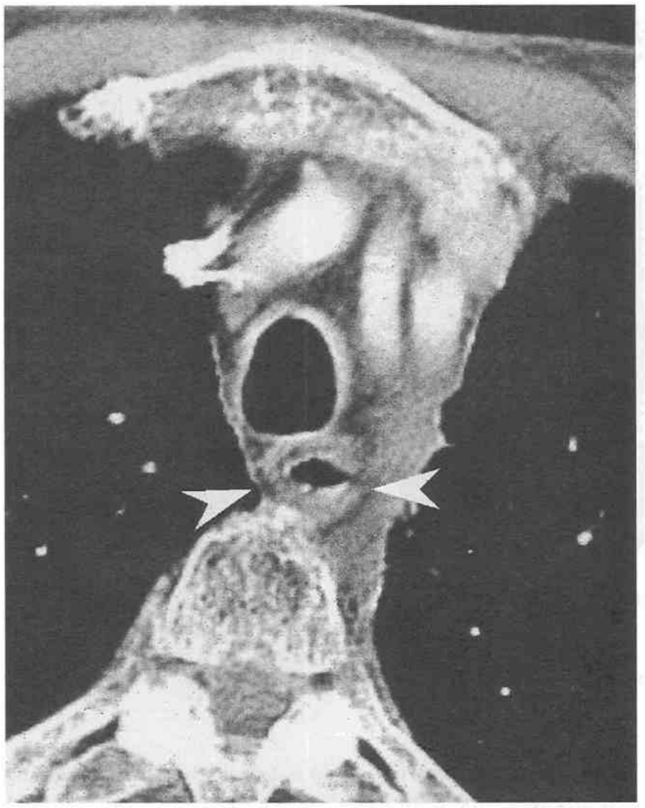

Figure 34–16. Esophagitis. CT scan shows circumferential esophageal wall thickening with the "target sign" *(arrowheads)*. The esophageal fat is preserved in esophagitis, which is a point of differentiation from esophageal carcinoma.

Pearlberg and coworkers[455] described the CT findings of esophageal intramural pseudodiverticulosis, which was associated with long-standing esophagitis and characterized by dilatation of the excretory ducts of esophageal mucous glands. CT features of this condition include intramural air collections at multiple levels within a thick-walled esophagus. Postinflammatory stricture may produce luminal narrowing without wall thickening. When circumferential soft tissue thickening is observed, it is due to fibrosis.[380]

The esophagus may be involved secondarily from adjacent mediastinal inflammatory processes. Histoplasmosis or TB may result in tracheoesophageal or bronchoesophageal fistula and subsequent aspiration pneumonia or lung abscess. The most common cause of esophageal TB is secondary involvement from adjacent tuberculous lymphadenitis rather than primary esophageal TB. CT is useful in detecting the fistula between the esophagus and mediastinal lymphadenopathy (Fig. 34–17).[42, 254, 602]

Im and associates[254] analyzed five patients with esophagomediastinal fistula caused by tuberculous lymphadenitis and observed amorphous gas collections along the fistulous tract with evidence of enlarged mediastinal lymph nodes. These findings in patients with tuberculous lymphadenitis should suggest the presence of an esophagonodal fistula.

Berkmen and Auh[42] also reported that CT could demonstrate the fistula that appeared as an air-filled communication between the esophagus and airway (Fig. 34–18). Thin section (2 to 4 mm) may be helpful in their detection.

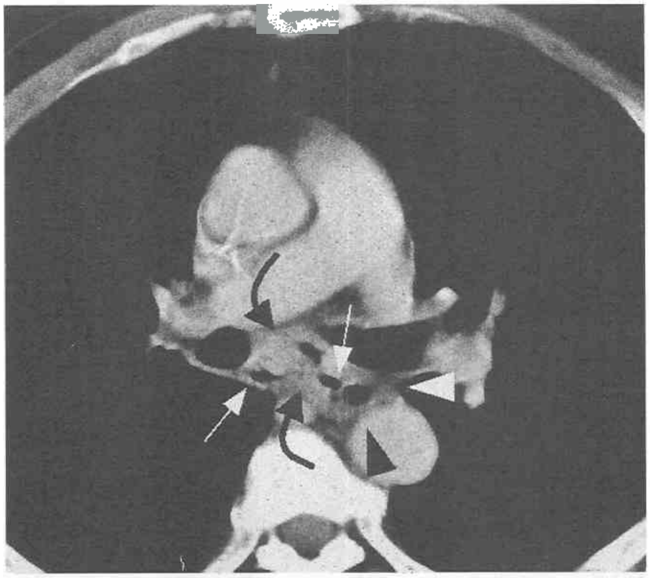

Figure 34–17. Fistula between the esophagus and tuberculous lymphadenopathy. CT scan demonstrates an air-filled fistulous tract *(arrows)* between the esophagus *(arrowheads)* and the enlarged subcarinal lymph node *(curved arrows)*.

Even when the actual fistula is not demonstrated, associated findings, including infiltration of mediastinal fat due to inflammation and fibrosis, pulmonary consolidation, pulmonary cavitation, and pleural fluid, help suggest the diagnosis.

Achalasia

Achalasia is an uncommon disease of the esophagus, with an incidence of 0.6 to 0.2 per 100,000 per year.[48, 478] It is caused by aperistalsis of the lower esophageal segment and by inadequate relaxation of the lower esophageal sphincter (LES). Although the pathogenesis of achalasia is obscure, the histologic basis is unknown.[478] There is no sex predilection. The condition usually occurs in middle-aged patients. Clinical symptoms are usually dysphagia, which is usually worse with liquids than with solids, although sometimes only nonspecific symptoms, such as heartburn, may be present.

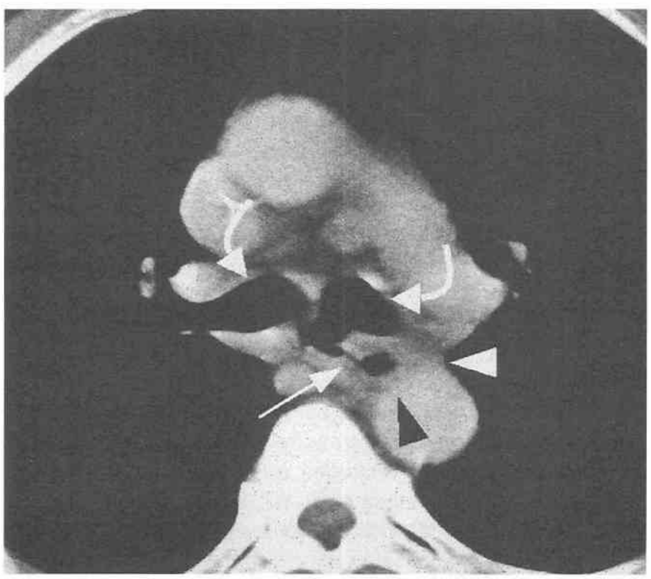

Figure 34–18. Tracheoesophageal fistula. CT scan shows an air-filled communication *(arrow)* between the esophagus *(arrowhead)* and the mainstem bronchus *(curved arrows)*.

The diagnosis of achalasia is usually made on the basis of esophagography, manometry, nuclear examination, and endoscopy. Radiographic findings of achalasia have been reported by many authors.[134, 359, 444] On barium study, the primary peristalsis is absent on all swallow studies. The lower end of the esophagus shows a smooth "beaklike" tapering located at the level of the esophageal hiatus. This tapering reflects LES dysfunction and failure of the barium bolus to distend the tonically contracted LES.[444]

CT features of achalasia have been described. Rabuschka and colleagues[478] reported that a unique CT feature of achalasia is moderate dilatation of the esophagus with a mean diameter of 1.4 cm at the carinal level, not combined with wall thickening in the distal segment of the esophagus (Fig. 34–19). They mentioned that normal wall thickness is the most important feature that distinguishes patients with achalasia from those with other esophageal diseases.

The role of CT in the evaluation of patients with achalasia exists not only to detect the disease and its complications but also to demonstrate atypical features that may indicate the presence of other diseases or superimposed benign or malignant processes. Other causes of LES narrowing that may mimic achalasia include intrinsic or extrinsic neoplasms, peptic stricture, and complications of scleroderma. Patients with tumor infiltration into the distal esophagus may report symptoms similar to achalasia. This entity has been named *pseudoachalasia*, and it is important to distinguish it from *primary achalasia*.

Esophageal cancer occurs in 2% to 7% of patients with long-standing achalasia.[429, 478, 608] In this situation, cancer develops in the midesophagus, and the etiologic mechanism has been presumed to be stasis and irritation of the esophagus.[478] When patients with achalasia experience rapid worsening of symptoms, the possibility of superimposed esophageal cancer is suggested.

Ott and coworkers,[445] investigating the relationship between achalasia and hiatal hernia, found that hiatal hernia is inversely related to achalasia; hiatal hernia is uncommon in patients with achalasia compared with the normal population. If patients with achalasia have hiatal hernia, another cause for the dysphagia and abnormal motility should be sought.

Varices

Esophageal varices may be classified as *uphill* or *downhill;* the former category is more common than the latter. Uphill varices develop by portal hypertension, in which increased portal venous pressure leads to hepatofugal venous flow through the coronary vein into a plexus of dilated esophageal and periesophageal veins. Downhill varices develop by obstruction of superior vena cava and result in reversal of flow into vein of the cervical and upper thoracic esophagus via the superior intercostal vein, bronchial vein, inferior thyroid vein, and other mediastinal collateral ves-

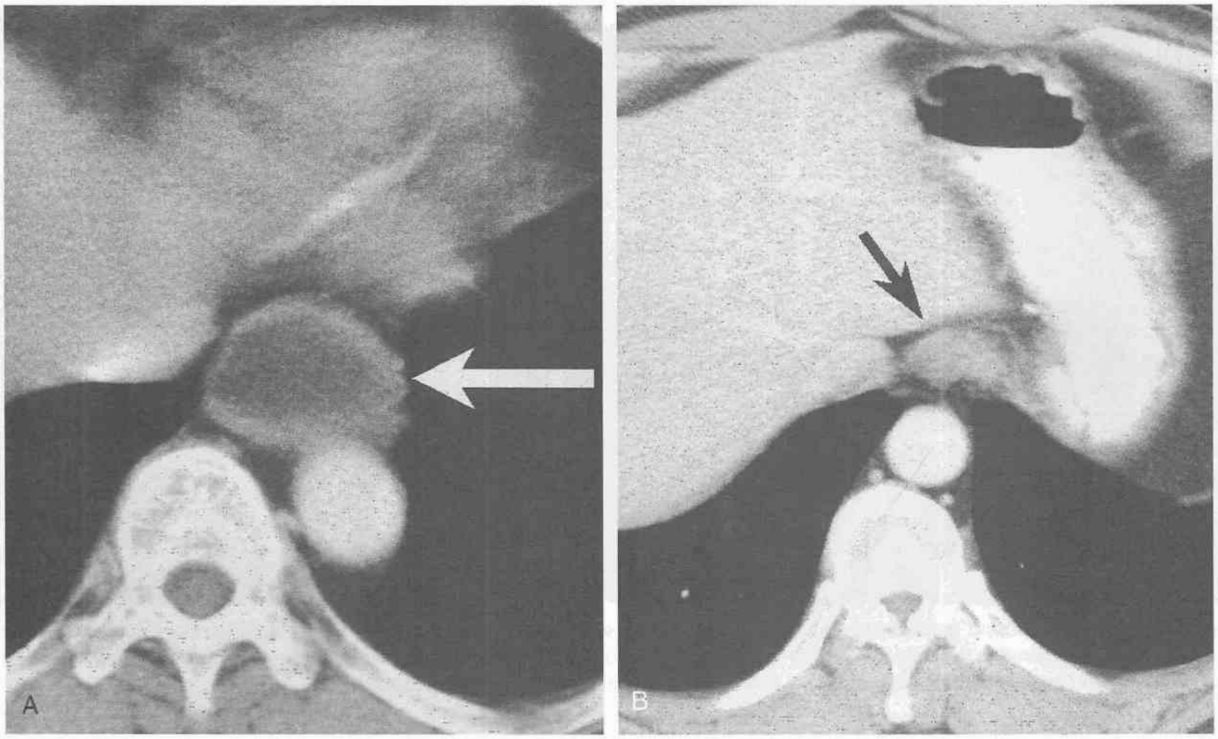

Figure 34–19. Achalasia in a 47-year-old woman. *A,* CT scan shows dilated, fluid-filled esophagus *(arrow). B,* In this patient, the distal esophageal wall thickness *(arrow)* is normal, in contrast with other obstructive causes of the esophagus.

sels.[235] Esophageal varices are important because of the potentially catastrophic consequences of variceal rupture and hemorrhage.

On CT scans, esophageal varices are recognized by the presence of a thickened, lobulated esophageal wall that is markedly enhanced after administration of IV contrast medium. Without such an infusion, the varices are indistinguishable from neoplasms or esophagitis.[22, 94, 386] Secondary signs in esophageal varices include the presence of hepatic disease, gastric varices, and recanalization of venous structures such as the umbilical vein.[428]

According to Balthazar and associates,[22] CT is superior to barium esophagography in evaluating the presence and extent of periesophageal varices and portal hypertension, although the sensitivities in detection of the lesion are similar. CT features of esophageal varices before and after endoscopic esophageal sclerotherapy include esophageal wall thickening; low attenuation within the wall, giving the esophagus a laminated appearance; a mediastinal effusion of predominantly low attenuation that is often masslike; obliteration of mediastinal fat planes; thickening of the diaphragmatic crura; pleural effusions; and subsegmental atelectasis (Fig. 34–20).[383]

On CT scans, therapeutically sclerosed esophageal varices may sometimes mimic esophageal carcinoma.[219] With the increasing use of sclerotherapy, the radiologist may expect to see an increasing number of nonenhancing esophageal varices on CT.

Trauma

Esophageal Hematoma

Esophageal hematoma is related to variable conditions such as abnormal hemostasis, endoscopic instrumentation, variceal sclerotherapy, foreign body ingestion, remote trauma, and vomiting.[120, 238, 619] Clinical manifestations include sudden onset of retrosternal chest pain, dysphagia, and hematemesis. Most esophageal hematomas resolve spontaneously with only conservative treatment and do not result in esophageal perforation.[336]

On barium studies, the hematoma appears as an ovoid or elongated submucosal mass in the esophagus. When a mucosal laceration is present (particularly after iatrogenic injury), contrast medium may dissect beneath the mucosa into the hematoma. This intramural dissection may produce a characteristic "double-barreled" appearance owing to parallel collections of contrast medium in both true and false lumina, separated by a thin, radiolucent stripe.[336, 457] However, intramural tracks can also be caused by Crohn's disease, *Candida* esophagitis, or tuberculous esophagitis.[457]

On CT scans, esophageal hematoma appears as a nonenhancing submucosal lesion with high attenuation or low attenuation in the middle and lower esophagus.

MRI reveals an intermediate signal intensity on T1-weighted images and a hyperintense signal on T2-weighted images.[120, 619]

Esophageal Perforation

Esophageal perforation is a catastrophic condition that may rapidly progress to fulminant mediastinitis and septic shock. Most cases are caused by endoscopy or other forms of esophageal instrumentation. In other cases, spontaneous perforation of the esophagus (Boerhaave's syndrome) may occur as a result of a sudden, rapid increase in intraluminal esophageal pressure.

The initial symptoms and signs include sudden onset of severe retrosternal chest pain, vomiting, and subcutaneous

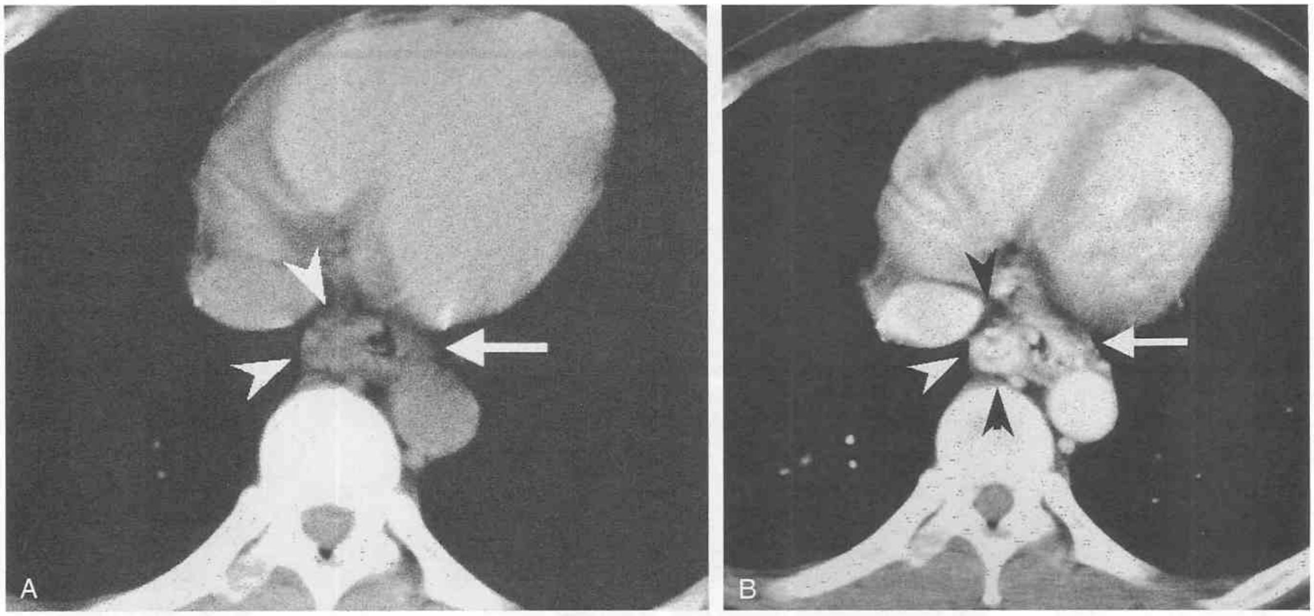

Figure 34–20. Esophageal and paraesophageal varices. *A*, On this unenhanced CT scan, esophageal wall *(arrow)* is slightly thickened and nodular lesions *(arrowheads)* adjacent to the esophageal wall are noted. *B*, After administration of intravenous contrast medium, the esophageal wall *(arrow)* and multiple nodular lesions *(arrowheads)* are strongly enhanced.

emphysema with crepitus in the soft tissues of the anterior chest wall *(mediastinal crunch)*. In some cases, however, the initial signs and symptoms are nonspecific and may consist of hypotension, sepsis, or fever, falsely suggestive of myocardial infarction, acute aortic dissection, or intra-abdominal abnormalities.[266, 274, 387, 454, 598] The prognosis is directly related to the interval between perforation and initiation of therapy; within 24 hours, the mortality rate for thoracic esophageal perforation exceeds 80%.[13]

In patients with spontaneous esophageal perforation, chest radiographs may reveal pneumomediastinum associated with left pleural effusion or, less commonly, right pleural effusion or bilateral effusions. Esophagography may demonstrate extravasation of contrast medium from the left lateral wall of the distal esophagus into the adjacent mediastinum. Often, however, the clinical features are atypical, and up to 10% of patients with esophageal perforation may have false-negative findings on contrast esophagogra-

CT features of esophageal perforation include esophageal wall thickening, periesophageal fluid, extraluminal air, pleural effusion, and pericardial effusion (Fig. 34–21). Pleural effusions are usually bilateral. CT is ideally suited for defining the extent of extraluminal air-fluid collection and for detecting small amounts of extravasated contrast material not appreciated at esophagography. In addition, CT may also be useful in monitoring the clinical course of patients treated conservatively.[14, 137, 143, 274, 460]

Foreign Body Impactions

Esophageal foreign body impaction usually occurs in children, who tend to ingest coins, toys, or other foreign materials. In adults, foreign body impaction in the esophagus is usually caused by an inadequately chewed bolus of food or bones. Unchewed food tends to lodge in a lower esophageal ring or stricture, whereas bones tend to lodge in the pharynx near the cricopharyngeus.[336] Most patients with food impaction present with sudden onset of chest pain, odynophagia, or dysphagia. In contrast, young children usually exhibit respiratory distress, drooling, or regurgitation.[556]

Esophageal perforation is rare, affecting fewer than 1% of all patients with foreign body impaction, but the risk of perforation increases significantly if the impaction persists

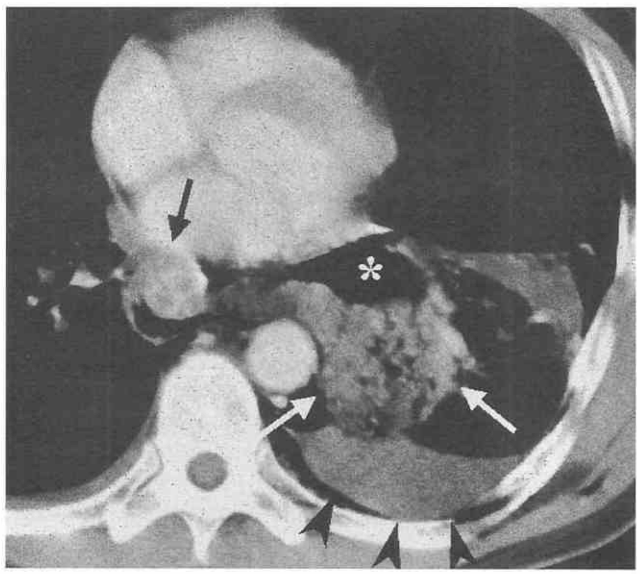

Figure 34–21. Esophageal perforation (Boerhaave's syndrome) in a 56-year-old man. After vigorous vomiting, the patient experienced sudden chest pain. CT scan shows a thickened esophageal wall *(arrow)*, pneumomediastinum *(asterisk)*, regurgitated gastric content *(white arrows)*, and pleural effusion *(arrowheads)*.

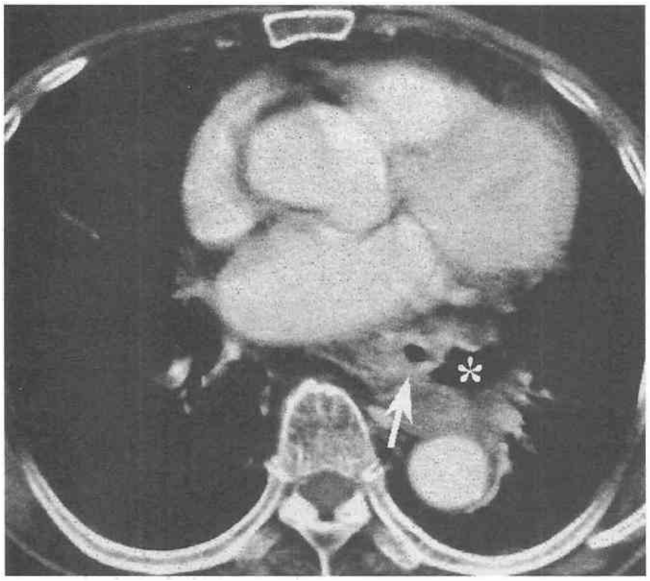

Figure 34–22. Sliding hernia. The stomach *(asterisk)* and esophagogastric junction *(arrow)* are located in the mediastinum. Note that the esophagogastric junction is above the diaphragm, which is a crucial criterion in differentiating sliding hernia from paraesophageal hernia.

longer than 24 hours and if the perforation of the cervical esophagus with a foreign body produces a retropharyngeal

Plain radiography, especially lateral radiographs of the neck, may occasionally demonstrate bones or other radiopaque foreign bodies.

Barium study is another option when a foreign body is suspected in the esophagus; barium can determine whether a foreign body is present and whether it is causing obstruction. The impacted foreign body typically appears as a polypoid filling defect in the esophagus with an irregular meniscus owing to barium outlining the superior border of the impacted food bolus.

CT is also useful in evaluating esophageal foreign body impaction. With its soft tissue and bone windows, CT may replace the barium swallow because of its superior detection of thin, small, minimally calcified foreign bodies that are often obscured by overlying tissues. CT can also visualize inflammatory changes in the adjacent structures.[46, 595]

Hiatal Hernia

Hiatal hernia is caused by a weakness or tear of the phrenoesophageal membrane. It can be divided into two types:

1. *Sliding* hernia, in which the gastroesophageal junction is above the esophageal hiatus of the diaphragm.
2. *Paraesophageal* hernia, in which all or portions of the stomach herniate into the chest but the gastroesophageal junction is below the diaphragm (Figs. 34–22 and 34–23).

Approximately 99% of hiatal hernias are sliding, and the remaining 1% are paraesophageal.[336] Although the incidence of paraesophageal hernia is much lower than that of sliding hernia, patients with a paraesophageal hernia have a higher risk for the development of volvulus, incarceration, and strangulation of a herniated portion.

Hiatal hernia can be readily detected on a single barium study, but CT and MRI also can demonstrate the size, content, and orientation of the herniated stomach within the lower thoracic cavity as well as the location of the gastroesophageal junction.[85, 320, 588]

In some instances, only omental fat can be herniated into the chest while the stomach remains in the abdomen; this is referred to as a *paraesophageal omental hernia*. On CT and MRI, this situation may mimic a mass containing fat in the mediastinum. Characteristic CT and MRI features of paraesophageal omental hernia include a bilobed, retrocardiac fatty mass, with branching blood vessels through-

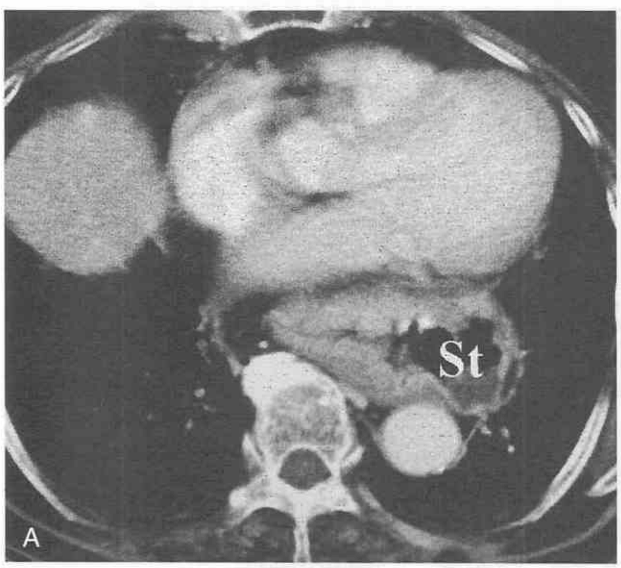

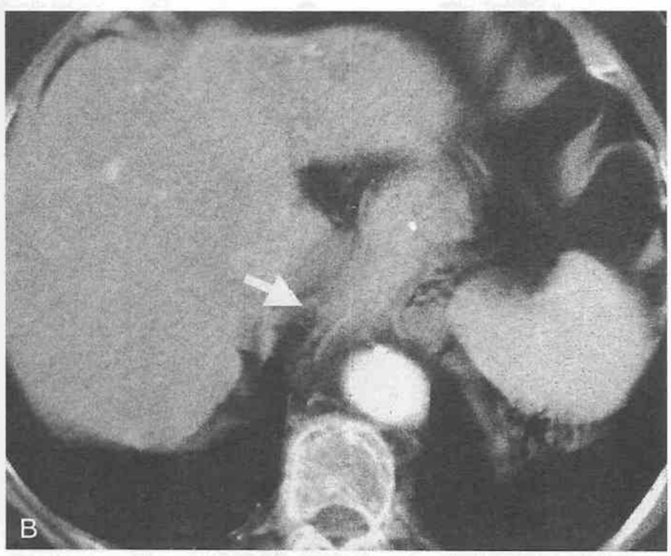

Figure 34–23. Paraesophageal hernia. The gastric fundus (St) has migrated u[redacted]ard into t[redacted]ediastinum ([redacted] whereas the esophagogastric junction *(arrow)* is normally located below the diaphragm *(B)*.

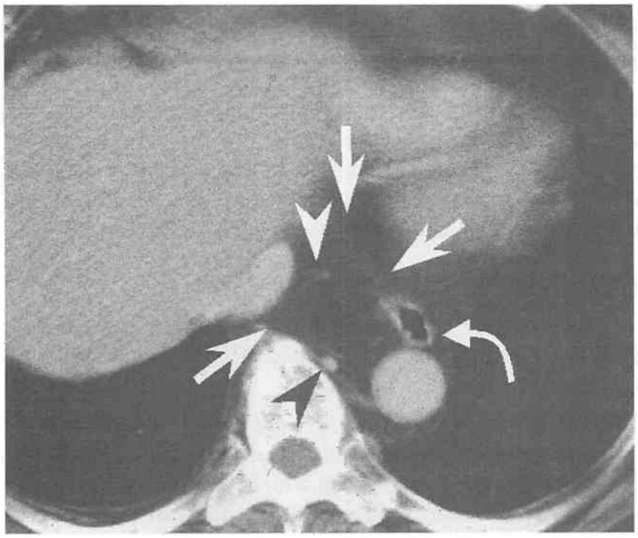

Figure 34–24. Paraesophageal omental hernia. Omental fat *(arrows)* has herniated into the mediastinum, displacing the esophagus *(curved arrow)*. Note the blood vessels within the lesion *(arrowheads)*, which indicates that the fatty mass is the herniated omental fat.

out, a midline septum, and extension through the diaphragm (Fig. 34–24).[324, 508]

Diverticula

Diverticula may be classified as *pulsion* and *traction* types. A pulsion diverticulum, the most common form, is caused by increased intraluminal pressure related to motility disorders; a traction diverticulum is caused by fibrosis in adjacent periesophageal tissues. Pulsion diverticula are further classified as a *Zenker's diverticulum* in the proximal esophagus and as an *epiphrenic diverticulum* in the distal esophagus.

Traction diverticula are usually located in the midesophagus.[556] These diverticula can be readily diagnosed on esophagography. Pulsion diverticula show one or more rounded outpouching barium collections from the esophagus (Fig. 34–25), whereas traction diverticula are manifested as a tented or triangular-shaped barium collection caused by scarring and retraction by granulomatous disease in adjacent subcarinal or hilar lymph nodes.[556]

Epiphrenic diverticula are typically demonstrated by CT as a thin-walled, air-filled or air-fluid–filled structure communicating with the esophagus (Fig. 34–26). However, those not associated with a distal esophageal obstruction (stricture, achalasia) may remain contracted in a resting state and thus may not be visible. Occasionally, the diverticulum may have to be differentiated from mediastinal abscess or tumors and even hiatus hernia.[295]

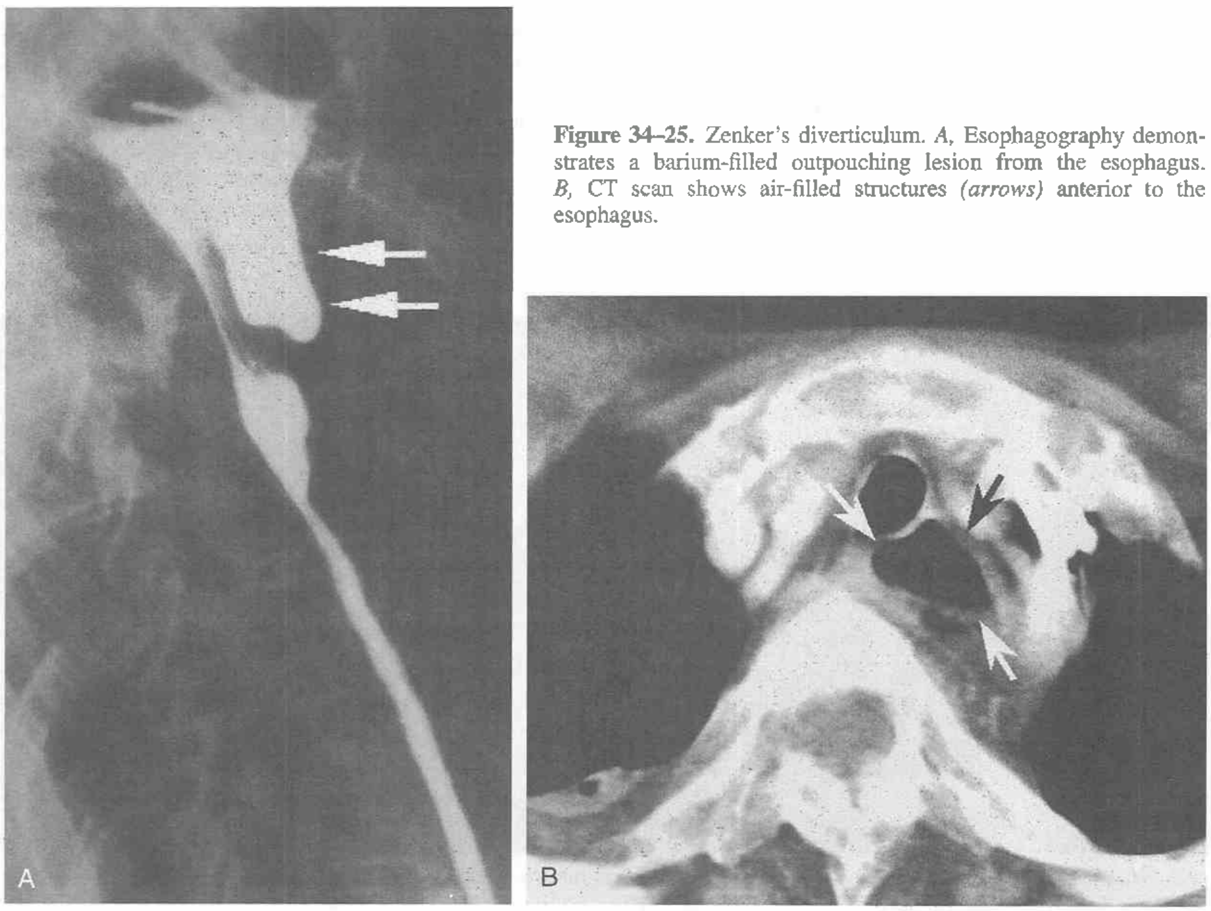

Figure 34–25. Zenker's diverticulum. *A,* Esophagography demonstrates a barium-filled outpouching lesion from the esophagus. *B,* CT scan shows air-filled structures *(arrows)* anterior to the esophagus.

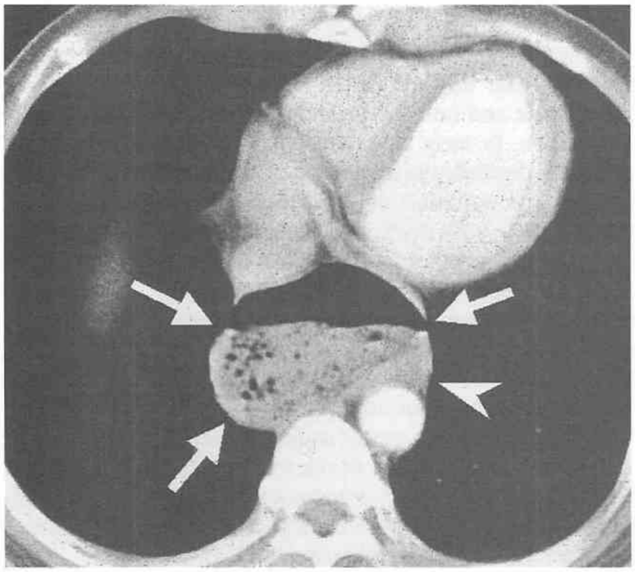

Figure 34–26. Epiphrenic diverticulum. CT scan demonstrates a thin-walled, air-fluid–filled structure *(arrows)* in the distal esophagus. The esophageal wall *(arrowhead)* is laterally displaced.

Stomach

Techniques and Normal Anatomy

Optimal luminal distention with either barium, water, or gas is the key for evaluating the gastric wall. In the evaluation of gastric cancer, new protocols using 5-mm incremental or helical scanning, drug-induced hypotonia, prone position, and water-filling methods have been advocated (Fig. 34–27).[132, 242, 513] Gastric distention is achieved by drinking as much as 1500 mL of water. Peristalsis is minimized by the administration of spasmolytics. This protocol may reduce the limitation of conventional CT caused by beam-hardening artifact, peristalsis, and suboptimal gastric distention.

The normal gastric wall is 2 to 5 mm thick, with 10 mm the upper limit for normal[187]; in an air-filled stomach, a 3-mm[507] or 5-mm[121] wall thickness is considered the upper normal limit. However, anatomic difficulty is most frequently encountered in the region of the gastroesophageal junction.[579] As the esophagus becomes an intra-abdominal organ and joins the stomach, it can produce a focal thickening and simulate a mass projecting into the gastric wall. Whenever a soft tissue mass is noted in this region, its relationship to the fissure plane anterior to the caudate lobe should be studied. If the mass and fissure plane are in the same or adjoining sections, a pseudotumor should be suspected. A wall thickness of more than 1 cm is considered abnormal in this region when the stomach is well distended.

In evaluations of the stomach, the most commonly encountered difficulty is the differentiating spurious gastric wall thickening produced by redundant mucosa in an incompletely filled stomach from pathologic thickening. In such instances, additional studies with different patient positioning may be important.

When air techniques are used, the right decubitus position is selected to evaluate the proximal stomach and gastroesophageal junction and the left decubitus position is best to evaluate the distal stomach and duodenum; this is the reversal of the patient's position when a high-density oral contrast agent is used.[579]

When conventional CT is used, the normal gastric wall enhances homogeneously but shows a two-layered or three-layered (multilayered) structure (Fig. 34–28).[88] The inner layer corresponding to the mucosal layer enhances markedly. The intermediate layer of low attenuation corresponds to the submucosal layer, and the occasionally seen outer layer of slightly higher attenuation corresponds to the muscular-serosal layer. This multilayered mural pattern, however, is difficult to appreciate when the wall measures less than 5 mm thick.[242]

The perigastric ligaments contain major vascular structures and lymph nodes, which are important pathways for lymphatic metastasis and direct extension of gastric pathologic processes. The gastrohepatic ligament is located in the most superior portion of the lesser omentum, containing the left gastric artery and coronary vein and lymph nodes. Any rounded structure larger than 8 mm within this ligament should suggest lymphadenopathy or collateral vessels. The gastrosplenic and gastrocolic ligaments con-

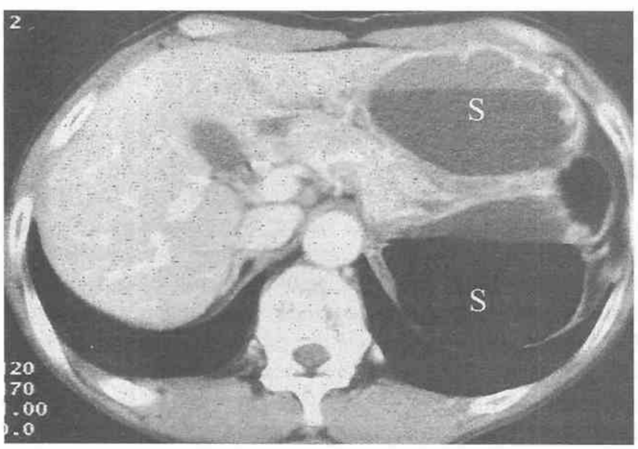

Figure 34–27. Prone position with the water-filling method for evaluation of the patient with gastric cancer.

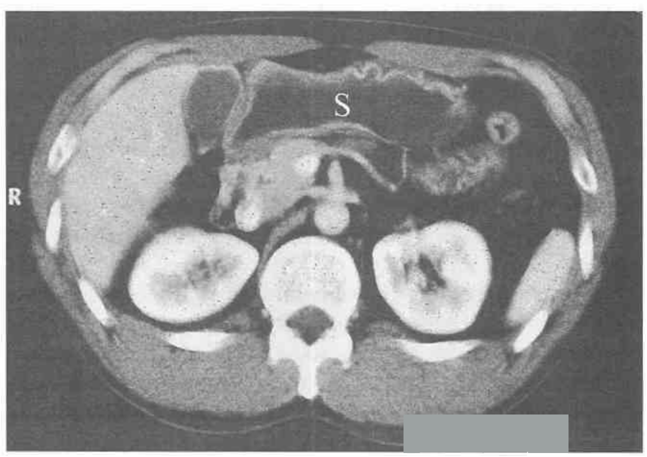

Figure 34–28. Normal gastric wall with layered appearance.

Table 34–3. Numbering of Upper Abdominal Lymph Node Stations

Station Number	Location
1/2	Right/left side of the cardia
3/4	Along the lesser/greater curvature
5	Suprapyloric, along the right gastric artery
6	Infrapyloric
7	Along the left gastric artery
8	Along the common hepatic artery
9	Around the celiac artery
10	At the splenic hilus
11	Along the splenic artery
12	In the hepatoduodenal ligament
13	Behind the pancreas head
14	At the root of the mesentery (superior mesenteric artery)
15	Along the middle colic artery
16	Para-aortic

tain the gastroepiploic vessels and lymph nodes that drain the greater curvature.

The stomach is supplied by several vessels, including the celiac axis, hepatic artery, and splenic artery. The lymph vessels drain from the following major areas (Table 34–3):

1. Cardia and most of the lesser curvature into left gastric nodes.
2. Pylorus and the distal lesser curvature into the right gastric and hepatic nodes.
3. Proximal portion of the greater curvature into the pancreaticosplenic nodes in the splenic hilum.
4. Distal portion of the greater curvature into the right gastroepiploic nodes in the greater omentum and the pyloric nodes at the head of the pancreas.

Many surgeons prefer to use the lymph node classification system proposed by the Japanese Research Society for Gastric Cancer.[265]

Malignant Gastric Tumors

Adenocarcinoma

Gastric carcinoma is a worldwide disease. Its incidence varies widely, being higher in Asian than in Western countries. Many factors affect prognosis in patients with gastric cancer, including age, symptoms, tumor size, lymph node involvement, depth of tumor invasion, distant metastasis, histopathologic type, and surgery performed. These tumors may be detected either in an early stage (in which case the mucosa or the submucosa is involved) or in an advanced stage. The gross visual appearance of advanced carcinoma is polypoid, fungating, ulcerated, or infiltrative, whereas that of early carcinoma is either protruded, flat, or depressed.

Vascular structures in patients with gastric cancer have been examined with angiography, microangiography, or both.[384, 539] In these studies, most gastric cancers showed neovascularity in the arterial and capillary phases and tumor stain in the venous phase of angiography. Neoplastic vessels became more numerous, more tortuous, and wider than normal vessels.[384]

Tumor Detection

When dynamic CT is performed, gastric cancers show moderate and marked heterogeneous enhancement in the early phase and homogeneous enhancement in the equilibrium phase. In early gastric cancer, CT sensitivity in tumor detection depends on the examination technique as well as on the type and size of the lesion. On conventional CT scans, gastric wall thickening in early cancer appears minimal, usually smaller than 1 cm. Furthermore, a flat or depressed type of early cancer may not be demonstrated by CT. Therefore, the reported sensitivity of CT for early gastric cancer reported may be approximately 50%[132, 174, 242]; however, use of dynamic helical CT with water ingestion improves the detection of cancer.

The early cancers appear as focal gastric wall thickening with strong enhancement in the most inner (mucosal) layer, especially in the arterial-dominant phase; however, an early gastric lesion smaller than 2 cm in diameter is still difficult to detect on CT.[132] The presence of a low-attenuation stripe in the middle layer differentiates early from advanced tumors.[318] Endoscopic three-dimensional (3D) CT, which can provide an overview of the tumor within the lumen of the stomach as seen in gastroscopy, improves the detection rate of early cancer.[319] However, this technique is time-consuming and is limited in detecting flat or small lesions.

Most advanced gastric adenocarcinomas appear as thickened or abnormally enhancing gastric wall in a localized or circumferential pattern (Fig. 34–29) or intraluminal polypoid mass. Sometimes an ulcer is detected within the thickened area of the gastric wall or within the mass. As a less common variety, there is a *scirrhous* type of gastric carcinoma in which the tumor cells (most commonly, the signet ring cell type) spread predominantly in the submucosa with no or minimal involvement of the mucosal layer (Fig. 34–30). In these cases, CT appears to be more diagnostic than endoscopy or barium study and shows diffuse, circumferential thickening of the gastric wall with a mean thickness of 1.8 cm (range, 1 to 3 cm).[28]

Because of marked desmoplastic response in mainly submucosal layer of the gastric wall, the thickened wall usually shows homogeneous and prolongs contrast enhancement, especially in the equilibrium phase.[28] In contrast with the submucosal layer, the muscularis propria shows edematous thickening in the absence of fibrous connective tissues and thus appears to be hypoattenuated on CT, occasionally causing a target appearance in the thickened gastric wall. Other CT features diagnostic for scirrhous cancer include preservation of a thin rim of hypoattenuated mucosal line, intramural calcifications, and high-grade gastric outlet obstruction.

The differential diagnosis of scirrhous carcinoma includes scirrhous metastases (lung, breast carcinoma); non-Hodgkin's or Hodgkin's lymphoma; and unusual chronic systemic or inflammatory conditions such as sarcoidosis, corrosive gastritis, amyloidosis, and Crohn's disease.[28] Calcified gastric carcinomas are rarely reported in the literature, and most of them are caused by mucin-producing adenocarcinoma (Fig. 34–31).[251] The calcifications in the thickened gastric wall are nodular, miliary, punctate, or homogeneously distributed and are also noted in metastatic lesions, such as lymph nodes and liver.[251]

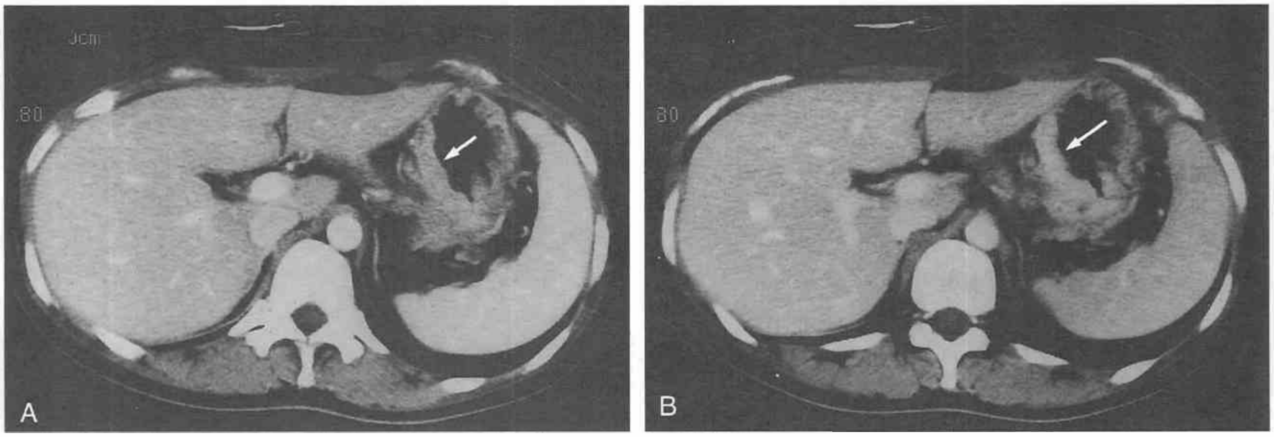

Figure 34–29. Gastric adenocarcinoma. Early phase *(A)* of a dynamic CT scan shows mild enhancement of thickened gastric wall *(arrow)*. Scan shows good enhancement in the equilibrial phase *(B)*.

In certain instances of gastric carcinoma, the tumor grows exophytically, thereby simulating a *stromal* tumor (Fig. 34–32). The presence of gastric wall thickening adjacent to an exogastric mass or a gastric outlet obstruction favors gastric cancer, allowing it to be distinguished from gastric stromal tumors.[317]

In contrast with early gastric cancer, the sensitivity of CT in detecting advanced gastric cancer is high (92% to 96%).[88, 132, 242, 408] However, gastric cancer situated on the horizontally oriented portion of the gastric wall, such as the greater curvature and gastric angle, is difficult to evaluate because of the partial-volume averaging effect.[88, 242] The use of multiplanar reconstruction (MPR) images following thin-slice thickness (5 mm) helical CT scans aids in the evaluation of these lesions (Fig. 34–33).[174]

Tumor Staging

Accurate tumor staging is essential for the appropriate management of patients with gastric cancer. The TNM classification is generally used.

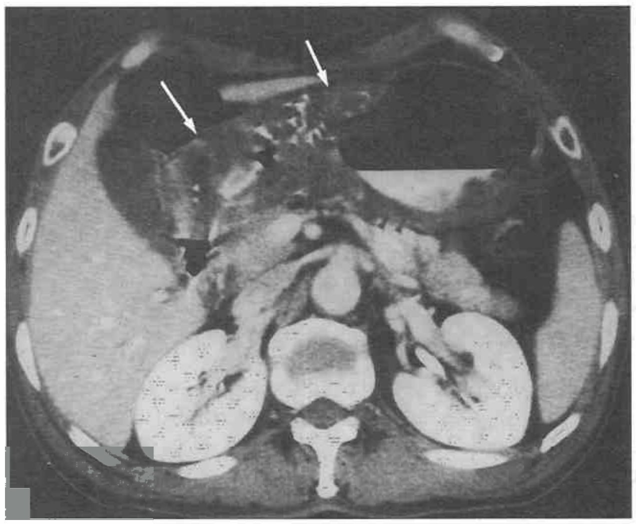

Figure 34–31. Mucinous adenocarcinoma of the stomach. CT scan shows gastric wall thickening *(arrows)* with poor contrast enhancement and calcifications.

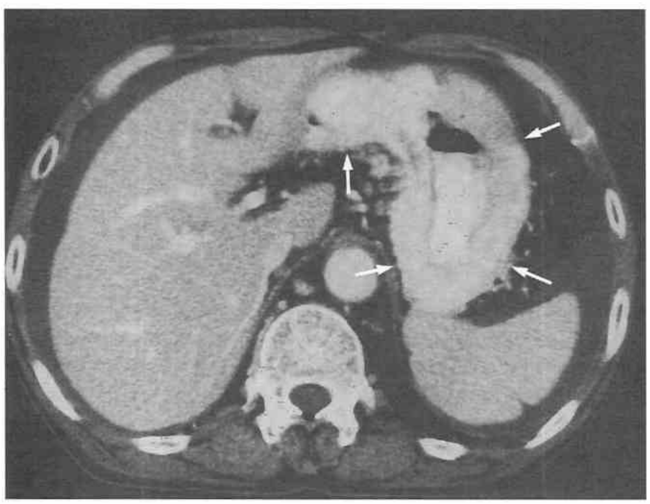

Figure 34–30. Scirrhous adenocarcinoma of the stomach. CT scan shows considerable gastric wall thickening *(arrows)* with a markedly enhanced submucosal layer and a poorly enhanced thin rim of mucosal layer. Ascites is also seen.

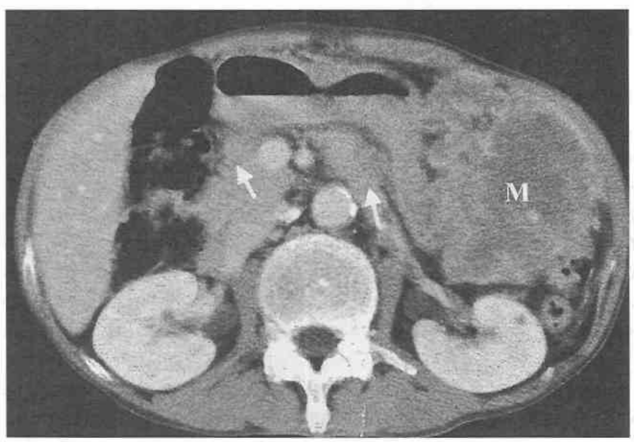

Figure 34–32. Gastric adenocarcinoma with exophytic tumor growth. CT scan shows a heterogeneous mass (M) in the left upper quadrant, simulating an exophytically growing malignant gastrointestinal stromal tumor. Enlarged perigastric lymph nodes *(arrows)* are seen along the lesser curvature of the stomach.

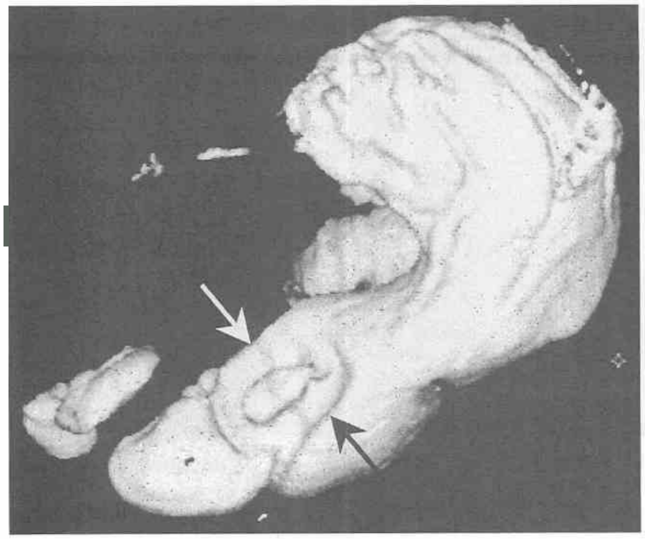

Figure 34–33. Three-dimensional spiral CT image of advanced ulcerofungating gastric cancer *(arrows)*.

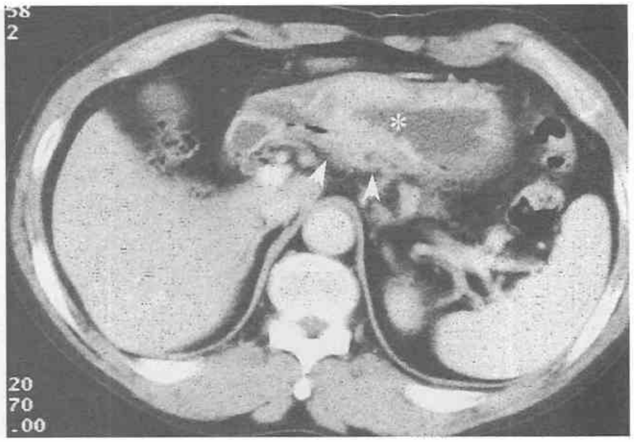

Figure 34–34. Gastric cancer with serosal invasion. CT scan shows circumferential gastric wall thickening *(asterisk)* with perigastric tumor infiltration *(arrowheads)*.

T Category

The T category (tumor invasion) includes the following:

- T0 (no tumor invasion)
- T1 (lamina propria or submucosal invasion)
- T2 (muscularis or subserosal invasion)
- T3 (extraserosal invasion)
- T4 (invasion of adjacent organs)

Although initial reports were encouraging, the efficacy of CT in T staging of gastric cancer has been controversial, and an overall accuracy of 42% to 82% has been reported.[132, 174, 513]

Some series have also stressed the importance of water filling (>400 mL), study with prone position, and gastric hypotonia to reduce peristalsis and beam-hardening artifacts and suboptimal gastric distention during CT for the evaluation of patients with gastric cancer.[132, 174, 513] However, use of such optimal techniques along with the introduction of helical CT scan does not appear to improve T staging significantly.[132]

The prognosis in surgically treated patients with gastric cancer is significantly affected by the presence or absence of intraperitoneal free cancer cells at the time of gastrectomy. According to a series by Kaibara and colleagues,[275] who analyzed the relationship between the spatial extent of invasion of the gastric serosa and their 5-year survival rate, intraperitoneal free cancer cells were detected by lavage of the Douglas cavity in 135 (44%) of 309 patients with gross evidence of serosal invasion. Their study also showed that the 5-year survival rate was worsening in patients with wider areas of serosal invasion.

Therefore, the primary role of CT in patients with a known history of gastric cancer is to assess the extragastric tumor extension (Fig. 34–34). The accuracy of CT for predicting serosal invasion ranges between 60% and 83%.[88, 132, 174] In most series,[88, 132, 174] understaging was more common than overstaging, probably as a result of CT's limited ability to detect microscopic invasion.

N Category

Besides depth of invasion, extent of node metastases is one of the most important prognostic factors in gastric cancer without distant metastases.[379] Therefore, preoperative evaluation of nodal involvement is essential.

The N category (regional lymph node involvement) includes the following:

- N0 (no involvement)
- N1 (perigastric lymph node metastasis within 3 cm of the edge of the primary tumor)
- N2 (metastasis in perigastric lymph nodes more than 3 cm from the edge of the primary tumor or in lymph nodes along the left gastric, common hepatic, splenic, or celiac arteries)

Compared with conventional CT, helical CT improves the detection of lymph nodes.[173] However, lymph nodes smaller than 5 mm in diameter cannot be accurately detected by available imaging techniques.[88, 173] Furthermore, lymph nodes situated in a small space and surrounded by soft tissue, such as the porta hepatis, may be difficult to detect by CT. Discrimination between benign and malignant nodes is usually difficult. However, in a study by Fukuya and coworkers,[173] hyperattenuation was more common in metastatic nodes, and low attenuation was more common in tumor-free nodes on the early phase of dynamic or helical CT scans.[88, 173]

Metastatic nodes tended to have larger short-to-long axis ratios (>0.7).[173] Until recently, CT diagnosis of lymph node metastasis had been based on size criteria. Most studies of GI tract tumors consider lymph nodes 10 mm or larger to have been infiltrated by metastases of solid tumors.[88, 173] According to this criterion, the sensitivity of CT in nodal staging of gastric cancer has been reported to be variable (range, 48% to 91%).[52, 88, 560] Understaging is the main drawback of CT because only lymph nodes with a diameter larger than 5 mm are visible and metastases in smaller nodes cannot be detected. Furthermore, the results of two reports[132, 415] appear to be pessimistic with regard to the nodal staging of CT.

In a study by Mönig and associates,[415] who analyzed

regional lymph nodes from 31 gastrectomy specimens of patients with gastric cancer, 55% of the metastatic lymph nodes were 5 mm or smaller in diameter and 80% of tumor-free lymph nodes were smaller than 5 mm in diameter. In another study by Düx and colleagues,[132] most metastatic lymph nodes were between 2 and 10 mm in diameter, and helical CT depicted 74% of histologic N0 stages, 45% of N1 stages, and only 32% of N2 stages. Therefore, it may be true that lymph node size is not a reliable indicator for lymph node metastasis; accordingly, CT is not an effective modality for N staging of gastric cancer.

Tumor Spread

The major methods of spread of cancer are by local invasion through contiguity and tissue planes, by the lymphatic system, by the vascular system, and by implantation.[95] Thus, gastric cancer spreads to the liver, lymph nodes, pancreas, duodenum, transverse mesocolon, peritoneal cavity, and ovary.

In clinical practice, one of the major questions of the surgeon for patients with gastric cancer who do not appear to have distant metastasis, according to CT, is whether there is pancreatic invasion because its presence precludes curative surgery. On CT, pancreatic invasion is suggested when the low-attenuation band of fat between the tumor and the pancreas is absent (Fig. 34–35) or when the gastric tumor abuts the pancreas. When this criterion was applied, the sensitivity of CT in detecting pancreatic invasion was poor (27%) in a series by Sussman and coworkers[560]; in this series, eight patients with intact fat planes had extension into the pancreas and five of another eight patients who were presumed to have pancreatic invasion on CT were eventually shown to have no tumor invasion.

According to a series by Cook and associates,[98] a sensitivity of 60% was reported. Furthermore, coexisting acute or chronic pancreatitis or associated inflammatory response also causes obliteration of the peripancreatic fat plane.[119] Therefore, application of this finding alone seems to have a significant limitation in determining the pancreatic invasion, and more strict criteria may be required.

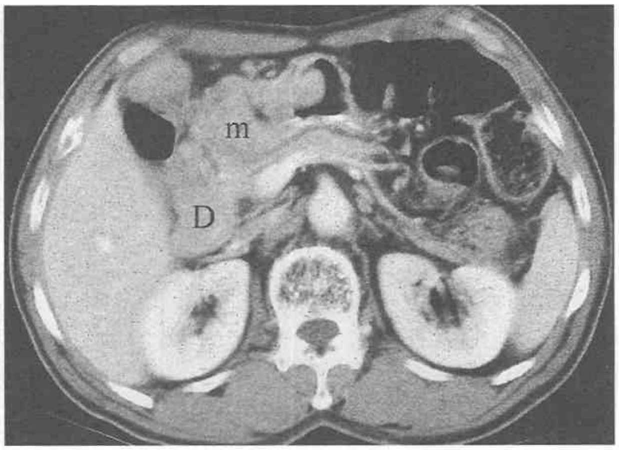

Figure 34–36. Intramural duodenal spread from gastric cancer. CT scan shows a large polypoid mass (m) in the stomach extending into the second portion of the duodenum (D).

The diagnostic value of the CT criterion of obliterated fat plane is increased when it is associated with prominent strandings in the perigastric fat plane as well as irregularity along the outer border of gastric wall involved by the tumor. Although additional studies with patients in a decubitus position are time-consuming, they may be helpful in determining focal or diffuse fixation between the pancreas and the stomach.

In certain instances, gastric cancer spreads into the duodenum through the pyloric canal (Fig. 34–36). The incidence varies greatly in surgical and postmortem series (range, 9% to 69%).[276] However, the incidence of radiographically detectable transpyloric spread has been reported as only 5% to 25%.[89] Such spread occurs by direct infiltration through the submucosa or subserosa or by lymphatic transport through the submucosal layer.[276] The 5-year sur-

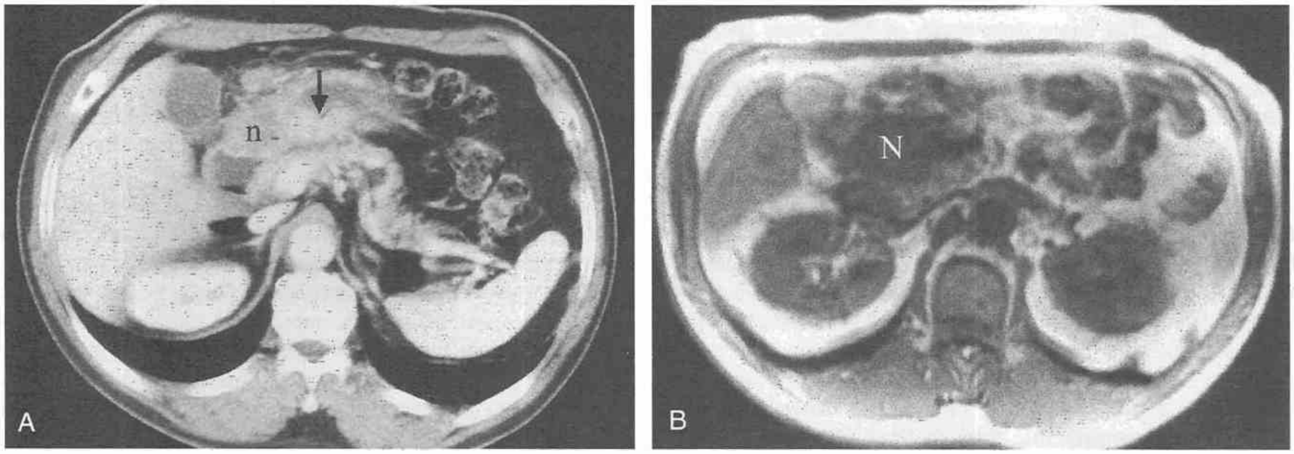

Figure 34–35. Gastric cancer with pancreatic invasion. *A,* CT scan shows obliterated interface *(arrow)* between the tumor in the stomach and pancreas along with linear strands. Enlarged perigastric nodes are also seen. *B,* Axial T1-weighted MR image at a lower level shows obliteration of the fat plane between the enlarged perigastric node and the uncinate process of the pancreas along with diffuse stranding. (From Sohn KM, Lee JM, Lee SY, et al: Comparing MR imaging and CT in the staging of gastric carcinoma. AJR Am J Roentgenol 174:1551–1557, 2000.)

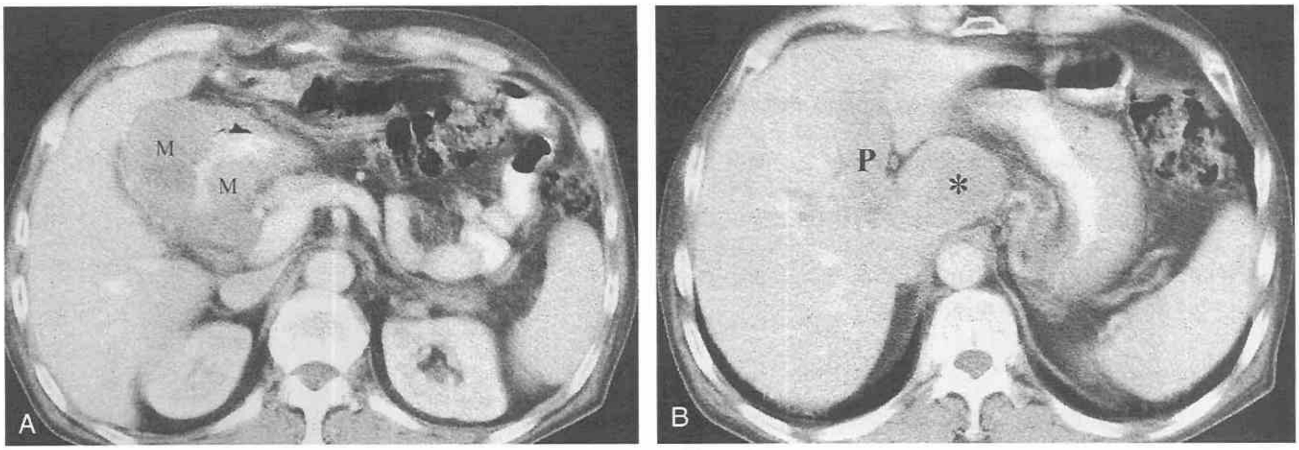

Figure 34–37. Hepatoid type of gastric adenocarcinoma. *A,* CT scan shows concentric gastric wall thickening (M) involving the antrum of the stomach. *B,* CT scan at a higher level shows a portal vein thrombus (P) and a metastatic lesion *(asterisk)* in the caudate lobe of the liver.

vival rate in these patients is poor compared with patients whose tumor is confined to the antrum.[276]

Rarely, portal venous thrombosis occurs in approximately 0.95% of patients with gastric cancer.[257] The thrombosis develops as a consequence of splenic vein involvement by the gastric tumor, and a high incidence of liver metastasis is reported in these patients.[257]

Hepatoid adenocarcinoma, an adenocarcinoma originating primarily from the gastric mucosa and containing wide and distinctive foci of hepatocellular differentiation, tends to invade portal or hepatic veins and to metastasize to the liver; the prognosis is poor (Fig. 34–37).[258] This tumor usually produces a large amount of serum alpha-fetoprotein, as high as the level released by hepatocellular cell carcinoma,[258] although one report showed that not all alpha-fetoprotein–producing adenocarcinomas have hepatoid features.[422]

Magnetic Resonance Imaging Staging of Gastric Adenocarcinoma

Until recently, MRI had not been popular for staging gastric cancer. The main drawbacks of MRI were its high cost and its lack of effectiveness in comparison with CT. However, the recent development of fast MRI techniques allows an examination during breath-holding for several seconds, thus providing high-quality images of the stomach (see Fig. 34–35). With the use of spoiled gradient-recalled acquisition in the steady state (GRASS) and the water-filling method, Matsushita and coworkers,[382] who analyzed 48 patients with gastric cancer, reported an overall accuracy rate of 88% in predicting serosal invasion by observing the changes in a low-signal-intensity band surrounding the gastric lesion.

A later article by Sohn and associates,[550] who compared CT with MRI for 30 patients with gastric cancer, showed that MRI was comparable with helical CT in T and N staging; the accuracies of MRI and CT were 73.3% and 66.7% for T staging and 55% and 58.6% for N staging, respectively. Although further investigation is necessary, MRI appears to be an alternative modality of choice for tumor staging in patients with gastric cancer.

Local Recurrence of Gastric Adenocarcinoma

Local recurrence of gastric carcinoma after surgery is defined as histologic evidence of a tumor in the surrounding tissues of the resected stomach (i.e., the gastric remnant, the esophageal anastomosis, the pancreas, the duodenal stump, the hepatic pedicle, the splenic hilum, the celiac axis area, and the abdominal wound).[450] According to autopsy studies, 80% of the patients who underwent gastrectomy for gastric cancer eventually experienced local recurrence with or without distant metastasis.[391] However, only 19% of all patients with recurrence had resectable lesions on re-exploration; almost 50% of stump recurrences were resectable, whereas only 2 of 34 patients with recurrence at an extragastric site had resectable lesions.[450]

Tumor recurrence at the gastric remnant may occur more commonly in patients with early-stage gastric cancers[450, 451] very late after surgery.[259] Also, the gastric cancers arising in the cardia were prone to anastomotic recurrence.[451] Because barium studies are associated with difficulty in their capability to fully assess the areas mentioned earlier, CT plays an important role in determining the extent of local tumor recurrence or distal metastasis. On CT, recurrence at gastric stump or anastomosis appears as a localized wall thickening or mass (Figs. 34–38 and 34–39). Afferent loop syndrome may be caused by development of the recurrent tumor near the orifice of the afferent loop (Fig. 34–40). However, potential sources of erroneous interpretation include improperly opacified bowel loop, food, surgical plication, gastritis, and gastritis cystica polyposa.[207]

The most frequently involved lymph nodes are those along the common hepatic artery, the celiac axis, and the hepatoduodenal ligament.[207] The presence of lymphadenopathy along the hepatoduodenal ligament may cause moderate to severe biliary tract obstruction. When the pancreas is involved, CT features are indistinguishable from those of primary pancreatic tumor, and enlarged peripancreatic lymph nodes can mimic tumor recurrence in the pancreas.

Most tumor recurrences at the abdominal incision are caused by iatrogenic dissemination of cancer cells during surgery (Fig. 34–41).[95] However, postoperative fibrosis,

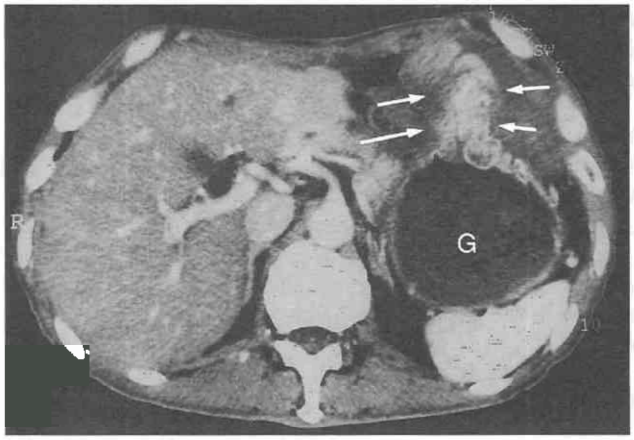

Figure 34–38. Local recurrence of gastric adenocarcinoma at the anastomotic site following subtotal gastrectomy. The bowel wall *(arrows)* at the surgical anastomosis is thickened and markedly enhanced along with marked distention of the remnant stomach (G).

hematoma, abscess, or granuloma cannot be differentiated from tumor recurrence at this site by imaging findings alone. Because tumor recurrences were most common within 2 years after surgery, follow-up CT scanning in a short interval is required at this period for early diagnosis.

Lymphoma

The stomach is the most frequent site of lymphomatous involvement of the GI tract. *Non-Hodgkin's lymphoma* accounts for approximately 80% of cases. Gastric involvement may be isolated but more commonly is part of a generalized disease process.[53] Among various prognostic factors that include gender, age, size and location of tumor, histologic type, depth of invasion, and nodal status, depth

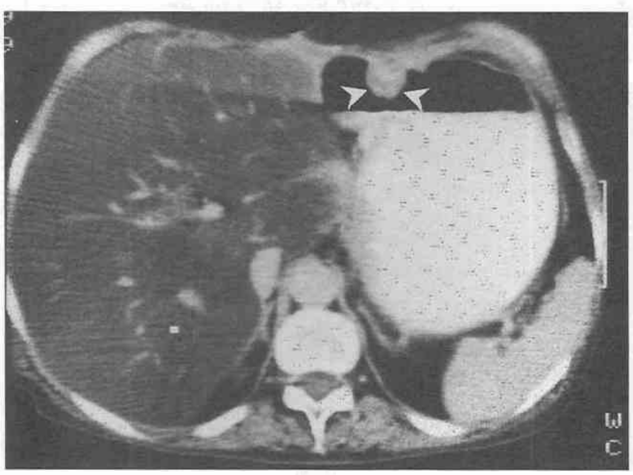

Figure 34–39. Tumor recurr[redacted] at the surgical plication. CT scan shows prominent surgical plication *(arrowheads)*. Surgery confirmed tumor infiltration at the plication. (From Ha HK, Kim HH, Kim HS, et al: Local recurrence after surgery for gastric carcinoma: CT findings. AJR Am J Roentgenol 161:975–977, 1993.)

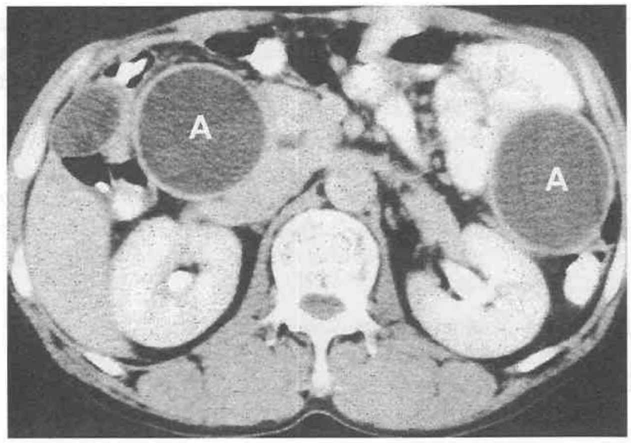

Figure 34–40. Afferent loop syndrome due to obstruction at the proximal afferent loop by recurrent tumor (not shown).

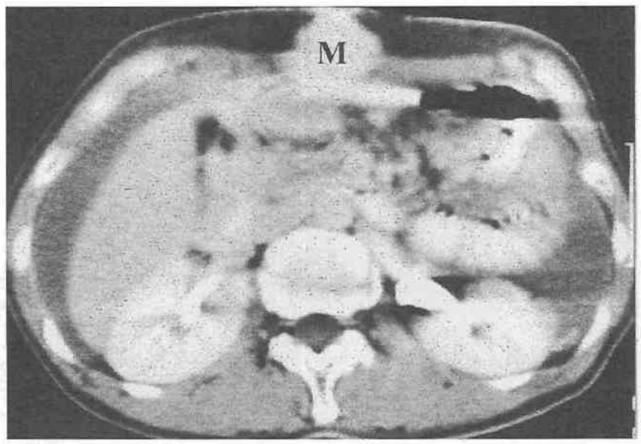

Figure 34–41. Tumor recurrence at the incisional wound after surgery for gastric cancer. CT scan shows a lobulated, well-enhancing mass (M) along the incisional wound as well as a large amount of ascites and peritoneal thickening due to peritoneal carcinomatosis. (From Ha HK, Kim HH, Kim HS, et al: Local recurrence after surgery for gastric carcinoma: CT findings. AJR Am J Roentgenol 161:975–977, 1993.)

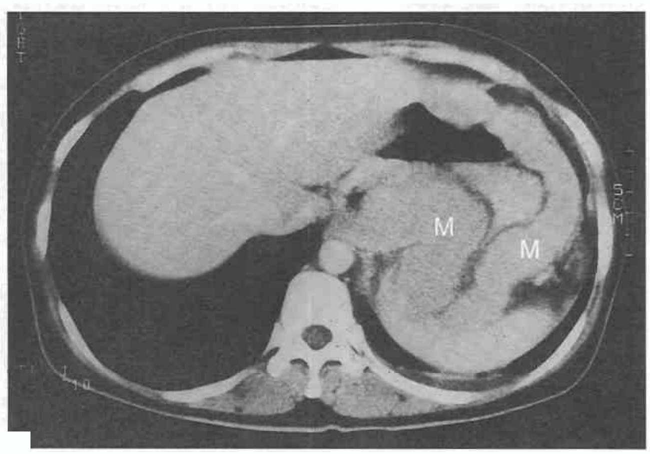

Figure 34–42. Gastric lymphoma. Gastric wall is markedly thickened (M) with predominant involvement of the submucosa. The mucosal layer is well preserved.

of invasion and regional lymph node involvement play a decisive role in survival.[60] Unlike carcinoma, lymphoma tends to spread laterally within the submucosal plane and spares the muscular coats until late in its course.

With its ability to directly image the entire gastric wall and adjacent structures, CT has proved capable of determining the extent of spread of gastric lymphoma with a high degree of accuracy.[69] According to Megibow and colleagues,[398] gastric wall involvement can be divided into three patterns, as seen with CT:

1. Diffuse infiltration involving more than 50% of the length of the stomach.
2. Segmental infiltration.
3. The localized polypoid form.

Gastric wall thickening is most commonly circumferential, with thickness greater than 4 cm. Thickening and distortion of the gastric rugal folds may be present but outlet obstruction is rare (Fig. 34–42).[69, 398] Dynamic CT and MRI clearly depict submucosal spread of the tumor within the normally enhanced mucosal layer (Fig. 34–43).[408] Lymphomatous tissues in the thickened gastric wall usually show poor and homogeneous contrast enhancement; this pattern may be due to lack of desmoplastic response in lymphoma in contrast with gastric adenocarcinoma.

Sometimes gastric lymphoma shows heterogeneous enhancement. In such cases, the hypoattenuated areas may be caused by the pathologic evidence of necrosis and hemorrhage.[232] The localized polypoid form is often associated with an ulcer. The perigastric fat plane is usually preserved. Most patients with gastric lymphoma have perigastric lymphadenopathy, and the presence of widespread retroperitoneal lymphadenopathy indicates systemic disease.

Perforation is an important complication affecting therapy and prognosis. It may occur in 9% to 47% of patients as a result of the lack of desmoplastic response, the rapid growth of the tumor, or a response to therapy.[393] Tumor extension into the esophagus is present in about 10% of patients, and spread across the pylorus into the duodenal bulb has been noted in approximately one third of patients.[245] Although not common, far-advanced cases of lymphoma can show diffuse peritoneal involvement with ascites, omental infiltration, and peritoneal implants, mimicking carcinomatosis (Fig. 34–44).[298]

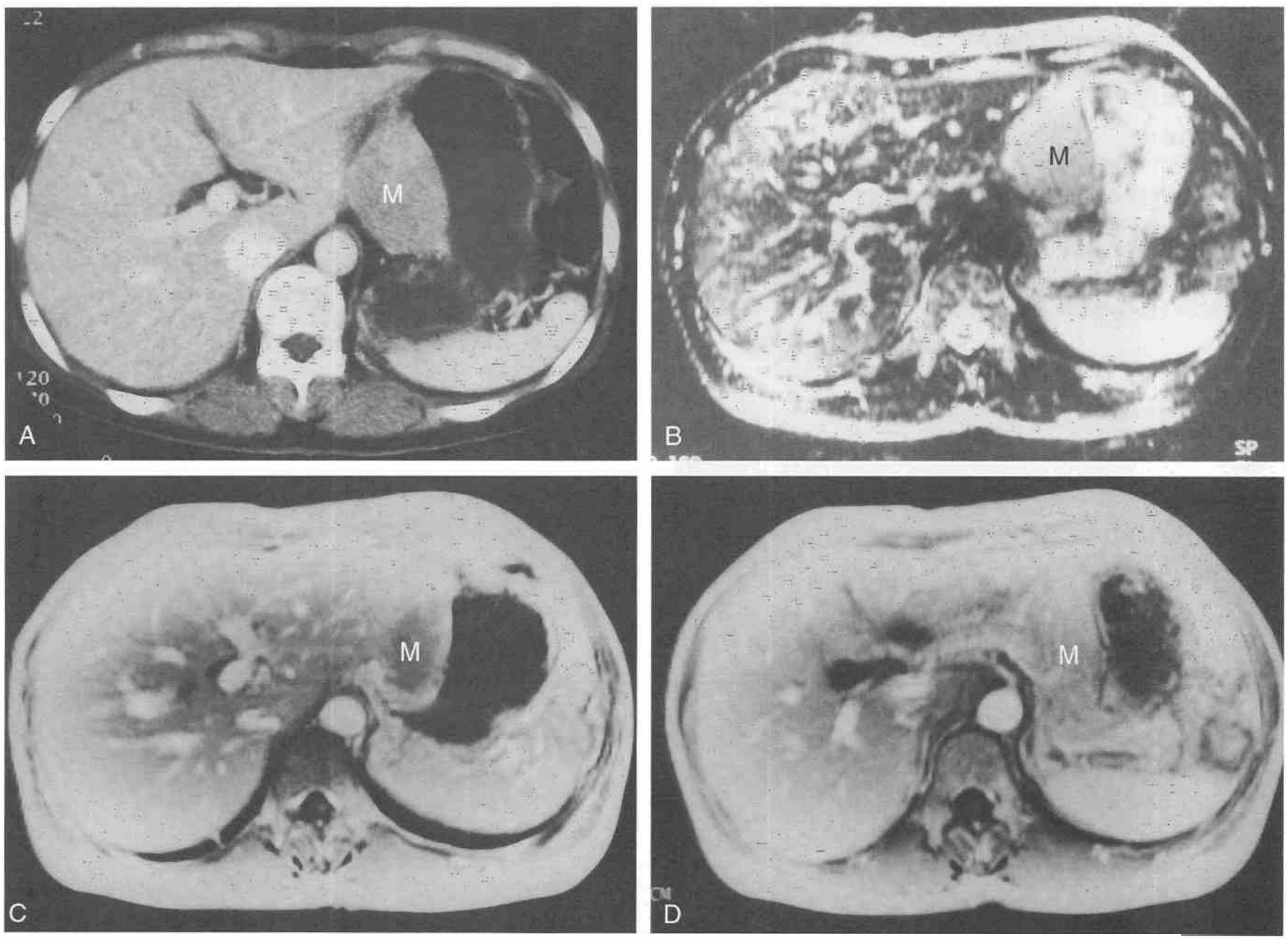

Figure 34–43. Gastric lymphoma. *A*, A mass (M) is seen in the gastric wall along the lesser curvature of the stomach on CT scan. *B*, T2-weighted MR image shows a mass (M) with intermediate signal intensity. *C* and *D*, Dynamic gadolinium-enhanced MR images show poor contrast enhancement of the mass (M) in the early phase *(C)* and isointensity to that of the liver in the delayed phase *(D)*.

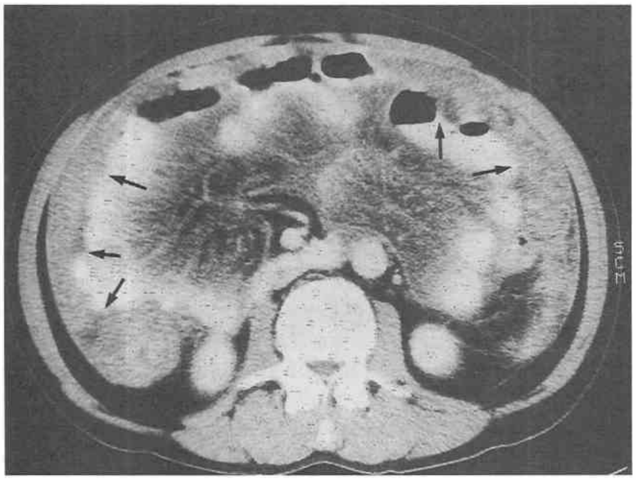

Figure 34–44. Peritoneal lymphomatosis. CT scan shows omental cake *(arrows)* and diffuse mesenteric infiltration.

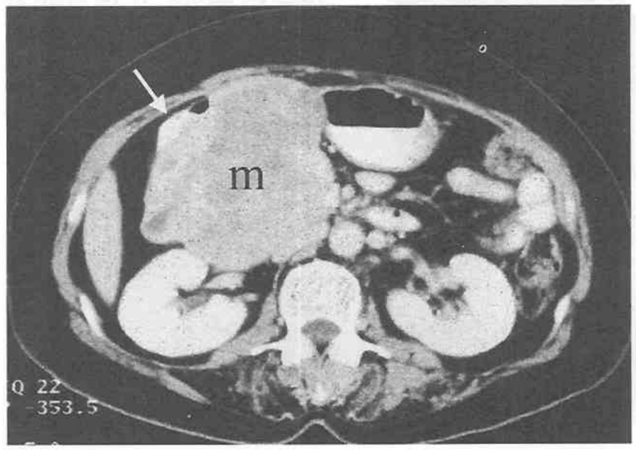

Figure 34–46. Malignant gastrointestinal stromal tumor. CT scan shows a large, heterogeneous mass (m) growing exophytically from the stomach *(arrow)*.

Gastrointestinal Stromal Tumor

GI stromal tumors are the most common primary nonepithelial neoplasms of the stomach and small bowel. For many years, they were all regarded as being basically of smooth muscle nature; they were designated as leiomyomas and leiomyosarcomas when composed of spindle cells and as benign or malignant leiomyoblastomas when composed of epithelioid cells.

GI stromal tumors can be divided into four major categories on the basis of their phenotypical features[510]:

1. Tumors with features of smooth muscle differentiation.
2. Tumors with features of neural differentiation.
3. Tumors with dual differentiation in smooth muscle and neural elements.
4. Tumors lacking differentiation in either cell type.

Tumors with features of neural differentiation are currently regarded as malignant, and tumors with dual differentiation and with none of smooth muscle and neural differentiation are regarded as malignant or potentially malignant. Tumors with features of smooth muscle differentiation may be benign, borderline, or malignant. Features favoring malignancy are size larger than 5 cm, necrosis, hemorrhage, hypercellularity, nuclear atypia, and mitotic activity.

The location of the tumor in the gastric wall is submucosal in about 60%, subserosal in about 30% and intramural in 10%. Ninety percent of gastric stromal tumors are in the fundus and body. Growth is usually in an exogastric fashion or dumbbell shaped.[397]

Dynamic CT may demonstrate the location of stromal tumor in the submucosal layer and the intact mucosal layer (Fig. 34–45). Most stromal tumors are enhanced heterogeneously on CT,[93] with common occurrence of low attenuated areas owing to internal hemorrhage, necrosis, or cystic changes (Fig. 34–46)[481]; the presence of hemorrhage produces fluid-fluid level within the mass. Areas of necrosis can give the appearance of multiple, thick septations within the tumor. Necrosis within the tumor mass may lead to excavation and communication with the GI tract or perforation into the peritoneal cavity.

In one series,[505] crescent-shaped necrosis caused by necrosis in the periphery of the extraluminal component of the mass was reported to be suggestive of a stromal tumor on CT. Ulceration of the overlying mucosa can be demonstrated on CT as the presence of air or an oral contrast agent. Another cause of gas within the mass may be superinfection of the necrotic tumor (Fig. 34–47).[522]

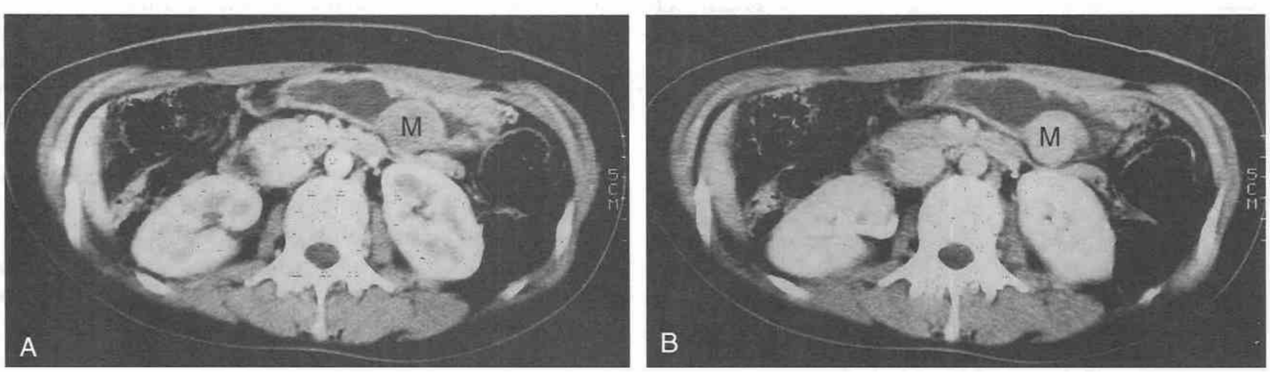

Figure 34–45. Benign gastrointestinal stromal tumor (M) of the stomach with poor contrast enhancement in the early phase *(A)* of the dynamic CT study and marked enhancement in the delayed phase *(B)*.

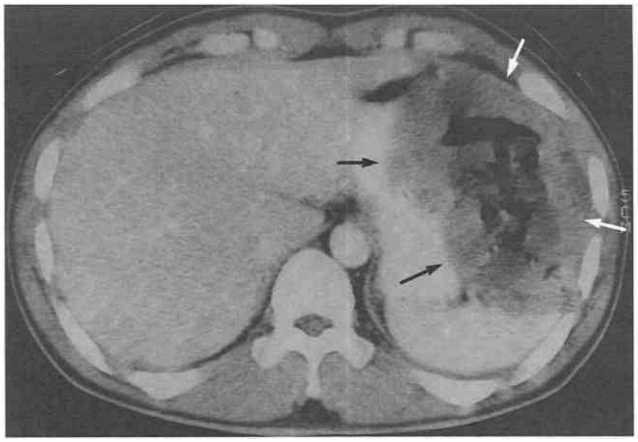

Figure 34–47. Infected malignant gastrointestinal stromal tumor of the stomach. CT scan shows a large, heterogeneous mass *(arrows)* with central cavitation and gas collection. The small orifice of the ulcer in the tumor was considered to be the cause of secondary infection.

Although not common, calcification is seen in stromal tumors (Fig. 34–48). Compared with adenocarcinoma, stromal tumors tend to show much less local invasiveness. Lymphatic spread and intraperitoneal fluid collection are also less common but do occur. The most common sites of metastases of stromal tumors are the liver, peritoneum, and lungs. Intraperitoneal tumor seeding (leiomyosarcomatosis) occurs directly along mesenteric reflections via ascitic fluid or embolic metastases.[405] The incidence is high in patients with tumors that are exposed to the peritoneal cavity along with local invasiveness. On follow-up CT scans, both paracolic gutters and pelvic cavity should be carefully evaluated for the presence of small nodule or granular infiltration. The CT appearance of leiomyosarcomatosis does not differ significantly from that of peritoneal carcinomatosis of other origin, but the incidence of peritoneal nodules was much higher in stromal tumors (see Fig. 34–82).[590]

Hasegawa and colleagues[226] reported the usefulness of MRI in nine patients with gastric stromal sarcomas. MRI was helpful not only in determining the relationships between the mass and gastric wall or surrounding organs but also in detecting intratumoral hemorrhage and necrosis. High-grade stromal tumors showed ill-defined borders, whereas low-grade tumors showed well-defined margins.

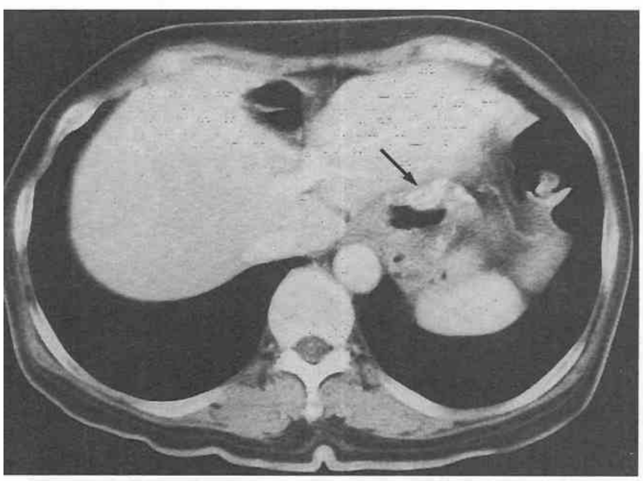

Figure 34–48. Benign gastrointestinal stromal tumor of the stomach. A calcified mass *(arrow)* is seen in the high body and fundus of the stomach.

Metastatic Tumor

Hematogenous metastases may be discovered during abdominal CT performed for other reasons. Malignant melanoma and breast and lung carcinoma are the usual primary lesions. Metastasis from a lobular carcinoma of the breast produces a linitis plastica pattern of gastric wall thickening (Fig. 34–49).[81] Squamous carcinoma of the esophagus reportedly involves the gastric cardia in up to 15% of patients and may simulate a primary mucosal or submucosal neoplasm.[182] Carcinomas of the transverse colon and tail of the pancreas metastasize to the gastric wall by direct extension via the gastrocolic and splenorenal-gastrosplenic ligaments, respectively.

Liposarcoma

Gastric liposarcoma originates in undifferentiated mesenchymal cells present within the submucosa and tunica muscularis of the gastric wall.[313] Pathologically, four forms are recognized: (1) differentiated, (2) myxoid, (3) round cell, and (4) pleomorphic.

The exuberant exophytic growth explains the lack of specific GI symptoms and the delayed diagnosis. The CT appearances correlate with the macroscopic appearance of the neoplasm. Fatty areas within the tumor is reported only in the differentiated form.[354] Undifferentiated liposarcomas commonly contain areas of necrosis and hemorrhage along with prominent enhancement of the solid zones.[152] Myxoid tumors present as a cystic form owing to the presence of gelatinous matrix.[152]

Plasmacytoma

Malignant neoplasms of plasma cells (plasmacytoma) appear in two forms. The *diffuse* form includes multiple myeloma or plasma cell leukemia; the *local* form is a solitary myeloma of bone or an extramedullary plasmacytoma. Ten percent of cases of extramedullary plasmacytoma occur in the GI tract; the small bowel is most commonly involved, followed by the stomach, colon, and esophagus. Primary gastric plasmacytoma accounts for approximately 5% of all extramedullary plasmacytomas.[230]

The diagnosis of primary gastric plasmacytoma is established by the absence of a serum M protein component; hence, there is no Bence-Jones proteinuria, no bone marrow infiltration, and no visceral involvement other than of the stomach.[517]

Pathologically, primary gastric plasmacytoma has been thought to originate from lymphoid follicles in the submucosa or from plasma cells in the lamina propria of the mucosa and can have various forms. Remingo and Klaum[497] grossly classified gastric plasmacytoma into four types: (1) *nodular*, (2) *infiltrative*, (3) *ulcerative*, and (4) *polypoid*. Of these four types, the nodular type was most commonly seen in their study. CT findings of gastric plasmacytoma simulate those of lymphoma or a mucinous type

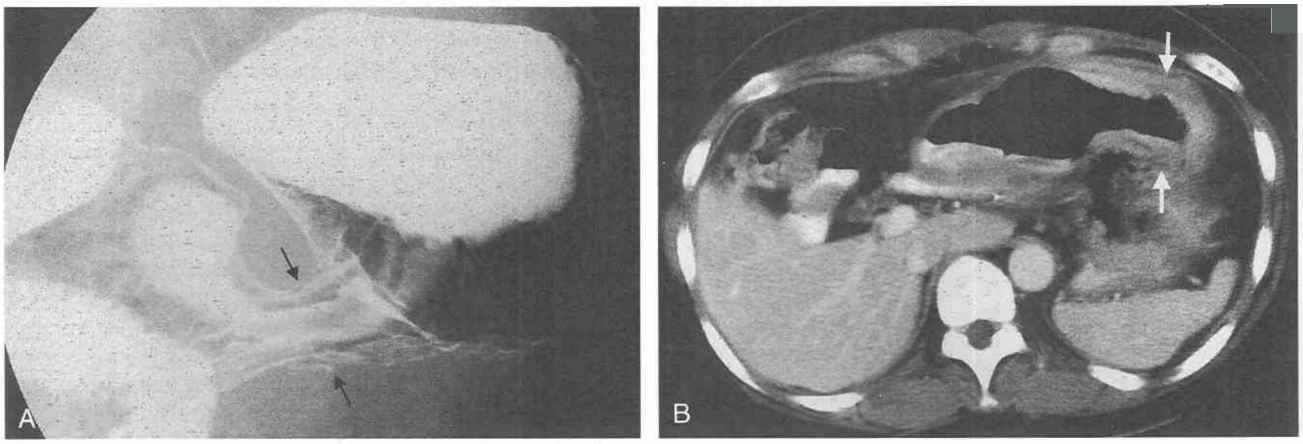

Figure 34–49. Metastasis to the stomach (linitis plastica) from breast cancer. *A*, Double-contrast upper gastrointestinal series shows focal luminal narrowing *(arrows)*, rigidity, and fold thickening in the proximal antrum and lower body of the stomach. *B*, CT scan shows involvement of the stomach by a scirrhous tumor.

of gastric cancer owing to poor contrast enhancement of the gastric wall (Fig. 34–50).[614] Deep endoscopic biopsy, combined with the immunohistochemical study of immunoglobulin, is essential in diagnosis.[532]

Benign Gastric Tumors

Gastric Polyp and Adenoma

Epithelial polyps of the stomach may be *hyperplastic* or *adenomatous*.

Hyperplastic polyps are not true neoplasms. They are believed to develop from excessive regeneration of superficial epithelium. Although most of these non-neoplastic polyps are often multiple and smaller than 1.5 cm in diameter, 9% are larger than 2 cm.[409]

In contrast, 80% of adenomatous polyps (adenoma) exceed that size.[409] CT may detect epithelial polyps that are larger than 2 cm in diameter when the stomach is well distended with air or when oral contrast material has been given (Fig. 34–51). No specific CT features that can distinguish these polyps from gastric malignancy have been reported. Rarely, pedunculated polyps may prolapse into the duodenum or may cause intussusception (Fig. 34–52).[216]

Lipoma

Gastric lipoma is a rare submucosal tumor that usually occurs in the antrum. Large lipomas ulcerate and produce

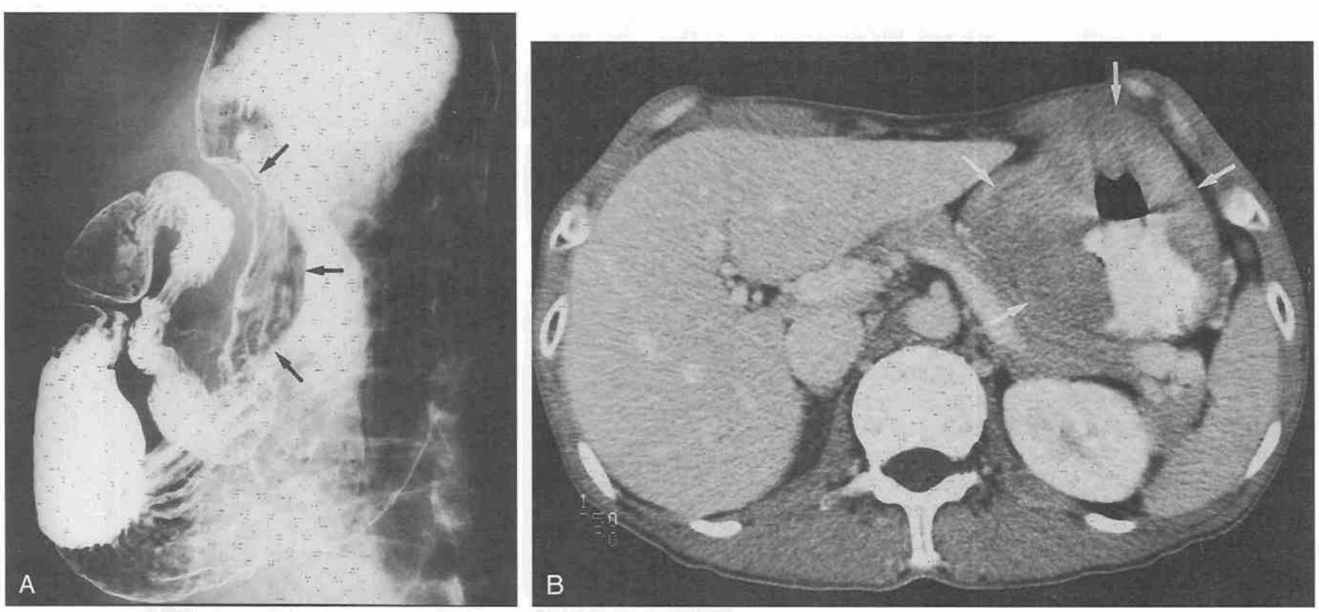

Figure 34–50. Gastric plasmacytoma. *A*, Upper gastrointestinal radiograph shows large gastric mass *(arrows)* with a sharply marginated border. *B*, CT scan shows marked gastric wall thickening *(arrows)* with poor contrast enhancement simulating lymphoma or adenocarcinoma. (From Yoon SE, Ha HK, Lee YS, et al: Upper gastrointestinal series and CT findings of primary gastric plasmacytoma: Report of two cases. AJR Am J Roentgenol 173:1266–1268, 1999.)

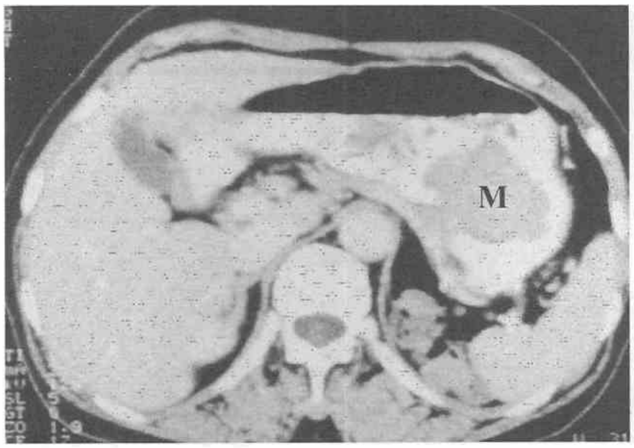

Figure 34–51. Gastric adenoma with malignant transformation. CT scan shows a polypoid mass (M) with a short, thick stalk.

clinically significant hemorrhage.[365] The CT finding of gastric mass having a CT attenuation equivalent to fat is pathognomonic of a gastric lipoma (Fig. 34–53).

Hemangioma

Gastric hemangiomas are rare neoplasms, constituting less than 2% of all benign tumors of the stomach. Pathologically, hemangiomas can be (1) cavernous, (2) capillary, or (3) mixed. The gross appearance varies according to the size and density of the plexus of vessels forming the lesion, the degree of arteriovenous shunting, and the presence of thrombosis or fibrosis.

Cavernous hemangiomas may be single or multiple, localized, or diffuse.[180, 285] Gastric hemangiomas are smooth submucosal masses that are radiographically indistinguishable from stromal tumors. Although rare, the presence of phleboliths, which are most often associated with the cavernous types, help in establishing an accurate diagnosis on CT.[537]

Figure 34–52. Gastroduodenal intussusception due to prolapsed gastric adenoma. *A,* Radiograph shows a large polypoid mass *(arrowheads)* in the antrum of the stomach. *B* and *C,* CT scans obtained 1 month later after an upper gastrointestinal series show large soft tissue mass *(arrows)* in the duodenum and beaklike narrowing *(small arrows)* of the distal stomach. (From Ha HK, Shinn KS, Kim IC, et al: Gastroduodenal intussusception due to a prolapsed gastric adenoma. AJR Am J Roentgenol 159:432, 1992.)

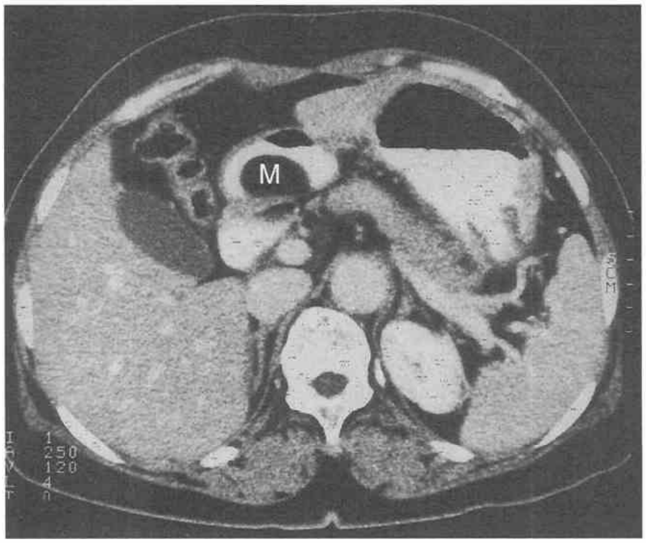

Figure 34–53. Gastric lipoma. A fatty mass (M) is seen in the antrum.

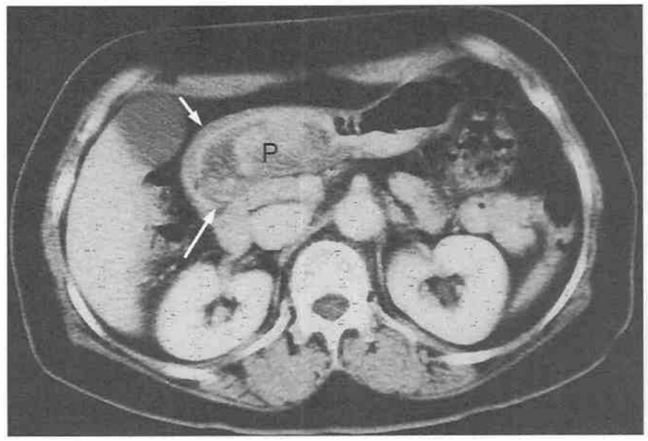

Figure 34–55. Benign gastric ulcer. The swollen gastric wall surrounding the gastric ulcer simulates a polypoid mass (P). Gastric wall thickening *(arrows)* is also present.

Inflammation and Other Conditions

Peptic Ulcer Disease

Although CT has no useful role in patients with uncomplicated peptic ulcer disease, it is effective in detecting its complications such as acute free perforation and penetration. The ulcers are frequently identified on CT as round, thin-walled collections of air or orally administered contrast medium, projecting beyond the confines of the gastric or duodenal lumen. Although direct visualization of the ulcer may be difficult on CT in many instances, the involved gastric or duodenal wall is mostly thickened with considerable mural edema (Figs. 34–54 and 34–55). If free perforation is present, CT may show free extravasation of oral contrast material or free intraperitoneal air, or both, along with evidence of diffuse peritonitis such as omental or mesenteric infiltration and intraperitoneal fluid collection.

Although CT is not very accurate in detecting the perforating site,[262, 366] the use of thin-section spiral CT may improve detection by demonstrating the interruption of well-enhanced gastric wall.[437] On occasion, peptic ulcers that extend beyond the serosa of the bowel wall may penetrate the adjacent structures (confined perforation or penetration). The most common site of penetration is the pancreas owing to an ulcer's proximity to the distal stomach and duodenum and fixation of its position[366]; other sites include the gastrohepatic omentum, the biliary tree, and the liver, with the omentum being involved by gastric ulcers and the biliary tree by duodenal ulcers.[227] On CT, the diagnosis of ulcer penetration can be confirmed when a low-density linear band (sinus tract) containing perigastric contrast material is identified or when an ectopic pocket of

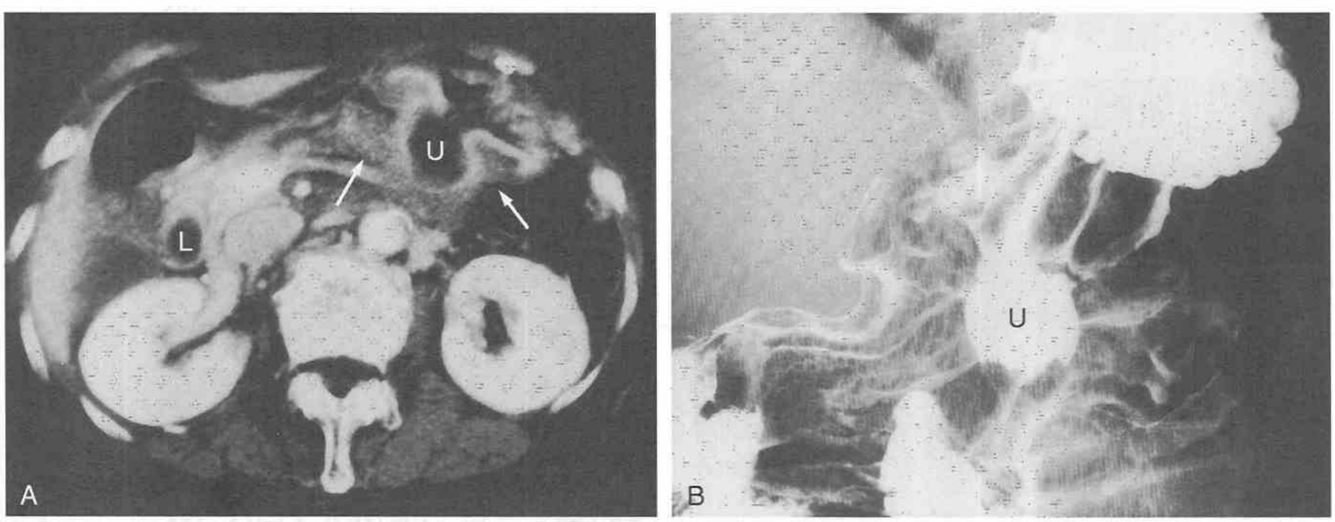

Figure 34–54. Benign gastric ulcer. *A,* A large, penetrating ulcer (U) is seen in the posterior wall of the stomach with markedly enhancing inner layer of the thickened gastric wall and edematous outer layer *(arrows).* Minimal perigastric infiltrate is also seen. A lipoma (L) is incidentally found in the duodenum. *B,* Double-contrast upper gastrointestinal series shows a large ulcer crater (U) with convergence of thickened gastric wall.

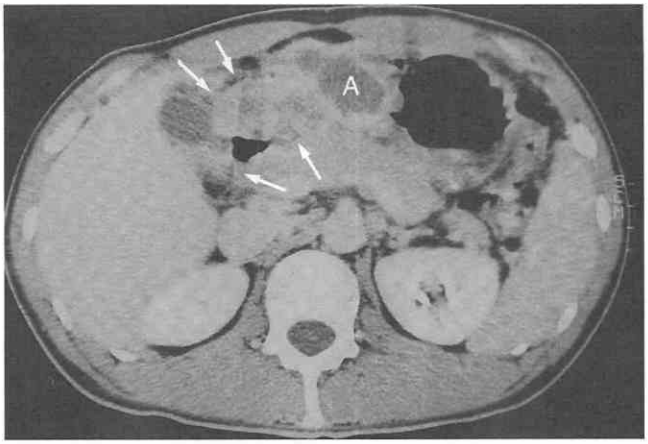

Figure 34–56. Confined peptic ulcer perforation. CT scan shows a perigastric cystic mass (A) with a thick peripheral wall in the perigastric region. The wall of the stomach and duodenum is considerably thickened with heterogeneous contrast enhancement *(arrows)* and evidence of perigastric infiltrates is present.

gas is demonstrated in the perigastric space adjacent to the suspected ulcer crater (Figs. 34–56 and 34–57).

In cases of pancreatic penetration, the fat plane between the ulcer and the pancreas is lost and the pancreas is focally enlarged with diminished CT attenuation, findings that are indistinguishable from those of acute pancreatitis. However, despite pancreatic enlargement, the remaining peripancreatic fat plane is commonly preserved, and only a small number of patients may show an increased level of serum amylase or lipase in such instances.[262] CT can also depict penetration of a gastric ulcer crater or its surrounding inflammatory mass into the splenic parenchyma.[181]

Gastritis and Other Conditions Causing Gastric Wall Thickening

Gastritis, recently associated with *Helicobacter pylori* infection, commonly involves the antrum and body of the stomach, with most cases involving the antrum.[584] Enlargement of gastric folds and thickening of the gastric wall may occur owing to a combination of mucosal inflammation, submucosal edema, and secondary hypertrophy and hyperplasia of the gastric mucosa. Gastritis appears as circumferential or focal gastric wall thickening on CT.[584]

Although CT is sensitive in detecting inflammatory processes in the stomach, it is not specific in differentiating gastritis from gastric malignancy. The absence of obliteration of the fat planes, perigastric infiltration, and lymphadenopathy may aid in diagnosis. Other infectious processes, such as toxoplasmosis and cryptosporidiosis, can also cause nonspecific gastric wall thickening.[548, 551]

In rare instances of acute infectious gastritis, an intramural gastric wall abscess develops, simulating a submucosal tumor.[104] In patients with emphysematous gastritis, CT may show an irregular, thickened gastric wall along with multiple intramural gas bubbles. When intramural gas is seen with noninfectious causes of gastric emphysema, such as secondary to gastric outlet obstruction, the gas is distributed as thin, uniform linear streaks.[377] Although rare, chronic granulomatous disease can involve the stomach, especially along the antrum, with diffuse nonspecific gastric wall thickening on CT.

Menetrier's disease shows diffuse thickening of the gastric mucosal folds, predominantly along the body and fundus of the stomach (Fig. 34–58).[157] In immunocompromised patients, graft-versus-host disease (GVHD) may demonstrate not only gastric wall thickening on CT but also a peculiar, persistent coating of the gastric and small-bowel mucosa with orally administered contrast material.[272] CT also demonstrates gastric fold or wall thickening in Zollinger-Ellison syndrome (Fig. 34–59), amyloidosis, sarcoidosis, and eosinophilic gastritis. An extragastric inflammatory process, such as acute pancreatitis, may involve the gastric wall with focal thickening or cystic mass formation (Fig. 34–60).

Congenital Conditions

Diverticula

Gastric diverticula generally arise from the posterior wall of the fundus. They appear as a thin-walled, cystic-

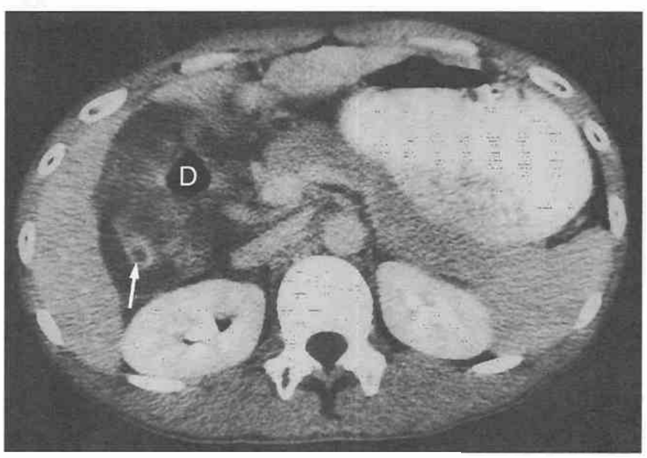

Figure 34–57. Confined duodenal ulcer perforation. CT scan shows edematous bowel wall thickening of the duodenum with an ulcer crater *(arrow)*. A small amount of fluid is collected in the paraduodenal space.

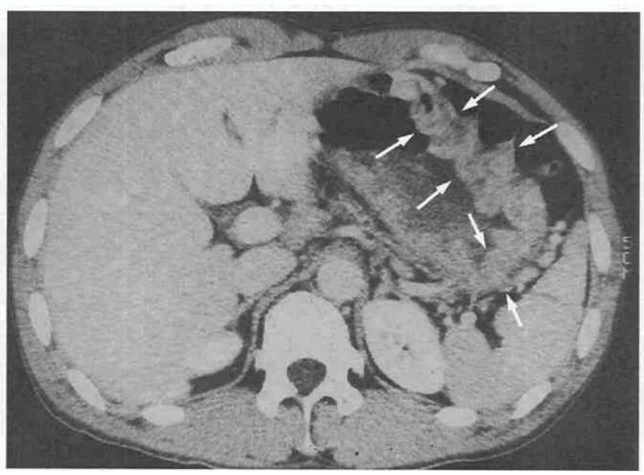

Figure 34–58. Ménétrier's disease of the stomach. CT scan shows marked thickening *(arrows)* of the gastric rugal folds along the greater curvature of the stomach.

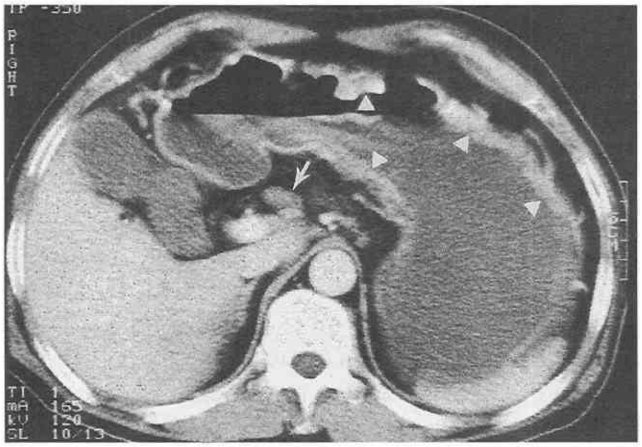

Figure 34–59. Gastric fold thickening due to gastrinoma. CT scan shows marked gastric distention and fluid excess with prominent and thickened mucosal folds *(arrowheads)*. A small mass *(arrow)*, which was confirmed as gastrinoma at surgery, is noted in the perigastric region.

appearing mass on CT (Fig. 34–61). If the diverticulum is not filled with air or orally administered contrast material, it simulates a cystic inflammatory or neoplastic condition of adjacent structures.

Ectopic Pancreatic Rest

The ectopic pancreas pathologically appears as a smooth nodule and, occasionally, as a mass with an irregular surface. It is usually situated in the submucosa and only occasionally expands into the muscularis. It most frequently occurs in the antrum within 3 to 6 cm of the pylorus and is on the greater curvature side of the posterior wall of the stomach; other sites include the second portion of the duodenum and the jejunum.[32] On barium study, demonstration of umbilication, which represents the filling of the rudimentary pancreatic duct, may suggest the proper diagnosis.[571] When a nodule exceeds 2 cm, it appears as a mural nodule on CT (Fig. 34–62).

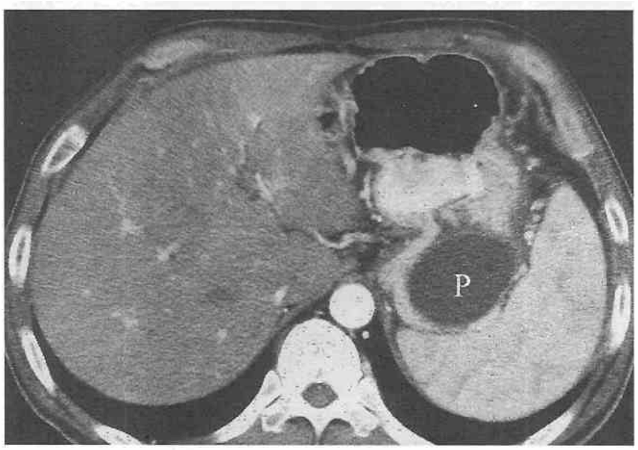

Figure 34–60. Gastric wall involvement in a patient with pancreatitis. CT scan shows a cystic mass (P) in the gastric wall due to extension of pancreatic pseudocyst.

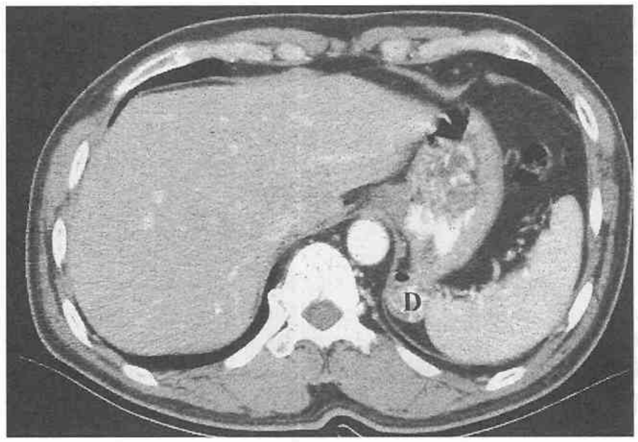

Figure 34–61. Gastric diverticulum. CT scan shows a diverticulum (D) arising from the posterior wall of gastric fundus, which is filled with oral contrast material and gas.

Gastric Duplication

Most gastric duplications occur during the first year of life, but 28% of cases have been detected in patients older than 12 years of age.[472] Approximately 82% are spherical cysts and do not communicate with the stomach; the remaining 18% are tubular and communicate with the gastric lumen.[601] Although rare, pedunculated type of duplication with a thin, fibrous strand is also reported.[309] The most common location is along the greater curvature, followed by posterior wall, lesser curvature, anterior wall, and pylorus.

Ectopic pancreatic tissue is found in the wall of up to 37% of gastric duplications[239] and is associated with pancreatitis and elevated amylase levels. Detection of associated vertebral anomalies such as spina bifida, hemivertebra, and complete vertebral body cleft is a helpful clue for the diagnosis.

Clinically, duplications occur twice as often in girls than

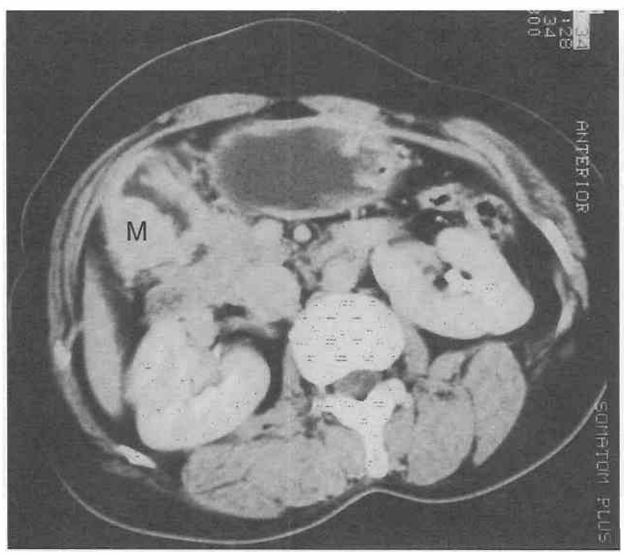

Figure 34–62. Ectopic pancreas in the stomach. CT scan shows a submucosal mass (M) in the prepyloric antrum of the stomach.

in boys. Clinical symptoms and signs include a palpable mass, gastric obstruction, abdominal pain, melena, or hematemesis. Gastric duplication may undergo torsion and may perforate and cause a surgical emergency.[531]

CT and MRI may be used to determine the nature, size, and extent of the mass, revealing a cystic mass contiguous with the stomach and containing fluid, gas, or debris. Curvilinear calcification is rarely detected on the wall of the duplication.[162]

The differential diagnosis with other disease entities such as pancreatic cyst and pseudocyst, mesenteric cyst, and various intramural tumors of the stomach cannot be easily made by imaging findings alone. Technetium 99m–pertechnetate may show uptake of the radiopharmaceutical agent in the gastric mucosal lining.

Other Conditions

Varices

Esophageal and gastric varices develop in patients with portal hypertension either as a consequence of intrahepatic obstruction (cirrhosis) or extrahepatic obstruction, such as portal or splenic vein occlusion. In contrast to the superficial location beneath the mucosa in esophageal varices, gastric varices tend to have a subserosal location and are thereby easily mistaken at endoscopy or radiographic studies for other submucosal masses.[79, 376]

In the stomach, the posteromedial border of the gastric fundus is the most common site, although any part of the stomach can be involved. CT is a sensitive tool for detecting gastric varices and for determining their primary cause. Gastric varices appear as well-defined clusters of markedly enhancing, rounded, and tubular lesions within the scalloped gastric wall (Fig. 34–63).[79] Intra-abdominal collateral venous channels may also be seen along the distribution of the left gastric, gastroepiploic, or short gastric vein.

Gastroduodenal Intussusception

Gastroduodenal intussusception is an uncommon condition reported to be caused by benign pedunculated gastric tumors such as stromal tumor, adenoma, and lipoma or Menetrier's disease.[122, 216] CT findings are characteristic. The site of the invagination is seen as a target-like mass in the duodenal region. Both CT and barium study may also show foreshortening and beaklike narrowing of the distal stomach as well as gastric outlet obstruction (see Fig. 34–52).[122, 216]

Jejunogastric Intussusception

Jejunogastric intussusception is a rare complication of gastric surgery that may present either in acute form or as a chronic recurrent process. According to the type of invaginated loop, it can be classified as an *afferent* loop invagination or as an *efferent* loop invagination or both.[534] The efferent loop invagination is most commonly seen.

Retrograde peristalsis is considered to be the main pathogenetic factor. Immediate laparotomy should be performed because an 80% mortality rate has been reported when treatment is delayed.[96]

Although the diagnosis can be made with an upper GI series or gastroscopy, CT is also useful in diagnosis and in early detection of possible strangulation in the intussuscepted jejunal loop. CT may show dilatation of the gastric remnant with evidence of intragastric position of the jejunal loop and mesentery (Fig. 34–64).[348, 353]

Gastric Herniation and Volvulus

The diagnosis of gastric herniation through the lacerated diaphragm is often delayed or missed because its plain radiographic appearance resembles that of pneumothorax, hemothorax, pleural effusion, pulmonary consolidation or collapse, or raised hemidiaphragm. In addition to the penetrating or blunt trauma to the diaphragm, laxity or absence of the tethering gastric ligaments as well as conditions that increase the size of the esophageal hiatus, such as rapid changes in intra-abdominal pressure (i.e., trauma), and de-

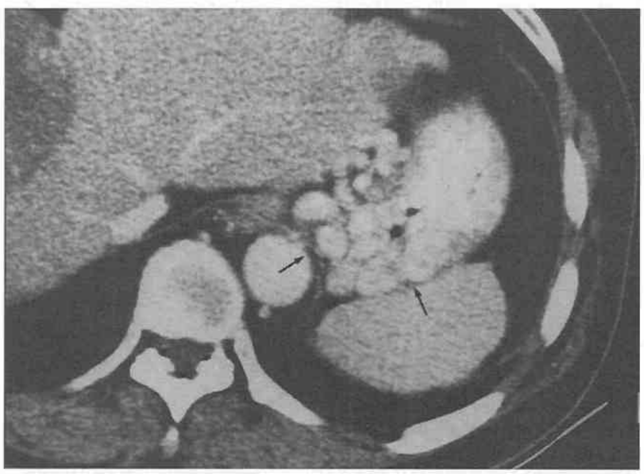

Figure 34–63. E[redacted]ageal varices after scl[redacted]herapy in a patient with liver cirrhosis. CT scan shows esophageal wall thickening with target appearance. The middle layer *(arrows)* appears hypoattenuated, presumably owing to mural hematoma or edema.

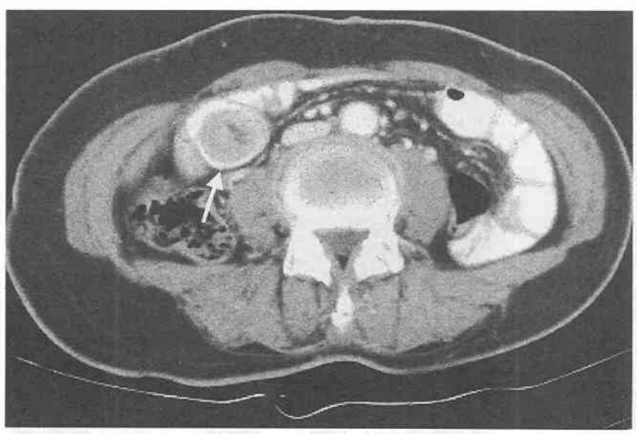

Figure 34–64. Transient jejunojejunal intussusception after gastrectomy. CT scan shows heterogeneous masslike lesion in the jejeunal loop caused by invagination of the regional mesentery into the bowel lumen. Small-bowel follow-through study (not shown) did not demonstrate any mass.

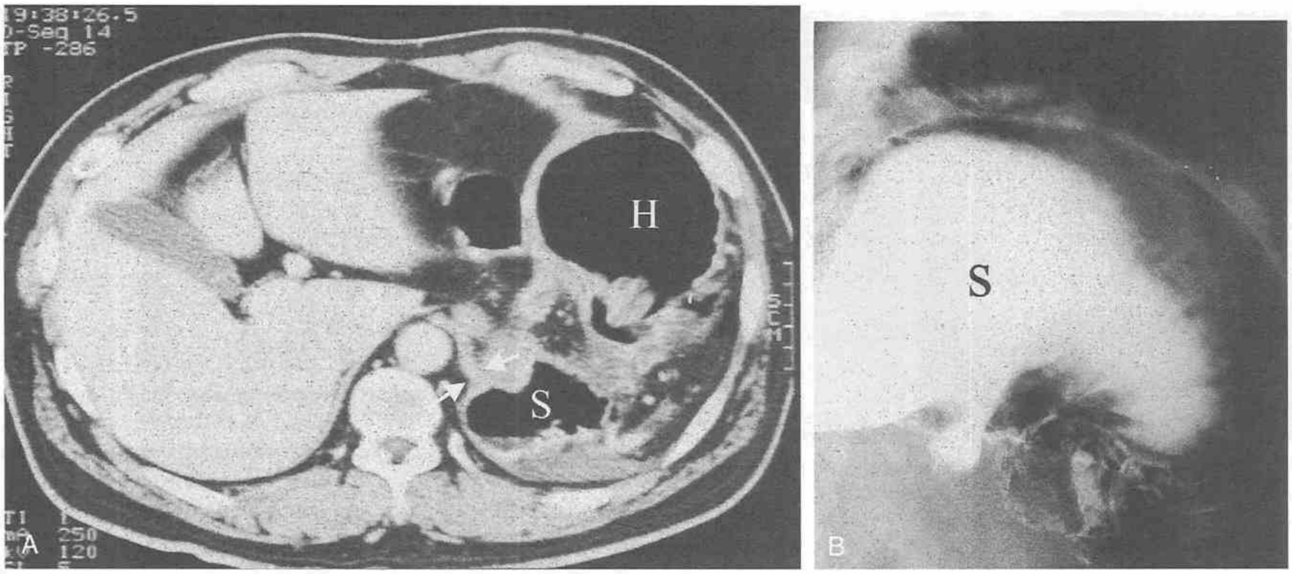

Figure 34–65. Delayed post-traumatic diaphragmatic hernia. *A,* CT scan shows herniation of the proximal part of the stomach (H) into the thorax as well as evidence of disruption of the left crus of the diaphragm *(arrows)*. *B,* Barium study shows gastric obstruction with markedly distended, herniated intrathoracic stomach (S).

generative changes (i.e., aging) may also predispose to herniation and volvulus of the stomach.

Herniation may involve the fundus only or much of the body and antrum. In this condition, a nasogastric tube may show a normal position at the esophagogastric junction but then pass up into the chest, although such findings can be seen in the presence of an elevated left diaphragm. A barium study may show the intrathoracic position of the herniated stomach as well as a waistlike constriction in the stomach where the stomach passes through the diaphragm.

Although CT may be suboptimal in evaluating the diaphragm, several reports acknowledge its success (Fig. 34–65).[228, 582] The use of additional reformatted images in coronal or sagittal plane helps to facilitate detection of diaphragmatic abnormalities. MRI, especially with coronal or sagittal T1-weighted images, is useful not only for establishing the diagnosis but also for localizing the site of lacerated diaphragm (Fig. 34–66). To determine the presence or absence of strangulation of the herniated stomach that is mainly caused by volvulus, IV infusion of the contrast material in both CT and MRI is mandatory.

Corrosive Gastric Injury

Corrosive agents produce extensive damage to the GI tract, with perforation or death occurring in the acute phase.

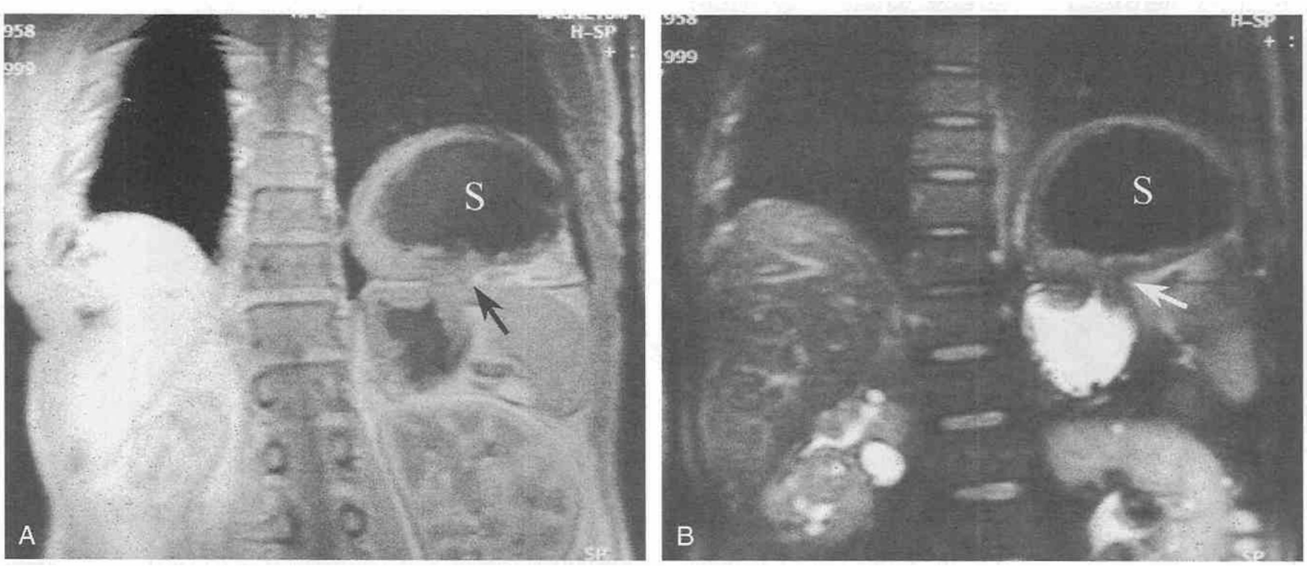

Figure 34–66. Delayed post-traumatic diaphragmatic hernia. Coronal T1-weighted *(A)* and half-Fourier acquisition single-shot turbo spin-echo (HASTE) *(B)* MR image clearly depicts gastric wasting *(arrow)* and the intrathoracic position of the herniated stomach (S). Note the hyperintense, thin diaphragm.

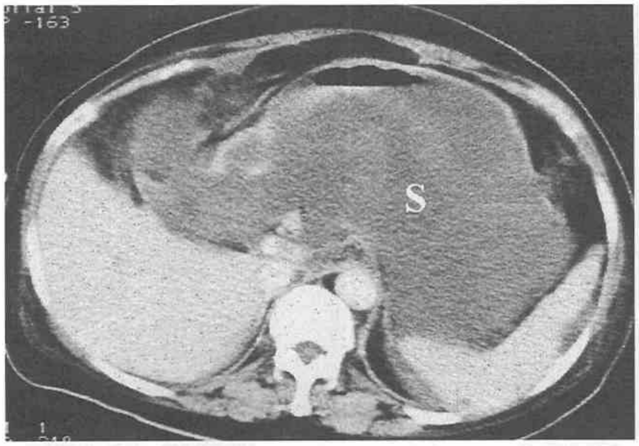

Figure 34–67. Corrosive gastritis after acid ingestion, with nearly complete loss of posterior wall of the stomach (S), as seen on this CT scan.

Alkaline caustic agents produce injury by liquefaction necrosis.[184] Fat and proteins become saponified, and blood vessels are thrombosed, leading to further cellular necrosis and degeneration. This characteristic of an alkali enhances its penetration into tissues, resulting in complete dissolution of the upper GI tract and damage of adjacent structures, including, in rare instances, even the transverse colon. In contrast to alkaline agents, concentrated acids produce a coagulative necrosis with a protective eschar that develops rapidly and may limit penetration to deeper muscle layer.[202]

The esophagus and stomach are the most common sites of involvement, but in severe cases significant liquefaction necrosis can occur both extraluminally and much more distally in the GI tract with the development of ischemia.[433] Diagnostic evaluation of patients with corrosive injury should include examination of the entire esophagus, stomach, and duodenum by endoscopic or noninvasive methods. However, CT is useful in the evaluation of structures beyond the first site of the injury, thus avoiding the risk of instrumental perforation associated with endoscopy (Figs. 34–67 and 34–68).

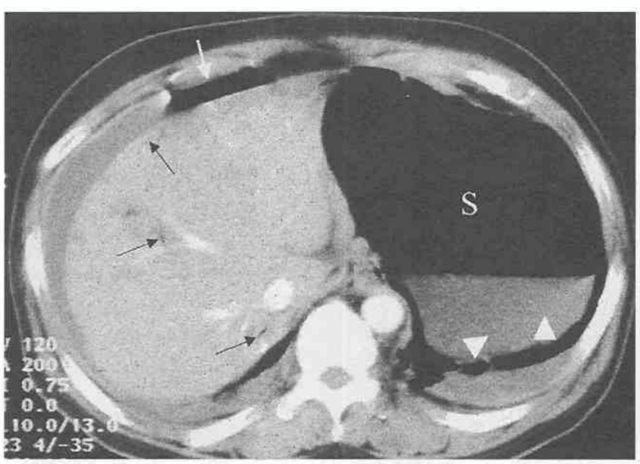

Figure 34–68. Corrosive gastritis with pneumatosis in the gastric wall and multifocal hepatic infarction. CT scan shows intramural gas *(arrowheads)* along with pneumoperitoneum *(white arrow)* and ascites due to gastric perforation. Also noted are intrahepatic portal vein gas *(thin arrows)* caused by hepatic infarction. (From Rha SE, Ha HK, Lee SH, et al: CT and MR imaging findings of bowel ischemia according to the various primary causes. Radiographics 20:29–42, 2000.)

Duodenum

Malignant Neoplasms

Primary Adenocarcinoma

Most cases of primary duodenal carcinomas usually occur in the periampullary region and in the third portions of the duodenum; the duodenal bulb involvement is extremely rare.[100] Duodenal adenocarcinoma may be associated with Gardner's syndrome, neurofibromatosis, celiac sprue, Crohn's disease, and Peutz-Jeghers syndrome.[510] Lesions situated more distally usually have a napkin-ring appearance and produce partial intestinal obstruction; about 20% have a predominantly polypoid or fungating appearance, probably caused by their origins in preexisting adenomatous polyps or villous adenomas.[58] Metastases are often present in the regional lymph nodes at the time of diagnosis, and thus the prognosis is poor.

On CT, primary duodenal adenocarcinomas appear as an intrinsic mass with a short segment of bowel wall thickening (Figs. 34–69 and 34–70).[145, 281] The incidence of duodenal obstruction is common. When tumors invade the pancreas and biliary ducts, it may be difficult to distinguish these tumors from pancreatic and biliary tumors. With primary adenocarcinomas, the duodenal wall is more circumferentially thickened with a lesser degree of biliary and pancreatic duct dilation.

Lymphoma

Duodenal lymphoma is rare because the distribution of lymphoma is proportionate to the amount of lymphoid tissue. Characteristic CT features include a long segment of a large annular wall thickening along with aneurysmal dilatation of the lumen and bulky regional or more widespread lymphadenopathy (Fig. 34–71). In contrast to cases of primary adenocarcinoma, bowel obstruction is uncom-

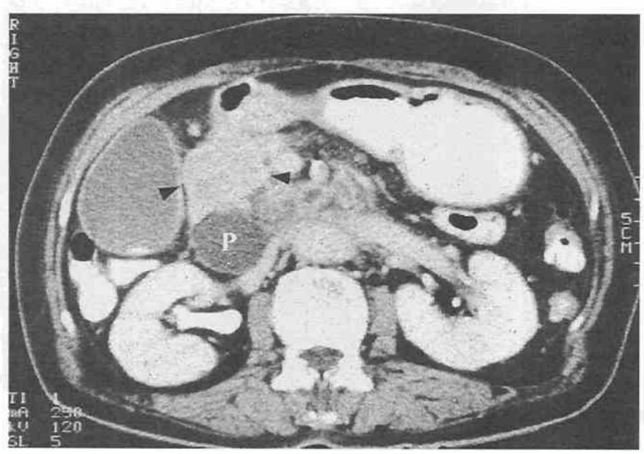

Figure 34–69. Primary duodenal adenocarcinoma.

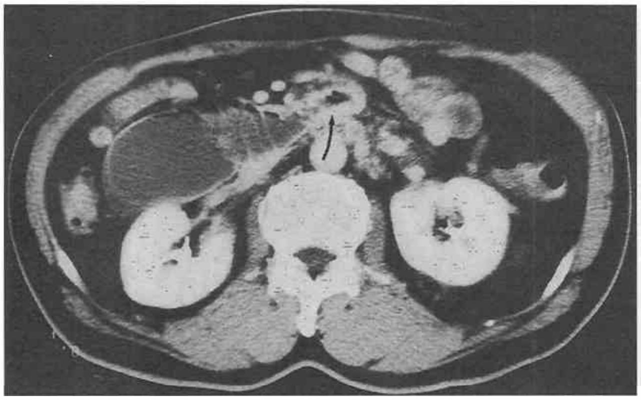

Figure 34–70. Primary duodenal carcinoma. CT scan shows concentrical bowel wall thickening *(arrow)*, producing low-grade bowel obstruction. Note lymphadenopathy in the paraortic and periduodenal regions.

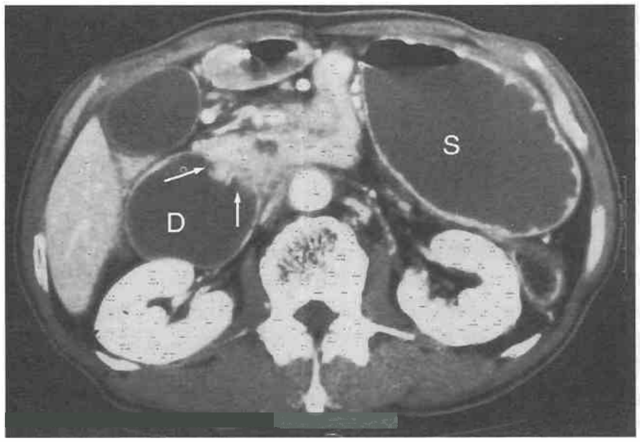

Figure 34–72. Duodenal obstruction caused by direct tumor invasion of pancreatic cancer into third portion of the duodenum. CT scan shows irregular soft tissue mass *(arrows)* obstructing the duodenum (D) with marked distention of the stomach (S). Pancreatic cancer is not shown.

mon. In rare instances, the lymphoma involving the ampulla may produce biliary tract obstruction.[50]

Metastatic Neoplasms

Direct invasion from tumors of the adjacent organs is the most important route for metastatic neoplasm of the duodenum. The primary tumor sites include the pancreas, stomach, gallbladder, liver, bile tract, right colon, and right kidney. In metastatic pancreatic or bile duct tumor, the medical aspect of the C-loop is involved with eccentric duodenal wall thickening. On the basis of CT findings alone, however, it may be difficult to ascertain whether the engulfing mass is of duodenal, bile duct, or pancreatic origin (Fig. 34–72).

Metastases from left colon carcinoma occur via the lymphatic drainage to the central mesenteric nodes surrounding the fourth portion of the duodenum or across the short fascial plane of the lateral reflection of the transverse mesocolon[145]; it may cause duodenal or jejunal obstruction. Hematogenous and lymphatic metastasis to the duodenum also occurs in lung and breast cancer (Fig. 34–73). In patients receiving chemotherapy for lung cancer, bowel obstruction and perforation may develop as a result of tumor necrosis in a metastatic lesion.[392] Gastric cancer may spread intramurally to the duodenum through submucosal lymphatic channels.[149]

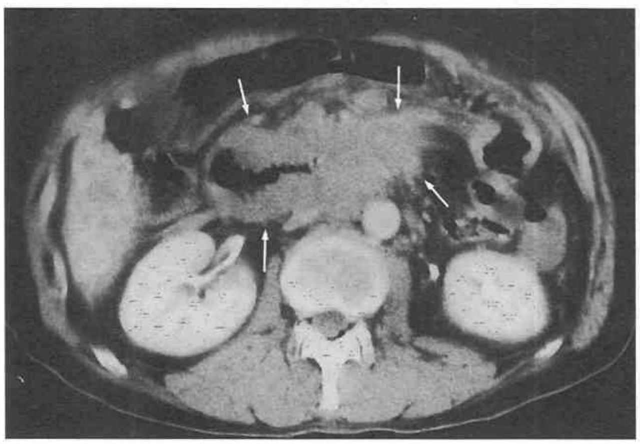

Figure 34–71. Duodenal lymphoma. CT scan shows irregular concentrical bowel wall thickening *(arrows)* in the duodenum. Note lymphadenopathy along the root of mesentery and lymphomatous nodules in the liver.

Non-neoplastic Conditions

Trauma

Because a large portion of the duodenum is within the retroperitoneum, most perforations occurring in these segments are clinically insidious. The horizontal segment

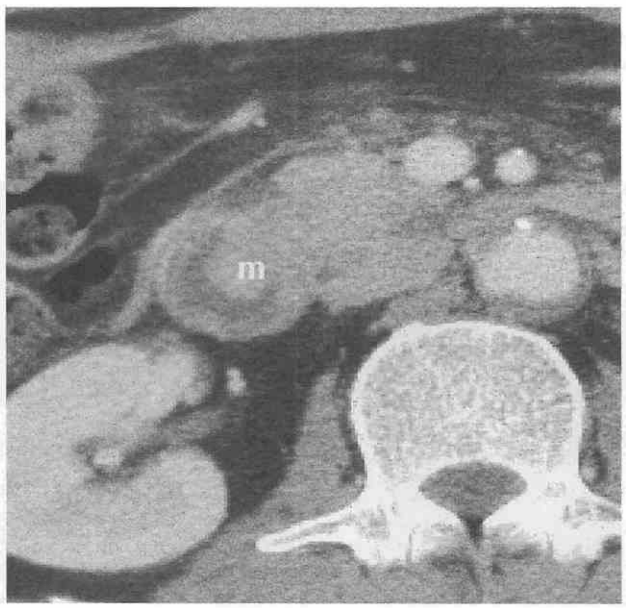

Figure 34–73. Metastasis to the duodenum from squamous cell carcinoma of the lung. CT scan shows a polypoid mass (m) protruding into the doudenal lumen.

of the duodenum crosses the vertebral column and is easily compressed against the spine by a direct blow. The distinction of duodenal perforation from an intramural hematoma without perforation is important because the latter condition does not require surgery.[344]

CT is becoming the most widely used modality for patients with abdominal trauma. The identification of extraluminal gas or extravasated oral contrast material or both in the right anterior pararenal space indicates the presence of duodenal perforation.[311] Intramural duodenal hematomas are manifested on CT as tubular or ovoid, circumferential, or eccentric and heterogeneous wall thickening (Fig. 34–74); a curvilinear area of high density *(ring sign)* can be demonstrated inside the margin of the hematoma.[615] When the hematoma is resolved, the hematomas become cystic. Because of contiguity with the duodenum, it is important to search for an associated injury of the head of the pancreas.

Pancreatitis

The inflammation in pancreatitis may spread from the pancreas at the site of direct contact with the nonperitonealized posterior surface of the second part of the duodenum.[38] Once the barrier is crossed, the inflammatory process may extend along the wall of duodenum. The duodenal involvement in pancreatitis can be identified on CT by nonspecific wall thickening (Fig. 34–75). In rare instances, intramural duodenal pseudocyst develops[388]; CT attenuation in this pseudocyst is related to the presence or absence of hemorrhage, cells, or proteinaceous material. In such cases, CT differentiation of duodenal pseudocyst from duodenal duplication cyst, choledochocele, or cystic dystrophy of the duodenal wall is often difficult.

Cystic Dystrophy

Cystic dystrophy of the duodenal wall is a rare lesion characterized by the presence of cysts within the duodenal wall that originate from ectopic pancreatic tissue. This lesion can be induced by inflammation of ectopic pancreatic tissue within the duodenal wall, secondary to obstruction of pancreatic excretory ducts.

Since the first report in 1970 by Potet and Duclert,[468] the radiologic appearances of this lesion have been described.[471] The pancreas may appear to be normal or may show evidence of chronic inflammation. In the cystic variant of cystic dystrophy, the cysts are easily demonstrated by both ultrasonography and CT between the duodenum and the pancreatic head. In contrast to a pseudocyst, the cystic variant is more frequently elongated or bilobate.[471] The solid variant of cystic dystrophy is depicted as thickening of the duodenal wall along with microcysts embedded within it.[471]

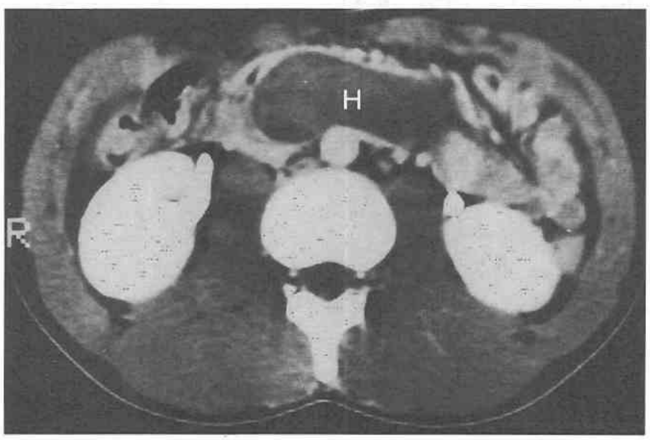

Figure 34–74. Intramural duodenal hematoma after blunt abdominal trauma. CT scan shows a sausage-like cystic lesion (H) in the wall of the duodenum.

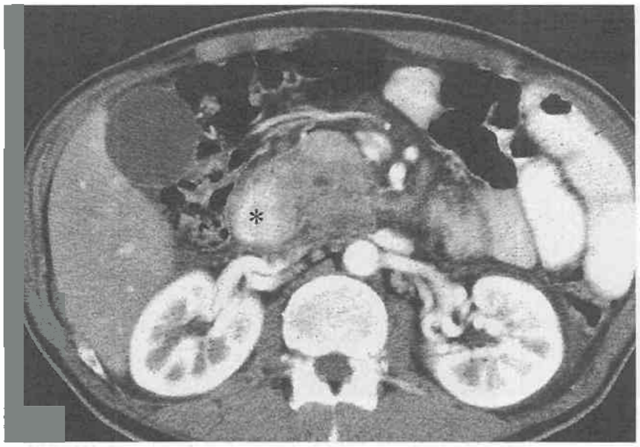

Figure 34–75. Pancreatitis with secondary duodenal involvement. CT scan shows concentrical duodenal wall thickening with heterogeneous contrast enhancement of the enlarged head of the pancreas.

Aortoduodenal Fistula

Aortoduodenal fistula is a rare and usually fatal disease. It may be primary or secondary.

The *primary* type is caused mainly by atherosclerotic aneurysms, accounting for more than 70% of cases. Other causes of aortic aneurysms complicated with aortoduodenal fistula are trauma and infections, including TB, syphilis, salmonellosis, and mycosis.[499] Although extremely rare, primary aortoduodenal fistula can also occur without an associated aortic aneurysm, the causes of which include carcinomas, irradiation, peptic ulcers, foreign bodies, cholecystitis, diverticulitis, and bacterial infections.[306]

The *secondary* type generally occurs as a complication of abdominal aortic aneurysm repair. The most common sites of involvement in all types of aortoduodenal fistula are the third and fourth parts of the duodenum. Clinical symptoms include abdominal or back pain, hematemesis, melena, and an abdominal pulsatile mass. Surgical therapy carries high mortality and morbidity rates, primarily because of the difficulty and delay in establishing the diagnosis.

CT may offer a quick, inexpensive, and accurate method of diagnosis. On CT, an aortoduodenal fistula should be considered if extraluminal gas is present in the periaortic region (Fig. 34–76). Gas may also be noted within the calcified rim of the aneurysm in association with an adherent loop of intestine. Other findings include pseudoaneurysm formation and focal bowel wall thickening. In patients who have undergone aortic reconstructive surgery, com-

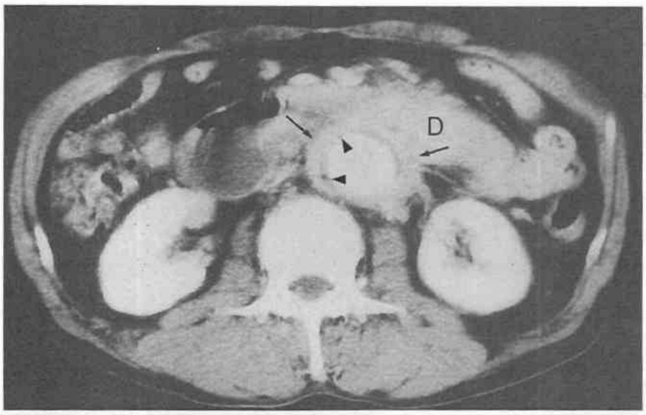

Figure 34–76. Primary aortoduodenal fistula in a patient with an aortic aneurysm. CT scan shows periaortic fibrosis *(arrows)* with subtle gas bubbles *(arrowheads)* in the periaortic region. The duodenal wall (D) adjacent to the aortic aneurysm is thickened, causing low-grade duodenal obstruction.

plete resolution of hematoma should occur in 2 to 3 months and no ectopic gas should be visualized at 3 to 4 weeks.[476] After that time, any amount of perigraft soft tissue, fluid, or ectopic gas should be considered a sign of graft infection or *aortoenteric* fistula. However, the differentiation between aortoenteric fistula and perigraft infection is difficult, although the presence of ectopic gas favors the diagnosis of aortoenteric fistula.[356]

Small Intestine

Technique and Normal Anatomy

For homogeneous filling and distention of the small intestine, one should decide on the type, amount, and time sequence of oral contrast agents as well as review the patient's history or previous radiologic studies. In general, patients generally tolerate 800 to 1000 mL of dilute barium suspension with reasonable results. Collapsed or poorly opacified small-bowel loops may simulate focal wall thickening or mass lesion. In certain instances, pharmacologic agents such as metoclopramide are necessary to stimulate motility of the upper GI tract. Metoclopramide increases the tone and amplitude of gastric contractions, relaxes the pyloric sphincter and duodenal bulb, and increases peristalsis of the duodenum and the jejunum. However, this drug is contraindicated in patients with known or suspected pheochromocytoma, bowel obstruction, bowel perforation, or GI bleeding.[492]

In general, use of oral contrast agents helps in the detection of abnormalities in the small intestine, but administration of the high-density contrast agents are not necessary for certain conditions, such as suspected mesenteric ischemia or small-intestinal obstruction due to adhesions, bands, or volvulus. Such a recommendation is attributable to the absence of or poor contrast enhancement in the bowel after infusion of the IV contrast material, which is one of the most important indicators for establishing the diagnosis of strangulated obstruction[208] or intestinal ischemia; therefore, this finding can be overlooked if high-density contrast agents are used. Furthermore, in patients with small-intestinal obstruction, the fluid in the distended bowel already provides a good contrast agent. In performing CT in patients with blunt trauma, use of both IV and oral contrast material is necessary. The oral contrast agent must be diluted enough to avoid causing reconstruction artifacts and must be administered 20 to 30 minutes before scanning to allow for good bowel opacification. Scans must extend through the pelvis.

On CT, the normal small-bowel wall thickness measures 2 to 3 mm; a wall thicker than 4 mm is considered abnormal except in the terminal ileum, where 5 mm is considered the upper limit for normal.[507] The thickness of valvulae conniventes also should not exceed 3 mm. When the intestine is collapsed or partially distended, the wall may appear to be 3 to 4 mm thick. If the wall seems to be concentrically and symmetrically thickened and is homogeneously enhanced, the clinical significance of a thickness greater than 4 mm should be interpreted cautiously and assessed in relation to the degree of distention of the small-bowel loop.[19] The fat in the mesentery has the same attenuation as fat elsewhere in the body. Major arteries and veins are identifiable as branching structures within mesenteric fat and do not exceed 3 mm in diameter.[263] Mesenteric lymph nodes are occasionally observed within mesenteric fat and do not exceed 3 mm in diameter.

Neoplasms

Although the small intestine represents about 75% of the total length of the GI tract and more than 90% of its total mucosal surface, it is the site of fewer than 25% of all GI neoplasms and fewer than 2% of all malignant neoplasms.[624] The most common histologic types of benign small-intestinal tumors are benign stromal tumor, lipoma, and adenoma, whereas malignant tumors include adenocarcinoma, carcinoid tumor, lymphoma, and malignant stromal tumor.

The nonspecific nature of symptoms contributes to the delayed diagnosis of small-intestinal tumors, generally resulting in the poor prognosis of these patients. Even though barium studies, such as enteroclysis, and small-bowel follow-through examinations have been used as primary diagnostic methods, CT and MRI not only have become a primary tool in cases with a palpable mass, small-bowel obstruction, or known lymphoma but also play a large role in preoperative staging and follow-up. According to a study that analyzed 35 patients with small-bowel neoplasms, the tumor detection rate by CT was 80%.[315] Dudiak and coworkers[131] were able to suggest a specific tumor diagnosis in 60% of the patients with adenocarcinomas, 58% of patients with lymphomas, and 33% of those with carcinoid tumors and malignant stromal tumors. CT is helpful in staging the small-bowel malignancy, but their reported accuracy was not high (47%) in a series that included 15 patients with small-bowel adenocarcinoma.[56]

Adenocarcinoma

Primary adenocarcinoma of the small intestine is rare, accounting for approximately 40% of malignant tumors of the small intestine. When this lesion occurs, it generally

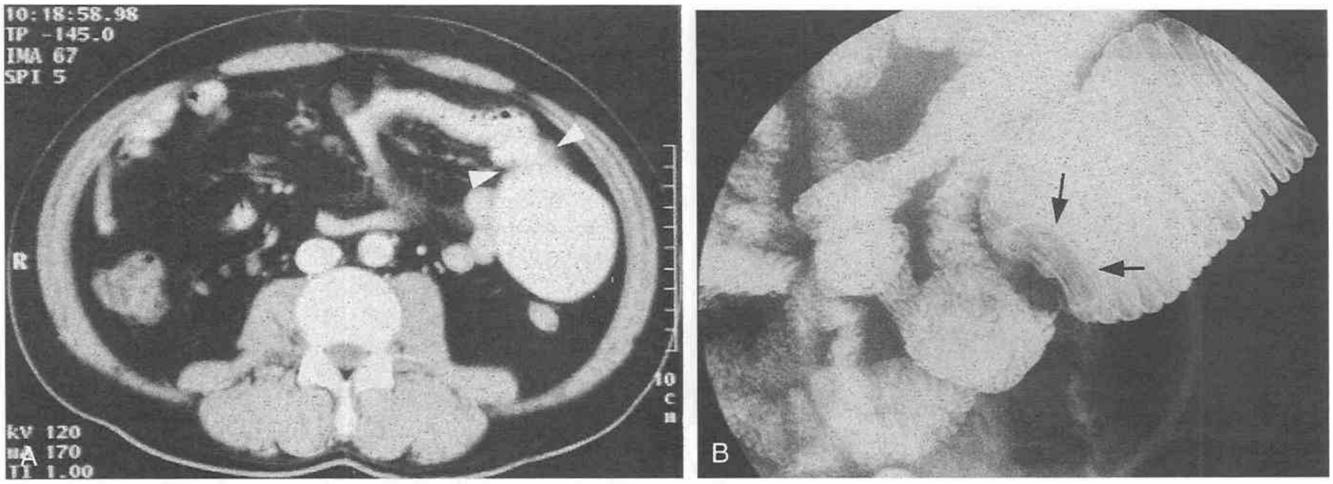

Figure 34–77. Primary jejunal carcinoma. *A,* CT scan shows bowel obstruction *(arrowheads)* at the site of the tumor. *B,* On small-bowel follow-through, a polypoid mass *(arrows)* and luminal narrowing are seen in the jejunum along with proximal bowel loop dilatation.

arises in the proximal jejunum. Risk factors for the development of small-bowel adenocarcinoma include a history of Crohn's disease, sprue, Peutz-Jeghers syndrome, Lynch syndrome II, congenital bowel duplication, ileostomy, or duodenal or jejunal bypass surgery. The most frequent gross types are infiltrative, resulting in early bowel obstruction, and ulcerative, as represented by bleeding. Polypoid forms are uncommon.

Adenocarcinomas tend to metastasize early to regional lymph nodes and to invade the mesenteric vessels when they are located near the mesenteric root. On CT scans, the tumor appears as an eccentric focal mass or a circumferential bowel wall thickening in a short segment (Figs. 34–77 and 34–78). Narrowing of the lumen and dilation of the proximal bowel are also common. However, tumors smaller than 2 cm in diameter may be missed by CT and are better detected by barium study.[315]

Carcinoid

After the appendix, the small bowel is the second most frequent site of carcinoid tumors, representing up to 20% of GI carcinoids. Ninety percent of these tumors are located in the ileum. Carcinoid tumors vary in appearance from a small submucosal lesion to a large intraluminal ulcerating lesion. The tumor tends to infiltrate the mesentery, causing characteristic desmoplastic mesenteric reactions such as angulation, kinking, rigidity, and separation of small-bowel loops.

Despite widespread metastases, the primary tumor itself may be difficult to detect on CT and even at laparotomy owing to its small size. Therefore, some researchers advocated the use of scintigraphy using meta-iodobenzylguanidine (mIBG) labeled with iodine 131 as a screening procedure in patients thought to have carcinoid tumors.[3] The *carcinoid syndrome*, which includes diarrhea, flushing, and

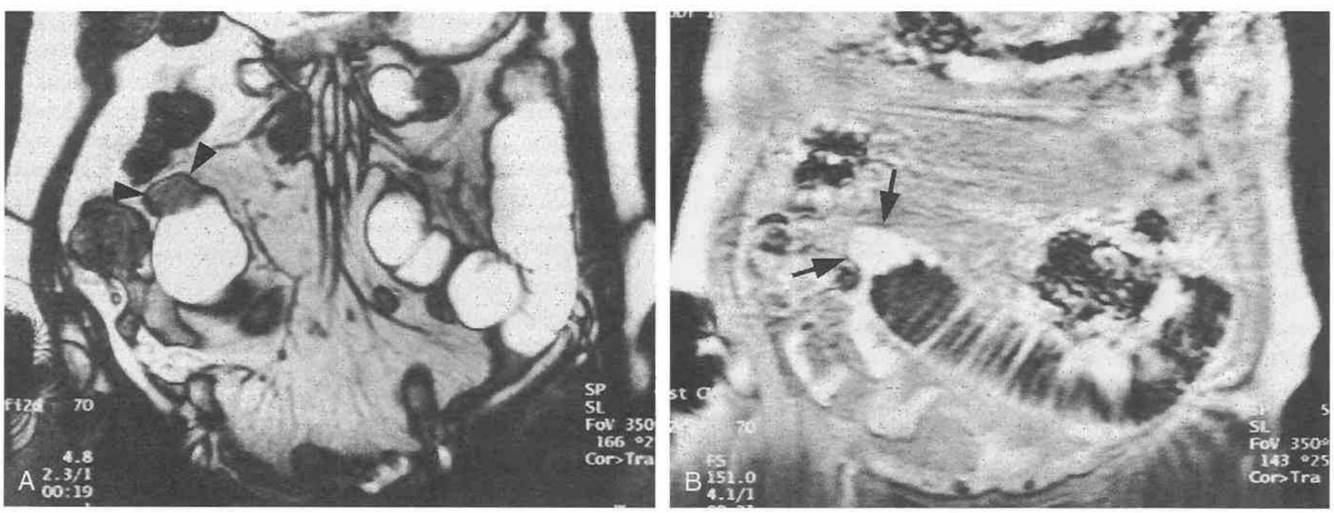

Figure 34–78. Primary jejunal adenocarcinoma. *A,* Coronal true fast imaging with steady-state precession (FISP) MR image shows a high-signal-intensity mass *(arrowheads)* obstructing the small-bowel loop. *B,* Gadolinium-enhanced MR image shows a high-signal-intensity mass *(arrows)* at the site of bowel obstruction.

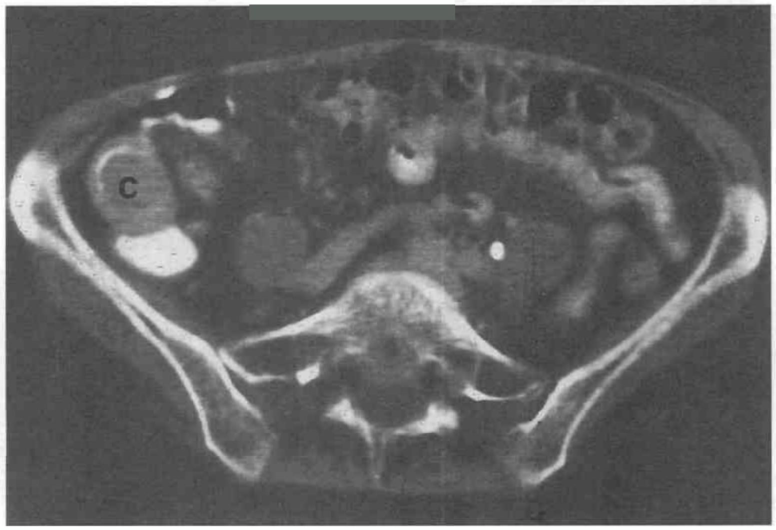

Figure 34–79. Carcinoid tumor. CT scan shows an intramural mass (C) in the bowel loop near the ileocecal region. Visualization of the primary carcinoid tumor is unusual. (From Megibow AJ, Balthazar EJ: CT of the Gastrointestinal Tract. St. Louis, CV Mosby, 1986.)

abdominal pain, occurs in 2% of cases of small-bowel carcinoid, but it is much more likely to be present in cases of hepatic metastasis.[558] CT may show virtually pathognomonic features, with a mesenteric mass associated with radiating linear or curvilinear soft tissue strands (Figs. 34–79 and 34–80). Calcifications are seen in approximately 70% of cases with mesenteric carcinoid tumor.[449] The occurrence of retroperitoneal lymphadenopathy is not rare.[465] CT features of small-bowel carcinoid tumor may be similar in appearance to those of lymphoma, metastasis, Crohn's disease, and mesothelioma.

Gastrointestinal Stromal Tumor

Stromal tumors are usually solitary, benign tumors that are categorized by their differentiation into smooth muscle or neural tissue. Tumors are classified as (1) benign, (2) borderline, or (3) malignant.

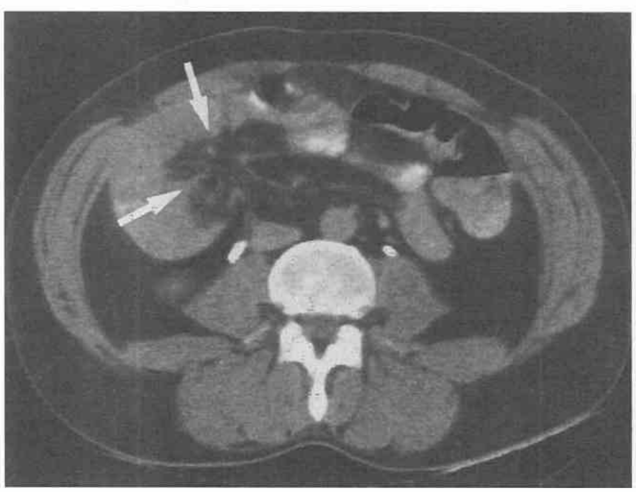

Figure 34–80. Mesenteric changes in a carcinoid tumor. Stellate, centripetally oriented, thickened mesenteric vessels are seen subtending a dilated, "kinked" loop of distal ileum *(arrows)*. The primary tumor is not visualized. (From Megibow AJ, Balthazar EJ: CT of the Gastrointestinal Tract. St. Louis, CV Mosby, 1986.)

In contrast to benign stromal tumors (leiomyomas) that occur anywhere in the small intestine, malignant stromal tumors (leiomyosarcomas) arise more commonly in the ileum than in the jejunum. Symptoms depend on the growth pattern, that is, submucosal, subserosal, or intraluminal.

On CT and MRI, this tumor appears as a large, heterogeneous mass with central necrotic areas, often growing in an exoenteric pattern with a large extraluminal component (Figs. 34–81 and 34–82). Severe hemorrhage within the mass, which is associated with hypervascular stromal tumors, produces a fluid-fluid level. Calcification is occasionally demonstrated.[93] Those tumors, located in the pelvis, often resemble ovarian neoplasms. The differentiation between benign and malignant stromal tumors is radiologically difficult, but CT findings favoring malignant stromal tumor include a large mass greater than 5 cm, lobulated contour, heterogeneity with central necrosis or liquefaction, mesenteric infiltration, regional lymphadenopathy, and exophytic growth.[93] Metastasis occurs by direct extension and by the hematogenous route. However, intraperitoneal spread (peritoneal leiomyosarcomatosis) may occur by intraperitoneal seeding via ascitic fluid or by embolic metastases.[405]

CT manifestations of leiomyosarcomatosis mimic those of peritoneal carcinomatosis, except for a much lower incidence of ascites and lymphadenopathy (see Fig. 34–82).[590] Hepatic metastasis may appear almost cystic on CT.

Lymphoma

Lymphoma accounts for approximately 20% of all small-bowel tumors. The small intestine closely follows the stomach as the most frequent site of disease, and multicentric involvement occurs in 10% to 25% of cases.[345] Almost all small-bowel lymphomas are non-Hodgkin's lymphoma; most of them are of B-cell origin, but the cases complicating celiac disease are of T-cell origin. Predisposing conditions include AIDS, celiac disease, systemic lupus erythematosus (SLE), Crohn's disease, and chemotherapy.[54] In children and young adults, lymphoma primarily affects the ileocecal region; in adults, the distal ileum is the most

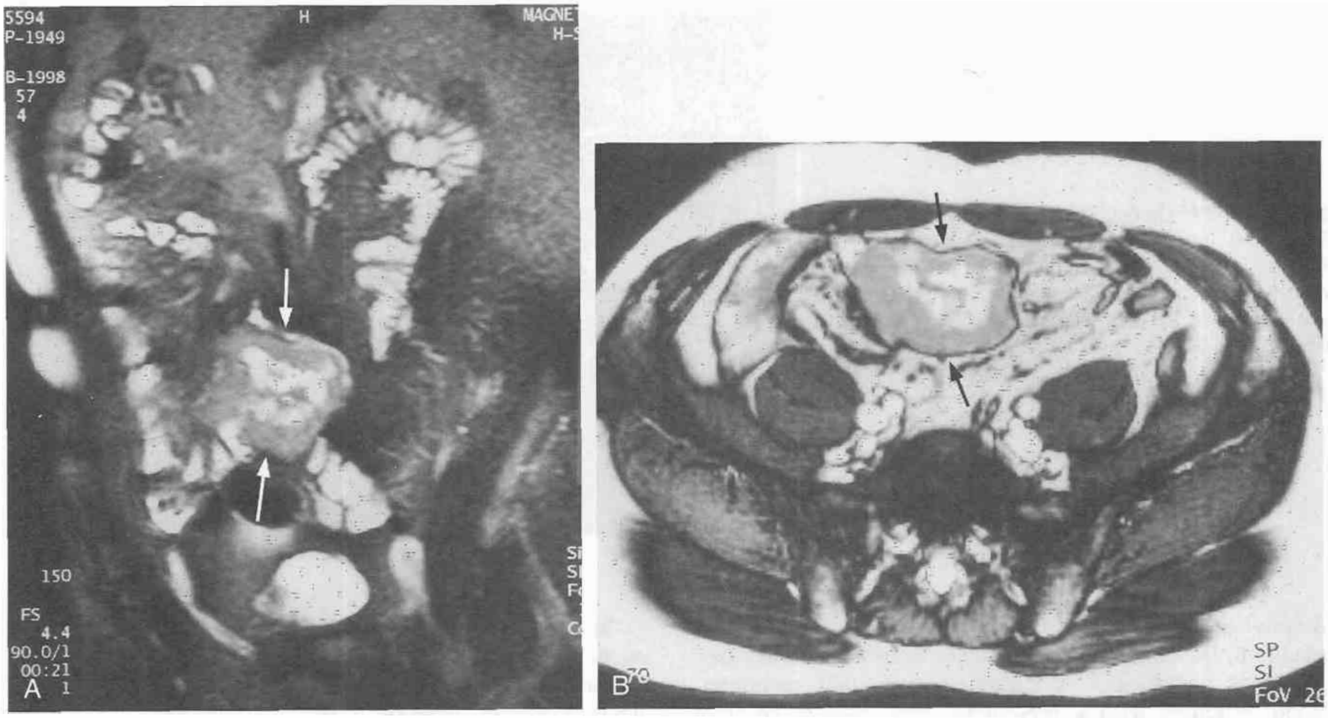

Figure 34–81. Malignant gastrointestinal stromal tumor of the ileum. Oblique coronal T2-weighted half-Fourier acquisition single-shot turbo spin-echo (HASTE) *(A)* and axial T2-weighted (true fast imaging with steady-state precession [FISP]) *(B)*. MR images show a mass *(arrows)* with a lobulated surface in the ileum. High signal intensity within the mass indicates tumoral necrosis.

frequent site of tumor.[345] In lymphoma complicating celiac disease, however, the proximal jejunum is usually involved.

Although the CT appearance of lymphomas is variable, these tumors can be classified as follows[516]:

1. *Circumferential* forms are characterized by concentric bowel wall thickening (Fig. 34–83). Aneurysmal dilatation of the lumen, which is regarded as one of the most characteristic features of the lymphoma, occurs in approximately 50% of cases.[131, 315] Except for cases with developing intussusception, bowel obstruction is rare because the tumor weakens the muscularis propria of the bowel wall and does not elicit a desmoplastic response.[516]
2. *Cavitary* forms are the second most commonly occurring pattern (Fig. 34–84). Cavitation of the tumor bulk results from ulceration of the mucosa with extension to the intramural portion of the tumor. Compared with stromal or epithelial tumors, the lymphomatous mass characteristically shows poorer contrast enhancement. Perforation of the tumor may occur secondary to a lack of desmoplastic response to tumor growth, as a

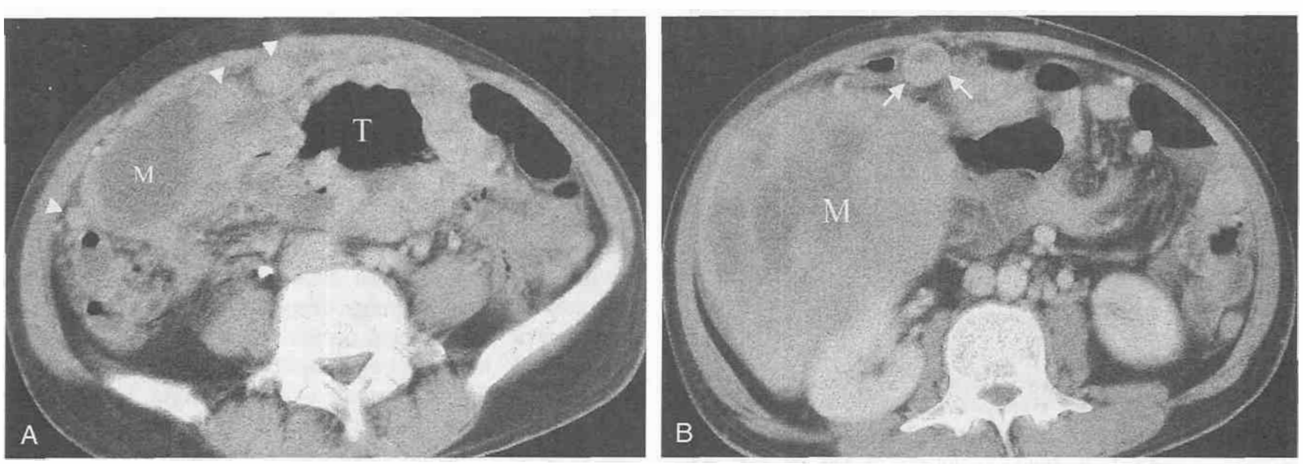

Figure 34–82. Leiomyosarcomatosis and hepatic metastasis in a malignant gastrointestinal stromal tumor of the jejunum. *A,* CT scan shows a large, exophytically growing cavitary mass (T) in the jejunum. Note multiple peritoneal nodules *(arrowheads)*. *B,* CT scan shows a large hepatic metastatic lesion (M) and peritoneal nodule *(arrows)* in the omentum.

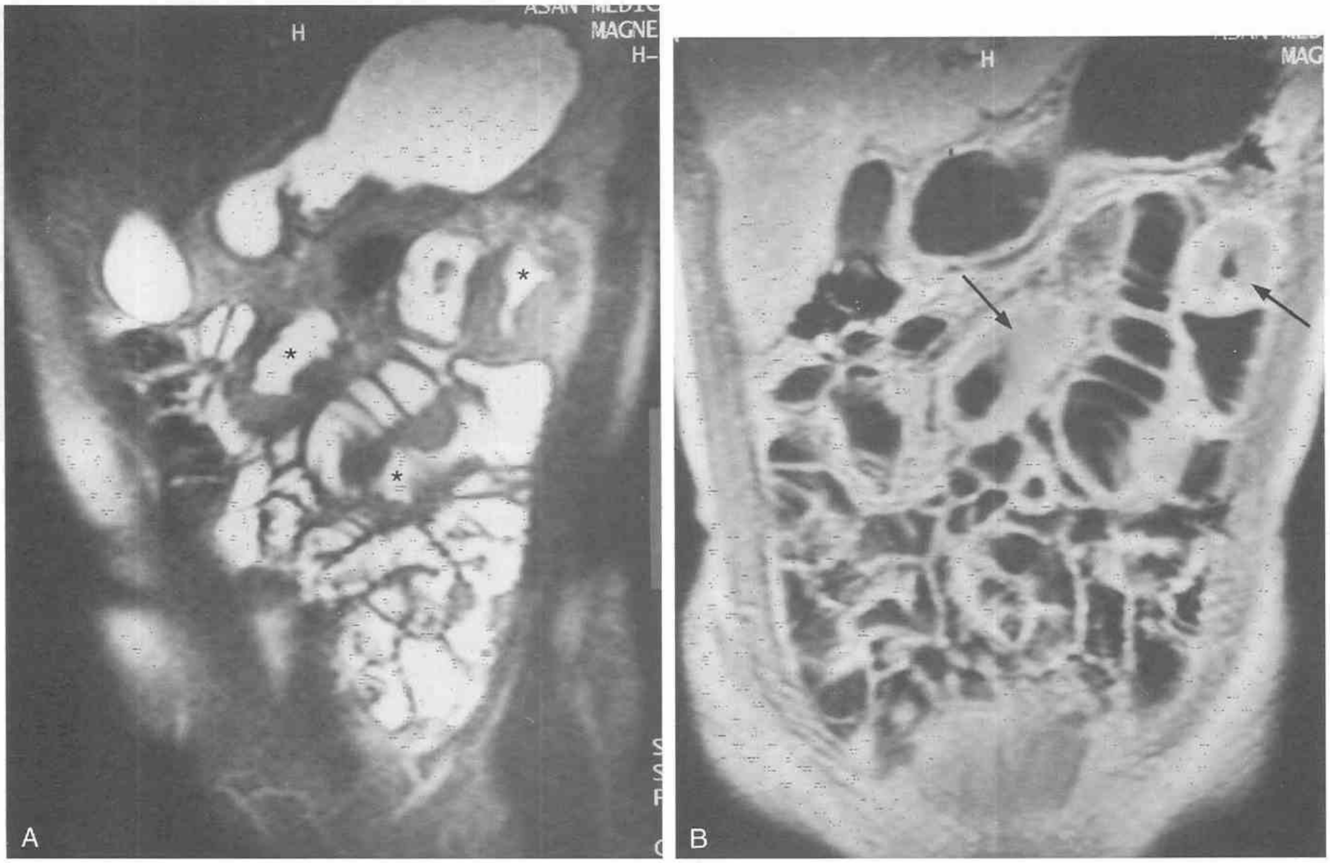

Figure 34–83. T-cell lymphoma involving the jejunum. *A*, Oblique coronal T2-weighted half-Fourier acquisition single-shot turbo spin-echo (HASTE) MR image shows multiple intramural nodules and bowel wall thickening *(asterisks)* in the jejunum. *B*, Gadolinium-enhanced coronal MR image clearly depicts lymphomatous involvement in the jejunal loop.

result of rapid tumor growth, or as a response to therapy (Fig. 34–85).[224] Fistulization to the skin, solid organs, or bladder develops in 5% to 15% of cases.[65]

3. *Mesenteric* forms are usually manifested as diffuse lymphadenopathy in the mesentery as well as in the retroperitoneum. A "sandwich" appearance is demonstrated when mesenteric masses surround mesenteric vessels but leave intact a thin rim of preserved perivascular fat. The small-bowel loops are displaced, focally invaded, or occasionally obstructed by mesenteric masses. Mesenteric lymphoma may also appear as an ill-defined confluent mass engulfing and encasing multiple

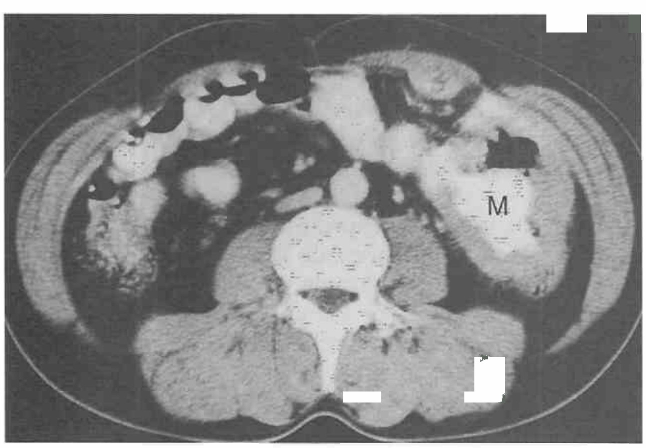

Figure 34–84. Small-bowel lymphoma of B-cell origin with a large cavitary mass (M) arising from the ileum.

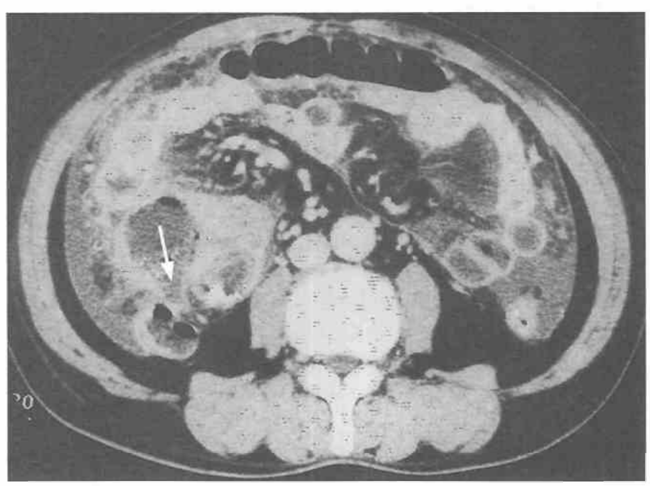

Figure 34–85. Perforated sma[redacted]wel lymphoma after chemotherapy. On CT scan, the bowe[redacted]ll involved with lymphoma is focally perforated *(arrow)* along with evidence of a large amount of ascites and diffuse omental infiltration.

loops of adjacent bowel or as a conglomerate mantle of mesenteric tissue.

MRI appears comparable to CT in demonstrating the morphologic changes in the GI tract as well as in the peritoneal cavity in patients with small-bowel lymphomas. Contrast-enhanced MRI had an advantage in depicting the submucosal tumor location by demonstrating a three-zone appearance: (1) a high-intensity mucosa, (2) an intermediate-intensity submucosal tumor infiltration, and (3) a low-intensity proper muscular layer.[91]

The prevalence of lymphomas has been reported to be increased in patients with AIDS or in post-transplantation patients. In nearly all cases, the pathologic type is non-Hodgkin's lymphoma. The CT appearance of lymphoma in these immunocompromised hosts is indistinguishable from that of lymphoma in nonimmunocompromised patients.

Metastases

Metastatic disease in the small intestine may spread by:

1. Intraperitoneal seeding (ovary, stomach, appendix, colon).
2. Direct invasion from contiguous tumor (colon, pancreas, kidney, ovary, uterus).
3. Hematogenous dissemination (breast, lung, melanoma).

Intraperitoneal Seeding

Intraperitoneal seeding produces ascites, and the ascitic fluid facilitates spread throughout the abdomen. Because of gravitational flow, the peritoneal implants tend to occur in four major areas: (1) the rectouterine or rectovesical pouch, (2) the lower small-bowel mesentery near the ileocecal valve, (3) the sigmoid mesocolon, and (4) the right paracolic gutter.

Direct Invasion

In the small intestine, the tumor cells are implanted on the mesenteric border of the bowel, causing a direct bowel wall invasion. Once the bowel wall becomes involved, the tumors tend to spread circumferentially and longitudinally through the submucosa or subserosa in a short or long length, occasionally producing a linitis plastica pattern of bowel wall thickening. In such cases, the target sign is commonly seen in the thickened bowel wall.[205] Malignant intestinal obstruction is also caused by recurrent tumor or by peritoneal carcinomatosis. The presence of a mass at the obstructed or prior surgical site or lymphadenopathy on CT favors the diagnosis of malignant rather than benign intestinal obstruction.[215] However, differentiating each condition is difficult in cases of intestinal obstruction without a demonstrable peritoneal mass. Other ancillary CT findings, such as omental infiltration, nodules or cakes, and peritoneal thickening, are also helpful in suggesting the diagnosis of peritoneal carcinomatosis.

Hematogenous Dissemination

In hematogenous dissemination of tumor to the small bowel, the involved sites are often multiple (Fig. 34–86).[392] The incidence of small-bowel metastasis from lung cancer is reported to be approximately 11% of cases.[392] In such cases, the presenting symptom may be bowel perforation, intestinal obstruction, malabsorption, or hemorrhage[330]; perforation is caused by tumor necrosis, obstruction by bulky tumor, hemorrhage by ulcerative lesions, and malabsorption by extensive involvement of mucosal surface. When metastatic tumor is found unexpectedly at laparotomy for perforated viscus in a heavy smoker after the fifth decade, lung cancer should be included as one of the possible sites of primary tumors.

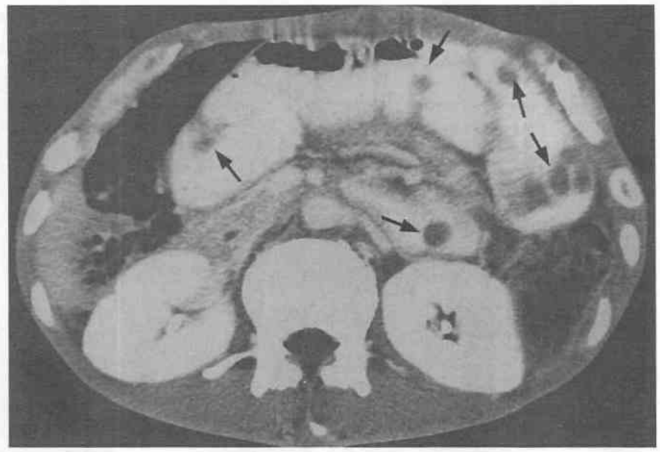

Figure 34–86. Hematogenous metastasis to the small intestine from sigmoid colon carcinoma. Multiple hypoattenuated nodules (*arrows*), noted in the dilated small intestinal loop, were confirmed to be metastatic neoplasm on surgery.

In metastatic lesions to the small intestine from breast cancer, a linitis plastica pattern of bowel involvement can also be seen.[195] Eighty percent of cases of melanoma metastatic to the GI tract involve the small bowel or mesentery. The site of hematogenously seeded tumor cells influences their radiologic appearance. On CT scans, metastatic melanoma may manifest as mucosal or submucosal masses, serosal implants, or carcinomatosis (Fig. 34–87).[280] Mucosal mass may often lead to intussusception. Necrosis and ulceration may occur in large submucosal masses, but obstruction is less frequent. Lymphatic spread is less common, but when it occurs lymphadenopathy may be marked.[390]

Benign Neoplasms

Five neoplasms, making up 95% of benign small-bowel tumors include benign stromal tumors, lipomas, adenomas, fibromas, and hemangiomas.[110]

Lipomas are slow-growing tumors composed of well-differentiated adipose tissue surrounded by a fibrous capsule. They are usually solitary, but small-bowel lipomatosis has been reported.[440] Of lipomas, 90% to 95% are submucosal and tend to prolapse into the bowel lumen. Lesions larger than 2 cm in diameter produce abdominal pain, diarrhea, constipation, or blood loss when the overlying mucosa is ulcerated, or intestinal obstruction develops secondary to intussusception.[568]

On CT, the diagnosis can be easily made by the tumor's characteristic fatty CT attenuation (Fig. 34–88). MRI is also useful in diagnosis because lipomas appear hyperintense on T1-weighted images. Focal area of soft tissue

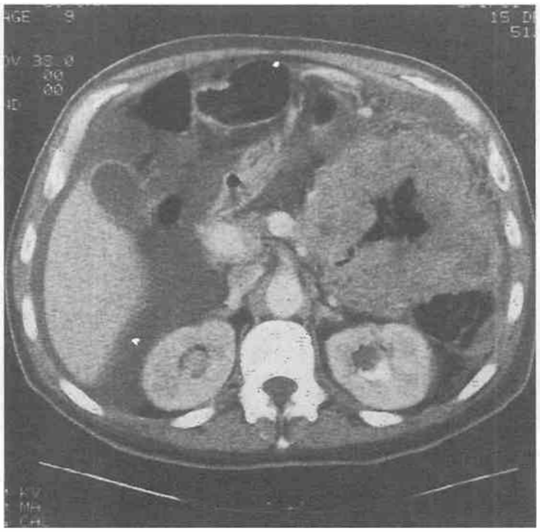

34–87. Metastatic melanoma to the jejunum. CT scan shows a large cavitary mass at the left upper quadrant. (From Megibow AJ: Computed Tomography and Magnetic Resonance Imaging of the Whole Body. St. Louis, CV Mosby, 1994.)

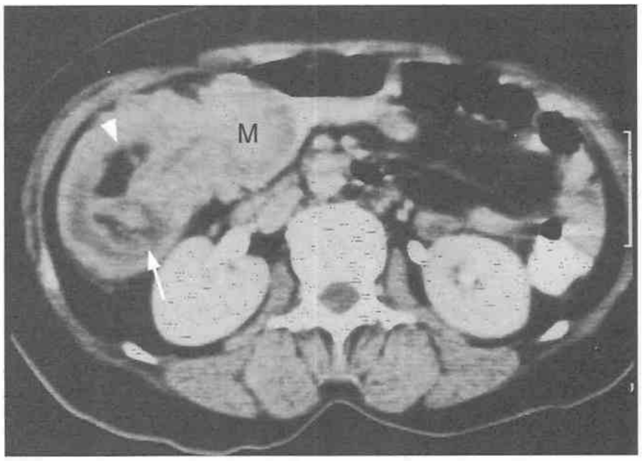

Figure 34–89. [redacted]roc[redacted]intussusception due to in[redacted]matory fibroid tumor [redacted]e i[redacted]. CT scan shows a he[redacted]geneous mass in the right-sided colon with interposed mesenteric fat *(arrowheads)* and vessels *(arrows)*. A round mass (M) is seen at the lead point.

attenuation may be occasionally seen on CT scans in a lipomatous mass, especially in cases with intussusception. This finding may be caused by focal ischemic change and does not indicate liposarcoma. Multiple hemangiomas have been reported to involve the bowel and represent an important diagnostic consideration in patients with hemangiomatosis of the lower extremity. Phleboliths are frequently detected within hemangiomatous masses, providing a clue to their nature.[421]

Apart from these five benign neoplasms, inflammatory fibroid polyps can develop in the small intestine, especially at the ileum in 70% of cases (Fig. 34–89). They originate primarily in the submucosa and are composed of fibroblasts, blood vessels, and inflammatory cells within an edematous and collagenous stroma. Most of the lesions are solitary and large, often causing bowel obstruction due to intussusception. No distinctive radiologic features have been noted between these tumors and other mural or intraluminal lesions.

Inflammatory Conditions

Intestinal Tuberculosis

By the middle of the 20th century, intestinal TB had declined dramatically; since the mid-1980s, however, the incidence of TB has increased, especially in urban areas, owing to AIDS. Intestinal TB occurs at any age and is equally prevalent in men and women. The chest radiograph may show active disease in only about 20% of patients with intestinal TB.

Intestinal TB may arise by several mechanisms[375]:

1. Swallowing of infected sputum in active pulmonary TB.
2. Ingestion of contagious milk.
3. Hematogenous spread.
4. Direct extension from adjacent organs.

After the tubercle bacillus enters the GI tract, it traverses the mucosa to lodge in the submucosa. Lymphangitis, endarteritis, and fibrosis ensue, leading to mucosal ulceration, caseating necrosis, and narrowing of the intestinal tract.

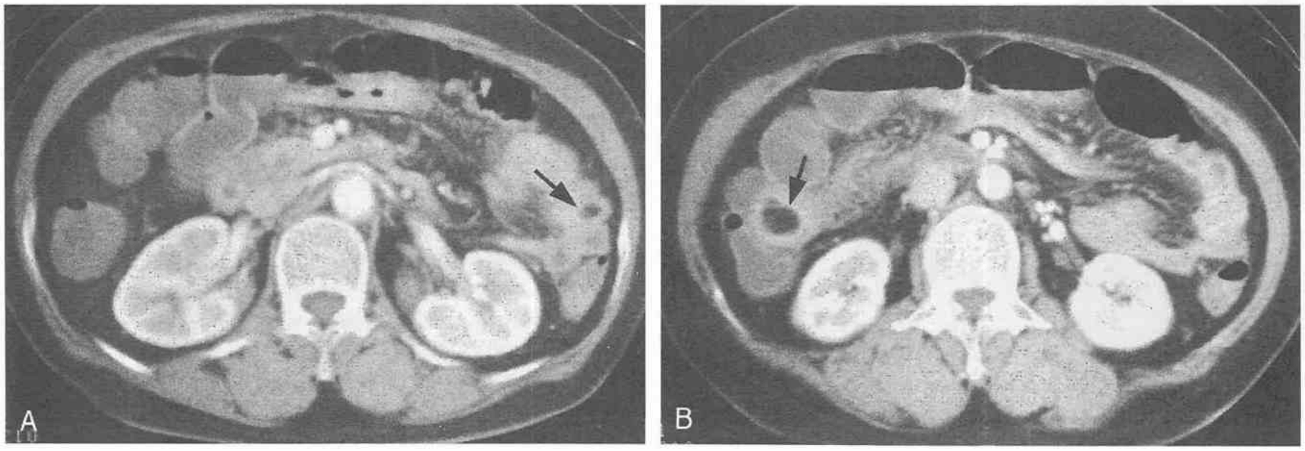

Figure 34–88. Multiple lipomas in the small intestine. *A* and *B,* CT scan shows multiple lipomas *(arrows)* in the small-bowel loops.

Intestinal TB manifests three gross pathologic types: (1) ulcerative, (2) hypertrophic, and (3) ulcerohypertrophic. The highest incidence of abdominal TB has been noted in the GI tract and in the peritoneum, followed by the mesenteric lymph nodes.[1] The affinity of the tubercle bacillus for lymphoid tissue and areas of physiologic stasis may be reasons that the ileocecum is the most common site of disease.[375]

There have been limited citations in the literature describing the CT features of intestinal TB. In our experience, however, CT is useful in determining the extent of disease, in detecting its complications, and for differentiating it from Crohn's disease. The common CT finding of tuberculous enteritis is bowel wall thickening, with a range of 1 to 2 cm in thickness (Fig. 34–90).[209] The thickened bowel may show homogeneous attenuation on CT, but mural stratification may be rarely seen. Multiple sites of involvement with skipped areas are common. Therefore, there seems to be no specific CT features of bowel wall involvement patterns in intestinal TB that can distinguish them from Crohn's disease.

Bowel loop separation can be caused by mesenteric lymphadenopathy or lymphadenitis, bowel wall thickening, intraperitoneal fluid collection, and, rarely, fibrofatty proliferation in the mesentery. Although not always the case, lymph nodal involvement patterns differ from those of Crohn's disease. The enlarged lymph nodes are commonly larger than 1 cm, may have low attenuation center caused by caseating necrosis, commonly involve the peripancreatic nodal chains, and may contain calcification (Fig. 34–91).[206] The incidence of peritonitis in patients with intestinal TB has not been well described, but the presence of peritonitis on CT scans may favor the diagnosis of TB rather than Crohn's disease when the differentiation between the two diseases should be made.[206, 371]

The CT findings of tuberculous peritonitis may mimic those of peritoneal carcinomatosis, including diffuse omental and mesenteric infiltration and nodules, peritoneal thickening, and ascites.[206] In addition, the incidence of splenic involvement is common in abdominal TB, which includes splenomegaly, hypoattenuated nodules, or calcifications.[206]

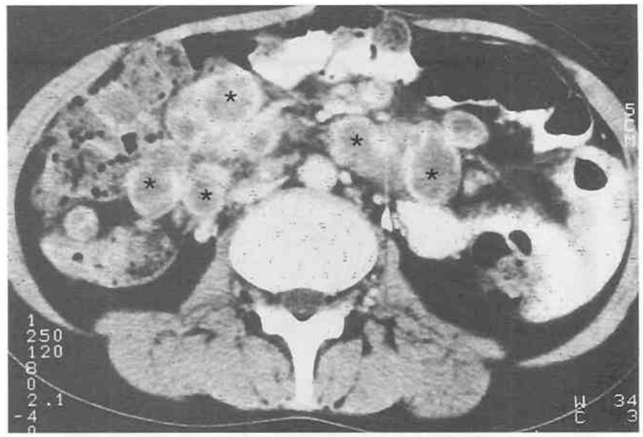

Figure 34–91. Abdominal tuberculosis with mesenteric lymphadenitis. Diffusely enlarged lymph nodes with central hypoattenuation *(asterisks)* are noted in the mesentery. (From Ha HK, Jung JI, Lee MS, et al: CT differentiation of tuberculous peritonitis and peritoneal carcinomatosis. AJR Am J Roentgenol 167:743–748, 1996.)

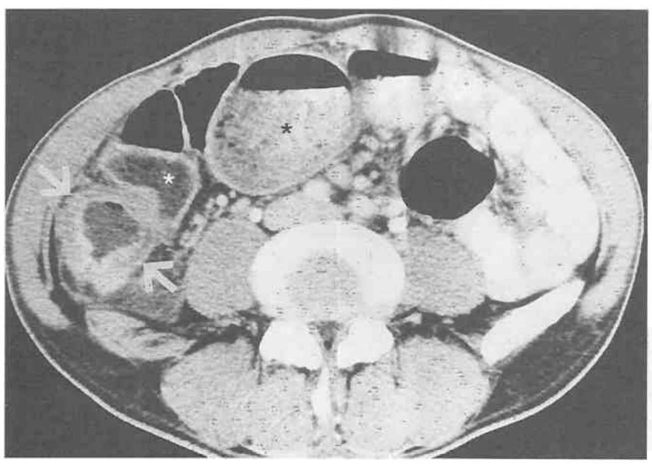

Figure 34–90. Intestinal tuberculosis. CT scan shows heterogeneous bowel wall thickening *(arrows)* of the ileum. The ileal loops are dilated *(asterisks)* as a result of bowel obstruction caused by strictures (not shown).

Although intestinal TB is a chronic disease, acute onset of abdominal symptoms may develop owing to their complications. A broad spectrum of complications include intestinal obstruction, bowel perforation, fistula, GI bleeding, enterolithiasis, venous thrombosis, and traction diverticula (Fig. 34–92).[45, 375] Intestinal obstruction is the most common complication of tuberculous enteritis, with an incidence of 12% to 60% of patients.[375] The mechanisms may include inflammatory thickening of the bowel wall, especially in cases of hypertrophic or ulcerohypertrophic type with a long length of stricture or multiple areas of involvement and intraperitoneal adhesion.[206] This complication commonly occurs during the medical therapy. Healing by cicatrization in the course of antituberculous therapy increases the tendency to result in obstruction, and the use of modern chemotherapeutic agents, such as rifampicin, also plays a partial role in producing cicatrization.[9]

Single or multiple bowel perforation may occur in patients with ulceration proximal to the obstruction[206]; although it may be confined to a localized area when preexisting adhesive change is present. The incidence of fistula formation is lower than that in Crohn's disease but may result from bacterial invasion of the necrotic area in the bowel, a penetrating abscess, or sequelae of the confined perforation.[452]

Crohn's Disease

Crohn's disease is a chronic transmural inflammation that may involve any part of the alimentary tract, from the mouth to the anus. One fourth to one third of patients present before age 20 years, and about 15% of patients experience an onset after 50 years of age. In the older age group, in contrast to younger people, the disease predominates in women, who show a higher frequency of colonic involvement than men. The most common sites of involvement include the distal small bowel and the proximal colon;

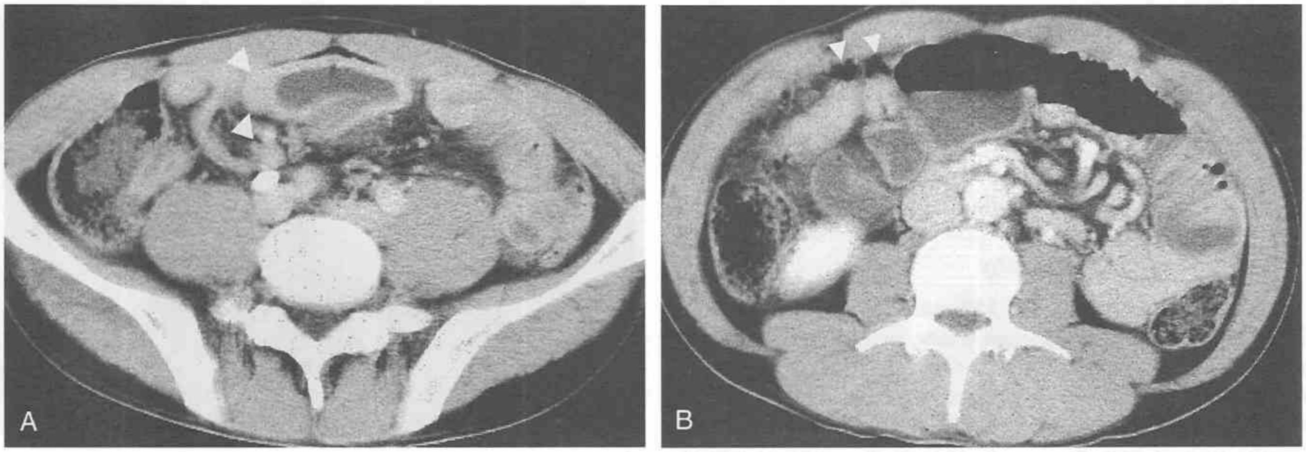

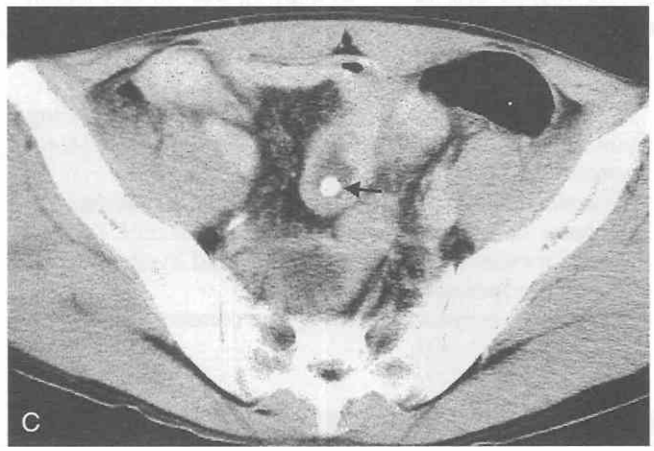

Figure 34–92. Bowel perforation in a patient with intestinal tuberculosis during medical therapy. *A,* CT scan shows a stricture *(arrowheads)* at the site of low-grade small-bowel obstruction. *B,* CT scan shows pneumoperitoneum *(arrowheads)* due to bowel perforation from the ulcer at the bowel loop proximal to the stricture. *C,* CT scan at a lower level shows an enterolith in the bowel proximal to the stricture.

the ileocecal area involvement occurs in approximately 50% of patients, the small bowel alone in 30% to 40%,[434] and the colon alone in 20% to 27%.[77]

An increased risk of small-bowel adenocarcinoma is likely to be present in patients with Crohn's disease, and the risk factors include Crohn's disease with duration of 20 years or longer, intestinal bypass surgery, and chronic enteric fistula.[198] An excessive rate of lymphomas has also been reported.[197] Other extraintestinal complications include hepatitis, pericholangitis, hydronephrosis, renal calculi, and gallstones. Recurrence of small-intestinal Crohn's disease depends on the preoperative disease distribution and severity and on the extent of resection. The disease recurs in 40% to 80% of patients following ileocecal or ileocolic resection, almost always in the neoterminal ileum and within 2 years.[621]

CT yields accurate information regarding the extent of inflamed segment of the bowel, and it can detect potential complications. Accordingly, CT may sometimes play a critical role in the management of patients with Crohn's disease; in one study of 80 patients with Crohn's disease, CT demonstrated unsuspected abnormalities that altered medical or surgical management in 28% of cases.[158]

Although CT scans are usually normal when the disease is limited to the mucosa, the most common CT finding in Crohn's disease is bowel wall thickening ranging from 1 to 2 cm (Fig. 34–93).[192] The presence of mural stratification (double-halo or target sign) in thickened wall on CT may indicate an acute phase of disease,[183, 190] and this CT finding appears to be caused by submucosal edema or fat infiltration.[603] With the development of long-standing disease and transmural fibrosis, the thickened wall becomes homogeneous in attenuation. The distribution of bowel involvement is commonly segmental with interposed loops of normal bowel.

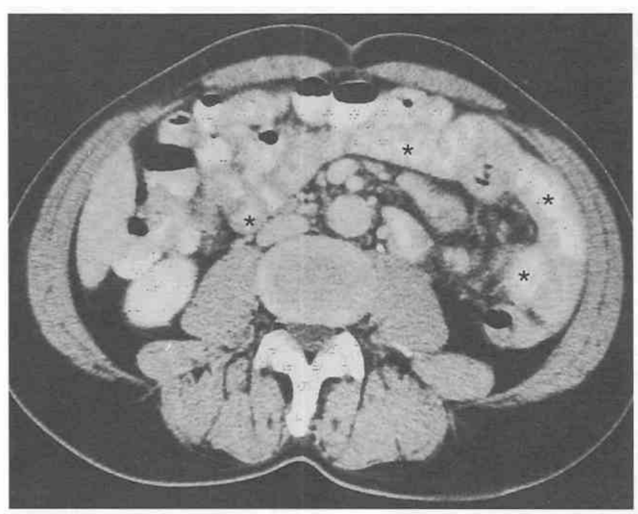

Figure 34–93. Crohn's disease. CT scan shows uneven, concentric bowel wall thickening *(asterisks)* of the small intestine.

A variety of conditions cause bowel loop separation or abdominal mass on small-bowel follow-through examination, and CT is useful in determining their primary causes. These causes are as follows:

- Abscess
- Phlegmon
- Fibrofatty proliferation within the mesentery
- Thickened bowel wall
- Mesenteric lymphadenopathy

Abscesses occur in about 15% to 20% of patients with Crohn's disease owing to sinus tracts, fistulas, perforations, or postsurgical complication.[302] On CT, they appear as a low-attenuation mass with a thick wall that may enhance with administration of IV contrast material, but the most specific finding may be the presence of gas bubbles within the mass (Fig. 34–94). CT is also useful for guiding percutaneous drainage of abscess collection, frequently obviating the need for surgical intervention.

A *phlegmon* produces a loss of definition of surrounding organs and a smudgy or streaky appearance of the adjacent mesenteric or omental fat.

Fibrofatty proliferation may present as an increase in the volume and attenuation of mesenteric fat on CT along with mild mesenteric lymphadenopathy and hypervascularity within the mesentery.[404]

Mesenteric lymphadenopathy is a common finding in patients with Crohn's disease, but lymph node sizes usually range from 3 to 8 mm (Fig. 34–95). When the lymph nodes are larger than 1 cm, the presence of lymphoma or carcinoma as a complication of Crohn's disease must be excluded.[541] Fistula and sinus tracts are hallmarks of Crohn's disease, occurring in about one third of patients.[183] Barium study may be limited in the identification of the

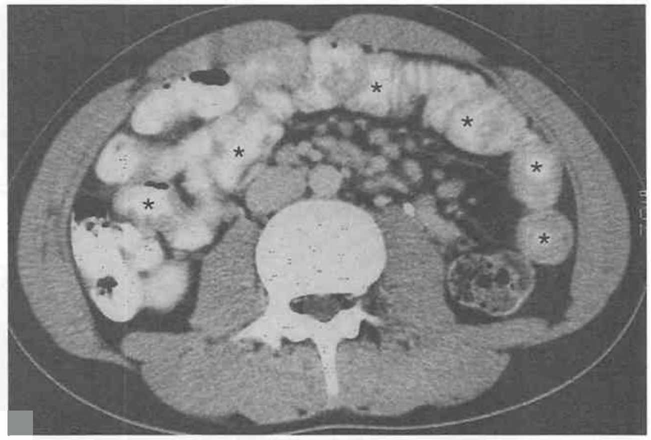

Figure 34–95. Crohn's disease. CT shows diffuse bowel wall thickening *(asteris*[redacted]f the small intestine with a skipped segment. Minimal lymphadenopathy is seen in the mesentery.

Figure 34–94. Peritoneal abscess complicating Crohn's disease. *A,* Coronal T1-weighted (2D fast low-angle shot [FLASH]) MR image shows a heterogeneous mass *(arrows)* in the peritoneal cavity. *B,* Coronal gadolinium-enhanced MR image clearly depicts multiseptated abscess cavity *(arrows)* with well-enhanced thick peripheral wall and internal septations.

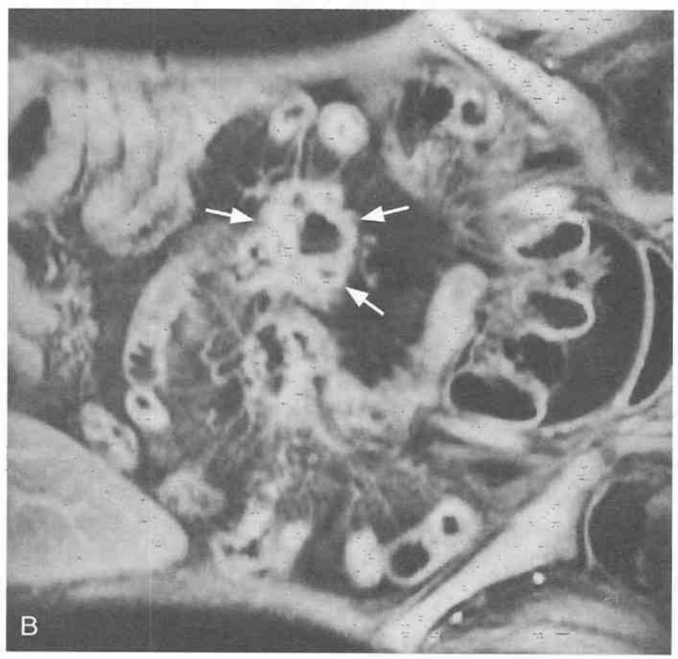

RoshanKetab TEHRAN - IRAN Tel: +98 (21) 66950639
Medical Publishers TelFax: +98 (21) 66963783_6

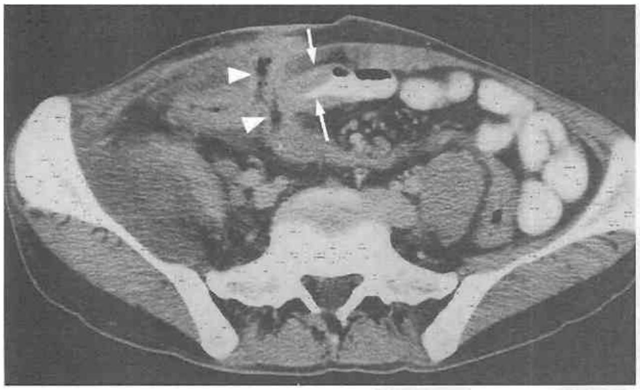

Figure 34–96. Enterocutaneous fi[redacted] wi[redacted]'s disease. CT scan shows a fistulou[redacted]wel wall thickening of the ileal loop.

origin, anatomic course, and site of communication of fistula and sinus tract, but CT may have an advantage in demonstrating their full extent (Fig. 34–96). In some instances, CT scans may show hypervascularity of the involved mesentery, producing vascular tortuosity, dilatation, prominence, and wide spacing of the vasa recta in a comblike manner *(comb sign)* (Fig. 34–97).[404] The presence of hypervascularity may suggest an acute exacerbation.[404]

MRI has been reported to be useful for demonstrating the intestinal and extraintestinal changes of Crohn's disease involving the GI tract (Fig. 34–98; see also Fig. 34–97).[210, 355] According to Shoenut and associates,[540] bowel wall thickness, length of diseased segment, and amount of enhancement with gadolinium correlated with disease activity.

Mycobacterium avium–intracellulare Enteritis

Mycobacterium avium–intracellulare (MAI) is the most common cause of systemic bacterial infection in patients with AIDS. It frequently affects the GI tract as well as the hepatobiliary system.[617] Patents typically present with progressive weight loss, watery diarrhea, malabsorption, fever, and chills. This disease is often called *pseudo-Whipple's disease* because of the clinical, histologic, and radiologic similarities.[467]

The single most sensitive test for the diagnosis of disseminated MAI is the peripheral blood culture, with a reported sensitivity of 86% to 98%.[617] CT may demonstrate bowel wall thickening especially in the jejunum (Fig. 34–99). The presence of low-attenuation mesenteric and retroperitoneal lymphadenopathy is characteristic. Unlike other infectious processes, the nodes in MAI infection are often bulky and may be impossible to distinguish from lymphoma.[243] Hepatosplenomegaly may be seen.

Eosinophilic Enteritis

Eosinophilic gastroenteritis is a rare inflammatory disorder characterized by focal or diffuse infiltration of the GI tract by eosinophils. It usually occurs during the third decade of life. Although the etiologic mechanism is unknown, an allergic or immunologic disorder is the most commonly proposed cause for this disease.[589] Peripheral eosinophilia (present in 60% to 96% of patients) is regarded as one of the most important clinical features for diagnosis.[303, 424] An allergic disorder such as bronchial asthma, food allergy, eczema, or atopic dermatitis occurs in approximately 50% of patients.[303] The clinical response to steroid treatment is usually dramatic.

The *Klein classification*[303] separates eosinophilic gastro-

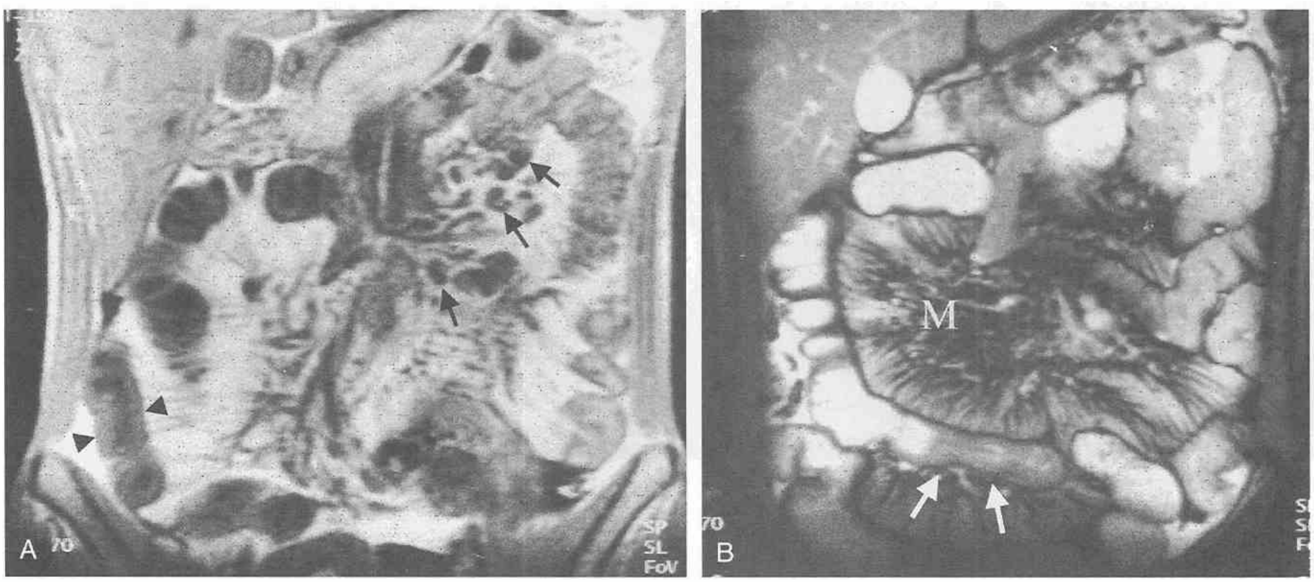

Figure 34–97. Crohn's disease. *A,* T1-weighted MR image shows mesenteric lymphadenopathy *(arrows),* especially along the jejunal branches of the mesenteric artery. Note the bowel wall thickening *(arrowheads)* of the ascending colon. *B,* Coronal true fast imaging with steady-state precession (FISP) MR image shows fibrofatty proliferation (M) with hypervascularity ("comb sign") of mesenteric vasculatures. Also note the focal bowel wall thickening *(arrows)* and pseudosacculation along the antimesenteric border of the adjacent bowel loop.

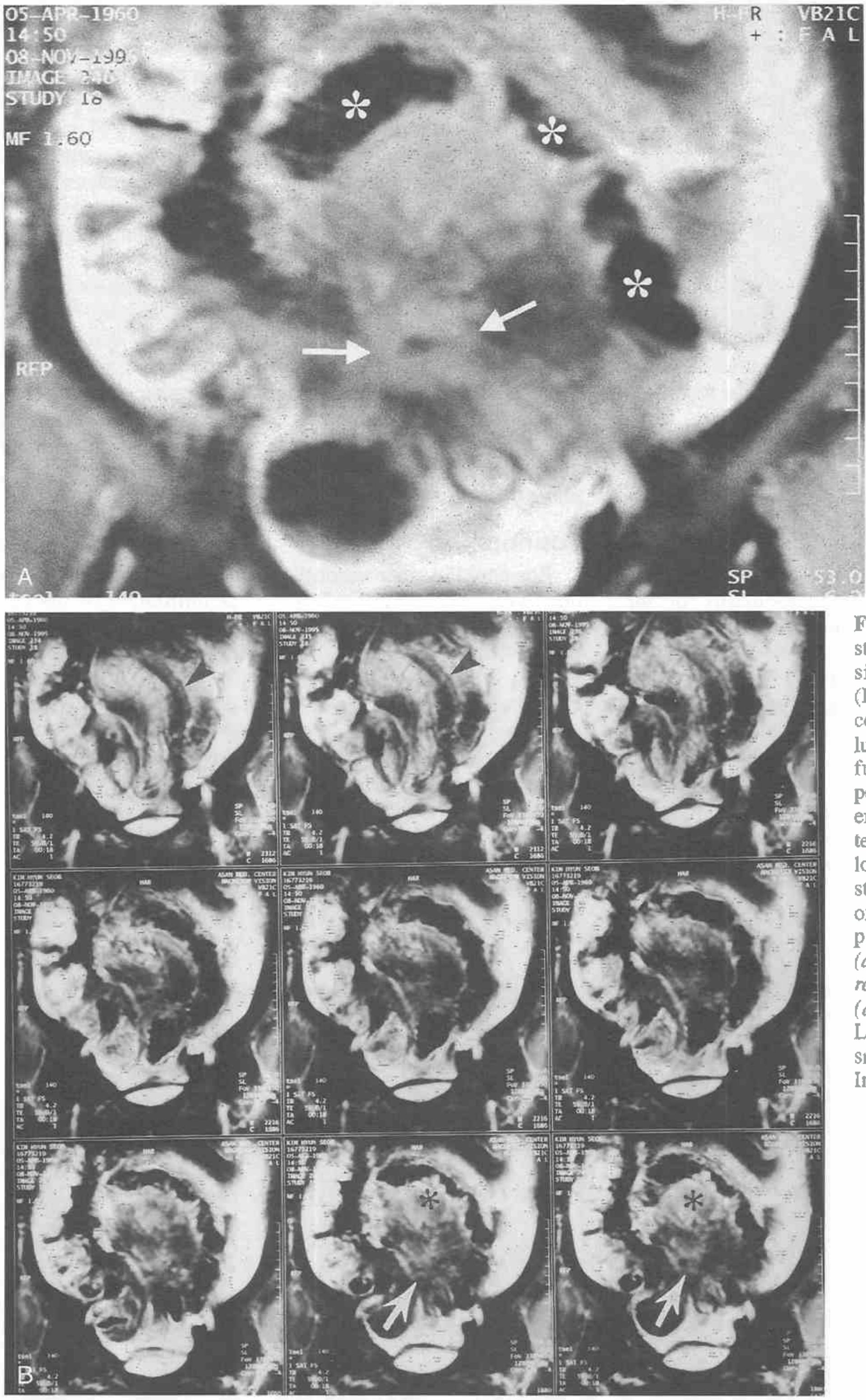

Figure 34–98. Crohn's disease with stricture. *A,* Coronal half-Fourier acquisition single-shot turbo spin-echo (HASTE) MR image shows irregular concentric bowel wall thickening and luminal narrowing *(arrows)* with diffuse inflammatory infiltration in the perienteric region. Bowel wall thickening is also present along the mesenteric border of the dilated small-bowel loop *(asterisks). B,* Multiplanar reconstruction images have the advantages of easy orientation of bowel wall and perienteric changes such as stricture *(arrows),* bowel wall thickening *(arrowheads),* and mesenteric infiltration *(asterisks).* (From Ha HK, Lee EH, Lim CH, et al: Application of MRI for small intestinal diseases. J Magn Reson Imaging 8:375–383, 1998.)

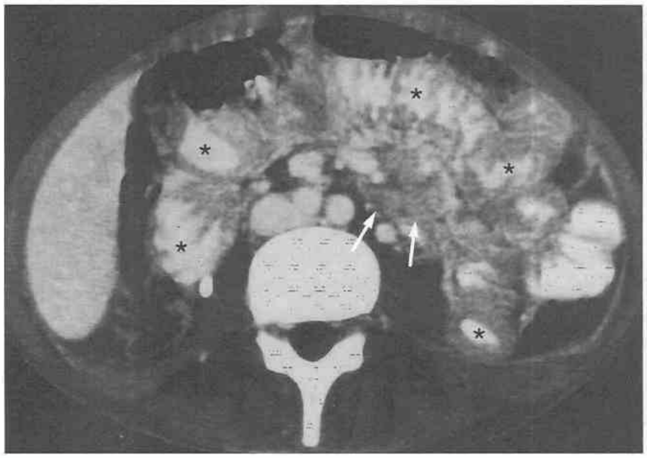

Figure 34–99. *Mycobacterium avium–intracellulare* enteritis. CT scan shows concentric bowel wall thickening *(asterisks)* of the small-bowel loops with evidence of bowel dilatation and fold thickening. Mesenteric lymphadenopathy *(arrows)* is also seen. (Courtesy of K. C. Cho, M.D., Newark, New Jersey.)

enteritis into three groups according to the predominant tissue layer of involvement in the GI tract:

- Predominant mucosal disease
- Predominant disease of the muscularis
- Predominant subserosal disease

Patients usually present with recurrent episodes of abdominal pain, vomiting, diarrhea, or malabsorption, but the clinical features depend on the location and depth of tissue involvement.

Mucosal involvement leads to protein-losing enteropathy, fecal blood loss, and malabsorption.

Involvement of muscle layer *(muscularis)* often causes obstruction of the gastric outlet or small bowel, and subserosal involvement manifests as eosinophilic ascites. The stomach and small bowel are most frequently affected; the stomach alone is involved in approximately 40% of cases, both the stomach and small bowel in approximately 50%, and the small bowel alone in about 10%.[424] However, the colon and esophagus may also be involved. The most common CT features include circumferential bowel wall thickening in the distal stomach and proximal small bowel (Fig. 34–100). A target appearance can be seen in the thickened wall.

When *subserosal* involvement is predominant, eosinophilic ascites, eosinophilic pleural effusions, lymphadenopathy, and diffuse omental and mesenteric infiltration may also be seen. Rarely, inflammatory mass in the involved bowel may develop, causing bowel obstruction.[543]

Giardia lamblia Infection

Giardiasis is a small-intestinal infection with the protozoan parasite, *Giardia intestinalis*. Isolates obtained from humans are commonly given the name *Giardia lamblia*. The major clinical impact of this infection is in young children in whom it can produce persistent diarrhea, intestinal malabsorption, and retardation of growth and development. Outbreaks have been linked to contaminated water supplies and situations involving person-to-person contact. Immunocompromised patients are especially at risk.

Most cases can be diagnosed by a single stool examination. CT findings show thickening of the wall of the duodenum and jejunum and mesenteric lymphadenopathy.[438]

Yersinia enterocolitica Infection

Yersinioses are primarily diseases of animals, but human infections are recognized with increased frequency all over the world. In humans, the alimentary tract is probably the portal of entry in most cases. The proposed modes of infection are (1) intake of contaminated food, (2) contact with infected animals, and (3) person-to-person transmission. Enteric infection causes mucosal ulcerations in the terminal ileum, necrotic lesions in Peyer's patches, and enlargement of mesenteric lymph nodes.

Although most patients are younger than 5 years of age, the clinical presentations vary with age, sex, and immunologic state of the host: acute enteritis (<5 years of age), mesenteric adenitis (5 to 15 years of age), acute terminal ileitis (10 to 20 years of age), gastroenteritis, erythema nodosum, and polyarthritis (adults).[151] Most cases are self-limited, but complications have included appendicitis, diffuse ulceration and inflammation of the small intestine and colon, intestinal perforation, peritonitis, ileocolic intussusception,[249] toxic megacolon, mesenteric venous thrombosis, and gangrene of the small bowel.[103]

A definitive diagnosis can be made by the isolation of *Yersinia enterocolitica* together with the demonstration of a rising antibody titer.[587] The terminal ileum is most commonly affected in a length approximately 10 to 20 cm. The most typical lesions consist of shallow, small, round aphthoid ulcers to longitudinal ulcers of 2 cm or more, resembling those seen in Crohn's disease. CT may help to detect bowel wall thickening of the distal ileum as well as enlarged mesenteric lymph nodes (Fig. 34–101).

Salmonellosis

Salmonellosis is one of the common causes of acute gastroenteritis. *Salmonella* species are gram-negative non-spore-forming bacilli, and in humans the disease is usually contracted by ingestion of contaminated foods, notably meat, dairy products, poultry, and eggs. Susceptibility to infection is heightened in patients with sickle cell anemia, hemolytic disease, and immunodeficiency. The terminal ileum may be mainly affected, although colonic changes are also seen. *Salmonella* organisms penetrate the wall of the small bowel, invading the lymphoid tissue of Peyer's patches with development of small, longitudinally oriented ulcers. Ileal inflammation is usually superficial and involves the mucosa and lamina propria. Once the patient recovers, intestinal lesions heal with minimal fibrosis so that stricture formation is unusual.

CT findings include circumferential and homogeneous thickening of the terminal ileum over a segment of 10 to 15 cm (Fig. 34–102).[21] The colonic wall can also be mildly thickened. Small-bowel perforation with peritonitis may occasionally occur.[168]

Whipple's Disease

Whipple's disease is a chronic, multisystemic condition resulting from a systemic infection with *Tropheryma whip-*

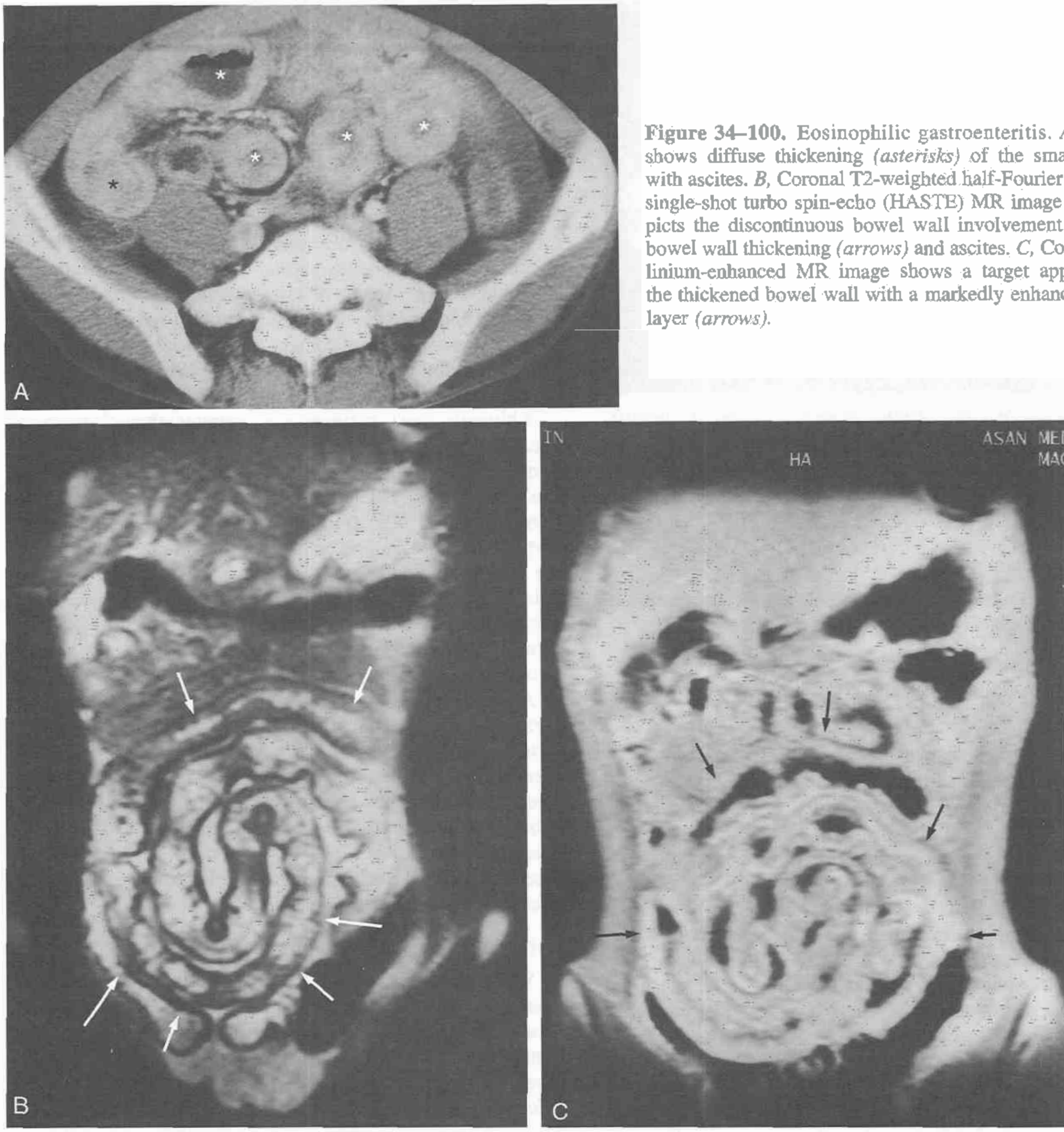

Figure 34–100. Eosinophilic gastroenteritis. *A,* CT scan shows diffuse thickening *(asterisks)* of the small intestine with ascites. *B,* Coronal T2-weighted half-Fourier acquisition single-shot turbo spin-echo (HASTE) MR image clearly depicts the discontinuous bowel wall involvement as well as bowel wall thickening *(arrows)* and ascites. *C,* Coronal gadolinium-enhanced MR image shows a target appearance of the thickened bowel wall with a markedly enhancing middle layer *(arrows).*

peli. It frequently involves the jejunum and ileum but usually spares the duodenum. There is a characteristic infiltration of the small-bowel mucosa and submucosa with foamy macrophages containing periodic acid–Schiff-positive glycoprotein granules.[161] The villi appear blunted and distorted by collections of foamy macrophages. Widespread fatty deposits and granulomas are present in the intestinal mucosa and intra-abdominal lymph nodes, reflecting lymphatic obstruction with fatty extravasation. The most common clinical presentation is a generalized malabsorption syndrome.

CT shows diffuse thickening of the small-bowel folds. Characteristically, the mesenteric or retroperitoneal nodes are of low CT attenuation owing to fatty deposits.[503] Ancillary CT findings include hepatosplenomegaly and ascites.

Lymphangiectasia

Intestinal lymphangiectasia, characterized by protein-losing enteropathy, hypoproteinemia, edema, malabsorption, and dilated lacteals, is a rare congenital obstructive defect of the lymphatics affecting primarily children and young adults. Hypoplastic visceral lymphatics obstruct lymph flow, causing increased intestinal lymphatic pressure and thereby dilating lymphatic vessels through the small bowel and mesentery. Hypoproteinemia and steatorrhea are secondary to rupture of the dilated lymphatic vessels with discharge of lymph into the bowel lumen. The condition may also develop secondary to inflammatory or neoplastic involvement of the lymphatics.[164]

In both primary and secondary lymphangiectasia, CT

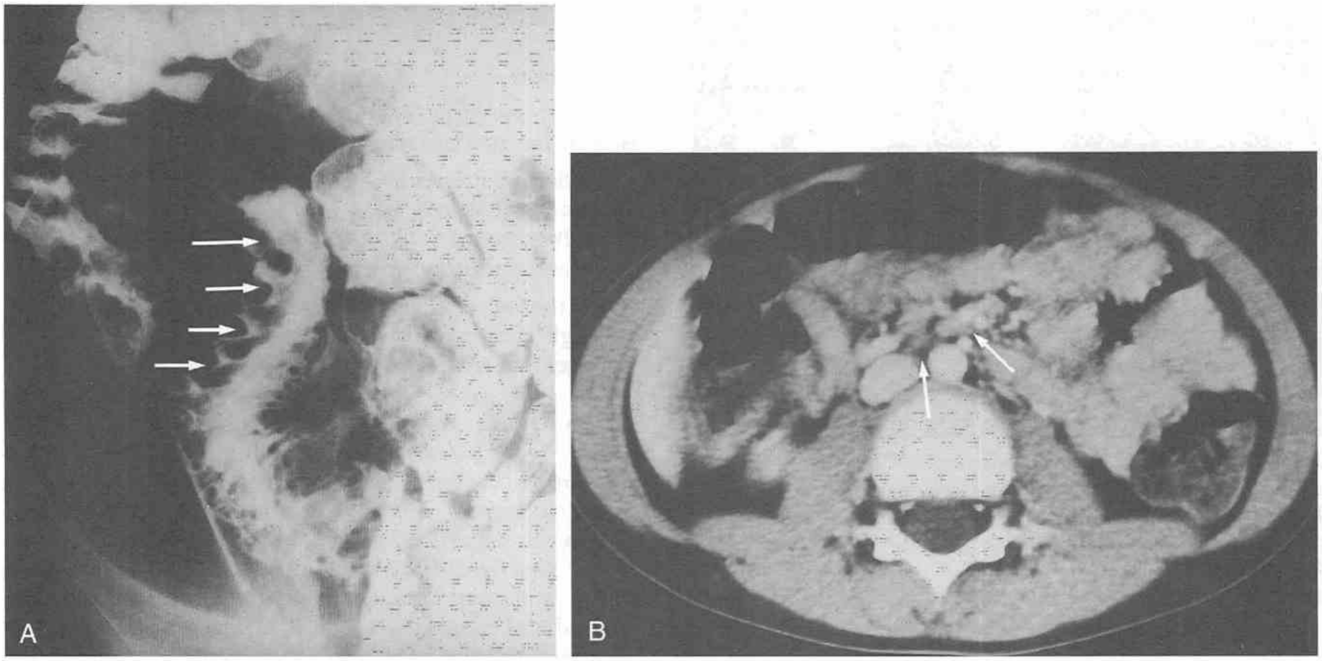

Figure 34–101. Yersiniosis. *A*, Small-bowel follow-through scan shows multiple nodular defects *(arrows)* in the distal ileum. *B*, CT scan shows minimal mesenteric lymphadenopathy *(arrows)*.

shows diffuse small bowel and fold thickening.[473, 555] A halo may be present within the wall owing to edema. The presence of mesenteric infiltration and retroperitoneal or mesenteric lymphadenopathy may suggest the secondary form because adenopathy is not usually present in the primary form.[555]

Mucormycosis

Mucormycosis, a relatively uncommon opportunistic fungal infection, is caused by fungi of the order Mucorales. The disease is known to occur especially in association with diabetes mellitus, leukemia, or lymphoma.[72] When the GI tract is involved, the stomach is the most common site of involvement and the intestinal form has a predilection for the terminal ileum and cecum.[361] GI involvement usually complicates local disease processes, such as intractable peptic ulceration, amebic colitis, persistent peritonitis, and malnutrition.[72, 329] However, a fulminant and rapidly fatal course can occur in certain instances.[361]

These fungi exhibit a remarkable tendency to infiltrate the walls of blood vessels, especially arteries. They grow profusely into the vessel lumen and initiate acute vasculitis and thrombosis of major blood vessels. As a result, ischemic infarction can occur in any organ.[329] In some instances, venous involvement with thrombosis causes hemorrhagic necrosis.[385]

CT studies show diffuse circumferential wall thickening of the small bowel, intermingled with areas of both intense and poor contrast enhancement (Fig. 34–103).[322] Pathologically, poorly enhanced areas coincide with the areas of necrosis and infarction, whereas intensely enhanced areas

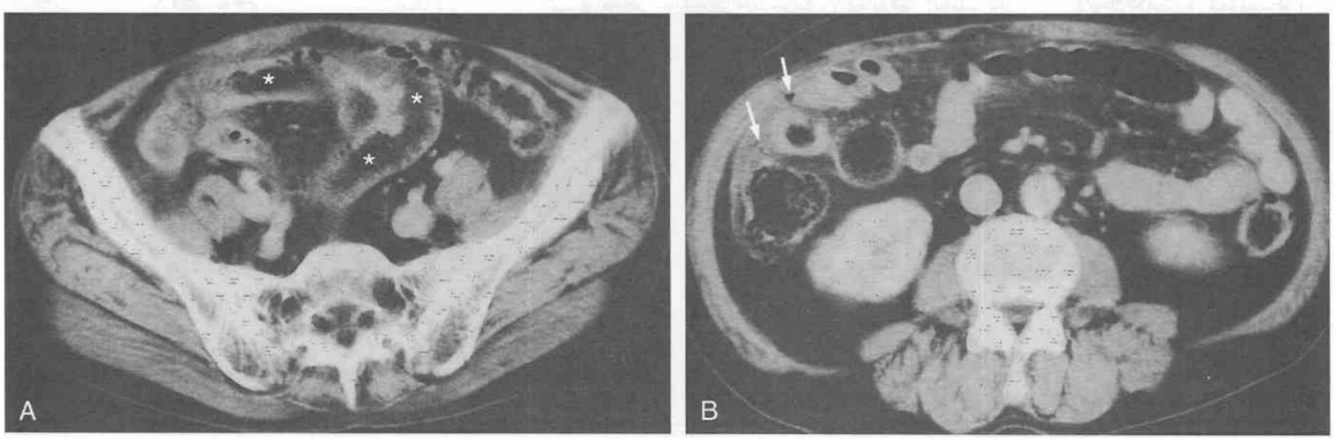

Figure 34–102. Perforated salmonellosis. *A* and *B*, The ileal wall is diffusely thickened *(asterisks)* with a small amount of intraperitoneal fluid and free gas *(arrows)*.

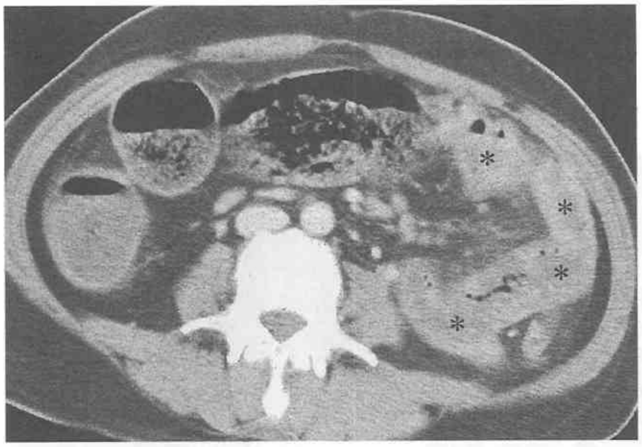

Figure 34–103. Intestinal mucormycosis. CT scan shows alternating areas of poor and prolonged contrast enhancement in the bowel wall of the small intestine *(asterisks)* along with regional mesenteric haziness. (From Lee JH, Ha HK, Yoo ES, et al: CT and sonographically guided biopsy in a patient with intestinal mucormycosis. AJR Am J Roentgenol 175:129–131, 2000.)

represent the areas of edema and hemorrhage in the submucosa and muscle layers due to congestive changes. Therefore, such CT findings can easily be confused with chemotherapy-induced necrotizing enteropathy if they have been seen in patients with lymphoma or leukemia who had received chemotherapeutic regimens.

Amyloidosis

Amyloidosis is a group of heterogeneous disorders caused by the extracellular deposition of a protein substance. Any part of the GI tract is involved, but the small intestine is most commonly affected. According to the traditional clinical classification,[312] there are five types of amyloidosis:

- Primary
- Secondary
- Familial
- Senile
- Localized

However, use of the classification based on the histochemistry of the amyloid fibril is preferred[562]:

- Amyloid A protein (AA)
- Light chain protein (AL)
- Prealbumin (AF)
- β_2-microglobulin (AH)

All four types of amyloid substance involve the GI tract, although each protein has its own specific mechanism of pathogenesis, radiologic findings, and clinical course. In the AL type, massive amyloid deposits commonly occur in the muscularis propria and submucosa of the intestinal wall.[562] Wide granular deposits in the lamina propria mucosa are much more commonly seen in the AA type than in the AL type.[178]

Vascular deposits of amyloid in the submucosa are commonly seen in all types of amyloidosis. As a result, the vessel walls are thickened, and the lumen is gradually reduced and eventually occluded, leading to ischemia, ulceration, infarction, and even perforation.[562] Although focal or diffuse symmetrical wall thickening of the affected bowel is a common CT finding, CT may not differentiate infiltrative from ischemic changes (Fig. 34–104). Intestinal hypomotility results in delayed transit of the oral contrast agent.[448] Adenopathy may be present but not as bulky or low attenuation as seen in Whipple's disease. Occasionally, bowel wall calcification can be seen.[243]

Cytomegalovirus Enteritis

CMV is a herpes virus that can be transmitted sexually or transmitted via infected organs, blood, or needles. CMV remains in a latent state in the host after the initial infection. With increasing impairment of cell-mediated immunity, particularly a CD4 lymphocyte count below 100 mm^3, viral reactivation may occur.[592] Clinically evident CMV infections most commonly affect immunosuppressed patients, including transplant recipients and patients with

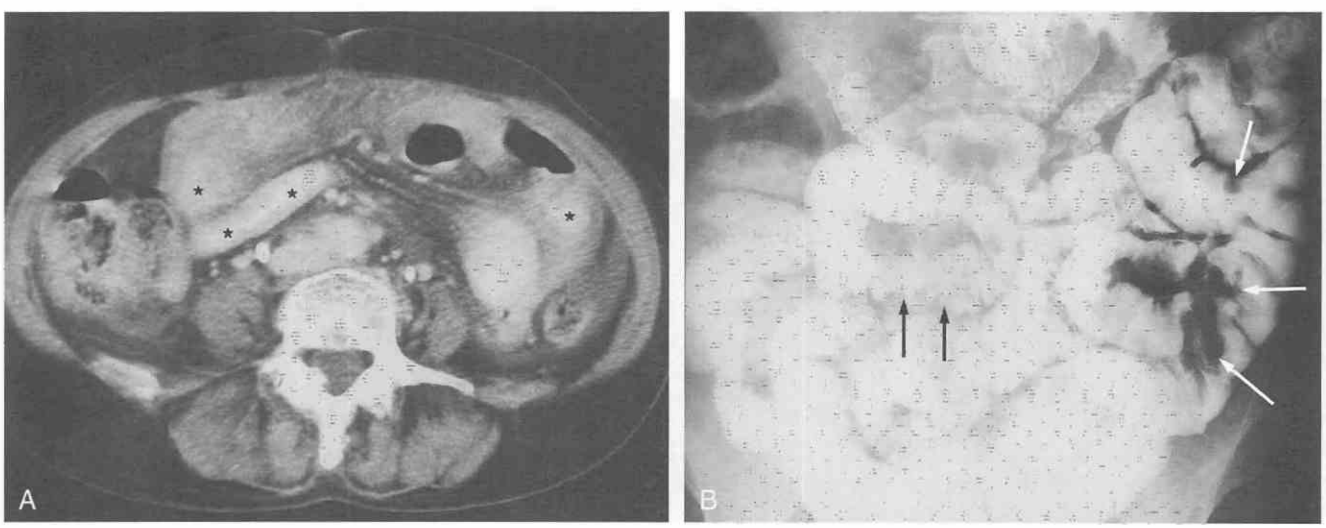

Figure 34–104. Amyloidosis. *A,* Mild bowel wall thickening is noted in the small intestine *(asterisks).* Note the small amount of ascites. *B,* Small-bowel follow-through scan shows nodular fold thickening *(arrows)* in both the jejunum and the ileum.

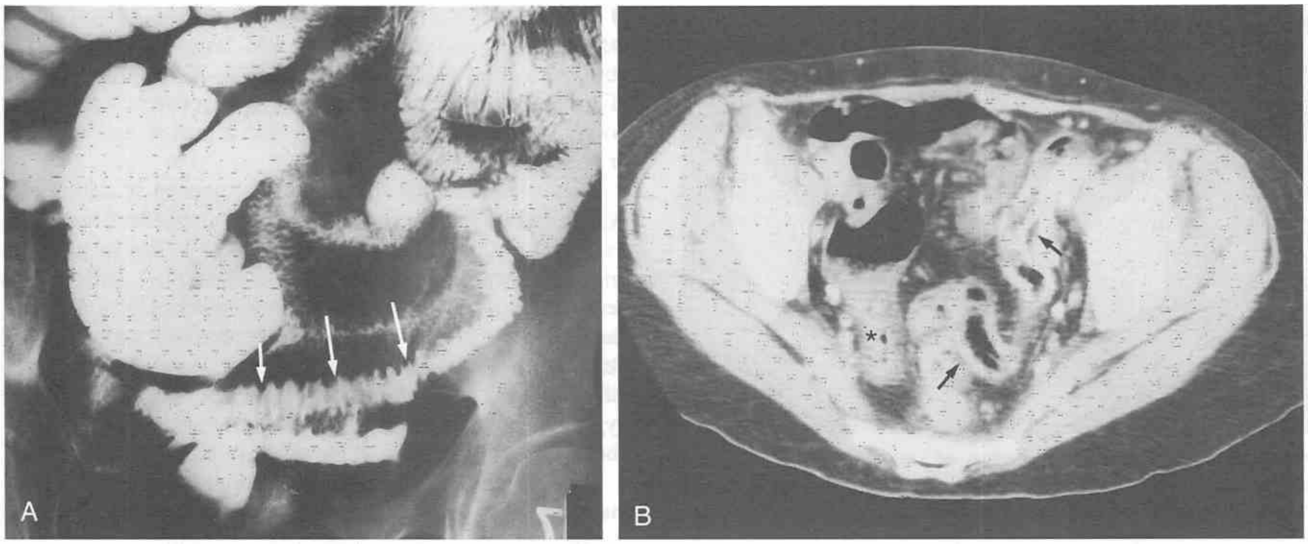

Figure 34–105. Cytomegalovirus enterocolitis. *A,* The circular folds of the ileum are diffusely thickened *(arrows)* with spastic narrowing of the lumen on a single-phase study of enteroclysis. *B,* Bowel wall at the involved segment of the ileum *(asterisk)* is minimally thickened with proximal loop dilatation. There is also diffuse concentric bowel wall thickening *(arrows)* of the rectosigmoid colon. (Courtesy of D. T. Maglinte, M.D., Indianapolis, Ind.)

AIDS; however, it may occasionally occur in nonimmunosuppressed individuals, including those with diabetes mellitus, those who receive corticosteroids or radiation therapy, and those who are elderly.[553]

Clinical manifestations usually include diarrhea, hematochezia, abdominal pain, and constitutional symptoms. Although the colon is the organ most commonly affected by CMV infection, the incidence of small-bowel involvement is not uncommon.[420, 570]

Radiographic features include ulcers of various sizes and depth along with mucosal fold thickenings and luminal narrowing.[570] The ulcers are usually numerous, round, or serpiginous, often reaching the muscular layer with subsequently common occurrence of bowel perforation; CMV inclusions in the capillaries and venules of the mucosa and submucosa may produce focal ischemias that are responsible for mucosal ulcerations.[186] These features simulate those of inflammatory bowel disease, bacterial or parasitic infection, ischemic bowel disease, lymphoma, and GVHD. CT may demonstrate bowel wall thickening in both the small and the large intestines, lymphadenopathy, and ascites (Fig. 34–105).[420]

Trauma

Bowel disruption due to blunt abdominal trauma is no longer rare and occurs in 5% to 25% of patients. The increasing frequency is attributed to the automobile and industrialization. The mechanisms of bowel disruption have been thought to be at least one of the following different types of stress:

1. Direct, crushing impingement of the bowel against the prominent, unyielding vertebral column.[439]
2. A tearing or shearing force at areas of the bowel where either the bowel or mesentery is relatively fixed.[111]
3. A sudden increase of intraluminal pressure in a closed loop of bowel, especially the duodenum.

It is generally agreed that the segments of the small intestine most commonly involved by blunt abdominal trauma are the duodenum near the ligament of Treitz, the proximal jejunum just beyond the ligament, and the ileum just proximal to the ileocecal valve, because these segments are relatively fixed. The relationship of intestinal injury to intra-abdominal adhesions has been well documented,[597] and the knowledge of a previous surgery should suggest possible intestinal damage. Similarly, fixation of the small intestine within an inguinal hernia has led to bowel perforation.[111]

Different types of injuries occur in the blunt wounds of the small intestine, including transection, perforations, avulsions, intramural hematoma, and serosal tears. Delayed perforation up to 10 days after injury may occur. Clinically, the classic triad of rigidity, absent or decreased bowel sounds, and tenderness occur in approximately one third of patients.[456]

Diagnostic peritoneal lavage following blunt trauma markedly improves sensitivity (94% to 100%) for detection of intraperitoneal injury but remains less sensitive for the detection of retroperitoneal trauma to the duodenum, colon, and kidney.[140, 153] Because lavage findings are nonspecific for the type or extent of organ injury, positive lavage results may lead to nontherapeutic laparotomy rates of 6% to 25% with associated morbidity.[153]

Although the accuracy of CT is controversial, CT is effective in detecting bowel and mesenteric injuries caused by blunt abdominal trauma and may be useful in predicting the need for either surgical repair or conservative management.[57, 130, 411, 506] In performing CT scan in patients with blunt trauma, use of both IV and oral contrast material is necessary. The oral contrast agent must be diluted enough to avoid causing reconstruction artifacts and must be ad-

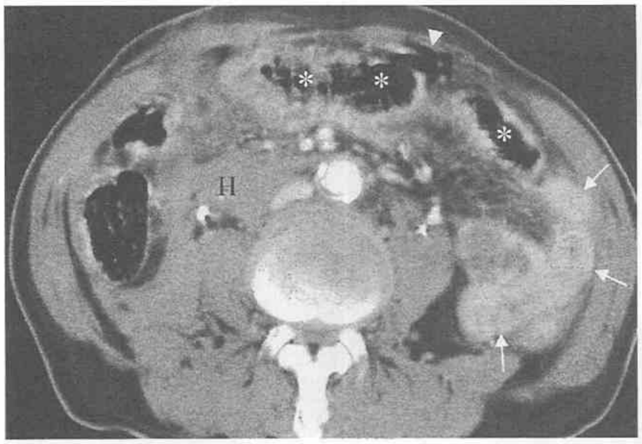

Figure 34–106. Bowel perforation of the transverse colon and jejunum after blunt abdominal trauma. CT scan shows bowel wall thickening of both the transverse colon *(asterisks)* and the jejunal loop *(arrows)* along with diffuse pericolonic and perienteric infiltration. Also note pneumoperitoneum *(arrowhead)*, intraperitoneal fluid collection, and right retroperitoneal hematoma (H).

ministered 20 to 30 minutes before scanning to allow for good bowel opacification. Scans must extend through the pelvis.

On CT, injury to the bowel may be manifested by bowel wall thickening, which is seen in 75% of patients with transmural laceration.[506] The two most specific CT signs of bowel injury include pneumoperitoneum and frank extravasation of oral contrast agent. Unfortunately, these findings are insensitive, with free air seen in 32% to 56% and extravasated oral contrast seen in only 12%.[331, 506] *Note:* Intraperitoneal gas may result from causes other than bowel perforation, such as pneumomediastinum or diagnostic peritoneal lavage.

Other highly specific signs requiring surgical repair are bowel wall thickening in combination with bowel wall discontinuity,[57] abnormally intense contrast enhancement of the bowel wall,[425] adjacent mesenteric hematoma or infiltration,[130] and intermediate and large amounts of free peritoneal fluid (Figs. 34–106 and 34–107).[506] The finding of moderate to large amounts of intraperitoneal fluid with no visible solid organ injury is also a useful sign of bowel or mesenteric injury.[57, 332]

Mesenteric fluid is extremely uncommon in solid organ injury, and its presence should be considered highly suggestive of bowel or mesenteric injury.[331, 425] The presence of only focal bowel wall thickening or hematoma indicates the need for close observation but not necessarily immediate surgical exploration without other definite indications.[127] Furthermore, bowel wall thickening may also occur in other conditions such as hypovolemic shock syndrome, hypoproteinemia, liver cirrhosis, inflammatory bowel, ischemia, heart failure, and incomplete bowel distention.

As demonstrated by several researchers,[236] blunt abdominal trauma is also one of the causes of segmental intestinal stenosis in association with acute ischemic insult to the intestine. Focal deprivation of the blood supply secondary to a tear in the mesenteric attachment is considered to be the main cause of the development of focal segmental ischemia. Although it depends on the site of the trauma, the stricture usually occurs near the proximal or distal extremes of the small intestine where mesenteric mobility commences.[373] Intestinal stenosis is characterized by the delayed onset of symptoms within a variable interval of months or years after the accident. Therefore, if a patient's history is overlooked, intestinal stenosis can be confused with other inflammatory or neoplastic GI diseases.

Radiographic features of tubular narrowing and circumferential ulcers in post-traumatic intestinal stenosis are similar to those in patients with chronic intestinal ischemia.[370] On CT, post-traumatic intestinal stenosis shows nonspecific bowel wall thickening with or without bowel obstruction (Fig. 34–108). In such cases, barium studies of the colon or small intestine appear to be more useful than CT in demonstrating the characteristic findings of tubular or circumferential luminal narrowing in a short segment.

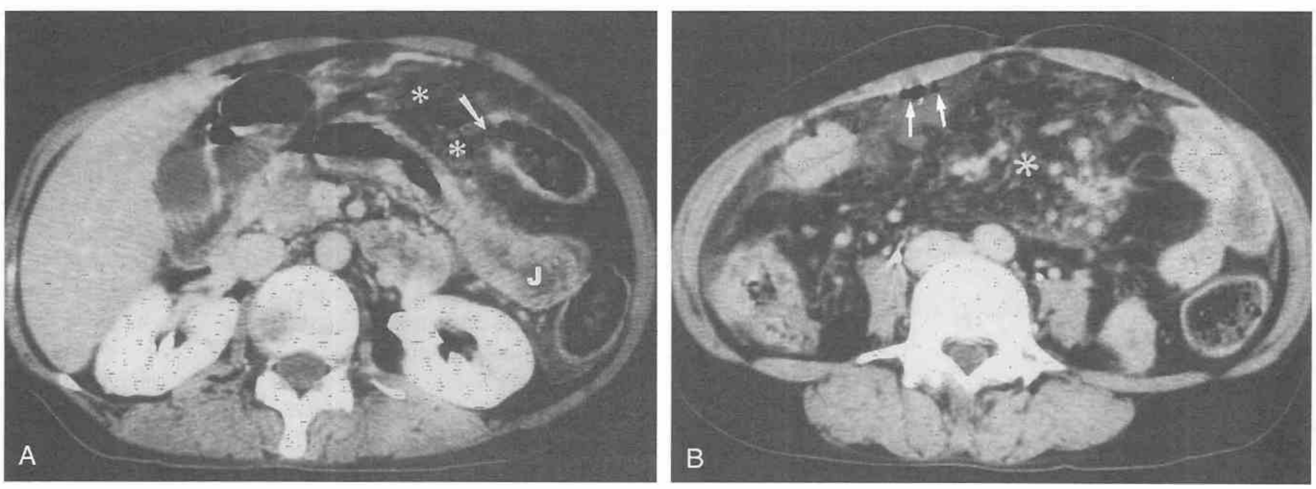

Figure 34–107. Blunt trauma with bowel perforation and mesenteric injury. *A,* Bowel perforation *(arrow)* is noted in the transverse colon with regional free gas collection *(asterisks)* and pericolonic infiltrates. The jejunal wall (J) is also thickened as a result of traumatic contusion. *B,* The mesenteric vessels *(asterisk)* are increased and prominent with their distorted courses, which resulted from mesenteric vascular injury. Intraperitoneal collection of free gas and fluid is also seen.

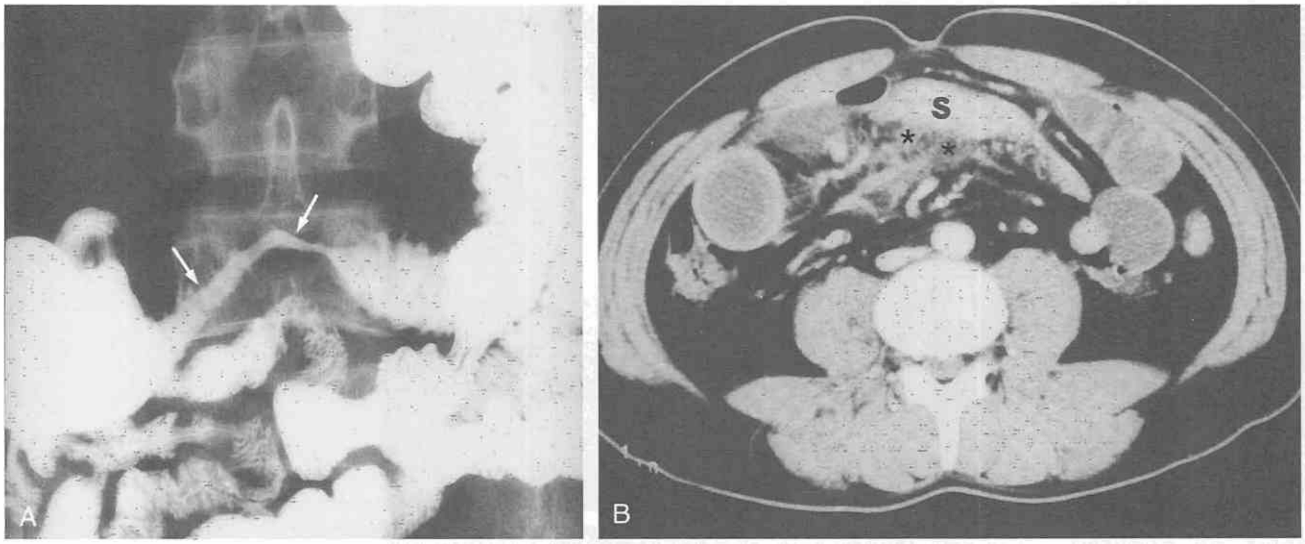

Figure 34–108. Post-traumatic intestinal stenosis following blunt abdominal trauma 1 month before. *A,* Small-bowel follow-through shows short segment of tapered, circumferential luminal narrowing *(arrows)* of the distal jejunum along with thickened folds and ulcerations. *B,* CT scan shows marked contrast enhancement of the thickened bowel wall *(arrows)*. Regional mesenteric vascular engorgement and haziness *(asterisks)* are also seen. (From Ha HK, Rha SE, Kim AY, et al: CT and MR diagnoses of intestinal ischemia. Semin Ultrasound CT MRI 21:40–55, 2000.)

Gastrointestinal Disease in the Immunocompromised Host: Complications after Transplantation

Human allogeneic bone marrow transplantation has been used with increasing frequency for treatment of lymphoma, leukemia, aplastic anemia, metabolic disorders of the hematopoietic system, and some metastatic disease. Preparatory regimens such as whole body irradiation and high doses of chemotherapy as well as immunosuppressive therapy can cause profound immunosuppression after bone marrow transplantation.

Apart from GVHD, a number of abdominal complications result from this immunosuppression, which include lymphoproliferative disorders, enteritis from direct radiation or chemotherapy toxicity, infective enteritis, neutropenic colitis, pseudomembranous colitis, pneumatosis intestinalis, abdominal abscess, and increased incidence of cancer.[150]

Graft-Versus-Host Disease

GVHD is a significant complication after transplantation as a consequence of immunologic assault of donor lymphoid cells against host target organs.[150] It develops when tissues containing immunocompetent cells (blood products, bone marrow, or solid organs) are transferred between persons. Acute GVHD occurs within 1 day or as late as 1 to 2 months after transplantation.[574] The incidence ranges from less than 10% to more than 80%.[150] The major target organs in acute GVHD are the immune system, skin, liver, and intestine.[150, 574] The initial organ involved in almost all cases is the skin; hepatic and intestinal involvement usually appear several days after the rash.[574] Therefore, the hallmarks of the disease include skin rash, jaundice, and profuse secretory diarrhea.[150, 574] Pathologically, the sine qua non of acute GVHD is selective epithelial damage of target organs.[150] The destruction of intestinal crypts results in mucosal ulceration that may be either patchy or diffuse. The esophagus is less commonly involved.

In acute GVHD, small-bowel follow-through studies show a combination of fold thickening and effacement of folds with a characteristic ribbon-like or tubular appearance, associated with separation of bowel loops, excess intraluminal fluid, and rapid small-bowel transit.[160, 512] These findings are more prominent in the ileum than in the jejunum. Unusual prolonged or persistent mucosal coating also has been reported[273]; the cause of this finding is unknown, but it seems likely that the barium may be adherent to mucosa, to submucosa, or to pseudomembranes or trapped in sloughed mucosa. However, the same finding also can be seen in GI inflammation due to viral infection.[273] Therefore, the differentiation between acute GVHD and viral enteritis is not possible on the basis of radiographic findings alone.[273]

Colonic changes include luminal narrowing, wall thickening, ulceration, edema, and a haustral appearance.[160, 512] CT findings are reminiscent of radiographic findings, including luminal narrowing, diffuse wall thickening, and prolonged contrast coating in the small intestine, colon or mesentery (Fig. 34–109).[272]

According to a report by Donnelly and Morris,[126] who analyzed CT findings of 16 patients with acute GVHD, acute GVHD characteristically appears on CT scans as multiple, diffuse, fluid-filled bowel loops with a thin, enhancing layer of bowel wall mucosa in all their patients; a thin, enhancing layer corresponded with mucosal destruction and replacement by a thin layer of granulation tissue. Bowel wall thickening is often absent.

Although chronic GVHD was initially defined as a GVHD presenting more than 100 days after bone marrow transplantation, it can develop 40 or 50 days after trans-

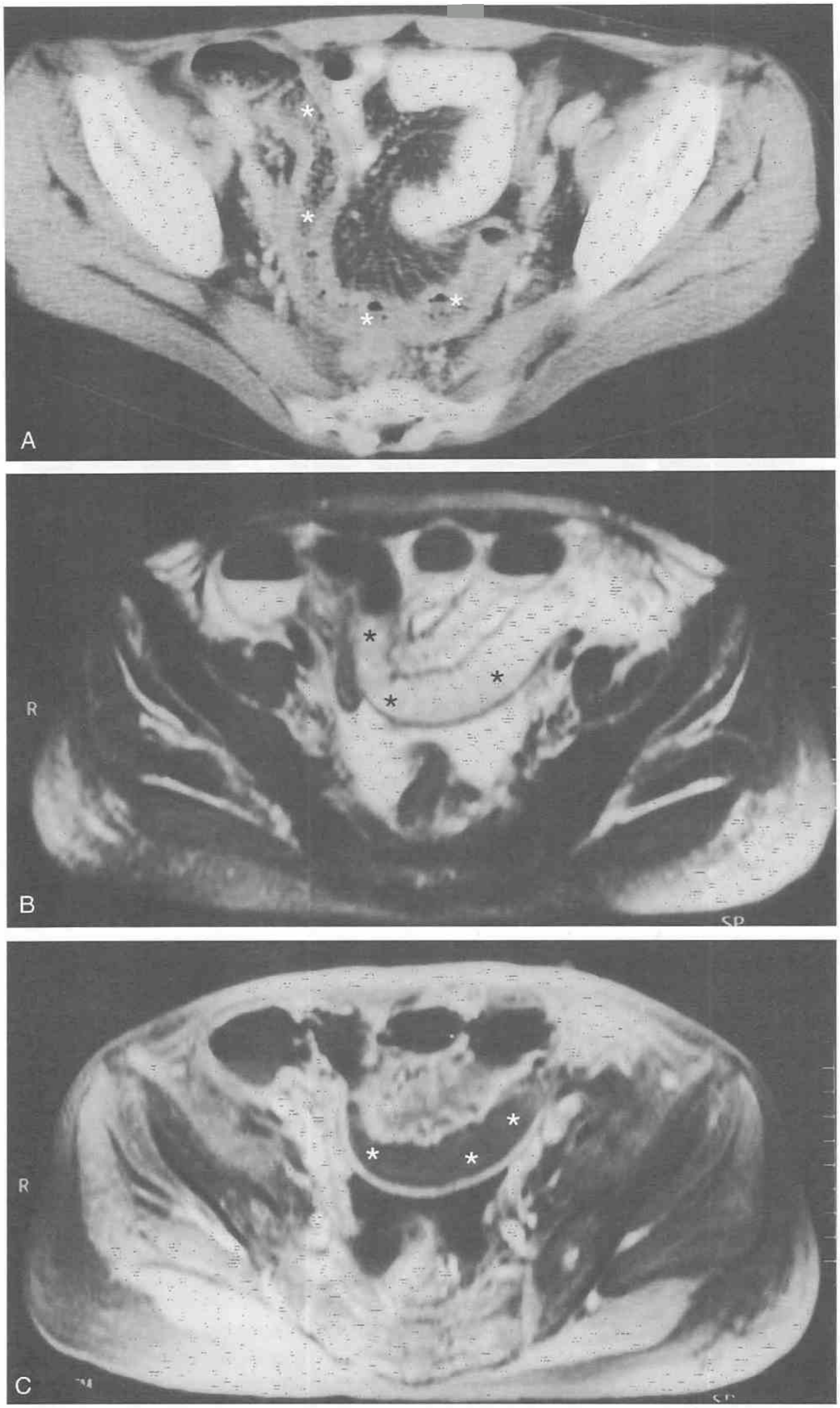

Figure 34–109. Graft-versus-host disease in a patient with bone marrow transplantation. *A*, CT scan shows diffuse thickening *(asterisks)* of the ileum. *B*, Axial T2-weighted half-Fourier acquisition single-shot turbo spin-echo (HASTE) MR image shows thickened ileal wall *(asterisks)* with ascites in the pelvic cavity. *C*, Axial gadolinium-enhanced MR image shows a well-enhancing, thickened wall in the ileum *(asterisks)*.

plantation.[150] Its incidence ranges from 30% to 60% of patients. As the number of long-term survivors increases, chronic GVHD has emerged as an increasingly frequent complication of allogeneic marrow transplantation. The clinicopathologic features resemble an overlap of several collagen vascular diseases with frequent involvement of the skin, liver, eyes, mouth, upper respiratory tract, and esophagus and less frequent involvement of the serosal surfaces and lower GI tract.[150, 542] In chronic GVHD, the distribution and histopathology of the lesions in the intesti-

nal tract differ from those of the acute form, particularly with regard to the esophagus. Esophageal involvement causes a characteristic desquamation of upper esophageal mucosa.[542] The small bowel and colonic mucosa seem to be spared in chronic GVHD.[150, 542]

Post-transplantation Lymphoproliferative Disorders

Post-transplantation lymphoproliferative disorders (PTLDs) are an uncommon but persistent complication of solid organ transplantation. When a primary infection with Epstein-Barr virus (EBV) occurs in an immunocompetent host, a transient lymphoproliferative disorder occurs. This proliferation of infected B lymphocytes is controlled by cytotoxic and suppressive T lymphocytes. When the infected host is immunodeficient, the proliferation of B cells may not be controlled and EBV-induced PTLD can occur.[423] It includes a spectrum of disease ranging from polyclonal B-cell hyperplasia to monoclonal B-cell lymphoma.

The reported incidence of PTLD varies from 12% in pancreas transplant recipients, to 9% in heart and lung transplant recipients, and to 1% to 2% in renal and liver transplant recipients.[357, 482] Early diagnosis of PTLD is important because reduction or cessation of immunosuppression results in tumor regression. The anatomic region of the transplant organ was the most common site of involvement in lung and liver transplant recipients.[463]

According to a series that analyzed 51 patients with PTLD,[463] CT manifestations of non-Hodgkin's lymphoma occurring in the general population and PTLD in transplant recipients demonstrated important differences. The most striking distinction was the relatively high frequency of extranodal disease (81%) and lower frequency of nodular disease (22%) in patients with PTLD; in contrast, extranodular disease occurred in approximately 25% of nonimmunosuppressed patients with non-Hodgkin's lymphoma.[55]

On CT, PTLD is similar in appearance to those of non-Hodgkin's lymphoma when solid abdominal organs and hollow viscus are involved (Fig. 34–110). The most common sites of involvement are the liver, small bowel, and kidney, but virtually any organ or space within the abdomen and pelvis can be affected. Although the CT appearance of GI involvement in PTLD mimics that of lymphoma, PTLD has a propensity for ulceration and perforation of the alimentary tract.[462]

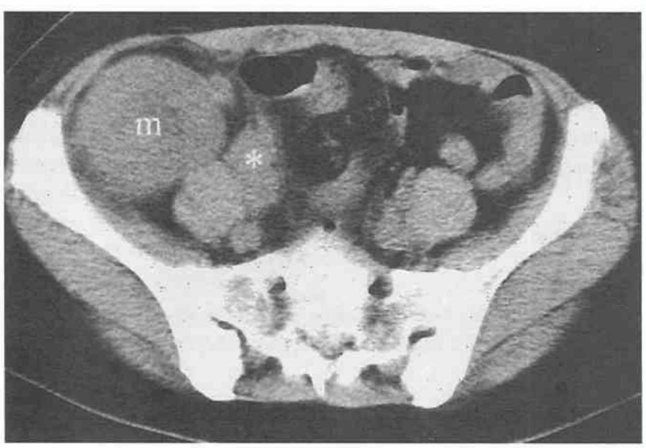

Figure 34–110. Post-transplantation lymphoproliferative disorder. Unenhanced CT scan shows an ill-defined mass in the transplanted kidney (m), which appeared as a heterogeneous mass lesion on ultrasound examination. Another mass *(asterisk)* is noted along the ureteral course.

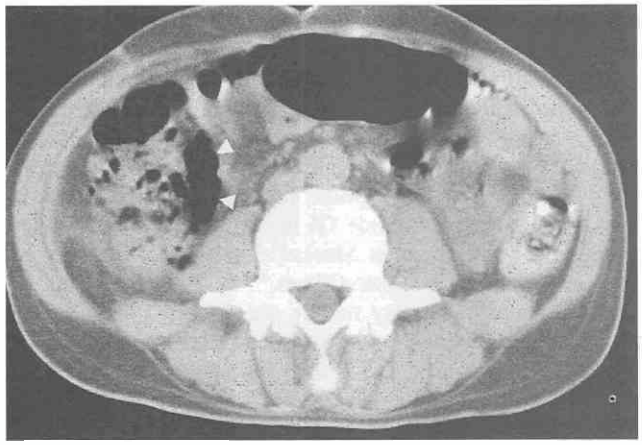

Figure 34–111. Pneumatosis *(arrowheads)* in the right-sided colonic wall after renal transplantation. The patient showed no clinical signs or symptoms of bowel necrosis.

Pneumatosis Intestinalis

Pneumatosis intestinalis can develop after transplantation. Contributing factors include mucosal damage from pretransplantation chemotherapy and radiation therapy, steroid therapy, acute GVHD, infectious colitis, small-bowel obstruction, and severe humoral and cellular immunodeficiency.[113] Day and colleagues[113] reported on 18 patients with pneumatosis after bone marrow transplantation. The colon, predominantly the right side, was involved in 17 of 18 cases. Seven of these patients died within 2 weeks after detection of pneumatosis and 1 needed hemicolectomy, whereas the remaining 10 responded well to the conservative treatment. Therefore, in the clinical context of systemic infection or shock, the finding of pneumatosis may be a poor prognostic sign (Fig. 34–111); if it is identified in asymptomatic patients, however, it is probably of little clinical significance.

Diverticular Diseases

Small-bowel diverticula are either congenital or acquired. A congenital diverticulum contains all three intestinal wall layers, usually as a Meckel's diverticulum located on the antimesenteric aspect of the ileum 30 to 60 cm from the ileocecal valve. Acquired diverticula have only mucosal and submucosal layers that herniate through the muscular and serosal layers; they occur at the mesenteric border, in contrast with the true congenital Meckel's diverticulum.

Jejunal diverticula are found twice as frequently in men than in women and occur almost exclusively in persons older than 40 years of age.[368] Diverticula tend to be larger and higher in number in the proximal jejunum and smaller

and fewer as one progresses caudally.[368] An exception is the terminal ileum, where the diverticula are often multiple.

Acute complications of congenital or acquired diverticula include diverticulitis, with or without abscess or perforation, massive GI hemorrhage, and intestinal obstruction.[115] Chronic symptomatology includes chronic abdominal pain, malabsorption, functional pseudo-obstruction, and chronic low-grade GI hemorrhage. Various types of neoplasm can occur in Meckel's diverticulum owing to the presence of heterotopic tissues.[611]

Small diverticula may not be recognized on CT scans because distinguishing between diverticula and bowel loops is usually impossible. CT findings that may be useful in identifying small-bowel diverticula include (1) large size of the diverticulum (>3 cm), (2) different contents of the diverticulum and adjacent small-bowel loops, and (3) absence of valvulae conniventes.[92]

Intestinal obstruction may occur as a result of pressure on the intestinal wall from distended diverticula, an inflammatory mass associated with diverticulitis, stricture or adhesions from recent or past diverticulitis, intussusception at the site of the diverticulum, enteroliths developed within the diverticula, or volvulus of the diverticula-containing segment.[33, 92] On CT scans, the presence of diverticulitis may mimic many other conditions, such as abdominal abscess associated with appendicitis or inflammatory bowel disease, perforated colon cancer, and perforated right-sided colonic diverticulitis. However, diverticulitis can be suggested when an inflammatory mass containing air or oral contrast material with edema of the adjacent mesentery is detected in an unusual location, distant from the area of the ileocecal valve, and from the sigmoid colon (Fig. 34–112); contrast material within a diverticulum may remain for several days after the CT scanning has been completed.

Endometriosis

Endometriosis is a common disease characterized by the presence of ectopic endometrial tissue in an extramyometrial site. About 10% to 15% of women in their reproductive years are affected.

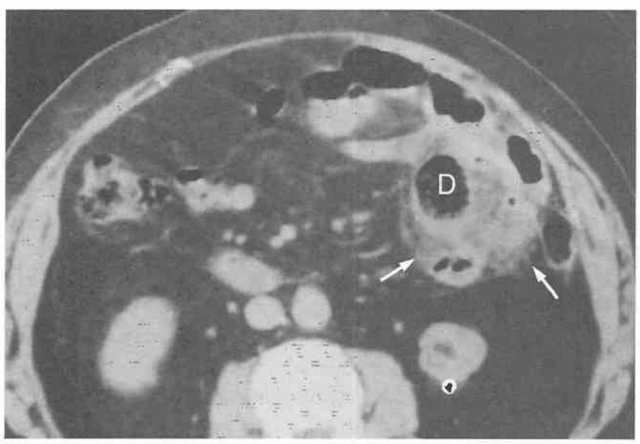

Figure 34–112. Jejunal diverticulitis. CT scan shows diverticular abscess (D) and diffuse perienteric haziness and infiltrates *(arrows)*. (Courtesy of K. C. Cho, Newark, New Jersey.)

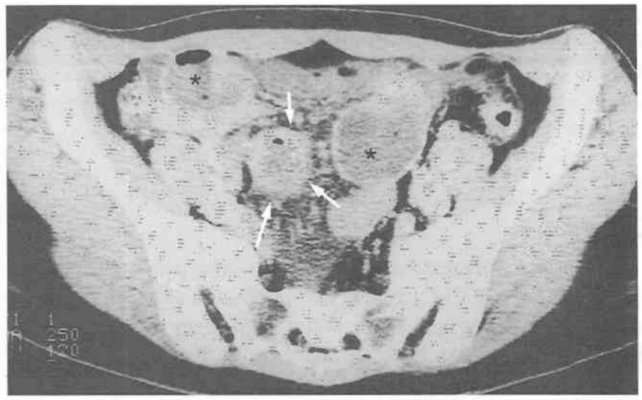

Figure 34–113. Small-bowel obstruction caused by endometrial implantation on the ileal loop. The small-bowel loop is dilated *(asterisks)* with mild bowel wall thickening *(arrows)*. Diffuse granular infiltrates are noted in the perienteric fat plane.

The most commonly accepted theory of pathogenesis is transtubal reflux with peritoneal implantation.[141] Alternatively, extrauterine growth of endometriotic tissue can occur as a result of metaplastic transformation of pluripotential peritoneal mesothelium.[141] GI tract lesions have been found in about 12% of patients with endometriosis, and 85% of these lesions involved the rectosigmoid, 7% the small bowel, 3% the cecum, and 3% the appendix.[362] Ileal endometriosis most often involves the terminal ileum within 10 cm of the ileocecal valve.[401] Endometriotic implants can also affect the proximal ileum or even the jejunum as far proximally as 30 cm from the duodenojejunal junction.

Small-bowel endometriosis may present as cyclic episodes of abdominal pain coinciding with the menstrual cycle, nausea and vomiting, diarrhea, or constipation; however, classic symptoms are seen in only 18% to 40% of patients.[410] Occasionally, this disease may result in acute, chronic, or intermittent small-bowel obstruction by kinking, stenosis, volvulus, or intussusception (Fig. 34–113).[217]

The common radiographic findings include extrinsic mass effect with variable spiculation and tethering of folds.[427] Endometrial implants may also present as short annular or plaquelike lesions.[427] Muscular hypertrophy and fibrotic reaction may be responsible for the narrowing, tethering, or spiculation of the ileum on barium studies.[427] Although colonic involvement commonly coexists, ileal endometriosis can occur in the absence of colonic disease.

Hernias

Abdominal hernias remain a common problem for both clinicians and radiologists. The main types of abdominal hernias are:

- External, or abdominal wall, hernias
- Internal hernias
- Diaphragmatic hernias

In the past, the diagnosis of a hernia was made clinically either with plain radiographs or with barium studies. Currently, specific diagnoses are confirmed more frequently

by CT, especially in patients with nonspecific abdominal complaints. In addition to revealing the anatomic location and type of hernia, CT may provide information regarding the contents and complications of the hernia.

External Hernias

Abdominal wall hernias account for most external hernias and include inguinal, femoral, umbilical, spigelian, and incisional types; rare forms include lumbar and obturator hernias. All abdominal wall hernias consist of a peritoneal sac that protrudes through a weakness or defect in the muscular layers of the abdomen. Abdominal contents may include properitoneal fat, greater omentum, and viscera. Weakness in the transversalis fascia is the main source of predilection for abdominal wall hernia, especially in the groin. Trauma is a rare cause of these hernias.

Inguinal Hernias

Inguinal hernias are either *indirect* or *direct*, depending on their relationship to the inferior epigastric vessels.

In patients with an indirect hernia, the peritoneal sac passes down the course of the inguinal canal anterior to the spermatic cord and lateral to the inferior epigastric vessels. In women, the hernia sac follows the course of the round ligament into the labium. The sac usually contains omentum and small bowel and, occasionally, ascites.

A direct hernia is almost always acquired rather than congenital. The neck of the hernia is medial to the inferior epigastric vessels and generally does not traverse the inguinal canal. Therefore, bowel strangulation is seldom a complication because of the blunt and diffuse character of the protrusion. CT and MRI define the relationship of the inferior epigastric vessels to the hernia sac.

Femoral Hernias

Femoral hernias are far less common than inguinal hernias. They are seldom seen in children and are more common in women. They occur below the inguinal ligament and lateral to the femoral vessels. Bowel strangulation is common.

The diagnosis is easily made by CT. A femoral hernia may be distinguished from an inguinal hernia on CT because its sac lies below and lateral to the pubic tubercle as it emerges from the femoral canal. Conversely, an inguinal hernia lies above and medial to the tubercle.[596]

Incisional Hernias

Incisional hernias are a complication of laparotomy. Most of these hernias develop during the first 4 months after surgery but may remain clinically silent for up to 5 years until their detection.[136] Vertical incisions are thought to be more likely to result in an incisional hernia than are transverse incisions. Incisional hernias can be seen with incisions as small as a puncture site for laparoscopic surgery.[524]

A common variation is the *parastomal hernia*, in which bowel and omental fat protrude through a fascial defect immediately adjacent to a colostomy or ileostomy stoma. This type has been reported to occur in as many as 36% of patients with an ileostomy.[138] If the hernia is left untreated, bowel loops may be incorporated into the hernia and may become incarcerated or strangulated. CT demonstrates the abdominal wall defects and the hernial contents as well as signs of bowel ischemia (Fig. 34–114).

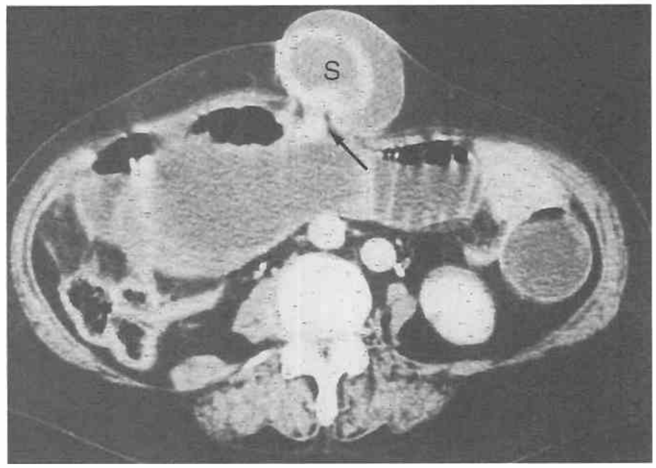

Figure 34–114. Incisional external hernia with intestinal strangulation. CT scan shows marked enhancement of a small-bowel loop (S) herniated in the hernia sac along with a narrowed hernia neck *(arrows)*. Fluid collection is present in the hernia sac.

Richter's Hernias

Richter's hernia is an uncommon type of hernia in which only part of the bowel wall becomes involved. Because only a portion of the intestinal wall is incorporated into the hernia, the lumen remains patent and there is no obstruction. Incarceration is uncommon.

Spigelian Hernias

Spigelian hernias occur at a weak point along the lateral border of the rectus muscle at a midpoint between the umbilicus and symphysis pubis. Although rare, they have a high frequency of bowel incarceration and strangulation.

On CT scans, a hernia sac protruding through the linear semilunaris and containing bowel or fat is identified. If it contains only peritoneal fat, it can be mistaken for an abdominal wall lipoma.[596] However, careful inspection of the images reveals the muscular defect at the linear semilunaris (Figs. 34–115 and 34–116).

Obturator Hernias

Obturator hernias protrude through the obturator foramen alongside the obturator vessels. They occur most often in thin, elderly women. About one third of patients have neuralgia involving the thigh as a result of compression of the obturator nerve in the obturator canal.[105]

The diagnosis is made by the presence of herniated bowel protruding through the obturator canal on CT scans or MR images.

Internal Hernias

Internal hernias are the result of herniation of a viscus through a normal or abnormal aperture within the confines of the peritoneal cavity. Hernias that arise when bowel

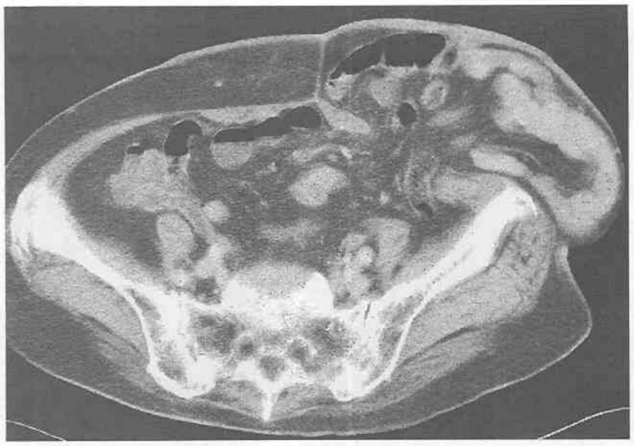

Figure 34–115. Spigelian hernia. CT scan shows herniation of the mesentery and small-bowel loop into the sac.

herniates through the mesentery or peritoneum do not have a hernia sac. Paraduodenal hernias account for approximately 50% of all internal hernias. Other internal hernias include pericecal, intersigmoid, transmesenteric, and retroanastomotic hernias and herniation through the foramen of Winslow.

Paraduodenal Hernias

Paraduodenal hernias are the most common type of internal hernia. They frequently present with acute intestinal obstruction but may also cause chronic intermittent postprandial abdominal pain. A right paraduodenal hernia results from incomplete rotation of the duodenum during development. They usually contain only small bowel. The anterior wall of the sac comprises transverse colon and mesentery of the ascending colon. The entrance into the hernia sac is most commonly via the mesentericoparietal fossa of Waldeyer, which is in the first part of the jejunal mesentery immediately behind the superior mesenteric artery (SMA) and inferior to the third part of the duodenum.[41, 406]

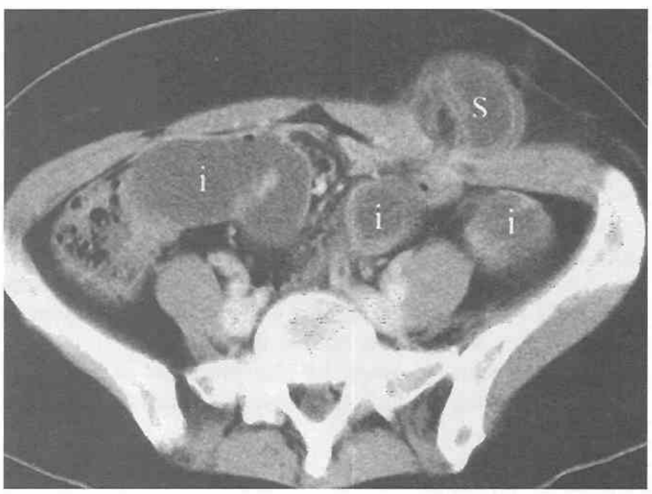

Figure 34–116. Incarcerated spigelian hernia. CT scan shows bowel thickening, with the "target sign" in the small-bowel loop (S) herniated into the hernia sac, along with diffuse small-bowel dilatation (i) caused by obstruction.

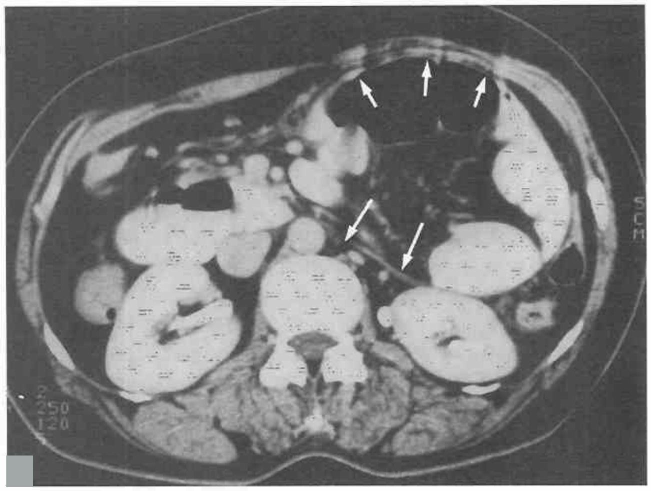

Figure 34–117. Left paraduodenal hernia. The jejunal loops are enveloped by thin capsule of the mesentery *(arrows)*, located at the subperitoneal space.

On CT, right paraduodenal hernias show a retroperitoneal mass, comprising an encapsulated cluster of dilated small-bowel loops, and displacing the right ureter (Fig. 34–117). The SMA and branches of the ileocolic artery are found in the anterior wall of the hernia. Left paraduodenal hernias also involve an anomaly of gut rotation. The bowel becomes entrapped behind the descending mesocolon in a hernia sac created by the fossa of Landzert.

CT may show an abnormal cluster of normal caliber or dilated bowel loops in an abnormal position either behind the body of the pancreas or between stomach and body of pancreas.[112, 453] The inferior mesenteric vein and ascending left colic artery are located at the anteromedial border of a left paraduodenal hernia.

Herniation through the Foramen of Winslow into the Lesser Sac

Herniation through the foramen of Winslow into the lesser sac may contain small-bowel loops, cecum, ascending and transverse colon, gallbladder, and omentum. CT findings include gas-containing bowel loops within the lesser sac medial and posterior to the stomach (Fig. 34–118). The cecum and ascending colon may be absent from their usual location if they are part of the herniated viscera.

Intussusception

Intussusception is the most common cause of intestinal tract obstruction occurring in young children, but it is relatively uncommon in adults; 5% of all intussusceptions occur in adults, and it accounts for up to 5% of all cases of bowel obstruction in adults.[37] In contrast with childhood intussusception, which is idiopathic in 90% of cases, adult intussusception has a demonstrable cause in more than 90% of cases.[37] As the intussusceptum enters into the intussuscipiens, the mesentery is carried forward and is trapped between the overlapping layers of bowel. Twisting

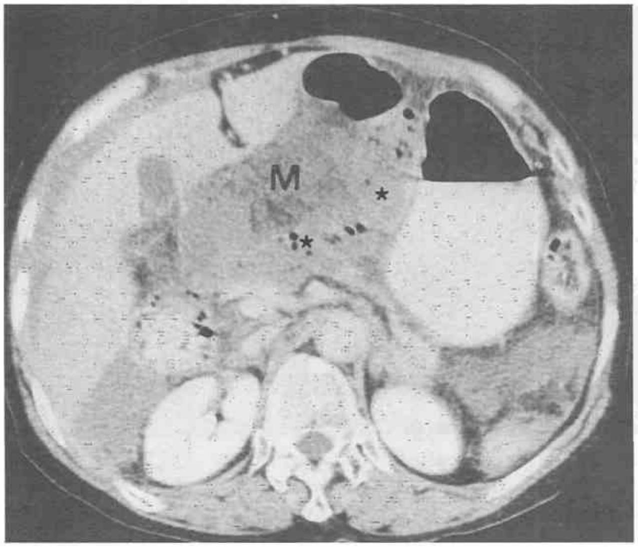

Figure 34–118. Internal (lesser sac) hernia with strangulated small-bowel obstruction. The dilated small-bowel loops *(asterisks)*, herniated in the lesser sac, are poorly enhanced because of intestinal strangulation. Diffuse regional mesenteric haziness (M) is also present. (From Ha HK, Kim HS, Lee MS, et al: Differentiation of simple and strangulated small bowel obstructions: Usefulness of known CT criteria. Radiology 204:507–512, 1997.)

or severe constriction of the mesenteric vessels may result in vascular compromise with subsequent edematous thickening of the involved bowel. Ischemic necrosis may develop if timely intervention is not undertaken.[249]

Intussusceptions may be *enteroenteric*, *ileocolic*, or *colocolic* types.

In general, most lead points in the *enteroenteric* intussusceptions are benign, including benign neoplasms, Meckel's diverticula, adhesions, lymphoid hyperplasia and adenitis, trauma, celiac disease, duplications, and inflammatory lesions; small-bowel malignancy (either primary or metastatic) may account for 6% to 30% of cases. Eight percent to 20% of enteroenteric intussusceptions may be idiopathic,[557] and transient nonobstructing enteric cases associated with physiologic status have also been reported.[594]

Colocolic intussusception is more likely to have a malignant etiology. Postoperative intussusception in adults has been also recognized as a distinct entity and may be related to a variety of predisposing factors, such as suture lines, oversewn ileum in jejunoileal bypass, previous jejunostomy site, adhesions, submucosal bowel edema, intestinal dysmotility, long intestinal tubes, and chronic bowel dilation.[4] The intussusceptions in patients with AIDS are generally ileum-based and may occur from lymphoma, atypical mycobacterial infection, or other unusual inflammatory process.[74] Presenting signs and symptoms of intussusception include recurrent intestinal obstruction, intermittent abdominal cramps, and rectal bleeding.

The diagnosis of intussusception is easily made by CT and MRI. The imaging appearance of a bowel-within-bowel configuration with or without contained fat and mesenteric vessels is pathognomonic (Fig. 34–119).[594] Depending on their orientation to the scanning axis, they may appear either as a round target-shaped mass or as an oblong

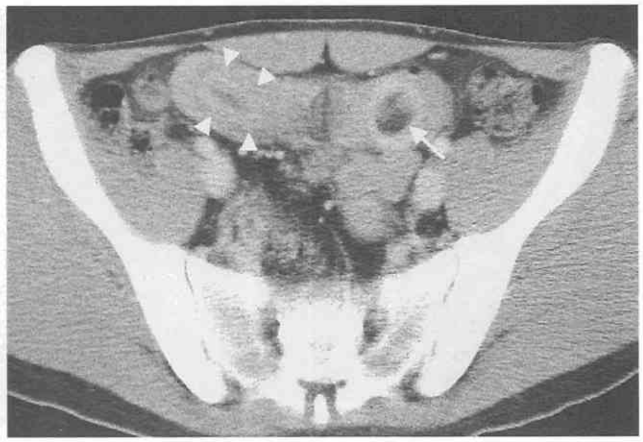

Figure 34–119. Ileal lipoma with intussusception. CT scan shows a "bowel-within-bowel" appearance *(arrowheads)*. A lipomatous mass *(arrow)* can be seen at the leading point.

sausage-shaped mass. The thick outer rim of soft tissue density represents the edematous wall of the intussusceptum with some contribution from bowel wall of the intussuscipiens.

Although CT and MRI are sensitive in detecting the intussusception, morphologic analysis of the lead point may not provide the clue for determining their primary cause in many instances, except for the cases of lipoma. According to a series by Warshauer and Lee,[594] enteroenteric intussusceptions caused by non-neoplastic lesions were shorter in length, smaller in diameter, and less likely to be associated with obstruction; no neoplastic enteric intussusceptions were shorter than 3.6 cm or smaller than 3.4 cm in diameter.

The determination of the presence or absence of intestinal necrosis in intussusception is important in patient management. On CT, the presence of severe engorgement or twisting (whirl sign) of the mesenteric vessels as well as evidence of loss of layered pattern, extraluminal fluid collection, and bowel perforation may suggest the diagnosis of intestinal necrosis (Fig. 34–120).[253, 260] The bowel necrosis may be confined to only intussuscepted segment or can extend to longer segment of the bowel.

Small-Bowel Obstruction

Small-bowel obstruction may be caused by several primary causes. According to degree, they may be *complete* or *high-grade partial obstructions* or *low-grade partial obstructions*. The diagnosis is usually made on the basis of clinical signs and patient's history. However, because the clinical symptoms and signs are often nonspecific, radiologic studies (e.g., plain radiograph and barium studies) are considered essential for a diagnosis. Nevertheless, plain radiographic study is diagnostic in only 46% to 80% of cases with common occurrence of false-positive and false-negative interpretations; up to 20% of patients may have no radiographic evidence of obstruction.[59, 166]

Although barium studies are the standard of reference in diagnosing and characterizing the intestinal obstruction, the results of these studies are sometimes mixed. Further-

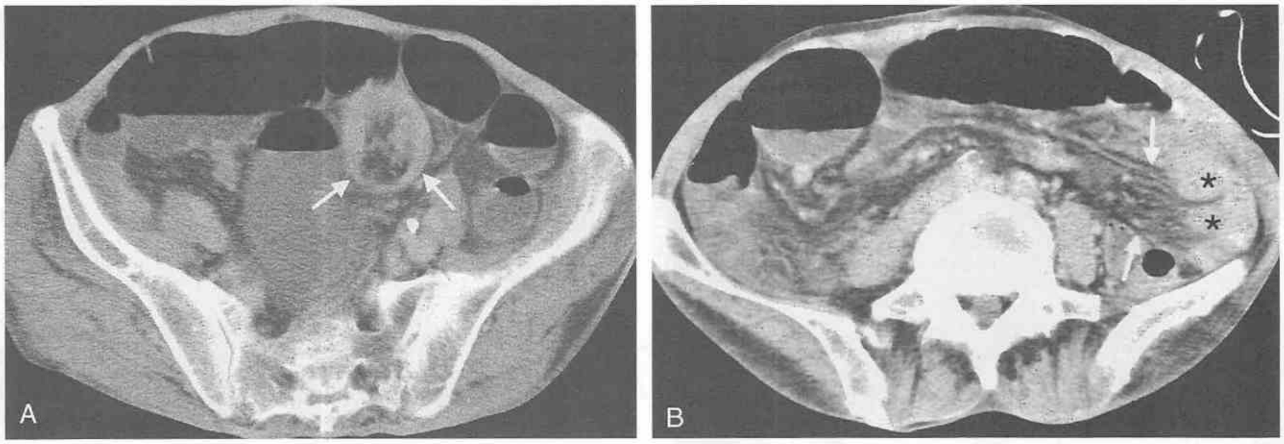

Figure 34–120. Intussusception with vascular compromise in a patient who underwent gastrectomy 1 year before. *A,* CT scan shows a heterogeneous mass *(arrows)* caused by invagination of the mesentery. *B,* CT scan at another level shows diffuse haziness and mesenteric vascular prominence *(arrows)* along with suspected bowel wall thickening *(asterisks)* in the loops proximal to the obstruction. At surgery, intestinal strangulation was noted in the small-bowel loops proximal to the intussuscepted site. Bowel adhesion was considered to be the primary cause of intussusception.

more, contrast studies are limited in the evaluation of changes in the peritoneal cavity and abdominal solid organs, may interfere with further diagnostic work-up, such as CT or ultrasonography, and may be misleading, especially when a contrast agent passes into the colon through a high-grade partial obstruction.

CT has been widely used for patients who were thought to have small-bowel obstruction because it is simple to perform and provides information about the site and cause of obstruction, the bowel wall and extraluminal changes, and the presence or absence of intestinal strangulation. With more experience, however, certain limitations are also identified in this examination.

Because of its multiplanar imaging capability and recent advances in technology, MRI can be used to evaluate small-bowel obstruction, especially in patients whose bowel is filled with residual barium suspension after barium study, who have hypersensitivity to the IV contrast material, or who are pregnant. In most instances, coronal MR images are more useful than axial images in searching for an obstructed site because they produce images comparable to those of small-bowel follow-through (Fig. 34–121). More-

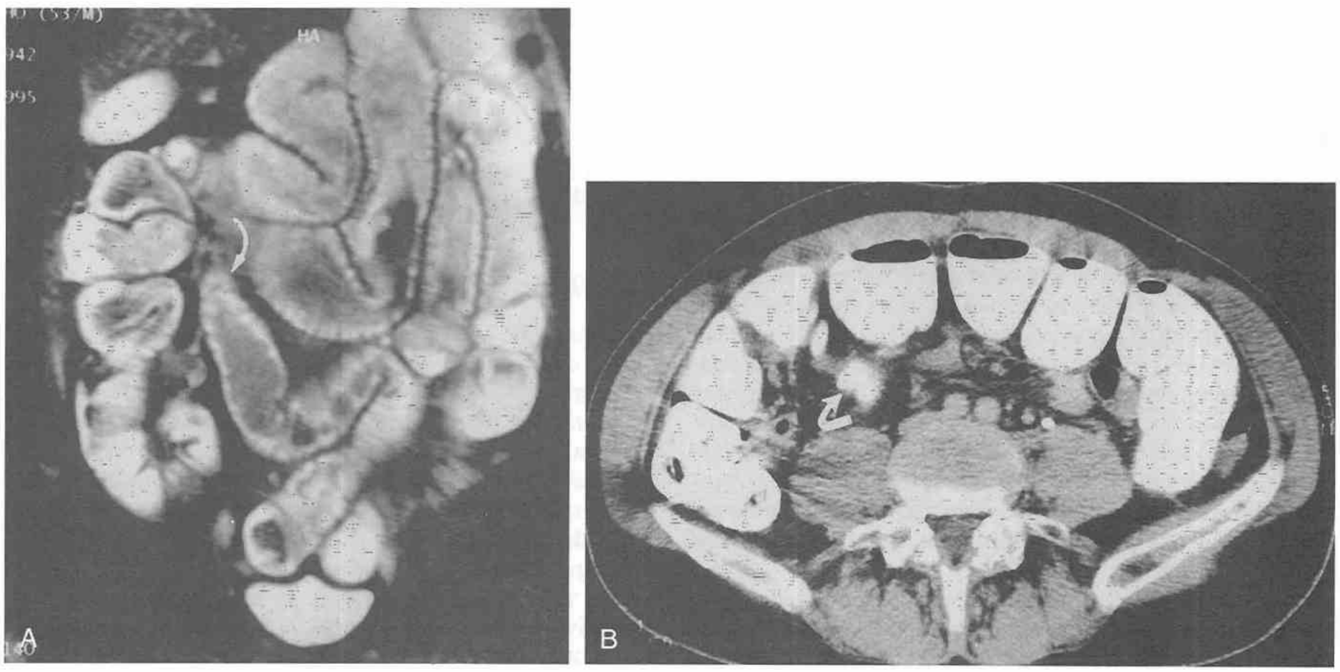

Figure 34–121. Simple intestinal obstruction caused by bowel adhesion. *A,* Coronal half-Fourier acquisition single-shot turbo spin-echo (HASTE) MR image shows diffuse small-intestinal loop dilatation with tapered luminal narrowing at the obstructed site *(arrow)*. *B,* CT scan shows end-on view of a narrowed intestinal segment *(arrow)* just above the obstructed site.

over, in equivocal cases, more detailed examination of the obstructed site or loops can be made with the help of multiplanar reconstruction or 3D reformatted images (see Fig. 34–98*B*). Therefore, in such patients it is important to obtain the images without an interslice gap.[210]

For determining the primary causes of small-bowel obstruction, MRI may be equal to or superior to CT. However, both MR and CT appear to have difficulty in determining the primary causes of obstruction when a short segmental stricture is present.

Complete or High-Grade Partial Obstruction

The CT diagnosis of bowel obstruction is based on the detection of a transition zone, dilated fluid or air-filled loops of small bowel proximal to the site of obstruction, and collapsed loops of small bowel or colon distal to the obstructed site. The bowel dilatation is indicated when the luminal diameter exceeds 2.5 cm[172] and should be continuous.[177]

Although CT is usually useful for evaluating high-grade obstruction, the transition zone is sometimes difficult to detect. In these circumstances, use of thin-section CT may be helpful not only to determine the level of obstruction but also to reveal their causes. The presence or absence of colonic fluid or gas is also used to distinguish paralytic ileus from small-bowel obstruction. In patients with high-grade small-bowel obstruction, the sensitivity of CT in diagnosis ranges between 81% and 100%.[166, 367]

Low-Grade Partial Obstruction

The presence of low-grade partial small-bowel obstruction is considered to be present on CT when small-bowel loops are mildly dilated with ill-defined transition zone, incomplete collapse of the distal bowel, and moderate colonic fluid and gas.[166] The diagnosis can be easily misinterpreted as paralytic ileus. Furthermore, because the transition zone is difficult to detect, CT has limitation in determining the level and cause of obstruction. Therefore, small-bowel follow-through or enteroclysis may be necessary for further evaluating patients with suspected low-grade small-bowel obstruction. In contrast to high-grade small-bowel obstruction, the sensitivity of CT in diagnosis of low-grade obstruction is not high (48%).[367] The occurrence of intestinal strangulation is rare in these patients.

Simple Small-Bowel Obstruction

Typical cases of simple obstruction may show diffuse bowel loop dilatation with a smooth transition zone or a smooth "beak" at the obstructed site on CT (Fig. 34–122). The bowel wall at the site of obstruction may be minimally thickened or of normal thickness. Mesenteric changes, such as vascular engorgement and haziness, are absent or minimal, and ascites is either absent or minimal (Fig. 34–123). However, the presence of such findings does not always indicate simple obstruction because these changes can also be seen in some patients with strangulated obstruction.

Closed-Loop Obstruction

Most cases of strangulated obstruction are related to closed-loop obstruction. Contrast radiography has no role in the acute clinical setting, but its value is in the further work-up of partial obstruction in the subacute or chronic setting when CT cannot answer questions relevant to management.[369] The most important CT indicators may include the whirl sign, convergence of mesenteric vessels toward the twisted site, and reversed position of the mesenteric artery and vein (Fig. 34–124)[204]; the whirl sign, however, is also seen in asymptomatic subjects.

Balthazar and coworkers[20] described additional signs of U-shaped or C-shaped configuration of dilated bowel loops and two adjacent collapsed, round, oval, or triangular loops with an "arrowhead" configuration. The *serrated beak sign* (Fig. 34–125), described by Ha and associates,[214] also indicates the presence of a closed loop associated with regional mesenteric vascular engorgement as well as bowel

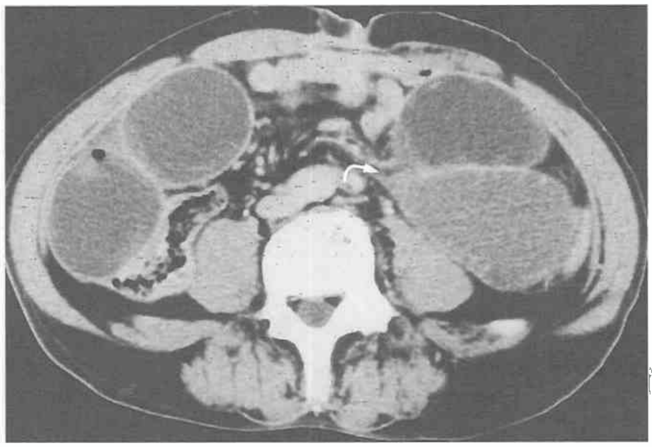

Figure 34–122. Simple small-bowel obstruction caused by adhesion and bands. CT scan shows diffuse dilatation of the small intestine with a smooth beak *(arrow)* at the site of obstruction. (From Ha HK, Rha SE, Kim JH, et al: CT diagnosis of strangulation in patients with small bowel obstruction: Current status and future direction. Emerg Radiol 2:47–55, 2000.)

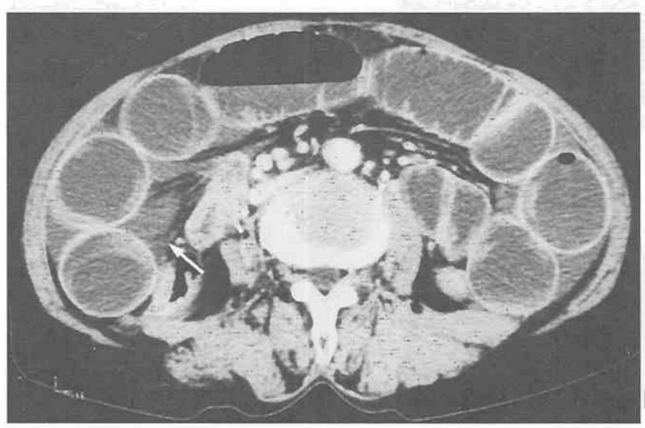

Figure 34–123. Simple small-bowel obstruction. CT scan shows diffuse dilatation of small-intestinal loops with ascites. Accumulated fluid collection *(arrow)* between the mesenteric layers mimics mesenteric haziness. (From Ha HK, Rha SE, Kim JH, et al: CT diagnosis of strangulation in patients with small bowel obstruction: Current status and future direction. Emerg Radiol 2: 47–55, 2000.)

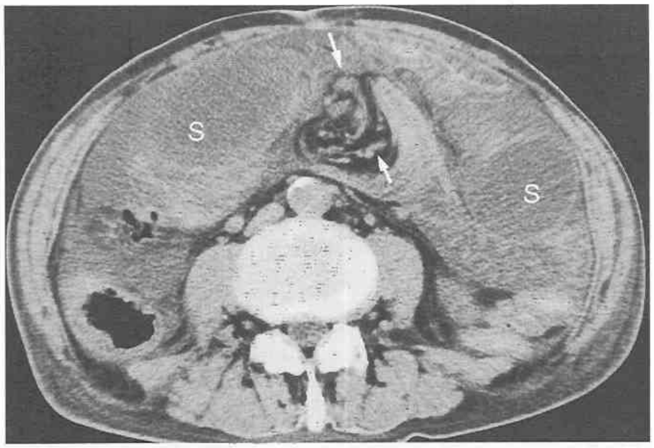

Figure 34–124. Closed-loop obstruction due to volvulus. CT scan shows twisting and engorgement of the mesenteric vessels ("whirl sign") *(arrows)* adjacent to the obstructed site. Note diffuse dilatation of the small intestine (S) and intraperitoneal fluid collection *(asterisks)*. At surgery, strangulation was present in the involved segment. (From Ha HK, Rha SE, Kim JH, et al: CT diagnosis of strangulation in patients with small bowel obstruction: Current status and future direction. Emerg Radiol 2: 47–55, 2000.)

wall thickening at the obstructed bowel; this sign also suggests strangulated obstruction.

Strangulated Small-Bowel Obstruction

Strangulation implies interference with the blood supply associated with an obstruction that may not necessarily be complete. In most instances, it occurs as a complication of intussusception, torsion, volvulus, or any other form of closed-loop obstruction. Interference with the blood supply may occur either from twisting of the bowel on the mesentery or from distention of an obstructed closed loop.

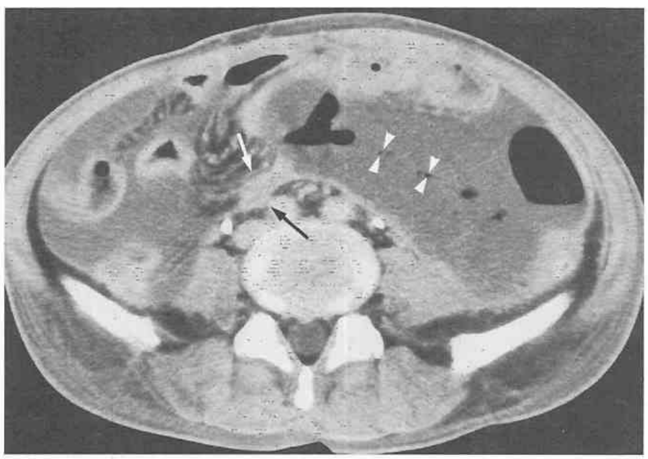

Figure 34–125. Strangulated small-bowel obstruction due to adhesions. CT scan shows a serrated beak *(arrows)* in the bowel loop at the site of obstruction. The bowel wall *(arrowheads)* in the strangulated segment has lost its definition. A large amount of ascites is present. (From Ha HK: CT in the early detection of strangulation in intestinal obstruction. Semin Ultrasound CT MRI 16:141–150, 1995.)

The incidence of strangulation is more than 40% in complete or high-grade obstruction[520] but may be less than 10% in low-grade obstruction.[47] Some researchers[139] distinguish between long, medium (8 to 20 inches), and short-loop strangulated obstructions as follows:

1. Long strangulated loops tend to cause death by sequestration of large quantities of plasma and blood from circulation.
2. Medium loops tend to cause shock and death by the formation of exotoxins of *Clostridium welchii*.
3. Short loops tend to perforate and cause peritonitis.

With prompt surgical intervention, the strangulating element may be removed before gangrene of the intestine ensues.

The sensitivity of CT in detecting the strangulated obstruction has been reported to range from 83% to 100% in the literature.[23, 165, 208] The proposed well-known diagnostic CT criteria for strangulated obstruction are as follows:

1. Portal or mesenteric venous gas, pneumatosis intestinalis.
2. Abnormal bowel wall enhancement.
3. Serrated beak sign.
4. Unusual mesenteric vascular course.
5. Diffuse mesenteric vascular engorgement and haziness.
6. Bowel wall thickening.
7. A large amount of ascites.

Although these CT criteria are useful in the diagnosis of intestinal strangulation, most of them, when used alone, are not sufficiently sensitive indicators of simple or strangulated obstruction. Furthermore, some of these findings are also noted in cases of simple intestinal obstruction. Therefore, use of a combination of highly specific findings may increase the diagnostic accuracy of CT in detecting strangulation. In addition, the importance of clinical criteria (abdominal tenderness, tachycardia, fever, and leukocytosis) should not be overlooked. In equivocal cases demonstrated by CT, the presence of none or one of the four clinical criteria had higher chance to have simple obstruction and the patients with three or all to have strangulated obstruction; the presence of two criteria did not help in distinction of strangulated and simple obstruction.

Portal or Mesenteric Venous Gas or Pneumatosis Intestinalis. Of the various findings reported, portal or mesenteric venous gas and pneumatosis intestinalis (Fig. 34–126) are perhaps the most specific signs[6, 146] and are representative of bowel gangrene. However, the incidence of these signs is very low[6, 208]; pneumatosis was noted in only one of the 19 patients in one series[6] and was not found in any of the 41 patients in another series.[208] Furthermore, some reports suggest that these findings are not always indicative of intestinal strangulation.[165, 566]

Abnormal Bowel Wall Enhancement. Absent or poor contrast enhancement in the bowel wall is also an important finding for identifying intestinal strangulation with a sensitivity of 34% and a specificity of 100% (see Figs. 34–125 and 34–126).[208] This finding in strangulated segments may be attributable mainly to a perfusion phenomenon, that is, delayed return of the venous blood with

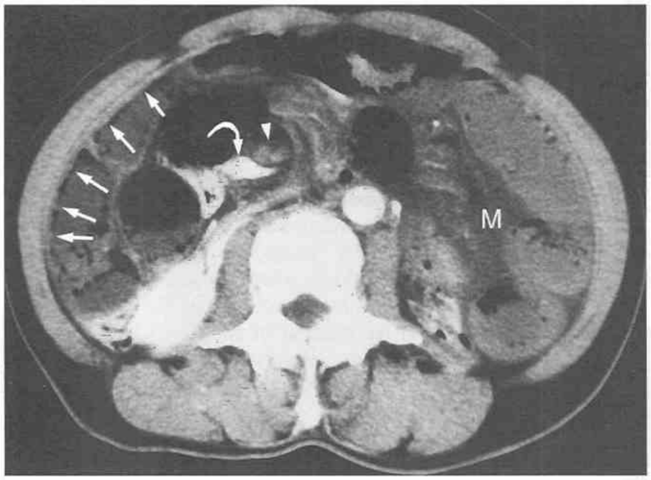

Figure 34–126. Strangulated small-bowel obstruction caus[redacted]y bands and adhesion. Early phase of the spiral CT scan shows pneumatosis *(arrows)* and poor contrast enhancement in the strangulated segment of the small-intestinal loops. At the site just proximal to the obstruction, the superior mesenteric artery *(arrowheads)* is poorly opacified with contrast material as compared with the well-opacified superior mesenteric vein *(curved arrow)*. Diffuse mesenteric haziness (M) is also noted. (From Ha HK, Rha SE, Kim JH, et al: CT diagnosis of strangulation in patients with small bowel obstruction: Current status and future direction. Emerg Radiol 2:47–55, 2000.)

subsequent slowing of the arterial supply or arteriospasm. Delayed enhancement may be observed in the strangulated segments in which early-phase spiral CT shows poor contrast enhancement (Fig. 34–127).[621]

The most reliable method of determining whether abnormally enhancing bowel is present is to compare adjacent bowel loops. Because of the importance of analyzing the contrast enhancement pattern, it is better to avoid the use of oral contrast medium and to use dynamic CT study in patients thought to have small-intestinal obstruction due to adhesions, bands, or hernia.

Serrated Beak Sign. This sign (see Fig. 34–125), described in one series,[214] is highly specific in the diagnosis of strangulation; however, CT interpretation of this sign is problematic. The configuration of beaklike narrowing changes with different imaging planes, causing low sensitivity of this sign and yielding poor interobserver agreement.[208]

Unusual Mesenteric Vascular Courses. Most strangulated obstructions are associated with torsion or twisting of both bowel and mesenteric vessels. Therefore, CT findings of an unusual mesenteric vascular course offer an important clue to the presence of closed-loop obstruction with intestinal strangulation. As described earlier, these findings include the whirl sign, converging of the mesenteric vessels toward one point, and reversed position of the mesenteric artery and vein (Fig. 34–128; see also Figs. 34–124 and 34–127). However, caution is needed when one is using CT to interpret these signs because they can be seen in asymptomatic subjects without closed-loop or strangulated obstruction (Fig. 34–129).

Diffuse Mesenteric Vascular Engorgement and Haziness. Although a mild degree of mesenteric changes, such as vascular engorgement and haziness, are seen in simple obstruction,[208, 214] diffuse or severe mesenteric change is one of the highly sensitive and specific CT signs of intestinal strangulation (see Figs. 34–126 and 34–127).[20, 208, 165] One should be cautious not to interpret the localized peritoneal fluid accumulated in the spaces between the two mesenteric layers as mesenteric haziness.

Bowel Wall Thickening. The likelihood of strangulated obstruction may increase when the bowel wall be-

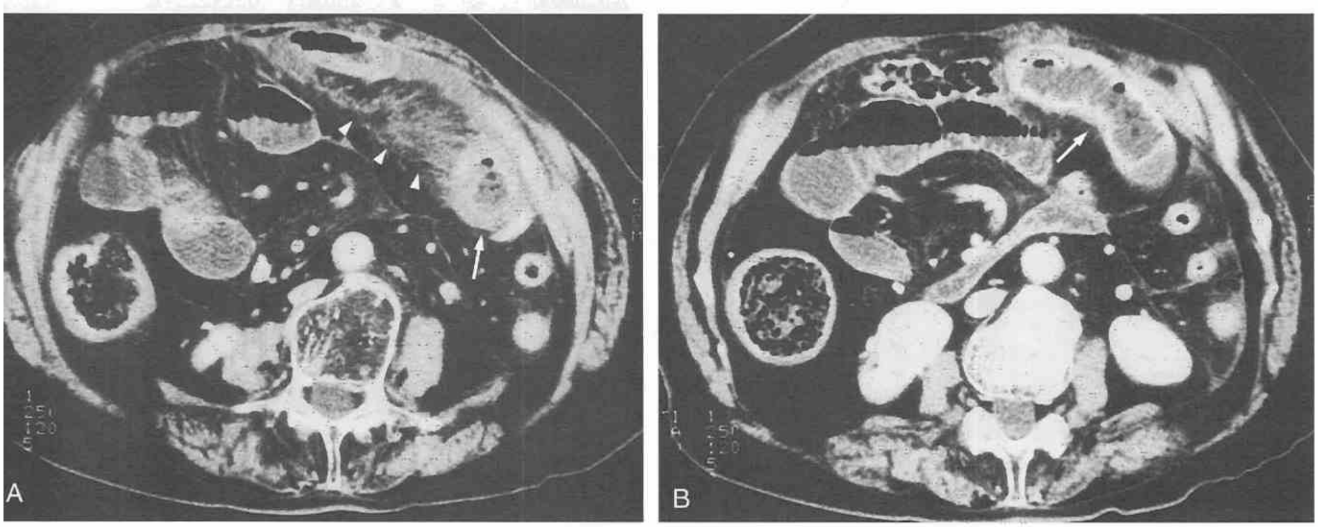

Figure 34–127. Strangulated small-bowel obstruction caused by bands and adhesion. *A* and *B*, CT scan shows different degrees of contrast enhancement *(arrows)* in the thickened bowel wall of the same strangulated segment. Diffuse engorgement and haziness *(arrowheads)* are seen in the vasa recta of the regional mesentery. (From Ha HK, Rha SE, Kim JH, et al: CT diagnosis of strangulation in patients with small bowel obstruction: Current status and future direction. Emerg Radiol 2:47–55, 2000.)

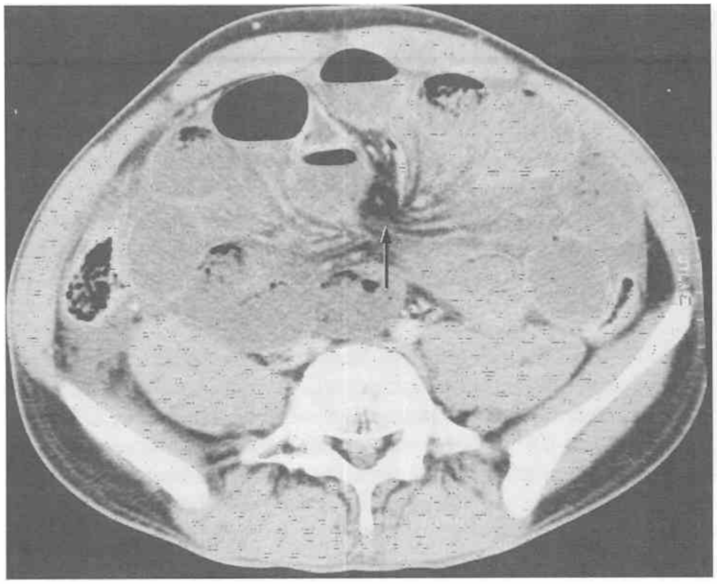

Figure 34–128. Closed-loop obstruction caused by volvulus. CT scan shows convergence *(arrow)* and engorgement of the mesenteric vessels. Small-intestinal loops are poorly enhanced compared with the colonic loops. Intestinal strangulation was confirmed at surgery. (From Ha HK, Kim HS, Lee MS, et al: Differentiation of simple and strangulated small bowel obstructions: Usefulness of known CT criteria. Radiology 204:507–512, 1997.)

comes thicker. To assess bowel wall thickness accurately, Maglinte and colleagues[367] stressed the importance of not using oral contrast material in patients who showed definite or probable small-intestinal obstruction on abdominal radiography because the presence of hyperattenuated intraluminal fluid made it difficult to determine wall thickening. When strict criteria (5 mm) were used, CT findings of bowel wall thickening showed high specificity (88%) with a sensitivity of 54% in distinguishing the simple from strangulated obstruction.[208] However, the bowel wall is thinned out or occasionally invisible when the bowel becomes gangrenous (see Fig. 34–122).

The thickened bowel wall may sometimes show the target sign (Fig. 34–130) due to submucosal edema or hemorrhage.

Ascites. In strangulated obstruction, there is rapid blood and plasma loss into the involved small-bowel loops or peritoneal cavity. It is therefore not surprising that the presence of a large amount of ascites is an indicator of strangulation (see Fig. 34–130).[208] However, the presence of a large amount of ascites in patients with small-bowel obstruction is not always related to the obstruction and can be caused by many other conditions. Therefore, before this finding is used as a specific indicator in the diagnosis of strangulation, it is necessary to exclude other diseases as necessary. If results are questionable, paracentesis should be performed because peritoneal fluid is reddish brown

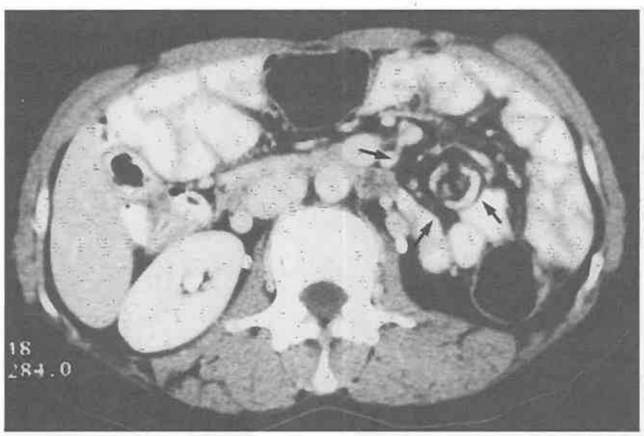

Figure 34–129. Subtotal gastrectomy with gastrojejunostomy performed for gastric cancer in an asymptomatic patient. The CT scan, obtained for routine follow-up study, shows twisting of the mesenteric vessels ("whirl sign") *(arrows)*. (From Ha HK, Rha SE, Kim JH, et al: CT diagnosis of strangulation in patients with small bowel obstruction: Current status and future direction. Emerg Radiol 2:47–55, 2000.)

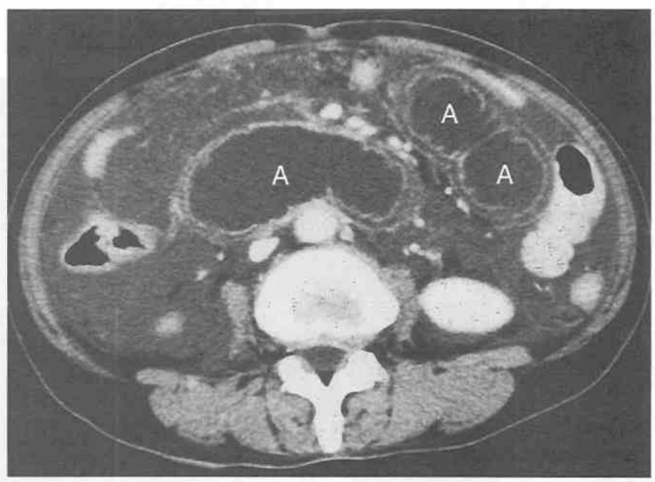

Figure 34–130. Strangulated small-bowel obstruction in an afferent loop in a 43-year-old man after subtotal gastrectomy with gastrojejunostomy for gastric cancer. CT scan shows bowel wall thickening of the afferent loop (A) with the "target sign." A large amount of ascites is present in the peritoneal cavity. (From Ha HK, Rha SE, Kim JH, et al: CT diagnosis of strangulation in patients with small-bowel obstruction: Current status and future direction. Emerg Radiol 2:47–55, 2000.)

or yields *Escherichia coli* with culture in patients with strangulated obstruction.[327]

Primary Causes of Obstruction

Small-bowel obstruction may be caused by three types of abnormalities:

1. Obturation of the intestinal lumen (polypoid tumor, gallstone, bezoars).
2. Intrinsic bowel lesions (congenital atresia or stenosis, adenocarcinoma).
3. Lesions extrinsic to the bowel (adhesions, hernia, peritoneal carcinomatosis).

Among these lesions, the most common cause is adhesions, followed by malignancy and hernia.[47] CT may determine the cause of obstruction in 73% to 85% of the cases.[166, 396]

Adhesions

In general, adhesions and bands themselves are not visible on CT because they are thin, fibrous connective tissues. However, indirect findings may help in their detection, which include close attachment of collapsed loops along the abdominal incisional wound, abrupt cut-off of the bowel in a linear orientation, and unusual clustering of the bowel loops.[204] The obstructed site caused by an adhesion or a band may appear as a beaklike luminal narrowing on CT. Inability to visualize an obstructive lesion, such as a tumor, intussusception, or abscess, may be diagnostic of obstruction caused by adhesions.[18]

Hernias

A variety of external and internal abdominal hernias can cause bowel obstruction. Although CT is excellent for detecting and characterizing types of hernias and for demonstrating the bowel, mesentery, or omentum within a hernia sac, it is especially valuable in patients who have symptoms of small-bowel obstruction, possibly resulting from hernia, but who have no hernia apparent on physical examination.

Incarceration usually occurs as a result of a narrow hernia ring, which leads to bowel obstruction and may cause strangulation of the hernia sac and its contents (see Fig. 34–114). Small-bowel obstruction caused by internal hernia can be predicted when CT shows abnormal location of bowel loops, crowding of small-bowel loops, and an unusual course of mesenteric vessels (see Fig. 34–118). Because the hernia may not be recognizable if it is reduced spontaneously, it is better to perform CT during symptomatic periods. Defects in the small-bowel mesentery, usually through a small hernia ring, may show a high frequency of strangulation and intestinal gangrene.

Bezoars

A phytobezoar is a concretion of poorly digested fibers, fruit seeds, and pulpy fruits, especially oranges and persimmons, causing small-intestinal obstruction usually after migration of a gastric phytobezoar. However, the obstruction is also caused by a primary bezoar (an enterolith) formed in the small intestine in association with underlying small-bowel diseases such as diverticula, strictures, or tumors.[169] Gastric surgery is the most predisposing factor for the development of phytobezoar; other factors include poor mastication, autonomic neuropathy, and overindulgence of foods with a high fiber content.[231] Early diagnosis is important because phytobezoars provoke decubitus ulcer, pressure necrosis, perforation, and even strangulation if the diagnosis is delayed.[231]

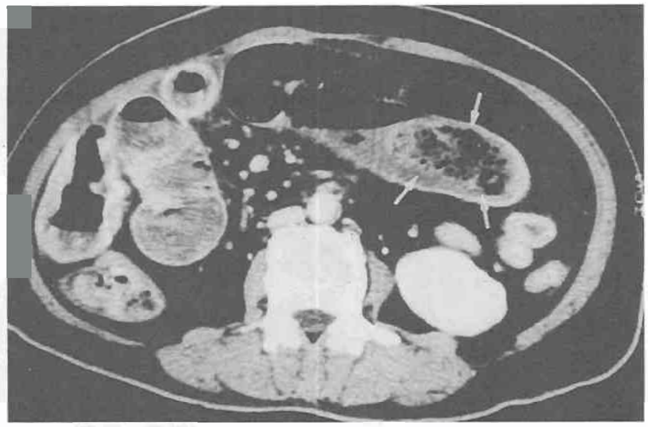

Figure 34–131. Intestinal obstruction caused by phytobezoar. CT scan shows an ovoid mass *(arrows)* containing mottled gas at the ileum along with diffuse small intestinal dilatation due to obstruction.

The most common CT findings of phytobezoars include a round or ovoid or a long sausage-shaped mass containing mottled gas at the obstructed site (Fig. 34–131).[305] Phytobezoars are rarely manifested as a soft tissue mass without gas, resembling an intraluminal tumor or intussusception. In these cases, barium study may give the clue in suggesting the diagnosis, and the diagnosis should be suspected when intraluminal filling defects appear to be mobile or multiple.

Some bezoars (enteroliths) appear as a calcified intraluminal mass with a laminated appearance.[231] In the differential diagnosis, small-bowel feces, which develop proximal to the obstructed site in patients with high-grade small-bowel obstruction, mimic those signs of phytobezoars on CT. With MRI, phytobezoars appear as a hypointense mass on T1-weighted and T2-weighted MR images, and the hypointensity may be due to their high fiber content and admixture of internal gas.

Gallstone Ileus

Gallstone ileus refers to erosion of a gallstone into the GI tract with subsequent development of bowel obstruction. This condition occurs in 0.3% to 0.5% of all cases of cholelithiasis.[114] Although the duodenum is the most common site, cholecystenteric fistula can occur in the colon or stomach.[114] Stones larger than 2.5 cm may cause obstruction. Bowel obstruction can occur preferentially at the narrow portion of the GI tract, such as the duodenum, the ligament of Treitz, the terminal ileum, or any area of stricture.

CT findings include gas in the gallbladder or biliary tree, calcified gallstone in the dilated bowel, and intestinal obstruction (Fig. 34–132).[201] The duodenal wall may appear

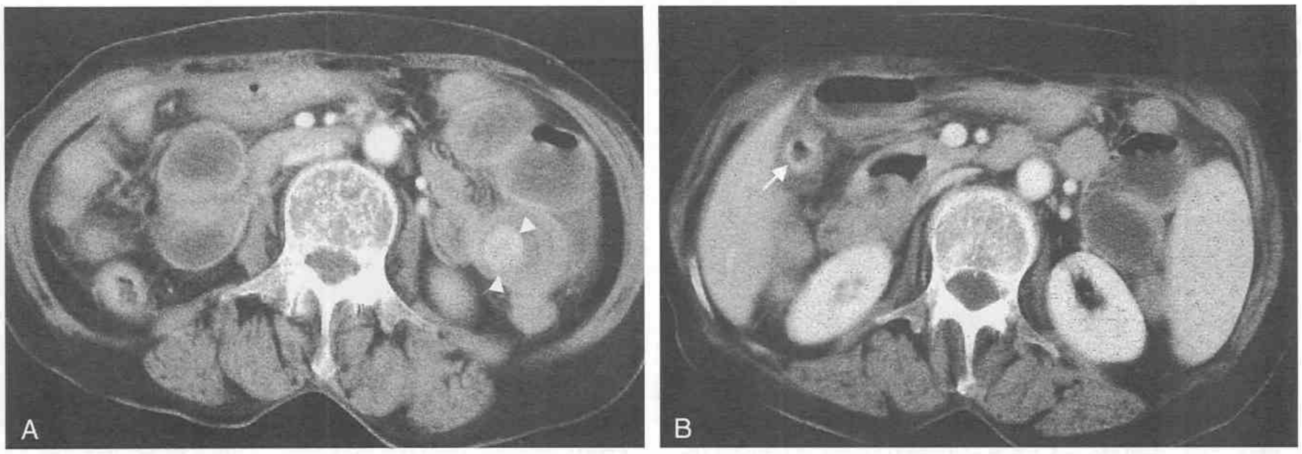

Figure 34–132. Gallstone ileus. *A,* CT scan shows a high-attenuated stone *(arrowheads)* obstructing the small-bowel loop. *B,* CT scan at higher level shows contracted and gas-filled gallbladder *(arrow)* with diffuse pericholecystic infiltration.

thickened with inflammatory infiltration in the pericholecystic space and focal or diffuse loss of interface between the gallbladder and duodenum.

Bowel Obstruction after Abdominal Surgery for Malignancy

Bowel obstruction in patients who have undergone abdominal surgery for malignancy remains a vexing problem in which the cause of obstruction may be benign postoperative adhesions, a focal malignant deposit, or peritoneal carcinomatosis. Approximately 25% of these cases are due to benign causes, a resectable or easily bypassed local recurrence, or a potentially curable new primary tumor.[286, 443] For this reason, patients with cancer who do not have proven recurrent tumor or peritoneal carcinomatosis should undergo aggressive treatment with early surgery in response to failure of conservative management.[68] Benign obstruction is more likely if pelvic irradiation was used in the management of the primary tumor, whereas the chance of malignant obstruction is increased if the patient had known metastatic cancer or if the primary cancer is in an advanced stage or of gynecologic origin.[286, 443]

When one is predicting the causes of intestinal obstruction, it is helpful to consider the time interval from the cancer surgery to the development of intestinal obstruction. The common causes of bowel obstruction during the early postoperative period (<3 months after surgery) are adhesions and bands, volvulus, or other benign conditions, such as stricture due to postsurgical fibrosis.[215, 552] The site of intestinal obstruction is also another useful indicator in differentiating malignant from benign obstruction. The presence of colonic obstruction favors the diagnosis of malignant obstruction.

According to a series by Megibow and coworkers,[396] CT was successful in determining the cause of obstruction in 12 of 13 patients. A later report by Ha and associates[215] showed that the diagnostic accuracy of CT in differentiating benign from malignant obstruction was 84%. The most diagnostic and specific CT findings to suggest malignant obstruction are the mass at the obstructed or prior surgical site and diffuse omental infiltration or cake (Fig. 34–133); however, if intestinal obstruction develops with implanted lesions smaller than 5 mm, they can be mistaken for a benign obstruction.

The lymphadenopathy in the para-aortic space or along the upper major vessels of the aorta favors the diagnosis of malignant obstruction, whereas the presence of hematogenous metastases to the other organs (e.g., liver, lung, or bone) may not.[215] In some instances, observation of bowel loop configuration at the site of obstruction on CT is also valuable. The transition zone at the site of obstruction is commonly abrupt in malignant obstruction and smooth in benign obstruction, whereas bowel wall thickening at obstructed sites is commonly irregular in malignant obstruction and smooth in benign obstruction. A large amount of ascites can be seen in both conditions.

Mesenteric Ischemia

Mesenteric ischemia is a devastating disease process that frequently poses a challenge to clinicians. This disease

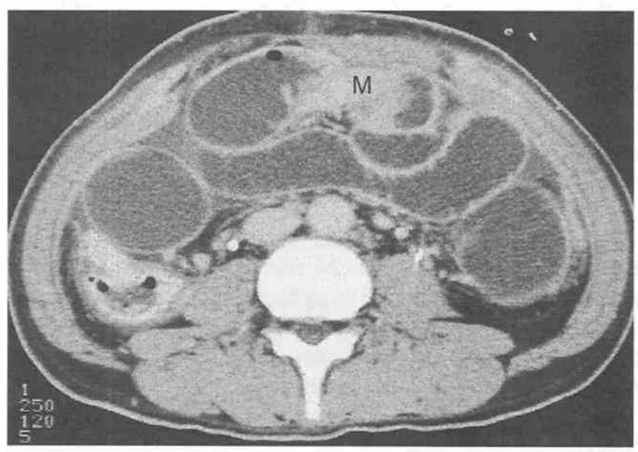

Figure 34–133. Malignant small-bowel obstruction due to peritoneal tumor seeding after surgery for gastric cancer. CT scan shows irregular mass (M) obstructing the small-bowel loop. (From Ha HK, Shin BS, Lee SI, et al: Usefulness of CT in patients with intestinal obstruction who have undergone abdominal surgery for malignancy. AJR Am J Roentgenol 171:1587–1593, 1998.)

can be classified as *acute* or *chronic* and has a *venous* or *arterial* origin. Bowel viability is not compromised in the chronic form because collateral blood flow will occur. In the acute form, infarction of bowel is more common. Ischemia of arterial origin occurs much more often than venous disease.[56]

The conditions most frequently leading to mesenteric ischemia include vascular occlusion due to arterial or venous disease and hypoperfusion associated with nonocclusive vascular disease. Many other diseases may also cause such vascular changes, including bowel obstruction, neoplasm, vasculitis, inflammatory conditions, trauma, and iatrogenic causes such as drug or radiation therapy. Irrespective of the cause of the ischemic insult, the end results are similar and range from transient alteration of bowel activity to transmural hemorrhagic necrosis.

CT has been used as a diagnostic tool in patients with suspected mesenteric ischemia. CT helps in detecting changes in the vessels and the bowel and reveals other ancillary abdominal findings. Furthermore, the use of dy-

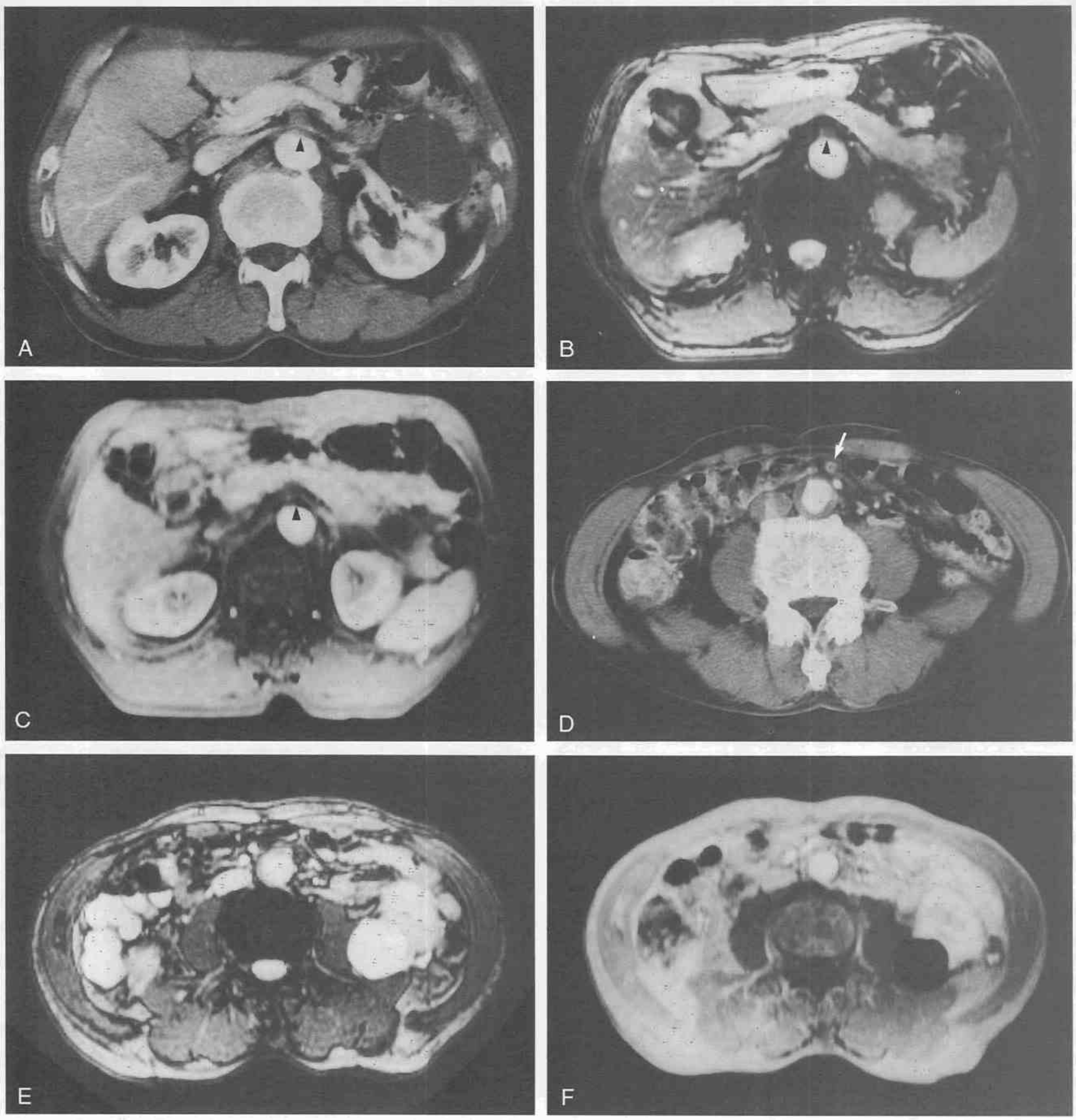

Figure 34–134. Intes[redacted] ischem[redacted]ue to multiple arterial emboli. CT scan *(A)* shows a hypoattenuated occlusive lesion *(arrowhead)* in the root of the sup[redacted] mesent[redacted] artery, w[redacted]well demonstrated on axial T2-weighted (true fast imaging with steady-state precession [FISP]) *(B)* and gadolinium-enhanced *(C)* MR images. CT scan *(D)* at a lower level shows a small embolus in the branch of the superior mesenteric artery; however, the embolus is difficult to see on true-FISP *(E)* and contrast-enhanced *(F)* MR images.

namic CT provides information regarding the hemodynamics of blood flow to the intestine. Specific CT signs for establishing the diagnosis include thromboembolism in the mesenteric vessel, intramural gas, portal venous gas, lack of bowel wall enhancement, and ischemia of other organs; nonspecific signs are bowel dilatation, bowel wall thickening, bowel obstruction, mesenteric edema and vascular engorgement, and ascites.[6, 302, 549, 566]

MRI has been attempted in cases of suspected mesenteric ischemia. Unenhanced MR images are comparable with CT for demonstrating changes in the bowel and adjacent mesentery, but a significant problem is posed in regard to detecting small thromboemboli in the peripheral mesenteric arterial branches (Fig. 34–134).[210] As in CT, use of a contrast infusion study may be mandatory not only to assess the dynamic changes in the bowel wall but also to detect small thromboemboli. In addition, some researchers have attempted to use the cine phase-contrast MRI to quantitate mesenteric vascular blood flow.[349] In the study by Li and colleagues,[349] the percentage change in SMA blood flow 30 minutes after meal intake seems to be a promising criterion for differentiating healthy subjects from patients with chronic mesenteric ischemia. However, further study with a large number of patients is warranted.

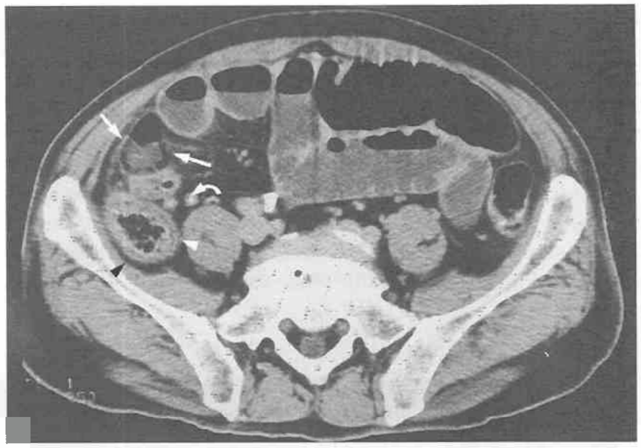

Figure 34–135. Bowel infarct caused by mesenteric arterial embolic occlusion with iodinated poppyseed oil (Lipiodol) after hepatic arterial embolization for hepatocellular carcinoma. CT scan shows concentric bowel wall thickening of the ileum with intestinal pneumatosis *(arrows)*. The wall of the ascending colon is also thickened *(arrowheads)*. A hyperattenuated Lipiodol *(curved arrow)* occludes the ileocolic branch of the superior mesenteric artery. (From Rha SE, Ha HK, Lee SH, et al: CT and MR imaging findings of bowel ischemia according to the various primary causes. Radiographics 20:29–42, 2000.)

Thromboembolism

Occlusive intestinal ischemia is usually caused either by arterial or venous disease, although arterial occlusion accounts for most cases.[56] More than 95% of patients with embolic occlusion of the SMA have documented histories of cardiac disease, with the emboli usually originating from a left atrial or ventricular mural thrombus. The embolus lodges at points of normal anatomic narrowing immediately distal to the origin of a major arterial branch. Most patients with SMA thrombosis also have a history of coronary, cerebrovascular, or peripheral arterial insufficiency, and thrombosis occurs at points of severe atherosclerotic narrowing, most often at the origin of the SMA.[56]

Before symptoms are expected, the degree of arterial narrowing must be severe, with narrowing of the cross-sectional area by 50% to 80%.[123] In addition to the arterial luminal narrowing, systemic blood pressure and the degree of collateral circulation also play a role in determining the severity of a patient's symptoms and the extent of ischemic insult.[31] If collateral circulation is adequate, bowel infarction may not develop even in cases with total occlusion of the main SMA or inferior mesenteric artery.

Although angiography remains the most valuable method of diagnosis and the immediate therapy of acute arterial occlusion, CT has recently been regarded as a valuable tool in a noninvasive diagnostic method. In the radiologic literature, reports of sensitivity of CT in diagnosis of acute mesenteric ischemia have varied. In an early report,[549] the sensitivity of CT was poor (only 39%); more recent series using high-quality infusion techniques[302, 566] have shown much higher sensitivity (ranges, 64% to 82%). Such improved diagnostic accuracy results mainly from higher detection rates of specific signs of mesenteric ischemia, such as thromboembolism in the mesenteric vessels and lack of bowel wall enhancement (Fig. 34–135). If good contrast enhancement is achieved in the mesenteric vessels, most of thromboemboli in the superior mesenteric vein and large branches of the SMA are easily detected on CT (Fig. 34–136; see also Fig. 34–134). However, it is likely that significant limitation is encountered in detecting small thromboemboli in the peripheral arterial branches. In fact, angiography appears to be not much better than CT in cases of thromboembolism in the peripheral or terminal mesenteric branches.

In one series,[566] only nonspecific CT findings of mesenteric ischemia, such as diffuse bowel dilatation, bowel wall thickening, ascites, and mesenteric haziness and vascular engorgement, were observed in 36% of the patients with proven mesenteric ischemia (Fig. 34–137). Furthermore, in many instances, it is difficult to obtain high-quality images because of the generally poor condition of patients with mesenteric ischemia; thus, specific CT findings can be easily missed. In such patients with nonspecific CT signs, it is difficult to differentiate mesenteric ischemia from other GI tract disease (e.g., inflammatory bowel disease, acute abdominal conditions). A high index of suspicion may be the key for early identification of acute mesenteric ischemia, especially in patients older than 50 years of age who have chronic heart disease and long-standing congestive heart failure and who show atheromatous vascular wall calcifications on CT studies.

Nonocclusive Mesenteric Ischemia

In patients with nonocclusive mesenteric ischemia, the mesenteric arteries and veins are patent but flow through them is too slow to deliver enough oxygenated blood to the bowel. This condition is most commonly related to primary cardiac dysfunction, such as cardiac failure, arrhythmia, myocardial infarction, sepsis, trauma, and vascular insufficiency. Most cases of colonic ischemia belong to this group. Flow to the viscera is reduced by progressive

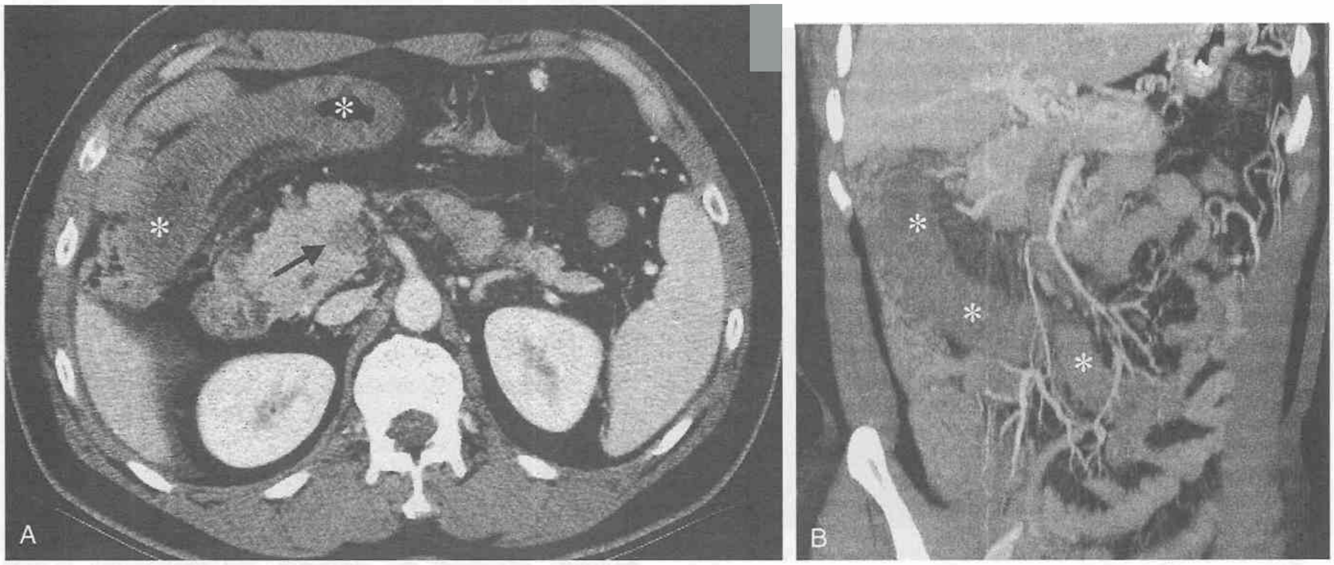

Figure 34–136. Intestinal ischemia resulting from mesenteric venous thrombosis. *A,* CT scan shows thrombus *(arrow)* in the superior mesenteric vein. Note diffuse bowel wall thickening *(asterisks)* of the small-bowel loop with poor contrast enhancement. *B,* Thick-slab (20-mm), coronal maximum intensity projection image shows favorable demonstration of the poorly enhancing ischemic intestinal segment *(asterisks)* as well as prominence of the regional vasa recta of the mesenteric vessels.

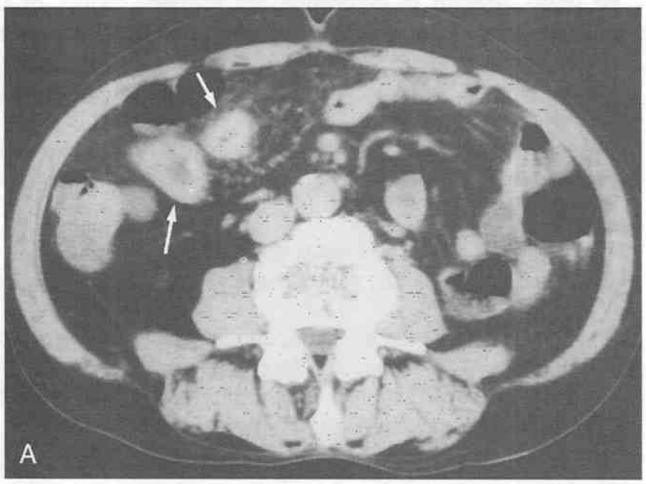

Figure 34–137. Intestinal ischemia due to mesenteric arterial occlusion. *A,* CT scan shows nonspecific bowel wall thickening *(arrows)* of the ileum with prominent mesenteric vessels in the regional mesentery. Thromboembolism is not definitively demonstrated. *B,* Arterial phase of the superior mesenteric artery (SMA) angiogram shows occlusion *(arrow)* of the ileocolic branch of the SMA. *C,* Venous phase of the SMA angiogram shows delayed pooling *(arrows)* of contrast material in the ischemic ileal segment. (From Ha HK: CT in the early detection of strangulation in intestinal obstruction. Semin Ultrasound CT MRI 16:141–150, 1995.)

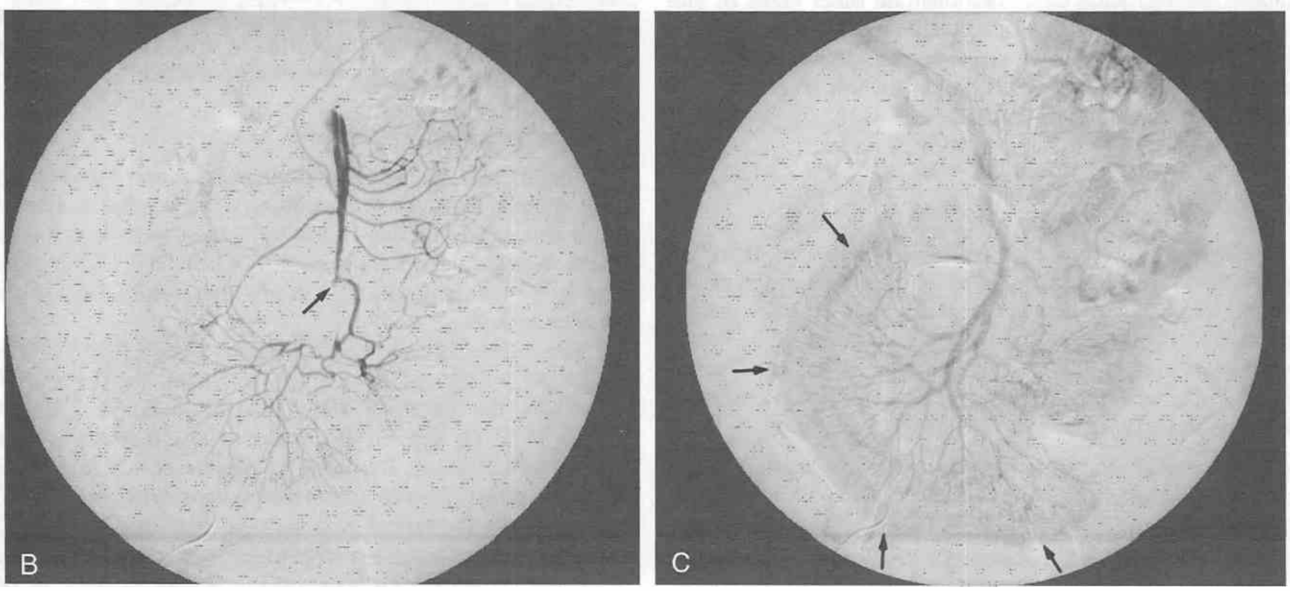

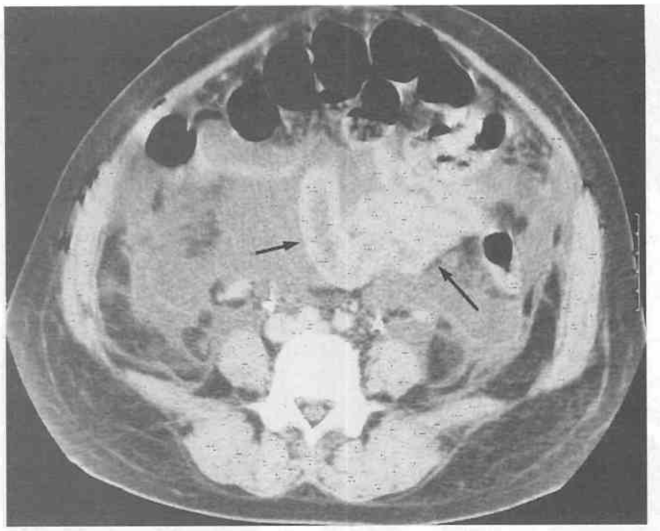

Figure 34–138. Shock bowel in a 26-year-old woman after cesarean section. CT scan shows diffuse bowel wall thickening in the ileum *(arrows)* with a large intraperitoneal fluid collection caused by hemoperitoneum. (From Rha SE, Ha HK, Lee SH, et al: CT and MR imaging findings of bowel ischemia according to the various primary causes. Radiographics 20:29–42, 2000.)

vasoconstriction, and persistent vasoconstriction of the splanchnic vasculature results in intestinal hypoxia.[56]

Shock bowel, caused by prolonged hypoperfusion due to hypovolemic shock, is a subtype of nonocclusive mesenteric ischemia. It is a transient phenomenon and resolves with restoration of hypovolemia. CT scans may show diffuse bowel wall thickening and contrast enhancement exclusively in the small intestine (Fig. 34–138).[412] Other reported CT manifestations include diminished caliber and increased enhancement of the inferior vena cava and aorta as well as intense contrast enhancement of the kidneys and mesentery.[547]

Shock bowel should be distinguished from diffuse edema of the small bowel that accompanies central venous hypertension due to aggressive volume resuscitation in a trauma setting. Such cases demonstrate other signs of elevated central venous pressure, including an enlarged inferior vena cava, periportal lymphedema, and accumulation of retroperitoneal fluid[536] and do not exhibit increased contrast enhancement of the small-bowel wall.

Vasculitis

Vasculitis can affect blood vessels of all sizes, resulting in necrosis and inflammation. The extent and clinical course depend on the size and location of the vessels involved.[529] In the 1990s, the predominant type of affected vessel was generally accepted as the criterion for classification.[268] According to this system, vasculitis can be classified into three types:

1. *Large-vessel* vasculitis includes Takayasu's arteritis and giant cell arteritis.
2. *Medium-sized vessel* vasculitis includes polyarteritis nodosa (see later) and Kawasaki's disease.
3. *Small-vessel* vasculitis comprises microscopic polyangiitis (hypersensitivity vasculitis), Wegener's granulomatosis, Churg-Strauss syndrome, Henoch-Schönlein syndrome, SLE, rheumatoid vasculitis, and Behçet's disease.

Systemic vasculitis affecting the GI tract is uncommon. The frequency of GI involvement depends on the type of vasculitis, with the highest incidence (50% to 70%) in cases of polyarteritis nodosa. With larger-vessel involvement, abdominal manifestations may be indistinguishable from those of mesenteric ischemia caused by emboli or thrombosis except for associated evidence of systemic disease.

Inflammation of medium-sized arteries may also lead to the formation of aneurysms, as commonly occurs in polyarteritis nodosa, and their rupture may cause GI or intra-abdominal hemorrhage. The vasa recta and intramural arteries and arterioles may be affected in virtually all disorders associated with systemic vasculitis. Ulceration and stricture formation are common, but perforation is less common with small-vessel involvement.

Until recently, the medical literature has not sufficiently dealt with the role of radiology in distinguishing ischemia caused by mesenteric vasculitides from that attributed to other causes. If only radiologic findings are used, it may be quite difficult to determine the primary causes of GI manifestations. Knowledge of the systemic clinical manifestations in patients with mesenteric ischemia not only would suggest the possibility of vasculitis but also would be helpful in establishing the specific diagnosis.

In our experience, CT helps to suggest the diagnosis of vasculitis. The possibility of vasculitis should be considered when:

1. Multiple abdominal organs are involved.
2. Mesenteric ischemic changes are suspected in young patients.
3. Involvement of the stomach, duodenum, or rectum coexists with small-bowel and large-bowel changes.
4. The bowel wall changes concomitantly involve both the small and large intestine.[268]

Ancillary findings occurring in other organs may also suggest the diagnosis because a high incidence of genitourinary tract involvement (nephritis, cystitis, or hydronephrosis) or splenomegaly has also been reported.[70]

Polyarteritis Nodosa

Polyarteritis nodosa is a fibrinoid necrotizing vasculitis that mainly involves the medium-sized muscular arteries. A characteristic finding is multiple aneurysm formation in these vessels, which are seen in 50% to 60% of the cases; the individual lesions affect the branch points and bifurcation of arteries.

The kidney is most commonly involved (80% to 90%), followed by the GI tract (50% to 70%), the liver (50% to 60%), the spleen (45%), and the pancreas (25% to 35%).[430, 583] Of the GI tract, the small intestine is most commonly affected, followed by the mesentery and colon.

Approximately two thirds of patients with polyarteritis nodosa have abdominal pain, nausea, vomiting, or other GI symptoms in association with organ damage due to ischemia and infarction; GI hemorrhage occurs in roughly 6%

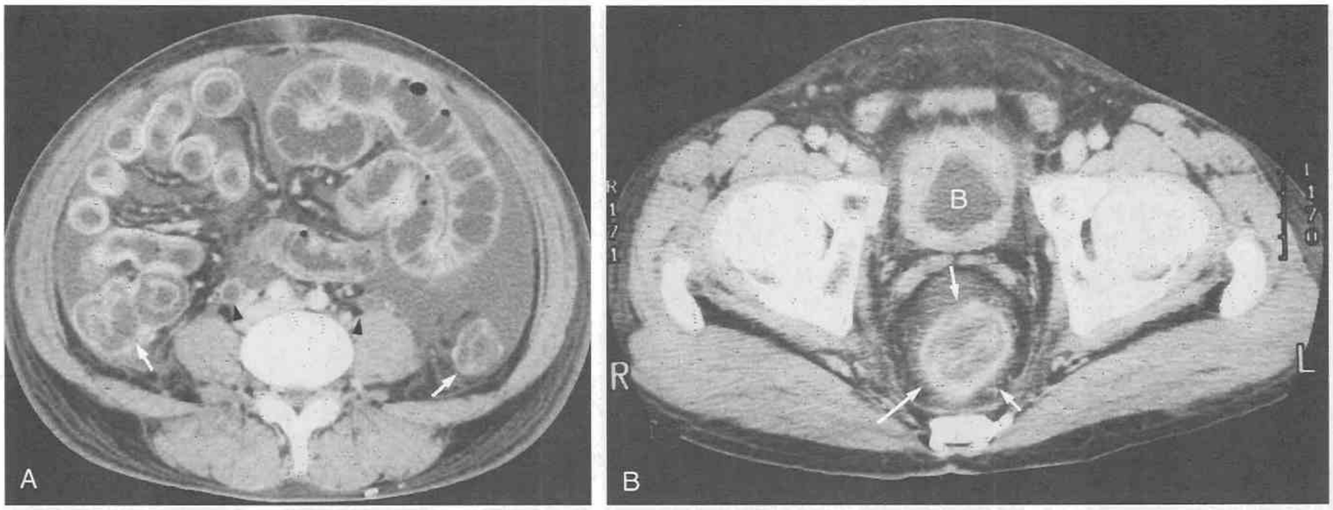

Figure 34–139. Polyarteritis nodosa. *A,* CT scan shows bowel wall thickening of the ileum and ascending and descending colon *(arrows)* with evidence of the "target sign." Also noted are a large amount of ascites and bilateral ureteral dilatation *(arrowheads). B,* CT scan shows rectal wall thickening *(arrows)* with the target sign. The bladder (B) is also diffusely thickened. (From Ha HK, Lee SH, Rha SE, et al: Radiologic features of vasculitis involving the gastrointestinal tract. Radiographics 20:779–794, 2000.)

of cases, bowel perforation in 5%, and bowel infarction in 1.4%.[71, 430] Therapy with corticosteroids and cyclophosphamide results in remission or cures in 90% of affected patients.[529]

The diagnosis can be suggested by the presence of aneurysms up to 1 cm in size within the renal, mesenteric, and hepatic vasculature on angiography; however, these visceral aneurysms are not always a pathognomonic finding because they are also seen in necrotizing angiitis associated with drug abuse[220] and other vasculitides, such as Wegener's granulomatosis and SLE.[583] Without angiography, the correct diagnosis is established by biopsy of subcutaneous nodules or skeletal muscle.[364]

CT may help in determining the extent of involvement in multiple abdominal organs. When the GI tract is involved, CT manifestations do not differ from intestinal ischemia resulting from other causes (Fig. 34–139).[267]

Microscopic Polyangiitis

Microscopic polyangiitis is characterized by pauci-immune necrotizing small-vessel vasculitis without clinical or pathologic evidence of necrotizing granulomatous inflammation.[268] The lesions are thought to represent a hypersensitivity reaction to drugs (e.g., penicillin), microorganisms, heterologous proteins, and tumor antigens,[529] and they involve the skin, mucous membranes, lung, brain, heart, GI tract, kidneys, and muscle. In many instances, the lesions are limited to the skin (cutaneous leukocytoclastic vasculitis). The radiologic findings, when the GI tract is involved, do not differ from findings of other types of vasculitis involving similar-sized vessels, and bowel infarction or perforation is rarely reported (Fig. 34–140).[293] In contrast to the findings of polyarteritis nodosa, visceral angiographic results are usually normal and do not reveal microaneurysms.

Henoch-Schönlein Syndrome

Henoch-Schönlein syndrome is one of the subgroups of hypersensitivity-related acute small-vessel vasculitis.[407] Although the cause is unknown, immunization, insect bites, medications, infections, and certain foods sometimes play a role in the development of this disease. The syndrome occurs most commonly in children between 3 and 10 years of age, but in some series, 30% of affected patients have been older than age 20 years.

The diagnosis is based on characteristic clinical signs and symptoms, such as skin rash, arthritis involving the large joints, colicky abdominal pain, GI bleeding, and hematuria.[407] The GI manifestations are thought to be related to edema and intramural hemorrhage. When GI symptoms predominate or precede skin lesions, the syndrome may mimic a number of acute abdominal diseases, resulting in unnecessary laparotomies. GI hemorrhage is confined mostly to the mucosa and submucosa, and full-thickness

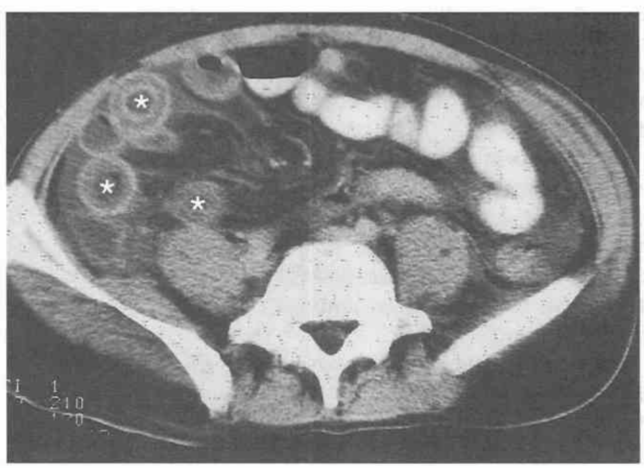

Figure 34–140. Microscopic polyangiitis (hypersensitivity vasculitis). CT scan shows bowel wall thickening of the ileum *(asterisks)* with the "target sign." A small amount of ascites is also visible. (From Ha HK, Lee SH, Rha SE, et al: Radiologic features of vasculitis involving the gastrointestinal tract. Radiographics 20:779–794, 2000.)

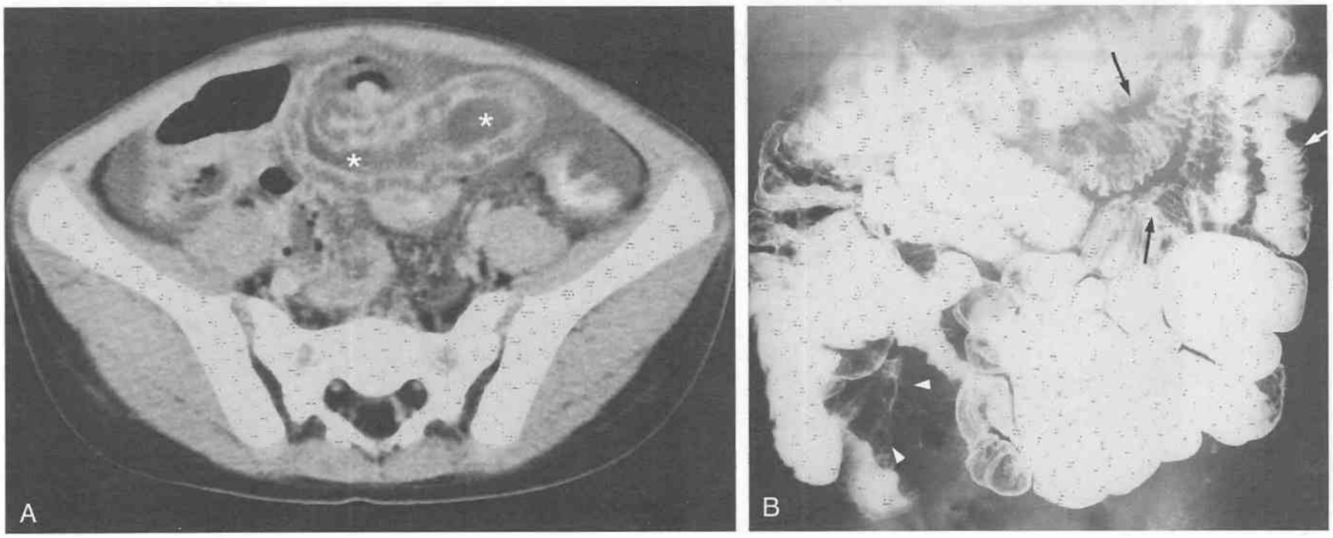

Figure 34–141. Henoch-Schönlein purpura with bowel infarct in a 6-year-old boy with symptoms of severe colicky abdominal pain, vomiting, and polyarthralgia. The patient had purpura on both buttocks on physical examination. The diagnosis was made on the basis of histopathologic results following surgery (segmental ileal resection). *A,* CT scan shows bowel wall thickening *(asterisks)* of the ileum with the "target sign." Ascites is also noted. *B,* Small-bowel follow-through shows luminal narrowing and circular fold thickening in both the jejunum *(arrows)* and the ileum *(arrowheads)* with skipped areas. (From Ha HK, Lee SH, Rha SE, et al: Radiologic features of vasculitis involving the gastrointestinal tract. Radiographics 20:779–794, 2000.)

necrosis and perforation of bowel loop are rare. Therefore, most GI manifestations are self-limited without residua, and only 3% to 5% of cases develop bowel infarction, perforation, or irreducible intussusception.[378]

No specific findings are seen on radiologic examinations, although the CT finding of multifocal bowel wall thickening with skipped areas under the clinical backgrounds is important to establish a diagnosis (Fig. 34–141).[269]

Systemic Lupus Erythematosus

SLE is an autoimmune disorder, affecting the musculoskeletal system, kidneys, GI tract, or skin.[564] Local deposition of antigen-antibody complexes or antibodies inducing necrotizing vasculitis is the presumptive cause of this disease. Most patients range between 16 and 41 years of age, with the most common occurrence during childbearing ages.

A diagnosis of SLE can be made with 98% specificity and 97% sensitivity if at least 4 of 11 diagnostic criteria are present at any time during the course of disease[564]; these criteria include malar rash; discoid rash; photosensitivity; oral ulcers; arthritis; serositis; antinuclear antibodies; and renal, neurologic, hematologic, and immunologic disorder.

SLE may involve any part of the GI tract from the esophagus to the colon, but the territory of the SMA is more preferentially affected. Other sites, such as the stomach, duodenum, colon, or rectum, may also be involved. Inflammation of the small blood vessels of the gut produces a spectrum of complications, including intestinal ischemia, hemorrhage, ileus, ulceration, infarction, and perforation.[301]

CT facilitates more accurate diagnosis of mesenteric arteritis. Common CT findings include dilated bowel, focal or diffuse bowel wall thickening, engorged mesenteric vessels with a comblike arrangement (comb sign), ascites, and lymphadenopathy (Figs. 34–142 and 34–143).[70] In most cases, the segments of bowel wall thickening are multifocal and are not confined to a single vascular territory because mesenteric vasculitis may affect several vessels simultaneously.[300] Rather than bowel wall changes, the ancillary findings occurring in other organs may suggest the diagnosis because a high incidence of genitourinary tract involvement (lupus nephritis, cystitis, or hydronephrosis) has been reported.[3] Hydronephrosis also occurs in other types of vasculitis (e.g., polyarteritis nodosa, Henoch-Schönlein syndrome) and seems to be caused either by detrusor muscle spasm with subsequent vesicoureteral reflux or by fibrosis of the ureterovesical junction.[63, 291]

Behçet's Syndrome

Behçet's syndrome is a well-recognized nonspecific necrotizing vasculitis that affects many organs; its well-known clinical manifestations include orogenital ulceration, uveitis, arthritis, and neurologic and GI involvement.[256, 381] Among patients with Behçet's syndrome, the GI tract has been reported to be involved in 10% to 40% of the cases[442]; the usual site is the ileocecal area, especially the terminal ileum.

The hallmark of the syndrome is the presence of large, deeply penetrating ulcerations of the submucosa, the muscle layer, or the entire intestinal wall. As a result, a high incidence of complications, such as perforation, hemorrhage, fistula, and peritonitis, has been reported.[277] An appropriate treatment, therefore, is of great importance in avoiding these complications.

Barium study shows a large ovoid or geographic ulcer with marked thickening of the surrounded intestinal wall at the sites of involvement, although in certain instances small, multiple, discrete, and punched-out ulcers can be

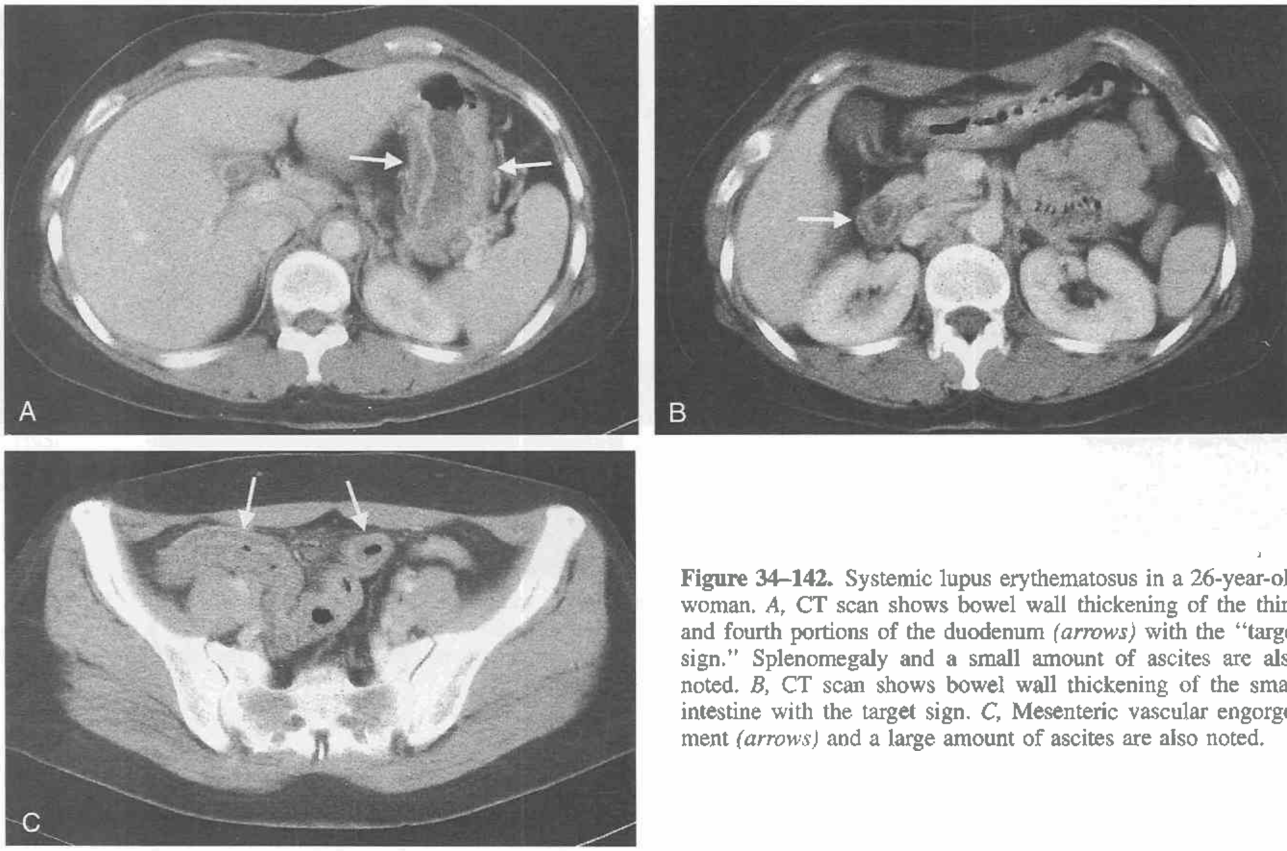

Figure 34–142. Systemic lupus erythematosus in a 26-year-old woman. *A,* CT scan shows bowel wall thickening of the third and fourth portions of the duodenum *(arrows)* with the "target sign." Splenomegaly and a small amount of ascites are also noted. *B,* CT scan shows bowel wall thickening of the small intestine with the target sign. *C,* Mesenteric vascular engorgement *(arrows)* and a large amount of ascites are also noted.

seen. CT has proved effective not only for detecting primary lesions but also for excluding extraluminal complications.[212] On CT scans, the involved bowel shows concentric bowel wall thickening or a polypoid mass (Figs. 34–144 and 34–145). The polypoid, masslike lesions may reach a diameter of 8 to 10 cm in some cases, with central ulceration in one third of these cases. Most of the thickened bowel wall may show marked contrast enhancement, presumably owing to vasculitis and perivasculitis.[212] Other CT findings include minimal lymphadenopathy of less than 1 cm in diameter and fibrofatty proliferation.

In patients with no complications, perienteric or pericolonic infiltrations are usually absent or minimal. In contrast, the presence of severe perienteric or pericolonic infiltra-

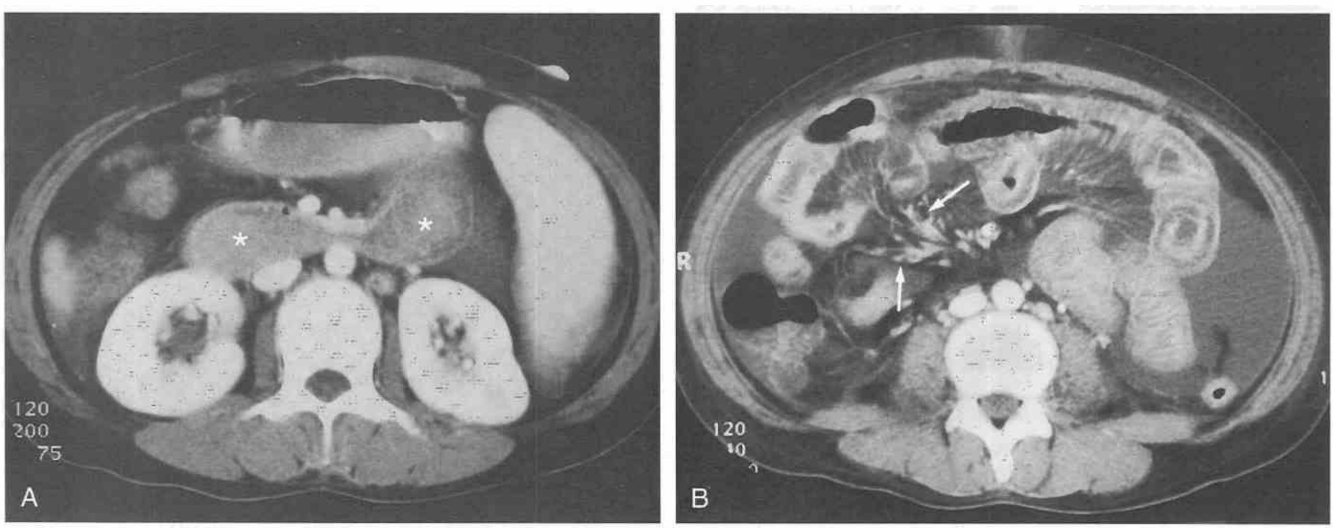

Figure 34–143. Systemic lupus erythematosus. *A,* CT scan shows edematous gastric wall thickening *(asterisks)*. *B,* The duodenal and ileal walls are also similarly thickened *(arrows)*. (From Ha HK, Lee SH, Rha SE, et al: Radiologic features of vasculitis involving the gastrointestinal tract. Radiographics 20:779–794, 2000.)

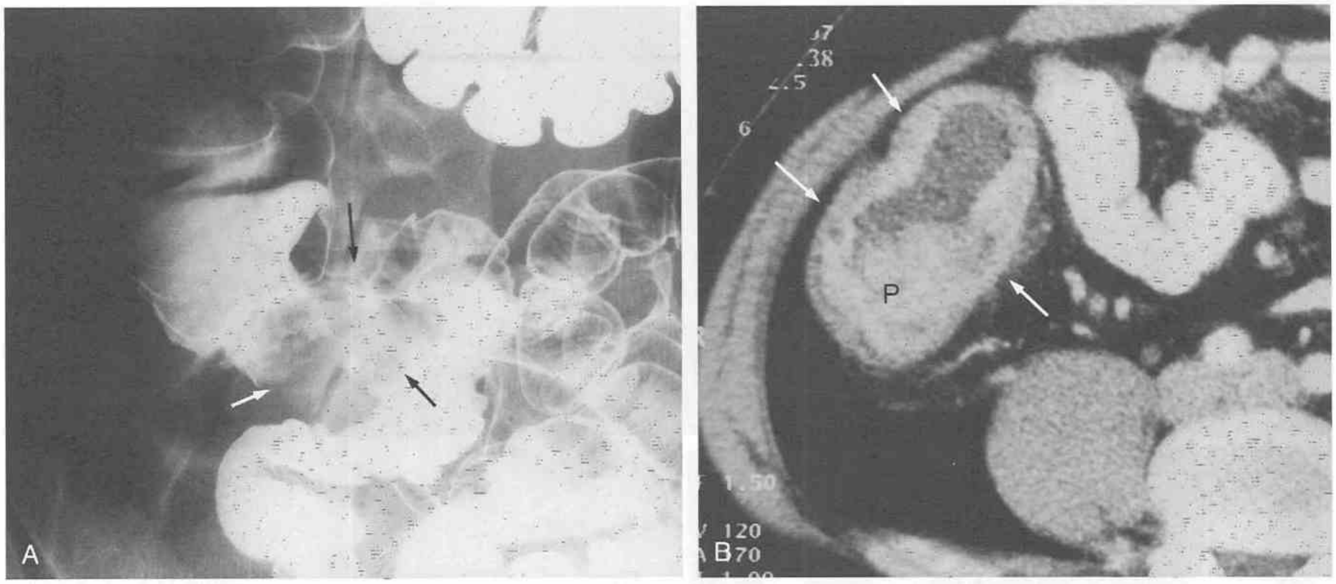

Figure 34–144. Behçet's syndrome. *A,* Double-contrast barium enema shows multiple, discrete ulcers with thickened mucosal folds *(arrows)* at the terminal ileum. *B,* CT scan shows both bowel wall thickening *(arrows)* and a polypoid masslike lesion (P) at the ileocecal region. (From Ha HK, Lee SH, Rha SE, et al: Radiologic features of vasculitis involving the gastrointestinal tract. Radiographics 20:779–794, 2000.)

tions raises the possibility of complications such as microperforation and localized peritonitis (Fig. 34–146).

Drug-Induced Enteropathy

A variety of medications can cause injury to any part of the GI tract by different mechanisms. Although GI reactions may be minor in many instances, serious drug-induced complications, such as bowel ischemia, perforation, peritonitis, or shock, are not uncommon and are sometimes fatal.

Oral contraceptives and estrogens are the well-known drugs causing an increased incidence of thromboembolic complications in the superior and inferior mesenteric arteries, celiac artery, superior and inferior mesenteric veins, and hepatic vein.[163] The duration of drug therapy with these agents before development of ischemic bowel disease ranges from 10 days to 11 years.[163] Many instances of oral contraceptive, steroid-induced mesenteric ischemia have mimicked Crohn's disease but are reversible on discontinuation of the agent.[569]

Digoxin and certain cardiovascular agents[347] can also

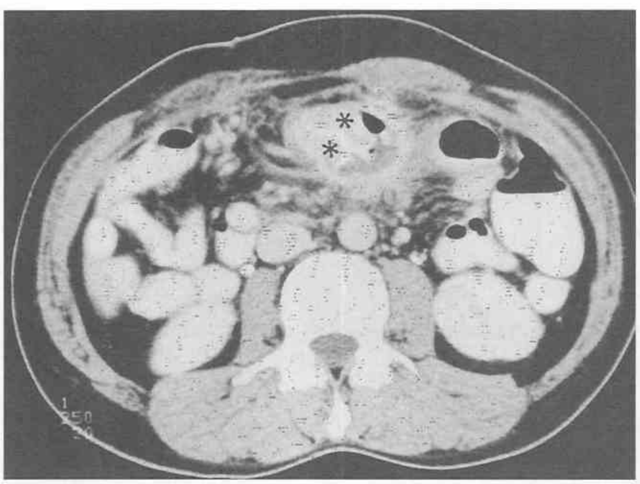

Figure 34–145. Recurrent Behçet's syndrome at the surgical anastomosis. CT scan shows concentric bowel wall thickening *(asterisks)* at the anastomotic site after right hemicolectomy. Perienteric infiltration and regional mesenteric vascular engorgement are also noted. (From Chung SY, Ha HK, Kim JH, et al: Radiological findings of Behçet's syndrome involving the gastrointestinal tract. Radiographics 21:911–924, 2001.)

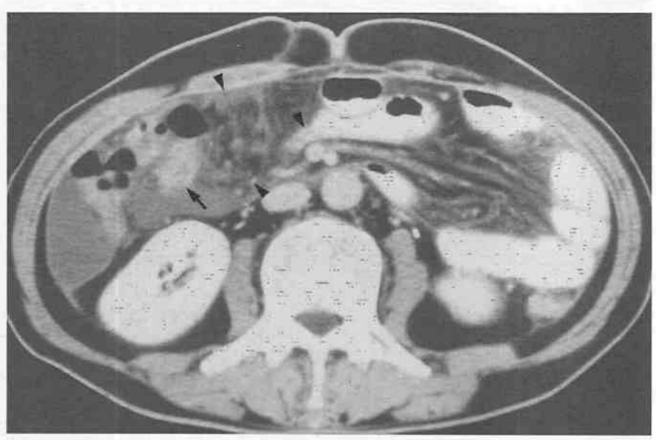

Figure 34–146. Behçet's syndrome with bowel perforation. CT scan shows intraperitoneal fluid collection and mesenteric infiltration *(arrowheads)* surrounding the involved bowel loop *(arrow)*. (From Ha HK, Lee SH, Rha SE, et al: Radiologic features of vasculitis involving the gastrointestinal tract. Radiographics 20:779–794, 2000.)

cause bowel ischemia by diminishing splanchnic flow or by stimulating the renin-angiotensin axis, leading to vasoconstriction. Other drugs causing bowel ischemia include various diuretics, antihypertensive medications, and ergot alkaloids.

Chemotherapeutic agents also produce GI toxicity ranging from mild clinical symptoms to acute surgical conditions due to peritonitis, perforation, or bowel necrosis. A high incidence of necrotizing lesions of the GI tract in patients with malignancy, lymphoma, or leukemia has been reported.

Dosik and associates,[128] separated 26 patients with malignancy (most received antineoplastic and antimicrobial regimens and died of necrotizing colitis) into three histologically distinct categories: (1) those with pseudomembranous colitis (69%), (2) those with agranulocytic (typhlitis) (19%), and (3) those with ischemic colitis (12%).

Amromin and Solomon[8] also classified necrotic enteric lesions (necrotizing enteropathy) in 63 patients with treated leukemia or lymphoma into the following four types according to the pathogenic mechanisms:

1. Shock with a superficial variety of necrosis.
2. Therapeutic necrosis of tumor or leukemic infiltrates of the intestinal mucosa.
3. Hemorrhage with necrosis of GI mucosa.
4. Traumatic erosions.

In their second group of patients, necrosis occurred at sites with the most abundant lymphoid tissue and, therefore, the terminal ileum or appendix was commonly involved. Because little or no supporting tissue remained, either normal or neoplastic, perforations and peritonitis were common in this group of patients.

Among various chemotherapeutic agents, 5-fluorouracil and its analogs are considered to be the most injurious.[347] Ischemic enteritis or enterocolitis can be seen in patients with intra-arterial infusion of floxuridine for the treatment of hepatic metastasis.[282, 469]

Even though numerous reports regarding the clinical and surgicopathologic aspects of drug-induced enteropathy have been published, studies of imaging results have been limited. This is attributable to the fact that in patients with mild GI symptoms during or following drug therapy of any kind, CT is not usually performed and may be confined to patients with severe symptoms. Furthermore, as symptoms develop with periods of varying intervals after therapy, abnormal CT findings may be commonly confused with other conditions. In our experience, CT findings of drug-induced enteropathy appear to be nonspecific, including mild small-bowel fold thickening, focal or diffuse bowel wall thickening, bowel obstruction, pneumatosis intestinalis, and signs of peritonitis (Figs. 34–147 and 34–148). Therefore, drug-induced enteropathy may be difficult to distinguish from ischemic or inflammatory bowel diseases. Multifocal involvement or patchy distribution in the GI tract may be one of the important features for suggesting the diagnosis.

Radiation Enteritis

Radiation enteritis is generally observed in patients who receive abdominal and pelvic radiation with doses of 4500 to 6000 rads (45 to 60 Gy).[518] The latent period between radiation therapy and the development of radiation damage is usually 6 to 24 months, although this interval can be longer than 20 years. Predisposing factors include diabetes, hypertension, atherosclerosis, prior abdominal surgery with adhesive bowel loops, and peritonitis before the radiation therapy.

The long-term effects of radiation on the vasculature may cause the involved vessel wall, especially of the small arterioles in the submucosa, to be obliterated with sufficient luminal narrowing, resulting in progressive occlusive vasculitis and diffuse collagen deposition with fibrosis.[538] Fewer than 2% of patients who receive radiation therapy

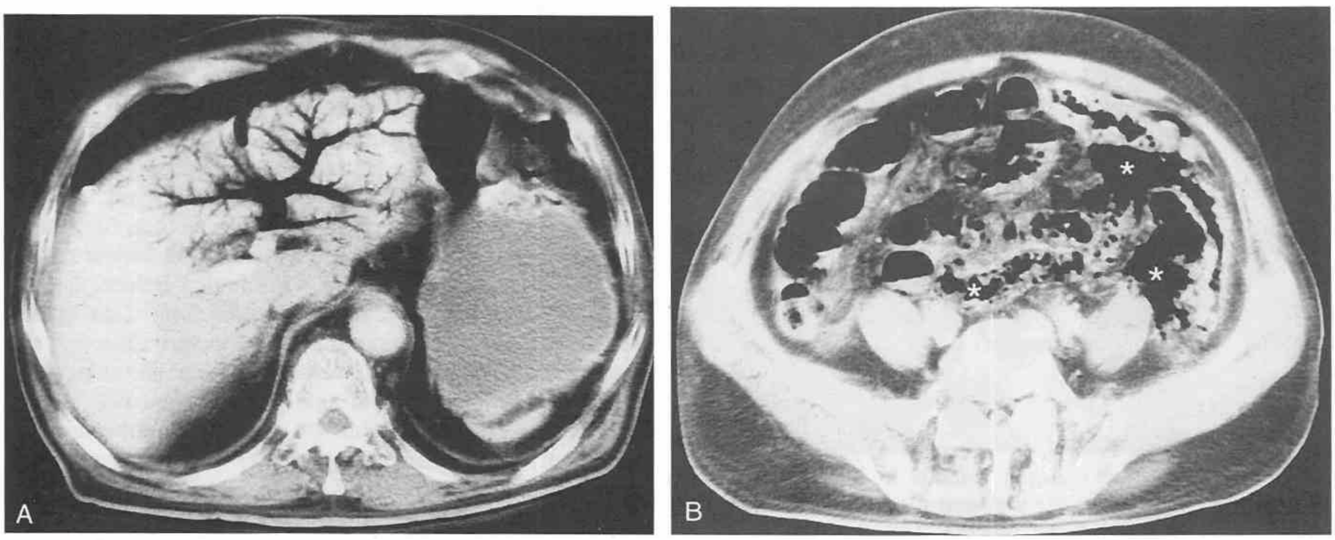

Figure 34–147. Chemotherapy-induced enteropathy with diffuse intestinal necrosis in a patient who received chemotherapy for central nervous system lymphoma. *A,* CT scan shows extensive intrahepatic portal venous gas. *B,* CT scan shows intestinal pneumatosis *(asterisks)* and gas in the mesenteric vascular branches. (From Rha SE, Ha HK, Lee SH, et al: CT and MR imaging findings of bowel ischemia according to the various primary causes. Radiographics 20:29–42, 2000.)

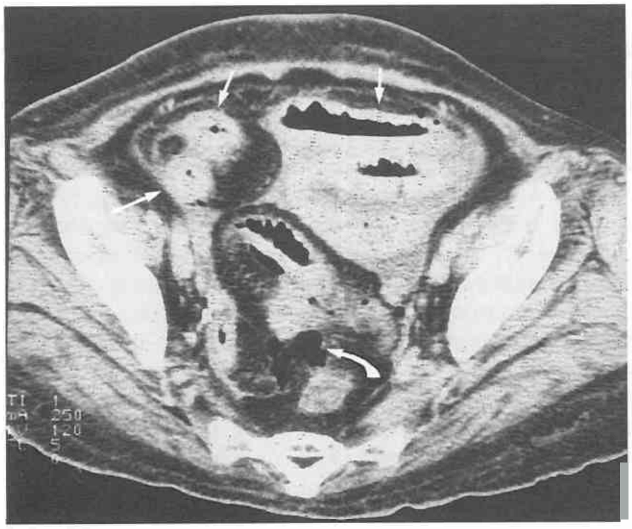

Figure 34–148. Chemotherapy-induced enteropathy with bowel necrosis and perforation in a patient receiving chemotherapy for leukemia. CT scan shows bowel wall thickening *(arrows)* of the ileum with free gas *(curved arrow)* in the pelvic cavity. Note the intraperitoneal fluid collection, which proved to be hemoperitoneum at surgery. (From Rha SE, Ha HK, Lee SH, et al: CT and MR imaging findings of bowel ischemia according to the various primary causes. Radiographics 20:29–42, 2000.)

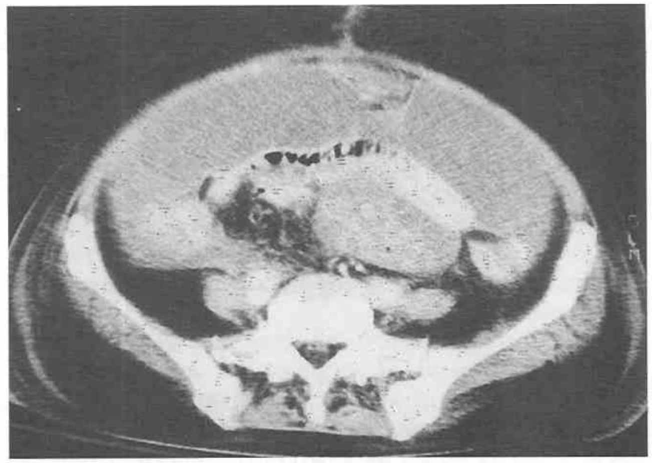

Figure 34–150. Perforated radiation enteritis in a patient with a history of radiation therapy for cervical cancer. CT scan shows bowel wall thickening of the ileum with a large amount of ascites and free gas (not shown).

ultimately require surgery because of perforation, bleeding, fistula, or stricture formation.[61] Although the involved bowel segments depend on the radiation mantle selected, the sigmoid colon, rectum, and terminal ileum are the most common sites affected by chronic radiation enteritis.

The diagnosis of chronic radiation enteritis is difficult because patients often present many years after treatment and the disease often simulates recurrent cancer or adhesion. CT findings of radiation enteritis are relatively nonspecific. CT may demonstrate a masslike confluence of adherent bowel loops with thickening of the bowel wall, thickening of adjacent mesentery, or increased density of mesenteric fat (Figs. 34–149 and 34–150).[159] The important CT findings that help to differentiate chronic radiation enteritis from other conditions, such as recurrent malignant disease, include the distribution of changes within the radiation therapy port and the absence of a mass.

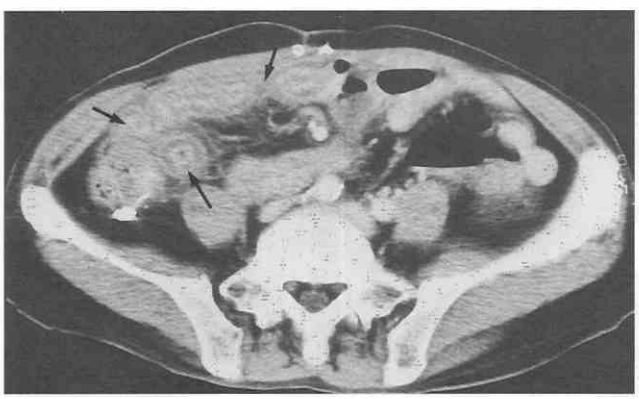

Figure 34–149. Acute radiation enteritis in a patient with a history of radiation therapy for periureteral metastases from rectal cancer. CT scan shows bowel wall thickening *(arrows)* of the ileal loops, with the target appearance confined to the radiation port. (From Rha SE, Ha HK, Lee SH, et al: CT and MR imaging findings of bowel ischemia according to the various primary causes. Radiographics 20:29–42, 2000.)

Large Intestine

Techniques and Normal Anatomy

The imaging protocols for achieving an adequate opacification and distention of the colon are variable, depending on the preferences of the radiologist, the time available for scanning, the types of contrast material used, and the purpose of the examination. Although we prefer a dilute (2% to 3%) barium suspension, the use of dilute iodinated contrast material is safer in patients with trauma or suspected bowel perforation. Patients with suspected enterovesical fistula should undergo pelvic imaging after administration of oral and rectal contrast medium but before administration of IV contrast medium.[261] This sequence may help to confirm the visualization of small amounts of oral contrast agent entering the bladder via a fistulous tract before the filling of the bladder with the contrast agent.

In general, administration of 400 to 600 mL of oral contrast material is given the evening before or 2 to 3 hours before CT scanning. Alternatively, the patient drinks 450 mL of contrast material 45 minutes before the CT procedure and ingests a tablet of metoclopramide, which hastens the transit of the oral contrast material through the small bowel. The use of metoclopramide eliminates the need for administration of oral contrast material on the evening before the examination and is recommended for outpatients and for emergency studies in inpatients.

The more proximal small bowel is opacified by taking a second cup of 450 mL of contrast agent 30 minutes before the examination. Immediately before CT scanning, another 250 mL of contrast agent is given to fill the stomach and duodenum. Air insufflation per rectum is another useful means of distending the colon.[400] It allows

accurate assessment of bowel wall thickness and detection of small intraluminal lesions. However, the air insufflation technique should not be used in patients with suspected perforation, clinically severe forms of colitis, radiation enterocolitis, or profound neutropenia.[261] A rectal contrast enema (200 to 500 mL) or air insufflation can be selectively used for the maximal distention of the distal colon and rectum. An injection of 1 mg of glucagon may reduce the colonic spasm, allowing more accurate assessment of bowel wall thickness through the maximum distention of the colorectum. Vaginal tampons are helpful to delineate the anatomic structures of the lower pelvis in women.

IV contrast material is now used in patients with suspected colonic pathology almost routinely regardless of inflammatory, vascular, or neoplastic diseases because an analysis of the contrast enhancement pattern of the involved bowel often suggests the diagnosis. Use of thin sections may reduce partial-volume averaging, allowing more accurate assessment of bowel wall thickness and extent of disease. Moreover, thin-section CT enables excellent multiplanar reformations.

A total of 150 mL of IV contrast agent is generally used at an injection rate of 2 mL/second. The entire abdomen and pelvis should be scanned in patients with suspected or proven colonic malignancy because many patients have metastatic intra-abdominal disease. In selected cases, and often in patients with recurrent colonic neoplasms in which the main focus may be the liver and upper abdomen, a dedicated liver protocol is obtained with thin axial sections through the liver.

On CT, the colon is visualized by its anatomic location and its typical haustral morphology. It appears as a ringlike or tubular structure, depending on the orientation and position relative to the scanning plane. Recognition of the cecum is facilitated by visualization of the terminal ileum, ileocecal valve, or appendix. The appendix appears as a small ringlike or tubular structure. The presence of air or contrast material in the appendix along with normal-appearing surrounded fat may not be indicative of appendicitis. The ascending and descending colons are within the anterior pararenal space and usually are surrounded by homogeneous fatty tissue. The transverse colon is suspended within the peritoneal cavity by the transverse mesocolon.

The rectum is about 12 to 15 cm in length. The peritoneum covers the anterior surface of the upper rectum, and the lower two thirds of the rectum is enveloped by extraperitoneal connective and adipose tissue. Within the subperitoneal space, a fascial plane (perirectal fascia) encloses the perirectal fatty tissue and separates it from the more peripherally located pararectal connective tissue.

The degree of development of the perirectal fascia varies among individuals, and it is rarely seen in normal patients. Thickening of perirectal fascia helps in early CT recognition of inflammatory or neoplastic involvement of perirectal and pararectal spaces.[194] The colon is commonly filled with fecal material that appears as gas-containing structures and often mimics a soft tissue mass. In certain instances, repeated CT with the patient in various positions may be required to differentiate fecal material from a polypoid colonic mass.

The wall of the normal colon measures 3 mm or less in thickness when the colon is distended with oral contrast material. Walls measuring between 4 and 6 mm in thickness suggest pathology, and a thickness of more than 6 mm is definitely abnormal. When the air-contrast technique is used, however, measurements of 3 mm for the rectum and 2 mm for the colon are at the upper limit of normal.[622] The luminal margin is usually smooth, being well outlined on the mucosal side by contrast or air. The outer colonic margin is sharply outlined by surrounding homogeneous pericolonic fat. Inflammation adjacent to the colonic wall obliterates the sharpness of the outer colonic margin by increasing the density of the pericolonic fat.

Benign Tumors

Adenoma

Hyperplastic or adenomatous polyps are the most common benign neoplasms of the colon. Because of their small size (<1 cm), however, imaging studies may play no role for the detection. In patients with larger polyps, CT may help in identifying these lesions, but no specific findings to distinguish adenocarcinoma have been reported. According to one series,[101] villous adenomas may have a characteristic CT appearance as a result of their high mucus content, producing a soft mass containing homogeneous low attenuation (Fig. 34–151).

Lipoma and Teratoma

Lipoma of the colon is a benign neoplasm arising from the submucosal layer of the intestinal wall. Lesions may be asymptomatic but may cause symptoms when they are large (>2 cm), especially in cases associated with intussusception or ulceration of the overlying mucosa. Seventy percent of the lesions are located in the right colon and usually in the cecum.[82] They are well demonstrated on CT scans because the masses present characteristic fatty attenuation. However, small lesions may be missed because of artifacts and mostly partial-volume averaging. Further-

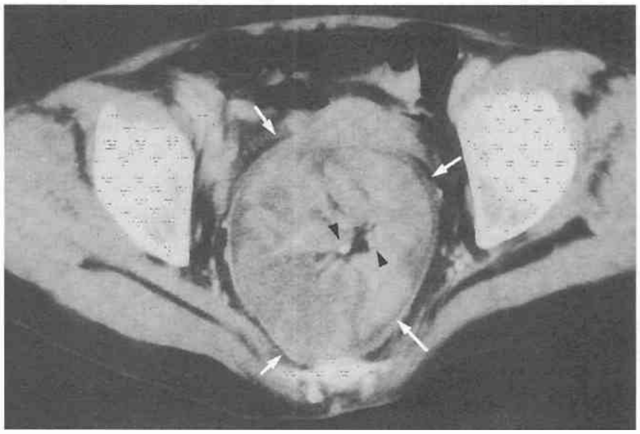

Figure 34–151. Villous adenoma with focal malignant transformation. A large polypoid mass *(arrows)* with heterogeneous contrast enhancement and a lobulated surface is seen in the rectum. Small vessels *(arrowheads)* supplying the pedicle are also visible within the mass.

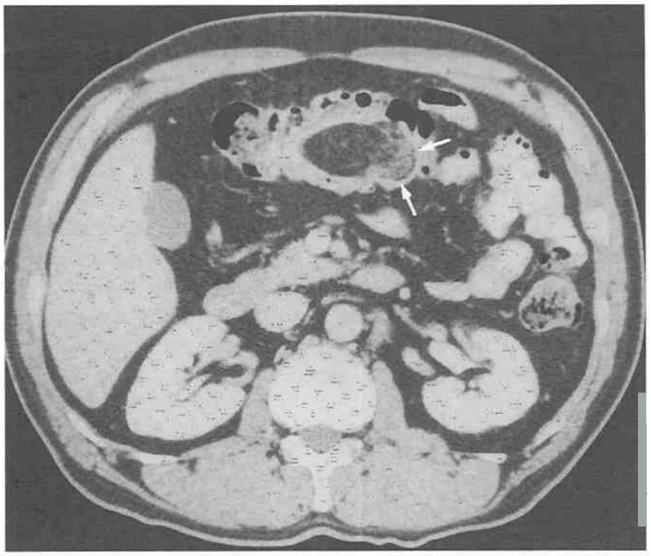

Figure 34–152. Colonic lipoma with focal fat necrosis. There is evidence of colocolic-type intussusception with a lipoma at the lead point. A focal area of high attenuation *(arrows)* in the lipoma results from focal fat necrosis.

more, the intussuscepted lipomas occasionally show focal or diffuse areas of soft tissue attenuation within the lesion and may be mistaken for other neoplasms (Fig. 34–152).

The changes in CT attenuation in such cases are directly related to the degree of infarction and fat necrosis within the lipoma.[67] Although uncommon, teratoma can occur in the colon. CT may show a mass made up of fatty and soft tissue components.[535] The presence of calcification may distinguish teratoma from lipoma.

Hemangioma

Diffuse cavernous hemangioma of the colon is an uncommon disease that affects mainly young adults. The rectosigmoid is the most common site in the GI tract. Chronic rectal bleeding is the main complaint of these patients. On gross examination, an extensive network of vascular lakes is found, involving the entire intestinal wall with infiltration into the surrounding connective tissue. On microscopic examination, the disease is characterized by large, thin-walled vessels with smooth muscle fibers and connective tissue stroma in a submucosal location.[99]

CT may show a transmural thickening of the involved segment, intramural and extrarectal phleboliths, vascular engorgement within the mesentery, and extrarectal lesions (Fig. 34–153).[458] MRI shows a markedly thickened rectosigmoid wall of very high signal intensity on T2-weighted images, which may result from slow flow in the vascular malformation and is considered to be a highly specific finding. Perirectal fat is also of very high signal intensity on T2-weighted images and exhibits heterogeneity related to serpiginous vascular structures.[360]

Cystic Lymphangioma

Cystic lymphangioma rarely occurs in the colon as a submucosal lesion. CT may show a sharply marginated, a

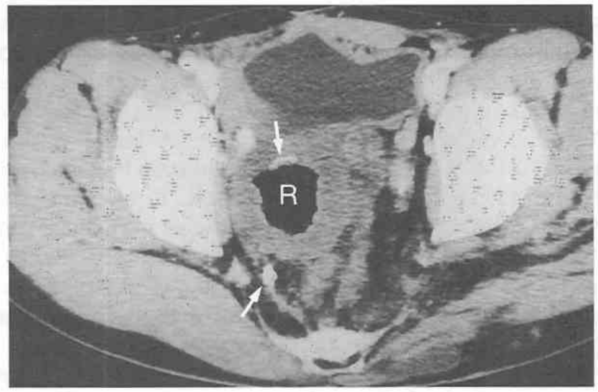

Figure 34–153. Hemangioma of the rectum. The bowel wall of the rectum (R) is concentrically thickened with poor contrast enhancement. Small phleboliths *(arrows)* are noted in the involved rectal wall as well as in the perirectal space.

multilocular, or a purely cystic mass.[618] Colitis cystica profunda may also have similar appearances on CT.

Colorectal Carcinoma

Primary Tumors

The ultimate goal of CT and MRI is to predict three factors that affect the patient's prognosis, including:

1. The depth of tumor penetration into the colonic wall.
2. The presence of regional or distant lymph node metastases.
3. The occurrence of distant metastases to other sites.

Except for the advanced colorectal tumors, CT and MRI have virtually no role in the initial diagnosis. On CT and MRI, a colorectal cancer appears as a discrete mass (Fig. 34–154) or focal wall thickening. Asymmetrical wall thickening with or without an irregular surface suggests a neoplastic process.

Generally, CT attenuation on contrast-enhanced scans correlates with tumor size but not with histologic type.[26] However, some series have shown that mucinous adenocar-

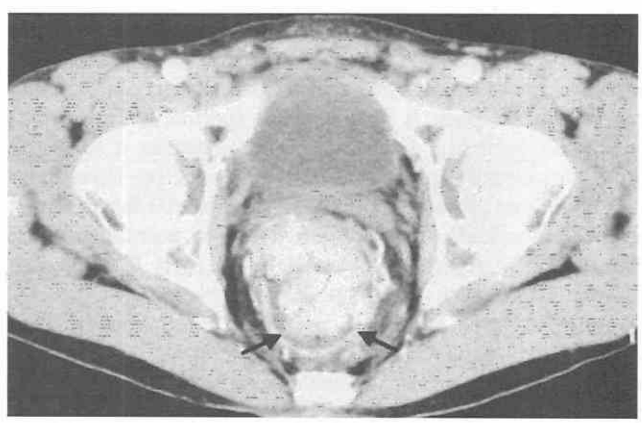

Figure 34–154. Polypoid rectal carcinoma. CT scan shows a large polypoid mass *(arrows)*, with a lobulated contour, protruding into the rectal lumen.

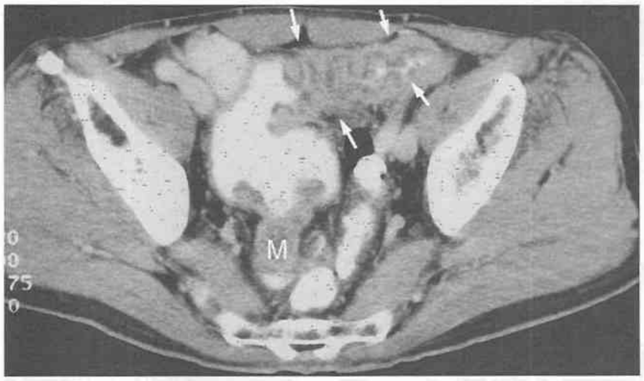

Figure 34–155. Rectal cancer in the proximal colon in a patient with colitis. CT scan shows a mass (M) in the sigmoid colon along with proximal colonic dilatation. Bowel wall thickening with a target appearance *(arrows)*, also shown in the proximal sigmoid colon, was confirmed as ischemic colitis on pathologic examination. Note the skipped area between tumoral and ischemic segments. (From Rha SE, Ha HK, Lee SH, et al: CT and MR imaging findings of bowel ischemia according to the various primary causes. Radiographics 20:29–42, 2000.)

cinoma was enhanced in a peripheral or heterogeneous, lacelike pattern as a result of excessive accumulation of extracellular mucin.[250] The presence of punctate or irregular calcifications within tumors may suggest the possibility of mucinous adenocarcinoma. Although rare, ossification may develop in the colorectal tumor.[35] In the area of the lower rectum and anus, internal hemorrhoids must be distinguished from a polypoid malignancy.

In 1% to 7% of cases of colorectal carcinoma, ischemic colitis may develop in the proximal colon. An understanding of this condition is important because the concomitant presence of an ischemic segment may give a false impression regarding tumor length or depth of tumor invasion. According to one series,[304] CT distinguished ischemic from tumoral segment in 75% of patients by the differences of both bowel wall thickness and contrast enhancement patterns (Fig. 34–155). In contrast to irregular thickening in the tumoral segment, the ischemic segment shows smooth and regular thickening; the target sign with low attenuation in the central zone was the most specific sign. Maximum thickness also differed, with a mean thickness of 2 cm in the tumoral segment and 1 cm in the ischemic segment.[304] In certain instances, the ischemic segment may be present in the proximal colon with intervening normal-appearing colonic mucosa.

In another series,[288] distal small bowel was affected in 10% of patients with right-sided colon cancer, especially the tumor involving the ileocecal region. The presence of both colonic and distal ileal thickening might be misinterpreted as inflammatory bowel disease or another neoplastic condition such as lymphoma, when CT imagers are not aware of a patient's history of colon cancer. The distal ileal involvement is caused either by direct tumor invasion or lymphatic spread or by non-neoplastic processes with edema and congestion (Fig. 34–156). Although a target sign in the thickened ileal wall favored the diagnosis of tumor extension, difficulty was encountered in differentiating tumoral from nontumoral involvement.[288]

Perforation occurring in 2.5% to 8% of patients with colorectal cancer is regarded as a poor prognostic sign. Because perforation is usually either localized or channeled into a fistulous tract, a significant percentage of patients with perforated colorectal cancer have no signs or symptoms of acute toxicity.[246] Except for the detection of enteroenteric fistulas, CT proved superior to barium studies in establishing the correct diagnosis. On CT scans, most of these patients showed a neoplastic mass with fluid-attenuation abscess or inflammatory changes in the pericolic or perirectal tissues (Fig. 34–157).[246]

The patterns of regional spread of disease in the lymph nodes may be predictable on CT. Left-sided colonic and rectal tumors tend to spread first to nodes in the mesocolic, left colic, and inferior mesenteric artery nodal groups.[196] Right-sided colonic tumors tend to spread first to lymph nodes at the root of the SMA and then into the retroperitoneum and to ascend along the paraaortic and aortocaval nodal groups.[389] Tumors of the hepatic flexure and proximal transverse colon initially spread to the paracolic nodal group and the nodes of the gastrocolic trunk, whereas distal transverse colon and splenic flexure tumors spread to nodes in the mesocolon along middle colic vessels.[389] Low rectal or anal tumors drain into the inguinal nodes.

Tumor Spread

When the tumor is confined to the wall of the colorectum, the outer margins of the large bowel appear smooth on CT scans and the perirectal or pericolonic fat has uniform low attenuation without soft tissue stranding. Extension of tumor beyond the bowel wall manifests as a mass with irregular outer borders with soft tissue stranding in the perirectal or pericolonic fat plane. Similar strandings can also be caused by fibrosis, inflammation, or congestive changes, and CT cannot detect microscopic invasion of the fat surrounding the colorectum. Therefore, a diagnosis of tumor invasion can be confirmed only when a tumor mass extends directly into an adjacent muscle (levator ani, obturator internus, coccygeus, piriformis, or gluteus maximus), obliterating the fat planes and enlarging the individual muscle or enveloping the neighboring structure (Figs. 34–158 through 34–160). In fact, the accuracy of conventional CT for detecting local tumor extension is not high (range, from 55% to 72%).[26, 170, 577] Accuracy increases with more advanced stages of disease, and most errors with CT have tended to overstage the tumors. Use of colonic preparation, air insufflation, water enema, and helical CT may improve the results to a certain degree.[10]

Several studies have evaluated the value of MRI in tumor staging. Major advantages of MRI are that tissue contrast is high and images can be obtained in multiple planes. Extension of tumor beyond the colonic wall is visible on T1-weighted images. Gadolinium enhancement can improve definition of tumor margins.

The reported sensitivities of MRI in staging perirectal invasion varies from 59% to 100%, depending on the method of examination technique. MRI would be equal or inferior to CT with the body-coil MR technique,[624] slightly better with the double-surface coil, and much better with the endorectal surface coil.[527] The most valuable merit of endorectal surface coil with T2-weighted MRI is its ability

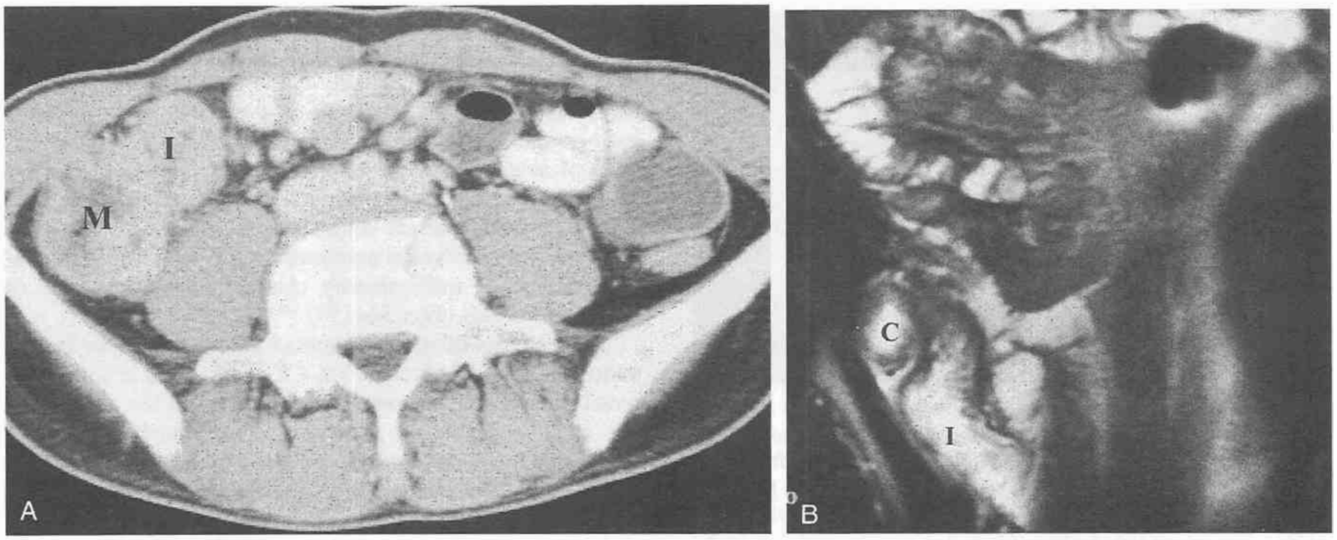

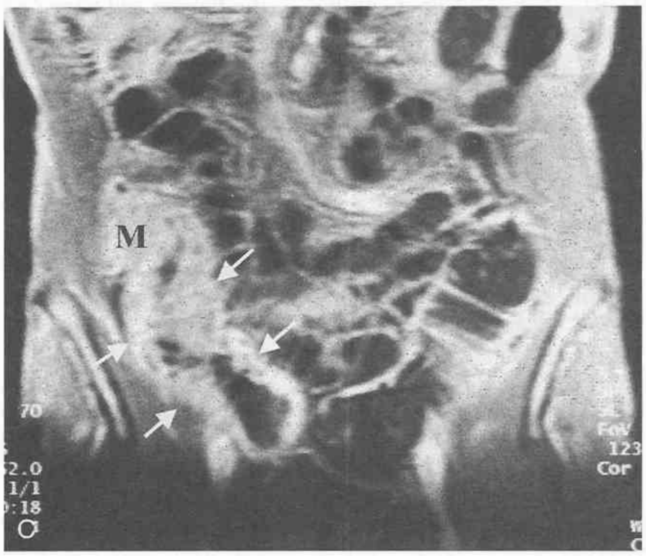

Figure 34–156. Adenocarcinoma of the ascending colon with extension to the distal ileum. *A,* CT scan shows a heterogeneous mass (M) in the ascending colon with irregular thickening of the distal ileum (I). *B,* Coronal half-Fourier acquisition single-shot turbo spin-echo (HASTE) MR image shows irregular thickening of the bowel wall in the ascending colon (C) and distal ileum (I). *C,* Coronal gadolinium-enhanced MR image shows irregular bowel wall thickening of the distal ileum *(arrows)* with heterogeneous contrast enhancement. A mass (M) is visible in the ascending colon.

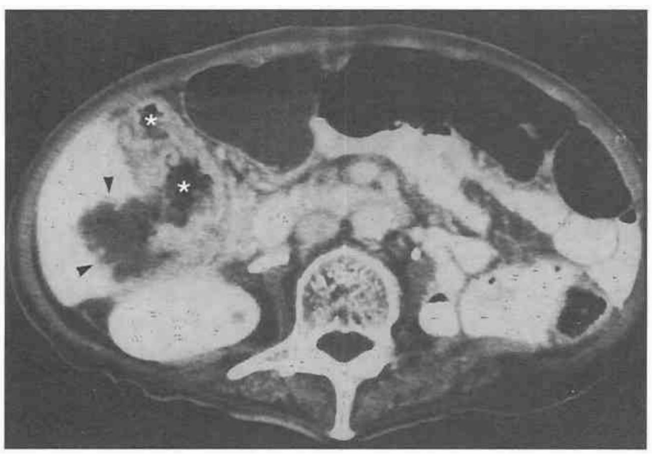

Figure 34–157. Perforated colon cancer. The colonic wall at the hepatic flexure is irregularly thickened *(asterisks)*, and its continuity is focally disrupted *(arrowheads)*. A hypoattenuated mass is formed in the adjacent hepatic parenchyma.

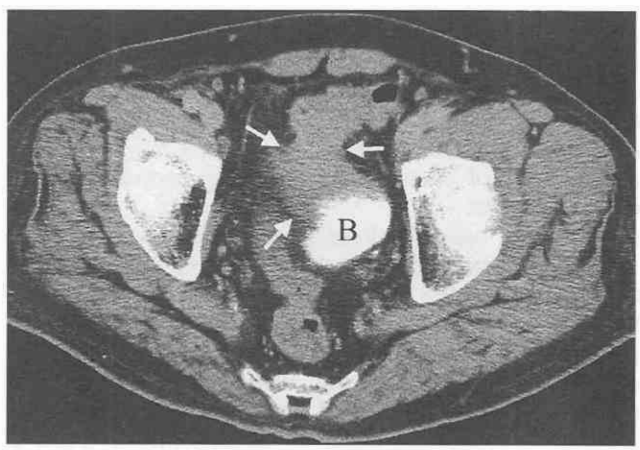

Figure 34–158. Sigmoid colon cancer with bladder invasion. CT scan shows irregular bowel wall thickening of the sigmoid colon *(arrows)*. The superior part of the bladder (B) is irregular because of direct tumor invasion.

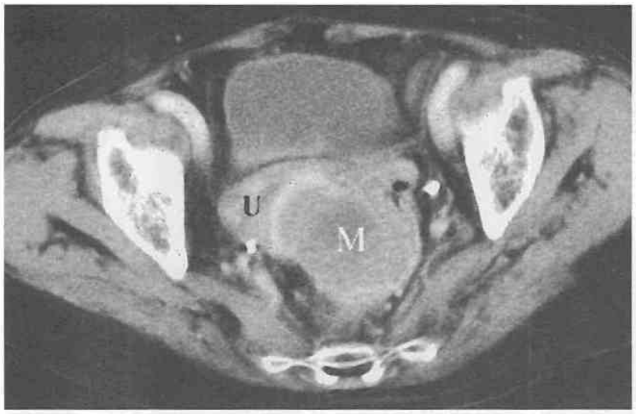

Figure 34–159. Rectal cancer with uterine invasion. CT scan shows a large heterogeneous rectal mass (M) with compression and direct invasion into the posterior wall of the uterus (U).

to discriminate the different layers of rectal wall; however, there is a tendency to overstage the lesion.[527]

Lymph Node Metastases

The detection of local adenopathy depends on nodal size, number, and clustering. Generally, lymph nodes measuring 1 cm or larger and clusters of three or more smaller nodes are considered abnormal. However, CT and MRI cannot distinguish hyperplastic and malignant nodes and cannot detect microscopic nodal involvement. Therefore, the reported sensitivity of CT and MRI is low (25% to 73%).[10, 26, 527, 577, 624] Thus, no currently available imaging modality may be used to identify, with certainty, lymph node involvement.[62] However, any nonenhancing nodes in the perirectal fat should be considered malignant lymphadenopathy, regardless of size, because hyperplastic lymph nodes do not occur in this region.

Distant Metastases

Hepatic metastases are the most common site of hematogenous spread in colorectal cancer and appear as areas of low attenuation on CT. Punctate or amorphous calcification can be seen in the hepatic metastasis from mucinous colonic adenocarcinoma.

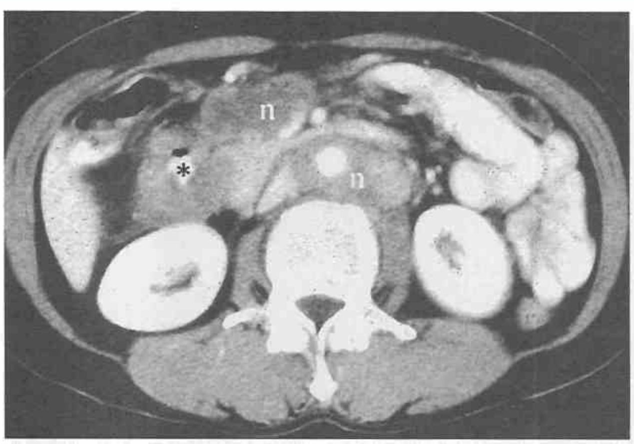

Figure 34–160. Ascending colon cancer (not shown) with duodenal invasion. CT scan shows heterogeneous duodenal wall thickening *(asterisk)* along with lymphadenopathy (n) in the retroperitoneum and peripancreatic region.

Dynamic studies using helical CT scanning may demonstrate varying appearances over time.[573] In the early phase, a contrast-enhanced and complete peripheral ring can be seen. If the scan is repeated in the portovenous phase, the lesion itself may enhance with a heterogeneous pattern or target lesions may become evident. Isoattenuation due to "fill-in over time" is the major cause of false-negative CT results in patients thought to have hepatic metastasis. Such lesion isoattenuation is particularly frequent, with smaller masses smaller than 2 cm and conventional, nonhelical CT scanners.

Sometimes a metastasis can appear identical to a simple benign cyst, an eosinophilic abscess, a granuloma, or a hemangioma. According to the surgical literature,[604] liver resection for hepatic metastases is considered if screening CT shows lesions only in one lobe of the liver as long as only one to four metastases are detected, no other lesions are present in the normal-appearing lobe, the lobe without lesions shows normal function, no focal adenopathy is identified, and no distant spread is evident. If results are equivocal, at least two imaging modalities should be used to exclude the presence of hepatic metastases.

Tumor Recurrence

Local recurrence of a rectal or sigmoid colon carcinoma is often encountered after surgery; it develops during the first 12 months in 50% of patients and within 24 months in more than 80%.[572] CT is highly sensitive in detection of pelvic masses, but lack of specificity limits it application (Figs. 34–161 and 34–162). The sensitivity of CT in diagnosis of local recurrence is greater in patients with abdominoperineal resection than in those with anterior resection.[402]

Findings indicative of tumor recurrence include invasion of surrounding structures (muscle, bladder), enlarged local lymph nodes, or a rounded soft tissue mass increasing in size on follow-up scans. Another important sign indicating recurrence is the presence of ischiorectal fossae invasion (Fig. 34–163).[500]

According to one series,[284] a soft tissue mass commonly develops in the presacral space or in the area of surgical

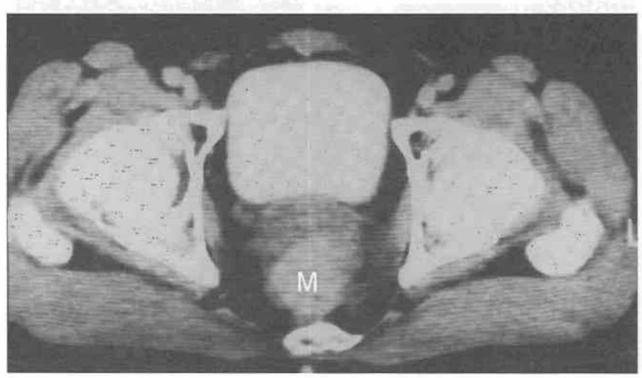

Figure 34–161. Recurrent rectal cancer following abdominoperineal resection. A well-enhancing soft tissue mass (M) is seen in the presacral space posterior to the prostate gland.

Figure 34–162. Postsurgical fibrosis following abdominoperineal resection for rectal cancer. A round, well-enhancing soft tissue mass *(arrows)* is seen in the presacral space.

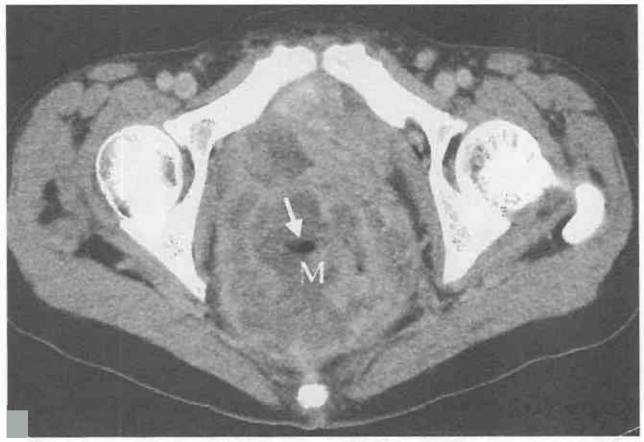

Figure 34–164. Mucinous adenocarcinoma of the rectum. CT scan shows a large heterogeneous mass (M) with areas of cystic components. Note marked luminal narrowing of the rectum *(arrow)*.

bed as a result of postoperative fibrous tissue, a displaced uterus or prostate gland, and nonopacified loops of small bowel. However, CT cannot accurately distinguish fibrosis from tumor recurrence (see Figs. 34–161 and 34–162).[283, 323] Because a single CT examination has an inherent limitation in suggesting the correct diagnosis, it is recommended that a baseline CT scan be performed 3 to 6 months after surgery to observe the evolution of changes in the operative bed and to detect early local recurrence in asymptomatic patients.[284]

MRI has been advocated as an alternative imaging method for the early assessment of tumor recurrence. An early study suggested that signal intensity on T2-weighted images was accurate in distinguishing tumor from fibrosis.[310] However, later studies have suggested that high signal intensity on T2-weighted images is not specific for recurrent tumor and can be seen in non-neoplastic, inflammatory changes or edema or in immature fibrosis that develops less than 1 year after surgery.[117] Moreover, low signal intensity can be found in both fibrosis and tumor with desmoplastic reaction.[117] In this regard, contrast-enhanced MRI, especially dynamic studies, may improve the results, although further investigation is required.[374, 418]

Mucinous Adenocarcinoma

Colorectal mucinous carcinoma has been regarded as a subtype of adenocarcinoma, with abundant extracellular mucin contained within the tumor. According to World Health Organization criteria for mucinous carcinoma, the mucin composition should be at least more than 50% of the tumor area for the diagnosis.[616] Compared with nonmucinous tumors, mucinous tumors are at a higher pathologic stage at diagnosis, have a greater tendency for metastasis and local recurrence, and carry an unfavorable prognosis.[561]

On CT scans, these tumors may show lower attenuation and commonly demonstrate intratumoral calcification than nonmucinous types (Figs. 34–164 and 34–165). On MR images, signal intensity is higher as a result of the presence of extracellular mucin.[250, 296] A peripheral or heterogeneous, lacelike contrast-enhancement pattern has been reported to be characteristic of these tumors.[250]

Figure 34–163. Perineal recurrence of rectal cancer following abdominoperineal resection. A heterogeneous soft tissue mass (M) extends to the left ischiorectal fossae.

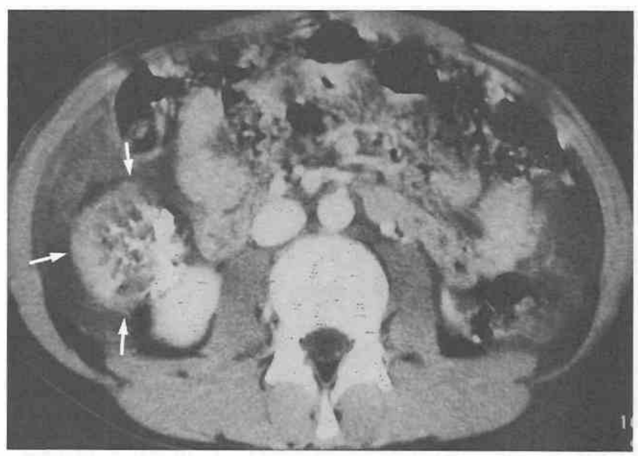

Figure 34–165. Development of mucinous colonic carcinoma in a patient with juvenile polyposis. A large mass *(arrows)* in the ascending colon contains multiple calcifications.

Primary Signet Ring Cell Carcinoma

Primary colorectal signet ring cell carcinoma is a rare condition, constituting between 0.1% and 2.4% of all colorectal carcinomas.[142] In the GI tract, it usually produces minimal mucosal alterations but permeates the wall extensively, thereby transforming the affected organ into a rigid and contracted structure. Therefore, this disease is also known as a *linitis plastica* type of carcinoma.

Compared with ordinary colorectal adenocarcinoma, signet ring cell carcinoma commonly occurs in younger patients and tends to spread to the pelvic lymph nodes, the ovaries, and the peritoneal surfaces with a low incidence of hepatic metastasis.[7] Moreover, its clinical course is aggressive, with a high incidence of local recurrence.[7]

Radiologically, it mimics an inflammatory lesion rather than a carcinoma owing to the long length of involvement. On CT scans, the most common feature of this tumor is a long segment of concentric bowel thickening (Fig. 34–166).[290] When the rectum is involved, extension to the level of anal verge is common.

Another important CT feature includes target appearance in the thickened colorectal wall. The inner zone of thickened bowel wall with target sign is markedly enhanced owing to abundant fibrous tissues secondary to desmoplastic response. However, these atypical features, such as long length of bowel wall thickening and target appearance, have been noted in approximately 50% of cases with signet ring cell carcionoma.[290]

Because of its long length of bowel wall thickening, primary colorectal signet ring cell carcinoma may simulate many other conditions; among those, metastatic linitis plastica from stomach, breast, gallbladder, bladder, or prostate[149] may have exactly the same CT appearance.[205] Therefore, without knowledge of the clinical history of tumor at other sites, CT differentiation of these two conditions may not be possible. Other conditions that should be considered in the differential diagnosis are lymphoma and inflammatory and vascular disorders (e.g., Crohn's disease, ulcerative colitis, pseudomembranous and ischemic colitis) and gynecologic diseases (e.g., endometriosis, actinomycosis).

Metastatic Tumor

As seen in the stomach and small bowel, metastatic disease can occur in the colon as a result of peritoneal seeding, direct invasion, and hematogenous or lymphatic spread. CT helps not only in discriminating primary from secondary neoplasms to the colon but also in identifying the primary tumor in other sites. The rectum may be affected by direct extension of tumor from the prostate or cervix. Secondary involvement by extension along mesenteric reflection is seen in the transverse colon where neoplasms of either gastric or pancreatic origin extend to the colon. The anterior wall of the rectum is the most common site of peritoneal seeding; other locations include the sigmoid and transverse colons and along the paracolic gutters.

Although not common, hematogenous metastases, especially from breast, melanoma, or lung cancers, produce polypoid masses in the colon and even cause intussusception.[544] In such instances, it may be difficult to differentiate mucosal polyps from primary colonic tumor. At other times, metastatic tumors may show diffuse involvement of the colonic wall with an annular or linitis plastica appearance on CT, mimicking primary colonic carcinoma or inflammatory bowel disease (Figs. 34–167 and 34–168).

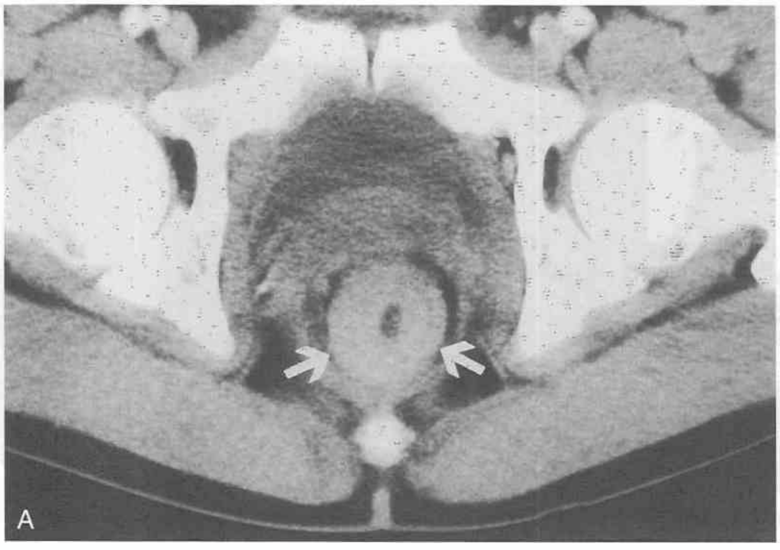

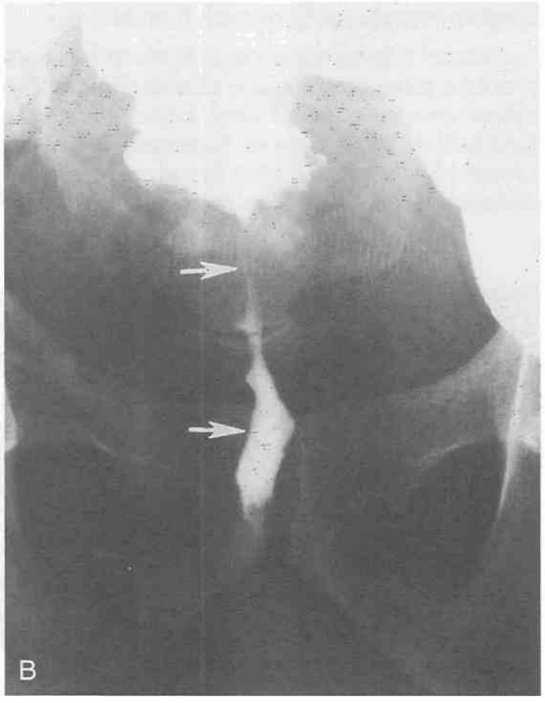

Figure 34–166. Primary "signet ring" cell carcinoma of the rectum. *A,* CT scan shows concentric bowel wall thickening *(arrows)* with the "target sign" in the rectum. *B,* Double-contrast barium enema shows a long segment of concentric luminal narrowing *(arrows)* along the rectum with minimal irregularity of the mucosal surface.

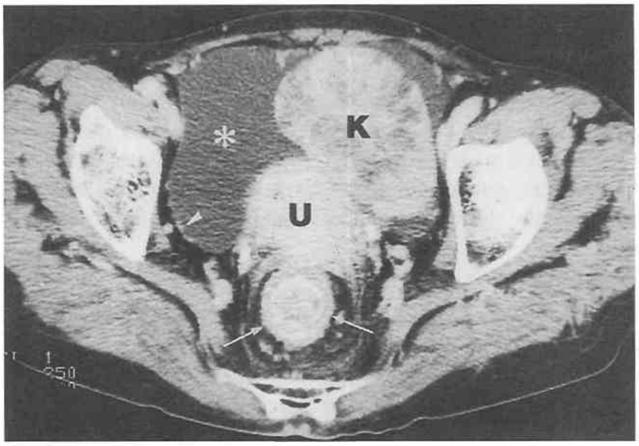

Figure 34–167. Metastatic tumor of the rectum with Krukenberg's tumor of the ovary after gastrectomy for gastric cancer. CT scan shows concentric thickening *(arrows)* of the rectal wall with the "target sign." The surface of the uterus (U) appears irregular, and there is evidence of a left ovarian mass (K), ascites *(asterisk)*, and focal thickening of the peritoneum *(arrowhead)*. (From Ha HK, Jee KR, Yu E, et al: CT features of metastatic linitis plastica to the rectum in patients with peritoneal carcinomatosis. AJR Am J Roentgenol 174:463–466, 2000.)

Such linitis plastica pattern of colonic involvement may result from the intramural spread of tumor cells through the submucosa or subserosa in association with bowel peristaltic movement.[149] Because an important pathologic characteristic of linitis plastica is the exuberant desmoplastic reaction in the submucosa and subserosa, the occurrence of a target sign in diffusely thickened wall is commonly seen on CT scans.[205]

Gastrointestinal Stromal Tumors

Stromal tumors occur rarely in the colorectum, with the rectum a more common site than the colon. These tumors appear as a submucosal mass growing toward the lumen *(endocolic)*, away from it *(exocolic)*, or in a combined *(dumbbell)* form. In certain instances, a constricted form occasionally has also been reported.[491] In general, clinical symptoms correlate with the types of tumor growth: *intramural* types cause pain, bowel habit changes, and intestinal obstruction; *pedunculated* tumors commonly develop intussusception or bleeding owing to degeneration; and *exocolic* tumors may have a common occurrence of peritoneal metastasis.[554]

Seventy percent of rectal stromal tumors are located in the lower rectum, 20% are in the midrectum, and 10% are in the upper rectum. In the remaining part, these tumors are located equally in the ascending colon, the transverse colon, and the descending colon.[352] Because of the high incidence of late recurrence, some investigators suggest that most colorectal stromal tumors should be regarded as potentially malignant neoplasms.[593]

Generally, stromal tumors have varying degrees of internal necrosis or cystic changes on CT, predominantly in cases of malignant forms (Fig. 34–169). The presence internal dystrophic calcification within a tumor suggests the possibility of stromal tumor in the colon, although this finding can be seen in both benign and malignant forms (Fig. 34–170). The tumor growth patterns may be helpful in differentiating the benign from malignant form; endophytic tumor growth favors the diagnosis of benign rather than malignant form.[93]

Stromal tumors arising from the rectum may be difficult to diagnose preoperatively. Many possibilities occur in considering the differential diagnosis, depending on the patient's gender or the direction of tumor growth. Tumors growing in an *anterorectal* direction may be easily confused with prostatic and gynecologic tumors, such as uterine, cervical, and ovarian tumors or a mass arising from the rectovaginal septum. Stromal tumors growing in the *retrorectal* direction should be differentiated from other unusual sarcomas or lymphomas.

In contrast with cases of rectal cancer, rectal stromal tumors usually show an absence or mild degree of obstruction owing to the position of the main tumoral component in the extraluminal space.[15] Except for its poor sensitivity for detection of internal tumoral calcification, MRI may be

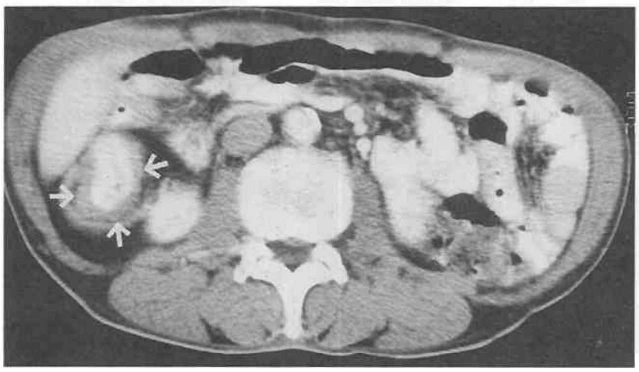

Figure 34–168. Metastatic linitis plastica involving the ascending colon in a patient who had undergone gastrectomy for gastric cancer. CT scan shows marked luminal narrowing of the ascending colon with concentric bowel wall thickening *(arrows)* in addition to the "target sign" markedly enhancing the inner zone.

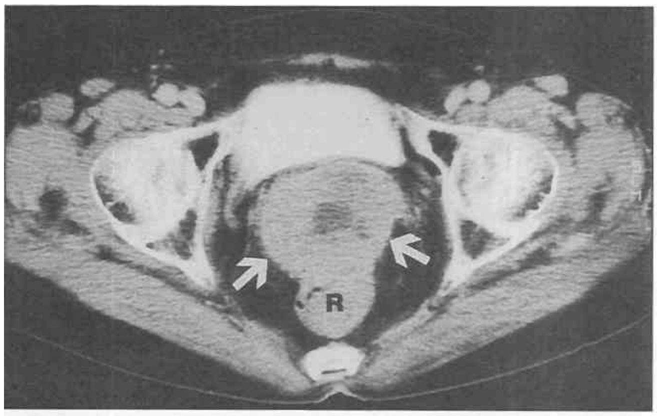

Figure 34–169. Rectal leiomyosarcoma. CT scan shows a heterogeneous mass *(arrows)* of rectal (R) origin growing exophytically and displacing the vagina anteriorly. (From Lee SH, Ha HK, Byun JY, et al: Radiological features of leiomyomatous tumors of the colon and rectum. J Comput Assist Tomogr 24:407–412, 2000.)

Figure 34–170. Rectal leiomyosarcoma. CT scan shows a calcified mass *(arrows)*, anterior to the rectum *(arrowhead)*, simulating a prostatic mass. (From Lee SH, Ha HK, Byun JY, et al: Radiological features of leiomyomatous tumors of the colon and rectum. J Comput Assist Tomogr 24:407–412, 2000.)

comparable to CT in evaluating the morphology of the tumors.[326]

Lymphoma

Primary lymphoma of the colon is relatively rare, constituting approximately 0.05% of all colonic neoplasms and fewer than 3% of all extranodal lymphoma.[124] Non-Hodgkin's lymphoma is the most predominant type, and the cecum and rectum are the most common sites of involvement. Colonic lymphoma may be (1) infiltrative, (2) polypoid, (3) cavitary, or (4) diffuse.

On CT, the *infiltrative* form is characterized by a long segment of concentric luminal narrowing by diffuse tumor infiltration into the submucosa, simulating primary colonic carcinoma (Fig. 34–171) However, in patients with lymphoma, the occurrence of aneurysmal dilatation is common, and the degree of contrast enhancement of the mass is usually poor owing to a lack of desmoplastic reaction.

CT may not distinguish a *polypoid* form of lymphoma from primary colonic adenocarcinoma (Fig. 34–172). However, lymphoma may be a possibility when the tumor extends to the terminal ileum, when diffuse mesenteric lymphadenopathy and splenomegaly are associated, and when the tumor shows no evidence of invasion or obstruction of neighboring viscera.[607] In the cavitary form of lymphoma, large tumors may excavate into the mesentery, producing a giant cavitated mass.

In the *diffuse* form of lymphoma characterized by multiple nodules of relatively small size, CT may not detect the nodules but helps in staging the tumor.

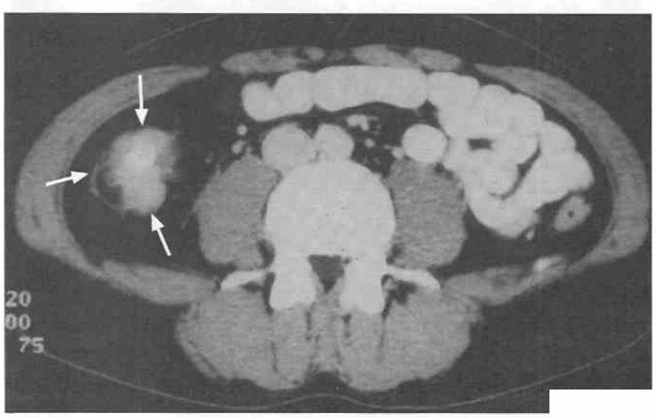

Figure 34–171. Colonic lymphoma. Bowel wall of the ascending colon *(arrows)* is irregularly thickened.

Mucocele

Mucocele of the appendix is a descriptive term for an abnormal mucus accumulation distending the appendiceal lumen, regardless of the underlying cause. Mucoceles usually result from obstruction of the appendiceal lumen. Both benign and malignant lesions can produce a mucocele, consisting of mucosal hyperplasia, mucinous cystadenoma, and mucinous cystadenocarcinoma.[233]

Preoperative diagnosis is important because of the possibility of rupture at surgery with the development of pseudomyxoma peritonei (described later). On CT, a mucocele appears as a low-attenuation, well-encapsulated mass with smooth, regular walls in the right lower quadrant. The degree of attenuation depends on the amount of mucin in the mass. No periappendiceal inflammation or abscess is the key differential point in excluding acute appendicitis. Calcification occasionally develops in the wall of the mucocele, owing to a dystrophic response to a chronic inflammatory process incited by the mucus; this can ultimately lead to a *porcelain appendix*.[106]

Although uncommon, intussusception may develop. *Myxoglobulosis*, a variant of mucocele, is seen in 0.35% to 8% of cases and is characterized by an appendix filled with "translucent globules," or a cluster of "frog eggs."[106] When these spheres calcify, they become evident on CT and may shift in the appendix with changes in body position. The presence of a thickened wall suggests the possibility of a neoplastic mucocele, and enhancing nodules favor the diagnosis of mucinous cystadenocarcinoma (Fig. 34–173).[297]

Rupture of a mucocele may result in pseudomyxoma peritonei, characterized by implants of mucinous epithelium on the peritoneal surfaces and mucus accumulation within the peritoneal cavity (Fig. 34–174).

Inflammation

Crohn's Disease

Patients with Crohn's disease are at increased risk for colorectal cancer. According to one study,[223] colorectal cancer occurred an average of 10 years earlier than sporadic cancer and is more often of the mucinous type. Rectal sparing is a characteristic of Crohn's disease that helps distinguish it from ulcerative colitis, but perirectal and perianal lesions occur in up to one third of patients, especially those with colonic involvement.

The most common CT finding of Crohn's colitis is bowel wall thickening (mean thickness, 11 mm).[461] It is often discontinuous and may have skip areas. Although a double-halo appearance of the bowel wall has been re-

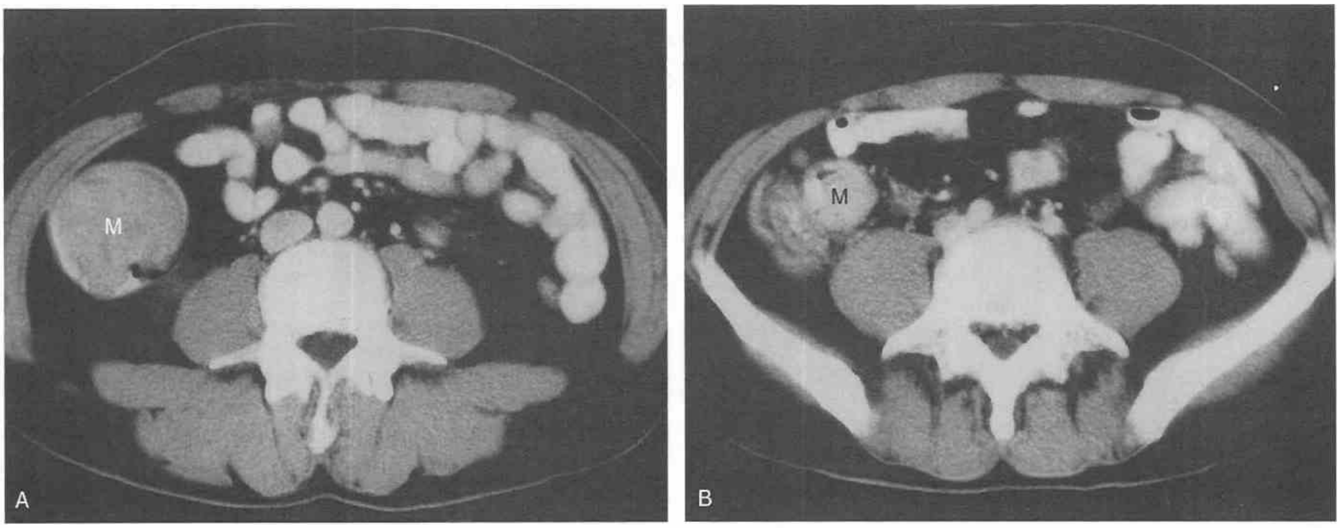

Figure 34–172. Colonic lymphoma. *A,* A polypoid mass (M) is [redacted] in the ascending colon. *B,* The mass (M) extends into the terminal ileum.

ported in Crohn's disease involving the small intestine,[167] most patients show homogeneously attenuated bowel wall thickening when the colon is involved (Fig. 34–175).[461] Marked contrast enhancement in the early phase of dynamic study and the presence of hypervascularity in the pericolic space and mesentery may indicate acute exacerbation of the disease. Perianal disorders, which are quite common in patients with Crohn's disease, include anal fissures and ulceration, perirectal abscess, and fistulas.

CT offers an excellent alternative to barium studies in fully defining the extent of perirectal disease, especially in patients with an exquisitely tender perineum or rectum in which the performance of barium enema and sinography is painful (Fig. 34–176).[494] In performing the CT scan for patients thought to have perianal disease, the scanning plane must continue caudal to the symphysis to include the entire perineum because of common occurrence of diseases beneath the level of the symphysis pubis.[619] Because of multiplanar capability, MRI is superior to CT in demonstrating the relationship between the pelvic and abdominal sinus tracts or fistulas and the levator ani muscle.[307]

In the differentiation with ulcerative colitis, Crohn's colitis may show even distribution between right-sided, left-sided, or bilateral disease and high frequency of both small-bowel involvement and abscess.[461] The presence of ascites is not common in Crohn's disease and instead suggests pseudomembranous, infectious, or ischemic colitis. Tuberculous colitis may have patterns of bowel wall changes similar to those of Crohn's disease. In tuberculous colitis, however, the occurrence of rectal involvement is rare; lymph nodes are larger than 1 cm and may show central necrosis. Moreover, the presence of CT findings of peritonitis, such as diffuse omental and mesenteric infiltra-

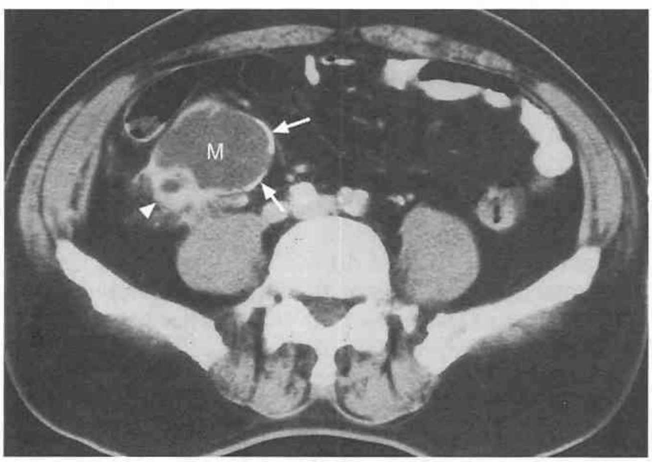

Figure 34–173. Mucinous cystadenoma of the appendix. A cystic mass (M) is noted in the pericecal region, which shows curvilinear calcification *(arrows)* in the periphery. The appendiceal wall *(arrowhead)* is concentrically thickened with minimal periappendiceal infiltrate.

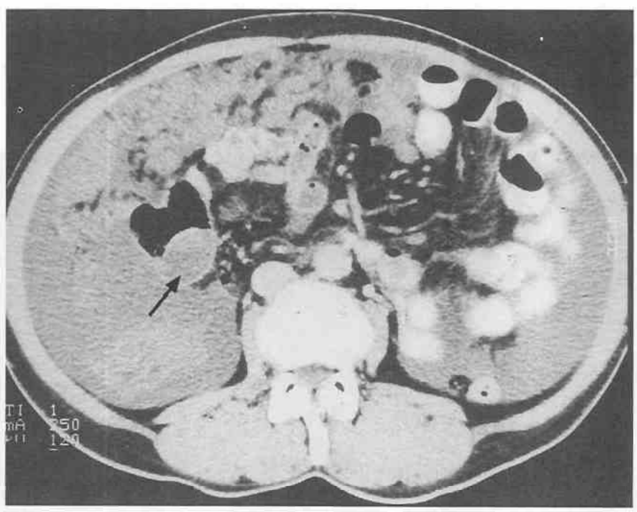

Figure 34–174. Mucinous cystadenocarcinoma of the appendix with pseudomyxoma peritonei. CT scan shows nodular omental infiltration and a large amount of ascites. A cystic mass *(arrow)* is seen in the pericecal region.

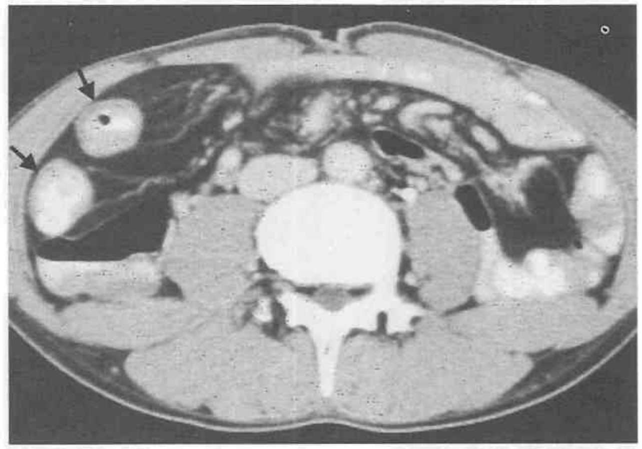

Figure 34–175. Crohn's disease. CT scan shows colonic wall thickening *(arrows)* with a faint demonstration of the "target sign" along with fibrofatty proliferation and prominent mesenteric vessels.

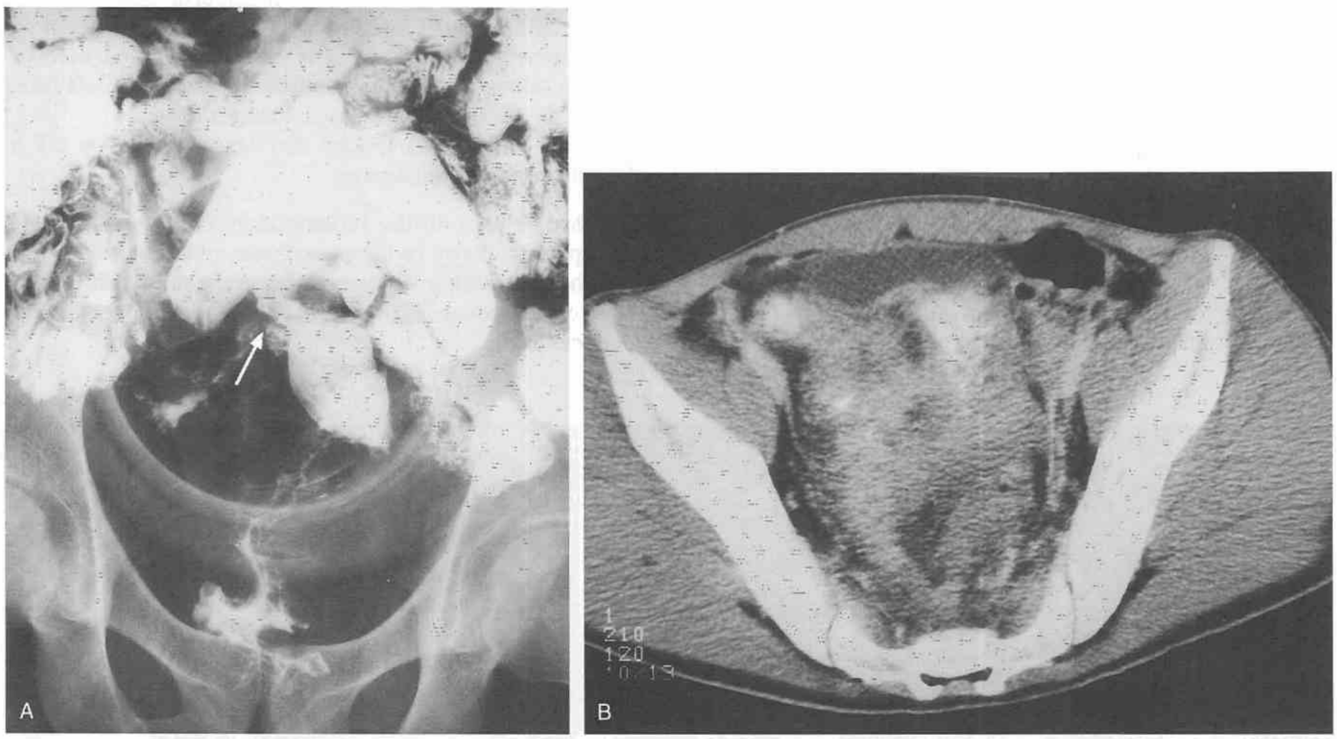

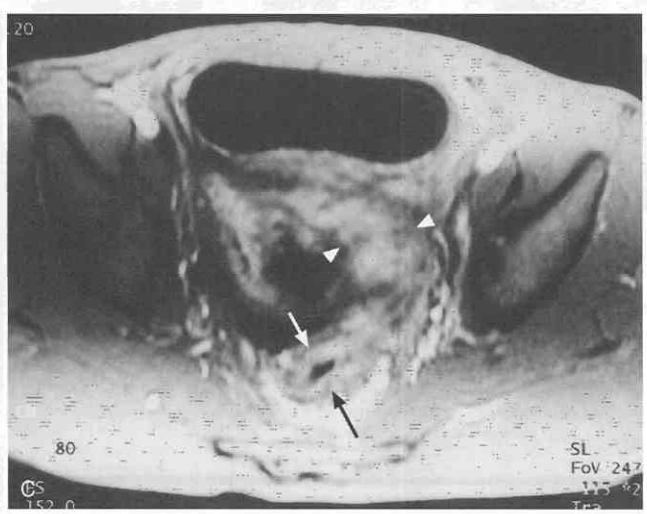

Figure 34–176. Crohn's disease with enterorectal fistula. *A,* Small-bowel follow-through examination shows an enterorectal fistula *(arrow)*. *B,* CT scan shows diffuse pericolonic, perirectal, and perienteric inflammatory infiltrates with bowel wall thickening of pelvic ileal loops. *C,* Gadolinium-enhanced MR image shows marked contrast enhancement in the thickened rectal wall *(arrows)* and inflammatory tissues *(arrowheads)* surrounding the fistula.

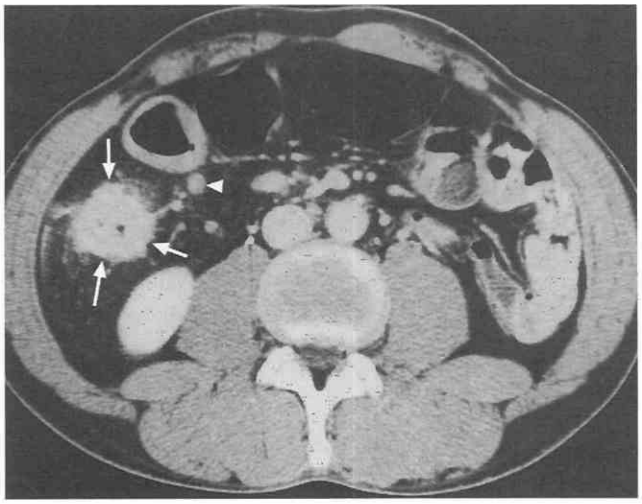

Figure 34–177. Tuberculous colitis. CT scan shows concentric bowel wall thickening *(arrows)* of the ascending colon with pericolonic stranding and minimal lymphadenopathy *(arrowhead).*

tion or nodules and ascites, may indicate tuberculous origin.

Tuberculous Colitis

Tuberculous colitis may have several forms, most commonly segmental colitis, inflammatory strictures, and hypertrophic lesions resembling polyps and tumors.[375] A rare form includes a diffuse type simulating ulcerative colitis.[17] The ileocecal area is involved in about 90% of the cases, and there is a decreasing frequency of involvement proximal and distal to the ileocecal valve.[1] Multiple sites of involvement are common with skip segments.[585] The length of stricture is usually shorter (<3 cm) than that of Crohn's disease.[565] Tuberculous lymphadenitis adjacent to the colon can result in colonic traction diverticula, bowel fixation, and sinus tract formation.[375] Although not common, anal TB may cause ulcers and fissures, fistulas, and abscesses.

On CT scans, the involved colon may show circumferential bowel wall thickening up to 3 cm. This thickening is usually homogenous in attenuation (Fig. 34–177); however, mural stratification (a double-halo or target sign) is rarely seen. Thickening of the ileocecal valve or the presence of inflammatory tissue (localized hypertrophic type), or segmental lesion in any sites of the colon may give the appearance of colonic carcinoma on CT. There are also no specific CT findings that can distinguish from Crohn's disease in the bowel wall involvement patterns, except for the distribution of disease; it is rare to see rectal involvement in tuberculous colitis, and the predominant left-sided colonic involvement may favor Crohn's disease.

Active tuberculous lesions may be suggested on CT in the following circumstances:

1. When there is diffuse inflammatory infiltrates or, rarely, hypervascularity in the pericolonic space.
2. When the enlarged lymph nodes in the pericolonic space or other sites are diffusely enlarged or show central low attenuation.

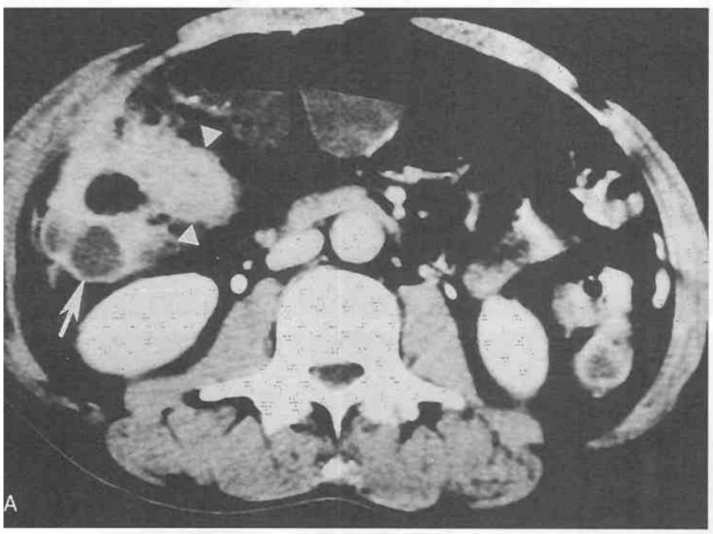

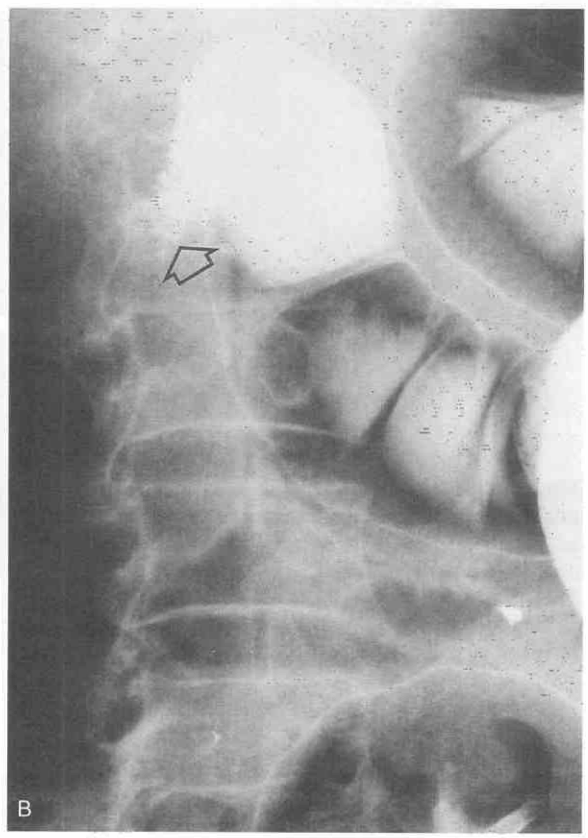

Figure 34–178. Perforated tuberculous colitis. *A,* CT scan shows mass-like bowel wall thickening *(arrowheads)* with colonic obstruction. Ill-defined soft tissue–attenuated lesion is seen in the pericolic space. There is also evidence of loculated fluid collection *(arrow). B,* Barium study shows nearly complete colonic obstruction at the hepatic flexure of the colon.

Figure 34–179. Ulcerative colitis. The bowel wall of the rectum and sigmoid colon is minimally thickened with a target appearance *(arrowheads)*.

3. When there is evidence of diffuse peritonitis, such as ascites, infiltration, or nodules in the omentum or mesentery, and peritoneal thickening.

The latter two findings also favor the diagnosis of tuberculous colitis rather than Crohn's disease. Although not common, fibrofatty proliferation can be seen in the pericolonic space. Healing of ileocecal lesions may result in shortening of the ascending colon. In such cases, the thickened terminal ileum may be easily misinterpreted as ascending colon on CT. In comparison with tuberculous enteritis, the incidence of colonic obstruction is low because of a larger luminal diameter in the colon, but it rarely occurs in hypertrophic type of tuberculous colitis. Colonic perforation due to tuberculous colitis is also rare (Fig. 34–178).

Ulcerative Colitis

Ulcerative colitis is characterized by a chronic mucosal disease with the inflammatory reaction that remains limited to the mucosa and the superficial portion of the submucosa. It usually starts in the rectum and then spreads more proximally, sometimes to involve the entire colon (pancolitis). In about one third of the cases, the ileum is involved by backwash ileitis. In active stages of the process, the mucosa shows a diffuse, uniformly granular, and erythematous, hemorrhagic appearance, and the entire bowel becomes fibrotic, narrowed, and shortened in the advanced stage.

When the disease is limited to the mucosa, the colon appears normal on CT scans; the presence of active ulceration does not significantly alter the CT appearance of the colonic wall. In patients with chronic disease, CT may show bowel wall thickening caused by hypertrophy of the muscularis mucosa and deposition of submucosal fat (Figs. 34–179 and 34–180).[192]

The mean bowel wall thickness is 7.8 mm in ulcerative colitis and 11 mm in Crohn's disease.[461] In about 70% of patients with ulcerative colitis, the thickened bowel wall may show heterogeneous attenuation, with a target appearance due primarily to submucosal fat. This target appearance is most commonly observed in the rectum but less frequently in the remainder of the colon.[271] Submucosal fat deposition is seen only in the chronic or subacute disease[461] and may result from a long-term use of corticosteroid therapy.

An additional CT feature favoring the diagnosis of ulcerative colitis includes widening of the presacral space, which results from a combination of increased presacral fat deposition, luminal narrowing of the rectum, rectal wall thickening, and stranding of the perirectal fat.[261] Although rarely seen, pneumatosis may develop in severe ulcerative colitis.[461]

MRI may be a new imaging modality in analyzing the mural changes in patients with ulcerative colitis,[179] but further experience is necessary to define its clinical role.

Local complications of ulcerative colitis include perforation with peritonitis and abscess (Fig. 34–181), toxic megacolon (Fig. 34–182), venous thrombosis, and carcinoma (Fig. 34–183). Because the risk of carcinoma is markedly increased in ulcerative colitis with a long-standing history (>10 years) or with pancolitis, CT findings of any focally exaggerated colonic wall thickening with pericolonic

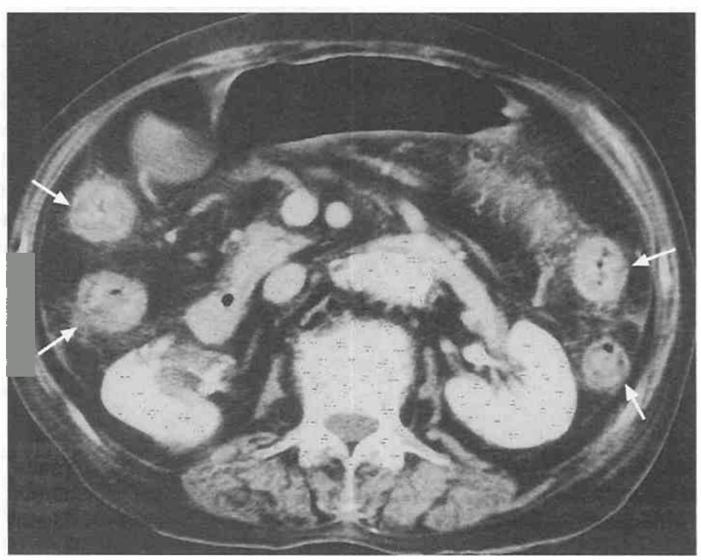

Figure 34–180. Ulcerative colitis. Heterogeneous bowel wall thickening *(arrows)* is noted in the ascending colon and descending colon. Minimal pericolonic infiltration is noted.

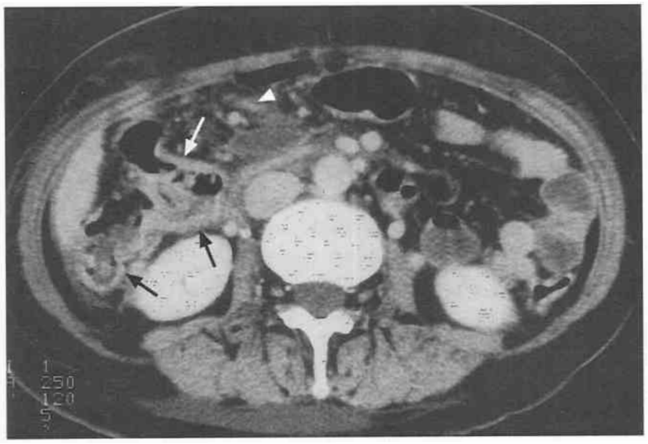

Figure 34–181. Bowel perforation in a patient with ulcerative colitis. The bowel wall *(arrows)* of the hepatic flexure of the colon is thickened with diffuse pericolonic infiltration and fluid collection. Free gas *(arrowhead)* is also noted.

lymphadenopathy in these patients should suggest the possibility of cancer development. The presence of toxic megacolon should be suspected on CT when the colonic lumen is considerably dilated (>8 cm).[191] Typically the bowel wall will be thinner rather than thick.

Diverticulitis

Colonic diverticulosis affects approximately 5% of the population, and acute inflammation occurs in 10% to 35% of these patients.[83] Diverticula are primarily caused by obstruction of diverticular neck with fecal material, subsequently resulting in distention and inflammation of the prediverticular tissues. In uncomplicated diverticulitis, the inflammatory process is confined to the colonic serosa. Microscopic perforations into the pericolic fat are usually walled off, forming focal abscesses; however, continued infection and inflammation can lead to peritonitis or fistulas. The inflammatory process can also dissect longitudinally within the wall of the colon, giving rise to intramural sinus tracts.

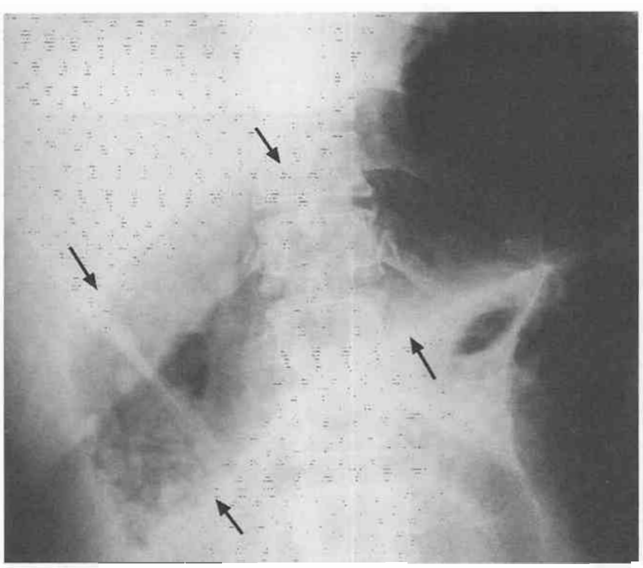

Figure 34–182. Toxic megacolon in a patient with ulcerative colitis. The transverse colon is markedly dilated *(arrows)* with nodular mucosal contour.

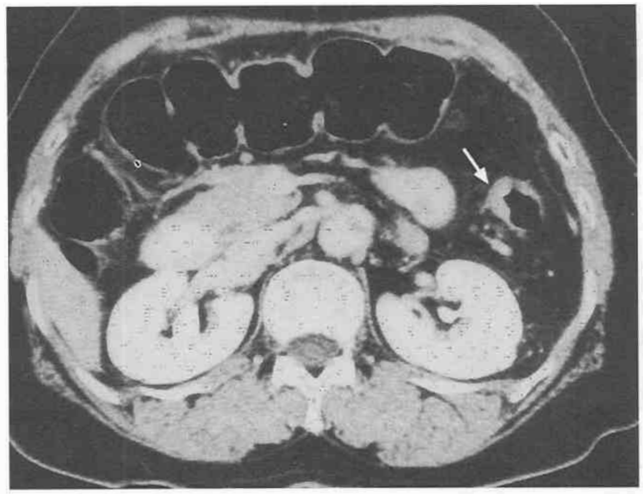

Figure 34–183. Colonic carcinoma complicating a long-standing ulcerative colitis. The splenic flexure of colon shows irregular bowel wall thickening *(arrow)* with proximal colonic dilatation caused by obstruction.

Although not common, diverticulitis also causes large-bowel and small-bowel obstruction,[289] portal and mesenteric vein gas,[599] venous thrombosis, and colovenous fistula to the inferior mesenteric vein.[514] The classic clinical symptoms and signs, especially in sigmoid diverticulitis, include left lower quadrant pain, tenderness, fever, and leukocytosis. Therefore, these signs may mimic many other acute abdominal conditions.

Although barium studies can be used, CT has been advocated as the initial procedure for radiologic evaluation for suspected acute diverticulitis. It is not only more suitable for grading the severity of pericolic inflammation but also more accurately depicts the presence, location, and size of pericolic abscesses.[90, 470] In addition, the use of CT is more effective in determining the alternative diagnosis.

The sensitivity of CT in diagnosis of diverticulitis is reported to range between 79% and 97%, with a specificity of 77% to 100%.[90, 270, 470, 484] According to some reports, the use of helical CT with thin-section CT[264] can improve the detection of diverticulitis. The most important CT findings of diverticulitis include diverticula, inflammatory bowel wall thickening, and pericolonic fat stranding (Figs. 34–184 to 34–186).[90] More severe cases may depict extraluminal air bubbles, phlegmon, pericolonic abscess, colonic fistula and sinus tracts, colonic obstruction, and peritonitis. In some instances, contrast material may collect in an arrowhead shape adjacent to focally inflamed colonic wall *(arrowhead sign)*,[488] and inflamed diverticulum appears as a thick, enhancing ring shadow within the area of inflamed peridiverticular tissues (see Fig. 34–184).[264]

A few reports[87, 446] have indicated an overlap with the imaging appearance of colon cancer in about 10% of cases of diverticulitis. The point of overlap includes colonic wall thickening of more than 1 cm, associated soft tissue mass, wall thickening with luminal narrowing, wall thickening

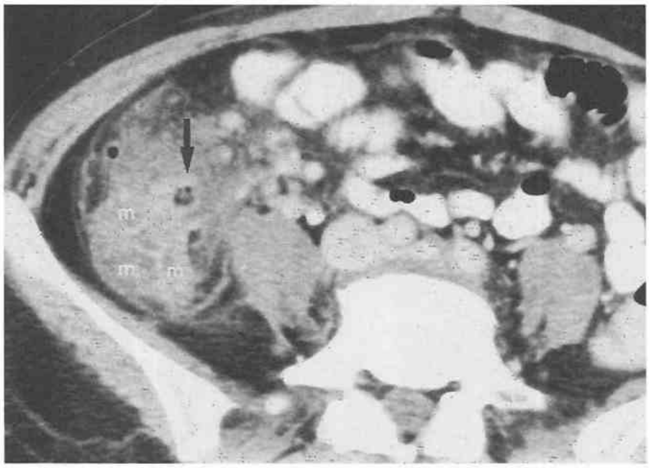

Figure 34–184. Acute diverticulitis. The inflamed diverticular wall *(arrow)* appears to be thickened, and there is diffuse mural edema (m) in the adjacent colonic wall. (From Jang HJ, Lim HK, Choi SH, et al: Acute diverticulitis of the cecum and ascending colon: Thin-section helical CT findings. AJR Am J Roentgenol 172:601–604, 1999.)

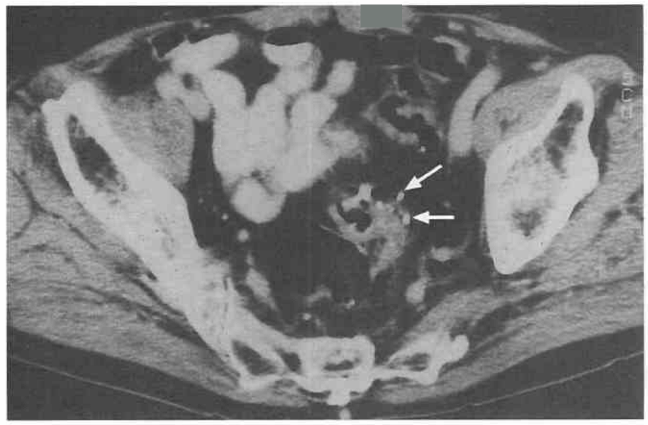

Figure 34–186. Diverculitis after response to antibiotic treatment. CT scan obtained after antibiotic therapy shows only multiple barium-filled diverticula *(arrows)* and minimal bowel wall thickening without pericolic inflammatory infiltrates.

without pericolic inflammation, and short segments of wall thickening.[87] CT findings favoring the diagnosis of acute diverticulitis include fluid at the root of the mesentery and vascular engorgement.[446] In contrast, an abrupt zone of transition with normal bowel, enlarged pericolic lymph nodes, and mural thickness greater than 1.5 cm favor colonic carcinoma (Fig. 34–187).[87]

Right-sided diverticulitis represents only about 5% of cases in Western populations but accounts for 17% in Asian patients.[351] Although CT findings are similar to those of left-sided diverticulitis, it may be difficult to differentiate cecal diverticulitis from appendicitis unless a normal appendix is seen. The presence of an intramural abscess or cecal diverticula, in association with an inflammatory process located cephalad to a normal-appearing cecal caput and the periappendicular region, should suggest the diagnosis.[25] The offending diverticulum may contain gas, fluid, contrast material, or calcified material.[264]

Appendicitis

Appendicitis is one of the most common causes of acute abdomen. Although the clinical diagnosis is usually made on the basis of history, physical examination, and laboratory data, approximately 20% to 33% of patients with suspected appendicitis present with atypical features.[346] Up to 20% negative appendectomy rates have been considered to be acceptable.[346]

CT is now regarded as the most accurate diagnostic test for excluding appendicitis. The reported diagnostic accuracies of CT range between 93% and 98%, with a sensitivity of 90% to 98% and a specificity of 83% to 98%; alternative diagnostic rates range between 48% and 80%.[27, 314, 483, 485]

A variety of CT techniques have been used for appendiceal imaging, including unenhanced and contrast-enhanced

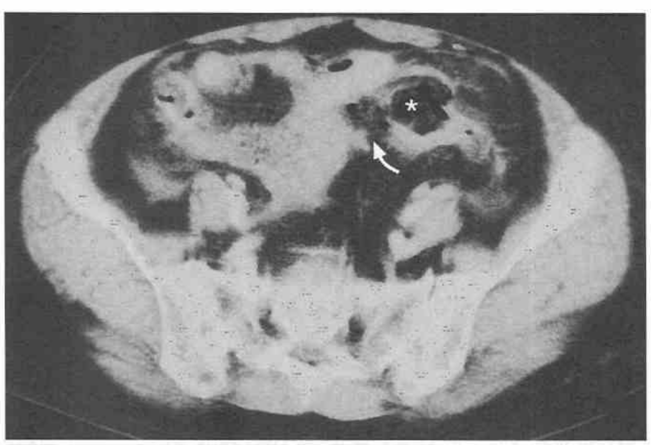

Figure 34–185. Diverticulitis of the sigmoid colon. The wall of the sigmoid colon *(asterisk)* is thickened. A small amount of free gas collection *(curved arrow)* and infiltrates is seen in the pericolonic space.

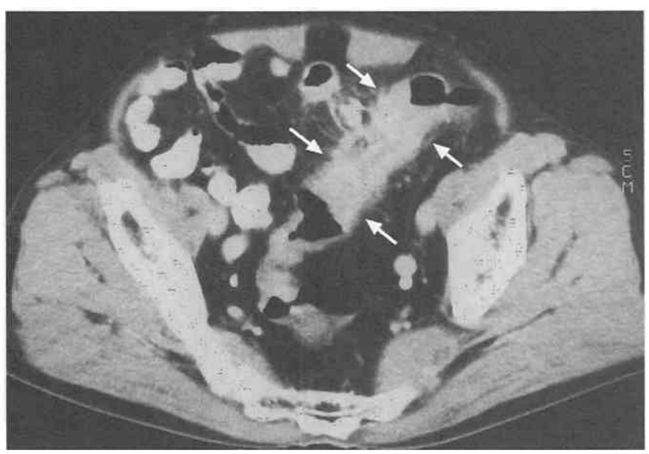

Figure 34–187. Colon cancer simulating diverticulitis. The sigmoid colon shows concentric bowel wall thickening *(arrows)* with an abrupt transition between normal and tumoral segments. Pericolonic stranding is also noted.

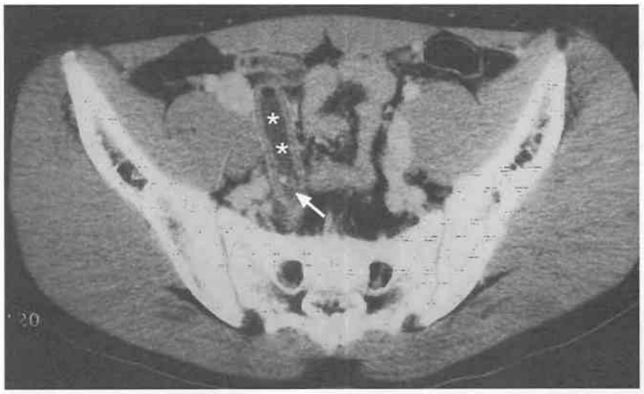

Figure 34–188. Acu[redacted]ppendicitis. The appendix *(asterisks)* is dilated with a thickened wall owing to mural edema. A small appendicolith *(arrow)* is also seen.

CT, conventional and helical CT scanning, full and limited abdominopelvic scanning, and various combinations of contrast materials.[27, 314, 483, 485] Among various techniques, use of both unenhanced and helical CT scans appear to have some merits.[314, 483, 485]

The advantage of unenhanced CT scans is that their use can eliminate the risk of an adverse reaction to IV contrast material and is less expensive. Helical CT scans may eliminate the risk of missing the appendix by misregistration; also, relatively thin-section images can be easily obtained. The importance of optimal cecal opacification and distention with contrast material has been stressed.[483, 485] Contrast material can be administered only through the colon or both by mouth and through the colon; however, each technique shows no statistical difference in achieving high diagnostic accuracy.[483, 485]

CT features in typical cases of acute appendicitis include an abnormal appendix, periappendiceal inflammation, and changes in the cecal apex. The abnormal appendix is distended and nonopacified, showing a diameter wider than 6

Figure 34–189. Periappendiceal abscess with small-bowel obstruction. A thick-walled, cystic mass *(arrows)* containing high-attenuated appendicolith *(arrowhead)* is seen at the right lower quadrant. Small-bowel loops are diffusely dilated as a result of bowel obstruction.

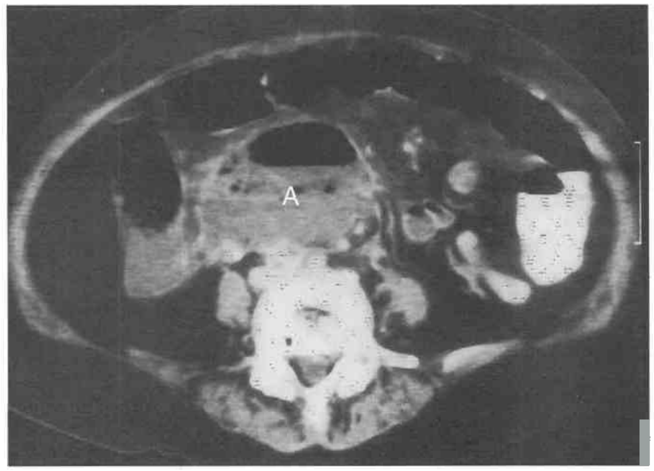

Figure 34–190. Perforated acute appendicitis with abscess. An abscess (A) with air-fluid level is noted in the root of the mesentery.

mm, wall thickening and enhancement after contrast infusion, and appendicoliths (Figs. 34–188 and 34–189). Periappendiceal inflammatory changes include fat stranding, phlegmon, fluid, free air bubbles, abscess, and adenopathy (Figs. 34–190 and 34–191).

Changes in the cecal apex include focal cecal apex thickening, an arrowhead sign, and a cecal bar; the arrowhead sign indicates a collection of contrast material between each side of the cecal apical thickening, and the cecal bar is a straight or slightly curved band of inflamed soft tissue that separates proximal calcified appendicolith from cecal lumen.[490] Although highly specific, the presence of appendicolith does not always indicate appendicitis and may be an incidental finding.

Variants of appendiceal disease include (1) recurrent, (2) chronic, (3) stump, and (4) distal appendicitis.

Stump appendicitis occurs after appendectomy with simple ligation without appendiceal stump invagination; the residual stump acts as a small appendix or diverticulum (Fig. 34–192).

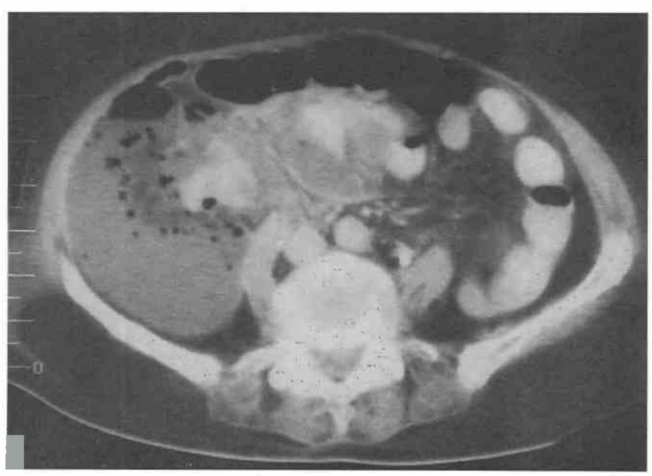

Figure 34–191. Acute appendicitis with free perforation into the peritoneal cavity. A large amount of intraperitoneal fluid collection with free gas is present.

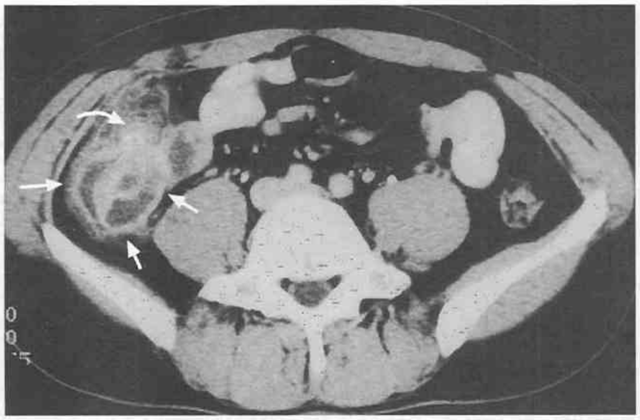

Figure 34–192. Stump appendicitis. A small appendicolith *(curved arrow)* is noted within the appendiceal stump. The wall of the cecum *(arrows)* is considerably thickened as a result of mural edema. There is also evidence of inflammatory infiltrates in the pericecal fat plane.

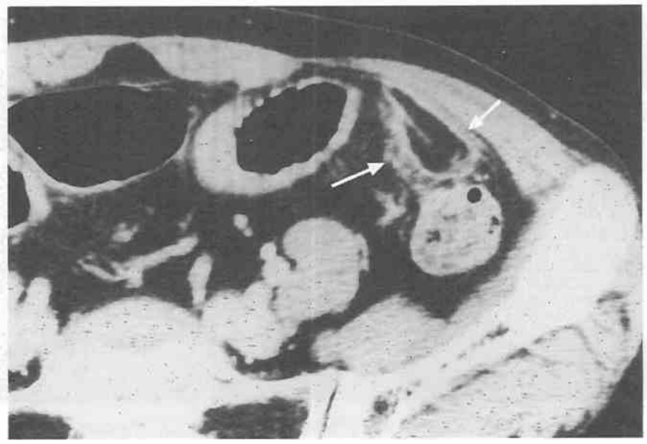

Figure 34–193. Appendagitis in patient with left lower abdominal pain and tenderness, mild fever, and leukocytosis. CT scan shows a pericolonic, oval-shaped, fatty lesion *(arrows)* with an enhancing peripheral wall. Pericolonic fat strands also surround this lesion.

Distal appendicitis is a potential cause of false-negative CT results, which may show a normal cecal apex and proximal appendix, a gradual or abrupt enlargement of the distal appendix, and periappendiceal fat stranding.[486]

MRI can also be used in the diagnosis of appendicitis.[255] Intense contrast enhancement of the inflamed appendiceal wall indicates the presence of appendicitis. However, MRI has inherent limitations in detecting appendicoliths.

Epiploic Appendagitis

Epiploic appendices (appendices epiploicae) are sacs of visceral peritoneum that are filled with fat and vascular structures and protrude from the serosal surface of the colon. The average person has approximately 100 appendices epiploica that are distributed from the cecum to the rectosigmoid junction. Rarely, epiploic appendages may undergo torsion or spontaneous venous thrombosis with subsequent ischemic infarction and inflammation; this condition is termed *primary epiploic appendagitis*.[575] The torsion has been reported to be related to heavy exercise or excessive stretching.[504]

Secondary epiploic appendagitis is caused by inflammation of adjacent organs (i.e., in diverticulitis, appendicitis, or cholecystitis).

Patients with primary epiploic appendagitis characteristically present with an abrupt onset of focal abdominal pain, mild fever, and mild elevation of the white blood cell count, which is often mistaken for appendicitis or diverticulitis. Most cases can be managed conservatively with the use of analgesics only.[489]

The diagnosis can be made confidently on CT, and this disease can be differentiated from other, far more common conditions such as appendicitis and diverticulitis. The important CT findings include pericolonic, oval-shaped lesions with fat attenuation, thickened peritoneal lining, and periappendageal fat stranding (Fig. 34–193).[109, 504] Additional findings include a central high-attenuating dot and a thickened nearby parietal peritoneum as well as mass effect, focal wall thickening of adjacent colon, or both. *Omental infarction* may produce similar CT findings, but it appears as a larger lesion without a well-defined rim of thickened visceral peritoneum.

Pseudomembranous Colitis

Pseudomembranous colitis is a potentially life-threatening acute infectious disorder associated with the overgrowth of *Clostridium difficile* after antibiotic use. Although virtually all antibiotics may produce the disorder, clindamycin, ampicillin, and cephalosporins are agents most commonly associated. Most cases occur when the drug is given orally rather than parenterally. Pseudomembranous colitis may also occur in other clinical settings such as bowel ischemia, intestinal obstruction, uremia, abdominal surgery, or chemotherapy.[509]

The disease usually involves the colon but may include only the small bowel or both colon and small bowel. In the colorectum, the rectum and sigmoid colon are typically involved. In approximately 30% to 40% of cases, however, pseudomembranous colitis can be limited to the right side of colon with sparing of the rectosigmoid or even the entire left side of colon.[156]

The classic clinical presentation includes abdominal pain, watery diarrhea, fever, and leukocytosis. CT is helpful not only in suggesting the diagnosis but also in evaluating the extent of disease. Common CT findings include colonic wall thickening, low-attenuation mural thickening corresponding to mucosal and submucosal edema, the accordion sign, the target sign, pericolonic stranding, and ascites (Figs. 34–194 and 34–195). The average colonic wall thickness (14.7 mm) is nearly twice that reported in the ulcerative colitis and more than that reported in Crohn's disease (7.8 and 13 mm, respectively).[156]

The accordion sign indicates alternating edematous haustral folds separated by transverse mucosal ridges filled with oral contrast material. Although this sign was once considered specific for the diagnosis of pseudomembranous colitis,[156] it can be seen in other edematous and inflammatory conditions affecting the colon, such as portal hypertensive colopathy and ischemic colitis.[363] Ascites is seen in

Figure 34–194. Pseudomembranous colitis. CT scan shows marked bowel wall thickening of the sigmoid colon and rectum *(asterisk),* producing a target appearance. Diffuse pericolic and perirectal infiltration is seen.

approximately 35% of cases.[156] Untreated cases of pseudomembranous colitis can result in toxic megacolon with subsequent perforation and peritonitis. However, CT does not help to distinguish patients requiring surgical intervention from patients requiring conservative management.[278]

Cytomegalovirus Colitis

CMV is a herpesvirus that can be sexually transmitted or transmitted via infected organs, blood, or needles. CMV remains in a latent state in the host after initial infection. With increasing impairment of cell-mediated immunity, particularly a CD4 lymphocyte count lower than 100 mm^3, reactivation may occur.[592]

Clinically evident CMV infections most commonly affect immunosuppressed patients, including transplant recipients and patients with AIDS. However, CMV infection may occasionally occur in nonimmunosuppressed individuals, including patients with diabetes mellitus, those who receive corticosteroids or radiation therapy, and elderly patients.[553]

Although the incidence of small-bowel involvement is not rare, the colon is the organ most commonly affected by CMV infection. Before the AIDS epidemic, the cecum was the most common site of colonic involvement, but in approximately 50% of patient with AIDS the disease was confined to the descending colon, particularly to the rectosigmoid region. In severe forms, multiple ulcerations and perforations occur; the vasculitis resulting from the CMV endothelial cell involvement in the wall or submucosal vessels leads to tissue edema and necrosis with ulceration, hemorrhage, and perforation.[234]

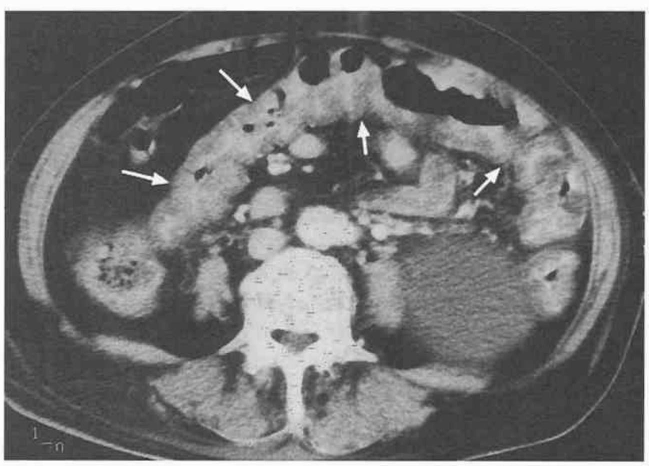

Figure 34–195. Pseudomembranous colitis. The colonic wall is diffusely thickened from the ascending colon through the rectum. The transverse colon shows the "accordion sign" *(arrows).*

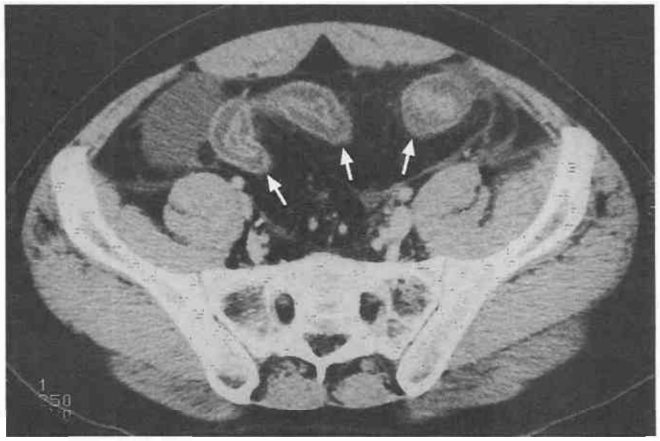

Figure 34–196. Cytomegalovirus colitis with bowel perforation. The sigmoid colon shows a thickened wall with a target appearance *(arrows).* Minimal pericolonic strands and a small amount of ascites are noted.

The clinical symptoms of CMV colitis are persistent diarrhea, fever, weight loss, abdominal pain, and hematochezia. The most prominent CT feature is colonic wall thickening with mural edema and deep ulceration (Fig. 34–196).[420] Other findings include pericolonic stranding, lymphadenopathy, and ascites. Because of nonspecificity of these findings, it is difficult to distinguish CMV infection from other colitides such as pseudomembranous colitis, although the relative high incidence of small-bowel involvement is a useful feature in this regard.[420]

Neutropenic Colitis (Typhlitis)

Neutropenic colitis, a necrotizing enterocolitis, occurs as a complication of acute leukemia or other neutropenic states such as aplastic anemia, SLE, or cyclic neutropenia. The cecum is most commonly involved, but the remaining colon and distal ileum may also be affected.

Various factors account for predominant cecal involvement by neutropenic colitis.[2] The cecum represents an area of relative stasis of bowel contents and is easily distensible. Mucosal ulcerations create a mural port of entry for the resident colonic microflora and allow the overgrowth of bacteria, viruses, or fungi, causing edema, thickening, and induration of the cecal wall.[2, 247]

Typical clinical features are fever, watery diarrhea, abdominal pain, and occasionally a palpable mass. CT findings are nonspecific and include concentric homogeneous or heterogeneous thickening of the bowel wall with intramural edema and necrosis, pericolic fluid, and pneumatosis intestinalis (Fig. 34–197).[171]

Figure 34–197. Development of typhlitis during chemotherapy for leukemia. CT scan shows concentric bowel wall thickening *(arrows)* of the cecum with poor contrast enhancement.

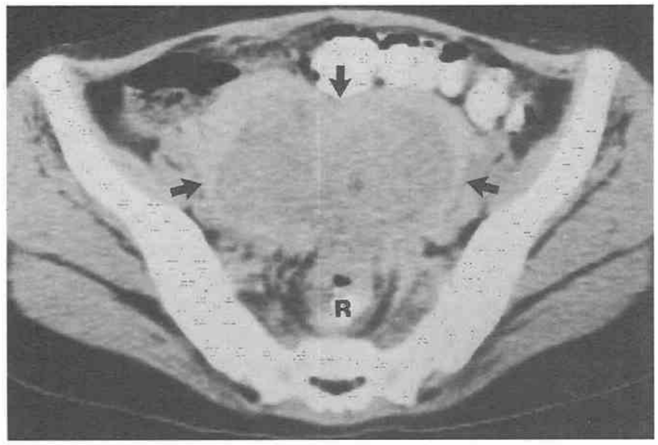

Figure 34–198. Actinomycosis. A large, bilobed, heterogeneous mass *(arrows)* in the ovary and bowel wall thickening of the rectum (R) are seen. (From Ha HK, Lee HJ, Kim H, et al: Abdominal actinomycosis: CT findings in 10 patients. AJR Am J Roentgenol 161:791–794, 1993.)

Uncomplicated neutropenic colitis is managed conservatively, if left untreated, neutropenic colitis progresses to transmural necrosis and colonic perforation, requiring surgery.[2]

Actinomycosis

Actinomycosis is a chronic, progressive, suppurative disease characterized by the formation of multiple abscesses, draining sinuses, abundant granulation, and dense fibrous tissue. This infection is considered to be caused by *Actinomyces* organisms (most commonly, *Actinomyces israelii*), which are gram-positive anaerobic bacteria; they are not regarded as virulent human pathogens and are best considered as opportunistic because they are normally present in healthy individuals, especially in the oral cavity, tonsillar crypts, and colon.[40] Dental caries are also common reservoirs of *Actinomyces*.[39]

A. israelii has a world-wide distribution and is present with equal frequency in urban and rural dwellers.[40] Although that there is no reported discemible sex predilection, most patients (94%) are women.[40, 612]

Human actinomycosis commonly occurs in three distinct forms. Most cases of clinical disease are *cervicofacial* (55%), with only 20% occurring in an *abdominopelvic* form and 15% as *thoracopulmonic* form.[39, 612] Abdominopelvic actinomycosis has been associated with abdominal surgery (such as appendectomy), bowel perforation, or trauma. The association with a long-standing intrauterine device has been emphasized as a risk factor in young women.[431] Various abdominal organs can be involved in abdominopelvic actinomycosis, including the GI tract, ovaries, liver, gallbladder, and pancreas.[40] In many instances, the GI tract appears to be secondarily involved and the rectosigmoid colon and ileocecal region, including the appendix, are most commonly involved.[40, 526]

The clinical features depend on which organs are involved, but common symptoms and signs include fever and leukocytosis.[40, 211] The presumptive diagnosis is made when "sulfur granules" are seen in the Papanicolaou smears of pus in the abscess or discharged material from the sinus tract.[203] Although histologic identification of actinomycotic granules or culture of *Actinomyces*[40] is important to establish a definitive diagnosis, the success rate is fewer than 50% of cases.[39]

The use of CT in patients with abdominopelvic actinomycosis is important for suggesting the diagnosis and determining the anatomic location and extent of disease as well as for monitoring the effectiveness of treatment and for follow-up in cases of possible recurrence.[211, 225]

Because of their aggressiveness and infiltrative nature, this disease can easily be mistaken for GI malignancy on CT scans, including carcinoid tumor, intestinal TB, Crohn's disease, diverticulitis, and other complicated GI infections. When the GI tract is involved, the main CT features include bowel wall thickening (mostly concentric) (Figs. 34–198 and 34–199). The mean wall thickness of 1.2 cm and

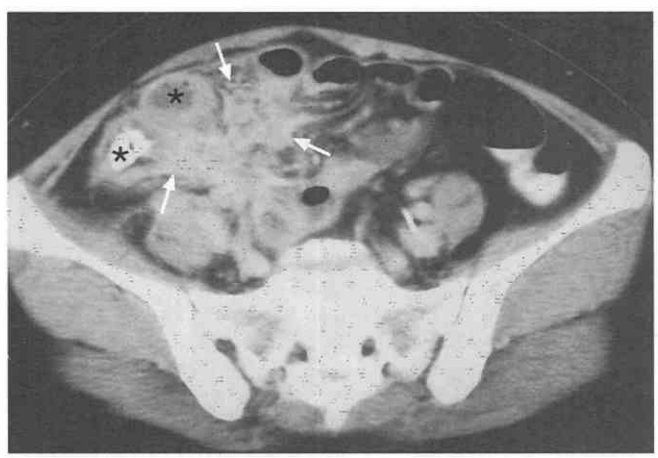

Figure 34–199. Actinomycosis infection involving the gastrointestinal tract. CT scan shows ill-defined soft tissue lesion *(arrows)* occupying the right lower abdomen as well as evidence of bowel wall thickening of the distal ileum *(asterisks)* and diffuse infiltration in the regional fat plane. (From Lee IJ, Ha HK, Park CM, et al: CT features of abdominopelvic actinomycosis involving the gastrointestinal tract. Radiology 220:76–80, 2001.)

the mean length of 8.3 cm overlap considerably with the parameters of other inflammatory bowel diseases. However, rather than bowel wall thickening, the most important CT feature for the correct diagnosis is the presence of a large mass adjacent to the involved bowel; we found that the mass was present in 17 of the 18 patients.[321] Such a mass appears to be predominantly cystic or solid.

The presence of abundant granulation and dense fibrous tissues in the solid components of these masses may cause hyperattenuation after infusion of contrast material. These lesions show an aggressive infiltration pattern with a propensity for crossing the fascial planes or boundaries and involve multiple compartments. These tendencies are attributed to the proteolytic enzyme produced by *A. israelii*. Soft tissue strandings are also prominent, surrounding the involved bowel or mass. Because of the size of the bacterium, the organism usually does not spread via the lymphatics; therefore, regional lymphadenopathy is uncommon or develops late.[36, 612]

Early diagnosis is important to minimize morbidity and to avoid unnecessary surgery because the response to treatment with high doses of penicillin is usually favorable.[39, 211]

Schistosoma Japonica Infection

Schistosoma japonica infection is confined to eastern Asia. Patients are infected by contact with fresh water that is infested with larvae. The schistosomal larvae penetrate the skin and pass via the systemic circulation to the portal vein and its tributaries. The eggs are the chief cause of tissue damage to the host. An intense granulomatous reaction is followed by irregular mucosal thickening, formation of granulomatous polyps, and, eventually, fibrosis. CT characteristically shows curvilinear or nodular calcification in the colon, appendix, or small bowel (Fig. 34–200).[325] The calcified eggs are deposited more extensively in the submucosa and serosa.[325]

Vascular and Miscellaneous Conditions

Colonic Ischemia

Colonic ischemia is one of the most common vascular disorders of the large bowel in elderly people. Several forms of ischemic colopathy are recognized[496]:

Figure 34–200. *Schistosoma japonica* infection. CT scan shows diffuse colonic wall calcification *(arrows)* in the rectum and sigmoid colon. (Courtesy of T. Araki, M.D., Yamanashi University, Japan.)

- Reversible colopathy (submucosal or intramural hemorrhage)
- Transient colitis
- Chronic ulcerating colitis
- Stricture
- Gangrene
- Fulminant universal colitis

Acute ischemia results from an acute reduction in blood flow through an intestinal segment caused by an acute occlusive event or decreased splanchnic blood flow. A number of predisposing factors have been suggested, including arteriosclerotic heart disease, hypotensive episodes, cardiac and aortic surgery, myocardial infarction, digitalis treatment, arrhythmias, vasculitis, colonic obstruction, colonic infection such as CMV, and hypercoagulable states.

Although the common denominator producing ischemia in most of these circumstances is hypoxia, no specific cause of the ischemia is usually identified. Although any region of the colon is subject to focal ischemia,[29] the segments commonly affected by ischemic colitis are the junction between the superior and inferior mesenteric arteries near the splenic flexure (Griffith's point) and the anastomotic plexus between the inferior mesenteric artery and hypogastric vessels near the rectosigmoid region (critical point of Sudeck).

According to one report,[546] isolated cecal ischemia may occur because the ileocecal region is also a "watershed area." The ischemic process tends to affect the mucosa initially; a severe and prolonged process causes involvement of only the muscularis propria. Mucosal damage is reversible, occurring as a self-limiting condition, whereas necrosis of the muscle layer can lead to the development of a fibrotic stricture or to necrosis with severe sepsis and perforation.

The diagnostic accuracy of CT in detection of colonic ischemia has not been well described in the literature, but improved contrast enhancement and scanning techniques may increase its sensitivity. On CT images, colonic ischemia appears as circumferential bowel wall thickening with or without a target sign, poor bowel wall enhancement, focal or diffuse bowel dilatation, mesenteric vascular thrombus, mesenteric vascular engorgement, pneumatosis intestinalis, portal or mesenteric venous gas, and pneumoperitoneum (Figs. 34–201 and 34–202).[6, 146] Although similar CT findings can be seen in a variety of inflammatory conditions (e.g., ulcerative or granulomatous colitis, pseudomembranous colitis, or CMV colitis), the occurrence of segmental colonic involvement is much more often seen in colonic ischemia.[29]

Differentiating reversible from irreversible ischemia may be important to establish the strategy of patient management. Except for the presence of portal air or intraperitoneal air, however, Balthazar and associates[29] observed that a single CT examination was limited in predicting the development of complications (stricture, infarction, perforation).

Radiation Colitis

Radiation colitis is generally observed in patients who receive abdominal and pelvic radiation with doses of 4500 to 6000 rads (45 to 60 Gy).[518] The latent period between

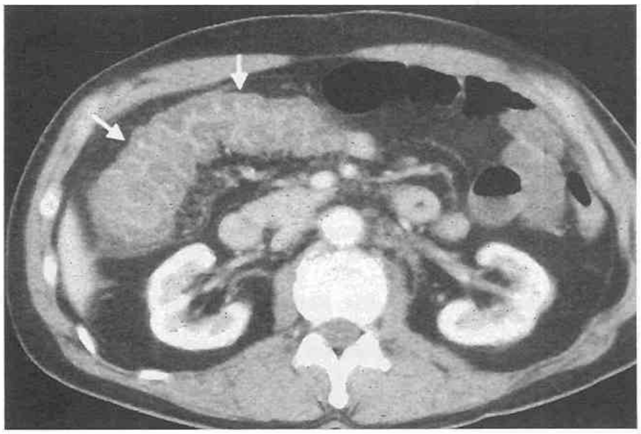

Figure 34–201. Colonic ischemia. CT scan shows heterogeneous colonic wall thickening *(arrows)* resulting from diffuse intramural hemorrhage or edema, which is confined to the right-sided colonic segment.

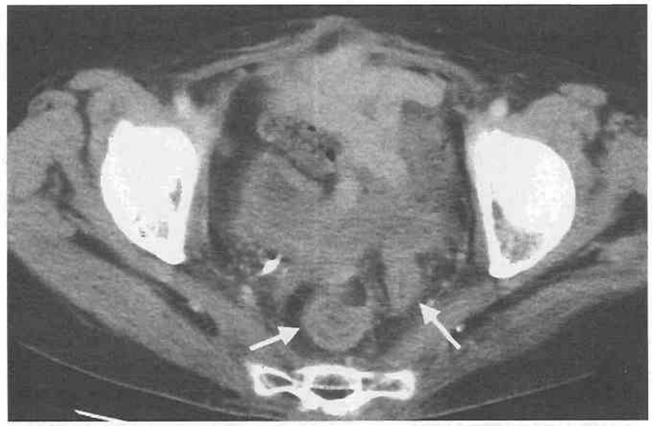

Figure 34–203. Radiation colitis after radiation therapy for cervical cancer. CT scan shows bowel wall thickening *(arrows)* of the rectum and sigmoid colon with the "target sign."

radiation therapy and the development of radiation damage is usually 6 to 24 months but can be longer than 30 years.[118] Predisposing factors include diabetes, hypertension, atherosclerosis, prior abdominal surgery with adhesive bowel loops, and peritonitis before the radiation therapy.

Although the small intestine is more radiosensitive than the rectum, radiation injury occurs more commonly in the rectosigmoid because the rectum is fixed in position and in close proximity to many sites of malignancy, such as the cervix, uterus, ovary, bladder, and prostate. Depending on the area irradiated, other sites of the colon can be involved.

In contrast to the acute radiation changes in which viable regenerating cells within the crypts of the intestinal epithelium are damaged by the direct effects of the radiation, late radiation injury can cause bowel ischemia due to obliterative endarteritis in the fine intestinal vasculature of the submucosa. Fewer than 2% of patients who receive radiotherapy ultimately require surgery resulting from perforation, bleeding, fistula, or stricture formation.[61]

CT may show bowel wall thickening and luminal narrowing of the irradiated bowel segment (Figs. 34–203 and 34–204). The thickened bowel wall commonly shows heterogeneous attenuation with target appearance. The perirectal changes include thickening of the perirectal fibrous tissue and increased perirectal fat, resulting in a widened presacral space.[129] Symmetrically proliferated fat immediately adjacent to the rectum and higher attenuation fibrous tissue surrounding it create a halo effect.[129] A fibrous connection between the sacrum and rectum may also be demonstrated. Because CT findings may closely simulate those of inflammatory bowel disease or colonic ischemia, correlation with the clinical history and radiation ports is necessary for a correct diagnosis.

MRI can also be used to evaluate suspected radiation

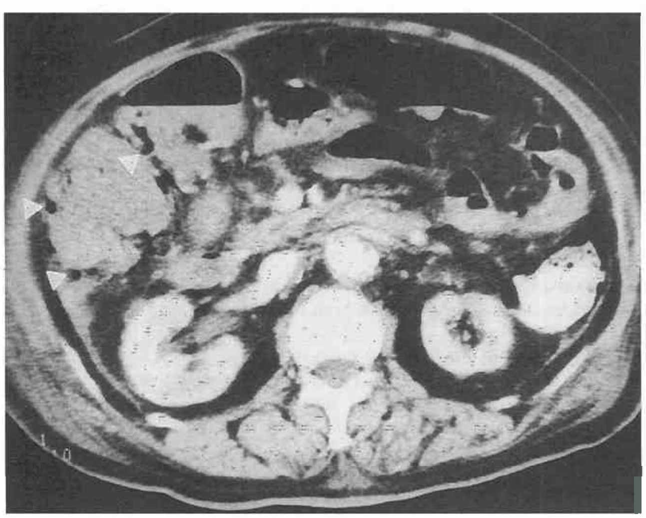

Figure 34–202. Colonic infarction. CT scan shows intramural gas *(arrowheads)* in the proximal transverse colon without well-defined bowel wall thickening. (From Ha HK: CT in the early detection of strangulation in intestinal obstruction. Semin Ultrasound CT MRI 16:141–150, 1995.)

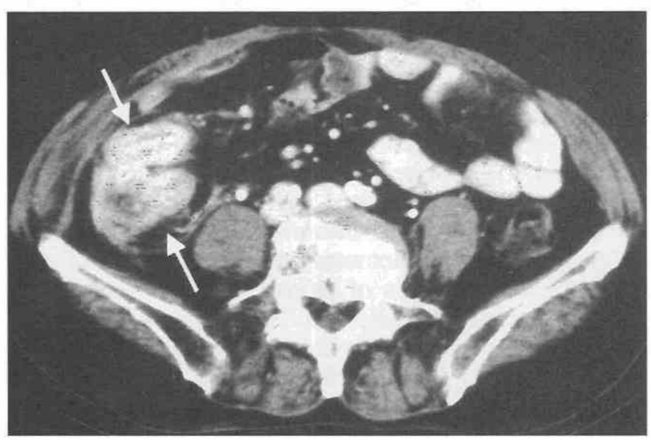

Figure 34–204. Development of radiation colitis after radiation therapy for cecal lymphoma. CT scan shows bowel wall thickening *(arrows)* of the distal ileum, cecum, and ascending colon with marked and heterogeneous contrast enhancement. Pericolonic infiltration is minimal without free gas. Histopathologic examination of the resected specimen showed transmural infarction with microperforation.

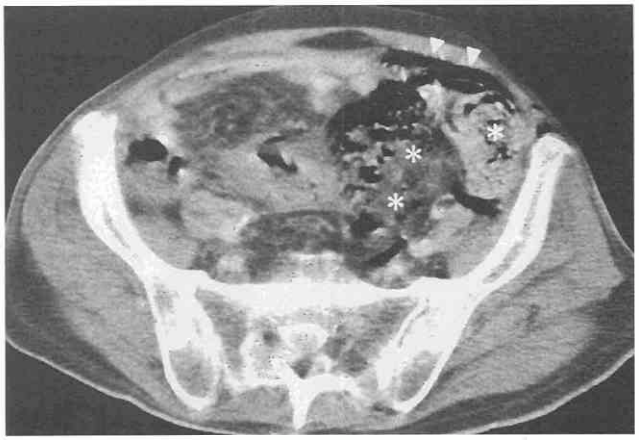

Figure 34–205. Pneumatosis in the colonic wall caused by bowel infarction. CT scan shows diffuse intramural gas in the left-sided colon *(asterisks)*.

colitis. According to a series by Sugimura and colleagues,[559] the frequency of MRI tissue changes increased with incremental radiation doses. In addition to the perirectal changes seen on CT scans, MRI may have advantages in revealing the muscle and bone marrow changes in the region of the radiation port; the signal intensity of the affected muscle is increased on T2-weighted images and that of the marrow becomes increased on T1-weighted images.[559]

In differentiating between radiation-induced changes and residual recurrent tumor, MRI has a limited role, except for the presence of bulky mass that favors the diagnosis of recurrent tumor. In cases of infiltrative tumor growth in the rectum or bladder, differentiation is difficult.

Pneumatosis Intestinalis

Pneumatosis intestinalis (intramural gas) is characterized by the presence of gas in the wall of the GI tract. The disorder can be *primary* (15%) or *secondary* (85%).[133] Although the primary type is not associated with any known GI disease, the secondary form is related to various GI, pulmonary, and other conditions.[133]

CT enables precise assessment of localization and extent of intramural gas accumulation (Fig. 34–205).[244] Pneumatosis cystoides intestinalis has a benign course and is occasionally self-limited. In contrast, pneumatosis intestinalis is commonly associated with severe disease such as bowel infarction and is characterized by a linear and small cystic appearance of intramural gas.[244] In addition, CT may allow for differentiation of primary and secondary forms and assessment of the prognosis.[523] Pneumatosis intestinalis may be occasionally overlooked as intraluminal gas; therefore, the use of lung window settings is necessary in equivocal cases.

References

1. Abrams JA, Holden W: Tuberculosis of the gastrointestinal tract. Arch Surg 89:282–293, 1964.
2. Abramson SJ, Berdon WE, Baker DH: Childhood typhlitis: Its increasing association with acute myelogenous leukemia. Radiology 146:61–64, 1983.
3. Adolph JMG, Kimming BN, Georgi P, et al: Carcinoid tumors: CT and I-131 meta-iodobenzylguanidine scintigraphy. Radiology 164: 199–203, 1987.
4. Agha FP: Intussusception in adults. Am J Roentgenol 146:527–531, 1986.
5. Agha FP, Keren DF: Spindle-cell squamous carcinoma of the esophagus: A tumor with biphasic morphology. Am J Roentgenol 145: 541–545, 1985.
6. Alpern MB, Glazer GM, Francis IR: Ischemic or infarcted bowel: CT findings. Radiology 166:149–152, 1988.
7. Amorn Y, Knight WA Jr: Primary linitis plastica of the colon: Report of two cases and review of the literature. Cancer 41:2420–2425, 1978.
8. Amromin GD, Solomon RD: Necrotizing enteropathy. JAMA 182: 133–139, 1962.
9. Anand BS, Nanda R, Sachdev GK: Response of tuberculous stricture to antituberculous treatment. Gut 29:62–69, 1988.
10. Angelelli G, Macarini L, Lupo L, et al: Rectal carcinoma: CT staging with water as contrast medium. Radiology 177:511–514, 1990.
11. Ascenti G, Racchiusa S, Mazziotti S, et al: Giant fibrovascular polyp of the esophagus: CT and MR findings. Abdom Imaging 24: 109–110, 1999.
12. Athanasoulis CA, Aral IM: Leiomyosarcoma of the esophagus. Gastroenterology 54:271–274, 1968.
13. Attar S, Hankins SR, Suter CM, et al: Esophageal perforation: A therapeutic challenge. Ann Thorac Surg 50:45–51, 1990.
14. Backer CL, LoCicero J III, Hartz RS, et al: Computed tomography in patients with esophageal perforation. Chest 98:1078–1080, 1990.
15. Baek JH, Rhim HC, Koh BH, et al: Rectal leiomyosarcoma: Report of two cases. J Korean Radiologic Soc 31:511–514, 1994.
16. Balfe DM, Mauro MA, Koehler RE, et al: Gastrohepatic ligament: Normal and pathologic CT anatomy. Radiology 150:485–490, 1984.
17. Balikian JP, Uthman SM, Kabakian HA: Tuberculous colitis. Am J Proctol 28:75–79, 1977.
18. Balthazar EJ: CT of small-bowel obstruction. AJR Am J Roentgenol 162:255–261, 1994.
19. Balthazar EJ: CT of the gastrointestinal tract: Principles and interpretation. AJR Am J Roentgenol 156:23–32, 1991.
20. Balthazar EJ, Birnbaum BA, Megibow AJ, et al: Closed-loop and strangulating intestinal obstruction: CT signs. Radiology 185:769–775, 1992.
21. Balthazar EJ, Charles HW, Megibow AJ: *Salmonella*- and *Shigella*-induced ileitis: CT findings in four patients. J Comput Assist Tomogr 20:375–378, 1996.
22. Balthazar EJ, Naidich DP, Megibow AJ, et al: CT evaluation of esophageal varices. AJR Am J Roentgenol 148:131–135, 1987.
23. Balthazar EJ, Leibeskind ME, Macari M: Intestinal ischemia in patients in whom small-bowel obstruction is suspected: Evaluation of accuracy, limitations, and clinical implications of CT in diagnosis. Radiology 205:519–522, 1997.
24. Balthazar EJ, Megibow AJ, Schinella RA, Gordon R: Limitations in the CT diagnosis of acute diverticulitis: Comparison of CT, contrast enema, and pathologic findings in 16 patients. AJR Am J Roentgenol 154:281–285, 1990.
25. Balthazar EJ, Megibow AJ, Gordon RB, Hulnick D: Cecal diverticulitis: Evaluation with CT. Radiology 162:79–81, 1987.
26. Balthazar EJ, Megibow AJ, Hulnick DH, et al: Carcinoma of the colon: Detection and preoperative staging by CT. AJR Am J Roentgenol 150:301–306, 1988.
27. Balthazar EJ, Megibow AJ, Siegel SE, Birnbaum BA: Appendicitis: Prospective evaluation with high-resolution CT. Radiology 180:21–24, 1991.
28. Balthazar EJ, Siegel SE, Megibow AJ, et al: CT in patients with scirrhous carcinoma of the GI tract: Imaging findings and value for tumor detection and staging. AJR Am J Roentgenol 165:839–845, 1995.
29. Balthazar EJ, Yen B, Gordon RB: Ischemic colitis: CT evaluation of 54 cases. Radiology 211:381–388, 1999.
30. Barki Y, Elias H, Tovi F, et al: A fibrovascular polyp of the oesophagus. Br J Radiol 54:142–144, 1981.
31. Bartnicke BJ, Balfe DM: CT appearance of intestinal ischemia and intramural hemorrhage. Radiol Clin North Am 32:845–860, 1994.
32. Basemann EF, Auerbach SH, Wolfe WW: The importance of roentgenologic diagnosis of aberrant pancreatic tissue in the gastrointestinal tract. Am J Roentgenol 107:71–76, 1969.

33. Baskin RH, Mayo CW: Jejunal diverticulosis: A clinical study of 87 cases. Surg Clin North Am 32:1185–1196, 1952.
34. Battifora H: Spindle cell carcinoma: Ultrastructural evidence of squamous origin and collagen production by the tumor cells. Cancer 37:2275–2282, 1976.
35. Beauchamp NJ, Pizer E, Hruban RH, Fishman EK: Ossification of a rectal tumor: CT evaluation. J Comput Assist Tomogr 21: 671–673, 1997.
36. Becker CD, Barbier P, Porcellini B: CT evaluation of patients undergoing transhiatal esophagectomy for cancer. J Comput Asssist Tomogr 10:607–611, 1986.
37. Begos DG, Sandor A, Modlin IM: The diagnosis and management of adult intussusception. Am J Surg 173:88–94, 1997.
38. Bellon EM, George CR, Schreiber H, Marshall JB: Pancreatic pseudocyst of the duodenum. Am J Roentgenol 133:827–831, 1979.
39. Bennhoff DF: Actinomycosis: Diagnostic and therapeutic considerations and a review of 32 cases. Laryngoscope 94:1198–1217, 1984.
40. Beradi RS: Abdominal actinomycosis. Surg Gynecol Obstet 149: 257–266, 1979.
41. Berardi R: Paraduodenal hernias: Collective review. Surg Gynecol Obstet 152:99–110, 1981.
42. Berkmen YM, Auh YH: CT diagnosis of acquired tracheoesophageal fistula in adults. J Comput Assist Tomogr 9:302–304, 1980.
43. Berkovich GY, Levine MS, Miller WT: CT findings in patients with esophagitis. AJR Am J Roentgenol 175:1431–1434, 2000.
44. Beyer KL, et al: Primary small cell carcinoma of the esophagus: Report of 11 cases and review of the literature. J Clin Gastoenterol 13:135–141, 1991.
45. Bhansali SK: Abdominal tuberculosis: Experiences with 300 cases. Am J Gastroenterol 67:324–337, 1977.
46. Bizakis JG, Segas J, Skoulakis H, et al: Retropharyngoesophageal abscess associated with a swallowed bone. Am J Otolaryngol 14: 354–357, 1993.
47. Bizer LS, Liebling RW, Delany HM, Gliedman ML: Small-bowel obstruction: The role of nonoperative treatment in simple intestinal obstruction and predictive criteria for strangulation obstruction. Surgery 89:407–413, 1981.
48. Blackwell JN, Castell DO: Motility disorders of the lower esophagus. Surv Dig Dis 1:157–168, 1983.
49. Bladerfren MR, Lowe JE, Postlethwait RW: Diagnosis and recommended management of esophageal perforation and rupture. Ann Thorac Surg 42:235–239, 1986.
50. Boddie AW Jr, Eisenberg BL, Mullins JD, et al: The diagnosis and treatment of obstructive jaundice secondary to malignant lymphoma: A problem in multidisciplinary management. J Surg Oncol 14: 111–123, 1980.
51. Boley SJ, Agrawal GP, Warren AR, et al: Pathophysiologic effects of bowel distention on intestinal blood flow. Am J Surg 117:228–234, 1969.
52. Botet JF, Lightdale CJ, Zauber AG, et al: Preoperative staging of gastric cancer: Comparison of endoscopic US and dynamic CT. Radiology 181:426–432, 1991.
53. Brady LW: Malignant lymphoma of the gastrointestinal tract. Radiology 98:132–139, 1980.
54. Brady LW, Asbell SO: Malignant lymphoma of the gastrointestinal tract. Radiology 137:291–298, 1980.
55. Bragg DG, Colby TV, Ward JH: New concepts in the non-Hodgkin lymphoma: Radiologic implications. Radiology 159:289–304, 1986.
56. Brandt LJ, Boley SJ: Ischemic and vascular lesions of the bowel. In Sleisenger MH, Fordtran JS (eds): Disease: Pathophysiology, Diagnosis, and Management, 6th ed. Philadelphia, WB Saunders, 1993, pp 1927–1961.
57. Breen DJ, Janzen DL, Zwirewich CV, Nagy AG: Blunt bowel and mesenteric injury: Diagnostic performance of CT signs. J Comput Assist Tomogr 21:706–712, 1997.
58. Bridge MF, Pezin KH: Primary adenocarcinoma of the jejunum and ileum: A clinicopathologic study. Cancer 36:1876–1887, 1975.
59. Brolin RE, Krasna MJ, Mast BA: Use of tubes and radiographs in the management of small-bowel obstruction. Ann Surg 206: 126–133, 1987.
60. Brooks JJ, Enterline HT: Primary gastric lymphomas: A clinical pathologic study of 58 cases with long-term follow-up and literature review. Cancer 51:701–711, 1983.
61. Brown FA: Gastrointestinal complications associated with radiation therapy: Characteristic, confusing or compounded. Am J Dig Dis 7: 1006–1025, 1962.
62. Brown G, Richards CJ, Newcombe RG, et al: Rectal carcinoma: Thin-section MR imaging for staging in 28 patients. Radiology 211: 215–222, 1999.
63. Bruce GR, Bishof NA, Jackson EC, et al: Bilateral ureteral obstruction associated with Henoch-Schönlein purpura. Pediatr Nephrol 11: 347–349, 1997.
64. Bruneton JN: Carcinoid tumors: Small intestine. In Bruneton JN (ed): Imaging of Gastrointestinal Tract Tumors. Berlin, Springer-Verlag, 1990, pp 252–256.
65. Bubenik O, Lopez MJ, Greco AO, et al: Gastrosplenic fistula following successful chemotherapy for disseminated histiocytic lymphoma. Cancer 52:994–996, 1983.
66. Buckley JA, Siegelman SS, Jones B, Fishman EK: The accuracy of CT staging of small-bowel adenocarcinoma: CT/pathologic correlation. J Comput Assist Tomogr 21:986–991, 1997.
67. Buetow PC, Buck JL, Carr NJ, et al: Intussuscepted colonic lipomas: Loss of fat attenuation on CT with pathologic correlation in 10 cases. Abdom Imaging 21:153–156, 1996.
68. Butler JA, Cameron BL, Morrow M, et al: Small-bowel obstruction in patients with a prior history of cancer. Am J Surg 162:624–628, 1991.
69. Buy JN, Moss AA: Computed tomography of gastric lymphoma. Am J Roentgenol 138:859–865, 1982.
70. Byun JY, Ha HK, Yu SY, et al: CT Features of systemic lupus erythematosus in patients with acute abdominal pain. Radiology 211:203–209, 1999.
71. Cabal E, Holtz S: Polyarteritis as a cause of intestinal hemorrhage. Gastroenterology 61:99–105, 1971.
72. Calle S, Klatsky S: Intestinal phycomycosis (mucormycosis). Am J Clin Pathol 45:264–272, 1966.
73. Camishion RC, Gibbon JH, Templeton JY: Leiomyosarcomas of the esophagus. Am Surg 153:951–956, 1961.
74. Cappell MS, Hassan T, Rosenthal S, Mascarenhas M: Gastrointestinal obstruction due to *Mycobacterium avium-intracellulare* associated with the acquired immunodeficiency syndrome. Am J Gastroenterol 87:1823–1827, 1992.
75. Carlisle JG, Quint LE, Francis IR, et al: Recurrence esophageal carcinoma: CT evaluation after esophagectomy. Radiology 189:271–275, 1993.
76. Carnovale RL, Goldstein HM, Zornoza J, et al: Radiologic manifestations of esophageal lymphoma. Am J Roentgenol 128:751–754, 1977.
77. Caroline DF, Friedman AC: The radiology of inflammatory bowel disease. Med Clin North Am 78:1353–1385, 1994
78. Carter MM, Kulkarni MV: Giant fibrovascular polyp of the esophagus. Gastointest Radiol 9:301–303, 1984.
79. Carucci LR, Levine MS, Rubsin SE, Laufer I: Tumorous gastric varices: radiographic findings in 10 patients. Radiology 212:861–865, 1999.
80. Caruso RD, Berk RN: Lymphoma of the esophagus. Radiology 95: 381–382, 1970.
81. Casjet CI, Scatarige JC, Fishman EK: Distribution of metastases in breast carcinoma: CT evaluation of the abdomen. Clin Imaging 15: 166–171, 1991.
82. Castro EB, Stearns MW: Lipoma of the large intestine: A review of 45 cases. Dis Colon Rectum 15:441–444, 1972.
83. Chappuis CW, Cohn I: Acute colonic diverticulitis. Surg Clin North Am 68:301–313, 1988.
84. Chen YM, Frederick MC: Barret esophagus and adenocarcinoma. Radiol Clin North Am 32:1167–1181, 1994.
85. Chiechi MV, Hamrick-Turner JE, Abbitt PL: Gastric herniation and volvulus: CT and MR appearance. Gastrointest Radiol 17:99–101, 1992.
86. Chintapalli KN, Chopra S, Ghiatas AA, et al: Diverticulitis versus colon cancer: Differentiation with helical CT findings. Radiology 210:429–435, 1999.
87. Chintapalli KN, Esola CC, Chopra S, et al: Pericolic mesenteric lymph nodes: An aid in distinguishing diverticulitis from cancer of the colon. AJR Am J Roentgenol 169:1253–1255, 1997.
88. Cho JS, Kim JK, Rho SM, et al: Preoperative assessment of gastric carcinoma: Value of two-phase dynamic CT with mechanical IV injection of contrast material. AJR Am J Roentgenol 163:69–75, 1994.
89. Cho KC, Baker SR, Alterman DD, Fusco JM, Cho S: Transpyloric spread of gastric tumors: Comparison of adenocarcinoma and lymphoma. AJR Am J Roentgenol 167:467–469, 1996.

90. Cho KC, Morehouse HT, Alterman DD, Thorhill BA: Sigmoid diverticulitis: Diagnostic role of CT—comparison with barium enema studies. Radiology 176:111–115, 1990.
91. Chou CK, Chen LT, Sheu RS, et al: MRI manifestations of gastrointestinal lymphoma. Abdom Imaging 19:495–500, 1994.
92. Chou CK, Mak CW, Hou CC, Chang JM: CT of large small-bowel diverticulum. Abdom Imaging 23:132–134, 1998.
93. Chun HJ, Byun JY, Chyn KA, et al: Gastrointestinal leiomyoma and leiomyosarcoma: CT differrentiation. J Comput Assist Tomogr 22: 69–74, 1998.
94. Clark KE, Foley WD, Lawson TL, et al: CT evaluation of esophageal and upper abdominal varices. J Comput Assist Tomogr 4: 510–515, 1980.
95. Cole WH: The mechanism of spread of cancer. Surg Gynecol Obstet 137:853–871, 1973.
96. Conklin EF, Markowitz AM: Intussusception, a complication of gastric surgery. Surgery 57:480–488, 1965.
97. Connor R, Jones B, Fishman EK, et al: Pneumatosis intestinalis: Role of computed tomography in diagnosis and management. J Comput Assist Tomogr 8:269–275, 1984.
98. Cook AO, Levine BA, Sirinek KR, Gaskill HV: Evaluation of gastric adenocarcinoma: Abdominal computed tomography does not replace celiotomy. Arch Surg 121:603–606, 1986.
99. Coppa GF, Eng K, Localio SA: Surgical management of diffuse cavernous hemangioma of the colon, rectum, and anus. Surg Gynecol Obstet 159:17–22, 1984.
100. Cortese AF, Cornell GN: Carcinoma of the duodenum. Cancer 29: 1010–1015, 1972.
101. Coscina WF, Arger PH, Herlinger H, et al: CT diagnosis of villous adenoma. J Comput Assist Tomogr 10:764–766, 1986.
102. Coulomb M, Lebas JF, Sarrazin R, et al: Oesophageal cancer extension: Diagnostic contribution and effects on therapy of computed tomography: Report on 40 cases. J Radiol 62:475–487, 1981.
103. Cover TL, Aber RC: *Yersinia enterocolitica*. N Engl J Med 32: 16–24, 1989.
104. Cruz FO, Soffia PS, Rio PMD, et al: Acute phlegmonous gastritis with mural abscess: CT diagnosis. AJR 159:767–768, 1992.
105. Cubillo E: Obturator hernia diagnosed by computed tomography. AJR Am J Roentgenol 140:735–736, 1983.
106. Dachman A, Lichtenstein J, Friedman A: Mucocele of the appendix pseudomyxoma peritonei. AJR 144:923–929, 1985.
107. Daffner RH: Computed tomography of the esophagus. Crit Rev Diagn Imaging 14:191–242, 1981.
108. Daffner RH, Halbr MD, Postlethwait RW, et al: CT of the esophagus: II. Carcinoma. AJR 133:1051–1055, 1979.
109. Danielson K, Chernin MM, Amberg JR, et al: Epiploic appendicitis: CT characteristics. J Comput Assist Tomogr 10:142–143, 1986.
110. Darling RC, Welch CE: Tumors of the small intestine. N Engl J Med 260:397–408, 1959.
111. Dauterive AH, Flancbaum L, Cox EF: Blunt intestinal trauma: A modern-day review. Am Surg 201:198–203, 1985.
112. Day DL, Drake DG, Leonard AS, et al: CT findings in left paraduodenal hernia. Gastrointest Radiol 13:27–29, 1988.
113. Day DL, Ramsay NKC, Letourneau JG: Pneumatosis intestinalis after bone marrow transplantation. AJR Am J Roentgenol 151: 85–87, 1988.
114. Day EA, Mark C: Gallstone ileus: Review of the literature and presentation of 34 new cases. Am J Surg 129:552–558, 1975.
115. De Bree E, Grammatikakis J, Christodoulakis M, Tsiftsis D: The clinical significance of acquired jejunoileal diverticula. Am J Gastroenterol 93:2523–2528, 1998.
116. De La Pava S, Karjoo R, Mukhtar R, et al: Melanosis of the esophagus. Cancer 16:48–50, 1963.
117. De Lange EE, Fechner RE, Wanebo HJ: Suspected recurrent rectosigmoid carcinoma after abdominoperineal resection: MR imaging and histopathologic findings. Radiology 170:323–328, 1989.
118. DeCosse JJ, Rhodes RS, Wentz WB, et al: The natural history and management of radiation-induced injury of the gastrointestinal tract. Ann Surg 170:369–384, 1969.
119. Dehn TCB, Reznek RH, Nockler IB, White FE: The preoperative assessment of advanced gastric cancer by computed tomography. Br J Surg 71:413–417, 1984.
120. Demos TC, Okrent DH, Studlo JD, et al: Spontaneous esophageal hematoma diagnosed by computed tomography. J Comput Assist Tomogr 10:133–135, 1986.
121. Desai RK, Tagliabue JR, Wegryn SA, et al: CT evaluation of wall thickening in the alimentary tract. Radiographics 11:771–783, 1991.
122. Deutsch JP, Mariette D, Moukarbel N, et al: Gastroduodenal intussusception secondary to Ménétrier's disease. Abdom Imaging 19: 207–209, 1994
123. Dick AP, Graff R, Gregg D, et al: An arteriographic study of mesenteric arterial disease: Large-vessel changes. Gut 8:206–220, 1967.
124. Dodd GD: Lymphoma of the hollow abdominal viscera. Radiol Clin North Am 28:771–783, 1990.
125. Donnelly LF, Frush DP, Marshall KW, White KS: Lymphoproliferative disorders: CT findings in immunocompromised children. AJR Am J Roentgenol 171:725–731, 1998.
126. Donnelly LF, Morris CL: Acute graft-versus-host disease in children: Abdominal CT findings. Radiology 199:265–268, 1996.
127. Donohue JH, Federle MP, Griffiths BG, Trunkey DD: Computed tomography in the diagnosis of blunt intestinal and mesenteric injuries. J Trauma 27:11–17, 1987.
128. Dosik GM, Luna M, Valdivieso M, et al: Necrotizing colitis in patients with cancer. Am J Med 67:646–656, 1979.
129. Doubleday LG, Bernardino ME: CT findings in the perirectal area following radiation therapy. J Comput Assist Tomogr 4:634–638, 1980.
130. Dowe MF, Shanmuganathan K, Mirvis SE, et al: CT findings of mesenteric injury after blunt trauma: Implications for surgical intervention. AJR Am J Roentgenol 168:425–428, 1997.
131. Dudiak KM, Johnson CD, Stephens DH: Primary tumors of the small intestine: CT evaluation. AJR Am J Roentgenol 152:995–998, 1989.
132. Dűx M, Richter GM, Hansmann J, et al: Helical hydro-CT for diagnosis and staging of gastric carcinoma. J Comput Assist Tomogr 23:913–922, 1999.
133. Earnest DL, Hixson LJ: Other disease of the colon and rectum. In Sleisenger M, Fordtran JS (eds): Gastrointestinal Disease: Pathophysiology, Diagnosis, and Management, 5th ed. Philadelphia, WB Saunders, 1989, pp 1537–1570.
134. Edwards DA: Achalasia: Symptoms and radiology. Postgrad Med J 50:209–210, 1974.
135. Ehrlich AN, Stalder G, Geller W, et al: Gastointestinal manifestations of malignant lymphoma. Gastoenterology 54:1115–1121, 1968.
136. Ellis H, Gajraj H, George CD: Incisional hernias: When do they occur? Br J Surg 70:290–291, 1983.
137. Endicott JN, Molony TB, Campbell G, et al: Esophageal perforation: The role of computerized tomography in diagnosis and management decisions. Laryngoscope 96:751–757, 1986.
138. Etherington RJ, Wiliams JG, Hayward MW, Hughes LE: Demostration of para-ileostomy herniation using computed tomography. Clin Radiol 41:333–336, 1990.
139. Evans EI: Mechanism of shock in intestinal strangulation: An experimental study. Ann Surg 117:28–38, 1943.
140. Fabian JC, Mangiante EC, White TJ, et al: A prospective study of 91 patients undergoing both computed tomography and peritoneal lavage following blunt abdominal trauma. J Trauma 26:602–608, 1986.
141. Fagan CJ: Endometriosis: Clinical and roentgenographic manifestations. Radiol Clin North Am 12:109–125, 1974.
142. Fahl JC, Dockerty MB, Judd ES: Scirrhous carcinoma of the colon and rectum. Surg Gynecol Obstet 3:759–766, 1960.
143. Faling LJ, Pugatch RD, Robbins AH: Case report: The diagnosis of unsuspected esophageal perforation by computed tomography. Am J Med Sci 28:31–34, 1981.
144. Falk GW, Richter JE: Why is esophageal adenocarcinoma increasing in incidence? Abdom Imaging 23:539–542, 1998.
145. Farah MC, Jafri SZH, Schwab RE, et al: Duodenal neoplasms: Role of CT. Radiology 162:839–843, 1987.
146. Federle MP, Chun G, Jeffrey RB, Raylor R: Computed tomographic findings in bowel infarction. AJR 142:91–95, 1984.
147. Fenlon HM, O'Keane C, Carney DN, et al: Imaging of small cell carcinoma of the oesophagus. Clin Radiol 50:634–638, 1995.
148. Ferguson MK, Skinner DB: Carcinoma of the esophagus and cardia. In Zuidema GA (ed): Shackerford's Surgery of the Alimentary Tract. Philadelphia, 1995, WB Saunders, pp 305–332.
149. Fernet P, Azar HA, Stout AP: Intramural (tubal) spread of linitis plastica along the alimentary tract. Gastroenterology 48:419–424, 1965.

150. Ferrara JLM, Deeg HJ: Graft-versus-host disease. N Engl J Med 324:667–674, 1991.
151. Ferrer MG, Pastor GP, Otero BM: *Yersinia enterocolitica:* Intestinal features. Dig Dis 8:313–321, 1990.
152. Ferrozzi F, Bova D, Garlaschi G: Gastric liposarcoma: CT appearance. Abdom Imaging 18:232–233, 1993.
153. Fischer RP, Beverlin BC, Engran LH, Benjamin CI, Perry JF. DPL: 14 years and 2586 patients later. Am J Surg 136:701–704, 1978.
154. Fisher JK: Computed tomographic diagnosis of volvulus in intestinal malrotation. Radiology 140:145–146, 1981.
155. Fisher JK. Normal colon wall thickness on CT. Radiology 145: 415–417, 1982.
156. Fishman EK, Kavuru M, Jones B, et al: Pseudomembranous colitis: CT evaluation of 26 cases. Radiology 180:57–60, 1991.
157. Fishman EK, Magid D, Jones SB, Siegelman SS: Menetrier disease. J Comput Assist Tomogr 7:143–145, 1983.
158. Fishman EK, Wolf EJ, Jones B, Bayless TM, Siegelman SS: CT evaluation of Crohn's disease: effect on patient management. AJR Am J Roentgenol 148:537–540, 1987.
159. Fishman EK, Zinreich ES, Jones B, Siegelman SS: Computed tomographic diagnosis of radiation ileitis. Gastrointest Radiol 9:149–152, 1984.
160. Fisk JD, Greening RR, McDonald GB, et al: Gastrointestinal radiographic features of human graft-versus-host disease. AJR 136:329–336, 1981.
161. Fleming JL, Weisner RH, Shorter RG: Whipple disease: Clinical, biochemical, and histopathologic features and assessment of treatment in 29 patients. Mayo Clin Proc 63:539–551, 1988.
162. Fletcher JD, Covell L, Shortsleeve MJ: Calcified gastric duplication. AJR Am J Roentgenol 163:994–995, 1994.
163. Fortson WC, Tedesco FJ: Drug-induced colitis: A review. Am J Gastroenterol 79:878–883, 1984.
164. Fox U, Lucani G: Disorders of the intestinal mesenteric lymphatic system. Lymphology 26:61–66, 1993.
165. Frager D, Baer JW, Medwid SW, et al: Detection of intestinal ischemia in patients with acute small-bowel obstruction due to adhesions or hernia: Efficacy of CT. AJR 166:67–71, 1966.
166. Frager D, Medwid SW, Baer JW, et al: CT of small-bowel obstruction: Value in establishing the diagnosis and determining the cause. AJR Am J Roentgenol 162:37–41, 1994.
167. Frager DH, Goldman M, Beneventano TC: Computed tomography in Crohn's disease. J Comput Assist Tomogr 7:819–824, 1983.
168. Francis RS, Berk RN: Typhoid fever. Radiology 112:583–585, 1974.
169. Frazzini VI, English WJ, Bashist B, Moore E: Small-bowel obstruction due to phytobezoar formation within Meckel diverticulum: CT findings. J Comput Assist Tomogr 10:390–392, 1996.
170. Freeny PC, Marks WM, Ryan JA, Bolen JW: Colorectal carcinoma evaluation with CT: Preoperative staging and detection of postoperative recurrence. Radiology 158:347–353, 1986.
171. Frick MP, Maile CW, Crass JR, et al: Computed tomography of neutropenic colitis. Am J Roentgenol 143:763–765, 1984.
172. Fukuya T, Hawes DR, Lu CC, et al: CT diagnosis of small-bowel obstruction: Efficacy in 60 patients. AJR Am J Roentgenol 158: 765–769, 1992.
173. Fukuya T, Honda H, Hayashi T, et al: Lymph node metastases: Efficacy of detection with helical CT in patients with gastric cancer. Radiology 197:705–711, 1995.
174. Fukuya T, Honda H, Kaneko K, et al: Efficacy of helical CT in T-staging of gastric cancer. J Comput Assist Tomogr 21:73–81, 1997.
175. Gamsu G, Webb WR: Computed tomography of the trachea: Normal and abnormal. Am J Roentgenol 139:321–326, 1982.
176. Gayer G, Zissin R, Apter S, et al: Acute diverticulitis of the small bowel: CT findings. Abdom Imaging 24:452–455, 1999.
177. Gazalle GS, Goldberg MA, Wittenberg J, et al: Efficacy of CT in distinguishing small-bowel obstruction from other causes of small-bowel dilatation. AJR Am J Roentgenol 162:43–47, 1994.
178. Gerz MA: Secondary amyloidosis (AA). J Intern Med 232:523–524, 1992.
179. Giovagnoni A, Misericordia M, Terilli F, et al: MR imaging of ulcerative colitis. Abdom Imaging 18:371–375, 1993.
180. Gladden JR: Hemangioma of the stomach. Am J Surg 56:495–498, 1942.
181. Glick SN, Levine MS, Teplick SK, Gasparaitis A: Splenic penetration by benign gastric ulcer: Preoperative recognition with CT. Radiology 163:637–639, 1987.
182. Glick SN, Teplick SK, Levine MS, Caroline DF: Gastric cardia metastasis in esophageal carcinoma. Radiology 160:627–630, 1986.
183. Goldberg HI, Gore RM, Margulis AR, et al: Computed tomography in the evaluation of Crohn disease. Am J Roentgenol 140:277–282, 1983.
184. Goldman LP, Weigert JM: Corrosive substance ingestion: A review. Am J Gastroenterol 79:85–90, 1984.
185. Goldstein HM, Zornoza J, Hopens T: Intrinsic disease of the adult esophagus: Benign and malignant tumors. Semin Roentgenol 16: 183–197, 1981.
186. Goodman MD, Porter DD: Cytomegalovirus vasculitis with fatal colonic hemorrhage. Arch Pathol 96:281–284, 1973.
187. Gore RM: Cross-sectional imaging of inflammatory bowel disease. Radiol Clin North Am 25:115–131, 1987.
188. Gore RM: CT of inflammatory bowel disease. Radiol Clin North Am 27:717–729, 1989.
189. Gore RM: Esophageal cancer: Clinical and pathologic features. Radiol Clin North Am 35:243–263, 1997.
190. Gore RM, Balthazar EJ, Ghahremain GG, Miller FH: CT features of ulcerative colitis and Crohn's disease. AJR Am J Roentgenol 167:3–15, 1996.
191. Gore RM, Laufer I: Ulcerative and granulomatous colitis. In Gore RM, Levine MS, Laufer I (eds): Textbook of Gastrointestinal Radiology. Philadelphia, WB Saunders, 1994, pp 1098–1141.
192. Gore RM, Marn CS, Kirby DF, et al: CT findings in ulcerative, granulomatous, and indeterminate colitis. Am J Roentgenol 143: 279–284, 1984.
193. Govoni AF: Hemangiomas of esophagus. Gastointest Radiol 7:113–117, 1982.
194. Grabbe, E, Lierse W, Winkler R: The perirectal fascia: Morphology and use in staging of rectal carcinoma. Radiology 149:241–246, 1983.
195. Graham WP III, Goldman L: Gastrointestinal metastasis from carcinoma of the breast. Ann Surg 159:477–480, 1964.
196. Granfield CAJ, Charnsangavej C, Dubrow RA, et al: Regional lymph node metastases in carcinoma of the left side of the colon and rectum: CT demonstration. AJR Am J Roentgenol 159:757–761, 1992.
197. Greenstein AJ, Gennuso R, Sachar DB, et al: Extraintestinal cancers in inflammatory bowel disease. Cancer 56:2914–2921, 1985.
198. Greenstein AJ, Sachar D, Pucillo A, et al: Cancer in Crohn's disease after diversionary surgery. Am J Surg 135:86–90, 1978.
199. Greenstein S, Jones B, Fishman EK, et al: Small-bowel diverticulitis: CT findings. Am J Roentgenol 147:271–274, 1986.
200. Gross BH, Agha FP, Glazer GM, et al: Gastric interposition following transhiatal esophagectomy: CT evaluation. Radiology 155:177–179, 1985.
201. Grumbach K, Levine MS, Wexler JA: Gallstone ileus diagnosed by computed tomography. J Comput Assist Tomogr 10:146–148, 1986.
202. Gumaste VV, Dave PB: Ingestion of corrosive substance by adults. Am J Gastroenterol 87:1–5, 1992.
203. Gupta PK, Hollander DH, Frost JK: Actinomycosis in cervicovaginal smears: An association with IUD usage. Acta Cytol 20:295–297, 1976.
204. Ha HK: CT in the early detection of strangulation in intestinal obstruction. Semin Ultrasound CT MR 16:141–150, 1995.
205. Ha HK, Jee KR, Yu E, et al: CT features of metastatic linitis plastica to the rectum in patients with peritoneal carcinomatosis. AJR Am J Roentgenol 174:463–466, 2000.
206. Ha HK, Jung JI, Lee MS, et al: CT differentiation of tuberculous peritonitis and peritoneal carcinomatosis. AJR Am J Roentgenol 167:743–748, 1996.
207. Ha HK, Kim HH, Kim HS, et al: Local recurrence after surgery for gastric carcinoma: CT findings. AJR Am J Roentgenol 161: 975–977, 1993.
208. Ha HK, Kim HS, Lee MS, et al: Differentiation of simple and strangulated small-bowel obstructions: Usefulness of known CT criteria. Radiology 204:507–512, 1997.
209. Ha HK, Ko GY, Yu ES, et al: Intestinal tuberculosis with abdominal complications: Radiologic and pathologic features. Abdom Imaging 24:32–38, 1999.
210. Ha HK, Lee EH, Lim CH, et al: Application of MRI for small intestinal diseases. J Magn Reson Imaging 8:375–383, 1998.
211. Ha HK, Lee HJ, Kim H, et al: Abdominal actinomycosis: CT findings in 10 patients. AJR Am J Roentgenol 161:791–794, 1993.

212. Ha HK, Lee HJ, Yang SK, et al: Intestinal Behçet syndrome: CT features of patients with and patients without complications. Radiology 209:449–454, 1998.
213. Ha HK, Lee SH, Rha SE, et al: Radiologic features of vasculitis involving the gastrointestinal tract. Radiographics 20:779–794, 2000.
214. Ha HK, Park CH, Kim SK, et al: CT analysis of intestinal obstruction due to adhesions: Early detection of strangulation. J Comput Assist Tomogr 17:386–389, 1993.
215. Ha HK, Shin BS, Lee SI, et al: Usefulness of CT in patients with intestinal obstruction who have undergone abdominal surgery for malignancy. AJR Am J Roentgenol 171:1587–1593, 1998.
216. Ha HK, Shinn KS, Kim IC, Bahk YW: Gastroduodenal intussusception due to a prolapsed gastric adenoma. AJR Am J Roentgenol 159:432, 1992.
217. Haines JD: Ileal endometriosis: A difficult preoperative diagnosis. Postgrad Med 85:145–147, 1989.
218. Halber MD, Daffner RH, Thompson WM: CT of the esophagus: I. Normal appearance. AJR 133:1047–1050, 1979.
219. Halden WJ, Harnsberger HR, Mancuso AA: Computed tomography of esophageal varices after sclerotheraphy. AJR 140:1195–1196, 1986.
220. Halpern M, Citro BP: Necrotizing angiitis associated with drug abuse. Am J Roentgenol 111:663–671, 1971.
221. Halvorsen RA, Thompson WM: Computed tomographic staging of gastrointestinal tract malignancies: I. Esophagus and stomach. Invest Radiol 22:2–16, 1987.
222. Halvorsen RA, Thompson WM: CT and MRI of the esophagus. In Levine MS (ed): Radiology of the Esophagus. Philadelphia, WB Saunders, 1989, pp 291–309.
223. Hamilton S: Colorectal carcinoma in patients with Crohn's disease. Gastroenterology 89:398–407, 1985.
224. Hande KR, Fisher RI, DeVita VT, et al: Diffuse histiocytic lymphoma involving the gastrointestinal tract. Cancer 41:1984–1989, 1978.
225. Harris LA, DeCosse JJ, Dannenberg A: Abdominal actinomycosis: Evaluation by computed tomography. Am J Gastroenterol 84:198–200, 1989.
226. Hasegawa S, Smelka RC, Noone TC, et al: Gastric stromal sarcomas: Correlation of MR imaging and histopathologic findings in nine patients. Radiology 208:591–595, 1998.
227. Haubrich WS, Pounder RE, Fraser AG: Peptic ulcer disease: Diagnosis, medical management, and complications. In Haubrich WS, Schaffner F, Berk JE (eds): Gastroenterology. Philadelphia, WB Saunders, 1994, pp 749–789.
228. Heiberg E, Wolverson MK, Hurd RN, et al: CT recognition of traumatic rupture of the diaphragm. AJR 135:369–372, 1980.
229. Heiken JP, Balfe DM, Roper CL: CT evaluation after esophagogastrectomy. AJR 143:555–560, 1984.
230. Hellwing AC: Extramedullary plasma cell tumors as observed in various locations. Arch Pathol 36:95–111, 1943.
231. Herbetko J, Brunton FJ: Enteroliths of small-bowel diverticula. Clin Radiol 43:311–313, 1991.
232. Hertzer NR, Hoerr SO: An interpretive review of lymphoma of the stomach. Surg Gynecol Obstet 143:113–124, 1976.
233. Higa E, Radai J, Pizzimbono CA, Wise L: Mucosal hyperplasia, mucinous cystadenoma, and mucinous cystadenocarcinoma of the appendix. Cancer 32:1525–1541, 1973.
234. Hinnant KL, Rotterdam HZ, Bell ET, Tapper ML: Cytomegalovirus infection of the alimentary tract: A clinicopathological correlation. Am J Gastroenterol 81:944–950, 1986.
235. Hirose J, Takashima T, Suzuki M, et al: "Downhill" esophageal varices demonstrated by dynamic computed tomography. J Comput Assist Tomogr 8:1007–1009, 1984.
236. Hirota C, Iida M, Aoyagi K, et al: Posttraumatic intestinal stenosis: Clinical and radiographic features in four patients. Radiology 194: 813–815, 1995.
237. Ho KJ, Herrera GA, Jones JM, et al: Small cell carcinoma of the esophagus: Evidence for a unified histogenesis. Hum Pathol 15: 460–468, 1984.
238. Hoffe N, Millan VG: Postemetic dissecting intramural hematoma of the esophagus. Radiology 9:293–295, 1984.
239. Holcomb GW, Gheissari A, O'Neill JA, et al: Surgical management of alimentary tract duplications. Ann Surg 209:167–174, 1989.
240. Holscher AH, Dittler HJ, Siewert JR: Staging of squamous esophageal cancer: Accuracy and value. World J Surg 18:312–320, 1994.
241. Hori S, Tsuda K, Murayama S, et al: Preliminary results with a new scanning technique. Radiographics 12:257–268, 1992.
242. Hori S, Tsuda K, Murayama S, et al: CT of gastric carcinoma: Preliminary results with a new scanning technique. Radiographics 12:257–268, 1992.
243. Horton KM, Corl FM, Fishman EK: CT of non-neoplastic disease of the small bowel: Spectrum of disease. J Comput Assist Tomogr 23:417–428, 1999.
244. Hosomi N, Yoshioka H, Sawai Y, et al: *Pneumatosis cystoides* intestinalis: CT findings. Abdom Imaging 19:137–139, 1994.
245. Hricak H, Thoeni RF, Margulis AR, et al: Extension of gastric lymphoma into the esophagus and duodenum. Radiology 135:309–312, 1980.
246. Hulnick DH, Megibow AJ, Balthazar EJ, et al: Perforated colorectal neoplasms: Correlation of clinical, contrast enema, and CT examinations. Radiology 164:611–615, 1987.
247. Hunter TB, Bjelland JC: Gastrointestinal complications of leukemia and its treatment. AJR 142:513–518, 1984.
248. Hurwitz A, Khafif RA: Acute necrotizing colitis proximal to obstructing neoplasms of the colon. Surg Gynecol Obstet 111:749–752, 1960.
249. Hurwitz LM, Gertler SL: Colonoscopic diagnosis of intussusception. Gastrointest Endosc 32:217–218, 1986.
250. Hussain SM, Outwater EK, Siegelman ES: Mucinous versus nonmucinous rectal carcinomas: Differentiation with MR imaging. Radiology 213:79–85, 1999.
251. Hwang HY, Choi BI, Han JK, et al: Calcified gastric carcinoma: CT findings. Gastrointest Radiol 17:311–315, 1992.
252. Hwang JC, Ha HK, Yoon KH, et al: Colonic wall thickening in cirrhotic patients: CT features and its clinical significance. Abdom Imaging 24:125–128, 1999.
253. Iko BO, Teal JS, Siram SM, et al: Computed tomography of adult colonic intussusception: Clinical and experimental studies. AJR 143: 769–772, 1984.
254. Im JG, Kim JH, Han MC, et al: Computed tomography of esophagomediastinal fistula in tuberculous mediastinal lymphadenitis. J Comput Assist Tomogr 14:89–92, 1990.
255. Incesu L, Coskun A, Selcuk MB, et al: Acute appendicitis: MR imaging and sonographic correlation. AJR Am J Roentgenol 168: 669–674, 1997.
256. International Study Group for Behçet's disease: Criteria for diagnosis of Behçet's disease. Lancet 335:1078–1080, 1990.
257. Ishida H, Konno K, Hamashima Y, et al: Portal tumor thrombus due to gastrointestinal cancer. Abdom Imaging 24:585–590, 1999.
258. Ishikura H, Kirimoto K, Shamoto M, et al: Hepatoid adenocarcinomas of the stomach. Cancer 58:119–126, 1986.
259. Iwanaga T, Koyama H, Furukawa H, et al: Mechanisms of late recurrence after radical surgery for gastric carcinoma. Am J Surg 135:637–640, 1978.
260. Jacob BZ, Albert S: Computed tomography in adult intussusception. Gastrointest Radiol 16:264–266, 1991.
261. Jacobs JE, Birnbaum BA: CT of inflammatory disease of the colon. Semin Ultrasound CT MR 16:91–101, 1995.
262. Jacobs JM, Hill MC, Steiberg WM: Peptic ulcer disease: CT evaluation. Radiology 178:745–748, 1991.
263. James S, Balfe DM, Lee JKT, et al: Small-bowel disease: Categorization by CT examination. AJR Am J Roentgenol 148:863–868, 1987.
264. Jang HJ, Lim HK, Choi SH, et al: Acute diverticulitis of the cecum and ascending colon: Thin-section helical CT findings. AJR Am J Roentgenol 172:601–604, 1999.
265. Japanese Research Society for Gastric Cancer: The general rules for the gastric cancer study in surgery and pathology: I. Clinical classification. Jpn J Surg 11:127–139, 1981.
266. Jaworski A, Fischer R, Lippman M: Boerhaave's syndrome: Computed tomographic findings and diagnostic considerations. Ann Intern Med 148:223–224, 1988.
267. Jee KN, Ha HK, Lee IJ, et al: Radiologic findings of abdominal polyarteritis nodosa. AJR Am J Roentgenol 174:1675–1679, 2000.
268. Jennette JC, Falk RJ, Andrassy K, et al: Nomenclature of systemic vasculitis. Arthritis Rheum 37:187–192, 1994.
269. Jeong YK, Ha HK, Yoon CH, et al: Gastrointestinal ivolvement in Henoch-Schönlein syndrome: CT Findings. AJR Am J Roentgenol 168:965–968, 1997.
270. Johnson CD, Baker ME, Rice RP, et al: Diagnosis of acute colonic diverticulitis: Comparison of barium enema and CT. AJR Am J Roentgenol 148:541–546, 1987.

271. Jones B, Fishman EK, Hamilton SR, et al: Submucosal accumulation of fat in inflammatory bowel disease: CT/pathologic correlation. J Comput Assist Tomogr 10:759–763, 1986.
272. Jones B, Fishman EK, Kramer SS, et al: Computed tomography of gastrointestinal inflammation after bone marrow transplantation. AJR 146:691–695, 1986.
273. Jones B, Kramer SS, Beschorner WE, et al: Gastrointestinal inflammation after bone marrow transplantation: Graft-versus-host disease or opportunistic infection? AJR Am J Roentgenol 150:277–281, 1988.
274. Jones WG II, Ginsberg RJ: Esophageal perforation: A continuing challenge. Ann Thorac Surg 53:534–543, 1992.
275. Kaibara N, Iitsuka Y, Kimura A, et al: Relationship between area of serosal invasion and prognosis in patients with gastric carcinoma. Cancer 60:136–139, 1987.
276. Kakeji Y, Tsujitani S, Baba H, et al: Clinicopathologic features and prognostic significance of duodenal invasion in patients with distal gastric carcinoma. Cancer 68:380–384, 1991.
277. Kasahara Y, Tanaka B, Nishino M, et al: Intestinal involvement in Behçet's disease: Review of 136 surgical cases in the Japanese literature. Dis Colon Rectum 24:103–106, 1981.
278. Kawamoto S, Horton KM, Fishman EK: Pseudomembranous colitis: Can CT predict which patients will need surgical intervention? J Comput Assist Tomogr 23:79–85, 1999.
279. Kawashima A, Sandler CM, Fishman EK, et al: Spectrum of CT findings in nonmalignant disease of the adrenal gland. Radiographics 18:393–412, 1998.
280. Kawashima A, Fishman EK, Kuhlman JE, Schuchter LM: CT of malignant melanoma: Patterns of small-bowel and mesenteric involvement. J Comput Assist Tomogr 15:570–574, 1991.
281. Kazerooni EA, Quint LE, Francis IR: Duodenal neoplasms: Predictive value of CT for determining malignancy and tumor resectability. AJR Am J Roentgenol 159:303–309, 1992.
282. Kelvin FM, Gramm HF, Gluck WL: Radiographic manifestations of small-bowel toxicity due to floxuridine therapy. AJR 146:39–43, 1986.
283. Kelvin FM, Korobkin M, Breiman RS: Recurrent rectal carcinoma in an asymptomatic patient. J Comput Assist Tomogr 6:180–188, 1982.
284. Kelvin FM, Korobkin M, Heaston DK, et al: The pelvis after surgery for rectal carcinoma: Serial CT observations with emphasis on nonneoplastic features. AJR 141:959–964, 1983.
285. Kerkes ES: Gastric haemangioma: A case report. Radiology 82: 468–469, 1964.
286. Ketcham AS, Hoye RC, Pilch YH, Morton DL: Delayed intestinal obstruction following treatment for cancer. Cancer 25:406–410, 1970.
287. Khalifa AA, Bong WL, Rao VK, et al: Leiomyosarcoma of the rectum: Report of a case and review of literature. Dis Colon Rectum 29:427–432, 1986.
288. Kim AY, Ha HK, Seo BK, et al: CT of patients with right-sided colon cancer and distal ileal thickening. AJR Am J Roentgenol 175: 1439–1444, 2000.
289. Kim AY: Small-bowel obstruction associated with sigmoid diverticulitis: CT evaluation in 16 patients. AJR Am J Roentgenol 170: 1311–1313, 1998.
290. Kim HJ, Ha HK, Cho KS, et al: CT features of primary colorectal signet-ring cell carcinoma. J Comput Assist Tomogr 25:225–230, 2001.
291. Kim HJ, Park MH: Obstructive uropathy due to interstitial cystitis in a patient with systemic lupus erythematosus. Clin Nephrol 45: 205–208, 1996.
292. Kim JK, Ha HK, Byun JY, et al: CT differentiation of mesenteric ischemia due to vasculitis and thromboembolic disease. J Comput Assist Tomogr 25:604–611, 2001.
293. Kim JK, Ha HK, Byun JY, et al: Intestinal infarction secondary to mesenteric venous thrombosis: CT-pathologic correlation. J Comput Assis Tomogr 17:382–385, 1993.
294. Kim JK, Ha HK, Byun JY, et al: CT differentiation of mesenteric ischemia due to vasculitis and thromboembolic disease. J Comput Assist Tomogr 25:604–611, 2001.
295. Kim KW, Berkmen YM, Auh YH, et al: Diagnosis of epiphrenic esophageal diverticulum by computed tomography. J Comput Assist Tomogr 12:25–28, 1988.
296. Kim MJ, Huh YM, Park YN, et al: Colorectal mucinous carcinoma: Findings on MRI. J Comput Assist Tomogr 23:291–296, 1999.
297. Kim SH, Lim HK, Lee WJ, et al: Mucocele of the appendix: Ultrasonographic and CT findings. Abdom Imaging 23:292–296, 1998.
298. Kim YS, Cho OK, Song SY, et al: Peritoneal lymphomatosis: CT findings. Abdom Imaging 23:87–90, 1998.
299. Kirby TJ, Rice TW: The epidemiology of esophageal carcinoma: The changing face of a disease. Chest Surg Clin North Am 4: 217–225, 1994.
300. Kirshy DM, Gordon DH, Atweh NA: Abdominal computed tomography in lupus mesenteric arteritis. Comput Med Imaging Graph 15: 369–372, 1991.
301. Kistin MG, Kaplan MM, Harrington JT: Diffuse ischemic colitis associated with systemic lupus erythematosus: Response to subtotal colectomy. Gastroenterology 75:1147–1151, 1978.
302. Klein HM, Lensing R, Klosterhalfen B, et al: Diagnostic imaging of mesenteric infarction. Radiology 197:79–82, 1995.
303. Klein NC, Hargrove RL, Sleisenger MH, Jeffries GH: Eosinophilic gastroenteritis. Medicine 49:299–319, 1970.
304. Ko GY, Ha HK, Lee HJ, et al: Usefulness of CT in patients with ischemia colitis proximal to colonic cancer. AJR Am J Roentgenol 168:951–956, 1997.
305. Ko SF, Lee TY, Ng SH: Small-bowel obstruction due to phytobezoar: CT diagnosis. Abdom Imaging 22:471–473, 1997.
306. Kodaira Y, Shibuya T, Matsumoto K, et al: Primary aortoduodenal fistula caused by duodenal tuberculosis without an abdominal aortic aneurysm: Report of a case. Jpn J Surg 27:745–748, 1997.
307. Koelbel G, Schmiedl U, Majer MC, et al: Diagnosis of fistulae and sinus tracts in patients with Crohn disease: Value of MR imaging. AJR Am J Roentgenol 152:999–1003, 1989.
308. Koga H, Iida M, Suekane H, et al: Rapidly growing esophageal leiomyosarcoma: Case report and review of the literature. Abdom Imaging 20:15–19, 1995.
309. Kremer RM, Lepoff RB, Izant RJ Jr: Duplications of the stomach. J Pediatr Surg 5:360–364, 1970.
310. Krestin GP, Steinbrich W, Friedmann G: Recurrent rectal cancer: Diagnosis with MR imaging versus CT. Radiology 168:307–311, 1988.
311. Kunin JR, Korobkin M, Ellis JH, et al: Duodenal injuries caused by blunt abdominal trauma: Value of CT in differentiating perforation from hematoma. AJR Am J Roentgenol 160:1221–1223, 1993.
312. Kyle RA, Greipp PR: Amyloidosis (AL): Clinical and laboratory features in 229 cases. Mayo Clin Proc 58:665–683, 1983.
313. Laky D, Stoica T: Gastric liposarcoma: A case report. Pathol Res Pract 181:112–117, 1986.
314. Lane MJ, Katz DS, Ross BA, et al: Unenhanced helical CT for suspected appendicitis. AJR Am J Roentgenol 168:405–409, 1997.
315. Laurent F, Raynaud M, Biset JM, et al: Diagnosis and categorization of small-bowel neoplasms: Role of computed tomography. Gastrointest Radiol 16:115–119, 1991.
316. Lee CM, Changchien CS, Chen PC, et al: Eosinophilic gastroenteritis: Ten years' experience. Am J Gstroenterol 88:70–74, 1993.
317. Lee DH, Choi BI, Park CM, et al: Exophytic adenocarcinoma of the stomach: CT findings. AJR Am J Roentgenol 163:77–80, 1994.
318. Lee DH, Ko YT: The role of 3D spiral CT in early gastric carcinoma. J Comput Assist Tomogr 22:709–713, 1998.
319. Lee DH: Three-dimensional imaging of the stomach by spiral CT. J Comput Assist Tomogr 22:52–58, 1998.
320. Lee GM, Cohen AJ: CT imaging of abdominal hernias. AJR Am J Roentgenol 161:1209–1213, 1993.
321. Lee IJ, Ha HK, Park CM, et al: Abdominopelvic actinomycosis involving the gastrointestinal tract: CT features. Radiology 220: 76–80, 2001.
322. Lee JH, Ha HK, Yoo ES, et al: CT and sonographically guided biopsy in a patient with intestinal mucormycosis. AJR Am J Roentgenol 175:129–131, 2000.
323. Lee JKT, Stanley RJ, Sagel SS, et al: CT appearance of the pelvis after abdominoperineal resection for rectal carcinoma. Radiology 141:737–741, 1981.
324. Lee MJ, Breathnach E: CT and MRI findings in paraoesophageal omental herniation. Clin Radiol 42:207–209, 1990.
325. Lee RC, Chiang JH, Chou YH, et al: Intestinal schistosomiasis japonica: CT-pathologic correlation. Radiology 193:539–542, 1994.
326. Lee SH, Ha HK, Byun JY, et al: Radiological features of leiomyomatous tumors of the colon and rectum. J Comput Assist Tomogr 24: 407–412, 2000.

327. Leffall LD Jr, Quander J, Syphax B: Strangulation intestinal obstruction: A clinical appraisal. Arch Surg 91:592–596, 1965.
328. Lehr L, Rupp N, Siewert JR: Assessment of resectability of esophageal cancer by computed tomography and magnetic resonance imaging. Surgery 103:344–350, 1988.
329. Lehrer RI, Howard DH, Sypherd PS, et al: Mucormycosis. Ann Intern Med 93:93–108, 1980.
330. Leidich RB, Rudolph LE: Small-bowel perforation secondary to metastatic lung carcinoma. Ann Surg 193:67–69, 1981.
331. Levine CD, Gonzales RN, Wachsberg RH, Ghanekar D: CT findings of bowel and mesenteric injury. J Comput Assist Tomogr 21:974–979, 1997.
332. Levine CD, Patel UJ, Eachsberg RH, et al: CT in patients with blunt abdominal trauma: Clinical significance of intraperitoneal fluid detected on a scan with otherwise normal findings. AJR Am J Roentgenol 164:1381–1385, 1995.
333. Levine MS: Other malignant tumors. In Gore RM, Levine MS, Laufer I (eds): Textbook of Gastrointestinal Radiology. Philadelphia, WB Saunders, 1994, pp 479–498.
334. Levine MS: Varices. In Gore RM, Levine MS, Laufer I (eds): Textbook of Gastrointestinal Radiology. Philadelphia, WB Saunders, 1994, pp 499–511.
335. Levine MS: Esophageal cancer: Radiologic diagnosis. Radiol Clin North Am 35:265–279, 1997.
336. Levine MS: Miscellaneous abnormalities. In Gore RM, Levine MS, Laufer I (eds): Textbook of Gastrointestinal Radiology. Philadelphia, WB Saunders, 1994, pp 512–530.
337. Levine MS, Buck JL, Pantongrag-Brown L, et al: Esophageal leiomyomatosis. Radiology 199:533–536, 1996.
338. Levine MS, Pantongrag-Brown L, Buck JL, et al: Small cell carcinoma of the esophagus: Radiographic findings. Radiology 199:703–705, 1996.
339. Levine MS, Buck JL, Pantongrag-Brown L, et al: Fibrovascular polyps of the esophagus: Clinical, radiographic, and pathologic findings in 16 patients. AJR Am J Roentgenol 166:781–787, 1996.
340. Levine MS, Buck JL, Pantongrag-Brown L, et al: Leiomyosarcoma of the esophagus: Radiographic findings in 10 patients. AJR Am J Roentgenol 167:27–32, 1996.
341. Levine MS, Halvorsen RA: Esophageal carcinoma. In Gore RM, Levine MS, Laufer I (eds): Textbook of Gastrointestinal Radiology. Philadelphia, WB Saunders, 1994, pp 446–478.
342. Levine MS, Herman JB, Fruth EE: Barrett's esophagus and esophageal adenocarcinoma: The scope of the problem. Abdom Imaging 20:291–298, 1995.
343. Levine MS, Rubesin SE, Pantongrag-Brown, et al: Non-Hodgkin's lymphoma of the gastrointestinal tract: Radiographic findings. AJR Am J Roentgenol 168:165–172, 1997.
344. Levison MA, Petersen SR, Sheldon GF, Trunkey DD: Duodenal trauma: Experience of a trauma center. J Trauma 24:475–480, 1984.
345. Lewin KJ, Ranchod M, Dorfman RF: Lymphomas of the gastrointestinal tract. Cancer 42:693–707, 1978.
346. Lewis FR, Holcroft JW, Boey J, Dunphy JE: Appendicitis: A critical review of diagnosis and treatment in 1000 cases. Arch Surg 110: 677–684, 1975.
347. Lewis JH: Gastrointestinal injury due to medicinal agents. Am J Gastroenterol 81:819–834, 1986.
348. Leyman P, Ponette E, Marchal G, et al: Computed tomography of acute jejunogastric intussusception. J Comput Assist Tomogr 13: 531–533, 1989.
349. Li KCP, Whitney WS, McDonnell CH, et al: Chronic mesenteric ischemia: Evaluation with phase-contrast cine MR imaging. Radiology 190:175–179, 1994.
350. Livstone EM, Skinner DB: Tumors of the esophagus. In Berk JE (ed): Gastroenterology. Philadelphia, WB Sanders, 1995, pp 818–850.
351. Lo CY, Chu KW: Acute diverticulitis of the right colon. Am J Surg 171:244–246, 1996.
352. Localio SA, Eng K, Cappa GF: Malignant tumors of the rectum. In Localio SA, Eng K, Copper GF (eds): Anorectal, Presacral and Sacral Tumors. Philadelphia, WB Saunders, 1987, pp 137–151.
353. López-Mut JV, Cubells M, Campos S, et al: Jejunogastric intussusception: A rare complication of gastric surgery. Abdom Imaging 23: 558–559, 1998.
354. López-Negrete L, Luyando L, Sala J, et al: Liposarcoma of the stomach. Abdom Imaging 22:373–375, 1997.
355. Low RN, Francis IR, Politoske D, Bennett M: Crohn's disease evaluation: Comparison of contrast-enhanced MR imaging and single-phase helical CT scanning. J Magn Reson Imaging 11:127–135, 2000.
356. Low RN, Wall SD, Jeffrey RB Jr, et al: Aortoenteric fistula and perigraft infection: Evaluation with CT. Radiology 175:157–162, 1990.
357. Lumbreras C, Fernandez L, Velosa J, et al: Infectious complications following pancreatic transplantation: Incidence, microbiological and clinical characteristics, and outcome. Clin Infect Dis 20:514–520, 1995.
358. Lunderquist A, Lunderquist A, Knutsson H: Angiography in Crohn's disease of the small bowel and colon. AJR 101:338–344, 1967.
359. Lundquist A, Olsson R, Ekberg O: Clinical and radiologic evaluation reveals high prevalence of abnormalities in young adults with dysphagia. Dysphagia 13:202–207, 1998.
360. Lupetin AR: Diffuse cavernous hemangioma of the rectum: Evaluation and MRI. Gastrointest Radiol 15:343–345, 1990.
361. Lyon DT, Schubert TT, Mantia AG, Kaplan MH: Phycomycosis of the gastrointestinal tract. Am J Gastroenterol 72:379–394, 1979.
362. MacAfee CH, Greer HL: Intestinal endometriosis: A report of 29 cases and a review of the literature. J Obstet Gynecol 67:539–555, 1960.
363. Macari M, Balthazar EJ, Megibow AJ: The accordion sign at CT: A nonspecific finding in patients with colonic edema. Radiology 211:743–746, 1999.
364. Maceiner SR, McDonald JR, Kerklin JW: Muscle biopsy in the diagnosis of periarteritis nodosa: An evaluation. Surg Clin North Am 32:1225–1233, 1952.
365. Maderal F, Hunter F, Fuselier G, et al: Gastric lipomas: An update of clinical presentation, diagnosis, and treatment. Am J Gastroenterol 79:964–967, 1984.
366. Madrazo BL, Halpert RD, Sandler MA, et al: Computed tomographic findings in penetrating peptic ulcer. Radiology 153:751–754, 1984.
367. Maglinte DDT, Balthazar EJ, Kelvin FM, Megibow AJ: The role of radiology in the diagnosis of small-bowel obstruction. AJR Am J Roentgenol 168:1171–1180, 1997.
368. Maglinte DDT, Chernish SM, DeWeese R, et al: Acquired jejunoileal diverticular disease: Subject review. Radiology 158:577–580, 1986.
369. Maglinte DDT, Herlinger H, Nolan DJ: Radiologic features of closed-loop obstruction: Analysis of 25 confirmed cases. Radiology 179:383–387, 1991.
370. Maglinte DDT, Herlinger H: Vascular disorders of the small intestine. In Herlinger H, Maglinte DDT (eds): Clinical Radiology of the Small Intestine. Philadelphia, WB Saunders, 1989, pp 453–478.
371. Makanjuola D: Is it Crohn's disease or intestinal tuberculosis? CT analysis. Eur J Radiol 28:55–61, 1998.
372. Mannell A: Carcinoma of the esophagus. Curr Probl Surg 19:553–647, 1982.
373. Marks CG, Nolan DJ, Piris J, et al: Small-bowel stricture after blunt abdominal trauma. Br J Surg 66:663–664, 1979.
374. Markus J, Morrissey B, deGara C, Tarulli G: MRI of recurrent rectosigmoid carcinoma. Abdom Imaging 22:338–342, 1997.
375. Marshall JB: Tuberculosis of the gastrointestinal tract and peritoneum. Am J Gastroenterol 8:989–999, 1993.
376. Marshall JP, Smith PD, Hoyumpa AM: Gastric varices: Problems in diagnosis. Am J Dig Dis 22:947–955, 1977.
377. Martin DF, Hartley G: Gastric emphysema demonstrated by computed tomography. Br J Radiol 59:505–507, 1986.
378. Martinez-Frontanilla LA, Hasse GM, Ernster JA, Bailey WC: Surgical complications in Henoch-Schönlein purpura. J Pediatr Surg 19: 434–436, 1984.
379. Maruyama K, Guven P, Okabayashi K, et al: Lymph node metastases of gastric cancer: General pattern in 1931 patients. Ann Surg 210: 596–602, 1989.
380. Marx MV, Balfe DM: Computed tomography of the esophagus. Semin Ultrasound CT MR 8:316–348, 1987.
381. Mason RM, Barnes CG: Behçet's syndrome with arthritis. Ann Rheum Dis 28:95–103, 1969.
382. Matsushita M, Oi H, Murakami T, et al: Extraserosal invasion in advanced gastric cancer: Evaluation with MR imaging. Radiology 192:87–91, 1994.
383. Mauro MA, Jaques PF, Swantkowski TM, et al: CT after uncomplicated esophageal sclerotheraphy. Am J Roentgenol 147:57–60, 1986.

384. McAlister WH, Margulis AR, Heinbecker P, Spjut H: Arteriography and microangiography of gastric and colonic lesions. Radiology 79: 769–782, 1962.
385. McBride RA, Corson JM, Dammin GJ: Mucormycosis: Two cases of disseminated disease with cultural identification of *Rhizopus*. Am J Med 28:832–846, 1960.
386. McCain AH, Bernardino ME, Sones PJ Jr, et al: Varices from portal hypertension: Correlation of CT and angiography. Radiology 154: 63–69, 1985.
387. McCartney J, Dobrow J, Hendrix TR: Boerhaave syndrome. Johns Hopkins Med 144:28–33, 1979.
388. McCowin MJ, Federle MP: Computed tomography of pancreatic pseudocysts of the duodenum. Am J Roentgenol 145:1003–1007, 1985.
389. McDaniel KP, Charnsangavej C, Dubrow RA, et al: Pathways of nodal metastasis in carcinomas of the cecum, ascending colon, and transverse colon: CT demonstration. AJR Am J Roentgenol 161: 61–64, 1993.
390. McDermott VG, Low VHS, Keogan MT, et al: Malignant melanoma metastatic to the gastrointestinal tract. AJR Am J Roentgenol 166: 809–813, 1996.
391. McNeer G, Vandenberg H Jr, Donn FY, Bowden L: A critical evaluation of subtotal gastrectomy for the cure of cancer of the stomach. Ann Surg 134:2–7, 1951.
392. McNeill PM, Wagman LD, Neifeld JP: Small-bowel metastases from primary carcinoma of the lung. Cancer 59:1486–1489, 1987.
393. Megibow AJ: Gastrointestinal lymphoma: The role of CT in diagnosis and management. Semin Ultrasound CT MR 7:43–57, 1986.
394. Megibow AJ: Techniques of gastrointestinal computed tomography. In Megibow AJ, Balthazar EJ (eds): Computed Tomography of the Gastrointestinal Tract. St. Louis, CV Mosby, 1986, pp 1–32.
395. Megibow AJ: The gastrointestinal tract. In Haaga JR, Alfidi RJ (eds): Computed Tomography of the Whole Body. St. Louis, CV Mosby, 1988, pp 1390–1428.
396. Megibow AJ, Balthazar EJ, Cho KC, et al: Bowel obstruction: Evaluation with CT. Radiology 180:313–318, 1991.
397. Megibow AJ, Balthazar EJ, Hulnick DH, et al: CT evaluation of gastrointestinal leiomyomas and leiomyosarcomas. Am J Roentgenol 144:727–731, 1985.
398. Megibow AJ, Balthazar EJ, Naidich DP, et al: Computed tomography of gastrointestinal lymphoma. AJR 141:541–547, 1983.
399. Megibow AJ, Balthazar EJ, Hulnick DH, et al: CT evaluation of gastrointestinal leiomyomas and leiomyosarcomas. AJR 144:727–731, 1985.
400. Megibow AJ, Zerthouni EA, Hulnick DH, et al: Air insufflation of the colon as an adjunct to computed tomography of the pelvis. J Comput Assist Tomogr 8:797–800, 1984.
401. Melody GF: Endometriosis causing obstruction of the ileum. Obstet Gynecol 8:468–472, 1956.
402. Méndez RJ, Rodríguez R, Kovacevich T, et al: CT in local recurrence of rectal carcinoma. J Comput Assist Tomogr 17:741–744, 1993.
403. Meyers MA, Ghahremani GG, Clements JL, et al: Pneumatosis intestinalis. Gastrointest Radiol 2:91–105, 1977.
404. Meyers MA, McGuire PV: Spiral CT demonstration of hypervascularity in Crohn disease: "Vascular jenunization of the ileum" or the "comb sign." Abdom Imaging 20:327–332, 1995.
405. Meyers MA, McSweeny J: Secondary neoplasms of the bowel. Radiology 105:1–11, 1972.
406. Meyers MA: Paraduodenal hernias: Radiologic and arteriographic diagnosis. Radiology 95:29–37, 1970.
407. Mills JA, Michel BA, Bloch DA, et al: The American College of Rheumatology 1990 criteria for the classification of Henoch-Schönlein purpura. Arthritis Rheum 33:1114–1121, 1990.
408. Minami M, Kawauchi N, Itai Y, et al: Gastric tumors: Radiologic-pathologic correlation and accuracy of T staging with dynamic CT. Radiology 185:173–178, 1992.
409. Ming S-C, Goldman H: Gastric polyps: A histogenetic classification and its relation to carcinoma. Cancer 18:721–726, 1965.
410. Minocha A, Davis MS, Wright RA: Small-bowel endometriosis masquerading as regional enteritis. Dig Dis Sci 39:1126–1133, 1994.
411. Mirvis SE, Gens DR, Shanmuganathan K: Rupture of the bowel after blunt abdominal trauma: Diagnosis with CT. AJR Am J Roentgenol 159:1217–1221, 1992.
412. Mirvis SE, Shanmuganathan K, Erb R: Diffuse small-bowel ischemia in hypotensive adults after blunt trauma (shock bowel): CT findings and clinical significance. AJR Am J Roentgenol 163:1375–1379, 1994.
413. Miyake H, Maeda H, Kurauchi S, et al: Thickened gastric walls showing diffuse low attenuation on CT. J Comput Assist Tomogr 13:253–255, 1989.
414. Moersh HJ, Harrington SW: Benign tumor of the esophagus. Ann Otal Laryngol 53:800–817, 1944.
415. Mönig SP, Zirbes TK, Schröder W, et al: Staging of gastric cancer: Correlation of lymph node size and metastatic infiltration. AJR Am J Roentgenol 173:365–367, 1999.
416. Mori M, Matsukuma A, Adachi Y, et al: Small cell carcinoma of the esophagus. Cancer 63:564–573, 1989.
417. Moss AA, Schnyder P, Thoeni RF, et al: Esophageal carcinoma: Pretherapy staging by computed tomography. AJR 136:1051–1056, 1981.
418. Müller-Schimpfle M, Brix G, Layer G, et al: Recurrent rectal cancer: Diagnosis with dynamic MR imaging. Radiology 189:881–889, 1993.
419. Murata Y, Suzuki S, Hashimoto H: Endoscopic ultrasonography of the upper gastrointestinal tract. Surg Endosc 2:180–183, 1988.
420. Murray JG, Evans SJJ, Jeffrey PB, Halvorsen RA Jr: Cytomegalovirus colitis in AIDS: CT features. AJR Am J Roentgenol 165: 67–71, 1995.
421. Nader PR, Margolin FR: Hemangioma causing gastrointestinal bleeding. Am J Dis Child 111:215–222, 1966.
422. Nagai E, Ueyama T, Yao T: Hepatoid adenocarcinoma of the stomach: A clinicopathologic and immunohistochemical analysis. Cancer 72:1827–1835, 1993.
423. Nalesnik MA, Makowka L, Starzl TE: The diagnosis and treatment of posttransplant lymphoproliferative disorders. Curr Probl Surg 25: 367–472, 1988.
424. Naylor AR, Pollet JE: Eosinophilic colitis. Dis Colon Rectum 28: 615–618, 1985.
425. Nghiem HV, Jeffrey RB Jr, Mindelzun RE: CT of blunt trauma to the bowel and mesentery. AJR Am J Roentgenol 160:54–58, 1993.
426. Nishimaki T, Suzuki T, Fukuda T, et al: Primary small cell carcinoma of the esophagus with ectopic gastrin production. Dig Dis Sci 38:767–771, 1993.
427. Nitsch B, Ho CS, Cullen J: Barium study of small-bowel endometriosis. Gastrointest Radiol 13:361–363, 1988.
428. Noh HM, Fishman EK, Forastiere AA, et al: CT of the esophagus: Spectrum of disease with emphasis on esophageal carcinoma. Radiographics 15:1113–1134, 1995.
429. Norton GA, Postlethwait RW, Thompson WM: Esophageal carcinoma: A survey of population at risk. South Med J 73:25–27, 1980.
430. Nuzum JC, Falk RJ: Small-vessel vasculitis. N Engl J Med 20: 1512–1523, 1997.
431. O'Connor KF, Bagg MN, Croley MR, Schabel SI: Pelvic actinomycosis associated with intrauterine devices. Radiology 170:559–560, 1989.
432. O'Sullivan SG: The accordion sign. Radiology 206:177–178, 1998.
433. Oakes DD: Reconsidering the diagnosis and treatment of patients following ingestion of liquid lye [editorial]. J Clin Gastroenterol l21:85–86, 1995.
434. Ogorek CP, Fisher RS: Differentiation between Crohn's disease and ulcerative colitis. Med Clin North Am 78:1249–1258, 1994.
435. Oguzkurt L, Karabulut N, Cakmakci E, et al: Primary non-Hodgkin's lymphoma of the esophagus. Abdom Imaging 22:8–10, 1997.
436. Olmsted WW, Lichtenstein JE, Hyams VJ: Polypoid epithelial malignancies of the esophagus. AJR 140:921, 1983.
437. Ongolo-Zogo P, Borson O, Carcia P, et al: Acute gastroduodenal peptic ulcer perforation: Contrast-enhanced and thin-section spiral CT findings in 10 patients. Abdom Imaging 24:329–332, 1999.
438. Orchard JL, Petorak V: Abnormal abdominal CT findings in a patient with giardiasis: Resolution after treatment. Dig Dis Sci 40: 346–348, 1995.
439. Orloff MJ, Charters AC: Injuries of the small bowel and mesentery and retroperitoneal hematoma. Surg Clin North Am 52:729–734, 1972.
440. Ormson MJ, Stephens DH, Carson HC: CT recognition of intestinal lipomatosis. AJR 144:313–314, 1985.
441. Orringer MB: The esophagus: Historical aspects and anatomy. In Sabiston DC (ed): Textbook of Surgery. Philadelphia, WB Saunders, 1986, pp 697–701.

442. Oshima Y, Shimizu T, Yokohari R, et al: Clinical studies on Behçet's syndrome. Ann Rheum Dis 22:36–45, 1963.
443. Osteen RT, Guyton S, Steele G Jr, Wilson RE: Malignant intestinal obstruction. Surgery 87:611–615, 1980.
444. Ott DJ: Motility disorders of the esophagus. Radiol Clin North Am 32:1117–1134, 1994.
445. Ott DJ, Hodge RG, Chen MY, et al: Achalasia associated with hiatal hernia: Prevalence and potential implications. Abdom Imaging 18: 7–9, 1993.
446. Padidar AM, Jeffrey RB Jr, Mindelzun RE, et al: Differentiating sigmoid diverticulitis from carcinoma on CT scans: Mesenteric inflammation suggests diverticulitis. AJR Am J Roentgenol 163: 81–83, 1994.
447. Palchick BA, Alpert MA, Holmes RA, et al: Esophageal hemangioma: Diagnosis with computed tomography and radionuclide angiography. South Med J 76:1582–1584, 1983.
448. Pandarinath GS, Levine SM, Sorokin JJ, Jacoby JH: Selective massive amyloidisis of the small intestine mimicking multiple tumors. Radiology 129:609–610, 1978.
449. Pantongrag-Brown L, Buetow PC, Carr NJ, et al: Calcification and fibrosis in mesenteric carcinoid tumor: CT findings and pathologic correlation. AJR Am J Roentgenol 164:387–391, 1995.
450. Parachristou DN, Fortner JG: Local recurrence of gastric adenocarcinomas after gastrectomy. J Surg Oncol 18:47–53, 1981.
451. Parachristou DN, Karas M, Fortner JG: Anastomotic recurrence in the oesophagus complicating gastrectomy for adenocarcinoma of the stomach. Br J Surg 66:609–612, 1979.
452. Partel MP, De I: Segmental tuberculosis of the colon with enterocolic fistula. Br J Radiol 45:150–152, 1972.
453. Passas V, Karavias D, Gulias D, et al: Computed tomography of left paraduodenal hernia. J Comput Assist Tomogr 10:542–543, 1986.
454. Patton AS, Lawson DW, Shannon JM, et al: Reevaluation of the Boerhaave syndrome. Am J Surg 137:560–565, 1979.
455. Pearlberg JL, Sandler MA, Madrazo BL: Computed tomographic features of esophageal intramural pseudodiverticulosis. Radiology 117:189–190, 1983.
456. Peitzman AB, Makoroin MS, Slasky BS, et al: Prospective study of CT in initial management of blunt abdominal trauma. J Trauma 26: 585–591, 1986.
457. Pellicano A, Watier A, Gentile J: Spontaneous double-barreled esophagus: Report of two cases and review of the literature. J Clin Gastroenterol 9:149–154, 1987.
458. Perez C, Andreu J, Llauger J, Valls J: Hemangioma of the rectum: CT appearance. Gastrointest Radiol 12:347–349, 1987.
459. Petrillo R, Balzarini L, Bidoli P, et al: Esophageal squamous cell carcinoma: MRI evaluation of mediastinum. Gastointest Radiol 15: 275–278, 1990.
460. Pezzulli FA, Aronson D, Goldberg N: Computed tomography of mediastinal hematoma secondary to unusual esophageal laceration: A Boerhaave variant. J Comput Assist Tomogr 13:129–131, 1989.
461. Philpotts LE, Heiken JP, Westcott MA, Gore RM: Colitis: Use of CT findings in differential diagnosis. Radiology 190:445–449, 1994.
462. Pickhardt PJ, Siegel MJ: Abdominal manifestations of posttransplantation lymphoproliferative disorder. AJR Am J Roentgenol 171: 1007–1013, 1998.
463. Pickhardt PJ, Siegel MJ: Posttransplantation lymphoproliferative disorder of the abdomen: CT evaluation in 51 patients. Radiology 213:73–78, 1999.
464. Picus D, Balfe DM, Koehler RE, et al: Computed tomography in the staging of esophageal carcinoma. Radiology 146:433–438, 1983.
465. Picus D, Glazer HS, Levitt RG, et al: Computed tomography of abdominal carcinoid tumors. Am J Roentgenol 143:581–584, 1984.
466. Plachta A: Benign tumor of the esophagus: Review of literature and report of 99 cases. Am J Gastroenterol 38:639–652, 1962.
467. Poorman JC, Katon RM: Small-bowel involvement by *Mycobacterium avium* complex in patients with AIDS: Endoscopic, histologic, and radiographic similarities to Whipple disease. Gastrointest Endosc 40:753–759, 1994.
468. Potet F, Duclert N: Dystrophie Kystique sur pancréas aberrant de la paroi duodénale. Arch Fr Mal Appl Dia 59:223–238, 1970.
469. Pozniak MA, Babel SG, Trump DL: Complications of hepatic arterial infusion chemotherapy. Radiographics 11:67–79, 1991.
470. Pradel JA, Adell JF, Taoureal P, et al: Acute colonic diverticulitis: Prospective comparative evaluation with US and CT. Radiology 205:503–512, 1997.
471. Procacci C, Graziani R, Zamboni G, et al: Cystic dystrophy of the duodenal wall: Radiologic findings. Radiology 205:741–747, 1997.
472. Pruksapong S, Donovan RJ, Pinit A, Heldreth FJ: Gastric duplication. J Pediatr Surg 14:83–85, 1979.
473. Puri AS, Aggarwl R, Gupta RK, et al: Intestinal lymphangiectasia: Evaluation by CT and scintigraphy. Gastrointest Radiol 17:119–121, 1992.
474. Quint LE, Glazer GM, Orringer MB, et al: Esophageal carcinoma: CT findings. Radiology 155:171–175, 1985.
475. Quint LE, Glazer GM, Orringer MB: Esophageal imaging by MR and CT: Study of normal anatomy and neoplasms. Radiology 156: 727–731, 1985.
476. Qvafordt PG, Reilly LM, Mark AS, et al: Computerized tomographic assessment of graft incorporation after reconstruction. Am J Surg 150:227–231, 1985.
477. Rabushka LS, Fishman EK, Kuhlman JE, et al: Diffuse esophageal leiomyomatosis in a patient with Alport syndrome: CT demonstration. Radiology 179:176–178, 1991.
478. Rabushka LS, Fishman EK, Kuhlman JE: CT evaluation of achalasia. J Comput Assist Tomogr 15:434–439, 1991.
479. Radin DR: Primary esophageal lymphoma in AIDS. Abdom Imaging 18:223–224, 1993.
480. Rainer WG, Brus R: Leiomyosarcoma of the esophagus. Surgery 58:343–350, 1965.
481. Ranchod M, Kempson RL: Smooth muscle tumors of the gastrointestinal tract and retroperitoneum. Cancer 39:255–262, 1977.
482. Randhawa PS, Yousem SA, Paradis IL, et al: The clinical spectrum, pathology, and clonal analysis of Epstein-Barr virus–associated lymphoproliferative disorders in heart-lung transplant recipients. Am J Clin Pathol 92:177–185, 1989.
483. Rao PM, Rhea JT, Novelline RA, et al: Helical CT technique for diagnosing appendicitis: Prospective evaluation of a focused appendix CT examination. Radiology 202:139–144, 1997.
484. Rao PM, Rhea JT, Novelline RA, et al: Helical CT with only colonic contrast material for diagnosing diverticulitis: Prospective evaluation of 150 patients. AJR Am J Roentgenol 170:1445–1449, 1998.
485. Rao PM, Rhea JT, Novelline RA, et al: Helical CT combined with contrast material administered only through the colon for imaging of suspected appendicitis. AJR Am J Roentgenol 169:1275–1280, 1997.
486. Rao PM, Rhea JT, Novelline RA: Distal appendicitis: CT appearance and diagnosis. Radiology 204:709–712, 1997.
487. Rao PM, Rhea JT, Novelline RA: Sensitivity and specificity of the individual CT signs of appendicitis: Experience with 200 helical appendiceal CT examinations. J Comput Assist Tomogr 21:686–692, 1997.
488. Rao PM, Rhea JT: Colonic diverticulitis: Evaluation of the arrowhead sign and the inflamed diverticulum for CT diagnosis. Radiology 209:775–779, 1998.
489. Rao PM, Wittenberg J, Lawrason JN: Primary epiploic appendagitis: Evolutionary changes in CT appearance. Radiology 204:713–717, 1997.
490. Rao PM, Wittenberg J, McDowell RK, et al: Appendicitis: Use of arrowhead sign for diagnosis at CT. Radiology 202:363–366, 1997.
491. Rao TDE, Vaas F: Leiomyosarcoma of the transverse and descending colon: Two case reports and review. Am J Gastroentenol 52: 150–156, 1969.
492. Raptopoulos V, Davidoff A, Karellas A, et al: CT of the pancreas with a fat-density oral contrast regimen. AJR Am J Roentgenol 150: 1303–1306, 1988.
493. Raptopoulos V, Davis MA, Davidoff A, et al: Fat-density oral contrast agent for abdominal CT. Radiology 164:653–656, 1987.
494. Raptopoulos V, Schwartz RK, McNicholas MMJ, et al: Multiplanar helical CT enterography in patients with Crohn's disease. AJR Am J Roentgenol 169:1545–1550, 1997.
495. Reinig JW, Stanley JH, Schabel SI: CT of thickened esophageal walls. AJR 140:931–934, 1983.
496. Reinus JF, Brandt LJ, Boley SJ: Ischemic disease of the bowel. Gastroenterol Clin North Am 19:319–343, 1990.
497. Remingo P, Klaum A: Extramedullary plasmacytoma of the stomach. Cancer 27:562–568, 1971.
498. Reubi JC, Mazzucchelli L, Laissue JA: Intestinal vessels express a high density of somatostatin receptors in human inflammatory bowel disease. Gastroenterology 106:951–959, 1994.
499. Reynolds JY, Galloway JMD: Primary aortoduodenal fistula: A case report and review of the literature. Ir J Med Sci 160:381–384, 1991.

500. Reznek RH, White FE, Young JWR, et al: The appearance on computed tomography after abdominoperineal resection for carcinoma of the rectum: A comparison between the normal appearances and those of recurrence. Br J Radiol 56:237–240, 1983.
501. Rha SE, Ha HK, Lee SH, et al: CT and MR imaging findings of bowel ischemia from various primary causes. Radiographics 20: 29–42, 2000.
502. Ribeiro MB, Greenstein AJ, Yamazaki Y, Aufses ATL: Intra-abdominal abscess in regional enteritis. Ann Surg 213:32–36, 1991.
503. Rijke AM, Falke TH, de Varies RR: Computed tomography in Whipple disease. J Comput Assist Tomogr 7:1101–1102, 1983.
504. Rioux M, Langis P: Primary epiploic appendagitis: Clinical, US, and CT findings in 14 cases. Radiology 191:523–526, 1994.
505. Rioux M, Mailloux C: Crescent-shaped necrosis: A new imaging sign suggestive of stromal tumor of the small bowel. Abdom Imaging 22:376–380, 1997.
506. Rizzo MJ, Federle MP, Griffiths BG: Bowel and mesenteric injury following blunt abdominal trauma: Evaluation with CT. Radiology 173:143–148, 1989.
507. Rockery DC, Halverson RA Jr, Higgins JL, Cello JP: Prospective evaluation of patients with bowel wall thickening. Am J Gastroenterol 90:99–103, 1995.
508. Rockoff SD, Aaron BL, Black C, et al: Diagnosis of paraesophageal omental hiatal hernia by magnetic resonance imaging. Chest 103: 285–287, 1993.
509. Ros PR, Buetow PC, Pantograg-Brown L, et al: Pseudomembranous colitis. Radiology 198:1–9, 1996.
510. Rosai J: Ackerman's Surgical Pathology. St. Louis, CV Mosby, 1996.
511. Rosenber SA, Diamond HD, Jaslowicz, et al: Lymphosarcoma: A review of 1269 cases. Medicine 40:31–84, 1961.
512. Rosenberg HK, Serota FT, Koch P, et al: Radiographic features of gastrointestinal graft-versus-host disease. Radiology 138:371–374, 1981.
513. Rossi M, Broglia L, Graziano P, et al: Local invasion of gastric cancer: CT findings and pathologic correlation using 5-mm incremental scanning, hypotonia, and water filling. AJR Am J Roentgenol 172:383–388, 1999.
514. Rossmann MD, Burr LJ, Thorpe PE: Colovenous fistula complicating diverticulitis: CT and radiographic findings. Abdom Imaging 22: 513–515, 1997.
515. Rubesin SE, Beatty SM: The postoperative esophagus. Semin Roentgenol 29:401–410, 1994.
516. Rubesin SE, Gilchrist AM, Bronner M, et al: Non-Hodgkin lymphoma of the small intestine. Radiographics 10:985–998, 1990.
517. Ruiz Montes F, Rene Espinet JM, Buenestado Garcia J, et al: Primary gastric plasmacytoma of rapid growth presenting with upper gastrointestinal bleeding. Am J Gastroenterol 90:1349–1350, 1995.
518. Russell JC, Welch JP: Operative management of radiation injuries of the intestinal tract. Am J Surg 137:433–442, 1979.
519. Sabate JM, Franquet T, Palmer J, et al: AIDS-related primary esophageal lymphoma. Abdom Imaging 22:11–13, 1997.
520. Sarr MG, Bulkley GB, Zuidema GD: Preoperative recognition of intestinal strangulation: Prospective evaluation of diagnostic capability. Am J Surg 145:176–182, 1983.
521. Saunders HS, Wolfman NT, Ott DJ: Esophageal cancer: Radiologic staging. Radiol Clin North Am 35:281–294, 1997.
522. Scatarige JC, Fishman EK, Jones B, et al: Gastric leiomyosarcoma: CT observation. J Comput Assist Tomogr 9:320–327, 1985.
523. Scheidler J, Stäbler A, Kleber G, Neidhardt D: Computed tomography in pneumatosis intestinalis: Differential diagnosis and therapeutic consequences. Abdom Imaging 20:523–528, 1995.
524. Schiller VL, Joyce PW, Sarti DA: Small-bowel obstruction due to hernia through the primary laparoscopic port: A complication of laparoscopic cholecystectomy [letter]. AJR Am J Roentgenol 163: 480–481, 1994.
525. Schmalfuss IM, Mancuso AA, Tart RP: Postcricoid region and cervical esophagus: Normal appearance at CT and MR imaging. Radiology 214:237–246, 2000.
526. Schmidt P, Koltai JL, Weltzein A: Actinomycosis of the appendix in childhood. Pediatr Surg Int 15:63–65, 1999.
527. Schnall M, Furth EE, Rosato E, Kressel HY: Rectal tumor stage: Correlation of endorectal MR imaging and pathologic findings. Radiology 190:709–714, 1994.
528. Schnall MD: Magnetic resonance of the hollow viscera. In Gore RM, Levine MS, Laufer I (eds): Textbook of Gastrointestinal Radiology. Philadelphia, WB Saunders, 1994, pp 113–126.
529. Schoen FJ, Cotran RS: Blood vessels. In Cotran RS, Kumar V, Collins T (eds): Robbins Pathologic Basis of Disease, 6th ed. Philadelphia, WB Saunders, 1999, pp 493–542.
530. Schung GE: Leiomyoma of the cardioesophageal junction. Arch Surg 65:342–346, 1952.
531. Schwartz DL, So HB, Becjer JM, Scheider KM: Ectopic gastric duplication arising from the pancreas and presenting with a pneumoperitoneum. J Pediatr Surg 14:187–188, 1979.
532. Scott FET, Dupont PA, Webb J: Plasmacytoma of the stomach: Diagnosis with the aid of immunoperoxidase technique. Cancer 41: 675–681, 1978.
533. Seremetis MG, Lyons WS, deGuzman VC, et al: Leiomyoma of the esophagus: An analysis of 838 cases. Cancer 38:2166–2177, 1976.
534. Shackman R: Jejunogastric intussusception. Br J Surg 27:475–480, 1940.
535. Shah RS, Kaddu SJ, Kirtane JM: Benign mature teratoma of the large bowel: A case report. J Pediatr Surg 31:701–702, 1996.
536. Shanmuganathan K, Mirvis SE, Amorosa M: Periportal low density on CT in patients with blunt trauma: Association with elevated venous pressure. AJR Am J Roentgenol 160:279–283, 1993.
537. Sharma S, Bandhu S, Gulati MS, Berry M: Gastric hemangioma associated with phleboliths: CT appearance. AJR Am J Roentgenol 173:859–860, 1999.
538. Sher ME, Bauer J: Radiation-induced enteropathy. Am J Gastroenterol 85:121–128, 1990.
539. Shibata S, Iwasaki N: Angiographic findings in diseases of the stomach. Am J Roentgenol 110:322–331, 1970.
540. Shoenut JP, Semelka RC, Silverman R, et al: Magnetic resonance imaging in inflammatory bowel disease. J Clin Gastroenterol 17: 73–78, 1993.
541. Shorter RG: Risks of intestinal cancer in Crohn's disease. Dis Colon Rectum 26:686–689, 1985.
542. Shulman HM, Sullivan KM, Weiden PL, et al: Chronic graft-versus-host syndrome in man: A long-term clinicopathologic study of 20 Seattle patients. Am J Med 69:204–217, 1980.
543. Shweiki E, West JC, Klena JW, Kelley SE: Eosinophilic gastroenteritis presenting as an obstructing cecal mass—a case report and review of the literature. Am J Gastroenterol 94:3644–3645, 1999.
544. Silverman JM, Hamlin JA: Large melanoma metastases to the gastrointestinal tract. Gut 30:1783–1785, 1989.
545. Silverman PM, Kelvin FM, Korobkin M, et al: Computed tomography of the normal mesentery. Am J Roentgenol 143:953–957, 1984.
546. Simon AM, Birnbaum BA, Jacobs JE: Isolated infarction of the cecum: CT findings in two patients. Radiology 214:513–516, 2000.
547. Sivit CJ, Taylor GA, Bulas DI, et al: Posttraumatic shock in children: CT findings associated with hemodynamic instability. Radiology 182:723–726, 1992.
548. Smart PE, Weinfeld A, Thompson NE, Defortuna SM: Toxoplasmosis of the stomach: A cause of antral narrowing. Radiology 174: 369–370, 1990.
549. Smerud MJ, Johnson CD, Stephens DH: Diagnosis of bowel infarction: A comparison of plain films and CT scans in 23 cases. AJR Am J Roentgenol 154:99–103, 1990.
550. Sohn KM, Lee JM, Lee SY, et al: Comparing MR imaging and CT in the staging of gastric carcinoma. AJR Am J Roentgenol 174: 1551–1557, 2000.
551. Soulen MC, Fishman EK, Scatarige JC, et al: Cryptosporidiosis of the gastric antrum: Detection using CT. Radiology 159:705–706, 1986.
552. Spears H, Petrelli NJ, Herrera L, Mittelman A: Treatment of bowel obstruction after operation for colorectal carcinoma. Am J Surg 155: 383–386, 1988.
553. Spiegel JS, Schwabe AD: Disseminated cytomegalovirus infection with gastrointestinal involvement: The role of altered immunity in the elderly. Am J Gastroenterol 73:37–44, 1980.
554. Stavorovsky M, Jaffa AJ, Papo J, et al: Leiomyosarcoma of the colon and rectum. Dis Colon Rectum 23:249–254, 1980.
555. Stevens RL, Jones B, Fishman EK: The CT halo sign: A new finding in intestinal lymphangiectasia. J Comput Assist Tomogr 21: 1005–1007, 1997.
556. Stewart ET, Dodds WJ: Radiology of the esophagus. In Freeny PC, Stevenson GW (eds): Alimentary Tract Radiology. St. Louis, CV Mosby, 1994, pp 192–271.

557. Stubenbord WT, Thorbjarnarson B: Intussusception in adults. Ann Surg 172:306–310, 1970.
558. Sugimoto E, Lorelius LE, Eriksson B, Oberg K: Midgut carcinoid tumors: CT appearance. Acta Radiol 36:367–371, 1995.
559. Sugimura K, Carrington BM, Quivey JM, Hricak H: Postirradiation changes in the pelvis: Assessment with MR imaging. Radiology 175:805–813, 1990.
560. Sussman SK, Halvorsen RA Jr, Illescas FF, et al: Gastric adenocarcinoma: CT versus surgical staging. Radiology 167:335–340, 1988.
561. Symonds DA, Vickery AL: Mucinous carcinoma of the colon and rectum. Cancer 37:1891–1900, 1976.
562. Tada S, Iida M, Yao T, et al: Gastrointestinal amyloidosis: Radiologic feature by chemical types. Radiology 190:37–42, 1994.
563. Takashima S, Takeuchi N, Shiozaki H, et al: Carcinoma of the esophagus: CT versus MR imaging in determining resectability. AJR Am J Roentgenol 156:297–302, 1991.
564. Tan EM, Cohen AS, Fries JF, et al: The 1982 revised criteria for the classification of systemic lupus erythematosus. Arthritis Rheum 25:1271–1277, 1982.
565. Tandon HD, Prakash A: Pathology of intestinal tuberculosis and its distinction from Crohn's disease. Gut 13:260–269, 1972.
566. Taourel PG, Deneuville M, Pradel JA, et al: Acute mesenteric ischemia: Diagnosis with contrast-enhanced CT. Radiology 199: 632–636, 1996.
567. Tateishi R, Taniguchi H, Wada A, et al: Argyrophil cell and melanocytes in esophageal mucosa. Arch Pathol 98:87–89, 1974.
568. Taylor JA, Stewart ET, Dodds W: Gastrointestinal lipomas: A radiologic and pathologic review. AJR Am J Roentgenol 155:1205–1210, 1990.
569. Tedesco FJ, Volpicelli NA, Moore FS: Estrogen- and progesterone-associated colitis: A disorder with clinical and endoscopic features mimicking Crohn's colitis. Gastrointest Endosc 28:247–249, 1982.
570. Texidor HS, Honig CL, Norsoph E, et al: Cytomegalovirus infection of the alimentary canal: Radiologic findings with pathologic correlation. Radiology 163:317–323, 1987.
571. Thoeni RF, Gedgaudas RK: Ectopic pancreas: Usual and unusual features. Gastrointest Radiol 5:37–42, 1980.
572. Thoeni RF: Colorectal cancer: Cross-sectional imaging for staging of primary tumor and detection of local recurrence. AJR Am J Roentgenol 156:909–915, 1991.
573. Thoeni RF: Colorectal cancer: Radiologic staging. Radiol Clin North Am 35:457–485, 1997.
574. Thomas ED, Storb R, Clift RA, et al: Bone-marrow transplantation. N Engl J Med 292:895–902, 1975.
575. Thomas JH, Rosato FE: Epiploic appendagitis. Surg Gynecol Obstet 138:23–25, 1979.
576. Thompson WM, Halvorsen RA, Foster WL Jr, et al: Computed tomography for staging esophageal and gastroesophageal cancer: Reevaluation. AJR 141:951–958, 1983.
577. Thompson WM, Halvorsen RA Jr, Foster WL Jr, et al: Preoperative and postoperative CT staging of rectosigmoid carcinoma. AJR 146: 703–710, 1986.
578. Thompson WM, Halvorsen RA Jr: Staging esophageal carcinoma: II. CT and MRI. Semin Oncol 21:447–452, 1994.
579. Thompson WM, Halvorsen RA, Foster W Jr, et al: Computed tomography of the gastroesophageal junction: Value of the left lateral decubitus view. J Comput Assist Tomogr 8:346–349, 1984.
580. Tio TL, Cohen P, Coene PP, et al: Endosonography and computed tomography of esophageal carcinoma: Preoperative classification compared to the new (1987) TNM system. Gastroenterology 96: 1478–1486, 1989.
581. Tominaga K, Arakawa T, Ando K, et al: Oesophageal cavernous haemangioma diagnosed histologically, not by endoscopic procedures. J Gastroenterol Hepatol 15:215–219, 2000.
582. Toombs BD, Sandler CM, Lester RG: Computed tomography of chest trauma. Radiology 140:733–738, 1981.
583. Travers RL, Allison DJ, Brettle RP, Hughes G: Polyarteritis nodosa: A clinical and angiographic analysis of 17 cases. Semin Arthritis Rheum 8:184–189, 1979.
584. Urban BA, Fishman EK, Hruban RH: *Helicobacter pylori* gastritis mimicking gastric carcinoma at CT evaluation. Radiology 179:689–691, 1991.
585. Vaidya MG, Sodhi JS: Gastrointestinal tract tuberculosis: A study of 102 cases including 55 hemicolectomies. Clin Radiol 29:189–195, 1978.
586. Valls C, Laforga AS, Benasco C: Oat-cell carcinoma of the esophagus. AJR Am J Roentgenol 163:1266–1267, 1994.
587. Vantrappen G, Agg HO, Geboes K, Ponette E: *Yersinia* enteritis. Med Clin North Am 66:639–653, 1982.
588. Vas W, Malpani AR, Singer J, et al: Computed tomographic evaluation of paraesophageal hernia. Gastrointest Radiol 14:291–294, 1989.
589. Vilellas KM, Bennett WF, Bova JG, et al: Radiographic manifestations of eosinophilic gastroenteritis. Abdom Imaging 20:406–413, 1995.
590. Villanueva A, Pérez C, Sabaté JM, et al: CT manifestations of peritoneal leiomyosarcomatosis. Eur J Radiol 17:166–169, 1993.
591. Wakefield AJ, Sawyer AM, Dhillon AP, et al: Pathogenesis of Crohn's disease: Multifocal gastrointestinal infarction. Lancet 2: 1057–1062, 1989.
592. Wall SD, Jones B: Gastrointestinal tract in the immunocompromised host: Opportunistic infections and other complications. Radiology 185:327–335, 1992.
593. Walsh TH, Mann CV: Smooth muscle neoplasm of the rectum and anal canal. Br J Surg 71:597–599, 1984.
594. Warshauer DM, Lee JKT: Adult intussusception detected at CT or MR imaging: Clinical-imaging correlation. Radiology 212:853–860, 1999.
595. Watanabe K, Kikuchi T, Katori Y, et al: The usefulness of computed tomography in the diagnosis of impacted fish bones in the oesophagus. J Laryngol Otol 112:360–364, 1998.
596. Wechsler RJ, Kurtz AB, Needleman L, et al: Cross-sectional imaging of abdominal wall hernias. AJR Am J Roentgenol 153:517–521, 1989.
597. Weiss M, Dreiling DA: Small-bowel perforation in blunt trauma: Its relationship to previous laparotomy. Am J Gastroenterol 50: 279–288, 1968.
598. White CS, Templeton PA, Attar S: Esophageal perforation: CT findings. AJR Am J Roentgenol 160:767–770, 1992.
599. White TB: Portal and mesenteric vein gas in diverticulitis: CT findings. AJR Am J Roentgenol 171:525–526, 1998.
600. Whitman GJ, Borkowski GP: Giant fibrovascular polyp of the esophagus: CT and MR findings. AJR Am J Roentgenol 152:518–520, 1989.
601. Wieczorek RL, Seidman I, Ramson JH, Ruoff M: Congenital duplication of the stomach: A case report and review of the English literature. Am J Gastroenterol 79:597–602, 1984.
602. Williford ME, Thompson WM, Hamilton JD, et al: Esophageal tuberculosis: Findings on barium swallow and computed tomography. Gastrointest Radiol 8:119–122, 1983.
603. Wills JS, Lobis IF, Denstman FJ: Crohn disease: State of the art. Radiology 202:597–610, 1997.
604. Wilson SM, Adson MA: Surgical treatment of hepatic metastases from colorectal cancers. Arch Surg 111:330–334, 1976.
605. Wolfel DA: Leiomyosarcoma of the esophagus. AJR 145:41–45, 1963.
606. Wolfman NT, Scharling ES, Chen MY: Esophageal squamous carcinoma. Radiol Clin North Am 32:1183–1201, 1994.
607. Wyatt SH, Fishman EK, Jones B: Primary lymphoma of the colon and rectum: CT and barium enema correlation. Abdom Imaging 18: 376–380, 1993.
608. Wychulis AR, Woolam GE, Andersen GE, et al: Achalasia and carcinoma of the esophagus. JAMA 215:1638–1641, 1971.
609. Wynder EL, Mabuch K: Cancer of the esophagus: Etiological and environmental factors. JAMA 226:1546–1548, 1973.
610. Yamada I, Murata Y, Izumi Y, et al: Staging of esophageal carcinoma in vitro with 4.7-T MR imaging. Radiology 204:521–526, 1997.
611. Yamaguchi M, Takeuchi S, Awazu S: Meckel's diverticulum: Investigation of 600 patients in Japanese literature. Am J Surg 136: 247–249, 1978.
612. Yeguez JF, Martinez SA, Sands LR, Hellinger MD: Pelvic actinomycosis presenting as malignant large bowel obstruction: A report and a review of the literature. Am Surg 66:85–90, 2000.
613. Yoo CC, Levine MS, McLarney JK, et al: Primary malignant melanoma of the esophagus: Radiographic findings in seven patients. Radiology 209:455–459, 1998.
614. Yoon SE, Ha HK, Lee YS, et al: Upper gastrointestinal series and CT findings of primary gastric plasmacytoma: Report of two cases. AJR Am J Roentgenol 173:1266–1268, 1999.
615. Yoshino MT: Duodenal hematoma: CT demonstration of the ring sign. Gastrointest Radiol 12:330–332, 1987.

616. Younes M, Katikaneni PR, Lechago J: The value of the preoperative mucosal biopsy in the diagnosis of colorectal mucinous adenocarcinoma. Cancer 72:3588–3592, 1993.
617. Young LS, Inderlied CB, Berlin ZG, Gottlieb MS: Mycobacterial infection in AIDS patents, with emphasis on the *Mycobacterium avium* complex. Rev Infect Dis 8:1024–1033, 1986.
618. Young TH, Ho AS, Tang HS, et al: Cystic lymphangioma of the transverse colon: Report of a case and review of the literature. Abdom Imaging 21:415–417, 1996.
619. Yousem DM, Fishman EK, Jones B: Crohn's disease: Perirectal and perianal findings at CT. Radiology 167:331–334, 1988.
620. Yuen EH, Yang WT, Lam WW, et al: Spontaneous intramural hematoma of the oesophagus: CT and MRI appearances. Australas Radiol 42:139–142, 1998.
621. Zalcman M, Gansbeke V, Lalmand B, et al: Delayed enhancement of the bowel wall: A new CT sign of small-bowel strangulation. J Comput Assist Tomogr 20:379–381, 1996.
622. Zalev AH, Prokipchuk EJ, Jeejeebhoy KN, et al: Recurrent Crohn's disease in the duodenum and jejunum following extensive small-bowel resection and jejunocolonic anastomosis: Radiologic findings in twenty-five patients. Abdom Imaging 24:538–543, 1999.
623. Zerhouni EA, Fishman EK, Jones B: Principles and techniques. In Fishman EK, Jones B (eds): Computed Tomography of the Gastrointestinal Tract. New York, Churchill Livingstone, 1988, pp 1–16.
624. Zerhouni EA, Rutter C, Hamilton SR, et al: CT and MR imaging in the staging of colorectal carcinoma: Report of the Radiology Diagnostic Oncology Group II. Radiology 200:443–451, 1996.
625. Zollinger RM, Sternfeld WC, Schrelber H: Primary neoplasms of the small intestine. Am J Surg 151:654–658, 1986.

35 Hepatic Mass Lesions

Jeffrey D. McTavish, Pablo R. Ros

Hepatic masses can be classified in the following categories: (1) primary benign neoplasms, (2) primary malignant neoplasms, (3) secondary malignant liver neoplasms, and (4) infectious lesions.

Primary hepatic neoplasms may arise from each one of the cellular components of the liver: hepatocytes, biliary epithelium, and mesenchymal tissues, which explains the varied gamut of liver tumors.[49] This chapter reviews primary benign and malignant liver lesions, then secondary malignant neoplasms and infectious lesions. We complete the chapter with our practical approach to the differential diagnosis of liver masses.

Computed tomography (CT) has assumed a primary role in the evaluation of hepatic masses. Magnetic resonance imaging (MRI) is often used to further characterize a mass found by CT or ultrasound and may be helpful in formulating a more specific differential diagnosis. The development of tissue-specific contrast agents for use in MRI holds promise for increased sensitivity and specificity.

Benign Liver Neoplasms

Hemangioma

The hemangioma, a benign tumor, is composed microscopically of multiple vascular channels lined by a single layer of endothelial cells that are supported by thin septa of fibrous stroma. Hemangiomas are grossly solitary, well circumscribed, and blood-filled, ranging in size from a few millimeters to larger than 20 cm.[49] Although early reports described them as a solitary lesions in 90% of cases, with the increased use of imaging there is mounting evidence that the number of multiple hemangiomas is higher than 10% and probably above 30%. By convention, *giant hemangiomas* are larger than 10 cm. On cut sections, areas of fibrosis are almost always present, with cystic zones and areas of necrosis often, but less frequently, seen.[123, 216]

The hemangioma is the most common benign liver tumor seen at imaging, with an incidence ranging from 0.4% to 20%, the higher figure coming from a prospective autopsy series that involved a dedicated search for this tumor.[123] Hemangiomas occur primarily in women and may be present at any age. Most hemangiomas are clinically silent, because of their small size, but may become symptomatic when enlarged or when they compress adjacent structures, only then becoming a surgical lesion primarily to relieve pain. The remote chance of rupture does not usually constitute an indication for surgery.

On unenhanced CT scans, hemangiomas appear as low-attenuation masses with lobulated, well-defined borders. Calcification may be present in up to 20% of cases, either amorphous or in the form of phleboliths.[213] Following intravenous (IV) contrast administration, large feeding vessels cause peripheral globular enhancement with centripetal fill-in of the lesion within 15 minutes (Figs. 35–1*A–D* and 35–2*A–D*).[76, 77] Unfortunately, some metastases can also have peripheral globular enhancement.

A study by Leslie and coauthors[140] found that 8% of metastases had peripheral globular enhancement. In this study, all of the metastases had enhancement that was hypointense to the aorta, whereas the enhancement in hemangiomas was isointense or hyperintense to the aorta. Although small (<2 cm) lesions may show complete enhancement, the large tumors may have central nonenhancing zones that result from fibrosis and hemorrhage.[226] The centripetal enhancement may be demonstrated by dynamic scanning through the liver at 30-second intervals for the first few minutes, potentially followed by longer intervals up until 20 minutes if the lesion does not completely opacify. Centripetal filling alone is not a characteristic sign of hemangioma because all benign and malignant liver tumors, except for *focal nodular hyperplasia* (FNH), may have peripheral vascular supply and thus enhancement. To diagnose a hemangioma by CT, a lesion must fulfill the diagnostic triad of enhancement, which is equal or hyperintense to the aorta, which persists on delayed imaging, and appears in a peripheral globular fashion. However, this technique has been largely replaced by the increased specificity of MRI with IV contrast in the evaluation of a suspected hemangioma.[97, 282]

MR imaging is used to evaluate suspected hemangiomas because of the tumor's characteristic appearance resulting from slow blood flow through the vascular channels of the lesion. On *T1-weighted* (T1W) images, hemangiomas are hypointense to the surrounding hepatic parenchyma with smooth, well-defined, often lobulated margins (Fig. 35–3*A* and *B*). On *T2-weighted* (T2W) images, they become significantly hyperintense to normal liver, increasing in relative signal intensity to the liver with increasing echo time (TE).[111, 112, 237]

Spin-echo pulse sequences with a repetition time (TR) of 2000 msec, with an increasing TE from 60 to 180 msec, are often used. Unfortunately, some malignant lesions, particularly hypervascular metastases, can also have quite long T2 values and can mimic hemangiomas on T2-weighted images. A prospective study[145] found that 39% of endocrine tumor metastases could not be distinguished from hemangiomas by T2 appearance. Thus, the diagnosis of hemangioma by MRI rests not only in the signal characteristics but also in morphologic features (e.g., sharp and geographic margins, lack of peripheral halo in T2-weighted images, and enhancement pattern).

Dynamic gradient-echo MR imaging, after IV injection

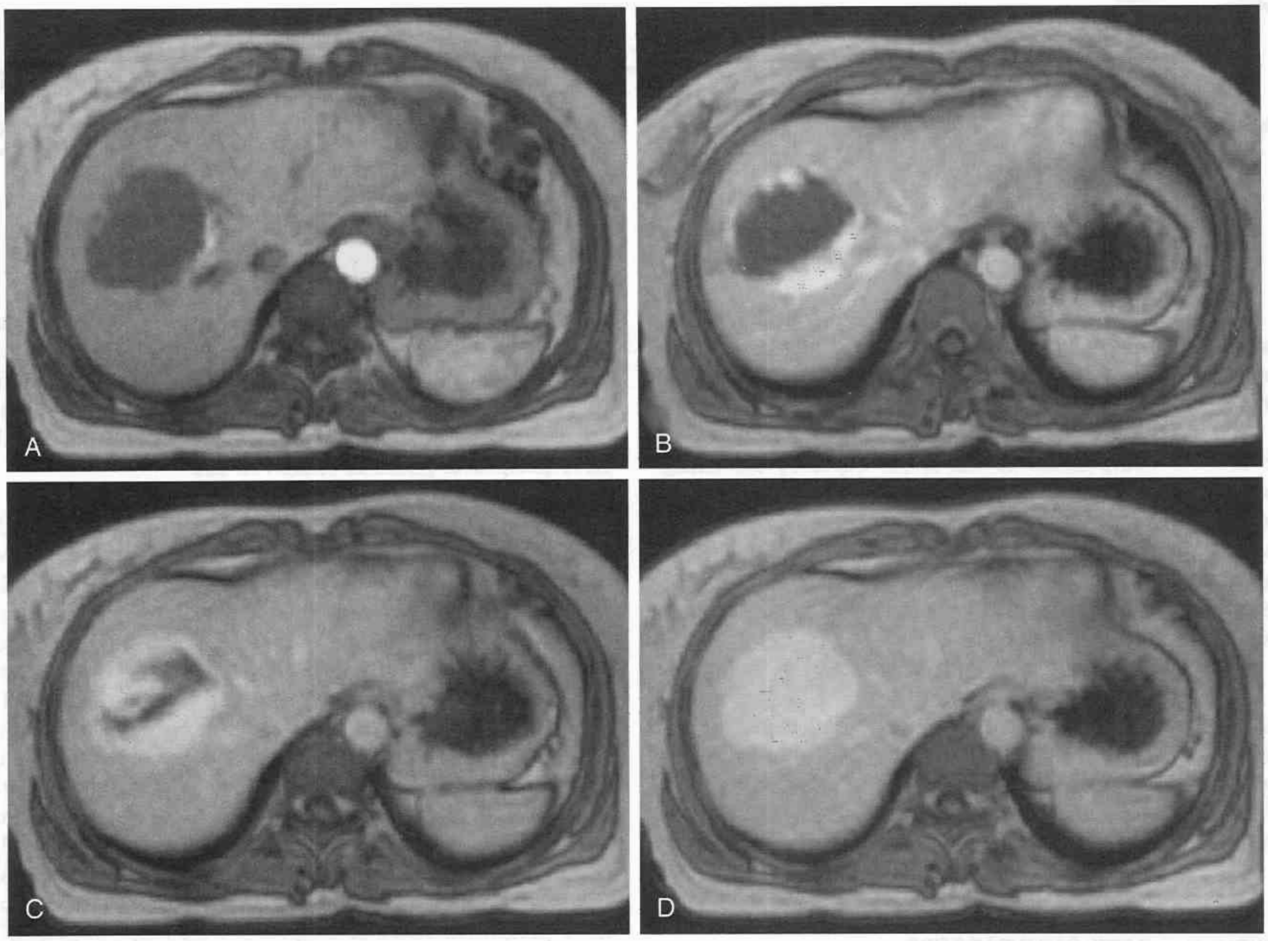

Figure 35–1. Hemangioma. *A–D,* a Large lesion in the right hepatic lobe after intravenous gadolinium (Gd-DTPA) administration. The lesion enhances in a peripheral, globular fashion and gradually fills in.

of an intravascular contrast agent, such as gadolinium-diethylenetriamine-pentaacetic acid (Gd-DTPA), is useful in increasing the specificity of MRI for the study of hemangiomas.[97, 282] Fast T1-weighted, gradient-echo images, such as fast low-angle shot (FLASH) or spoiled gradient-recalled acquisition in the steady state (SPGR, or spoiled GRASS), are obtained before contrast, which are repeated at approximately 30-second intervals following contrast injection(0.05 mmol/kg). With current technology, most of the liver can be scanned using this technique, obviating the need for "single-level" scanning.

Peripheral globular enhancement with centripetal fill-in, similar to that demonstrated by CT, is observed. Central areas lacking enhancement, especially in large tumors, correspond to areas of fibrosis that appear as low attenuation on CT.[40] These fibrotic areas appear hypointense on T2-weighted images, which may aid the imager in distinguishing a large heterogeneous hemangioma (containing areas of fibrosis) from a necrotic malignancy in which the necrotic areas are hyperintense on T2-weighted images. After administration of ultra-small superparamagnetic iron oxide (USPIO), hemangiomas demonstrate signal loss because their slowly flowing vascular spaces represent blood pool (Fig. 35–4).

Focal Nodular Hyperplasia

FNH is a benign tumor-like condition characterized by a central fibrous scar surrounded by nodules of hyperplastic hepatocytes and small bile ductules.[49] Vessels are prominent throughout the lesion but are most abundant in the fibrous scar. FNH is believed to be a hyperplastic response to an underlying arteriovenous malformation (AVM).[266]

FNH is well circumscribed, usually solitary (95%), is often present on the liver surface, and may be pedunculated. Although FNH is sharply marginated, there is no capsule. Most lesions are smaller than 5 cm, with a mean diameter of 3 cm at discovery. Occasionally, FNH may replace an entire lobe of the liver *(lobar FNH).*[49]

FNH is the second most common benign tumor of the liver seen at imaging, representing 8% of primary hepatic tumors.[49] It is more prevalent in women and has been associated with oral contraceptive use, although not as often as with hepatocellular adenoma.[41] It is usually discovered in the third to fifth decades of life as an incidental finding during imaging, surgery, or autopsy; fewer than one third of cases (usually large lesions) are discovered because of clinical symptoms, such as epigastric pain and right upper quadrant pain.

Figure 35–2. Multiphase enhancement of a hemangioma. *A,* Arterial phase, enhancing mass in the right hepatic lobe. *B,* Parenchymal phase. Progressive enhancement is seen. Note enhancement of portal veins without hepatic venous opacification. *C,* Hepatic venous phase. All of the hepatic vessels are enhanced. Parenchymal enhancement is maximal during this phase. *D,* An intrahepatic mass and the hepatic vessels are demonstrated on this 3D image.

On unenhanced CT scans, FNH appears as a homogeneous, low-attenuation mass, often with a central low-density area representing the central scar. After IV contrast injection, the tumor becomes isodense to slightly hyperdense to normal liver while low attenuation of the central scar may remain.[156, 273] If a low-density central scar is not present, the tumor may be quite subtle, producing a bulge or deformity of the liver if it is only peripherally located.[219] On delayed images, contrast medium accumulates within the scar. This sign has been described as highly indicative of FNH.[156]

On unenhanced T1-weighted MR images, FNH is typi-

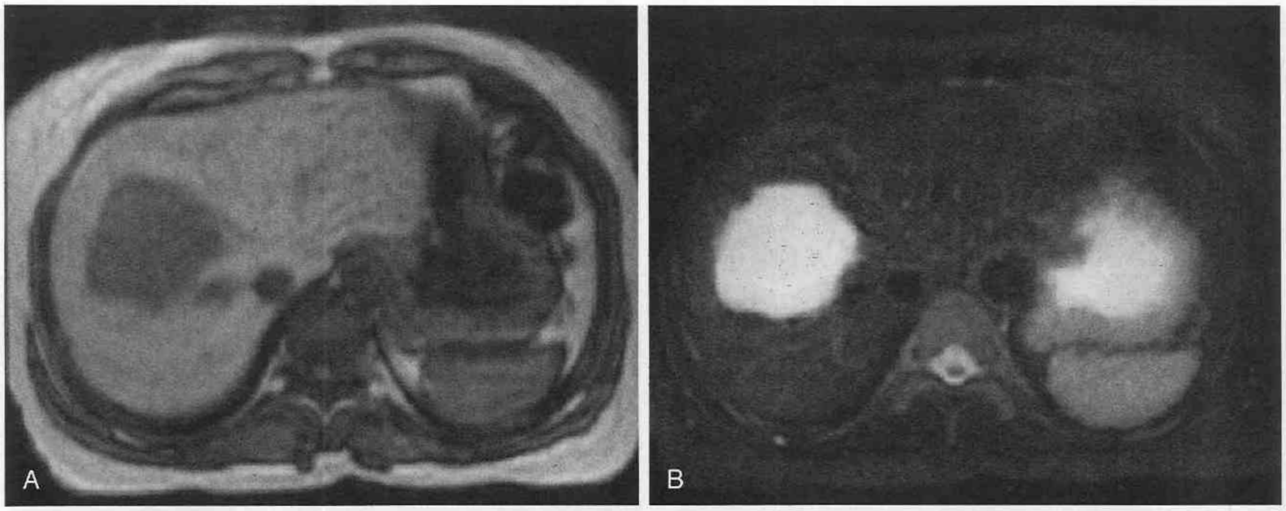

Figure 35–3. Hemangioma. *A,* Unenhanced T1-weighted image demonstrates a large lesion in the right hepatic lobe with low signal intensity. *B,* Unenhanced T2-weighted image demonstrates very high signal intensity, or a "light bulb" appearance.

cally isointense to liver, becoming isointense to slightly hyperintense on T2-weighted images. The central scar, when apparent, is usually hypointense on T1-weighted images and hyperintense on T2-weighted images (Fig. 35–5).[139, 162, 221, 260] Unenhanced MR imaging has 70% sensitivity and 98% specificity in the diagnosis of FNH.[37] Following injection of an extracellular contrast agent (e.g., Gd-DTPA, Gd-DOTA), there is a high degree of enhancement during the early arterial phase[153, 158]; further, there is often delayed enhancement of the central scar owing to its excellent vascularity.[158, 251]

SPIO particles are coated crystalline iron oxide particles, which are taken up by the reticuloendothelial system. In a magnetic field, these particles become strongly magnetized, a phenomenon termed *magnetic susceptibility.* SPIO particles create magnetic field inhomogeneity, which promotes dephasing of protons and results in T2 signal loss. SPIO particles are phagocytosed by FNH because they contain Kupffer cells and have an excellent vascular supply. Studies have demonstrated significant uptake of SPIO by FNH[92, 200, 206]; however, the relative signal intensity of an FNH after administration of SPIO varies. In one study, most FNHs lost less signal than liver parenchyma (which, on average, loses 74% to 78% of its signal after SPIO[165, 200]), some lost more signal than liver, and some FNHs lost no signal (Fig. 35–6).[92] After SPIO administration, FNH may also lose signal (Fig. 35–7).

Because FNHs contain hepatocytes, they often take up hepatobiliary agents as well (e.g., Gd-EOB-DTPA), appearing hyperintense to liver parenchyma.[261]

Hepatocellular Adenoma

Hepatocellular adenoma (HCA), a benign lesion, consists of hepatocytes arranged in cords that occasionally

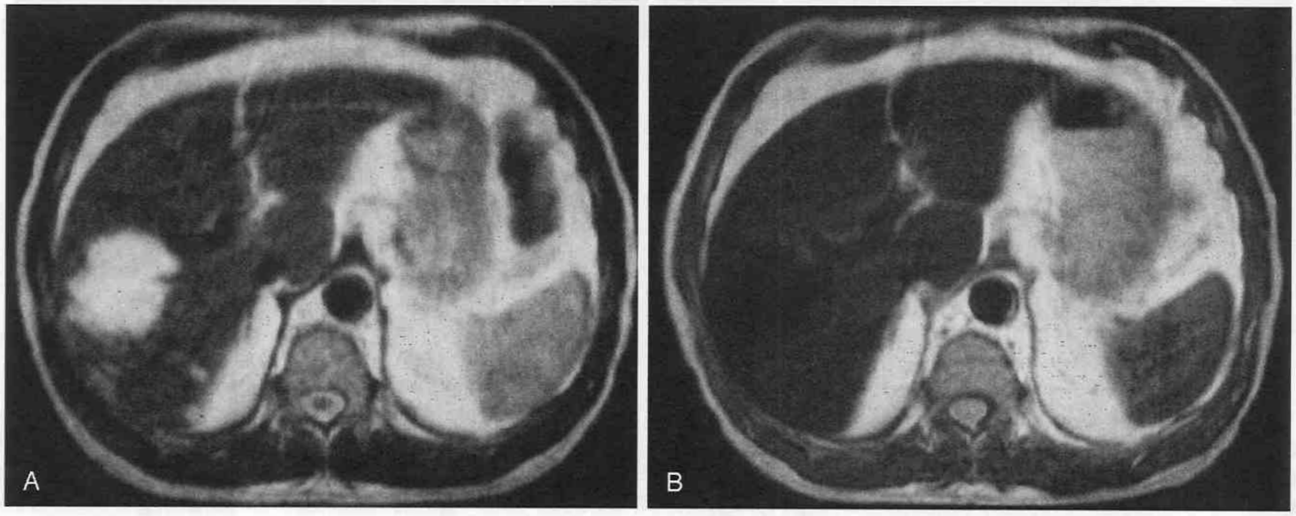

Figure 35–4. Hemangioma. *A,* Unenhanced T2-weighted image demonstrates a 4-cm lesion in the right hepatic lobe. *B,* T2-weighted image after ultra-small superparamagentic iron oxide (USPIO) administration demonstrates signal loss, reflecting blood pool effects.

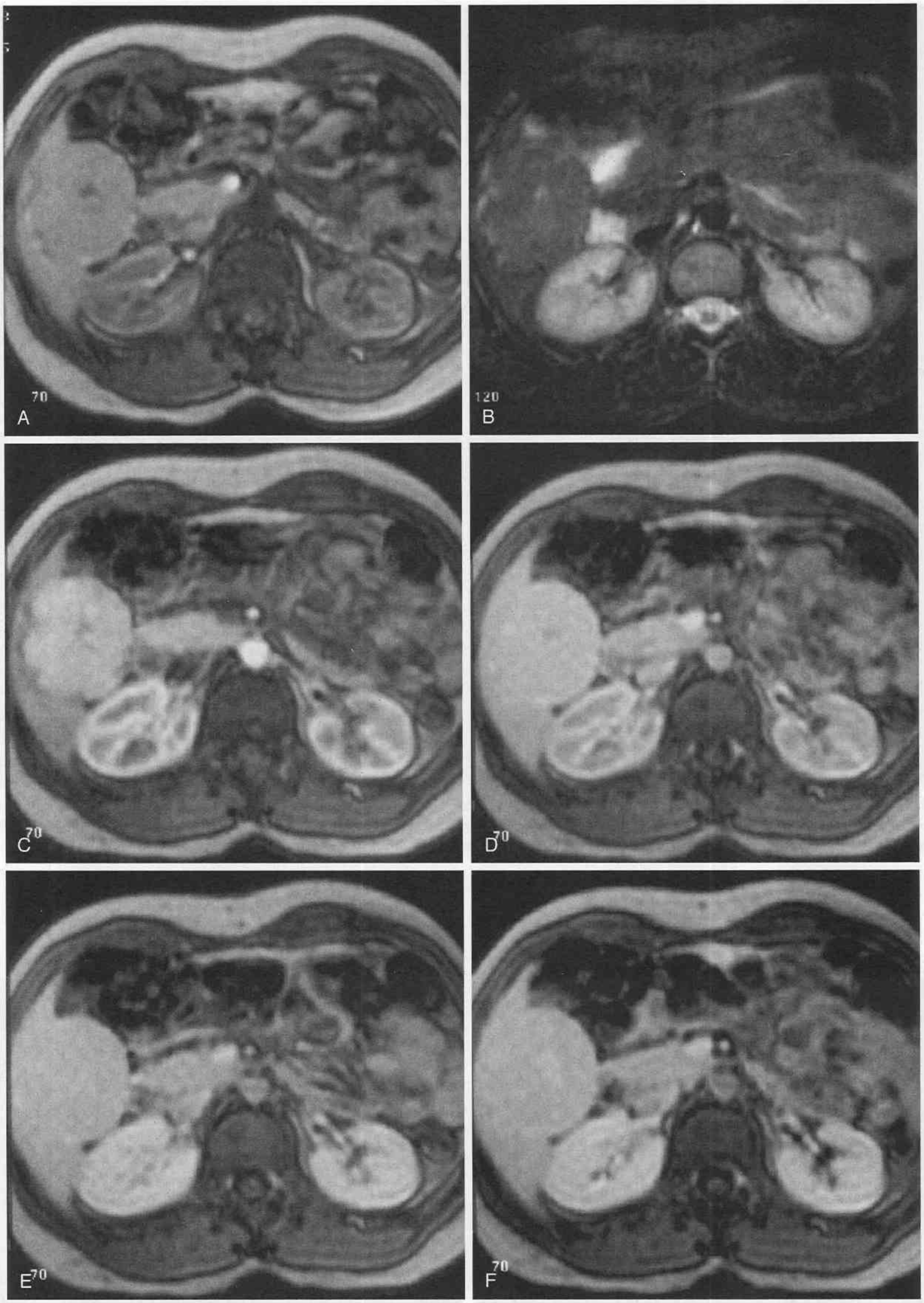

Figure 35–5. Focal nodular hyperplasia. *A,* Unenhanced T1-weighted image demonstrates an exophytic lesion, extending from the right hepatic lobe, that is isointense to hepatic parenchyma. *B,* Unenhanced T2-weighted image demonstrates the lesion to be isointense to hepatic parenchyma. *C–F,* T1-weighted images after gadolinium (Gd-DTPA) administration demonstrate early arterial phase enhancement with rapid washout. The central scar is hypoattenuating during the arterial phase and enhances in the later phases.

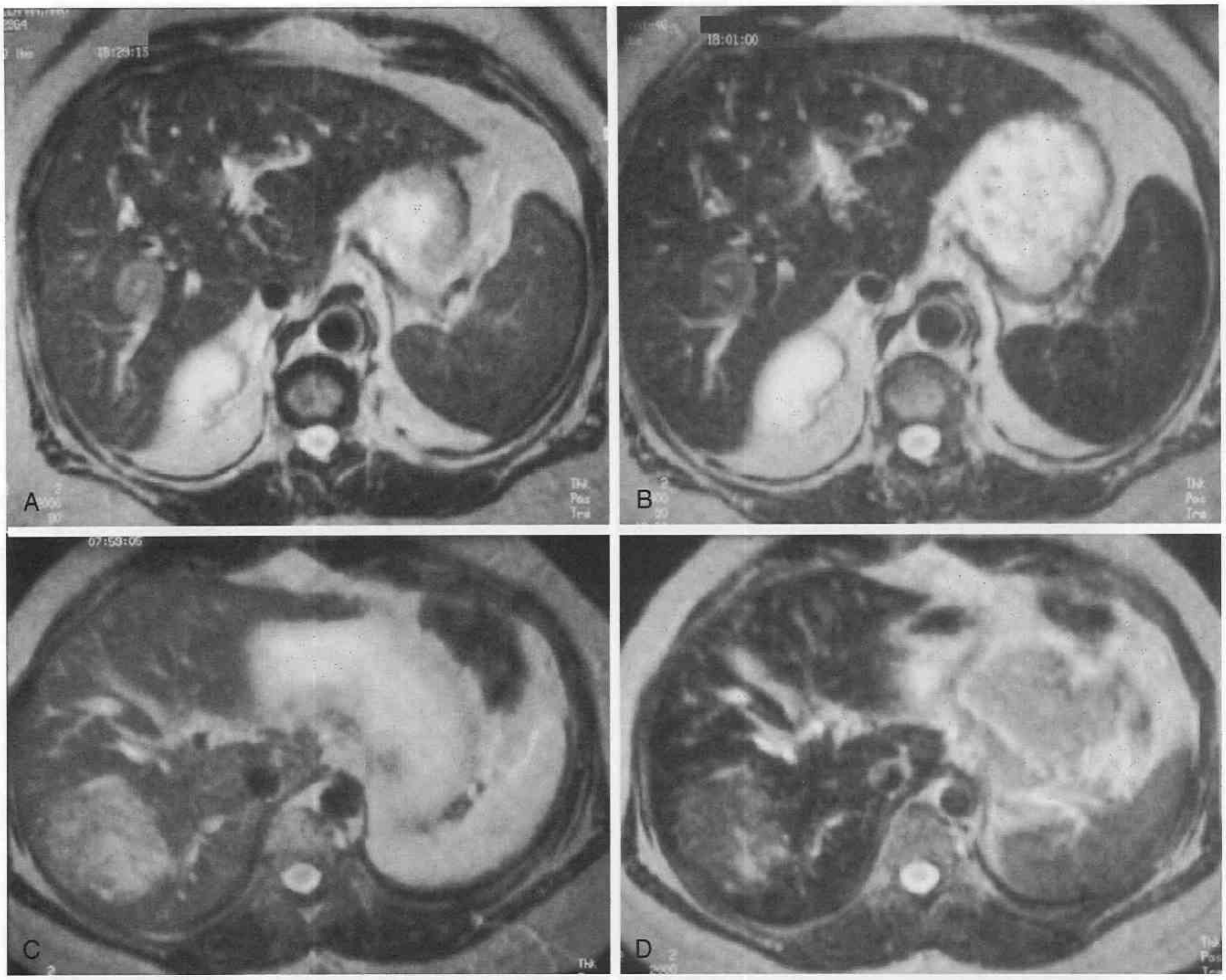

Figure 35–6. Focal nodular hyperplasia. *A,* Unenhanced T1-weighted image demonstrates a 2-cm lesion in the right hepatic lobe. *B,* T2-weighted image after superparamagnetic iron oxide (SPIO) enhancement demonstrates signal loss of the lesion. *C,* Signal loss is seen in a different patient between unenhanced T2-weighted images. *D,* SPIO-enhanced imaging.

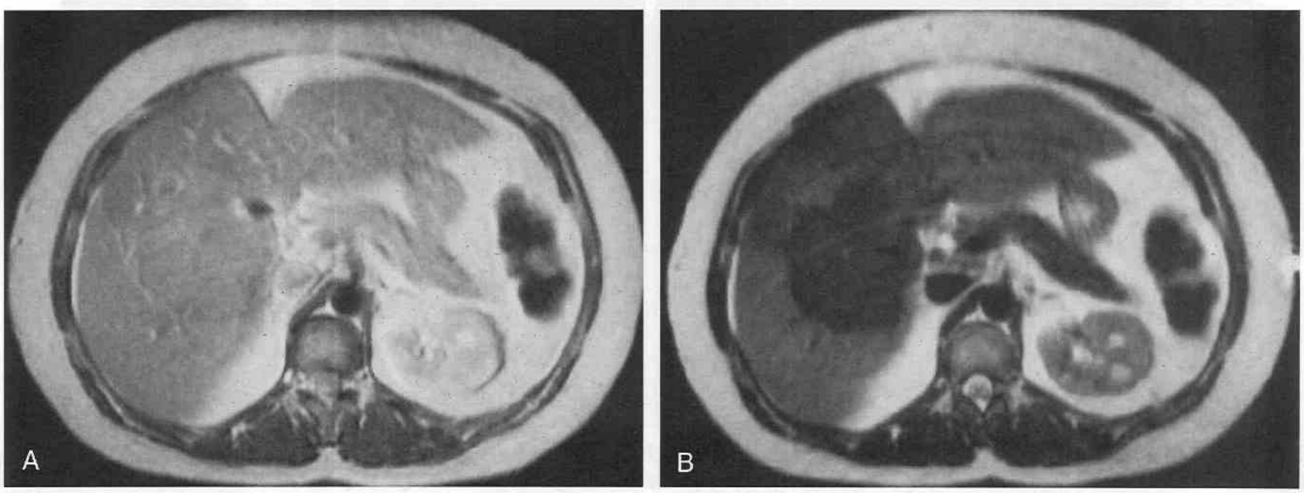

Figure 35–7. Focal nodular hyperplasia. *A,* Unenhanced T2-weighted image demonstrates a large lesion in the right hepatic lobe. *B,* T2-weighted image after superparamagnetic iron oxide (USPIO) administration demonstrates signal loss.

form bile.[49] Although known to contain Kupffer cells, this tumor lacks portal tracts, hepatic veins, and biliary canaliculi.[89] Fat and glycogen-rich hepatocytes are often present.

Grossly, hepatocellular adenoma is usually single, 8 to 10 cm in diameter at discovery, with pedunculation present in 10% of cases.[49] A capsule containing large vessels is often present. On cut section, the tumor often contains areas of hemorrhage or infarction, with internal hemorrhage one of its hallmarks. Rupture of an adenoma may result in hemoperitoneum. In rare instances, multiple adenomas may be seen, usually involving both hepatic lobes; this situation is called *multiple hepatocellular adenomatosis*.[36, 150] Multiple hepatocellular adenomas have been associated with type 1 glycogen storage disease.[44]

Most cases of HCA are found in women of childbearing age who have used oral contraceptives; the estimated overall incidence is 4 per year per 100,000 users,[41, 210] which declines to 1 per million in women who have not used oral contraceptives in the preceding 2 years. When the tumor is large, upper abdominal pain may lead its discovery.

Although benign, this tumor is considered surgical because of its potential for rupture. On unenhanced CT scans, HCA appears as a low-attenuation mass because of the fat and glycogen contained within the tumor.[156, 273] Areas of increased attenuation that correlate with fresh hemorrhage may be seen, creating a heterogeneous appearance. After IV contrast administration, enhancement of the peripheral vessels occurs early with a centripetal enhancement pattern somewhat similar to hemangioma (see Figs. 35–5*A* and 35–9*A*).[156] Unlike the case of hemangioma, however, contrast enhancement does not persist in later phases because of arteriovenous shunting present within the HCA.[213]

On T1-weighted MR images, areas of mildly increased signal intensity may be demonstrated because of the presence of fat and hemorrhage associated with this lesion (Figs. 35–8 and 35–9*B*).[81, 173, 185, 212, 221] The appearance on T2-weighted images is often heterogeneous, with hypointense, isointense, and hyperintense areas, depending on the nature of the lesion and the stage of hemorrhage (Fig. 35–9*C*). The heterogeneous appearance on both T1-weighted and T2-weighted images makes it difficult to distinguish from hepatocellular carcinoma. A capsule often appears as a hypointense rim surrounding the tumor and may contain large vessels.[81, 212]

SPIO uptake is common in these lesions,[92, 200] depending on the variable presence of reticuloendothelial cells (Fig.

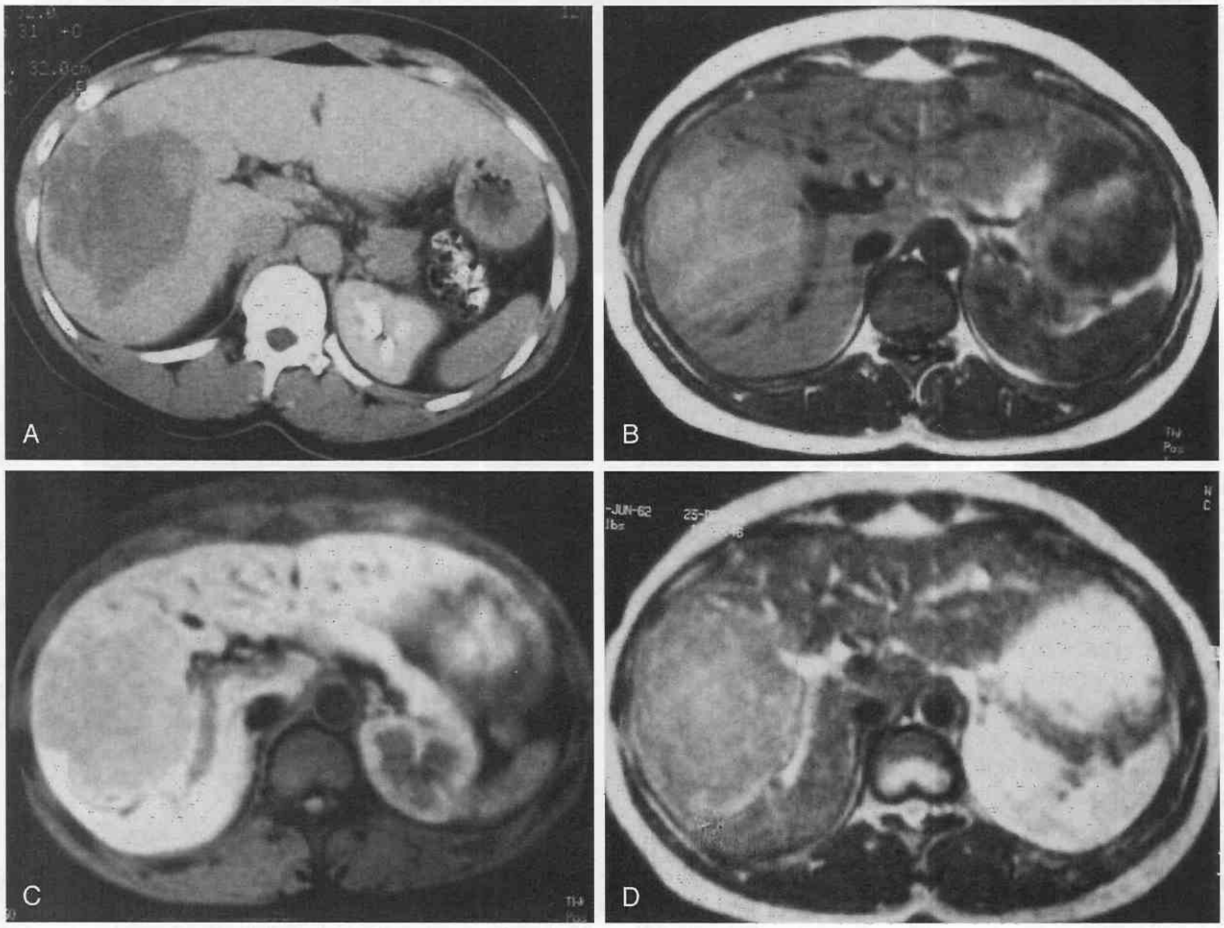

Figure 35–8. Hepatocellular adenoma in a 29-year-old woman. *A,* Contrast-enhanced CT scan demonstrates a large mass of mixed attenuation in the right hepatic lobe. *B,* T1-weighted image (TR = 450 msec, TE = 15 msec) shows the mass to have slightly increased signal intensity relative to the liver. *C,* Fat-suppression T1-weighted image (TR = 550 msec, TE = 15 msec) now shows the lesion to be lower in signal intensity relative to the liver. This indicates that the mass has a fatty composition. *D,* T2-weighted image (TR = 2000 msec, TE = 90 msec) shows the mass to be slightly hyperintense relative to the liver.

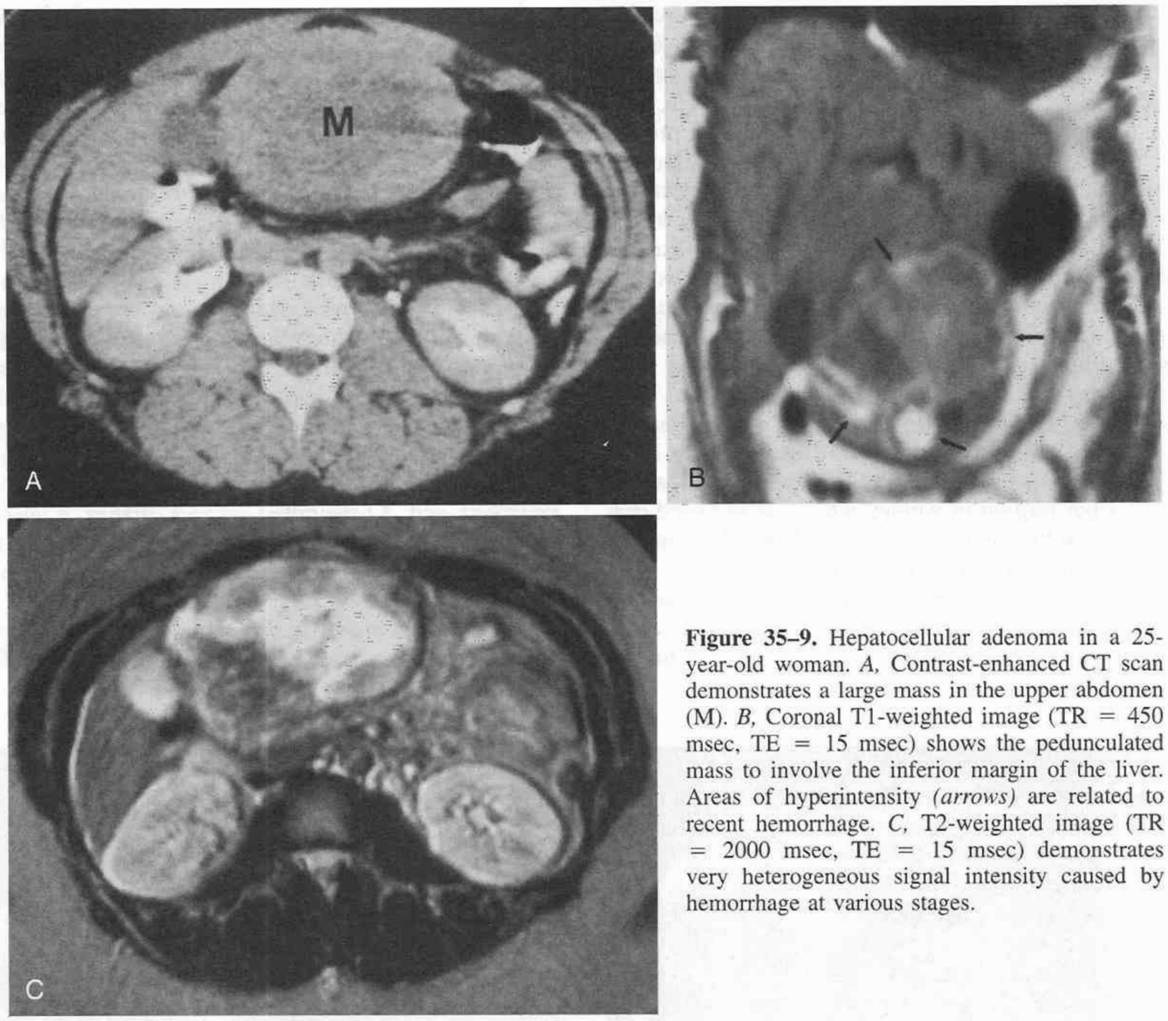

Figure 35–9. Hepatocellular adenoma in a 25-year-old woman. *A,* Contrast-enhanced CT scan demonstrates a large mass in the upper abdomen (M). *B,* Coronal T1-weighted image (TR = 450 msec, TE = 15 msec) shows the pedunculated mass to involve the inferior margin of the liver. Areas of hyperintensity *(arrows)* are related to recent hemorrhage. *C,* T2-weighted image (TR = 2000 msec, TE = 15 msec) demonstrates very heterogeneous signal intensity caused by hemorrhage at various stages.

35–10). In their series, Grandin and coworkers[92] found that adenomas had similar signal loss to that of FNH. These lesions take up hepatobiliary contrast agents (e.g., manganese-DPDP, Gd-EOB-DTPA)[98] as a result of the presence of functioning hepatocytes.

Nodular Regenerative Hyperplasia

Nodular regenerative hyperplasia (NRH) of the liver is defined as the presence of diffuse, multiple regenerative nodules not associated with fibrosis.[241] The nodules consist of cells that resemble normal hepatocytes. The absence of fibrosis is an important distinction between NRH and regenerating nodules of cirrhosis.[245] Multiple diffuse, bulging nodules are present on the liver surface and vary in size from a few millimeters to several centimeters in diameter.

NRH (also called nodular transformation of the liver, diffuse nodular hyperplasia, and noncirrhotic nodulation),[49] is a rare condition that is discovered incidentally or during the evaluation of portal hypertension. Several drugs (e.g., steroids and antineoplastic medications) as well as multiple systemic conditions (e.g., myeloproliferative, lymphoproliferative, immunologic, and collagen vascular disorders) have been associated with NRH.[52, 180, 245, 267] It is the leading cause of noncirrhotic portal hypertension in the Western Hemisphere. Complications include esophageal varices and ascites.[170]

The CT appearance of NRH may range from that of a normal liver to that of focal liver nodules of varied but predominantly low attenuation.[52] Hemorrhage may occur, resulting in a complex mass of mixed density. Descriptions in the literature regarding the MRI appearance of NRH are limited. Casillas and colleagues described the appearance in five patients, which was subtly hypointense or hyperintense before contrast administration. Enhancement was similar to that of normal hepatic parenchyma.[32]

Adenomatous Hyperplastic Nodule

Adenomatous hyperplastic nodule (AHN), also referred to as *adenomatoid hyperplasia* or *regenerative nodule*, is a benign but premalignant lesion that appears in cirrhotic livers. When larger than other regenerative nodules of the cirrhotic liver, it has been called a *macroregenerative nodule*. Histologically, it contains portal tracts and bile ducts but has no capsule.[49]

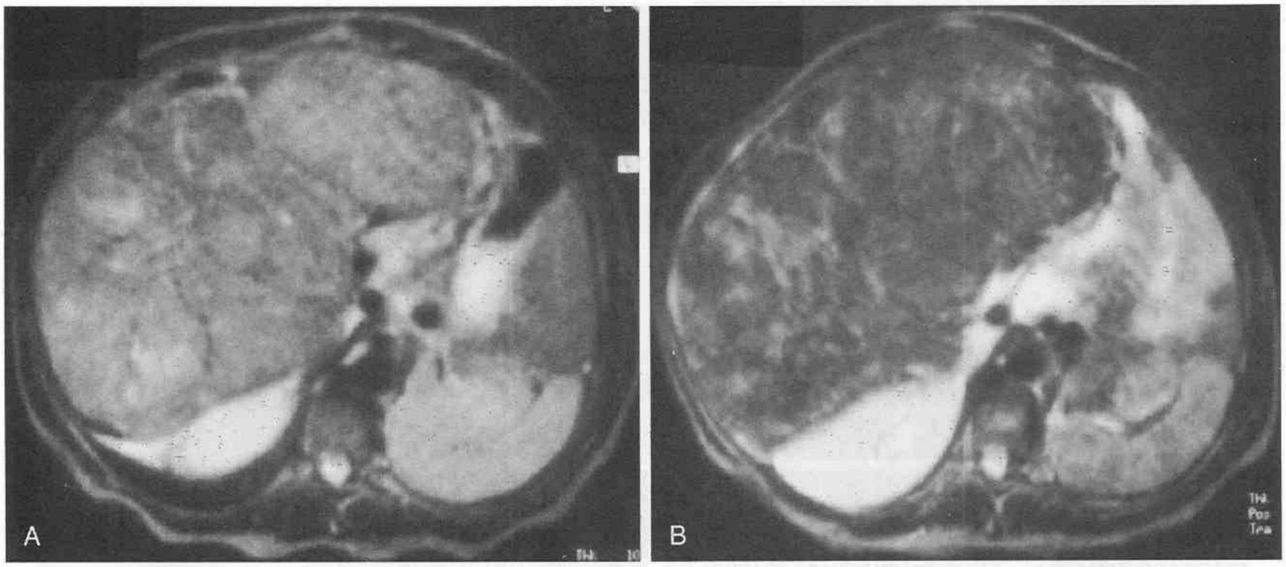

Figure 35–10. Hepatocellular adenoma. *A,* Unenhanced T2-weighted image demonstrates a very large hepatic lesion. *B,* T2-weighted image after superparamagnetic iron oxide (SPIO) enhancement demonstrates signal loss from the lesion.

Unenhanced CT scans show a low-attenuation nodule that is indistinguishable from a small hepatocellular carcinoma (HCC). CT arterial portography (CTAP) is useful because an AHN is not apparent (because of its portal blood flow), whereas HCC is seen as a hypoattenuating lesion (because of a lack of portal flow).[161] CTAP, however, is seldom used as a result of its invasive nature.

MRI is also useful for distinguishing AHN from HCC.[160] On T1-weighted images, AHN is frequently hyperintense, whereas T2-weighted images demonstrate a hypointense nodule (Fig. 35–11).[110, 160, 188] This is in contrast to HCC, which is often hyperintense on T2-weighted images. The finding of a "nodule within a nodule" on gradient-echo and T2-weighted images, consisting of a large, low-intensity nodule containing a smaller nodule of isointensity or hyperintensity relative to liver, suggests the development of a small HCC within a hyperplastic nodule.[167] After injection of an extracellular contrast agent, an AHN typically does not enhance to a greater degree than liver parenchyma, thus further differentiating it from HCC.[178]

Lipomatous Tumors

In rare cases, benign hepatic tumors consisting of fat cells may be seen. These include lipoma, hibernoma, and mixed tumors such as angiomyolipomas (fat and blood vessels), myelolipoma (fat and hematopoietic tissue), and angiomyolipoma (fat, blood vessels, and hematopoietic tissue).[87] Hepatic lipomatous tumors usually are round, well-

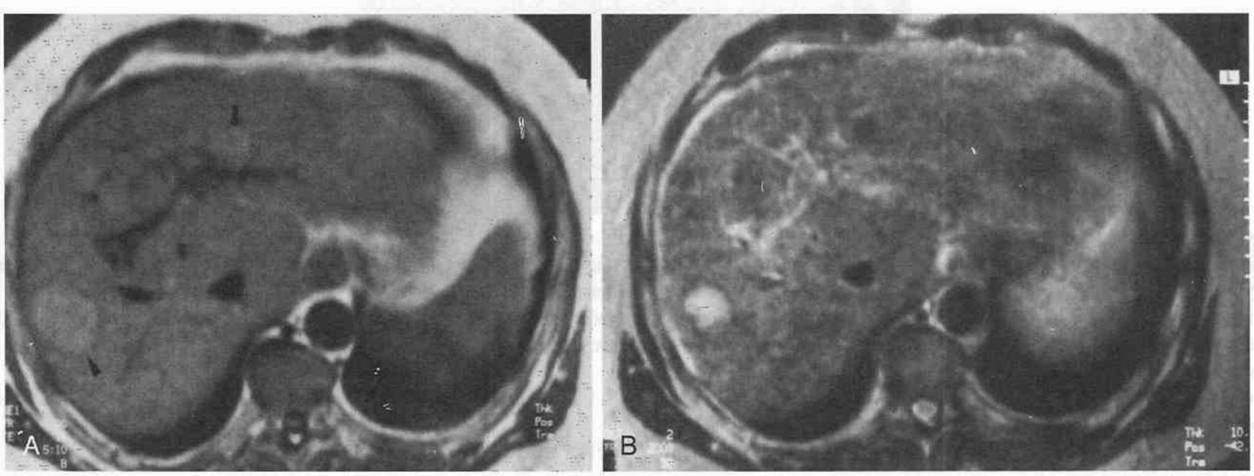

Figure 35–11. Adenomatous hyperplastic nodules in a man with hepatocellular carcinoma. *A,* T1-weighted image (TR = 300 msec, TE = 15 msec) shows a small hyperintense nodule of the left hepatic lobe *(arrow)* and a larger hyperintense nodule of the right hepatic lobe *(arrowhead). B,* T2-weighted image (TR = 2000 msec, TE = 90 msec) demonstrates the adenomatous hyperplastic nodule of the left hepatic lobe to be of low signal intensity whereas the hepatocellular carcinoma of the right hepatic lobe is of high signal intensity.

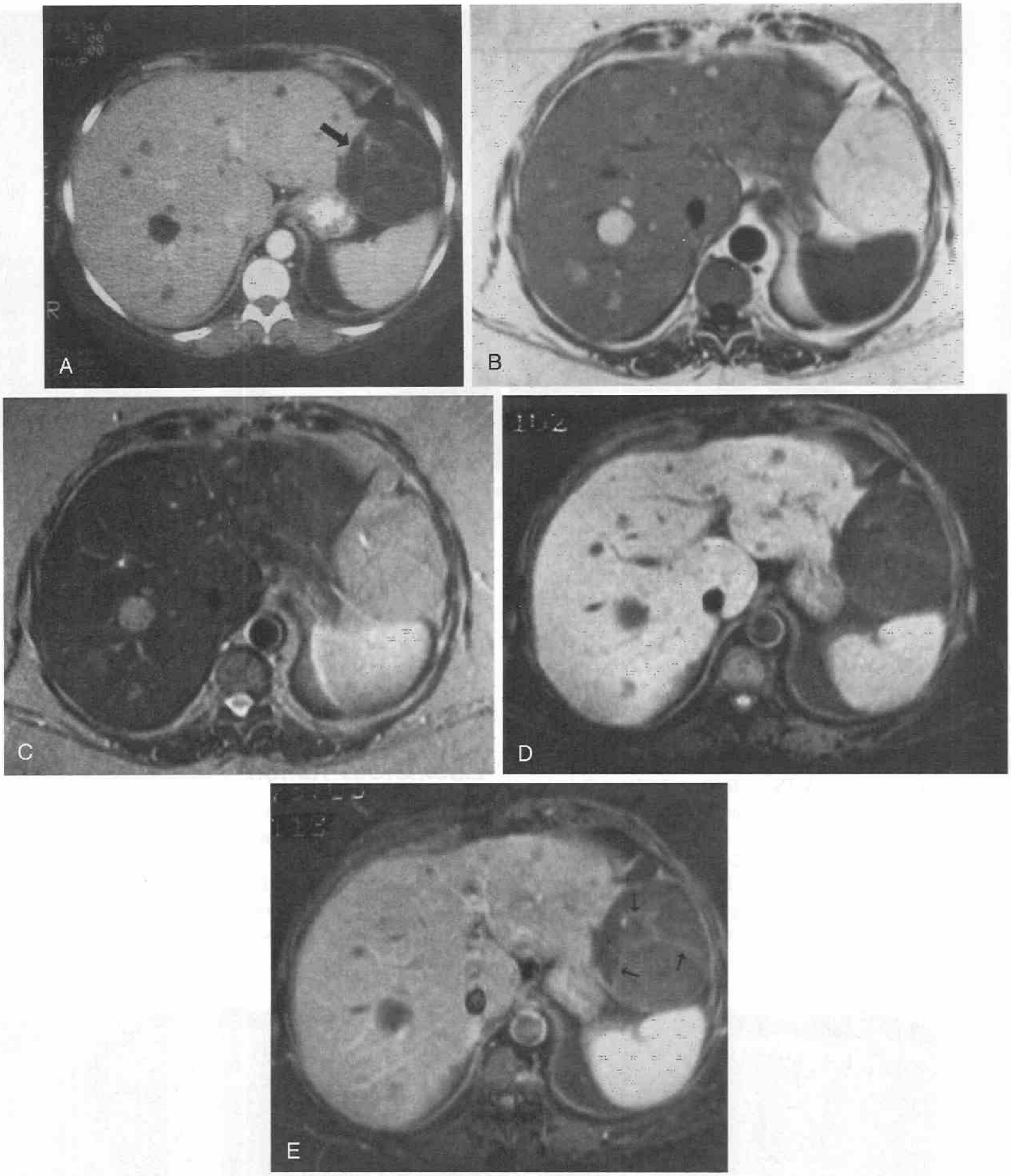

Figure 35–12. Tuberous sclerosis in a woman with angiomyolipomas of the liver and kidneys.

A, Contrast-enhanced CT scan demonstrates multiple lipomatous lesions of the liver having fat attenuation. A large pedunculated angiomyolipoma *(arrow)* is present in the lateral segment of the left hepatic lobe.

B, T1-weighted image (TR = 300 msec, TE = 15 msec) demonstrates the multiple lipomatous tumors of the liver to be of increased signal intensity similar to that of the subcutaneous and retroperitoneal fat. Fibrous septa of the angiomyolipoma of the left hepatic lobe have low signal intensity.

C, T2-weighted image (TR = 2400 msec, TE = 90 msec) shows the lesions to continue to have signal intensity similar to that of other fatty areas.

D, Fat-suppression T1-weighted image (TR 800 msec, TE = 15 msec) demonstrates the fatty lesions to be of low signal intensity similar to that of other fatty areas.

E, Fat-suppression T1-weighted image (TR = 800 msec, TE = 15 msec) obtained after intravenous gadolinium (Gd-DTPA) demonstrates mild enhancement of the septa *(arrows)* of the angiomyolipoma of the left hepatic lobe, similar to that seen on CT.

defined, solitary lesions that occur in a noncirrhotic liver.[88] Their microscopic appearance is similar to that seen in lipomatous lesions of soft tissues.[49]

Hepatic lipomatous tumors may occur in approximately 10% of patients with tuberous sclerosis and renal angiolipomas (Fig. 35–12),[208] although solitary liver lipomas may be present without other lesions (Fig. 35–13). Most are found incidentally and are asymptomatic; occasionally, however, they may hemorrhage, causing abdominal pain.

Benign lipomatous tumors of the liver have the characteristic CT appearance of a lesion with fat attenuation (see Figs. 35–12 and 35–13).[22, 208] In a reported case of the MRI findings of a hepatic lipoma, the lesion appeared homogeneous and well defined, with similar signal intensity to retroperitoneal fat on all pulse sequences (Fig. 35–13*B*).[22]

Infantile Hemangioendothelioma

Infantile hemangioendothelioma (IHE) is a benign vascular tumor consisting of vascular channels formed by proliferating endothelial cells. Although usually presenting as multiple spongy nodules that vary in diameter from a few millimeters to 15 cm or more, a solitary lesion is a less common variant.[163] Nodules may become fibrotic with age.[219]

Microscopically, IHE consists of a proliferation of vascular channels with an endothelial cell lining. Areas of hemorrhage, thrombosis, fibrosis, and calcification are common. Cavernous areas are also seen.[49]

IHEs are the most common liver tumor during the first 6 months of life; 90% of them are discovered during that period. IHE accounts for 12% of all childhood hepatic tumors, with girls being affected more often than boys.[56] Hepatomegaly, congestive heart failure (up to 25% of cases), thrombocytopenia (due to trapping of platelets by the tumor), and occasional rupture with hemoperitoneum may be seen.[26, 141] Cutaneous hemangiomas may be associated with the multinodular form of IHE (in up to 40% of patients) and may involve other organs.[49] Although IHE may enlarge with resulting hemodynamic compromise, spontaneous involution occurs with time if the child survives.[195]

On CT scans, IHE demonstrates an appearance similar to that of hemangioma.[149] On precontrast scans, it appears as a well-defined mass that may contain calcifications (Fig. 35–14*A*). After IV contrast administration, peripheral enhancement occurs (Fig. 35–14*B*). On delayed CT scans, a variable degree of centripetal enhancement is seen with prolonged and persistent contrast enhancement, similar to that seen with hemangioma.[126]

MR images of IHE demonstrate a heterogeneous appearance on both T1-weighted and T2-weighted images because of the presence of hemorrhage, necrosis, and fibrosis (Fig. 35–15). The vascular nature of the lesion produces various degrees of hyperintensity on T2-weighted images, similar to the hyperintensity of a hemangioma.[126]

Mesenchymal Hamartoma

Mesenchymal hamartoma is a benign cystic developmental lesion consisting of gelatinous mesenchymal tissue with cyst formation and remnants of normal hepatic parenchyma.[55, 244] It is large, usually 15 cm or more in diameter at diagnosis, with cysts present in 80% of cases.[106] It is a well-defined tumor that may be encapsulated or pedunculated.[215] On cut section, this tumor may have either mesenchymal predominance (a solid appearance) or cystic predominance (multiloculated cystic masses). Microscopically, it consists of cysts, remnants of portal triads, hepatocytes, and fluid-filled mesenchyme.

Mesenchymal hamartoma is uncommon and accounts for only 8% of all childhood liver masses.[106] Most cases are discovered by the time the child is 3 years of age, and

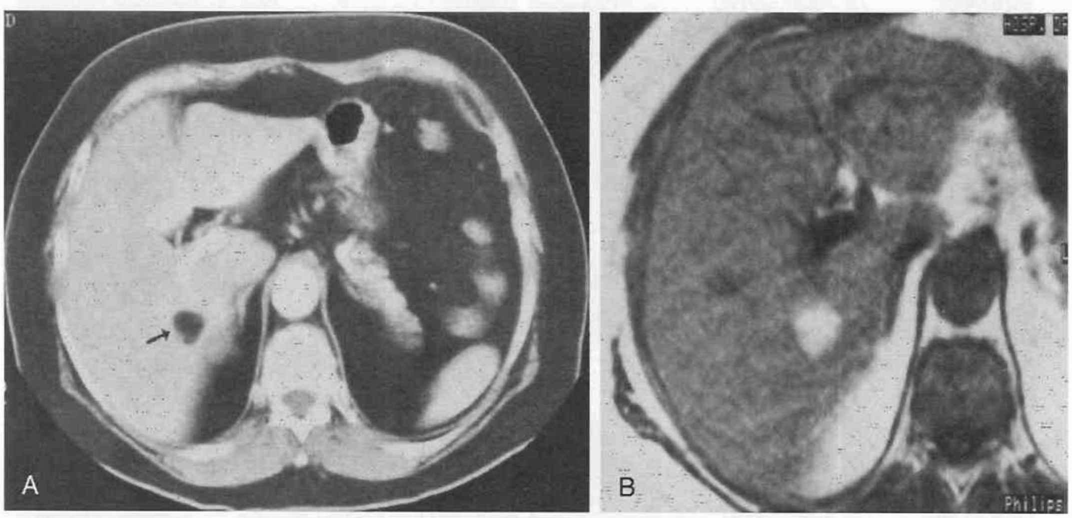

Figure 35–13. Lipoma of the liver. *A,* Contrast-enhanced CT scan demonstrates a lesion of low attenuation *(arrow)*, with similar attenuation to subcutaneous and retroperitoneal fat. *B,* T1-weighted image demonstrates the lesion's high signal intensity, similar to that of other fatty areas. (From Marti-Bonmati L, Menor F, Vizcaino J, et al: Lipoma of the liver: US, CT and MRI appearance. Gastrointest Radiol 14:155–157, 1989.)

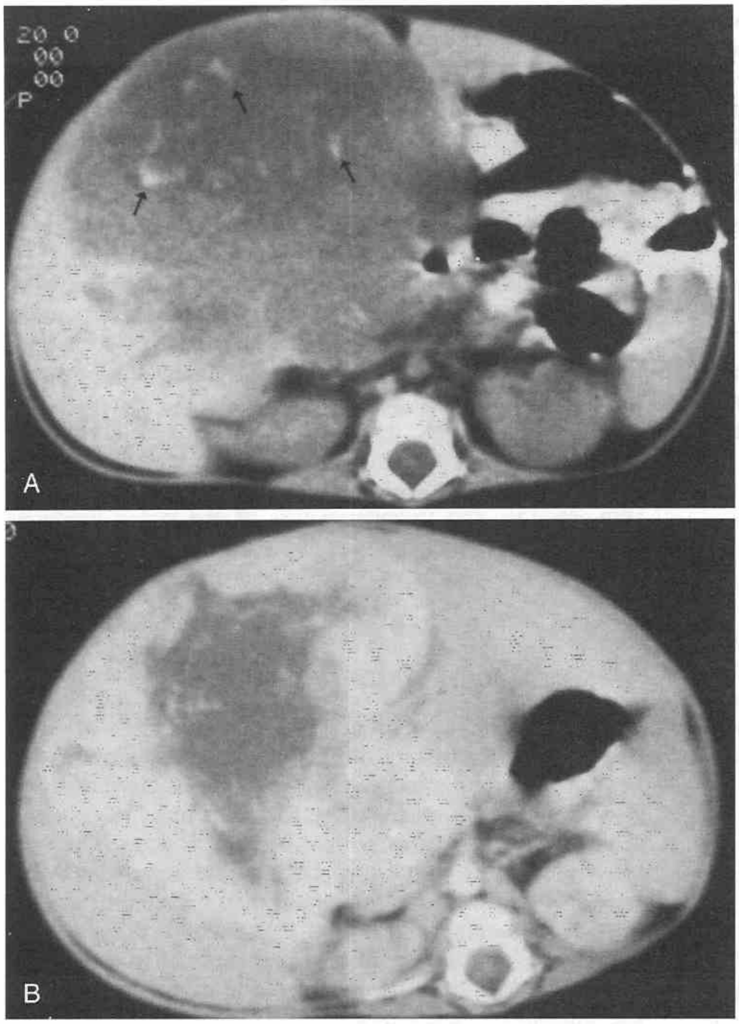

Figure 35–14. Infantile hemangioendothelioma in a 1-month-old boy. *A,* Unenhanced CT scan shows a large mass of the liver containing calcifications *(arrows)*. *B,* Contrast-enhanced CT scan shows the enhancement beginning in the periphery, similar to that seen with hemangioma.

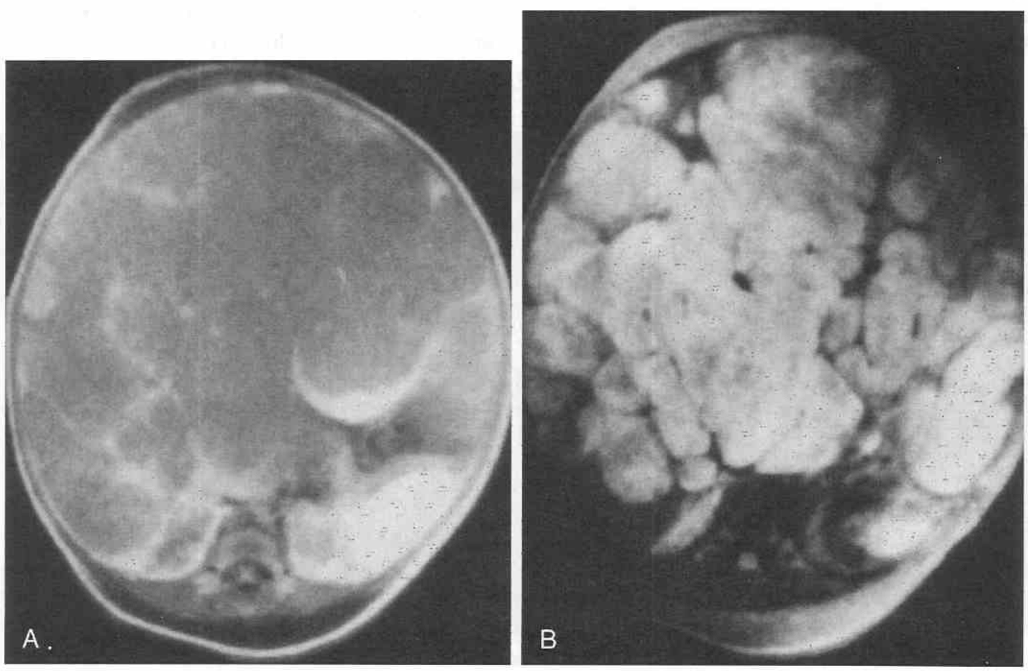

Figure 35–15. Infantile hemangioendothelioma in an infant girl. *A,* T1-weighted image, obtained with the patient in the decubitus position, reveals a large, multinodular hepatic lesion of heterogeneous signal intensity that fills the abdomen. *B,* T2-weighted image shows that the lesion has predominantly high signal intensity because of its vascular nature.

there is a slight male predominance.[244] Although slow, progressive, and painless abdominal enlargement is seen, occasionally sudden enlargement may result from rapid fluid accumulation in the cysts. Mass effect from the bulky tumor may cause respiratory distress and lower extremity edema.[247] Extensive surgery is not necessary because mesenchymal hamartoma is not a neoplasm but a failure of normal development; thus, simple excision, marsupialization, or incisional drainage may be all that is required for treatment.[215]

On CT scans, mesenchymal hamartoma appears as a well-defined mass with central areas of low density and internal septa (Fig. 35-16*A*). Both solid and cystic areas are seen.[215, 236]

The MRI appearance of mesenchymal hamartomas depends on their mesenchymal (stromal) or cystic predominance. Lesions of mesenchymal predominance have lower intensity than normal liver on T1-weighted images because of their fibrotic tissue content. Cystic-predominant lesions are of variable intensity on T1-weighted images and are significantly hyperintense on T2-weighted images because of the cyst's contents (see Fig. 35–16*B* and *C*). Multiple septa are best seen on T2-weighted images, which demonstrates the complex nature of the cystic mass.[190]

Simple Hepatic Cysts

A simple hepatic cyst, or *bile duct cyst*, is defined as a solitary, unilocular cyst with a lining composed of a single layer of cuboidal bile duct epithelium.[49] Its wall is a thin (<1 mm thick) layer of fibrous tissue, surrounded by normal hepatic parenchyma. Although the simple hepatic cyst is thought to be of congenital, developmental origin, usually it is discovered in adults.[147]

The incidence of simple hepatic cysts ranges from 1% to 14% in autopsy series. These cysts tend to occur more frequently in women than in men by a 5:1 ratio.[49] They are usually found incidentally but may cause mass effect, resulting in abdominal pain or jaundice.[223] If the cyst is symptomatic, surgical excision or percutaneous aspiration with alcohol sclerotherapy may be helpful.[11, 119, 147, 223]

On CT scans, a simple hepatic cyst appears as a well-defined intrahepatic mass having water attenuation, a round or oval shape, smooth thin walls, no internal structure, and no enhancement after IV contrast administration.[9, 179] Usually solitary and peripheral, the cysts may be multiple and occur more centrally. When more than 10 cysts are present, the diagnosis of polycystic disease should be considered.[24] Cysts that become complicated by hemorrhage

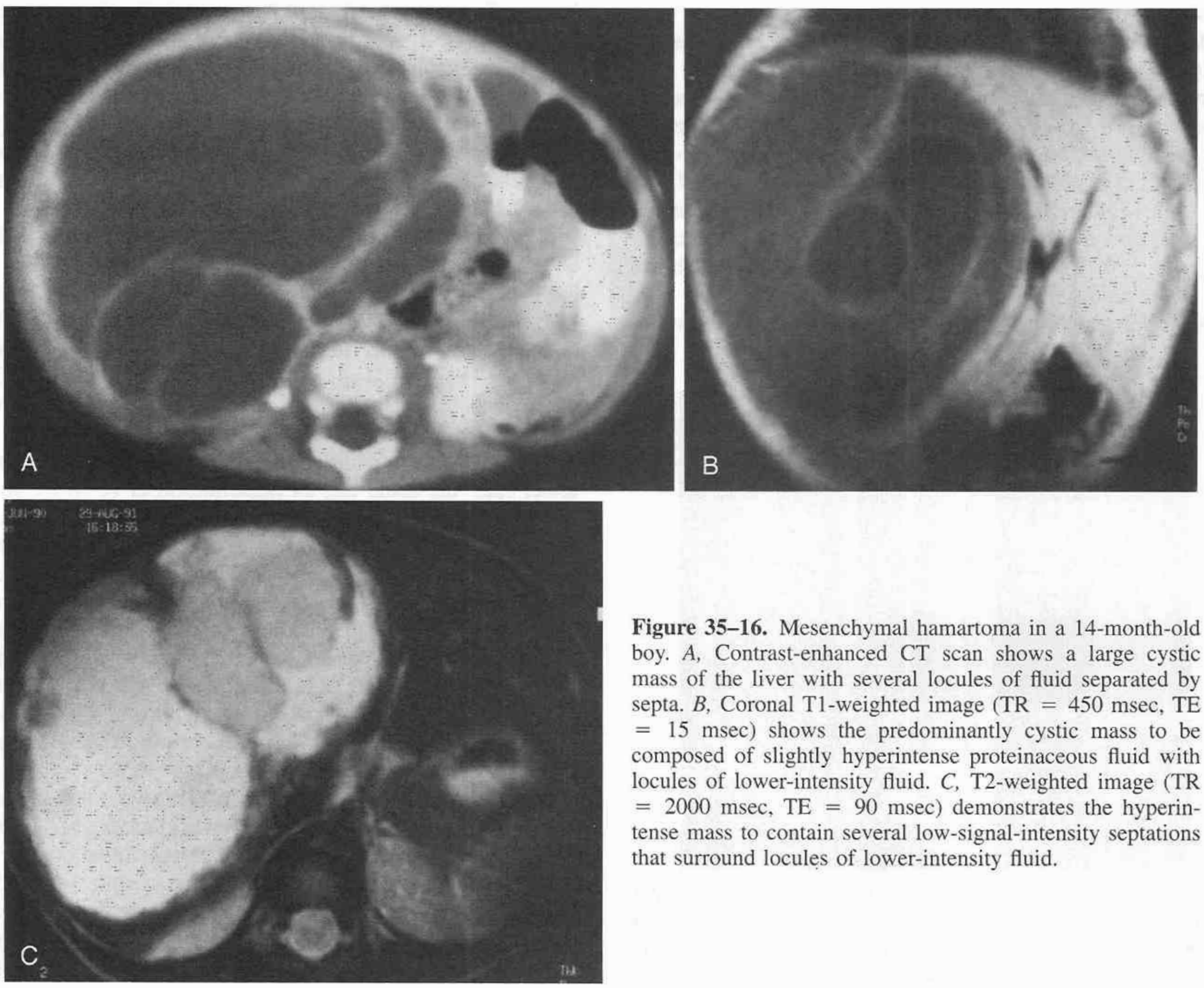

Figure 35–16. Mesenchymal hamartoma in a 14-month-old boy. *A,* Contrast-enhanced CT scan shows a large cystic mass of the liver with several locules of fluid separated by septa. *B,* Coronal T1-weighted image (TR = 450 msec, TE = 15 msec) shows the predominantly cystic mass to be composed of slightly hyperintense proteinaceous fluid with locules of lower-intensity fluid. *C,* T2-weighted image (TR = 2000 msec, TE = 90 msec) demonstrates the hyperintense mass to contain several low-signal-intensity septations that surround locules of lower-intensity fluid.

or infection may have septations and internal debris as well as wall enhancement.

MRI of simple hepatic cysts demonstrates hypointensity on T1-weighted images and hyperintensity on T2-weighted images.[278] It is difficult to differentiate a cyst from a hemangioma without the use of IV contrast agents.

Congenital Hepatic Fibrosis and Polycystic Liver Disease

Congenital hepatic fibrosis and polycystic liver disease are part of the spectrum of *fibropolycystic disease* of the liver. Congenital hepatic fibrosis is characterized by periductal fibrosis and aberrant bile duct proliferation.[49] Typically, the cysts are visible only with magnification. However, numerous large and small cysts, which are identical on pathologic examination to simple or bile duct cysts, are present with fibrosis in the polycystic liver disease variant.

In the patient with polycystic liver and/or kidney disease, hepatic tissue surrounding the cysts is not normal and commonly contains von Meyenburg's complexes and increased fibrous tissue. Hepatic involvement occurs in approximately 30% to 40% of patients with autosomal dominant (adult) polycystic kidney disease.[119] Occasionally, hepatic cysts occur without radiologically evident renal cysts; approximately 70% of patients with polycystic liver disease also have autosomal dominant polycystic kidney disease.[24]

Most patients with congenital hepatic fibrosis present in childhood with complications of portal hypertension, such as bleeding varices.[125] In patients with polycystic disease, lesions are often found incidentally on imaging studies.

CT demonstrates multiple cysts of the liver and may reveal calcification of the cyst walls (Figs. 35–17 and 35–18*A*). Hemorrhage into cysts may occur, as in the kidneys, and results in increased attenuation of the cystic contents.[24, 142, 179] Contrast enhancement of a cyst should not occur unless the cyst becomes infected.

MRI demonstrates simple, noncomplicated cysts as having decreased signal intensity on T1-weighted images and increased signal intensity on T2-weighted images (Fig. 35–18*B* and *C*). Calcifications of cyst walls appear as areas of signal void, although detection may be difficult. When hemorrhage occurs, variations in signal intensity on all pulse sequences may be seen.[275]

Figure 35–17. Polycystic kidney and liver disease in a 60-year-old woman. Noncontrast CT scan demonstrates multiple cysts of varying attenuation involving the liver. A few calcifications *(arrows)* of the cyst walls are present.

Malignant Hepatic Tumors

Hepatocellular Carcinoma

The most common primary malignant hepatic tumor and one of the most prevalent malignancies in the world, HCC is characterized by malignant hepatic cells that mimic normal hepatocytes.[49] On microscopic examination, it is often difficult to distinguish the cells of HCC from normal hepatocytes or hepatocellular adenoma; this problem affects the accuracy of cytologic needle aspiration biopsy.[184] The malignant hepatocytes may be so well differentiated in some tumors as to even produce bile, which is found in the tumor cells and in biliary canaliculi. Fat and glycogen are often present in the cytoplasm of HCC hepatocytes.

Several growth patterns occur. The most common is the *trabecular* pattern, which may give the tumor a pseudoglandular or acinar appearance. When the trabeculae grow together, a *solid* pattern is produced.

Grossly, three major patterns of growth are seen: (1) a large solitary mass, (2) nodular or multifocal masses, and (3) diffuse or cirrhotomimetic HCC. A variant of the solitary form, encapsulated HCC, may carry an improved prognosis because of easier resectability.[75, 217] In all forms of growth, HCC is a soft tumor with frequent necrosis and hemorrhage as a result of its lack of stroma. Vascular invasion of portal and hepatic veins is common, although biliary invasion is uncommon.[246]

The incidence of HCC is highest in sub-Saharan Africa and Asia, with its peak incidence in Japan.[176, 181] In the high-incidence areas, presentation is often at a young age (30 to 45 years). Men are affected eight times more frequently than women. The primary etiologic factors in these areas are hepatitis B virus and aflatoxin exposure. HCC is aggressive in these patients and may present with both rupture of the liver and hemoperitoneum.

In the Western Hemisphere, where HCC occurs at a lower rate, the usual age of presentation is 70 to 80 years, with a male-to-female ratio of 2.5:1.[176] Most patients have underlying cirrhosis caused by alcohol abuse, hemochromatosis, or toxin exposure, with hepatitis B virus increasingly becoming the responsible agent, especially in younger patients. Symptoms are insidious in onset and include malaise, fever, and abdominal pain. Jaundice is rare, and liver function test results may be normal except for an elevated α-fetoprotein level. Paraneoplastic syndromes may occur, including erythrocytosis, hypercalcemia, hypoglycemia, hypercholesterolemia, and hirsutism.

Unenhanced CT scans usually demonstrate HCC as a large, hypodense mass, often with central areas of low attenuation representing areas of necrosis. On unenhanced CT scans, the tumor is occasionally isodense to the liver.[134, 249] Calcification is rarely present.[133, 247] In North American and European patients, associated cirrhosis (60%) or hemochromatosis (20%) is often present (Fig. 35–19).[75] After

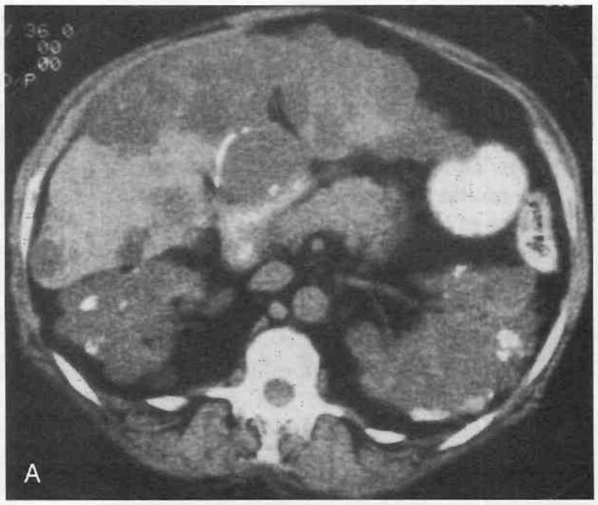

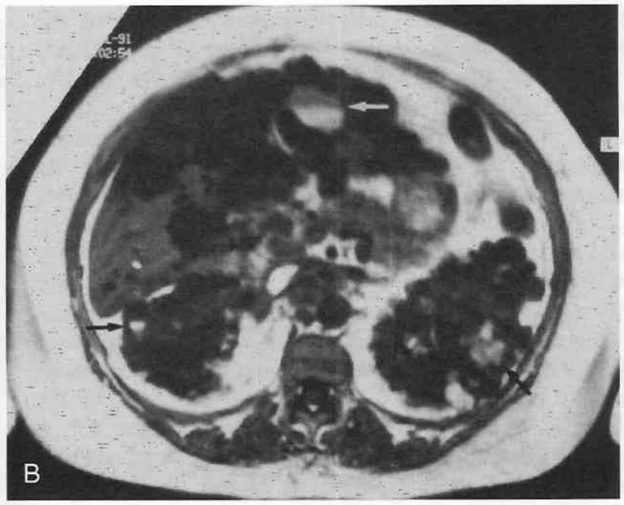

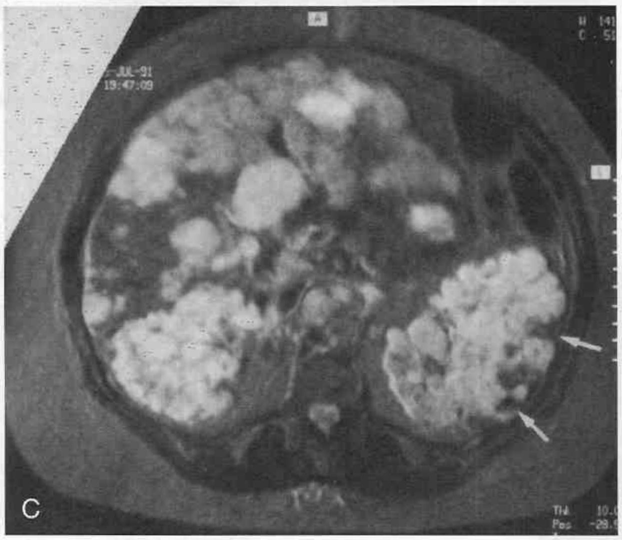

Figure 35–18. Polycystic kidney and liver disease in a 48-year-old woman. *A,* Noncontrast CT scan shows multiple cysts involving the liver and both kidneys. Several calcifications are demonstrated. *B,* T1-weighted image (TR = 450 msec, TE = 15 msec) shows multiple low-signal-intensity cysts of both the liver and kidneys. Several cysts demonstrate high-signal intensity, which corresponds to hemorrhage *(arrows). C,* T2-weighted image (TR = 2500 msec, TE = 90 msec) shows the cysts with varying degrees of hyperintensity. Areas of signal void that correspond to calcifications are better visualized *(arrows).*

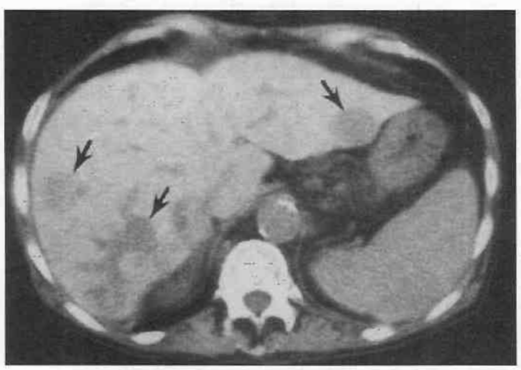

Figure 35–19. Hemochromatosis with multifocal hepatocellular carcinoma. Unenhanced CT scan demonstrates multiple masses of low attenuation relative to the overall increased density of the liver as a result of the high levels of iron in the liver. The lesion of the posterior segment of the right hepatic lobe has portal vein invasion, which causes the venous dilatation peripheral to the lesion.

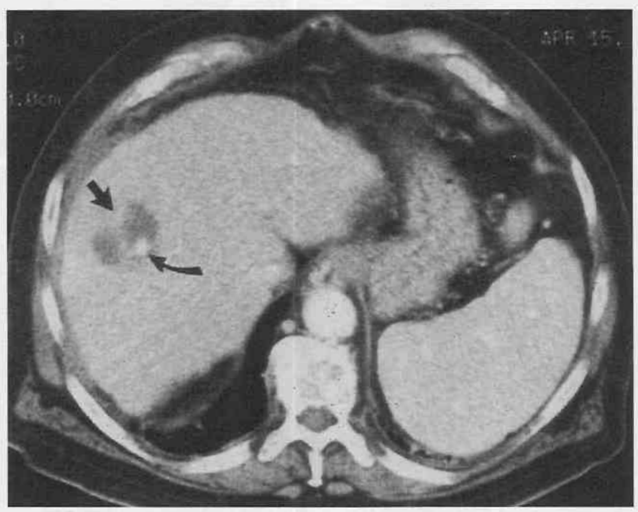

Figure 35–20. Hepatocellular carcinoma in a 70-year-old man with a cirrhotic liver. Contrast-enhanced CT scan demonstrates a predominantly low-attenuation mass with enhancement of the non-necrotic area of the tumor *(straight arrow).* An enhancing vessel *(curved arrow)* is well demonstrated on this dynamic bolus-enhanced scan. A rim of ascites is present.

IV contrast administration, the non-necrotic areas of the tumor may enhance and appear hyperdense (Fig. 35–20).[75] If a capsule is present, it appears as an enhancing rim around the tumor (Fig. 35–21).[217]

In the *solid* histologic forms of HCC, the postcontrast attenuation of the lesion may be similar to that of the surrounding liver; in these instances, lesion detection relies on a change in liver contour. Low attenuation persists in areas of necrosis and fat.[134, 283] Vascular invasion of venous structures, including the portal veins, hepatic veins, and inferior vena cava, may be seen after contrast administration (Fig. 35–22).[157, 169, 246] CTAP, CT after iodized oil (Lipiodol) injection, and intraoperative ultrasound are more sensitive than IV bolus dynamic CT in detecting HCCs smaller than 3 cm.[248] However, contrast-enhanced CT is more accurate than abdominal sonography for identifying and staging HCC.[169] Intraperitoneal rupture of HCC may be demonstrated by CT as high-density blood adjacent to a peripheral mass, and its occurrence may be predicted in patients with very large peripheral tumors with extrahepatic protrusion (Fig. 35–23).[122]

MR images of HCC reveal a variable appearance on T1-weighted images, depending on the degree of fatty change, internal fibrosis, hemorrhage, and dominant histologic pattern (Fig. 35–24*C*; see Fig. 35–22*A*).[58, 114, 221] T2-weighted images usually show HCC as hyperintense relative to the liver, with higher intensity seen in areas of necrosis (Fig. 35-25; see Figs. 35–22*D* and 35–24*B*). A low-signal-intensity rim on T1-weighted images, which represents the tumor capsule, may be seen. This capsule appears on T2-weighted images as a double layer of inner low signal and outer high signal in approximately 50% of encapsulated HCCs; the inner layer represents fibrous tissue and the outer layer consists of compressed vessels and bile ducts.[114]

Gradient-echo MRI and other flow techniques are sensitive in detecting hepatic and perihepatic vascular invasion.[187] As with CT, local staging of HCC may be aided by multiplanar imaging or three-dimensional (3D) reconstruction. Contrast-enhanced MRI of HCC reveals variable enhancement of the lesion after IV gadolinium administration as a result of the tumor's hypervascular nature.[189, 282] Intravenous SPIO increases the sensitivity in the detection of HCC, even in the setting of cirrhosis,[281] by decreasing the signal intensity of normal parenchyma (see Fig. 35–25).[67] Well-differentiated HCC has been reported to take

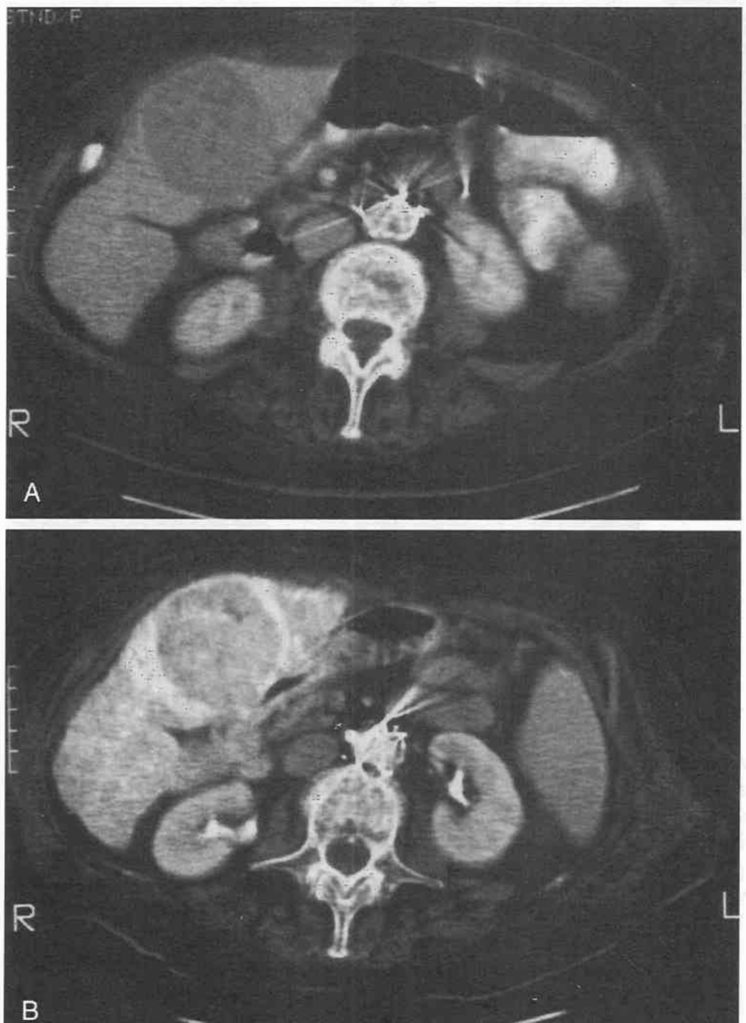

Figure 35–21. Encapsulated hepatocellular carcinoma in a cirrhotic liver. *A*, Contrast-enhanced CT scan demonstrates the well-defined, low-attenuation mass, which deforms the liver contour. *B*, CT scan performed during hepatic arterial injection of contrast more accurately demonstrates the enhancing rim.

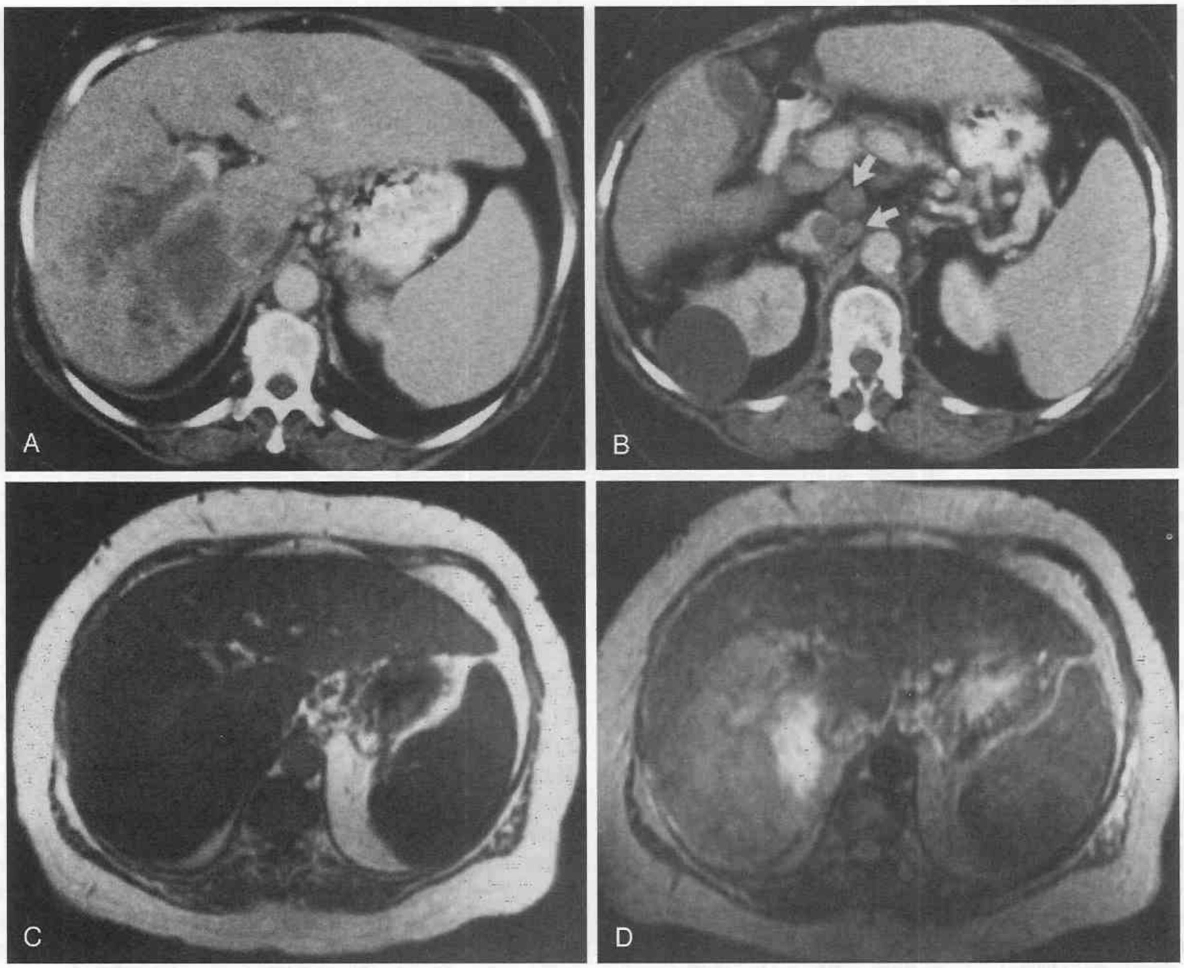

Figure 35–22. Hepatocellular carcinoma and metastases in a 63-year-old woman.

A, Contrast-enhanced CT scan demonstrates a large, mixed-attenuation mass of the posterior segment of the right hepatic lobe with thrombus involving the right portal vein and inferior vena cava (IVC).

B, At a more caudal level to that seen in *A,* lymphadenopathy *(arrows)* is demonstrated with extension of the IVC thrombus. Multiple venous collaterals are present. Incidentally noted are a large right renal cyst and thickening of the gallbladder wall.

C, T1-weighted image (TR = 350 msec, TE = 20 msec) shows the large, hypointense mass. There is slightly higher signal in the right portal vein and in the IVC.

D, T2-weighted image (TR = 2500 msec, TE = 80 msec) shows that the mass is moderately to significantly hyperintense relative to the remainder of the liver. Abnormal signal intensity of the right portal vein and the IVC is again noted.

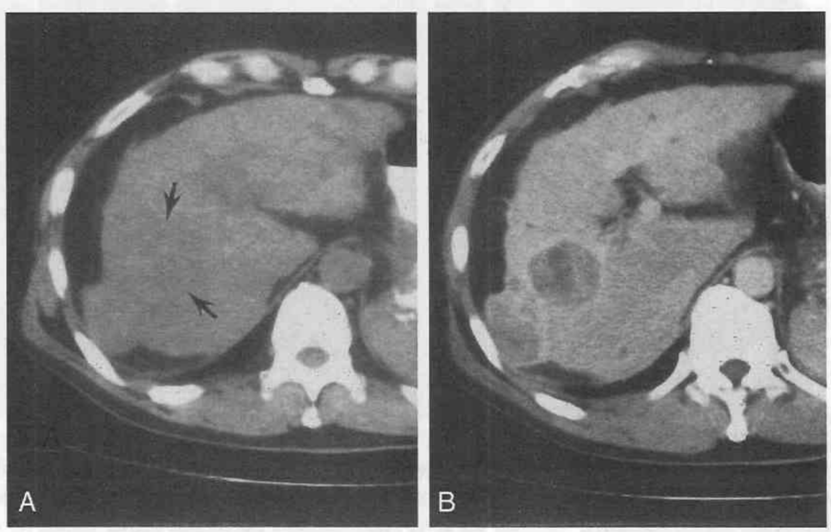

Figure 35–23. Multifocal hepatocellular carcinoma in a cirrhotic liver as a result of chronic active hepatitis B. *A,* Unenhanced CT scan shows two low-density lesions in the right hepatic lobe, one protruding from the liver margin and the other defined by a slightly hypodense peripheral rim *(arrows). B,* Contrast-enhanced CT scan shows peripheral rim enhancement and heterogeneous internal density. The protruding lesion is at increased risk for rupture.

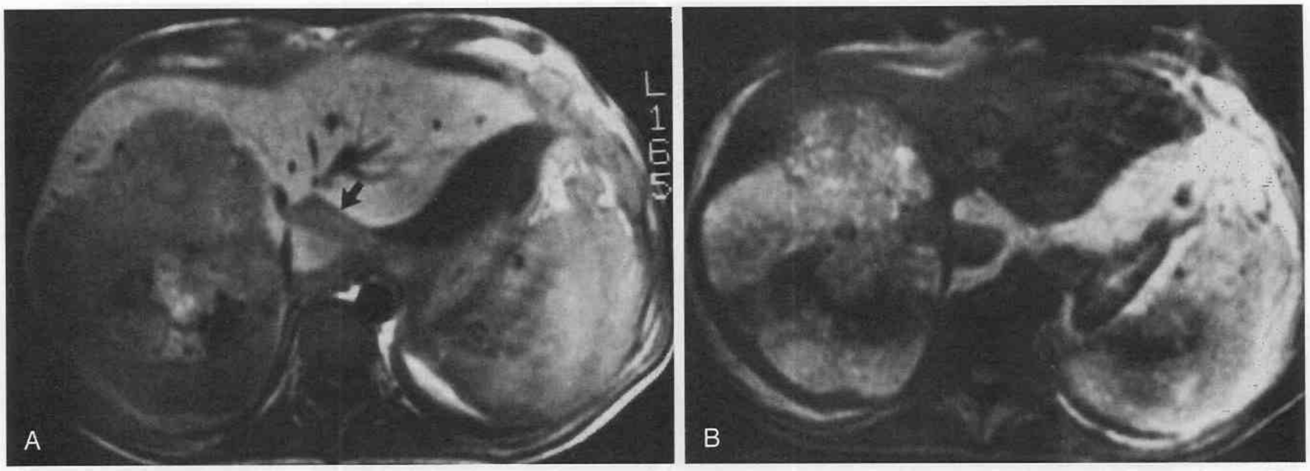

Figure 35–24. Hepatocellular carcinoma in a 46-year-old man. *A,* Fat-suppression T1-weighted image (TR = 550 msec, TE = 20 msec) reveals the large mass to be predominantly hypointense with central hemorrhage of mixed signal intensity. Regional extension of tumor is present *(arrow)*. *B,* T2-weighted image (TR = 2500 msec, TE = 80 msec) reveals the heterogeneous hyperintense mass with low signal intensity in the region of hemorrhage, indicating the presence of hemosiderin. The signal intensity of the ascitic fluid is higher than that of the area of regional spread.

up SPIO, although usually in a heterogeneous fashion, and to a lesser degree than normal liver (Fig. 35–26).

Fibrolamellar Carcinoma

Fibrolamellar carcinoma (FLC) is a slow-growing malignant tumor of hepatocellular origin that arises in a noncirrhotic liver. Composed of neoplastic hepatocytes separated into cords by lamellar fibrous strands, these lesions have a distinctive histologic pattern with eosinophilic malignant hepatocytes that contain prominent nuclei.[49, 50, 209] The α-fetoprotein body inclusions that are usually seen in HCC are not present in FLC. A fibrous central scar may be seen in larger lesions.[49]

Grossly, FLC usually arises in a normal liver; only 20% of patients have cirrhosis.[209] Satellite lesions are often seen. FLC may be similar in appearance to FNH because both tumors may have central scars and multiple fibrous septa. Hemorrhage and necrosis are rarely seen in FLC.

FLC usually occurs in adolescents and adults younger than 40 years of age; there is no sex predilection.[209] The mean survival (45 to 60 months) is much better than that of HCC (only 6 months), and FLC has more potential for cure (40%) after surgical resection.[16] Most patients with FLC present with pain, malaise, and weight loss. Jaundice may occur if occasional biliary tree invasion is present. In two thirds of patients with FLC, a palpable mass is found.[72] Usually, α-fetoprotein levels are normal.

Unenhanced CT scans show FLC as a well-defined, low-attenuation mass.[72, 79] The central scar has a lower-attenuation appearance. Calcifications are common and

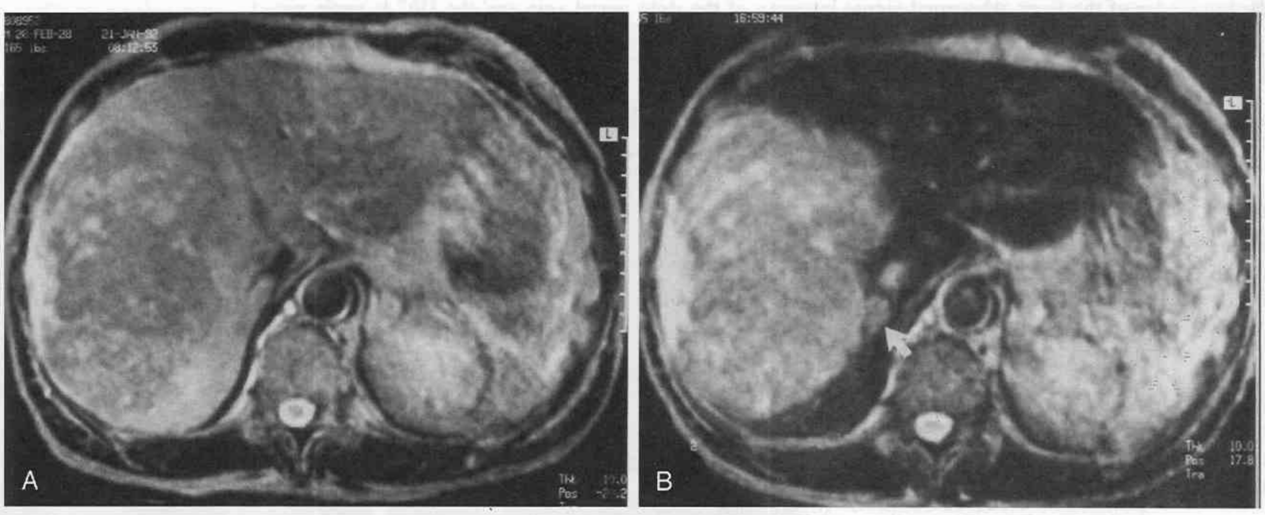

Figure 35–25. Hepatocellular carcinoma in a 63-year-old man with cirrhosis. *A,* T1-weighted image (TR = 2000 msec, TE = 90 msec) demonstrates ascites and heterogeneous slightly increased signal intensity involving the right hepatic lobe. *B,* T2-weighted image (TR = 2000 msec, TE = 90 msec) postintravenous superparamagnetic iron oxide (SPIO) shows the large mass to be defined as increased signal intensity, whereas the liver demonstrates decreased signal intensity. A satellite lesion is now demonstrated *(arrow)*.

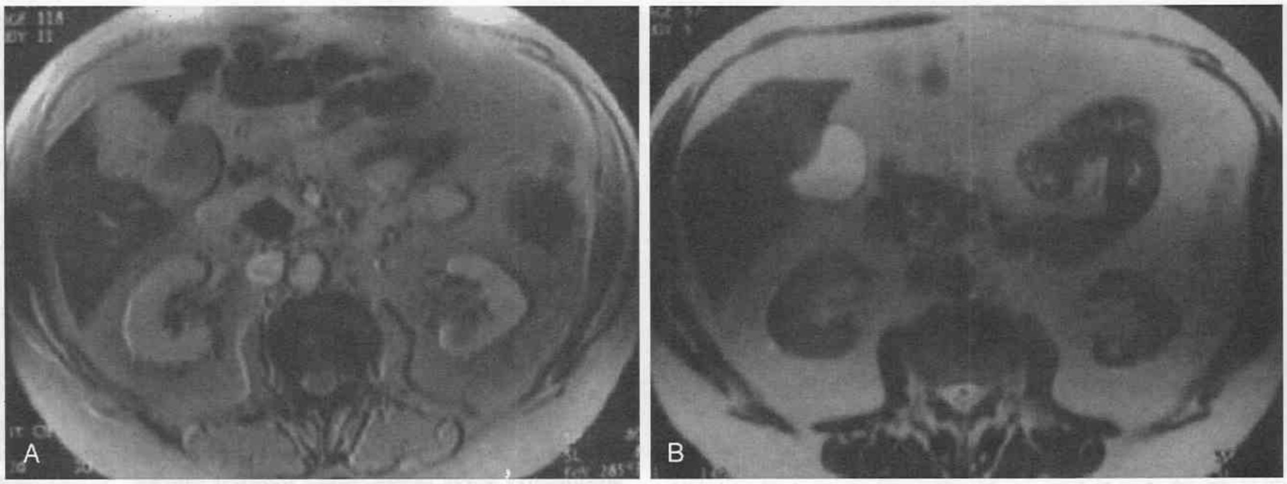

Figure 35–26. Hepatocellular carcinoma. *A,* Unenhanced T2-weighted image demonstrates a 3-cm lesion next to the gallbladder. *B,* T2-weighted image after superparamagnetic iron oxide (SPIO) administration demonstrates signal loss.

may occur within the scar in a stellate pattern. After IV contrast administration, enhancement of the tumor occurs because of its perivascularity (Fig. 35–27*A*).[72, 79]

MRI shows FLC to be isointense relative to normal liver on T1-weighted images (Fig. 35–27*B*).[162, 256] On T2-weighted images, it remains isointense to slightly hyperintense, occasionally hypointense, relative to liver (Fig. 35–27*C*). A distinguishing feature from hepatocellular carcinoma is its lack of hemorrhage and necrosis. The central scar of FLC remains hypointense on T1-weighted and T2-weighted images because of its fibrous nature. This hypointensity of the central scar of FLC often aids in differentiating this lesion from FNH, which has a hyperintense central scar.[253]

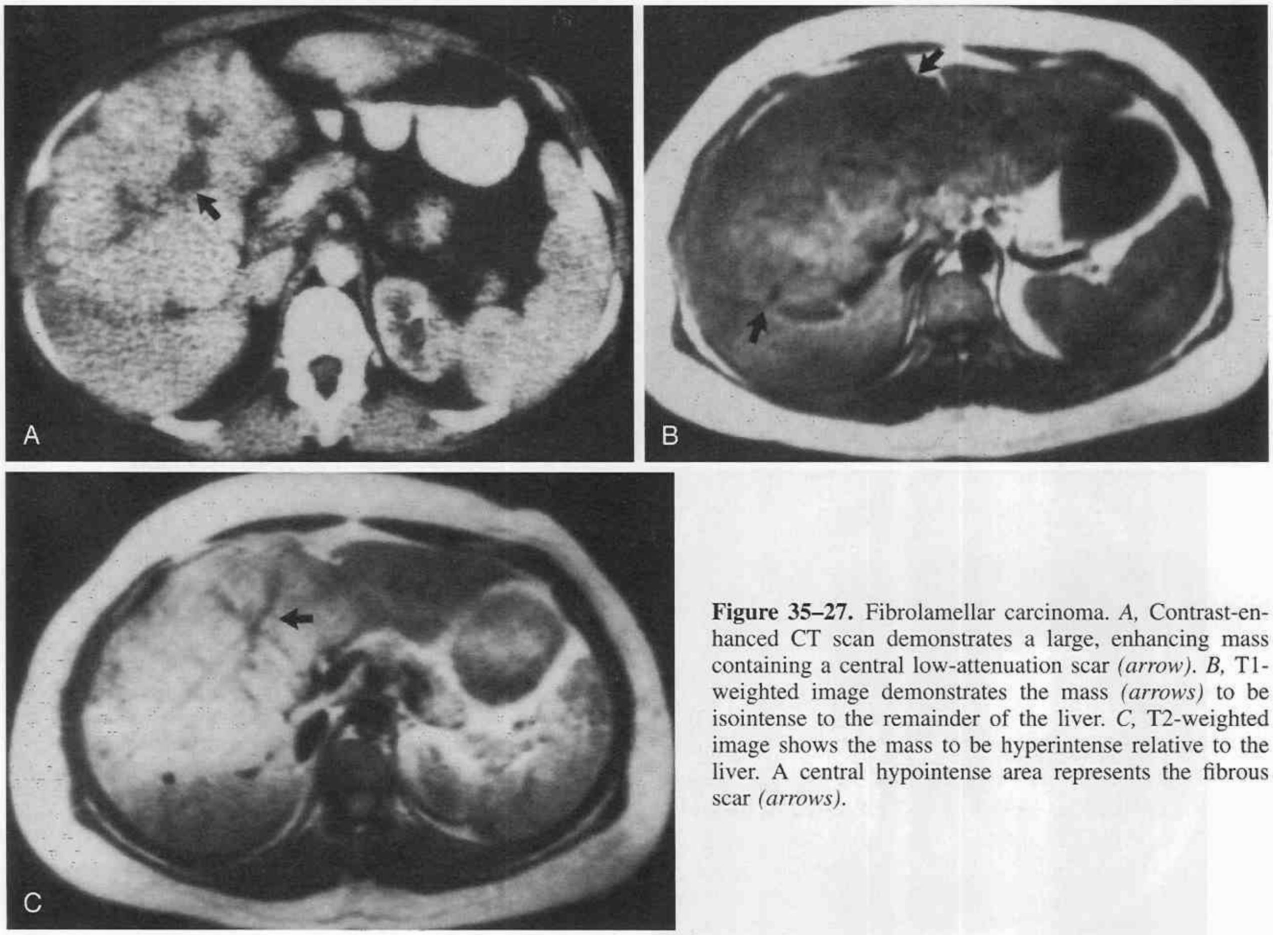

Figure 35–27. Fibrolamellar carcinoma. *A,* Contrast-enhanced CT scan demonstrates a large, enhancing mass containing a central low-attenuation scar *(arrow)*. *B,* T1-weighted image demonstrates the mass *(arrows)* to be isointense to the remainder of the liver. *C,* T2-weighted image shows the mass to be hyperintense relative to the liver. A central hypointense area represents the fibrous scar *(arrows)*.

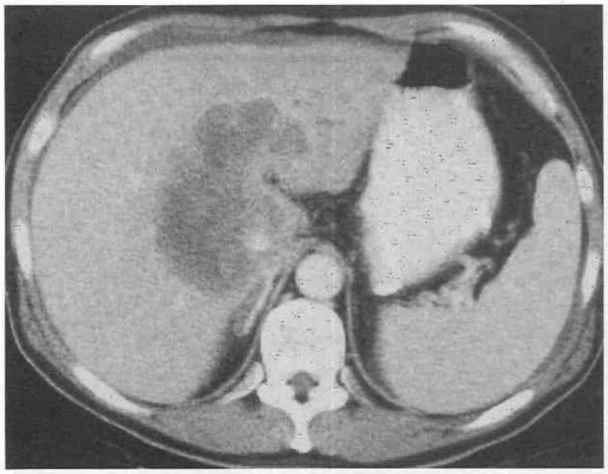

Figure 35–28. Intrahepatic cholangiocarcinoma in a 45-year-old man. Contrast-enhanced CT scan demonstrates a large central, predominantly hypointense mass with peripheral enhancement. The lobulated mass encases the inferior vena cava, which remains patent.

Intrahepatic Cholangiocarcinoma

Intrahepatic cholangiocarcinoma (I-CAC), an adenocarcinoma that originates in the small intrahepatic ducts, represents approximately 10% of all cholangiocarcinomas.[49, 128, 172] These tumors are usually large, firm masses with abundant fibrous tissue. Rarely do they contain internal necrosis or hemorrhage.[214] Mucin and calcification are often demonstrated microscopically, and desmoplastic reaction may be prominent.

The second most common primary hepatic malignancy in adults, I-CAC is usually discovered in the seventh decade of life, with a slight male predominance.[49] Symptoms are often vague until the tumor has enlarged, causing abdominal pain and a palpable mass. Jaundice is rarely a presenting symptom because the tumor arises in the peripheral biliary ducts.

On unenhanced CT scans, I-CAC usually has the appearance of a homogeneous, hyperdense mass.[33, 109, 113, 254] Mild, diffuse centripetal enhancement is often seen after IV contrast administration, with persistent, small, low-attenuation areas representing internal fibrosis. When these lesions are peripheral, associated capsular retraction may occur as a result of its fibrous nature. Satellite nodules and tumor extension through the hepatic capsule with invasion of adjacent organs may be present. Encasement of large vascular structures, such as the portal and hepatic veins, is often present but usually without tumor thrombus (Figs. 35–28 and 35–29*A*).

MRI demonstrates I-CAC as a large central mass with irregular borders, hypointense on T1-weighted imaging and hyperintense on T2-weighted imaging relative to the liver (Fig. 35–29*B* and *C*).[63, 211] Small satellite nodules may be

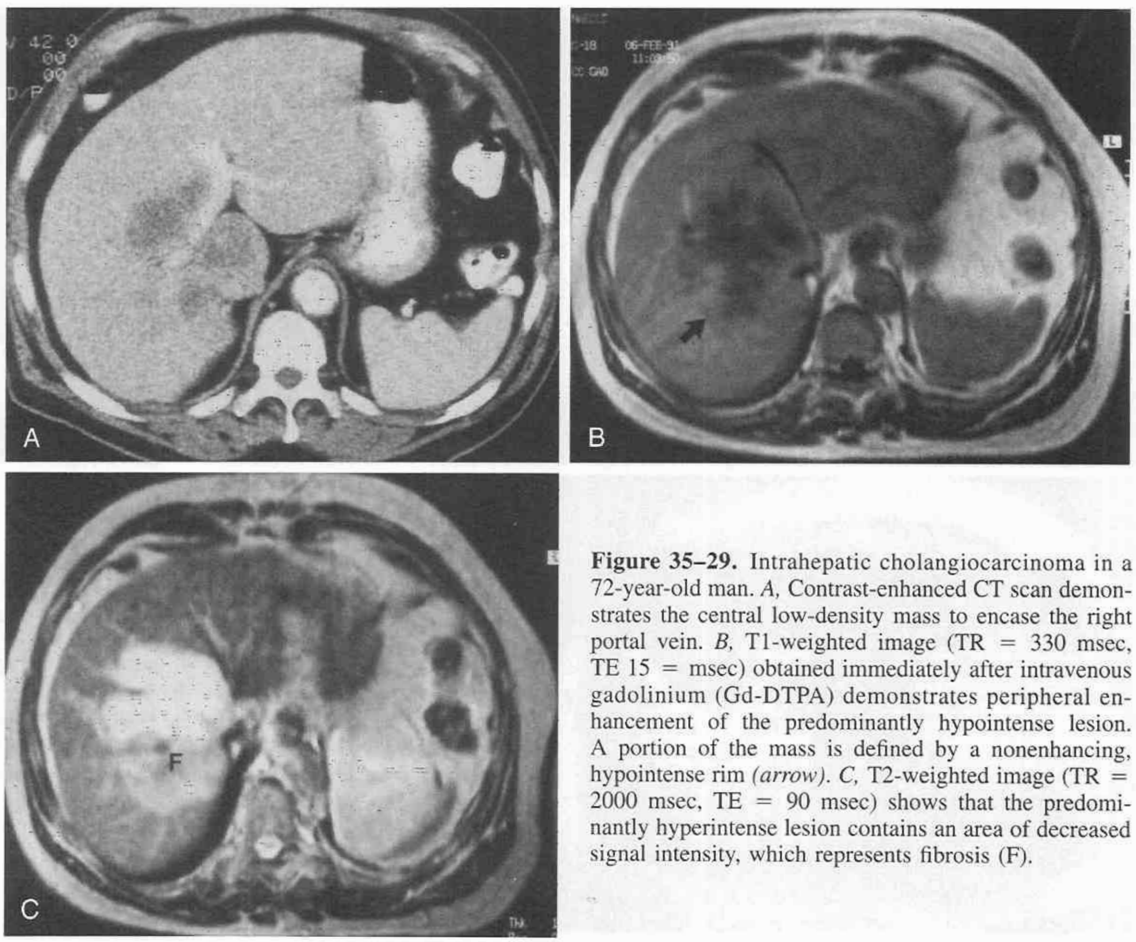

Figure 35–29. Intrahepatic cholangiocarcinoma in a 72-year-old man. *A,* Contrast-enhanced CT scan demonstrates the central low-density mass to encase the right portal vein. *B,* T1-weighted image (TR = 330 msec, TE 15 = msec) obtained immediately after intravenous gadolinium (Gd-DTPA) demonstrates peripheral enhancement of the predominantly hypointense lesion. A portion of the mass is defined by a nonenhancing, hypointense rim *(arrow)*. *C,* T2-weighted image (TR = 2000 msec, TE = 90 msec) shows that the predominantly hyperintense lesion contains an area of decreased signal intensity, which represents fibrosis (F).

seen. On T2-weighted images, large central areas of fibrosis in the mass cause hypointensity and an overall heterogeneous appearance. The periphery of I-CAC may be more hyperintense than its center on T2-weighted images, suggesting the presence of a central scar. Progressive, concentric enhancement is common after IV gadopentetate dimeglumine administration (see Fig. 35–29*B*). As in CT, this may result in the appearance of delayed enhancement relative to the liver parenchyma. This centripetal enhancement pattern spares central areas of fibrosis and reflects the presence of viable peripheral tumor. The typical finding of vascular encasement without tumor thrombus seen in I-CAC is well demonstrated by gradient-echo images and MR angiography.[211]

Biliary Cystadenoma and Cystadenocarcinoma

Two forms of a disease spectrum, biliary cystadenoma and cystadenocarcinoma are rare tumors. They represent only 5% of all intrahepatic cysts of bile duct origin, with most cases corresponding to the bile duct or simple cysts.[179] Cystadenocarcinoma is the overtly malignant form of the disease, whereas cystadenoma has a high propensity for recurrence and malignant transformation.[108, 274]

The tumors occur most often in middle-aged women and are probably congenital in origin because of the presence of aberrant bile ducts.[49] Although the tumors are most commonly mucinous, a serous variety is recognized. These tumors contain locules that are lined by columnar, cuboidal, or flattened epithelium. Papillary areas and polypoid projections are often present. Focal calcification within the well-formed wall is occasionally seen. Biliary-type epithelium overlies a compact mesenchymal stroma in the cystadenoma, whereas malignant epithelial cells line the cysts of cystadenocarcinoma.

Grossly, the tumor is usually solitary but is often large, measuring up to 30 cm in diameter.[49] Multiple communicating locules of varying size are contained within the tumor and have a predominantly smooth lining with papillary excrescences and mural nodules projecting from the cyst wall. There is no consistent distinction grossly between the benign and malignant forms of the disease.

On CT scans, both cystadenomas and cystadenocarcinomas are seen as large, low-attenuation intrahepatic masses, often with thick, irregular walls (Figs. 35–30 and 35–31*A*).[4, 39, 131] Although cystadenocarcinomas tend to have more solid components and are more irregular than cystadenomas, these signs are not reliable. The presence of adenopathy or metastatic disease usually indicates cystadenocarcinoma.

MRI shows the multiple locules of cystadenoma or cystadenocarcinoma to be of variable signal intensity on T1-weighted and T2-weighted images, depending on the protein content or presence of hemorrhage within the locules.[192, 212] Septations are seen as low-intensity bands (Fig. 35–31*B* and *C*).[124]

Angiosarcoma

Angiosarcoma of the liver is a tumor that consists of malignant endothelial lining cells, occurring primarily in adults exposed to chemical agents and radiation.[49, 113, 130] The malignant endothelial cells line vascular channels of sizes vary from cavernous to capillary and attempt to form sinusoids. When associated with thorium dioxide (Thorotrast) exposure, the Thorotrast particles may be found within the malignant endothelial cells.

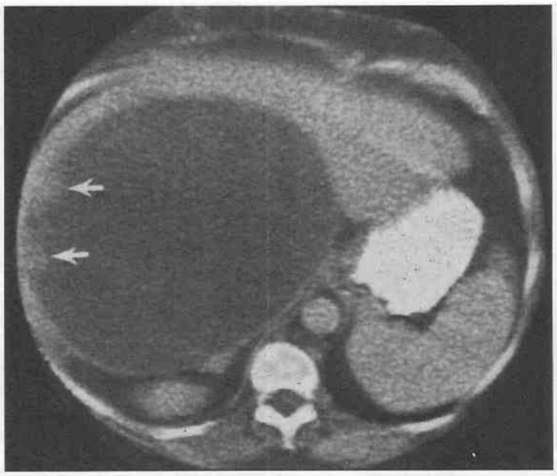

Figure 35–30. Biliary cystadenocarcinoma. Contrast-enhanced CT scan shows this large cystic mass of the liver containing mural nodules *(arrows)*, distinguishing it from a large simple cyst.

Grossly, most angiosarcomas are multiple and are characterized by internal hemorrhage.[130] When the lesion appears as a large single mass, it often has cystic areas of bloody debris and does not have a capsule. Concurrent cirrhosis is common.

A rare neoplasm that is 30 times less common than HCC, angiosarcoma occurs most often in men in the seventh decade of life.[103] It is associated with previous exposure to radiation, Thorotrast, or toxins such as polyvinyl chloride (PVC), arsenic, and steroids; it has also been associated with hemochromatosis. Patients may present with weakness, weight loss, abdominal pain, ascites, and hepatomegaly. Platelet segregation in a large angiosarcoma may cause thrombocytopenia. Rupture with hemoperitoneum may occur in rare instances.[104, 148]

On unenhanced CT scans, single or multiple hypodense masses may appear except for slightly hyperdense nodules seen with recent hemorrhage.[143, 234] After IV contrast administration, a centripetal enhancement pattern similar to that seen with hemangioma has been reported.[234] When related to Thorotrast exposure, the reticular pattern of thorium dioxide (Thorotrast) deposition may be well visualized in the liver, with significantly increased density in the spleen and lymph nodes (Fig. 35–32*A* and *B*). If rupture occurs, hemoperitoneum may be demonstrated.[153]

In our experience, circumferential displacement of Thorotrast to the periphery of a nodule is a characteristic finding of angiosarcoma. Even though the literature on the MRI appearance of angiosarcoma is limited,[211] we have found that angiosarcoma usually appears as a hypointense mass relative to the liver on T1-weighted images and is hyperintense on T2-weighted images (Fig. 35–32*C* and *D*). Peripheral rim enhancement is present after administration of IV gadolinium, with persistent enhancement, seen in

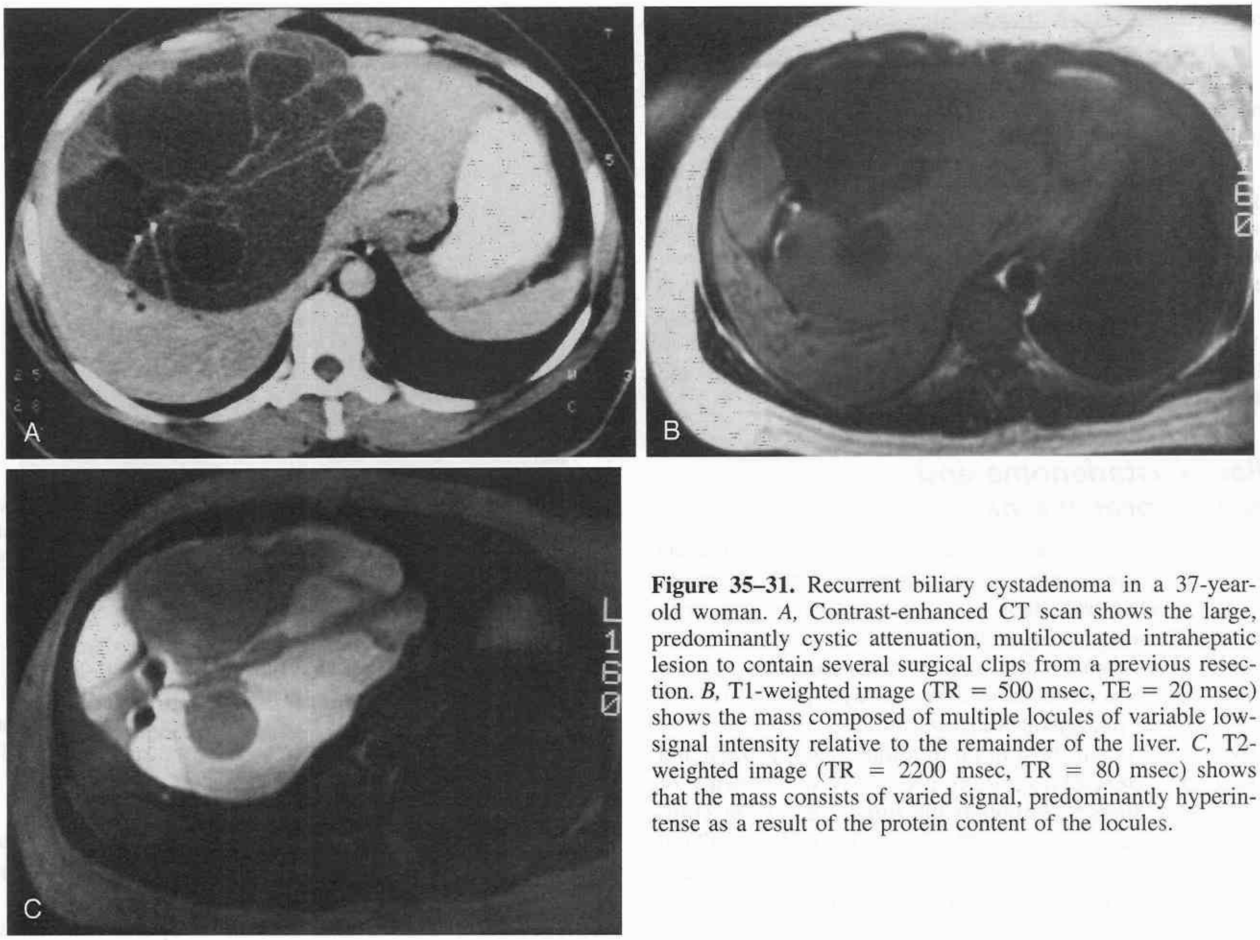

Figure 35–31. Recurrent biliary cystadenoma in a 37-year-old woman. *A,* Contrast-enhanced CT scan shows the large, predominantly cystic attenuation, multiloculated intrahepatic lesion to contain several surgical clips from a previous resection. *B,* T1-weighted image (TR = 500 msec, TE = 20 msec) shows the mass composed of multiple locules of variable low-signal intensity relative to the remainder of the liver. *C,* T2-weighted image (TR = 2200 msec, TR = 80 msec) shows that the mass consists of varied signal, predominantly hyperintense as a result of the protein content of the locules.

delayed images that may mimic the appearance of hemangioma (Fig. 35–32*E*). The presence of Thorotrast is not detectable by MRI.

Epithelioid Hemangioendothelioma

Epithelioid hemangioendothelioma (EHE) is a very rare malignant hepatic neoplasm of vascular origin.[49] EHE develops in adults and should not be confused with infantile hemangioendothelioma, which occurs in young children. These tumors are often multiple, consisting of neoplastic cells that infiltrate the sinusoids, hepatic veins, and portal vein branches. Although usually an incidental finding, EHE may occasionally cause jaundice, hepatic failure, and rupture with hemoperitoneum.[107] It is more common in women than men.

The prognosis of EHE is more favorable than that of angiosarcoma, with extrahepatic metastases occurring in only one third of reported cases. Metastatic or synchronous lesions may also be found in the lungs and soft tissues.

On unenhanced CT scans, EHE appears as multiple peripheral nodules that coalesce to form large, confluent, low-attenuation masses.[168, 201, 258] After IV contrast administration, peripheral portions of the mass become isodense relative to the liver, thus resulting in less sensitive identification of tumor extent compared with that of unenhanced scans. The lesions often cause capsular retraction or flattening and may contain calcifications. A peripheral hypodense hypovascular rim and venous invasion may be seen after contrast administration.

MRI of epithelioid hemangioendothelioma accurately depicts tumor extent.[168, 258] Variable signal intensity, predominantly low to isointense relative to the liver, has been described on T1-weighted images. On T2-weighted images, the lesions are of heterogeneous increased signal intensity. On both T1-weighted and T2-weighted images, peripheral low-signal-intensity rims are often seen.

After IV Gd-DTPA administration, concentric layers of alternating signal intensity are seen with an outer, nonenhancing hypointense rim that corresponds with the hypovascular, hypodense rim seen with contrast-enhanced CT. Capsular retraction or flattening over the multiple peripheral nodules, which coalesce into confluent masses, is revealed by MRI similar to the images depicted by CT.

Mesenchymal Sarcoma

Tumors that arise in the mesenchymal elements of the liver are very rare. These include angiomyosarcoma, leiomyosarcoma, fibrous sarcoma, malignant fibrous histiocytoma, and rhabdomyosarcoma.[45, 69, 154] These mesenchymal sarcomas usually appear as large, solitary masses that may be smoothly lobulated and contain fibrous septa, often with central necrosis and hemorrhage.

CT usually demonstrates primary hepatic sarcoma as a

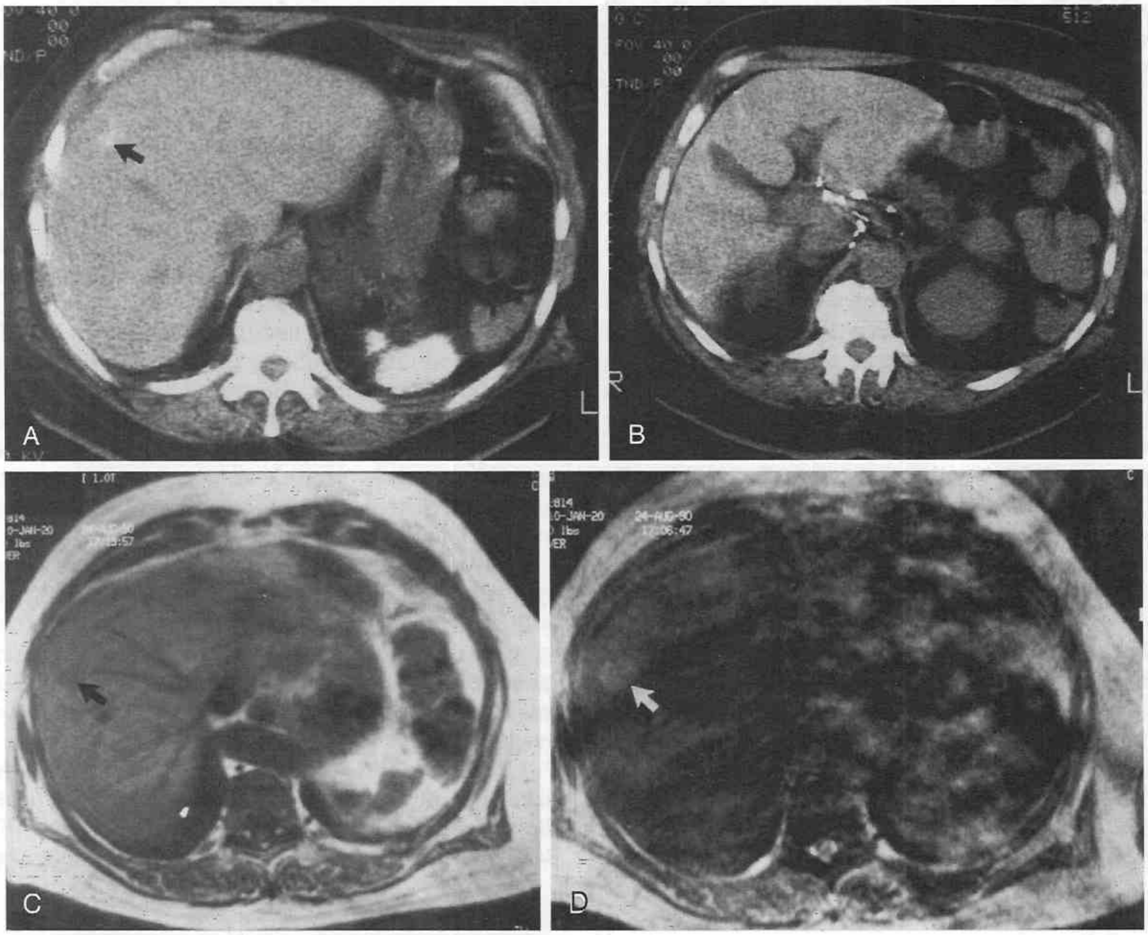

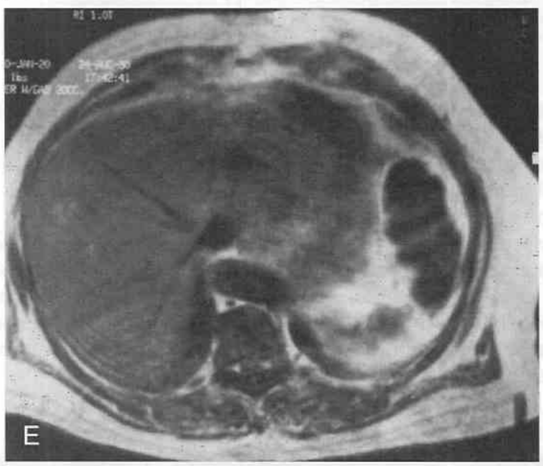

Figure 35–32. Angiosarcoma in a 70-year-old man with history of thorium dioxide (Thorotrast) exposure.

A, Unenhanced CT scan without oral contrast reveals that the spleen is of increased attenuation. High-density Thorotrast is retained in the right hepatic lobe *(arrow)*.

B, Unenhanced CT scan at a more caudal level to that in *A* shows other areas of high attenuation in the liver as a result of retained Thorotrast and high-attenuation nodes containing Thorotrast in the porta hepatis.

C, T1-weighted image (TR = 500 msec, TE = 15 msec) demonstrates a 1-cm hypointense lesion *(arrow)* not demonstrated by CT.

D, T2-weighted image (TR = 2000 msec, TE = 80 msec) shows the lesion to be of slightly increased signal intensity *(arrow)*.

E, T1-weighted image (TR = 501 msec, TE = 15 msec) following intravenous gadolinium (Gd-DTPA) demonstrates persistent enhancement of the lesion.

large, noncalcified, low-attenuation homogeneous mass on unenhanced scans. After IV contrast administration, there is inhomogeneous peripheral enhancement. The MRI appearance is nonspecific, with the mass having low signal intensity relative to the liver on T1-weighted images and increased signal intensity on T2-weighted images.[211]

Hepatoblastoma

Hepatoblastoma, the most common primary liver neoplasm of childhood, is a malignant neoplasm of hepatocyte origin that often contains mesenchymal tissues.[105] It is classified histologically as *epithelial* or *mixed (epithelial-mesenchymal)*.[49] The epithelial hepatoblastoma is composed of malignant fetal and/or embryonal hepatocytes. The mixed hepatoblastoma consists of both an epithelial (hepatocyte) component and a mesenchymal component composed of primitive mesenchymal tissue and osteoid material, cartilage, or both.[268]

This histologic classification is useful for predicting clinical outcome. The epithelial type, especially that with a fetal hepatocyte predominance, is associated with the best

prognosis.[94, 268] Tumors with the embryonal epithelial cell type carry a poor prognosis. A rare anaplastic form of hepatoblastoma has the poorest prognosis of all types.[49]

Grossly, the hepatoblastoma is usually a large, solitary, well-circumscribed mass with a nodular or lobulated surface. In 20% of cases, it may be multifocal.[49] Epithelial hepatoblastomas are homogeneous internally; mixed hepatoblastomas with osteoid and cartilage may have large calcifications, fibrotic bands, and an overall heterogeneous appearance.[268]

Hepatoblastoma usually is found in the first 3 years of life; the peak incidence is between 18 and 24 months of age. However, it may be present at birth or may develop in adolescents and young adults.[94] It is more frequent in boys than girls. The child with hepatoblastoma may present with abdominal swelling, often with anorexia or weight loss. The serum α-fetoprotein level is usually significantly elevated. Metastatic disease to the lungs is often present at diagnosis.[51]

Hepatoblastomas appear on unenhanced CT scans as large, solid, low-attenuation masses that may contain calcifications.[51] Bands of fibrosis, when present, may cause a lobulated pattern. Calcification is most extensive in the mixed form. Following IV contrast administration, enhancement may be extensive because of the tumor's hypervascular nature. Vascular invasion may be present (Fig. 35–33*A*).

With MRI, the hepatoblastoma is hypointense relative to the liver on T1-weighted images and hyperintense on T2-weighted images (Fig. 35–33*B* and *C*).[21] Fibrotic septa, when present, appear as low-signal-intensity bands on T2-weighted images. Vascular invasion when present is well demonstrated by gradient-echo imaging or MR angiography.

Undifferentiated Embryonal Sarcoma

Undifferentiated embryonal sarcoma (UES) is a malignant tumor and the fourth most common hepatic neoplasm of childhood, after hepatoblastoma, IHE, and HCC.[243] It consists of primitive, undifferentiated spindle cells that resemble primitive (embryonal) cells with frequent mitoses and a myxoid stroma. Grossly, UES is a large, usually solitary mass having well-defined margins with an occasional pseudocapsule. Internally, it has various-sized cystic areas that contain necrotic debris, hemorrhage, blood, or gelatinous material.[102, 243] Predominantly cystic tumors are more common than solid tumors.

UES usually occurs in older children, 6 to 10 years of age, with 90% of patients below age 15 years. UES occurs with almost equal frequency in boys and girls.[243] Presenting symptoms are usually a painful abdominal mass; fever, jaundice, weight loss, and gastrointestinal complaints are less common. Serum α-fetoprotein levels are usually not elevated.

CT shows UES to be a low-attenuation mass that may have a cystic or heterogeneous appearance, depending on the degree of necrosis and hemorrhage present (Fig. 35–34*A*).[218] Septa and solid portions of the tumor appear as

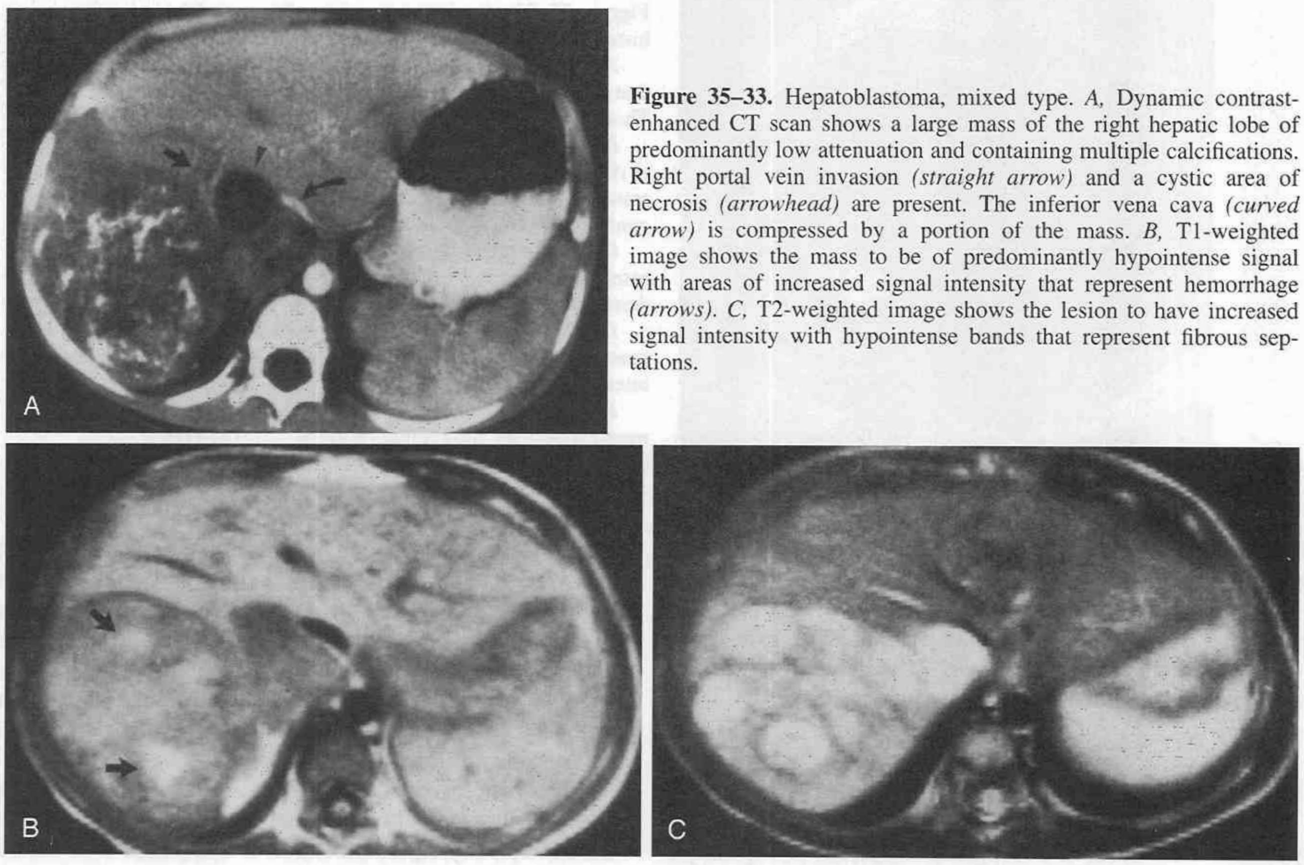

Figure 35–33. Hepatoblastoma, mixed type. *A,* Dynamic contrast-enhanced CT scan shows a large mass of the right hepatic lobe of predominantly low attenuation and containing multiple calcifications. Right portal vein invasion *(straight arrow)* and a cystic area of necrosis *(arrowhead)* are present. The inferior vena cava *(curved arrow)* is compressed by a portion of the mass. *B,* T1-weighted image shows the mass to be of predominantly hypointense signal with areas of increased signal intensity that represent hemorrhage *(arrows)*. *C,* T2-weighted image shows the lesion to have increased signal intensity with hypointense bands that represent fibrous septations.

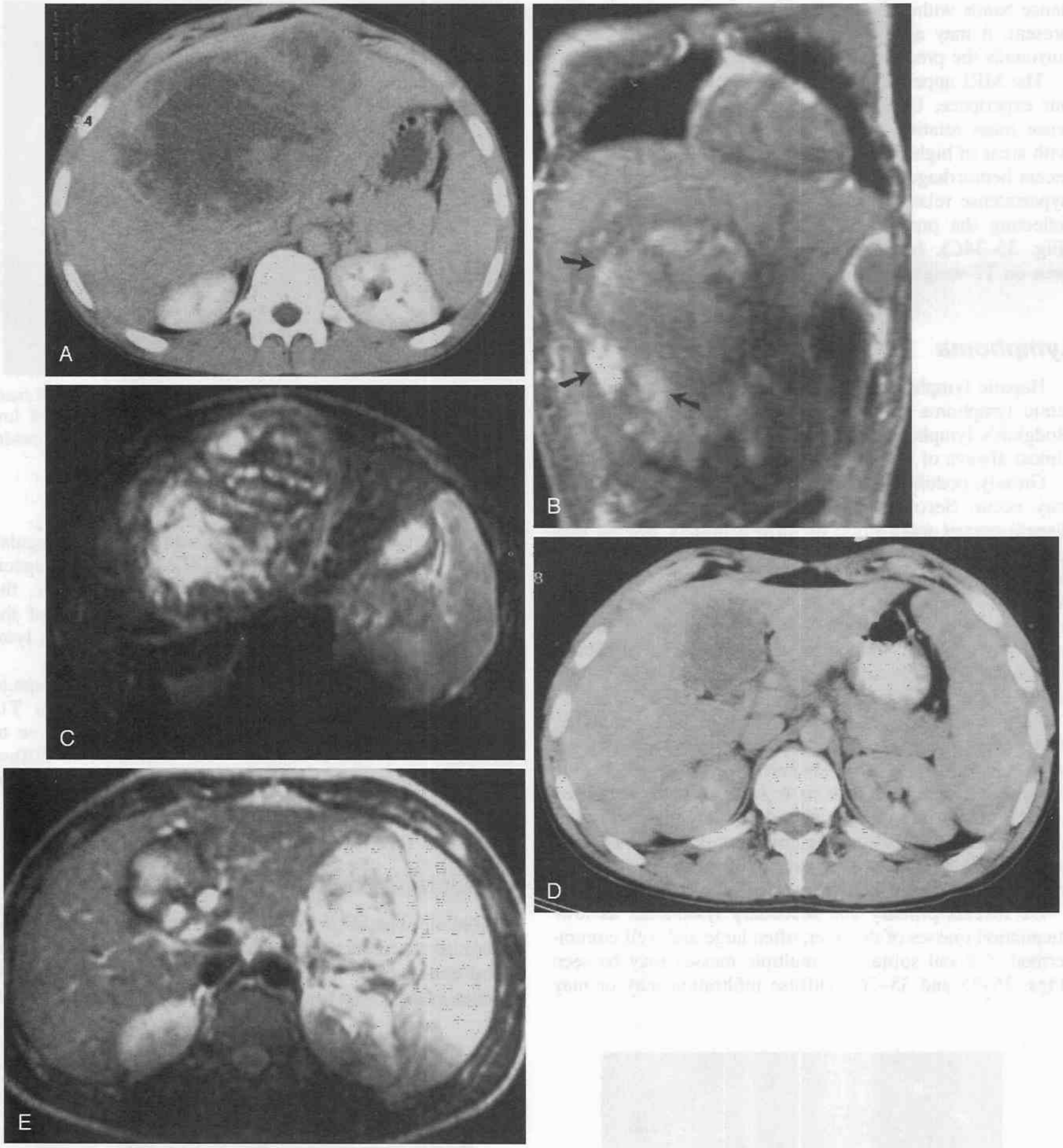

Figure 35–34. Undifferentiated embryonal sarcoma in a 15-year-old boy.

A, Contrast-enhanced CT scan demonstrates a very large, central, predominantly low-attenuation mass with a very heterogeneous appearance.

B, Coronal T1-weighted image (TR = 400 msec, TE = 12 msec) demonstrates the large mass to have areas of high signal intensity, corresponding to hemorrhage *(arrows).*

C, T2-weighted image (TR = 2000 msec, TE = 90 msec) shows the mass to be of predominantly very high signal intensity.

D, After chemotherapy, this contrast-enhanced CT scan demonstrates a significant reduction in the size of the mass.

E, T2-weighted image (TR = 2200 msec, TE = 80 msec) after chemotherapy shows the mass continuing to be of mixed signal intensity. The hypointense rim, which represents a pseudocapsule, is demonstrated as low signal intensity. Following the excellent response to chemotherapy, the mass was successfully resected.

dense bands within the cystic tumor. If a pseudocapsule is present, it may appear as a thin rim of dense tissue that surrounds the predominantly cystic mass.

The MRI appearance of UES has not been reported. In our experience, UES appears as a predominantly hypointense mass relative to the liver on T1-weighted images, with areas of high signal intensity corresponding to areas of recent hemorrhage (Fig. 35–34*B*). The mass is significantly hyperintense relative to the liver on T2-weighted images, reflecting the predominantly cystic nature of the lesion (Fig. 35–34*C*). Internal debris and septations are easily seen on T2-weighted images.

Lymphoma

Hepatic lymphoma usually occurs in the setting of systemic lymphoma in both Hodgkin's disease and in non-Hodgkin's lymphoma. Rarely, it may be a primary lesion, almost always of the non-Hodgkin's large-cell type.[222]

Grossly, nodular and diffuse forms of hepatic lymphoma may occur. Secondary hepatic lymphoma of Hodgkin's disease occurs more often as diffuse miliary lesions than as focal masses. Hodgkin's disease of the liver is almost always associated with splenic involvement, with an increased likelihood of hepatic involvement when splenic involvement is extensive.[30, 91] In both Hodgkin's disease and non-Hodgkin's lymphoma, the portal area is typically involved initially because this is the region where lymphatic tissue of the liver is present.

Although primary hepatic lymphoma was previously found most frequently in middle-aged white men, today it is found with increasing frequency in patients who are immunocompromised, such as organ transplant recipients or patients with acquired immunodeficiency syndrome (AIDS).[233] The liver may or may not be enlarged, and patients may present with right upper quadrant pain or a tender mass of the upper abdomen.[20]

CT reveals primary and secondary lymphoma as low-attenuation masses of the liver, often large and well circumscribed.[231] Focal solitary or multiple masses may be seen (Figs. 35–35 and 35–36). Diffuse infiltration may or may not cause hepatomegaly and may be difficult to distinguish from normal liver tissue (Fig. 35–37). Whereas the specificity of CT for hepatic lymphoma is almost 90%, the sensitivity approaches only 60%, mainly because of the difficulty in detecting the infiltrative form of hepatic lymphoma.[35, 284]

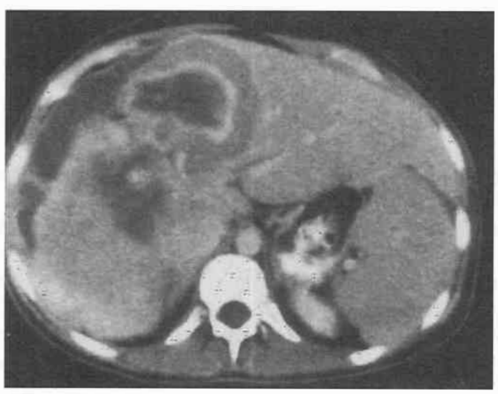

Figure 35–35. Primary hepatic lymphoma. The contrast-enhanced CT scan shows a large mass of varying attenuation, with contrast enhancement of the tumor lining the necrotic central component. The outer zone of hypovascular tumor remains relatively unenhanced.

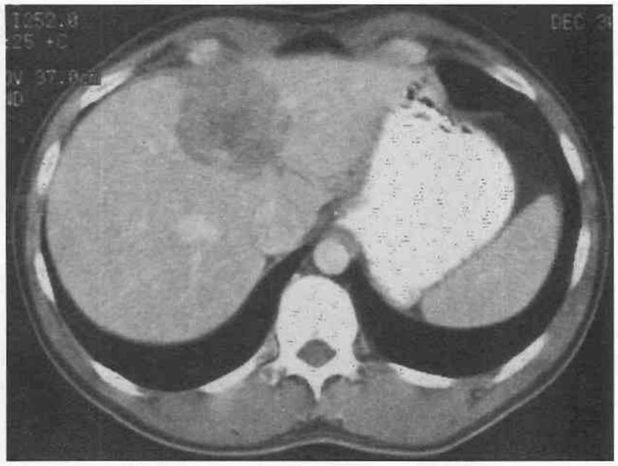

Figure 35–36. Non-Hodgkin's lymphoma in a 34-year-old man. Contrast-enhanced CT scan demonstrates a focal mass of low attenuation that extended into the portal region on more caudal images.

MRI demonstrates focal masses of hepatic lymphoma to be of low signal intensity relative to the liver on T1-weighted images and of high signal intensity relative to liver on T2-weighted images.[272] As with CT, the diffuse infiltrative form of hepatic lymphoma is not reliably detected by MRI.

Metastatic Disease

Hepatic metastatic disease is the most common malignancy of the noncirrhotic liver, surpassed in incidence of focal lesions only by hemangioma, focal fatty change, and simple cysts. Metastases occur 30 times more often than

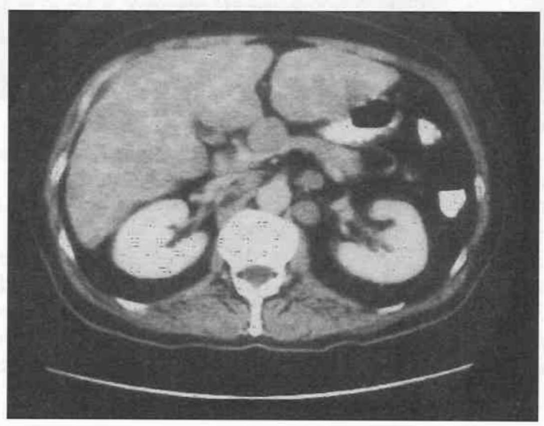

Figure 35–37. Diffuse infiltrative lymphoma. Contrast-enhanced CT scan demonstrates diffuse involvement of the liver. Lymphadenopathy is present.

other malignancies in the noncirrhotic liver. In the cirrhotic liver, however, HCC remains about nine times more common than metastatic disease.[161]

The liver is second in prevalence only to regional lymph nodes as a site of metastatic disease. Approximately 25% to 50% of all patients who die of malignant disease have metastatic disease of the liver at autopsy. The most common primary neoplasms to cause hepatic metastases are colon (42%), stomach (23%), pancreas (21%), breast (14%), and lung (13%). A silent primary neoplasm with hepatic metastasis is most often found to be a result of pancreatic, stomach, or lung carcinomas. The highest percentages of liver metastases occur in primary carcinomas of the gallbladder, pancreas, colon, and breast; the lowest occurs in prostate carcinoma.[59, 60]

In patients who died of metastatic disease of the liver, approximately 50% had signs or symptoms of liver disease. Hepatomegaly (31%) is the most common finding, followed by ascites (18%) and jaundice (14.5%). Liver function tests are very insensitive in the detection of hepatic metastatic disease, with normal results in 25% to 50% of patients with metastases. These results may be abnormal because of parenchymal replacement by tumor, biliary ductal obstruction, chemotherapy, or hepatotoxicity. Therefore, radiologic imaging has become essential in the evaluation of hepatic metastatic disease.[85, 269, 276]

Hepatic metastases may vary in size, consistency, uniformity of growth, response of surrounding tissue, and vascularity.[59, 60] Lesions may be infiltrative, expansive, or miliary. The primary source of metastasis and the mode of spread influence all of these factors. Individual metastatic liver lesions may differ greatly in appearance in the same patient because of variations in cellular differentiation, fibrosis, necrosis, hemorrhage, and blood supply (Fig. 35–38). This is most common in the vascular metastatic tumors of renal cell carcinoma, carcinoid, choriocarcinoma, and some types of lung cancer.

A zone of venous stasis may be observed to surround a metastatic lesion, extending up to 1 cm, in approximately 25% of patients.[59, 60] The zone is uniformly circumferential, and either all or none of the metastatic lesions show this finding in a given patient. This zone of venous stosis is seen most commonly with lung cancer and least commonly with colon carcinoma.

Tumor thrombi that occlude the portal or hepatic vein may be seen in approximately 7% to 15% of patients with hepatic metastatic disease.[56, 57] When the large portal veins are penetrated, metastases disseminate throughout peripheral portal branches. When the hepatic veins are penetrated, pulmonary metastases may result.

The vascular supply of liver metastases is almost entirely from the hepatic artery.[1] Although hepatic metastases from gastrointestinal tract neoplasms originally derive their blood supply from the portal vein, their blood supply progressively becomes arterial. If therapeutic arterial ligation is performed, however, the blood supply may revert to the portal vein. Metastases may develop calcification that is detectable by CT scanning in the presence of mucin, necrosis, and phosphatase activity. This is most commonly seen in metastases of mucinous adenocarcinomas of the colon, pancreas, and stomach.

Diagnostic challenges in the radiologic evaluation of metastatic disease include staging and follow-up in patients with a known malignancy and the evaluation of resectability in patients with solitary or few metastases (Fig. 35–39). Dynamic CT during the bolus administration of IV water-soluble iodinated contrast material has gained widespread acceptance as the primary modality in the staging and follow-up of metastatic disease. This technique exploits the attenuation difference between tumor and liver, which varies according to the phase of enhancement.

Most gastrointestinal malignancies are best demonstrated in the *portal-venous phase*, 60 to 70 seconds after the start of contrast injection, when they are hypoattenuating to the liver parenchyma. So-called hypervascular metastases (e.g., neuroendocrine tumors, carcinoid tumor, renal cell carcinoma) are best imaged in the *arterial phase*, 20 to 30 seconds after contrast injection, when they are hyperattenuating to the liver.

Paushter and coworkers found the bolus technique supe-

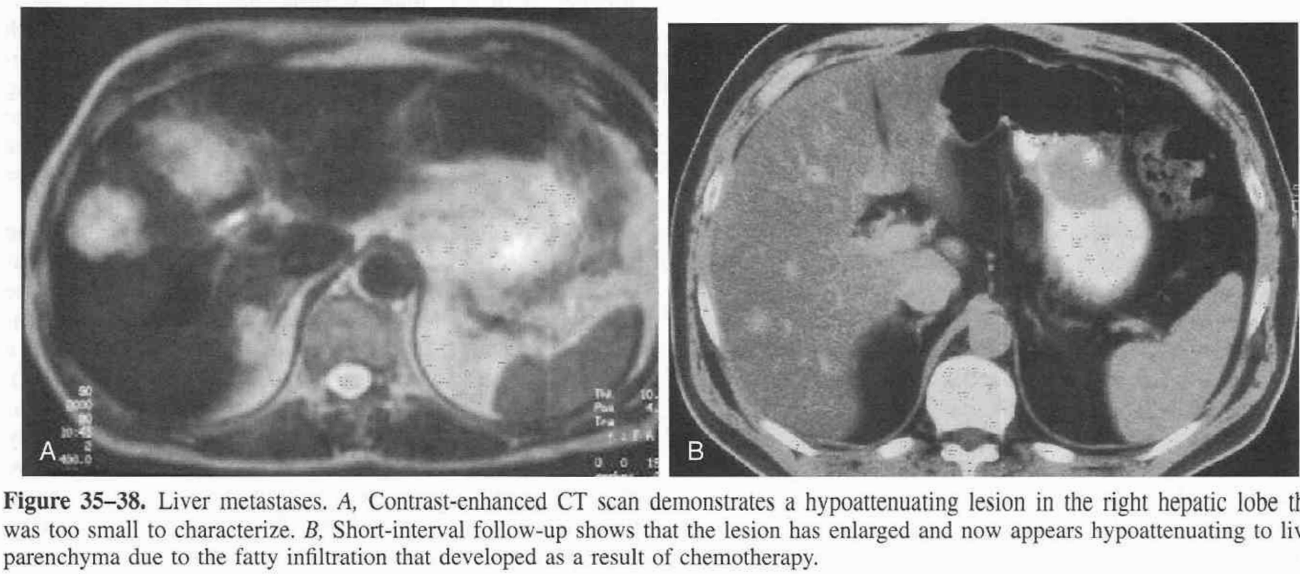

Figure 35–38. Liver metastases. *A,* Contrast-enhanced CT scan demonstrates a hypoattenuating lesion in the right hepatic lobe that was too small to characterize. *B,* Short-interval follow-up shows that the lesion has enlarged and now appears hypoattenuating to liver parenchyma due to the fatty infiltration that developed as a result of chemotherapy.

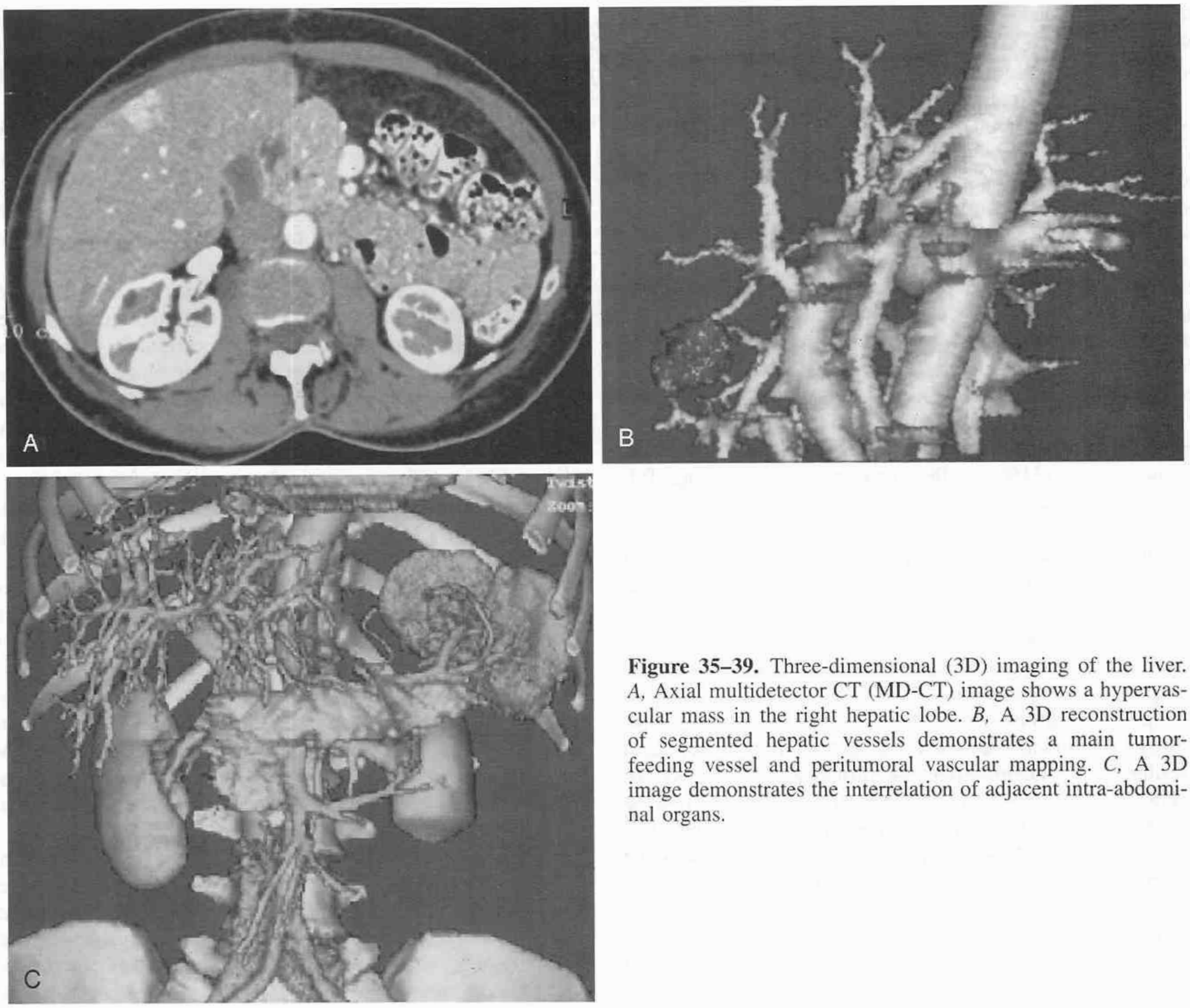

Figure 35–39. Three-dimensional (3D) imaging of the liver. *A,* Axial multidetector CT (MD-CT) image shows a hypervascular mass in the right hepatic lobe. *B,* A 3D reconstruction of segmented hepatic vessels demonstrates a main tumor-feeding vessel and peritumoral vascular mapping. *C,* A 3D image demonstrates the interrelation of adjacent intra-abdominal organs.

rior to the bolus–plus–drip-infusion technique for detecting metastases.[196] The latter technique results in scanning of the liver during the *equilibrium phase*, when the intravascular and interstitial concentrations of contrast material have equilibrated, yielding reduced difference in attenuation between lesions and normal liver than the bolus technique. Bolus injection rates of 3.0 and 4.5 mL/second produce higher CT hepatic contrast enhancement than those reported previously with other techniques.[99]

On CT scans, metastatic lesions may be hyperdense, isodense, hypodense, hypodense with peripheral enhancement, cystic, complex, calcified, or diffusely infiltrative. The CT appearance depends on tumor size, vascularity, hemorrhage, and necrosis as well as the type of IV contrast bolus and timing of scanning.[10, 14, 71, 78, 242]

Hyperdense metastases usually are hypervascular in nature, resulting from primary neoplasms such as melanoma, carcinoid, renal cell carcinoma, pancreatic islet cell tumor, choriocarcinoma, pheochromocytoma, and thyroid carcinoma. Breast and bronchogenic carcinoma may also occasionally result in hypervascular metastases. During contrast-enhanced CT scanning, the lesions may become isodense to the normal hepatic parenchyma, leading some authors to recommend that precontrast scans be obtained before contrast is given (Fig. 35–40).[27]

Some metastases may have a cystic appearance, with an attenuation of less than 20 Hounsfield units (HU). These "cystic" lesions may be seen with adenocarcinomas such as mucinous carcinoma of the colon and cystadenocarcinoma of the ovary (Fig. 35–41). Other neoplasms having rapid growth leading to necrosis and a cystic appearance include sarcoma, melanoma, carcinoid, and lung carcinoma (Fig. 35–42). Occasionally, a fluid-debris level may be present.[277]

Most liver metastases are hypodense relative to the normal liver. Because these lesions are usually hypovascular, administration of IV contrast material increases the density difference between the lesion and the normal parenchyma. Centrally, low attenuation may be present if a lesion has central necrosis or cystic change (Fig. 35–43). Rim enhancement representing the vascularized viable tumor periphery may be seen. The borders of metastases may be sharply defined, ill-defined, or nodular, and their shape may be ovoid, round, or irregular. Calcifications, when present, are well displayed by CT and are better seen on unenhanced scans (Fig. 35–44).[18, 227] Portal vein invasion

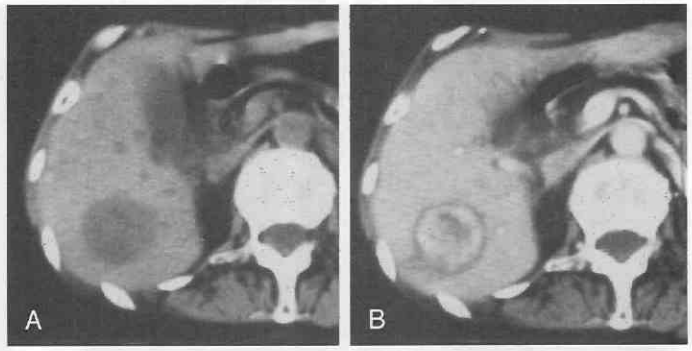

Figure 35–40. Hypervascular leiomyosarcoma metastases. *A,* Unenhanced CT scan demonstrates a large low-attenuation mass. *B,* Contrast-enhanced CT scan demonstrates central enhancement with a circumferential unenhancing peripheral rim.

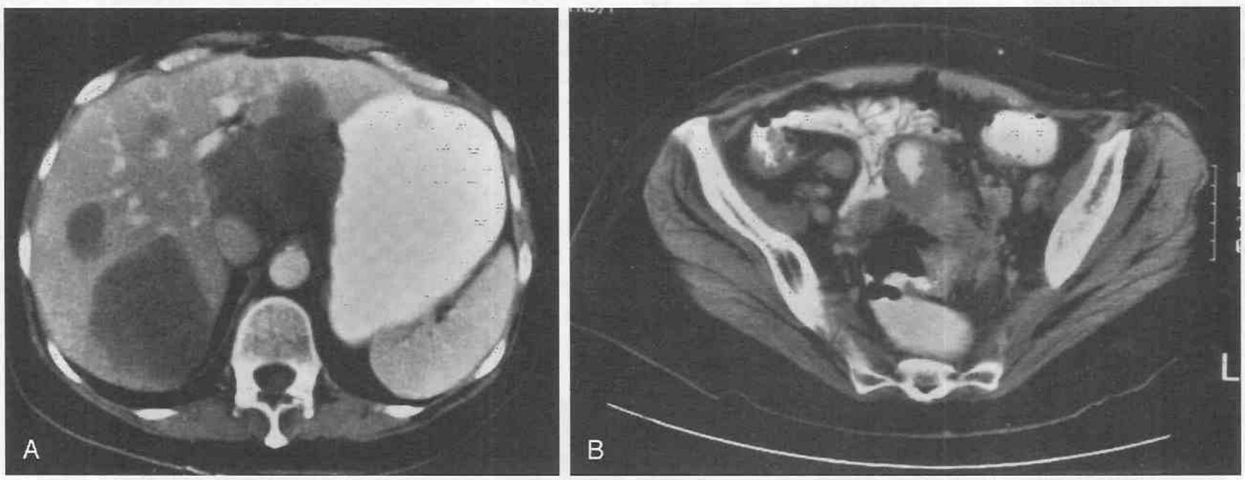

Figure 35–41. Mucinous carcinoma of the sigmoid colon and "cystic" metastases in a 56-year-old woman. *A,* Contrast-enhanced CT scan demonstrates multiple low-attenuation lesions of the liver that have a cystic appearance. *B,* A large mass of the sigmoid colon is demonstrated with evidence of regional spread.

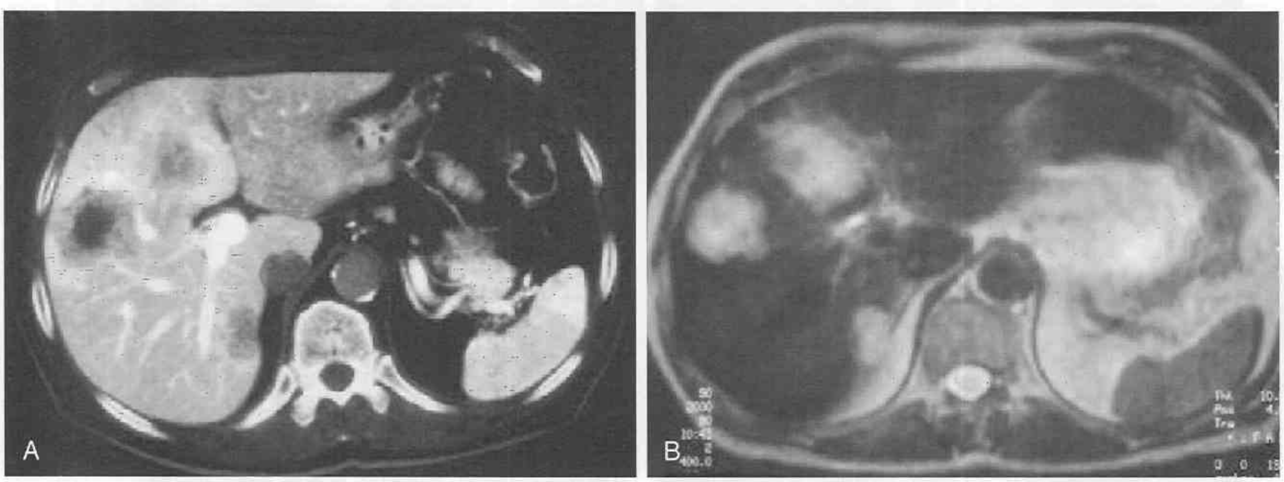

Figure 35–42. Liver metastases. *A,* Contrast-enhanced CT scan demonstrates multiple hepatic lesions, with abnormal enhancement involving most of the anterior segment. *B,* T2-weighted image after superparamagnetic iron oxide (SPIO) administration more clearly identifies the margins of the lesions.

Figure 35–43. Metastatic breast carcinoma in a 54-year-old woman. Contrast-enhanced CT scan shows a metastatic lesion having very low attenuation centrally, suggesting necrosis.

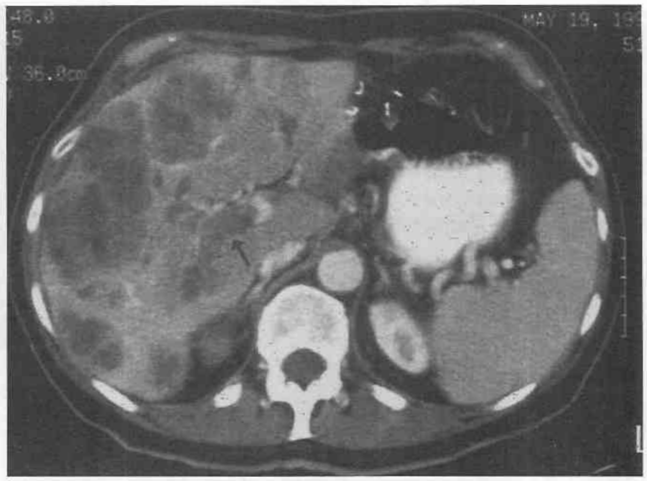

Figure 35–45. Extensive gastric adenocarcinoma metastases and portal vein thrombosis in a 68-year-old man. Contrast-enhanced CT scan shows multiple low-attenuation masses of the liver with thrombus present in the right portal vein *(arrow)*. Surgical clips are present related to previous partial gastrectomy.

is best displayed after IV contrast administration (Fig. 35–45).

Bernadino and coworkers showed that delayed CT scanning performed 4 to 6 hours after a IV bolus injection of a 60-g dose of iodinated contrast material led to increased lesion detection when compared with conventional dynamic bolus-enhanced hepatic CT scanning.[17] The delayed CT scanning technique is based on the normal hepatobiliary secretion of 1% to 2% of the iodine dose, which results in a difference of 20 HU in liver density between precontrast

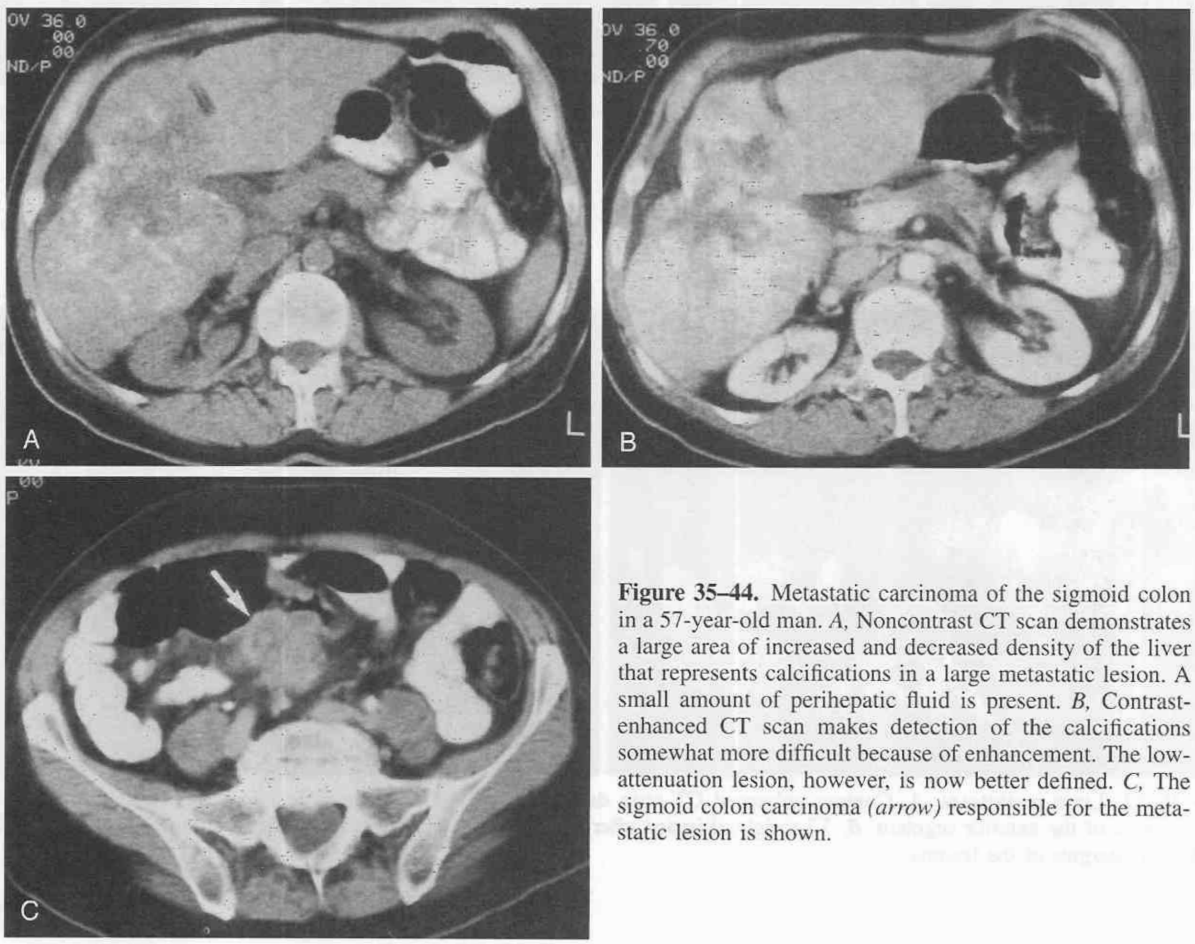

Figure 35–44. Metastatic carcinoma of the sigmoid colon in a 57-year-old man. *A,* Noncontrast CT scan demonstrates a large area of increased and decreased density of the liver that represents calcifications in a large metastatic lesion. A small amount of perihepatic fluid is present. *B,* Contrast-enhanced CT scan makes detection of the calcifications somewhat more difficult because of enhancement. The low-attenuation lesion, however, is now better defined. *C,* The sigmoid colon carcinoma *(arrow)* responsible for the metastatic lesion is shown.

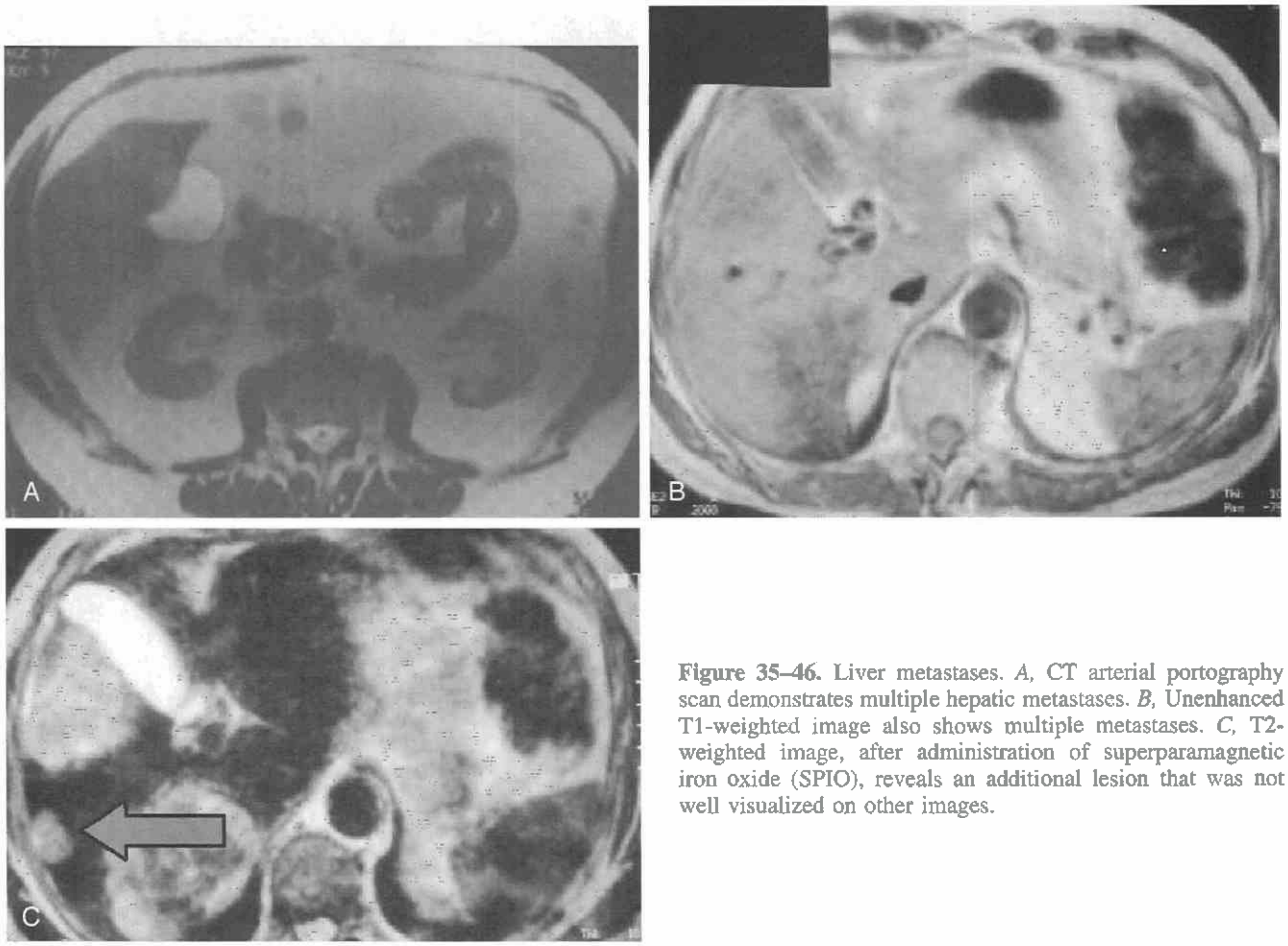

Figure 35–46. Liver metastases. *A*, CT arterial portography scan demonstrates multiple hepatic metastases. *B*, Unenhanced T1-weighted image also shows multiple metastases. *C*, T2-weighted image, after administration of superparamagnetic iron oxide (SPIO), reveals an additional lesion that was not well visualized on other images.

scans and those obtained 4 to 6 hours later. Iodine secretion is not naturally present in focal benign or malignant hepatic lesions not containing hepatocytes. Therefore, this technique results in lower attenuation of the lesion compared with the increased attenuation of the adjacent liver (Fig. 35–46). If liver function is abnormal, as in the setting of biliary obstruction or diffuse hepatic disease, this technique may be less successful.

CTAP, mentioned earlier, is a technique designed to maximize the difference in contrast enhancement between normal hepatic parenchyma (which receives approximately 75% to 80% of its blood supply from the portal vein), and hepatic neoplasms (which receive their blood supply from the hepatic artery). Iodinated contrast material is injected through a catheter placed in the superior mesenteric artery. This enhances normal hepatic parenchyma, although most hepatic lesions are hypoattenuating as a result of their predominantly arterial blood supply.

Although CTAP has gained some acceptance as a sensitive preoperative method of detecting liver metastases, with its great strength in its ability to detect lesions smaller than 1 cm in diameter,[8, 100, 182] a significant false-positive rate, stemming from benign lesions and perfusion variations in normal hepatic parenchyma, persists (Fig. 35–47). Peripheral wedge-shaped and flat perfusion defects are almost always benign. Benign perfusion defects have also been identified in two characteristic locations: (1) in the anteromedial aspect of the medial segment adjacent to the intersegmental fissure and (2) within the posterior aspect of the medial segment, immediately anterior to the porta hepatis.[197]

MRI is also used for staging and follow-up of metastatic disease. The T1 and T2 relaxation times of liver metastases vary greatly, depending on the primary tumor and on the degree of necrosis, hemorrhage, and vascularity. However, the T1 and T2 relaxation times of metastases are longer than those of normal liver and are usually shorter than those of simple cysts and hemangiomas (except in some hypervascular metastases). Many morphologic appearances of liver metastases have been described.

On T1-weighted images, metastatic liver lesions usually appear as low-signal-intensity masses. In some cases, there is a distinct central region of even lower signal intensity, a pattern often seen with larger lesions and with those that undergo necrosis. However, metastases containing mucin, fat, hemorrhage, or melanin may have a relatively high signal intensity on T1-weighted images.[277]

On T2-weighted images, most metastatic lesions have increased signal intensity. Spherical metastatic lesions with smooth, sharply defined borders and very high signal intensity have been described as having a "light bulb" appearance. This may be due to (1) complete tumor necrosis and liquefaction, (2) true cystic components, or (3) hypervascularity from primary tumors such as pheochromocytoma,

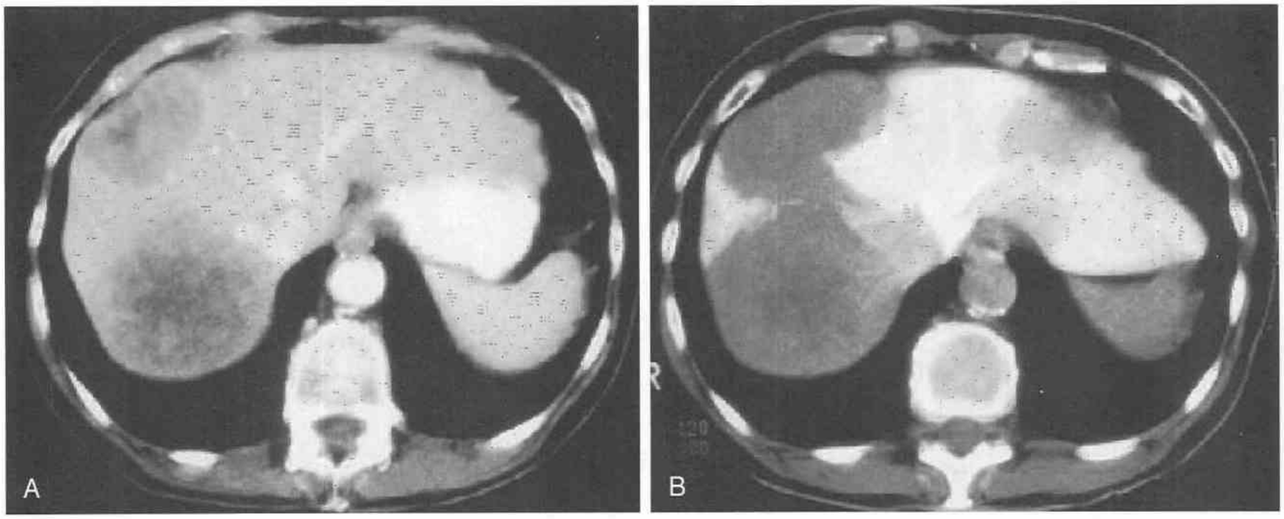

Figure 35–47. Liver metastases. *A*, Contrast-enhanced CT scan demonstrates two metastatic lesions in the right hepatic lobe. *B*, CT arterial portography image shows the same two lesions; however, the presence of a flow-related artifact in the left hepatic lobe suggests a third lesion.

carcinoid, and islet cell tumor.[84, 138, 191, 277] Some metastatic lesions appear to have a central area of high signal intensity surrounded by a rim of somewhat weaker signal intensity. This pattern is also commonly seen in large lesions and in those with necrosis.[138, 191, 277]

Other metastases have variable increased signal intensity on T2-weighted images with inhomogeneous and featureless contents. These amorphous lesions have outer margins that tend to be round and indistinct.[277] Some metastases may change in both size and shape with different pulse sequences. This may be due to peritumoral edema, which is caused by tumor compromise of the circulation of the more peripheral tissues.[277]

A pattern that is often described in colorectal metastases is a rim or "halo" on T2-weighted images of increased intensity from 2 to 10 mm in thickness, which encircles a lesion of somewhat lower signal intensity. The lower signal intensity may reflect the presence of fibrosis, coagulative necrosis, or mucin. The halo is probably a manifestation of increased water content. Although some suggest that it may represent peritumoral edema incited by tumor cell infiltration, more likely it represents viable tumor and should be considered when one is estimating tumor volume and planning resection.[138, 191, 277]

Compared with CT or ultrasound, gadolinium-enhanced MRI has been found to be more sensitive in detecting metastases. Compared with CTAP, MRI has similar sensitivity and shows better specificity for malignancy. Indications for MRI include patients for whom iodinated contrast is contraindicated (e.g., a history of serious reaction to contrast medium[206]) or additional characterization of lesions thought to represent fatty change or hemangioma.[61] With Gd-DTPA, hypervascular metastases can be distinguished from hemangioma because of the specific persistence of contrast enhancement seen in hemangiomas (Fig. 35–48).

Compared with CT and unenhanced MRI, IV SPIO shows improved detection rates of lesions (Figs. 35–49 to 35–51; see Fig. 35–46).[29] Compared with CTAP, IV SPIO is more accurate in detecting metastases. Additional liver specific contrast agents are being evaluated, including Gd-EOB-DTPA, Mn-DPDP, and Gd-BOPTA (Figs. 35–52 to 35–55).

Infectious Lesions

Bacterial (Pyogenic) Liver Abscess

Bacterial abscess of the liver may develop from several routes, most commonly via the biliary tree, secondary to ascending cholangitis from benign or malignant biliary obstruction.[6, 121] Other sources of abscess include:

1. Portal vein or superior mesenteric vein phlebitis related to appendicitis, diverticulitis, pancreatitis, or other gastrointestinal (GI) infectious source.
2. Arterial septicemia caused by endocarditis, pneumonitis, or osteomyelitis.
3. Direct extension from contiguous organs, such as a perforated ulcer, pneumonia, or pyelonephritis.
4. Trauma.
5. Iatrogenic causes.

In patients with diabetes mellitus, a cryptogenic abscess may occur with no identifiable source. Metastases may also become infected.

Anaerobic or mixed anaerobic and aerobic organisms account for most bacterial liver abscesses. Facultative gram-negative enteric bacilli, anaerobic gram-negative bacilli, and microaerophilic streptococci are often the responsible organisms. In adults, *Escherichia coli* is most commonly isolated, while *Staphylococcus* is most often isolated from pediatric liver abscesses.[25]

Although the incidence of pyogenic abscesses has decreased in the United States, these abscesses do remain the most common infectious lesion of the liver. Individuals between 40 and 60 years of age are most often affected, with a slight female predominance. Tender hepatomegaly, fever, malaise, rigors, weight loss, and nausea and vomiting

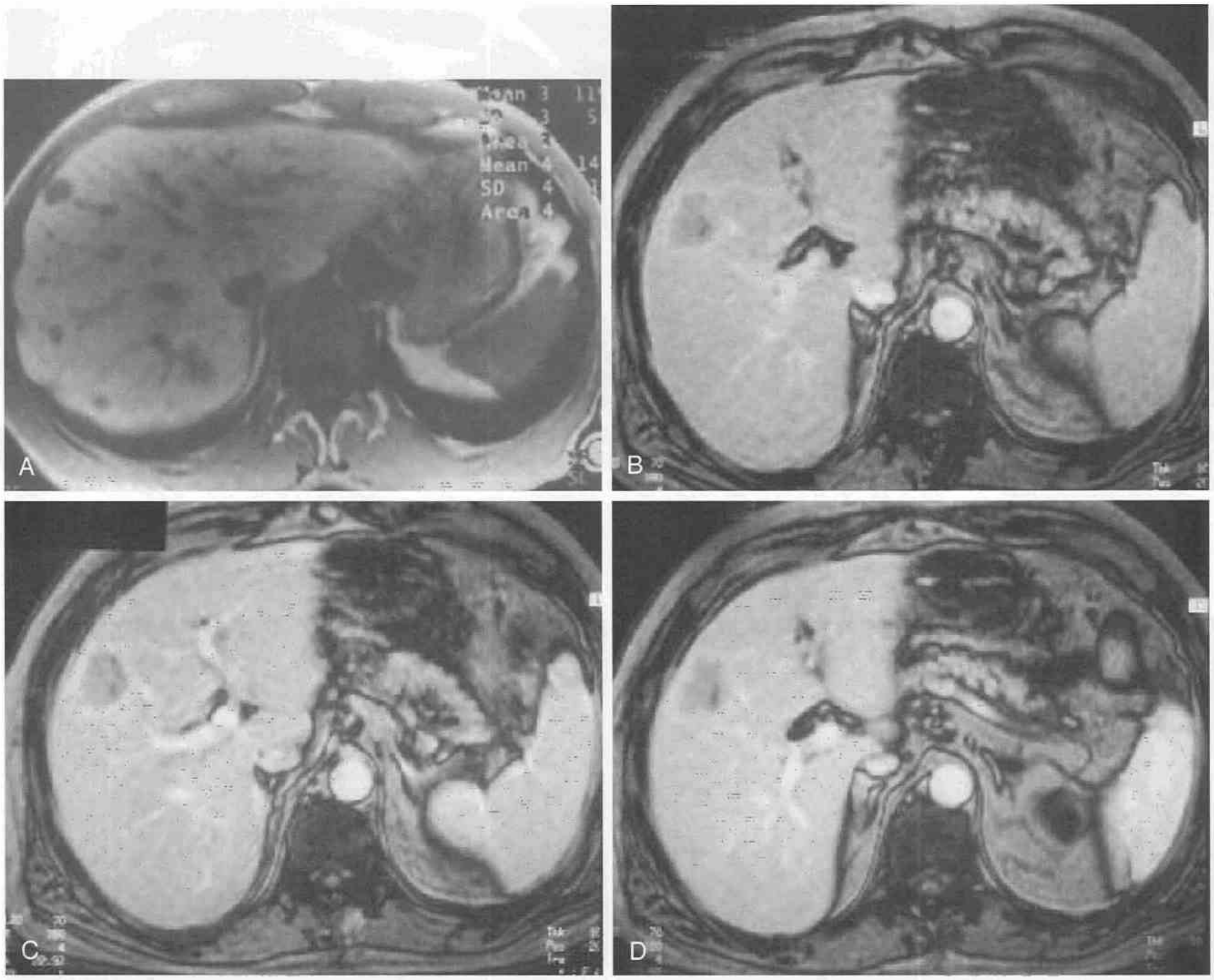

Figure 35–48. Liver metastases. *A,* Unenhanced T1-weighted image demonstrates a lesion in the right hepatic lobe. *B,* After administration of gadolinium (Gd-DTPA), the lesion shows rim enhancement. *C,* As the liver parenchyma enhances, the rim of tumoral enhancement becomes less apparent. *D,* On portal venous phase imaging, the rim of enhancement is no longer able to be identified.

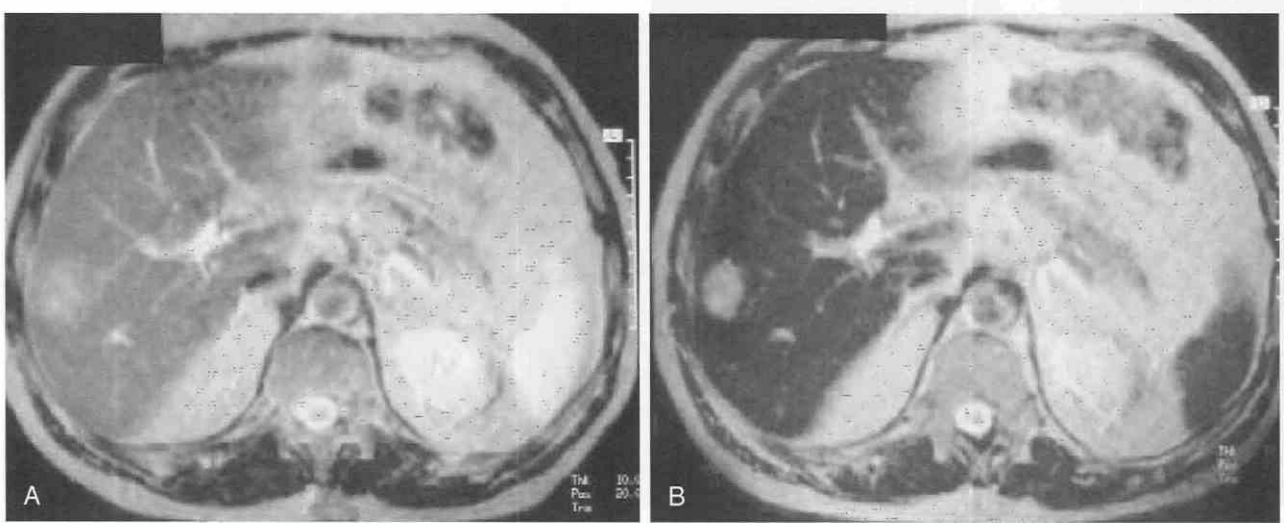

Figure 35–49. Liver metastases. *A,* Unenhanced T2-weighted image demonstrates a solitary lesion in the right hepatic lobe. *B,* T2-weighted image after administration of superparamagnetic iron oxide (SPIO) shows a second lesion, anterior to the portal vein, not seen on the unenhanced images.

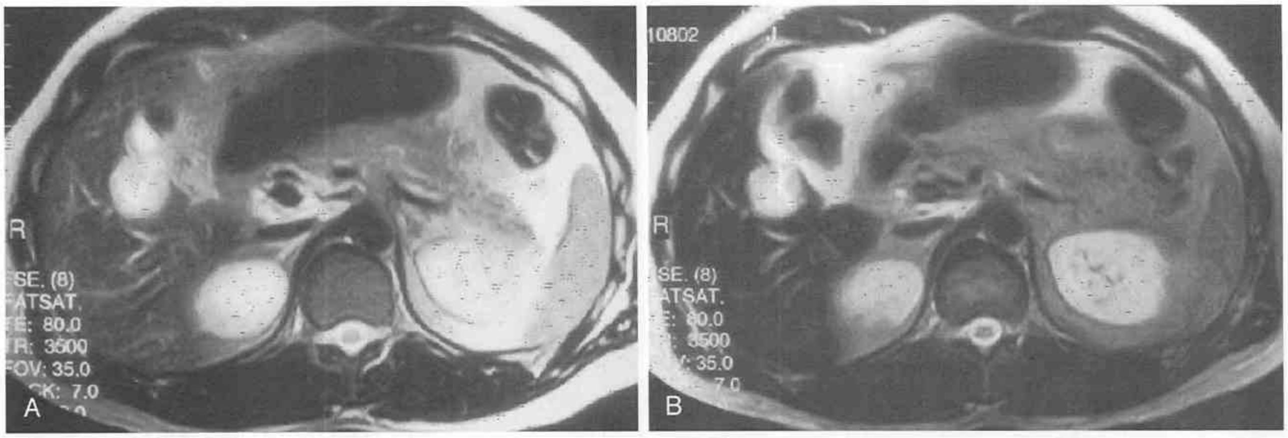

Figure 35–50. Liver metastasis. *A,* Unenhanced T2-weighted image demonstrates a single bright lesion. *B,* T2-weighted image after administration of superparamagnetic iron oxide (SPIO) reveals loss of signal in the haptic parenchyma without loss of signal in the lesion.

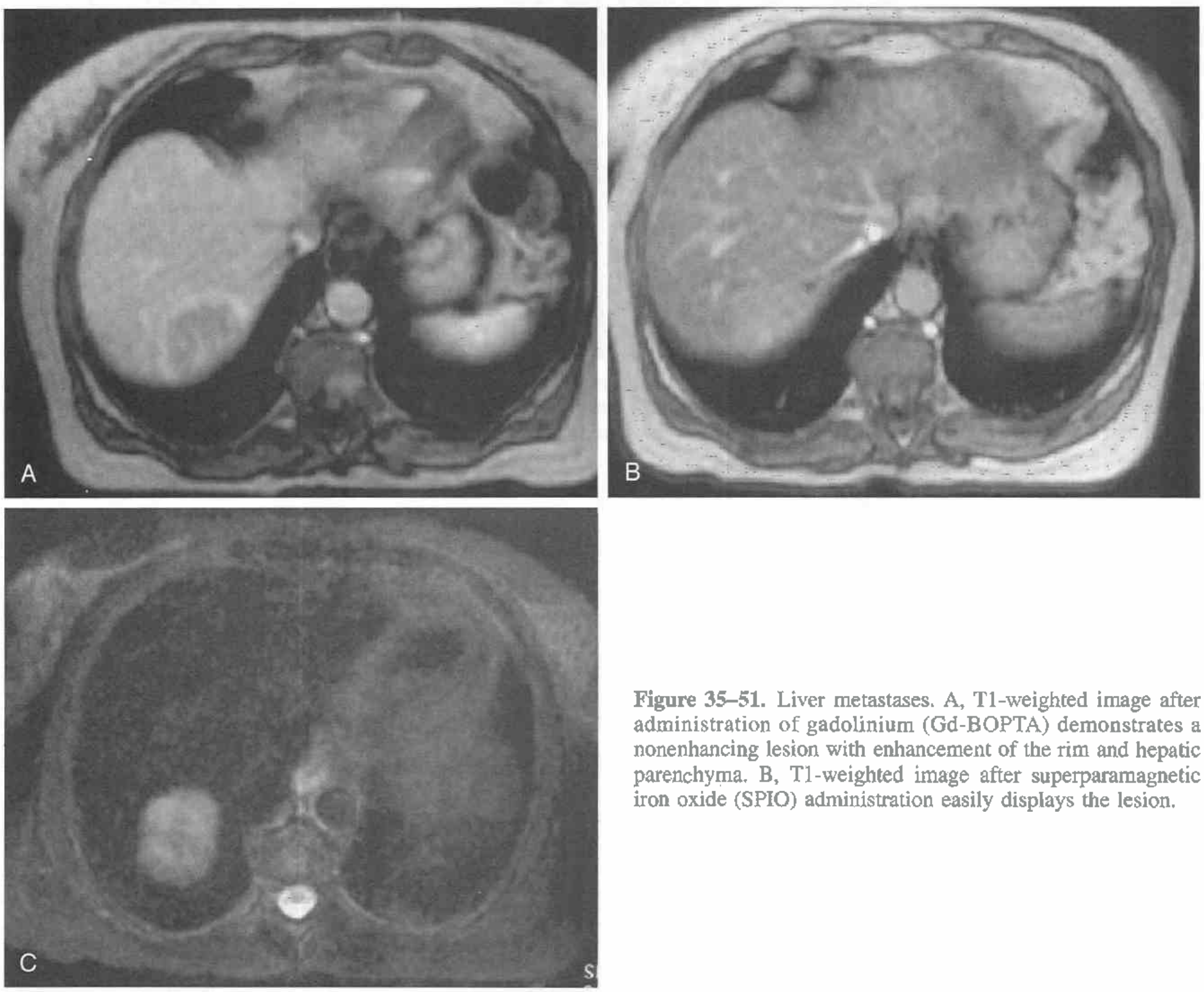

Figure 35–51. Liver metastases. A, T1-weighted image after administration of gadolinium (Gd-BOPTA) demonstrates a nonenhancing lesion with enhancement of the rim and hepatic parenchyma. B, T1-weighted image after superparamagnetic iron oxide (SPIO) administration easily displays the lesion.

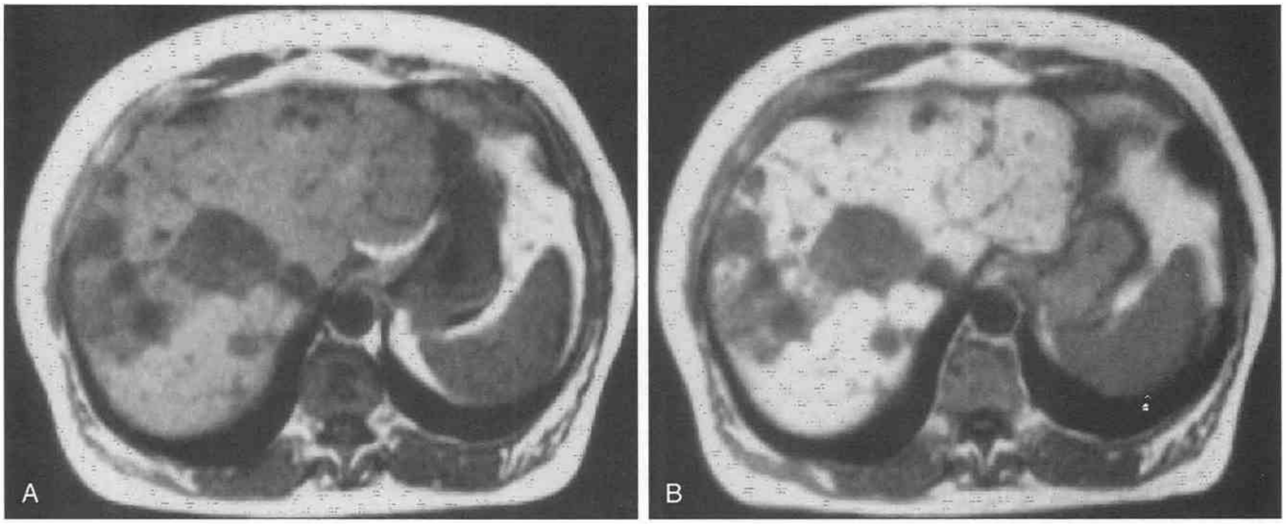

Figure 35–52. Liver metastases. *A,* Unenhanced T1-weighted image demonstrates multiple hepatic lesions. *B,* T1-weighted image after manganese-DPDP administration shows enhancement of the normal liver with improved conspicuity of the proven liver masses.

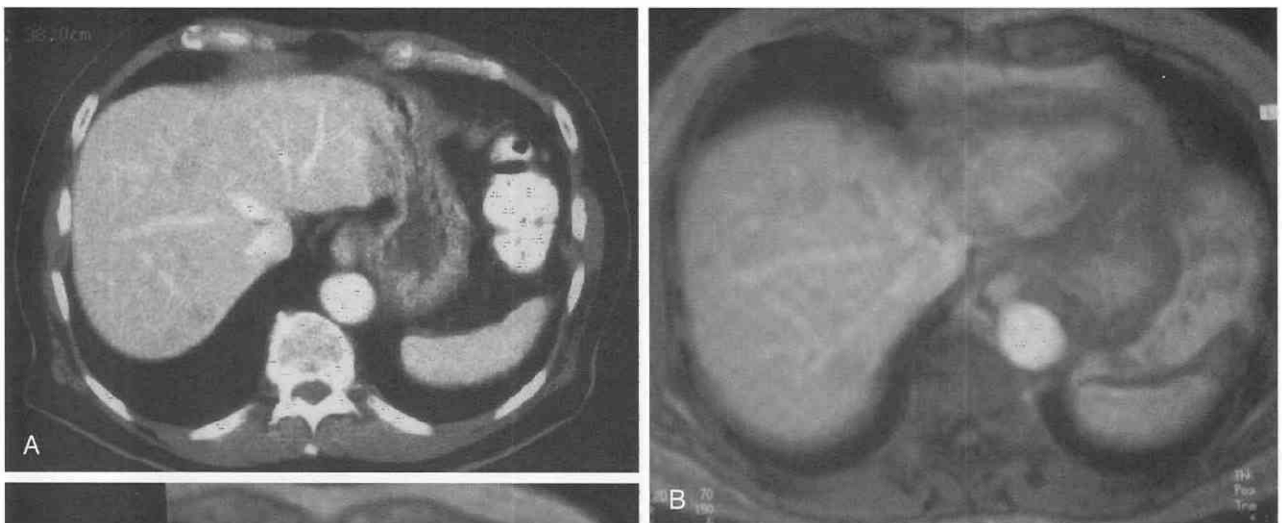

Figure 35–53. Metastases. *A,* Enhanced CT scan demonstrates multiple hypoattenuating hepatic lesions. *B* and *C,* T1-weighted MR image after gadolinium (Gd-BOPTA) administration in portovenous and delayed phases. Delayed imaging identified many more lesions.

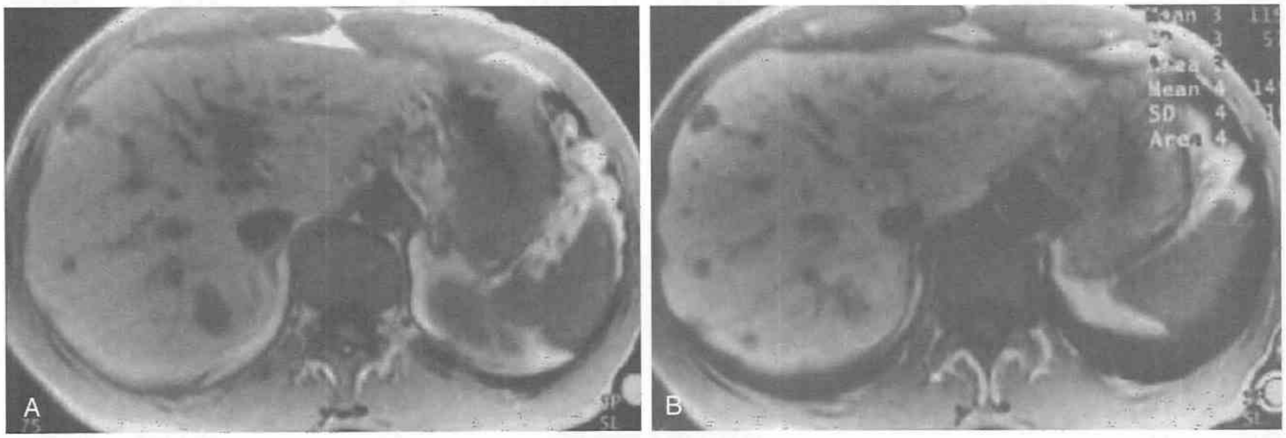

Figure 35–54. Metastases. *A,* Unenhanced T1-weighted MR image demonstrates multiple hepatic lesions. *B,* T1-weighted MR image after manganese-DPDP administration identified additional lesions.

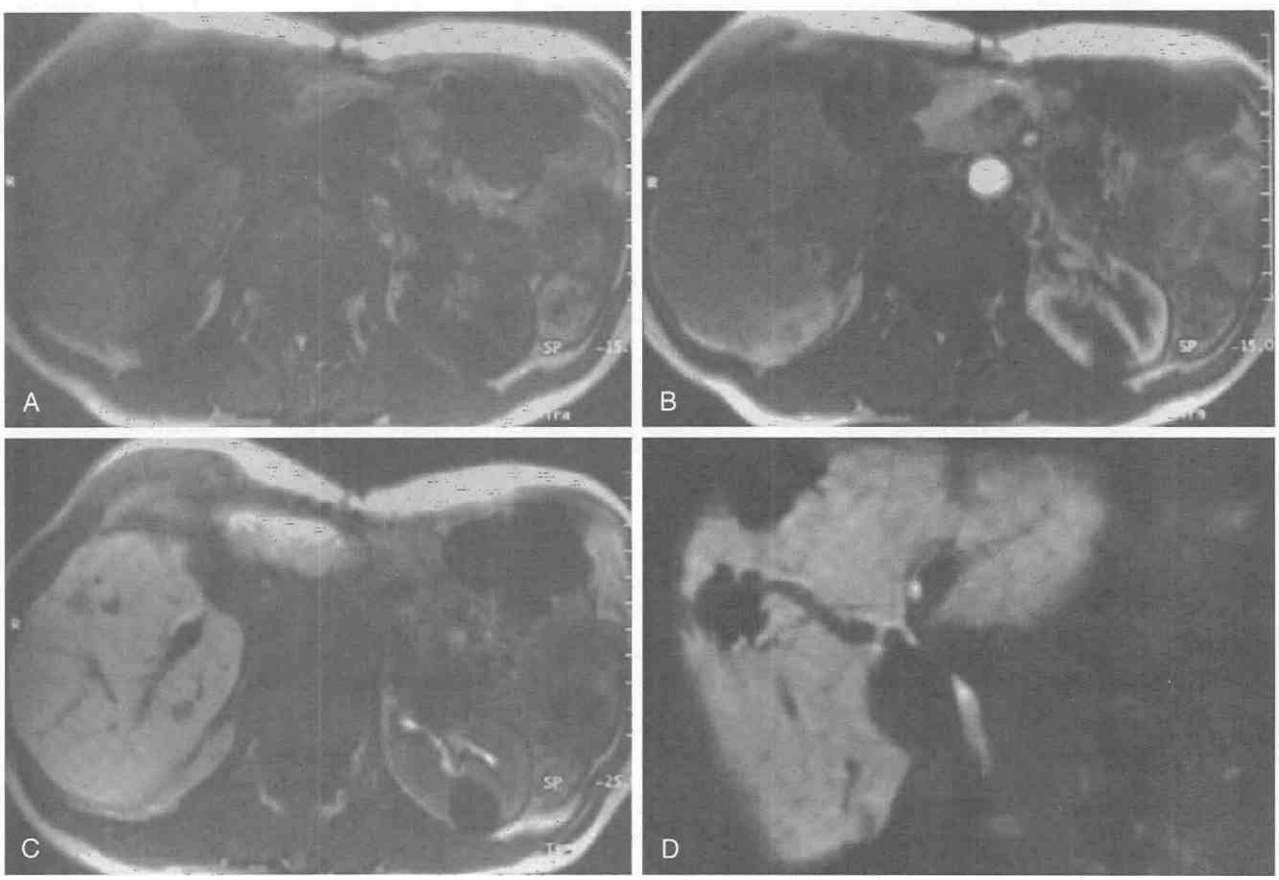

Figure 35–55. Metastases. *A,* Unenhanced T1-weighted MR image demonstrates few low-signal-intensity lesions. *B,* T1-weighted MR image after gadolinium (Gd-EOB-DTPA) administration in the arterial phase shows ring enhancement of the lesions. *C* and *D,* The lesions were much more conspicuous on delayed imaging.

are the most common signs and symptoms of pyogenic liver abscess. Leukocytosis, elevated serum alkaline phosphatase, hypoalbuminemia, and prolonged prothrombin time are the most common laboratory findings.[25, 54, 199]

Abscesses that are of biliary origin are usually multiple, involving both hepatic lobes in 90% of cases. Abscesses from portal vein sources are often solitary, with 65% occurring in the right lobe, 12% in the left lobe, and 23% in both lobes. This distribution has been attributed to the pattern of mesenteric blood flow in the portal vein.[199]

Treatment of pyogenic liver abscess includes elimination of the abscess as well as the source of infection. Therapeutic options for abscess treatment include surgical drainage, antibiotics alone, percutaneous aspiration with antibiotics, and percutaneous catheter drainage with antibiotics. Complications of pyogenic liver abscess include septic shock, secondary infection to other organs, perforation with peritonitis, and fistula formation.

CT has greater than 90% sensitivity for the detection of hepatic abscesses, which appear as low-attenuation, rounded masses on both noncontrast and contrast-enhanced scans (Figs. 35-56 and 35–57).[96] The attenuation range between 0 and 45 HU overlaps with that of other lesions (e.g., cysts, bilomas, and neoplasms); however, most abscesses have an enhancing peripheral rim or capsule. Although usually sharply defined, some abscesses have a lobulated contour and circumferential "transition zones" of intermediate attenuation.[159] The *cluster sign* may also be seen, with small lesions less than 2 cm in diameter clustering together with apparent coalescence into a large abscess (Fig. 35–58).[115] These described findings are nonspecific, with aspiration required for diagnosis. Gas bubbles or an

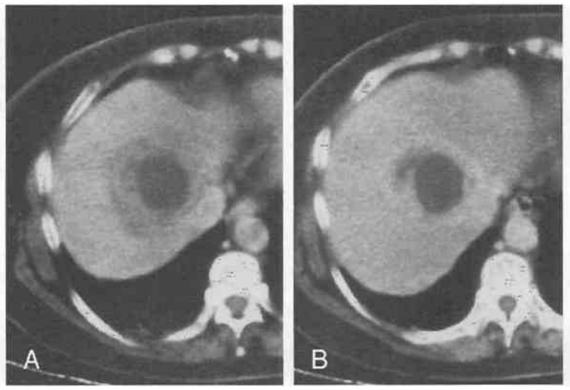

Figure 35–57. Pyogenic abscess. *A,* Unenhanced CT scan shows a zone of intermediate densities that surrounds the central low-attenuation cavity. *B,* Contrast-enhanced CT scan reveals the hyperemic peripheral zone to enhance.

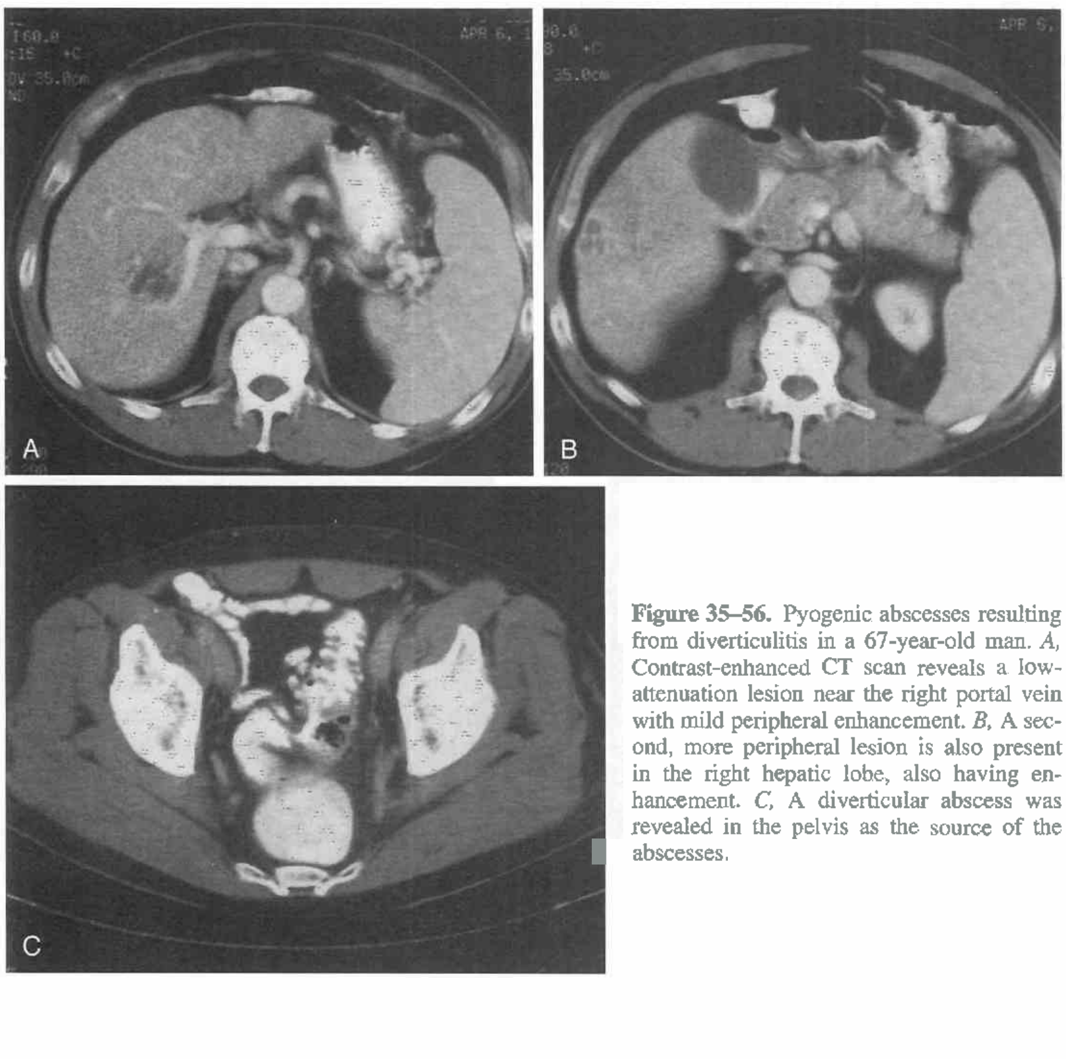

Figure 35–56. Pyogenic abscesses resulting from diverticulitis in a 67-year-old man. *A,* Contrast-enhanced CT scan reveals a low-attenuation lesion near the right portal vein with mild peripheral enhancement. *B,* A second, more peripheral lesion is also present in the right hepatic lobe, also having enhancement. *C,* A diverticular abscess was revealed in the pelvis as the source of the abscesses.

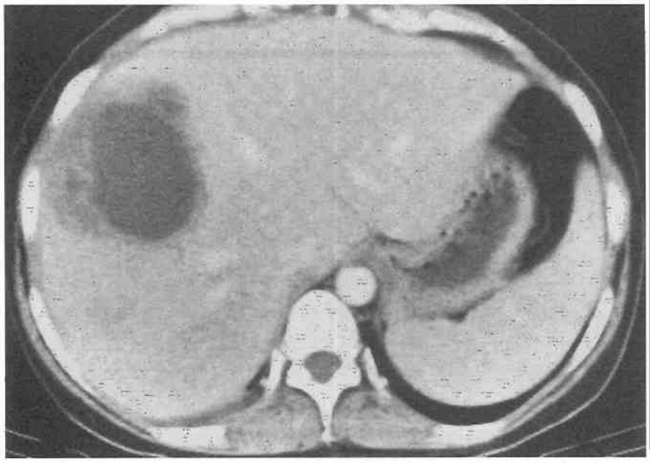

Figure 35–58. Pyogenic abscess. Contrast-enhanced CT scan demonstrates the "cluster" sign with two small lesions adjacent to the large central cavity.

air-fluid level are specific signs but are present in fewer than 20% of cases (Fig. 35–59).[96] The presence of an air-fluid or fluid-debris level may indicate the formation of an enteric communication with the abscess.

MRI of pyogenic liver abscesses is nonspecific, with hypointensity on T1-weighted images and hyperintensity on T2-weighted images relative to the liver, as with other focal hepatic lesions.[265] The abscess cavity may be homogeneous or heterogeneous, depending on its contents and degree of necrosis and debris. The capsule may appear as a low-intensity rim. After IV Gd-DTPA administration, rapid enhancement of the abscess wall is followed by a slower increase in signal intensity centrally.[227, 267]

Fungal Abscesses

Candidiasis, the most frequently occurring systemic fungal infection in immunocompromised patients, is becoming more common with the increase in incidence of AIDS and with bone marrow transplantation, chemotherapy, and radiation therapy. At autopsy, hepatic candidiasis is found in up to 70% of patients with acute leukemia and in 50% with lymphoma. Concurrent splenic involvement, or *hepatosplenic candidiasis*, is very common. Detection may be difficult because blood cultures are positive in only 50% of patients.[73, 90, 250] Although aspiration for culture and diagnosis may be needed, treatment usually is by antifungal therapy alone without percutaneous drainage.

The most common appearance of hepatic candidiasis on CT scans is that of multiple, small, round areas of decreased attenuation for which both precontrast and postcontrast scans are required in order to be visualized (Fig. 35–60). On noncontrast scans, areas of scattered increased density that represent calcification may be seen. Periportal fibrosis appearing as increased attenuation may also be present.[15, 231, 232]

MRI of microabscesses of the liver and spleen caused by *Candida* shows multiple, small lesions of intermediate signal intensity on T1-weighted images and increased signal intensity on T2-weighted images relative to the liver. Conspicuity of the lesions is improved in patients with increased hepatosplenic iron deposition secondary to multiple blood transfusions. This is because the decreased signal intensity of the liver and spleen creates a dark background that highlights the hyperintense microabscesses.[38]

Amebic Abscess

Amebiasis occurs most often in tropical or subtropical zones of the world. It is becoming more prevalent in the Western Hemisphere as a result of travel and migration, in institutionalized patients, and in homosexual populations.[205] Caused by the protozoan parasite *Entamoeba histolytica*, amebic liver abscess is the most common extraintestinal manifestation of amebiasis.[93, 118, 129, 205, 230] Amebic liver abscesses result when the parasite crosses the colonic mucosa and enters the portal circulation (most commonly) or

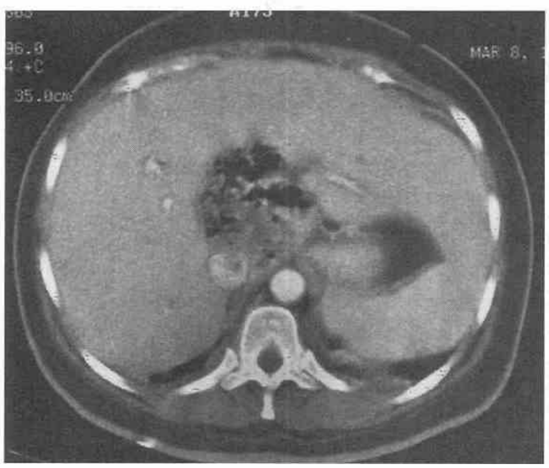

Figure 35–59. Gram-negative pyogenic abscess of unknown etiology in a 52-year-old woman with diabetes. Contrast-enhanced CT scan demonstrates multiple air-fluid levels in this large central hepatic abscess.

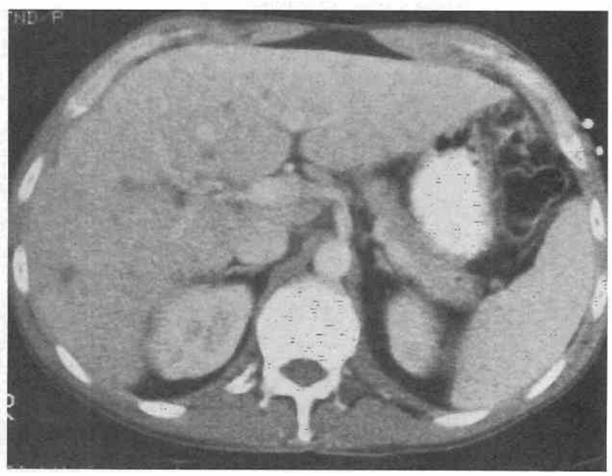

Figure 35–60. The patient is an immunocompromised man with leukemia and hepatic candidiasis. Contrast-enhanced CT scan demonstrates multiple low-attenuation foci of the liver.

the lymphatics or when it passes directly into the liver from the hepatic flexure.[93, 199]

The cavitary amebic abscess occurs as liver tissue is focally destroyed. Initially, the lesion contains necrotic tissue, including the viable organism. As the lesion becomes larger, central cavitation occurs and the active organism lies within the necrotic tissue lining the cavity. Surrounding this layer is an inflammatory zone of hepatic parenchyma that is invaded by the organisms. Centrally, the cavity is often filled by a thick fluid that resembles anchovy paste. Frequently solitary, the abscess is most often located in the right lobe. The preferential occurrence of these lesions in the right lobe is related to the venous drainage from the usually infected right colon, via the superior mesenteric vein to the portal vein.[198] Complications include rupture of the abscess through the diaphragm into the pleural space or the lung or into the pericardium or peritoneum.[118, 199, 230]

Although serologic testing is often useful for the detection of amebiasis,[93, 129, 205] percutaneous aspiration is occasionally needed for diagnosis. Biopsy of the abscess wall, which contains the living parasite, is more likely to be diagnostic than is aspiration of the thick, reddish brown, "anchovy paste" fluid. Percutaneous drainage may be helpful in the uncommon situation in which medical therapy fails.[203, 224, 257, 259]

On CT scans, amebic abscesses of the liver appear as low-attenuation lesions, with the density of a lesion dependent on its stage of development and internal contents.[96, 202] Lesions that are early in development may have an appearance similar to that of solid tumors, whereas older abscesses are more cystic in appearance. If lesions are multiple, their appearance may vary as a result of different stages of development. On unenhanced CT scans, the zone of inflammation, of variable thickness and density, is isodense to hypodense and usually enhances after contrast administration. A thin outer rim of lower attenuation may surround the enhancing layer, giving the lesion a target appearance, and defines the outer boundary of the inflamed hepatic parenchyma (Fig. 35–61).

On unenhanced MR images, amebic abscesses have a well-defined appearance with a rim of varying signal intensity (Fig. 35–62*A* and *B*).[62, 204] On T1-weighted images, the central cavity is usually of decreased signal intensity relative to the normal liver. The central cavity has increased signal intensity on T2-weighted images and often is surrounded by a ring of higher signal intensity that corresponds to the reactive zone. Adjacent high signal intensity on T2-weighted images is thought to represent edema. After Gd-DTPA administration, the hyperemic reactive zone demonstrates enhancement similar to that seen with contrast-enhanced CT (Fig. 35–62*D*). After successful medical therapy, MRI shows a reduced signal intensity of the hyperintense area that surrounded the abscess cavity on T2-weighted images.

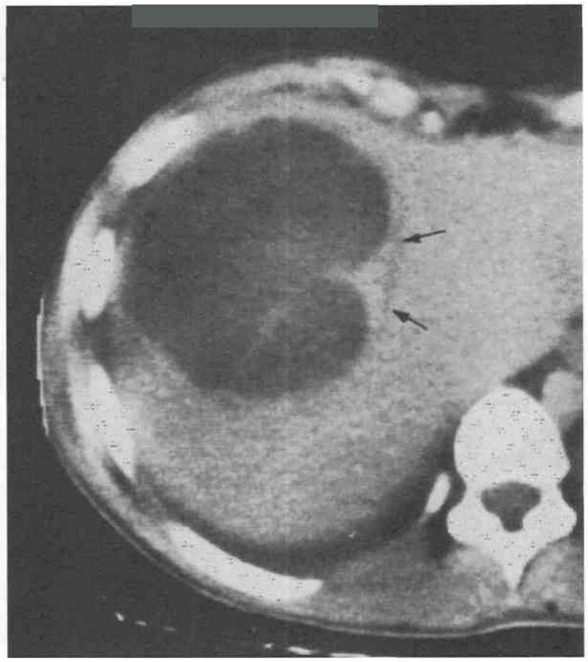

Figure 35–61. Amebic abscess. Contrast-enhanced CT scan shows that the peripheral low-attenuation rim *(arrows)* defines the outer limit of the inflammatory wall. An internal septum is present in the large, low-attenuation central cavity.

Echinococcal Disease

Hydatid disease of the liver, caused by the larvae of a tapeworm, has two forms. The cystic form, caused by *Echinococcus granulosus*, is more common, occurring in Mediterranean countries, South America, Australia, and New Zealand. The alveolar form, caused by *Echinococcus multilocularis (alveolaris)*, is found in central Europe, the Soviet Union, and other areas of the northern hemisphere, including Alaska.[136]

In echinococcal disease caused by *E. granulosus*, dogs are usually the definitive hosts and sheep are the most common intermediate hosts. In some areas, about 50% of dogs and up to 90% of sheep and cattle may be infected. Humans who ingest material contaminated by dog feces that contain eggs may become intermediate hosts. The eggs hatch within the intestinal tract of the host and penetrate the intestinal mucosa, entering the lymphatics and portal venous system. Most are then filtered by the liver and lungs, thus accounting for the high rate of cyst development in the liver (up to 75% of cases) and lungs.

The cysts, which may be solitary or multiple, grow slowly to reach a large size. The wall of the cyst contains three layers: (1) the *pericyst*, an outer layer formed by the reactive tissue of the host organ; (2) the *endocyst*, an inner germinal layer containing the growing parasite; and (3) the *ectocyst*, an intermediate layer consisting of a proteinaceous membrane.

Daughter cysts may develop within the parent cyst as a result of fragmentation of the germinal layer. Brood capsules, also produced by the germinal layer, give rise to scolices, or infectious miniature tapeworms. When brood capsules and scolices separate from the germinal layer, debris *(hydatid sand)* that falls to the dependent portion of the cyst is formed. Calcification of the ectocyst alone may occur, and when the parasite dies, the true cyst wall (both ectocyst and endocyst) may also calcify or may separate from the pericyst.[46, 136, 177]

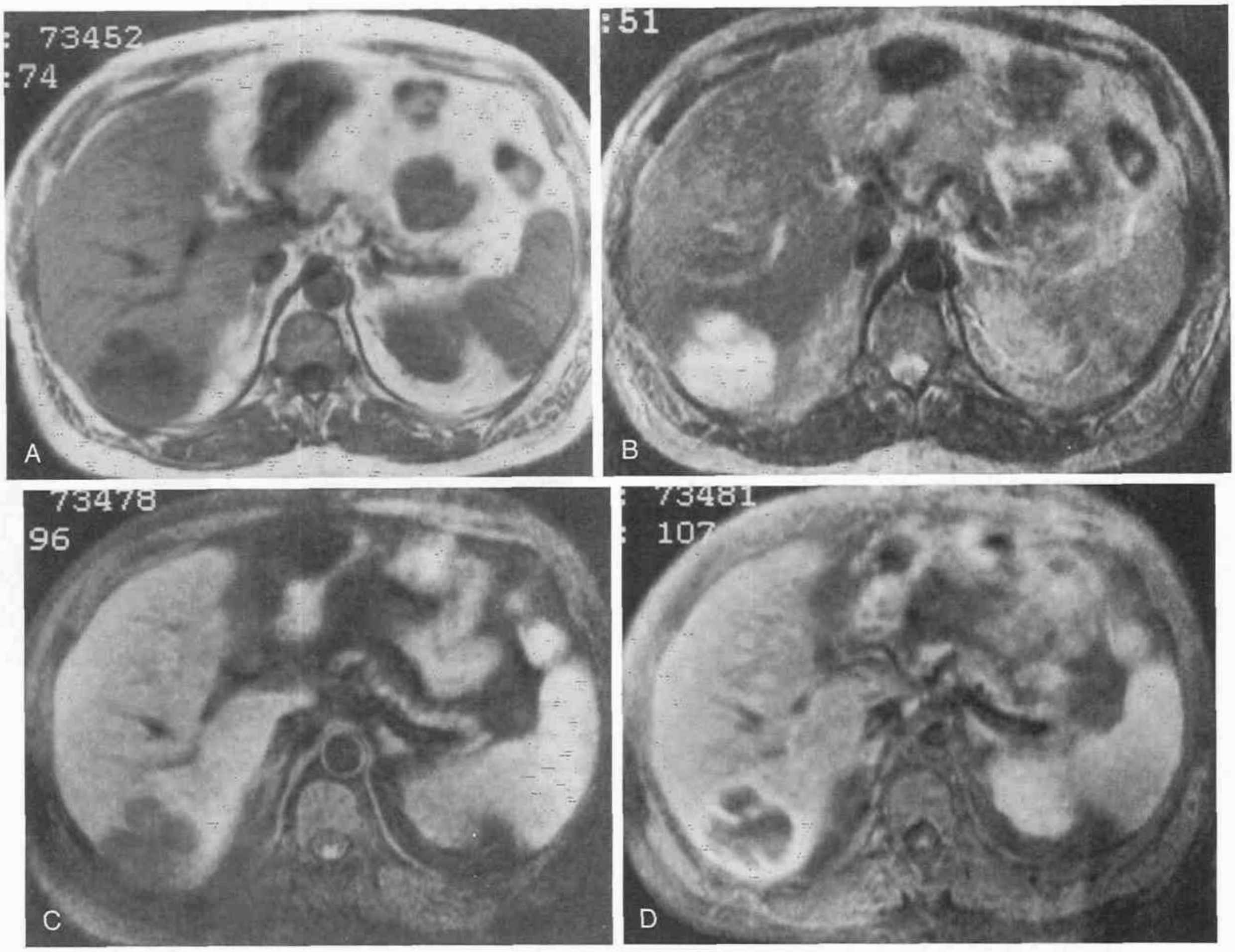

Figure 35–62. Amebic liver abscess in a 60[redacted]-old man. *A*, T1-weighted image (TR = 300 msec, TE = 15 msec) demonstrates a lobulated, low-signal-intensity lesion of the posterior segment of the right hepatic lobe. *B*, T2-weighted image (TR = 2400 msec, TE = 90 msec) demonstrates the lesion to be of high signal intensity relative to the liver. The internal septa are of low signal intensity. *C*, Fat-suppression T1-weighted image (TR = 800 msec, TE = 15 msec) demonstrates the lesion continuing to be of low signal intensity. *D*, Fat-suppression T1-weighted image (TR = 800 msec, TE = 15 msec) after intravenous gadolinium (Gd-DTPA) demonstrates enhancement of the rim and internal septa.

Hydatid cysts of the liver often remain asymptomatic for many years, becoming painful only after growing very large.[86] They are often discovered incidentally during radiologic imaging performed for other reasons. Most complications from hydatid cysts are related to rupture of the cyst into surrounding structures (biliary tree, pleura, peritoneum).[23,144] If peritoneal rupture or spillage during surgical excision occurs, a serious anaphylactic reaction may result.

Serologic results for echinococcal disease are positive in more than 80% of patients with hepatic lesions.[86] Treatment includes antiparasitic drug therapy and surgical removal.[12,137] Several reports describe successful percutaneous drainage. Medical therapy before drainage is advocated to reduce the risk of anaphylactic reaction in case of accidental spillage.

On CT scans, hepatic echinoccocal cysts appear as well-defined round or oval cystic masses with a density near that of water (Fig. 35–63).[2, 120, 178, 194, 228] Daughter cysts, indicating viability, give the lesion a multilocular appearance (Fig. 35–64*A*). The outer wall may be outlined peripherally by a line of slightly lower attenuation, or it may contain calcification. Extensive calcification, however, usually indicates that the lesion is no longer viable. When detached from the pericyst, the true cyst wall may appear as a thin, wavy membrane within the fluid-filled cyst.[2] After IV contrast administration, the hyperemic ectocyst may enhance slightly.

On MR images, hydatid cysts have decreased T1-weighted signal intensity and increased T2-weighted signal intensity relative to the normal liver.[101, 155, 262, 279] A low-signal-intensity rim, best seen on T2-weighted images, corresponds to the collagen-rich pericyst. The internal architecture is well demonstrated by MRI, with the daughter cysts being hypointense to isointense on T1-weighted images and isointense on T2-weighted images relative to the hyperintense hydatid fluid and sand of the mother cyst (Fig. 35–64*B*). The floating membranes seen in a cyst undergoing degeneration appear as low-intensity structures. Intraparenchymal rupture of the wall may be seen as a defect in the low-intensity rim.[151, 262] Calcifications, when present, are not as well demonstrated by MRI but may produce a signal void.

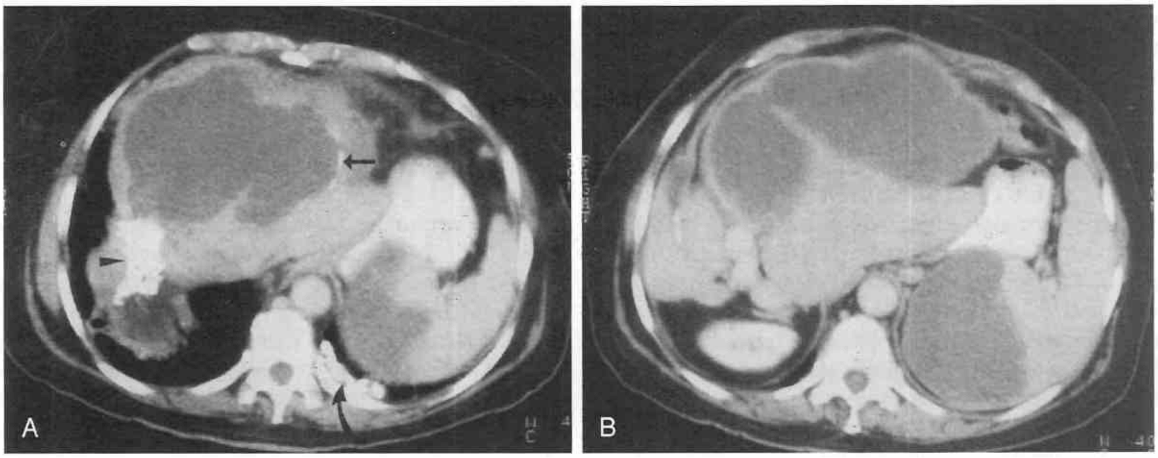

Figure 35–63. The patient is a 77-year-old woman with echinococcal cysts of the liver and spleen. *A,* Contrast-enhanced CT scan shows a large cyst of the liver with calcification of the cyst wall *(straight arrow).* An area of dense calcification *(arrowhead)* is related to a previous resection. Involvement of the spleen is present. Calcification in the left lung base *(curved arrow)* is related to prior involvement of the pleural space. *B,* Several centimeters more caudal to *A,* additional cysts involving the liver as well as the large splenic cyst are shown.

The alveolar form of echinococcal disease is distinct from the cystic form in several aspects.[253] The main definitive host is the fox, with small rodents being the usual intermediate hosts. Humans become infected by ingesting contaminated materials or by coming into direct contact with infected foxes. This disease, in contrast to the expansile cysts of *E. granulosus,* is characterized by the formation of one or more infiltrative liver lesions that stimulate a granulomatous reaction. Internal necrosis, cavitation, and calcification may be seen within the lesion. The CT and MR imaging appearances of the predominantly solid lesion of *E. multilocularis* are indistinguishable from those of primary or secondary malignant liver neoplasms.[42, 53, 228] Atrophy of a lobe or segment of the liver may occur when the lesion is located centrally in the liver.[220]

Serologic testing and percutaneous biopsy may be useful for diagnosis when alveolar echinococcal disease is suspected. It should be included in the differential diagnosis of hepatic lesions in patients who live in or have traveled to endemic regions of the world.

Schistosomiasis

Schistosomiasis is a common parasitic infection, with a prevalence of 70% in endemic areas; 10% of patients in these areas experience hepatosplenic involvement.[186] *Schistosoma japonicum* occurs in coastal areas of China, Japan, Formosa, and the Philippines. *S. mansoni* is found in parts of Africa, in the Middle East, in the West Indies, and in the northern regions of South America. *S. haematobium* occurs in North Africa, in Mediterranean countries, and in southwest Asia.

The larvae are shed by snails—the intermediate hosts—into fresh water, where human infection occurs when the parasite penetrates skin or mucous membranes.

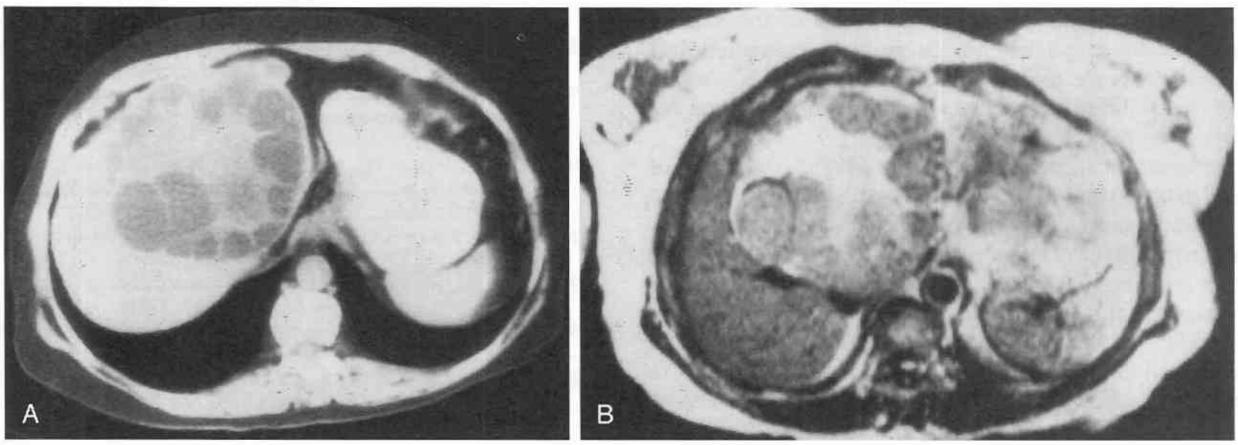

Figure 35–64. Echinococcal cyst. *A,* Contrast-enhanced CT scan shows a large cyst [redacted]e liv[redacted]hat contains multiple daughter cysts, which indicate viability. *B,* T2-weighted image demonstrates the low-signal-intensity rim that corresponds to the collagen-rich pericyst. The daughter cysts are slightly hyperintense relative to the liver but hypointense relative to the very high signal intensity of the internal hydatid fluid.

The schistosomes migrate via venules and lymphatics, reaching the heart and then passing through the pulmonary circulation. All die except those that reach the mesenteric circulation, maturing within the intrahepatic portal venous system. A granulomatous reaction to the ova occurs, leading to periportal fibrosis and sometimes resulting in portal hypertension. The life cycle of the blood fluke is completed after the mature female worm, which has lived with the male in the portal vein for 10 to 15 years, swims to reach the venules of the urinary bladder (*S. haematobium*) or gut (*S. mansoni* and *S. japonicum*) to lay its eggs. The eggs then pass through the wall of the bladder or intestine to be excreted via urine or feces to infect snails. Schistosomiasis is associated with an increased incidence of hepatocellular carcinoma.

On CT scans, peripheral hepatic septal or capsular calcification is characteristic of *S. japonicum* infection.[7,171] Gross pseudoseptations with geographic bands of calcification and notches of the liver margin are also noted. Septal, capsular, and amorphous enhancement may be seen after IV contrast administration.[171] Periportal low-density areas may be apparent. *S. mansoni* infection appears as round, low-attenuation foci with linear branching low-attenuation fibrotic bands engulfing the portal tracts. These bands occasionally show enhancement after IV contrast administration but do not usually calcify.[64]

MRI features of schistosomiasis infection include the morphologic changes and associated findings of portal hypertension. The regions of calcification and fibrosis may be demonstrated as curvilinear areas of low signal intensity.

Practical Approach to Imaging

Advances in radiologic imaging have led to the detection of additional and smaller hepatic lesions. The detection of lesions smaller than 15 mm may be problematic because of their uncertain clinical significance. A study using CT demonstrated that a single, small (<1.5 cm) lesion was benign in 65% of patients, whereas two to four small lesions were benign in 59% of patients.[117] As the number of lesions increased or when a large lesion was present, the likelihood of malignancy increased. Even when an extrahepatic malignancy was present, 51% of these small lesions proved to be benign. In patients with dominant metastases who are under consideration for hepatic resection, the possibility that other smaller lesions may be benign must be considered.

A systematic approach to the differential diagnosis of hepatic mass lesions should include both clinical information and the imaging appearance. The most important clinical information is (1) the patient's age and sex and (2) whether an extrahepatic malignancy, cirrhosis, infection, or immunocompromise is present.

In adults younger than 40 years of age, hemangioma, metastases, FLC, FNH, and HCA are most common. In patients older than 50 years of age, hemangioma, metastases, HCC, I-CAC, and angiosarcoma are most frequently seen.

In children, IHE is seen before 6 months of age, whereas the peak incidences of hepatoblastoma and mesenchymal hamartoma are similar at 18 months. In older children and adolescents, HCC and UES may be seen. Benign primary hepatic tumors are generally more common in women, whereas malignant primary hepatic tumors are more frequent in men. Overall, metastatic disease is much more common than primary liver neoplasms in adults as well as in the pediatric age groups, except in cirrhotic patients, in whom HCC is more common.[164]

Other important clinical information includes the long-term use of steroids or oral contraceptives. Neoplasms related to such use include HCA and (to a lesser degree) FNH, NRH, hemangioma, and HCC.[41] With multiple hepatic masses, note that metastases, although common, are not the only cause of multiple hepatic lesions. Abscesses, cysts, multifocal or diffuse HCC, I-CAC, angiosarcoma, NRH, and hemangioma may all present as multiple liver lesions.

The major goal in the evaluation of a suspected hepatic neoplasm is determining whether it is a *surgical* or *nonsurgical* lesion. The two most common nonsurgical primary hepatic neoplasms in adults are hemangioma and FNH. All other primary hepatic neoplasms are surgical lesions if resectable. In children, hepatoblastoma, UES, HCC, and mesenchymal hamartoma are considered surgical lesions. IHE need not be resected if the patient can survive with supportive care or embolization until the tumor spontaneously regresses.

References

1. Ackerman NB, Lin WM, Conde ES, et al: The blood supply of experimental liver metastases: I. Distribution of hepatic artery and portal vein blood to "small" and "large" tumors. Surgery 66: 1067, 1969.
2. Acunas B, Rozanes I, Acunas G, et al: Hydatid cyst of the liver: Identification of detached cyst lining on CT scans obtained after cyst puncture. AJR Am J Roentgenol 156:751–752, 1991.
3. Acunas B, Rozanes I, Celik L, et al: Purely cystic hydatid disease of the liver: Treatment with percutaneous aspiration and injection of hypertonic saline. Radiology 182:541–543, 1992.
4. Agildere AM, Haliloglu M, Akhan O: Biliary cystadenoma and cystadenocarcinoma. AJR Am J Roentgenol 156:1113, 1991.
5. Allard JC, Kuligowska E: Percutaneous treatment of an intrahepatic abscess caused by a penetrating duodenal ulcer. J Clin Gastroenterol 95:603–606, 1987.
6. Altmeir WA, Schowenger DT, Whiteley DH: Abscess of the liver: Surgical considerations. Arch Surg 101:258–267, 1982.
7. Araki T, Hayakawa K, Okada J, et al: Hepatic schistosomiasis japonica identified by CT. Radiology 157:757–760, 1985.
8. Balfe DM: Hepatic metastases from colorectal cancer: Radiologic strategies for improved selection. Radiology 185:18–19, 1992.
9. Barnes PA, Thomas JL, Bernardino ME: Pitfalls in the diagnosis of hepatic cysts by computed tomography. Radiology 141:129–133, 1981.
10. Baron RL, Freeny PC, Moss AA: The liver. In Moss AA, Gamsu G, Genant HK (eds): Computed Tomography of the Whole Body, 2nd ed. Philadelphia, WB Saunders, 1992, pp 735–822.
11. Bean WJ, Rodan BA: Hepatic cysts: Treatment with alcohol. Am J Roentgenol 144:237–241, 1985.
12. Behans KE, van Heerden JA: Surgical management of hepatic hydatid disease. Mayo Clin Proc 66:1193–1197, 1971.
13. Berland LL: Additional comment: Dynamic hepatic CT. Radiology 181:22–23, 1991.
14. Berland L, Lee JKT, Stanley RJ: Liver and biliary tract. In Lee JKT, Sagel SS, Stanley RJ (eds): Computed Body Tomography with MRI Correlation, 2nd ed. New York, Raven Press, 1989, pp 593–660.
15. Berlow ME, Spirt BA, Weil L: CT follow-up of hepatic and splenic fungal microabscesses. J Comput Assist Tomogr 8:42–45, 1984.
16. Berman MA, Burnham JA, Sheahan DG: Fibrolamellar carcinoma of the liver: An immunohistochemical study of nineteen cases and a review of the literature. Hum Pathol 19:784–794, 1988.

17. Bernardino ME, Ervin BC, Steinberg HV, et al: Delayed hepatic CT scanning: Increased confidence and improved detection of hepatic metastases. Radiology 159:71–74, 1986.
18. Bernardino ME: Computed tomography of calcified liver metastases. J Comput Assist Tomogr 3:32–35, 1979.
19. Bertel CK, Van Heerden JA, Sheedy PF: Treatment of pyogenic hepatic abscesses. Arch Surg 121:554–558, 1986.
20. Biemer JJ: Hepatic manifestations of lymphoma. Ann Clin Lab 14: 252–260, 1984.
21. Boechat MI, Kangarloo H, Ortega J, et al: Primary liver tumors in children: Comparison of CT and MR imaging. Radiology 169: 727–732, 1988.
22. Marti-Bonmati L, Menor F, Vizcaino J, et al: Lipoma of the liver: US, CT and MRI appearance. Gastrointest Radiol 14:155–157, 1989.
23. Marti-Bonmati L, Serrano FM: Complications of hepatic hydatid cysts: Ultrasound, computed tomography, and magnetic resonance diagnosis. Gastrointest Radiol 15:119–125, 1990.
24. Bosniak MA, Ambos MA: Polycystic kidney disease. Semin Roentgenol 10:133–143, 1975.
25. Brandborg LL, Goldman IS: Bacterial and miscellaneous infections of the liver. In Zakim D, Boyer TD (eds): Hepatology. Philadelphia, WB Saunders, 1990, pp 1086–1098.
26. Braun P, Ducharme JC, Riopelle JL, et al: Hemangiomatosis of the liver in infants. J Pediatr Surg 10:121–126, 1975.
27. Bressler EL, Alpern MB, Glazer GM, et al: Hypervascular hepatic metastases: CT evaluation. Radiology 162:49–54, 1987.
28. Bret PM, Fond A, Bretagnolle M, et al: Percutaneous aspiration and drainage of hydatid cysts in the liver. Radiology 168:617–620, 1980.
29. Bruneton J-N, Falewee M-N, Francois E, et al: Liver, spleen, and vessels: Preliminary clinical results of CT with perfluorooctylbromide. Radiology 170:179–183, 1989.
30. Bruneton JN, Schnider M: Radiology of Lymphoma. New York, Springer-Verlag, 1986.
31. Bydder GM: Magnetic resonance imaging of the liver. In Wilkins RA, Nunnerly HB (eds): Imaging of the Liver, Pancreas, and Spleen. Oxford, Blackwell Scientific, 1990, pp 49–66.
32. Casillas C, Marti-Bonmati L, Galant J: Pseudotumoral presentation of nodular regenerative hyperplasia of the liver: Imaging in five patients including MR imaging. Eur Radiol 7:654–658, 1997.
33. Carr DH, Hadjis NS, Banks LM, et al: Computed tomography of hilar cholangiocarcinoma: A new sign. Am J Roentgenol 145: 53–56, 1985.
34. Carrel TP, Matthews JB, Baer HU, Blumgart LH: Etiology, diagnosis and treatment of hepatic abscesses after biliary tract surgery. Ann Chir 44:746–751, 1990.
35. Castellino RA, Hoppe RT, Blank N, et al: Computed tomography, lymphography and staging laparotomy: Correlations in initial staging of Hodgkin's disease. Am J Roentgenol 143:37–41, 1984.
36. Chen KT, Bocian JJ: Multiple hepatic adenomas. Arch Pathol Lab Med 107:274–275, 1983.
37. Cherqui D, Rahmouni A, Charlotte F, et al: Management of focal nodular hyperplasia and hepatocellular adenoma in young women: A series of 41 patients with clinical, radiological, and pathological correlations. Hepatology 22:1674, 1995.
38. Cho J, Kim EE, Varma DGK, Wallace S: MR imaging of hepatosplenic candidiasis superimposed on hemochromatosis. J Comput Assist Tomogr 14:774–776, 1990.
39. Choi B, Lim JH, Han MC, et al: Biliary cystadenoma and cystadenocarcinoma: CT and sonographic findings. Radiology 171:57, 1989.
40. Choi BI, Han MC, Park JH, et al: Giant cavernous hemangioma of the liver: CT and MR imaging in 10 cases. AJR Am J Roentgenol 152:1221–1226, 1989.
41. Christopherson WM, Mays ET, Barrows G: A clinicopathologic study of steroid-related tumors. Am J Surg Pathol 1:31–41, 1977.
42. Claudon M, Bessieres M, Regent D, et al: Alveolar echinococcosis of the liver: MR findings. J Comput Assist Tomogr 14:608–614, 1990.
43. Cohen JL, Martin FM, Rossi RL, et al: Liver abscess: The need for complete gastrointestinal evaluation. Arch Surg 124:561–564, 1989.
44. Coire CI, Qizilbash AH, Castelli MF: Hepatic adenomata in type Ia glycogen storage disease. Arch Pathol Lab Med 111:166–169,1987.
45. Conran RM, Stocker JT: Malignant fibrous histiocytoma of the liver: A case report. Am J Gastroenterol 80:813–815, 1985.
46. Cotran RS, Kumar V, Robbins SL: Robbins Pathologic Basis of Disease, 4th ed. Philadelphia, WB Saunders, 1989, pp 421–422.
47. Cox IH, Foley WD: Right window for dynamic hepatic CT. Radiology 181:18–21, 1991.
48. Cox IH, Foley WD: Dynamic hepatic CT: Drs. Cox and Foley reply. Radiology 181:23–24, 1991.
49. Craig GR, Peters RL, Edmonson HA: Tumors of the liver and intrahepatic bile ducts. Atlas of Tumor Pathology, Second Series. Washington, DC, Armed Forces Institute of Pathology, 1989.
50. Craig JR, Peters RL, Edmondson JL: Fibrolamellar carcinoma of the liver. Cancer 46:372–379, 1980.
51. Dachman AH, Parker RL, Ros PR, et al: Hepatoblastoma: A radiologic-pathologic correlation in 50 cases. Radiology 164:15–19, 1987.
52. Dachman AH, Ros PR, Goodman ZD, et al: Nodular regenerative hyperplasia of the liver: Clinical and radiologic observations. Am J Roentgenol 148:717–722, 1987.
53. Didier D, Weiler S, Rohmer P, et al: Hepatic alveolar echinococcosis: Correlative US and CT study. Radiology 154:179–186, 1985.
54. De Cock KM, Reynolds TB: Amebic and pyogenic liver abscess. In Schiff L, Schiff ER (eds): Diseases of the Liver, 6th ed. Philadelphia, JB Lippincott, 1987, pp 1235–1255.
55. Dehner LP, Ewing SL, Sumner HW: Infantile mesenchymal hamartoma of the liver: Histologic and ultrastructural observations. Arch Pathol Lab Med 99:379–382, 1975.
56. Dehner LP: Hepatic tumors in the pediatric age group: A distinctive clinicopathologic spectrum. Perspect Pediatr Pathol 4:217–268, 1978.
57. Do H, Lambiase RE, Deyoe L, et al: Percutaneous drainage of hepatic abscesses: Comparison of results in abscesses with and without intrahepatic biliary communication. AJR Am J Roentgenol 157:1209–1212, 1991.
58. Ebara M, Ohto M, Wantanabe Y, et al: Diagnosis of small hepatocellular carcinoma: Correlation of MR imaging and tumor histologic studies. Radiology 159:371–377, 1986.
59. Edmunson HA, Craig JR: Neoplasms of the liver. In Schiff L, Schiff ER (eds): Diseases of the Liver, 8th ed. Philadelphia, JB Lippincott, 1987, pp 1109–1158.
60. Edmunson HA, Peters RL: Tumors of the liver: Pathologic features. Semin Roentgenol 18:75–83, 1983.
61. Egglin TK, Rummeny E, Stark DD, et al: Hepatic tumors: Quantitative tissue characterization with MR imaging. Radiology 176:107–110, 1990.
62. Elizondo G, Weissleder R, Stark DD, et al: Amebic liver abscess: Diagnosis and treatment evaluation with MR imaging. Radiology 165:795–800, 1987.
63. Fan ZM, Yamashita Y, Harada M, et al: Intrahepatic cholangiocarcinoma: Spin-echo and contrast-enhanced dynamic MR imaging. AJR Am J Roentgenol 161:313–317, 1993.
64. Fatar S, Bassiony H, Satyanath S: CT of hepatic schistosomiasis mansoni. Am J Roentgenol 145:63–66, 1985.
65. Fernandez MDP, Murphy FB: Hepatic biopsies and fluid drainages. Radiol Clin North Am 29:1311–1328, 1991.
66. Ferrucci JT: MR imaging of the liver. Am J Roentgenol 147: 1103–1116, 1986.
67. Ferrucci JT, Stark DD: Iron oxide–enhanced MR imaging of the liver and spleen: Review of the first five years. AJR Am J Roentgenol 155:943–950, 1990.
68. Filice C, Strosselli M, Brunetti E, et al: Percutaneous drainage of hydatid liver cysts. Radiology 184:579, 1992.
69. Alberti-Flor JJ, O'Hara MF, Weaver F, et al: Malignant fibrous histiocytoma of the liver. Gastroenterology 89:890–893, 1985.
70. Foley WD: Dynamic hepatic CT. Radiology 170:617–622, 1989.
71. Foley WD, Jochem RJ: Computed tomography: Focal and diffuse disease. Radiol Clin North Am 29:1213–1233, 1991.
72. Francis IR, Agha FP, Thompson NW, et al: Fibrolamellar hepatocarcinoma: Clinical, radiologic and pathologic features. Gastrointest Radiol 11:67–72, 1986.
73. Francis IR, Glazer GM, Amendola MA, et al: Hepatic abscesses in the immunocompromised patient: Role of CT in detection, diagnosis, management, and follow-up. Gastrointest Radiol 2:257–262, 1986.
74. Freeny PC: Comparison of uniphasic versus biphasic bolus contrast material injections for dynamic hepatic CT. Radiology 181(P):95, 1991.
75. Freeny PC, Baron RL, Teefey SA: Hepatocellular carcinoma: Reduced frequency of typical findings with dynamic contrast-enhanced CT in a non-Asian population. Radiology 182:143–148, 1992.
76. Freeny PC, Marks WM: Hepatic hemangioma: Dynamic bolus CT. Am J Roentgenol 147:711–719, 1986.

77. Freeny PC, Marks WM: Patterns of contrast enhancement of benign and malignant hepatic neoplasms during bolus dynamic and delayed CT. Radiology 160:613–618, 1986.
78. Friedman AC, Fishman EK, Radecki PD, et al: Focal disease. In Friedman AC (ed): Radiology of the Liver, Biliary Tract, Pancreas and Spleen. Baltimore, Williams & Wilkins, 1987, pp 151–264.
79. Friedman AC, Lichtenstein JE, Goodman Z, et al: Fibrolamellar hepatocellular carcinoma. Radiology 157:583–587, 1985.
80. Reference deleted.
81. Gabata T, Matsui O, Kadoya M, et al: MR imaging of hepatic adenoma. AJR AM J Roentgenol 155:1009–1011, 1990.
82. Giacomantonio M, Ein SH, Mancer K, et al: Thirty years of experience with pediatric primary malignant liver tumors. J Pediatr Surg 19:523–526, 1984.
83. Giorgio A, Tarantino L, Francica G, et al: Unilocular hydatid liver cysts: Treatment with US-guided, double percutaneous aspiration and alcohol injection. Radiology 184:705, 1992.
84. Goldberg MA, Saini S, Hahn PF, et al: Differentiation between hemangiomas and metastases of the liver with ultrafast MR imaging: Preliminary results with T2 calculations. AJR AM J Roentgenol 157:727–730, 1991.
85. Golding SJ, Fletcher EWL: The radiology of secondary malignant neoplasms of the liver. In Wilkins RA, Nunnerly HB (eds): Imaging of the Liver, Pancreas and Spleen. Oxford, Blackwell Scientific, 1990, pp 198–219.
86. Goldman JS, Brandborg LL: Parasitic diseases of the liver. In Zakim D, Boyer TD (eds): Hepatology. Philadelphia, WB Saunders, 1990, pp 1061–1065.
87. Goodman ZD: Benign tumors of the liver. In Okuda K, Ishak KG (eds): Neoplasms of the Liver. Tokyo, Springer-Verlag, 1987, pp 105–125.
88. Goodman ZD, Ishak DG: Angiomyolipomas of the liver. Am J Surg Pathol 8:745–750, 1984.
89. Goodman ZD, et al: Kupffer cells in hepatocellular adenomas. Am J Surg Pathol 11:191–196, 1987.
90. Gordon SC, Watts JC, Vener RJ, et al: Focal hepatic candidiasis with perihepatic adhesions: Laparoscopic and immunohistologic diagnosis. Gastroenterology 88:214–217, 1990.
91. Gowing NFC: Modes of death and post mortem studies. In Smithers D (ed): Hodgkin disease. Edinburgh, Churchill Livingstone, 1973, pp 163–166.
92. Grandin C, Van Beers BE, Robert A, et al: Benign hepatocellular tumors: MRI after superparamagnetic iron oxide administration. J Comput Assist Tomogr 19:412–418, 1995.
93. Gupta RK: Amebic liver abscess: A report of 100 cases. Int Surg 69:261–264, 1984.
94. Haas JE, Muczynski KA, Krallo M, et al: Histopathology and prognosis in childhood hepatoblastoma and hepatocarcinoma. Cancer 64:1082–1095, 1989.
95. Hahn PF, Stark DD, Weissleder R, et al: Clinical application of superparamagnetic iron oxide to MR imaging of tissue perfusion in vascular liver tumors. Radiology 174:361–366, 1990.
96. Halvorsen RA, Korobkin M, Foster WL, et al: The variable CT appearance of hepatic abscesses. Am J Roentgenol 141:941–946, 1984.
97. Hamm B, Fischer E, Taupitz M: Differentiation of hepatic hemangiomas from metastases by dynamic contrast-enhanced MR imaging. J Comput Assist Tomogr 14:205–216, 1990.
98. Hamm B, et al: Focal liver lesions: MR imaging with Mn-DPDP: Initial clinical results in 40 patients. Radiology 182:167–174, 1992.
99. Harmon BH, Berland LL, Lee JY: Effect of varying rates of low-osmolarity contrast media injection for hepatic CT: Correlation with indocyanine green transit time. Radiology 184:379–382, 1992.
100. Heiken JP, Weyman PJ, Lee JKT, et al: Detection of focal hepatic masses: Prospective evaluation with CT, delayed CT, CT during arterial portography, and MR imaging. Radiology 171:47–51, 1989.
101. Hoff FL, Aisen AM, Walden ME, Glazer GM: MR imaging in hydatid disease of the liver. Gastrointest Radiol 12:39–42, 1987.
102. Horowitz ME, Etcubanas E, Webber BL, et al: Hepatic differentiated (embryonal) sarcoma and rhabdomyosarcoma in children: Results of therapy. Cancer 59:396–402, 1987.
103. Ishak KG: Mesenchymal tumors of the liver. In Okuda K, Peter RL (eds): Hepatocellular Carcinoma. New York, John Wiley & Sons, 1976, pp 228–587.
104. Ishak KG: Pathogenesis of liver diseases. In Farber E, Philips MJ, Kaufman N (eds): International Academy of Pathology, Monograph No. 28. Baltimore, Williams & Wilkins, 1987, pp 314–315.
105. Ishak KG, Glunz PR: Hepatoblastoma and hepatocarcinoma in infancy and childhood: Report of 47 cases. Cancer 20:396–422, 1967.
106. Ishak KG, Rabin L: Benign tumors of the liver. Med Clin North Am 59:995–1013, 1975.
107. Ishak KG, Sesterhenn IA, Goodman MD, et al: Epithelioid hemangioendothelioma of the liver: A clinicopathologic and follow-up study of 32 cases. Hum Pathol 15:839–852, 1984.
108. Ishak KG, Willis GW, Cummins SD, et al: Biliary cystadenoma and cystadenocarcinoma: Report of 14 cases and review of the literature. Cancer 39:322–338, 1977.
109. Itai Y, Araki T, Furui S, et al: Computed tomography of primary intrahepatic biliary malignancy. Radiology 147:485–490, 1983.
110. Itai Y, Ohnishi S, Ohtomo K, et al: Regenerating nodules of liver cirrhosis: MR imaging. Radiology 165:419–423, 1987.
111. Itai Y, Ohtomo K, Furui S, et al: Noninvasive diagnosis of small cavernous hemangioma of the liver: Advantage of MRI. Am J Roentgenol 145:1195–1199, 1985.
112. Itoh K: Differentiation between small hepatic hemangiomas and metastases on MR images: Importance of size-specific quantitative criteria. AJR Am J Roentgenol 155:61–65, 1990.
113. Ito Y, Kojiro M, Nakashima T, et al: Pathomorphologic characteristics of 102 cases of Thorotrast-related hepatocellular carcinoma, cholangiocarcinoma, and hepatic angiosarcoma. Cancer 62:1153–1162, 1988.
114. Itoh K, Nishimura K, Togashi K, et al: Hepatocellular carcinoma: MR imaging. Radiology 164:21–25, 1987.
115. Jeffrey RB, Tolentino CS, Chang FC, et al: CT of small pyogenic hepatic abscesses: The cluster sign. AJR Am J Roentgenol 151: 487–489, 1988.
116. Johnson RD, Mueller PR, Ferrucci JT, et al: Percutaneous drainage of pyogenic liver abscesses. Am J Roentgenol 144:463–467, 1985.
117. Jones EC, Chezmar JL, Nelson RC, et al: The frequency and significance of small ($\leq$15 mm) hepatic lesions detected by CT. AJR Am J Roentgenol 158:535–539, 1992.
118. Juimo AG, Gervez F, Angwafo FF: Extraintestinal amebiasis. Radiology 182:181, 1992.
119. Kairaluoma M, Leinonen A, Stahlberg MM, et al: Percutaneous aspiration and alcohol sclerotherapy for symptomatic hepatic cysts. Ann Surg 210:208–215, 1989.
120. Kalovidouris A, Pissiotis C, Pontifex G, et al: CT characterization of multivesicular hydatid cysts. J Comput Assist Tomogr 8:839–845, 1984.
121. Kandel G, Marion NE: Pyogenic liver abscess: New concepts of an old disease. Am J Gastroenterol 79:65–71, 1984.
122. Kanematsu M, Imaeda T, Yamawaki Y, et al: Rupture of hepatocellular carcinoma: Predictive value of CT findings. AJR 158:1247–1250, 1992.
123. Karhunen PJ: Benign hepatic tumors and tumor-like conditions in men. J Clin Pathol 39:183–188, 1986.
124. Kennedy SJ: Biliary. In Ros PR, Bidgood WD (eds): Abdominal Magnetic Resonance Imaging. St. Louis, Mosby–Year Book, 1992, pp 246–251.
125. Kerr DN, Harrison CV, Sherlock S, et al: Congenital hepatic fibrosis. Q J Med 30:91–133, 1961.
126. Keslar PJ, Buck JL, Selby DM: Infantile hemangioendothelioma of the liver revisited. Radiographics 13:657–670, 1993.
127. Khuroo MS, Zargar SA, Mahajan R: *Echinococcus granulosus* cysts in the liver: Management with percutaneous drainage. Radiology 180:141–145, 1991.
128. Klatskin G: Adenocarcinoma of the hepatic duct at its bifurcation within the porta hepatis. Am J Med 38:241–256, 1965.
129. Knight R: Hepatic amebiasis. Semin Liver Dis 4:277–292, 1984.
130. Kojiro M, Nakashima T, Ito Y, et al: Thorium dioxide–related angiosarcoma of the liver: Pathomorphic study of 29 autopsy cases. Arch Pathol Lab Med 109:853–857, 1985.
131. Korobkin MT, Stephens DH, Lee JKT, et al: Biliary cystadenoma and cystadenocarcinoma: CT and sonographic findings. AJR Am J Roentgenol 153:507–511, 1989.
132. Kressel HY, Abbas YA: The liver and pancreas. In Higgins CB, Hricak H, Helms CA (eds): Magnetic Resonance Imaging of the Body, 2nd ed. New York, Raven Press, 1992, pp 721–760.
133. Kunstlinger F, et al: Computed tomography of hepatocellular carcinoma. Am J Roentgenol 134:431–437, 1980.

134. LaBerge JM, Laing FC, Federle MP, et al: Hepatocellular carcinoma: Assessment of resectability by computed tomography and ultrasound. Radiology 152:485–490, 1984.
135. Lambiase RE, Deyoe L, Cronan JJ, Dorfman GS: Percutaneous drainage of 335 consecutive abscesses: Results of primary drainage with 1-year follow-up. Radiology 184:167, 1992.
136. Langer B, Gallinger S: Cystic disease of the liver. In Zuidema GD (ed): Shackelford's Surgery of the Alimentary Tract, 3rd ed. Philadelphia, WB Saunders, 1991, pp 428–442.
137. Langer JC, Rose DB, Keystone JS, et al: Diagnosis and management of hydatid disease of the liver. Ann Surg 199:412–417, 1984.
138. Lee MJ, Saini S, Compton CC: MR demonstration of edema adjacent to a liver metastasis: Pathologic correlation. AJR Am J Roentgenol 157:499–501, 1991.
139. Lee MJ, Saini S, Hamm B, et al: Focal nodular hyperplasia of the liver: MR findings in 35 proved cases. AJR AM J Roentgenol 156: 317–320, 1991.
140. Leslie DF, Johnson CD, MacCarty RL, et al: Single-pass CT of hepatic tumors: Value of globular enhancement in distinguishing hemangiomas from hypervascular metastases. AJR Am J Roentgenol 165:1403–1406, 1995.
141. Levick CB, Rubie J: Hemangioendothelioma of the liver simulating congenital heart disease in infants. Arch Dis Child 28:49–51, 1953.
142. Levine E, Cook LT, Grantham JJ: Liver cysts in autosomal-dominant polycystic kidney disease: Clinical and computed tomographic study. Am J Roentgenol 145:229–233, 1985.
143. Levy DW, Rindsberg S, Friedman AC, et al: Thorotrast-induced hepatosplenic neoplasia: CT identification. Am J Roentgenol 146: 997–1004, 1986.
144. Lewall DB, McCorkell SJ: Rupture of echinococcal cysts: Diagnosis, classification, and clinical implications. Am J Roentgenol 146: 391–394, 1986.
145. Li KC, Glazer GM, Quint LE, et al: Distinction of hepatic cavernous hemangioma from hepatic metastases with MR imaging. Radiology 169:409–415, 1988.
146. Lim KO, Stark DD, Leese PT, et al: Hepatobiliary MR imaging: First human experience with Mn-DPDP. Radiology 178:79–82, 1991.
147. Litwin DEM, Taylor BR, Greig P, Langer B: Nonparasitic cysts of the liver: The case for conservative surgical management. Ann Surg 205:45–48, 1987.
148. Locker GY, Doroshow JH, Zwelling LA, et al: The clinical features of hepatic angiosarcoma: A report of four cases and a review of the English literature. Medicine (Baltimore) 58:48–64, 1979.
149. Lucaya J, Enriquez G, Amat L, et al: Computed tomography of infantile hepatic hemangioendothelioma. Am J Roentgenol 144:821–826, 1985.
150. Lui AF, Hirotza LF, Hirose FM: Multiple adenomas of the liver. Cancer 45:1001–1004, 1980.
151. Lupetin AR, Dash N: Intrahepatic rupture of hydatid cyst: MR findings. AJR Am J Roentgenol 151:491–492, 1988.
152. Mahfouz A-E, Hamm B, Taupitz M, et al: Hypervascular liver lesions: Differentiation of focal nodular hyperplasia from malignant tumors with dynamic gadolinium-enhanced MR imaging. Radiology 186:133, 1993.
153. Mahony B, Jeffrey RB, Federle MP: Spontaneous rupture of hepatic and splenic angiosarcoma demonstrated by CT. Am J Roentgenol 183:965–966, 1982.
154. Maki HS, Hubert BC, Sajjad SM, et al: Primary hepatic leiomyosarcoma. Arch Surg 122:1193–1196, 1987.
155. Marani SAD, Canossi GC, Nicoli FA, et al: Hydatid disease: MR imaging study. Radiology 175:701–706, 1990.
156. Mathieu D, Bruneton JN, Drouillard J, et al: Hepatic adenomas and focal nodular hyperplasia: Dynamic CT study. Radiology 160: 53–58, 1986.
157. Mathieu D, Grenier P, Larde D, et al: Portal vein involvement in hepatocellular carcinoma. Dynamic CT features. Radiology 152: 127–132, 1984.
158. Mathieu D, Rahmouni A, Anglade M-C, et al: Focal nodular hyperplasia of the liver: Assessment with contrast-enhanced turboFLASH MR imaging. Radiology 180:25–30, 1991.
159. Mathieu D, Vasile N, Fagniez P, et al: Dynamic CT features of hepatic abscesses. Radiology 154:749–752, 1985.
160. Matsui O, Kadoya M, Kameyama T, et al: Adenomatous hyperplastic nodules in the cirrhotic liver: Differentiation from hepatocellular carcinoma with MRI. Radiology 173:123–126, 1989.
161. Matsui O, Kadoya M, Suzuki M, et al: Dynamic sequential computed tomography during arterial portography in the detection of hepatic neoplasms. Radiology 146:721–727, 1983.
162. Mattison GR, Glazer GM, Quint LE, et al: MR imaging of hepatic focal nodular hyperplasia: Characterization and distinction from primary malignant hepatic tumors. Am J Roentgenol 148:711–715, 1987.
163. McLean RH, Moller JH, Warwick WJ: Multinodular hemangiomatosis of the liver in infancy. Pediatrics 49:563–573, 1972.
164. Melato M, Laurino L, Mueli E, et al: Relationship between cirrhosis, liver cancer, and hepatic metastases: An autopsy study. Cancer 64: 455–459, 1989.
165. Mergo PJ, Engelken JD, Helmberger T, Ros PR: MRI in focal liver disease: A comparison of small and ultra-small superparamagnetic iron oxide as hepatic contrast agents. J Magn Res Imaging 8: 1073–1078, 1998
166. Miedema BW, Dineen P: The diagnosis and treatment of pyogenic liver abscesses. Ann Surg 200:328–335, 1984.
167. Mitchell DG, Rubin R, Siegelman ES, et al: Hepatocellular carcinoma within siderotic regenerative nodules: Appearance as a nodule within a nodule on MR images. Radiology 178:101–103, 1991.
168. Miller WJ, Dodd GD III, Federle MP, et al: Epithelioid hemangioendothelioma of the liver: Imaging findings with pathologic correlation. AJR Am J Roentgenol 159:53–57, 1992.
169. Miller WJ, Federle MP, Campbell WL: Diagnosis and staging of hepatocellular carcinoma: Comparison of CT and sonography in 36 liver transplantation patients. AJR Am J Roentgenol 157:303–306, 1991.
170. Mones JM, Saldana MJ: Nodular regenerative hyperplasia of the liver in a 4-month-old infant. Am J Dis Child 138:79–81, 1984.
171. Monzawa S, Uchiyama G, Ohtomo K, Araki T: Schistosomiasis japonica of the liver: Contrast-enhanced CT findings in 113 patients. AJR Am J Roentgenol 161:323–327, 1993.
172. Mori W, Nagasako K: Cholangiocarcinoma and related lesions. In Okuda K, Peters RL (eds): Hepatocellular Carcinoma. New York, John Wiley & Sons, 1976, pp 227–246.
173. Moss AA, Goldberg HJ, Stark DD, et al: Hepatic tumors: Magnetic resonance and CT appearance. Radiology 150:141–147, 1984.
174. Mueller PR, Dawson SL, Ferrucci JT, et al: Hepatic echinococcal cyst: Successful percutaneous drainage. Radiology 155:627–628, 1985.
175. Mueller PR, White EM, Glass-Royal M, et al: Infected abdominal tumors: Percutaneous catheter drainage. Radiology 173:627–629, 1989.
176. Munoz M, Bosch Y: Epidemiology of hepatocellular carcinoma. In Okuda K, Ishak KG (eds): Neoplasms of the Liver. Tokyo, Springer-Verlag, 1987, pp 3–19.
177. Munzer D: New perspectives in the diagnosis of *Echinococcus* disease. J Clin Gastroenterol 13:415–423, 1991.
178. Murakami T, Kim T, Nakamura H: Hepatitis, cirrhosis, and hepatoma. J Magn Res Imaging 8:346–358, 1998.
179. Murphy BJ, Castillas J, Ros PR, et al: The CT appearance of cystic masses of the liver. Radiographics 9:307–322, 1989.
180. Nakanuma Y, Ohta G, Sasaki K: Nodular regenerative hyperplasia of the liver associated with polyarteritis nodosa. Arch Pathol Lab Med 108:133–135, 1984.
181. Nakashima T, Okuda K, Kojiro M, et al: Pathology of hepatocellular carcinoma in Japan: 232 consecutive cases autopsied in ten years. Cancer 51:863–877, 1983.
182. Nelson RC, Chezmar JL, Sugarbaker PH, et al: Hepatic tumors: Comparison of CT during arterial portography, delayed CT, and MR imaging for preoperative evaluation. Radiology 172:27–34, 1989.
183. Nelson RC, Moyers JH, Chezmar JL, et al: Hepatic dynamic sequential CT: Section enhancement profiles with a bolus of ionic and nonionic contrast agents. Radiology 178:499–502, 1991.
184. Noguchi S, Yamamoto R, Tatsuta M, et al: Cell features and patterns in fine-needle aspirates of hepatocellular carcinoma. Cancer 58: 321–328, 1986.
185. Nokes SR, Baker ME, Spritzer CE, et al: Hepatic adenoma: MR appearance mimicking focal nodular hyperplasia. J Comput Assist Tomogr 12:885–887, 1988.
186. Nompleggi DJ, Farraye FA, Singer A, et al: Hepatic schistosomiasis: Report of two cases and literature review. Am J Gastroenterol 86: 1658–1664, 1991.
187. Ohtomo K, Itai Y, Fururi S, et al: MR imaging of portal vein

thrombus in hepatocellular carcinoma. J Comput Assist Tomogr 9: 328–329, 1985.

188. Ohtomo K, Itai Y, Yoshida H, et al: Regenerating nodules of liver cirrhosis: MR imaging with pathologic correlation. AJR Am J Roentgenol 154:505–507, 1990.
189. Ohtomo K, Itai Y, Yoshikawa K, et al: Hepatic tumors: Dynamic MR imaging. Radiology 163:27–31, 1987.
190. O'Neil J, Ros PR: Knowing hepatic pathology aids MRI of liver tumors. Diagn Imaging 11:58–65, 1989.
191. Outwater E, Tomaszewski JE, Daly JM, et al: Hepatic colorectal metastases: Correlation of MR imaging and pathologic appearance. Radiology 180:327–332, 1991.
192. Palacios E, Shannon M, Solomon C, et al: Biliary cystadenoma: Ultrasound, CT, and MRI. Gastrointest Radiol 15:313–316, 1990.
193. Paling MR, Abbitt PL, Mugler JP, et al: Liver metastases: Optimization of MR imaging pulse sequences at 1.0 T. Radiology 167: 695–699, 1988.
194. Pandolfo I, Blandino G, Scribano E, et al: CT findings in hepatic involvement by *Echinococcus granulosus*. J Comput Assist Tomogr 8:839–845, 1984.
195. Pardes JG, Bryan PJ, Gauderer MWL: Spontaneous regression of infantile hemangioendotheliomatosis of the liver. J Ultrasound Med 1:349–353, 1982.
196. Paushter DM, Zeman RK, Schiebler MJ, et al: CT evaluation of suspected hepatic metastases: Comparison of techniques for IV contrast enhancement. AJR Am J Roentgenol 152:267–271, 1989.
197. Peterson MS, Baron RL, Dood GD III, et al: Hepatic parenchymal perfusion defects associated with CTAP: Imaging-pathologic correlation. Radiology 185:149–155, 1992.
198. Pitt HA: Surgical management of hepatic abscesses. World J Surg 14:498–504, 1990.
199. Pitt HA: Liver abscess. In Zuidema GD (ed): Shackelford's Surgery of the Alimentary Tract, 3rd ed. Philadelphia, WB Saunders, 1991, pp 443–465.
200. Poeckler-Schoeniger C, Koepke J, Gueckel F, et al: MRI with superparamagnetic iron oxide: Efficacy in the detection and characterization of focal hepatic lesions. Magn Res Imaging 17:383–392, 1999.
201. Radin DR, Craig JR, Colletti PM: Hepatic epithelioid hemangioendothelioma. Radiology 169:145–148, 1988.
202. Radin DR, Ralls PW, Colletti PM, et al: CT of amebic liver abscess. AJR Am J Roentgenol 150:1297–1301, 1988.
203. Ralls PW, Barnes PF, Johnson MB, et al: Medical treatment of hepatic amebic abscess: Rare need for percutaneous drainage. Radiology 165:805–807, 1987.
204. Ralls PW, Henley DS, Colletti PM, et al: Amebic liver abscess: MR imaging. Radiology 165:801–804, 1987.
205. Reed SL: Amebiasis: An update. Clin Infect Dis 14:385–393, 1992.
206. Reimer P, Tombach B: Hepatic MRI with SPIO: Detection and characterization of focal liver lesions. Eur Radiol 8:1198–1204, 1998.
207. Reinig JW: Differentiation of hepatic lesions with MR imaging: The last word. Radiology 179:601–602, 1991.
208. Roberts JL, Fishman EK, Hartman DS, et al: Lipomatous tumors of the liver: Evaluation with CT and US. Radiology 158:613–617, 1986.
209. Rolfes DB: Fibrolamellar carcinoma of the liver. In Ishak KG, Okuda K (eds): Neoplasms of the Liver. Tokyo, Springer-Verlag, 1987, pp 137–142.
210. Rooks JB, Ory HW, Ishak KG, et al: Epidemiology of hepatocellular adenoma: The role of contraceptive steroid use. JAMA 242:644–648, 1979.
211. Ros PR: Malignant liver tumors. In Ros PR, Bidgood WD (eds): Abdominal Magnetic Resonance Imaging. St. Louis, Mosby–Year Book, 1993, pp 208–218.
212. Ros PR: Benign tumors and tumor-like conditions. In Ros PR, Bidgood WD (eds): Abdominal Magnetic Resonance Imaging. St. Louis, Mosby–Year Book, 1993, pp 195–208.
213. Ros PR: Computed tomography-pathologic correlations in hepatic tumors. In Ferrucci JT, Mathieu DG (eds): Advances in Hepatobiliary Radiology. St. Louis, Mosby–Year Book, 1990, pp 75–108.
214. Ros PR, Buck JL, Goodman ZD, et al: Intrahepatic cholangiocarcinoma: Radiologic-pathologic correlation. Radiology 167:689–693, 1988.
215. Ros PR, Goodman ZD, Ishak KG, et al: Mesenchymal hamartoma of the liver: Radiologic-pathologic correlation. Radiology 158:619–624, 1986.
216. Ros PR, Lubbers PR, Olmsted WW, Morillo G: Hemangioma of the liver: Heterogeneous appearance on T2-weighted images. Am J Roentgenol 149:1167–1170, 1987.
217. Ros PR, Murphy BJ, Buck JL, et al: Encapsulated hepatocellular carcinoma: Radiologic findings and pathologic correlation. Gastrointest Radiol 15:233–237, 1990.
218. Ros PR, Olmsted WW, Dachman AH, et al: Undifferentiated (embryonal) sarcoma of the liver: Radiologic-pathologic correlation. Radiology 160:141–145, 1986.
219. Ros PR, Rasmussen JF, Li KCP: Radiology of malignant and benign liver tumors. Curr Probl Diagn Radiol 18:95–155, 1989.
220. Rozanes I, Acunas B, Celik L, et al: CT in lobar atrophy of the liver caused by alveolar *Echinococcus*. J Comput Assist Tomogr 16: 216–218, 1992.
221. Rummeny E, Weissleder R, Stark DD, et al: Primary liver tumors: Diagnosis by MR imaging. AJR Am J Roentgenol 152:63-72, 1989.
222. Ryan J, Straus DJ, Lange C: Primary lymphoma of the liver. Cancer 61:370–375, 1988.
223. Sanfelippo PM, Beahrs OH, Weiland LK: Cystic diseases of the liver. Ann Surg 179:922–925, 1974.
224. Saraswat VA, Agarwal DK, Baijal SS, et al: Percutaneous catheter drainage of amebic liver abscess. Clin Radiol 45:187, 1992.
225. Saremi F: Percutaneous drainage of hydatid cysts: Use of a new cutting device to avoid leakage. AJR Am J Roentgenol 158:83–85, 1992.
226. Scatarige JC, Kenny JM, Fishman EK, et al: CT of giant cavernous hemangioma. Am J Roentgenol 149:83–85, 1987.
227. Scatarige JC, et al: Computed tomography of calcified liver masses. J Comput Assist Tomogr 7:83–89, 1983.
228. Scherer U, Weinzerl M, Sturm R, et al: Computed tomography of hydatid disease of the liver: A report on 13 cases. J Comput Assist Tomogr 2:612–617, 1978.
229. Schmiedl U, Paajanen H, Arakawa M, et al: MR imaging of liver abscesses: Application of Gd-DTPA. Magn Reson Imaging 6:9–16, 1988.
230. Sherlock S: Diseases of the Liver and Biliary System. Oxford, Blackwell Scientific, 1981, pp 431–435.
231. Shirkhoda A: CT findings in hepatosplenic and renal candidiasis. J Comput Assist Tomogr 11:795–798, 1987.
232. Shirkhoda A, Lopez-Berestein G, Holbert JM, et al: Hepatosplenic fungal infection: CT and pathologic evaluation after treatment with liposomal amphotericin B. Radiology 159:349–353, 1986.
233. Shirkhoda A, Ros PR, Farah J, et al: Lymphoma of the solid abdominal viscera. Radiol Clin North Am 28:785–799, 1990.
234. Silverman PM, Ram PC, Korobkin M: CT appearance of induced angiosarcoma of the liver. J Comput Assist Tomogr 4:655–658, 1983.
235. Stain SC, Yellin AE, Donovan AJ, et al: Pyogenic liver abscess. Arch Surg 126:991–996, 1991.
236. Stanley P, Hall TR, Woolley MM, et al: Mesenchymal hamartomas of the liver in childhood: Sonographic and CT findings. Am J Roentgenol 147:1035–1039, 1986.
237. Stark DD, Felder RC, Wittenberg J, et al: Magnetic resonance imaging of cavernous hemangioma of the liver: Tissue-specific characterization. Am J Roentgenol 145:213–222, 1985.
238. Stark DD, Weissleder R, Elizondo G, et al: Superparamagnetic iron oxide: Clinical application as a contrast agent for MR imaging of the liver. Radiology 168:297–301, 1988.
239. Stark DD, Wittenberg J, Butch RJ, et al: Hepatic metastases: Randomized, controlled comparison of detection with MR imaging and CT. Radiology 165:399–406, 1987.
240. Stark DD, Wittenberg J, Edelman RR, et al: Detection of hepatic metastases: Analysis of pulse sequence performance in MR imaging. Radiology 159:365–370, 1986.
241. Steiner PE: Nodular regenerative hyperplasia of the liver. Am J Pathol 49:943–953, 1959.
242. Stephens DHL: The liver. In Haaga JR, Alfidi RJ (eds): Computed tomography of the whole body. St. Louis, Mosby–Year Book, 1988, pp 792–853.
243. Stocker JT, Ishak KG: Undifferentiated (embryonal) sarcoma of the liver: Report of 31 cases. Cancer 42:336–348, 1978.
244. Stocker JT, Ishak KG: Mesenchymal hamartoma of the liver: Report of 30 cases and review of the literature. Pediatr Pathol 1:245–267, 1983.

245. Stromeyer FW, Ishak KG: Nodular transformation (nodular "regenerative" hyperplasia) of the liver: A clinicopathological study of 30 cases. Hum Pathol 12:60–71, 1981.
246. Subramanyan BR, Balthazar EJ, Hilton S, et al: Hepatocellular carcinoma with venous invasion: Sonographic-angiographic correlation. Radiology 150:793–796, 1984.
247. Sutton CA, Eller JL: Mesenchymal hamartoma of the liver. Cancer 22:29–34, 1968.
248. Takayasu K, Moriyama N, Muramatsu Y, et al: The diagnosis of small hepatocellular carcinomas: Efficacy of various imaging procedures in 100 patients. AJR Am J Roentgenol 155:49–54, 1990.
249. Teefey SA, et al: Computed tomography and ultrasonography of hepatoma. Clin Radiol 37:339–345, 1986.
250. Thaler M, Pastakia B, Shawker TH, et al: Hepatic candidiasis in cancer patients: The evolving picture of the syndrome. Ann Intern Med 108:88–100, 1988.
251. Tham R, et al: Focal nodular hyperplasia of the liver: Features on Gd-DTPA–enhanced MR. AJR Am J Roengenol 153:884–885, 1989.
252. Thoeni RF: Clinical applications of magnetic resonance imaging of the liver. Invest Radiol 26:266–273, 1991.
253. Thompson WM, Chisholm DP, Tank R: Plain film roentgenographic findings in alveolar hydatid disease: *Echinococcus multilocularis*. Am J Roentgenol 116:345–358, 1972.
254. Thorsen MK, Quiroz F, Lawson TL, et al: Primary biliary carcinoma: CT evaluation. Radiology 142:479–483, 1984.
255. Titelbaum DS, Burke DR, Meranze SG, et al: Fibrolamellar hepatocellular carcinoma: Pitfalls in nonoperative diagnosis. Radiology 167:25–30, 1988.
256. Titelbaum DS, Hatabu H, Schiebler ML, et al: Fibrolamellar hepatocellular carcinoma: MR appearance. J Comput Assist Tomogr 12: 588–591, 1988.
257. Van Allan RJ, Katz MD, Johnson MB, et al: Uncomplicated amebic liver abscess: Prospective evaluation of percutaneous therapeutic aspiration. Radiology 183:827, 1992.
258. Van Beers B, Roche A, Mathieu D, et al: Epithelioid hemangioendothelioma of the liver: MR and CT findings. J Comput Assist Tomogr 16:420–424, 1992.
259. VanSonnenberg E, Mueller PR, Schiffman HR, et al: Intrahepatic amebic abscesses: Indications for and results of percutaneous catheter drainage. Radiology 156:631–635, 1985.
260. Vilgrain V, Flejou J-F, Arrivé L, et al: Focal nodular hyperplasia of the liver: MR imaging and pathologic correlation in 37 patients. Radiology 184:699–703, 1992.
261. Vogl TJ, Kommel S, Hammerstingl R, et al: Liver tumors: Comparison of MR imaging with Gd-EOB-DTPA and Gd-DTPA. Radiology 200:59, 1996.
262. von Sinner W, te Starke L, Clark D, Sharif H: MR imaging in hydatid disease. AJR Am J Roentgenol 157:741–745, 1991.
263. Walkey MM: Dynamic hepatic CT: Dr. Walkey replies. Radiology 181:22–23, 1991.
264. Walkey MM: Dynamic hepatic CT: How many years will it take 'til we learn? Radiology 181:17–18, 1991.
265. Wall SD, Fisher MR, Amparo EG, et al: Magnetic resonance imaging in the evaluation of abscesses. Am J Roentgenol 144:1217–1221, 1985.
266. Wanless IR, Mawdsley C, Adams R: Pathogenesis of focal nodular hyperplasia. Hepatology 5:1194–1200, 1985.
267. Wanless IR, Solt LC, Kortan P, et al: Nodular regenerative hyperplasia of the liver associated with macroglubulinemia. Am J Med 170: 1203–1209, 1981.
268. Weinberg AG, Finegold MJ: Primary malignant tumors of childhood. Hum Pathol 14:512–537, 1983.
269. Weiss L, Gilbert HA: Liver Metastases. Boston, GK Hall, 1992.
270. Weissleder R, Saini S, Stark DD, et al: Pyogenic liver abscess: Contrast-enhanced MR imaging in rats. AJR Am J Roentgenol 150: 115–120, 1988.
271. Weissleder R, Stark DD: MRI of the liver. In Silverman PM, Zeman RK (eds): CT and MRI of the liver and biliary system. New York, Churchill Livingstone, 1990, pp 39–62.
272. Weissleder R, Stark DD, Elizondo G: MRI of hepatic lymphoma. Magn Reson Imaging 6:675–681, 1988.
273. Welch TJ, Sheedy PF, Johnson CM, et al: Radiographic characteristics of benign liver tumors: Focal nodular hyperplasia and hepatic adenoma. Radiographics 5:673–682, 1985.
274. Wheeler DA, Edmondson HA: Cystadenoma with mesenchymal stroma (CMS) in the liver and bile ducts: A clinicopathologic study of 17 cases, 4 with malignant change. Cancer 56:1434–1445, 1985.
275. Wilcox DM, Weinreb JC, Lesh P: MR imaging of a hemorrhagic hepatic cyst in a patient with polycystic liver disease. J Comput Assist Tomogr 9:183–185, 1985.
276. Wilson MA: Metastatic disease of the liver. In Wilson MA, Ruzicka FF (eds): Modern Imaging of the Liver. New York, Marcel Dekker, 1989, pp 631–659.
277. Wittenberg J: MRI of hepatic metastatic disease. In Ferrucci JT, Stark DD (eds): Liver Imaging: Current Trends and New Techniques. Boston, Andover Medical Publishers, 1990, pp 153–161.
278. Wittenberg J, Stark DD, Forman BH, et al: Differentiation of hepatic metastases from hepatic hemangiomas and cysts by using MR imaging. AJR Am J Roentgenol 151:79–84, 1988.
279. Wojtasek DA, Teixidor HS: Echinococcal hepatic disease: Magnetic resonance appearance. Gastrointest Radiol 14:158–160, 1989.
280. Wooten WB, Bernardino ME, Goldstein HM: Computed tomography of necrotic hepatic metastases. Am J Roentgenol 131:839–842, 1978.
281. Yamamoto H, Yamashita Y, Yoshimatsu S, et al: Hepatocellular carcinoma in cirrhotic livers: Detection with unenhanced and iron oxide–enhanced MR imaging. Radiology 195:106–112, 1995.
282. Yoshida H, Itai Y, Ohtomo K, et al: Small hepatocellular carcinoma and cavernous hemangioma: Differentiation with dynamic FLASH MR imaging with Gd-DTPA. Radiology 171:339–342, 1989.
283. Yoshikawa J, Matsui O, Takashima T, et al: Fatty metamorphosis in hepatocellular carcinoma: Radiologic features in 10 cases. AJR Am J Roentgenol 151:717–720, 1988.
284. Zornoza J, Ginaldi S: Computed tomography in hepatic lymphoma. Radiology 138:405–410, 1981.

36 Liver: Normal Anatomy, Imaging Techniques, and Diffuse Diseases

Elmar M. Merkle, Thorsten R. Fleiter,
Daniel T. Boll, Hans-Juergen Brambs

Normal Anatomy

The liver is the largest abdominal organ. Encapsulated by a dense layer of connective tissue, it resides in the upper right abdominal quadrant, although it can reach into the epigastrium and, sometimes, as far as the spleen. The liver's external structure features a convex diaphragmatic and a concave visceral surface.

The diaphragmatic surface is affixed to a triangular section of the lumbar part of the diaphragm—the bare area, or area nuda. The bare area is demarcated by folds of the parietal and visceral peritoneum forming the coronary ligament of the liver. To the right and left, the coronary ligament extends into the right and left triangular ligaments. Toward the ventral aspect of the liver, both limbs of the coronary ligament merge to form the falciform ligament, which serves to divide the liver "anatomically" into right and left hepatic lobes. These ligaments together anchor the liver to the diaphragm. Besides the bare area, only the fossae of the gallbladder and the inferior vena cava (IVC) are not covered by peritoneum.

On the visceral surface of the organ, the individual lobes are demarcated by several fossae and fissures. Two sagittally running fissures are joined by a transverse fissure, forming an H-like structure. The transverse fissure contains the porta hepatis. The left sagittal fissure, which separates the left and right hepatic lobes on the inferior aspect of the liver, contains at its ventral end the ligamentum teres (a remnant of the umbilical vein) and at its dorsal end the ligamentum venosum, which represents the obliterated ductus venosus. (*Note:* In the fetus, the ductus venosus forms a bypass linking the IVC and the umbilical vein.)

The right sagittal fissure contains the gallbladder and, dorsal to it, the IVC. Anterior to the porta hepatis is the slight prominence of the quadrate lobe; posterior to it is the caudate lobe. In the porta hepatis, the hepatoduodenal ligament contains the hepatic artery and portal vein as well as the common hepatic duct, whereby the hepatic artery usually lies between the latter two structures. The hepatic artery carries oxygenated blood to the liver. This blood constitutes about 20% to 25% of the total blood volume in the organ.

The portal vein, in contrast, carries nutrient-rich blood from the digestive system (75% to 80% of total blood volume). The hepatic artery and the portal vein ramify parallel to each other. In healthy subjects, the caliber of the portal vein's branches is larger than the branches of the hepatic artery. Venous return takes place through the hepatic veins, which drain directly into the IVC.

Advances in surgical procedures on the liver have made the anatomic division of the liver (into right, left, quadrate, and caudate lobes) obsolete, and this division has yielded to a functionally oriented segmentation. This segmentation is based primarily on the surgical definition of feasible intrahepatic boundaries of resection.[6, 13, 21, 59] Computed tomography (CT), magnetic resonance imaging (MRI), and, to a lesser extent, the other cross-sectional imaging techniques provide excellent visualization of the segmental structure of the liver and of the anatomic relationship of hepatic structures to adjacent abdominal viscera.

Centrally placed in each segment is a branch of the portal vein and the hepatic artery as well as a bile duct. The hepatic veins lie between the individual segments. Over the last 50 years, several systems have been proposed for classifying the segments of the liver. Although many of these are similar, the most common is the nomenclature proposed by Bismuth-Couinaud (Figs. 36–1 and 36–2).

In the *Bismuth-Couinaud system*, liver segment I corresponds to the caudate lobe. Because of its vascular supply, this segment is in the unique position of receiving branches from both the main trunk of the portal vein and from its right and left lateral branches. Furthermore, it drains not into the hepatic veins but directly into the IVC.

Liver segments II to VIII are defined by their positions relative to branches of the portal vein and the hepatic veins. The portal vein divides early into a left and a right branch, whereby the left branch supplies segments II through IV and the right branch supplies segments V through VIII. The liver can also be divided by the regions drained by the left, median, and right hepatic veins, which all run obliquely, from ventrocaudal to dorsocranial, into the IVC.

The Bismuth-Couinaud classification also defines a so-

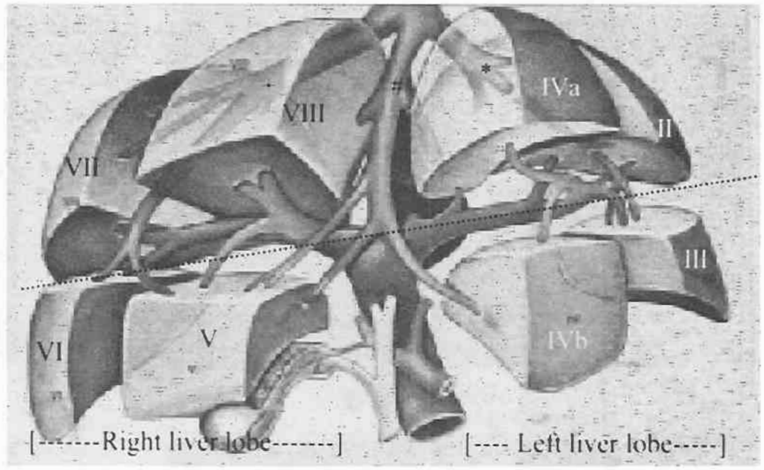

Figure 36–1. Schematic division of liver segments (II to VIII) according to the Bismuth-Couinaud classification. The definition of the individual segments corresponds to the portal venous supply as well as to separation by the right (+), middle (#), and left (*) hepatic veins. Segment I, corresponding to the caudate lobe, because of its special vascularization, is not included. The *dashed line* represents the horizontal plane separating the cranial from the caudal hepatic segments.

called portal vein plane (see Figs. 36–1 and 36–2). This is simply the transverse plane intersecting the liver at the level of the portal vein bifurcation into right and left branches. In the functional left liver lobe, segment II lies above the portal vein plane to the left of and laterally to the left hepatic vein. Segment III lies beneath this plane, also to the left of and laterally to the left hepatic vein. Segment IV, delineated by the left and median hepatic veins, may be further subdivided into segments IVa (above the portal vein plane) and IVb (beneath this plane).

To the right of and lateral to the median hepatic vein are segments V through VIII, forming the functional right liver lobe. Segment V lies between the median and right hepatic veins below the portal vein plane. Segment VI also lies beneath the portal vein plane, but posterolateral to the right hepatic vein. Segment VII lies directly cranial to segment VI, thus, above the portal vein plane. Finally, segment VIII lies between the median and right hepatic veins above the portal vein plane.

The Bismuth-Couinaud system serves as the basis for describing the location of hepatic focal lesions. Interindividual variability of the vessels, particularly in the right liver lobe, however, is significant. In up to 20% of subjects, there may be reduplication of the right hepatic vein. Data from three-dimensional (3D) reconstructions of the right hepatic vein and of the portal venous system have shown that only an anterosuperior sector and a posteroinferior sector are constantly visualized in the right hepatic lobe.[69] The scissura between the anterosuperior and posteroinferior sectors shows an angled orientation; that is, its cranial part is tilted posteriorly (~60 degrees), and its caudal part is tilted slightly anteriorly, in relation to the coronal plane. Furthermore, portal branches often cross the plane of the right hepatic vein, and no portal venous plane can be seen separating the anterosuperior and posteroinferior sector; hence, the right hepatic vein cannot serve as a reliable landmark for dividing the anteromedial and posterolateral segments of the right hepatic lobe.

The left liver lobe presents fewer variations in vascular anatomy. Reduplication of the median hepatic vein is seen in about 5% of subjects; of the left hepatic vein, in about 15%.

There may also be some variation in arterial structure, particularly in segment IV. In about 8% of cases, the dorsal portion of segment IV is supplied by the right hepatic artery, hence from the contralateral side, functionally speaking.[33]

In about 30% of patients, accessory portal segments, analogous to the caudate lobe (segment I), may be observed; each is supplied directly from the main portal venous trunk or from its right branch.[5, 69] The presence of a Riedel's lobe (Fig. 36–3), usually resulting from a prominent, inferiorly positioned narrow right lobe of the liver (which significantly extends the expected confines of the liver), should be identified and differentiated from extracapsular extension caused by a liver tumor. When the caudate lobe is prominent, and even with a normal caudate lobe, the inferior caudate extension (or *papillary process*) can simulate a mass in the portocaval region.[4] One can determine the correct diagnosis by recognizing the continuity of this process with the caudate lobe on contiguous axial sections.

Following segmental hepatic resections, rapid hypertrophy of the remaining liver segments occurs. This results in a distortion of the expected anatomy because the major vessels become displaced by the enlarging segments.

Besides diffuse liver diseases (e.g., hepatic cirrhosis), which produce a nodular contour in the organ, a nodular surface structure may be seen as a normal variation in some subjects (Fig. 36–4). Also important are indentations of the liver's surface resembling the furrows made by the drawing in of a sack with strings, which reflect the structure of the muscular bundles forming the diaphragm and which are more commonly seen in patients with lung diseases (Fig. 36–5).

Because of the significant interindividual variation in vascularity, modern surgical practice has been to reduce reliance on a rigid schematic division of the liver into segments and consider, instead, the patient's individual vascular situation in operations involving segments or even subsegments of the liver.[19, 46, 65, 67] A liver segment is defined solely by its vascular supply. On the basis of contrast-enhanced helical CT data sets, it is possible to construct

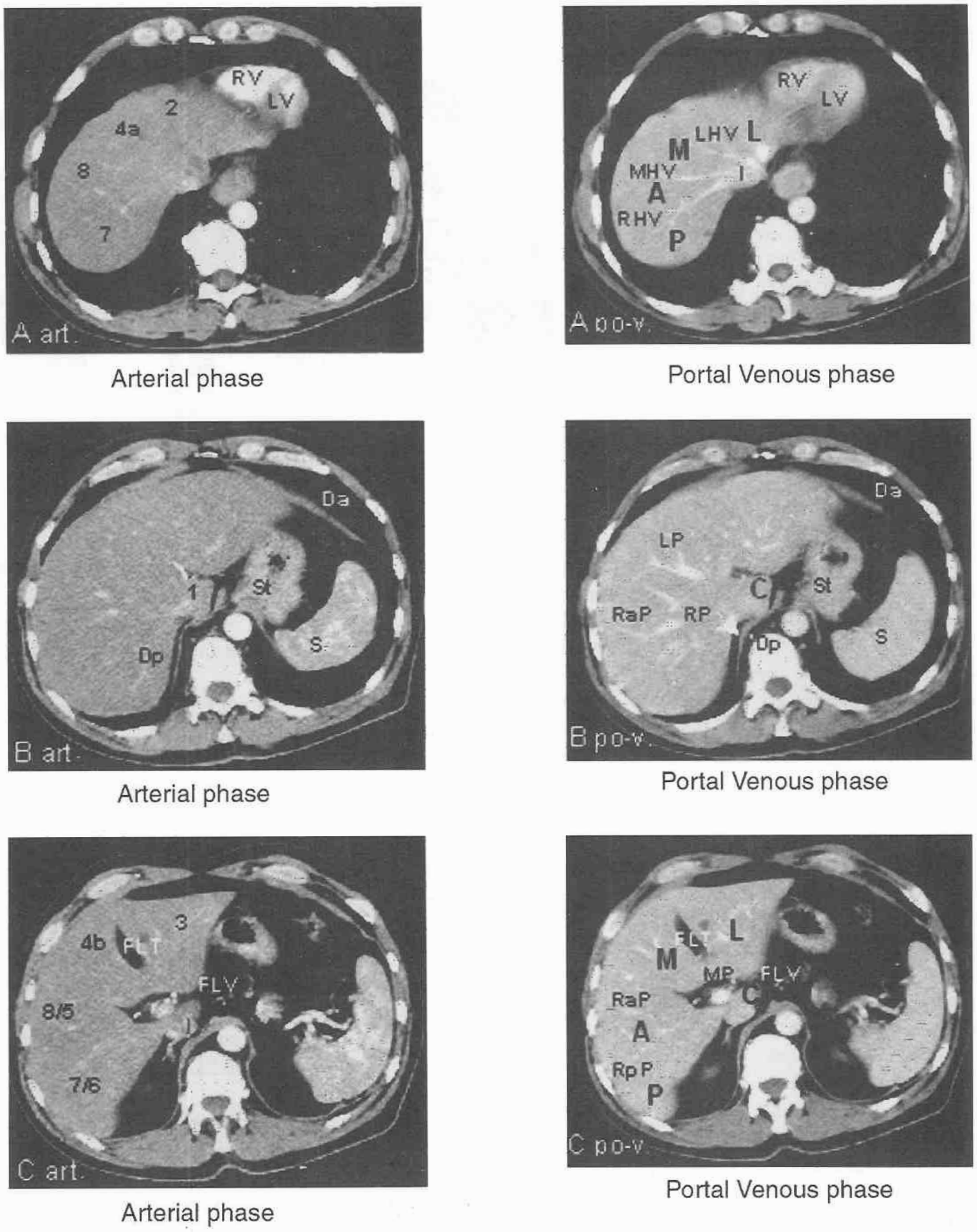

Figure 36–2. *A–E,* Dual-phase-contrast, enhanced liver scans on different levels. *A,* The liver is shown to the right of the midline. Both the left ventricle (LV) and the right ventricle (RV) of the contrast-enhanced heart are clearly seen above the diaphragm in the left side of the chest. The hepatic venous branches are clearly identified, with the right hepatic vein (RHV) coursing between the posterior (P) and the anterior (A) segments of the right lobe. The middle hepatic vein (MHV) courses between the anterior segment (A) of the right lobe and the medial segment (M). The left hepatic vein (LHV) courses between the medial segment (M) and the lateral segment (L) of the left lobe. According to the Bismuth Classification (see arterial phase image, *left*), the segments 2, 4a, 7, 8 represent the superior aspect of each of the traditional segments. The inferior vena cava (I) enters its intrahepatic portion. *B,* Level 30 mm caudal to *A* shows the right portal vein (RP) and left portal vein (LP). Note the anterior branch of the right portal vein (RaP). According to the Bismuth Classification, this is the craniocaudal demarcation level, separating the superior segments (2, 4a, 7, 8) and the inferior segments (3, 4b, 5, 6). The adjacent organs at this level can be easily identified with the stomach (St) to the left and the diaphragm (Da) seen anteriorly (Da) and posteriorly (Dp, indicated by an arrow). S, spleen. *C,* Level 22 mm caudal to *B* shows the main portal vein (MP), giving rise to the right portal vein, which bifurcates into anterior branches (RaP) and posterior branches (RpP). The fissure of the ligamentum teres (FLT) with the obliterated remnants of the round ligament is seen, separating the lateral (L) and medial (M) segments of the left lobe of the liver. According to the Bismuth Classification, segments 3 and 4b can be seen in the left liver lobe (lying inferior to the level of the transverse scissura). The right liver lobe is displayed at the junction between the superior and inferior segments of the anterior (A) (8/5) and the posterior (P) part (7/6). The fissure of the ligamentum venosum (FLV) separates the lateral part of the left liver lobe (L) and the caudate lobe (C).

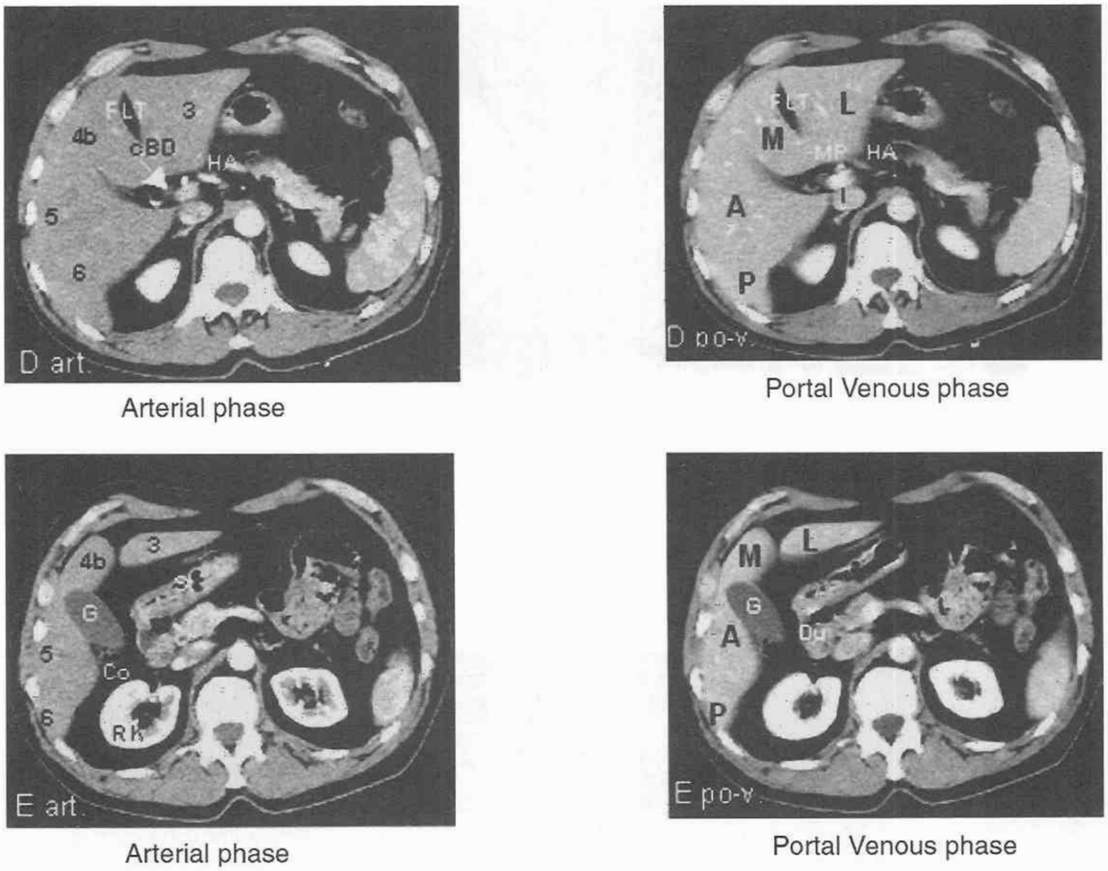

Figure 36–2. *Continued. D,* Level 18 mm caudal to *C* shows the main portal vein(MP) in the porta hepatis. The hepatic artery (HA) can be seen anterior and medial to the main portal vein (MP). Note the common bile duct (cBD) *(arrow)*. Bismuth segments 3, 4b, 5, and 6 are caudal to the transverse scissura. *E,* Level 30 mm caudal to *D* shows the superior aspect of the gallbladder (G) and the gallbladder fossa, separating the medial inferior segment (M) 4b and the anterior segment (A) 5. The demarcation between the anterior segment (A), segment 5, and posterior segment (P), segment 6, can only be approximated. Organs bordering the liver are the stomach, colon (Co), duodenum (Du), and right kidney (RK).

3D images of the liver, which assist the surgeon in exact preoperative planning of the procedure (Fig. 36–6).

The 5-year survival rate in patients undergoing resection of both solitary and multiple hepatic metastases can be significantly enhanced if the following three conditions are met:

1. Absence of extrahepatic metastases.
2. Complete excision of all malignant tissue in the liver.
3. Adequate volume of intact residual hepatic parenchyma (at least 30% of the original organ volume).

Figure 36–3. Riedel's lobe *(arrows)* in a 77-year old woman has resulted from a prominent, inferiorly positioned narrow right hepatic lobe, which significantly extends the expected confines of the liver.

CT Appearance and Imaging Technique

Despite increasing competition from MRI over the last decade, the role of CT in the diagnosis of diseases of the liver has not been significantly affected. Besides the general availability of the method, the dominance of CT is due primarily to its excellent visualization of anatomic relationships and of the liver's position relative to adjacent organs (see Fig. 36–2). These capabilities have been further enhanced by technologic developments that fundamentally affect the method.

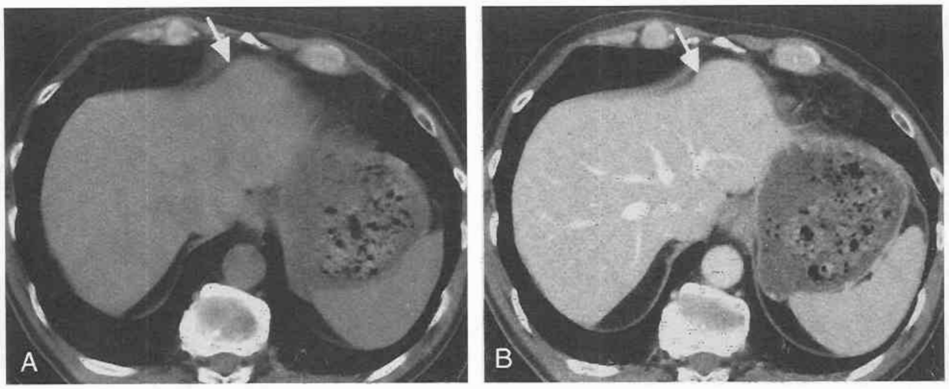

Figure 36–4. Protuberant liver *(arrows)* in a 64-year-old man. Both unenhanced *(A)* and intravenous contrast-enhanced *(B)* scans show normal liver parenchyma but do not visualize a tumor responsible for this protrusion.

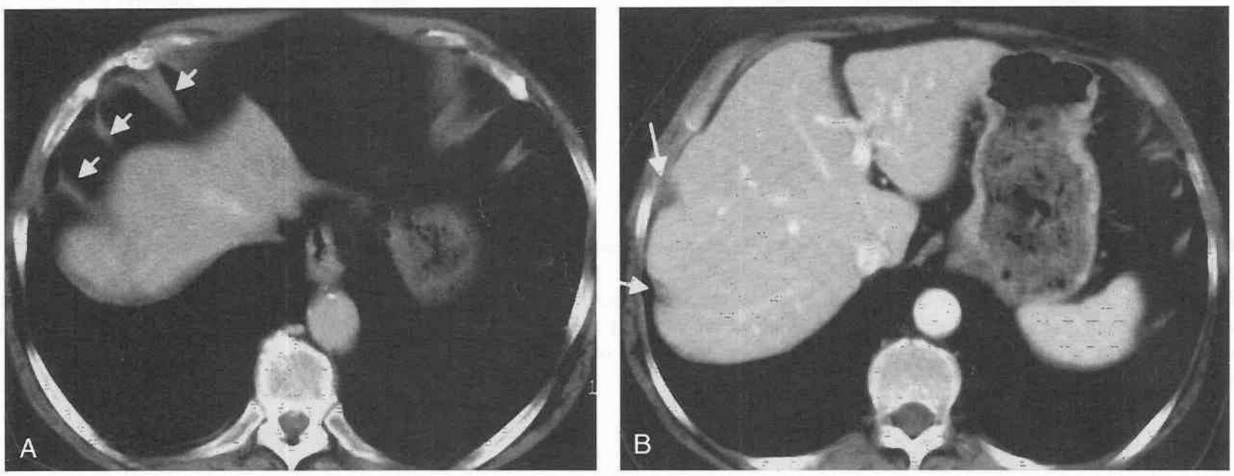

Figure 36–5. Chronic obstructive pulmonary disease in a 52-year-old woman. On the diaphragmatic surface *(A)*, the liver displays a wavelike contour caused by the impression of muscular bundles *(arrows)* of the diaphragm. This phenomenon *(arrows)* is also apparent in more caudally placed sections of the liver *(B)*.

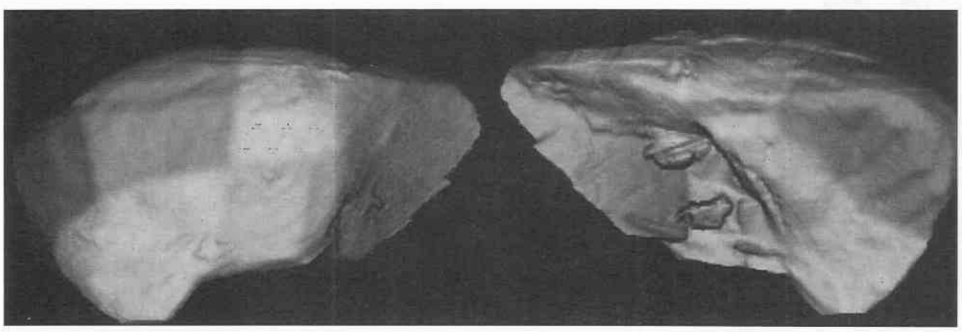

Figure 36–6. Volume rendering of the various liver segments defined by the portal venous branches.

The most important of these has been the introduction of single-slice helical CT, in the early 1990s, whose rapid and continuous data acquisition has proved advantageous.[31] Other important technologic advances over the past decade include the drastic reduction in scan times owing to significantly shorter gantry rotation times (as short as 0.5 second).

Another advance was the development of multiple slice helical CT scanners; as of early 2000, up to sixteen parallel CT slices per tube rotation (with partial reconstructions) could be simultaneously acquired.

The normal CT attenuation of the liver in unenhanced studies varies interindividually between 38 and 80 Hounsfield units (HU). Intraindividually, the normal liver appears homogeneous at CT visualization, and its attenuation exceeds that of the spleen in healthy subjects by about 10 HU.

The relatively large interindividual range in attenuation values is due to the fat and glycogen content of the organ. The increased, diffuse deposition of fat leads to a reduction in attenuation, whereas increased glycogen is reflected in an increase in CT measured density.[17] Valid indications for unenhanced CT scans of the liver include:

1. The search for calcifications (e.g., in primary tumors, such as hemangioendotheliomas (Fig. 36–7); in secondary tumors, such as the calcified metastases of mucinous adenocarcinoma; in postinflammatory calcifications, such as in cases of alveolar echinococcosis; and in intrahepatic CT-opaque bile duct concrements).
2. Visualization of hemorrhage, either subcapsular or into the hepatic parenchyma (Fig. 36–8).
3. Visualization of the Lipiodol distribution pattern following completed intra-arterial embolization of liver tumors (Fig. 36–9).

Because of the biphasic nature of the blood supply to the liver, the pattern of contrast medium uptake in the liver and the associated changes in attenuation values in the hepatic parenchyma over time are complex. Three phases can be differentiated:

1. *Arterial phase*. There is a rapid increase in attenuation values in the abdominal aorta, with a peak occurring immediately following completion of contrast medium injection. Attenuation values in the liver also increase, reaching about 50% of the extent of enhancement in the aorta. As a rule, assuming normal circulatory conditions, the arterial phase begins about 20 seconds after the start of contrast medium injection and lasts 10 to 15 seconds.
2. *Redistribution phase*. Attenuation values within the abdominal aorta decrease rapidly, although enhancement of the hepatic parenchyma, caused by the beginning portal uptake, remains nearly constant or sometimes even slowly increases.
3. *Equilibrium phase*. Attenuation values in both the aorta and the liver slowly and continuously decrease in relation to renal elimination of the contrast medium.

The contrast medium uptake pattern of the liver also depends on the following:

- Amount of contrast medium administered
- Iodine content of the contrast agent
- Site of injection
- Cardiovascular circulation time
- Extent of perfusion of the liver and the other intra-abdominal viscera

At present, application of contrast medium by means of a mechanical injector has become standard; arterial access

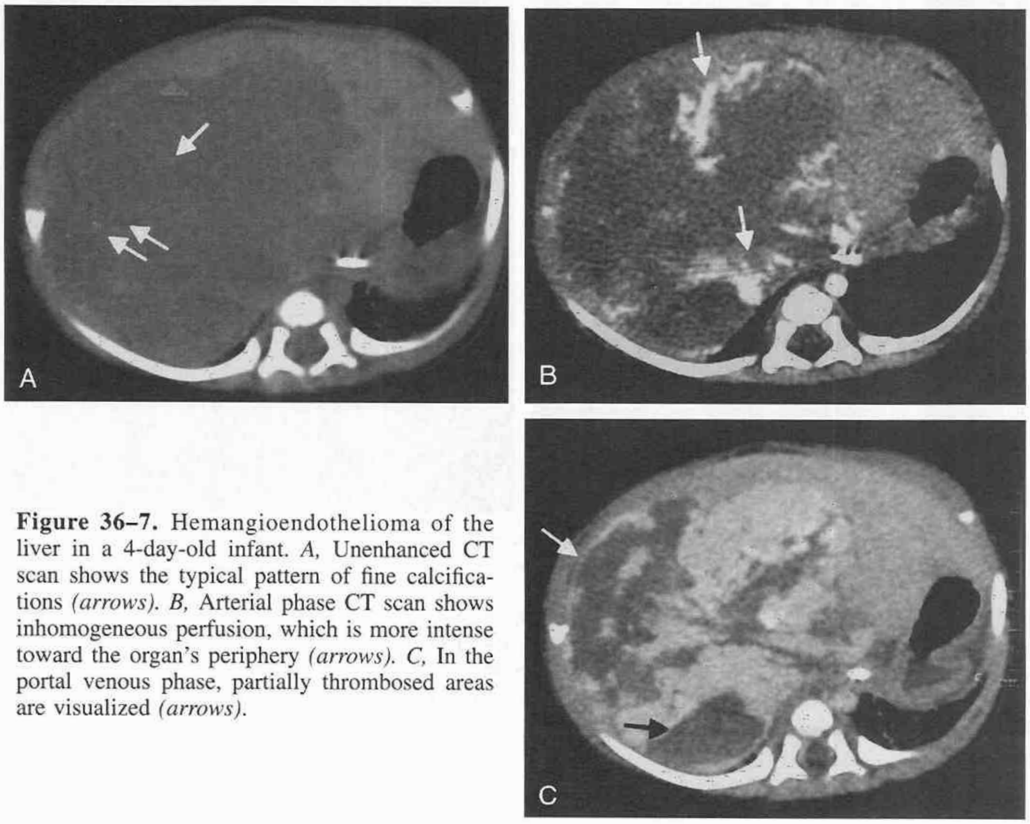

Figure 36–7. Hemangioendothelioma of the liver in a 4-day-old infant. *A,* Unenhanced CT scan shows the typical pattern of fine calcifications *(arrows). B,* Arterial phase CT scan shows inhomogeneous perfusion, which is more intense toward the organ's periphery *(arrows). C,* In the portal venous phase, partially thrombosed areas are visualized *(arrows).*

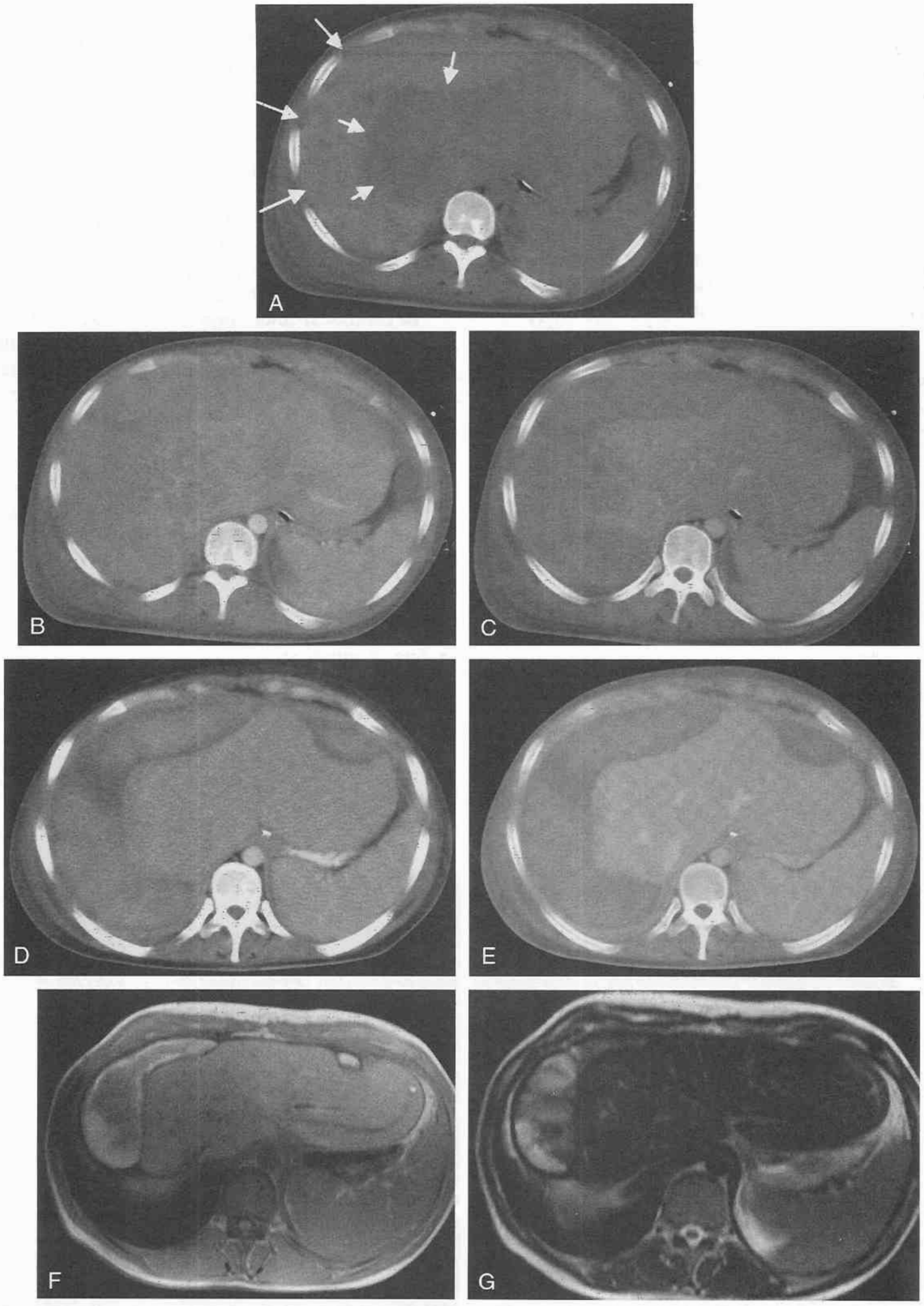

Figure 36–8. Hepatic bleeding in a 23-year-old woman. *A,* Unenhanced CT scan shows extensive subcapsular hematoma *(long arrows),* which is hyperdense in comparison with normal hepatic parenchyma *(short arrows). B,* In the early arterial phase, the CT attenuation values of perfused liver tissue and of the hematoma become almost equal. *C,* In the portal venous phase, the liver becomes hyperdense in comparison with the hematoma. *D* and *E,* Two weeks later, the hematoma appears, much less dense as a result of hemolysis. *F* and *G,* After 3 months, the reduced hematoma appears inhomogeneously hyperintense in both T1-weighted (FLASH gradient-echo sequence TR/TE/NSA/FA/TA 84.2/4.1/1/70°/14) and T2-weighted (TSE sequence TR/TE/NSA/ETL/TA 3000/138/1/29/22) images. ETL, echo train length; FA, flip angle; FLASH, fast low-angle shot; TE, echo time; TR, repetition time; NSA, *n*umber of *s*ignals *a*veraged; TA, *a*cquisition *t*ime; TSE, *t*urbo *s*pin *e*cho.

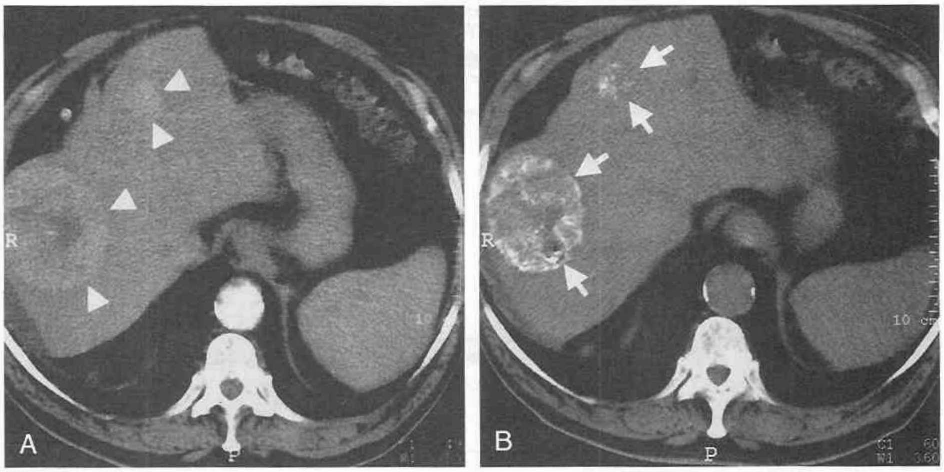

Figure 36–9. Hepatocellular carcinoma of both liver lobes in a 72-year-old man. *A,* Two tumor nodules *(arrowheads)* are visualized by contrast-enhanced CT (arterial phase). *B,* One day after transarterial chemoembolization (mitomycin C mixed with Lipiodol), the embolisate is well distributed in both tumor nodules *(arrows).*

is usually through an 18- to 20-gauge indwelling catheter placed in a cubital vein. Non-ionic contrast media with an iodine concentration of 300 mg/mL are most commonly used and are applied at a flow rate of 1 to 5 mL/second.

The recommended maximum amount of applied iodine is 35 to 45 g; this amount will probably not change significantly despite introduction of the multiple-slice helical CT scanners. This is because the important factor in liver imaging is the degree of maximum contrast enhancement of the hepatic parenchyma, which is determined primarily by the amount of iodine applied, independent of the duration of the examination.[35, 40]

The concentration of contrast medium actually becomes more crucial in the case of multiple-slice helical CT studies because of the short duration of the arterial perfusion phase. A higher contrast medium uptake can be achieved either by increased concentration or by an increased flow rate. Because increases in the flow rate of the injection are subject to certain limits, the concentration of the contrast medium solution (the total applied amount of iodine being held constant) appear to be the more important parameter. The following example can clarify this principle:

At the end of the arterial phase, following application of 120 mL of contrast medium containing 300 mg/mL of iodine (36 g total iodine), only 80 mL (containing 24 g of iodine) contributes to contrast enhancement within the liver during the arterial phase. When a more highly concentrated contrast medium solution (97 mL of solution containing 370 mg/mL of iodine, total iodine dose = 36 g) at an identical flow rate and comparable transit time from the cubital vein to the liver is selected, 80 mL of contrast medium is sufficient to perfuse the liver with 30 g of iodine, resulting in a 25% increase in the iodine concentration during the arterial phase.

Because of the short window provided by the arterial phase (10 to 15 seconds) and interindividually variable perfusion conditions (cardiac output, blood volume, visceral perfusion), the need for the capability to track the contrast medium bolus (i.e., using a software program for automatic or semiautomatic determination of expected arrival time of the contrast medium bolus installed directly in the CT unit) becomes apparent.[34, 36, 56, 57] With its high acquisition speed, multislice CT is superior to single-slice CT in its utilization of this narrow window, permitting visualization of the entire liver during this phase of early contrast medium uptake.

Sequential low-dose scans are obtained at the level of the liver hilum during bolus tracking, usually beginning 10 to 15 seconds after the contrast medium injection is begun. Sequential enhancement values (postcontrast minus precontrast) of the liver, portal vein, and aorta are immediately displayed graphically after image reconstruction. When aortic enhancement reaches a predefined threshold (e.g., 150 HU), scanning begins. The lag time between in vivo contrast enhancement, graphic display on the console, and subsequent initiation of helical scanning is less than 5 seconds.

Tables 36–1 and 36–2 present current liver scan proto-

Table 36–1. Liver Computed Tomography (CT) Standard Protocol Using a Single-Slice Helical CT Contrast Medium*

Scan parameter	Unenhanced	Arterial phase	Portal venous phase
Slice thickness	7 mm	7 mm	7 mm
Pitch factor	1.3	1.6	1.3
Reconstruction interval	3 mm	3 mm	3 mm
Table speed gantry rotation	9.1 mm	11.2 mm	9.1 mm
Complete gantry rotation	1 sec	1 sec	1 sec
Tube current	250 mA	200 mA	250 mA
Delay from initiation of bolus		20 sec	50 sec
Scan time	20 sec	16 sec	20 sec

*Contrast medium, 120 mL; iodine, 300 mg/mL; injection rate, 4 mL/second.

Table 36–2. Liver Computed Tomography (CT) Standard Protocol Using a Multislice Helical CT Contrast Medium*

Scan parameter	Unenhanced	Arterial phase	Portal venous phase
Detector configuration	4 × 3.75 mm	4 × 3.75 mm	4 × 3.75 mm
Primary slice thickness	5 mm	5 mm	5 mm
Pitch factor	0.75	0.75	0.75
Reconstruction interval	3.75 mm	3.75 mm	3.75 mm
Table speed/gantry rotation	11.25 mm	11.25 mm	11.25 mm
Complete gantry rotation	0.8 sec	0.8 sec	0.8 sec
Tube Current	160 mA	160 mA	160 mA
Delay from initiation of bolus		20 sec	55 sec
Scan time	11 sec	11 sec	11 sec

*Contrast medium, 120 mL; iodine, 300 mg/mL; injection rate, 4 mL/second.

cols for single-slice and multiple slice CT units, respectively.

The introduction of helical CT scanning has resulted in the displacement of previously used techniques, such as dynamic stationary CT and angiography-assisted CT.

Dynamic stationary CT uses contrast medium uptake behavior to more precisely characterize a known hepatic lesion by documenting the change in attenuation over time; for example, a slice through the lesion is acquired every 5 seconds. On the basis of the resulting data, it is possible to determine whether a focal hepatic lesion is fed arterially or through the portal vein and whether the lesion is primarily hypervascular, hypovascular, or avascular. On the whole, the method is considered obsolete and is applied only in exceptional cases.

Angiography-assisted CT consists of the introduction of a catheter into the common femoral artery whose tip is then advanced into the common hepatic artery (CT arteriography) or the superior mesenteric artery (CT portography). Once the catheter has been positioned, the patient is transferred to the CT unit. During the CT examination, contrast medium is injected through the intra-arterial catheter at a flow rate of 2 mL/second. (*Note:* For this method, the contrast medium must be diluted with normal saline solution: 1:2 for CT angiography, 1:1 for CT portography.) The delay time is about 6 seconds with CT angiography and about 20 seconds with CT portography. Because of its invasivity, the use of angiography-assisted CT is somewhat restricted today.

MRI Appearance and Technique

Examination of the abdomen in general, and of the liver in particular, has become a versatile technique in recent years. Numerous technical improvements, such as the development of more powerful gradient systems and phased-array body coils, permit breath-hold examination of the liver with both T1 and T2 weighting. To date, the liver has the distinction of being the only organ for which an organ-specific contrast medium—superparamagnetic iron oxide (SPIO)—has been developed and approved by the U.S. Food and Drug Administration (FDA). These advances have underscored the significant potential of hepatic MRI not only for tumor detection but also for tumor characterization.

Indications for MRI of the liver include:

1. Characterization of hepatic lesions of uncertain histology.
2. Determination of the extent and segment localization of hepatic malignancies prior to planned partial liver resection.
3. Follow-up in cases of known primary or secondary hepatic malignancies.

In current practice, hepatic MRI studies are performed using phased-array body coils with the patient supine. If a dynamic contrast-enhanced examination is planned, it is best to place an indwelling cannula intravenously in an antecubital vein before the examination is begun. The cannula is then attached by an extension to a contrast medium injection pump that is operated directly from the control room.

Despite the multiplanar imaging that is possible with MRI, axial slices remain standard in hepatic imaging, which also facilitates comparison with any previous CT scan findings that may have been obtained. Should any questions remain, axial images can be supplemented with coronal or sagittal slices. The standard MRI examination of the liver includes native T1-weighted and T2-weighted sequences. The examination technique for MRI systems using medium (0.5 tesla [T]) and high (1.0 to 1.5 T) field strengths is discussed next.

T1-Weighted Imaging

Multislice gradient-echo (GRE) sequences are considered the standard today, particularly in systems with high field strengths. In healthy subjects, MRI visualization reveals the liver to be homogeneous and hyperintense in relation to the spleen (Fig. 36–10). GRE sequences permit examination of the patient in breath-hold technique, and because of the very short echo time (TE), about 4 msec, T1-weighted contrast is very good. Depending on the capabilities of the gradient system, it is possible to acquire between 5 and 25 slices per breath-hold; hence, the entire liver may be scanned in one to three breath-hold phases.

If rapid GRE sequences are not available, spin-echo (SE) techniques or GRE sequences with multiple data transfers represent viable alternatives. These methods, however, extend the required examination time to several minutes. On the other hand, multiple data transfer results in a reduction in motion artifacts while at the same time in-

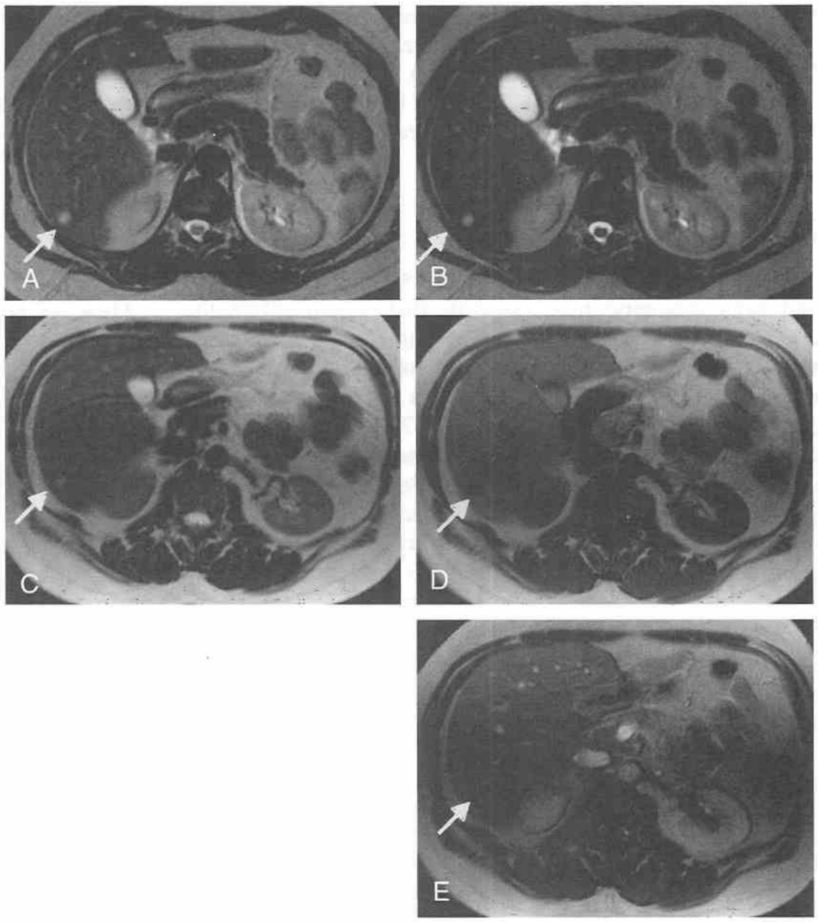

Figure 36–10. Solitary hemangioma of the liver *(arrow)* in a 44-year-old woman. In the first echo of the T2-weighted turbo spin-echo (TSE) sequence *(A)* (TR/TE/NSA/ETL/TA 5136/83/3/9/405), a hypointense lesion in segment VI, in the second echo *(B)* (TR/TE/NSA/ETL/TA 5136/165/3/9/405), continues to increase in signal relative to the surrounding parenchyma, as is typical of hemangioma. *(C)* The hemangioma is also clearly visualized on the breath-hold T2-weighted TSE sequence (TR/TE/NSA/ETL/TA 3000/138/1/29/22). On T1-weighting, the hemangioma appears hypointense on unenhanced scans *(D)* but hyperintense after application of gadolinium-pentetic acid (Gd-DTPA) *(E)* (FLASH gradient-echo sequence TR/TE/NSA/FA/TA 84.2/4.1/1/70°/14).

creases the signal-to-noise ratio with consecutive improvement of contrast, image quality, and recognition of anatomic details.

Because the T1 relaxation time depends on the magnetic field strength (Table 36–3), sequence parameters differ for medium and high field strengths:

1. *Medium.* A repetition time (TR) of 250 to 350 msec at a TE of 10 to 15 msec for SE sequences (5 to 10 msec for GRE sequences) is recommended.
2. *High.* The TR must be increased to 400 to 500 msec with SE sequences.

If the TE is adjusted for T1-weighted GRE sequences, scans can be obtained with water and lipid protons either *in-phase* or *opposed-phase*.[43, 44, 51] On in-phase images, the signal from both water and fat protons contributes to tissue signal intensity. On opposed-phase images, signal from fat protons cancels that of water protons.

The choice of TE for in-phase images and for opposed-phase images depends on field strength: using a 1.5-T high field system, the TE is 4.4 msec and 2.2 msec for in-phase and opposed-phase images, respectively (mid-field: in-phase TE = 14 ms, opposed-phase TE = 7 msec). This

Table 36–3. Tissue Relaxation Time of Normal Liver and Focal Liver Lesions

	Mid Field (0.5 T)		High Field (0.1–1.5 T)	
	*Relaxation Time**		*Relaxation Time†*	
Tissue	*T1 (msec)*	*T2 (msec)*	*T1 (msec)*	*T2 (msec)*
Normal liver tissue	327–518	55–62	547 ± 80b 568 ± 59	51 ± 11b 56 ± 11
Primary or secondary cancer	1013 ± 605	83 ± 24	1004 ± 234b 1191 ± 196c	80 ± 18b 92 ± 6c
Hemangioma	1105 ± 326	150 ± 45	1337 ± 216b	178 ± 40b

T, tesla

* Data from Stark DD, Felder RC, Wilterbery J, et al: Am J Roentgenol 145: 213–222, 1985.[61]

† Data from Goldberg MA, Hahn PF, Saini S, et al: AJR Am J Roentgenol 160: 1011–1017, 1993[23]; and Van Lum, Brown JJ, Perman WH, et al: Magn Reson Imaging 9: 165–171, 1991.[70]

technique is useful in evaluating focal or diffuse fatty infiltration to detect lesions and characterize tissue (e.g., *incidentalomas* in the adrenal glands). Usually, the boundaries between tissues with different water or fat content appear black on opposed-phase images.

T2-Weighted Imaging

There are no significant differences between medium and high magnetic field strength that would affect the choice of T2-weighted imaging parameters. T2-weighted images may be obtained with conventional SE sequences using a long TR and a long TE or a combination of two different TEs, one in the range of 70 to 80 msec (first echo) for lesion detection and the other TE of 140 to 160 msec (second echo) for lesion characterization.

Because of the long acquisition times, conventional SE sequences have been increasingly replaced by rapid sequences in recent years. In turbo SE sequences, multiple echoes can be acquired per excitation, each of which can be phase-coded differently. Acquisition time is reduced by the factor of the acquired echoes. In Figure 36–10*C*, echo train length = 29; that is, the acquisition time is reduced by a factor of 29 from 10 minutes 38 seconds to 22 seconds; thus, an examination in a breath-hold technique is possible in instances of inadequate local resolution.

With the so-called single-shot techniques, such as rapid acquisition with relaxation enhancement (RARE) or half-Fourier acquisition single-shot turbo SE (HASTE) sequences with an echo train length of more than 100, acquisition times may fall below 1 second per image in certain cases. The lesion-liver contrast on these images is compromised but may be improved with fat-suppression techniques or with an inversion recovery prepulse that provides short inversion time, inversion recovery-like additive T1-weighted, proton density–weighted, and T2-weighted contrast.[20]

Echoplanar MRI (EPI) may also be able to replace slower T2-weighted sequences for some indications and might be able to contribute additional diagnostic capabilities, such as lesion characterization, although its routine use in liver imaging had not been recommended by early 2000.

Use of Intravenous Contrast Agents

Various intravenous (IV) contrast agents have been developed to improve the diagnostic capabilities of hepatic MRI. At present, only the nonspecific extracellular gadolinium chelate agents, SPIOs, and manganese-based hepatobiliary agents have been approved for use in the United States.

Nonspecific Extracellular Gadolinium Chelate Agents

With regard to their method of application and their in vivo pattern of distribution, these agents are comparable to non-ionic radiographic contrast media but with a much better biologic tolerability. Although these contrast media were used infrequently in abdominal studies, their use has become increasingly routine in recent years as part of dynamic triphasic examinations. After bolus administration of a gadolinium chelate, at 0.1 mmol/kg of body weight, rapid GRE images are acquired in the arterial (20 to 60 seconds), portal venous (60 to 100 seconds), and equilibrium (5 minutes) phases (Fig. 36–11). The timing of data acquisition can be optimized by precisely determining the

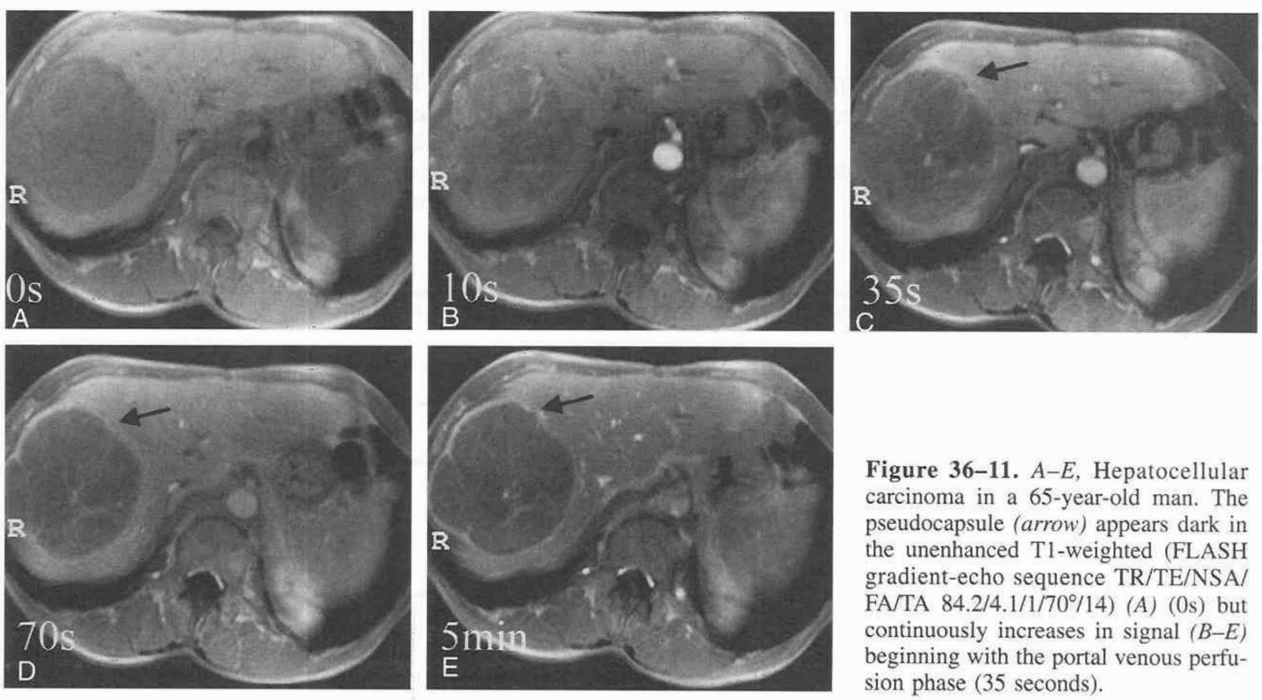

Figure 36–11. *A–E,* Hepatocellular carcinoma in a 65-year-old man. The pseudocapsule *(arrow)* appears dark in the unenhanced T1-weighted (FLASH gradient-echo sequence TR/TE/NSA/FA/TA 84.2/4.1/1/70°/14) *(A)* (0s) but continuously increases in signal *(B–E)* beginning with the portal venous perfusion phase (35 seconds).

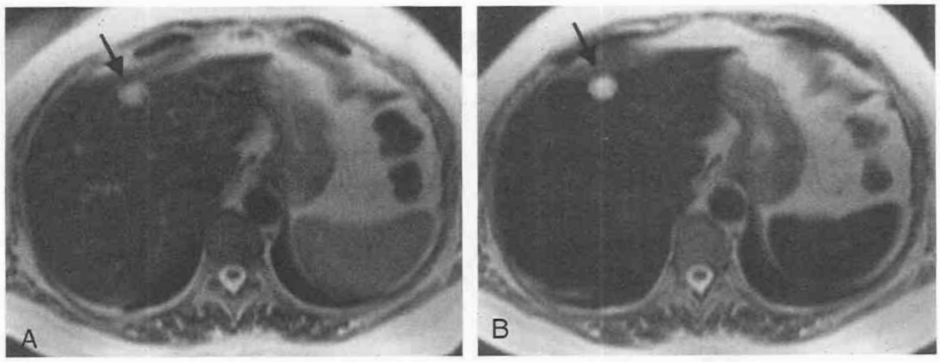

Figure 36–12. Simple liver cyst *(arrow)* in a 32-year-old woman appears hyperintense in the T2-weighted image (TSE: TR/TE/NSA/ETL/TA 3000/138/1/29/22). *A*, Forty minutes after administration of an iron-containing contrast medium *(B)*, images generated at unchanged sequence parameters show significant reduction of the liver signal intensity caused by uptake of iron in Kupffer's cells. Also of interest is the drop in signal intensity in the spleen.

individual circulation time with a bolus tracking system using 2.0 mL of a gadolinium contrast agent.[18]

Superparamagnetic Iron Oxides

Ferrumoxides are administered as an intravenously injectable colloid, associated with dextran. The colloid is taken up by the Kupffer cells (which make up 2% of the liver volume) as a part of the reticuloendothelial system. Liver uptake is approximately 80% of administered ferrumoxides; the remaining 20% is stored in the spleen and bone marrow. The iron uptake in the macrophages causes local magnetic field inhomogeneties with a decrease in liver signal intensity caused by shortening of T2 relaxation time. Ferrumoxides, diluted with a 5% dextrose solution, are administered intravenously at least 30 minutes before imaging at a dosage of 10 μmol/kg of body weight, but imaging can also occur up to 4 hours after administration (Fig. 36–12).[53]

Hepatobiliary Contrast Agents

Hepatobiliary contrast agents, based on either manganese (Mn-DPDP) or gadolinium (Gd-BOPTA, Gd-EOB-BOPTA), are taken up by the hepatocytes. Unlike the extracellular gadolinium chelates, these liver-specific contrast agents produce long-lasting enhancement, thus providing a wide imaging window after administration.[28, 52, 72]

Diffuse Diseases of the Liver

Storage Diseases

Fatty Infiltration

Hepatic steatosis is the result of excessive accumulation of triglycerides within hepatocytes. It is seen in association with several clinical disorders, including alcoholic liver disease, diabetes mellitus, obesity, malnutrition, severe hepatitis, corticosteroid use, and chemotherapy. Although it is most commonly a diffuse process, fatty infiltration can also be focal and inhomogeneous, thus mimicking a tumorous mass.

On unenhanced CT scans, fatty infiltration results in a lowering of the attenuation of the liver parenchyma. In normal adults, the attenuation value of the liver is consistently higher than that of the spleen, with a mean difference of 8 HU.[63] Milder degrees of diffuse fatty infiltration can be diagnosed when the attenuation value of the liver parenchyma is less than that of the spleen. Marked steatosis leads to a characteristic CT appearance in which the attenuation of the liver is even lower than that of the blood vessels (e.g., the portal venous branches and IVC) (Fig. 36–13).

Although fatty infiltration can be depicted on contrast-enhanced scans, with liver parenchyma seen as having lower attenuation than that of the spleen, contrast images are less reliable and less specific in detecting steatosis. After contrast administration, significant fatty infiltration is a suggested diagnosis if attenuation of the liver is less than that of muscle.

Both focal fatty infiltration and residual foci of normal unaffected liver parenchyma surrounded by fatty infiltration may be confused with a neoplastic lesion (Fig. 36–14). Focal fatty infiltration commonly has a segmental or lobar distribution, often with a straight line margin providing a clue to diagnosis. These large, irregular-shaped lesions typically extend to the liver capsule, usually without associated bulging of the liver contour. In addition, vessels coursing through the area of abnormality are not displaced. Common locations of nodular fatty infiltration are the anterior part of segment IV adjacent to the falciform ligament and the fissure for the ligamentum teres.

Conversely, focal areas of higher attenuation within a region of fatty change may represent neoplastic masses or foci of uninvolved liver tissue (Fig. 36–15).[27] The diagnosis of focal hepatic sparing is suggested when a geographic area of higher attenuation is identified in a typical location, such as along the gallbladder fossa adjacent to the interlobar fissure, next to the ligamentum teres, or in a subcapsular location.

MRI is an excellent tool in differentiating nodular fatty infiltration from neoplasms.[39, 43, 44] Using in-phase and opposed-phase images, the radiologist can readily diagnose fatty infiltration simply by comparing signal intensity. On opposed-phase images, focal fatty infiltration appears as a region of decreased signal intensity; on in-phase images, signal intensity is present in the corresponding area.

Iron Overload

In a discussion of iron storage diseases, congenital and acquired disease forms should be differentiated and the cellular site of iron deposition must be considered.

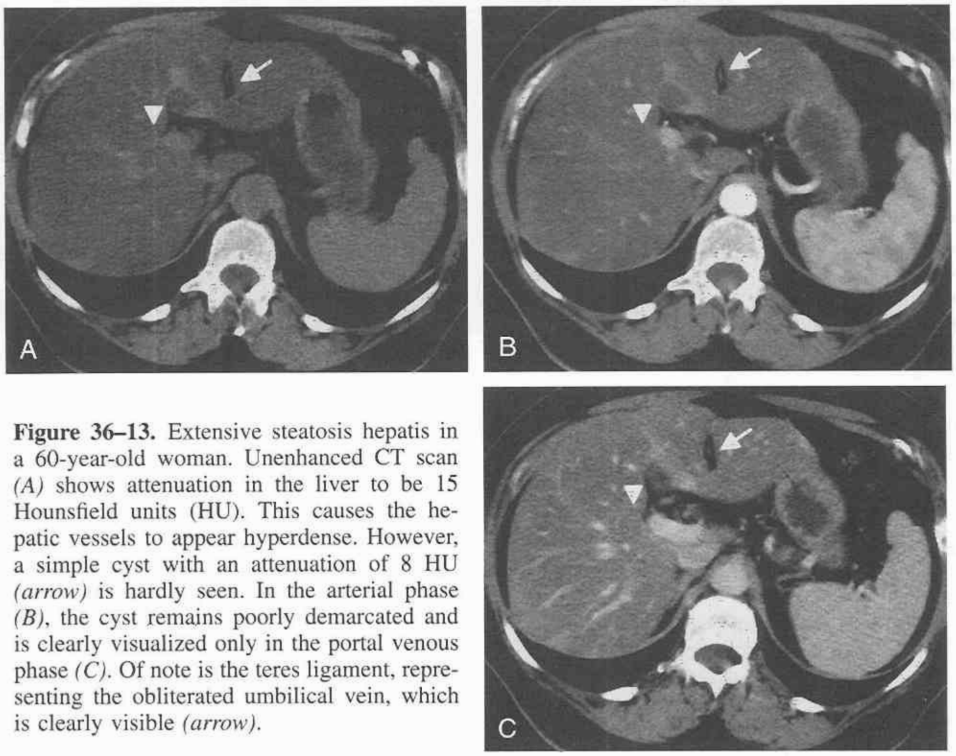

Figure 36–13. Extensive steatosis hepatis in a 60-year-old woman. Unenhanced CT scan *(A)* shows attenuation in the liver to be 15 Hounsfield units (HU). This causes the hepatic vessels to appear hyperdense. However, a simple cyst with an attenuation of 8 HU *(arrow)* is hardly seen. In the arterial phase *(B)*, the cyst remains poorly demarcated and is clearly visualized only in the portal venous phase *(C)*. Of note is the teres ligament, representing the obliterated umbilical vein, which is clearly visible *(arrow)*.

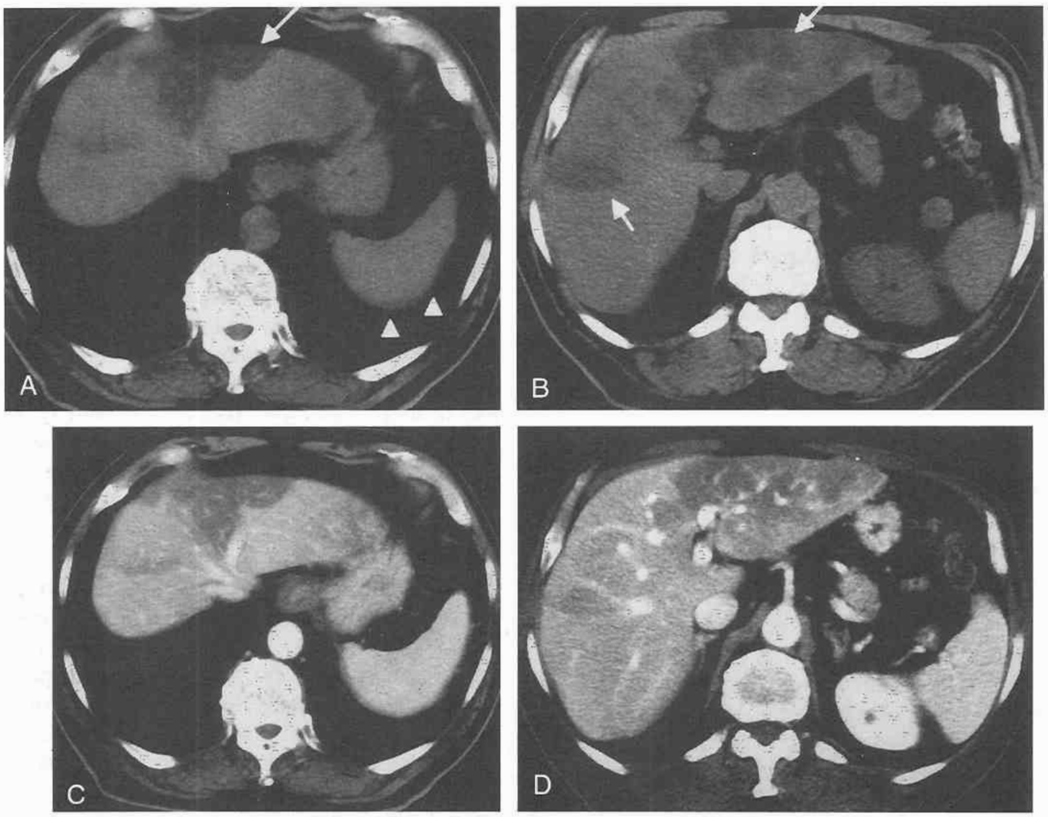

Figure 36–14. Hyperechoic lesion, visualized by ultrasound, in a 60-year-old man with a prior history of colorectal carcinoma. *A* and *B*, Unenhanced CT scans show hypodense areas in both liver lobes *(arrows)* without the impression of tumor with attenuation similar to fat; compare the splenic parenchyma *(arrowheads)*. *C* and *D*, Contrast medium application does not lead to visualization of displacement of the blood vessels. These findings are pathognomonic of focal fatty infiltration.

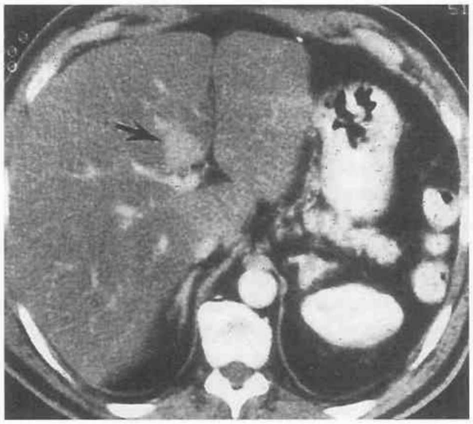

Figure 36–15. Diffuse, fatty infiltration of the liver with focal sparing simulating a neoplastic lesion. Contrast-enhanced CT scan shows a diffuse, low-attenuation appearance of the liver as a result of fatty infiltration. In segment IV, a rounded focus of higher attenuation *(arrows)* represents a focus of unaffected, normal liver parenchyma. (Courtesy of Richard L. Baron, M.D.)

In human lymphocyte antigen (HLA)-associated primary hemochromatosis, a defect in the intestinal mucosa leads to increased gastrointestinal (GI) resorption of iron. As a consequence, iron is deposited first in the hepatocytes and then, as the disease progresses, in other tissues (e.g., pancreas, GI tract, kidneys, heart, joints and endocrine glands), with resulting destruction of these tissues. The disease is usually manifested during the fourth or fifth decade with hepatomegaly, ultimately leading to cirrhosis of the organ.

Hepatocellular carcinoma (HCC) is a late complication and occurs in up to 30% of cases. Secondary hemochromatosis presents, as a rule, with the same symptoms and is encountered in patients with chronic anemias who have received multiple blood transfusions. Further disease forms include congenital transferrin deficiency, porphyria cutanea tarda, cirrhosis of the liver, excessive iron ingestion, and complications of portocaval shunting.

The characteristics of hemosiderosis differ. Unlike hemochromatosis, the primary site of iron deposition is not the hepatocytes but, rather, the reticuloendothelial system, including the spleen, lymph nodes, bone marrow, and Kupffer's cells in the liver.

Iron deposition in the various organs can be detected by both CT and MRI. Increased attenuation within the hepatic parenchyma to levels in excess of 70 HU on unenhanced CT scans is considered characteristic for iron overload.[8, 26] However, mild forms of iron overload (Fig. 36–16) or cases of coexistent steatosis hepatis may appear normal at CT. The differential diagnosis in patients with CT attenuation values within the hepatic parenchyma exceeding 70 HU includes the following:

1. Glycogen storage disease (or hyperalimentation).[17]
2. Wilson's disease with increased copper deposition in the liver and brain.
3. Cardiac arrhythmias in a patient taking amiodarone.[24]
4. A history of thorium dioxide (Thorotrast) application (Fig. 36–17).[50, 68]

Cisplatin therapy and colloidal gold used in the treatment of arthritis have also been reported to result in increased liver attenuation.[3, 12]

MRI is much more sensitive and specific, compared with unenhanced CT, in detecting milder forms of iron storage diseases. Signal reduction is due to the paramagnetic effect of the ferric ions (Fe^{3+}), which shortens the T1 and T2 relaxation times of nearby protons.[62] T2 shortening is the predominant effect and accounts for the reduction in hepatic signal intensity, which is seen best on GRE T2-weighted images (because of the lack of a 180-degree

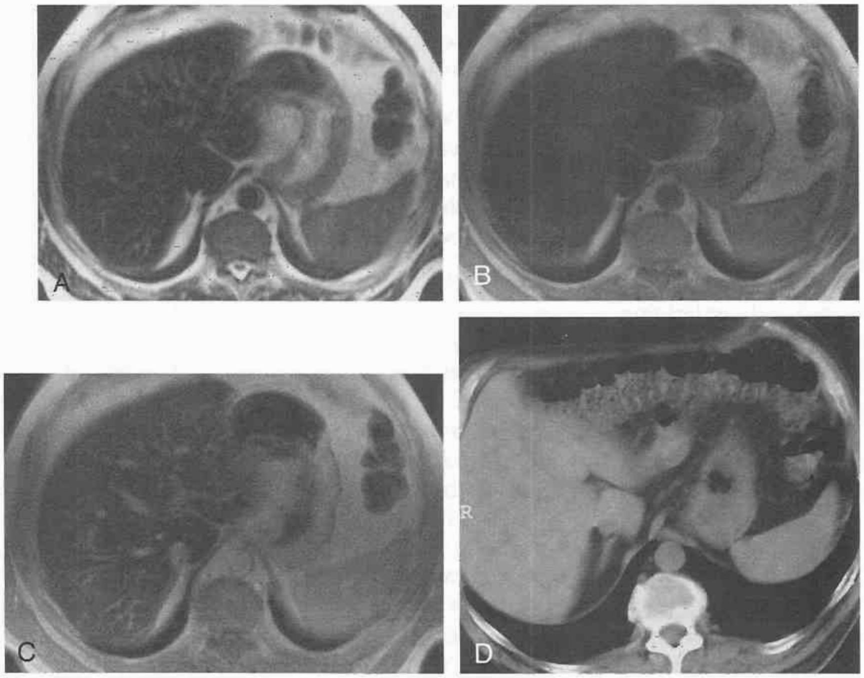

Figure 36–16. Primary hemochromatosis in a 68-year-old man. In both the T2-weighted image *(A)* (TSE sequence TR/TE/NSA/ETL/TA 3000/138/1/29/22) and the T1-weighted image (FLASH gradient-echo sequence TR/TE/NSA/FA/TA 84.2/4.1/1/70°/14) before *(B)* and after *(C)* application of gadolinium-DTPA (Gd-DTPA), signal intensity is significantly reduced. Unenhanced CT scan *(D)* shows a normal liver with attenuation of the hepatic parenchyma at 61 HU.

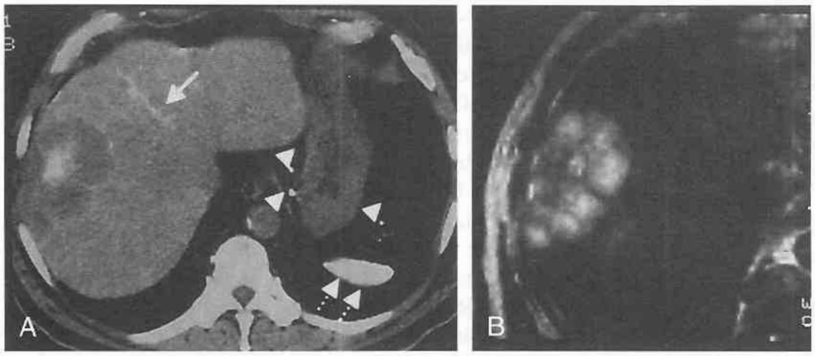

Figure 36–17. Hemangiosarcoma in a patient with a history of thorium dioxide (Thorotrast) exposition. Unenhanced CT scan *(A)* shows deposition of Thorotrast throughout the entire reticuloendothelial system, particularly in the spleen *(dashed arrows)*, in the perigastric lymph nodes *(arrowheads)*, and in the liver *(arrow)*. In the right liver lobe, the hemangiosarcoma with its cystic appearance and hypodense central sections is seen. The cystic character of the tumor is even more clearly visualized on the T2-weighted MR image *(B)*. (Courtesy of J. Görich, Ulm.)

refocusing pulse). In many cases, iron overload within hepatocytes (hemochromatosis) can be distinguished from iron deposition within the reticuloendothelial system (hemosiderosis) on the basis of recognition of extrahepatic signal intensity changes.[55]

In hemosiderosis, the liver and spleen each demonstrate low signal intensity (as seen after IV administration of SPIO containing contrast medium) (see also Fig. 36–12*B*). In hemochromatosis, however, signal intensity in the spleen is not altered, whereas low signal intensity in the pancreas can be documented.

One study has suggested that GRE imaging to estimate hepatic iron content can obviate the need for percutaneous liver biopsy. In this study, GRE imaging showed a close correlation between the hepatic iron concentration and the natural logarithm of the ratio of the signal intensity of liver to the standard deviation of background noise ($r = -.94$) with a low coefficient of variation (12%).[7]

Vascular Diseases

Budd-Chiari Syndrome

Budd-Chiari syndrome occurs secondary to obstruction of hepatic venous outflow caused by occlusion of the major hepatic veins with or without thrombosis of the IVC[32, 41]:

Type I involves occlusion of the IVC with or without secondary occlusion of the hepatic veins.
Type II consists of occlusion of the major hepatic veins.
Type III is veno-occlusive disease of the liver, or a progressive thrombotic occlusion of small centrilobular veins.

Venous obstruction may be idiopathic in origin or associated with underlying diseases, including hypercoagulopathy, pregnancy, oral contraceptive use, trauma, obstructing tumors (renal, liver, right atrial, IVC leiomyosarcoma, adrenal), and fibrous webs in the IVC. Clinically, patients present with hepatomegaly and liver dysfunction, which lead to portal hypertension and, ultimately, liver failure.[60]

Classical CT imaging findings are based on alteration in the visualization of vessels and of hepatic parenchymal blood flow, including small or absent intrahepatic veins, a small or constricted IVC, enlarged extrahepatic collateral vessels, and patchy liver enhancement in combination with a normal appearance of the caudate lobe owing to its separate drainage directly into the IVC (Fig. 36–18). The caudate lobe is often enlarged, whereas the periphery of the liver may be atrophied. In chronic cases, nodular regenerative hyperplasia can occur.

One study described 23 patients with liver nodules who were being monitored for Budd-Chiari syndrome. Whereas 4 patients had HCC with one to three lesions, 19 patients had multiple benign regenerative nodules.[71]

Distinguishing hepatic veno-occlusive disease from Budd-Chiari syndrome types I and II is a key point in differential diagnosis. In hepatic veno-occlusive disease, the IVC and main hepatic veins are patent, but the terminal hepatic venules are partially or completely destroyed.

With MRI, an absent blood flow in patients with Budd-Chiari syndrome may be difficult to interpret on SE images because, depending on the sequence parameters chosen and the scan orientation relative to the vessel direction, flowing blood may appear as a signal void or as a flow-related increase in contrast. Depending on age and composition, thrombotic material may also exhibit various appearances at MRI. When cross-sectional images do not provide an unequivocal diagnosis, MRI angiography in most instances can clarify the situation.[32]

Portal Venous Thrombosis

Partial or complete thrombosis of the portal vein can be caused by a variety of disorders, most commonly neoplasms (with extrinsic compression or direct invasion), infection, trauma, hypercoagulopathy, and pancreatitis.[49]

Thrombosis is best seen on helical CT scans during the portal venous phase, appearing as a low-attenuation defect in the portal vein. Collateral vessels, characteristically seen in the porta hepatis and referred to as a *cavernous transformation*, are another typical finding.[45] When portal vein thrombosis is segmental, the liver may show decreased attenuation on unenhanced CT scans and increased enhancement during the arterial perfusion phase, thus mimicking an infiltrating tumor. At MRI, intraluminal thrombi demonstrate variable signal intensities, often appearing isointense on T1-weighted images with increased signal intensity on T2-weighted images.[54]

Liver Infarction

Hepatic infarction is rare, in large part because of the dual blood supply provided by the hepatic artery and the portal vein. It is most commonly seen in liver transplant

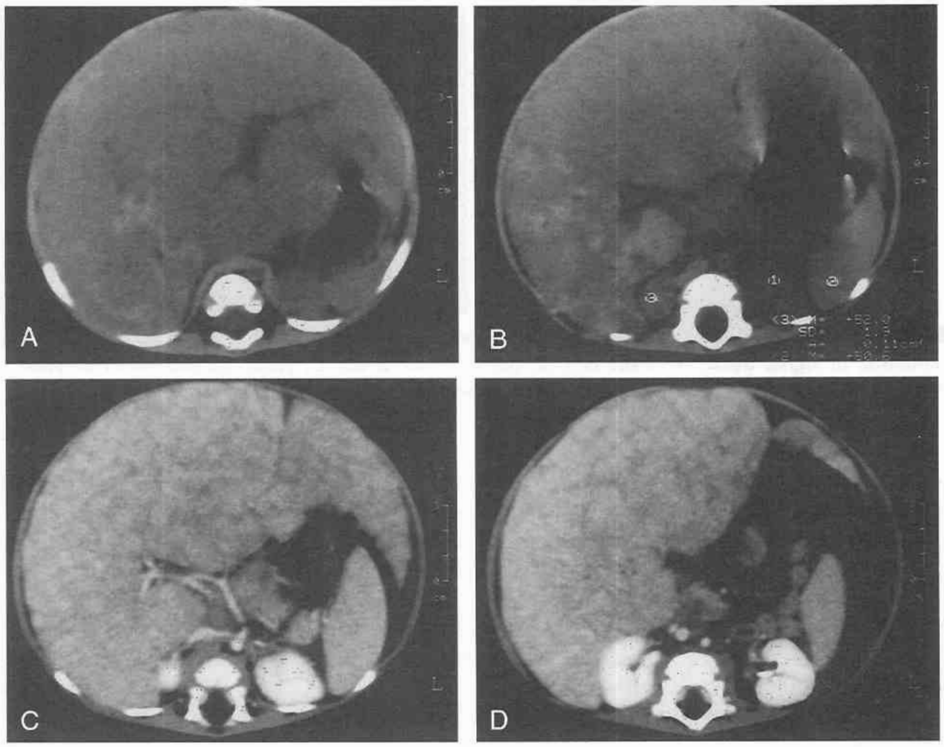

Figure 36–18. Hepatomegaly, ascites, and abdominal pain in a boy aged 4 months. *A* and *B*, Unenhanced CT scans reveal an inhomogeneously hyperdense liver. The hypertrophy of the caudate lobe is of interest. *C* and *D*, After contrast medium administration, a nodular, spotty pattern of contrast enhancement is seen. Note the absence of visible hepatic veins.

recipients.[22] Other causes include hepatic artery thrombosis, embolism, and occlusion following surgical procedures (e.g., laparoscopic cholecystectomy), hypercoagulopathy, and shock.[2, 37, 38] It may also be seen in preeclamptic or postpartum patients as part of the HELLP (hemolytic anemia, elevated liver enzymes, low platelets) syndrome (Fig. 36–19).[37, 74]

The typical CT appearance of liver infarction is a peripheral, wedge-shaped area of low attenuation on contrast-enhanced CT. Larger infarcts may have a more geographic distribution. At MRI, lesions are typically hypointense on T1-weigted images but hyperintense on T2-weighted images. Although the diagnosis of liver infarction is obvious in most cases, it may be confused with focal fatty infiltration, abscess, or even a tumor. It is notable that hepatic infarction does not demonstrate either mass effect or abnormal enhancement. Further, vessels coursing through the lesion (as seen in focal fatty infiltration) are typically *not* seen in hepatic infarction.

Hepatitis and Cirrhosis

Hepatitis can be caused by a variety of disorders; the most common cause is infection. Other causes include ingestion and autoimmune and drug-associated factors. In most cases of hepatitis, the CT and MRI appearances of the hepatic parenchyma are normal. In severe and fulminant cases, however, liver edema may be present, with diffuse lowering of the parenchymal attenuation. Other common CT findings are hepatomegaly, ascites, and splenomegaly (Fig. 36–20). MRI shows diffuse signal reduction on T1-weighted images and diffuse signal increase on T2-weighted images. In general, the value of imaging techniques is minor, and the correct diagnosis is usually made as a result of microscopic findings following percutaneous biopsy of the organ.

Chronic hepatitis may lead to liver *cirrhosis*, representing irreversible hepatic fibrosis bridging the portal tracts. Other conditions leading to cirrhosis include alcohol abuse, hemochromatosis, chemical and drug toxicity, chronic bili-

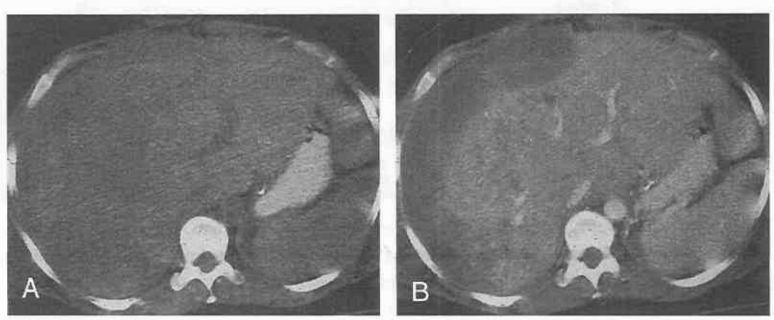

Figure 36–19. HELLP syndrome in a 23-year-old woman. Unenhanced CT scan *(A)* shows an extensive subcapsular hematoma. After administration of contrast medium *(B)*, further hypodense areas corresponding to infarctions are visualized. HELLP, hemolysis, elevated liver enzymes, and low platelets.

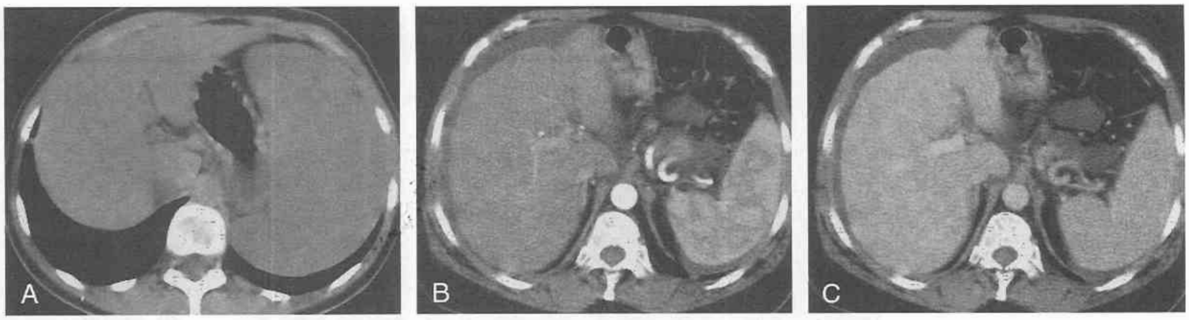

Figure 36–20. Autoimmune hepatitis in a 66-year-old woman. *A,* Unenhanced CT scan shows splenomegaly without significant reduction in signal intensity of the hepatic parenchyma. *B* and *C,* After application of contrast medium, ascites becomes more visible. As is typically the case, the liver itself appears normal.

ary obstruction (primary sclerosing cholangitis, primary biliary cirrhosis), infections, and other rare entities. If the inciting cause is unknown, the process is referred to as *cryptogenic cirrhosis*. Liver cirrhosis affects the contour of the organ, the size of the lobes and segments, and maycause benign as well as malignant focal lesions within the liver (Fig. 36–21). Processes associated with cirrhosis include ascites and evidence of portal hypertension.

Splenomegaly is the most common finding of portal hypertension, and varices are also often found. These collateral vessels can be seen as enhancing tortuous vessels in the paraesophageal and gastric cardial region, the porta hepatis, in the peritoneal cavity, retroperitoneum, and even passing through the liver via paraumbilical collaterals (Fig. 36–22).

Another common finding in patients with liver cirrhosis is the presence of mesenteric, omental, or retroperitoneal edema, which may be seen in up to 80% of cases (see Fig. 36–21).[10] Edema is usually mild but may be severe in approximately 25% of patients. The CT appearance is patchy in about 65% of patients and diffuse in another third. The appearance is purely infiltrative in most cases

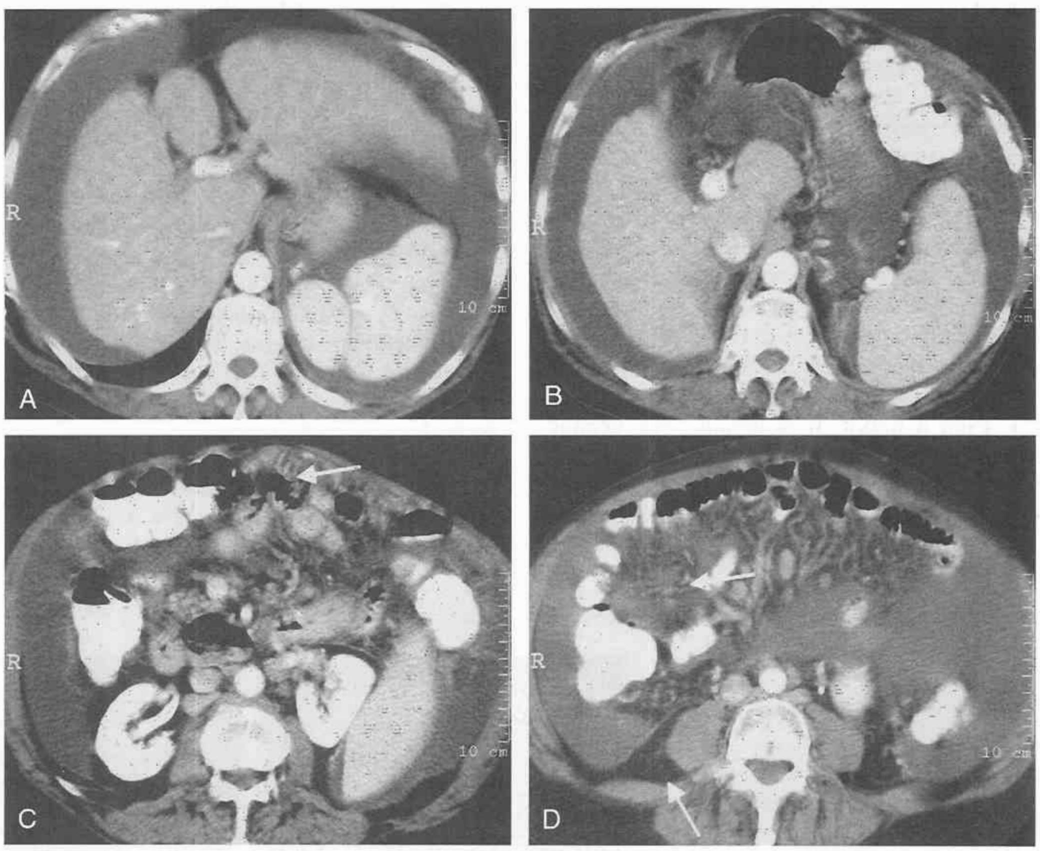

Figure 36–21. Cirrhosis of the liver secondary to alcohol abuse in a 68-year-old man. *A* and *B,* Contrast-enhanced CT scans show hypertrophy of the caudate lobe and of segments II and III. Conversely, segments IV to VIII appear unusually small. Other signs of liver cirrhosis include splenomegaly and ascites. *C* and *D,* Abdominal scans show another typical secondary sign: edema in the greater omentum and of the mesenterium and retroperitoneum *(arrows).*

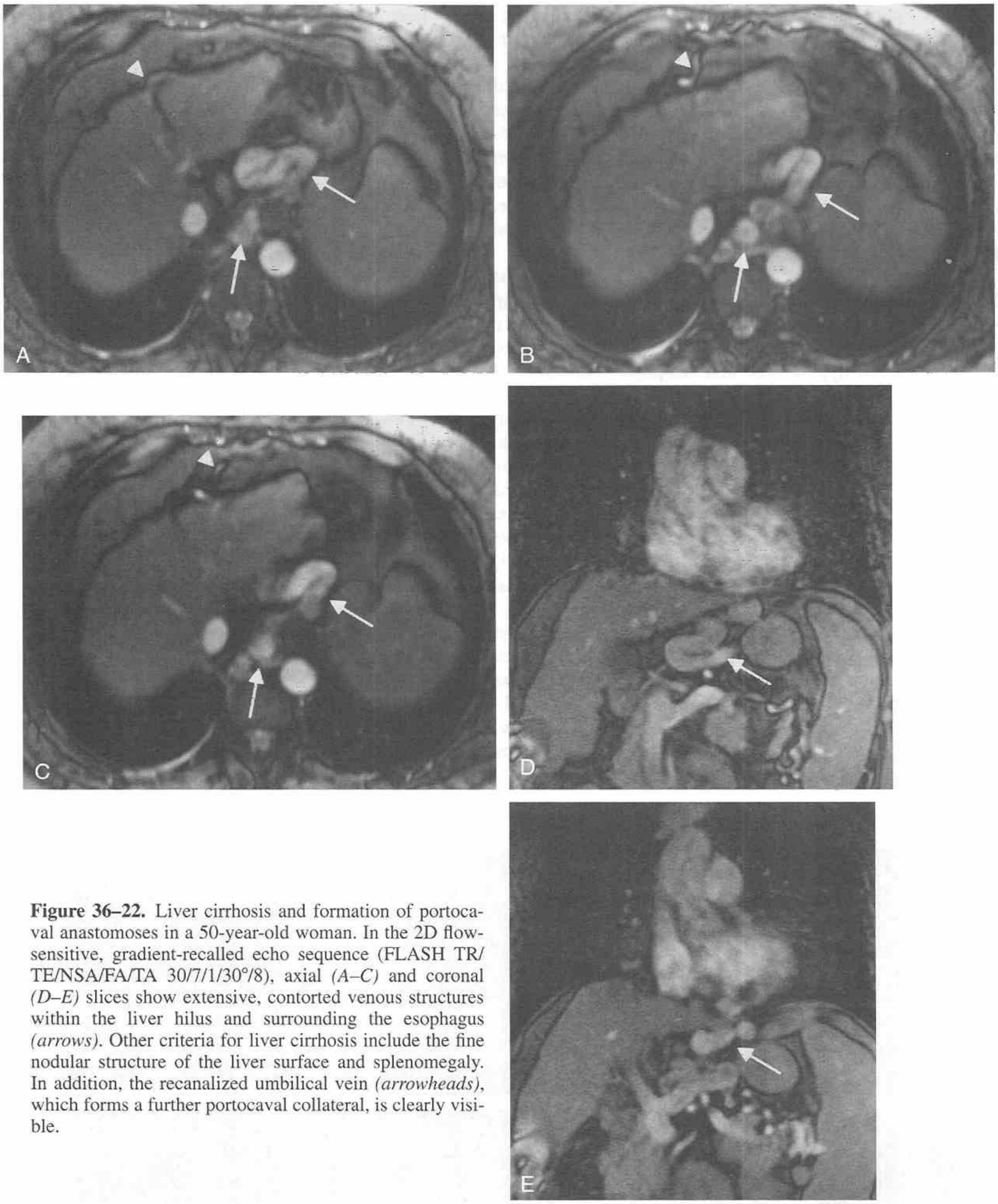

Figure 36–22. Liver cirrhosis and formation of portocaval anastomoses in a 50-year-old woman. In the 2D flow-sensitive, gradient-recalled echo sequence (FLASH TR/TE/NSA/FA/TA 30/7/1/30°/8), axial *(A–C)* and coronal *(D–E)* slices show extensive, contorted venous structures within the liver hilus and surrounding the esophagus *(arrows)*. Other criteria for liver cirrhosis include the fine nodular structure of the liver surface and splenomegaly. In addition, the recanalized umbilical vein *(arrowheads)*, which forms a further portocaval collateral, is clearly visible.

but occasionally shows features of infiltration with superimposed masslike nodules.

In some cases of cirrhosis, adenopathy can be seen in the porta hepatis and in the peripancreatic region. Occasionally, these nodes can be large and bulky, mimicking neoplastic involvement. These lymph nodes are the most prominent in cases of primary biliary cirrhosis.[48]

Cirrhosis markedly distorts the hepatic parenchyma, producing either a smooth, nodular, or lobular appearance of the hepatic capsule in most cases.[15] In patients with micronodular cirrhosis, margins that are either smooth or deformed by multiple small nodules are typical. These micronodules underlying the surface of the liver often are not visualized on CT or MR images. At present, high-

resolution transabdominal sonography with a 7.5-MHz transducer may represent the best imaging tool for visualizing these small nodules.[58] The result of macronodular cirrhosis is coarse nodularity of the margin.

Finally, a lobular liver is usually caused by marked segmental atrophy and hypertrophy rather than by large regenerative nodules.[14] Tremendous overlap in the frequency of smooth and nodular livers among patients with different etiologic mechanisms of cirrhosis usually prevents the physician from being able to distinguish the cause. However, a lobular liver margin is more frequently seen in patients with primary sclerosing cholangitis.[14]

Approximately 25% of end-stage cirrhotic livers appear normal in size and shape in all cross-sectional imaging modalities,[15] whereas another third may be diffusely atrophic. Most end-stage cirrhotic livers exhibit a combination of segmental hypertrophy and atrophy,[66] with the predominant finding being hypertrophy of liver segments I to III (see Fig. 36–21). Focal atrophy is most common in segments IV to VIII and may range from mild to complete involution of the affected segments. Occasionally, segments II/III and VI/VII may be atrophic. This finding is most often seen in patients with primary sclerosing cholangitis. Another rare finding in these patients is a higher attenuation in segment I, causing a pseudotumor in the caudate lobe.[14] Diffuse hypertrophy of the liver, however, may be seen in patients with primary biliary cirrhosis.

In approximately 25% of all patients with end-stage cirrhosis, unenhanced CT and T2-weighted MRI images reveal an inhomogeneous appearance in all parts of the liver.[15] Pathologic examination reveals three causes: (1) diffuse fibrosis, (2) fat, and (3) iron (Fig. 36–23). On cross-sectional imaging, four different patterns of diffuse fibrosis may be seen:[15]

1. Patchy, poorly defined regions of low attenuation on unenhanced CT.
2. Thin perilobular bands of low attenuation on unenhanced CT.
3. Thick fibrosis bridging of low attenuation surrounding regenerative nodules (most often in patients with primary biliary cirrhosis).
4. Diffuse fibrosis, causing a high-attenuation perivascular cuffing (usually in patients with primary biliary cirrhosis).

As a result of the reduced portal venous flow in patients with end-stage cirrhosis, contrast-enhanced CT scans during the portal venous phase is usually not helpful in demonstrating fibrosis. On (turbo) SE T2-weighted MRI images, fibrosis appears as an area of high signal intensity. On unenhanced T1-weighted images, fibrosis usually cannot be visualized. Following administration of contrast medium, however, in cases with thin perilobular bands or perivenous cuffing, the fibrous tissue may show mild enhancement on CT and T1-weighted MRI scans.

Another characteristic sign of liver cirrhosis is the development of a spectrum of focal lesions ranging from benign regenerative nodules to malignant HCC.[64] In 1995, the International Working Party introduced a new nomenclature for hepatocellular nodules, in which the term *dysplastic nodule* replaces such former pathologic descriptions as *adenomatous hyperplasia*, *macroregenerative nodule*, and other terms (Table 36–4).[1]

By definition, *regenerative nodules* are present in all cirrhotic livers; however, these nodules are visualized on only 25% of unenhanced CT scans and on approximately 50% of MR images.[16] These nodules usually present as high-attenuation lesions on unenhanced CT scans as a

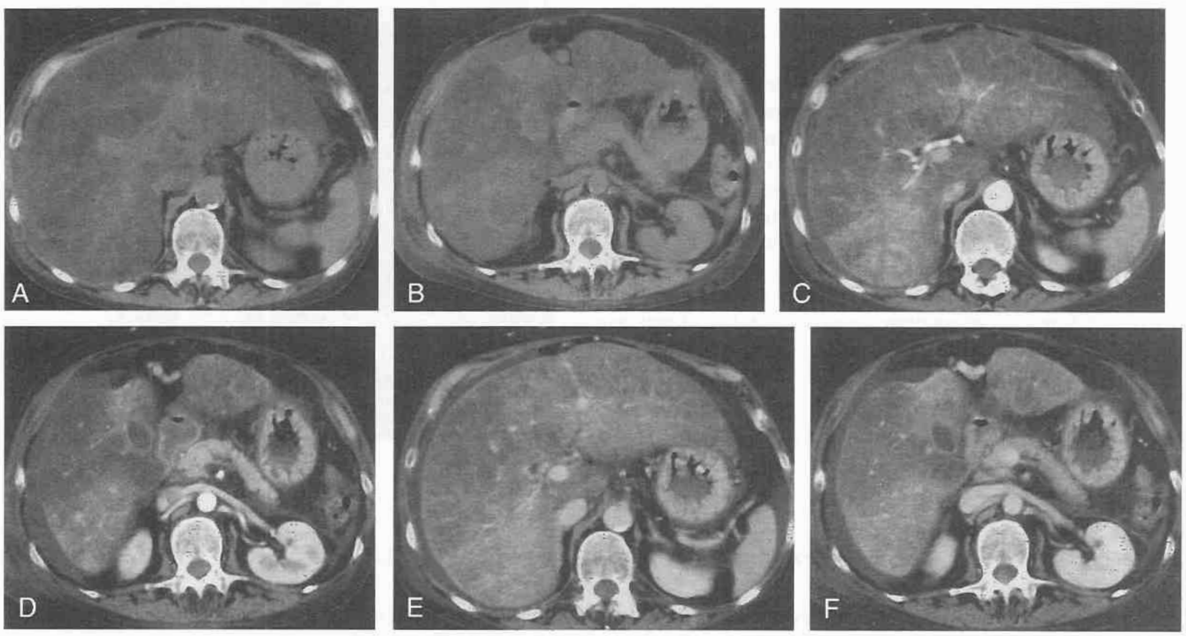

Figure 36–23. Alcohol–toxic liver cirrhosis in a 56-year-old woman. Unenhanced CT scans *(A* and *B)* show reduced attenuation of the hepatic parenchyma, suggestive of steatosis. The parenchyma, particularly in the more caudal sections, is very inhomogeneous. The early arterial contrast phase *(C* and *D)* shows irregular, spotty enhancement, which remains visible into the portal venous phase *(E* and *F)*. Also of note is the significant ramification of the intrahepatic portal vessels.

Table 36–4. Terminology of Hepatocellular Nodules in Cirrhotic Livers

New Terminology	Old Terminology
Regenerative nodule	Regenerative nodule
Low-grade dysplastic nodule	Macrogenerative nodule type I; ordinary adenomatous hyperplasia
High-grade dysplastic nodule	Macrogenerative nodule type II; adenomatous hyperplasia with atypia; borderline hepatocellular lesion
Dysplastic nodule with subfocus of HCC	Early HCC; macrogenerative nodule with microscopic HCC; adenomatous hyperplasia with microscopic HCC
HCC or small HCC (if < 2 cm)	Adenomatous hyperplasia with macroscopic HCC; early advanced HCC; advanced HCC; hepatoma

HCC, hepatocellular carcinoma.

result of their iron or glycogen content or, simply, because they are surrounded by lower-attenuation fibrosis. On portal phase, contrast-enhanced scans, these nodules are rarely revealed. On MR images, these focal lesions can appear hypointense, isointense, or hyperintense on T1-weighted images. An isointense appearance is the most usual, and a hyperintense appearance is the most unusual. On T2-weighted images, they typically appear as hypointense nodules. (Iron causes local magnetic field inhomogeneties with decrease of liver signal intensity because of shortening of T2 relaxation time.)

Dysplastic nodules are premalignant lesions that represent an intermediate step in the pathway of hepatocarcinogenesis in cirrhotic livers.[64] These lesions are present in approximately 10% of all end-stage cirrhotic livers; unfortunately, however, they are detected only rarely by cross-sectional imaging.[16] If visualized, these dysplastic nodules appear slightly hyperdense or isodense on unenhanced CT scans and isodense or hypodense on all contrast-enhanced (arterial phase, portal phase, and delayed) scans. With MRI, dysplastic nodules appear hyperintense on T1-weighted images and isointense to hypointense on T2-weighted images.[9, 29]

The incidence of HCC in end-stage cirrhosis is high (range, 3% to 11%).[11, 16, 42, 47] It occurs most often in cirrhosis secondary to hepatitis.[16] Unfortunately, as many as 40% of all HCC nodules in the cirrhotic liver are not detected by cross-sectional imaging.

Furthermore, carcinogenesis of HCC changes the hemodynamic properties and vascular supply of the tumor nodules resulting in a different enhancement pattern for early and advanced HCCs. In early HCC, the combination of normal hepatic artery degeneration and preserved portal veins results in low attenuation on CT arteriography and isoattenuation on CT during arterial portography. In advanced HCC, the combination of neoplastic (abnormal) arterial development by angiogenesis and obliteration of portal veins results in high attenuation on CT arteriography and low attenuation on CT during arterial portography.[30]

At MRI, various appearances may be seen on T1-weighted images, ranging from hypointense to hyperintense nodules. However, almost all HCCs appear bright on T2-weighted images, which allows dysplastic nodules to be differentiated from HCCs.

Small HCCs may be seen only on early gadolinium-enhanced, triphasic, multiphase, dynamic T1-weighted MR images and appear as hyperintense enhancing nodules.[73]

Another characteristic finding in patients with HCC is the presence of a pseudocapsule, usually consisting of connective fibrous tissue, that appears hypointense on T1-weighted and T2-weighted MRI sequences.[25] After administration of gadolinium-containing contrast medium, this pseudocapsule usually shows early enhancement but becomes more prominent on portal venous phase images.

Fibrosis can occur as a confluent mass that replaces even the cirrhotic, regenerating parenchyma in approximately 30% of patients.[16] Focal confluent fibrosis may be seen in all types of cirrhosis, but it occurs most commonly in primary sclerosing cholangitis and least commonly in primary biliary cirrhosis. Important imaging features are as follows:

1. Focal retraction of the liver capsule over the area of fibrosis.
2. Incomplete involvement of liver segments with accompanying atrophy.
3. Characteristic location in segments IVa, IVb, V, and VIII with a wedge-shaped structure radiating from the porta hepatis.

On unenhanced CT scans, focal confluent fibrosis usually appears as a lesion with low attenuation. After contrast medium administration, approximately 50% of the lesions become isoattenuating with the surrounding parenchyma. In rare instances, contrast enhancement of the fibrotic area may simulate a neoplastic process, which typically necessitates percutaneous biopsy. Focal confluent fibrosis appears bright on T2-weighted MR images and hypointense on T1-weighted MR images.

References

1. Anonymous: Terminology of nodular hepatocellular lesions. Hepatology 22:983–993, 1995.
2. Adler DD, Glazer GM, Silver TM: Computed tomography of liver infarction. Am J Roentgenol 142:315–318, 1984.
3. Aihara T, Fujioka M, Yamamoto K: Increased CT density of the liver due to *cis*-diaminedichloro platinum (II). Pediatr Radiol 17: 75–76, 1987.
4. Auh YH, Rosen A, Rubenstein WA, et al: CT of the papillary process of the caudate lobe of the liver. Am J Roentgenol 142:535–538, 1984.
5. Auh YH, Rubenstein WA, Zirinsky K, et al: Accessory fissures of the liver: CT and sonographic appearance. Am J Roentgenol 143: 565–572, 1984.
6. Bismuth H: Surgical anatomy and anatomical surgery of the liver. World J Surg 6:3–9, 1982.
7. Bonkovsky HL, Rubin RB, Cable EE, et al: Hepatic iron concentration: Noninvasive estimation by means of MR imaging techniques. Radiology 212:227–234, 1999.
8. Chezmar JL, Nelson RC, Malko JA, Bernardino ME: Hepatic iron overload: Diagnosis and quantification by noninvasive imaging. Gastrointest Radiol 15:27–31, 1990.
9. Choi BI, Han JK, Hong SH, et al: Dysplastic nodules of the liver: Imaging findings. Abdom Imaging 24:250–257, 1999.
10. Chopra S, Dodd GD, Chintapalli KN, et al: Mesenteric, omental, and retroperitoneal edema in cirrhosis: Frequency and spectrum of CT findings. Radiology 211:737–742, 1999.
11. Colombo M, de Franchis R, Del Ninno E, et al: Hepatocellular carcinoma in Italian patients with cirrhosis. N Engl J Med 325: 675–680, 1991.

12. De Maria M, De Simone G, Laconi A, et al: Gold storage in the liver: Appearance on CT scans. Radiology 159:355–356, 1986.
13. Dodd GD: An American's guide to Couinaud's numbering system. AJR Am J Roentgenol 161:574–575, 1993.
14. Dodd GD, Baron RL, Oliver JH, Federle MP: End-stage primary sclerosing cholangitis: CT findings of hepatic morphology in 36 patients. Radiology 211:357–362, 1999.
15. Dodd GD, Baron RL, Oliver JH, Federle MP: Spectrum of imaging findings of the liver in end-stage cirrhosis: Part I. Gross morphology and diffuse abnormalities. AJR Am J Roentgenol 173:1031–1036, 1999.
16. Dodd GD, Baron RL, Oliver JH, Federle MP: Spectrum of imaging findings of the liver in end-stage cirrhosis: Part II. Focal abnormalities. AJR Am J Roentgenol 173:1185–1192, 1999.
17. Dwyer A, Doppman JL, Adams AJ, et al: Influence of glycogen on liver density: Computed tomography from a metabolic perspective. J Comput Assist Tomogr 7:70–73, 1983.
18. Earls JP, Rofsky NM, DeCorato DR, et al: Hepatic arterial-phase dynamic gadolinium-enhanced MR imaging: Optimization with a test examination and a power injector. Radiology 202:268–273, 1997.
19. Fasel JH, Selle D, Evertsz CJ, et al: Segmental anatomy of the liver: Poor correlation with CT. Radiology 206:151–156, 1998.
20. Gaa J, Hatabu H, Jenkins RL, et al: Liver masses: Replacement of conventional T2-weighted spin-echo MR imaging with breath-hold MR imaging. Radiology 200:459–464, 1996.
21. Gazelle GS, Haaga JR: Hepatic neoplasms: Surgically relevant segmental anatomy and imaging techniques. AJR Am J Roentgenol 158: 1015–1018, 1992.
22. Glockner JF, Forauer AR: Vascular or ischemic complications after liver transplantation. AJR Am J Roentgenol 173:1055–1059, 1999.
23. Goldberg MA, Hahn PF, Saini S, et al: Value of T1 and T2 relaxation times from echoplanar MR imaging in the characterization of focal hepatic lesions. AJR Am J Roentgenol 160:1011–1017, 1993.
24. Goldman IS, Winkler ML, Raper SE, et al: Increased hepatic density and phospholipidosis due to amiodarone. Am J Roentgenol 144: 541–546, 1985.
25. Grazioli L, Olivetti L, Fugazzola C, et al: The pseudocapsule in hepatocellular carcinoma: Correlation between dynamic MR imaging and pathology. Eur Radiol 9:62–67, 1999.
26. Guyader D, Gandon Y, Deugnier Y, et al: Evaluation of computed tomography in the assessment of liver iron overload: A study of 46 cases of idiopathic hemochromatosis. Gastroenterology 97:737–743, 1989.
27. Halvorsen RA, Korobkin M, Ram PC, Thompson WM: CT appearance of focal fatty infiltration of the liver. Am J Roentgenol 139: 277–281, 1982.
28. Hamm B, Staks T, Muhler A, et al: Phase I clinical evaluation of Gd-EOB-DTPA as a hepatobiliary MR contrast agent: Safety, pharmacokinetics, and MR imaging. Radiology 195:785–792, 1995.
29. Hayashi M, Matsui O, Ueda K, et al: Correlation between the blood supply and grade of malignancy of hepatocellular nodules associated with liver cirrhosis: Evaluation by CT during intraarterial injection of contrast medium. AJR Am J Roentgenol 172:969–976, 1999.
30. Honda H, Tajima T, Kajiyama K, et al: Vascular changes in hepatocellular carcinoma: Correlation of radiologic and pathologic findings. AJR Am J Roentgenol 173:1213–1217, 1999.
31. Kalender WA, Seissler W, Klotz E, Vock P: Spiral volumetric CT with single-breath-hold technique, continuous transport, and continuous scanner rotation. Radiology 176:181–183, 1990.
32. Kane R, Eustace S: Diagnosis of Budd-Chiari syndrome: Comparison between sonography and MR angiography. Radiology 195:117–121, 1995.
33. Kobayashi K, Matsui O, Yoshikawa J, et al: Right hepatic arterial supply to the posterior aspect of segment IV of the liver: Analysis by CT during hepatic arteriography. Abdom Imaging 24:591–593, 1999.
34. Kopka L, Funke M, Fischer U, et al: Parenchymal liver enhancement with bolus-triggered helical CT: Preliminary clinical results. Radiology 195:282–284, 1995.
35. Kopka L, Grabbe E: Biphasic liver diagnosis with multiplanar-detector spiral CT. Radiologe 39:971–978, 1999.
36. Kopka L, Rodenwaldt J, Fischer U, et al: Dual-phase helical CT of the liver: Effects of bolus tracking and different volumes of contrast material. Radiology 201:321–326, 1996.
37. Kronthal AJ, Fishman EK, Kuhlman JE, Bohlman ME: Hepatic infarction in preeclampsia. Radiology 177:726–728, 1990.
38. Lev-Toaff AS, Friedman AC, Cohen LM, et al: Hepatic infarcts: New observations by CT and sonography. Am J Roentgenol 149: 87–90, 1987.
39. Levenson H, Greensite F, Hoefs J, et al: Fatty infiltration of the liver: Quantification with phase-contrast MR imaging at 1.5 T vs. biopsy. AJR Am J Roentgenol 156:307–312, 1991.
40. Luboldt W, Straub J, Seemann M, et al: Effective contrast use in CT angiography and dual-phase hepatic CT performed with a subsecond scanner. Invest Radiol 34:751–760, 1999.
41. Mathieu D, Vasile N, Menu Y, et al: Budd-Chiari syndrome: Dynamic CT. Radiology 165:409–413, 1987.
42. Miller WJ, Baron RL, Dodd GD, Federle MP: Malignancies in patients with cirrhosis: CT sensitivity and specificity in 200 consecutive transplant patients. Radiology 193:645–650, 1994.
43. Mitchell DG: Focal manifestations of diffuse liver disease at MR imaging. Radiology 185:1–11, 1992.
44. Mitchell DG, Kim I, Chang TS, et al: Fatty liver. Chemical shift phase-difference and suppression magnetic resonance imaging techniques in animals, phantoms, and humans. Invest Radiol 26:1041–1052, 1991.
45. Nakao N, Miura K, Takahashi H, et al: Hepatic perfusion in cavernous transformation of the portal vein: Evaluation by using CT angiography. AJR Am J Roentgenol 152:985–986, 1989.
46. Nghiem HV, Dimas CT, McVicar JP, et al: Impact of double helical CT and three-dimensional CT arteriography on surgical planning for hepatic transplantation. Abdom Imaging 24:278–284, 1999.
47. Oka H, Kurioka N, Kim K, et al: Prospective study of early detection of hepatocellular carcinoma in patients with cirrhosis. Hepatology 12: 680–687, 1990.
48. Outwater E, Kaplan MM, Bankoff MS: Lymphadenopathy in primary biliary cirrhosis: CT observations. Radiology 171:731–733, 1989.
49. Parvey HR, Raval B, Sandler CM: Portal vein thrombosis: Imaging findings. AJR Am J Roentgenol 162:77–81, 1994.
50. Rao BK, Brodell GK, Haaga JR, et al: Visceral CT findings associated with Thorotrast. J Comput Assist Tomogr 10:57–61, 1986.
51. Rofsky NM, Weinreb JC, Ambrosino MM, et al: Comparison between in-phase and opposed-phase T1-weighted breath-hold FLASH sequences for hepatic imaging. J Comput Assist Tomogr 20:230–235, 1996.
52. Rofsky NM, Weinreb JC, Bernardino ME, et al: Hepatocellular tumors: Characterization with Mn-DPDP–enhanced MR imaging. Radiology 188:53–59, 1993.
53. Ros PR, Freeny PC, Harms SE, et al: Hepatic MR imaging with ferumoxides: A multicenter clinical trial of the safety and efficacy in the detection of focal hepatic lesions. Radiology 196:481–488, 1995.
54. Saddik D, Frazer C, Robins P, et al: Gadolinium-enhanced three-dimensional MR portal venography. AJR Am J Roentgenol 172: 413–417, 1999.
55. Siegelman ES, Mitchell DG, Rubin R, et al: Parenchymal versus reticuloendothelial iron overload in the liver: Distinction with MR imaging. Radiology 179:361–366, 1991.
56. Silverman PM, Brown B, Wray H, et al: Optimal contrast enhancement of the liver using helical (spiral) CT: Value of SmartPrep. AJR Am J Roentgenol 164:1169–1171, 1995.
57. Silverman PM, Roberts S, Tefft MC, et al: Helical CT of the liver: Clinical application of an automated computer technique, SmartPrep, for obtaining images with optimal contrast enhancement. AJR Am J Roentgenol 165:73–78, 1995.
58. Simonovsky V: The diagnosis of cirrhosis by high-resolution ultrasound on the liver surface. Br J Radiol 72:29–34, 1999.
59. Soyer P, Roche A, Gad M, et al: Preoperative segmental localization of hepatic metastases: Utility of three-dimensional CT during arterial portography. Radiology 180:653–658, 1991.
60. Stanley P: Budd-Chiari syndrome. Radiology 170:625–627, 1989.
61. Stark DD, Felder RC, Wittenberg J, et al: Magnetic resonance imaging of cavernous hemangioma of the liver: Tissue-specific characterization. Am J Roentgenol 145:213–222, 1985.
62. Stark DD, Moseley ME, Bacon BR, et al: Magnetic resonance imaging and spectroscopy of hepatic iron overload. Radiology 154: 137–142, 1985.
63. Stephens DH, Sheedy PF, Hattery RR, MacCarty RL: Computed tomography of the liver. Am J Roentgenol 128:579–590, 1977.
64. Theise ND, Schwartz M, Miller C, Thung SN: Macroregenerative nodules and hepatocellular carcinoma in forty-four sequential adult liver explants with cirrhosis. Hepatology 16:949–955, 1992.
65. Togo S, Shimada H, Kanemura E, et al: Usefulness of three-dimen-

sional computed tomography for anatomic liver resection: Sub-sub-segmentectomy. Surgery 123:73–78, 1998.
66. Torres WE, Whitmire LF, Gedgaudas-McClees K, Bernardino ME: Computed tomography of hepatic morphologic changes in cirrhosis of the liver. J Comput Assist Tomogr 10:47–50, 1986.
67. Uchida M, Ishibashi M, Abe T, et al: Three-dimensional imaging of liver tumors using helical CT during intravenous injection of contrast medium. J Comput Assist Tomogr 23:435–440, 1999.
68. van Kaick G, Bahner ML, Liebermann D, et al: Thorotrast-induced liver cancer: Results of the German Thorotrast study. Radiologe 39: 643–651, 1999.
69. van Leeuwen MS, Noordzij J, Fernandez MA, et al: Portal venous and segmental anatomy of the right hemiliver: Observations based on three-dimensional spiral CT renderings. AJR Am J Roentgenol 163: 1395–1404, 1994.
70. Van Lom KJ, Brown JJ, Perman WH, et al: Liver imaging at 1.5 tesla: Pulse sequence optimization based on improved measurement of tissue relaxation times. Magn Reson Imaging 9:165–171, 1991.
71. Vilgrain V, Lewin M, Vons C, et al: Hepatic nodules in Budd-Chiari syndrome: Imaging features. Radiology 210:443–450, 1999.
72. Vogl TJ, Pegios W, McMahon C, et al: Gadobenate dimeglumine: A new contrast agent for MR imaging. Preliminary evaluation in healthy volunteers. AJR Am J Roentgenol 158:887–892, 1992.
73. Yu JS, Kim KW, Kim EK, et al: Contrast enhancement of small hepatocellular carcinoma: Usefulness of three successive early image acquisitions during multiphase dynamic MR imaging. AJR Am J Roentgenol 173:597–604, 1999.
74. Zissin R, Yaffe D, Fejgin M, et al: Hepatic infarction in preeclampsia as part of the HELLP syndrome: CT appearance. Abdom Imaging 24:594–596, 1999.

37 The Gallbladder and Biliary Tract

John R. Haaga, Thomas E. Herbener

The Gallbladder

The gallbladder is a blind pear-shaped pouch lying along the undersurface of the liver. The gallbladder fossa is located in the plane of the interlobar fissure, which lies between the right and left hepatic lobes (Fig. 37–1). It is approximated by a plane passing longitudinally through the middle hepatic vein and the inferior vena cava. Knowledge of the normal gallbladder location aids in differentiating the gallbladder from other structures and in determining whether the gallbladder location is normal or ectopic.

Normal Anatomy

On axial CT images, the gallbladder is a rounded structure with a maximum diameter of less than 4 to 5 cm and an average volume of 30 to 50 mL in the distended state (see Fig. 37–1).[98] On consecutive axial images, the diameter of the gallbladder usually increases from the more cephalad and medially located neck to the more caudal and typically more laterally located fundus. The neck of the gallbladder may not be readily obvious except on thin-section axial images focused on the porta hepatis or reconstructions (see Fig. 37–2). If contracted, the gallbladder is a smaller tubular structure with a readily discernible wall (Figs. 37–2 and 37–3). Visualization of the gallbladder wall depends on the degree of gallbladder distention, the clarity of visualization of the gallbladder, or the presence of abnormality. Several values for normal gallbladder wall thickness have been published; these range from 1 to 3.5 mm.[204, 207, 208, 223, 236] In a series by Whitehouse and colleagues[237] 95% of normal patients had a gallbladder wall thickness of less than 2.8 mm. As with ultrasonography, 3 mm is therefore a reasonable upper limit of normal. The accuracy of the wall thickness measurement will depend on technical factors such as small pixel size, thin-slice collimation, field of view, and appropriate window width and level. In addition, contrast medium administration may aid in defining the wall. There can be enhancement in the gallbladder wall normally after intravenous contrast medium administration, especially if the agent is given in bolus form with dynamic scanning.[212, 236] A 20-HU increase in gallbladder wall density has been shown in normal gallbladder walls after contrast agent administration.[119, 236] Enhancement may persist normally in the gallbladder wall up to 2 hours after angiographic studies if more than 37 g of iodine was administered.[212]

The density of the gallbladder lumen is usually that of water (0 to 20 HU).[98] After intravascular contrast medium

Figure 37–1. Multislice CT scan of normal gallbladder, with images formatted in 3D plane. Wall of the normal gallbladder is very thin. *Open arrow* shows dilated pancreatic duct.

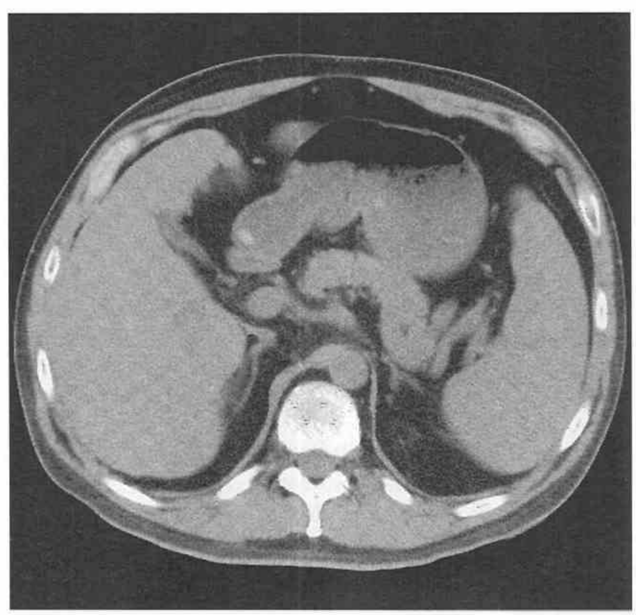

Figure 37–2. Thin-section axial CT scan showing neck of gallbladder.

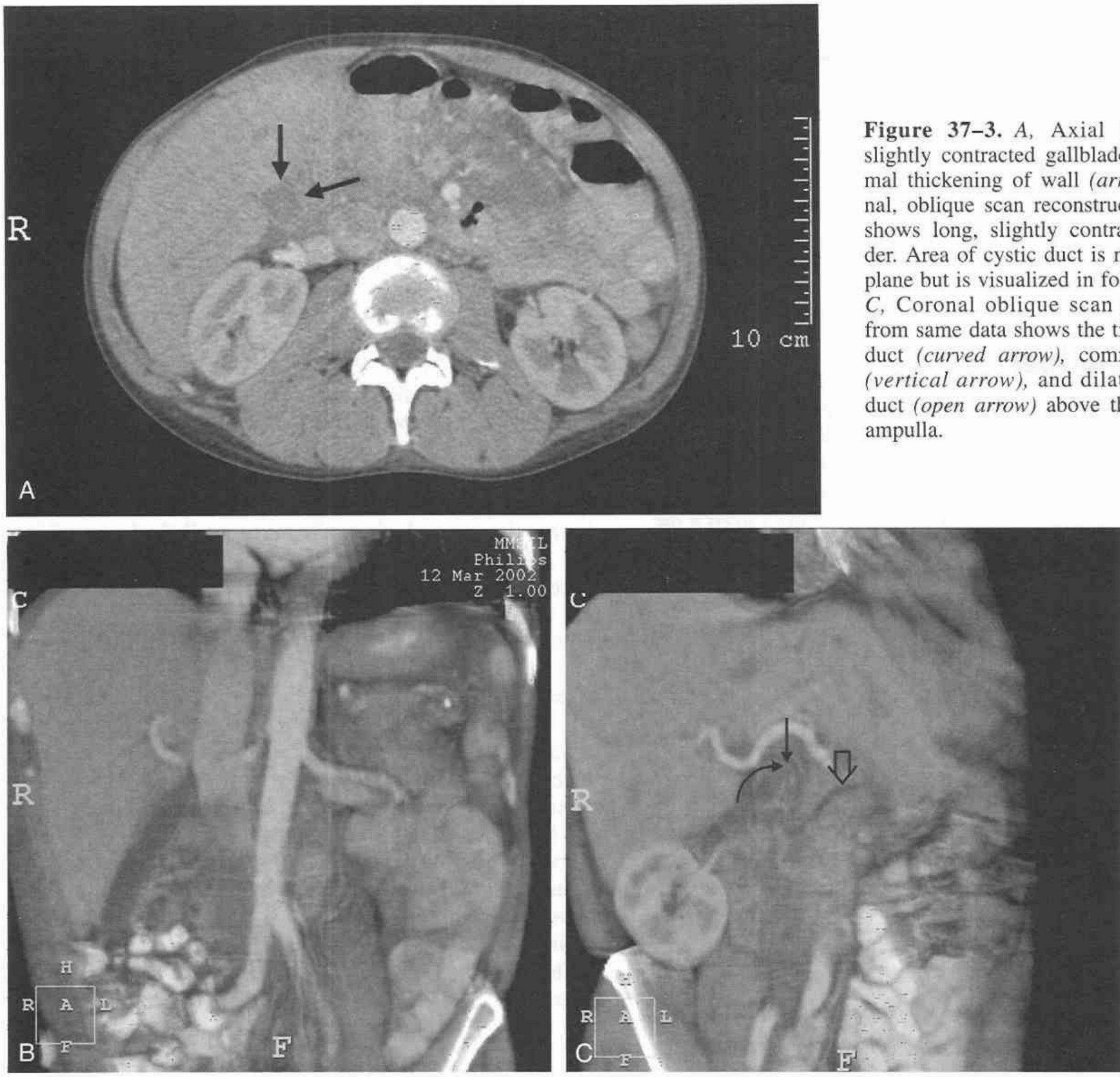

Figure 37–3. *A,* Axial image shows slightly contracted gallbladder with minimal thickening of wall *(arrow). B,* Coronal, oblique scan reconstructed from data shows long, slightly contracted gallbladder. Area of cystic duct is not seen in this plane but is visualized in following image. *C,* Coronal oblique scan reconstructed from same data shows the tip of the cystic duct *(curved arrow),* common bile duct *(vertical arrow),* and dilated pancreatic duct *(open arrow)* above the level of the ampulla.

administration, an increase in density of the gallbladder lumen can be seen normally on CT. This is caused by normal hepatic excretion of a small fraction of the contrast agent into the biliary tree. This amount is usually too small to be seen on plain film but can be seen on CT because of the superior contrast sensitivity.[212, 228] In the setting of abnormal renal function, hepatobiliary excretion of contrast agent may be pronounced with increased density of the gallbladder lumen on CT and plain films (Fig. 37–4).[203, 212] Certainly, oral cholecystographic agents will increase the density of bile and have been used to perform CT cholangiography.[89, 90]

Abnormal density of bile in the gallbladder lumen can be seen in various pathologic conditions by CT. Hemobilia can increase the density of bile toward that of blood (50 to 60 HU) as in hepatobiliary trauma or hemorrhage from a neoplasm or vascular abnormality (Fig. 37–5).[130] Multiple tiny stones may appear simply as increased bile density in the gallbladder lumen if the stones are too small to be individually resolved (Fig. 37–6). However, the most com-

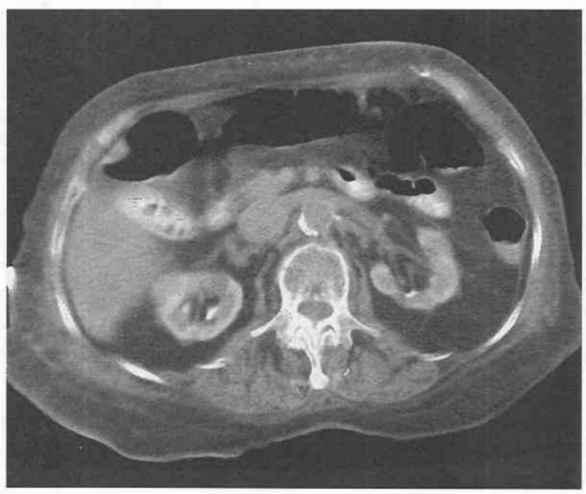

Figure 37–4. CT scan of patient with renal failure shows concentration of contrast material in the gallbladder, which permits visualization of radiolucent gallstones.

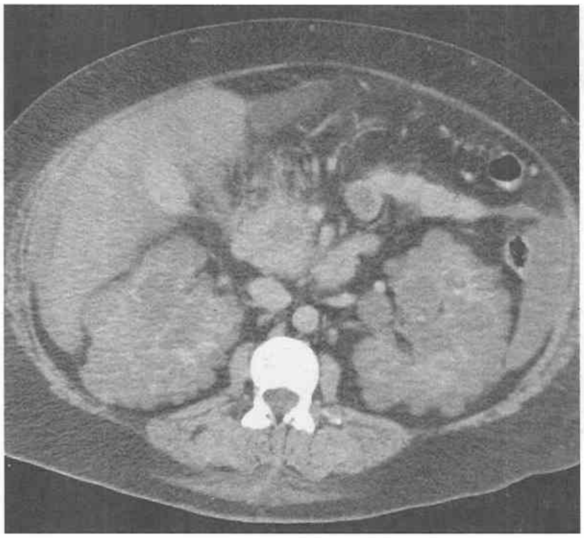

Figure 37–5. High-density material in gallbladder representing blood in a patient with excess anticoagulation.

mon cause of increased bile density in the gallbladder lumen is due to cystic duct obstruction secondary to an impacted stone or neoplasm. In acute and chronic cholecystitis, the density of the gallbladder lumen may be increased because of inflammatory debris (Fig. 37–7).[227, 228] More commonly, however, milk of calcium bile, which is a suspension of calcium carbonate and calcium bilirubinate, will form with cystic duct obstruction (Figs. 37–8 and 37–9). This calcium salt suspension may form from a change in bile alkalinity as a result of cystic duct obstruction and inflammation or may result from secretion of calcium by the injured gallbladder mucosa. It also has been described in the setting of ischemic injury to the gallbladder after transcatheter embolization of the cystic artery.[39, 228] Milk of calcium bile may completely fill the gallbladder or produce a fluid-fluid level with the denser calcium salt

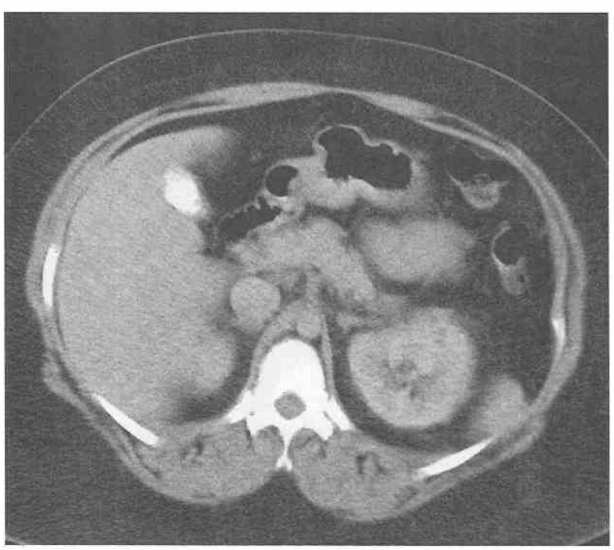

Figure 37–6. Numerous, very tiny calcified gallstones are too small to be individually resolved.

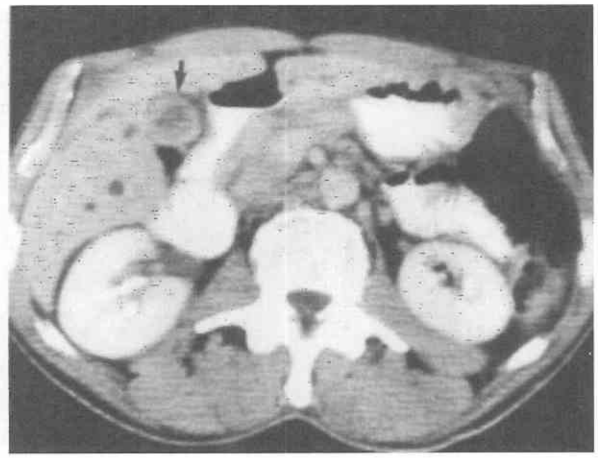

Figure 37–7. Chronic cholecystitis with contracted gallbladder *(arrow)* with thickened wall and internal debris with increased density of bile.

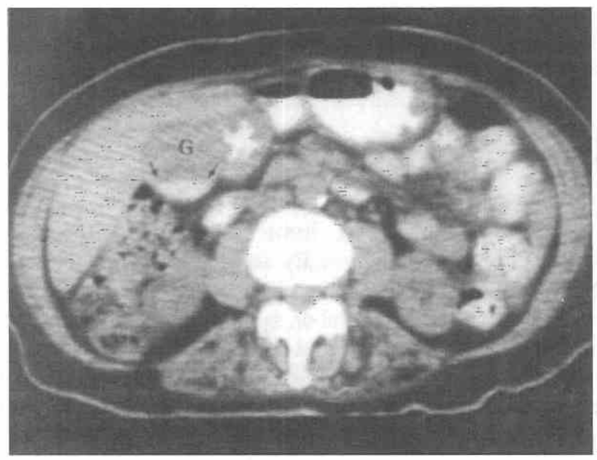

Figure 37–8. Gallbladder (G) with milk of calcium bile *(arrows)*.

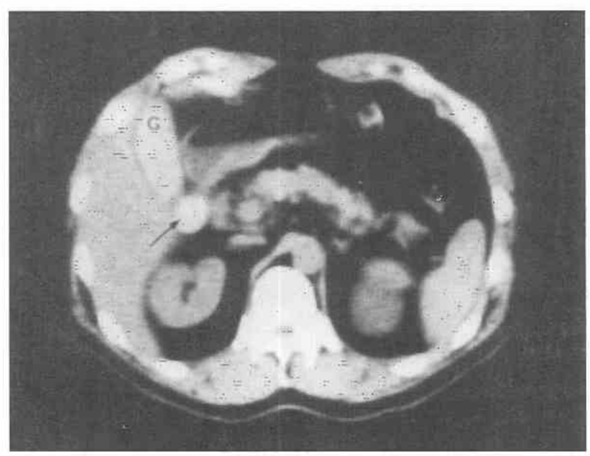

Figure 37–9. Milk of calcium bile. The intraluminal contents of the gallbladder (G) are hyperdense rather than the normal water-density bile. There is also an obstructing calcified gall stone *(arrow)* in the gallbladder neck. Bile stasis, often secondary to cystic duct obstruction, is the cause of milk of calcium bile. (Courtesy of Dr. Avram Pearlstein, Mount Sinai Hospital, Cleveland, Ohio.)

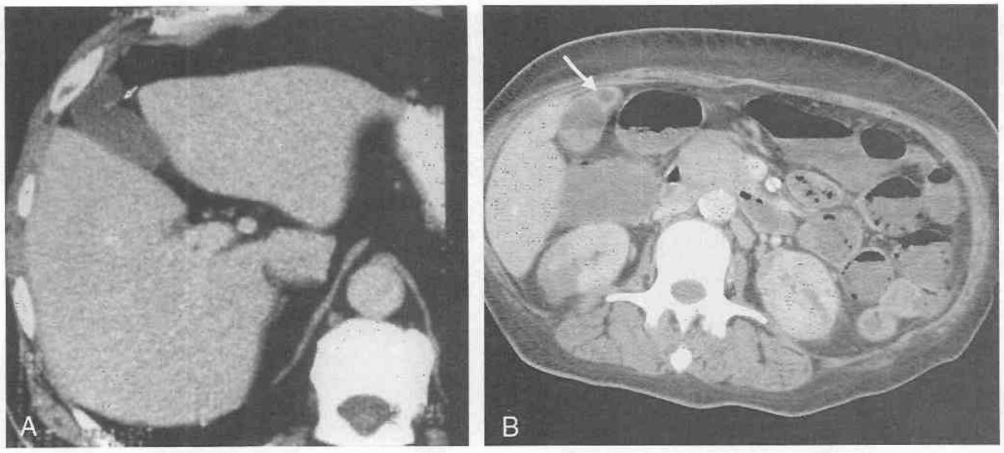

Figure 37–10. *A*, Phrygian cap with small luminal septation *(arrow)*. *B*, Phrygian cap is the most common variant *(arrow)*. This scan shows thickened wall and numerous low-density stones in the dependent portion.

suspension layering dependently. Blood is usually less dense (less than 90 HU) than milk of calcium bile, which may have a density as high as 1000 HU (Fig. 37–5; see also Figs. 37–25 and 37–103).[106]

Congenital Variants

Most anomalies of the gallbladder occur as a result of alterations in budding from the primitive foregut or recanalization of the originally solid gallbladder anlage.[197] Abnormalities in gallbladder form, number, and location occur. Abnormalies in number, such as agenesis or duplication, have been described and are rare.[146]

The most common anomalies are those of form, particularly septations of the gallbladder lumen. The most common anomaly of the entire biliary tree is a septation in the distal fundus, which gives the configuration called a phrygian cap (Fig. 37–10). Septations may occur elsewhere in the gallbladder but are less common and may be multiple. Septations may predispose to bile stasis and stone formation.[146] In addition, septations in the gallbladder may cause an appearance that mimics pericholecystic fluid collections (Fig. 37–11).

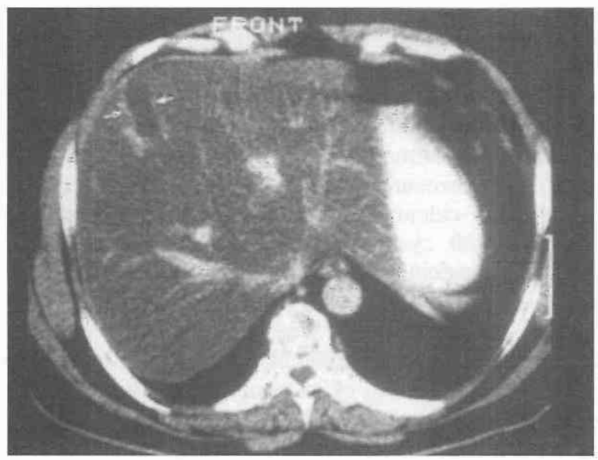

Figure 37–12. Intrahepatic gallbladder *(arrows)* surrounded by liver parenchyma infiltrated with fat.

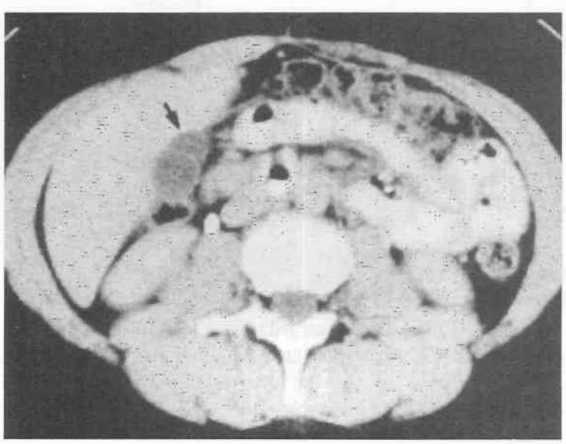

Figure 37–11. A septation in the gallbladder may give appearance of a pericholecystic fluid collection *(arrow)*.

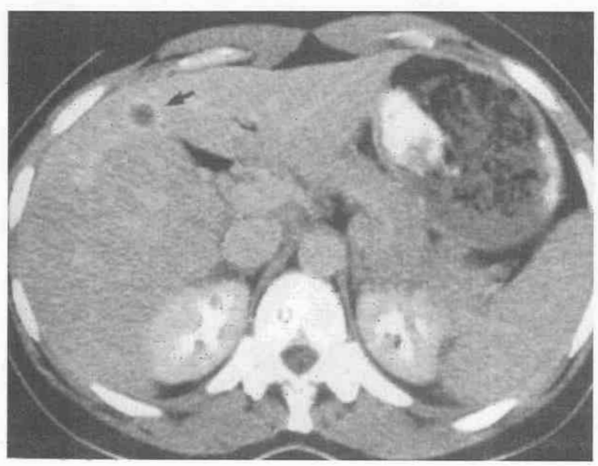

Figure 37–13. Intrahepatic gallbladder *(arrow)* surrounded by liver parenchyma.

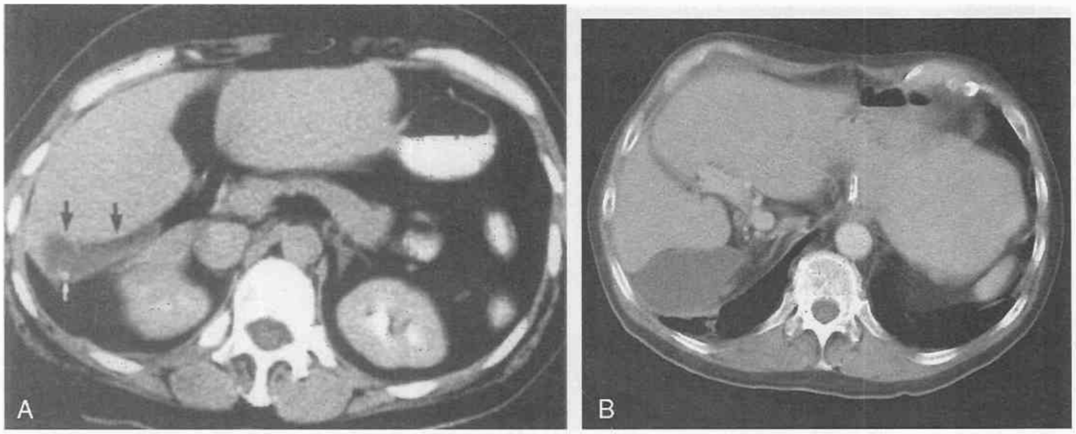

Figure 37–14. *A,* Retroplaced gallbladder *(black arrows)* secondary to hypoplasia of the right hepatic lobe. Note small gallstone *(white arrow). B,* Retroplaced dilated gallbladder on posterior surface of the liver. Note congenital absence of the right lobe.

Anomalies of gallbladder position are rare. The most common ectopic locations are under the left lobe, intrahepatic, transverse, and retroplaced.[146, 160] The intrahepatic gallbladder is typically subcapsular in location along the anteroinferior aspect of the right hepatic lobe and may be surrounded by fat (Figs. 37–12 and 37–13).[25] With hypoplasia, aplasia, atrophy, or hypertrophy of one of the hepatic lobes, the gallbladder may be displaced or rotated abnormally to one side.[146] With cirrhosis and associated atrophy of the right hepatic lobe, the gallbladder may be retroplaced and be posterior to the liver (Fig. 37–14).[163] A suprahepatic gallbladder was described with hypoplasia of the right hepatic lobe and eventration of the diaphragm (Fig. 37–15).[69] Patients with situs inversus will have a gallbladder in the left upper quadrant, and those with polysplenia syndrome may have a spectrum of hepatobiliary anomalies, including a centrally located gallbladder.[78]

Approximately 10% of gallbladders are completely sur-

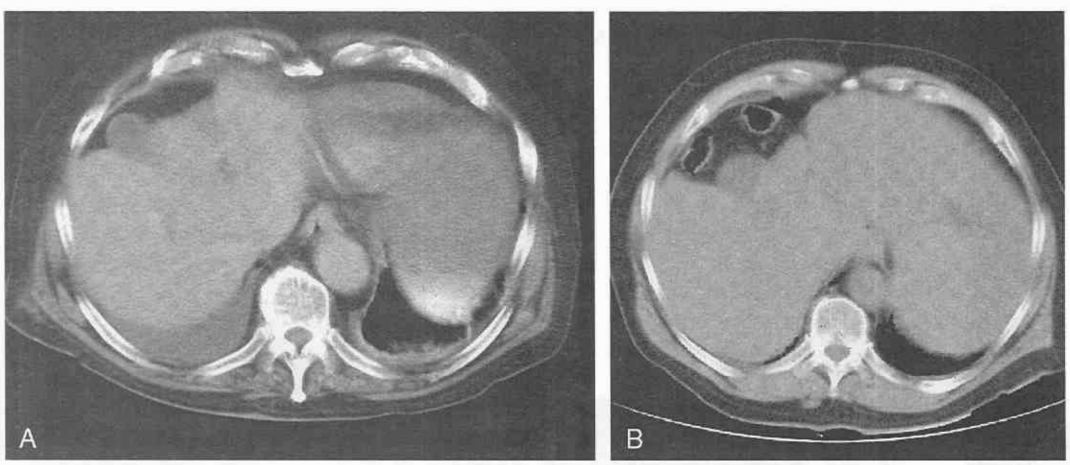

Figure 37–15. *A,* Ectopic gallbladder on the anterior surface of the diaphragm. *B,* Ectopic gallbladder on anterior surface of diaphragm with some atrophy of anterior right lobe. *C,* Ectopic gallbladder in patient with absence of medial segment of left lobe.

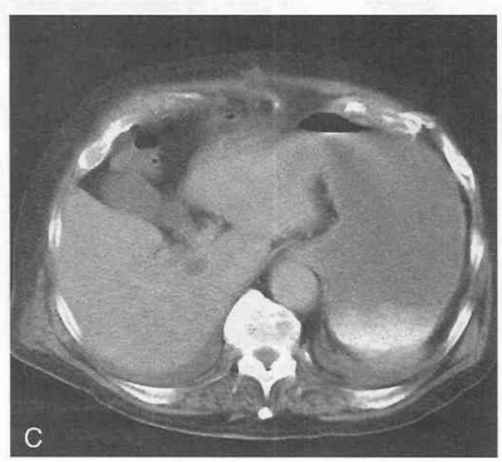

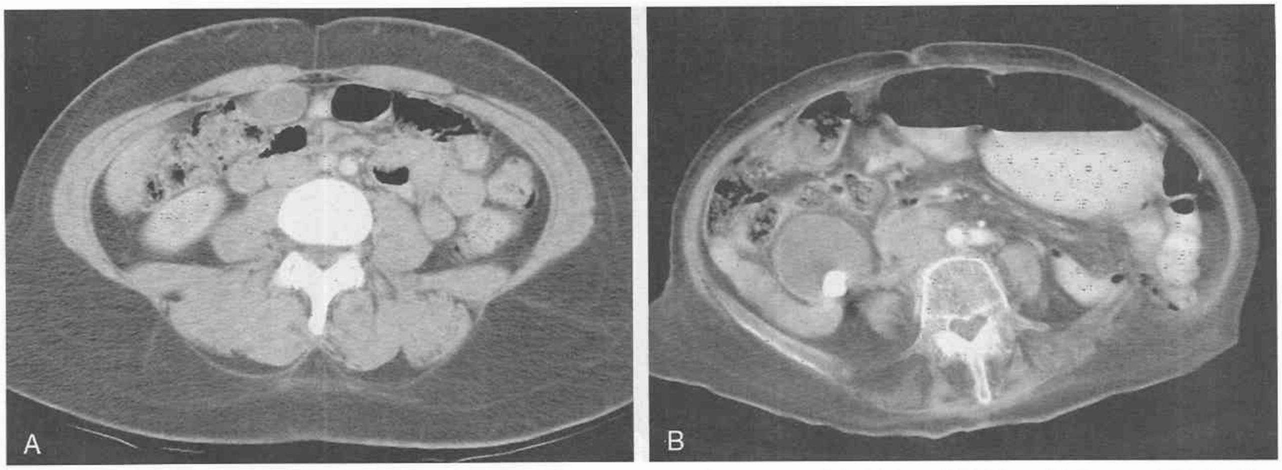

Figure 37–16. *A,* Mobile gallbladder due to long mesentery, located in mid abdomen. *B,* Mobile gallbladder with large calcified calculus.

rounded by peritoneum and may have a long mesentery that allows the gallbladder to lie in abnormal locations such as the pelvis (Fig. 37–16). These are the so-called floating gallbladders. These gallbladders may be prone to torsion or volvulus.[197] In one reported case, such a gallbladder presented as a mass in the region of the head of the pancreas (Fig. 37–17).[160]

Patients with disease in an ectopic gallbladder may present diagnostic challenges because their symptoms may be atypical particularly as to the location of the pain (see Fig. 37–14). The key to the diagnosis on CT is absence of the gallbladder in its typical location in the gallbladder fossa. Identifying the abnormally located gallbladder is imperative to ensure the appropriate surgical approach if needed.

Cholecystitis

The findings on CT of cholecystitis are individually nonspecific. Gallbladder wall thickening, gallbladder distention, gallbladder wall enhancement, gallstones, and pericholecystic fluid can be seen in both acute and chronic cholecystitis but also in other conditions such as gallbladder carcinoma. The overall specificity of CT depends on both the constellation of radiographic findings and the appropriate clinical setting. Because the clinical presentation of patients with cholecystitis is often unclear, CT may be the first examination performed. Knowledge of the characteristics of cholecystitis on CT will be helpful for appropriate diagnosis.

Acute Cholecystitis. The most common finding on CT

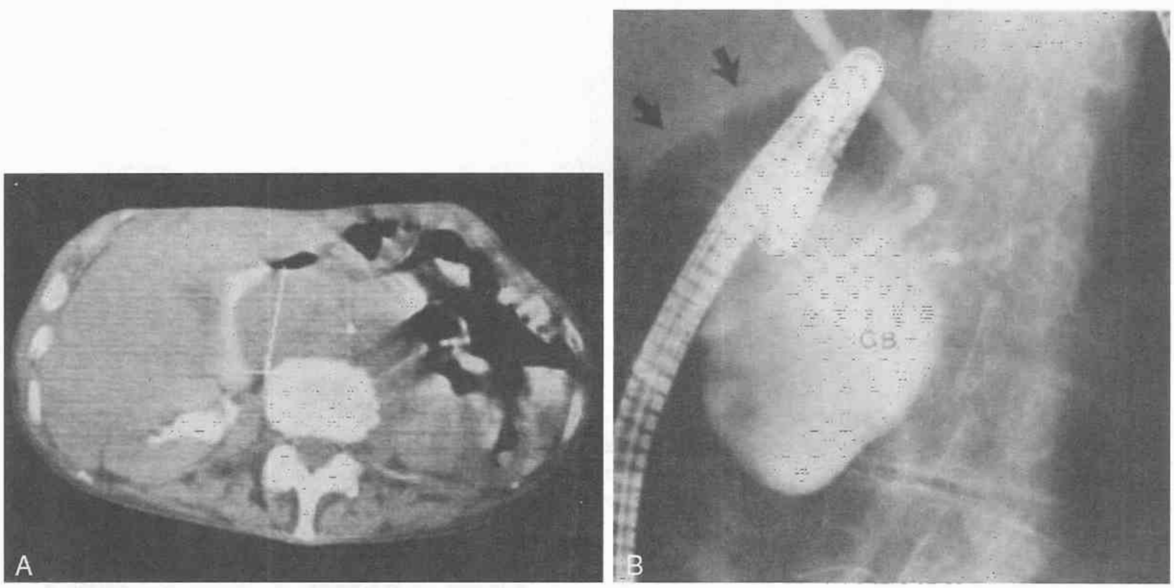

Figure 37–17. *A,* The ectopic, floating gallbladder appears as a mass in the region of the head of the pancreas. Associated indentation of the medial wall of the contrast medium–filled duodenum is seen. *B,* Endoscopic retrograde cholangiopancreatography (ERCP) reveals normal pancreatic and common bile ducts. The normal contrast medium–filled gallbladder (GB) is located medial to the air-filled C loop of the duodenum *(arrows).* (From Morse JMD, Lakshman S, Thomas E: Gastrointest Radiol 10:111, 1985.)

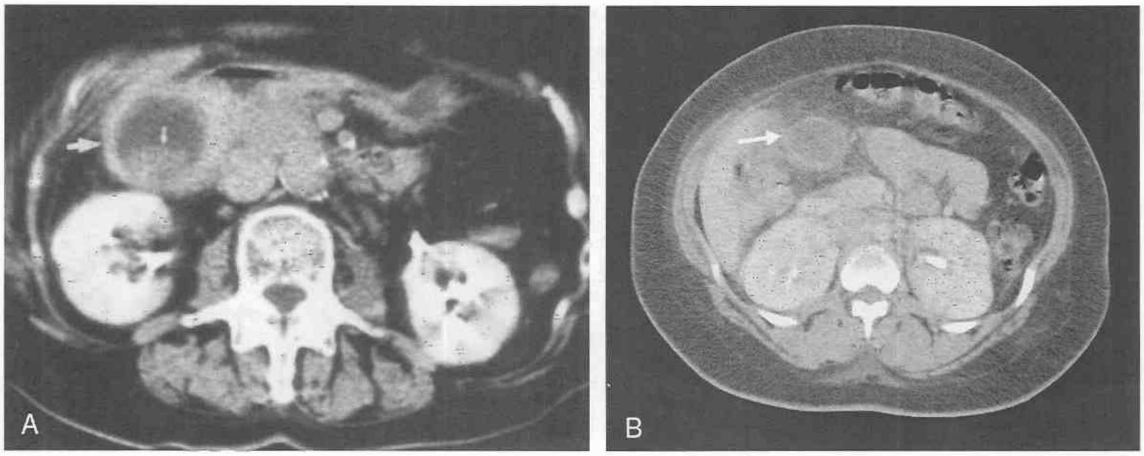

Figure 37–18. *A,* Acute cholecystitis with thickened gallbladder wall *(large arrow)* and debris in the gallbladder lumen *(small arrow). B,* Acute cholecystitis showing edema in the peritoneal fat, thick wall, and focal area of subserosal edema *(arrow).* This is a free-floating gallbladder with a long mesentery, so it appears detached from the liver.

of acute cholecystitis is thickening of the gallbladder wall, often nodular in contour (Fig. 37–18).[121, 222] Thickening of the wall alone is not specific for acute cholecystitis and can be seen in a contracted gallbladder, cirrhosis, hepatitis, ascites, pancreatitis, congestive heart failure, renal failure, hypoalbuminemia, adenomyomatosis, portal hypertension, multiple myeloma, and gallbladder carcinoma (Fig. 37–19; see also Figs. 37–48, 37–49, and 37–51).[36, 120, 135, 166, 176] The wall thickness in acute cholecystitis is 3 to 5 mm or more and is caused by mural inflammation and edema. Subserosal edema may present as a hypodense rim surrounding inner, more dense layers of the wall (Fig. 37–20; see also Fig. 37–23).[166] On CT, differentiation of this subserosal edema from pericholecystic fluid may be difficult. Pericholecystic fluid, however, tends to be more focal, and mural edema is more circumferential (see Fig. 37–20). With mural edema, an inner enhancing layer of mucosa and an outer enhancing layer of serosa will "sandwich" the hypodense layer of mural edema.[88] Pericholecystic fluid will not be surrounded by an enhancing serosa. In addition, enhancing blood vessels may be seen passing through the mural edema but not through the pericholecystic fluid.[88]

Distention of the gallbladder to greater than 5 cm in diameter can be seen in acute cholecystitis. This, however, is also a nonspecific finding if it is the only abnormality. Diabetes, toxic hepatitis, and distention secondary to neoplastic obstruction of the common bile duct can produce enlarged gallbladders.[98, 119] In these settings, however, the gallbladder wall is usually not thickened. Distention and wall thickening together are more specific for cholecystitis.

Poor definition of the gallbladder wall and inflammatory changes in the pericholecystic fat are important findings of cholecystitis on CT. The strandlike water and soft tissue densities in the pericholecystic fat represent edema and inflammation (Figs. 37–21 and Fig. 37–22). Transmural inflammation with edema in the tissues around the gallbladder wall will cause loss of sharpness of the wall; and the fatty interface between the gallbladder and adjacent liver parenchcyma will be obscured. One report suggests that these pericholecystic changes are one of the most reliable signs of acute cholecystitis on CT.[221]

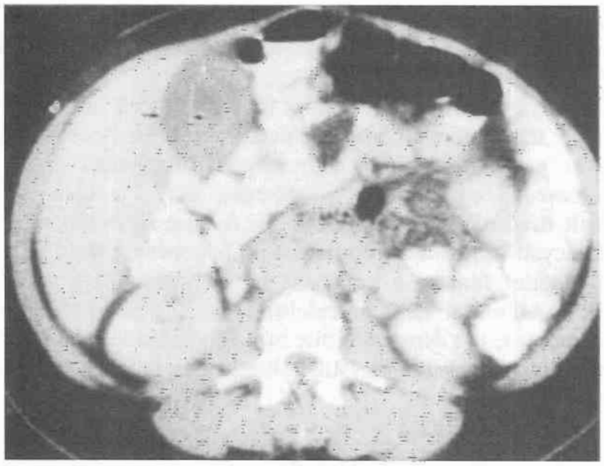

Figure 37–19. Thickened gallbladder wall *(between black arrows)* due to hepatitis. Note enhancing mucosa along inner wall *(white arrow).*

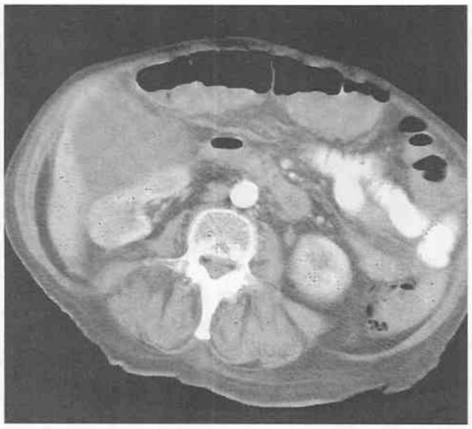

Figure 37–20. Gangrenous cholecystitis with findings of edema, wall thickening, and subserosal edema. Note the bulge medially representing local perforation.

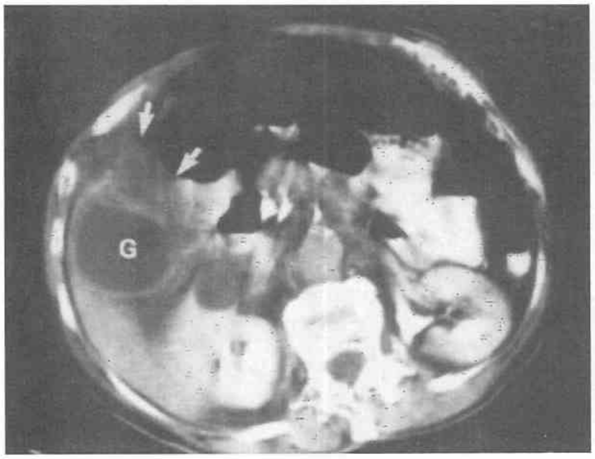

Figure 37–21. Acute cholecystitis with pericholecystic inflammatory changes *(arrows)* and distended gallbladder (G).

Gallstones alone are not themselves a reliable sign of the presence of acute cholecystitis, because they may be seen with or without inflammation of the gallbladder. In addition, CT is not as sensitive as ultrasound for detecting gallstones (see Fig. 37–49). Pure cholesterol stones may not be visualized on CT, owing to the similar density with adjacent bile. Finally, acalculous cholecystitis may demonstrate similar CT findings as acute calculous cholecystitis, such as wall thickening, pericholecystic fluid, and pericholecystic inflammation but without demonstrable gallstones (Fig. 37–23).[151, 229]

Complicated Cholecystitis. CT is helpful in diagnosing complications of acute cholecystitis because it demonstrates the pericholecystic abnormalities better than ultrasound.[229] Progression to complicated cholecystitis such as empyema, gangrene, and perforation occurs in 25% to 30% of cases of acute cholecystitis.[133, 222] As transmural inflammation progresses, ischemia and necrosis may develop and lead to perforation. A focal pericholecystic fluid collection in the setting of gallstones, wall thickening, and pericholecystic edema should suggest acute gangrenous cholecystitis (see Fig. 37–20).[221, 229]

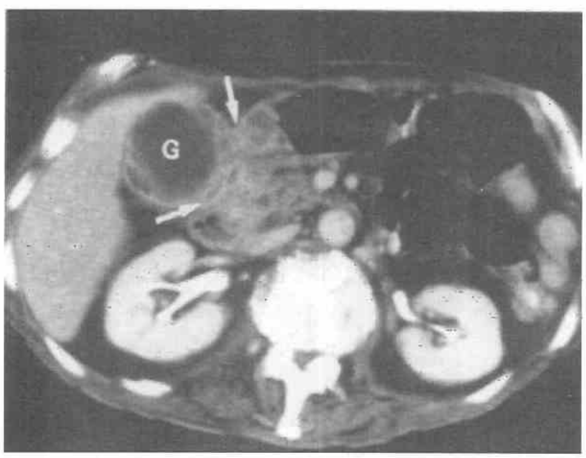

Figure 37–22. Acute cholecystitis (G) with pericholecystic inflammation *(arrows)* extending into adjacent bowel.

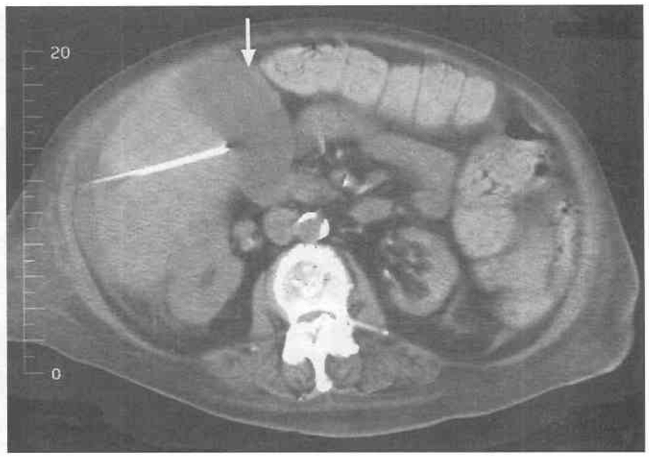

Figure 37–23. Acalculus cholecystitis showing large gallbladder with thick wall *(arrow).* The patient's symptoms were so severe percutaneous cholecystotomy was performed. Needle is noted entering the hepatic side of the gallbladder.

Fidler and associates[73] studied the various findings related to cholecystitis and their usefulness for diagnosis. In 29 cases, they studied the frequency of various findings. The most common findings were wall thickening in 17, pericholecystic stranding in 15, distention in 12, pericholecystic fluid in 9, subserosal edema in 9, high-density bile in 7, and sloughed membrane in 1. When the standard criteria were used, 14 patients were not diagnosed by means of the standard criteria.

Bennett and colleagues[22] studied the findings associated with gangrenous cholecystitis in 23 cases and correlated them with comparable groups of simple cholecystitis and normal gallbladder. The four criteria most specific were gas in the wall or lumen, intraluminal membranes, irregular or absent wall, and abscess.

Phlegmon or a complex abscess adjacent to the gallbladder may have a density higher than bile in the gallbladder lumen. In addition, with perforation, gallstones may be detected outside the gallbladder lumen. These stones may erode into adjacent structures such as the duodenum, colon, and biliary tree, causing fistulas. If there is communication into bowel, air may be seen in the gallbladder and biliary tree. Gallstone ileus can occur when a stone erodes into the small bowel with subsequent small bowel obstruction (Fig. 37–24).

Empyema of the gallbladder may not appear differently on CT than uncomplicated acute cholecystitis because pus in the gallbladder lumen may have normal water density. Increased luminal density, however, may be seen as a result of the inflammatory debris. A case of hemorrhagic cholecystitis has been reported with hyperdense fluid in the gallbladder lumen, as a result of hemorrhage (Fig. 37–25).[119] Although milk of calcium bile and contrast agent can increase the density of bile in the gallbladder, empyema and hemorrhagic cholecystitis should be another consideration.

Gallbladder Perforation

Kim and colleagues[127] reported on the appearance of gallbladder perforation and compared findings on ultraso-

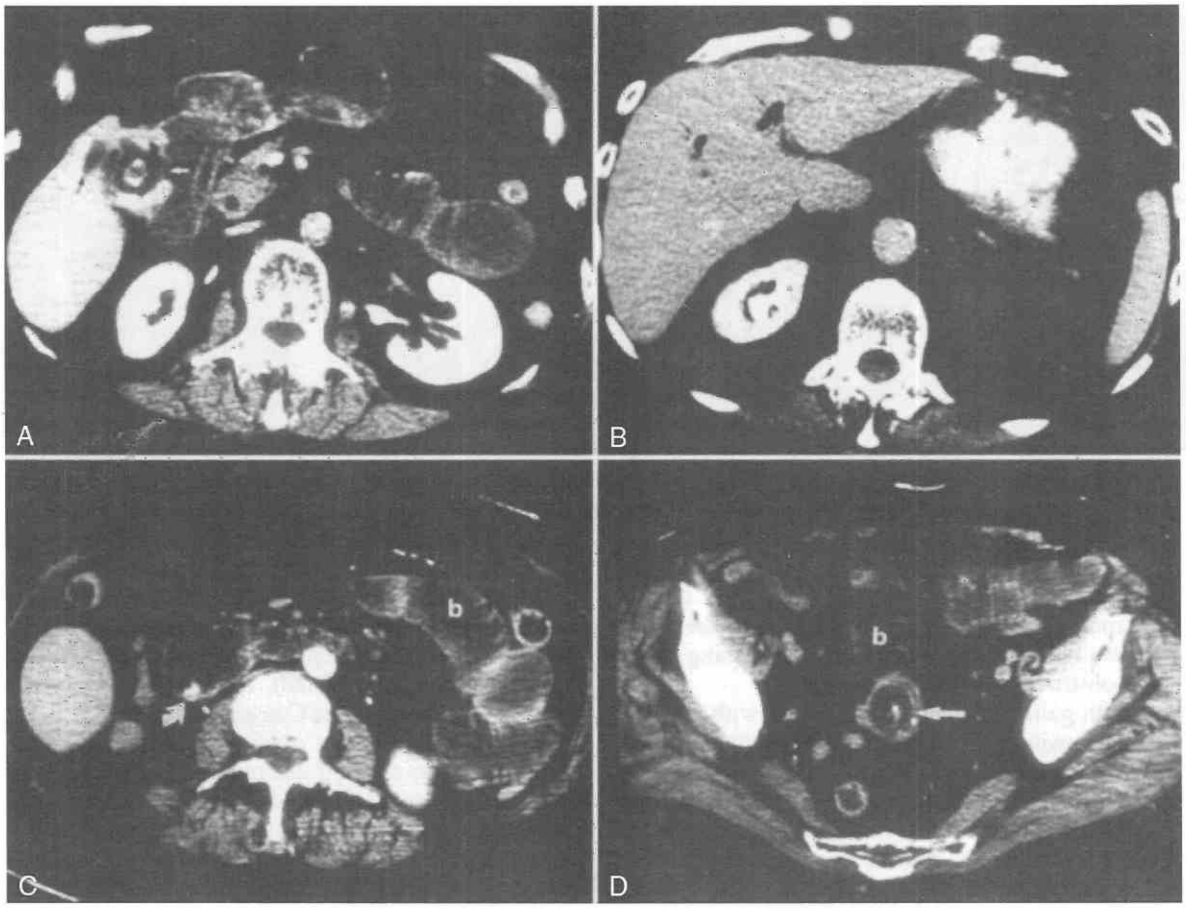

Figure 37–24. Gallstone ileus. *A,* A stone (S) is seen in the gallbladder with a visible fistula between the gallbladder and the adjacent duodenum (*white arrow* shows defect in medial gallbladder wall). *Black arrow* shows pericholecystic fluid. *B,* Pneumobilia *(black arrows). C,* Stone in second portion of dilated duodenum *(arrow).* Note dilated small bowel (b) due to distal obstruction. *D,* Stone in distal small bowel lumen *(arrow)* causing obstruction with dilated small bowel (b) proximally.

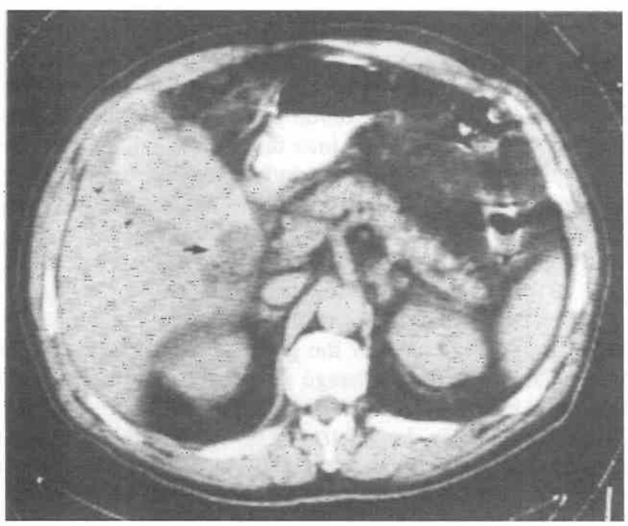

Figure 37–25. Hemorrhagic cholecystitis. The gallbladder wall is thickened *(arrowheads),* and its intraluminal contents are abnormally increased in density, representing blood mixed with bile. The rounded area of decreased density within the neck of the gallbladder *(arrow),* is a calculus. (From Jenkins M, Golding RH, Cooperberg PL: Am J Roentgenol 140:1197–1198, © by American Roentgen Ray Society, 1983.)

nography and CT. The findings common to both modalities were the presence of pericholecystic fluid, layering of gallbladder wall, streaky edema in the mesentery, and a bulge or defect in the wall at the site of the perforation. The defect in the wall was seen in 38.5% of cases on ultrasonography and in 69.2% on CT examination.

Emphysematous Cholecystitis. The only single specific sign for acute cholecystitis on CT is gas in the wall or lumen of the gallbladder, as seen in emphysematous cholecystitis.[5, 145] The gas develops in acute cholecystitis with bacterial infection secondary to gas-producing organism, such as *Escherichia coli, Enterobacter aerogenes,* and *Clostridium.* The gas may appear as bubbles in the gallbladder lumen, or it may be within the gallbladder wall, giving a gas density rim to the gallbladder that is pathognomonic (Figs. 37–26 and 37–27). CT is an excellent technique to diagnose emphysematous cholecystitis because it detects and localizes gas easily as a result of its superior contrast and spatial resolution. No intravenous or oral contrast agent is required and, unlike on plain film or ultrasound, bowel gas is usually readily differentiated.

Gallstone Ileus. Gallstone ileus is an uncommon complication of chronic cholecystitis in which a gallstone erodes through the gallbladder wall and into adjacent

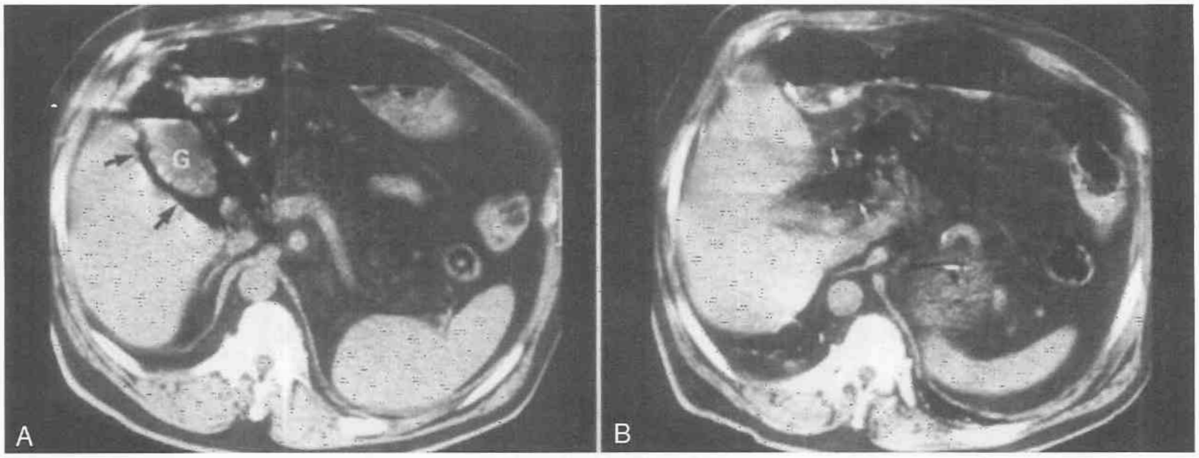

Figure 37–26. *A,* Emphysematous cholecystitis with gas in the gallbladder wall *(arrows)* surrounding the gallbladder lumen (G). *B,* Emphysematous cholecystitis with gas extending into porta hepatis *(arrows).*

bowel, causing subsequent bowel obstruction. The duodenum is the most common site of erosion, with the stone migrating distally in the bowel lumen and causing distal small bowel obstruction.

Patients with gallstone ileus often present with nonspecific abdominal pain. Biliary symptoms are often absent. The preoperative diagnosis is difficult to make. The plain film findings have been described and include the triad of small bowel obstruction, pneumobilia, and an ectopic gallstone. However, not all gallstones are radiopaque on plain film, and pneumobilia may not be present. Therefore, plain film diagnosis may be difficult and is seen in only 30% to 35% of cases.[92]

The findings on CT have been described and include dilated loops of small bowel, pneumobilia with air in the bile ducts and gallbladder, and a stone within the bowel lumen—usually distal small bowel.[92]

Mirizzi Syndrome. Mirizzi syndrome is the condition of biliary obstruction of the common hepatic duct at the level of the gallbladder neck caused by inflammation associated with an impacted gallstone in the gallbladder neck or cystic duct (Fig. 37–28). It is typically a complication of chronic cholecystitis. Congenital anomalies of the extrahepatic bile ducts may predispose patients to this condition.[20] Because of the inflammation, fibrosis, and distortion of structures at the level of obstruction, both preoperative and intraoperative diagnoses are difficult.

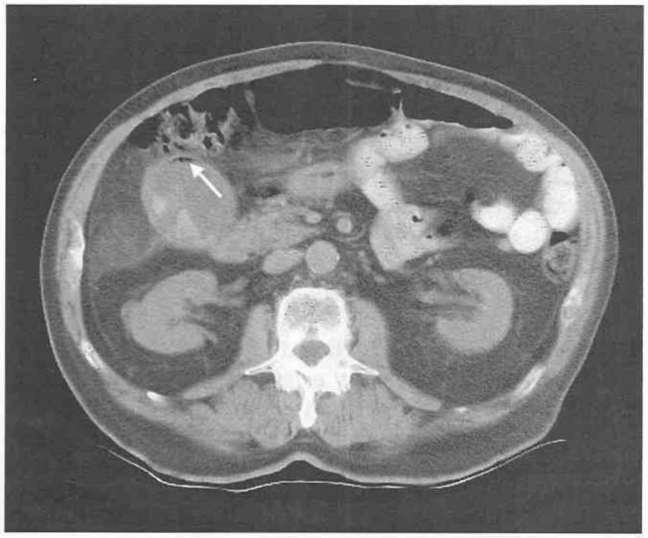

Figure 37–27. Gram-negative gas forming infection in gallbladder. CT scan shows enlarged gallbladder with thick wall, small amount of air *(arrow),* and faceted gallstones.

These patients typically present with symptoms suggestive of gallbladder disease and jaundice. Ultrasonography and CT are often the initial examination performed to evaluate such a clinical presentation. On CT, dilated bile ducts may be seen with the common hepatic duct (CHD) dilated to the level of the gallbladder neck or cystic duct (Fig. 37–29).[20, 24] Often a stone may be seen in the neck or cystic duct at this level. The CHD diameter abruptly decreases below the level of the stone. Nonspecific signs of cholecystitis may be present.

The stone in the neck of the gallbladder or cystic duct may obstruct the CHD as a result of extrinsic compression. However, the stone may erode into the CHD by pressure necrosis, or it may erode into the surrounding tissues of the hepatoduodenal ligament and be detected outside the bile duct. A cholecystobiliary fistula may occur but will be difficult to directly visualize on CT.[20] Cholangiography (endoscopic retrograde [ERCP] or percutaneous transhepatic [PTC]) is the gold standard to evaluate for a fistula.

Mirizzi syndrome may mimic a malignancy especially if the stone in the neck of the gallbladder or cystic duct is not visualized. Abrupt change in caliber of the CHD can be seen in malignancy such as cholangiocarcinoma (CCA). PTC or ERCP may demonstrate a stricture in the CHD that also may mimic malignancy. Carcinoma of the cystic duct has been described as mimicking Mirizzi syndrome because of associated CHD obstruction.[181] However, CT, especially high-resolution CT, will show no evidence of mass or lymphadenopathy in the setting of Mirizzi syndrome as expected with malignancy; this is an extremely important observation.[24]

Chronic Cholecystitis. Chronic cholecystitis may have

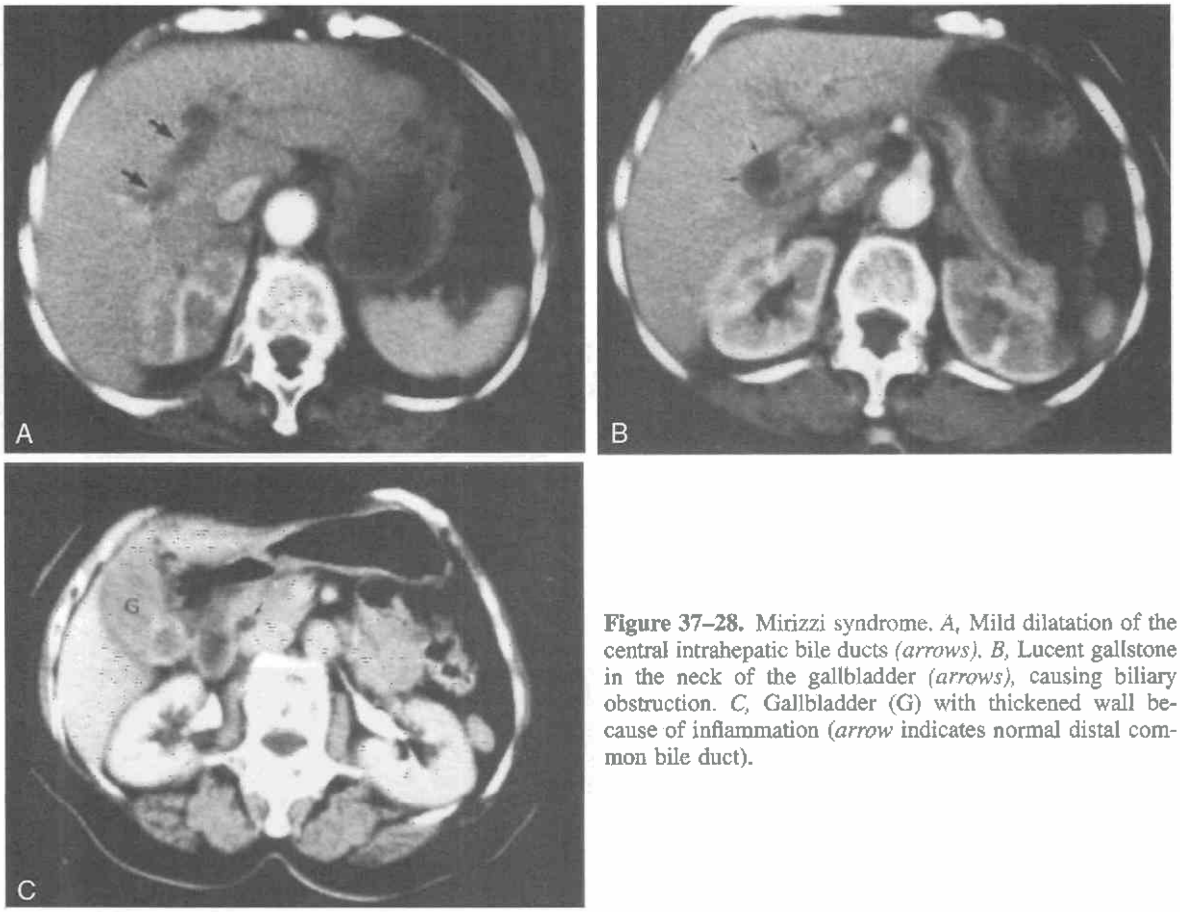

Figure 37–28. Mirizzi syndrome. *A,* Mild dilatation of the central intrahepatic bile ducts *(arrows)*. *B,* Lucent gallstone in the neck of the gallbladder *(arrows)*, causing biliary obstruction. *C,* Gallbladder (G) with thickened wall because of inflammation (*arrow* indicates normal distal common bile duct).

similar findings as acute cholecystitis, such as wall thickening, stones, and wall enhancement (Figs. 37–29 to 37–31). The gallbladder, however, often is contracted around the gallstones rather than distended. A "porcelain" gallbladder is an uncommon manifestation of chronic cholecystitis where calcium is deposited in the gallbladder wall. The calcium may be found in coarse plaques in the muscularis or as diffuse punctate foci in the mucosa (Fig. 37–32). Although plain films and ultrasonography may demonstrate a porcelain gallbladder, CT is better at detecting and localizing the calcium to the wall of the gallbladder.[122] In addition, because of the association of porcelain gallbladder and gallbladder carcinoma, the CT examination should be carefully viewed for any sign of carcinoma (Fig. 37–33).[79, 106, 175]

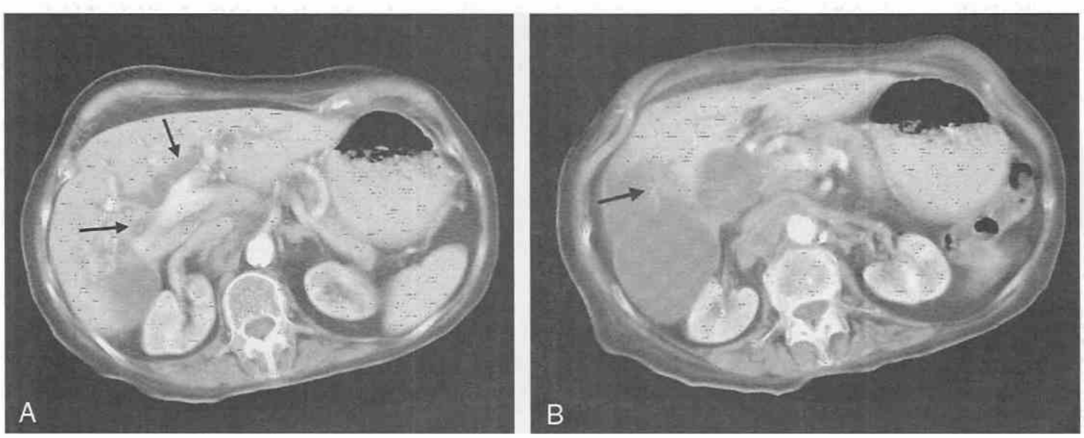

Figure 37–29. *A,* Large loculated fluid collection in porta hepatis by common bile duct causing intrahepatic dilatation *(arrows)*. *B,* Large ectopic gallbladder with rupture, with inflammatory fluid spreading to porta region. Single gallstone is noted in the anterior portion *(arrow)*.

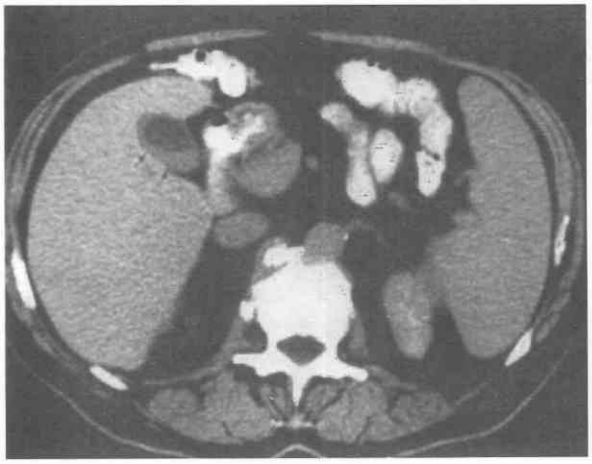

Figure 37–30. Chronic cholecystitis with thickened gallbladder wall *(arrows)*.

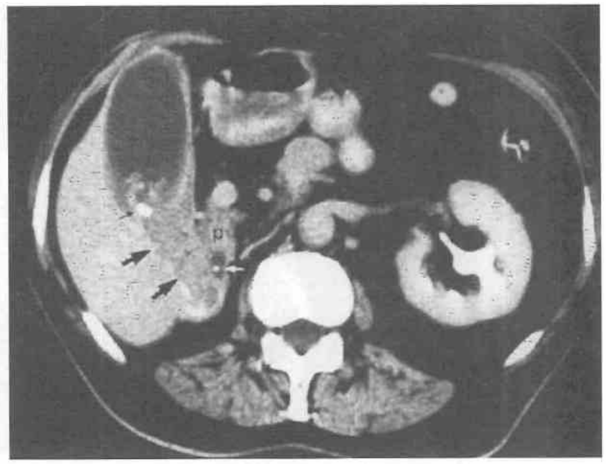

Figure 37–31. Chronic cholecystitis with thickened gallbladder wall *(large black arrows)*, gallstones *(small black arrow)*, and distal common bile duct stone *(small white arrow)* in the head of the pancreas (p).

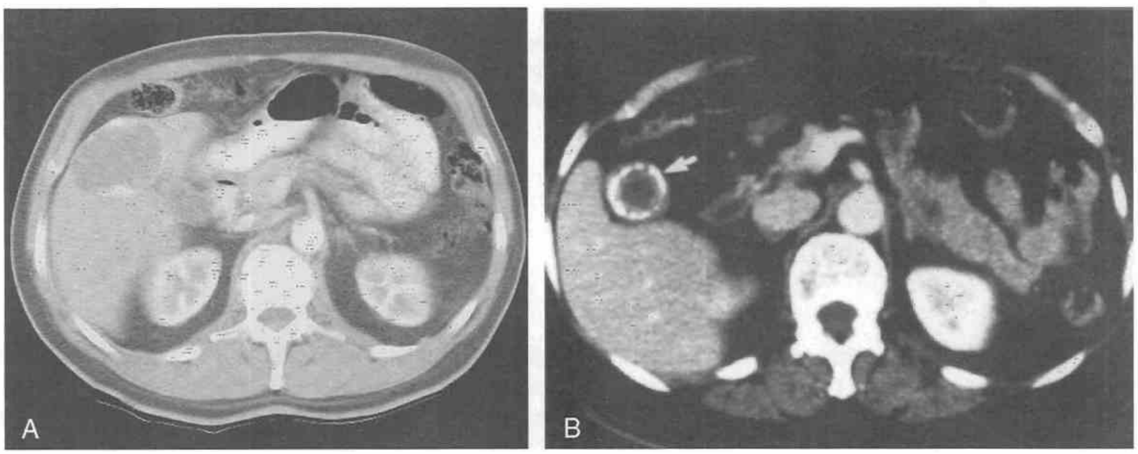

Figure 37–32. Porcelain gallbladder. *A*, Scattered calcium in wall of gallbladder, some more discrete and dense. *B*, Diffuse calcific plaques throughout gallbladder wall.

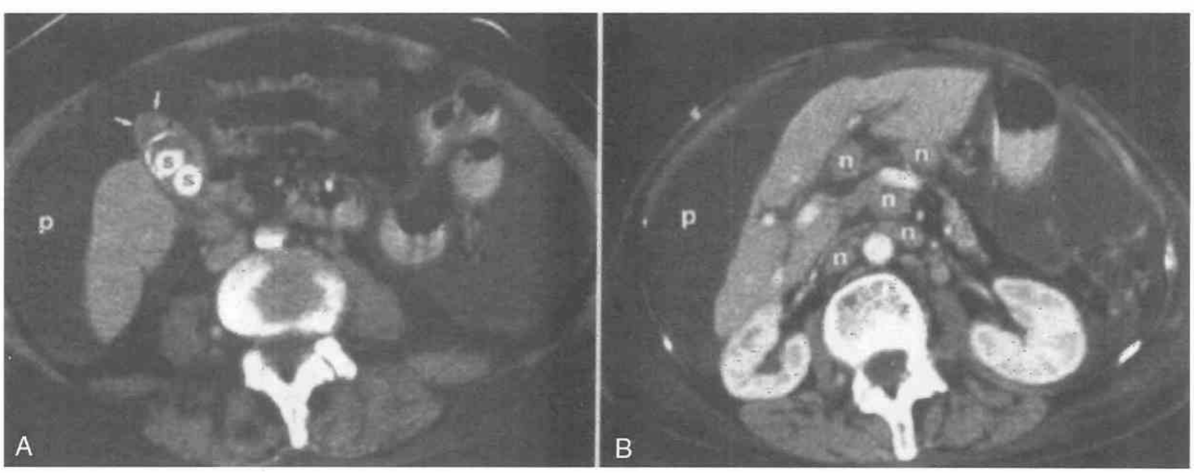

Figure 37–33. Gallbladder carcinoma arising from a porcelain gallbladder. *A*, Gallbladder containing dense stones (s) and calcified mural plaque *(black arrows)* with focal carcinoma in the wall *(white arrows)*. p, ascites. *B*, Diffuse metastatic lymphadenopathy (n) and ascites (p) with peritoneal metastases.

Porcelain gallbladders may, in fact, be removed prophylactically because of the association with carcinoma. Occasionally, the calcified rim of a large gallstone may mimic calcification in the wall of the gallbladder.

Xanthogranulomatous Cholecystitis. Xanthogranulomatous cholecystitis is a rare condition associated with chronic recurrent inflammation of the gallbladder due to gallstones. It is a benign process but may mimic gallbladder malignancy with its slow insidious onset and its appearance on imaging studies. Preoperative diagnosis is rare.[58, 64]

Pathologically, this process consists of a mixed inflammatory infiltrate in the gallbladder wall with foamy histiocytes, foreign body giant cells, and diffuse fibrotic reaction. This is a similar xanthogranulomatous reaction as elsewhere in the body. Grossly, diffuse nodules may appear in the gallbladder wall, a large "tumor" mass may form, or an ill-defined infiltrative process may occur.[58]

On CT, irregular thickening of the gallbladder wall is the most common abnormality in addition to gallstones. However, a mass may be present in the gallbladder fossa.[54] The appearance may be impossible to separate from that of gallbladder carcinoma on both ultrasound evaluation and CT. However, no evidence of metastases or biliary dilatation will be seen with xanthogranulomatous cholecystitis.[58, 64]

Chun and associates[48] studied the features of xanthogranulomatous cholecystitis and gallbladder carcinoma and to define criteria to differentiate the two. They concluded one can differentiate the two only when the gallbladder is largely occupied by large hypoattenuated nodules. Without such nodules, the thickening and mass effect are indistinguishable.

Hyperplastic Cholecystoses. The hyperplastic cholecystoses are noninflammatory conditions of the gallbladder that consist of benign proliferation of normal tissue of the gallbladder and include cholesterolosis and adenomyomatosis. Cholesterolosis consists of multiple focal deposits of cholesterol-laden macrophages in the lamina propria of the gallbladder wall and formation of cholesterol polyps. These are very small, however, and not typically seen on CT but better appreciated on ultrasound evaluation.

The CT findings in adenomyomatosis have been described. This condition consists of thickening of the muscular wall of the gallbladder with proliferation of mucosal epithelium and outpouching of the mucosa into or through the wall, forming intramural diverticula. CT demonstrates the gallbladder wall thickening, which may be focal and may show the intramural diverticula especially if an oral cholecystographic agent is administered or if small stones are within the diverticula (Figs. 37–34 and 37–35).[29, 50, 113, 153] Fatty proliferation in the subserosal portion of the gallbladder has been reported.[153] Thickening of the gallbladder wall may be the only finding on CT, and exclusion of other processes such as cholecystitis or gallbladder carcinoma may be difficult (see Fig. 37–55).[113]

Polypoid Lesions

Furukawa and colleagues[77] evaluated the use of CT for the detection and characterization of polypoid lesions. They studied a group of 20 patients who had CT examination followed by cholecystectomy. With unenhanced scans, only 40% were detected, whereas 100% were detected in the enhanced studies. The polypoid lesions were classified into three types: pedunculated, sessile, and mass-forming. Cholesterol and hyperplastic polyps were all pedunculated. Adenomyomatoses were mass-forming in the two cases. Adenocarcinomas were sessile in four of five cases and pedunculated in one. Density differences were of no benefit in distinguishing among the various entities.

Figure 37–34. Focal adenomyomatosis *(large arrow)* in fundus of gallbladder with small gallstones in the lumen *(small arrow).*

Postcholecystectomy. After cholecystectomy via laparotomy (open cholecystectomy), CT can be used to evaluate patients with persistent fever, abdominal pain, or abnormal liver function tests. Biliary scintigraphy (DISIDA) and cholangiography will often be the first-line examinations

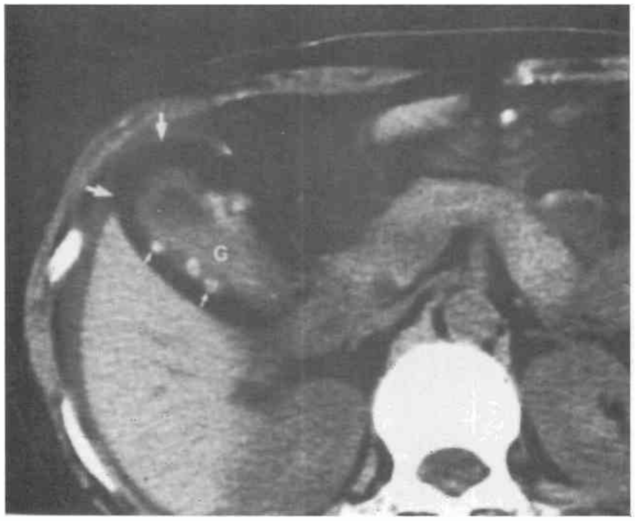

Figure 37–35. Adenomyomatosis with proliferation of subserosal fat *(large arrows),* intramural diverticula containing stones *(small arrows),* and soft tissue mass (G) in gallbladder lumen. (From Miyake H, Aikawa H, Hori Y, et al: Adenomyomatosis of the gallbladder with subserosal fatty proliferation. CT findings in two cases. Gastrointest Radiol 17:21, 1992.)

to evaluate for bile leak or duct injury.[80] However, CT may be used to evaluate for abscess, hematoma, or an unexpected postoperative complication. Subhepatic fluid collections have been shown by ultrasound in 20% of postcholecystectomy patients.[143] In addition, 44% of such patients have been shown in one series to have bile leaks on DISIDA scans, with the majority being clinically insignificant.[232] CT can identify these collections but unfortunately often cannot differentiate a postoperative seroma, abscess, hematoma, or biloma, unless percutaneous aspiration is performed (Fig. 37–36).

Laparoscopic cholecystectomy is rapidly becoming a popular treatment for gallbladder disease. Typical postoperative changes on CT have been described and include pneumoperitoneum, subcutaneous emphysema, subhepatic fluid collections, ascites, and gallbladder fossa edema.[143] Small fluid collections in the gallbladder fossa immediately in the postoperative period are common and probably represent small bile leaks because of disruption of ducts of Luschka, which are accessory ducts draining directly from liver parenchyma into the gallbladder (Fig. 37–37). Significant bile leakage is one of the more common postoperative complications and occurs as a result of injury to the extrahepatic bile ducts, leak from the cystic duct remnant, or leak from transection of large unrecognized accessory bile ducts. A DISIDA scan will be the most useful examination in demonstrating the bile leak, and ERCP can define the exact site of leakage. CT will demonstrate a fluid collection in the porta hepatis, subhepatic fluid, or diffuse ascites. Endoscopic management of such leaks has been shown to be nearly 95% successful.[232] If the DISIDA and ERCP are not helpful, CT may be used to examine the patient for other postoperative complications such as abscess or hematoma. Ligation of aberrant bile ducts or unrecognized accessory bile ducts may be demonstrated on CT and has been reported as focally dilated subsegmental intrahepatic bile ducts typically in the posterior portion of the right lobe of the liver.[49]

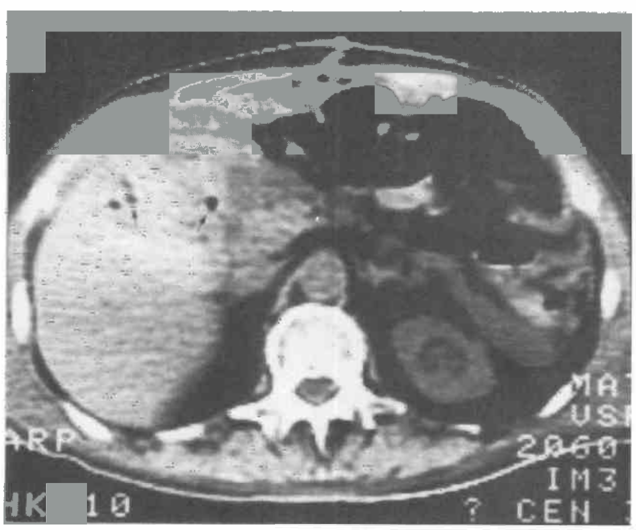

Figure 37–36. After cholecystectomy, abnormal soft tissue density, with a few small collections of gas *(arrows)*, is present in the region of the gallbladder fossa. On aspiration, this proved to be an infected hematoma.

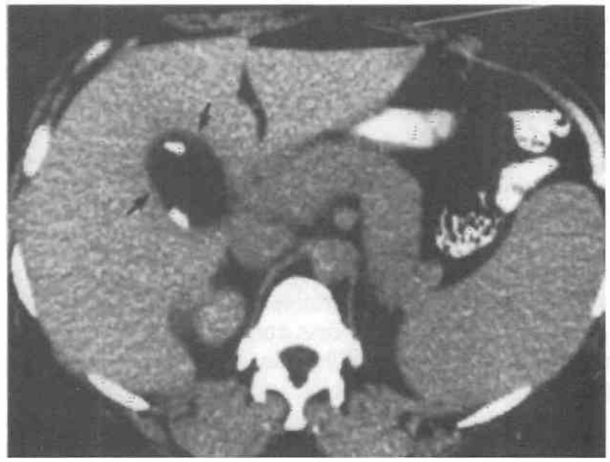

Figure 37–37. Abscess *(arrows)* in the gallbladder fossa following laparoscopic cholecystectomy.

Cystic Duct Remnant. After cholecystectomy, a small remnant of the cystic duct remains in place. Rarely, patients may develop symptoms because of the residual cystic duct that mimic symptoms of cholecystitis or cholelithiasis (Fig. 37–38).[87] The remnant itself can enlarge over time and may function as a gallbladder, developing similar diseases such as gallstones and even carcinoma (Fig. 37–39).[192]

Gallstones

The appearance of gallstones on CT depends on the complex relationship of several factors. The major determinant of appearance is the composition of the stone. Gallstones may be composed of, in general, three components: bile pigments, cholesterol, and calcium. Pure cholesterol or pure bile pigment stones are rare. Pure cholesterol stones will have a low density compared with bile (−100 HU in vitro).[75] Most stones, however, are a mixture of calcium, bile pigment, and cholesterol. The density of the mixed stone will vary, depending on the amount of each component present. There is some controversy in the literature as

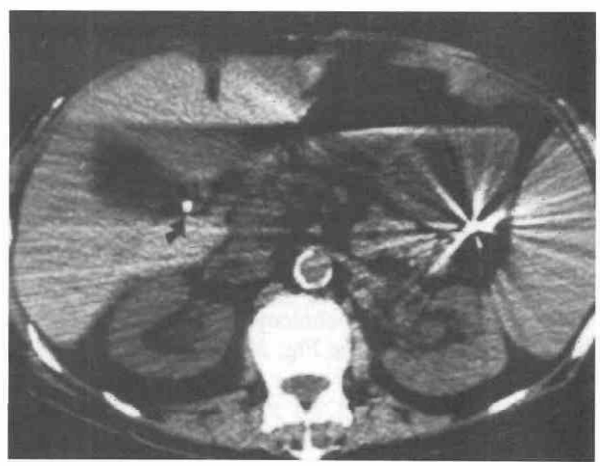

Figure 37–38. Retained stone within cystic duct remnant *(arrow)*.

Figure 37–39. Dilated cystic duct remnant *(large arrow)* containing dense stone *(arrowhead).*

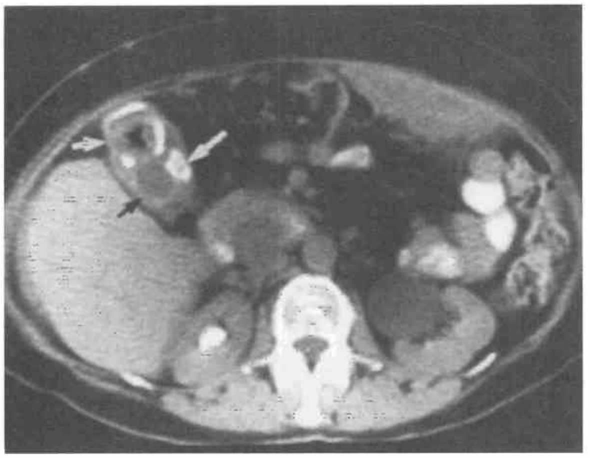

Figure 37–41. Gallbladder containing rim of calcified stone with central gas *(short white arrow)* and relatively lucent stone *(black arrow),* with coarse calcified plaque *(long white arrow)* in gallbladder wall (porcelain gallbladder).

to whether calcium or cholesterol plays the predominant role in determining stone density on CT.[14, 17, 18, 30, 33, 242] In general, calcium content is responsible for increasing the density of the stone. Up to 60% of gallstones demonstrate calcium on CT scan in vivo and are dense.[11, 33] Other mixed-composition stones with less calcium may have a density equal to bile and may be difficult to visualize on CT (Figs. 37–40 to 37–47.[11, 13, 21, 75]

The pattern in which the components of the stone are distributed will affect the appearance of the stone. Calcium bilirubinate stones are often homogeneously dense (see

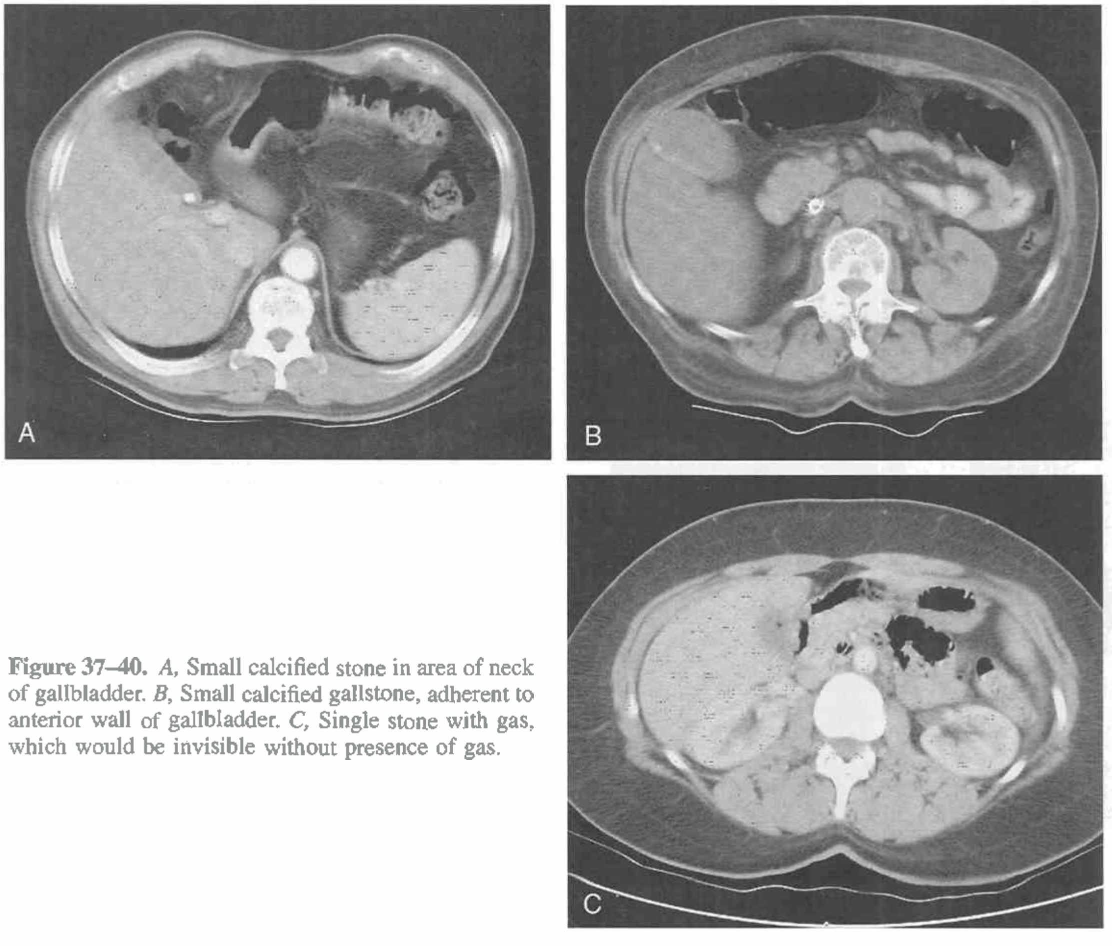

Figure 37–40. *A,* Small calcified stone in area of neck of gallbladder. *B,* Small calcified gallstone, adherent to anterior wall of gallbladder. *C,* Single stone with gas, which would be invisible without presence of gas.

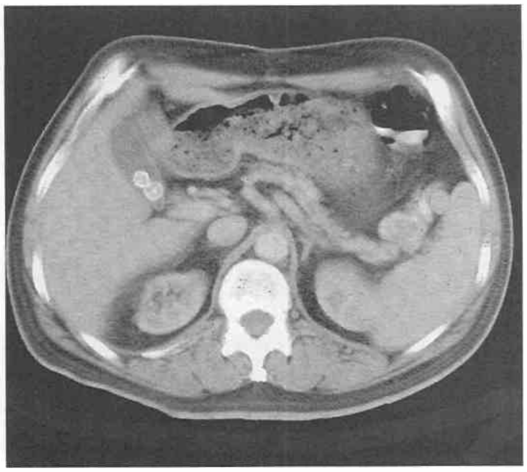

Figure 37–42. Multiple laminated stones, with subtle internal pattern.

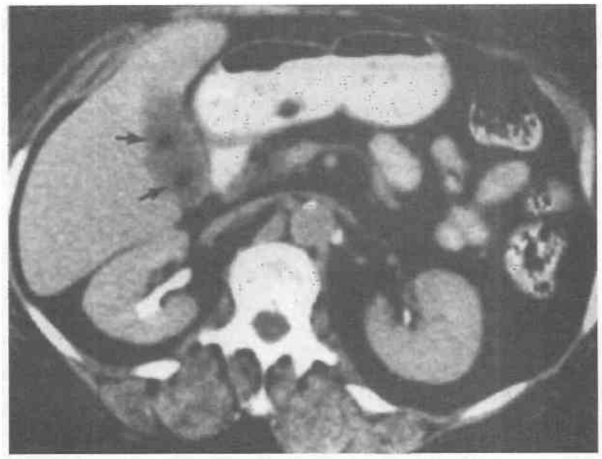

Figure 37–44. Gas centrally in gallstones *(arrows)*. These isodense stones would not be visible without the gas.

Fig. 37–39). Mixed-composition stones may have several patterns, depending on the distribution of calcium. They may have a dense rim of calcium peripherally with a low-density cholesterol center (see Figs. 37–41 and 37–42). They may also have a laminated appearance with alternating layers of calcification. Also, these stones may have punctate foci of increased density scattered throughout.

Stones may also have clefts centrally in their matrix that contain gas (see Figs. 37–41 and 37–43). Gas in these clefts appears as low-density fissures in various patterns, giving the so-called Mercedes-Benz sign, crow's feet sign, or seagull sign. Gas probably forms after shrinkage of the stone matrix.[75] The gas consists mostly of nitrogen. The significance of the gas clefts is little if any, except that it may contribute to floating of gallstones and it may aid in detecting stones on CT that are otherwise isodense with bile (see Fig. 37–44).

The ability of CT to detect gallstones depends on several factors, including stone composition, size, number, shape, bile density, and scanning technique. There have been numerous reports of varying degrees of sensitivity of CT for detecting stones ranging from 78% to 83%.[11, 13, 30, 33, 98, 106, 226] Uchida[226] reported a 100% sensitivity for calcified stones. Havrilla reported a 78% sensitivity prospectively with a 94% sensitivity retrospectively.[98] The stone composition greatly affects the detection rate. Calcified stones that are hyperdense will be seen more readily than will composite stones, which are isodense to bile (see Fig. 37–45). In addition, the presence of matrix gas will increase detection rate (see Fig. 37–44). The size of stones will also affect detection rate, with small stones being missed because of partial voluming. Large stones that completely fill the lumen may not be detected if they are isodense with bile (see Fig. 37–46). In addition, if there are multiple tiny stones, they may layer and mimic milk of calcium bile. The density of bile may also affect stone detection (see Fig. 37–5). If the bile density is increased, lower density stones will appear as negative filling defects whereas higher-density stones may be obscured (see Fig. 37–47). Oral cholangiographic agents have been used to increase the density of bile to improve CT detection rates of gallstones. Finally, the technique of the CT examination will determine detection rates of stones. High-resolution CT that is targeted to the gallbladder with thin collimation is recommended.[14]

In recent years, a large volume of literature has considered the use of CT in selecting patients for nonsurgical therapy of gallstones. The nonsurgical options include extracorporeal shock-wave lithotripsy (ESWL), direct-contact dissolution with methyl tert-butyl ether (MTBE), and oral agents (cheno- and ursodeoxycholic acid). In the past, plain film was used to detect gallstones containing calcium, which precluded nonsurgical therapy. The problem is that 14% of patients with lucent stones based on plain films have pigment stones that are not candidates for dissolution. In addition, 33% of dense stones on plain film are cholesterol stones and would be candidates for nonsurgical therapy.[14] Therefore, CT has been proposed as a more accurate method to evaluate which stones would be ideal for the nonsurgical therapies.

Studies have shown correlation between the CT attenuation of gallstones and the cholesterol and calcium content of the stone, and both in vitro and in vivo studies have

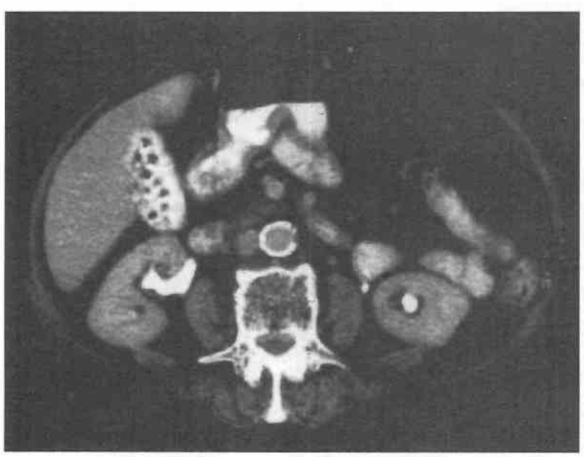

Figure 37–43. Multiple small lucent stones floating in gallbladder presenting as negative filling defects owing to contrast medium in gallbladder after ERCP.

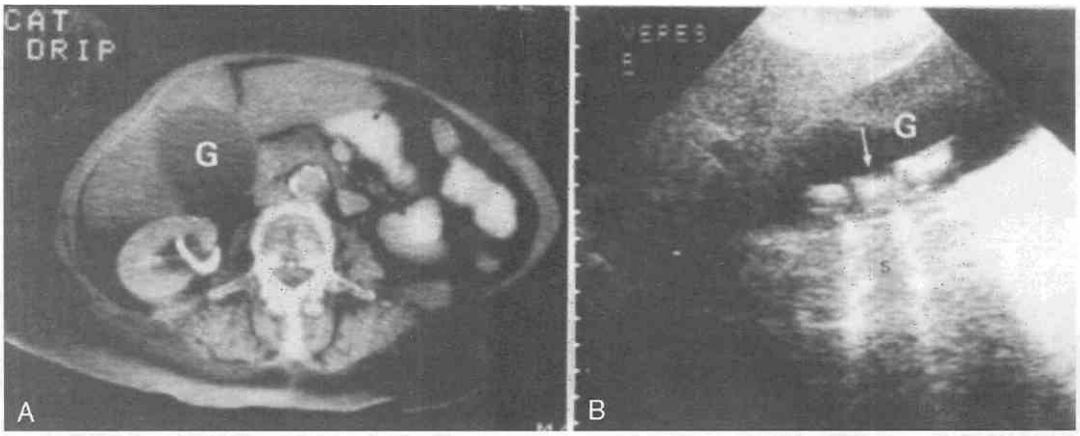

Figure 37–45. *A,* The gallbladder (G) is distended, but no filling defects are perceptible on this CT scan. *B,* Sagittal ultrasound scan through the gallbladder (G) demonstrates large, echogenic structures *(arrow)* within the gallbladder lumen, with associated acoustic shadowing (s) diagnostic of gallstones.

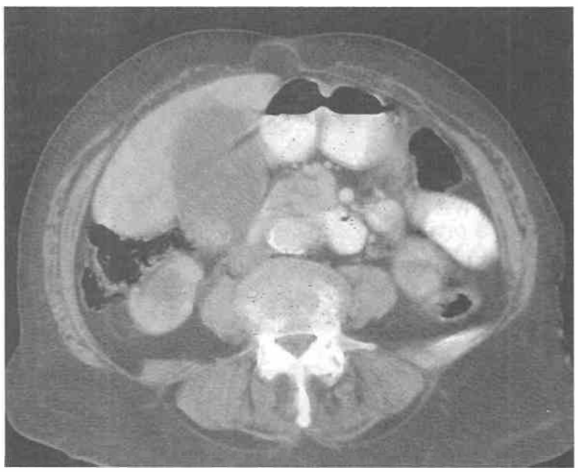

Figure 37–46. Enlarged gallbladder with thickened wall and large low-density stone in dependent portion.

Figure 37–47. Low-density gallstone *(arrow)* presents as negative filling defect because of high-density bile in gallbladder (G).

demonstrated this finding.[8, 14, 30, 115, 243] Although there have been disagreements over whether it is the calcium or the cholesterol content that most determines the CT attenuation number, the basic finding is that the homogeneously dense stone with high attenuation numbers contains high levels of calcium and is a poor candidate for nonsurgical therapy. The less dense the stone, with lower attenuation values, the better the success with nonsurgical therapy. Unfortunately, the issue is not this straightforward. Concerning the success of dissolution, Baron and colleagues reported that the pattern of calcium within the stone may play a more important role than does simply the amount of calcium.[18] For example, densely calcified stones do poorly with MTBE dissolution. However, if the calcium is arranged in lamina or a peripheral rim, the stone dissolves well. Those that dissolve best are isodense or hypodense with bile and contain a high amount of cholesterol. In addition, stones with a central nidus of calcium or peripheral rim of calcium have been shown to fragment with ESWL; these have now been approved for such therapy.[33] Therefore, success at nonsurgical treatment may not simply depend on the attenuation number of the stone but on multiple factors such as the pattern of calcification in the stone. CT may therefore be important in evaluating which patients will have the greatest success with the nonsurgical therapies; however, large-scale clinical trials will have to be performed.

Gallbladder Neoplasms

Gallbladder carcinoma is the most common malignant tumor of the gallbladder. Adenocarcinoma is the most common histologic type, in 90% of cases. Squamous carcinomas, mixed-type carcinomas, and sarcomas have been described in the gallbladder (Fig. 37–48).

Many benign neoplasms of the gallbladder have been reported such as a fibroma, lipoma, myxoma, granular cell tumor, leiomyoma, hemangioma, and neurofibroma.[105, 159] The most common benign tumor of the gallbladder is the adenoma, which appears on CT as a small mass along the gallbladder wall.

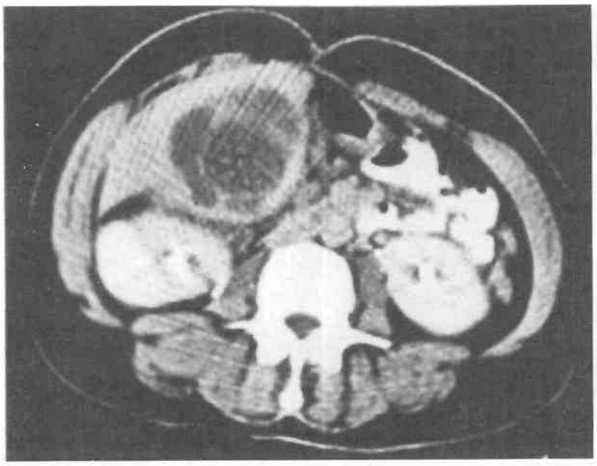

Figure 37–48. Squamous cell carcinoma of the gallbladder (m).

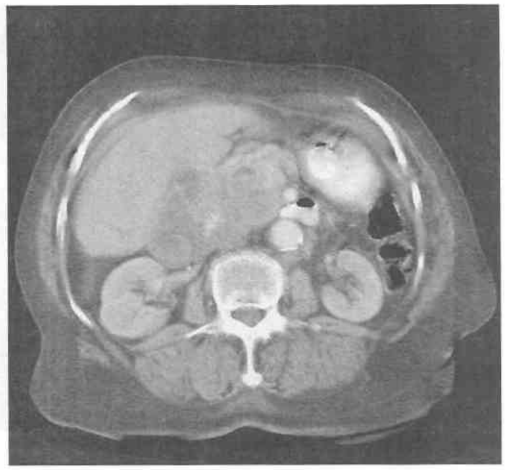

Figure 37–49. Gallbladder carcinoma spreading into the porta hepatis and head of pancreas.

Gallbladder carcinoma is the most common malignancy of the biliary tree and is the fifth most common gastrointestinal malignancy. Its peak occurrence is in the sixth decade or older, and there is a female predilection of 3–4:1.[147, 204] The female predominance may be related to underlying inflammatory disease, and gallstones are detected in 65% to 95% of gallbladder carcinoma cases.[147, 204] With new therapeutic methods for treating gallstones, such as lithotripsy or stone dissolution, that spare the gallbladder and leave it in place, surveillance of the gallbladder is recommended because of the increased risk of carcinoma.[205] Calcification in the gallbladder wall (porcelain gallbladder) is associated with gallbladder carcinoma in 11% to 33% of cases (see Fig. 37–31).[79, 106, 175] In addition, an increased risk of gallbladder carcinoma has been reported in patients with choledochal cysts.[244]

The clinical presentation of gallbladder carcinoma is often nonspecific and mimics other right upper quadrant diseases such as cholecystitis. Symptoms of jaundice and weight loss may not appear until the carcinoma has spread. Local extension of tumor is seen in 75% to 85% of patients at the time of presentation.[147] Therefore, a large portion of patients have tumors that are unresectable at presentation, and prognosis is poor, with a 5-year survival rate of less than 12% even if the carcinoma is incidentally detected.[147] An estimated 1% of gallbladder carcinoma is detected incidentally at the time of cholecystectomy.[234]

The appearance on CT is also nonspecific and often mimics benign disease. The typical findings of gallbladder carcinoma include three patterns: a mass replacing the gallbladder fossa, an intraluminal mass, and gallbladder wall thickening. The mass replacing the gallbladder fossa is the most common appearance in several series (Figs. 37–48 to 37–54).[107, 111, 234, 242] Such a mass may contain gallstones within it and demonstrate central necrosis when large. A normal gallbladder cannot be detected (see Fig. 37–49). This form typically has invaded adjacent structures at the time of presentation. The thickened gallbladder wall type is less common but is very difficult to differentiate from benign cholecystitis (see Fig. 37–50). Kumar and Aggarwal[131] reported a series of 50 cases and characterized the findings as follows. They divided their cases into two groups, group 1 in whom the gallbladder could be recognized and group 2 in whom the gallbladder could not be recognized. In group 1, the cases were further divided into type 1, mass filling the entire gallbladder lumen; type 2, a polypoidal mass projecting into the lumen; and type 3, an infiltrating tumor producing local or diffuse wall thickening. In 80% of cases the localized invasion into the adjacent liver was noted. The wall is usually 4 to 13 mm or greater in thickness, often asymmetrically thickened, and often nodular.[107] The intraluminal mass type is less common and presents as a polypoid mass in the gallbladder lumen (see Fig. 37–51). Lesions less than 10 mm in diameter are difficult to detect on CT.[106] Such lesions are difficult to differentiate from benign polyps or low-density adherent stones.

Associated findings on CT typically involve the spread of the tumor and aid in diagnosis. Gallbladder carcinoma most commonly spreads by direct invasion into adjacent structures, such as liver, porta hepatic structures, colon, duodenum, and pancreas. The liver is the most common

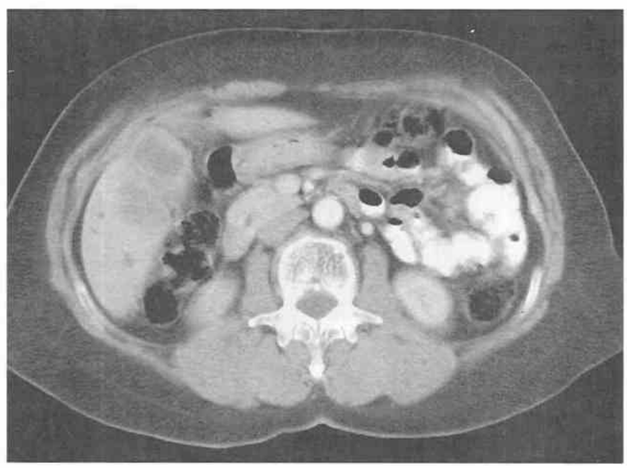

Figure 37–50. Thickening of the gallbladder wall from carcinoma. Local spread into the right lobe of the liver has occurred. Note blurring of adjacent liver margin. Without the spread to the liver, distinction from inflammatory thickening would be impossible.

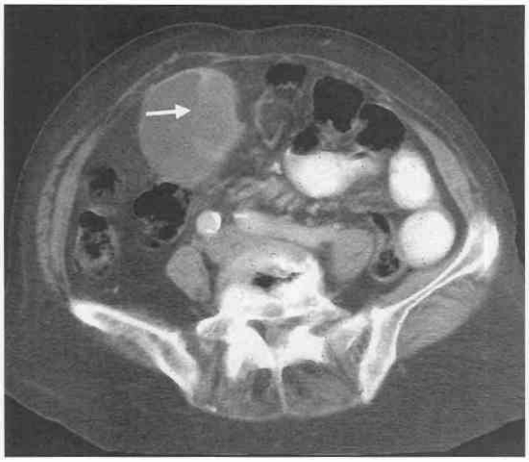

Figure 37–51. Intraluminal gallbladder neoplasm eccentrically placed along the medial wall *(arrow).*

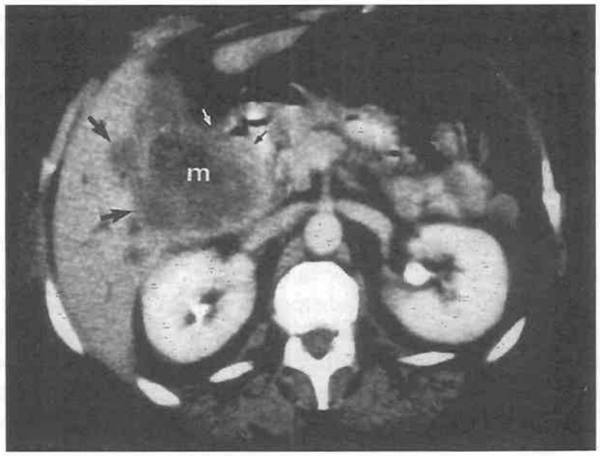

Figure 37–53. Gallbladder carcinoma presenting as mass in the gallbladder fossa (m) with invasion into adjacent liver *(large arrows)* and duodenum *(small arrows).*

site of invasion in 34% to 89% of patients depending on the series, at the time of presentation.[204] When the tumor invades the liver, the medial segment of the left lobe and the anterior segment of the right lobe are the most common targets (see Fig. 37–52). The area of invasion is usually hypodense relative to surrounding liver parenchycyma on enhanced CT scan. Direct invasion of the liver versus simple contact of the tumor with the liver surface may be difficult to differentiate on CT. An irregular boundary with normal liver parenchyma suggests invasion (see Figs. 37–50 and 37–53).

Gallbladder carcinoma can metastasize to local nodes or distantly, primarily to the liver. Lymph nodes in the porta hepatis peripancreatic region and celiac axis may be involved. Engels reported that the foramen of Winslow

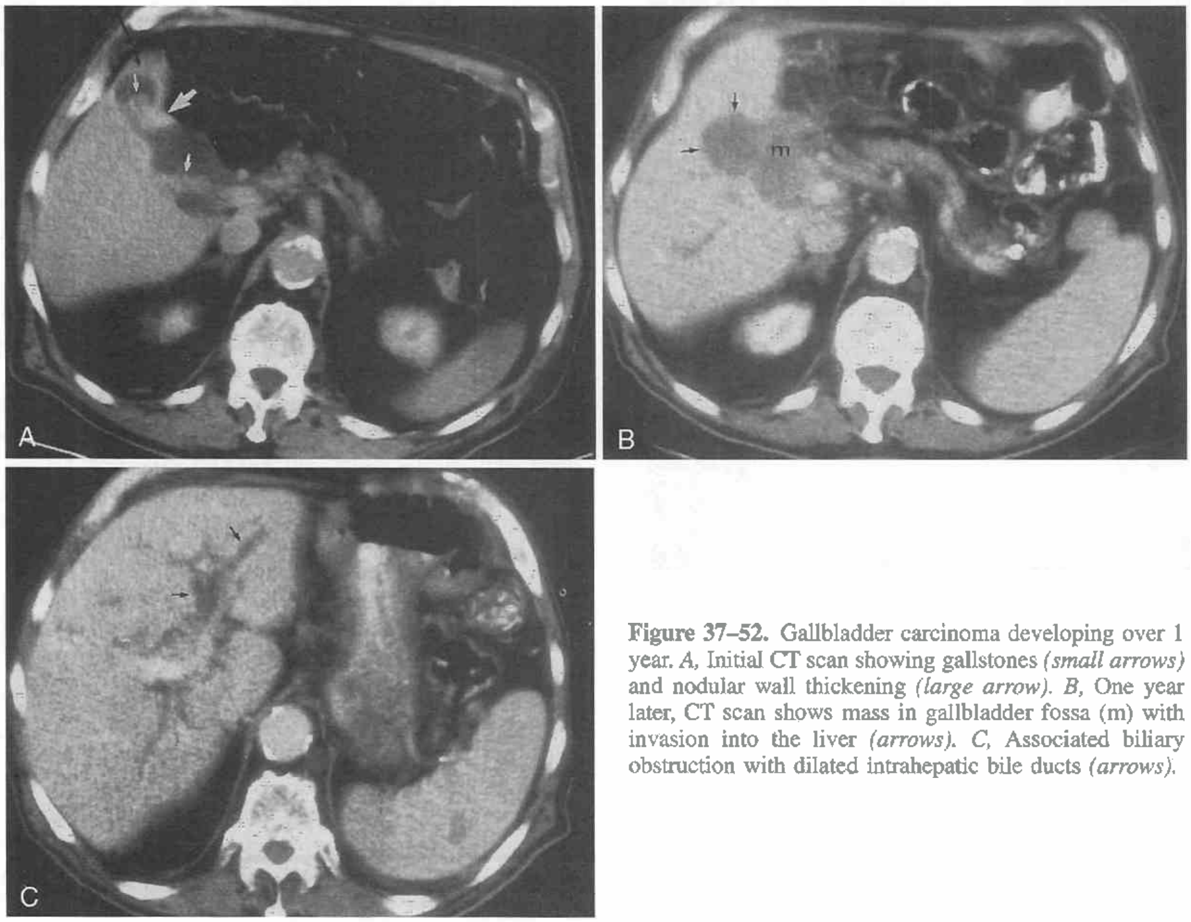

Figure 37–52. Gallbladder carcinoma developing over 1 year. *A,* Initial CT scan showing gallstones *(small arrows)* and nodular wall thickening *(large arrow). B,* One year later, CT scan shows mass in gallbladder fossa (m) with invasion into the liver *(arrows). C,* Associated biliary obstruction with dilated intrahepatic bile ducts *(arrows).*

lymph node and the superior pancreaticoduodenal node are the most frequent sites of nodal metastases (see Fig. 37–49).[67] Nodal masses may cause biliary obstruction and mimic a primary pancreatic tumor.[234] Distant metastases to the liver appear as hypodense lesions relative to adjacent liver parenchyma on enhanced CT scans. Hepatic metastases are less common, however, than direct invasion.[106] Peritoneal carcinomatosis may occur.

Biliary obstruction is reported in 50% of cases of gallbladder carcinoma.[147] This may be due to direct invasion into the porta hepatis, obstructing lymphadenopathy, or intraductal spread of tumor. Intraductal spread of tumor was reported in only 4% of cases by Weiner and associates but is difficult to differentiate from cholangiocarcinoma (Figs. 37–52, 37–54, and 37–55); also see Figures 37–92 and 37–93.[234]

The differential diagnosis of gallbladder carcinoma on CT scan may be difficult. Gallbladder carcinoma often mimics cholecystitis (acute, chronic, and xanthogranulomatous), polyps, and occasionally adenomyomatosis (Fig. 37–56) radiographically and clinically. Findings common to both on CT include gallbladder wall thickening, gallstones, mass in the gallbladder fossa, edema in pericholecystic fat, and thickening of the hepatoduodenal ligament. A hypodense "halo" in the thickened gallbladder wall has been described as a helpful sign on CT of cholecystitis rather than carcinoma (see Fig. 37–19).[204] The halo represents mural edema. Direct invasion into the liver suggests carcinoma; however, in rare cases, abscess formation may occur in liver parenchyma adjacent to gangrenous cholecystitis. Smathers and colleagues reported signs on CT that were helpful to differentiate gallbladder carcinoma from complicated cholecystitis including a mass less than half the size of the gallbladder, direct invasion of the liver with focal bulge of the anterior contour of the liver, biliary obstruction at the level of the porta hepatis, and lymphadenopathy.[204]

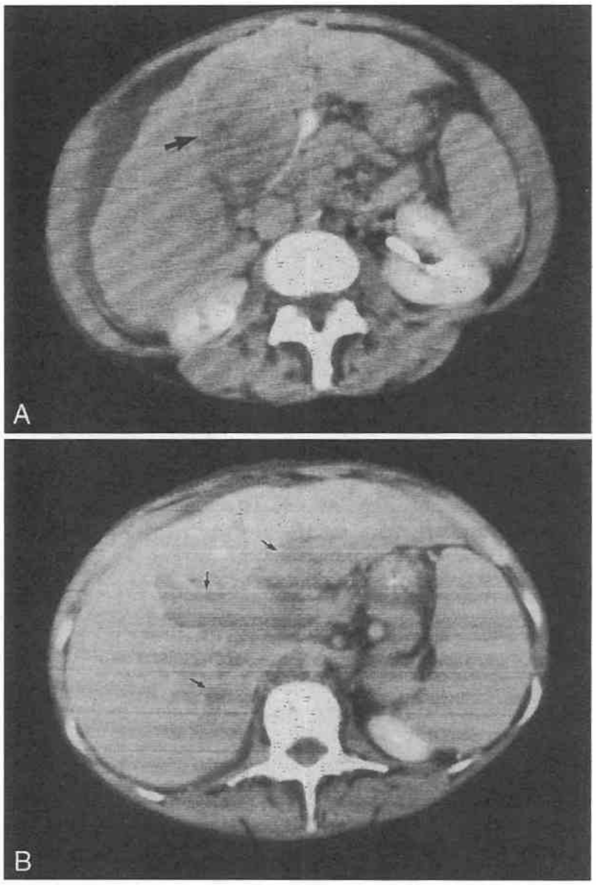

Figure 37–54. Gallbladder carcinoma. *A*, Mass in gallbladder fossa *(arrow)*. *B*, Intraductal spread of tumor throughout the biliary tree *(arrows)*.

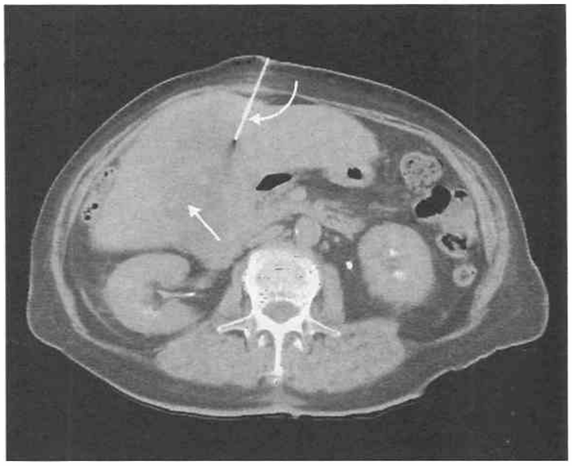

Figure 37–55. CT scan shows biopsy needle *(curved arrow)* in mass in central liver, representing gallbladder carcinoma from intrahepatic gallbladder. Note the faceted stone *(arrow)* surrounded by fluid in the central liver.

Primary malignant tumors of the liver may extend into the gallbladder fossa and mimic gallbladder carcinoma. Visualizing a normal gallbladder on CT, even if displaced by tumor, suggests a hepatic primary rather than gallbladder primary. Occasionally, the scirrhous type of gallbladder carcinoma may present as a contracted gallbladder with a thickened wall, mimicking a cholangiocarcinoma.[147]

The diagnostic accuracy of CT scan with gallbladder carcinoma has been reported in several series. Itai reported successful detection of 27 of 30 cases of gallbladder carcinoma on CT for an accuracy of 90%.[106] In addition, CT and ultrasonography were compared by Weiner and associates and of 22 cases, ultrasonography detected 7 of 11 cases and CT detected 10 of 11 cases.[234] The conclusion was that CT and ultrasonography were complementary.

Metastases

Metastases to the gallbladder are rare and often detected incidentally at autopsy. The most common primary malignancies with metastases reported to the gallbladder are pancreatic, gastric, renal cell, ovarian, and melanoma.[28, 35, 147] Typically, metastases are focal nodular thickenings of the gallbladder wall and are often serosal in location. Such a finding in a patient with a known primary malignancy should raise the suspicion of gallbladder metastasis.

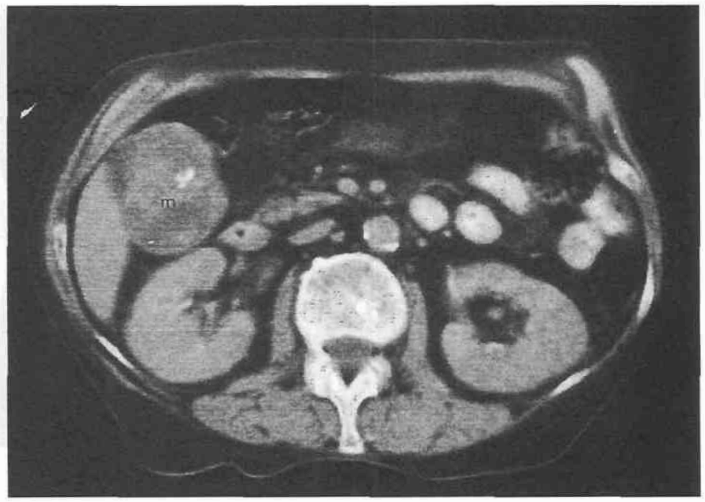

Figure 37–56. Adenomyomatosis presenting as a mass in the gallbladder fossa (m) and mimicking gallbladder carcinoma. (From Gerard PS, Berman D, Zafarnloss S: J Comput Assist Tomogr 14:490, 1990.)

The Biliary Tract

Normal Anatomy

Normal intrahepatic bile ducts (IHBDs) can be visualized in the liver parenchyma, especially on the newer-generation high-resolution CT scanners. In 40% of their patients, Liddell and colleagues reported seeing normal IHBDs as linear water density structures accompanying the portal vein branches peripherally in the liver parenchyma.[136] The normal IHBDs measure less than 3 mm, are few in number, and are randomly scattered throughout the liver. Such random scattering is a key observation, because visualization of IHBDs confluent with the hilum should raise suspicion of obstruction (Fig. 37–57). In addition, certain pathologic conditions may be difficult to differentiate from visualization of normal IHBDs. For example, sclerosing cholangitis and biliary obstruction in cirrhosis may present as a few, scattered, and small visible IHBDs (see Fig. 37–70*A*). The clinical setting will aid in differentiating these conditions. Finally, normal IHBDs are linear structures seen along one side of the portal vein. In contrast, periportal lymphedema will appear as low density accompanying the portal vein branches but will completely surround the portal vein and usually will be confluent with the hilum (Fig. 37–58).[129, 233]

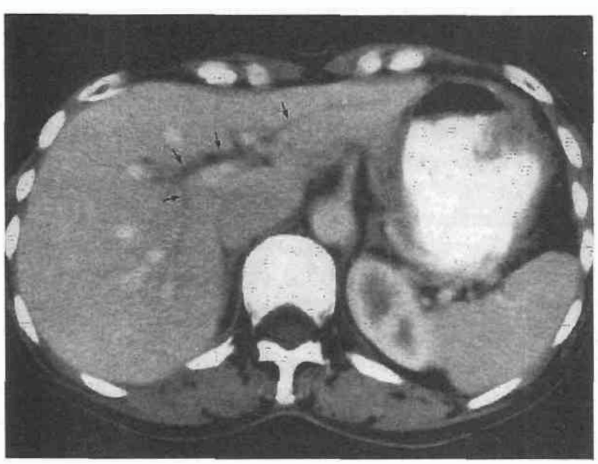

Figure 37–57. Mild intrahepatic biliary dilatation *(arrows)*. Note the confluence of the ducts into the hilum.

The normal IHBDs may lie on any side of the accompanying portal vein. As they course toward the hilum, the IHBDs from each lobe unite to form the right and left hepatic ducts, which have a constant location just anterior to the main portal vein bifurcation (Fig. 37–59*A*). The right and left hepatic ducts unite in the hilum to form the common hepatic duct (CHD). The CHD is usually imaged as a round or elliptical structure sitting anterior and often slightly lateral to the main portal vein (see Fig. 37–59*B*). On consecutive axial images, the CHD usually courses along a 40- to 45-degree oblique plane with reference to the midline sagittal plane (Fig. 37–59*C* and *D*).[171, 172] It may, however, lie transversely; previously, this was considered a sign of obstruction and is now known to be an anatomic variant.[89, 114] The CHD lies to the right and lateral to the proper hepatic artery. The right hepatic artery typically branches off the proper hepatic artery and passes between the CHD and main portal vein in 75% to 85% of patients.[235] Contrast medium enhancement often aids in differentiating the water-density CHD from the enhanced hepatic artery and portal vein.

The common bile duct (CBD) forms when the cystic duct joins with the CHD. This union can occur at varying levels from high in the porta hepatis to near the ampulla of Vater. The confluence is rarely imaged on CT. The CBD enters the pancreas and typically lies along the posterior and lateral aspect of the pancreatic head. It can be used as a landmark to indicate the lateral border of the pancreatic head (see Fig. 37–59*E*).

The extrahepatic bile ducts (EHBDs: CHD and CBD) are readily visualized if the anatomy is recognized and the study tailored appropriately. Schulte and associates demonstrated the CHD in 66% of their patients and CBD in 82%.[199] The CHD usually measures 3 to 6 mm in short-axis diameter, and the CBD usually measures up to 8 mm.[13] The diameter should be measured in short axis because the duct often courses obliquely through the axial image, making the long-axis diameter inaccurate.[74] In some patients, the CBD may be larger than 8 mm, and in postcholecystec-

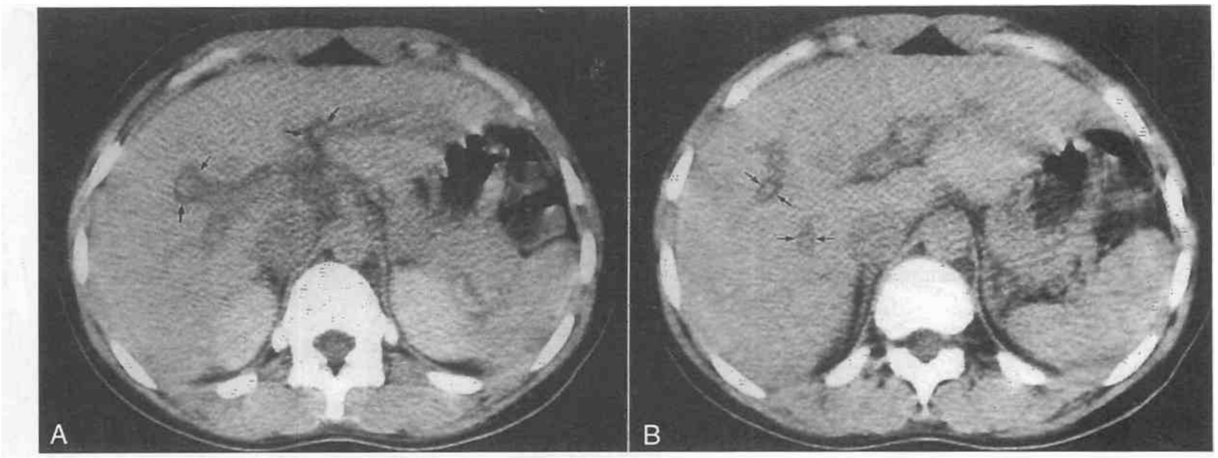

Figure 37–58. Periportal edema. *A*, Edema around hilar portal vein branches *(arrows)*. *B*, Edema forms lucent "collar" around portal vein branches *(arrows)*. Note how low density completely surrounds the vein.

tomy patients it may measure up to 10 mm without obstruction.[13, 51] The wall of the CHD and CBD can normally be visualized and measures less than 1.5 mm.[199] The wall may also enhance normally and be brighter than the adjacent pancreas (see Fig. 37–83*B*).

The CT examination should be tailored to examine the EHBDs. Narrow collimation of 4 to 5 mm at 5- to 10-mm intervals with bolus intravenous contrast agent enhancement injected at 1 to 2 mL/sec can be used. In addition, a small field of view should be used with the image targeted to the porta hepatis and pancreatic head (see Fig. 37–59). Oral cholangiographic agents have been used to demonstrate the biliary tree on CT scan[89, 90]; however, these are probably not needed with the new higher-resolution scanners.

Congenital Biliary Anomalies

Biliary Atresia. In extrahepatic biliary atresia, ultrasonography and a DISIDA scan are typically the imaging studies performed initially to evaluate the biliary tree. Extrahepatic biliary atresia, however, is associated with other anomalies in 10% to 23% of patients.[78] Such anomalies include polysplenia, bilateral bilobed lungs, azygous continuation of the inferior vena cava, intestinal malrotation, and situs inversus.[57] CT can be used to demonstrate these associated anomalies. In addition, CT can be used to assess patients who, after corrective surgery, develop cholangitis, bile duct dilatation, bilomas, or intrahepatic calculi (see Fig. 37–96).[56] CT can also evaluate the development of cirrhosis, varices, splenomegaly, and ascites and play an important role in pre–liver transplant evaluation in such patients.

Choledochal Cyst. Congenital dilatation of the biliary tract, the so-called choledochal cyst, may occur and has been classified based on the spectum of morphologic changes in the bile ducts.[34] The most common classification scheme of Alonso-Lej includes type I, which is dilatation of the CBD; type II, which is a diverticulum of the CBD; and type III, which is the rare choledochocele. Type I has been subdivided into cystic dilatation of the entire CBD and CHD, a small cyst of the distal CBD, or diffuse fusiform dilatation of the CBD. Todani and colleagues added to this classification type IV-A, representing multiple cysts of the IHBDs and EHBDs; type IV-B, representing multiple cysts of the EHBDs; and type V, representing multiple cysts of the IHBDs, or Caroli disease.[196, 225] Placing a patient into a specific category is not as important to the patient's management as is describing the extent of involvement of the IHBDs and EHBDs.

The choledochal cyst is not truly a cyst of the biliary tract but rather some variation of duct dilatation. The etiology of this condition is not clear but may be multifactorial. Laing proposed that biliary atresia, neonatal hepatitis, and choledochal cyst are part of the same spectrum of disease.[132] In addition, biliary atresia may be coexistent with choledochal cyst.[219] An anomalous union of the distal CBD and pancreatic duct has been reported in patients with a choledochal cyst; this may lead to pancreatic enzyme reflux into the CBD, causing dilatation. This anomalous union is seen in 10% to 58% of such patients.[196] The choledochocele may have a different cause and may form as a result of obstruction at the ampulla with formation of a diverticulum of the sphincter, or it may represent a distal choledochal cyst that prolapses into the duodenum.

On CT, choledochal cyst can have varying appearances depending on the extent of ductal involvement and the degree of dilatation. There may only be mild EHBD dilatation (Fig. 37–60) or a large water-density mass in the porta hepatis or adjacent to the head of the pancreas (Fig. 37–61). Reportedly, 60% of patients with choledochal cyst will have associated congenital IHBD dilatation. This is usually limited to the central IHBDs.[6, 239] Congenitally dilated IHBDs often have a lobulated cystic appearance with an abrupt transition zone at the junction with the normal ducts. Acquired biliary dilatation usually does not have the lobulated cystic appearance, and the dilated ducts usually taper gradually toward the periphery of the liver. With congenitally dilated ducts, the gallbladder is often normal. Direct communication of the cystic duct to the dilated EHBDs will aid in making the diagnosis of choledochal cyst, but this connection is often difficult to visualize on

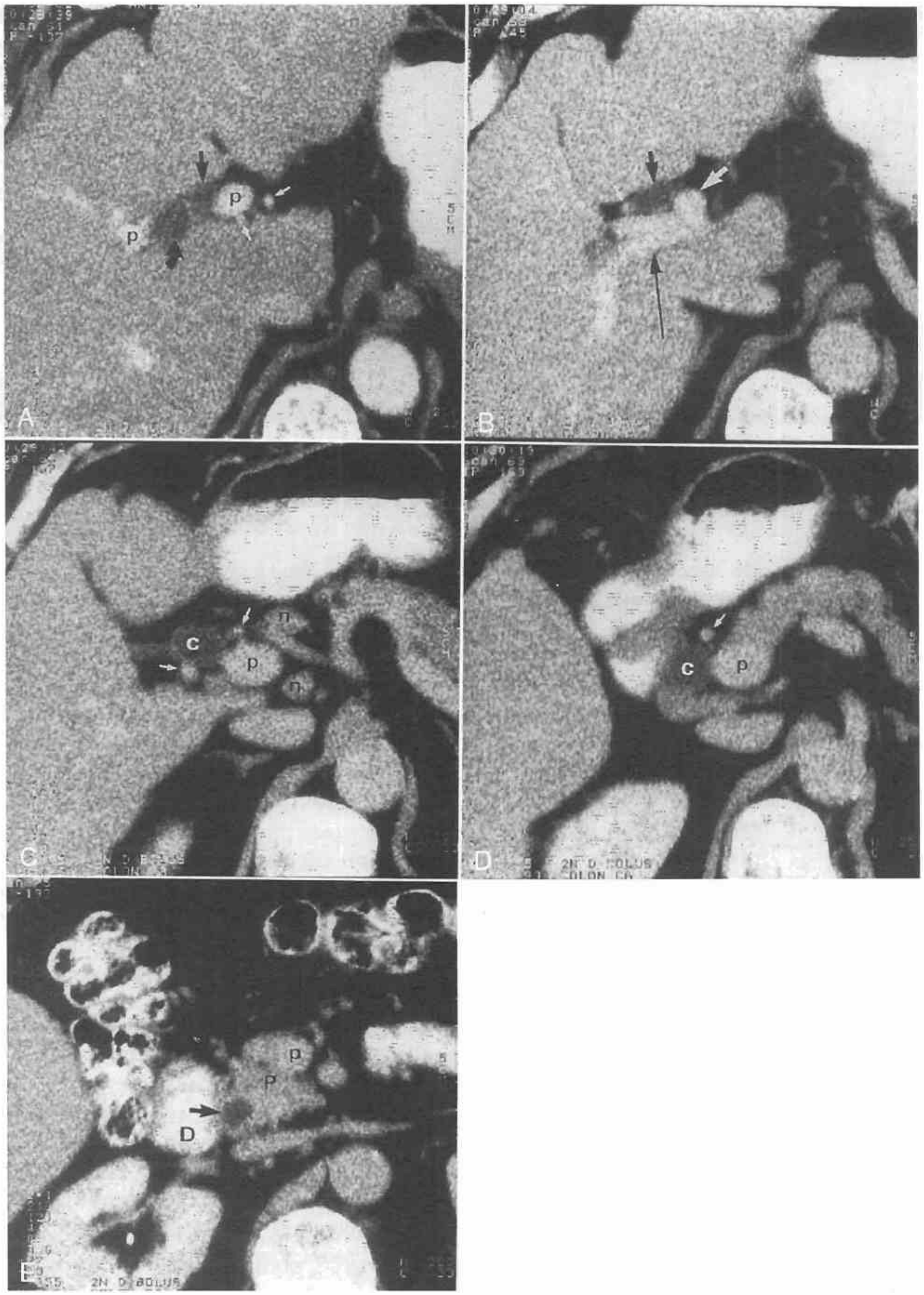

Figure 37–59. Normal anatomy of extrahepatic bile duct. Exam is high-resolution study with 4-mm-thick images, with bolus intravenous contrast medium enhancement and targeted field of view. *A,* First level at the confluence of the right hepatic duct *(curved black arrow)* with the left hepatic duct *(straight black arrow).* Portal vein branches (p) and hepatic artery branches *(white arrows). B,* Level 8 mm caudal to *A.* CHD *(short black arrow)* has formed and lies anterior to bifurcation of portal vein into right *(long black arrow)* and left *(large white arrow)* branches. Hepatic artery branch *(small white arrow). C,* Level 12 mm caudal to *B.* Common duct (c) lies anterolateral to main portal vein (p). Branches of hepatic artery *(small white arrows);* small lymph nodes (n). *D,* Level 12 mm caudal to *C.* Common duct (c) is lateral to main portal vein (p) and posterolateral to the hepatic artery *(small white arrow). E,* Level 24 mm caudal to *D* at the level of the pancreatic head. Distal common duct *(black arrow)* lies in posterolateral aspect of pancreatic head (P). The descending duodenum (D) is filled with contrast medium just lateral to the pancreatic head. Superior mesenteric vein (p).

CT. Direct communication of nondilated ducts with the dilated portion is important to visualize and can be seen on CT unless the choledochal cyst is large. The differential diagnosis of choledochal cysts will include gastrointestinal tract duplication cysts, mesenteric cysts, hepatic cysts, pseudocysts, ovarian cyst, and a renal cyst.

Ultrasonography and CT can make the diagnosis if direct communication with the biliary tree and the choledochal cyst is demonstrated. Often this cannot be accomplished, and a DISIDA scan is required. CT cholangiography can be diagnostic and has been described revealing a contrast-fluid level within the choledochal cyst.[239]

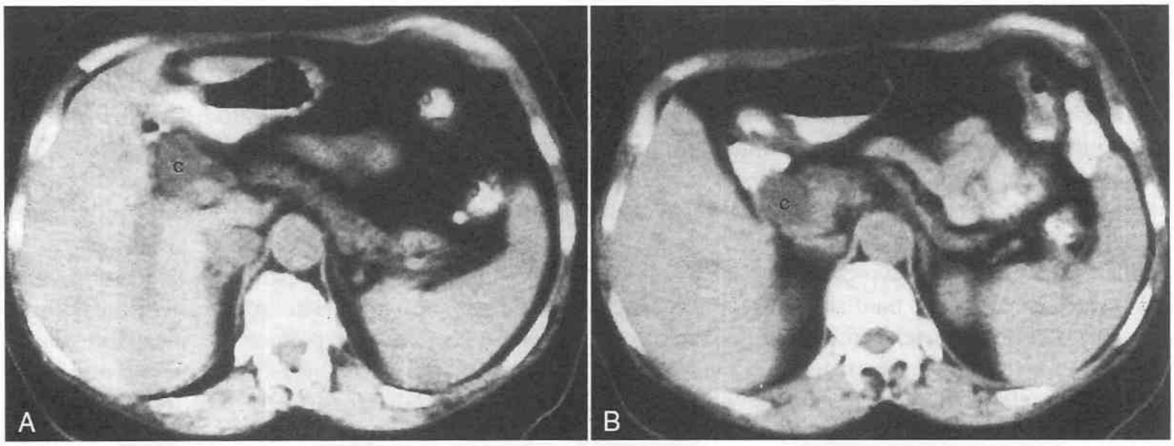

Figure 37–60. Choledochal cyst. *A,* Dilatation of th[redacted]trahepatic common bile duct (c). *B,* Dilated common bile duct (c) down to the pancreatic head. No intrahepatic biliary dilatation is present.

The choledochocele is typically seen as a round fluid-density structure in or medial to the pancreatic head, or it may lie completely within the lumen of the duodenum (Fig. 37–62). If an oral contrast agent has been given, the lesion may be circumscribed by the agent. The IHBDs and EHBDs are often not dilated. Differential diagnostic considerations would include an intraluminal duodenal diverticulum, small pseudocyst, duodenal duplication cyst, or small cystic neoplasm of the pancreas. CT cholangiography with administration of an oral cholangiographic agent may make the diagnosis.[13, 53]

Most patients with choledochal cyst present with jaundice; therefore, imaging usually with CT or ultrasonography is performed. Only about 25% of patients present with the classic triad of pain, jaundice, and a right upper quadrant mass. Surgical correction is usually required and involves excision with a biliary-enteric anastomosis.

Complications of the choledochal cyst usually involve bile stasis with stone formation and infection, pancreatitis, biliary cirrhosis, and portal hypertension. There is, however, a reported increased incidence (4% to 28%) of malignancy involving the hepatobiliary system.[6, 18, 86, 196, 244] The increased risk of malignancy is most likely caused by chronic mucosal irritation, but it is not limited only to the choledochal cyst. Malignancy can develop anywhere in the biliary tree in such patients.[244] CCA arising in the choledochal cyst will appear as a soft tissue density mass or irregular thickening of the cyst wall (see Fig. 37–98). Tumor arising in a choledochal cyst that was bypassed but not excised has been reported.[219] Gallbladder carcinoma has been reported in patients with a choledochal cyst and will appear as described previously in this chapter.

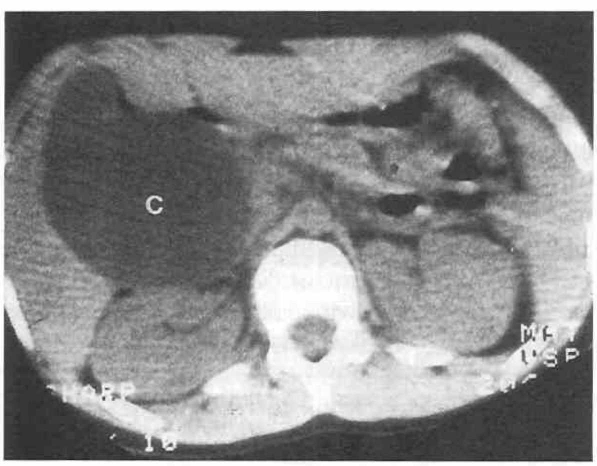

Figure 37–61. Large choledochal cyst (c).

Caroli Disease. Caroli disease is also called communicating cavernous ectasis of the biliary tract. This is a rare disease that is part of the spectrum of congenital anomalies affecting the biliary tree and the kidney. The uncommon pure form of this entity involves congenital saccular dilatation of only the IHBDs. The second more common or "classic" form consists of the saccular bile duct dilatation with associated congenital hepatic fibrosis and portal hypertension.[47, 195] In addition, there may be associated congenital dilatation of the EHBDs, suggesting that Caroli disease is part of the spectrum of choledochal cyst. Two thirds of such patients have been reported to have extrahepatic biliary abnormalities.[196] In addition, there is a high association with renal tubular ectasis and other renal cystic disease that may be part of the same underlying disorder.

On CT, the saccular cystic dilatation of the IHBDs may mimic multiple hepatic cysts. Several signs, however, aid in differentiating Caroli disease. Most importantly, the cystic areas often can be shown to communicate directly with the bile ducts.[13] The distribution of cystic dilatation is often segmental. Finally, the "central dot sign" has been suggested as a pathognomonic sign of Caroli disease (Fig. 37–63).[47] This sign consists of cystic dilatation of the IHBDs with a small focus or "dot" of increased density lying apparently within the lumen of the duct. This "dot" represents the portal radicle, which has become engulfed by the dilating adjacent bile duct. The vessel is not truly in the lumen but is surrounded by the duct. The "dot" will enhance with intravenous contrast medium administration. One case report documented the "central dot sign" being seen with large hepatic cysts that occurred centrally in the

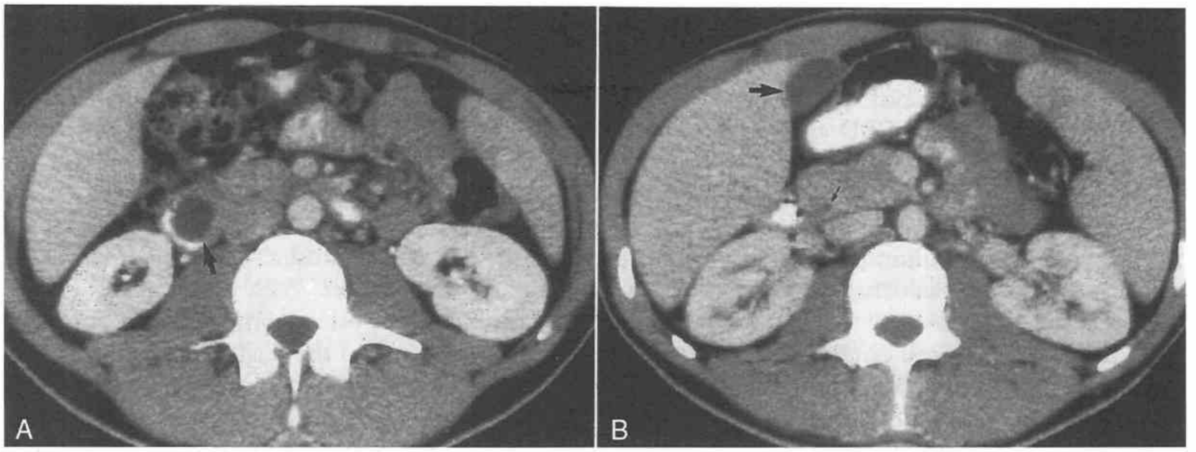

Figure 37–62. *A,* Choledochocele *(arrow)* appears as fluid density mass pushing laterally into barium-filled duodenum. *B,* Note common bile duct *(small arrow)* proximal to the choledochocele is not dilated, nor is gallbladder distended *(large arrow).*

liver and most likely represented retention cysts in periductal glands.[101]

Complications of Caroli disease will include problems with bile stasis such as stone formation and cholangitis. In addition, pancreatitis, abscess formation, hepatic amyloidosis, and biliary malignancy have been associated with Caroli disease.[102, 137] CT can document the extent of the disease and the presence of intrahepatic calculi, abscess formation, and so on. With congenital hepatic fibrosis, CT can document the presence of splenomegaly and varices. Finally, because of the association with renal cystic disease, the kidneys should be carefully evaluated for the presence of obvious cysts or calculi.

Cholangitis

Suppurative Cholangitis. Acute cholangitis is typically found in patients with obstruction or stone disease. Gram-negative organisms, such as *Escherichia coli,* are often responsible. The disease can become quite severe and life-threatening, requiring immediate relief of the obstruction as well as antibiotic therapy.

On CT, dilatation of the IHBDs and EHBDs may be present unless early obstruction or partial obstruction is present.[13] There may be increased density of the bile within the ducts because of purulent material (Fig. 37–64). The bile duct wall may be thickened concentrically and diffusely with prominent contrast agent enhancement (see Fig. 37–64).[199] High-resolution CT will best demonstrate this finding. Finally, gas-forming organisms can cause pneumobilia, which can be seen on CT especially in the nondependent portion of the biliary tract, typically in the left lobe.

CT can also be used to assess for complications of suppurative cholangitis, such as abscesses, which will appear as hypodense or fluid density areas adjacent to the bile ducts. Areas of liver parenchyma enhancement around the bile ducts may represent focal pyogenic hepatitis (see Fig. 37–68).[41]

AIDS Cholangitis. Several abnormalities in the biliary tract have been described in patients with AIDS. Although difficult to directly prove, the major cause of these biliary abnormalities is opportunistic infection, with the typical agents being *Cryptosporidium,* cytomegalovirus, *Mycobacterium avium-intracellulare, Candida albicans,* and *Klebsiella pneumoniae.*[40, 188]

One of the most common biliary abnormalities is diffuse gallbladder wall thickening. This may be caused by edema in the gallbladder wall and can rapidly change over time. The exact cause of the wall edema is not clear but may be lymphatic obstruction, as has been shown in patients with adenopathy secondary to Kaposi's sarcoma or lymphoma.[188] The gallbladder wall thickening may also be caused by inflammation associated with acalculous cholecystitis. Both *Cryptosporidium* and cytomegalovirus have been implicated in causing acalculous cholecystitis in patients with AIDS.[220, 221] The diagnosis may be difficult with imaging studies. However, if there is pericholecystic fluid or inflammatory changes on CT or ultrasonography, acalculous cholecystitis should be suspected in the appropriate clinical setting over noninflammatory gallbladder wall edema.

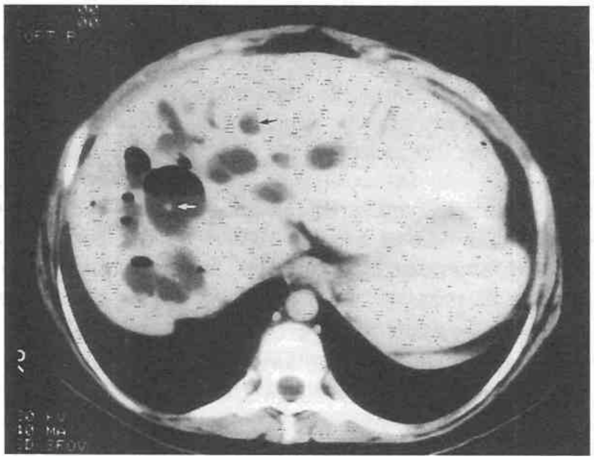

Figure 37–63. Caroli disease with cystic dilatation of the intrahepatic bile ducts. *Arrows* show "central dot sign." Air in ducts is caused by previous intervention. (Courtesy of R.L. Baron, M.D.)

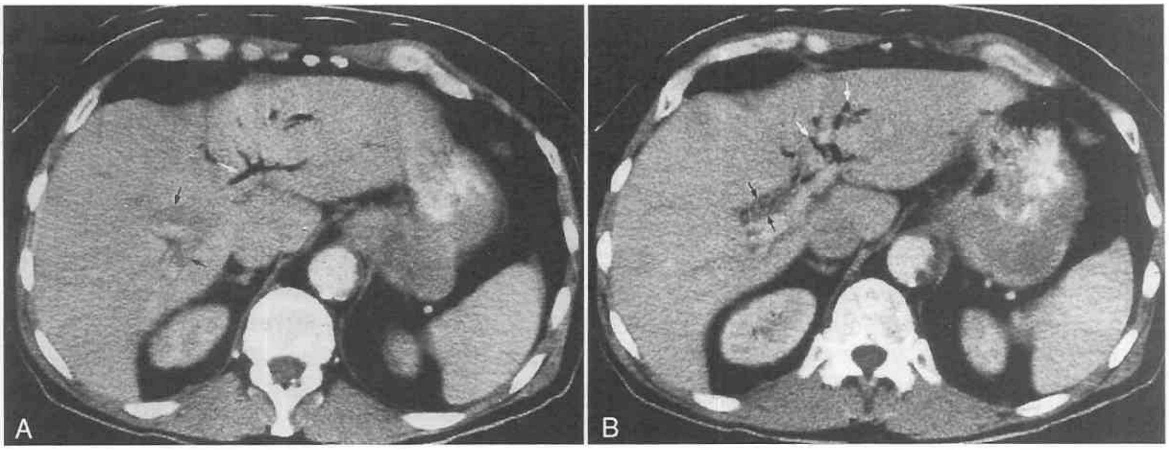

Figure 37–64. *A*, Suppurative cholangitis with dilated intrahepatic ducts *(black arrows)* filled with dense inflammatory debris. Pneumobilia *(white arrow)* secondary to previous biliary enteric anastomosis. *B*, Suppurative cholangitis. Note thickened wall of the hepatic ducts *(black arrows)* and pneumobilia *(white arrows).*

Bile duct abnormalities in patients with AIDS can be arranged into two patterns. The first pattern involves narrowing only of the distal CBD; this may be due to acute papillitis or stricture and may mimic papillary stenosis.[60, 220, 221] The remainder of the biliary tract in those cases may be dilated but otherwise normal. Acute inflammation or an inflammatory stricture of the distal CBD ampulla had been attributed to infection by *Cryptosporidium* and cytomegalovirus, both of which have been isolated on ampullary biopsy specimens.[60]

The second pattern of bile duct abnormalities mimics primary sclerosing cholangitis (PSC) with multiple strictures occurring throughout the biliary tree with or without distal CBD/ampullary strictures (Fig. 37–65). Focal dilatation of the ducts and pruning of the intrahepatic ducts can occur as in PSC.[60] Thickening of the duct wall can be appreciated on CT or ultrasonography. The cause of these strictures has been linked to *Cryptosporidium* and cytomegalovirus.

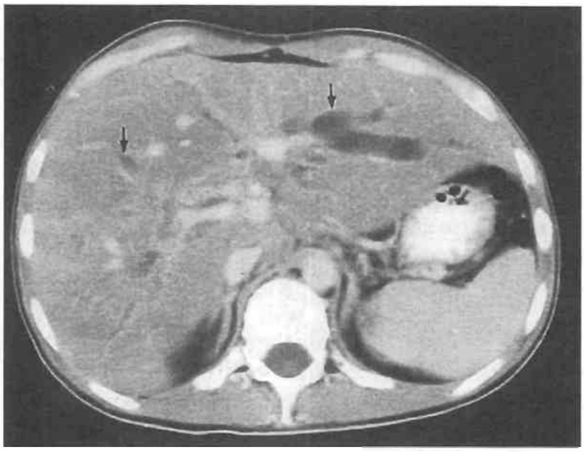

Figure 37–65. AIDS cholangitis with dilated intrahepatic ducts *(arrows).* Note asymmetry of dilatation with greater dilatation of the left ducts. (From Dolmatch BL, Laing FC, Federle MP, et al: AIDS-related cholangitis: radiographic findings in nine patients. Radiology 163:313, 1987.)

AIDS patients with such biliary infections usually present with recurrent nonspecific abdominal pain, nausea, vomiting, fever, diarrhea, and cholestasis. Ultrasonography and CT can be performed to evaluate the biliary tract and rule out other abnormalities such as stone disease. The biliary abnormalities in AIDS patients may rapidly progress; therefore, ultrasonography and CT can be used for follow-up examinations.[221] ERCP is helpful in evaluating these patients by allowing for simultaneous ductal evaluation, biopsy, and papillotomy if required.

Parasitic Cholangitis. Parasitic infection of the biliary tract is rare in the United States. It is seen, however, in areas where there are large populations of immigrants particularly from Southeast Asia. *Clonorchis sinensis* and *Ascaris lumbricoides* are the two major biliary tract parasites.

Ascariasis can involve the biliary tract when the worms migrate through the ampulla. This may produce biliary colic, pyogenic cholangitis, and acalculous cholecystitis.[182] Stones may form around the worms or ova, and ductal stricture formation may occur as a result of inflammatory reaction. Liver abscesses may develop secondary to infected and obstructed bile ducts. On CT, signs of cholangitis may be visualized with biliary dilatation, increased density of bile, pneumobilia, and parenchymal abscesses.[182]

Clonorchiasis typically appears on CT scan as biliary dilatation. The degree of biliary dilatation will vary but is usually mild and involves only the IHBDs (Fig. 37–66). The EHBDs are characteristically not dilated. Dilatation of the IHBDs is caused by obstruction by the parasites or associated inflammatory debris. Thickening of the bile duct walls and the parasites themselves are usually not seen on CT but may be appreciated on ultrasonography.[45] CT may, however, demonstrate complications of the infection such as calculi, suppurative cholangitis, abscesses, or cholangiohepatitis. There is an increased incidence of CCA associated with chronic *Clonorchis* infection. If prominent biliary dilatation is seen, an underlying biliary neoplasm should be suspected because significant biliary dilatation is not common with *Clonorchis* infection alone.[43, 45] Finally, CT

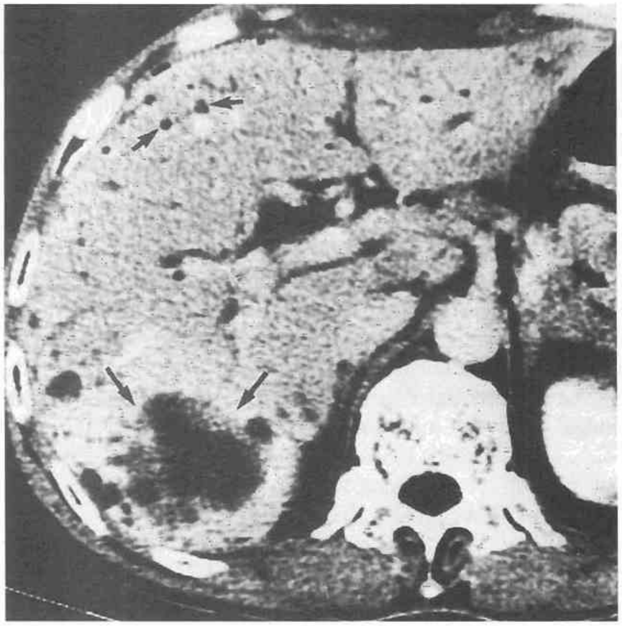

Figure 37–66. *Clonorchis* infection with dilated intrah[redacted]c bile ducts *(short arrows)* and an intrahepatic cholangiocarcinoma *(long arrows)*. (From Choi BI, Kim HJ, Han MC: CT findings of clonorchiasis. AJR Am J Roentgenol 152:281, 1989.)

may demonstrate an intrahepatic mass due to CCA (see Fig. 37–66).

Recurrent Pyogenic Cholangitis. Recurrent pyogenic cholangitis (RPC) or oriental cholangiohepatitis is a common disease in Asia and is being seen more in Western countries because of immigration. It is reported to be a very common cause of an acute abdomen requiring surgery in Southeast Asia.[117] The disease involves recurrent episodes of infectious cholangitis that eventually leads to bile duct strictures, ductal obstruction, and biliary calculi. Clinically, the patients present with episodic abdominal pain, sepsis, and jaundice.

The findings on CT reflect the pathologic changes. There is usually significant intrahepatic and extrahepatic biliary dilatation. "Pruning" of the IHBDs can occur where there is notable dilatation of the duct, blunting of the peripheral end of the duct, and nonvisualization of the secondary duct branches. Debris and calculi are often seen within the ducts (Fig. 37–67). The stones are usually bile pigment stones with varying degrees of calcium content. Depending on the calcium content, the stones may vary from isodense to hyperdense with bile.[13, 71] CT demonstrates the stones better than can ultrasonography, because often these stones are the consistency of paste and do not shadow on ultrasonography.[71, 117, 186] In addition, pneumobilia is often present, which limits the ability to visualize the ducts optimally with ultrasound.

The IHBDs in the left lobe of the liver are usually the most common site of involvement and often the most severely involved.[41] There may be diffuse areas of involvement in the liver with varying degrees of severity. However, solitary segmental involvement may occur. CT can demonstrate the areas of involvement quite well; this is important for surgical treatment planning.

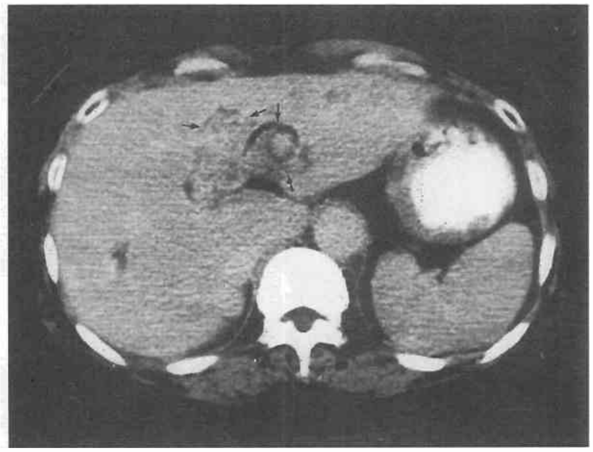

Figure 37–67. Recurrent pyogenic cholangitis with significantly dilated intrahepatic bile ducts containing debris and stones *(between arrows)*.

Periductal and duct wall enhancement can be seen on enhanced CT scans. This suggests acute inflammation (Fig. 37–68).[41] In addition, periductal hepatic abscesses can be detected as a complication of acute episodes. Chronically, the disease can lead to lobar atrophy, cirrhosis, and portal hypertension.

The EHBD is often significantly dilated up to as much as 3 to 4 cm in diameter. The grossly distended common duct may be full of stones and debris, producing a cast of the duct (Fig. 37–69). This finding is very suggestive of RPC.[117] On high-resolution CT, the wall of the common duct may be seen to be eccentrically and diffusely thickened.[199] Differential diagnosis of RPC includes PSC. However, the ducts are usually not as dilated in PSC and intrahepatic calculi are more common in RPC. Caroli's disease may be difficult to differentiate from RPC, but the extrahepatic bile duct is usually not as dilated in Caroli's disease.

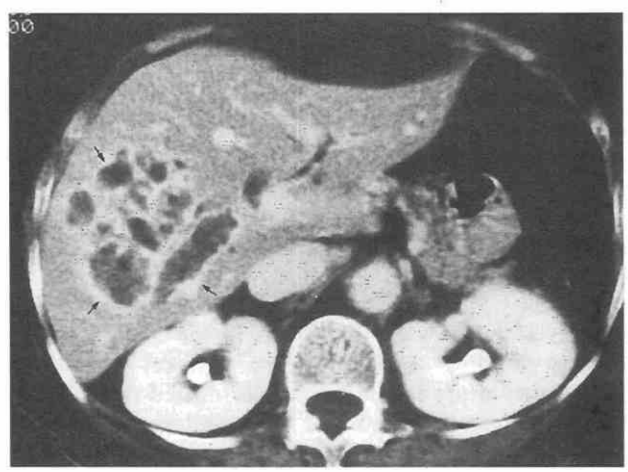

Figure 37–68. Acute exacerbation of recurrent pyogenic cholangitis with dilated right intrahepatic bile ducts and periductal enhancement *(arrows)*. (From Chan F, Man SW, Leong LL, Fan ST: Evaluation of recurrent pyogenic cholangitis with CT: Analysis of 50 patients. Radiology 170:165, 1989.)

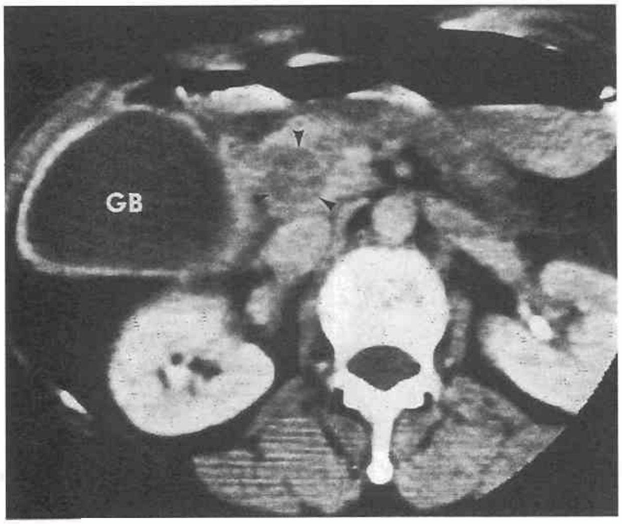

Figure 37–69. *Arrowheads* show dilated common duct in the pancreatic head, filled with a calculus of higher attenuation than bile in the gallbladder (GB). (From Choi BI, Kim HJ, Han MC: CT findings of clonorchiasis. Am J Roentgenol 152:281, 1989.)

CT is probably the best examination for evaluating patients with RPC. Because the biliary tree in these patients is colonized with bacteria and parasites, biliary sepsis can occur from an invasive procedure such as ERCP and PTC. CT, however, will noninvasively demonstrate the distribution, extent, and severity of ductal and hepatic parenchymal involvement.

Sclerosing Cholangitis. Sclerosing cholangitis is a rare disease of the biliary tract that may be primary, in which case it is idiopathic, or associated with several diseases, such as nlcerative colitis, Crohn's disease, retroperitoneal fibrosis, and Reidel's stroma. It has been described in association with histiocytosis X, angioimmunoblastic lymphadenopathy, and AIDS.[168] Secondary sclerosing cholangitis can occur as a result of stone disease, previous biliary surgery, or recurrent infection, and these conditions must be excluded to diagnose PSC. The clinical course is insidious and manifested by intermittent jaundice. Cirrhosis may result because of chronic cholestasis.

The pathology of sclerosing cholangitis is characterized by ductal and periductal fibrosis causing focal strictures with alternating areas of ductal dilatation. This pattern produces the "beaded" appearance of the ducts on cholangiography. Classically, both the IHBDs and EHBDs are involved. However, cases have been reported of only the EHBDs being involved.[4]

The classically described findings of sclerosing cholangitis on CT reflect the cholangiographic and pathologic findings.[4, 184, 217, 218] Randomly scattered, focal areas of bile duct dilatation are seen. The focally dilated ducts do not directly communicate, nor are they confluent with the hilum (Fig. 37–70*A*). There often is a segmental distribution to the involved ducts. The dilated ducts may demonstrate a beaded appearance reflecting alternating areas of strictures and dilatation. Pruning of the ducts may be seen where there is dilatation of the segmental ducts without dilatation of their secondary branches (see Fig. 37–70*B*). Teefey and associates[218] reported a series of 100 patients in which pruning and beading of the IHBD was not specific for PSC but was also seen in infectious and malignant processes. Skip dilatations or areas of alternating stricture and duct dilatation were considered the strongest sign for PSC, especially in the absence of a mass or evidence of recurrent pyogenic cholangitis.

In PSC, the EHBD is often not dilated but may have a serpentine course. With high-resolution CT of the EHBD, subtle changes in the wall of the duct may be appreciated. Teefey and colleagues[217] described such findings in the EHBD, including wall thickening with enhancement, mural nodules, and focal ductal stenosis (see Fig. 37–70*E*).

The differential diagnosis of sclerosing cholangitis includes recurrent infectious cholangitis, diffuse sclerosing CCA, early Caroli's disease, ductal sclerosis after transcatheter arterial chemotherapy administration, and post-traumatic stricture.[27, 174] The clinical setting may allow differentiation of several of these entities, but the CT appearances are often similar. Diffuse sclerosing CCA is difficult to differentiate and often requires a biopsy for the diagnosis. Brush biopsies of the ducts may not be helpful, because of the large component of fibrosis found in both PSC and sclerosing CCA. There is an increased incidence of CCA in sclerosing cholangitis, and sclerosing cholangitis is considered to be a premalignant condition.[165] In a series of patients receiving liver transplants for PSC, 10% of the patients were found to have CCA in their native livers.[100] Some of these cases were not discovered until later when the hepatectomy specimens were histologically examined. In sclerosing cholangitis, ductal dilatation is often not dramatic; this is caused by periductal fibrosis. However, if prominent duct dilatation, particularly segmental dilatation, is seen in a patient with known sclerosing cholangitis, or if ductal dilatation rapidly progresses, CCA should be suspected (see Fig. 37–70*C*).[187] Lymphadenopathy in the upper abdomen has been reported in PSC without CCA.[168] Such enlarged nodes often occur in the gastrohepatic ligament and in the pancreaticoduodenal chain. Lymphadenopathy in the porta hepatis has been reported as a sign suggesting a malignant biliary process (see Fig. 37–70*D*).[187] However, in PSC the mere presence of lymphadenopathy is not as useful. Therefore, biopsy of the lymph nodes may be required.

PTC and ERCP have been the gold standards for demonstrating sclerosing cholangitis. However, cholangiographically, ducts peripheral to tight strictures may not be filled adequately, and CT may show these areas better. In addition, given the possibility of underlying CCA, CT can evaluate for an extraductal mass or lymphadenopathy better than can cholangiography.

Biliary Obstruction

CT is often the initial examination performed in patients with clinical presentation of jaundice, or CT may be performed as a correlative examination after ultrasonography. The main goals of the CT examination are to determine the presence of obstruction, determine the level and extent of obstruction, and determine the cause. The overall accu-

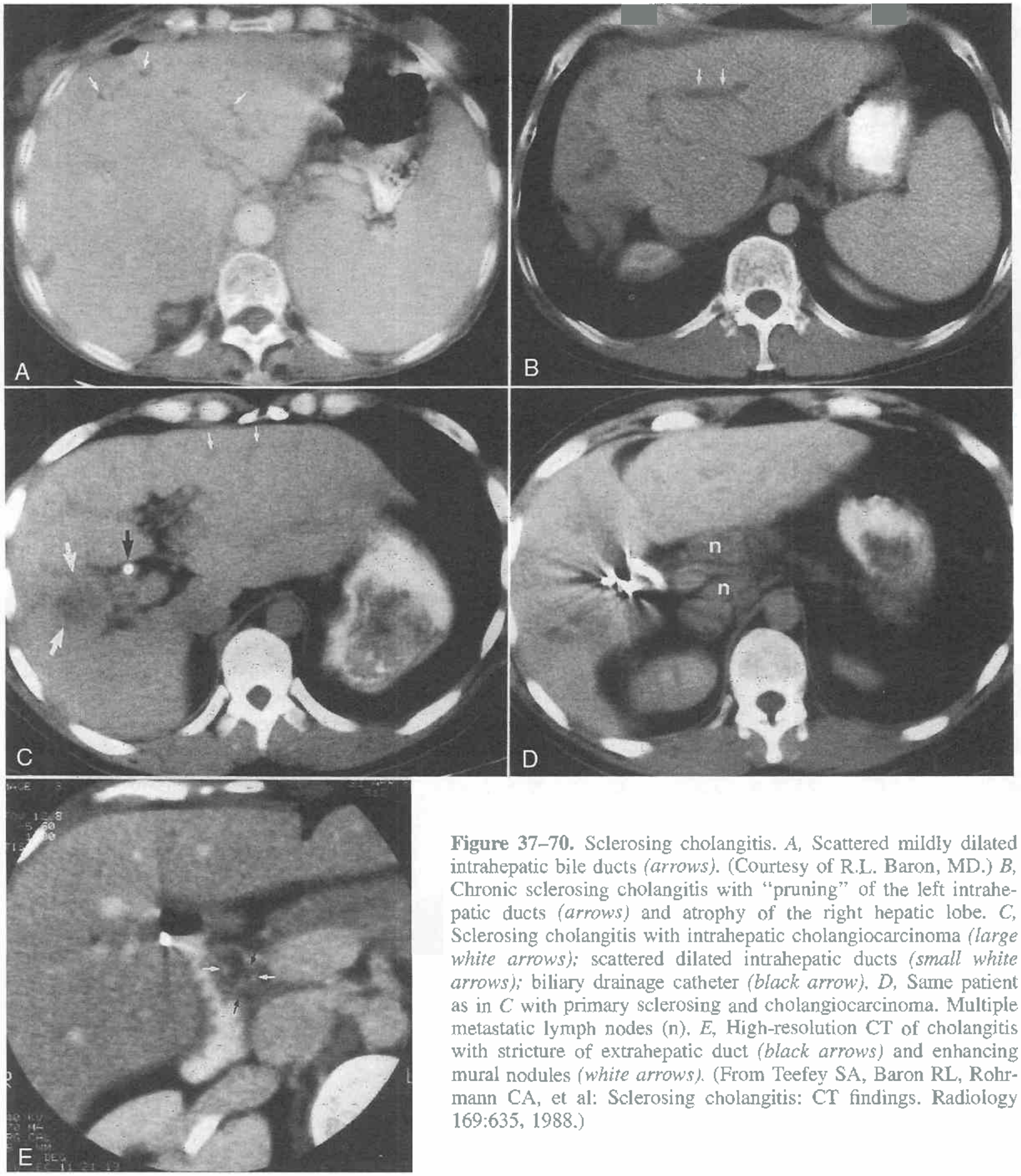

Figure 37–70. Sclerosing cholangitis. *A,* Scattered mildly dilated intrahepatic bile ducts *(arrows).* (Courtesy of R.L. Baron, MD.) *B,* Chronic sclerosing cholangitis with "pruning" of the left intrahepatic ducts *(arrows)* and atrophy of the right hepatic lobe. *C,* Sclerosing cholangitis with intrahepatic cholangiocarcinoma *(large white arrows);* scattered dilated intrahepatic ducts *(small white arrows);* biliary drainage catheter *(black arrow). D,* Same patient as in *C* with primary sclerosing and cholangiocarcinoma. Multiple metastatic lymph nodes (n). *E,* High-resolution CT of cholangitis with stricture of extrahepatic duct *(black arrows)* and enhancing mural nodules *(white arrows).* (From Teefey SA, Baron RL, Rohrmann CA, et al: Sclerosing cholangitis: CT findings. Radiology 169:635, 1988.)

racy of CT for diagnosing biliary obstruction has been reported at 85% to 97%.[15, 134, 157, 224] The hallmark of biliary obstruction on CT is biliary dilatation (Figs. 37–71 to 37–77). Such intrahepatic dilatation appears as confluent linear structures of water density that course with the portal vein branches and gradually increase in size as they course toward the hilum. As mentioned previously, normal IHBDs may occasionally be visualized, but these are few in number, scattered, and not confluent (see Figs. 37–56 and 37–57). The dilated EHBD measures greater than 8 to 10 mm in short-axis measurement. With intravenous enhancement, dilated bile ducts can more easily be differentiated from enhancing vascular structures.

False negatives for biliary obstruction being diagnosed by CT do exist. For example, biliary dilatation may not be present in early obstruction. Animal studies have demonstrated that 4 days may be required before dilatation occurs after duct obstruction.[13] In addition, obstruction may be present in certain cases without dilatation, as can happen in cirrhosis and in liver transplants.[13, 132, 246] In such cases, cholangiography is required to make the diagnosis. In partial or intermittent obstruction, ductal dilatation may not be present. Choledocholithiasis has been reported to cause partial and intermittent obstruction without dilatation. A number of series have reported the lack of sensitivity of CT to detect obstruction in cases of distal common duct

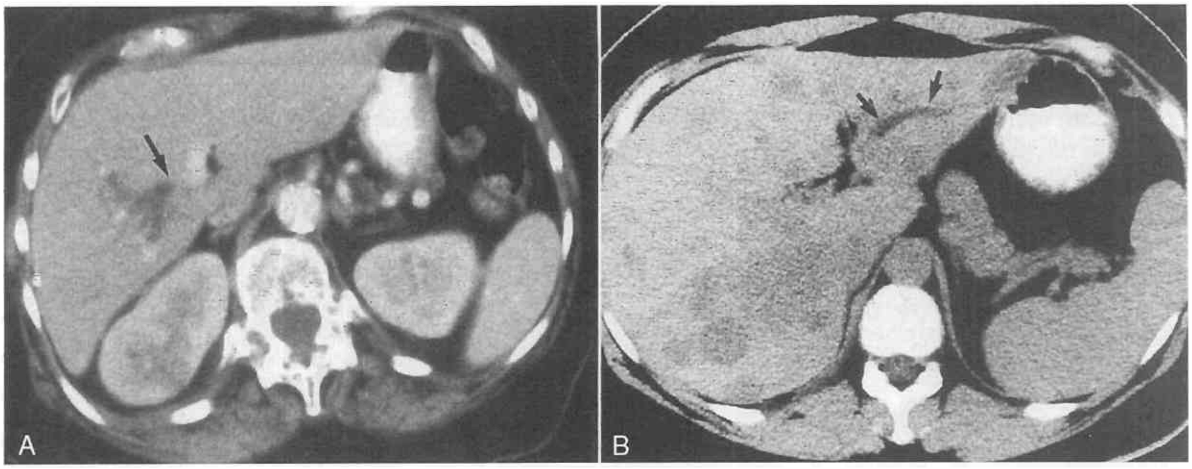

Figure 37–71. Focal intrahepatic dilatation. *A,* Isolated intrahepatic biliary dilatation in the posterior segment of the right hepatic lobe because of focal stricture *(arrow)* secondary to stone disease and cholangitis. *B,* Focal intrahepatic biliary dilatation *(arrows)* due to breast carcinoma metastases.

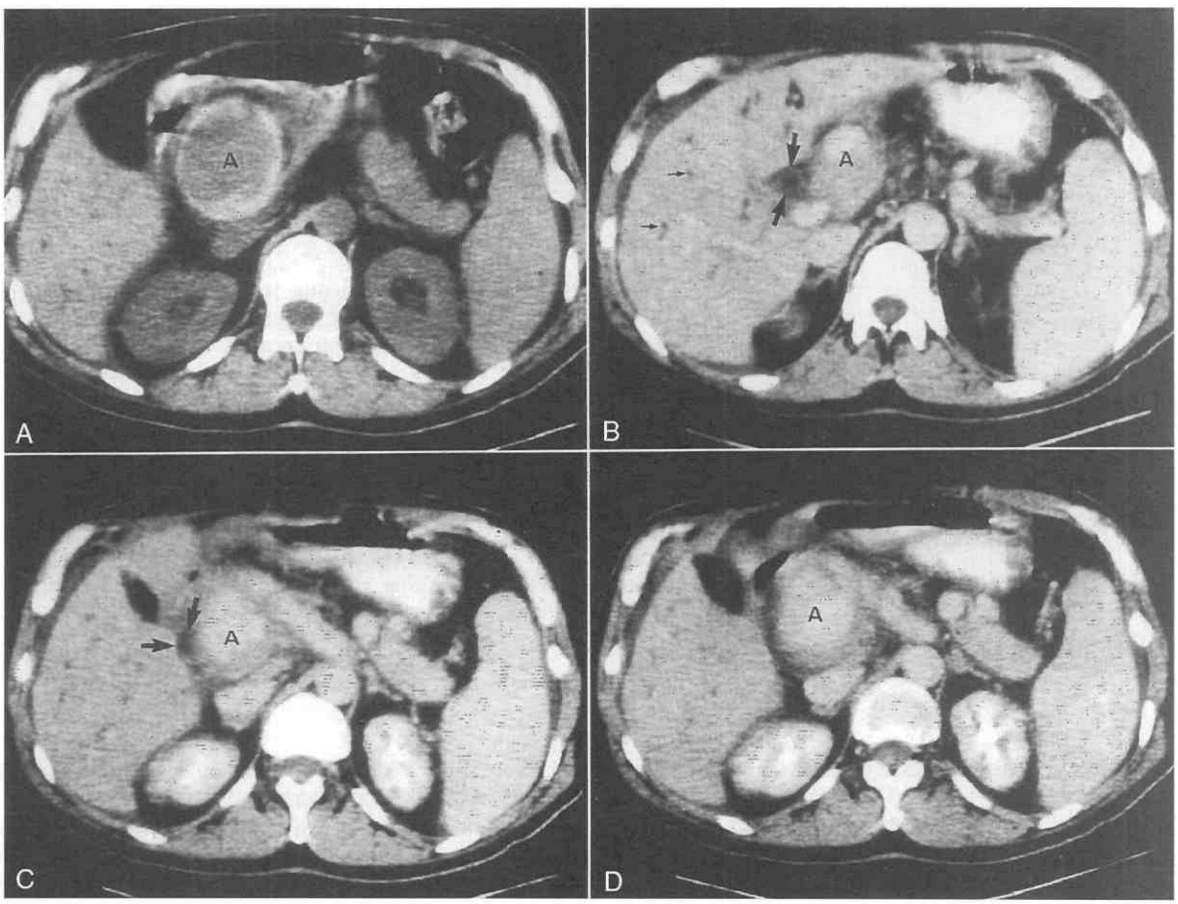

Figure 37–72. Obstruction of suprapancreatic portion of common duct by aneurysm of gastroduodenal artery. *A,* Precontrast scan of HIV-positive patient showing dense gastroduodenal artery aneurysm (A). *B,* Postcontrast scan at level of common hepatic duct *(large arrows)* with mild intrahepatic biliary duct dilatation *(small arrows)* and enhancing aneurysm (A). *C,* Level caudad to *B,* shows compression of common duct *(arrows)* by aneurysm (A). *D,* Level caudad to *C* shows aneurysm (A), which has occluded the common duct.

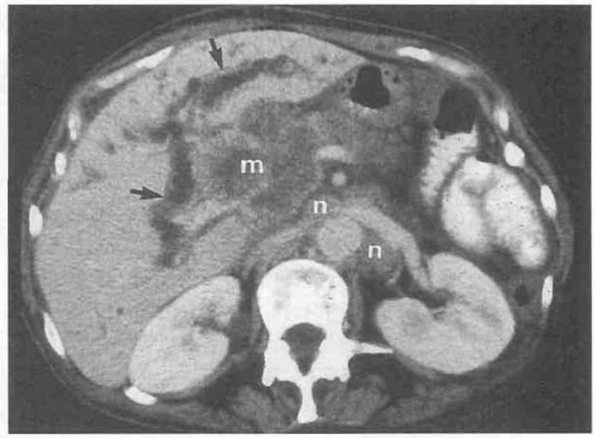

Figure 37–73. Obstruction of suprapancreatic portion of common duct by metastatic nodal mass (m) from lung carcinoma. Note dilated intrahepatic ducts *(arrows)* and lymphadenopathy (n).

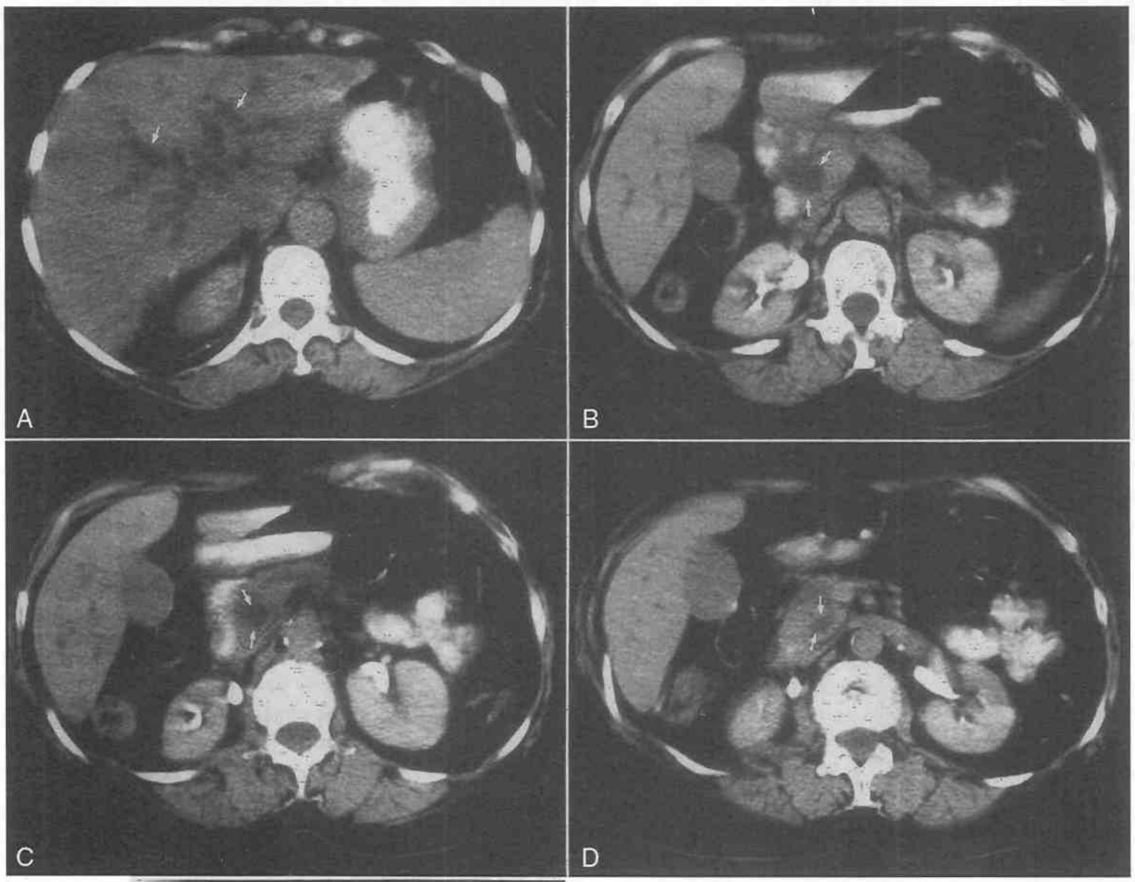

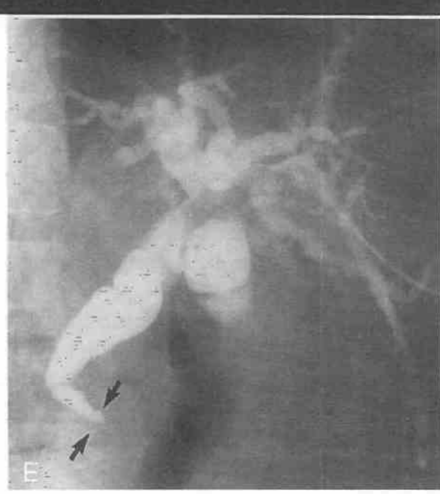

Figure 37–74. Benign distal common duct stricture with tapering of the common duct. *A,* Dilated intrahepatic bile ducts *(arrows)* throughout liver. *B,* Dilated common duct *(arrows).* This level is at top of pancreatic head. *C* and *D,* Common duct *(arrows)* slowly narrows over several levels in the head of pancreas. *D* is several millimeters caudad to *C. E,* Cholangiogram shows tapering of distal common duct *(arrows)* as a result of the benign stricture.

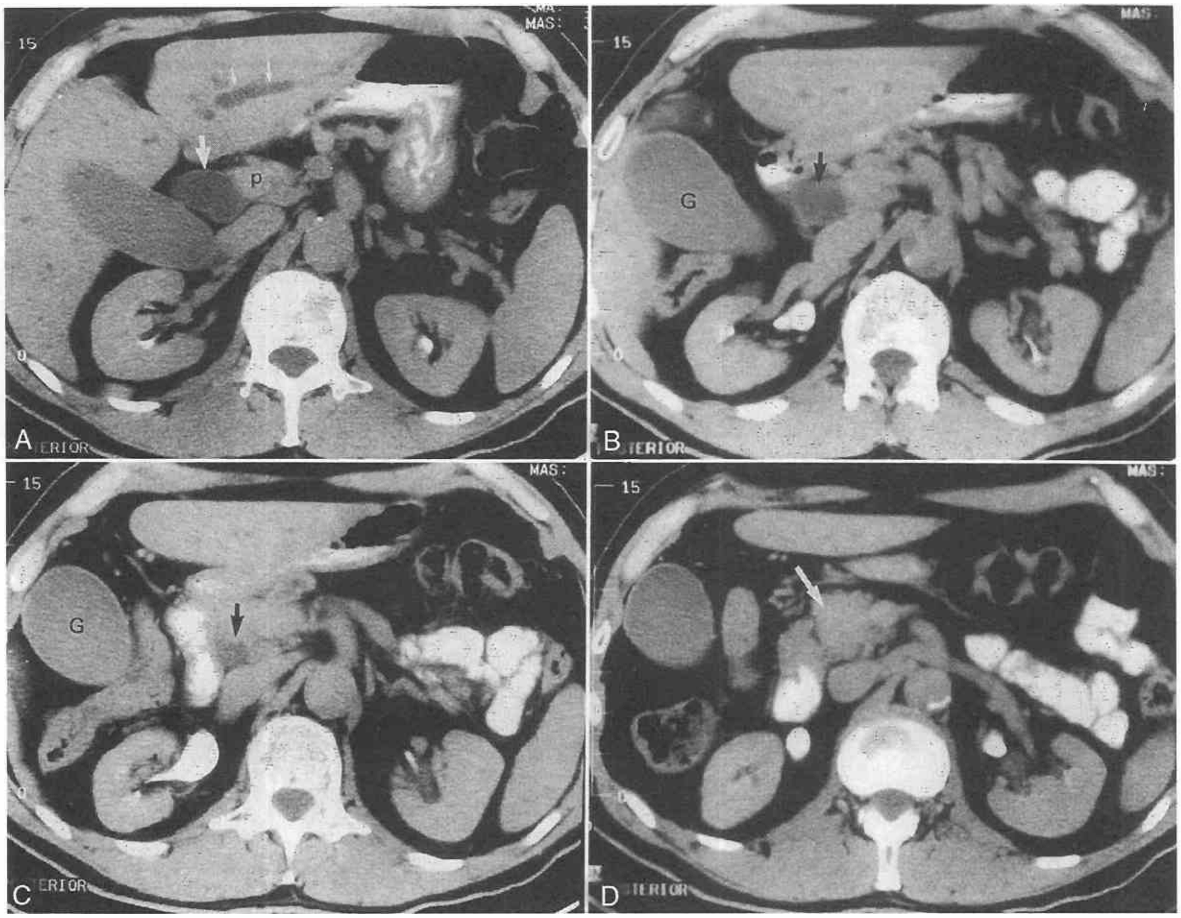

Figure 37–75. Distal biliary obstruction secondary to pancreatic carcinoma. *A*, Dilated common duct *(large arrow)* next to portal vein (p) with dilated intrahepatic ducts *(small arrows)*. *B*, Dilated common duct *(arrow)* at level 8 mm caudal to *A*. Note dilated gallbladder (G). *C*, Dilated common duct *(arrow)* in head of pancreas. Note irregularity in ventral wall of dilated duct *(at arrow tip)* secondary to pancreatic carcinoma. Dilated gallbladder (G). *D*, Level just caudad to *C* shows abrupt termination of common duct with mass *(arrow)*, which is the pancreatic carcinoma.

stones because of the lack of dilatation (Fig. 37–78).[13, 55, 84, 85, 169] Finally, ductal dilatation, particularly intrahepatic, may be difficult to detect in the setting of diffuse fatty infiltration of the liver because of less contrast between the water-density ducts and the fatty liver (Fig. 37–79).[179]

In CT, false positives for biliary dilatation, hence obstruction, do exist. Morehouse reported a case of metastatic pancreatic carcinoma extending along the portal vein branches mimicking biliary dilatation.[157] In addition, I have seen a case of a neurofibroma in the porta hepatis with extension along the portal vein branches mimicking biliary dilatation on ultrasonography, CT, and MRI (Fig. 37–80). Periductal tumor will often enhance and thereby be differentiated from dilated bile ducts. Periportal lymphedema and ascites tracking along the hepatoduodenal ligament may also mimic ductal dilatation (see Fig. 37–58). Finally, thrombosis of the portal vein can mimic dilated bile ducts.[157]

In early obstruction and in some cases of prolonged obstruction, only extrahepatic biliary dilatation may be seen.[16, 199, 202] This has been described with common bile duct stones. In postcholecystectomy patients, the EHBD is considered normal in size up to 10 mm in short-axis diameter.[13, 50, 161, 199] If there is any question of obstruction in such patients, a fatty meal challenge or intravenous cholecystokinin may be given with measurement of the EHBD before and 10 to 15 minutes after administration. A normal response is seen if the duct remains stable or decreases in diameter. If there is an increase in the size of the duct or onset of pain, the response is abnormal.[13] Further evaluation of the duct with ERCP will be necessary.

Level and Extent of Obstruction. Depending on the series, the accuracy of CT for determining the level of obstruction has been reported to be 80% to 97%.[15, 85, 171, 172] The dilated bile ducts can be traced on the same image or consecutive images to the transition point at which the caliber of the duct decreases or the duct disappears. This transition point is best demonstrated with thin-collimation axial images along the course of the biliary tree. Associated findings may aid in determining the level. Gallbladder dilatation can be seen with distal duct obstruction, but it is not a sensitive indicator and may be seen only in 50% of cases.[16] Pancreatic duct dilatation points to an obstructing lesion in the distal common duct or even the ampulla (see Fig. 37–76).

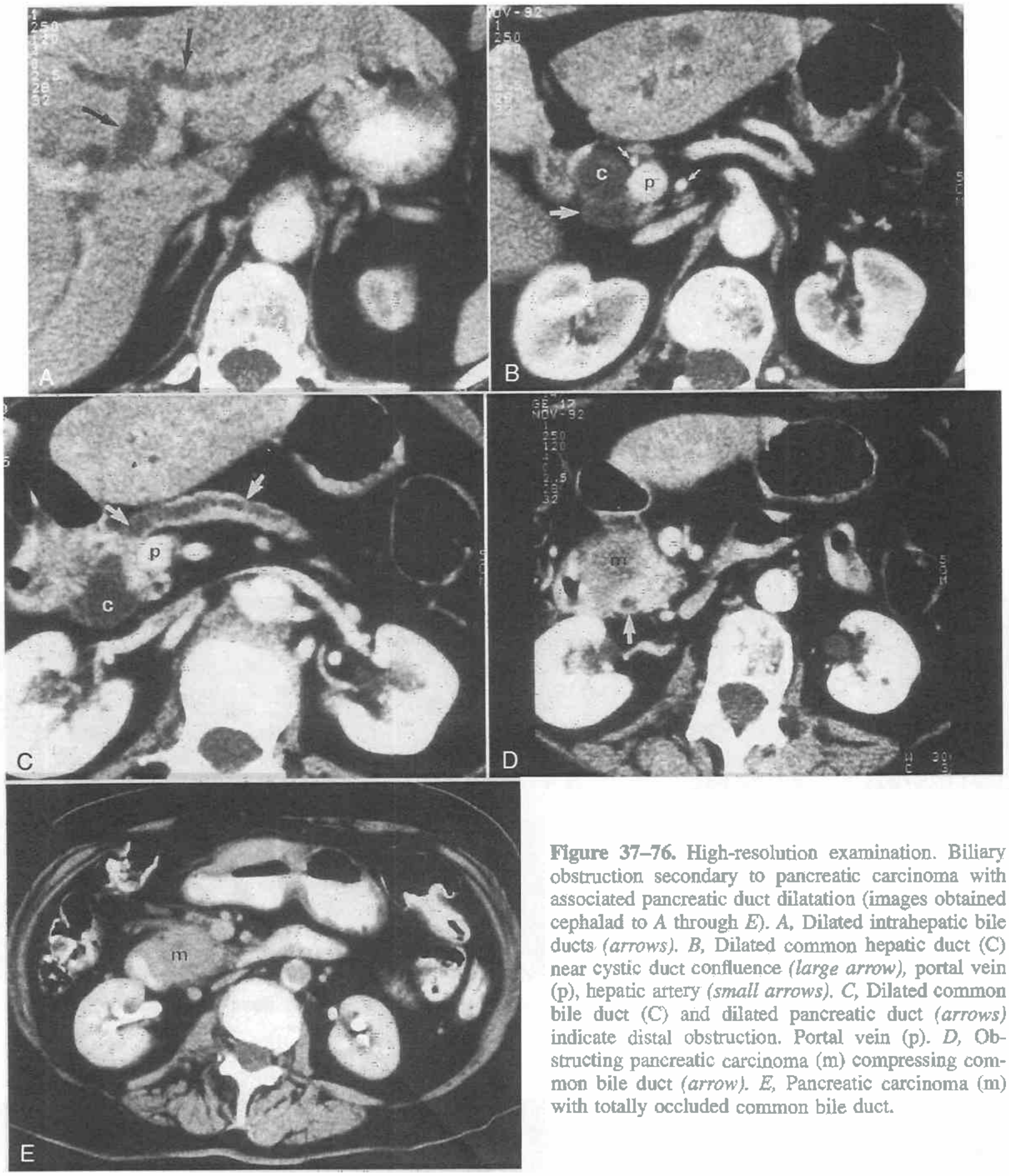

Figure 37–76. High-resolution examination. Biliary obstruction secondary to pancreatic carcinoma with associated pancreatic duct dilatation (images obtained cephalad to *A* through *E*). *A*, Dilated intrahepatic bile ducts *(arrows)*. *B*, Dilated common hepatic duct (C) near cystic duct confluence *(large arrow)*, portal vein (p), hepatic artery *(small arrows)*. *C*, Dilated common bile duct (C) and dilated pancreatic duct *(arrows)* indicate distal obstruction. Portal vein (p). *D*, Obstructing pancreatic carcinoma (m) compressing common bile duct *(arrow)*. *E*, Pancreatic carcinoma (m) with totally occluded common bile duct.

The extent of the biliary tree that is obstructed can be determined by CT and can aid in therapy planning. For example, intrahepatic biliary obstruction proximal to the right or left hepatic duct is rarely amenable to surgical correction. Such obstruction is usually treated with percutaneous transhepatic catheter drainage. CT can demonstrate which dilated segmental ducts communicate and whether more than one catheter is required.[187] If the ducts in more than three segments are obstructed and do not communicate, these cases are poor candidates for surgery and catheter drainage. More distal EHBD obstruction is usually more amenable to surgical correction and percutaneous or endoscopic intervention.

Cause of Obstruction. The reported accuracy of CT for determining the cause of biliary obstruction ranges from 63% to 94%.[15, 84, 85, 171, 172] The wide range of accuracies is most likely caused by different generations of CT scanners, different scanning techniques, and different types of pathology in each series. High-resolution scanning of the bile ducts with small field of view and thin collimation is the optimum technique (see Figs. 37–76 and 37–92). However, even with optimum technique, certain pathologic conditions such as cholesterol stones in the common duct are difficult to detect (see section on choledocholithiasis).

Differential diagnostic categories can be formulated based on the level at which obstruction occurs. Intrahepatic

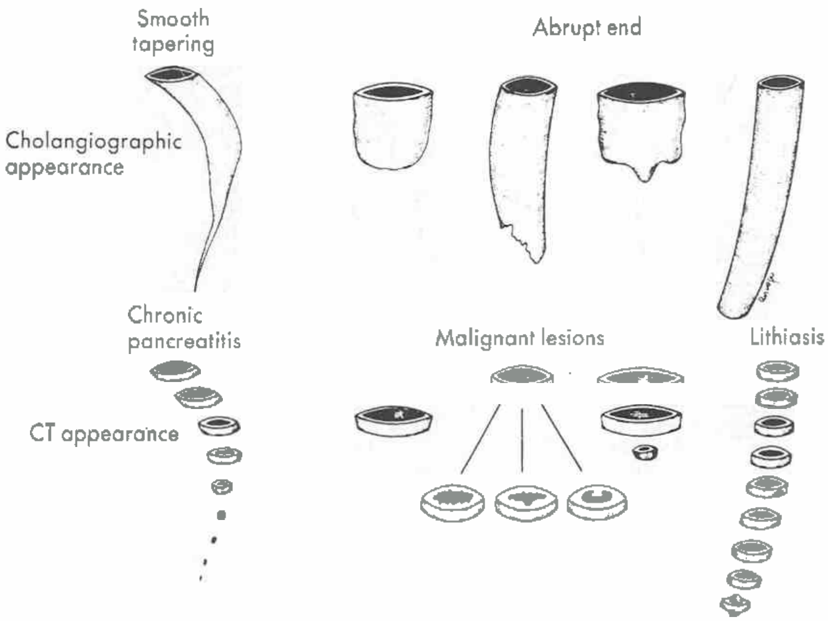

Figure 37–77. Diagrammatic representation of cholangiographic and CT appearance of the bile duct in the most common lesions. (From Pedrosa CS, Casanova R, Lezana AH, Fernandez MC: Computed tomography in obstructive jaundice: II. The level of obstruction. Radiology 139:635, 1981.)

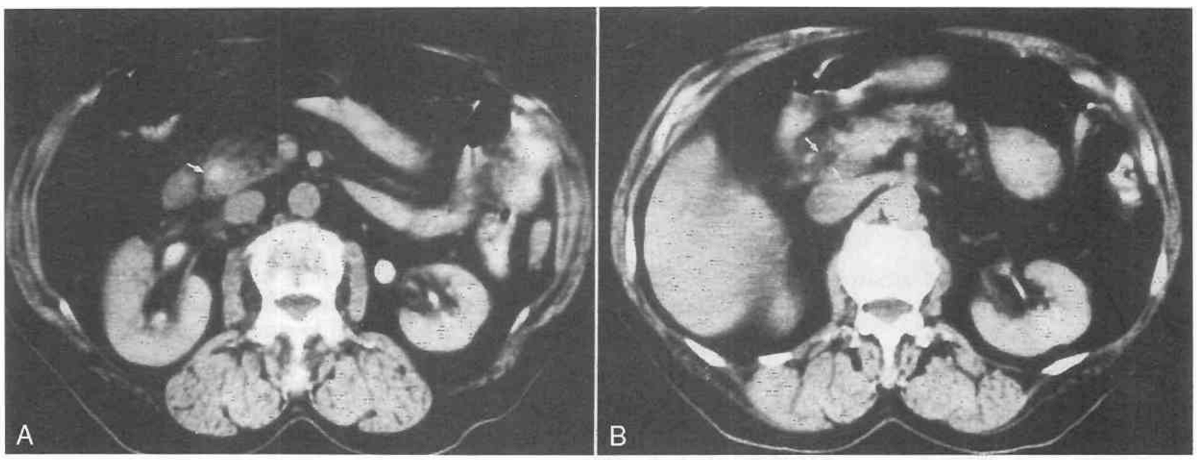

Figure 37–78. [redacted]l common bile duct stone without biliary dilatation. *A,* Dense stone in distal duct *(arrow). B,* Nondilated duct *(arrows)* just ab[redacted]evel of s[redacted].

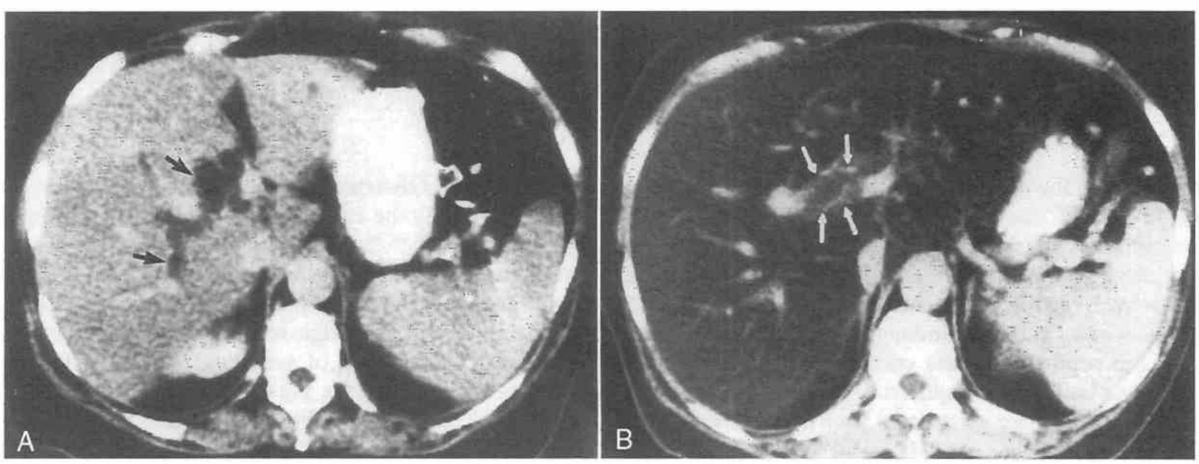

Figure 37–79. Biliary dilatation in a fatty liver. *A,* Postcontrast CT scan shows mild fatty infiltration of the liver with biliary dilatation *(arrows). B,* Five months after *A,* dilated bile ducts *(arrows)* are indistinguishable from the hypodense fatty liver on this postcontrast scan. (From Quint LE, Glazer GM: CT evaluation of the bile ducts in patients with fatty liver. Radiology 153:755, 1984.)

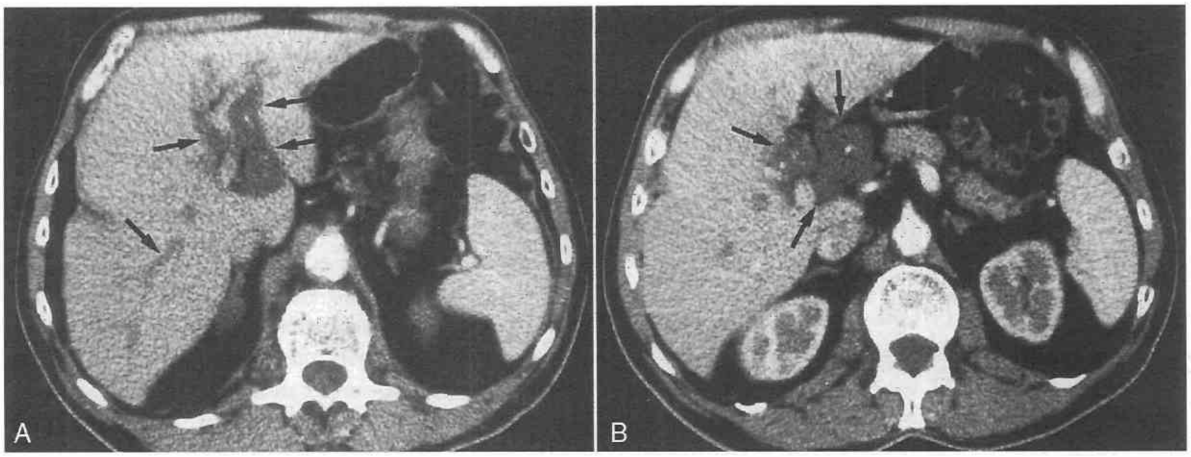

Figure 37–80. Peribiliary neurofibroma. *A*, Hypodense structures *(arrows)* mimicking dilated bile ducts are actually a neurofibroma branching along the biliary tract and portal structures. No dilated ducts were seen on ERCP. *B*, Hypodense neurofibroma *(arrows)* in the porta hepatis mimics dilated bile ducts.

ductal obstruction can be caused by strictures secondary to sclerosing cholangitis, infection, or neoplasm such as cholangiocarcinoma (see Fig. 37–72*A*). Rarely, metastases may cause intrahepatic ductal obstruction (see Fig. 37–72*B*). Christiansen reported focal dilatation of IHBDs limited to a subsegment in the posterior segment of the right hepatic lobe as a result of inadvertent ligation of an aberrant right hepatic duct during cholecystectomy.[49] At the hilum, obstruction is commonly a result of tumor such as CCA or a hepatic neoplasm extending into the hilum (see Figs. 37–88 to 37–90). In the suprapancreatic portion of the EHBD, strictures can be caused by benign disease such as sclerosing cholangitis, infectious cholangitis, surgery, or trauma. However, malignant strictures caused by CCA or secondary involvement by tumor of the gallbladder, pancreas, liver, or duodenum may occur (see Fig. 37–72). In addition, adenopathy secondary to inflammatory conditions or malignancy may obstruct the suprapancreatic duct (see Fig. 37–73). Finally, obstruction of the distal common duct can be a result of benign inflammatory strictures caused by cholangitis or pancreatitis, common duct stones, adenopathy, or tumor (pancreatic carcinoma or ampullary carcinoma) (see Figs. 37–74 to 37–76 and 37–81).

Once the level of obstruction is determined and various causes are considered, CT can be used to narrow the possibilities. A clue to the cause of obstruction is the manner in which the duct terminates at the site of obstruction (see Fig. 37–77). Different pathologic processes may have different appearances at the level of obstruction. Gradual tapering of the bile duct over a distance of 1 cm or greater is typically caused by benign disease, such as an inflammatory stricture (see Fig. 37–74). However, abrupt termination of the dilated bile duct over less than 5 mm is highly suggestive of malignancy, especially if seen in the suprapancreatic portion of the duct or near the ampulla (see Figs. 37–75 and 37–92). In a series by Reiman and colleagues abrupt termination of the suprapancreatic common duct was seen in all cases of malignancy but also in 50% of benign causes of obstruction.[187] Benign strictures occasionally may cause abrupt termination of the duct.[13] In addition, obstructing cholesterol stones in the common duct may cause abrupt termination of the duct and escape visualization because of its density being similar to bile (Figs. 37–82 and 37–83). However, if a soft tissue mass or lymphadenopathy is seen with the abrupt ductal termination, then malignancy should be suspected (see Fig. 37–92).[84, 85, 187] CT is much better than cholangiography for demonstrating a mass outside the duct or periductal lymphadenopathy.

Schulte and colleagues described the appearance of the bile duct at or proximal to the level of obstruction as being helpful in determining the cause of obstruction.[199] High-resolution CT with thin collimation of images is optimum for this evaluation. Thickening of the duct wall (greater than 1.5 mm) can be observed and classified as concentric or eccentric and as focal or diffuse.[199] Focal concentric thickening in the distal common duct was nonspecific and attributed to stones, pancreatitis, or pancreatic carcinoma (see Fig. 37–83*B*). Diffuse concentric wall thickening was relatively specific and seen in infectious cholangitis (see Fig. 37–64*B*). Focal concentric or eccentric thickening else-

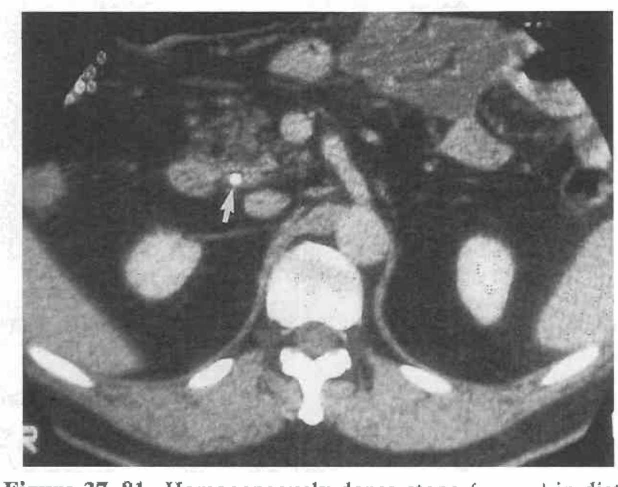

Figure 37–81. Homogeneously dense stone *(arrow)* in distal common bile duct on high-resolution axial image at level of uncinate process of pancreas.

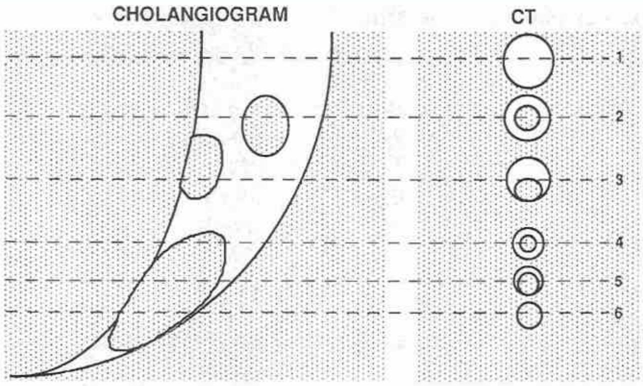

Figure 37–82. Appearance of distal common bile duct seen on cholangiogram *(left)* and CT *(right)*. *1,* CT shows rounded duct with only water-density bile. *2,* Target sign shows central, the stone, surrounded by water-density bile "halo" (see *4*). *3,* Crescent sign shows rim of water-density bile anterior to dependent stone (see *5*). *4,* Target sign can be seen when the image cuts through only one end of the stone. *5,* Crescent sign can be seen when the stone does not fill the duct. *6,* If stone is soft tissue density, no duct may be seen at this level, mimicking abrupt termination of the duct as if due to carcinoma. (From Baron RL: Computed tomography of the biliary tree. Radiol Clin North Am 29:1235, 1991.)

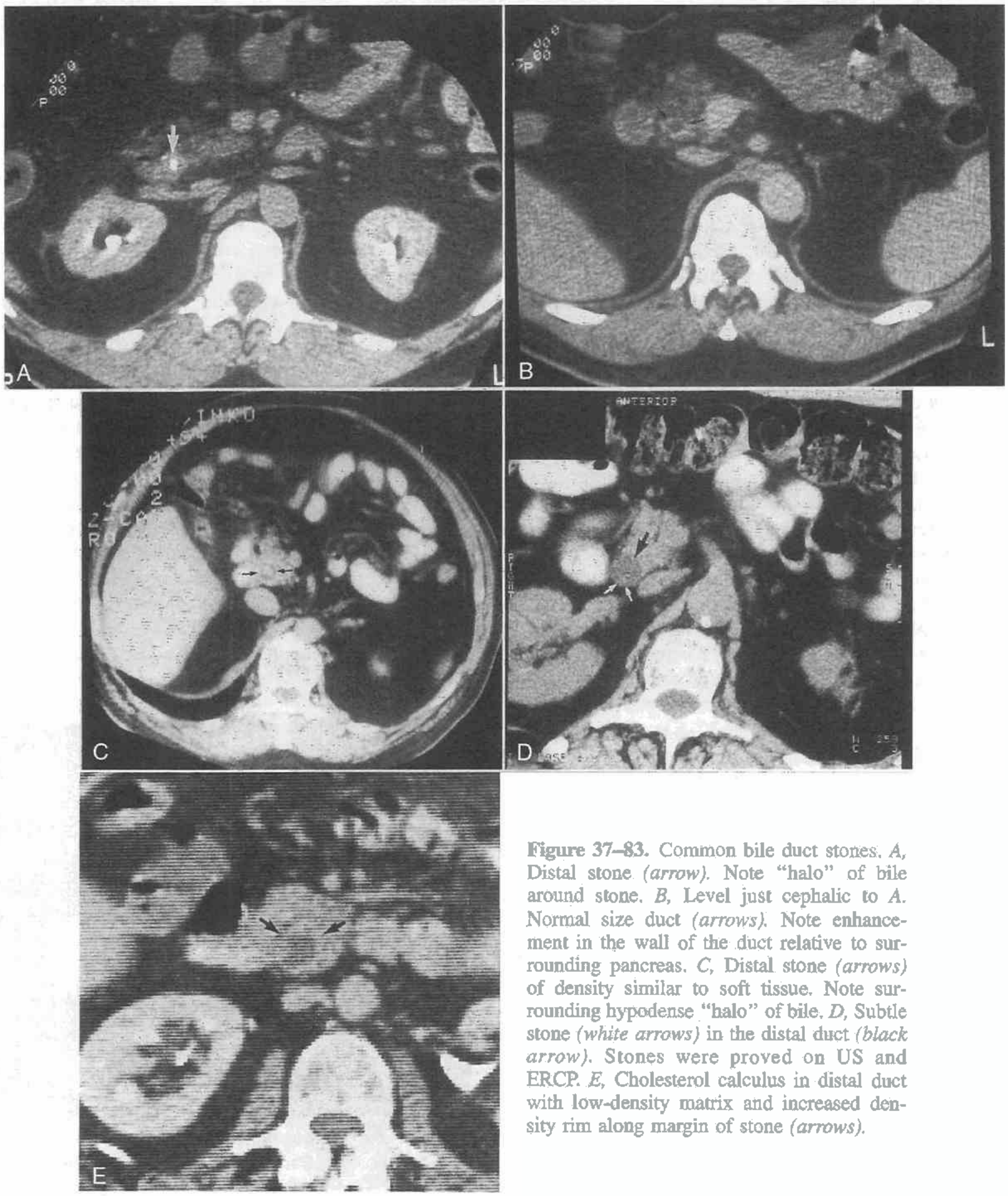

Figure 37–83. Common bile duct stones. *A,* Distal stone *(arrow)*. Note "halo" of bile around stone. *B,* Level just cephalic to *A*. Normal size duct *(arrows)*. Note enhancement in the wall of the duct relative to surrounding pancreas. *C,* Distal stone *(arrows)* of density similar to soft tissue. Note surrounding hypodense "halo" of bile. *D,* Subtle stone *(white arrows)* in the distal duct *(black arrow)*. Stones were proved on US and ERCP. *E,* Cholesterol calculus in distal duct with low-density matrix and increased density rim along margin of stone *(arrows)*.

where in the common duct may be seen in PSC, but this pattern may also be seen in CCA, especially with pronounced wall thickening (see Figs. 37–70*E* and 37–92).

Choledocholithiasis. The diagnosis of common duct stones can be difficult to make on noninvasive imaging. Ultrasonography is often the first-line study requested to evaluate the patient with biliary colic or jaundice. Its reported sensitivity ranges up to 80% to 82%, but many series suggest lower sensitivity.[169] These studies are limited by the patient's body habitus, bowel gas, and experience of the operator. CT, on the other hand, is not limited by bowel gas or the patient's body habitus. The reported sensitivities of CT for choledocholithiasis vary but range up to 90%.[12, 13, 15, 118, 172] The sensitivity of CT greatly depends on the type of stone in the duct and the technique of the examination. Although invasive, ERCP remains the gold standard technique for diagnosing common duct stones.

Strict attention to the technique of the CT examination will improve the ability to detect common duct stones. High-resolution CT should be performed with a small field of view targeted to the right upper quadrant with specific attention to the distal common duct. Thin collimation of axial images (3 to 5 mm thick) should be used with contiguous spacing at 3- to 5-mm intervals. Baron suggests that overlapping images are helpful in the distal common duct.[12] Intravenous contrast medium is helpful in defining structures in the porta hepatis. Contrast agent enhancement will aid in detecting subtle intrahepatic biliary dilatation and will also increase the visibility of the distal common duct contrasted to the pancreatic head. Oral administration of contrast medium may confuse the picture because dense contrast in the duodenum may obscure or mimic a calcified stone near the ampulla (Fig. 37–84). Therefore, studies should be performed without oral contrast agent administration. In addition, glucagon administered intravenously or intramuscularly will decrease artifact from bowel peristalsis. Finally, these examinations should be closely monitored so that they may be tailored to the individual patient.

Even given optimum scan technique, common duct stones may elude detection because of the stone composition. Some stones are isodense with bile and may not be detected within the dilated common duct (see Fig. 37–82). Mixed-composition stones may have densities similar to soft tissue and may be difficult to detect when surrounded by pancreatic tissue. Calcium bilirubinate stones are the easiest to detect and appear as radiopaque calcified filling defects in the duct (see Figs. 37–81 and 37–83). However, calcium bilirubinate stones are the minority of stones (15% to 20%), with pure cholesterol and mixed-composition stones being the most common (80% to 85%). Secondary signs of common duct stones must be employed to detect these noncalcified stones.

The primary sign of a stone in the common duct is a radiopaque filling defect in the lumen (see Figs. 37–81 and 37–83). This sign may be detected even if the duct is not dilated (see Fig. 37–78). Common duct stones may not have associated biliary dilatation in 24% to 36% of cases even with obstruction.[13, 54] Another sign, the target sign, consists of higher central density (the stone surrounded by a water-density "halo" of bile, which is surrounded by the duct wall (see Fig. 37–83). If the stone lies in the dependent portion of the duct, the surrounding bile will form a crescent of lower density anteriorly. Rarely, a papillary tumor may project into the lumen of the duct, giving a target sign and mimicking a stone (Fig. 37–85).

Secondary signs of duct stones include abrupt termination of the common duct without an associated mass. This sign, however, is not specific for stones and can be seen with obstructing malignancies, particularly pancreatic carcinoma. A second sign is a thin rim of increased density around a central portion of lower density (see Fig. 37–83*E*). The whole complex is thought to represent an impacted stone with the high-density rim representing a peripheral calcified layer in the stone. The density of the central portion will be hypodense or isodense with bile if the stone is composed of cholesterol, and soft tissue density if of mixed composition. It has been reported, however, that the thin dense rim represents the wall of the common duct and not part of the stone.[13] There may be inflammation

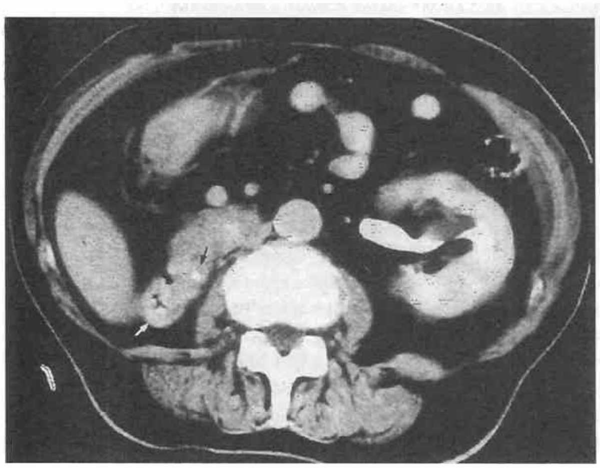

Figure 37–84. Barium in duodenum *(black arrow)* mimics stones in distal common duct. *White arrow* shows barium and gas in descending duodenum.

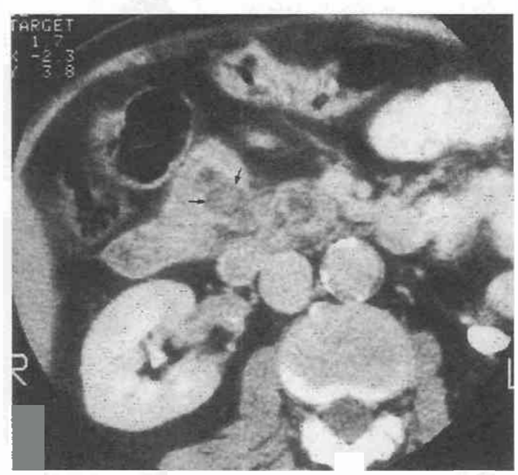

Figure 37–85. Protrusion of pancreatic carcinoma into distal common duct *(arrows)* mimics soft tissue density stone. (From Baron RL: Computed tomography of the biliary tree. Radiol Clin North Am 29:1235, 1991.)

in the wall of the duct at the level of an impacted stone, which on high-resolution CT will show prominent contrast enhancement and concentric thickening.[199] A final secondary sign of a common duct stone is subtle soft tissue densities in the lumen of the duct; this may represent areas of different composition within the stone matrix (see Fig. 37–83*D*). Unfortunately, none of these secondary signs are specific for choledocholithiasis. Intraluminal neoplasm may demonstrate any of these signs. If there is an irregular termination to the dilated duct, visible mass, or lymphadenopathy, then neoplasm rather than a stone should be suspected. For calcified distal common duct stones, there are several false positives. Barium in the duodenum adjacent to the ampulla may mimic a common duct stone especially if the barium is within a duodenal diverticulum (see Fig. 37–84). Barium may reflux into the distal duct if there is a sphincterotomy or incompetent sphincter. In addition, a pancreatic duct stone or calcification in the pancreatic parenchyma may mimic a common duct stone. With high-resolution CT, most of these entities can be differentiated.

Intrahepatic Calculi. Intrahepatic biliary calculi are rare in Western countries. They typically occur in the setting of an underlying biliary abnormality such as congenital duct dilatation strictures, cholangitis, or previous biliary surgery.[147] They do occur in patients with biliary atresia status post portoenterostomy and in cystic fibrosis.[68] The density of the stones on CT depends on the amount of calcium within the stone. CT, however, demonstrates the location of intrahepatic stones well and, unlike ultrasonography, is not inhibited by pneumobilia in visualizing these stones. (See section on recurrent pyogenic cholangitis).

Neoplasms of the Biliary Tree

Bile duct carcinoma or CCA is a rare malignancy comprising 0.5% to 1.0% of all malignancies.[164] It is much less common than the other hepatobiliary tumors, and much less common than hepatocellular or gallbladder carcinomas. The vast majority of bile duct malignancies are adenocarcinomas, but squamous carcinoma, carcinoid, leiomyosarcoma, and rhabdomyosarcoma of the bile ducts have been reported.[76, 147, 224, 230] The peak age at onset for adenocarcinoma is usually in the sixth to seventh decade, although patients with predisposing inflammatory bowel disease or PSC may present earlier.[140] There is a slight male predominance (1.5:1.0), but this is not as great as with hepatocellular carcinoma.

The clinical presentation depends on where in the biliary tree the tumor arises. If the tumor arises intrahepatically, it usually presents late with abdominal pain. However, if the tumor arises in the hilum or the extrahepatic bile duct, presentation is usually earlier with painless jaundice.

There are a number of predisposing conditions for CCA, including inflammatory bowel disease (ulcerative colitis

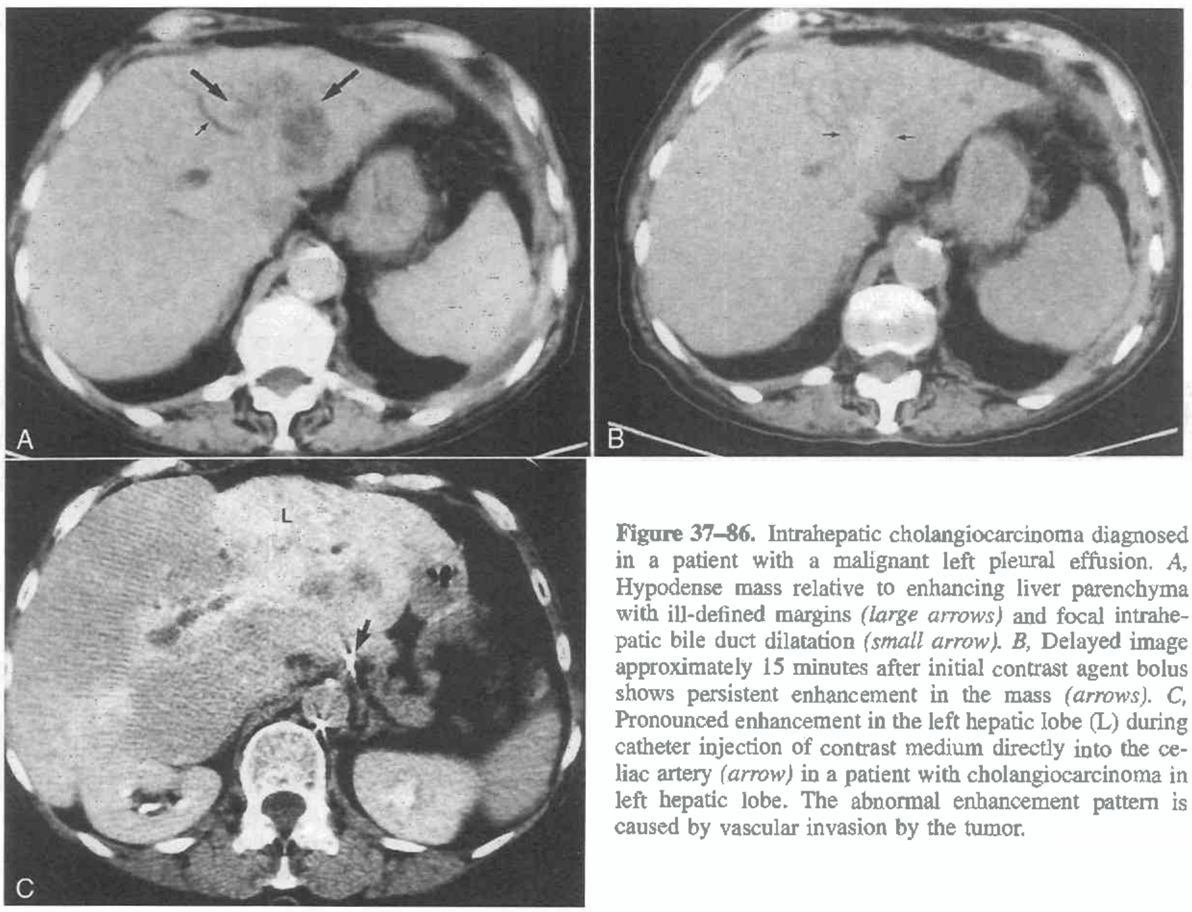

Figure 37–86. Intrahepatic cholangiocarcinoma diagnosed in a patient with a malignant left pleural effusion. *A*, Hypodense mass relative to enhancing liver parenchyma with ill-defined margins *(large arrows)* and focal intrahepatic bile duct dilatation *(small arrow)*. *B*, Delayed image approximately 15 minutes after initial contrast agent bolus shows persistent enhancement in the mass *(arrows)*. *C*, Pronounced enhancement in the left hepatic lobe (L) during catheter injection of contrast medium directly into the celiac artery *(arrow)* in a patient with cholangiocarcinoma in left hepatic lobe. The abnormal enhancement pattern is caused by vascular invasion by the tumor.

and Crohn's disease), sclerosing cholangitis, *Clonorchis sinensis* infestation, biliary-enteric anastomosis, biliary tract stones and gallstones, Thoratrast exposure, choledochal cyst, Caroli's disease, congenital hepatic fibrosis, and pancreaticocholedochal junction anomalies.[43, 45, 65, 139, 147, 230] A case of CCA arising in a patient with cystic fibrosis has been reported.[1] Chronic inflammation of the bile ducts seems to be a common element leading to CCA. Sclerosing cholangitis with chronic biliary inflammation and fibrosis is most likely the underlying cause of an increased risk of CCA in patients with ulcerative colitis and Crohn's disease. Chronic inflammation is also probably the underlying cause of predisposition to CCA with chronic *Clonorchis* (liver fluke) infestation, stone disease, choledochal cyst, and biliary-enteric anastomoses.[43, 45, 99, 155]

If CCA arises peripherally in the liver parenchyma from small IHBDs, it usually presents as a well-defined mass (Figs. 37–86 and 37–87; see also Fig. 37–93). Rarely, a diffusely infiltrating or sclerosing type can occur.[165] The mass is usually heterogeneous but hypodense relative to the liver on unenhanced scans. High-attenuation areas in the mass may be seen because of the presence of mucinous material.[47] These tumors can produce mucin, which may accumulate in adjacent bile ducts and, if dense, may mimic stones. Low-attenuation areas in the mass may be due to mucin or necrosis.[109] With intravenous contrast, heterogeneous enhancement is seen, often peripherally. The differential diagnostic considerations of such a mass would include hepatocellular carcinoma, biliary cystadenoma or cystadenocarcinoma, and metastases. Hepatocellular carcinoma is much more common than CCA and typically arises in cirrhotic livers. The serum α-fetoprotein is usually not elevated in CCA, but the bilirubin may be higher than typically seen with hepatocellular carcinoma.[147] In addition, if intrahepatic biliary dilatation is associated with the mass, then CCA should be suspected over hepatocellular carcinoma. Biliary cystadenoma and cystadenocarcinoma may mimic this form of CCA, but they are usually more cystic than is CCA. Finally, metastases may have a similar appearance to this form of CCA and are far more common (Fig. 37–88). Percutaneous needle biopsy is usually the only definite way to differentiate these lesions.

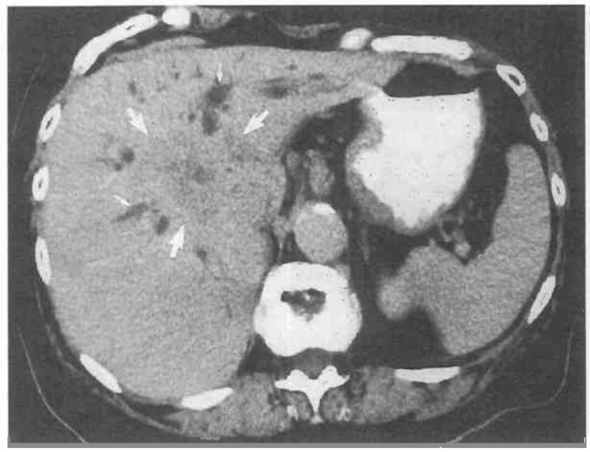

Figure 37–88. Ill-defined mass in hilum of liver *(large white arrows)* causing biliary dilatation *(small white arrows)*. The mass proved to be metastatic adenocarcinoma but mimicked cholangiocarcinoma.

CCA arising from the EHBDs is the most common form of this tumor. Grossly, the extrahepatic type of tumor is typically sclerosing and infiltrative, although it may be exophytic with an associated mass or polypoid with an intraluminal mass. The most common extrahepatic site is the confluence of the right and left hepatic ducts with the CHD. Such hilar CCA comprise up to 85% of extrahepatic CCA, depending on the series.[12, 13, 230] A distinct pathologic variant of CCA found at the hilum is the so-called Klatskin tumor which spreads along the ducts with extensive fibrosis.[65] These infiltrating tumors are often difficult to visualize directly on CT scans because there may only be focal thickening of the duct wall and little associated mass (Fig. 37–89). A reported sensitivity of CT for such a hilar CCA has been reported in the range of only 40%.[46, 240] The typical finding on CT is dilatation of the IHBDs in both the right and left lobes with nonunion of the dilated ducts at the hilum. Occasionally, a mass may be detected at the hilum, and it is typically hypodense relative to adjacent

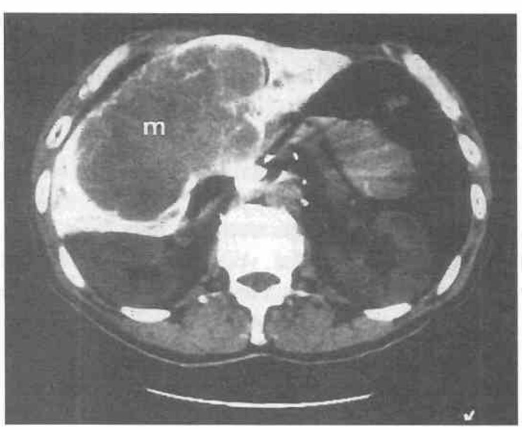

Figure 37–87. Mass (m) arising in liver with pathology revealing a mixed tumor containing cholangiocarcinoma and hepatoma. Note the density of the liver is increased because of previous Thoratrast administration.

Figure 37–89. Subtle infiltrative type of hilar cholangiocarcinoma presents as only mild thickening of the walls of the right and left hepatic ducts *(arrows)*. Note dilated intrahepatic ducts.

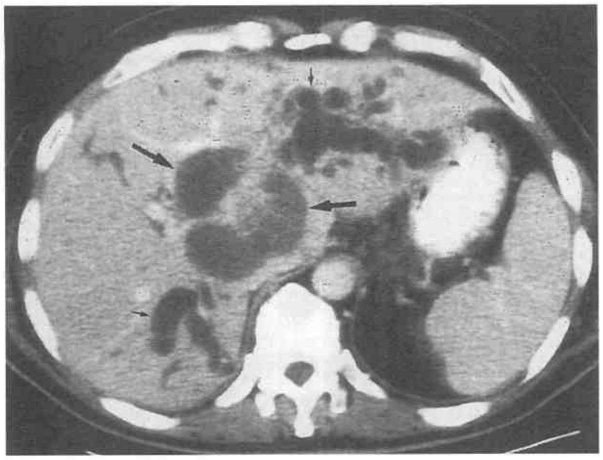

Figure 37–90. Hilar cholangiocarcinoma *(large arrows)* presenting as a hypodense mass expanding out into the hepatic parenchyma. Because of the location of the tumor, intrahepatic biliary dilatation in both lobes of the liver occurs *(small arrows)*.

liver parenchyma on enhanced scans (Fig. 37–90). Yamashita, however, reported a hypervascular densely enhancing exophytic-type mass as one appearance of hilar CCA.[240] The density of the hypodense masses may increase relative to liver parenchyma on delayed scans (8 to 15 minutes post injection) (see Fig. 37–86).[214]

CCA can arise elsewhere in the remainder of the EHBDs. Typically, these tumors are of the infiltrating type, with little detectable mass (Fig. 37–91) Biliary dilatation down to the level of the tumor will be present, and the appearance may mimic a benign stricture or obstruction secondary to a cholesterol stone. Thin-section CT targeted to this area, however, may reveal wall thickening or a small intraluminal mass consistent with tumor (Fig. 37–92).[13, 199] CCA should be suspected if there is an abrupt end to the biliary dilatation without a visible mass, especially if it occurs between the hilum and the pancreatic head.[13]

Hilar CCA tends more to present early because of earlier biliary obstruction than does the peripheral intrahepatic form of CCA. However, Thorsen and associates reported that in 57% of their patients with hilar CCA the tumors were nonresectable at presentation because of local liver invasion.[224] Resectability depends on location of the tumor and local or distant metastasis. If there is extensive ductal involvement, liver or vascular invasion, or nodal involvement, resection is difficult. Generally, distal duct tumors tend to be more resectable than are proximal tumors. Proximal tumors invade locally with nodal metastases earlier than do distal tumors. Common sites for nodal metastases involve primarily the foramen of Winslow node, superior pancreaticoduodenal nodes, and posterior pancreaticoduodenal nodes (see Fig. 37–70*D*). Distant metastases to liver, lung, and bones may occur, but late in the disease. Portal vein invasion occurs less frequently with CCA than with hepatocellular carcinoma grossly (Fig. 37–93). However, microscopically, portal vein invasion is common (89% to 90%).[241] Enhancement of liver parenchyma peripheral to a CCA may be altered as a result of portal vein invasion. Increased enhancement of the liver parenchyma distal to the tumor on bolus-enhanced CT and decreased enhancement of the same area on CT arterioportography has been described in the setting of portal vein invasion. The same area may appear hyperintense on T2-weighted MRI.[111]

Lobar atrophy has been described with CCA, particularly hilar CCA (Fig. 37–94). The exact mechanism of lobar atrophy is not clear. One of the major causes is biliary obstruction, which secondarily leads to diversion of portal vein flow with resultant atrophy of the affected hepatic parenchyma.[38, 213] Some have argued that lobar atrophy is a sign of nonresectability because it implies portal vein invasion.[38, 230] However, others have demonstrated lobar atrophy with only biliary obstruction without venous involvement, and therefore these tumors are still resectable.[187] Lobar atrophy was once used as a sign of the presence of malignancy but also has been reported in benign biliary disease.

The staging of CCA is best performed by ultrasonography, CT, and cholangiography (PTC and ERCP) (Figs. 37–95 to 37–98). The overall accuracy of ultrasonography, CT, and cholangiography at staging CCA is reported at 70% to 90%.[85, 164] Cholangiography demonstrates the extent of bile duct involvement better than do ultrasonography and CT especially for infiltrative tumors, and it provides a route for biopsy. MRI is gaining in its use for staging because of its sensitivity for vascular invasion and invasion into the hepatoduodenal ligament. Itoh compared ultrasonography, CT, and MRI for staging hilar or proximal bile duct carcinoma and concluded that CT was the best overall examination for tumor depiction but that MRI was more useful for evaluating portal vein invasion.[112] Nesbit and associates reported a 78% accuracy by CT for determining unresectability of CCA but only a 44% accuracy in suggesting resectability. False negatives were caused by metastases to lymph nodes and liver or portal vein invasion detected at surgery that were not detected by CT examination. Normal-sized positive lymph nodes and small hepatic metastases (<1 to 2 cm) may not be detected on CT.[164] Tailoring of the CT examination with thin-collimation axial images, bolus administration of intravenous contrast me-

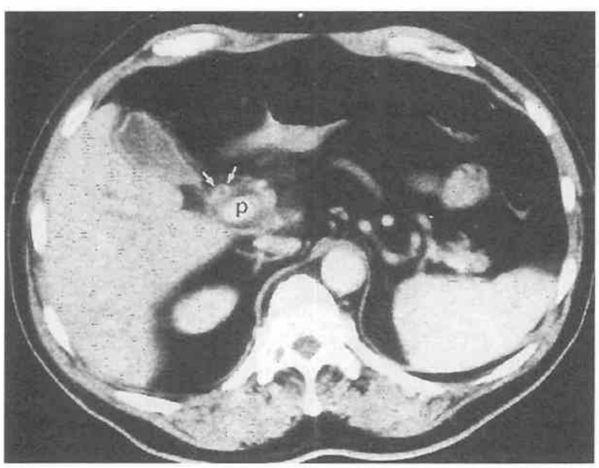

Figure 37–91. Infiltrative type of cholangiocarcinoma causing wall thickening of the common hepatic duct *(white arrows)*; p = portal vein.

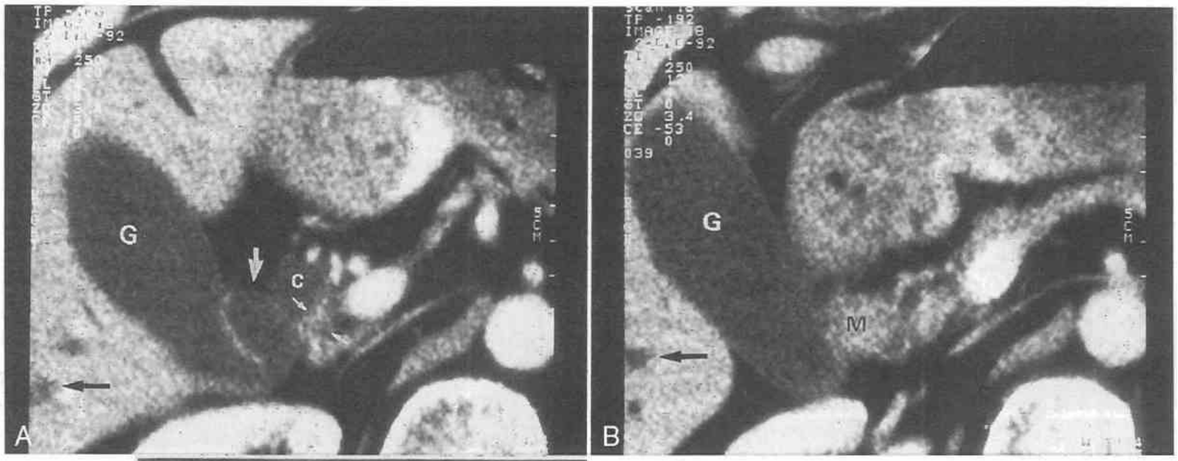

Figure 37–92. Cholangiocarcinoma in a patient with a history of prostate carcinoma and elevated liver function tests. *A,* High-resolution image showing a dilated common hepatic duct (c) with focal, eccentric thickening of the posterior wall *(small white arrows),* intrahepatic biliary dilatation *(black arrow);* gallbladder, neck of the gallbladder, and cystic duct *(large white arrow). B,* Image 6 mm caudad to *A* shows abrupt termination of the common duct with a small mass (M) at the level of termination; G = gallbladder, *black arrow* = intrahepatic biliary dilatation. *C,* ERCP showing dilatation of the intrahepatic bile ducts and the extrahepatic duct down to the level of a tight stricture *(white arrows),* which correlates with the level of the mass in *B.*

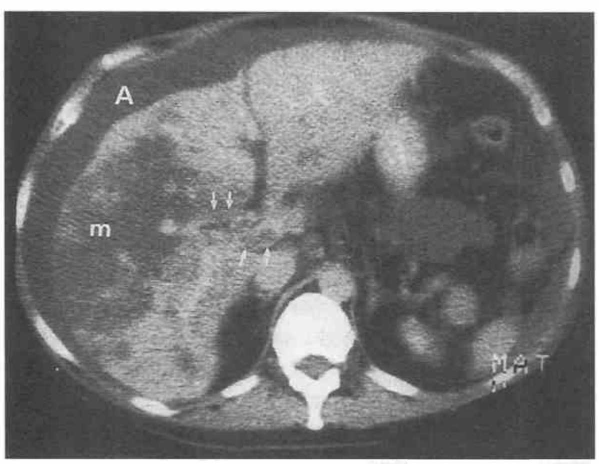

Figure 37–93. Multiple intrahepatic foci of cholangiocarcinoma (m) presenting as hypodense masses. Note thrombus in the main and right branch of the portal vein *(arrows).* A = ascites.

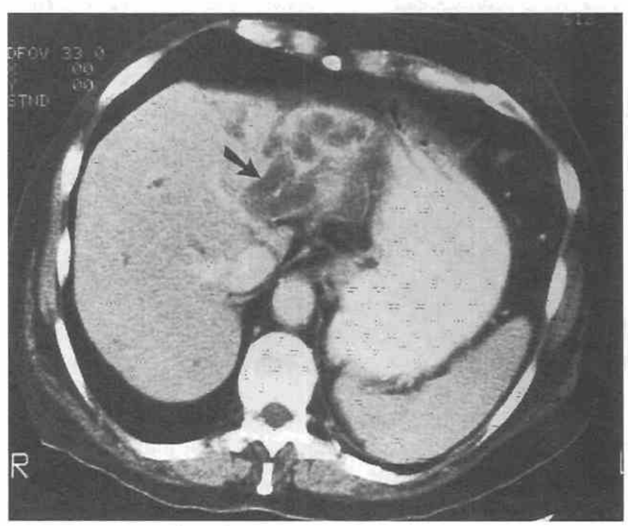

Figure 37–94. Biliary dilatation *(arrow)* and atrophy of the left hepatic lobe as a result of cholangiocarcinoma. (From Vazquez JL, Thorsen MK, Dodds WJ, et al: Atrophy of the left hepatic lobe caused by a cholangiocarcinoma. Am J Roentgenol 144: 542, 1985.)

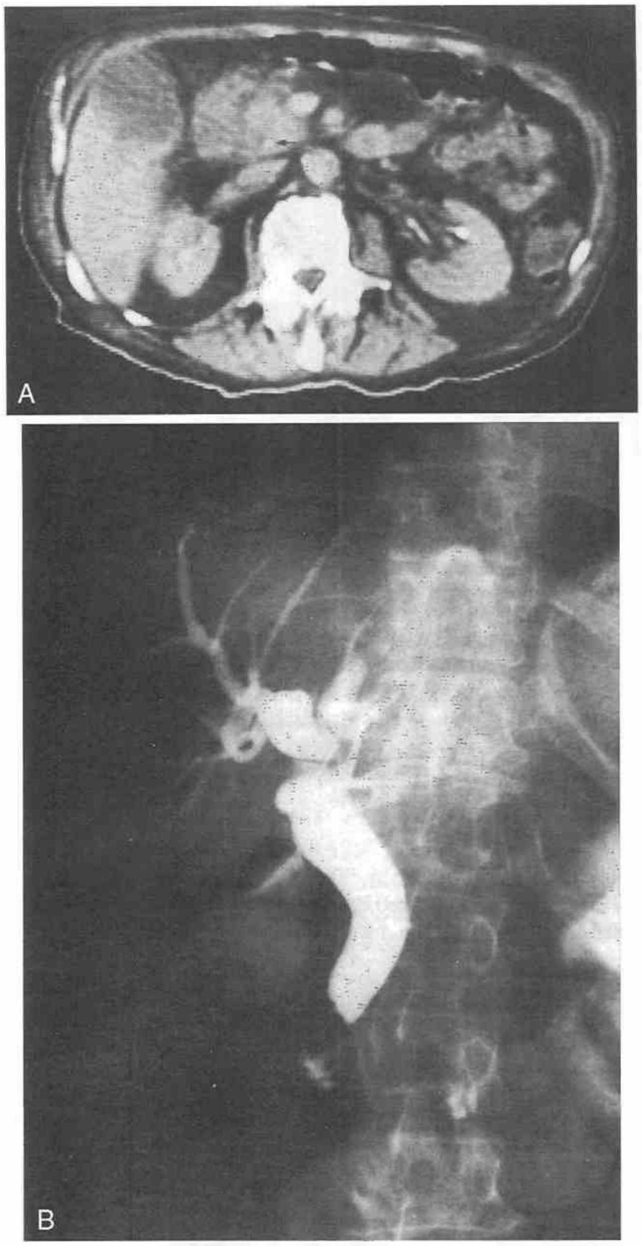

Figure 37–95. *A,* This scan shows a calcification *(arrow)* below the level of a dilated bile duct that was believed to be a calculus. Gallstones were present on another scan. *B,* The transhepatic cholangiogram shows a dilated common bile duct with narrowing distally, which is diagnostic of a malignancy.

dium, and a targeted small field of view will improve the ability to stage CCA.

Biliary Cystadenoma and Cystadenocarcinoma. The biliary cystadenoma and cystadenocarcinoma are rare neoplasms of the biliary tree. They typically arise from IHBDs but in rare cases are found in EHBDs. The vast majority arise in women and in patients older than 30 years of age. These lesions are usually large, well-defined, solitary masses that are multiloculated and hypodense relative to liver (Fig. 37–99).

Rarely, they may be multifocal.[44] There have been case

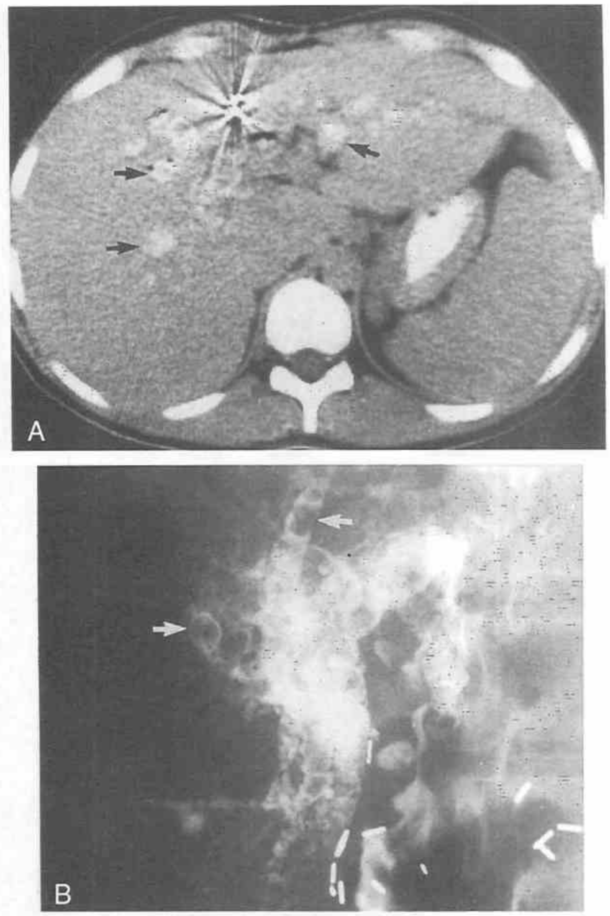

Figure 37–96. Patient with biliary atresia, cirrhosis, and portoenterostomy. *A,* Multiple intrahepatic calculi *(arrows)*. *B,* Cholangiogram revealing multiple filling defects consistent with stones *(arrows)*.

reports of unilocular lesions, but most have multiple septations. The septations in the benign cystadenoma are usually thin, whereas those seen in the cystadenocarcinoma are often thicker with nodularity or papillary projections. These septations typically enhance on CT. Often, these

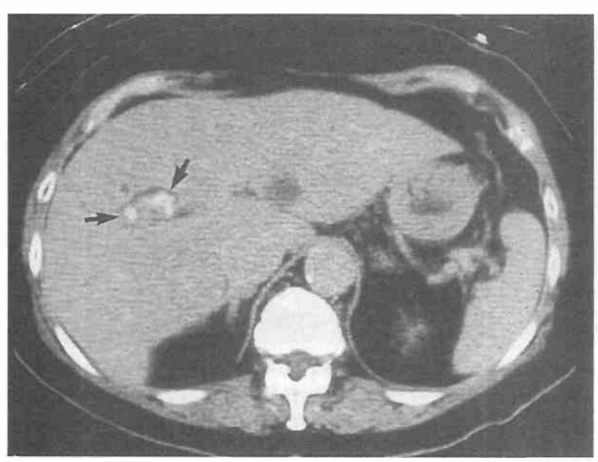

Figure 37–97. Intrahepatic biliary calculi *(arrows)* in patient with repeated episodes of cholangitis.

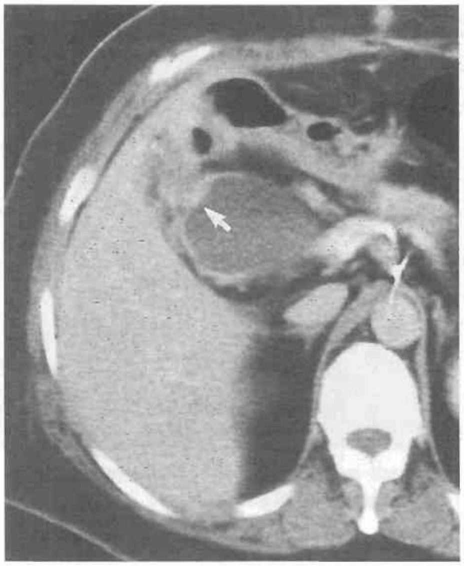

Figure 37–98. Cholangiocarcinoma arising in a choledochal cyst. The tumor presents as a focal thickening in the cyst wall *(arrow)*. (From Baron RL: Computed tomography of the biliary tree. Radiol Clin North Am 29:1235, 1991.)

lesions contain mucin and are low in density. However, the cystic spaces may vary in density because of the presence of serous fluid, pus, or high amounts of cholesterol.[82] They may communicate with the IHBDs and secrete mucinous material into the ducts. Calcifications may be present in the septations; when coarse and associated with nodular projections, they are more suggestive of cystadenocarcinoma.[128]

The differential diagnosis of these lesions would include a complex benign cyst, abscess, hematoma, echinoccocal cyst, mesenchymal hamartoma, undifferentiated embryonal sarcoma, and cystic metastases. Diagnosis has been performed with percutaneous biopsy.[42, 104] Resection of these lesions is usually complete and leads to cure.

Other Neoplasms of the Biliary Tract. Other benign neoplasms of the bile ducts are very rare. Papillomas, bile duct hamartomas, neurofibromas, and granular cell tumors have been reported (see Fig. 37–80).[65, 66, 147] These lesions may appear as intraluminal filling defects or may simply occur with ductal obstruction. Cholangiography is typically most helpful at evaluating such lesions.

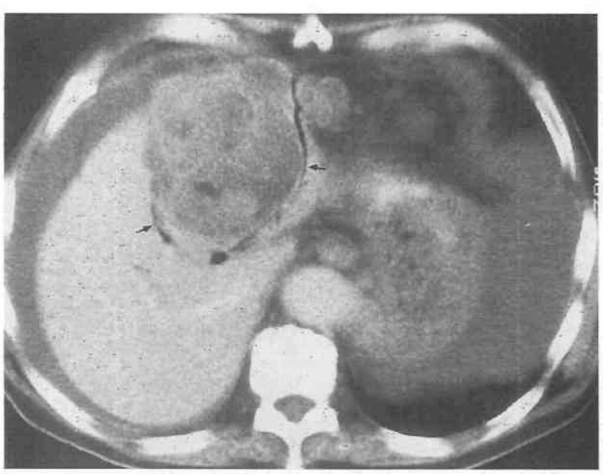

Figure 37–99. Papillary cystadenocarcinoma appears as a multiseptated mass with areas of high and low density. Pneumobilia around mass *(arrows)* is secondary to recent biliary intervention.

Lymphoma in the bile ducts has been described.[216] Typically, lymphomatous involvement of the biliary tract involves extrinsic compression by hepatoduodenal ligament and pancreaticoduodenal lymph nodes. Direct infiltration of the bile duct wall can occur, and it may cause biliary obstruction with a smooth structure. Only bile duct wall thickening may be seen without apparent mass on CT scan (Fig. 37–100).

Trauma to the Biliary Tree

Trauma to the gallbladder and biliary tree is uncommon and is almost always associated with hepatic injury.[81, 206] Because of the location of the gallbladder, it is protected from injury to some degree by ribs and the liver. With blunt trauma, however, perforation, avulsion, or contusion of the gallbladder can occur in rare cases.

Perforation or laceration of the gallbladder is the most common type of injury and can result in bile leakage. Unfortunately, such leakage may not be detected for days to weeks.[10, 56] On CT, ascites or a localized fluid collection around the gallbladder may be seen. The diagnosis can be made more accurately with aspiration of the fluid or a DISIDA scan.

A contusion of the gallbladder may simply appear as gallbladder wall thickening on CT, a nonspecific finding. Avulsion of the gallbladder is usually associated with bile ascites or hemoperitoneum on CT.[116] Both conditions are difficult radiologic diagnoses.

Trauma to the bile ducts is usually associated with a hepatic injury. Bilomas may occur, particularly with perihilar hepatic injuries.[150] Such bilomas may develop slowly over several days to weeks and may be asymptomatic. On CT, these bilomas will be focal collections of water density and may mimic abscesses or old hematomas. The diagnosis, however, can be made with DISIDA scans, aspiration, or cholangiography.

Hemobilia is a rare occurrence with hepatobiliary trauma but can result in increased density in the gallbladder or biliary tree on CT scan (Fig. 37–101). The differential diagnostic considerations for hemobilia include vicarious excretion of intravascular contrast agent, milk of calcium bile, or multiple small stones (see Figs. 37–4, 37–5, 37–8, 37–9, and 37–25).

Bilomas

Bilomas are focal collections of bile that may occur in a variety of locations such as intrahepatic, subcapsular, in the porta hepatis, and subhepatic (Fig. 37–102). Typically, they appear on CT as near water-density collections, although if infected or associated with hemorrhage, the density may be higher. Most bilomas occur after surgery, such as cholecystectomy or liver transplantation. However, they

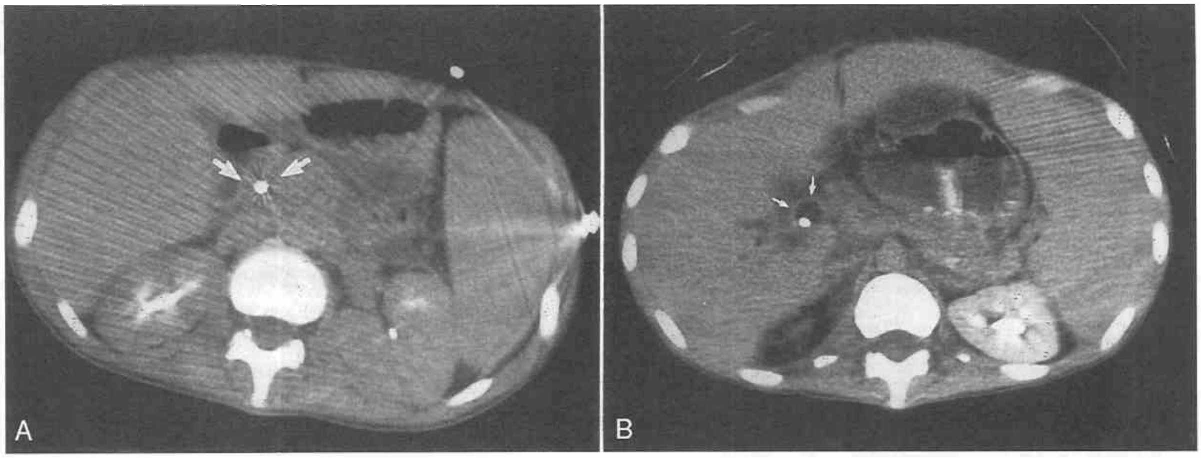

Figure 37–100. Lymphoma involving wall of distal common bile duct. *A,* Pretreatment examination shows thickened tissue *(arrows)* around biliary stent. *B,* Post-treatment examination shows residual thickening of duct wall *(arrows).*

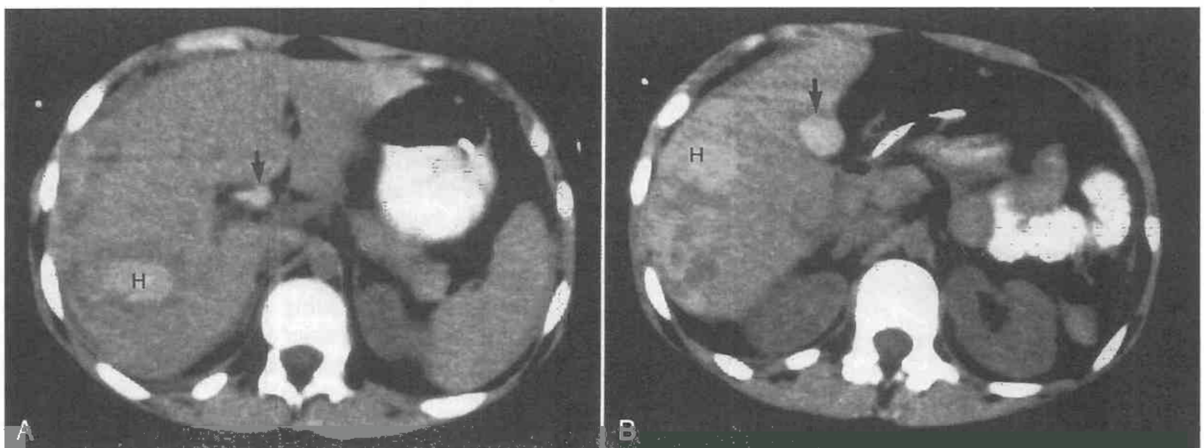

Figure 37–101. Hemobilia secondary to liver trauma. *A,* Hyperdense blood in central bile ducts *(arrow). B,* Hyperdense blood in gallbladder *(arrow).* H = liver hematoma.

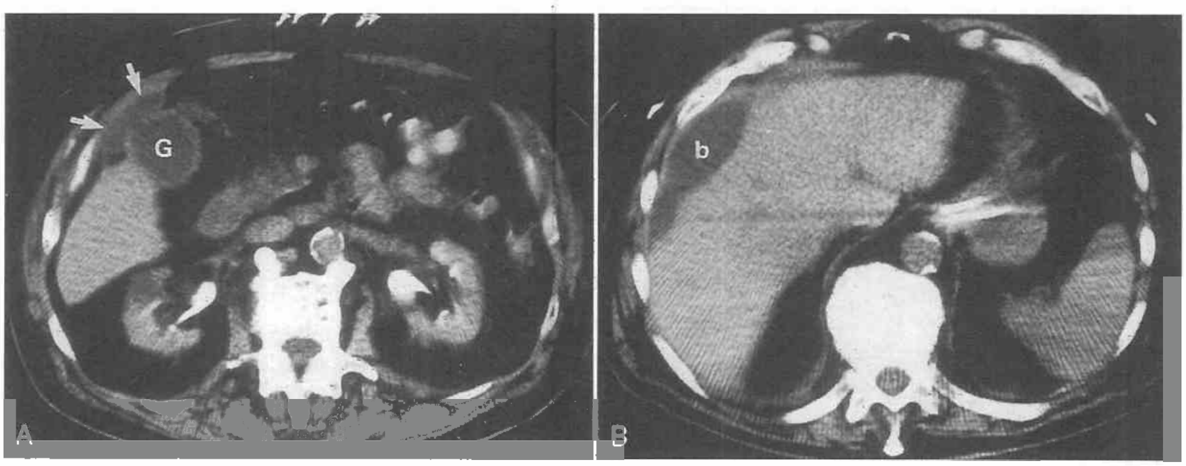

Figure 37–102. Biloma secondary to gallbladder perforation. *A,* Gallbladder (G) with adjacent biloma *(arrows). B,* Biloma (b) tracking superiorly along the right side of the liver.

can occur as a result of trauma particularly with blunt trauma to the gallbladder or with a penetrating laceration of the liver.[81, 150] They may also occur iatrogenically after a liver biopsy. Bilomas may rarely occur after gallbladder perforation owing to severe acute cholecystitis; however, most pericholecystic fluid collections associated with acute cholecystitis are abscesses. Rare reports of spontaneous perforation of the CBD described bile leakage with biloma formation occurring spontaneously, particularly in children. The cause is not known but may be related to occult distal biliary obstruction or congenital weakness in the duct wall near the cystic duct and CBD junction.[95]

CT cannot definitively diagnose a biloma, because it appears like other fluid collections. DISIDA scans or cholangiography better define leaks and bilomas. However, CT can be used to percutaneously aspirate or drain such collections.

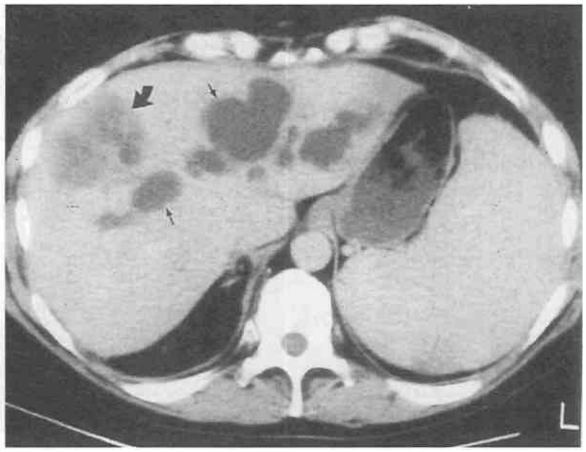

Figure 37–103. Liver transplant with hepatic arterial occlusion and resultant hepatic infarct *(large arrow)* and bile duct necrosis with formation of bilomas *(small arrows)*.

Biliary Complications in Liver Transplants

Biliary complications after liver transplantation are the second most common cause of hepatic dysfunction after rejection and may occur in up to 20% of patients.[167, 246–248] Biliary obstruction and bile leak are the two major categories of post-transplant biliary complications. Although cholangiography is the gold standard method for evaluating biliary complications, the clinical presentation of such problems is often nonspecific, and CT scans are initially obtained as general surveys of the abdomen. Therefore, recognition of the CT appearance of these biliary complications can aid in directing the work-up and therapy.

Bile leaks typically occur at the duct anastomosis. The preferred type of anastomosis is the duct-duct or choledochocholedochostomy, which preserves the recipient ampulla of Vater. If the recipient duct is diseased, as for example in recurrent cholangitis, then a biliary-enteric anastomosis or choledochojejunostomy is performed. In the latter case, a Roux loop of bowel is brought up into the porta hepatis and connected to the donor CBD. The Roux loop itself may be fluid-filled and mimic a fluid collection such as a biloma in the porta hepatis.[91] Bile leaks will appear as focal fluid collections in the porta hepatis, or if nonfocal they may appear as ascites. Unfortunately, CT cannot differentiate bile from other fluid such as lymph, blood, or pus. A DISIDA scan or cholangiogram will be required to more definitively diagnose a bile leak. CT, however, can be used to percutaneously aspirate or drain such collections.

Bile leaks with associated bilomas can occur away from the anastomosis and should be recognized as a sign of a hepatic arterial complication, particularly thrombosis.[245] In liver allografts, the biliary tree is highly dependent on the hepatic artery for its blood supply. Hepatic arterial occlusion results in bile duct necrosis with bile leak and biloma formation. Bilomas in the liver appear as focal fluid collections along the biliary tree (Fig. 37–103). They may or may not become infected. Hepatic infarcts may also be seen presenting as hypodense areas of liver parenchyma.

Biliary obstruction can occur because of strictures, occluded or trapped internal stent, T-tube dysfunction, common duct redundancy, stones, or mucocele of the cystic duct.[167] A stricture at the biliary anastomosis is the most common cause of obstruction. Cholangiography is the best method for evaluating post-transplant biliary obstruction and can provide subsequent therapy via stenting or balloon dilatation. The hallmark of biliary obstruction on CT or ultrasonography is duct dilatation. However, in liver allografts, dilatation may not be present at the time that biliary obstruction is clinically suspected, and biliary obstruction may not be diagnosed by CT or ultrasonography.[246] Cholangiography would be required in such cases. Obstructing stones or sludge may be recognized on CT as increased density in the bile ducts. In addition, a mucocele of the cystic duct remnant has been reported as a small round collection in the porta hepatis on CT.[248] On cholangiography, it can be seen to compress the EHBD and cause obstruction. The differential diagnosis of such a small collection should include a seroma, abscess, pseudoaneurysm of the hepatic artery, hematoma, biloma, or Roux limb of the biliary-enteric anastomosis.

Diffuse dilatation of the EHBD after liver transplantation has been reported and may be seen with or without obstruction. This generalized dilatation of only the EHBD can occur gradually and may be caused by sphincter of Oddi dysfunction or denervation and devascularization of the duct during surgery.[37, 149, 167, 247] Clinically, the patient may present with signs of biliary obstruction, or the dilatation may simply occur with no apparent obstruction to bile flow. If the degree of dilatation is significant, some element of obstruction should be suspected and further investigation with a DISIDA scan or cholangiography should be performed.

MRI of the Biliary Tract

Only a brief overview of MRI of the biliary tract will be provided here because currently it is not one of the primary imaging modalities of the biliary tract. Cholangiography, ultrasonography, and CT are more useful in evaluating the biliary tract. However, familiarity with the MR

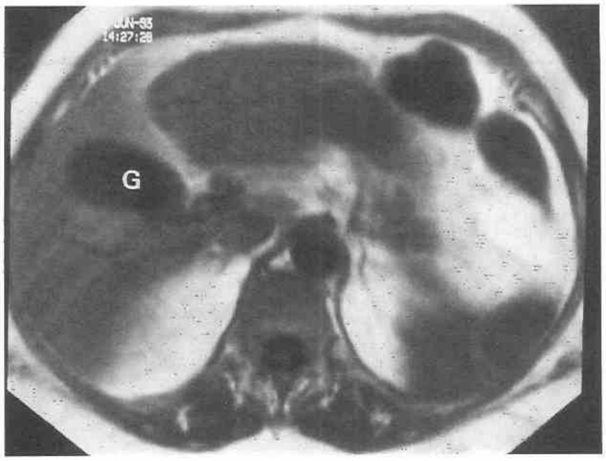

Figure 37–104. Normal appearance of gallbladder on short TR (T1-weighted) image. Note hypointense signal of gallbladder (G). TR = 700; TE = 10.

appearance of the biliary tract and biliary diseases is essential when interpreting MRI examinations of the upper abdomen.

Bile has varying signal on MRI, depending on the fasting state of the individual, the pulse sequence used, and the presence of pathology.[62, 103, 123, 124] In a fasting individual, bile is concentrated with little water content and increased concentrations of bile acids, cholesterol, and phospholipids. The T1 value of concentrated bile is shortened and on short TR/TE images (T1-weighted images) it can appear hyperintense compared with other body fluids such as cerebrospinal fluid.[103, 123] On long TR/TE images (T2-weighted images), concentrated bile will still have high signal comparable to cerebrospinal fluid. In the nonfasting individual with rapid release of bile, concentration does not occur and the water content remains relatively high. Such bile behaves similar to other fluid such as cerebrospinal fluid with hypointensity on T1-weighted images and hyperintensity on T2-weighted images (Fig. 37–104). Layering of various concentrations of bile can occur in the gallbladder. Because of a higher specific gravity, the more concentrated bile will layer dependently (Fig. 37–105).

Lack of concentrating ability of the gallbladder in fasting patients has been reported with acute cholecystitis.[144] Such patients demonstrate low signal intensity while on T1-weighted images rather than the high signal of concentrated bile. This finding in a fasting patient is suggestive of a concentrating problem in the gallbladder, as can be seen in acute cholecystitis. Unfortunately it is not a consistent finding in all cases of acute cholecystitis.[124, 144, 236] In chronic cholecystitis, the concentrating function of the gallbladder is typically preserved so that the signal of bile is as expected in fasting and nonfasting patients.[124] Therefore, the signal characteristics of the gallbladder bile alone are not diagnostic for cholecystitis on MRI but must be used in conjunction with other signs such as gallbladder wall thickening, gallstones, and pericholecystic fluid.

Gallstones typically have no signal on MRI because of their solid nature, with little free water, rather than their chemical composition (Figs. 37–106 and 37–107).[18, 156] There may, however, be retraction clefts centrally in the stone that contain fluid and appear hyperintense on T2-weighted images.[94] An atypical appearance of gallstones on MRI was reported where the stones demonstrated high signal on T1-weighted images because of high fatty acid content.[154]

Carcinoma of the gallbladder has been described as a mass in the gallbladder fossa with hypointensity on T1-weighted images and hyperintensity on T2-weighted images relative to liver.[191, 194, 238] Low signal gallstones may be seen within the gallbladder or engulfed within the mass. MRI is helpful in evaluating spread of tumor into the liver with hyperintensity of the tumor relative to liver parenchyma on T2-weighted images. In addition, MRI is reported to be more accurate than CT or ultrasonography for invasion of the hepatoduodenal ligament or spread to pancreaticoduodenal lymph nodes.[194] MRI performs as well as CT for direct spread to the liver and for hepatic metastases. The ability of MRI to detect small gallbladder tumors is not yet evident.

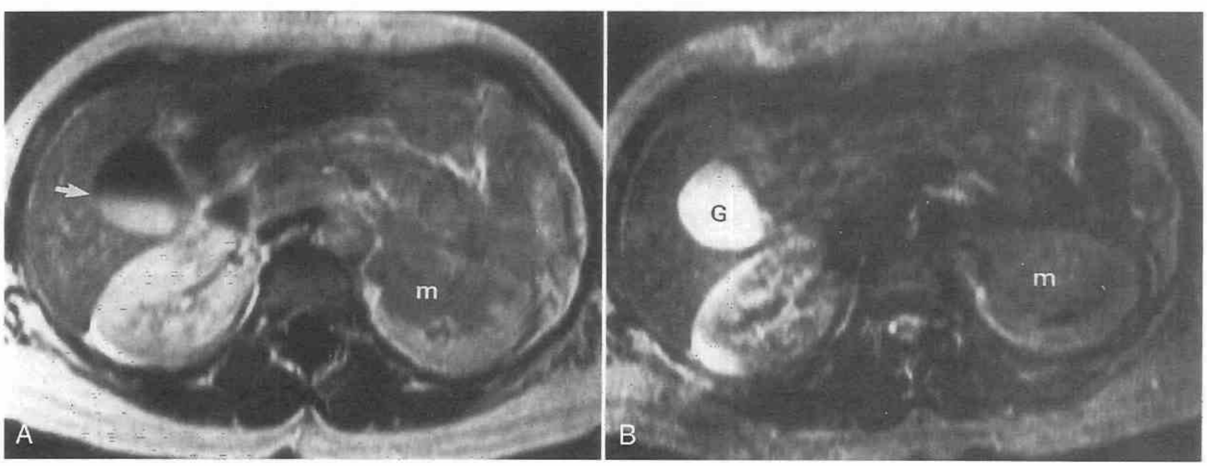

Figure 37–105. Layering bile in gallbladder. Note patient also has left renal neoplasm (m). *A*, T1-weighted image showing concentrated bile (hyperintense) layering dependently beneath the less concentrated bile (hypointense) in the gallbladder *(white arrow)*. TR = 700; TE = 10. *B*, T2-weighted image showing all bile in gallbladder (G) turned hyperintense. TR = 2000; TE = 80.

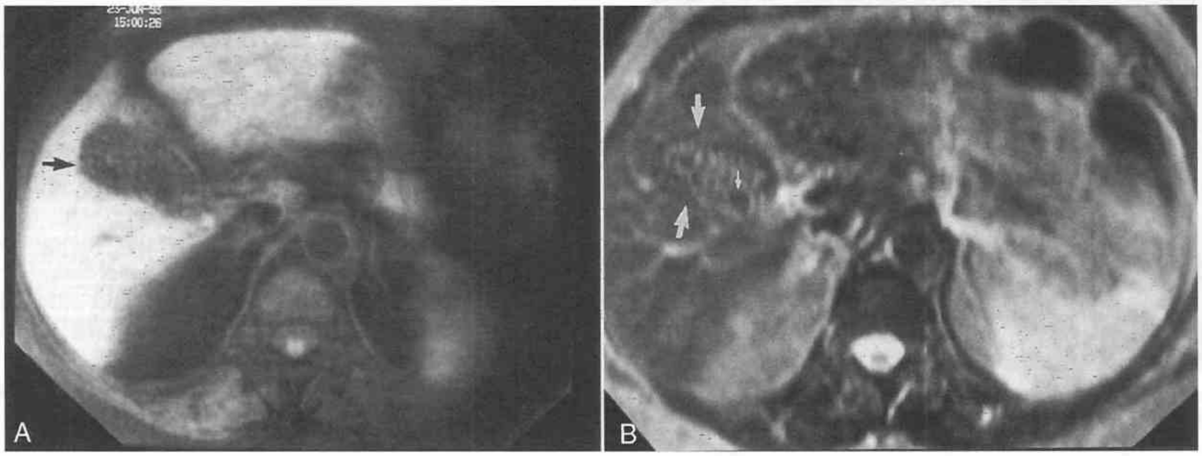

Figure 37–106. Gallstones. *A,* Fat-suppression T1-weighted image showing gallbladder *(arrow)* with multiple tiny stones presenting as signal voids. *B,* T2-weighted image of same patient showing gallbladder *(large arrows)* and gallstones *(small arrow).*

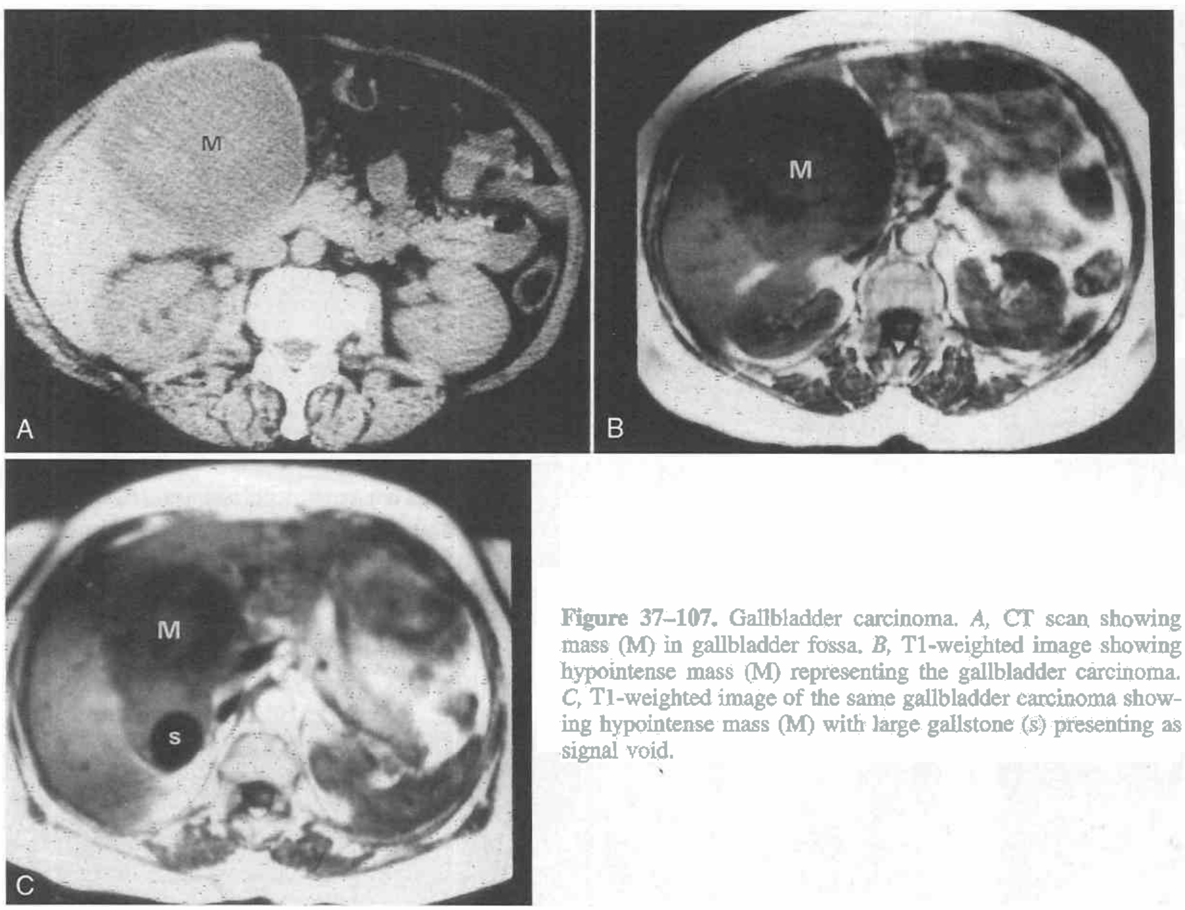

Figure 37–107. Gallbladder carcinoma. *A,* CT scan showing mass (M) in gallbladder fossa. *B,* T1-weighted image showing hypointense mass (M) representing the gallbladder carcinoma. *C,* T1-weighted image of the same gallbladder carcinoma showing hypointense mass (M) with large gallstone (s) presenting as signal void.

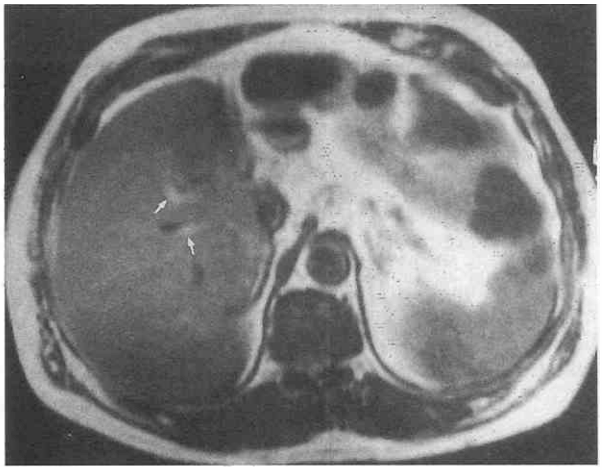

Figure 37–108. T1-weighted image of subtle intrahepatic biliary dilatation *(arrows)*. The dilated ducts are hyperintense because of the concentration of the bile. Adjacent vessels have relatively low signal. TR = 500; TE = 20.

Visualization of the IHBDs on MRI depends on the size of the ducts, concentration of the bile, pulse sequences used, motion artifact, and periportal high signal. Rapid pulse sequences, as in single breath-hold techniques, reduce respiratory and motion artifact and aid in evaluating the IHBDs, which are normally not visible. In our experience, T1- and T2-weighted sequences with fat suppression techniques are required for visualizing the IHBDs especially if they are only mildly dilated. Detecting mildly dilated IHBDs may still be difficult even with optimum imaging because the signal characteristics of bile will vary, depending on its concentration (Fig. 37–108). Signal contrast between the bile ducts and the liver therefore may be low, depending on the bile concentration. CT and ultrasonography are more sensitive for evaluating mild IHBD dilatation than is MRI.[61, 94]

The EHBD can be visualized with varying normal diameters being reported (Fig. 37–109). The upper limit of normal size of the EHBD on T1-weighted images is 10 mm, and on T2-weighted images it is 11.8 mm.[211] The distal CBD appears as a relatively hypointense round structure in the posterolateral portion of the pancreatic head on

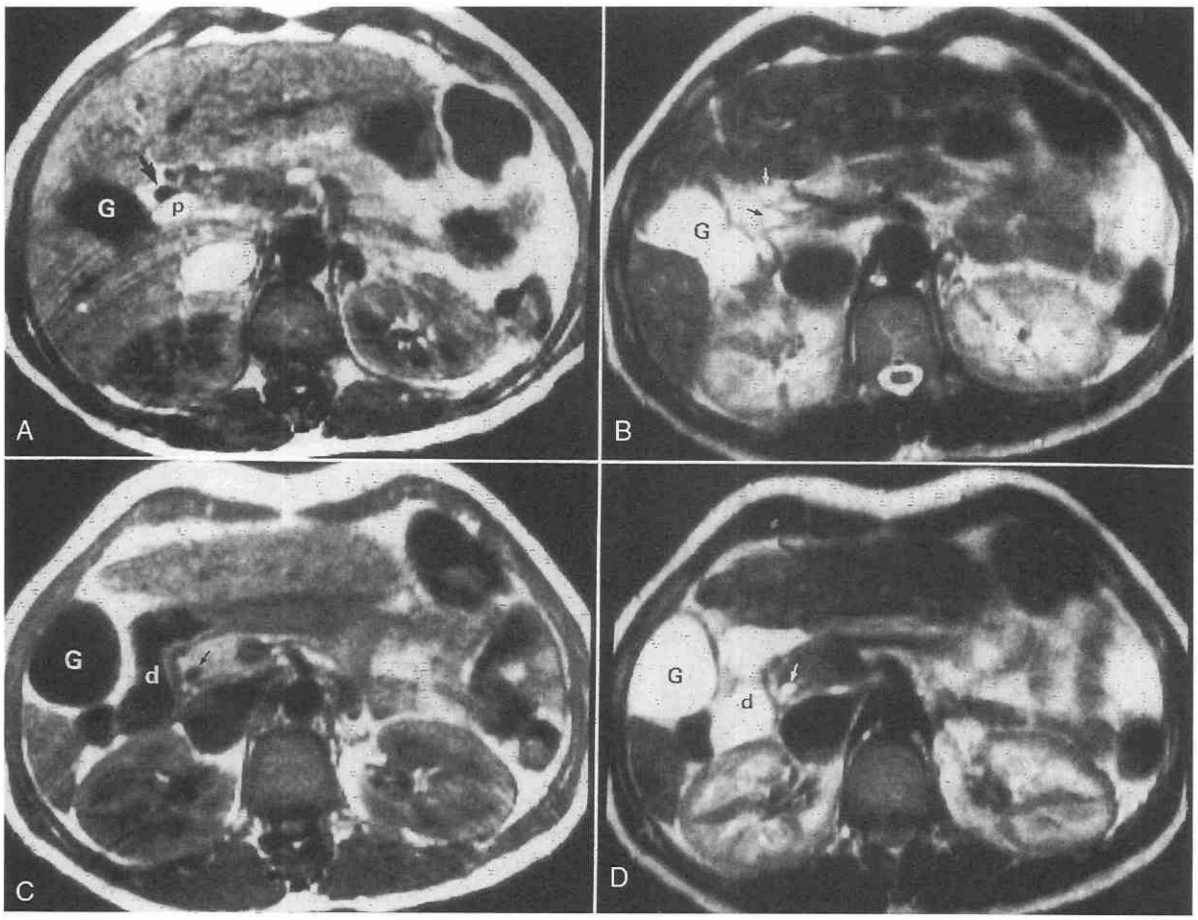

Figure 37–109. Normal extrahepatic bile duct. *A,* Common hepatic duct *(arrow)* is hypointense on the T1-weighted image. Gallbladder (G); portal vein (p). TR = 578; TE = 15. *B,* T2-weighted image at level comparable to *A*. Common hepatic duct *(white arrow)* is now hyperintense. Gallbladder (G); portal vein *(black arrow)*. TR = 1995; TE = 90. *C,* T1-weighted image of distal common bile duct *(arrow)* in pancreatic head also shows gallbladder (G) and duodenum (d). TR = 578; TE = 15. *D,* T2-weighted image at comparable level to *C*. Note distal common bile duct *(arrow)* now turns hyperintense. G = gallbladder; d = duodenum; TR = 1995; TE = 90.

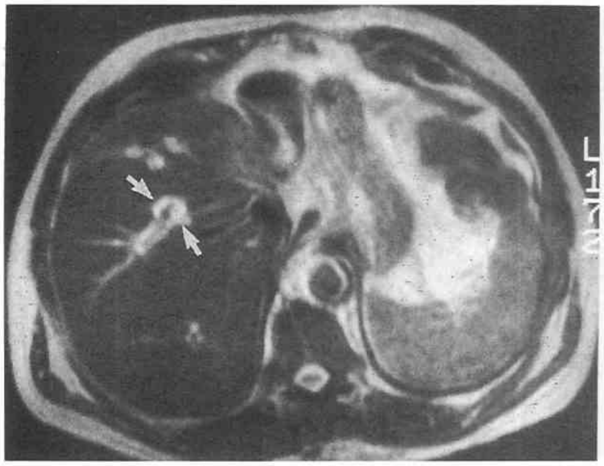

Figure 37–110. Periportal high-signal intensity *(arrows)* seen around low-signal vessel centrally, in patient with liver disease. TR = 2000; TE = 80.

T1-weighted images and is relatively hyperintense on T2-weighted images.

The characteristics of several types of bile duet pathology on MRI have been described. The appearance of a choledochal cyst has been reported as a mass near the porta hepatis with a long T1 and T2 signal with associated biliary dilatation.[3, 26] CCA has two basic appearances on MRI. Peripheral CCA often appears as a focal well-defined mass with homogeneous relatively high signal as compared with the liver on T2-weighted images. There may be a central scar and satellite nodules.[70, 96] The detection rate of such tumors has been reported to be 78% to 100%.[215] This appearance, however, is not diagnostic for CCA, and other liver lesions such as hepatomas may have a similar appearance.[70, 193] The second type of CCA is the more infiltrative and scirrhous type that may have relatively low signal on all sequences because of high fibrous tissue content.[62] Biliary dilatation that abruptly terminates is an important sign for malignancy as on CT, ultrasonography, and cholangiography. MRI is not as sensitive as CT for showing subtle duct wall thickening associated with CCA because of the lower spatial resolution and more artifacts. MRI, however, can demonstrate the hepatic lobar or segmental tumor location and detect intrahepatic metastases well. In addition, MRI may be quite useful at determining resectability.[112, 201] It can demonstrate vascular invasion by showing loss of normal vascular flow void, tumor enhancement within the vessel, or abnormal signal in the liver parenchyma affected by the vascular invasion or occlusion.[111]

Abnormal signal can be seen surrounding intrahepatic vascular structures and has been described by Matsui as periportal abnormal intensity.[142] Periportal abnormal intensity is a nonspecific finding seen in diseases affecting the biliary tract, such as cholangitis, CCA, obstructive jaundice of any cause, and lymphedema secondary to malignant portal lymph nodes. Matsui reported that periportal abnormal intensity was not seen in cases of choledocholithiasis, pancreatic disease, or nonobstructive biliary dilatation.[142] However, similar abnormal signal can be found in a variety of conditions including trauma, congestive heart failure, and rejection in liver allografts, and it has been described on CT as periportal lymphedema.[7, 125, 129, 141, 233] Matsui reported that the periportal abnormal intensity represents edema, ductal proliferation, dilated lymphatics, and inflammatory infiltrates in periportal tissues.[142] Typically, the periportal abnormal intensity is low signal on T1-weighted images and relatively high signal on T2-weighted images. It differs from biliary dilatation in that periportal abnormal intensity completely surrounds the portal vein, whereas dilated bile ducts are found on only one side of the vessel (Fig. 37–110).

Recently literature has been published concerning three-dimensional MR cholangiography. The technique employs two- and three-dimensional fast scanning sequences with multiplanar reconstruction so that the biliary tree can be visualized in three-dimensional projections (Figs. 37–111 and 37–112).[158] Such techniques will provide similar information as direct cholangiography, without the risks of an invasive procedure such as ERCP or PTC.

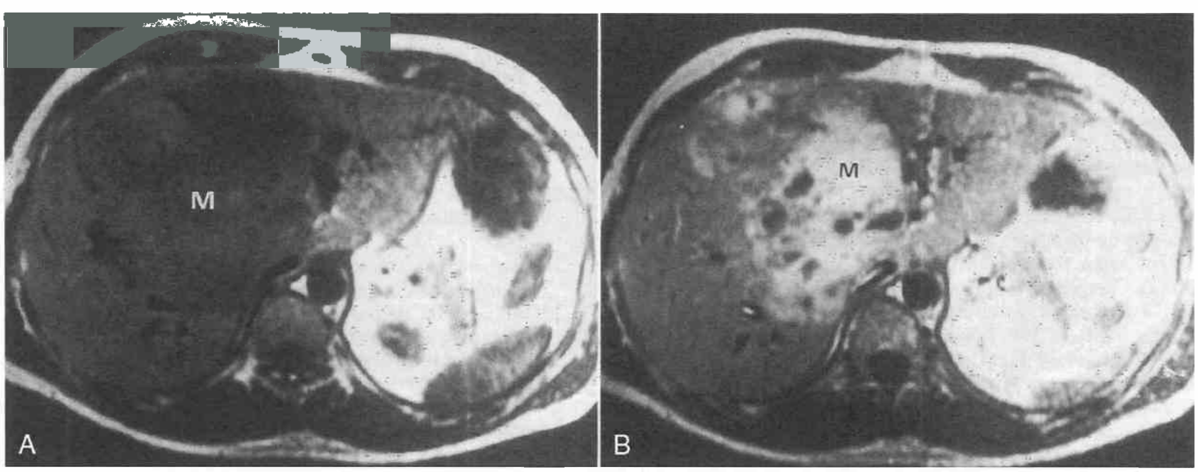

Figure 37–111. Gallbladder carcinoma invading liver. *A*, Invasion into liver appears as hypointense mass (M) on T1-weighted image. TR = 500; TE = 15. *B*, Tumor invasion into liver (M) becomes hyperintense on T2-weighted image. TR = 2357, TE = 80.

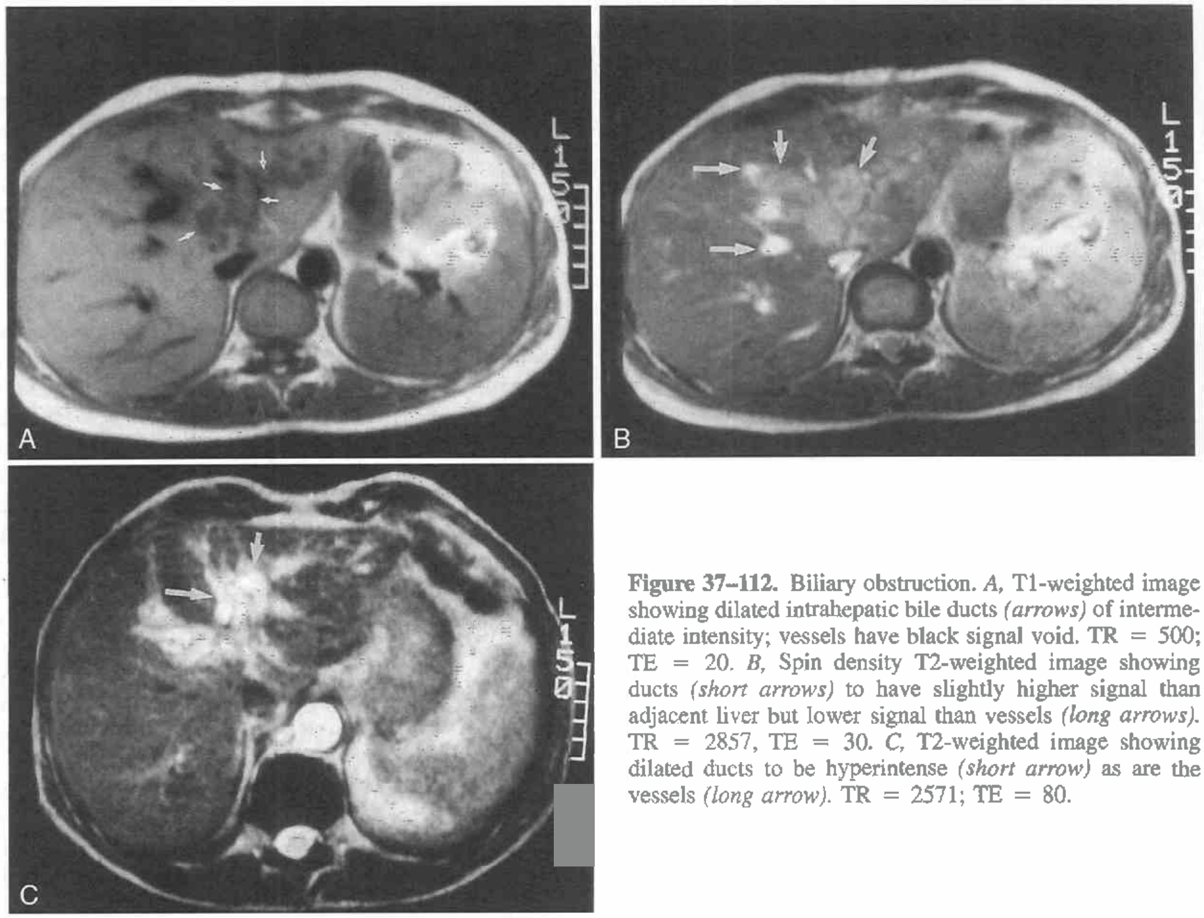

Figure 37–112. Biliary obstruction. *A,* T1-weighted image showing dilated intrahepatic bile ducts *(arrows)* of intermediate intensity; vessels have black signal void. TR = 500; TE = 20. *B,* Spin density T2-weighted image showing ducts *(short arrows)* to have slightly higher signal than adjacent liver but lower signal than vessels *(long arrows).* TR = 2857, TE = 30. *C,* T2-weighted image showing dilated ducts to be hyperintense *(short arrow)* as are the vessels *(long arrow).* TR = 2571; TE = 80.

References

1. Abdul-Karim FW, King TA, Dahms BB, et al: Carcinoma of extrahepatic biliary system in an adult with cystic fibrosis. Gastroenterology 82:758, 1982.
2. Alagille D: Extrahepatic biliary atresia. Hepatology 4:75, 1984.
3. Alexander MC, Haaga JR: MR imaging of the choledochal cyst. J Comput Assist Tomogr 9:357, 1985.
4. Ameut AE, Haaga JR, Wiedenmann SD, et al: Primary sclerosing cholangitis: CT findings. J Comput Assist Tomogr 7:795, 1983.
5. Andreu J, Perez C, Caceres J, et al: Computed tomography as the method of choice in the diagnosis of emphysematous cholecystitis. Gastrointest Radiol 12:315, 1987.
6. Araki T, Itani Y, Tasaka A: CT of choledochal cyst. Am J Roentgenol 135:739, 1980.
7. Aspestrand F, Schrumpf E, Jacobsen M, et al: Increased lymphatic flow from the liver in different intra- and extrahepatic disease demonstrated by CT. J Comput Assist Tomogr 15:560, 1991.
8. Auteri AG, Maler PF: Radiographic imaging to predict gallstone dissolution: More than meets the eye. Gastroenterology 98(6):1715, 1990.
9. Baker ME, Silverman PM, Halvorsen RA Jr, Cohan RH: Computed tomography of masses in periportal/hepatoduodenal ligament. J Comput Assist Tomogr 11:258, 1987.
10. Balt DS, Friedman AC, Radecki PD, Caroline DF: Avulsed gallbladder. CT appearance. J Comput Assist Tomogr 12:538, 1988.
11. Berakus JA, Ralls PW, Lapin SA, et al: Cholelithiasis: evaluation with CT. Radiology 162:415, 1987.
12. Baron RL: Common bile duct stones: Reassessment of criteria for CT diagnosis. Radiology 162:419, 1987.
13. Baron RL: Computed tomography of the biliary tree. Radiol Clin North Am 29:1235, 1991.
14. Baron RL: Role of CT in characterizing gallstones: An unsettled issue. Radiology 178:635, 1991.
15. Baron RL, Stanley RJ, Lee JK, et al: A prospective comparison of the elevation of biliary obstruction using computed tomography and ultrasonography. Radiology 146:91, 1982.
16. Baron RL, Stanley RJ, Lee JK, et al: Computed tomographic features of biliary obstruction. Am J Roentgenol 140:1173, 1988.
17. Baron RL, Rohrmann CA Jr, Lee SP, et al: CT evaluation of gallstones in vitro: Correlation with chemical analysis. Am J Roentgenol 151:1123, 1988.
18. Baron RL, Kuyper SJ, Lee SP, et al: In vitro dissolution of gallstones with MTBE: Correlation with characteristics of CT and MR imaging. Radiology 173:117, 1989.
19. Barwick KW, Rosai J: Liver. In Ackerman's Surgical Pathology, 7th ed. St. Louis, CV Mosby, 1989.
20. Becker CD, Hassler H, Terrier F: Preoperative diagnosis of the Mirizzi syndrome: Limitations of sonography and computed tomography. Am J Roentgenol 143:591, 1984.
21. Becker CD, Vock P: Appearance of gas-containing gallstones on sonography and computed tomography. Gastrointest Radiol 9:323, 1984.
22. Bennett GL, Rusinek H, Lisi V, et al: CT Findings in acute gangrenous cholecystitis. AJR Am J Roentgenol 178(2):275, 2002.
23. Berk RN, Ferrucci JT Jr, Fordtran JS, et al: The radiologic diagnosis of gallbladder disease: an imaging symposium. Radiology 141:49, 1981.
24. Berland LL, Lawson TL, Stanley RJ: CT appearance of Mirizzi syndrome. J Comput Assist Tomogr 8:165, 1984.
25. Blanton DE, Bream CA, Mandel SR: Gallbladder ectopia: A review of anomalies of position. Am J Roentgenol 121:396, 1974.
26. Boechant MI: Magnetic resonance imaging of abdominal and pelvic masses in children. Top Magn Reson Imaging 3:25, 1990.
27. Botet JF, Watson RC, Kemeny N, et al: Cholangitis complicating intraarterial chemotherapy in liver metastasis. Radiology 156:335, 1985.
28. Botting AL, et al: Metastatic hypernephroma masquerading as a polypoid tumor of the gallbladder and review of metastatic tumors of the gallbladder. Mayo Clin Proc 38:225, 1963.

29. Boukadoum M, Siddiky MA, Zerhouni EA, Stitik FP: CT demonstration of adenomyomatosis of the gallbladder. J Comput Assist Tomogr 8:177, 1984.
30. Brakel K, Lameris JS, Nijs HG, et al: Predicting gallstone composition with CT: In vivo and in vitro analysis. Radiology 174:337, 1990.
31. Brandon JC, Velez MA, Teplick SK, et al: Laparoscopic cholecystectomy: Evolution, early results, and impact on nonsurgical gallstones therapies. AJR Am J Roentgenol 157:235, 1991.
32. Brandt DJ, McCarty RL, Charboneau JW, et al: Gallbladder disease in patients with primary sclerosing cholangitis. AJR Am J Roentgenol 150:571, 1988.
33. Brink JA, Ferrucci JT: Use of CT for predicting gallstone composition: A dissenting view. Radiology 178:633, 1991.
34. Brodey PA, Fisch AE, Fertig S, Roberts GS: Computed tomography of choledochocele. J Comput Assist Tomogr 8(1):162, 1984.
35. Bundy AL, Ritchie WG: Ultrasonic diagnosis of metastatic melanoma of the gallbladder presenting as acute cholecystitis. J Clin Ultrasound 10:285, 1982.
36. Burrell MI, Zeman RK, Simeone JF, et al: The biliary tract: imaging for the 1990's. AJR Am J Roentgenol 157:223, 1991.
37. Campbell WL, Foster RG, Miller WJ, et al: Changes in extrahepatic bile duct caliber in liver transplant recipients without evidence of biliary obstruction. AJR Am J Roentgenol 158:997, 1992.
38. Carr DH, Hadjis NS, Bants LM, et al: Computed tomography of hilar cholangiocarcinoma: A new sign. Am J Roentgenol 53, 1985.
39. Carrasco CH, Freeny PC, Chuang VP, Wallace S: Chemical cholecystitis associated with hepatic artery infusion chemotherapy. Am J Roentgenol 141:703, 1983.
40. Cello JP: Acquired immunodeficiency syndrome cholangiopathy: spectrum of disease. Am J Med 86:539, 1989.
41. Chan FL, Man SW, Leong LL, Fan ST: Evaluation of recurrent pyogenic cholangitis with CT: Analysis of 50 patients. Radiology 170:165, 1989.
42. Cheung YK, Chen FL, Leong LL, et al: Biliary cystadenoma and cystadenocarcinoma: some unusual features. Clin Radiol 43:183, 1991.
43. Choi BI, Park JH, Kim YI, et al: Peripheral cholangiocarcinoma and cholanorchiasis: CT findings. Radiology 169:149, 1988.
44. Choi BI, Lim JH, Han MC, et al: Biliary cystadenoma and cystadenocarcinoma: CT and sonographic findings. Radiology 171:57, 1989.
45. Choi BI, Kim HJ, Han MC, et al: CT findings of clonorchiasis. AJR Am J Roentgenol 152:281, 1989.
46. Choi BI, Lee JH, Han MC, et al: Hilar cholangiocarcinoma: comparative study with sonography and CT. Radiology 172:689, 1989.
47. Choi BI, Yeon KM, Kim SH, Han MC: Caroli disease: Central dot sign in CT. Radiology 174:161, 1990.
48. Chun KA, Ha HK, Yu ES, et al: Xanthogranulomatous cholecystitis: CT features with emphasis on differentiation from gallbladder carcinoma. Radiology 203:93, 1997.
49. Christiansen RA, et al: Inadvertent ligation of the aberrant right hepatic duct at cholecystectomy: radiologic diagnosis and treatment. Radiology 183:549, 1992.
50. Clouston JE, Thorpe RJ: Case report: CT findings in adenomyomatosis of gallbladder. Australas Radiol 35:86, 1991.
51. Co CS, Shea WJ Jr, Goldberg HI: Evaluation of common bile duct diameter using high resolution computed tomography. J Comput Assist Tomogr 10:424, 1986.
52. Cooperberg PL, Gibney RG: Imaging of the gallbladder. Radiology 163:605, 1987.
53. Cory DA, Don S, West KW: CT cholangiography of a choledochocele. Pediatr Radiol 21:73, 1990.
54. Cossi AF, Scholz FJ, Aretz HT, Larsen CR: Computed tomography of xanthogranulomatous cholecystitis. Gastrointest Radiol 12:154, 1987.
55. Cronan JJ, Mueller PR, Simeone JF: Prospective diagnosis of choledocholithiasis. Radiology 146:467, 1983.
56. Daneman A, Matzinger MA, Martin DJ: Post-traumatic hemorrhage into the gallbladder. J Comput Tomogr 7:59, 1983.
57. Day DL, Mulcahy PF, Dehner LP, Letourneau JG: Postoperative abdominal CT scanning in extrahepatic biliary atresia. Pediatr Radiol 19:379, 1989.
58. DeGaetano AM, et al: Xanthogranulomatous cholecystitis: echographic and CT patterns. RAYS (Roma) 10(2):63, 1985.
59. Demas BE, Hricak H, Moseley M, et al: Gallbladder bile: An experimental study in dogs using MR imaging and proton MR spectroscopy. Radiology 157:453, 1985.
60. Dolmatch BL, Laing FC, Federle MP, et al: AIDS-related cholangitis: radiographic findings in nine patients. Radiology 163:313, 1987.
61. Dooms GC, Fisher MR, Higgins CB: MR imaging of the dilated biliary tract. Radiology 158:337, 1986.
62. Dooms GC, Kerlan RK Jr, Hricak H, et al: Cholangiocarcinoma: Imaging by MR. Radiology 159:89, 1986.
63. Doppman JL, Dwyer A, Vermess M, et al: Segmental hyperlucent defects in the liver. J Comput Assist Tomogr 8:50, 1984.
64. Duber C, Storkel S, Wagner PK, Muller J: Xanthogranulomatous cholecystitis mimicking carcinoma of the gallbladder: CT findings. J Comput Assist Tomogr 8:1195, 1984.
65. Edmondson HA, Peters RL: Liver. In Kissane JM (ed): Anderson's Pathology. St. Louis, CV Mosby, 1985, p. 1194.
66. Eisenberg D, Hurwitz L, Yo AC: CT and sonography of multiple bile duct hamartomas simulating malignant liver disease (case report). Am J Roentgenol 147:279, 1986.
67. Engels JT, Balfe DM, le JKT: Biliary carcinoma: CT evaluation of extrahepatic spread. Radiology 172:35, 1989.
68. Enriquez G, Lucaya J, Allende E, Garcia-Pena P: Intrahepatic biliary stones in children. Pediatr Radiol 22:283, 1992.
69. Faintuch J, Machado MCC, Raia AA: Suprahepatic gallbladder with hypoplasia of the right lobe of the liver. Arch Surg 115:658, 1980.
70. Fan ZM, Yamashita Y, Harada M, et al: Intrahepatic cholangiocarcinoma: Spin-echo and contrast-enhanced dynamic MR imaging. AJR Am J Roentgenol 161:313, 1993.
71. Federle MP, Cello JP, Lang FC, Jeffrey RB Jr: Recurrent pyogenic cholangitis in Asian immigrants: Use of ultrasonography, computed tomography, and cholangiography. Radiology 143:151, 1982.
72. Ferrozzi F, Rossi A: Gallbladder metastasis: CT appearance. Rays 13(2):23, 1988.
73. Fidler J, Paulson EK, Layfield L: CT evaluation of acute cholecystitis: Findings and usefulness in diagnosis. AJR Am J Roentgenol 166:1085, 1996.
74. Foley WD, Wilson CR, Quiroz FA, Lawson TL: Demonstration of the normal extrahepatic biliary tree with computed tomography. J Comput Assist Tomogr 4:48, 1980.
75. Fork FT, Nyman UIF, Sigurjonnson S: Recognition of gas in gallstones in routine computed tomograms of the abdomen. J Comput Assist Tomogr 7:805, 1983.
76. Friedburg H, Kauffman GW, Bohm N, et al: Sonographic and computed tomographic features of embryonal rhabdomyosarcoma of the biliary tract. Pediatr Radiol 14:436, 1984.
77. Furukawa H, Takayasu K, Mukai K, et al: CT evaluation of small polypoid lesions of the gallbladder. Hepatogastroenterology 42:800, 1995.
78. Gagner M, Munson JL, Scholz FJ: Hepatobiliary anomalies associated with polysplenia syndrome. Gastrointest Radiol 16:167, 1991.
79. Gale ME, Robbins AH: Computed tomography of the gallbladder: Unusual disease. J Comput Assist Tomogr 9:439, 1985.
80. Gelman R, Alexander MS, Zucker KA, Bailey RW: The use of radionuclide imaging in the evaluation of suspected biliary damage during laparoscopic cholecystectomy. Gastrointest Radiol 16:201, 1991.
81. Gembala RB, Flynn DE, Radecki PD, et al: Sonographic diagnosis of traumatic gallbladder avulsion. J Ultrasound Med 5:399, 1993.
82. Genkins SM, Tucker JA, Seigler HF, Dunnick NR: Biliary cystadenoma with mesenchymal stroma: CT and angiographic appearance. J Comput Assist Tomogr 12:527, 1988 (Case Report).
83. Gerard PS, Berman D, Zafarnloss S: CT and ultrasound of gallbladder adenomyomatosis mimicking carcinoma. J Comput Assist Tomogr 14:490, 1990.
84. Gibson RN: Suprapancreatic biliary obstruction: CT evaluation. Radiology 165:875, 1987 (Letter to the Editor).
85. Gibson RN, Yeung E, Thompson JN, et al: Bile duct obstruction: Radiologic evaluation of level, cause and tumor resectability. Radiology 160:43, 1986.
86. Ginaldi S: Cholangiocarcinomas arising in a choledochal cyst: Diagnostic value of computed tomography and ultrasonography. Gastrointest Radiol 12:212, 1987.
87. Goldstein F: Cystic duct syndrome. In Bockus HL (ed): Gastroenterology. Philadelphia, WB Saunders, 1976.
88. Goldstein RB, Wing VW, Laing FC, Jeffrey RB: Computed tomography of the thick-walled gallbladder mimicking pericholecystic fluid. J Comput Assist Tomogr 10:55, 1986.

89. Greenberg M, Robin JM, Greenberg BM: Appearance of the gallbladder and biliary tree by CT cholangiography. J Comput Assist Tomogr 7:788, 1983.
90. Greenberg M, Greenberg BM, Rubin JM, Greenberg IM: Computed tomographic cholangiography: A new technique for evaluating the head of the pancreas and distal biliary tree. Radiology 144:363, 1982.
91. Greenler DP, Sumkin JH, Campbell WL: CT appearance of the Roux limb following choledochojejunostomy in liver transplantation. Gastrointest Radiol 16:41, 1991.
92. Grumbach K, Levine MS, Exler JA: Gallstone ileus diagnosed by computed tomography. J Comput Assist Tomogr 10:146, 1986.
93. Gulliver DJ, Baker ME, Cheng CA, et al: Malignant biliary obstruction: Efficacy of thin-section dynamic CT in determining resectability. AJR Am J Roentgenol 159:503, 1992.
94. Gupta RK, Kakar AK, Jena A, et al: Magnetic resonance in obstructive jaundice. Australas Radiol 33:245, 1989.
95. Haller JO, Condon VR, Berdon WE, et al: Spontaneous perforation of the common bile duct in children. Radiology 172:621, 1989.
96. Hamrick-Turner J, Abbitt PL, Ros PR: Intrahepatic cholangiocarcinoma: MR appearance. AJR Am J Roentgenol 158:77, 1992.
97. Harshfield DL, Teplick SK, Stanton M, et al: Obstructing villous adenoma and papillary adenomatosis of the bile duct. AJR Am J Roentgenol 154:1217, 1990.
98. Havrilla TR, Reich NE, Haaga JR, et al: Computed tomography of the gallbladder. Am J Roentgenol 130:1059, 1978.
99. Herba MJ, Casola G, Bret PM, et al: Cholangiocarcinoma as a late complication of choledochoenteric anastomoses. Am J Roentgenol 147:513, 1986.
100. Herbener TE, et al: Recurrent cholangiocarcinoma of the biliary tree after liver transplantation. Radiology 1969:642, 1988.
101. Herman TE, Siegel MJ: Central dot sign on CT of liver cysts. J Comput Assist Tomogr 14:1019, 1990.
102. Hopper KD: The role of computed tomography in the evaluation of Caroli disease. Clin Imaging 13:68, 1989.
103. Hricak H, Filly RA, Margulis AR, et al: Nuclear magnetic imaging of the gallbladder. Radiology 147:481, 1983.
104. Iemoto Y, Kondo Y, Nakano T, et al: Biliary cystadenocarcinoma diagnosed by liver biopsy performed under ultrasonographic guidance. Gastroenterology 84:399, 1983.
105. Ilie B, Behar AJ: Solitary neurofibroma of the gallbladder: report of three cases and literature review. Mt Sinai J Med 52:473, 1985.
106. Itai Y: Computed tomographic evaluation of gallbladder disease CRC Crit Rev Diagn Imaging 27:113, 1987.
107. Itai Y, Ataki T, Yoshikawa K, et al: Computed tomography of gallbladder carcinoma. Radiology 137:713, 1980.
108. Itai Y, Ataki T, Furui S, et al: Computed tomography and ultrasound in the diagnosis of intrahepatic calculi. Radiology 136:399, 1980.
109. Itai Y, Ataki T, Furui S, et al: Computed tomography of primary intrahepatic biliary malignancy. Radiology 147:485, 1983.
110. Itai Y, Ohtomo K, Kokubo T, et al: CT of hepatic masses: Significance of prolonged and delayed enhancement. Am J Roentgenol 146:729, 1986.
111. Itai Y, Ohtomo K, Kokubo T, et al: Segmental intensity differences in the liver on MR images: A sign of intrahepatic portal flow stoppage. Radiology 167:17, 1988.
112. Itoh K, et al: Staging of bile duct cancer: comparative study of US, CT, and MR imaging, presented at RSNA meeting 1992.
113. Izumi N, Koyama W, Irie T, et al: Ultrasonography and computed tomography in adenomyomatosis of the gallbladder. Acta Radiol Diagn 26:689, 1985.
114. Jacobson JB, Brodey PA: The transverse common duct. Am J Roentgenol 136:91, 1981.
115. Janowitz P, Zoller A, Swobodnik W, et al: Computed tomography evaluation of radiolucent gallstones in vivo. Gastrointest Radiol 15:58, 1990.
116. Jeffrey RB Jr, Federle MP, Laing FC, Wing VW: Computed tomography of blunt trauma to the gallbladder. J Comput Assist Tomogr 10:756, 1986.
117. Jeffrey RB Jr: Diagnosis of intrahepatic calculi and choledocholithiasis. In Ferrucci JT, Mathieu DG (eds): Advances in Hepatobiliary Radiology. St. Louis, CV Mosby, 1990.
118. Jeffrey RB, Federle MP, Laing FC, et al: Computed tomography of choledocholithiasis. Am J Roentgenol 140:1179, 1983.
119. Jenkins M, Golding RH, Cooperberg PL: Sonography and computed tomography of hemorrhagic cholecystitis. Am J Roentgenol 140:1197, 1983.
120. Juttner H, Ralls PW, Quinn MF, Jenney JM: Thickening of the gallbladder wall in acute hepatitis: Ultrasound demonstration. Radiology 142:465, 1982.
121. Kane RA, Costella P, Duszlak E: Computed tomography in acute cholecystitis: New observations. Am J Roentgenol 141:697, 1983.
122. Kane RA, Jacobs R, Katz J, Costello P: Porcelain gallbladder: Ultrasound and CT appearance. Radiology 152:137, 1984.
123. Kang YS, et al: Alternatives in MR relaxation of normal canine gallbladder bile during fasting. Magn Reson Imaging 4:399, 1986.
124. Kanzer GK, Weinreb JC: Magnetic resonance imaging of diseases of the liver and biliary system. Radiol Clin North Am 29:1259, 1991.
125. Kaplan SB, Zajko AB, Koneru B: Hepatic bilomes due to hepatic artery thrombosis in liver transplant recipients: percutaneous drainage and clinical outcome. Radiology 174:1031, 1990.
126. Kaplan SB, Sumkin JH, Campbell WL, et al: Periportal low attenuation areas on CT: value as evidence of liver transplant rejection. Am J Roentgenol 152:285, 1989.
127. Kim PN, Lee KS, Kim IY, et al: Gallbladder perforation: Comparison of US findings with CT. Abdom Imaging 19:239, 1994.
128. Korobkin M, Stephens DH, Lee JK, et al: Biliary cystadenoma and cystadenocarcinoma: CT and sonographic findings. Am J Roentgenol 153:507, 1989.
129. Koslin DB, Stanley RJ, Berland LL, et al: Hepatic perivascular lymphedema: CT appearance. Am J Roentgenol 150:111, 1988.
130. Krudy AG, Doppman JL, Bissmette MB, Girton M: Hemobilia: Computed tomographic diagnosis. Radiology 148:785, 1983.
131. Kumar A, Aggarwal S: Carcinoma of the gallbladder: CT findings in 50 cases. Abdom Imaging 19:304, 1994.
132. Laing FC, et al: Biliary dilatation: Defining the level and cause by real-time US. Radiology 160:36, 1986.
133. Lamki N, Raval B, St Ville E: Computed tomography of complicated cholecystitis. J Comput Assist Tomogr 10:319, 1985.
134. Levitt RG, Sagel SS, Stanley RJ, Jost RG: Accuracy of computed tomography of the liver and biliary tract. Radiology 124:123, 1988.
135. Lewandowski BJ, Winsberg F: Gallbladder wall thickness distortion by ascites. Am J Roentgenol 137:519, 1981.
136. Liddell RM, Baron RL, Ekstrom JE, et al: Normal intrahepatic bile ducts: CT depiction. Radiology 176:633, 1990.
137. Lindsay KA, Hall JRW, Chapman AH: Radiology of excessive mucus production as a complication of congenital bile duct abnormalities. Clin Radiol 46:43, 1992.
138. Loflin TG, Simeone JF, Mueller PR, et al: Gallbladder bile in cholecystitis, in vitro MR evaluation. Radiology 157:457, 1985.
139. MacCarty RL, LaRusso NF, Wiesner RH, Ludwig J: Primary sclerosing cholangitis: Findings on cholangiography and pancreatography. Radiology 149:39, 1983.
140. MacCarty RL, LaRusso NF, May GR, et al: Cholangiocarcinoma complicating primary sclerosing cholangitis: Cholangiographic appearance. Radiology 156:43, 1985.
141. Marincek B, Barbier PA, Becker CD, et al: CT appearance of impaired lymphatic drainage in liver transplants. Am J Roentgenol 147:519, 1986.
142. Matsui O, Kadoya M, Takashima T: Intrahepatic periportal abnormal intensity on MR images: an indication of various hepatobiliary diseases. Radiology 171:335, 1989.
143. McAllister JD, D'Altori RA, Synder A: CT findings after uncomplicated percutaneous laparoscopic cholecystectomy. J Comput Assist Tomogr 15:770, 1991.
144. McCarthy S, Hricak H, Cohen M, et al: Cholecystitis: Detection with MR imaging. Radiology 158:333, 1986.
145. McMillin K: Computed tomography of emphysematous cholecystitis. J Comput Assist Tomogr 9:330, 1985.
146. Meilstrup JW, Hopper KD, Hieme GA: Imaging of gallbladder variants. Am J Roentgenol 152:1205, 1991.
147. Menu Y, Lorphelin JM, Arrive L: Tumors of the gallbladder and bile ducts. In Ferrucci JT, Mathieu DG (eds): Advances in Hepatobiliary Radiology. St. Louis, CV Mosby, 1990.
148. Menu Y, Lorphelin JM, Scherrer A, et al: Sonographic and computed tomographic evaluation of intrahepatic calculi. Am J Roentgenol 145:579, 1985.
149. Miller WJ, Campbell WL, Zajko AB, et al: Obstructive dilatation of extrahepatic recipient and donor bile ducts, complicating orthotopic liver transplantation: imaging and laboratory findings. Am J Roentgenol 157:959, 1991.

150. Mirvis SE, Whitley NO: Computed tomography in hepatobiliary trauma. In Ferrucci JT, Matthieu DG (eds): Advances in Hepatobiliary Radiology. St. Louis, CV Mosby, 1990.
151. Mirvis SE, Vainright JR, Nelson AW, et al: The diagnosis of acute acalculous cholecystitis: A comparison of sonography, scintigraphy, and CT. Am J Roentgenol 147:1171, 1986.
152. Mitchell SE, Clark KA: A comparison of computed tomography and sonography in choledocholithiasis. Am J Roentgenol 142:729, 1984.
153. Miyake H, Aikawa H, Hori Y, et al: Adenomyomatosis of the gallbladder with subserosal fatty proliferation: CT findings in two cases. Gastrointest Radiol 17:21, 1992.
154. Moeser PM, Julian S, Karstaedt N, Sterchi M: Unusual presentation of cholelithiasis on T_1-weighted MR imaging. J Comput Assist Tomogr 12:150, 1988.
155. Montana MA, Rohromann CA: Cholangiocarcinoma in a choledochal cyst: Preoperative diagnosis. Am J Roentgenol 147:516, 1986.
156. Moon KL Jr, Hricak H, Margulis AR, et al: Nuclear magnetic resonance imaging characteristics of gallstones in vitro. Radiology 148:753, 1983.
157. Morehouse H, Leibman AJ, Biempica L, Hoffman J: Infiltrating periductal neoplasm mimicking biliary dilatation on computed tomography. J Comput Assist Tomogr 7:721, 1983.
158. Morimoto K, Shimoi M, Shirakawa T, et al: Biliary obstruction: Evaluation with three-dimensional MR cholangiography. Radiology 183:578, 1992.
159. Morizumi H, Sano T, Hirose T, Hizawa K: Neurofibroma of the gallbladder seen as a papillary polyp. Acta Pathol Jpn 38:259, 1988.
160. Morse JMD, Lakshman S, Thomas E: Gallbladder ectopia simulating pancreatic mass on CT. Gastrointest Radiol 10:111, 1985.
161. Mueller PR, Ferrucci JT Jr, Simeone JF, et al: Postcholecystectomy bile duct dilatation: Myth or reality? Am J Roentgenol 136:355, 1981.
162. Muhletaler C, Gerlock AJ Jr, Fleischer AC, James AE Jr: Diagnosis of obstructive jaundice with nondilated bile ducts. Am J Roentgenol 134:1149, 1980.
163. Nardi PM, Yaghoobian J, Ruchman RB: CT demonstration of retrohepatic gallbladder in severe cirrhosis. J Comput Assist Tomogr 12: 968, 1988.
164. Nesbit GM, Johnson CD, James EM, et al: Cholangiocarcinoma: Diagnosis and evaluation of resectability by CT and sonography as procedures complementary to cholangiography. Am J Roentgenol 151:933, 1988.
165. Nichols DA, MacCarty RL, Gaffey TA: Cholangiographic evaluation of bile duct carcinoma. Am J Roentgenol 141:1291, 1983.
166. Nyman U, Rimer U, Aspelin P, et al: Intravenous computed tomographic cholangiography in acute cholecystitis. Acta Radiol Diagn 25:289, 1984.
167. Oliver JH 3rd, Federle MP, Campbell WL, Zajko A: Imaging the hepatic transplant. Radiol Clin North Am 29:1285, 1991.
168. Outwater E, Kaplan MM, Bankoff MS: Lymphadenopathy in sclerosing cholangitis: Pitfall in the diagnosis of malignant biliary obstruction. Gastrointest Radiol 17:157, 1992.
169. Pasanen P, Eskelinen M, Partanen K, et al: Ultrasonography, CT and ERCP in the diagnosis of choledochal stones. Acta Radiol 33: 53, 1992.
170. Pastakia B, Shawker TH, Horvath K: Biliary neoplasm simulating dilated bile ducts: Role of computed tomography and ultrasound. J Ultrasound Med 6:333, 1987.
171. Pedrosa CS, Casanova R, Rodriguez R: Computed tomography in obstructive jaundice: I. The level of obstruction. Radiology 139: 627, 1981.
172. Pedrosa CS, Casanova R, Lezana AH, Fernandez MC: Computed tomography in obstructive jaundice: II. The cause of obstruction. Radiology 139:635, 1981.
173. Phillips G, Pochaczevsky R, Goodman J, Kumari S: Ultrasound patterns of metastatic tumors in the gallbladder. J Clin Ultrasound 10:379, 1982.
174. Pien EH, Zeman RK, Benjamin SB, et al: Iatrogenic sclerosing cholangitis following hepatic arterial chemotheraphy infusion. Radiology 156:329, 1985.
175. Polk HC Jr: Carcinoma and calcified gallbladder. Gastroenterology 50:582, 1966.
176. Pollack M, Shirkhoda A, Charnsangavej C: Computed tomography of choledochocele. J Comput Assist Tomogr 9:360, 1985.
177. Pombo F, Arrojo L, Soler R: Left hepatic atrophy in Mirizzi syndrome: CT appearance. Eur J Radiol 10:181, 1990.
178. Quinn SF, Fazzio F, Jones E: Torsion of the gallbladder: Findings on CT and sonography and role of percutaneous cholecystostomy. AJR Am J Roentgenol 148:881, 1987.
179. Quint LE, Glazer GM: CT evaluation of the bile ducts in patients with fatty liver. Radiology 153:755, 1984.
180. Radin DR, Cohen H, Halls JM: Acalculous inflammatory disease of the biliary tree in acquired immunodeficiency syndrome: CT demonstration. J Comput Assist Tomogr 11:775, 1987.
181. Radin DR, Parkrama C, Ralls PW: Carcinoma of the cystic duct. Gastrointest Radiol 15:49, 1990.
182. Radin DR, Vachon LA: CT findings in biliary and pancreatic ascariasis. J Comput Assist Tomogr 10:508, 1986.
183. Raghavendra BN: Ultrasound features of primary carcinoma of the gallbladder: Report of five cases. Gastrointest Radiol 5:239, 1980.
184. Rahn NH 3rd, Koehler RE, Weyman PJ, et al: CT appearance of sclerosing cholangitis. Am J Roentgenol 141:549, 1983.
185. Ralls PW, Quinn MF, Juttner HU, et al: Gallbladder wall thickening: patients without intrinsic gallbladder disease. Am J Roentgenol 137: 65, 1981.
186. Ralls PW, Colletti PM, Quinn MF, et al: Sonography in recurrent oriental pyogenic cholangitis. Am J Roentgenol 136:1010, 1981.
187. Reiman TH, Balfe DM, Weyman PJ: Suprapancreatic biliary obstruction: CT evaluation. Radiology 163:49, 1987.
188. Romano AJ, van Sonnenberg E, Casola G, et al: Gallbladder and bile duct abnormalities in AIDS: sonographic findings in eight patients. AJR Am J Roentgenol 150:123, 1988.
189. Ros PR, Buck JL, Goodman ZD, et al: Intrahepatic cholangiocarcinoma: radiologic pathologic correlation. Radiology 167:689, 1988.
190. Rosai J: Gallbladder and extrahepatic bile ducts. In Ackerman's Surgical Pathology, 7th ed. St. Louis, CV Mosby, 1989.
191. Rossman MD, et al: MR imaging of gallbladder carcinoma. AJR Am J Roentgenol 148:143, 1987.
192. Roth JL, Berk JE: Symptoms after cholecystectomy. In Bockus HL (ed): Gastroenterology, 3rd ed. Philadelphia, WB Saunders, 1976.
193. Rummeny E, Weissleder R, Stark DD, et al: Primary liver tumors: Diagnosis by MR imaging. AJR Am J Roentgenol 152:63, 1989.
194. Sagoh T, Itoh K, Togashi K, et al: Gallbladder carcinoma: Evaluation with MR imaging. Radiology 174:131, 1990.
195. Sarno RC, Carter BL: Computed tomography in Caroli's disease. Comput Radiol 7:287, 1983.
196. Savader SJ, Benenati JF, Venbrux AC, et al: Choledochal cysts: Classification and cholangiographic appearance. AJR Am J Roentgenol 156:327, 1991.
197. Schoenfield LJ: Gallstones and other biliary diseases. Clin Symp CIBA, 34(4), 1982.
198. Schoenfield LJ: Gallstones: An update. Am J Gastroenterol 84: 999, 1987.
199. Schulte SJ, et al: CT of the extrahepatic bile ducts: Wall thickness and contrast enhancement in normal and abnormal ducts. AJR Am J Roentgenol 154:79, 1990.
200. Schulman A: Non-western patterns of biliary stones and the role of ascariasis. Radiology 162:425, 1987.
201. Semelka RC, Shoenut JP, Kroeker MA, et al: Bile duct disease: Prospective comparison of ERCP, CT, and fat suppression MRI. Gastrointest Radiol 17:347, 1992.
202. Shanser JD, Korobkin M, Goldberg HI, Rohlfing BM: Computed tomographic diagnosis of obstructive jaundice in the absence of intrahepatic ductal dilatation. Am J Roentgenol 131:389, 1978.
203. Shea TE, Pfister RC: Opacification of the gallbladder by urographic contrast media reflection of an alternate excretory pathway. Am J Roentgenol Radium Ther Nucl Med 107:763, 1969.
204. Smathers RL, Lee JKT, Heiken JP: Differentiation of complicated cholecystitis from gallbladder carcinoma by computed tomography. Am J Roentgenol 143:255, 1984.
205. So CB, Gibney RG, Swdamore CH: Carcinoma of the gallbladder: A risk associated with the gallbladder-preserving treatments for cholelithiasis. Radiology 174:127, 1990.
206. Soderstrom CA, Maekawa K, DuPriest RW Jr, Cowley RA: Gallbladder injuries resulting from blunt abdominal trauma. Ann Surg 193:60, 1981.
207. Solomon A, Kreel L, Pinto D: Contrast computed tomography in the diagnosis of acute cholecystitis. J Comput Assist Tomogr 3: 585, 1979.
208. Somer K, Kivisaari L, Standertskjold-Nordenstam CG, Kalima TV: Contrast enhanced computed tomography of the gallbladder in acute pancreatitis. Gastrointest Radiol 9:31, 1984.

209. Sons HV, Borchard F: Carcinoma of the extrahepatic bile ducts: A postmortem study of 65 cases and review of the literature. J Surg Oncol 34:6, 1987.
210. Sood GK, Mahapatra JR, Khurana A, et al: Caroli disease: Computed tomographic diagnosis. Gastrointest Radiol 16:243, 1991.
211. Spritzer C, Kressel HY, Mitchell D, Axel L: MR imaging of normal extrahepatic bile ducts. J Comput Assist Tomogr 11:248, 1987.
212. Strax R, Toombs BD, Kam J, et al: Gallbladder enhancement following angiography: a normal CT finding. J Comput Assist Tomogr 6: 766, 1982.
213. Takayasu K, Muramatsu Y, Shima Y, et al: Hepatic lobar atrophy following obstruction of the ipsilateral portal vein from hilar cholangiocarcinoma. Radiology 160:389, 1986.
214. Takayasu K, Ikeya S, Mukai K, et al: CT of hilar cholangiocarcinoma: Late contrast enhancement in six patients. AJR Am J Roentgenol 154:1203, 1990.
215. Tani K, Kubota Y, Yamaguchi T, et al: MR imaging of the peripheral cholangiocarcinoma. J Comput Assist Tomogr 15:975, 1991.
216. Tartar VM, Balfe DM: Lymphoma in the wall of the bile ducts: Radiologic imaging. Gastrointest Radiol 15:53, 1990.
217. Teefey SA, Baron RL, Rohrmann CA, et al: Sclerosing cholangitis: CT findings. Radiology 169:635, 1988.
218. Teefey SA, Baron RL, Schulte SJ, et al: Patterns of intrahepatic bile duct dilatation at CT: Correlation with obstructive disease processes. Radiology 182:139, 1992.
219. Teele RL, Share JC: Ultrasound of Infants and Children, Philadelphia, WB Saunders, 1991.
220. Teixidor HS, Godwin TA, Ramirez EA: Cryptosporidiosis of the biliary tract in AIDS. Radiology 180:51, 1991.
221. Teixidor HS, Honig CL, Norsoph E, et al: Cytomegalovirus infection of the alimentary canal: Radiologic findings with pathologic correlation. Radiology 163:317, 1987.
222. Terrier F, Becker CD, Stoller C, Triller JK: Computed tomography in complicated cholecystitis. J Comput Assist Tomogr 8:58, 1984.
223. Thomas JL, Bernadino ME: Segmental biliary obstruction: Its detection and significance. J Comput Assist Tomogr 4:155, 1980.
224. Thorsen MK, et al: Primary biliary carcinoma: CT evaluation. Radiology 152:479, 1984.
225. Todani T, Watanabe Y, Narusue M, et al: Congenital bile duct cysts: Classification, operative procedures, and review of 37 cases including cancer arising from a choledochal cyst. Am J Surg 1134: 263, 1977.
226. Uchida H, et al: Computed tomography of gallstones. Jpn Clin Exp Med 62:2411, 1985.
227. Ueda J, Kobayashi Y, Nishida T: Computed tomography evaluation of high-density bile in the gallbladder. Gastrointest Radiol 15:22, 1990.
228. Ueda J, Hara K, Ohishi H, Uchida H: High density bile in the gallbladder observed by computed tomography. J Comput Assist Tomogr 7:801, 1983.
229. Varma DGK, Faust JM: Computed tomography of gangrenous acute postoperative acalculous cholecystitis. J Comput Assist Tomogr 12: 29, 1988.
230. Vazquez JL, Thorsen MK, Dodds WJ, et al: Atrophy of the left hepatic lobe caused by a cholangiocarcinoma. Am J Roentgenol 144:547, 1985.
231. Vujic I, Young JW, Gobien RP, et al: Computed tomographic demonstration of hemobilia. J Comput Assist Tomogr 7:219, 1983.
232. Walker AT, Shapiro AW, Brooks DC, et al: Bile duct disruption and biloma after laparoscopic cholecystectomy: Imaging evaluation. AJR Am J Roentgenol 158:785, 1992.
233. Wechsler RJ, Munoz SJ, Needleman L, et al: The periportal collar sign: A CT sign of liver transplant rejection. Radiology 165:57, 1987.
234. Weiner SN, Koenigsberg M, Morehouse H, Hoffman J: Sonography and computed tomography in the diagnosis of carcinoma of the gallbladder. Am J Roentgenol 142:735, 1984.
235. Weinstein JB, Heiken JP, Lee JK, et al: High resolution CT of the porta hepatis and hepatoduodenal ligament. Radiographics 6: 55, 1986.
236. Weissleder R, Stark DD, Compton CC, et al: Cholecystitis: Diagnosis by MR imaging. Magn Reson Imaging 6:345, 1988.
237. Whitehouse RW, Martin DF: Contrast-enhanced computed tomography of the normal and abnormal gallbladder. Br J Radiol 59:1083, 1986.
238. Wilbur AC, Gyi B, Renigers SA: High-field MRI of primary gallbladder carcinoma. Gastrointest Radiol 13:142, 1988.
239. Wolfe B: Contrast layering in a choledochal cyst: A new CT observation. J Can Radiol Assoc 39:51, 1988.
240. Yamashita Y, Takahashi M, Kanazawa S, et al: Hilar cholangiocarcinoma: an evaluation of subtype with CT and angiography. Acta Radiol 33:351, 1992.
241. Yamashita Y, Takahashi M, Kanazawa S, et al: Parenchymal changes of the liver in cholangiocarcinoma: CT evaluation. Gastrointest Radiol 17:161, 1992.
242. Yeh H: Ultrasonography and computed tomography of carcinoma of the gallbladder. J Comput Assist Tomogr 133:167, 1979.
243. Yoneda M, Tamasawa N, Makino I, et al: Measurement of calcium content of gallstones by computed tomography and the relationship between gallbladder function and calcification of gallstones. Gastroenterol Jpn 25:478, 1990.
244. Yoshida H, Itai Y, Minami M, et al: Biliary malignancies occurring in choledochal cysts. Radiology 173:389, 1989.
245. Zajko AB, Campbell WL, Logsdon GA, et al: Cholangiographic findings in hepatic artery occlusion after liver transplantation. AJR Am J Roentgenol 149:485, 1987.
246. Zajko AB, Zemel G, Skolnick ML, et al: Percutaneous transhepatic cholangiography rather than ultrasound as a screening test for postoperative biliary complications in liver transplant patients. Transplant Proc 20:678, 1988.
247. Zajko AB, Campbell WL, Bron KM, et al: Diagnostic and interventional radiology in liver transplantation. Gastroenterol Clin North Am 17:105, 1988.
248. Zajko AB, Bennett MJ, Campbell WL, Koneru B: Mucocele of the cystic duct remnant in eight liver transplant recipients: findings at cholangiography, CT and US. Radiology 177:691, 1990.
249. Zeman RK, Schiebler M, Clark LR, et al: The clinical and imaging spectrum of pancreaticoduodenal lymph node enlargement. AJR Am J Roentgenol 144:1223, 1985.
250. Zirinsky K, Auh YH, Rubenstein J, et al: The portacaval space: CT with MR correlation. Radiology 156:453, 1985.

38 The Pancreas

John R. Haaga

During the past 25 years, the modern imaging techniques of computed tomography (CT) and magnetic resonance imaging (MRI) have made considerable improvement in the quality of life as well as in health care. A survey in the journal *Health Affairs* polled a group of 225 clinical physicians to determine what innovations they considered the most significant to the improvement and practice of medicine. An overwhelming number, 75%, responded that these two imaging modalities were the greatest innovations among many techniques and procedures, even including cancer treatments, angiographic stents, and cardiac bypass. The next closest innovation was angiotensin-converting enzyme inhibitors, which were regarded as the most important innovation in their practice by 54% of respondents.[72]

This historical revolution is on the verge of being eclipsed by the newest methods of CT and MRI, especially multislice CT imaging. I noted in earlier editions of this book that prior to modern imaging techniques, the pancreas was a hidden organ. Early CT scanners afforded the first opportunities to actually visualize the exact anatomic characteristics of the pancreas and peripancreatic region. With the development of the spiral scanners, the diagnosis and treatment of pancreatic disease were no longer restricted by the lack of anatomic detail but rather by the inherent nature of the disease and the limitations of therapeutic regimens.

The development of multislice scanners and cone-beam multislice scanners ushers in a new age of medical diagnosis and treatment, the potential of which is almost unimaginable. These new tools provide the general anatomic information displayed by older scanners but with almost microscopic detail. The speed of imaging is so fast that temporal studies can be performed to assess physiologic function affected by molecular interactions. Although it is unlikely that such scanners will be used to visualize molecules themselves, they will indirectly permit assessment of molecular function.

This chapter discusses the normal anatomic appearance, relationships, and pathologic conditions of the pancreas as visualized by CT and MRI. The very latest information related to multislice scanners and cone-beam sources is included if available.

CT Anatomy

The pancreatic chapter in earlier editions of this book used multiple imaging modalities and artists' renditions to display anatomy and the routine axial, reconstructed images. The vascular images of modern imaging devices are so superior to these earlier images that few other modalities are used in this chapter. It is truly a milestone event when even the classic drawings of Dr. Frank Netter are no longer needed to demonstrate relationships. The illustrations by Dr. Netter used in the first three editions of this book have been retired in favor of the new three-dimensional (3D) renderings now available with multislice scanners.

The pancreas is an exocrine and endocrine organ measuring approximately 15 cm in length and weighing 60 to 100 g. Its gross anatomic relationships with the stomach, duodenum, colon, and spleen are fairly constant, but individual variations do occur (Fig. 38–1). The pancreas is located in the anterior pararenal space of the retroperitoneum, just anterior to the perirenal (Gerota's) fascia and posterior to the parietal peritoneum (see Fig. 38–1). The uncinate portion of the pancreas (congenitally the ventral aspect of the pancreas) is in the inferior-most portion of the head of the pancreas, just posterior to the superior mesenteric artery and vein (Fig. 38–2*A*). The normal uncinate portion is triangular or wedge-shaped with the narrow portion beneath the superior mesenteric artery and vein (Fig. 38–2*A*). The head of the pancreas is medial and posterior to the bulb of the duodenum, bounded laterally by the second and inferiorly by the third portions of the duodenum (Fig. 38–2*B*). The neck of the pancreas is ante-

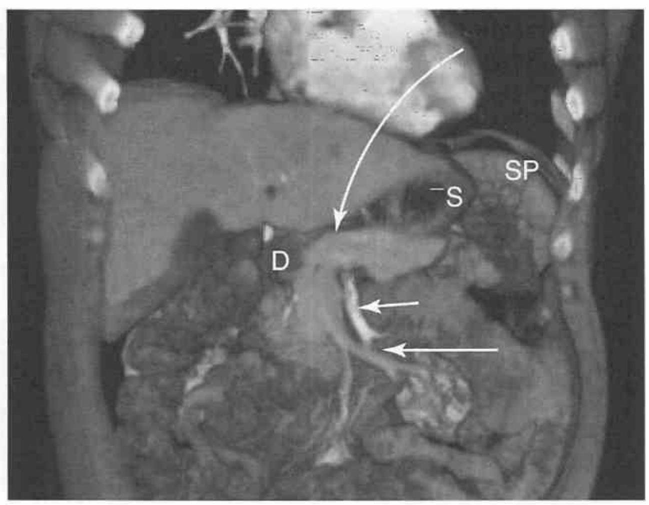

Figure 38–1. Reconstructed view from multislice scanner in 3D mode shows the general relationships of the pancreas (*curved arrow*) to adjacent structures such as the duodenum (D), stomach (S), spleen (SP), superior mesenteric artery (*short horizontal arrow*), and superior mesenteric vein (*long horizontal arrow*). One can also see without any special reconstruction techniques the pancreatic duct; data manipulation can even provide multiplanar views of the duct as well as internal endoscopic views.

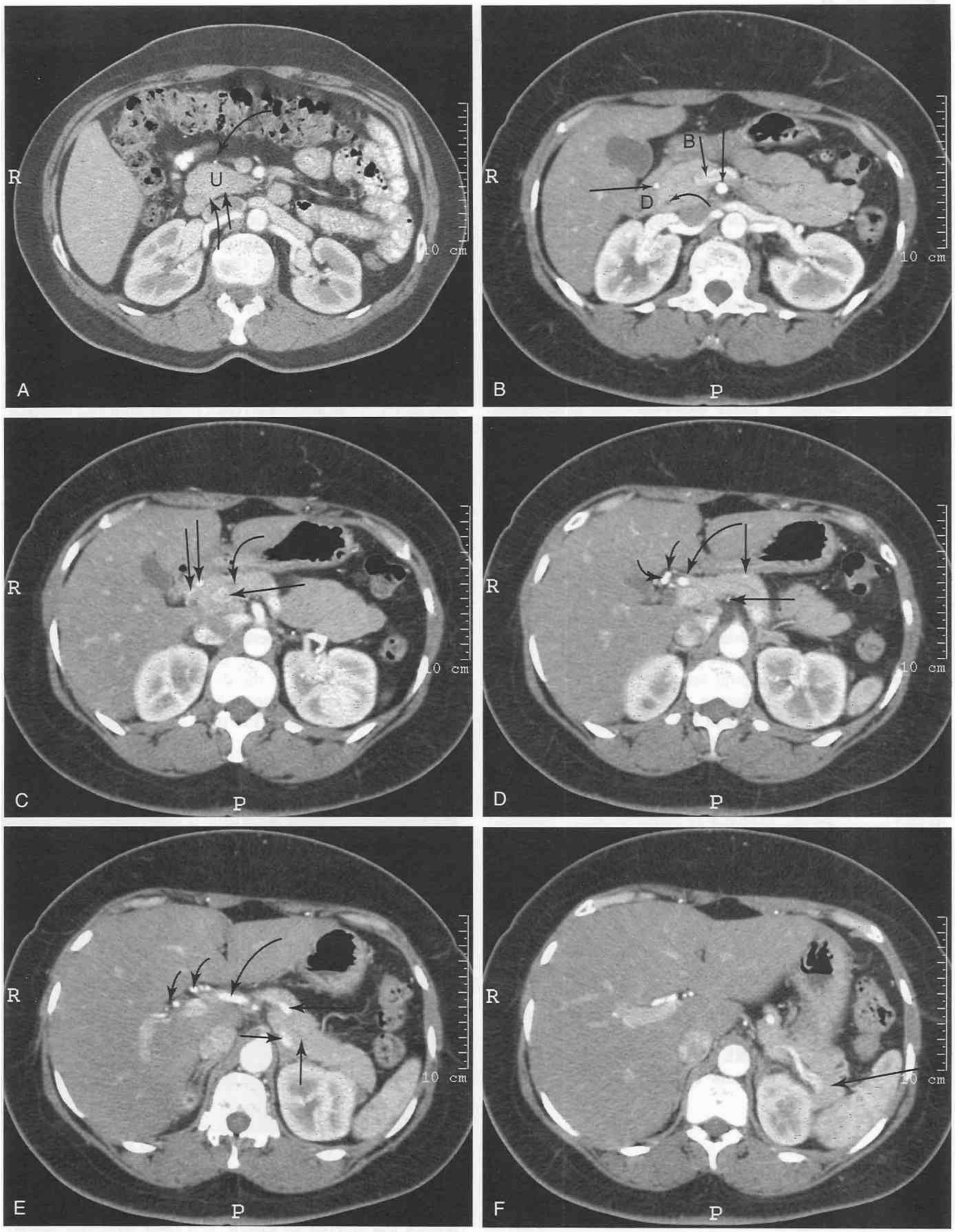

Figure 38–2. *See legend on opposite page*

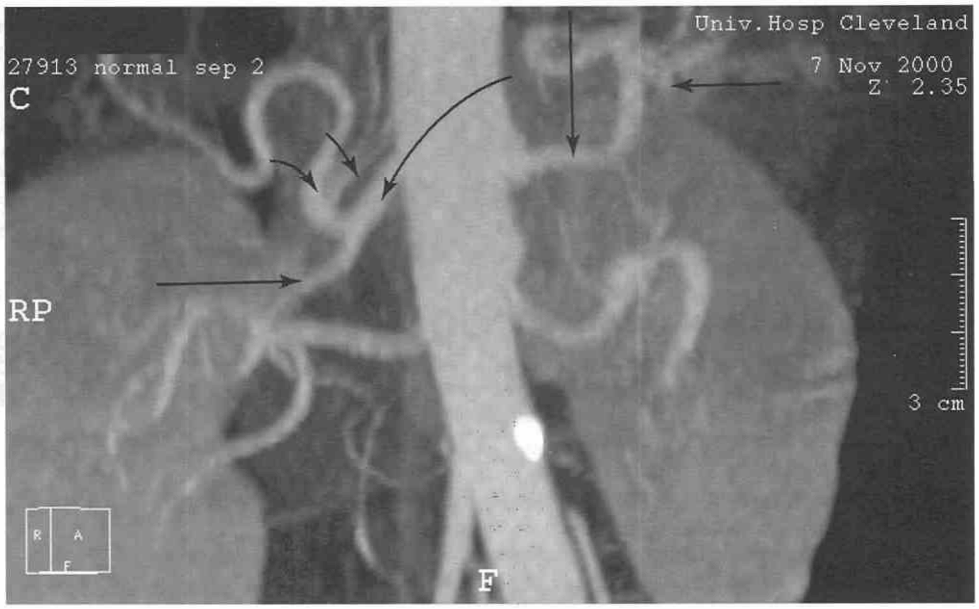

Figure 38–3. Arterial reconstruction of the vessels in the same patient correlates well with the axial slices. The splenic artery (*short vertical arrow*), common hepatic artery (*large curved arrow*), right and left hepatic arteries (*small curved arrows*), and gastroduodenal artery (*long horizontal arrow*) feeding the pancreaticoduodenal arcades are seen.

rior to the superior mesenteric artery and varies in thickness depending on the specific configuration (Fig. 38–2*D* and see Fig. 38–5). The tail and body of the pancreas lie immediately posterior to the fundus and antrum of the stomach (Fig. 38–2*C* and *D*). The omental bursa, or lesser peritoneal sac, is a potential space between the stomach and the pancreas that is never visualized unless it is filled with fluid. The entrance to this space, Winslow's foramen, is behind the free edge of the lesser omentum or the hepatoduodenal ligament, which contains the portal vein, common bile duct, and hepatic artery (Fig. 38–2*C* and *D*). The tail of the pancreas is adjacent to the hilum of the spleen, just anterior to the left adrenal gland, the upper pole of the left kidney, and the medial portion of the spleen. The tail usually tapers gradually in a constant plane, but occasionally it may be bulbous or angulated at the end. The tail may also be closely adherent to the left kidney or surrounded by the peritoneum in unusual cases.

Vascular anatomy in and adjacent to the pancreas has always been well displayed with spiral scanners, but the vascular detail with the multislice scanners is nothing short of spectacular. With the thin slice images of multislice imaging, the overall vascular anatomy can be reconstructed to give a traditional angiographic representation (Fig. 38–3). The axial slices show remarkable clarity, so that not only the major vessels but also the very tiny branches and parenchymal feeding vessels can be seen. The major vessels such as the splenic, hepatic, and superior mesenteric arteries are obvious, but the third order of most vessels is seen. The gastroduodenal artery, pancreaticoduodenal arcade, transverse pancreatic artery, and parenchymal arteries are clearly depicted (Fig. 38–2). Calcifications occur com-

Figure 38–2. *A,* In most patients, the uncinate process (U) is wedge-shaped and extends behind the superior mesenteric artery as seen in this image. Small pancreatic artery (*curved arrow*) is seen on anterior surface of the pancreatic head, as are small unopacified vessels on the posterior surface of the pancreatic head (*vertical arrows*).

B, The head of the pancreas is posterior to the bulb and antrum (B) and medial to the second portion of the duodenum (D). This slightly higher scan in the same patient shows the confluence of the superior mesenteric vein (*short vertical arrow*) with the first portion of the portal vein just anterior to the superior mesenteric artery (*long vertical arrow*). The large pancreaticoduodenal artery (*horizontal arrow*) is just lateral to the pancreatic head. The distal end of the common bile duct is seen in the head of the pancreas (*curved arrow*).

C, Higher scan shows the confluence point between the head and the body of the pancreas. The *horizontal arrow* indicates the partially opacified portal vein as it courses toward the liver. The *vertical arrows* point to the gastroduodenal artery with its arcade branches lateral to the head of the pancreas; the larger medial vessels represent the gastroduodenal artery, whereas the more lateral branches are the beginning portions of the arcade.

D, Next scan in this sequence shows the main portion of the pancreatic body with the main duct. Small vessels are exquisitely displayed, including the tiny parenchymal vessel entering the anterior gland (*vertical arrow*) and portions of the transverse pancreatic artery behind the pancreas (*horizontal arrow*). The main pancreatic duct is in the gland; with multislice scanning, it is seen in almost every case. The two major vessels in the porta hepatis are the common hepatic artery (*large curved arrow*), and the small, more lateral arteries (*small curved arrows*) are the proper hepatic forming branches to the right and left lobes.

E, Higher scan shows most cephalad portion of the gland, with the main portion of the body and tail, adjacent to the spleen. The splenic artery (*horizontal arrow*) "overlies" the body, the main hepatic artery (*long curved arrow*), the right and left hepatic arteries (*small curved arrows*), the splenic vein (*small horizontal arrow*), and pancreatic duct (*large vertical arrow*).

F, Very highest scan shows the upper portion of the tail (*arrow*) adjacent to the splenic hilum.

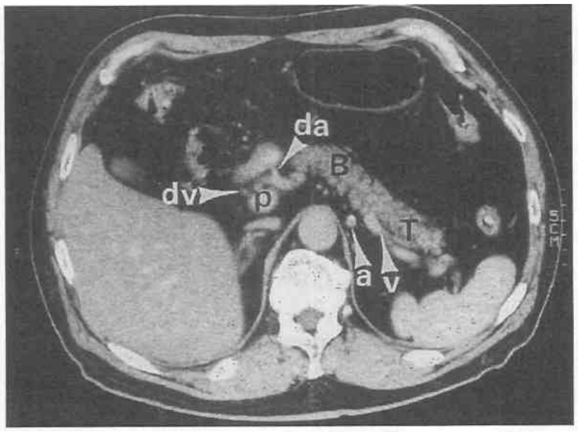

Figure 38–4. This pancreas [redacted] normal tapering of the tail and also a variation of density and texture very commonly seen. The gland shows discrete parenchymal lobules interspersed with fat. The pancreaticoduodenal artery (da), pancreaticoduodenal vein (dv), portal vein (p), splenic artery (a), and splenic vein (v) are noted adjacent to the body (B) and tail (T) of the gland. The splenic artery is usually quite tortuous, so only circular, cross-sectional portions are seen.

monly in the splenic artery and others and should not be mistaken for pancreatic calcifications.

The configuration and density of the pancreas may vary. There are several basic shapes; perhaps the most common is the gradually tapered pancreas in which the head is larger than either the body or the tail (Fig. 38–4). The narrowest portion is the neck, just anterior to the superior mesenteric artery. Another common variant is a dumbbell-shaped pancreas, which has a larger head and tail and a narrow neck immediately anterior to the superior mesenteric artery (Fig. 38–5). The tail of the pancreas may vary in its appearance, with the head being bulbous, angled, or especially close to the left kidney (Fig. 38–6). In some patients, in whom the peritoneal spaces have developed

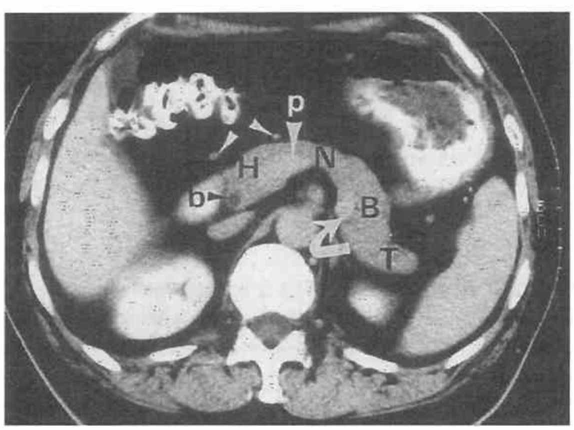

Figure 38–5. Slightly different configuration of the normal gland is seen. Almost all portions of the gland, including the head (H), neck (N), body (B), and tail (T), are seen. This level of the gland has a "dumbbell" shape, in which the head (H) and body (B) are almost equal in size. Also seen are the common bile duct (b), splenic artery (*curved arrow*), and pancreatic arteries (*arrowheads*).

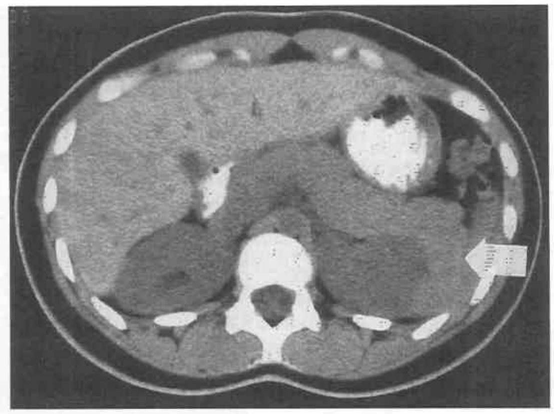

Figure 38–6. Variation of the tail (*arrow*) may be slightly bulbous and alm[redacted] the kidney.

abnormally in utero, the splenic flexure of the colon may actually be posterior to the pancreas and within the hilum of the spleen; in such cases, the pancreatic tail and the spleen are partially peritonealized.

One should be familiar with these various configurations, because pathologic processes may on occasion mimic them (Figs. 38–7 through 38–9), and the only clue may be disproportion in the different portions of the gland. With the most common tapering configuration, there should be a gentle decrease in the size of the gland from the head to the tail. A pathologic process may cause the head to be normal and the rest to be atrophied (see later sections). If a dumbbell-shaped gland is present, the two ends should be about equal in size. If the head or body is larger than the other, a pathologic process should be considered.

The size of the normal pancreas may be measured several ways.[34, 52] An average size or a range of sizes in the different regions of the pancreas can be used. The best anteroposterior measurements of the normal gland were made by Kreel and Sandin[139] as follows: head, 23 (± 3) mm; neck, 19 (± 2.5) mm; body, 20 (± 3) mm; and tail, 15 (± 2.5) mm. These measurements with CT differ from those with ultrasonography because ultrasonography is typ-

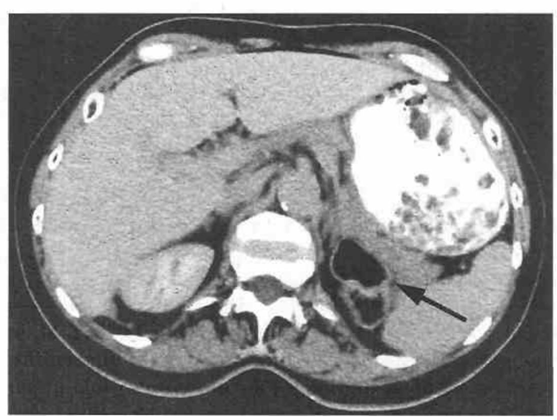

Figure 38–7. Scan shows a variation of the pancreatic tail in which the splenic flexure of the colon (*arrow*) is posterior to the tail of the pancreas. This variation implies incomplete fusion of the retroperitoneal fascia.

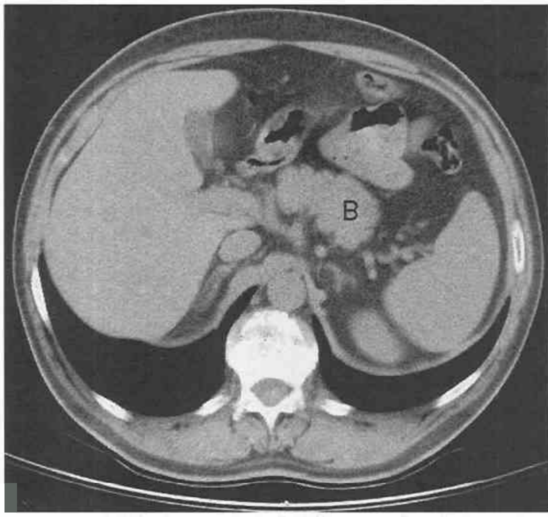

Figure 38–8. Pancreas with "short" body (B) without tail.

ically better for visualization of the splenic vein and artery, and so accordingly the ultrasonographic measurements tend to be smaller. The most accurate and noteworthy study of pancreatic size was performed by Muranaka and colleagues,[182] who studied the anteroposterior diameter of the head and body in various age groups. They reconfirmed the observations by others that the size of the gland decreases with age, but the ratio of the head to the body remains almost constant.

Little attention was given to the craniocaudad measurement of the gland until the description of pancreas divisum, as described later. The first to measure the maximal craniocaudad dimension were Pochhammer and associates.[205] They found that the mean length in women was 5.9 cm, with a range of 4.2 to 7.8 cm; the mean length in men was 6.2 cm, with a range of 4.8 to 7.6 cm. These measurements were made from older scanning devices, so the upper value limits are probably greater than they should be; later measurements have been made in conjunction with diagnosis of pancreas divisum (see later).

The main pancreatic duct—Wirsung's duct—runs the length of the pancreas and joins the common bile duct at Vater's ampulle (Fig. 38–10). The accessory pancreatic duct—Santorini's duct—is in the upper portion of the pancreas and is more horizontal than Wirsung's duct (Figs. 38–2*D* to *F* and 38–11). The common bile duct travels with the portal vein and hepatic artery in the edge of the lesser omentum or the hepatoduodenal ligament. The common bile duct appears as a low-density structure in the posterior portion of the head of the pancreas (see Fig. 38–2*C*). It and the normal pancreatic duct are seen during rapid injection of intravenous contrast material as described in the technique section. Although both of these ducts are commonly visualized, their clear delineation is also variable.

The density or attenuation of the pancreas is normally the same as that of soft tissue, or somewhere between 30 and 50 HU, depending on whether contrast material has been administered. The normal pancreas increases in density after intravenous administration of urographic contrast material; the more rapid the administration (i.e., dynamic), the denser the enhancement.[138, 164] If a bolus injection is administered, normal enhancement can be visualized during arterial, capillary, and venous phases. This enhancement of the normal gland has become an important differential sign for excluding necrosis in pancreatitis (see later section on necrosing pancreatitis). The margin of the pancreas may be smooth or somewhat irregular (see Fig. 38–4). In the normal gland, variable normal fat tissue may be present, either interspersed along the margin of the gland or within the glandular portions. The entire pancreas may be replaced by fat, and the patient may not have any clinical symptoms. Some pathologic conditions, however, produce infiltration of fat when atrophy of the gland occurs, such as cystic fibrosis.

Figure 38–9. [redacted] questionable mass can be seen in the head of the pancreas, on a spiral scan. *B,* Second scan shows, quite clearly, sharp delineation of the margins of the head, clear definition of the vascular margins, and the normal density of the head parenchyma. What was suspicious for a mass on an older spiral scanner is very definitely normal on a multislice scanner.

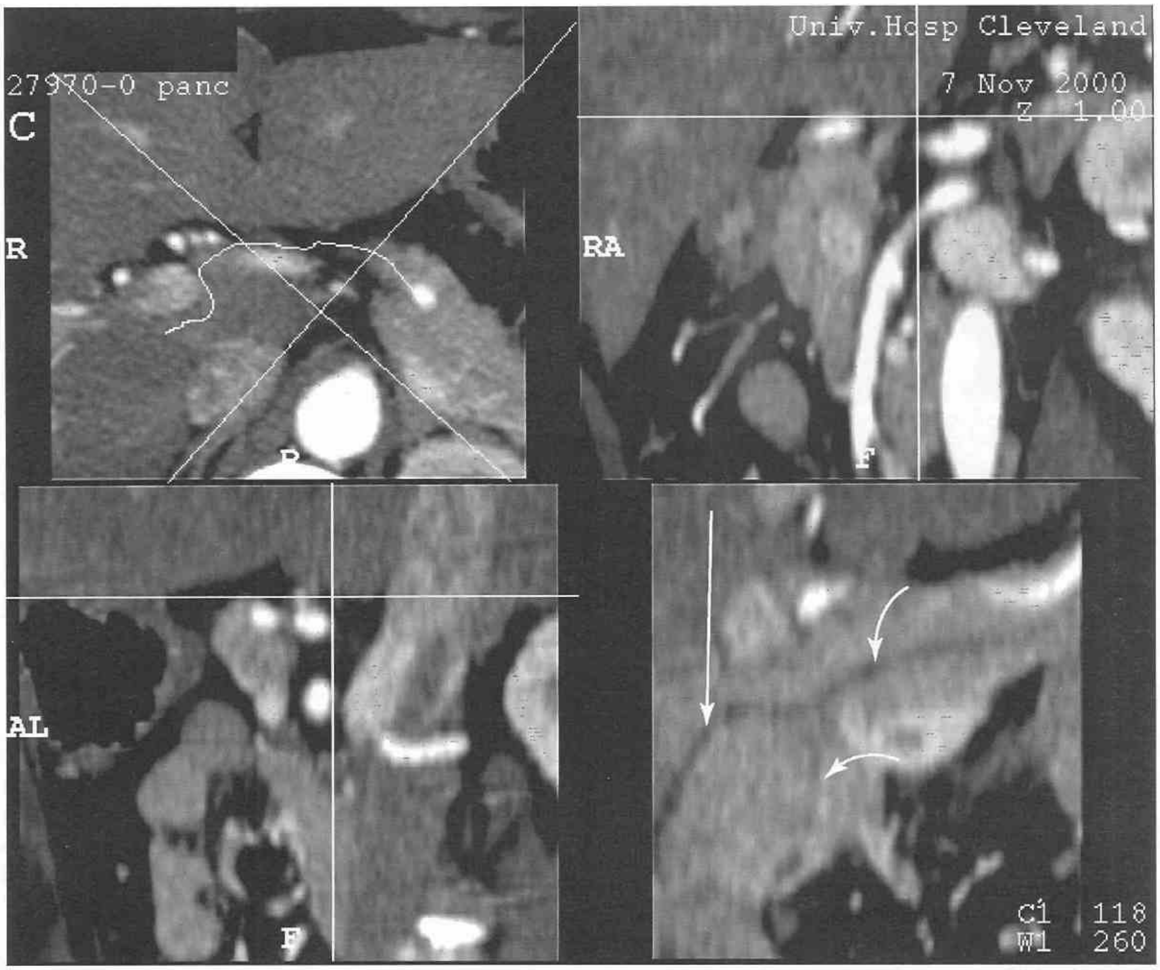

Figure 38–10. 3D Reconstruction of the pancreas, with a contour pathway, shows both major and minor pancreatic ducts as they converge and course toward the ampulla of Vater. The accessory duct (*vertical arrow*), also known as the duct of Santorini, is larger in this patient than the main duct (*lower curved arrow*), also known as the duct of Wirsung. The main duct (*upper curved arrow*) is seen in the tail.

The position of the pancreas may also vary. In most patients, the head is more caudad than the tail, and the tail is located adjacent to the hilum of the spleen. In some patients, the head and tail may be more horizontal and below the spleen, and in others, the tip of the tail may be high. In postnephrectomy cases or with agenesis of the kidney, the appropriate portion of the gland moves posteriorly to partially fill in the space vacated by the kidney. One should not mistake the soft tissue density of the retropositioned pancreas for recurrent tumor.

Pancreatic Vessels and Lymphatic Drainage

The vascular anatomy of the pancreas consists of arteries originating from the celiac and superior mesenteric arteries and veins that drain into the tributaries of the superior mesenteric and portal veins (see Figs. 38–2 and 38–3). The main arteries, consisting of the dorsal pancreatic, great pancreatic, transverse pancreatic, and pancreaticoduodenal branches, are almost always present, but the origin, size, and type of collateral supply may vary. The draining veins are also constant in that they parallel the arteries, and they drain into the pancreaticoduodenal, superior mesenteric, splenic, or portal veins. Small circular structures representing these vessels may be seen in and around the pancreas, but specific identification may be difficult. When pathologic occlusion of any of these vessels occurs, collateral vessels may open and become visible. A vein that has been reported to do this consistently is the posterior pancreaticoduodenal vein, as noted later.

The lymphatic drainage of the pancreas parallels the venous drainage. Small lymph nodes around vessels and in the various ligaments are commonly seen, but if nodes are 10 mm or larger, one should suspect neoplasm.

Impact of Multislice Scanners

The impact of multislice scanners has yet to be felt, but many significant improvements will occur. With the high-resolution, high-speed scans, the anatomy is absolutely exquisite. There is perfect visualization of even the most subtle change in density or margin of structures. The small-

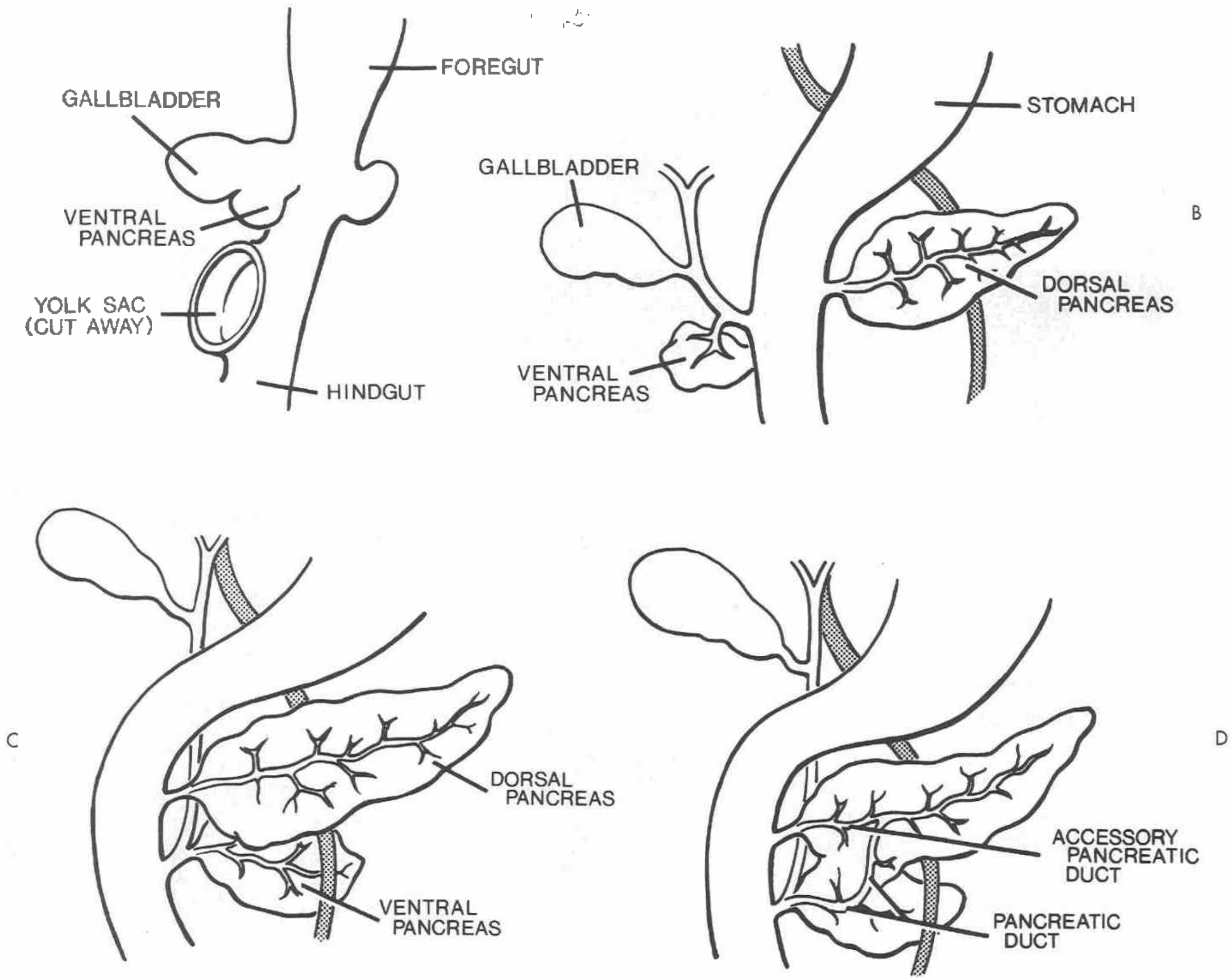

Figure 38–11. *A,* Embryologic evolution of the pancreas. This diagram shows the ventral and dorsal bud of the pancreas forming off the primitive gut. *B,* Dorsal and ventral pancreas evolves from the pancreatic buds. *C,* Without fusion of the dorsal and ventral pancreas, pancreas divisum develops. *D,* Normal fusion of the gland should result in atrophy of the accessory duct to the duodenum with maintenance of main duct patency. Compare this with a normal duct in Figure 38–10.

est vessels can be visualized, even the tiny ones entering the glandular parenchyma itself. The end result of this improvement is better definition of detail in both normal and abnormal conditions. In some cases, when an older spiral scan demonstrates a subtle variation in contour suggesting an early neoplasm, a multislice scan clarifies a spurious finding (see Fig. 38–9).

Furthermore, with the remarkably vivid anatomy and the multiplanar reconstructions, it is clear to see that in the near future, endoscopy will be completely replaced except for the interventional procedures (Fig. 38–12; see also Figs. 38–113 and 38–136). I expect further refinement of the associated techniques that will permit accurate assessment of normal and abnormal ducts and glandular function. It is quite clear that as further techniques using pharmacology are developed, the function of the gland, as reflected by blood flow, will be assessed by hormonal stimulation or suppression.

Normal MRI of the Pancreas

The appearance of the normal gland on MRI depends partially on the specific pulsing sequence used, but the overall configuration and intensity appearances are consistent. As one can note in Figure 38–13, the gland, with its uniform texture and the adjacent blood vessels, is easily appreciated. The relationship of the splenic vessels, gastroduodenal vessels, common bile duct, and other structures is consistent. With either less than optimal signal characteristics or motion artifacts, the best approach is to identify the location of the splenic vein and then extrapolate from that structure. Considering the many pulsing sequences that

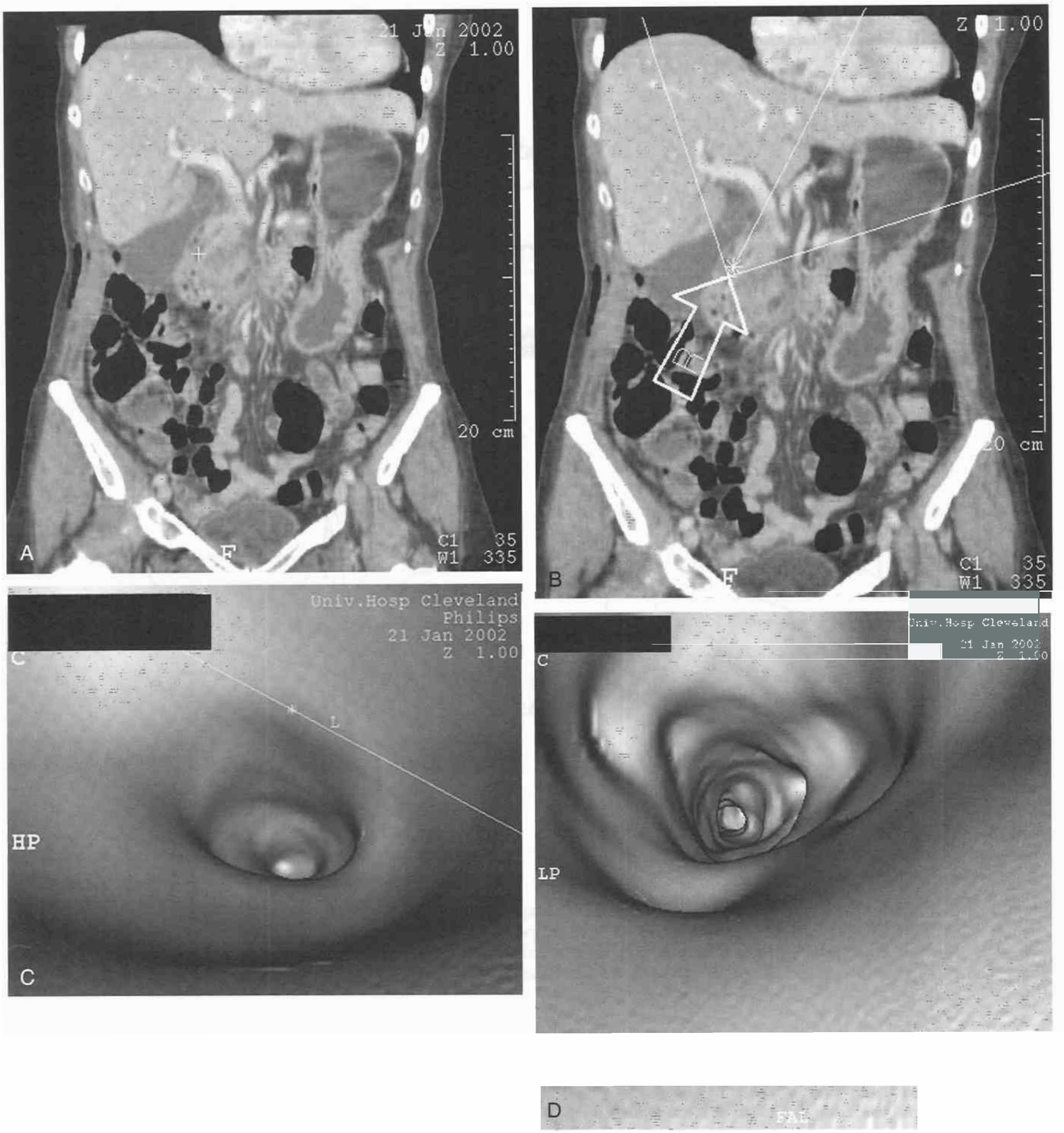

Figure 38–12. *A*, Multislice images permit accurate reconstructions as shown in this coronal image of the pancreas. The pancreatic duct is dilated but better characterization of the duct is difficult. *B*, Image shows navigational tools superimposed on the image, the arrow path will follow the dilated duct. *C*, Proximal duct shows dilatation but is smooth along the wall. *D*, At a more distal site in the duct, the sacculations and irregularities can be better appreciated in the wall.

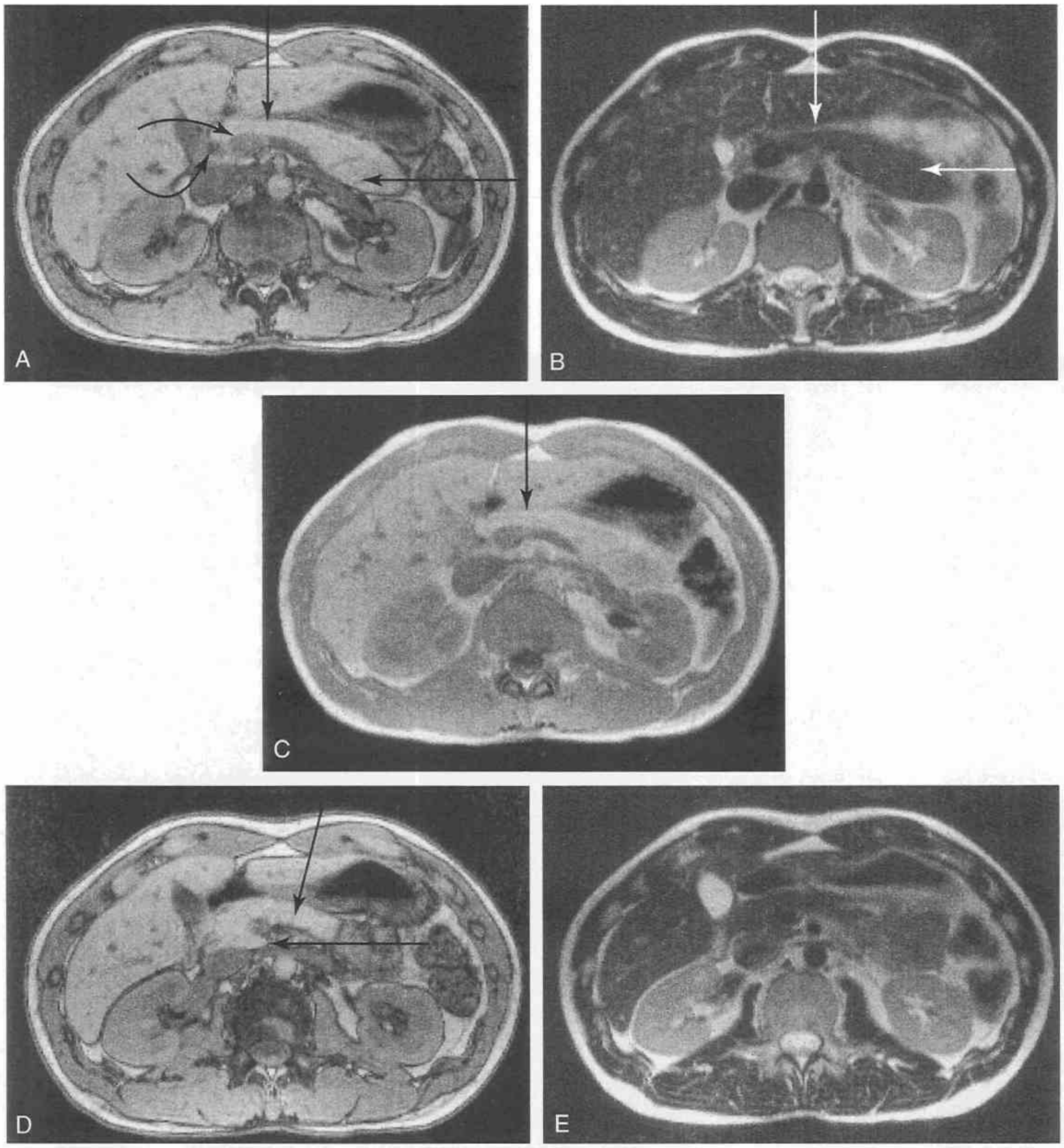

Figure 38–13. Normal-appearing gland with various pulsing sequences; see MRI section for specific technique. *A,* Normal gland, T1 weighting out of phase, shows discrete gland with the neck portion (*vertical arrow*) and tail of gland (*horizontal arrow*). The portal vein (*large curved arrow*) is seen behind the head, and the common bile duct (*small curved arrow*) is seen. *B,* Same slice with in-phase T1. Note the change in the visualization in the margins of the organs. The neck (*vertical arrow*) and tail (*horizontal arrow*) are again seen. *C,* Appearance of the gland during T2-weighted sequences. Note the effects of the change in sequence on the delineation of the margins of organs. *D,* Lower axial slice in same patient shows segment of the uncinate portion (*horizontal arrow*) of the gland behind the superior mesenteric artery, with T1 weighting out of phase. The neck (*vertical arrow*) is again seen. *E,* Lower axial slice with T2 weighting in the region of the head; compare with *D.*

are now available, it is not possible to perform them all in every patient. The best two sequences that I have found are the standard spin-echo T1-weighted images, which give good anatomic detail with relatively high signal intensity. A variety of breath-holding "flash" images are now available that minimize patient motion (see section on MRI technique).

Embryology and Congenital Variants

Although the embryology of many organs is well known to most physicians, knowledge of pancreatic development is less prevalent. In the early stages of the embryo, there are a dorsal and a ventral pancreas, which are located on opposite sides of the gut. When the rotation of the bowel occurs, the dorsal and ventral pancreas fuse into a single gland. The dorsal portion becomes the body and tail, and the ventral portion becomes the head and uncinate portion of the gland (see Figs. 38–2 and 38–4).

As one might anticipate, the outcome of these complex events is variable, and the final form of the gland has a wide spectrum of variation, including a prominence of the head in the approximate area of the fusion, agenesis of the dorsal or ventral portion, annular pancreas, pancreas

divisum, and left-sided pancreas.[85] Furthermore, this embryologic information explains the wide variation in the ductal system.[165]

Ductal Variations

Before the refinements of CT, discussion of ductal anatomy and variation was not relevant. With the current high-resolution systems and spiral scanning systems, one should be aware of possible variations because of the consistent visualization of the ductal systems during normal and pathologic states. The main pancreatic duct in the dorsal pancreas combines with the ventral component to form the main duct, Wirsung's duct, which enters through the main papilla and ampulla of Vater. In most instances, the minor duct, Santorini's duct, becomes atretic. If the accessory Santorini's duct stays patent, it enters by means of the minor papilla (see Fig. 38–11). The multislice scanners permit reconstruction and display of the normal pancreatic duct and subtle variations. Although no studies have been performed comparing reconstructions to endoscopic retro-

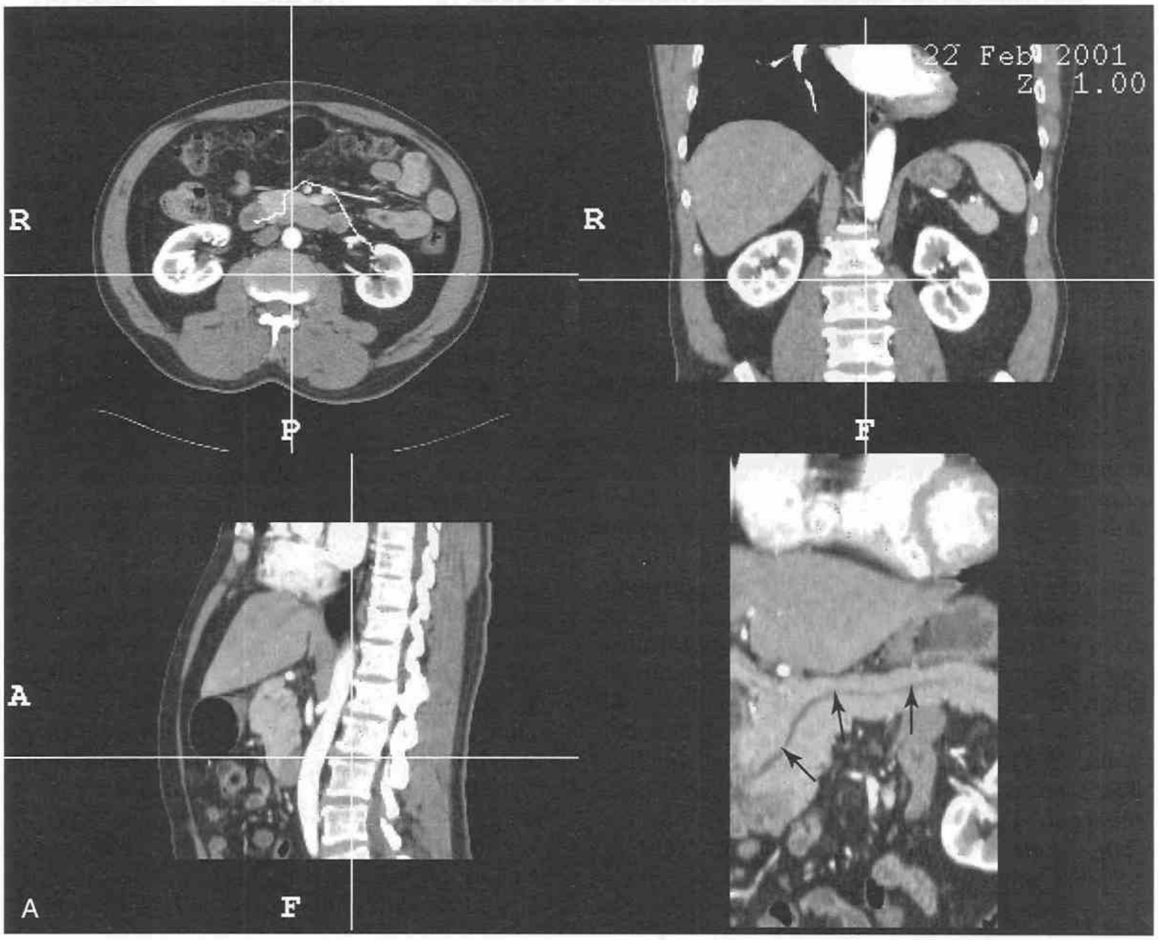

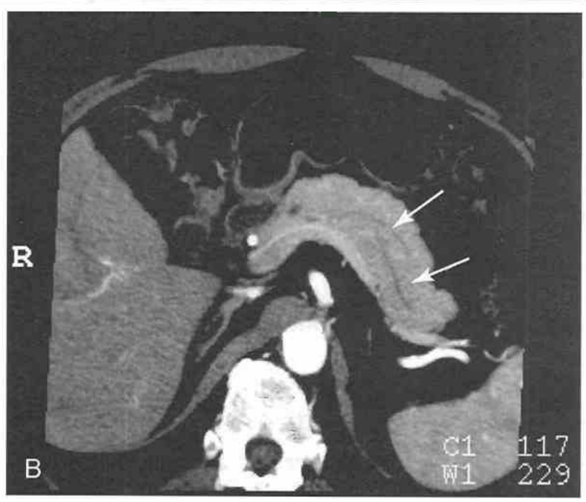

Figure 38–14. *A,* Reconstruction of pancreatic duct shows main duct throughout length of gland. *B,* Multiplanar reconstruction of the same duct system in a slightly oblique axial mode shows a duplication of the main duct, which was not suspected and is probably of no clinical significance.

grade cholangiopancreatography (ERCP), it is very probable that ductograms by CT or MRI will replace routine diagnostic ERCP in the future (Fig. 38–14 and see Fig. 38–112).

Prominent Fusion Anomaly

One permutation of the variable anatomy is a prominent head of the pancreas at the junction point between the head and neck of the gland, close to the main portal vein. The contour of the gland may be so prominent that there may be a concern about an early neoplasm. Fortunately, with experience one can learn to identify this normal variant by carefully noting the density resulting from intravenous contrast enhancement and the appearance of the uncinate portion of the gland. With contrast enhancement, the density of the normal head is increased in a comparable amount relative to the adjacent gland. Virtually all non–islet cell tumors are hypovascular and show a lower density than normal, whereas most islet cell tumors are hypervascular and show an increase in density. Notwithstanding this information, the clinical suspicion may occasionally be so high that percutaneous biopsy is performed (see Chapter 61).

Pancreas Divisum

One of the most common anomalies is *pancreas divisum,* the nonfusion of the dorsal and ventral ductal system. Frequency by autopsy studies is reported between 4% and 14%, whereas ERCP confirmation of this entity is stated to be between 1% and 7%. Normally, during the 8 weeks of embryologic life, fusion of the ductal bud occurs to form the adult system. When such fusion does not occur, two separate entry points through the major and minor papilla form, which are the exclusive ductal paths from the dorsal and ventral gland.

The mere presence of this problem is not in itself significant, but patients with it are considered at risk for pancreatitis in the dorsal portion because of frequent narrowing of the duct at the papilla. Such pancreatitis is recurring unless corrective action is taken to eliminate the narrowing.

Diagnosis of this entity is best made on ERCP, but CT findings may suggest the correct diagnosis.[154, 233, 234] Two findings appear to be consistent among the various articles reporting on this topic: the increase in the craniocaudal length and the occasional presence of a fat cleft separating the dorsal and ventral elements. Soulen and others[233, 234] reported a size variation of the pancreas in a group of 12 patients with pancreatic divisum. These researchers noted an increase in both the anteroposterior and the craniocaudal dimensions; in the anteroposterior size, they noted a measurement of 3.2 cm compared with 2.7 cm for normals, and in the craniocaudal size, a measurement of 5.4 cm in pancreas divisum compared with 4.4 cm in the normal gland. Lindstrom and Ihse[154] found that the craniocaudal length of the pancreatic head was 40% greater in patients with pancreas divisum than in normal patients. They found that the anteroposterior dimensions and the total volume of

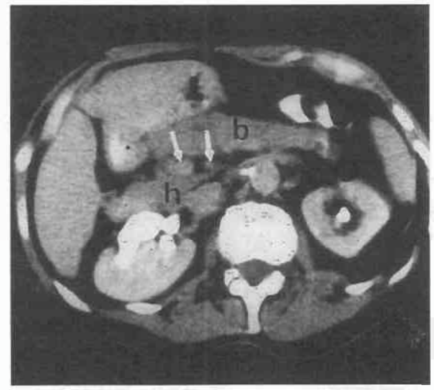

Figure 38–15. Pancreas divisum, which shows a fat cleft separating the head (h) from the body (b). The superior mesenteric vessels (*arrows*) are noted within the cleft. This appearance was seen on all sections through the gland.

the gland did not vary between the two groups. Zeman and colleagues[270] reported the occasional presence of the fat cleft separating the two segments (Fig. 38–15). An associated finding that is not specific is that the dorsal duct was visualized in a high percentage of cases, which incidentally was said to be normal; the ventral duct was infrequently seen.

With the occurrence of pancreatitis, secondary changes in the gland, such as focal enlargement, irregularity of the margins, and calcifications, can occur. These changes have been noted in the reports on pancreas divisum and have been recognized as sequelae of the inflammation rather than primary findings of the problem. One author believed that the increased anteroposterior size noted by Soulen and others[233, 234] might have been due to inflammation. Gold and coworkers[79] reported a case of pseudocyst associated with pancreas divisum.

Annular Pancreas

When rotation of the embryologic analogues does not occur and fusion takes place, an annular pancreas results.[186] In such cases, the CT appearance suggests a mass in the head of the pancreas. Although most case reports have described these findings as false-positive cases for tumors, the prospective diagnosis should be possible with an adequate contrast enhancement, correlative studies, and clinical information (Fig. 38–16).

Agenesis of the Gland or Short Pancreas

Several case reports showing agenesis of the dorsal pancreas have been published under the topic of congenital short pancreas.[93, 100] In these cases, the head of the pancreas is in a normal location, but the body and tail of the pancreas distal to the neck are absent (Fig. 38–17). Congenitally short pancreas has a high association with polysplenia and other gastrointestinal anomalies, such as partial situs inversus, common mesentery with or without malrotation, preduodenal portal vein, lobulation of the liver, agenesis of

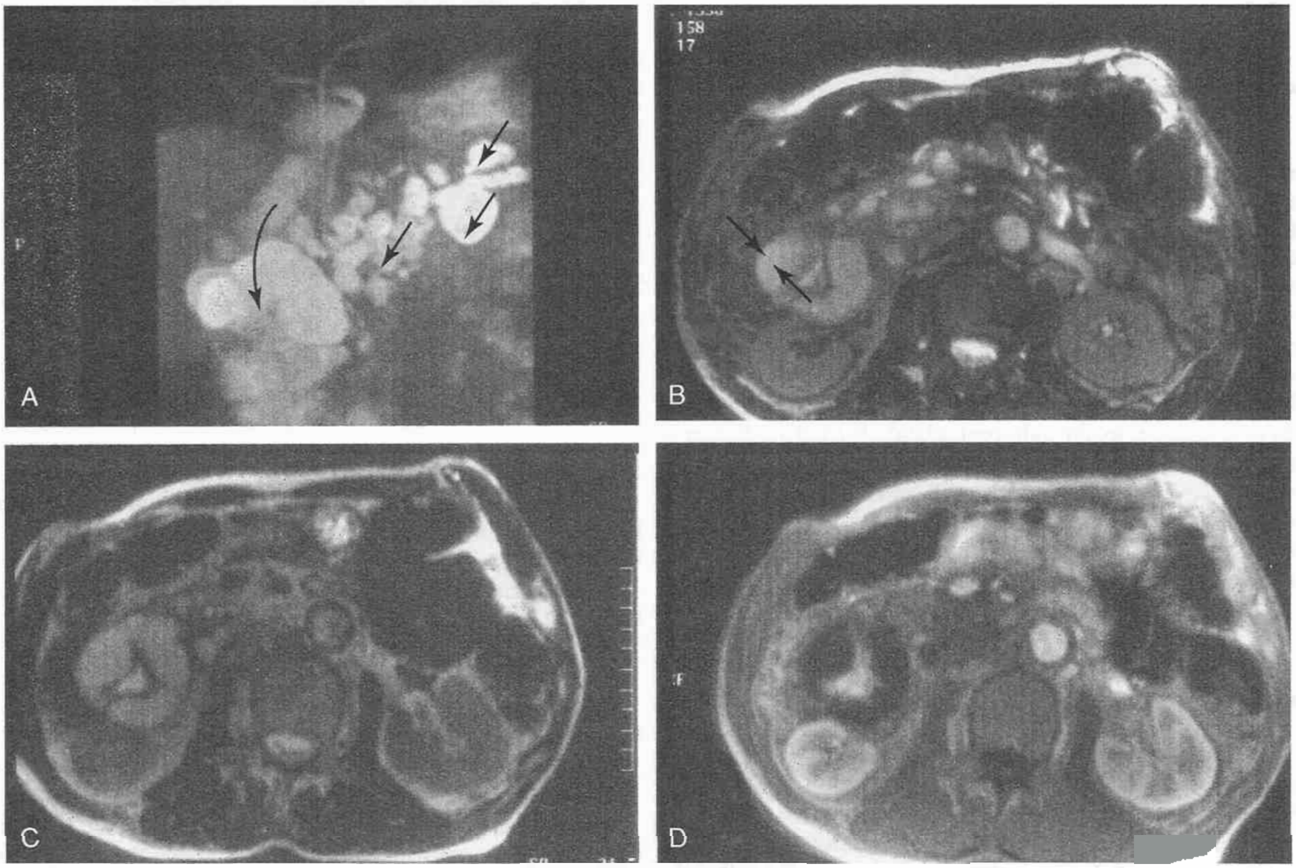

Figure 38–16. *A,* MR pancreatogram in a patient with an annular pancreas. The pancreatic duct is very dilated owing to chronic pancreatitis. Note the cystic enlargement of the duct in the body and tail (*arrows*) as well as the massive dilatation of the duct in the head. The head of the pancreas circumferentially surrounds the second portion of the duodenum (*curved arrow*). *B,* Axial image with true FISP sequencing, showing the dilated annular pancreatic duct (*arrows*), around the duodenum. *C,* Same image with T2 weighting. *D,* T1-weighted image obtained after instillation of gadolinium shows cystic duct and vascular enhancement. Courtesy of Elmer Merkel, University Hospitals of Cleveland.

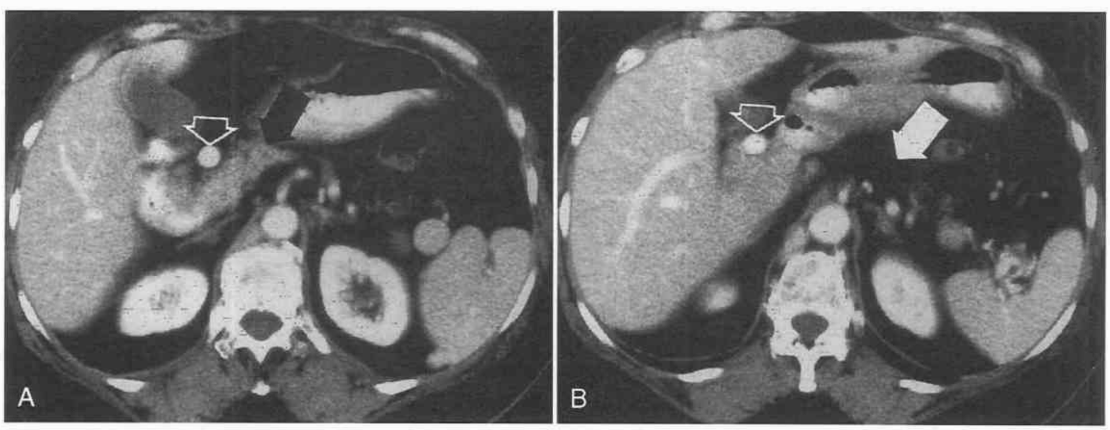

Figure 38–1[redacted]nge[redacted] pancreas or age[redacted]dorsal gl[redacted] This level shows the head of the gland (*black arrow*) behind the s[redacted] Note [redacted]enal portal vein [redacted]). *B,* A h[redacted]r section through the gland shows absence of the gland in the body and tail (*white arrow*). The preduodenal portal vein (*short arrow*) is again seen.

the gallbladder, biliary atresia, and absence of the omentum. The associated pancreatic anomalies reported include intraperitoneal location and annular shape. There has been a single case report of a carcinoma in such a case.

Ectopic Pancreas

The most common sites for ectopic pancreatic tissue are the esophagus, stomach, duodenum, jejunum, and Meckel's diverticulum. Ectopic tissue can produce a mass in such areas if the primordial ductal system and acinar elements produce and retain excretions.

Other Variants

In some other variants, the configuration of the gland varies or confusion arises because of embryologic or pathologic changes that occur in the adjacent structures. Several problems occur that are associated with anomalous rotation of the bowel and formation of the peritoneum. The splenic flexure may reside between the tail of the pancreas and the spleen, with associated abnormal contour and size. When malrotation of the duodenum occurs, the third portion of the duodenum does not cross beneath the superior mesenteric artery and vein. Other authors[18] have stated that a reversal of the position of the superior mesenteric vein and artery helps diagnose this entity (our cases did not show this finding).[187] There has been a single case report[226] of a torsion of the tail of the pancreas, which probably occurred as a result of abnormal fusion of the peritoneum and retroperitoneum (Fig. 38–18).

Several unusual problems can produce the findings of a spurious mass.[184] In patients with severe scoliosis, the acute angulation of the body can distort the gland so its anteroposterior dimension may be increased because of "buckling." A spurious mass can also be produced by an enlarged caudate lobe of the liver (Fig. 38–19), accessory spleen, fluid-filled diverticulum, or benign lymph node enlargement.

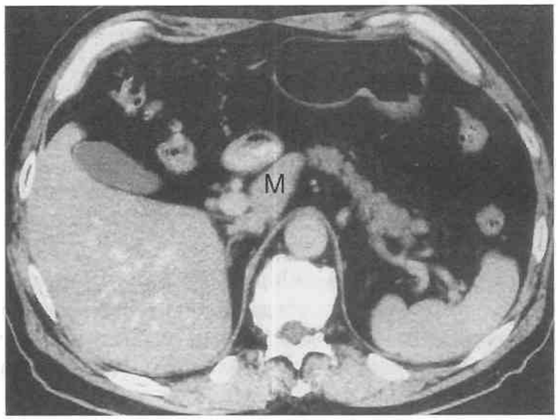

Figure 38–19. This image shows the slightly higher-density spurious "mass" (M) in the head of the pancreas. The mass is the caudate lobe of the liver projecting down and effacing the normal gland.

General Indications and Selection of Imaging Studies

Since the advent of the modern imaging technologies ultrasonography, CT, and MRI, evaluation and controversy about the appropriate roles and selection of the different modalities have continued. These topics, however, represent "moving targets" because of the remarkable advances that continue at an unprecedented pace. In general terms, however, it has become apparent that some inherent limitations can now be identified related to speed of data acquisition, signal-to-noise limitations, and inherent properties of imaging various biologic tissues. These three modalities have their own advantages and disadvantages, which are discussed later, but it is now apparent that CT is emerging as the preeminent imaging modality for the pancreas.

Ultrasonography continues to improve, with progress in signal refinement such as harmonic imaging and sophisticated Doppler strategies. Of course, there is no radiation with ultrasonography, making it a very safe examination.

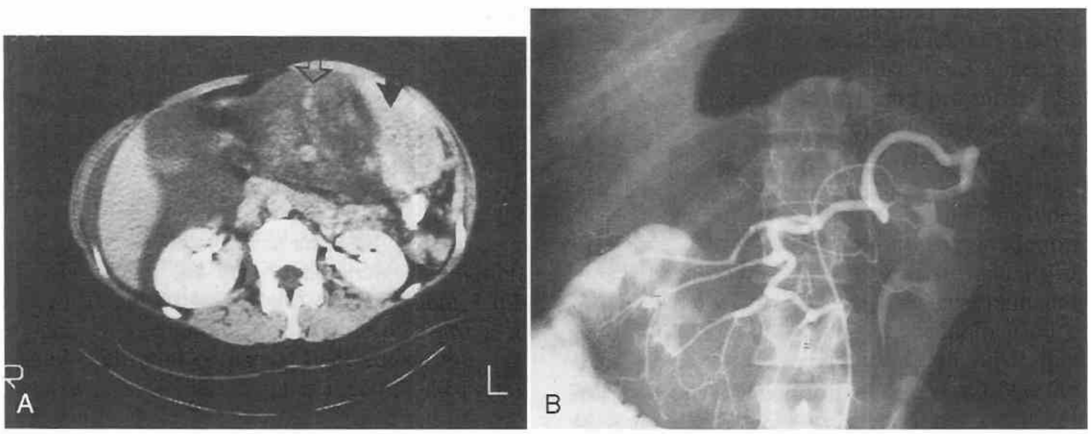

Figure 38–18. *A,* Large mass in the midabdomen (*open arrow*) that is adjacent to the spleen (*arrow*). The mass was the tail of the pancreas, which was edematous because of torsion of the gland. *B,* Angiogram shows a circular configuration of the splenic artery and a cutoff at the end. (From Sheflin JR, Lee CM, Kretchmar KA: Torsion of wandering spleen and distal pancreas. AJR 142:100; copyright by American Roentgen Ray Society, 1984.)

There still remain inherent problems with imaging deep anatomy in large patients, because for high resolution, high-megahertz transducers are required. Such high-megahertz systems are limited by penetration and interference from high selective surfaces, such as air, bone, and metal. On the other hand, when the anatomy is accessible, Doppler ultrasonography is far superior to either CT or ultrasonography for measurement of vascular flow or other vascular characteristics.

In superficial structures, ultrasonography is unparalleled for the definition of texture changes and anatomic detail, for example, in the thyroid or the ovaries. The importance of close proximity and high resolution can be best appreciated by looking at the detail provided by endoscopic ultrasonography; because of the close proximity of the pancreas to the duodenum, high-resolution devices can be used, and the detail is spectacular. Therefore, for the accurate routine evaluation of the pancreas, ultrasonography at this time takes a secondary role to CT.

The refinements in MRI have been spectacular in recent years. This modality has the advantages of no radiation and being very good in the definition of anatomy and display of tissue characteristics. Because of the sophisticated pulsing sequences now available, definition of deep anatomy is not a problem, although accurate detection of calcification and air still presents a problem. In a given case, calcification or gas can be problematic because MRI cannot accurately detect small amounts nor distinguish between the two because of the absence of mobile protons in either material. Gadolinium contrast material is, of course, necessary for the best quality of scanning, and fortunately, there is no cross-reactivity with the iodinated contrast agents used in CT; this adds an important alternative for imaging in patients with pancreatic disease in whom allergy precludes the possibility of a contrast-enhanced CT scan.

The greatest strength of MRI is the measurement and display of subtle tissue signal changes related to a T1- and T2-weighting and proton density. The new high-speed techniques permit rapid imaging of tissue signals, contrast enhancement, and fat suppression which are quite accurate for unusual tumors of the pancreas, such as mucinous tumors and endocrine tumors. Another useful quality has been the ability to use multiple planes in the assessment of anatomy. Because of these properties, MRI is the modality of choice for unusual pancreatic tumors or problem-solving in the pancreas.

CT with multislice technology is now the absolute mainstay of pancreatic diagnosis for actually the very same reasons originally identified for CT. Over the past 20 years, comparing the qualities of the different modalities was quite difficult because the pace of innovation, development, and refinement varied among the three modalities. At this time, the new developments in multislice CT have clearly shown that the remarkable qualities of CT will give it the technologic edge for a number of years to come.

CT has no limitations related to definition of anatomy and density measurements. Prior shortcomings related to speed of acquisition and 3D anatomy have been eliminated. Size of patient, location of anatomy, proximity or presence of calcium, air, or metal, and even some patient motion have no adverse effect on CT imaging. The issues related to radiation dose have been minimized because of the new techniques and methods used to minimize radiation dose now implemented by manufacturers. These methods are based on direct measurements of photon flux during the scan with adjustments "on the fly" or through assessment of body size or diameter and adjustment of the dose.

The speed and definition of new CT scanners are so remarkable because true 3D imaging is possible. Because the imaging voxel is symmetrical, measuring less than 1 mm in all planes, axial and reconstructed images have identical resolution. The only real disadvantage of the new CT scanners is that intravenous contrast material is required for most examinations. The issues related to allergic reactions and renal function have been managed for many years so the real impact of this issue for the future is minimal.

General CT Technique

The technique for CT examination of the pancreas is straightforward but may vary depending on some unusual circumstances, anatomy, and the information sought. Most commonly, the patient is examined in the supine position, and a large amount of intravenous contrast material is administered.

Multislice Scanner

With the modern multislice scanners, the techniques for scanning are remarkably simplified because of the exquisite imaging detail. With the very small isotropic pixels and the ability to evaluate the anatomy in three dimensions, there are never any problems visualizing very thin fat planes, small vessels, overlapping intestinal loops, or unusual congenital variations. Authors for many years have recognized the theoretical benefit of isotropic data sets, but the multislice scanners now permit such data collection.[19]

For definitive evaluation of the pancreas, it is appropriate to administer oral and intravenous contrast material. The amount of intravenous contrast material required is much less than with older spiral devices. A single injection of 90 mL of contrast material is more than sufficient to scan and rescan the pancreas multiple times. For the best results, one can use a bolus tracking program, or a simple manual delay will suffice. For best visualization of subtle disease and possible arterial reconstruction, it is appropriate to use 3-mm-thick scans. If ductal disease is suspected, 1-mm sections should be performed.

The pancreatic area should be scanned in three phases—baseline, arterial, and venous—for the following reasons: The baseline scan is critical for the detection and accurate localization of any calcification, which is obviously important to diagnosing and differentiating ductal calculi, chronic pancreatitis, vascular aneurysms (to distinguish pseudoaneurysm from true aneurysm), tumor calcification, and chronic infections.

The arterial phase with reconstructions defines normal or abnormal vessels. This is important in tumors for evaluating the presence of aberrant vessels or encasement. Aberrant vessels or anomalies are important to guide surgical intervention. Encasement is critical to determine inopera-

bility. Increased vascular enhancement is common in primary endocrine tumor and metastatic disease of the pancreas. The passage of contrast material may be so rapid that such enhancement may not be visible during the later venous or equilibration phase. The venous phase is critical to assess the homogeneous enhancement of the normal glandular parenchyma in order to detect subtle low-density lesions, which can be produced by cancer or focal inflammation, as well as venous enhancement.

McNulty and associates[173] studied the effects of contrast-enhanced multiphasic imaging with the multidetector row helical CT on the the visualization of the vasculature. In a group of 49 patients, 21 normal and 28 with cancer, they studied the visualization of the vessels and enhancement of the parenchyma. With multiple scanning sequences, they evaluated the arterial phase (AP), pancreatic parenchymal phase (PPP), and the portal venous phase (PVP). As one might expect, they found that maximum arterial enhancement was seen during the PPP and maximum venous enhancement in the PVP. The pancreatic adenocarcinoma was best seen in PPP and PVP. They recommended that the AP be reserved for patients in whom angiography was required. Unfortunately, this recommendation is less useful because one can reliably plan a technique to trigger only on the arterial phase, so refinement of the technique (excluding the AP) is difficult at this time. In the future further work on the bolus chasing or detection programs will permit selection of the contrast phases to permit scanning during the venous phase. Reliable scanning of the venous phase is important because numerous researchers have shown that small veins are excellent indicators of local spread of tumor and inoperability.[257, 267]

Standard Spiral Scanner

Assuming that one has a traditional spiral scanner, the injection should be made through a moderate-sized needle with a rapid injection rate. In most centers, a loading dose of 25 to 55 mL is given immediately, followed by an infusion rate of 1 to 1.5 mL/second to a maximal accumulated dose of 150 to 200 mL. The amount of contrast material given must be varied according to the patient's clinical and renal status. When modern equipment with either cluster or spiral scanning is used, the pancreatic area is scanned over several minutes. If one does not have the luxury of a high-speed scanner, the contrast material should be given with a 50-mL loading dose followed by a constant infusion during the entire period of the scan; administration rates may need to be adjusted according to the scanning time. Appropriate amounts of intravenous contrast material are important to provide enhancement, which highlights and distinguishes tumors, vascular or avascular, and blood vessels, whether they are normal, neovascular, collaterals, or aneurysmal.[132]

Because most of the studies are performed during the course of a general examination, the scan slices are typically contiguous 8-mm slices or spiral scans over the entire upper abdomen. In special cases, if one is aware of pancreatic disease and one wishes to optimize visualization of the pancreatic duct, thin sections of 4 or 2 mm may be used. One should be aware of two shortcomings with these techniques, related to contrast material and radiation dosage. Because the thin sections require more time to cover the anatomy, the rate of contrast administration must be changed. Furthermore, because more x-ray output is required to make the images acceptable, the patient receives a higher radiation exposure.

It is also important to administer oral contrast material for opacification of the duodenum and the bowel. Although iodinated materials can be given, they are less palatable, and they stimulate peristalsis, which can produce a large number of artifacts. Dilute barium solutions are better accepted by patients because of the pleasant taste, and they seldom produce artifacts. With slow scanning devices or with iodinated oral contrast material, one should be careful to distinguish the contrast material from pancreatic calcification so as not to miss or overestimate calcifications.

On occasion, even with modern scanners, portions of the pancreatic tail or head may be difficult to visualize if there is a paucity of fat in the retroperitoneum in front of the gland with the patient in a supine position. In such cases, examining the patient in the decubitus position after the ingestion of oral contrast material is helpful. This particular technique is valuable because it eliminates three troublesome false-positive possibilities: (1) with contrast material gravitating into the antrum of the stomach and duodenum,[88, 128, 185] those structures cannot be confused for masses in the head of the pancreas; (2) air in the fundus of the stomach eliminates the pseudomass that can be produced by the partial volume effect of the fluid-filled stomach fundus; and (3) the jejunum moves away from the body and tail of the pancreas, eliminating another pseudomass.

Scanning Parameters and Radiation Dose

This is a complicated time for discussing scanning parameters because a large number of older spiral scanning devices are still in common use but a rapid replacement of these devices with multislice technology is occurring. With either device, the same clinical principles are valid. One should tailor the scanning parameters to best visualize the disease being sought. In general, one should use thicker slices for general survey of the pancreatic area, but thin sections should be used for high resolution of ductal anatomy and disease.

Scanning parameters on the CT scanner must be appropriately planned according to whether the scan is being performed for a general survey of the abdomen or a specific examination of the pancreas. The same principles of physics and clinical judgment must be exercised with either the multslice devices or the standard spiral devices, except that the considerations are somewhat reversed. With the older spiral scanning devices, it is easier to perform thick slices because of limitations of the x-ray tube and longer scanning times. With those devices, one consciously makes the decision to use thin sections when specific high-resolution detail is required. The path of least resistance is to not perform thin sections routinely.

With the multislice device, the equipment is so powerful and fast that it is almost easier to perform thin sections of

1 mm or less on every patient. The path of least resistance is to scan everyone with such thin sections and to perform multiple repetitive scans over the pancreas routinely. The temptation to produce so many scans must be avoided, and the study planned rationally. If one does not routinely plan the approach for each patient, there is a great risk that patients will receive excessive radiation doses for no clinical benefit.

Using these guidelines ensures that excessive radiation dose will not be administered to patients. These issues can be addressed by both selection of the appropriate technique and technologic improvements provided by the vendors. With older CT scanners, the highest kilovoltage possible should be used combined with the lowest suitable milliampere-second (mAs) value. It is the responsibility of the radiologist, during the installation of equipment and software, to ensure the standard radiation exposure is set to appropriate levels. This is, of course, very important for children. With the newer scanners, the vendors have introduced new hardware and software that permit dynamic adjustment of the radiation dose. It is estimated that new techniques reduce the radiation dose for a single scan by 30% to 50%.

I find it gratifying to note that vendors have unknowingly taken advice from the previous edition, in which I stated, "It would seem logical that commercial vendors would be more receptive to making devices that would permit adjustable doses either automatically (why not photimed CT scans?) or manually to minimize the radiation dose to small patients and to ensure good quality scans in large patients."

MRI Technique

As for many other organ areas, MRI pulsing and scanning techniques for the pancreas vary significantly among the many groups reporting in the literature. The art and

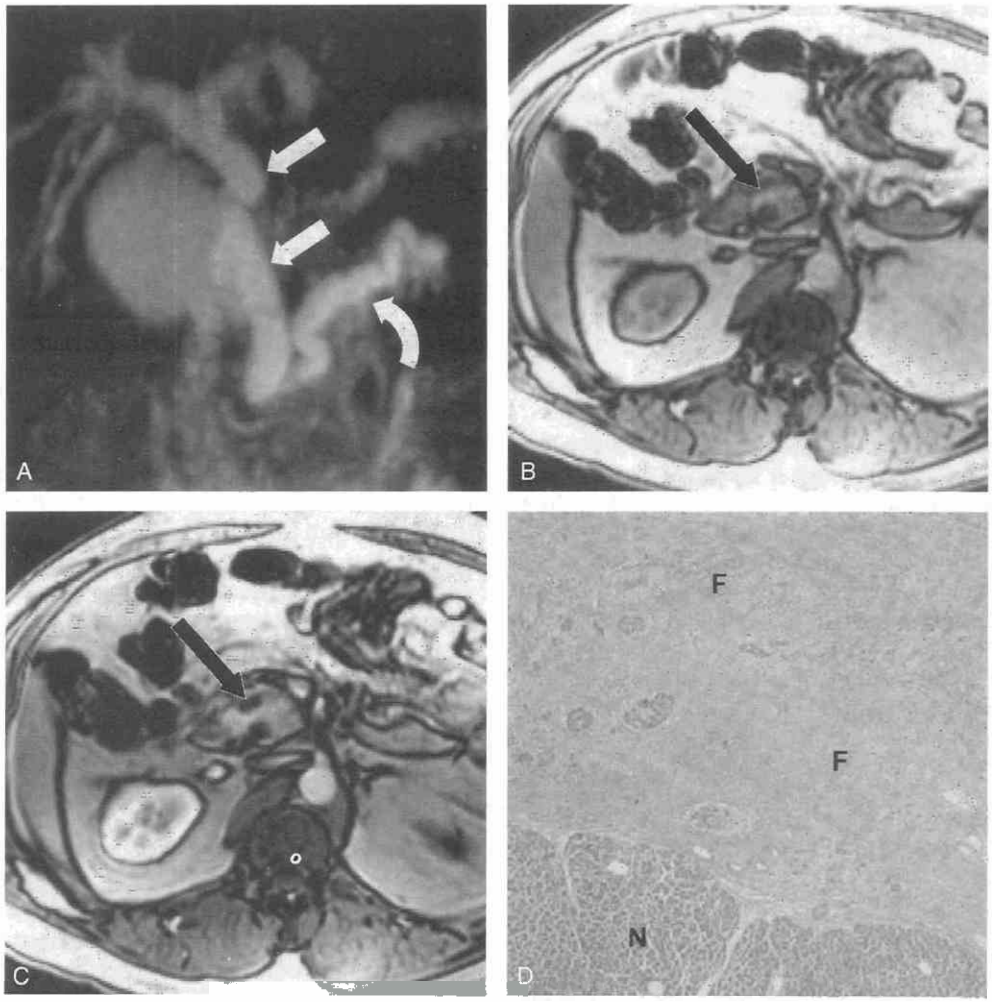

Figure 38–20. Enhancement [redacted]eatic carcinoma. *A,* Reconstructed MR cholangiographic image (TR = 12000 msec, TE = 255 msec) shows distal obstruction of the common bile duct (*straight arrows*) and pancreatic duct (*curved arrow*) due to a pancreatic adenocarcinoma near the ampulla. T1-weighted gradient-echo images (TR = 155 msec, TE = 2.2 msec) taken before gadolinium chelate injection (*B*) and during the arterial phase of gadolinium enhancement (*C*) show enhancement of the tumor (*arrows*), which is less than that of normal pancreatic parenchyma. *D,* Photomicrograph shows extensive fibrosis (F) throughout the tumor, bordering normal pancreatic parenchyma (N). (From Johnson PT, Outwater EK: Pancreatic carcinoma versus chronic pancreatitis: Dynamic MR imaging. Radiology 212:213–218, 1999.)

science of MRI continue to evolve very rapidly, so one must constantly consult the current literature for the latest pulsing sequences. In our laboratory, the favored pulse sequences for optimal visualization of the pancreas are as follows (see Fig. 38–13):

After acquisition of multiplanar gradient-echo localizing images, the pancreas imaging protocol consists of the following breath-hold sequences. Sequences 2 through 4 are acquired either axially or parallel to the main pancreatic duct to depict the whole pancreas within one slice.

1. Multislice 2D HASTE (half-Fourier acquisition single-shot turbo spin echo) (TR [repetition time] = 4.4 msec, TE [echo time] = 90 msec, NEX = 1, FA = 130 degrees, ST = 6 mm, matrix = 176 × 256, TA = 22 sec), scan orientation coronal.
2. Multislice turbo spin echo T2-weighted sequence (TR = 5130 msec, TE = 138 msec, NEX = 1, FA = 180 degrees, ST = 6 mm, matrix = 116 × 256, TA = 26 sec).
3. Multislice 2D, in phase and out of phase, T1-weighted gradient-echo sequence (TR = 144 msec, TE = 2.7 and 5.3 msec, NEX = 1, FA = 70 degrees, ST = 6 mm, matrix = 119 × 256).
4. Contrast-enhanced fat-saturated (using chemical shift technique multislice 2D FLASH (fast low-angle shot) (TR = 152 msec, TE = 4.1 msec, NEX = 1, FA = 80 degrees, ST = 6 mm, matrix = 117 × 256, TA = 17 sec), after IV administration of gadopentetate dimeglumine (0.5 mol/L; Multihance [Bracco]), 0.2 mL per kg of body weight; delay times are 20 seconds and 70 seconds after start of the contrast injection.

The administration of intravenous gadolinium is as important for accurate diagnosis with MRI as the use of iodinated contrast material is for accurate diagnosis with CT scanning. Johnson and Outwater[121] demonstrated clearly, in their article on MRI of the pancreas, that both chronic pancreatitis and carcinoma produce decreased gadolinium enhancement (Figs. 38–20 and 38–21).

Pancreatic Disease Detected by MRI

MRI has been used extensively to study virtually all pancreatic disease. The consensus in the literature is that

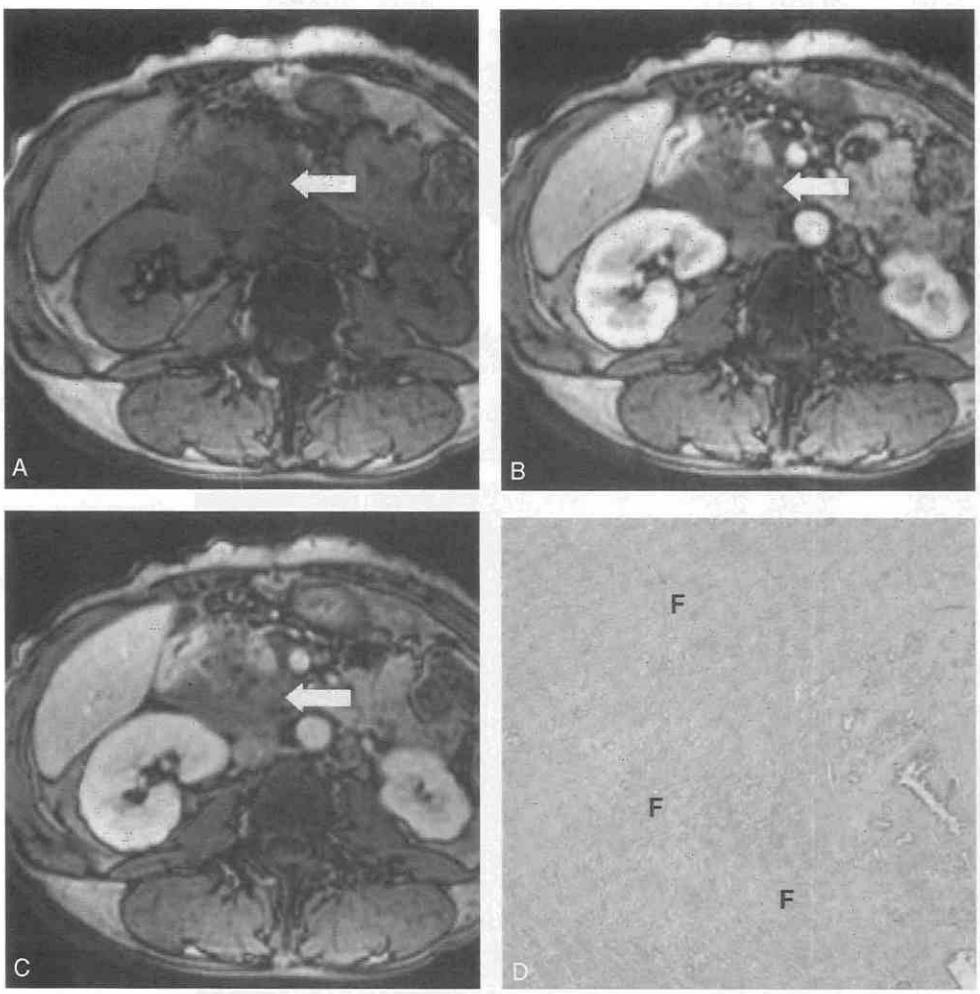

Figure 38–21. Enhancement of chronic pancreatitis. T1-weighted gradient echo images (TR = 140 msec, TE = 2.5 msec) before gadolinium chelate injection (*A*), during the arterial phase of gadolinium enhancement (*B*), and during the portal venous phase of enhancement (*C*). There is lower than normal enhancement of the pancreatic parenchyma (*arrows*). *D,* Histologic photomicrograph shows the extensive fibrosis (F) throughout the chronic pancreatitis. (From Johnson PT, Outwater EK: Pancreatic carcinoma versus chronic pancreatitis: Dynamic MR imaging. Radiology 212:213–218, 1999.)

MRI remains a secondary tool for general evaluation of the pancreas but is the modality of choice for unusual pancreatic tumors.

The obvious advantages of MRI are several. The technique does not use ionizing radiation and has no proven ill effects from the magnetic fields or radiofrequency pulses. The contrast resolution of soft tissues is remarkable and shows subtle changes based on proton density, especially edema and relaxation times. This quality suits it well for detecting subtle tissue relaxation differences, enabling the optimal imaging of unusual tumors such as endocrine or cystic tumors.

The disadvantages of MRI are associated with consistency of image quality and difficulty with visualization of certain tissue components. Although in most cases the images of the pancreas and the immediate area are of good quality, the spatial fidelity and image clarity still do not match those of CT scans. When fast pulse sequences are used to visualize anatomy, the signal-to-noise ratio can be compromised and the clarity of the images may be affected. Two tissue components, air and calcium, are important to detect and characterize for optimal diagnosis of pancreatic disease. Unfortunately, MRI is not reliable in displaying subtle collections of either component; in fact, air and calcium can be confused for each other on MRI.

MRI Pancreatography

In the last several years, the technique has been refined to a reliable method to visualize ductal anatomy and disease. Numerous authors have reported the consistent visual-

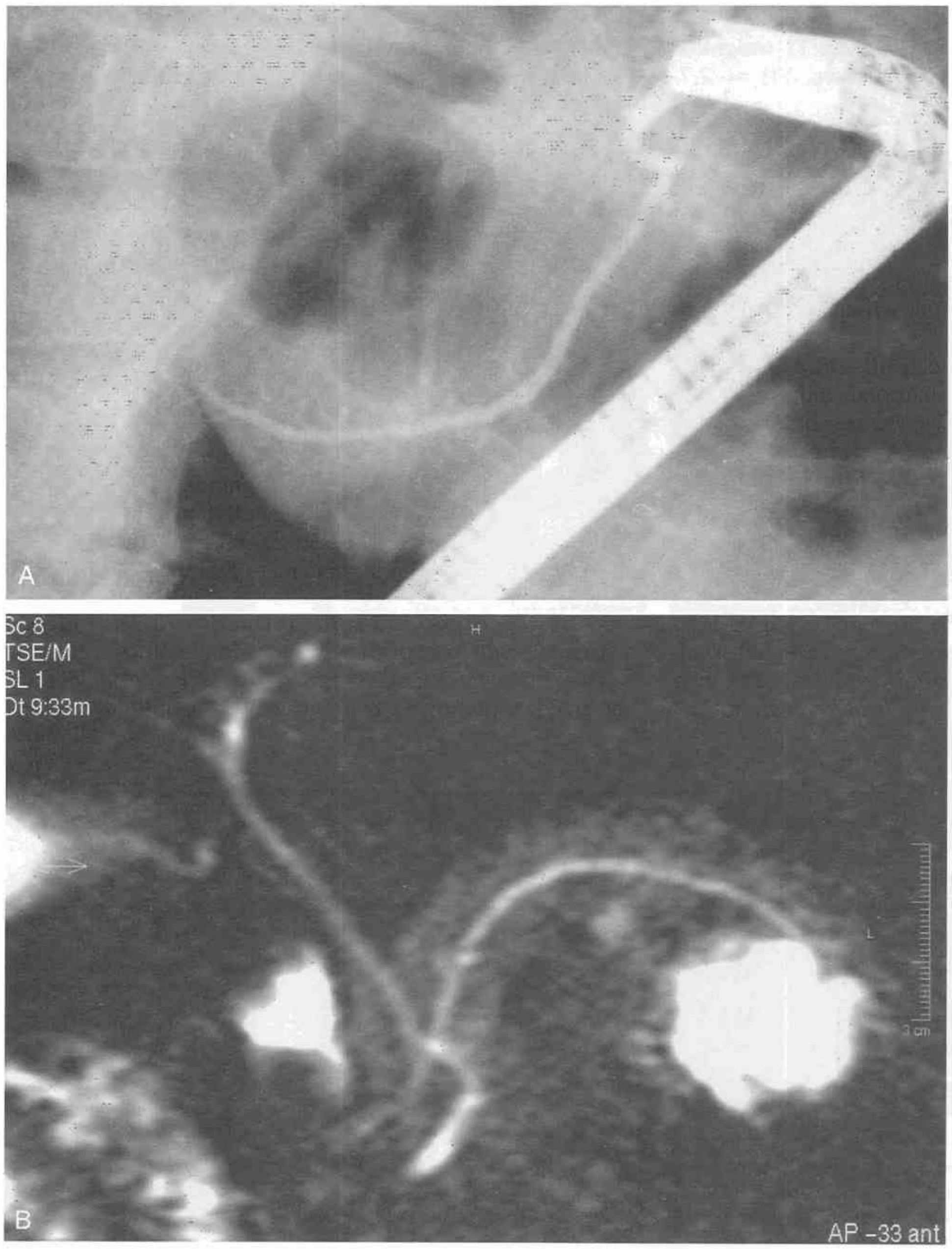

Figure 38–22. *A,* Pancreatic duct during endoscopic retrograde cholangiopancreatography (ERCP). *B,* MR cholangiopancreatogram (MRCP) showing acinar filling. (From Matos C, Deviere J, Cremer M, et al: Acinar filling during secretin-stimulated MR pancreatography. AJR Am J Roentgenol 171: 165–169, 1998.)

ization of normal duct and congenital variations. Manfredi and coworkers[163] reported a large series of patients evaluated by magnetic resonance cholangiopancreatography (MRCP) in which they successfully diagnosed 5 cases of pancreas divisum and three cases of santorinicele. Sica and colleagues[229] found an excellent correlation between MRCP and ERCP. Furthermore, other authors have demonstrated the benefit of using MR pancreatography with secretin stimulation for assessment of exocrine function (Fig. 38–22).

Pancreatitis

Imaging of acute pancreatitis is possible with the newer sequences. Several authors, most recently Semelka and colleagues,[224] have shown that the acute changes are quite consistently imaged with the new fast acquisition images.

The findings that can be noted include the overall morphology of the gland, presence of edema, enlargement of the pancreatic duct, formation of fluid collections, and presence of fibrotic tissue. Edema or fluid within the parenchyma shows as a decrease in intensity with T1-weighted images and an increase in intensity with T2-weighted images. The evolution of the disease, with either an increase in fluid during exacerbation or a decrease in fluid during improvement, can be seen (Figs. 38–23 and 38–24). The dilatation of the pancreatic duct is seen as a tubular fluid density structure within the gland. The signal intensity varies from bright to dark depending on weighting of the signal (see Fig. 38–23).

Piironen and associates[202] demonstrated in a swine model that hemorrhagic necrotizing pancreatitis could be demonstrated with turboflash imaging during the injection of gadolinium. These authors noted that the appearance was very similar to that noted with CT contrast studies and remarked that their findings encourage the use of MRI as an alternative for diagnosing necrotizing pancreatitis.

As the disease evolves, any pseudocyst is visualized as a fluid collection showing the appropriate signal intensity. T1-weighted images are dark (see Fig. 38–23*A*), and T2-weighted images are bright.

As chronic disease develops in the gland, fibrosis and calcification may occur. Fibrosis characteristically shows an absence of signal on both T1- and T2-weighted imaging. Kim and associates[130] and Johnson and Outwater[121] demonstrated that fibrosis visible on MRI correlates with histologic findings. Furthermore, there is no reliable way to

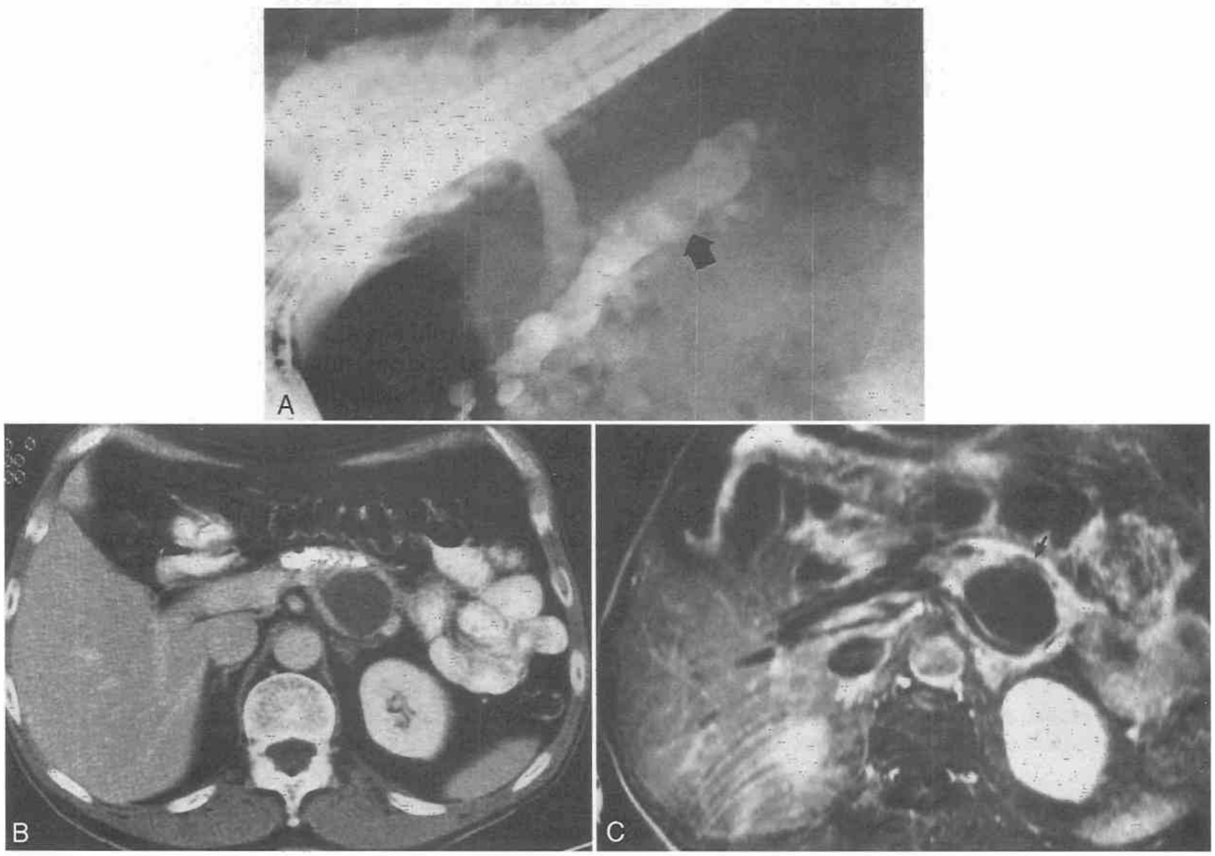

Figure 38–23. Chronic pancreatitis with pseudocysts. *A,* ERCP shows dilatation of the pancreatic duct (*arrow*) with calcifications throughout the pancreas. No communication between the duct and pseudocyst is shown. *B,* Contrast-enhanced, 5-mm CT scan shows extensive calcification along the wall of the pancreatic duct and clearly shows the pseudocyst arising from the posterior aspect of the body of the pancreas. *C,* Gadolinium-enhanced fast spin echo (FSE) (TR = 500 msec, TE = 15 msec) MR image clearly shows that the pancreatic duct (*arrow*) is anterior to the pseudocyst. Dilated duct and calcification could not be clearly distinguished. (From Semelka RC, Kroeker MA, Shoenut JP, et al: Pancreatic disease: Prospective comparison of CT, ERCP, and 1.5-T MR imaging with dynamic gadolinium enhancement and fat suppression. Radiology 181:785–791, 1991.)

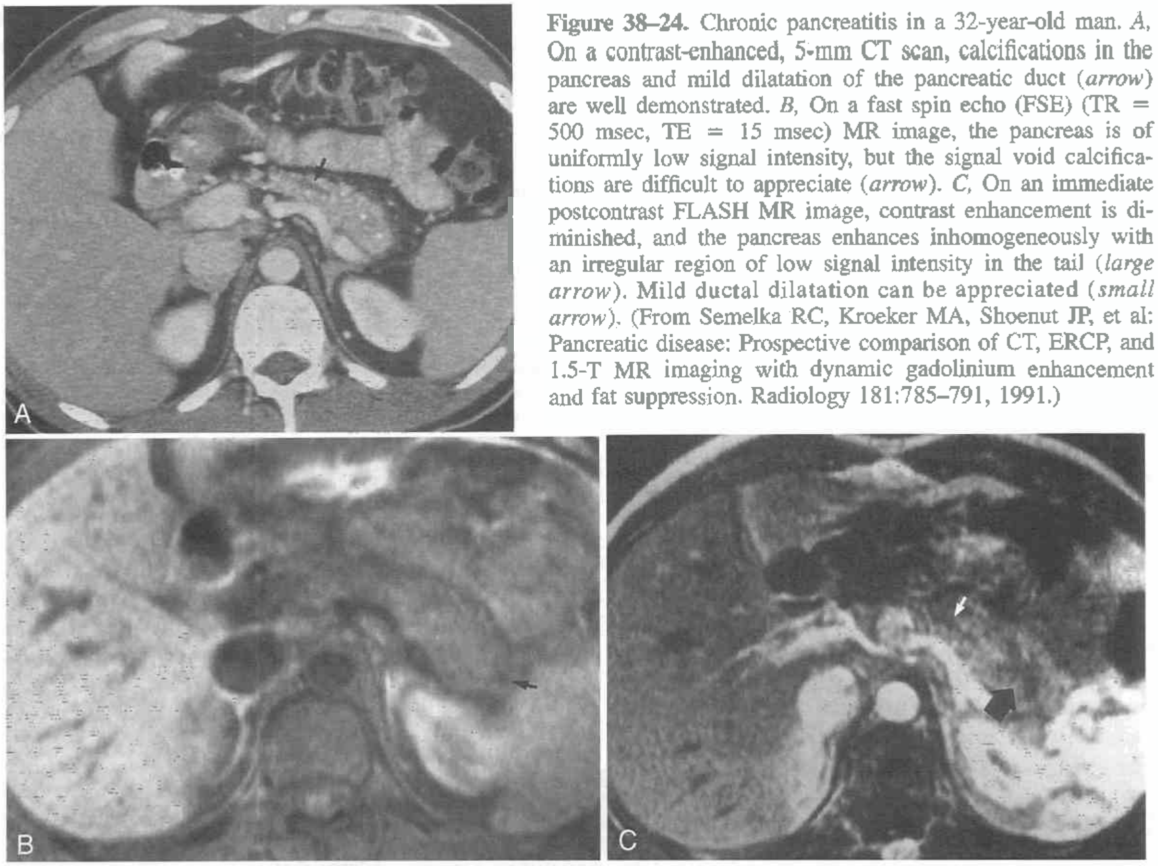

Figure 38–24. Chronic pancreatitis in a 32-year-old man. *A*, On a contrast-enhanced, 5-mm CT scan, calcifications in the pancreas and mild dilatation of the pancreatic duct (*arrow*) are well demonstrated. *B*, On a fast spin echo (FSE) (TR = 500 msec, TE = 15 msec) MR image, the pancreas is of uniformly low signal intensity, but the signal void calcifications are difficult to appreciate (*arrow*). *C*, On an immediate postcontrast FLASH MR image, contrast enhancement is diminished, and the pancreas enhances inhomogeneously with an irregular region of low signal intensity in the tail (*large arrow*). Mild ductal dilatation can be appreciated (*small arrow*). (From Semelka RC, Kroeker MA, Shoenut JP, et al: Pancreatic disease: Prospective comparison of CT, ERCP, and 1.5-T MR imaging with dynamic gadolinium enhancement and fat suppression. Radiology 181:785–791, 1991.)

differentiate such a finding from neoplasm (see Figs. 38–20 and 38–21).

Calcifications may show a signal void on all signals if the calcium is quite mature or a normal signal depending on the amount of hydration of the calcium (see Fig. 38–23*A* and *C*). All authors reporting note that the inability to detect and characterize calcium consistently is a definite disadvantage.

Cystic Fibrosis

MRI has been used to evaluate cystic fibrosis by numerous researchers. These authors have noted that because MRI visualizes fat well, patterns of change resulting from atrophic changes were well seen. Tham and associates[252] reported on 15 cases and noted three appearances: complete replacement of the gland by fat, resulting in a lobulated, enlarged gland; small atrophic gland with partial fat replacement; and diffuse atrophy of the gland.

Pancreatic Transplants

The ability of MRI to detect edema of the pancreas makes it well suited for evaluation of pancreatic transplants. The most notable article on this topic is by Yuh and colleagues.[268] These authors noted that configuration and density changes related to edema and rejection can be well evaluated by MRI. They found that the progression and regression of rejection could be followed by monitoring the increase and decrease in the amount of fluid within the gland. Chronic rejection showed as a progressive decrease in size as well as the decrease in signal associated with the development of fibrosis.

Another potential use of MRI is the prediction of rejection or infarction based on changes in enhancement produced by injection of gadopentetate dimeglumine (Figs. 38–25 to 38–27). After injection of 0.1 mmol/kg, Yuh and colleagues obtained numerous gradient echo scans in the same anatomic location over the pancreas. They found that the normal gland in six cases increased enhancement by 98% during the first minute, whereas the rejecting gland increased enhancement at 1 minute by 42% (6 of 6 rejections). They found that there was little or no change in the calculated T2 value. The abnormal scans preceded chemical evidence of rejection (urinary amylase levels) in four cases (4 of 6 rejection cases). They concluded that T2 intensity was a poor indicator for rejection and favored the use of this new enhancement method.

Pancreatic Nonendocrine Tumors

Most tumors in the pancreas are adenocarcinomas, which produce characteristic configuration changes and occasional signal change. The two most significant reports on MRI of tumors are those by Steiner and associates[244] and Semelka and colleagues.[224] As with CT, these tumors produce contour alterations that exceed normal measurements

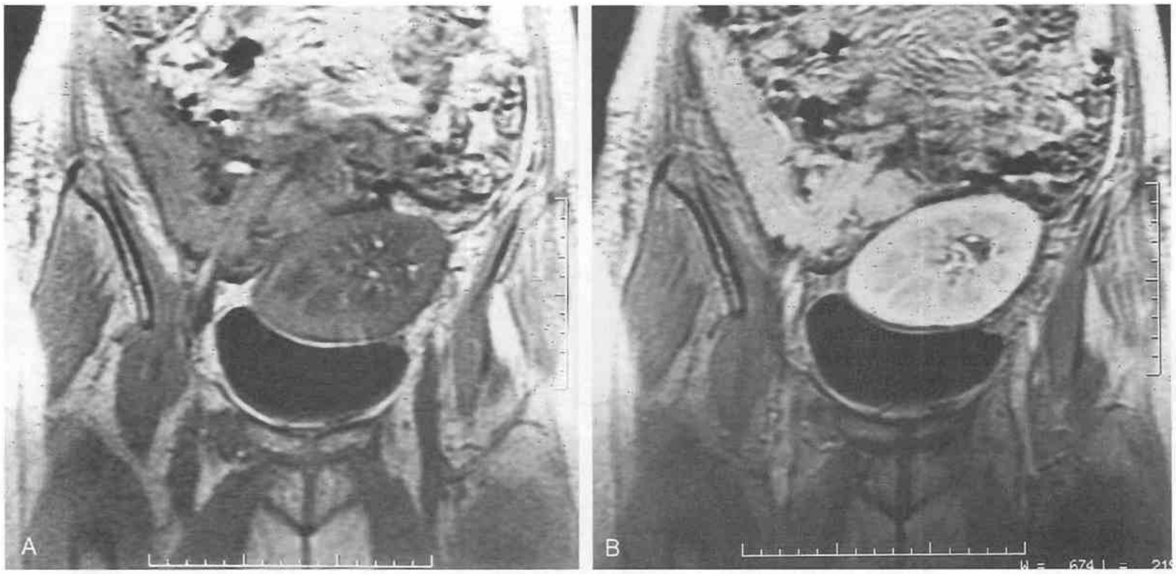

Figure 38–25. Coronal fast multiplanar, spoiled, gr[redacted]nt-recalled e[redacted]MR ima[redacted](TR [redacted]50 msec, TE = 4.2 msec, 60-degree flip angle) obtained in a patient with normal pancreas allograft, as confirmed at percutaneous biopsy. Unenhanced image (*A*) and image obtained 1 minute after the administration of gadolinium-based contrast material (*B*) demonstrate avid enhancement through a normal-sized pancreatic allograft. Note the adjacent enteric anastomosis and renal allograft. (From Krebs TL, Daly B, Wong-You-Cheong JJ, et al: Acute pancreatic transplant rejection: Evaluation with dynamic contrast-enhanced MR imaging compared with histologic analysis. Radiology 210:437–442, 1999.)

Figure 38–26. Coronal fast multiplanar, spoiled, gradient-recalled echo MR image (TR = 150 msec, TE = 4.2 msec, 60-degree flip angle) obtained 1 minute after the administration of gadolinium-based contrast material in a patient with moderate acute rejection of pancreatic allograft, as confirmed at percutaneous biopsy. Image demonstrates diminished enhancement compared with the enhancement in the pancreas in Figure 38–25*B*. Mild hydronephrosis of the renal transplant is noted. (From Krebs TL, Daly B, Wong-You-Cheong JJ, et al: Acute pancreatic transplant rejection: Evaluation with dynamic contrast-enhanced MR imaging compared with histologic analysis. Radiology 210:437–442, 1999.)

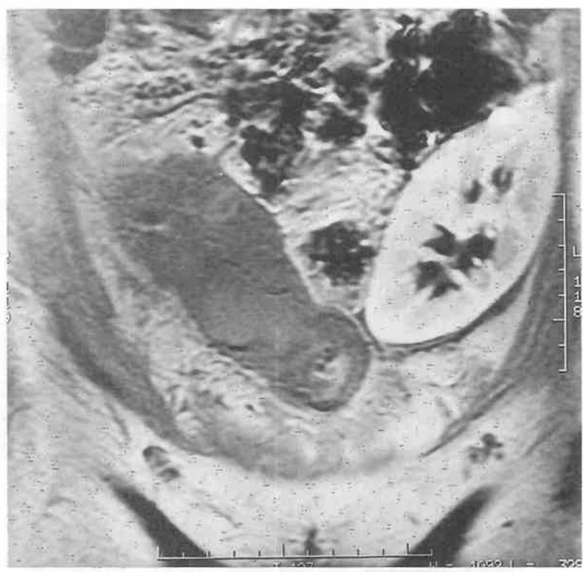

Figure 38–27. Coronal fast multiplanar, spoiled, gradient-recalled echo MR image (TR = 150 msec, TE = 4.2 msec, 60-degree flip angle) obtained 1 minute after the administration of gadolinium-based contrast material in a patient with pancreatic allograft infarction that was proved at surgical explantation. There is no enhancement in the enlarged pancreatic allograft or in the duodenal cuff. (From Krebs TL, Daly B, Wong-You-Cheong JJ, et al: Acute pancreatic transplant rejection: Evaluation with dynamic contrast-enhanced MR imaging compared with histologic analysis. Radiology 210:437–442, 1999.)

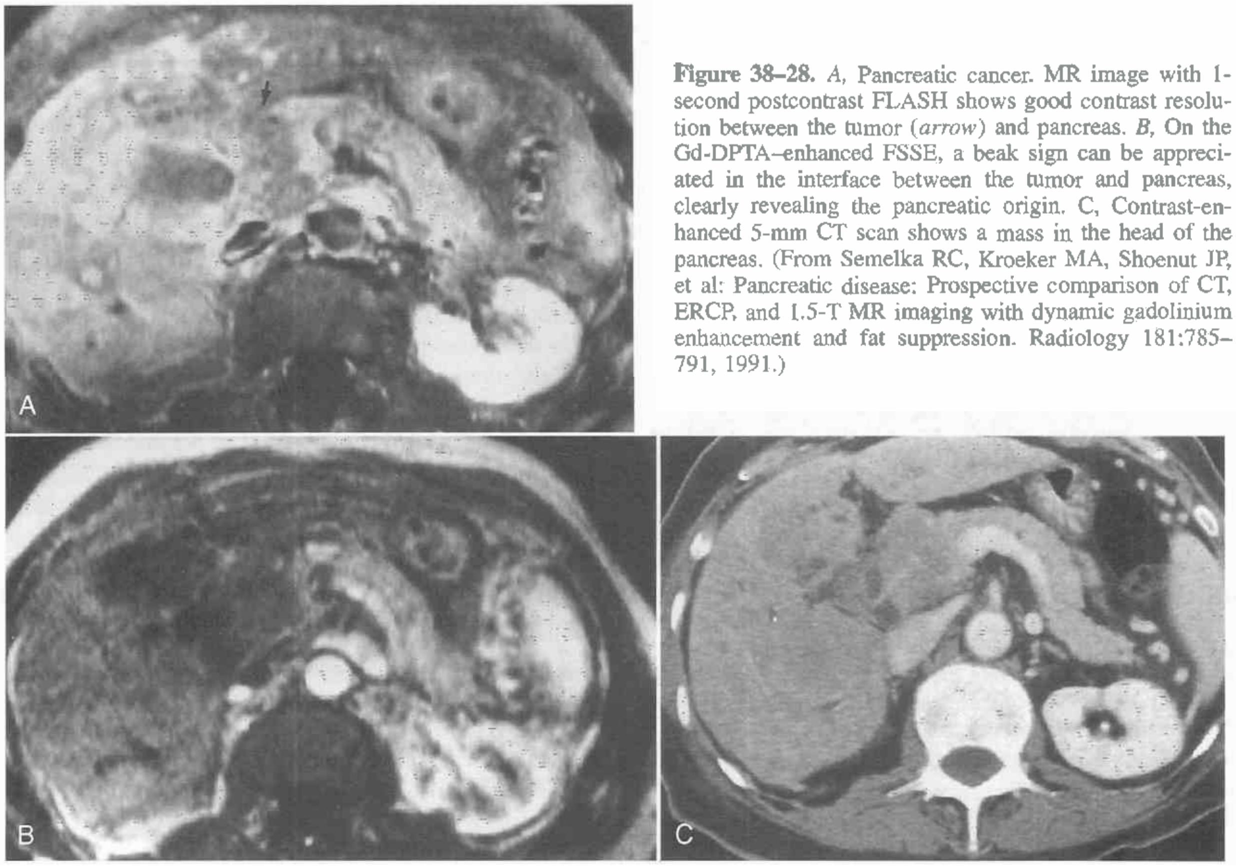

Figure 38–28. *A,* Pancreatic cancer. MR image with 1-second postcontrast FLASH shows good contrast resolution between the tumor (*arrow*) and pancreas. *B,* On the Gd-DPTA–enhanced FSSE, a beak sign can be appreciated in the interface between the tumor and pancreas, clearly revealing the pancreatic origin. C, Contrast-enhanced 5-mm CT scan shows a mass in the head of the pancreas. (From Semelka RC, Kroeker MA, Shoenut JP, et al: Pancreatic disease: Prospective comparison of CT, ERCP, and 1.5-T MR imaging with dynamic gadolinium enhancement and fat suppression. Radiology 181:785–791, 1991.)

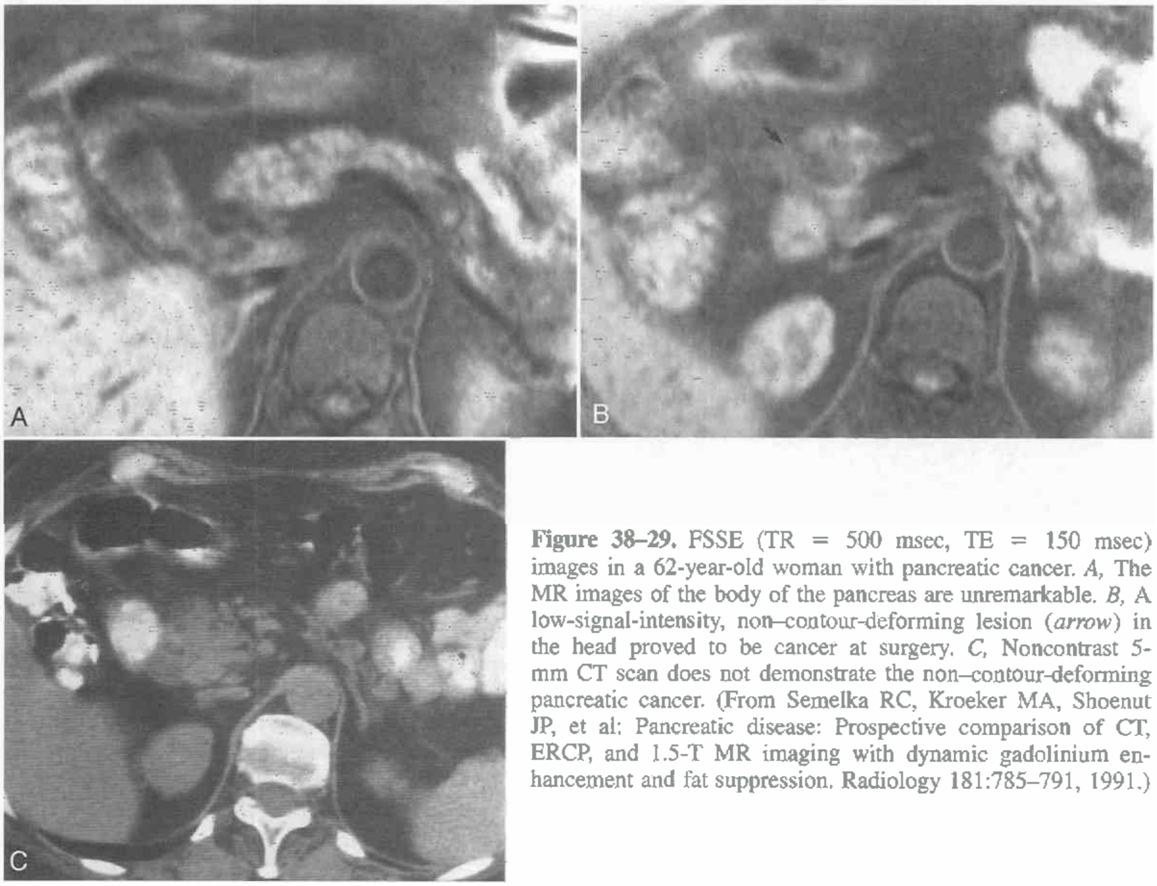

Figure 38–29. FSSE (TR = 500 msec, TE = 150 msec) images in a 62-year-old woman with pancreatic cancer. *A,* The MR images of the body of the pancreas are unremarkable. *B,* A low-signal-intensity, non–contour-deforming lesion (*arrow*) in the head proved to be cancer at surgery. *C,* Noncontrast 5-mm CT scan does not demonstrate the non–contour-deforming pancreatic cancer. (From Semelka RC, Kroeker MA, Shoenut JP, et al: Pancreatic disease: Prospective comparison of CT, ERCP, and 1.5-T MR imaging with dynamic gadolinium enhancement and fat suppression. Radiology 181:785–791, 1991.)

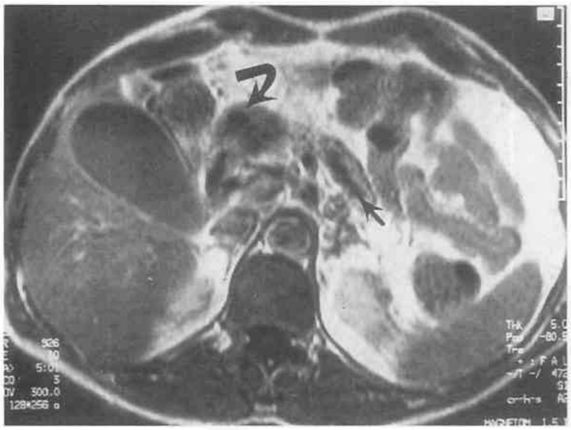

Figure 38–30. MR ima[redacted]SE 926/10) shows pancreatic cancer (*curved arrow*) in the head of the pancreas, producing distal ductal dilatation (*arrow*).

or apparent discrepancy between various portions of the gland. On unenhanced scans, Steiner and associates[244] reported, 61% (20 of 32) of the tumors had an intensity less than that of normal pancreas, whereas 40% (13 of 32) of the tumors had intensities greater than that of the normal gland. In a similar way that the avascular tumor produces a decreased density with intravenous urographic contrast material on CT, gadolinium-enhanced MR images can show a difference in the intensity of such tumors compared with the normal gland (Figs. 38–28 to 38–30).

Although the point has not been emphasized, it is apparent that if problematic cases of staging for operability arise, MRI would be extremely well suited to evaluate the status of the peripancreatic vascular system. Encroachment of the portal or superior mesenteric vein would be quite easily detected on MRI.

MRI offers a viable alternative to CT if a specific case is problematic or allergy to contrast agents is an issue. No authors have asserted that MRI is the preeminent study for tumor, but all, including my colleagues and I, recognize the potential for the future.

Authors who have reported indicate that MRI offers no significant advantages over CT for evaluating the pancreas for neoplasia. Further progress is needed in refinement of signal-to-noise ratio, spatial resolution, motion suppression, and bowel opacification before MRI might become competitive with CT.

Cystic Tumors

There is only one extensive report in the literature about the usefulness of MRI for the diagnosis and evaluation of cystic tumors of the neoplasm, by Minami and associ-

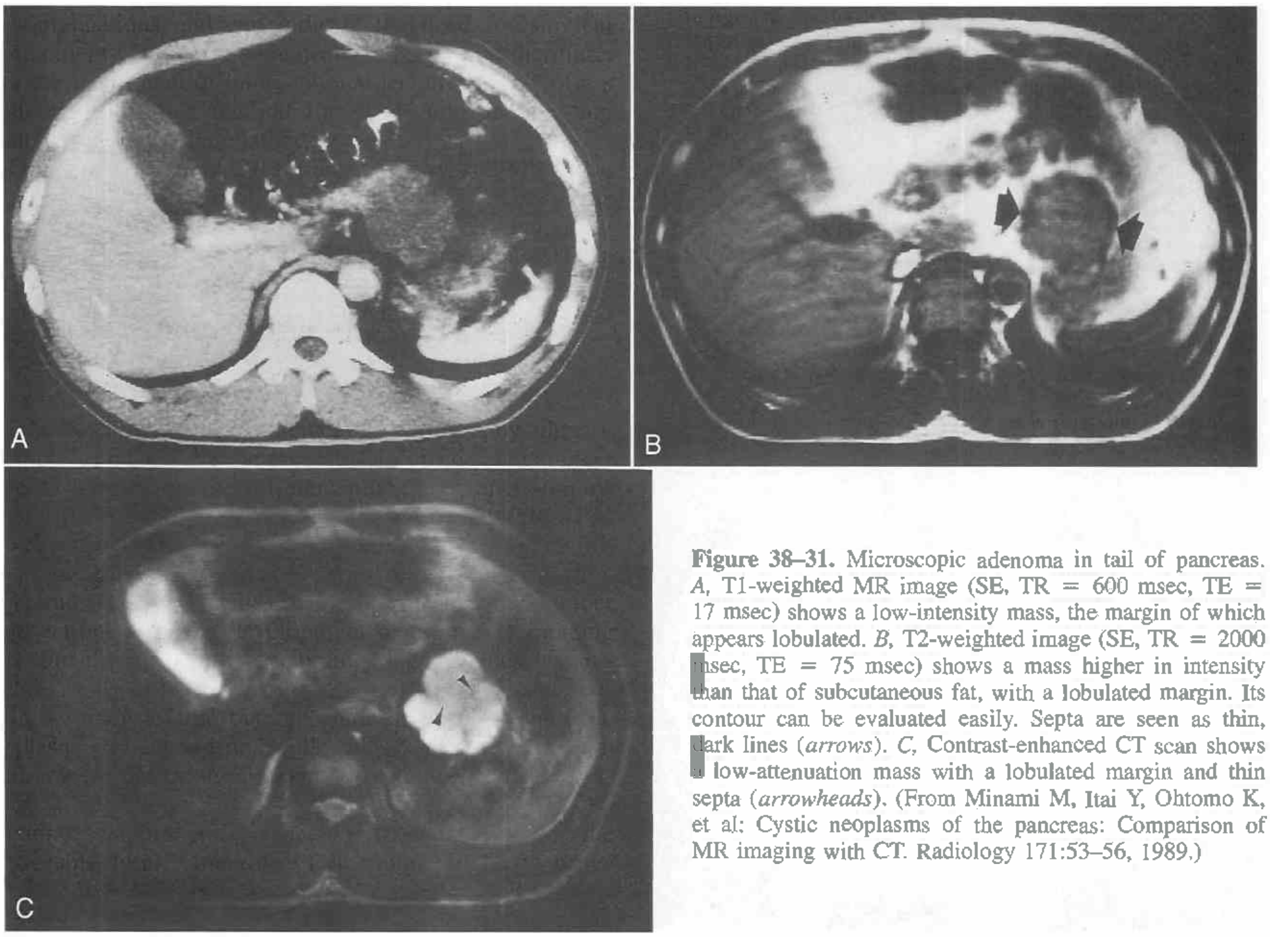

Figure 38–31. Microscopic adenoma in tail of pancreas. *A*, T1-weighted MR image (SE, TR = 600 msec, TE = 17 msec) shows a low-intensity mass, the margin of which appears lobulated. *B*, T2-weighted image (SE, TR = 2000 [redacted]sec, TE = 75 msec) shows a mass higher in intensity [redacted]han that of subcutaneous fat, with a lobulated margin. Its contour can be evaluated easily. Septa are seen as thin, [redacted]ark lines (*arrows*). *C*, Contrast-enhanced CT scan shows [redacted] low-attenuation mass with a lobulated margin and thin septa (*arrowheads*). (From Minami M, Itai Y, Ohtomo K, et al: Cystic neoplasms of the pancreas: Comparison of MR imaging with CT. Radiology 171:53–56, 1989.)

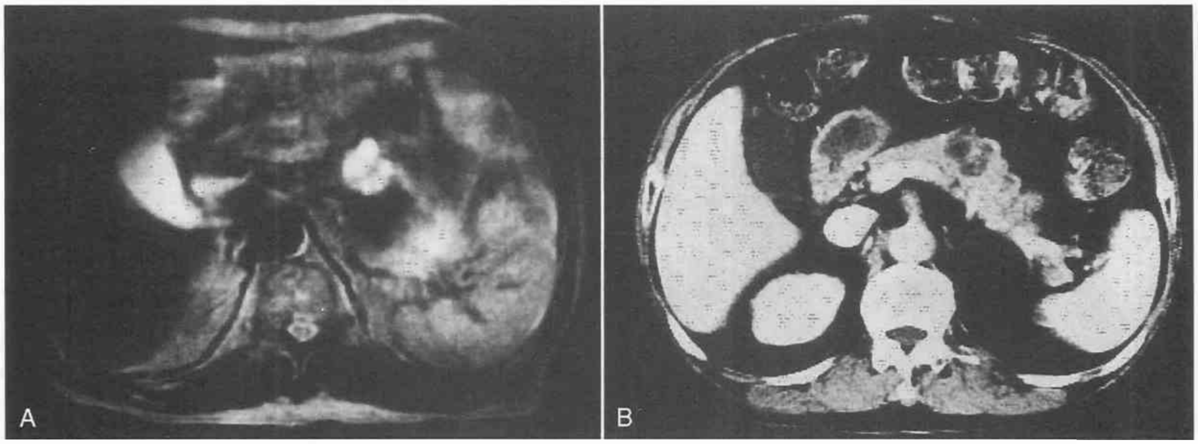

Figure 38–32. Microcystic adenoma in the body of the pancreas. *A,* T2-weighted MR image (SE, TR = 2000 msec, TE = 75 msec) shows a hyperintense tumor that appears inhomogeneous in intensity owing to the low intensity of a central scar. *B,* Enhanced CT scan shows a lobulated tumor with a calcified central stellate scar. (From Minami M, Itai Y, Ohtomo K, et al: Cystic neoplasms of the pancreas: Comparison of MR imaging with CT. Radiology 171:53–56, 1989.)

ates.[178a] These researchers studied five microcystic adenomas and seven mucinous (macrocystic) neoplasms (study was not prospective or blinded). Three cystadenomas and four cystadenocarcinomas were studied with both CT and MRI. The observations and conclusions of the authors were that MRI was equivalent to or slightly better than CT for these tumors because MRI was better able to demonstrate the cystic content by virtue of the different signal (Fig. 38–31). The cystic material was low intensity on the T1-weighted images and high intensity on the T2-weighted images (Figs. 38–32 and 38–33). Attempts to characterize lesions as either microcystic and mucinous or to distinguish

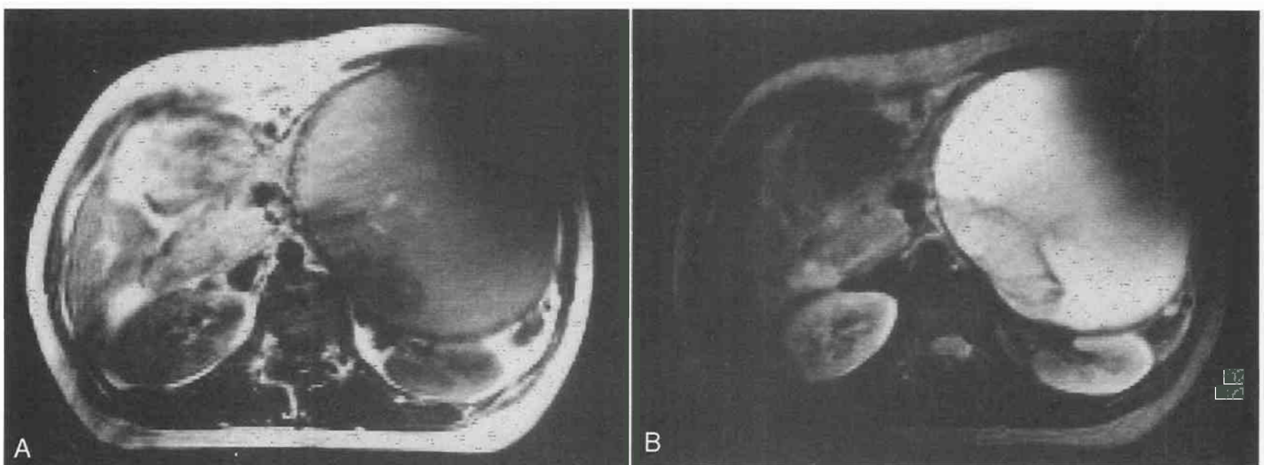

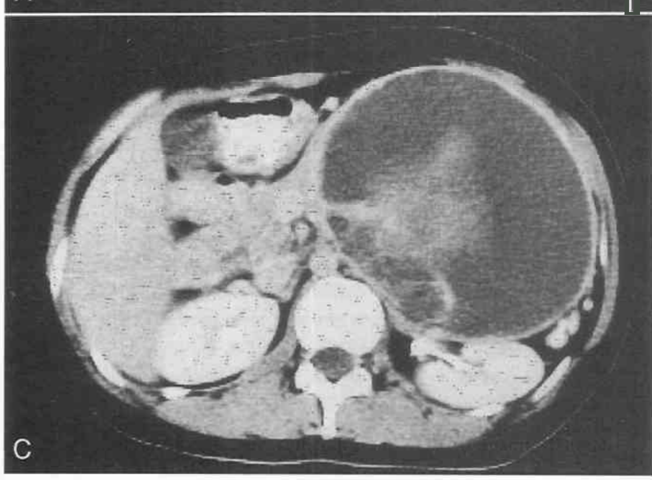

Figure 38–33. Mucinous cystadenocarcinoma in the tail of the pancreas. *A,* T1-weighted MR image (SE, TR = 400 msec, TE = 35 msec) shows a large, round mass with two compartments. The larger one is higher in intensity and has small high-intensity spots. *B,* T2-weighted image (SE, TR = 1600 msec, TE = 70 msec) shows septa of the tumor as low-intensity lines. The two compartments also have slightly different signal intensities. *C,* Enhanced CT scan shows a large cystic mass with a bizarre septum of irregular thickness and papillary projections. The cystic compartments are almost equal in attenuation. (From Minami M, Itai Y, Ohtomo K, et al: Cystic neoplasms of the pancreas: Comparison of MR imaging with CT. Radiology 171:53–56, 1989.)

benign from malignant (cystadenoma from cystadenocarcinoma) were not possible on the basis of MRI appearance alone. Variation in signal between different loculations is more common with mucinous tumors, but it can also occur with serous tumors.

The authors' conclusion was optimistic but cautious in stating that MRI was equivalent or slightly superior to CT by virtue of sensitivity to difference in intensity of the different cavities and the better definition of the outer contour of the masses. They also noted that further improvement would be important if better spatial resolution and differentiation between serous and mucinous material were to be achieved.

Endocrine Tumors

A variety of endocrine tumors have been studied with MRI and reported in the literature. Although my colleagues and I have not accumulated a large number of such cases, we have observed the same advantages reported by others for MRI in evaluating these cases.

The signal intensity of endocrine tumors of the pancreas is much different from that for nonendocrine tumors. Such tumors show configuration changes as one might expect, but also, the intensity of the tumor is higher on T2-weighted images than that of the normal pancreas or the typical pancreatic adenocarcinoma (Figs. 38–34 and 38–35).

With the evolution and development of MRI, its usefulness for the detection of endocrine tumors is proven without question. Early reports using slow pulsing sequences showed disappointing results for detection of these lesions by imaging, with the greatest diagnostic success achieved by angiography. Because these tumors are very rare and the literature is rather sparse, I have included the older data as well as the new data so that the reader will have appropriate perspective when considering the topic.

One of the larger studies, reported by Frucht and colleagues,[71] evaluated the prospective usefulness of various imaging modalities, including CT, ultrasonography, MRI, and angiography, for the detection of gastrinoma (outside of the liver). The results are rather surprising considering the theoretical advantage of MRI and CT. The authors used spin-echo (SE) imaging with T1 and T2 weighting as well as some short T1 inversion recovery imaging. Of the 22 cases of extrahepatic gastrinoma, 17 were within the pancreas and 3 were outside. MRI was successful in detecting lesions in only 4 of the group, and CT was successful in detecting the lesion in only 9 of the group (Fig. 38–36). The most effective imaging system used was angiography, which detected 16 lesions. The addition of MRI or CT did

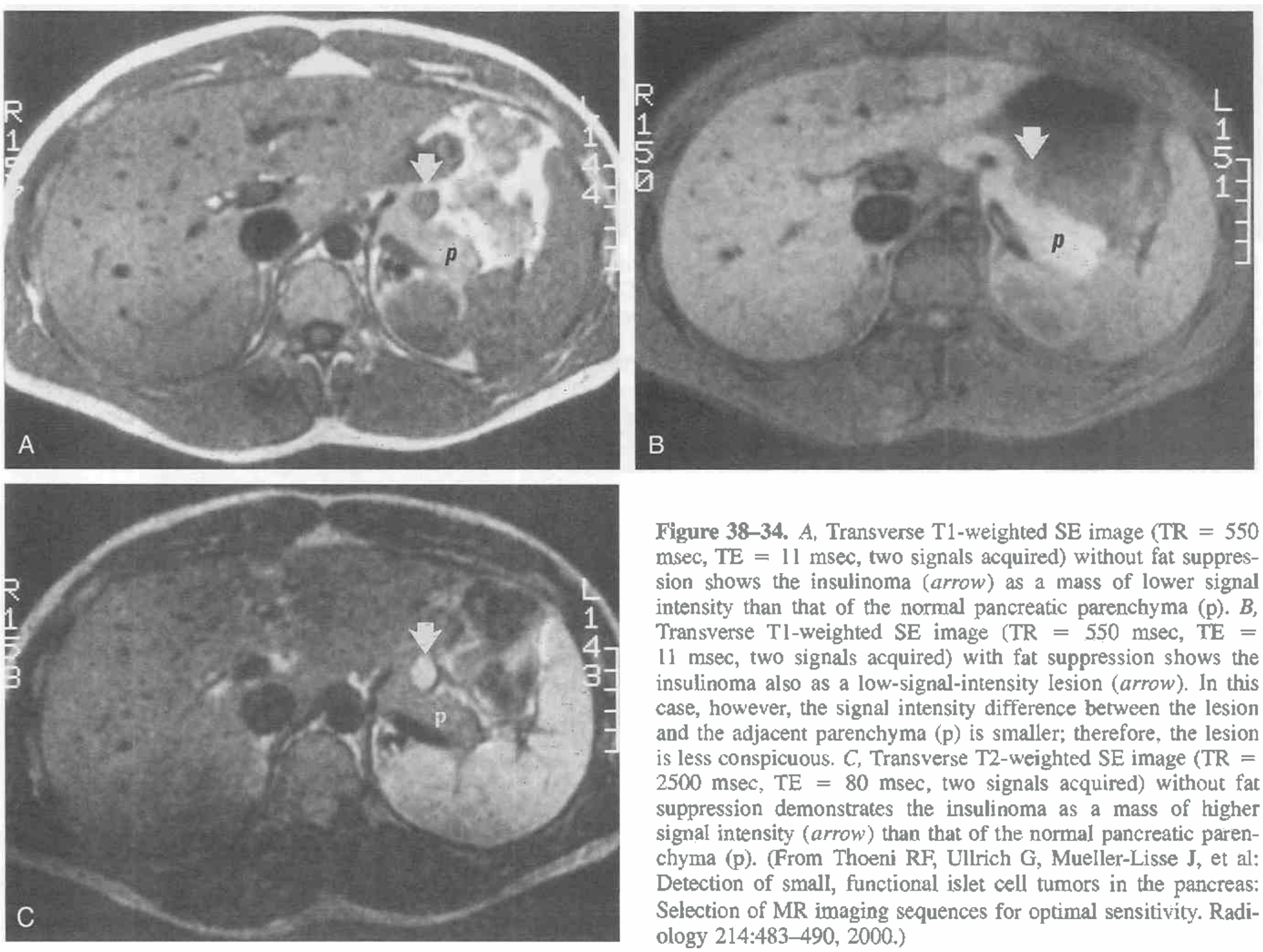

Figure 38–34. *A,* Transverse T1-weighted SE image (TR = 550 msec, TE = 11 msec, two signals acquired) without fat suppression shows the insulinoma (*arrow*) as a mass of lower signal intensity than that of the normal pancreatic parenchyma (p). *B,* Transverse T1-weighted SE image (TR = 550 msec, TE = 11 msec, two signals acquired) with fat suppression shows the insulinoma also as a low-signal-intensity lesion (*arrow*). In this case, however, the signal intensity difference between the lesion and the adjacent parenchyma (p) is smaller; therefore, the lesion is less conspicuous. *C,* Transverse T2-weighted SE image (TR = 2500 msec, TE = 80 msec, two signals acquired) without fat suppression demonstrates the insulinoma as a mass of higher signal intensity (*arrow*) than that of the normal pancreatic parenchyma (p). (From Thoeni RF, Ullrich G, Mueller-Lisse J, et al: Detection of small, functional islet cell tumors in the pancreas: Selection of MR imaging sequences for optimal sensitivity. Radiology 214:483–490, 2000.)

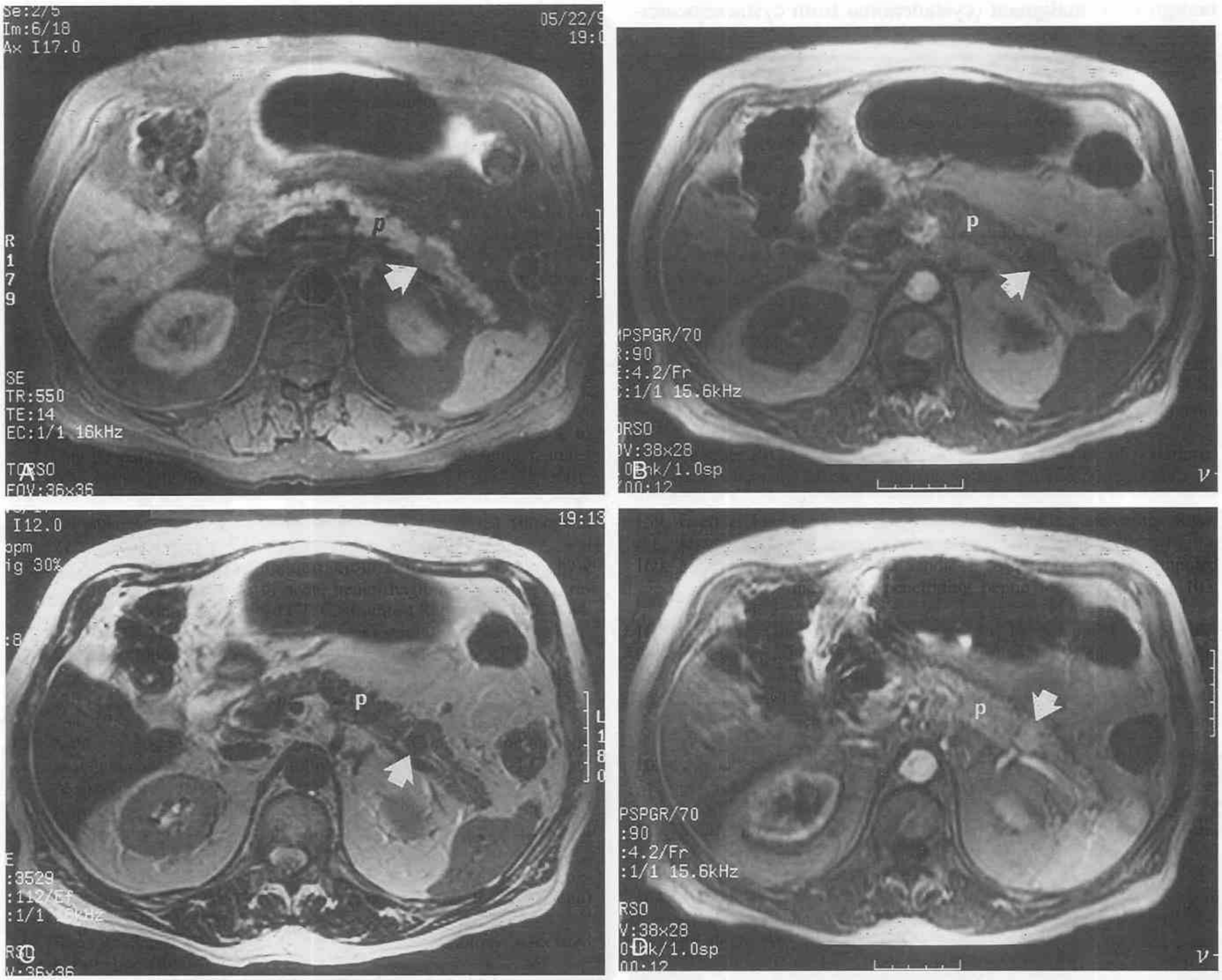

Figure 38–35. *A*, T[redacted]verse T1-weighted S[redacted] (TR = 550 ms[redacted] acq[redacted]ession shows a 1.5-cm les[redacted] (*arrow*) near the tail [redacted] pancreas (p). CT [redacted] patie[redacted]ma. *B*, Transverse breath-hold T1-weighted fast multiplanar spoiled gradient-recalled echo (GRE) image (TR = 120 msec, TE = 4.2 msec, one signal acquired, 70-degree flip angle) also demonstrates the insulinoma (*arrow*), but less conspicuously. *p*, = pancreas. *C*, Transverse T2-weighted fast SE image (TR = 4000 msec, TE = 102 msec/[effective], three signals acquired) without fat suppression shows the lesion (*arrow*) as a mass of low signal intensity. p, pancreas. *D*, Transverse breath-hold fast multiplanar spoiled GRE image (TR = 120 msec, TE = 4.2 msec, one signal acquired) with gadopentetate dimeglumine enhancement shows the mass (*arrow*) as an enhancing lesion of higher signal intensity than that of the normally enhancing parenchyma (p). (From Thoeni RF, Ullrich G, Mueller-Lisse J, et al: Detection of small, functional islet cell tumors in the pancreas: Selection of MR imaging sequences for optimal sensitivity. Radiology 214:483–490, 2000.)

not improve the results because no other lesions were found by the techniques. Tham and others[250–252] made similar observations, noting that MRI was superior to CT for detecting endocrine tumors (Fig. 38–37), but angiography was still superior to both.

With the advent of faster pulsing sequences and refinement of the contrast agent administration, the current success rate of MRI for detection is excellent. In its current state, proper MRI scanning can diagnose 85% of islet cell tumors 2 cm or smaller. The most significant article on this topic was by Thoeni and associates, [254] who studied 28 consecutive patients. In this group, they successfully diagnosed 17 of 20 patients with tumors and had 8 true-negative evaluations. The specificity was 100%; positive predictive value was 100%, and negative predictive value was 73%. The most successful pulsing sequences were the T1-weighted SE images with fat suppression and nonenhanced gradient recalled echo (GRE) images, which showed 75% of lesions (see Figs. 38–34 and 38–35). T2-weighted conventional SE with fat suppression diagnosed 65%. Other useful sequences were gadolinium-enhanced, spoiled GRE in 12 (60%), and T2-weighted fast SE in 7 of 10 patients (70%). This later work is extremely important, because before MRI had been developed, there was no simple means of preoperative diagnosis of these tumors. Endoscopic ultrasonography was capable of detecting such lesions, but the technique is quite expensive and rather invasive. Intraoperative ultrasonography is virtually 100%

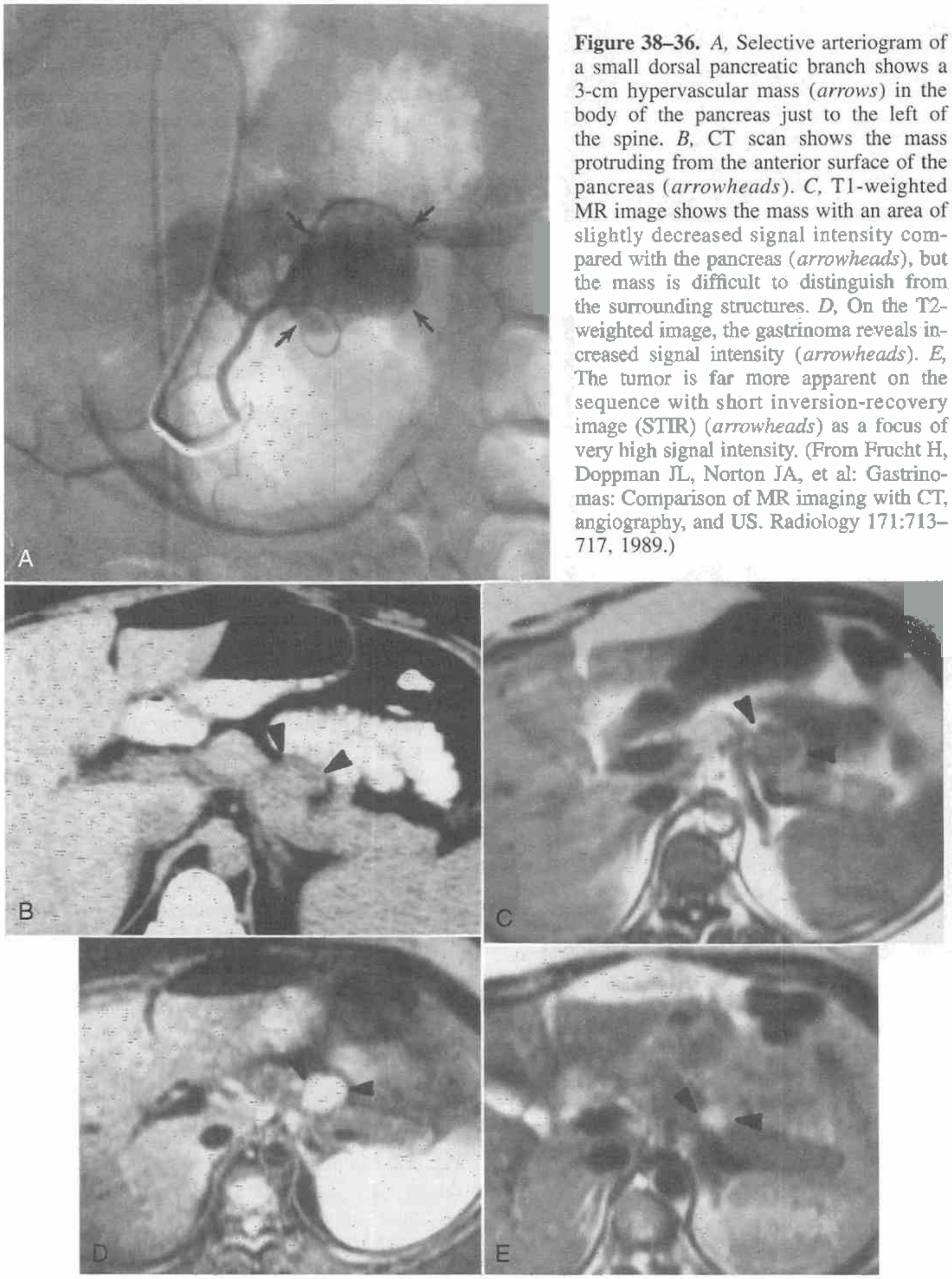

Figure 38–36. *A,* Selective arteriogram of a small dorsal pancreatic branch shows a 3-cm hypervascular mass (*arrows*) in the body of the pancreas just to the left of the spine. *B,* CT scan shows the mass protruding from the anterior surface of the pancreas (*arrowheads*). *C,* T1-weighted MR image shows the mass with an area of slightly decreased signal intensity compared with the pancreas (*arrowheads*), but the mass is difficult to distinguish from the surrounding structures. *D,* On the T2-weighted image, the gastrinoma reveals increased signal intensity (*arrowheads*). *E,* The tumor is far more apparent on the sequence with short inversion-recovery image (STIR) (*arrowheads*) as a focus of very high signal intensity. (From Frucht H, Doppman JL, Norton JA, et al: Gastrinomas: Comparison of MR imaging with CT, angiography, and US. Radiology 171:713–717, 1989.)

accurate, but an accurate noninvasive test such as MRI permits better procedure planning and can avoid laparotomy in selected cases.

CT Imaging of Pancreatic Disease

Pancreatic Duct

The best technique to visualize the pancreatic duct in both normal and abnormal situations requires the administration of urographic contrast material and selection of optimal scanning parameters.[62, 95]

For best visualization, maximal enhancement of the parenchyma relative to the duct should be produced by a sustained intravenous injection of urographic contrast material by mechanical injector with simultaneous or immediately subsequent CT scanning of the pancreas. The recommendations of exact injection rates may vary from one institution to the next, but the dosage and rate suggested in the previous section on technique are adequate.

Occasionally, the normal duct can be visualized with 8-

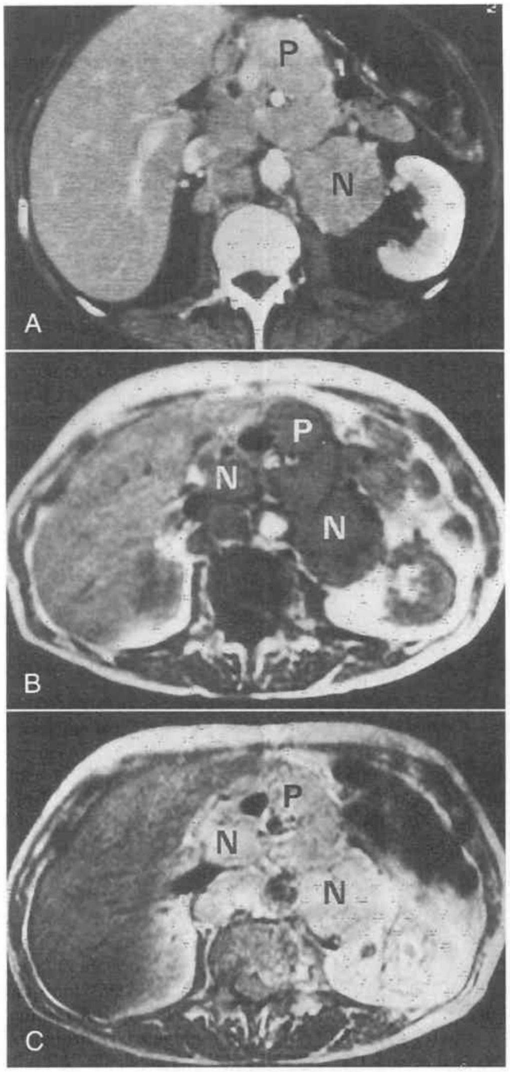

Figure 38–37. A 55-year-old woman with multiple endocrine neoplasia type I and Zollinger-Ellison syndrome for 18 years exhibits a tumor of the body of the pancreas with lymph node and bone metastases. *A*, CT scan after intravenous contrast administration demonstrates enlargement of the body of the pancreas (*P*) and lymph node metastases (*N*) that are isodense. *B*, T1-weighted (SE, TR = 300 msec, TE = 20 msec) MR image shows the pancreatic tumor (*P*) and the lymph node metastases (*N*) with a homogeneous low signal intensity compared with that of the normal liver parenchyma. The sharply delineated contours of the multiple lesions are readily visible. *C*, T2-weighted (SE, TR = 2000 msec, TE = 50 msec) MR image reveals the slightly inhomogeneous high signal intensity of the pancreatic tumor (*P*) and lymph node metastases (*N*). (From Tham RTOTA, Falke THM, Jansen JBM, Lamers CBHW: CT and MR imaging of advanced Zollinger-Ellison syndrome. J Comput Assist Tomogr 13:821–828, 1989.)

mm-thick scan slices. More consistent visualization of the duct can also be achieved by setting the scanning parameters to optimize contrast and spatial resolution. The best approach is to optimize the spatial resolution in the XY as well as the longitudinal plane. Resolution in the XY plane is improved by using a small field of view to maximize the number of pixels within the anatomy being imaged and using thin scan slices of 2 to 4 mm. These thin sections are necessary to minimize the partial volume effect in the longitudinal plane, considering that the diameter of the normal duct is 2 to 6 mm. The advantage of the thick slices is that the entire duct can be seen through the length of the gland, and most cases of pathologic dilatation can be routinely imaged without the optimized scanning parameters. Thin slices are advantageous in that the anatomy is better defined, but in most cases, the segments of the duct appear on different scans. With multislice scanners, the normal pancreatic duct is visible on virtually all scans because the routine slice thickness is always 3 mm or less (see Figs. 38–2 and 38–14).

Pancreatitis Effects on Duct

Acute pancreatitis may produce dilatation of the duct, especially if there is superimposition of acute inflammation on a baseline of chronic changes (Fig. 38–38) or, rarely, an acute obstruction of the duct by a calculus (Fig. 38–39) or pseudocyst (Fig. 38–40).

Chronic inflammation produces fibrosis, which, depending on its anatomic location and extent, may result in diffuse dilatation, diffuse stenosis, or segmental narrowing of the duct; the CT scan or MR image directly reflects these gross anatomic findings. In patients who have diffuse narrowing of the ductal system that is significantly attenuated, the CT scan is unlikely to show any positive findings.

When fibrosis occurs close to the head of the gland and is producing partial obstruction, moderate dilatation of the duct, which appears as a fluid-density tubular structure within the gland, occurs. When fibrosis occurs intermittently along the length of the duct, a string of ectatic areas is produced, resulting in the appearance of sacculations on the duct on the CT scan. On occasion, one portion of the duct is more isolated than the others, and a buildup of fluid in a localized area, which appears as a cystic mass on the scan, is produced. This cyst mass, which cannot be distinguished from a pseudocyst by imaging alone, is called a *retention cyst* (Figs. 38–40 and 38–41). It differs from a pseudocyst in that the wall is lined by epithelium of the duct; if the epithelium remains in place for a sufficient time, the ductal lining may atrophy, so ductal elements may not be detectable on pathologic examination. Differentiation of retention cysts from pseudocysts may be difficult because pseudocysts may coexist with or cause ductal dilatation. The nature of a cystic abnormality can be best differentiated by ERCP. Dilatation of the secondary ductules produces clusters of cysts (see Fig. 38–41), which are typically fluid density but may calcify if chronic disease persists.

Ductal Calcification

The calcium deposits that can occur in the parenchyma of the gland can also occur in the wall or the lumen of the duct (Figs. 38–42 and 38–43). The cause and pathophysiology of this process are not well understood. The presence of such deposits, however, should be detected at the earliest time so that corrective measures, such as surgical ductal

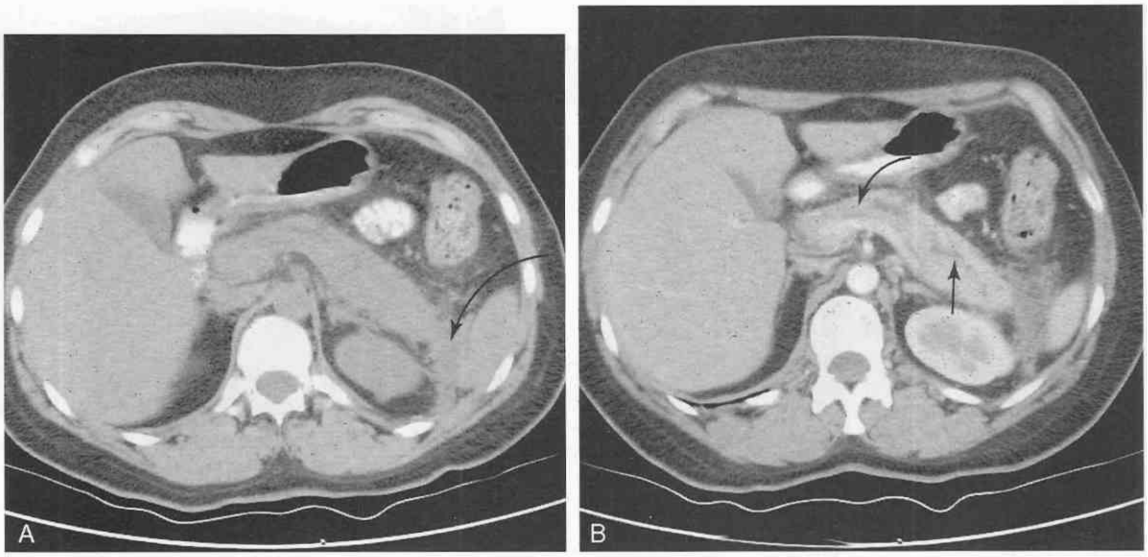

Figure 38–38. *A,* Pancreatic duct dilatation may occur in association with acute pancreatitis superimposed on chronic pancreatitis. This unenhanced scan shows inflammatory fluid adjacent to the distal tail and hilum of spleen (*curved arrow*). Without intravenous contrast material, visualization of parenchymal or ductal changes is difficult. *B,* After intravenous administration of contrast material, ductal dilatation (*vertical arrow*), is seen as well as subtle decreased density in the head (*curved arrow*).

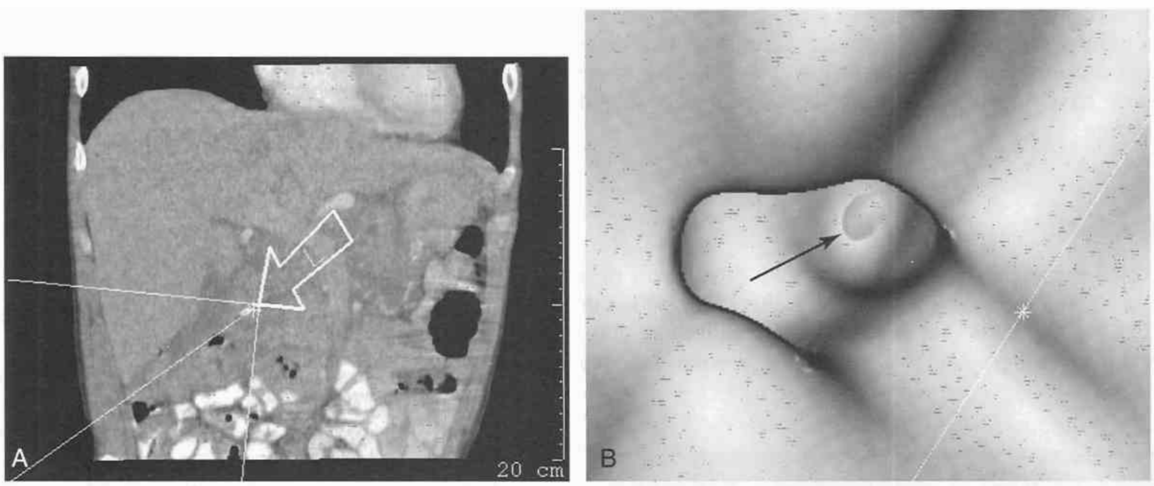

Figure 38–39. *A,* Longitudinal reconstruction from multislice scans of pancreas shows stone in pancreatic duct, designated by the large, open arrow. *B,* Reconstruction endoscopic view of the pancreatic duct shows calculus in the head of the pancreas (*arrow*), at the end of the view of the duct.

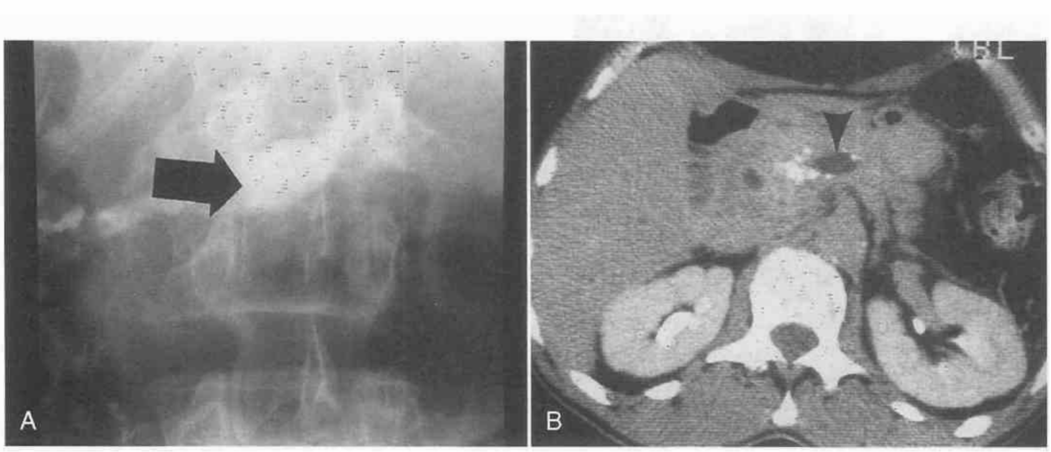

Figure 38–40. *A,* Pancreatogram shows diffuse dilatation with a central ectasi (*arrow*). *B,* CT scan shows central dilatation of the main pancreatic duct, resulting in a small retention cyst (*arrowhead*).

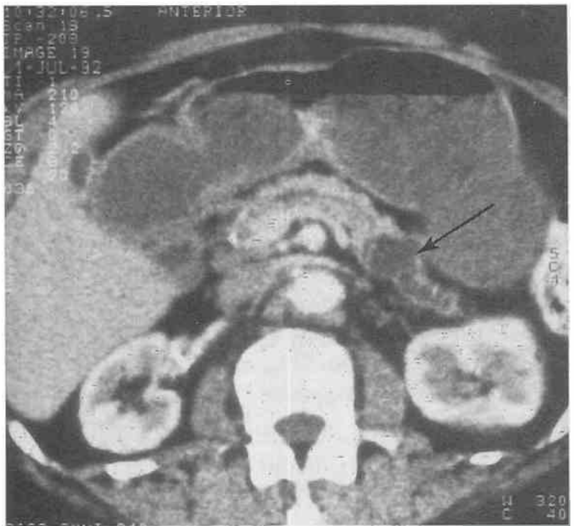

Figure 38–41. CT scan shows mild dilatation of the central portion of the duct with saccular dilatation distally (*arrow*), resulting in a retention cyst.

drainages, can be contemplated if clinically indicated. The spectrum of symptoms associated with a calculus in the duct is quite wide. Some patients are asymptomatic, some experience atrophy of the gland (Fig. 38–44), and some may even have life-threatening inflammation after ductal enterostomy.

Ductal Gas

Air can appear in the duct, which may be a result of a fistula or other more benign conditions. Air can also occur after ERCP (Fig. 38–45*A*), as a result of papillotomy (Fig. 38–45*B*), from surgery (Fig. 38–45*C*), or in some patients

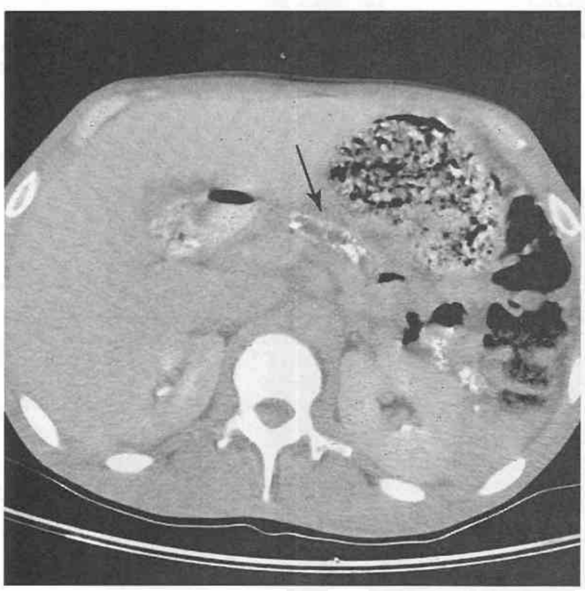

Figure 38–42. CT scan shows dilatation of pancreatic duct with calcifications in the wall (*arrow*).

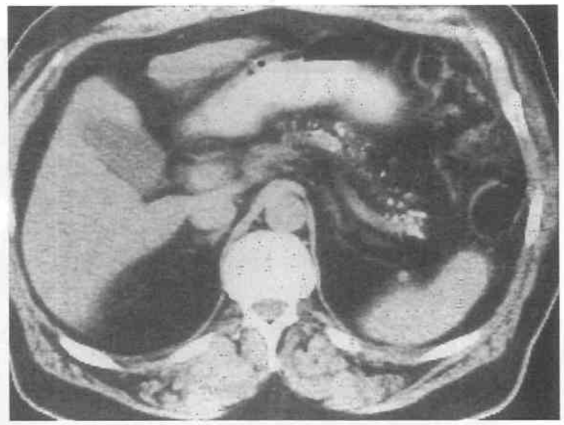

Figure 38–43. Chronic inflammation has produced intense calcification in the pancreatic duct, atrophy of the gland, and calcifications of the secondary ductules of the gland.

simply as a result of a patulous sphincter of Oddi (Fig. 38–45*D*). One could certainly hypothesize that cholangitis or another infectious process could spread gas to the duct, but I have not observed this nor seen it reported.

Ductal Changes from Neoplasm

Several authors have reported on ductal changes seen in neoplasm, including Berland and colleagues,[22] Freeny and others,[64–67] and Muranaka and associates.[182] There is a consensus among authors that high-quality modern CT and MRI reliably demonstrate the appearance and status of the duct. Recognizing the changes produced by inflammation as noted previously, these authors point out that uniform, severe dilatation of the duct can be produced by either inflammation or neoplasm (Fig. 38–46). The frequency and reliability of MRI and CT in differentiating inflammation from neoplasm have been variable among these studies.

Karasawa and coworkers[127] reported their experience with CT pancreatogram in patients with pancreatitis and carcinoma. They stated that ductal dilatation caused by these entities could be distinguished in a large number of cases. They reported that smooth or beaded dilatation was commonly associated with carcinoma; dilatation occurred in 56% of patients with neoplasm. Ductal dilatation occurred in 58% of patients with pancreatitis, and irregular dilatation was seen in 73% of these patients. The researchers found that patients with carcinoma tended to have a larger duct, average 8.7 mm compared with 6.7 mm in patients with pancreatitis. They also noted that the ratio of the duct to the overall dimension of the gland was greater with carcinoma because of atrophy of the acinar elements associated with complete obstruction; if the ratio of duct to gland was greater than 0.5, carcinoma was likely.

Freeny and others[64–67] reported that 108 of 159 patients (68%) had ductal dilatation. In 90 of 108 patients, the margins of the duct were smooth and parallel. In 18 of 108, they appeared beaded or irregular. Pancreatic parenchyma was atrophic in 82% of the patients with ductal dilatation.

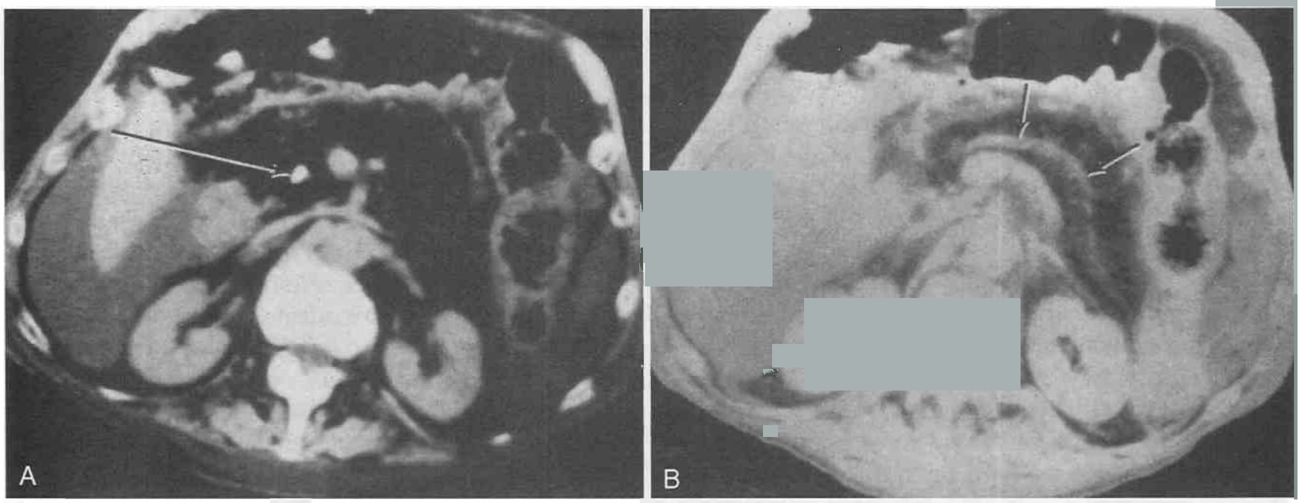

Figure 38–44. *A,* A calcul[redacted] the ampulla (*arrow*). *B,* Obstru[redacted]n of the pan[redacted]tic duct (*arrows*) resulting from calculus. The pancreas has autolyzed so only the fat remains within the parenchymal area. (From Patel S, Bellon EM, Haaga J, et al: Fat replacement of the exocrine pancreas. AJR 135:843–845; copyright by American Roentgen Ray Society, 1980.)

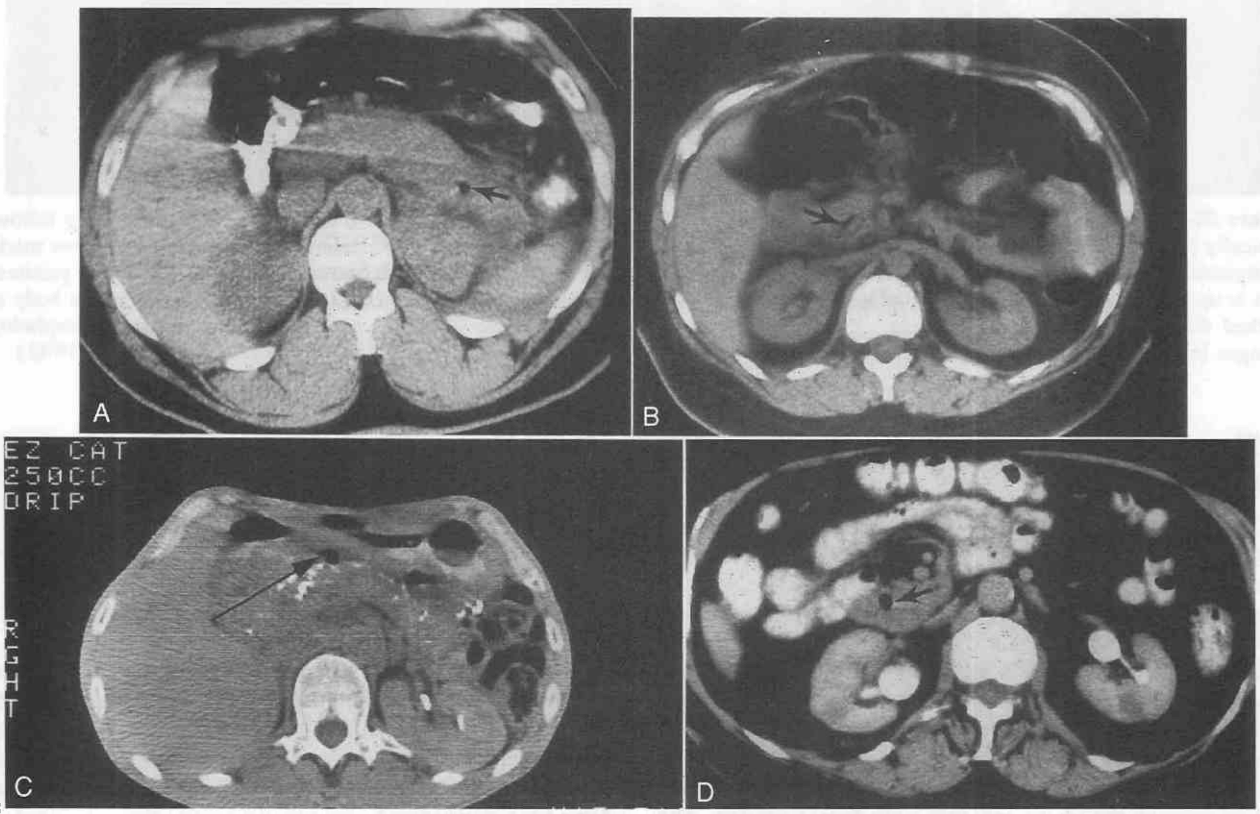

Figure 38–45. *A,* Small bubbles of gas (*arrow*) can be introduced into the ductal system by pancreatograms. *B,* Postsphincterotomy at ERCP. After interventional procedures on the common or pancreatic duct, small air collections can be seen within the head of the gland (*arrow*). *C,* Patient with calcifications has air (*arrow*) in the duct containing calculi. Air has refluxed from the bowel through an anastomosis through the duct from a Puestow procedure. *D,* Air (*arrow*) has refluxed into the common duct because of an incompetent sphincter of Oddi.

Figure 38–46. Sequential changes in the pancreatic body on CT in patients with pancreatic head carcinoma. This patient was followed clinically because of poor respiratory function. Carcinoma was confirmed by postmortem examination. *A*, Initial CT scan shows marked enlargement of the pancreatic body. *B*, Two months later, the width of the pancreatic body is decreased, and a smooth, narrow pancreatic duct is seen continuously. *C*, Four months later, the pancreatic body has become normal in size. *D*, Atrophy of the pancreatic body and marked dilatation of the pancreatic duct with a beaded contour are demonstrated 7 months later. (From Muranaka T: Morphologic changes in the body of the pancreas secondary to a mass in the pancreatic head: Analysis by CT. Acta Radiol 31:483–488, 1990.)

Differentiating Disease According to Ductal Changes

The information provided by the studies cited in the preceding section is helpful for an overall perspective of pancreatic duct assessment, but the most definitive work to date on this topic was by Muranaka and coworkers.[182] These researchers noted that differentiation of benign from malignant disease in the specific case is still not always possible. The configuration and size of the duct depend on the degree and duration of obstruction. Muranaka and coworkers[182] reported that pancreatic duct dilatation is relatively uncommon in small tumors but dilatation of the duct and atrophy of the gland progress with tumor growth. The increased ratio of duct to gland occurs with late tumor progression. Neoplasms and inflammatory processes can produce partial or complete and slow or quick obstruction of the duct. The guidelines proposed by earlier authors are beneficial; that is, if the ratio of the diameter of the duct to the overall diameter of the parenchyma is 0.5 or greater, the chance of a neoplastic origin is more likely (Fig. 38–47). The detailed analysis of these findings provided by Muranaka and coworkers[182] is illuminating as a reference source (Table 38–1).

Pancreatitis

Inflammation of the pancreas is produced by the release of proteolytic, lipolytic, and other enzymes; the acute process produces a serious clinical state that has numerous life-threatening complications. Chronic pancreatitis is associated with recurrent acute bouts and produces significant long-term morbidity.[5]

Causes of pancreatitis are numerous and include gallbladder disease, trauma,[162] alcohol ingestion, drug use, hypercalcemia, hyperlipidemia, vascular disease, infection, uremia, diabetic coma, heredity, and unknown causes. Regardless of the initiating cause, once there has been activation of the various enzymes, severe inflammation ensues. The spectrum of acute pancreatitis is broad, and it may

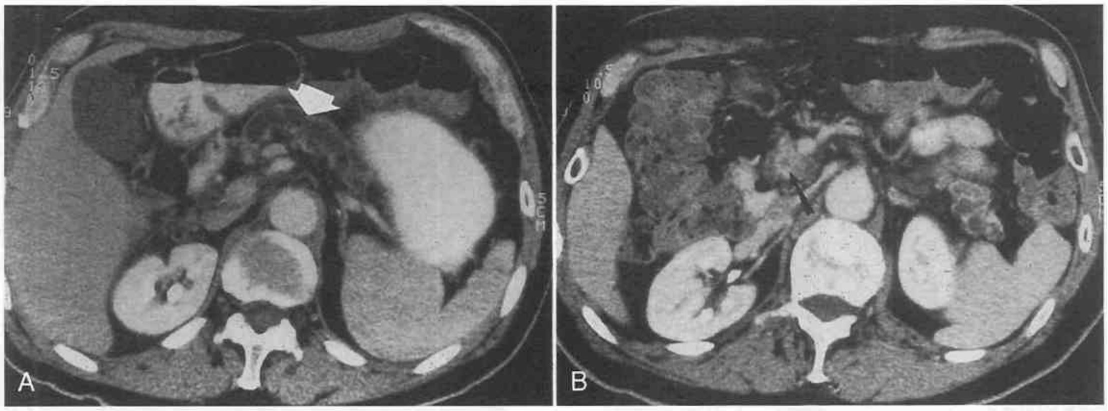

Figure 38–47. *A,* CT scan of a patient with chronic pain, which shows severe dilatation of the pancreatic duct. The diameter of the duct is more than 0.5 the diameter of the gland (*arrow*). The duct is somewhat tortuous, which some authors suggest may be consistent with pancreatitis. *B,* A lower section on CT scan shows a small high-density mass (*arrow*) within the fat density gland, which proved to be cancer at surgery.

produce a benign, self-limited episode or worsen into a self-perpetuating fulminant course.

The symptoms of pancreatitis include abdominal pain, nausea, and vomiting. Classic laboratory findings include elevated levels of serum amylase and lipase and depressed levels of serum calcium. Occasionally there are also elevations of serum glucose and triglycerides.

Although the diagnosis of either acute or chronic pancreatitis is usually made clinically, imaging procedures at times may provide valuable information about the cause, course, progression, prognosis, and complications of the disease.[4, 264] The following sections discuss the different forms of pancreatitis and are intended to make the radiologist an integral part of the clinical team that cares for such patients.

Causative Factors

The most valuable contribution that can be made by CT examination is the detection of the primary cause of the inflammatory process so that remedial steps can be taken. The most important finding on a study of a patient with pancreatitis is the presence of biliary or gallbladder calculi. Calculi can be the cause of severe pancreatitis, and they are one of the few problems that can be easily remedied. The specific appearance of calculi is discussed in Chapter 37, but one should bear in mind that CT is not the modality of choice for biliary or gallbladder calculi. A CT scan may be normal in the presence of gallstones simply because there is minimal density between the stones and the surrounding bile. Ultrasonography is the study of choice and should be performed in all patients with pancreatitis.

In cases of trauma, direct damage can be seen as well as significant trauma in the adjacent structures. In children with pancreatitis, the presence of calcification usually indicates familial pancreatitis. In most instances, the cause of pancreatitis is unknown, let alone detectable on CT or other imaging techniques. The sensitivity of CT for detecting pancreatitis is exceptional, considering that even clinically asymptomatic pancreatitis caused by ERCP can be detected by CT, as noted by Thoeni and associates.[253]

Acute Edematous Pancreatitis

Acute pancreatitis is well suited for examination by CT because CT scanning is not impaired by gas as is ultrasonography. If there is an associated ileus or sentinel loop, it will not impede CT examination but may preclude an examination by ultrasonography. The diagnostic signs of pancreatitis include pancreatic and peripancreatic edema, contour changes, duct dilatation (see prior section on the pancreatic duct), and alteration of pancreatic density.

The contour of the gland may change significantly depending on the enlargement of the gland and the amount of fluid and edema (Figs. 38–48 to 38–51). The anterior and posterior margins of the gland may be difficult to delineate because of the presence of edema or fluid in the immediate area of the gland. A slight amount of edema posteriorly makes the fat plane between the gland and vessels slightly denser, whereas a large amount of high-

Table 38–1. Incidence of Pancreatic Duct Visualization on CT Scans in Pancreatic Head Masses*

	Pancreatic Carcinomas					
	T1	*T2*	*T3*	*T4*	Focal Inflammatory Masses	Pseudocysts
No.	2	10	14	10	8	12
Percentage	18	71	70	91	80	100

* Incidence of pancreatic duct visualization in carcinoma 36/56 (64%). See page 0000.
Adapted from Muranaka T: Morphologic changes in the body of the pancreas secondary to a mass in the pancreatic head: Analysis by CT. Acta Radiol 31:483–488, 1990.

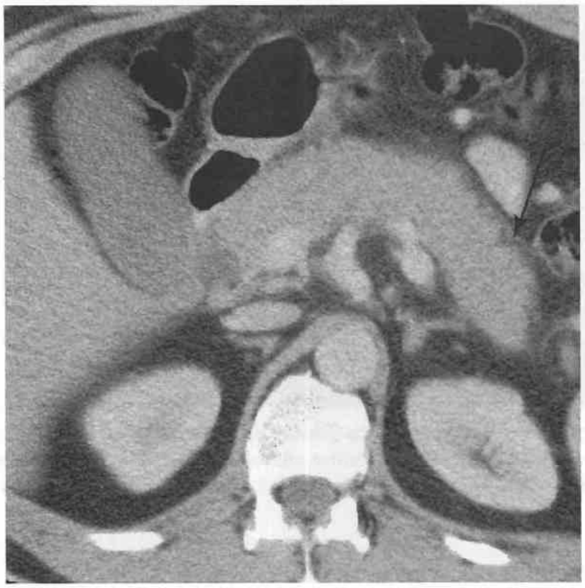

Figure 38–48. Early edematous pancreatitis shows enlargement of the gland diffusely and subtle amounts of edema fluid along the margins of the gland (*arrow*).

density fluid may totally obscure the margins of the splenic vessels. The pancreas may increase or decrease in size, depending on the stage of inflammation (Figs. 38–52 and 38–53). Edema fluid may extend along the anterior ligamentous pathways, such as the mesentery, hepatoduodenal ligament, or the mesocolon (Fig. 38–54). With the mesocolon originating from the anterior surface of the pancreas, spread of the inflammation resulting in a sentinal loop is quite common in the hepatic, transverse, or splenic flexure portion of the colon.

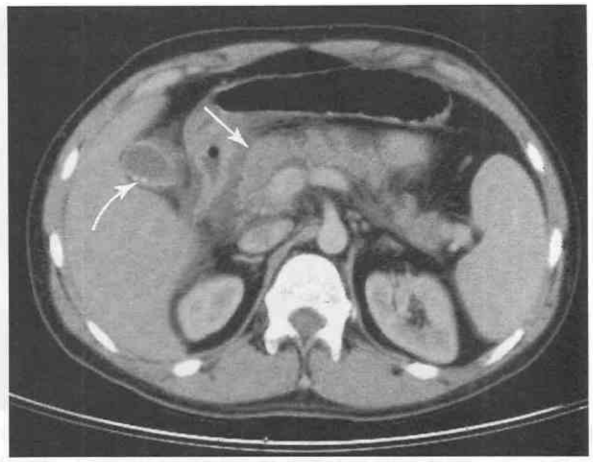

Figure 38–50. CT scan shows subtle fluid around the body of the gland but early accumulation of fluid in the lesser sac (*arrow*) behind the antrum of the stomach and in front of the pancreas. Also note the small gallstones in the gallbladder (*curved arrow*).

Density alterations within the gland result from either fluid accumulation (see Figs. 38–52 and 38–53) or necrosis. Edematous pancreatitis can be differentiated from necrotizing pancreatitis by the injection of contrast material (see Fig. 38–51) because the normal gland enhances but the avascular necrosis does not. Maier[161] found in operatively confirmed cases that edematous pancreatitis maintains uniform enhancement without alterations of density; necrotic devascularized areas do not enhance. In subtle cases, there may be no positive laboratory findings; the serum amylase and lipase levels may be normal.

Further progression of the inflammation most commonly produces ascites, which can fill the adjacent peritoneal

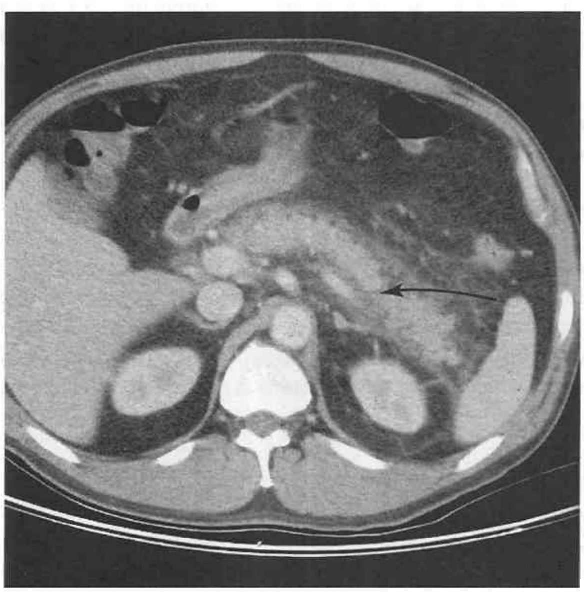

Figure 38–49. With large accumulations of fluid, the fat plane between the gland and the splenic vein becomes higher in density (*arrow*). Note also the subtle edema spread throughout the midportion of the mesentery.

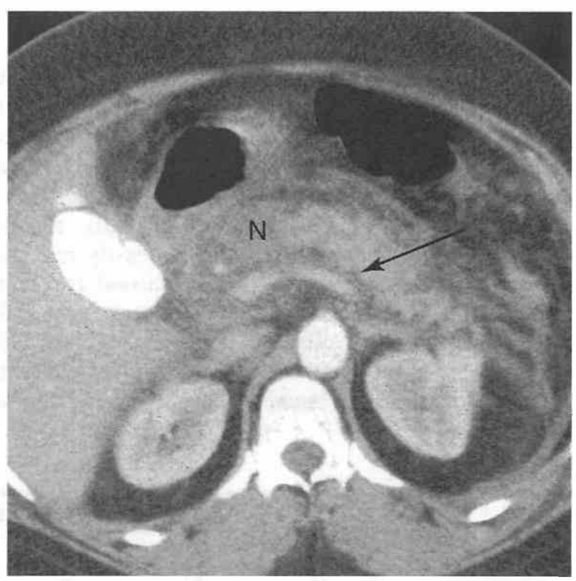

Figure 38–51. Severe pancreatitis produces large amounts of pancreatic and peripancreatic edema. The fat plane (*arrow*) between the splenic vein and the gland is dense. Also note the early necrosis (N) in the head, which shows decreased enhancement compared with adjacent normal parenchyma.

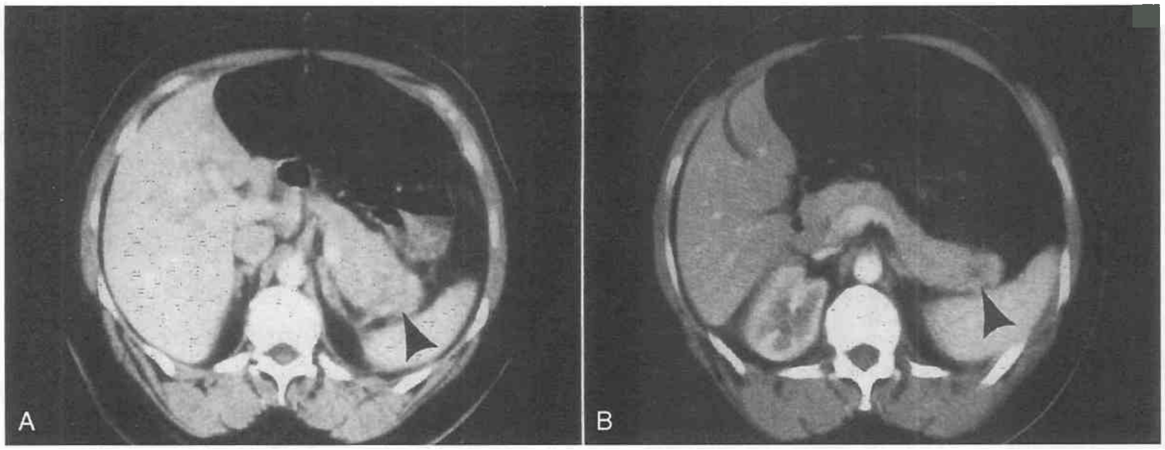

Figure 38–52. *A,* CT scan shows focal enlargement of the tail (*arrowhead*) secondary to pancreatitis. *B,* After resolution, the gland returned to normal size (*arrowhead*), but residual focus of fibrosis remains.

space, including the greater peritoneal cavity and lesser sac. Involvement of the general cavity produces ascitic fluid in the adjacent dependent spaces, such as the paracolic gutters and Morrison's pouch. The lesser sac, being immediately anterior to the gland, is the space most commonly involved by accumulation of fluid (see Fig. 38–50). Fluid collections or subsequent pseudocysts can occur in either the inferior or the superior medial recesses of the lesser sac (Fig. 38–55).

The anatomic area second in frequency of involvement by continued inflammation is the anterior perirenal fascia on either the right or left side depending on whether the head or the body of the gland is involved. The fluid may extend either cephalad to involve the bare area behind the liver or spleen or caudad to involve the retroperitoneum down into the pelvis by the psoas muscle. The amount of the fluid can be so great that it produces distention of the fascia, creating a mass (see Fig. 38–56). With the sparing of the perinephric fat, this appearance has been given the name "halo sign" by Susman and colleagues.[246]

Progressive inflammation and spread of edema can produce pronounced extension into contiguous organs or bowel.[178] Inflammatory involvement of the mesentery and mesocolon may produce sufficient edema to cause lymphatic and venous congestion, leading to an ileus or sentinal loop of the adjacent bowel. Involvement of the stomach and edema can produce such severe thickening that they may simulate a mass. Digestion of the enzymatic material along the vasculature of the ligaments or through fascia can result in direct involvement of the liver, spleen, or even the kidney with ultimate formation of pseudocysts in those organs.

One specific area of inflammatory spread that has been the source of some controversy is the perivascular fat plane around the superior mesenteric artery. Traditional teaching has held that only tumors can produce this appearance of encasement, but Schulte and colleagues[223] and other researchers have documented the occurrence of loss of the fat plane with pancreatitis in addition to neoplastic inflammation. This finding can be seen in both acute and chronic pancreatitis.

Chronic Pancreatitis Mimicking Adenocarcinoma

Numerous authors, including Johnson and Outwater,[121] Kim and associates,[131] and Kusano and coworkers,[142] have

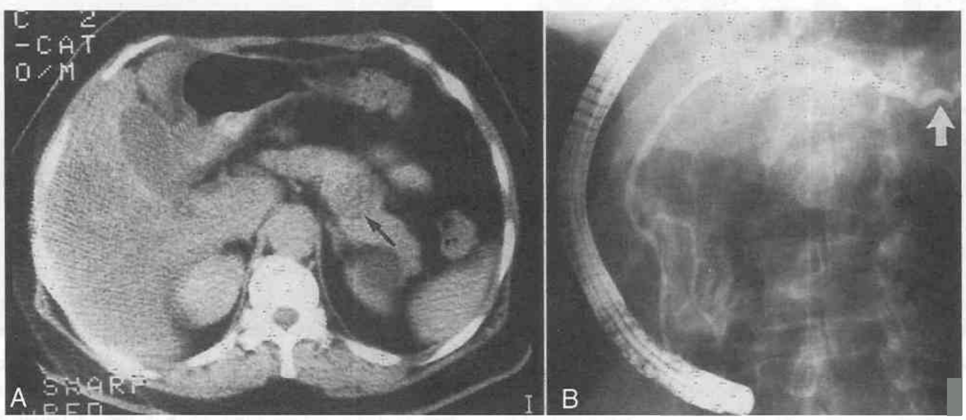

Figure 38–53. *A,* CT scan shows an area of decreased density (*arrow*) within the gland that represents focal pancreatitis. *B,* ERCP shows enlargement of the duct (*arrow*) in the central part of the gland; enlargement is typical of pancreatitis.

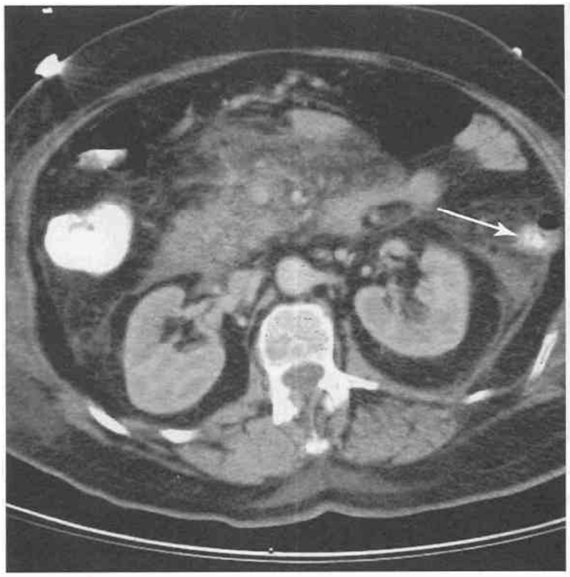

Figure 38–54. Large amount o[redacted]ema spreads throughout the mesentery and into the perirenal [redacted]cia. Note the wall thickening of the descending colon. It is my belief that secondary infection of fluid collections occurs when bacteria are cleared through the lymphatics but become lodged in fluid collections and propagate.

reported that chronic pancreatitis can look virtually identical to pancreatic adenocarcinoma on CT and MRI studies. Johnson and Outwater[121] studied a group of 28 patients with adenocarcinomas and 7 patients with chronic pancreatitis, using the best available MRI sequences at the time and gadolinium injection. Normal glands enhanced in a predictable fashion, but both tumor and fibrotic areas of pancreatitis showed delayed enhancement patterns that were indistinguishable (see Figs. 38–20 and 38–21). Kim and associates[131] studied 7 patients with focally enlarged masses in the pancreas, using the current MRI and CT techniques with the appropriate contrast enhancement. In all patients pathologic analysis confirmed local fibrosis in the masses. The imaging appearance of all of the masses mimicked that of focal adenocarcinoma, with no specific differentiating findings.

Evolution of Inflammation

Pancreatic inflammation has many different appearances as it evolves through various stages. In the earliest phases, it appears as a subtle increase in the density of the fat. As fluid accumulates, it may fill tissue spaces until it develops well-defined margins. Although no formal study correlating the appearance with fluid composition has been made, it has been my perception that if the process becomes more severe, the density of the fluid increases. If the inflammatory fluid remains low in density or changes from high density to low density, it seems that resolution soon follows. The resolution of the edema and fluid collections may be complete, but some may remain as residual collections of enzymatic material, thereby creating pseudocysts (see Fig. 38–67).

Although observations about the extent and nature of fluid distribution are important, the most significant diagnostic signs that should be sought are those related to necrosis and possible infection. Both of these problems can have a devastating effect on a patient if they are not treated promptly and correctly. A number of surgeons and clinicians, including Maier,[161] have stressed that both necrosis and infection are accurate predictors of the ultimate outcome of severe pancreatitis and also have used them as indications for surgical intervention, as noted in the later section on necrosing pancreatitis.

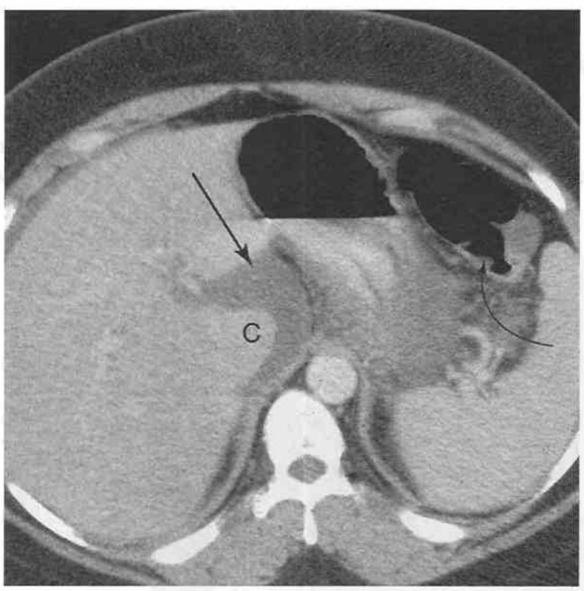

Figure 38–55. With sustained inflammation, ascitic fluid accumulates in spaces such as the superior recess of the lesser sac, which borders the caudate lobe C of the liver (*straight arrow*). Also note thickening of the splenic flexure of the colon (*curved arrow*).

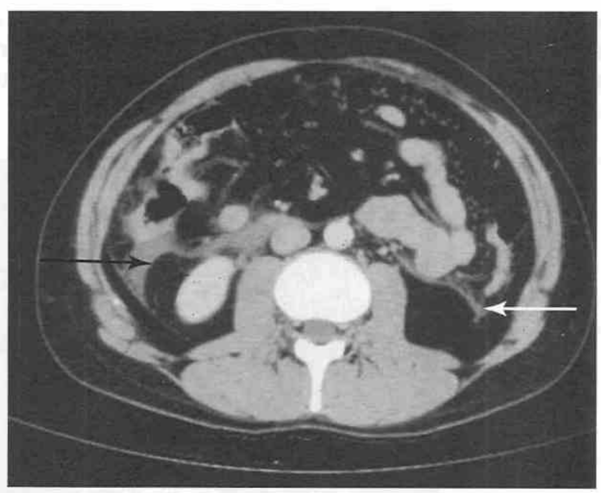

Figure 38–56. CT scan showing extensive fluid collections extending caudally into retroperitoneal fascia (*arrows*). The right side is more severe than the left side. Distention of fascia around normal peripheral fat has been called a "halo sign" by Susman and associates.[246]

Differentiating Inflammatory Mass from Neoplasm. Thickening of the perirenal fascia, a nonspecific sign, can be associated with any entity that produces edema or obstructs the flow of lymphatics (e.g., masses, infection). As a practical matter, however, thickening of the perirenal fascia is more common with inflammation in both acute and chronic pancreatitis.[187a] Published data have shown that thickening of the left perirenal fascia occurs infrequently in early pancreatic carcinoma. This is not an absolutely reliable finding, because in occasional cases, pancreatic cancer can coexist with inflammation. Another finding commonly mistaken as pathognomonic of neoplasm is loss of the perivascular fat plane, which can occur with inflammation as well as neoplasm.[143, 148, 183]

Differentiating Tissue Edema from Fluid Collection. When inflammation is severe, a large amount of edema occurs as well as the accumulation of fluid. Differentiation of these two entities can be made by looking for the presence of small "fat islands" within the fluid density. These areas represent intact areas of normal tissue and fat uninvolved with edema fluid, thereby distinguishing them from collections of liquefied tissue or fluid that may require drainage.

Spontaneous Hemorrhage with Acute Pancreatitis. A sudden loss of blood sufficient to produce a sudden drop in a patient's hematocrit value, can occur in an inflamed area. Such a sudden blood loss in the area of the pancreatic bed is easily detectable on CT as an increased-density collection of material in the inflamed area. This blood loss can result from a diffuse leakage of inflamed granulation tissue or a break in a vessel damaged by digestive enzymes. Hemorrhage associated with pancreatitis should not be confused with *hemorrhagic pancreatitis,* a term that has been used in the past to refer to severe or life-threatening pancreatitis.

From experience with CT procedures and surgical procedures, it is clear that virtually all fluid or inflammatory material obtained from an acute inflammatory process appears bloody regardless of the severity of the disease. The irrelevance of the hemorrhagic nature of inflammatory fluid was noted by both Isikoff and colleagues[109] and Lawson and others.[144–146] They reported detecting high-density material believed to be blood in the inflammation associated with pancreatitis. Both groups noted that the finding was not consistently related to the severity of the disease, and Lawson stated, "There did not appear to be any correlation between the mortality, severity of the illness, or extent of retroperitoneal necrosis and the presence or absence of hemorrhage as observed at surgery."

Severe Necrosing Pancreatitis. Severe pancreatitis, regardless of the descriptive terms or the method of categorization, is a devastating disease with a reported mortality rate between 33% and 100%.[122, 161, 262] Before CT scanning, the objective assessment of the anatomic extent of pancreatic inflammation and determination of the degree of involvement were difficult to achieve.[191]

Clinically, this entity has been virtually impossible to distinguish from severe edematous pancreatitis. Previously the most reliable method of assessing the severity of the disease was careful examination and correlation of clinical signs and relevant serum laboratory values, such as serum calcium, serum methemalbumin, and hematocrit. Paracentesis was occasionally performed to obtain fluid for analysis. Data published by surgeons have shown that the standard clinical method for grading severity of disease, such as Ranson's criteria or the APACHE (Acute Physiology and Chronic Health Evaluation) II, are not good indicators for either operative intervention or prognostication.

The most valuable diagnostic method for evaluating the status of the pancreas with severe inflammation is a good-quality CT scan enhanced by adequate doses of intravenous contrast material, as noted in the technique section.[43, 120, 133, 136] The normal gland shows considerable enhancement as a homogeneous pancreatogram. The devascularized or necrotic gland shows a lack of this enhancement in the focal area of necrosis (Figs. 38–51 and 38–57). Furthermore, authors have shown that the larger the area of devascularized necrosis, the poorer the outcome for the patient, accompanied by a greater probability of secondary infection. The significance of this sign has been studied by several groups, but the importance of this finding was best demonstrated by Block and colleagues.[25] These authors compared the effectiveness of CT and ultrasonographic procedures with clinical staging for identifying pancreatic necrosis. They studied 93 patients in a prospective fashion, who subsequently underwent surgical exploration. The group found that CT with enhancement was superior for detection of pancreatic necrosis. Ninety percent of cases of severe necrosis and 79% of cases of minor necrosis were demonstrated with enhanced CT. Ultrasonography was not diagnostic in 24% because of the presence of meteorism. Other observations made by these authors are also noteworthy. They noted that even with CT, there is the risk that the area of necrosis may be larger and that occasionally, an avascular area may be ischemic but not necrotic. Maier[161] reported that the contrast-enhanced CT evaluation for pancreatic necrosis was a better indicator for surgery than

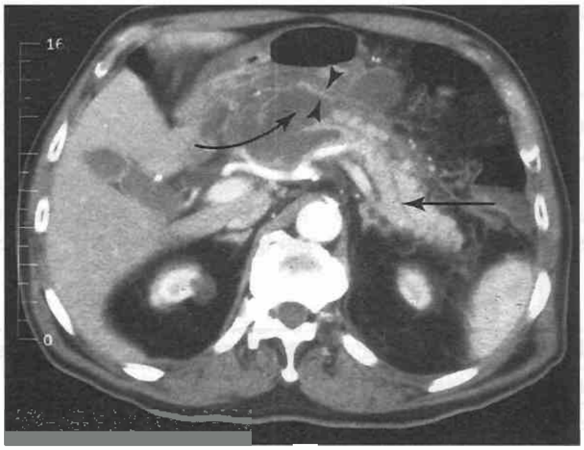

Figure 38–57. CT scan performed during contrast enhancement shows large fluid mass in the central portion of the pancreas corresponding to an area of necrosis. Dilated pancreatic duct (*horizontal arrow*) and fluid extension to stomach (*curved arrow*) can be seen. Gastric wall is distended with inflammatory fluid on both the anterior and posterior surfaces (*arrowheads*).

any of the currently accepted clinical methods for grading severity of disease.

Once the diagnosis is made, a diversity of therapeutic regimens is recommended, including conservative management, sump drainage, and pancreatectomy. Serious complications, such as pancreatic abscess, pseudocyst, fistula formation, and endocrine and exocrine deficiency, can result. Despite the fact that diverging opinions on the modes of therapy can be found, all authors agree that expeditious, accurate diagnosis of the problem is needed.[133, 149] Morbidity and mortality rates for severe pancreatitis are still high.

Distinguishing Infected and Sterile Necrosis. Bittner and colleagues[23] and others[21, 25, 161] pointed out the importance of differentiating pancreatic abscesses (well-marginated fluid collections) from pancreatic necrosis and infected pancreatic necrosis. The outcome of pancreatitis depends not on the amount or severity of inflammation but rather on the presence or absence of infection. Although abscesses can usually be drained by percutaneous methods, infected necrosis requires surgical evacuation of all infected material and institution of postoperative lavage of the lesser sac. Necrosis tends to become infected, and it is critical that infection be detected.

The inflammatory material with necrotic matter, blood, and enzymes is a good culture medium and has a high susceptibility for secondary infection.[8] Unfortunately, it is not possible to detect any transition from necrosis to infection on the basis of a CT scan. Serial aspiration samples for culture must be obtained if an infectious process is suspected or if any air is present. In such cases, it is absolutely imperative that the diagnostic aspiration be completely and technically precise, without contamination from intestinal material; passage through bowel negates the reliability of the culture because false-positive findings may result and, more important, contamination with the gastrointestinal contents may introduce an inoculation, which can lead to infection. (It might be hypothesized that one could distinguish between contamination and infection in the culture results on the basis of the mixed colonic flora obtained. This is incorrect because most authors believe the major source of infection is small gastrointestinal fistulas.)

Anatomic Staging and Prediction of Clinical Severity. With the seriousness of pancreatitis and the difficulty in predicting the outcome, several authors have attempted to devise a method for predicting the outcome of pancreatitis. One imaging approach developed by Balthazar and others[13–15] parallels Ranson's criteria and has been somewhat useful for staging the inflammatory process in a slightly different fashion from the simple method of looking for necrosis.[11, 13]

Balthazar and others[13–15] devised the following grading system on the basis of CT findings: grade A, normal pancreas; grade B, focal or diffuse enlargement of the gland (includes nonhomogeneous attenuation of gland, dilatation of duct, and foci of fluid within the gland, as long as there is no extrapancreatic edema); grade C, peripancreatic edema and intrinsic abnormalities of grade B; grade D, single ill-defined fluid collections or phlegmon; and grade E, two or more fluid collections or the presence of gas. These researchers found that the patient's hospital course correlated well with these findings and the grading system. Abscess occurred in 21.6% of all patients and in 80% of patients with grade E pancreatitis. The researchers also point out the use of CT to pick up associated findings, such as gallstones and peritoneal and pleural fluid. All deaths occurred in grades C, D, or E pancreatitis, with the majority in grade E.

Balthazar and others[13–15] also noted that the longer the hospital stay, the higher the grade of pancreatitis. Patients with grade A stayed 13 days; grade B, 17 days; grade C, 25 days; grade D, 31 days; and grade E, 52 days. They also found a correlation between CT findings and the clinical prognostic signs previously described by Ransom; the signs are listed in Tables 38–2 and 38–3.

This information provides a mechanism for effectively communicating in a concise fashion the severity of a patient's pancreatic inflammation. This system, however, does not always correctly predict the outcome. Despite these attempts to predict and manage acute situations, the outcomes are remarkably different from expectations. Sometimes, disease with fairly benign-appearing inflammation can have a precipitous course (Fig. 38–58). Conversely, individuals with more anatomically extensive disease can do well.

Prognostic Indicators. The best method of predicting clinical outcome was evaluated by De Sanctis and colleagues,[53] who prospectively compared the merits of the contrast-enhanced computed tomographic (CECT) criteria of disease severity and the APACHE II system. In their study, 35 consecutive inpatients were scanned and a consensus interpretation was performed to provide determination of the CECT grade of the severity index. The APACHE II score was calculated within 24 hours of the CECT.

In my opinion, this is the most significant work performed in the evaluation of pancreatitis in the last 25 years. The imaging field and the clinical science have been refined

Table 38–2. Early Prognostic Signs of Acute Pancreatitis* According to Ranson

Admissions or Diagnosis	Initial 48 Hours
Over 55 years of age	Hematocrit falls more than 10%
White blood cell count over $16 \times 10^3/\mu L$ ($16 \times 10^9/L$)	Blood urea nitrogen level rises more than 5 mg/dL (1.79 mmol/L)
Blood glucose level over 200 mg/dL (11 mmol/L)	Serum calcium level falls below 8 mg/dL (2 mmol/L)
Serum lactic dehydrogenase level over 350 μ/mL	Arterial Po_2 below 60 mm Hg (7.98 kPa)
Serum glutamate oxaloacetate transaminase level over 250 μ/mL	Base deficit greater than 4 mEq/L (4 mmol/L)
	Estimated fluid sequestration more than 6000 mL (6 L)

* Each sign counts as 1 for score.
From Balthazar EJ, Ranson JH, Naidich DP, et al: Acute pancreatitis: Prognostic value of CT. Radiology 156:767, 1985.

Table 38–3. Relationship Between Prognostic Signs and Clinical Course

No. of Patients	Prognostic Signs*	Average Fasting Days	Average Days Hospitalized	No. of Abscesses	No. of Deaths with Abscess
56	0–2	16.4	24.6	7 (12.5%)	—
22	3–5	28.9	40.6	7 (31.8%)	2 (9.1%)
5	6–8	39.7	48.0	4 (80.0%)	3 (60%)

* See Table 38–2 for signs.
From Balthazar EJ, Ranson JH, Naidich DP, et al: Acute pancreatitis: Prognostic value of CT. Radiology 156:767, 1985.

over this period, so there can be no question as to the validity of this study. The results show that the APACHE II score is the best predictor of the need for admission to intensive care or severity of systemic disease. The CECT, because it provides an assessment of anatomic information, is the best predictor of local complications. This is only logical, because it is known that ultimate mortality of severe disease depends directly on fluid collections, which may be infected, or pseudoaneurysms, which have a propensity to bleed. The most effective strategy is to triage the patient to an acute care environment according to an immediately calculated APACHE II score. Imaging assessment can be performed as clinically indicated.

Presence of Infection

Relative to infection, many studies have noted that no imaging method can determine the presence or absence of infection. The only effective way to do so is to perform a diagnostic aspiration for culture, as discussed in Chapter 62. Several short comments are appropriate. CT is extremely well suited to use during aspirations because of its ability to detect fluid collections and guide accuracy of the procedure. During such procedures, several technical points are relevant. It is always prudent to perform an intense bolus injection to demonstrate possible pseudoaneurysms. The trajectory planning of any diagnostic aspiration should be made to avoid intestinal loops, because contamination of the needle could result in a spurious culture result or, potentially, contamination of any fluid collection. Finally, one should realize that infection is a dynamic event and may occur during different phases of the pancreatic inflammation. Diagnostic aspirations should be repeated whenever there is a consideration of infection; spontaneous development of infection can occur at any time, so a negative prior aspiration result is meaningless.

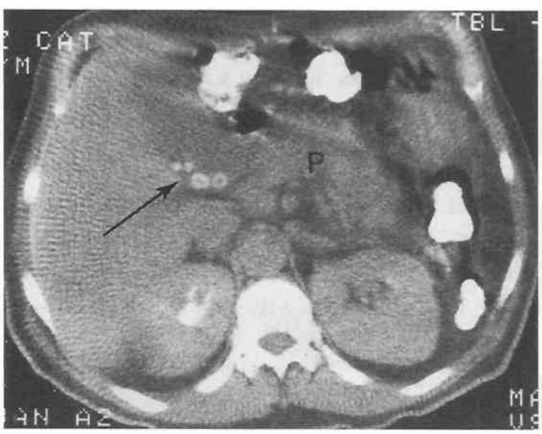

Figure 38–58. Patient who died within 24 hours after admission and 8 hours after this study has minimal signs of inflammatory disease around the pancreas (P), even though the cause of death was pancreatitis. Note calculi in gallbladder (*arrow*).

Once infection has been discovered, proper management is critical, because the outcome of infected pancreatitis depends on effective drainage. In a limited number of cases, percutaneous methods may work if a fluid collection is well confined and contains very thin material. In many cases, patient survival is contingent on effective surgical drainage.[28, 29, 241]

Emphysematous Pancreatitis

Emphysematous pancreatitis is a diagnostic term originating from plain-film radiography that describes a life-threatening pyogenic infection of the pancreas caused by gas-forming bacteria. When applied to CT imaging, however, the term describes a wide spectrum of disorders, some of which are severe and some of which are benign and self-limited.

Gas-forming pyogenic infection superimposed on pancreatitis can result from a variety of causes, including spontaneous, hematogenously seeded colonization from gastrointestinal fistula or secondarily from surgical procedure (usually cystotomy). The organisms that most commonly produce gas are *Escherichia coli, Enterobacter aerogenes,* and *Clostridium.* The most infamous of these bacteria are the *E. coli,* which classically produce emphysematous pancreatitis associated with a high mortality rate in diabetic patients. Because plain-film radiography has a much lower contrast resolution than CT, it is virtually impossible to detect gas in the pancreas in an early phase of development on plain-film radiography. Conversely, the slightest amount of gas can be detected with CT; the presence of gas caused by a multitude of disorders is possible.

With the advent of CT, with its superlative axial anatomic images and contrast resolution, the diagnosis of gas in the pancreas has become much easier from a detection standpoint but more complex because of the multitude of entities that can be seen and must be differentiated.

A number of authors have noted that there may be a discrepancy between the imaging appearance of the gland and the clinical appearance in many cases of emphysematous pancreatitis.[177] A high percentage of cases of emphysematous pancreatitis have resolved without aggressive treat-

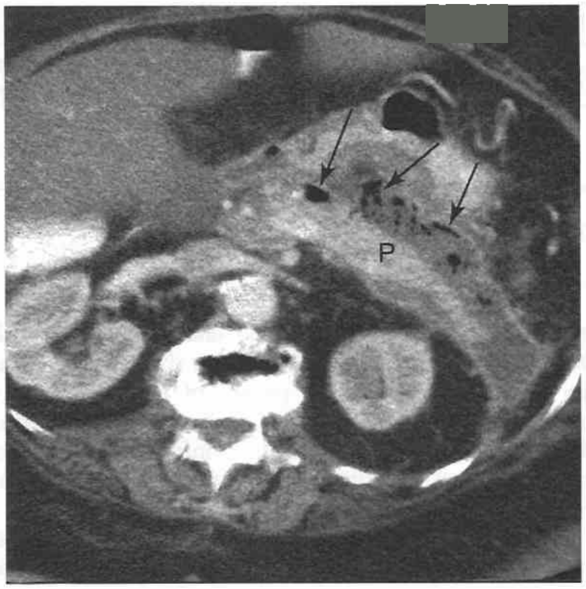

Figure 38–59. Scan of patient with emphysematous pancreatitis shows fluid collection surrounding the enhancing pancreas (P). Air is distributed in the fluid around the gland as well as in the gland itself (*arrows*).

ment by drainage (Fig. 38–59). A smaller percentage of cases have a disastrous outcome, regardless of adequate treatment.

In most seriously ill patients with emphysematous changes, there are significant associated problems, such as a gastrointestinal fistula,[8, 199] which may have developed because of an ulcer,[160] perforation, or another problem. Such patients may do well temporarily, but most eventually experience sepsis and do poorly unless proper expeditious drainage and correction of the basic problem are accomplished. In the case illustrated in Figure 38–59, the patient initially appeared well, and the clinical physicians were not convinced of his serious situation until he suffered cardiorespiratory collapse. While connected to a respirator and supported with vasopressive agents, the patient underwent percutaneous drainage of the pancreas, which effected a cure.

The cause of the gas in patients who do well is in question. Two plausible hypotheses explain these observations. The first explanation is that the gas is a by-product of necrosis. The gas may be nitrogen or another gaseous material, not from gas-forming bacteria but from tissue necrosis. An alternative theory, which I propose, is that the gas is produced by gas-forming organisms or from a small gastrointestinal fistula that closed spontaneously and that may or may not adversely affect the patient, depending on immune status. I have scanned several patients with gas in the pancreas produced by pyogenic organisms who have recovered without surgery or antibiotics. The presence of pyogenic bacteria in both cases was proved by diagnostic aspiration, the specimen for which was obtained by an aseptic method (avoiding bowel) (Fig. 38–60).

The outcome in patients with emphysematous pancreatitis probably depends on their immune status. Some patients who have a competent immune system can handle a borderline colonization or infection from their own flora. Those who are immunocompromised or become debilitated are unable to mobilize or sustain the competence of the immune system to handle the infection. Such patients become severely ill and can even die.

Management. The management and disposition of patients who have emphysematous pancreatitis should be based on clinical, laboratory, and imaging data. First, it is important to ensure clear communication among the internist, surgeon, and radiologist. Close cooperation ensures that all physicians are aware of any change in clinical status or imaging appearance so adjustment in patient care can be made without delay.

There does not appear to be any controversy about the best treatment for symptomatic patients with pancreatic gas. These patients require early surgical or percutaneous drainage of infected areas around the pancreas. The methods for draining such areas are discussed in Chapter 62.

In asymptomatic patients, aspiration should be performed under CT guidance at the earliest time, with careful avoidance of intestinal loops or bowel (assuming that other causes of gas have been excluded) (see next section). Careful avoidance of bowel loops is important if the culture of the sample is to be valid. The sample obtained must be

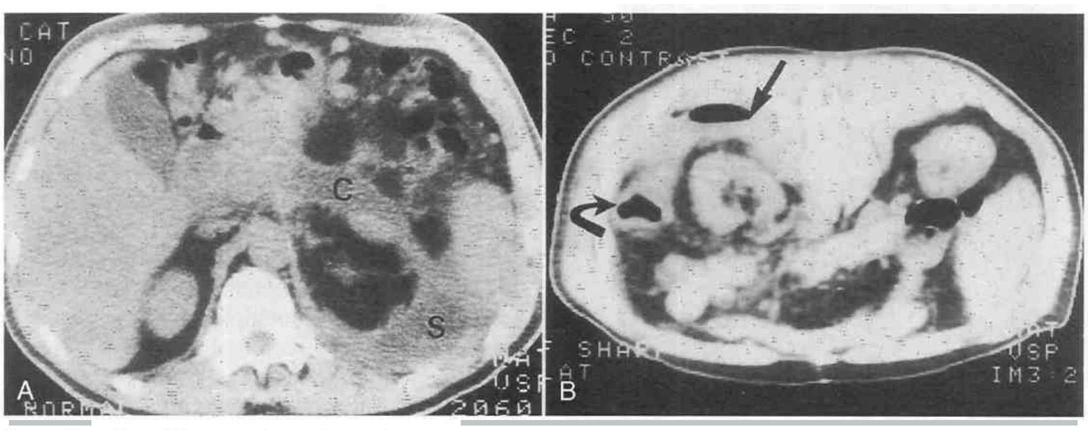

Figure 38–60. *A*, Baseline CT scan of a patient with a pseudocyst in whom a colonic fistula developed. This scan shows a pseudocyst (C) with an extension to the splenorenal ligament (S). *B*, Second scan taken 2 days later with the patient prone shows air (*arrow*) in the posterior fluid collection and fluid extending around the colon (*curved arrow*).

free of bowel contents. Second, enteric bacteria must not be introduced into a pancreatic fluid collection; such a contaminant could cause an abscess if the pyogenic bacteria grew.

Management of asymptomatic patients should be based on the results of the culture. If the culture is negative, the patient should be observed and CT examinations should be performed regularly until the gas disappears. Any clinical or CT sign of deterioration should result in a re-evaluation, and surgery should be considered.

If the gas does not resolve within 1 week, a second aspiration should be performed in case a sampling or handling error was on the first sample.

If the culture result is positive, one of several courses of action can be taken. First, if the sample aspirated is culture positive, the proper antibiotic medication should be chosen, and surgical drainage considered. If the patient is a poor surgical candidate, percutaneous procedure may be performed to stabilize him or her. This procedure decreases the "toxic load" and, it is hoped, stabilizes homeostasis (e.g., nutrition, cardiovascular system). If the patient remains stable with antibiotic therapy and the emphysematous appearance on the CT scan resolves, no further intervention is required. If the patient improves generally but the gas remains, further investigation is required to determine the origin of the infection (e.g., penetrating ulcer or gastrointestinal fistula) (see Fig. 38–60).

Other Causes of Gas. One of the most common benign causes of gas in the pancreas is a duodenal diverticulum. The air collection is usually single, well defined, and located just medial to the second portion of the duodenum or in the lower portion of the uncinate process just cephalad to the third portion of the duodenum (Fig. 38–61). The diverticulum may contain a fluid level or even barium if an oral contrast agent has been given.

A penetrating ulcer has one of two appearances. If the ulcer penetration seals, only a single minute collection of gas in the pancreas just adjacent to the duodenal or stomach wall is usually seen. In some cases, edema of the wall can be seen. If a large penetration has occurred and it is not sealed, a large amount of air may be scattered throughout the omental bursa or into an adjacent structure.

Gastrointestinal fistula also produces air in and adjacent to the pancreas (Figs. 38–62 and 38–63). The gas is ill defined and closely related to the stomach, jejunum, duodenum, or colon. It is difficult to ascertain the origin of the fistula on the CT scan; contrast studies of the bowel and injection of contrast material after drainage are most useful.

Other common causes for benign gas in the pancreas are iatrogenic and are usually the result of a recent or remote surgery or interventional procedure. Puestow procedures (enterostomy to the duct) or papillotomy can produce gas in the duct. Freed and colleagues[63] reported that with Puestow procedures, when the anastomosis or Roux-en-Y loop was collapsed and contained fluid and gas, confusion with a peripancreatic abscess was very possible. Patients who have undergone internal drainage procedures on pseu-

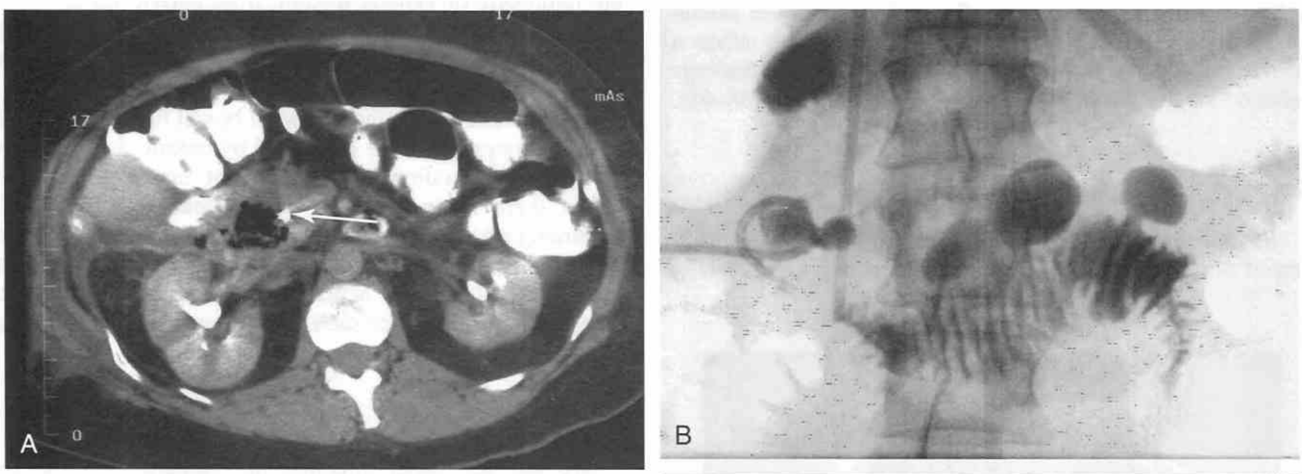

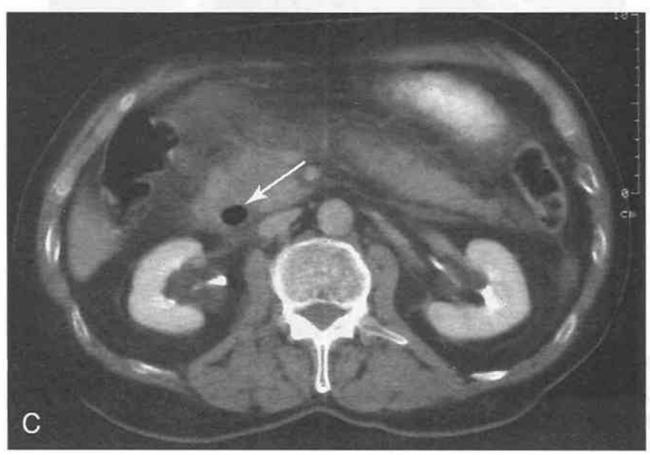

Figure 38–61. *A,* CT scan shows a gas collection in the area of the head of the pancreas, which has some ill-defined densities within. Because the patient was febrile, a drainage catheter was inserted (*arrow*). *B,* Fluoroscopic study showing contrast material in duodenum and multiple diverticuli; the catheter remains in diverticulum. *C,* In CT scan obtained after the drainage catheter was removed, the air cavity has reduced in size and has a better-defined margin. This case of duodenal diverticulitis required no further treatment.

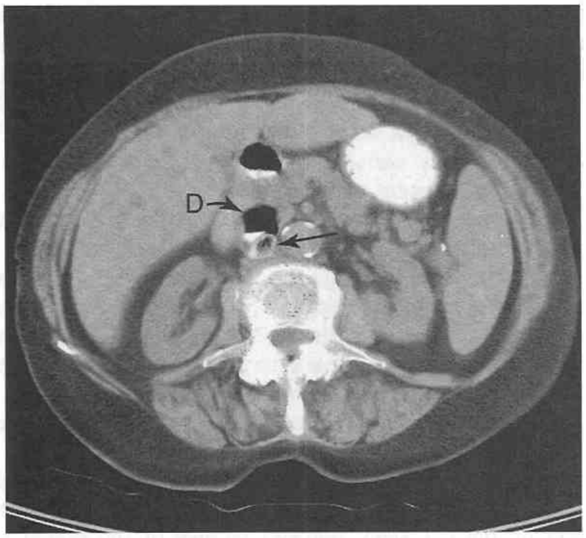

Figure 38–62. CT scan shows a large air collection with a contrast level in the cavity behind the head of the pancreas, anterior to the vena cava. Small amounts of air (*arrow*) are noted in the vena cava due to ulcer in diverticulum (D), which penetrated posteriorly.

docysts (e.g., cystogastrostomies) can have variable amounts of gas and fluid in the cavity (see Fig. 38–61*A*). Immunocompromised patients experience a long delay in the healing of such cavities (Fig. 38–64). Occasionally, some asymptomatic elderly patients have a patulous sphincter, and spontaneous reflux of air into the ductal system occurs. Rarely gas can appear in vessels when a penetration occurs into adjacent vessels. Spurious findings related to partial-volume effects may be seen (Fig. 38–65).

Pancreatic Abscess

Pancreatic abscesses are a severe, life-threatening problem if not correctly treated. As has been noted previously, the outcome of pancreatic inflammation occasionally depends on the presence or absence of infection. Pyogenic infection of the pancreas can be caused by a variety of organisms introduced by different mechanisms.

Virtually any organism can infect the pancreas,[54] but most are bacteria or fungi from the gastrointestinal tract. They include many gram-negative and gram-positive organisms and *Candida albicans*. Hurley and Vargish[106] showed significant differences among infections caused by different organisms. In their series, gram-negative infections were polymicrobial and had a high mortality, whereas gram-positive infections were monomicrobial and had a low mortality. (In immunocompetent patients, primary infection from *Candida* probably does not occur; it is probably opportunistic initially after treatment with broad-spectrum antibiotics.) If the causative organism is not gas forming, the appearance of fluid on the CT study is indistinguishable from the appearance in a typical case of suppurative or hemorrhagic pancreatitis.[58] If there is any question of possible infection in a patient, a percutaneous diagnostic aspiration should be performed.

The mechanisms for introduction of the infection are the same as for emphysematous pancreatitis; they include hematogenous seeding, lymphatic spread, gastrointestinal perforation or fistula,[99] and iatrogenic responses to some type of procedure. Hematogenous seeding is most likely to occur superimposed on a gland that has some type of baseline problem, such as pancreatic necrosis. It is our impression that patients who have large amounts of fluid around the colon are at risk for infection because of possible lymphatic or venous seeding from enteric flora.

Iatrogenic causes of abscess can also occur after surgical drainage procedures, ERCP,[54] or percutaneous instrumentation. After an internal drainage procedure during which a stoma between a cyst and a loop of bowel has been created, the pseudocysts become colonized by enteric flora. In most instances, this colonization does not create a problem, but if there is an anatomic region that does not freely communicate with the bowel, a local accumulation of material can result in an abscess. Considering the number of bacteria involved, it is actually surprising that more infections do not occur after such procedures (see Fig. 38–64).

Immune Status

As with any other infection the immune status of the patients with pancreatitis is critical. Those who are immunocompromised may have delayed clinical responses to treatment as well as delayed resolutions of anatomic findings. In such cases, the resolution of the fluid or air collection may take longer than it would in a patient with a normal immune status.

Abscesses Caused by Other Pathogens

In addition to the typical bacteria, abscesses may be caused by fungi, tuberculosis,[40, 237] parasites, and other pathogens.[148] In such cases, especially if percutaneous culture specimens are to be obtained, proper handling of the material for culture must be ensured. Experience shows

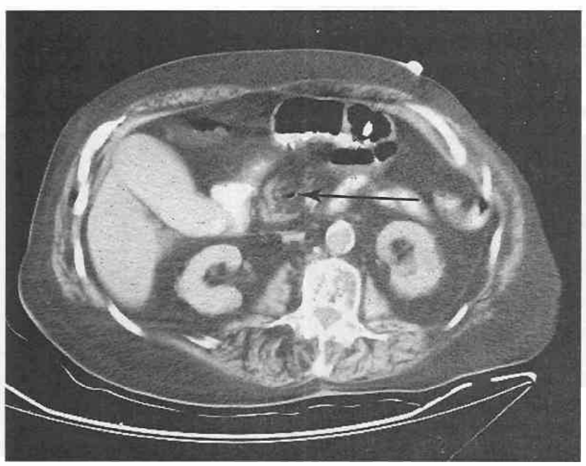

Figure 38–63. CT scan of peripancreatic region shows a small collection of gas in the superior mesenteric vein (*arrow*). This was secondary to a perforated diverticulum in the small bowel that had tracked into the vein.

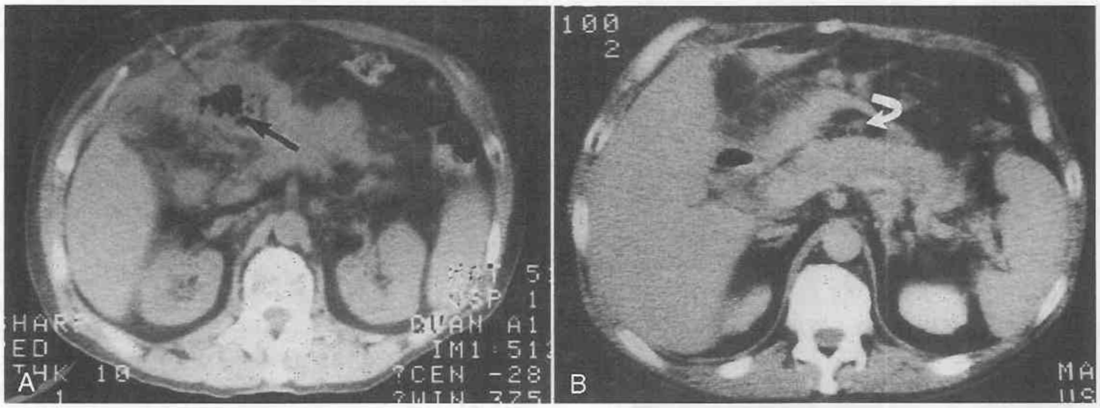

Figure 38–64. *A,* In immunocompromised patients, resolution of the pseudocyst cavity takes a long time, even after surgical internal drainage. The cavity contains a large amount of fluid and air (*arrow*) that could be mistaken for an abscess; sinogram showed enteric anastomosis as intact. *B,* Study performed after removal of the internal drain shows a small residual cavity (*arrow*) containing minimal air and fluid.

that the appearance of abscesses is nonspecific except for those due to *Echinococcus* (Fig. 38–66). All abscesses appear as fluid collections with variable density depending on the amount of blood and debris. With echinococcal disease, however, daughter cysts should be visible.[6, 269] Also, in patients with acquired immunodeficiency syndrome (AIDS), one can expect a variety of unusual opportunistic pathogens. Lederman[147] had a patient with toxoplasmosis microabscesses of the pancreas. Noncaseating granulomatous disease such as sarcoidosis of the pancreas has also been reported by Sagalow and associates.[217]

Pseudocysts

A *pseudocyst* is a fluid collection consisting of necrotic material, proteinaceous debris, and enzymatic material that is confined by a fibrous capsule. The term *pseudocyst* notes the difference between it and other fluid collections within the pancreas that are true cysts (with an endothelial lining) or retention cysts (with a ductal cell lining).[219]

The exact pathogenesis of pseudocysts is not well understood, especially the initiating process, although it is well known that a pseudocyst can result from any significant inflammatory process—either acute or chronic inflammation or acute injury such as trauma. Some authors believe that the fluid in such pseudocysts results from tissue damage, whereas others believe it results from the rupture of ductal elements, which contribute significant amounts of pancreatic secretions. Obviously, both processes must occur, and the cause has no effect on detection, therapy, or prognosis.

Pseudocysts are unique entities because of their protean

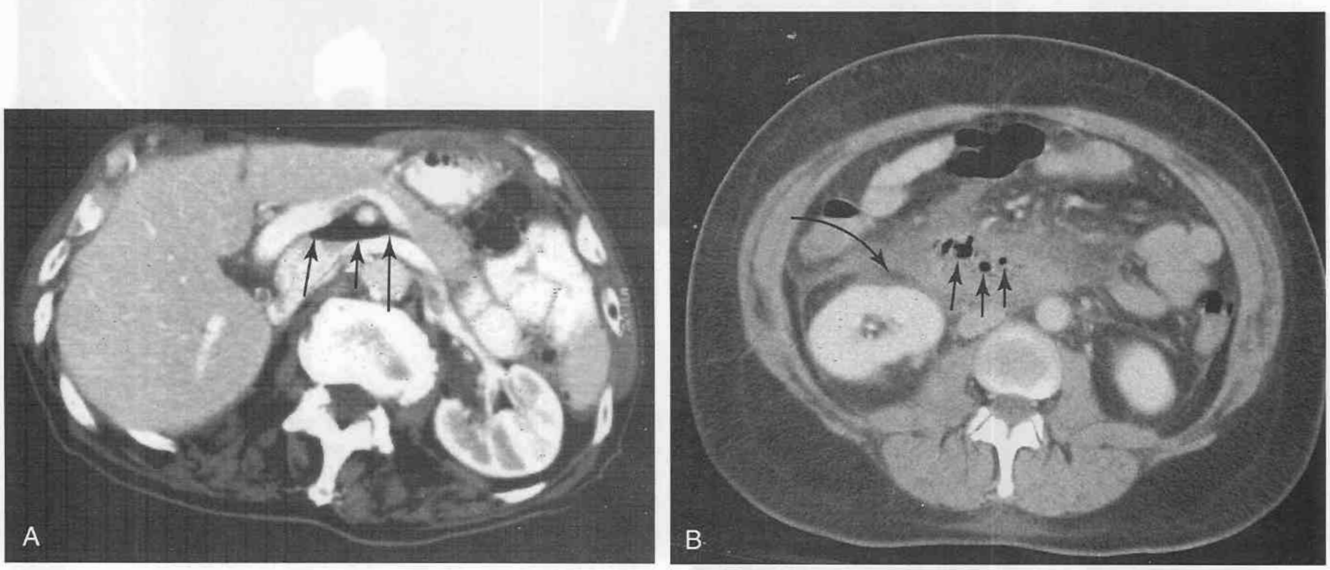

Figure 38–65. *A,* CT scan illustrates an unusual caveat. In this patient, an air density is visible behind the superior mesenteric artery (*arrows*), which is simply due to an incidental herniation of a portion of a loop of small bowel, below the artery. This finding was of no clinical significance. *B,* A partial volume averaging of a loop of jejunum adjacent to an area of edema gives a spurious impression of emphysematous pancreatitis. Gas bubbles (*small arrows*) are trapped in the valvulae conniventes of the duodenum. Note the edema in the retroperitoneal fascia (*curved arrow*).

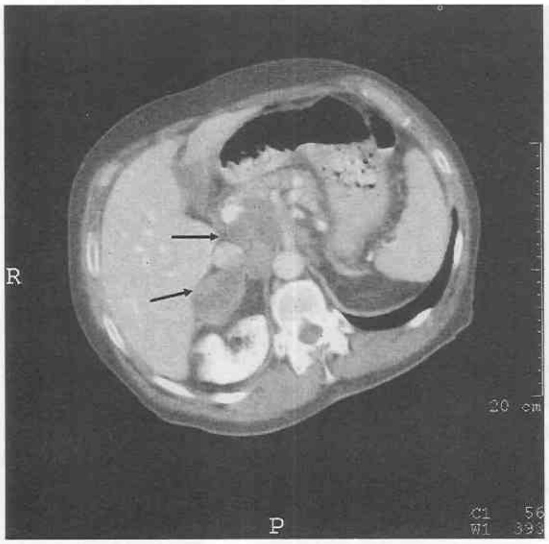

Figure 38–66. Unusual infections of the pancreas can occur. This CT scan shows a cystic mass (*top arrow*) with several components adjacent to the head of the pancreas and adrenal gland (*lower arrow*). The infectious agent proved to be *Echinococcus.* (Printed with permission of Dr. Elmar Merkel, Cleveland, Ohio.)

manifestations, the many locations in which they can appear, and the many complications with which they can be associated.[20, 26, 29] The location and size of the cyst can produce symptoms and problems for the patient, but the complications can be life-threatening. With prompt, adequate treatment, most pseudocysts can be managed effectively.

Symptoms associated with pseudocysts depend on the amount and severity of pancreatitis and the size and speed of their growth. Patients may experience significant, ill-defined pain associated with pancreatitis and have small pseudocysts. Large pseudocysts can cause pain secondary to the inflammatory process, displacement of or effect on adjacent structures, or the amount of pressure within the pseudocysts.

Some patients show an evolution of pseudocysts on sequential examinations, first having a large amount of edema in the area of the pancreas, which usually obscures the margin of the gland and extends into various adjacent areas. As the inflammation resolves, the fluid may coalesce into a well-defined pseudocyst with a clearly defined wall (Fig. 38–67). In other patients, the pseudocyst appears to evolve from necrosis within the pancreas. The necrosis begins as a subtle area of low density and progresses to a well-defined cavity.

Figure 38–67. *A,* CT scan taken early in the patient's disease shows mild edema around the gland. *B,* Later scan shows increased edema between the head of the pancreas and the stomach. *C,* After a number of days, the inflammatory fluid coalesced into a pseudocyst (*arrow*).

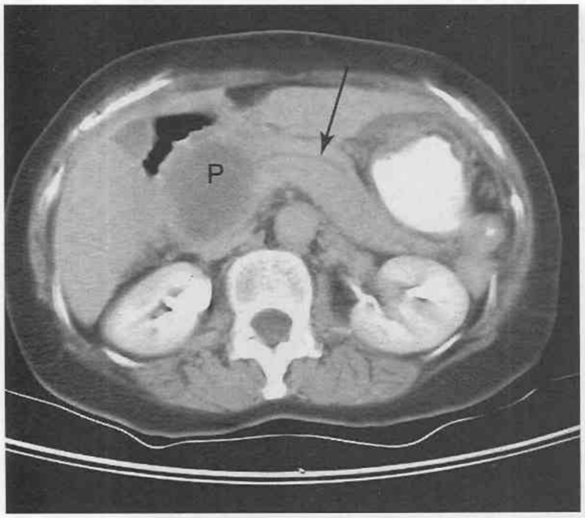

Figure 38–68. Typical appearance of a pseudocyst (p) in the head of the pancreas. Also note dilated pancreatic duct (*arrow*).

The administration of intravenous urographic contrast material enhances the margins of such collections and makes the central portion appear less dense. Because of the high protein content of such pseudocysts, the density may appear high, and the appreciation of the cystic nature of a lesion may not be apparent without the use of intravenous contrast material.

Anatomic Location

Pseudocysts are typically located in the pancreas and the immediate peripancreatic region. They can be associated with other severe or minimal findings of pancreatitis (Figs. 38–68 and 38–69). In some cases, however, pseudocysts may extend to more remote anatomic areas, by dissection along or through fascial planes, along areolar tissue around vessels (intermesenteric space according to a new concept of retroperitoneum; see Chapter 43), through capsules, or into the substance of solid organs.

The omental bursa is the second most common location of pseudocysts, according to Siegelman and associates.[230] The inflammation causes closure of Winslow's foramen, and the fluid fills the entire omental bursa or is confined to a local region of the bursa.[140]

When located in the inferior portion of the omental bursa, pseudocysts produce anterior displacement of the body and antrum of the stomach. When located in the splenic portion of the inferior recess, they produce anterior displacement of the fundus (Fig. 38–70*A* and *B*). Those extending into the superior medial recess of the lesser sac lie adjacent to the caudate lobe of the liver (see Fig. 38–55). In such cases, it is important to use oral contrast material or the decubitus position because the pseudocyst otherwise can be mistaken for fluid-filled stomach or duodenum.

If the patient is too ill for these technique modifications, a large pseudocyst might be confused for the distended fundus of the stomach.[172] If adequate intravenous contrast material is given, the gastric wall enhances, permitting distinction from the wall of the pseudocyst. Pseudocysts located in the splenic recess may reveal themselves by producing a circular interface with the air in the stomach rather than the normal level air-fluid interface (bezoar, retained food, or gastric mass may give a similar appearance) (Fig. 38–70*B*).

If a pseudocyst is large and aggressive, it may erode from the lesser bursa into adjacent contiguous areas. Extending inferiorly, it may split the leaves of the omentum, producing a mass that projects below the surface of the stomach in an anterior position (Fig. 38–71). The inflammatory fluid may also digest through the lining of the omental bursa and dissect into the hepatogastric ligament and even beneath the capsule of the liver (Fig. 38–72*A*) or spleen (Fig. 38–72*B*). A pseudocyst may also proceed cephalad from the superior medial recess next to the caudate lobe into the posterior mediastinum[191] adjacent to the esophagus (see Fig. 38–55).

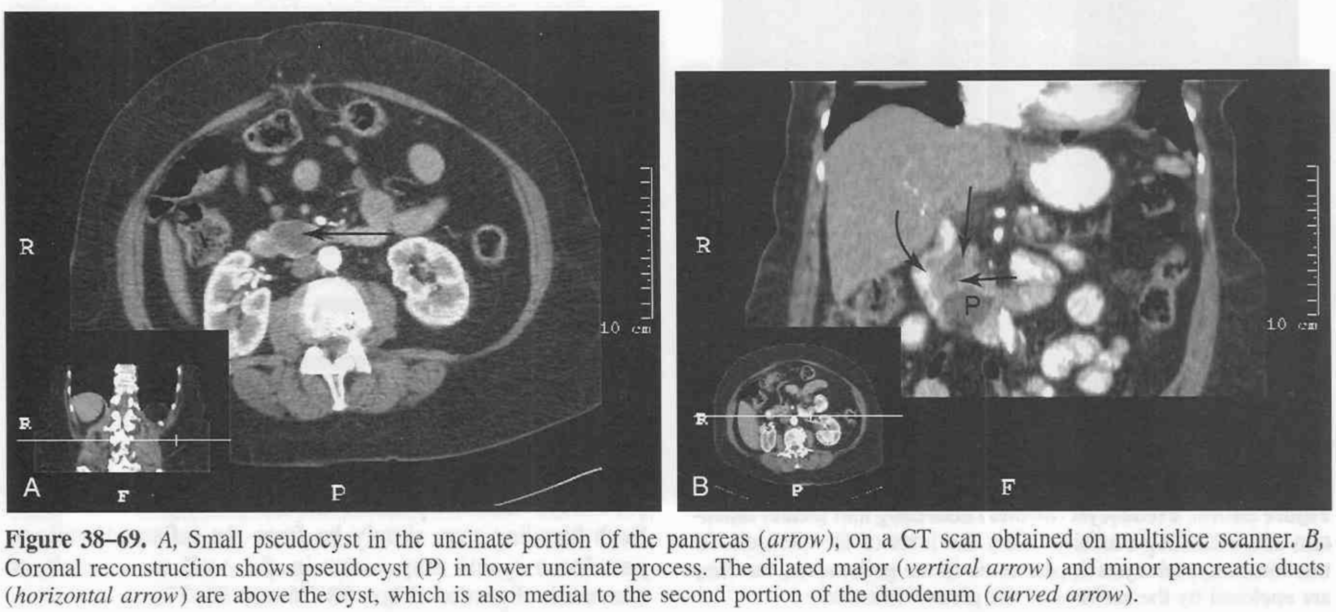

Figure 38–69. *A,* Small pseudocyst in the uncinate portion of the pancreas (*arrow*), on a CT scan obtained on multislice scanner. *B,* Coronal reconstruction shows pseudocyst (P) in lower uncinate process. The dilated major (*vertical arrow*) and minor pancreatic ducts (*horizontal arrow*) are above the cyst, which is also medial to the second portion of the duodenum (*curved arrow*).

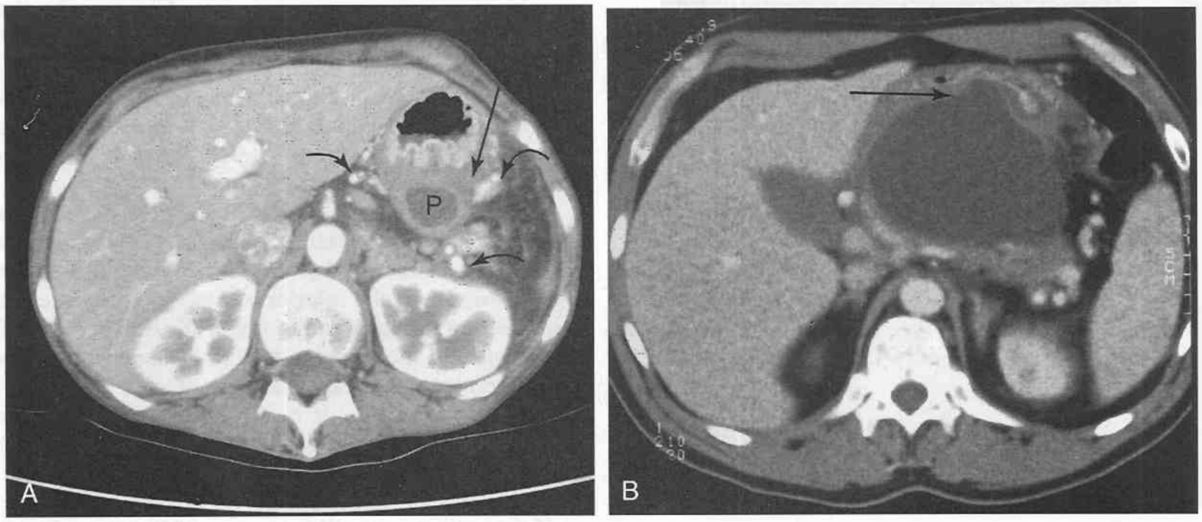

Figure 38–70. *A,* Small pseudocyst (P) in splenic portion of inferior portion of the lesser sac (*arrow*) is visible effacing the posterior surface of the stomach fundus. Note the thickening of the gastric wall (*left curved arrow*) and the dilated varices in and adjacent to the wall of the stomach (*right curved arrows*). Even the mucosa of the stomach is enhancing remarkably. *B,* Very large pseudocysts on the posterior surface of the stomach can give the deceptive appearance of a dilated stomach fundus, unless appropriate oral and intravenous contrast agent is used. For many patients undergoing this examination, the "NPO" status precludes the use of oral contrast material. With use of intravenous contrast material, the anterior surface of the pseudocyst effacing the gastric mucosa (*arrow*) can be recognized.

As with the spread of material during the acute inflammatory phase, a pseudocyst may develop or digest through fascia[96, 210] and capsules directly into a solid organ. This may occur in the spleen (Fig. 38–72*B*), liver, or kidney (Fig. 38–73). Such pseudocysts can be diagnosed from knowledge of the patient's history or through a search for signs of pancreatitis, but in many instances, diagnostic aspiration is required, as suggested by Baker and coworkers.[12]

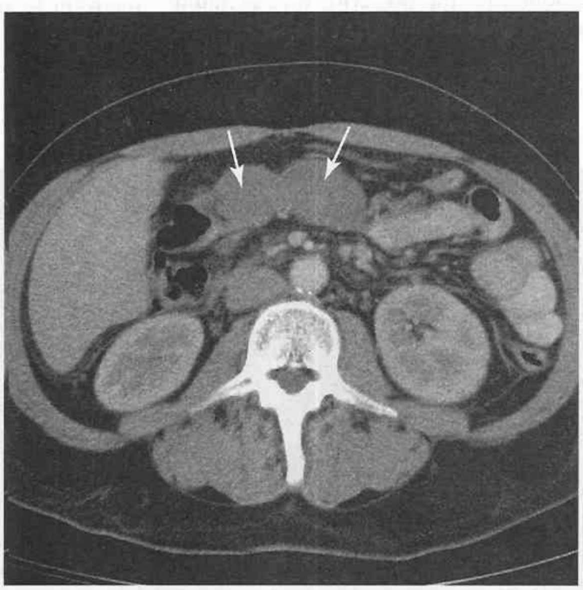

Figure 38–71. Pseudocyst (*arrows*) dissecting into greater omentum and extending caudally below the level of the stomach. At this location, such cysts appear to be in the peritoneum, but they are enclosed by the surfaces of the greater omentum.

Resolution

Pseudocysts may spontaneously resolve simply from resorption of fluid or drainage into a loop of bowel. Both mechanisms are commonly observed. When evacuation into bowel occurs, residual gas may be seen in the cyst or a small pathway between the cyst and the bowel loop (Fig. 38–74).

Beebe and colleagues[20] found that pseudocysts less than 4 cm in diameter were more likely to resolve spontaneously than larger pseudocysts. Kolars and colleagues[135] found that the outcome and recurrence of pseudocysts did not depend on their size, multiplicity, anatomic location, or communication with the pancreatic duct.

Complications

Pseudocysts must be treated to avoid a number of severe complications. Pseudocysts can rupture into the peritoneum or a loop of bowel. Rupture into the peritoneum can be catastrophic, producing a generalized chemical peritonitis (Fig. 38–75). Rupture into a loop of bowel can be catastrophic or curative. The outcome probably depends on the loop of bowel that is entered, the degree of bacterial colonization, and the immune competence of the patient. Rupture into colon is potentially more threatening than rupture into other bowel because of the nature of the gram-negative flora. The patient with an incompetent immune system or an overwhelming bacterial inoculum may succumb if prompt, effective treatment is not given.

Finally, hemorrhage can occur in association with a pseudocyst and can produce life-threatening loss of blood. Such bleeding may simply be from the inflamed wall, or pseudoaneurysms may occur in the wall as a result of enzymatic digestion (Figs. 38–76 and 38–77).

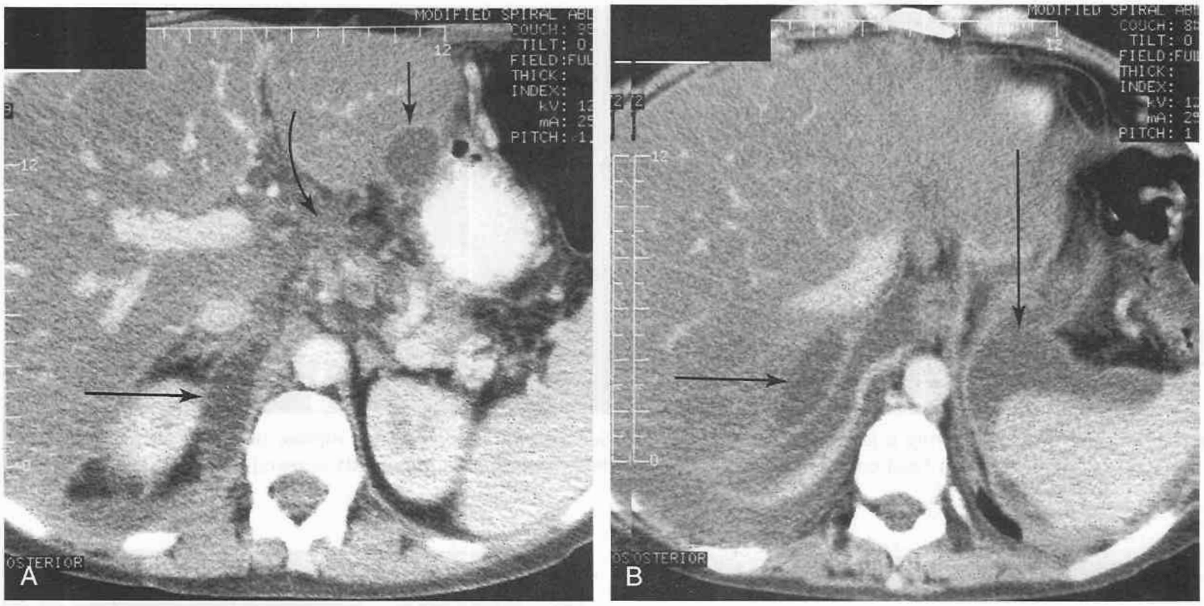

Figure 38–72. *A,* CT scan taken at a high level shows cystic fluid in the subcapsular region of the liver (*arrow*), the porta hepatis (*curved arrow*), and the retroperitoneum behind the right kidney (*horizontal arrow*). *B,* Scan taken at a slightly different level shows inflammatory fluid around the spleen (*vertical arrow*) and bare area of the liver (*horizontal arrow*) by the adrenal gland.

Figure 38–73. Pseudocysts may cross the fascia into the perirenal space. This scan shows a large pseudocyst (*arrow*) in the perirenal space on the left side.

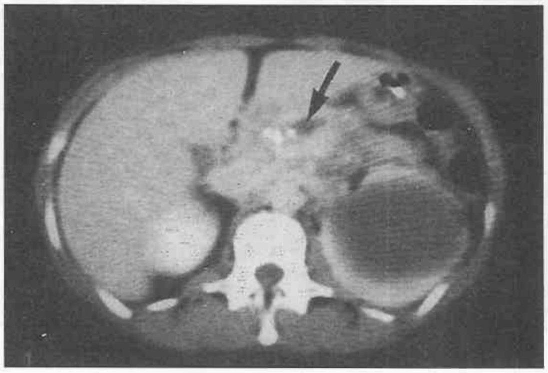

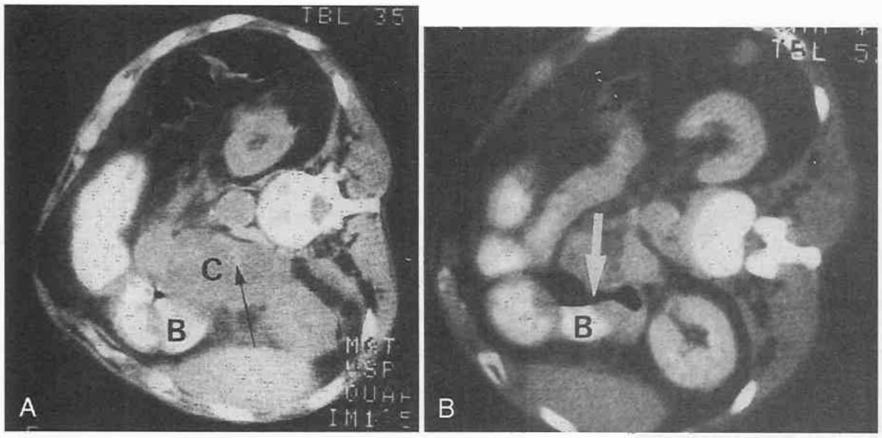

Figure 38–74. *A,* Large retroperitoneal pseudocyst (C) around the vena cava (*arrow*), which is located behind the duodenal bulb (B). *B,* Follow-up study shows an "empty pseudocyst" containing air (*arrow*) beside the bulb (B). Note the normal size of the vena cava.

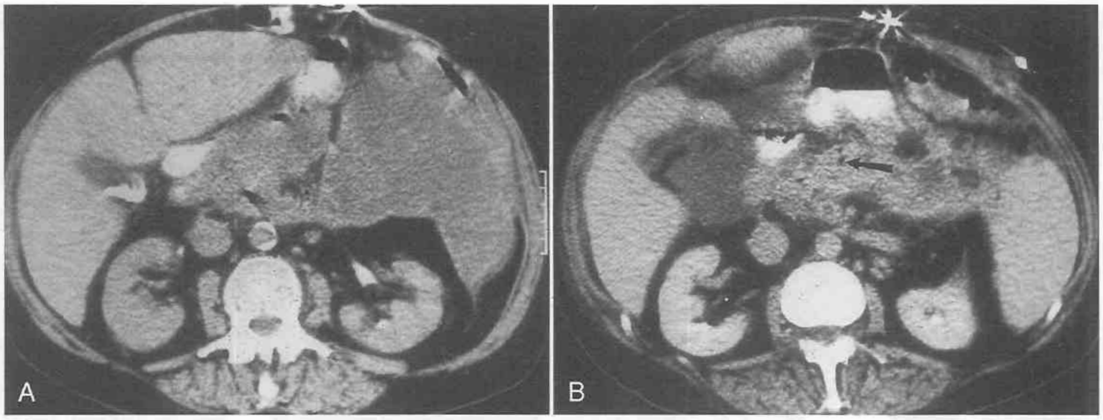

Figure 38–75. *A,* CT scan showing a large fluid collection in the left side of abdomen after rupture of a pseudocyst. *B,* Scan showing small gas bubble (*arrow*) within fluid collection in the pancreatic bed; aspiration subsequently showed this area to be infected.

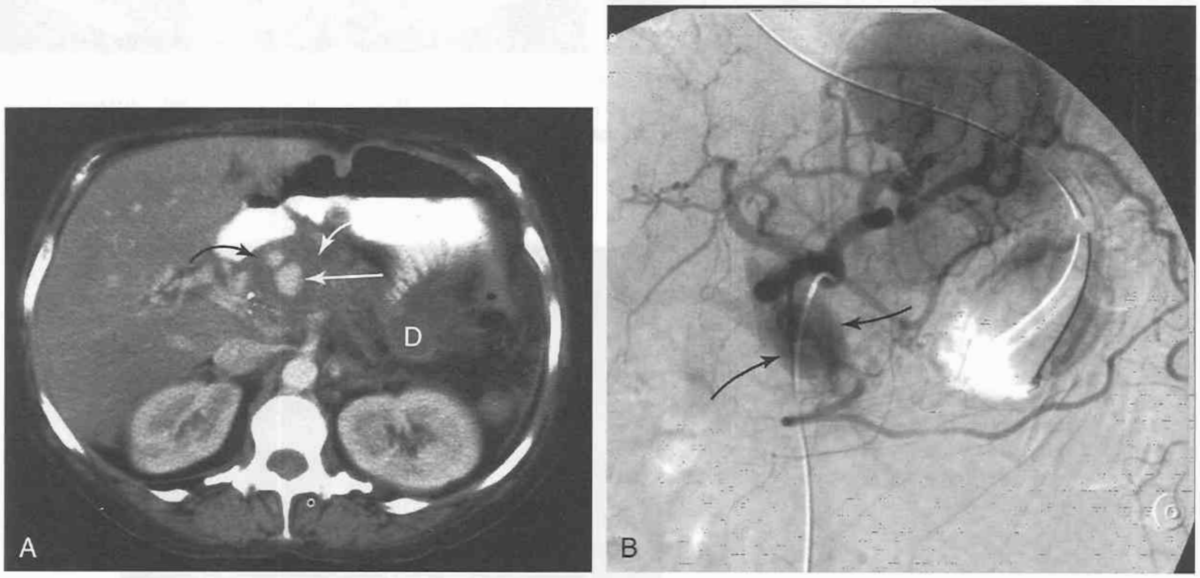

Figure 38–76. *A,* Axial CT scan shows enhancing focus in the head of the pancreas (*straight arrow*) posterior to the portal vein coursing toward the porta hepatis region. It is located in an inflammatory mass (*curved arrows*). Note the severely dilated pancreatic duct (D). *B,* Traditional angiogram shows "pooling" of contrast material in a pseudoaneurysm (*arrows*).

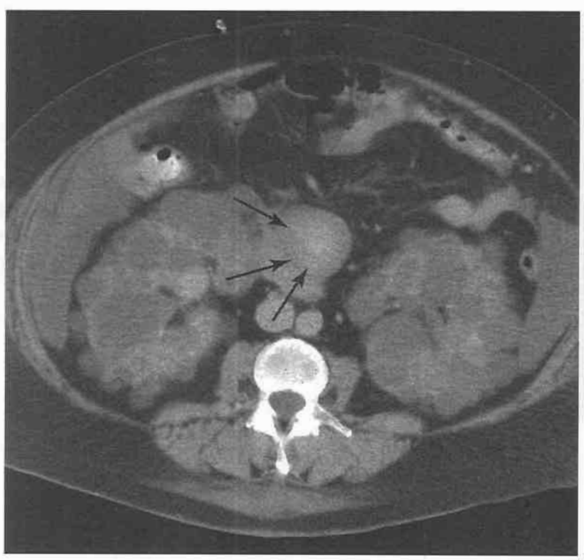

Figure 38–77. CT scan in a patient with polycystic disease of the kidneys shows massively enlarged kidneys with many cysts. Blood density mass is seen in the head of the pancreas, representing hemorrhage into a small pseudocyst (*arrows*).

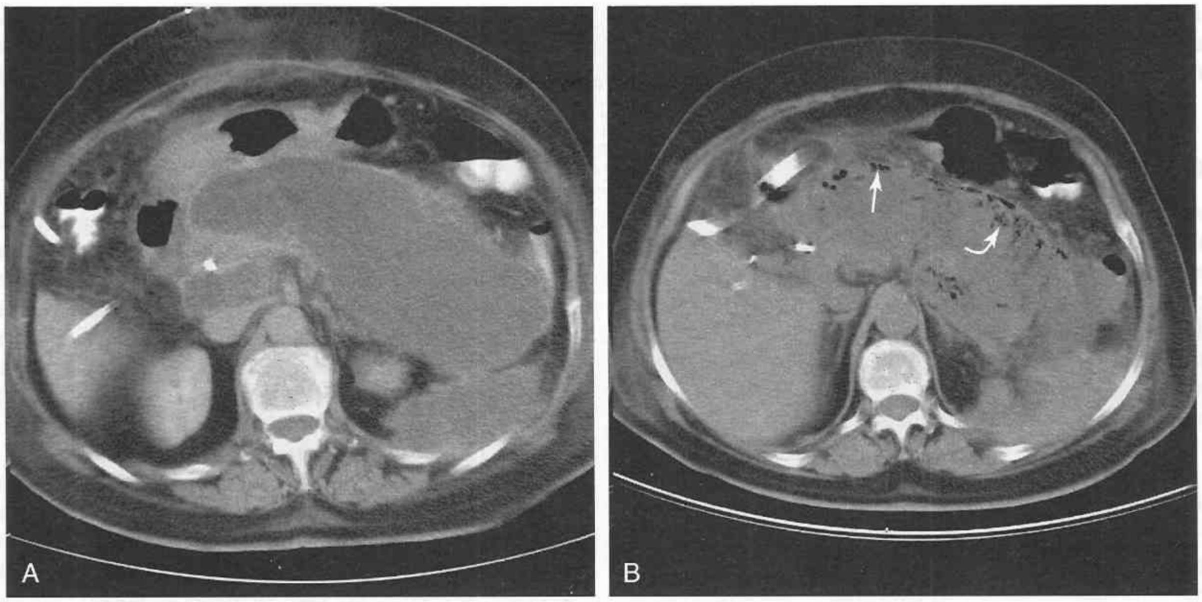

Figure 38–78. *A,* A very large pseudocyst is visible in the body and tail of the pancreas. *B,* Repeat scan of the same pseudocyst shows multiple pockets of gas (*arrows*), which represent infection with a gas-forming organism.

Pseudocysts with Air: Abscess or Fistula

Gas in pseudocysts suggests the following possibilities: (1) fistula formation, (2) gas-forming infection (Fig 38–78), (3) surgically produced internal cystotomy (Fig. 38–79), and (4) any combination of these three.

Several reports in the literature provide useful insights into gas in pseudocysts. Torres and colleagues,[256] Alexander and coworkers,[3] and Petruschak and associates[199] have reported seeing gas in pseudocysts from gastrointestinal fistulas (Fig. 38–79). A common observation is that patients who have gas in pseudocysts should be evaluated to determine the type, size, and nature of the fistula. In some patients, the fistula can be found by radiologic methods before surgery, but in other patients it may be detectable only at surgery.

Depending on the site of the fistula, treatment may be easy or difficult. In most patients, a traditional bowel study using a water-soluble iodinated contrast agent or a barium sulfate contrast suffices (i.e., upper or lower study). In other patients, it may be helpful to perform a percutaneous aspiration for a diagnostic sample, drainage, or sinogram.

Fistulas occurring in the stomach or duodenum may drain a pseudocyst effectively (see Fig. 38–74), and surgical intervention may not be needed. In patients who have fistulas in the colon, the prognosis is not so good, because colonic pathogens are more likely to cause serious infections and sequelae; the traditional surgical method requires immediate débridement and bowel diversion in this case. The circumstances of each patient must be considered, however, because rarely, a patient may tolerate a colonic fistula and not require surgery. The following factors determine the outcome of such a problem: the immune status of the patient, the size and nature of the fistula, the size of

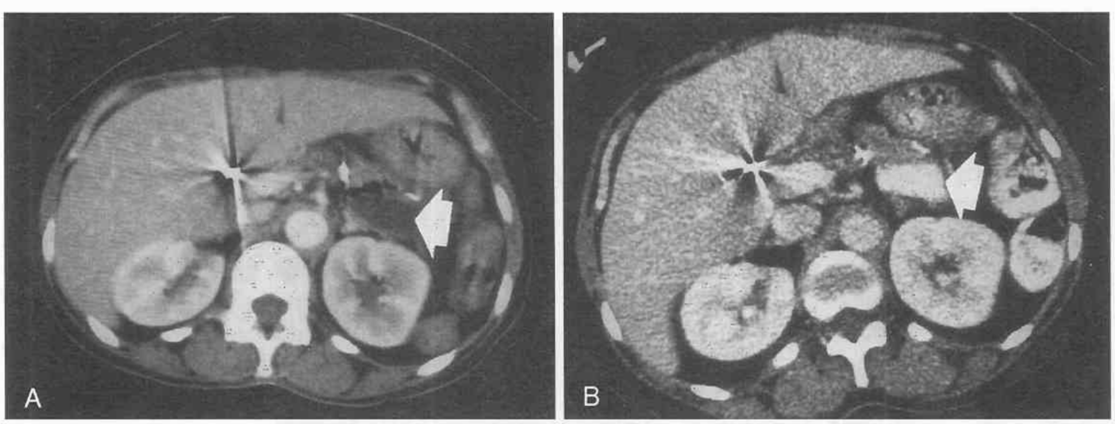

Figure 38–79. *A,* Appropriate surgery for pseudocysts is gastrocystotomy. CT scan shows fluid-filled and air-filled cavity (*arrow*) behind the stomach. *B,* Subsequent scan shows contrast material (*arrow*) filling the cyst cavity, indicating the nature of the cavity and communication with the stomach. Note the high-density suture line between the stomach and cyst.

the inoculum, and the virulence of the pathogens. Healthy immunocompetent patients may tolerate such events well, and immunocompromised patients may not.

Vascular Problems

Pancreatitis and pseudocysts can cause a number of vascular problems, including vascular occlusion, pseudoaneurysms, and spontaneous hemorrhage.

Occlusion of many vessels, but most commonly the splenic vein and artery, can occur. In such cases, only the secondary effects, such as varix formation or shrinkage of the spleen, may be seen.

Pseudoaneurysms occur in pancreatitis in 10% of patients as a result of enzymatic digestion of the vessel wall. Proper diagnosis and treatment are important because hemorrhage is associated with bleeding 37% of the time.[24, 194, 245] Pseudoaneurysms can occur in any vessel in the peripancreatic area, but the most common vessel is the splenic, followed by the gastroduodenal[178] and branches of the pancreaticoduodenal arteries.[31, 33, 238] In some patients, diagnosis of a pseudoaneurysm is not made prospectively, but the patients have acute hemorrhage associated with a pseudocyst.

Sometimes a clearly definable pseudoaneurysm in the area of the pancreas can be confused with a pseudocyst.[149, 228] Careful scrutiny of the CT scan shows a circular area of low density, which may correspond to a clot within the aneurysm. Because of the potential for such pseudoaneurysms, it is imperative that a dynamic intravenous study be performed before any interventional procedure[26] (see Fig. 38–76; Fig. 38–80).

Natural History of Pseudocysts

The natural history of undisturbed pseudocysts has been extensively studied by several authors,[129] including Bradley and others[28, 29] and Pollack and associates.[207] In Bradley's series, 54 patients had serial studies over many months; the authors were able to follow the outcomes accurately.

Of 54 patients who had serial, clinical, and sonographic evaluations, 10 (or 40%) had spontaneous resolution.[29] Five (20%) experienced complications, including abscess, rupture, and biliary obstruction. In patients with pseudocysts lasting 7 to 12 weeks, the proportion of spontaneous resolutions and the frequency of complications remained constant at 46% (6 of 13 cases). Spontaneous resolution did not occur in 12 patients observed between weeks 13 and 18, but the rate of complication increased to 75% (8 of 12 cases). These complications included spontaneous rupture in five patients, secondary infection in one, obstructive jaundice with sepsis in another, and a spontaneous cystogastric fistula in another. This last patient died after massive gastrointestinal hemorrhage. Of five patients studied for more than 19 weeks, three had complications and two did not complete follow-up. Seven deaths occurred as a direct result of the pseudocyst, and complications occurred on an average of 13.5 weeks after initial development.

In another study, by Pollack and associates,[207] similar findings were noted in a group of 54 patients. The authors treated patients with nonoperative means until sepsis occurred or until the pseudocyst had persisted more than 3 weeks. They reported that 29 patients underwent elective surgery during the initial hospitalization, and 6 patients who did not undergo surgery had abscesses and died.

Surgical Treatment

Good information exists on selected surgical treatment based on pseudocyst evolution. Bradley and others[28, 29] and Bodurtha and colleagues[26] have recommended that surgical intervention not be performed in the first 6 weeks because of the high incidence of spontaneous resolution. Furthermore, they recommend that treatment be deferred during this time because the inflammation usually does not have a well-defined fibrous wall that could hold the sutures required for a cystogastrostomy. In such cases, external instead of internal drainage would be required. External drainage has a high rate of infections, fistulas, and complications. Between 6 and 13 weeks, the pseudocyst wall becomes well defined; thus internal drainage is possible. If a pseudocyst is well defined and has a thick fibrous wall, internal drainage by cystotomy is the preferred method of treatment because it has the greatest success rate and the lowest complication and recurrence rates. Waiting longer

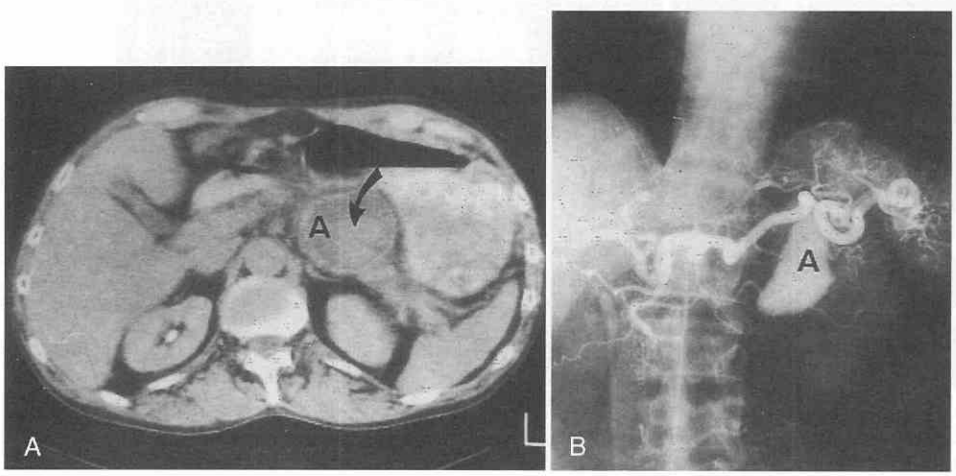

Figure 38–80. *A,* CT scan shows a low-density mass (A) with a central, high-density region (*arrow*) that represents a pseudoaneurysm of the splenic artery. *B,* Angiogram shows the large pseudoaneurysm (A) coming from the splenic artery.

than 13 weeks creates a greater risk for spontaneous complications.

As one might anticipate, development of radiologic procedures paralleled the surgical experience. Initial methods of external drainage were used with some success, but these methods had problems similar to the surgical ones. More recently, certain radiologic methods have had some success.

Imaging Follow-up of Internal Drainage

Patients who undergo an internal drainage procedure show a consistent pattern of resolution on CT scan. Initially the pseudocyst appears as a total fluid density, but immediately after surgery it contains air. As long as patency with the bowel exists, such cysts fill with gastrointestinal contrast material. With further resolution, the amount of air and fluid lessens (see Figs. 38–64 and 38–79). In patients who do not show prompt resolution, abscess due to colonized bacteria that have sequestered a portion of the pseudocyst should be suspected.

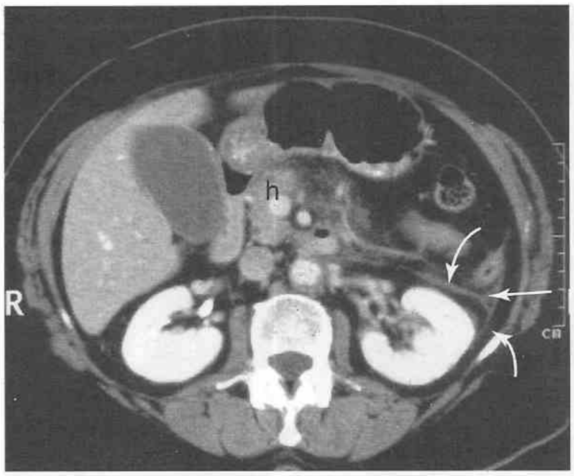

Figure 38–82. Axial CT scan shows that the head (*h*) of the pancreas is normal but the body and tail are atrophied. Also note that chronic infection has produced thickening of the lateroconal fascia (*straight arrow*) and the perirenal fascia, both anterior and posterior (*curved arrows*).

Chronic Pancreatitis

Once the acute phase of pancreatitis has resolved, the pancreas may return to normal. Chronic changes may occur, however, resulting in persistent or permanent alterations in the pancreatic function or morphologic features.

Pathologically, fibrosis and scarring may alter the morphologic characteristics and density of the parenchyma and duct system.[166] The entire gland may be affected, but only a focal area may be involved. Focal changes may occur in the acinar or ductal portions and may involve the deposit of calcium salts.

Clinically, the patient may have chronic symptoms such as upper abdominal pain, back pain, and steatorrhea, diabetes, or recurrent inflammation. Diagnosis of chronic pancreatitis is important because a plausible explanation for a number of clinical signs can be given if its presence can be documented on scanning. Furthermore, a more definite statement about the presence of new findings can be made if it is known that a patient previously had pancreatitis. In such cases, comparison scans are important.

Diagnostic Signs

In chronic pancreatitis, the overall size of the gland may be normal, enlarged, or reduced, depending on the amount of fibrosis or atrophy, and the level of activity of the inflammation.[60] Atrophy or reduction of the size of the gland, like enlargement, can occur in either a diffuse or focal fashion (Fig. 38–81). In addition to these findings, the thickening of the renal fascia, which is seen in the acute form of the disease, may become chronic (Fig. 38–82). Chronic fibrosis can produce loss of the fat plane

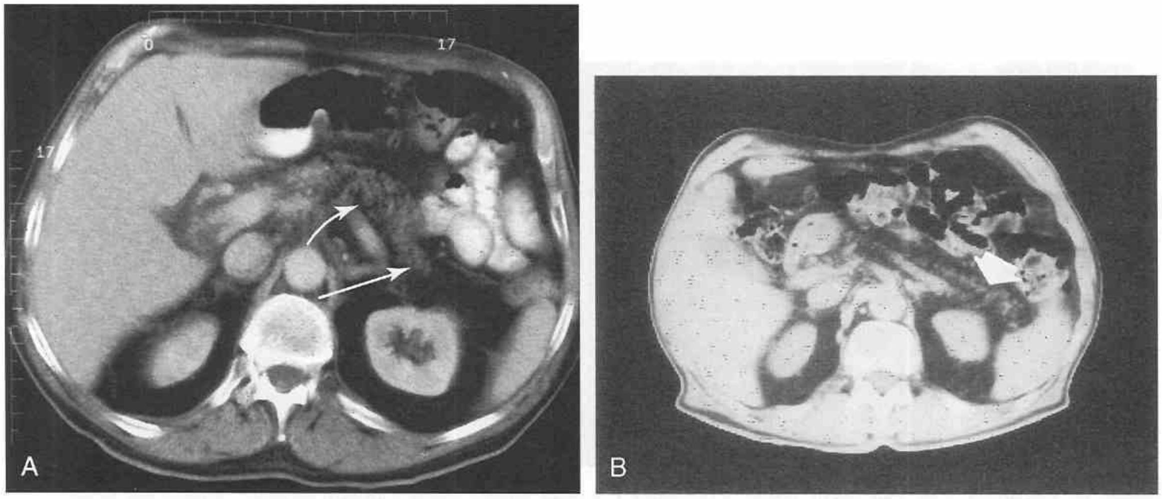

Figure 38–81. *A,* CT scan shows low density with atrophy of two portions of the pancreas (*arrows*). *B,* Chronic inflammation may result in complete atrophy of the glandular elements so that the only residual is a faint pattern of the ductal system (*arrow*).

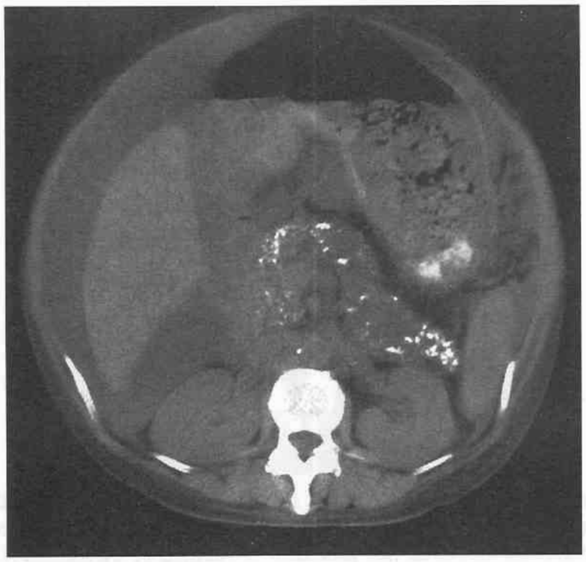

Figure 38–83. Deposition of calcium is the best indicator of chronicity. Scan shows fine calcifications scattered throughout all portions of the gland.

around the vessels and can be mistaken for tumor encasement.[11, 116, 158] Chronic pancreatitis is usually associated with intermittent episodes of recurrent inflammation, which can produce alterations in the baseline appearance of a diseased gland.

Acute edema and swelling may be superimposed on the fibrotic gland and may fluctuate with the activity of the disease. With resolution of the acute process, follow-up studies show a return to the baseline appearance. If the mass does not diminish or if it increases in size, a coexisting neoplasm must be considered. A percutaneous biopsy should be performed. If the biopsy result is negative and follow-up studies show no definite progress, one can accept the premise that the chronic inflammation is establishing a new baseline with an increased size.

Calcifications. The hallmark of chronic inflammation is the deposition of calcium.[220, 260] With inflammation and necrosis in the pancreas, the local chemical changes produce the deposit of calcium carbonate and calcium phosphate. The deposit of calcium salts can vary in location and amount. Most commonly, calcification first occurs in the head, but with continued inflammation, calcification occurs in the body and tail. Calcifications can occur within the parenchymal or ductal portions; either area can be involved first (Fig. 38–83). It is important to note whether the duct is involved, because various surgeons believe that relieving pancreatic duct obstruction may be beneficial to some patients.

Although the typical pattern is one of progressive deposit, it is possible to observe the reverse—decalcification[7] (Fig. 38–84). This is a rare phenomenon, but it has been observed on plain radiographs as well as CT scans. Initially, decalcification was thought to indicate the development of a neoplasm, but researchers have refuted this point. To our knowledge, decalcification is neither good nor bad. One should not mistake the change in configuration for calcification that can occur with changes in size of the gland (Fig. 38–85).

CT is the most sensitive of all radiographic procedures for detection and accurate localization of calcifications. A number of processes other than inflammation can produce calcifications, and some materials can simulate calcium. First, a variety of tumors produce calcifications in a large percentage of cases (see section on tumors). Second, the most common entity producing calcification in this area is probably arteriosclerotic changes in vessels or aneurysms. Finally, foreign bodies (swallowed objects, surgical sutures, catheters, or other devices) and iron-filled lymph nodes in hemochromatosis appear opaque and simulate calcification.

Pancreatic Duct. The changes that occur in the pancreatic duct are discussed earlier. In summary, one can make some statement about the probability of malignancy or inflammation from the size and the configuration; but these relationships are not absolute. The factors depend on the benign or malignant nature of the process and the duration or completeness of the obstruction (Fig. 38–86).

Frequency of Signs in Chronic Disease. The frequency of inflammatory signs in pancreatitis has been ex-

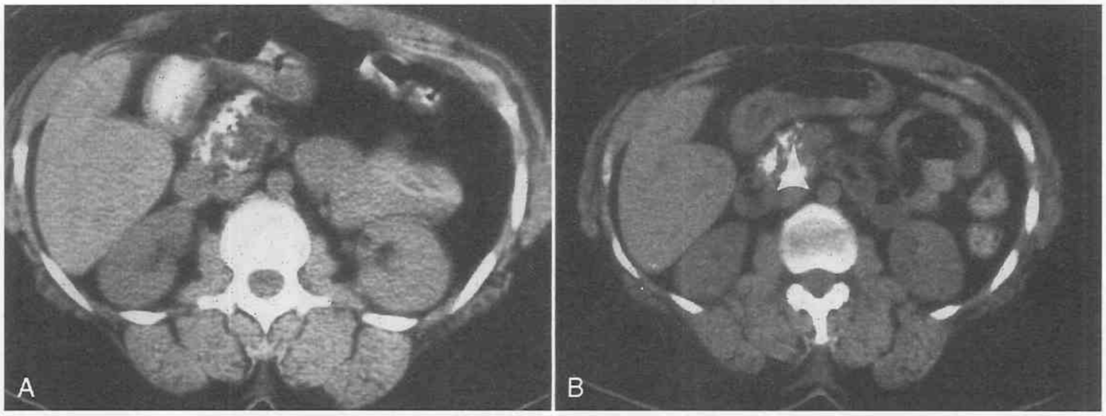

Figure 38–84. *A,* Decalcification can occur rarely. This early CT scan shows dense calcium deposits within the head. *B,* Later scan demonstrates that the overall size of the gland has not changed but the density of the anterior calcification (*arrowhead*) has decreased owing to decalcification.

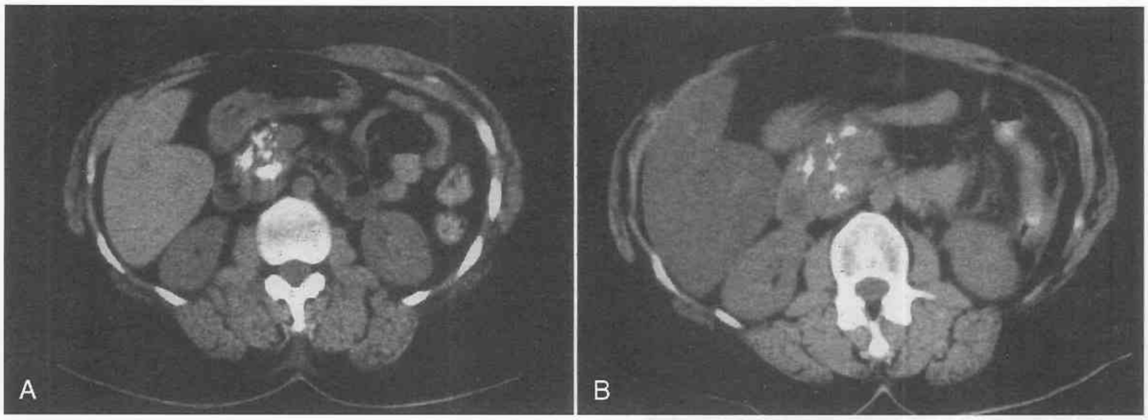

Figure 38–85. *A,* CT scan obtained before resumption of inflammation shows dense calcification within the head of the gland. *B,* Subsequent scan shows enlargement of the head of the gland, demonstrating that the calcifications have moved peripherally as the gland has enlarged.

tensively studied, but one of the better reviews of the findings related to chronic pancreatitis was by Luetmer and others.[158, 159] They studied 56 consecutive patients with documented pancreatitis and without surgical intervention, in whom contrast-enhanced CT scans were obtained. Dilatation of the pancreatic duct was seen in 68% of the cases, pancreatic atrophy in 54%, pancreatic calcifications in 50%, fluid collections in 30%, focal enlargement in 30%, biliary dilatation in 29%, and fascial plane or perivascular fat changes in 16%. Although there has been some variation among the various reports as to the frequency of these signs, the constellations of findings are all similar.

Trauma

Pancreatic trauma is common in patients with injury to the abdomen. The most common types of injury are contusion, tear, and damage to the duct; late sequelae include pseudocysts, abscesses, and fistulas. Because CT is a commonly used tool for early evaluation of abdominal injury, it is important to become familiar with its usefulness and limitations.[114–118, 204]

The largest evaluation of the pancreas by CT was by Jeffrey and others.[115–118] In 13 cases, they found that CT was helpful for detecting some injury to the pancreas but was limited in determining the exact nature or extent of the problem (Fig. 38–87). They observed nonspecific thickening of the left anterior renal fascia in 8 of 11 cases. They were able to identify fracture or laceration of the gland in some cases, but the actual planes were not easy to visualize. ERCP is indicated if there is significant injury to the gland.

After acute injury to the pancreas and formation of a fluid collection with or without secondary infection, CT is well suited to detect and determine the extent of any such process (Fig. 38–88).

Miscellaneous Disorders

Hereditary Pancreatitis

Hereditary pancreatitis is relapsing pancreatitis among multiple family members. The symptoms, signs, and patho-

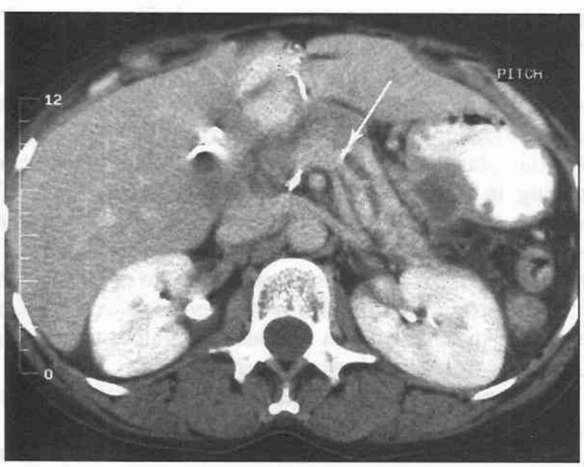

Figure 38–86. Ductal dilatation in body of pancreas with single calculus (*arrow*) in the main duct.

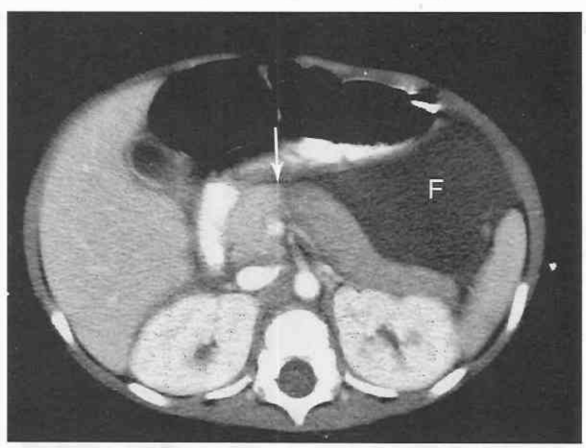

Figure 38–87. Axial CT scan shows transection (*arrow*) of the pancreas in the area of the neck. Note the difference in density of the body and tail compared with the head, indicating decreased vascular enhancement and edema. Also, there is a large amount of free fluid (F).

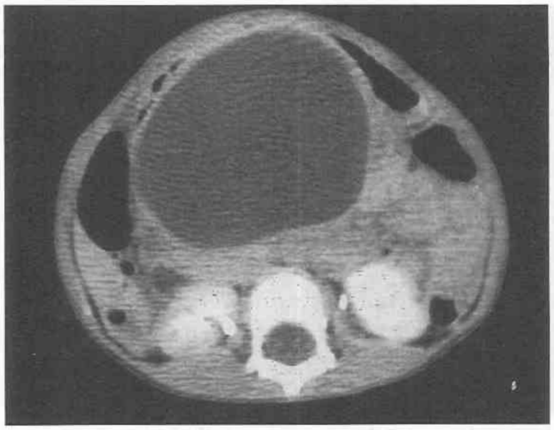

Figure 38–88. CT scan showing a large pseudocyst, which has developed after a severe injury to the gland.

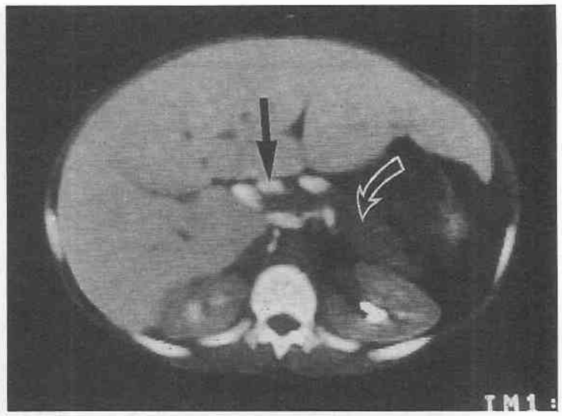

Figure 38–90. Some patients with iron overload have increased density of lymph nodes (*arrow*) in the peripancreatic area and not in the gland (*open arrow*).

physiologic process of this type of pancreatitis are no different from those of the other types of pancreatitis discussed. It has been suggested but not proved that factors such as hyperlipidemia, hypercalcemia, and alcohol consumption may play a role in this disease. There are, however, two unique traits of the disease. The onset is typically in children around the age of 10 years, and there are usually calcifications within the gland in both the parenchyma and the duct system.[17, 222, 236] Reportedly, calcification occurs more commonly in the duct system than in the parenchyma.

The majority of the patients seen with hereditary pancreatitis have been children. In our experience, calcifications occurred in the parenchymal portion as much as in the ductal portion (Fig. 38–89). They are the same types of inflammation and pseudocysts seen with adults. The best treatment has been obtained with pancreatectomy.

Hemochromatosis

Hemochromatosis results from excessive accumulation of iron in the body. The disease has a primary form, which is idiopathic, and a secondary form, which results from ingestion of exogenous iron or from multiple transfusions.[57]

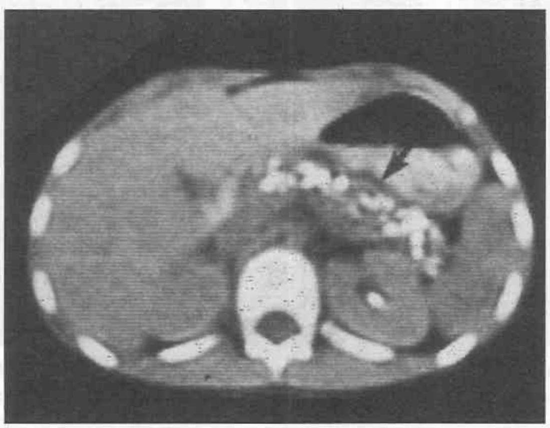

Figure 38–89. Hereditary pancreatitis produces calcifications (*arrow*) in the pancreas of this 6-year-old child.

CT characteristically shows an increased density in the pancreas and adjacent peripancreatic lymph nodes; similar findings have been reported by Long and associates[156] and Mitnick and colleagues.[179] Long and associates[156] did not find a correlation between the amount of increased density and the pancreatic dysfunction or insufficiency. Dense nodes in the porta hepatis and peripancreatic, periaortic, and perisplenic nodes should be noted (Fig. 38–90). These findings should not be confused with calcifications. Unopacified vessels may give the spurious impression of a low-density mass in the pancreas in some cases. The use of intravenous contrast material eliminates any question of a possible mass (Fig. 38–91).

Cystic Fibrosis

Cystic fibrosis, or *mucoviscidosis,* is a hereditary generalized disease affecting all mucus-producing exocrine glands of the body. The disease results in abnormally thick secretions that obstruct most exocrine glands, including the pancreas. Studies have shown that there is a greater concentration of protein in the pancreatic fluids, which may account for increased viscosity. It is postulated that inspissation of the material can produce ductal ectasia. A variety of changes can result in varied clinical situations with a wide range of findings on CT scan.

Most patients with cystic fibrosis have problems that are associated with exocrine function. The gland usually appears completely replaced with fat (Fig. 38–92). Presumably, the gland has complete and long-term obstruction, resulting in complete atrophy of the acinar portions. The islet cells are not usually affected, and the endocrine functions remain intact, without development of diabetes or other problems. This process would seem to parallel studies with laboratory animals, that show complete autolysis and atrophy of the gland when the duct is ligated; the function of the islet cells is typically not affected.

Also reported and considered to be a different entity along the same spectrum is cystosis of the pancreas.[101, 201] Although this is an uncommon disorder, a number of large cysts scattered throughout the course of the pancreas can be observed. The cysts are typically thin walled and cannot

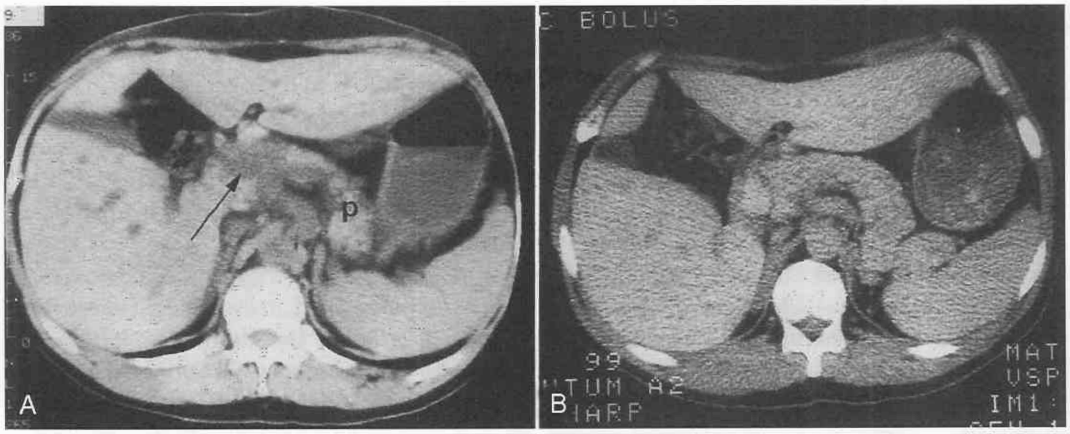

Figure 38–91. *A,* In this patient with iron overload, there is increased density of the gland (*p*) and not the portal vein (*arrow*). The vessels should not be mistaken for an intrapancreatic tumor. *B,* After intravenous contrast administration, the vessels are opacified, dispelling the question of a tumor.

be distinguished from pseudocysts (Fig. 38–93). In some patients, lesser variations are seen, which include presence of a fluid-filled duct or smaller cysts. The fluid has calcium and eosinophilic concretions. The fluid is said to be antigenically identical to serum and contains increased amounts of inactive trypsinogen; this finding indicates that autodigestion has no major role in the process.

In another group of patients with a mild form of cystic fibrosis, the exocrine function of the gland may be preserved with or without any pulmonary symptoms. Patients with pulmonary problems who have a normal-appearing pancreas and no associated abdominal problems have been observed. Other patients who do not suffer from pancreatic insufficiency may experience recurrent, severe pancreatitis. The incidence of pancreatitis is said to be approximately 0.05% of all patients. Pancreatitis may develop in some patients who have a mild but undiagnosed form of cystic fibrosis without pulmonary symptoms. Masaryk and Achkar[169] reported several patients with active clinical pancreatitis thought to originate from functional obstruction of the pancreatic duct. The diagnosis of cystic fibrosis had not even been considered until pancreatitis occurred. Although these authors did not postulate the etiologic conditions, it seems logical to assume that inspissated pancreatic fluid creates partial obstruction of the duct. It is not sufficient to destroy the acinar portion but is sufficient to impair flow, producing inflammation.

Fatty Pancreas

A fat-density pancreas can be entirely normal (see section on normal variations), but a number of entities have been reported to produce fat replacement of the gland.[198] These include pancreatic duct obstruction, malnutrition, Shwachman's syndrome, hemochromatosis, viral infection, Cushing's syndrome, steroid therapy, and an unusual entity called lipomatous pseudohypertrophy of the pancreas. Specific reports on these entities have not yet appeared, but one would anticipate future reports on this topic.

Benign Tumors

Fatty Tumors

See Figure 38–94 for cases in which CT revealed fatty masses of the pancreas.

Figure 38–92. Typically, in patients with cystic fibrosis who have pancreatic atrophy, the pancreas (*arrowhead*) is completely replaced with fat.

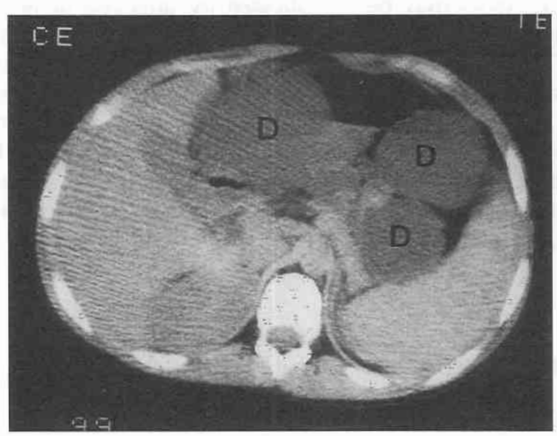

Figure 38–93. Rarely, cystic fibrosis produces a massive cyst formation of residual ducts (D), which are occluded. Such changes have been called *cystosis.*

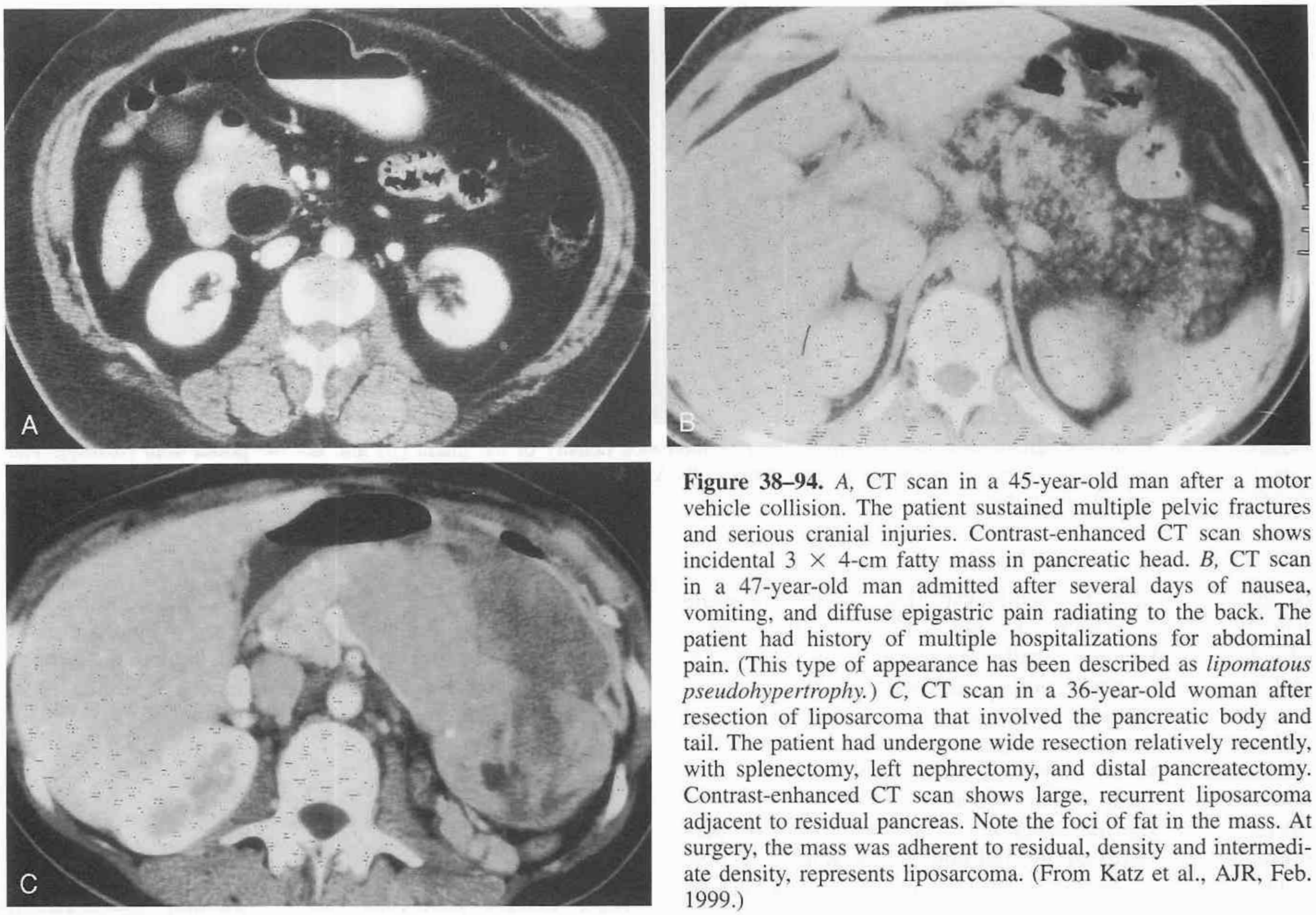

Figure 38–94. *A,* CT scan in a 45-year-old man after a motor vehicle collision. The patient sustained multiple pelvic fractures and serious cranial injuries. Contrast-enhanced CT scan shows incidental 3 × 4-cm fatty mass in pancreatic head. *B,* CT scan in a 47-year-old man admitted after several days of nausea, vomiting, and diffuse epigastric pain radiating to the back. The patient had history of multiple hospitalizations for abdominal pain. (This type of appearance has been described as *lipomatous pseudohypertrophy.*) *C,* CT scan in a 36-year-old woman after resection of liposarcoma that involved the pancreatic body and tail. The patient had undergone wide resection relatively recently, with splenectomy, left nephrectomy, and distal pancreatectomy. Contrast-enhanced CT scan shows large, recurrent liposarcoma adjacent to residual pancreas. Note the foci of fat in the mass. At surgery, the mass was adherent to residual, density and intermediate density, represents liposarcoma. (From Katz et al., AJR, Feb. 1999.)

Cysts

True cysts of the pancreas differ from pseudocysts and retention cysts through origin, histologic appearance, and clinical significance. True cysts are believed to be anomalously developed from remnants of the embryologic ductal systems. Histologically, they may have a lining of epithelial cells, but with pressure changes the lining may atrophy. In such cases, the wall may consist of smooth, fibrous tissue. Rarely, cysts may be complicated by infection or hemorrhage (although not with the frequency of pseudocysts).

They can appear incidentally but most commonly occur with multicystic[227] or von Hippel–Lindau disease. Levine and associates[151] reported on 31 patients with a history of von Hippel–Lindau disease. Five of the patients had pancreatic cysts. The CT appearance of this entity is identical to that of any other well-defined cystic abnormality (Fig. 38–95).

Lymphangioma

A single case of lymphangioma of the pancreas has been reported.[193] CT scan demonstrated a "cystic" mass that was indistinguishable from a cystadenoma; the diagnosis can be made only on pathologic analysis.

Adenomas

A number of benign solid tumors, some of ductal origin and some of acinar cell origin, do occur, but no specific reports have appeared in the literature. We have encountered one case of adenoma of the pancreas that was palpated and examined by biopsy at surgery but did not show any morphologic or density changes on CT scan that would distinguish it from a neoplasm (Fig. 38–96). Further experi-

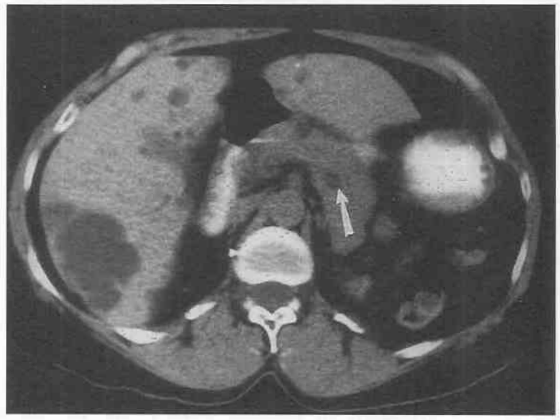

Figure 38–95. True cysts of the pancreas (*arrow*) may occur with polycystic disease.

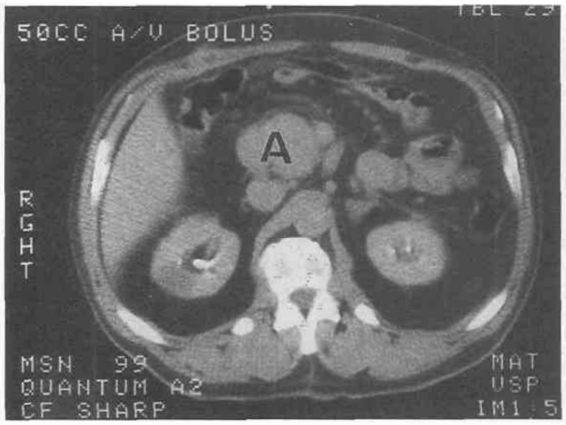

Figure 38–96. Adenoma of the head of the pancreas (A).

ence must be reported before any generalizations of the CT appearance of adenoma can be made.

Von Hippel–Lindau Disease

Von Hippel–Lindau disease is a hereditary disease with a dominant trait. It can be associated with a number of abnormalities, including angiomas of the central nervous system and eye as well as neoplasms and cysts of the pancreas, kidney, adrenal glands, and epididymis.

Pancreatic involvement by this disease consists of cysts, serous cystadenomas, solid nonfunctional islet cell tumors, and adenocarcinomas. The earliest signs are said to be small cysts, but calcifications are common. Progression of the disease can result in steatorrhea and diabetes. Solid tumors usually represent nonfunctional islet cell tumors or adenocarcinoma.

Periodic monitoring of diagnosed patients and screening for the disease in unaffected family members are appropriate. This approach enables genetic counseling for family planning. Also, early detection of problems with high morbidity and mortality can permit earlier effective treatment.

Levine and associates[151] and Choyke and colleagues[42] have reported on screening of visceral problems. Choyke and colleagues found CT to be more accurate than MRI and ultrasonography. CT detected all pancreatic and renal abnormalities in a group of 14 patients, whereas ultrasonography and MRI each missed abnormalities in three cases, including two pancreatic masses that were seen only on CT.

The recommended screening modality depends on the age of the patient. Choyke and colleagues[42] recommended ultrasonography and MRI for evaluation of the abdomen and central nervous system in patients younger than 11 years. Contrast-enhanced CT was recommended for patients older than 16 years.

Vascular Abnormalities

Because the pancreas lies in a location surrounded by vascular structures, a number of vascular entities occur in the region and can be associated or confused with pathologic conditions of the pancreas. Abnormalities can be related to inflammatory, arteriosclerotic, or neoplastic involvement of the vessels.

Splenic Artery Aneurysms and Pseudoaneurysms

Splenic artery aneurysms are common and characteristic. Surgical repair of such aneurysms is required only when they are more than 3 cm in diameter or if they occur in women who are of child-bearing age or are taking oral contraceptives. This latter group is at risk for spontaneous rupture. The aneurysms appear as circular soft tissue densities or curvilinear calcification in the area of the splenic artery (Fig. 38–97). On some occasions, when there is no extensive calcification of the aneurysm, it may simulate a focal mass. Aneurysms can be definitively diagnosed only on a dynamic bolus scan or with an infusion of contrast material at a high rate (Fig. 38–98). Identification is important because of the possibility that they can be mistaken for a mass in the gland. Spontaneous hemorrhage into the pancreatic duct has been reported with a splenic aneurysm.

Other Aneurysms

Aneurysms in the peripancreatic vessels can occur based on arteriosclerotic disease, but they are rare anomalies. They most commonly contain calcifications, and the diagnosis is best made with dynamic bolus scanning. Historically, these vessels are likely to rupture, so most authors recommend surgical correction in the appropriate patients. The aneurysms may be seen in the gastroduodenal, hepatic, or other vessels.

Hepatic Artery Aneurysms. Hepatic artery aneurysms represent 19% of splanchnic aneurysms and are atherosclerotic, traumatic, or mycotic. Surgical treatment is recommended because 44% of such aneurysms rupture. Therapy consists of ligation of aneurysmectomy; the extensive collateral network provides an adequate blood supply.

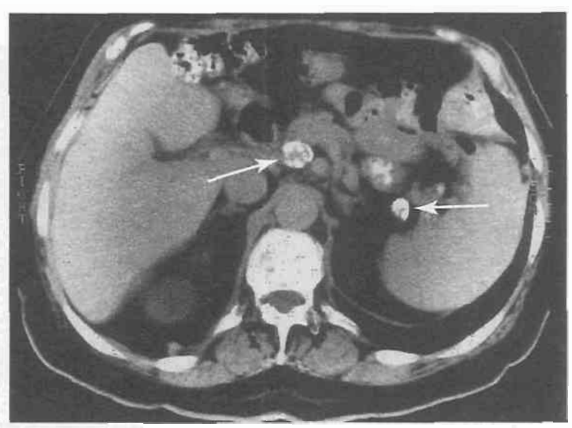

Figure 38–97. Aneurysms of the hepatic artery and splenic artery may demonstrate calcified dilatations, as noted in this case (*arrows*).

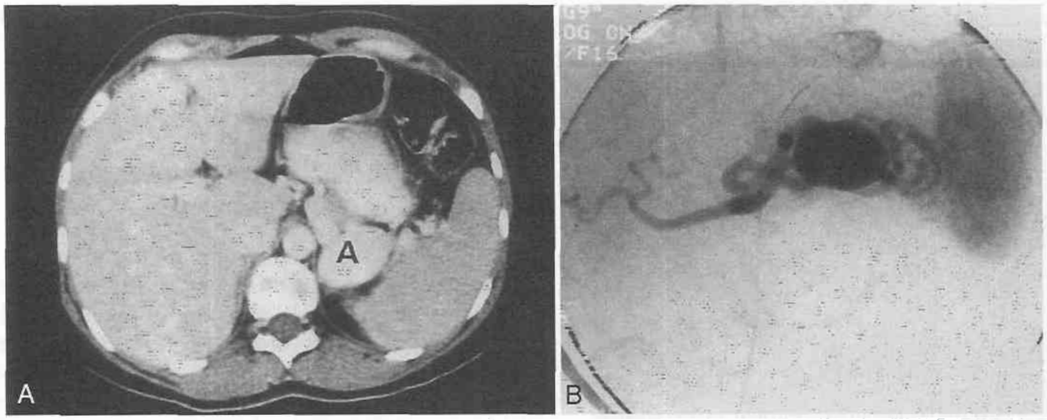

Figure 38–98. *A*, Although the patient was referred because of suspected tumor, the correct diagnosis of noncalcified splenic artery aneurysm was made preoperatively. CT scan with bolus dynamic contrast injection shows a high-density mass (A) in the area of the splenic pedicle, suggestive of an aneurysm. Digital subtraction angiography (DSA) was performed to document it. *B*, DSA shows the large aneurysm.

On CT, a hepatic artery aneurysm is a mass of blood density that enhances with bolus injection of contrast material. It may be adjacent to the artery or peripheral in the liver (Fig. 38–99).

Superior Mesenteric Artery Aneurysms. Superior mesenteric artery aneurysms are the third most common splanchnic aneurysms, of which 63% are mycotic lesions, and most are associated with endocarditis on the left side. Most other causes are secondary to medial degenerative disease. Operative treatment is justified because of the common occurrence of rupture or arterial occlusion (Fig. 38–100).

Celiac Artery Aneurysms. Celiac artery aneurysms are uncommon and are mainly atherosclerotic in origin. Approximately 20% rupture. Surgical treatment is recommended and consists of resection or ligation.

Cavernous Transformation of the Portal Vein

Cavernous transformation of the portal vein is a vascular anomaly that consists of multiple venous collaterals in the area of the portal vein. The incidence is small, and only one series of 16 cases has been reported, by Mathieu and coworkers.[170] Although it was once thought to be a congenital problem, it is now thought to result from portal vein occlusion or compromise. Because the numerous vascular channels can occur in any portion of the porta hepatis, a network of vascular channels adjacent to the pancreatic head can simulate a pancreatic mass. Correct diagnosis depends, of course, on familiarity with the entity and an appropriate scanning technique, which includes ample enhancement with an intravenous contrast agent.

The correct diagnosis can be easily made if the channels are large and the dynamic bolus scan has been administered properly (Fig. 38–101*A*). Diagnosis is more difficult when the vascular channels are not as well formed, are smaller, and are located in the area of the portal vein. In such cases, the diagnosis can sometimes be suggested by the presence of small amounts of fat irregularly interspersed within the porta hepatis region. It is very difficult to distinguish from another unusual entity, such as an arteriovenous malformation of the pancreas (Fig. 38–101*B*). In difficult cases, an angiogram may be required. In our early experience, before we were familiar with the appearance of this entity, we

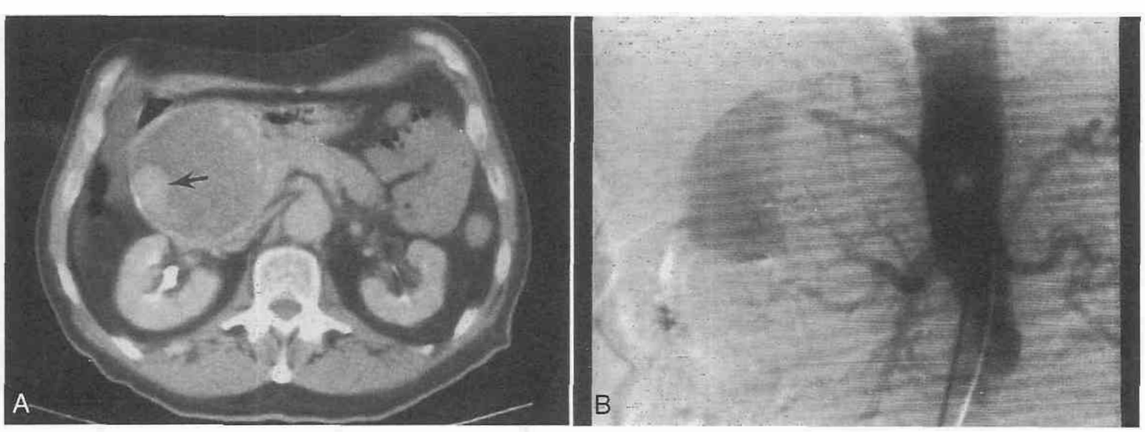

Figure 38–99. Massive aneurysms or pseudoaneurysms may simulate fluid-density pseudocysts. Note the large area of low-density clot surrounding the small area of high density, representing flowing blood in this large aneurysm.

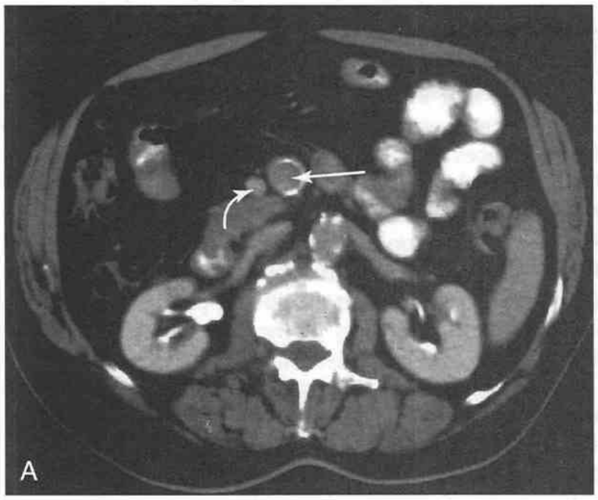

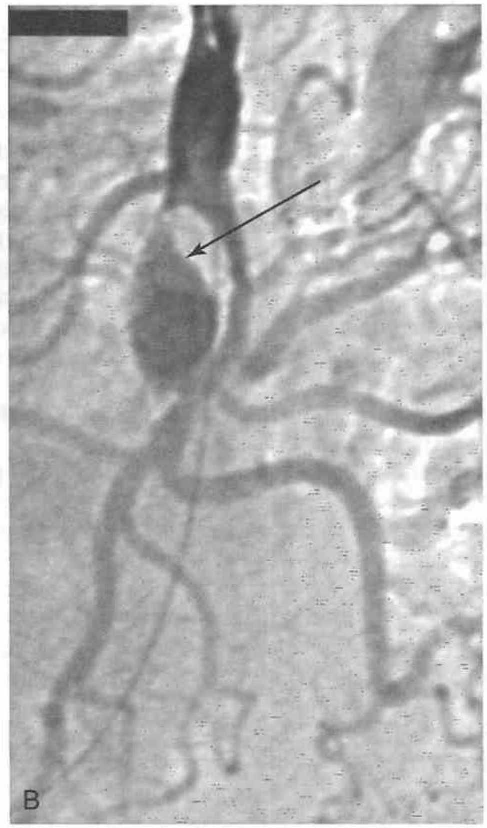

Figure 38–100. *A,* Axial CT scan shows circular calcium density (*arrow*), representing an aneurysm of superior mesenteric artery, to the left of the superior mesenteric vein (*curved arrow*). *B,* Angiogram shows large aneurysm with "neck" (*arrow*) coming from the superior mesenteric artery.

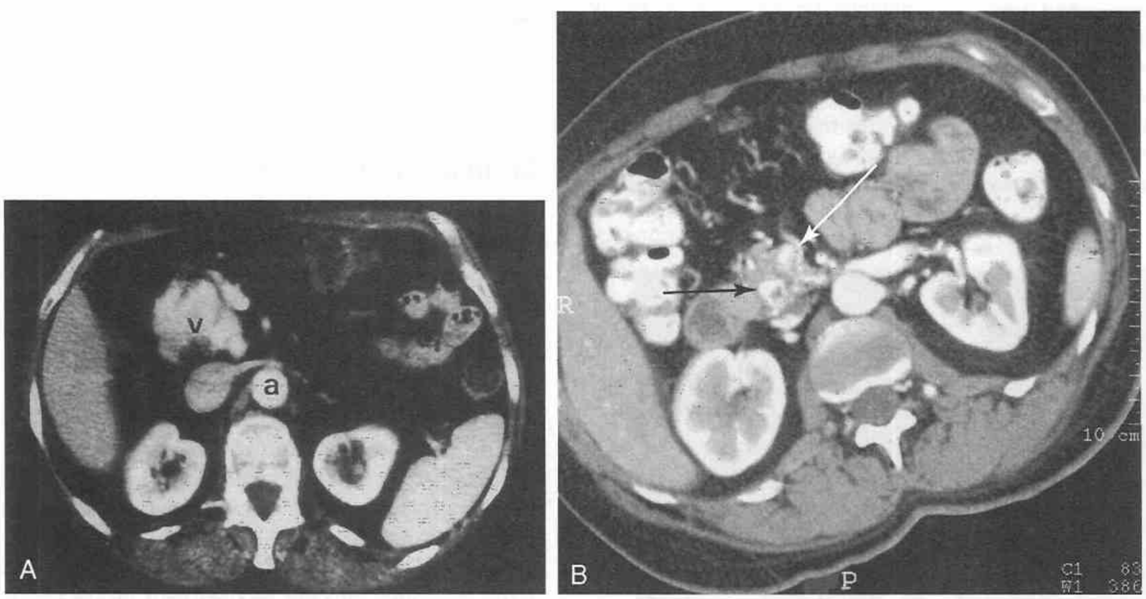

Figure 38–101. *A,* Mass in the head of the pancreas shows increased enhancement with contrast material, a finding consistent with a cavernous transformation [redacted] portal [redacted]n. *B,* Enhancing mass in the head of the pancreas, representing arteriovenous malformation of the head (*arrows*).

inadvertently performed biopsies using fine-needle aspiration on three patients with cavernous transformation that was producing a pseudomass in the head of the gland. No ill effects or blood loss occurred.

Portal Systemic Collaterals and Varices

Because of the close physical proximity to the pancreas and the possible effect of pancreatitis on adjacent structures, venous abnormalities of the portal vein and splenic vein are discussed. An enlarged splenic or portal vein may be visualized in cases of massive splenomegaly as a result of increased flow. Other entities, such as occlusion, thrombosis, or encasement of the splenic, superior mesenteric, or portal vein, result in portal hypertension and portal systemic collaterals (see Fig. 38–70*A*).[168, 239]

When the obstruction to flow is intrahepatic, such as occurs with cirrhosis, dilatation of the portal, splenic, and other veins occurs.[167, 171] Assessing enlargement of the portal and splenic vessels is subjective, but the appearance is usually obvious. When portal pressure has been present for long periods, calcifications may occur in the wall (Fig. 38–102).

With portal hypertension, a number of portal systemic collaterals appear.[123, 125] A common finding in such cases is recanalization of the umbilical vein in the falciform ligament, which can feed superficial periumbilical veins that form the classic caput medusae. There is dilatation of the inferior mesenteric vein coming off the splenic vein in some patients with portal systemic collaterals. In such cases, the dilated inferior mesenteric vein courses on the left side of the aorta, down to the perirectal hemorrhoidal veins.[108]

Large esophageal varices may be seen as a mass of serpiginous structures that enhance on bolus injection of contrast material. Systemic collaterals forming a splenorenal shunt can be well seen as enhancing tubular structures in the splenorenal ligament (see Fig. 38–70*A*). The collateral pathway is through small veins from the medial surface of the spleen, through the adrenal veins, and into the left renal vein. There may be a significant change in the caliber of the vena cava above and below the renal vessels, probably because of the difference in blood flow at these two levels. We have seen these vessels persist in a patient with such a shunt, with even-flowing splenectomy. In this case, tumor was considered until a bolus-dynamic scan was performed.

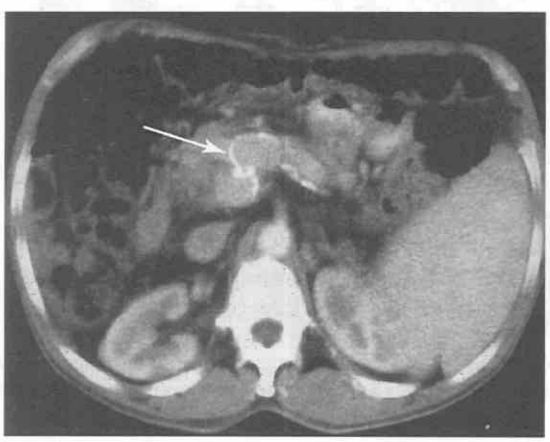

Figure 38–102. Chronic portal hypertension may rarely produce calcifications in the walls of the portal vein and splenic vein (*arrow*), as noted in this scan.

The accuracy of detecting varices has not been defined, but a number of authors have discussed the CT appearances. Primary diagnosis by CT scan is probably not as good as that by endoscopy or barium swallow study, but varices should be recognized when they are present. Such information may be helpful as an additional clue for correct and complete interpretation and is a critical factor if a percutaneous interventional procedure is being considered.

If thrombosis of the veins is suspected as the primary problem, administration of contrast material for a dynamic bolus study is essential. In instances of thrombosis of the portal or mesenteric vein, clot within the vessel is visualized as a filling defect (Fig. 38–103). If the clot extends into the intrahepatic portion of the liver, it may give the spurious impression of biliary dilatation.

Malignant Tumors

In contrast to some other cancers, pancreatic carcinoma has risen in incidence in recent years. In the United States and the United Kingdom, it is now the fourth leading cause of cancer death in men and the sixth leading cause of cancer death in women. Contributing causes have not been well defined, and previous associations with pancreatitis and alcohol abuse have been disproved.[150] Some related factors may be smoking, high-fat diet, diabetes, industrial exposure, and perhaps coffee.

Tumors of the pancreas other than adenocarcinoma are rare, and no change in their incidence has been noted. The diagnosis of all tumors has improved as a result of laboratory, clinical, and imaging studies.

Clinical Syndromes

Several syndromes that have specific symptoms have been associated with exocrine gland tumors. The most familiar sign is the association of adenocarcinoma neoplasms with migratory thrombophlebitis, called *Trousseau's sign.* The exact cause of Trousseau's sign is not clear, but the most commonly proposed mechanism is the release of tumor proteins from necrosis that act like tissue thromboplastin material. This material triggers the normal coagulation system to form thrombi in various veins.

A somewhat characteristic perineoplastic syndrome has been associated with acinar cell carcinoma. The syndrome consists of peripheral fat necrosis, polyarthralgia, and eosinophilia. It is thought that the release of lipase and other active enzymes into the bloodstream produces digestion of fat in the marrow and other areas, causing the symptoms.

The endocrine types of islet cell tumors produce clinical syndromes related to excessive secretion of their respective products. At least eight different cell lines in the islets of Langerhans and specific syndromes related to most of these cell lines have been reported. The endocrine products caus-

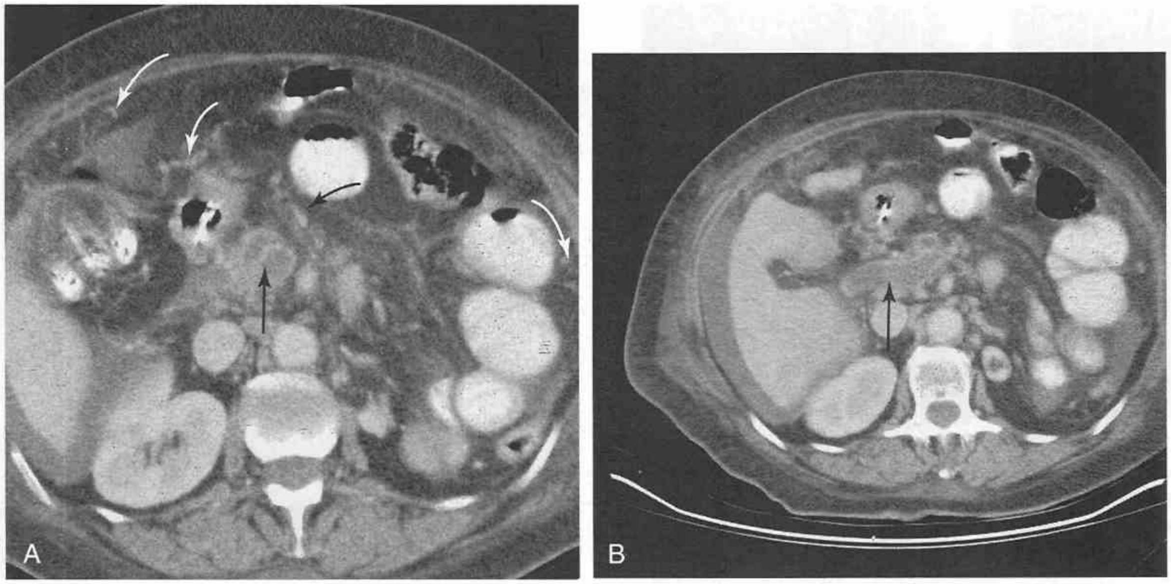

Figure 38–103. *A*, CT scan taken at the level of the lower pancreas shows low-density filling defects in the superior mesenteric veins (*arrow*) to the right of the superior mesenteric artery. In such cases, the vein may be mistaken for a dilated common bile duct. Distinction can be made by following the anatomy on contiguous sections. Also, note the excessive number of venous collaterals in the peritoneal cavity (*curved arrows*). *B*, Scan taken at a higher level shows the large clot in the portal vein (*arrow*), extending toward the porta hepatis region.

ing these syndromes include insulin, glucagon, gastrin, somatostatin, and vasoactive polypeptide; the signs and symptoms are discussed later.

Nonendocrine Tumors

Pancreatic Adenocarcinoma. Ductal cell adenocarcinoma constitutes 80% of the neoplasms of the pancreas and occurs most commonly in the head (65%). It is most common in older patients and has a higher incidence among men. Patients frequently have weight loss, pain, and jaundice, but a variety of other symptoms related to the gastrointestinal tract or metastatic spread can occur.[26]

The treatment and outcome have not significantly changed in recent years. The overall long-term results from surgery and chemotherapy have not been good, but there is reason for some optimism. With the availability of modern CT equipment, proliferation of medical information, and greater experience, two positive trends exist. At least with current technology, it has been possible to avoid surgery in patients for whom it would be inappropriate, especially since such surgery can have a high morbidity.[88–92] Similarly, because more likely candidates are undergoing surgery, it is my belief that outcome data in the future will show an improvement in survivorship. Second, several new chemotherapeutic agents have produced remarkable improvements in the short term.

Diagnostic Signs. Tumors may demonstrate one or a combination of the following diagnostic signs.[88–92, 94, 152, 225, 240]

1. Morphologic and contour changes.
2. Mass effect.
3. Density changes (i.e., low density or calcification).
4. Contrast enhancement.
5. Pancreatic duct changes.
6. Secondary signs.

Morphologic and Contour Changes. The morphology of the normal gland is discussed in previous sections. Complete familiarity with the variations of shape and contour is important if one is to diagnose subtle pancreatic tumors. In most cases, alteration in the morphology caused by the mass is so remarkable that it is hard to discern even the normal margins of the remaining gland. In other cases, the changes may be so subtle that only careful attention to detail reveals the nature of the problem.[35, 152]

Masses of the head of the pancreas are usually obvious because of their size, but subtleties can occur that require attention to diagnostic details (Fig. 38–104). Such masses may have smooth contours or a lobulated appearance (Figs. 38–105 to 38–107). Masses of considerable size displace adjacent structures, such as bowel and blood vessels. If aggressive local invasion occurs, the margin of the adjacent bowel can be involved, and there may be encasement of vessels, resulting in vascular compromise and formation of collateral vessels. Vessel involvement is an indicator of tumor unresectability (see later section).

When appreciation of a mass in the head is difficult, it may be helpful to note the presence of any discrepancy between the sizes of the head and the neck and tail. Although this discrepancy was initially believed to be an early sign of malignancy, a study indicates that it is simply a common appearance and does not necessarily indicate the presence of early disease.

An extensive study of morphologic changes was made by Muranaka and colleagues,[182] who studied the overall

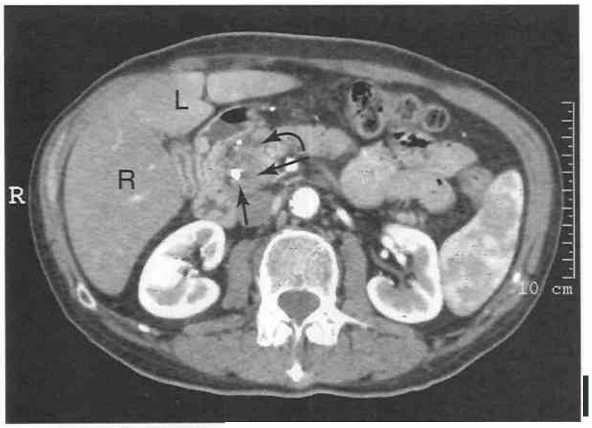

Figure 38–104. Pancreatic mass (*arrows*) in this patient is rather subtle because the contour is changed only on the medial portion of the gland. Because of the low density of the tumor and the adjacent dilatation of the pancreatic duct, the mass can be appreciated. The liver shows an increased enhancement in the left lobe (L) and low enhancement of the right lobe (R), due to reduced right portal blood flow.

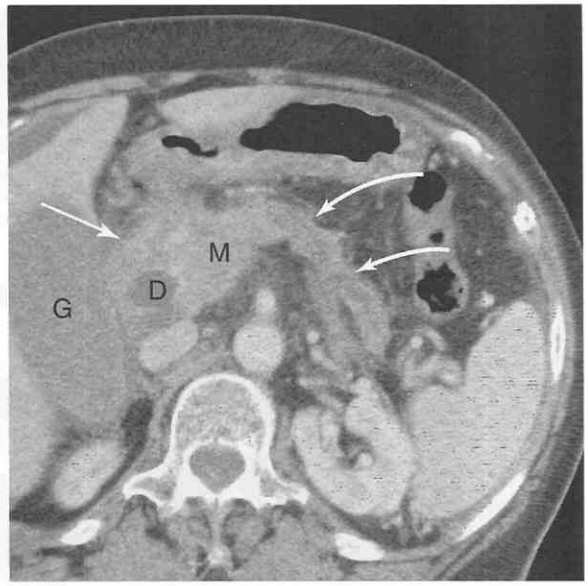

Figure 38–106. Low-density mass (M) of adenocarcinoma (*straight arrow*) is seen in the pancreatic head. Irregular dilatation of the pancreatic duct is seen (*curved arrows*). There is invasion of the tumor into the porta region, producing dilatation of the common bile duct (D) and the gallbladder (G).

size relationships of the head and body of the pancreas as well as the size and configuration of the pancreatic duct. The authors classified the body of the gland as enlarged when it exceeded 2.2 cm and atrophic when it measured less than 1.0 cm (see Table 38–1). They classified the head mass of the pancreas into four grades depending on the anteroposterior measurement: T1, 0 to 2 cm; T2, 2.1 to 4 cm; T3, 4.1 to 6.0 cm; and T4, more than 6 cm. In their series of 72 patients, there were 11 patients with T1, 14 patients with T2, 20 patients with T3, and 11 patients with T4 masses. They evaluated the size of normal and cancerous glands and assessed the ratio of the head and body to validate or refute earlier observations about size discrepancy.

Results of the study by Muranaka and colleagues[182] showed that the normal gland varied in size as follows (see Fig. 38–46): The head varied between 19.8 and 29.5 cm, and the body varied between 12.1 and 21.4 cm. Although the size decreased with age, the ratio of head and body remained constant at 1.45 ± 0.03. The ratio of the head and body in carcinoma patients was $3.4 + 0.9$. An interesting finding in this series was that contrary to the traditional thinking that a discrepancy between the head and body can be found in small tumors, these researchers found that in more than half of the patients with small tumors, the body of the pancreas was actually larger than normal, resulting

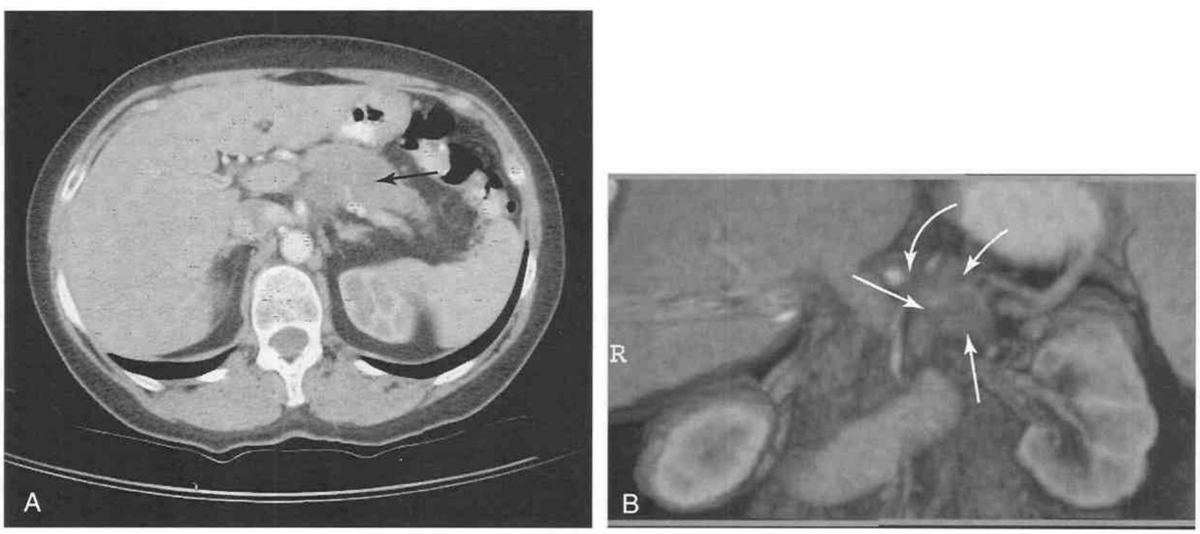

Figure 38–105. *A,* A large mass in the body of the pancreas shows low density owing to lack of enhancement (*arrow*) and encasement of the splenic artery. *B,* 3D reconstruction of the mass shows a large mass in the midportion of the gland (*arrows*), adjacent to the vessels. *Curved arrow* indicates encasement around the celiac artery.

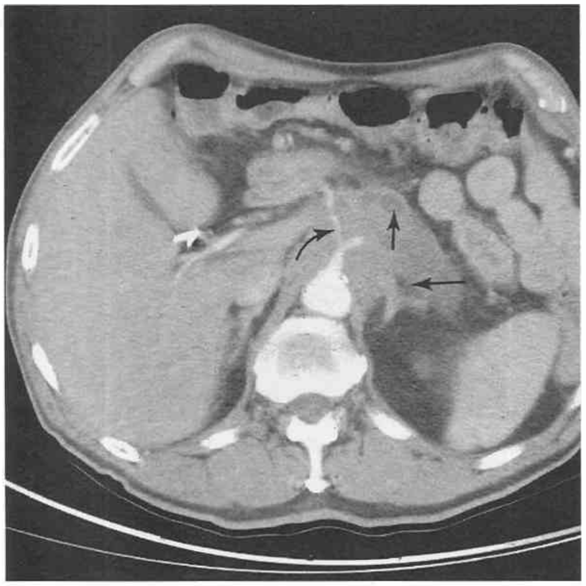

Figure 38–107. CT scan shows a large mass in the head of the pancreas that is encasing (*curved arrow*) the hepatic artery, originating from the celiac artery. Dilatation of the pancreatic duct is so severe that it is producing a retention cyst (*vertical arrow*). Left adrenal gland (*horizontal arrow*) is partially invaded on the medial surface.

in a ratio less than normal (between 1.0 and 1.5 cm). As the tumors increased in size, the pancreatic ratio rose as previously noted. These findings contrasted with the ratio noted in patients with inflammation. The ratio with pancreatitis was close to normal despite the large size of any mass because of concomitant enlargement of the body.

Tumors of the neck and body commonly produce enlargement of the gland and local extension to the splenic pedicle (Fig. 38–108). When a mass is immediately adjacent to the stomach, it may be difficult to appreciate unless there is adequate contrast material in the fundus. In such cases, it may be helpful to turn the patient to a decubitus position, which shifts the anatomy somewhat and clarifies the appearance. Although most tumors enlarge in the plane of the axial slice (i.e., anterior, posterior, right or left sides), they may grow in a cephalad-caudad direction and be difficult to identify as a pancreatic tumor.

Wittenberg and associates[265] noted that carcinoma may appear as enlargement of almost the entire gland. They found that three or more portions of the gland (head, neck, body, and tail) were involved in 27% of cases, and they recommended that multiple biopsies might be required to differentiate between neoplastic and secondary inflammatory components.

One of the most disappointing facts is that despite the remarkable evolution of the diagnostic equipment and advanced experience level, carcinoma of the pancreas can occur without any distortion of the contour (Fig. 38–109). In such cases, the tumor may become manifest many months later.

Other Problems Simulating a Pancreatic Mass. A variety of problems can cause difficulties in interpreting a "mass" in the head of the gland. (See the section on normal variants and pseudomasses.) If the contrast material is not adequate to opacify the venous structures, a prominent portal vein, or the vena cava, an overall impression of "fullness" in the area of the pancreas may be noted. In such cases, a second study using adequate contrast material or an ultrasound examination can clarify the findings. When a mass abuts the stomach or duodenum, administration of oral contrast material and examining the patient in the decubitus position may be helpful.

On other occasions, enlargement of the caudad lobe of the liver by cirrhosis or another problem may produce the spurious finding of a "mass." Another confusing abnor-

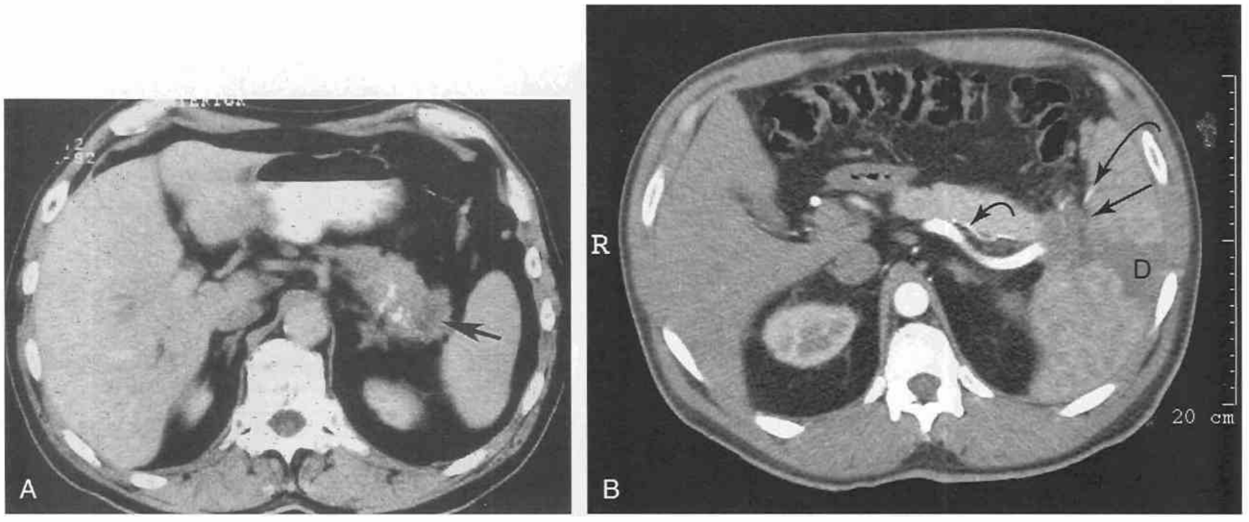

Figure 38–108. Tumors in the pancreatic tail. *A*, Patient with adenocarcinoma of the tail of the pancreas (*arrow*). Note the decreased density as well as the small calcifications in the tail. It is difficult to determine whether the calcifications are related to the tumor or to previous pancreatitis. *B*, Tumor in the hilum of the spleen (*straight arrow*) of a different patient has almost completely occluded the splenic artery (*small curved arrow*), which appears as a tiny vessel because of reduced blood flow. Infarction of the spleen has produced an infarct defect (D) in the spleen. Also note the small collateral arteries (*large curved arrow*) attempting to supply the spleen.

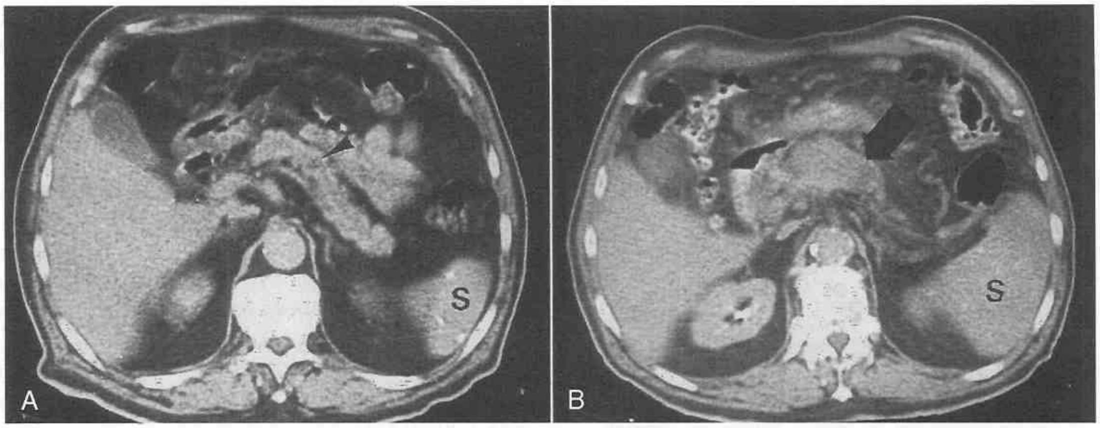

Figure 38–109. Small intraglandular tumor. *A,* CT scan performed early in the clinical course shows a subtle enlargement of the pancreatic duct and a tiny low-density area in the body (*arrowhead*). Note the normal-sized spleen (S). This study was not read as abnormal. *B,* Repeat CT scan months later shows a large mass in the body of the gland (*arrow*). There are numerous collateral vessels in the mesentery and enlargement of the spleen (S), indicating definite occlusion of the splenic vein.

mality is enlargement of lymph nodes in the retroperitoneum adjacent to the head of the pancreas. Finally, another unusual entity that can cause an apparent mass is a partial malrotation of the duodenum. Because Treitz's ligament is in an abnormal location and the path of the bowel is redundant, the duodenum can produce a "clump" that looks like a mass. A fluid-filled duodenal diverticulum may also produce a "mass."

Density Changes. Although early scanning devices did not demonstrate many density differences between tumor and normal gland, modern CT consistently shows decreased density in almost all non–islet cell tumors with contrast enhancement. Freeny and others[64–67] noted diminished density in 83% of patients with focal masses. Without the use of intravenous contrast material, many adenocarcinomas have an almost isodense appearance (compared with the rest of the gland). This low density observed on the CT scan is thought to be due to decreased vascularity of the neoplasm compared with the normal gland (Fig. 38–110). Necrosis or low-density fluid production may be visible in many tumors with or without contrast material[126]; this is common with mucinous adenocarcinomas, cystadenomas or cystadenocarcinomas, adenosquamous carcinomas, papillary adenocarcinoma, and any necrotic tumor resulting from necrosis or mucinous material.

A paradoxically unusual finding can occur in patients who have the normal variation of extensive fatty infiltration of the gland. Because the tumor does not contain the same amount of fat as seen in the parenchyma, it is higher in density than the normal gland (Fig. 38–111). Interestingly, one of the tumors we have observed became isodense with the rest of the gland after administration of a contrast agent. This is comparable to seeing lesions in a fat-density liver.

Another obvious change in the density of tumors is calcifications, which occur in a number of different tumor

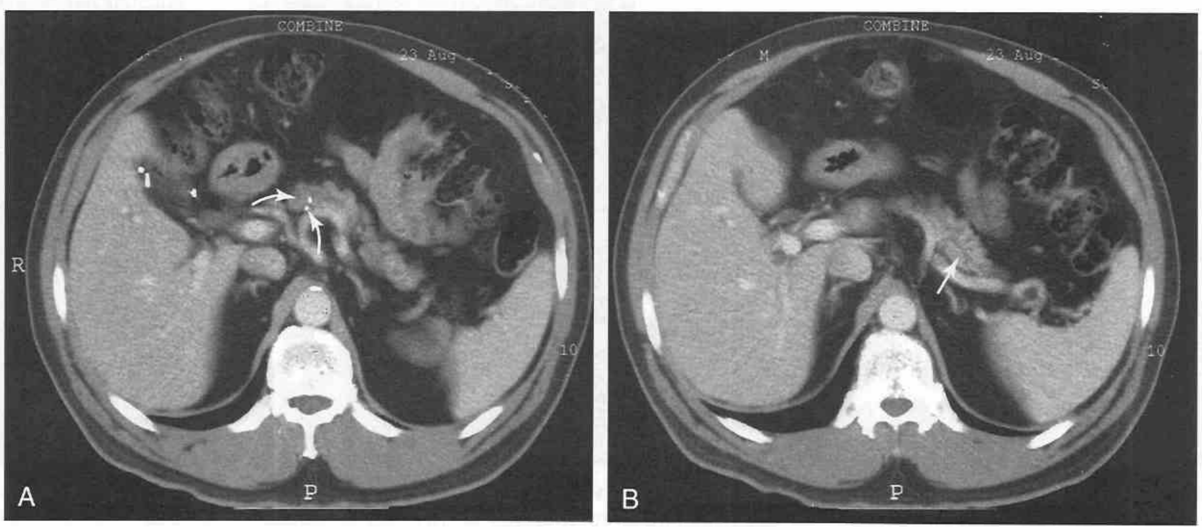

Figure 38–110. *A,* Small low-density tumor (*curved arrows*) is seen in the head adjacent to a calcification from chronic pancreatitis. Note the subtle dilatation of the pancreatic duct. *B,* A scan obtained at a slightly higher level shows subtle dilatation of the duct (*arrow*) as well as dilatation of the side branches of the pancreatic duct.

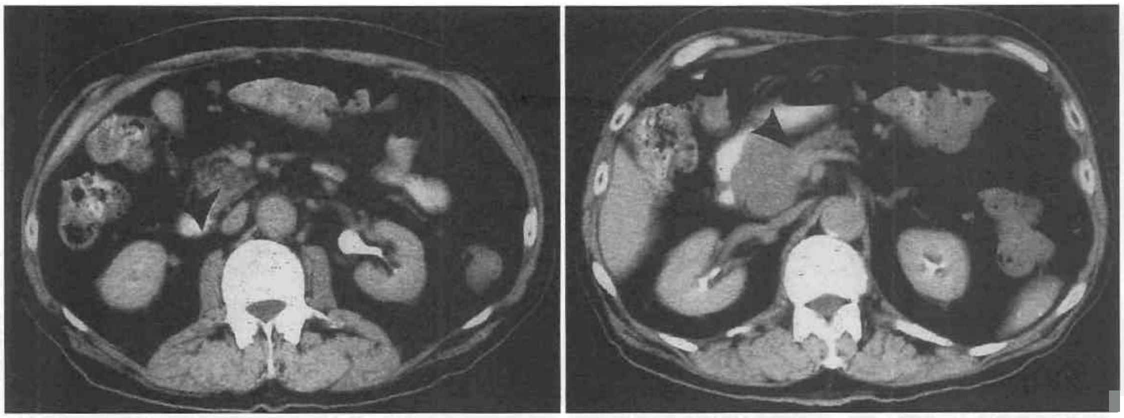

Figure 38–111. *A,* This and the subsequent scan show the paradoxical increased density of a neoplasm compared with the normal gland. Note that the pancreatic head has a low density owing to fat infiltration (*arrowhead*). *B,* Slightly higher-level scan shows a higher-density mass in the head of the gland. *Arrowhead* points to the junction point with the neck and body, which is slightly atrophied and has a lower density owing to fat infiltration.

types in the de novo state. Typically, adenocarcinoma only rarely calcifies (see Fig. 38–108*A*), and calcium is considered typical for other unusual pancreatic tumors. The nonfunctioning islet cell tumor is the most common. The configuration of the calcifications is not helpful because they may vary in both amount and size. Other, rarer tumors that may also contain calcifications are mucinous adenocarcinomas, cystadenomas, cystadenocarcinomas, papillary epithelial tumors, fibromas, and glucagonomas, which are discussed later.[102] Dystrophic calcifications may occur in any type of tumor after treatment if necrosis has resulted. Dastur and Lewin[51] reported a case of adenocarcinoma that showed calcification in the primary tumor and metastases after chemotherapy.

Contrast Enhancement. The effects of contrast enhancement vary according to the method of contrast administration, enhancement by generalized equilibration or by dynamic bolus injection aided by mechanical injector. The optimal method, as noted previously, is enhancement with mechanical injection. With this method, the relatively decreased density of the tumor is better visualized as well as any vascular collaterals that may exist in the peripancreatic area (see Figs. 38–104 and 38–106). When contrast material has been given as a single bolus or drip infusion, it has equilibrated between the intravascular and extravascular spaces. (Experimental work indicates that it takes only a few minutes for this equilibration to occur.) Direct arterial injection through arterial catheters has been performed in specific cases and can be helpful in finding a small vascular endocrine tumor.

The importance of giving adequate contrast material was noted by Hosoki,[104] who discussed the benefit of dynamic bolus injection for the diagnosis of neoplasms. As others have noted, he observed that contrast material permitted better visualization of the pancreatic duct. He thought this procedure facilitated (1) correct evaluation of the tumor vascularity, allowing a differential diagnosis, (2) location of the boundary between tumor and nontumor tissue, (3) detection of small tumors, and (4) visualization of pancreatic invasion by peripancreatic tumors. He found that tumors were more likely to appear isodense compared with the normal gland if contrast material was given as a slow bolus before the scan, whereas they appeared hypodense compared with the normal gland if rapid contrast injection was given. He also confirmed findings reported by other authors about the vascularity of cystic and islet cell tumors (see later).

Ductal Dilatation and Cyst Formation. Ductal dilatation can occur in either pancreatitis or neoplasm. Several observations based on the size and configuration of the pancreatic duct can be helpful. (See the section on the pancreatic duct.)

Dilatation occurs in patients in whom the duct is obstructed by a neoplasm. As noted earlier, visibility of the duct is improved by intravenous injection of contrast material, which highlights the density of the glandular tissue around the fluid-density duct. In most cases, dilatation of the duct is uniform, but on occasion there may be some tortuosity or beading of the duct. In unusual cases, obstruction of the duct may produce ectasia and enlargement of a localized segment, producing a retention cyst or pseudocyst distally (Fig. 38–112; also see earlier).

Biliary Obstruction. Biliary obstruction occurs with great frequency in the patient with a mass in the head of the gland. In these cases, the course of the dilated biliary system from the liver through the porta hepatis and down the length of the common bile duct should be followed,[83, 198] and the level of the obstruction determined. In most cases, the dilatation ends just above the level of the pathologic condition (unless there are metastatic nodes in the porta hepatis) (Fig. 38–113).

The configuration of the common bile duct may have a characteristic finding that can help to distinguish between neoplastic and inflammatory narrowing of the duct. The complete details are noted in Chapter 38. In pancreatitis, sequential concentric narrowing of the distal duct occurs as it passes through the inflammatory mass. An abrupt end to the duct on sequential scans or an irregular margin of the dilated common bile duct is expected with neoplasm. These findings parallel those seen on cholangiography. The

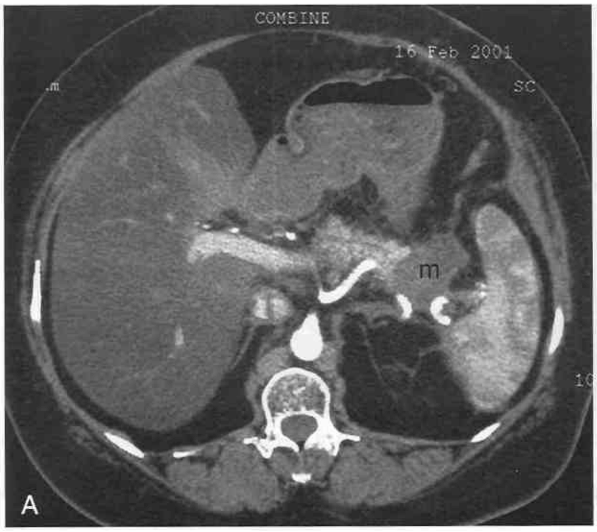

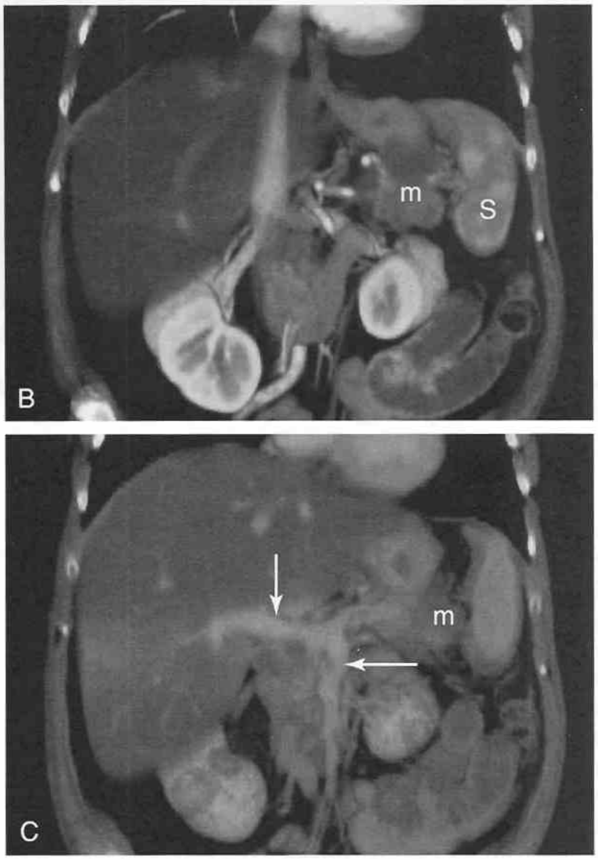

Figure 38–112. *A,* Mass in the tail of the pancreas (*m*) has both solid and cystic components. The vasculature is intact. Also, there is some thickening of the fascial planes, which might suggest the presence of pancreatitis. Note the patency of the splenic artery and the mottled but homogeneous appearance of the spleen, which is due to the timing of the contrast injection. Compare this scan with that in *B. B,* 3D image produced on a multislice scanner shows tumor (*m*) adjacent to the hilum of the spleen (S), with the preservation of the vessels and the normal size of the spleen. *C,* Another level of the 3D reconstruction shows the mass (*m*) in the hilum as well as the intact portal vein (*vertical arrow*) and the superior mesenteric vein (*horizontal arrow*).

changes in the distal duct and duodenum can be appreciated on 3D CT reconstructions.

Local Extension. Local invasion of adjacent structures can be easy or difficult to see, depending on the nature or degree of involvement. In most instances, the margins of the contiguous anatomic structures are displaced and distorted by an extension of the soft tissue mass. In other cases, infiltration of the vascular planes around the superior mesenteric artery and vein or the portal venous system must be carefully sought. Acute obstruction of the portal system produces clinical symptoms and collateral vessels that are best seen with dynamic contrast studies.

Contiguous spread into adjacent organs occurs commonly and is obvious most of the time. The tumor extension usually follows the areolar tissue containing the vessels, lymph nodes, and lymphatic system with the various peritoneal reflections or ligaments. When the tumor invasion is subtle or there is associated inflammation, the appearance may be confused with edema, which can occur with pancreatitis.[259] Extension may occur along the lines of the splenic hilum and the splenorenal peritoneal reflection. It can produce focal areas of neoplasm or necrosis within the spleen.

Invasion into the duodenum or stomach can cause gastric or duodenal obstruction. In most instances, displacement and massive involvement occur, but in some cases, the infiltration can be so subtle that the bowel can be affected without any significant soft tissue mass.

Direct tumor invasion into or from the bowel can occur along the mesocolon, especially at the hepatic or splenic flexures. If a fistula to the bowel is created, gas in the tumor may produce an appearance suggestive of an abscess. The amounts may be so remarkable that distinction from an abscess or infected pseudocyst may be difficult (Fig. 38–114). Comparison studies are helpful because affected patients may be only slightly more ill when they are seen than other patients with tumors.

Spread of the tumor along the margins of the vasculature[223] may result in narrowing or encasement of the arteries and veins (Fig. 38–115). In such cases, venous occlusion usually occurs first, and numerous venous collaterals can usually be seen in the adjacent tissues (Fig. 38–116). When occlusion of the artery is complete, it may produce vascular compromise of the involved organ, such as the spleen, which shows characteristic changes. Several authors, including Megibow and colleagues[174] and Itai and others,[111–113] have compared CT and angiography for the study of encasement of the vessels. They report that the finding of the loss of the fat plane around arteries on CT is as accurate for encasement as the angiographic finding of narrowing (Fig. 38–117).

A corollary sign of tumor invasion of the venous system is the dilatation of the posterior superior pancreaticoduode-

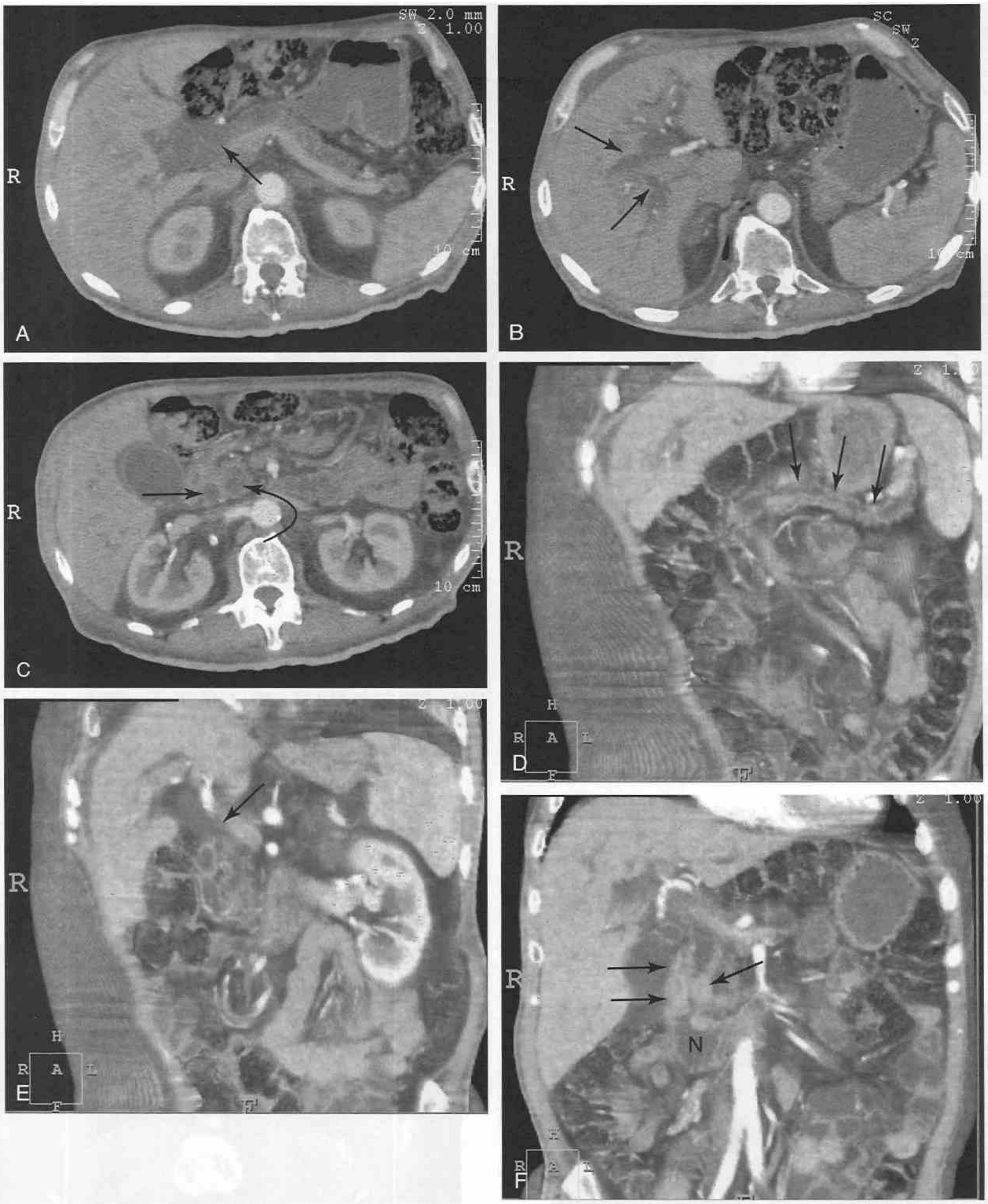

Figure 38–113. Scans demonstrating the remarkable benefit of the 16-slice multislice scanners. The images in both the axial scans and the 3D reconstructions are so numerous that it is very difficult to display them in the standard printed book. *A,* This scan shows an axial slice at the level of the head of the pancreas. The dilated common bile duct is noted (*arrow*). *B,* Higher scan shows that the biliary dilatation extends throughout the upper biliary system as well (*arrows*). *C,* Lower scan shows dilated biliary (*arrow*) and pancreatic duct (*curved arrow*) adjacent to the duodenum. No definite mass is identified. *D,* Oblique 3D image shows the dilated pancreatic duct (*arrows*) in the main part of the gland but no definite mass in the gland. *E,* Oblique 3D image at different level shows the dilated common bile duct (*arrow*) above the level of the duodenum but still no definite mass. *F,* A more coronal 3D scan shows the duodenum adjacent to the duct. The lower, second portion of the duodenum shows thickening of the duodenal wall (*arrows*) adjacent to the normal portion (N). This appearance is quite clearly consistent with the patient's proven diagnosis of villous adenocarcinoma of the duodenum.

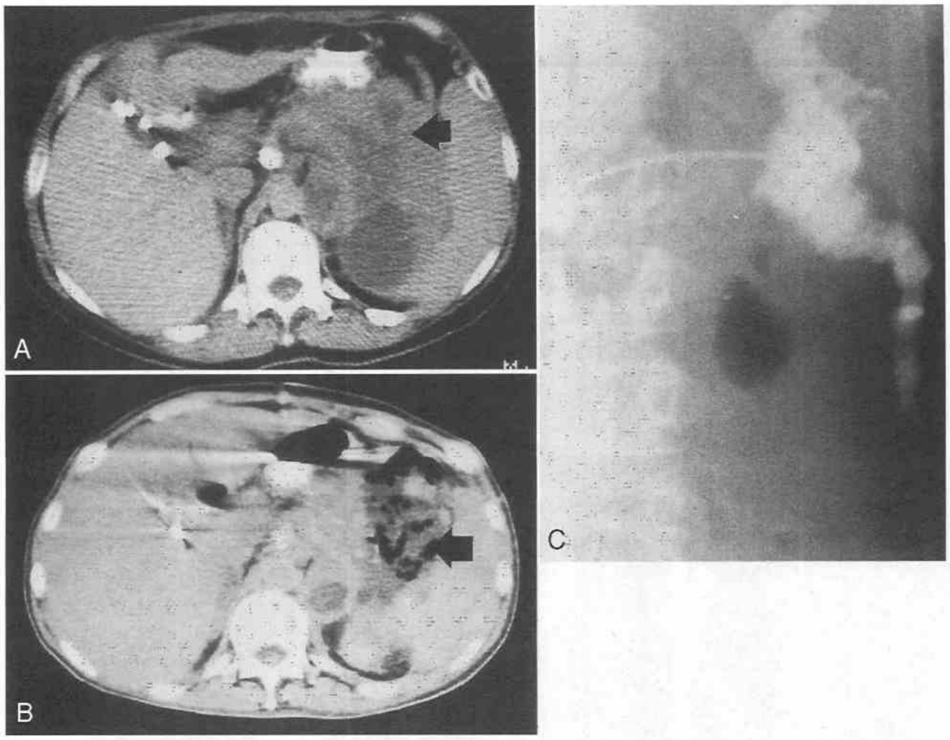

Figure 38–114. *A,* Baseline scan of a patient with a tumor of the tail of the pancreas that is producing a soft tissue mass (*arrow*) in the hilum. *B,* Later scan shows "air" within the mass (*arrow*); the origin of the air was not known. *C,* Percutaneous puncture followed by injection of contrast material shows a fistula to the colon.

nal vein reported by several authors. The essence of this sign is that with occlusion of the normal anterior venous pathways by tumor, there is increased flow through the posterior pancreaticoduodenal vein, which becomes more apparent[113] (Fig. 38–118).

Lymph Node Involvement. Lymph node involvement is common with pancreatic tumors.[5] The first nodes to be involved are usually those around the vessels in the immediate peripancreatic and porta hepatis regions (see Fig. 38–115). Lymph channels follow the veins (see arteriogram, Fig. 38–3). Accordingly, the pancreatic lymph nodes are located in their prospective peritoneal reflections (e.g., hepatoduodenal area, root of the mesentery). Direct spread within the areolar tissue of the peritoneal reflection also occurs.

Liver Metastases. Metastatic disease of the liver occurs frequently with adenocarcinoma and does not have a specific appearance. Metastatic foci appear low density within the enhanced liver and may be well circumscribed or diffuse.

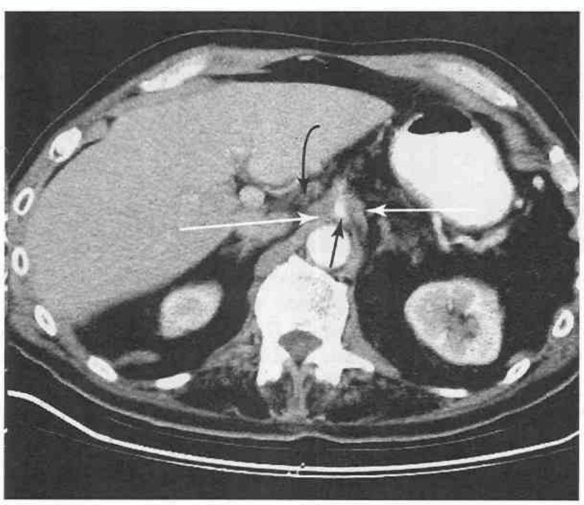

Figure 38–115. Axial CT scan shows encasement (*horizontal arrows*) of the celiac artery (*vertical arrow*). Small lymph node is noted in the porta hepatis region (*curved arrow*).

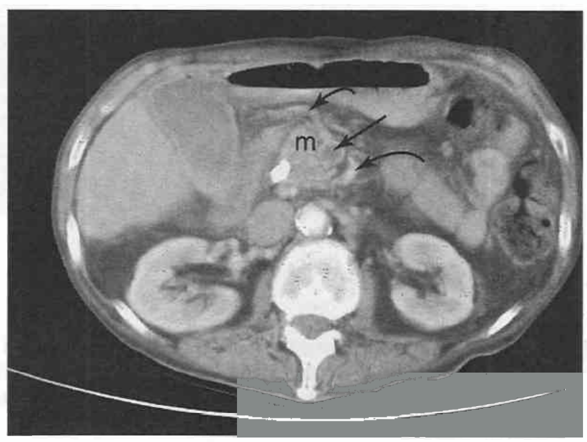

Figure 38–116. Mass (m) in the head of the pancreas has interfered sufficiently with the flow of blood in the superior mesenteric vein that a clot (*straight arrow*) has formed. In such cases, one must be careful not to overdiagnose the findings because incorrect timing of the bolus of contrast material might produce a spurious finding owing to unopacified blood. Note the presence of associated venous varices in the mesentery, which supports the diagnosis of occlusion (*curved arrows*).

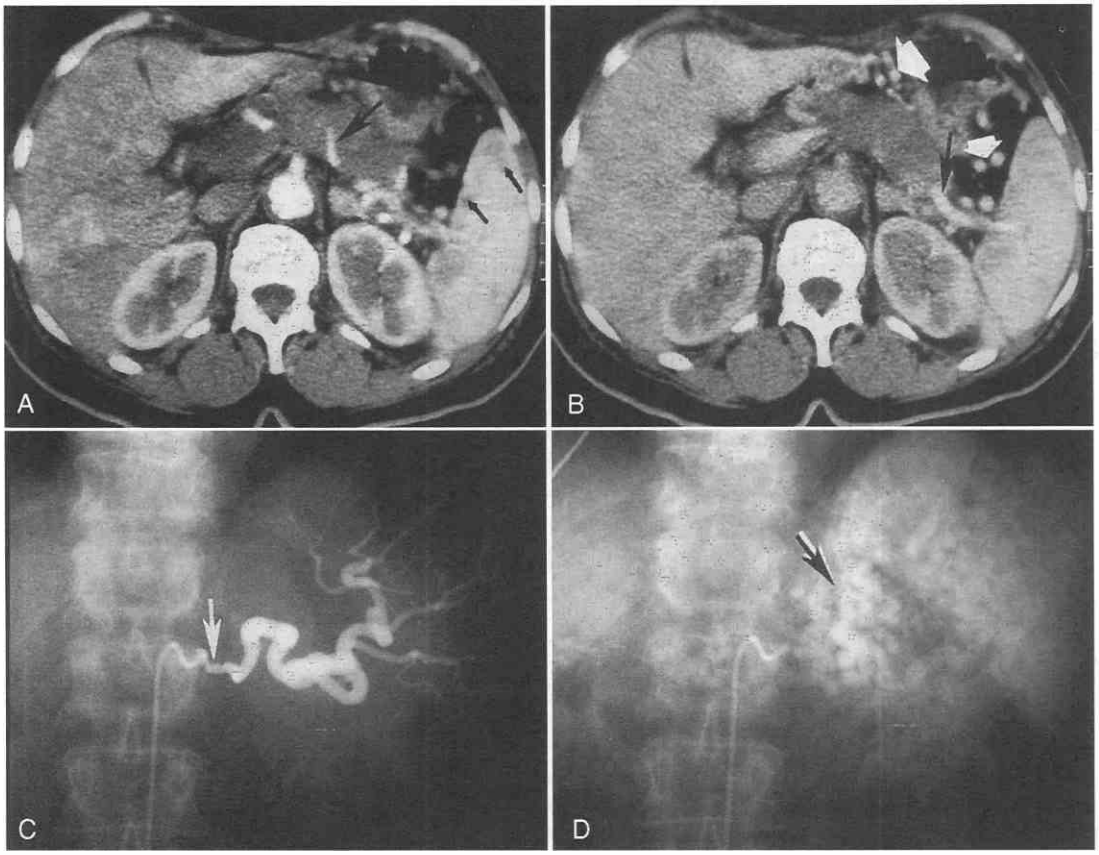

Figure 38–117. This set of images has been retained for historical purposes. With the advent of the new multislice devices, it is very likely such direct angiograms for diagnosis of pancreatic cancer will never be performed in the future. *A,* CT scan of pancreatic mass with encasement of the splenic artery (*large arrow*), which is producing low-density areas (*small arrows*) in the spleen. *B,* Scan taken at a later phase shows the splenic vein (*black arrow*) and collateral veins in the perisplenic area and the left gastric area (*white arrows*). *C,* Arteriogram showing encasement (*arrow*) of the origin of the splenic artery. *D,* Numerous venous collaterals in the perisplenic area (*arrow*) produced by occlusion of the splenic vein.

Staging and Operability

With a tumor type as lethal as pancreatic carcinoma, the practical goal of staging with imaging studies is to definitely identify patients who are not surgical candidates. At the same time, such determinations must be made with a great deal of reliability to ensure that patients with curable disease are not excluded from appropriate surgical treatment.

Of the 27,000 cases that are diagnosed each year in the United States, 75% to 90% are ductal adenocarcinoma. The untreated survival rate is 3 to 6 months, and the 5-year survival after a Whipple procedure is 18% to 20%.[248] The numbers of patients qualifying for the different treatments vary according to the reporting institutions, but generally, 90% of patients presenting for care have locally advanced or disseminated disease; 95% succumb to disease within the first year. Only 20% to 25% of those undergoing surgical exploration have resectable disease. For this group, there is a 15% to 20% survival. These percentages provide a practical perspective on the potential for treatment of pancreatic carcinoma.

The traditional TNM classification is still the standard used by most authors. In view of the dismal response of past treatment methods, there is a tendency to avoid specific staging because it seems futile. In reality, it is important that staging approaches continue because there are very innovative diagnostic and treatment strategies in development that promise to improve the outcome of pancreatic cancer. This classification, as shown in Table 38–4, depends on location, extension, lymph node involvement, involvement of vessels, and metastases.

Surgical Strategies

Whipple Procedure. Resection of the pancreas and duodenum was first performed by Kausch in Berlin in 1912.[235] The procedure was popularized in the 1940s by Whipple and colleagues. With this procedure, the pancreatic tumor of the head is resected en bloc. with the duodenum. Anastomotic attachments are then made with the small bowel, biliary system, and pancreatic duct. This procedure was originally used only for ampullary cancer, but now has been extended to cases with periampullary tumor and local tumor with limited staging. Over the years, the survivorship of the procedure has not changed significantly, but the mortality and morbidity of the procedure have improved. The mortality has improved from 20% to less than 4%. Current data also indicate a difference in mortality between

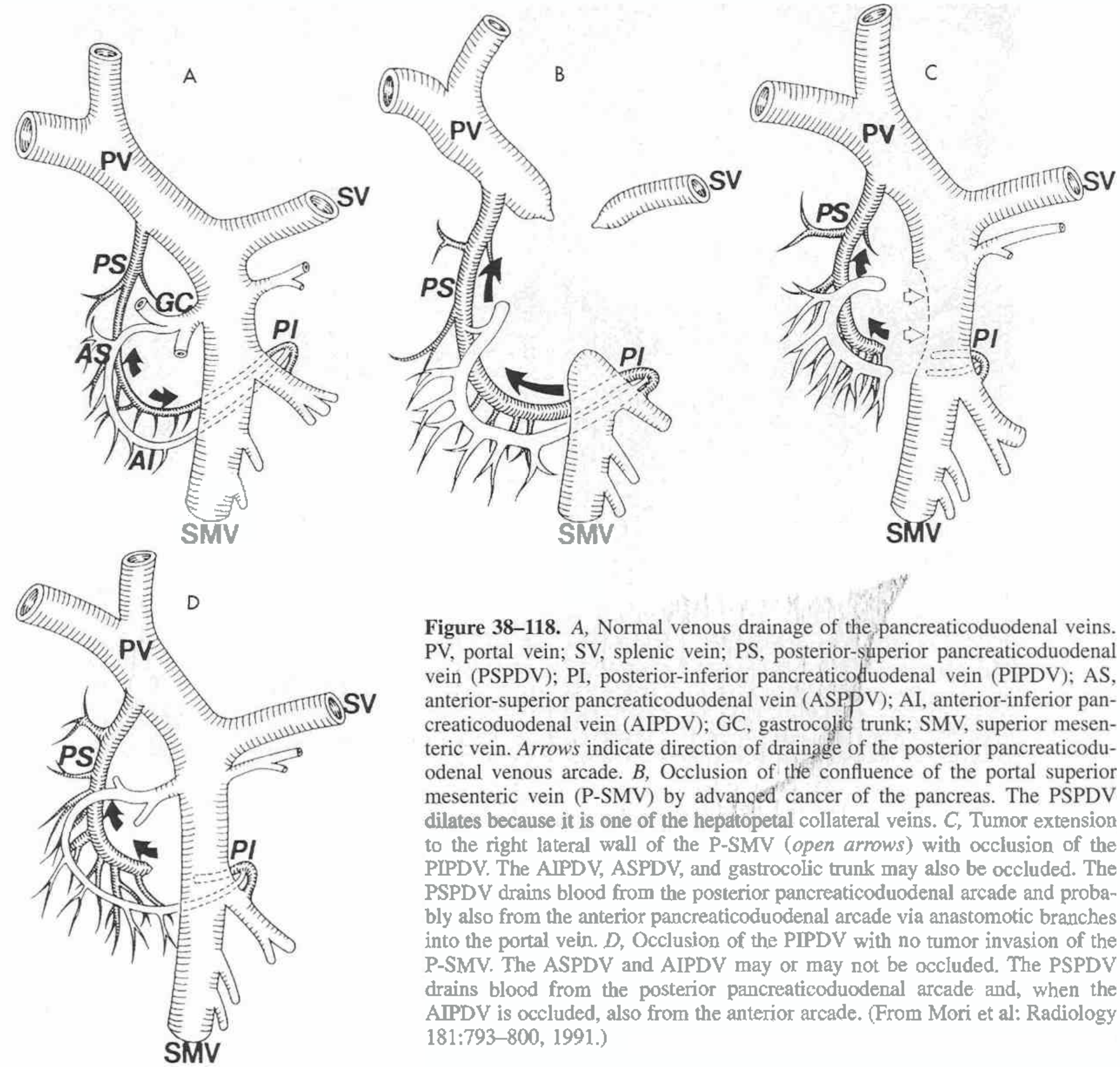

Figure 38–118. *A*, Normal venous drainage of the pancreaticoduodenal veins. PV, portal vein; SV, splenic vein; PS, posterior-superior pancreaticoduodenal vein (PSPDV); PI, posterior-inferior pancreaticoduodenal vein (PIPDV); AS, anterior-superior pancreaticoduodenal vein (ASPDV); AI, anterior-inferior pancreaticoduodenal vein (AIPDV); GC, gastrocolic trunk; SMV, superior mesenteric vein. *Arrows* indicate direction of drainage of the posterior pancreaticoduodenal venous arcade. *B*, Occlusion of the confluence of the portal superior mesenteric vein (P-SMV) by advanced cancer of the pancreas. The PSPDV dilates because it is one of the hepatopetal collateral veins. *C*, Tumor extension to the right lateral wall of the P-SMV (*open arrows*) with occlusion of the PIPDV. The AIPDV, ASPDV, and gastrocolic trunk may also be occluded. The PSPDV drains blood from the posterior pancreaticoduodenal arcade and probably also from the anterior pancreaticoduodenal arcade via anastomotic branches into the portal vein. *D*, Occlusion of the PIPDV with no tumor invasion of the P-SMV. The ASPDV and AIPDV may or may not be occluded. The PSPDV drains blood from the posterior pancreaticoduodenal arcade and, when the AIPDV is occluded, also from the anterior arcade. (From Mori et al: Radiology 181:793–800, 1991.)

tertiary centers (2% to 4%) and low-volume hospitals (12% to 14%). The morbidity has diminished from 50% to 40%.[208] The most common complication is anastomotic leakage.

Whipple Procedure with Pylorus Sparing. This procedure is identical to the standard Whipple, except that pylorus is preserved to permit gastric reservoir function and a more normal gastrointestinal physiology. Patients who undergo this modified procedure have shorter operative times, reduced blood loss and fewer transfusions, comparable gastric function, and comparable survival.

Regional Pancreatectomy. This procedure consists of more extensive surgery with removal of local lymph nodes and some vein resection. The lymph nodes from the diaphragm to the level of the inferior mesenteric artery are removed, including the periaortic, portal, and perirenal lymph nodes. The limited data available do not clearly demonstrate any improvement in survival with regional pancreatectomy.

Vascular Resection. The purpose of vascular resection was to improve resection rates and rates of achievement of negative resection margins. Local involvement of venous structures is present in almost one third of cases and was the single barrier to resection in those cases. Although long-segment involvement of the portal or superior mesenteric vein is considered unresectable, isolated tumor adherence in a local site is not considered a contraindication.[73a, 94a, 146a] Repair of the resected vein can be accomplished by an end-to-end anastomosis or a vein graft. As one might expect, the resection of veins prolongs operative time and increases blood loss and need for transfusion.

Total Pancreatectomy. The rationale behind total pancreatectomy was based on theoretical advantages of eliminating multifocal disease, achieving wider resection mar-

Table 38–4. Standard Classification of Tumors of the Pancreas

Staging			
Stage I	T1	N0	M0
	T2	N0	M0
Stage II	T3	N0	M0
Stage III	Any T	N1	M0
Stage IV	Any T	Any N	M1

Primary Tumor (T)	
TX	Primary tumor cannot be assessed
T0	No evidence of primary tumor
T1	Tumor limited to the pancreas
	T1a Tumor 2 cm or less in greatest dimension
	T1b Tumor more than 2 cm in greatest dimension
T2	Tumor extends directly to the duodenum, bile duct, or peripancreatic tissues
T3	Tumor extends directly to the stomach, spleen, colon, or adjacent large vessels
Regional Lymph Nodes (N)	
NX	Regional lymph nodes cannot be assessed
N0	No regional lymph node metastasis
N1	Regional lymph node metastasis
Distant Metastasis (M)	
MX	Presence of distant metastasis cannot be assessed
M0	No distant metastasis
M1	Distant metastasis

gins, avoiding tumor cell spillage, and preventing complications of pancreatic anastomotic leak. The procedure resulted, however, in significantly higher morbidity and worse overall survival.

Distal Pancreatectomy. This procedure is less commonly discussed because (1) only 25% of tumors involve the body and tail and (2) the disease is silent and more likely present in an advanced stage. Body and tail tumors are more likely to be larger and have a higher incidence of metastatic disease. If comparable staging paramenters are present, the survival rates are similar to those of head tumors. Preservation of the spleen is not critical to survival. As one might expect, the incidence of infections, blood loss, and hospital stay are improved in patients in whom the spleen is preserved.[235]

Role of Staging by Various Modalities

Formerly, there was great controversy about the role of various modalities for imaging the pancreas. Those opinions have now converged, so there is general agreement about the use of the many techniques available.

Because ultrasonography is so ubiquitous and easily available, it has assumed the role of initial screening for the pancreas. With the new technical refinements, it is well suited to evaluate patients with upper abdominal pain in a preliminary fashion. The method is very accurate for the detection and characterization of biliary and peripancreatic disease. Dilatation of the biliary system is easily detected and assessed by ultrasonography, so the associated findings of pancreatic mass, inflammation, or calculi can be defined. When the primary problems are related to the biliary system, little additional investigation is required, because ultrasonography is so accurate for the gallbladder, the common bile duct, and the main portion of the pancreas. When a tumor is detected, however, the accurate definition of the extent, invasion, encasement, and characterization of unusual features typically must be accomplished with CT or MRI.

Positron emission tomography (PET) nuclear studies have yet to find an accepted role in the evaluation of pancreatic carcinoma. Although PET is capable of detecting generally any malignancies, its accuracy has been less than anticipated because of false-negative results in patients with hyperglycemia and false-positive results in patients with pancreatitis.[53a, 70a]

MRI has been widely studied and found to be very worthwhile for the characterization of some unusual pancreatic tumors, such as endocrine tumors and also cystic types of tumors. Only the very highest-technology MRI scanners appear to be capable of accurately characterizing anatomic detail sufficiently to permit accurate staging. One of the few studies to compare CT and MRI for the staging of cancer, by Nishiharu and colleagues,[188] reported that the thin-section, dynamic CT is more accurate with the use of a receiver operator curve (ROC) analysis for depicting local invasion into local tissues, portal veins, and peripancreatic arteries.

Even before the introduction of the new multislice scanners, the thin-slice spiral CT scans were extremely accurate as reported in the literature. With the very thin, very high-speed, isotropic scanning of the multislice scanners, the diagnostic capabilities approximate perfection.[107] Philosophically, the goal of radiologic imaging is to provide imaging that closely approximates the gross anatomic findings of the pathologists. With the new submillimeter imaging, radiology is ready to cross the next threshold into microscopic or molecular imaging.

In relation to the TNM classification for pancreatic cancer, certain imaging findings are quite straightforward, such as the visualization of lymph nodes and metastases. The evaluation of local extension and involvement of the vasculature, however, is very critical to selection of patients for curative versus palliative surgical procedures.

For the detection of liver metastases, CT is well suited, as discussed in the chapter on the liver. Specific study of the technique for the evaluation of liver metastases from pancreatic cancer has been performed by Furukawa and coworkers.[77] They studied the two major CT methods for enhancing the liver, arterial portography (CTAP) and intravenous contrast-enhanced CT (IVCT). The two approaches yielded equivalent diagnostic accuracy, indicating that the clinically more complicated method, CTAP, conferred no advantage.

General local invasion of the serosa, retroperitoneum, and vessels was evaluated by Tabuchi and colleagues relative to the phase of contrast enhancement, early or late.[247] They concluded that the early phase CT (arterial) was better than the venous or late phase for revealing tumors, tumor size, and retroperitoneal invasion.

The importance of detecting involvement of arterial invasion or encasement has been appreciated for many years. Early workers studying direct angiography were the first to observe that encasement or narrowing of the arteries was a definite indicator of inoperability (see Fig. 38–117). Early authors Megibow and colleagues[174] and Itai and associates[113] showed clearly that even with older CT devices, the detection of encasement on CT, as manifested by loss of the perivascular fat plane, was equivalent to or more accurate than standard angiography. There is therefore little question that even though the newer spiral or multislice scanners can produce aesthetically pleasing 3D images of the vasculature, the clinical significance of these methods is small.[218] Baek and associates[10] evaluated axial, 2D multiplanar, and 3D vascular CT. They reported interobserver and intraobserver errors for assessing vascular involvement to be favorable for the axial scans but very poor for the reformatted images alone. Reformatted images are worthwhile when used in conjunction with the axial scans and may on occasion be useful for revealing the major anatomic variations of the vasculature, which can affect the planning of surgical procedures. A pertinent example is the demonstration of a hepatic artery originating from the superior mesenteric artery, which might facilitate the planning of a Whipple procedure.

As the resolution of scanning devices has improved, researchers have tried to further refine the subtle variations in vascular encasement. The intent of these studies was to further define these characteristics as they related to resectability in an effort to expand the group of patients selected for curative surgical resections. The thin-section scanning techniques obviously demonstrate the perivascular fat planes better than prior methods, so a number of authors have classified the degree of encasement and correlated it with the surgical findings and resections. Lu and associates[157] graded the degree of circumferential involvement of the artery on a scale between 0 and 4: no involvement of the fat plane was 0, 0 to 25% was grade 1, 25% to 50% was grade 2, 50% to 75% was grade 3, and more than 75% was grade 4 (Fig. 38–119). Their final conclusion was that contiguity of the tumor more than one half of the arterial circumference was highly specific for unresectability. Park and colleagues[197] studied patients with encasement of vessels and looked at the length and extent of involvement as well as at the number of vessels involved. The group found that relative to judgments made at the time of surgery, a curative resection in preference to a palliative procedure was performed in patients with less than a 2-cm length of vascular involvement. Unfortunately, there were no differences in the survival between the resected and unresected groups.

The other types of vessels that must be considered when determining operability are the venous structures. The assessment of the major veins—portal, splenic, and superior mesenteric veins—can be made on either CT or MRI. Involvement of the larger veins can be determined by looking at the margin of the vessels during maximal enhancement and also at the associated formation of collaterals around the porta hepatis or the spleen. Assessment of subtle changes of the portal vein or the confluence of the portal and the superior mesenteric veins is best made with high-resolution endoscopic ultrasonography.

Involvement of the smaller peripancreatic veins provide insights about local invasion of tissues and can indicate when surgical resection is inappropriate. Yamada and associates[267] and Vedantham and colleagues[257] have noted the importance and consistency of visualizing normal veins as well as those in patients with cancer. Occlusion or narrowing of the veins by tumor produces flow of blood away from the tumor through established collateral channels. In patients who have invasion of the third portion of the duodenum, the inferior veins are occluded, producing dilatation of the more superior veins. When the second portion of the duodenum is invaded, the superior/anterior veins are likely to be included, so the more inferior veins are likely to be dilated.

Laparoscopy has recently been considered as an important adjunct after routine imaging studies and preceding surgical resection. Some workers at Massachusetts General Hospital advocate the use of laparoscopy. Warshaw and colleagues[261] recommend the use of laparoscopy and peritoneal cytology to improve the detection of peritoneal metastases. Others have shown that this approach excludes from surgery only 4% to 13% of patients whose tumors have been staged with optimal CT techniques.[203]

The simplest and most reliable factor indirectly related to favorable tumor staging is the size of lesions. Manabel and coworkers[162a] previously reported a 4-year survival of 37% for patients with a tumor smaller than 2 cm. Similarly, Pantalone and associates[194] reported that patients whose tumors were completely confined to the gland had a survival of 31%.

Unrelated to the anatomic staging as discussed here is the histologic characteristics of the various tumors. Kloppel and Maillet[134] demonstrated that patients with poorly differentiated adenocarcinoma tumor have the poorest prognosis, all of their patients having died within 15 months. Similarly, Fukushima and coworkers[75] confirmed that even in patients presenting with intraductal carcinoma, who generally have a better prognosis than those with other forms of pancreatic tumors, poorly differentiated intraductal tumors have a very high mortality; there were no survivors after 3 years in their study.

Prognosis Based on Staging. One of the most complete studies of staging and prognosis was by Freeny and others,[66] who evaluated the accuracy of CT staging relative to operative findings and also looked at the overall outcome

of their patients. They studied a series of 174 patients over a 6-year period. They judged tumors as resectable if there was an isolated pancreatic mass with or without ductal dilatation or combined pancreas–bile duct dilatation without an identifiable pancreatic mass. Tumors were judged unresectable if one or more ancillary findings of carcinoma were present, including local tumor extension, contiguous organ invasion, metastases, ascites, and vascular involvement.

Although the data in the literature about the current outcome of pancreatic carcinoma are discouraging,[32, 47, 48, 59] they clearly demonstrate that CT has a definitive role for diagnosing, staging, and predicting the outcome of surgical treatment. CT is and will be especially helpful for following the course of the disease during the development of study of new therapeutic regimens (Fig. 38–120). Further refinement of MRI may assist in these goals.

Distinguishing Between Carciuoma and Pancreatitis. Most authors agree that it is difficult to make a distinction between carcinoma and pancreatitis on the basis of imaging studies alone.[143, 148, 183] Carcinoma can coexist with pancreatitis, even though there is no proof that a close relationship exists. Kim and associates[131] reported that the intrapancreatic fibrotic changes, as visualized on enhanced CT or MRI, cannot be distinguished from carcinoma.

Several diagnostic points are helpful in distinguishing the two diseases. The most definitive method for distinguishing them is evidence for spread of malignancy, such as liver metastases or extensive local spread. Factors that

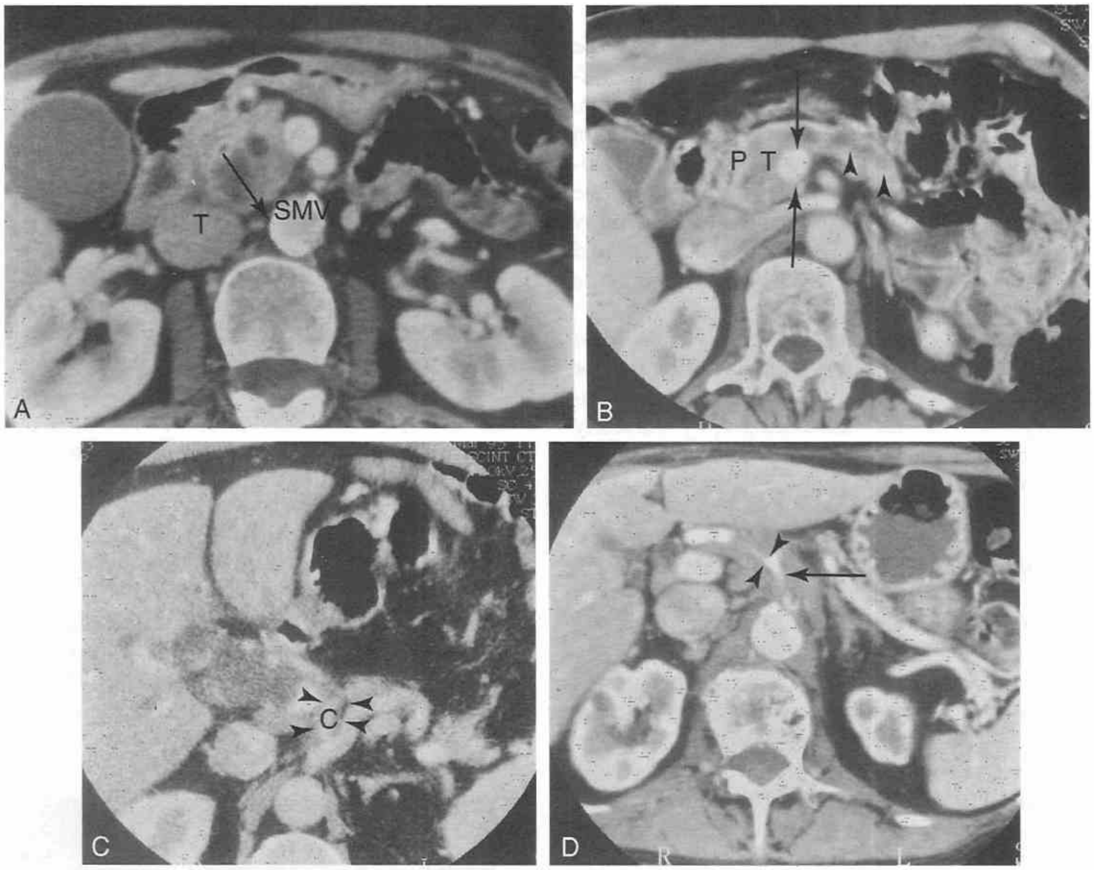

Figure 38–119. *A,* CT scan of a 67-year-old woman with grade 1 vessel involvement. Pancreatic-phase thin-section CT image of pancreatic head adenocarcinoma (T) shows minimal tumor contiguity to the superior mesenteric vein (SMV) (*arrow*). Contiguity is less than one quarter the circumference of the vessel. At surgery, the SMV was found to be free of tumor.

B, A 59-year-old woman with resectable grade 2 vessel involvement. Pancreatic-phase thin-section CT image of pancreatic head adenocarcinoma (T) shows contiguity of the tumor to the lateral wall of the superior mesenteric vein (SMV) for up to almost one half the circumference (*between arrows*). At surgery, the tumor was easily freed from the SMV. Note the marked pancreatic ductal dilatation (*arrowheads*) and normal enhancing pancreatic parenchyma (P).

C, A 62-year-old man with unresectable grade 3 vessel involvement. Pancreatic-phase thin-section CT image of the celiac axis (C) with pancreatic head and neck adenocarcinoma is shown. Note the cuff of tumor on both sides of the hepatic artery (*arrowheads*); images inferior to the slice showed main tumor bulk, and the image immediately above the slice showed no tumor cranial to the hepatic artery, indicating grade 3 involvement. Hepatic artery was adherent and unresectable at surgery.

D, A 72-year-old woman with unresectable grade 4 vessel involvement. Pancreatic-phase thin-section CT image of pancreatic neck and body adenocarcinoma reveals circumferential encasement of the celiac artery (*arrow*) as well as the hepatic artery (*arrowheads*) and proximal splenic artery.

(From Lu DSK, Reber HA, Krasny RM, et al: Local staging of pancreatic cancer. Criteria for unresectability of major vessels as revealed by pancreatic-phase, thin-section helical CT. AJR Am J Roentgenol 168:1439–1443, 1997.)

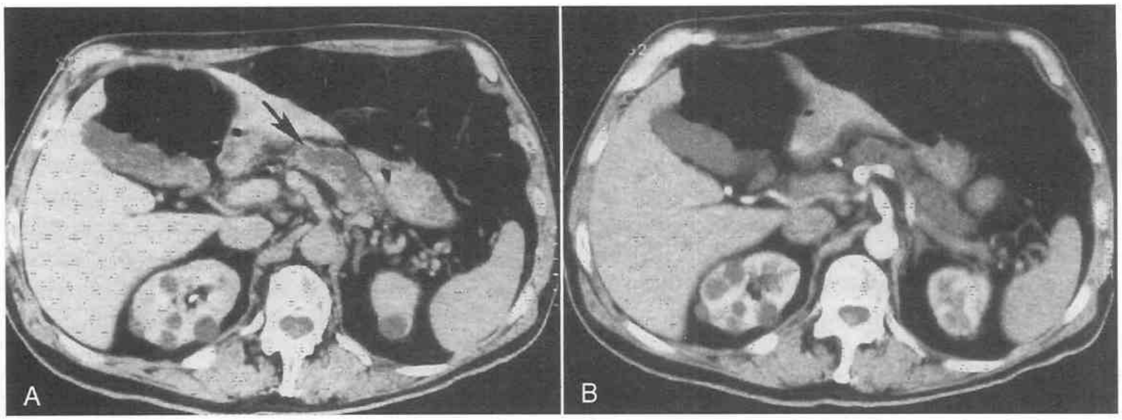

Figure 38–120. *A,* Patient with adenocarcinoma, before treatment. CT scan shows an enlarged pancreatic duct (*arrow*) that has a duct-to-gland diameter ratio less than 0.5. *B,* After chemotherapy, the pancreatic duct returned to normal size.

would support pancreatitis are not as definite but may be suggestive. Pancreatitis is also more likely to produce diffuse changes in the gland and peripancreatic inflammation. The peripancreatic findings of thickened fascia occur in almost all cases of pancreatitis and only seldom in neoplasms. The appearance of the distal dilated common bile duct and the configuration of a dilated pancreatic duct may also be helpful. It is also true that loss of fat planes around arteries occurs more commonly in neoplasm, but it may be observed occasionally in pancreatitis.

In the final analysis, no imaging system is capable of absolutely differentiating carcinoma from inflammation or benign masses in the pancreatic area. Pathologic confirmation is necessary.[90, 110] CT and ultrasonography currently provide remarkable assistance for percutaneous sampling procedures, and MRI promises to provide the same capability.

CT Combined with ERCP. Frick and associates[68] reported on patients studied by CT immediately after injection of contrast material during ERCP. The authors did not specifically alter the ERCP study to optimize the CT study in any way. They found that the normal gland demonstrated diffuse homogeneous enhancement that persisted for several minutes on CT. Areas of pancreatitis showed irregular contrast distribution, presumably resulting from duct distortion. Obliteration of the duct by neoplasms resulted in absence of "stain" on the pancreatogram and clear delineation of the mass on the CT image. This combined technique has not gained widespread support, so at this time it represents merely a historical perspective. Perhaps, however, future work with the high-resolution multislice scanners will be performed.

Squamous or Adenosquamous Carcinoma. Squamous or adenosquamous carcinoma is a rare variant with some specific differential pathologic and radiographic findings, but the outcome and prognosis are not much different from those in ordinary adenocarcinoma. In several large series, squamous or adenosquamous carcinoma occurred in less than 0.5% of all cases of carcinoma.

This carcinoma is said to occur predominantly in men. The clinical presentation and outcome are said to be no different from those in regular adenocarcinoma. The appearance is somewhat characteristic because the density of the tumor appears to be low as a result of necrosis within the mass (Figure 38–121).

Acinar Cell Tumors. Acinar cell tumors, which arise from acinar elements of the pancreas, are rare, occurring in 1% to 3% of all cases. An association with subcutaneous and intraosseous fat necrosis has occurred in only 20 cases.

Acinar cell tumors have a constellation of unique clinical signs. Symptoms are due to panniculitis or fat necrosis and consist of joint swelling, tenderness, and cutaneous nodules resembling those of erythema nodosum. Laboratory studies usually show leukocytosis, eosinophilia, and elevated lipase levels. Radiographs can show lytic areas involving medullary or cortical bone. These later changes are presumed to be due to a release of excessive amounts of lipase into the blood.

The prognosis of the disease is poor, the patient living 2 to 12 months. Most cases of the disease are not diagnosed until autopsy.

Radin and associates[209] and Lim and Ko[153] have reported cases of acinar cell carcinoma. CT showed a well-circumscribed mass with some central necrosis (Figs. 38–122 and 38–123). The unique aspect of these cases is the presence

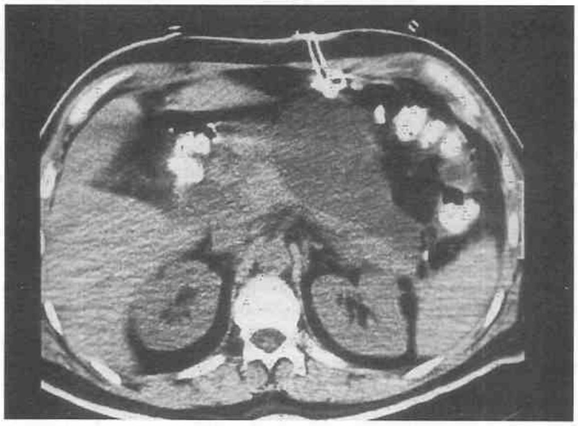

Figure 38–121. Large soft tissue mass in pancreas is low in density and had the appearance of a fluid mass. It proved to be a necrotic squamous cell carcinoma.

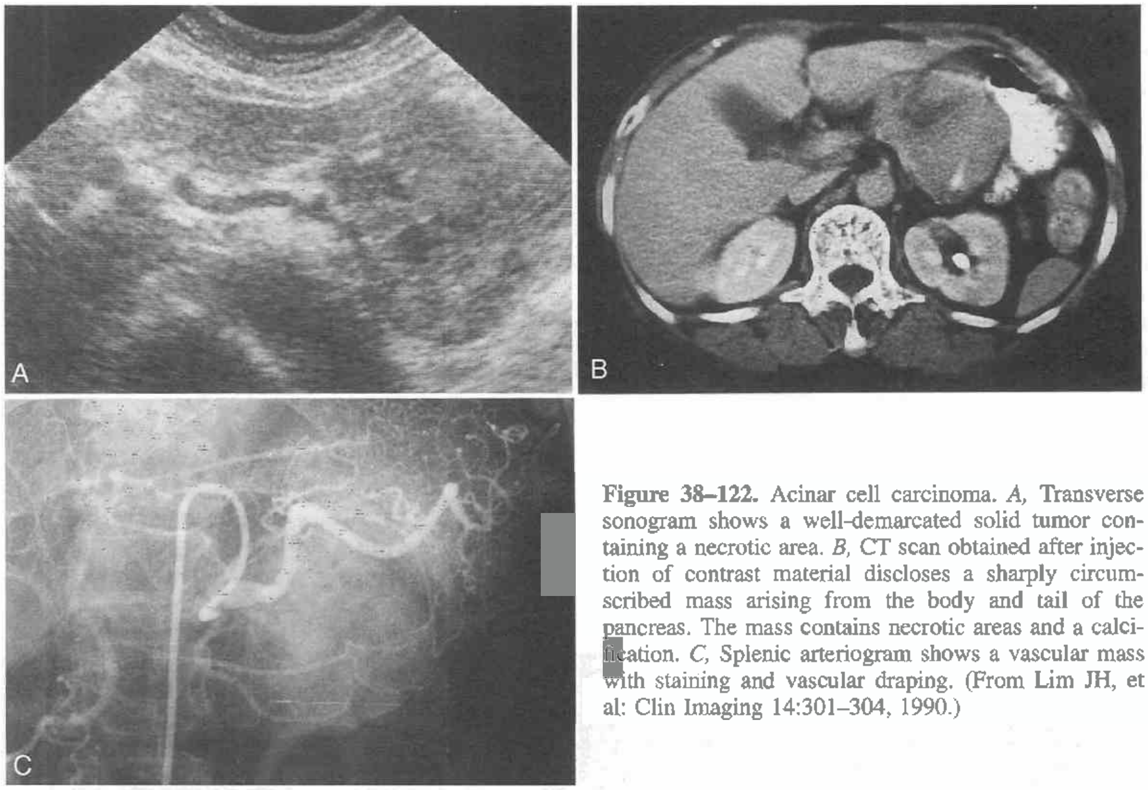

Figure 38–122. Acinar cell carcinoma. *A,* Transverse sonogram shows a well-demarcated solid tumor containing a necrotic area. *B,* CT scan obtained after injection of contrast material discloses a sharply circumscribed mass arising from the body and tail of the pancreas. The mass contains necrotic areas and a calcification. *C,* Splenic arteriogram shows a vascular mass with staining and vascular draping. (From Lim JH, et al: Clin Imaging 14:301–304, 1990.)

of a permeative lytic process, which may involve the phalanges of the hands and feet. A radionuclide bone scan also showed diffuse periarticular uptake around the peripheral joints.

Other Tumors. A variety of other tumors can arise in the pancreas from connective or lymphatic tissue, including lymphoma, fibrosarcoma, leiomyosarcoma, fibrous histiocytoma, pancreatoblastoma, lymphangioma, and plasmacytoma.[76, 193, 249, 263]

Specifically, lymphomas of the pancreas have no pathognomonic features, but Merkle and associates[177] reported several suggestive findings. They noted that adenocarcinoma of the pancreas was more likely to produce ductal dilatation than lymphoma. Lymph node involvement below the level of the renal pedicles was more characteristic of lymphoma than of adenocarcinoma.

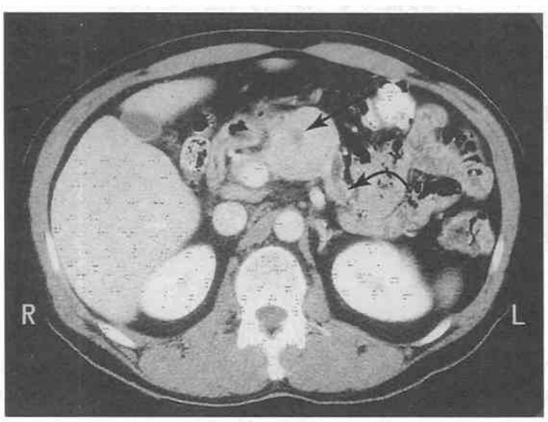

Figure 38–123. Acinar cell carcinoma. CT scan shows a well defined mass with a small area of necrosis. A dilated pancreatic duct is noted distally. (From Mustert B, et al: Appearance of acinar cell carcinoma of the pancreas on dual-phase CT. AJR Am J Roentgenol 171:709, 1998.)

Ductal and Parenchymal Cystadenoma and Cystadenocarcinoma. If one takes a long-term perspective on pancreatic tumors, it is apparent that the basic pathologic conditions and processes of pancreatic tumors have not changed but rather that our imaging capabilities have improved. The disease processes have not changed significantly, but our understanding of the various stages and presentation of these tumors has evolved. The basic purpose of radiologic imaging is and has been to display and portray the general anatomic appearance of disease processes. When imaging modalities were rather primitive with relatively poor resolution, the end-stage processes were typically displayed, and assumptions relative to those observations were made. Now that imaging devices have isotropic volume pixels and rapid data acquisition, and using the experience gained over the past 25 years, we can better understand the appearances of the cystic and mucinous tumors of the pancreas.

Review of current literature on cystic tumors reveals that a consensus has developed about these tumors. Authors note that intraductal mucinous tumors may develop in either the main duct or side duct, whereas the classic cystic mucinous tumor develops from ductal cells in the periphery of the gland without direct communication with the duct. Because the intraductal variety originates within the duct, symptoms invariably develop related to ductal obstruction, such as pain and pancreatitis, while the classic mass is

silent and without symptoms until the mass effect causes the patient to present to a physician.

Intraductal Papillary Mucinous Neoplasms. This tumor is also called mucinous ductal ectasia, ductectatic cystadenoma or cystadenocarcinoma, mucin-hypersecreting tumor, mucinous villous adenomatosis, intraductal papillary mucinous tumor, and intraductal papillary neoplasm. Intraductal papillary mucinous tumor was originally described by Itai and colleagues,[112] who noted its common occurrence in the uncinate portion of the gland. Another early author, Agostini,[1] noted that the tumor typically produced a cluster of thin-walled cysts. Although the clinical experience of these unusual tumors is somewhat limited, it is clear that they have a number of distinctive features. Accurate preoperative diagnosis is important because it has been shown that surgical treatment can have excellent outcome. The differences from the classic cystic tumor occur in the clinical presentation, site of development, and imaging appearance.

The clinical presentation of the ductal tumors differs greatly from the classic traditional cystic tumors. The tumors cause ductal obstruction, so symptoms due to pancreatitis, pain, and pancreatic insufficiency may occur. The cystic tumors are usually asymptomatic and are found incidentally at physical examination or imaging.

Fukukura and associates[74] and Grogan and colleagues[84] have best described the various imaging and clinical parameters related to this tumor (Fig. 38–124). Fukukura and associates[74] noted that the most common features in their patients were a dilated main pancreatic duct and a lobulated multilocular cystic lesion in the uncinate portion of the gland (Fig. 38–125). The dilated main pancreatic duct had certain features of importance for determining malignancy as well as characterizing the nature of the papillary component. These researchers also observed that lesions that were malignant produced dilatation of the duct greater than 10 mm and that papillary projections into the ducts could be seen on thin-section CT (Fig. 38–126).

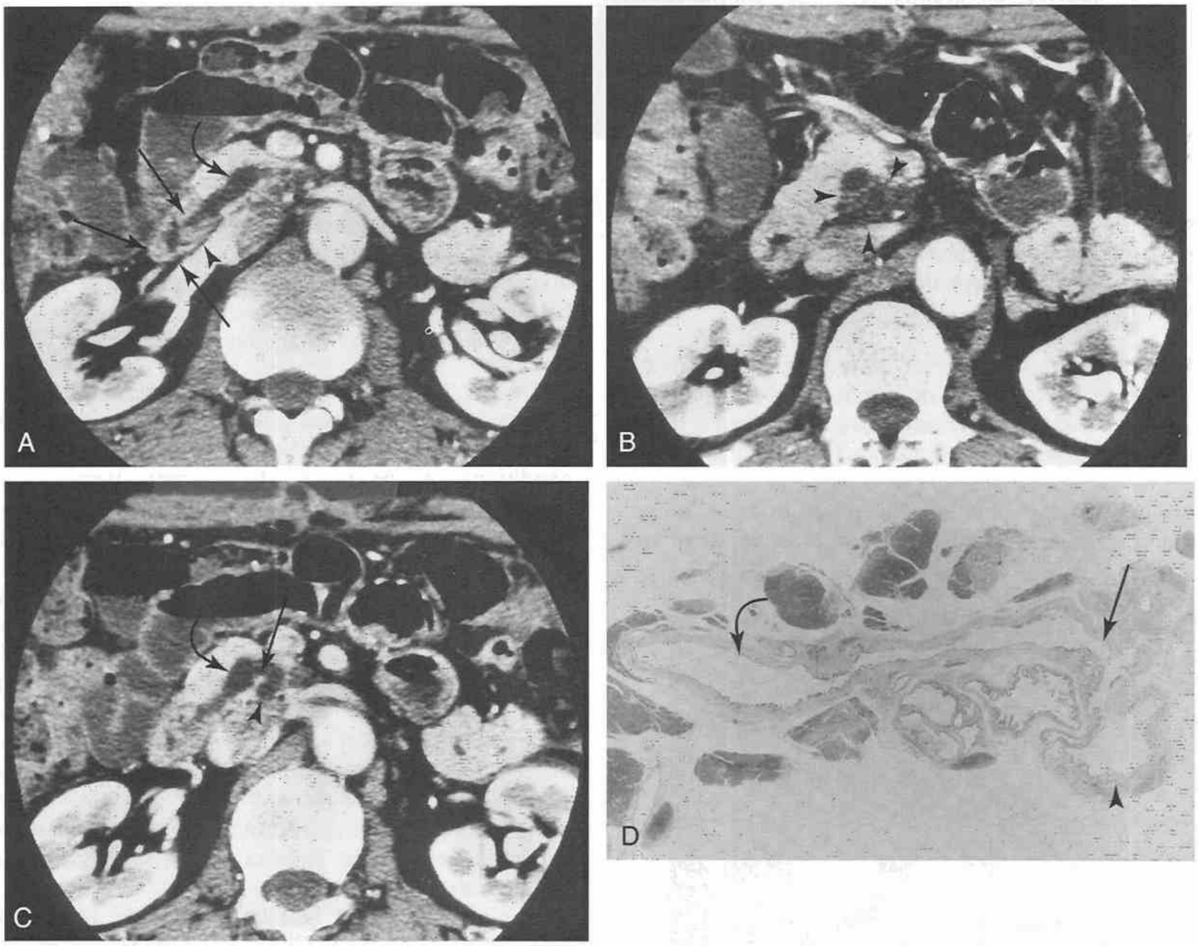

Figure 38–124. CT scan of a 68-year-old man with benign intraductal papillary mucinous tumor. *A*, Helical CT scan shows papilla (*arrowheads*) bulging into duodenal lumen (*straight arrows*). Note that papilla is contiguous with main pancreatic duct (*curved arrow*). *B*, Helical CT scan shows multilocular cystic lesion (*arrowheads*) without papillary projections in uncinate process. *C*, Helical CT scan obtained at level directly below that of *B* shows communication (*straight arrow*) between dilated main pancreatic duct (*curved arrow*) and cystic lesion (*arrowhead*). *D*, Histologic specimen shows communication (*straight arrow*) between main pancreatic duct (*curved arrow*) and cystic lesion (*arrowhead*) covered by papillary epithelium smaller than 1 mm. (H and E, ×1.) (From Fukukura Y, Fujiyoshi F, Sasaki M, et al: Intraductal papillary mucinous tumors of the pancreas: Thin-section helical CT findings. AJR Am J Roentgenol 174: 441–447, 2000.)

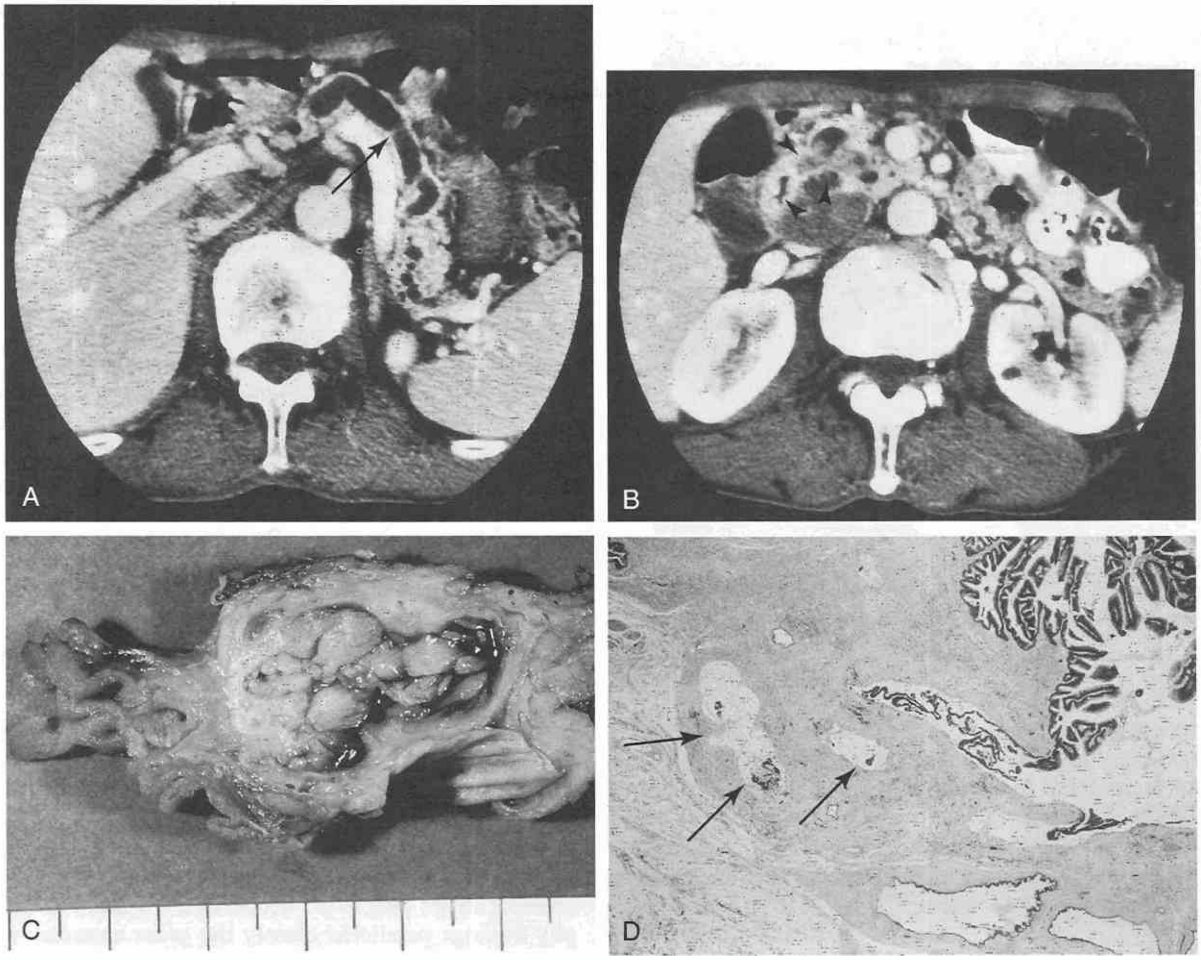

Figure 38–125. A 75-year-old man with a malignant intraductal papillary mucinous tumor. *A*, Helical CT scan shows dilatation of main pancreatic duct (*arrow*). Pancreatic parenchyma is markedly atrophic. *B*, Helical CT scan shows papillary neoplasms (*arrowheads*) as slightly heterogeneous soft tissue in dilated pancreatic duct. Invasive carcinoma in pancreatic parenchyma is not seen. *C*, Photograph of excised specimen corresponding to *B* shows dilated main pancreatic duct filled with 8-mm papillary neoplasms. *D*, Photomicrograph of histologic specimen corresponding to *B* and *C* shows invasive adenocarcinoma components (*arrows*) in pancreatic parenchyma. (H and E, ×5.) (From Fukukura Y, Fujiyoshi F, Sasaki M, et al: Interductal papillary mucinous tumors of the pancreas: Thin-section helical CT findings. AJR Am J Roentgenol 174:441–447, 2000.)

Grogan and colleagues[84] noted the classic appearance of the large defined tumors and the newly described appearances of the intraductal tumors. The typical ductal tumor may begin in the main duct, resulting in a focal unilocular mass, and may have the appearance of a pseudocyst (Figs. 38–127 and 38–128). Even if an aggressive surgical approach is taken, such tumors may progress, leading to death. When such tumors involve the side branches, the entire ductal system may become distended and have the appearance of grape clusters.

The prognosis of intraductal papillary mucinous tumors is quite good with appropriate surgical management. Cuillerier and associates[50] reported the outcome of a group of 45 cases treated with total or partial pancreatectomy. The 3-year survival was 83%. The authors recommend partial resection for noninvasive carcinoma, guided by frozen-section examination, until disease-free margins are obtained. Total pancreatectomy is likely to cure patients with invasive carcinoma, but potential morbidity and mortality should be considered.

Cystadenoma and Cystadenocarcinoma. Cystadenomas and cystadenocarcinomas are rare tumors thought to originate from the ductal epithelium. They are distinctly different in presentation, histologic appearance, imaging characteristics, treatment, and prognosis. Several terms have been applied to them, but they are divided into two types, one thought to be a benign type, called *microcystic cystadenoma* (serous cystadenoma or glycogen-rich cystic tumor), and a premalignant or malignant type, called *macrocystic cystadenoma* (mucinous cystadenoma). Patients with these tumors usually have a gradually increasing tumor mass. They may or may not have pain and weight loss.

Considerable attention has been focused on these two lesions and the methods to distinguish them. In 1962, Campbell and Cruickshank[36] observed that the two entities could be differentiated by pathologic criteria. In the benign type, they noted a relatively uniform population of cells without any evidence of malignant changes. In the malignant type, they noted a distinctly different pattern that showed malignant changes scattered throughout the tumor.

Figure 38–126. Small cystic mass (*arrow*) in the neck of the pancreas proved on histology to be a macrocystic tumor with mucinous components.

Although these researchers did not actually observe the transition in a patient, they postulated that malignant degeneration occurred in the latter type. Histologically, they found the benign tumor had cuboidal epithelium, with little secretion of mucus. The tumor with scattered changes of malignant tissue had tall, mucus-secreting epithelium and large, mucin-filled cystic spaces.

In 1978, Compagno and Oertel[45, 46] clearly defined the histologic difference between what they termed *benign microcystic* (glycogen-rich or serous) *cystadenomas* and *mucinous cystic neoplasms* (cystadenocarcinoma and cystadenoma) with overt and latent malignancy. They also noted distinct differences in the clinical data between the patients with the two distinctly different tumors.

Microcystic adenomas occur more commonly in patients 60 to 70 years old and equally in men and women. Some patients were symptomatic, with local pain or discomfort related to the mass, whereas others had no symptoms; some were tumors found incidentally at autopsy. The tumors had a mean diameter of 10.8 cm and showed small cysts with glycogen but little or no mucin. They most commonly occurred in the head of the gland. Fatalities most commonly occurred from complications of surgery or obstruction of the gastrointestinal or biliary system.

Clinical data about mucinous cystic (macrocystic) neoplasms or cystadenocarcinoma differed greatly from the microcystic tumors. Mucinous cystic neoplasms occurred in a younger group of patients, most commonly female, with mean and median ages of 49 years. The symptoms were similar to those of microcystic cystadenomas but were more diffuse and severe. Patients had epigastric pain or discomfort, with some radiation of pain to the back. They had also anorexia, weakness, and weight loss. The tumors commonly appeared in the body and tail of the pancreas. Histologically, the masses showed larger cystic areas that were lined with columnar, mucin-producing epithelium.

Imaging Appearance. Although these tumors are fairly uncommon, a considerable experience has now been reported in the literature that characterizes their imaging appearance.[18, 69, 119, 137, 196, 215]

One of the first reports, by Friedman and coworkers,[69] detailed the radiologic and pathologic correlation in 35 cases of cystic pancreatic neoplasms. CT and ultrasonography findings paralleled closely the gross anatomic appearance of the tumors. Microcystic adenomas have a mixed variety of appearances that are similar to the gross anatomic findings. CT scan with contrast enhancement showed a mixture of connective tissue and fluid density. Ultraso-

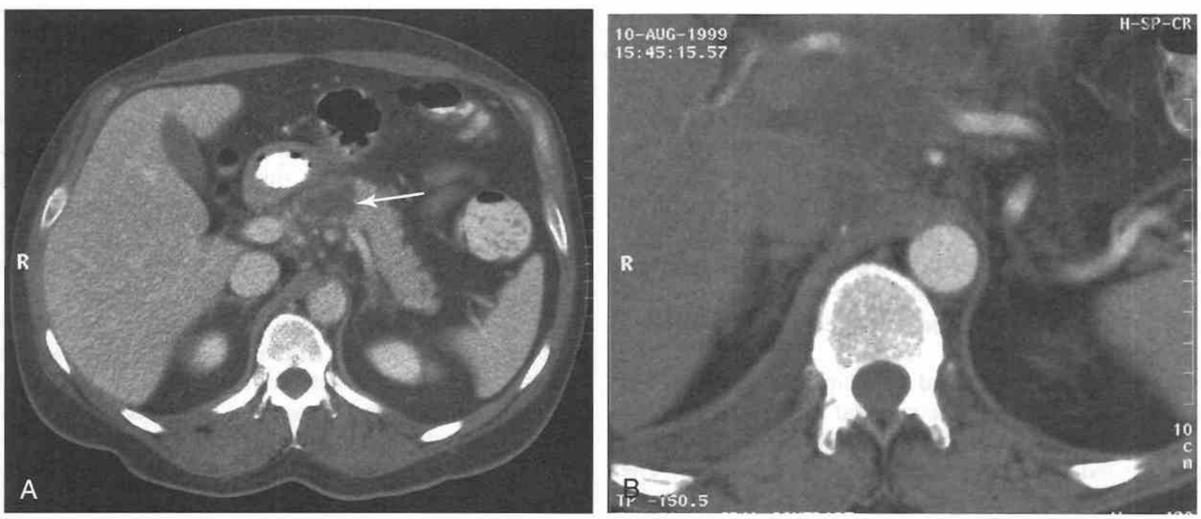

Figure 38–127. *A*, CT scan shows a cystic mass in the pancreatic head (*arrow*), which has caused adjacent atrophy of parenchyma, although the distal portion of gland is intact. Contrast this scan with that shown in Figure 38–124. Both appearances are typical variations of intraductal mucinous tumors. *B*, Later scan in same patient shows that the cystic tumor has broken through the pancreas and is invading the porta hepatis region. Tumor invasion of the fat planes around the portal and arterial structures is seen. Because such mucinous tumor is not as "hard" as the sclerotic adenocarcinoma, typical encasement of the arteries is not so prevalent.

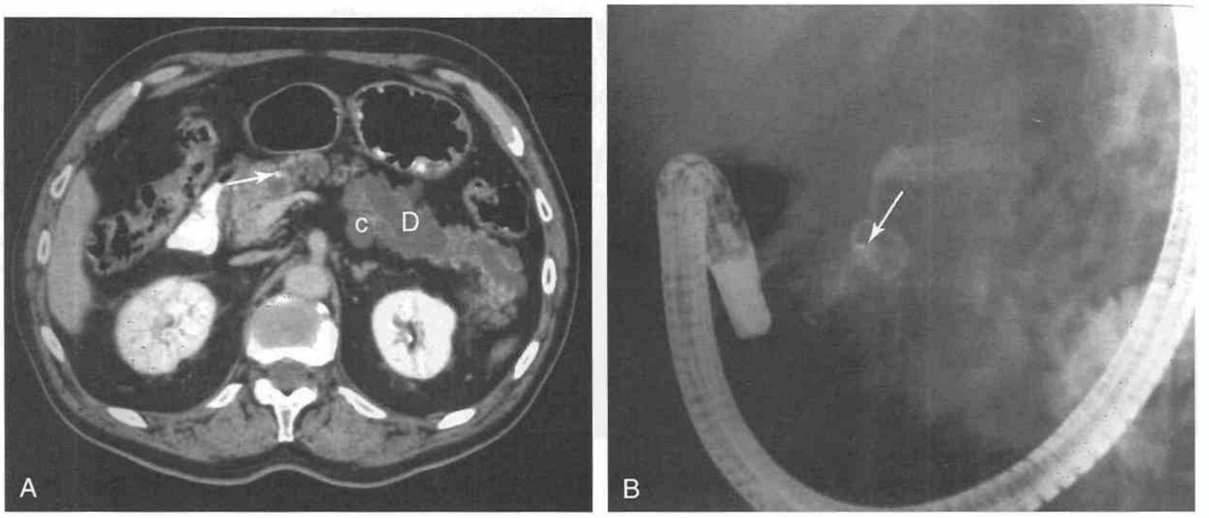

Figure 38–128. *A*, Intraductal papillary mucinous tumor of the midportion of the pancreas shows characteristic changes. There is severe dilatation of the pancreatic duct (D) with dilatation of the side branches (c), producing cystlike structures. In the head, the dilated duct, with small central calcification (*arrow*), can be seen. Dystrophic calcifications can occur in concretions of chronic mucin plugs. *B*, ERCP shows dilated pancreatic duct, with filling defect with small calcifications (*arrow*) in same patient. (*A* from Grogan JR, Saeian K, Taylor AJ, et al: Making sense of mucin-producing pancreatic tumors. AJR 176:921–929, 2001.)

nography revealed a mixed pattern; angiography showed hypervascularity. Mucinous neoplasms showed large cystic changes on CT and sonography. Both types of cystic tumors had calcifications. Other authors, including Freeny and associates[64–67] and Carroll and Sample,[38] have reported similar findings. Itai and associates[112] reported that all tumors they studied appeared cystic in nature, with the major distinction being the number and size of the cystic areas. The macrocystic (mucinous) form was said to have larger and fewer cystic areas, compared with the microcystic form. Wolfman and coworkers[266] reported several cases of the microcystic type appearing solid on the ultrasonography and CT.

Two additional studies were informative relative to the appearance of these tumors. One study, by Johnson and associates,[119] evaluated the various imaging criteria as applied by a number of blinded readers, and a second study, by Warshaw and colleagues,[261] evaluated a large series of cystic tumors and made observations concerning the clinical, radiologic, and pathologic findings.

Johnson and associates[119] studied 45 cystic tumors, which included 16 microcystic adenomas, 17 mucinous cystadenomas, and 12 mucinous cystadenocarcinomas. They evaluated the number of cysts, size of cysts, and presence of calcifications (Figs. 38–129 to 38–132). The authors concluded that one should be cautious in using imaging studies for making the diagnosis of microcystic or mucinous tumors because there is considerable overlap with pseudocysts and other tumors, such as ductal adenocarcinoma, papillary and solid epithelial neoplasms, and pancreatic lymphangiomas. They did observe that the typical appearances as described subsequently were present in 50% of the microcystic adenomas and about 90% of the mucinous cystadenomas and cystadenocarcinomas. Signs for the microcystic adenomas include multiple cysts smaller than 2 cm; the macrocystic adenomas were larger than 2 cm. Calcifications were present in both tumors.

Warshaw and colleagues[261] commented about the calcifications and noted that the calcifications were not specific. Only 2 of the 18 patients with microcystic adenomas showed the typical starburst configuration.

The latest study, by Fugazzola and coworkers,[73] reconfirmed the findings of earlier researchers on more current scanners. They noted that 7 of 11 tumors became partly or diffusely hyperdense after intravenous contrast administration compared with normal pancreatic tissue. One of their patients had a multiseptated mass with calcified walls. Calcifications were visible in three other cases. Metastases from these tumors may or may not parallel the findings of calcifications and increased vascularity.

In my experience, the described findings apply in most cases, but several points should be clarified. These tumors are vascular with good contrast enhancement. When the

Figure 38–129. Large microcystic tumors of the pancreas may demonstrate considerable enhancement, as shown here. Note that the cystic changes are so small that definition of small cystic spaces is difficult.

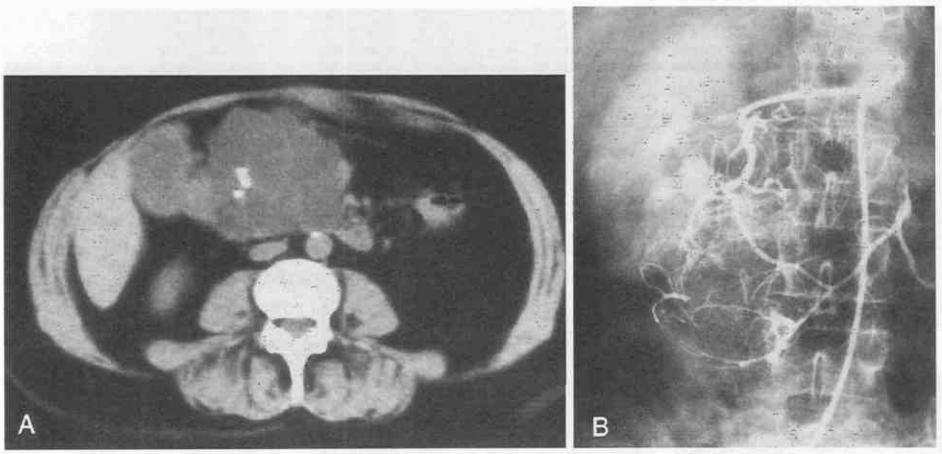

Figure 38–130. Microcystic adenoma. *A,* Plain CT scan. Large, lobulated cystic mass with foci of central calcifications. *B,* Selective angiography. Enlarged pancreatic feeding arteries from the gastroduodenal artery. (From Mathieu D, Guigui B, Valette PJ, et al: Pancreatic cystic neoplasms. Radiol Clin North Am 27:163–176, 1989.)

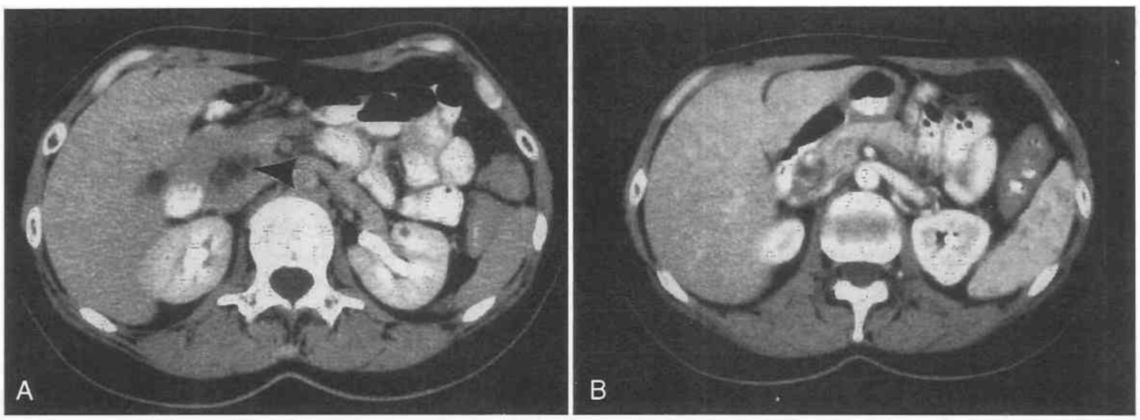

Figure 38–131. *A,* [redacted]ocystic [redacted]oma[redacted]). Low-d[redacted]ass in the head of the pancreas was appropriately resected. *B,* Dynamic scan of the[redacted] mass [redacted]s e[redacted]f the cy[redacted]r.

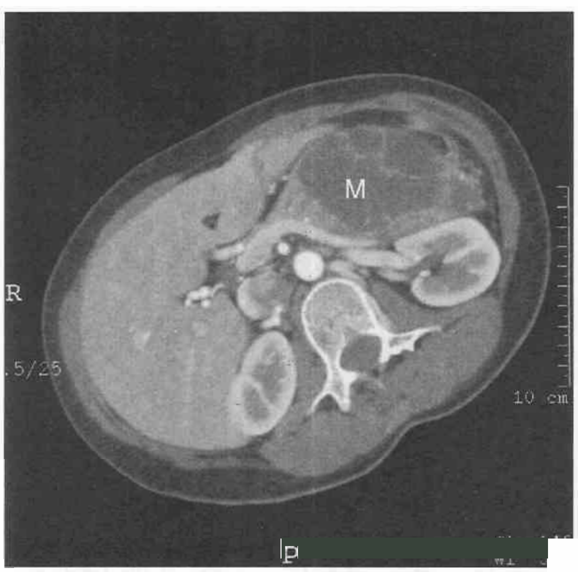

Figure 38–132. More t[redacted]l macrocyst[redacted] (M[redacted]hows a large mass in the body [redacted] pancreas, [redacted]front of [redacted]splenic vein.

tumor is small overall, it is difficult to characterize the cysts within it. Furthermore, I am convinced that imaging appearance (CT or other) is not sufficiently characteristic to differentiate the two tumor types, as some authors imply. Using the imaging traits previously listed, I saw two cases that progressed contrary to what I would have predicted. These two cases should have been classified as microcystic on the basis of the imaging appearance, yet both patients over the course of several years had growth of the tumor and subsequently died from carcinoma (Fig. 38–133). Several authors have reported on the benefits of percutaneous procedures for diagnosing the presence of cystadenocarcinoma, but even they recommend removal of the tumors regardless of the outcome of the cytologic study.[73] I believe that all tumors should be surgically removed until definitive data appear indicating that a preoperative differentiation can be made by imaging or biopsy (see Chapter 61).

Papillary Neoplasms. Papillary neoplasms (solid and papillary epithelial carcinoma, papillary carcinoma, papillary-cystic carcinoma) are unique because their surgical resection is associated with a good prognosis.[41, 70, 200] The diagnosis, however, can be difficult to make preoperatively. In one case, the patient was healthy at the end of several years, and the original diagnosis, cystadenocarcinoma, was

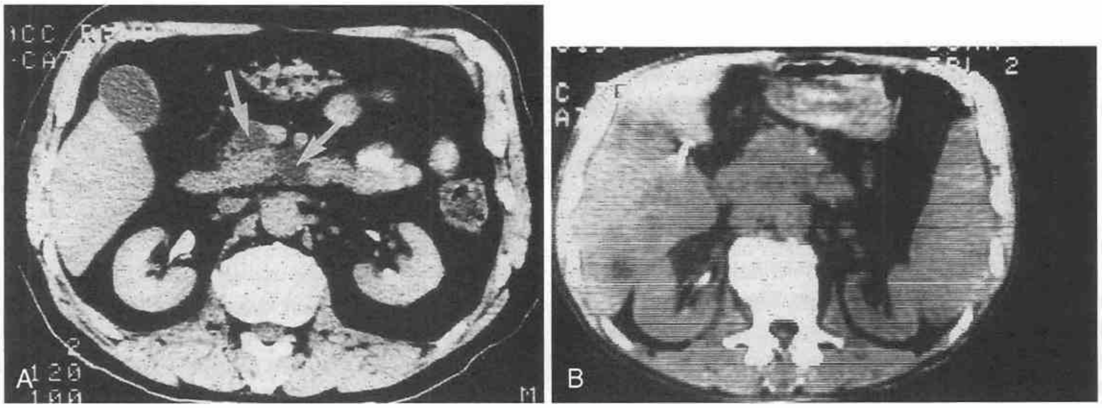

Figure 38–133. *A,* Completely asymptomatic tumor with small cysts (*arrows*) measuring less than 2 cm; the tumor should be microcystic according to the criteria in the literature. The patient refused surgery. *B,* The patient had widespread pancreatic carcinoma 6 months later (autopsy proven).

changed retrospectively to papillary carcinoma (Fig. 38–134).

Demographically and histologically, papillary neoplasms vary significantly from other tumors. They usually occur in women around 26 years of age. The symptoms are related to vague abdominal symptoms, in turn related to the large size of the tumor; papillary neoplasms have even been found incidentally during surgery for other problems.

Pathologically, these tumors lack the microacinar patterns common to islet cell tumors and contain papillae as well as cysts of different sizes. The numerous small cysts and myxoid stroma may suggest microcystic adenomas, but they lack the glycogen. The nature of these tumors is not aggressive, and they seldom metastasize; surgical removal may produce good chances for survival.

The first report of CT findings was by Balthazar and associates[14] in 1984. The characteristic CT findings were described as somewhat specific. These researchers described the papillary neoplasm as a sharply defined nonhomogeneous mass of uneven soft tissue density undergoing central necrosis. Contrast infusion produces no central enhancement and only slight peripheral enhancement. Although ill-defined cystic components should be expected, a sharply outlined, septate appearance, central scarring, or calcification would be unusual. Ultrasonography in their study showed a diffuse echogenic mass with no through transmission. Angiographically, the vessels should be displaced and stretched but not encased.

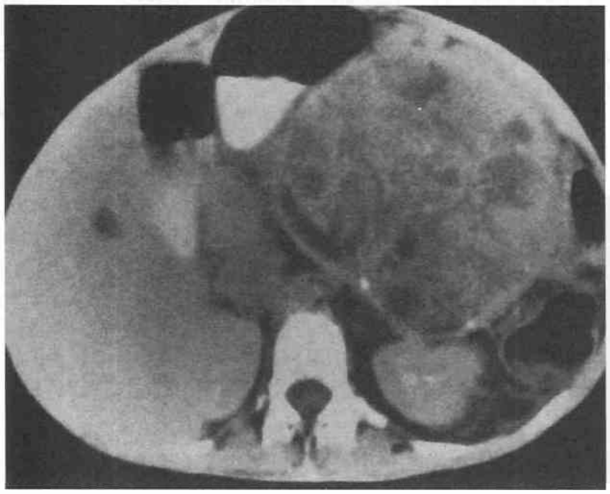

Figure 38–134. Papillary epithelial tumor. The patient has a large mass with cystic areas and a well-encapsulated margin. The true nature of this lesion was not shown until the patient survived many years and a review of the pathologic sections was made. Diagnosis was changed from cystadenocarcinoma to papillary epithelial tumor. (Courtesy of Dr. D.H. Stephens, Rochester, MN.)

Kim and coworkers[130] reported a similar appearance on CT, but the ultrasonographic findings differ from those reported by Balthazar and associates[14]: a sonolucent rather than an echogenic mass.

Friedman and associates[70] reported on nine cases from the Armed Forces Institute of Pathology, which provided imaging information on seven. The tumors were large, averaging 11.5 cm. CT showed mixed cystic-solid appearance in seven cases, and two tumors were chiefly cystic, with thick walls. In one patient, there was enhancement of the edge with contrast enhancement on CT. The exact appearance on ultrasonography was not specifically noted, the authors saying only that the findings paralleled the histologic information. Choi and coworkers[41] reported six additional cases and confirmed similar findings on CT.

Endocrine Tumors

Islet Cell Tumors. Islet cell tumors differ from neoplasms of the acinar portion of the gland because they originate in the various cell lines of the islets of Langerhans.[49] The cell types and their corresponding products according to the Lausanne classification are A cell, glucagon; B cell, insulin; D cell, somatostatin; D1 cell, vasoactive intestinal polypeptide; EC cell, 5-hydroxytryptamine; G cell, gastrin; P cell, bombesin; and PP cell, pancreatic polypeptide.[81]

Depending on the tumor's degree of function, signs and symptoms may or may not be associated with endocrine secretion. Tumors reported to cause syndromes include glucagonoma, insulinoma, gastrinoma, vipoma (watery diarrhea, hypokalemia, and anacidity), and somato-

statinoma.[81, 212] There have been reports relating to CT evaluation of these rare entities.

In addition to being isolated, these endocrine tumors can also be associated with the multiple endocrine neoplasia syndrome, specifically type I (Wermer's syndrome). Type I includes pituitary, pancreas, and parathyroid tumors; type II (Sipple's syndrome) includes thyroid, adrenal medulla, and parathyroid tumors; and type III includes thyroid, adrenal medulla, mucosal nerve, and ganglion cell tumors.[81, 255]

Nonfunctioning Islet Cell Tumors. There may be both benign and malignant islet cell tumors that do not function. Benign tumors are seldom seen because they do not produce hormones and do not grow large enough to appear as abdominal masses. The patient with malignant tumors usually has vague abdominal symptoms produced by the large size of the tumor mass.[255] It is important to differentiate these malignant tumors from the typical adenocarcinoma of acinar origin, because the prognosis and treatment vary considerably. In these tumors, special stains may demonstrate endocrine products; a clinical syndrome from excessive products may not be present.

As reported by Eelkema and associates,[55] the typical CT appearance of this mass includes three specific findings: The tumors are typically large, contain calcification, and show increased enhancement with dynamic bolus arterial studies (Figs. 38–135 and 38–136). Slight differences among the various series were noted in the size and homogeneity of the mass. Stark and colleagues[242, 243] noted calcification in only one of five cases. Eelkema and associates,[55] in a report about 27 patients, noted that the soft tissue mass could have a variable density (i.e., either homogeneous or heterogeneous); when comparison was possible, most of these tumors were isodense with the normal gland, and only a few were more or less dense than the normal gland. Finally, nonfunctioning islet cell tumors grow slowly, and they show minimal change over long periods, even years. In most cases, oncologists delay treatment until symptoms are present regardless of imaging appearance.

General Localization of Functioning Islet Cell Tumors. Although absolute localization of the endocrine-producing tumors depends on imaging methods as described subsequently, Howard and coworkers[105] have described a general localization of the various tumors. Studying their data on endocrine tumors, they found a bimodal distribution of the various tumors. In cluster 1, which included gastrinomas, pancreatic polypeptide-secreting tumors, and somatostatinomas, the tumors occurred in 75% of cases to the right of the superior mesenteric artery. In cluster 2, which included insulinomas and glucagonomas, 75% of the tumors occurred to the right of the superior mesenteric artery. These researchers further noted that the distribution paralleled the expected density of the various islet cell precursors in the gland. They finally speculated that the distribution might be a consequence of embryologic development, with cluster 1 tumors originating from the ventral bud, and cluster 2 tumors originating from the dorsal bud.

Insulinoma. When a tumor of the B cells develops, the patient usually has hypoglycemia and high serum insulin levels. Whipple's triad, a set of clinical features that should suggest the diagnosis, consists of the following findings: (1) spontaneous hypoglycemia, followed by central nervous system and vasomotor symptoms, (2) blood glucose values consistently less than 50 mg/mL, and (3) relief of symptoms by administration of glucose.

These insulin-secreting tumors are generally small and usually less than 2.0 cm in diameter.[49] In 90% of cases, they are solitary and benign, being malignant in only 10% of cases. They are multiple in 8% of cases and may present as a diffuse hyperplasia or microadenomatosis in 2% of cases. Most reports show a predilection for the head of the gland.

Because insulin produces such profound hormonal symptoms, the abnormality is usually diagnosed from clinical signs and serum hormonal assays. The role of imaging is not to diagnose the problem but rather to determine the number, location, and size of the abnormality. A variety of diagnostic methods have been used, including angiography, ultrasonography, CT, percutaneous venous sampling for hormone, and intraoperative sampling of glucose correlated with palpation. The vascular sampling techniques are usually used as a method of last resort if the other methods have failed, so are not discussed here (references are provided for additional information).

Angiography was an accurate method for detecting these

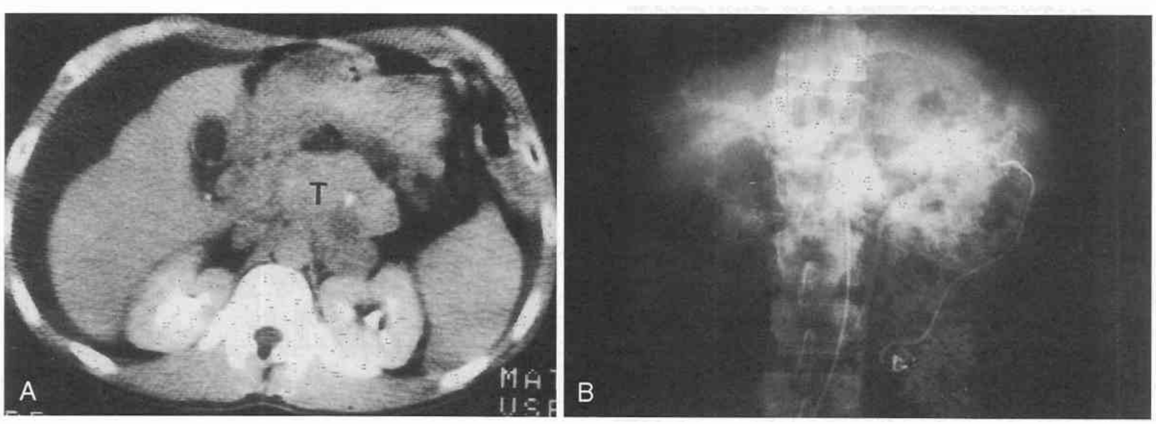

Figure 38–135. *A,* Nonfunctioning islet cell tumor (T) shows necrotic areas and calcifications. *B,* Angiogram demonstrates greater enhancement during celiac arteriogram.

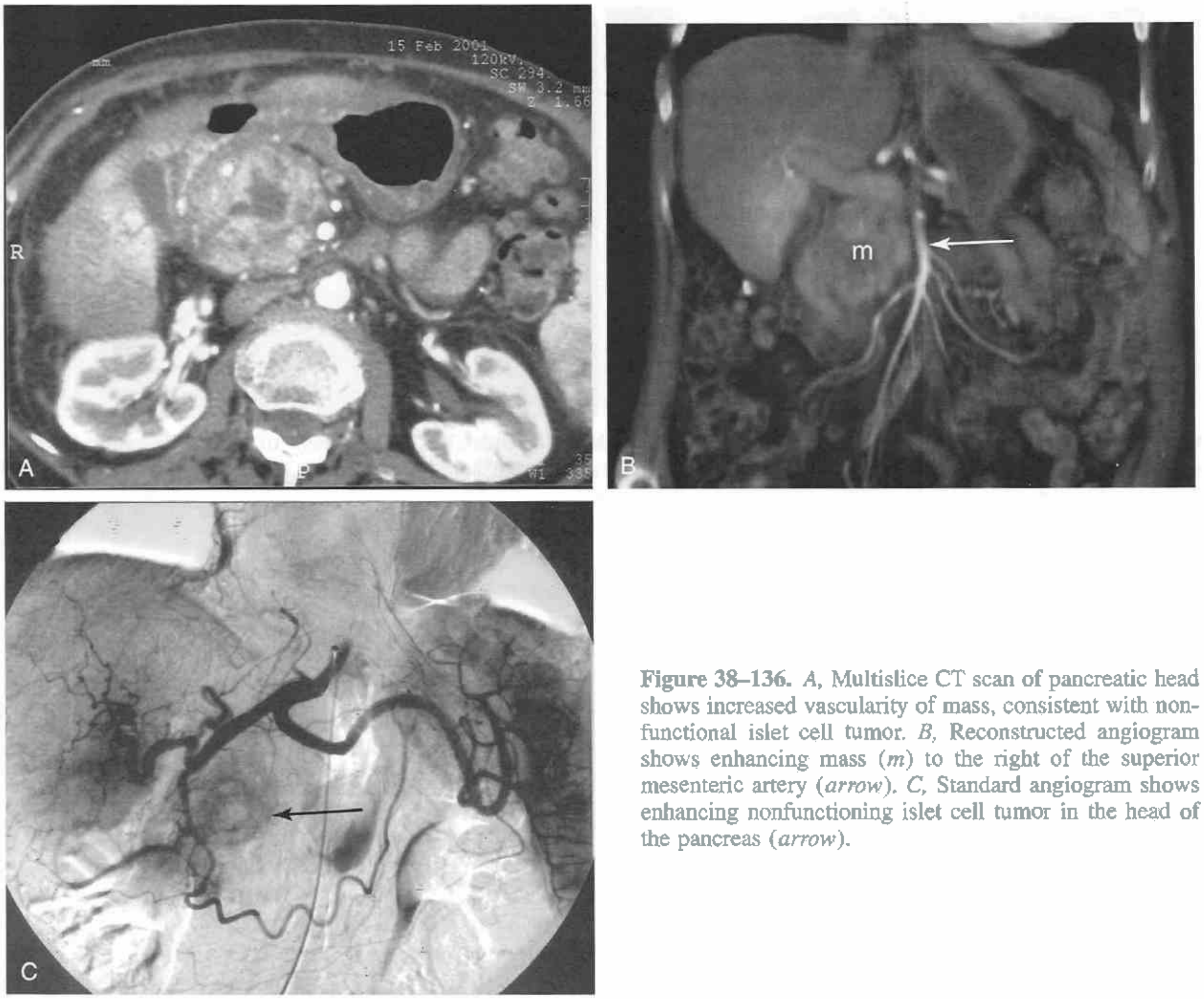

Figure 38–136. *A,* Multislice CT scan of pancreatic head shows increased vascularity of mass, consistent with nonfunctional islet cell tumor. *B,* Reconstructed angiogram shows enhancing mass (*m*) to the right of the superior mesenteric artery (*arrow*). *C,* Standard angiogram shows enhancing nonfunctioning islet cell tumor in the head of the pancreas (*arrow*).

tumors[192] before the refinement of CT and ultrasonography. Insulinomas are well suited for this method because the tumors demonstrate hypervascularity that is clearly visualized during angiographic study. Historically, angiography has been accepted as the most accurate method, with accuracy varying between 29% and 91%, but authors such as Rossi and associates[213, 214] have shown that angiography and high-quality CT scanning are essentially equivalent for the detection of insulinoma. Most authors suggest that because of the invasive nature of angiography, this study should be deferred until other diaguostic methods have been used. A combination of CT and angiography was reported by Krudy and colleagues[141] and Ahlstrom and coworkers,[2] but this method has not gained acceptance[61] because state-of-the-art scanners combined with dynamic contrast injection by mechanical injectors produce almost equivalent images.

CT scanning combined with high-dose intravenous contrast material administration by mechanical injection has been demonstrated as quite accurate for the detection of insulinomas. Numerous authors have confirmed the merits of CT for detecting this abnormality. Because these lesions tend to be small but hypervascular, the essential elements of an accurate examination include intense intravenous contrast enhancement and high-resolution scanning. Characteristically, the lesions are isodense with the normal unenhanced gland but show intense enhancement with contrast material, which may be uniform or target-like. The likelihood of detection also depends on size; tumors larger than 2 cm are detected between 90% and 100% of the time, and tumors less than 1 cm are detected with an accuracy of 45% to 50%.

Unusual findings may include small calcifications, low density,[232] or a cystic appearance. Pogany and coworkers[206] reported an unusual cystic insulinoma.

Ultrasonography. Before the development of high-quality real-time ultrasonography, detection of insulinomas by ultrasonography was unreliable. Using real-time ultrasonography, many groups have reported favorable results for detecting insulinomas preoperatively.[39, 44, 78, 80, 82, 86, 87, 211, 231] Using meticulous technique to ensure visualization of all parts of the gland, Charboneau and colleagues reported accuracies of 60% and 63%. Most insulinomas are sonolucent in appearance, but occasionally they are echogenic or isoechoic. When they are isoechoic, one can detect them by observing the presence of a sonolucent "halo" (Fig. 38–137).

Although the transabdominal method[45] is comparable to the detection rate as reported by CT, there is no question

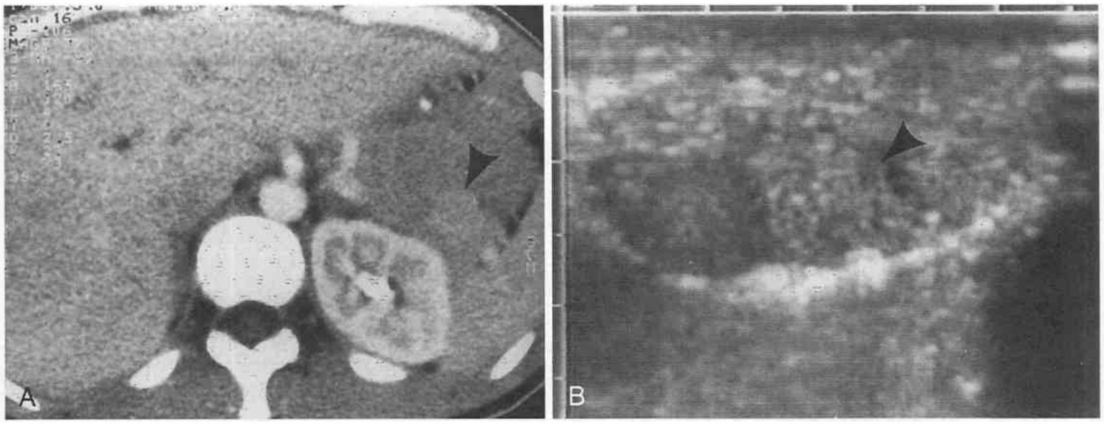

Figure 38–137. *A,* CT scan with intense contrast enhancement shows considerable enhancement of small pancreatic insulinoma. *B,* Intraoperative ultrasound scan shows small echogenic mass with hypoechoic "halo" (*arrowhead*). This procedure still has the highest detection rate, but MRI can provide accurate preoperative diagnosis.

that the experience with intraoperative ultrasonography shows superiority of that method. The accuracy for intraoperative ultrasonography varies between 86% and 100% and has been confirmed by numerous authors.[2, 80, 86, 87, 190] Although little data are available, a study by Thoeni and colleagues[254] indicates that MRI with appropriately selected pulsing sequences will become the diagnostic modality of the future (see Figs. 38–34 and 38–35). These authors, in a cohort of 28 patients, showed a specificity and positive predictive accuracy of 100%. As a preoperative method, MRI appears to be the modality of choice, because intraoperative ultrasonography will be used for final localization and surgical planning.

It is my opinion that diagnostic aspiration serves no purpose in patients with suspected endocrine tumors. The probability for a catastrophic event is high, and I believe that aspiration is not in the best interest of the patient. There has been one case report about percutaneous fine-needle aspiration performed on a patient with unsuspected insulinoma, and no problems were encountered (the lesion was "cystic"). Experience with other endocrine tumors, such as the adrenal gland, has resulted in some deaths.

Gastrinoma. Gastrinomas originate in the cells of the pancreas and are associated with a specific syndrome, known as the Zollinger-Ellison syndrome. This syndrome is associated with hypersecretion of stomach acid and associated multiple peptic ulcerations refractory to traditional treatment methods; removal of the tumor, which is the source of gastrin, is the most effective treatment.

The appearance reported in the literature is as follows: The masses are of soft tissue density and may have a heterogeneous appearance because of necrosis. The lesions are vascular with dynamic bolus scanning or arterial enhancement (Fig. 38–138). Two of nine patients in one series had calcifications.

Krudy and associates[141] reported on nine gastrinomas that were evaluated by CT, dynamic CT, angiography, venous sampling, and ultrasonography. The gastrinoma was in the pancreas in only one case; this was a 1-cm lesion in the uncinate process. In the other eight cases, the gastrinoma was in lymph nodes adjacent to the pancreas or represented a recurrence. In five cases, the lesions were near the gland. Angiography detected six of the nine cases, routine CT detected five of the nine lesions, and dynamic CT detected two additional gastrinomas. Two lesions in small lymph nodes next to the gland were not seen by any method. Routine ultrasonography detected two of the nine lesions. Percutaneous portal vein sampling was performed in three cases and was helpful in two.

Krudy and associates[141] found that all the lesions shown on dynamic scanning were demonstrated by angiography before CT (except one in the psoas muscle). Angiography was used to identify the location for the dynamic scan. Although the lesions probably could have been detected without CT, the surgeons found CT helpful in guiding the exploration. The limitation of the CT dynamic scan is that a large amount of contrast material must be used for sequential bolus injection; it is not practical to use CT in a primary study because of the number of boluses that would be required (see Fig. 38–138).

Stark and colleagues[242, 243] reported a series of nine cases of gastrinoma. They found CT to be accurate for the detection and staging of gastrinomas. CT was accurate for showing the extent of the disease; in their series, four of nine tumors were curable by surgery. Angiography detected only lesions larger than 2 cm, whereas CT detected 6 of 12 lesions smaller than 2 cm.

A report by London and coworkers[155] defines the roles of CT, ultrasonography, and angiography for detecting and staging gastrinomas. They found that ultrasonography and CT were almost equal for the detection of hepatic gastrinomas but that CT was slightly better for extrahepatic lesions. Angiography was superior to both methods for both of these areas.

Reports by Tham and associates[250, 251] discussed the merits of CT and MRI for detection of gastrinomas. They found no clear advantage of MRI over CT but also noted that MRI showed promise for future improvement. Because MRI showed increased intensity on T2-weighted images, these researchers speculated that with future refinements related to motion compensation and imaging time, MRI might prove to be the modality of choice for the future

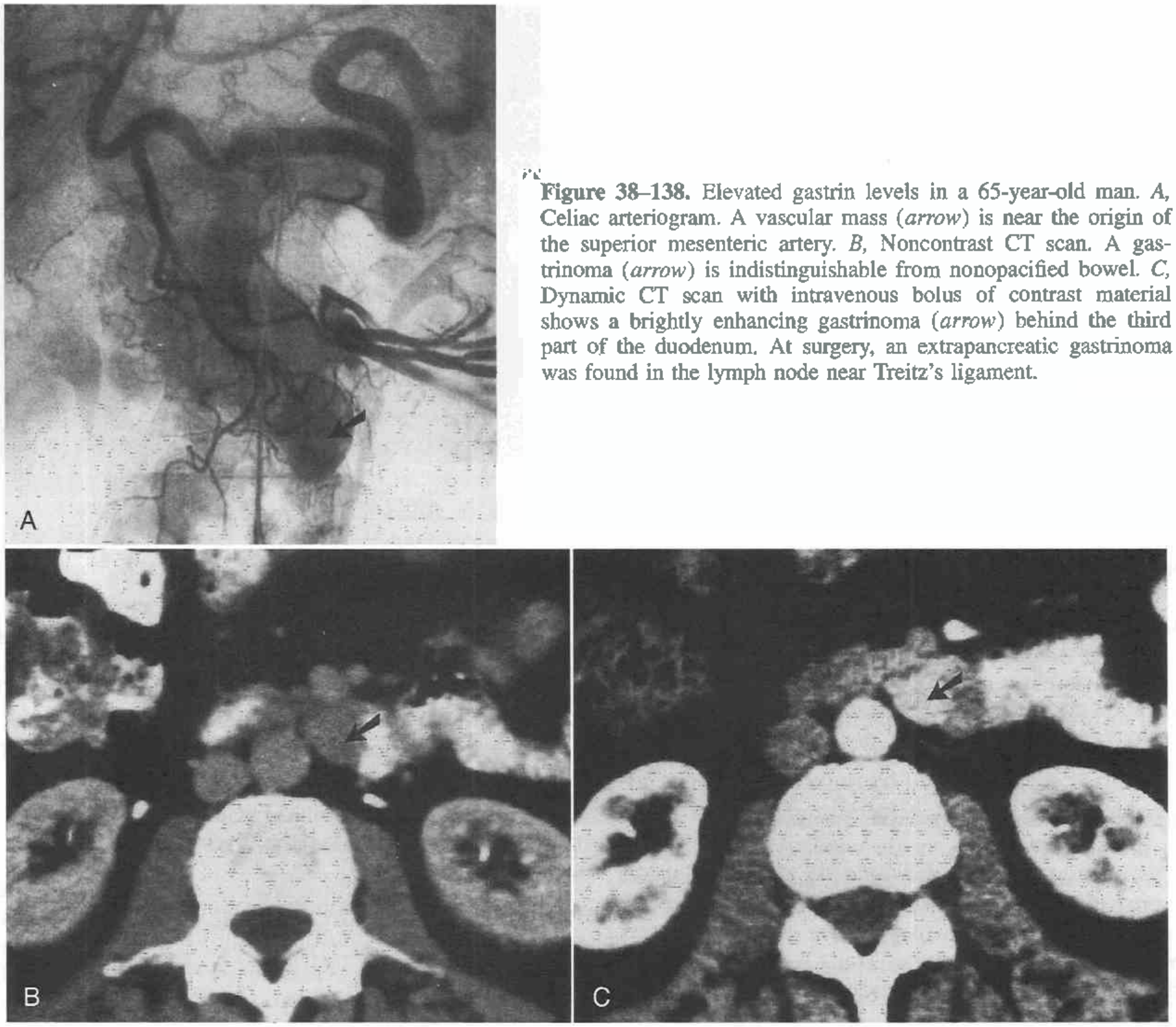

Figure 38–138. Elevated gastrin levels in a 65-year-old man. *A,* Celiac arteriogram. A vascular mass (*arrow*) is near the origin of the superior mesenteric artery. *B,* Noncontrast CT scan. A gastrinoma (*arrow*) is indistinguishable from nonopacified bowel. *C,* Dynamic CT scan with intravenous bolus of contrast material shows a brightly enhancing gastrinoma (*arrow*) behind the third part of the duodenum. At surgery, an extrapancreatic gastrinoma was found in the lymph node near Treitz's ligament.

(there were no consistent signal characteristics on T1-weighted images).

If one considers the available data, it is clear that both CT and angiography are needed for the preoperative evaluation of gastrinoma. If these methods are unsuccessful in detecting a pancreatic lesion, intraoperative ultrasonography will undoubtedly be useful for detection of small lesions.

The study by Thoeni and colleagues[254] indicates that MRI in its current, refined form will become the modality of choice for preoperative diagnosis of gastrinoma. These workers were quite successful in accurately showing gastrinomas smaller than 2 cm that were confined to the gland. Although the number of cases diagnosed by MRI is limited, it is clear that it will be the modality of choice. As with insulinomas, surgeons will continue to use intraoperative ultrasonography for final confirmation prior to resection.

Glucagonoma. Tumors of the A islet cells result in a clinical syndrome consisting of a rash, diabetes mellitus, and weight loss. When benign, the lesion may be surgically extirpated, but when malignant, it responds favorably to chemotherapeutic agents.

The largest experience reported to date has been by Breatnach and coworkers,[30] who reported on seven patients. Six cases showed histologic proof of glucagonoma, and one case clinical proof. Five of the six cases with histologic proof were malignant.

The masses varied from 2.5 to 6 cm in size. Densities of the masses were less than those of the normal gland after the administration of intravenous contrast material. In most cases, the tumors had clearly defined margins (in contrast to the infiltration of the planes that occurs with adenocarcinoma). Calcifications occurred in three of the six cases. The authors did not comment on the use of dynamic bolus scanning in these patients. All six patients underwent angiography, which demonstrated hypervascular lesions in all cases. Venous samplings were not mentioned.

Somatostatinoma. Somatostatinoma is the rarest of all islet cell tumors. Only eight cases have been reported, and only one case with CT findings. Somatostatinoma produces a hormone, somatostatin, that has some effect on insulin and glucagon that may account for diabetes. It is a direct antagonist of cholecystokinin, which inhibits gallbladder contractility. The clinical findings associated with this en-

tity are not as clearly defined as with other entities, but patients with this disorder have shown glucose intolerance and cholecystitis. Half have had diarrhea and weight loss.

The tumor size in the case reported with CT findings[212] and in the other cases was quite large, 3 to 10 cm. CT findings were nonspecific and showed only a soft tissue mass. No mention of vascularity or calcifications was made. It was the author's belief that CT should be capable of detecting such lesions because of their large size.

Vipoma. Since the previous edition of this book, there has been a single report on CT and MRI imaging of a vipoma by Tham and associates.[250, 251] They noted the tumor on CT was large, measuring 5 × 7 cm, and showed heterogeneous density with contrast enhancement. On MRI study, the tumor was isointense with T1-weighted images and hyperintense with T2-weighted images. There were no distinguishing features that would permit a preoperative diagnosis without the clinical information.

Percutaneous Biopsy. I believe that percutaneous procedures are not prudent in patients who have endocrine-secreting tumors. It is not inconceivable that a surge of endocrine products that might threaten the patient or cause a bad result could be released. An aspiration was performed without difficulty in one patient with a cystic insulinoma. The authors were not aware of the diagnosis before the procedure.

Small Bowel and Metastatic Tumors. Small bowel tumors are fairly common in the region of the third and fourth portions of the duodenum (see Fig. 38–113). In such cases, careful attention to detail is necessary to ensure proper diagnosis. Careful study of the normal anatomy around the uncinate process and Treitz's ligament enables identification of tumors in this region because of the effacement of the contrast material.

Metastatic tumors in the pancreas are not uncommon.[182, 216] The cell types that may occur include breast, lung (Fig. 38–139), colon (Fig. 38–140), gastric, renal, pulmonary, ovarian, and gallbladder tumors as well as hepatoma, melanoma, lymphoma, angiosarcoma, and leiomyosarcoma. The most frequent are lung and breast tumors and lymphoma. Gastric, colon, or renal cells can contiguously spread through the adjacent ligaments. They have no distinguishing features except, at times, extension of the tumor margins from the stomach, colon, or kidney.

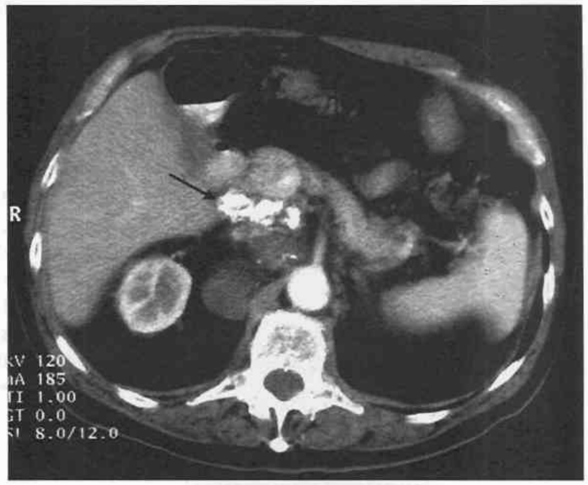

Figure 38–140. Calcified mass (*arrow*), behind the head of the pancreas, secondary to colon metastasis.

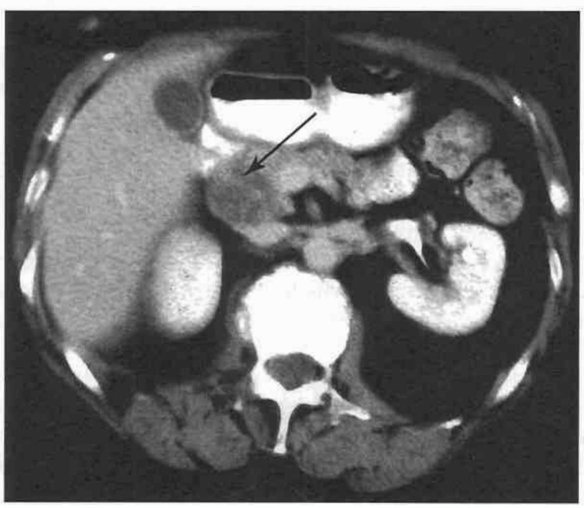

Figure 38–139. Axial CT scan shows low-density mass posterior to the head of the pancreas (*arrow*) from metastatic breast tumor.

Postoperative Evaluation

Two types of postoperative evaluation should be discussed—one for changes associated with displacement of the gland after surgery on adjacent organs and the other for changes associated with surgery on the gland itself. In most patients who undergo resection of the kidneys or the spleen, the pancreas changes location slightly, moving toward the area where the adjacent organ has been removed. Once movement has occurred, the position remains stable, and one must then simply monitor the appearance on any subsequent examinations.

After pancreatectomy, several findings can be seen, depending on the location and type of resection. Because some type of gastric bypass will have been performed, the appearance of the surgical anastomosis of the bowel must be monitored (Fig. 38–141). If the bowel is excessively motile, administration of glucagon may be needed to immobilize it, as suggested by Heiken and associates.[97]

Overall Diagnostic Accuracy

With the continued refinement of CT imaging and contrast enhancement techniques, CT scanning has continued to be the mainstay for diagnosis of pancreatic disease. In the early years of CT, considerable work was performed to compare its diagnostic accuracy with that of ultrasonography. These classic articles showed the superiority of CT.[9, 16, 124, 181]

The largest and most comprehensive study about the pancreas evaluated the diagnostic accuracy of ultrasonography and CT.[103] In this series, which included 279 patients

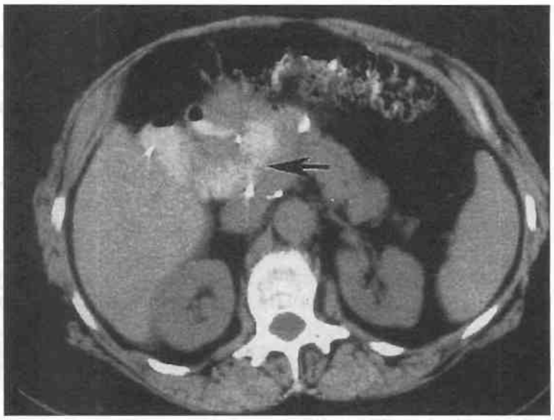

Figure 38–141. CT scan of postoperative pancreas shows dilute barium in bowel adjacent to the pancreas (*arrow*).

(146 normal and 133 abnormal pancreases), the accuracy rate was evaluated using receiver operator curves (ROCs). Hessel and colleagues[103] found that CT was more accurate than ultrasonography for determination of normal tissue, inflammation, or neoplasm. When 44 suboptimal ultrasonographic studies were excluded, CT proved to be better. In detecting a lesion as abnormal and identifying it as malignant or inflammatory, CT had a sensitivity level of 0.84 and ultrasonography a level of 0.56.

For the evaluation of inflammatory processes, CT is superior to all other modalities. It is capable of determining the full extent of inflammatory processes and the presence of complications and can indicate the need for surgical débridement when pancreatic necrosis occurs. Furthermore, with the refinement of interventional techniques, CT offers a superior guidance method for diagnosing and treating pseudocysts and inflammatory processes.

Despite the fact that CT, ultrasonography, and MRI have improved visualization of tumors, a positive effect on the outcome of pancreatic tumors has not been seen. The mortality rate and detection rate of resectable cases have not significantly changed. It does appear, however, that diagnoses are being made earlier, with fewer studies and greater ease for the patient.

In 1983, Savarino and associates[221] reviewed the outcome of two groups of tumor patients, one evaluated before and the other after the development of angiography, ultrasonography, and CT. Accuracy rates for resectable tumors were as follows for the different modalities: angiography, 85%; ERCP, 88%; ultrasonography, 73%; and CT, 81%. The sensitivity levels for unresectable tumors were as follows: angiography, 88%; ERCP, 90%; ultrasonography, 75%; and CT, 85%. There was no difference in the number of resections after the development of the newer imaging tests, but the number of exploratory laparotomies was reduced.

In a review of the outcome and staging of pancreatic neoplasms by Freeny and colleagues,[66] there was a high accuracy for detection and staging of tumors, but the outcome of the patients was uniformly poor (see earlier section on tumor staging and prognosis). It seems that for the foreseeable future, the role of imaging will be to prove inoperability of tumors to prevent needless morbidity, mortality, and expense for treating incurable patients.

Cost Efficacy

CT has decreased the role of other diagnostic tests. This, of course, translates into monetary and emotional economy for the patient and the health care system. Freeny and colleagues[65] looked at two groups of patients, one group of 278 studied before CT and the other group of 300 studied after. CT enabled the correct diagnosis without the aid of other studies in 74% of the cases. Additional studies required in the other cases are as follows: ERCP, 15%; angiography, 5%; and ERCP and angiography, 5%. The accumulative diagnostic accuracy rate, for normal tissue, pancreatitis, and neoplasm, was 99% for the pre-CT group and 97% for the post-CT group. For the post-CT group, CT reduced the use of ERCP by 68% and of angiography by 54%; there was also an overall reduction in cost of radiologic diagnosis by 47%. This was an absolute dollar-value change from $863 per case to $459.

Fine-needle biopsy combined with CT scanning has been described by Mitty and associates.[180] They evaluated the total cost for initial diagnosis and palliation of pancreatic carcinoma in patients in whom radiologic biopsy and drainage procedures were performed. They then compared it with the cost of standard surgical methods. For 53 patients, there was an overall cost savings of $169,800, mostly from avoidance of laparotomy and reduced hospitalization.

References

1. Agostini S. Mucinous pancreatic duct ectasia in the body of the pancreas. Radiology 170:815–816, 1989.
2. Ahlstrom H, Magnusson A, Grama D, et al: Preoperative localization of endocrine pancreatic tumors by intra-arterial dynamic computed tomography. Acta Radiol 31:171–175, 1990.
3. Alexander ES, Clark RA, Federle MP: Pancreatic gas: Indication of pancreatic fistula. AJR 139:1089, 1982.
4. Alfidi RJ, Evens RG, Glenn W: Special report: New indications for computed body tomography. Society for Computed Body Tomography. AJR 133:115, 1979.
5. Ammann R: Acute pancreatitis. In Bockus HL (ed): Gastroenterology, vol 3. Philadelphia, WB Saunders, 1976.
6. Andrew WK, Thomas RG: Hydatid cyst of the pancreatic tail. S Afr Med 59:235, 1981.
7. Andriole JG, Haaga JR, Bolwell BJ: Spontaneous pancreatic calcification—case report. J Comput Assist Tomogr 7:534–535, 1983.
8. Arenholz DH, Simmons RL: Fibrin in peritonitis. I. Beneficial and adverse effects of fibrin in experimental *E. coli* peritonitis. Surgery 88:41, 1980.
9. Ariyama J, Shirakabe H, Shimaguchi S, Autenrieth J: Critical comparison of methods of examination for the diagnosis of pancreatic carcinoma. ROFO 133:6, 1980.
10. Baek SY, Sheafor DH, Keogan MT, et al: Two dimensional multiplanar and three-dimensional volume-rendered vascular CT in pancreatic carcinoma: Interobserver agreement and comparison with standard helical techniques. AJR 176:1467–1473, 2000.
11. Baker ME, Cohan RH, Nadel SN, et al: Obliteration of the fat surrounding the celiac axis and superior mesenteric artery is not a specific CT finding of carcinoma of the pancreas. AJR 155: 991–994, 1990.
12. Baker MK, Kopecky KK, Wass JL: Perirenal pancreatic pseudocysts: Diagnostic management. AJR 140:729, 1983.
13. Balthazar EJ, Robinson DL, Megibow AJ, Ranson JHC: Acute pancreatitis: Value of CT in establishing prognosis. Radiology 174: 331–336, 1990.
14. Balthazar EJ, Subramanyan BR, Lefleur RS, Barone CM: Solid and papillary epithelial neoplasm of the pancreas: Radiographic, CT, sonographic, and angiographic features. Radiology 150:39, 1984.

15. Balthazar EJ, Ranson JH, Naidich DP, et al: Acute pancreatitis: Prognostic value of CT. Radiology 156:767, 1985.
16. Barkin J, Vining D, Miale A, et al: Computerized tomography, diagnostic ultrasound, and radionuclide scanning: Comparison of efficacy in diagnosis of pancreatic carcinoma. JAMA 238:2040, 1977.
17. Bartholomew LG: Hereditary and familial pancreatitis. In Bockus HL (ed): Gastroenterology, vol 3. Philadelphia, WB Saunders, 1976.
18. Bastid C, Sahel J, Sastre B, et al: Mucinous cystadenocarcinoma of the pancreas. Acta Radiol 30:45–47, 1989.
19. Baum U, Lell M, Nomayr A, et al: Multislice spiral CT for the diagnosis of pancreatic tumors. Radiologe 39:958–964, 1999.
20. Beebe DS, Bubrick MP, Onstad OR, Hitchcock GR: Management of pancreatic pseudocysts. Surg Gynecol Obstet 195:562–564, 1984.
21. Beger HG, Maier W, Block S, Buchler M: How do imaging methods influence the surgical strategy in acute pancreatitis? In Malfertheiner P, Ditschuneit H (eds): Diagnostic Procedures in Pancreatic Disease. Berlin, Springer-Verlag, 1986.
22. Berland LL, Lawson TL, Foley WD, et al: Computed tomography of the normal and abnormal pancreatic duct: Correlation with pancreatic ductography. Radiology 141:715, 1981.
23. Bittner R, Block S, Buchler M, Beger HG: Pancreatic abscess and infected pancreatic necrosis. Different local septic complications in acute pancreatitis. Dig Dis Sci 32:1082–1087, 1987.
24. Bivens BA, Sachatello CR, Chuang UP: Hemosulcus pancreaticus: Gastrointestinal hemorrhage due to rupture of a splenic artery aneurysm. Radiology 129:276, 1978.
25. Block S, Maier W, Bittner R, et al: Identification of pancreas necrosis in severe acute pancreatitis: Imaging procedures versus clinical staging. Gut 27:1035–1042, 1986.
26. Bodurtha AJ, Dajee H, You CK: Analysis of 29 cases of pancreatic pseudocyst treated surgically. Can J Surg 23:432, 1980.
27. Borlaza GS, Kuhns LR, Seigel R, et al: Computed tomographic and angiographic demonstration of gastroduodenal artery pseudoaneurysm in a pancreatic pseudocyst. J Comput Assist Tomogr 3:612, 1979.
28. Bradley EL: Management of infected pancreatic necrosis by open drainage. Ann Surg 206:542–550, 1987.
29. Bradley EL, Clements JL, Gonzalez AC: The natural history of pancreatic pseudocysts: A unified concept of management. Am J Surg 137:135, 1979.
30. Breatnach ES, Han SY, Rahatzad MT, Stanley RJ: CT evaluation of glucagonomas. J Comput Assist Tomogr 9:25, 1985.
31. Bretagne JF, Heresbach D, Darnault P, et al: Pseudoaneurysms and bleeding pseudocysts in chronic pancreatitis: Radiological findings and contribution to diagnosis in 8 cases. Gastrointest Radiol 15: 9–16, 1990.
32. Brooks JR, Culebras JM: Cancer of the pancreas: Palliative operation, Whipple procedure, or total pancreatectomy? Am J Surg 131: 516, 1976.
33. Burke JW, Erickson SJ, Kellum CD, et al: Pseudoaneurysms complicating pancreatitis: Detection by CT. Radiology 161:447, 1986.
34. Callen PW, London SS, Moss AA: Computed tomographic evaluation of the dilated pancreatic duct: The value of thin-section collimation. Radiology 134:253, 1980.
35. Callen PW, Breiman RS, Koroblum M, et al: Carcinoma of the tail of the pancreas: An unusual CT appearance. AJR 133:135, 1979.
36. Campbell JR, Cruickshank AH: Cystadenoma and cystadenocarcinoma of the pancreas. J Clin Pathol 15:432, 1962.
37. Cappeliez O, Delhaye M, Devière J, et al: Chronic pancreatitis: Evaluation of pancreatic exocrine function with MR pancreatography after secretin stimulation. Radiology 215:358–364, 2000.
38. Carroll B, Sample WF: Pancreatic cystadenocarcinoma: CT body scan and gray scale ultrasound appearance. AJR 131:339, 1978.
39. Charboneau JW, James EM, Von Heerden JA, et al: Intraoperative real-time ultrasonographic localization of pancreatic insulinoma: Initial experience. Radiology 151:853, 1984.
40. Cho KC, Lucak SL, Delany HM, et al: CT appearance in tuberculous pancreatic abscess. J Comput Assist Tomogr 14:152–154, 1990.
41. Choi BI, Kim KW, Han MC, et al: Solid and papillary epithelial neoplasms of the pancreas: CT findings. Radiology 166:413–416, 1988.
42. Choyke PL, Fillings Katz MR, Shawker TH, et al: Von Hippel–Lindau disease: Radiologic screening for visceral manifestations. Radiology 174:815–820, 1990.
43. Clavien PA, Hauser H, Meyer P, Rohner A: Value of contrast-enhanced computerized tomography in the early diagnosis and prognosis of acute pancreatitis: A prospective study of 202 patients. Am J Surg 155:457–466, 1988.
44. Clyne CAC, Greene WJ, Paisey RB: Intra-operative ultrasound localization of an insulinoma undetected pre-operatively. J Clin Ultrasound 19:419–420, 1991.
45. Compagno J, Oertel JE: Microcystic adenomas of the pancreas (glycogen-rich cystadenomas): A clinicopathologic study of 34 cases. Am J Clin Pathol 69:289, 1978.
46. Compagno J, Oertel JE: Mucinous cystic neoplasms of the pancreas with overt and latent malignancy (cystadenocarcinoma and cystadenoma): A clinicopathologic study of 41 cases. Am J Clin Pathol 69: 573, 1978.
47. Cooperman AM, Herker FP, Marboe CA, et al: Pancreatoduodenal resection (PDR) and total pancreatectomy (TP): An institutional review. Surgery 90:707–712, 1981.
48. Crile G: The advantages of bypass operations over radical pancreatoduodenectomy in the treatment of pancreatic carcinoma. Surg Gynecol Obstet 130:1049, 1970.
49. Cubilla AL, Hajdu SI: Islet cell carcinoma of the pancreas. Arch Pathol 99:204–207, 1975.
50. Cuillerier E, Cellier C, Palazzo L, et al: Outcome after surgical resection of intraductal papillary and mucinous tumors of the pancreas. Am J Gastroenterol 95:441–445, 2000.
51. Dastur KJ, Lewin JR: Computed tomography demonstration of tumor calcification after chemotherapy in a case of pancreatic carcinoma [abstract]. Radiology 143:592, 1982.
52. Dembner AG, et al: A new computed tomographic sign of pancreatitis. AJR 133:477, 1979.
53. De Sanctis JT, Lee MI, Gazelle GS, Beland GW, et al: Prognostic indicators in acute pancreatitis: CT vs APACHE II. Clin Radiol 52: 842–848, 1997.
53a. Diederichs CG, Shreve PD: Pancreatic cancer. In Wieler HJ, Coleman RE (eds): PET in Clinical Oncology. Darmstadt, Steinkop II Verlag, 2000, pp 211–224.
54. Doherty DE, Falko JM, Lefkowitz N, et al: *Pseudomonas aeruginosa* sepsis following retrograde cholangiopancreatography. Dig Dis Sci 27:169–170, 1982.
55. Eelkema EA, Stephens DH, Ward EM, Sheedy PF 2nd: CT features of nonfunctioning islet cell carcinoma. AJR 143:943, 1984.
56. Elechi EN, Callender CO, Leffall LD Jr, Kurtz LH: The treatment of pancreatic pseudocysts by external drainage. Surg Gynecol Obstet 148:707, 1979.
57. Ertman R, Hausdorf G, Landbeck G: Pancreatic sonography in thalassemia major. Klin Padiatr 195:97, 1983.
58. Federle MP, Jeffrey RB, Crass RA, Van Dalen V: Computed tomography of pancreatic abscesses. AJR 136:879, 1981.
59. Feduska MJ, Dent TL, Lindenauer SM: Results of palliative operation for carcinoma of the pancreas. Arch Surg 103:330, 1971.
60. Ferrucci JR, et al: Computed body tomography in chronic pancreatitis. Radiology 130:175, 1979.
61. Fink IJ, Krudy AG, Shawker TH, et al: Demonstration of an angiographically hypovascular insulinoma with intraarterial dynamic CT. AJR 144:555, 1985.
62. Fishman A, Isikoff MB, Barlan JS, Friedland JT: Significance of a dilated pancreatic duct on CT examination. AJR 133:225, 1979.
63. Freed KS, Paulson EK, Frederick MG, et al: Abdomen after a Puestow procedure: Postoperative CT appearance, complications, and potential pitfalls. Radiology 203:790–794, 1997.
64. Freeny PC: Portal vein tumor thrombus: Demonstration by computed tomographic arteriography. J Comput Assist Tomogr 4:268, 1980.
65. Freeny PC, Marks WM, Ball TJ: Impact of high-resolution computed tomography of the pancreas on utilization of endoscopic retrograde cholangiopancreatography and angiography. Radiology 142:35, 1982.
66. Freeny PC, Marks WM, Ryan JA, Traverso LW: Pancreatic ductal adenocarcinoma: Diagnosis and staging with dynamic CT. Radiology 166:125–133, 1988.
67. Freeny PC, Weinstein CJ, Taft DA, Allen FH: Cystic neoplasms of the pancreas: New angiographic and ultrasonographic findings. AJR 131:795, 1978.
68. Frick MP, O'Leary JP, Salomonowitz E, et al: Pancreas imaging by computed tomography after endoscopic retrograde pancreatography. Radiology 150:191, 1984.

69. Friedman AC, Lichtenstein JE, Dachman AH: Cystic neoplasms of the pancreas. Radiology 149:45, 1983.
70. Friedman AC, Lichtenstein JE, Fishman EK, et al: Solid and papillary epithelial neoplasm of the pancreas. Radiology 154:333, 1985.
70a. Frohach A, Diederichs CG, Staib L, et al: Detection of liver metastases from pancreatic cancer using FDG PET. J Nucl Med 40: 250–255, 1999.
71. Frucht H, Doppman JA, Norton JA, et al: Gastrinomas: Comparison of MR imaging with CT, angiography, and U.S. Radiology 171: 713–717, 1989.
72. Fuchs VR, Sox HC Jr: Physicians' view of the relative importance of thirty medical innovations. Health Affairs 20:30–42, 2001.
73. Fugazzola C, Procaccia C, Bergano Andreis IA, et al: Cystic tumors of the pancreas: Evaluation by ultrasonography and computed tomography. Gastrointest Radiol 16:53–61, 1991.
73a. Fuhrman GM, Leach SD, Staley CA, et al: Rationale for en bloc vein resection in the treatment of pancreatic adenocarcinoma adherent to the superior mesenteric-portal vein confluence. Ann Surg 223: 154–162, 1996.
74. Fukukura Y, Fujiyoshi F, Sasaki M, et al: Intraductal papillary mucinous tumors of the pancreas: Thin-section helical CT findings. AJR Am J Roentgenol 174:441–447, 2000.
75. Fukushima N, Sakamoto M, Mukai K, Kanai Y, et al: Intraductal papillary components in invasive ductal carcinoma of the pancreas are associated with long-term survival of patients. Hum Pathol 32: 834–841, 2001.
76. Fukuya T, Yoshimitsu K, Kitagawa S, et al: Plasmacytoma of the pancreatic head. Gastrointest Radiol 14:226–228, 1989.
77. Furukawa H, Iwata R, Moriyama N: Is CT during arterial portography useful for the preoperative evaluation of liver metastases from pancreatic carcinoma? Pancreas 22:200–202, 2001.
78. Galiber AK, et al: Pancreatic insulinoma localization: A comparison of preoperative and intraoperative US with angiography, CT and MR imaging. Scientific Program E394, presented at the Radiological Society of North America (RSNA) Conference, Chicago, 1986.
79. Gold RP, Berman H, Fakhry J, et al: Pancreas divisum with pancreatitis and pseudocyst. AJR 143:1343, 1984.
80. Gorman B, Charboneau JW, James EM, et al: Benign pancreatic insulinoma: Preoperative and intraoperative sonographic localization. AJR 147:929–934, 1985.
81. Gould V, DeLellis RA: The neuroendocrine system: Its tumors, hyperplasia, and dysplasia. In Principles and Practice of Surgical Pathology. New York, John Wiley & Sons, 1983.
82. Grant CS, van Heerden J, Charboneau JW, et al: Insulinoma: The value of intraoperative ultrasonography. Arch Surg 123:843–848, 1988.
83. Greenberg M, Greenberg RM, Rubin JM, Greenberg IM: Computed-tomographic cholangiography: A new technique for evaluating the head of the pancreas and distal biliary tree. Radiology 144:363, 1982.
84. Grogan JR, Saeian K, Taylor AJ, et al: Making sense of mucin-producing pancreatic tumors. AJR Am J Roentgenol 176:921–929, 2001.
85. Gunn GD, Gibson RN: The left-sided pancreas. Radiology 159: 713, 1986.
86. Gunther RW, Klose KJ, Ruckert K, et al: Localization of small islet-cell tumors. Preoperative and intraoperative ultrasound, computed tomography, arteriography, digital subtraction angiography and pancreatic venous sampling. Gastrointest Radiol 10:145–152, 1985.
87. Gunther RW, Klose RJ, Ruckert K, et al: Islet cell tumors: Detection of small masses with computed tomography and ultrasound. Radiology 148:485, 1983.
88. Haaga JR, Alfidi RJ: CT scanning of the pancreas. J Belg Radiol 59:281, 1976.
89. Haaga JR, Alfidi RJ: Computed tomographic scanning of the pancreas. Radiol Clin North Am 15:367, 1977.
90. Haaga JR, Alfidi RJ: Diagnostic procedures: Computed tomography. In Cooperman AM, Hoerr SO (eds): Surgery of the Pancreas. St. Louis, CV Mosby, 1977.
91. Haaga JR, Reich N: Computed Tomography of Abdominal Abnormalities. St. Louis, CV Mosby, 1978.
92. Haaga JR, Alfidi RJ, Zelch MG, et al: Computed tomography of the pancreas. Radiology 120:589, 1976.
93. Hadar H, Gadoth N, Herskovitz P, Heifetz M: Short pancreas in polysplenia syndrome. Ann Radiol 32:299–301, 1991.
94. Haertel M, Zaunbauer W, Fuchs WA: Computed tomographic morphology of pancreatic carcinoma. ROFO 133:1, 1980.
94a. Harrison LE, Klimstra DS, Brennan MF: Isolated portal vein involvement in pancreatic adenocarcinoma: A contradiction for resection? Ann Surg 224:342–349, 1996.
95. Hauer H, Battikha JG, Wettstein P: Computed tomography of the dilated main pancreatic duct. J Comput Assist Tomogr 4:53, 1980.
96. Havrilla TR: Pseudocyst of the pancreas with perirenal extension: Demonstration by computed tomography. Comput Axial Tomogr 1: 199, 1977.
97. Heiken JP, Balfe DM, Picus D, et al: Radical pancreatectomy: Postoperative evaluation by CT. Radiology 153:211, 1984.
98. Henrick AJ, Thomas CY, Friesen SR: Importance of pathologic staging in the surgical management of adenocarcinoma of the exocrine pancreas. Am J Surg 127:653, 1974.
99. Henderson JM, MacDonald JAE: Fistula formation complicating pancreatic abscess. Br J Surg 63:233, 1976.
100. Herman TE, Siegel MJ: Polysplenia syndrome with congenital short pancreas. AJR Am J Roentgenol 156:799–800, 1991.
101. Heranz-Schulman M, Teele RL, Perez-Atayde A: Pancreatic cystosis in cystic fibrosis. Radiology 158:629, 1986.
102. Hertzanu Y, Bar-Ziv J, Freund U: Computed tomography of unusual calcified pancreatic tumors. J Comput Assist Tomogr 13:75–76, 1989.
103. Hessel SJ, Siegelman SS, McNeil BJ, et al: A prospective evaluation of computed tomography and ultrasound of the pancreas. Radiology 143:129, 1982.
104. Hosoki T: Dynamic CT of pancreatic tumors. AJR 140:939, 1983.
105. Howard TJ, Stebile BE, Zinner MJ, et al: Anatomic distribution of pancreatic endocrine tumors. Am J Surg 159:258–264, 1990.
106. Hurley JE, Vargish T: Early diagnosis and outcome of pancreatic abscesses in pancreatitis. Am Surg 53:29–33, 1987.
107. Ishiguchi T, Ota T, Naganawa S, et al: CT and MR imaging of pancreatic cancer. Hepatogastroenterology 48:923–927, 2001.
108. Ishikawa T, Tsukune Y, Ohyana Y, et al: Venous abnormalities in portal hypertension demonstrated by CT. AJR 134:271, 1980.
109. Isikoff MB, Hill MC, Silverstein W, Barkin J: The clinical significance of acute pancreatic hemorrhage. AJR 136:679, 1981.
110. Isler RJ, Ferrucci JT Jr, Wittenberg J, et al: Tissue core biopsy of abdominal tumors with a 22 gauge cutting needle. AJR 136: 725, 1981.
111. Itai Y, Moss AA, Goldberg HI: Pancreatic cysts caused by carcinoma of the pancreas: A pitfall in the diagnosis of pancreatic carcinoma. Radiology 147:309, 1983.
112. Itai Y, Moss AA, Ohtomo K: Computed tomography of cystadenoma and cystadenocarcinoma of the pancreas. Radiol 145:419, 1982.
113. Itai Y, Araki Y, Tasaka A, Maruyama M: Computed tomographic appearance of resectable pancreatic carcinoma. Radiology 143:719, 1982.
114. Ivancev K, Kullendorff C-M: Value of computed tomography in traumatic pancreatitis in children. Acta Radiol [Diagn] (Stockh) 24: 441, 1983.
115. Jeffrey RB, Federle M, Crass RA: Computed tomography of pancreatic trauma. Radiology 147:491, 1983.
116. Jeffrey RB, Federle MP, Laing FC: Computed tomography of mesenteric involvement in fulminant pancreatitis. Radiology 147:185, 1983.
117. Jeffrey RB, Laing FC, Wing VW: Extrapancreatic spread of acute pancreatitis: New observations with real-time US. Radiology 159: 707, 1986.
118. Jeffrey RB, Federle MP, Cello JP, Crass RA: Early computed tomographic scanning in acute severe pancreatitis. Surg Gynecol Obstet 154:170, 1982.
119. Johnson CD, Stephens DH, Charboneau JW, et al: Cystic pancreatic tumors: CT and sonographic assessment. AJR Am J Roentgenol 151:1133–1138, 1988.
120. Johnson CD, Stephens DH, Sarr MG: CT of acute pancreatitis: Correlation between lack of contrast enhancement and pancreatic necrosis. AJR Am J Roentgenol 156:93–95, 1991.
121. Johnson PT, Outwater EK: Pancreatic carcinoma versus chronic pancreatitis: Dynamic MR imaging. Radiology 212:213–218, 1999.
122. Jordan GL, Spjut HJ: Hemorrhagic pancreatitis. Arch Surg 104: 489, 1972.
123. Juttner HU, Jenney JM, Ralls PW, et al: Ultrasound demonstration of portosystemic collaterals in cirrhosis and portal hypertension. Radiology 142:459, 1982.

124. Kamin PD, Bernardino ME, Wallace S, Jing BS: Comparison of ultrasound and computed tomography in the detection of pancreatic malignancy. Cancer 46:2410, 1980.
125. Kane RA, Katz SG: The spectrum of sonographic findings in portal hypertension: A subject review and new observations. Radiology 142:453, 1982.
126. Kaplan JO, Isikoff MB, Bakin J, Livingstone AS: Necrotic carcinoma of the pancreas: "The pseudo-pseudocyst." J Comput Assist Tomogr 4:166, 1980.
127. Karasawa E, Goldberg HI, Moss AA, et al: CT pancreatogram in carcinoma of the pancreas and chronic pancreatitis. Radiology 148: 489, 1983.
128. Kaye MD, Young SW, Hayword R, Castellino RA: Gastric pseudotumor on CT scanning. AJR 135:190, 1980.
129. Kellokumpu-Lehtinen P, Huovinen R, Tuominen J: Pancreatic cancer: Evaluation of prognostic factors and treatment results. Acta Oncol 28:481–484, 1989.
130. Kim SY, Lim JH, Lee JD: Papillary carcinoma of the pancreas: Findings of US and CT. Radiology 184:338, 1988.
131. Kim T, Murakami T, Takamura M, et al: Pancreatic mass due to chronic pancreatitis: Correlation of CT and MR imaging features with pathologic findings. AJR Am J Roentgenol 77:367–371, 2001.
132. Kivisaari L, Korman M, Rantakokko V: Contrast enhancement of the pancreas in computed tomography. J Comput Assist Tomogr 3: 772, 1979.
133. Kivisaari L, Somer K, Standertskjold-Nordenstam CG: A new method for the diagnosis of acute hemorrhagic-necrotizing pancreatitis using contrast enhanced CT. Gastrointest Radiol 9:27–30, 1984.
134. Kloppel G, Maillet B: Classification and staging of pancreatic nonendocrine tumors. Radiol Clin North Am 27:108–119, 1969.
135. Kolars JC, Allen MO, Ansel H, et al: Pancreatic pseudocysts: Clinical and endoscopic experience. Am J Gastroenterol 84:259–264, 1989.
136. Kolmannskog F, Kolbenstvedt A, Aakhus T: Computed tomography in inflammatory mass lesions following acute pancreatitis. J Comput Assist Tomogr 5:169, 1981.
137. Kolmannskog F, Schrumpf E, Valnes K: Computed tomography and angiography in pancreatic apudomas and cystadenomas. Acta Radiol [Diagn] (Stockh) 23:365, 1982.
138. Kolmannskog F, Swensen T, Vatn MH, Larsen S: Computed tomography and ultrasound of the normal pancreas. Acta Radiol [Diagn] (Stockh) 23:443, 1982.
139. Kreel L, Sandin B: Changes in pancreatic morphology associated with aging. Gut 14:952, 1973.
140. Kressel HY, Margulis AR, Gooding GW, et al: CT scanning and ultrasound in the evaluation of pancreatic pseudocysts: A preliminary comparison. Radiology 126:153, 1978.
141. Krudy AG, Doppman JL, Jensen RT, et al: Localization of islet cell tumors by dynamic and venous sampling. AJR 143:588, 1984.
142. Kusano S, Kaji T, Suglura Y, Tamai S: CT demonstration of fibrous stroma in chronic pancreatitis: Pathologic correlation. J Comput Assist Tomogr 23:297–300, 1999.
143. Lammer J, Herlinger H, Zalaudek G, Hofler H: Pseudotumorous pancreatitis. Gastrointest Radiol 10:59, 1985.
144. Lawson DW, Daggett WM, Civetta JM, et al: Surgical treatment of acute necrotizing pancreatitis. Ann Surg 4:605, 1970.
145. Lawson TL: Inflammatory disease of the pancreas: Computed tomographic evaluation. Syllabus for Society of Computed Body Tomography Meeting, Tarpon Springs, Fla, Feb. 15–18, 1982.
146. Lawson TL: Acute pancreatitis and its complications: Computed tomography and sonography. Radiol Clin North Am 21:495, 1983.
146a. Leach SD, Lee JE, Charnsangavej C, et al: Survival following pancreaticoduodenectomy with resection of superior mesenteric-portal vein confluence for adenocarcinoma of the pancreatic head. Br J Surg 85:611–617, 1998.
147. Lederman M: Personal communication, 1988.
148. Lee JKT, Stanley RJ, Melson GL, et al: Pancreatic imaging by ultrasound and computed tomography: A general review. Radiol Clin North Am 16:105, 1979.
149. Lee MJ, Saini S, Geller SC, et al: Pancreatitis with pseudoaneurysm formation: A pitfall for the interventional radiologist. AJR Am J Roentgenol 136:97–98, 1991.
150. Legg M, Khettry: The pancreas and extrahepatic biliary system. In Principles and Practice of Surgical Pathology. New York, John Wiley & Sons, 1983.
151. Levine E, Collins DL, Horton WA, Schimke RN: CT screening of the abdomen in von Hippel–Lindau disease. AJR 139:505, 1982.
152. Levitt RG, Geisse GG, Sagel SS: Complementary use of ultrasound and computed tomography in studies of the pancreas and kidneys. Radiology 126:149, 1978.
153. Lim JH, Ko YT: Clonorchiasis of the pancreas. Clin Radiol 41: 195–198, 1990.
154. Lindstrom E, Ihse I: Computed tomography findings in pancreas divisum. Acta Radiol 6:609–613, 1989.
155. London JF, Shawker TH, Doppman JL, et al: Zollinger-Ellison syndrome: Prospective assessment of abdominal US in the localization of gastrinomas. Radiology 178:763–767, 1991.
156. Long JA Jr, Doppman JL, Nienhus AW, Mills SR: Computed tomographic analysis of beta-thalassemic syndromes with hemochromatosis: Pathologic findings with clinical and laboratory correlations. J Comput Assist Tomogr 4:159, 1980.
157. Lu DSK, Reber HA, Krasny RM, et al: Local staging of pancreatic cancer: Criteria for unresectability of major vessels as revealed by pancreatic-phase, thin-section helical CT. AJR Am J Roentgenol 168:1439–1443, 1997.
158. Luetmer PH, Stephens DH, Fischer AP: Obliteration of periarterial retropancreatic fat on CT in pancreatitis: An exception to the rule. AJR Am J Roentgenol 153:63–64, 1989.
159. Luetmer PH, Stephens DH, Ward EM: Chronic pancreatitis: Reassessment with current CT. Radiology 171:383–387, 1989.
160. Madrazo BL, Halport RD, Sandles MA, Pearlberg JL: Computed tomographic findings in penetrating peptic ulcer. Radiology 103: 751, 1984.
161. Maier W: Grading of acute pancreatitis by computed tomography morphology. In Malfertheiner P, Ditschuneit H (eds): Diagnostic Procedures in Pancreatic Disease. Berlin, Springer Verlag, 1986.
162. Mailberger E, Edoute Y, Nagler A: Rare complications after transabdominal fine needle aspiration. Am J Gastroenterol 79:458–460, 1984.
162a. Manabel T, Miyashita T, Ohshio G, et al: Small carcinoma of the pancreas: Clinical and pathologic evaluation of 17 patients. Cancer 62:135–141, 1988.
163. Manfredi R, Costamagna G, Brizi MG, et al: Pancreatic divisum and "santorinicele": Diagnosis with dynamic MR cholangiopancreatography with secretin stimulation. Radiology 217:403–408, 2000.
164. Marchal G, Baert AL, Wilms G: Intravenous pancreaticography in computed tomography. J Comput Assist Tomogr 3:727, 1979.
165. Friedman AC, Markle BM, Dachman AH, et al: Anomalies and Congenital Disorders: Radiology of the Liver, Biliary Tract, Pancreas, and Spleen. Baltimore, Williams & Wilkins, 1987.
166. Marks IN, Bank S: Chronic pancreatitis, relapsing pancreatitis, calcifications of the pancreas II: Clinical aspects. In Bockus HL (ed): Gastroenterology, vol 3. Philadelphia, WB Saunders, 1976.
167. Marn CS, Glazer GM, Williams DM, Francis IR: CT-angiographic correlation of collateral venous pathways in isolated splenic vein occlusion: New observations. Radiology 175:375–380, 1990.
168. Marx M, Scheible W: Cavernous transformation of the portal vein. J Ultrasound Med 1:167, 1982.
169. Masaryk TJ, Achkar E: Pancreatitis as initial presentation of cystic fibrosis in young adults: A report of two cases. Dig Dis Sci 28: 874, 1983.
170. Mathieu D, Vasile N, Dibie C, Grenier P: Portal cavernoma: Dynamic CT features and transient differences in hepatic attenuation. Radiology 154:743–748, 1985.
171. McCain AH, Bernardino ME, Sones DJ Jr, et al: Varices from portal hypertension: Correlation with CT and angiography. Radiology 154: 63, 1985.
172. McCowin MJ, Federle MP: Computed tomography of pancreatic pseudocysts of the duodenum. AJR 154:1003, 1985.
173. McNulty NJ, Francis IR, Platt JF, et al: Multi-detector row helical CT of the pancreas: Effect of contrast-enhanced multiphasic imaging on enhancement of the pancreas, peripancreatic vasculature, and pancreatic adenocarcinoma. Radiology 220:97–102, 2001.
174. Megibow AJ, Bosniak MA, Ambos MA, Beranbaum ER: Thickening of the celiac axis and/or superior mesenteric artery: A sign of pancreatic carcinoma on computed tomography. Radiology 141: 449, 1981.
175. Mendez G Jr, Isikoff MB: Significance of intrapancreatic gas demonstrated by CT: Review of nine cases. AJR Am J Roentgenol 132: 59, 1979.

176. Mercer D, Ghent WR: Gastroduodenal artery aneurysm associated with chronic relapsing pancreatitis. Can Med Assoc J 136:1068, 1982.
177. Merkle EM, Bender GN, Brambs HJ: Imaging findings in pancreatic lymphoma: Differential aspects. AJR Am J Roentgenol 174:671–675, 2000.
178. Meyers MA, Evans JA: Effects of pancreatitis on the small bowel and colon: Spread along mesenteric planes. AJR 119:151–165, 1973.
178a. Minami M, Itai Y, Ohtomo K, et al: Cystic neoplasms of the pancreas: Comparison of MR imaging with CT. Radiology 171: 53–56, 1989.
179. Mitnick JS, Bosniak MA, Megibow AJ, et al: CT in β-thalassemia: Iron deposition in the liver, spleen, and lymph nodes. AJR 136: 1191, 1981.
180. Mitty HA, Efremidis SC, Yeh H-C: Impact of fine-needle biopsy on management of patients with carcinoma of the pancreas. AJR 137: 1119, 1981.
181. Moss AA, Federle M, Shapiro HA, et al: The combined use of computed tomography and endoscopic retrograde cholangiopancreatography in the assessment of suspected pancreatic neoplasm: A blind clinical evaluation. Radiology 134:159, 1980.
182. Muranaka T, Teshima K, Honda H, et al: Computed tomography and histologic appearance of pancreatic metastases from distant sources. Acta Radiol 30:615–619, 1989.
183. Neff CC, Simeone JF, Wittenberg J, et al: Inflammatory pancreatic masses: Problems in differentiating focal pancreatitis from carcinoma. Radiology 150:35, 1984.
184. Neumann CH, Buttner CH: Pancreatic tail pseudotumor: CT demonstration of an anatomic variation of the pancreatic tail responsible for abnormal finding on conventional radiographs and ultrasonographic abdominal examinations. [German]. Computertomographie 3:80, 1983.
185. Neumann CH, Hessel SJ: CT of the pancreatic tail. AJR 135: 741, 1980.
186. Nguyen KT, Pace R, Groll A: CT appearance of annular pancreas: A case report. J Can Assoc Radiol 40:322–323, 1989.
187. Nicholas DM, Li DK: Superior mesenteric vein rotation: A CT sign of midgut malrotation. AJR 141:707–708, 1983.
187a. Nicholson RL: Abnormalities of the perinephric fascia and fat in pancreatitis. Radiology 139:125, 1981.
188. Nishiharu T, Yamashita Y, Abe Y, et al: Local extension of pancreatic carcinoma: Assessment with thin-section helical CT versus with breath-hold FAST MR imaging—ROC analysis. Radiology 212: 445–452, 1999.
189. Nordestgaard AG, Wilson SE, Williams RA: Early computerized tomography as a predictor of outcome in acute pancreatitis. Am J Surg 152:127–132, 1986.
190. Norton JA, Shawker TH, Doppman JL, et al: Localization and surgical treatment of occult insulinomas. Am Surg 212:615–620, 1990.
191. Owens GR, Arger PH, Mulhern CB Jr, et al: CT evaluation of mediastinal pseudocyst. J Comput Assist Tomogr 4:256, 1980.
192. Paivansalo M, Makarainen H, Siniluoto T, et al: Ultrasound compared with computed tomography and pancreatic arteriography in the detection of endocrine tumours of the pancreas. Eur J Radiol 9: 173–178, 1989.
193. Pandolfo I, Sanbaro E, Gaeta M, et al: Cystic lymphangioma of the pancreas: CT demonstration. J Comput Assist Tomogr 9:209, 1985.
194. Pantalone D, Ragionieri I, Nesi G: Improved survival in small pancreatic cancer. Dig Surg 18:41–46, 2001.
195. Pantongrag-Brown L, Suwanwela N, Arjhansiri K, et al: Demonstration on computed tomography of two pseudoaneurysms complicating chronic pancreatitis. Br J Radiol 64:754–757, 1991.
196. Parienty RA, et al: Cystadenomas of the pancreas: Diagnosis by computed tomography. J Comput Assist Tomogr 4:364, 1980.
197. Park D, Lee JK, Kim JE, et al: The analysis of resectability and survival in pancreatic cancer patients with vascular invasion. J Clin Gastroenterology 32:231–234, 2001.
198. Patel S, Bellon EM, Haaga J, et al: Fat replacement of the exocrine pancreas. AJR 135:843–845, 1980.
199. Petruschak MJ, Haaga JR, Pardes JG: CT demonstration of spontaneous internal drainage of a pancreatic pseudocyst. CT 5:534, 1981.
200. Phillips GWL, Chou ST, Mulhauser J: Papillary cystic tumour of the pancreas: Findings at computed tomography and ultrasound. Br J Radiol 64:367–369, 1991.
201. Phillips HE, Cox KL, Reid MH, McGahan JP: Pancreatic sonography in cystic fibrosis. AJR 137:69, 1981.
202. Piironen A, Kivisaari R, Pitkaranta P, et al: Contrast-enhanced magnetic resonance imaging for the detection of acute haemorrhagic necrotizing pancreatitis. Eur Radiol 7:17–20, 1997.
203. Pisters PW, Lee JE, Vauthey JN, et al: Laparoscopy in the staging of pancreatic cancer. Br J Surg 88:325–327, 2001.
204. Pistolesi GF, Marzoli GP, Colosso PQ, et al: Computed tomography in surgical pancreatic emergencies. J Comput Assist Tomogr 2: 165, 1978.
205. Pochhammer KF, Szekessy T, Frentzel-Beyme B, Hollstein H: [Craniocaudad extension of the head of the pancreas]. Digit Bilddiagn 4:118, 1984.
206. Pogany AC, Kerlan RK Jr, Karam JH, et al: Cystic insulinoma. AJR 142:951, 1984.
207. Pollack EW, Michas C, Wolfman EF Jr: Pancreatic pseudocyst management in fifty-four patients. Am J Surg 135:199, 1978.
208. Poon RTP, Fan ST: The pancreas revisited II: Benign and malignant tumors—an interdisciplinary approach. Surg Clin North Am 81: 1–12, 2001.
209. Radin DR, et al: Pancreatic acinar cell carcinoma with subcutaneous and intraosseous fat necrosis. Radiology 158:67, 1986.
210. Raptopoulos V, Kleinman PK, Marks S Jr: Renal fascial pathway: Posterior extension of pancreatic effusions within the anterior pararenal space. Radiology 158:367, 1986.
211. Rifkin MD, Weiss SM: Intraoperative sonographic identification of nonpalpable pancreatic masses. J Ultrasound Med 3:409–411, 1984.
212. Roberts L Jr, Dunnick NR, Foster WL Jr, et al: Somatostatinoma of the endocrine pancreas: CT findings. J Comput Assist Tomogr 8: 1015, 1984.
213. Rossi P, Baert A, Marchal W, et al: Multiple bolus techniques: Single bolus or infusion of contrast medium to obtain prolonged contrast enhancement of the pancreas. Radiology 144:929, 1982.
214. Rossi P, Baert A, Passariello R, et al: CT of functioning tumors of the pancreas. AJR 144:57, 1985.
215. Rubin GD, Jeffrey RB, Walter JF: Pancreatic microcystic adenoma presenting with acute hemoperitoneum: CT diagnosis. AJR 156: 749–750, 1991.
216. Rumancik WM, Megibow AJ, Bosniak MA, et al: Metastatic disease to the pancreas: Evaluation by computed tomography. J Comput Assist Tomogr 8:829, 1984.
217. Sagalow BR, Miller CL, Wechsler RJ: Pancreatic sarcoidosis mimicking pancreatic cancer. J Clin Ultrasound 16:131–134, 1988.
218. Saldinger PF, Reilly M, Reynolds K, et al: Is CT angiography sufficient for prediction of resectability of periampullary neoplasms? J Gastrointest Surg 4:233–237; discussion 238–239, 2000.
219. Sandy JT, Taylor RH, Christensen RM, et al: Pancreatic pseudocyst: Changing concepts in management. Am J Surg 14:574, 1981.
220. Sarles H, Payan H, Tasso F, et al: Chronic pancreatitis, relapsing pancreatitis, calcifications of the pancreas. I: Pathology. In Bockus HL (ed): Gastroenterology, vol 3. Philadelphia, WB Saunders, 1976.
221. Savarino V, Masi C, Bistolfi L, et al: Failure of new diagnostic aids in improving detection of pancreatic cancer at a resectable stage. Dig Dis Sci 28:1078, 1983.
222. Schmidt H, Creutzfeldt W: Etiology and pathogenesis of pancreatitis. In Bockus HL (ed): Gastroenterology, vol 3. Philadelphia, WB Saunders, 1976.
223. Schulte SJ, Baron RL, Freeny PC, et al: Root of the superior mesenteric artery in pancreatitis and pancreatic carcinoma: Evaluation with CT. Radiology 180:659–662, 1991.
224. Semelka RC, Kroeker MA, Shoenut JP, et al: Pancreatic disease: Prospective comparison of CT, ERCP, and 1.5-T MR imaging with dynamic gadolinium enhancement and fat suppression. Radiology 181:785–791, 1991.
225. Sheedy PF II, Stephens DH, Hattery RR, MacCarty RL: Computed tomography in the evaluation of patients with suspected carcinoma of the pancreas. Radiology 124:731, 1977.
226. Sheflin JR, Lee CM, Kretchmar KA: Torsion of wandering spleen and distal pancreas. AJR 142:100, 1984.
227. Shirkhoda A, Mittel Staedt CA: Demonstration of pancreatic cysts in adult polycystic disease by computed tomography and ultrasound. AJR 131:1074, 1978.
228. Shultz S, Drury EM, Friedman AC: Common hepatic artery aneurysm: Pseudopseudocyst of the pancreas. AJR 144:1287, 1985.
229. Sica GT, Braver J, Cooney MJ, et al: Comparison of endoscopic

retrograde cholangiopancreatography with MR cholangiopancreatography in patients with pancreatitis. Radiology 210:605–610, 1999.
230. Siegelman SS, et al: CT of fluid collections associated with pancreatitis. AJR 134:1121, 1980.
231. Sigel B, Copeland BE, Saba GP, et al: Localization of insulinomas of the pancreas at operation by real-time ultrasound scanning. Surg Gynecol Obstet 156:145–147, 1983.
232. Smith TR, Koenigsberg M: Low-density insulinoma on dynamic CT. AJR 155:995–996, 1990.
233. Soulen MC, Zerhouni EA, Fishman EK, et al: Enlargement of the pancreatic head in patients with pancreas divisum. Clin Imag 13: 51–57, 1989.
234. Soulen MC, et al: Pancreatic divisum: CT scanning and ERCP correlation. Radiology 161:145, 1986.
235. Spanknebel K, Kevin CP, Conlon MD: Advances in the surgical management of pancreatic cancer. Cancer J 7:312–323, 2001.
236. Spencer JA, Lindsell DRM, Isaacs D: Hereditary pancreatitis: Early ultrasound appearances. Pediatr Radiol 20:293–295, 1990.
237. Stambler JB, et al: Tuberculous abscess of the pancreas. Gastroenterology 83:922, 1982.
238. Stanley J: Splanchnic aneurysms. In Rutherford RB (ed): Splanchnic Artery Aneurysms. Philadelphia, WB Saunders, 1977.
239. Stanley P: Portal hypertension. In Stanley P, Miller J (eds): Pediatric Angiography. Baltimore, Williams & Wilkins, 1982.
240. Stanley RJ, Sagel SS, Levitt RG: Computed tomography evaluation of the pancreas. Radiology 124:715, 1977.
241. Stanten R, Frey CF: Comprehensive management of acute necrotizing pancreatitis and pancreatic abscess. Arch Surg 125:1269–1275, 1990.
242. Stark DD, Moss AA, Goldberg HJ, Deveney CW: CT of pancreatic islet cell tumors. Radiology 150:491–494, 1984.
243. Reference deleted.
244. Steiner E, Stark DD, Hahn IF, et al: Imaging of pancreatic neoplasms: Comparison of MR and CT. AJR 152:487–491, 1989.
245. Steckman ML, Dooley MC, Jaques PF, Powell DW: Major gastrointestinal hemorrhage from peripancreatic blood vessels in pancreatitis: Treatment by embolotherapy. Dig Dis Sci 29:486, 1984.
246. Susman N, Hammerman AM, Cohen E: The renal halo sign in pancreatitis. Radiology 142:323, 1982.
247. Tabuchi T, Itoh K, Ohshio G, et al: Tumor staging of pancreatic adenocarcinoma using early- and late-phase helical CT. AJR Am J Roentgenol 73:375–380, 1999.
248. Tamm E, Chusilp C: Pancreatic cancer: Current concepts in imaging for diagnosis and staging. Cancer J 7:298–311, 2001.
249. Teefey SA, Stephens DH, Sheedy PF II: CT appearance of primary pancreatic lymphoma. Gastrointest Radiol 11:41, 1986.
250. Tham RTOTA, Falke THM, Jansen JBM, Lamers CBHW: CT and MR imaging of advanced Zollinger-Ellison syndrome. J Comput Assist Tomogr 13:821–828, 1989.
251. Tjon A, Tham RT, Jansen JB, et al: MR, CT, and ultrasound findings of metastatic vipoma in pancreas. J Comput Assist Tomogr 13: 142–144, 1989.
252. Tham RTOTA, et al: Cystic fibrosis: MR imaging of the pancreas. Radiology 179:183–186, 1991.
253. Thoeni RF, Fell SC, Goldberg HI: CT detection of asymptomatic pancreatitis following ERCP. Gastrointest Radiol 15:291–295, 1990.
254. Thoeni RF, Ullrich G, Mueller-Lisse, et al: Detection of small, functional islet cell tumors in the pancreas: Selection of MR imaging sequences for optimal sensitivity. Radiology 214:483–490, 2000.
255. Tisell LE, Ahlman H: Treatment of the pancreatic disease of multiple endocrine neoplasia type 1 (MEN 1). Acta Oncol 28:415–417, 1989.
256. Torres WE, Clements JL Jr, Sones PJ, Knopf DR: Gas in the pancreatic bed without abscess. AJR 137:1131, 1981.
257. Vedantham S, Lu DSK, Reber HA, Kadell D: Small peripancreatic veins: Improved assessment in pancreatic cancer patients using thin-section pancreatic phase helical CT. AJR 377–383, 1998.
258. Vernacchia FS, Jeffrey RB Jr, Federle MP, et al: Pancreatic abscess: Predictive value of early abdominal CT. Radiology 162:435–438, 1987.
259. Ward E, Stephens DH, Sheedy PF II: Computed tomographic characteristics of pancreatic carcinoma: Analysis of 100 cases. Radiographics 3:547, 1983.
260. Warren KW: Chronic pancreatitis, relapsing pancreatitis, calcifications. III. Surgery. In Bockus HL (ed): Gastroenterology, vol 3. Philadelphia, WB Saunders, 1976.
261. Warshaw AL, Compton CC, Lewandrowski K, et al: Cystic tumors of the pancreas: New clinical radiologic and pathologic observations in 67 patients. Ann Surg 212:432–445, 1990.
262. White EM, Wittenberg J, Mueller PR, et al: Pancreatic necrosis: CT manifestations. Radiology 158:343, 1986.
263. Wilson TE, Korobkin M, Francis IR: Pancreatic plasmacytoma: CT findings. AJR 152:1227–1228, 1989.
264. Silverstein W, Isikoff MB, Hill MC, Barkin J: Diagnostic imaging of acute pancreatitis: Prospective study using CT and sonography. AJR 137:497, 1981.
265. Wittenberg J, Simeone JF, Ferruca JT Jr, et al: Non-focal enlargement in pancreatic carcinoma. Radiology 144:131, 1982.
266. Wolfman NT, Karstaedt N, Kawamoto EH: Pleomorphic carcinoma of the pancreas: Computed-tomographic, sonographic, and pathologic findings. Radiology 154:329, 1985.
267. Yamada Y, Mori H, Kiyosue H, et al: CT assessment of the inferior peripancreatic veins: Clinical significance. AJR 174:677–684, 2000.
268. Yuh WTC, Hunsicker LG, Nghiem DD, et al: Pancreatic transplants: Evaluation with MR imaging. Radiology 170:171–177, 1989.
269. Zakari S, Ajani A, Dhobb OH: Ultrasonographic features of hydatid cyst of the pancreas: Report of 2 cases. Radiology 156:266, 1985.
270. Zeman RK, McVay LV, Silverman PM, et al: Pancreas divisum: Thin-section CT. Radiology 169:395–398, 1988.

39 The Spleen

Dean A. Nakamoto, Raymond P. Onders

The spleen can be evaluated well with current cross-sectional imaging modalities. The primary imaging technique is computed tomography (CT), although magnetic resonance imaging (MRI) continues to improve. Ultrasonography is also frequently utilized, although it has limitations because of the subcostal location of the spleen and adjacent bowel gas. The advantages of CT are that it is readily available and that it allows concurrent evaluation of the other abdominal and pelvic organs.

Techniques of Examination

Current CT imaging utilizes helical scanning during a single breath-hold and intravenous (IV) administration of a contrast agent. Typically, 400 mL of dilute water-soluble oral contrast (2% to 5%) is given 30 to 40 minutes prior to the study. A mechanical injector and an angiocatheter at least 20 gauge, 100-mL bolus of nonionic contrast agent (Optiray 240 [ioversol 51%]) is administered at a rate of 2 to 3 mL/sec. Scanning is performed 45 seconds after the bolus is given. This approach typically provides uniform enhancement of the spleen and enhancement of the liver during the portal venous phase. Routine images are acquired at 8-mm intervals with a pitch of 1:1 to 1:1.5. Occasionally, thin-section images can be obtained at 4- to 5-mm intervals. For any patient being evaluated for trauma, delayed scans taken 2 to 3 minutes after the bolus often help exclude lacerations of the spleen or other organs.

MRI Protocol

Because of continuing advances in MR technology, we are always refining our MRI protocols. Our current protocol for imaging the spleen, which we also use to image the liver, is as follows. After acquiring multiplanar gradient echo localizing images, we perform following breath-hold sequences:

1. Coronal multi-slice two-dimensional (2D) HASTE (half-Fourier acquisition single-shot turbo spin-echo) sequence (TR = 4.4 msec, TE = 90 msec, NEX = 1, flip angle (FA) = 130 degrees, ST = 6 mm, matrix = 176 × 256, TA = 22 sec).
2. Axial multi-slice, turbo spin-echo, T2-weighted sequence (TR = 5130 msec, TE = 138 msec, NEX = 1, FA = 180 degrees, ST = 6 mm, matrix = 116 × 256, TA = 26 sec) with and without fat saturation.
3. Axial multi-slice 2D, in- and out-of-phase, T1-weighted gradient echo sequence (TR = 144 msec, TE = 2.7 msec [in-phase] and 5.3 msec [out-of-phase], NEX = 1, FA = 70 degrees, ST = 6 mm, matrix = 119 × 256).
4. Axial contrast-enhanced, fat-saturated (with use of a chemical shift technique), multi-slice 2D FLASH (fast low-angle shot) sequence (TR = 152 msec, TE = 4.1 msec, NEX = 1, FA = 80 degrees, ST = 6 mm, matrix = 117 × 256, TA= 17 sec), obtained after IV administration of gadopentetate dimeglumine (Magnevist; Berlex), 0.2 mL per kg of body weight. Delay times are 20 seconds, 70 seconds, 3 minutes, and 5 minutes after the start of the contrast injection.

The goal of this protocol is to image the organ as quickly as possible; examination time is about 25 minutes. The dynamic post-gadolinium images are usually the most important images. It is often helpful to employ a T2-weighted sequence with a long TE to aid in the evaluation of potential hemangiomas.

Normal Anatomy and Variants

Normal Spleen

The spleen normally lies within the left upper quadrant. The typical size of the adult spleen is 12 × 7 × 4 cm, and it weighs 100 to 200 g.[46] The maximum craniocaudal length is 12 to 15 cm. The spleen is a network of white and red pulp. The white pulp consists of lymphocytes, plasma cells, and macrophages. The red pulp contains splenic cords, splenic sinuses, terminal branches of the central arteries, and pulp veins. The visceral surface of the spleen is adjacent to the stomach, left kidney, splenic flexure of the colon, and tail of the pancreas. The normal spleen may have rib notching, which should not be confused with lacerations in patients who have experienced trauma.

The spleen is usually a completely peritonealized organ. The splenorenal ligament, which connects the splenic hilum to the left kidney, contains the tail of the pancreas and the splenic artery and vein. The gastrosplenic ligament is formed by the union of the peritoneum of the lesser and greater sacs and connects the splenic hilum to the stomach. The phrenicocolic ligament connects the lower pole of the spleen to the splenic flexure of the colon and the diaphragm.

On nonenhanced CT scanning, the normal splenic parenchyma is homogeneous; it measures 40 to 60 Hounsfield units (HU), usually 5 to 10 HU less than normal liver. On T1-weighted MR images, the normal spleen has a signal

intensity equal to or less than that of normal liver, whereas on T2-weighted images, the spleen has high signal intensity. After IV contrast enhancement, the spleen can have a heterogeneous appearance on the early arterial phase images on both CT and MRI. This appearance is believed to be due to the differential enhancement of red and white pulp (Fig. 39–1). Typically, this differential enhancement can give an arciform appearance to the spleen. Occasionally, however, the enhancement pattern can simulate a mass lesion, producing a pseudomass appearance in the spleen. It is therefore important to obtain delayed images (see Fig. 39–1).

Normal Variants

Splenic clefts are common. They can usually be easily recognized because of their sharp, smooth borders. They are typically located superiorly and medially in the spleen but may occur anywhere. In patients with trauma, one should avoid misinterpreting a congenital cleft as a splenic laceration. Splenic clefts are not associated with perisplenic edema (Fig. 39–2*A*).

A retrorenal spleen occurs when the posterior border of the spleen lies posterior to the posterior border of the left kidney. In one series, this finding was described in 15% to

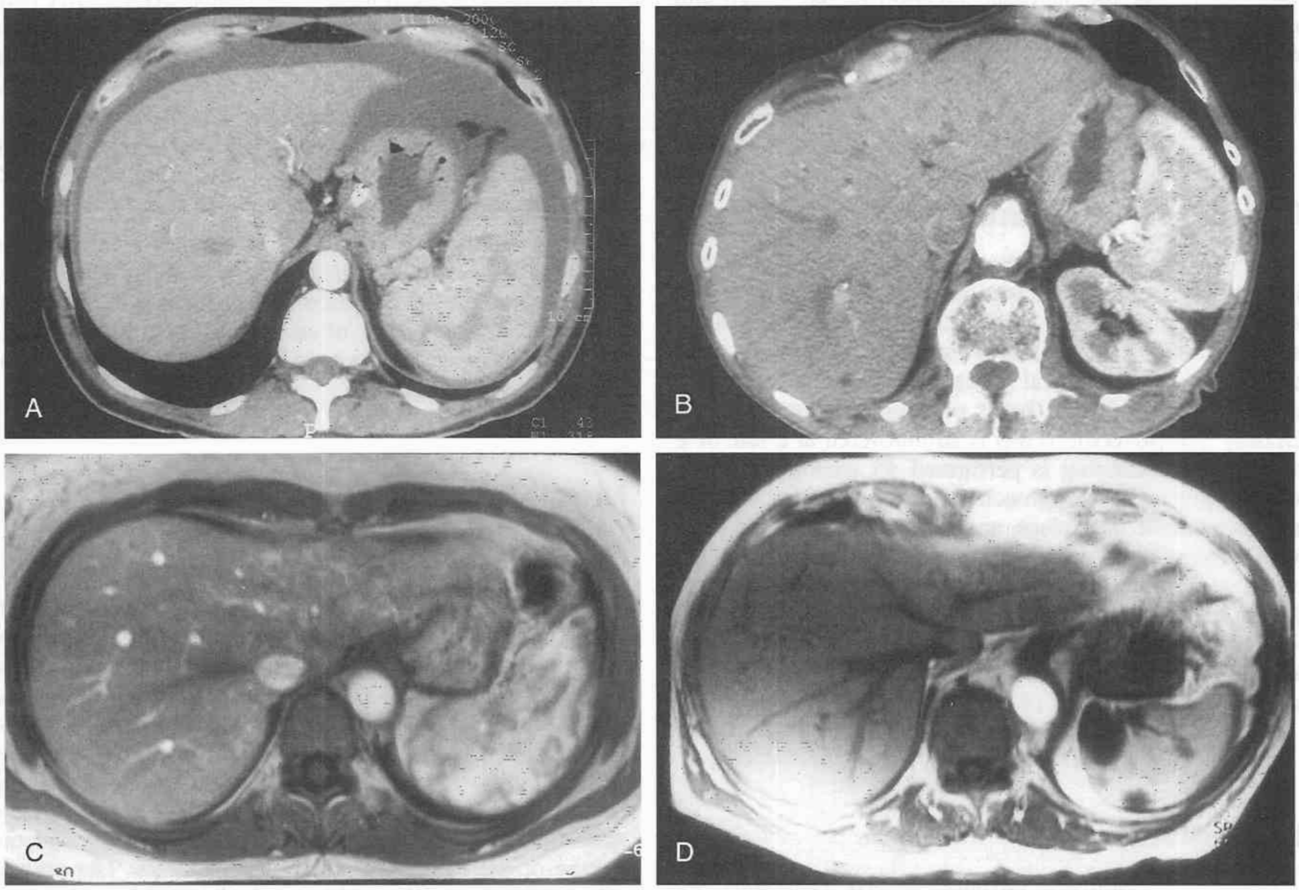

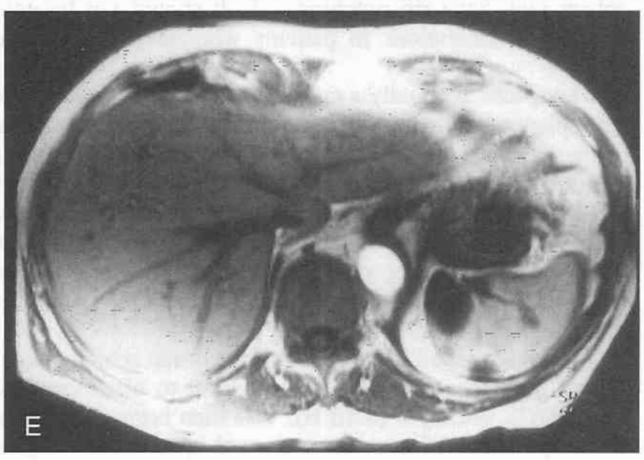

Figure 39–1. Normal splenic enhancement. Early arterial phase images may demonstrate a variety of patterns. Typically, there is an arciform appearance. Masses may be simulated, producing a pseudomass appearance, particularly during the MRI immediate after intravenous administration of the bolus of contrast agent. Therefore, delayed images are important. All of these patterns become homogeneous on delayed images. *A*, Normal early post-contrast, arterial phase CT scans, arciform. *B*, Peripheral pattern of enhancement on CT scan. *C*, Arciform pattern on T1-weighted, gadolinium-enhanced MR image, arterial phase. *D*, Hypointense splenic pseudomass on a T1-weighted gadolinium-enhanced MR image, arterial phase. *E*, Hypointense splenic pseudomass on a T1-weighted, gadolinium-enhanced MR image, arterial phase. Also note the rim-enhancing liver metastases.

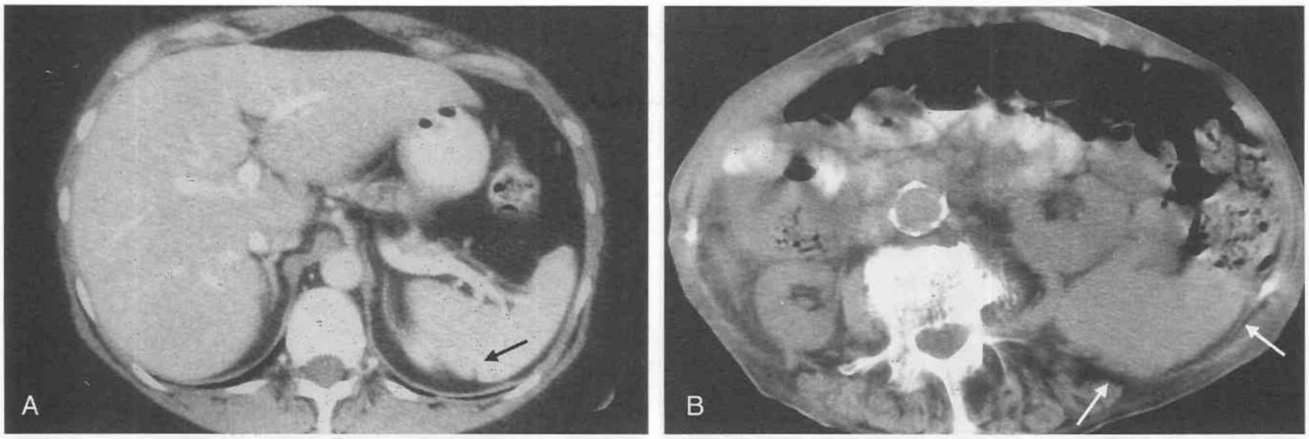

Figure 39–2. Normal splenic variants. *A*, CT scan showing splenic cleft (*arrow*). *B*, CT scan showing retrorenal spleen (*arrows*). Note how the splenic location would make a left renal biopsy difficult.

20% of patients.[62] It is more common in elderly patients (Fig. 39–2*B*).

Accessory spleens are common. They are typically located near the splenic hilum, but they can be found anywhere in the peritoneal cavity (Fig. 39–3). Accessory spleens may hypertrophy after surgical removal of primary spleen.

Congenital Variants

Congenital variations in the spleen are described in Chapter 55.

Lymphoma and Splenic Neoplasms

Lymphoma

Splenic lymphoma, probably the most common splenic malignancy, is usually seen as a manifestation of generalized (secondary) lymphoma.[93, 114] Primary splenic lymphoma is rare, representing 1% to 2.6% of all lymphomas; most of the primary splenic lymphomas are non-Hodgkin's lymphomas.[1, 31] The definition of primary splenic lymphoma is controversial.[1, 43] In general, a history of normal bone marrow findings, clinical detection of peripheral adenopathy, or both, combined with imaging data and surgical findings were used to exclude generalized lymphoma.[1, 31] Most of the primary splenic lymphomas are non-Hodgkin's lymphoma.[1, 31] Because primary lymphoma is rare, this discussion focuses on the features of generalized lymphoma.

The imaging appearance of lymphoma of the spleen depends on its pathologic appearance, which consists of (1) homogeneous enlargement without a discrete mass, (2) a solitary mass, (3) multifocal lesions, and (4) diffuse infiltration. Splenomegaly is the most common imaging finding, but it may be absent in up to one third of patients with lymphoma (Fig. 39–4).[46, 117, 125] Conversely, in 30% of the enlarged spleens found in patients with lymphoma, the enlargement is benign in origin.[43, 46, 132] Focal lesions are more common in non-Hodgkin's lymphoma than in Hodgkin's lymphoma.

Although imaging plays an important role in the detection of abnormalities in patients with lymphoma, staging of lymphomas with imaging can be limited. Forty-five percent to 70% of splenic lymphoma lesions may manifest

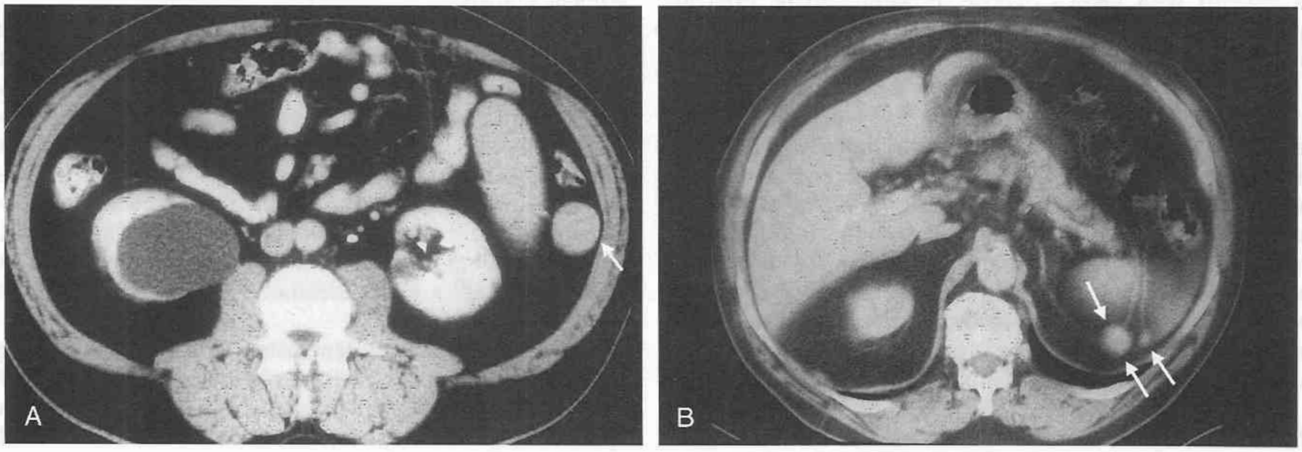

Figure 39–3. CT scans showing accessory spleens in unusual locations. *A*, Accessory spleen (*arrow*) lateral to the spleen's lower pole. *B*, Accessory spleens (*arrows*) inferior and lateral to the spleen's lower pole.

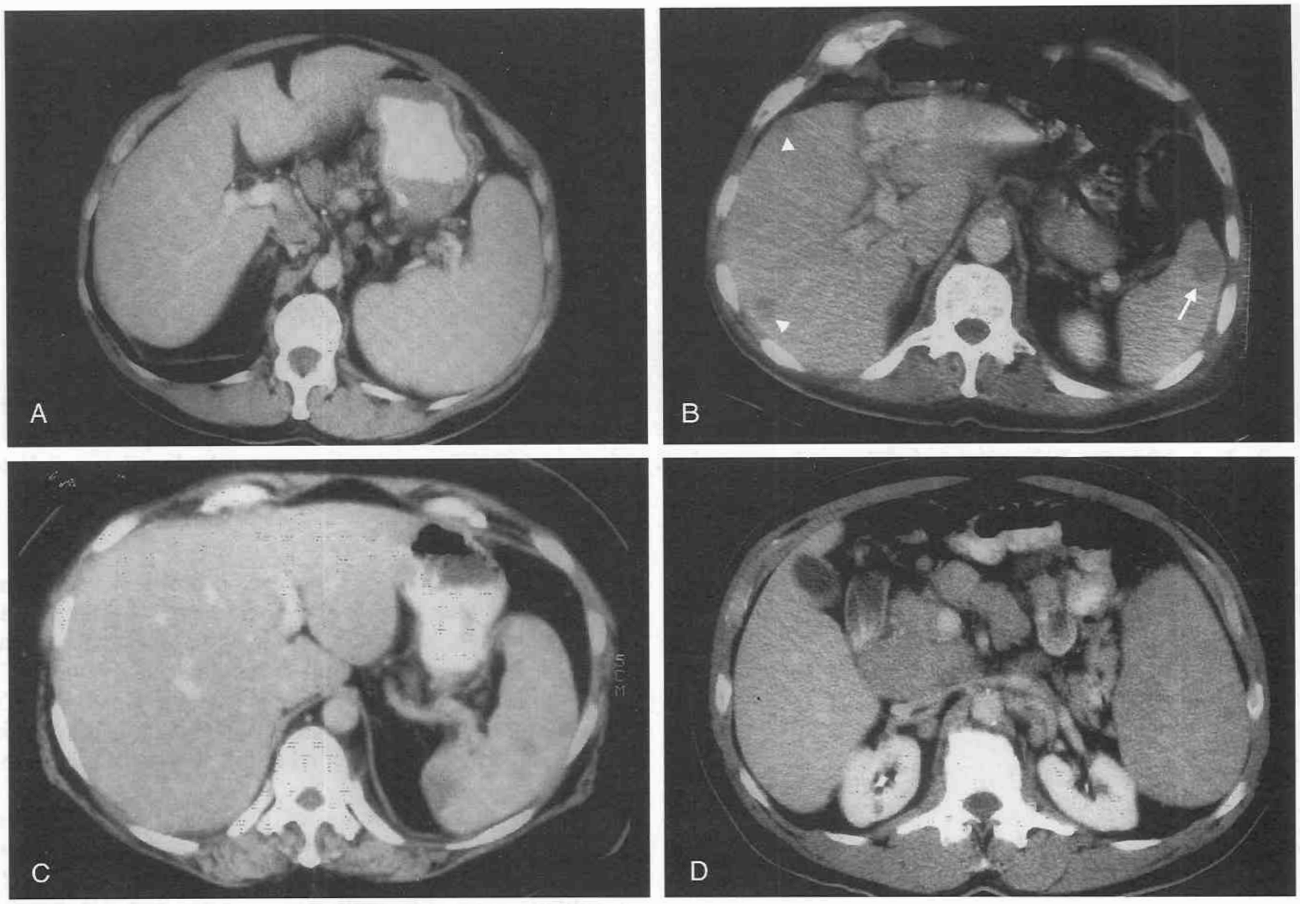

Figure 39–4. CT scans of splenic lymphoma. *A*, Spleen of a patient with non-Hodgkin's lymphoma and diffuse splenic enlargement with no focal splenic lesions. *B*, Spleen of a patient with non-Hodgkin's lymphoma reveals a focal low-attenuation splenic lesion (*arrow*). There are focal low-attenuation lesions in the liver as well (*arrowheads*). *C*, Multifocal low-attenuation splenic lesions in a patient with non-Hodgkin's lymphoma. *D*, Diffuse low-attenuation splenic infiltration can be seen in this patient with non-Hodgkin's lymphoma. Retroperitoneal and peripancreatic adenopathy is present as well.

as diffuse infiltration or tumor foci smaller than 1 cm.[93, 132] Occasionally, tumor foci can be seen only microscopically; on gross visual inspection, the spleen may appear normal. Such small lesions may be difficult or impossible to visualize even with state-of-the-art CT and MRI modalities. This difficulty makes staging of lymphoma difficult. However, in patients with known disease, imaging can be used to upgrade staging—that is, to detect new retroperitoneal or mediastinal lymph nodes.

CT is the primary tool for diagnosing lymphoma and monitoring the response to therapy.[43, 93] Helical CT scanning with IV contrast enhancement may improve the detection of smaller lesions.[125] Typically, lymphoma lesions do not enhance with contrast material during CT or MRI. It is important to realize that there are potential pitfalls with current CT and MRI techniques, because of the heterogeneous enhancement of the normal spleen during dynamic bolus imaging. As previously described, delayed scanning may be helpful, but occasionally, the lesions may enhance to the same level as the remaining spleen (Fig. 39–5).

In general, MRI is less reliable than CT, because both the normal spleen and lymphomatous tissue may have similar T1 and T2 relaxation times and proton densities.[93, 122] Use of superparamagnetic iron oxide has been proposed to improve detection of lymphoma lesions on MRI.[132] If lymphoma is present in the liver, the spleen is practically always involved as well.[114] Although rare, calcifications can be seen with splenic lymphoma both before and after treatment. They are most likely dystrophic calcifications secondary to necrosis, hemorrhage, and subsequent fibrosis.[93]

The other role of cross-sectional imaging in patients with lymphoma is to differentiate between lymphoma and other disease processes. For example, patients with lymphoma may undergo chemotherapy and become immunocompromised and may thus be susceptible to disseminated fungal infections such as candidiasis. Fungal infections may be difficult to diagnose, and fungal microabscesses should not be mistaken for foci of splenic lymphoma. MRI with gadolinium enhancement has been shown to be an effective modality to differentiate between fungal abscess and lymphoma lesions.[108]

Splenic abscess may demonstrate clinical and imaging features similar to those of lymphoma—that is, fever, left upper quadrant pain, malaise, and cystic lesions within the spleen. In general, splenic abscesses rarely occur with lymphadenopathy; this fact can be helpful in differentiating between these two entities.[43, 93] Even with current imaging

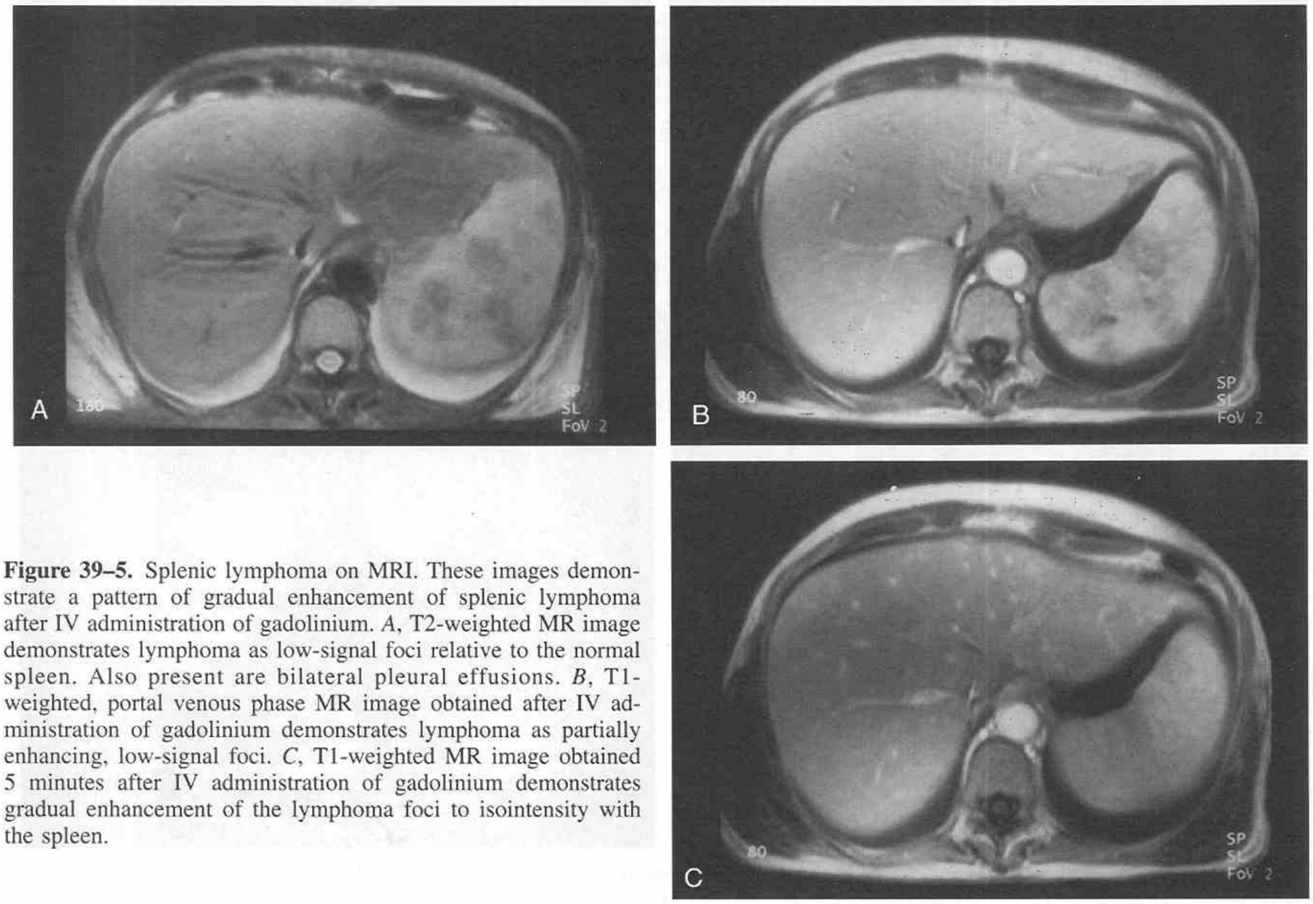

Figure 39–5. Splenic lymphoma on MRI. These images demonstrate a pattern of gradual enhancement of splenic lymphoma after IV administration of gadolinium. *A*, T2-weighted MR image demonstrates lymphoma as low-signal foci relative to the normal spleen. Also present are bilateral pleural effusions. *B*, T1-weighted, portal venous phase MR image obtained after IV administration of gadolinium demonstrates lymphoma as partially enhancing, low-signal foci. *C*, T1-weighted MR image obtained 5 minutes after IV administration of gadolinium demonstrates gradual enhancement of the lymphoma foci to isointensity with the spleen.

technology, however, differentiating lymphoma from abscess can occasionally be difficult. For example, necrotic lymphoma lesions may appear cystic and look similar to splenic abscess. Although necrosis of lymphoma lesions is rare,[93] larger lesions can manifest as cystic-appearing masses or may have cystic components.[125] Gas within a cystic-appearing splenic lesion suggests infection, although gas can also be seen with necrosis only. Splenic infarcts may occur in conjunction with lymphoma. Typically, infarcts are peripheral, wedge-shaped lesions.

Splenic lymphoma may be associated with human immunodeficiency virus (HIV). Single or multiple low-attenuation foci may be present. Focal splenic lesions are more common in patients with lymphoma related to acquired immunodeficiency syndrome (AIDS) than in patients with lymphoma unrelated to AIDS.[123] The diagnosis of non-Hodgkin's lymphoma in a patient with HIV infection fulfills the criteria for the diagnosis of AIDS.[123] In general, AIDS-related lymphomas are aggressive and often manifest with multiple sites of abdominal involvement.[123]

Splenic Angiosarcoma

Splenic angiosarcoma is a rare neoplasm of the spleen, which may be primary or metastatic. It has a poor prognosis and may be complicated by splenic rupture.[24] There appear to be two types of angiosarcomas. Some angiosarcomas appear to be related to exogenous administration of substances such as thorium dioxide, vinyl chloride, and arsenic; they arise in the liver and can have a few metastases to the spleen. The angiosarcomas unrelated to such toxic substances arise in both the liver and the spleen.[24] Angiosarcomas can manifest as multiple nodules of various sizes or show permeative growth into the spleen; some may have hemorrhage.[42, 93] Like hepatic hemangiomas, angiosarcomas may show varying degrees of enhancement.[93]

Splenic Metastases

Although metastases to the spleen are more common than primary neoplasm, they tend to occur in patients with widely disseminated tumor. Primary tumors that commonly metastasize to the spleen include melanoma and lung, breast, and ovarian carcinomas. Direct invasion may also occur from gastric, pancreatic, or colon carcinoma (Fig. 39–6).

Cysts

Various types of focal lesions of the spleen may appear cystic on cross-sectional imaging. They include congenital

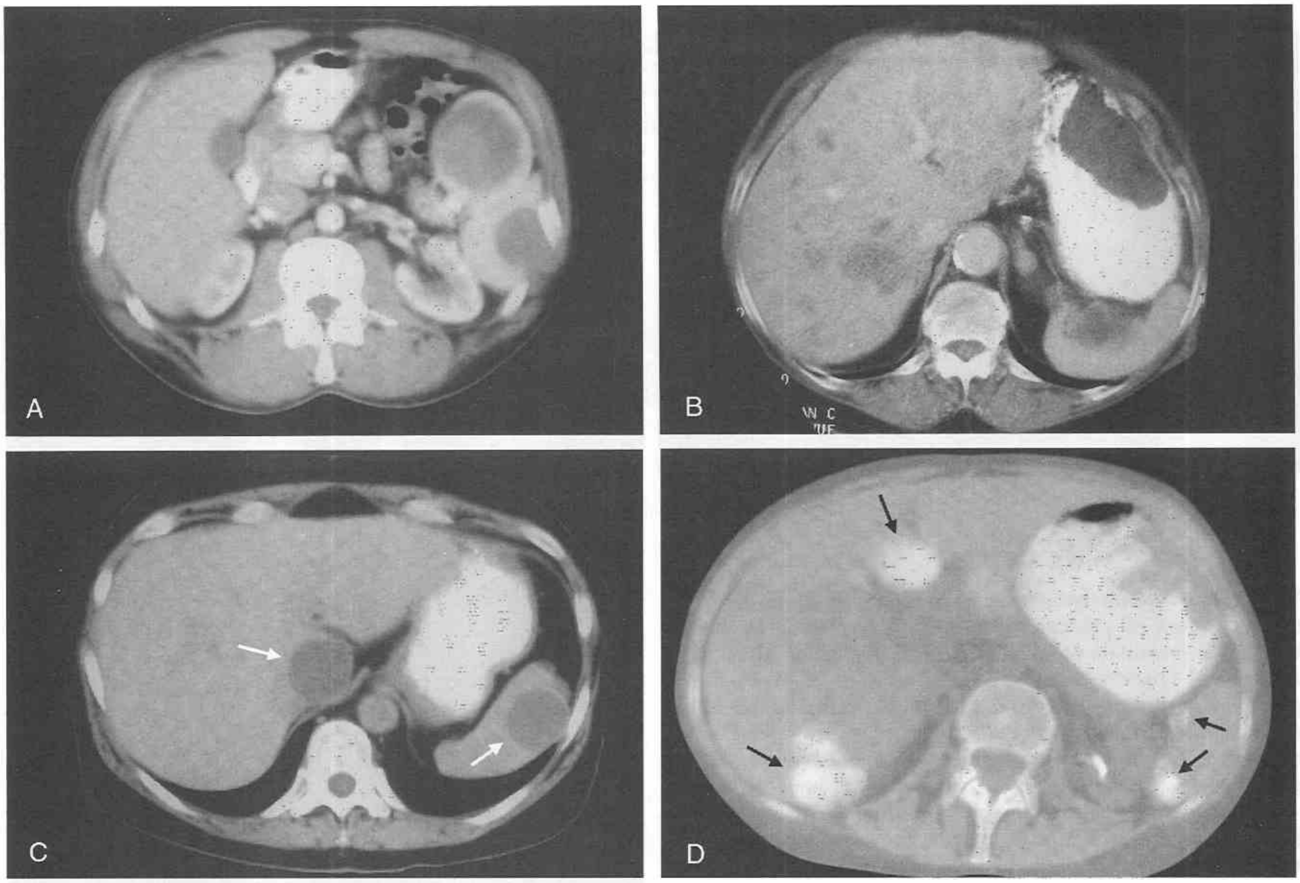

Figure 39–6. CT scans showing spleen metastases. *A*, Low-attenuation melanoma metastases to the spleen. *B*, Low-attenuation breast cancer metastases to the spleen, liver, and left adrenal gland. *C*, Ovarian carcinoma with cystic spleen and liver metastases (*arrows*). *D*, Ovarian carcinoma with calcified spleen and liver metastases after treatment (*arrows*).

(true) cysts, nonpancreatic pseudocysts (post-traumatic hematoma), cystic neoplasms (i.e., lymphangiomas, hemangiomas, lymphomas, and metastases), inflammatory lesions (abscesses and parasitic cysts), and vascular lesions (infarction, peliosis).[32, 88, 126] Congenital cysts are generally classified as "true" cysts and contain an epithelial lining (also called epidermoid, epithelial or congenital cysts), whereas "false" cysts or pseudocysts do not have an epithelial lining.[32] True cysts are believed to be developmental in origin. Possible explanations for the development of the epithelial lining include infolding of peritoneal mesothelium and collections of peritoneal mesothelial cells trapped within the splenic sulci.[32, 37, 126] False cysts are presumed to be post-traumatic in origin, may be hemorrhagic or serous, and may be the end stage of intrasplenic hematoma.[32, 88, 126] Post-traumatic false cysts probably account for 75% to 80% of all splenic cysts.[88, 126] Because splenic cysts have been found in women of childbearing age, it is thought that congestion and infarction of the spleen during pregnancy cause hemorrhage and secondary cyst formation.[37]

True and false cysts can appear identical on cross-sectional imaging. Typically, both are well-defined, homogeneous, and unilocular (although septations may be present). Although it may be impossible to differentiate between true and false cysts on imaging studies, there are a few differential points to consider. False cysts, which tend to be smaller, have internal debris and peripheral calcifications.[126] Peripheral calcifications are less common in true cysts.[32] The diagnosis of false cyst should also be favored when (1) there is a clear history of trauma, (2) the patient is older than the fourth decade, or (3) there is hematoma elsewhere in the spleen.[32] On CT scans, both true and false cysts have an attenuation value near or equal to that of water, their walls are either thin or imperceptible, and they do not enhance after IV administration of a contrast agent (Fig. 39–7). On MRI, both types of cysts appear to contain fluid with a signal intensity similar to or slightly greater than that of water. After administration of gadolinium, the cysts show no central or rim enhancement.[65]

It may be difficult to differentiate the various cystic lesions of the spleen. The clinical and imaging features may have to be considered together to narrow the differential diagnosis, which includes echinococcal cysts (which often appear multiseptated), large solitary abscess or hematoma (usually distinguished on basis of clinical history), and cystic neoplasms of the spleen.[32]

Hemangioma

Splenic hemangioma is the most common benign splenic neoplasm. Its incidence is 0.03% to 14% in autopsy series.[1]

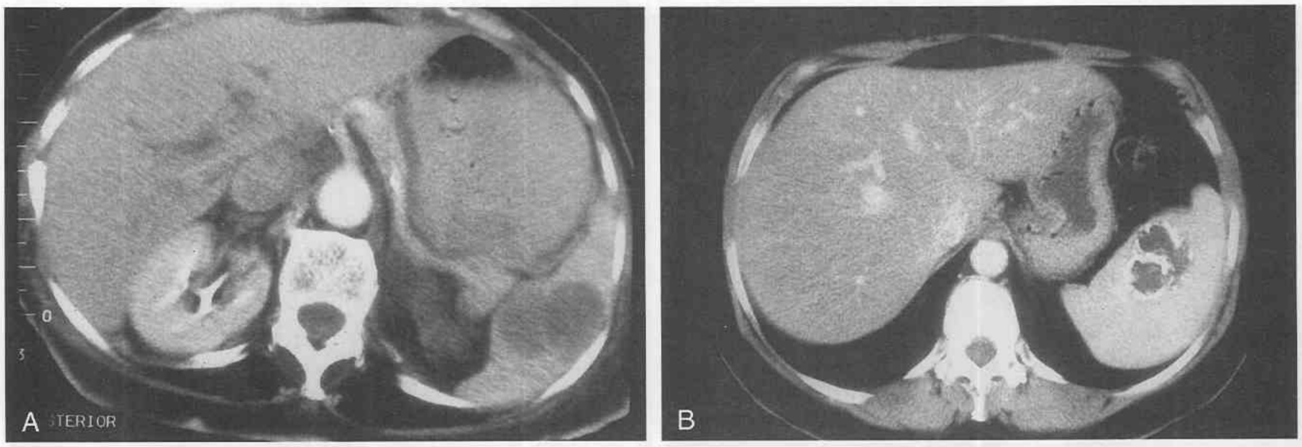

Figure 39–7. CT scans showing splenic cysts. *A*, Splenic cyst with septations. *B*, Splenic cyst with peripheral calcifications.

Hemangiomas of the spleen may be single or multiple and may occur as part of a generalized angiomatosis (Klippel-Trenaunay-Weber syndrome).[96] Splenic hemangiomas are usually cavernous in subtype, although they may be capillary or mixed. Infarction, thrombosis, or fibrosis may occur in splenic hemangiomas, just as in hemangiomas in other parts of the body.[96]

Solitary hemangiomas are usually asymptomatic and are often incidentally discovered in adults. Hemangiomas may grow slowly and, as they enlarge, can produce symptoms such as pain and fullness in the left upper quadrant. Up to 25% of splenic hemangiomas may manifest acutely because of rupture.[96] Anemia, thrombocytopenia, and coagulopathy (Kasabach-Merritt syndrome) have been reported with large hemangiomas, likely secondary to the sequestration of red cells and platelets and consumption of clotting factors.[98]

On CT, solitary splenic hemangiomas are usually small and solid. However, larger hemangiomas may be more complex and may have both solid and cystic components. Rarely, central and punctate or peripheral and curvilinear calcifications may be noted.[98] On nonenhanced scans, solid splenic capillary hemangiomas are typically isodense to hypodense relative to normal spleen; after IV administration of a contrast agent, they enhance from the periphery to the center, like hepatic hemangiomas (Fig. 39–8).[98] However, cavernous hemangiomas of the spleen tend to have mixed solid and cystic components, and unlike their classic appearance in the liver, they demonstrate discrete mottled areas of heterogeneous density on delayed images after administration of a contrast agent (Fig. 39–9).[42]

Splenic hemangiomas have low signal on T1-weighted MR images and higher signal (> 120 msec) on T2-weighted images, particularly with prolonged TE. Complex hemangiomas may have mixed signal on T1- and T2-weighted images. After IV administration of gadolinium, splenic hemangiomas demonstrate peripheral enhancement with progressive central fill-in. Ramani and associates[96] found that 19 of 22 hemangiomas had peripheral enhancement with centripetal fill-in. Only two lesions in their series demonstrated a clearly defined peripheral nodular type of enhancement; the remaining lesions demonstrated a periph-

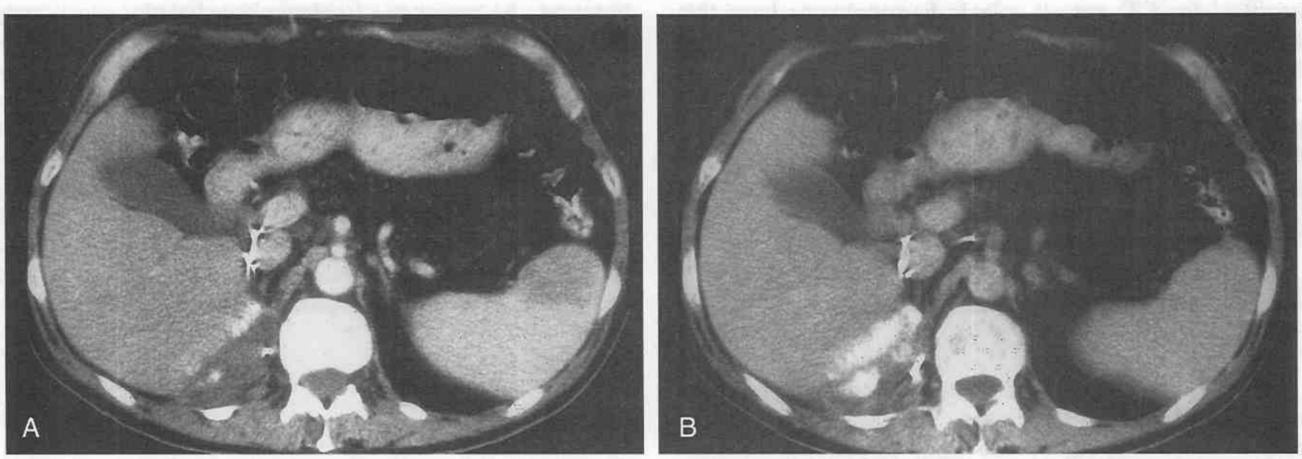

Figure 39–8. CT scans showing hemangioma of the spleen. *A*, Initial post-contrast image demonstrates a low-attenuation lesion (*arrow*). *B*, Delayed scan obtained at 3 minutes shows complete enhancement.

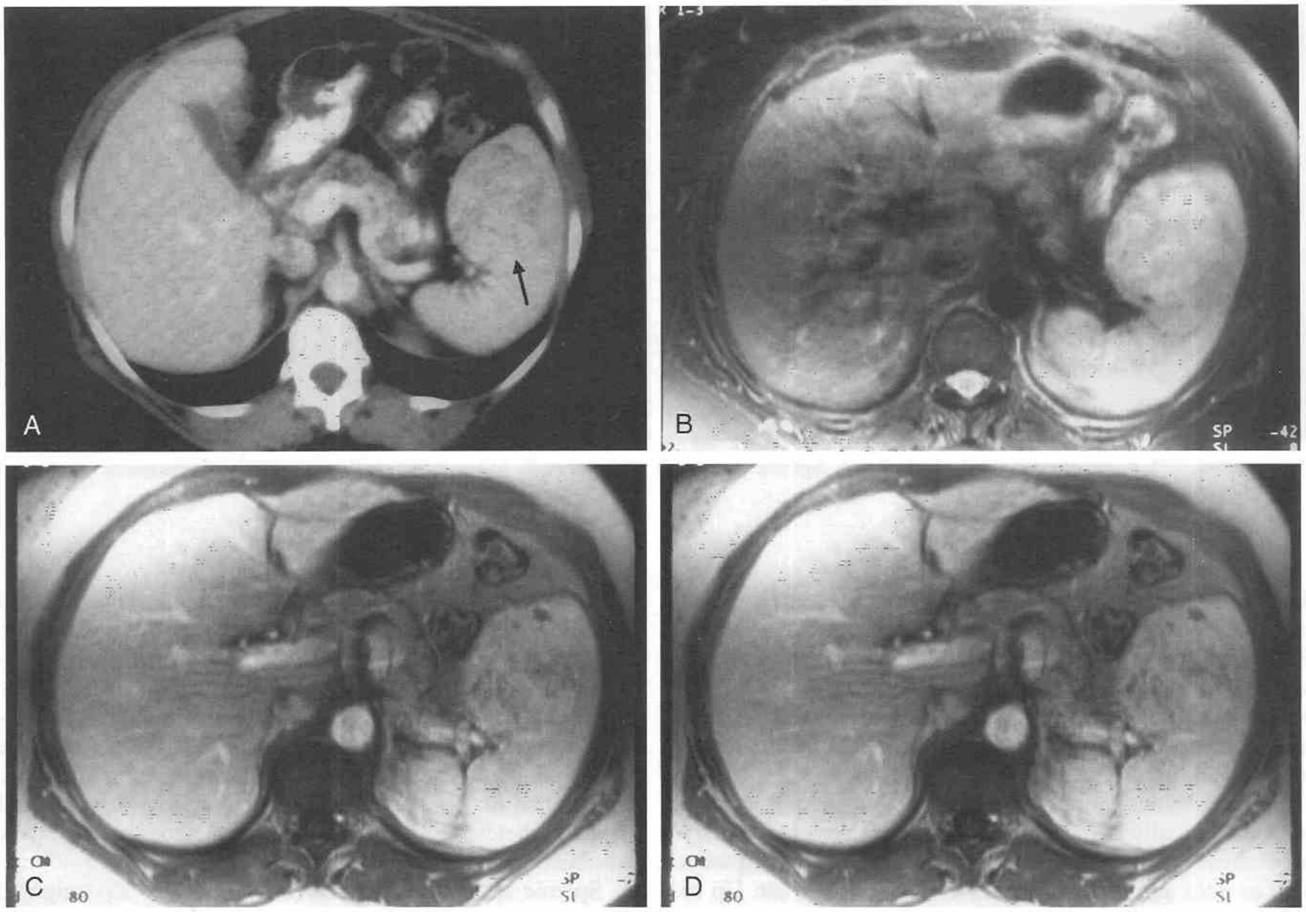

Figure 39–9. Hemangioma of the spleen, demonstrated on both CT and MRI. *A*. CT scan obtained during the arterial phase shows a heterogeneously enhancing hemangioma in the spleen (*arrow*). *B*, T2-weighted MR image demonstrates the heterogeneously high signal of the hemangioma. *C*, T1-weighted, portal venous phase MR image obtained after IV administration of gadolinium demonstrates heterogeneous enhancement of the hemangioma, similar to the CT appearance on *A*. *D*, T1-weighted MR image obtained 5 minutes after IV administration of contrast agent image demonstrates near-complete enhancement of the hemangioma.

eral rim of variable thickness with irregular inner margins. One hemangioma had central enhancement. Splenic hemangiomas also demonstrate retention of contrast material on delayed images, like hepatic hemangiomas. However, as described for CT, not all splenic hemangiomas have this classic pattern of enhancement on MRI (Figs. 39–10 and 39–11).

Differentiation of splenic hemangiomas from other splenic neoplasms can be difficult. Positive result of red blood cell scintigraphy can establish the diagnosis of hemangioma of the spleen.[39]

Splenic Lymphangioma and Lymphangiomatosis

Lymphangiomas are rare, slow-growing, benign tumors composed of lymphatic vessels. Splenic lymphangiomas are considered very rare.[42] They may be solitary but more often appear as multiple, thin-walled, well-marginated cysts that may be subcapsular in location.[92, 129] When lymphangiomas are diffuse, their presence is called *lymphangiomatosis*.

The prognosis of isolated splenic lymphangioma or lymphangiomatosis is believed to be good. In some cases, however, the presence of splenic lymphangiomatosis may signal multisystem involvement, known as cystic angiomatosis, consisting of lymphangiomatous or hemangiomatous involvement of bone, soft tissues, and viscera. This multisystem form can be progressive and can have a poor prognosis.[129]

On CT and MRI, splenic lymphangiomas appear as multiloculated cystic lesions that do not enhance on arterial or delayed phase imaging (Fig. 39–12).[65] Angiography demonstrates multiple, well-defined, avascular lesions of various sizes that give the spleen a "Swiss cheese" appearance.

Splenic Hamartoma

Rare lesions, splenic hamartomas are usually solitary masses. They are classified as white pulp or red pulp

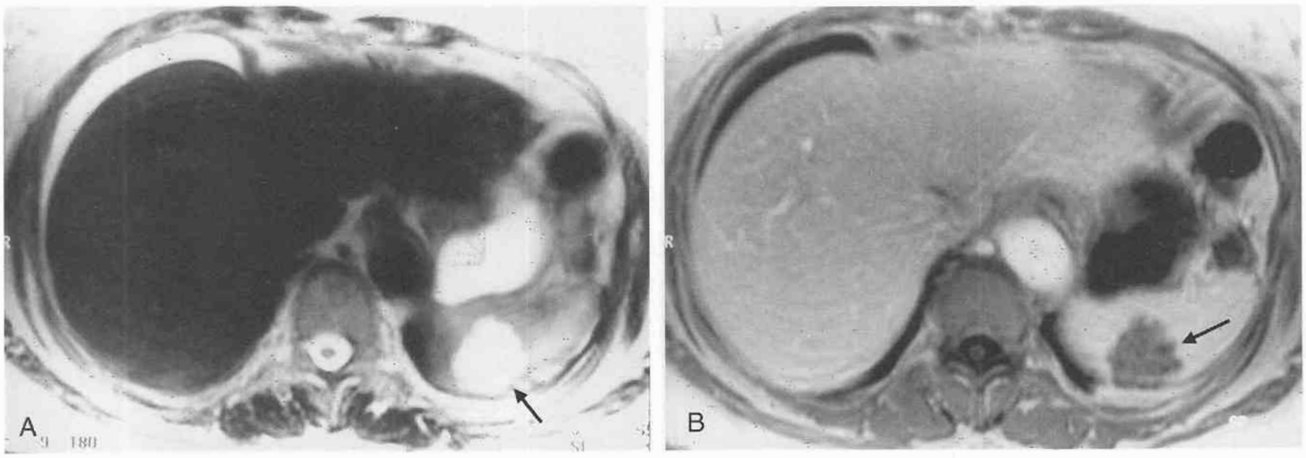

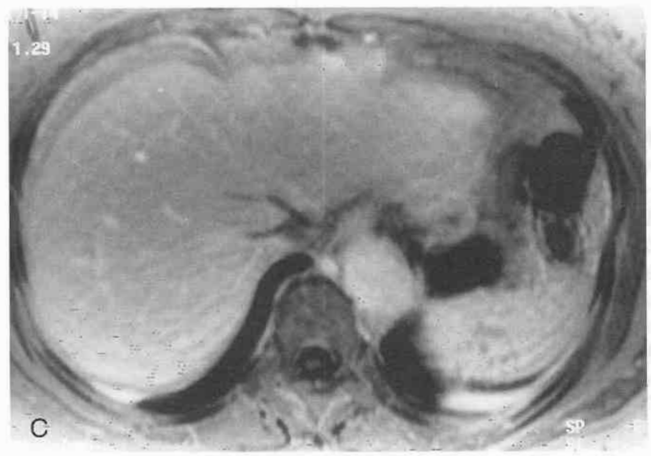

Figure 39–10. MR images of the same patient showing hemangioma of the spleen. *A*, T2-weighted image shows a high-signal hemangioma (*arrow*) on prolonged TE (TR = 5046 msec, TE = 165 msec). *B*, T1-weighted image obtained 45 seconds after IV administration of gadolinium reveals that the hemangioma is low in signal and has not yet enhanced (*arrow*). *C*, On another T1-weighted image obtained 5 minutes after IV administration of gadolinium, the hemangioma retains contrast agent but does not completely enhance and has a mottled appearance.

hamartomas; most are a mixture of the two cell types.[96] They can be cystic or solid and may have punctate or stellate calcifications. Rarely, these tumors can be symptomatic, causing splenomegaly, pancytopenia, fatigue, and anorexia.[121]

On MRI, the solid lesions may be isointense on T1-weighted images and hyperintense on T2-weighted images relative to the spleen. Unlike hemangiomas, however, hamartomas do not demonstrate an increase in signal intensity similar to that of cerebrospinal fluid when images with higher T2 weighting (TE = 120 to 150 msec) are performed.[121] After IV administration of a contrast agent, hamartomas demonstrate diffuse heterogeneous enhancement. Hamartomas may be difficult to distinguish from malignant lesions. Splenic hamartomas may demonstrate radiotracer uptake on sulfur colloid scintigraphy; this finding may be helpful in differentiating these lesions from malignant neoplasms and hemangiomas.

Infections and Diffuse Diseases

Splenic Abscess

Splenic abscesses are uncommon, having been reported in 0.14% to 0.70% of the large autopsy series.[7, 25, 26] The observed rise in their incidence is believed to be due to an increase in the number of immunocompromised patients, such as oncology patients undergoing current aggressive chemotherapeutic regimens, critically ill patients in intensive care units, and growing numbers of HIV-infected patients.[38] The development of a splenic abscess may require both bacteremia and intrinsic splenic disease that alters splenic architecture, such as infarct, hematoma, or sickle cell disease. Alternatively, splenic abscesses result from direct extension of infection from adjacent organs, such as the pancreas[72] or the stomach.[67] Aerobic organisms account for 57% of splenic abscesses, with the majority being due to *Staphylococcus*, *Escherichia coli*, and *Salmonella*; 26% of abscesses are caused by fungi, predominantly *Candida*, and 18% by anaerobic organisms.[81] The mortality rates range from 15% in otherwise healthy patients with unilocular splenic abscess to 80% in immunocompromised patients with multiple abscesses.[3]

On cross-sectional imaging, splenic abscesses may appear solitary or multiple. CT is the study of choice. The solitary abscesses and multiloculated abscesses tend to be bacterial. Septations may be present, and there may be an enhancing capsule. The CT appearance of an abscess may overlap with that of an infarct, hematoma, or neoplasm. The lack of mass effect helps differentiate infarct from abscess or other tumor. The presence of gas within the lesion is diagnostic of abscess; however this finding is rare. Gas is more readily apparent on CT than on MRI (Fig.

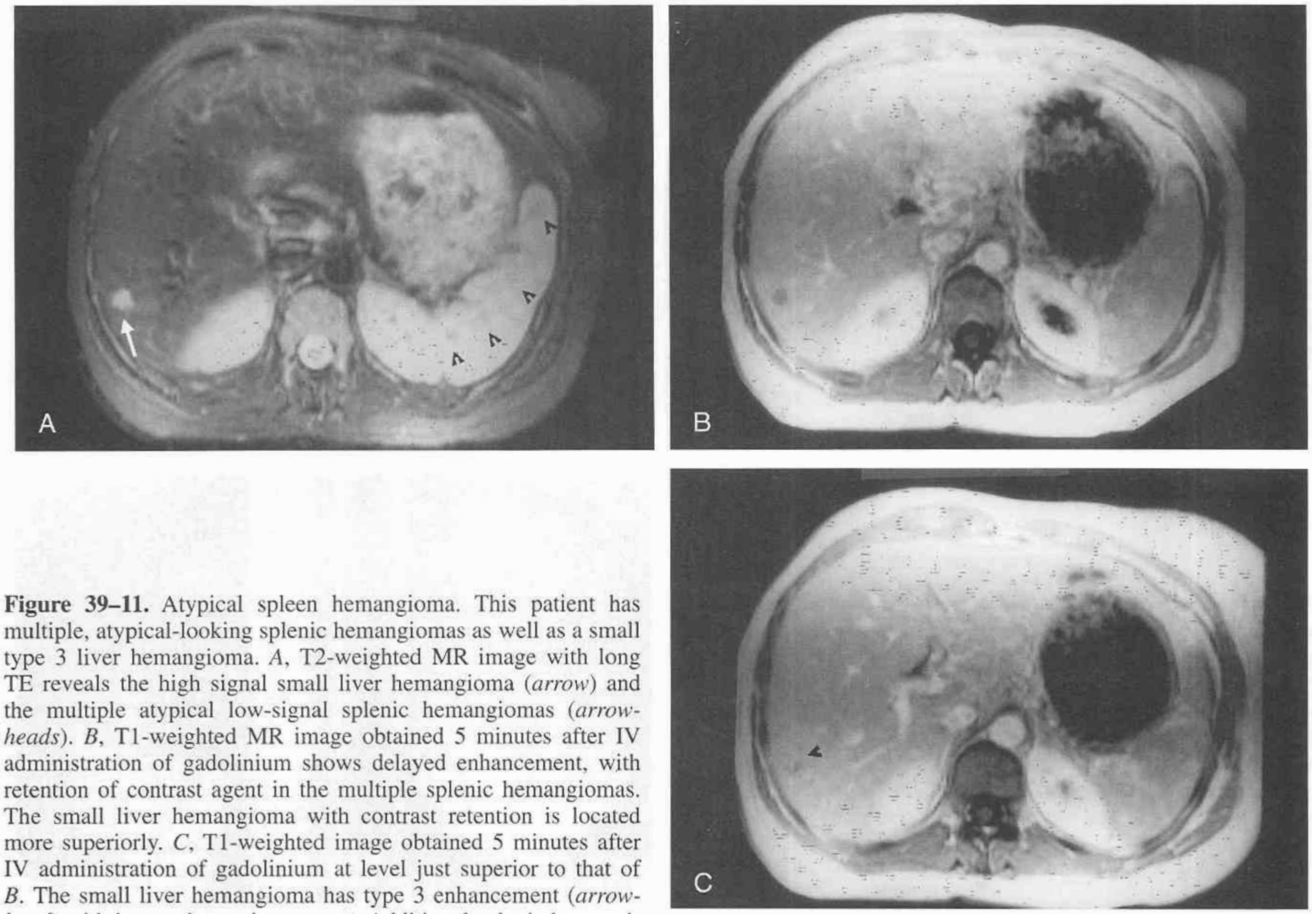

Figure 39–11. Atypical spleen hemangioma. This patient has multiple, atypical-looking splenic hemangiomas as well as a small type 3 liver hemangioma. *A*, T2-weighted MR image with long TE reveals the high signal small liver hemangioma (*arrow*) and the multiple atypical low-signal splenic hemangiomas (*arrowheads*). *B*, T1-weighted MR image obtained 5 minutes after IV administration of gadolinium shows delayed enhancement, with retention of contrast agent in the multiple splenic hemangiomas. The small liver hemangioma with contrast retention is located more superiorly. *C*, T1-weighted image obtained 5 minutes after IV administration of gadolinium at level just superior to that of *B*. The small liver hemangioma has type 3 enhancement (*arrowhead*) with incomplete enhancement. Additional splenic hemangiomas can be seen.

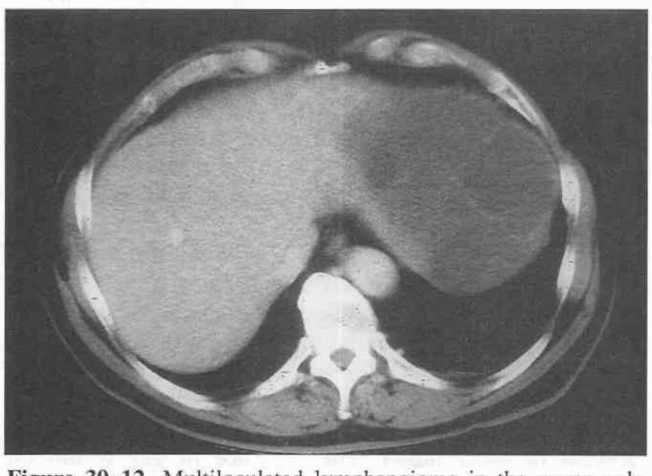

Figure 39–12. Multiloculated lymphangioma in the upper pole of the spleen, incidentally noted on a chest CT scan.

39–13). In patients with high surgical risk, percutaneous abscess drainage can be performed.

Multiple small splenic abscesses (microabscesses) are typically nonbacterial in origin and are most commonly associated with fungal infections. The liver is also usually involved. Fungal infections occur primarily in neutropenic patients, most commonly in patients with acute leukemia or other lymphoproliferative disorders who are undergoing high-dose chemotherapy with or without bone marrow transplantation.[99, 108] An increase in the incidence of fungal abscesses of the spleen has resulted from the widespread use of aggressive chemotherapy.[81] Prior to the development of helical CT and current MRI techniques, it was difficult to establish the diagnosis of hepatosplenic candidiasis. The lesions were often undetectable because of (1) their small size on imaging, (2) the often nonspecific clinical signs and symptoms, and (3) the commonly negative results of blood culture.[73, 99] Percutaneous needle biopsy may also yield a false-negative result.[89] Typically, these lesions of hepatosplenic candidiasis are smaller than 2 cm, usually measuring 5 to 10 mm in diameter. However, they may also be less than 5 mm (miliary). On CT, they often have low attenuation (Fig. 39–14), although there can be a focus of high attenuation or a "wheel-within-a-wheel" pattern.

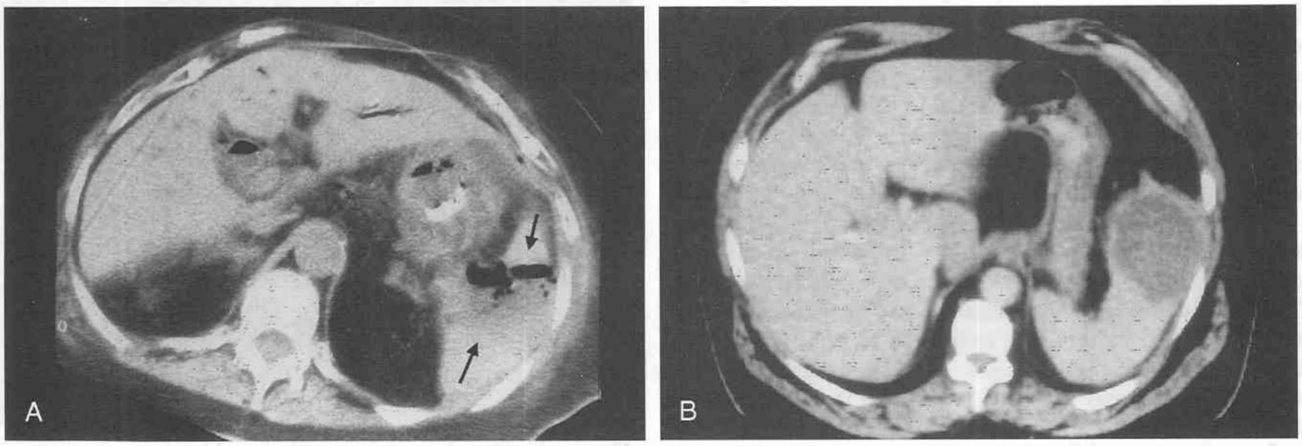

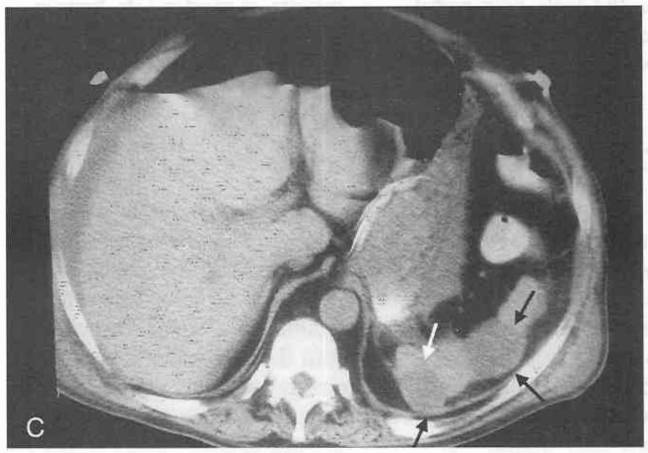

Figure 39–13. CT scans showing splenic abscesses. *A*, Unenhanced scan demonstrates a low-attenuation splenic abscess (*arrows*) with gas. *B*, Splenic abscess mass effect and complex fluid. *C*, Unenhanced scan shows two abscesses in the lower pole of the spleen (*arrows*).

MRI is the modality of choice to evaluate for hepatosplenic candidiasis. Semelka and colleagues[108] have described the appearance of hepatosplenic candidiasis on MRI, which they have used to distinguish the acute, subacute, and chronic phases of infection. Although MRI is very accurate in the diagnosis of acute hepatosplenic fungal disease, the findings may be falsely negative if the patient is neutropenic and is unable to mount an immune response to the infection.

Semelka and colleagues[108] described acute microabscesses as small (<1 cm), round lesions best demonstrated on T2-weighted images as hyperintense foci. On T1-weighted images, they are often poorly seen as low-signal foci and are only moderately demonstrated with gadolinium enhancement (Fig. 39–15).

After treatment, acute microabscesses become necrotizing granulomas with central abscess and peripheral fibrosis

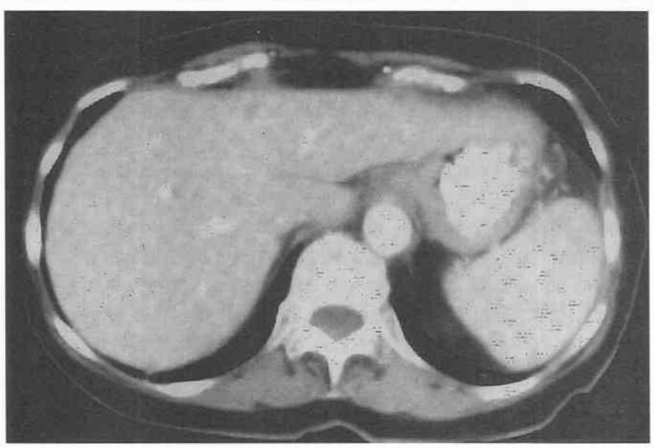

Figure 39–14. Enhanced CT scan demonstrates multiple low-attenuation candidal microabscesses in this patient with chronic lymphocytic leukemia. A hepatic fungal microabscess is present as well.

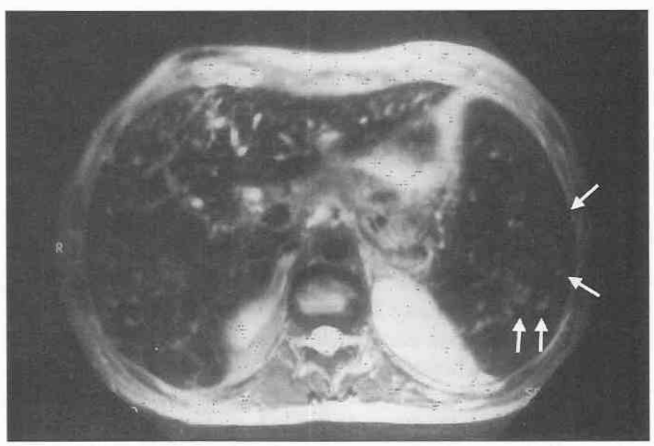

Figure 39–15. T2-weighted MR image demonstrates multiple small foci of increased signal (*arrows*) in both the spleen and the liver consistent with acute fungal abscesses. The spleen and liver are diffusely decreased in signal because of iron overload from multiple transfusions.

surrounded by a zone of lymphocytes and macrophages. In the setting of multiple blood transfusions, the macrophages contain iron,[68] which produces a low-signal ring around the lesions on all MRI sequences. The lesions are still small, typically less than 1 cm in diameter. The subacute treated lesions are intermediate to mildly high in signal intensity on T1- and T2-weighted MRI sequences and have a perilesional ring nearly void of signal intensity.

If the therapy is successful, the subacute granulomas progress to chronic healed lesions composed of fibrous tissue of differing densities and degrees of vascularization. Chronic healed fungal abscesses are low in signal intensity on T1-weighted images and isointense to mildly hyperintense on T2-weighted images. They have an irregular polygonal shape and measure 1 to 3 cm in diameter. No perilesional dark ring is noted. These lesions are best noted on the early post-gadolinium images as moderately hypointense foci. They are minimally hypointense on delayed post-gadolinium images.

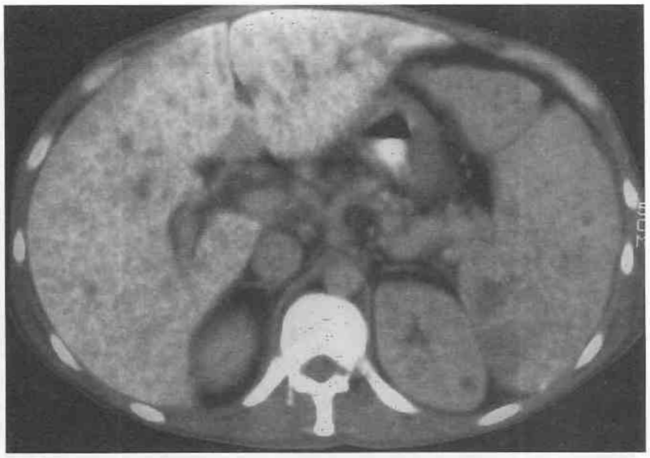

Figure 39–16. CT scan in a 38-year-old man with acquired immunodeficiency syndrome shows multiple foci of *Pneumocystis carinii* in the spleen and liver.

Other Infectious Processes

Other organisms, including *Mycobacterium tuberculosis*, *Mycobacterium avium-intracellulare*, and *Pneumocystis carinii*, may also infect the liver and spleen. Such infections tend to be miliary. *M. tuberculosis* infection can be seen in patients with immunodeficiency states associated with alcoholism, diabetes, steroid therapy, cancer, and HIV infection. Acutely, only splenomegaly may be present without focal lesions. Subsequently, microabscesses may form and may appear on CT as low-attenuation lesions. They may then progress to scattered punctate calcifications, innumerable calcifications throughout the spleen, and then to almost complete splenic calcifications.[46] In patients with HIV who have disseminated *M. tuberculosis*, the spleen is more commonly involved than the liver.[80]

CT is the preferred modality for evaluation of disseminated processes such as mycobacterial infections, because other intra-abdominal manifestations, such as lymphadenopathy and bowel wall thickening, are better appreciated on CT than on MRI. Splenic microabscesses are generally intermediate in signal intensity on T1-weighted MR images and measure from a few millimeters to 1 to 2 cm in diameter. They may show ring enhancement after administration of gadolinium. On T2-weighted images, the microabscesses are high in signal intensity. As the lesions calcify, they become low in signal intensity on both T1- and T2-weighted images.[122]

M. avium-intracellulare and *P. carinii* infections occur more commonly in patients with HIV infection. *M. avium-intracellulare* infection occurs as a late manifestation of AIDS. Differentiating between *M. tuberculosis* and *M. avium-intracellulare* can be difficult in patients with HIV. Focal splenic or hepatic lesions are noted in about 30% of patients with HIV who are infected with *M. tuberculosis* but are rarely noted in those infected with *M. avium-intracellulare* infection. Marked splenomegaly is more common in *M. avium-intracellulare* infection than in *M. tuberculosis* infection.[80, 93, 94]

P. carinii infections occur very commonly in patients with AIDS, typically as pneumonia. However, with improvements in therapies for *P. carinii* pneumonia, extrapulmonary *P. carinii* has become more common. When involved, the spleen may be enlarged with focal lesions that may become progressively calcified either in a rimlike or punctate fashion over a few months.[93, 95] However, not all lesions demonstrate calcification, even at follow-up (Fig. 39–16).[95]

Peliosis

Peliosis is a rare disorder characterized by multiple blood-filled spaces that may involve the liver and spleen. It can lead to portal hypertension and organ rupture.[75, 113] The disorder is associated with some drugs, including anabolic steroids and corticosteroids. However, peliosis is primarily associated with HIV and AIDS. In patients with AIDS, visceral peliosis is due to infection by *Bartonella henselae*, a treatable manifestation of AIDS. Infection by *B. henselae* affects multiple organ systems, including the skin, airway, mucous membranes, visceral organs, bone, and brain.[77] Kaposi's sarcoma may have a similar presentation in patients with AIDS. If Kaposi's sarcoma is clinically suspected in patient with AIDS, the treatable infection bacillary angiomatosis should be considered in the differential diagnosis.[77]

In bacillary angiomatosis, multiple, blood-filled cavities ranging in size from a few millimeters to 1 to 2 cm are noted in the liver and spleen. Such cavities may or may not have an endothelial lining and may communicate with dilated sinusoids.[94] Some of the cavities may be thrombosed. The imaging findings depend on the pathologic appearance. On CT, the liver lesions appear as multiple small, low-attenuation foci that become isodense with IV administration of a contrast agent, whereas the splenic lesions can be variable, ranging from nonenhancing hypodense nodules up to 1.5.cm in diameter to nodules with a target appearance and central enhancement. The thrombosed cavities remain low in attenuation with contrast enhancement.[75, 94] On MRI, multiple foci may be seen,

with increased signal intensity on T2-weighted images and variable signal intensity on T1-weighted images. The thrombosed cavities may show mixed signal on T2-weighted images because of the presence of deoxyhemoglobin and methemoglobin.[75] The diagnosis can be confirmed histologically.[76]

Sarcoidosis

Sarcoidosis is a systemic disease of unknown etiology. It involves primarily the thorax (mediastinal and hilar lymph nodes and lung parenchyma), skin, and eyes. Less commonly it involves the liver and spleen. Mesenteric and retroperitoneal lymph nodes can also be involved. The appearance can be similar to that of lymphoma, particularly non-Hodgkin's lymphoma, and to metastases. However, involvement of retrocrural nodes by sarcoidosis is rare. This feature may help distinguish sarcoidosis from non-Hodgkin's lymphoma, in which retrocrural node involvement is common.

The most common finding is nonspecific hepatosplenomegaly, although sarcoidosis may also manifest as nodular lesions.[107] Scott and associates[107] evaluated the various patterns of nodular hepatosplenic sarcoidosis. They found the single most common pattern of nodular involvement to be isolated splenic involvement. The other patterns, listed in order of frequency, were hepatosplenic involvement with splenic predominance, comparable hepatic and splenic involvement, and isolated hepatic involvement. Hepatosplenic involvement with hepatic predominance was the least common presentation.

On CT, the nodules of sarcoidosis are low in attenuation without contrast enhancement (Fig. 39–17).[60, 107] On MRI, nodular sarcoidosis has been described as having multiple low-signal intensity foci on T1- and T2-weighted images and no substantial enhancement.[122, 130]

Hydatid Disease

Splenic involvement is uncommon in hydatid disease, occurring in less than 2% to 8% of all patients with *Echinococcus*.[45, 90] The liver, lung, bone, and brain are more commonly affected than the spleen. Systemic dissemination and intraperitoneal spread from a ruptured liver cyst constitute the two main sources of spread to the spleen.[45] Hydatid cysts are not often seen except in areas where *Echinococcus* is endemic, such as Argentina, Greece, and Spain.[126]

The appearance of splenic hydatid cysts varies according to the age of the cyst and the associated complications, such as rupture and secondary infection. On CT, an uncomplicated cyst may have homogeneous fluid content with water attenuation; however, such a cyst may also contain debris, hydatid sand, or inflammatory cells that can cause high attenuation.[45] Peripheral calcifications may also be present. Classically, small daughter cysts, formed by invaginations of the inner layer of the cyst, are noted at the periphery of the main cyst.[126]

Hydatid cysts are prone to rupture. Although rupture can be clinically silent, there are many potential complications, including anaphylaxis, infection, peritoneal seeding, perforation of hollow viscera, and hematogenous spread.[90] Infection can occur if there is cyst rupture. Infected cysts may appear solid, may have a mixed solid and cystic pattern, or may contain air or air-fluid levels. CT and ultrasonography are the most useful modalities for diagnosis, with CT being preferred in cases of suspected infection.[90]

Splenomegaly

There are numerous causes of splenomegaly. Although CT or MRI can accurately determine splenic volume, the cause of the splenomegaly may not always be apparent from imaging alone. Splenomegaly can be due to congestion (e.g., portal hypertension, splenic vein thrombus), storage disease (i.e., Gaucher's disease, histiocytosis, amyloid), infection (i.e., infectious mononucleosis, tuberculosis), hematologic disorders (i.e., myelofibrosis, polycythemia vera), or neoplasms (i.e., leukemia, lymphoma). Splenomegaly is a nonspecific finding, but some of the possible causes of massive splenomegaly are chronic myelogenous leukemia, lymphoma, polycythemia vera, myelofibrosis, and chronic malaria (Fig. 39–18).[117]

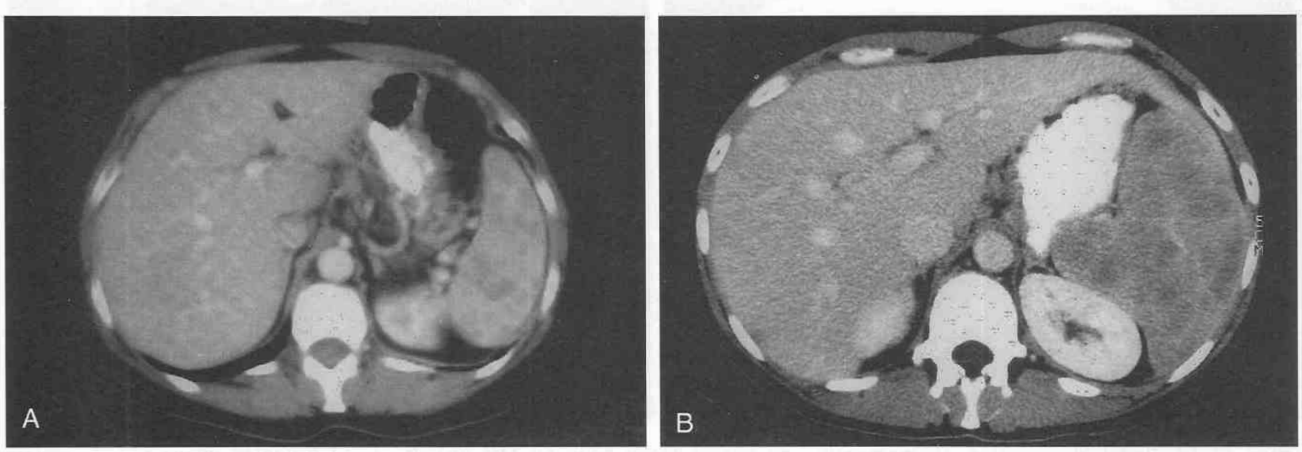

Figure 39–17. CT scans showing sarcoidosis of the spleen. *A*, Multiple small, nonenhancing foci of sarcoidosis in the spleen. The liver is not involved. *B*, Diffuse involvement of the spleen by sarcoid. The lesions are nonenhancing, and splenomegaly is present.

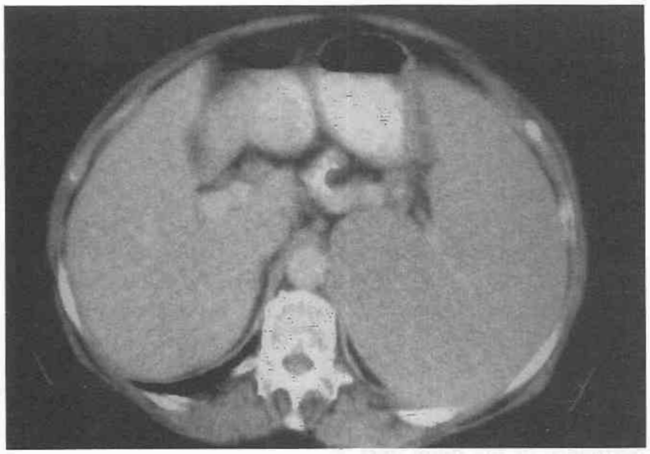

Figure 39–18. This CT scan reveals massive splenomegaly in a patient with non-Hodgkin's lymphoma.

Portal Hypertension

Portal hypertension is a frequent cause of splenomegaly. In addition to splenomegaly, there is enlargement of the splenic vein, formation of varices, and formation of gamna-gandy bodies, which are small remnants of intrasplenic hemorrhage composed of hemosiderin, fibrous tissue, and calcium.[122] On MRI, the gamna-gandy bodies are low in signal on T1- and T2-weighted images, appearing as multiple foci of signal void (Figs. 39–19 and 39–20).

Gaucher's Disease

Gaucher's disease is a metabolic disorder in which glucocerebroside accumulates abnormally in the reticuloendothelial system because of a deficiency of the enzyme glucocerebrosidase. Affected patients have hepatosplenomegaly, thrombocytopenia, and anemia. In one study, focal lesions were described on MRI in 30% of 46 patients with Gaucher's disease.[59] Both red and white types of nodules were noted. The white foci of solid Gaucher cells in the spleen were judged to be isointense on the T1-weighted images and low in signal on T2-weighted images, but the red focal lesions contained sinusoids and behaved more like hemangiomas, showing increased signal on T2-weighted images.[59] Infarcts were also noted.

Hemochromatosis

Hemochromatosis results from iron deposition in multiple organs, including the spleen. Primary hemochromatosis, an autosomal recessive disorder, causes organ damage such as cirrhosis and possible hepatocellular carcinoma. Secondary hemochromatosis is caused by deposition of iron into the reticuloendothelial system (spleen, bone marrow, liver Kupffer cells), usually from blood transfusions or rhabdomyolysis. On MRI, a decrease in signal intensity is seen on both T1- and T2-weighted images because the tissue iron is superparamagnetic (Fig. 39–21).

Trauma

The abdomen is one of the most frequently injured sites in both blunt and penetrating trauma; the spleen is the most commonly injured organ. A missed splenic injury is one of the most common causes of preventable death in patients with trauma.[133] Iatrogenic splenic injuries also occur, the most common being intraoperative injury. The spleen may also be inadvertently injured during percutaneous needle procedures, such as left thoracentesis, kidney biopsy, and colonoscopy.[118]

Splenic injuries due to blunt trauma are produced by (1) rapid deceleration with compression through the posterolateral chest wall, in which energy is transmitted to the spleen, or (2) a puncture of the spleen through adjacent rib fractures. The forces on the spleen result in capsular avulsions along the various ligamentous attachments. Because 5% of the cardiac output goes to the spleen, which has an extensive arterial supply, injuries to the spleen can cause significant hemorrhage.

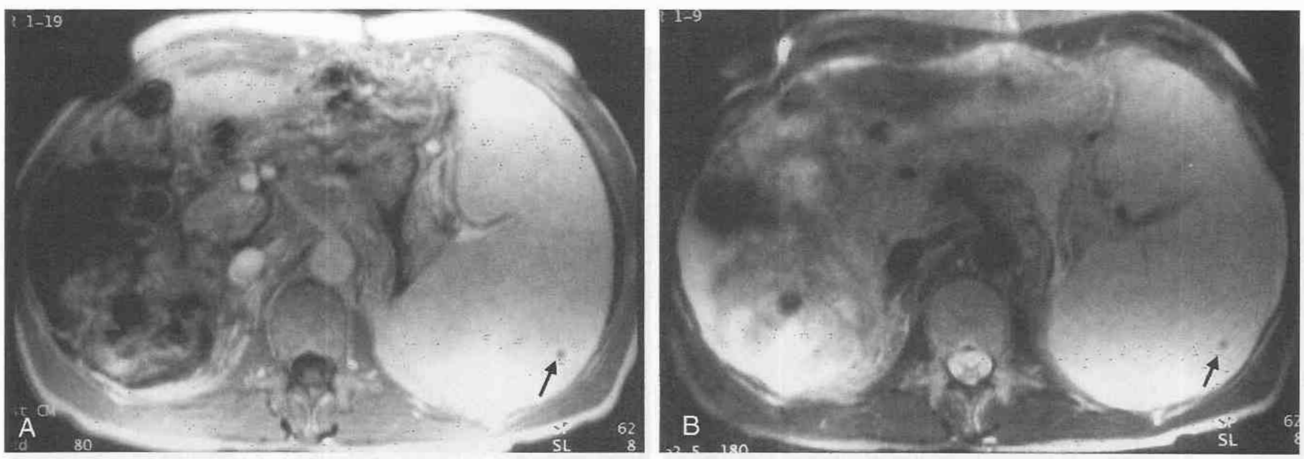

Figure 39–19. Portal hypertension, splenomegaly, and gamna-gandy body on MR images. *A*, T1-weighted image reveals massive splenomegaly. A gamna-gandy body is noted as low-signal, nonenhancing focus (*arrow*). *B*, T2-weighted image shows that the gamna-gandy body is low in signal (*arrow*).

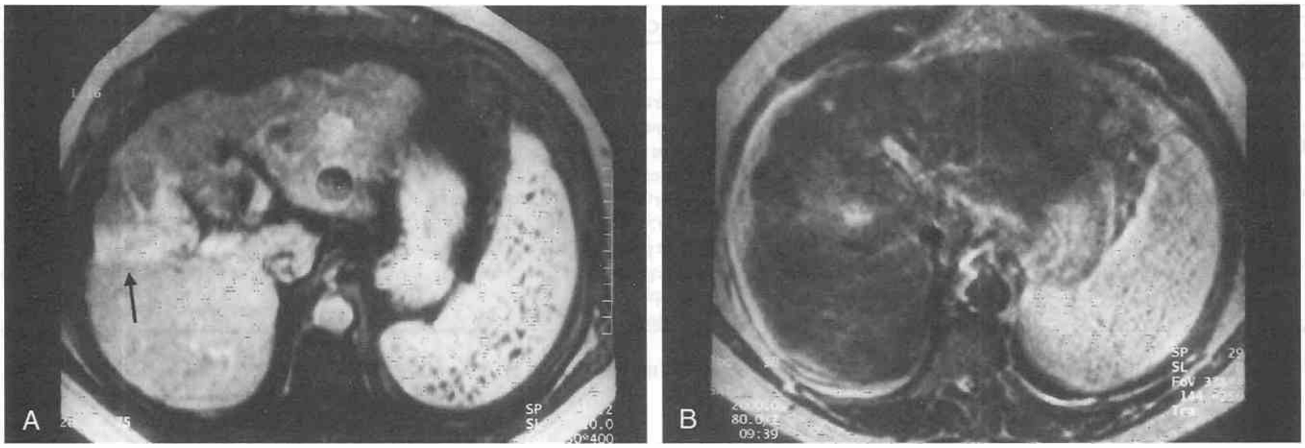

Figure 39–20. MR images showing multiple gamna-gandy bodies. *A*, T1-weighted image demonstrates multiple low-signal foci in the spleen consistent with gamna-gandy bodies. There is also an enhancing hepatocellular carcinoma in the liver (*arrow*). *B*, T2-weighted image reveals the low-signal splenic gamna-gandy bodies.

The clinical evaluation of the abdomen by physical examination may be limited at times because of a patient's altered mental status due to head trauma, alcohol, or drugs. A patient with labile blood pressure and tachycardia should be rapidly assessed for intra-abdominal blood with either diagnostic peritoneal lavage (DPL) or abdominal ultrasonography (FAST [focused assessment with sonography for trauma]; see later); if blood is detected, the patient must undergo surgery immediately. More stable patients may be evaluated for splenic injury by DPL, FAST, or CT scanning. Hemodynamically stable patients are often initially evaluated with ultrasonography. If free fluid is detected on ultrasonography, an abdominal CT scan is obtained to identify the source of bleeding, search for other intra-abdominal injuries, and determine the severity of the spleen injury.

The key to patient management involves grading the spleen injury after review of the CT images or careful inspection of the mobilized spleen in the operating room. The revised 1994 American Association for the Surgery of Trauma (AAST) standard for grading of splenic injury has now been adopted universally to facilitate clinical investigation and outcomes research (Table 39–1)[77]; the grades are as follows:

Grade I: A subcapsular hematoma involving less than 10% of the splenic surface area or a laceration less than 1 cm deep.

Grade II: A subcapsular hematoma involving 10% to 50% of the splenic surface area, an intraparenchymal hematoma less than 5 cm in diameter, or a laceration 1 to 3 cm deep that does not involve a trabecular vessel.

Grade III: A subcapsular hematoma involving more than 50% of the splenic surface area, ruptured subcapsular or parenchymal hematoma, intraparenchymal hematoma greater than 5 cm, or a laceration more than 3 cm deep or involving the trabecular vessels.

Grade IV: A hilar laceration and devascularization of more than 25% of the splenic mass.

Grade V: A shattered or early completely devascularized spleen.

The decision to proceed to surgical intervention is multifaceted and depends on more than the results of any radiologic test. Generally, however, most patients with grade IV or grade V injuries require surgery. Patients with active extravasation may require endovascular or surgical intervention, even for grade II or III injuries.[40]

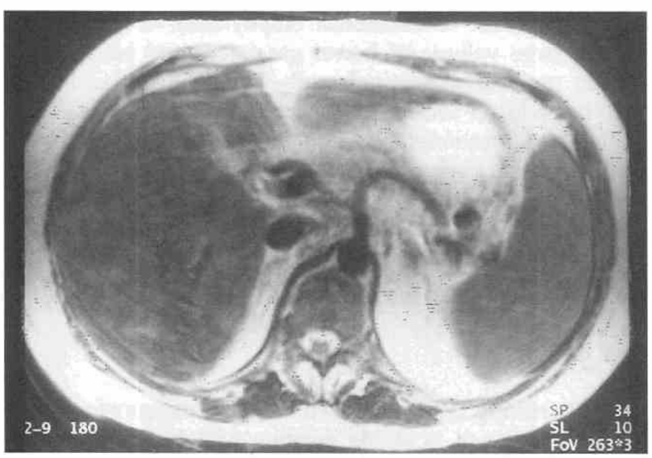

Figure 39–21. A T2-weighted MR image demonstrates diffusely decreased signal intensity of the spleen in this patient who has received multiple transfusions (TR = 5000 msec, TE = 83 msec).

Goals and Strategy

The initial emergency room evaluation for any patient who has experienced trauma involves stabilization and resuscitation according to Advanced Trauma Life Support (ATLS) guidelines.

Patients with a splenic injury are ideally managed at a trauma center with experience in all of the therapeutic options. At many centers, CT is considered the standard for evaluation for trauma. However, many centers also employ FAST in the emergency department setting.

Table 39–1. Splenic Injury Scale of the American Association for the Surgery of Trauma

Grade*	Type of Injury	Description
I	Hematoma	Subcapsular, <10% surface area
	Laceration	Capsular tear, ≤1-cm parenchymal depth
II	Hematoma	Subcapsular, 10–50% surface area; intraparenchymal, <5 cm in diameter
	Laceration	1–3-cm parenchymal depth that does not involve a trabecular vessel
III	Hematoma	Subcapsular, >50% surface area or expanding; ruptured subcapsular or parenchymal hematoma; intraparenchymal, >5 cm or expanding
	Laceration	>3-cm parenchymal depth or involving trabecular vessels
IV	Laceration	Laceration involving segmental or hilar vessels producing major devascularization (>25% of spleen)
V	Laceration	Completely shattered spleen
	Vascular	Hilar vascular injury that devascularizes spleen

* Advance one grade for multiple injuries, up to grade III.
From Moore EE, Cogbill TH, Jurkovich GJ, et al: Organ injury scaling: Spleen and liver (1994 revision). J Trauma 38:323–324, 1995.

Focused Assessment with Sonography for Trauma

A limited form of ultrasonography known as FAST has emerged as a new modality for the assessment of the injured torso. The 1992 introduction of this modality with the first published study in the United States rapidly changed the assessment of the trauma patient, so that by 1999, 79% of Level I trauma centers utilized FAST.[10, 124]

The use of ultrasonography as a FAST examination is indicated in the initial trauma evaluation of patients in whom there is a concern about intraperitoneal blood. The most important application is in the evaluation of hemodynamically unstable patients who have multiple injuries, so that a quick decision regarding surgery can be made. The place for ultrasonography in stable patients is less clear. In such patients, CT scanning is important for staging the injury because nonoperative management has become so prominent.

Technique

The FAST examination is performed as part of the primary survey in hemodynamically unstable patients or during the secondary survey in the trauma resuscitation area. This procedure evaluates for the presence of fluid in the following four areas: the subxiphoid region for the pericardial sac; the right upper quadrant in Morison's pouch; the left upper quadrant in the splenorenal recess; and the pelvis in the pouch of Douglas. The examination is performed in these four areas for the specific purpose of identifying hemoperitoneum or tamponade. It can be done at the patient's bedside at the same time as other procedures or evaluations. With the use of real-time imaging, physicians can receive instantaneous information to augment the trauma examination

The stable patient with a negative FAST result is followed clinically rather than evaluated with CT. The stable patient with a negative FAST result who has a high-energy pelvic ring fracture, the seatbelt sign, or a significant head injury may require abdominal CT.[6, 109] The stable patient with a positive FAST result should undergo a CT scan for grading of the splenic or liver injury. Generally, the unstable patient with a positive FAST result requires urgent exploratory laparotomy.

Efficacy

The sensitivity of FAST ranges from 85% to 99% with a specificity of 97% to 100%. False-negative results occur with retroperitoneal and hollow viscus injuries. Bode and colleagues[9] used ultrasonography to evaluate 353 patients with blunt trauma and found the technique to have 93% specificity and a 99% accuracy rate.[9] Rothlin and associates[100] reported that ultrasonographic assessment of intra-abdominal injuries in 290 patients had a sensitivity of 90% and a specificity of 99%.[100]

Boulanger and coworkers[10] reported in 1999 on their review of the utilization of the FAST examination. A survey of 96 Level I trauma centers in the United States and Canada found that 79% routinely use FAST; the examination is performed by surgeons in 39% of institutions, by surgeons and emergency departments in 21%, by emergency departments in 5%, and by radiologists in 35%.[10] The introduction of FAST has also changed management of patients with trauma in that CT scans and DPL are now used less for initial management.

The advantages of FAST are as follows: (1) it can be performed immediately at the bedside, making evaluation of the patient more efficient, (2) it is inexpensive, (3) it is noninvasive, and (4) it can be easily repeated. Its disadvantages involve the fact that it is examiner dependent. Assessment can be more difficult in the obese patient, the patient with significant subcutaneous emphysema, or the patient with a large volume of bowel gas interposed between the spleen and the abdominal wall. The FAST examination also has a lower sensitivity for free fluid volumes less than 500 mL. Ultrasonography can miss a solid organ injury that is not actively bleeding. The abdominal evaluation cannot grade splenic injuries. Other important injuries, such as bowel perforation, pancreatic fracture, and retroperitoneal injuries, may not be detected by ultrasonography.[109]

CT Scan

CT scanning is still the most common means of evaluating the abdomen in stable patients with blunt abdominal trauma, although the use of ultrasonography is rapidly increasing. The overall diagnostic accuracy of CT scanning is approximately 95%.[41, 66] The goals are to ascertain a diagnosis, to categorize the injury, and to reliably rule out

other concomitant injures in the management of the patient who has sustained blunt trauma to the abdomen. The indications for an abdominal CT scan are blunt trauma, hemodynamic stability, unreliable physical examination, and assessment for duodenal and pancreatic trauma because of the mechanism of injury. Contraindications for abdominal CT scans include clear indications for exploratory laparotomy, hemodynamic instability, and severe agitation.

State-of-the-art helical CT scans can very rapidly image the head, chest, abdomen, and pelvis as needed. Typically, a contrast agent is given both orally and intravenously as a bolus with a mechanical injector. The patient receives 400 mL of a dilute (2% to 5%) water-soluble contrast agent orally or through a nasogastric tube at least 30 to 50 minutes prior to the scan, usually while still in the trauma room. Once positioned inside the CT scanner, the patient should be given 100 mL of Optiray 240 (ioversol 51%, 240 mg I/mL) intravenously, at a rate of 2 to 3 mL per second via an automated injector, 45 to 60 seconds prior to image acquisition. Images obtained too early after the bolus of IV contrast agent is started often show heterogeneous enhancement of the spleen because of differential enhancement of the red and white pulp. Splenic lacerations may not be visualized during this phase of enhancement. If the spleen demonstrates this type of enhancement or if corticomedullary differentiation is still noted in the kidneys, delayed scans should be performed. Ideally, delayed scans should be performed within 2 to 3 minutes after initiation of the IV bolus. Uncooperative patients should be sedated to minimize motion artifacts.

Ideally, the presence of an experienced radiologist at the time of the scan will greatly enhance the value of the study. Injured patients are often imaged while still on a fracture board and with monitor wires overlying them; the board and wires can cause multiple artifacts on the images. Care should be taken to avoid misinterpreting such an artifact as a laceration. The entire abdomen and pelvis should be evaluated. Usually, the appearance of free abdominal fluid without solid organ injury on a CT scan should raise the suspicion of mesenteric, intestinal, or bladder injury, and an exploratory laparotomy may be warranted. Subtle signs of bowel injury should also be assessed, such as free intraperitoneal air, focal wall thickening, and mesenteric edema or fluid.[115]

Splenic subcapsular hematomas may be isodense to the spleen on nonenhanced CT scans. They are better visualized after IV administration of a contrast agent because they do not enhance unless there is active hemorrhage. Most subcapsular hematomas have some mass effect on the adjacent splenic parenchyma; this finding differentiates them from perisplenic hematomas, which do not deform the spleen. Splenic lacerations are linear, low-attenuation parenchymal defects. A *fracture* is a laceration traversing two capsular surfaces. Multiple lacerations and fractures appear as a shattered spleen. Intraparenchymal hematomas appear as low-attenuation, rounded areas. Lack of enhancement of part or all of the spleen suggests injury or thrombosis of the splenic artery or segmental artery (Fig. 39–22). In addition to the size of the splenic injury, the presence of active bleeding should be assessed. *Active bleeding* is defined as CT evidence of focal intrasplenic or perisplenic collection that has attenuation values similar to those of the aorta or a major adjacent artery and greater than the attenuation value of the spleen.[40, 49, 110] As stated previously, the presence of active bleeding may necessitate surgery even for a relatively low-grade splenic injury.[40]

Although most splenic injuries are well demonstrated on CT, there are various sources of false-negative and false-positive interpretations. A perisplenic clot (*sentinel clot*) may be seen with splenic injury. Both hemoperitoneum and a sentinel clot may be noted in cases of splenic injury without obvious visualization of a laceration.[134] Sources of potential false-positive interpretations include congenital clefts, splenic cysts, beam-hardening artifacts, and images obtained too early after the IV contrast bolus is given. Congenital clefts through the spleen should not be mistaken for lacerations. Splenic clefts are common variants. They can occur anywhere but tend to be in the superomedial aspect of the spleen (see Fig. 39–1). A lack of perisplenic hematoma would suggest a congenital cleft and not a laceration. Splenic cysts are usually spherical and low in attenuation.

A prospective multi-institutional study found that patients with negative abdominal CT scan results do not require the usual 24 to 48 hours of hospitalization for observation.[74] The initial abdominal CT scan had a negative predictive value of 99.63% on the basis of the subsequent need for laparotomy. This excellent study of more than 2000 patients showed that even a patient with abdominal tenderness could be sent home if CT scan results are negative, because CT scan findings are diagnostic for the presence or absence of abdominal injury but physical examination findings are not.

However, delayed rupture of the spleen can occur up to 10 days after injury. This complication is believed to be associated with subtle low-grade injury to the spleen that is not detectable on CT, ultrasonography, or DPL.[71] The exact incidence of delayed rupture of the spleen is not known.

Diagnostic Peritoneal Lavage

DPL, initially described in 1965, was the standard diagnostic procedure for blunt trauma for the next two decades.[60] The procedure is a rapid and accurate test used to identify intra-abdominal injuries in patients who are hypotensive or are unresponsive after incurring blunt trauma to the abdomen but who have no obvious indication for abdominal exploration.

Indications include equivocal physical findings, unexplained shock, altered sensorium, and general anesthesia for extra-abdominal procedures. DPL is still indicated (1) for the unstable patient with an indeterminate FAST result and (2) to rule out a bowel injury in the stable patient in whom FAST and CT scans show free fluid with no solid organ injury. Contraindications to DPL include a clear indication for exploratory laparotomy. Some relative contraindications are previous exploratory laparotomy, pregnancy, and obesity.

DPL is highly sensitive to the presence of intraperitoneal blood, with sensitivities approaching 99%; however, its specificity is lower. Significant injures that can be missed

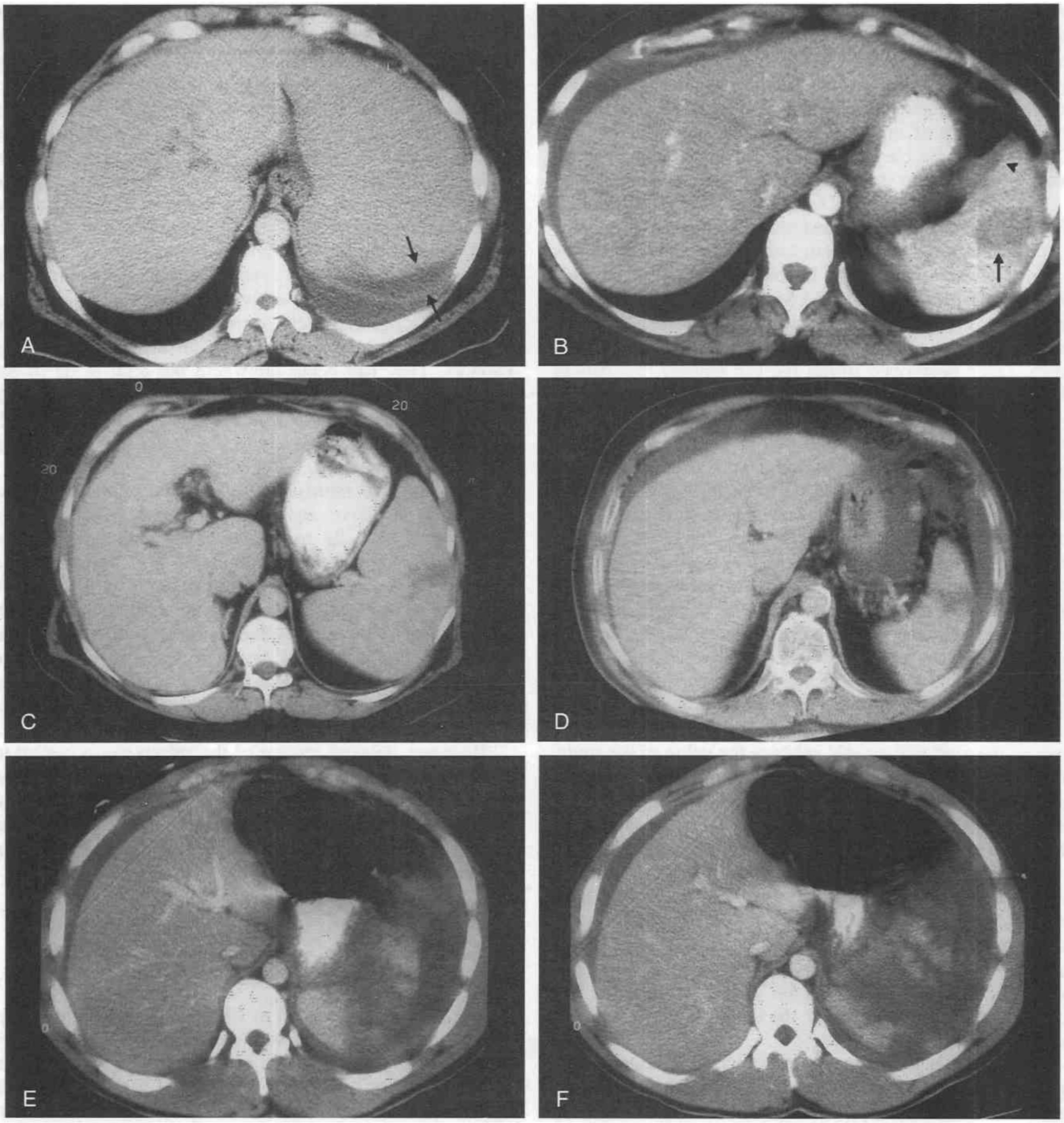

Figure 39–22. CT scans showing classification of trauma to the spleen. *A*, Grade I injury: A small subcapsular hematoma (*arrows*) can be seen in a patient with an enlarged spleen from chronic lymphocytic leukemia. There is also a left pleural effusion. *B*, Grade II injury: A 4-cm intraparenchymal hematoma (*arrow*) and a 30% subcapsular hematoma (*arrowhead*) are seen in a patient after a fall. *C*, Grade II injury: A 3-cm laceration without involvement of trabecular vessels is shown in the lateral aspect of the spleen. *D*, Grade III injury: There is a 4-cm laceration near the hilum. *E*, Grade IV injury: Hilar laceration with devascularization of approximately 50% of the spleen can be seen. *F*, Grade V injury: The spleen is shattered, and only minimal parenchyma remains.

by DPL include retroperitoneal hematomas and diaphragmatic tears as well as renal, pancreatic, duodenal, and extraperitoneal bladder injuries. DPL may give false-positive results in the presence of a pelvic fracture, because of bleeding from the retroperitoneum into the peritoneal cavity.

The major advantage of DPL is that it requires no specialized equipment and is a rapid, sensitive technique to determine whether there is intraperitoneal blood. As CT began to be utilized, it became apparent in some hemodynamically stable patients, small splenic injuries could cause a positive DPL result and lead to nontherapeutic laparotomy. In other words, for stable patients, DPL was too sensitive.

Nonoperative Management

Blunt traumatic injury to the spleen is no longer considered to require immediate exploratory laparotomy. The lifelong susceptibility of these patients who have undergone surgery to infectious complications has prompted splenic conservation whenever safe and feasible. In most hemodynamically stable patients with blunt splenic trauma, management has evolved from splenectomy to splenorrhaphy to nonoperative management. Nonoperative management is not an easy approach, however, because it requires close monitoring, serial clinical examinations, and a high level of vigilance and familiarity with the course of splenic injuries. The goal is to preserve the spleen's role in the immune system and to save the patient the morbidity of exploratory surgery.

The spleen's anatomy holds the key to successful observation in splenic injury. In children, the splenic capsule is relatively thicker than in adults and can contract, thus leading to tamponade. This ability lessens with age as the vessels harden, making the spleen more friable in older patients. The spleen in such patients has a thinner capsule and is less able a to contract, so observation as treatment is less successful in older patients with blunt splenic injury.

Pediatric patients were the first to benefit from the nonoperative approach to splenic injuries, with success rates of 97%.[65] In the 1990s, the success rate for nonoperative treatment of hemodynamically stable adult patients with blunt splenic injuries exceeded 90%. Such treatment has always been less successful than in adults in children, probably because of (1) the greater severity of adult injuries and (2) the higher number of associated extra-abdominal and intra-abdominal injuries in adult patients, which preclude a nonsurgical approach in patients with injured spleens (Fig. 39–23).[91]

Angiography

Angiography has become an integral part of the nonsurgical armamentarium available for the care of the patient with trauma. In the appropriate setting, angiography is indicated for such patients in whom contrast extravasation and active hemorrhage are demonstrated on initial CT scan. If a bleeding vessel or pseudoaneurysm is noted, embolization can be performed. Scalfani and associates[104] have documented a splenic salvage rate of 93% to 97%. Pachter and colleagues[86] report a 98% salvage rate with no mortality for the use of angio-embolization if (1) active hemorrhage is detected on initial CT scan, (2) the patient's hematocrit drops, or (3) a new or worsening injury is demonstrated on a second CT scan. Selective arteriography is relatively contraindicated in patients with hemodynamic instability, peritonitis, or other indications for emergent surgery. It remains unclear whether splenic artery embolization has any detrimental effect on the spleen's immune function.

Splenic Infarcts

Splenic infarcts occur commonly and have various causes. The splenic arterial branches are end arteries with no intercommunication. Causes of splenic infarcts include embolic disease (i.e., mitral valve disease, endocarditis, atheromatous plaques), arteritis, splenic artery aneurysm or occlusion (pancreatic disease), sickle cell disease (thrombo-

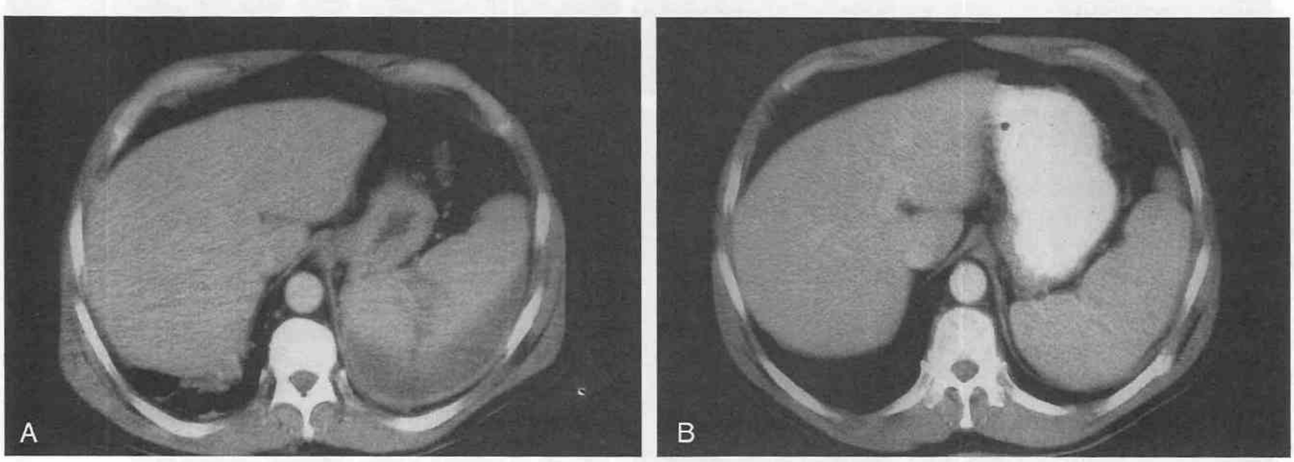

Figure 39–23. CT scans following the conservative management of a grade III splenic injury in an adult. *A*, Initial CT scan demonstrates a grade III injury with a large subcapsular hematoma and a 5-cm laceration. *B*, Follow-up CT obtained at 3 months shows complete healing.

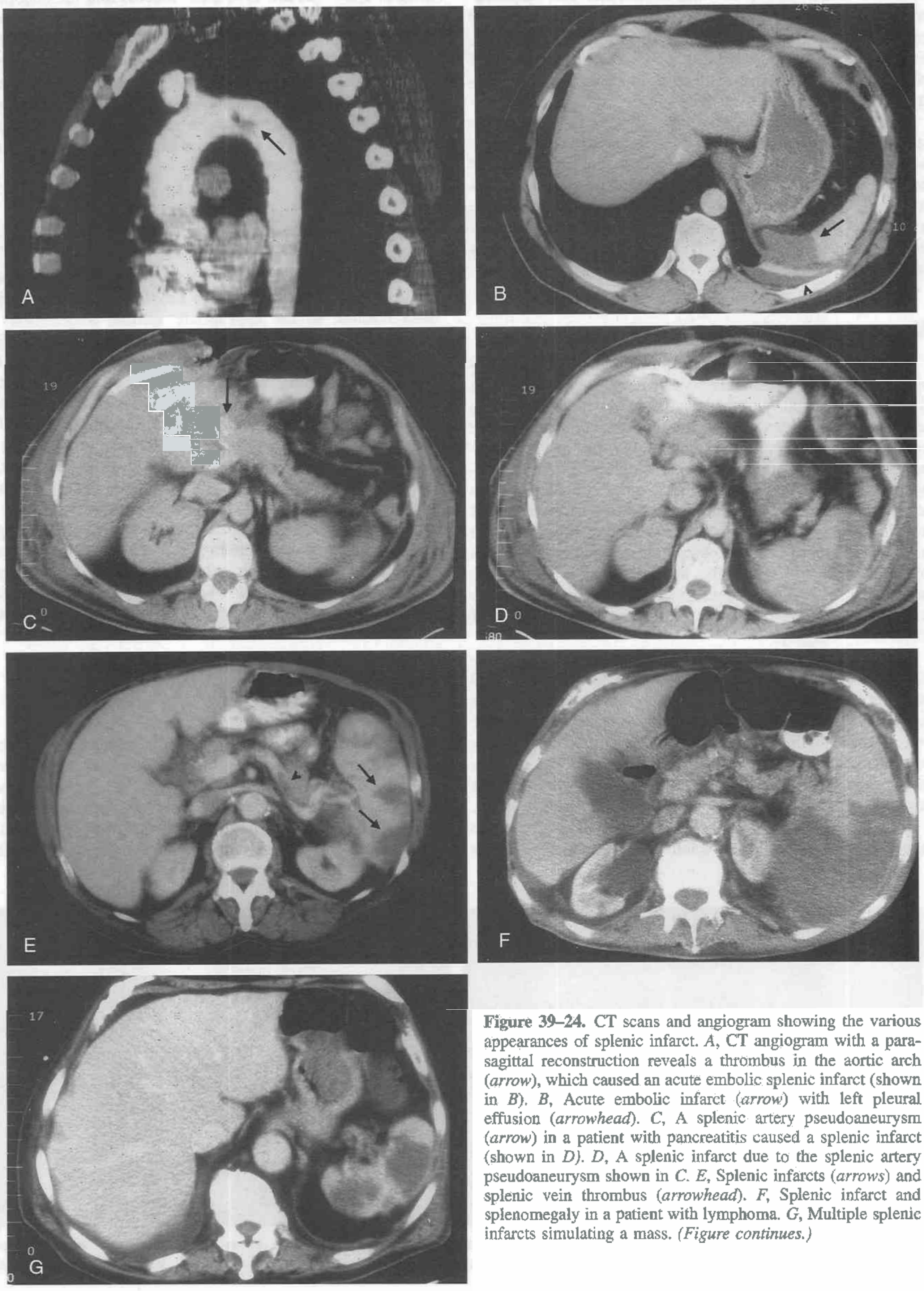

Figure 39–24. CT scans and angiogram showing the various appearances of splenic infarct. *A*, CT angiogram with a parasagittal reconstruction reveals a thrombus in the aortic arch (*arrow*), which caused an acute embolic splenic infarct (shown in *B*). *B*, Acute embolic infarct (*arrow*) with left pleural effusion (*arrowhead*). *C*, A splenic artery pseudoaneurysm (*arrow*) in a patient with pancreatitis caused a splenic infarct (shown in *D*). *D*, A splenic infarct due to the splenic artery pseudoaneurysm shown in *C*. *E*, Splenic infarcts (*arrows*) and splenic vein thrombus (*arrowhead*). *F*, Splenic infarct and splenomegaly in a patient with lymphoma. *G*, Multiple splenic infarcts simulating a mass. *(Figure continues.)*

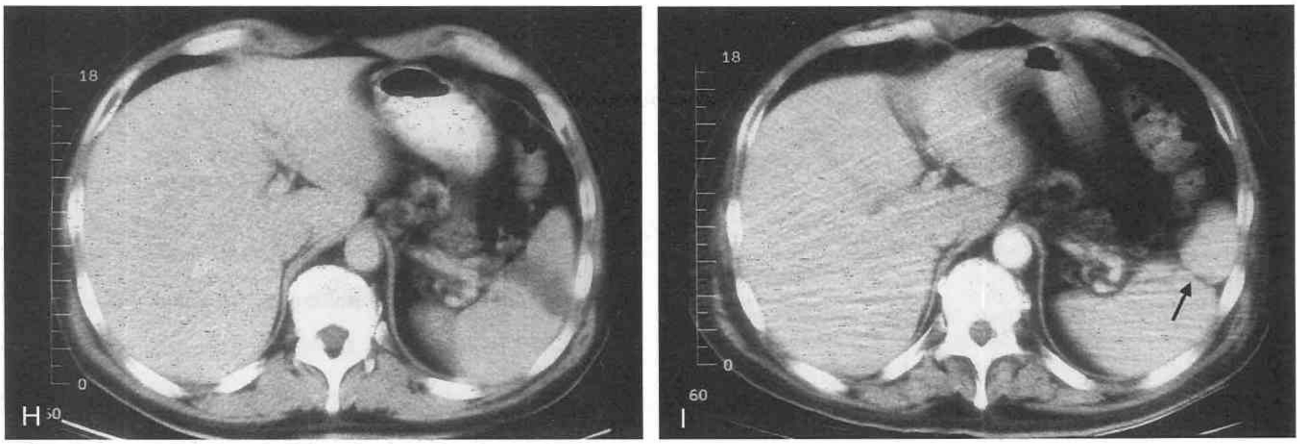

Figure 39–24. *Continued. H* and *I,* Evolution of a splenic infarct. The acute splenic infarct (*H*) heals to become fissure-like (*arrow*) at 9-month follow-up (*I*).

sis), or mass lesions. Most cases are asymptomatic, although some patients have acute onset of left upper quadrant pain. The infarcts are typically focal but can be diffuse. Infarcts in younger patients are due more often to thrombosis from a hematologic disorder; infarcts in older patients tend to be embolic (Fig. 39–24).

On CT and MRI, infarcts are usually wedge-shaped but may be irregular in contour. Although the infarct has no enhancement, there can be peripheral enhancement of the capsule. Infarcts can also be multiple. As described previously, differentiating between infarct and abscess or tumor can sometimes be difficult. A lack of mass effect and perisplenic changes suggests infarct. Over time, infarcts decrease in size. Any increase in size would be suspicious for superimposed infection. On MRI, the signal of the infarct can vary, depending on its composition and age.[65] Hemorrhagic infarcts may be high in signal on T1- and T2-weighted images.[65]

Chronic splenic infarction, as seen in homozygous sickle cell anemia, leads to near-complete calcification and atrophy of the spleen. Adults with heterozygous hemoglobinopathies may have enlarged spleens with subcapsular calcification (Fig. 39–25).

Miscellaneous Disorders of the Spleen

Splenosis

Splenosis is caused by autotransplantation of splenic tissue. It usually occurs after trauma. The implants are located throughout the peritoneum. The diagnosis can be confirmed by a nuclear medicine heat-damaged red cell scan.

Inflammatory Pseudotumor

Inflammatory pseudotumor of the spleen is a rare, benign lesion composed of localized areas of inflammatory cells.[64] The etiology is uncertain. On CT, such areas are

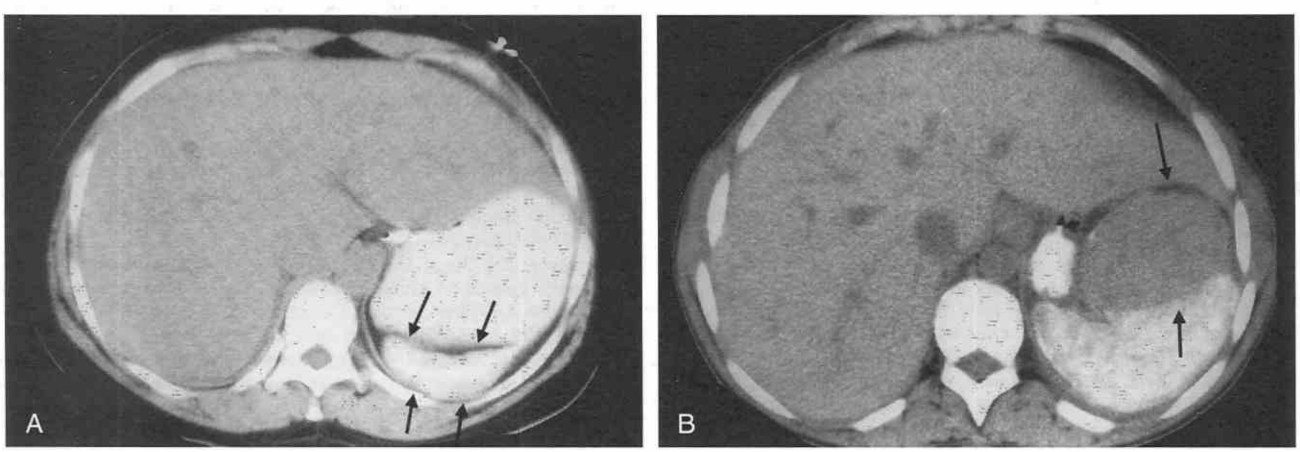

Figure 39–25. CT scans in sickle cell disease. *A,* Calcified, shrunken spleen in a patient with homozygous sickle cell anemia (*arrows*). *B,* Scan in an adult patient with homozygous sickle cell anemia and nearly complete splenic calcification, with a subcapsular hematoma (*arrows*), after undergoing exploratory laparotomy. The liver is also diffusely increased in attenuation, suggesting iron overload.

low in attenuation on nonenhanced images and show progressive opacification after IV administration of a contrast agent.[93] Calcifications may be present. Inflammatory pseudotumors have been described as being low in signal on T2-weighted MR images with delayed enhancement on T1-weighted images after IV administration of gadolinium; however, because there are few reports, the imaging characteristics of these lesions have not been established.[64]

References

1. Ahmann DL, Kiely JM, Harrison EG, Payne WS: Malignant lymphoma of the spleen. Cancer 19:461–469, 1996.
2. Al-Salem AH, Qaisaruddin S, Nasserallah Z, et al: Splenectomy in patients with sickle-cell disease. Am J Surg 172:254–258, 1996.
3. Allen KB, Andrews G: Pediatric wandering spleen—the case for splenopexy: Review of 35 reported cases in the literature. J Pediatr Surg 24:432–436, 1989.
4. Alonso Cohen MA, Galera MJ, et al: Splenic abscess. World J Surg 14:513–517, 1990.
5. Badaloow AV, Singhal A, Forrester TE, et al: The effect of splenectomy for hypersplenism on whole body protein turnover, resting metabolic rate and growth in sickle cell disease. Eur J Clin Nutr 50: 672–675, 1996.
6. Ballard RB, Rozycki GS, Newman PG, et al: An algorithm to reduce the incidence of false-negative FAST examinations in patients at high risk for occult injury. J Am Coll Surg 189:145–150, 1999.
7. Balthazar EJ, Hilton S, Naidich D, et al: CT of splenic and perisplenic abnormalities in septic patients. AJR Am J Roentgenol 144: 53–56, 1985.
8. Barone JE, Burns G, Svehlak SA, et al: Management of blunt splenic trauma in patients older than 55 years: Southern Connecticut Regional Trauma Quality Assurance Committee. J Trauma 46:87–90, 1990.
9. Bode PJ, Niezen RA, van Vught AB, et al: Abdominal ultrasound as a reliable indicator for conclusive laparotomy in blunt abdominal trauma. J Trauma 34:27–31, 1993.
10. Boulanger BR, Kearney PA, Brenneman FD, et al: Utilization of FAST (Focused Assessment with Sonography for Trauma) in 1999: Results of a Survey of North American Trauma Centers. Am Surgeon 66:1049–1055, 2000.
11. Boulanger BR, McLellan BA, Brenneman FD, et al: Emergent abdominal sonography (EAS) as a screening test in a new diagnostic algorithm for blunt trauma. J Trauma 40:867–874, 1996.
12. Boulanger BR, McLellan BA, Brenneman FD, et al: Prospective evidence of the superiority of a sonography-based algorithm in the assessment of blunt abdominal injury. J Trauma 47:632–637, 1999.
13. Bouvet M, Babiera GV, Termuhlen PM, et al: Splenectomy in the accelerated or blastic phase of chronic myelogenous leukemia: A single-institution, 25-year experience. Surgery 122:20–25, 1997.
14. Branney SW, Moore EE, Cantrill SV, et al: Ultrasound based key clinical pathway reduces the use of hospital resources for the evaluation of blunt abdominal trauma. J Trauma 42:1086–1090, 1997.
15. Brigden ML: Overwhelming postsplenectomy infection still a problem. West J Med 157: 440–443, 1992.
16. Britt AR, Francis IR, Glazer GM, Ellis JH: Sarcoidosis: Abdominal manifestations at CT. Radiology 178:91–94, 1991.
17. Brodsky J, Abcar A, Styler M: Splenectomy for non-Hodgkin's lymphoma. Am J Clin Oncol 19:558–561, 1996.
18. Brunt LM, Langer JC, Quesebarth MA, Whitman ED: Comparative analysis of laparoscopic versus open splenectomy. Am J Surg 172: 596–601, 1996.
19. Bunt TJ, Hackler MT, Greene FL: Isolated splenic vein thrombosis: The curable variceal hemorrhage. South Med J 76:936–941, 1983.
20. Bussel J, Cines D: Immune thrombocytopenic purpura, neonatal alloimmune thrombocytopenia and posttransfusion purpura. In Hofffman R (ed): Hematology: Basic Principles and Practice, 3rd ed. Philadelphia, Churchill Livingstone, 2000, pp 2096–2105.
21. Buzzas GR, Kern SJ, Smith S, et al: A comparison of sonographic examinations for trauma performed by surgeons and radiologists. J Trauma 44:604–608, 1998.
22. Cala Z, Cvitanovic B Laparoscopic treatment of nonparasitic cysts of the spleen and liver. J Laparoendosc Surg 6:387–391, 1996.
23. Caplan ES, Botansky H, Snyder MJ, et al: Response of traumatized splenectomized patients to immediate vaccination with polyvalent pneumococcal vaccine. J Trauma 23:801–805, 1983.
24. Chen KTK, Bolles JC, Gilbert EF: Angiosarcoma of the spleen: A report of two cases and review of the literature. Arch Pathol Lab Med 103:122–124, 1979.
25. Chulay JD, Lankerani MR: Splenic abscess: Report of 10 cases and review of the literature. Am J Med 61:513–522, 1976.
26. Chun CH, Raff MJ, Contreras L, et al: Splenic abscess. Medicine 59:50–65, 1980.
27. Cocanour CS, Moore FA, Ware DN, et al: Delayed complications of nonoperative management of blunt adult splenic trauma. Arch Surg 8:322–325, 1998.
28. Cole JT, Flaum MA: Postsplenectomy infections. South Med J 85: 120–124, 1992.
29. Coon WW: Splenectomy for massive splenomegaly. Surg Gynecol Obstet 169:235–237, 1989.
30. Cusak JC, Symour JF, Lerner S, et al: Role of splenectomy in chronic lymphocytic leukemia. J Am Coll Surg 185:237–243, 1997.
31. Dachman AH, Buck JL, Krishnan J, et al: Primary non-Hodgkin's splenic lymphoma. Clin Radiol 53:137–142, 1998.
32. Dachman AH, Ros PR, Murari PJ, et al: Nonparasitic splenic cysts: A report of 52 cases with radiologic-pathologic correlation. AJR Am J Roentgenol 147:537–542, 1986.
33. Davis KA, Fabian TC, Croce MA, et al: Improved success in nonoperative management of blunt splenic injuries: Embolization of splenic artery pseudoaneurysms. J Trauma 44:1008–1015, 1998.
34. Delaitre B, Maignien BL: Laparoscopic splenectomy—technical aspects. Surg Endosc 6:305–308,1992.
35. Delaitre B, Pitre J: Laparoscopic splenectomy versus open splenectomy: A comparative study. Hepatogastroenterology 44:45–49, 1997.
36. Diez J, Eisenstat M, Chung R: A case controlled study of laparoscopic splenectomy. Am J Surg 171:348–350, 1997.
37. Doolas A, Nolte M, McDonald OG, Economou SG: Splenic cysts. J Surg Oncol 10:369–387, 1978.
38. Emery KH: Splenic emergencies. Radiol Clin North Am 35:831–843, 1997.
39. Eshaghi N, Ros PR: Imaging of splenic masses. Contemp Diagn Radiol 12:1–6, 1989.
40. Federle MP, Courcoulas AP, Powell M, et al: Blunt splenic injury in adults: Clinical and CT criteria for management, with emphasis on active extravasation. Radiology 206:137–142, 1998.
41. Federle MP, Goldberg HI, Kaiser JA, et al: Evaluation of abdominal trauma by computed tomography. Radiology 138:637–644, 1981.
42. Ferrozzi F, Bova D, Draghi F, Garlaschi G: CT findings in primary vascular tumors of the spleen. AJR Am J Roentgenol 166:1097–1101, 1996.
43. Fishman EK, Kuhlman JE, Jones RJ: CT of lymphoma: Spectrum of disease. Radiographics 11:647–669, 1991.
44. Flowers JL, Lefor AT, Steers J, et al: Laparoscopic splenectomy in patients with hematologic diseases. Ann Surg 224:19–28, 1996.
45. Franquet T, Montes M, Lecumberri FJ, et al: Hydatid disease of the spleen: Imaging findings in nine patients. AJR Am J Roentgenol 154:525–528, 1990.
46. Freeman JL, Jafri SZ, Roberts JL, et al: CT of congenital and acquired abnormalities of the spleen. Radiographics 13:597–610, 1993.
47. Friedman RL, Hiatt JR, Korman JL, et al: Laparoscopic or open splenectomy for hematologic disease: Which approach is superior? J Am Coll Surg 185:49–54, 1997.
48. Gadacz TR: Splenic abscess. World J Surg 9:410–415, 1985.
49. Gavant ML, Schurr M, Flick PA, et al: Predicting clinical outcome of nonsurgical management of blunt splenic injury: Using CT to reveal abnormalities of splenic vasculature. AJR Am J Roentgenol 168:207–211, 1997.
50. George JN, Woolf SH, Raskob GE, et al: Idiopathic thrombocytopenia purpura: A practice guideline developed by explicit methods for the American Society of Hematology. Blood 88:3–40, 1996.
51. Gigot JF, Jamar F, Ferrant A, et al: Inadequate detection of accessory spleen and splenosis with laparoscopic splenectomy: A shortcoming of the laparoscopic approach in hematologic diseases. Surg Endosc 12:101–106, 1998.
52. Glasgow RE, Yee LF, Mulvihill SJ: Laparoscopic splenectomy: The emerging standard. Surg Endosc 11:108–111, 1997.
53. Glatstein E, Guernsey JM, Rosenberg SA, et al: The value of laparotomy and splenectomy in the staging of Hodgkin's disease. Cancer 24:709–718, 1969.

54. Gleich S, Wolin DA, Berbsman H: A review of percutaneous drainage of splenic abscess. Surg Gynecol Obstet 167:211–216, 1988.
55. Godley CD, Warren RL, Sheridan RL, et al: Nonoperative management of blunt splenic injury in adults: Age over 55 years as a powerful predicator of failure. J Am Coll Surg 183:133–140, 1996.
56. Gollard R, Lee TC, Piro LD, et al: The optimal management of hairy cell leukemia. Drugs 49:921–931, 1995.
57. Grosfeld JL: American Board of Surgery. Bull Am Coll Surg 81: 57, 1996.
58. Hagiwara A, Yukioka T, Ohta S, et al: Nonsurgical management of patients with blunt splenic injury: Efficacy of transcatheter arterial embolization. AJR Am J Roentgenol 167:159–166, 1996.
59. Hill SC, Damaska BM, Ling A, et al: Gaucher disease: Abdominal MR imaging findings in 46 patients. Radiology 184:561–566, 1992.
60. Hoeffel C, Bokemeyer C, Hoeffel JC, et al: CT hepatic and splenic appearances with sarcoidosis. Eur J Radiol 23:94–96, 1996.
61. Holdsworth RJ, Irving AD, Cuschieri A: Postsplenectomy sepsis and its mortality rate: Actual vs perceived risks. Br J Surg 78: 1031–1038, 1991.
62. Hopper KD, Chantelois AE: The retrorenal spleen: Implications for percutaneous left renal procedures. Invest Radiol 24:592–595, 1989.
63. Husni EA: The clinical course of splenic hemangioma. Arch Surg 83:681–688, 1961.
64. Irie H, Honda H, Kaneko K, et al: Inflammatory pseudotumors of the spleen: CT and MRI findings. J Comput Assist Tomogr 20: 244–248, 1996.
65. Ito K, Mitchell DG, Honjo K, et al: MR imaging of acquired abnormalities of the spleen. AJR Am J Roentgenol 168:697–702, 1997.
66. Jeffrey RB, Laing FC, Federle MP, Goodman PC: Computed tomography of splenic trauma. Radiology 141:729–732, 1981.
67. Joffe N, Antonioli DA: Penetration into the spleen by benign gastric ulcers. Clin Radiol 32:177–181, 1981.
68. Johnson TL, Barnett JL, Appelman HD, Nostrant T: *Candida* hepatitis: Histopathologic diagnosis. Am J Surg Pathol 12:716–720, 1988.
69. Kathouda N, Hurwitz MB, Rivera RT, et al: Laparoscopic splenectomy outcome and efficacy in 103 consecutive patients. Ann Surg 228:568–578, 1998.
70. King H, Shumacker HB: Splenic studies. I: Susceptibility to infection after splenectomy performed in infancy. Ann Surg 136:239–241, 1952.
71. Kluger Y, Douglas DB, Raves JJ, et al: Delayed rupture of the spleen—myths, facts and their importance: Case reports and literature review. J Trauma 36:568–571, 1994.
72. Lankisch PG: The spleen in inflammatory pancreatic disease. Gastroenterology 98:509–516, 1990.
73. Lewis JH, Hasmukh RP, Zimmerman HJ: The spectrum of hepatic candidiasis. Hepatology 2:479–487, 1982.
74. Livingston DH, Lavery RF, Passannante MR, et al: Admission or observation is not necessary after a negative abdominal computed tomographic scan in patients with suspected blunt abdominal trauma: Results of a prospective, multi-institutional trial. J Trauma 44:273–282, 1998.
75. Maves CK, Caron KH, Bisset GS, Agarwal R: Splenic and hepatic peliosis: MR findings. AJR Am J Roentgenol 158:75–76, 1992.
76. Moore EE, Cogbill TH, Jurkovich GJ, et al: Organ injury scaling: Spleen and liver (1994 revision). J Trauma 38:323–324, 1995.
77. Moore EH, Russell LA, Klein JS, et al: Bacillary angiomatosis in patients with AIDS: Multiorgan imaging findings. Radiology 197: 67–72, 1995.
78. Morel P, Dupriez B, Gosselin B, et al: Role of early splenectomy in malignant lymphomas with prominent splenic involvement. Cancer 71:207–215, 1993.
79. Morgenstern L, Rosenberg J, Geller SA: Tumors of the spleen. World J Surg 9:486–476, 1985.
80. Murray JG, Patel MD, Lee S, et al: Microabscesses of the liver and spleen in AIDS: Detection with 5-MHz sonography. Radiology 197: 723–727, 1995.
81. Nelken N, Ignatius J, Skinner M, Christensen N: Changing clinical spectrum of splenic abscess. Am J Surg 154:27–33, 1987.
82. Nelson EW, Mane MC: Splenectomy in high risk patients with splenomegaly. Am J Surg 178:581–586, 1999.
83. Oksenhendler E, Bierling P, Chevret S, et al: Splenectomy is safe and effective in human immunodeficiency virus–related immune thrombocytopenia. Blood 82:29, 1993.
84. Onders RP, Stellato TA: Utility of laparoscopy in evaluating and treating lymphomas [abstract]. Surg Endosc 12:S39, 1998.
85. Pachter HL, Hofstetter S: Splenic salvage procedures: Therapeutic options. In Cameron JL (ed): Current Surgical Therapy, 6th ed. St. Louis, Mosby, 1998, pp 551–556.
86. Pachter HL, Hofstetter SR, Guth AA, et al: Changing patterns in the management of splenic trauma: The impact of non-operative management. Ann Surg 227:708–719, 1998.
87. Park A, Gagner M, Pomp A: The lateral approach to laparoscopic splenectomy. Am J Surg 173:126–130, 1997.
88. Park JY, Song KT: Splenic cyst: A case report and review of the literature. Am Surg 37:544–547, 1971.
89. Pastakia B, Shawker TH, Thaler M, et al: Hepatosplenic candidiasis: Wheels within wheels. Radiology 166:417–421, 1988.
90. Pedrosa I, Saiz A, Arrazola J, et al: Hydatid disease: Radiologic and pathologic features and complications. Radiographics 20:795–817, 2000.
91. Powell M, Courcoulas A, Gardner M, et al: Management of blunt splenic trauma: Significance differences between adults and children. Surgery 122:654–660, 1997.
92. Pyatt RS, Williams ED, Clark M, Gaskins R: CT diagnosis of splenic cystic lymphangiomatosis. J Comput Assist Tomogr 5:446–448, 1981.
93. Rabushka LS, Kawashima A, Fishman EK: Imaging of the spleen: CT with supplemental MR examination. Radiographics 14:307–332, 1994.
94. Radin DR: Intraabdominal *Mycobacterium tuberculosis* vs. *Mycobacterium avium-intracellulare* infections in patients with AIDS: Distinction based on CT findings. AJR Am J Roentgenol 156: 487–491, 1991.
95. Radin DR, Baker EL, Klatt EC, et al: Visceral and nodal calcification in patients with AIDS-related *Pneumocystis carinii* infection. AJR Am J Roentgenol 154:27–31, 1990.
96. Ramani M, Reinhold C, Semelka RC, et al: Splenic hemangiomas and hamartomas: MR imaging characteristics or 28 lesions. Radiology 202:166–172, 1997.
97. Root HD, Hauser CW, McKinely CR: Diagnostic peritoneal lavage. Surgery 57:633–637, 1965.
98. Ros PR, Moser RP, Dachman AH, et al: Hemangioma of the spleen: Radiologic-pathologic correlation in ten cases. Radiology 162:73–77, 1987.
99. Rossetti F, Brawner DL, Bowden R, et al: Fungal liver infection in marrow transplant recipients: Prevalence at autopsy, predisposing factors, and clinical features. Clin Infect Dis 20:801–811, 1995.
100. Rothlin MA, Naf R, Amgwerd M, et al: Ultrasound in blunt abdominal and thoracic trauma. J Trauma 34:488–495, 1993.
102. Rutherford EJ, Livengood J, Higginbotham M, et al: Efficacy and safety of pneumococcal revaccination after splenectomy for trauma. J Trauma 39:448–452, 1995.
103. Scalea TM, Rodriguez A, Chiu WC, et al: Focused assessment with sonography for trauma (FAST): Results from an international consensus conference. J Trauma 46:466–472, 1999.
104. Scalfani JAS, Shaftan GW, Scalea TM, et al: Nonoperative salvage of computed tomography-diagnosed splenic injuries: Utilization of angiography for triage and embolization for hemostasis. J Trauma 39:507–513, 1995.
105. Schurr MJ, Fabian TC, Gavant M, et al: Management of blunt splenic trauma: Computed tomographic contrast blush predicts failure of non-operative management. J Trauma 39:507–513, 1995.
106. Schwartz SI: The role of splenectomy in hematologic disorders. World J Surg 20:1156–1159, 1996.
107. Scott GC, Berman JM, Higgins JL: CT patterns of nodular hepatic and splenic sarcoidosis: A review of the literature. J Comput Assist Tomogr 21:369–372, 1997.
108. Semelka RC, Kelekis NL, Sallah S, et al: Hepatosplenic fungal disease: Diagnostic accuracy and spectrum of appearances on MR imaging. AJR Am J Roentgenol 169:1311–1316, 1997.
109. Shanmuganathan K, Mirvis SE, Sherbourne CD, et al: Hemoperitoneum as the sole indicator of abdominal visceral injuries: A potential limitation of screening abdominal US for trauma. Radiology 212: 423–430, 1999.
110. Shanmugnathan K, Mirvis SE, Sover ER: Value of contrast-enhanced CT in detecting active hemorrhage in patients with blunt abdominal or pelvic trauma. AJR Am J Roentgenol 161:65–69, 1993.
111. Shaw JHP, Print CG: Postsplenectomy sepsis. Br J Surg 76:1074–1081, 1989.

112. Shilling RF: Estimating the risk for sepsis after splenectomy in hereditary spherocytosis. Ann Intern Med 122:187–188, 1995.
113. Shimono T, Yamaoka T, Nishimura K, et al: Peliosis of the spleen: Splenic rupture with intraperitoneal hemorrhage. Abdom Imaging 23:201–202, 1998.
114. Shirkhoda A, Ros R, Farah J, et al: Lymphoma of the solid abdominal viscera. Radiol Clin North Am 155:805–810, 1990.
115. Shuman WP: CT of blunt abdominal trauma in adults. Radiology 205:297–306, 1997.
116. Sutherland GA, Burghard FF: The treatment of splenic anaemia by splenectomy. Lancet 2:1819, 1910.
117. Taylor AJ, Dodds WJ, Erickson SJ, Stewart ET: CT of acquired abnormalities of the spleen. AJR Am J Roentgenol 157:1213–1219, 1991.
118. Taylor FC, Frankl HD, Riemer KD: Late presentation of splenic trauma after routine colonoscopy. Am J Gastroenterol 84:442–443, 1989.
119. Taylor MA, Kaplan HS, Nelsen TS: Staging laparotomy with splenectomy for Hodgkin's disease: The Stanford experience. World J Surg 9:449–460, 1985.
120. Thiebault C, Mamazza J, Letourneau R, Puolin E: Laparoscopic splenectomy: Operative technique, and preliminary report. Surg Laparosc Endosc 2:248–253, 1992.
121. Thompson SE, Walsh EA, Cramer BC, et al: Radiological features of a symptomatic splenic hamartoma. Pediatr Radiol 26:657–660, 1996.
122. Torres GM, Terry NL, Mergo PJ, Ros PR: MR imaging of the spleen. MRI Clin North Am 3:39–50, 1995.
123. Townsend RR: CT of AIDS-related lymphoma. AJR Am J Roentgenol 156:969–974, 1991.
124. Tso P, Rodriguez A, Cooper C, et al: Sonography in blunt abdominal trauma: A preliminary progress report. J Trauma 33:39–44, 1992.
125. Urban BA Fishman EK: Helical CT of the spleen. AJR Am J Roentgenol 170:997–1003, 1998.
126. Urrutia M, Mergo PJ, Ros LH, et al: Cystic masses of the spleen: Radiologic-pathologic correlation. Radiographics 16:107–129, 1996.
127. Velanovich V, Tapper D: Decision analysis in children with blunt splenic trauma: The effect of observation, splenorrhaphy or splenectomy on quality-adjusted life expectancy. J Pediatric Surg 28:179–184, 1993.
128. Velmahos GC, Chan LS, Kamel E, et al: Nonoperative management of splenic injuries: Have we gone too far? Arch Surg 135:674–681, 2000.
129. Wadsworth DT, Newman B, Abramson SJ, et al: Splenic lymphangiomatosis in children. Radiology 202:173–176, 1997.
130. Warshauer DM, Semelka RC, Ascher SM: Nodular sarcoidosis of the liver and spleen: Appearance on MR images. J Magn Reson Imaging 4:553–557, 1994.
131. Wasvary H, Howells G, Villalba M, et al: Nonoperative management of adult blunt splenic trauma. Am Surg 63:694–699, 1997.
132. Weissleder R, Elizondo G, Stark DD, et al: The diagnosis of splenic lymphoma by MR imaging: Value of superparamagnetic iron oxide. AJR Am J Roentgenol 152:175–180, 1989.
133. West JG, Trunkey DD, Lim RC: Systems of trauma care: A study of two counties. Arch Surg 114:455–460, 1979.
134. Wolfman NT, Bechtold RE, Scharling ES, Meredith JW: Blunt upper abdominal trauma: Evaluation by CT. AJR Am J Roentgenol 158:493–501, 1992.
135. Yavorski C, Greason K, Egan M: Splenic cysts: A new approach to partial splenectomy—case report and review of the literature. Am Surg 64:795–798, 1998.

40 The Adrenal Glands

Timothy J. Welch, Patrick F. Sheedy II

The adrenal glands play an important role in endocrine function. First described by Eustachius in 1563, they continued to be studied over the next 400 years until the 20th century, when their important endocrine and physiologic functions were defined. More recently, powerful imaging techniques such as ultrasound, computed tomography (CT), and magnetic resonance imaging (MRI) have played an important role in defining pathologic conditions of the adrenal glands. This has resulted in remarkable advances in our understanding of the normal physiology and pathologic states involved in adrenal disease.

Normal Anatomy

The adrenal glands develop from mesenchyme adjacent to the urogenital ridge and appear in the fetus at the 7- to 8-mm stage.[13] By the time the fetus reaches the 20- to 25-mm stage, a distinction between the two zones of the adrenal glands can be made. When the baby is born, the adrenal glands weigh approximately 5 g each. They then undergo involution over the next several weeks. This fall in weight is secondary to degeneration of the fetal zone within the cortex.[73] Maturation of the cortical and medullary portions of the adrenal gland generally occurs within the first several years of life.

The right adrenal gland is located in an area just superior to the right kidney, medial to the right lobe of the liver, lateral to the crus of the right hemidiaphragm, and posterior to the inferior vena cava. Its shape is variable but may resemble an elongated comma lying in the crease between the liver and the crus of the diaphragm (Fig. 40–1). It also may be shaped like an inverted letter V or Y. The lateral limb of the adrenal gland lies close to the right lobe of the liver and can sometimes be difficult to separate from the surface of the liver.

The left adrenal gland is located above and extends anterior to the upper pole of the left kidney in a triangle formed by the left lateral margin of the aorta, the posterior surface of the body and tail of the pancreas, and the anterior superior medial surface of the upper pole of the left kidney (Fig. 40–2). It is shaped like an inverted letter V or Y or an inverted or reversed letter L. It may also be triangular.

The right adrenal gland is usually in a clearly suprarenal location in the retroperitoneum, whereas the position of the left adrenal gland in the retroperitoneum is frequently in front of the anterior surface of the left kidney. The superoinferior length of the gland is variable but can extend from 2 to 6 cm. The right gland maintains a constant relationship with the posterior surface of the inferior vena cava. Its lateral limb is known to extend more inferiorly than the medial limb. The superior portion of the left gland, behind the pancreas, often abuts the splenic vessels, and its inferior margin extends to the superior aspect of the left renal vein.

The normal adult adrenal gland weighs approximately 4 g in both men and women.[13, 59] Its outer cortex, which is yellow, surrounds an inner medulla, which is pale gray. The medulla, which is usually absent from the tail of the glands, generally makes up between 10% and 20% of the total weight of the adrenal gland. The degree of thickness of the adrenal cortex overlying the medulla varies according to location, and at times it can be difficult to distinguish between the two zones.

The adrenal glands have a unique blood supply, in that they are supplied by multiple arteries, including branches from the inferior phrenic artery, aorta, and ipsilateral renal artery.[15] These arteries branch to form a vascular plexus just beneath the capsule of the adrenal gland. A great degree of variability exists in the arterial supply to the adrenal glands. The venous drainage of the right adrenal gland differs from left to right. The right adrenal vein drains directly into the inferior vena cava between the right renal vein and the hepatic veins. The left adrenal vein joins the left renal vein several centimeters away from the inferior vena cava. Thus, the unique blood supply, together with the vascular nature of the adrenal gland, plays an important role in the imaging characteristics of adrenal abnormalities and their appearance at biopsy.

The apparent thickness of both adrenal glands depends on their orientation relative to the plane of imaging. They appear thicker if obliquely oriented and thinner if vertically oriented in transaxial images. Rarely does the thickness of a normal adrenal gland exceed 10 mm; more commonly, the gland is 5 to 6 mm thick. Variability in the appearance of the glands is due to differences in abdominal fat content, the orientation of the glands with respect to the plane of the scan, and differences in anatomic location.

Adrenal Physiology

The adrenal glands are made up of two distinctly functioning portions: the adrenal cortex and the adrenal medulla.

Cortex

The adrenal cortex synthesizes three main groups of hormones: glucocorticoids, mineralocorticoids, and adrenal androgens.[49] All of these are derived from cholesterol and share a common structural formula.

The cortex is divided into three zones: the zona glomer-

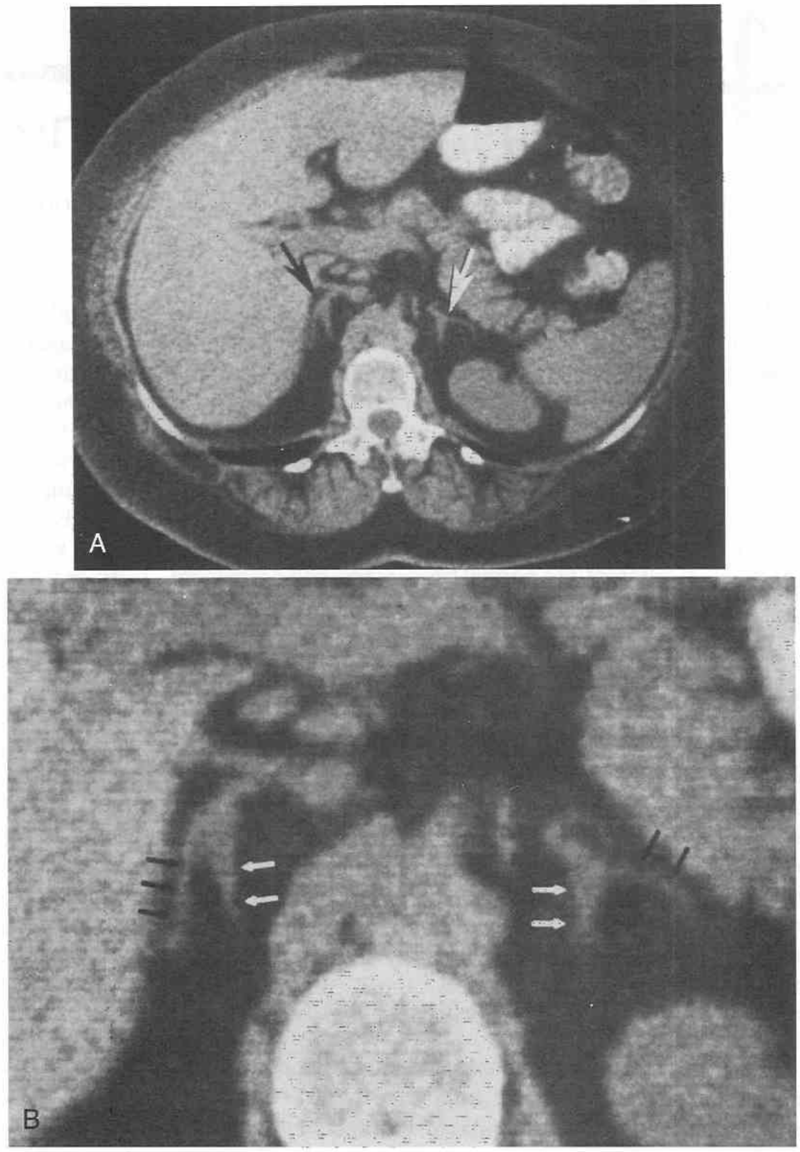

Figure 40–1. Normal adrenal glands. *A,* Typical location and appearance of the right gland *(black arrow),* which is shaped like an upside-down V. On the left, the gland is located in a triangle bounded by the pancreas, aorta, and kidney. It is shaped like an upside-down Y *(white arrow). B,* Magnification view of the same scan shows the medial *(white arrows)* and lateral *(black arrows)* limbs of the gland to better advantage. The limbs are thinner than the apex of the gland.

ulosa, the zona fasciculata, and the zona reticularis. Steroid synthesis differs in each zone. The zona glomerulosa is a major source of glucocorticoids. The zona fasciculata and the zona reticularis are thought to act as a unit in the production of cortisols and androgens. Unique to the zona fasciculata are large, clear lipid-laden cells. The degree to which the zona fasciculata is present plays an important role in the imaging characteristics of many adrenal lesions.

Medulla

The adrenal medulla is derived from neuroectodermal tissue and contains catecholamine-producing cells known as chromaffin cells.[13] The primary catecholamines produced by the adrenal medulla include norepinephrine and epinephrine. These chemicals act primarily on the α-adrenergic and β-adrenergic receptors present in the body. The main endocrine effects of these catecholamines are in the cardiovascular system and in glucose metabolism.

Imaging Modalities

Imaging of the adrenal glands can be accomplished via many different modalities, including plain films, ultrasonography, nuclear medicine imaging, CT, and MRI. In recent years, CT and MRI have become the imaging modalities of choice in adult patients. Although ultrasound can be used to detect adrenal abnormalities, it is not used as a primary imaging modality because of its inability to depict the entire adrenal gland in adults. In children, however, ultrasound is more commonly used to evaluate adrenal disease.

Since its introduction in the 1970s, CT has become the primary imaging tool for adrenal imaging because of its superior spatial resolution, its widespread availability, and the speed in which examinations can be performed. The advent of spiral CT, and more recently multidetector-row helical (spiral) CT, has allowed rapid thin-slice imaging through the adrenal glands during various phases of contrast enhancement.

The rapidity of CT has allowed the use of precontrast

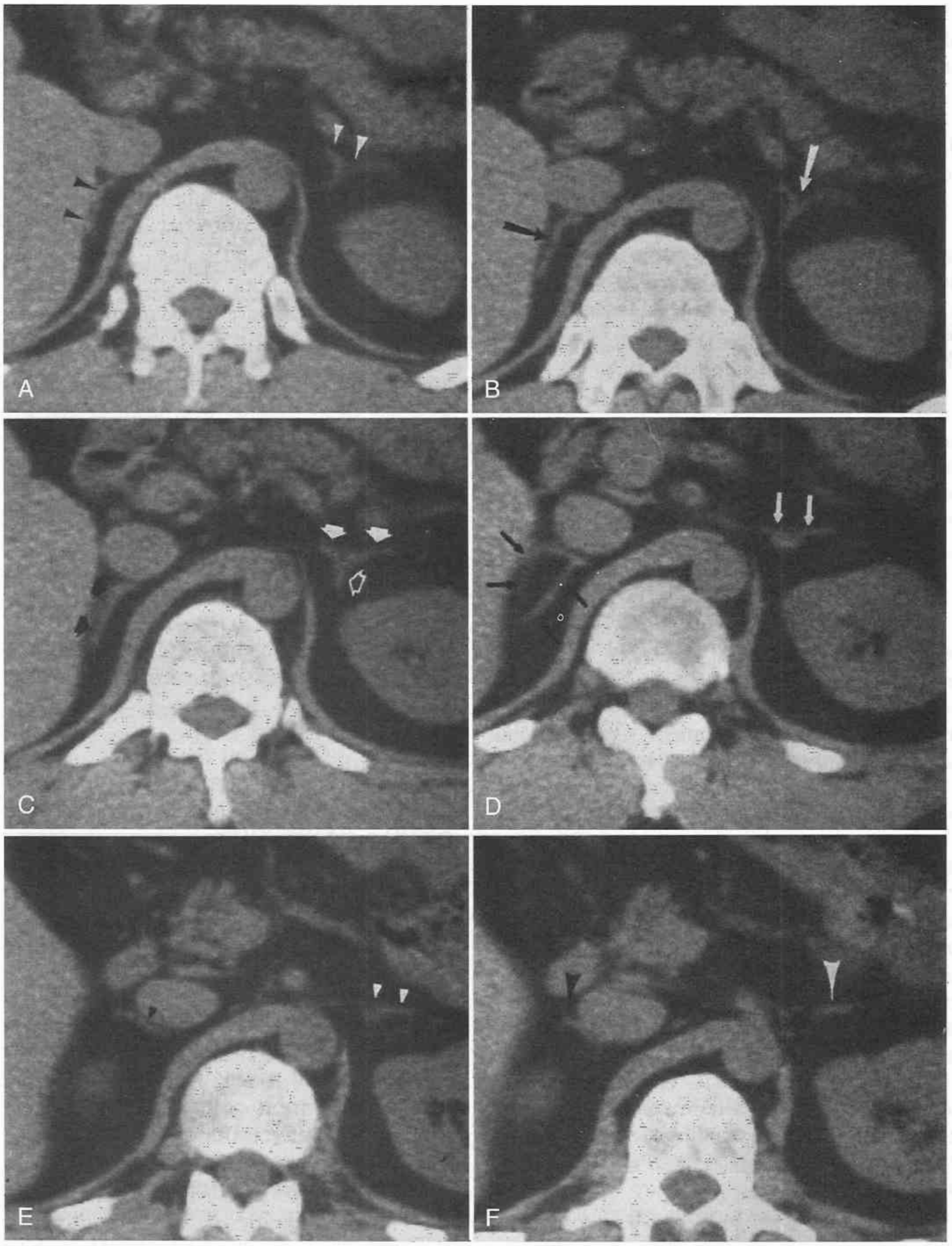

Figure 40–2. Normal adrenal glands. Scans at six different levels (5-mm-thick slices) reveal variability in the size, shape, and configuration of the right *(black arrows, arrowheads)* and left *(white arrows, arrowheads)* glands at different levels in the same patient. For instance, the medial limb of the right gland extends superiorly *(A–C)*. On the right *(black arrows)*, both medial and lateral limbs are visible at only one level *(D)*. The lateral limb extends inferiorly (*black arrowheads* in *A* and *F*). On the left, both limbs are visible on the upper three scans (*white arrows* and *arrowheads* in *A–C*). The lateral limb is visible only on the lower three scans (*white arrows* and *arrowheads* in *D–F*).

scans as well as post-intravenous (IV) contrast-enhanced scans to become routine. Oral contrast material can also be helpful in examination of the adrenal glands because unopacified (nonradiopaque) stomach or loops of bowel may be opacified so that adrenal "pseudomasses" can be clearly defined as bowel and not adrenal lesions. The use of oral contrast material is especially helpful after nephrectomy, when loops of bowel may fall into the renal fossa and can make evaluation of the adrenal glands difficult.

In general, when CT is used to study the adrenal glands, the entire abdomen through the aortic bifurcation is scanned. The complete examination of the abdomen is helpful for staging or for evaluating possible ectopic adrenal lesions that may occur in certain disease processes.

In recent years, MRI has become the other primary imaging modality for identifying adrenal pathology. Initially, most adrenal lesions were evaluated with standard T1-weighted and T2-weighted, spin-echo images with magnets of low and medium field strength. With the advent of higher-field-strength magnets (1.5 tesla), chemical shift imaging and dynamic gadolinium-enhanced MRI have been added to the process of adrenal gland evaluation.

Chemical shift imaging is based on the fact that the resonant frequency of a given atom's nucleus is affected by its chemical environment. This is secondary to slight variations in local magnetic field strength caused by the shielding effects of nearby orbiting electrons. The change that occurs during an MR signal as a result of this effect is referred to as a chemical shift.

The chemical shift is used primarily to identify protons within the body that are located either within water molecules or within lipid molecules. This allows a separation of fat from water contributions in an image. Conventional spin-echo imaging results in water and lipid protons that are *in phase*; their magnetic moments are oriented in the same direction at the same time of the spin echo. When the imaging is *out of phase*, or *opposed*, signal detection occurs when lipid and water protons are oriented in opposite directions. The resulting image expresses the signal difference between water and lipid protons and therefore enables areas that are predominantly lipid to be distinguished from those that are predominantly water. This capability plays an important role in certain adrenal conditions, since certain adrenal lesions contain significant amounts of lipid.

The most common contrast agents used in MRI today involve gadolinium bound to diethylenetriamine-penta-acetic acid (DTPA). The physiologic characteristics of gadolinium agents are similar to those of iodinated contrast material. The distributions within the body and renal clearances are also similar, but the safety margin of gadolinium is greater than that of iodinated contrast material. The similarity to iodinated contrast material allows the principles of CT IV contrast enhancement to be extended to MRI. These techniques, along with the inherent strengths of MRI, which include the ability to obtain routine coronal and sagittal images and its superior contrast resolution compared with that of CT, have made MRI a mainstay in evaluating adrenal pathology.

Radionuclide imaging of the adrenal gland has been largely limited to the use of metaiodobenzylguanidine (MIBG) scans. MIBG is an analog of norepinephrine and is a useful agent for use in detecting functionary medullary tumors. β-Iodomethyl-19-norcholesterol (Np-59) has been used to detect glucocorticoid, mineralocorticoid, and androgen-secreting tumors. The advances made with both CT and MRI have largely eliminated the use of Np-59 imaging for adrenal imaging.

More recently, the increased availability of positron emission tomography (PET) has led to the development of several compounds as possible staging agents for tumors of the adrenal glands.[42] The use of fluorodeoxyglucose (FDG)-PET for evaluating tumor metabolism in other sites of the body has been assessed. Malignant lesions demonstrate abnormally increased uptake of FDG. Whole body FDG-PET scanning allows detection of malignancies and differentiation of malignant from benign masses, and this capability has been applied to the adrenal glands. FDG-PET scanning also has a role in staging extra-adrenal tumor sites.

Several inherent problems are associated with FDG-PET imaging:

1. Its lack of widespread availability.
2. The fact that pathologic lesions in the adrenal glands are often small and thus difficult to image.
3. Uptake in other abdominal structures, such as the renal pelvis, that can obscure the adrenal gland.

In past years, adrenal venous sampling was more commonly used to evaluate functioning adrenal tumors. It is now reserved for differentiating functioning adenoma from hyperplasia in patients with documented hyperaldosteronism; this is useful in aiding the endocrinologist and the surgeon to decide whether surgical treatment for hyperaldosteronism is indicated.

The general approach to imaging the adrenal glands has been the use of CT for screening and for depicting smaller lesions (3 cm or less) because of its superior spatial resolution. MRI is commonly used to further define lesions that have already been documented on CT scans or to evaluate larger adrenal lesions. Both CT and MRI play complementary roles in detection of most pathologic changes in the adrenal glands.

Functioning Adrenal Tumors

Conn's Syndrome

Primary hyperaldosteronism (Conn's syndrome) is a rare cause of hypertension, accounting for fewer than 1% of all cases of hypertension. It is a heterogeneous disease characterized by hypersecretion of aldosterone, moderate hypertension, and hypokalemia.[5] In 70% of cases, this disease process is the result of an aldosterone-secreting adrenal adenoma. In this subsegment of cases, unilateral adrenalectomy is the treatment of choice.

These tumors are universally small, generally less than 2 cm in diameter (Fig. 40–3). There is a female predilection, with a peak incidence occurring within the fourth and fifth decades of life. On histologic evaluation, these aldosterone-secreting adenomas reveal primarily lipid-laden cells of the zona fasciculata. As a result, the lesions generally show low density on imaging studies (Figs. 40–4 and 40–5).

Most of the remainder (30%) of primary hyperaldosteronism are the result of adrenal hyperplasia, usually bilateral (Fig. 40–6), which is treated medically with pharmacologic agents.[16] Histologic evaluation of patients with adrenal hyperplasia reveals hypertrophy of the zona fasciculata with underlying microscopic and macroscopic nodules. This results in the appearance of enlarged, irregular adrenal glands.

Rarer causes of primary hyperaldosteronism (<5% of all cases) include primary adrenal hyperplasia, renin-responsive aldosterone-secreting adenomas, and glucocorticoid-remediable aldosteronism.

The imaging approach to suspected primary hyperaldosteronism is to distinguish to the referring physician those

Figure 40–3. Aldosterone-producing adenoma. *A,* A tiny mass in the left adrenal gland *(black arrows)* preserves the configuration of the left adrenal gland but indents the central portion of the gland *(arrowheads). B,* Inspection of the gross specimen reveals both a tumor *(arrows)* and a portion of the normal glands *(arrowheads).*

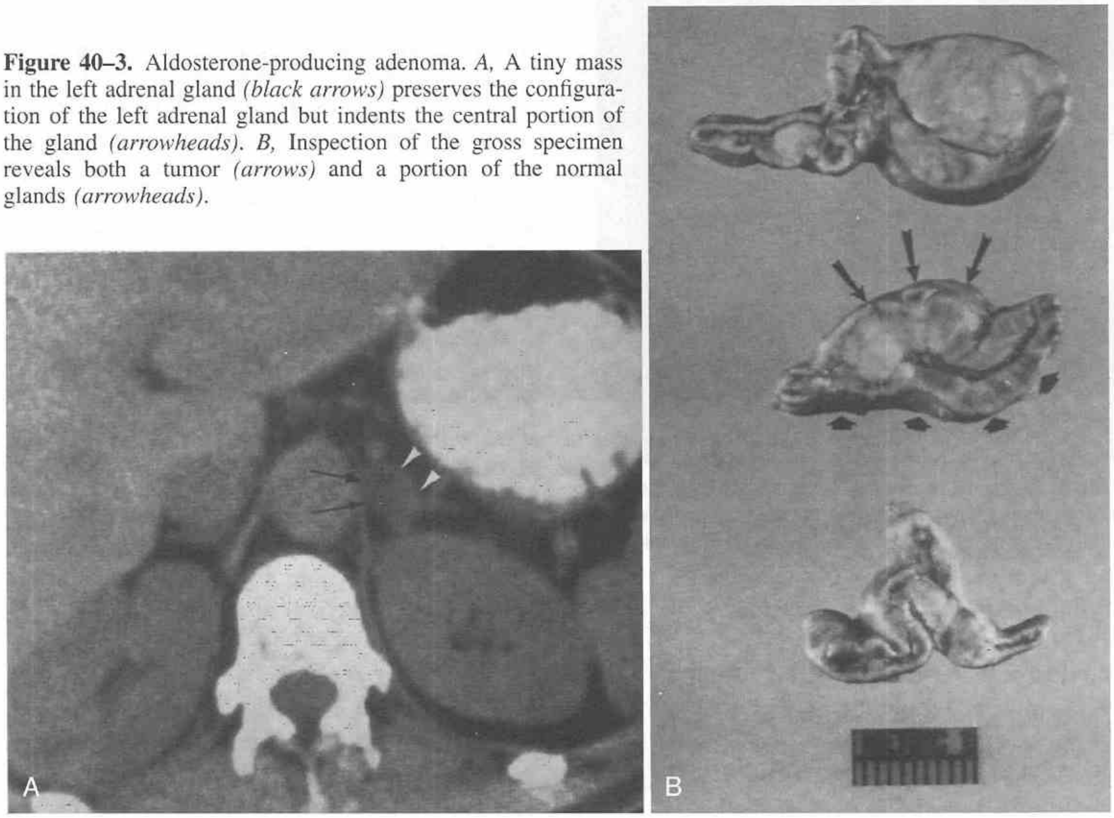

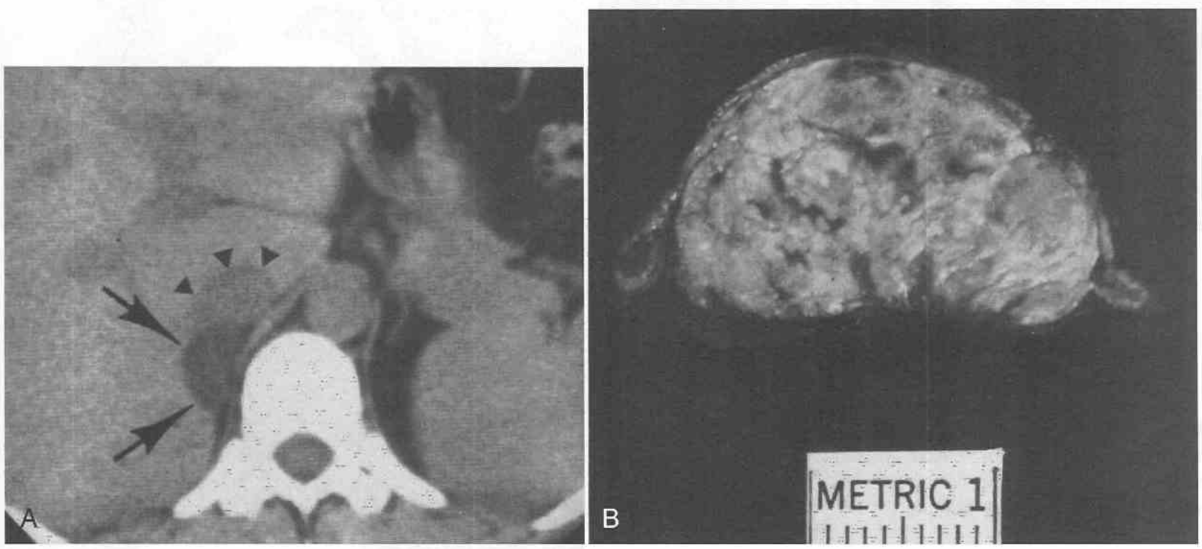

Figure 40–4. Aldosterone-producing adenoma. A mass 1.5 cm in diameter in the right adrenal gland *(arrows)* is located posterior to, and is lower in density than, the inferior vena cava *(arrowheads). B,* Examination of the gross specimen revealed a high cholesterol content.

Figure 40–5. Aldosterone-producing adenoma. An adenoma 1 cm in diameter arises from the lateral limb of the right adrenal gland *(arrow)*. The left adrenal gland *(arrowhead)* is normal.

patients with adrenal cortical adenomas as a cause of this disease process from patients with adrenal hyperplasia. The imaging modality of choice for evaluating patients with suspected primary hyperaldosteronism is CT because of its superior spatial resolution in depicting these small tumors.[17, 22] The advent of helical CT and, more recently, multidetector-row helical CT has allowed one to routinely perform thin-slice imaging through the adrenal glands in a single breath-hold. Slices of the adrenal glands 2.5 mm thick or less can be obtained to evaluate aldosterone-secreting adenomas smaller than 2 cm in size. For these scans, IV contrast material is not required.

The lesions seen in hyperaldosteronism secondary to a solitary adenoma generally appear as a low-density oval mass under 2 cm in size and frequently eccentric within the gland.[26, 32] Blood samples from each adrenal vein can be assayed for elevated aldosterone levels. This test is confirmatory but is not done in all cases because of its invasive nature.

Primary hyperaldosteronism secondary to adrenal hyperplasia generally results in adrenal glands that are mildly enlarged and have an irregular surface because of the presence of underlying microscopic and macroscopic nodules.[16, 17] Usually, no single dominant nodule can be seen with the adrenal glands. Up to one third of these patients,

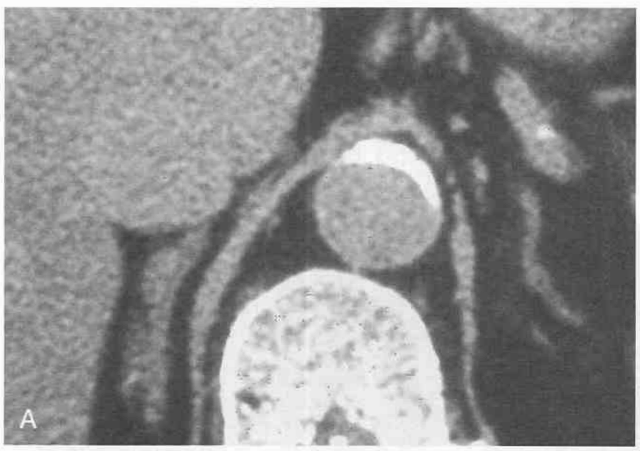

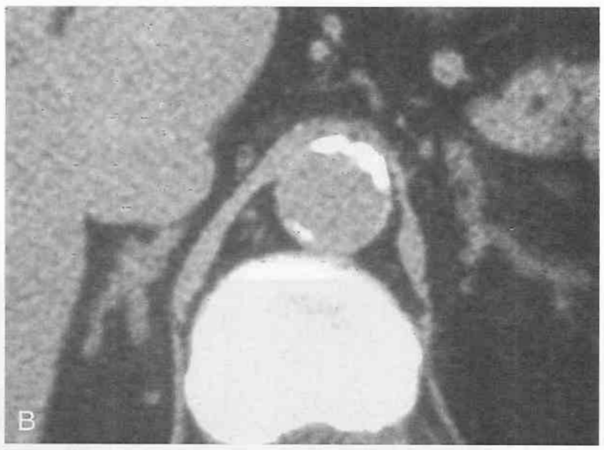

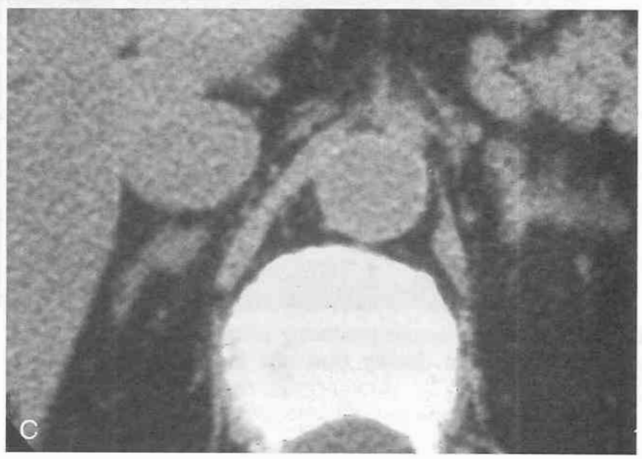

Figure 40–6. *A–C,* Conn's syndrome. Thin-section CT imaging of the adrenal glands reveals multinodular hyperplasia of both adrenal glands, resulting in primary hyperaldosteronism (Conn's syndrome) in this patient.

however, have normal-appearing adrenal glands on imaging studies.[60] When a patient with suspected primary hyperaldosteronism has either normal-appearing adrenal glands or glands that are mildly enlarged with multiple nodules, adrenal venous sampling is performed to aid in the diagnosis and localization of the disease process.

Cushing's Syndrome

Cushing's syndrome is a well-documented disease of chronic excess of circulating glucocorticoids.[25, 70] The clinical features, which appear in varying degrees of severity, include obesity, plethora, bruising, abdominal striae, and muscle wasting. Frequently, osteoporosis and delayed wound healing are also present. As a result of the effects of glucocorticoids on glucose metabolism, 10% to 15% of the patients have diabetes mellitus.

The causes of Cushing's syndrome are many. In 70% of cases, the cause is pituitary disease secondary to an adrenocorticotropic hormone (ACTH [corticotropin])–secreting adenoma.[72] Five percent of cases result from ectopic ACTH secretion; this usually occurs in certain types of malignancy, including lung carcinomas, islet cell tumors, and ovarian neoplasms.

In 20% of cases, Cushing's syndrome is secondary to an adrenal adenoma. These adenomas are larger than those seen in Conn's syndrome, usually 2 to 4 cm in size. They contain a large amount of lipid-laden cells, giving them a characteristic low-density appearance on CT scans (Fig. 40–7).[48, 49]

The final major etiologic mechanism in approximately 5% of cases of Cushing's syndrome is adrenal cortical carcinoma. These generally large tumors occupy much of the right or left upper quadrant, depending on the adrenal gland involved. Frequently there is associated necrosis and hemorrhage. Only 10% of adrenal cortical carcinomas function to a level that results in Cushing's syndrome.

The initial imaging of the adrenal glands is usually performed with CT because of its superior spatial resolution and the ability to perform routine thin-slice imaging. The imaging process is facilitated by the large amount of retroperitoneal fat that is usually present in patients with Cushing's syndrome. The low-density imaging appearance of these 2- to 4-cm adenomas is the result of the large amount of lipid in the cytoplasm of their cells (Fig. 40–8).

It is vital that the radiologist observe the thickness of the unaffected limbs of the adrenal gland when evaluating a patient with an adrenal nodule for Cushing's syndrome.[10] Cortisol-producing adenomas suppress ACTH levels, resulting in atrophy of the remaining adrenal tissue. If normal adrenal thickness is observed, the adrenal lesion is not responsible for Cushing's syndrome.

Adrenal gland hyperplasia secondary to pituitary or ectopic causes of Cushing's syndrome can have several imaging appearances (e.g., normal-appearing glands, bilateral uniform adrenal enlargement, adrenal glands with irregular small nodules on the surface, or a multinodular gland with larger dominant nodules).[29] The most common pattern of adrenal hyperplasia is diffuse bilateral enlargement without a focal mass (Fig. 40–9). In some cases of Cushing's syndrome secondary to hyperplasia, when evaluation of the pituitary gland does not reveal an adenoma, petrosal venous sampling may be valuable in determining the cause.

MRI has played a secondary role in the evaluation of patients with Cushing's syndrome because CT can better evaluate the smaller adrenal masses. MRI signal intensity seen in adrenal hyperplasia closely follows that of the normal adrenal gland, rendering MRI less sensitive than CT in evaluating adrenal hyperplasia.

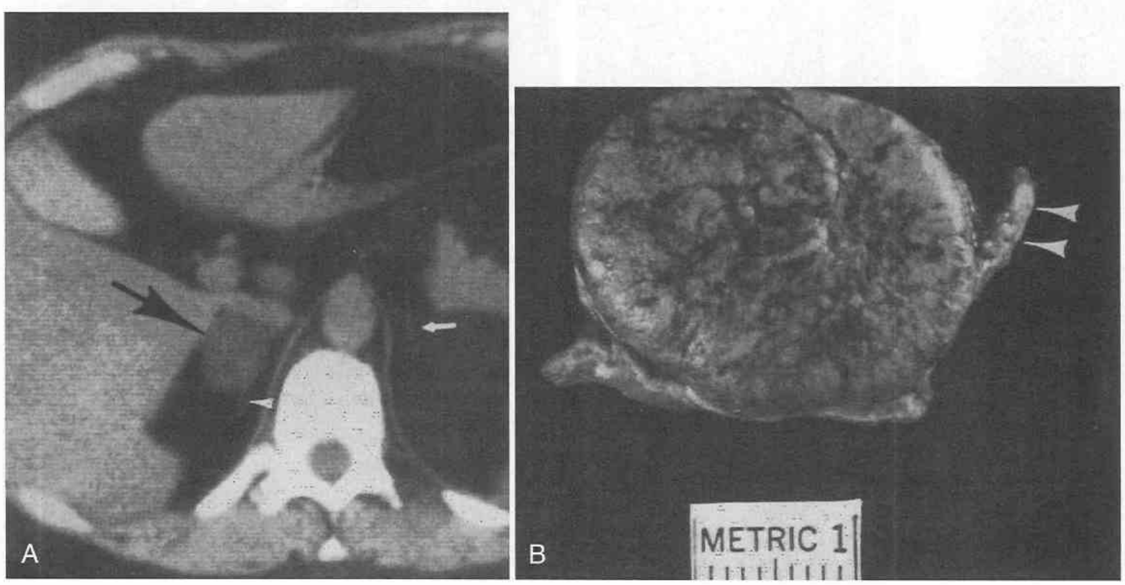

Figure 40–7. Right adrenal gland adenoma in a patient with Cushing's disease. *A,* A tumor 2 cm in diameter in the right adrenal gland *(black arrow)* is associated with a hypoplastic ipsilateral remnant *(arrowheads).* The left gland is also hypoplastic *(white arrow). B,* The gross specimen includes the hypoplastic remnant *(arrowheads).*

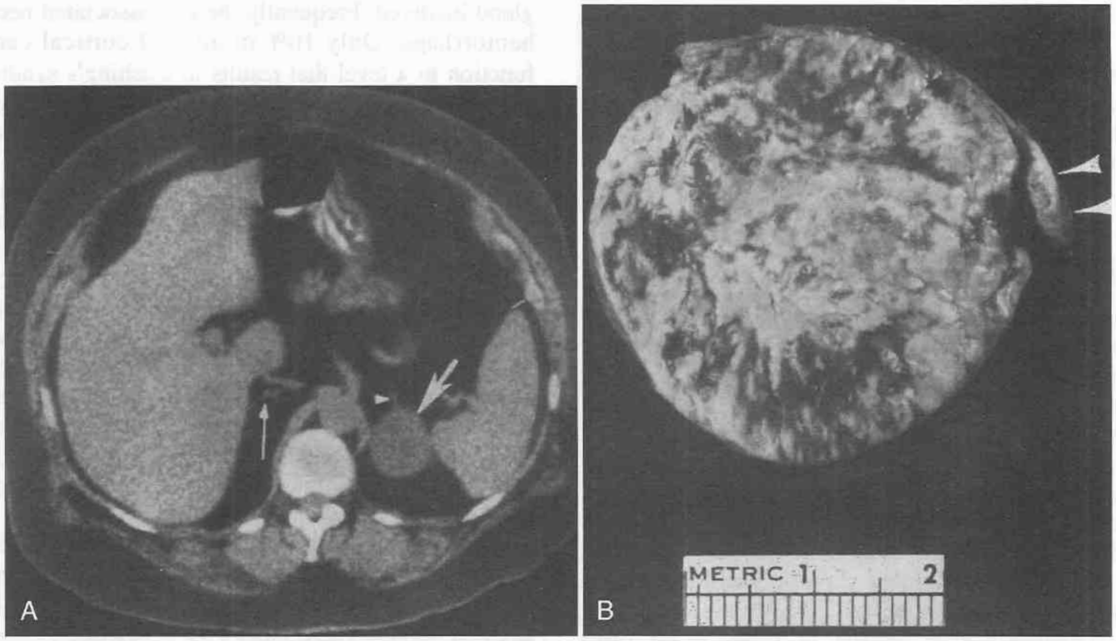

Figure 40–8. Left adrenal gland adenoma in a patient with Cushing's disease. *A,* A mass 2.5 cm in diameter can be seen in the left adrenal gland *(large white arrow).* Also visible is a hypoplastic remnant of the left adrenal gland *(arrowhead).* The right adrenal gland *(small white arrow)* is hypoplastic. *B,* The gross specimen includes the hypoplastic remnant *(arrowheads).*

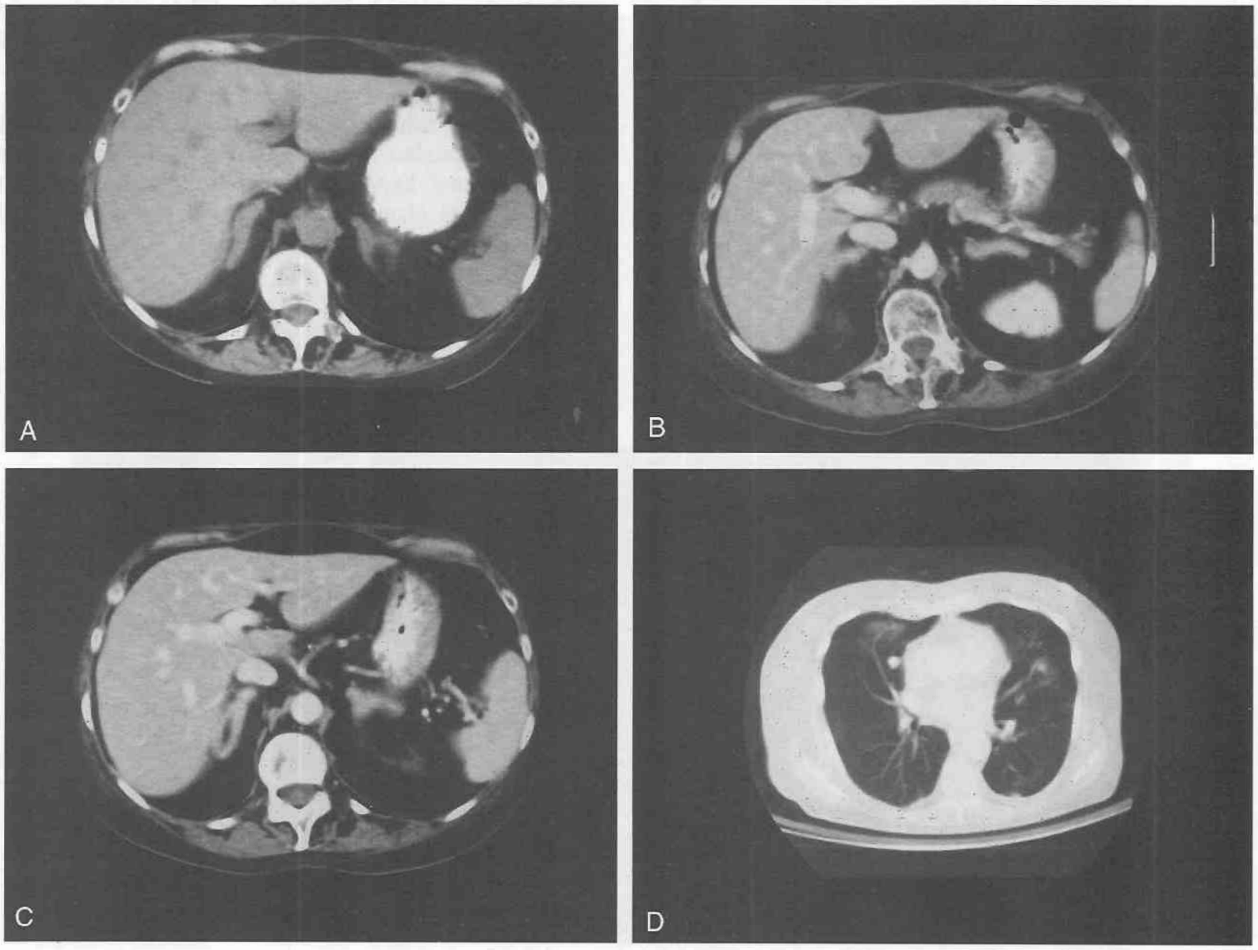

Figure 40–9. Cushing's syndrome. *A–C,* Non–contrast-enhanced and contrast-enhanced CT scans of the adrenal glands reveal symmetrical hypertrophy. *D,* CT scan of the chest demonstrates a 1-cm nodule in the right middle lung. The nodule was a bronchial carcinoid ectopically secreting adrenocorticotropic hormone, which resulted in Cushing's syndrome. (Courtesy of Mayo Foundation.)

Adrenogenital Syndrome

Adrenogenital syndrome is characterized by excessive secretion of sex hormones and causes virilization, feminization, or precocious puberty, depending on the hormones secreted and the age of the patient.[2–4] Androgen excess is the most common form of this syndrome; of the cases diagnosed clinically, 80% occur in female patients. In prepubertal girls, the consequences are clitoral hypertrophy, development of male secondary sex characteristics, and early closure of bony epiphyses. In prepubertal boys, changes include precocious puberty. In adults, men usually

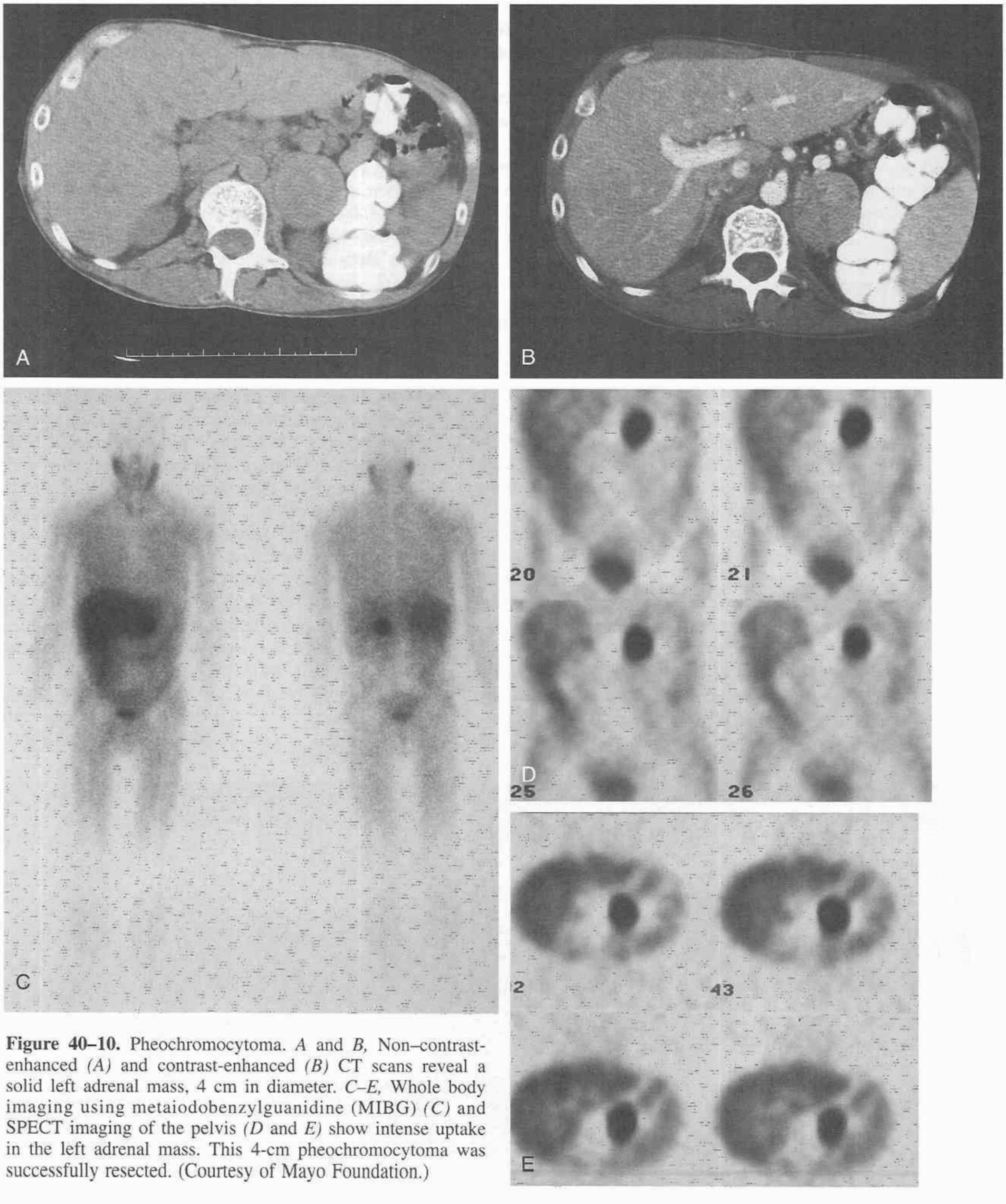

Figure 40–10. Pheochromocytoma. *A* and *B,* Non–contrast-enhanced *(A)* and contrast-enhanced *(B)* CT scans reveal a solid left adrenal mass, 4 cm in diameter. *C–E,* Whole body imaging using metaiodobenzylguanidine (MIBG) *(C)* and SPECT imaging of the pelvis *(D* and *E)* show intense uptake in the left adrenal mass. This 4-cm pheochromocytoma was successfully resected. (Courtesy of Mayo Foundation.)

undergo testicular atrophy secondary to pituitary suppression, whereas women undergo changes including amenorrhea, hirsutism, and virilization. Less commonly, the presence of estrogen-secreting tumors results in precocious puberty in girls and feminization in males.

Adrenogenital syndrome is most often caused by congenital adrenal hyperplasia secondary to an enzymatic deficiency in adrenal steroid synthesis, resulting in an overproduction of androgens. Approximately 25% of patients have associated overproduction of mineralocorticoids as well. The imaging findings in patients with congenital adrenal hyperplasia are generally those of uniformly enlarged adrenal glands.

Both benign adrenal adenomas and adrenal cortical carcinomas can give rise to adrenogenital syndrome. These lesions have the imaging characteristics of both tumors. In general, in adults a higher proportion of malignant adrenal cortical tumors results in adrenogenital syndrome than in benign lesions.

Pheochromocytoma

Pheochromocytoma is a rare tumor of the chromaffin cells of the adrenal medulla; it affects approximately 1 in 200,000 individuals in the general population.[12, 78] The biochemical diagnosis is facilitated by characteristic symptoms and signs attributable to excessive release of catecholamines. Pheochromocytomas usually secrete both epinephrine and norepinephrine. The characteristic clinical findings include severe headaches, palpitations, excessive sweating, tremor, anxiety, and sustained hypertension.

Pheochromocytomas are extra-adrenal in 10% of cases, multicentric in 10%, bilateral in 5%, and malignant in 10%. They are relatively large (~5 cm in size), but sizes range from 1 cm to above 20 cm. Smaller tumors may be seen when bilateral pheochromocytomas are present or in patients with multiple endocrine neoplasia (MEN).

Pheochromocytomas are associated with MEN types 2A and 2B, von Hippel–Lindau disease, neurofibromatosis, Sturge-Weber syndrome, and Carney's triad. They are generally well-defined adrenal lesions with occasional areas of necrosis or cystic changes. Treatment is surgical excision of the tumor, which is curative in almost all cases.

The initial imaging findings in benign and malignant pheochromocytomas are nearly identical. Only the presence of metastasis can clearly define a pheochromocytoma as malignant.

Imaging is performed to localize a tumor that has already been diagnosed biochemically. Urinary or serum catecholamine levels are measured to confirm the diagnosis. The radiologist's role is to identify whether the pheochromocytoma is intra-adrenal and whether it is unilateral or bilateral.[78]

Ectopic pheochromocytomas can occur anywhere neural crest cells are present in the body. Tumors have been reported from the base of the brain to the epididymis, making preoperative localization imperative. The most common extra-adrenal site of pheochromocytoma is the organ of Zuckerkandl at the aortic bifurcation.

CT has long been the primary method of diagnosis. On scans, intra-adrenal pheochromocytomas appear as round or oval, discrete masses whose density is homogeneous (Fig. 40–10).[78] Central necrosis, calcification, and cystic changes may be present in a minority of cases (Fig. 40–11).[20] These vascular lesions enhance uniformly after administration of contrast material. The use of IV iodinated contrast material in patients with pheochromocytoma has been controversial because it may cause a hypertensive crisis; however, the use of low-osmolarity iodinated contrast material has largely eliminated that concern. The incidence of elevated circulating serum catecholamines with low-osmolarity contrast material is generally negligible.[47]

In patients with suspected adrenal pheochromocytoma, CT scans of the entire abdomen through the aortic bifurcation are generally obtained to identify possible ectopic tumor (Fig. 40–12). Helical scanning done at 5-mm increments with IV contrast material is the preferred technique. The accuracy of CT in detecting intra-adrenal pheochromocytomas is nearly 100%.[78]

MRI is also excellent for evaluating intra-adrenal pheochromocytomas.[11, 34, 37, 39] Because these are generally larger

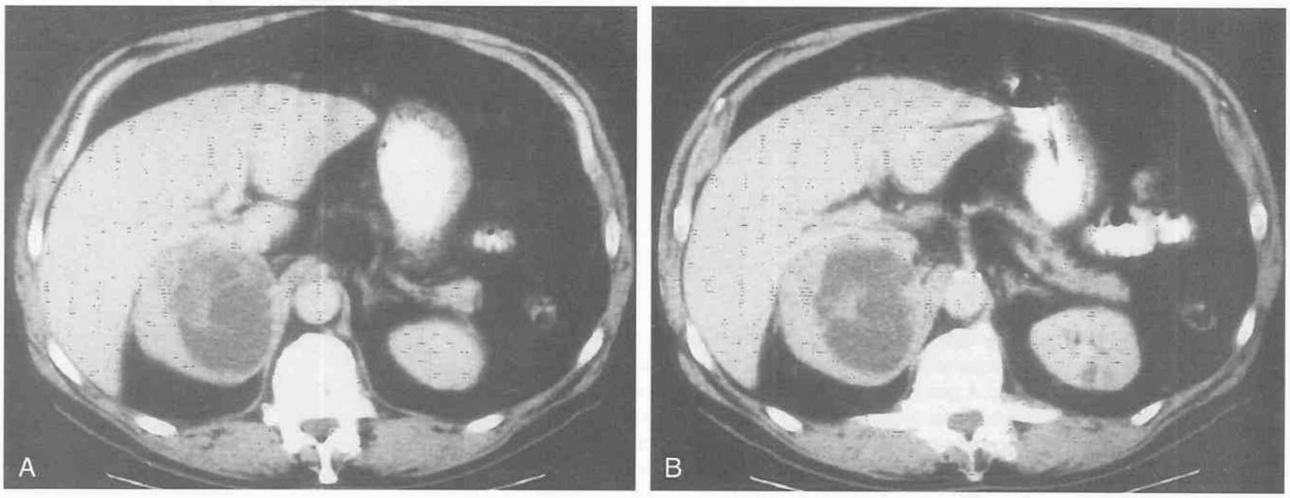

Figure 40–11. Pheochromocytoma. *A* and *B*, Contrast-enhanced CT scans of the abdomen demonstrate a 6-cm cystic right adrenal pheochromocytoma. (Courtesy of Mayo Foundation.)

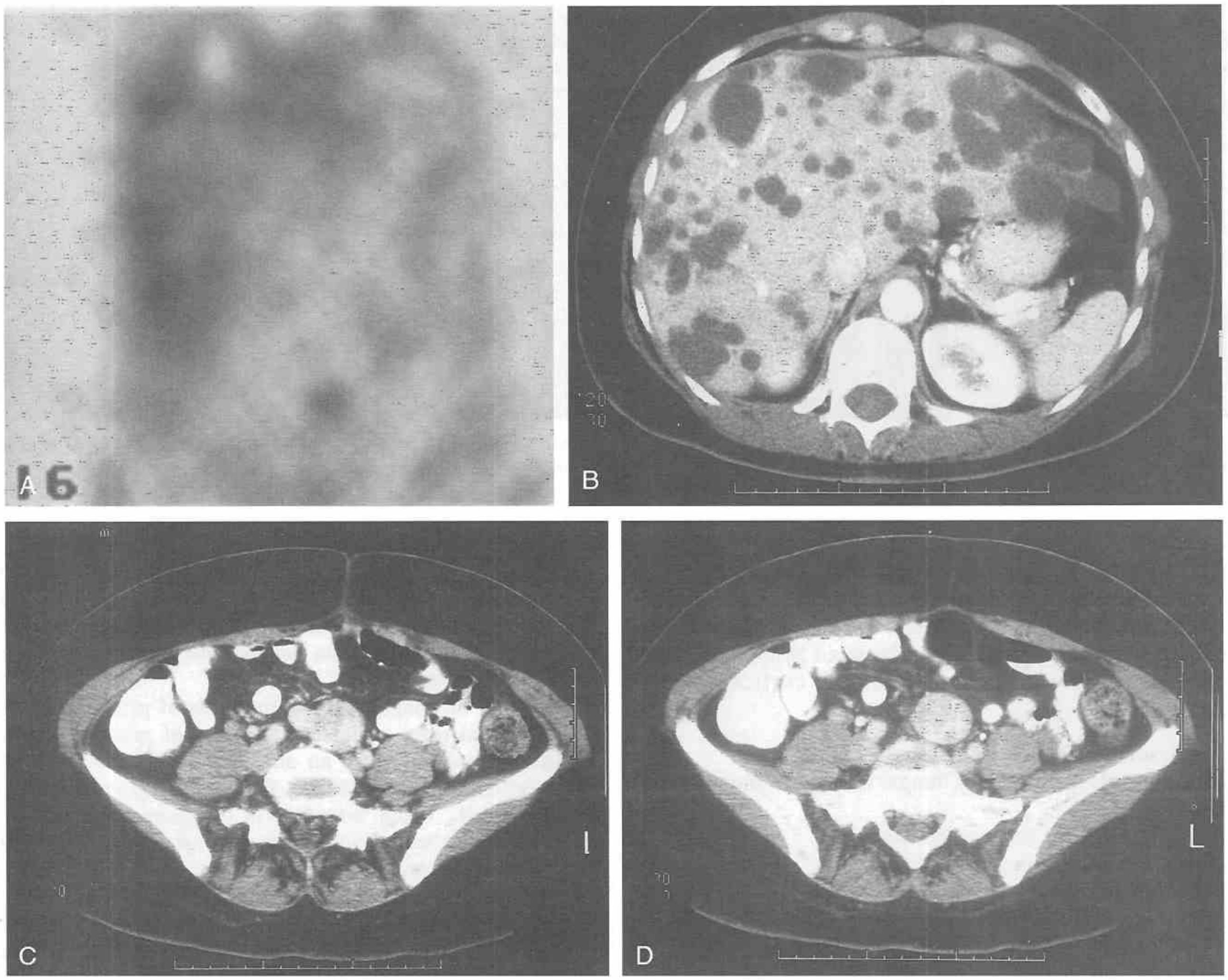

Figure 40–12. Pheochromocytoma. *A,* Whole-body metaiodobenzylguanidine (MIBG) scan demonstrates uptake in the lower abdomen and upper pelvis. *B–D,* Contrast-enhanced CT scans of the abdomen and pelvis demonstrate normal-appearing adrenal glands; multiple cysts are present in the liver. A solid, 3-cm enhancing mass at the aortic bifurcation is compatible with a pheochromocytoma in the organ of Zuckerkandl. This tumor was successfully resected. (Courtesy of Mayo Foundation.)

tumors (5 cm), the poorer spatial resolution of MRI is usually not a problem. On T1-weighted images, pheochromocytomas have a signal intensity similar to or slightly lower than that of other solid organs of the abdomen. On T2-weighted images, they tend to have a hyperintense signal as a result of their long T2 times (Fig. 40–13).[11, 34, 37, 63] Although this finding is almost uniformly seen with pheochromocytomas, a percentage of adrenal metastases have overlapping imaging findings.

MIBG scanning can play a complementary role in evaluating intra-adrenal pheochromocytomas. The combination of an adrenal mass seen on a CT scan or an MR image and uptake on MIBG scanning is definitive in the diagnosis of pheochromocytoma. This approach is limited by the lack of availability of MIBG scanning equipment in some settings.

The imaging of extra-adrenal and recurrent pheochromocytomas is more complex, and MIBG scintigraphy is extremely valuable in these situations. MIBG is a precursor of catecholamines and therefore is actively taken up in catecholamine-producing tissues. After recurrent, metastatic, or extra-adrenal lesions are initially discovered via whole body MIBG scanning, CT or MRI can then be performed for more accurate anatomic localization of the lesion to be resected (Fig. 40–14).

Adrenal Hypofunction

Hypofunction of the adrenal gland primarily refers to disorders of the adrenal cortex. Currently, no syndromes of adrenal medullary hypofunction are known. Initial work on hypofunctioning adrenal cortex was pioneered by Thomas Addison.[1] Hypofunction of the adrenal cortex may result either from its destruction (secondary to many disease processes) or from inadequate stimulation of the adrenal by the pituitary gland. These are classified as *primary* and *secondary* hypofunction, respectively.

Hypoadrenocorticism is a diagnosis that is often overlooked or delayed in many patients. The symptoms of

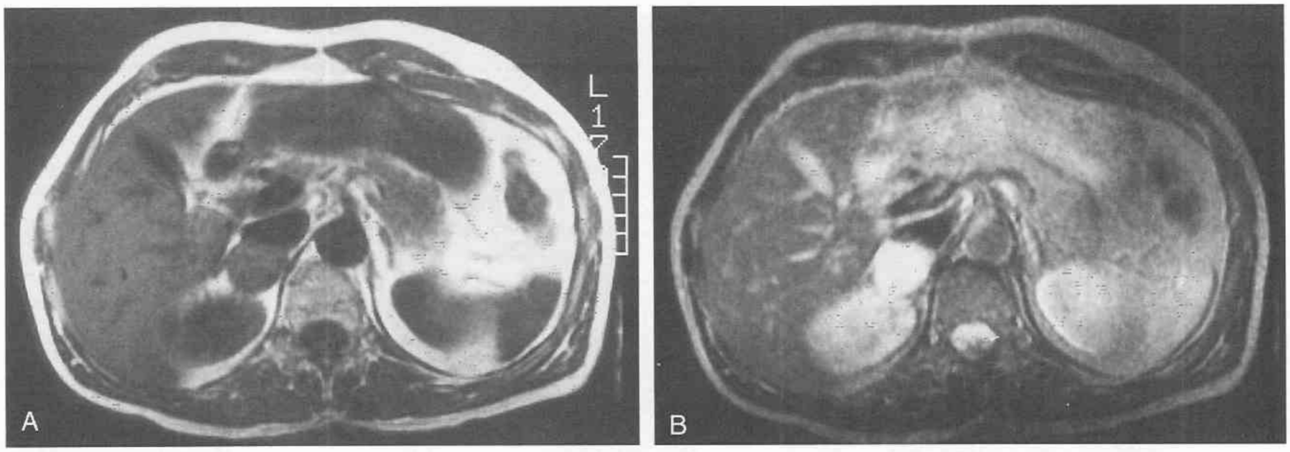

Figure 40–13. Pheochromocytoma. *A* and *B*, MR scans of a 3.5-cm solid right intra-adrenal pheochromocytoma. On T2-weighted images, this tumor demonstrates the hyperintense signal intensity commonly seen in intra-adrenal pheochromocytomas.

lethargy, fatigue, and weakness are uniform among these patients, but may be confused with other clinical entities. Weight loss, anorexia, abdominal pain, and hypotension are further clinical signs and symptoms of hypoadrenalism.

Potential causes of primary adrenal cortical failure include[53, 81–84]:

- Autoimmune disorders
- Infection (most commonly, fungal infections and tuberculosis)
- Drugs that inhibit cortical synthesis
- Drugs that increase cortical clearance
- Hemorrhage
- Metastasis
- Sarcoidosis
- Hemochromatosis
- Amyloidosis

The most common drug that inhibits cortisol synthesis is ketoconazole; drugs that increase cortisol clearance and result in this syndrome include barbiturates and phenytoin (Dilantin). Hypocortisolism occurs with equal frequency in adults of both genders.

The role of imaging in the diagnosis of primary adrenal hypofunction is to evaluate the causes of primary adrenal failure. In patients with an autoimmune disease and primary adrenal cortical failure, the adrenal glands are uniformly small. When infection is the primary cause, the glands may be acutely enlarged or, in the case of chronic infection, may contain areas of calcification.

On a CT scan, hemorrhage caused by septicemia or anticoagulant therapy is seen as a characteristic high-density mass or infiltrating process in one or both adrenal glands. The high-density material follows the normal pattern of blood on CT scanning; the density diminishes over

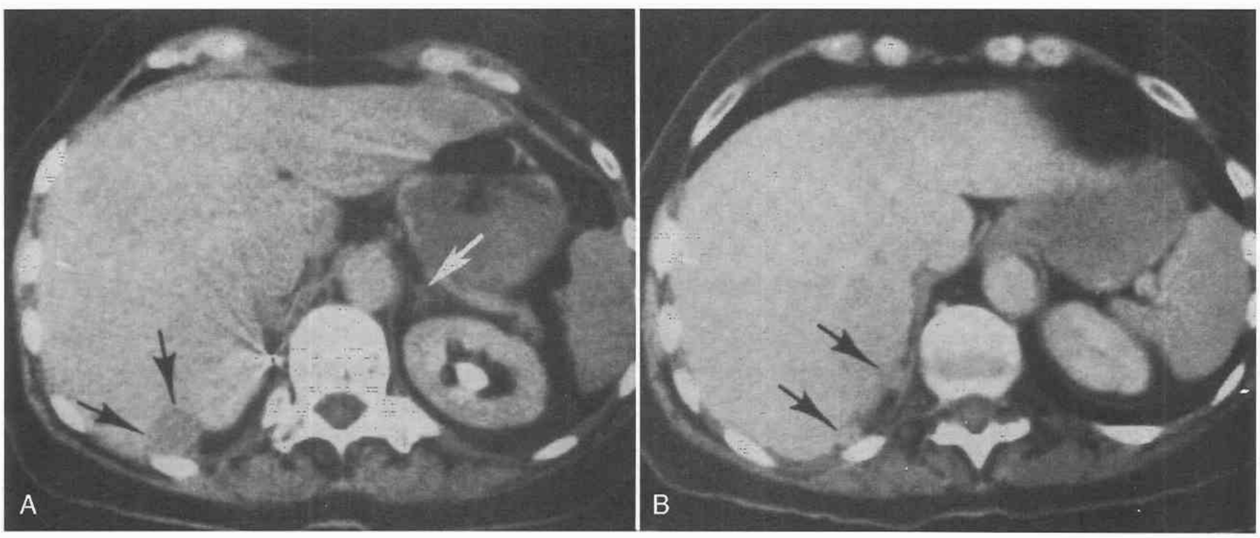

Figure 40–14. Recurrent pheochromocytoma. CT was performed to evaluate the left adrenal gland in a patient with biochemical evidence of a recurrent pheochromocytoma. The original tumor had been removed several years previously. *A*, CT scan at one level shows normal left adrenal gland *(white arrow)* but also reveals a low-density mass, 1.5 cm in diameter, in the operative site *(black arrows)*. *B*, CT scan at a slightly higher level shows two additional nodules *(arrows)* between the right lobe of the liver and the diaphragm. At surgery, these were found to be three nodules of pheochromocytoma "rests."

the next several weeks.[30, 31] When metastases are the cause of primary adrenal cortical failure, the adrenal gland shows the characteristic appearance of the metastases.

Usually, 85% to 90% of the adrenal cortex must be destroyed before adrenal hypofunction is classified as a clinically relevant syndrome. Thus, adrenal hypofunction occurs in a minority of such patients because these disease processes often do not destroy enough adrenal cortex to result in hypofunction.

Nonfunctioning Adrenal Gland Disease Processes

Adrenal Cortical Adenomas

Adrenal cortical adenomas are common benign tumors found in 3% of autopsies and in 1% of all patients undergoing abdominal CT.[46] Benign nonfunctioning adenomas are asymptomatic and usually discovered incidentally in an imaging study.[18] Histologically, they are composed of an admixture of clear, lipid-rich cells arranged in small cords.[24] The cause is thought to be overgrowth of adrenal cortical cells in response to previous injury or vascular insult. Nonfunctioning adenomas appear to increase with age and hypertension. Nonfunctioning adrenal adenomas tend to be small (usually less than 3 cm), sharply marginated, homogeneous masses.

CT often demonstrates a sharply marginated, rounded, homogeneous mass that shows low density.[27, 30, 32] The use of nonenhanced CT for characterization of benign adrenal masses relies on the fact that adrenal adenomas contain a large number of lipid-rich cells, often resulting in Hounsfield unit (HU) values near or below zero (Figs. 40–15 and 40–16).

The literature contains reports of more than 500 adrenal lesions that have been analyzed on unenhanced CT scans.[7, 20, 30, 35, 38, 44, 45, 68] These series present data for different manufacturers and slice thicknesses. In general, the unenhanced scans of adrenal lesions with attenuation values of 18 HU or less exhibit a sensitivity of 86% and a specificity of 88% in identifying benign adrenal adenomas. As the HU value falls toward zero, the specificity increases, reaching 100% at 2 HU. To obtain the HU value in the region of interest, at least half of the cross-sectional area of the lesion should be included on the selected CT slice.

Much attention has been focused on the use of delayed contrast-enhanced CT to differentiate benign adrenal adenomas from nonadenomas. Reports were based on the demonstration that adrenal adenomas had significantly lower attenuation than that of nonadenomas on delayed contrast-enhanced CT scans at arbitrarily chosen times (between 3 and 50 minutes) after contrast infusion.[36, 75] In several studies, attenuation thresholds of 24 HU or less after contrast administration indicated that the lesions were benign.[6, 74] Results varied according to the volume and type of contrast material infused, how it was infused, and the type of scanner used.

The washout of contrast material at the delayed times was assessed in several studies involving contrast-enhanced CT. The results showed that adenomas enhanced significantly more than nonadenomas did at 30, 60, and 90 seconds after contrast infusion. When scans were delayed as long as 30 minutes after contrast infusion, the loss of contrast enhancement and the relative percentage of loss of contrast enhancement were significantly greater for adenomas than for nonadenomas.

Two methods of evaluating contrast washout are used. The patient is scanned without contrast material, then again at 70 seconds, and then 15 minutes after IV contrast administration. The percent enhancement washout is calculated by the formula

$$\frac{E - D}{E - U} \times 100$$

where

E is the 70-second IV postcontrast enhancement value
D is the 15-minute IV postcontrast enhancement value
U is the unenhanced value

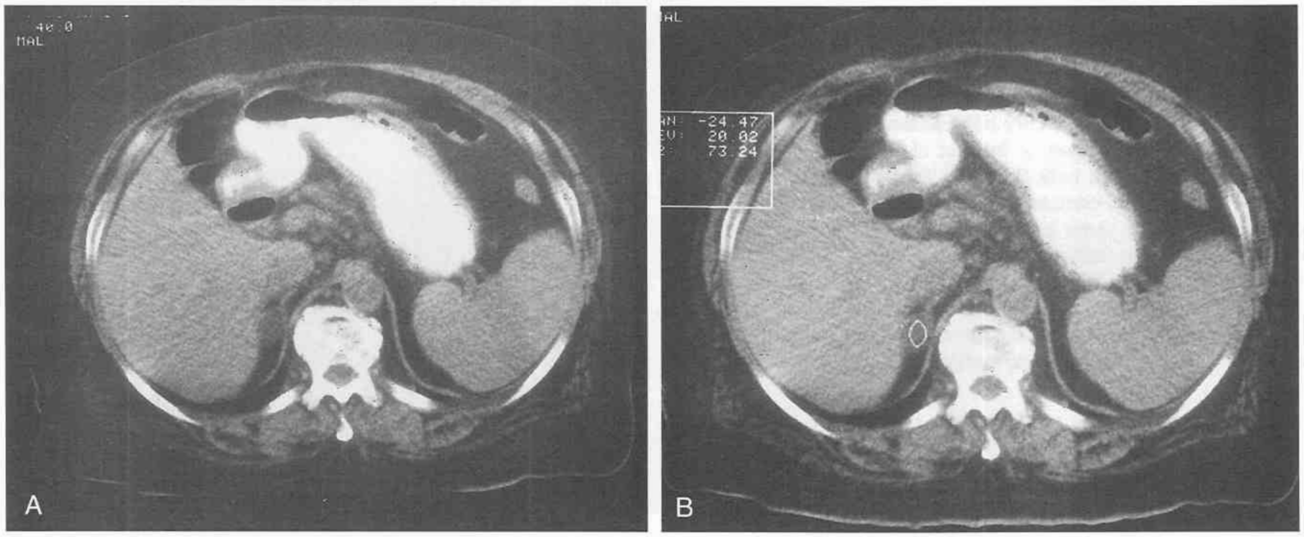

Figure 40–15. Adenoma. *A* and *B*, Non–contrast-enhanced CT scans demonstrate a 1.5-cm low-density mass in the right adrenal gland. The mass measured −24 Hounsfield units (HU), indicating that this is a benign adenoma.

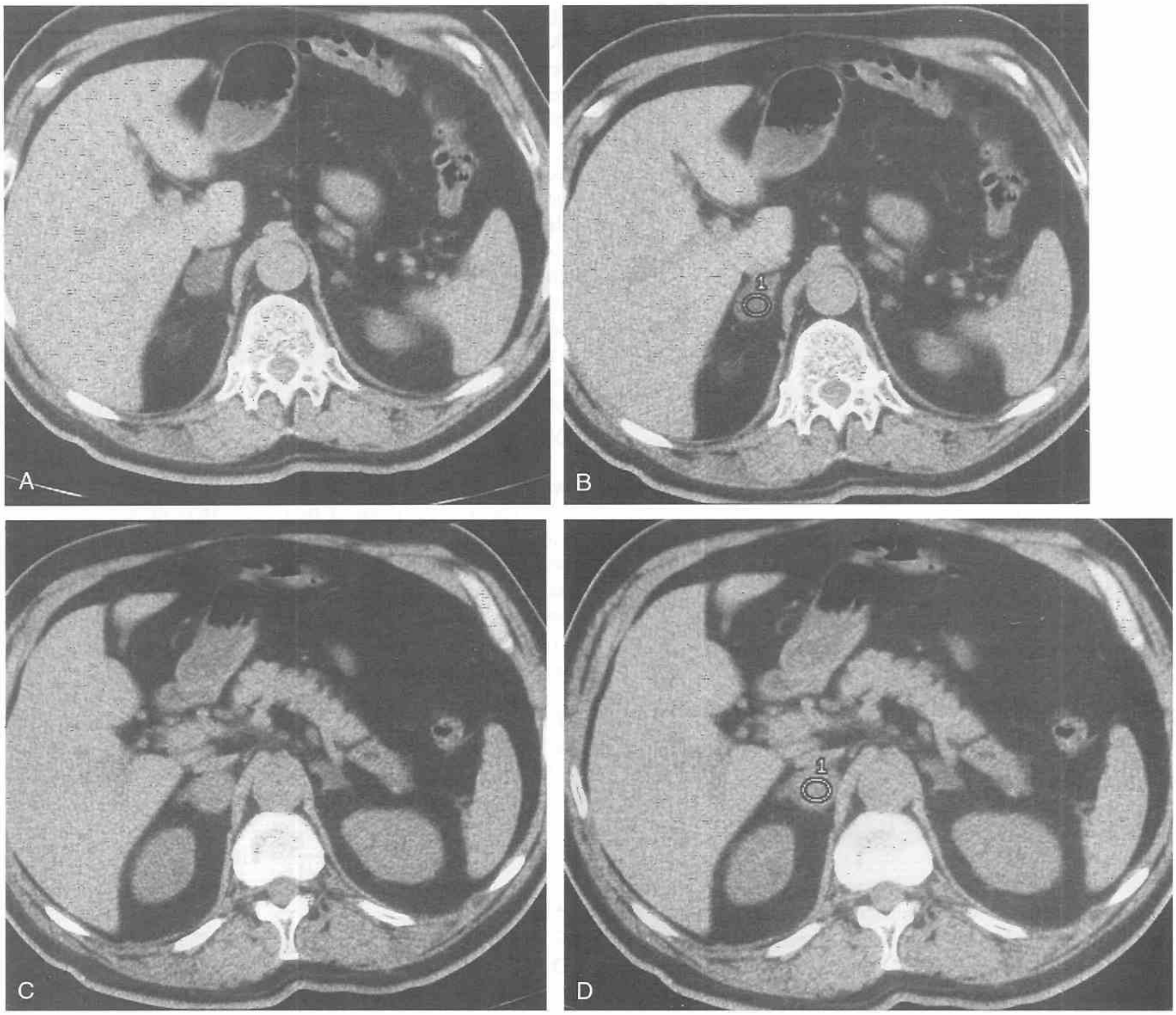

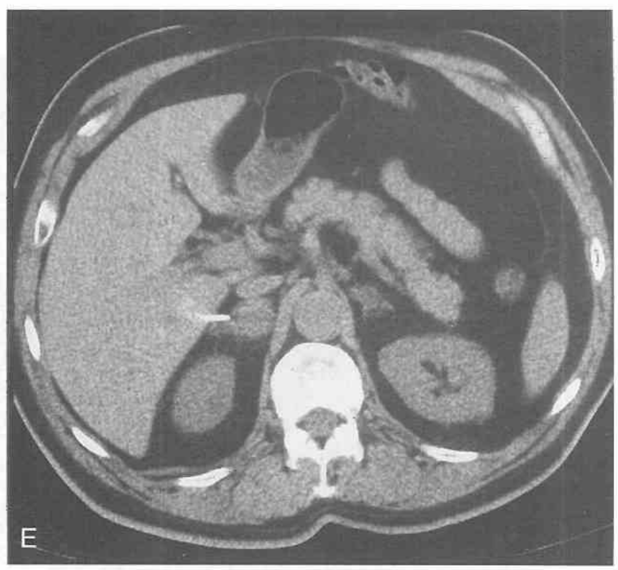

Figure 40–16. Adenoma. *A* and *B,* Nonenhanced CT scans demonstrate a 2-cm low-density right adrenal mass. The attenuation value for the region of interest in this mass was −10 Hounsfield units (HU), indicating that this was a benign adenoma. *C* and *D,* Non–contrast-enhanced CT scans at a slightly lower level in the same patient demonstrated a solid-appearing, 2-cm right adrenal mass. The region of interest in this mass measured 20 HU, which did not clarify whether it was benign or malignant. *E,* Percutaneous biopsy of the solid mass via a transhepatic approach revealed a benign adenoma. Incidentally noted was a 9-mm benign adenoma in the opposite adrenal gland.

All values are in HU.

If percent enhancement washout is greater than 60%, the lesion is benign.

If no enhanced values are available, the relative washout can be used. The formula for relative washout is

$$\frac{E - D}{E} \times 100$$

If the value is greater than 40%, the lesion is benign.[33a]

MRI has been used to distinguish benign adenomas from nonadenomas. Initial reports using low-field-strength magnets and comparing the density of the adrenal lesion to that of other solid abdominal organs showed initial promise, but there was significant overlap with nonadenomas.[24, 43, 55, 63, 66, 67] This technique has not been regarded as useful for evaluating benign adrenal adenomas.

The technique of chemical shift imaging to detect lipid within an adrenal mass has become one of the most common techniques of evaluating adrenal adenomas (Fig. 40–17).[67–69] Because most adrenal adenomas contain lipids but nonadenomas do not, chemical shift imaging readily reveals adrenal masses as adenomas when they lose signal and appear dark on opposed-phase images compared with their appearance on in-phase images.

More recently, the use of dynamic gadolinium-enhanced MRI has also been successfully applied to differentiate benign adrenal adenomas from nonadenomas.[39, 68] With this technique, imaging is usually performed through the adrenal lesion at 20- to 30-second intervals starting with the infusion of the initial bolus of gadolinium and continuing for 5 minutes. Generally, gadolinium in a dose of 1.1 mmol/kg of body weight is used. The principles of gadolinium-enhanced studies are similar to those of contrast-enhanced CT studies. Adenomas show moderate enhancement initially, with quick washout, whereas malignant tumors and other benign tumors, such as pheochromocytomas, show stronger overall contrast enhancement with slower washout. The overall specificities and sensitivities of chemical shift and gadolinium-enhanced MRI for differentiating adrenal adenomas from nonadenomas range from 81% to 100% and from 80% to 100%, respectively.

Both unenhanced CT and delayed contrast-enhanced CT as well as MRI using chemical shift or dynamic gadolinium-enhanced techniques are accurate for differentiating most adrenal adenomas from nonadenomas. The diagnosis is based on the presence of lipid within these lesions or the characteristic enhancement pattern of adenomas versus nonadenomas. Unfortunately, a significant number of adenomas, as many as 10%, do not have a high-enough lipid content or do not behave characteristically in contrast enhancement, rendering the techniques ineffective.[50] In such cases, patients can be monitored at 6-month intervals for changes in the adrenal lesion, or they can undergo percutaneous biopsy.

Adrenal "Incidentalomas" (Incidentally Discovered Adrenal Lesions)

The workup of clinically silent and incidentally discovered adrenal lesions can present a challenge. Increasingly, CT and MRI techniques have helped in their evaluation.

The size of an adrenal lesion is important in predicting its behavior.[45] Benign adrenal lesions generally grow slowly; 87% of adrenal masses smaller than 3 cm in diameter are benign, whereas 95% of masses larger than 3 cm are malignant. Lesions greater than 6 cm in diameter are almost always malignant.[56] In most cases, lesions this large should undergo biopsy or should be treated without further diagnostic study.

The most practical and cost-effective way to evaluate nonfunctioning, incidentally discovered adrenal lesions is to use the imaging modality by which they were discovered. For example, if a lesion is discovered on a CT scan, unenhanced or delayed-contrast imaging can be performed

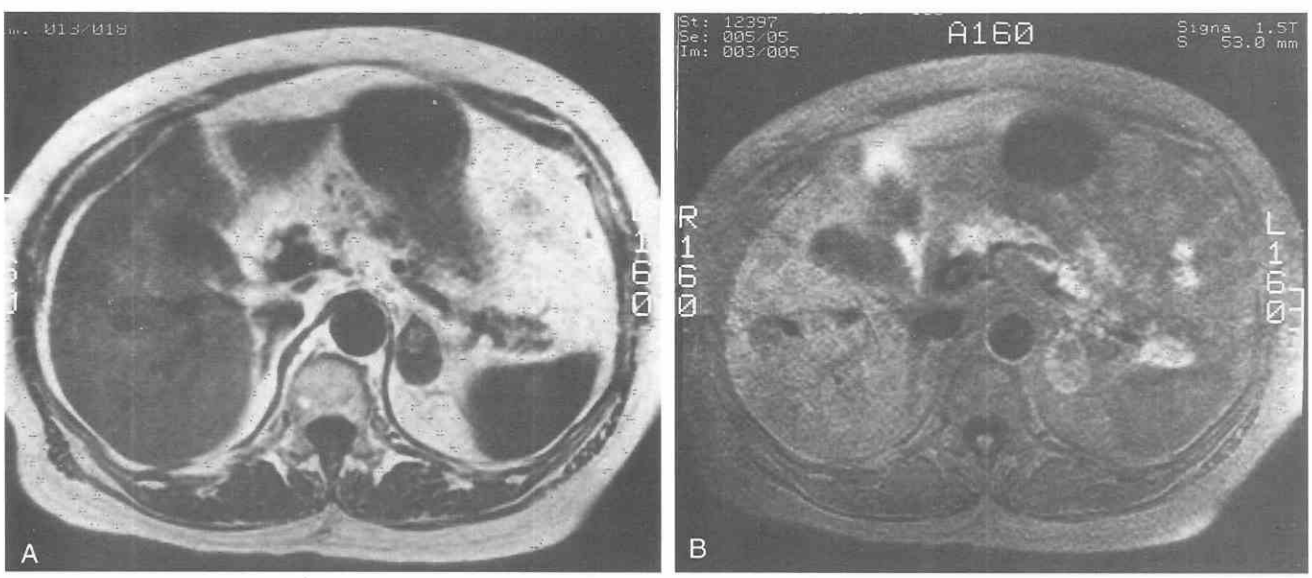

Figure 40–17. Adenoma. *A* and *B*, MR images of a 2.5-cm left adrenal mass. Loss of signal on opposed-phase chemical shift imaging showed that this lesion was a benign adenoma.

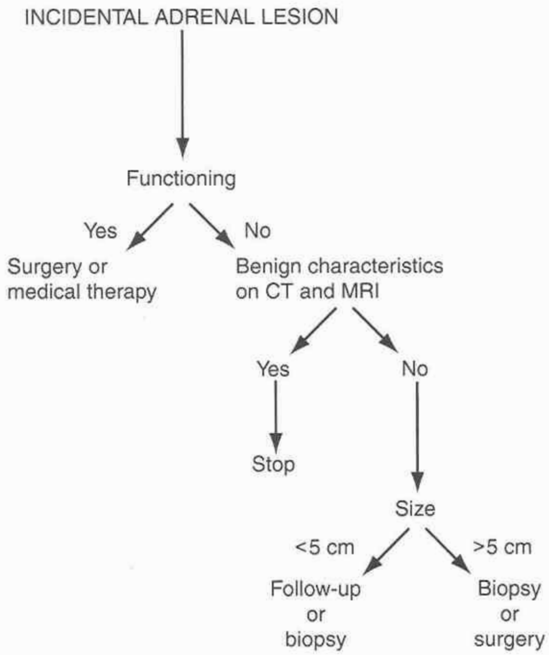

Figure 40–18. Algorithm for evaluating an incidentally discovered adrenal lesion.

at that time to further characterize it. If the lesion is discovered via MRI, chemical shift imaging or dynamic gadolinium enhancement can be performed.

Note that there are no imaging criteria that clearly distinguish benign nonfunctioning adenomas from benign functioning adenomas other than the clinical presentation. Figure 40–18 presents a suggested workup of the incidentally discovered adrenal lesion, summarized as follows:

1. Use clinical and laboratory analyses to decide whether the tumor is functioning. If the tumor is functioning, recommend medical or surgical therapy.
2. If the tumor is nonfunctioning, perform CT, MRI, or both to determine whether it is benign. If the tumor is shown to be benign, stop the workup.
3. If the lesion does not have the characteristics of a benign lesion, determine its size.
4. If the lesion is smaller than 5 cm, follow up at an interval of 6 months.
5. If the patient has an underlying malignancy, however, and the lesion is smaller than 5 cm, recommend biopsy.
6. If the lesion is larger than 5 cm and does not have benign characteristics, recommend percutaneous biopsy or surgery.

Recent data suggest that 5% to 25% of patients with adrenal incidentalomas have some form of subclinical hormonal dysfunction and may represent a population at higher risk for metabolic and cardiovascular disease. The adrenal incidentaloma will continue to be an evolving subject of research and clinical evaluation in the future.[47a]

Adrenal Cortical Carcinomas

Adrenal cortical carcinomas are unusual neoplasms, occurring in less than 0.1% of the population. These tumors affect women more frequently than men, with a bimodal age distribution consisting of an initial peak in the first two decades of life and a second peak in the fifth and sixth decades.[2]

Ten percent of these tumors are clinically functional. When functional, they usually coexist with Cushing's syndrome or a mixed endocrine manifestation.[9] The patient usually presents with a large abdominal mass and experiences symptoms of abdominal pain and weight loss. At the time of presentation, these tumors are often larger than 10 cm in size and are invasive. By the time of diagnosis, they are either locally invasive or metastatic in nearly 90% of patients.[9, 77]

Determining malignancy can be difficult because of the subtle differences between benign and malignant cortical tumors. Adrenal cortical carcinomas can especially be difficult to differentiate from those benign adrenal adenomas that tend to be large (>5 cm in size) and contain large areas of degeneration, hemorrhage, calcification, and necrosis.[50]

The radiologic findings show a large mass that usually envelops much of the area surrounding the involved adrenal gland.[20, 39, 44] Most such masses show degenerative and cystic changes, and 33% contain calcifications. CT and MRI findings reflect the pathologic changes that occur within these large, frequently necrotic, and sometimes calcified tumors. Contrast-enhanced CT shows them to be relatively vascular in certain areas. With MRI, the masses show low signal intensity on T1-weighted images and higher signal intensity on T2-weighted images when compared with the liver. Signal intensity generally increases on opposed-phase chemical shift imaging.

When CT or MRI is performed, the tumors should be staged. They tend to be locally invasive, especially in vascular structures such as the adrenal vein, the renal vein, and the inferior vena cava (Fig. 40–19). In case reports,[34] smaller adrenal cortical carcinomas have showed decreased signal intensity on opposed-phase chemical shift imaging compared with in-phase imaging, but this should not dissuade the radiologist from looking for the other signs of malignancy usually associated with these tumors.

Treatment of adrenal cortical carcinomas consists of surgical resection.

Adrenal Metastases

At autopsy, metastases to the adrenal glands are found in up to 27% of patients dying of cancer. Certain tumors are more likely than others to metastasize to the adrenal glands.[41, 52, 65] Of breast and lung carcinomas that are metastatic, 30% to 40% have adrenal metastases. Of melanomas, 50% show metastatic lesions to the adrenal glands. Less common causes of adrenal metastasis include gastrointestinal tumors and renal cell carcinoma.

Metastases generally involve the boundary between the cortex and the medulla, but spread to either part of the organ occurs. Metastases are usually asymptomatic, but in rare cases hypoadrenalism can occur. Because of the incidence of benign adrenal adenomas in patients with documented underlying malignancies, 50% of all adrenal lesions in patients with malignancies still represent benign adrenal adenomas.

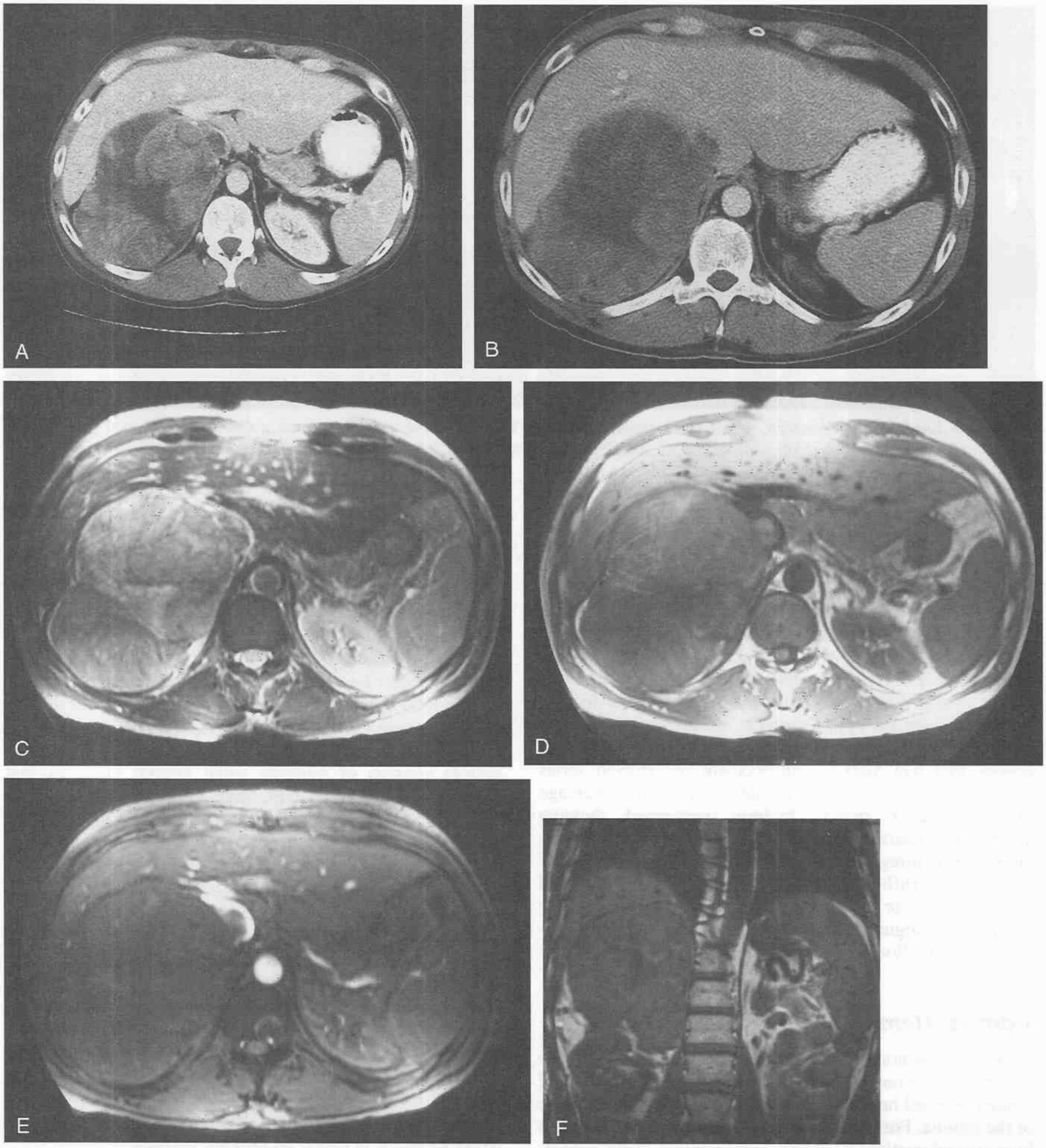

Figure 40–19. Adrenal cortical carcinoma. *A* and *B,* Contrast-enhanced CT scans of the abdomen demonstrate a large heterogeneous right adrenal mass invading the inferior vena cava. *C–F,* MR images demonstrate a large right adrenal cortical carcinoma with invasion of the inferior vena cava.

The CT findings of metastatic disease to the adrenal gland demonstrate that metastases tend to be larger and less well defined, with inhomogeneous central areas that have thick, irregularly enhancing rims. The metastases are frequently bilateral (Fig. 40–20).[20, 32, 37]

Metastases usually demonstrate an attenuation of more than 20 HU on unenhanced CT scans. On delayed contrast-enhanced CT, the value is generally higher and the metastases tend to remain enhanced longer than adrenal adenomas; at 30 minutes, metastases show an attenuation of more than 40 HU.

MRI has been used to differentiate metastatic disease

Figure 40–20. Adrenal metastasis. *A* and *B,* Contrast-enhanced CT scans of the abdomen reveal a 4.5-cm left adrenal mass that is inhomogeneous and irregular. The patient had an underlying lung carcinoma; percutaneous biopsy indicated left adrenal metastasis.

from benign adrenal tumors. Initially, T1-weighted and T2-weighted signal intensities were studied in other organs in an attempt to differentiate metastases from adenomas. Unfortunately, because of signal intensity overlap in 20% to 30% of cases, these methods were not useful.

Next, dynamic gadolinium-enhanced MRI and chemical shift imaging were studied for their ability to evaluate adrenal masses. Chemical shift imaging demonstrated that it is rare for nonadenomatous lesions to have a loss of signal intensity on opposed-phase images compared with in-phase images. On dynamic gadolinium-enhanced scans, lesions that had marked enhancement on delayed series were more likely to be malignant. In a small percentage of lesions, these imaging findings overlapped, showing appearances characteristic of both adenomas (particularly large degenerating ones) and metastases. When neither CT nor MRI is sufficient to determine whether an adrenal mass is benign or malignant, a patient with a suspected or diagnosed malignancy should undergo percutaneous adrenal biopsy to allow histopathologic examination.

Adrenal Hemorrhage

Adrenal hemorrhage and infarction can have multiple causes, both *traumatic* and *nontraumatic*.[31] In the case of trauma, adrenal hemorrhage is usually unilateral to the side of the trauma. For example, in a patient who has undergone liver transplantation, unilateral right adrenal gland hemorrhage and infarction tend to occur after ligation and division of the right adrenal vein.[8]

Nontraumatic causes include physiologic stress, usually secondary to surgery or sepsis.[51] Other causes include a bleeding diathesis an underlying adrenal tumor, and certain idiopathic conditions.[58, 71] The clinical manifestations of nontraumatic adrenal hemorrhage depend on (1) the amount of hemorrhage and its rate of onset, (2) the presence or absence of hemorrhage into the perinephric space, and (3) the patient's underlying hematologic status.

Patients may be asymptomatic or may present with sudden or gradual onset of upper abdominal flank or back pain. If the hemorrhage is massive, signs and symptoms of blood loss can occur.

It is unusual for adrenal insufficiency to result from adrenal hemorrhage, but when this occurs, it can be life-threatening because the patient is often under other critical physiologic stresses. Generally, more than 90% of the adrenal gland must be destroyed before insufficiency occurs.[83]

The unique blood supply of the adrenal gland results in a predisposition to adrenal hemorrhage. The vascular system of the adrenal gland is termed a *vascular dam*.[15] The system consists of multiple small arterial branches that form a subcapsular plexus, and there are few draining venules. With physiologic stress, the vascularity of the adrenal gland increases, venous pressure becomes elevated, and venous constriction can occur. As a result, this intrinsically vulnerable network is susceptible to hemorrhage.

Imaging findings of acute adrenal hemorrhage are usually discovered incidentally. On CT scans, the adrenal glands appear as round or oval masses that may have stranding if hemorrhage into the periadrenal fat is present. Acute to subacute hemorrhages contain areas of high attenuation, usually between 50 and 90 HU on nonenhanced CT scans (Fig. 40–21). Adrenal hematomas generally regress over time and almost always resolve completely. Calcification can occur but usually not within the first year after hemorrhage. If a hematoma organizes and becomes relatively cystic, it is called an *adrenal pseudocyst*.

In the *acute* stage, adrenal hematomas displayed by MRI generally demonstrate isointense or slightly hypointense signal on T1-weighted images and markedly hypointense signal on T2-weighted images. The findings on T2-weighted images are caused by a high concentration of intracellular deoxyhemoglobin, which leads to the T2 proton relaxation characteristics.

In the *subacute* stage, about 7 to 10 days after the initial hemorrhage, the hematoma appears hyperintense on both T1-weighted and T2-weighted images. The T1 shortening that occurs during this time is caused by the paramagnetic

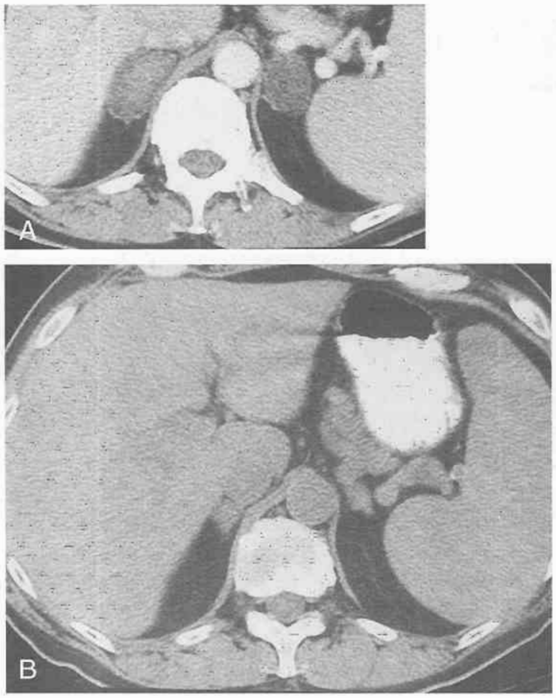

Figure 40–21. Adrenal masses. *A,* Contrast-enhanced CT scan of the abdomen indicates bilateral adrenal masses that contain high-density material compatible with adrenal hemorrhage. *B,* Follow-up scan performed 7 months later reveals regression of the bilateral adrenal masses, which is compatible with resolution of adrenal hemorrhage.

effect of free methemoglobin, which is produced as the hematoma ages.

In the *chronic* stage, usually 2 to 3 months after the hemorrhage, a hypointense rim can be seen on both T1-weighted and T2-weighted images. Gradient-echo imaging is helpful to demonstrate the "blooming," or magnetic susceptibility effect, that results from hemosiderin deposition at this stage. Appreciating adrenal hemorrhage is important in the management of patients who have undergone significant injury or physiologic stress.

Myelolipomas

Myelolipomas are benign and relatively uncommon adrenal tumors. They contain a variable mixture of fat and hemopoietic elements that frequently resemble bone marrow.[14, 24, 33, 62] Myelolipomas almost always occur within the adrenal gland but have been reported in other locations in the retroperitoneum. Most of these lesions are asymptomatic and are found on routine imaging for other reasons.

Occasionally, acute hemorrhage occurs within these lesions, or certain functional conditions such as Cushing's syndrome or Conn's syndrome can occur. When myelolipomas undergo acute hemorrhage, patients usually present with a sudden onset of pain, hypotension, and documented blood loss. Myelolipomas that spontaneously hemorrhage are usually larger than 10 cm in size. No malignant potential is associated with these lesions.

The hallmark of imaging these tumors by CT, ultrasound, or MRI is identification of the areas of fat within the lesion (Fig. 40–22). On CT scans, layers of fat are usually interspersed with areas of high-attenuation tissue (Fig. 40–23). Ultrasound shows myelolipomas as generally hyperechoic masses, with the more hypoechoic regions representing the myeloid components.

On MR images, the predominantly fatty areas demonstrate increased signal intensity on T1-weighted images. The appearance on T2-weighted images is more complex because of the admixture of marrow and soft tissue elements within the fat. Chemical shift opposed-phase imaging, also used for identifying benign adrenal adenomas, should demonstrate low signal intensity in areas that contain fat.

Management generally involves observation unless the tumor is functioning or acute hemorrhage occurs.

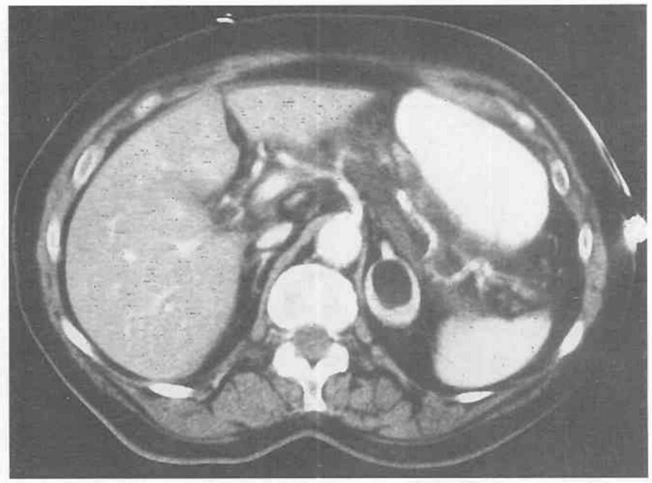

Figure 40–22. Adrenal myelolipoma. Contrast-enhanced CT scan of the abdomen demonstrates a 3.5-cm left adrenal mass containing a large amount of fat. This mass is characteristic of an adrenal myelolipoma.

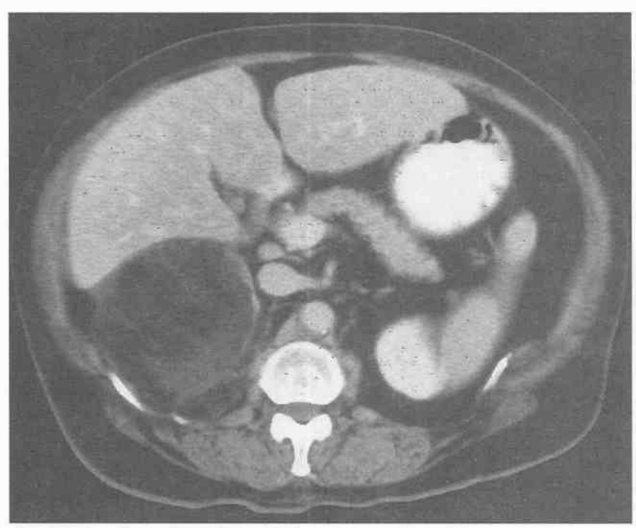

Figure 40–23. Myelolipoma. Contrast-enhanced CT scan of the abdomen reveals a 6-cm by 7-cm right adrenal mass containing both fat and soft tissue elements. This appearance is compatible with a myelolipoma.

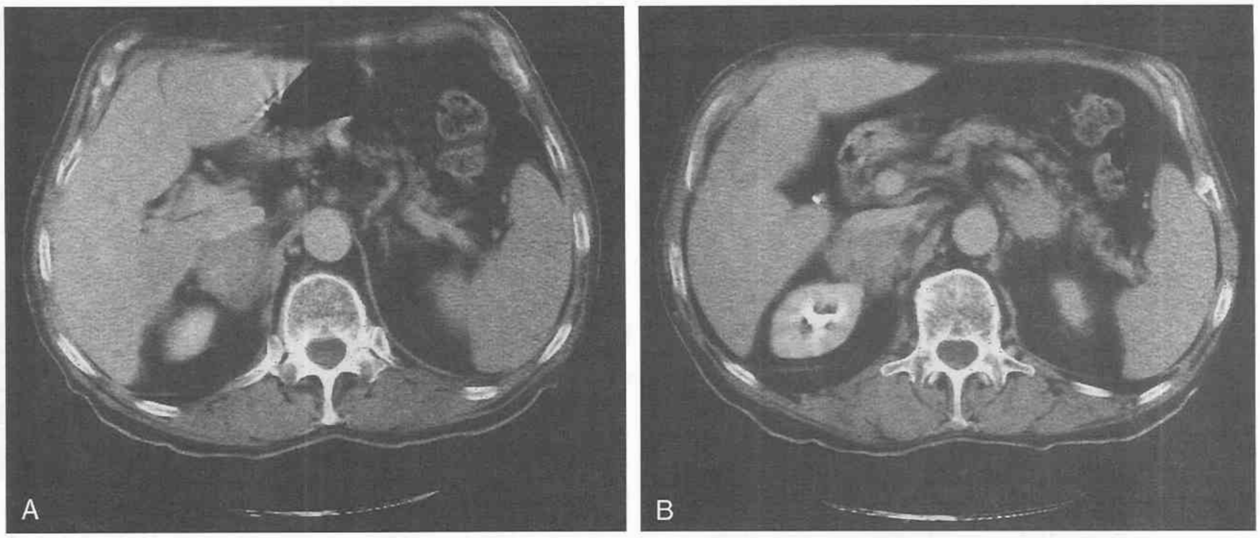

Figure 40–24. Lymphoma. *A* and *B*, Contrast-enhanced CT scans of the abdomen demonstrate bilateral infiltrating soft tissue masses within both adrenal glands. The appearance is compatible with that of a lymphoma. Involvement of the liver can be seen on the lower-level scan of the series. The patient underwent percutaneous adrenal biopsy, which resulted in a diagnosis of non-Hodgkin's lymphoma.

Lymphoma

Adrenal glands are an unusual site for primary lymphoma. At autopsy, however, the adrenal gland has been found to be involved in up to 25% of patients with disseminated non-Hodgkin's lymphoma. In all age groups, involvement of the adrenal glands occurs more often in patients with non-Hodgkin's lymphoma than in those with Hodgkin's disease. Involvement is bilateral in 70% of cases (Fig. 40–24). Although lymphoma of the adrenal glands may present as a solid mass or as solid masses, the most common presentation is of diffuse bilateral enlargement of the adrenal glands (Fig. 40–25).

Generally, treatment of lymphoma in the adrenal glands is similar to that of other sites.[21]

Miscellaneous Adrenal Conditions

Cysts

Adrenal cysts are rare lesions that are usually found incidentally at imaging or autopsy. The cysts are endothelial in 45% of cases, pseudocysts in approximately 40%, epithelial in 10%, and parasitic in 5%.[19, 28] Endothelial cysts are most often lymphangiomatous and contain clear fluid (Fig. 40–26). Pseudocysts usually result from previous adrenal injury or hemorrhage and contain fibrinous walls with no obvious lining (Fig. 40–27). Epithelial cysts are usually degenerated benign neoplasms or embryonal cysts. Parasitic cysts are usually secondary to echinococcal infections.

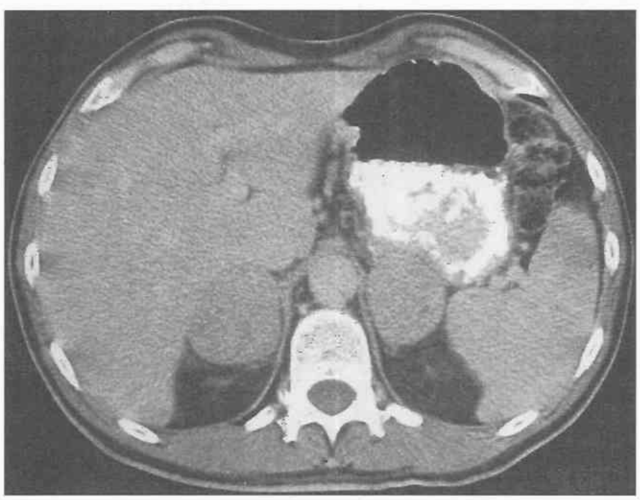

Figure 40–25. Non-Hodgkin's lymphoma. Contrast-enhanced CT scan of the abdomen demonstrates solid bilateral adrenal masses. Biopsy revealed the diagnosis.

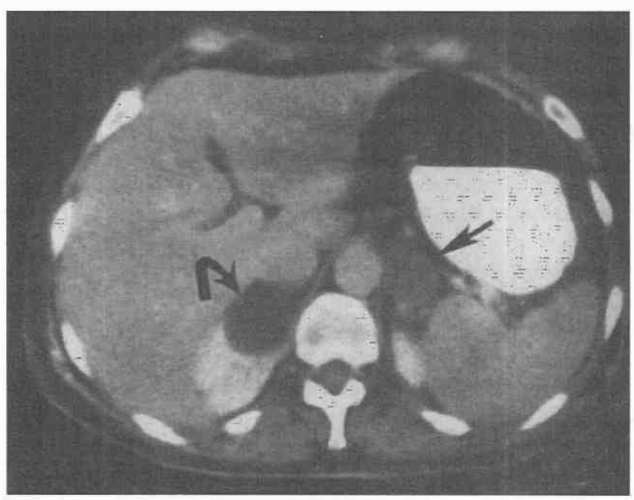

Figure 40–26. Adrenal and renal cysts. Oval, low-density mass with a thin wall can be seen in the left adrenal gland *(arrow)*. The density of the left adrenal cyst is slightly greater than that of the cyst in the upper pole of the right kidney *(curved arrow)*, but the attenuation value is compatible with a diagnosis of a cyst.

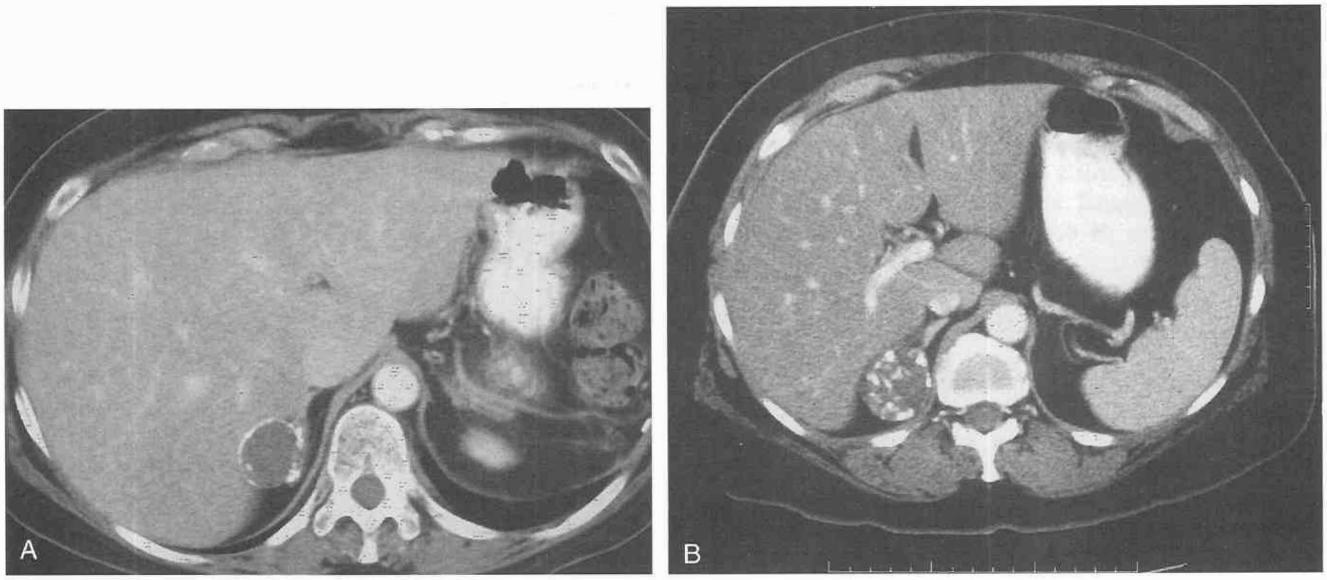

Figure 40–27. Adrenal pseudocysts. *A* and *B*, Contrast-enhanced CT scans of two patients reveal nodular calcification in right adrenal cystic lesions. These lesions, which remained stable over several years, were thought to represent adrenal pseudocysts resulting from previous trauma.

Imaging findings are similar to those of simple cysts found elsewhere in the body. Pseudocysts or echinococcal cysts appear as more complex cystic masses that can be difficult to differentiate from cystic neoplasms.[64]

Infection

Infection in the adrenal glands is most commonly fungal or tubercular.[80–82] Adrenal gland involvement is often bilateral and in the acute setting results in diffuse enlargement of the adrenal glands (Fig. 40–28). Patients with underlying immune compromise, including those with acquired immunodeficiency syndrome (AIDS), are more susceptible to *Mycobacterium avium–intracellulare* infection.[23] The adrenal glands may appear normal on imaging studies. In the chronic stage of infection, a calcified mass or diffuse adrenal calcification can be seen.

Solid Lesions

Several solid lesions that involve the adrenal glands are extremely rare[54]:

- Adrenal hemangiomas
- Ganglioneuromas
- Adrenal angiosarcomas
- Primary malignant melanomas

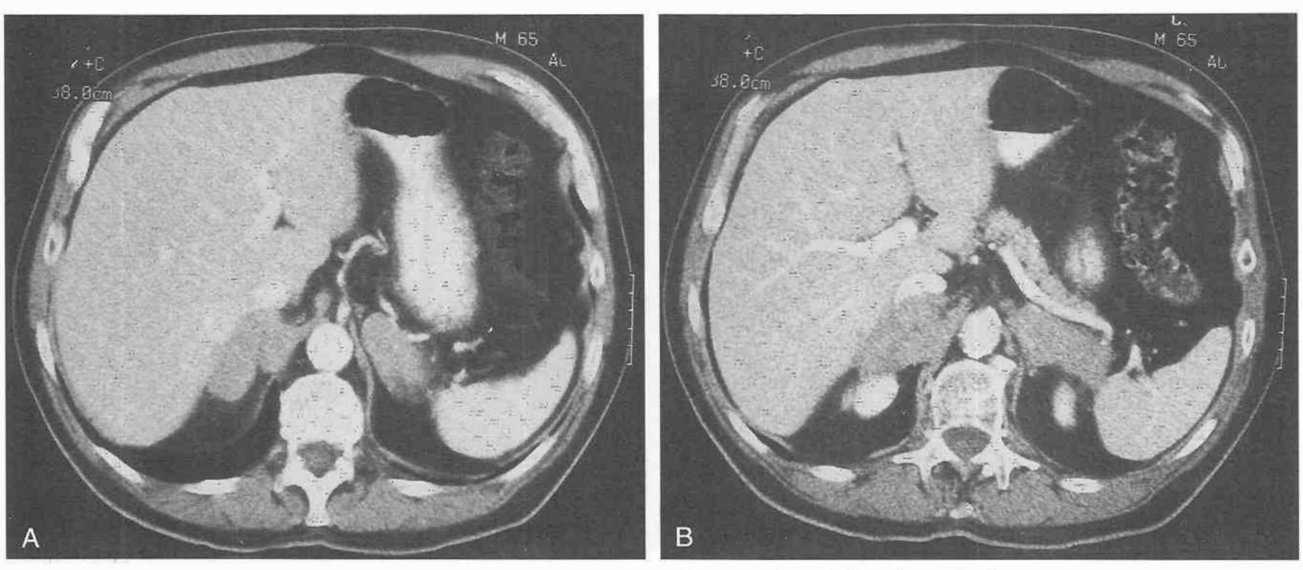

Figure 40–28. Tuberculous infection. *A* and *B*, Contrast-enhanced CT scans show infiltrating soft tissue masses shaped like adrenal glands. Percutaneous biopsy indicated acute tuberculous infection of the adrenal glands in an immunocompromised patient.

Adrenal Hemangiomas

Adrenal hemangiomas are generally asymptomatic and usually involve the adrenal cortex. Calcifications are common, and on contrast-enhanced CT scans peripheral nodular enhancement is seen. Complete enhancement is unusual because of inner necrosis and fibrosis. MRI findings usually consist of high signal intensity on T2-weighted images, with central areas of decreased signal intensity resulting from fibrotic scar.

Ganglioneuromas

Ganglioneuromas are rare, benign neoplasms that originate from sympathetic ganglia.[61] Most patients are older than 40 years of age and have no symptoms. The tumors present as well-defined, oval, discrete masses. With contrast enhancement, delayed heterogeneous uptake of contrast material results in incomplete filling of the tumor. On T1-weighted MRI images, ganglioneuromas demonstrate hypointensity. On T2-weighted images, they show heterogeneous but marked hyperintensity.

Adrenal Angiosarcomas

Angiosarcomas are malignant mesenchymal tumors that originate from the smooth muscle of the walls of adrenal veins. These tumors generally appear vascular on imaging studies.

Primary Malignant Melanoma

Primarily malignant melanoma of the adrenal glands is extremely rare. This tumor can occur within the adrenal gland because of the neuroectodermal origin of the adrenal medulla. Chromaffin cells and melanocytes have a common embryogenesis and similar histologic appearance. For a diagnosis of primary adrenal melanoma, the patient must have unilateral involvement of the adrenal, no previous history of melanoma, and an absence of extra-adrenal lesions.

Percutaneous Adrenal Biopsy

Percutaneous biopsy of an adrenal mass has become a standard diagnostic procedure for evaluating adrenal abnormalities. The most common indication for an adrenal biopsy is to exclude metastasis in patients with a known malignancy. Biopsy is also performed to identify primary adrenal tumors, infectious disease of the adrenal gland, and adrenal hemorrhage.[79]

Adrenal biopsy is generally performed under CT guidance, which gives superior spatial resolution for visualizing the deep retroperitoneum. The *coaxial* technique, in which a guiding needle is placed next to the lesion, is performed (Fig. 40–29). Through the guiding needle, multiple passes can be made with a biopsy gun to obtain a significant amount of tissue for cytologic and histologic studies.

For the right adrenal gland, the approach to biopsy is generally transhepatic or posterior; for the left adrenal gland, the approach is generally posterior. For a posterior approach to either adrenal gland, the patient is placed in the decubitus position with the biopsy side down. This position helps to prevent the lung from intervening along the biopsy path. The anterior approach to the left adrenal gland is generally avoided because of the close proximity of the pancreas and vascular structures, which can increase the risk of complication.

The patient's breathing should be controlled during percutaneous adrenal biopsy because of the proximity of the pleura and the lung. The use of full expiration generally helps to obtain very reproducible results, acts as a breathing marker, and does not allow lung tissue to intervene through the chosen pathway. An 18-gauge biopsy gun can obtain cores of tissue for histologic study. When tracking deep into the retroperitoneum, these larger needles tend to be deflected less often compared with thinner needles. There is no difference in the complication rates for 18-gauge needles compared with needles used for smaller lesions.

The accuracy of image-guided biopsy of the adrenals generally approaches 95% in experienced hands.[79] The complication rate is 3%. The most common complication is adrenal hemorrhage because of the unique blood supply and the gland's vascular dam physiology. Most complica-

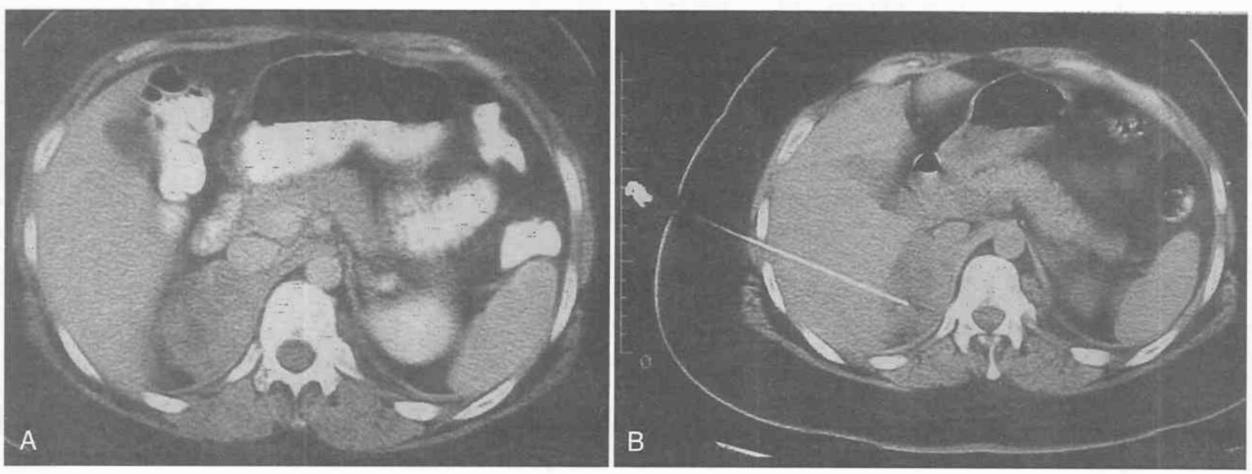

Figure 40–29. Possible adrenal metastases in a 66-year-old patient. *A*, Large infiltrating right adrenal mass. *B*, Transhepatic biopsy specimen of adrenal metastases in the right adrenal gland.

tions are benign and self-limiting and do not require surgery.

Pneumothorax and pancreatitis, two other potential major complications, can be minimized by:

1. Avoiding the pancreas by not using an anterior approach to the left adrenal gland.
2. Ensuring that no lung tissue intervenes along the path of the biopsy needle.

Percutaneous adrenal biopsy has become important for evaluating adrenal pathology and has reduced the use of more invasive procedures. A new trend in percutaneous intervention is the use of percutaneous ablation.[40, 76] Generally applied to malignant tumors, percutaneous ablation is performed by injection of alcohol or by radiofrequency heating devices. Use of the technique has been limited in the adrenal gland, although adrenal cyst ablation and functioning adrenal tumor ablation using percutaneous injection of either absolute alcohol or acetic acid has been performed (Fig. 40–30).[40, 76] The exact role of percutaneous ablation for other adrenal conditions continues to evolve and appears to have a promising future.

Multiple Endocrine Neoplasia

MEN comprises a group of disorders in which tumor or hyperplasia develops in two or more endocrine organs in a single patient. It exists as three main types: MEN1, MEN2A, and MEN2B.[57] Autosomal dominant inheritance occurs in all three types.

MEN Type 1

MEN1 primarily affects the adrenal cortex by the formation of either nodules or functioning adenomas. Rarely do functional adrenal cortical adenomas occur; if they do, they present as either hyperaldosteronism or Cushing's syndrome. The other endocrine abnormalities involved with MEN1 include parathyroid hyperplasia or adenoma, gastrinoma, insulinoma, vipoma, and glucagonoma of the pancreatic islet cells. The anterior pituitary gland can be involved through adenomas that secrete prolactin, growth hormone, or ACTH. Carcinoid tumors can also occur, as can multiple lipomas and thyroid nodules.

MEN Types 2A and 2B

MEN2A is characterized by pheochromocytomas in the adrenal medulla. Associated medullary thyroid carcinoma and parathyroid hyperplasia or adenomas may occur. MEN2B is characterized by pheochromocytomas of the adrenal medulla and by medullary thyroid carcinoma, soft tissue neuromas, and ganglioneuromatosis of the intestine

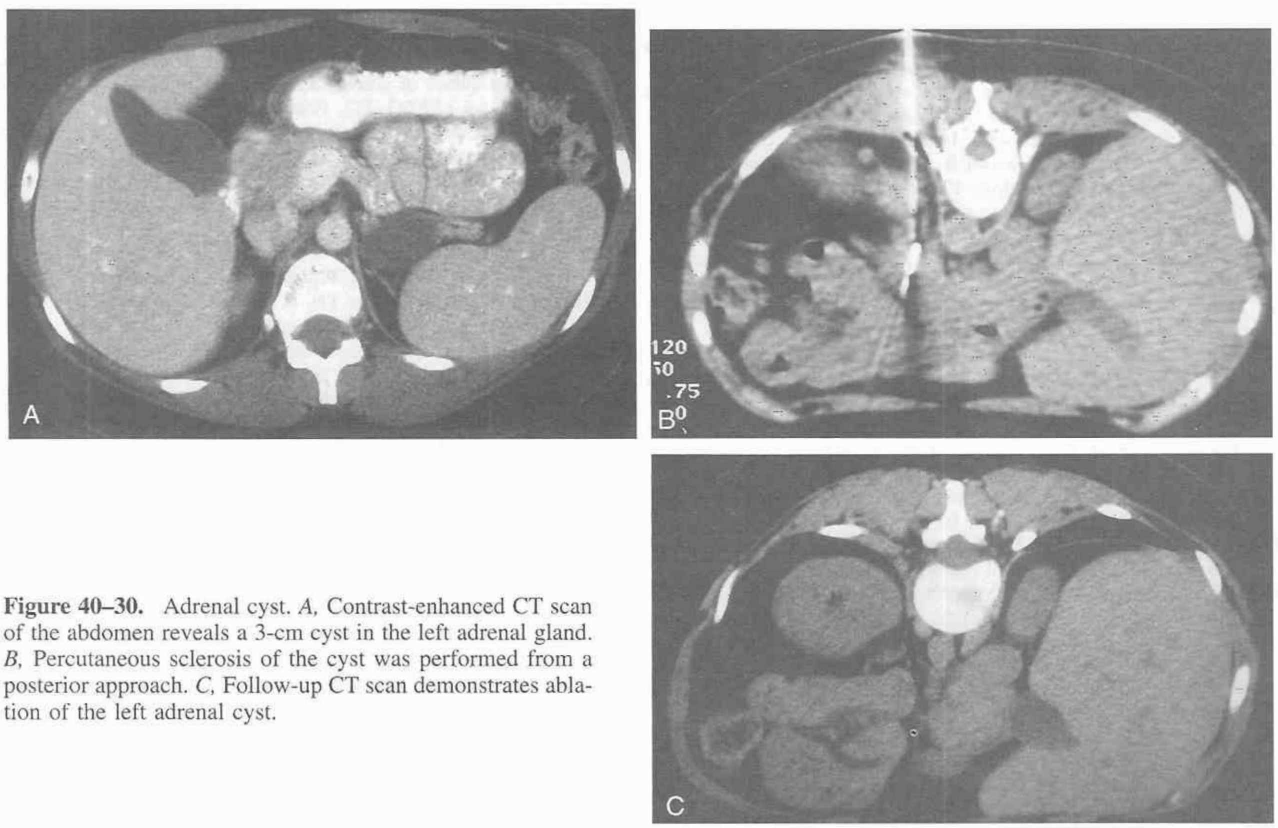

Figure 40–30. Adrenal cyst. *A,* Contrast-enhanced CT scan of the abdomen reveals a 3-cm cyst in the left adrenal gland. *B,* Percutaneous sclerosis of the cyst was performed from a posterior approach. *C,* Follow-up CT scan demonstrates ablation of the left adrenal cyst.

with Marfan-like build. The pheochromocytomas that occur in MEN2A and MEN2B are often smaller than isolated intra-adrenal pheochromocytomas and more frequently bilateral. An increased incidence of extra-adrenal pheochromocytomas also occurs in patients with MEN2A or MEN2B.

Carney's Syndrome

Carney's syndrome is a related disorder characterized by the presence of gastric leiomyogenic neoplasms, extra-adrenal pheochromocytomas or paragangliomas, and pulmonary chondromas. Accurate imaging to define the extra-adrenal pheochromocytomas or paragangliomas, which are often functional, is important for preoperative localization. The combination of MIBG scanning with MRI or CT has been successful.

References

1. Addison T: On the constitutional and local effects of disease of the suprarenal capsules. 1855. In a collection of the published writings of the late Thomas Addison, M.D., physician to Guy's Hospital, London, 1868. Med Classics 2:244–293, 1937.
2. Agrons GA, Lonergan GJ, Dickey GE, et al: Adrenocortical neoplasms in children: Radiologic-pathologic correlation. Radiographics 19:989–1008, 1999.
3. Avila NA, Shawker TS, Jones JV, et al: Testicular adrenal rest tissue in congenital adrenal hyperplasia: Serial sonographic and clinical findings. AJR Am J Roentgenol 172:1235–1238, 1999.
4. Avila NA, Premkumar A, Merke DP: Testicular adrenal rest tissue in congenital adrenal hyperplasia: Comparison of MR imaging and sonographic findings. AJR Am J Roentgenol 172:1003–1006, 1999.
5. Blevins LS Jr, Wand GS: Primary aldosteronism: An endocrine perspective. Radiology 184:599–600, 1992.
6. Boland GW, Hahn PF, Pena C, et al: Adrenal masses: Characterization with delayed contrast-enhanced CT. Radiology 202:693–696, 1997.
7. Boland GW, Lee MJ, Gazelle GS, et al: Characterization of adrenal masses using unenhanced CT: An analysis of the CT literature. AJR Am J Roentgenol 171:201–204, 1998.
8. Bowen A, Keslar PJ, Newman B, et al: Adrenal hemorrhage after liver transplantation. Radiology 176:85–88, 1990.
9. Brennan MF: Adrenocortical carcinoma. CA Cancer J Clin 37:348–353, 1987.
10. Choyke PL, Doppman JL: Case 18: Adrenocorticotropic hormone–dependent Cushing syndrome. Radiology 214:195–198, 2000.
11. Cirillo RL, Bennett WF, Vitellas KM, et al: Pathology of the adrenal gland: Imaging features. AJR Am J Roentgenol 170:429–435, 1998.
12. Coupland RE: The development and fate of catecholamine-secreting endocrine cells. In Parvez H, Parvez S (eds): Biogenic Amines in Development. Amsterdam, Elsevier, 1980, pp 3–28.
13. Crowder RE: Development of the adrenal gland in man with special reference to origin and ultimate locations of cell types and evidence of favour of cells migration theory. Contrib Embryol 36:193–210, 1975.
14. Cyran KM, Kenney PJ, Memel DS, et al: Adrenal myelolipoma. AJR Am J Roentgenol 166:395–400, 1996.
15. Dobbie JW, Symington T: The human adrenal gland with special reference to the vasculature. J Endocrinol 34:479–489, 1966.
16. Doppman JL, Gill JR Jr, Miller DL, et al: Distinction between hyperaldosteronism due to bilateral hyperplasia and unilateral aldosteronoma: Reliability of CT. Radiology 184:677–682, 1992.
17. Dunnick NR, Leight GS Jr, Roubidoux MA, et al: CT in the diagnosis of primary aldosteronism: Sensitivity in 29 patients. AJR Am J Roentgenol 160:321–324, 1993.
18. Dunnick NR, Korobkin M, Francis I: Adrenal radiology: Distinguishing benign from malignant adrenal masses. AJR Am J Roentgenol 167:861–867, 1996.
19. Foster DG: Adrenal cysts. Arch Surg 92:131–143, 1966.
20. Francis IR, Gross MD, Shapiro B, et al: Integrated imaging of adrenal disease. Radiology 184:1–13, 1992.
21. Frick MP, Salomonowitz E, Hanto DW, et al: CT of abdominal lymphoma after renal transplantation. Am J Roentgenol 142:97–99, 1984.
22. Geisinger MA, Zelch MG, Bravo EL, et al: Primary hyperaldosteronism: Comparison of CT, adrenal venography, and venous sampling. Am J Roentgenol 141:299–302, 1983.
23. Glasgow BJ, Steinsapir KD, Anders K, et al: Adrenal pathology in the acquired immune deficiency syndrome. Am J Clin Pathol 84: 594–597, 1985.
24. Heinz-Peer G, Honigschnabl S, Schneider B, et al: Characterization of adrenal masses using MR imaging with histopathologic correlation. AJR Am J Roentgenol 173:15–22, 1999.
25. Hensen J, Buhl M, Oelkers W: The functional spectrum of adrenocortical adenomas. Med Hypotheses 40:217–222, 1993.
26. Huebener KH, Treugut H: Adrenal cortex dysfunction: CT findings. Radiology 150:195–199, 1984.
27. Hussain S, Belldegrun A, Seltzer SE, et al: Differentiation of malignant from benign adrenal masses: Predictive indices on computed tomography. Am J Roentgenol 144:61–65, 1985.
28. Incze JS, Lui PS, Merriam JC, et al: Morphology and pathogenesis of adrenal cysts. Am J Pathol 95:423–432, 1979.
29. Jey RK, van Heerden JA, Carpenter PC, et al: Ectopic ACTH syndrome: Diagnostic and therapeutic aspects. Am J Surg 149:276–282, 1985.
30. Kawashima A, Sandler CM, Fisherman EK, et al: Spectrum of CT findings in nonmalignant disease of the adrenal gland. Radiographics 18:393–412, 1998.
31. Kawashima A, Sandler CM, Ernst RD, et al: Imaging of nontraumatic hemorrhage of the adrenal gland. Radiographics 19:949–963, 1999.
32. Kenney PJ, Berlow ME, Ellis DA: Current imaging of adrenal masses. Radiographics 4:743–783, 1984.
33. Kenney PJ, Wagner BJ, Rao P, et al: Myelolipoma: CT and pathologic features. Radiology 208:87–95, 1998.
33a. Korobkin M: CT characterization of adrenal masses: The time has come. Radiology 217:629–632, 2000.
34. Korobkin M, Lombardi TJ, Aisen AM, et al: Characterization of adrenal masses with chemical shift and gadolinium-enhanced MR imaging. Radiology 197:411–418, 1995.
35. Korobkin M, Brodeur FJ, Yutzy GG, et al: Differentiation of adrenal adenomas from nonadenomas using CT attenuation values. AJR Am J Roentgenol 166:531–536, 1996.
36. Korobkin M, Brodeur FJ, Francis IR, et al: CT time-attenuation washout curves of adrenal adenomas and nonadenomas. AJR Am J Roentgenol 170:747–752, 1998.
37. Krebs TL, Wagner BJ: MR imaging of the adrenal gland: Radiologic-pathologic correlation. Radiographics 18:1425–1440, 1998.
38. Lee MJ, Hahn PF, Papanicolaou N, et al: Benign and malignant adrenal masses: CT distinction with attenuation coefficients, size, and observer analysis. Radiology 179:415–418, 1991.
39. Lee MJ, Mayo-Smith WW, Hahn PF, et al: State-of-the-art MR imaging of the adrenal gland. Radiographics 14:1015–1029, 1994.
40. Liang HL, Pan HB, Lee YH, et al: Small functional adrenal cortical adenoma: Treatment with CT-guided percutaneous acetic acid injection: Report of three cases. Radiology 213:612–615, 1999.
41. Macari M, Rofsky NM, Naidich DP, et al: Non–small cell lung carcinoma: Usefulness of unenhanced helical CT of the adrenal glands in an unmonitored environment. Radiology 209:807–812, 1998.
42. Maurea S, Mainolfi C, Bazzicalupo L, et al: Imaging of adrenal tumors using FDG PET: Comparison of benign and malignant lesions. AJR Am J Roentgenol 173:25–29, 1999.
43. Mayo-Smith WW, Lee MJ, McNicholas MMJ, et al: Characterization of adrenal masses (<5 cm) by use of chemical shift MR imaging: Observer performance versus quantitative measures. AJR Am J Roentgenol 165:91–95, 1995.
44. McLoughlin RF, Bilbey JH: Tumors of the adrenal gland: Findings on CT and MR imaging. AJR Am J Roentgenol 163:1413–1418, 1994.
45. McNicholas MM, Lee MJ, Mayo-Smith WW, et al: An imaging algorithm for the differential diagnosis of adrenal adenomas and metastases. AJR Am J Roentgenol 165:1453–1459, 1995.
46. Miyake H, Maeda H, Tashiro M, et al: CT of adrenal tumors: Frequency and clinical significance of low-attenuation lesions. AJR Am J Roentgenol 152:1005–1007, 1989.
47. Mukherjee JJ, Peppercorn PD, Reznek RH, et al: Pheochromocytoma: Effect of nonionic contrast medium in CT on circulating catecholamine levels. Radiology 202:227–231, 1997.
47a. National Institutes of Health: Management of the Clinically Inappar-

ent Adrenal Mass or Incidentaloma. NIH Consensus Panel Program, February 4–6, 2002.
48. Neville AM, Symington T: The pathology of the adrenal gland in Cushing's syndrome. J Pathol Bacteriol 93:19–35, 1967.
49. Neville AM, O'Hare MJ: The Human Adrenal Cortex: Pathology and Biology: An Integrated Approach. Berlin, Springer-Verlag 1982.
50. Newhouse JH, Heffess CS, Wagner BJ, et al: Large degenerated adrenal adenomas: Radiologic-pathologic correlation. Radiology 210: 385–391, 1999.
51. O'Hara SM, Donnelly LF: Intense contrast enhancement of the adrenal glands: Another abdominal CT finding associated with hypoperfusion complex in children. AJR Am J Roentgenol 173:995–997, 1999.
52. Oliver TW Jr, Bernardino ME, Miller JI, et al: Isolated adrenal masses in nonsmall-cell bronchogenic carcinoma. Radiology 153: 217–218, 1984.
53. Oppong FC, Brodribb AJ, Hunt AC, et al: Bilateral adrenal lymphoma presenting as Addison's disease and hypercalcaemia. Eur J Surg Oncol 17:395–396, 1991.
54. Otal P, Escourrou G, Mazerolles C, et al: Imaging features of uncommon adrenal masses with histopathologic correlation. Radiographics 19:569–581, 1999.
55. Outwater EK, Siegelman ES, Radecki PD, et al: Distinction between benign and malignant adrenal masses: Value of T1-weighted chemical-shift MR imaging. AJR Am J Roentgenol 165:579–583, 1995.
56. Outwater EK, Mitchell DG, Rubenfeld IG: Correction to a previously published case: Recurrence of invasive adrenocortical tumor after excision of atypical adenoma. Radiology 202:531–532, 1997.
57. Ponder BAJ: Clinical and molecular genetics of multiple endocrine neoplasia type 2 (MEN 2). In Brandi ML, White R (eds): Hereditary Tumours. New York, Raven Press, 1991, pp 49–54.
58. Provenzale JM, Ortel TL, Nelson RC: Adrenal hemorrhage in patients with primary antiphospholipid syndrome: Imaging findings. AJR Am J Roentgenol 165:361–364, 1995.
59. Quinan C, Berger AA: Observations on human adrenals with especial reference to the relative weight of the normal medulla. Ann Intern Med 6:1180–1192, 1933.
60. Radin DR, Manoogian C, Nadler JL: Diagnosis of primary hyperaldosteronism: Importance of correlating CT findings with endocrinologic studies. AJR Am J Roentgenol 158:553–557, 1992.
61. Radin R, David CL, Goldfarb H, et al: Adrenal and extra-adrenal retroperitoneal ganglioneuroma: Imaging findings in 13 adults. Radiology 202:703–707, 1997.
62. Rao P, Kenney PJ, Wagner BJ, et al: Imaging and pathologic features of myelolipoma. Radiographics 17:1373–1385, 1997.
63. Reinig JW, Stutley JE, Leonhardt CM, et al: Differentiation of adrenal masses with MR imaging: Comparison of techniques. Radiology 192: 41–46, 1994.
64. Rozenblit A, Morehouse HT, Amis ES: Cystic adrenal lesions: CT features. Radiology 201:541–548, 1996.
65. Sandler MA, Pearlberg JL, Madrazo BL, et al: Computed tomographic evaluation of the adrenal gland in the preoperative assessment of bronchogenic carcinoma. Radiology 145:733–736, 1982.
66. Schwartz LH, Panicek DM, Koutcher JA, et al: Echoplanar MR imaging for characterization of adrenal masses in patients with malignant neoplasms: Preliminary evaluation of calculated T2 relaxation values. AJR Am J Roentgenol 164:911–915, 1995.
67. Schwartz LH, Panicek DM, Koutcher JA, et al: Adrenal masses in patients with malignancy: Prospective comparison of echo-planar, fast spin-echo, and chemical shift MR imaging. Radiology 197:421–425, 1995.
68. Schwartz LH, Panicek DM, Doyle MV, et al: Comparison of two algorithms and their associated charges when evaluating adrenal masses in patients with malignancies. AJR Am J Roentgenol 168: 1575–1578, 1997.
69. Shifrin RY, Bechtold RE, Scharling ES: Metastatic adenocarcinoma within an adrenal adenoma: Detection with chemical shift imaging. AJR Am J Roentgenol 167:891–892, 1996.
70. Simpson ER, Waterman MR: Regulation by ACTH of steroid hormone biosynthesis in the adrenal cortex. Can J Biochem Cell Biol 61:692–707, 1983.
71. Sivit CJ, Ingram JD, Taylor GA, et al: Posttraumatic adrenal hemorrhage in children: CT findings in 34 patients. AJR Am J Roentgenol 158:1299–1302, 1992.
72. Sohaib SA, Hanson JA, Newell-Price JDC, et al: CT appearance of the adrenal glands in adrenocorticotrophic hormone–dependent Cushing's syndrome. AJR Am J Roentgenol 172:997–1002, 1999.
73. Stoner HB, Whiteley HJ, Emery JL: Effect of systemic disease on adrenal cortex of children. J Pathol Bacteriol 66:171–183, 1953.
74. Szolar DH, Kammerhuber F: Quantitative CT evaluation of adrenal gland masses: A step forward in the differentiation between adenomas and nonadenomas. Radiology 202:517–521, 1997.
75. Szolar DH, Kammerhuber FH: Adrenal adenomas and nonadenomas: Assessment of washout at delayed contrast-enhanced CT. Radiology 207:369–375, 1998.
76. Tung GA, Pfister RC, Papanicolaou N, et al: Adrenal cysts imaging and percutaneous aspiration. Radiology 173:107–110, 1989.
77. Weiss LM, Medeiros LJ, Vickery AL Jr: Pathologic features of prognostic significance in adrenocortical carcinoma: Therapeutic implications. Am J Surg Pathol 12:202–206, 1989.
78. Welch TJ, Sheedy PF II, van Heerden JA, et al: Pheochromocytoma: Value of computed tomography. Radiology 148:501–503, 1983.
79. Welch TJ, Sheedy PF II, Stephens DH, et al: Percutaneous adrenal biopsy review of a 10-year experience. Radiology 193:341–344, 1994.
80. Westra SJ, Zaninovic AC, Hall TR, et al: Imaging of the adrenal gland in children. Radiographics 14:1323–1340, 1994.
81. Wilms GE, Baert AL, Kint EJ, et al: Computed tomographic findings in bilateral adrenal tuberculosis. Radiology 146:729–730, 1983.
82. Wilson DA, Muchmore HG, Tisdal RG, et al: Histoplasmosis of the adrenal glands studied by CT. Radiology 150:779–783, 1984.
83. Wolverson MK, Kannegiesser H: CT of bilateral adrenal hemorrhage with acute adrenal insufficiency in the adult. Am J Roentgenol 142: 311–314, 1984.
84. Wulffraat NM, Drexhage HA, Bottazzo GF: Autoimmune aspects of Addison's disease. In James VHT (ed): The Adrenal Gland. New York, Raven Press, 1992, pp 263–288.

41

The Kidney

Vikram Dogra
Errol Levine

Computed tomography (CT) is a rapid, easily performed, and safe diagnostic imaging technique that provides valuable information about a wide spectrum of renal disorders. CT is highly accurate for determining the nature and extent of renal masses and plays a valuable role in assessing patients with renal cystic disease, renal trauma, renal infections, renal blood flow disturbances, and hydronephrosis of unknown cause. Multidetector CT (multislice CT) promises to provide even more rapid assessment of the kidneys and a higher accuracy in the evaluation of renal masses and of the renal blood vessels than is currently provided by single-detector helical CT.

The technology of magnetic resonance imaging (MRI) has advanced rapidly, and MRI is now almost equivalent to CT in detecting and characterizing renal masses. However, because CT is less expensive, quicker, and more generally available, renal MRI is mainly used for evaluating patients in whom CT findings are equivocal or contrast-enhanced CT is contraindicated because of (1) previous reactions to intravenous iodinated contrast medium or (2) the presence of renal failure.

This chapter has been fully revised with updated information and most current references; additional images have also been included. The introduction of new applications of CT, such as in the evaluation of renal stone study protocol, is also discussed, as are newly described entities, such as medullary carcinoma. This chapter addresses and analyzes the most updated roles of CT and MRI in uroradiologic diagnosis.

Normal CT Anatomy

The kidneys are surrounded by perinephric fat, which in turn is enveloped by a dense connective tissue sheath called the renal fascia (Fig. 41–1). The anterior renal fascia (Gerota's fascia) covers the kidney anteriorly, while the posterior renal fascia (Zuckerkandl's fascia) covers the kidney posteriorly (Fig. 41–1). The renal fascial layers divide the general retroperitoneal space into three compartments extending from the diaphragm to the pelvic brim—the anterior pararenal space, the perinephric space, and the posterior pararenal space (see Fig. 41–1).[181] Because it differentiates between fat and fascial tissue, CT usually shows the renal fascia and major extraperitoneal compartments (Fig. 41–2).

Perinephric Space

The perinephric space contains the kidney, adrenal gland, inferior vena cava, lower aorta, renal pelvis, proximal ureter, renal blood vessels, renal capsular vessels, and perinephric fat (see Fig. 41–1). It is bound by the anterior and posterior renal fascial layers and is demarcated by their sites of fusion. Above the adrenal glands, the two fascial layers fuse and adhere firmly to the diaphragmatic fascia; laterally the layers fuse behind the ascending or descending colon to form the lateroconal fascia (see Fig. 41–1). Medially, the anterior renal fascia blends into the connective tissue near the midline (see Fig. 41–1)[74, 181]; the posterior

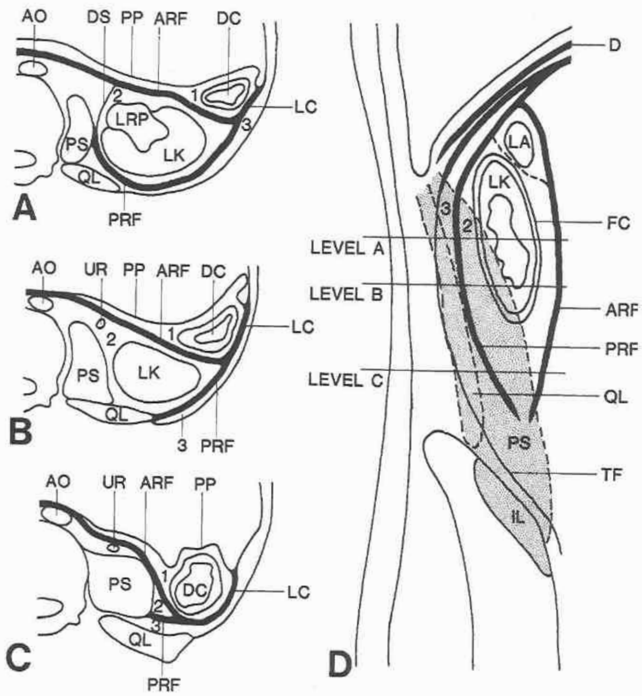

Figure 41–1. Transverse (*A* to *C*) and parasagittal (*D*) sections of the left flank. Sections *A* to *C* show the cross-sectional anatomy at the three levels indicated in *D*—the level of the renal hilus (*A*), the lower renal pole (*B*), and above the iliac crest (*C*). In *D*, the approximate positions of the psoas and quadratus lumborum muscles (*stippled areas*) are indicated by dashed lines. AO = aorta; PS = psoas muscle; QL = quadratus lumborum muscle; LK = left kidney; LRP = left renal pelvis; UR = ureter; PP = parietal peritoneum; ARF = anterior renal fascia; PRF = posterior renal fascia; LC = lateroconal fascia; DS = deeper stratum of renal fascia; DC = descending colon; 1 = anterior pararenal space; 2 = perinephric space; 3 = posterior pararenal space; D = diaphragm; LA = left adrenal; FC = fibrous capsule of kidney; TF = transversalis fascia; IL = iliacus muscle. (From Feldberg MA, Koehler PR, van Waes PF: Psoas compartment disease studied by computed tomography: Analysis of 50 cases and subject review. Radiology 148:505–512, 1983.)

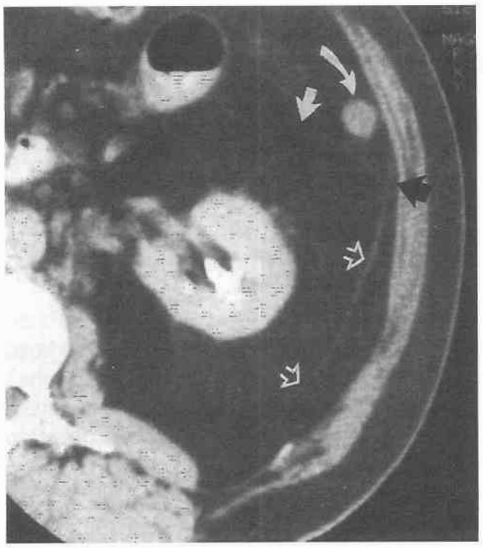

Figure 41–2. Normal CT anatomy. The posterior renal fascia (*open arrows*) separates the perinephric and posterior pararenal spaces. The anterior renal fascia (*straight white arrow*) separates the perinephric and anterior pararenal spaces. The lateroconal fascia (*black arrow*) extends lateral to the descending colon (*curved arrow*).

renal fascia fuses with the psoas or quadratus lumborum fascia. The renal fascial cone extends inferior to the kidney, forming a caudal extension of the main perinephric space containing the proximal ureter and gonadal vessels (see Fig. 41–1).[181] Right and left perirenal spaces communicate with each other anterior to the inferior vena cava and below the level of the renal hilum.[11, 271]

The perinephric space is divided into multiple compartments by fibrous lamellae, the bridging septa (Fig. 41–3).[2, 136] Some arise from the renal capsule and extend to the anterior and posterior renal fascia. Others are attached only to the renal capsule and are arranged nearly parallel to the renal surface (see Fig. 41–3). One of the more constant of these is the posterior renorenal bridging septum. It arises from the renal capsule at its posteromedial aspect and runs nearly parallel to the posterior surface of the kidney, inserting into the posterolateral aspect of the renal capsule. Still other bridging septa directly connect the anterior and posterior leaves of the renal fascia.[136] The bridging septa determine the distribution of blood, pus, or urine collections in the perinephric space.[2, 136]

Kidneys

On CT, the transverse contour of the kidney is smooth and oval, with an anteromedial break in the renal outline at the hilus where the vascular pedicle enters (Fig. 41–4). The renal sinus is a potential space contained by the renal parenchyma. The space is filled with fatty tissue and contains the renal arteries, veins, lymphatics, and pelvicalyces. The renal sinus fat is directly continuous with the perinephric fat through the renal hilus. On unenhanced CT scans, the normal renal parenchyma has an attenuation value of 30 to 50 Hounsfield Units (HU), depending on patient hydration, and the cortex and medulla show no visible density differences.

After a rapid, intravenous injection of contrast medium, helical CT scanning shows a cortical nephrogram in which there is clear demarcation of the renal cortex and columns of Bertin from the renal medulla (Fig. 41–5). However, the cortical nephrogram phase is transient and a homogeneous tubular nephrogram rapidly develops (see Fig. 41–5). The renal veins are usually densely opacified during dynamic CT scanning and are shown anterior to the renal pelvis as tubular structures joining the inferior vena cava. However, during dynamic scanning the inferior vena cava often shows significantly less contrast enhancement than the renal veins; this difference is due to mixing of opacified blood from the renal vein and unopacified blood from the lower extremities (Fig. 41–6). This appearance should not be mistaken for vena caval thrombosis or tumor extension.

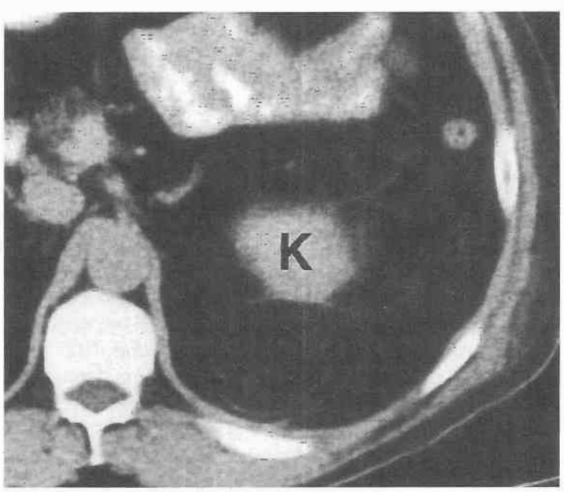

Figure 41–3. Bridging septa in perinephric space. Multiple delicate fibrous bridging septa traverse the upper part of the left perinephric space. K = kidney.

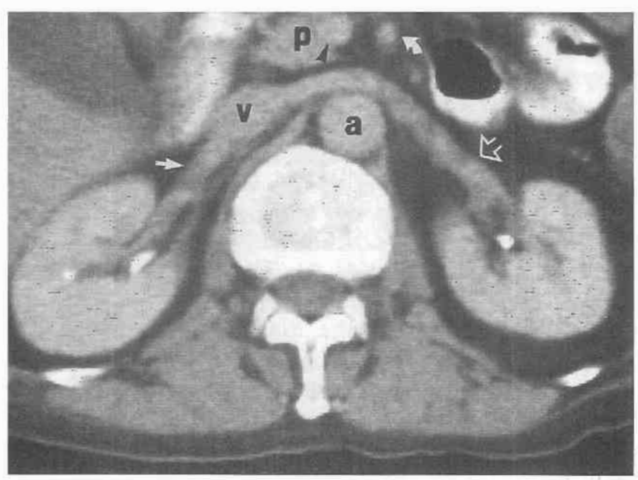

Figure 41–4. Normal CT renal anatomy. The longer left renal vein (*open arrow*) passes between the aorta (a) posteriorly and the superior mesenteric artery (*curved arrow*) and vein (*arrowhead*) anteriorly. It joins the inferior vena cava (v) at the level of the uncinate process of the pancreas (p). The right renal vein (*arrow*) is shorter.

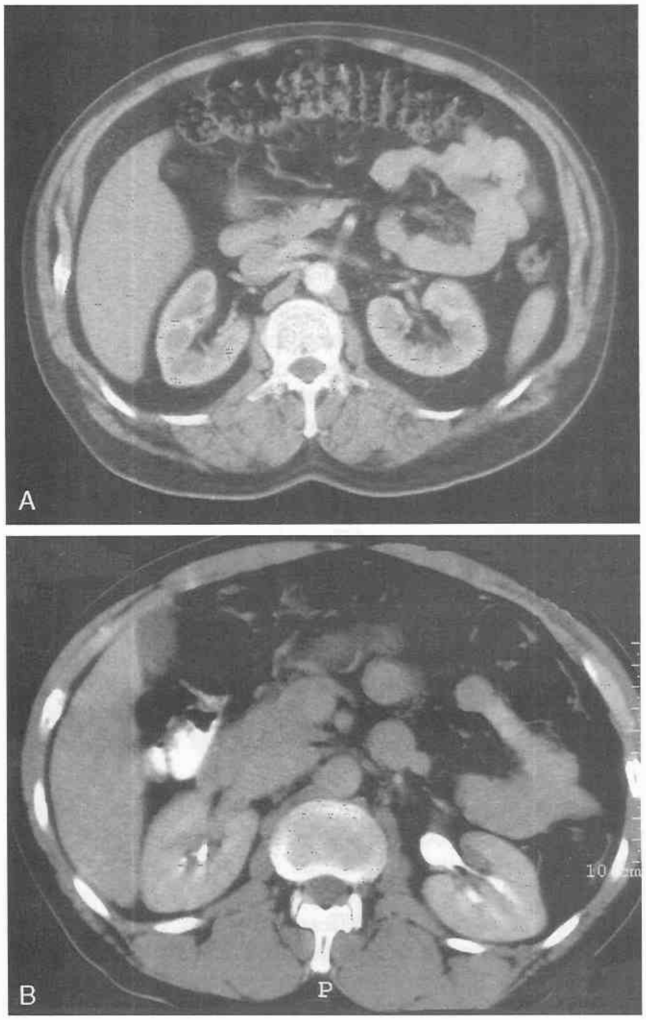

Figure 41–5. Normal CT. *A,* The corticomedullary phase demonstrates dense enhancing cortex with minimal enhancement of renal medulla. *B,* After a brief delay, the parenchymal enhancement becomes uniform, resulting in the nephrographic phase; in late nephrographic phase calyces may be opacified.

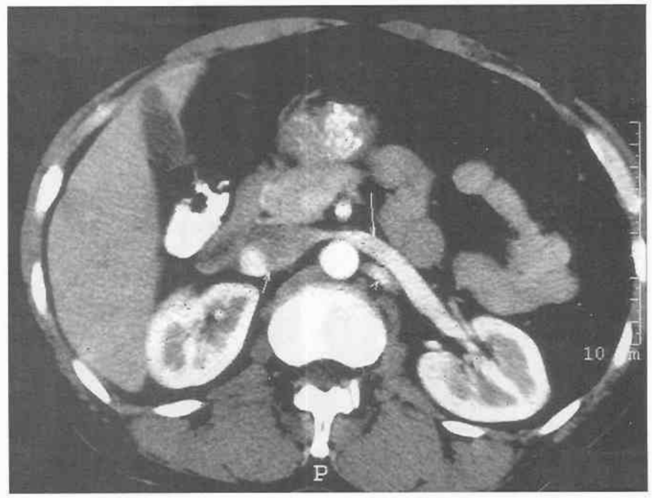

Figure 41–6. Normal renal vasculature. In the corticomedullary phase, the renal veins (*long arrow*) and arteries (*short arrow*) have maximal opacification. The inferior vena cava (*medium arrow*) appears less dense because of mixing of opacified blood from the renal vein and unopacified blood from the lower extremities. This appearance should not be confused with vena caval thrombus.

The longer left renal vein crosses the retroperitoneum between the aorta posteriorly and the superior mesenteric vessels anteriorly, and joins the inferior vena cava at the level of the uncinate process of the pancreas. The right renal vein usually has a shorter, more oblique course (see Figs. 41–4 and 41–6). The renal arteries are located posterior to the renal veins and are usually smaller. Normal renal arteries are seen by helical (spiral) CT, performed during breath-holding with the use of narrow scan collimation.[230]

Developmental renal anomalies and minor anatomic variants are commonly encountered and are usually evaluated by excretory urography. However, CT is sometimes necessary for further evaluation when urographic findings are confusing (Figs. 41–7 and 41–8). For example, on excretory urography, renal sinus lipomatosis may masquerade as a mass lesion in the renal sinus. CT reveals the benign nature of the process by showing that the renal sinus is occupied by tissue with a fat-attenuation value. Normal variants, such as a dromedary hump in the left

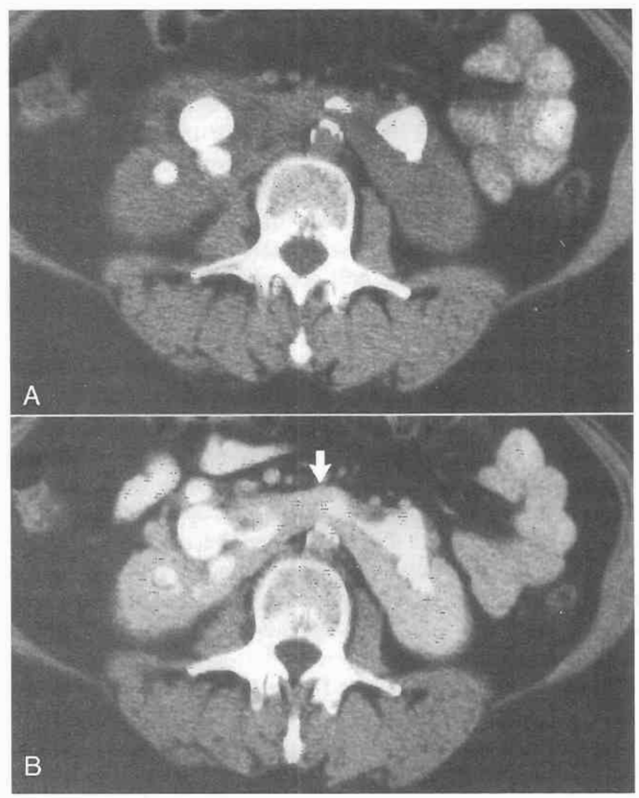

Figure 41–7. Horseshoe kidney. *A,* Unenhanced scan shows staghorn calculi involving both elements of a horseshoe kidney. *B,* Contrast-enhanced CT scan shows malrotation of both kidneys with the renal pelves directed anteriorly. The kidneys are joined by an isthmus (*arrow*) of functioning renal parenchyma.

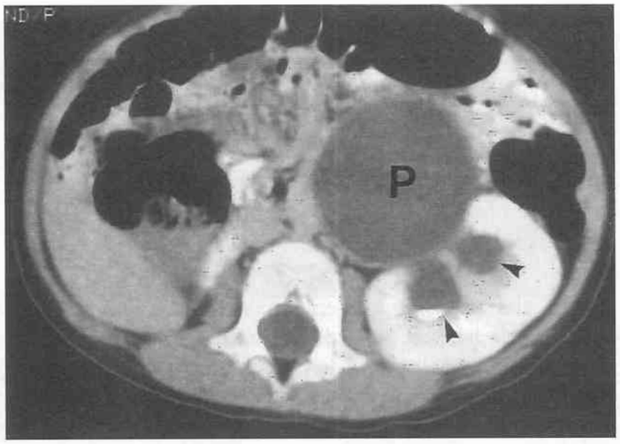

Figure 41–8. Agenesis of the right kidney and congenital left ureteropelvic junction obstruction in an infant. The left renal pelvis (P) is markedly dilated, and there is also calyceal dilatation (*arrowheads*).

kidney and prominent columns of Bertin, may simulate renal masses on excretory urography. CT easily recognizes these variants, which enhance to the same degree as normal renal parenchyma after intravenous administration of contrast medium.

CT Technique

Single-detector and multidetector spiral CT have dramatically refined the diagnostic evaluation of renal disorders by allowing rapid image acquisition through the entire kidney during various phases of contrast enhancement after the administration of a single bolus of intravenous contrast material.[133, 265] The technique should be tailored according to the specific clinical problem involved. However, there are some aspects common to all dedicated renal CT studies. Since unopacified bowel loops may simulate perinephric masses and retroperitoneal adenopathy, patients undergoing renal CT should receive oral contrast medium.

CT protocol for evaluation of the kidneys consists of both nonenhanced and contrast-material enhanced CT scans obtained in suspended respiration, to overcome the motion artifact. To avoid artifactual differences in attenuation values, the same peak kilovoltage, milliampere-second setting, section thickness, and field of view should be used for both precontrast and postcontrast scans when small renal masses are being evaluated. The accuracy of attenuation values should also be tested by measuring the attenuation value of the gallbladder contents before and after intravenous administration of contrast medium. Apparent enhancement of the gallbladder contents suggests that mild enhancement of a renal mass may be spurious.[26]

Images should be acquired with 1- to 3-mm collimation, subsecond scan time, and a pitch of up to 2:1 to allow coverage of the area of interest in single breath-hold. Multislice scanners allow 1- to 2.5-mm slices through the region of interest in single breath-hold. Unenhanced scans permit contrast enhancement of a renal lesion to be measured and also ensure that renal parenchymal calcifications, renal calculi, renal and perinephric hemorrhage and fat, and calcification in a renal mass will not be obscured by contrast medium. Unenhanced scans also help differentiate hyperdense cyst from renal solid tumor.[244]

Corticomedullary Phase. Administration of intravenous contrast medium is a fundamental requirement for CT evaluation of most renal lesions. Enhancement of a mass indicates that the lesion is vascular and is therefore possibly a neoplasm. Contrast medium should be administered rapidly with a mechanical injector via an antecubital vein as a 150-mL bolus containing 40 to 45 g of iodine at a rate of 2 to 4 mL per second. The corticomedullary phase occurs between 25 and 70 seconds after the start of contrast administration. The corticomedullary phase begins as contrast material enters the cortical capillaries and peritubular spaces and filters into the proximal cortical tubules.[234] Renal cortex can be differentiated from renal medulla at this stage because (1) the vascularity of the cortex is greater than that of the medulla and (2) contrast material has not yet reached the distal aspect of the renal tubules (Fig. 41–9).[68, 234] The resultant CT nephrogram has been termed a *cortical nephrogram.* Corticomedullary phase images should always be obtained when information about the renal vasculature is desired or when there is a possibility that a detected renal mass may represent an aneurysm or an arteriovenous malformation or fistula.[296] Maximal opacification of the renal vein and arteries occurs during this phase, allowing confident diagnosis of tumor extension to the vein.

Nephrographic Phase. This begins as contrast material proceeds from the cortical vessels and extracellular-interstitial space and enters the loops of Henle and collecting tubules. A homogeneous or tubular nephrogram results in which corticomedullary differentiation is lost (Fig. 41–10).[18] The nephrographic phase starts about 80 seconds and lasts up to 180 seconds after the start of injection, and offers the best opportunity for discrimination between the normal renal medulla and a renal mass.[265, 296] The nephrographic phase is the most valuable for detecting renal masses and characterizing indeterminate lesions.[17, 41, 265]

Excretory Phase. Approximately 180 seconds after the start of contrast injection, the excretory phase begins. The

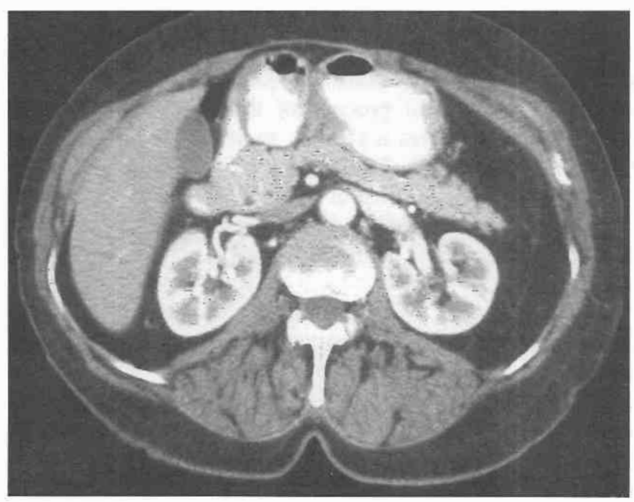

Figure 41–9. Corticomedullary phase. The corticomedullary phase demonstrates dense enhancing cortex with minimal enhancement of renal medulla.

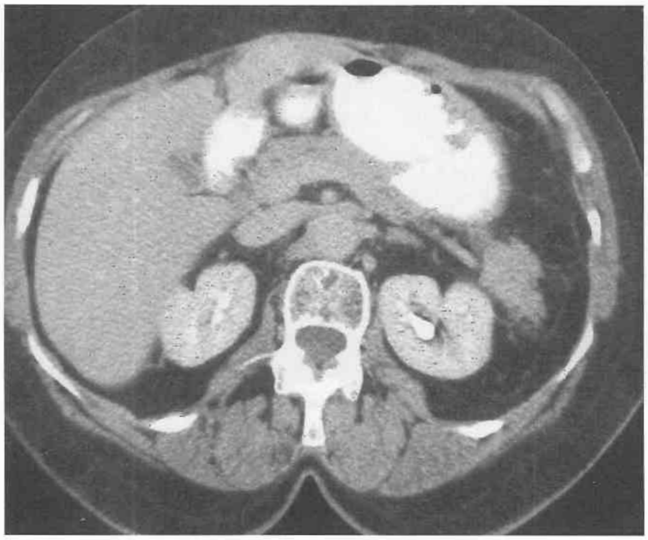

Figure 41–10. Nephrographic phase. The renal parenchyma enhances uniformly, and corticomedullary differentiation is lost.

contrast material is excreted into the collecting system, so the attenuation of the nephrogram progressively decreases (Fig. 41–11). This phase is occasionally helpful to better delineate the relationship of a centrally located mass with the collecting system.[244] This phase is also useful for evaluating urothelial masses.

MRI Techniques and Anatomy

Gadolinium-enhanced renal MRI is attractive as an alternative to other techniques for evaluation of native and transplanted kidneys, because it can be used in patients with renal failure or iodine allergies.[224]

Dynamic gadolinium-enhanced gradient-echo imaging achieves coverage of the entire kidney during breath-holding, thereby reducing respiration-induced phase artifacts.[240] Gadolinium-enhanced fat-suppressed T1-weighted spin-echo technique images the kidneys with significantly fewer artifacts than does conventional spin-echo imaging.[241] The ability of dedicated renal CT scanning and gadolinium-enhanced MRI to detect and characterize renal lesions greater than 1 cm is similar, although MRI is superior in detecting polar lesions because of its ability to image directly in nonaxial planes.[223] Since CT is generally available, quicker, and less expensive than MRI, it is usually preferred to MRI for evaluating patients with suspected renal masses.

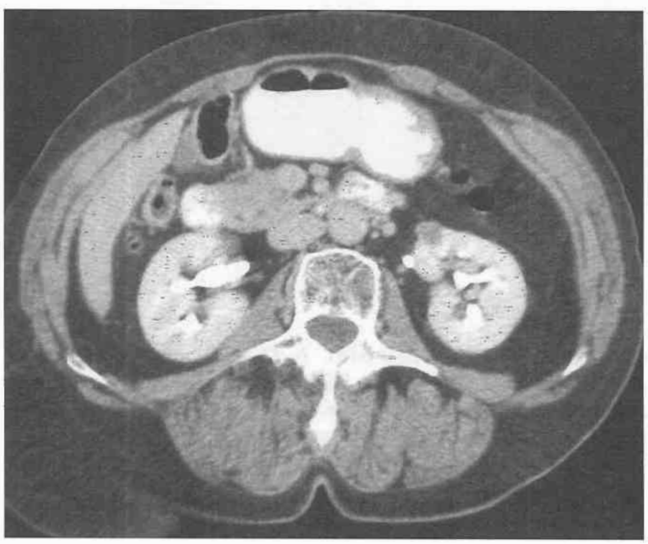

Figure 41–11. Excretory phase. The attenuation of the nephrogram progressively decreases, and calyces demonstrate contrast. Left kidney shows renal carcinoma.

MRI is the preferred modality, however, for determining the cephalic extent of an intracaval tumor in a patient with renal cell carcinoma when this finding is not adequately documented by CT.[209] Other indications for renal MRI are differentiation between hemorrhagic renal cysts and renal neoplasms, characterization of small renal masses that are indeterminate on CT or ultrasonography,[26] evaluation of renal donors,[301] visualization of renal blood vessels (MR angiography [MRA]),[235] and evaluation of transplanted kidneys.[108]

The MRI pulse sequences and the precise imaging parameters used depend on the nature of the available MRI equipment and on the clinical problem. Conventional spin-echo sequences may be used for evaluating the kidneys; the development of newer and faster imaging techniques, such as fast spin-echo and gradient-echo imaging, are preferred. T1-weighted, gradient-echo, in- and out-of-phase images from the top of the liver to the inferior pole of the kidney are obtained to study the anatomy and also evaluate the liver for any metastatic disease from renal tumor. This technique also allows assessment of the presence of fat within the renal lesion.

A T2-weighted fast spin-echo sequence with fat saturation is obtained in axial plane corresponding to the T1-weighted gradient sequence. Coronal T2-weighted (very long echo time [TE], such as half-Fourier acquisition single-shot turbo spin-echo [HASTE] and single-shot fast spin-echo [SSFSE]) images are also acquired to identify renal cysts. T1- and T2-weighted sequences help identify hemorrhagic cysts (Fig. 41–12). Gradient-echo images are helpful for evaluating renal masses.

Precontrast images of the kidneys are first obtained (Fig. 41–13). A 2D or 3D gradient-echo breath-hold sequence with and without gadolinium enhancement is obtained in the arterial phase (corticomedullary phase; 20 seconds), venous phase (nephrographic phase; 70 seconds), and delayed phase (excretory phase; 180 seconds). Gadopentetate dimeglumine (Gd) is injected intravenously by power injector in a dose of 0.1 to 0.2 mmol/kg over 5 seconds with the patient positioned in the bore of the magnet. The coronal plane is often advantageous because it allows evaluation of both kidneys, renal vessels, and the inferior vena cava.[209] Imaging is started during breath-holding at 20 seconds after a rapid saline flush of the intravenous catheter has been performed. Images are also obtained at 70 seconds and 3 minutes after the start of injection.

Corticomedullary phase imaging demonstrates corticomedullary differentiation and also significant enhancement of the renal vein blood (see Fig. 41–13). This phase is optimal for assessing tumor extension to the veins. The

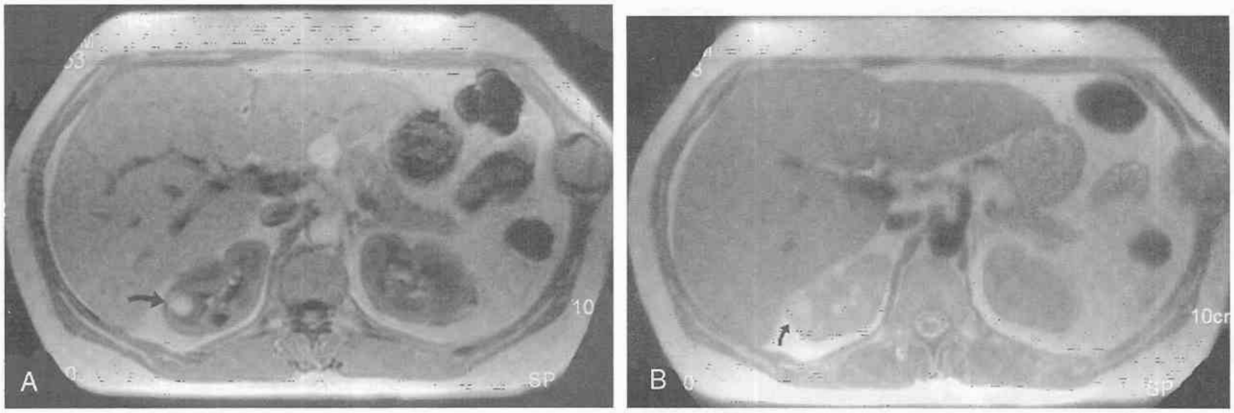

Figure 41–12. Hemorrhagic cyst. *A,* Axial T1-weighted gradient images demonstrate a small right renal upper pole cyst with increased signal (*arrow*). *B,* Corresponding T2-weighted image demonstrates increased signal (*arrow*) compared with the renal cortex. Previously diagnosed fibrous dysplasia of left ninth rib is incidental finding.

nephrographic phase is the best sequence to detect a renal mass.

Renal Cysts

Renal cysts usually represent notably dilated nephrons or collecting ducts.[83] A cystic kidney is a kidney with three to five or more cysts. The term *renal cystic disease* refers to any disorder that results from the presence of multiple renal cysts.

Simple Cysts

Simple cysts are the most common renal masses. Most are clinically insignificant, being discovered incidentally at autopsy or on imaging studies. Their frequency increases with age, with only rare examples reported in children. Although the cause of renal cysts is unknown, their frequent occurrence in older patients suggests that they are acquired lesions.[198] Although most simple cysts are asymptomatic, they occasionally cause pressure symptoms because of their large size, and cyst hemorrhage or infection

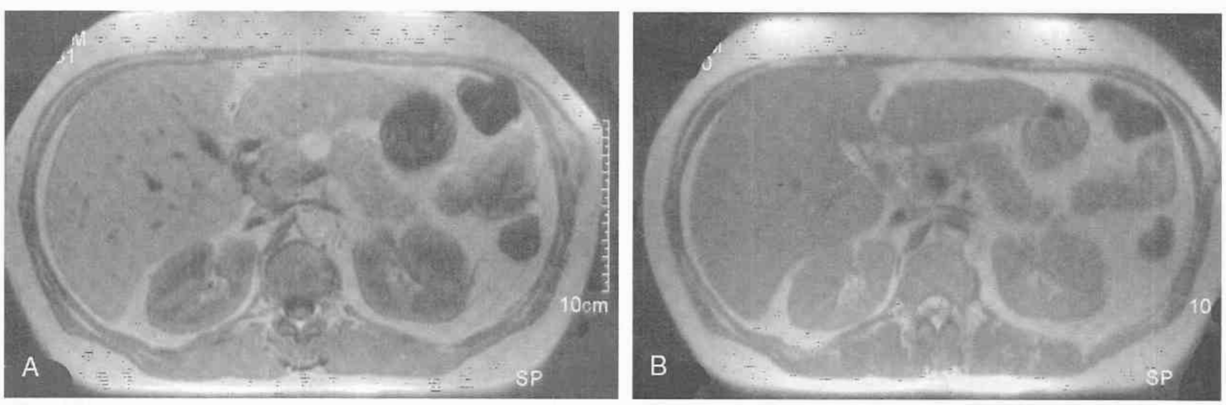

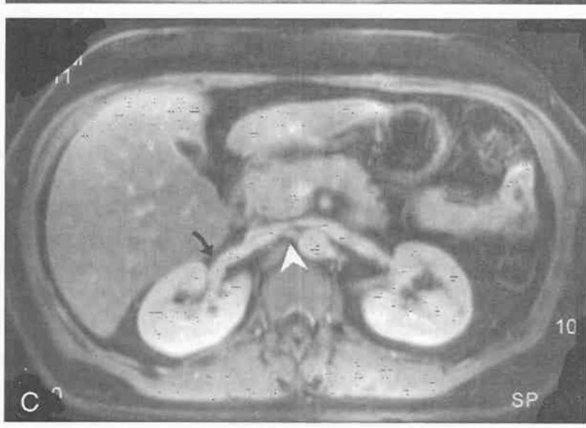

Figure 41–13. Normal renal MRI. A T1-weighted (gradient, out-of-phase) image (*A*) and a T2-weighted axial image (*B*) demonstrate the normal appearance of the kidneys. *C,* T1-weighted axial gadolinium-enhanced images reveal normal enhancing renal parenchyma. Renal vein (*arrow*) and renal artery (*arrowhead*) are also seen.

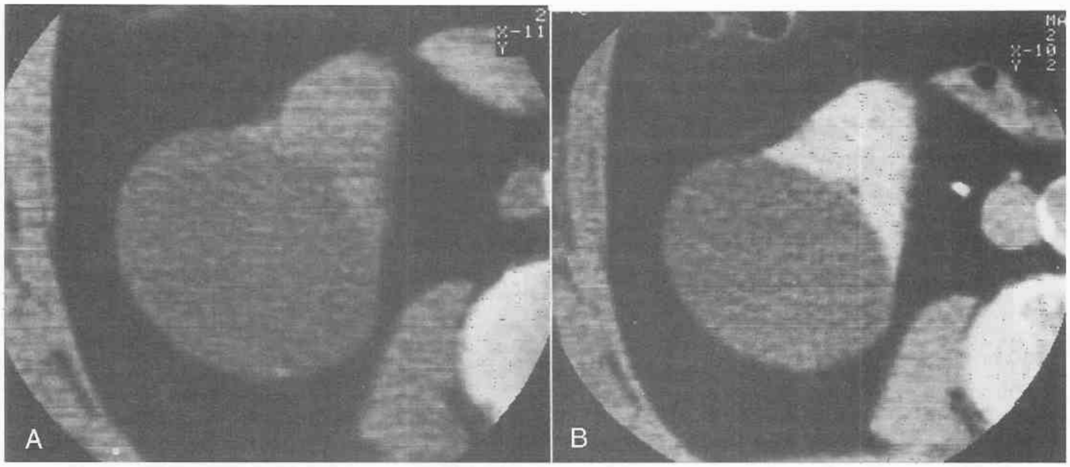

Figure 41–14. Simple renal cyst. Unenhanced (*A*) and contrast-enhanced (*B*) CT scans show that the mass is round, with a smooth margin and distinct margination from adjoining renal parenchyma. It has a homogeneous water density and does not enhance (precontrast and postcontrast attenuation value = 7 HU) and has no discernible wall thickness.

may cause pain and hematuria. Simple renal cysts may be solitary or multiple and are commonly bilateral. Ultrasonography is usually considered the most appropriate next investigation for further evaluation of a presumed renal cyst discovered on excretory urography. However, renal cysts are currently often found on abdominal CT scanning performed for nonrenal complaints. Such cysts may vary in size from less than 1 cm to 10 to 15 cm (Figs. 41–14 and 41–15).

CT Features

The accuracy of CT diagnosis of a simple renal cyst approaches 100% if a renal mass strictly fulfills the following well-established criteria: (1) sharp margination and demarcation from surrounding renal parenchyma, (2) a smooth, thin wall, (3) a homogeneous, water-density content with an attenuation value of 0 to 20 HU, and (4) no enhancement after intravenous administration of contrast medium (see Fig. 41–14).[24, 170] If a renal mass fulfills these CT criteria, no further evaluation is necessary.

In routine CT, performed for nonrenal complaints, usually only intravenous contrast–enhanced scanning is performed; therefore, the presence or absence of contrast enhancement in renal masses often cannot be determined.[24] A simple cyst can usually be diagnosed even without this information, however, if the other CT criteria listed previously are fulfilled (see Fig. 41–15).[24] If CT findings are atypical or if the patient is referred because of symptoms such as hematuria, nonenhanced scans should also be obtained. Obtaining both sets of scans permits contrast enhancement to be measured and also precludes misinterpretation of nonenhancing high-density renal cysts as solid renal masses.[24]

Although CT is accurate in diagnosing simple renal cysts, interpretation of CT findings has some potential pitfalls. Small renal cysts may be volume-averaged with normal renal tissue, causing spuriously high attenuation values,[170] or falsely high attenuation values may be caused by streak artifacts.[26] In these circumstances, ultrasonography should be performed to determine whether the lesion is a cyst or a neoplasm. If ultrasonographic findings are indeterminate, dedicated renal CT with special attention to the lesion should be performed.[24]

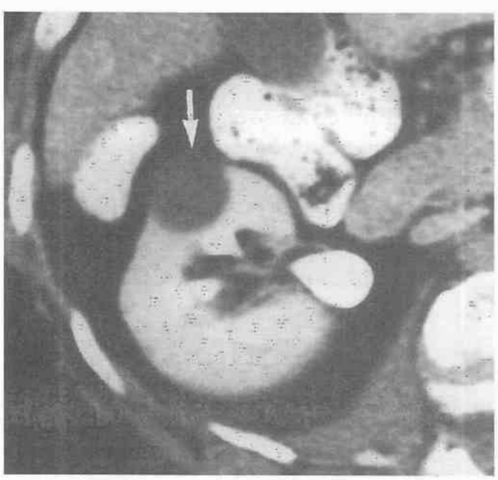

Figure 41–15. Simple renal cyst. Lesion (*arrow*) has attenuation value of 9 HU and was detected during survey CT scan performed only with intravenous contrast enhancement. Even though an unenhanced scan is unavailable, the diagnosis of a cyst can be made with confidence because of the low-attenuation value, smooth rounded shape, sharp margination, and demarcation from surrounding renal parenchyma and thin wall where the lesion projects beyond the renal outline.

MRI Features

The use of gadolinium-enhanced MRI, particularly with gradient-echo imaging techniques applied during breath-hold is helpful in the evaluation of renal cystic lesions in patients with contraindications to iodinated intravenous contrast medium, such as chronic renal failure or previous reactions to contrast media.[224, 241] Even a small, simple renal cyst can be diagnosed on contrast-enhanced MRI if it fulfills the following criteria: (1) sharp margination and demarcation from surrounding renal parenchyma, (2) a

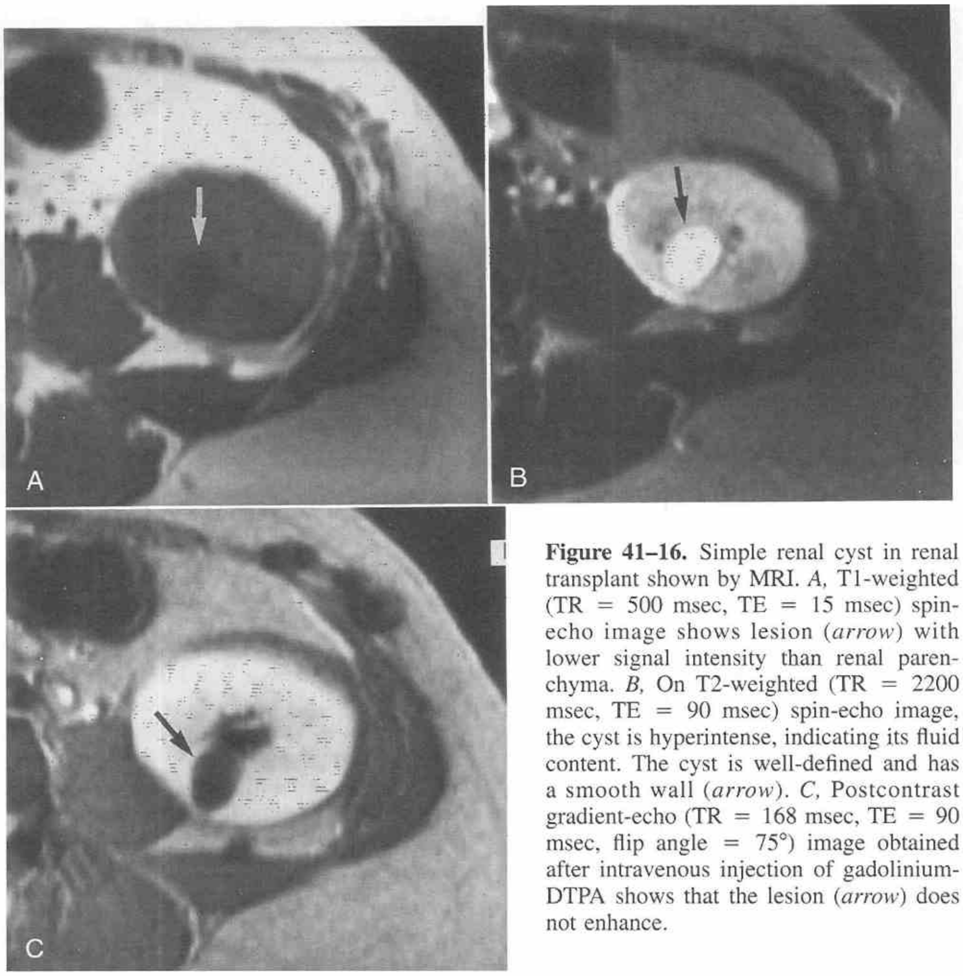

Figure 41–16. Simple renal cyst in renal transplant shown by MRI. *A,* T1-weighted (TR = 500 msec, TE = 15 msec) spin-echo image shows lesion (*arrow*) with lower signal intensity than renal parenchyma. *B,* On T2-weighted (TR = 2200 msec, TE = 90 msec) spin-echo image, the cyst is hyperintense, indicating its fluid content. The cyst is well-defined and has a smooth wall (*arrow*). *C,* Postcontrast gradient-echo (TR = 168 msec, TE = 90 msec, flip angle = 75°) image obtained after intravenous injection of gadolinium-DTPA shows that the lesion (*arrow*) does not enhance.

smooth, thin wall, (3) homogeneous contents with signal characteristics of water (such lesions have a low signal intensity on T1-weighted spin-echo images and a high signal intensity on T2-weighted spin-echo images), and (4) no enhancement after intravenous injection of gadolinium-DTPA (diethylene triaminepenta-acetic acid) (Fig. 41–16).[241] Subsecond T2-weighted pulse sequence (SSFSE on GE machines and their equivalent on other machines) is better suited for detection of simple renal cysts, especially those smaller than 1 cm.[182]

Atypical Cysts and Cystic Neoplasms

Many renal cystic lesions do not fulfill the criteria for simple cysts listed previously. Such lesions vary from minimally complicated simple cysts that usually do not require surgery to cystic renal neoplasms that generally need resection. Complicated cysts often result from bleeding in a simple cyst. Bosniak has suggested the categorization of cystic renal masses according to CT criteria in an attempt to separate lesions that require surgery from those that do not.[24] The application of Bosniak's classification is most useful in evaluating and managing cystic renal lesions.[6]

Category I Lesions. In Bosniak's classification, category I lesions are classic simple cysts as described previously (see Figs. 41–14 to 41–16). They require no further evaluation or management.

Category II Lesions. Category II lesions are minimally complicated cysts that also usually do not require surgery.

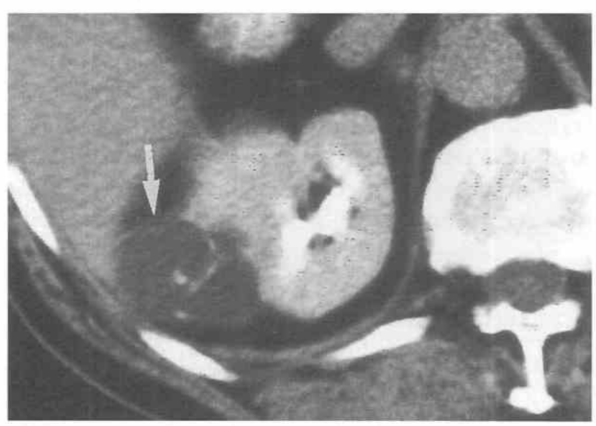

Figure 41–17. Minimally calcified benign cyst (*arrow*); category II lesion. A contrast-enhanced CT scan reveals fine linear calcification in the cyst wall and septa. The lesion shows a thin wall, and no focal nodules or areas of enhancement. The fluid in the cyst measured 12 HU.

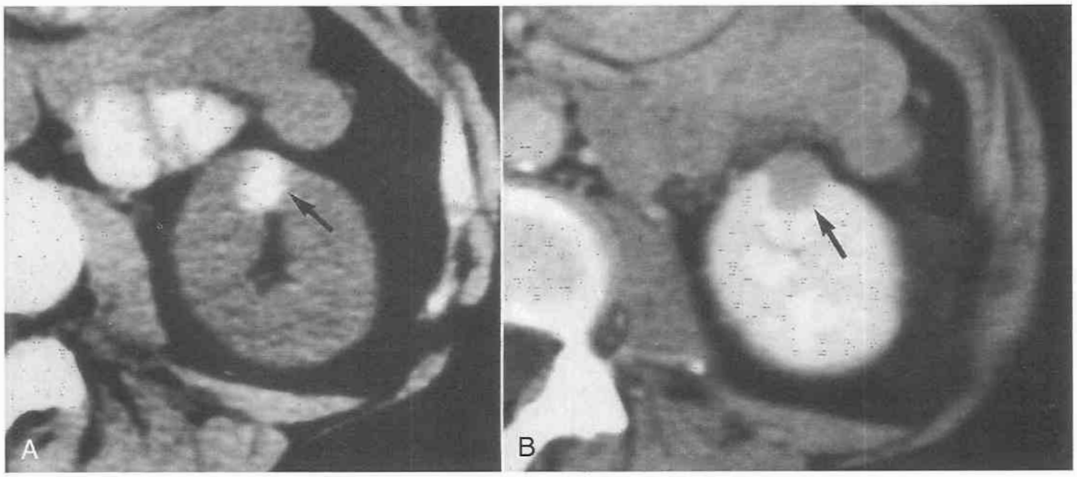

Figure 41–18. Hyperdense benign renal cyst; category II lesion. Unenhanced CT scan (*A*) shows a high-density mass (92 HU) (*arrow*) located anteriorly in the kidney. On contrast-enhanced CT scan (*B*), the lesion (*arrow*) did not enhance; it is homogeneous and reveals a smooth margin where it projects beyond the renal outline.

Occasional thin (less than 1 mm), smooth septa, or small, smooth plaques of fine linear calcification in the cyst wall or septa occur in these lesions (Fig. 41–17).

Also included in category II are high-density cysts (Fig. 41–18). These lesions have attenuation values ranging from 40 to 100 HU on unenhanced CT scans and are usually caused by a high protein content or previous hemorrhage.[120] Most high-density renal cysts are benign and can simply

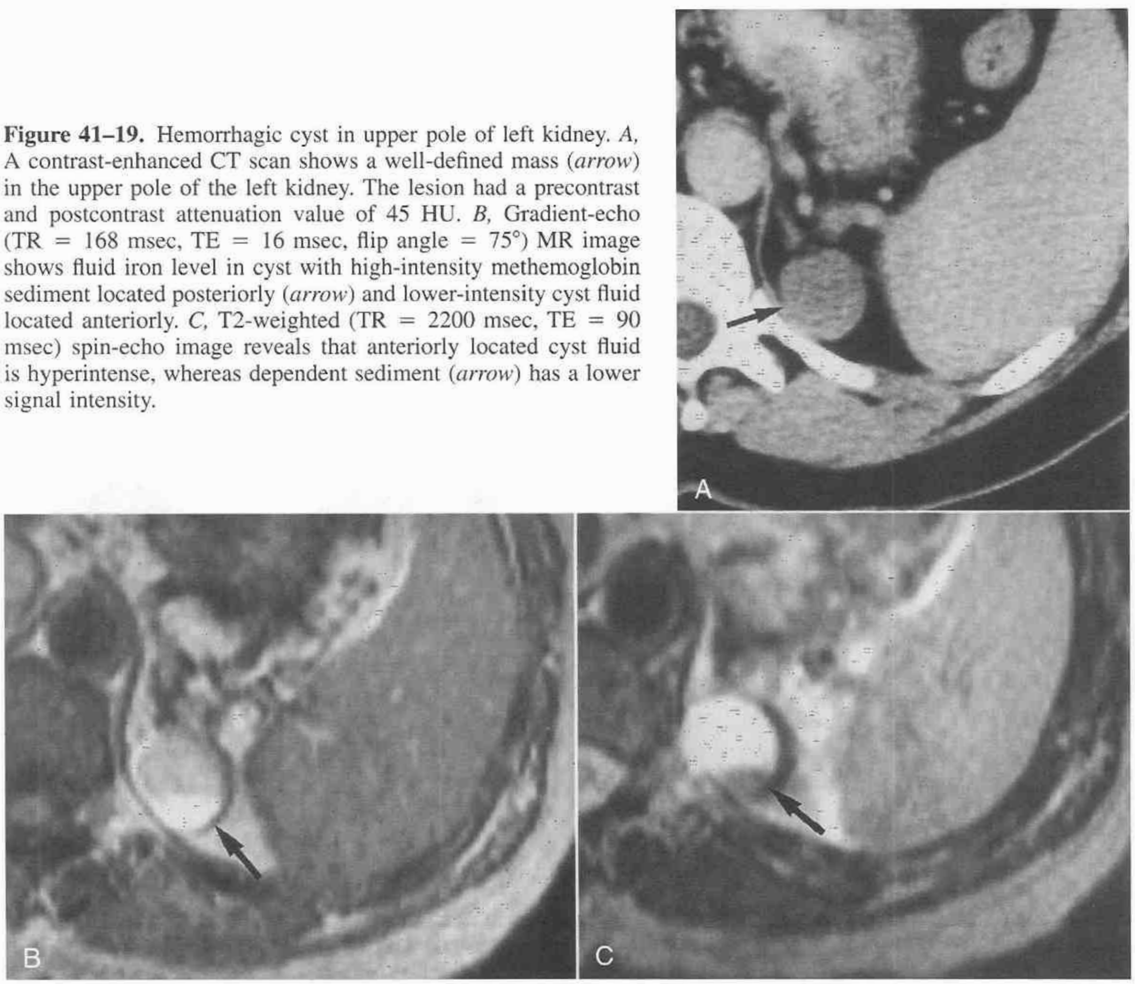

Figure 41–19. Hemorrhagic cyst in upper pole of left kidney. *A,* A contrast-enhanced CT scan shows a well-defined mass (*arrow*) in the upper pole of the left kidney. The lesion had a precontrast and postcontrast attenuation value of 45 HU. *B,* Gradient-echo (TR = 168 msec, TE = 16 msec, flip angle = 75°) MR image shows fluid iron level in cyst with high-intensity methemoglobin sediment located posteriorly (*arrow*) and lower-intensity cyst fluid located anteriorly. *C,* T2-weighted (TR = 2200 msec, TE = 90 msec) spin-echo image reveals that anteriorly located cyst fluid is hyperintense, whereas dependent sediment (*arrow*) has a lower signal intensity.

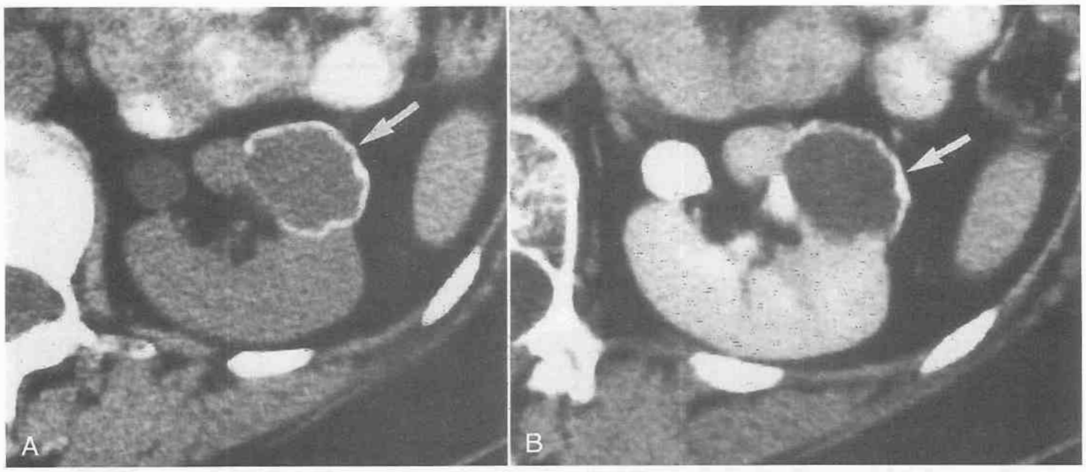

Figure 41–20. Hemorrhagic benign renal cyst; category III lesion. The lesion (*arrow*) shows thick, irregular mural calcification. The lesion has an attenuation value of 12 HU on an unenhanced CT scan (*A*) and shows no enhancement after contrast administration (*B*). The kidney was explored, and a local resection of the lesion was performed.

be monitored with serial imaging, provided that the following CT criteria are fulfilled: (1) the lesion must be perfectly smooth, round, sharply marginated, and homogeneous; (2) the lesion should not enhance with intravenous contrast medium; (3) at least one fourth of the lesion's circumference should extend outside the kidney so that the smoothness of some of the wall can be evaluated; and (4) the lesion should be less than 3 cm in diameter.[26] Although most lesions meeting these criteria are benign hemorrhagic cysts,[25] cystic renal cell carcinoma may rarely show similar characteristics on CT.[100]

MRI may also help in characterizing high-density renal cysts that do not fulfill all the preceding CT criteria or that show internal echoes on ultrasonography. Hemorrhagic cysts appear on MRI as sharply marginated, smooth, round, homogeneous lesions. They have high signal intensity on both T1- and T2-weighted sequences,[146] and they do not enhance after intravenous administration of gadolinium-DTPA (see Fig. 41–16). In addition, hemorrhagic cysts often show fluid-iron levels on MRI, probably because of dependent settling of methemoglobin containing sediment (Fig. 41–19).[146]

Category III Lesions. Lesions in category III are more complicated cystic lesions. They exhibit some findings seen in malignant lesions, including thick, irregular mural or septal calcification (Fig. 41–20), numerous or thick (>1 mm), irregular septa (Fig. 41–21), and uniform or slightly nodular wall thickening.[24] Some category III lesions are benign (e.g., multilocular cystic nephromas and hemorrhagic renal cysts); others are cystic renal cell carcinomas (see Fig. 41–21). All such lesions should undergo surgical exploration, unless the procedure is contraindicated because of the patient's advanced age or poor general medical condition.[24]

Category IV Lesions. Category IV lesions are clearly malignant lesions with large cystic components; they should be resected.[24] They may show marginal irregularity or solid vascular elements (Fig. 41–22).

Figure 41–21. Multilocular cystic renal cell carcinoma; category III lesion. A contrast-enhanced CT scan reveals a well-defined, mainly fluid-containing mass in the right kidney. Enhancing septa are seen throughout the lesion. A right nephrectomy was performed.

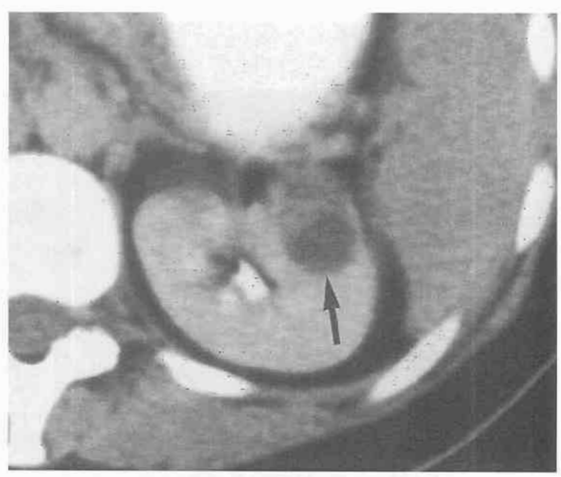

Figure 41–22. Cystic renal cell carcinoma; category IV lesion. Contrast-enhanced CT scan shows a cystic mass (*arrow*) with irregular and enhancing solid elements located anteriorly.

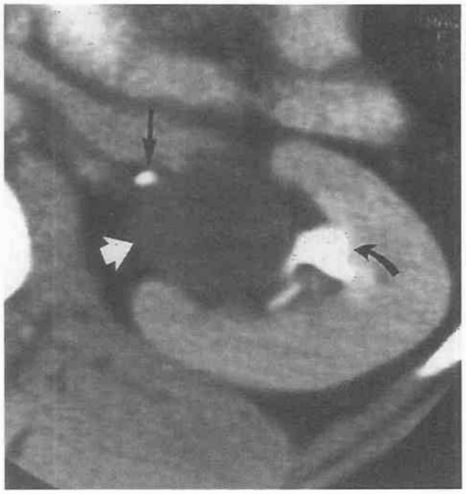

Figure 41–23. Renal sinus (parapelvic) cyst. A contrast-enhanced CT scan reveals that the cyst (*white arrow*) is surrounded by a halo of renal sinus fat, indicating its extrarenal origin. The nondilated collecting system (*curved arrow*) and ureter (*long arrow*) are displaced by the cyst.

Renal Sinus Cysts

Renal sinus (parapelvic) cysts are benign extraparenchymal cysts located in the renal sinus.[107] They are not true renal cysts, but are probably lymphatic in origin.[107] They may be unilocular or multilocular and are often bilateral (Figs. 41–23 and 41–24).[107] They do not communicate with the renal collecting system. Most renal sinus cysts are asymptomatic and are discovered incidentally on imaging studies.[107] They may in rare cases cause hypertension, hematuria, or hydronephrosis, or may become secondarily infected.

Renal sinus cysts display the same CT features as simple renal parenchymal cysts.[107] They have attenuation values in the water range (0 to 20 HU) and are difficult to distinguish from dilated or extrarenal renal pelvis on unenhanced CT scans. After intravenous administration of contrast medium, the cysts remain of water density and cause displacement of the renal pelvis and calyces (see Fig. 41–24). Differentiation from hydronephrosis is thus readily made on contrast-enhanced CT.[107] On CT, the characteristic feature of a renal sinus cyst is a surrounding halo of renal sinus fat, indicating its extrarenal origin (see Fig. 41–23).[44]

CT easily distinguishes between a renal sinus cyst and renal sinus lipomatosis, which causes a similar deformity of the collecting system on excretory urography.[107] In renal sinus lipomatosis, the attenuation value of the tissue is in the fat range. Solid masses in the renal sinus, such as lymphoma and invasive transitional cell carcinoma, are readily differentiated from renal sinus cysts because of their soft tissue attenuation values.

Renal Cystic Disease

Renal cystic disease includes a wide variety of disorders. Although imaging studies help greatly in the evaluation of renal cystic disease, they are seldom diagnostic per se because many types of cystic kidneys show similar imaging findings. Therefore, interpretation of imaging findings should always include knowledge of the patient's age, family history, symptoms, clinical findings, and renal functional status.

Multicystic Dysplastic Kidney

Multicystic dysplastic kidney (MDK) is the most common form of cystic disease in infants, usually presenting as an asymptomatic flank mass. The disorder is associated with intrauterine ureteral obstruction or atresia.[233] The renal artery may also be hypoplastic or atretic.[197] Contralateral renal anomalies are detected in 41% of patients with MDK and include obstruction of the ureteropelvic junction, renal agenesis, renal hypoplasia, vesicoureteral reflux, and bilateral MDK. Bilateral MDK is seen in 19% and contralateral agenesis is seen in 11% of patients with MDK.[130] Two types of MDK may be shown by imaging, pelvo-infundibular atresia and the hydronephrotic type.[261] In the classic type, pelvo-infundibular atresia, no discernible renal pelvis is demonstrated on imaging.[232] The kidney may be small, normal in size, or enlarged and contains multiple variably-sized noncommunicating renal cysts (Fig. 41–25).[197, 232] No perfusion of the affected kidney occurs on renal scintigraphy, and contrast-enhanced CT shows no evidence of contrast excretion by the affected kidney.[261]

Figure 41–24. Bilateral renal sinus cysts. The cysts cause displacement and attenuation of the opacified collecting systems. A simple renal cyst is also present anteriorly in the left kidney (*arrow*).

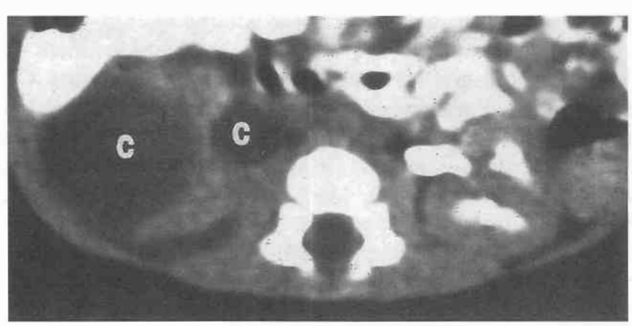

Figure 41–25. Multicystic dysplastic kidney in a neonate. The right kidney was replaced by cysts (c), one of which is larger than the other. The right kidney did not excrete contrast medium. The left kidney is normal.

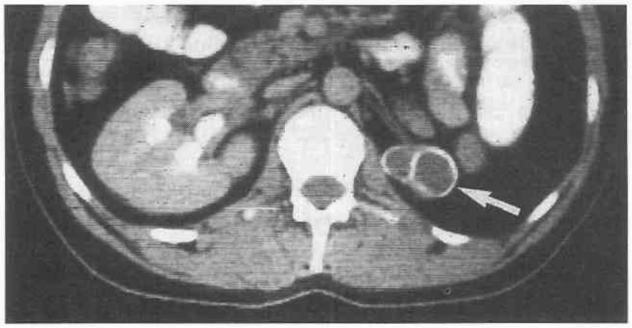

Figure 41–26. Multicystic dysplasia of left kidney in a 27-year-old man with microscopic hematuria. The left kidney is small and is composed of cysts with mural calcification (*arrow*). There is compensatory hypertrophy of the right kidney.

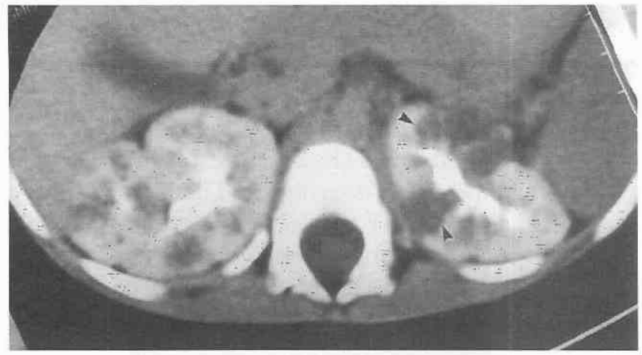

Figure 41–27. Autosomal recessive polycystic kidney disease in a 30-month-old infant with normal renal function. A contrast-enhanced CT scan shows dilated collecting ducts in the renal medulla (striated nephrogram) bilaterally and relative preservation of the renal cortex. Occasional macroscopic cysts (*arrowheads*) are present in the left kidney.

The hydronephrotic form of MDK is characterized by dilatation of the renal pelvis and calyces. Differentiation of this type of MDK from simple hydronephrosis is based on the imaging demonstration of parenchymal cysts that do not communicate with the collecting system.[197, 232] Currently, most cases of unilateral MDK are managed nonsurgically and are followed with serial ultrasonography.[188, 197] The affected kidney may remain unchanged, but it frequently undergoes spontaneous regression.[197, 281] MDK may occasionally be detected first in adults in whom imaging studies show a small kidney with calcified cysts (Fig. 41–26) or an enlarged dysfunctional kidney.[264] T2-weighted pulse sequence can be used to diagnose MDK, especially in utero.[110]

Polycystic Kidney Disease

Hereditary polycystic kidney disease may be transmitted as an autosomal recessive or autosomal dominant trait.

Autosomal Recessive Polycystic Disease

Autosomal recessive polycystic kidney disease (ARPKD) is characterized by ectasia of the renal collecting ducts, interstitial fibrosis, and variable degrees of portal hepatic fibrosis (congenital hepatic fibrosis), which often causes portal hypertension.[158] Ten percent to 90% of the collecting ducts are involved. Severity of the disease depends on, and is inversely related to, the age at presentation. Patients with milder renal involvement may present at any age from infancy to early adulthood. The severity of renal involvement and extent of liver involvement in these patients are inversely related. On noncontrast CT examination, the kidneys are smooth, enlarged, and low in attenuation, likely a reflection of the large fluid volume in the dilated ducts. Upon administration of contrast medium, a *striated nephrogram* is seen, representing accumulation of contrast in the dilated tubules Tubular ectasia is confined mainly to the renal medulla with only occasional macrocysts. The renal cortex is less severely affected (Fig. 41–27).[158] CT may also show evidence of congenital hepatic fibrosis and portal hypertension.[48] The liver contour is often irregular, and dilated intrahepatic bile ducts, ascites, splenomegaly, and enlarged portal-systemic collateral veins may be seen (Fig. 41–28). Liver cysts are not usually

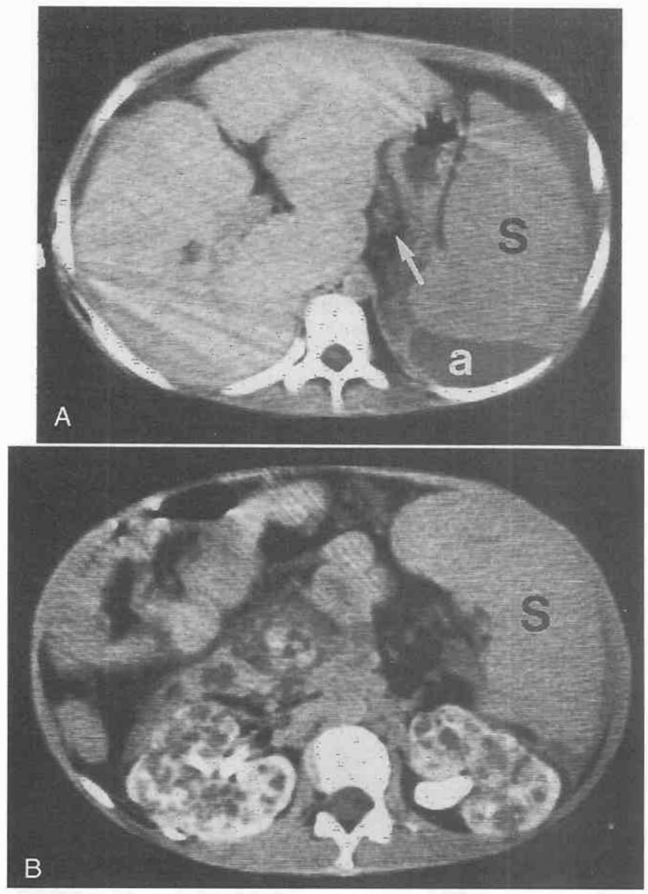

Figure 41–28. Autosomal recessive polycystic kidney disease in a 14-year-old girl with normal renal function. *A,* The liver contour is irregular as a result of congenital hepatic fibrosis. The spleen (S) is enlarged because of portal hypertension. Ascites (a) is present, and there is an enlarged left gastric vein (*arrow*) in the hepatogastric ligament. *B,* A more caudal scan shows mild nephromegaly and multiple medullary cysts with relative preservation of the renal cortex. (From Levine E: Computed tomography of renal masses. Crit Rev Diagn Imaging 24:91–200, 1985.)

evident. However, some patients have large liver cysts of biliary origin because of the presence of Caroli's disease.[54] Increased signal intensity of renal parenchyma is seen on T2-weighted MRI in ARPKD.[127, 128, 183]

Autosomal Dominant Polycystic Kidney Disease. ADPKD is one of the most commonly inherited diseases in the United States. It affects nearly 500,000 Americans and accounts for 5% to 10% of patients with end-stage renal disease (ESRD).[12] ADPKD comprises at least three phenotypically indistinguishable but genetically distinct entities, caused by mutations in three autosomal genes: PKD1 (chromosome 16p13.3) is present in about 85% of patients; PKD2 (chromosome 4q21–23) in 10%; PKD3 (unknown chromosome) in a few families.[242] The mean patient age at presentation with symptoms in ADPKD-1 is 44.8 years, versus 69.1 years for ADPKD-2.[193] New mutations or non-familial development of ADPKD occurs in 1% to 2% of ADPKD. Whites of European descent have the highest disease rates.[33] ADPKD is associated with severely impaired renal function, but only 2% to 5% of the nephrons are directly affected by the cystic changes.[35] Only 35% to 45% of patients with ADPKD experience ESRD.[39]

Cysts originate from renal tubules and collecting ducts. The ADPKD genotypes are characterized by bilateral kidney cysts, hypertension, hematuria, renal infection, stones, and renal insufficiency. ADPKD is a systemic disorder; cysts appear with decreasing order of frequency in the kidneys, liver, pancreas, brain, spleen, ovaries, and testis. Cardiac valvular disorders, abdominal and inguinal hernias, and aneurysms of cerebral and coronary arteries and the aorta are also associated with ADPKD. Colonic diverticula occur in about 80% of patients with the disease.[76]

Although the disorder usually manifests in adults (Fig. 41–29), it may be diagnosed during infancy and childhood. Patients with fully developed ADPKD often show dramatic CT findings (see Fig. 41–29). CT is slightly more sensitive than ultrasonography for detecting small renal cysts in the asymptomatic progeny of patients with ADPKD (Fig. 41–30).[82]

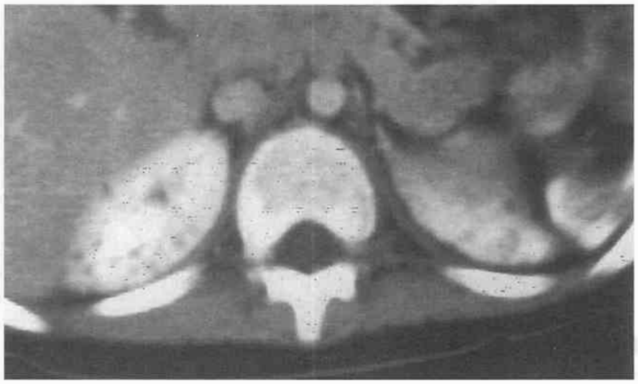

Figure 41–30. Autosomal dominant polycystic kidney disease in an asymptomatic 14-year-old boy whose father has the disease. A contrast-enhanced CT scan shows multiple, tiny bilateral renal cysts.

Flank pain and hematuria, the most common symptoms of ADPKD, may be due to cyst hemorrhage, calculi, or renal infection. Cyst hemorrhage is a common cause of pain in ADPKD and can be detected by CT in about 69% of patients.[145] Hemorrhagic cysts have attenuation values of 40 to 100 HU on unenhanced scans, do not enhance after intravenous administration of contrast medium, and are homogeneously hyperdense and well defined (Fig. 41–31). Pseudoenhancement of 10 Hu can be seen in cysts smaller than 2 cm.[42] They may rupture into the perinephric space, causing large hematomas (Fig. 41–32).[146] Hemorrhagic cysts often develop mural calcification (Fig. 41–33).

Renal calculi occur in 20% to 36% of patients with ADPKD, and they commonly cause flank pain.[144] About 57% of calculi in ADPKD are composed predominantly of uric acid and are therefore radiolucent on conventional tomography.[273] Such calculi are best evaluated by CT (Fig. 41–34).[144] Urinary tract infections are more common in women with ADPKD and may cause cyst infection. Cyst infection is difficult to diagnose on CT; it is suggested by the finding of a cyst larger than surrounding cysts with

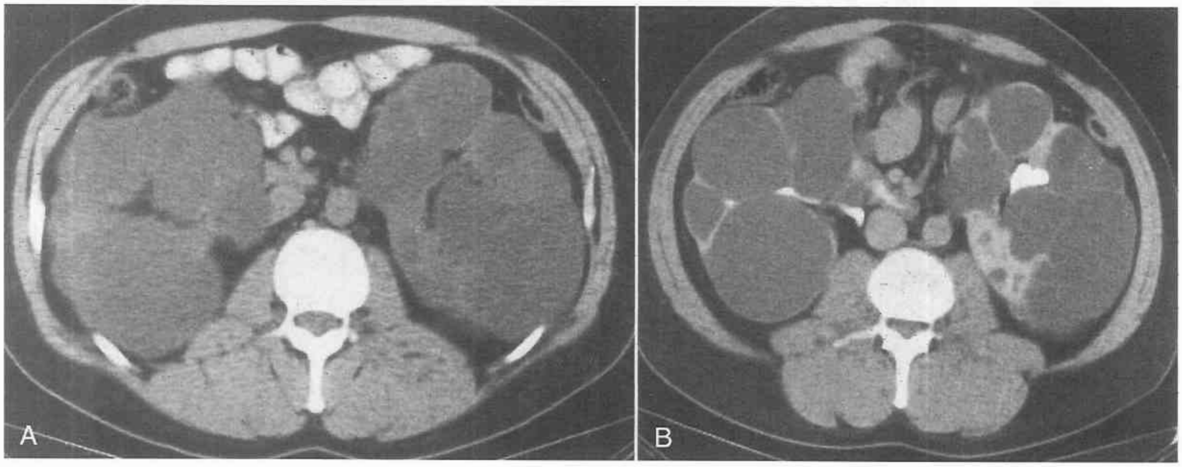

Figure 41–29. Autosomal dominant polycystic kidney disease in a 39-year-old man with hypertension and mildly impaired renal function. Unenhanced CT scan (*A*) shows bilateral nephromegaly. Contrast-enhanced CT scan (*B*) reveals large renal cysts with enhancing residual parenchyma between the cysts.

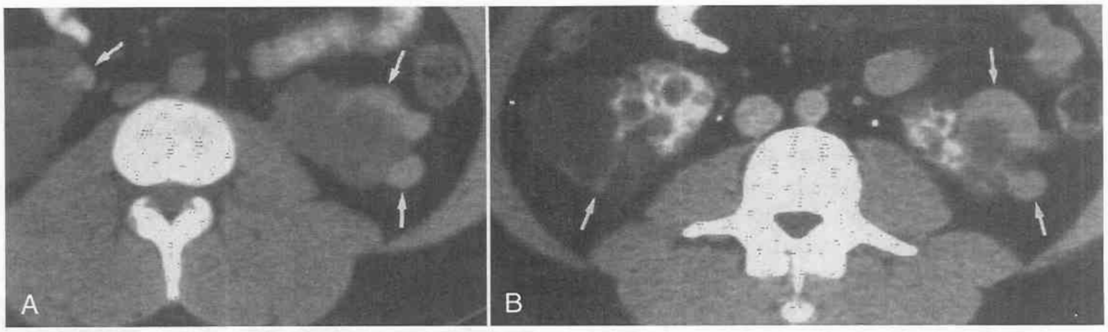

Figure 41–31. Hemorrhagic renal cysts in autosomal dominant polycystic kidney disease. *A,* Unenhanced CT scan shows bilateral subcapsular high-density cysts (*arrows*). *B,* After IV contrast enhancement, the high-density cysts (*arrows*) are hypodense relative to enhanced residual renal parenchyma. Many fluid-density cysts are present. The high-density cysts had an average attenuation value of 70 HU on both precontrast and postcontrast scans.

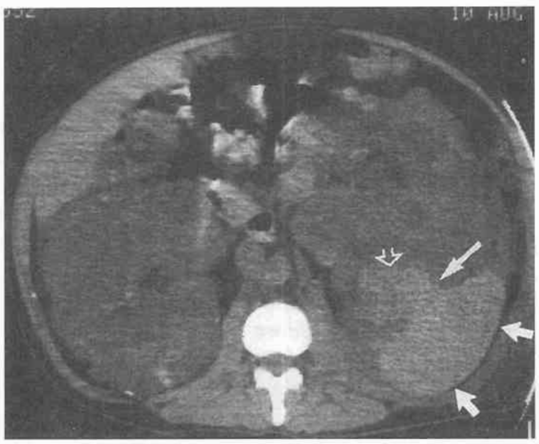

Figure 41–32. Autosomal dominant polycystic kidney disease with perinephric hemorrhage. Unenhanced CT scan reveals bilateral nephromegaly and multiple cysts. A posterior perinephric hematoma (*short arrows*) causes anterior displacement of the left kidney. A ruptured hemorrhagic cyst (*open arrow*) communicates (*long arrow*) with the hematoma. (From Levine E, Grantham JJ: Perinephric hemorrhage in autosomal dominant polycystic kidney disease: CT and MR findings. J Comput Assist Tomogr 11: 108–111, 1987.)

Figure 41–33. Autosomal dominant polycystic kidney disease with multiple curvilinear calcifications in cyst walls.

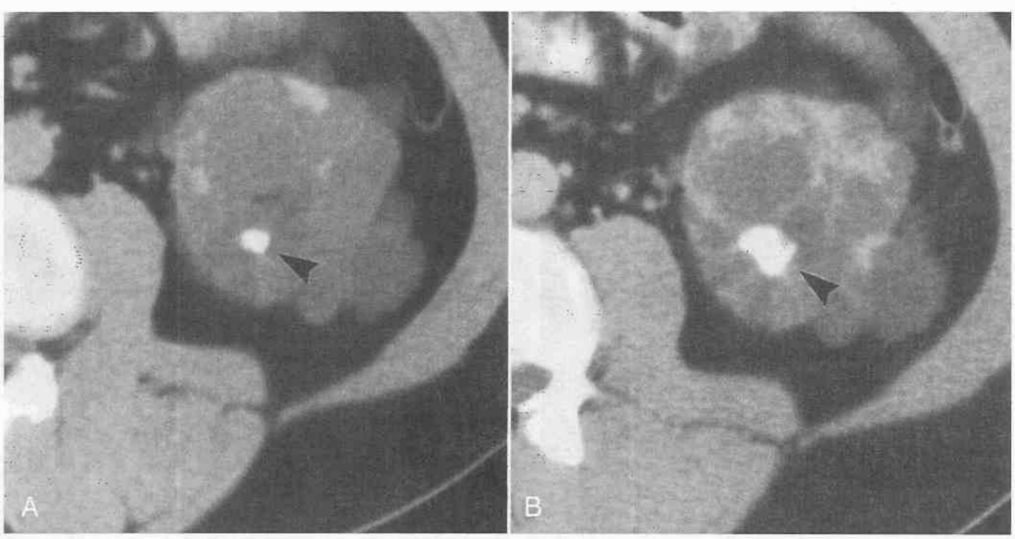

Figure 41–34. Autosomal dominant polycystic kidney disease with a calculus in the lower pole of the left kidney. *A,* An unenhanced CT scan shows a small, rounded calcification (*arrowhead*). *B,* A contrast-enhanced CT scan reveals that the calcification is located in an opacified calyx (*arrowhead*). (From Levine E, Grantham JJ: Calcified renal stones and cyst calcifications in autosomal dominant polycystic kidney disease: Clinical and CT study in 85 patients. AJR Am J Roentgenol 159:77–81, 1992.)

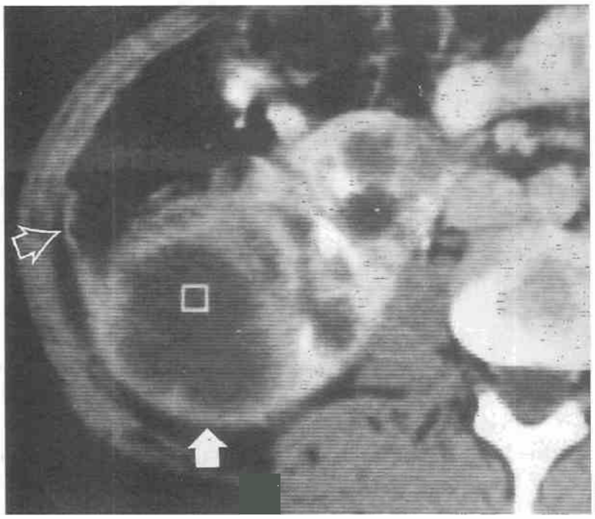

Figure 41–35. Acute pyelonephritis complicated by cyst infection in autosomal dominant polycystic kidney disease. A lower pole cyst (*solid arrow*) is larger than adjacent cysts and shows an irregular, thickened wall and adjacent renal fascial thickening (*open arrow*). The patient demonstrated a response to antibiotic therapy, and a follow-up sonogram showed absence of the large cyst, suggesting rupture into the collecting system. (From Levine E, Grantham JJ: Calcified renal stones and cyst calcifications in autosomal dominant polycystic kidney disease: Clinical and CT study in 85 patients. AJR Am J Roentgenol 159:77–81, 1992.)

thickening and irregularity of its wall, an increase in the attenuation value of its contents, and localized thickening of the adjacent renal fascia (Fig. 41–35). Radionuclide scanning using gallium citrate 32– or indium III–labeled white blood cells may help confirm the diagnosis of cyst infection by showing increased tracer activity at the cyst periphery.[236]

Cysts of the liver are present in 70% to 75% of cases of ADPKD. The cysts are thought to arise from Meyenburg's complexes. Hepatic cysts develop later than renal cysts and women are more commonly affected.[35] The CT appearance can vary from occasional small cysts (Fig. 41–36) to multiple, large cysts that cause hepatomegaly (Fig. 41–37). Abnormal liver function values suggest the development of such complications as common hepatic duct compression by cysts, cyst infection, and cholangiocarcinoma arising from the cyst lining (Fig. 41–38).[149, 268] The risk of renal cancer in patients with ADPKD who are not undergoing dialysis is probably not increased; however, patients under-

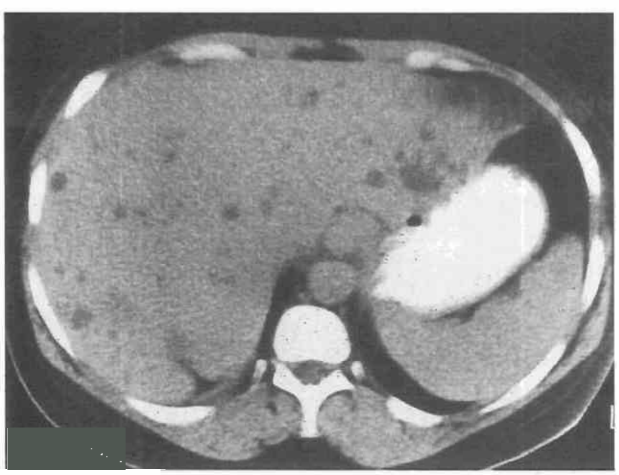

Figure 41–36. Multiple small liver cysts in autosomal dominant polycystic kidney disease.

Figure 41–37. Significant hepatomegaly caused by liver cysts in a 45-year-old woman with autosomal dominant polycystic kidney disease. (From Levine E, Cook LT, Grantham JJ: Liver cysts in autosomal-dominant polycystic kidney disease: Clinical and computed tomographic study. AJR Am J Roentgenol 145:229–233, 1985.)

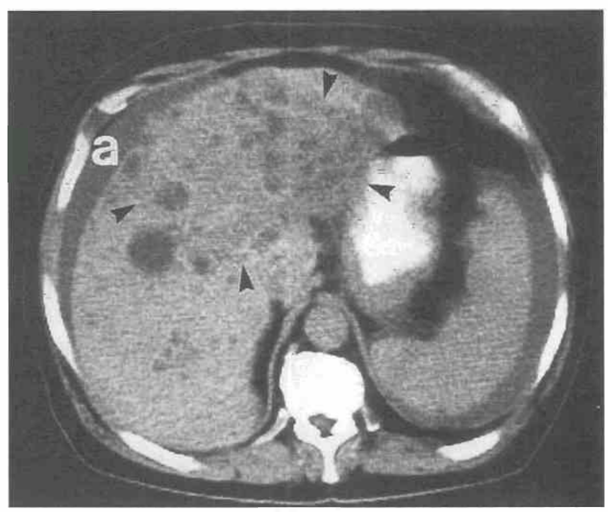

Figure 41–38. Autosomal [redacted]nt polycystic kidney disease complicated by cholangiocarcinoma in a 69-year-old man complaining of abdominal pain and weight loss. Liver function values were notably abnormal. CT scan shows several cysts in the right lobe of the liver. A poorly defined, low-density mass (*arrowheads*) involves the left lobe and part of the anterior segment of the right lobe. Ascites (a) is present. The neoplasm was not resectable, and the patient died from metastatic disease. (From Levine E, Cook LT, Grantham JJ: Liver cysts in autosomal-dominant polycystic kidney disease: Clinical and computed tomographic study. AJR Am J Roentgenol 145:229–233, 1985.)

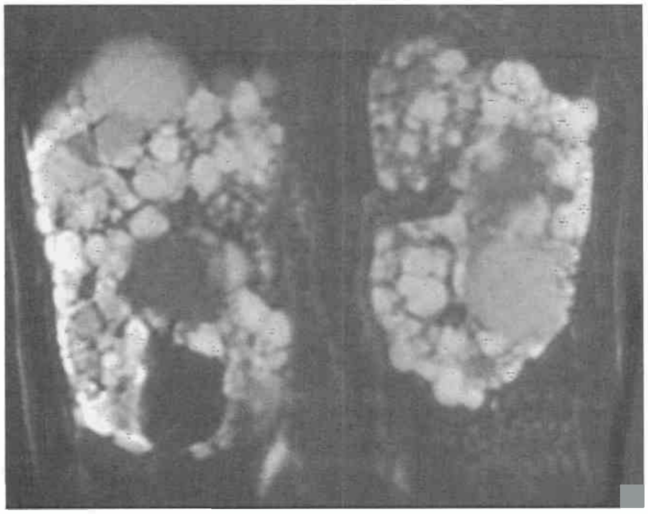

Figure 41–39. MRI of polycystic kidney. Coronal single-shot fast spin-echo images (TR = 67,500 msec, and effective TE = 637 msec) demonstrate nephromegaly with multiple cysts that have variable signal intensities secondary to hemorrhage or high protein content.

going dialysis are at greater risk for development of renal malignancy relative to the general population.[35]

Living related kidney donors (with a family history of ADPKD) require screening for ADPKD, most commonly by ultrasonography. Ultrasound examination has a negative predictive value (NPV) of 100% for donors older than 30 years, but of only 96% for donors 20 to 30 years old. Heavily T2-weighted MRI in coronal and axial planes may be a more sensitive screening method for ADPKD in younger kidney donors (Fig. 41–39).[301]

Unilateral (Localized) Renal Cystic Disease

In unilateral renal cystic disease (URCD), also known as localized renal cystic disease, most of one kidney is replaced by multiple cysts and the other kidney is normal. The affected patient usually has no family history of renal cysts, and the condition is not related to ADPKD.[45, 132, 147, 250] Liver cysts and renal failure do not occur in this condition. Affected patients range in age from childhood to the sixth decade and may have hypertension, flank pain, or hematuria.[147] On CT, the cysts are seen to be separated by enhancing bands of normal renal parenchyma so that no distinct encapsulated renal mass is found (Fig. 41–40). The affected kidney may be enlarged and shows normal excretion of contrast medium. Although the cysts may predominate in one part of the affected kidney, careful assessment of the CT scan usually shows multiple smaller cysts elsewhere in the renal parenchyma.[147]

The absence of cysts in the other kidney on CT in adults usually excludes the diagnosis of ADPKD, but one must use caution in making a definitive diagnosis of URCD in children. In ADPKD, renal cysts develop slowly during childhood and may become apparent earlier in one kidney.[205] Accordingly, in children, follow-up CT should be performed after an appropriate interval before a final diagnosis of URCD is made.

Acquired Cystic Kidney Disease

Acquired cystic kidney disease (ACKD) is characterized by the development of multiple renal cysts in patients with chronic renal failure but without a history of hereditary renal cystic disease.[140] ACKD is seen in 90% of patients after 5 to 10 years of renal dialysis (hemodialysis or peritoneal dialysis); however, ACKD may be encountered in as many as 8% to 13% of patients with ESRD who are not undergoing dialysis.[119, 167] Nephrosclerosis, diabetic nephropathy, and chronic glomerulonephritis account for a large percentage of ACKD patients undergoing dialysis.[167] The condition is usually asymptomatic but may become symptomatic when associated with a complication such as cyst or retroperitoneal hemorrhage, cyst infection, renal calculi, erythrocytosis, or renal neoplasm.[34, 140]

The radiologic diagnosis of ACKD is best established with contrast-enhanced CT, although ultrasonography and MRI are useful for evaluating patients with ESRD who are not being treated with dialysis. The diagnosis is based on detection of at least three to five cysts in each kidney in a patient who has chronic renal failure not due to hereditary renal cystic disease.[154] The affected kidneys are usually small (Fig. 41–41). However, ACKD is a progressive disorder, and nephromegaly may eventually develop (see Fig. 41–41).[119] On MRI, renal cysts in ACKD are best shown on gadolinium-enhanced images (Fig. 41–42).

Hemorrhagic cysts occur in about 50% of patients with

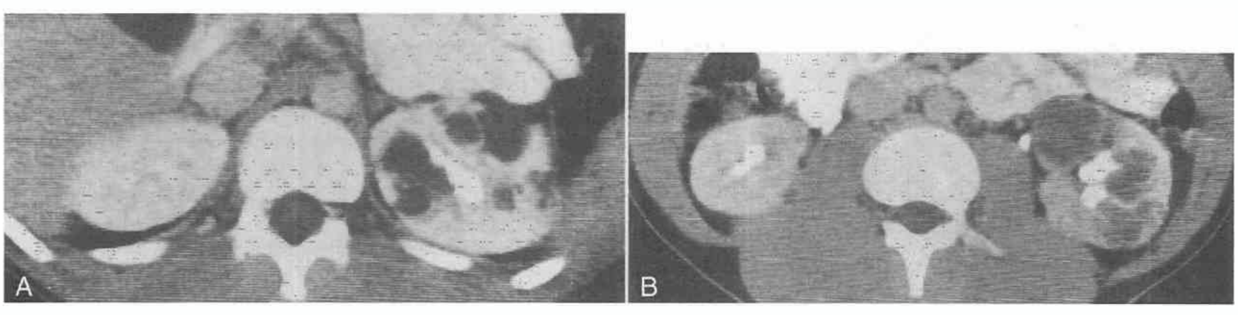

Figure 41–40. Unilateral renal cystic disease in a 15-year-old male with intermittent gross hematuria starting at 5 years of age. Contrast-enhanced CT scans (*A* and *B*) show partial replacement of the left kidney by many cysts that are separated by enhancing bands of normal parenchyma. The right kidney is free of cysts, and a follow-up CT scan 7 years later showed no change.

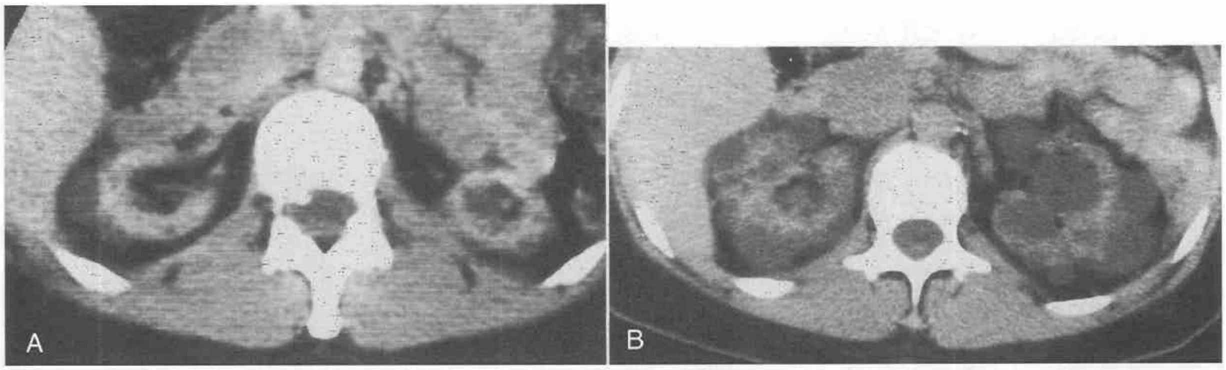

Figure 41–41. Acquired renal cystic disease in a 45-year-old man undergoing long-term hemodialysis. *A,* CT scan after 4 years of dialysis shows bilateral small cysts in shrunken kidneys. *B,* A follow-up CT scan obtained 4 years later shows enlargement of cysts and kidneys.

ACKD and sometimes attain a large size.[153] On CT, hemorrhagic cysts manifest as well-defined masses with attenuation values ranging from 40 to 100 HU on unenhanced CT scans (Fig. 41–43). Differentiation of these lesions from renal neoplasms on CT is suggested by lack of contrast enhancement and a homogeneous appearance on contrast-enhanced CT scans (see Fig. 41–43).[153] A nonhemorrhagic cyst that is more than 1 cm in diameter may show pseudo-enhancement of less than 10 HU.[7] Sonography may help in establishing the cystic nature of such a lesion by showing anechoic center, posterior acoustic enhancement, and a smooth wall. On MRI, hemorrhagic cysts often have high signal intensity on both T1- and T2-weighted images and do not enhance after gadolinium administration (Fig. 41–44). Subcapsular and perinephric hematomas, which occur in as many as 13% of patients with ACKD, are usually due to rupture of hemorrhagic cysts (Fig. 41–45).[153]

The primary concern in patients with ACKD is the increased incidence (5% to 19%) of renal cell carcinoma (RCC). The incidence is about 12 to 18 times higher than that in the general population, and the cancers may be asymptomatic (Fig. 41–46).[119] RCC in patients undergoing dialysis occurs at an average age of 49 years, compared with 62 years in nonazotemic patients.[206] The development of RCC in patients undergoing dialysis depends on the duration of dialysis (incidence rises after 3 years of dialysis), the size of the kidneys, and male gender (seven times higher).[34, 140] Small renal neoplasms (<3 cm in diameter) are significantly more common than large carcinomas and occur in about 7% of patients undergoing dialysis (Fig. 41–47).[140] Most such lesions remain unchanged with prolonged follow-up. However, some gradually enlarge and may become locally invasive or even metastasize (see Fig. 41–47).[150] Because of their propensity to develop malignant renal neoplasms, the native kidneys of patients undergoing dialysis should be evaluated with CT if the patients experience flank pain or hematuria. Annual imaging of the native kidneys in asymptomatic patients undergoing dialysis should be restricted to those with a good general medical condition and a good life expectancy.[153]

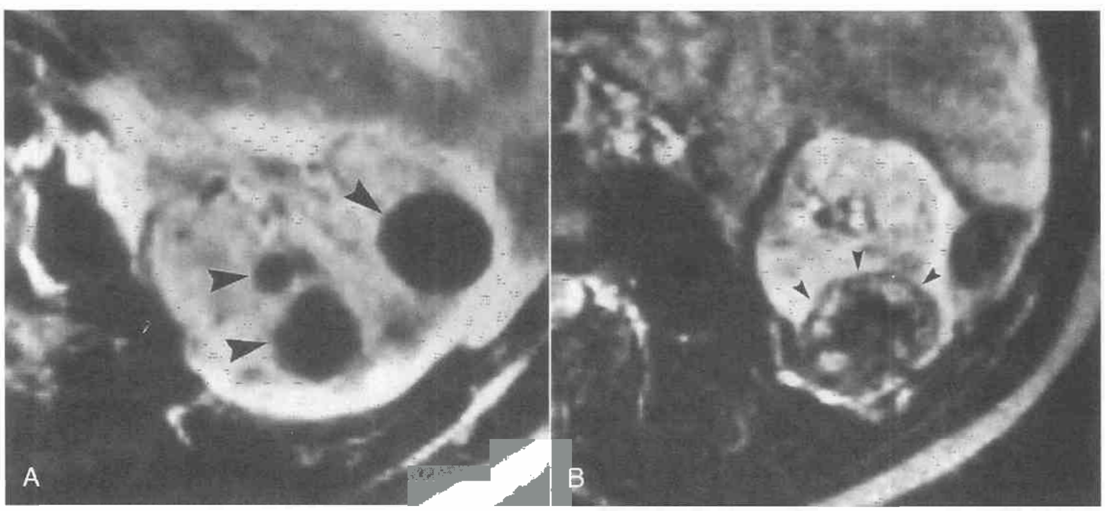

Figure 41–42. Acquir[redacted] cystic diseas[redacted]d left renal cell carcinoma in[redacted]year-old[redacted] with azotemia not treated with dialysis. *A,* T1-weighted (TR =[redacted]sec, TE = [redacted]msec) spin-echo MR image af[redacted]gadoliniu[redacted]TPA administration shows several well-defined cysts (*arrowheads*) of low signal intensity in the left kidney. *B,* T2-weighted (TR = 2100 msec, TE = 90 msec) image without gadolinium administration reveals a heterogeneous, 3.5-cm lower-pole carcinoma (*arrowheads*).

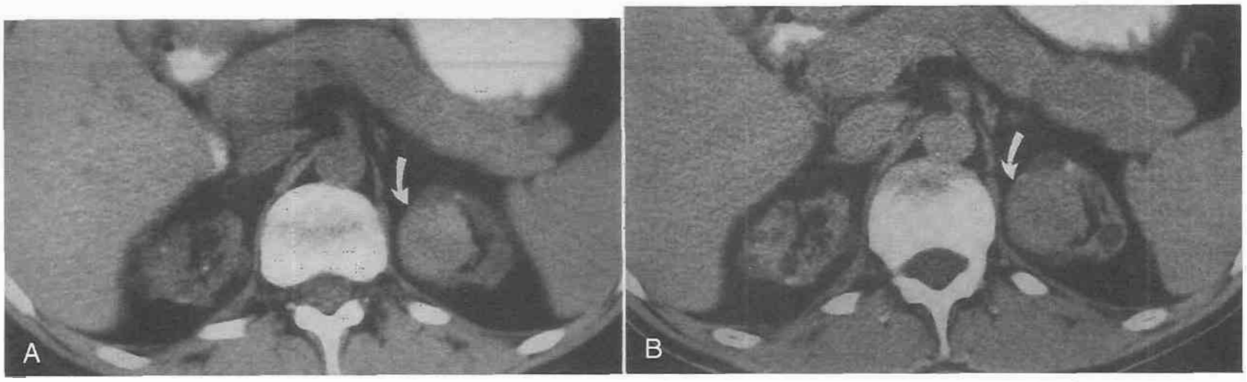

Figure 41–43. Acquired renal cystic disease with cyst hemorrhage in a 41-year-old man with gross hematuria. *A*, An unenhanced CT scan shows a 3.8-cm high-density (44 HU) mass (*arrow*) in the upper pole of the left kidney. *B*, After contrast enhancement, the attenuation value of the mass (*arrow*) was 43 HU. Multiple bilateral fluid-density cysts are also present. The mass resolved completely on a follow-up CT scan obtained 3 months later, suggesting a hemorrhagic cyst that had ruptured into the collecting system. (From Levine E, Slusher SL, Grantham JJ, Wetzel LH: Natural history of acquired renal cystic disease in dialysis patients: A prospective longitudinal CT study. AJR Am J Roentgenol 156:501–506, 1991.)

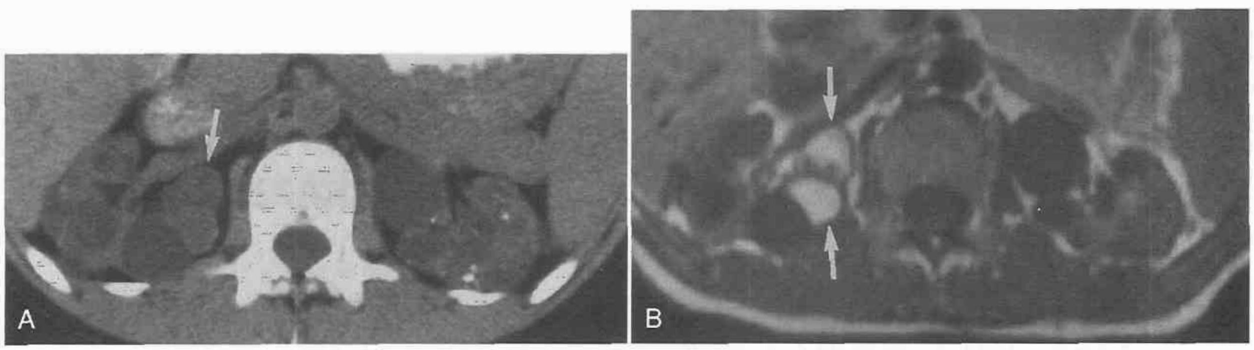

Figure 41–44. Hemorrhagic cysts in acquired renal cystic disease. *A*, Unenhanced CT scan shows multiple bilateral fluid-density cysts with cyst wall calcifications. An area (*arrow*) located medially in the right kidney was considered suspicious for a neoplasm. *B*, T1-weighted (TR = 500 msec, TE = 15 msec) spin-echo MR image shows that most cysts have low signal intensity. However, two lesions (*arrows*) located medially in the right kidney have a high signal intensity, which persisted on T2-weighted images (not shown), findings consistent with cyst hemorrhage.

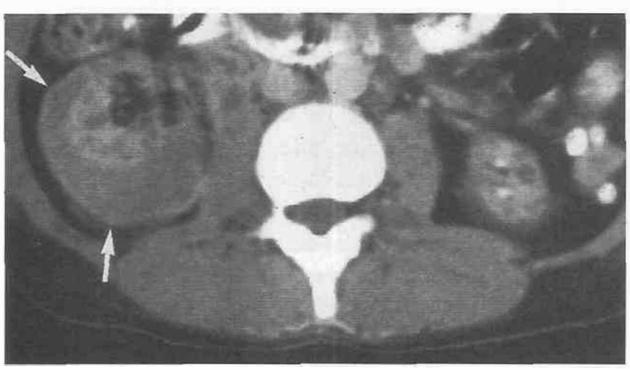

Figure 41–45. Acquired renal cystic disease and a right perinephric hematoma (*arrows*) in a patient undergoing long-term dialysis. (From Levine E, Grantham JJ, Slusher SL, et al: CT of acquired cystic kidney disease and renal tumors in long-term dialysis patients. AJR Am J Roentgenol 142:125–131, 1984.)

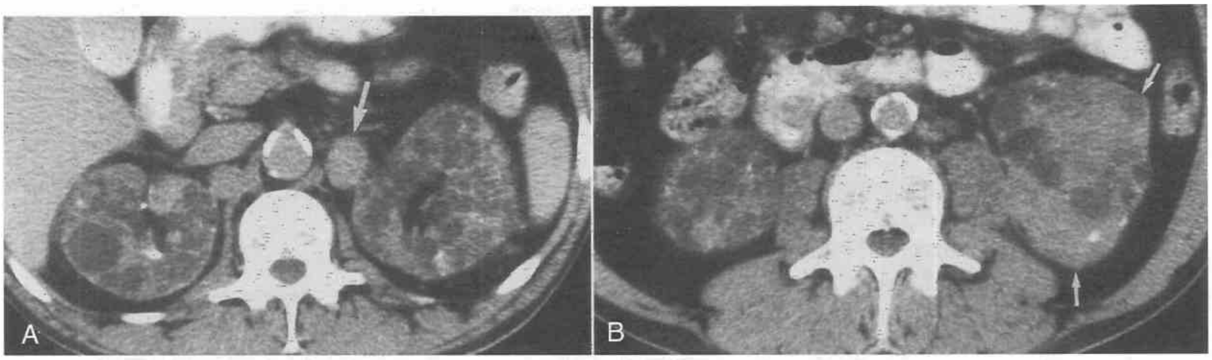

Figure 41–46[redacted]cquired renal cystic disease a[redacted]static renal cell carcinoma in a 46-year-old man treated with hemodialysis for 120 months. *A*, Contrast-enhanced CT scan shows multiple bilateral renal cysts and nephromegaly. The enlarged left renal hilar lymph node (*arrow*) is due to a metastasis. *B*, A caudal CT scan reveals two solid, heterogeneous masses (*arrows*) with irregular contours and focal calcifications in the lower pole of the left kidney. The masses enhanced by 30 HU. (From Levine E, Slusher SL, Grantham JJ, Wetzel LH: Natural history of acquired renal cystic disease in dialysis patients: A prospective longitudinal CT study. AJR Am J Roentgenol 156:501–506, 1991.)

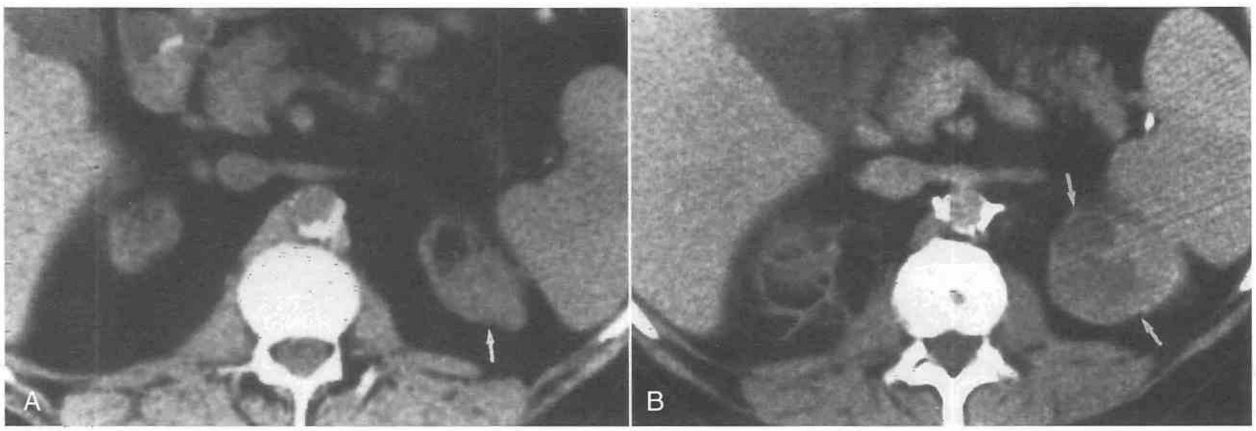

Figure 41–47. Growth of renal cell carcinoma in a patient with acquired renal cystic disease who was undergoing hemodialysis. *A*, The first CT scan shows a small mass (*arrow*) in the upper pole of the left kidney. *B*, A CT scan performed 18 months later during an episode of gross hematuria reveals that the left renal mass (*arrows*) has enlarged and become heterogeneous, suggesting renal cell carcinoma. On pathologic examination, the lesion had invaded the renal capsule. Linear strands related to the right kidney resulted from perinephric hemorrhage. (From Levine E, Grantham JJ, MacDougall ML: Spontaneous subcapsular and perinephric hemorrhage in end-stage kidney disease: Clinical and CT findings. AJR Am J Roentgenol 148:755–758, 1987.)

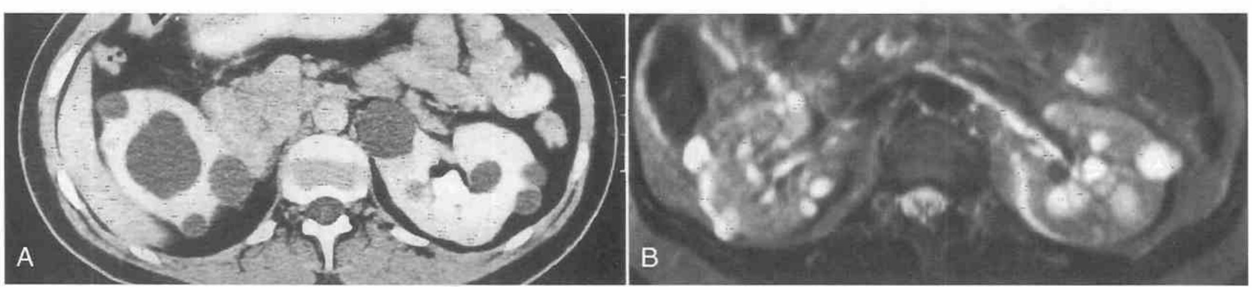

Figure 41–48. Multiple renal cysts in two different patients with von Hippel-Lindau disease. *A*, Contrast-enhanced CT scan shows multiple bilateral renal cysts. *B*, T2-weighted (TR = 2200 msec, TE = 90 msec) spin-echo MR image shows multiple cysts with high signal intensities involving both kidneys.

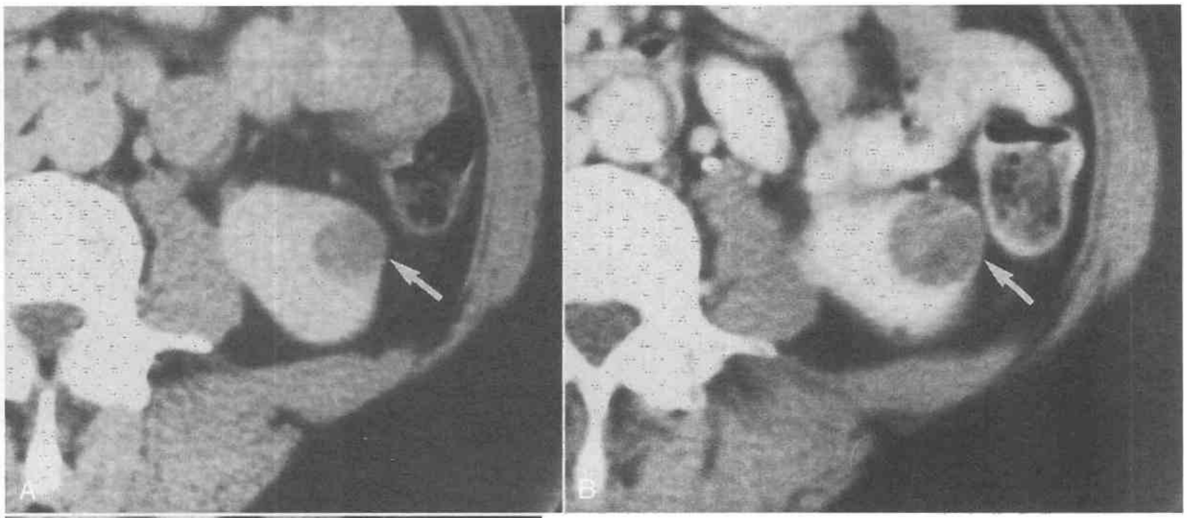
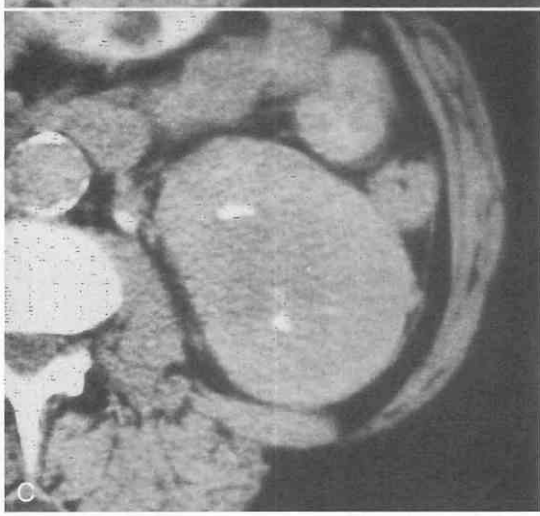

Figure 41–49. Growth of a renal cell carcinoma in a patient with von Hippel-Lindau disease. The right kidney was previously resected because of renal cell carcinoma. The patient refused surgery for the left renal lesion until after the third CT scan. *A*, There is a 1.8-cm solid mass (*arrow*) in the lower pole of the left kidney. *B*, A follow-up CT scan obtained 2 years after *A* shows that the lesion (*arrow*) had enlarged to 2.2 cm as well as mild heterogeneity. *C*, A CT scan obtained 3 years after *B* shows that the lesion has now replaced most of the left kidney. A left nephrectomy was performed, and hemodialysis was started.

Hereditary Syndromes

Von Hippel-Lindau Disease

It is estimated that approximately 7000 patients in the United States have von Hippel-Lindau disease (VHLD) The incidence of VHLD is approximately 1 in 40,000 live births. The disease, inherited as an autosomal dominant trait with high penetrance, is caused by a genetic defect in the short arm of chromosome 3.[249] Manifestations of VHLD include retinal angiomas, central nervous system hemangioblastomas, pancreatic cysts, islet cell tumors, pheochromocytomas, endolymphatic sac tumors, cystadenomas of the epididymis, and broad ligament and renal cysts and tumors.[35] The abdominal lesions are best detected on CT.[37, 38] VHLD that is not associated with pheochromocytoma is subclassified as VHLD1 and VHLD that is associated with pheochromocytoma as VHLD2. Multiple bilateral renal cysts and cystic and solid neoplasms are the most common manifestation of VHLD (Fig. 41–48). Most cysts remain stable with long-term CT follow-up and transformation from typical simple cysts to solid lesions is rare.[35, 37] However, complex lesions with both cystic and solid elements may transform into solid lesions and therefore require careful imaging follow-up.[37]

RCC is reported to develop in 24% to 45% of patients with VHLD and is often multifocal and bilateral.[164, 165] VHLD-associated renal cysts are lined by hyperplastic epithelium that is commonly intermixed with foci of tumor.[207]

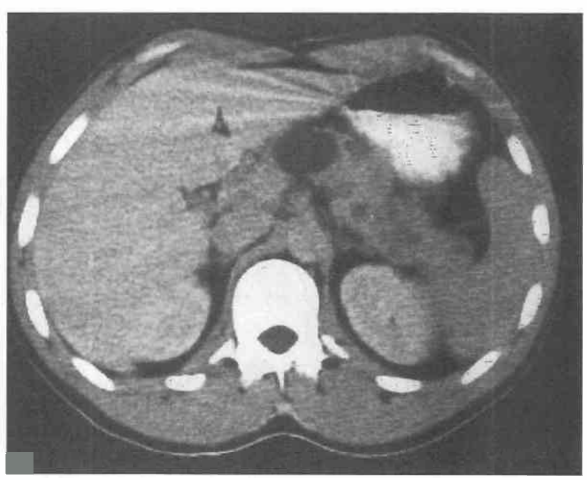

Figure 41–50. Multiple pancreatic cysts with mild pancreatic enlargement in von Hippel-Lindau disease.

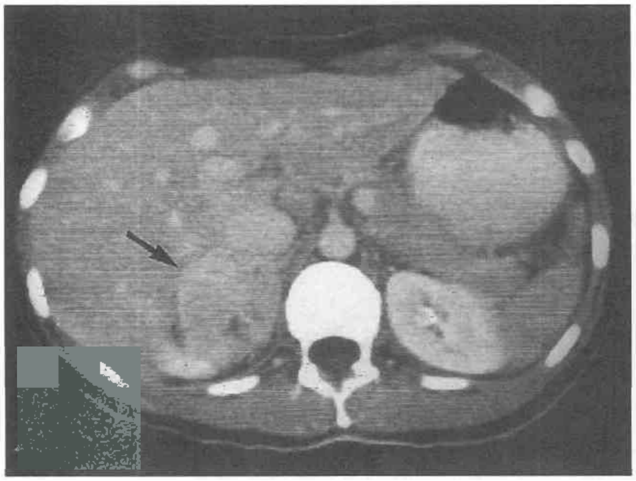

Figure 41–51. Right adrenal pheochromocytoma (*arrow*) in von Hippel-Lindau disease.

Once solid renal lesions develop, they grow at rates similar to those of sporadic RCCs (Fig. 41–49).[37] Predominantly cystic lesions with solid components are characteristic of VHLD. The solid component usually represents RCC.[207]

The pancreas is commonly involved in VHLD, with pancreatic cysts occurring in about 30% of patients (Fig. 41–50). Solid pancreatic lesions, including nonfunctional islet cell tumor and ductal carcinoma, occur less commonly in VHLD. Pheochromocytomas, which occur in 10% of patients with VHLD, are often multiple and ectopic; approximately 50% to 80% are bilateral (Fig. 41–51).[148, 219]

Screening in families affected by VHLD permits timely genetic counseling and early identification of potentially life-threatening lesions. Abdominal CT should first be performed late in the second decade in at-risk individuals (i.e., primary relatives of patients with the diagnosis). The frequency of imaging thereafter depends on the initial findings. Patients with suspicious renal lesions may require annual CT evaluation.

Tuberous Sclerosis Complex

Tuberous sclerosis complex (TSC) may be inherited as an autosomal dominant trait or may occur sporadically. Tuberous sclerosis is an autosomal dominant disorder often associated with a chromosome 9 (TSC1) and chromosome 16 (TSC2) abnormality, although up to 60% of cases occur spontaneously. The incidence of the disorder is between 1 in 10,000 and 100,000 live births, and it leads to multiple organ and skeletal abnormalities.[35, 70] The classic triad of epilepsy, mental retardation, and adenoma sebaceum defines the syndrome clinically.[70] Renal lesions, seen in 50% of patients with TSC, include multiple cysts, angiomyolipomas (AMLs), tumors and perirenal cystic collections, or lymphangiomas.[35, 303] Other associated abnormalities are subependymal nodule, giant cell astrocytoma, peripheral tubers, retinal hamartoma, cardiac rhabdomyoma, lymphangioleiomyomatosis, shagreen patch, subungual fibroma, and bone cyst.[35] Multiple renal AMLs are the sine qua non of TSC and are usually bilateral; they occur in about 15% of patients, mostly females.[303] The AMLs are benign renal tumors composed of fat, smooth muscle, and abnormal blood vessels. Abnormal vessels (aneurysmal dilatations) predispose the lesions to hemorrhage. The rate of hemorrhage within TSC-related AMLs is higher than that found in sporadic AMLs.[35]

CT scans usually demonstrate a large fatty mass intermixed with areas of tissue density that may represent nonfatty parts of the tumor or areas of hemorrhage (Fig. 41–52). The tumor commonly extends into the perinephric space and is often complicated by intratumoral or perinephric hemorrhage. CT is also useful in identifying perinephric extension and hemorrhage. The CT appearance of AMLs that are composed primarily of smooth muscle, or in which intratumoral hemorrhage has obscured the fatty part of the tumor, is indistinguishable from that of other solid renal tumors.[243]

Renal cystic disease in TSC may sometimes be the earliest and only clinical manifestation of the disorder in infancy and childhood.[178] The kidneys are often signifi-

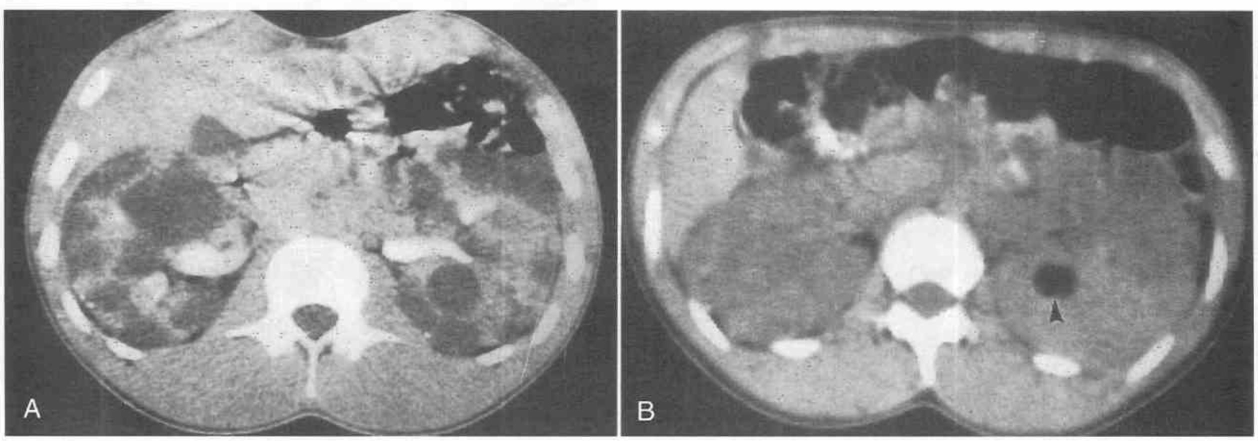

Figure 41–52. Tuberous sclerosis with renal cystic disease in a 15-year-old female. *A*, Contrast-enhanced CT scan shows enlarged kidneys with multiple fluid-density cysts. The appearances closely resemble that of autosomal dominant polycystic kidney disease. *B*, Unenhanced CT scan shows a 1.9-cm rounded lesion (*arrowhead*) in the left kidney with a fat attenuation value of 110 HU. The findings indicate an angiomyolipoma and strongly suggest tuberous sclerosis. (From Mitnick JS, Bosniak MA, Hilton S, et al: Cystic renal disease in tuberous sclerosis. Radiology 147:85–87, 1983.)

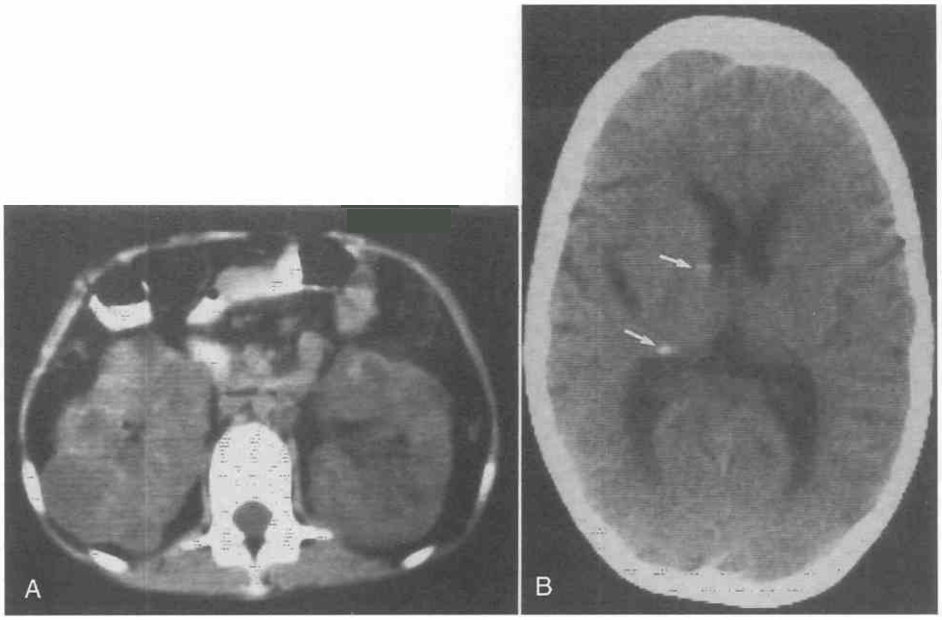

Figure 41–53. **Tuberous sclerosis with renal [redacted] disease in a 14-[redacted]-old female.** *A,* Unenhanced CT scan [redacted] kidneys containing multiple cysts. No fat-containing angiomyolipomas were detected. *B,* A cranial CT scan reveals paraventricular calcifications (*arrows*), indicating diagnosis of tuberous sclerosis and permitting differentiation from autosomal dominant polycystic kidney disease.

cantly enlarged in such patients and are replaced by multiple cysts of varying size (see Fig. 41–52). The cysts involve the renal cortex and medulla, and the findings are similar to those of ADPKD.[174] The cysts in TSC are not a diagnostic feature, occurring at an earlier age than in ADPKD.

The combination of renal cysts and AMLs is strongly suggestive of tuberous sclerosis.[174] If no renal AMLs are found in a patient suspected of having TSC, cranial CT may help establish the diagnosis of TSC by showing small, high-attenuation periventricular subependymal nodules (Fig. 41–53).[269]

Renal Lymphangiectasia

Renal lymphangiectasia is probably due to developmental obstruction of the larger lymphatics draining the kidney through the renal pedicle.[21, 156, 200] The condition is usually bilateral and is characterized on imaging studies by large lymphatic cysts in the renal sinuses, perinephric tissues, and central retroperitoneum, as well as diffuse intrarenal lymphangiectasia (Fig. 41–54).[180, 214] Renal lymphangiectasia is usually discovered clinically because of abdominal masses due to nephromegaly. The disorder may be complicated during pregnancy by large perinephric lymph collections and ascites (Fig. 41–55).[171] These findings may be secondary to lymphatic rupture due to increased renal lymph flow during pregnancy in the presence of lymphatic obstruction.[171]

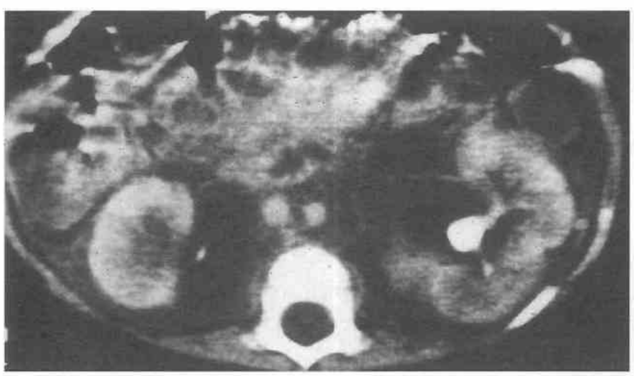

Figure 41–54. Renal lymphangiectasia in a 10-month-old boy with abdominal masses on routine physical examination and normal renal function. A contrast-enhanced CT scan reveals nephromegaly and many renal sinus, perinephric, and central retroperitoneal lymphatic cysts. (From Blumhagen JD, Wood BJ, Rosenbaum M: Sonographic evaluation of abdominal lymphangiomas in children. J Ultrasound Med 6:487–495, 1987.)

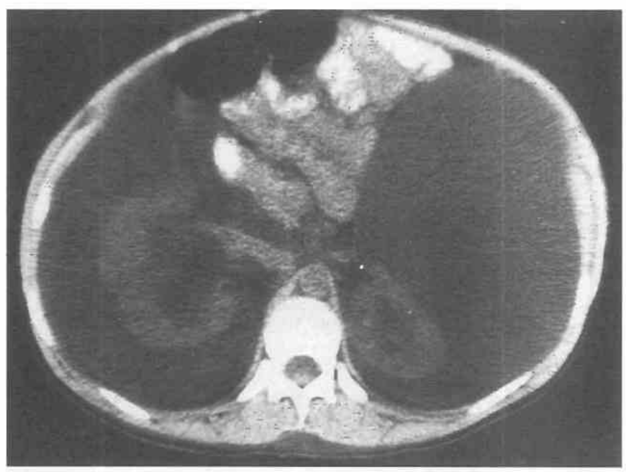

Figure 41–55. Renal lymphangiectasia in a 25-year-old woman who experienced severe abdominal distention during pregnancy. An unenhanced CT scan shows large bilateral perinephric lymph collections and renal sinus lymphatic cysts. (From Meredith WT, Levine E, Ahlstrom NG, Grantham JJ: Exacerbation of familial renal lymphangiomatosis during pregnancy. AJR Am J Roentgenol 151:965–966, 1988.)

Renal Parenchymal Neoplasms

Malignant renal parenchymal neoplasms may be either primary or secondary. RCC is the most common primary renal cancer, accounting for about 86% of all primary malignant renal parenchymal neoplasms. Of the remainder, 12% are Wilms' tumors and 2% are renal sarcomas.[142] Secondary neoplasms of the renal parenchyma include malignant lymphoma and metastases. The most common renal neoplasm overall, is metastases.[203]

Renal Cell Carcinoma

RCC is a common urologic malignant lesion in adults and accounts for 2% of all cancers. It may occur at any age, although most patients are more than 40 years, and persons in the seventh and eighth decades of life are most commonly affected.[209] In children over 5 years, only 0.3% to 1.3% of all cases of RCC present in childhood.[86] Known risk factors are cigarette smoking, exposure to petroleum products, obesity, ACRD, VHLD, TSC, and hereditary papillary renal cancer.[179, 209]

Current imaging techniques have had a notable effect on tumor detection. Kidney cancers are being diagnosed at an earlier stage and with greater precision.[166] Small early-stage carcinomas are now commonly identified during abdominal CT or ultrasonography performed for nonrenal complaints (Fig. 41–56).[151] Indeed, almost as many new RCCs are currently being detected incidentally as are being found in patients investigated because of hematuria or flank pain.

CT Technique and Imaging

Scanning protocol for RCC consists of a combination of unenhanced (or CT imaging) in the corticomedullary and nephrographic phases. The corticomedullary phase (25 to 70 seconds from the start of injection of contrast material) is best for evaluating venous extension of RCC. The nephrographic phase (80 to 180 seconds after the start of injection) is best for evaluating the renal mass.[244]

Single-detector and multidetector spiral CT allows rapid image acquisition through the entire kidney in single breath-hold during various phases of contrast enhancement after the administration of a single bolus of intravenous contrast material.[244] CT is the primary modality for the detection, diagnosis, and staging of RCC. The precontrast CT appearance of RCC varies considerably, depending on the gross pathologic features. Neoplasms may be hypodense, isodense (see Fig. 41–56), or hyperdense (Fig. 41–57) compared with normal renal parenchyma on unenhanced CT scans.[300] Most RCCs are solid lesions with attenuation values of 20 HU or greater on unenhanced CT.[248] Tumor calcification occurs in as many as 31% of cases and may take the form of amorphous internal calcification (Figs. 41–57 and 41–58) or curvilinear calcification (Fig. 41–59), which may be peripheral or central.[300]

After administration of intravenous contrast medium, most RCCs enhance, but usually to a lesser extent than normal renal parenchyma (see Figs. 41–56 and 41–57). This feature is best seen in nephrographic phase,[17, 265] the most important phase for detecting renal masses.[244] Enhancement is often heterogeneous because of tumor hemorrhage or necrosis (see Figs. 41–57 and 41–58).[142] The mass often shows an indistinct interface with the surrounding parenchyma and frequently has a lobulated or irregular outer margin. Small RCCs, however, often have distinct, smooth margins.[242, 300]

MRI assumes a primary role in tumor detection and staging in patients in whom contrast-enhanced CT scanning is contraindicated because of either previous major reactions to contrast material or renal failure.[64, 223] MRI may be used as a supplement to CT in patients who have renal carcinoma and venous tumor extension and in whom the status of the vena cava is not clearly established.[64, 69, 91]

The usual appearance of RCC on MR imaging is that of a lesion which is hypointense to isointense to renal parenchyma on T1-weighted images, heterogeneously hyperintense on T2-weighted images and demonstrates less enhancement than renal parenchyma after administration of gadolinium. The appearance can vary, however, depending on tumor histology, the presence or absence of intratumoral

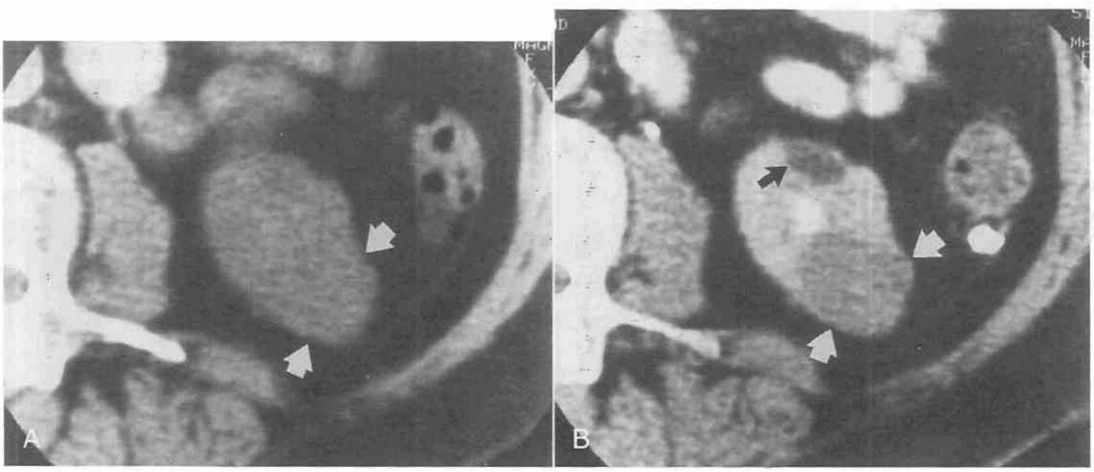

Figure 41–56. Renal cell carcinoma. *A*, The neoplasm (*arrows*) has a similar density to normal renal parenchyma on an unenhanced CT scan. *B*, A contrast-enhanced CT scan shows a homogeneous 2.3-cm mass (*white arrows*) with a slightly irregular outline. The attenuation value increased from 37 to 87 HU. A small renal cyst (*black arrow*) is seen anteriorly.

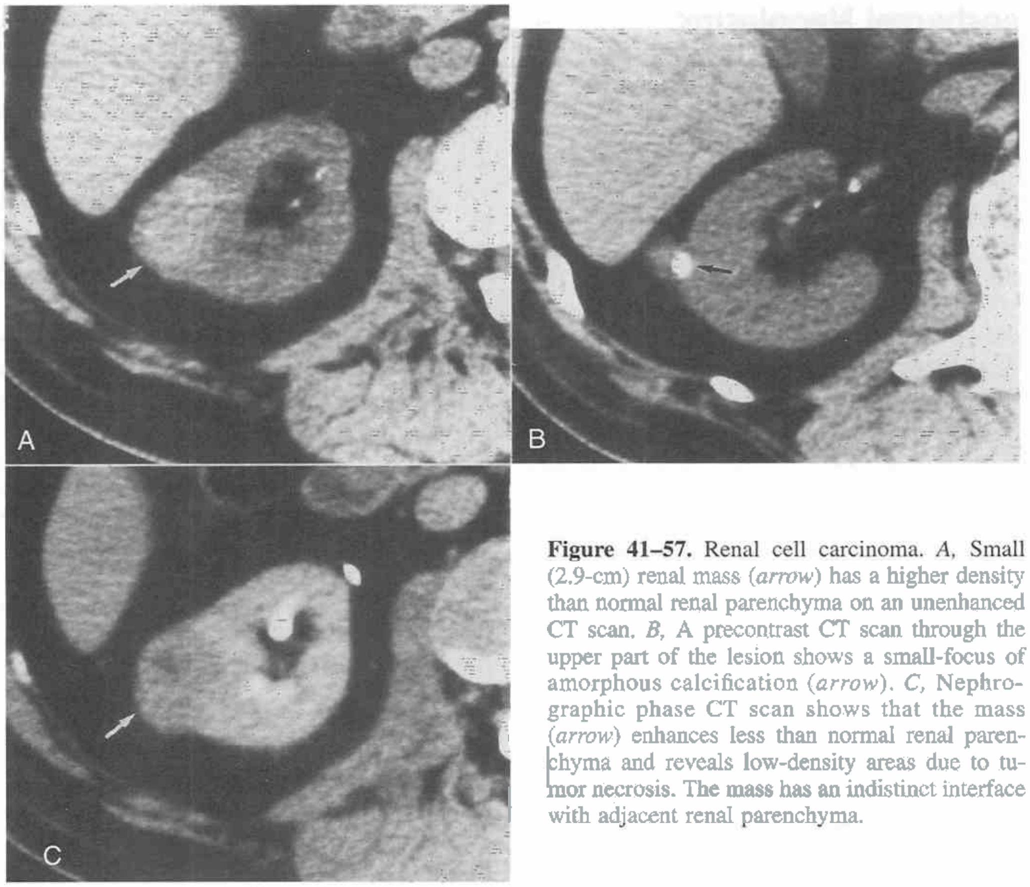

Figure 41–57. Renal cell carcinoma. *A,* Small (2.9-cm) renal mass (*arrow*) has a higher density than normal renal parenchyma on an unenhanced CT scan. *B,* A precontrast CT scan through the upper part of the lesion shows a small-focus of amorphous calcification (*arrow*). *C,* Nephrographic phase CT scan shows that the mass (*arrow*) enhances less than normal renal parenchyma and reveals low-density areas due to tumor necrosis. The mass has an indistinct interface with adjacent renal parenchyma.

lipid, hemorrhage, and necrosis.[209, 245] RCC may be hyperintense, hypointense, or isointense to normal renal parenchyma on both T1- and T2-weighted images. The use of intravenous gadolinium enhancement with fat suppression on T1-weighted imaging makes tumors much more conspicuous.[240, 241] Solid RCCs often show contrast enhancement and may reveal irregular, ill-defined margins and heterogeneity (Fig. 41–60). Tumor calcification is difficult to appreciate on MRI.

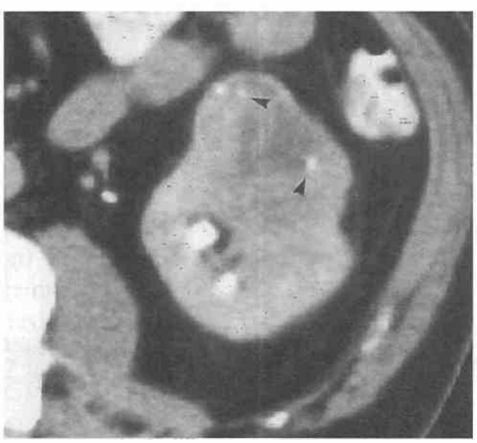

Figure 41–58. Renal cell carcinoma. Small foci of amorphous calcification (*arrowheads*) are present in a left renal carcinoma. The mass has an indistinct interface with adjacent renal parenchyma, and it is heterogeneous.

Staging of Renal Cell Carcinoma

The prognosis of patients with RCC depends mainly on histologic tumor grade and the anatomic extent or stage of the disease when first seen. RCC is most commonly staged according to the system proposed by Robson and colleagues[221]; alternatively, the TNM classification may be used (Table 41–1). In the Robson system, stage I RCC consists of tumor confined within the renal capsule, stage II of perinephric extension, including the ipsilateral adrenal

Figure 41–59. Renal cell carcinoma. Left renal carcinoma (*arrows*) shows peripheral curvilinear calcification. The right kidney is small because of renal artery stenosis.

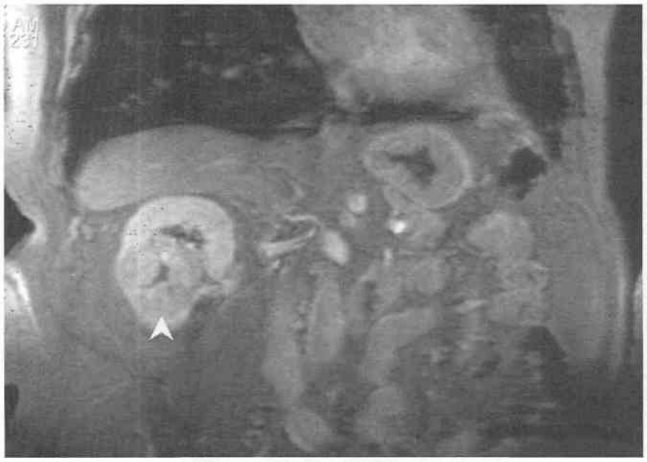

Figure 41–60. Gadolinium-enhanced MR image of renal cell carcinoma. Coronal (T1-weighted and fat-suppressed sequence with gadolinium) image in the nephrographic phase demonstrates a mass that enhances less than the adjoining renal parenchyma in the midpole of the right kidney.

gland, stage IIIA of venous invasion (renal vein that may extend into the inferior vena cava), stage IIIB of regional lymph node metastases, and stage IIIC of both venous tumor extension and regional lymph node metastases. Stage IVA neoplasms extend through the Gerota's fascia to involve adjacent organs, and stage IVB neoplasms have distant metastases.

Radiologic staging of RCC has an important influence on management. Small stage I neoplasms (<3 cm) are managed by partial nephrectomy in many institutions (Fig. 41–61).[209] A radical nephrectomy is usually required for stage II tumors. The operation includes removal of the kidney, adrenal gland, perirenal fat, and Gerota's fascia with or without a regional lymph node dissection.[199] Lymphadenectomy is commonly employed, but its effectiveness has not been definitively proved. Stage III tumors are also managed with radical nephrectomy with extension of surgery to remove the entire renal vein and caval thrombus and a portion of the vena cava as necessary.[101] Preoperative detection of venous tumor thrombus is important, because the surgical approach changes according to the cephalad extent of the tumor extension into the inferior vena cava.[190] Treatment of stage IV RCC differs from center to center. Almost all cases are incurable. Tumor embolization, external-beam irradiation, and nephrectomy can aid in the palliation of symptoms due to the primary tumor or to related ectopic hormone production. The main chemotherapeutic agents in use are interleukin-2 and interferon alfa.[189, 288]

CT is the single most effective modality for staging RCC, with an overall accuracy of about 90%.[10, 61] CT and MRI achieve approximately equal accuracy in the local staging of RCC.[10] Perinephric invasion is suggested by a perinephric soft tissue mass at least 1 cm in diameter (Fig. 41–62), but lesser degrees of perinephric involvement are difficult to diagnose with CT (Fig. 41–63).[111, 133] Perinephric soft-tissue stranding is an unreliable indicator of perinephric tumor invasion. Venous tumor invasion can be

Table 41–1. Staging Systems for Renal Cell Carcinoma and Their CT Criteria

Tumor Position	Robson Stage	TNM Class	CT Findings	CT Pitfalls
Confined within renal capsule	I	...	Soft tissue mass enhances less than normal renal parenchyma; central necrosis in large renal cell carcinoma	...
Small (<7 cm diameter)	...	T1	...	...
Large (≥7 cm diameter)	...	T2	...	...
Spread to perinephric fat	II	T3a	Perinephric stranding; perinephric collateral vessels	Not reliable or specific; found in 50% of T1 and T2 tumors; false-negative if spread is microscopic
			Soft tissue mass in perinephric space	Specific, not sensitive in 45%–50% of cases
Venous thrombus	IIIA	...	Filling defect within a distended vein; direct continuity of thrombus with primary mass; IV contrast enhancement indicates tumor thrombus; collateral veins	False-negative: right renal vein and IVC obscured by large renal cell carcinoma; false-negative: enhancing thrombus obscured; false-positive: venous enlargement due to increased flow; false-positive: streaming of unopacified blood in IVC (perform delayed scanning)
Renal vein only	...	T3b	...	...
IVC infradiaphragmatic	...	T3c	...	...
IVC supradiaphragmatic	...	T4b	...	...
Regional lymph node metastases	IIIB	N1–N3	Lymph nodes 1 cm in diameter or larger	False-negative rate: 4%; false-positive: enlarged inflammatory nodes
Direct invasion of adjacent organs	IVA	T4a	Obliteration of normal soft tissue planes between tumor and adjacent organs	False-positive: partial volume averaging; false-positive: tumor adherent but not directly invading
Distant metastases	IVB	M1a–d	Metastases enhance with IV contrast material; hepatic metastases best in arterial phase	Hypervascular metastases may be obscured in portal venous phase
	...	N4	...	...

IV = intravenous; IVC = inferior vena cava.

With permission from Sheth S, Scatarige JC, Horton KM, et al: Current concepts in the diagnosis and management of renal cell carcinoma: Role of multidetector CT and three-dimensional CT. Radiographics 21(Spec No):S237–S254, 2001.

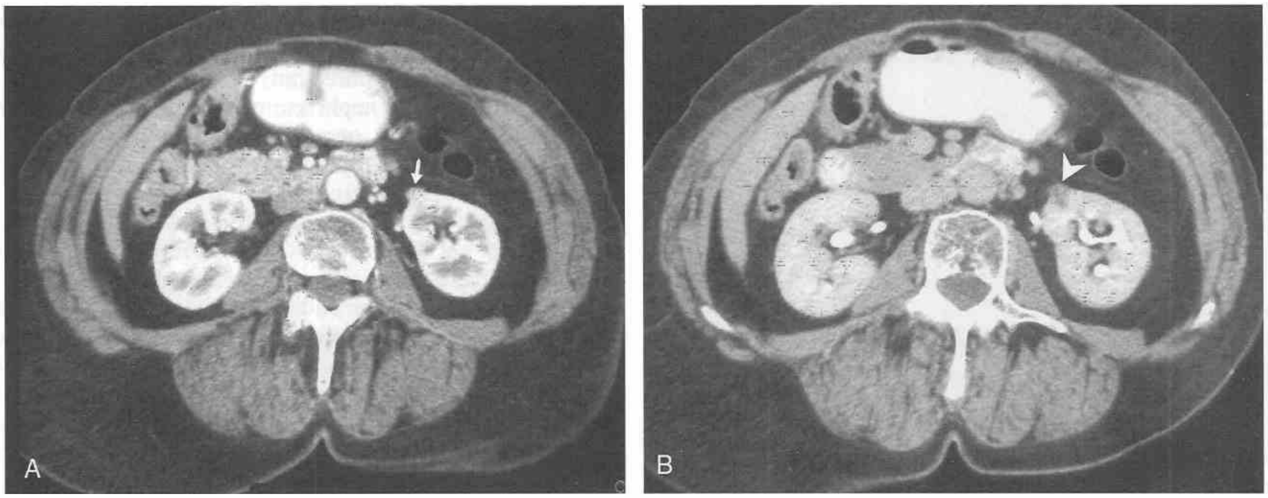

Figure 41–61. Renal cell carcinoma. *A,* Corticomedullary phase demonstrates a small exophytic mass in the midpole of the left kidney, isodense to the renal cortex (*arrow*). *B,* The nephrographic phase demonstrates that the mass (*arrowhead*) enhances less than the renal parenchyma. The patient underwent partial nephrectomy.

definitely diagnosed on CT only if there is identifiable thrombus in the renal vein (Figs. 41–64 and 41–65) or inferior vena cava (see Fig. 41–65) with or without venous enlargement.[302] Ipsilateral renal vein enlargement on CT without identifiable tumor thrombus is not a reliable sign of venous tumor extension (Fig. 41–66). Although such enlargement may reflect the presence of tumor thrombus, it more frequently results from increased blood flow due to a hypervascular tumor (see Fig. 41–66).[302] Errors in diagnosis of venous tumor extension on CT often occur when large right-sided tumors cause notable distortion of the ipsilateral renal vein and inferior vena cava.[111, 152] Tumor thrombus is distinguished from a bland thrombus by the former's heterogeneous enhancement on corticomedullary phase and continuity with the primary tumor.[244, 298]

MRI is superior in detecting venous tumor involvement and its extent and is a suitable alternative when CT findings

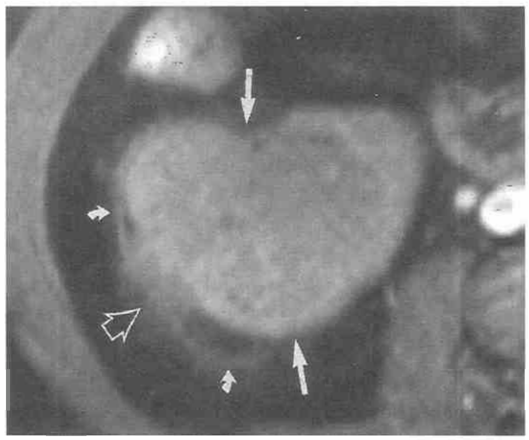

Figure 41–63. Renal cell carcinoma with early perinephric extension. Unenhanced fat-suppressed T1-weighted MR image (TR = 600 msec, TE = 15 msec) shows a large neoplasm (*straight arrows*) in the lower pole of the right kidney. There are early extension into the perinephric fat (*open arrow*) and associated renal fascial thickening (*curved arrows*).

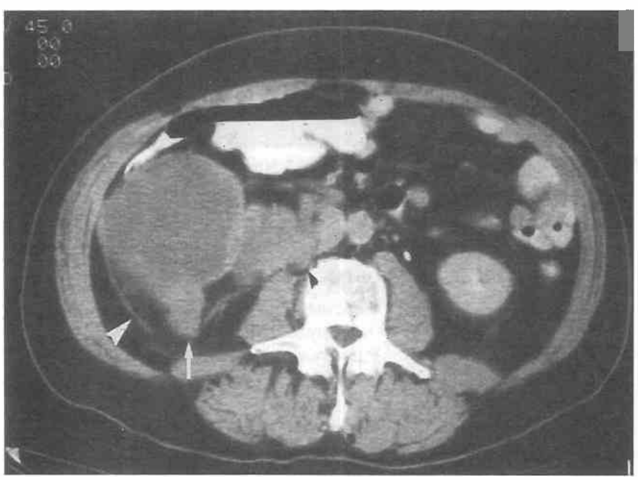

Figure 41–62. Renal cell carcinoma. A right-sided tumor has invaded the perinephric fat posteriorly (*arrow*) and medially (*black arrowhead*). The medial perinephric mass indents the inferior vena cava. The renal fascia (*white arrowhead*) is thickened.

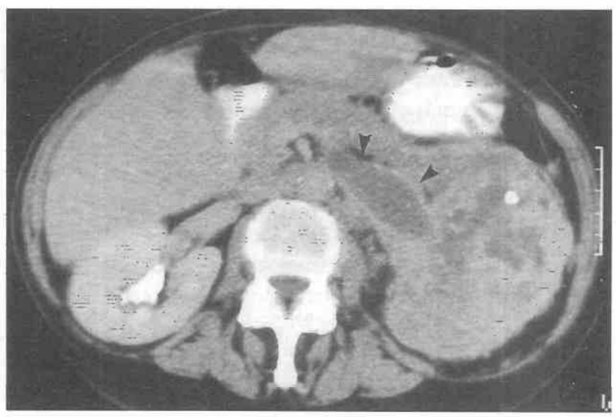

Figure 41–64. Left renal cell carcinoma with venous extension. The proximal part of the left renal vein is enlarged (*arrowheads*) and is occupied by low-density tumor.

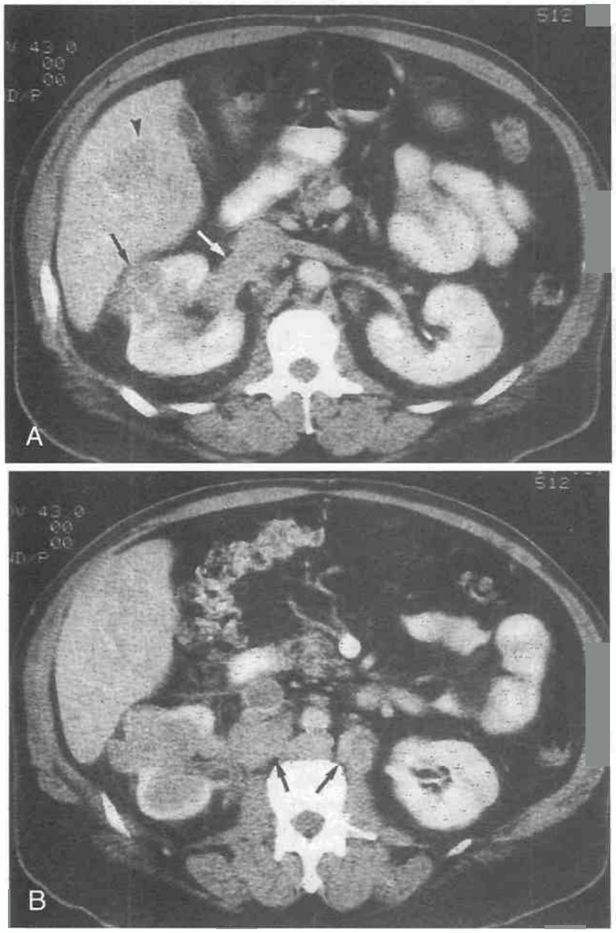

Figure 41–65. Renal cell carcinoma with venous extension and regional lymph node metastases. *A,* Contrast-enhanced CT scan shows a right renal mass (*black arrow*). The right renal vein (*white arrow*) is enlarged and occupied by tumor, which has also extended into the inferior vena cava. There is a metastasis in the right lobe of the liver. *B,* Multiple enlarged, central retroperitoneal lymph nodes (*arrows*) were due to metastatic disease.

are indeterminate (see Figs. 41–66 and 41–67). Tumor thrombus in the renal vein and vena cava may be suspected on T1- and T2-weighted conventional imaging if the signal void of flowing blood is replaced by relatively high signal which is due to tumor thrombus (Fig. 41–68). Tumor thrombus has signal intensity similar to that of the primary neoplasm (see Fig. 41–68). Gradient-echo images are also useful for detecting venous tumor extension.[78, 225] On such images, flowing blood has significantly increased signal intensity and appears white, whereas tumor thrombus has medium signal intensity and appears as an intravenous filling defect (Fig. 41–69).[78, 225] MR angiographic 2D or 3D gradient-echo sequences with gadolinium enhancement are most widely used. The 3D slab is centered over the renal vessels in coronal plane.[209] Sagittal or coronal MRI accurately evaluates the superior extent of vena caval thrombus relative to the diaphragm, hepatic veins, and right atrium.[91, 225] The sensitivity of MRI has been reported at 90% for detection of inferior vena caval thrombus, compared with 79% for CT (Fig. 41–70).[115]

Regional lymph nodes are considered to be involved by tumor if they are at least 1 cm in diameter in the short axis. However, lymph nodes may be 1 to 2 cm in diameter because of reactive hyperplasia.[111] Lymph nodes larger than 2 cm in size are usually due to metastases (see Fig. 41–65).[111, 152] Adjacent organ invasion is diagnosed only if there is enlargement, density change, or both, of an adjacent structure (Fig. 41–71). The loss of a fat plane between the tumor and an adjacent organ is not reliable evidence of tumor invasion (see Fig. 41–71).[111] RCC most commonly metastasizes to the lungs and mediastinum, bones, and liver (see Fig. 41–65). Less common sites are the adrenal glands, kidney, brain, pancreas, mesentery, and abdominal

Postnephrectomy Evaluation. Recurrence of neoplasm in the renal bed occurs in about 5% of patients after radical nephrectomy, as detected on follow-up CT. Patients with large, invasive tumors have a higher risk of local recurrence than those with small, early-stage tumors.[89] Renal bed recurrence is most likely within 2 years of nephrectomy.[290] The liver, ascending colon, second part of duode-

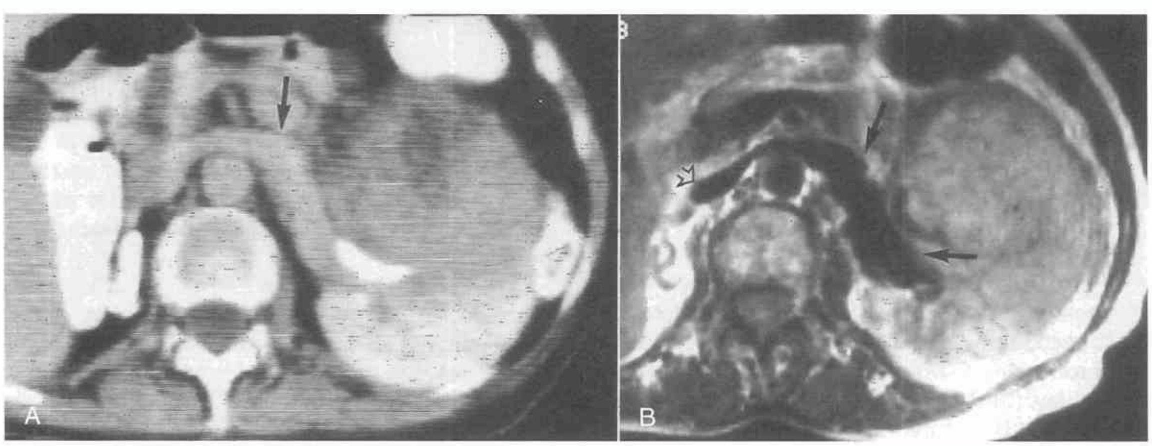

Figure 41–66. Left renal cell carcinoma with renal vein enlargement (*arrow*) on contrast-enhanced CT scan (*A*). The right kidney is atrophic. On MRI (*B*) (spin-echo, TR = 2100 msec, TE = 30 msec), the [redacted] renal v[redacted] (*arrows*) is enlarged but shows a normal signal void, indicating that venous enlargement is probably due to increased blood flow rather than tumor extension. The inferior vena cava (*open arrow*) is also normal.

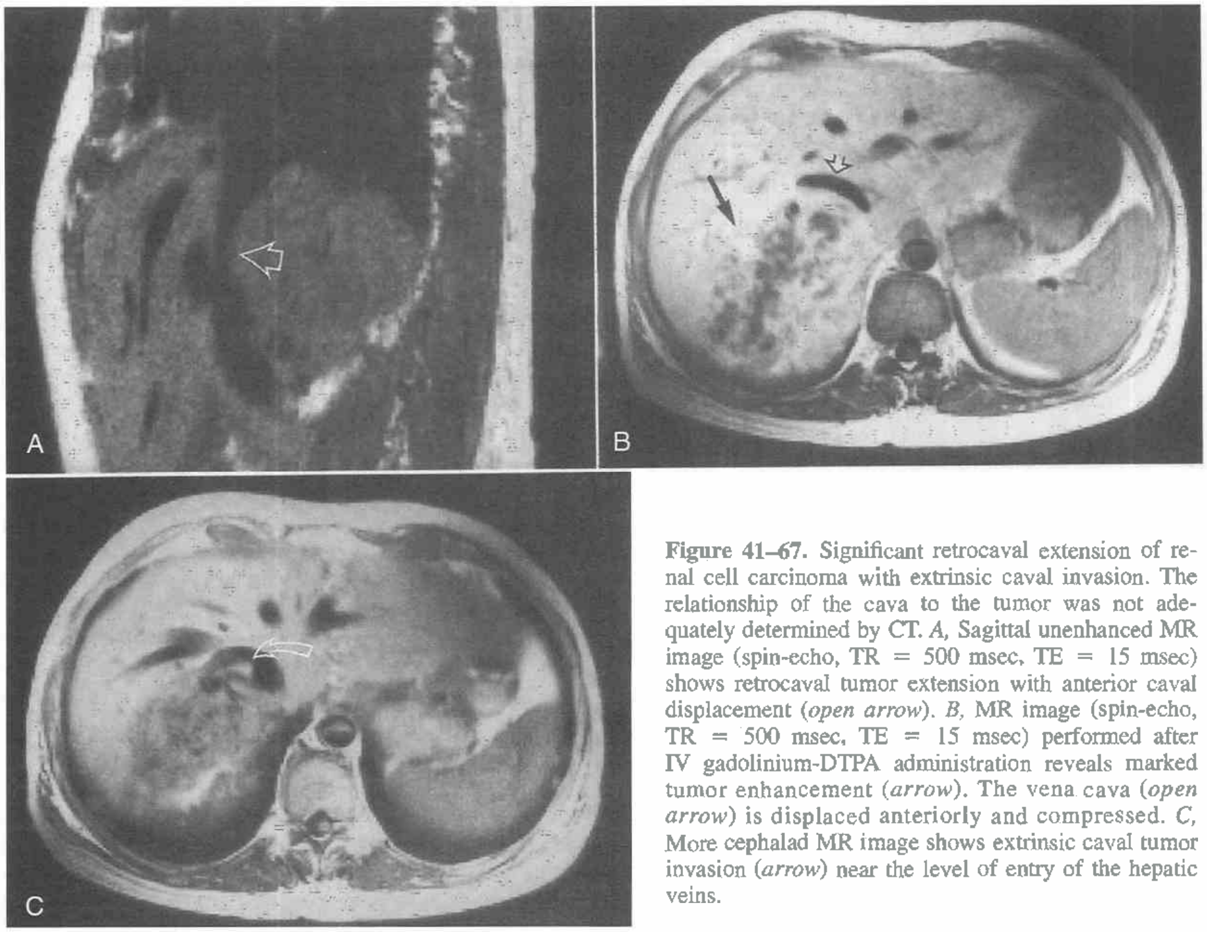

Figure 41–67. Significant retrocaval extension of renal cell carcinoma with extrinsic caval invasion. The relationship of the cava to the tumor was not adequately determined by CT. *A,* Sagittal unenhanced MR image (spin-echo, TR = 500 msec, TE = 15 msec) shows retrocaval tumor extension with anterior caval displacement (*open arrow*). *B,* MR image (spin-echo, TR = 500 msec, TE = 15 msec) performed after IV gadolinium-DTPA administration reveals marked tumor enhancement (*arrow*). The vena cava (*open arrow*) is displaced anteriorly and compressed. *C,* More cephalad MR image shows extrinsic caval tumor invasion (*arrow*) near the level of entry of the hepatic veins.

num, pancreatic head, and small bowel migrate into the right renal fossa; the pancreatic tail, spleen, and large and small bowel migrate into the left renal fossa. Interpretational errors can be avoided in patients who have undergone nephrectomy by ensuring adequate bowel opacification with oral contrast medium. Postoperative scarring in the renal fossa is distinguished from neoplasm recurrence if the area shows no change on serial CT examinations.[4]

Local recurrence of neoplasms may also be suggested by enlargement or irregularity of the psoas muscle on the side of the nephrectomy (Fig. 41–72), although this finding may also be caused by postoperative scarring.[15] In all patients undergoing radical nephrectomy or partial nephrectomy for RCC, a baseline postoperative CT scan of the abdomen should be obtained, and CT scanning should be performed at regular intervals thereafter.

Partial Nephrectomy

Nephron-sparing surgery is the treatment of choice when radical nephrectomy would render the anephric patient with a subsequent need for dialysis.[244] Current accepted indications for nephron-sparing surgery are (1) RCC in a solitary functioning kidney, (2) RCC in a patient with compromised renal function, and (3) multiple bilateral tumors, which are common in VHLD and hereditary RCC.[209, 244] The most suitable lesion for nephron-sparing nephrectomy is smaller than 4 cm, polar, cortical, and far from the renal hilum and collecting system.[244]

Renal Medullary Carcinoma

Renal medullary carcinoma is a rare tumor of the kidney, first described by Davis and colleagues in 1995.[55] This tumor occurs exclusively in young black patients with sickle cell trait (HbSA and HbSC) but not sickle cell anemia.[32, 55] Affected patients range from 11 to 39 years in age.[55] Flank pain and hematuria are the most common presenting complaints.[286] The exact histologic origin of this tumor is controversial. It has been suggested that renal medullary carcinoma represents a particular aggressive form of collecting duct carcinoma.[256] Metastatic involvement of regional lymph nodes, liver, and lungs at presentation is common.[129]

Renal medullary carcinoma is thought to arise at the renal pelvis–mucosa interface. The tumor quickly grows to fill the renal pelvis and invade vascular and lymphatic structures. Intraparenchymal satellite nodules are frequently present.[160]

The radiologic appearance of renal medullary carcinoma is that of a prototypical infiltrative lesion. An ill-defined mass centered in the renal medulla with extension into the renal sinus and cortex is characteristic; caliectasis may be seen, and the reniform contour of the kidney is maintained (Fig. 41–73).[203] The tumors are heterogeneous on ultrasonography and contrast-enhanced CT, reflecting the characteristic tumor necrosis.[51] The prognosis is extremely poor, with advanced disease at the time of diagnosis. The tumor responds poorly to chemotherapy or radiation therapy, with

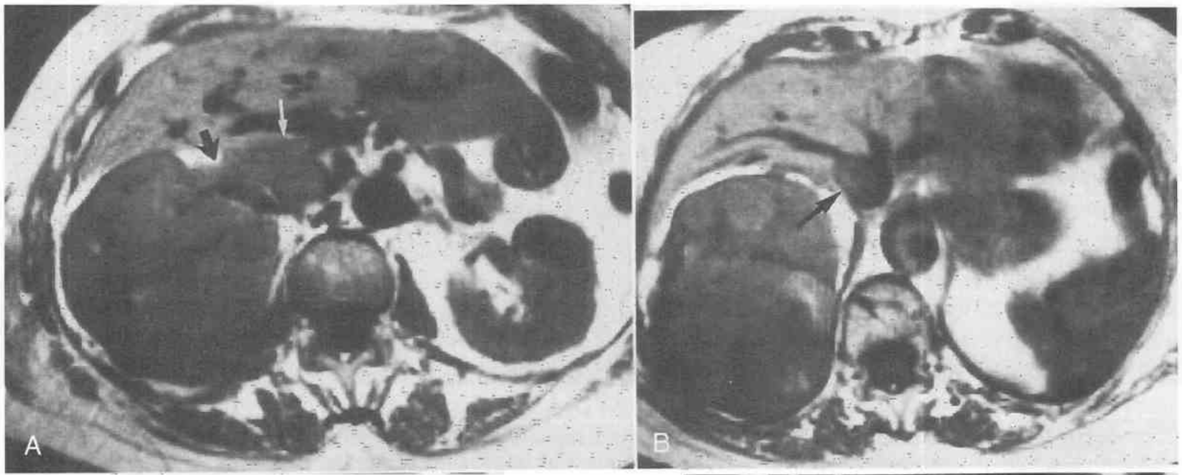

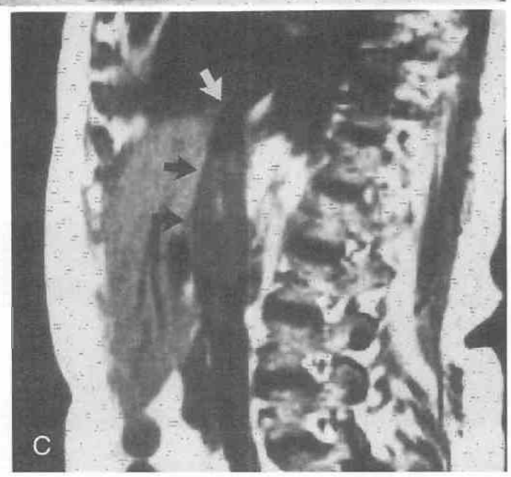

Figure 41–68. Inferior vena caval extension of right renal cell carcinoma. *A*, Unenhanced MR image (spin-echo, TR = 500 msec, TE = 17 msec) shows neoplasm extension into the right renal vein (*black arrow*) and the inferior vena cava (*white arrow*). The venous tumor has a signal intensity similar to that of the primary neoplasm. *B*, More cephalad MR image shows intracaval tumor (*arrow*) at the level where the three hepatic veins join the cava. *C*, Sagittal MR image shows intracaval tumor (*black arrows*). The supradiaphragmatic part of the cava (*white arrow*) is not affected.

Figure 41–69. Inferior vena caval extension of left renal cell carcinoma. A gradient-echo MR image (TR = 60 msec, TE = 12 msec, flip angle = 60°) shows tumor extension along the left renal vein (*arrow*) and into the inferior vena cava. Flowing blood in the cava appears white and the tumor is shown as a filling defect (*arrowhead*). (Courtesy of Richard L. Ehman, M.D., Rochester, Minn.)

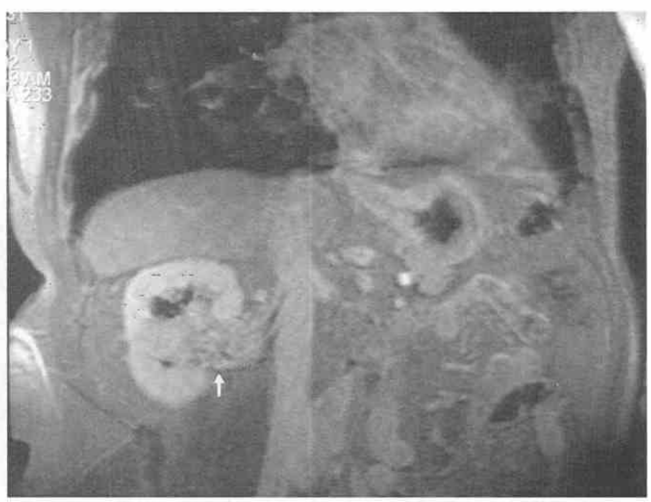

Figure 41–70. MR image obtained after gadolinium enhancement, in the same patient shown in Figure 41–62, demonstrates enlarged renal vein with enhancement (*arrow*). At surgery, the enlargement was confirmed to be tumor extension into the renal vein.

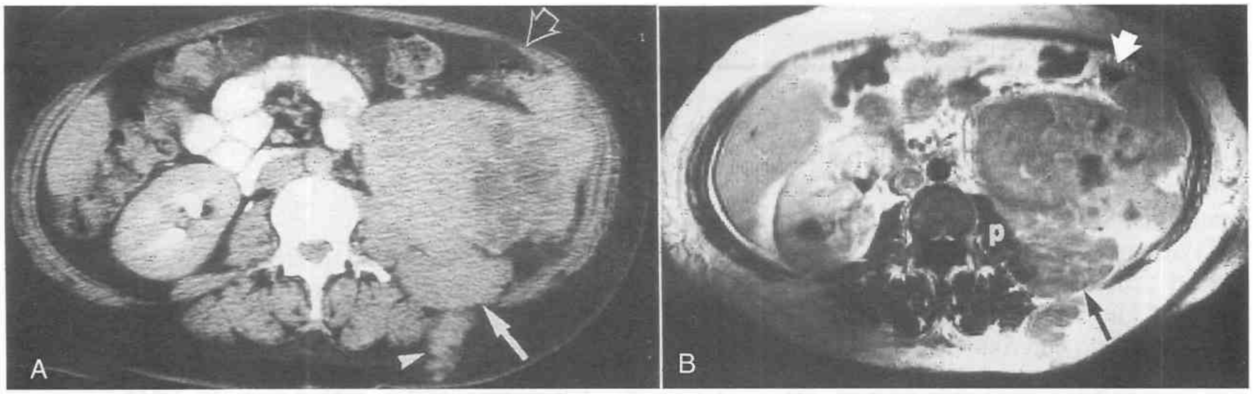

Figure 41–71. Left renal cell carcinoma with extension beyond the renal fascia. *A,* The tumor invades the abdominal wall in the region of the left quadratus lumborum muscle (*arrow*). Tumor has grown along a needle biopsy track in the subcutaneous tissues (*arrowhead*). Tumor invasion of the descending colon (*open arrow*) was confirmed at surgery. Although the neoplasm abuts the left psoas muscle, there was no actual muscle invasion. *B,* Contrast-enhanced MR image (spin-echo, TR = 500 msec, TE = 15 msec) reveals that the neoplasm does not invade the psoas muscle (p). However, tumor has invaded the abdominal wall (*long arrow*) and the colon (*short arrow*).

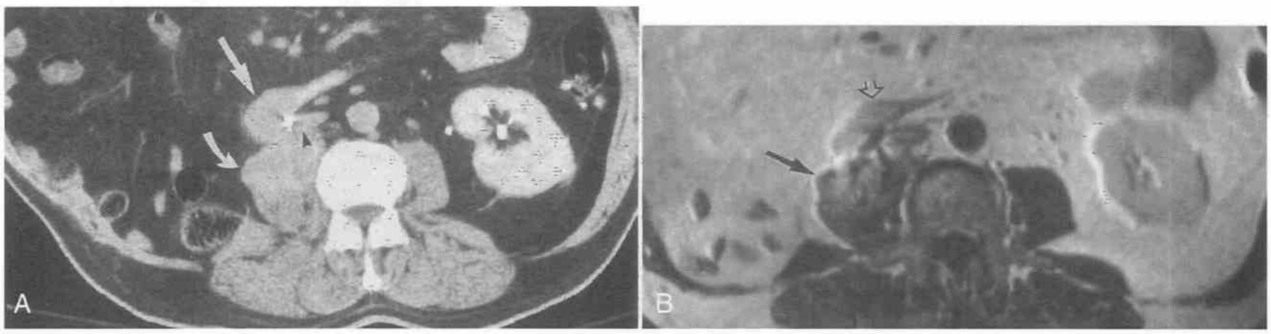

Figure 41–72. Local recurrence of renal cell carcinoma 7 years after nephrectomy for right renal cell carcinoma. Patient presented with upper gastrointestinal bleeding. *A,* An enhancing mass (*curved arrow*) causes enlargement of the right psoas muscle. The third part of the duodenum (*straight arrow*) and the inferior vena cava (*arrowhead*) are adherent to the mass. *B,* MRI (spin-echo, TR = 500 msec, TE = 15 msec) performed after IV injection of gadolinium-DTPA shows an enhancing mass (*arrow*) involving the right psoas muscle. Endoscopy with biopsy showed clear cell carcinoma invading the third part of the duodenum (*open arrow*).

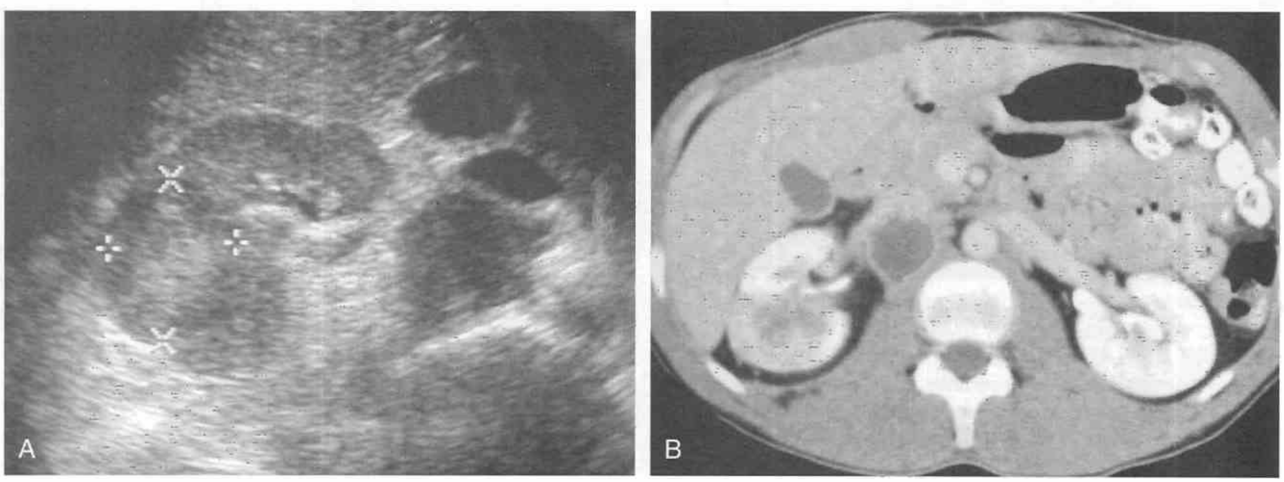

Figure 41–73. Medullary carcinoma. Transverse oblique view *(A)* of ri[redacted]idney s[redacted] an upper pole hyperechoic mass. *(B)* Contrast-enhanced axial CT shows heterogeneous enhancement of mass. (Courtesy of Pickhardt PJ: Abdominal Imaging, 1998.)

a mean survival of 15 weeks from diagnosis. The constellation of renal medullary mass, black race, sickle cell trait, and hemoglobin SC disease suggests the diagnosis.[160]

Collecting Duct Carcinoma

Collecting duct carcinoma (Bellini duct carcinoma), originating from the collecting ducts of the kidney accounts for only 1% of renal carcinomas.[118] The age at presentation ranges from 16 to 62 years with median age of 43 years.[60] Hematuria is the most common presentation and most patients have metastases at presentation.[60, 169] Collecting duct tumors demonstrate aggressive behavior; a maximum survival of approximately 2 years is reported.[60, 124, 169]

CT demonstrates renal medullary involvement with an infiltrative appearance and renal sinus encroachment. The reniform contour of the kidney is preserved except when an expansile component is present (Fig. 41–74). Collecting duct carcinomas are hypointense on T2-weighted images and hypovascular on angiography.[201–203]

Wilms' Tumor. Wilms' tumor accounts for 87% of pediatric renal neoplasms.[114, 220] Approximately 80% of children with this tumor present between 1 and 5 years of age, with the peak incidence between 3 and 4 years.[31] Occasional cases are encountered during adult life.[79] Most patients present because of an enlarging abdominal mass.[104] Less common presenting symptoms include abdominal pain, fever, and microscopic or gross hematuria.[86] The lung

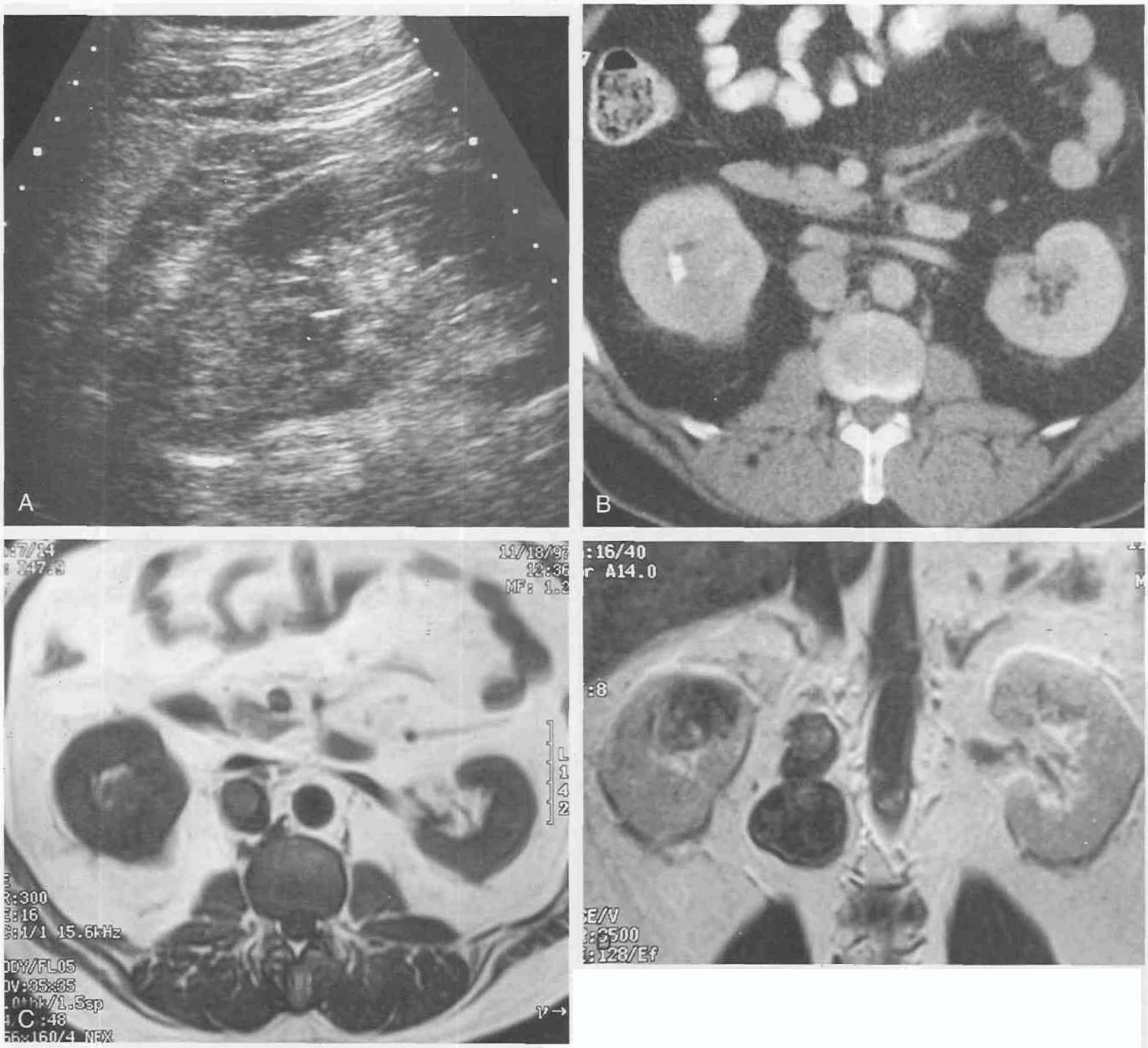

Figure 41–74. Collecting duct carcino[redacted], Sagittal view of right kidney shows a hyperechoic mass in the upper pole. *B,* Axial contrast-enhanced CT scan demonstrates low-attenuating right renal mass that abuts the renal sinus. Axial T1-weighted image (*C*) and coronal T2-weighted image (*D*) reveal the mass to be isointense to renal parenchyma on T1-weighted and hypointense on T2-weighted sequences relative to the renal parenchyma. (From Pickhardt PJ, Lonergan GJ, Davis CJ, et al: From the Archives of the AFIP: Infiltrative renal lesions: Radiologic-pathologic correlation. Radiographics 20:215–243, 2000.)

is the most frequent site of metastatic disease, and the liver is less frequently involved.

With appropriate therapy about 95% of patients with Wilms' tumor can be cured.[291] Tumor histology and stage are the most useful predictors of patient outcome and help determine the nature of therapy. Although all Wilms' tumors require surgical resection, preoperative imaging helps determine tumor stage and resectability, therefore influencing decisions about preoperative chemotherapy or radiation therapy.[47, 291] Ultrasonography is the most common method for initial diagnosis of Wilms' tumor. However, CT and MRI have been found to be more accurate than ultrasonography in tumor staging.[47, 246] Chest and abdominal CT may be performed during the same examination, thereby determining the presence or absence of lung metastases.[86]

On CT, a Wilms' tumor usually appears as a large, spherical, intrarenal mass, very often with a well-defined rim of compressed renal parenchyma or pseudocapsule surrounding it (Fig. 41–75). Tumors that arise in the peripheral cortex may grow in an exophytic manner with most of the tumor mass outside the kidney.[79] The tumor is less dense than normal renal parenchyma on contrast-enhanced CT scans; areas of low attenuation coincide with tumor necrosis, fat deposition, or both (Fig. 41–76).[86] About 13% of Wilms' tumors contain calcifications as seen on unenhanced CT scans.[79, 86] About 10% of patients show poor or absent function of the involved kidney because of either venous tumor extension, compression of the collecting system, or extensive tumor infiltration throughout the kidney.

Perinephric tumor extension thickens the renal fascia and obliterates the perinephric fat, but subtle perinephric extension may be missed on CT. Central retroperitoneal adenopathy may be detected on CT, although the distinction between nodes enlarged as a result of metastases and those enlarged because of reactive changes is usually not possible.[47, 246] Renal vein and inferior vena caval tumor extension is best shown after an intravenous bolus injection of contrast medium. The thrombus may be seen as a low-density intraluminal filling defect. CT may also identify bilateral Wilms' tumors (Fig. 41–77), present in about 10% of patients,[160] and liver and pulmonary metastases.[47, 216]

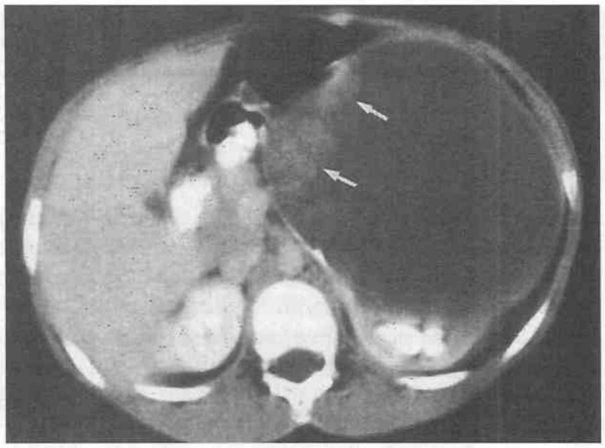

Figure 41–76. Wilms' tumor of left kidney with extensive necrosis. A contrast-enhanced CT scan shows that the tumor has a mainly fluid density. Solid and enhancing tumor elements are present medially (*arrows*).

On MRI, Wilms' tumor appears as a large, well-defined mass with relatively distinct margins (Fig. 41–78). It has low signal intensity on T1-weighted images and high signal intensity on T2-weighted images.[160] The tumor often appears heterogeneous on both T1- and T2-weighted images. Although MRI is sensitive for detecting regional lymph node enlargement, it cannot predict the cause of the enlargement.[246] Currently, CT and MRI appear equivalent for staging Wilms' tumor. However, MRI shows venous extension better than CT (see Fig. 41–78).[246]

Nephroblastomatosis. Nephrogenesis is normally complete by 34 to 35 weeks of gestation. However, metanephric blastema may persist into infancy and childhood. Foci of persistent metanephric tissue are designated as nephrogenic "rests." The presence of multiple nephrogenic rests is termed *nephroblastomatosis.* There is wide acceptance of nephroblastomatosis as a precursor lesion to Wilms' tumor. Thirty percent to 34% of Wilms' tumors arise from these

Figure 41–75. A large heterogeneous Wilms' tumor is present in the left kidney. The residual renal parenchyma is displaced medially (*arrows*).

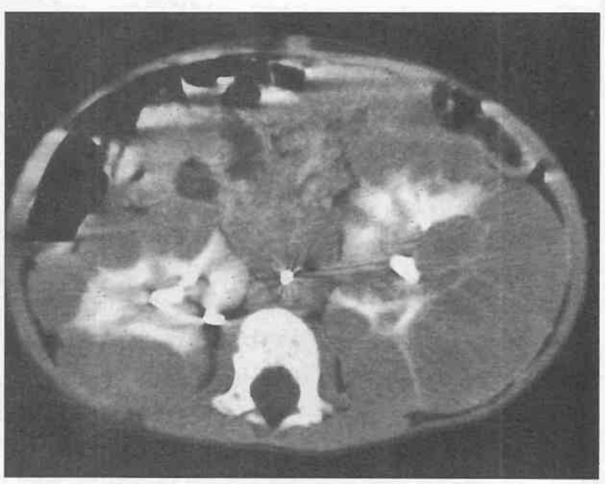

Figure 41–77. Multicentric and bilateral Wilms' tumors. The tumors have a low density, and they compress residual enhancing renal tissue.

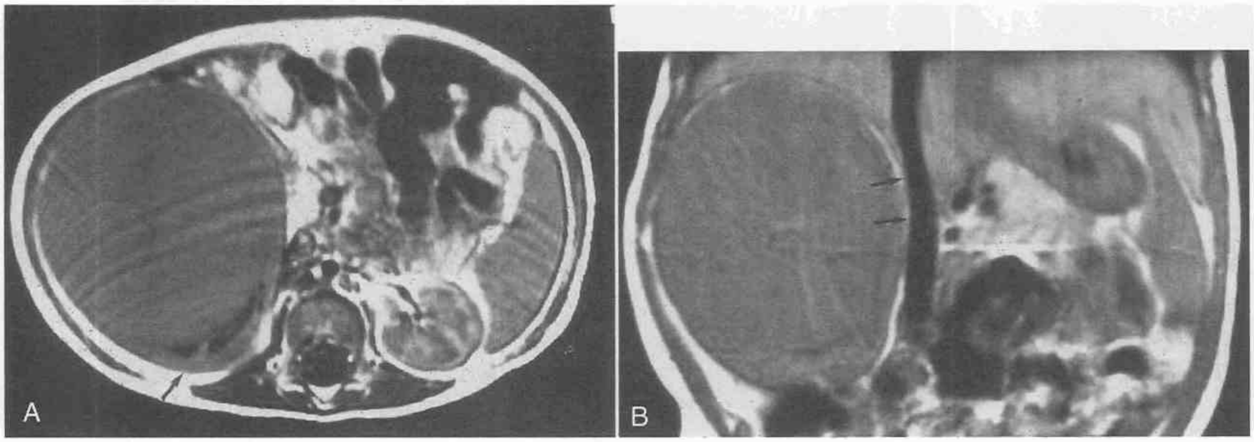

Figure 41–78. Wilms' tumor of right kidney shown by MRI (spin-echo, TR = 600 msec, TE = 15 msec). *A,* An axial image reveals that the mass is well defined and displaces normal renal tissue (*arrow*) posteriorly. *B,* A coronal image shows that the mass indents the inferior vena cava (*arrows*), but does not extend to the vena cava.

rests. Approximately 35% of patients with diffuse nephroblastomatosis eventually have Wilms tumor.[159] Hyperplastic nephrogenic rests are macroscopic and plaquelike (Fig. 41–79). Any macroscopic nephrogenic rest that is nodular and enlarges over time is considered neoplastic.[289] Nephroblastomatosis occurs most often in neonates and is characterized by multiple-bilateral subcapsular masses.[160]

CT is the technique of choice for detection of this disorder. On contrast-enhanced CT, in addition to nephromegaly, the kidney may show striate enhancement. The rests enhance less than adjacent normal parenchyma.[203] CT is particularly useful for evaluating the other kidney in the child with Wilms' tumor, for renal screening in children with syndromes associated with Wilms' tumor, and for follow-up evaluation for neoplastic changes in patients with known nephroblastomatosis.[75, 289] The hallmark of neoplastic transformation of a benign nephrogenic rest is enlargement on serial CT scans.[289]

On MRI, nephroblastomatosis tends to be hypointense to renal cortex on T1-weighted images and isointense to cortex on T2-weighted images.[95] Gadolinium enhancement adds to the conspicuity of these lesions, although contrast-enhanced studies have not been found superior to unenhanced studies for lesion detection.[86]

Renal Sarcoma. Primary renal sarcomas are rare (accounting for approximately 1% of malignant renal parenchymal tumors) mesenchymal tumors that generally have a poor prognosis. Subtypes of renal sarcoma include leiomyosarcoma, angiosarcoma, hemangiopericytoma, liposarcoma, rhabdomyosarcoma, fibrosarcoma, and osteosarcoma. The biologic behavior of the various types of sarcoma is highly variable.[203,257] Leiomyosarcoma is the most common renal sarcoma, accounting for about 58% of all sarcomas.[71] Hemangiopericytoma and liposarcoma each account for about 20% of renal sarcomas.[71] Renal rhabdomyosarcoma and osteogenic sarcoma occur rarely. Capsular localization, a feature of more than 50% of these tumors,[71] should suggest the diagnosis on CT (Figs. 41–80 and 41–

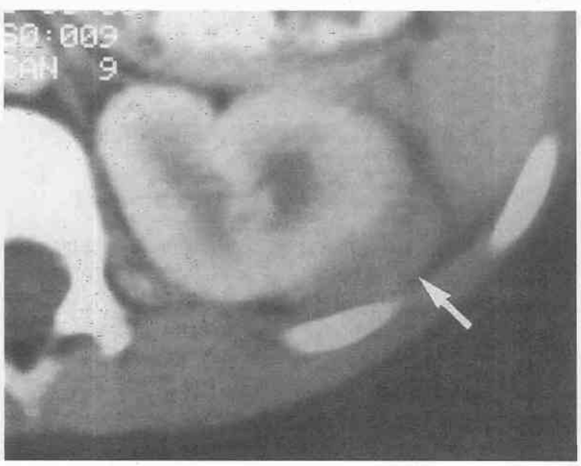

Figure 41–79. A hyperplastic intralobar nephrogenic rest presents as a low-density subcapsular mass (*arrow*) on a contrast-enhanced CT scan.

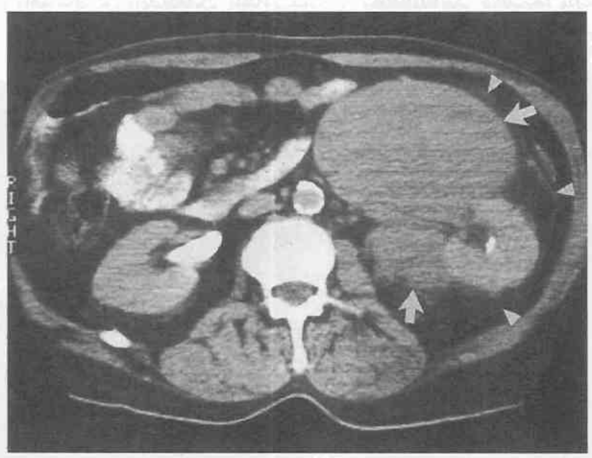

Figure 41–80. Undifferentiated liposarcoma (*arrows*) arising in the perinephric fat. The neoplasm is confined within the renal fascia (*arrowheads*). The left kidney is displaced laterally, but the tumor has not invaded the renal parenchyma.

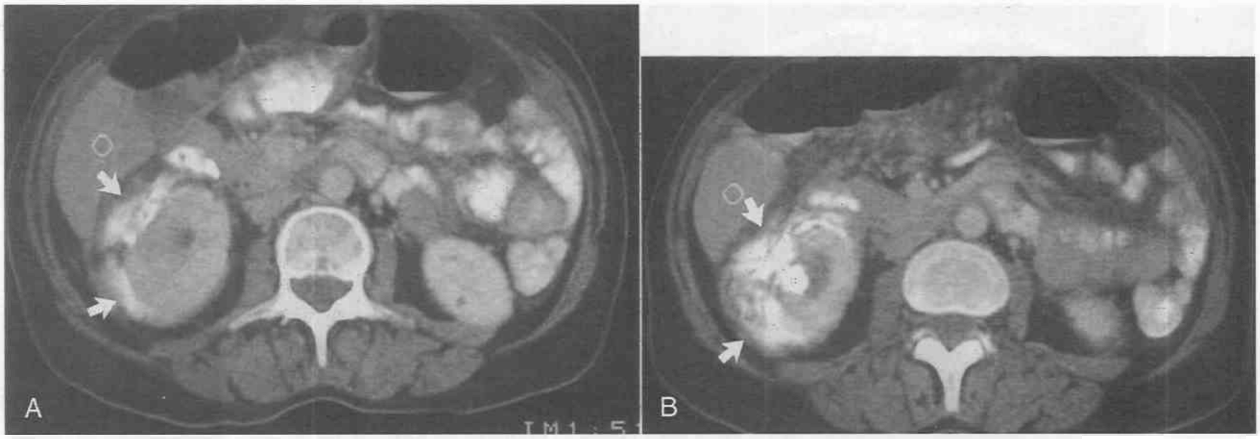

Figure 41–81. *A* and *B*, Renal osteosarcoma. A densely ossified mass (*arrows*) arises peripherally in the lower pole of the right kidney. (Courtesy of Clive Levine, M.D., Columbia, Mo.)

81). When these neoplasms arise in the renal parenchyma, however, they are indistinguishable from RCC on CT.

Renal liposarcomas usually arise in the renal capsule or perinephric fat (see Fig. 41–80).[71] On CT, liposarcomas cause compression without invasion of the renal parenchyma and show a variety of appearances correlating closely with their gross and histologic features.[137] Tumors containing a large amount of mature fat show negative attenuation values. Myxoid liposarcomas contain little mature fat, and their predominantly fluid and connective tissue composition results in attenuation values nearer those of water.[137] On CT, undifferentiated liposarcomas are indistinguishable from other types of sarcoma (see Fig. 41–80). The diagnosis of renal osteogenic sarcoma is suggested on CT by a peripherally located renal mass containing dense ossification (see Fig. 41–81).[297]

Renal Lymphoma

Renal involvement by lymphoma is usually secondary to systemic disease, because the kidney does not contain lymphoid tissue.[40, 203, 276] However, secondary renal involvement occurs commonly either from generalized hematogenous dissemination of lymphoma or by direct extension of retroperitoneal disease.[40] Bilateral renal involvement occurs more frequently, being present in 75% of all patients with lymphoma. Renal involvement occurs significantly more commonly in non-Hodgkin's lymphoma than in Hodgkin's disease.[276] Five CT patterns of renal lymphoma are as follows: 1) multiple renal masses, 2) solitary mass, 3) renal invasion from contiguous retroperitoneal disease, 4) perirenal disease, and 5) diffuse renal infiltration.[276]

With the extensive use of abdominal CT for lymphoma staging, renal lymphoma is now recognized on CT in about 8% of patients with lymphoma.[40] Multiple renal nodules are the most common CT manifestation of renal lymphoma, occurring in about 59% of cases (Fig. 41–82).[40, 217] The nodules range from 1 to 3 cm, are less dense than normal renal parenchyma on contrast-enhanced CT scans, and typically show a homogeneous appearance. As multiple renal nodules grow, coalesce, and replace nephrons, the kidneys are almost diffusely replaced by lymphoma (Fig. 41–83). However, the multinodular nature of the disease process usually remains apparent. In most patients, the renal arteries and veins remain patent despite tumor encasement, a finding that is characteristic for lymphoma.[276] Retroperitoneal lymph node enlargement is not visible on CT in a significant percentage of patients with renal lymphoma that

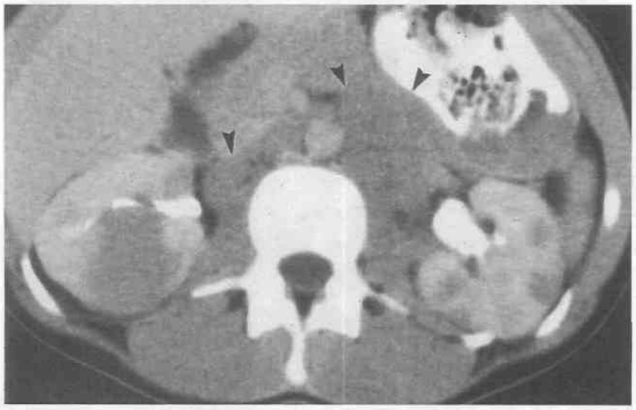

Figure 41–82. Non-Hodgkin's lymphoma with bilateral multiple renal masses. There is extensive retroperitoneal adenopathy (*arrowheads*).

Figure 41–83. Bilateral renal replacement and mild nephromegaly in non-Hodgkin's lymphoma. There is no enlargement of retroperitoneal lymph nodes.

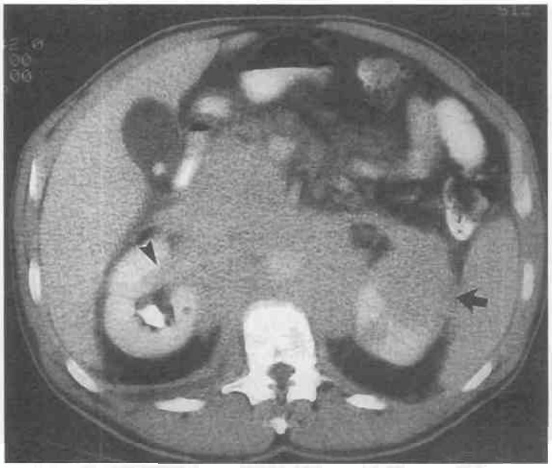

Figure 41–84. Renal involvement from retroperitoneal non-Hodgkin's lymphoma. There is extensive central retroperitoneal adenopathy causing lateral displacement of the kidneys. The upper pole of the left kidney (*arrow*) is invaded through the renal capsule. Tumor extends into the right kidney via the renal sinus (*arrowhead*).

is not due to direct spread of retroperitoneal tumor (see Fig. 41–83).[40, 217]

Renal involvement from retroperitoneal lymphoma commonly occurs either by invasion through the renal capsule or by extension through the renal sinus (Fig. 41–84). This pattern accounts for about 28% of patients with renal lymphoma. Retroperitoneal adenopathy is invariably present, and many patients show obstructive hydronephrosis. Rarely, a solitary mass in one kidney is the only CT manifestation of renal lymphoma (about 3% of cases) (Fig. 41–85). Some patients (about 10%) show a predominance of perinephric disease without extensive parenchymal or retroperitoneal disease (Fig. 41–86).

On MRI, renal lymphoma tends to be hypointense relative to the renal cortex on T1-weighted images and heterogeneously hypointense or isointense on T2-weighted images. Minimal enhancement is generally detected, although renal lymphoma enhances considerably less than normal renal parenchyma. MRI characteristics of treated lymphoma are variable.[40, 209]

Figure 41–85. Hodgkin's disease with solitary heterogeneous left renal mass.

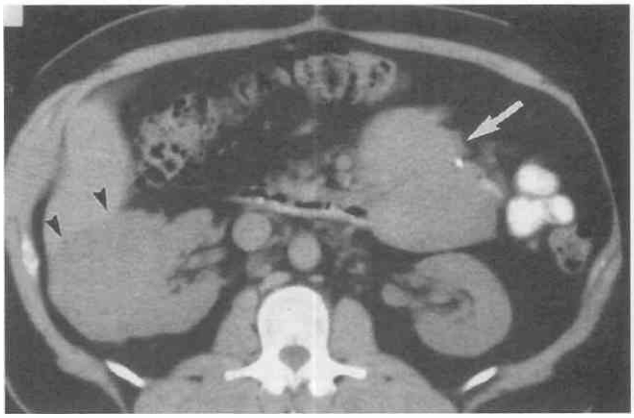

Figure 41–86. Right perinephric mass (*arrowheads*) shown on unenhanced CT scan in a patient with non-Hodgkin's lymphoma. A large nodal mass (*arrow*) involves the small bowel mesentery.

Metastases

The frequency of metastases to the kidney in patients with cancer is 7% to 13% in large autopsy series.[30, 196] The kidney is the fifth most common site of metastases in the body, after lung, liver, bone, and adrenals; most metastases reach the kidney via the hematogenous route.[175] The three neoplasms with the highest frequency of renal metastases are lung carcinoma, breast carcinoma, and carcinoma of the other kidney.

Renal metastases are usually discovered incidentally during abdominal CT performed for tumor staging. However, some patients have hematuria and flank pain.[175] The most common pattern on CT is that of multiple discrete bilateral lesions. Solitary exophytic metastases are more common in patients with colon cancer, and perinephric tumor extension is typical of melanoma (Fig. 41–87).[36] These lesions are best seen on contrast-enhanced CT scans.

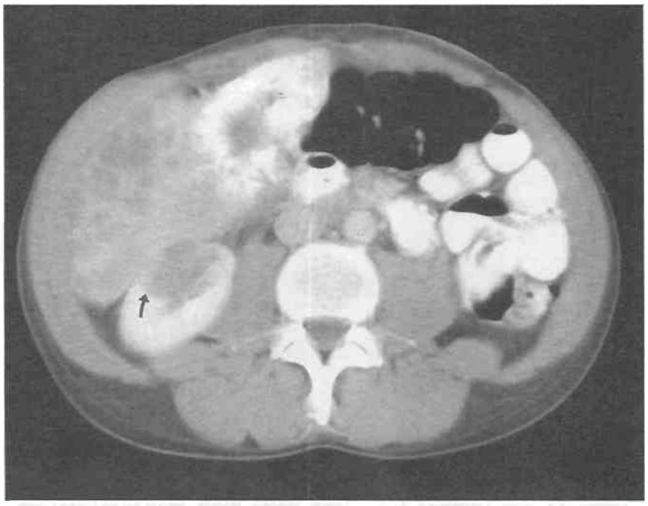

Figure 41–87. Renal metastases from colonic carcinoma. Axial contrasted-enhanced CT scan shows a low-attenuating mass with minimal enhancement in the inferior pole of right kidney (*arrow*). Multiple low-attenuating lesions are also seen in the liver, which are metastases from colonic carcinoma.

Figure 41–88. Left renal metastasis (*arrow*) and retrocrural adenopathy (*arrowhead*) in a patient with small cell lung cancer. A follow-up scan after 3 weeks of chemotherapy showed complete resolution of the renal mass and adenopathy.

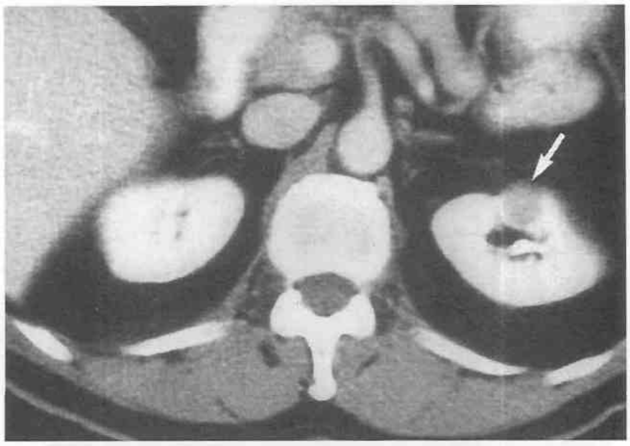

Figure 41–90. Small (1.8-cm) renal cell carcinoma (*arrow*) detected incidentally by CT.

Although metastases are usually homogeneous on CT, larger lesions may show central necrosis.[175] Occasionally, patients with metastases have solitary renal masses.[36] If the patient has other areas of metastatic disease and a current known primary neoplasm, such solitary renal lesions can usually be safely assumed to be metastases, and pathologic proof of their nature is unnecessary (Fig. 41–88).[36, 175] However, in the patient with no other metastases, it is difficult to determine whether the renal lesion is a synchronous RCC or a renal metastasis (Fig. 41–89). In these circumstances, further investigation is necessary, particularly if there has been an apparent remission of the primary neoplasm. Tissue sampling is usually necessary in such cases.

Benign Neoplasms

Adenoma. During the last decade, there has been a significant increase in detection of asymptomatic renal tumors 3 cm or less in diameter by sonography and CT (Fig. 41–90).[151, 283] Most such tumors are neoplasms of tubular origin. In the past, such lesions were often classified as renal adenomas, because they rarely metastasize. However,

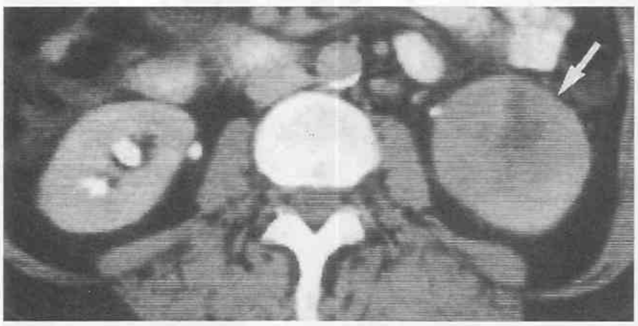

Figure 41–89. Solitary renal metastasis from squamous cell carcinoma of the lung. The patient underwent a left upper lobectomy. Two years later, he demonstrated left flank pain and hematuria. CT scan shows a heterogeneous left renal mass (*arrow*). No other lesions were found. A renal cell carcinoma was suspected, but percutaneous biopsy revealed metastatic squamous carcinoma.

serial imaging shows that they often gradually enlarge (Fig. 41–91)[19] and that even small tumors may metastasize (Fig. 41–92).[254] Indeed, such lesions are histologically indistinguishable from larger carcinomas more commonly encountered in the kidneys, and they often have histologic grades indicating a definite potential for malignant behavior. Accordingly, most investigators believe that these lesions should be regarded as carcinomas in an early stage of evolution and should not be classified as adenomas.[19, 151] On CT, these small renal tumors are usually well-defined and homogeneous in appearance (see Fig. 41–90).[151, 254] Less commonly, they show marginal irregularity, heterogeneity, or central calcification (see Fig. 41–57), findings that may suggest pathologically high-grade tumors.[26] These lesions are best managed with partial nephrectomy[262, 278] provided that the other kidney is normal.

Oncocytoma. The renal oncocytoma is a solid epithelial neoplasm with a generally benign course.[57] It represents between 10% and 15% of small (<3 cm) solid renal neoplasms.[223] They arise from proximal tubular epithelium (oncocyte) and range in size from 1.5 to 13 cm with a mean of 6.3 cm.[106]

On CT, oncocytomas typically are well-defined masses with smooth, rounded margins (Fig. 41–93).[53] Tumor calcification occurs rarely, and oncocytomas are sometimes multiple and bilateral.[46, 109] Small oncocytomas are usually homogeneous in appearance on contrast-enhanced CT scans, although they are occasionally heterogeneous because of the presence of central scars (Fig. 41–94). On CT, small oncocytomas are usually indistinguishable from slowly growing small RCCs that lack hemorrhage or necrosis.[53] A central, sharply defined stellate scar (Fig. 41–95) is present in 25% to 33% of large oncocytomas and strongly suggests the diagnosis.[213]

The classic angiographic findings for the oncocytoma are a spoke-wheel pattern, a homogeneous nephrogram, and a sharp, smooth rim. The finding of a homogeneous blush or a spoke-wheel pattern greatly increases the possibility of an oncocytoma, though an RCC may have any or all of the classic findings described for an oncocytoma.[287] However, CT criteria are usually poor discriminants for distinguishing between oncocytoma and RCC, regardless

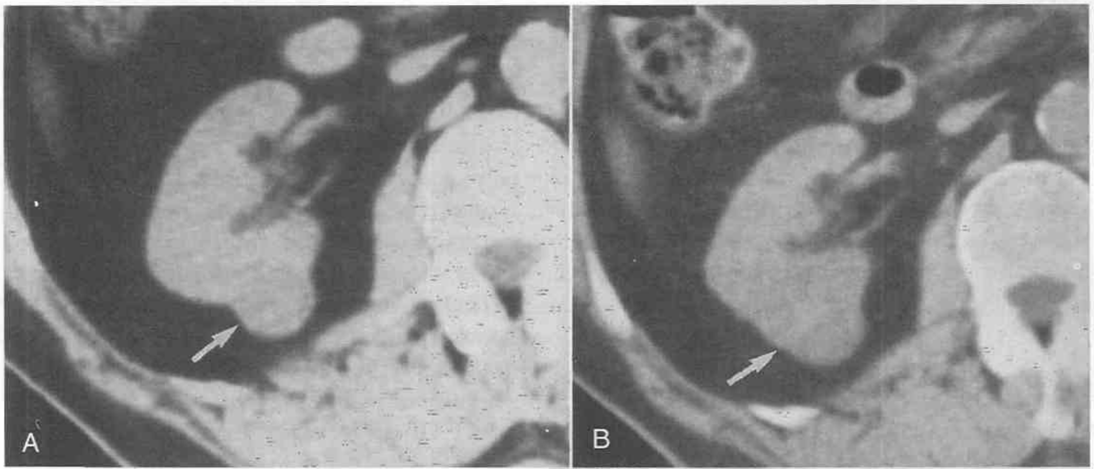
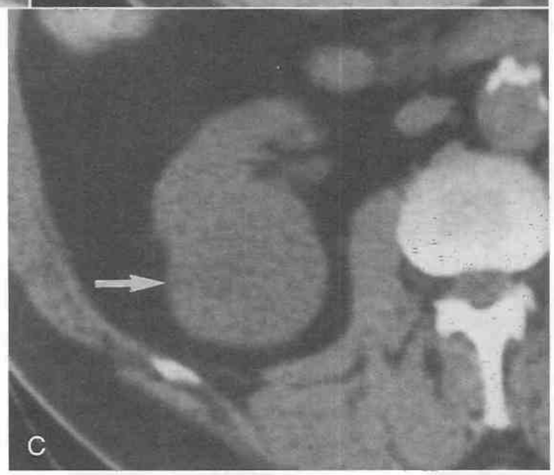

Figure 41–91. Progression of renal cell carcinoma shown by serial CT in a 70-year-old man who underwent bladder carcinoma resection 6 years previously. The patient initially refused surgery. *A,* Contrast-enhanced CT scan shows a 2.5-cm renal mass (*arrow*). *B,* Follow-up scan obtained 3 years later shows that the mass (*arrow*) has enlarged to 3.8 cm. *C,* Unenhanced CT scan obtained 2 years after *B* shows further enlargement of the mass (*arrow*), which measures 6.5 cm.

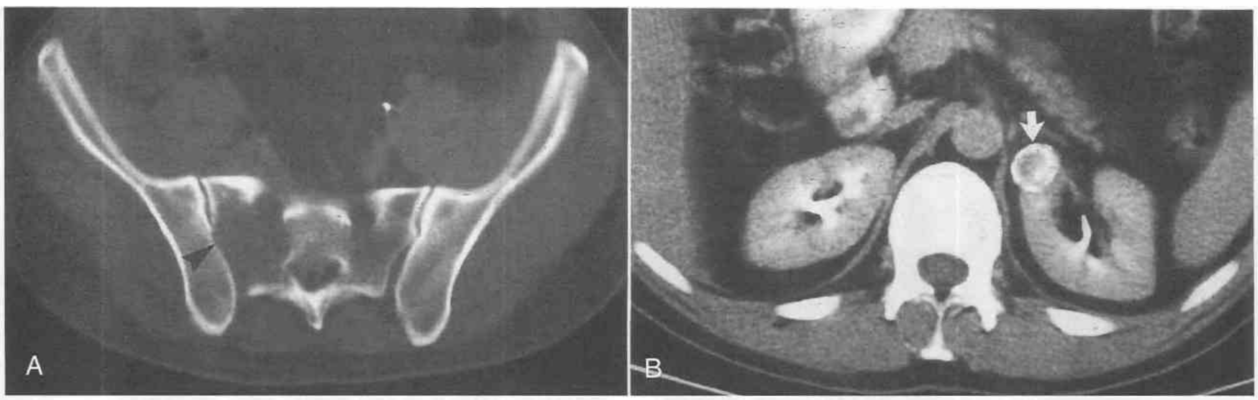

Figure 41–92. Small renal cell carcinoma with sacral metastasis. The patient was a 42-year-old man who complained of low back pain. *A,* A lytic metastasis (*arrowhead*) is present in the right sacral ala. *B,* CT performed to search for a primary neoplasm shows a small mass (*arrow*) with dense peripheral calcification in the left kidney. Histologic examination revealed a high-grade left renal cell carcinoma.

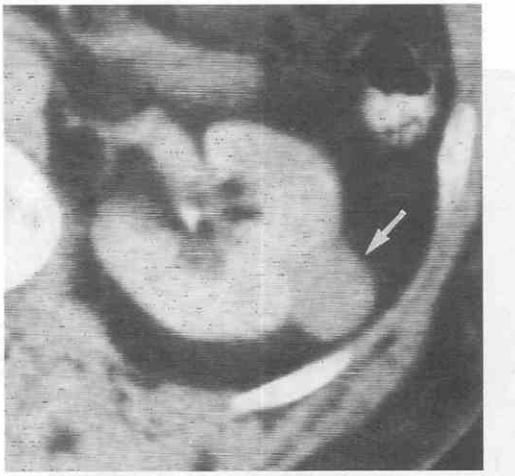

Figure 41–93. Left renal oncocytoma. A contrast-enhanced CT scan shows a homogeneously enhancing, well-circumscribed, exophytic renal mass (*arrow*).

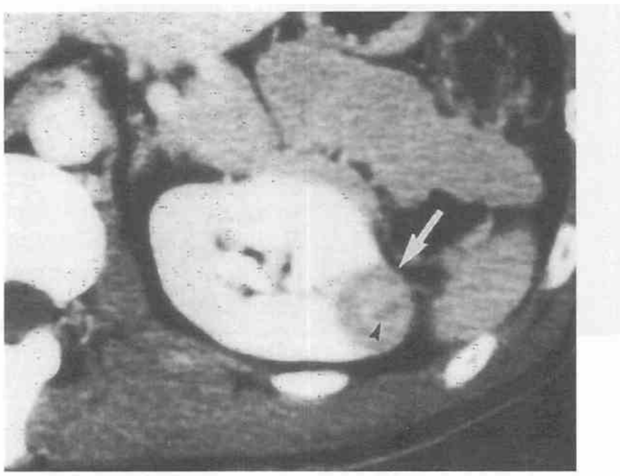

Figure 41–94. Left renal oncocytoma (*arrow*) with eccentric scar (*arrowhead*). Distinction from a small renal cell carcinoma is not possible on CT.

Figure 41–95. Large left renal oncocytoma (*arrow*). The centrally placed, sharply defined, stellate area of low attenuation (*arrowheads*) suggests the diagnosis of oncocytoma.

of tumor size.[53] Fine-needle aspiration cytology has been shown to be successful in discriminating between RCC and renal oncocytoma.[157] If the diagnosis of oncocytoma is suspected preoperatively, small tumors may be treated with partial nephrectomy because of the excellent prognosis.[210] On MRI, oncocytoma is generally isointense to hypointense to normal parenchyma on T1-weighted images and has a variable appearance on T2-weighted images. The presence of a central scar suggests the diagnoses (Fig. 41–96). Oncocytomas do enhance with gadolinium administration but less than renal parenchyma.

Juxtaglomerular Neoplasm (Reninoma).[185] Renin-producing tumors of juxtaglomerular cells (reninomas) are a rare,[65] but curable, cause of hypertension. Two thirds of juxtaglomerular cell tumors of the kidney occur in young women in their reproductive years.[104] Plasma renin and aldosterone values are usually elevated. None of the reported neoplasms has been invasive or has metastasized. Reninomas are usually well shown on contrast-enhanced CT scans on which they show a smooth outline and sharp margination. Small foci of hemorrhage may cause a heterogeneous tumor appearance. Because of their benign nature, reninomas may be managed by partial nephrectomy.[185]

On MRI, reninomas are isointense to hypointense to normal cortex on T1-weighted images and hypointense to normal cortex on T2-weighted images. These tumors tend to enhance less than normal cortex on MRI because of their relative hypovascularity.[1, 117, 209]

Multilocular Cystic Renal Tumor. Multilocular cystic renal tumor (MCRT) refers to two types of generally benign tumors: cystic nephroma (CN) and cystic poorly differentiated nephroblastoma (CPDN).[113] These are well-encapsulated, multilocular, noninfiltrating cystic lesions with no solid components. MRCT manifests in young children (usually boys) as a painless abdominal mass. Affected females usually are over 4 and the tumor demonstrates a biphasic age distribution, occuring in girls 4 to 20 years of age and in women in their fifth and sixth decades of life.[163] The masses are often large, averaging 8 to 10 cm in diameter, are single, are unilateral, and involve only part of the kidney. Individual cysts may vary from microscopic to 2 to 4 cm.[186] CPDN resembles CN in every feature on histopathology and imaging examinations, except that the septa contain blastemal cells with or without other embryonal stromal cells.

On CT, MCRT presents as a well-defined encapsulated mass containing multiple cysts separated by septa (Fig. 41–97). The septa may be as thick as several millimeters, but they do not display significant nodularity. On contrast-enhanced CT, septa within the mass may enhance.[163] Excretion of contrast by the affected kidney is usually normal. However, the lesion frequently herniates into the renal pelvis causing a filling defect and, sometimes, obstructive calycectasis (Fig. 41–98).[163] MRI does not add much information to that provided by CT (see Fig. 41–98). MRI shows encapsulated multilocular mass with capsule that has low signal on all pulse sequences, variable signal intensity of cyst contents on T1-weighted images, and high signal intensity of cyst contents on T2-weighted images.[86] CN and CPDN are indistinguishable by imaging or by

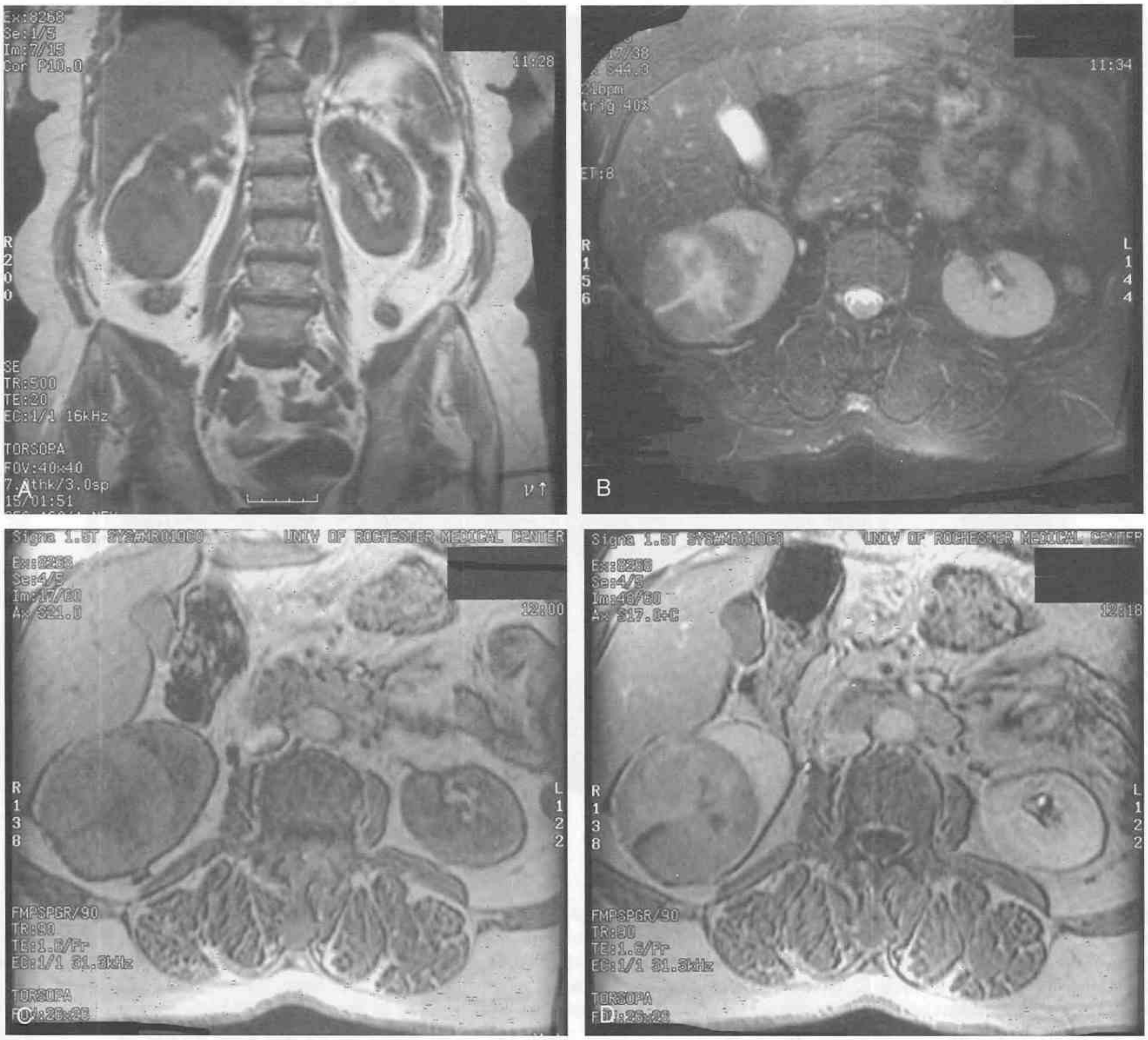

Figure 41–96. A 78-year-old woman with oncocytoma. *A,* Coronal T1-weighted MR image shows a mass in the inferior pole of right kidney; the mass is slightly hyperintense to the renal parenchyma. *B,* T2-weighted fast spin-echo image shows mass to be hyperintense to the surrounding renal parenchyma with a high signal central scar. Precontrast T1-weighted axial fast multiplanar spoiled gradient image (*C*) shows mass to be slightly hyperintense to the renal parenchyma with low signal central scar, which demonstrates enhancement on post–gadolinium enhancement sequences (*D*).

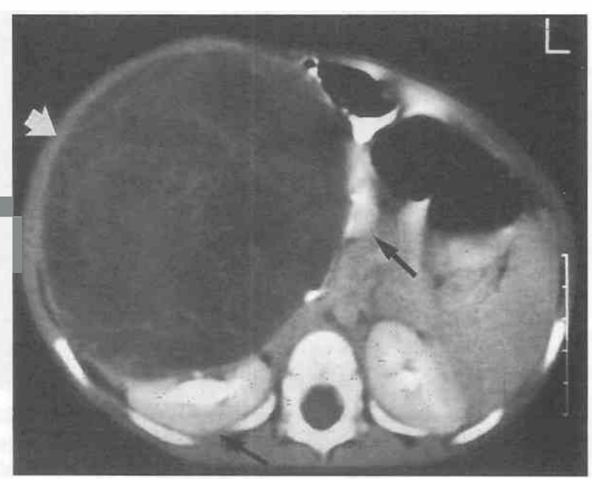

Figure 41–97. Multilocular cystic nephroma (*white arrow*) in the right kidney in an infant. Multiple septa separate the fluid-containing locules. The renal parenchyma is displaced medially and posteriorly (*black arrows*).

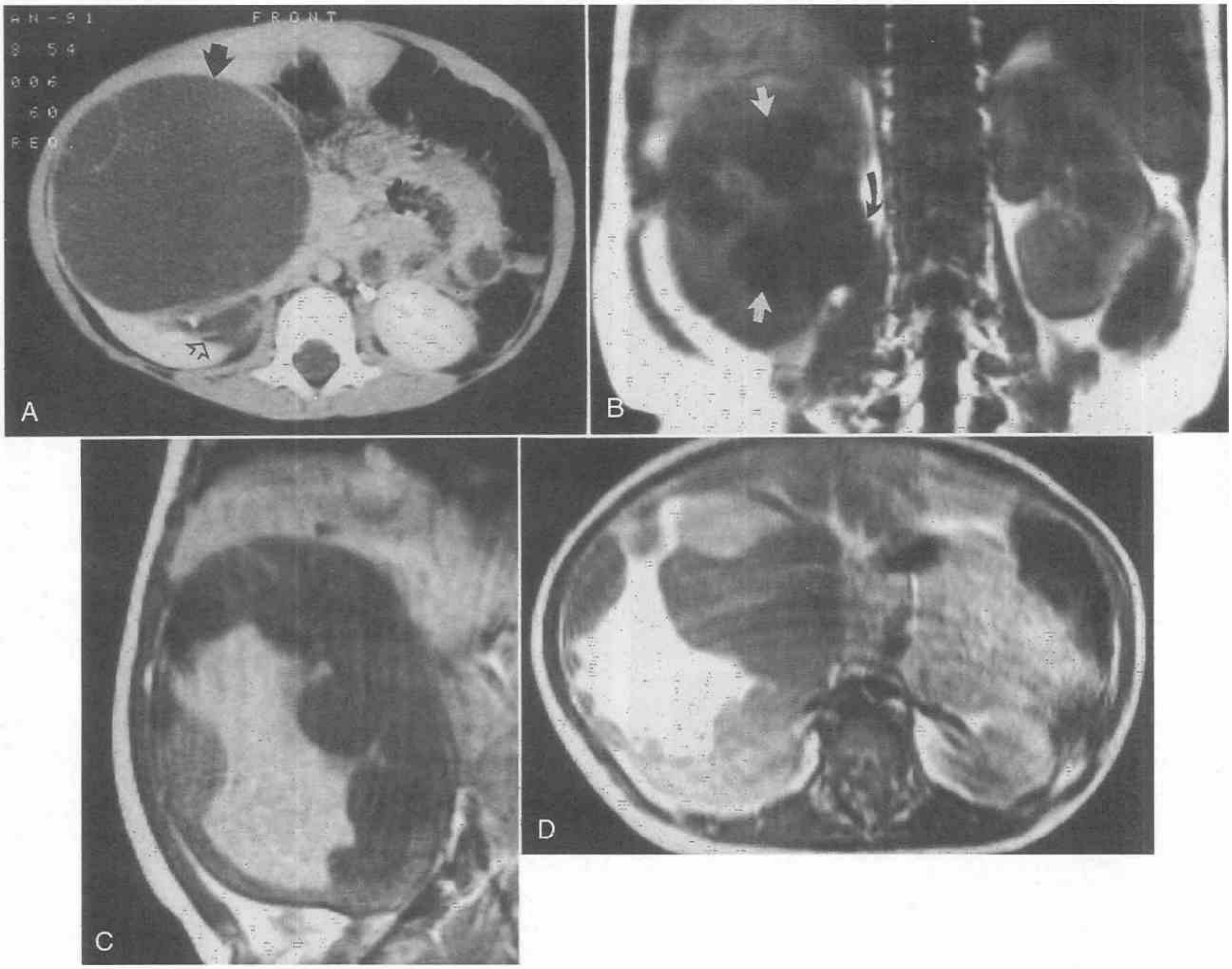

Figure 41–98. Multilocular cystic nephroma occurring in the right kidney in an infant. *A,* CT scan shows fine septa in well-defined cystic renal mass (*arrow*). Hydronephrosis (*open arrow*) was due to herniation of the tumor into the right renal pelvis. *B,* Coronal MR image (spin-echo, TR = 350 msec, TE = 15 msec) obtained posteriorly through the right kidney shows dilated calyces (*white arrows*) and renal pelvis (*curved arrow*). *C,* Coronal T1-weighted MR image (spin-echo, TR = 350 msec, TE = 15 msec) shows that the tumor has a heterogeneous appearance with area of high signal intensity probably due to hemorrhage or high protein content in cyst fluid. *D,* Axial proton-density–weighted MR image (TR = 2000 msec, TE = 22 msec) shows that fluid locules have significantly variable signal intensities.

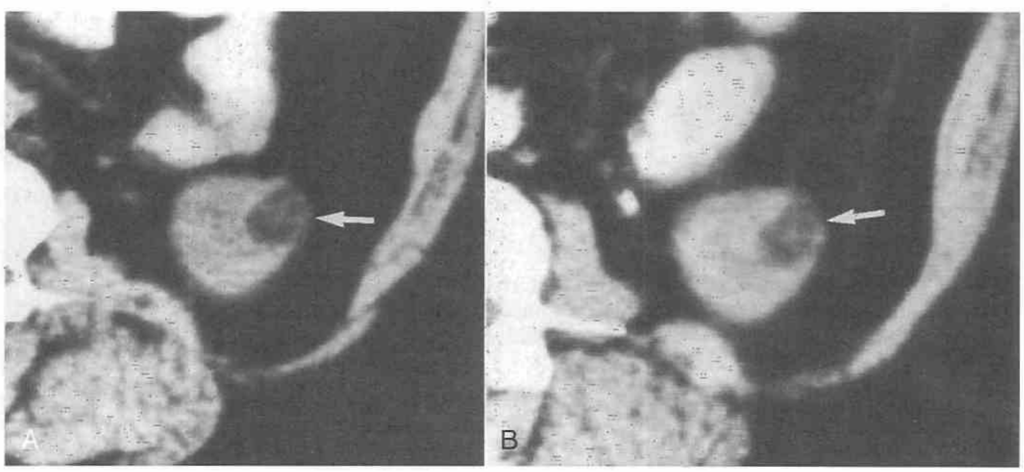

Figure 41–99. Small renal angiomyolipoma. *A,* Unenhanced CT scan shows a low-density mass (*arrow*) in the lower pole of the left kidney. Attenuation values as low as −42 HU, indicating the presence of fat, were found in the lesion through the use of small regions of interest. *B,* On a contrast-enhanced CT scan, the attenuation values of the lesion (*arrow*) were in the soft tissue range.

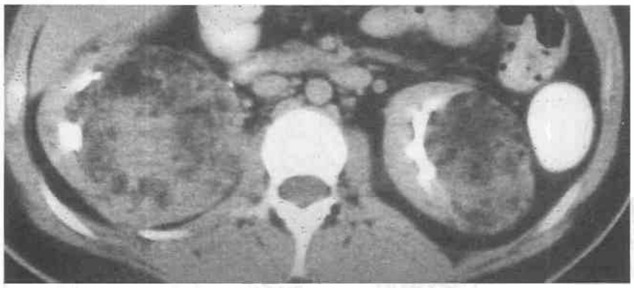

Figure 41–100. Tuberous sclerosis with multiple bilateral renal angiomyolipomas. The lesions contain low-density areas consistent with fat.

gross appearance. The treatment for MCRT is complete resection, with noninvasive imaging for follow-up if the tumor proves to be CPDN.[86]

Angiomyolipoma. AMLs are benign hamartomas composed of blood vessels, smooth muscle, and fatty tissue. AML is seen in two distinct clinical forms, sporadic (isolated) and in association with tuberous sclerosis. Although exact figures are difficult to obtain, the sporadic form accounts for approximately 80% to 90% of cases of AML.[282] The sporadic form is typically seen in middle-aged patients (mean age, 43 years) and is more common in women by at least a 4:1 ratio. Up to 80% of all patients with TSC, including adults and children, have AMLs.[86] When found in children, AMLs are almost exclusively associated with TSC.[86] Masses less than 4 cm in diameter are usually asymptomatic, but those larger than 4 cm often cause flank pain, hematuria, and anemia and carry a significant risk of intratumoral or perinephric hemorrhage.[260, 279]

AMLs are seen on CT as well-circumscribed renal masses. They vary in size from tiny renal nodules to large tumors (Fig. 41–99). Patients with TSC often have extensive bilateral renal involvement by AMLs (Fig. 41–100). The presence of intratumoral fat is almost diagnostic of AMLs,[29] although in rare cases, fat has been reported in Wilms' tumor in children[195] and in renal oncocytomas.[46] Retroperitoneal lymph node involvement may be discovered in patients with AML.[267]

The presence of fat is best shown by CT. Thin-section (3 to 5 mm) technique is preferred to avoid volume averaging, which might prevent demonstration of low attenuation in the tumor. The use of intravenously administered contrast material is not necessary (see Fig. 41–99).[282] Fatty tissue is considered to be present in a tumor if a region-of-interest attenuation measurement of −10 HU or lower is found within the tumor. Lesions without detectable fat cannot be distinguished from other renal neoplasms on CT (Fig. 41–101). Approximately 5% of AMLs do not show fat attenuation on CT scans and cannot be differentiated from RCC.[282] Extensive intratumoral hemorrhage may also obscure the presence of fat. AMLs are always benign. However, the tumors may exhibit extrarenal extension. Large perinephric tumor components may be found (Fig. 41–102), and AMLs may extend into the renal vein and inferior vena cava.[86]

MRI may also detect the presence of fat in renal AMLs (Fig. 41–103). The MRI characteristics of AML depend on the relative amounts of fat and other tissue components. The presence of macroscopic fat in a lesion is very specific for AML, although rarely, RCC can also contain fat.[103] If an AML is suspected on chemical shift imaging, the diagnosis can be confirmed by acquiring fat-saturated, T1-weighted and water-saturated, T1-weighted gradient-echo sequences.[209]

Surgery and biopsy are rarely needed in asymptomatic patients with typical imaging findings of AML. Patients with extensive intratumoral or perinephric hemorrhage can usually be managed conservatively (Fig. 41–104). Partial nephrectomy or selective catheter embolization is advocated for masses larger than 4 cm.[125, 279] Generally, asymptomatic patients with an AML approaching 4 cm in diameter are followed annually with CT or ultrasonography although in most of these patients the lesions will show

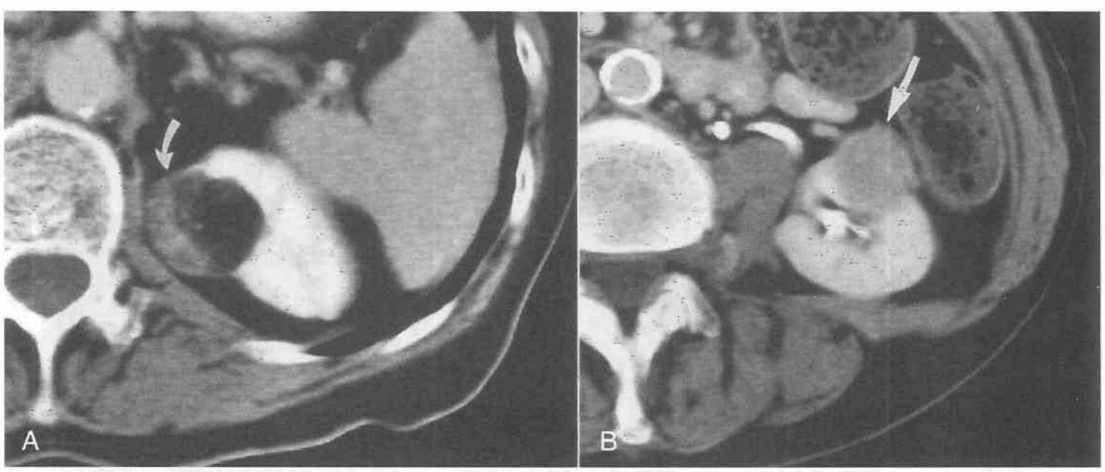

Figure 41–101. Two left renal angiomyolipomas in a patient without tuberous sclerosis. *A,* A lesion (*curved arrow*) in the upper pole of the left kidney contains fat, indicating the diagnosis of angiomyolipoma. *B,* A mass (*arrow*) in the midregion of the kidney contained no detectable fat and was therefore indistinguishable from a renal cell carcinoma. Nephrectomy revealed that both lesions were angiomyolipomas, although the lesion shown in *B* had only a minimal fat content.

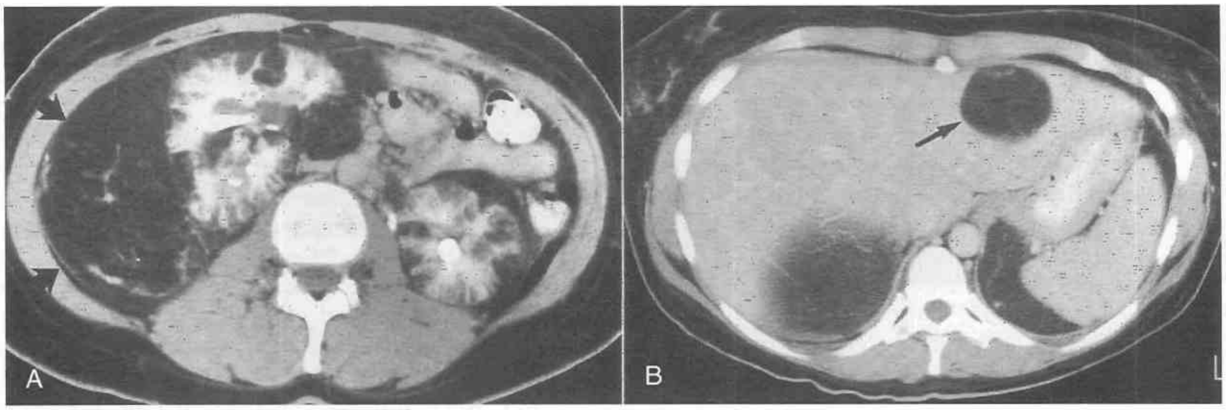

Figure 41–102. Tuberous sclerosis with renal and liver involvement. *A,* The kidneys show multiple fat-containing lesions. On the right side, there is extensive involvement of the perinephric space by an angiomyolipoma (*arrows*) containing fat and prominent blood vessels. The right kidney is displaced anteromedially. *B,* A fat-containing mass (*arrow*) is present in the left lobe of the liver. (Courtesy of Randi W. Hart, M.D., Waukesha, Wis.)

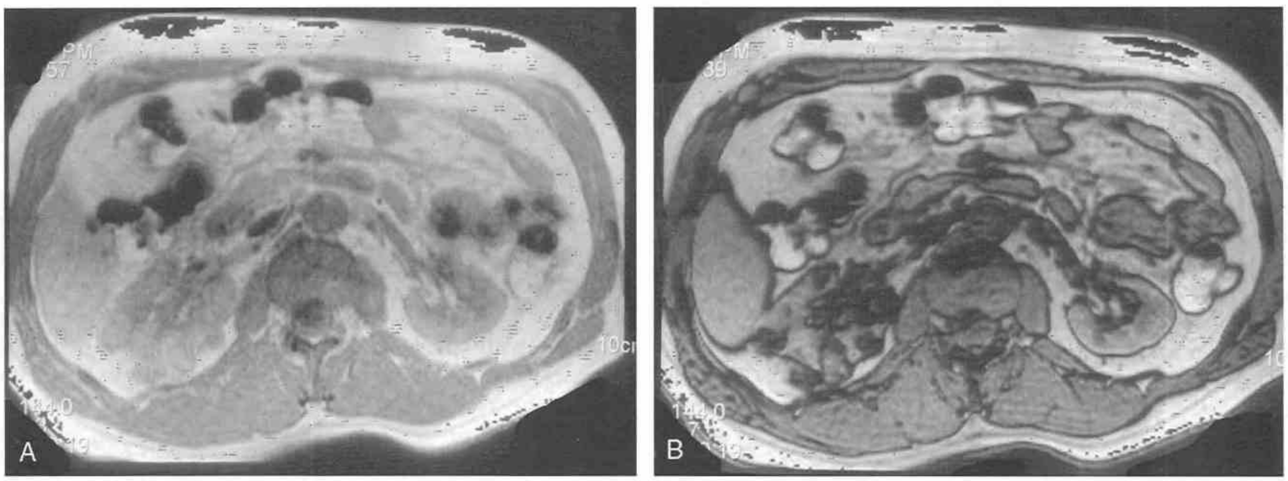

Figure 41–103. Multiple angiomyolipoma. In- and out-of-phase MR image in axial projection (*A*) demonstrates multiple small lesions in the right kidney that have a slightly higher signal compared with the surrounding renal parenchyma. *B,* Out-of-phase pulse sequence demonstrates a significant drop in the signal of these lesions, consistent with the presence of fat. Post–gadolinium enhancement images (*not shown*) did not reveal any enhancement.

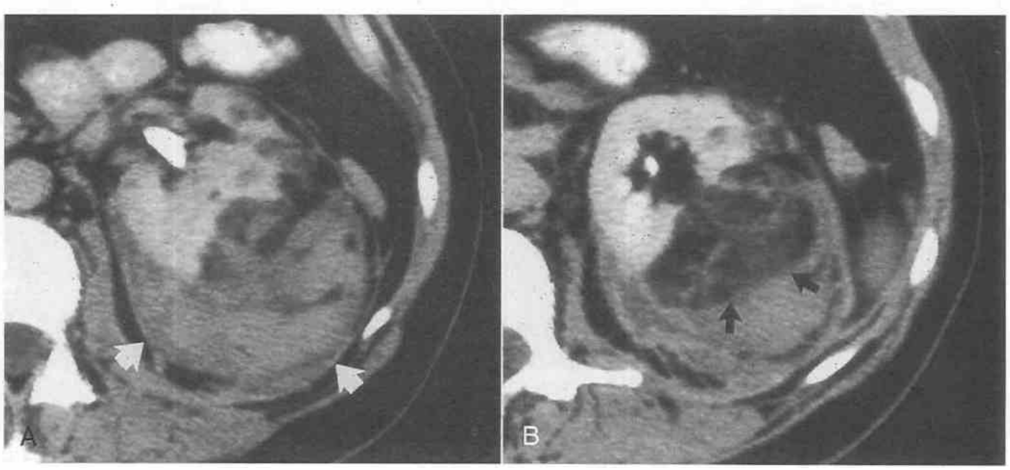

Figure 41–104. Extensive left perinephric hematoma due to hemorrhage from a renal angiomyolipoma. *A,* The hematoma (*arrows*) is partially contained by the posterior renorenal bridging septum. *B,* A more cephalad scan shows a fat-containing angiomyolipoma (*arrows*) closely related to the hematoma. The bleeding responded to conservative management.

little change over time. Patients with lesions larger than 4 cm can be evaluated at shorter intervals.[282]

Pelvicalyceal and Ureteral Neoplasms

Primary neoplasms of the renal pelvis, calyces, and ureter are relatively uncommon. CT plays a limited but often important role in the diagnosis and staging of these tumors.

Pelvicalyceal Neoplasms

About 90% of pelvicalyceal cancers are transitional cell carcinomas, about 9% are squamous cell carcinomas, and less than 1% are adenocarcinomas.[93, 138] Occupational exposure to industrial dyes, phenacetin abuse, cigarette smoking, prior cyclophosphamide therapy, and urinary stasis associated with horseshoe kidneys predispose an individual to the development of transitional cell carcinoma.[138, 143] Squamous cell carcinoma of the renal pelvis is commonly associated with chronic irritation secondary to renal calculi and chronic infection. Transitional cell carcinoma has a peak frequency in the sixth and seventh decades of life, and about 68% of affected patients are men. Patients present with painless hematuria.[186] Transitional cell carcinoma of the renal pelvis is frequently multicentric with either synchronous or metachronous tumor involvement of the ureter, bladder, and contralateral renal pelvis.[186, 293]

CT Diagnosis

Imaging findings in urothelial cancer consist of a calyceal or renal pelvic filling defect, hydronephrosis with a nonfunctioning kidney, and extensive renal parenchymal infiltration.[138] The diagnosis of pelvicalyceal cancer is usually established by various combinations of excretory urography, retrograde pyelography, retrograde brush biopsy, ureteroscopy, and biopsy. CT helps in establishing the extent of renal parenchymal invasion including the perinephric and periureteral extents of tumor.

CT evaluation of pelvicalyceal filling defects of unknown nature shown by excretory urography or retrograde pyelography requires unenhanced, corticomedullary, nephrographic, and excretory-phase images through the abdomen and pelvis using a slice thickness of 3 to 5 mm. Small pelvicalyceal neoplasms may be difficult to detect on precontrast scans, although occasional neoplasms show coarse, punctate calcification.[62] Contrast-enhanced CT demonstrates collecting system filling defects with smooth, lobulated, or irregular margins (Fig. 41–105).[8] Precontrast attenuation values of pelvicalyceal cancers range from 20 to 46 HU.[194] Although characteristically hypovascular on angiography, pelvicalyceal tumors often show mild enhancement on CT after intravenous administration of contrast medium. Postcontrast attenuation values range from 64 to 84 HU.[194] Contrast enhancement differentiates pelvicalyceal neoplasms from other filling defects that occur in the collecting system.

Radiolucent renal calculi are usually composed predominantly of uric acid and appear as densities with attenuation values greater than 200 HU on unenhanced CT scans (Fig. 41–106).[73, 239] The attenuation values of recent pelvicalyceal blood clots on unenhanced CT scans range from 45 to 75 HU; these values are higher than those of urothelial cancer and lower than those of urate calculi.[138] Moreover, blood clots do not have contrast enhancement and follow-up studies show disappearance of blood clots with time.[138] CT enables the recognition that an apparent intrinsic pelvic filling defect is produced by extrinsic compression of the renal pelvis by renal sinus lipomatosis, renal sinus cysts, RCCs, and lymphoma.

The hydronephrotic form of urothelial cancer with a nonfunctioning kidney is due to ureteropelvic junction obstruction and may present a diagnostic problem on excretory urography.[138] Although retrograde pyelography may suggest the diagnosis, CT sometimes provides a definitive diagnosis (Fig. 35–107).[237] An enhancing soft-tissue mass

Figure 41–105. Polypoid transitional cell carcinoma (*arrow*) of the right renal pelvis. The lesion invaded to but not beyond the muscularis. Compared with the unenhanced CT scan, the lesion enhanced on this scan by 36 HU.

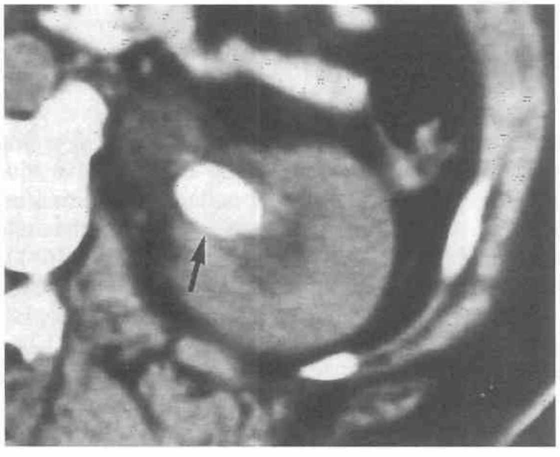

Figure 41–106. Urate calculus (*arrow*) in the left renal pelvis. Excretory urography showed a pelvic filling defect, but the lesion was radiolucent on conventional tomography. The stone has an attenuation value of 458 HU.

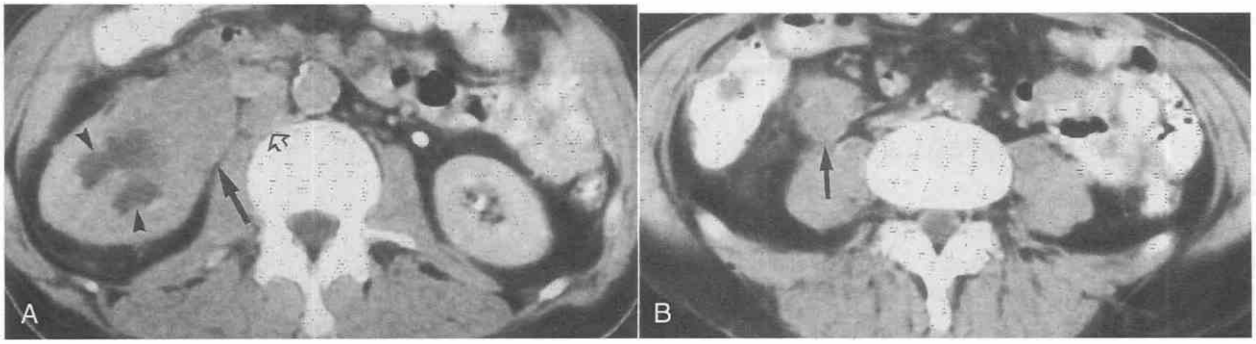

Figure 41–107. Hydronephrosis due to transitional cell carcinoma of the right renal pelvis. *A,* A soft-tissue mass (*arrow*) fills the right renal pelvis. Dilated calyces (*arrowheads*) are seen in the right kidney. An enlarged retrocaval lymph node (*open arrow*) was involved by metastatic disease. *B,* The tumor also involved the upper half of the right ureter (*arrow*).

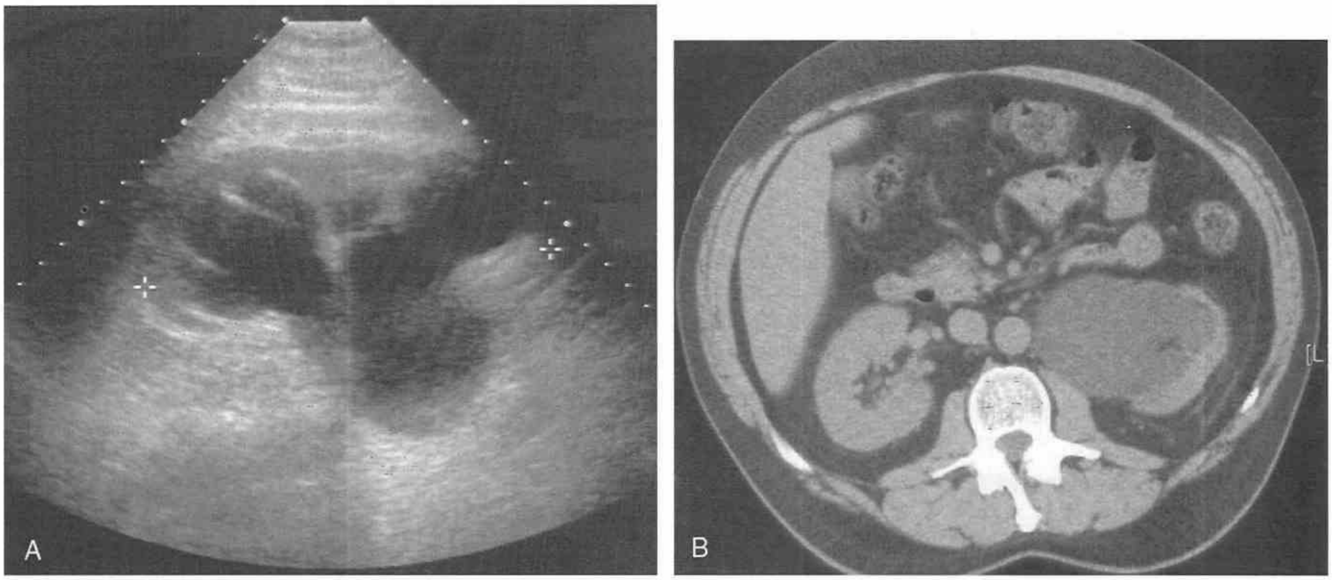

Figure 41–108. [redacted]genital ureteropelvic junction obstruction. *A,* Longitudinal sonogram of left kidney shows marked hy[redacted]ephrosis with medial tap[redacted] of the renal pelvis. *B,* Corresponding CT scan reveals the medial tapering of the renal pelvis [redacted] marked hydronephrosis. The ureter beyond the junction was collapsed. The patient underwent pyeloplasty.

at the apex of a dilated renal pelvis or diffuse thickening of the renal pelvic wall on CT indicates a tumor causing ureteropelvic junction obstruction. The proximal ureter may be thickened and filled from invasion by the neoplasm (see Fig. 41–107).[138] Most cases of ureteropelvic junction obstruction are congenital in origin, and on CT, a dilated renal pelvis with a smooth wall and a smooth transition at the ureteropelvic junction to the collapsed proximal ureter is seen (Fig. 41–108).[237] A calculus impacted at the ureteropelvic junction is easily shown by CT (Fig. 41–109). Extrinsic lesions causing ureteropelvic junction obstruction (e.g., enlarged lymph nodes or retroperitoneal neoplasms) are also easily diagnosed on CT.[237]

Another presentation of urothelial cancer is that of extensive parenchymal infiltration of the kidney.[203] Urothelial cancer is centrally located, and its pattern of renal invasion differs from the eccentric origin and invasion of the renal sinus seen in RCC. Urothelial cancers do not usually distort the shape of the kidney. The demonstration of a central mass that is less dense than normal renal parenchyma and

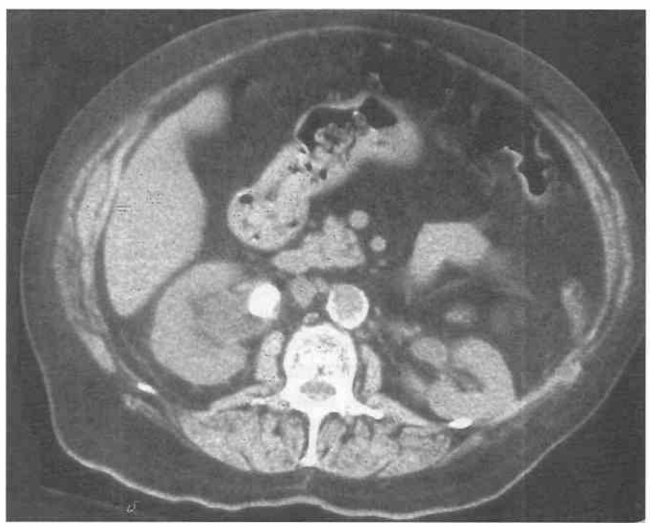

Figure 41–109. Axial CT scan demonstrates a large right ureteropelvic junction calculus.

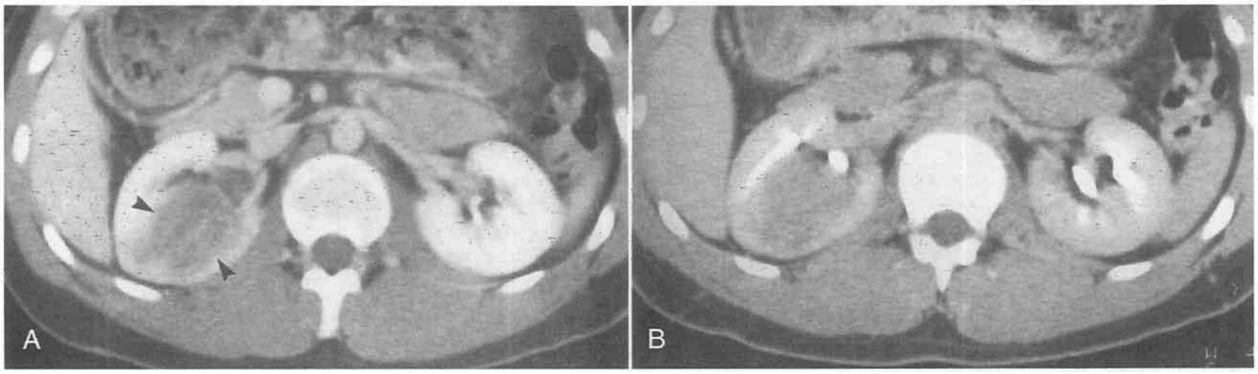

Figure 41–110. Transitional cell carcinoma of the right renal pelvis in a 20-year-old man associated with cyclophosphamide therapy administered 6 years earlier. *A,* Dynamic CT scan obtained immediately after bolus injection of contrast material shows an enhancing mass (*arrowheads;* attenuation value = 71 HU) in the right renal pelvis. The precontrast attenuation value was 43 HU. The mass obliterates and invades the renal sinus fat. A poorly defined margin between the tumor and the renal parenchyma indicates parenchymal invasion. *B,* A CT scan obtained 5 minutes after *A* shows displacement of the opacified collecting system. (From Levine E: Transitional cell carcinoma of the renal pelvis associated with cyclophosphamide therapy. AJR Am J Roentgenol 159:1027–1028, 1992.)

shows minimal tumor enhancement strongly suggests a urothelial cancer (Fig. 41–110).[138] The renal sinus fat may be obliterated, and there is often a poorly defined margin between the tumor and the renal parenchyma.[138] The calyces may be displaced, compressed, or dilated.

Tumor Staging

Conservative therapy is considered an option in patients with a solitary functioning kidney, bilateral tumor, and renal insufficiency. However, nephroureterectomy with excision of a bladder cuff is considered the standard treatment and should be performed whenever possible.[102] When conservative surgery is planned, CT is helpful for tumor staging.[173] Patients with high-grade or high-volume pelvicalyceal cancers have a high frequency of metastases, primarily to regional lymph nodes, lung, bones, and liver in decreasing order of frequency.

Although CT cannot demonstrate the depth of tumor invasion in the renal pelvic wall (see Fig. 41–105), it can show whether the tumor has extended beyond the tunica muscularis into the renal sinus fat.[8] Invasion of renal sinus fat is suggested by obliteration of the peripelvic fat stripe, which is the renal sinus fat separating the anterior and posterior cortical hilar lips from the renal pelvic adventitia (see Fig. 41–110).[8] Invasive renal pelvic tumors may become attached to the aorta and inferior vena cava and may invade the psoas muscle (Fig. 41–111). In rare cases, tumor extension into the renal vein and inferior vena cava may be shown by CT.[85] CT may also demonstrate regional lymph node metastases (Fig. 41–112), although the technique sometimes leads to "understaging" of tumors with metastases in normal-sized central retroperitoneal lymph nodes.[8] MRI is not used frequently in the diagnosis and management of urothelial tumors. However, it may help determine local extent of tumor.

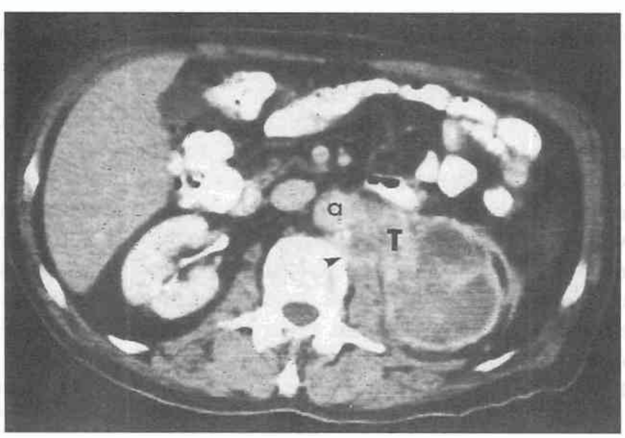

Figure 41–111. Invasive transitional cell carcinoma of the left renal pelvis. The tumor (T) causes left hydronephrosis. It extends through the wall of the renal pelvis and is attached to the aorta (a) and the left psoas muscle (*arrowhead*). Complete resection was not possible.

Ureteral Neoplasms

Transitional cell carcinoma accounts for about 93% of ureteral neoplasms. Of the remainder, 5% are squamous cell carcinomas, and 2% are adenocarcinomas. The age and gender distribution, symptoms, and causes are similar to those for pelvicalyceal carcinoma. Tumors have a predi-

Figure 41–112. Transitional cell carcinoma of the right renal pelvis with extensive parenchymal invasion and regional nodal metastases (*arrows*).

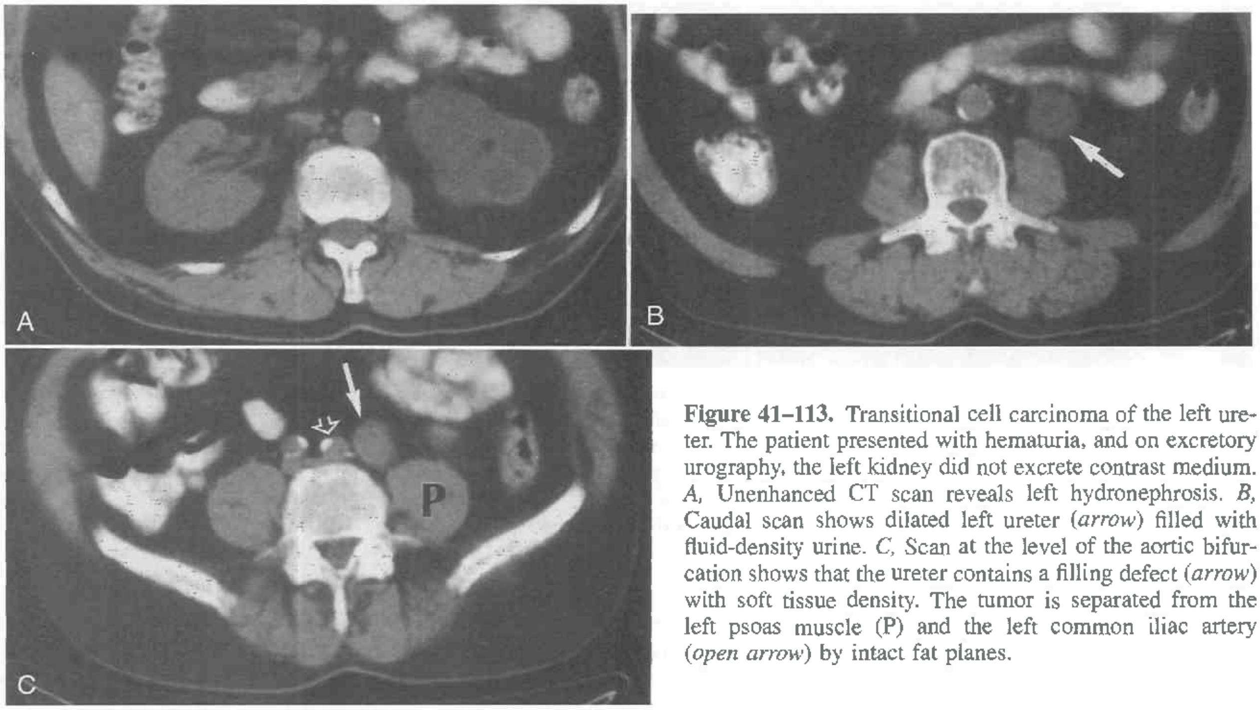

Figure 41–113. Transitional cell carcinoma of the left ureter. The patient presented with hematuria, and on excretory urography, the left kidney did not excrete contrast medium. *A*, Unenhanced CT scan reveals left hydronephrosis. *B*, Caudal scan shows dilated left ureter (*arrow*) filled with fluid-density urine. *C*, Scan at the level of the aortic bifurcation shows that the ureter contains a filling defect (*arrow*) with soft tissue density. The tumor is separated from the left psoas muscle (P) and the left common iliac artery (*open arrow*) by intact fat planes.

lection for the middle and distal ureter. The diagnosis of ureteral carcinoma is usually readily established with a combination of excretory urography and retrograde pyelography. However, CT may help by confirming that a ureteric filling defect represents a neoplasm and not a radiolucent calculus or blood clot. Ureteral neoplasms manifest on CT as soft tissue intraluminal filling defects (Fig. 41–113), often with ureteral widening or thickening of the ureteral wall.

These are findings can also occur in inflammatory conditions and ureteral metastases.[138] CT also helps determine whether a ureteral neoplasm has extended outside the tunica muscularis to involve the retroperitoneal fat (see Fig. 41–113) and surrounding structures, or whether it has metastasized to regional lymph nodes.

An important use of CT is to determine whether ureteral obstruction is due to an intrinsic neoplasm or to extrinsic disease when excretory urography and retrograde pyelography have failed to do so.[28] CT is particularly useful in detecting such causes of extrinsic ureteric obstruction as idiopathic and malignant retroperitoneal fibrosis, inflammatory aortic aneurysm, and lymphomatous and metastatic retroperitoneal adenopathy.[28]

Renal Infections

Acute Bacterial Renal Infection

Acute bacterial renal infection in adults frequently causes fever, chills, flank pain, leukocytosis, and pyuria. It occurs significantly more commonly in women. Vesicoureteric reflux is sometimes an important predisposing factor in children, but it is only rarely found in adults with acute pyelonephritis. *Escherichia coli* bacteria usually cause the typical ascending acute renal infection, whereas the hematogenous disease is often caused by *Staphylococcus aureus*.[191] The diagnosis of acute bacterial renal infection is usually made clinically, and about 95% of patients with uncomplicated infections treated with appropriate antibiotics become afebrile in 48 hours, and nearly 100% do so in 72 hours.[255] Such patients do not need renal imaging. However, imaging studies are valuable in patients with severe refractory renal infections. Imaging is needed to determine if there are complications requiring prolonged antibiotic therapy or surgical intervention (e.g., renal and perinephric abscess or pyonephrosis). Imaging is also useful for excluding abnormalities that predispose to refractory infections, such as nephrolithiasis or ureteric obstruction.

Acute Bacterial Pyelonephritis. In patients with acute bacterial renal infection, CT scans are acquired with contrast enhancement during the corticomedullary phase (30 seconds after initiation of injection and during either the nephrographic phase (70–90 seconds after injection) or the excretory phase (5 minutes after injection).[277] A striated nephrogram on contrast-enhanced CT that consists of discrete rays of alternating attenuation extending to the cortex is characteristic of pyelonephritis and is better demonstrated on CT than on excretory urography.[203] Striations result from stasis of contrast material within edematous tubules that demonstrates increasing attenuation over time.[277] Some patients with acute pyelonephritis show diffuse renal involvement on CT. This is manifested by poor renal contrast enhancement, delay to absence of excretion of contrast medium, and global renal enlargement (Fig. 41–114). Other patients show unifocal or multifocal renal abnormalities with extensive areas of apparently uninvolved renal parenchyma.[90] These abnormalities are seen on contrast-enhanced CT scans as wedge-shaped zones of decreased attenuation (Fig. 41–115). They often manifest

Figure 41–114. Acute pyelonephritis with diffuse renal involvement. The affected left kidney shows diminished contrast enhancement, global enlargement, and delayed contrast excretion. The right kidney is normal.

straight borders, radiate from the collecting system to the renal capsule, and are widest at the periphery of the kidney.[90, 255, 270] Severe tubulo-interstitial inflammation may progress to form a hypodense mass or masses with rounded or irregular contours and bulging of the renal surface (Fig. 41–116). If treated too late or inadequately, such lesions may develop single or multiple small areas of liquefaction (i.e., small abscesses).[90] These areas are often irregular and of near water attenuation (20 to 30 HU); they do not enhance after intravenous administration of contrast medium (Fig. 41–117).

Renal and Perinephric Abscesses. If inadequately treated, acute pyelonephritis may progress to tissue necrosis, resulting in renal abscess. On contrast-enhanced CT scans, renal abscesses usually have attenuation values of about 30 HU; this feature distinguishes them from fluid-density renal cysts.[255] Their contents do not enhance. They may have distinct, rounded margins and thick, enhancing walls (Figs. 41–118 and 41–119).[141, 255] Alternatively, ab-

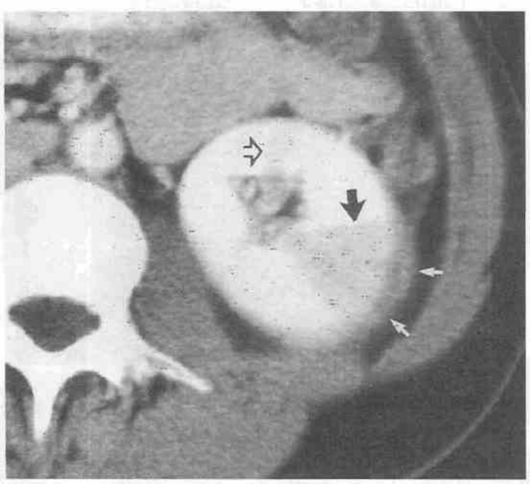

Figure 41–115. Acute pyelonephritis. The kidney shows a wedge-shaped zone (*black arrow*) of decreased attenuation. The lesion exhibits straight borders, radiates from the collecting system to the renal capsule, and is widest at the kidney periphery. There is inflammatory change in the adjacent perinephric fat and localized renal fascial thickening (*white arrows*). A similar but smaller zone of inflammation (*open arrow*) is present anteriorly.

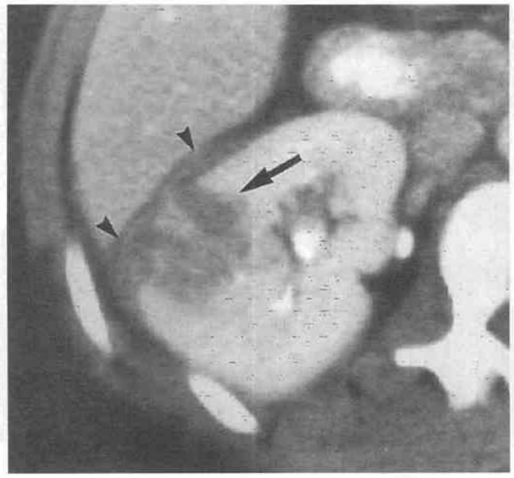

Figure 41–116. Acute pyelonephritis with focal mass formation. The kidney shows a rounded, heterogeneous mass (*arrow*) with a poorly defined margin. Inflammatory changes in the adjacent perinephric fat and renal fascial thickening (*arrowheads*) are also present.

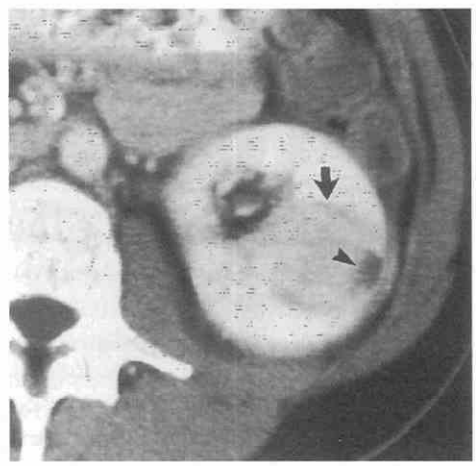

Figure 41–117. Acute pyelonephritis with early abscess formation. The inflammatory mass (*arrow*) shows a small, peripheral area of liquefaction (*arrowhead*).

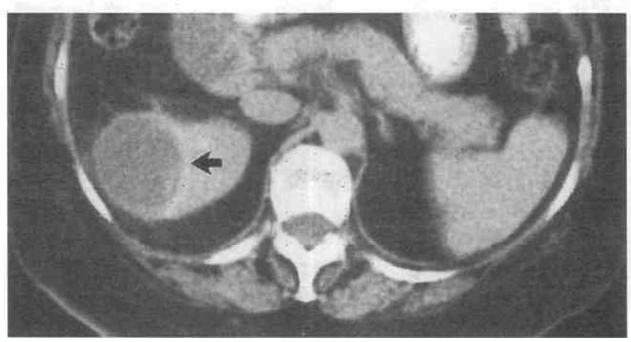

Figure 41–118. Right renal abscess (*arrow*) shows a thick wall and low density (30 HU). Inflammatory stranding is present in the perinephric fat.

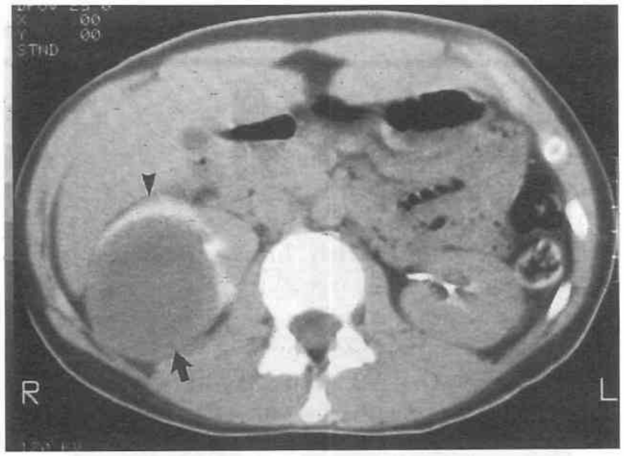

Figure 41–119. Lar[redacted]w) has an attenuation value[redacted]. High-density renal parenchyma on its anteromedial aspect (*arrowhead*) is probably due to retention of contrast medium in compressed and obstructed renal tubules on the periphery of the abscess.

scesses may be ill-defined and surrounded by zones of decreased parenchymal enhancement, representing inflammation that has not yet progressed to necrosis. Gas is occasionally found in renal abscesses.[177] Focal thickening of the adjacent renal fascia and stranding in the adjacent perinephric fat are common CT findings.[141] A perinephric abscess may ultimately result if the infection extends through the renal capsule (Fig. 41–120). Although small renal abscesses may respond to antibiotic therapy alone, percutaneous drainage is usually the treatment of choice for larger renal abscesses. Perinephric abscesses always require drainage.[177] Abscesses can be drained with the use of CT or ultrasonographic guidance.

Emphysematous Pyelonephritis (EPN). Emphysematous pyelonephritis is a relatively uncommon life-threatening bacterial infection characterized by gas formation within the renal parenchyma or the perinephric space.[191] Most patients with EPN are diabetic with an average age of 55 years. *E. coli* is the commonest bacteria found in patients with EPN; other bacteria found include *Klebsiella, Pseudomonas,* and *Proteus.* Two types of EPN have been defined. Type I is characterized by destruction of more than one third of the renal parenchyma with absence of fluid or fluid collection. A smaller gas collection may be present. Type II is characterized by either renal or perirenal fluid collection with bubbly or loculated gas or gas in the collecting system and destruction of less than one third of the renal parenchyma. Type I EPN has a mortality rate of 69%, and Type II a rate of 18%.[284] CT is the most sensitive method for establishing the diagnosis and can also distinguish among gas in the collecting system, parenchymal gas, and gas in the perinephric tissues (Fig. 41–121).[220] Gas in the renal pelvis or calyces is a benign entity and may be related to emphysematous pyelitis, representing gas-forming urinary tract infection that is associated with gas localized in only the renal collecting system (Fig. 41–122). Other causes of gas in the collecting system are ureteral instrumentation, a surgical or interventional radiologic procedure, and a fistulous connection with a hollow viscus.[226]

At present nephrectomy remains the primary therapeutic interventional modality for EPN, although CT-guided drainage appears to have good results in patients in whom surgery is contraindicated, or who have a solitary kidney, bilateral disease, or disease with renal or perirenal fluid collections.[96, 222, 299]

Pyonephrosis. Pyonephrosis is the accumulation of pus in an obstructed pelvicalyceal system. It may appear when

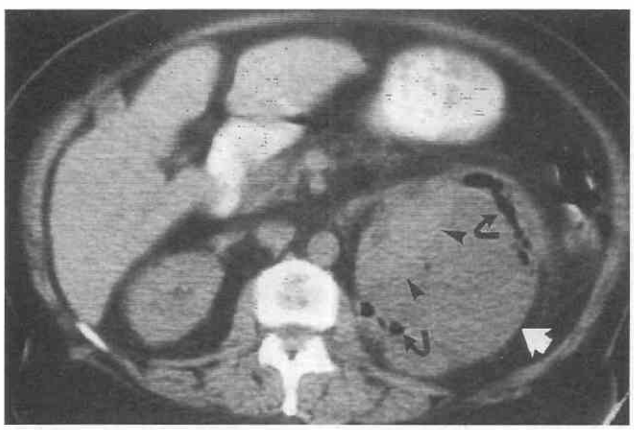

Figure 41–120. Unenhanced CT scan shows a perinephric abscess (*white arrow*) complicating acute pyelonephritis in a diabetic patient. Gas collections (*curved arrows*) are present in the abscess, and the left kidney (*arrowheads*) is displaced anteriorly.

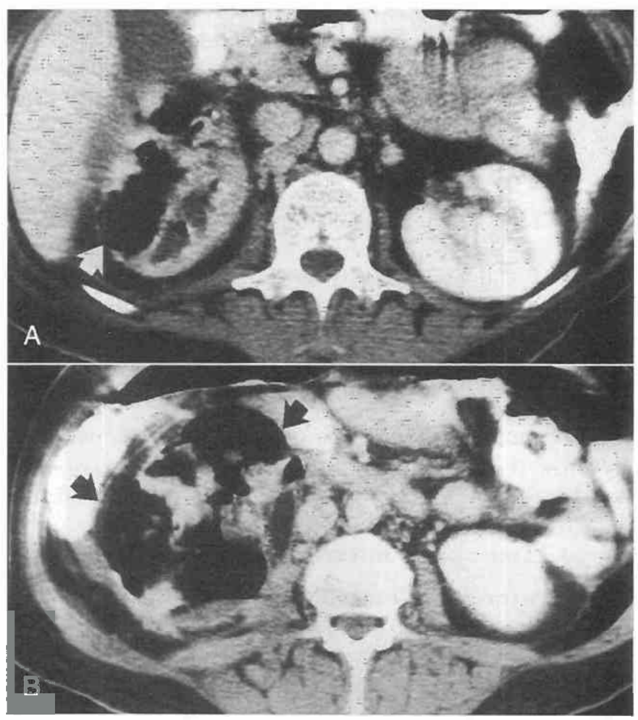

Figure 41–121. E[redacted]ysematous pyelonephritis[redacted]a diabetic patient. There is ex[redacted]ve destruction of the rig[redacted]kidney (*A* and *B*), which is largely replaced by gas (*white arrow*). Gas is also present in the perinephric space (*black arrows*) (*B*). A right nephrectomy was performed.

Figure 41–122. Emphysematous pyelitis in a diabetic patient. Gas is present in both collecting systems (*arrows*), but the right kidney is more significantly involved. The renal parenchyma is uninvolved, and the infection responded to antibiotic therapy.

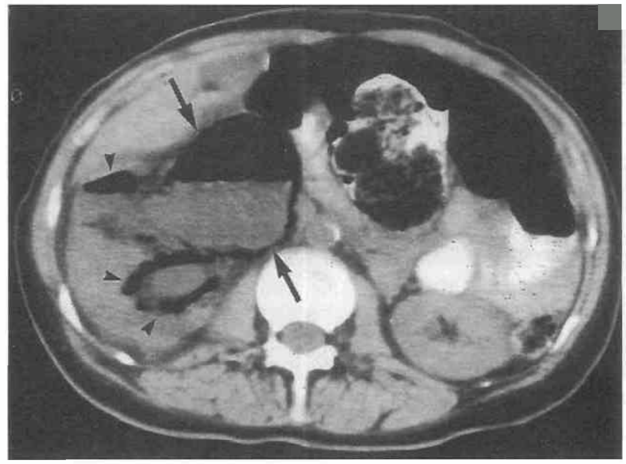

Figure 41–124. Pyonephrosis complicating congenital uretero-pelvic junction obstruction in a diabetic patient. The significantly dilated right renal pelvis (*arrows*) shows a gas-fluid level, and gas is also present in dilated calyces (*arrowheads*).

urinary tract infection occurs in patients with ureteric obstruction due to calculi, strictures, developmental ureteric anomalies, or malignant disease.[191] Pyonephrosis is often associated with severe urosepsis. It represents a true urologic emergency requiring either urgent percutaneous nephrostomy or passage of a ureteral stent to bypass the obstruction (Fig. 41–123). The preferred examination is contrast-enhanced CT. On CT, patients with pyonephrosis may have increased pelvic wall thickness, inflammatory changes in the perinephric fat, and, in rare cases, layering of intravenously injected contrast material anterior to the pus in the dilated renal pelvis.[81,295] Pelvicalyceal system gas in the absence of a history of urinary tract instrumentation, although uncommon, is a strong diagnostic indicator of pyonephrosis (Fig. 41–124).[81] However, CT usually cannot reliably distinguish between infected and uninfected hydronephrosis (Fig. 41–123). The presence of both clinical signs of infection and hydronephrosis is an indicator more sensitive than CT findings of pyonephrosis. CT may show the site and cause of urinary tract obstruction (Fig. 41–123).[191]

Chronic Renal Infections

Xanthogranulomatous Pyelonephritis. Xanthogranulomatous pyelonephritis (XGP) is a chronic renal inflammatory disease associated with indolent bacterial infection. The inflammatory process begins in the renal pelvis and later extends into the medulla and cortex, which are gradually destroyed and replaced by lipid-laden macrophages (xanthoma cells).[92] The disease is usually diffuse but may be focal. Patients are typically middle-aged women. Systemic symptoms include malaise, fever, chills, and weight loss. Nonspecific urinary symptoms include flank pain, increased frequency of micturition, dysuria, and nocturia. *E. coli* or *Proteus mirabilis* organisms are commonly cultured from the urine. CT is valuable in diagnosis and preoperative planning.[92] Nephrectomy is usually required, particularly in the diffuse form of the disease.

On CT, findings of diffuse XGP are pathognomonic in most cases: diffuse reniform enlargement with ill-defined central low attenuation, apparent cortical thinning, staghorn calculus, and unilateral decrease or (more commonly) absence of renal excretion of contrast material (Fig. 41–125).[9,203] Less commonly a small, contracted kidney with replacement lipomatosis is found (Fig. 41–126).[92] A staghorn calculus is present in up to 70% of cases (see Fig. 41–126).[272] Multiple, fluid-density, rounded areas almost

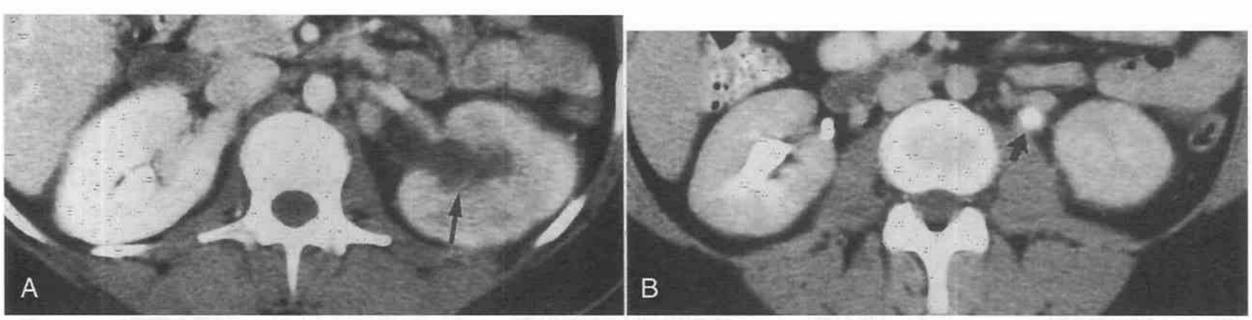

Figure 41–123. CT Scans of pyonephrosis and severe urosepsis due to an obstructing left ureteric urate calculus not visible on plain films. *A*, There is decreased enhancement of the left renal parenchyma, and the left renal pelvis is dilated with delayed contrast excretion (*arrow*). *B*, An obstructing calculus (*arrow*) is present in the proximal ureter. Differentiation between simple hydronephrosis and pyonephrosis could not be made by CT. However, the diagnosis of pyonephrosis was suggested by clinical findings. The patient showed rapid response to percutaneous nephrostomy.

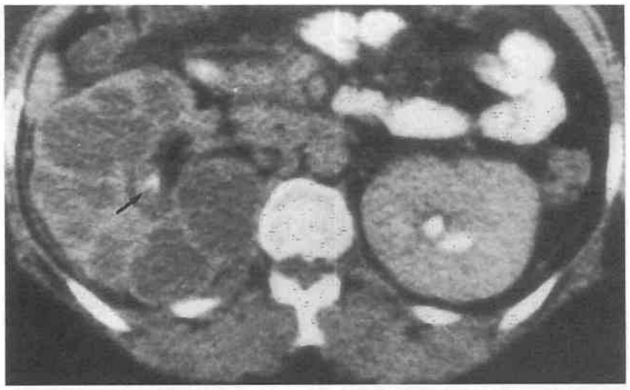

Figure 41–125. Xanthogranulomatous pyelonephritis. The right kidney is globally enlarged, shows no contrast excretion, and is replaced by multiple, rounded, fluid-density areas. A calculus (*arrow*) is present in a nondilated renal pelvis with a thickened wall. (Courtesy of David S. Hartman, M.D., Hershey, Pa.)

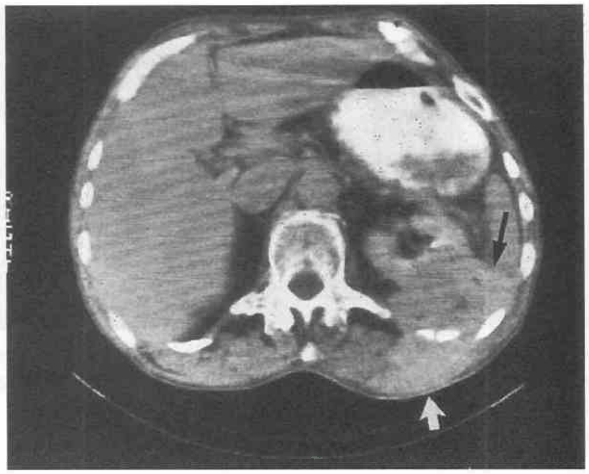

Figure 41–127. Renal parenchymal malacoplakia. CT scan shows a nonspecific soft tissue mass (*black arrow*) extending from the left kidney and invading the perinephric space and the left flank (*white arrow*). (Courtesy of David S. Hartman, M.D., Hershey, Pa.)

completely replace the renal parenchyma (see Fig. 41–125). Pathologically, these areas represent either dilated calyces or focal areas of parenchymal destruction filled with pus or debris. Histologically, these cavities are lined by xanthoma cells.[92] Rim enhancement of the low-density areas often occurs. Extrarenal extension of the inflammatory process is common and may involve the perinephric space, pararenal spaces, ipsilateral psoas muscle, flank muscles, diaphragm, and skin (see Fig. 41–126).[92] Perinephric and psoas muscle abscesses often occur. In the focal form of XGP, CT shows a poorly enhancing mass adjacent to a calyx or in one pole of a kidney. Associated calculi may be found. The focal form may be misdiagnosed as a renal neoplasm.[126]

Malacoplakia. Malacoplakia is a rare inflammatory disease usually associated with chronic *E. coli* infection. The urinary collecting system (especially the bladder) is most frequently involved, but the renal pelvis, ureter, kidney, and other organs outside the genitourinary tract may be affected. Affected patients are usually middle-aged women with recurrent urinary tract infections.[26] Malacoplakia is attributed to abnormal macrophage response. The histologic hallmark of the disorder is the presence of basophilic inclusions, called *Michaelis-Gutmann bodies,* within large eosinophilic macrophages.[63] Renal parenchymal malacoplakia is usually unilateral but can be bilateral. Contrast-enhanced CT demonstrates multiple poorly defined hypodense cortical masses and associated decreased excretion of the contrast material in cases with extensive parenchymal replacement.[99, 275] Nephromegaly and perinephric extension of disease may occur.[126] The CT findings are nonspecific, and renal parenchymal malacoplakia may be indistinguishable from a neoplasm (Fig. 41–127).

Tuberculosis. Renal tuberculosis usually results from hematogenous dissemination of a pulmonary infection. The diagnosis is usually best made on excretory urography, which shows typical calyceal and ureteric abnormalities. CT may show a variety of abnormalities, many of which are nonspecific. Obstruction of a single major calyx or of a group of minor calyces often occurs because of scarring. The obstructed calyces are dilated and show no excretion of contrast medium, and thinning of the overlying renal parenchyma occurs.[126] Tuberculosis of the renal pelvis is manifested as either hydronephrosis secondary to ureteropelvic junction obstruction or diffuse pelvic contraction with fibrosis extending down a thickened ureter. The vari-

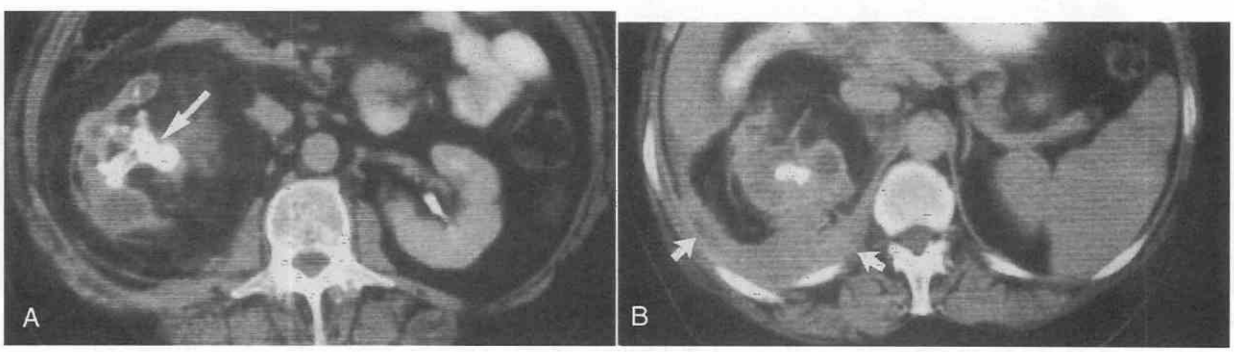

Figure 41–126. Xanthogranulomatous pyelonephritis with a contracted kidney. *A,* A staghorn calculus (*arrow*) is present in the right renal pelvis. The right kidney is small and replaced by oval, fluid-density areas. *B,* A more cephalad CT scan shows extensive chronic inflammatory change (*arrows*) in the posterior pararenal space.

Figure 41–128. Renal tuberculosis with diffuse parenchymal calcification involving most of the right kidney (*arrow*) as shown on an unenhanced CT scan. (Courtesy of David S. Hartman, M.D., Hershey, Pa.)

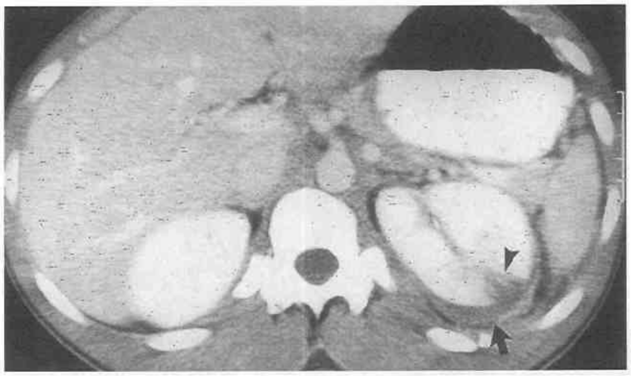

Figure 41–130. Category I renal trauma. There is a small cortical laceration (*arrowhead*) involving the left kidney. An associated small perinephric hematoma is present (*arrow*).

ous patterns of hydronephrosis seen at CT depend on the site of the stricture and include focal caliectasis, caliectasis without pelvic dilatation, and generalized hydronephrosis.[285] Low-density parenchymal lesions, probably representing areas of caseous necrosis, may be seen.[126] The calcifications within the renal parenchyma may be amorphous, granular, curvilinear, or lobar ("putty kidney") (Fig. 41–128).[97] In a tuberculous putty kidney, large, round or oval, dense renal calcifications representing calcified caseating material in medullary cavities and dilated calyces are found. This condition, also called tuberculous autonephrectomy, is due to the superimposition of ureteral obstruction on renal parenchymal tuberculosis (Fig. 41–129).

Renal Trauma

Renal trauma may be caused by both blunt and penetrating abdominal injuries. Blunt trauma is responsible for most renal injuries. Such injuries are usually mild and heal without specific therapy.[168] Serious renal injury is often associated with damage to other structures, such as the liver, spleen, bowel, pancreas, or chest. Multiorgan involvement occurs in about 80% of patients with penetrating injuries and in about 75% of those with blunt trauma.[66, 231]

Imaging Classification and Management

Categorization of renal injuries according to severity provides a helpful guide to patient management. Renal injuries are classified into four categories on the basis of imaging findings.[72] Category I lesions (75% to 85% of cases) are clinically insignificant; they consist of contusions and small corticomedullary lacerations that do not communicate with the collecting system (Fig. 41–130). They are managed nonoperatively.[66, 72] Category II lesions (10% of cases) are more serious and comprise major lacerations through the renal cortex extending to the medulla or collecting systems with or without urinary extravasation (Fig. 41–131). Many of these lesions are managed nonoperatively. However, surgery is sometimes required in patients with extensive hemorrhage or urinary extravasation and a large amount of nonviable renal tissue.[122] Category III lesions (5% of cases), which are catastrophic, consist of shattered kidney (multiple deep lacerations) (Fig. 41–132) and injury to the renal pedicle (Figs. 41–132 to 41–134). The rare entities of ureteropelvic junction avulsion and laceration of the renal pelvis are designated as category IV lesions. Category III and IV renal lesions usually require surgical intervention. Subcapsular and perinephric hematomas may occur in any of the categories of renal trauma,

Figure 41–129. Renal tuberculosis. The left kidney shows large, oval, dense calcifications (*arrow*) representing calcified caseating material in medullary cavities and dilated calyces (tuberculous autonephrectomy). Low-density areas in the right kidney probably represent foci of caseous necrosis.

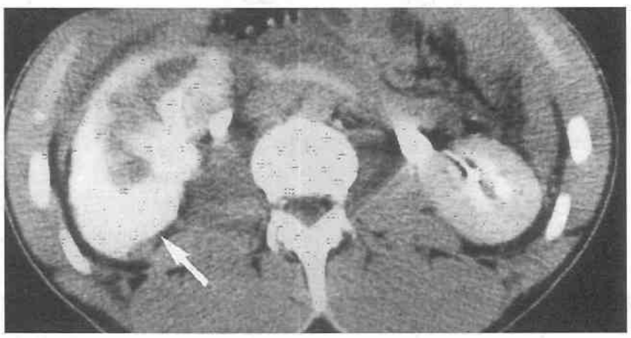

Figure 41–131. Category II renal trauma. A renal laceration (*not shown*) involved the collecting system, resulting in contrast extravasation into the right perinephric space (*arrow*). The lesion responded to conservative management.

Figure 41–132. Category III renal trauma—shattered kidney. There are multiple right renal lacerations with the fragments separated by blood clot. An associated perinephric hematoma (*arrow*) is present. A right nephrectomy was performed.

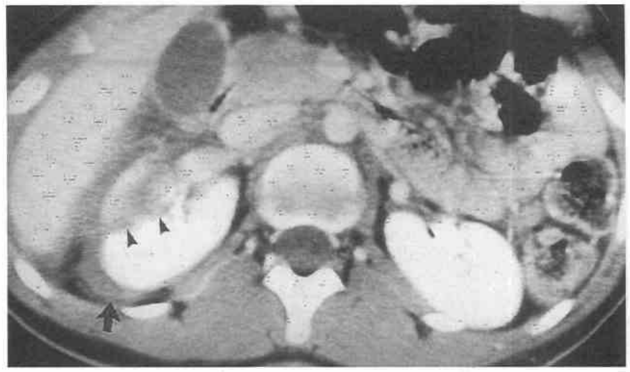

Figure 41–134. Deep renal laceration (*arrowheads*) extending into the renal medulla without involvement of the collecting system. A small perinephric hematoma (*arrow*) is present.

but when they occur in isolation, they are assigned to category I. Although an image-based classification of renal trauma is useful in guiding management, treatment is often ultimately determined by the patient's clinical status.

Imaging of Renal Trauma

Gross hematuria is the most reliable indication of potentially serious renal damage.[122] However, the absence of hematuria does not preclude significant renal injury; absence of hematuria has been reported in up to 24% of patients with renal artery thrombosis and in one-third of cases of uretero-pelvic junction injury.[22, 258] Contrast-enhanced CT is the preferred modality for evaluation of patients with blunt or penetrating abdominal trauma with scans obtained at 70 seconds and 3 minutes after the start of injection of contrast material.[122]

The three basic types of renal injury demonstrable by CT are contusions, lacerations, and infarcts, any of which may be further complicated by intrarenal or extrarenal hematomas or by urinary extravasation. The mildest form of renal injury is the contusion, characterized by an amorphous, interstitial extravasation of blood and edema. On unenhanced CT scans, the affected kidney zones may show focal swelling and irregular infiltrates of high-density fresh blood. On contrast-enhanced CT, renal contusions appear as ill-defined, round or ovoid areas of hypoattenuation. They may also appear as small interstitial accumulations of contrast material staining on delayed images (striated nephrogram).[72, 122, 204]

Superficial lacerations are limited to the renal cortex; deep lacerations extend into the medulla (see Fig. 41–134), where they may enter the collecting system or transect the kidney.[204] Contrast extravasation is often seen in the perinephric space (see Fig. 41–131). In patients with multiple lacerations (shattered kidney), the fragments are separated and surrounded by blood clot (see Fig. 41–132).[204] Thrombosis or laceration of a segmental branch of the renal artery produces a focal area of renal infarction. Infarcts typically appear as peripherally based, wedge-shaped areas of parenchyma that fail to enhance during both the corticomedullary and pyelographic phases of CT (Fig. 41–135).[98] Post-traumatic bleeding is commonly associated with all injuries to the kidney. Hematomas may be intrare-

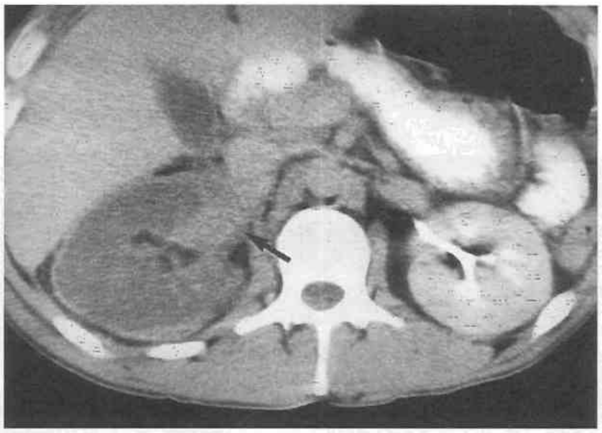

Figure 41–133. Category III renal trauma—occlusion of the right main renal artery. The right kidney shows absence of contrast enhancement except for a subcapsular rim of renal tissue perfused via capsular collateral vessels. Aortography showed occlusion of the main right renal artery. A hematoma (*arrow*) is present around the renal vascular pedicle.

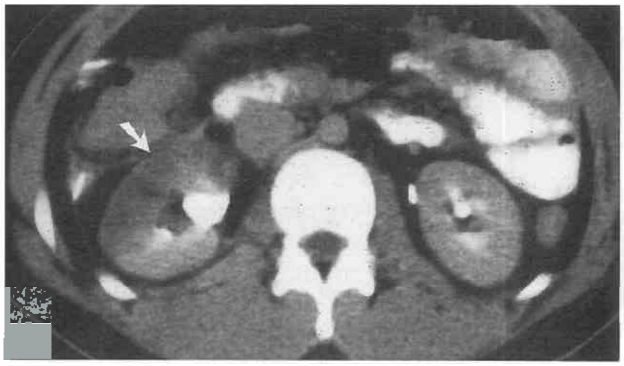

Figure 41–135. Focal renal infarction after blunt trauma. The nephrogram is absent anteriorly (*arrow*) in the right kidney. "Rim" cortical perfusion of the infarct is present.

Figure 41–136. Left perinephric urinoma (*arrows*) secondary to blunt trauma to a hydronephrotic left kidney. Hydronephrosis was due to congenital ureteropelvic junction obstruction.

nal or subcapsular or may involve the perinephric or pararenal spaces. The most significant vascular injury after blunt trauma is thrombosis of the main renal artery.[123] Main renal artery injuries can be diagnosed on CT through the use of the criterion of absence of renal contrast enhancement with or without cortical rim sign (see Fig. 41–133).[187] Other findings that suggest the diagnosis of pedicle injury include a hematoma surrounding the renal hilus (see Fig. 41–133) and abrupt cutoff of the contrast-filled renal artery.[72] Acute renal vein occlusion may be suspected if the kidney is enlarged and shows thrombus in the renal vein. Venography may be performed if injuries to the renal vein and inferior vena cava are suspected, because CT may not reliably detect venous laceration.[122]

Ureteropelvic junction injuries are rare. In these patients CT typically demonstrates excellent excretion of contrast material with an intact intrarenal collecting system, but with medial perinephric urinary extravasation rather than lateral urinary extravasation in category II injuries with involvement of the collecting system. A circumrenal urinoma may be seen around the affected kidney, but typically, there is no perinephric hematoma.[122]

Abnormal kidneys, including hydronephrotic kidneys (Fig. 41–136), ectopic kidneys, and horseshoe kidneys (Fig. 41–137) as well as kidneys containing neoplasms or cysts, may sustain injury secondary to minor trauma.[218] Gadolinium-enhanced MRI may be used to assess suspected renal injury when the use of iodinated contrast material is contraindicated.[139]

Renal Blood Flow Disorders

Renal Hemorrhage

CT is the most valuable examination in the evaluation of patients with suspected acute renal hemorrhage because it accurately diagnoses the presence and location of such hemorrhage and often shows the underlying cause.[14, 238] Renal hemorrhage may be suburothelial, intraparenchymal, subcapsular, perinephric, or pararenal in location or may involve the renal sinus.[56, 80, 135, 192]

Causes. The most common cause of renal hemorrhage is trauma, either blunt or penetrating (Figs. 41–137 and 41–138). Extracorporeal shock wave lithotripsy for nephrolithiasis is another form of renal trauma not infrequently associated with parenchymal and perinephric hemorrhage (Fig. 41–139).[192] Spontaneous (nontraumatic) renal hemorrhage may be caused by anticoagulation, blood dyscrasias

Figure 41–137. Injury of horseshoe kidneys. *A*, Bilateral perinephric hematomas (*arrows*) are present. *B*, A caudal CT scan shows a hematoma (*white arrow*) involving the isthmus connecting the two kidneys. There is contrast extravasation (*black arrow*) from the left collecting system because of a laceration.

Figure 41–138. Fat-suppressed T1-weighted MR image (TR = 600 msec, TE = 17 msec) shows a high-intensity left perinephric hematoma (*arrow*) due to a renal biopsy performed 2 weeks earlier. Loss of corticomedullary differentiation is due to chronic renal disease.

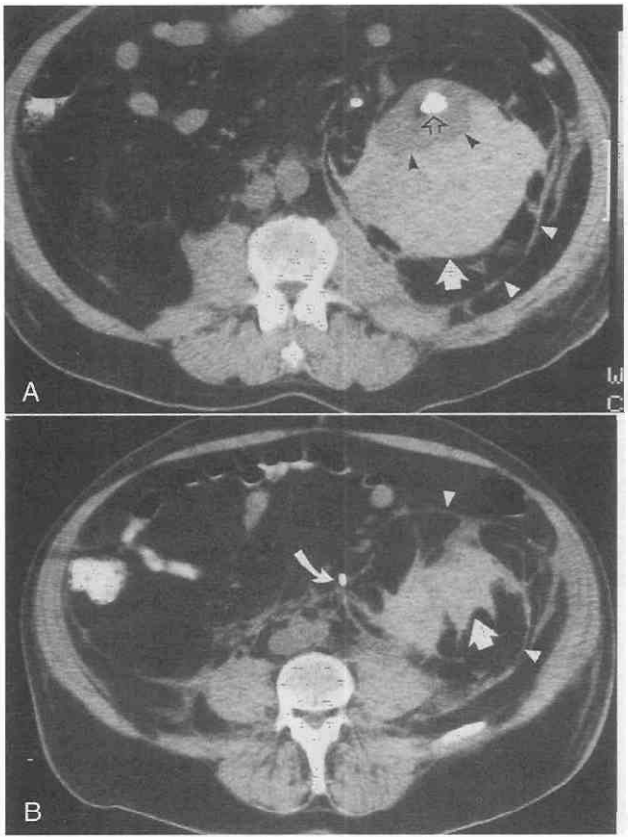

Figure 41–139. Left perinephric hematoma secondary to extracorporeal shock wave lithotripsy. *A,* An unenhanced CT scan reveals anterior displacement of left kidney (*black arrowheads*) by high-density hematoma (*arrow*). There is a calculus (*open arrow*) in the collecting system. The hematoma is limited posteriorly by the posterior renorenal bridging septum, which separates it from the thickened posterior renal fascia (*white arrowheads*). *B,* The hematoma (*white arrow*) extends into the infrarenal fascial cone (*arrowheads*). Infrarenal extension confirms the perinephric location of the hematoma and distinguishes it from a subcapsular hematoma. The left ureter (*curved arrow*) contains a stent and is displaced anteriorly.

(Fig. 41–140), renal infarction, polyarteritis nodosa (Fig. 41–141), renal aneurysms and arteriovenous malformations, RCC, AML, (see Fig. 41–104), renal abscess, renal vein thrombosis, and rupture of hemorrhagic solitary cysts (Fig. 41–142) or of hemorrhagic cysts in renal cystic disease (see Figs. 41–32 and 41–45).[14, 146, 150] Some cases are idiopathic.[14] RCC is probably the most common cause of spontaneous subcapsular and perinephric hemorrhage.

Findings on CT. Recent renal hemorrhage is characterized by high-attenuation blood (50 to 90 HU), which are best shown by unenhanced CT scans (see Fig. 41–139). Postcontrast scans should also be obtained to facilitate identification of disorders such as small neoplasms causing spontaneous renal hemorrhage. Suburothelial hemorrhage is characterized on CT by thickening of the wall of the renal pelvis and upper ureter by blood that has a high-attenuation value on unenhanced scans.[135] Spontaneous hemorrhage into the renal sinus is characterized by a high-density blood collection in the renal sinus with displacement of the renal pelvis (Fig. 41–143).[80] Renal sinus hematomas usually resolve spontaneously, as shown by follow-up CT. Both suburothelial and renal sinus hemorrhage occur most commonly in patients undergoing anticoagulation therapy or with bleeding or coagulation disorders.[80, 135]

On an unenhanced CT scan, a recent subcapsular hematoma is characterized by a mass with a higher attenuation value than that of adjacent renal parenchyma (see Fig. 41–140). Pressure on the underlying renal parenchyma characteristically causes flattening of the kidney, elevation of the renal capsule, and medial displacement of the collecting system. Sometimes, subcapsular hematomas fail to resolve, causing chronic fluid collections that compress the renal parenchyma. This, in turn, may cause hypertension by reducing renal blood flow, thereby triggering the renin-angiotensin-aldosterone system. This clinical entity is called the *Page kidney.*[122] The walls of chronic subcapsular hematomas may eventually calcify (Fig. 41–144).

Perinephric hematomas involve the fat between the renal capsule and the renal fascia. The configuration of such hematomas is determined largely by the bridging septa in the perinephric fat.[136] When a hematoma is confined by the

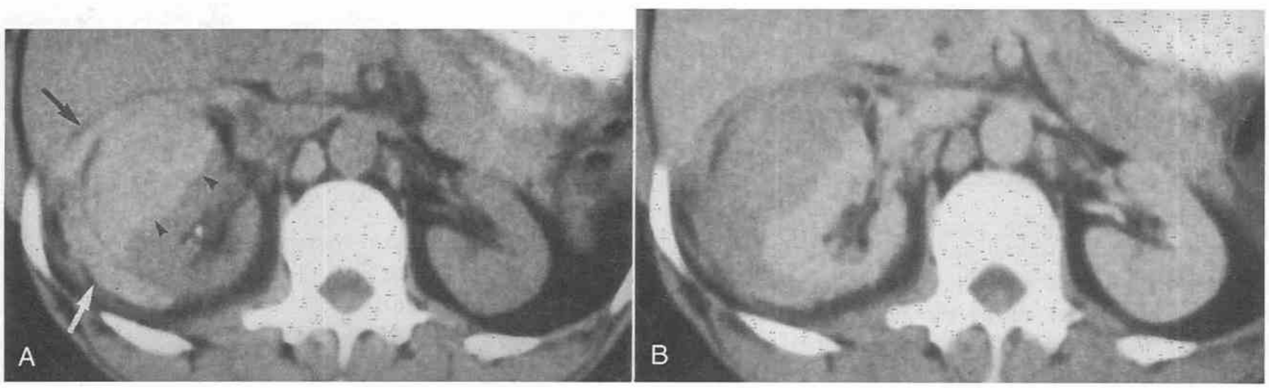

Figure 41–140. Right subcapsular and perinephric hemorrhage associated with idiopathic thrombocytopenia. *A,* An unenhanced CT scan shows indentation of the lateral border (*arrowheads*) of the right kidney by a denser subcapsular hematoma. A smaller perinephric hematoma (*arrows*) is also present. *B,* A contrast-enhanced CT scan shows that the hematoma is less dense than the enhanced renal parenchyma. (From Levine E, Grantham JJ, MacDougall ML: Spontaneous subcapsular and perinephric hemorrhage in end-stage kidney disease: Clinical and CT findings. AJR Am J Roentgenol 148:755–758, 1987.)

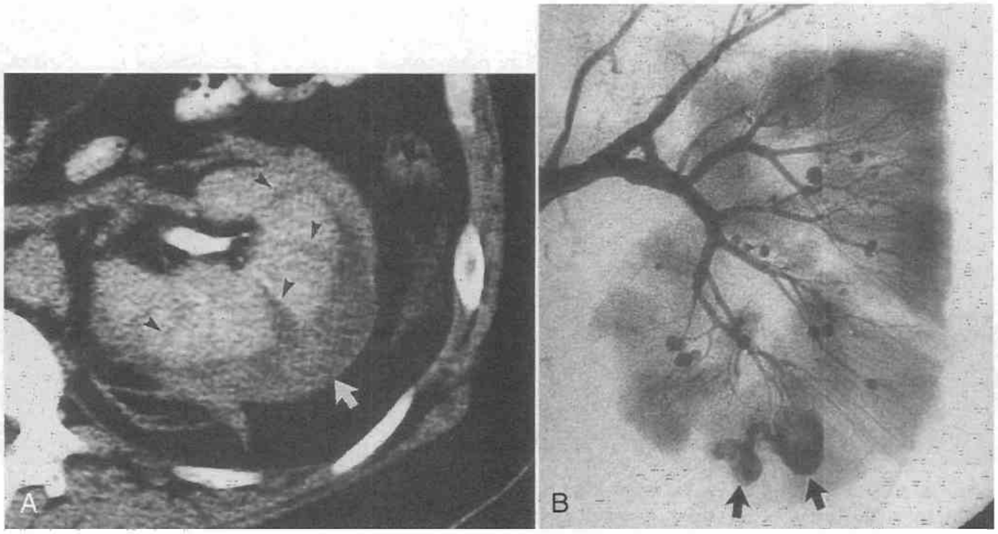

Figure 41–141. Multiple renal infarcts and perinephric hemorrhage complicating polyarteritis nodosa. *A,* A left perinephric hematoma (*arrow*) is contained by the posterior renorenal bridging septum. There are several wedge-shaped infarcts (*arrowheads*) involving the renal parenchyma. *B,* A left selective renal arteriogram shows multiple small aneurysms arising from interlobar arteries. Active contrast extravasation (*arrows*) in the lower pole indicates bleeding from a ruptured aneurysm. The patient showed response to selective embolization of the feeding artery. (Courtesy of James Bergh, M.D., Overland Park, Kan.)

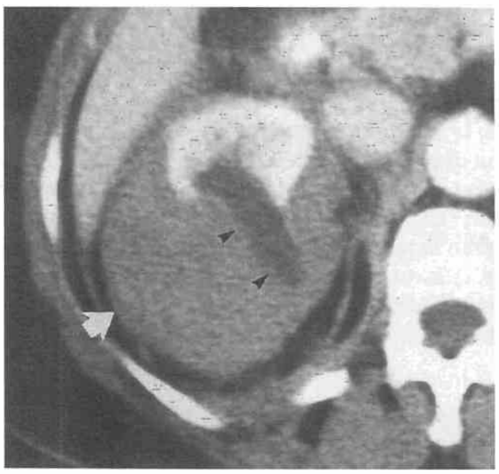

Figure 41–142. Right perinephric hematoma (*arrow*) probably due to rupture of a simple renal cyst. The cyst (*arrowheads*) is flattened by the hematoma.

Figure 41–143. Acute hemorrhage (*arrow*) in the left renal sinus associated with anticoagulant therapy displaces the renal pelvis.

posterior renorenal bridging septum, it may compress and indent the renal surface, and because it is separated from the renal fascia, it may simulate a subcapsular hematoma (see Figs. 41–139 and 41–141).[136] However, although subcapsular hematomas are confined to the kidney by the renal capsule, perinephric hematomas often extend caudally below the kidney into the cone of renal fascia (see Fig. 41–139).

CT often shows the cause of spontaneous subcapsular and perinephric hematomas.[238] RCCs or AMLs associated with such hematomas may be suspected on CT from the presence of a distinct mass clearly different in character from the surrounding hemorrhage.[14] RCCs present as heterogeneous, enhancing solid masses or as cystic masses, manifest whereas an AML is suggested by the presence of tumor fat (see Fig. 41–104).[14] CT may show that hemorrhage originated in either a solitary renal cyst (see Fig. 41–142)[56] or a cyst associated with hereditary or acquired renal cystic disease (see Figs. 41–32 and 41–45).[146, 150] If CT shows no cause for hemorrhage, renal angiography may help with diagnosis by demonstrating underlying disorders such as angiitis, renal aneurysms, arteriovenous malformations, and polyarteritis nodosa (see Fig. 41–141).[14]

Management. CT is valuable in the follow-up and management of renal hemorrhage whether spontaneous or due to trauma. RCCs complicated by hemorrhage are managed with nephrectomy, whereas underlying hemorrhagic renal cysts, renal infarcts, or AMLs can usually be managed conservatively.[14, 150] When the bleeding is extensive and the patient is unstable, renal angiography with embolization (see Fig. 41–141) or, occasionally, surgery may be necessary to stop the bleeding.[27, 150] Patients with spontaneous renal hemorrhage who have no demonstrable cause for the bleeding or for whom the diagnosis of the cause of the hemorrhage is in doubt should also receive conservative management. To exclude an underlying RCC, however,

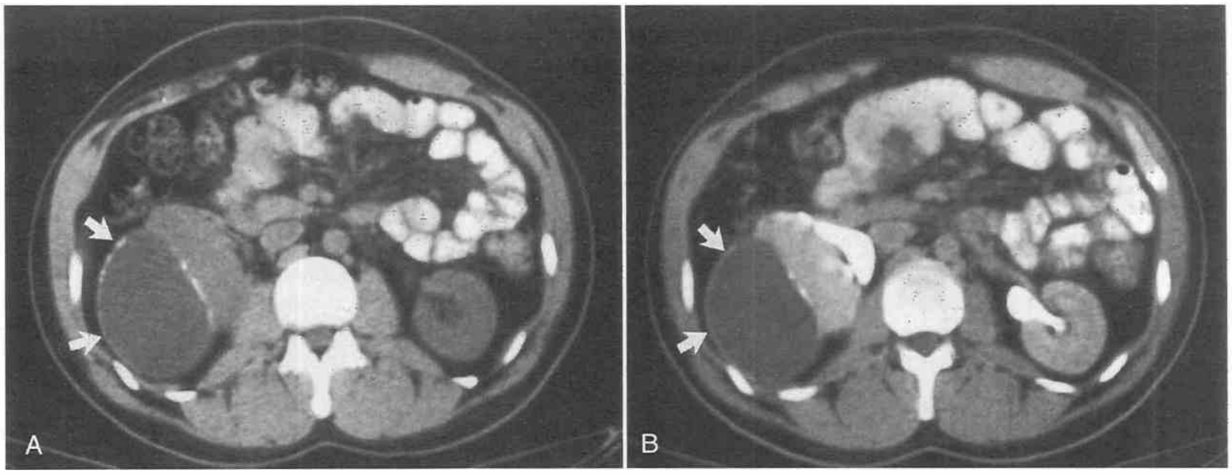

Figure 41–144. Chronic calcified subcapsular hematoma in a hypertensive man. The low-density (17 HU) posterolateral mass with peripheral calcification (*arrows*) causes anteromedial displacement of the right kidney as seen on unenhanced (*A*) and contrast-enhanced (*B*) CT scans.

serial CT should be used to monitor such patients until the hematoma completely resolves.[14] This approach avoids unnecessary nephrectomy in patients who have spontaneous renal hemorrhage with benign renal disease or no underlying disease.[14, 27]

Renal Infarction

Renal infarction may be due to renal artery thrombosis or embolism, vasculitis as in polyarteritis nodosa, trauma, sickle cell disease, or aortic dissection. The most common cause is thromboembolism from cardiovascular disease.[123] CT findings depend on both the extent and age of the infarction. The size and shape of a renal infarct is determined by the size of the occluded artery. If the main renal artery is occluded, global infarction of the kidney occurs (see Fig. 41–133). On contrast-enhanced CT scans, the affected kidney shows lack of enhancement, apart from a high-density cortical rim reflecting perfusion of the preserved outer rim of the cortex by collateral vessels (see Fig. 41–133).[116] The renal collateral circulation is supplied via renal capsular vessels, peripelvic vessels, and periureteral vessels.

If a major renal artery branch is occluded, an acute focal infarct results, which manifests as a wedged-shape low-attenuation renal parenchymal lesion on a contrast-enhanced CT scan. The base of the wedge is contiguous with the renal capsule and the apex is directed toward the renal hilus.[98] There is usually sharp margination between infarcted tissue and the adjacent normal nephrogram (Fig. 41–145). A rim sign is often seen on the capsular margin of the infarct. Emboli and vasculitis cause multiple, often bilateral, focal renal infarcts (Fig. 41–146).[292] Unilateral infarcts are often the result of renal trauma, which is also a common cause of global renal infarction (see Fig. 41–133).[292] When smaller intrarenal arteries are occluded, the CT findings are less specific and consist of multiple low-attenuation defects that are scattered throughout the nephrogram although usually peripherally located. Vascular thrombosis in sickle cell disease causes multiple foci of "slitlike" areas of low attenuation.[292]

Both acute focal and global infarcts may be associated with subcapsular or perinephric blood or fluid collections and thickening of the renal fascia (see Fig. 41–146).[292] Old infarcts manifest on CT as renal cortical scars or as a small, shrunken kidney (Fig. 41–147).[123]

The main CT differential diagnosis of acute renal infarction is acute pyelonephritis, because both conditions (1) often demonstrate wedge-shaped, low-attenuation renal lesions on CT and (2) often manifest as acute onset of flank pain and fever. A cortical rim sign should strongly suggest the diagnosis of renal infarction (see Fig. 35–146), because it is usually not seen in acute pyelonephritis.[292] Small renal infarcts may also be confused with focal lymphomatous lesions or metastases on CT.

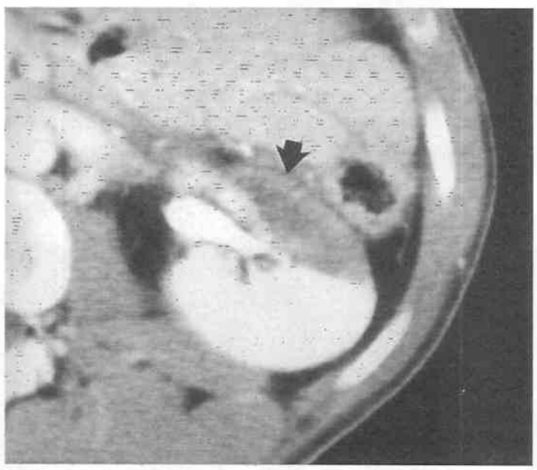

Figure 41–145. Focal renal infarct associated with emboli from a prosthetic mitral valve. The lesion (*arrow*) manifests as a wedge-shaped zone of low attenuation. The base of the wedge is contiguous with the renal capsule, and the apex is directed toward the renal hilus. There is a straight, sharp margin between the infarct and normal renal tissue. A rim of perfused tissue is seen on the capsular margin of the infarct.

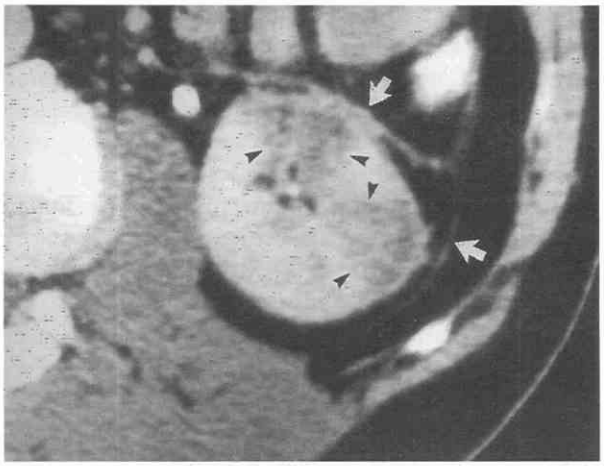

Figure 41–146. Left renal infarcts [redacted] with fibrodysplastic occlusions of bran[redacted] Both lesions show subcapsular rims of perfused tissue, and there is associated thickening of the anterior and posterior renal fascia (*arrows*).

Renal Artery Stenosis

Secondary hypertension due to diseases of the renal arteries (i.e., renovascular hypertension) accounts for about 1% to 5% of all cases of hypertension.[176] Atherosclerosis and fibrodysplastic disease are the most common causes of significant renal artery narrowing. Although there are several tests for evaluating patients with suspected renovascular hypertension, the standard for the diagnosis of renal artery stenosis is angiography, with response to treatment the proof of its significance.[215] CT angiography (CTA) and MRA provide noninvasive means to obtain anatomic information. CTA and gadolinium-enhanced three-dimensional MRA seem to be preferred in patients referred for evaluation of renovascular hypertension.[280]

Computed Tomography. The renal arteries are not always well shown by conventional CT. However, significant renal artery disease may be suspected from conventional dynamic CT scans if the affected kidney shows prolonged corticomedullary differentiation in comparison with the normal side (Fig. 41–148). Global loss of renal parenchyma, if present, may be ancillary evidence of chronic arterial stenosis or occlusion (see Fig. 41–148).[16]

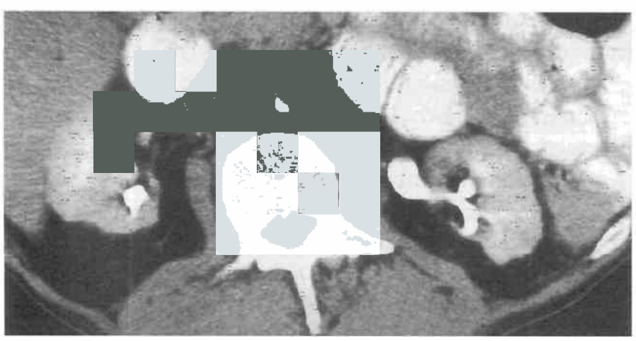

Figure 41–147. Bilateral renal scarring due to old infarcts in a hypertensive patient.

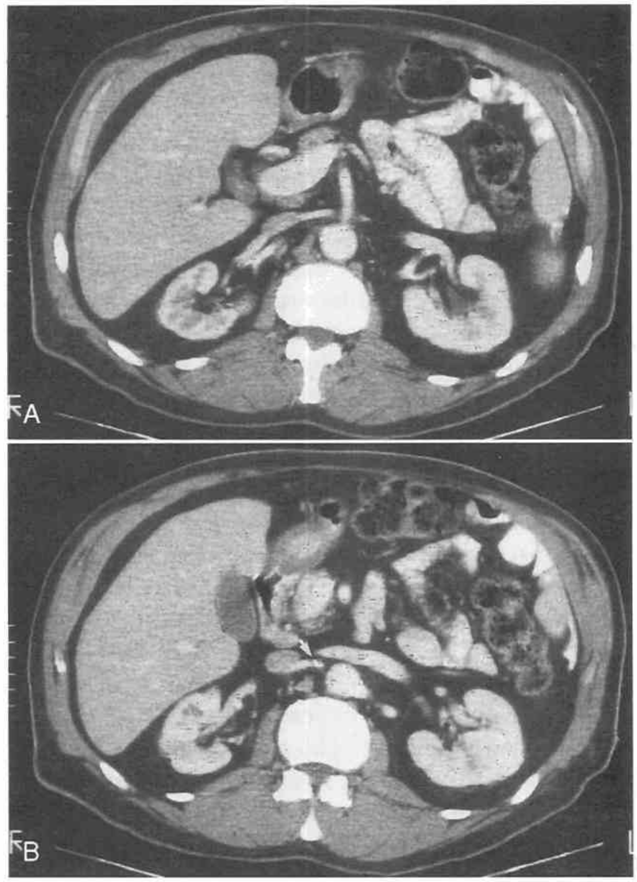

Figure 41–148. Right renal artery stenosis. *A,* Dynamic CT scan after a rapid intravenous injection of contrast agent shows prolonged corticomedullary differentiation in the right kidney as compared with the left kidney, for which the nephrogram is almost homogeneously dense. The right kidney also shows global atrophy. *B,* A contiguous caudal image reveals a calcified atherosclerotic plaque (*arrow*) at the origin of the right renal artery. (From Birnbaum BA, Bosniak MA, Megibow AJ: Asymmetry of the renal nephrogram on CT: Significance of the unilateral prolonged cortical nephrogram. Urol Radiol 12:173–177, 1991.)

The development of helical (spiral) CT and now multidetector (multislice) CT with subsecond speed allows volumetric acquisitions to be obtained during a single breath-hold. Multislice CT systems allow the simultaneous acquisition of multiple slices per gantry rotation. In combination with faster gantry rotation times of 0.5 second, the abdominal structures can be displayed in higher spatial and temporal resolution. The advantage of this technique is that it eliminates the respiratory misregistration that often degrades the image quality.[134] Sensitivity and specificity for significant renal artery stenosis with single-slice helical CT are 88% to 97% and 83% to 89%, respectively, compared with catheter angiography.

Multislice CTA exceeds MRA in spatial resolution and is now able to display even small vascular side branches.[212] Compared with catheter angiography, CTA has a sensitivity of 95% to 100% and a specificity of 99% to 100% for detection of accessory renal arteries (Fig. 41–149).[77] The renal vascularity is evaluated during the vascular phase, which occurs approximately 15 to 25 seconds after the

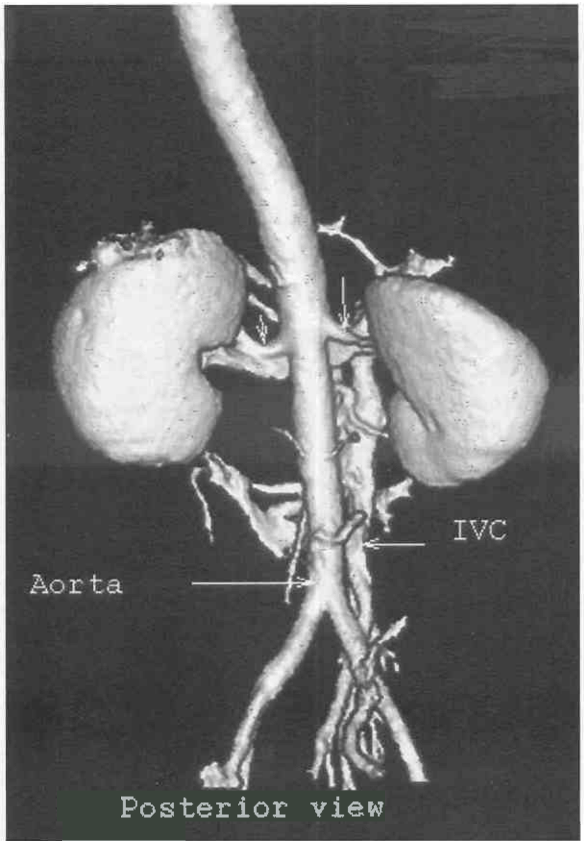

Figure 41–149. 3D multiplanar reconstruction, posterior view. There is slight narrowing of the right renal artery in its midcourse, and both renal arteries are of normal caliber at their origin (*arrows*). IVC = inferior vena cava.

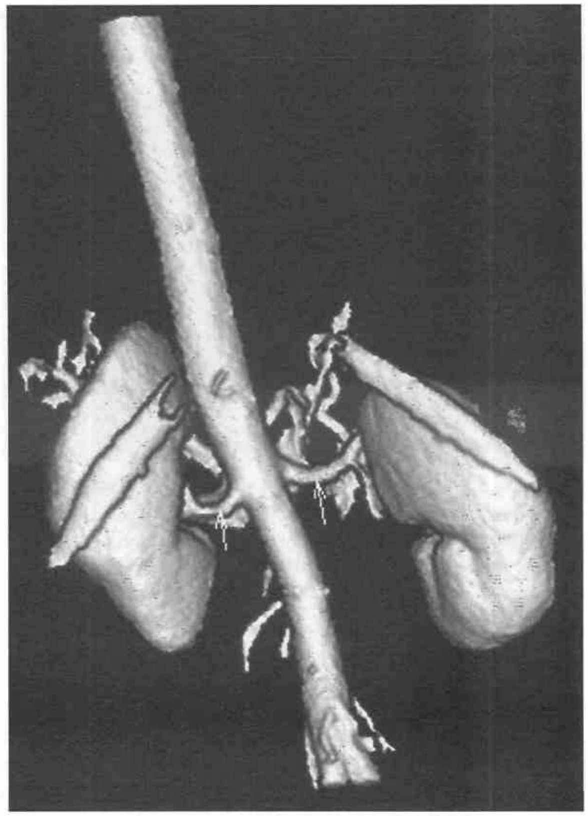

Figure 41–150. 3D multiplanar reconstruction, posterior view, with overlying 12th rib. *Arrows* point to the renal arteries.

start of injection of intravenous contrast material adminstration.[123] Typical acquisition parameters for CTA of the renal artery include a collimation of 3 mm, a pitch of 1.5 to 2.0, a reconstruction interval of 1 to 2 mm, a scan delay of 25 seconds after the start of contrast material, and an injection rate of 3 ml/sec or greater.[208, 228, 229] Images should be reconstructed with 50% overlap to improve detection of renal artery stenosis and 3D reconstruction.

Commonly used 3D visualization techniques include surface rendering, maximum intensity projection (MIP), and volume rendering. Volume rendering is superior to MIP and surface rendering because it uses the volume data and can provide lifelike images, including color. This permits multiplanar reconstruction (MPR) in any plane (Fig. 41–150). This technique is very useful in the pretransplantation evaluation of renal donors and in presurgical planning.

MR Angiography. MRA with gadolinium enhancement has a sensitivity of 100% and a specificity in the range of 93% to 97% for detection of proximal renal artery stenosis (Fig. 41–151).[58, 211, 259] In the past, both time-of-flight imaging and phase-contrast imaging were used; both methods have been virtually replaced by breath-hold 3D gadolinium MRA (3D-Gd). 3D-Gd breath-hold sequences prevent image degradation from respiratory motion, reduce the acquisition time, and overcome the problem of saturation of in-plane blood flow.[235] The dose of gadolinium is usually 0.2 mmol/kg. The typical injection rates are 2 to 3 mL/sec. Commonly, four different degrees of stenosis are assessed, based on the reduction of vessel diameter: normal (0%); mild (<50%); moderate (50% to 75%); or severe (75%) (Fig. 41–152).[235] In about 20% to 30% of patients, the kidney is supplied by more than one renal artery (Fig. 41–153).[235] 3D-Gd–enhanced MRA allows an accurate diagnosis of proximal renal artery stenosis without the risks associated with nephrotoxic contrast agents, ionizing radiation, or arterial catheterization.

Following is a general outline of the renal artery stenosis protocol. A torso coil centered at midabdomen is used, with peripheral gating and respiratory bellows. An 18-gauge intravenous line is placed in the antecubital vein. The following sequences are obtained:

1. Breath-hold coronal-large field of view of the upper abdomen.
2. Non–breath-hold, sagittal T1-weighted spin-echo image over the aorta (6–8 slices) about 4–6 mm thick, giving a good target for Smartprep tracker placement.
3. Breath-hold coronal SSFSE of the kidneys (for cysts) prescribe off series 2.
4. Precontrast coronal 3D enhanced fast GRE (EFGRE) sequence through the territory of interest (trial run); 3 mm thick (no gap because it is 3D). Cover from the celiac axis to groin. Keep scan time under 25 to 30

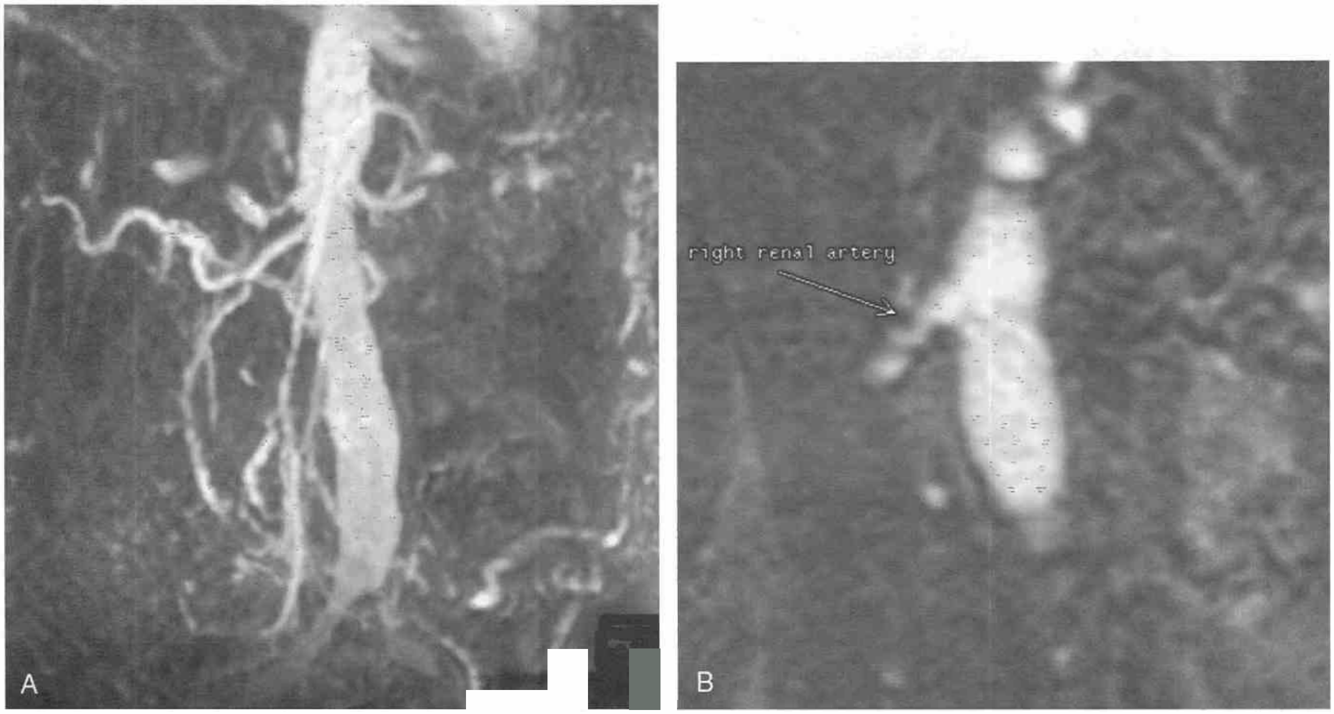

Figure 41–151. *A* and *B*, Gadolinium-enhanced MR angiogram shows stenosis of proximal right renal artery.

seconds for renal arteries. Maximize spatial resolution, increasing phase-encoding steps (can be 224 or 256 for some patients), using partial number of excitations (NEX).

5. Repeat step 4: Coronal plane 3D EFGRE with tracker placed just above the origin of renal arteries + gadolinium, with the patient's arms positioned up above the head to avoid the wrap-around artifact. Run this sequence two times successively, allowing the patient to take three deep breaths before each run.

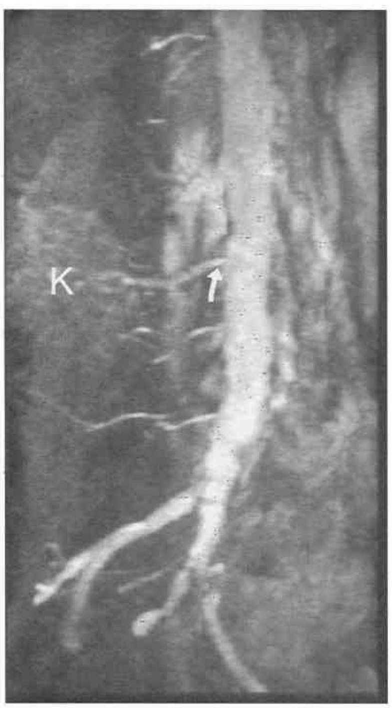

Figure 41–152. Gadolinium-enhanced MR angiogram shows severe stenosis of right renal artery at its origin (*arrow*). K = kidney.

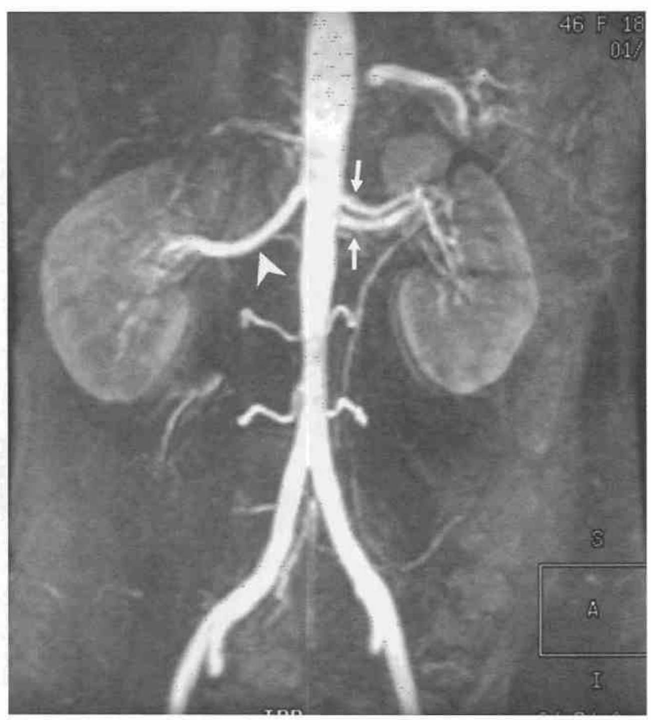

Figure 41–153. Gadolinium-enhanced MR angiogram (EFGRE 3D) composite image shows two left renal arteries (*arrows*) and a single right renal artery (*arrowhead*).

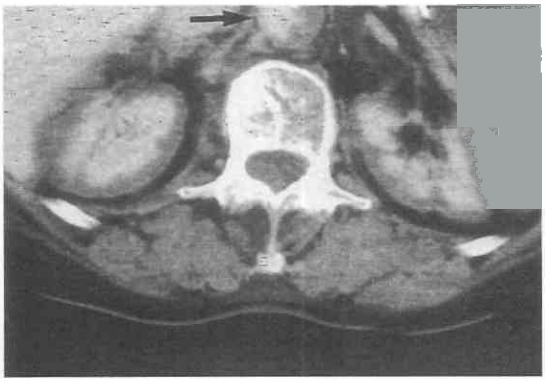

Figure 41–154. Bilateral acute renal cortical necrosis complicating aortic dissection (*arrow*). There is no enhancement of the renal cortex apart from a thin subcapsular rim perfused by capsular collateral vessels. Enhancement of the renal medulla is preserved. (Badiola-Varela CM: Acute renal cortical necrosis: Contrast-enhanced CT and pathologic correlation. Urol Radiol 14: 159–160, 1992.)

6. Optional: Flow-gradient axial from origin of the celiac axis to the iliac arteries in an elderly patient if an aneurysm is suspected; this helps visualization of the outer wall of the aneurysm.

Acute Cortical Necrosis

Acute cortical necrosis, a rare form of acute renal failure, results from ischemic necrosis of the renal cortex with sparing of the medulla.[123] The most common cause is hemorrhage in the third trimester of pregnancy, most often associated with placental abruption. Other causes are septic abortion, severe trauma with shock, transfusion reaction, severe dehydration, certain toxins including snake venom, the hemolytic-uremic syndrome, and acute aortic dissection.[112] Some of these conditions appear to act by producing renal cortical vasoconstriction, causing necrosis of the renal cortex.[52] The condition is usually bilateral, but may occasionally be unilateral.[112]

Contrast-enhanced CT shows a distinctive nephrographic pattern characterized by a zone of unenhanced cortex between a rim of enhancing subcapsular cortex and the enhancing juxtamedullary cortex and medulla (Fig. 41–154).[112, 172] Global atrophy of the kidneys occurs within a few months, leading to small, smooth kidneys. A dense linear "tram-line" calcification can form in the renal-cortex.[67]

Renal Artery Aneurysm and Arteriovenous Communications

Renal artery aneurysms may be saccular, fusiform, or intrarenal. The most common cause of aneurysms of the renal artery is atherosclerosis.[162] Other causes include medial fibrodysplasia, pregnancy, neurofibromatosis, and Ehlers-Danlos syndrome. Intrarenal aneurysms are usually associated with polyarteritis nodosa and Wegener's granulomatosis.[123] Most aneurysms are extrarenal (Fig. 41–155). Aneurysms of the main renal artery or its major branches may show rimlike calcification (Fig. 41–156) and significant enhancement on CT scans. Renal infarcts secondary to emboli from mural thrombus in the aneurysm may be seen on contrast-enhanced CT.[123] Demonstration of small intrarenal aneurysms requires selective renal arteriography.

Renal arteriovenous communications that are developmental are called arteriovenous malformations. Arteriovenous fistulas (AVFs) account for 70% to 80% of arteriovenous communications in the kidney.[43] Penetrating trauma is the most common cause of AVF; other causes include

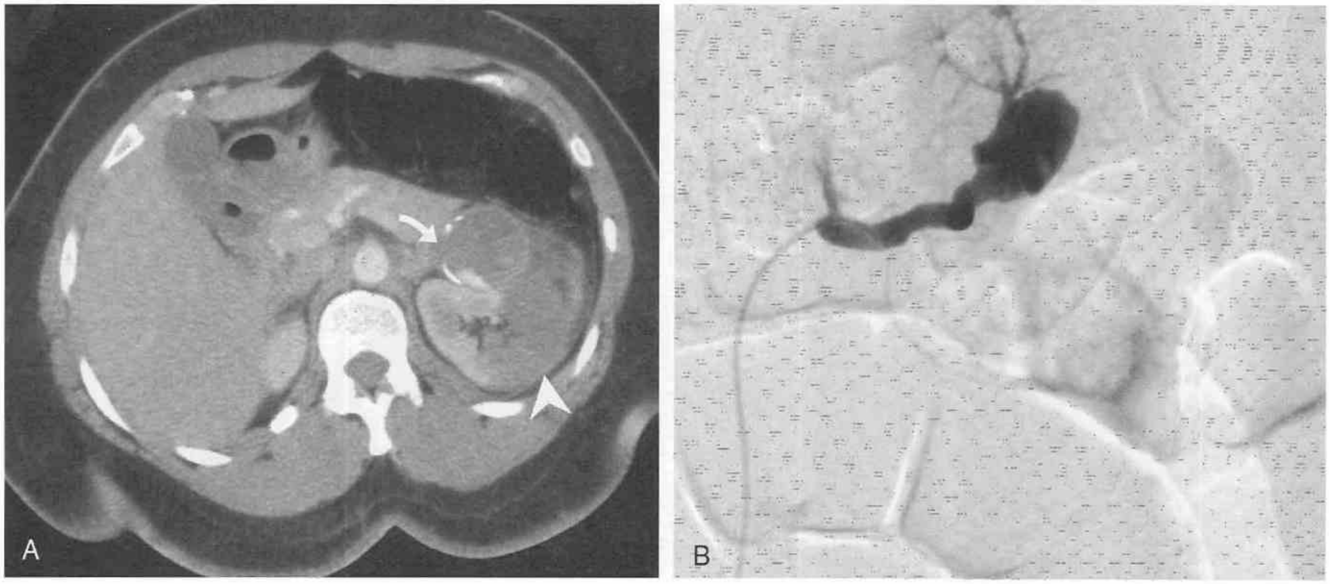

Figure 41–155. Left renal aneurysm *A,* Contrast-enhanced axial CT shows an extrarenal large aneurysm with thrombus (*arrow*) and focal calcification in its wall posteriorly. The embolus from the aneurysm has resulted in segmental infarct (*large arrowhead*). *B,* The selective angiogram of the left kidney confirms the extrarenal aneurysm of the renal artery.

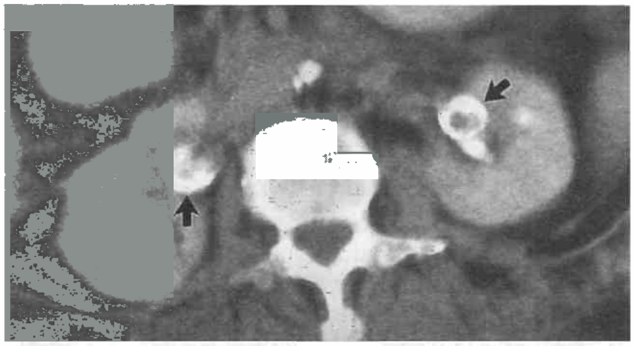

Figure 41–156. Bilateral atherosclerotic renal artery aneurysms (*arrows*) with peripheral calcification.

surgery, tumors, and inflammation; AVFs may also be idiopathic.[123] Small intrarenal AVFs or arteriovenous malformations are best diagnosed with selective renal arteriography. However, larger lesions may be calcified and may occur in the renal sinus where they may be confused with other renal masses (Fig. 41–157). These vascular lesions are best assessed on contrast-enhanced CT. A nonthrombosed lesion enhances to the same extent as the adjacent aorta. A thrombosed lesion shows no contrast enhancement (see Fig. 41–157). Visualization of an enlarged feeding renal artery and draining vein confirms the nature of an AVF (see Fig. 41–157).

Renal Vein Occlusion

Renal vein occlusions may be categorized into the following five groups:

1. Extrinsic occlusion of the renal vein by an adjacent neoplasm, e.g., pancreatic carcinoma or lymphoma.[155]
2. Direct renal vein extension of RCC or adrenal neoplasms.[111]
3. Renal vein thrombosis associated with primary renal disease. About 20% of patients with the nephrotic syndrome due to such causes as membranous glomerulonephritis, lupus erythematosus, and amyloidosis have renal

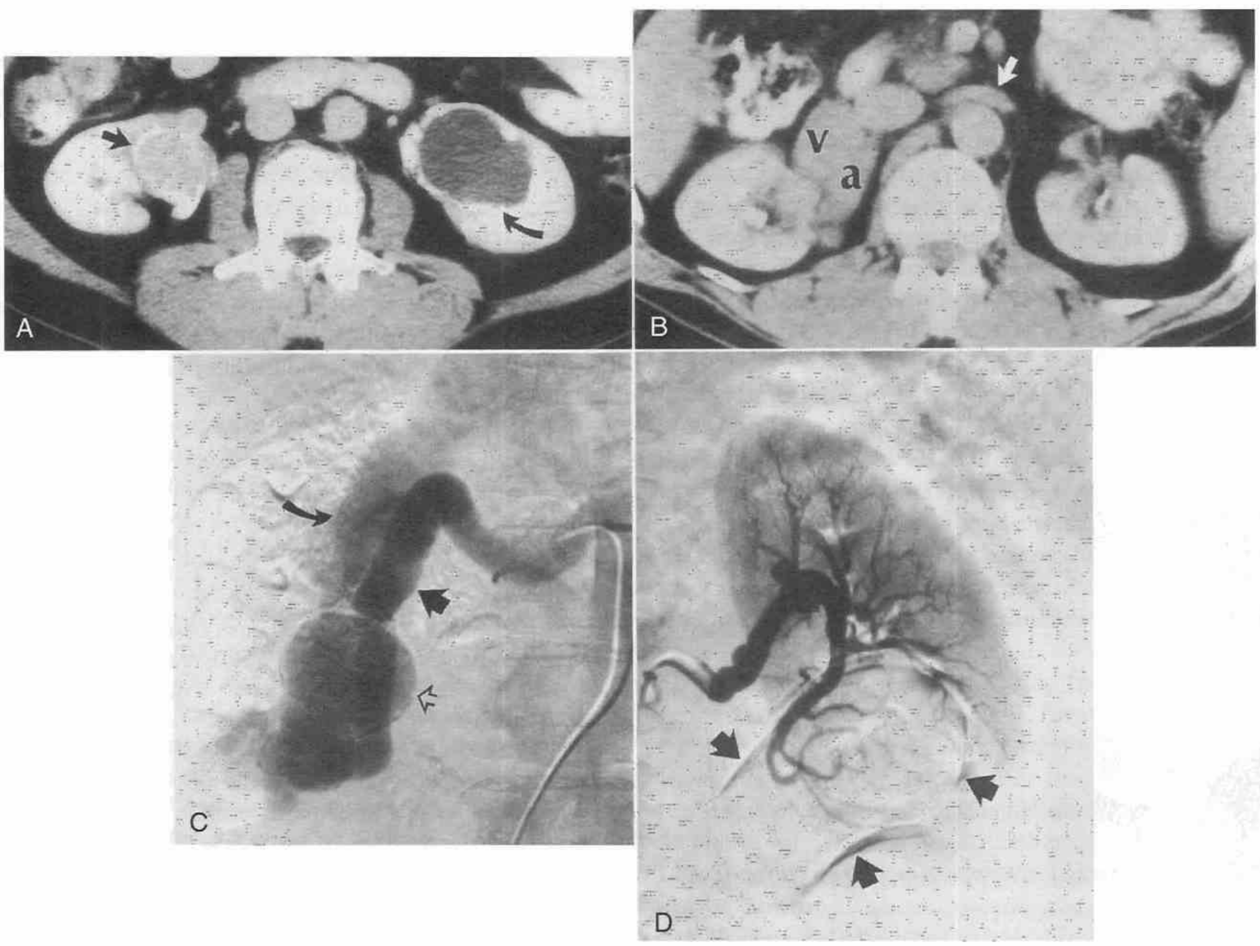

Figure 41–157. Bilateral renal artery pseudoaneurysms in a patient with a history of previous trauma. *A,* Contrast-enhanced CT scan shows an enhancing mass with peripheral calcification (*arrow*) in the lower part of the right renal hilus. There is also a nonenhancing mass with peripheral calcification (*curved arrow*) in the lower part of the left renal hilus. *B,* Cephalad scan reveals significant enlargement of the right renal artery (a) and vein (v), indicating an arteriovenous fistula. The left renal vein (*arrow*) is normal in size. *C,* Right selective renal arteriogram reveals enlargement of the right renal artery (*arrow*) and vein (*curved arrow*). The calcified pseudoaneurysm is opacified (*open arrow*). *D,* The left renal artery pseudoaneurysm (*arrows*) does not opacify because of thrombosis.

vein thrombosis, which may be acute or chronic.[294] In adults, the most common underlying abnormality is membranous glomerulonephritis.[123]

4. Secondary renal vein occlusion or thrombosis may occur when the inferior vena cava is thrombosed after caval extension of thrombus from pelvic or leg veins.
5. Renal vein thrombosis, which may occur as a primary phenomenon in infants with a history of maternal diabetes, sickle cell disease, hemoconcentration states such as diarrhea and sepsis, and hypoxia in cyanotic congenital heart disease.[94] Adults with hypercoagulable states may also experience renal vein thrombosis.

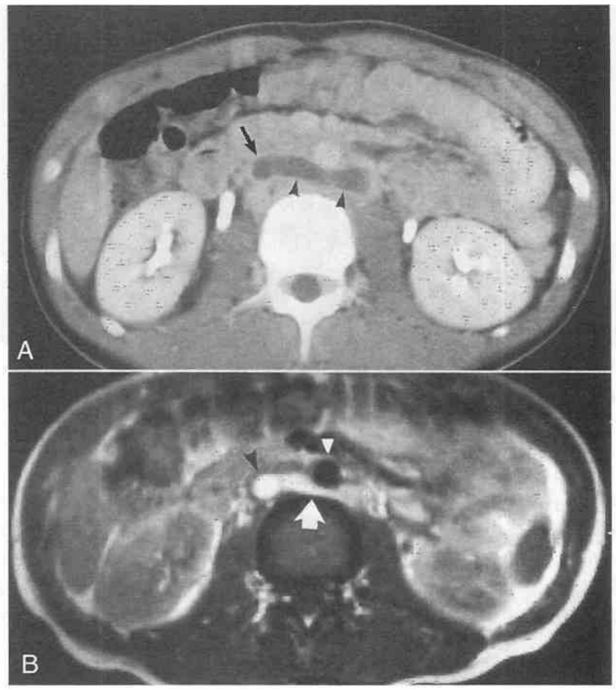

Figure 41–159. Renal vein thrombosis associated with the nephrotic syndrome. *A*, Low-density thrombus is present in a retroaortic left renal vein (*arrowheads*) and in the adjacent inferior vena cava (*arrow*). B, Spin-echo MR image (TR = 650 msec, TE = 30 msec) shows high signal thrombus in the retroaortic left renal vein (*arrow*) and in the adjacent inferior vena cava (*black arrowhead*). The aorta (*white arrowhead*) shows normal blood flow.

The clinical and imaging findings in renal vein thrombosis depend on the severity of occlusion, the rapidity of onset, the location of the thrombus, and the cause. Left renal vein thrombosis is more common. A classic acute presentation consists of flank pain, hematuria, and loss of renal function.[123] Patients with chronic renal vein occlusion are usually asymptomatic.

Contrast-enhanced CT is an excellent method for the noninvasive diagnosis of renal vein thrombosis, provided that renal function is normal. CT permits differentiation between acute renal vein thrombosis and conditions that have similar clinical presentations, such as acute pyelonephritis, acute renal infarction, and acute renal obstruction.[88]

Renal vein thrombosis is generally unilateral. In acute and subacute cases, an enlarged, swollen kidney is seen on CT. The nephrogram in the affected kidney is initially diminished because of impaired renal perfusion; however, once the nephrogram develops, it persists for a prolonged period and there is often prolonged enhancement of the renal cortex relative to the renal medulla (Fig. 41–158).[123] Calyceal opacification is often delayed, diminished, or absent in the affected kidney. Stranding of the perinephric fat due to edema and thickening of the renal fascia may occur. Enlarged perirenal collateral veins are often noted. Perinephric hemorrhage may occur. On CT, the renal vein is commonly enlarged and may show a filling defect because of thrombus (see Fig. 41–158).[87, 247] Thrombosis of the inferior vena cava at or near the renal vein orifices occurs in about 40% to 50% of patients with renal vein thrombosis (Fig. 41–159).

Demonstration of venous thrombus is facilitated by scanning during the peak phase of vascular opacification after bolus injection of contrast medium and by obtaining 5-mm-thick sections (see Fig. 41–158). Infarction of the affected kidney may occur, and long-term follow-up by CT may reveal severe atrophy and poor function in the affected kidney.[87]

Chronic renal vein thrombosis is often a silent complication of the nephrotic syndrome.[84] CT frequently shows the presence of venous thrombus (see Fig. 41–159). In the chronic phase of renal vein thrombosis, the affected renal vein becomes attenuated because of retraction of the clot and extensive collateral vessels develop along the proximal to middle ureter and around the kidney.[123]

MRI is widely used for detecting renal vein extension of RCC; it can also be used in the evaluation of nonneoplastic renal vein thrombosis. MRI is most useful for evaluating patients with significant renal functional impairment and symptoms suggesting renal vein thrombosis. Renal vein thrombus may be shown on T1-weighted spin-echo pulse sequences when the signal void of flowing blood in the renal vein is replaced by high signal because of thrombus (see Fig. 41–159). Gradient-echo technique shows thrombus as a filling defect of medium signal intensity that

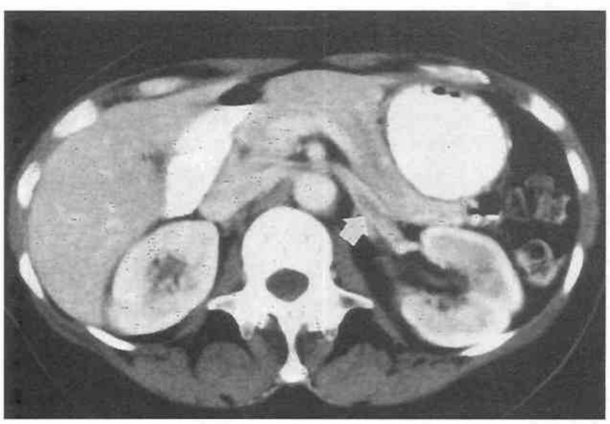

Figure 41–158. Renal vein thrombosis. Dynamic CT scan shows a low attenuation clot (*arrow*) in a partially thrombosed left renal vein. There is prolonged corticomedullary differentiation in the left kidney compared with the right kidney, which exhibits a homogeneous nephrogram. (From Birnbaum BA, Bosniak MA, Megibow AJ: Asymmetry of the renal nephrogram on CT: Significance of the unilateral prolonged cortical nephrogram. Urol Radiol 12:173–177, 1991.)

replaces the high signal of flowing blood (see Fig. 41–69). Coronal MRI helps determine the extent of vena caval involvement. MRI in patients with acute renal vein thrombosis may also show loss of corticomedullary differentiation on T1-weighted spin-echo images, increased signal in the affected kidney on T2-weighted images, renal fascial thickening, and renal enlargement.[131]

Helical CT of Urinary Tract Stones

Plain film radiography, excretory urography, retrograde pyelography, and ultrasonography are utilized in various combinations for the diagnosis of urinary tract stones in patients presenting with flank pain. CT has virtually replaced all other imaging modalities for this purpose. Unenhanced helical CT for the evaluation of patients with flank pain was first described by Smith and associates in 1994 in 1995.[252] Helical unenhanced CT is superior to other imaging modalities in diagnosis of urinary tract calculi. Also, it can diagnose other causes of flank pain such as appendicitis, diverticulitis, pancreatitis, bowel obstruction, and intussusception.[161, 251]

Technique

The CT examination for suspected ureterolithiasis is performed from the top of the kidneys to the base of the bladder, without the use of intravenous or oral contrast material. A collimation of 5 mm with a pitch of 1 is recommended for single-detector spiral CT; 2.5-mm collimation with reconstruction at 2.5 mm and a pitch of 0.8 to 1 for multidetector CT is preferred. The presence of distended urinary bladder at the time of imaging better defines the ureteral insertions.[251] Utilizing a pitch of 2 results in decreased radiation exposure without much sacrifice in the quality of scan.[59] The helical CT data are acquired in breath-holding, thus avoiding the respiratory misregistration artifact and allowing the retrospective reconstruction to delineate small calculi. The introduction of multidetector CT has further reduced the scan performance time, enabling the study to be completed in about 10 to 15 seconds.

CT Findings

Virtually all stones (including uric acid stones) are of sufficient radiographic attenuation to be readily visible on CT,[251] except for stones associated with protease inhibitors used for treating human immunodeficiency virus (indinavir).[20, 263] In the presence of flank pain, the primary CT finding in ureteral obstruction is the identification of a stone within the lumen of the ureter (Fig. 41–160).[251] Even calculi of submillimeter size can be easily identified. The most common sites of impaction are the ureteropelvic junction (35%) (Fig. 41–161), midureter (7%), distal ureter (33%), and ureterovesicular junction (18%). (Fig. 41–162). In one study 8% of the stones were already present in the bladder at the completion of the CT examination.[50] The search for the ureteric calculi should extend from the renal pelvis to the bladder. There is no substitute for establishing

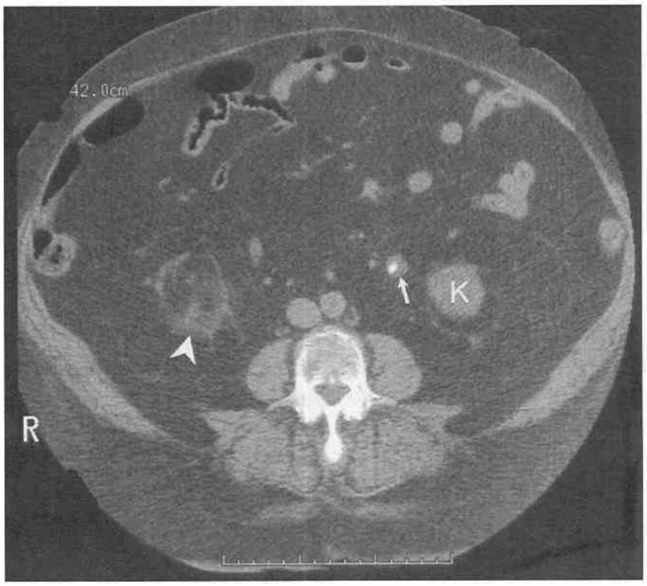

Figure 41–160. Non-contrast renal CT protocol. Axial image demonstrates a left ureteric calculus with surrounding ureteric wall edema called the soft tissue rim sign (*arrow*). Part of the left kidney (K) is seen. There is some right perinephric edema (*arrowhead*) because the patient had bilateral ureteric calculi (*not shown*).

continuity of a calcification within the ureteral lumen on sequential images.[49] The *soft tissue rim sign* (see Fig. 41–160) can be used to identify the ureter; it represents edema of the ureteral wall at the level where a stone has become impacted.[105, 252] Approximately 77% of ureteral stones have the soft tissue rim sign.[49] Presence of this sign is specific for the diagnosis of ureterolithiasis, however, absence of the sign does not preclude such a diagnosis.[121]

Differentiating between a phlebolith and a ureteric calculus is a significant problem especially in patients with minimal retroperitoneal fat. Phleboliths, which are common

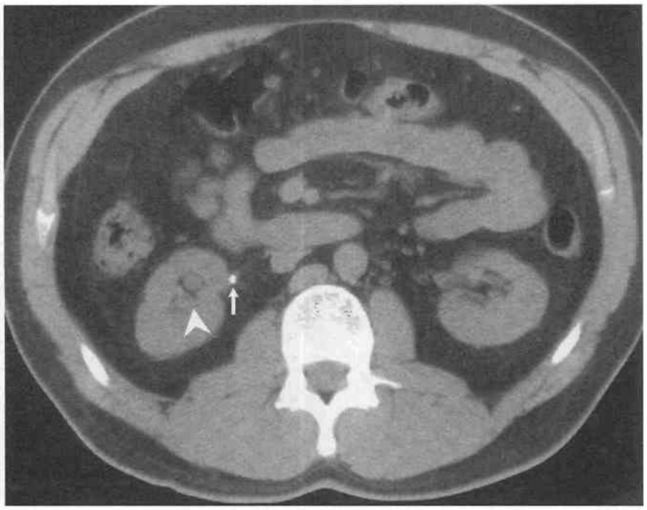

Figure 41–161. Non-contrast renal CT protocol. Axial image demonstrates a 3- to 4-mm calculus (*arrow*) in the right ureteropelvic junction with mild hydronephrosis (*arrowhead*).

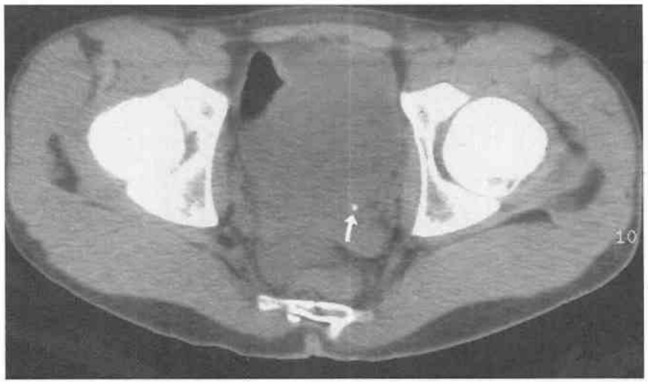

Figure 41–162. Non-contrast renal CT protocol. Axial image demonstrates a 2- to 3-mm calculus in the ureterovesicular junction (*arrow*) in a patient with left flank pain and hematuria.

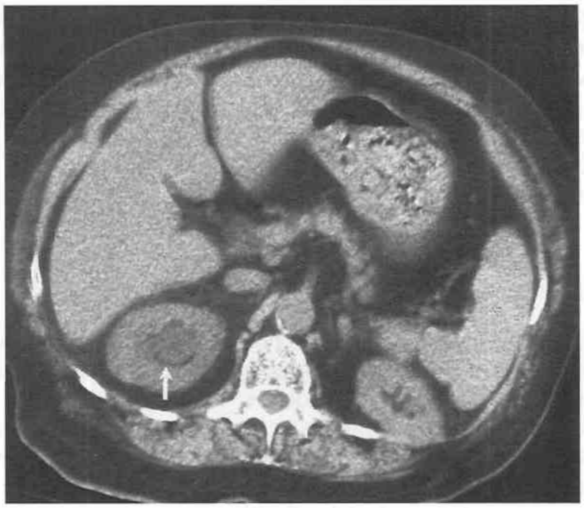

Figure 41–164. Non-contrast renal CT protocol. Axial image shows dilated calyx in the right renal upper pole (*arrow*) secondary to obstruction of the ureteropelvic junction (*not shown*).

in the pelvis, arise from thrombi in the pelvic veins and are not often seen in the mid- and upper abdomen except when present in gonadal veins. The presence of the *comet tail sign*—an adjacent eccentric, tapering soft tissue mass corresponding to the noncalcified portion of a pelvic vein—helps differentiate between ureteric calculus and phlebolith.[13, 23] CT is poor in identifying the central lucency present in a phlebolith on plain radiographs[274] and is not helpful in the differentiation of phlebolith and calculus.

When present, two important secondary CT signs of obstruction, ureteral dilatation and perinephric stranding (Fig. 41–163), are helpful in the diagnosis of ureteral obstruction.[251] Presence of ureteral dilatation has a positive predictive value of 90% and a negative predictive value of 89% for diagnosis of ureteral obstruction.[50] The dilated, urine-filled ureter, a reliable guide to the point of obstruction, is followed with sequential CT images until a change of caliber is seen (see Fig. 41–113). The mean diameter of the normal ureter on CT is 1 to 2 mm. The symptomatic side is compared with the normal side; it is important not to mistake a ureter for the gonadal vein.

Stranding of the perinephric fat on the symptomatic side represents fluid within the bridging septa due to increased lymphatic pressure.[49] This finding has a positive predictive value of 92% and a negative predictive value of 84% for diagnosis of ureteral obstruction.[253] Perinephric stranding is most commonly seen in patients with acute or chronic ureteral obstruction; however, in the absence of obstruction, stranding can be seen in pyelonephritis, renal vein thrombosis, renal infarction, trauma, and renal tumor with hemorrhage.[251] Periureteral stranding is less common and is rarely seen in the absence of perinephric stranding.

Collecting system dilatation is best identified in the upper pole and lower poles. Dilated calyces and infundibula appear as rounded, fluid-filled structures that partially obliterate the renal sinus fat when compared with the contralateral side (Fig. 41–164).[49] Its presence yields a positive predictive value of 93%.[253] After ureteral obstruction, renal enlargement may be seen; its presence has a

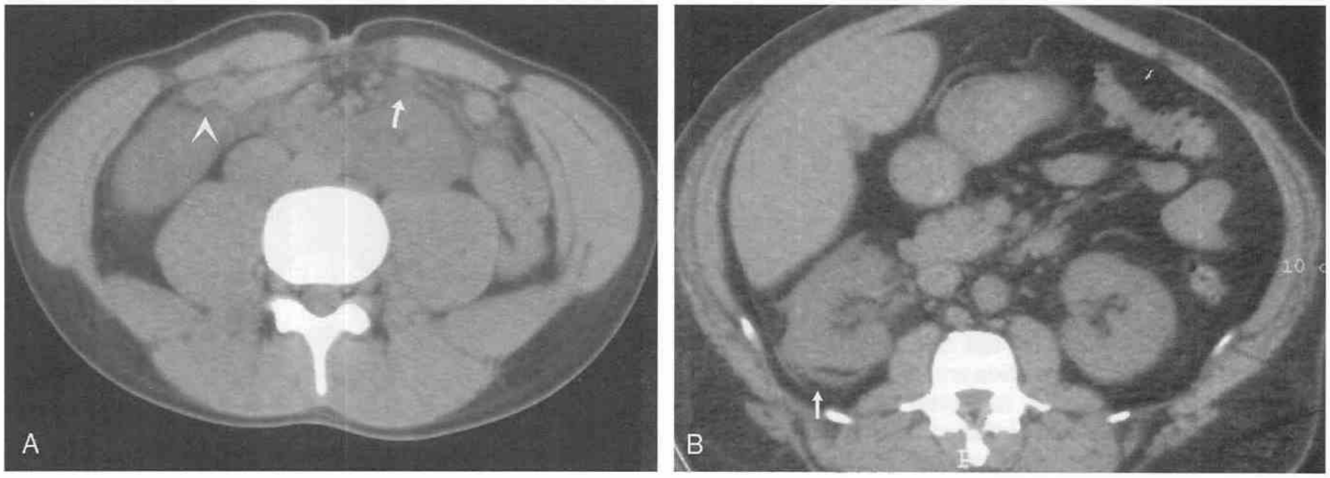

Figure 41–163. Non-contrast renal CT protocol. *A*, Axial image shows left ureteric dilatation (*arrow*); compare it with contralateral ureter (*arrowhead*) in a patient with horseshoe kidney. He had a small left ureterovesicular calculus (*not shown*). *B*, Right perinephric stranding (*arrow*) secondary to distal ureteric calculus (*not shown*).

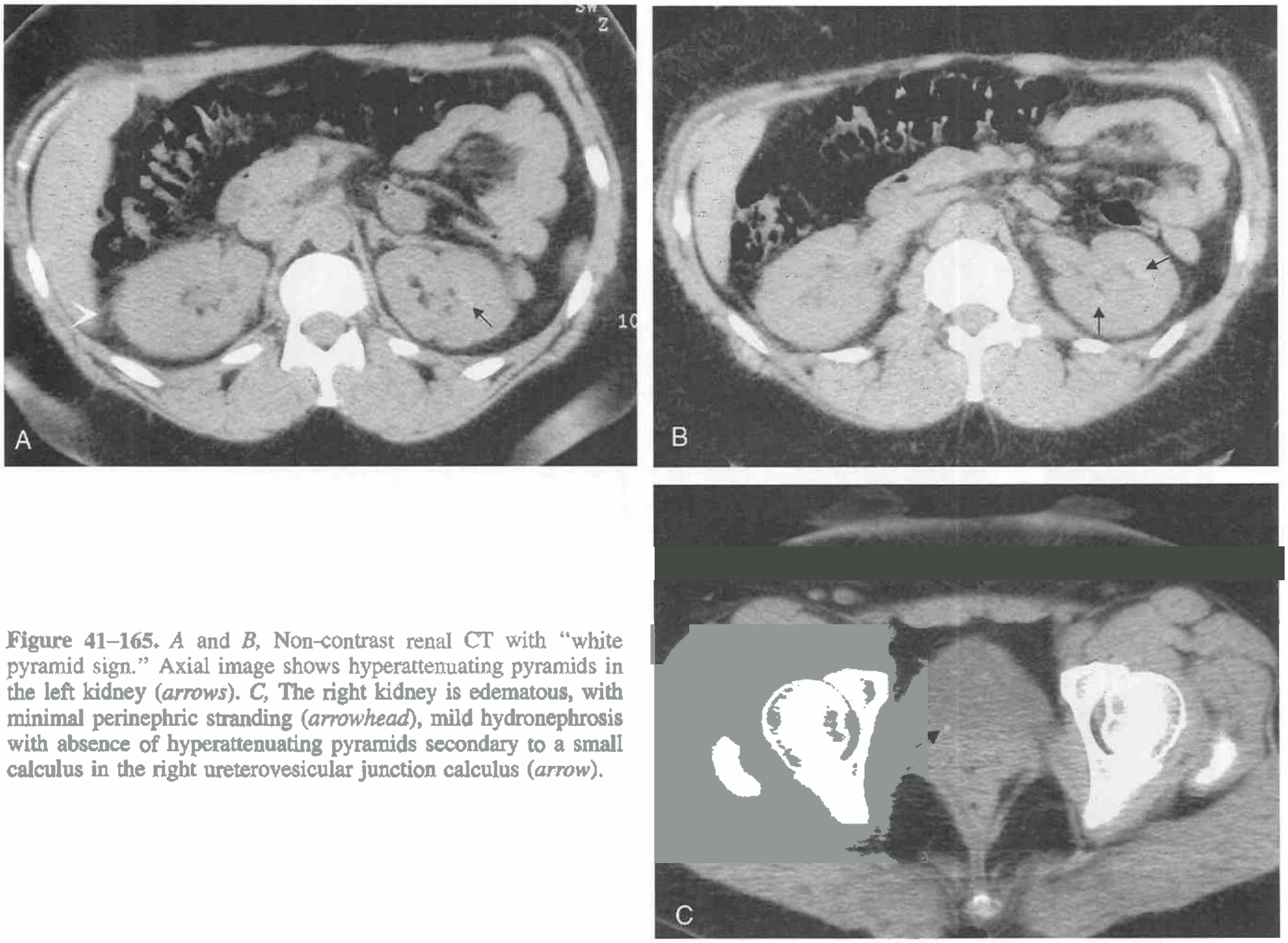

Figure 41–165. *A* and *B,* Non-contrast renal CT with "white pyramid sign." Axial image shows hyperattenuating pyramids in the left kidney (*arrows*). *C,* The right kidney is edematous, with minimal perinephric stranding (*arrowhead*), mild hydronephrosis with absence of hyperattenuating pyramids secondary to a small calculus in the right ureterovesicular junction calculus (*arrow*).

positive predictive value of 86% for diagnosis of ureteral obstruction.[253]

Unilateral absence of the "white pyramid" has been described as an additional secondary sign of urinary tract obstruction (Fig. 41–165).[227] Bilateral high-attenuation renal pyramids are an occasional incidental finding. Ureteral obstruction may result in tubular hydronephrosis, decreasing the attenuation of the medullary pyramid on the obstructed side. The finding of high-attenuation medullary pyramids in only one kidney suggests the presence of obstruction in the other kidney.[49]

Nephrolithiasis is found in 46% of patients with ureteral stones.[253] Approximately 5% of patients have ureteral dilatation and perinephric stranding without any demonstrable ureteral calculus[50]; this constellation of findings should prompt a differential diagnosis of a passed stone, stone too small to visualize, pyelonephritis, or obstruction unrelated to stone disease. However, the constellation of findings in a patient who is undergoing treatment with a protease inhibitor such as indinavir should suggest the diagnosis of indinavir stone disease (Fig. 41–166).[49] Indinavir stones are nonopaque on CT scans.[20] If the patient shows no evidence of infection, and has never been treated with protease inhibitors, CT scanning should be repeated with intravenous contrast material for further evaluation.

The other common diagnoses detected on unenhanced CT in patients with flank pain that are unrelated to the urinary tract include ovarian masses (with torsion or hemorrhage), appendicitis, diverticulitis, choledocholithiasis, Crohn's disease, and pancreatitis. The two most common diagnoses detected on unenhanced CT that are related to the urinary tract but are unrelated to stone disease are pyelonephritis and bladder outlet obstruction.[50]

Retroperitoneal Fibrosis

CT is particularly helpful in evaluating patients with ureteric obstruction secondary to retroperitoneal fibrosis. Retroperitoneal fibrosis may be due to a variety of causes. About 70% of cases are idiopathic (Fig. 41–167). Other causes are various drugs (especially methysergide), previous abdominal surgery or radiation therapy, inflammatory aortic aneurysm (Fig. 41–168), and inflammatory bowel diseases. Retroperitoneal fibrosis may also be caused by a desmoplastic reaction secondary to retroperitoneal spread of some neoplasms, notably lymphomas, and of carcinomas of the breast, stomach, lung, colon, and bladder (Fig. 41–169).[5]

Urinoma

Continued leakage of urine from the collecting system in the presence of urinary obstruction may lead to an

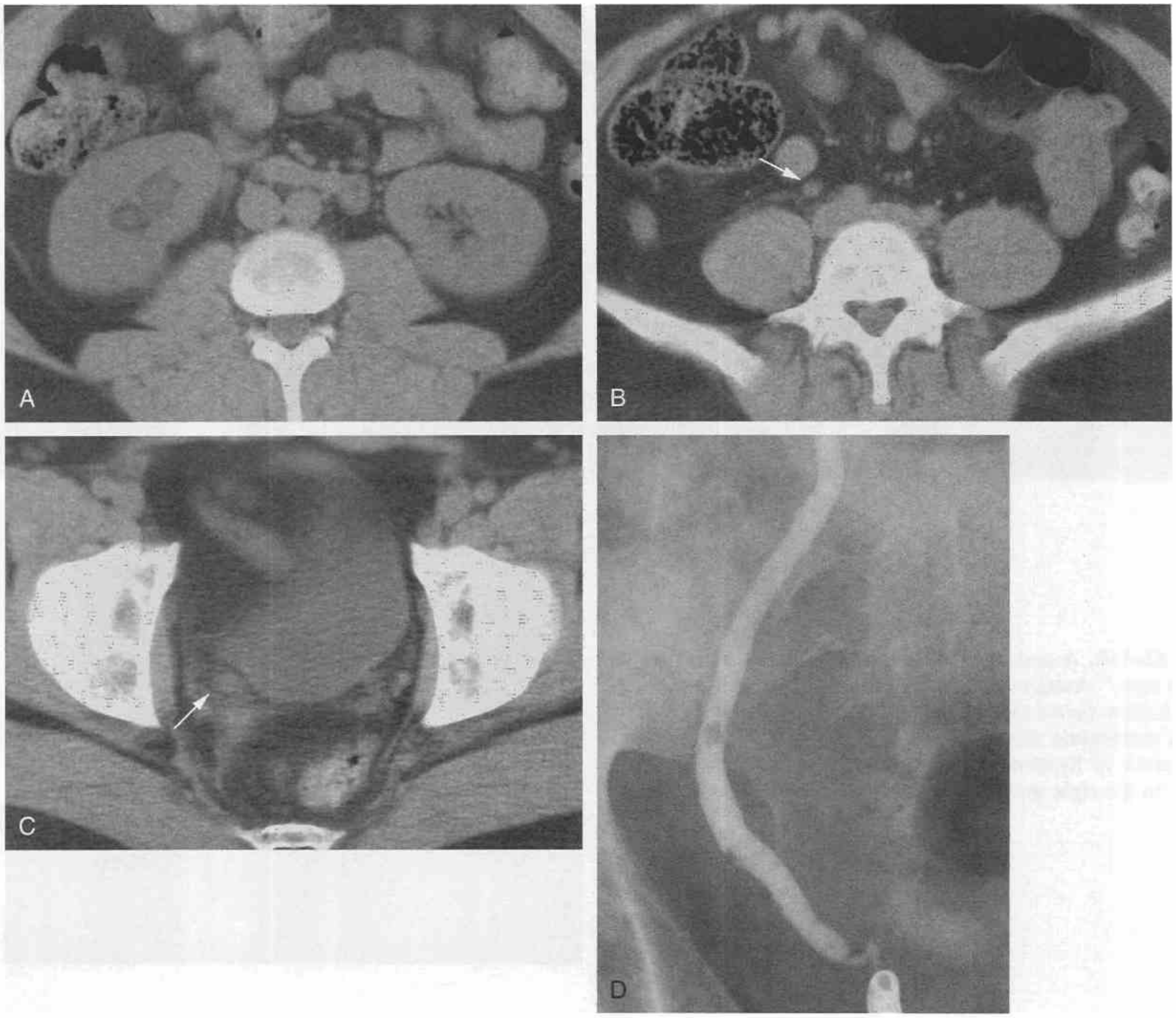

Figure 41–166. Protease inhibitor deposition in a 35-year-old man with human immunodeficiency virus disease who is undergoing indinavir therapy. *A,* Axial non-contrast CT scan reveals hydronephrosis and minimal perinephric stranding of the right kidney. *B,* A more caudal scan shows hydroureter (*arrow*). *C,* More caudal scan demonstrates the persistence of hydroureter to the level of the ureterovesicular junction (*arrow*). No calcification was identified. *D,* Retrograde ureterogram shows multiple filling defects in the distal right ureter. Stricture of the ureter distal to the indinavir fragments is likely caused by recent stone impaction near the ureterovesicular junction. (From Dalrymple NC, Casford B, Raiken DP, et al: Pearls and pitfalls in the diagnosis of ureterolithiasis with unenhanced helical CT. Radiographics 20:439–447, 2000.)

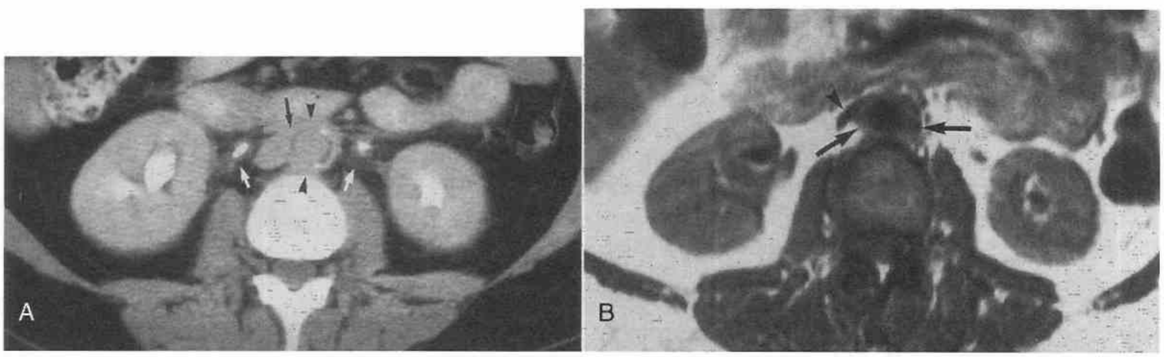

Figure 41–167. Idiopathic retroperitoneal fibrosis. *A,* A rim of fibrous tissue (*arrowheads*) surrounds the aorta, which contains calcified atherosclerotic plaques. The fibrous tissue obscures the plane between the aorta and the vena cava (*black arrow*). Fibrous tissue strands (*white arrows*) extend laterally to surround the ureters, which contain stents. There is bilateral calyceal dilatation. *B,* Proton-density weighted MR image (spin-echo, TR = 1800 msec, TE = 15 msec) obtained 6 months after bilateral ureterolysis reveals a periaortic rim of fibrous tissue (*arrows*) with a signal intensity higher than that of muscle. The inferior vena cava (*arrowhead*) is patent but is attached to the fibrous tissue.

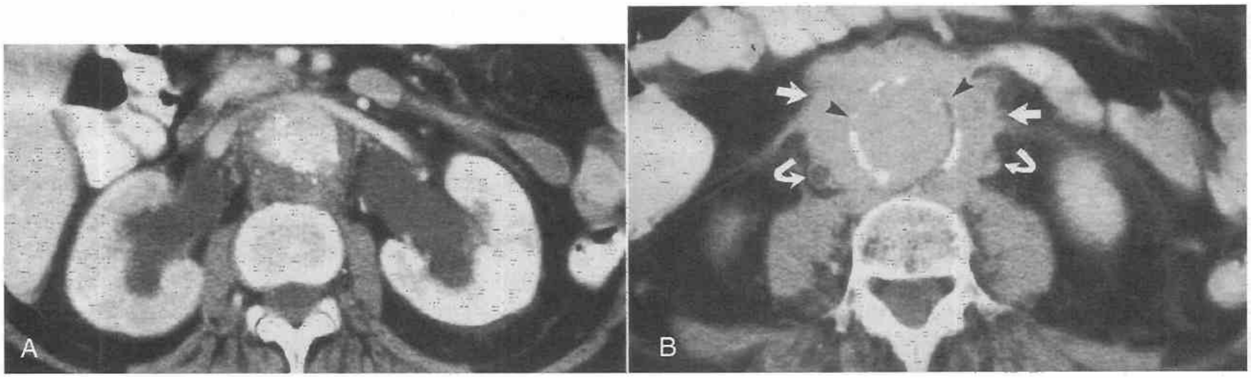

Figure 41–168. Retro[redacted]toneal fibrosis and ureteric obstruction due to an inflammatory aortic aneurysm. *A*, There is bilateral hydronephrosis. *B*, Caudal scan shows a calcified atherosclerotic aortic aneurysm (*arrowheads*) surrounded by thick fibrous tissue (*arrows*) that entraps the ureters (*curved arrows*).

Figure 41–169. Malignant retroperitoneal fibrosis due to metastat[redacted] gastric carcinoma. There is bilateral hydronephrosis with no contra[redacted] excretion on the right. The contrast-enhanced aorta (a) is surrounded by an ill-defined mantle of tissue (*arrows*) that displaces the vena cava (*arrowhead*) to the right. There is bilateral renal fascial thickening.

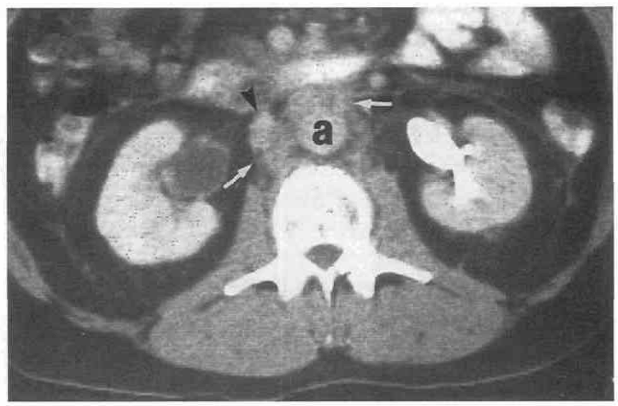

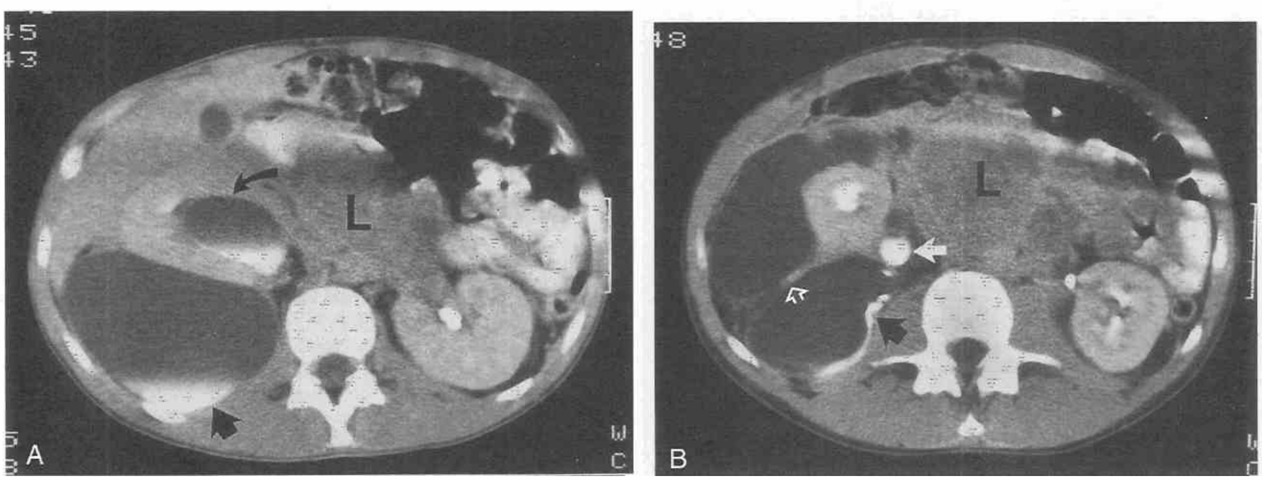

Figure 41–170. Right perinephric urinoma secondary to ureteric obstruction caused by lymph node metastases from a testicular carcinoma. *A*, Perinephric fluid collection causes anterior displacement of the right kidney. Contrast material (*arrow*) is present posteriorly in the perinephric space. The right renal pelvis (*curved arrow*) is dilated. Enlarged retroperitoneal lymph nodes (L) are evident. *B*, Caudal scan exhibits contrast material (*black arrow*) tracking posteriorly from a dilated and obstructed right ureter (*white arrow*). There is a bridging septum (*open arrow*) between the renal capsule and the posterior renal fascia.

encapsulated retroperitoneal urine collection called a *urinoma*. Urinomas may be associated with ureteropelvic junction obstruction, retroperitoneal fibrosis, retroperitoneal malignancy, cancer of the renal pelvis, ureter, or bladder, and a variety of conditions that cause bladder outlet obstruction.[266] Urinomas may also occur in patients who have experienced penetrating abdominal trauma, renal surgery, or urinary tract instrumentation.[266]

On CT, a urinoma is usually demonstrated to be confined to the perinephric space by the cone of the renal fascia and often to extend into the infrarenal part of the space. Most urinomas occur posterior to the kidney, which is displaced upward anteriorly and sometimes laterally (Figs. 41–170 and 41–171).[266] They often have a thickened wall, which may contain dystrophic calcification (see Fig. 41–171). Urinomas usually contain fluid of uniform water density. Hydronephrosis is usually present and is aggravated by ureteric compression due to the urinoma. The nature of a urinoma may be confirmed by contrast-enhanced CT, which sometimes shows layering of contrast medium in the dependent part of the collection (see Fig. 41–170). Management of urinomas due to urinary obstruction consists of overcoming the obstruction and excision or drainage of the urinoma.[266]

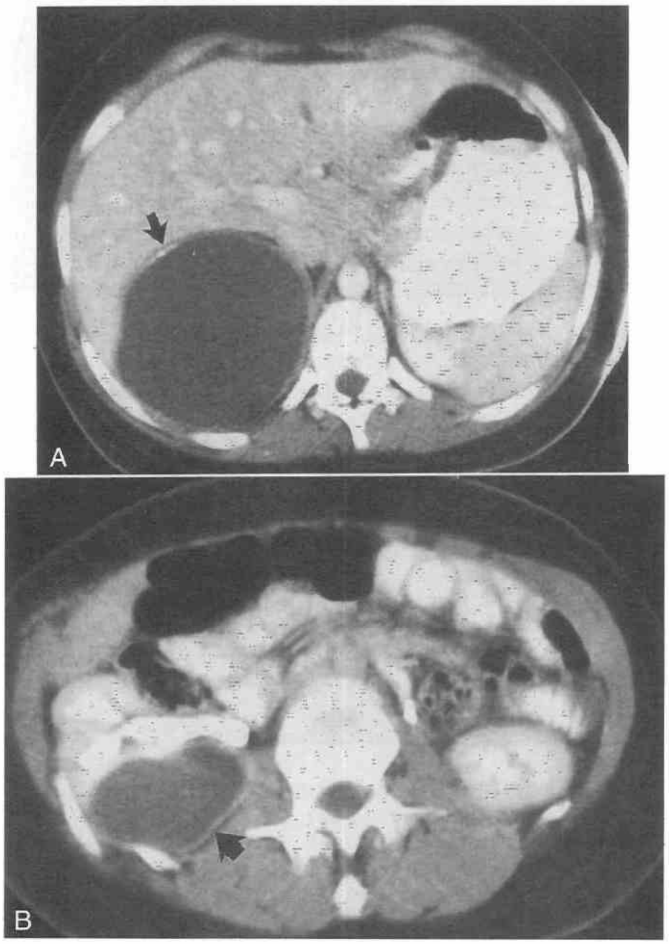

Figure 41–171. Chronic asymptomatic urinoma secondary to renal surgery during childhood. *A,* A fluid-density mass with peripheral calcification (*arrow*) extends above the right kidney. *B,* A caudal scan reveals that the mass (*arrow*) extends posterior to the kidney in the perinephric space.

Renal Transplants

Radiologic evaluation for suspected surgical complications and of kidney dysfunction in patients with renal transplants is best achieved by renal scintigraphy and ultrasonography. Peritransplant fluid collections, including hematomas, lymphoceles, abscesses, and urinomas, are readily assessed on ultrasonography. Unenhanced CT and MRI are reserved for cases in which ultrasonography fails either because of lack of access due to a recent surgical incision or because the transplant area is obscured by intestinal gas. Contrast-enhanced CT should be avoided because of the potential for nephrotoxicity.

MRI is a suitable alternative in the evaluation of the transplanted kidney and peritransplant region[3, 184]; however, sonography and sonographic-guided biopsy remain the primary imaging and interventional modalities.

References

1. Agrawal R, Jafri SZ, Gibson DP, et al: Juxtaglomerular cell tumor: MR findings. J Comput Assist Tomogr 19:140–142, 1995.
2. Aizenstein RI, Owens C, Sabnis S, et al: The perinephric space and renal fascia: Review of normal anatomy, pathology, and pathways of disease spread. Crit Rev Diagn Imaging 38:325–367, 1997.
3. Ali MG, Coakley FV, Hricak H, Bretan PN: Complex posttransplantation abnormalities of renal allografts: Evaluation with MR imaging. Radiology 211:95–100, 1999.
4. Alter AJ, Uehling DT, Zwiebel WJ: Computed tomography of the retroperitoneum following nephrectomy. Radiology 133:663–668, 1979.
5. Amis ES Jr: Retroperitoneal fibrosis. AJR Am J Roentgenol 157: 321–329, 1991.
6. Aronson S, Frazier HA, Baluch JD, et al: Cystic renal masses: Usefulness of the Bosniak classification. Urol Radiol 13:83–90, 1991.
7. Bae KT, Heiken JP, Siegel CL, Bennett HF: Renal cysts: Is attenuation artifactually increased on contrast-enhanced CT images? Radiology 216:792–796, 2000.
8. Baron RL, McClennan BL, Lee JK, Lawson TL: Computed tomography of transitional-cell carcinoma of the renal pelvis and ureter. Radiology 144:125–130, 1982.
9. Beachley MC, Ranniger K, Roth FJ: Xanthogranulomatous pyelonephritis. Am J Roentgenol Radium Ther Nucl Med 121:500–507, 1974.
10. Bechtold RE, Zagoria RJ: Imaging approach to staging of renal cell carcinoma. Urol Clin North Am 24:507–522, 1997.
11. Bechtold RE, Dyer RB, Zagoria RJ, Chen MY: The perirenal space: Relationship of pathologic processes to normal retroperitoneal anatomy. Radiographics 16:841–854, 1996.
12. Beebe DK: Autosomal dominant polycystic kidney disease. Am Fam Physician 53:925–931, 1996.
13. Bell TV, Fenlon HM, Davison BD, et al: Unenhanced helical CT criteria to differentiate distal ureteral calculi from pelvic phleboliths. Radiology 207:363–367, 1998.
14. Belville JS, Morgentaler A, Loughlin KR, Tumeh SS: Spontaneous perinephric and subcapsular renal hemorrhage: Evaluation with CT, US, and angiography. Radiology 172:733–738, 1989.
15. Bernardino ME, deSantos LA, Johnson DE, Bracken RB: Computed tomography in the evaluation of post-nephrectomy patients. Radiology 130:183–187, 1979.
16. Birnbaum BA, Bosniak MA, Megibow AJ: Asymmetry of the renal nephrograms on CT: Significance of the unilateral prolonged cortical nephrogram. Urol Radiol 12:173–177, 1991.
17. Birnbaum BA, Jacobs JE, Ramchandani P: Multiphasic renal CT: Comparison of renal mass enhancement during the corticomedullary and nephrographic phases. Radiology 200:753–758, 1996.

18. Birnbaum BA, Jacobs JE, Langlotz CP, Ramchandani P: Assessment of a bolus-tracking technique in helical renal CT to optimize nephrographic phase imaging. Radiology 211:87–94, 1999.
19. Birnbaum BA, Bosniak MA, Megibow AJ, et al: Observations on the growth of renal neoplasms. Radiology 176:695–701, 1990.
20. Blake SP, McNicholas MM, Raptopoulos V: Nonopaque crystal deposition causing ureteric obstruction in patients with HIV undergoing indinavir therapy. AJR Am J Roentgenol 171:717–720, 1998.
21. Blumhagen JD, Wood BJ, Rosenbaum DM: Sonographic evaluation of abdominal lymphangiomas in children. J Ultrasound Med 6: 487–495, 1987.
22. Boone TB, Gilling PJ, Husmann DA: Ureteropelvic junction disruption following blunt abdominal trauma. J Urol 150:33–36, 1993.
23. Boridy IC, Nikolaidis P, Kawashima A, et al: Ureterolithiasis: Value of the tail sign in differentiating phleboliths from ureteral calculi at nonenhanced helical CT. Radiology 211:619–621, 1999.
24. Bosniak MA: The current radiological approach to renal cysts. Radiology 158:1–10, 1986.
25. Bosniak MA: Difficulties in classifying cystic lesions of the kidney. Urol Radiol 13:91–93, 1991.
26. Bosniak MA: The small (less than or equal to 3.0 cm) renal parenchymal tumor: Detection, diagnosis, and controversies. Radiology 179:307–317, 1991.
27. Bosniak MA: Spontaneous subcapsular and perirenal hematomas. Radiology 172:601–602, 1989.
28. Bosniak MA, Megibow AJ, Ambos MA, et al: Computed tomography of ureteral obstruction. AJR Am J Roentgenol 138:1107–1113, 1982.
29. Bosniak MA, Megibow AJ, Hulnick DH, et al: CT diagnosis of renal angiomyolipoma: The importance of detecting small amounts of fat. AJR Am J Roentgenol 151:497–501, 1988.
30. Bracken RB, Chica G, Johnson DE, Luna M: Secondary renal neoplasms: An autopsy study. South Med J 72:806–807, 1979.
31. Breslow N, Beckwith JB, Ciol M, Sharples K: Age distribution of Wilms' tumor: Report from the National Wilms' Tumor Study. Cancer Res 48:1653–1657, 1988.
32. Bruno D, Wigfall DR, Zimmerman SA, et al: Genitourinary complications of sickle cell disease. J Urol 166:803–811, 2001.
33. Chauveau D, Knebelmann B, Grunfeld JP: Inherited kidney diseases: Polycystic kidney disease and Alport syndrome. Adv Intern Med 40:303–339, 1995.
34. Choyke PL: Acquired cystic kidney disease. Eur Radiol 10:1716–1721, 2000.
35. Choyke PL: Inherited cystic diseases of the kidney. Radiol Clin North Am 34:925–946, 1996.
36. Choyke PL, White EM, Zeman RK, et al: Renal metastases: Clinicopathologic and radiologic correlation. Radiology 162:359–363, 1987.
37. Choyke PL, Glenn GM, Walther MM, et al: The natural history of renal lesions in von Hippel–Lindau disease: A serial CT study in 28 patients. AJR Am J Roentgenol 159:1229–1234, 1992.
38. Choyke PL, Glenn GM, Walther MM, et al: von Hippel–Lindau disease: Genetic, clinical, and imaging features. Radiology 194: 629–642, 1995.
39. Churchill DN, Bear JC, Morgan J, et al: Prognosis of adult onset polycystic kidney disease re-evaluated. Kidney Int 26:190–193, 1984.
40. Cohan RH, Dunnick NR, Leder RA, Baker ME: Computed tomography of renal lymphoma. J Comput Assist Tomogr 14:933–938, 1990.
41. Cohan RH, Sherman LS, Korobkin M, et al: Renal masses: Assessment of corticomedullary-phase and nephrographic-phase CT scans. Radiology 196:445–451, 1995.
42. Coulam CH, Sheafor DH, Leder RA, et al: Evaluation of pseudoenhancement of renal cysts during contrast-enhanced CT. AJR Am J Roentgenol 174:493–498, 2000.
43. Crotty KL, Orihuela E, Warren MM: Recent advances in the diagnosis and treatment of renal arteriovenous malformations and fistulas. J Urol 150:1355–1359, 1993.
44. Crummy AB, Madsen PO: Parapelvic renal cyst: The peripheral fat sign. J Urol 96:436–438, 1966.
45. Curry NS, Chung CJ, Gordon B: Unilateral renal cystic disease in an adult. Abdom Imaging 19:366–368, 1994.
46. Curry NS, Schabel SI, Garvin AJ, Fish G: Intratumoral fat in a renal oncocytoma mimicking angiomyolipoma. AJR Am J Roentgenol 154:307–308, 1990.
47. Cushing B, Slovis TL: Imaging of Wilms' tumor: What is important! Urol Radiol 14:241–251, 1992.
48. D'Agata ID, Jonas MM, Perez-Atayde AR, Guay-Woodford LM: Combined cystic disease of the liver and kidney. Semin Liver Dis 14:215–228, 1994.
49. Dalrymple NC, Casford B, Raiken DP, et al: Pearls and pitfalls in the diagnosis of ureterolithiasis with unenhanced helical CT. Radiographics 20:439–447, 2000.
50. Dalrymple NC, Verga M, Anderson KR, et al: The value of unenhanced helical computerized tomography in the management of acute flank pain. J Urol 159:735–740, 1998.
51. Davidson AJ, Choyke PL, Hartman DS, Davis CJ Jr: Renal medullary carcinoma associated with sickle cell trait: Radiologic findings. Radiology 195:83–85, 1995.
52. Davidson AJ, Hartman DS, Choyke PL, Wagner BJ: Davidson's Radiology of the Kidney and Genitourinary Tract. Philadelphia, WB Saunders, 1999, pp 157–235.
53. Davidson AJ, Hayes WS, Hartman DS, et al: Renal oncocytoma and carcinoma: Failure of differentiation with CT. Radiology 186: 693–696, 1993.
54. Davies CH, Stringer DA, Whyte H, et al: Congenital hepatic fibrosis with saccular dilatation of intrahepatic bile ducts and infantile polycystic kidneys. Pediatr Radiol 16:302–305, 1986.
55. Davis CJ Jr, Mostofi FK, Sesterhenn IA: Renal medullary carcinoma: The seventh sickle cell nephropathy. Am J Surg Pathol 19: 1–11, 1995.
56. Davis JM 3rd, McLaughlin AP: Spontaneous renal hemorrhage due to cyst rupture: CT findings. AJR Am J Roentgenol 148: 763–764, 1987.
57. De Carli P, Vidiri A, Lamanna L, Cantiani R: Renal oncocytoma: Image diagnostics and therapeutic aspects. J Exp Clin Cancer Res 19:287–290, 2000.
58. De Cobelli F, Vanzulli A, Sironi S, et al: Renal artery stenosis: Evaluation with breath-hold, three-dimensional, dynamic, gadolinium-enhanced versus three-dimensional, phase-contrast MR angiography. Radiology 205:689–695, 1997.
59. Diel J, Perlmutter S, Venkataramanan N, et al: Unenhanced helical CT using increased pitch for suspected renal colic: An effective technique for radiation dose reduction? J Comput Assist Tomogr 24: 795–801, 2000.
60. Dimopoulos MA, Logothetis CJ, Markowitz A, et al: Collecting duct carcinoma of the kidney. Br J Urol 71:388–391, 1993.
61. Dinney CP, Awad SA, Gajewski JB, et al: Analysis of imaging modalities, staging systems, and prognostic indicators for renal cell carcinoma. Urology 39:122–129, 1992.
62. Dinsmore BJ, Pollack HM, Banner MP: Calcified transitional cell carcinoma of the renal pelvis. Radiology 167:401–404, 1988.
63. Dobyan DC, Truong LD, Eknoyan G: Renal malacoplakia reappraised. Am J Kidney Dis 22:243–252, 1993.
64. Dunnick NR: Renal lesions: Great strides in imaging. Radiology 182:305–306, 1992.
65. Dunnick NR, Hartman DS, Ford KK, et al: The radiology of juxtaglomerular tumors. Radiology 147:321–326, 1983.
66. Dunnick NR, Sandler CM, Amis ESJ, Newhouse JH: Urinary Tract Trauma: Textbook of Uroradiology. Baltimore, Williams & Wilkins, 1997, pp 297–324.
67. Dyer RB, Chen MY, Zagoria RJ: Abnormal calcifications in the urinary tract. Radiographics 18:1405–1424, 1998.
68. Dyer RB, Munitz HA, Bechtold R, Choplin RH: The abnormal nephrogram. Radiographics 6:1039–1063, 1986.
69. Eilenberg SS, Lee JK, Brown J, et al: Renal masses: Evaluation with gradient-echo Gd-DTPA-enhanced dynamic MR imaging. Radiology 176:333–338, 1990.
70. Evans JC, Curtis J: The radiological appearances of tuberous sclerosis. Br J Radiol 73:91–98, 2000.
71. Farrow GM, Harrison EG Jr, Utz DC, ReMine WH: Sarcomas and sarcomatoid and mixed malignant tumors of the kidney in adults I. Cancer 22:545–550, 1968.
72. Federle MP: Evaluation of renal trauma. In Pollack HM (ed): Clinical Urography. Philadelphia, WB Saunders, 1990.
73. Federle MP, McAninch JW, Kaiser JA, et al: Computed tomography of urinary calculi. AJR Am J Roentgenol 136:255–258, 1981.
74. Feldberg MA, Koehler PR, van Waes PF: Psoas compartment disease studied by computed tomography: Analysis of 50 cases and subject review. Radiology 148:505–512, 1983.
75. Fernbach SK, Feinstein KA, Donaldson JS, Baum ES: Nephroblastomatosis: Comparison of CT with US and urography. Radiology 166:153–156, 1988.

76. Fick GM, Gabow PA: Natural history of autosomal dominant polycystic kidney disease. Annu Rev Med 45:23–29, 1994.
77. Fielding JR, Silverman SG, Rubin GD: Helical CT of the urinary tract. AJR Am J Roentgenol 172:199–206, 1999.
78. Finn JP, Goldmann A, Edelman RR: Magnetic resonance angiography in the body. Magn Reson Q 8:1–22, 1992.
79. Fishman EK, Hartman DS, Goldman SM, Siegelman SS: The CT appearance of Wilms tumor. J Comput Assist Tomogr 7:659–665, 1983.
80. Fishman MC, Pollack HM, Arger PH, Banner MP: Radiographic manifestations of spontaneous renal sinus hemorrhage. AJR Am J Roentgenol 142:1161–1164, 1984.
81. Fultz PJ, Hampton WR, Totterman SM: Computed tomography of pyonephrosis. Abdom Imaging 18:82–87, 1993.
82. Gabow PA: Autosomal dominant polycystic kidney disease—more than a renal disease. Am J Kidney Dis 16:403–413, 1990.
83. Gardner KD Jr: Pathogenesis of human cystic renal disease. Annu Rev Med 39:185–191, 1988.
84. Gatewood OM, Fishman EK, Burrow CR, et al: Renal vein thrombosis in patients with nephrotic syndrome: CT diagnosis. Radiology 159:117–122, 1986.
85. Geiger J, Fong Q, Fay R: Transitional cell carcinoma of renal pelvis with invasion of renal vein and thrombosis of subhepatic inferior vena cava. Urology 28:52–54, 1986.
86. Geller E, Smergel EM, Lowry PA: Renal neoplasms of childhood. Radiol Clin North Am 35:1391–1413, 1997.
87. Glazer GM, Francis IR, Gross BH, Amendola MA: Computed tomography of renal vein thrombosis. J Comput Assist Tomogr 8: 288–293, 1984.
88. Glazer GM, Gross BH, Orringer MB, et al: Computed tomography of pericardial masses: Further observations and comparison with echocardiography. J Comput Assist Tomogr 8:895–899, 1984.
89. Gofrit ON, Shapiro A, Kovalski N, et al: Renal cell carcinoma: Evaluation of the 1997 TNM system and recommendations for follow-up after surgery. Eur Urol 39:669–674, 2001.
90. Gold RP, McClennan BL, Rottenberg RR: CT appearance of acute inflammatory disease of the renal interstitium. AJR Am J Roentgenol 141:343–349, 1983.
91. Goldfarb DA, Novick AC, Lorig R, et al: Magnetic resonance imaging for assessment of vena caval tumor thrombi: A comparative study with venacavography and computerized tomography scanning. J Urol 144:1100–1103, 1990.
92. Goldman SM, Hartman DS, Fishman EK, et al: CT of xanthogranulomatous pyelonephritis: Radiologic-pathologic correlation. AJR Am J Roentgenol 142:963–969, 1984.
93. Grabstald H, Whitmore WF, Melamed MR: Renal pelvic tumors. JAMA 218:845–854, 1971.
94. Greene A, Cromie WJ, Goldman M: Computerized body tomography in neonatal renal vein thrombosis. Urology 20:213–215, 1982.
95. Gylys-Morin V, Hoffer FA, Kozakewich H, Shamberger RC: Wilms tumor and nephroblastomatosis: Imaging characteristics at gadolinium-enhanced MR imaging. Radiology 188:517–521, 1993.
96. Hall JR, Choa RG, Wells IP: Percutaneous drainage in emphysematous pyelonephritis—an alternative to major surgery. Clin Radiol 39: 622–624, 1988.
97. Harisinghani MG, McLoud TC, Shepard JAO, et al: Tuberculosis from head to toe [CME available in print version and on RSNA Link]. Radiographics 20:449–470, 2000.
98. Harris AC, Zwirewich CV, Lyburn ID, et al: CT findings in blunt renal trauma. Radiographics 21(Spec No):S201–S214, 2001.
99. Hartman DS, Davis CJ Jr, Lichtenstein JE, Goldman SM: Renal parenchymal malacoplakia. Radiology 136:33–42, 1980.
100. Hartman DS, Weatherby E 3rd, Laskin WB, et al: Cystic renal cell carcinoma: CT findings simulating a benign hyperdense cyst. AJR Am J Roentgenol 159:1235–1237, 1992.
101. Hatcher PA, Anderson EE, Paulson DF, et al: Surgical management and prognosis of renal cell carcinoma invading the vena cava. J Urol 145:20–23, 1991.
102. Hauser S, Studer UE: [Therapy of carcinoma of the kidney pelvis]. Urologe A 40:452–455, 2001.
103. Helenon O, Chretien Y, Paraf F, et al: Renal cell carcinoma containing fat: Demonstration with CT. Radiology 188:429–430, 1993.
104. Henderson NL, Mason RC: Juxtaglomerular cell tumor in pregnancy. Obstet Gynecol 98:943–945, 2001.
105. Heneghan JP, Dalrymple NC, Verga M, et al: Soft-tissue "rim" sign in the diagnosis of ureteral calculi with use of unenhanced helical CT. Radiology 202:709–711, 1997.
106. Hes O, Michal M, Sulc M, et al: [Oncocytoma of the kidney—morphologic variation in 102 cases]. Cesk Patol 37:51–56, 2001.
107. Hidalgo H, Dunnick NR, Rosenberg ER, et al: Parapelvic cysts: Appearance on CT and sonography. AJR Am J Roentgenol 138: 667–671, 1982.
108. Hohenwalter MD, Skowlund CJ, Erickson SJ, et al: Renal transplant evaluation with MR angiography and MR imaging. Radiographics 21:1505–1517, 2001.
109. Honda H, Bonsib S, Barloon TJ, Masuda K: Unusual renal oncocytomas: Pathologic and CT correlations. Urol Radiol 14:148–154, 1992.
110. Huppert BJ, Brandt KR, Ramin KD, King BF: Single-shot fast spin-echo MR imaging of the fetus: A pictorial essay. Radiographics 19: 215–227, 1999.
111. Johnson CD, Dunnick NR, Cohan RH, Illescas FF: Renal adenocarcinoma: CT staging of 100 tumors. AJR Am J Roentgenol 148: 59–63, 1987.
112. Jordan J, Low R, Jeffrey RB Jr: CT findings in acute renal cortical necrosis. J Comput Assist Tomogr 14:155–156, 1990.
113. Joshi VV, Beckwith JB: Multilocular cyst of the kidney (cystic nephroma) and cystic, partially differentiated nephroblastoma: Terminology and criteria for diagnosis. Cancer 64:466–479, 1989.
114. Julian JC, Merguerian PA, Shortliffe LM: Pediatric genitourinary tumors. Curr Opin Oncol 7:265–274, 1995.
115. Kallman DA, King BF, Hattery RR, et al: Renal vein and inferior vena cava tumor thrombus in renal cell carcinoma: CT, US, MRI and venacavography. J Comput Assist Tomogr 16:240–247, 1992.
116. Kamel IR, Berkowitz JF: Assessment of the cortical rim sign in posttraumatic renal infarction. J Comput Assist Tomogr 20:803–806, 1996.
117. Kashiwabara H, Inaba M, Itabashi A, et al: A case of renin-producing juxtaglomerular tumor: Effect of ACE inhibitor or angiotensin II receptor antagonist. Blood Press 6:147–153, 1997.
118. Kasper HU, Buhtz P, Kruger G, et al: Bellini duct carcinoma of the kidney—a case report. Gen Diagn Pathol 143:237–241, 1997.
119. Kawamura K, Ikeda R, Suzuki K: [Acquired renal cystic disease]. Hinyokika Kiyo 46:651–656, 2000.
120. Kawashima A, Goldman SM, Sandler CM: The indeterminate renal mass. Radiol Clin North Am 34:997–1015, 1996.
121. Kawashima A, Sandler CM, Boridy IC, et al: Unenhanced helical CT of ureterolithiasis: Value of the tissue rim sign. AJR Am J Roentgenol 168:997–1000, 1997.
122. Kawashima A, Sandler CM, Corl FM, et al: Imaging of renal trauma: A comprehensive review. Radiographics 21:557–574, 2001.
123. Kawashima A, Sandler CM, Ernst RD, et al: CT evaluation of renovascular disease. Radiographics 20:1321–1340, 2000.
124. Kennedy SM, Merino MJ, Linehan WM, et al: Collecting duct carcinoma of the kidney. Hum Pathol 21:449–456, 1990.
125. Kennelly MJ, Grossman HB, Cho KJ: Outcome analysis of 42 cases of renal angiomyolipoma. J Urol 152:1988–1991, 1994.
126. Kenney PJ: Imaging of chronic renal infections. AJR Am J Roentgenol 155:485–494, 1990.
127. Kern S, Zimmerhackl LB, Hildebrandt F, et al: Appearance of autosomal recessive polycystic kidney disease in magnetic resonance imaging and RARE-MR-urography. Pediatr Radiol 30:156–160, 2000.
128. Kern S, Zimmerhackl LB, Hildebrandt F, Uhl M: RARE-MR-urography—a new diagnostic method in autosomal recessive polycystic kidney disease. Acta Radiol 40:543–544, 1999.
129. Khan A, Thomas N, Costello B, et al: Renal medullary carcinoma: Sonographic, computed tomography, magnetic resonance and angiographic findings. Eur J Radiol 35:1–7, 2000.
130. Kleiner B, Filly RA, Mack L, Callen PW: Multicystic dysplastic kidney: Observations of contralateral disease in the fetal population. Radiology 161:27–29, 1986.
131. Koch KJ, Cory DA: Simultaneous renal vein thrombosis and bilateral adrenal hemorrhage: MR demonstration. J Comput Assist Tomogr 10:681–683, 1986.
132. Kohno A, Yunoki M: Unilateral renal cystic disease. Radiat Med 17:423–426, 1999.
133. Kopka L, Fischer U, Zoeller G, et al: Dual-phase helical CT of the kidney: Value of the corticomedullary and nephrographic phase for

evaluation of renal lesions and preoperative staging of renal cell carcinoma. AJR Am J Roentgenol 169:1573–1578, 1997.
134. Kopka L, Rogalla P, Hamm B: [Multislice CT of the abdomen—current indications and future trends]. Rofo Fortschr Geb Rontgenstr Neuen Bildgeb Verfahr 174:273–282, 2002.
135. Kossol JM, Patel SK: Suburothelial hemorrhage: The value of preinfusion computed tomography. J Comput Assist Tomogr 10:157–158, 1986.
136. Kunin M: Bridging septa of the perinephric space: Anatomic, pathologic, and diagnostic considerations. Radiology 158:361–365, 1986.
137. Lane RH, Stephens DH, Reiman HM: Primary retroperitoneal neoplasms: CT findings in 90 cases with clinical and pathologic correlation. AJR Am J Roentgenol 152:83–89, 1989.
138. Leder RA, Dunnick NR: Transitional cell carcinoma of the pelvicalices and ureter. AJR Am J Roentgenol 155:713–722, 1990.
139. Leppaniemi A, Lamminen A, Tervahartiala P, et al: Comparison of high-field magnetic resonance imaging with computed tomography in the evaluation of blunt renal trauma. J Trauma 38:420–427, 1995.
140. Levine E: Acquired cystic kidney disease. Radiol Clin North Am 34:947–964, 1996.
141. Levine E: Computed tomography of renal abscesses complicating medullary sponge kidney. J Comput Assist Tomogr 13:440–442, 1989.
142. Levine E: Malignant renal parenchymal tumors in adults. In Pollack HM (ed): Clinical Urography: An Atlas and Textbook of Urological Imaging. Philadelphia, WB Saunders, 1990.
143. Levine E: Transitional cell carcinoma of the renal pelvis associated with cyclophosphamide therapy. AJR Am J Roentgenol 159:1027–1028, 1992.
144. Levine E, Grantham JJ: Calcified renal stones and cyst calcifications in autosomal dominant polycystic kidney disease: Clinical and CT study in 84 patients. AJR Am J Roentgenol 159:77–81, 1992.
145. Levine E, Grantham JJ: High-density renal cysts in autosomal dominant polycystic kidney disease demonstrated by CT. Radiology 154: 477–482, 1985.
146. Levine E, Grantham JJ: Perinephric hemorrhage in autosomal dominant polycystic kidney disease: CT and MR findings. J Comput Assist Tomogr 11:108–111, 1987.
147. Levine E, Huntrakoon M: Unilateral renal cystic disease: CT findings. J Comput Assist Tomogr 13:273–276, 1989.
148. Levine E, Collins DL, Horton WA, Schimke RN: CT screening of the abdomen in von Hippel–Lindau disease. AJR Am J Roentgenol 139:505–510, 1982.
149. Levine E, Cook LT, Grantham JJ: Liver cysts in autosomal-dominant polycystic kidney disease: Clinical and computed tomographic study. Am J Roentgenol 145:229–233, 1985.
150. Levine E, Grantham JJ, MacDougall ML: Spontaneous subcapsular and perinephric hemorrhage in end-stage kidney disease: Clinical and CT findings. AJR Am J Roentgenol 148:755–758, 1987.
151. Levine E, Huntrakoon M, Wetzel LH: Small renal neoplasms: Clinical, pathologic, and imaging features. AJR Am J Roentgenol 153: 69–73, 1989.
152. Levine E, Lee KR, Weigel J: Preoperative determination of abdominal extent of renal cell carcinoma by computed tomography. Radiology 132:395–398, 1979.
153. Levine E, Slusher SL, Grantham JJ, Wetzel LH: Natural history of acquired renal cystic disease in dialysis patients: A prospective longitudinal CT study. AJR Am J Roentgenol 156:501–506, 1991.
154. Levine E, Grantham JJ, Slusher SL, et al: CT of acquired cystic kidney disease and renal tumors in long-term dialysis patients. AJR Am J Roentgenol 142:125–131, 1984.
155. Lien HH, Lund G: Collateral veins in inferior caval vein occlusion demonstrated via CT. Eur J Radiol 3:319–323, 1983.
156. Lindsey JR: Lymphangiectasia simulating polycystic disease. J Urol 104:658–662, 1970.
157. Liu J, Fanning CV: Can renal oncocytomas be distinguished from renal cell carcinoma on fine-needle aspiration specimens? A study of conventional smears in conjunction with ancillary studies. Cancer 93:390–397, 2001.
158. Lonergan GJ, Rice RR, Suarez ES: Autosomal recessive polycystic kidney disease: Radiologic-pathologic correlation. Radiographics 20: 837–855, 2000.
159. Lonergan GJ, Martinez-Leon MI, Agrons GA, et al: Nephrogenic rests, nephroblastomatosis, and associated lesions of the kidney. Radiographics 18:947–968, 1998.
160. Lowe LH, Isuani BH, Heller RM, et al: Pediatric renal masses: Wilms tumor and beyond. Radiographics 20:1585–1603, 2000.
161. Lumerman J, Gershbaum MD, Hines J, et al: Unenhanced helical computed tomography for the evaluation of suspected renal colic in the adolescent population: A pilot study. Urology 57:342–346, 2001.
162. Lumsden AB, Salam TA, Walton KG: Renal artery aneurysm: A report of 28 cases. Cardiovasc Surg 4:185–189, 1996.
163. Madewell JE, Goldman SM, Davis CJ Jr, et al: Multilocular cystic nephroma: A radiographic-pathologic correlation of 58 patients. Radiology 146:309–321, 1983.
164. Maher ER, Iselius L, Yates JR, et al: Von Hippel–Lindau disease: A genetic study. J Med Genet 28:443–447, 1991.
165. Maher ER, Yates JR, Harries R, et al: Clinical features and natural history of von Hippel–Lindau disease. Q J Med 77:1151–1163, 1990.
166. Marshall FF, Stewart AK, Menck HR: The National Cancer Data Base: Report on kidney cancers. The American College of Surgeons Commission on Cancer and the American Cancer Society. Cancer 80:2167–2174, 1997.
167. Matson MA, Cohen EP: Acquired cystic kidney disease: Occurrence, prevalence, and renal cancers. Medicine (Baltimore) 69:217–226, 1990.
168. Matthews LA, Spirnak JP: The nonoperative approach to major blunt renal trauma. Semin Urol 13:77–82, 1995.
169. Matz LR, Latham BI, Fabian VA, Vivian JB: Collecting duct carcinoma of the kidney: A report of three cases and review of the literature. Pathology 29:354–359, 1997.
170. McClennan BL, Stanley RJ, Melson GL, et al: CT of the renal cyst: Is cyst aspiration necessary? AJR Am J Roentgenol 133: 671–675, 1979.
171. Meredith WT, Levine E, Ahlstrom NG, Grantham JJ: Exacerbation of familial renal lymphangiomatosis during pregnancy. AJR Am J Roentgenol 151:965–966, 1988.
172. Mertens PR, Duque-Reina D, Ittel TH, et al: Contrast-enhanced computed tomography for demonstration of bilateral renal cortical necrosis. Clin Invest 72:499–501, 1994.
173. Millan-Rodriguez F, Palou J, de la Torre-Holguera P, et al: Conventional CT signs in staging transitional cell tumors of the upper urinary tract. Eur Urol 35:318–322, 1999.
174. Mitnick JS, Bosniak MA, Hilton S, et al: Cystic renal disease in tuberous sclerosis. Radiology 147:85–87, 1983.
175. Mitnick JS, Bosniak MA, Rothberg M, et al: Metastatic neoplasm to the kidney studied by computed tomography and sonography. J Comput Assist Tomogr 9:43–49, 1985.
176. Mitty HA, Shapiro RS, Parsons RB, Silberzweig JE: Renovascular hypertension. Radiol Clin North Am 34:1017–1036, 1996.
177. Morehouse HT, Weiner SN, Hoffman JC: Imaging in inflammatory disease of the kidney. AJR Am J Roentgenol 143:135–141, 1984.
178. Moss JG, Hendry GM: The natural history of renal cysts in an infant with tuberous sclerosis: Evaluation with ultrasound. Br J Radiol 61: 1074–1076, 1988.
179. Motzer RJ, Bander NH, Nanus DM: Renal-cell carcinoma. N Engl J Med 335:865–875, 1996.
180. Murray KK, McLellan GL: Renal peripelvic lymphangiectasia: Appearance at CT. Radiology 180:455–456, 1991.
181. Myers MA: Dynamic radiology of the abdomen: Normal and pathological anatomy. New York, Springer-Verlag, 1994.
182. Nascimento AB, Mitchell DG, Zhang XM, et al: Rapid MR imaging detection of renal cysts: Age-based standards. Radiology 221:628–632, 2001.
183. Nasu K, Yoshimatsu J, Anai T, et al: Magnetic resonance imaging of fetal autosomal recessive polycystic kidney disease. J Obstet Gynaecol Res 24:33–36, 1998.
184. Neimatallah MA, Dong Q, Schoenberg SO, et al: Magnetic resonance imaging in renal transplantation. J Magn Reson Imaging 10: 357–368, 1999.
185. Niikura S, Komatsu K, Uchibayashi T, et al: Juxtaglomerular cell tumor of the kidney treated with nephron-sparing surgery. Urol Int 65:160–162, 2000.
186. Nocks BN, Heney NM, Daly JJ, et al: Transitional cell carcinoma of renal pelvis. Urology 19:472–477, 1982.
187. Nunez D Jr, Becerra JL, Fuentes D, Pagson S: Traumatic occlusion of the renal artery: Helical CT diagnosis. AJR Am J Roentgenol 167:777–780, 1996.
188. Oliveira EA, Diniz JS, Vilasboas AS, et al: Multicystic dysplastic kidney detected by fetal sonography: Conservative management and follow-up. Pediatr Surg Int 17:54–57, 2001.

189. Oliver RT, Nethersell AB, Bottomley JM: Unexplained spontaneous regression and alpha-interferon as treatment for metastatic renal carcinoma. Br J Urol 63:128–131, 1989.
190. Oto A, Herts BR, Remer EM, Novick AC: Inferior vena cava tumor thrombus in renal cell carcinoma: Staging by MR imaging and impact on surgical treatment. AJR Am J Roentgenol 171:1619–1624, 1998.
191. Papanicolaou N, Pfister RC: Acute renal infections. Radiol Clin North Am 34:965–995, 1996.
192. Papanicolaou N, Stafford SA, Pfister RC, et al: Significant renal hemorrhage following extracorporeal shock wave lithotripsy: Imaging and clinical features. Radiology 163:661–664, 1987.
193. Parfrey PS, Bear JC, Morgan J, et al: The diagnosis and prognosis of autosomal dominant polycystic kidney disease. N Engl J Med 323:1085–1090, 1990.
194. Parienty RA, Ducellier R, Pradel J, et al: Diagnostic value of CT numbers in pelvicalyceal filling defects. Radiology 145:743–747, 1982.
195. Parvey LS, Warner RM, Callihan TR, Magill HL: CT demonstration of fat tissue in malignant renal neoplasms: Atypical Wilms' tumors. J Comput Assist Tomogr 5:851–854, 1981.
196. Pascal RR: Renal manifestations of extrarenal neoplasms. Hum Pathol 11:7–17, 1980.
197. Pedicelli G, Jequier S, Bowen AD, Boisvert J: Multicystic dysplastic kidneys: Spontaneous regression demonstrated with US. Radiology 161:23–26, 1986.
198. Peterson RO: Urologic Pathology. Philadelphia, JB Lippincott, 1992.
199. Phillips E, Messing EM: Role of lymphadenectomy in the treatment of renal cell carcinoma. Urology 41:9–15, 1993.
200. Pickering SP, Fletcher BD, Bryan PJ, Abramowsky CR: Renal lymphangioma: A cause of neonatal nephromegaly. Pediatr Radiol 14:445–448, 1984.
201. Pickhardt PJ: Collecting duct carcinoma arising in a solitary kidney: Imaging findings. Clin Imaging 23:115–118, 1999.
202. Pickhardt PJ, Siegel CL, McLarney JK: Collecting duct carcinoma of the kidney: Are imaging findings suggestive of the diagnosis? AJR Am J Roentgenol 176:627–633, 2001.
203. Pickhardt PJ, Lonergan GJ, Davis CJ, et al: From the Archives of the AFIP: Infiltrative renal lesions: Radiologic-pathologic correlation. Radiographics 20:215–243, 2000.
204. Pollack HM, Wein AJ: Imaging of renal trauma. Radiology 172: 297–308, 1989.
205. Porch P, Noe HN, Stapleton FB: Unilateral presentation of adult-type polycystic kidney disease in children. J Urol 135:744–746, 1986.
206. Port FK, Ragheb NE, Schwartz AG, Hawthorne VM: Neoplasms in dialysis patients: A population-based study. Am J Kidney Dis 14: 119–123, 1989.
207. Poston CD, Jaffe GS, Lubensky IA, et al: Characterization of the renal pathology of a familial form of renal cell carcinoma associated with von Hippel-Lindau disease: Clinical and molecular genetic implications. J Urol 153:22–26, 1995.
208. Pozniak MA, Balison DJ, Lee FT Jr, et al: CT angiography of potential renal transplant donors. Radiographics 18:565–587, 1998.
209. Pretorius ES, Wickstrom ML, Siegelman ES: MR imaging of renal neoplasms. Magn Reson Imaging Clin North Am 8:813–836, 2000.
210. Pretorius ES, Siegelman ES, Ramchandani P, et al: Renal neoplasms amenable to partial nephrectomy: MR imaging. Radiology 212: 28–34, 1999.
211. Prince MR, Narasimham DL, Stanley JC, et al: Breath-hold gadolinium-enhanced MR angiography of the abdominal aorta and its major branches. Radiology 197:785–792, 1995.
212. Prokop M: Multislice CT angiography. Eur J Radiol 36:86–96, 2000.
213. Quinn MJ, Hartman DS, Friedman AC, et al: Renal oncocytoma: New observations. Radiology 153:49–53, 1984.
214. Ramseyer LT: Case 34: Renal Lymphangiectasia. Radiology 219: 442–444, 2001.
215. Rankin SC, Saunders AJ, Cook GJ, Scoble JE: Renovascular disease. Clin Radiol 55:1–12, 2000.
216. Reiman TA, Siegel MJ, Shackelford GD: Wilms tumor in children: Abdominal CT and US evaluation. Radiology 160:501–505, 1986.
217. Reznek RH, Mootoosamy I, Webb JA, Richards MA: CT in renal and perirenal lymphoma: A further look. Clin Radiol 42:233–238, 1990.
218. Rhyner P, Federle MP, Jeffrey RB: CT of trauma to the abnormal kidney. AJR Am J Roentgenol 142:747–750, 1984.
219. Richard S, Chauveau D, Chretien Y, et al: Renal lesions and pheochromocytoma in von Hippel–Lindau disease. Adv Nephrol Necker Hosp 23:1–27, 1994.
220. Ritchey ML, Azizkhan RG, Beckwith JB, et al: Neonatal Wilms tumor. J Pediatr Surg 30:856–859, 1995.
221. Robson CJ, Churchill BM, Anderson W: The results of radical nephrectomy for renal cell carcinoma. J Urol 101:297–301, 1969.
222. Rodriguez-de-Velasquez A, Yoder IC, Velasquez PA, Papanicolaou N: Imaging the effects of diabetes on the genitourinary system. Radiographics 15:1051–1068, 1995.
223. Rofsky NM, Bosniak MA: MR imaging in the evaluation of small (< or = 3.0 cm) renal masses. Magn Reson Imaging Clin North Am 5:67–81, 1997.
224. Rofsky NM, Weinreb JC, Bosniak MA, et al: Renal lesion characterization with gadolinium-enhanced MR imaging: Efficacy and safety in patients with renal insufficiency. Radiology 180:85–89, 1991.
225. Roubidoux MA, Dunnick NR, Sostman HD, Leder RA: Renal carcinoma: Detection of venous extension with gradient-echo MR imaging. Radiology 182:269–272, 1992.
226. Roy C, Pfleger DD, Tuchmann CM, et al: Emphysematous pyelitis: Findings in five patients. Radiology 218:647–650, 2001.
227. Roychowdhary A, Makris J, Colby JM: Unilateral absence of the white pyramid sign on noncontrast CT: A sign of tubular hydronephrosis. Presented at the 98th meeting of the American Roentgen Ray Society, San Francisco, California, April 26–May 1, 1998.
228. Rubin GD: Helical CT of potential living renal donors: Toward a greater understanding. Radiographics 18:601–604, 1998.
229. Rubin GD, Dake MD, Napel S, et al: Spiral CT of renal artery stenosis: Comparison of three-dimensional rendering techniques. Radiology 190:181–189, 1994.
230. Rubin GD, Walker PJ, Dake MD, et al: Three-dimensional spiral computed tomographic angiography: An alternative imaging modality for the abdominal aorta and its branches. J Vasc Surg 18: 656–664, 1993.
231. Sagalowsky AI, McConnell JD, Peters PC: Renal trauma requiring surgery: An analysis of 185 cases. J Trauma 23:128–131, 1983.
232. Sanders RC, Hartman DS: The sonographic distinction between neonatal multicystic kidney and hydronephrosis. Radiology 151: 621–625, 1984.
233. Sanders RC, Nussbaum AR, Solez K: Renal dysplasia: Sonographic findings. Radiology 167:623–626, 1988.
234. Saunders HS, Dyer RB, Shifrin RY, et al: The CT nephrogram: Implications for evaluation of urinary tract disease. Radiographics 15:1069–1085, 1995.
235. Schoenberg SO, Prince MR, Knopp MV, Allenberg JR: Renal MR angiography. Magn Reson Imaging Clin North Am 6:351–370, 1998.
236. Schwab SJ, Bander SJ, Klahr S: Renal infection in autosomal dominant polycystic kidney disease. Am J Med 82:714–718, 1987.
237. Schwartz JM, Bosniak MA, Hulnick DH, Megibow AJ: The use of computed tomography in the diagnosis of carcinoma of the renal pelvis causing ureteropelvic junction obstruction. Urol Radiol 9: 204–209, 1988.
238. Sebastia MC, Perez-Molina MO, Alvarez-Castells A, et al: CT evaluation of underlying cause in spontaneous subcapsular and perirenal hemorrhage. Eur Radiol 7:686–690, 1997.
239. Segal AJ, Spataro RF, Linke CA, et al: Diagnosis of nonopaque calculi by computed tomography. Radiology 129:447–450, 1978.
240. Semelka RC, Hricak H, Stevens SK, et al: Combined gadolinium-enhanced and fat-saturation MR imaging of renal masses. Radiology 178:803–809, 1991.
241. Semelka RC, Shoenut JP, Kroeker MA, et al: Renal lesions: Controlled comparison between CT and 1.5-T MR imaging with nonenhanced and gadolinium-enhanced fat-suppressed spin-echo and breath-hold FLASH techniques. Radiology 182:425–430, 1992.
242. Sessa A, Ghiggeri GM, Turco AE: Autosomal dominant polycystic kidney disease: Clinical and genetic aspects. J Nephrol 10:295–310, 1997.
243. Sherman JL, Hartman DS, Friedman AC, et al: Angiomyolipoma: Computed tomographic-pathologic correlation of 17 cases. AJR Am J Roentgenol 137:1221–1226, 1981.
244. Sheth S, Scatarige JC, Horton KM, et al: Current concepts in the diagnosis and management of renal cell carcinoma: Role of multidetector CT and three-dimensional CT. Radiographics 21(Spec No):S237–S54, 2001.
245. Shinmoto H, Yuasa Y, Tanimoto A, et al: Small renal cell carcinoma: MRI with pathologic correlation. J Magn Reson Imaging 8:690–694, 1998.

246. Siegel MJ: MR imaging of pediatric abdominal neoplasms. Magn Reson Imaging Clin N Am 8:837–851, 2000.
247. Si-Hoe CK, Thng CH, Chee SG, et al: Abdominal computed tomography in systemic lupus erythematosus. Clin Radiol 52:284–289, 1997.
248. Silverman SG, Lee BY, Seltzer SE, et al: Small (< or = 3 cm) renal masses: Correlation of spiral CT features and pathologic findings. AJR Am J Roentgenol 163:597–605, 1994.
249. Singh AD, Shields CL, Shields JA: Von Hippel–Lindau disease. Surv Ophthalmol 46:117–142, 2001.
250. Slywotzky CM, Bosniak MA: Localized cystic disease of the kidney. AJR Am J Roentgenol 176:843–849, 2001.
251. Smith RC, Levine J, Rosenfeld AT: Helical CT of urinary tract stones: Epidemiology, origin, pathophysiology, diagnosis, and management. Radiol Clin North Am 37:911–952, 1999.
252. Smith RC, Rosenfield AT, Choe KA, et al: Acute flank pain: Comparison of non-contrast-enhanced CT and intravenous urography. Radiology 194:789–794, 1995.
253. Smith RC, Verga M, Dalrymple N, et al: Acute ureteral obstruction: Value of secondary signs of helical unenhanced CT. AJR Am J Roentgenol 167:1109–1113, 1996.
254. Smith SJ, Bosniak MA, Megibow AJ, et al: Renal cell carcinoma: Earlier discovery and increased detection. Radiology 170:699–703, 1989.
255. Soulen MC, Fishman EK, Goldman SM, Gatewood OM: Bacterial renal infection: Role of CT. Radiology 171:703–707, 1989.
256. Srigley JR, Eble JN: Collecting duct carcinoma of kidney. Semin Diagn Pathol 15:54–67, 1998.
257. Srinivas V, Sogani PC, Hajdu SI, Whitmore WF Jr: Sarcomas of the kidney. J Urol 132:13–16, 1984.
258. Stables DP, Fouche RF, de Villiers van Niekerk JP, et al: Traumatic renal artery occlusion: 21 cases. J Urol 115:229–233, 1976.
259. Steffens JC, Link J, Grassner J, et al: Contrast-enhanced, K-space-centered, breath-hold MR angiography of the renal arteries and the abdominal aorta. J Magn Reson Imaging 7:617–622, 1997.
260. Steiner MS, Goldman SM, Fishman EK, Marshall FF: The natural history of renal angiomyolipoma. J Urol 150:1782–1786, 1993.
261. Stuck KJ, Koff SA, Silver TM: Ultrasonic features of multicystic dysplastic kidney: Expanded diagnostic criteria. Radiology 143:217–221, 1982.
262. Sullivan M, Frydenberg M: Nephron-sparing surgery for small incidental renal cell carcinoma. Aust N Z J Surg 71:349–353, 2001.
263. Sundaram CP, Saltzman B: Urolithiasis associated with protease inhibitors. J Endourol 13:309–312, 1999.
264. Suzuki K, Kurokawa S, Muraishi O, Tokue A: Segmental multicystic dysplastic kidney in an adult woman. Urol Int 66:51–54, 2001.
265. Szolar DH, Kammerhuber F, Altziebler S, et al: Multiphasic helical CT of the kidney: Increased conspicuity for detection and characterization of small (< 3-cm) renal masses. Radiology 202:211–217, 1997.
266. Talner LB: Urinary obstruction. In Pollack HM (ed): Clinical Urography: An Atlas and Textbook of Urological Imaging. Philadelphia, WB Saunders, 1990.
267. Taylor RS, Joseph DB, Kohaut EC, et al: Renal angiomyolipoma associated with lymph node involvement and renal cell carcinoma in patients with tuberous sclerosis. J Urol 141:930–932, 1989.
268. Telenti A, Torres VE, Gross JB Jr, et al: Hepatic cyst infection in autosomal dominant polycystic kidney disease. Mayo Clin Proc 65: 933–942, 1990.
269. Thibaut H, Parizel PM, Van Goethem J, De Schepper AM: Tuberous sclerosis: CT and MRI characteristics. Eur J Radiol 16:176–179, 1993.
270. Thornbury JR: Acute renal infections. Urol Radiol 12:209–213, 1991.
271. Thornton FJ, Kandiah SS, Monkhouse WS, Lee MJ: Helical CT evaluation of the perirenal space and its boundaries: A cadaveric study. Radiology 218:659–663, 2001.
272. Tolia BM, Iloreta A, Freed SZ, et al: Xanthogranulomatous pyelonephritis: Detailed analysis of 29 cases and a brief discussion of atypical presentations. J Urol 126:437–442, 1981.
273. Torres VE, Wilson DM, Hattery RR, Segura JW: Renal stone disease in autosomal dominant polycystic kidney disease. Am J Kidney Dis 22:513–519, 1993.
274. Traubici J, Neitlich JD, Smith RC: Distinguishing pelvic phleboliths from distal ureteral stones on routine unenhanced helical CT: Is there a radiolucent center? AJR Am J Roentgenol 172:13–17, 1999.
275. Trillo A, Lorentz WB, Whitley NO: Malakoplakia of kidney simulating renal neoplasm. Urology 10:472–477, 1977.
276. Urban BA, Fishman EK: Renal lymphoma: CT patterns with emphasis on helical CT. Radiographics 20:197–212, 2000.
277. Urban BA, Fishman EK: Tailored helical CT evaluation of acute abdomen [CME available in print version and on RSNA Link]. Radiographics 20:725–749, 2000.
278. Uzzo RG, Novick AC: Nephron sparing surgery for renal tumors: Indications, techniques and outcomes. J Urol 166:6–18, 2001.
279. van Baal JG, Smits NJ, Keeman JN, et al: The evolution of renal angiomyolipomas in patients with tuberous sclerosis. J Urol 152: 35–38, 1994.
280. Vasbinder GB, Nelemans PJ, Kessels AG, et al: Diagnostic tests for renal artery stenosis in patients suspected of having renovascular hypertension: A meta-analysis. Ann Intern Med 135:401–411, 2001.
281. Vinocur L, Slovis TL, Perlmutter AD, et al: Follow-up studies of multicystic dysplastic kidneys. Radiology 167:311–315, 1988.
282. Wagner BJ, Wong-You-Cheong JJ, Davis CJ Jr: Adult renal hamartomas. Radiographics 17:155–169, 1997.
283. Wagner BJ: The kidney: Radiologic-pathologic correlation. Magn Reson Imaging Clin N Am 5:13–28, 1997.
284. Wan YL, Lee TY, Bullard MJ, Tsai CC: Acute gas-producing bacterial renal infection: Correlation between imaging findings and clinical outcome. Radiology 198:433–438, 1996.
285. Wang LJ, Wong YC, Chen CJ, Lim KE: CT features of genitourinary tuberculosis. J Comput Assist Tomogr 21:254–258, 1997.
286. Warren KE, Gidvani-Diaz V, Duval-Arnould B: Renal medullary carcinoma in an adolescent with sickle cell trait. Pediatrics 103: E22, 1999.
287. Weiner SN, Bernstein RG: Renal oncocytoma: Angiographic features of two cases. Radiology 125:633–635, 1977.
288. Weiss GR, Margolin KA, Aronson FR, et al: A randomized phase II trial of continuous infusion interleukin-2 or bolus injection interleukin-2 plus lymphokine-activated killer cells for advanced renal cell carcinoma. J Clin Oncol 10:275–281, 1992.
289. White KS, Kirks DR, Bove KE: Imaging of nephroblastomatosis: An overview. Radiology 182:1–5, 1992.
290. Wiesner C, Jakse G, Rohde D: Therapy of local recurrence of renal cell carcinoma. Oncol Rep 9:189–192, 2002.
291. Wilms' tumor: Status report, 1990. By the National Wilms' Tumor Study Committee. J Clin Oncol 9:877–887, 1991.
292. Wong WS, Moss AA, Federle MP, Cochran ST, London SS: Renal infarction: CT diagnosis and correlation between CT findings and etiologies. Radiology 150:201–205, 1984.
293. Wong-You-Cheong JJ, Wagner BJ, Davis CJ: Transitional cell carcinoma of the urinary tract: Radiologic-pathologic correlation. Radiographics 18:123–142, 1998.
294. Wu ZL, Zhou KR, Liao L: Renal vein thrombosis and selective arterial or venous thrombolytic therapy. J Thromb Thrombolysis 3: 67–70, 1996.
295. Yoder IC, Pfister RC, Lindfors KK, Newhouse JH: Pyonephrosis: Imaging and intervention. AJR Am J Roentgenol 141:735-740, 1983.
296. Yuh BI, Cohan RH: Different phases of renal enhancement: Role in detecting and characterizing renal masses during helical CT. AJR Am J Roentgenol 173:747–755, 1999.
297. Zagoria RJ, Dyer RB: Computed tomography of primary renal osteosarcoma. J Comput Assist Tomogr 15:146–148, 1991.
298. Zagoria RJ, Bechtold RE, Dyer RB: Staging of renal adenocarcinoma: Role of various imaging procedures. AJR Am J Roentgenol 164:363–370, 1995.
299. Zagoria RJ, Dyer RB, Harrison LH, Adams PL: Percutaneous management of localized emphysematous pyelonephritis. J Vasc Interv Radiol 2:156–158, 1991.
300. Zagoria RJ, Wolfman NT, Karstaedt N, et al: CT features of renal cell carcinoma with emphasis on relation to tumor size. Invest Radiol 25:261–266, 1990.
301. Zand MS, Strang J, Dumlao M, et al: Screening a living kidney donor for polycystic kidney disease using heavily T2-weighted MRI. Am J Kidney Dis 37:612–619, 2001.
302. Zeman RK, Cronan JJ, Rosenfield AT, et al: Renal cell carcinoma: Dynamic thin-section CT assessment of vascular invasion and tumor vascularity. Radiology 167:393–396, 1988.
303. Zimmerhackl LB, Rehm M, Kaufmehl K, et al: Renal involvement in tuberous sclerosis complex: A retrospective survey. Pediatr Nephrol 8:451–457, 1994.

42

Peritoneum and Mesentery

John R. Haaga

As experience with imaging within the abdomen has accumulated, it has become apparent that computed tomography (CT) and magnetic resonance imaging (MRI) are useful for the diagnosis of the many peritoneal and mesenteric problems. Even if a primary peritoneal problem does not exist, many secondary signs that can add valuable insights about other disorders may be observed.

This chapter discusses the normal anatomy and physiology of the peritoneum and mesentery as well as the wide spectrum of pathologic disorders that affect the area. I have also included information on the retroperitoneum as it interrelates to the peritoneum. Inclusion of this material permits a more comprehensive understanding of abdominal problems.

Embryology

The gastrointestinal (GI) tract is formed when the entoderm develops in a tube within the coelomic cavity. It acquires a single-layer covering of mesodermal cells, which evolve from the space between the ectoderm and the endoderm (Fig. 42–1*A*). The dorsal or posterior mesoderm forms the dorsal mesentery, which eventually composes the visceral peritoneum of the abdomen (the pericardium and pleura in the chest) (Fig. 42–1*A*).

The anterior splanchnic mesoderms fuse to form the ventral (anterior) mesentery and later completely disappear, leaving the falciform ligament of the liver as the only remnant (Fig. 42–1*B*, *C*). Within the transverse septum (from which the diaphragm evolves), the liver forms and moves into the coelomic cavity, carrying an investment of peritoneum. The only attachments of the liver to the transverse septum are small portions of the peritoneum, which become the triangular and coronary ligaments (behind which are the "bare areas" of the liver).

The blood vessels (e.g., lymphatics) to the various developing viscera course the posterior or dorsal mesentery. The anterior attachment of the mesentery between the liver and the stomach, esophagus, and duodenum becomes the lesser omentum with two portions, the gastrohepatic and the gastroduodenal ligaments (Fig. 42–1*B* and *C*).

One might best understand the relationships of the pancreas to the omental bursa by considering the rotation of the bowel and changes in the dorsal mesentery. The pancreas forms from entodermal buds of the duodenum, the (ventral) anterior bud being slightly caudad but close to the common bile duct and the (dorsal) posterior bud being directly opposite to it. As the "C" loop of the duodenum rotates, the two pancreatic buds come together and fusion occurs at the level of the head. The ventral segment remains as the uncinate and head portion. The spleen forms in the (dorsal) posterior mesentery and is carried laterally as the omental bursa forms. The dorsal mesentery containing the pancreas fuses with the posterior abdominal peritoneum (Fig. 42–1*D*). The multiple layers of the embryologic mesentery as it relates to the retroperitoneum, pancreas, and colon can be seen (Fig. 42–1*D*).

The lesser omentum and the omental bursa are formed by the rotation of the stomach and duodenum and the posterior movement of the pancreas (Fig. 42–1*B* and *C*). The anterior aspect of the bursa consists of the lesser omentum, composed of the hepatoduodenal and the gastroduodenal ligaments, the posterior wall of the stomach, the gastrocolic ligament, and the mesocolon. The posterior wall is bounded by the peritoneum over the top of the pancreas. (This peritoneum is on the right side of the dorsal mesentery, which is on the anterior surface of the pancreas.) The lateral wall consists of the gastrocolic, gastrosplenic, and splenorenal ligaments (Fig. 42–1*C*). The other boundaries of the omental bursa are described under the "Normal Peritoneal Anatomy."

As the bowel and the colon rotate, the mesentery of the mesocolon fuses posteriorly with the covering of the retroperitoneum (Fig. 42–1*E*). If the fusion is complete, the spaces remain intact and conform to the traditional anatomic concepts of the retroperitoneum and the peritoneum (i.e., the peritoneal space is the anterior space and has a number of different compartments).[65] Traditionally, the retroperitoneum is divided into three parts: the anterior pararenal, posterior pararenal, and perirenal spaces. After extensive CT experience, it has become apparent that the traditional concept does not always explain some observations. Dodds et al[19, 20] have reviewed the embryologic formation of the retroperitoneum and proposed a new concept that reconciles some inconsistent observations.

Peritoneum

The peritoneum is a serous membrane covered with a single layer of mesothelial cells that envelops all portions of the abdomen. The total surface area is about 1.7 m^2, but the functional area (physiologic conditions described in the next section) is about 1 m^2.[42] The cavity is closed except for the fallopian tubes and contains 50 to 75 mL of clear fluid, which has a specific gravity of 1.016, and fewer than 3000 cells/mm^2. The cells are lymphocytes,

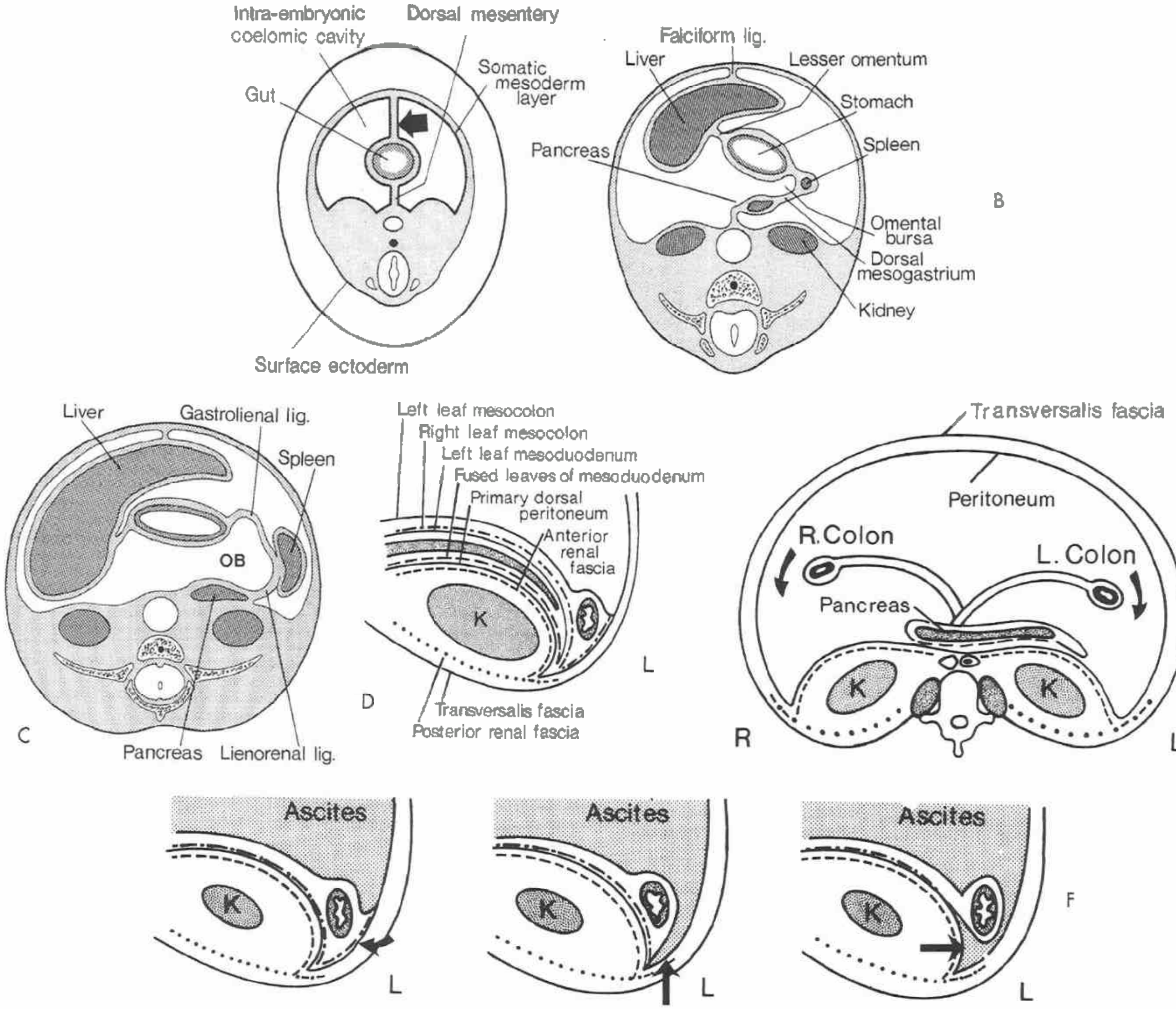

Figure 42–1. Embryology of gastrointestinal tract.

A, Diagram shows the embryologic formation of the gut as the entodermal canal within the layers of the mesoderm and ectoderm. The entoderm is attached posteriorly by the dorsal mesentery and anteriorly by the ventral mesentery *(arrow).* The coelomic cavity (later to be the peritoneal cavity) is lined by mesodermal cells (later to be the peritoneum).

B, A later stage in the embryo shows the liver having formed in the anterior or ventral mesentery. This mesentery persists as the falciform ligament and the lesser omentum between the liver and the stomach. The spleen and dorsal pancreas form in the posterior or dorsal mesentery. A folding of the posterior mesentery and mesogastrium forms the omental bursa. The kidney and adrenal gland are located in the retroperitoneum. (According to Dodds et al., the space within the mesentery is and should continue to be called the intermesenteric space, regardless of any changes in configuration.)

C, This diagram approximates the adult configuration, with the liver having moved to the right. The rotation of the stomach, spleen, lienorenal ligament, and pancreas produces the margins of the omental bursa.

D, Adult retroperitoneal spaces at the level of the left kidney. The primary retroperitoneum is divided by the anterior renal fascia *(dashed lines)* and the posterior renal fascia *(dotted lines)* into perirenal and posterior pararenal spaces. The fusion of the anterior renal fascia to the primary dorsal peritoneum eliminates any anterior pararenal space. Ventral to the primary retroperitoneum, a secondary retroperitoneum forms, consisting of a pancreaticoduodenal space overlying a retroperitoneal colonic space. These secondary spaces are demarcated by folded, laminated leaves of mesentery that fuse with one another or the primary dorsal peritoneum. K, Kidney; L, left.

E and *F,* Schematics of retroperitoneal colonic space. K, Kidney; R, right; L, left. Right leaf of the mesocolon, *long* and *short dashes;* anterior perirenal fascia, *short dashes;* posterior perirenal fascia, *dots;* and lateral fascia, *dots* and *dashes. E,* Axial section through the pancreas of a 14-week-old human fetus. During colonic rotation *(arrows),* the left and right colon swing toward the flanks so their dorsal mesentery, or mesocolon, lies flat against the posterior abdominal wall. At this stage, the mesentery of the duodenum and pancreas has already fused with the posterior peritoneum to form the pancreaticoduodenal space. Thus, bilateral retroperitoneal colonic spaces come to lie ventral to pancreaticoduodenal space but extend more caudad. *F,* Depending on complete or incomplete fusion of these spaces *(arrow),* the pericolic space may be very shallow, extend slightly posteriorly *(vertical arrow),* or even medially into the fascia *(horizontal arrow).* These changes are only appreciated when ascites is present.

D and *E,* From Dodds WJ, Darweesh RM, Lawson TL, et al: The retroperitoneal spaces revisited: Pictorial essay. Am J Roentgenol 147:1155, copyright by American Roentgen Ray Society, 1986.)

macrophages, eosinophils, mast cells, and rare free mesothelial cells. The peritoneum is normally sterile and free of bacteria.

Peritoneal Function

The function of the peritoneum can be separated into fluid dynamics and particle clearance. The peritoneal membrane is a semipermeable membrane that permits bidirectional diffusion of water and solutes. Fluid and solute exchange are related to membrane area and permeability. The permeability and transfer of material depend on blood flow, vasoactive compounds, and tonicity of the peritoneal fluid (or osmotic pressure of blood).[68, 119] Hyperosmotic fluid, inflammation, chemical irritants (bile, gastric acid, pancreatic fluid), or vascular agents can cause a net flow of water as high as 300 to 500 mL/hour into the cavity.[43, 60]

Although the passive exchange of fluids and solutes occurs over the entire surface, the clearance of particulate material (e.g., bacteria, cellular metastases) is restricted to the diaphragmatic surface of the peritoneum.[3, 4, 68] Through stomata between mesothelial cells, particulate material and fluid can be absorbed into specialized lymphatic vessels called *lacunae*.[3, 4, 109, 111] The material is transported through the diaphragm and into the retrosternal and anterior mediastinal lymphatic vessels to the right thoracic duct; reverse flow is prevented by lymphatic valves (Fig. 42–2).[11, 46] The stomata have been shown to accommodate particles smaller than 20 μm in size (using polystyrene beads); the size varies with respiratory movement.

In conjunction with the active flow of fluid through the diaphragm, respiratory motion of the diaphragm, gravitational pull on the liver, and normal peristalsis of the bowel enhance the flow of fluid cephalad. Normal peristalsis displaces fluid to the lateral gutters where the upward flow occurs. The respiratory movement of the diaphragm creates a negative subphrenic pressure, which enhances upward flow (Fig. 42–3*A*). Also the gravitational pull on the liver creates a negative pressure above the liver that enhances the flow upward. The sum of these influences is generally an upward movement of fluid toward the diaphragm covered by the peritoneum with the lacunae as noted previously. The net result and influence can be seen in Figure 42–4*A*, *B*.

Anything that alters the normal pattern of respiratory motion or affects motility of the bowel inhibits this normal flow. An ileus created by a laparotomy or other problem delays clearance time of the peritoneum. Positive pressure ventilation, increased intra-abdominal pressure, or phrenic neurectomy alters the physiologic processes and movements and thereby impairs normal clearance.

Gravity also plays an important role in the flow of fluid and particulate material.[7, 79, 114] The *in vivo* effects of gravity

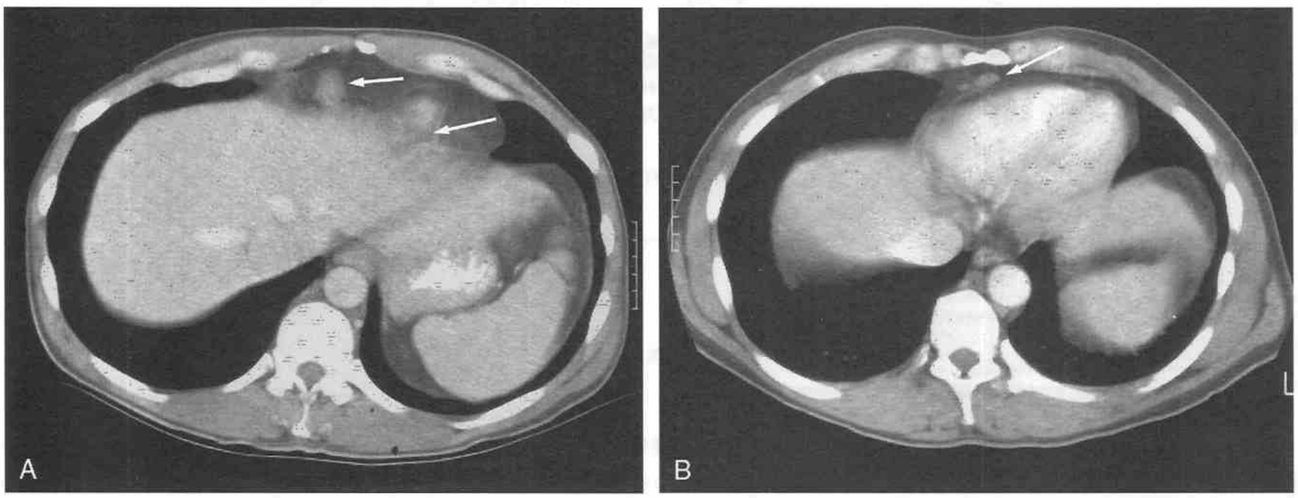

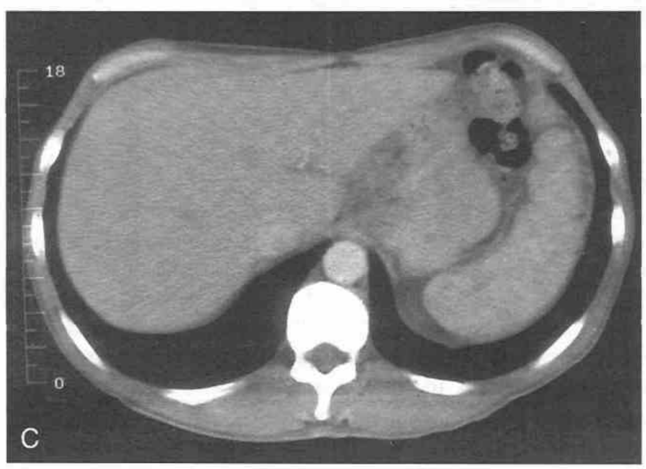

Figure 42–2. Location of the lymph nodes that filter material from the abdomen. *A,* CT scan through the upper abdomen of a patient with abdominal inflammation shows enlarged lymph nodes below the surface of the diaphragm *(arrows)*. *B,* Higher scan in the same patient shows enlarged lymph nodes in the anterior mediastinum in front of the pericardium *(arrow)*. Lymphatic material enters the lacunae on the undersurface of the diaphragm and enters the lymphatics of the mediastinum. *C,* Later scan performed at the level of the liver shows the shrinkage of the lymph nodes after inflammation has resolved.

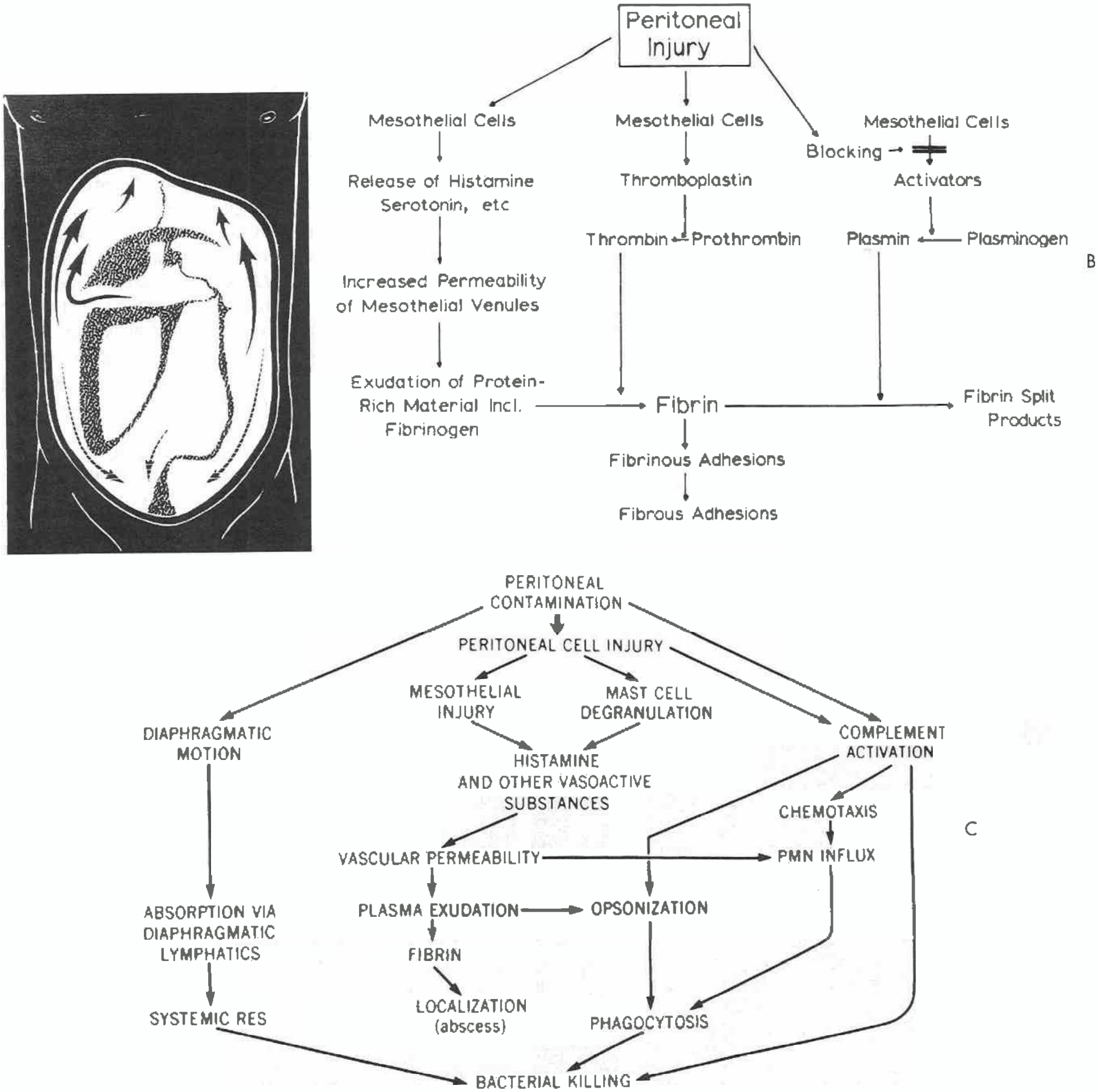

Figure 42–3. Peritoneal dynamics and physiology. *A,* Diagram showing the directions of fluid flow and clearance within the peritoneum. The relative size of the arrows indicates the relative contribution from each area. *B,* Pathogenesis of peritoneal adhesions. *C,* Diagram of bacterial interaction with the immune systems, and their clearance mechanisms. PMN, polymorphonuclear neutrophils; RES, reticuloendothelial system.

on particle distribution were studied by looking at clearance of contrast material injected into peritoneal cavities after routine appendectomy and cholecystectomy. Material injected into the ileocecal region goes preferentially to the pelvis, right paracolic area, and right subhepatic area. A smaller amount passes to the left pericolic gutter and the left subhepatic space. Material injected into the right subhepatic space next to the duodenum spreads to the right subphrenic space, the left infrahepatic space, the right pericolic gutter, and the pelvis (see Fig. 42–3). The infracolic spaces were not involved in either case, even when contrast material was injected into the ileocolic region, probably because the net flow of fluid is from the bowel loop surfaces laterally, as noted previously.

Response to Infection

There are two effective defensive mechanisms against pyogenic infections in the peritoneum: the mechanism of

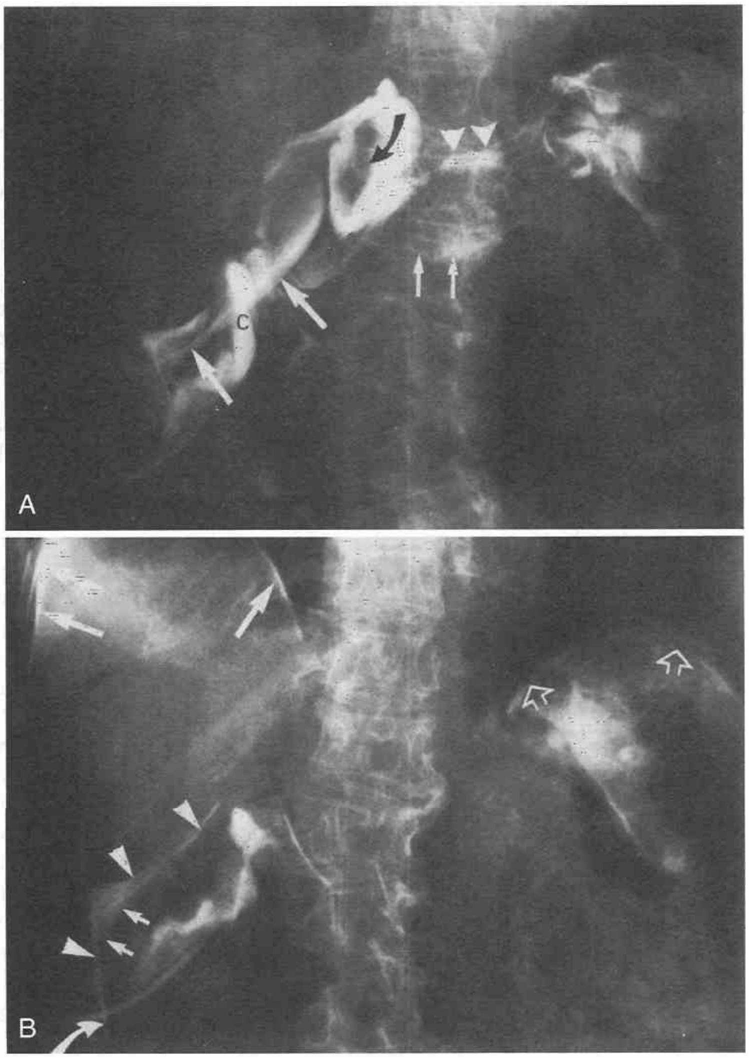

Figure 42–4. Fluid flow in peritoneum. *A*, This radiograph was taken after the injection of contrast material through a T-tube tract (C), which was displaced from the common bile duct and into the subhepatic recess. The edge of the right lobe of the liver *(large arrows)* is seen. The falciform ligament *(curved arrow)* is surrounded by contrast material. Contrast material flows to the left side into the anterior portion of the left subdiaphragmatic space *(arrowheads)* adjacent to the stomach. Some material has entered the omental bursa *(small arrows)* through Winslow's foramen. (The patient is rotated because of scoliosis.) *B*, In this later radiograph, contrast material is better seen in the subhepatic recess (Morison's pouch) *(arrowheads)*. It flowed cephalad into the right subdiaphragmatic space *(large arrows)*. The impression of the kidney on the subhepatic recess is seen *(small arrow)*. (The space appears to be located more medially because of the patient's rotation.) The left subdiaphragmatic space is also seen *(open arrows)*.

particulate clearance[68, 78, 119] and the typical immune response (involving antibodies and white cells) (see Fig. 42–3*B*). Absorption of bacteria into the diaphragmatic lymphatic system permits eradication of the bacteria by the systemic defense mechanisms of fixed tissue macrophages, reticuloendothelial cells, and polymorphonuclear leukocytes.[36, 37] Laboratory models have shown that bacteria begin to disappear from the peritoneum even before the influx of phagocytic cells. In such cases, bacteria have been isolated from mediastinal lymph channels within 6 minutes from the time of peritoneal injection.

The attraction of phagocytes, which can lyse bacteria, into the peritoneum[104] occurs by chemotaxis (see Fig. 42–3*C*). Chemotaxis occurs after activation of various complement components and attraction of phagocytes.[7] Killing of the bacteria with intracellular chemicals occurs after phagocytosis. Ingestion by phagocytes may occur unaided, but at times opsonization by complement (C3) or immunoglobulin G (IgG) may be required with encapsulated organisms.[105]

Fibrin also serves as a local defense mechanism, which is useful in one regard but detrimental in others. With peritoneal injury, a release of histamine and other permeability factors that may permit leakage of a protein-rich material containing fibrinogen occurs. This material, combined with tissue thromboplastin, causes the polymerization of fibrin. Normally, fibrin may be split and removed as needed by the activation of plasminogen to plasmin; however, when injury to the mesothelium or peritonitis occurs, no fibrinolytic activity takes place.[40, 119]

Although fibrin localizes the pathogens to a nearby area instead of permitting them to spread, it impairs eradication of the bacteria.[65, 119] Fibrin hinders the clearance of bacteria into the lymphatic system. Fibrin also protects the bacteria from phagocytic activity and impairs exposure to antibiotics.[37–39, 80] This latter problem is being addressed in percutaneous abscess drainages by the use of fibrinolytic agents (see "Abscesses" later).

An abscess occurs when further tissue destruction results from enzyme release from the phagocytes and bacteria. Further growth of the bacteria and mobilization of the immune system may rarely eradicate the abscess, or it may progress with more inflammation and destruction. Once a large inoculum of bacteria is established in an abscess, a low oxidation potential results[37] and impairs phagocytosis and antibiotic activity. In most cases, drainage is required.

Normal Peritoneal Anatomy

Because of the extensive work and educational efforts by Meyers[79] and Whalen,[114] knowledge of the anatomic spaces has become widespread among the radiologic community. I have relied heavily on these sources for the information in this chapter, but I have also drawn on additional physiologic data and clinical experience. The general orientation of the anatomy can be appreciated by studying radiographs with contrast injection delineating the perihepatic spaces (see Fig. 42–4*A* and *B*).[93]

Normal anatomy in this chapter is shown in axial, coronal, and sagittal images provided by thin sections from a new multislice scanner. Using 1-mm sections and subsecond scanning, these reconstructions show remarkably accurate anatomic relationships (Figs. 42–5 to 42–7; see Fig. 42–4).

Supracolic and Infracolic Spaces

The peritoneal spaces are potential spaces that are not normally visualized unless they are distended with fluid or unless the fascia is thick.

The abdomen can be divided into the supracolic, infracolic, pericolic (pericolonic), and pelvic spaces. The supracolic and the infracolic spaces are separated by the transverse colon and its mesentery (see Figs. 42–5*B* and *C*, 42–6*D*, and 42–7*A–D*. Anteriorly, the greater omentum is located between the peritoneal wall and the bowel (see Figs. 42–6*E* and 42–7*D*).

The supracolic spaces include the perihepatic spaces and the omental bursa. The infracolic space is divided into the right and left spaces by the root of the mesentery, which extends right to left from Treitz's ligament to the ileocecal area. Laterally, the pericolonic gutters communicate with the perihepatic spaces and the pelvic region.

Perihepatic Spaces

The perihepatic spaces consist of the subphrenic (subdiaphragmatic) spaces and subhepatic spaces. There are right, left, anterior, and posterior spaces in each area.

The right subphrenic space is continuous with the right subhepatic space and the right pericolic space. The right subphrenic space lies adjacent to the lateral and superior portion of the liver between the diaphragm and the body wall (see Figs. 42–5*A–C*, 42–6*A–C*, and 42–7). On axial and coronal images, the posterior margin of the subphrenic space ends at the anterior edge of the coronary ligaments (which encompasses the bare area of the liver against the posterior surface of the abdominal cavity) (see Figs. 42–5*C* and *D*, 42–6*A*, and 42–7*A*).

The right subphrenic space is limited medially by the falciform ligament (see Fig. 42–6*A*) in the upper portion of the abdomen. Because of variability in size, the ligament may or may not serve as an effective barrier to the spread of material to the left side (see Figs. 42–5*A* and 42–6*A*).

The left subphrenic space is beneath the left diaphragm and surrounds the fundus of the stomach anteriorly, the spleen, and the space between the liver and the stomach (see Figs. 42–6*A–D* and 42–7*D*). Fluid can also be localized into various areas of the space (e.g., anterior, posterior). The left subhepatic space is immediately continuous with the anterior part of the left subphrenic space (see Figs. 42–5*B* and 42–6*A* and *B*). The lateral perisplenic portion is immediately continuous with the left pericolic space (see Fig. 42–6*D*). Although it is traditionally taught that the phrenicolic ligament restricts flow of material from the left pericolic space to the left subphrenic space, in reality, it seldom is an effective barrier (see Fig. 42–5*A* and *B*). CT scans in numerous patients have shown variability in size, shape, and location of the ligament, which explains the inconsistent performance of the ligament as a barrier to infection.

The subhepatic spaces consist of a right subhepatic and a left subhepatic space (see Figs. 42–5*A*, 42–6*B*, and 42–7*A* and *D*). The right subhepatic space is adjacent to the gallbladder and extends posteriorly back to the anterior surface of retroperitoneum over the right kidney (see Figs. 42–5*A* and *C*, 42–6*D*, and 42–7*A*). It is immediately adjacent to the duodenum and Winslow's foramen, whose anterior edge consists of the edge of the lesser omentum, which contains the hepatic artery, portal vein, common bile duct, and lymph nodes (virtually all nodes from the perihepatic area—except the lower portion of the colon—converge at this area) (see Figs. 42–5*B*, 42–6*B* and *C*, and 42–7*B* and *C*).

The left subhepatic space is the space immediately beneath the left lobe of the liver and is continuous with the anterior part of the left subphrenic space (see Figs. 42–5*A*, 42–6*A*, and 42–7*D*). It is bounded posteriorly by the lesser omentum and on the sides by the capsular surface of the left liver lobe and the stomach.

The omental bursa (lesser sac)[19] is behind the stomach and anterior to the pancreas (see Figs. 42–5*A* and *B*, 42–6*B* and *C*, and 42–7*B* and *C*). The left margin is the gastrolienal (gastrosplenic) ligament, and the anterior margin is the gastrohepatic ligament; the right margin is the medial surface of the coronary ligament and the edge of lesser omentum, which is the boundary of the superior recess. The caudal boundary of the omental bursa is the gastrocolic reflection and the mesocolon. The greater omentum extends caudad from the anterior edge of the fundus of the stomach and the gastrocolic ligament. It contains a potential space in the fused membranes that may be split into a true space by an active process (i.e., bleeding or infection). The omental bursa can be divided into an inferior and superior recess of the omental bursa by the reflection over the left gastric artery (see Figs. 42–5*A* and *B* and 42–6*A–C*).

The superior recess is a potential space in the right side of the omental bursa and is seldom seen in patients with a transudative effusion. In cases of pseudocysts, infection, or processes that incite a pressure phenomenon, it may be visualized. The margins of these spaces are variable from one patient to another and may extend high beside the caudate lobe, vena cava, and into the porta hepatis (see Figs. 42–6*A* and 42–7*C*).

Pericolic Spaces

The right and left pericolic spaces are spaces that are contiguous with the pelvic region and the subphrenic spaces (see Figs. 42–5*A–C* and 42–6*E–G*). These spaces receive flowing fluid displaced from around the small

Text continued on page 1621

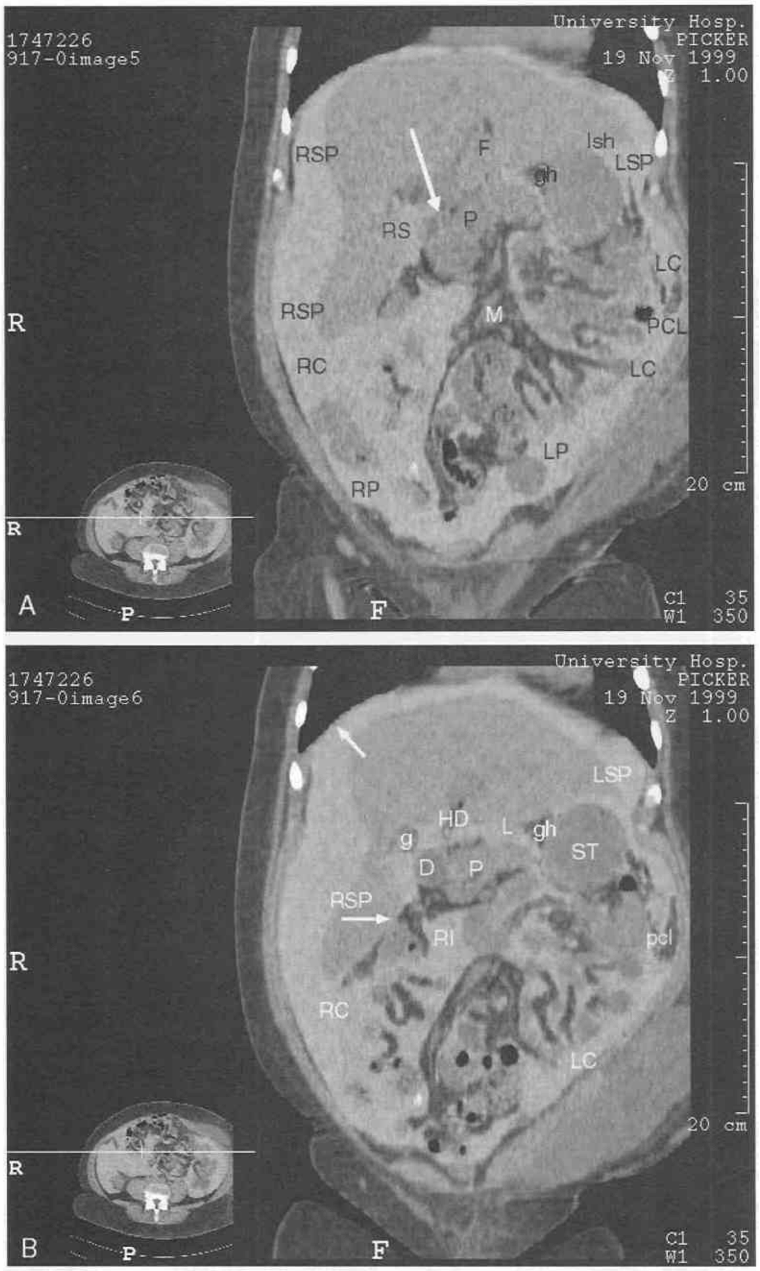

Figure 42–5. Peritoneal spaces in three dimensions. *A*, Coronal image of the anterior abdomen in a patient with dilute contrast material injected into the peritoneum. The various portions of the peritoneal cavity can be identified. The right subphrenic space (RSP) extends from the falciform ligament (F) laterally between the abdominal wall and the liver. This space then communicates with the pericolic space (RC) and the right subhepatic space (RS). The right pericolic space flows into the right side of the pelvis. The left subphrenic space (LSP) communicates with the left subhepatic space (lsh). Flow from these spaces is limited caudally by the phrenicocolic ligament (PCL). The left pericolic space (LC), extends caudally into the left side of the pelvis (LP). In the region of the suprahepatic spaces, the right subhepatic space (RS) is below the right lobe of the liver and extends into the lesser sac *(vertical down arrow)* beneath the edge of the lesser omentum, which contains the portal vein, hepatic artery, and common bile duct. This is immediately adjacent to the pancreas (P). The upper margin of the lesser sac is bounded by the gastrohepatic ligament (gh) containing the gastric vessels. The mesentery (M) is noted in the midline containing the mesenteric vessels.

B, Coronal scan of a patient with dilute contrast in the peritoneum. The peritoneum is generally divided into supracolic and infracolic (RI) spaces by the mesocolon *(horizontal arrow)*, which extends from the anterior margin of the pancreas (P). The supracolic space encompasses all of the subphrenic, perihepatic, and perisplenic spaces. The right subphrenic space extends from the upper space below the diaphragm *(oblique arrow)* and laterally around the liver (RSP). The falciform ligament is not seen, which demonstrates why it may not always serve as a complete barrier between the right and left sides. The subphrenic space communicates with the right pericolic space (RC), which extends into the right pelvis. The right subphrenic space communicates with the right subhepatic space *(horizontal arrow)* (see Fig. 42–4*B*), which is adjacent to the gallbladder (g) and duodenum (D). This space extends into the lesser sac (L) under the hepatoduodenal ligament (HD), which contains the portal vein, hepatic artery, and common duct. The lesser sac continues behind the stomach (ST), which is better seen on the sagittal views to follow. The superior boundary is the gastrohepatic ligament (gh). The left subphrenic space (LSP) is located below the diaphragm, around the left lobe and the stomach. It is limited inferiorly by the phrenicocolic ligament (pcl). The left pericolic space (LC) extends into the pelvis.

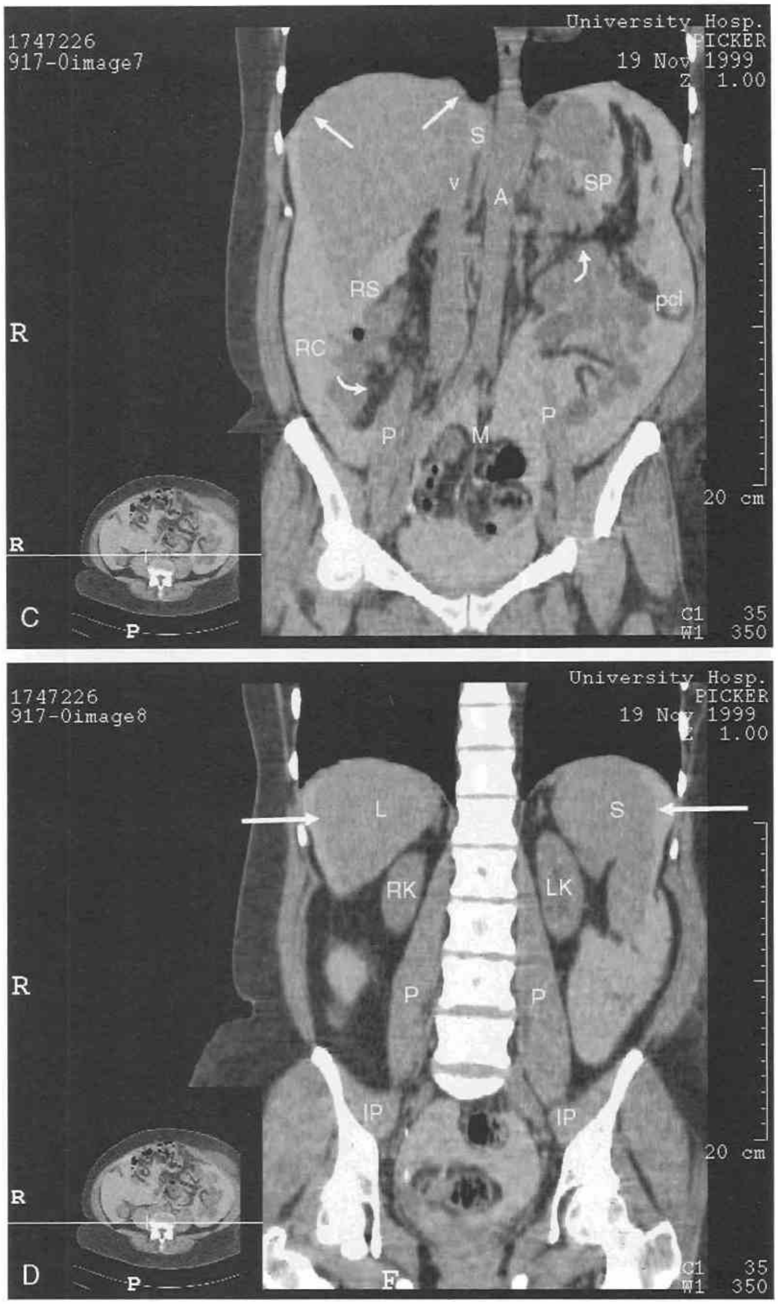

Figure 42–5 *Continued. C,* Coronal image more posterior than *B.* This level demonstrates the attachment *(arrows)* of the coronary ligaments of the right liver[redacted]e *(straight arrows)* to the more posterior portion of the diaphragm and abdominal cavity. The communication of the right subphrenic space to the pericolic (RC) and right subhepatic space (RS) is well seen. The broad attachment of the mesentery located on the posterior abdominal wall extends from the ligament of Treitz *(upward curved arrow)* to the right lower quadrant *(curved arrow).* The recesses of the lesser sac, the superior recess (S) adjacent to the vena cava (v), and the splenic recess (SP) behind the stomach are seen. Aorta (A) is noted. The phrenicocolic ligament (pcl) is again noted in the midportion of the left pericolic space (see Fig. 42–4*B*). The mesentery of the small bowel (M) and the psoas muscles (P) are seen. Contrast material in the pelvis is also noted.

D, Posterior coronal section shows the retroperitoneum and posterior portions of the peritoneum. The most posterior portions of the liver (L) and spleen (S) have medial and posterior "bare areas." Note the contrast material in the most posterior portions of the right and left subphrenic spaces *(horizontal arrows).* The retroperitoneum contains the right (RK) and left (LK) kidneys, which are surrounded by a cone-shaped space containing fat. The highest extent of the pararenal spaces extends cephalad under the diaphragm, contains the adrenal glands, and merges with the bare areas. The psoas muscles (P) extend distally and merge with the iliopsoas muscles (IP).

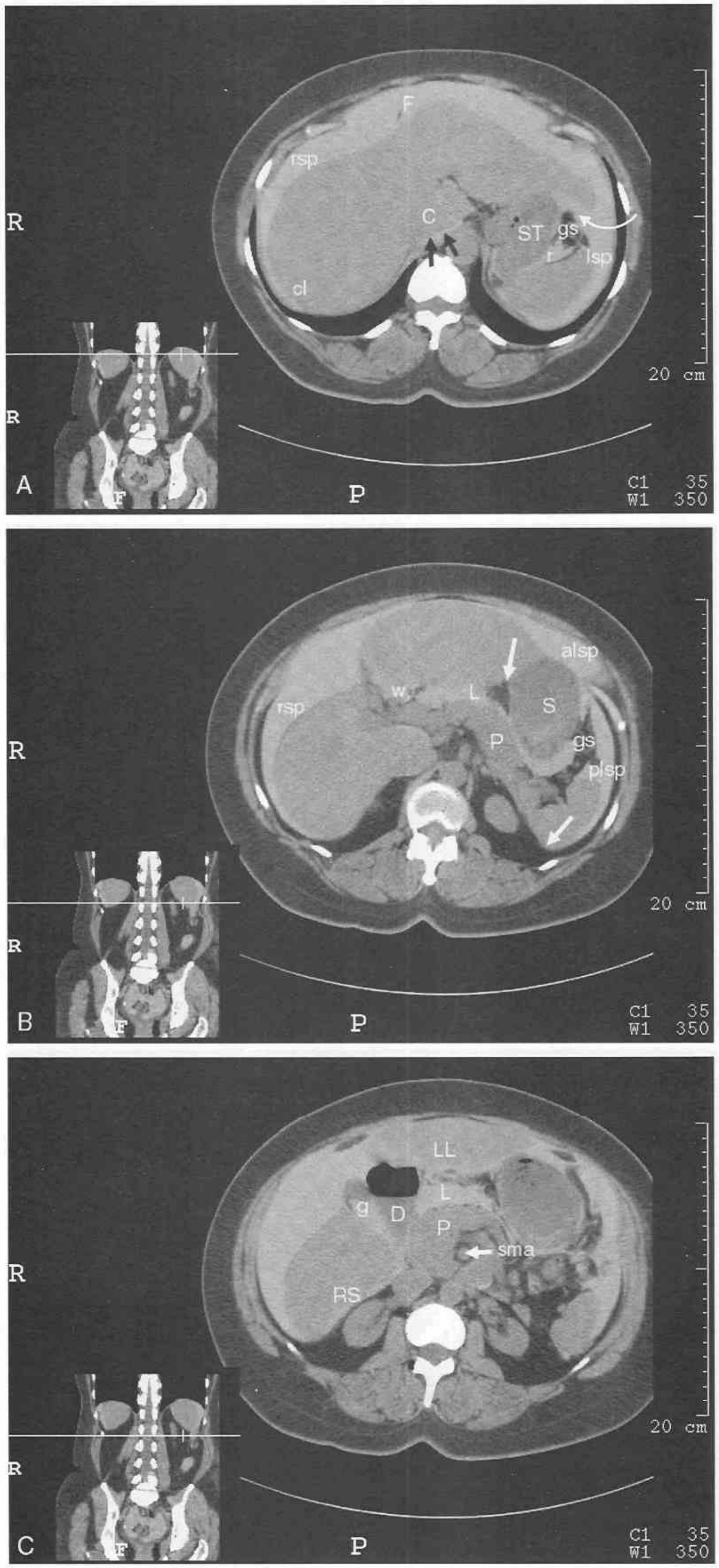

Figure 42–6. Coronal images of peritoneum. *A,* Axial scan through the upper abdomen shows the perihepatic spaces in the supracolic region. The right subphrenic space (rsp) extends from the falciform ligament (F), anteriorly around the liver and posteriorly to the coronary ligaments (cl). Behind these ligaments is the "bare area" of the liver, which is the most cephalad portion of the retroperitoneum. The left subphrenic space (lsp) extends posteriorly around the left lobe of the liver, stomach, and spleen. At this high level, the peritoneal space surrounds the spleen on all surfaces; the attached bare area of the spleen is attached posteriorly at the level of the splenic pedicle (see *C*). The left subhepatic space is contiguous with the left subphrenic space. Also at this level, the superior recess *(arrows)* of the lesser sac is seen around the caudate lobe of the liver (C). The splenic recess (r) of the lesser sac is noted behind the stomach (ST). The gastrohepatic ligament and the gastrosplenic ligament (gs) are noted.

B, This axial scan is at a slightly lower level over the lesser sac. The right subphrenic space (rsp) is noted lateral to the liver; inflammatory processes may sequester collections into anterior and posterior components. The left subphrenic space can be subdivided into the anterior (alsp) and posterior (plsp) spaces, and it ends posteriorly at the bare area of the spleen. The anatomic boundaries of the lesser sac are noted. The sac (L) is anterior to the pancreas (P) and extends posteriorly behind the stomach (S). The margin of the foramen of Winslow (w) contains the portal vein, the hepatic artery, and the common bile duct. The classic boundary within the lesser sac is the left gastric artery, which resides in the gastrohepatic ligament *(vertical arrow)* and the gastrosplenic ligament (gs). This peritoneal reflection over the gastric artery divides the inferior and superior components of the lesser sac. At this level, the spleen has a retroperitoneal component, which begins at its posterior margin *(arrow)*. The retroperitoneum around the kidney consists of several planes (see Fig. 42–1).

C, Axial scan at the level of the pancreatic head shows the perihepatic spaces, as noted in *A* and *B,* as well as additional peripancreatic anatomy. The inferior portion of the lesser sac (L) is anterior to the pancreas. The right subhepatic space (RS) is behind the gallbladder (g). The anterior boundary consists of the gastrohepatic ligament *(horizontal arrow pointed left)*. The head of the pancreas (P), superior mesenteric artery (sma), left lobe of the liver (LL), and air-filled duodenum (D) are seen.

Illustration continued on following page

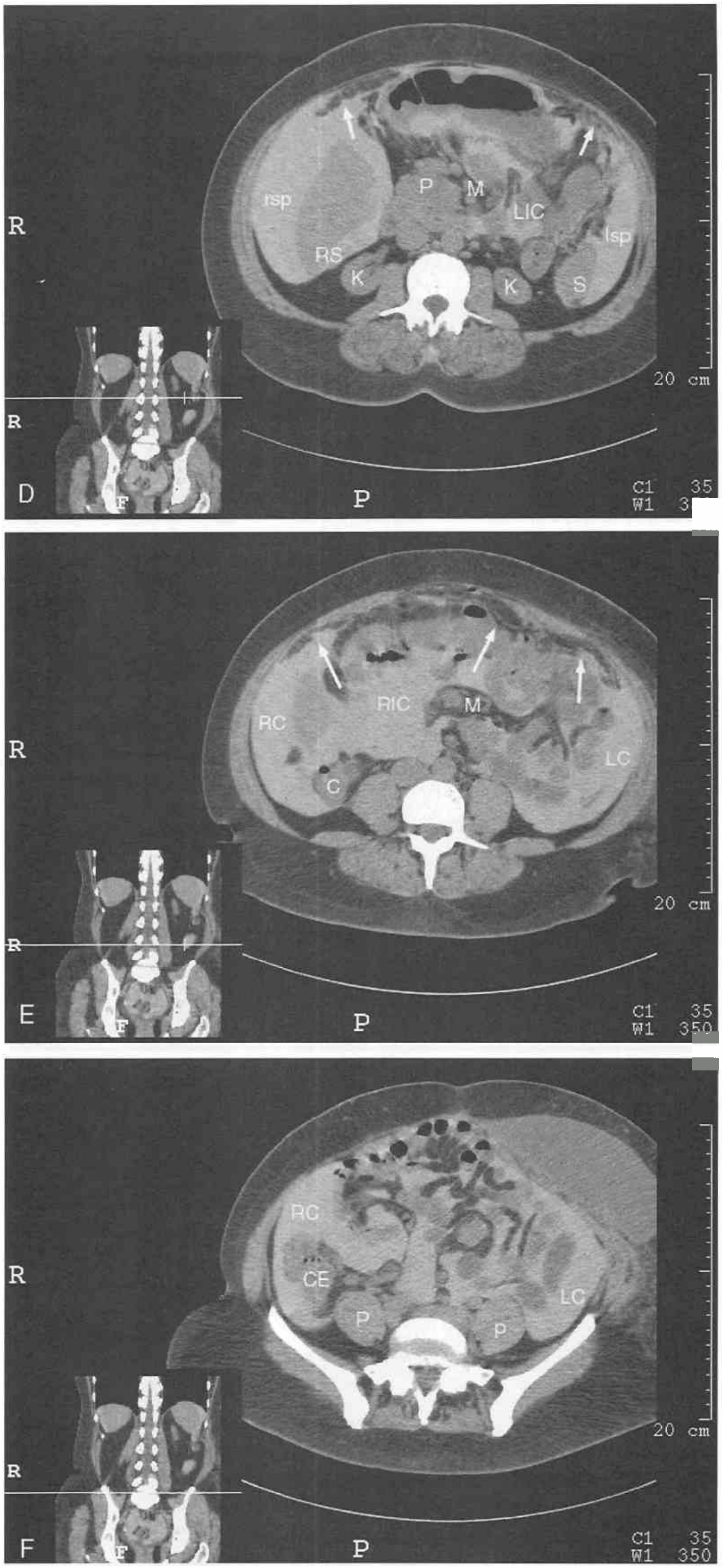

Figure 42–6 *Continued. D,* Axial scan at lower level than *C.* At this level, the right subphrenic space (rsp) merges with the posterior right subhepatic space (RS) (also known as Morison's pouch). The left subphrenic space (lsp) also begins to merge with the left pericolic space at this level. The left infracolic space (LIC) is seen to the left of the mesentery (M) and head of pancreas (P). The stomach is anterior and the greater omentum *(arrows)* lies anteriorly on either side. The kidneys (K) and spleen (S) are noted.

E, Axial scan at level below *D.* The right subphrenic space lateral to the liver converges with the right pericolic space (RC) adjacent to the cecum (C). The left pericolic space (LC) is on the left. The right infracolic space (RIC) adjacent to the mesentery (M) and the left pericolic space (LC) are noted. The fat-density greater omentum *(arrows)* is noted in the anterior peritoneum.

F, Lower axial scan shows the upper pelvis. The right (RC) and the left (LC) spaces are noted; the right space is lateral to the cecum (CE). The psoas muscles (P) are noted posteriorly, medial to the retroperitoneum below the renal fossa.

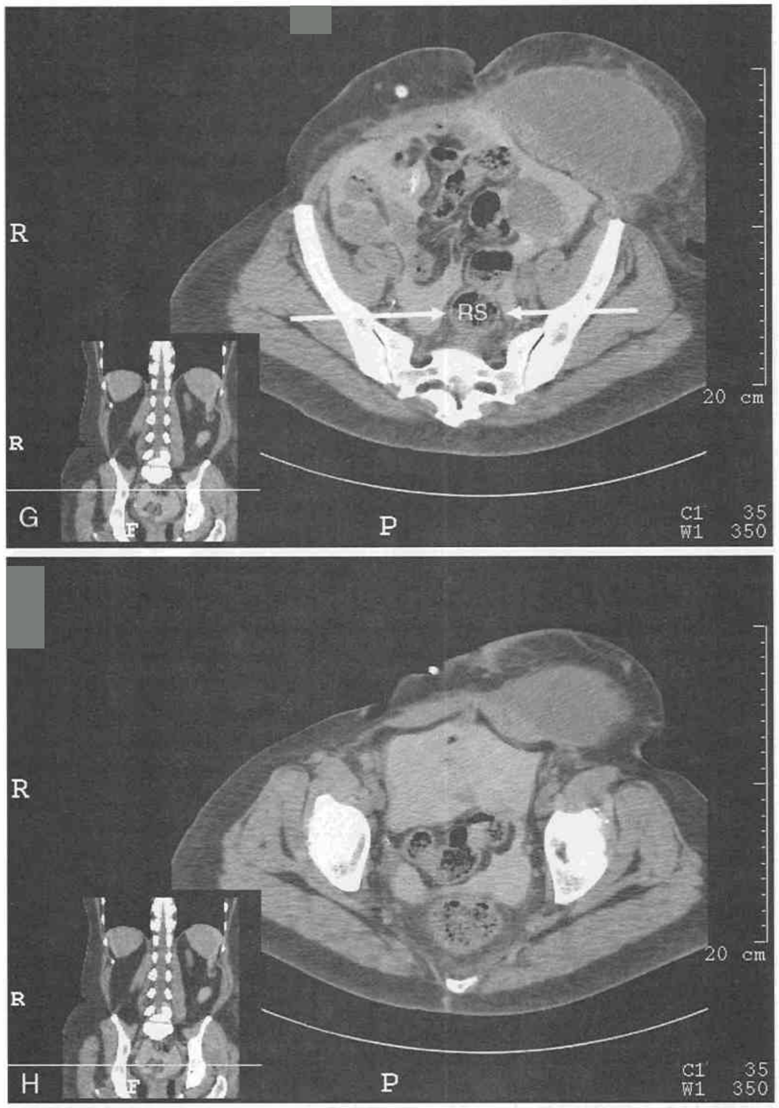

Figure 42–6 *Continued. G,* Axial scan in the pelvis shows communication of the pericolic spaces into the pelvis. Perirectal spaces *(horizontal arrows)* are lateral to the rectosigmoid (RS).

H, Scan taken through lowest part of pelvis, showing perirectal spaces.

bowel and are bounded laterally by the peritoneum of the abdominal wall and medially by the peritoneum over the colon. The depth and configuration of these spaces may vary, depending on the completeness of the fusion of mesentery in the embryologic state. The pericolic space may in such cases extend posteriorly, adjacent to the kidney.[97] The posterior extension occurs most commonly on the right side, which accounts for the observation that the right paracolic space is deeper than the left. This common variation has prompted new theories about the retroperitoneal spaces (see "New Concepts of Retroperitoneum and Peritoneum" later).

If a portion of the colon, such as the splenic flexure, is not in the normal location, the configuration of such spaces may be difficult to predict. Regardless of the anatomic variation, however, one can be confident that CT accurately displays the precise pathologic anatomy (even if there is some controversy about the nomenclature).

Infracolic Spaces

The right and left infracolic spaces are separated by the mesentery, which extends from Treitz's ligament in the left upper quadrant to the ileocecal region in the right lower quadrant (see Figs. 42–5*B,* 42–6*D,* and 42–7*A* and *D*). The left infracolic space communicates with the lower portions of the abdomen, but the right infracolic space is confined by the mesocolon, ascending colon, and the posterior attachment of the mesentery.

Pelvis

The right pericolic, left pericolic, and left infracolic spaces have pathways into the pelvis. On the left side, the mesentery of the sigmoid provides a surface on which neoplastic or inflammatory processes may center (see Fig. 42–5*A* and *B*). In addition, the broad ligaments of the uterus create a surface on which processes become involved.

From an anatomic standpoint, the pelvis can be subdivided into an anterior portion, which has certain fossae common to both men and women, and a posterior portion, which has some differences between men and women. The anterior divisions are less consistently visualized, depending on individual anatomy (Fig. 42–8; see Fig. 42–6*H*).

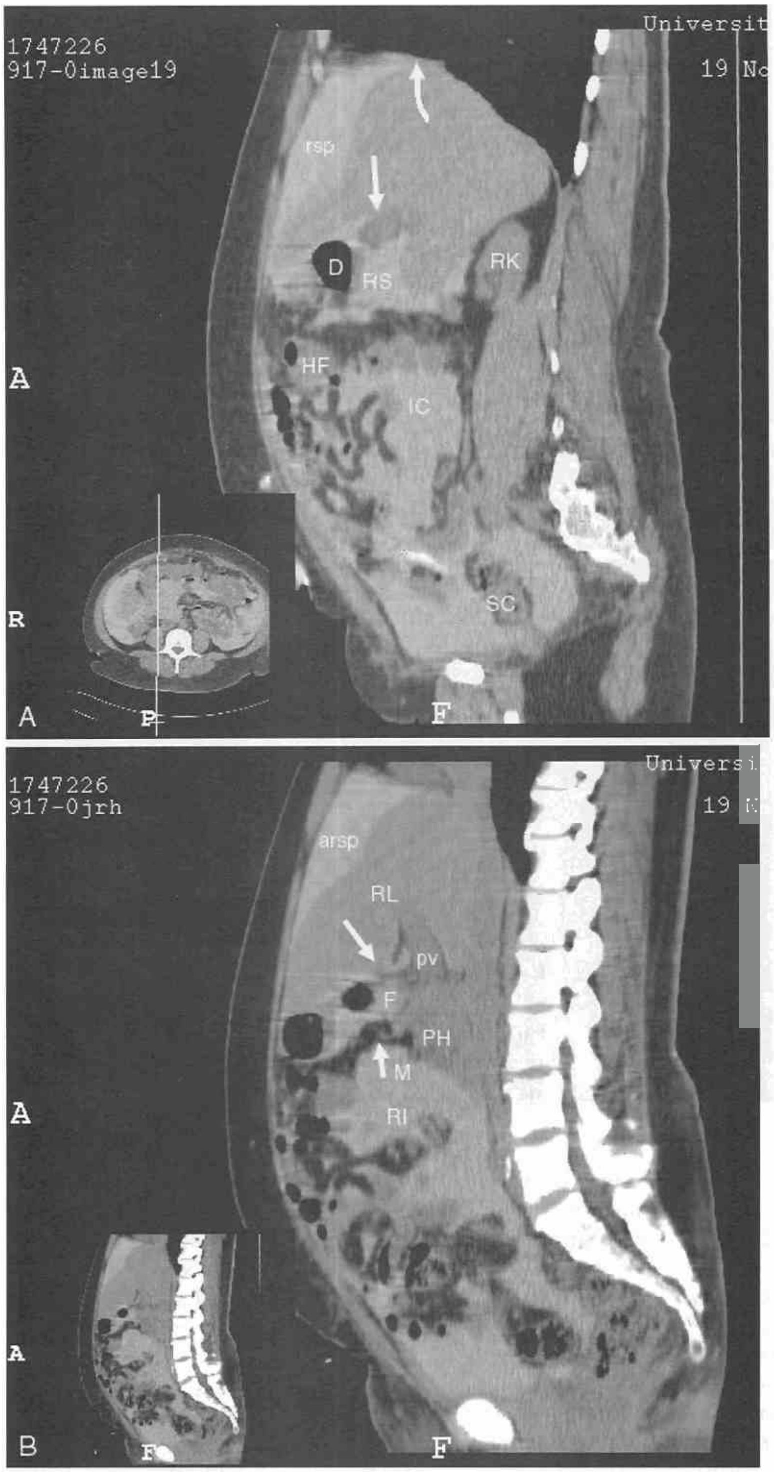

Figure 42–7. Sagittal images of peritoneum. *A,* Sagittal scan to the right of midline. The anterior right subphrenic space (rsp) is seen anterior to the liver, and the right subhepatic space (RS) is below the right lobe. The posterior attachment of the phrenic space limits the space posteriorly *(curved arrow).* The duodenum (D) and the upper portion of the hepatoduodenal ligament *(vertical arrow)* are noted adjacent to the subhepatic space (RS). Also noted are the hepatic flexure (HF) of the colon, the right kidney (RK), the infracolic space (IC), and the sigmoid colon (SC).

B, Sagittal scan slightly lateral to midline. The liver (RL), the anterior right subphrenic space (arsp), and the infracolic space (RI) are seen. The area of the foramen of Winslow (F) at the entrance of the lesser sac is noted. The lesser sac is limited posteriorly by the pancreatic head (PH), inferiorly by the transverse mesocolon (M), and anteriorly by the hepatoduodenal ligament *(arrow).* The portal vein (pv) is in the margin of the ligament.

The anterior pelvis is divided into several smaller fossae by peritoneal ligaments over certain vestigial remnants. These include the supravesical fossa in the midline, bounded laterally by reflections over the closed umbilical arteries. The medial umbilical fold, which reflects over the vestigial remnant of the urachus, is in the midline of this space. Immediately lateral to these reflections, the medial inguinal fossa can be seen on the right and left; they are bounded laterally by the reflection over the inferior epigastric arteries. Lateral to these are the lateral inguinal fossae, which are lateral to the inferior epigastric arteries. There is little clinical significance of these spaces except to distinguish between direct inguinal hernias, which are lateral to the epigastric artery, and indirect inguinal hernias, which are medial to the epigastric artery.

The posterior pelvic space is divided into areas that are determined by gender. In women, there is a space between the uterus and the bladder called the *vesicouterine space.*

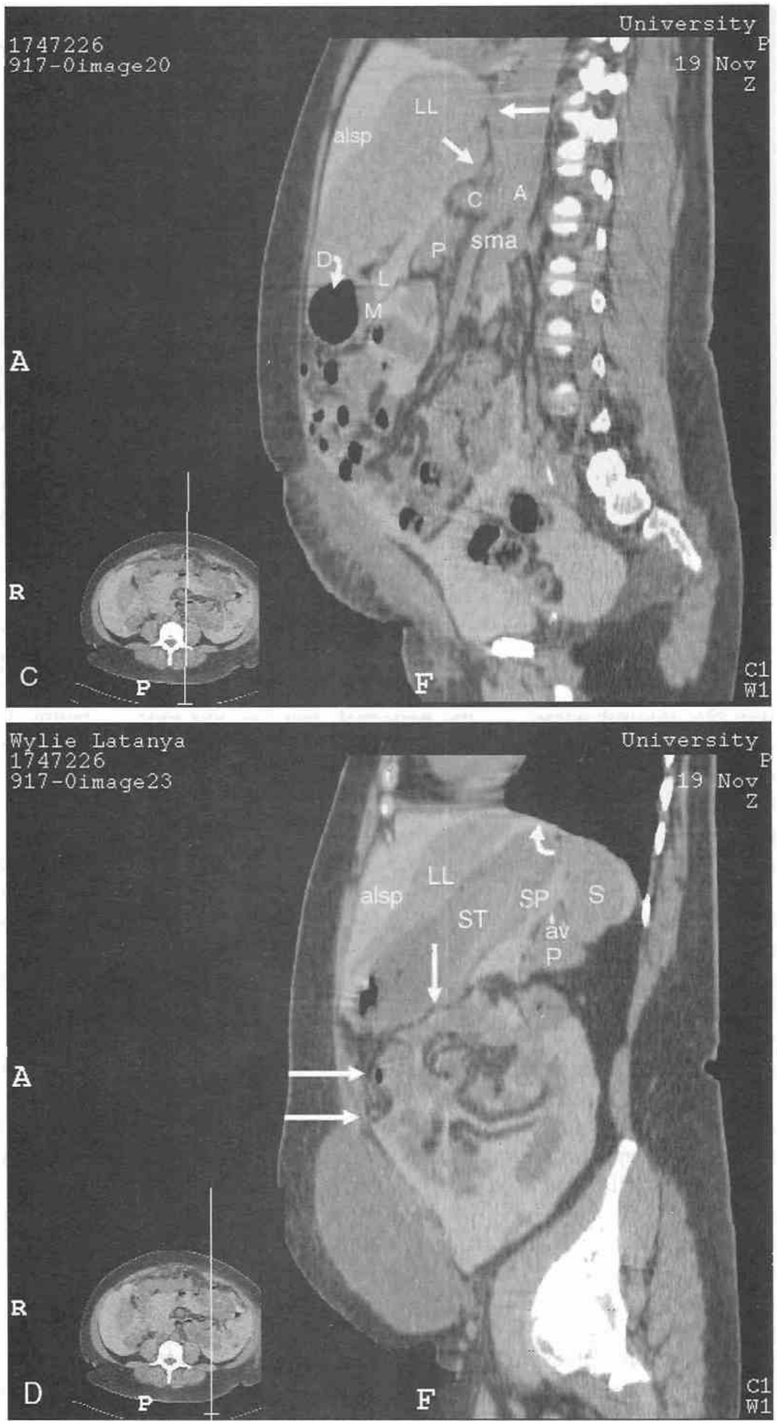

Figure 42–7 *Continued. C,* Sagittal image close to midline. The liver (LL) and adjacent structures are seen, including the anterior left subphrenic space (alsp), the superior recess of the lesser sac *(small arrow),* and the "bare area" of liver *(horizontal arrow).* The lesser sac (L) is seen bounded anteriorly by the edge of the gastrohepatic ligament and the hepatoduodenal ligament containing the duodenum (D), posteriorly by the pancreas (P), and inferiorly by the mesocolon (M). The aorta (A), with the celiac artery (C) and the superior mesenteric artery (sma), is seen.

D, Sagittal section to the left of midline. The left lobe of the liver (LL) is attached by the triangular ligaments to the diaphragm *(curved arrow).* The anterior left subphrenic space (alsp) is in front of the liver; the left subhepatic space is between the liver and the stomach (ST). The splenic recess (SP) is behind the stomach, in front of the spleen (S) and the pancreas (P). The splenic artery and vein (av) are seen in the hilum. The mesocolon *(vertical arrow),* with the splenic flexure, is seen, clearly separating the supracolic and infracolic spaces. Anteriorly, the greater omentum *(horizontal arrows)* is seen extending from the margin of the stomach.

The rectouterine space is between the uterus and the rectum. The spaces on each side of the rectum are called the *right* and *left pararectal spaces.* Some have also designated an ovarian fossa adjacent to the ovaries.

Men have fewer spaces in the pelvis, the rectovesicular space, and the right and left pararectal spaces. There is no space associated with the prostate, which is below the bladder.

In women, the ovarian fossae and vesicouterine space vary according to the size, configuration, and angulation of the uterus. The right and left pararectal spaces may also vary in size. In some patients, the right side may predominate with no space on the left. In other patients, the pararectal spaces may extend posteriorly around the rectum and extremely low, almost to the level of the coccyx.

Retroperitoneum

Traditionally, the retroperitoneum is said to have different compartments, depending on the level. At the level of the kidney, the space behind the peritoneum can be divided

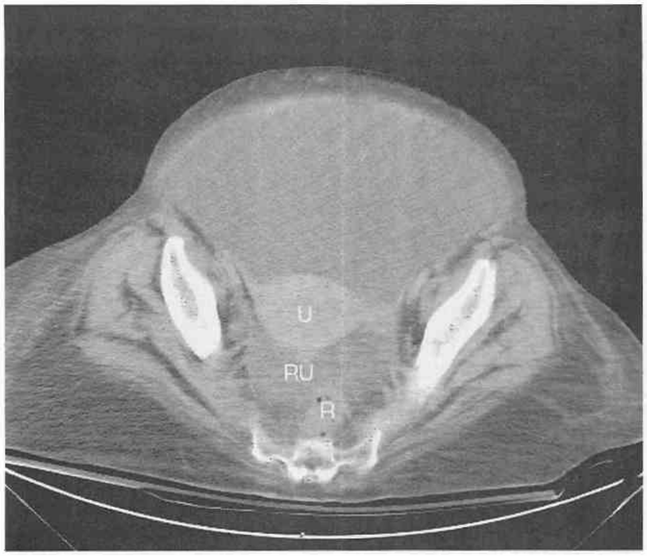

Figure 42–8. Axial scan through the female pelvis shows the uterus (U), rectum (R), and the rectouterine space (RU). The tubes and broad ligaments extend laterally.

into the anterior pararenal, the perirenal, and the posterior pararenal spaces (Fig. 42–9; see Fig. 42–1*D* and *E*). The division of this space is made based on the perirenal fascia. Gerota's fascia is the posterior portion, and Zuckerkandl's is the anterior one. The anterior pararenal space is bordered anteriorly by the peritoneum on the retroperitoneum, posteriorly by the anterior perirenal fascia, and laterally by the lateroconal fascia. The perirenal space is the space around the kidney bordered anteriorly by the renal fascia and the posterior renal fascia. The posterior pararenal space is bordered anteriorly by the posterior renal fascia and posteriorly by the fascia over the psoas muscle, which is continuous with the transversalis fascia.

Below the level of the kidneys, the retroperitoneal spaces are a single space with direct contiguity between the anterior and the posterior portions.

The cephalic and caudal relationships of the spaces should also be discussed. The perirenal space is the shape of an inverted cone (open at the bottom and closed at the top) (see Figs. 42–4, 42–5*D*, and 42–7*A*). The cone is attached superiorly to the diaphragm, whereas the open end of the cone is open to the pelvis. Both the anterior and the posterior pararenal spaces extend into the pelvis and cephalad to the level of the diaphragm. On the right side, the upper extent of this space is the bare area of the liver, and on the left, it is the bare area of the spleen. With certain pathologic processes, the mediastinum can communicate with either of these areas.

New Concepts of Retroperitoneum and Peritoneum

With the extensive experience gained with CT over the years, it has become apparent that the traditional description of the retroperitoneum and the posterior portions of the peritoneum does not fit some observations that have been made.

The inconsistencies of the traditional approach have related predominantly to the relationship of the anterior pararenal space to the retroperitoneum and the peritoneum.[20, 92] Authors have noted that the lateroconal fascia is not constant in its location and does not really function as a barrier to the spread of fluid or inflammation. Fluid from the pancreas region does not always spread to the margins of the colon, which are supposedly in the same space.

After reviewing the embryologic information, Dodds and colleagues[19, 20] came to several conclusions that differed from the traditional description. During embryologic development, the gut and its derivatives form in the intermesenteric space; they remain in this space regardless of any migration, folding, or fusion. Communication between the various components of the intermesenteric space follows the areolar connective tissue (the course of which can be followed by noting the vasculature) (see Fig. 42–1*B–D*). Communication between the retroperitoneum and the intermesenteric space is therefore only by means of spaces along the vessels predominantly at the root of the mesentery. A number of rotations and fusions occur before the adult form results. With the rotation of the bowel, the ventral pancreas and dorsal pancreata come to fuse and, with the duodenum, lie against the embryologic peritoneum. Fusion of the left side of the dorsal mesentery and the retroperitoneal embryologic peritoneum occurs at a line that the traditionalists have called the *anterior renal fascia* (see Fig. 42–1*D*, *E*), which Dodds et al[20] have called the *retropancreatic peritoneal recess*. It has been given this name because it represents a potential space that can be "split" by certain pathologic processes in the area.[9]

At about this time, the colon rotates and the mesocolon fuses to the mesentery over the pancreaticoduodenal space and laterally to the posterior parietal peritoneum (see Fig. 42–1*E*). Most commonly the fusion is complete and extends from the ascending colon and the cecum on the right to the descending colon by the sigmoid on the left (see Fig. 42–1*A–G*). If fusion is complete, the right and left colon are "sandwiched" between the flattened pancreaticoduodenal space and the retroperitoneum. If the fusion is not complete, a variation in the spaces results.

Without complete fusion, the colon has a mesentery (cecum or right colon in 10% to 20% of cases) and there is no colonic retroperitoneal space. When this occurs in some cases, the splenic flexure can occasionally be located medial to the spleen. In the adult, the distribution of ascitic fluid in the paracolic gutter depends on the shape of the recess and the extent of fusion of the mesocolon with the retroperitoneum. Without fusion, fluid or bowel can go posterior to the kidney by the psoas muscles.

When this approach is used, the compartments of retroperitoneal spaces differ. The anterior renal fascia fuses with the primordial peritoneum over the retroperitoneum (thus, there is no anterior pararenal space). The posterior renal fascia fuses posteriorly with the fascia over the psoas and quadratus lumborum muscles. Laterally, it fuses with the peritoneum, which extends anteriorly inside the properitoneal fat.

The cephalic and caudal boundaries also differ in the new concept. First, below the level of the renal fascia, there are two separate spaces (anterior and posterior), which are different areas of the intermesenteric space and do not

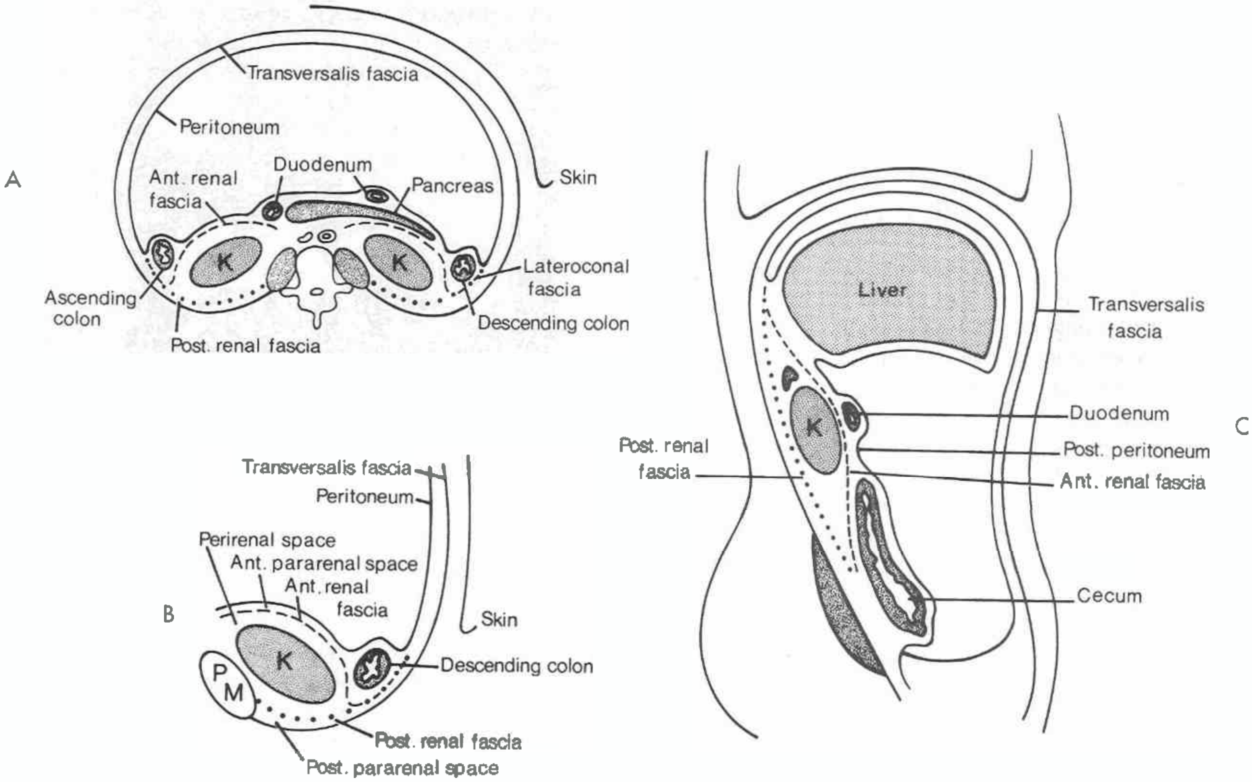

Figure 42–9. Schematic of retroperitoneal spaces based on the traditional concept of retroperitoneal anatomy. K, Kidney; PM, psoas muscle. Anterior *(dashed)* and posterior *(dotted)* perirenal fascia join to form lateroconal fascia *(dot-dashed)*. These fasciae divide the retroperitoneum into (1) the anterior pararenal space that contains the duodenum, pancreas, and right and left colon; (2) the perirenal space that contains the kidney and adrenal gland; and (3) the posterior pararenal space that contains fat. *A*, Axial section of the pancreas. *B*, Axial section of the left upper quadrant just caudal to the pancreatic tail. The anterior pararenal space is subtended ventrally by the posterior peritoneum and dorsolaterally by the anterior renal fascia and lateroconal fascia. The posterior pararenal space is demarcated ventrally by the posterior perirenal fascia and lateroconal fascia and dorsolaterally by transversalis fascia. *C*, Parasagittal section through the right kidney. The bare area of the liver is in continuity with the anterior pararenal space. The posterior pararenal space communicates with the anterior pararenal space in the iliac fossa, below the perirenal space. (See Fig. 42–1*D–F*, for an explanation of the newer concept.) (*B*, From Dodds WJ, Darweesh RM, Lawson TL, et al: The retroperitoneal spaces revisited: A pictorial essay. Am J Roentgenol 147:1155, 1986. Copyright by American Roentgen Ray Society, 1986.)

communicate directly. The anterior space contains the vessels of the sigmoid and ascending colon. The posterior space contains the retroperitoneal structures. The cephalad relationships also change. The anterior renal fascia is said not to extend above the adrenal glands; the bare area of the liver and spleen would then correspond to the posterior pararenal space.

The new approach can be summarized as follows. The previously designated anterior pararenal space is called the *intermesenteric space*, which is separated into two compartments, one for the colon and one for the pancreas and the duodenum. Communication between the different components, such as the pancreaticoduodenal and the colonic intermesenteric space, is along the vessels. When fusion of the mesothelium is not complete, there may be separation of the potential spaces by pathologic processes. With pancreatitis, for example, the primordial space splits with inflammatory fluid (which looks like the splitting of what was previously called the *anterior pararenal space*).[9, 78] The depth of the paracolonic spaces can vary posteriorly, and the position of colic mesentery can vary, depending on fusion of mesentery. The retroperitoneum above and below the cone of Gerota's fascia varies from the traditional viewpoint because there is only a posterior pararenal space (no anterior spaces).

Peritoneal Reflections or Ligaments

The various "ligaments" of the peritoneum are actually peritoneal reflections over tissue containing areolar tissue, arteries, veins, lymphatics, vessels, and lymph nodes. The margins of the ligaments are not definable except when the edges of the peritoneum are seen because of fluid or contrast material.

Understanding the reflections is important because they serve as boundaries to the peritoneal spaces and also as possible conduits for the contiguous spread of inflammation or neoplasms. These ligaments have been discussed under the category of the subperitoneum at various material meetings.

Coronary and Triangular Ligaments

The coronary and triangular ligaments represent attachments between the liver and the parietal peritoneum over

the abdominal wall. The coronary ligaments are contiguous with the capsule of the liver and attach the right lobe of the liver to the posterior abdominal wall (see Figs. 42–5*D*, 42–6*A* and *B*, and 42–7*A* and *B*). The triangular ligaments (Fig. 42–7*D*) are extensions of Glisson's capsule and attach the left lobe to the diaphragm. Although they are typically called *suspensory ligaments*, it is not clear what mechanical support they really provide. The triangular ligaments are virtually never seen on CT scans, uuless air is in the peritoneum, which highlights their margins. Although typically one thinks of the peritoneum and its spaces as completely constant, congenital variations may also occur. Authors have noted considerable variation in the size and position of the triangular ligaments.

Both sets of ligaments have little involvement with intra-abdominal processes except that they provide boundaries for the subphrenic and the right subhepatic spaces. When a retroperitoneal process occurs on the right side, it may extend into the bare area of the liver behind the right coronary ligaments or cross from one side to the other.

Falciform Ligament

This is a vestigial remnant that represents a peritoneal reflection (see Figs. 42–5*A* and 42–6*A*) over the closed umbilical vein, which remains as the ligamentum teres. In inflammatory disease of the pancreas, inflammation can extend along the fascial tissues around the porta hepatis, around the ligamentum teres, and to the abdominal wall. In patients with portal hypertension, the ligamentum teres may recanalize, resulting in a patent umbilical vein, which courses to the abdominal wall.

Finally, in the presence of tumors, such as ovary, stomach, colon, and pancreas, the falciform ligament may be a site of peritoneal seeding or extension. The normal ligament is not seen on CT scan unless free air or fluid within the abdomen provides better visualization.

Gastrohepatic, Gastrosplenic (Gastrolienal), and Gastrocolic Ligaments

These three ligaments are in direct contiguity with the margins of the stomach. They provide the peritoneal boundaries of the omental bursa in conjunction with the peritoneal surfaces of the hilum of the liver,[8] the posterior wall of the stomach, and the parietal peritoneum over the retroperitoneum. Because they contain the arteries, veins, lymphatics, vessels, and lymph nodes, they are conduits for the contiguous spread of disease.

A neoplasm beginning in the stomach can spread through any of these pathways into the lymph nodes along corresponding vessels (Fig. 42–10). Spreading may occur along the left gastric artery and coronary vein in the gastrohepatic ligament, along the celiac trunk and base of the hepatic artery in the hepatoduodenal ligament, along the gastroepiploic and short gastric vessels in the gastrosplenic ligament, and along the gastroepiploic vessels in the gastrocolic ligament.

Tumor involvement in the gastrohepatic ligament produces impression or impingement on the lesser curvature of the stomach. Involvement of the gastroduodenal ligament produces impingement on the stomach antrum. Gastrosplenic involvement shows pressure on the greater curvature of the stomach, and gastrocolic involvement produces changes on the upper portion of the colon. Conversely, processes that begin in the colon can spread to the stomach by these pathways. Processes from the duodenum or pancreas can spread along the hepatoduodenal ligament.

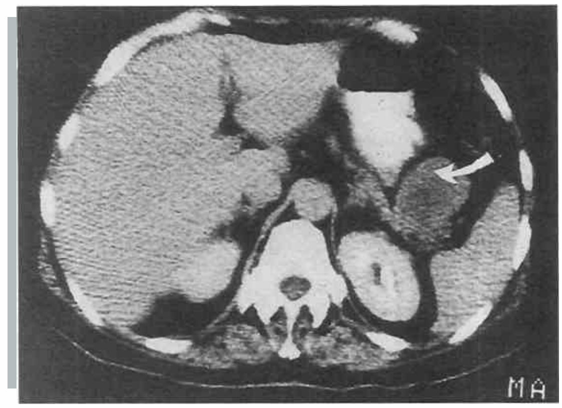

Figure 42–10. Scan of a patient with a single metastatic deposit in the gastrosplenic ligament *(arrow)*.

Extension within these various ligaments can also occur in some cases of pancreatitis or hemorrhage. The fluid may dissect within the ligaments and may even extend to the subcapsular areas.

Phrenicocolic Ligament and Mesocolon

The mesocolon attached on the anterior surface of the pancreas has a lateral attachment on the left side called the *phrenicocolic ligament*. The mesocolon containing the various colic vessels and lymph nodes can also serve as a pathway for disease. Spread of inflammation or neoplasms from the colon to the pancreas is possible by either of these paths.

Splenorenal (Lienorenal) Ligament

The splenorenal ligament is the connection between the spleen and the kidney. It contains the tail of the pancreas, the splenic vessels, and small vessels to the retroperitoneum. They are of little significance except as a landmark to distinguish between peritoneal and pleural fluid. Tumor can spread, and systemic portal collaterals can develop in this space.

Ileocolic Ligament

Mesentery at the ileocolic region may serve as a site for tumor implantation. Occurrence of this is infrequent (Fig. 42–11).

Sigmoid Mesentery

The mesentery of the sigmoid colon in the left lower quadrant acts as a barrier or a margin along which processes can collect. At times, it serves as a medial or caudal boundary for the spread of material down the left pericolic space (Fig. 42–12).

Broad Ligaments and Cul-de-Sac

The broad ligaments and cul-de-sac represent two low peritoneal reflections that border the lower portions of the

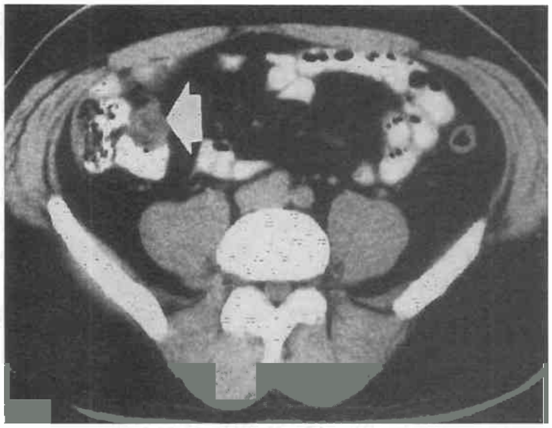

Figure 42–11. Patient with carcinoma of the pancreas has metastatic implant *(arrow)* adjacent to the ileocecal valve by the cecum.

cavity (see Fig. 42–8). Tumors within the peritoneal cavity can seed to either location; most commonly, ovary, colon, or gastric tumors involve these areas.

Mesentery

The small bowel mesentery containing the superior mesenteric vessels extends from the left upper quadrant at Treitz's ligament to the right lower quadrant at the ileocecal valve (see Figs. 42–5*C*, 42–6*D*, and 42–7*C*). It serves as a dividing point between the right and the left infracolic spaces.

Specific areas of the mesentery should be noted because they show changes with pathologic processes. These areas are the neurovascular bundles, the root of the mesentery, and the margin of the small bowel. Normally the neurovascular bundles are quite thin and are barely perceptible as thin lines within the fat-density mesentery (see Figs. 42–5*C* and 42–6*D*). The mesentery as a whole shows fat density and normally extends quite high into the abdomen, permitting the small bowel loops to appose themselves closely to the anterior abdominal peritoneum.[101] The margins of the fat on the inner surface of the small bowel are typically poorly defined because the course of the bowel is quite irregular and overlapping. When pathologic processes occur, the bowel dilates, the wall thickens, and the peristaltic motion lessens. Because the margins are more tuberlike, they are better defined and the junction between the mesentery and the bowel wall is better seen (see "Inflammatory Processes"). Retroperitoneal, mesenteric, and peritoneal processes can produce changes along the mesentery.[115]

Greater Omentum

The greater omentum originates along the margin of the greater curvature of the stomach and can cover a broad expanse of the anterior abdominal wall. The function and role of the greater omentum is not really defined, but removal does not produce any adverse effects in peritoneal function.

The normal omentum is usually imperceptible on routine scan. It is visualized only when fluid is present (see Figs. 42–6*D*, *E* and 42–7*D*) or it is pathologically involved. Two signs that can be helpful are the density of the omentum and the location of small bowel loops. The normal omentum shows fat density and is not seen; when it has infectious processes or neoplasms, it increases in density and becomes thicker and therefore can produce a mass effect on the small bowel loops.

Peritoneal Fluid and Peritonitis

Ascitic fluid occurs whenever there is active formation of peritoneal fluid or interference with its removal. It can be caused by anything that produces inflammation, venous obstruction, lymphatic obstruction, or albumin deficiency, including liver failure, caval or portal vein obstruction, infection, and neoplasms. Ascitic fluid can be detected quite well with CT, and with certain diseases, some specific ancillary findings may be provided to suggest the origin of the ascitic fluid (Fig. 42–13). For example, in patients with cirrhosis, there may be associated findings in the liver.

Figure 42–12. Two metastatic implants *(arrows)* on the right and left side of the sigmoid mesentery.

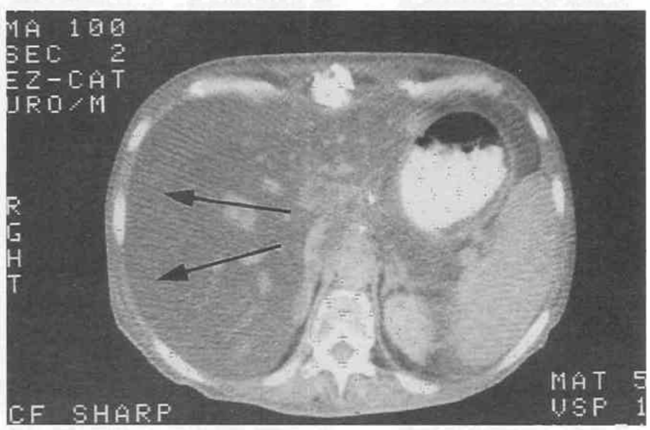

Figure 42–13. CT scan shows a fatty liver, which has a perihepatic fluid collection. It is difficult in some cases to see the adjacent fluid next to the liver capsule *(arrows)*.

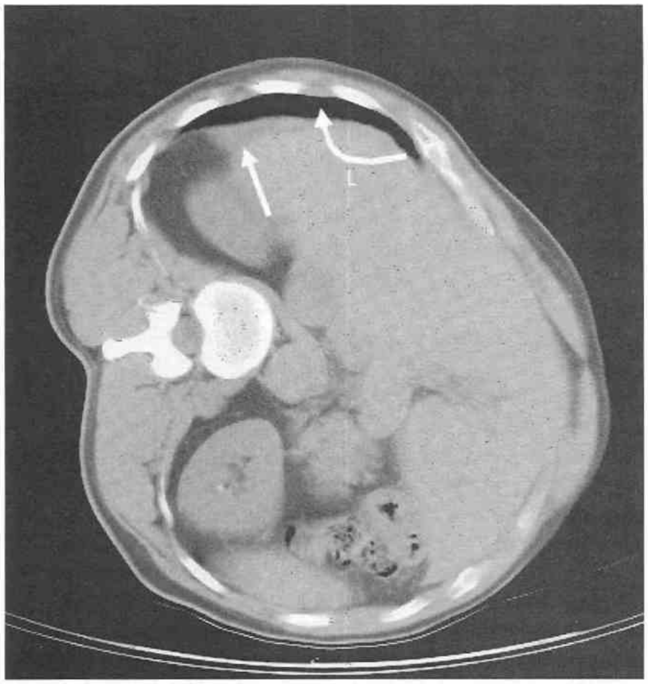

Figure 42–14. CT scan taken through the level of the subphrenic space shows the most posterior extent of the right subphrenic space *(arrow)* containing fluid. Its relationship to the adjacent bare area of the liver (L) containing the kidney *(curved arrow)* and the pleural space is well visualized.

Similarly, with pancreatitis, there may be enlargement of the gland and thickening of the perirenal fascia.[9] If neoplasms of the liver, pancreas, lymph nodes, or ovaries are present, the tumor masses may be noted.

The distribution and progression of ascitic fluid can be easily visualized with CT. In early ascites when the fluid is free moving and small in amount, it localizes in the cul-de-sac or pericolic gutters or the subhepatic space. Gravity causes the fluid to collect in the pelvis or the right subhepatic space. Negative pressure beneath the diaphragm "pulls" fluid beneath the diaphragm (Fig. 42–14). Fluid can loculate in unusual locations when the distribution is altered by adhesions or fibrinous material. When ascitic fluid becomes massive, it distends the peritoneal spaces.

Some authors have attempted to characterize the density of ascitic fluid in the disease processes,[14, 16, 40] but this has not been consistent. Some specialists have asserted that purulent ascites has a higher density than transudative fluid. Although it is true that the higher the protein content of the fluid, the higher the attenuation number, I have not found the high density specific enough to be uniformly helpful except in the presence of intraperitoneal bleeding. One important diagnostic point about detecting small amounts of fluid should be made. Intravenous (IV) contrast material is helpful because it permits opacification of normal structures, which enhance compared with fluid.

Rather than using the density as a critical factor, I have found the mobility of fluid and the presence of effacement more helpful (Fig. 42–15). If intraperitoneal fluid is localized to a single area, I place the patient in a decubitus position to see if the fluid moves. In a patient who is not immunosuppressed, infected fluid does not move, whereas sterile fluid usually shifts (see Fig. 42–15*B*). In an immunosuppressed patient, this has not been a useful sign.

Although the finding of focal displacement or effacement of organs may suggest infection, this sign has limitations with loculated ascites. Any active process, inflammatory, neoplastic, or other, can deposit fibrin at the margins

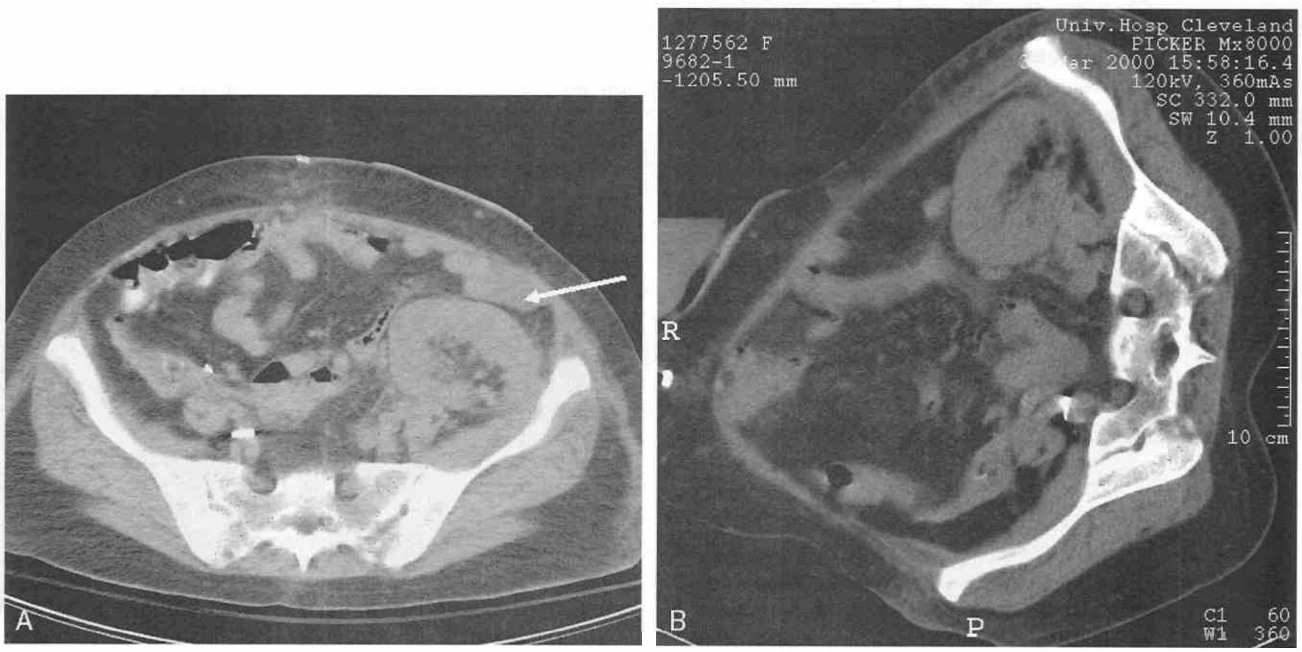

Figure 42–15. *A,* With the patient in the supine position, fluid *(arrow)* adjacent to the small bowel suggests an abscess. *B,* When the patient is scanned in the decubitus position, the fluid moves away, indicating that it was not loculated and was unlikely to be an abscess.

of a space and thereby produce a fluid collection under pressure, when there is active production of fluid. On the basis of the CT image alone, it is virtually impossible to distinguish loculated ascites, abscess, or loculated neoplastic fluid. The only way to clarify the diagnosis is to obtain fluid by percutaneous aspiration, to inspect it, and to inoculate it onto culture medium.

If the pyogenic peritonitis is produced by intestinal perforation or if there are gas-forming organisms, free gas can be seen within the peritoneum.[44, 70, 104] In a rare but deadly type of peritonitis produced by gas-forming organisms such as *Clostridium*, the amount and distribution of gas may be so extensive and diffuse that it is difficult to determine the extraluminal nature. I misdiagnosed one case of clostridial peritonitis in a patient with an extensive sarcoma because I mistakenly thought the free "gas" around clumps of tumor was the gas in the bowel being compressed by a large mass.

Tuberculous and Granulomatous Peritonitis

Tuberculous peritonitis is said to occur in 3.5% of patients with pulmonary tuberculosis.[35, 73] It is a rare disease that is a result of disseminated miliary tuberculosis of the bowel and peritoneum. It is thought to be a result of hematogenous spread or local spread from GI involvement (penetration of involved bowel or lymph nodes draining into the peritoneum).[44, 45]

Classically, it is divided into a "wet" form with large exudates, and a "dry" form,[73, 115, 120] which has large amounts of inflammation caused by fibrinous exudates and tubercules.

There have been several reports about tuberculous peritonitis. Soft tissue densities produce thickening of the mesentery, omentum, and bowel wall. The lymph nodes in the mesentery and retroperitoneum may be increased in number and size (Fig. 42–16). The findings are not specific, and this entity cannot be diagnosed without a high index of clinical suspicion. On occasion, histoplasmosis may involve the abdomen and produce lymph node enlargement in the abdomen (Fig. 42–17).

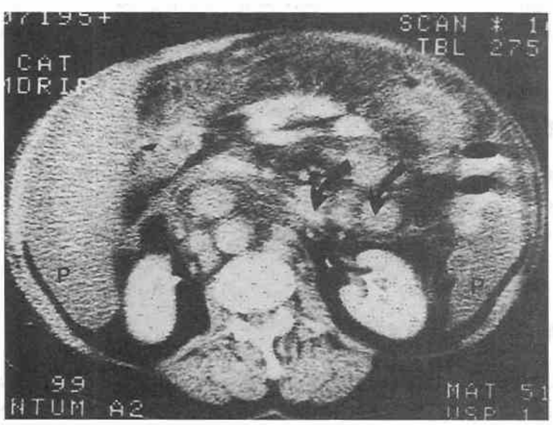

Figure 42–16. CT scan of a patient with intra-abdominal tuberculosis. There is fluid in the pericolic spaces (p) and large lymph nodes *(arrows)* in the retroperitoneum and mesentery.

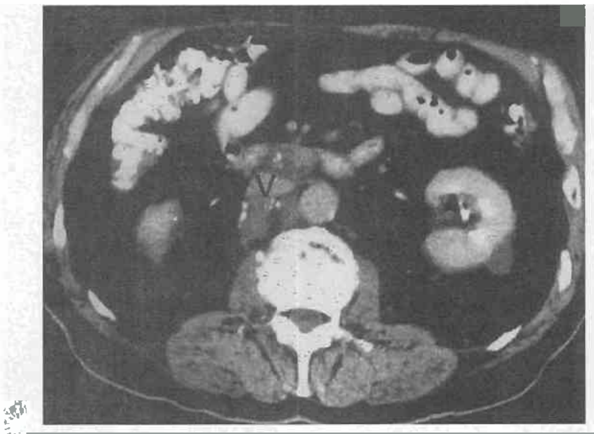

Figure 42–17. CT scan shows enlarged lymph nodes beside the aorta and behind the vena cava (V), resulting from histoplasmosis.

Hemorrhage

With hemorrhage into the peritoneum, the blood can be visualized quite easily (Fig. 42–18). When the earliest signs of hemorrhage are sought, the organ and the adjacent peritoneal spaces should be looked at quite carefully. The right subhepatic space, pericolic spaces, pelvis, and renal fascia should be examined (Figs. 42–19 to 42–21). When splenic injury is suspected, the most posterior portion of the pericolic space or the anterior renal fascia should be examined. Because the posterior of the space is dependent, blood accumulates there. The renal fascia may become thick if bleeding into the bare area behind the spleen occurs.

In contrast to other areas of the body where the breakdown of blood changes density over a period of days or weeks, density changes are much more rapid within the

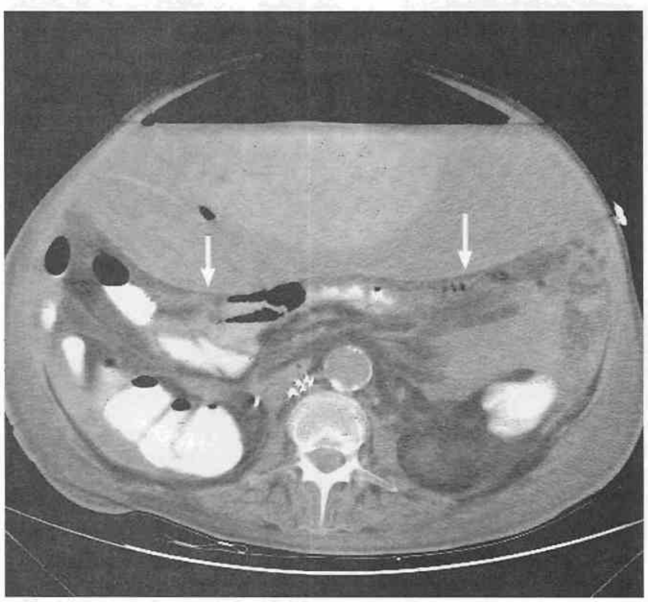

Figure 42–18. Large collection of blood in the anterior peritoneum. CT scan shows a large fluid collection containing internal clot. *Arrows* define the posterior wall.

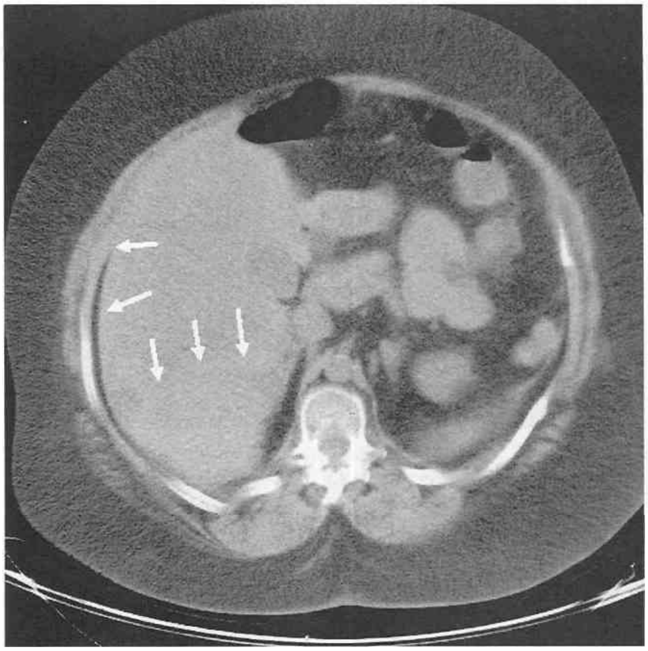

Figure 42–19. High-density hematoma (H) outlines the margin of the liver *(arrows)*. Because the peritoneum has significant fibrinolytic activities, the presence of intact hematoma usually indicates acute bleeding.

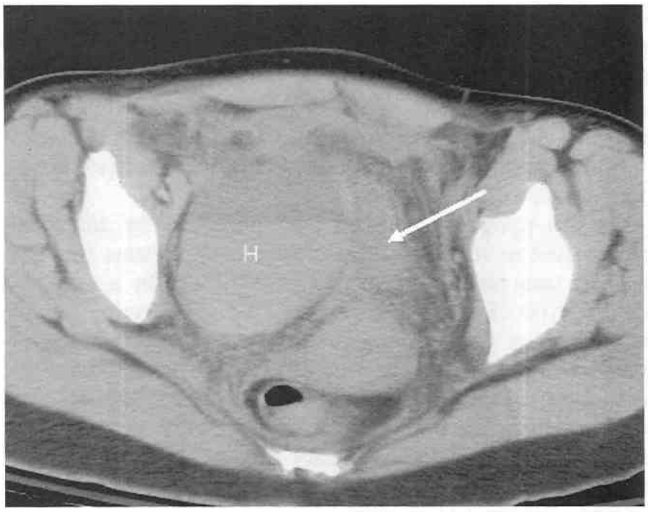

Figure 42–21. Extraperitoneal hematoma (H) contains serum and blood products. It is displacing the bladder *(arrow)* to the left.

peritoneum. Because of the fibrinolytic activity of the peritoneum and rapid influx of fluid, the density changes occur quickly, over a matter of hours. Such lysed blood shows a low density, similar to any other fluid. When the hemorrhage is recent or the bleeding is rapid, the peritoneum does not have sufficient time to lyse the clots, and blood appears as a high-density collection in the peritoneum or adjacent to the injured organ.

If a high-density "blood clot" is seen, it does not mean that the bleeding is stabilized but that the bleeding has been recent or rapid. Careful observation or intervention is needed (Fig. 42–22).

In cases of massive extraperitoneal bleeding, there may initially be some difficulty in defining the extraperitoneal location of the blood. With careful inspection, one can usually define the proper location by noting that the peritoneum is displaced inwardly. In the pelvis, the anterior extraperitoneal space indents the peritoneum posteriorly and may extend caudally below the cul-de-sac and above the bladder and rectum.

Hematomas in the abdomen go through the same evolution in density as other body areas. In early stages, a hematoma shows a homogeneous soft tissue density and then this changes to a mixed appearance of high density clot and serous fluid. Next, it usually evolves to a fluid density and then lessens in size until it is resorbed. In some unusual cases, the hematoma may simply shrink as a soft tissue mass.

Abscesses

Intra-abdominal abscesses are uniformly fatal if untreated and usually curable if properly treated.[5] CT has proved useful in the detection and treatment of this entity.

Clinical Presentation

An abscess is an isolated collection of purulent material and is the result of an unsuccessful attempt by the body to eradicate organisms from a focus of infection. Before an abscess develops, the inoculation of a bacterium or yeast occurs and the body responds with antibodies and leuko-

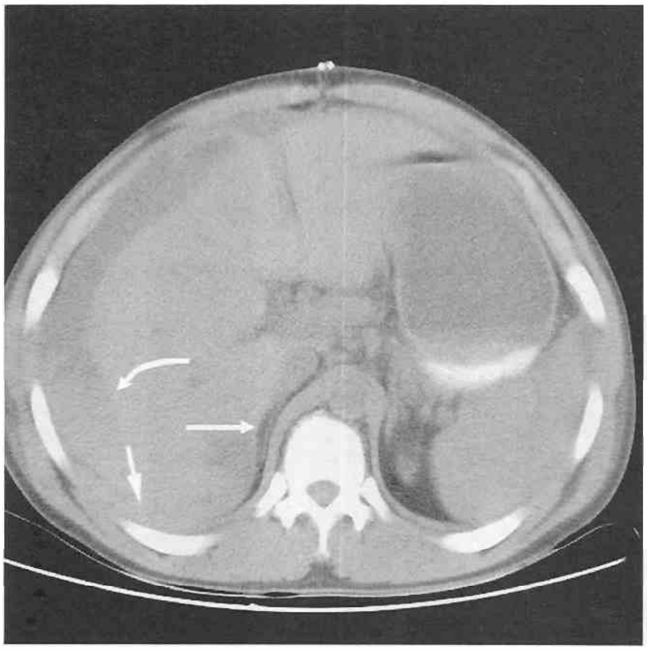

Figure 42–20. A hematoma in the right subphrenic space shows separation in the low-density serum component anteriorly, from the high-density blood products *(curved arrow)* posteriorly. The posterior margin *(vertical arrow)* of the subphrenic space is noted adjacent to the bare area *(horizontal arrow)* of the liver.

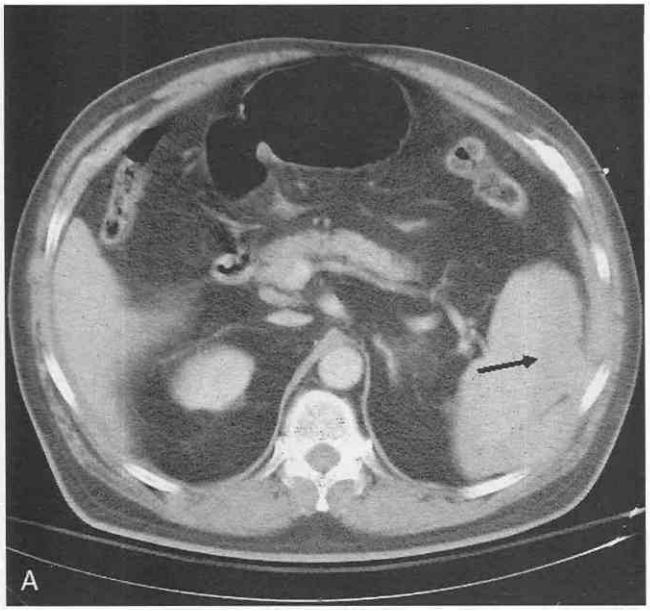

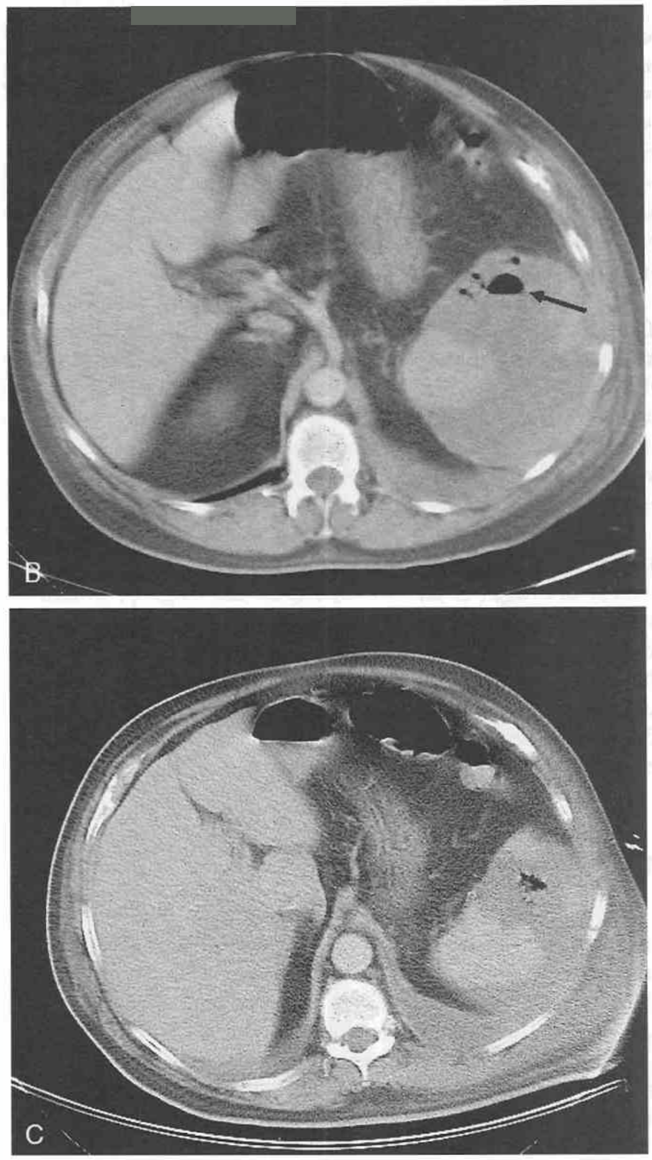

Figure 42–22. Post-traumatic subphrenic blood in evolution. *A,* CT scan shows hematoma *(arrow)* around the margin of the spleen, resulting from traumatic injury. The high-density material indicates that the spleen was unstable, and an angiographic embolization was performed to prevent catastrophic bleeding. *B,* After the embolization of the spleen, the fluid collection contains high-density clot and air *(arrow).* The patient stabilized. *C,* A later scan shows spontaneous reduction in the amount of fluid and air around the spleen.

cytes to eliminate the infection. At this stage, there is a focal inflammation, phlegmon, or cellulitis. If the body defenses prevail, the cellulitis clears;[38, 39, 102] if the organisms prevail and the focus of infection continues, a collection of purulent material results. With CT, it is usually not possible to detect an infection before it forms a fluid collection; in some cases, however, the process can be observed in evolution.

Normal Immune System

Patients with a normal immune system and an abscess have a typical clinical presentation. They have fever, tachycardia, leukocytosis, and symptoms localized to the area of the abscess. The localization of symptoms depends on the site of the abscess. Pain from the visceral peritoneum is carried by the splanchnic nerves and is poorly localized. When the parietal peritoneum is involved, the pain is more precisely localized. In such patients, the typical appearance of an abscess, which consists of well-defined fluid collections producing effacement of any adjacent anatomy, can be seen.

Immunocompromised Patients

Immunocompromised patients are a unique group that should be considered separately because of the lack of clinical signs and symptoms that may occur as a result of the altered immune system. Such patients may not exhibit fever or leukocytosis or discomfort by clinical examination.

Immunosuppression can be caused by a large number of factors, including corticosteroid medication, immunosuppressive agents, acquired immunodeficiency syndrome (AIDS), chemotherapy, or radiotherapy; patients with chronic diseases, such as hepatic cirrhosis, chronic renal failure, or malnutrition, may be immunocompromised. Some immunocompetent patients with abscesses initially appear to be handling an infection well, but after a short time they may unexpectedly decompensate. Fry and colleagues[21] found clinical signs in only 7% of 143 immunocompromised patients.

CT is important because it can detect subtle abscesses, even if immunocompromised patients lack localizing symptoms. In some such cases, a fluid collection may have findings typical of an abscess; in other patients, little fluid may be seen and may not produce the typical pressure effacement. The fluid in an immunocompromised patient may not loculate, but it may be widely disseminated throughout all of the peritoneal spaces. In such cases, the only practical way to assess the significance of the fluid collection is to sample it by needle aspiration.

A good example of this dynamic process is the evolution of an infection in the kidney or liver. An early focal infection of the kidney produces focal interstitial nephritis, which has the appearance of a soft tissue mass. It may further evolve into an area of necrosis and finally a fluid collection, producing an abscess. In very early abscess, there may be only subtle density change without clearly defined liquefaction (Fig. 42–23).

An understanding of this evolution is especially important because of the widespread use of CT in detecting abscess drainage. If an infection is in the stage of inflammation that has no fluid to be drained, surgical or percutaneous drainage is not indicated. Attempts to drain such phlegmons fail and may lead to complications, such as hemorrhage.[30] Occasionally such abscesses may be treated effectively with antibiotic medications and require no drainage.

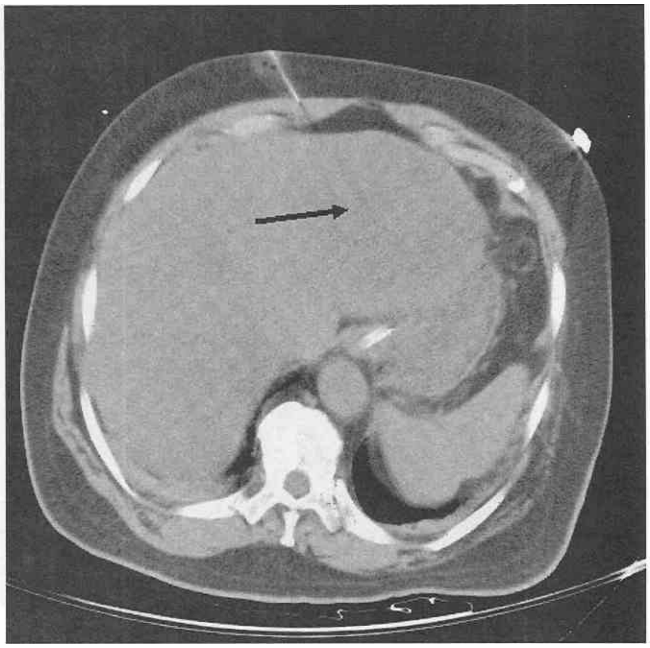

Figure 42–23. Large abscess *(arrow)* in the left lobe of the liver shows subtly decreased density, which represents a poorly liquefied inflammatory site. Administration of IV contrast material is critical to visualize such areas.

Imaging Appearance

The CT appearance of an abscess is quite characteristic. An abscess appears as an area of fluid density with well-defined or irregular margins, and it may contain multiple septations in the cavity (Figs. 42–23 and 42–24). Depending on the amount of debris, blood, or proteinaceous material, the attenuation value of that material may be the same as that of water or somewhat higher. Abscesses may contain gas, which appears in the CT scan as black densities. Gas may be abundant and produce an air-fluid level, or it may be scattered throughout the fluid-density area as small microbubbles. Approximately one third of abscesses contain gas (Fig. 42–25), which may be the result of a GI fistula or gas-forming organisms (most commonly, *Escherichia coli, Enterobacter aerogenes,* and *Klebsiella* and *Clostridium*). In some cases, there may be no well-defined fluid collections, or small pockets of gas may be the only sign of infection.

The most common example of gas as the only sign of infection is the presence of small gas bubbles around an infected aortic graft or emphysematous pyelonephritis. One diagnostic caveat is that of extremely small gas bubbles that may not measure −1000 Hounsfield units (HU) because of the partial-volume effect; such bubbles may measure only −200 to −300 HU. The nature of such gas bubbles, however, can easily be confirmed by adjusting the window center until the adjacent fat appears gray. Any structure darker than the gray fat represents gas.

CT and MRI are capable only of detecting a fluid or gas density but cannot determine whether such densities represent infection. For example, low-density fluid masses can be produced not only by abscesses but also by old hematomas, lobulated ascites, lymphoceles, necrotic tumors, mucinous tumors, and benign cysts. Thus, aspiration may be necessary for diagnosis in these cases (see "Imaged Guided Microsurgery" chapter).

Although free air within the peritoneum may be due to abscesses, it also may be secondary to surgery or to a perforated bowel. In fact, parenchymal gas can occur after any surgical or percutaneous procedure, such as emboliza-

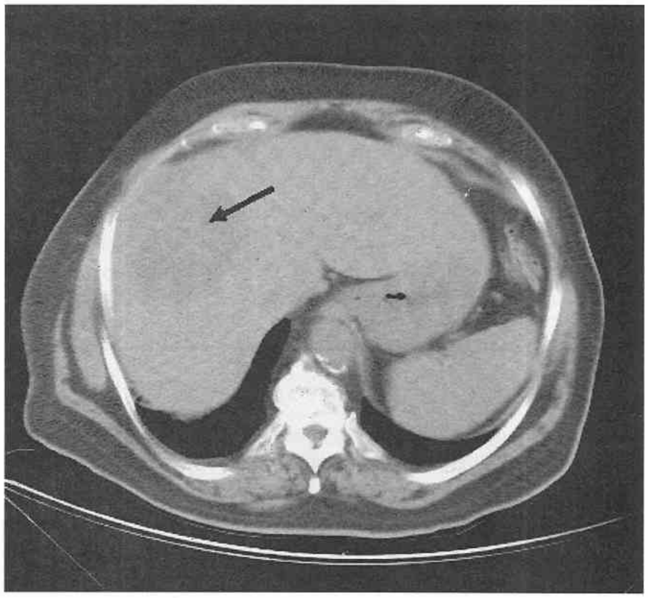

Figure 42–24. Large abscess *(arrow)* in the right lobe is significantly liquefied, showing a much better defined fluid collection, characteristic of an abscess.

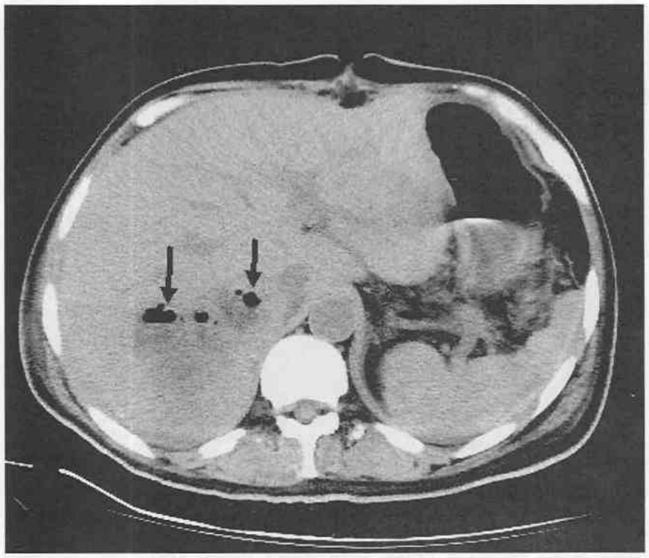

Figure 42–25. Abscess cavity in a hepatic abscess shows air collections *(arrows)*. Gas is typically present from gas-forming organisms, but it may also originate from fistulas.

tion that introduces minute amounts of air by tissue necrosis (see Fig. 42–22*B* and *C*).[67, 70] The gas appears on the scan, but there may be the spurious diagnosis of infection. A large number of free, small gas bubbles may be the result of a perforated ulcer without any drainable purulent material. Careful scrutiny can distinguish small amounts of gas in bowel, which may be confusing (Figs. 42–26 and 42–27).

The fluid densities of virtually all abscesses are identical in appearance, whether the causative organism is a bacterium, yeast, or a parasite. The only exception is when tuberculosis or echinococcosis may occasionally be associated with calcification.

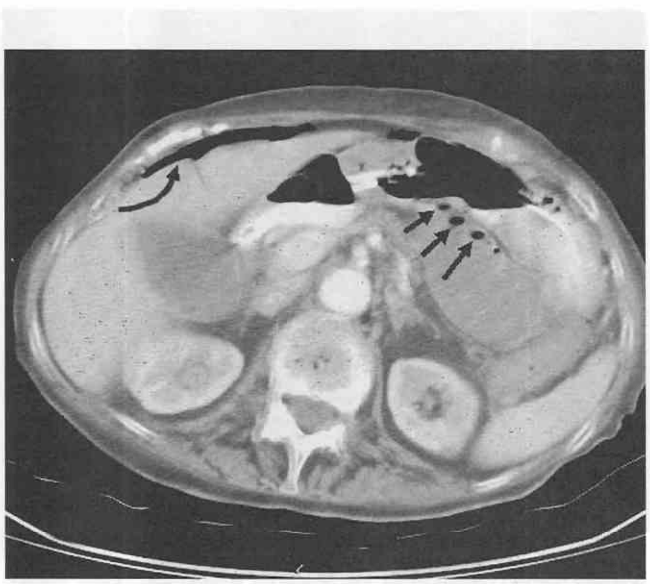

Figure 42–26. Small air collections in the bowel can be distinguished from abscess air by noting that the small pockets of air *(arrows)* are trapped in the margins of the small bowel valvulae. Free air *(curved arrow)* is noted anteriorly, in front of the liver.

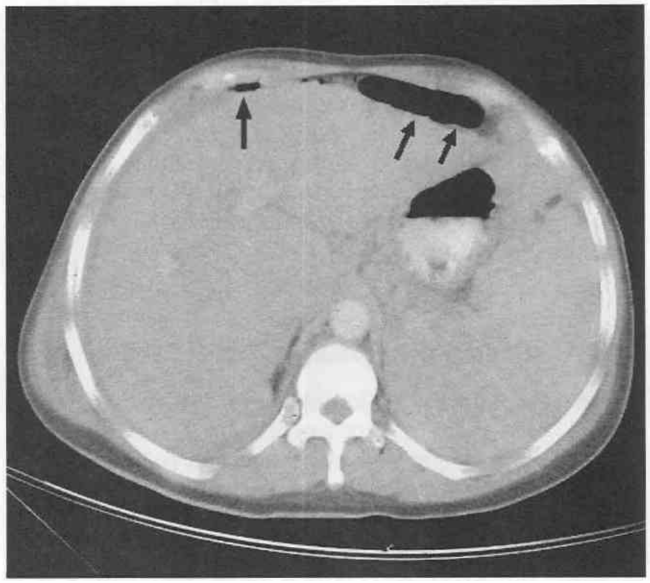

Figure 42–27. Another patient shows air beneath the diaphragm anteriorly. The collection on the right *(large arrow)* is free air, whereas the air on the left side is located in a loop of small bowel. Careful scrutiny shows the small indentations from the bowel markings *(small arrows)*, indicating this is intraluminal.

Technical Factors

When one is evaluating for an intra-abdominal abscess, two technical factors should be remembered. First, it is important to administer IV urographic contrast material in all instances (Fig. 42–28; see Figs. 42–23 and 42–25). Second, oral contrast material in either an iodinated or a barium solution should always be administered for opacification of the bowel. This is especially important for the

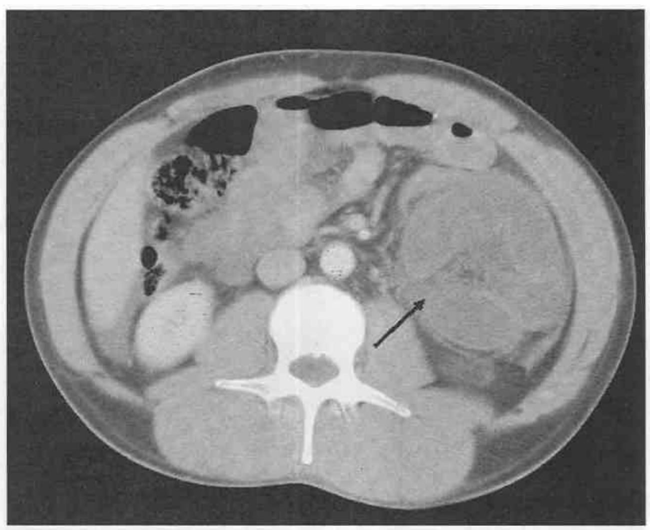

Figure 42–28. CT scan shows how beneficial IV contrast material is for a correct diagnosis. The fluid-density clump of bowel *(arrow)*, representing an internal hernia, can be correctly identified because the contrast material enhances the bowel wall and valvulae. Without contrast material, it would exhibit a fluid density indistinguishable from that of an abscess.

evaluation of abscesses in the left subdiaphragmatic space, the omental bursa, or the interloop region.

Abscesses in each of the organ systems and anatomic areas have some unique clinical characteristics and appearances on CT images. In addition, each of the anatomic areas has some potential false-positive findings associated with the variants of normal and other abnormalities, which should be sought to avoid an incorrect diagnosis of intra-abdominal abscesses.

Right Subdiaphragmatic Abscesses

Abscesses in the right subdiaphragmatic space are caused by a variety of disorders because this area has open access from the right pericolic gutter and right subhepatic recess. Virtually any inflammatory process in the abdomen can reach this area. The most common cause of an abscess, however, is appendicitis or a perforated viscus, gallbladder, or ulcer. The whole abscess may show fluid density, or it may contain gas (Fig. 42–29).

The most important diagnostic point is that the peritoneal space ends at the coronary ligaments immediately lateral to the bare area of the liver. A pleural effusion should not be mistaken for a subdiaphragmatic abscess (see Fig. 42–14). If the fluid of abscess is behind the fat that is posterior to the bare area of the liver, it represents a pleural effusion and not a subdiaphragmatic abscess. Any fluid or gas within the fat of this bare area is in the superiormost portion of the pararenal space. If both a pleural effusion and a subdiaphragmatic abscess exist, a decubitus view may permit the pleural fluid to move and confirm the diagnosis. In some unusual cases, a bolus injection of contrast material with dynamic scanning may have to be used to visualize the diaphragm, which enhances because of its rich blood supply. Any fluid in the subdiaphragmatic space can resemble an abscess, whether it be bile, blood, necrotic tumor, or loculated ascites.

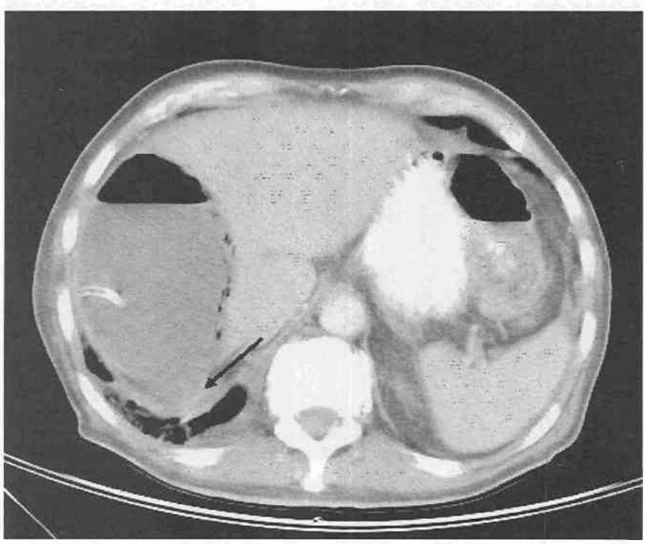

Figure 42–29. Subphrenic abscess containing fluid and air. The posterior margin *(arrow)* of the space borders the bare area of the liver.

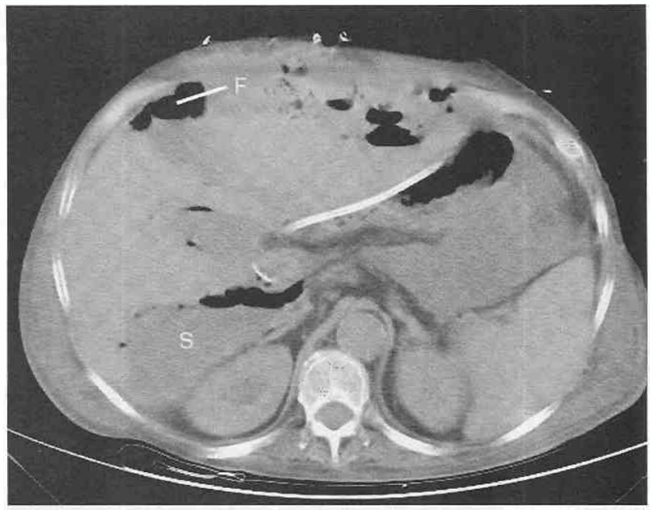

Figure 42–30. CT [redacted]ows free [redacted] (F) in the anterior subhepatic space adjacent to the gallbladder fossa. The posterior right subhepatic space (S) lies so high that it gives the erroneous impression of a hepatic fluid collection.

Right Subhepatic or Hepatorenal Abscesses

The right subhepatic space is located between the right lobe of the liver and the anterior surface of the kidney. It has been divided into anterior and posterior (Morison's pouch) compartments, a functional division based on etiologic conditions (Figs. 42–30 and 42–31). The most common cause of abscesses in the anterior portion is a perforated gallbladder that borders immediately on this area. The posterior portion of the space is a dependent area within the peritoneum that can collect fluid from the paracolic

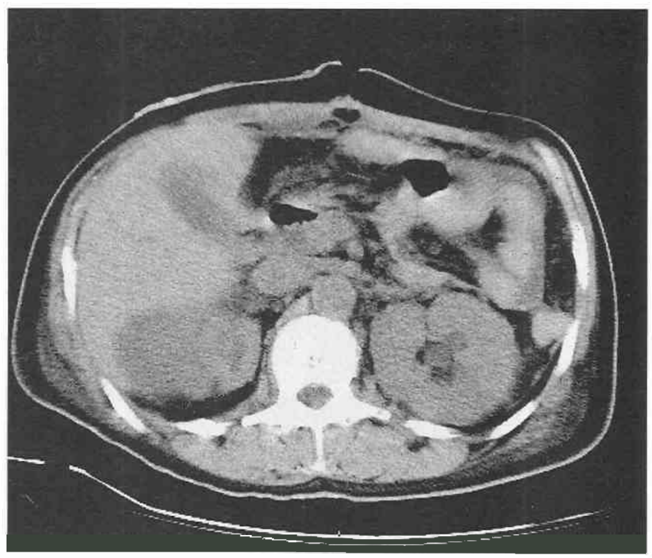

Figure 42–31. Abscess in the posterior subhepatic space (Morison's pouch) between the liver and kidney. On occasion, as here, the curved surfaces create a partial volume effect, which may make it difficult to distinguish the abscess from a renal or perirenal fluid collection.

gutters, the subphrenic space, or direct extension from the duodenum, liver, or bowel.

Because this is such a common site for fluid collection, even with ascites, a distinction may have to be made between ascites and purulent material. In such cases, it is best to place the patient in a decubitus position to let the fluid move out of the space. Ascites moves, whereas inflammatory collections (in the immunocompetent patient) do not; this is a good differential point to mark the need for aspiration in some patients.

Another uncommon problem is that sometimes the cephalic extent of this space is high. When an axial scan is taken above the typical location of the space in such cases, it may give the spurious impression of an intrahepatic abscess.

Left Subdiaphragmatic Abscesses

An abscess in the left subdiaphragmatic space can be caused by a number of abnormalities. It has traditionally been said that access to this anatomic area is limited from other peritoneal spaces because of the phrenicocolic and falciform ligaments. The typical origin is the stomach or colon, secondary to a gastric ulcer; postoperative leaks; or a perforated neoplasm, left colon, or esophagus. In some cases of a perforated esophagus, the inflammatory process involves the retroperitoneal space rather than the subdiaphragmatic space; if a portion of the stomach is involved, however, the subdiaphragmatic space is also involved.

Most abscesses can involve the entire diaphragmatic space, but they also may loculate in an anterior or posterior segment (Figs. 42–32, 42–33, and 42–34). Although it is traditionally taught that a process cannot extend from the left pericolic space or the right subphrenic space, experience has shown that, depending on individual anatomic variations or the nature of the inflammatory process, the falciform ligament and phrenicocolic ligaments may not serve as effective barriers to the spread of infection (see Figs. 42–5*A* and 42–6*A*).

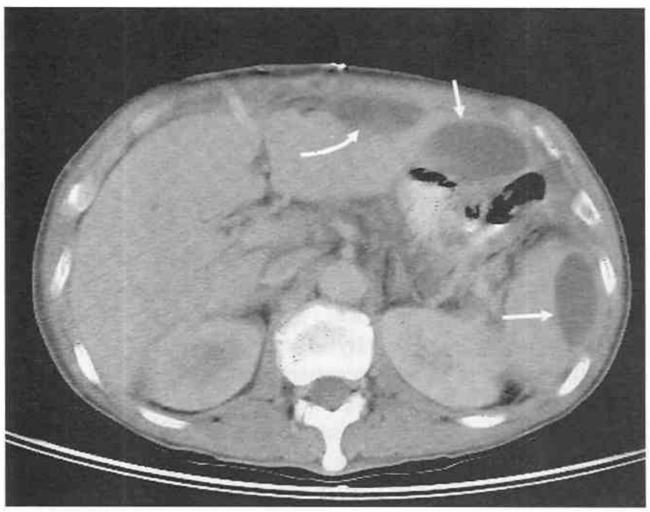

Figure 42–32. Three abscesses in different areas of the left subphrenic space. The most anterior portion of the space *(curved arrow)* is in front of the liver. An abscess is in the gastrohepatic space *(vertical arrow)*, sometimes known as the left subhepatic space. The posterior subphrenic space *(horizontal arrow)* is around the spleen.

To detect a small abscess in the left subdiaphragmatic space, one must always administer oral contrast material to fill the stomach. At times, a fluid-filled stomach may resemble an abscess, or vice versa. The contrast material clearly defines the stomach and eliminates any question of the diagnosis.

Left-sided pleural effusion should not be mistaken for a left subdiaphragmatic abscess. The region between the upper pole of the left kidney and the spleen, which contains the splenic pedicle and tail of the pancreas, represents the splenorenal ligament. This region located behind the fat is within the pleural space and not the subdiaphragmatic peritoneal space.[33] Any fluid within this area is in the superiormost area of the retroperitoneum rather than in the left subdiaphragmatic space. Above the level of the splenorenal ligament, fluid can surround the spleen entirely and may become interposed between the diaphragm and the spleen (see pararenal space abscesses later). Any problems distinguishing pleural effusions from subphrenic collections can be overcome by putting the patient in the decubitus position.

It is often difficult to differentiate a subphrenic abscess from inversion of the diaphragm by a large pleural effusion. In the latter case, a large pleural effusion is seen adjacent to the diaphragm.

On first glance, it is difficult to distinguish a pleural effusion from a subphrenic collection, but if one looks carefully, the fluid is behind the spleen and the bare area of the spleen. A decubitus view or sagittal reconstruction may clarify the nature of the inversion.

Left Subhepatic Abscesses

Abscesses in the left subhepatic space are caused by the same processes as those causing the subphrenic abscesses. They may spread from the right side, beneath the falciform ligament, or from other portions of the left subphrenic space (see Fig. 42–34).

Omental Bursa Abscesses

Abscesses in the omental bursa may be secondary to a process extending through Winslow's foramen, inflammation from the pancreas, a penetrating ulcer, or a tumor from the stomach or duodenum. The inferior recess of the omental bursa is anterior to the pancreas and is most commonly involved through penetrating ulcers or a pancreatic process. A small amount of air may be the only sign of a perforated ulcer. As was noted previously, the splenic recess of the omental bursa is located directly behind the fundus of the stomach (Figs. 42–35 and 42–36). The medial superior recess extends cephalad adjacent to the caudate lobe and vena cava (see Figs. 42–37 and 42–38).

It is important to administer oral contrast material to see the posterior wall of the stomach and to distinguish it from an abscess in the splenic recess of the omental bursa

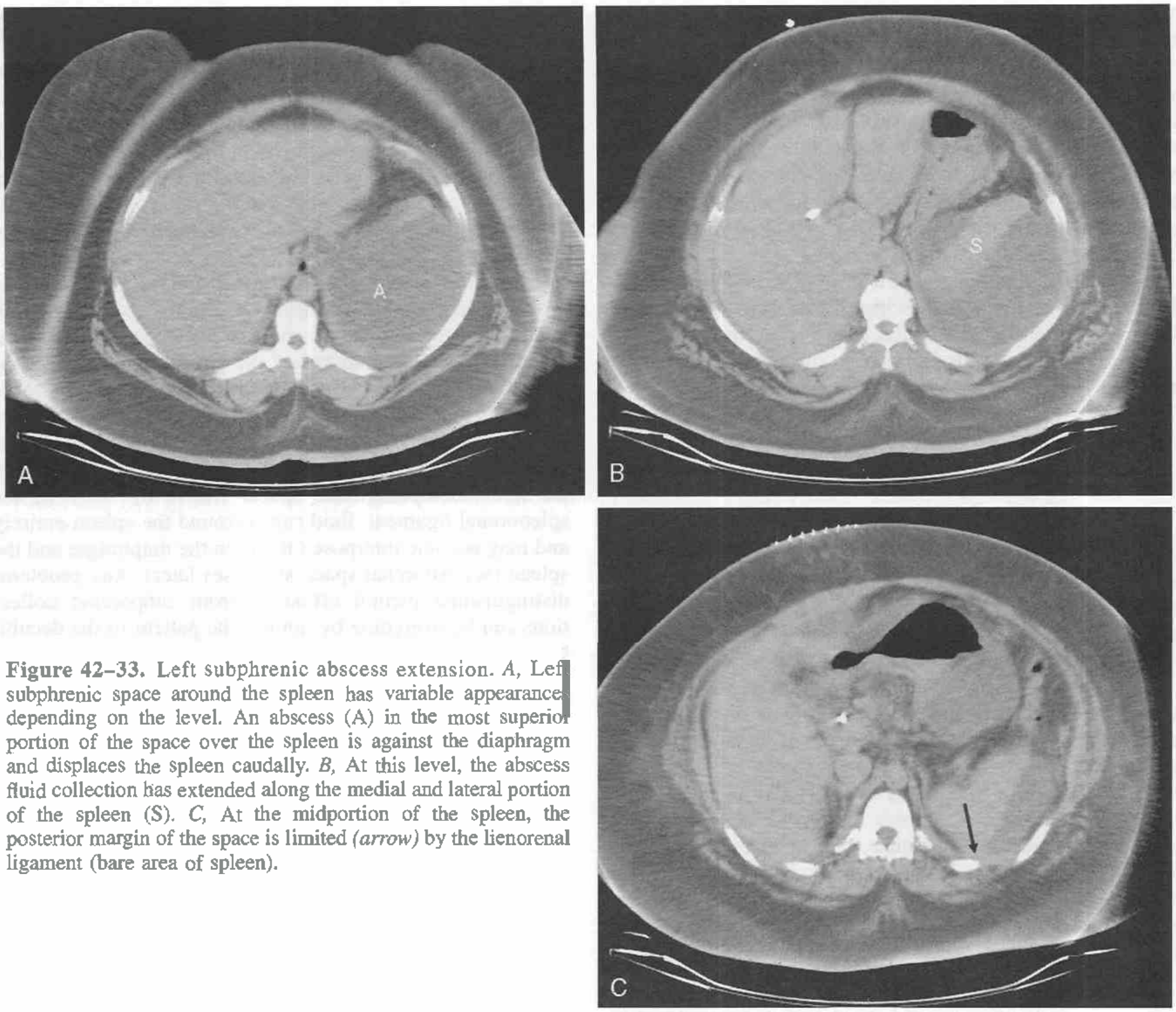

Figure 42–33. Left subphrenic abscess extension. *A,* Left subphrenic space around the spleen has variable appearances depending on the level. An abscess (A) in the most superior portion of the space over the spleen is against the diaphragm and displaces the spleen caudally. *B,* At this level, the abscess fluid collection has extended along the medial and lateral portion of the spleen (S). *C,* At the midportion of the spleen, the posterior margin of the space is limited *(arrow)* by the lienorenal ligament (bare area of spleen).

Figure 42–34. Abscess *(arrow)* in the left subhepatic (gastrohepatic) space behind the left lobe and adjacent to the stomach.

(Figs. 42–37 and 42–38). Air may remain in the omental bursa for several days after a surgical procedure and should not be mistaken for an abscess.

Pericolic and Interloop Abscesses

Pericolic abscesses can occur as a result of virtually any inflammatory process within the abdomen, such as a perforated colon or bowel, appendicitis, or a ruptured gallbladder because the physiologic movement of fluid is into the pericolic space (see earlier discussions of peritoneal function). Such abscesses are usually associated with a subhepatic or subdiaphragmatic abscess. On CT scans, a pericolic abscess appears as a mass of fluid density bordered on the lateral surface by the parietal peritoneum and medially by the serosa of the colon (Fig. 42–39). Such abscesses may spread into the right subhepatic or subdiaphragmatic space.

Interloop abscesses can be caused by the same conditions as any abscess but are more commonly associated with fistulas from the bowel. They can occur between

Figure 42–35. Abscess in a small child lying in the right decubitus position. CT scan shows a large abscess (A) in the space behind the stomach (S), anterior to the pancreas (P) and medial to the splenic flexure of the colon (C).

isolated loops of bowel or within the infracolic spaces. In such cases, it is best to give ample amounts of contrast material to try to opacify the bowel, but many times there is sufficient contrast enhancement of the bowel wall and the contents (see Fig. 42–28) to distinguish the abscesses.

When an abscess is present, bowel adjacent to the inflammation may be paralytic and may not carry the contrast. In such cases, a fluid-filled or gas-filled abscess can be distinguished from the normal bowel because the wall of the abscess is smooth and lacks the irregular contour of the bowel wall produced by typical haustra or valvulae. Moreover, the fluid in the bowel has a varied appearance with different densities, whereas an abscess is completely homogeneous.

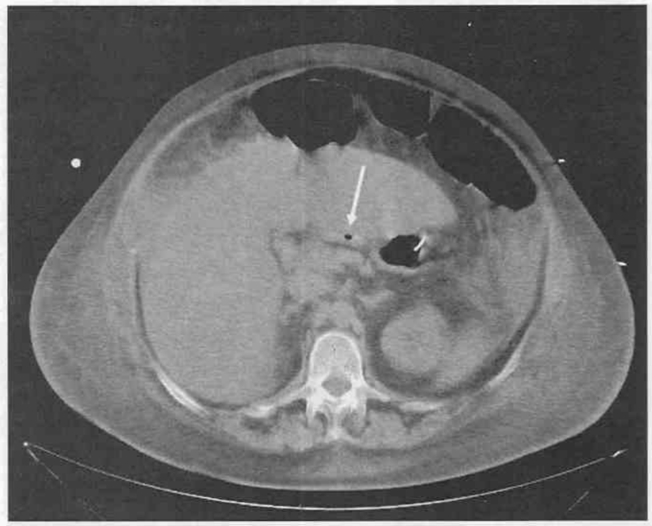

Figure 42–37. CT scan shows a small collection of contrast medium and air in the lesser sac *(arrow)* from a small gastric perforation.

Pelvic Abscesses

The pelvis, the lowest point in the abdomen and the area to which exudates gravitate, is one of the most com-

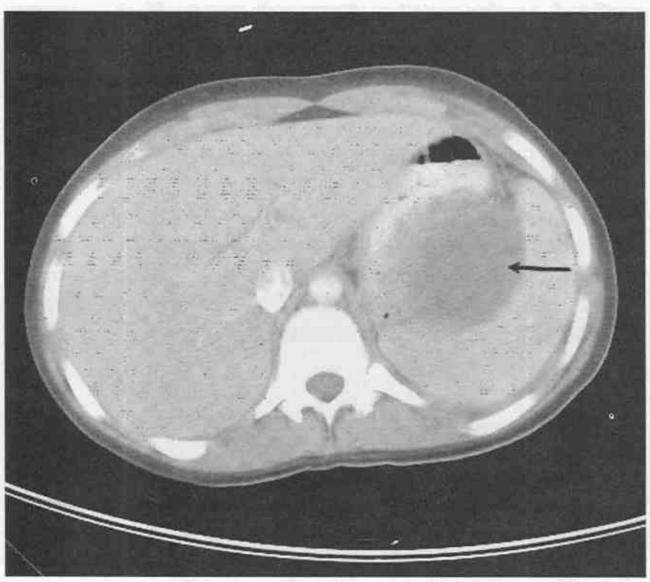

Figure 42–36. Abscess in a patient lying in the supine position. CT scan shows a large abscess *(arrow)* in the splenic recess of the lesser sac, which is effacing the stomach anteriorly.

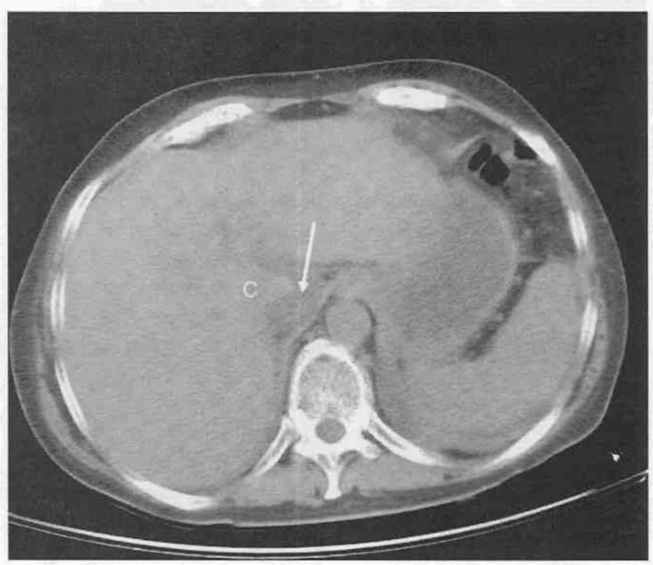

Figure 42–38. Fluid collection *(arrow)* in the superior recess of the lesser sac, around the caudate lobe (C) of the liver. (See Figs. 42–4, 42–5, and 42–6.)

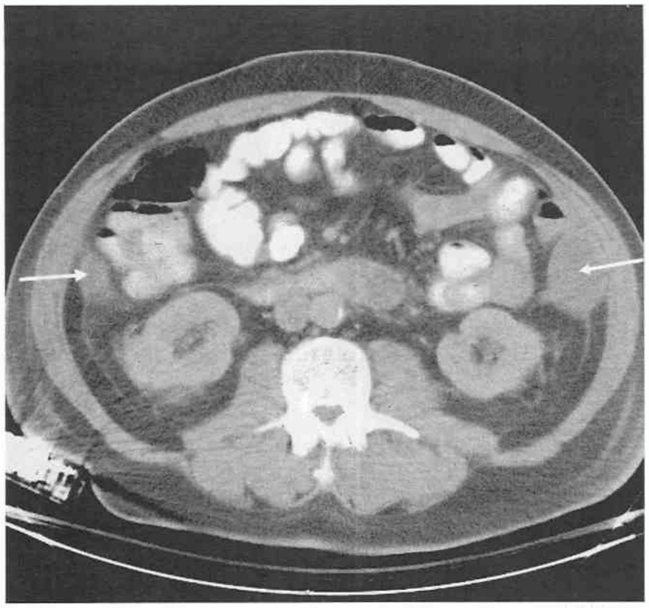

Figure 42–39. Pericolic abscesses *(arrows)* on the right and left sides of the peritoneum.

mon locations for intra-abdominal abscesses. Abscesses in this area may result from diverticulitis, appendicitis, a perforated viscus, peritonitis, or trauma (Fig. 42–40*A* and *B*).

On CT scans, the abscess has a typical appearance, being low in density and well marginated; it may or may not contain gas. It is important to administer both IV and urographic contrast material to opacify the rectum and colon. Administration of both contrast materials should eliminate any false-positive results, especially in patients with ascites; the ascitic fluid in the pelvis may produce an area of fluid density on the image, which may be confusing.

Posterior Pararenal Space Abscesses

The posterior pararenal space is bounded posteriorly by the transverse fascia and anteriorly by the posterior renal fascia (Fig. 42–41*A*). This space extends caudad to the pelvis and cephalad to the diaphragm (see Fig. 42–41*B*). Although most clinicians are familiar with the posterior pararenal space in the area of the kidneys, the pararenal space in the area adjacent to the diaphragm is not as familiar. In the space between the medial portion of the spleen and the upper pole of the kidney is the splenorenal ligament, which represents the farthest extension of the pararenal space on the left side. There is an analogous space in the right side in the bare area of the liver. It has been my experience that both the anterior and posterior pararenal spaces communicate into these areas on the right and left sides, although this is not the traditional teaching.

Inflammatory processes in the posterior pararenal space usually result from a ruptured aortic aneurysm, pancreatitis, osteomyelitis from the rib or spine, intestinal or esophageal perforation, or trauma. Abscesses may remain localized laterally within the pararenal space or become confluent with the psoas muscles. Processes from the aorta or spine may spread laterally. In addition to the abscess collection, there is concomitant thickening of the fascial planes. A psoas abscess produces enlargement of the psoas muscles.[91] This abscess typically shows fluid density but occasionally the density may be similar to that of the muscle (Fig. 42–42). In cases of bilateral psoas abscesses associated with destruction of the vertebral body, tuberculosis should still be considered.

Although little information is available in the literature, several cases indicate that the posterior pararenal space communicates with the posterior mediastinum. Esophageal perforations or other problems may extend caudally into the right or left posterior pararenal spaces, or vice versa.

Anterior Pararenal Space Abscesses

The anterior pararenal space is bounded anteriorly by the posterior parietal peritoneum and posteriorly by the anterior renal fascia; this space is bounded laterally by the lateroconal fascia (which is the fused anterior and posterior perirenal fasciae). This compartment contains several alimentary organs, including the pancreas and ascending and descending colon. (This anatomic discussion is based on the traditional viewpoint; a new concept of the retroperitoneum proposes that there is no free communication between the space around the pancreas and the colon but that they are interconnected only through the attachment of the mesentery. In addition, the new concept no longer uses the term *anterior pararenal space* but considers these areas the *intermesenteric spaces*; see "New Concepts of Retroperitoneum and Peritoneum" earlier.)

Most inflammatory processes in this area originate from the colon, appendix, pancreas (see Fig. 42–41*A*), or duodenum as a result of perforations from tumors, diverticulitis, inflammatory bowel disease, or trauma. Perforations of the bowel can produce gas, abscesses, or both, depending on the site of involvement. A localized perforation of the colon may occur in the retroperitoneal area and remain confined to the anterior pararenal space. If the process occurs below Gerota's fascia, it can move superiorly into both the anterior and the posterior pararenal spaces. The most cephalic extension of the pararenal spaces on the right is the retroperitoneum behind the bare area of the liver, and on the left it is the retroperitoneum medial to the spleen.

Another sign I have found to be valuable in cases of inflammation is thickening of the renal fascia. For example, in some cases it may be difficult to distinguish a loop of bowel with the density of fluid from an abscess; with an abscess, the renal fascia is thickened.

Liver Abscesses

Pyogenic hepatic abscesses usually occur as a result of intra-abdominal infection, such as appendicitis, suppurative cholangitis, hematogenous dissemination by the portal vein draining the bowel, or hematogenous spreading from a distant focus.[49, 86] The most common pyogenic organisms include gram-negative organisms, especially *E. coli;* less commonly, anaerobes, such as *Clostridium* or *Bacteroides*

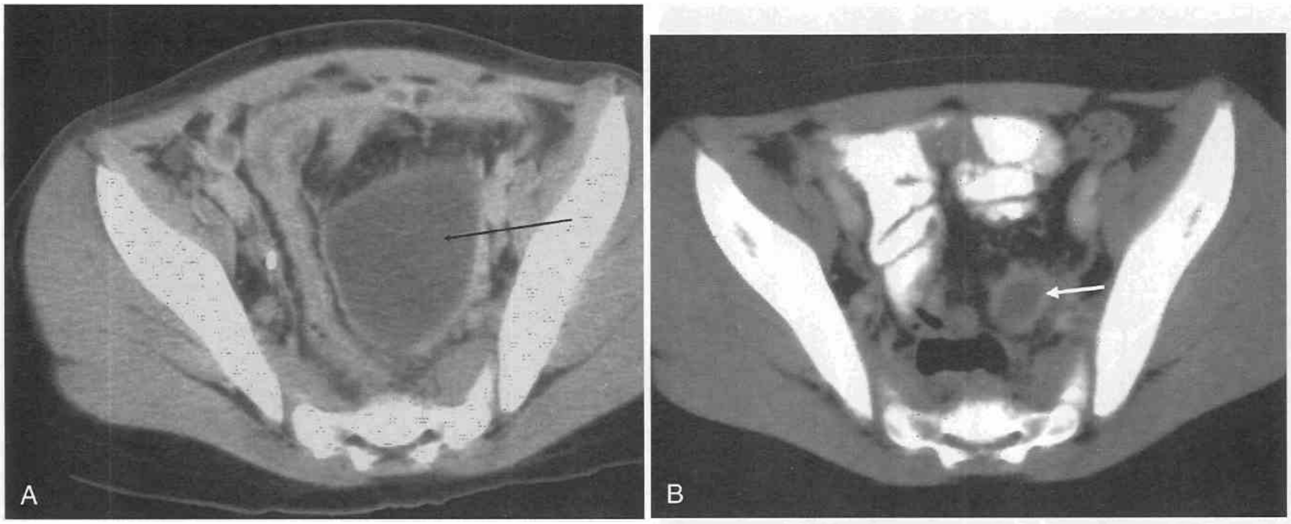

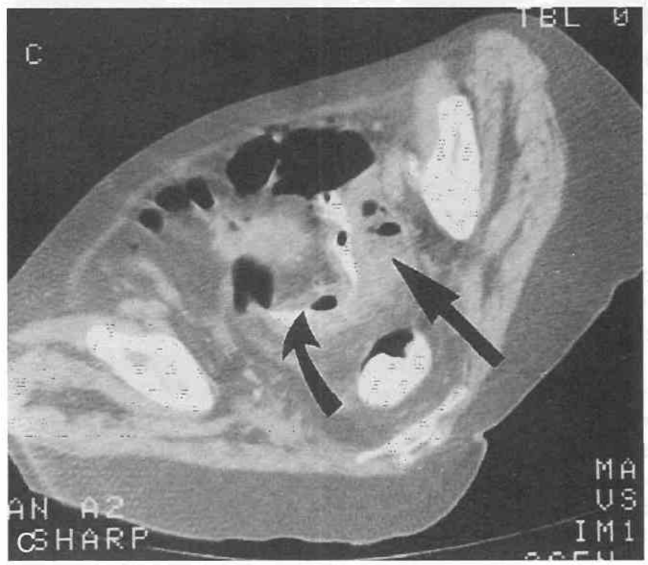

Figure 42–40. Pelvic abscesses. *A,* Pelvic abscess (*horizontal arrow*) shows large abscess anterior to the rectum. This unusual abscess resolved with only antibiotic therapy. *B,* After almost complete resolution of the abscess *(arrow)*, the patient did not require drainage. *C,* In a different patient, CT scan through the upper portion of the pelvis shows an abscess with an air-fluid level *(straight arrow)* next to a loop of sigmoid *(curved arrow)*.

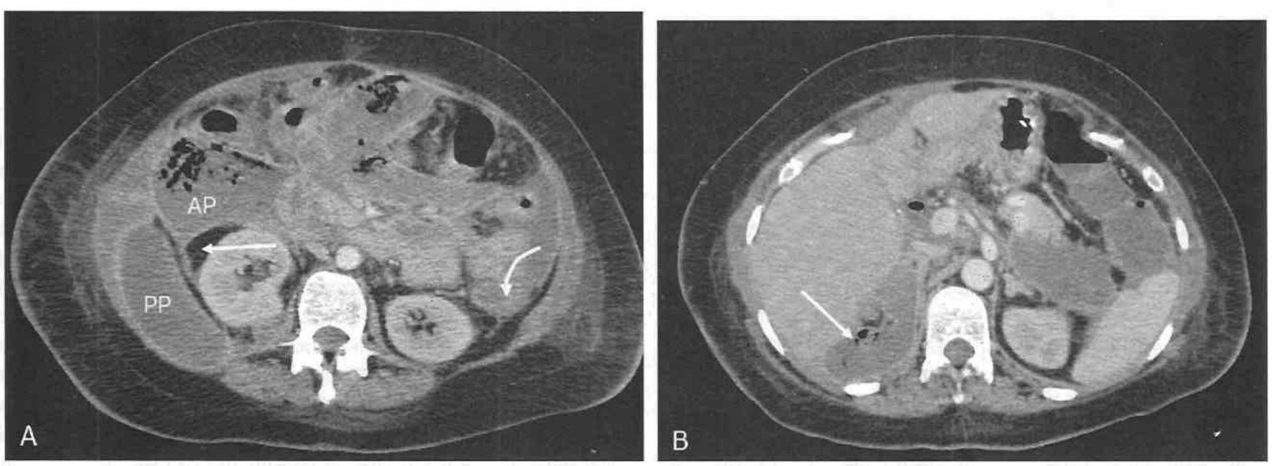

Figure 42–41. *A,* Retroperitoneal abscess in the pararenal spaces, anterior (AP) and posterior (PP). Fat *(arrow)* is seen within the renal fascia, bounded anteriorly by the fascia of Gerota and posteriorly by the Zuckerkandl fascia. Slightly thickened fascia *(curved arrow)* can also be noted on the left. *B,* The superior-most extent of this retroperitoneal abscess *(arrow)* continues in the bare area behind the liver.

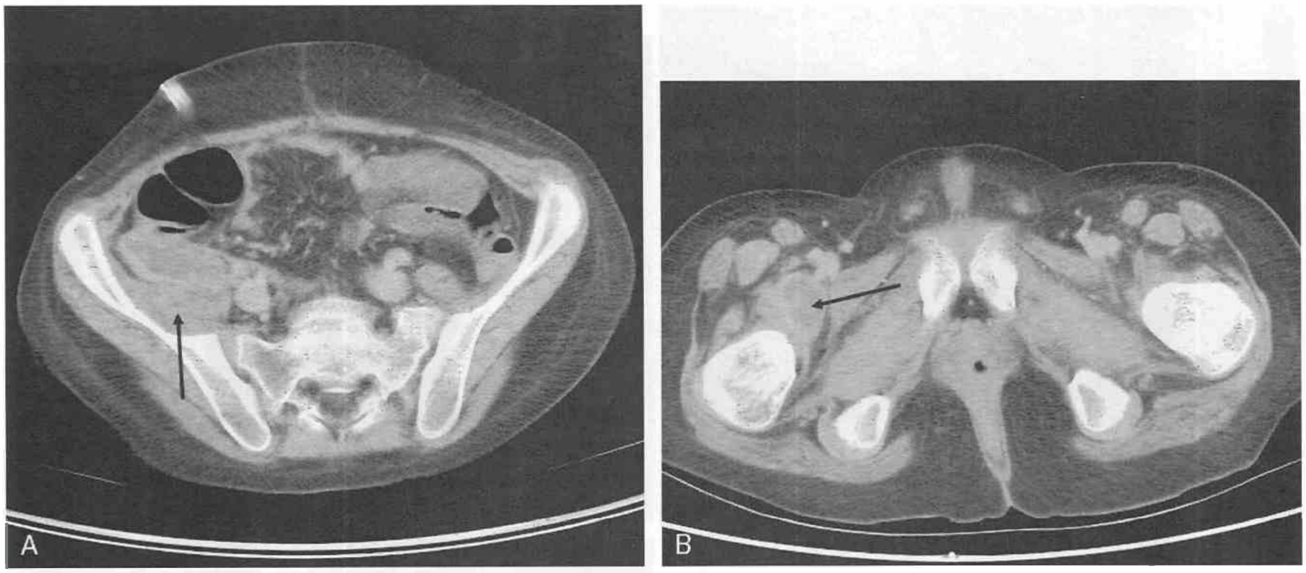

Figure 42–42. *A,* CT scan of a child with vasculitis and local perforation of bowel. A retroperitoneal abscess is seen in the right iliopsoas muscle *(arrow). B,* Abscess extends caudad through the psoas muscle and over the area of the lesser trochanter *(arrow).*

species, also may be involved. Antibiotic therapy and drainage, either surgical or percutaneous, are indicated. The typical CT appearance of a hepatic abscess is a circumscribed mass with the density of fluid (Fig. 42–23). Amebic abscesses and echinococcosis are also types of hepatic abscesses (see next).

Two potential false-positive findings are commonly associated with the liver. The first is the partial-volume effect produced by the upper pole of the right kidney. The space between the two is not clearly visualized but appears lower in density as a soft tissue mass; this may simulate a perirenal collection on the right side. The key to differentiating this partial-volume error from a real perirenal collection is that there is ipsilateral thickening of perirenal fascia if an abscess is present.

The second potential false-positive finding is a high hepatic flexure of the colon entering the porta hepatis. The course of the transverse colon to the hepatic flexure of the colon should be carefully traced; at times, a decubitus view may be required to confirm the diagnosis.

Amebic Abscesses

Amebic abscesses are a complication of colonic infestation by *Entamoeba histolytica.* The disease is produced when material contaminated with amebae is ingested. Amebae reach the liver either by the portal drainage or by the lymphatic vessels from the bowel.[49] Once in the liver, the amebae release autolytic enzymes and inflammation progresses until an abscess is produced. Such abscesses can become secondarily infected by pyogenic organisms, which may or may not be gas producing. The treatment of amebic abscesses consists of antibiotic therapy or surgical drainage, or both. Total resolution of the amebic abscess can occur without complete drainage with proper medical therapy consisting of metronidazole. (The material aspirated from such amebic abscesses has the appearance of anchovy pate and consists of autolyzed liver tissue.) Surgical drainage may be required in some abscesses that have become superinfected with pyogenic organisms. The CT scan appearance of an amebic abscess is identical to that of a pyogenic abscess.[58] It appears as well-delineated masses of fluid density within the liver substance (Fig. 42–43).

Fungal Infections

A number of different fungal infections can cause focal infections, *Candida* the most common. With most fungi, the early foci may show low density and be poorly defined, but they may liquefy into well-marginated fluid collections (Fig. 42–44).

Echinococcosis

Echinococcosis, or hydatid disease of the liver, is a parasitic abscess caused by the larvae of *Echinococcus multilocularis* (alveolaris) or *E. granulosus.* The dog is the host, and sheep are the intermediate hosts; humans may become intermediate hosts by ingesting food contaminated by the ova. The pathophysiologic conditions follow: After ingestion of the ova, the embryo, which penetrates the intestinal wall and is transported to the liver by the portal system, is released. (Although echinococcosis can occur virtually anywhere in the body, the liver is the most common organ involved.) Once in the liver, the larva establishes itself, and inflammation proceeds. The hepatic cyst produced is composed of the endocysts, comprising the parasitic elements of the germinal membrane and daughter cysts, and the surrounding percyst, which is the compressed hepatic parenchyma and inflammatory reaction.

Pathologically the two types of *Echinococcus* organisms differ. *E. granulosus* may have (1) a unilocular cavity,

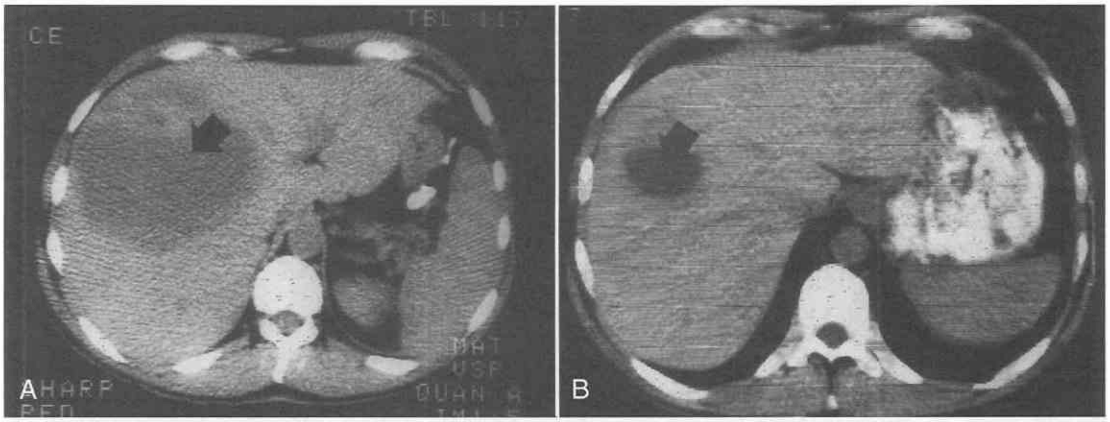

Figure 42–43. *A,* A large amebic abscess *(arrow),* which looks similar to other abscesses. *B,* Resolution of the amebic abscess occurred over a number of months after administration of antibiotic medications.

which is usually fertile, or (2) a multilocular cavity with irregular edges, which does not metastasize. Calcifications may indicate sterility. *E. multilocularis* produces small, numerous cysts that multiply by exogenous budding to produce the malignant hydatid cyst, which can become confluent throughout the liver or metastasize to other organs.

Although the liver is the most common site of echinococcal involvement,[53] lung and kidney are not uncommon sites. Unusual reports of many other sites, including pancreas, aorta, and brain, have occurred.[52]

Treatment of an echinococcal abscess has historically been possible only by surgical drainage,[22] but medical drainage methods have improved. Several chemical agents have been effective. For example, mebendazole has proved effective in a large percentage of patients,[109] with cure in 40%. Changes are produced in cyst appearance, such as a totally echogenic appearance on ultrasound, increased density of cysts, reduction of cyst size, detachment of endocysts from the wall, and calcification of the cyst wall.

Percutaneous drainage can be performed if a "killing" solution (10% povidone-iodine [Betadine], 20% sodium chloride, or ethyl alcohol) is injected and meticulous technique is used to prevent spillage, but it should not be performed unless significant symptoms or complications exist. Surgical drainage consists of complete removal of the intact cyst after the killing solution has been injected into the cyst. (Formalin has been abandoned because of adverse effects.) The greater omentum is usually sutured over the remaining cavity in the liver to preclude any spillage of residual fluid or cysts into the peritoneal cavity.

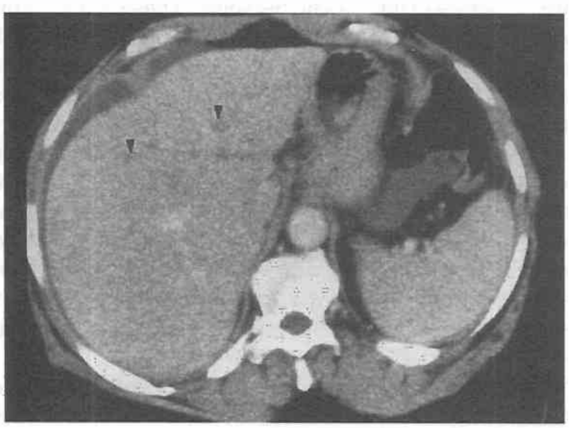

Figure 42–44. Fungal granulomas appear as small, low-density masses *(arrowheads)* in the right and left lobes of the liver.

In recent years, percutaneous treatment and drainage have become common, with several techniques reported.[89] These are discussed in Chapter 61. Lewall and Nyak[63] have cautioned that percutaneous drainage should be avoided and surgical drainage encouraged when echinococcal cysts show dilatation of the biliary system or an exophytic component that is likely to rupture.

The CT follow-up of such cases is informative because of the clear visualization of the anatomy. Before surgical treatment, the large mother cysts containing the daughter cysts are clearly seen (Fig. 42–45). With some of the new chemotherapeutic agents available, temporary improvement in the cysts can occasionally be seen, as evidenced by some dissolution of the walls of the daughter cysts. Whether such medical treatment will be effective in the long term is not known.

After surgery, the residual cavity can be clearly distinguished from the evacuated cyst and the fat density of the omentum, which is used to seal the cavity (see Fig. 42–45*D*). For several weeks, the size of the cavity shrinks and the amount of fat seen decreases as the fibrosis of healing continues.

In some cases, there may be secondary infection of daughter cysts by colonization from a biliary fistula. In such cases, air may be seen within the cysts from either pyogenic bacteria or a biliary fistula, which usually accompanies the infection. On some occasions, the pyogenic organisms can actually destroy the daughter cysts by enzymatic digestion (see Fig. 42–45*B, C*). Diagnostic aspiration should be avoided because of potential spillage of the daughter cysts and anaphylaxis from the foreign protein. Sensitization of the patient to the protein is necessary for anaphylaxis to occur; this usually follows a previous spillage of material, although it may occur without such an event.

Complications associated with the disease include rup-

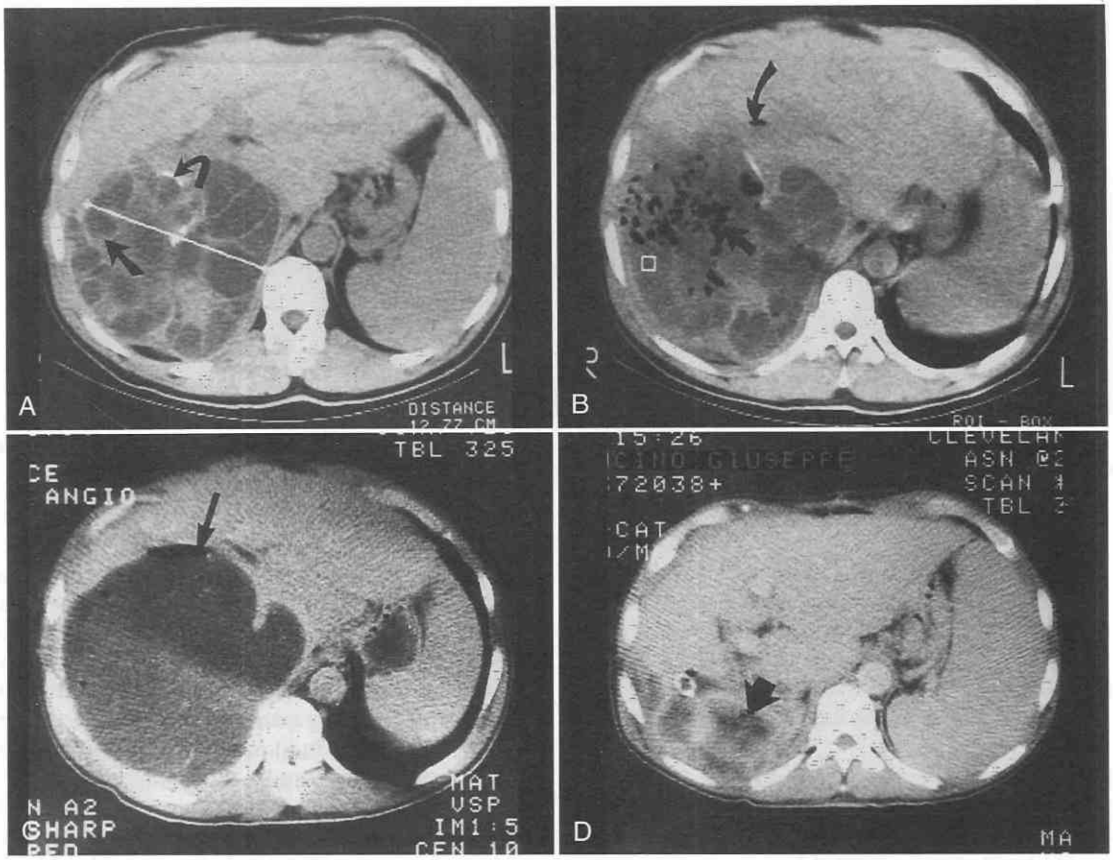

Figure 42–45. Echinococial cyst evolution with treatment. *A,* CT scan of echinococcal cys[redacted]hows calcification in the wall *(curved arrow)* and daughter cysts *(arrow)* within the mother cyst. *B,* After secondary infection, air [redacted]e seen within a cyst. This scan shows multiple air pockets within the cyst and air within the biliary system *(curved arrow). C,* With persistent infection, dissolution of the daughter cysts can be seen. Note the air *(arrow)* in the upper portion of the cyst and the absence of daughter cysts. *D,* After surgery, the cavity, filled with fat-density omentum *(arrow)*, can be seen.

ture of the mother cyst and spillage into the peritoneum or adjacent structures. In approximately 10% of cases, secondary infection may occur because of erosion into the bowel or the biliary system.

Since the early reports of the CT appearance of echinococcosis,[83] numerous articles discussing the CT detection and appearance of echinococcal cysts of the liver have appeared.[52, 53, 63, 110] Scherer and colleagues[99] reported on the CT evaluation of 13 cases of echinococcosis and noted two distinct appearances. In six of eight cases involving *E. granulosus,* the cysts appeared as masses of fluid density (3 to 30 HU) with a radiodense rim. In six of eight cases, there was calcification, and in five of those six, the calcifications were either crescent or ring shaped. Daughter cysts were visible in the larger cyst in six cases.

In five patients infected by *E. multilocularis,* the lesions were seen as low-density masses (14 to 38 HU), without a well-defined membrane. In four of five cases, small nodular calcifications were present (never ring-shaped). Gonzalez and coworkers[28] reported on the accuracy of detecting hepatic echinococcosis with CT. They reported that CT diagnosis was correct in 19 of 19 cases. They noted that CT was the preferred modality because it "clearly and precisely shows the existence, number, size, and location of cysts and also yields data allowing assumption as to their vitality."

Splenic Abscesses and Splenitis

Splenic involvement directly or indirectly by infection is quite common. In addition to abscesses, a wide spectrum of inflammatory changes can occur with pyogenic or granulomatous disease.

Pyogenic systemic infections can cause diffuse acute splenitis or focal fluid-density abscesses. Pathologically, small septic infarcts with systemic sepsis, which have been called "milk-flecked," may be seen. These small collections may be below the level of resolution of the CT scanner, so they can be missed. With larger amounts of inflammation and infection, the typical intrasplenic abscesses, which are associated with endocarditis, AIDS, or IV drug abuse, can be seen (Fig. 42–46). Granulomatous processes, such as tuberculosis and histoplasmosis, are quite easily seen as clearly delineated calcium deposits. From gross pathology, it is known that granulomatous processes are associated with infarcts. There is limited information available on this point, but I have noted the association of infarct-like areas in the spleen with such patients (Fig. 42–47).

Nonspecific splenomegaly without splenitis can occur with a variety of systemic disorders, including parasitic infestations, systemic sepsis, and AIDS-related disease. In many cases of patients with myeloproliferative disorders,

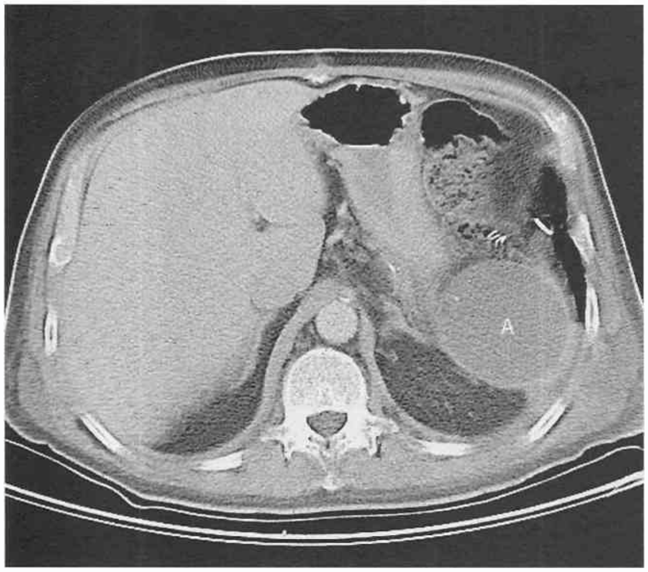

Figure 42–46. Splenic abscess (A) is totally replacing the spleen.

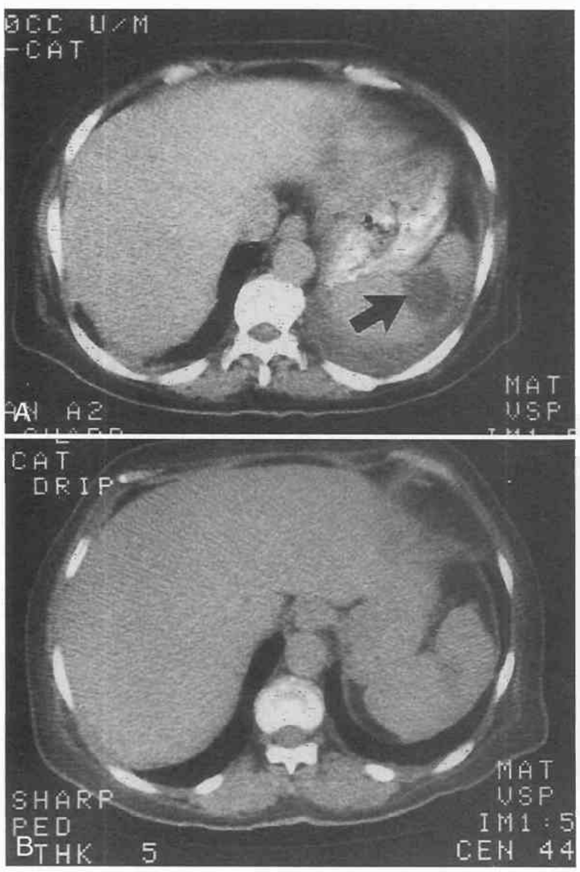

Figure 42–47. Tuberculosis. *A,* CT scan shows a low-density area *(arrow)* in the spleen, believed to be early changes of tuberculosis. *B,* A follow-up scan shows resolution of the area several months after the institution of antituberculous therapy.

such splenomegaly may be associated with the underlying disease or borderline infection.

Renal Abscesses

Renal abscesses may be caused by hematogenous "seeding," in which the organism is usually *Staphylococcus,* or a urinary tract infection, in which the organism is usually *E. coli, Proteus mirabilis,* or *Enterobacter aerogenes.* An intrarenal abscess is low in density and well marginated and may resemble a renal cyst (Fig. 42–48). More commonly, an abscess has a more irregular margin and higher density and produces unilateral thickening of the renal fascia, whereas cysts seldom do this. When the infection is still an inflammatory phlegmon and not a fluid collection, there may be a focal area of enlargement that is isodense with a normal enhanced kidney but low in density with IV contrast enhancement. This area of localized inflammation and focal enlargement is the focal nephritis, or nephronia.[96] If the infection resolves, the kidney may return to normal; if it progresses, an abscess may form (Fig. 42–49).

Emphysematous pyelonephritis is an uncommon disease produced by gas-forming organisms and usually occurs in patients with diabetes (Fig. 42–50). On CT scans, the kidney may show small gas densities within the parenchyma, or may appear as a gas-filled structure barely recognizable as a kidney. A spurious finding of "gas" can be produced by embolization or infarction.[116]

An earlier form of the disease in the infectious spectrum shows even more subtle, temporary changes in the kidney. With diffuse pyelonephritis, a striated appearance, or focal areas of decreased enhancement, can be seen. These areas usually resolve with adequate therapy.

Polycystic renal disease associated with an abscess is a difficult clinical problem. By looking at the CT image, one cannot distinguish an infected cyst from the multitude of other cysts within the kidney. In such cases, a gallium scan is helpful in finding an infected cyst among the other cysts of fluid density.

Perirenal Space Abscesses

Abscesses of the perirenal space, confined by the renal fascia, are usually caused by spread of renal infection. The most common infecting organisms are *E. coli, E. aerogenes,* and *P. mirabilis.*

The cross-sectional CT findings of a perirenal abscess are an area of fluid density surrounding the kidneys, bounded by the renal fascia (Figs. 42–49 and 42–50). In all cases, there is concomitant thickening of the renal fascia (Fig. 42–51). The partial-volume effect associated with the right kidney and medial margin of the liver should not be mistaken for a perirenal collection.

Other Considerations

One of the greatest advantages of CT is its ability to image all areas completely. This accurate localization is especially important for the preoperative evaluation of ab-

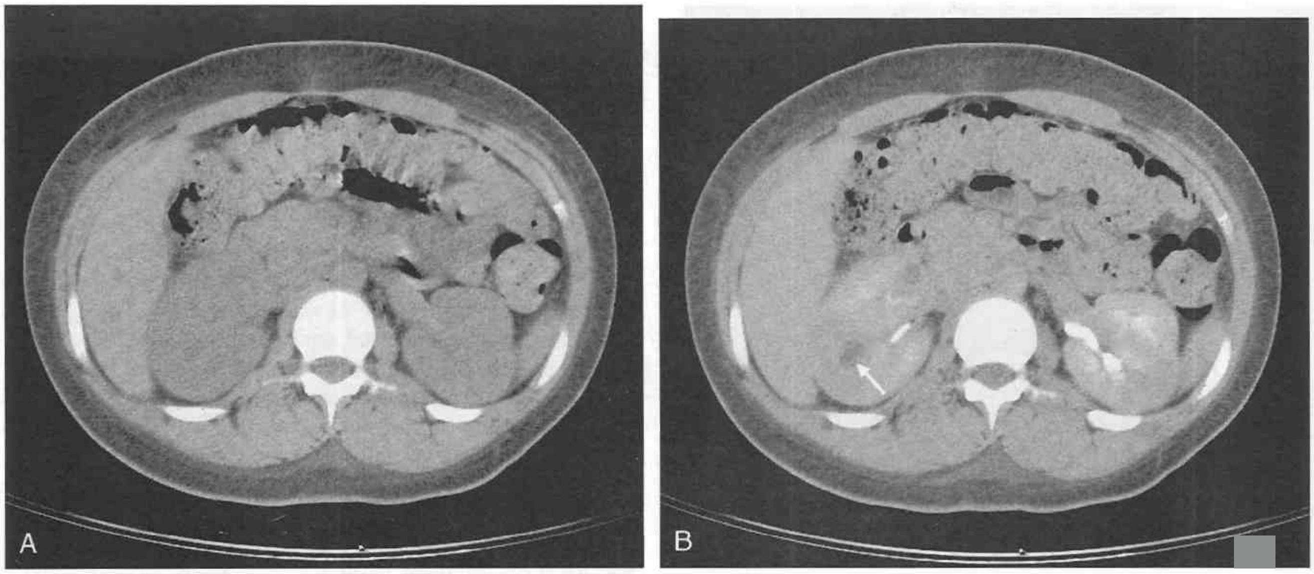

Figure 42–48. Abscess. The importance of administering IV contrast material. *A,* Before administration of contrast material, the CT scan shows no visible abnormality. *B,* After administration of intravenous contrast material, the CT scan shows enhancement of the renal parenchyma, but the abscess exhibits very low density and a clearly defined margin *(arrow).*

scesses to facilitate their drainage. With CT, it is possible to determine the full extent of an inflammatory process and to detect multiple concurrent abscesses. This latter point is especially important because one must always be concerned about the occurrence of multiple, concurrent abscesses. This information is especially important in regard to patients who are to undergo surgical procedures, but it is absolutely critical if percutaneous drainage is considered.[24, 29–32] For accurate localization of abscesses before percutaneous drainage procedures, the consensus in the literature is that CT is superior to other imaging systems and is the modality of choice.[59] Given equal availability of the instrumentation, CT should be used as the initial diagnostic modality when percutaneous aspiration drainage of an intra-abdominal abscess is anticipated.

Finally, another important advantage of CT is its ability to determine the initiating cause of abscesses. Entities such as appendicitis, diverticulitis, cholecystitis, and penetrating ulcers can sometimes be suspected or recognized. With appendicitis, the diagnosis is suggested by a fluid collection

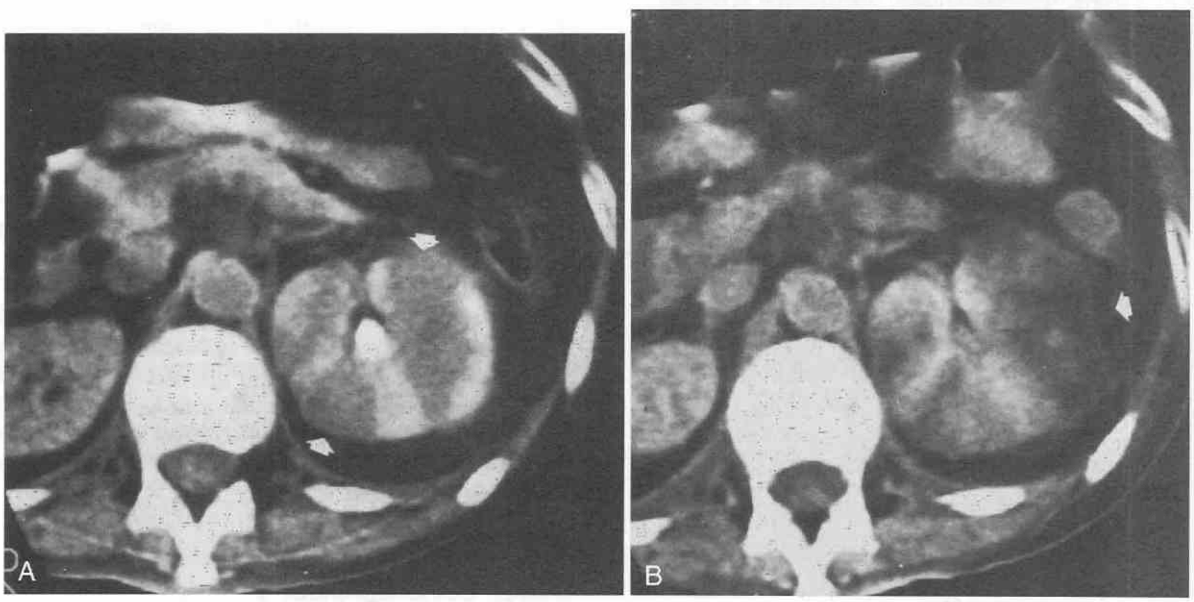

Figure 42–49. Progression of multifocal bacterial nephritis to a frank abscess. *A,* Post–contrast-enhanced image of the kidney demonstrates the typical defects of multifocal bacterial nephritis *(arrows).* Pre–contrast-enhanced images were normal. *B,* Post–contrast-enhanced image 1 week later demonstrates more severe changes of bacterial nephritis and liquefaction *(arrow),* with extension beyond the renal capsule. Surgery revealed an abscess in a "dead" kidney.

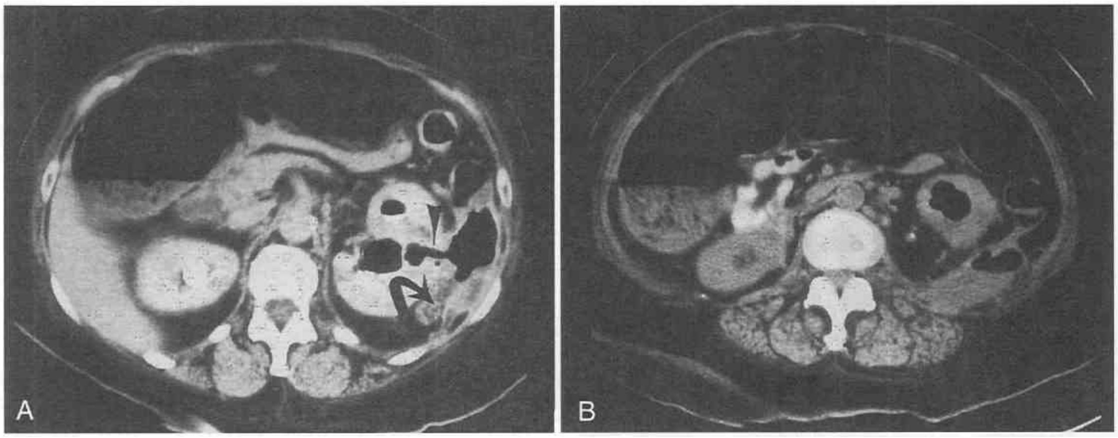

Figure 42–50. Emphysematous pyelonephritis. *A,* CT scan showing fistula *(arrowhead)* from the colon into the left kidney. Note the abscess extension *(curved arrow)* into the posterior pararenal space. *B,* This lower scan shows air within the left kidney and the air-fluid level in the pararenal space *(arrow).*

adjacent to the cecum or edema in the retroperitoneal fascia. With diverticulitis, the air-filled diverticuli adjacent to the abscess, which is of fluid density, can be recognized. Penetrating ulcers cannot be seen, but because of gas adjacent to the duodenum or in the omental bursa, the diagnosis should be suspected. In other cases, CT may not provide enough information, and other radiologic procedures or investigations are needed.

Mycotic Aneurysms

Mycotic aneurysms of native vessels are a rare event. It is believed that such infection must be superimposed on a diseased vessel and that it occurs as a result of hematogenous or direct spread. In cases of non–gas-forming organisms, there may only be a fluid collection in direct proximity to the vessel. In patients with a gas-forming infection, small bubbles of gas can be seen.

Infected Synthetic Grafts

Infection of synthetic grafts is a disastrous complication of vascular reconstructive surgery. The incidence of graft infections is as high as 6%, and they are associated with a high rate of morbidity and mortality. The potential causes of the infection are contamination, small GI fistulas, or hematogenous seeding. Gram-positive organisms that can cause infection of grafts include *Staphylococcus epidermidis,* other *Staphylococcus* species, and *Streptococcus faecalis.* The gram-negative organisms commonly encountered in such graft infections include *E. coli* (the most common) and *Klebsiella, Enterobacter, Proteus, Pseudomonas,* and *Bacteroides.* Before CT, the diagnosis of graft infection depended on such standard radiographic techniques as GI studies or angiography. By the time such studies revealed the infection, however, the patient was often beyond the point of cure, even with proper surgical therapy. With CT, it is now possible to detect accurately fluid and gas collections that may indicate infection in and around synthetic grafts (Fig. 42–52).

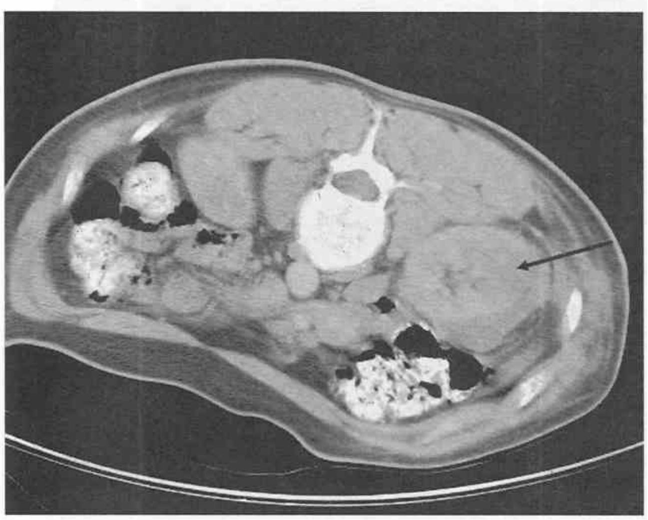

Figure 42–51. Perinephric abscess *(arrow),* contiguous with the renal parenchyma.

The typical findings of infected aortic grafts depend on the type of organism involved. Gram-positive cocci that do not produce gas produce a fluid collection in the aneurysm bed or adjacent to the graft itself (Fig. 42–53*A* and *B*). When the infecting organism is gas forming, such as *E. coli,* or there is a small enteric fistula (Fig. 42–54), there are small microbubbles of gas in and around the graft. Several possible causes of false-positive findings exist in such cases. If a significant amount of blood or old hematoma is around the graft in the aneurysm, it too appears to be an area of fluid density. Normal postoperative gas may also be present within the aneurysm bed adjacent to the graft 7 to 10 days after surgery.[94]

Because of the high mortality rate associated with this disease, radiologists have now adopted an aggressive approach for confirming the presence or absence of infection. In any case of a possible infected aortic graft, we now think that a CT-guided aspiration through the retroperitoneum is imperative to obtain a culture of the material around the aneurysm directly and determine whether infection is present (see Fig. 42–53*B* and *C*). This is important because in infected patients, expeditious surgical treatment consisting of removal of the graft and an axillofemoral bypass is typically performed. When aspiration results are normal, an extensive, complicated, and difficult surgical procedure

Figure 42–52. CT scan shows a fluid colle[redacted] containing gas bubbles *(arrows)*, adjacent to the area of the aortic bifurcation.

may be avoided. With the improved diagnostic accuracy of CT and the more potent antibiotics, some surgeons are now deferring surgery if the infectious area is not adjacent to the anatomic site. Advances with urokinase enhancement of percutaneous drainage may improve the outcome of percutaneous treatment in such cases.[57, 88]

Accuracy in Relation to Other Modalities

Since the introduction of CT, several authors have discussed its usefulness for detecting abscesses. The first article by our group[31] reported a correct diagnosis for 20 of 22 abscesses. Since this first report, numerous others (including Callen,[15] Gerzof et al,[23] Aronberg et al,[6] Korobkin et al,[56] Levitt et al,[62] Wolverson et al,[117] and Knochel et al,[55]) have confirmed the high detection rate of CT for abscesses. Data are sparse, but some comparative information is available about other imaging systems, such as ultrasound and gallium 67 citrate. In our initial report, CT was correct for 20 of 22 abscesses, gallium was correct in six of nine abscesses, and ultrasound was correct in one of two abscesses. Korobkin and colleagues[56] reported CT correct in 9 of 9 abscesses, gallium in 9 of 12, and ultrasound in 12 of 12. Levitt and coworkers[62] found CT to be correct in six of six abscesses and gallium correct in nine of nine.

More recently, Knochel and colleagues[55] presented larger numbers of cases with which to compare CT and

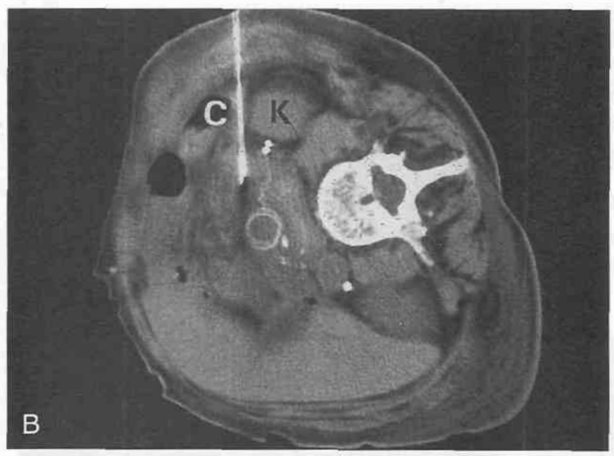

Figure 42–53. Suspected graft infection. *A,* CT scan of a patient in the decubitus position before needle procedure. There is a large amount of fluid and old blood in front of and behind the prosthetic graft (A). *B,* To separate cultures and prevent cross-contamination, separate aspirations from the anterior and posterior areas were taken. The needle is carefully guided between the colon (C) and kidney (K) to ensure sterility. The "double" appearance of the needle is the result of motion. *C,* A more posterior approach was taken for the aspiration of the posterior fluid collection. A trajectory was planned through the psoas muscle to prevent any possible contamination.

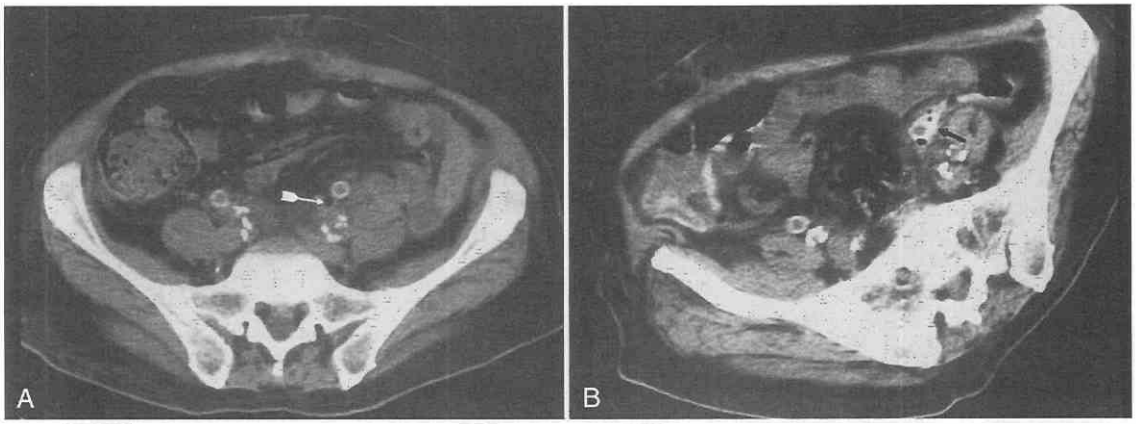

Figure 42–54. Infection caused by fistula. *A*, CT scan shows a small air collection *(arrow)* adjacent to the left iliac limb of a prosthetic graft. *B*, Communication with the colon is verified by leakage of contrast material *(arrow)* from the bowel to the graft.

ultrasound, but they did not include gallium isotope scanning. In their series, CT was the most accurate modality, with a sensitivity rate of 97.5% and a specificity rate of 95%, whereas ultrasound had a sensitivity rate of 82% and a specificity rate of 94.5%.

In the literature and at meetings, there is always a controversial debate about whether the use of CT is justified when ultrasound is also good and only 10% to 13% less accurate. Proponents of ultrasound argue that it is less expensive and does not use radiation. CT advocates point out that abscesses are curable, and therefore the 10% increased accuracy is worth the additional expense and radiation.

I have formulated an approach to these modalities on the basis of several principles. According to the guideline about medical decision making set by McNeil and colleagues,[76] any false-negative results must be minimized with a curable disease, and therefore significant costs and efforts to find and treat such a disease are justifiable. With this reasoning, I can rationalize using CT for all patients. Realistically, however, a CT device is a limited resource; thus one must maximize the diagnostic return and not overuse it improperly. I believe that CT, ultrasound, and gallium scanning are complementary, in that the patient can best be cared for by taking into account the advantages and disadvantages of each modality. An acutely ill patient does not have the luxury of waiting hours or even days for the results of an isotope test.[72]

Therefore, I prefer using an immediate imaging system, such as CT or ultrasound. Considering the various anatomic areas within the abdomen and technical considerations of each modality, the best-suited method for each case can be selected. Thus, if the patient is acutely ill and has focal symptoms in the right upper quadrant, retroperitoneum, or pelvis, ultrasound should be the modality of choice. If the ultrasound results are normal in these areas and the patient is toxic, examination with CT is appropriate. If the patient has focal symptoms in the left upper quadrant, pancreatic area of midabdomen, CT is the preferred modality. If the patient is acutely ill or immunocompromised with general symptoms and no focal signs, CT is the modality of choice because it can evaluate all areas without difficulty.

Finally, if the acutely ill patient has drains, wounds, or external appliances, CT is better suited immediately after surgery because it does not require a coupling agent to the skin. If the patient is chronically ill, a gallium scan should be performed to locate the potential area of infection. Depending on the region of uptake, one should use ultrasound (in the right upper quadrant, pelvis, and flank) or CT (in the left upper quadrant, pancreas, and abdomen).

Peritoneal and Mesenteric Abnormalities

Only a limited number of benign and malignant tumors affect the mesentery and peritoneum. The most common of these abnormalities are neoplastic diseases, but less commonly benign abnormalities of the mesentery can be seen.

Peritoneal Cysts

Peritoneal cysts are unusual cystic masses that may be attached to the mesentery or peritoneum. The origin of these abnormalities is poorly understood, but some believe they are related to lymphatic abnormalities that produce sequestered secondary cysts. They are typically lined with endothelium. The cysts may be unilocular or multilocular. Clinically, they produce the same symptoms as an abdominal mass; surgical treatment is curative.

On CT images, these cysts appear as large, low-density masses with clearly demarcated fibroconnective tissue walls (Fig. 42–55). No unique imaging features distinguish these cysts from other low-density masses, such as mucinous metastases, abscesses, or hematomas. In such cases, the clinical history is important, and if indicated, a percutaneous puncture for cytologic or bacteriologic study can be performed.

The differential diagnosis of peritoneal cysts includes lymphangioma, nonpancreatic pseudocysts, enteric cysts, duplication cysts, and cystic mesotheliomas. According to Ros and coworkers,[95] differentiation among these entities is not possible using current imaging techniques.

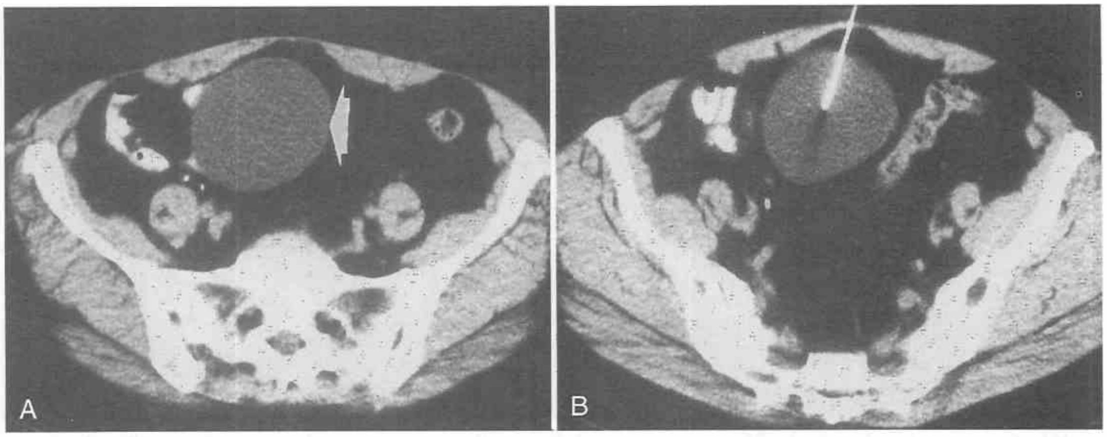

Figure 42–55. Mesenteric cyst. *A,* CT scan shows a mass *(arrow)* [redacted] proved to be a mesenteric cyst. *B,* CT-guided procedure proved the true nature of the mass. The trajectory chosen avoids any loops of bowel, thereby preventing the possibility of contamination.

Desmoid Fibromas

Desmoid fibromas are unencapsulated infiltrating fibromas occurring predominantly in women and in any part of the body, including the abdomen.[69] There is a high association of fibromas of the abdominal wall and peritoneum with familial polyposis syndrome,[75] and fibromas are one of the classic signs of Gardner's syndrome. In one series of 44 intra-abdominal desmoid fibromas, 41 occurred within the mesentery.[75] The main clinical problem that arises with such desmoid fibromas is distinguishing these tumors from neoplastic masses resulting from colonic carcinoma. Pathologically, the tumor is benign but difficult to distinguish from a low-grade fibrosarcoma; however, there have been no reported metastases. Occasionally, the lesion may cavitate and enlarge quickly by the imbibition of fluid. The treatment is surgical excision, but unless complete and meticulous resection is performed, recurrence is the rule.

On a CT scan, a desmoid fibroma appears as a mass of soft tissue density within the peritoneum, displacing other intra-abdominal organs (Fig. 42–56). No unique imaging traits distinguish these fibromas from neoplastic masses, such as lymphomas and metastatic disease, or even from other benign masses, hematomas, or high-density peritoneal cysts (Fig. 42–57).

Retractile Mesenteritis

Retractile mesenteritis is an unusual disorder of the mesentery consisting of diffuse inflammatory thickening of the mesenteric fat.[18, 54] The cause of the abnormality is unknown. Pathologically, there is fibrosis, inflammation, and fatty infiltration. *Retractile mesenteritis* is the term used when fibrosis predominates. The process originates in the root of the mesentery and then can extend diffusely throughout the mesenteric fat. The disease process is confined to the mesentery, and there are no abnormalities of the intestines or vessels.[54]

On CT scans, the mesentery does not appear to be of normal fat density but appears as an area of soft tissue density (Fig. 42–58). The bowel is not in its normal anterior location but is retracted posteriorly. One group[26] reports calcifications in some unusual cases of retractile mesenteritis and some resolution of the mesenteritis after treatment with steroids. In unusual cases, narrowing and rigidity of

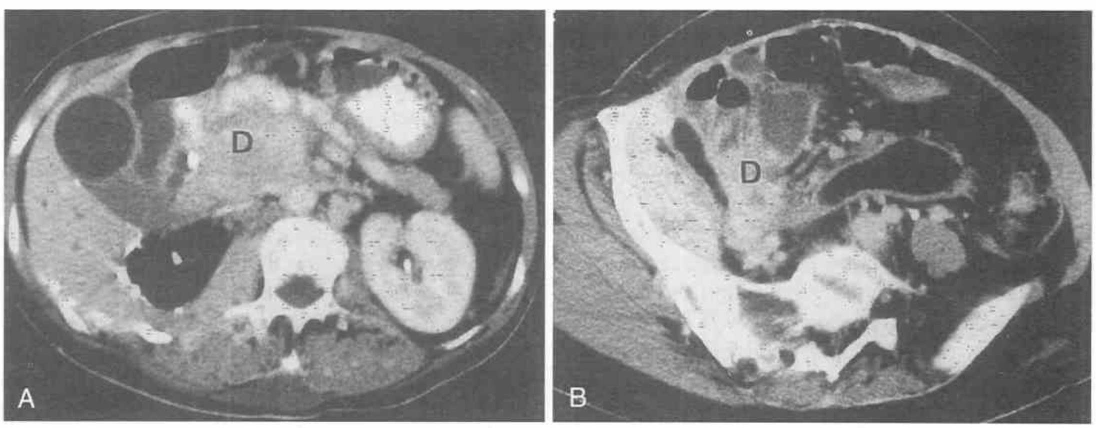

Figure 42–56. *A,* Desmoid fibroma ([redacted]nvolving the pancreas, which simu[redacted]s a n[redacted]asti[redacted] Infiltration into the biliary system and portal hepatis is occurring and pr[redacted]cing benign, aggressive extension [redacted] al[redacted] "[redacted]" properties. *B,* Lower scan taken through the pelvis shows an ill-defined mass behind the cecum and adjacent to the psoas.

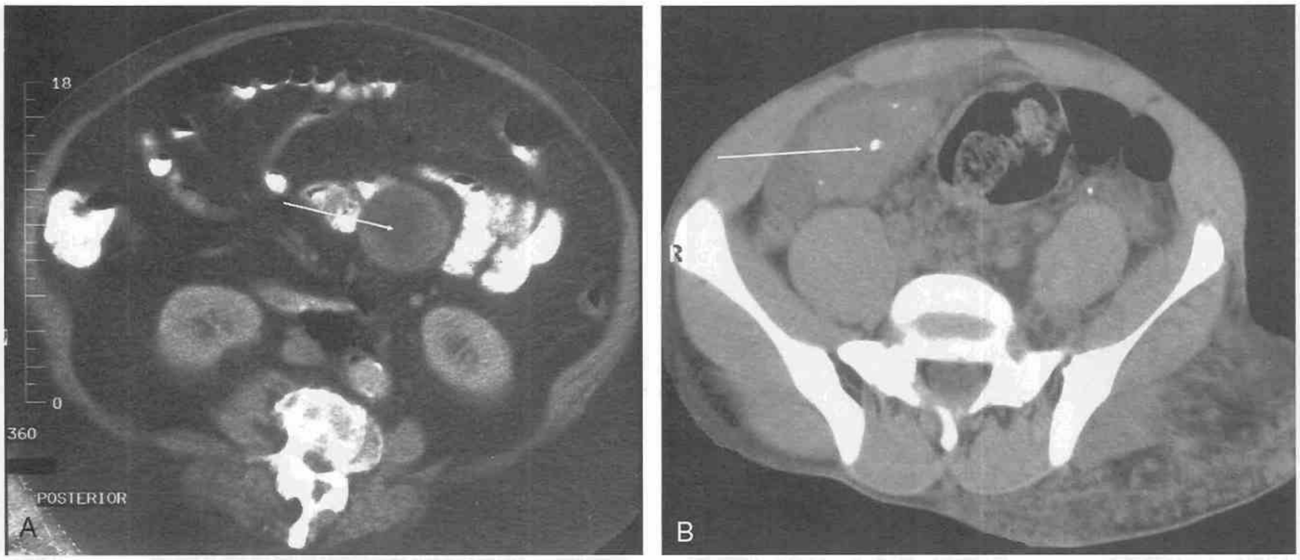

Figure 42–57. *A,* A number of mesenchymal tumors have a soft tissue density appearance that is nonspecific. This scan shows a leiomyoma of small bowel *(arrow),* which is exophytic. *B,* Hemangiomatous mass in mesentery has well-defined margins with some calcification *(arrow).*

the colon with thumbprinting or displacement of bowel by mesenteric masses may be seen.[106] Han and coworkers[34] reported a case involving the colon that produced transmural thickening of the colon.

With extensive metastatic disease to the peritoneum and mesentery, findings may simulate retractile mesenteritis (Fig. 42–59). In such cases, tumor implants in the mesentery produce increased density and may also restrict movement of bowel as visualized with ascites.

Inflammatory Processes

A number of inflammatory processes associated with the bowel, peritoneum, and mesentery produce certain predictable changes on CT scan. The findings of edema, bowel wall thickening, fluid distention, and fibrosis are nonspecific.

Crohn's disease causes transmural inflammation of the bowel, which produces fairly typical findings. Characteristically, thickening of the bowel wall associated with soft tissue density, edema, and fibrous reaction is seen. On occasion, an increased amount of fat separating several loops of bowel is seen; it has been said that this represents proliferation of fat, but the cause of such fat accumulation is not known.

Ulcerative colitis produces only thickening of the bowel wall without producing changes within the mesentery. Dilatation of the colon and some loss of the haustral markings can also be seen.

Pseudomembranous colitis produces thickening of the colonic wall and changes in the lateroconal fascia and the perirenal fascia. The entire colon usually is involved, but there may also be segmental involvement.

Diverticulitis consistently shows changes recognizable on the CT scan.[44, 66] First, small air pockets that represent air-filled diverticuli are seen on the wall of the colon. Inflammation from the diverticulitis produces edema in the fat adjacent to the bowel.

Appendicitis produces edema and inflammation adjacent to the end of the cecum. The normal appendix can be located in the peritoneum, pelvis, or retrocecal region. With inflammation, there is edema and thickening of the adjacent fascial planes.

Whipple's Disease

A single report exists in the literature about Whipple's disease of the small bowel.[64] Clinically the disease is associated with abdominal pain, malabsorption, and diarrhea. Some arthralgias may also be associated. In a report by Li and Rennie,[64] the specific diagnostic points included enlarged lymph nodes in the 2- to 3-cm range in the mesentery and retroperitoneum. In addition, abnormal changes in the small bowel pattern similar to the findings noted on traditional barium studies were noted. The lymph nodes were low in density because of fat content. Some had necrosis within the center (see Chapter 35).

Amyloidosis

Systemic amyloidosis consists of systemic deposition of amyloid throughout organs and tissues. GI involvement is said to occur in 70% of patients with primary and 55.5% with secondary amyloidosis.[2]

A single report exists in the literature about the findings of secondary amyloidosis of the mesentery. In the case reported by Allen and colleagues,[2] there was diffuse thickening of the mesentery and encasement of the mesenteric vessels, resulting in the appearance of diffuse carcinomatosis. Diagnosis can be established only by biopsy (see Chapter 35).

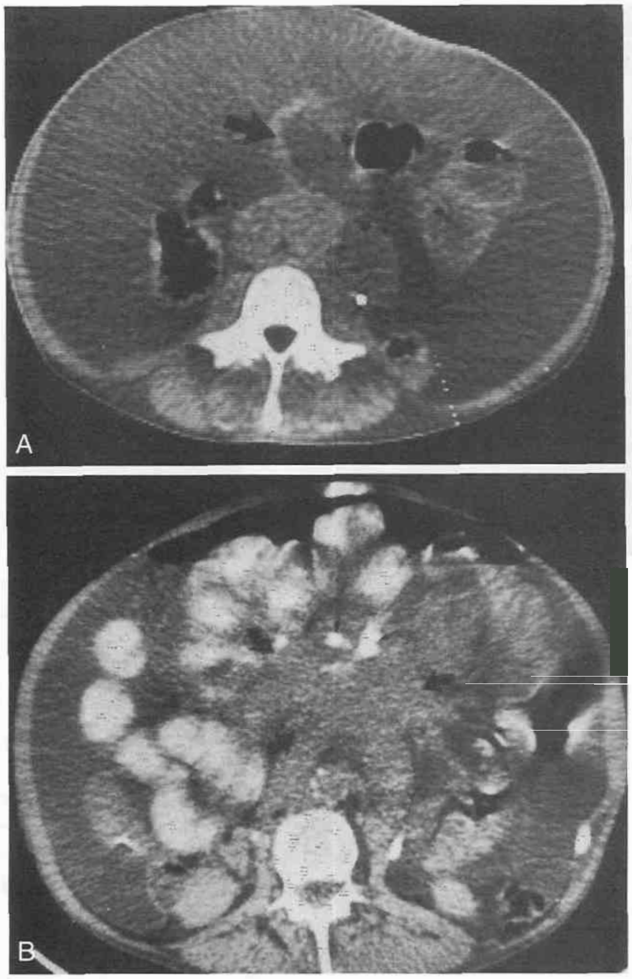

Figure 42–58. *A,* Retractile mesenteritis produces a thickening of the mesentery *(arrow),* which may retract loops of the bowel posteriorly. (Compare the posterior location of these bowel loops with those pictured in Fig. 42–63*C*.) *B,* A mass *(curved arrows)* with calcifications *(small arrows)* caused by retractile mesenteritis. (*B,* courtesy Dr. Richard Palmer Gold, Columbia-Presbyterian Medical Center, New York.)

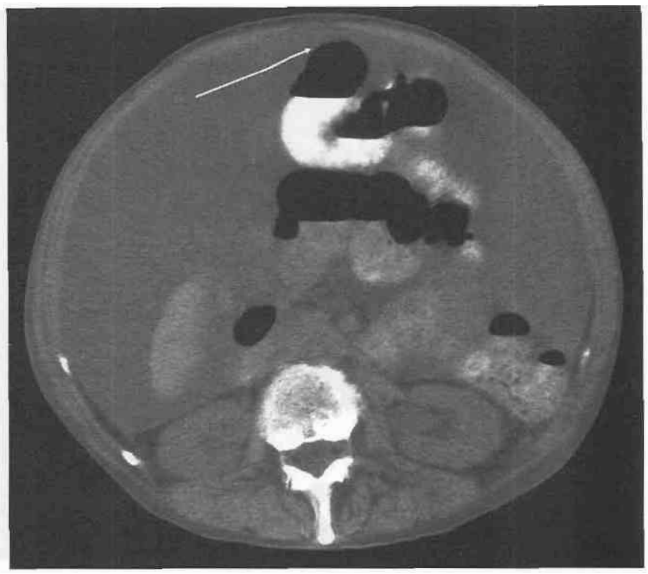

Figure 42–59. Diffuse metastatic disease to the peritoneum may produce thickening of the mesentery that produces changes similar to those of retractile mesenteritis. This CT scan of a patient with metastases to the mesentery shows increased density to the mesentery with retraction of the bowel so that the loops do not float against the anterior peritoneum *(arrow).*

AIDS

AIDS is becoming more significant because of its almost uncontrolled spread among certain risk groups.[13, 48] It is caused by the human immunodeficiency virus (HIV). Identified risk factors include homosexuality, IV drug abuse, and heterosexual exposure to prostitution.

These patients are at great risk for development of any infectious process, including many opportunistic infections. In addition, they are predisposed to the development of a number of malignancies, including Kaposi's sarcoma and a severe form of large cell lymphoma.

Jeffrey and coworkers[48] wrote an excellent article about AIDS within the abdomen. A review of this article is highly recommended for more specific details.

AIDS-related complex (ARC) is a constellation of symptoms and signs that predate the development of AIDS. Symptoms include fever, weight loss, diarrhea, malaise, and night sweats. There is associated lymphadenopathy in the mesentery and retroperitoneum secondary to reactive lymphoid hyperplasia. The triad of CT findings previously reported for this entity are lymphadenopathy, splenomegaly, and perirectal thickening (presumably owing to venereal infection). The lymph nodes in this state are seldom larger than 1.5 cm in diameter; any enlargement beyond this should suggest neoplasm or infection and probably warrants a CT-guided biopsy.

Opportunistic infections with AIDS are common and can consist of many forms, including *Candida* esophagitis and small bowel or colon infection with *Cryptosporidium,* cytomegalovirus, herpes simplex, or *Mycobacterium avium–intracellulare.* These problems cause nonspecific changes in those portions of the gastrointestinal tract. Both tuberculosis and *M. avium–intracellulare* can produce enlargement of mesenteric and retroperitoneal lymph nodes.[84, 108]

The two most common malignancies associated with AIDS include Kaposi's sarcoma and non-Hodgkin's lymphoma. Kaposi's sarcoma can show lymphadenopathy or GI involvement in the form of wall thickening. It may involve virtually any abdominal organ and may produce many unusual intra-abdominal lesions, which may be easily amenable to CT procedures.

The lymphoma associated with AIDS usually is a non-Hodgkin's type (Hodgkin's disease occasionally occurs), which typically has an increased incidence of extranodal involvement. Sites of occurrence may include brain, bone marrow, viscera, and mucocutaneous sites. The lymphoma is especially aggressive, and response to treatment has been generally poor.

Neoplastic Lesions

Peritoneal Mesotheliomas

Peritoneal mesothelioma is a rare neoplasm arising in the peritoneal lining of the abdomen. The disease is be-

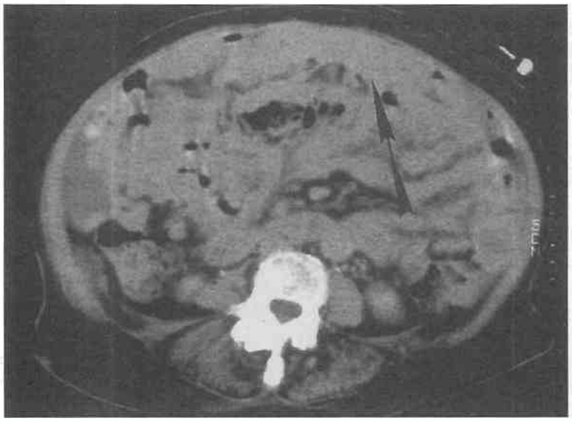

Figure 42–60. Extensive soft tissue thickening in the anterior abdomen produced by mesothelioma *(arrow)*. The tumor is infiltrating throughout the mesentery in an irregular pattern.

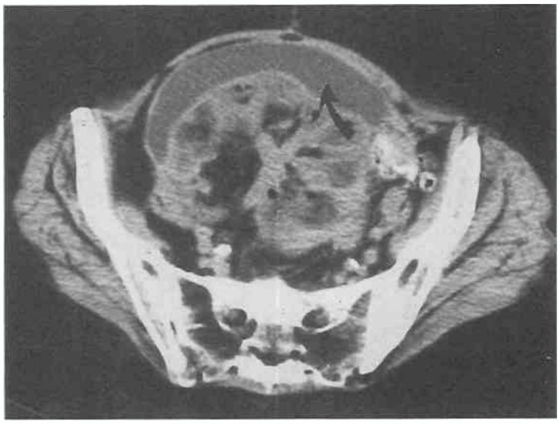

Figure 42–61. CT scan of a patient with primary papillary carcinoma of the peritoneum. There is a fluid density anteriorly *(arrow)*, which represents a neoplastic loculation.

lieved to be associated with exposure to asbestos. Pathologically, it occurs in several forms: sarcoma, polygonal cell type, and tubular papillary type. All types have a uniformly poor prognosis, and most patients die within 2 years of the diagnosis. In my experience, the appearance of the tumor coincided with the timing reported in the literature.

On CT examination, (Fig. 42–60)[17] the tumor appears as an area of soft tissue density within the abdomen. It may conform to the contour of the liver or produce a mass effect on adjacent structures. No features distinguish it clearly from other types of benign or malignant tumor with a benign fibrotic reaction. A number of authors have recommended signs for suggesting the diagnosis of mesothelioma.[10, 85, 115, 118]

Primary Papillary Tumors of the Peritoneum

Since 1976, primary papillary tumor of the peritoneum has been recognized as a separate entity, although for a time, it was thought to be related to either mesothelioma or ovarian tumors.[51, 90]

The tumor is thought to originate from mesothelial cells of the peritoneum, which are somewhat similar to ovarian cells. Clinical presentation of the patients is related to the involvement of multiple areas of the peritoneum. It is not possible to distinguish a metastatic focus from a localized origination point; the possibility of multicentric origin has been suggested.[51] The disease in patients having these tumors is consistently more extensive than in patients of the same age who have ovarian tumors.

Treatment of the disease is similar to that of disseminated ovarian tumor. The outcome has not been good.

CT findings of this disease are nonspecific. Scans may show a discrete tumor mass over the peritoneum or simply collections of loculated fluid (Fig. 42–61).

Lymphomas

According to Goffinet and colleagues,[25] 61% of the non-Hodgkin's lymphomas involve the mesentery, whereas only 5% of Hodgkin's lymphomas do so. When involved, the mesentery contains a mass of soft tissue density, which may extend from the bowel loops to the root of the mesentery and the retroperitoneum (Fig. 42–62). The normal mesenteric vessels are not clearly seen in such cases. In other cases, there may be localized masses within the mesentery adjacent to loops of bowel. To diagnose small mass lesions, it is important to attempt total opacification of the bowel loops with either iodine or dilute barium solution. Even if this opacification is not total, such lesions can be distinguished in a normal bowel by a sufficiently characteristic appearance with fluid and gas.

After treatment, the tumors shrink gradually, but they may leave residual fibrous tissue. Such tissue may be prominent but should not be confused for active tumor. Treatment of such masses is usually continued until no interval shrinkage occurs in the mass.

Primary Mesenchymal Tumors

A variety of tumors that have no specific traits, except liposarcoma, originate from mesenchymal origin. Virtually

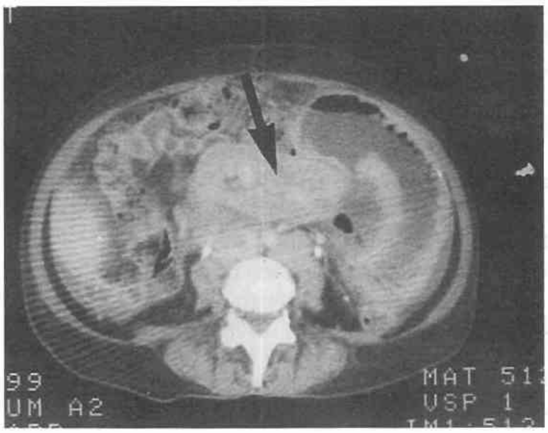

Figure 42–62. Lymphoma. CT scan shows a large soft tissue mass *(arrow)* in the root of the mesentery. The tumor extends to the wall of the small bowel, which is quite thick. Even when the bowel is distended, the mucosal markings can be seen.

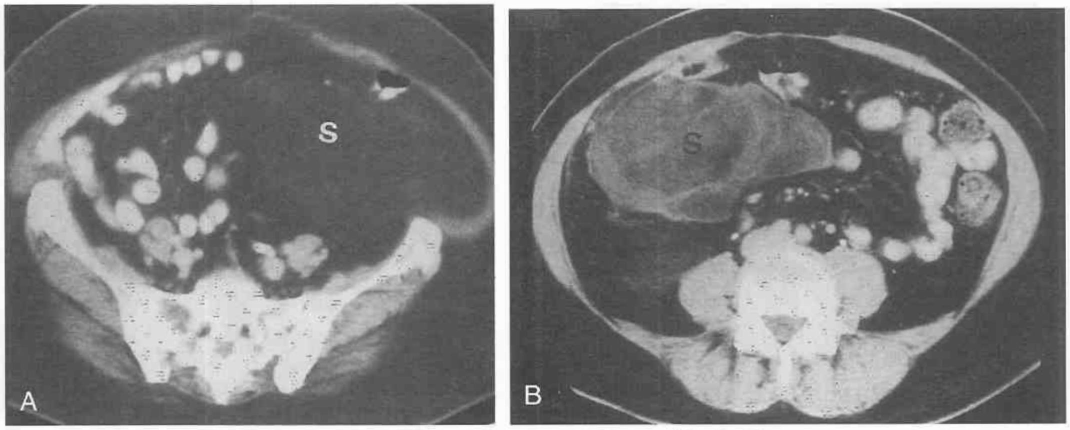

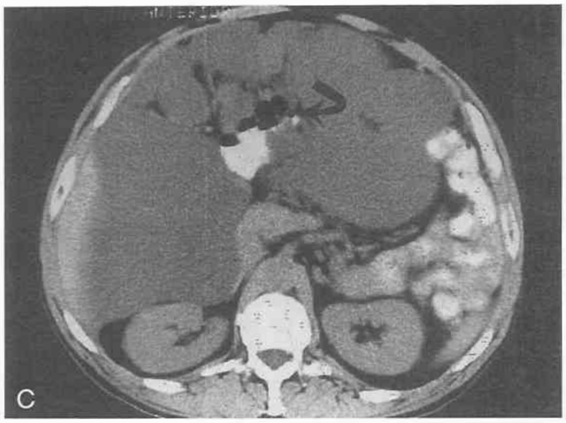

Figure 42–63. Liposarcoma varies in its density depending on the degree of differentiation. Mesenchymal tumors may have a variable appearance, but liposarcomas are somewhat typical, as can be seen in the following scans. *A,* The well-differentiated liposarcomas (S) appear low in density, as does normal mesenteric fat. *B,* This scan shows a well-defined, higher-density tumor (S) that has an intermediate differentiation. *C,* This scan shows a poorly differentiated liposarcoma, with myxoid changes. It is producing a pseudomyxomatous invasion of the peritoneum. The loops of the small bowel *(curved arrow)* are compressed centrally by the low-density tumor, which appears almost like fluid. The bowel does not float as with normal ascites. The contrast-filled small bowel is compressed posteriorly on the left.

all such tumors show soft tissue density without any distinguishing features. Well-differentiated liposarcoma can show a fat density that is indistinguishable from normal fat (Fig. 42–63), whereas poorly differentiated tumors are slightly higher in density.

Metastatic Disease

Metastatic involvement of the omentum and mesentery is quite common with neoplasms,[12] the most common being from the ovary, stomach, pancreas, and colon.[47] Spread within the peritoneum can be along the surface of the peritoneum or within the ligaments (areolar tissue surrounded by peritoneum), which contain the lymph nodes draining a specific area. Lymphatic spread can occur along the neurovascular muscular bundles within the intermesenteric space. When fibrosis is associated with the lesions, there may be retraction in the mesentery.

When metastatic lesions are on the peritoneal surface, several findings may be noted. First, if they are large enough, they may be seen as discrete nodular lesions (Figs. 42–64 to 42–66). If the tumor is of mucinous origin, such as ovary or colon, it may show soft tissue or fluid density. When the sizes of the lesions are below the resolving power of CT, collections of fluid indistinguishable from any other fluid may be produced. The metastatic sites of the ovarian tumor can be completely fluid in appearance.[77] In such cases, the tumors may have the appearance of

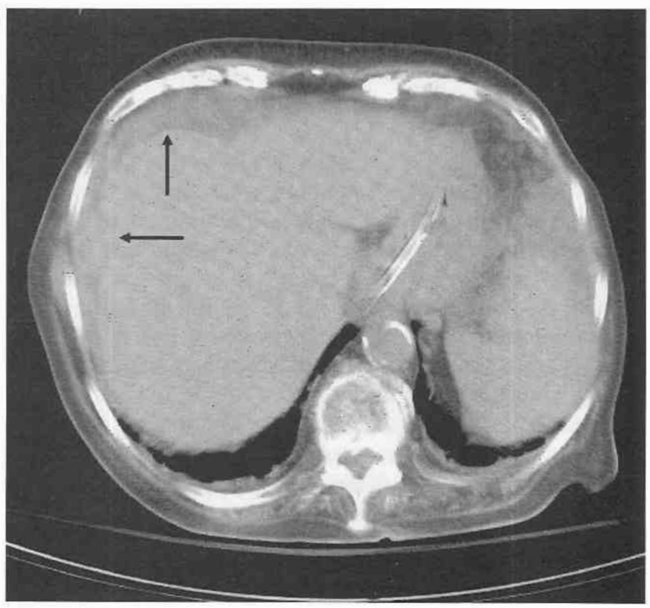

Figure 42–64. Peritoneal tumor implants are more likely to occur along the undersurface of the diaphragm because of the anatomic structure of the peritoneum. CT scan shows small tumor implants *(arrows)* on the undersurface of the diaphragm.

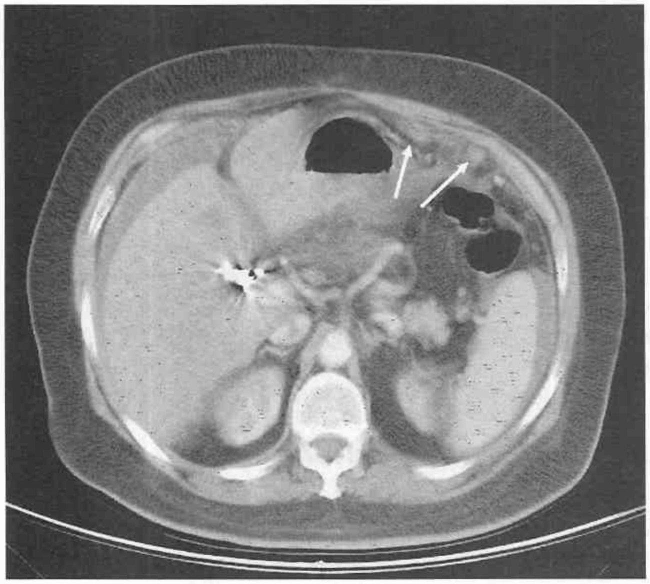

Figure 42–65. Small tumor implants *(arrows)* are noted under the anterior surface of the left diaphragm. Without fluid loculation, they are more difficult to appreciate.

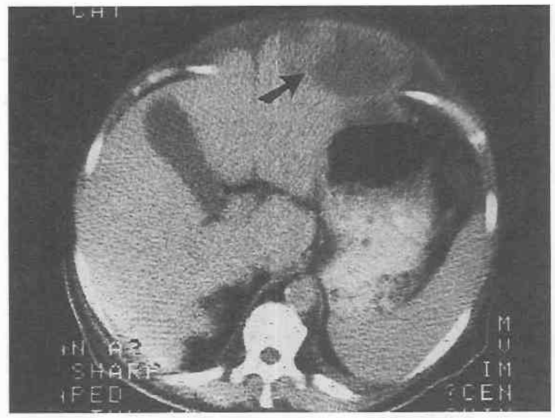

Figure 42–67. Certain tumors, such as ovary and stomach, are thought to have a propensity for the falciform ligament *(arrow).*

subcapsular collections or they may implant on specific ligaments such as the falciform ligament (Fig. 42–67).

Regardless of size, mucinous or other treated tumors can produce small calcifications throughout the peritoneum.[87] Mitchell and colleagues[82] reported a series of 15 patients with carcinoma of the ovary and found calcifications in six peritoneal sites of implant, perihepatic calcifications in five sites, and lymph node calcifications in one (Fig. 42–68).

Making the diagnosis of a peritoneal metastasis can be difficult at times if the mass is not big enough to cause displacement of the bowel and if total opacification of the bowel has not been achieved.[112] The normal bowel, however, does have a characteristic appearance that shows small amounts of fluid and gas in a diffuse pattern. Sometimes, even after administration of contrast material, there may be a problem distinguishing an adynamic loop of bowel from a mass. In such cases, IV administration of contrast material may be helpful because the wall of the bowel enhances well, or placing the patient in a decubitus position permits moving "gas" to reveal the true nature of a loop of bowel.

Omental Changes

The thickened omentum produced by "caking" appears as a large soft tissue mass with poorly defined edges. The fat plane between the anterior abdominal wall and the intestinal loops may be obscured. When the omentum (which shows fat density) is not thick, soft tissue masses within or on it may be seen.

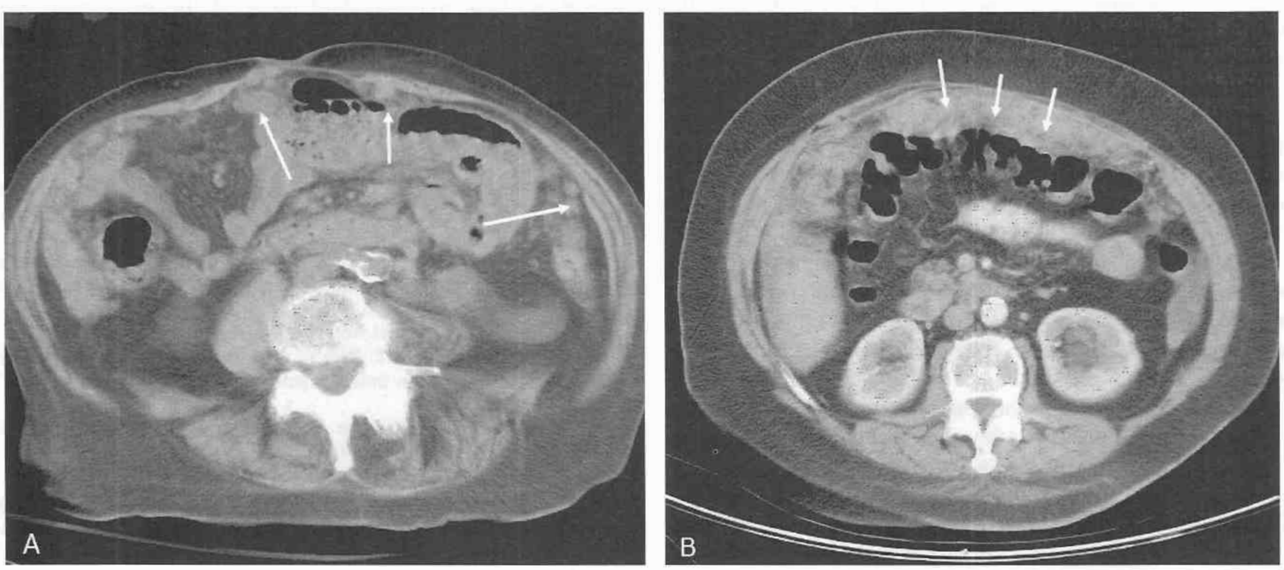

Figure 42–66. Omental metastases. *A,* Early tumor implantation on the omentum produces small masses *(arrows)* throughout the anterior peritoneum. *B,* More extensive tumor implantation produces a thick soft tissue density *(arrows),* displacing the colon from the anterior peritoneum.

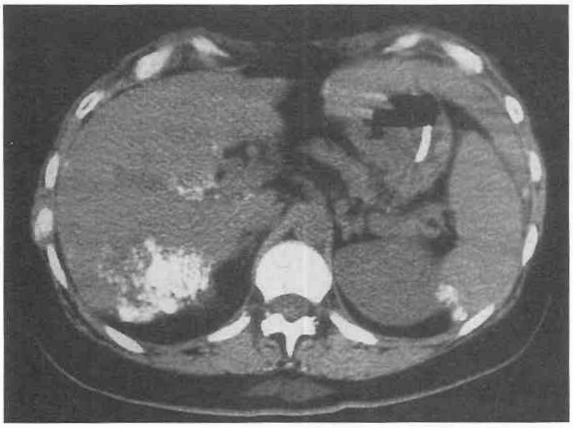

Figure 42–68. On occasion, mucinous or necrotic tumors contain dystrophic calcifications. Note the high-density material on the posterior right hepatic lobe, porta hepatis, and posterior spleen.

Sites of Implants

It has been suggested that the ligaments at the reflection of the sigmoid colon, the ileocolic region, and broad ligaments are the first location of implantation with malignancy.[79, 103, 114] Data have shown, however, that for the earliest detection of peritoneal seeding (at least with ovarian neoplasms), biopsy of the diaphragmatic areas is more likely to show early peritoneal involvement.[27] This is presumably a result of the circulation of peritoneal fluid. Common metastases of ovarian or gastric cancers to the falciform ligament may also be a result of this normal upward flow toward the diaphragm.

General Diagnostic Signs

Whitley[115] has evaluated a group of 370 patients who had mesenteric tumors and recommended some diagnostic signs that are helpful in approaching mesenteric disease. The following diagnostic signs characterize the lesions according to their appearance: rounded, ill-defined, cakelike, and stellate.

Rounded masses were caused by non-Hodgkin's disease in 33 of 41 cases, leukemia in 2 of 26 cases, and ovarian tumor in 3 of 38 cases. Whitley also noted a 30% occurrence in the nodes of the small bowel mesentery.[115] Other authors have noted an overall occurrence of 50% if nodes at the root of the mesentery are included.

Ill-defined masses, the next most common type of involvement, occurred in 27 patients. Of this group, the non-Hodgkin's and ovarian carcinomas were the most common type of involvement, followed by colon, pancreas, stomach, and other masses.

Cakelike masses of the mesentery occurred with ovarian tumors, non-Hodgkin's lymphoma, and leukemia.

Stellate infiltration of the neurovascular bundles of the mesentery occurred with all types of metastatic disease except lymphomas and leukemia. The stellate pattern is produced by the infiltration along the inner margins of the mesentery.

Levitt and coworkers[61] reported the detection of metastases in 18 of 27 cases. They noted that CT did not show microscopic lesions, masses smaller than 1 cm, or omental metastases, such as pancreatic and gastric carcinomas that are immediately adjacent to primary masses.

An article by Goldhirsch and colleagues[27] indicates that CT was not as accurate as second-look surgical exploration. A positive CT scan is a useful guide for the surgeon, but a negative study does not obviate the need for a second-look surgical procedure.

Early authors used contrast peritoneography to demonstrate the normal peritoneal spaces.[93] More recently, workers have used positive contrast as a method of clearly defining small peritoneal implants especially close to the diaphragm.[107]

Pseudomyxoma Peritonei

Pseudomyxoma peritonei is a rare disease resulting from the diffuse dissemination of mucinous material derived from neoplasms. Typically, the neoplasms producing the peritoneal seeding are mucinous cystadenocarcinomas of either the ovary or the appendix, but it may occur unusually with tumors of the urachus, uterus, or omphalomesenteric duct. The disease is quite indolent, and massive deposition of material may occur before it is noticed. On CT scans, this seems to have two appearances.[71, 74, 77, 100, 113] It may appear as discrete, low-density cystic masses located in multiple anatomic spaces. In other cases, the peritoneum is completely filled and resembles ascitic fluid, sometimes producing mass effects on adjacent organs. Calcifications may occur following chemotherapy.[81]

Carcinoid Tumors

A carcinoid is a serotonin-producing tumor commonly involving the terminal ileum; it can produce changes within the mesentery, creating a desmoplastic fibrotic reaction. If the tumor is small or microscopic, no abnormality is seen on the scan. If a significant desmoplastic reaction occurs, however, there may be thickening of the mesentery with areas of soft tissue density. By the time the disease is first seen, there are liver metastases, which also may be an associated finding on CT scans.

References

1. Ahrenholz DH, Simmons RL: Fibrin in peritonitis: I. Beneficial and adverse effects of fibrin in experimental *E. coli* peritonitis. Surgery 88:41, 1980.
2. Allen HA 3rd, Vick CW, Messmer JM, Parker GA: Diffuse mesenteric amyloidosis: CT, sonographic, and pathologic findings. J Comput Assist Tomogr 9:196, 1985.
3. Allen L: The peritoneal stomata. Anat Rec 67:89, 1936.
4. Allen L, Weatherford T: Role of fenestrated basement membrane in lymphatic adsorption from the peritoneal cavity. Am J Physiol 197: 551, 1959.
5. Altemeier WA, Culbertson WR, Fullen WD, Shook CD: Intra-abdominal abscesses. Am J Surg 125:70, 1973.
6. Aronberg DJ, Stanley RG, Levitt RG, Sagel SS: Evaluation of abdominal abscess with computed tomography. J Comput Assist Tomogr 2:384, 1978.
7. Autio V: The spread of intraperitoneal infection. Acta Chir Scand 321 (suppl):1, 1964.
8. Balfe DM, Mauro MA, Koehler RE, et al: Radiology 150:485, 1984.
9. Balthazar EJ, Ranson JH, Naidich DP, et al: Acute pancreatitis: Prognostic value of CT. Radiology 156:767, 1985.

10. Banner MP, Gobel VK: Peritoneal mesothelioma. Radiology 129: 637, 1978.
11. Bercovici B, Michel J, Miller J, Sacks TG: Antimicrobial activity of human peritoneal fluid. Surg Gynecol Obstet 141:885, 1975.
12. Bernardino ME, Jing BS, Wallace S: Computed tomography diagnosis of mesenteric masses. Am J Roentgenol 132:33, 1979.
13. Brody JM, Miller DK, Zeman RK, et al: Gastric tuberculosis: Manifestation of acquired immunodeficiency syndrome. Radiology 159:347, 1986.
14. Bydder GM, Kreel L: Attenuation values of fluid collections within the abdomen. J Comput Assist Tomogr 4:145, 1980.
15. Callen PW: Computed tomographic evaluation of abdominal abscesses. Radiology 131:171, 1979.
16. Callen PW, Marks WM, Filly RA: Computed tomography and ultrasonography in the evaluation of the retroperitoneum in patients with malignant ascites. J Comput Assist Tomogr 3:581, 1979.
17. Dach J, Patel N, Patel S, Petasnick J: Peritoneal mesothelioma: CT, sonography and gallium-67 scan. Am J Roentgenol 135:614, 1980.
18. Day DL, Sane S, Dehner LP: Inflammatory pseudotumor of the mesentery and small intestine. Pediatr Radiol 16:210, 1986.
19. Dodds WJ, Foley WD, Lawson TL, et al: Anatomy and imaging of the lesser peritoneal sac. Am J Roentgenol 144:567, 1985.
20. Dodds WJ, Darweesh RM, Lawson TL, et al: The retroperitoneal spaces revisited: A pictorial essay. Am J Roentgenol 147:1155, 1986.
21. Fry DE, Garrison RN, Heitsch RC, et al: Determinants of death in patients with intraabdominal abscess. Surgery 88:517, 1980.
22. Galematis B, Delikaris P: Treatment of echinococcal cyst. In Nyhus L, Baker R (eds): Mastery of Surgery. Boston, Little, Brown, 1984.
23. Gerzof SG, Robbins AH, Birkett DH: Computed tomography in the diagnosis and management of abdominal abscesses. Gastrointest Radiol 3:287, 1978.
24. Gerzof SG, Robbins AH, Birkett DH, et al: Percutaneous catheter drainage of abdominal abscesses guided by ultrasound and computed tomography. Am J Roentgenol 133:1, 1979.
25. Goffinet DR, Castellino RA, Kim H, et al: Staging laparotomies in unselected previously untreated patients with non-Hodgkin's lymphomas. Cancer 32:672, 1973.
26. Gold R: Personal communication, 1983.
27. Goldhirsch A, Triller JK, Greiner R, et al: Computed tomography prior to second-look operation in advanced ovarian cancer. Obstet Gynecol 62:630, 1983.
28. Gonzalez LR, Marcos J, Illanas M, et al: Radiologic aspects of hepatic echinococcosis: Value of the intravenous viscerogram and computed tomography. Radiology 130:21, 1979.
29. Haaga JR, Alfidi RJ: Precise biopsy localization by computed tomography. Radiology 118:603, 1976.
30. Haaga JR, Weinstein AJ: CT-guided percutaneous aspiration and drainage of abscesses. Am J Roentgenol 135:1187, 1980.
31. Haaga JR, Alfidi RJ, Havrilla TR, et al: CT detection and aspiration of abdominal abscesses. Am J Roentgenol 128:465, 1977.
32. Haaga JR, Reichi NE, Havrilla TR, Alfidi RJ: Interventional CT scanning. Radiol Clin North Am 15:449, 1977.
33. Halvorsen RA Jr, Fedyshin PA, Korobkin M, et al: Ascites or pleural effusion? CT differentiation: Four useful criteria. Radiographics 6: 135, 1986.
34. Han SY, Kochler RE, Keller FS, et al: Retractile mesenteritis involving the colon: Pathologic and radiologic correlation (case report). Am J Roentgenol 147:268, 1986.
35. Hanson RD, Hunter TB: Tuberculosis peritonitis: CT appearance. Am J Roentgenol 144:931, 1985.
36. Hau T, Ahrencholz DH, Simmons RL: Secondary bacterial peritonitis: The biological basis of treatment. Curr Probl Surg 16:1, 1979.
37. Hau T, Hoffman R, Simmons RL: Mechanisms of the adjuvant effect of hemoglobin in experimental peritonitis: I. In vivo inhibition of peritoneal leukocytosis. Surgery 83:223, 1978.
38. Hau T, Nishikawa RA, Phuangsab A: Treatment of peritonitis with systemic antibiotics. Clin Pharmacol Ther 29:251, 1981.
39. Hau T, Nishikawa RA, Phuangsab A: The effect of bacterial trapping by fibrin on the efficacy of systemic antibiotics in experimental peritonitis. Surg Gynecol Obstet 156:252, 1983.
40. Hau T, Payne WD, Simmons RL: Fibrinolytic activity of the peritoneum during experimental peritonitis. Surg Gynecol Obstet 148: 415, 1979.
41. Hauser H, Gurret JP: Miliary tuberculosis associated with adrenal enlargement: CT appearance. J Comput Assist Tomogr 10:254, 1986.
42. Henderson LW: The problem of peritoneal membrane area and permeability. Kidney Int 3:409, 1973.
43. Henderson LW, Nolph KD: Altered permeability of the peritoneal membrane after using hypertonic peritoneal dialysis fluid. J Clin Invest 48:992, 1969.
44. Hulnick DH, Megibow AJ, Balthazar EJ, et al: Computed tomography in the evaluation of diverticulitis. Radiology 152:491, 1984.
45. Hulnick DH, Megibow AJ, Naidich DP, et al: Abdominal tuberculosis: CT evaluation. Radiology 157:199, 1985.
46. Illig L: Die terminale Strombahn. Berlin, Springer-Verlag, 1961.
47. Jeffrey RB Jr: CT demonstration of peritoneal implants. Am J Roentgenol 135:323, 1980.
48. Jeffrey RB Jr, Nyberg DA, Bottles K, et al: Abdominal CT in acquired immunodeficiency syndrome. Am J Roentgenol 146:7, 1986.
49. Jeffries GH: The hepatic diseases. In Besson PB, McDermott W (eds): Cecil-Loeb Textbook of Medicine. Philadelphia, WB Saunders, 1971.
50. Jolles H, Coulan CM: CT of ascites: Differential diagnosis. Am J Roentgenol 135:315, 1980.
51. Kannerstein M, Churg J, McCaughey WT, Hill DP: Papillary tumors of the peritoneum in women: Mesothelioma or papillary carcinoma. Am J Obstet Gynecol 127:306, 1977.
52. Karapinar K, Ergul Z, Keskin A, et al: Hydatid cyst of the abdominal aorta and bilateral common iliac arteries: A case report. J Cardiovasc Surg (Torino) 40:583–585, 1999.
53. Katranci N, Elmas N, Yilmaz F, Mentes A: Correlative CT, MRI and histological findings of hepatic echinococcus alveolaris: A case report. Comput Med Imaging Graph 23:155–159, 1999.
54. Kipfer RE, Moertel CG, Dahlin DC: Mesenteric lipodystrophy. Ann Intern Med 80:582, 1974.
55. Knochel JQ, Koehler PR, Lee TG, Welch DM: Diagnosis of abdominal abscesses with computed tomography, ultrasound, and ^{111}In leukocyte scans. Radiology 137:425, 1980.
56. Korobkin M, Callen PW, Filly RA, et al: Comparison of computed tomography, ultrasonography, and gallium-67 scanning in the evaluation of suspected abdominal abscesses. Radiology 129:89, 1978.
57. Lahorra JM, Haaga JR, Stellato T, et al: Safety of intracavitary urokinase with percutaneous abscess drainage. AJR Am J Roentgenol 160:171–174, 1993.
58. Landay MJ, Setiawan H, Hirsch G, et al: Hepatic and thoracic amebiasis. Am J Roentgenol 135:449, 1980.
59. Lang RK, Springer RM, Glorioso LW 3rd, Cammarata CA: Abdominal abscess drainage under radiologic guidance: Causes of failure. Radiology 159:329, 1986.
60. Leak LV, Just EE: Permeability of peritoneal mesothelium: A TEM and SEM study. J Cell Biol 70:423, 1976.
61. Levitt RG, Sagel SS, Stanley RJ: Detection of neoplastic involvement of the mesentery and omentum by computed tomography. Am J Roentgenol 131:835, 1978.
62. Levitt RG, Biello DR, Sagel SS, et al: Computed tomography and ^{67}Ga citrate radionuclide imaging for evaluating suspected abdominal abscesses. Am J Roentgenol 132:529, 1979.
63. Lewall DB, Nyak P: Hydatid cysts of the liver: Two cautionary signs. Br J Radiol 71:37–41, 1998.
64. Li DKB, Rennie CS: Abdominal computed tomography in Whipple's disease. J Comput Assist Tomogr 5:249, 1981.
65. Lieberman JM, Haaga JR: Duodenal malrotation (case report). J Comput Assist Tomogr 6:1019, 1982.
66. Lieberman JM, Haaga JR: Computed tomography of diverticulitis. J Comput Assist Tomogr 7:431, 1983.
67. Long JA, Dunnick NR, Doppman JL: Non-inflammatory gas formation following embolization of adrenal carcinoma. J Comput Assist Tomogr 3:840, 1979.
68. MacCallum WG: On the mechanism of adsorption of granular materials from the peritoneum. Bull Johns Hopkins Hosp 14:105, 1903.
69. Magid D, Fishman EK, Jones B, et al: Desmoid tumors in Gardner syndrome: Use of computed tomography. Am J Roentgenol 142: 1141, 1984.
70. Marks WM, Filly RA: Computed tomographic demonstration of intraarterial air following hepatic artery ligation. Radiology 135: 665, 1979.
71. Masaryk TJ, Chilcote WA: CT of pseudomyxoma peritonei: Case report. Radiology 152:861, 1984.
72. Matthews AW, Gough KR, Davies ER, et al: The use of combined

ultrasonic and isotope scanning in the diagnosis of amoebic liver disease. Gut 14:50, 1973.
73. Mathieu D, Ladeb MF, Guigui B, et al: Periportal tuberculous adenitis: CT features. Radiology 161:713, 1986.
74. Mayes BG, Chuang VP, Fisher RGL: CT of pseudomyxoma peritonei. Am J Roentgenol 136:807, 1981.
75. McAdam WAF, Goligher JC: The occurrence of desmoids in patients with familial polyposis coli. Br J Surg 57:618, 1970.
76. McNeil B, Keeler E, Adelstein FJ: Primer on certain elements of medical decision making. N Engl J Med 293:211, 1975.
77. Megibow AJ, Lulnick DH, Bosniak MA, Balthazar EJ: Ovarian metastases: Computed tomographic appearances. Radiology 156: 161, 1985.
78. Mendez G, Isikoff MB, Hill MC: Retroperitoneal processes involving the psoas demonstrated by computed tomography. J Comput Assist Tomogr 4:78, 1980.
79. Meyers MA: Dynamic Radiology of the Abdomen: Normal and Pathological Anatomy, 2nd ed. New York, Springer-Verlag, 1976.
80. Miles AA, Miles EM, Burke J: The value and derivation of defense reactions of the skin to the primary lodgement of bacteria. Br J Exp Pathol 38:79, 1957.
81. Miller DL, Udelsman R, Sugarbaker PH: Calcification of pseudomyxoma peritonei following intraperitoneal chemotherapy: CT demonstration. J Comput Assist Tomogr 9:1123, 1985.
82. Mitchell DG, Hill MC, Hill S, Zaloudek C: Serous carcinoma of the ovary: CT identification of metastatic calcified implants. Radiology 158:649, 1986.
83. Newmark H, Smith JJ, Burrows R, Silberman EL: Echinococcal cyst of the liver seen on computed tomography. J Comput Assist Tomogr 2:231, 1978.
84. Nyberg DA, Federle MP, Jeffrey RB, et al: Abdominal CT findings of disseminated *Mycobacterium avium-intracellulare* in AIDS. Am J Roentgenol 145:297, 1985.
85. O'Neil JD, Ross PR, Storm BL, et al: Cystic mesothelioma of the peritoneum. Radiology 170:333–337, 1989.
86. Ochsner A: Pyogenic abscess. In Bockus HL (ed): Gastroenterology. Philadelphia, WB Saunders, 1976.
87. Pandolfo I, Blandino A, Gaeta M, et al: Calcified peritoneal metastases from papillary cystadenocarcinoma of the ovary: CT features. J Comput Assist Tomogr 10:545, 1986.
88. Park JK, Kraus FC, Haaga JR: Fluid flow during percutaneous drainage procedures: An in vitro study of the effects of fluid viscosity, catheter size, and adjunctive urokinase. Am J Roentgenol 160: 165–169, 1993.
89. Pelaez V, Kugler C, Correa D, et al: PAIR as percutaneous treatment of hydatid liver cysts. Acta Trop 75:197–202, 2000.
90. Pickhardt PJ, Fisher AJ, Balfe DM, et al: Desmoplastic small round cell tumor of the abdomen: Radiologic-histopathologic correlation. Radiology 210:633–638, 1999.
91. Ralls PW, Boswell W, Henderson R, et al: CT of inflammatory disease of the psoas muscle. Am J Roentgenol 134:767, 1980.
92. Raptopoulos V, Kleinman PK, Marks S Jr, et al: Renal fascial pathway: Posterior extension of pancreatic effusions within the anterior pararenal space. Radiology 158:367, 1986.
93. Roub LW, Drayer BP, Orr DP, Oh KS: Computed tomographic positive contrast peritoneography. Radiology 131:699, 1979.
94. Rhodes R: Personal communication, 1988.
95. Ros PR, Olmsted WW, Moser RP Jr, et al: Mesenteric and omental cysts: Histologic classification with imaging correlation. Radiology 164:327–332, 1987.
96. Rosenfield AT, Glickman MG, Taylor KJ, et al: Acute focal bacterial nephritis (acute lobar nephronia). Radiology 132:553, 1979.
97. Rubenstein WA, Auh YH, Zirinsky K, et al: Posterior peritoneal recesses: Assessment using CT. Radiology 156:461, 1985.
98. Runyon BA, Hoefs JC: Peritoneal lymphomatosis with ascites: Characterization. Arch Intern Med 156:887, 1986.
99. Scherer U, Weinzierl M, Sturm R, et al: Computed tomography in hydatid disease of the liver: A report of 13 cases. J Comput Assist Tomogr 2:612, 1978.
100. Seshol MB, Coulam CM: Pseudomyxoma peritonei: Computed tomography and sonography. Am J Roentgenol 136:803, 1981.
101. Silverman PM, Kelvin FM, Korobkin M, Dunnick NR: Computed tomography of the normal mesentery. Am J Roentgenol 143:953, 1984.
102. Silverman PM, Baker ME, Casper C, Kelvin FM: CT appearance of diffuse mesenteric colon. J Comput Assist Tomogr 10:67, 1986.
103. Silverman PM, Baker ME, Cooper C, Kelvin FM: Computed tomography of mesenteric disease. Radiographics 7:309–320, 1987.
104. Steinberg B: Infections of the Peritoneum. New York, Paul Hoeber, 1944.
105. Talley FP: Determinants of virulence in anaerobic bacteria. Microbiology 34:219, 1979.
106. Thompson GT, Fitzgerald ER, Somers SS: Retractile mesenteritis of the sigmoid colon. Radiology 157:565, 1985.
107. Tipaldi L, Giunta L: Personal communication, 1987.
108. Vincent ME, Robbins AH: *Mycobacterium avium-intracellulare* complex enteritis: Pseudo-Whipple disease in AIDS. Am J Roentgenol 144:921, 1985.
109. von Recklinghausen FT: Zur Fettresorption. Arch Pathol Anat Physiol 26:172, 1983.
110. Vutova K, Mechkov G, Vachkov P, et al: Effect of mebendazole on human cystic echinococcosis: The role of dosage and treatment duration. Ann Trop Med Parasitol 93:357–365, 1999.
111. Wang N-S: The performed stomas connecting the pleural cavity and the lymphatics in the parietal pleura. Am Rev Respir Dis 111: 12, 1975.
112. Warde P, Rideout DF, Herman S, Majesky IF: Computed tomography in advanced ovarian cancer: Inter- and intraobserver reliability. Invest Radiol 21:31, 1986.
113. Weigert F, Lindner P, Rohde U: Computed tomography and magnetic resonance of pseudomyxoma peritonei. J Comput Assist Tomogr 9: 1120, 1985.
114. Whalen J: Radiology of the Abdomen. Philadelphia, Lea & Febiger, 1976.
115. Whitley NO: Mesenteric disease. In Meyers MA (ed): Computed Tomography of the Gastrointestinal Tract: Including the Peritoneal Cavity and Mesentery. New York, Springer-Verlag, 1986.
116. Wilms G, Baert AL, Bruneel M: CT demonstration of gas formation after renal tumor embolization. J Comput Assist Tomogr 3:838, 1979.
117. Wolverson MK, Jagannadharao B, Sundaram M, et al: CT as a primary diagnostic method in evaluating intraabdominal abscesses. Am J Roentgenol 133:1089, 1979.
118. Yeh HC, Chaninian AP: Ultrasonography and computed tomography of peritoneal mesothelioma. Radiology 135:705, 1980.
119. Zinsser HH, Pryde AW: Experimental study of physical factors, including fibrin formation influencing the spread of fluids and small particles within and from the peritoneal cavity of the dog. Ann Surg 136:818, 1952.
120. Zirinsky K, Auh YH, Kneeland JB, et al: Computed tomography, sonography and MR imaging of abdominal tuberculosis. J Comput Assist Tomogr 9:961, 1985.

43 The Retroperitoneum

Ashok K. Gupta, Richard H. Cohan

The retroperitoneum is that portion of the abdomen located posterior to the peritoneal cavity. It extends from the diaphragm to the pelvic inlet and includes portions of the colon, duodenum, pancreas, kidneys, adrenal glands, abdominal aorta, inferior vena cava (IVC), lymph nodes, fat, and much of the abdominal wall musculature.[94]

Cross-sectional imaging has had a profound effect on the diagnosis and treatment of retroperitoneal diseases. This chapter presents the computed tomography (CT) and magnetic resonance imaging (MRI) appearances of normal retroperitoneal anatomy. CT and MRI manifestations of abnormalities involving the retroperitoneal spaces, aorta, IVC, and retroperitoneal lymph nodes are described and illustrated. Disease processes confined to the retroperitoneum, including primary retroperitoneal tumors, retroperitoneal fibrosis, and abnormalities related to the iliopsoas muscles, are also discussed.

Retroperitoneal Spaces

Normal Anatomy

The retroperitoneum is commonly divided into three spaces by the anterior and posterior renal fasciae (Fig. 43–1).[129]

The *anterior pararenal space* is bordered anteriorly by the parietal peritoneum, posteriorly by the anterior renal fascia (Gerota's fascia), and posterolaterally by the lateral continuation of the renal fasciae and the lateroconal fascia. This space contains the pancreas, retroperitoneal portions of the duodenum, and ascending and descending colon.[129]

The *perirenal space*, the largest retroperitoneal compartment, lies within the anterior and posterior renal fasciae and contains the kidneys, adrenals, proximal renal collecting systems, and renal hilar vessels.[210] The perirenal fasciae fuse medially and blend with the retroperitoneal fat surrounding the great vessels and adjacent lymph nodes. The perirenal spaces therefore theoretically communicate with one another across the midline via a narrow potential space anterior to the caudal aspects of the aorta and the IVC.[129] The large amount or perirenal fat in the perirenal space is subdivided by bridging septa, which are often able to confine pathologic perirenal processes to portions of the perirenal space. These septa are thought to prevent most perirenal processes from spreading into the central retroperitoneum and crossing the midline to involve the contralateral perirenal space.[212]

The *posterior pararenal space* is the smallest of the three retroperitoneal spaces. It is located posterior to the posterior renal fascia and contains only a small amount of fat. Although it is located posterior to the kidneys, it continues anterolaterally.[129] Indeed, posterior pararenal space fat is responsible for the properitoneal fat stripe seen on plain abdominal radiographs.

The *psoas compartment*, sometimes considered a fourth retroperitoneal space, is located within and immediately adjacent to the psoas muscles. It is immediately adjacent to the posteromedial aspect of the posterior pararenal space.

Some controversy exists about whether the retroperitoneal spaces communicate with the pelvis. Some communication has always been suspected, since pelvic hematomas have been observed to extend cephalad into abdominal retroperitoneal tissue. It has long been thought that the inferior aspect of the perirenal space is open, allowing this space to freely communicate with the other retroperitoneal spaces and the retroperitoneal tissue in the pelvis.[129] This was apparently confirmed in a study of cadavers imaged with CT, in which injected contrast material was found to track caudad from the perirenal space into the extraperitoneal spaces of the pelvis.[169] Communication between the anterior and posterior pararenal spaces and the pelvic extraperitoneum was also demonstrated.

In contrast, when Raptopoulos and colleagues injected latex into the perirenal spaces of cadavers, they found that none of the latex tracked into the pelvis, suggesting that the inferior aspect of the perirenal space is closed.[211] It has been postulated that this discrepancy may be explained on the basis of the ability of fluid within closed retroperitoneal

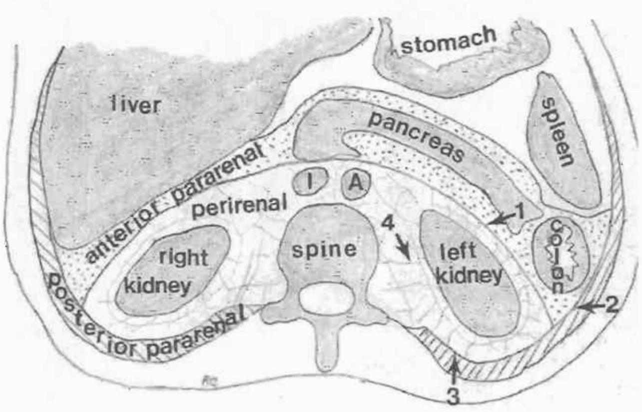

Figure 43–1. Anatomy of the retroperitoneum. 1, anterior perirenal fascia; 2, lateroconal fascia; 3, posterior perirenal fascia; 4, bridging septa in the perirenal space; A, aorta; I, inferior vena cava.

spaces to track inferiorly by entering the easily dissected planes between these spaces. It is these planes that freely communicate with the pelvic extraperitoneum.[171]

Pathologic Conditions

Identification of the retroperitoneal spaces in which retroperitoneal masses or fluid collections are seen on CT and MRI examinations may help elucidate their causes. Because the anterior and posterior renal and lateroconal fasciae are identified on CT and MRI as pencil-thin, linear, soft tissue densities enveloping the perirenal fat and extending toward the, lateral abdominal wall, the retroperitoneal spaces are usually easily identified.[129]

Fluid collections in the anterior pararenal space often result from pancreatitis or hematomas (Fig. 43–2). Although these commonly involve only one side of the retroperitoneum, they may spread across the midline. This is particularly seen in patients with pancreatitis.[210]

Abscesses, hematomas, urinomas, and neoplasms can all develop in the perirenal space. In most cases, these are the result of abnormalities of the kidneys, adrenals, or proximal renal collecting systems, although extension from the aorta and pancreas is also common. Perinephric space hemorrhage is usually caused by blunt trauma (Fig. 43–3), a ruptured abdominal aortic aneurysm (AAA), or bleeding from a renal mass.[21, 129] Abnormal perirenal space fluid may be in either of two locations: within the renal capsule (subcapsular) or outside the capsule in the perinephric fat.

These two types of fluid collections can often be differentiated from one another. Subcapsular fluid collections usually produce distortion of the renal parenchyma, whereas perinephric collections do not. Unfortunately, there is frequently overlap. This is because when a perinephric fluid collection develops between the renal capsule and the posterior renorenal septum (one of the bridging perinephric septa), the renal parenchyma may be compressed and the CT or MRI appearance may be indistinguishable from that of a subcapsular hematoma.[129]

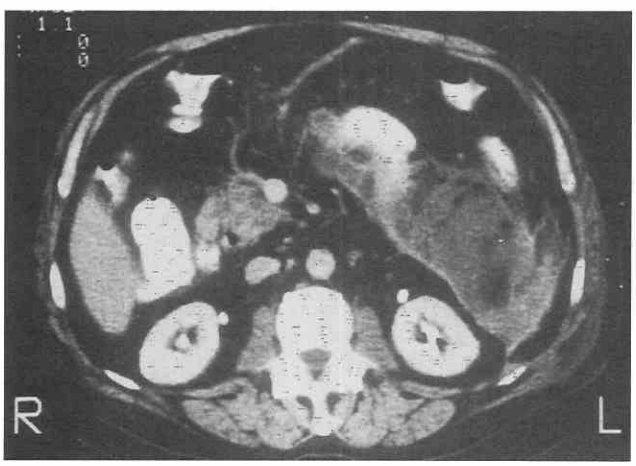

Figure 43–2. Fluid in the anterior pararenal space. Intravenous contrast-enhanced CT scan in a patient with acute pancreatitis demonstrates peripancreatic fluid in the left anterior pararenal space.

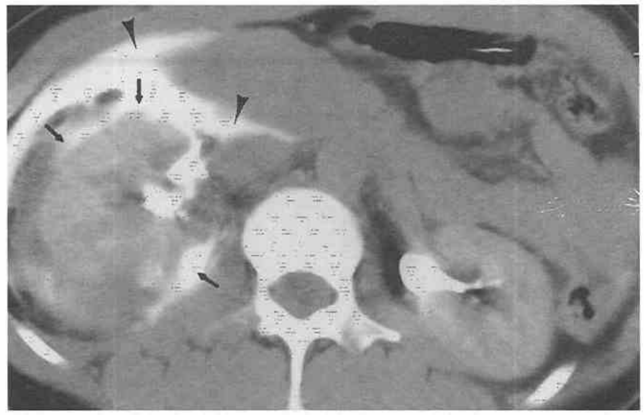

Figure 43–3. Fluid in the perirenal space. Delayed contrast-enhanced image through the midabdomen of a patient who sustained blunt abdominal trauma and injury to the renal collecting system shows accumulation of contrast-enhanced urine in the right perirenal space *(arrows)*. A portion of the urinoma also extends into the right anterior pararenal space *(arrowheads)*.

Abnormalities in the posterior pararenal space are much less common than abnormalities in the anterior pararenal space or the perirenal space. When present, these are most commonly the result of spread of pathologic processes in the pelvis. Causes can include hematoma (Fig. 43–4), infection, and neoplasm. In a minority of patients, peripancreatic fluid or phlegmon may spread through or around the fascial layers into the posterior from the anterior pararenal space.

Localization of retroperitoneal fluid within one of the major compartments is sometimes difficult. This is nowhere more apparent than in the retrorenal region. Retrorenal collections may reside within any of the retroperitoneal

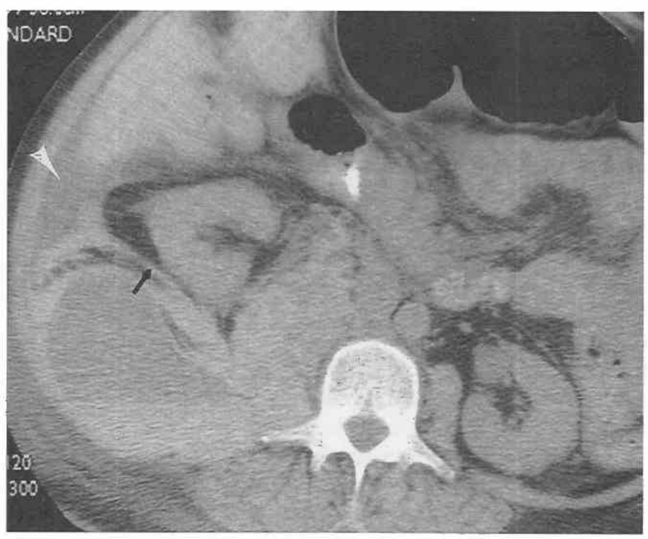

Figure 43–4. Fluid in the posterior pararenal space. Unenhanced CT scan of the right posterior pararenal space in a patient given anticoagulation agents demonstrates a fluid-fluid level within a large hematoma. The fluid displaces the posterior perirenal fascia *(arrow)* anteriorly. Intraperitoneal fluid is also present *(arrowhead)*.

spaces.[129] In some patients, the anterior renal fascia, posterior renal fascia, and lateroconal fascia meet in a more dorsal location, and this results in a portion of the anterior pararenal space lying posterior to the kidney. Also, perirenal fluid can layer in front of or behind the kidney.

Because the anterior, posterior, and lateroconal fasciae are often not seen as three distinct layers but instead as a multilayered complex, fluid may migrate within the leaves of this fascial network.[210] Some inflammatory processes, such as pancreatitis with its proteolytic enzymes and neoplasms, can destroy fascial barriers, further complicating attempts at fluid localization. In addition, the paracolic gutters of the peritoneal cavity occasionally may extend posterolateral to the kidney.[129] Thus, intraperitoneal fluid may also occasionally have a retrorenal location.

Inflammatory and neoplastic processes in any of the three major retroperitoneal spaces can cause thickening of the retroperitoneal fasciae. This response is nonspecific, and even in patients with an adjacent malignancy it does not necessarily indicate infiltration of these layers with tumor cells.

Aorta

Normal Anatomy

The aorta extends from the diaphragmatic hiatus to the level of the umbilicus or fourth lumbar vertebral body, where it bifurcates into the two common iliac arteries. The normal aorta is located just to the left of midline and is surrounded by retroperitoneal fat. In one autopsy series, the mean diameter of the normal infrarenal abdominal aorta was 1.75 cm for men and 1.64 cm for women.[52] The aorta usually enlarges as individuals age. In the same series, the mean "normal" aortic diameters for men and women between 19 and 29 years of age were 1.51 and 1.39 cm, respectively; those for men and women between 80 and 92 years of age were 1.96 and 1.82 cm.[52] Generally, a normal-caliber abdominal aorta never exceeds 3 cm in maximal diameter.[45]

The aorta is easily visualized on abdominal CT and MRI examinations. The celiac, superior mesenteric, and inferior mesenteric artery origins can also be identified in most patients. The renal arteries are less reliably visualized on routine abdominal and pelvic studies, but they are easily detected when CT or MR angiography (MRA) is performed. CT or MRI measurements of the abdominal aortic caliber are comparable to those obtained in autopsy series. On CT, for example, the mean normal aortic diameter at the level of the renal hilum has been measured to be between 1.5 cm in women in their fourth decade and 2.1 cm in men in their eighth decade. Mean infrarenal aortic diameters are 1.4 cm and 2.0 cm in the same two patient populations.[233]

Abnormalities of the Abdominal Aorta

The most important abdominal aortic abnormality is aneurysm formation and its consequences (aortic rupture). The ensuing paragraphs review the imaging of aortic aneurysms and patients with suspected aneurysm ruptures. The CT and MRI appearances of aortic dissections extending into the abdominal aorta and with penetrating ulcers are also reviewed. The significance of the small aorta is addressed. Imaging of the treated abdominal aortic aneurysm, including the appearance of normal surgical grafts and endovascular grafts and of complications of graft insertion, is also provided.

CT and MRI Technique

With CT, the aorta can be identified on either routine noncontrast or dynamic bolus contrast-enhanced scans obtained at contiguous 7- to 10-mm intervals through the abdomen. When detailed evaluation of the aorta is required, however, CT arteriography is most helpful. For CT arteriography, a dynamic bolus injection of contrast material, 60% by weight, is administered by a mechanical injector at a rate of 4 to 5 mL/second. After a delay of 25 to 40 seconds, thinly collimated (2.5- to 3-mm-thick) images are usually obtained. Images may then be reconstructed at overlapping intervals (usually with 50% overlap) so that three-dimensional (3D) reconstructions can be obtained.

Helical scanning is essential. CT angiography cannot be adequately performed when conventional axial scanners are used because of the lengthy time required for image acquisition and the large number of images that must be obtained. The most thinly collimated images can be obtained most rapidly on the new multidetector CT scanners, on which hundreds of images can be generated in less than 30 seconds. Indeed, the advent of multidetector helical CT has revolutionized CT angiography allowing it to compete successfully with both conventional and MR angiography.

Once helically obtained axial images are acquired, 3D reformatted images can be created with the use of a workstation to which the obtained images are forwarded. Excellent-quality images can be reconstructed in a variety of formats (standard coronal and sagittal planes, oblique planes, curved multiplanar images, and a variety of 3D techniques); however, today the most popular 3D reconstruction algorithms for visualization of the aorta are maximum intensity projection and volume-rendered images. Three-dimensional image reconstructions can be created from the entire data set or from a portion of the data set. Although 3D image reconstruction was time-consuming in the past, improvements in computer software and hardware now allow for images to be created in less than 10 minutes. Modifications have been made to the shaded-surface display and volume-rendered techniques such that both calcifications in the aorta and the surface of the aorta can be visualized together. Angioscopic images can also now be created.[237]

It must be emphasized that all of the information is on the retrospectively obtained (usually overlapping) axial images. These can be accurately interpreted by careful review of the images in a cine loop on the console. Furthermore, information can be lost on reconstructed images, leading to erroneous diagnoses, so that 3D reconstructions must be carefully created by knowledgeable and experienced radiologists or technologists.[233]

One potential drawback of CT arteriography is a relatively large intravenous (IV) bolus of potentially nephro-

toxic contrast material is required (with volumes of injected contrast material usually approaching 150 mL of 60% by weight contrast media). Concerns about nephrotoxicity are substantial in this patient population because many patients with aortic disease have associated severe renovascular disease.

Some researchers have responded to this concern by performing CT arteriography after administration of the MRI contrast agent gadopentetate dimeglumine. Gadopentetate dimeglumine is, in fact, more radiopaque than iodinated contrast material. It has a significantly higher rate of x-ray absorption than does the same concentration and volume of iodinated radiographic contrast media. Unfortunately, much lower total doses of gadopentetate (in comparison with iodinated contrast media) have been approved for intravascular use. When these lower doses are used, vessel radiopacity is generally much less than that seen after injection of standard volumes of iodinated contrast material.[200] This limits the quality of CT arteriography performed with this MRI contrast agent.

MRA is best performed on a 1.5-tesla (T) magnet with a body coil. The protocol used at the University of Michigan Hospital is as follows. Initially, T1-weighted (TR = 333 msec, TE = 25 msec) sagittal images can be obtained for localization. Then, an IV injection of 42 mL (two bottles) of gadolinium chelate is administered while a coronal 3D spoiled gradient-echo sequence is performed (TR = 24 msec, TE = 6.9 msec; flip angle = 40 degrees; bandwidth = 16 kHz; 28 slices with 2.5- to 2.8-mm thickness; matrix 256 × 256; frequency encoding, superior to inferior; flow compensation; field of view = 36 cm; 1 NEX). Subsequently, sagittal 2D time-of-flight, axial 2D time-of-flight, and 3D phase-contrast images can be obtained. The 3D images obtained with MRA can be processed in a fashion similar to those acquired during CT arteriography (Fig. 43–5). Of course, MRA cannot be performed if there are contraindications (e.g., presence of an indwelling pacemaker).

Figure 43–5. Normal aorta in a 28-year-old man. Magnetic resonance angiogram shows that the aorta is smoothly contoured and tapers gradually to the level of the aortic bifurcation.

Aortic Aneurysms: Prevalence, Growth, and Imaging Appearance

Abdominal aortic aneurysms (AAAs), defined as focal areas of aortic dilatation that usually exceed 3 cm in maximal diameter, occur in 1% to 4.5% of older adults.[75, 221, 227] It has been thought that most AAAs result from atherosclerosis; however, it is now postulated that these "atherosclerotic" aneurysms actually form as a result of an inflammatory process in the aorta that leads to plaque formation and vessel dilatation. It has been suggested that the term *atherosclerosis* be replaced with the term *degenerative* or *nonspecific* in reference to these most commonly encountered types of aortic aneurysms.[82] Other causes of aortic aneurysms include trauma, infection, cystic medial necrosis, Marfan's syndrome, Takayasu's arteritis, and syphilis.[135] AAAs are often asymptomatic, although patients may present with a pulsatile abdominal mass.[79]

Most AAAs originate below the level of the renal arteries. Between 2% and 20% of AAAs are believed to be *juxtarenal* (extending to within 1.0 to 1.5 cm of the renal artery origins but not involving these vessels) or *pararenal* (involving one or both renal arteries).[65] It is indeed fortunate that most aneurysms are infrarenal, because surgical repair of juxtarenal and pararenal aneurysms is much more complex than repair of infrarenal aortic aneurysms and patient morbidity and mortality are higher.[65] Also, standard endovascular stent-graft insertion is not possible when aneurysms are juxtarenal or pararenal.

Over time, at least 80% of AAAs enlarge.[64] Unfortunately, it is not possible to predict which detected aneurysms will enlarge and which will remain stable. Most aneurysms enlarge slowly. Larger aneurysms usually enlarge at a more rapid rate than smaller aneurysms. In general, aneurysms measuring 5 cm or more in maximal diameter enlarge by 4 to 8 mm per year. Aneurysms measuring between 4 and 5 cm in maximal diameter enlarge by 3 to 7 mm per year. Aneurysms measuring less than 4 cm in maximal diameter enlarge by 2 to 5 mm per year.[28, 48, 86, 148]

AAAs are easily visualized with CT and MRI (Figs. 43–6 and 43–7). The aortic wall is at least partially calcified in nearly every patient in whom "atherosclerosis" was the cause of the aneurysm, and this calcification is easily visualized on CT scans.[75, 154] CT-detected mural thrombus most often surrounds the patent aortic lumen but may be crescentic. Occasionally, an aneurysm thrombus may partially calcify, and this appearance may be confused with displaced intima in an aortic dissection.[99, 154]

Inflammatory Aneurysms and Perianeurysmal Fibrosis

In 5% to 15% of cases, aortic aneurysms are surrounded by inflammatory or fibrotic tissue.[57, 75, 213] This represents perianeurysmal fibrosis, which is believed to result from a fibrotic autoimmune reaction to material in atherosclerotic

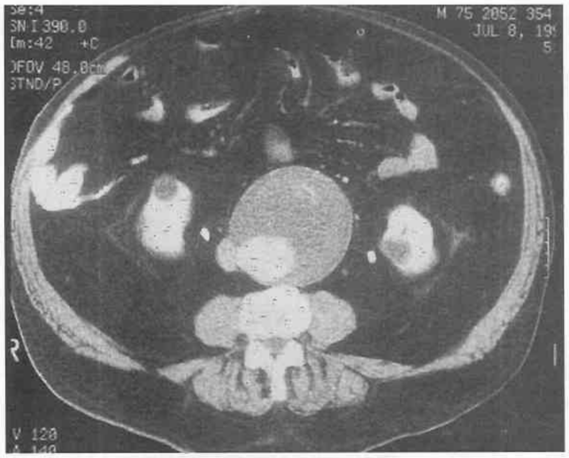

Figure 43–6. Abdominal aortic aneurysm. Dynamic, intravenous contrast-enhanced CT scan demonstrates a large amount of thrombus within the aneurysm. Some of the thrombus is calcified. An arteriogram on this patient would significantly underestimate the size of the aneurysm because only the patent part of the lumen containing flowing blood would be opacified.

plaques.[130] Currently, most researchers believe that the process involved in the formation of these inflammatory aneurysms is similar to, but more extensive than, that involved in the formation of aneurysms that are not surrounded by any inflammation or fibrosis.[55, 213] This is because similar inflammatory changes are found in the walls of both inflammatory and noninflammatory aneurysms.

Patients with inflammatory aneurysms may present with abdominal or back pain. The erythrocyte sedimentation rate (ESR) is often elevated. Treatment is similar to that of a noninflammatory aneurysm. Although the rupture rate is considered to be lower for inflammatory aneurysms than that encountered for comparably sized noninflammatory aneurysms (possibly because of the additional aortic wall thickening and the surrounding reaction), rupture may occur in these patients.[55] Thus, large aneurysms surrounded by perianeurysmal fibrosis must be repaired. Surgery in these patients is difficult because of the extensive inflammatory and fibrotic changes in the retroperitoneum. After treatment of the aneurysm, the retroperitoneal changes regress in many patients.

Both CT and MRI can often, but not always, be used to detect perianeurysmal fibrosis (Fig. 43–8). In one study, CT allowed identification of perianeurysmal fibrosis in only 9 of 15 patients in whom this inflammatory reaction was subsequently identified at surgery.[56] In another study, CT was used to identify the fibrosis in 13 of 15 patients.[55]

One report suggested that MRI may be more sensitive than CT in detected perianeurysmal fibrosis.[250] In this series, CT was successfully used to identify the perianeurysmal changes in only 7 of 15 patients with inflammatory aneurysms, whereas MRI was 100% sensitive, detecting characteristic alternating bands of high and low signal intensity in the periaortic tissue on T1-weighted spin-echo images.[250]

Mycotic Aneurysms

Infected or mycotic aneurysms account for nearly 3% of AAAs. These aneurysms, which are usually encountered in IV drug abusers or immunocompromised patients, can be suspected if an aneurysm is identified in a patient who is unlikely to have atherosclerotic disease and who has a fever and leukocytosis. Recognition of mycotic aneurysms as a distinct group on CT scans or MR images is important because these aneurysms are more prone to rupture than comparably sized atherosclerotic aneurysms.

In a small series, Sueyoshi and associates found an increase in periaortic fat to be one of the earliest signs of aneurysm infection.[245] Clearly, this finding can be assessed only when sequential CT scans are available. An aneurysm can also be suspected to be mycotic when its contour is irregular (Fig. 43–9), although most irregularly shaped aortic aneurysms are atherosclerotic.[233] Rapid enlargement of an aneurysm (again, assessable only when more than one cross-sectional imaging study is available), lack of calcification, and unusual (noninfrarenal) location should also suggest a mycotic origin. Perianeurysmal air and enlarged

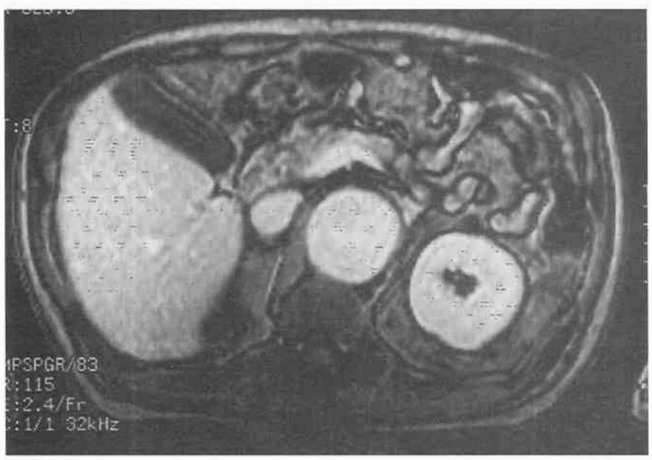

Figure 43–7. Suprarenal abdominal aortic aneurysm, as seen on a fat-suppressed, limited flip-angle MR image. There is no thrombus in this aneurysm.

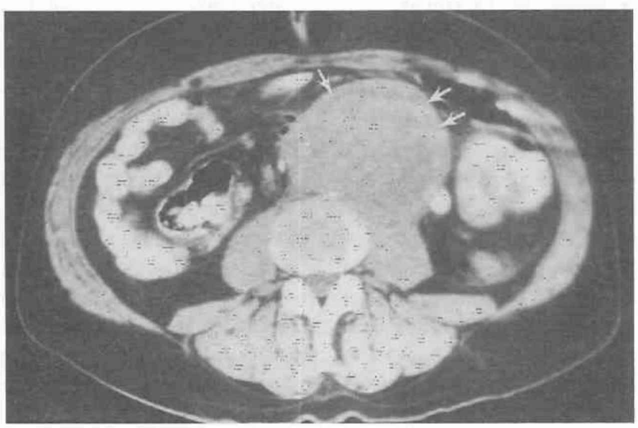

Figure 43–8. Perianeurysmal fibrosis. Unenhanced CT scan shows a rind of soft tissue *(arrows)* surrounding the anterior and lateral aspects of a large abdominal aortic aneurysm.

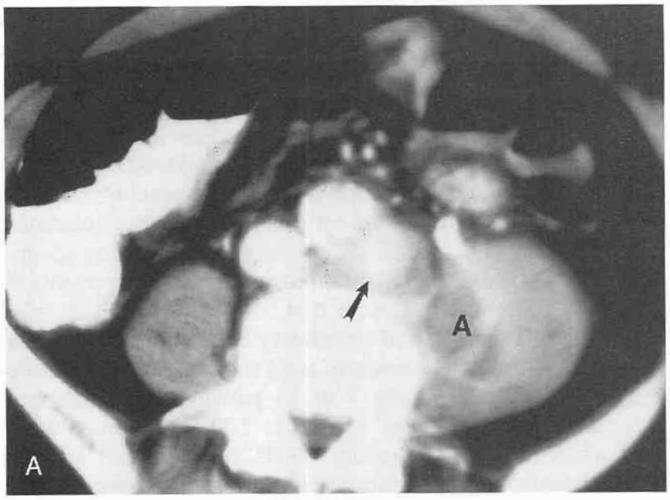

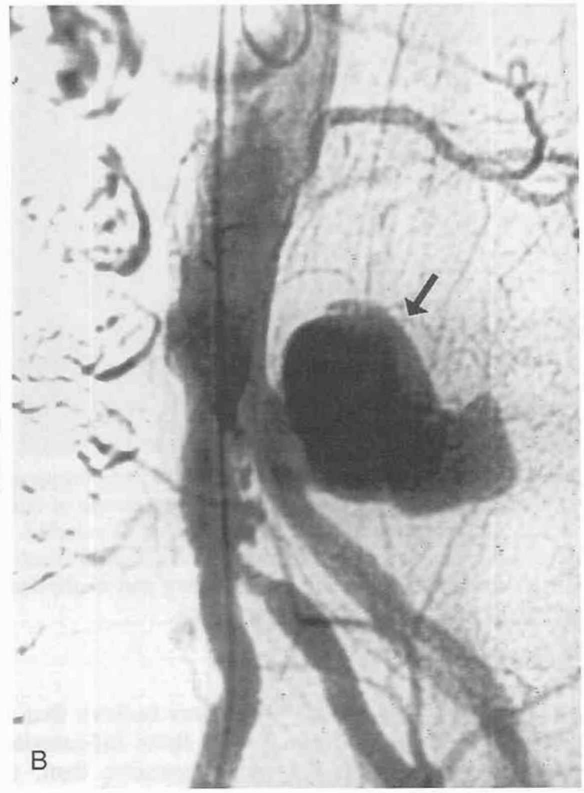

Figure 43–9. Mycotic abdominal aortic aneurysm. *A,* CT scan of a left psoas abscess (A) in a 66-year-old man also demonstrates a mycotic aneurysm as a focal outpouching of contrast-enhanced blood from the left posterolateral aspect of the aorta *(arrow). B,* A digital subtraction image from an aortogram better demonstrates the irregular shape of this mycotic aneurysm *(arrow).*

retroperitoneal lymph nodes may be other accompanying signs suggestive of infection.

Abdominal Aortic Aneurysms: Are Some More Likely to Rupture?

Given long enough patient survival, virtually all enlarging aneurysms rupture. Repair of AAAs is strongly preferred prior to rupture because morbidity and mortality are much higher in patients undergoing emergency aneurysm repairs (after aneurysm rupture) than in those undergoing elective or semielective repairs. Interestingly, the operative mortality for elective aneurysm repair has decreased dramatically in the past few decades, to well below 10%, whereas the mortality for emergency aneurysm repair has remained stable, at more than 50% in some studies.[233, 266] Long-term patient morbidity and mortality are also considerably higher after emergency aneurysm repair than after elective aneurysm repair.[40]

According to many vascular surgeons, operative repair of AAAs is indicated when they exceed 5 cm in maximal diameter, since the tendency to rupture increases dramatically once aneurysms reach this size. In one series, the percentage of aneurysms measuring 5 cm in diameter that could be predicted to rupture in 1 year was 2.5%.[259] In another, the maximum potential rupture rate (actual rupture rate plus elective surgery rate) for AAAs of 4.5 to 5.9 cm maximal diameter was found to be 10.2% per year.[228] There are only isolated reports of ruptures occurring in smaller aneurysms.[186]

Although patients with an aortic aneurysm 5 cm or greater in diameter and who are good operative candidates should undergo surgical repair, patients with smaller aneurysms are usually monitored by serial ultrasound studies.[258] Most recommend repeating the ultrasound examination every 6 months; however, because aneurysm growth is slow, aneurysm enlargement may not be detected unless the current study is compared with several previous examinations. Interobserver and intraobserver variability in measurements obtained during sonography can be substantial. The smallest measured difference in ultrasound-measured aneurysm diameter that has been found to reliably indicate true interval growth is 8 mm.[229] This greatly exceeds the typical, expected 6-month growth rate of even the largest aneurysms. The variability in aneurysm measurement with sonography generally greatly exceeds that encountered with CT.[138]

As an alternative to monitoring small aneurysms with sonography, some researchers now recommend surgical repair *before* the aneurysm reaches the threshold maximal diameter of 5 cm.[12, 186] This is because operative morbidity and mortality rates may be lower for these generally younger and healthier patients, and aneurysm repair is easier to perform when the aneurysm is small.

A number of researchers have attempted to identify features in AAAs, aside from maximal diameter, that may indicate probability of rupture. If such features could be described, it might be possible to identify a subset of patients with AAAs, including aneurysms less than 5 cm in maximal diameter, in whom prompt surgery is indicated.

Several ominous imaging findings have been identified. As previously noted, mycotic aneurysms as a group are more likely than atherosclerotic aneurysms to rupture. If an aneurysm increases in size by 1 cm or more in maximal diameter over 6 months, the risk of rupture is thought to be greatly increased.[233]

Identification of a high-attenuation crescent within an aneurysm wall or in a thrombus on either unenhanced or IV contrast-enhanced CT scans may also indicate an increased tendency to rupture (Fig. 43–10). Mehard and colleagues identified a high-attenuation crescent in the thrombi or walls of AAAs in 19 of 149 unenhanced CT scans of patients before AAA repair.[162] Ten of these 19 patients had frank AAA ruptures (4 patients), contained ruptures (3 patients), or intramural hemorrhage (3 patients) found during subsequent surgery. In only nine patients was no evidence of a rupture found on follow-up.

Siegel and colleagues found similar high-attenuation crescents in the thrombi of 11 of 52 patients with ruptured AAAs who were evaluated with either enhanced or unenhanced CT.[232] No such crescents were found in the thrombi of any of the 56 nonruptured aneurysms used as a control group. It is thought that the crescent is caused by dissection or leaking of blood into the thrombus or the wall of an AAA, an event that may be an early step in the development of a true aortic rupture.[7, 226]

Whatever the cause, these studies suggest that when CT detects a high-attenuation crescent in the thrombus of an AAA or adjacent to the wall of an AAA, the patient should, at the least, receive careful follow-up. The likelihood of rupture occurring sooner rather than later may be higher than in patients whose aneurysms are not characterized by this finding.

Another finding that may indicate an aneurysm likely to rupture or one that has already ruptured is the *draped aorta sign*. In patients with this sign, the wall of the aneurysmally dilated aorta is not clearly visualized posteriorly, and the posterior portion of the aorta is closely applied to one or several vertebral bodies and follows their contours on one or both sides. The aorta appears to be "draped over" adjacent vertebral bodies (Fig. 43–11). In one series of 10 patients whose CT examinations demonstrated this appearance, seven had contained leaks, two had weakened aortic walls resulting from a mycotic aneurysm, and the final patient had an anastomotic pseudoaneurysm (which developed after aortic graft surgery).[92]

Several other features, including aneurysm and thrombus shape, amount of thrombus, and amount or distribution of wall calcification, do not appear to be related to the tendency of an aneurysm to rupture.[233]

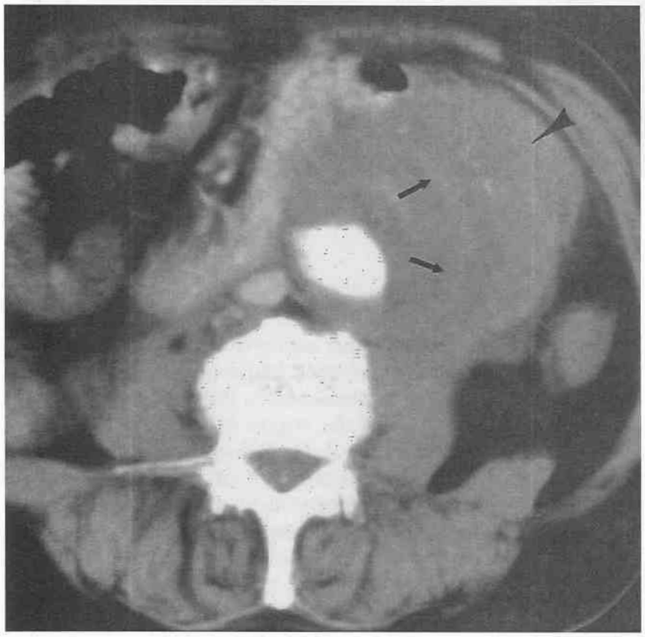

Figure 43–10. Large abdominal aortic aneurysm with crescent sign. Contrast-enhanced CT scan shows a crescent of high attenuation *(arrows)* in the aneurysm thrombus. This finding is believed to indicate that the aneurysm is likely to rupture in the near future. Indeed, rupture has already occurred, as evidenced by the poorly defined hematoma *(arrowhead)* located peripheral to calcification in the aortic wall.

Preoperative Evaluation of Abdominal Aortic Aneurysms

CT angiography and MRA have gradually replaced aortography as the procedures of choice for preoperative imaging of AAAs.[223, 233] This is the case for patients who are being considered for standard aneurysm repair and for those who are poor operative candidates and in whom an endovascular stent-graft is being considered. Preoperative assessment of AAAs with CT or MRI is valuable for delineation of proximal and distal extent, determination of maximal aneurysm diameter, detection of venous anomalies, and assessment of the periaortic tissues (for perianeurysmal fibrosis).[223] CT angiography and MRA can also accurately determine the number and locations of the renal arteries and the presence of any renal artery stenoses, or iliac artery stenoses and aneurysms.[223]

As previously stated, although most aneurysms are infrarenal, demonstration of renal artery involvement is cru-

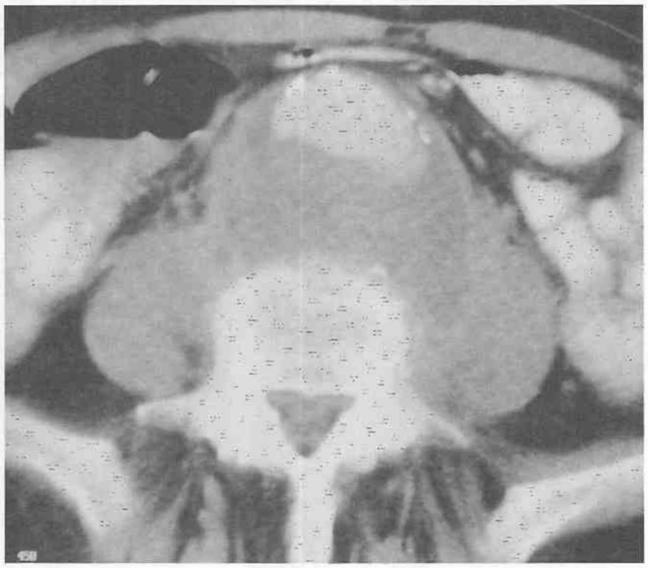

Figure 43–11. Draped aorta sign. Contrast-enhanced CT scan in an elderly man shows a large abdominal aortic aneurysm that appears to be draped over the adjacent lumbar vertebral body. The fat plane between the aorta and the vertebral body has been obliterated. This finding is ominous and indicates that free aneurysm rupture is likely in the near future.

cial, as this indicates that subsequent surgery will be much more complicated. Additionally, extension into the iliac arteries, discrete iliac artery aneurysms, or atherosclerotic occlusive aortoiliac disease may require the insertion of a Y graft rather than a simple aortic graft.[139]

CT angiography, with rapid bolus IV injections of contrast media and helical scanning, can provide images that are nearly as good as those obtained with angiography, especially if multidetector helical CT technology is used and if 3D reconstructions are obtained (Fig. 43–12). CT angiography technique has already been described (see "CT and MRI Technique").

CT and CT angiography measurements of aneurysm diameter and aortoiliac length are highly accurate, with interobserver variability being minimal.[8] In one study, interobserver variability in aneurysm diameter, measured by radiologists in the same department, exceeded 2 mm in only 10% of patients.[138] Furthermore, CT angiography also accurately identifies accessory renal arteries and vascular anatomic variants.[223] These findings confirm that CT angiography can completely replace aortography and produces accurate images of AAAs, before both open surgery and endovascular stent-graft insertion.

MRA evaluation of AAAs (see Fig. 43–7) is probably just as diagnostic as CT and can also be performed instead of conventional arteriography.[201, 206] In a study of 43 pa-

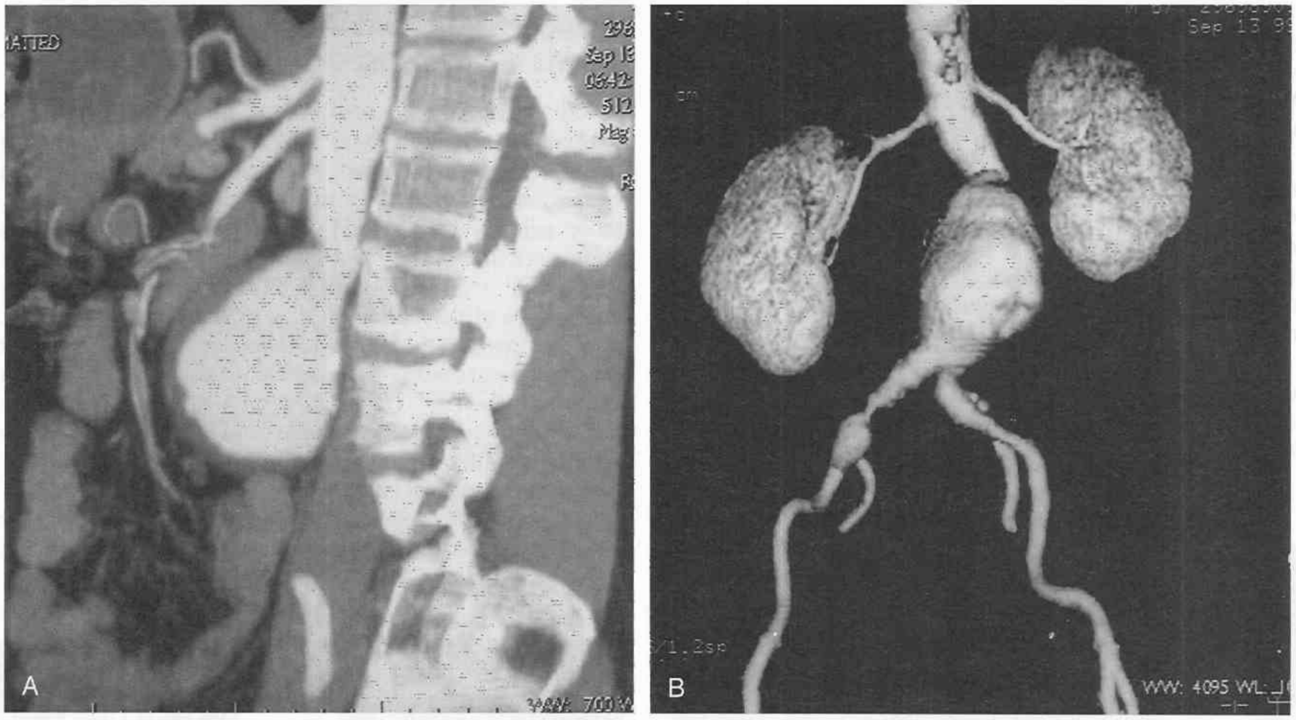

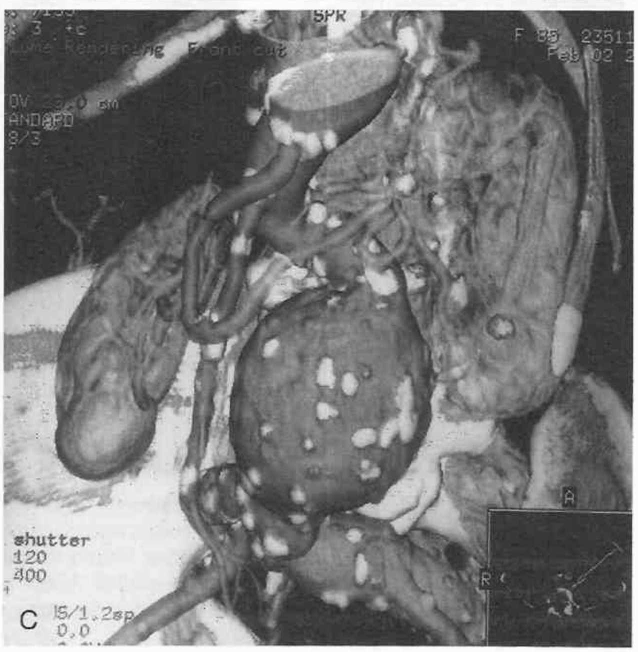

Figure 43–12. Abdominal aortic aneurysms, 3D CT reconstruction images. *A,* Sagittal reformatted image of a large infrarenal abdominal aortic aneurysm demonstrates that the aneurysm begins well below the level of the origins of the celiac axis and the superior mesenteric artery. *B,* Shaded-surface display image in the coronal plane (with subtraction of overlying osseous structures) shows the same aneurysm to originate well below the level of single renal arteries bilaterally. *C,* Volume-rendered image in another patient reveals another infrarenal abdominal aortic aneurysm. The reconstruction algorithm here allows for two different thresholds to be used: a *lower*-attenuation threshold to determine the aortic caliber and a *higher*-attenuation threshold for aortic wall calcification.

tients with AAAs who underwent aneurysm repair, Prince and colleagues found that AAA extent was properly delineated in all patients.[207] MRA also revealed significant arterial stenoses, with a 94% sensitivity and a 98% specificity. The authors also point out some advantages of MRA over CT angiography, including the lack of ionizing radiation and the lack of need for administration of potential nephrotoxic iodinated contrast material.

In another study, MRA was found to be significantly better than conventional axial (nonhelical) CT at imaging the AAAs of 82 patients before endoluminal stent-graft insertion.[183]

Ultrasonography is not used for preoperative evaluation of AAAs. It cannot reliably assess the periaortic tissue, and it occasionally is able to only imply the relationship of the aneurysm to the renal arteries because the latter are not always visualized. Because the superior mesenteric artery originates in close proximity to the renal vessels, an aneurysm may be presumed to be infrarenal if it begins more than 1.5 to 2 cm caudad to this artery, even when the renal arteries cannot be imaged.

Aortic Aneurysm Rupture

Aneurysm leak or rupture is a catastrophic event. If the rupture is untreated, mortality is 100%. Only about 50% of patients survive long enough to be admitted to the hospital.[118] Emergency aortic aneurysm repair is indicated in any operative candidate, since the alternative is certain death. Even when surgery is performed, patient survival is poor, with between 30% and 65% of patients still living at 30 days.[30, 118] Traditionally, emergency aortic aneurysm repair usually involves prompt transfer to the operating room, rapid clamping of the aorta to establish hemostasis, usually at the level of the diaphragm, and then aortic graft insertion. Endovascular stent-graft insertions have been performed successfully in patients who are poor operative risks.[191]

A patient presenting with abdominal or back pain, a pulsatile mass (thought to be an aortic aneurysm), and severe hypotension should proceed directly to surgery. Many vascular surgeons also recommend that when the diagnosis is certain clinically (i.e., the patient has a known large AAA and abdominal pain), the patient should proceed directly to the operating room even if he or she is hemodynamically stable.[46, 233]

Unfortunately, only a minority of patients with ruptured aneurysms come to the emergency department with the classic triad of symptoms,[233] and only slightly more than half have characteristic acute back or abdominal pain or both.[2] Conversely, in many patients thought to have a ruptured aneurysm, other causes of abdominal pain are ultimately identified. In one series, only 18 of 65 stable patients with suspected aneurysms and abdominal pain had AAA ruptures.[133] Initial misdiagnoses (with false-negative as well as false-positive clinical diagnoses) can occur in as many as 60% of patients.[2] For this reason, CT is recommended as the procedure of choice for evaluation of *hemodynamically* stable patients with a suspected aneurysm when other diagnoses are also considered. Although some authors (Buss and coworkers[31]) disagree, it is generally believed that the delay imposed by obtaining a rapid, emergency CT scan in appropriately selected patients does not adversely affect patient morbidity or mortality.[133]

CT is quite sensitive in detecting aortic ruptures and can also identify other causes of abdominal pain in some patients when ruptures are not present. In addition to revealing whether a rupture is present, the CT scan can be used to assess the size and extent of an AAA. In fact, it may even be used to predict whether a ruptured aneurysm is infrarenal, juxtarenal, pararenal, or suprarenal.[46]

CT is preferred over MRI for imaging of a suspected ruptured aneurysm, because gravely ill patients are generally managed much better in the CT suite. CT technique in these patients requires only that a rapid examination be performed. Use of oral contrast material may be helpful for distinguishing duodenum from periaortic hematoma in a few patients; however, this is not commonly a problem. Administration of IV contrast material is not mandatory; however, in a few instances it may facilitate differentiation of perianeurysmal fibrosis from a contained leak. This is because fibrotic tissue demonstrates detectable enhancement, whereas periaortic hematoma does not enhance—unless free extravasation of contrast-enhanced blood from the aortic aneurysm occurs, in which case the diagnosis of rupture is easily made.

CT images should be acquired quickly, because even normotensive patients may suddenly become hemodynamically unstable. In fact, the false sense of security that sometimes develops when stable patients with ruptured aneurysms are being evaluated and prepared for surgery may lead to delays that subsequently adversely affect patient mortality.[266] CT images are usually obtained through the abdomen and pelvis with a collimation of 7 to 10 mm. Images should be reconstructed at contiguous 7- to 10-mm intervals.

When seen on CT scans, aneurysm ruptures are often extensive and easy to identify (Fig. 43–13). Acute extraluminal blood shows soft tissue attenuation. It has a vermi-

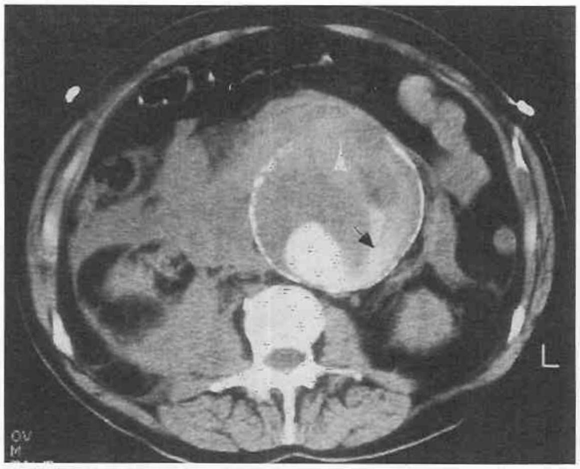

Figure 43–13. Ruptured abdominal aortic aneurysm. Contrast-enhanced CT scan demonstrates active intravasation of blood into the extensive aneurysm thrombus *(black arrow)*. Blood is also extravasating into the retroperitoneum through a large defect in the anterior wall of the aorta *(white arrowhead)*. Disruption of the aortic calcification can be seen.

form, finger-like appearance as it infiltrates between fascial planes in the retroperitoneum.[105, 233] Most often, blood accumulates in the perinephric space,[129, 233] although leaks into other retroperitoneal compartments, the duodenum, psoas muscle, IVC, and even into the peritoneal cavity have been observed.[68, 75]

Identification of the exact site of aortic rupture is possible only in some cases, when a focal disruption in aortic wall calcification is visualized or when there is an area of indistinctness between the aneurysm and the periaortic hematoma. Fortunately, emergency aortic aneurysm repair is performed in a similar fashion (by initially clamping the aorta near the level of the diaphragm), regardless of the exact site of leak; therefore, its identification is not essential.[233]

Occasionally, areas of rupture may be small and contained, and detection of extraluminal blood may be difficult or even impossible.[233] These areas may represent subacute, warning (or sentinel) bleeding episodes. These patients are at risk of massive rupture at any time.[68] Small, contained ruptures can produce a tiny amount of fluid or soft tissue–attenuation material adjacent to the aorta (Fig. 43–14). Slight changes in the distribution of aortic wall calcification, which can be difficult to identify if comparison studies are not available, may be produced by the aortic wall defect. As previously described, the presence of the draped aorta sign (in which the aortic wall is not identified posteriorly and the posterior aspect of the aorta is closely opposed to the vertebral bodies and follows their contour) strongly suggests that a contained leak may be present even when no periaortic fluid or soft tissue is identified.[92]

In some symptomatic patients, CT may demonstrate only an AAA without a draped aortic contour and with no obvious or subtle evidence of contained or free rupture. Greatorex and colleagues encountered six patients with surgically diagnosed ruptured AAAs; emergency CT examinations performed on these six patients within 24 hours of surgery were interpreted as showing no evidence of rupture.[84] In only one patient was the scan retrospectively believed to have been erroneously interpreted as negative for rupture. In one symptomatic patient, massive retroperitoneal hemorrhage was easily visualized on a subsequent CT scan obtained 28 minutes after the initial scan had revealed no extraluminal blood. The authors therefore suggest that even if an apparently nonruptured aneurysm is present in a patient with abdominal pain and in whom a diagnosis of aneurysm rupture is being considered, hospital admission and close monitoring of the patient are crucial. Emergency surgery may still be strongly considered in these patients regardless of the lack of evidence of aneurysm rupture according to the CT examination.

Alternatively, hemodynamically stable patients with large symptomatic aneurysms but no CT evidence of rupture may be able to undergo semielective aneurysm repair (after 24 to 48 hours of close monitoring). In some series, operative mortality falls drastically (to 17% from between 35% and 50%) when the patient can be prepared and when surgery can be performed in a semielective fashion.[233]

Many patients who are examined by CT to rule out aortic rupture have truly negative CT findings.[233] Nonetheless, because large aneurysms with no rupture cannot be reliably distinguished from those with small, subacute, contained, or impending ruptures, semielective repair may still be indicated if no other cause of abdominal pain can be identified. Fortunately, sometimes with a CT scan that is negative for rupture, other nonvascular causes of abdominal pain can be identified.

False-positive CT diagnoses of aneurysm rupture can be minimized if the radiologist is aware of certain potential pitfalls. Asymmetrical aneurysm thrombus and volume averaging of periaortic tissue with the aneurysm lumen at the level of the aneurysm neck can lead to the misdiagnosis of small contained ruptures in some instances. Perianeurysmal fibrosis can be confused with periaortic hemorrhage, particularly if scans are performed without IV contrast material (Fig. 43–15). As previously noted, if the duodenum is not opacified with oral contrast material, the third and fourth portions can sometimes be confused with periaortic hemor-

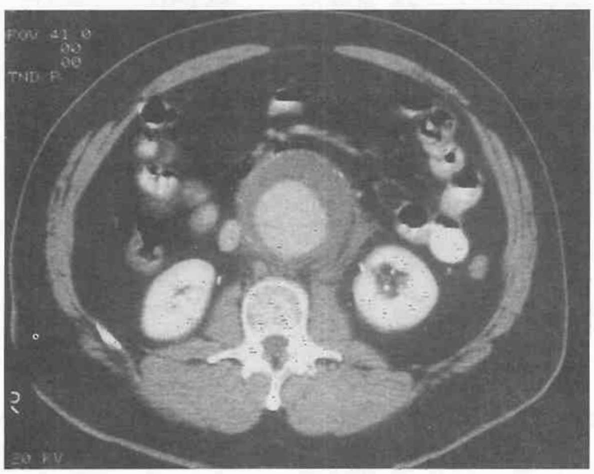

Figure 43–14. Ruptured abdominal aortic aneurysm. A small "contained" rupture is visualized along the left posterolateral aspect of this aneurysm on this contrast-enhanced CT image.

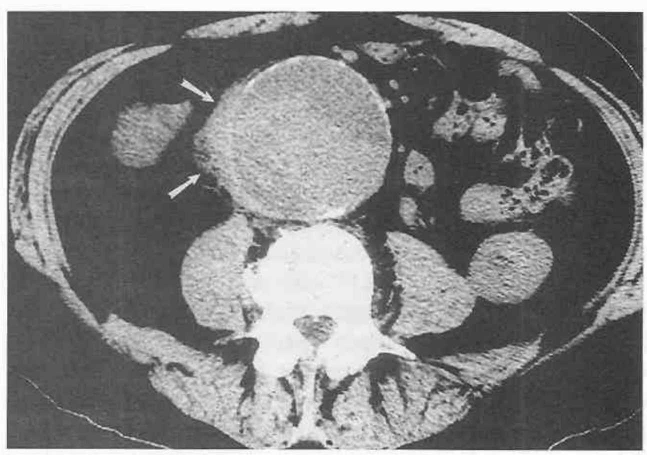

Figure 43–15. Perianeurysmal fibrosis mimicking aortic rupture. Poorly defined soft tissue attenuation material surrounds the right lateral aspect of the abdominal aorta *(arrows)* on an unenhanced CT scan. The patient had presented with acute severe back pain. The periaortic soft tissue was suspected to represent a small contained aneurysm rupture. At emergency surgery, only retroperitoneal fibrosis was found.

Figure 43–16. Enlarged lymph nodes (N) mimicking retroperitoneal hemorrhage in a patient with an abdominal aortic aneurysm (A) and metastatic prostate cancer. Nondynamically enhanced scan shows rounded and well-defined retroperitoneal nodes. The patient had presented with back pain.

rhage. Rarely, retroperitoneal lymphadenopathy can be mistaken for blood (Fig. 43–16).

Aortic ruptures have been rarely encountered in the absence of aneurysmal dilatation. These have been reported after blunt abdominal injury and as a result of nonaneurysmal bacterial aortitis.[155, 233] The latter diagnosis should, in fact, be considered in a patient who has a fever, positive blood cultures, atherosclerotic changes in the abdominal aorta, and periaortic soft tissue identified on CT or MRI.[45]

Once in a while, a large retroperitoneal hemorrhage develops in a patient who happens to have a large AAA (Fig. 43–17). Usually, the lack of relationship between the hematoma and the aneurysm can be delineated. The fat planes between the aorta and the surrounding hematoma are preserved. No disruption in aneurysm wall calcification is seen, and the aortic wall is not indistinct.

Other causes of retroperitoneal hemorrhage include blood dyscrasias, vasculitides, and renal infections.[43, 175] Nonspontaneous causes have included trauma, translumbar aortography, and renal biopsy.[43]

Aortic Dissection

Aortic dissections are relatively rare, accounting for only 1 in 10,000 hospital admissions.[103] Mortality rates of untreated dissections are extremely high, approaching 25% at 24 hours, 50% at 1 week, and 75% at 1 month.[6] Generally, a dissection involving only the descending aorta (DeBakey type III or Stanford type B) is treated with antihypertensive medication. If the ascending aorta is involved (DeBakey types I and II or Stanford type A), surgery (repair of the proximal extent or origin of the dissection) is required; however, exceptions occur. If flow to abdominal visceral organs or the extremities is compromised, emergency angiography may be warranted, during which time additional communications (fenestrations) between true and false lumina may be created or endovascular stents may be inserted.

When dissections involve the abdominal aorta, they almost always have originated in the thorax. An aortic dissection originating in the abdominal aorta is exceedingly rare and is usually produced iatrogenically (e.g., retrograde intimal tears produced by arteriographic catheters, guide wires, or intra-aortic balloon bumps) or develops as a result of blunt trauma.[203]

CT is extremely sensitive in depicting the intimal flap and the true and false lumina in both the chest and the abdomen of patients with an aortic dissection (Fig. 43–18). Today CT angiography is performed, clearly mandating that the patient receive a rapid bolus of IV contrast material. After the ascending aorta is evaluated, more scans are obtained farther into the abdomen to assess the inferior extent of the dissection and to determine whether the dissection is extending into the major aortic branch vessels. The intimal flap may extend into any of the major branch

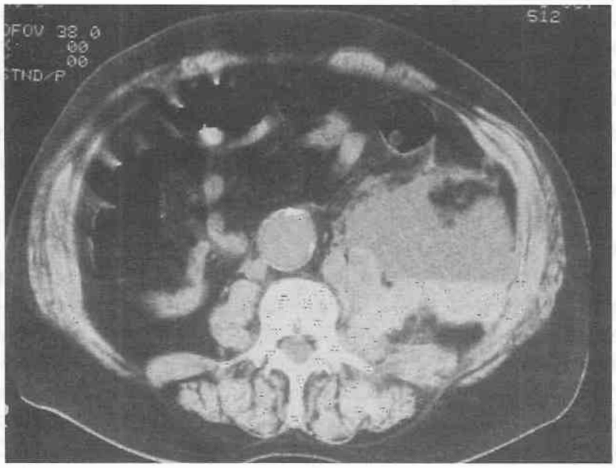

Figure 43–17. Retroperitoneal hematoma in a patient with a small abdominal aortic aneurysm. Unenhanced CT scan shows that the hematoma is separated from the aneurysm by uninfiltrated fat. The patient, who had received anticoagulation therapy, experienced sudden flank pain soon after cardiac catheterization.

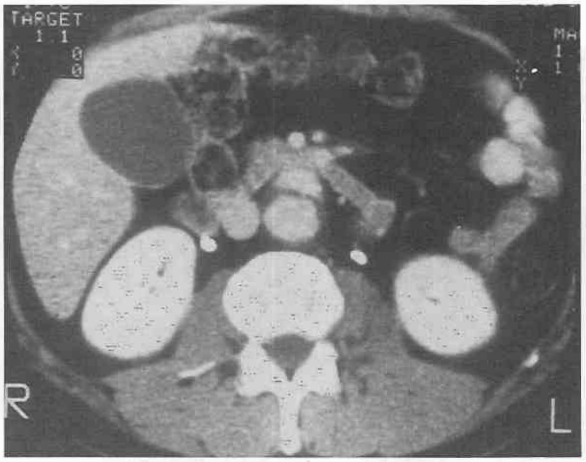

Figure 43–18. Aortic dissection. CT enhanced scan shows an aortic dissection in the midabdomen. The scan easily demonstrates the intimal flap between the anterior true lumen and the posterior false lumen.

Figure 43–19. Aortic dissection. *A,* Contrast-enhanced CT scan reveals extension of an intimal flap from a type III dissection into the left renal artery; the true *(arrowhead)* and false *(arrow)* lumina are easily identified. The renal artery involvement resulted in left renal hypoperfusion. Endovascular stent insertion was required to restore renal artery blood flow. *B,* The extension of the false lumen into the left renal artery is well seen on a coronal reformatted image. A small projection from the true lumen into the false lumen *(arrow)* may represent a penetrating atherosclerotic ulcer.

vessels (Fig. 43–19). Indeed, it is important to identify which major visceral artery branches communicate with which (true or false) lumina. Compromised blood flow in a branch vessel may necessitate emergency therapy.

Although MRI is sensitive in detecting aortic dissections, it is reserved primarily for problematic situations (e.g., when the CT arteriographic results are equivocal or when the patient cannot tolerate iodinated radiographic contrast media because of allergy or renal failure) (Fig. 43–20).[5] Differences in flow rate, and hence in signal intensity, between true and false lumina may facilitate correct MRI identification of a dissection, but they may also cause confusion. Slow-flowing blood can be mistaken for hematoma. Additionally, severely ill patients (and patients with suspected aortic dissections are often acutely ill) are more difficult to manage and observe in most MRI suites than in most CT rooms.

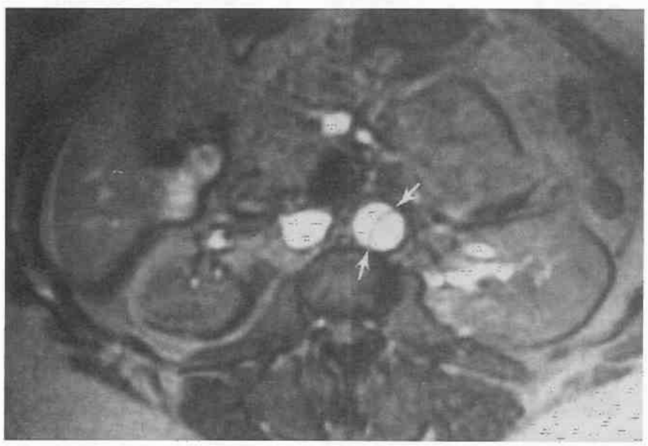

Figure 43–20. Aortic dissection. Limited flip-angle MR image demonstrates the intimal flap *(arrows)* between the bright signal in the true and false lumina.

Occasionally, the false lumen of an aortic dissection is completely thrombosed when first detected. Distinguishing an AAA from a chronic dissection containing a clotted false lumen may not be extremely difficult by CT or MRI.[273] The thrombus may have a similar appearance in both instances.

Heiberg and coworkers compared CT scans of 36 patients with aneurysms to scans of 24 patients with dissections.[99] Linear peripheral calcifications were more common in patients with aneurysms (70%) than in patients with dissections (20%), although neither the appearance nor the location of the aortic calcification was completely specific. Increased density of a thickened aortic wall on precontrast scans was seen in only one patient with an aneurysm but in 44% of patients with dissections. The residual lumen was round in 94% of patients with aneurysms but in only 29% of those with dissections. Differences in wall thickness or aortic size could not be demonstrated. The authors concluded that in some instances these features might be used to predict whether an aortic thrombus resides within a completely thrombosed dissection or within a thoracoabdominal aortic aneurysm.

Not surprisingly, medically treated aortic dissections may evolve with time. Yamaguchi and colleagues demonstrated that serial CT studies showed changes in false lumen size or the degree of thrombus in 7 of 13 patients with DeBakey type III dissections.[273] In each of their three patients whose false lumina were completely thrombosed initially, the false lumen disappeared or shrank by 1 to 2 months after the first scan. These authors concluded that CT might be used to monitor patients with medically treated dissections. Thus, serial CT or MRI examinations may prove helpful when a dissection is suspected and treated but the initial CT appearance is not diagnostic.

Penetrating Atherosclerotic Ulcers

Penetrating atherosclerotic ulcers of the aorta may lead to hemorrhage in the wall of the aorta and intimal displacement away from the media.[123] This leads to the creation of a false aortic lumen. Although penetrating ulcers, conceivably, may develop anywhere along the course of the aorta, they have almost always been identified in the descending thoracic aorta.

To our knowledge, only one case of a penetrating ulcer developing in the infrarenal abdominal aorta has been reported, and it resulted in development of an intramural hematoma.[177] When penetrating ulcers are present, the ulcers are frequently visualized on CT scans as focal irregular outpouchings extending off the aortic lumen (see Fig. 43–19*B*).

Treatment is controversial. Although a conservative (nonsurgical) approach has been effective in some hemodynamically stable patients, some authors recommend that all patients with penetrating ulcers be treated surgically.[177]

Small Aorta

In rare instances, the caliber of the aorta may actually be smaller than normal. This situation is commonly a result of either atherosclerotic aortic occlusive disease (with extensive atherosclerotic aortic calcification usually present) or severe hypotension (which is always clinically obvious) (Fig. 43–21).

Treatment of Abdominal Aortic Aneurysms

The preferred surgical treatment of AAAs is an end-to-end anastomosis with endoaneurysmorrhaphy. The proximal and distal ends of the graft are attached to uninvolved portions of the aorta, iliac, or femoral arteries in an end-to-end manner after incision and partial resection of the anterior wall of the aneurysm. The remaining aneurysm sac is then wrapped loosely around the graft and sutured closed.

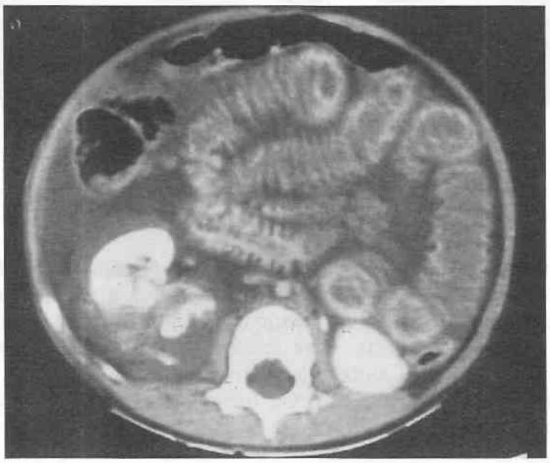

Figure 43–21. A small aorta and a slitlike inferior vena cava are noted on this contrast-enhanced CT scan. This pediatric patient was severely hypotensive. The right renal laceration, enhancing bowel, and hemoperitoneum can be seen.

This approach is recommended because blood flow patterns are physiologic (in contrast to end-to-side proximal anastomoses). In addition, the endoaneurysmorrhaphy is thought to lessen the incidence of injury to the vena cava, iliac veins, and lumbar vessels. Postoperatively, persistence of the aneurysmal shell around the graft provides an additional protective layer between the graft and the overlying duodenum, decreasing the frequency of postoperative aortoenteric fistulas.

Although endovascular stent-graft insertion is usually reserved for patients who are poor operative candidates, at some institutions this much less invasive alternative is now being performed as an alternative to elective aneurysm repair.[159] Preliminary studies have demonstrated that the mortality and long-term survival rates are similar for patients receiving standard operative grafts and for those receiving endovascular grafts; however, the expenditure of hospital resources (blood transfusions, time spent in the operating room or the intensive care unit, and time spent in the hospital) is much lower for patients treated with endovascular grafts.[173] It must be emphasized, however, that vascular surgeons must be available to perform emergency aneurysm repairs in any patient undergoing stent-graft insertion, since catastrophic complications such as aortic rupture, although very rare, may occur during the procedure.[178]

Endovascular stent-graft insertion appears to represent an excellent alternative to open surgical aortic aneurysm repair in some patients, but whether this procedure will ultimately replace surgery is not yet clear. The significance of the relatively common short-term complication of stent-graft leakage is not yet known, although some vascular radiologists now perform selective arterial embolization at the time of graft insertion in an attempt to reduce its incidence. Also, long-term morbidity has not yet been assessed.

Evaluation of the Post-treatment Abdominal Aorta

After Aortic Aneurysm Repair

CT is the imaging study of choice for evaluation of patients with suspected complications of aortic graft repair.[233] Several authors have recommended that CT also be performed for follow-up of patients long after aortic graft insertion even when no complications are clinically suspected.[122] This is because up to 14% of patients may develop additional areas of aneurysmal dilatation, either at the graft anastomoses or elsewhere. A significant minority of these complications may be significant, and additional treatment is required.

CT evaluation of these patients is best performed through the abdomen and pelvis at contiguous 7- to 10-mm intervals after dynamic bolus IV contrast enhancement. Although CT angiography is necessary for preoperative aortic aneurysm imaging, it is not necessary here. Visualization of the aortic branch vessels in great detail is not required. Use of IV contrast material is essential, however,

because it facilitates the distinction between anastomotic aneurysms and other perigraft fluid collections (e.g., hematomas, abscesses, seromas). In general, scans should be obtained after oral contrast material has been administered.

Although additional CT image acquisition prior to administration of oral contrast material has occasionally aided the detection of extravasation of contrast-enhanced blood from the graft into bowel in some patients with aortoenteric fistulas, usually no such extravasation can be identified even when these fistulas are present. Further, indirect signs of a fistula are almost always easily identified.

During CT or MRI evaluation after open aortic aneurysm repair, it is important to determine the presence of any perigraft fluid or air or aneurysm formation at the graft anastomoses. Normal aortic aneurysm grafts with endoaneurysmorrhaphy may have a CT or an MRI appearance strikingly similar to that of unrepaired aortic aneurysms. Initially, a thrombus in the wraparound aneurysmal sac may look like a thrombus around a centrally opacified blood-containing lumen in an aneurysm.

Subtle differences often exist. The lumen of the aortic graft is usually smooth and circular; however, the lumen of an aneurysm is commonly at least slightly irregular. The graft itself may have relatively high attenuation on CT and thus may be identifiable on precontrast scans (Fig. 43–22); after contrast enhancement, however, this distinctive feature is usually not apparent. On immediate postoperative scans, it is not unusual to see some perigraft fluid or air (Figs. 43–23 and 43–24). With time, the space between the aneurysm wrap and the graft should diminish. Usually, all perigraft air has disappeared by 3 weeks and all perigraft fluid by 3 months. Only a minimal amount of perigraft soft tissue, most likely corresponding to perigraft fibrosis, should be visible after several months have passed.

After Endovascular Stent-Graft Insertion

Helical CT or MRI is recommended for imaging patients after endovascular stent-graft insertion. In these patients, CT or MR arteriography may be helpful. Thus, in this instance, thinly collimated images should be obtained and images reconstructed at contiguous or overlapping intervals. Oral contrast material should not be administered to any patient in whom 3D reconstructions are to be created because it will produce artifacts and limit the utility of the reconstructed images. Although a number of studies have demonstrated that arterial phase images are the most sensitive for detecting stent-graft leaks,[80] biphasic scanning (during which time both arterial and portal venous phase images are obtained) has been found to be most accurate in one series.[77]

Endovascular stent-grafts are usually easily identified on CT scans because of their metallic components (Fig. 43–25).[78] On MR images, the metallic graft is not specifically seen and many stents may create susceptibility artifacts.

Several important observations should be made on CT

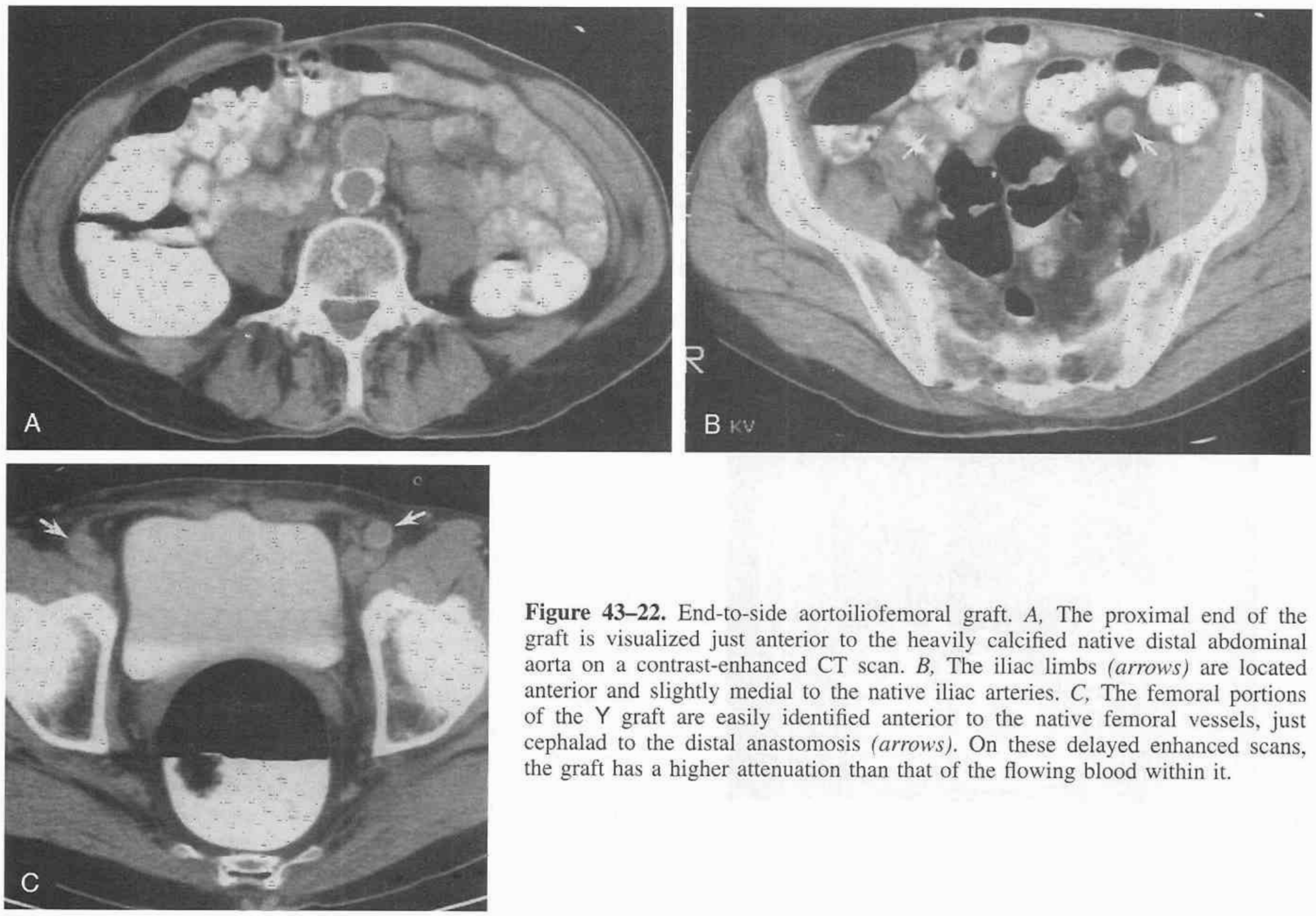

Figure 43–22. End-to-side aortoiliofemoral graft. *A,* The proximal end of the graft is visualized just anterior to the heavily calcified native distal abdominal aorta on a contrast-enhanced CT scan. *B,* The iliac limbs *(arrows)* are located anterior and slightly medial to the native iliac arteries. *C,* The femoral portions of the Y graft are easily identified anterior to the native femoral vessels, just cephalad to the distal anastomosis *(arrows)*. On these delayed enhanced scans, the graft has a higher attenuation than that of the flowing blood within it.

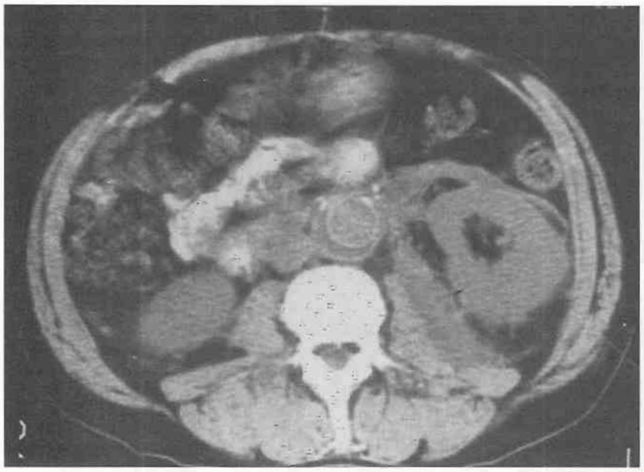

Figure 43–23. Endoaneurysmorrhaphy shortly after aortic aneurysm repair. Unenhanced CT scan demonstrates the partially calcified wall of the native aorta surrounding thrombus or perigraft fluid, which in turn surrounds the aortic graft. On this scan, the aortic graft is of higher attenuation than that of the blood in the aortic lumen. Extensive persistent hematoma from a recent aneurysm rupture in the retroperitoneum can be seen on the left.

scans or MR images obtained in patients after stent-graft insertion:

1. The widest diameter of the AAA should be measured because reduction in aneurysm diameter is considered to be the best indicator of adequate aneurysm exclusion by the graft.[78] Indeed, an increased aneurysm diameter should be viewed with concern, since an endograft leak may be present even when the CT scan does not demonstrate it directly.[255]
2. The diameters of the proximal and distal aneurysm necks should be measured because they may increase after stent insertion.[78]

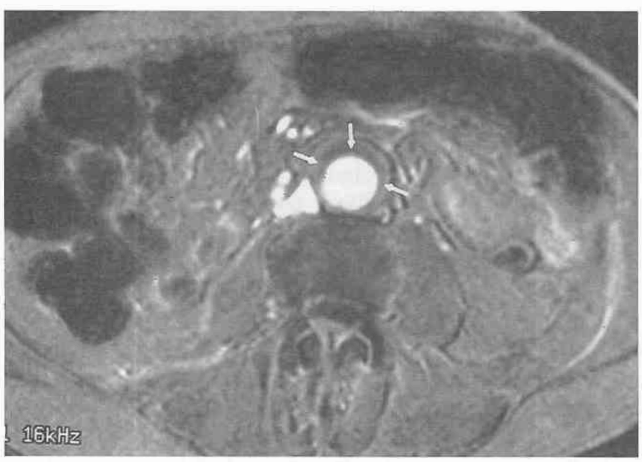

Figure 43–24. Endoaneurysmorrhaphy shortly after aortic aneurysm repair. Gradient-echo MR image reveals the high signal intensity of flowing blood within the aortic graft, but the blood and fluid between the graft and the native aorta *(arrows)* demonstrate low signal intensity. Normally, within about 3 months of surgery, most of the fluid between the graft and the aneurysm wrap is resorbed.

3. The images should be scrutinized for evidence of perigraft leaks (see later).
4. The patency of the inferior mesenteric and lumbar arteries should be assessed because these vessels, if patent, can serve as the source of perigraft leaks (resulting from retrograde filling of the aneurysm).
5. The configuration of the graft should be assessed. Graft deformation, angulation, or change in caliber can lead to migration.
6. The patency of the graft should be determined to ensure that thrombosis has not developed.[78]

Complications of Abdominal Aortic Aneurysm Treatment

Complications of conventional abdominal aortic graft surgery include the following:

- Graft infections (1% to 6%)[203]
- Aortoenteric fistulas (1% to 5%)
- Anastomotic aneurysms (up to 5%)
- Graft leak or rupture[233]

Surgical repair, usually with graft resection, is indicated in any patient in whom intra-abdominal and deep pelvic extension of graft infection, an aortoenteric fistula, or large or symptomatic pseudoaneurysm formation is identified.

Complications of endovascular stent-graft insertion may include leaks (20% to 47% of patients).[18, 77, 78, 81, 159, 160, 173] In one series, for example, leaks were detected in 13 of 50 patients 1 week (12 patients) or 3 months (1 patient) after stent-graft insertion.[77] Stent-graft occlusions and migrations may also be encountered.

Graft Infections

Aortic graft infections are potentially catastrophic early complications of aortic bypass surgery.[246] In most patients, groin infections develop initially at the distal anastomoses of aortobifemoral bypass grafts. In these instances, the diagnosis is obvious. If the groin infection remains undetected until 6 weeks or more after surgery, usually it has spread into the pelvis and sometimes the retroperitoneum.

Graft infection with extension into the pelvis or retroperitoneum often results in the formation of fluid collections and/or air in the vicinity of the aortic graft; both fluid collections and air are easily visualized on CT scans. The fluid collections are often irregular and septate.[88] Perigraft fluid and hematomas may be confused with abscesses in the immediate postoperative period (within 6 weeks of surgery), since air and fluid are normally visible in the operative bed.[190] Follow-up CT scans can be obtained when infection is considered likely in patients in whom retroperitoneal air visualized by CT may be secondary to recent surgery. Pathologic gas collections (often posterior and multilocular in relation to the graft) increase in size over time, whereas postsurgical collections of air (usually unilocular and anterior) should diminish.[190] Indium-labeled white blood cell scans may prove useful in some instances (Fig. 43–26). Ultimately, CT-guided needle aspiration may be necessary for a definitive diagnosis.[233]

CT diagnosis of graft infection in patients who are not

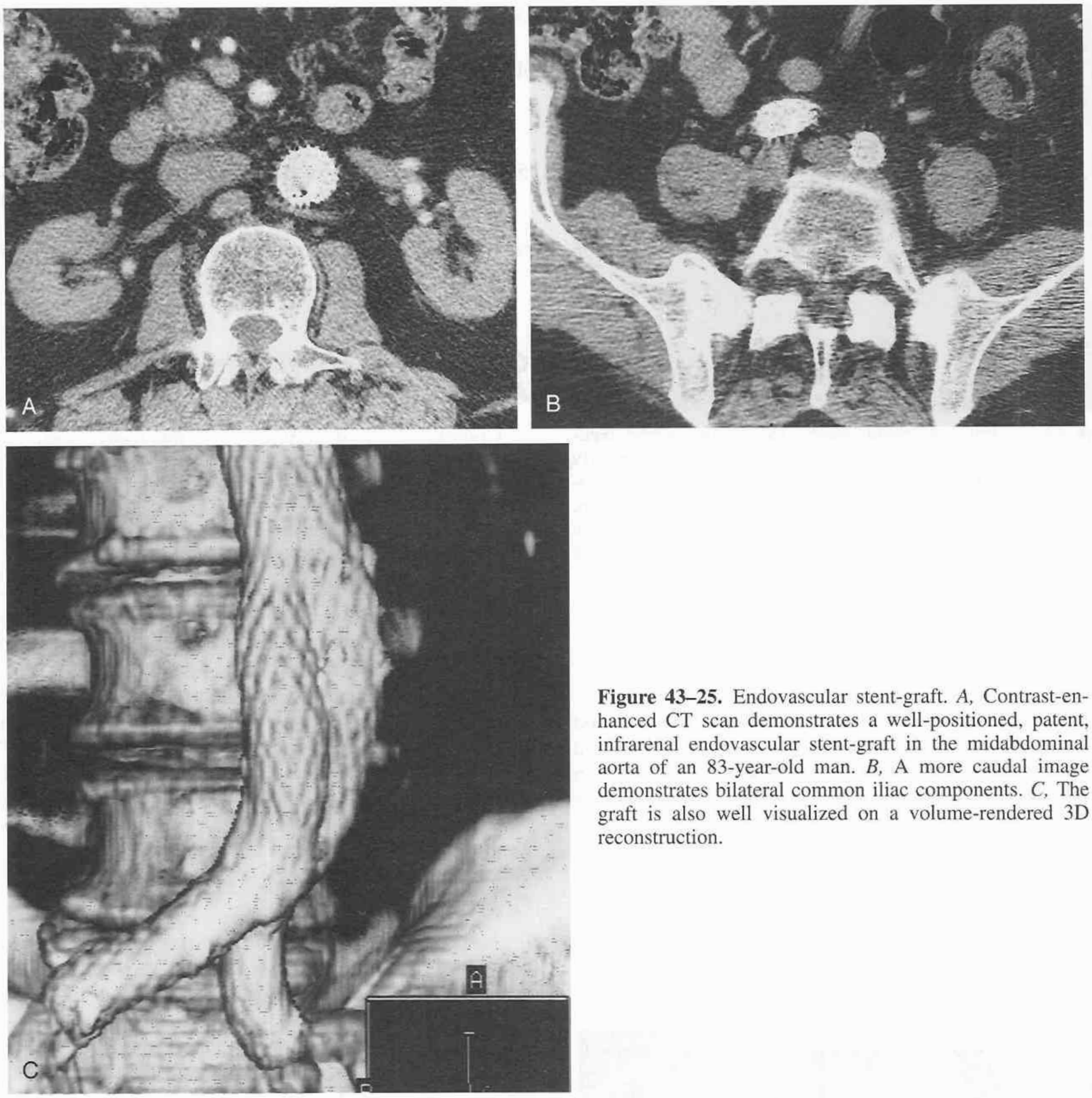

Figure 43–25. Endovascular stent-graft. *A,* Contrast-enhanced CT scan demonstrates a well-positioned, patent, infrarenal endovascular stent-graft in the midabdominal aorta of an 83-year-old man. *B,* A more caudal image demonstrates bilateral common iliac components. *C,* The graft is also well visualized on a volume-rendered 3D reconstruction.

in the immediate postoperative period (>3 months after surgery) is not nearly as difficult.[64] Any perigraft soft tissue, fluid, or air in these patients almost always suggests infection (Fig. 43–27).[190]

Treatment of graft infections varies, depending on the extent of the infection. A localized groin infection can occasionally be treated conservatively with antibiotics; however, once intra-abdominal spread occurs, most vascular surgeons recommend complete graft removal with extra-anatomic bypass.[230] Some researchers have successfully performed in situ graft replacement in these patients (after débridement and antibiotic irrigation of the graft bed), although the reinfection rate is still relatively high at over 20%.[277] Partial graft excision is considered to be a suboptimal treatment, resulting in the need for additional surgical procedures in as many as 60% of patients.[19]

Some radiologists have advocated the use of percutaneous techniques as a precursor to surgery or for definitive treatment of infected grafts in patients who are not good operative candidates.[222] Belair and colleagues treated 11 patients with percutaneous drainage of infected perigraft fluid collections.[20] Sepsis resolved in nine patients, four of whom were treated with percutaneous drainage and antibiotics alone. Graft resection followed percutaneous drainage in the remaining five patients. Perioperative mortality and complication rates were actually lower in the patients whose surgery was preceded by percutaneous treatment than in patients who proceeded directly to surgery.

Aortoenteric Fistulas

Aortoenteric fistulas result from the persistent pulsatile pressure of the proximal graft anastomosis on the duodenum or from a low-grade infection that disrupts the suture

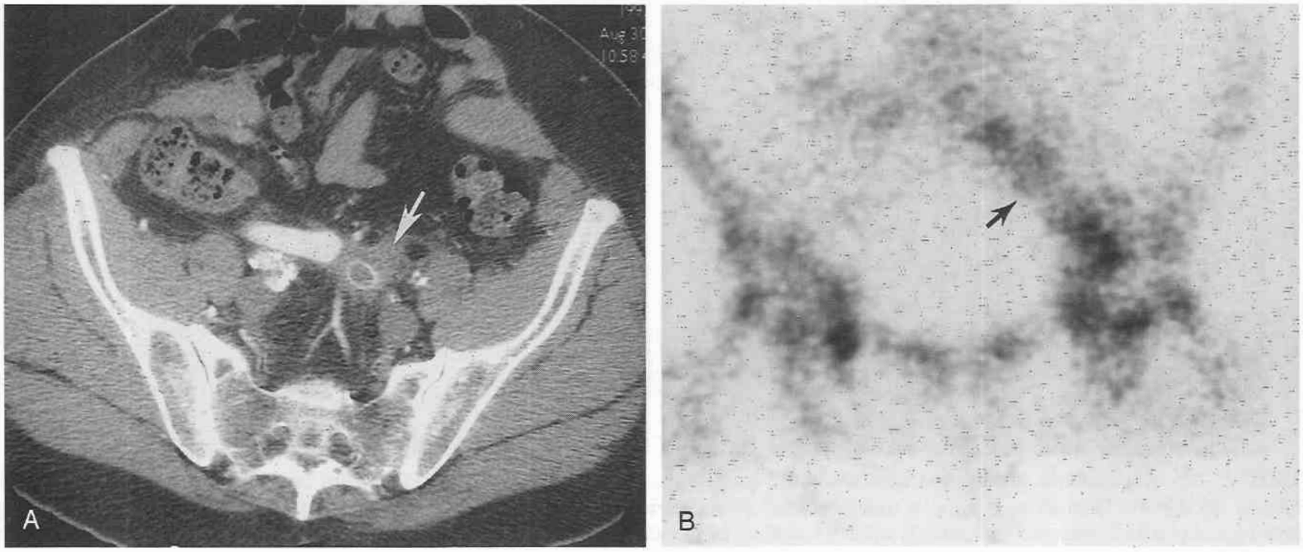

Figure 43–26. Infected aortic graft. *A,* Unenhanced CT scan shows fluid-attenuation material *(arrow)* surrounding the left iliac limb of an aortobifemoral Y graft. In this case, the infection is not caused by a gas-producing organism. *B,* Anterior view from an indium-labeled leukocyte scan demonstrates increased uptake in the left external iliac region *(arrow)* corresponding to the infected aortobifemoral graft.

line. Usually, these fistulas do not develop until many months after surgery. In one series, aortoenteric fistulas were not encountered until a mean of 32 months after surgery (range, 8 to 52 months).[17] The fistulas usually develop between the aortic graft and adjacent duodenum, although communication with the jejunum, ileum, and colon has also been observed.[233]

The main clinical manifestation is gastrointestinal (GI) tract bleeding; however, bleeding may be occult in some patients. If bleeding remains untreated, however, life-threatening hemorrhage eventually develops in all patients.[17]

CT is able to detect aortoenteric fistulas, usually by showing indirect signs of their presence (i.e., extraluminal air and adjacent bowel wall thickening) (Fig. 43–28). Extravasation of high-attenuation, contrast-enhanced blood from the aorta into the duodenum can be seen only in a patient given IV, but not oral, contrast material (Fig. 43–29). Even when this technique is employed, visualization of such extravasation is extremely rare in a patient stable enough to undergo CT (probably because bleeding is either intermittent or very slow in most patients referred for CT). For this reason, CT examinations are usually performed after administration of oral and IV contrast material.

On many occasions, patients with aortoenteric fistulas may have perigraft fluid and soft tissue and extraluminal air but no identifiable bowel wall thickening. In these instances, a specific diagnosis cannot be made and differentiation from aortic graft infection is not possible.[151] Because treatment of aortoenteric fistulas and treatment of infected grafts are similar (usually consisting of graft resection), the inability to distinguish between these two complications is not crucial. Although extra-anatomic bypass is often performed if evidence of overt infection is seen, in situ replacement of the graft is now commonly performed.[17, 233]

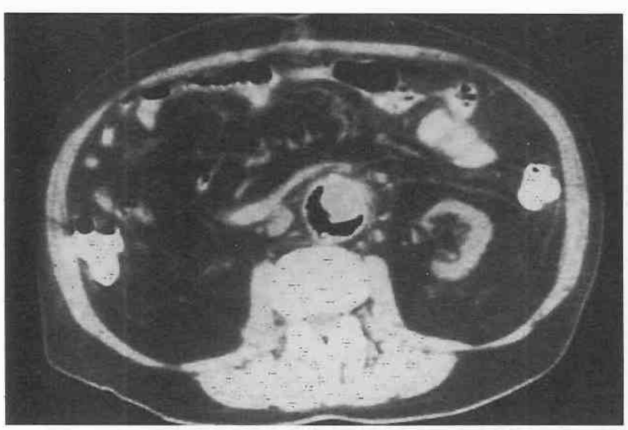

Figure 43–27. Infected aortic graft. Air has accumulated within the space between the graft and the surrounding native aorta on this unenhanced CT scan. The patient had undergone endoaneurysmorrhaphy.

Anastomotic Aneurysms

Anastomotic aneurysms occur most frequently in the femoral area and usually are identified well after surgery. In one series, they were detected an average of 6.2 years after aortic aneurysm repair.[50] The incidence of anastomotic aneurysms is estimated to be 0.8% at 5 years, 6.2% at 10 years, and 36% at 15 years.[165, 176] These aneurysms may originate either from pseudoaneurysm formation, as a result of breakdown of the suture line, or from true aneurysm formation, secondary to progression of atherosclerotic disease proximal or distal to one of the anastomoses. In one series, for example, 7 of 10 anastomotic aneurysms were pseudoaneurysms and the remaining 3 were true aneurysms.[176]

Dynamically enhanced CT can often be used to facilitate a specific diagnosis by its ability to identify a mass or collection contiguous with the aorta or iliac or femoral vessels at the level of one of the anastomoses in which

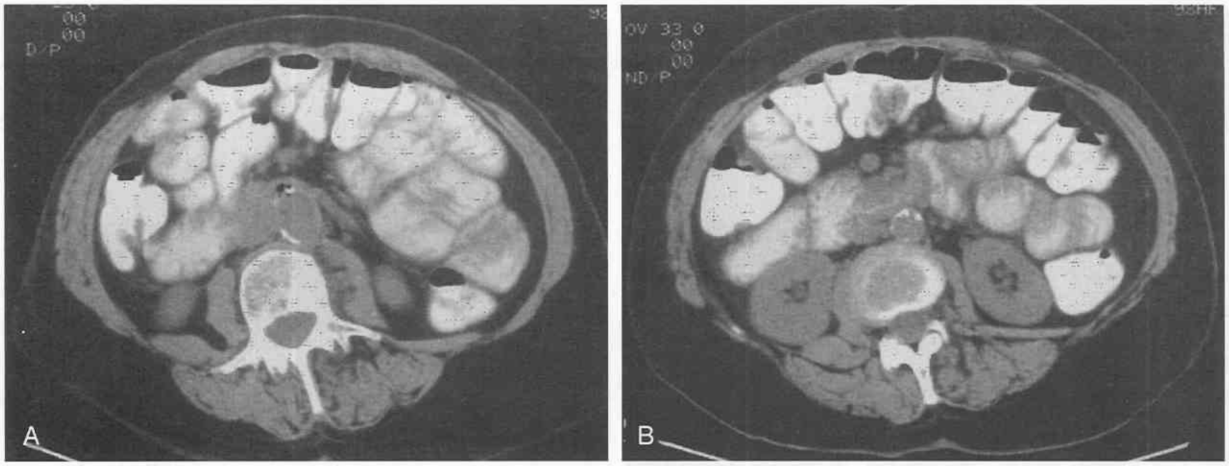

Figure 43–28. Aortoenteric fistula. *A,* Unenhanced CT scan shows a small amount of air, identified between the aortic graft and the adjacent duodenum. Distinction cannot be made between aortoenteric fistula and graft infection on the basis of this image. *B,* A slightly more cephalic scan (same patient) reveals mild thickening of the third portion of the duodenum. This finding, coupled with a history of gastrointestinal tract bleeding, suggested the correct diagnosis.

contrast-enhanced flowing blood can be visualized (Fig. 43–30). On unenhanced CT scans, however, anastomotic aneurysms must be distinguished from other perigraft masses and collections (e.g., hematomas, abscesses, lymphoceles). Such a distinction is crucial, particularly if percutaneous aspiration is considered in a patient with a suspected graft infection (because aspiration of a pseudoaneurysm is not desirable).

Treatment of large (>2 cm in maximal diameter) or symptomatic aneurysms consists of resection. Small, asymptomatic aneurysms can be followed.

Graft Rupture

Rupture of a prosthetic graft is an uncommon late complication, usually occurring 8 to 20 years after its placement.[236] Presentation may be acute (with ischemia, pain, or shock), or indolent (with rest pain or a groin mass). The cause of graft rupture may be rupture of an anastomotic pseudoaneurysm or a defect in the graft, possibly from fabric deterioration. Graft degeneration more commonly involves the distal branches in a Y graft but may also involve the main aortic segment.

Treatment depends on the site of graft deterioration. If distal deterioration has occurred, resection of the graft defect is performed. If the proximal portion of the graft has deteriorated, the graft is replaced. CT usually demonstrates either a pseudoaneurysm or dilatation of the graft.[233]

Endovascular Stent-Graft Leaks

It is not yet clear whether the fairly common development of graft leaks will have a significant adverse effect on long-term prognosis after endovascular stent-graft insertion. There are several types of endovascular stent-graft leaks[18]:

Type I (perigraft leak): A leak may develop at the proximal or distal insertion site. This leak may develop immediately or may occur over time as the relationship of the endovascular graft to the aorta changes, since the aortic diameter and orientation is expected to change as a response to graft insertion and aneurysm exclusion.

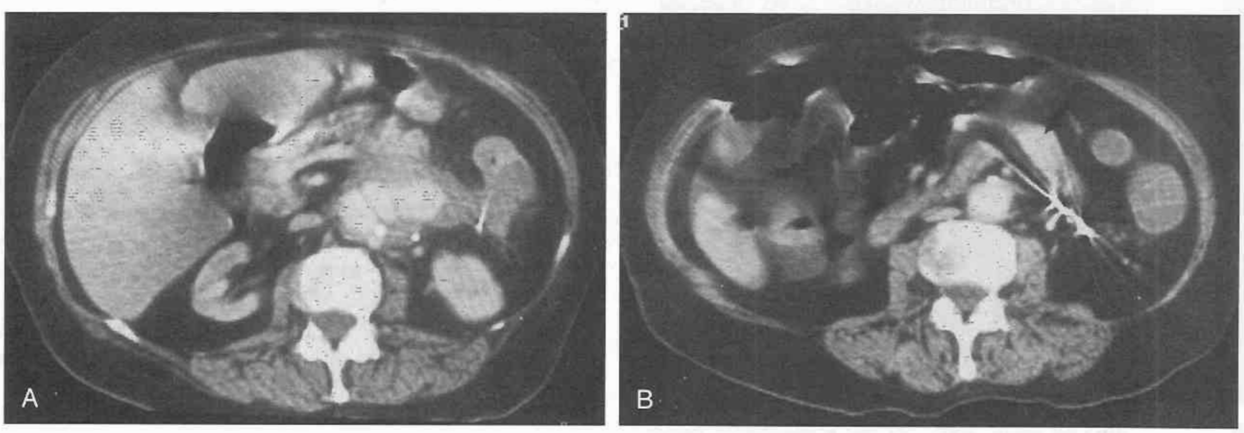

Figure 43–29. Aortoenteric fistula. This patient was studied before oral (but after intravenous) administration of contrast medium. *A,* Contrast-enhanced blood extends from the aorta (in a pseudoaneurysm) toward bowel in the left upper quadrant. *B,* A more cephalic scan demonstrates contrast-enhanced blood in the proximal jejunum *(arrow)*, confirming the diagnosis of aortoenteric fistula.

Figure 43–30. Anastomotic aneurysm in an 84-year-old woman who had undergone aortic aneurysm repair years earlier. CT scan demonstrates a large mass in the left periaortic region at the level of the proximal anastomosis *(arrows)*. Contrast-enhanced flowing blood can be identified in the center of this anastomotic aneurysm.

Type II (endoleak): A leak may also occur as a result of retrograde flow into the aneurysm sac from patent aortic branch vessels, most commonly via the inferior mesenteric or lumbar artery.

Types III and IV: Less commonly, a graft leak may be caused by graft fabric tears, disintegration, or flow through the graft itself as a result of the porous graft wall.

At present, many persistent leaks are treated aggressively, often by angiographic embolization, because it is believed that these leaks predispose patients to aortic rupture, much as did the original untreated aneurysm.[17, 18] Some suggest, however, that leaks developing through retrograde flow through aortic branch vessels can be treated conservatively (i.e., merely followed with sequential CT examinations), provided that the diameter of the aneurysm sac decreases over time, since these are least likely to eventually lead to rupture.[112] Leaks at the proximal ends of the stent-grafts are thought to be at greatest risk of rupture.[78]

Endograft leaks are often identified on CT or MRI as focal collections of contrast-enhanced blood external to the graft. These collections may or may not be within the aneurysm (Fig. 43–31). Some have suggested that endograft leaks should be suspected if the CT or MRI examination demonstrates an increase in the diameter of the excluded aneurysm, even when the leak itself is not visualized.[112] In one report, aneurysm rupture developed 16 months after stent-graft insertion.[255] The patient had undergone two CT scans, the first immediately after stent-graft insertion and the second 7 months later. Neither scan demonstrated a leak; however, the aneurysm size had increased on a follow-up scan.

Helical CT is thought to be superior to MRI in detecting endograft leaks because the endograft can be visualized directly on CT scans, whereas it appears merely as an area of signal void on MR images. Despite the perceived advantages of CT, MRI can certainly be used to detect endograft leaks as well, and both are considered superior

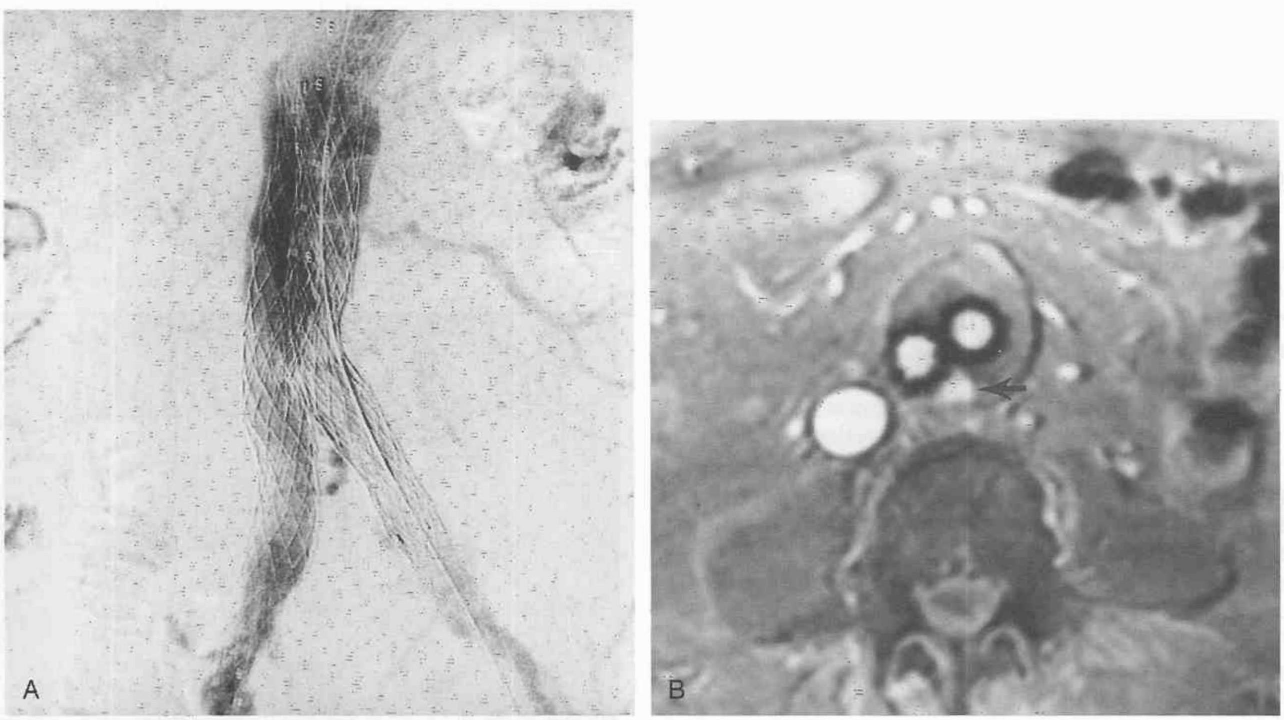

Figure 43–31. Endovascular stent-graft with leak. *A,* Digital radiograph obtained at the time of insertion demonstrates a long endovascular stent-graft extending from the abdominal aorta into both common iliac arteries. *B,* Gadolinium-enhanced, T1-weighted MR image reveals a focal collection of high signal intensity external to the stent but within the aneurysmally dilated aorta *(arrow)*; this indicates a leak. On other images, this leak was noted to be contiguous with a lumbar artery, indicating that it was caused by retrograde flow from this vessel. The signal void created by the graft can be seen.

to aortography. In one series, helical CT identified leaks in 13 patients with endografts.[77] In contrast, aortography identified the leak in only 8 of these 13 patients. Selective or superselective injections were required for angiographic identification of leakage in the remaining five patients.

CT and MRI may also be used to detect the cause of an identified endograft leak, thereby facilitating treatment planning. Leaks that lie outside the aortic aneurysm (perigraft leaks) are usually caused by mechanical problems related to graft insertion or to the changing orientation of the graft with the aneurysm. Intra-aneurysmal leaks that are separate from the prosthesis and anterior are probably the result of retrograde flow from the inferior mesenteric artery.[77] Intra-aneurysmal leaks that are posterior and lateral and that have a base with the aneurysm margin are probably caused by retrograde flow through the median sacral or lumbar arteries (see Fig. 43–31).

Endovascular Stent-Graft Migration and Other Complications

Other long-term complications of endovascular stent-graft insertion include:

- Thrombosis (reported in 0% to 15% of patients)
- Peripheral embolization distal to the graft
- Migration
- Disconnection of components of modular or multiple grafts[95, 253]

Stent-graft migration can produce additional complications. In one report, migration and kinking of a stent-graft resulted in formation of an aortoenteric fistula 20 months after insertion.[95] Thrombosis of the graft and change in graft position or morphology can easily be detected by CT (Fig. 43–32).

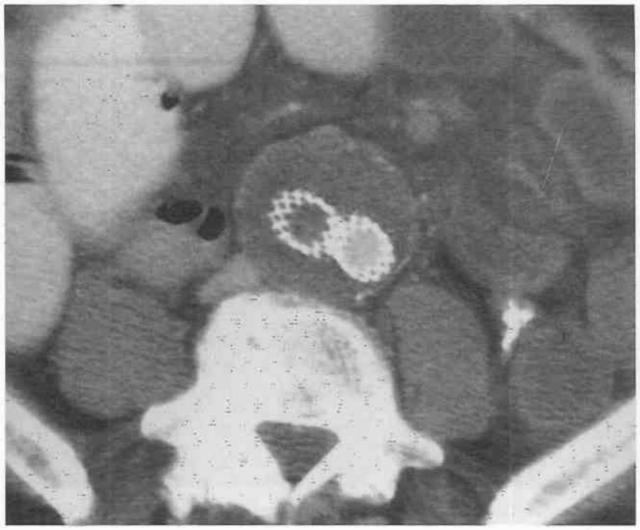

Figure 43–32. Endovascular stent-graft with thrombosis of a limb. Intravenous contrast-enhanced CT scan in a 68-year-old man who had undergone insertion of an endovascular stent-graft (2 months earlier) reveals contrast-enhanced blood flowing through the left common iliac limb but no enhancement in the right common iliac limb. The right limb is completely thrombosed. The aortic aneurysm surrounding the graft is also completely thrombosed but is still quite large, probably because the thrombus there has not had time to be resorbed.

Veins

Normal Anatomy

The IVC is formed by the confluence of the two common iliac veins, usually at the level of the fourth or fifth lumbar vertebral bodies, just caudad to the aortic bifurcation. The IVC courses to the right of the aorta, becoming slightly more ventral in location just before it traverses the diaphragm.[128]

The IVC is formed by the development and partial regression of the three paired venous systems in the embryo: the postcardinal veins, the subcardinal veins, and the supracardinal veins. Normally, the right supracardinal vein becomes the infrarenal portion of the IVC, the subcardinal vein and its anastomoses become the perirenal and suprarenal portion of the inferior vena, and the confluence of the hepatic veins forms the intrahepatic portion of the IVC. The upper portions of the right and left supracardinal veins form the azygous and hemizygous systems.[47] The normal IVC is easily identified on essentially all CT and MRI examinations.

The gonadal veins are located just lateral to the ureter and anterior to the psoas muscles in the lower abdomen. They ascend parallel to and cross anteriorly over the ureters (about half-way between the IVC bifurcation and the level of the renal hila) and then continue cephalad just medially to the ureters, usually emptying into the left renal vein (left gonadal vein) or the IVC (right gonadal vein). Despite their relatively small size in many patients, the gonadal veins are commonly visualized. On occasion, they may appear prominent in patients with no identifiable pathologic cause of dilatation (Fig. 43–33). This prominence, therefore, is probably a normal variant.

Venous Abnormalities

A variety of abnormalities of the retroperitoneal veins can be encountered, including a number of IVC venous

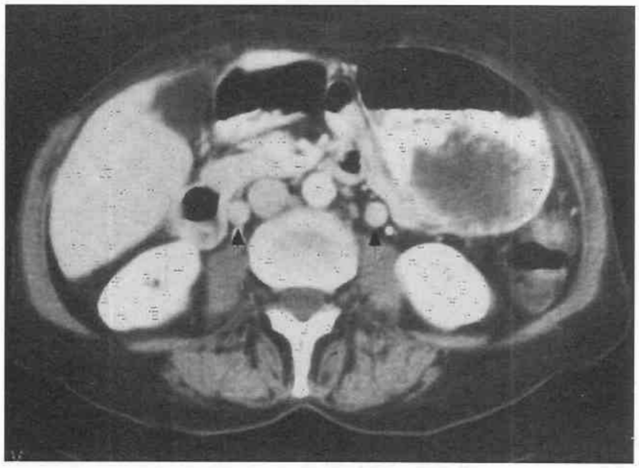

Figure 43–33. Prominent gonadal veins *(arrows)* are visualized on this dynamically enhanced CT scan. They should not be confused with enlarged retroperitoneal lymph nodes.

congenital anomalies. A thrombus may form in the IVC and gonadal veins, either because of spread of more distally located thrombi or as a result of a neoplasm. The retroperitoneal veins may become dilated, providing a pathway for collateral blood flow. On rare occasions, air can be identified in the IVC.

Cross-sectional imaging is now performed occasionally to assist interventional radiologists in planning treatment of venous thrombosis. By showing the extent of the thrombus, these studies can assist the interventionist in planning for insertion of the IVC filter.

In the text that follows, the common venous anomalies and abnormalities of the IVC and gonadal veins are detailed. CT evaluation of patients before and after placement of the IVC filter is reviewed next.

CT and MRI Technique

Retroperitoneal venous abnormalities are usually detected on CT studies performed to evaluate other structures. For this reason, CT scans are often obtained with relatively wide image collimation (of 7 to 10 mm) and relatively large reconstruction intervals (of 7 to 10 mm). When detailed evaluation of the retroperitoneal veins is required, however, it is prudent to obtain contiguous or even overlapping reconstructions of more thinly collimated images; these scans should be obtained following dynamic IV injection of contrast material.

In most instances, a rapid bolus of contrast material can help differentiate a blood vessel from a lymph node. Both the ability to follow a rounded structure on sequential images (indicating the vessel's tubular shape) and the higher attenuation of enhanced and flowing blood within the vessel lumen are helpful in making this distinction. Helical CT scanning is most efficient. If 3D reconstructions are to be created, image collimation should be 2.5 to 3 mm, with images reconstructed at 1.25-mm intervals.

Because of its capability to distinguish blood vessels from other retroperitoneal structures, MRI is preferred over CT when retroperitoneal venous imaging is specifically desired. Coronal and sagittal images are also easily obtained. Both "black-blood" (T1-weighted and T2-weighted spin-echo) and "bright-blood" (gradient-echo and 2D and 3D time-of-flight) imaging sequences can be employed. In particular, gradient-echo images in both the axial and the sagittal plane are rapid sequences that can provide good evaluation of anatomy and can facilitate assessment of veins for intraluminal thrombi. MRI contrast agents (e.g., gadolinium) produce brisk venous enhancement. When this approach is coupled with use of 3D reconstruction techniques (e.g., maximum intensity projection), excellent images of the retroperitoneal veins can be obtained.

Venous Anomalies

Failure of normal embryologic development may result in many possible venous anomalies, but only a small number have actually been reported. Recognition of these variants with CT and MRI prevents them from being confused with other abnormalities. Furthermore, knowledge of these anomalies is helpful before surgery, particularly in patients undergoing a shunt procedure for portal hypertension, kidney donation, AAA repair, or nephrectomy. In one series, for example, it was found that 40% of retroaortic left renal veins had been injured in a large group of patients undergoing abdominal aortic surgery.[27]

Circumaortic Left Renal Vein

Circumaortic left renal veins are thought to result from partial persistence of the posteriorly located left supracardinal vein and a midline left-to-right supracardinal anastomosis. In one series of 433 patients undergoing CT examinations, 4.4% were found to have this condition.[217]

When a circumaortic vein is present, the ventral portion of the left renal vein is usually normal in location. This component drains the inferior and ventral portions of the left kidney and traverses anterior to the abdominal aorta before inserting into the IVC. After draining the kidney, the dorsal vein, which drains the superior and dorsal aspects of the left kidney, continues posterior to the abdominal aorta and usually inserts several centimeters more caudad into an area of saclike dilatation of the IVC.[252]

The ventral vein is always equal in size to or larger than the dorsal vein.[217] Both ventral and dorsal components of circumaortic left renal veins are commonly identified with CT and MRI. The presence of the retroaortic component is suggested, however, even when it is not directly seen, if a medially located triangular diverticulum off the IVC is identified at or below the level of the ventral left renal vein.[132] The detection of a circumaortic left renal vein is usually an incidental observation. As previously noted, this usually does not affect patient care unless surgery is anticipated.

Retroaortic Left Renal Vein

A retroaortic left renal vein forms when the ventral component of a circumaortic renal vein has involuted. This anomaly is less common than a circumaortic left renal vein, having been reported in 1% to 3.3% of patients.[217, 252] In the previously cited review of 433 CT examinations, retroaortic renal veins were detected by CT in 1.8% of patients.[217] Cross-sectional imaging findings are notable for absence of the ventral left renal vein (Fig. 43–34). The dorsally located renal vein is often visualized just caudad to the level of the renal hila.

Transposition of the Inferior Vena Cava (Left-Sided Inferior Vena Cava)

A left-sided IVC, resulting from persistence of the infrarenal left supracardinal vein and regression of the right supracardinal vein, occurs in 0.2% to 0.5% of the population.[161] It appears as a round, tubular structure to the left of the aorta that extends superiorly to the left renal vein. The suprarenal portion of the IVC continues cephalad in its normal right-sided location because the subcardinal portion of the IVC is not involved.[128]

Duplication of the Inferior Vena Cava

Duplication of the IVC, occurring with an incidence of 0.2% to 3%, results from the persistence of both the infrare-

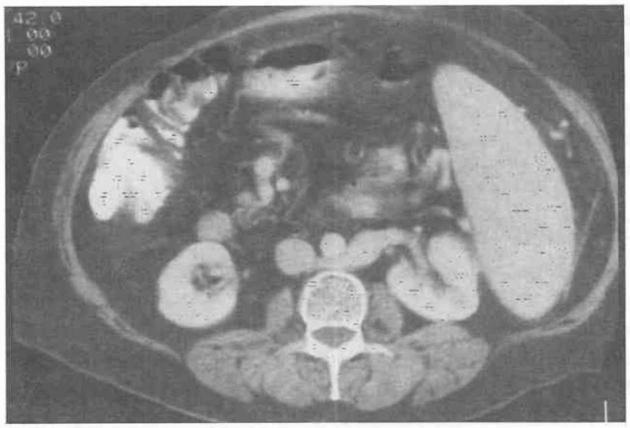

Figure 43–34. Retroaortic left renal vein in a patient with splenomegaly, as seen on a dynamically enhanced CT scan.

nal right and the infrarenal left supracardinal veins.[115, 161, 254] Usually, the left-sided IVC drains into the right by emptying into the left renal vein. Only a right-sided IVC is seen cephalad to this level (since subcardinal development is again normal) (Figs. 43–35 and 43–36). It is not uncommon for one of the vessels to be dominant. Bolus CT examination may not result in simultaneous or equal enhancement of both the right and the left portions of the IVC because contrast media may flow preferentially into the dominant vessel.[115]

Periureteric Venous Ring, Circumcaval or Retrocaval Ureter

Occasionally, an abnormally positioned IVC or a periureteric venous ring at the level of the third or fourth lumbar vertebral body medially displaces the right ureter. This abnormality, termed the *circumcaval ureter*, or *retrocaval ureter*, occurs with a frequency of 0.9 per 1000 patients.[188] Most patients have a single right preureteric IVC, which is thought to represent persistence of the right posterior cardinal vein with failure of development of the infrarenal right supracardinal vein.[188, 226]

Symptoms (secondary to obstruction), when present, usually appear late. CT and MRI can be used to identify a circumcaval ureter if the right ureter partially encircles the inferior cava, passing first posteriorly and then medially to the IVC (Fig. 43–37).[136] Lateral positioning of the upper abdominal IVC in relation to the right ureter without an identifiable retrocaval component of the ureter, although seen in all patients with circumcaval ureters, is usually a normal variant (visualized in 6% of the general population).[136]

Azygous Continuation of the Inferior Vena Cava

Azygous continuation of the IVC results both from failure of the hepatic and right subcardinal veins to merge and from persistence of a suprarenal right subcardinal–to–right supracardinal anastomosis, allowing venous drainage to continue up the azygos vein to the superior vena cava.[42]

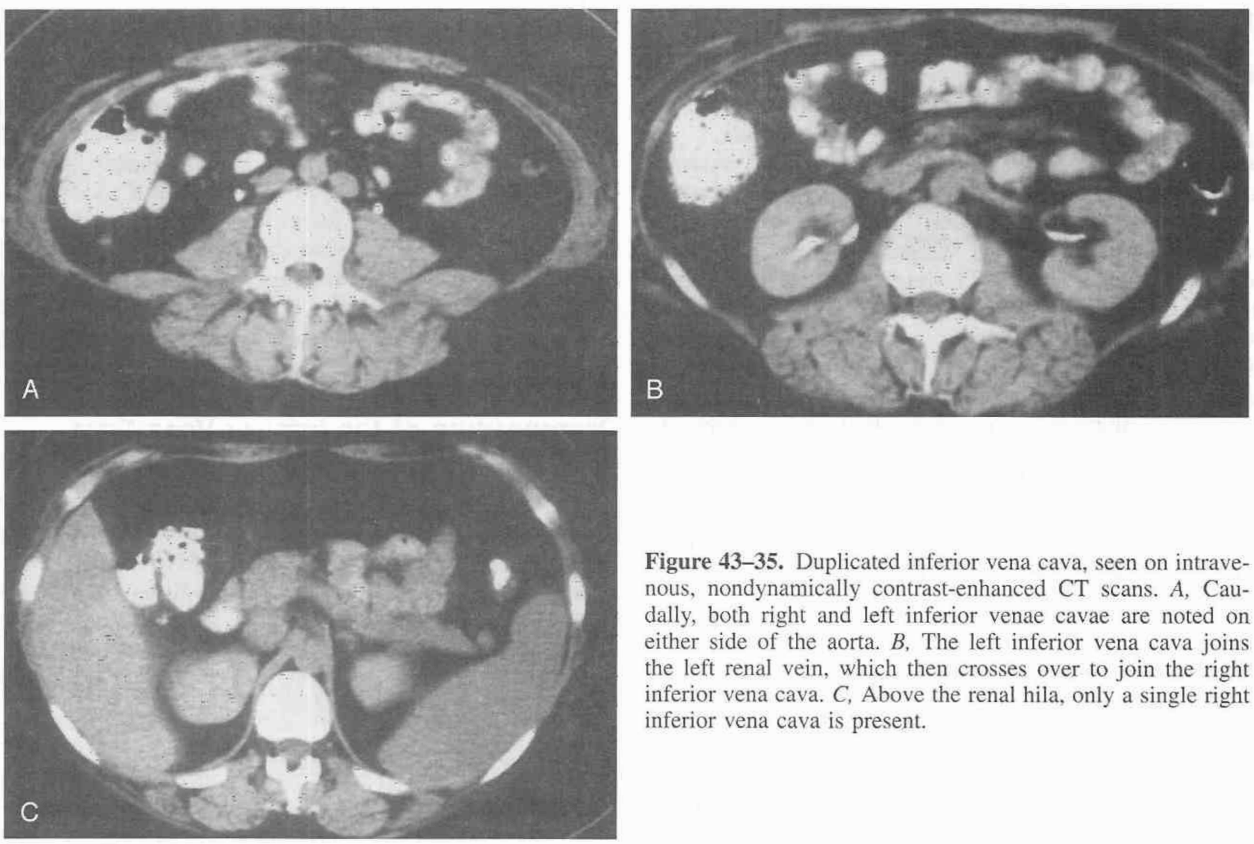

Figure 43–35. Duplicated inferior vena cava, seen on intravenous, nondynamically contrast-enhanced CT scans. *A,* Caudally, both right and left inferior venae cavae are noted on either side of the aorta. *B,* The left inferior vena cava joins the left renal vein, which then crosses over to join the right inferior vena cava. *C,* Above the renal hila, only a single right inferior vena cava is present.

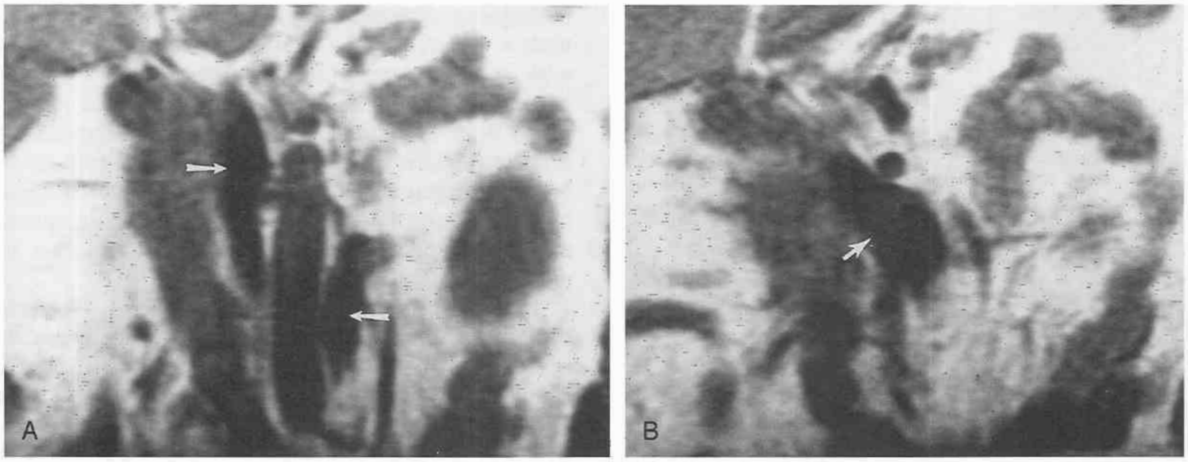

Figure 43–36. Duplicated inferior vena cava. *A,* Coronal T1-weighted, spin-echo MR image shows portions of both the right and left inferior venae cavae *(arrows).* The left inferior vena cava is located entirely caudad relative to the level of the left renal vein. *B,* MR image in a more anterior location demonstrates the enlarged left renal vein (into which the left inferior vena cava has emptied) *(arrow)* crossing the midline to drain into the right inferior vena cava.

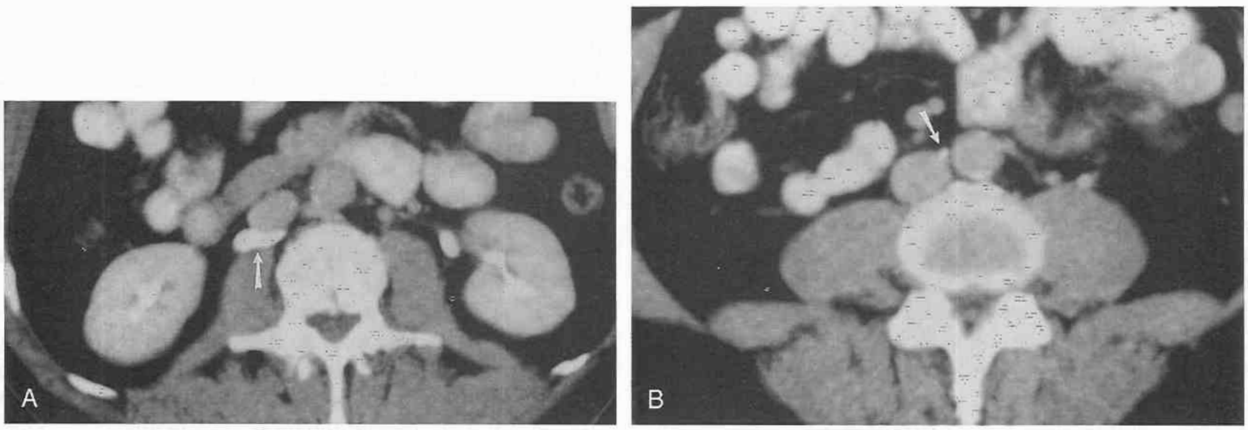

Figure 43–37. Circumcaval ureter. *A,* CT scan demonstrates the proximal portion of the right ureter *(arrow)* posterior to the inferior vena cava as it courses medially from the ureteropelvic junction. *B,* On a slightly more caudal image, the ureter *(arrow)* is located quite medially before continuing inferiorly in its more normal lateral position.

This anomaly is observed only rarely. In a series of 1055 noncardiac patients, none demonstrated this abnormality.[115] Associated abnormalities include asplenia, polysplenia, and abnormal abdominal or cardiac situs.

CT or MRI reveals enlarged azygous and hemizygous systems in the upper abdomen and chest (Fig. 43–38).[158] These vessels may be confused with enlarged retrocrural lymph nodes, although their tubular nature and the brisk enhancement after bolus injection of contrast material usually allow for their correct identification. Cases of accessory azygous continuation of a left-sided IVC also have been reported (Fig. 43–39).[60]

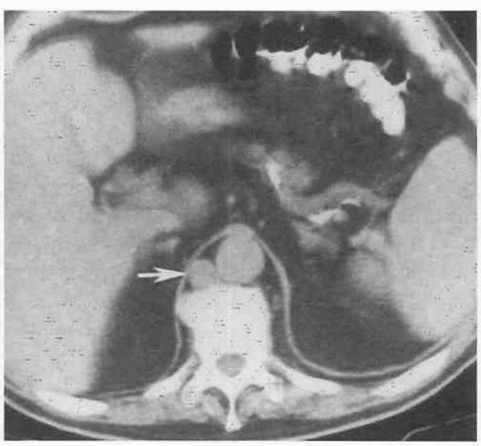

Figure 43–38. Azygous continuation of the inferior vena cava. Nondynamically enhanced CT scan demonstrates marked enlargement of the azygos vein *(arrow).* The subhepatic, suprarenal portion of the inferior vena cava is absent.

Venous Thrombosis

Thrombus formation may be detected in the IVC or its branches[69] (Figs. 43–40 and 43–41). Retroperitoneal tumor thrombus formation can be seen in patients with a multi-

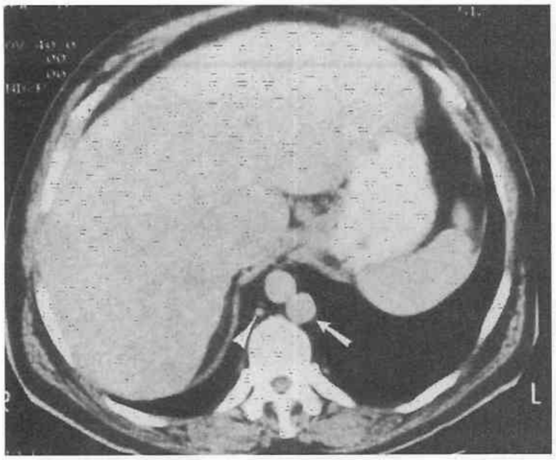

Figure 43–39. Hemiazygous continuation of a left inferior vena cava. Nondynamically enhanced CT scan shows an enlarged hemiazygos vein *(arrow)* but a normal-sized azygos vein *(arrowhead)*. The subhepatic, suprarenal portion of the inferior vena cava is absent. The liver is enlarged and heterogeneous because of the presence of infiltrative metastatic disease.

tude of various primary cancers. The most common include renal[121] and adrenal cancers, but thrombi have also been demonstrated to be a result of direct extension of other primary neoplasms, including pancreatic cancers, sarcomas, and endocrine neoplasms. IVC thrombi may also be seen as an extension of lower extremity or pelvic deep vein thrombosis. Thrombi may occasionally be encountered in patients with coagulation disorders. Some of these patients with coagulopathy have isolated blood dyscrasias and others have paraneoplastic syndromes.

Gonadal vein thrombosis is being diagnosed with increasing frequency, probably because it is easy to identify with CT and MRI. Although gonadal vein thrombosis has been seen traditionally in postpartum women, in women with endometritis or pelvic inflammatory disease, or after gynecologic surgery (Fig. 43–42), it is now occasionally detected in patients with malignancies (particularly those

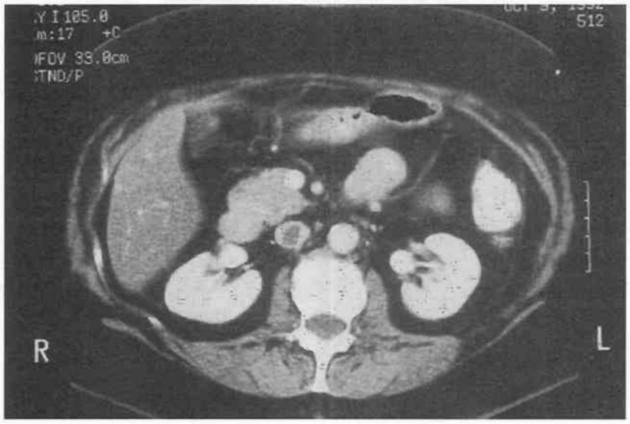

Figure 43–40. Inferior vena cava (IVC) thrombus. Dynamically enhanced CT scan shows the margin between the clot and the wall of the IVC to be sharply defined. Delayed images would not reveal any significant change in this appearance.

undergoing chemotherapy) (Fig. 43–43) and in patients with a variety of GI inflammatory diseases.[113, 114] Patients with typical postpartum or postgynecologic surgery gonadal vein thrombosis have infected thrombi and must be given both antibiotics and anticoagulant agents. Appropriate treatment for patients with gonadal vein thrombosis related to malignancy or GI tract inflammation has not yet been determined with certainty; however, it appears that antibiotics are not indicated and anticoagulation is often unnecessary.[113, 114]

In contrast to gonadal vein thrombosis, isolated septic thrombosis of the IVC is a rare finding, usually encountered in the critically ill. These patients must be managed aggressively with antibiotics and anticoagulants and, occasionally, even with surgical ligation of the IVC.

When imaging patients with suspected retroperitoneal venous thrombosis, the practitioner must determine not only whether a thrombus is present but also the extent of any thrombus that is identified. This information may be crucial for determining treatment. For example, it may be used to help direct subsequent IVC filter placement in a patient with a sterile inferior vena caval thrombus.[102]

CT affords easy identification of a thrombus in retroperitoneal vessels. The involved vessel is usually enlarged on the CT scan. Prominent collateral vessels may be present. If IV contrast material has been administered, the thrombus itself is identified as a low-attenuation filling defect, in which case, a definitive diagnosis can be made without the need for any additional imaging (see Fig. 43–40). The wall of the thrombosed vessel enhances brightly. When a tumor thrombus is present, the tumor vessels within the thrombus can be seen to enhance, facilitating distinction from a bland thrombus (see Fig. 43–41).[121]

It is important not to confuse heterogeneous IVC enhancement (a *pseudothrombus*), often seen on early images of a dynamically enhanced CT scan, with a *thrombus* (Fig. 43–44). Such heterogeneous contrast enhancement is caused by the low attenuation of unenhanced centrally located blood (from the lower extremities and pelvis) surrounded by higher-attenuation enhanced blood (entering the IVC from the renal veins) on CT images obtained early in the course of a bolus injection of contrast material. Unenhanced central blood in a patient with this pseudothrombus is usually not nearly as well defined as is a true thrombus. Dynamic CT flow artifact disappears as time passes; it is not be present if subsequent images are obtained.

MRI offers several advantages over CT in the assessment of potentially thrombosed veins:

1. Imaging can be performed in any plane.
2. IV contrast medium is not required.
3. Sensitivity, specificity, and accuracy of noncontrast MRI in detecting a venous thrombus are all exceedingly high (ranging between 97% and 98%).[242]

The accuracies of several noncontrast MRI techniques have been evaluated.[9, 242] Although both spin-echo and gradient-echo images have high sensitivities, gradient-echo images are much more specific.[242] A combination of both techniques is most accurate.[238, 242]

With MRI, errors in interpretation are most likely to be made when small, partially occluding thrombi are present.

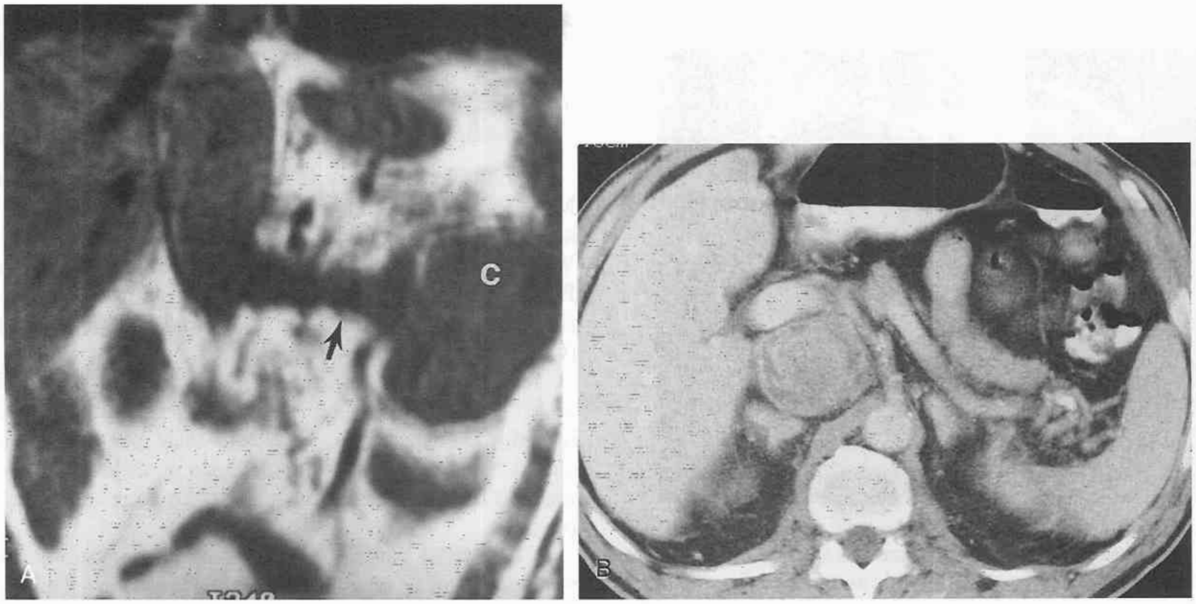

Figure 43–41. Inferior vena cava thrombus. *A,* Coronal T1-weighted MR image of a large left renal cancer (C) in a 68-year-old man reveals a large amount of thrombus extending into the left renal vein *(arrow)* and inferior vena cava. *B,* A contrast-enhanced CT image through the inferior vena cava thrombus demonstrates it to be very heterogeneous because it contains areas of contrast enhancement. This indicates that tumor thrombus (which contains its own blood vessels) is present. Identification of a tumor thrombus, rather than a bland thrombus, does not necessarily alter subsequent treatment.

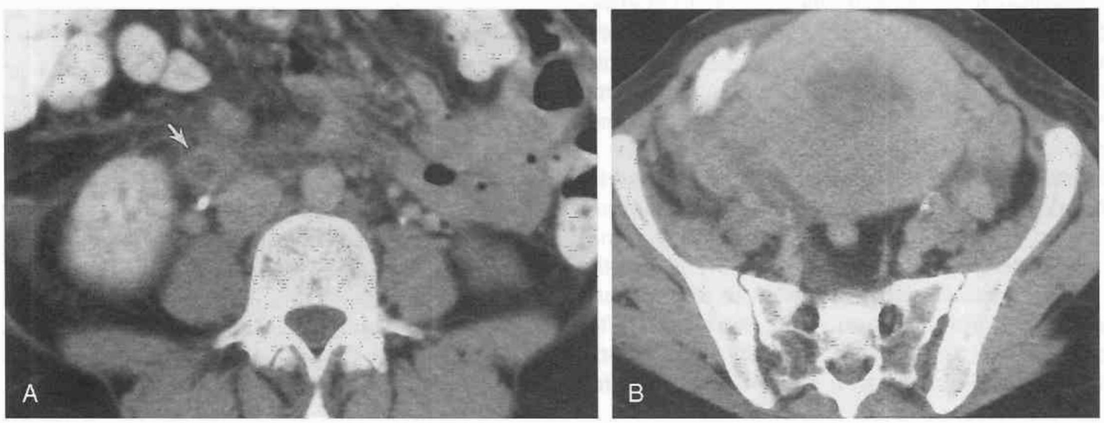

Figure 43–42. Gonadal vein thrombosis. *A,* Contrast-enhanced CT scan shows low-attenuation material within the lumen *(arrow)* of the right ovarian vein in a 22-year-old woman in whom a fever developed 24 hours after delivery. The wall of the vein is enhancing. The appearance is specific for venous thrombosis. *B,* A CT image through the pelvis reveals the enlarged uterus after delivery.

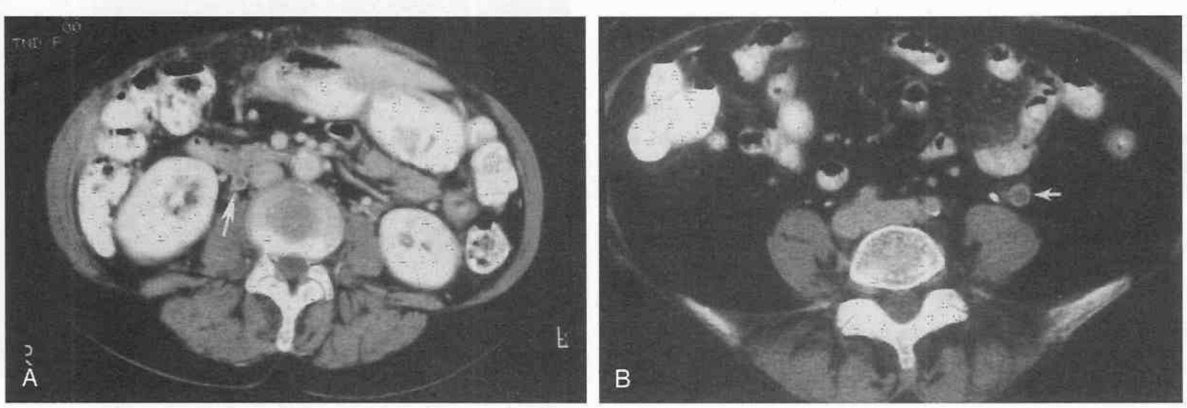

Figure 43–43. Gonadal vein thrombosis. *A,* Enhanced CT scan shows a low-attenuation clot in the right gonadal vein *(arrow)* of a patient with breast carcinoma. She had been receiving high-dose chemotherapy. *B,* On this enhanced CT scan from another patient with cancer, the thrombus is easily visualized in the left gonadal vein *(arrow).*

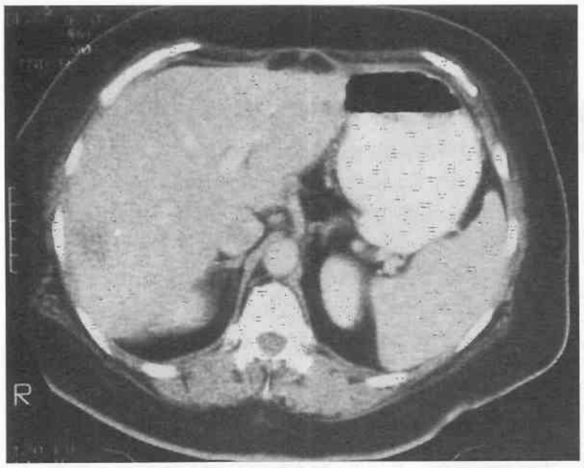

Figure 43–44. Inferior vena cava pseudothrombus. Early images on this dynamically enhanced CT scan demonstrate centrally, not yet enhanced inferior vena cava blood from the pelvis and lower extremities, surrounded by already enhanced blood from the renal veins. On delayed images, the inferior vena cava became homogeneous. Low-attenuation liver lesions are also present.

Occasionally, when spin-echo images are interpreted, false-negative diagnoses can be made because a low- to intermediate-signal-intensity thrombus can be mistaken for slowly flowing blood. In contrast, on spin-echo images false-positive diagnoses of thrombosis may result from misinterpretation of slowly flowing blood as thrombus; and on gradient-echo images, misdiagnosis may result from inability to detect high-intensity signal in small patent branch vessels.

MRI enhanced with gadolinium diethylenetriamine-penta-acetic acid (Gd-DTPA) can usually easily depict retroperitoneal venous thrombosis, particularly when the IVC is involved. Contrast-enhanced MRI can also be used to distinguish bland thrombi from tumor thrombi.[70] After contrast enhancement, the signal intensity of tumor thrombus may increase significantly in a fashion similar to that of the primary tumor.

MRI can identify the presence or absence of a thrombus, and with its multiplanar ability it is also extremely accurate in identifying the extent of tumor and components of a bland thrombus.[122] It has also been suggested that MRI can determine the age of a thrombus. In a study by Soler and colleagues, an acute thrombus (clinically evident for less than 1 week) was seen to have homogeneous signal 86% of the time on spin-echo images.[238] Heterogeneous signal intensity was seen in 75% of nonacute thrombi thought to be related to methemoglobin formation in the clot.

Inferior Vena Cava Filters

IVC filters may be indicated for the following:

1. Patients with lower extremity or pelvic venous thrombosis and recurring pulmonary emboli despite anticoagulation therapy.
2. Patients with lower extremity or pelvic venous thrombosis for whom anticoagulation therapy is contraindicated.[247]
3. Patients for whom anticoagulation therapy must be discontinued (e.g., because a complication has developed).[247]
4. Patients with a free-floating IVC thrombus even when anticoagulation agents can be safely administered.

A number of types of IVC filters are on the market. Most filters used today are permanent. The most well known is the Greenfield filter (Meditech/Boston Scientific, Watertown, Mass.). Others include the Vena-Tech filter (B. Braun Medical, Evanston, Ill.), the Simon Nitinol filter (Bard Radiology, Covington, Ga.), and the Bird's Nest filter (Cook, Bloomington, Ind.).

Temporary and retrievable filters have also been developed.[168] These filters must be removed within 2 weeks of insertion because after 3 weeks they become endothelialized.[163] The role of such devices is undefined, but they may be used increasingly in the future for short-term prophylaxis.

CT or MRI can be used to evaluate the retroperitoneal venous anatomy before IVC filter placement. This is done to identify the location and extent of any venous thrombi and to identify congenital abnormalities of the IVC and other veins in the abdomen that may affect the placement of the filter. For example, if there is a duplicated IVC, two separate filters may need to be placed (one in each infrarenal IVC).

CT is at least as accurate as venography in determining whether the filter is positioned at the proper level (Fig. 43–45). The normal filter position is usually between the IVC bifurcation and the renal veins. In some patients (e.g., those in whom thrombus extends more cephalad, as may occur in patients with renal cancer and renal vein and IVC tumor invasion), a suprarenal position may be safely used.[102] CT and plain abdominal radiographs can also help determine whether the filter is appropriately angulated.[166]

Complications of filter placement are not uncommon. It has been estimated that strut perforation may occur in as many as 40% of patients, although, fortunately, it is rarely symptomatic.[50] Filter malposition at the time of insertion

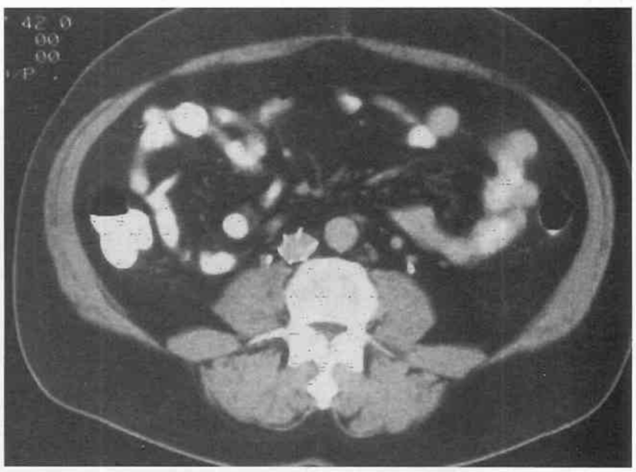

Figure 43–45. Inferior vena cava filter. Nondynamically enhanced CT scan shows that the metallic struts of this Greenfield filter are relatively evenly distributed, abutting all sides of the inferior vena cava.

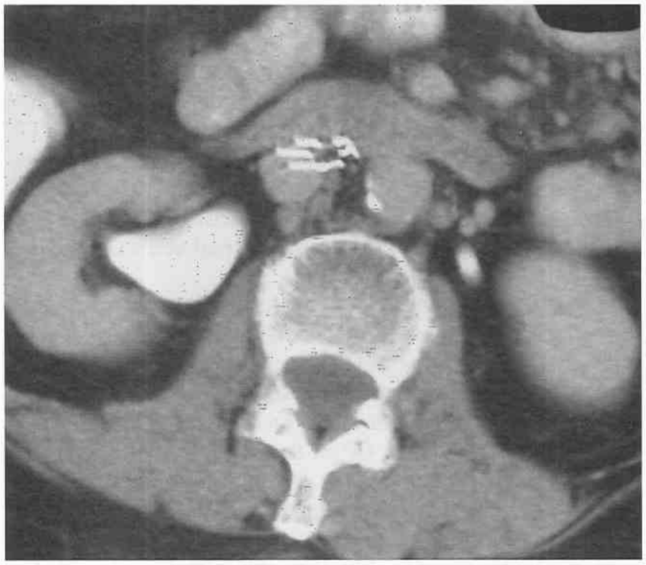

Figure 43–46. Perforation of an inferior vena cava wall by an inferior vena cava filter. The Greenfield filter has migrated almost completely through the inferior vena cava. All of the struts are located either anteromedial to or along the anteromedial wall of the inferior vena cava.

is not infrequent, having been encountered in up to 10% of patients, and probably relates to the experience of the interventionalist.[50] CT can be used to identify these potential complications and others, including hematomas, pseudoaneurysms, infections, IVC occlusion, vessel disruption, incomplete filter opening, filter fractures, and migration (Fig. 43–46).[215]

MRI can be performed safely in patients with an IVC filter. The newer Greenfield filters are made of titanium, which is less ferromagnetic than stainless steel. The Simon Nitinol filter is composed of a nickel and titanium alloy that is relatively nonferromagnetic.[147, 264] Even filters that are ferromagnetic can be safely imaged. In vitro experiments have not detected any evidence that the small amount of magnetic torque that develops at a field strength of 1.5 T results in filter migration.[147, 249] However, Liebman and colleagues caution that when filters are angulated, greater torque is exerted and the risk of filter movement increases.[147]

Although MRI is at least as effective as CT in evaluating patients before filter placement, it is of little or no use in evaluation after filter insertion; this is partly because the filter is not directly seen. Instead, the imager can infer the position only by the presence of signal void. Furthermore, these magnetic susceptibility artifacts, which are caused by most filter types,[249] degrade image quality to such an extent that abdominal MRI studies in these patients are of limited quality. In contrast, MRI of the head, pelvis, spine, and extremities is usually free of artifacts and can be performed without complication.[264]

Dilated Veins

Dilatation of the veins has several causes. Dilated azygos, hemiazygos, and lumbar veins may develop in patients with IVC obstruction. In the presence of portal hypertension, the portal venous system may spontaneously decompress into the left renal vein or, more rarely, into the lumbar or gonadal veins, and the increased blood flow often causes vessel enlargement.[216] The gonadal veins may enlarge during pregnancy or may enlarge as a normal variant (see Fig. 43–33).[216]

Normal retroaortic anastomoses between the azygos and hemiazygos veins may be prominent and may be confused with pathologic retrocrural nodes.[248] Dilated retroperitoneal veins may occasionally be confused with enlarged para-aortic lymph nodes because both may have the same shape and distribution.[60] This is particularly true on CT examinations performed without IV contrast material or in those rare instances in which abnormal retroperitoneal lymph nodes enhance briskly (as with highly vascular retroperitoneal lymph node metastases). Fortunately, distinction between veins and lymph nodes is usually easily accomplished with contrast-enhanced CT and MRI (when any technique is used).

On enhanced CT studies, retroperitoneal veins are usually of much higher attenuation compared with retroperitoneal lymph nodes. On MR images, in most instances, patent veins are characterized by signal void on spin-echo sequences and high signal intensity on gradient-echo images. Sometimes, however, when flow through collateral vessels is slow or when retroperitoneal vessels are thrombosed, flow may not be demonstrated on either contrast-enhanced CT or MRI. The CT or gradient-echo MRI appearance of the retroperitoneal veins in these patients may mimic that of enlarged retroperitoneal lymph nodes.[234]

Small Inferior Vena Cava

Although the size of the IVC varies greatly, a flattening or significant decrease in the short-axis diameter of the IVC, giving it a slitlike appearance, is cause for concern. This has been observed on CT scans or MR images obtained in hypovolemic patients (see Fig. 43–21).[116] The venous pressures of any trauma patient with this finding should be carefully monitored.

Primary Malignancies of the Inferior Vena Cava

Primary IVC malignancies are exceedingly rare. These tumors are most commonly found in middle-aged to elderly women. Leiomyosarcoma is the most frequently encountered cell type, although a primary malignant fibrous histiocytoma has been reported at least once.[125]

Primary IVC leiomyosarcomas may produce intraluminal inferior vena caval abnormalities (thrombosis or vessel enlargement); however, extrinsic circumferential growth or the IVC without identifiable intraluminal extension is more common.[25] Thus, on CT scans or MR images, these tumors usually appear as bulky retroperitoneal masses centered around the IVC. The appearance is similar to that of other primary retroperitoneal malignancies that are not directly related to the IVC. The IVC may contain thrombus or be extrinsically occluded.

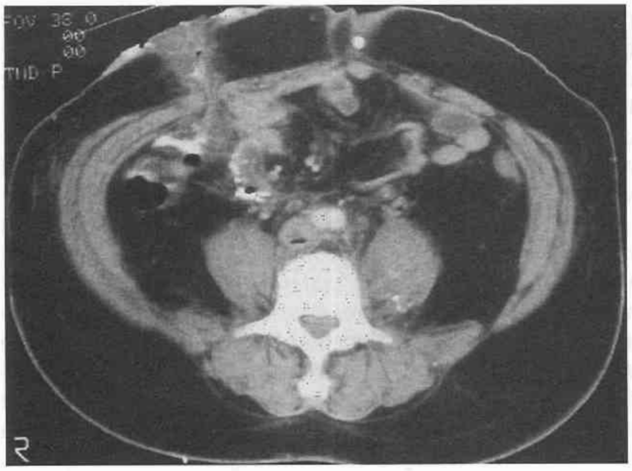

Figure 43–47. Infected inferior vena cava thrombus. Enhanced CT scan shows a punctate collection of air adjacent to inferior vena cava thrombus. This indicates infection in this patient with a right lower quadrant ostomy.

IV contrast enhancement is, at best, moderate because of the relative hypovascularity of most of these tumors.[25] Although leiomyosarcomas of the IVC grow slowly, they are associated with a poor prognosis.[276] The prognosis is worst for tumors that are large at the time of presentation.[25]

Pericaval Fat

Occasionally, fatty material can be identified adjacent to the IVC, most commonly in its intrahepatic portion. Although this finding can mimic a lipoma, it often merely represents localized pericaval fat (a normal variant).[196]

Gas in the Inferior Vena Cava

On occasion, air or gas can be seen within the IVC (Fig. 43–47). Causes include recent intervention or line placement, an infected or septic thrombosis, or a bowel venous fistula. The air is usually readily identified by CT, but it can be more difficult to correctly identify with MRI, particularly on spin-echo images, in which it can be difficult to distinguish from signal void that is caused by flowing blood.

Lymph Nodes

Normal Anatomy

Normal retroperitoneal lymph nodes, commonly seen with CT, appear as small, soft tissue masses adjacent to the great vessels. Of the intra-abdominal nodes that can be identified, the retrocrural nodes are the most cephalic. Normal retrocrural nodes do not exceed 6 mm in diameter.[59] Occasionally, they may be confused with other retrocrural structures, including azygos and hemiazygos veins or their anastomoses, or the thoracic duct.

Para-aortic and *paracaval* lymph nodes usually are well visualized by CT because the great vessels are often surrounded by fat, allowing a sharp contrast between small lymph nodes and the surrounding retroperitoneum. Single para-aortic lymph nodes are considered normal on CT scans if they measure 10 mm or less in short-axis diameter.[59] Para-aortic lymph nodes may be confused with unopacified loops of small bowel and retroperitoneal nerves and vessels, including dilated or collateral veins (in particular, dilated left gonadal vein).

Pelvic lymph nodes are more difficult to identify than retrocrural or para-aortic nodes. They follow the iliac vessels, dividing into internal (hypogastric) and external iliac groups. Thus, pelvic lymph nodes may be confused with unopacified loops of bowel, tortuous iliac vessels, or adnexal masses in women. Of all the pelvic lymph nodes, the obturator nodes are the most important because they are the first site of lymph node spread from most pelvic tumors. These nodes, belonging to the external iliac chain, are best seen medially to the obturator internus muscle on CT images obtained just above the acetabula.

In general, as in the abdomen, all pelvic lymph nodes exceeding 10 mm in short-axis diameter should be considered abnormally enlarged[128, 174]; however, some have suggested that the size cut-off for identifying pathologic lymph nodes in all but the external iliac chains should be lower. Vinnicombe and colleagues suggest that normal internal iliac lymph nodes should never exceed 7 mm in maximal short-axis diameter, obturator lymph nodes 8 mm in maximal short-axis diameter, and common iliac lymph nodes 9 mm in maximal short-axis diameter.[262]

Abnormalities of Lymph Nodes

In general, abnormal lymph nodes can be detected on CT or MRI only when their size is increased. Thus, although many diseases may produce lymph node pathology, there is tremendous overlap in their CT appearances.

In the text that follows, we discuss the use of various imaging modalities for evaluating abnormal retroperitoneal lymph nodes. Many processes that produce lymph node enlargement are discussed, including non-Hodgkin's and Hodgkin's lymphoma, and metastases from testicular cancer, prostate cancer, and other pelvic malignancies. Additionally, the significance of lymph node enlargement in patients with human immunodeficiency virus (HIV) infection is addressed. Benign causes of lymph node enlargement are also reviewed.

CT and MRI Technique

Computed Tomography

CT evaluation of retroperitoneal lymph nodes is most commonly performed in patients with a known or suspected malignancy to rule out malignant lymph node enlargement. Occasionally, CT is also performed to assess for retroperitoneal lymph node involvement in evaluation of patients with benign disease. CT demonstrates lymph node abnormalities only by identifying enlargement. It cannot detect tumor or inflammation in normal-sized lymph nodes.

CT scanning for evaluation of patients with possible retroperitoneal lymph node enlargement must be performed after administration of oral contrast material to maximally opacify any adjacent bowel. IV contrast medium is not mandatory but is helpful in distinguishing lymph nodes from vessels, especially in the pelvis. As is usually the case, contrast material should be injected as a dynamic bolus. Contiguous scans of 7- to 10-mm thickness are usually obtained from the diaphragm to the pubic symphysis.

Although most visualized retroperitoneal and pelvic lymph nodes over 10 mm in maximal short-axis diameter contain tumor cells, some do not; their enlargement may represent reactive hyperplasia, fatty replacement, reaction to chemotherapy or radiation therapy, or infection. In contrast, normal-sized lymph nodes may contain microscopic metastases that are missed by CT. This is particularly true in patients with Hodgkin's lymphoma and many of the primary pelvic malignancies.

Magnetic Resonance Imaging

Normally, lymph nodes have T1 values much longer than those of fat but only slightly longer than that of muscle. Lymph node T2 values are similar to those of fat but longer than that of muscle. Thus, lymph nodes show a signal intensity lower than that of fat on T1-weighted, spin-echo images but closer to that of fat on T2-weighted images. Lymph nodes in the midabdomen and upper abdomen are easily distinguished from retroperitoneal fat on T1-weighted, spin-echo sequences, and it is these images that are generally obtained for detection of enlarged retroperitoneal lymph nodes.

In the lower abdomen and pelvis, differentiation of lymph nodes from adjacent iliopsoas muscles may be more problematic. In these instances, T2-weighted images can be obtained for differentiation, since lymph nodes generally show considerably higher signal intensity than muscle on T2-weighted images.[140]

Unlike CT, MRI allows easy distinction between lymph nodes and vessels on T1-weighted and T2-weighted, spin-echo sequences because normally flowing blood emits no signal. On occasion, however, it may be difficult to distinguish enlarged lymph nodes from adjacent bowel. For this reason, some have advocated use of oral MR contrast agents in problematic cases.[63]

As with CT, untreated abnormal retroperitoneal lymph nodes can usually be reliably identified only on noncontrast MRI examinations and only by their abnormal size. In most cases, signal intensity criteria cannot be used to distinguish benign from malignant lymph nodes. In these instances, however, one potential advantage of MRI over CT is the ability of MRI to detect osseous or bone marrow involvement with greater sensitivity.[104]

The only untreated neoplasm that may have typically different signal characteristics on unenhanced MRI examinations is metastatic melanoma. Lymph nodes infiltrated with melanoma often have high signal intensity on T1-weighted images, theoretically permitting identification of tumor even in normal-sized lymph nodes.

Still, noncontrast MRI may have potential advantages over CT in evaluating patients with treated lymph node metastases because unenhanced MRI can sometimes distinguish residual tumor from fibrosis.[184, 205] When treated tumor shows low signal intensity on T2-weighted images, it is likely that any residual masses primarily consist of fibrotic tumor and that little, if any, viable tumor remains. Conversely, treated lymph node masses that show high signal intensity on T2-weighted images may contain residual tumor. Unfortunately, this distinction is not absolute. Small foci of tumor may be present in predominantly fibrotic retroperitoneal lymph node masses that have low signal intensity on T2-weighted images. Similarly, high signal intensity on T2-weighted images may be detected in successfully treated lymph node masses for up to 12 months after successful therapy, presumably as a result of to edema.[63] Additionally, increased signal intensity on T2-weighted images may be the result of inflammation.

In comparison with unenhanced MRI for measurement of lymph node signal intensity changes, contrast-enhanced MRI may permit identification of some untreated tumor cells in both abnormal- and normal-sized retroperitoneal lymph nodes. Barentsz and associates found that dynamic gadolinium-enhanced lymph nodes that were infiltrated with metastatic bladder cancer enhanced more rapidly than did uninvolved lymph nodes.[14] Metastatic lymph node enhancement was similar to that of the primary tumor. This difference permitted detection of metastatic tumor in some normal-sized lymph nodes in their series.

Detection of lymph node metastases may also be facilitated when another MR contrast agent, iron oxide, is administered.[93] Iron oxide particles are phagocytized and taken up in the lymphatic system. They accumulate in normal lymph nodes and thereby reduce lymph node signal intensity on T2-weighted or T2*-weighted images. Conversely, when lymph nodes are infiltrated with tumor, lymph node signal intensity either is not decreased or is heterogeneously decreased. In theory, this difference may also allow for MRI detection of nonenlarged metastatic lymph nodes. Unfortunately, there is some overlap, since some inflammatory lymph nodes do not demonstrate reduction in signal intensity on T2-weighted or T2*-weighted images.

Lymphography

In the past, lymphography was considered to be very valuable for evaluating patients with a wide variety of tumors because it demonstrated alterations in the internal architecture of normal-sized nodes as well as lymph node enlargement.[156] In recent years, however, the role of lymphography has been reduced dramatically. This is probably related as much to the decreasing expertise of most radiology departments in performing these "technically difficult" procedures as to the emergence of studies demonstrating that lymphography is not as clinically useful as was once thought.

As an example, lymphography has long been thought to be most useful in patients with Hodgkin lymphoma and with cervical and testicular carcinoma because of the propensity of these tumors to invade lymph nodes without enlarging them. Lipson and colleagues, however, found that of 39 patients with a low clinical stage of Hodgkin's

lymphoma and normal CT findings, 10 had positive lymphography results.[149] In only 2 of these 10 patients were the positive findings the result of tumor infiltration. In the other eight patients, the abnormalities were found to be caused by lymphoid hyperplasia at surgery, and these can be considered to represent false-positive diagnoses of tumor. The authors concluded that lymphography no longer has a role in the management of patients with Hodgkin's lymphoma.

CT and MRI have several important advantages over lymphography:

1. CT and MRI are able to image many more lymph node groups. Although lymphography opacifies most lymph nodes in the external and common iliac chains, the para-aortic, aortocaval, and paracaval nodes,[117] the para-aortic nodes not immediately contiguous to the aorta and cava are often not visualized.[174] In addition. with lymphography, hypogastric and presacral pelvic nodes are opacified only occasionally, and retrocrural, renal hilar, splenic, peripancreatic, periportal, and mesenteric nodes are never filled with lymphographic contrast media.[117] CT and MRI can be used to assess all of these lymph node groups.
2. CT and MRI can show other organs with possible tumor involvement (i.e., liver, spleen, adrenal glands).
3. CT and MRI can demonstrate the extent of local spread of a primary tumor.

Positron Emission Tomography

Positron emission tomography (PET), which is usually performed with either ^{18}F-fluorodeoxyglucose (FDG) or ^{11}C-methionine, has shown great promise in identifying lymph nodes containing metastatic tumor (whether abnormally enlarged or normal in size) by detecting abnormally increased metabolic activity in tumor cells. In one series, for example, PET with ^{18}F-FDG was more sensitive than CT in detecting lymph node regions involved with lymphoma.[172] In this study, in the 740 lymph node regions evaluated, 160 diseased locations were identified by both CT and PET; however, PET depicted 25 additional involved areas (7 of which were confirmed histologically and 2 of which were believed to be false-positive diagnoses). CT demonstrated six additional abnormal lymph node regions, at least three of which were ultimately found to be false-positive diagnoses.

The degree of metabolic activity of lymphomatous lymph nodes identified on PET studies has also been shown to correlate with disease activity and patient prognosis.[218]

CT-Guided and MRI-Guided Biopsy

CT-guided biopsy of abnormally enlarged retroperitoneal lymph nodes is easily performed. Biopsy of potentially lymphomatous masses should be performed with core (not aspiration) biopsy needles because pathologists often require histologic rather than cytologic specimens for accurate tumor characterization and grading. Core biopsy material is usually placed in sterile saline rather than Formalin to allow specific tissue analyses to be performed. CT fluoroscopy, which is being performed at an increasing number of institutions, can result in a quicker biopsy procedure.

MRI-guided biopsy of suspected pelvic lymph nodes is also usually easily performed.[13] MRI guidance is more expensive, and many radiology departments are not equipped to do biopsies in the MR suite because nonferromagnetic biopsy needles, among other items, are necessary; however, MRI offers the potential advantage over CT of allowing imaging in nonstandard planes.

Lymphoid Malignancies

Non-Hodgkin Lymphoma

Non-Hodgkin lymphoma (NHL) comprises a diverse group of lymphocytic neoplasms. Certain populations are particularly susceptible to NHL. Patients who have had renal transplants, patients with acquired immunodeficiency syndrome (AIDS), and patients who are immunocompromised for other reasons are all at increased risk.

Lymphomas are generally classified as low-grade, intermediate-grade, or high-grade, although controversies about classification continue.[218] Low-grade lymphomas are often disseminated widely when first detected, yet they are slow-growing and patients may survive for years after diagnosis. Treatment may be deferred initially. Chemotherapy and radiation therapy are used for palliation and not cure. Over time, these neoplasms may occasionally transform into high-grade lymphomas.

Intermediate-grade or high-grade lymphomas are less often widespread when discovered but are much more aggressive. Potent chemotherapy is required, and the goal of treatment is remission or even cure. Five-year survival statistics are much lower for these lymphomas (23% to 45%) than for low-grade lymphomas (50% to 70%).

Lymphomas are staged according to the Ann Arbor system as follows:

Stage I disease: involvement of one lymph node group
Stage II disease: involvement of more than one lymph node group on the same side of the diaphragm
Stage III disease: involvement of lymph nodes on both sides of the diaphragm
Stage IV disease: spread outside the lymphatic system

Patients with symptoms such as weight loss, nocturnal sweating, and/or fever are considered to have "B" disease; those without these symptoms are considered to have "A" disease.

CT and MRI at Presentation

CT has been the preferred imaging modality for evaluation of the retroperitoneum in patients presenting with NHL because the involved nodes are usually enlarged. CT is strongly advocated for measuring the extent of the lymphoma prior to initiation of treatment. It can be of great assistance in planning ports for radiation therapy.[26]

Most patients with NHL (compared with fewer than half with Hodgkin lymphoma) have abdominal involvement. Bulky para-aortic lymph node enlargement is common. CT easily detects the enlarged retroperitoneal lymph nodes (Fig. 43–48). Mesenteric disease, which is seen in more

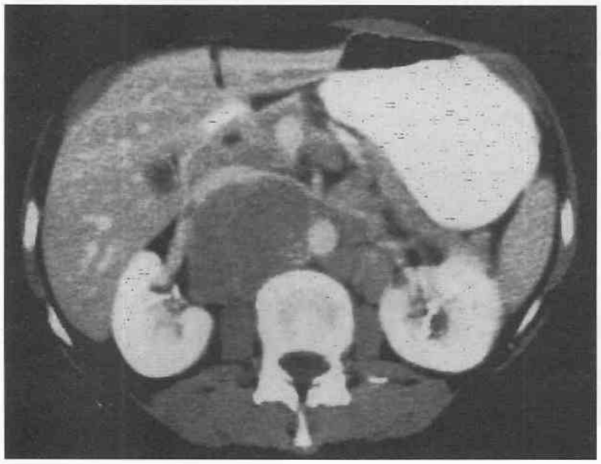

Figure 43–48. Non-Hodgkin lymphoma. Dynamically enhanced CT scan shows large lymph node masses in the para-aortic lymph node chains. The inferior vena cava is displaced anteriorly.

than half of the patients (versus fewer than 5% of those with Hodgkin disease), is also easily visualized.[174] The detected enlarged lymph nodes may appear as discrete masses or as confluent soft tissue obliterating the retroperitoneal fat, resulting in loss of definition of the fat planes between the aorta and the IVC. Many other lymph node groups (in addition to para-aortic lymph nodes), such as retrocrural, gastrohepatic, paraceliac, periportal, peripancreatic, posterior iliac crest, and pelvic chains, are frequently involved.[36, 61]

Although most enlarged lymphomatous lymph nodes show an attenuation similar to that of muscle on contrast-enhanced CT scans and are therefore easily distinguished from adjacent vessels, others may demonstrate enhancement that is similar to that of the retroperitoneal and pelvic vasculature. In one study, for example, 4 of 25 patients with lymphoma demonstrated lymph nodes that enhanced by a mean of about 60 Hounsfield units (HU) after injection of contrast material.[204]

CT can also be helpful in evaluating the specific group of patients with cutaneous T-cell lymphomas (except those with low-grade mycosis fungoides, in whom positive CT findings are unusual). Abnormal CT findings have been detected in nearly one third of these patients.[15] Lymph node abnormalities often consist of an increased number of normal-sized lymph nodes, which can occasionally be located in the retroperitoneum, although axillary and inguinal lymph nodes are most commonly involved. The involved lymph nodes may contain lymphoma or may be reactive (e.g., in dermatopathic adenopathy), and the prognosis is adversely affected in either case.[15]

MRI demonstrates enlarged lymphomatous lymph nodes with an accuracy comparable to that of CT, again facilitating staging (Fig. 43–49). In one study, MRI was actually superior to the combination of CT and bone marrow biopsy; it detected enlarged lymph nodes that were seen on CT as well as focal areas of marrow involvement that would not have been detected during standard iliac wing bone marrow sampling.[104]

CT and MRI for Follow-up of Non-Hodgkin Lymphoma

CT and MRI are commonly used to follow disease after treatment, with CT the preferred study at most institutions. Response to treatment is usually indicated by a reduction in overall abdominal lymph node enlargement, which can often be quite dramatic.[192] Increased retroperitoneal and mesenteric stranding is commonly noted in these patients (Fig. 43–50).

In some patients, lymph node attenuation values may decrease as an appropriate response to treatment with or without overall reduction in lymph node size and/or increased mesenteric stranding. Post-treatment dystrophic calcification of lymphomatous masses is also encountered occasionally.[137]

In some patients, treatment does not completely eradicate the lymphoma and persistent enlarged involved lymph nodes are demonstrated on CT. Conversely, it is not uncommon for patients with lymphoma who have responded to therapy to have post-treatment inflammatory or fibrotic masses containing no identifiable residual tumor.[145] In general, the larger the lymphomatous masses are before treatment, the larger the residual fibrotic masses will be after treatment.[218]

Thus, in patients with treated NHL, failure to completely eradicate retroperitoneal lymph node masses does not necessarily indicate that viable tumor cells are present. Residual masses after treatment can either be benign or contain persistent tumor. Unfortunately, there are no CT characteristics that reliably allow differentiation between benign and malignant residual masses. Patients with residual masses after treatment should be monitored closely on follow-up examinations to determine whether these masses remain stable over time, which would indicate that they are probably benign.

As noted, several studies have found that MRI may be helpful in distinguishing residual tumor from fibrosis. Many tumor masses remain bright on T2-weighted images, and chronic fibrosis or scar is often dark (see Lee and Glazer[141]). In some instances, MRI might be helpful in evaluating patients in whom recurrent or residual tumor is suspected despite stable CT findings. Unfortunately, there is much overlap. Although low-signal-intensity residual masses on T2-weighted images are unlikely to contain viable tumor, high signal intensity in residual masses on T2-weighted images can result from viable tumor or from a number of benign causes, including inflammation and edema. PET has shown greater promise in this area, occasionally revealing residual tumor because of its greater metabolic activity.[218]

HIV-Related Non-Hodgkin Lymphoma

HIV-related NHL is often characterized by exuberant lymph node enlargement, which is often widespread. Abdominal visceral organ involvement (resulting in hepatic, splenic, and GI tract masses) and omental disease are much more commonly seen than in other lymphoma patients.[256] AIDS-related lymphomas tend to be poorly differentiated and aggressive. Advanced disease is often present at the time of diagnosis, and the prognosis is poor.

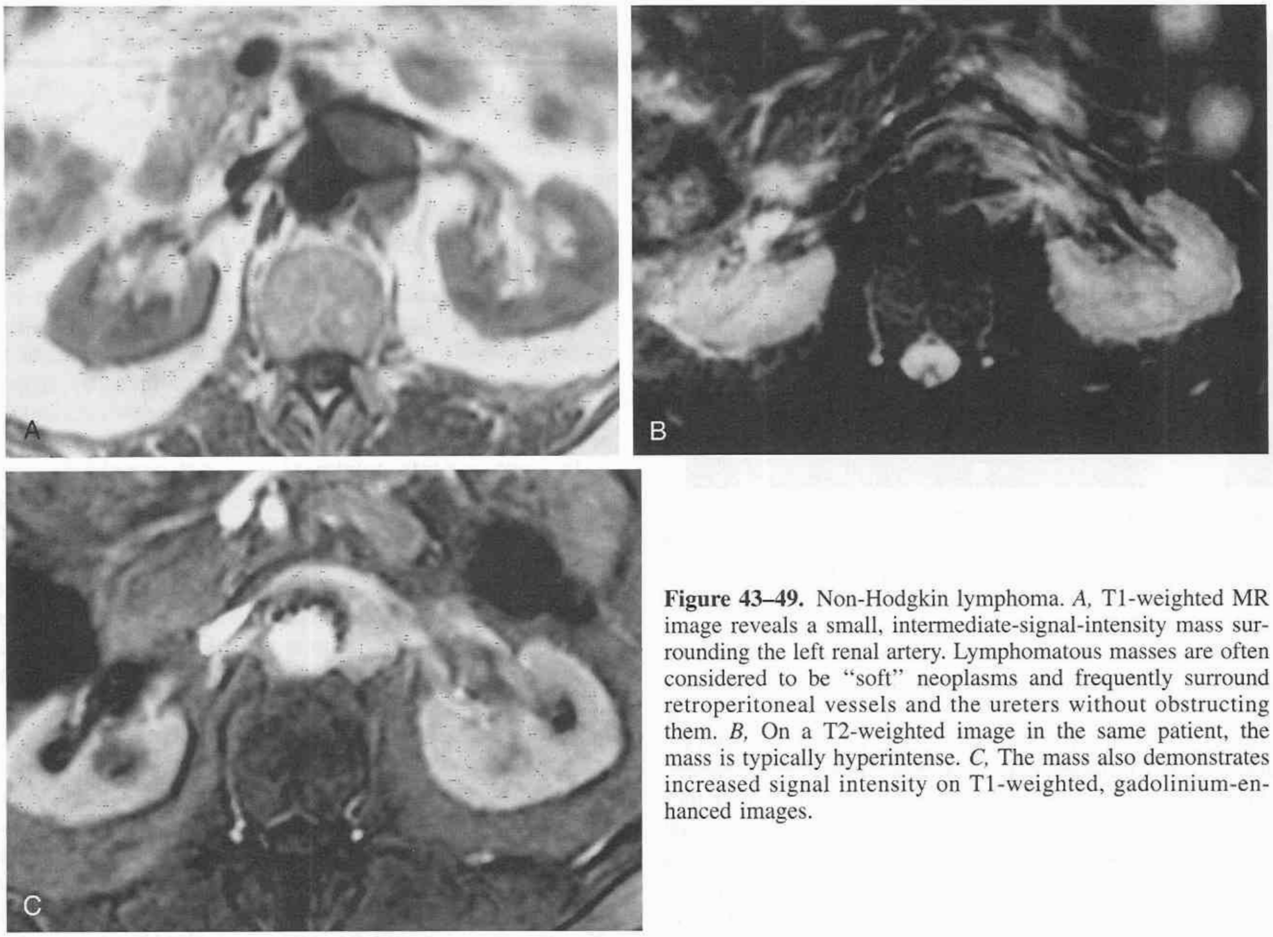

Figure 43–49. Non-Hodgkin lymphoma. *A,* T1-weighted MR image reveals a small, intermediate-signal-intensity mass surrounding the left renal artery. Lymphomatous masses are often considered to be "soft" neoplasms and frequently surround retroperitoneal vessels and the ureters without obstructing them. *B,* On a T2-weighted image in the same patient, the mass is typically hyperintense. *C,* The mass also demonstrates increased signal intensity on T1-weighted, gadolinium-enhanced images.

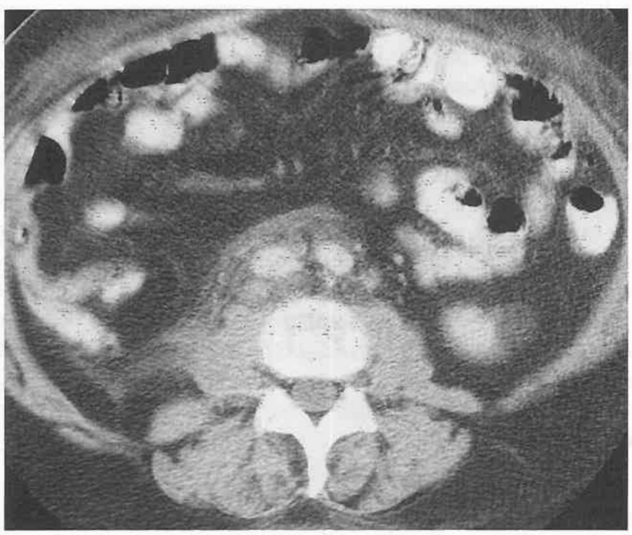

Figure 43–50. Treated non-Hodgkin lymphoma. Contrast-enhanced CT scan demonstrates residual soft tissue in the para-aortic and paracaval regions of the retroperitoneum in a patient who has undergone chemotherapy. The poorly defined soft tissue stranding is frequently identified in patients with treated lymphoma. Although all of the remaining tissue might represent fibrosis, the possibility of residual viable tumor cannot be excluded. In this patient, the soft tissue remained stable on scans over several years, suggesting that no residual tumor was present.

Hodgkin Lymphoma

Hodgkin's lymphoma is more common in adults in higher socioeconomic groups and peaks in both the third and the fifth decades of life. The hallmark of Hodgkin lymphoma is the Reed-Sternberg cell. Unfortunately, this cell is relatively uncommon in pathologic specimens, and aspiration biopsies are often inadequate for establishing the diagnosis.[35]

Histologically, Hodgkin lymphoma is classified into several forms. The *nodular sclerosing* type is most frequent (50% to 80% of cases) and of intermediate aggressiveness. *Lymphocyte-predominant* Hodgkin lymphoma, which carries the best prognosis, and *lymphocyte-depletion* Hodgkin lymphoma, which carries the worst, are considerably less common (5% to 10% each). The *mixed cellularity* forms occur with somewhat higher frequencies (15% to 40%).[35] Staging of Hodgkin lymphoma is similar to that of NHL.

CT is now used for pretreatment evaluation of nearly all patients with Hodgkin lymphoma. Staging laparotomies for Hodgkin lymphoma are performed only infrequently today. Hodgkin lymphoma tends to spread by involving contiguous lymph nodes. This pattern of spread contrasts with that of NHL, in which many different and widely separated lymph node chains can be involved at the same time. For this reason, when abdominal CT examinations are performed in patients with thoracic Hodgkin disease, the upper abdominal lymph nodes must be carefully scrutinized. Involvement of lower abdominal or pelvic lymph

nodes is unlikely unless the upper abdominal lymph nodes are also involved.

Lymph node involvement in Hodgkin's disease, in contrast to that in NHL, less commonly results in bulky enlargement. Therefore, unfortunately, CT and MRI are less sensitive in detecting abdominal spread. This has led to the recommendation by some (e.g., Castellino and coworkers[34]) that lymphography be performed instead of CT or MRI for evaluation of patients with Hodgkin lymphoma even though others now think that lymphography no longer has any role in the workup of patients with this disease.[149] While lymphography may still play a role in the evaluation of some patients with Hodgkin lymphoma, CT is generally performed before lymphography, and lymphography is restricted to patients with negative CT findings. Lymphography is not used at many institutions today because experience in performing this procedure is very limited. PET may eventually serve as an effective replacement.

CT and MRI can also be used to evaluate possible splenic involvement. Unfortunately, correlation between spleen size and splenic Hodgkin lymphoma is poor. Only about one third of patients with splenomegaly have splenic involvement, whereas one third of patients with normal-sized spleens have intrasplenic spread of Hodgkin lymphoma.[1] Only massive splenomegaly correlates well with the spread of Hodgkin disease. Single or multiple discrete, low-attenuation masses detectable by CT are seen infrequently.

Treatment of Hodgkin lymphoma that is confined to the mediastinum usually consists of radiation therapy, which can be curative when all areas of tumor involvement are included in the radiation port.[33] In advanced disease, chemotherapy and radiation therapy are often used jointly, often with favorable results. The 10-year survival rate has been reported at 85% in adults.[35] For this reason, careful follow-up of patients over many years is required.

Other Lymphoid Malignancies

Retroperitoneal and pelvic lymph node enlargement can be encountered in many patients with *Waldenström's macroglobulinemia*, a low-grade lymphoid malignancy that is encountered only rarely, usually in older adults. Clinically, patients typically present with fatigue, weight loss, hepatosplenomegaly, and peripheral lymph node enlargement.

Imaging studies commonly detect hepatosplenomegaly and enlarged lymph nodes as well as bone marrow involvement; the bone marrow involvement is best assessed by MRI. In one study, enlarged lymph nodes were noted in 10 (43%) of 23 patients with this disease, with multiple lymph node groups being involved in most instances (usually the retrocrural, para-aortic, iliac, and inguinal lymph node chains).[180] On lymphography, these lymph nodes usually appear hyperplastic.

Testicular Neoplasms

Testicular tumors are the most common cancers in men between the ages of 15 and 34 years.[62] Recent advances in therapeutic regimens have met with excellent success in prolonging patient survival.

Testicular neoplasms are divided into *germinal* and *non-germinal* cell types. The most common germinal tumor is the *seminoma*. Seminomas are extremely responsive to radiation, and for this reason retroperitoneal surgery (lymph node dissection) and chemotherapy are reserved for patients with advanced disease. The lack of routine lymphadenectomy after orchiectomy in these patients explains why there is some difficulty in acquiring data on the accuracy of CT in staging. Surgical follow-up is rarely available.

The nonseminomatous germ cell tumors include teratocarcinoma, teratoma, choriocarcinoma, embryonal cell neoplasms, and yolk sac tumors. Mixed cancers containing seminomatous and nonseminomatous elements may also be considered in this group because the clinical course often follows that of the nonseminomatous cells.[62] Although some testicular tumors appear quite homogeneous on CT and MRI scans, teratomatous neoplasms often appear heterogeneous because they contain areas of necrosis, fat, and calcification (Fig. 43–51). These neoplasms have been treated by orchiectomy followed by staging lymphadenectomy in many institutions.

Lymphatics from the testicle drain into ipsilateral para-aortic midabdominal lymph nodes near the renal vein insertions. Only rarely do testicular lymphatics drain into ipsilateral external iliac nodes. Lymph node metastases from testicular neoplasms, therefore, tend to develop first in these "landing zones" rather than in pelvic lymph nodes. Specifically, the landing zone for left testicular tumors is in the left para-aortic region just caudad to the level of the left renal vein; for right testicular tumors, it is in the right paracaval region, just caudad to the level of the right renal vein. When CT or MRI scans are being reviewed in patients with testicular cancers, it is imperative that these regions be scrutinized for lymph node enlargement.

Although testicular metastases often enlarge involved nodes, tumor spread is found in normal-sized nodes in many instances.[128] Furthermore, the lymph node enlargement seen on CT scans is occasionally not caused by spread of tumor. Thus, the detection rate of lymph node metastases by both CT and MRI has been disappointing.

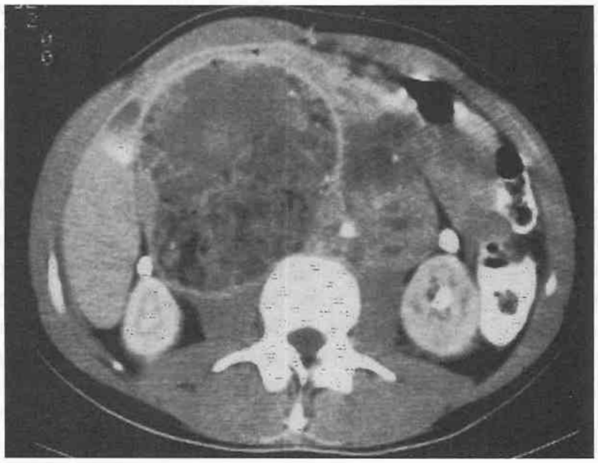

Figure 43–51. Metastatic testicular teratocarcinoma. Nondynamically enhanced CT scan shows retroperitoneal lymph node metastases. Huge nodal masses with areas of fat, fluid, and calcification are characteristic.

In general, lymph node status is appropriately assessed in only about 70% of patients.[32, 131] The errors probably result primarily from the inability of CT to identify microscopic lymph node metastases; however, false-positive diagnoses are not uncommon. In one study, for example, CT failed to detect any enlarged lymph nodes in 49 patients with nonseminomatous germ cell tumors, 18 of whom were found to have lymph node metastases at lymph node dissection.[32] Furthermore, of 15 patients in whom CT showed enlarged lymph nodes, only 7 were confirmed to have lymph node metastases at surgery.

False-negative and false-positive diagnoses have not decreased dramatically in the past few years, even though image quality has improved with the use of third-generation, fourth-generation, and now helical and multidetector CT scanners. For example, in a study that included 201 patients with testicular cancer, state-of-the-art CT in patients with clinically localized nonseminomatous germ cell tumors still had a 33% false-negative rate for detecting involved lymph nodes.[179] To reduce the number of false-negative scans, these authors suggested that identification of any lymph node (no matter what the size) in the landing zone areas should be considered suspect.

In another series, 143 CT examinations were performed on patients with low-stage nonseminomatous germ cell tumors.[142] It was found that when a size threshold of 10 mm was used, the false-negative rate for diagnosis of lymph node metastases in the landing zones was 25%. In contrast, the sensitivity in detecting metastatic lymph nodes increased to over 90% and the negative predictive value to over 90% when any visualized lymph nodes (regardless of size) in the landing zone of a known testicular primary neoplasm were considered abnormal. Certainly, such an increase in sensitivity and negative predictive value comes at the expense of low specificity (~50%) and positive predictive value (~50%).

In summary, unless size criteria are reduced or eliminated, CT and MRI are not exceedingly sensitive for detecting lymph node metastases in patients with testicular cancer. CT and MRI appear to be most accurate in these patients when they identify enlarged lymph nodes. False-positive diagnoses are considerably less common than false-negative diagnoses. Interestingly, PET has also been somewhat disappointing in these patients because ^{18}F-FDG may not be taken up in metastases that contain extensive, well-differentiated teratomatous cells.[131]

In many patients, lymph node metastases from testicular cancer show soft tissue attenuation on CT scans; however, low-attenuation lymph node masses (<30 HU) are occasionally encountered. In one series, 10 of 57 patients evaluated by CT had such masses.[227] Low-attenuation lymph nodes in patients with NHL are nearly always the result of treatment; however, they may be encountered in untreated patients with testicular cancer. Such low-attenuation lymph nodes often contain teratomatous elements, often reflecting cellular components of the primary tumor.

Residual masses, which may be of soft tissue or of low (near-water) attenuation, have been detected in patients with testicular cancer after apparently successful treatment (Fig. 43–52). As in patients with NHL, the persistence of these masses does not necessarily indicate that malignant or even benign teratomatous cells remain, and this can sometimes be a problem.[240] Follow-up CT examinations cannot distinguish among three possibilities: (1) residual cancer, (2) residual benign teratoma, or (3) fibrosis. Differentiation is important because treatment varies for each of these three types of masses. Patients with residual malignant tumor cells must receive additional chemotherapy. Benign mature teratomas, which may develop from treated malignant nonseminomatous germ cell tumors, must be surgically removed because they may undergo malignant transformation. Treatment of purely fibrotic masses is not warranted. In any given case, CT features do not reliably permit distinction of one of these masses from another.[244] MRI has not proved any more helpful than CT in facilitating these distinctions to date.

Figure 43–52. Retroperitoneal teratoma after treatment of metastatic testicular cancer. Contrast-enhanced CT scan demonstrates a large, predominantly cystic mass in the left para-aortic region in a young patient who had undergone orchiectomy and chemotherapy for testicular cancer. On the basis of the CT appearance, this mass might represent malignant disease (teratocarcinoma), teratoma, or fibrosis and necrosis. At surgery, this mass was found to represent a teratoma.

We recommend that patients with testicular neoplasms be followed up with serial CT examinations and serum tumor markers. Percutaneous fine-needle aspiration biopsy can be performed on a residual mass if a patient has rising markers or if the mass has changed in size or morphologic features. In many cases, surgery is required for diagnosis.

Prostate Cancer

Accuracy of CT and MRI in detecting lymph node metastases from prostate cancer has been disappointing, with sensitivities ranging from 27% to 75% and specificities from 66% to 100%.[194] In contrast, local staging of prostate cancer with endorectal coil MRI is considered to be far more accurate. It is thought that the primary reason for the low accuracy rate of CT and MRI in detecting lymph node metastases is that prostate cancer can spread to retroperitoneal lymph nodes without enlarging them; thus, metastatic disease is undetectable on CT or MRI, leading to many false-negative diagnoses.

Some authors have suggested that CT accuracy in lymph node staging of prostate cancer might be increased by

lowering the threshold for identifying lymph node enlargement and by generous performance of percutaneous biopsy. In their series of 285 patients with clinically localized prostate cancer, Oyen and colleagues considered all lymph nodes measuring 6 mm or more to be abnormal.[194] This would be expected to increase both true- and false-positive rates; however, percutaneous biopsy of one lymph node was performed in each patient in whom at least one abnormal lymph node was identified. Positive biopsy results were required to confirm the presence of metastatic disease. Use of biopsy along with the lower size threshold for detecting suspected lymph node metastases reduced the number of false-positive diagnoses. With this combination of techniques, sensitivity, specificity, and accuracy in detecting lymph node metastases from prostate cancer improved to 77.8%, 100%, and 96.5%, respectively. Although these results are intriguing, it is not yet clear that such considerable effort is warranted in all patients with this common pelvic malignancy.

Despite the relatively low accuracy of CT in local staging of prostate cancer and in detecting lymph node metastases from prostate cancer, many physicians request that staging CT be performed prior to treatment. In an attempt to limit the number of CT examinations that are requested, many urologists restrict the use of CT to patients with elevated serum prostate-specific antigen (PSA) levels. Indeed, it has been found that in an asymptomatic patient with a newly diagnosed and untreated prostate cancer, the likelihood of abdominal and pelvic CT demonstrating an abnormal finding is extremely low (<1%) if the serum PSA level is 20 ng/mL or lower.[109] When the serum PSA is elevated above 20 ng/mL, however, abnormal CT findings are detected in more than 10% of patients.[109]

CT and MRI are occasionally performed for follow-up evaluation of patients with prostate cancer after therapy. For example, images can be obtained to assess response of previously diagnosed lymph node metastases to hormonal therapy (Fig. 43–53).

Follow-up imaging has been performed in patients treated with a combination of transperineal radioactive seed implantation and laparoscopic lymph node dissection. In a study of 73 patients, 42 were found to have low-attenuation masses along abdominal and pelvic lymph node chains; these masses resembled necrotic lymph nodes but were subsequently believed to represent lymphoceles.[72] Awareness of this possible finding may reduce the number of false-positive diagnoses in these patients.

Other Malignancies

Retroperitoneal lymph node enlargement can also be encountered in patients with renal cell cancer (Fig. 43–54). Other pelvic tumors that commonly metastasize to pelvic and retroperitoneal lymph nodes are bladder, endometrial, and cervical carcinomas; less often, metastases may come from ovarian carcinomas.[96] Although the local manifestations of all of these pelvic tumors appear to be better assessed with MRI than with CT, both modalities appear equally effective in detecting retroperitoneal lymph node metastases.

CT and MRI are usually helpful only when bulky metastatic disease is present. Unfortunately, these pelvic neoplasms frequently metastasize to normal-sized or only slightly enlarged nodes, so that identification of tumor spread to pelvic and retroperitoneal nodes by CT and even MRI is often impossible.[128] Reported sensitivities for detecting abdominal and pelvic lymph node involvement range from 30% to 100% for bladder cancer and from 80% to 85% for cervical cancer. Specificities have also been less than optimal, ranging from 46% to 100%.[117, 265, 267] Detection of lymph node involvement in some patients (with cervical carcinoma) has not been substantially improved even when high-resolution MRI is performed with phase-array coils.[96]

Some work has demonstrated that MRI lymph node enhancement with gadolinium-based contrast material is more rapid when metastases from bladder cancer are pres-

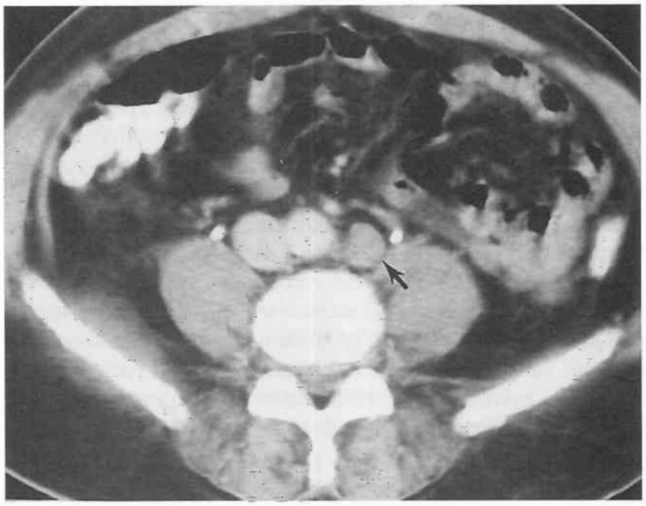

Figure 43–53. Prostate cancer metastatic to retroperitoneal lymph nodes. Contrast-enhanced axial CT image demonstrates a large lymph node metastasis in the left para-aortic region *(arrow)* of a 60-year-old man. This lymph node can be followed on serial CT scans once hormonal therapy is instituted.

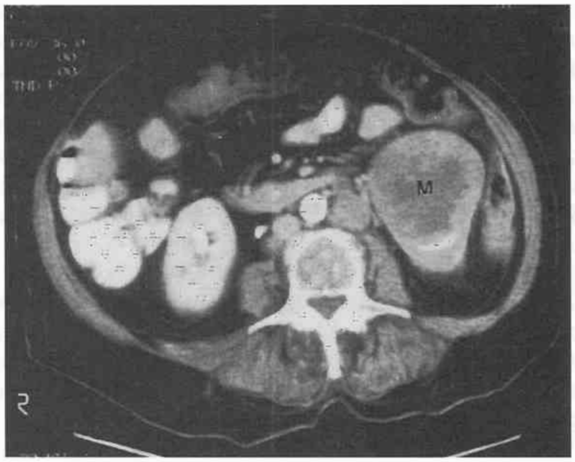

Figure 43–54. Retroperitoneal, para-aortic lymph node enlargement resulting from metastases due to a large left renal adenocarcinoma (M), as seen on a dynamically enhanced CT scan.

ent.[14] This difference in enhancement rate between lymph nodes that contain tumor and those that do not has resulted in MRI detection of metastatic disease even in normal-sized lymph nodes. On CT scans, however, lymph nodes invaded with metastatic tumor occasionally enhance with contrast material to the same extent as adjacent vessels. Such enhancement, which has been observed in some patients with bladder cancer[110] and some with other nonpelvic primary neoplasms (e.g., thyroid, renal, oat cell cancer and carcinoid),[204] may lead to the erroneous impression that the lymph nodes actually represent abnormal dilated vessels.

Currently, lymphography (followed by percutaneous biopsy of suspect nodes) is rarely performed in patients with cervical cancer whose cross-sectional imaging studies do not demonstrate metastatic disease. Lymphography is not used in patients with bladder, prostate, ovarian, or endometrial cancer. Any of these patients whose CT findings do not demonstrate metastatic disease must proceed to staging lymphadenectomy either at laparotomy or via laparoscopy.

Enlarged Lymph Nodes in HIV Infection

Enlarged abdominal lymph nodes are present in most (>60%) patients with HIV infection.[39, 209, 225] Lymph node enlargement is commonly not massive. In about 50% of all patients, the short-axis diameter of the largest lymph node measures only 10 to 15 mm.[209] Although in some HIV-infected patients, enlargement results only from reactive hyperplasia, many other diseases may be responsible.[39] For this reason, it has been recommended that lymph node biopsy be considered in any symptomatic patient with enlarged lymph nodes in whom no known cause of lymph node enlargement exists (other than HIV infection itself).[209]

Studies have demonstrated that when abdominal CT is performed in symptomatic HIV-infected patients, a cause of patient symptoms can be demonstrated in nearly 70% of instances.[225] Thus, CT often contributes to patient management, although it rarely leads directly to patient diagnosis. In patients with fever of unknown origin, however, CT appears to assist in patient management in a minority of cases.[225]

Occasionally, the CT characteristics of the enlarged lymph nodes and the identification or lack of identification of specific additional findings may facilitate a more focused differential diagnosis. For example, when lymph nodes are of homogeneous soft tissue attenuation (Fig. 43–55), the most likely diagnosis is *Mycobacterium avium* complex (MAC) infection or AIDS-related NHL.[209] Other, less common causes of enlarged, soft tissue–attenuation lymph nodes include Kaposi's sarcoma, disseminated histoplasmosis, and Hodgkin's lymphoma.

M. avium complex infections generally occur only in patients in advanced stages of AIDS with very low CD4+ lymphocyte counts (50 cells/μL or less). Although patients with mycobacterial infections can have enlarged retroperitoneal lymph nodes, they usually have disproportionately larger mesenteric lymph nodes.[108, 208]

When IV contrast-enhanced scans of lymph nodes in HIV-infected patients show central or diffuse low attenuation (Fig. 43–56), disseminated *M. tuberculosis* infection is the most likely cause; lymphoma, *M. avium* complex infection, histoplasmosis, and coccidioidomycosis are less likely.[209] More than 80% of patients with tuberculosis have enlarged lymph nodes, some or all of which are of diminished attenuation.[208, 209] Many patients with tuberculosis also have small, low-attenuation visceral organ lesions.

When enhancement of lymph nodes in HIV-infected patients shows them to have densities comparable to or higher than those of adjacent muscles, a diagnosis of Kaposi's sarcoma should be considered. Lymph nodes involved with Kaposi's sarcoma are often quite hyperenhancing, probably because of their vascularity.[209] In one series,

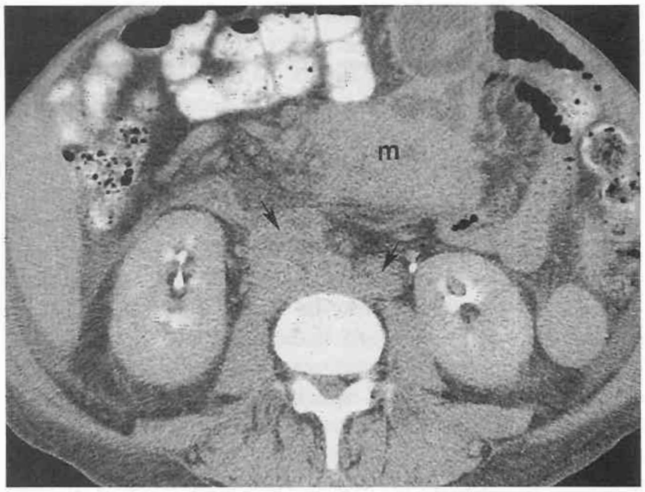

Figure 43–55. *Mycobacterium avium–intracellulare* in a patient with human immunodeficiency virus (HIV) infection and a low CD4+ count. Enlarged para-aortic and paracaval lymph nodes *(arrows)* along with a large mesenteric mass (m) are identified on this CT nondynamically enhanced scan. The lymph nodes show characteristic soft tissue attenuation. Low-attenuation lymph nodes are more commonly seen in patients with tuberculosis.

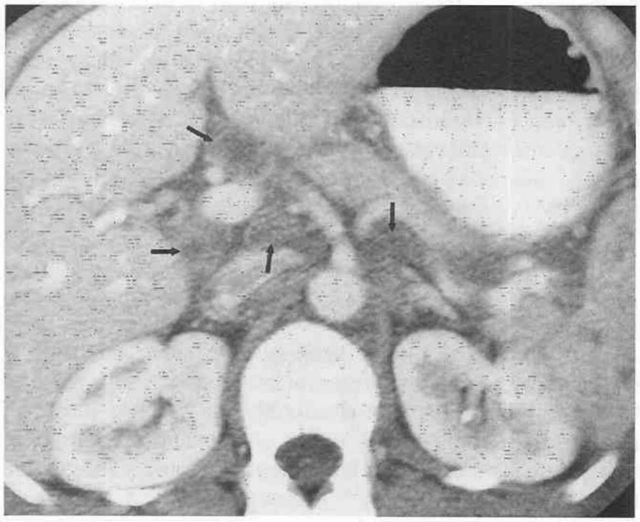

Figure 43–56. *Mycobacterium tuberculosis* infection in a 50-year-old man with human immunodeficiency virus (HIV) infection. Enlarged, low-attenuation lymph nodes are identified on this contrast-enhanced CT image in the periportal, portocaval, and paraceliac regions *(arrows)*.

lymph nodes that were enlarged because patients had the generalized form of Kaposi's sarcoma enhanced to a higher attenuation value than for adjacent muscles in 26 of 38 patients.[101] The authors suggest that whenever briskly enhancing lymph nodes are encountered, a diagnosis of Kaposi's sarcoma should be considered even when no such diagnosis has previously been made.

When calcifications are noted in lymph nodes, extrapulmonary *Pneumocystis carinii* infection is likely. Other associated findings of extrapulmonary pneumocystis infection include multiple focal low-attenuation splenic lesions, liver lesions, and pleural and peritoneal fluid.[152] Calcification has been noted to develop over time in all of these structures as well as in the renal cortices and adrenal glands. Visceral organ calcifications have also been reported to develop in rare patients with disseminated *M. avium* complex and cytomegalovirus infections.[209]

When lymph node enlargement is massive (with maximal diameters exceeding 3 cm, for example), lymphoma becomes the most likely diagnosis.[209]

Benign Causes of Retroperitoneal Lymphadenopathy

The presence of enlarged retroperitoneal lymph nodes is certainly not definitively diagnostic of malignancy. Occasionally, enlarged lymph nodes, seen on CT or MRI scans in patients with lymphomas or pelvic neoplasms, contain only reactive hyperplasia. Although hyperplastic lymph nodes can undergo fatty replacement, which has a characteristic appearance on CT or MRI scans, this finding is frequently absent.

Several inflammatory diseases have been specifically identified as causing, or being associated with, retroperitoneal lymph node enlargement. Benign enlarged lymph nodes are not uncommonly detected in patients with end-stage cirrhosis; in one series, they were identified in as many as 50% of patients.[58] Interestingly, lymph node enlargement is encountered at the highest frequency in patients with cirrhosis related to biliary tract disease. They have been seen in 86% of patients with primary biliary cirrhosis, 69% of patients with primary sclerosing cholangitis, and 64% of patients with cryptogenic biliary cirrhosis.[58] In comparison, lymph node enlargement is noted at the lowest frequency in patients with hepatitis or alcohol-induced cirrhosis (46% and 37%, respectively).[58] Although the enlarged lymph nodes associated with liver disease are most commonly seen in the periportal and portacaval spaces, they can also be identified in the retroperitoneum.

Retroperitoneal lymph node enlargement may also be encountered in patients with mycobacterial infections (with or without concomitant HIV infection). In these patients, mesenteric and peripancreatic lymph node enlargement frequently overshadows enlargement of the retroperitoneal nodes, perhaps reflecting the drainage routes of hematogenously seeded GI tract organs. As already described, in a significant minority of patients with tuberculosis (up to 40%), enlarged lymph nodes have low-attenuation centers, a finding that occurs in some patients with malignant disease as well as in patients with other bacterial infections, Whipple's disease, and lymphangioleiomyomatosis.[101, 108, 208, 209]

Enlarged retroperitoneal lymph nodes have also been observed in patients with sarcoidosis (Fig. 43–57).[11] In one series, lymph node enlargement was detected in 16 (31%) of 52 patients with this disease whose CT scans were obtained through the upper abdomen and midabdomen.[263] In several older studies, lymph node enlargement had been identified much more frequently, in 60% to 75% patients.[11, 164] The porta hepatis and para-aortic retroperitoneal lymph nodes are most commonly affected.

Interestingly, only rarely is abdominal lymph node enlargement present without mediastinal lymph node involvement. Further, although the extent of abdominal and pelvic CT findings is often related to clinical disease activity, these findings do not necessarily correlate with the chest radiographic stage. This indicates that abdominal involvement and chest involvement may occur at different times and with differing severities.

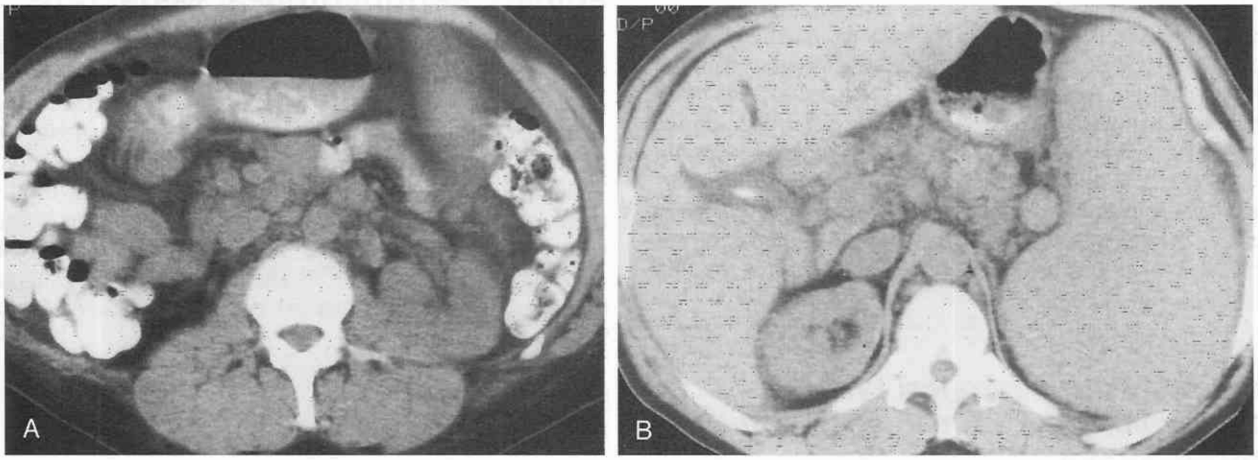

Figure 43–57. Retroperitoneal lymph node enlargement in a 41-year-old patient with sarcoidosis. *A,* Unenhanced CT image demonstrates multiple, mildly enlarged lymph nodes in the para-aortic region of the retroperitoneum. *B,* CT image at the upper abdomen level reveals a massively enlarged spleen and several mildly enlarged retrocrural lymph nodes. All of these abnormalities are a result of sarcoidosis.

Castleman disease is occasionally also associated with development of enlarged retroperitoneal fibrotic masses or nodes.[83] In many cases, the CT or MRI appearance of these enlarged lymph nodes is not specific. It has been suggested, however, that identification of intense and uniform contrast enhancement in lymph nodes can suggest the diagnosis, since such enhancement is uncommon in lymph nodes involved with metastatic tumor (which are most often from hypovascular pelvic primaries rather than from Kaposi's sarcoma) or with infections.[83] When seen in Castleman's disease, brisk lymph node enhancement usually indicates presence of the localized and more commonly encountered hyaline-vascular type (occurring in 90% of patients) rather than of the plasma-cell type.

In rare instances, patients with primary or secondary amyloidosis may have involved retroperitoneal or pelvic lymph nodes, which can enlarge to massive size.[74, 231] In some patients, the lymph node enlargement can represent the dominant or the only site of disease. The appearance of lymph node enlargement resulting from amyloidosis is not specific, although several case reports have noted that irregularly speckled calcifications may develop, as shown by Segalov and colleagues.[231]

Bulky retroperitoneal lymph node enlargement can also be encountered in patients with lymphangioleiomyomatosis. This rare disease, in which smooth muscle proliferation occurs in lymph nodes and lymphatics, usually affects young women of childbearing age. Although benign, this disease is often relentlessly progressive. Some patients may be stabilized with medical therapy; however, many who are treated for years eventually die of respiratory failure secondary to the characteristic pulmonary involvement unless lung transplantation can be performed. On abdominal and pelvic CT scans, the enlarged lymph nodes may show cystic, low-attenuation components. In fact, when bulky, enlarged lymph nodes are identified in a young woman of childbearing age *and* when these lymph nodes contain areas that show low (near-water) attenuation, a diagnosis of lymphangioleiomyomatosis should be suggested.[271]

Abnormal lymph nodes have also been identified in patients with *Kikuchi's disease*, a benign self-limited process lasting no more than 3 months and usually occurring in people under 30 years of age.[167] Affected patients usually present with asymptomatic lymph node enlargement. One third of patients experience fevers. Only rarely are other signs and symptoms (e.g., weight loss, diarrhea, chills, sweating) present. On CT examination, patients generally have increased numbers of normal-sized lymph nodes. Cervical, axillary, and inguinal lymph nodes are commonly affected. Retroperitoneal lymph node involvement is not common but in rare instances may represent an isolated site of disease.

Abnormal Retroperitoneal Lymph Nodes Simulating Normal or Abnormal Vascular Structures

Occasionally, abnormal pelvic lymph nodes may demonstrate contrast enhancement similar to that of adjacent vessels. This may be confusing and may lead to misdiagnosis of an abnormal lymph node as a dilated vessel. As mentioned earlier, such abnormal enhancement has been seen in patients with NHL, Kaposi's sarcoma, various metastatic neoplasms, and the hyaline-vascular type of Castleman's disease.

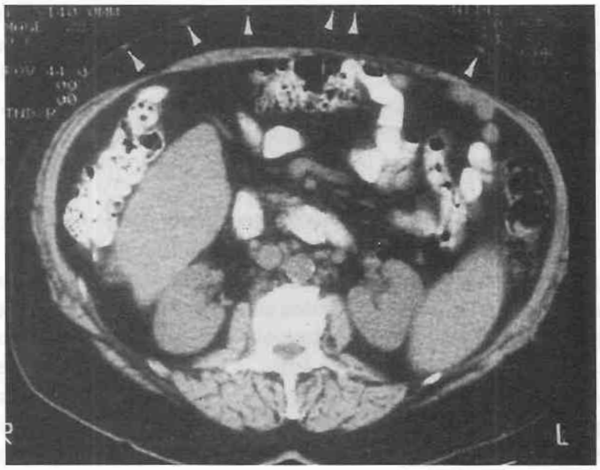

Figure 43–58. Collateral vessels mimicking "borderline"-sized to mildly enlarged lymph nodes in a patient with upper abdominal inferior vena cava occlusion. Unenhanced CT scan also demonstrates the presence of subcutaneous collateral vessels *(arrowheads)*.

Mimics

A variety of retroperitoneal structures can be confused with enlarged retroperitoneal lymph nodes, including collateral vessels (Fig. 43–58), dilated lymphatics, retroperitoneal hemorrhage, retroperitoneal fibrosis, and primary retroperitoneal tumors.[269] Usually, the distinctive features of each abnormality allow the radiologist to determine that the retroperitoneal masses do not represent pathologic lymph nodes.[110, 204]

Primary Retroperitoneal Neoplasms

Primary retroperitoneal neoplasms, rare tumors originating in the retroperitoneum, are generally derived from mesenchymal cells, neurogenic cells, or embryonic rests. Although these neoplasms usually present in middle-aged patients, they have been encountered in all age groups. These neoplasms do not produce symptoms until they are quite large, probably because they are able to grow unimpeded in the retroperitoneal space without compromising adjacent organ function.[94, 197] The average size of malignant tumors ranges from 11 to 20 cm and of benign tumors, from 4 to 7 cm.[134]

Malignant Neoplasms

Most primary retroperitoneal tumors are malignant.[90, 91, 134, 251] The frequency of diagnosis of the various malignant retroperitoneal tumor cell types depends on the pathologist's classification system.

Liposarcomas are considered by many to be most frequent,[44, 90] although in some studies, *malignant fibrous histiocytomas* are more commonly diagnosed.[134] *Leiomyosarcomas* are encountered slightly less often, and a variety of other malignancies *(fibrosarcomas, teratomas, rhabdomyosarcoma,* and *hemangiopericytomas)* are seen only occasionally.

Although identification of a specific cell type on CT scans or MR images is not of any help in determining treatment or prognosis, several primary retroperitoneal tumors demonstrate CT and MRI characteristics that allow diagnosis of a specific cell type to be made.

The preferred treatment of all primary retroperitoneal malignancies, regardless of cell type, is surgical resection, provided that the neoplasms are not widely metastatic. Additionally, only tumor grade and resectability affect prognosis. Nonetheless, the CT and MRI characteristics of specific primary retroperitoneal malignant cell types have been described in many earlier reports and are briefly reviewed here.

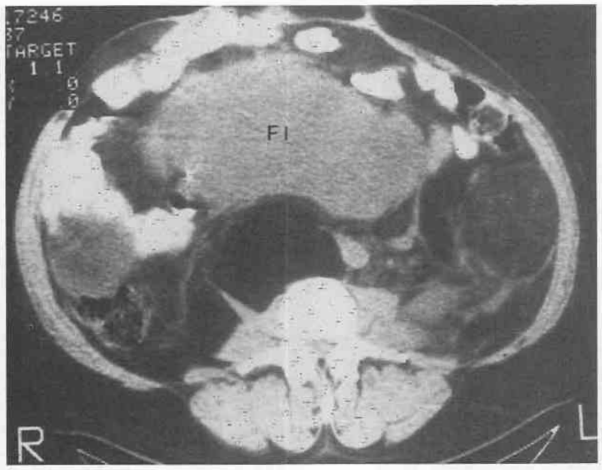

Figure 43–60. Liposarcoma. Nondynamically enhanced abdominal CT scan reveals a large area of fluid attenuation (Fl) surrounded by fat.

Liposarcomas

CT or MRI can suggest a diagnosis of liposarcoma when fat is detected within a retroperitoneal mass (Fig. 43–59). Fat in liposarcomas can often be detected because it demonstrates characteristically low attenuation on CT scans (measuring −10 HU or less). Fat can also be identified by its high T1-weighted and high T2-weighted signal intensity on spin-echo MRI images and by signal loss on fat-saturated, T1-weighted, spin-echo MRI images.

The amount of identifiable fat in liposarcomas varies widely. It is nearly always seen in patients with well-differentiated (lipogenic) liposarcomas (which usually also contain a minimal amount of material showing soft tissue attenuation).[44] Although well-differentiated sclerosing liposarcomas, intermediate-grade myxoid liposarcomas, and high-grade pleomorphic or poorly differentiated liposarcomas may contain recognizable fat, these neoplasms sometimes show only soft tissue attenuation on CT except for occasional areas that show near-water attenuation, which represent necrosis.[127, 153] More rarely, some retroperitoneal liposarcomas contain areas of homogeneously dispersed soft tissue and fatty elements, which average to water attenuation, thereby causing these regions to look cystic (Fig. 43–60).[44]

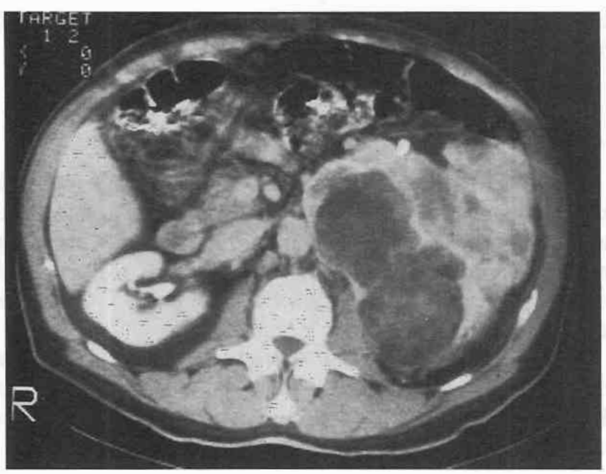

Figure 43–59. Liposarcoma. Nondynamically enhanced CT scan shows a huge liposarcoma demonstrating heterogeneous attenuation. The tumor contains components that show fat and soft tissue attenuation.

Definitive differentiation of retroperitoneal liposarcomas, (particularly of the lipogenic type, from benign lipomas is not possible with CT or MRI, although some CT or MRI findings suggest that a fatty mass is more likely to be malignant than benign. These findings include identification of soft tissue septa more than 2 mm thick within a fatty retroperitoneal mass, septal irregularity or bulging, and obvious enhancement.[106]

Differentiation of liposarcoma from lipoma may be difficult even for the pathologist. Percutaneous biopsy and evaluation of the resected tumor may not resolve the issue. For this reason, many surgeons and oncologists rely on clinical findings to determine whether a fatty tumor should be considered benign or malignant. Since malignant fatty tumors of the retroperitoneum—in contrast to those in the extremities—are much more common than benign fatty tumors, a fatty retroperitoneal tumor should generally be considered to be a liposarcoma and should be resected.

Leiomyosarcomas

Leiomyosarcomas are large, heterogeneous masses (Fig. 43–61). They often have low-attenuation or high T2-weighted–signal intensity components that represent necrosis and do not contain fat or calcification.[134] Although their appearance is never distinctive, their heterogeneity (as well as that of other retroperitoneal sarcomas of soft tissue attenuation) can be contrasted with the homogeneity usually found in the large lymphomatous masses with which they may otherwise be confused. In one series, 11 of 12 large homogeneous retroperitoneal masses were lymphomas and 20 of 26 heterogeneous soft tissue masses were retroperitoneal sarcomas (9 of these being leiomyosarcomas).[44]

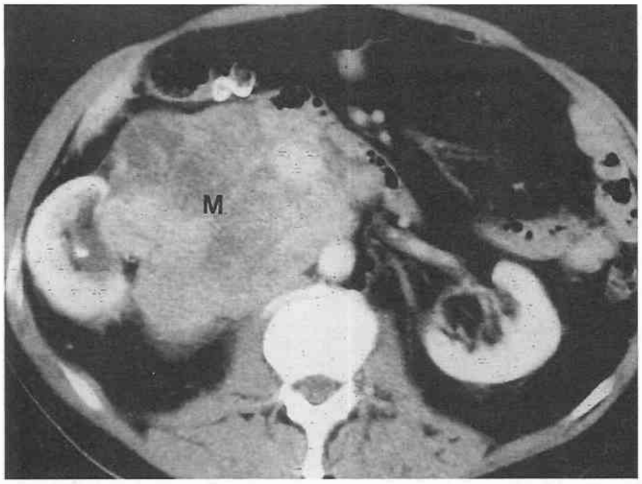

Figure 43–61. Leiomyosarcoma. Contrast-enhanced CT image at the midabdomen level in a 65-year-old man shows a large retroperitoneal mass (M) on the right. At surgery, this mass, which was subsequently determined to represent a leiomyosarcoma, was found to have invaded the inferior vena cava and right kidney. Any non–fat-containing primary retroperitoneal malignancy cell type may have this appearance.

Malignant Fibrous Histiocytomas

Malignant fibrous histiocytomas are often high-grade tumors. These tumors are usually visualized with CT scans and MRI as large, heterogeneous soft tissue–attenuation masses containing areas that show low attenuation or high T2-weighted signal intensity, probably representing necrosis.[220] The appearance is usually not distinctive; however, up to 25% of malignant fibrous histiocytomas contain dystrophic calcification, a finding that is extremely uncommon in other retroperitoneal malignancies (Fig. 43–62).[134]

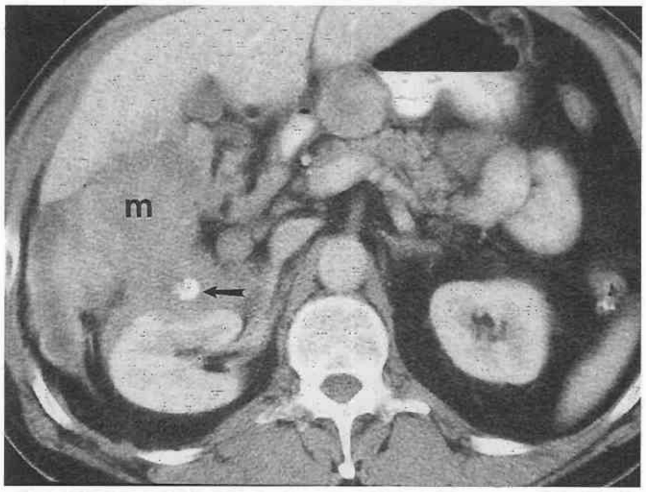

Figure 43–62. Malignant fibrous histiocytoma. Contrast-enhanced CT image obtained through the abdomen in a 61-year-old man shows a large heterogeneous mass (m) anterior to the right kidney and posterior to the liver. Although many primary retroperitoneal malignancies can appear heterogeneous, the presence of calcification *(arrow)* suggests the specific diagnosis of malignant fibrous histiocytoma.

Hemangiopericytomas

Hemangiopericytomas are thought to originate from blood vessel walls. These tumors, not surprisingly, are very vascular and tend to demonstrate brisk enhancement on dynamic bolus CT or gadolinium-enhanced MRI studies.[76] Such enhancement is not seen with most other primary retroperitoneal malignancies. In one report, 1 of 17 hemangiopericytomas also contained amorphous calcification.[76]

Primary Extragonadal Germ Cell Tumors

Only 1% to 10% of germ cell tumors originate outside the gonads, and most of these occur in the mediastinum. For this reason, the testes and ovaries should be carefully examined and imaged in any patient presenting with a retroperitoneal germ cell tumor because it is more likely that this represents metastatic disease in retroperitoneal lymph nodes than a true primary neoplasm.

Primary extragonadal germ cell tumors tend to affect young adults in their 20s and 30s.[24, 54, 187] They are commonly heterogeneous and usually show soft tissue attenuation, making them indistinguishable from most other primary retroperitoneal neoplasm cell types (Fig. 43–63). When teratomatous elements are present, however, these tumors may contain distinctive combinations of fat, calcification, and fluid. These three elements are not typically seen together in other primary retroperitoneal neoplasms.

Other Malignancies

Fibrosarcomas and *neurofibrosarcomas* are tumors that show soft tissue density on CT scans, with attenuation values equal to or just below that of muscle. They are usually heterogeneous and thus identical in appearance to leiomyosarcomas as well as some liposarcomas and malignant fibrous histiocytomas.[134]

Neuroblastomas and *ganglioneuroblastomas* often contain calcification. These two types of neoplasms are usually seen in children.[134]

Rhabdomyosarcomas are quite rare and are also seen in pediatric patients. They can be quite heterogeneous.[44]

Occasionally, *primary retroperitoneal adenocarcinomas* are encountered. These neoplasms are also usually heterogeneous soft tissue masses and do not have a characteristic appearance.

Benign Neoplasms

Benign primary retroperitoneal neoplasms are rare and, except for neural tumors in symptomatic patients with neurofibromatosis and paragangliomas, are usually diagnosed at surgery. Unlike surgery for many patients with primary malignant retroperitoneal neoplasms, surgery in patients with benign tumors is curative.

Most benign lesions tend to originate from neural tissue or neural crest remnants. For example, in one series, 22 of 31 benign neoplasms were paragangliomas, neurofibromas, neurilemomas, or ganglioneuromas.[134]

Paragangliomas

About 10% of all pheochromocytomas are extra-adrenal; most of these extra-adrenal pheochromocytomas, or para-

Figure 43–63. Extragonadal germ cell tumor. Contrast-enhanced CT scan from a 33-year-old man demonstrates a large, predominantly low-attenuation mass *(arrow)* in the paracaval region of the retroperitoneum. The differential diagnosis includes any primary retroperitoneal neoplasm.

gangliomas, lie in the retroperitoneum. The most common site is the para-aortic region, from the level of the adrenal glands to the aortic bifurcation; the latter is where the organ of Zuckerkandl is found.

Only some patients have the classic symptoms of episodic headaches, palpitations, and diaphoresis, and some patients have asymptomatic hypertension. Thus, some paragangliomas may not be clinically active. In one report of 31 tumors in 28 patients, 24 patients had hypertension, although 14 were asymptomatic; however, catecholamine levels were elevated in all 18 patients studied.[98]

Although most paragangliomas are benign, a small minority (e.g., 4 of 28 patients in the preceding series) are considered malignant. A diagnosis of malignancy is usually difficult for a pathologist to make on the basis of histologic analysis of the tumor cells; it is usually necessary to demonstrate local organ invasion or distant metastases.

CT and MRI usually show paragangliomas to be well-defined soft tissue masses in the immediate para-aortic region. A retroperitoneal mass not located adjacent to the aorta probably does not represent a paraganglioma. Most small paragangliomas are homogeneous; however, the more frequently encountered larger lesions are commonly heterogeneous because they can undergo central necrosis or hemorrhage and they may even contain calcification.[63] On MR images, adrenal pheochromocytomas and paragangliomas often demonstrate extremely high signal intensity on T2-weighted images.[63] Occasionally when hemorrhage is present within a paraganglioma, a ring of lower signal intensity can be seen on T2-weighted images, probably related to hemosiderin deposition.

Paragangliomas are generally hypervascular, and most enhance briskly after injection of IV contrast material; however, because ionic iodinated IV contrast material may promote catecholamine release and subsequent hypertensive crises in patients with adrenal pheochromocytomas and extra-adrenal paragangliomas, these contrast agents are not administered routinely if these patients are not receiving α-adrenergic blocking medication. These paragangliomas are usually quite large at the time of diagnosis, however, and are easily detected even on unenhanced CT scans. The effect of gadolinium-based contrast material on catecholamine release has not been well studied.

The likelihood of precipitating catecholamine release is greatest during percutaneous biopsy. Thus, biopsy in patients who have not received α-adrenergic blocking medication is absolutely contraindicated.

Neurofibromas

Neurofibromas are commonly retroperitoneal in location and are often seen in patients with neurofibromatosis.[134] Nerves generally course directly through these tumors and thus cannot be dissected away from them. For this reason, percutaneous biopsy of neurofibromas may be extremely painful. Surgical resection can be performed, but involved nerves will be damaged.

When imaged on CT, neurofibromas are seen as well-defined, sharply marginated, homogeneous masses that demonstrate near-water attenuation.[16, 134] This low attenuation reflects averaging of soft tissue and the extensive intracellular fat contained in these neural sheath tumors.

These neoplasms are often located adjacent to the vertebral column or deep to the psoas muscles (Fig. 43–64). Adjacent bone, particularly the neural foramina, may be smoothly eroded. Malignant degeneration can occur and is suggested if the mass is heterogeneous, demonstrating atypical soft tissue and cystic areas, as noted by Bass and coworkers.[16] Change in morphology or in size of a neurofibroma on sequential CT scans also suggests malignant degeneration.[16]

Neurilemmomas

Neurilemmomas or schwannomas are encapsulated tumors arising from peripheral nerve sheaths, usually seen in young to middle-aged adults.[126] Although most of these tumors are benign, malignant neurilemmomas have been reported.[97] Neurilemmomas most often occur in the soft tissues of the head and neck and in the extremities. Less commonly, the retroperitoneum is involved. Nerve fibers do not traverse neurilemmomas but instead are usually confined to the capsule of these tumors. Thus, often neurilemmomas can be surgically dissected away from adjacent nerves and removed.

On CT and MRI scans, neurilemmomas usually appear as heterogeneous soft tissue masses. Although they may contain cystic areas, they usually have large solid components. Thus, in comparison with neurofibromas, their ap-

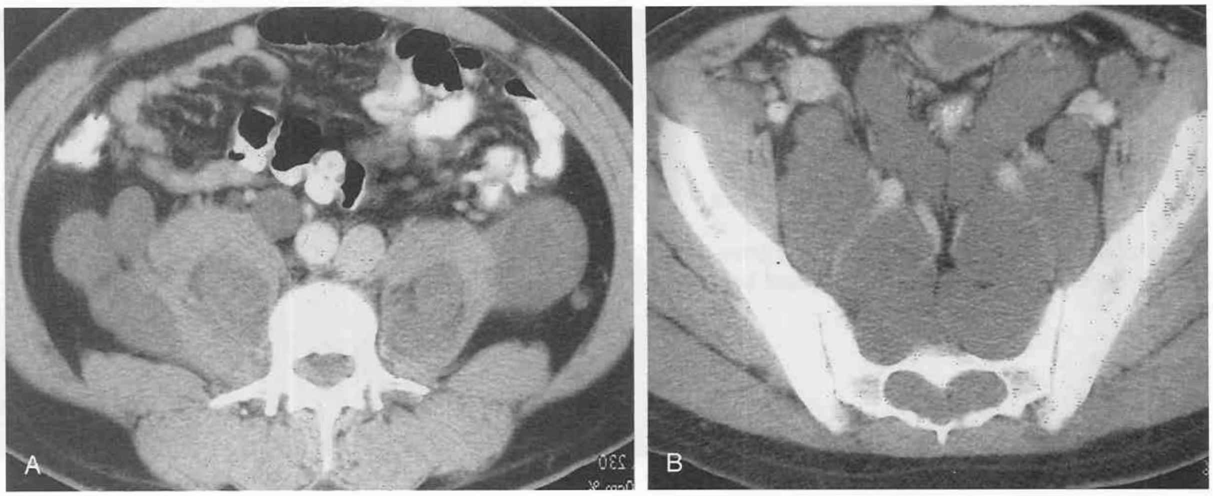

Figure 43–64. Plexiform neurofibromas in a 28-year-old man with type I neurofibromatosis. *A,* Low-attenuation masses are identified on this contrast-enhanced CT image within and lateral to the psoas muscles. *B,* A more caudal CT scan reveals plexiform neurofibromas in the presacral space in the pelvis as well as within the spinal canal. Neurofibromas in the spinal canal are expanding the sacral foramina.

pearance is nonspecific. They are usually primarily of soft tissue attenuation on CT. Most neurilemmomas are isointense on T1-weighted, spin-echo MR images and very hyperintense on T2-weighted images.[97] No CT or MRI features permit distinction between less aggressive and more aggressive neurilemmomas.[97]

Teratomas

The teratoma is one of the easiest tumors to characterize radiographically. This congenital neoplasm contains components of all three germ layers. CT may demonstrate calcification or even osseous elements. Fat-attenuation components may be visualized on both CT and MRI. A fat-fluid level, representing fat that floats on a denser layer of fluid and debris, is occasionally present (Fig. 43–65).[67] Sometimes, a dermoid plug is seen as a soft tissue mass projecting from the wall into a cystic cavity.[67]

Although the incidence of malignant degeneration is small (<1%), teratomas are usually removed because their continued growth can lead to complications (e.g., rupture, infection, torsion).[67] Even benign teratomas may adhere to adjacent structures.

Malignant degeneration is more common in postmenopausal women and usually occurs in the dermal plug. Although microscopic invasion cannot be excluded, CT or MRI visualization of an intact fat plane around the tumor usually indicates that the capsule has not been penetrated and that the tumor has not invaded and is not adherent to adjacent structures. Absence of a fat plane around the tumor does not necessarily indicate local invasion or adherence. This finding may be observed in the absence of any adjacent organ involvement, particularly in thin patients.

Lipomas

Lipomas are well-defined neoplasms composed of mature fat cells and bounded by a thin capsule. Except for

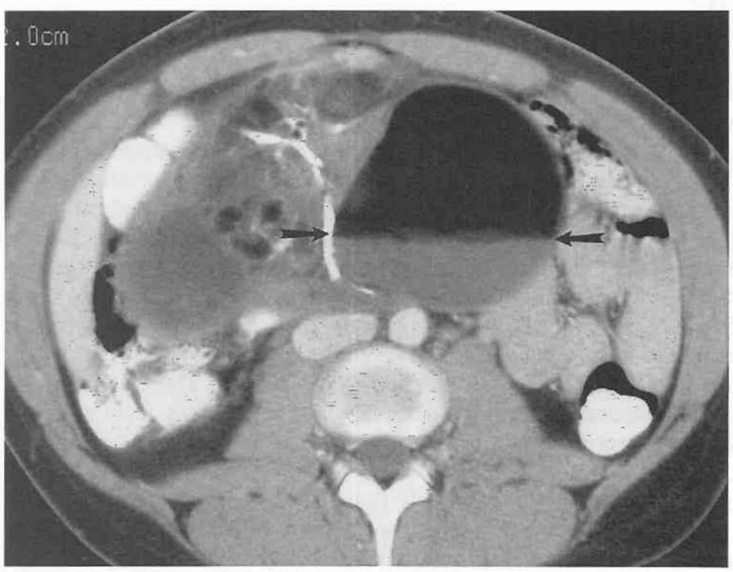

Figure 43–65. Teratoma. Contrast-enhanced abdominal CT scan reveals a large heterogeneous teratoma in the midabdomen of a 24-year-old woman. The teratoma contains elements that show the attenuation of calcification, soft tissue, fluid, and fat. A fat-fluid level can be seen in one component *(arrows).*

fine septa that may be seen traversing lipomas, they are relatively homogeneous and show fat density (Fig. 43–66).[261] As discussed, retroperitoneal lipomas can never be distinguished from lipogenic liposarcomas by the radiologist, by the surgeon, or often even by the pathologist.

Hemangiomas

Hemangiomas are unusual benign retroperitoneal tumors. On CT scans, they demonstrate soft tissue density. Unlike most retroperitoneal masses, they enhance briskly with IV contrast material. They may contain calcification.

Other Benign Neoplasms

Other benign retroperitoneal tumors, encountered only extremely rarely in adults, include lymphangiomas, desmoid tumors, retroperitoneal xanthogranulomas, granular cell tumors, sclerosing fibromas, xanthofibromas, and lymphangiomyomas.[91, 100, 189, 241, 260]

Lymphangiomas are usually smooth, well-defined, near-water-attenuation masses (Fig. 43–67), most commonly discovered incidentally in young children. Desmoid tumors are masses that show soft tissue attenuation. Retroperitoneal xanthogranulomas, representing either a local inflammatory reaction or a true benign neoplasm,[100] lymphangiomyomas (seen in a patient with lymphangioleiomyomatosis),[241] and other unusual benign masses have been encountered in only a few patients.

No distinguishing characteristics of these masses have been identified. The CT and MRI appearance of all of these lesions is nonspecific, showing inhomogeneous soft tissue attenuation and soft tissue signal intensity. Thus, the diagnosis of these entities before biopsy or surgery is not possible.

Imaging at Presentation

CT and MRI are the imaging modalities of choice for evaluation of patients with known or suspected retroperitoneal masses. When large retroperitoneal masses are detected by CT or MRI, the differential diagnosis usually includes retroperitoneal neoplasm, lymphoma, and occasionally retroperitoneal lymph node metastases and retroperitoneal fibrosis. Rarely, hematoma and infection can produce retroperitoneal masses.

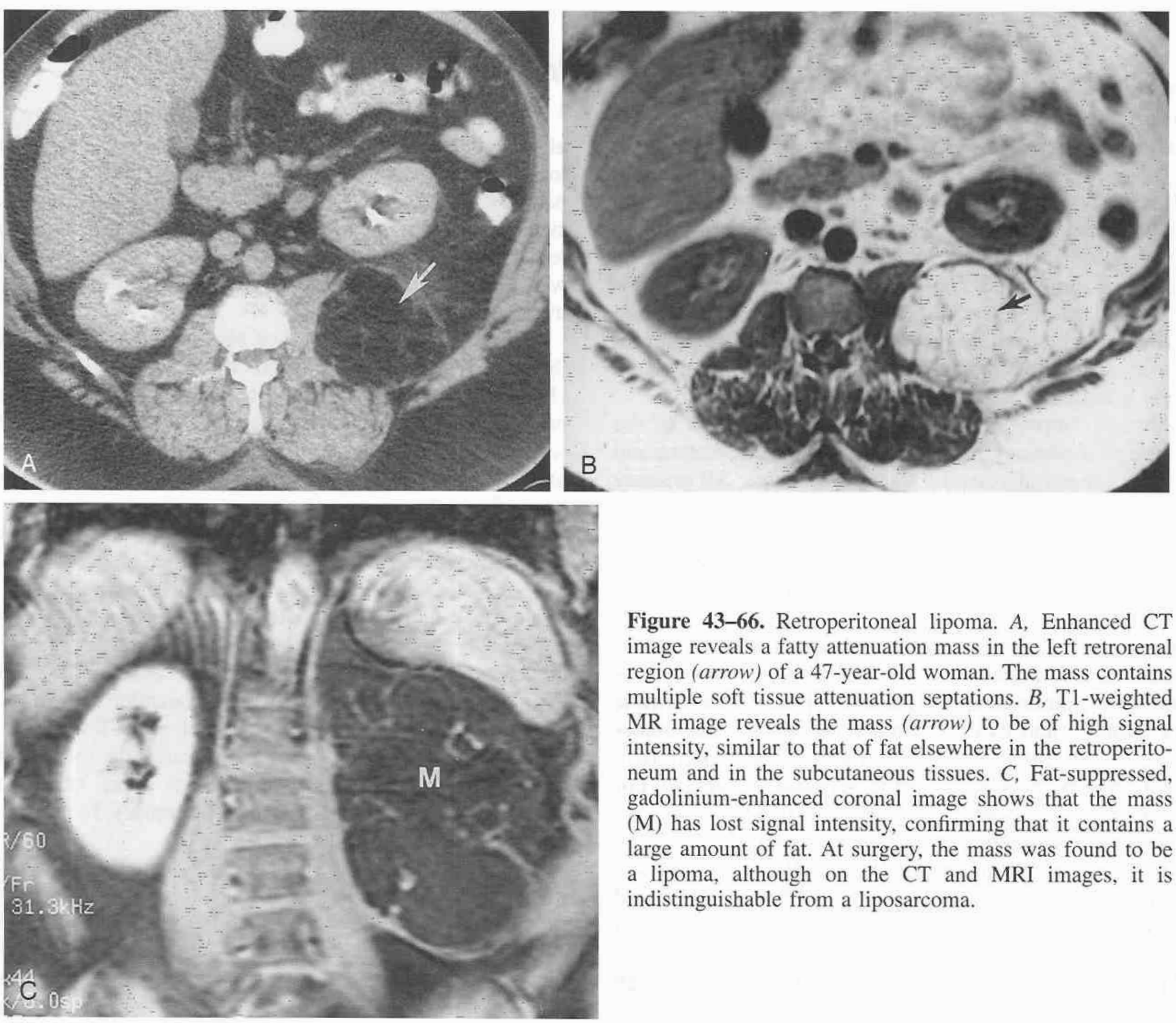

Figure 43–66. Retroperitoneal lipoma. *A,* Enhanced CT image reveals a fatty attenuation mass in the left retrorenal region *(arrow)* of a 47-year-old woman. The mass contains multiple soft tissue attenuation septations. *B,* T1-weighted MR image reveals the mass *(arrow)* to be of high signal intensity, similar to that of fat elsewhere in the retroperitoneum and in the subcutaneous tissues. *C,* Fat-suppressed, gadolinium-enhanced coronal image shows that the mass (M) has lost signal intensity, confirming that it contains a large amount of fat. At surgery, the mass was found to be a lipoma, although on the CT and MRI images, it is indistinguishable from a liposarcoma.

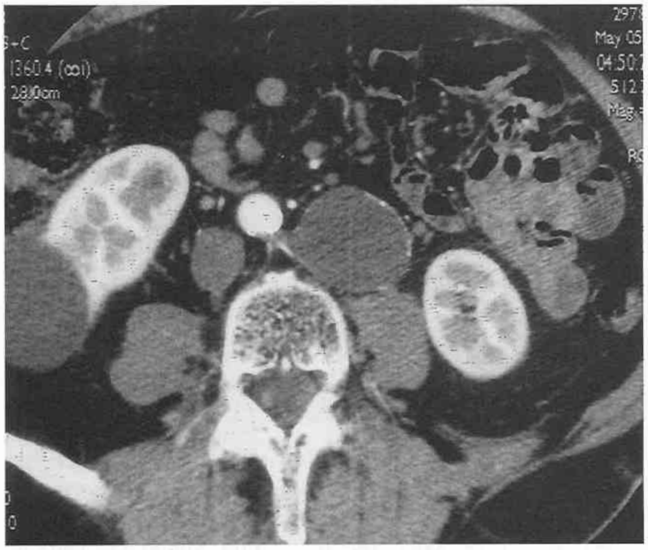

Figure 43–67. Retroperitoneal lymphangioma. CT scan demonstrates a large water-attenuation mass in the left para-aortic region of the retroperitoneum in an asymptomatic 71-year-old man. A thin rim of calcification along the periphery of the mass suggests that it has been present for a long time. The mass was resected. Pathologic examination confirmed the diagnosis of lymphangioma.

Percutaneous biopsy, which is often technically easy to perform because of the large size of these masses, can be extremely helpful in differentiating among these possibilities. Biopsies should be obtained with cutting or core needles because pathologic analysis often requires histologic samples, and distinction from lymphoma is more easily made.[197] As already noted, pathologists may have difficulty distinguishing benign from malignant retroperitoneal tumors even when surgical specimens are obtained, and clinical behavior (e.g., presence or absence of adjacent organ invasion and distant metastases) may be used to classify a tumor as benign or malignant.

Although biopsy may also permit identification of the cell type of a primary retroperitoneal tumor, treatment and prognosis are *not* affected by specific cell type. All primary retroperitoneal neoplasms must be treated surgically if possible (see later). Furthermore, only tumor resectability and grade affect patient survival.[3, 23, 235] Patients with completely resected tumors and with low-grade tumors are most likely to live the longest.

Once the diagnosis of primary retroperitoneal neoplasm has been made, presumably by percutaneous biopsy, the CT or MRI examination should be reviewed to determine tumor location and extent. Primary retroperitoneal tumors tend to directly invade adjacent structures, and multiorgan removal may be necessary during subsequent surgery. For this reason, it is essential to determine which organs are proximal to the neoplasms and which are definitely or possibly invaded by tumor. In theory, MRI has an advantage over CT because of its ability to image in coronal and sagittal planes and thus to better define the relationship of the tumor mass to the abdominal organs and vasculature.

CT and or MRI studies should be performed through the chest, abdomen, and pelvis. This is because patients must be assessed for possible regional or distant metastases, such as separate enlarged retroperitoneal lymph nodes, liver lesions, and lung nodules. Whereas extremity sarcomas usually metastasize to the lungs first, retroperitoneal sarcomas frequently metastasize to other abdominal organs, before or in addition to the lungs.

Treatment

Most primary retroperitoneal neoplasms in adults are treated surgically. Complete removal of the mass is preferred; however, in many patients with both benign and malignant tumors, only debulking is possible. When complete resection is performed, benign neoplasms are cured; however, recurrences are common in patients with malignant primary retroperitoneal neoplasms, even when initial surgical resection is believed to have been complete.[87]

When complete resection cannot be performed, chemotherapy and/or external beam radiation of malignant tumors may be used, although each of these techniques has limited effectiveness in most patients.[37, 73, 146, 239] Fortunately, because many malignant retroperitoneal neoplasms are relatively slow-growing, patients with unresectable tumors may still live for many years after the initial surgery.[87]

Imaging after Surgery

Tumor recurrences frequently develop relatively soon after surgery, even when the initial resection was believed to have been curative. For example, in one series of 33 patients with recurrent primary retroperitoneal malignancies, 25 recurred within the first 2 years.[87] Interestingly, recurrences developed at similar time intervals in patients with high-grade tumors and in those with low-grade tumors.

Given the limited benefit of chemotherapy and radiation therapy, when recurrences are detected, the treatment of choice is usually additional surgery. Tumor re-resection may be curative; however, re-recurrences often develop, which may be treated with still more surgery. It is not unusual for second and even third debulking procedures to be performed.

Given the high rate of tumor recurrence, patients with surgically treated primary retroperitoneal malignancies are usually followed closely with regular cross-sectional imaging by either CT or MRI. Because the likelihood of completely resecting a tumor recurrence is highest if the recurrence is small when detected, it is essential to identify recurrent tumor masses as early as possible.[87]

Since tumor recurrences are most often located in the operative bed, this region must be carefully evaluated on follow-up CT or MRI examinations. Next, other intra-abdominal sites (e.g., peritoneum, mesentery, liver) and the lungs should be scrutinized.

Although recurrent tumor masses usually have CT or MRI characteristics that are similar to those of the original neoplasm, tumors may recur at higher grades or with different morphology. In one study, for example, four of eight recurrent liposarcomas that initially contained identifiable fat on CT recurred as masses of entirely soft tissue attenua-

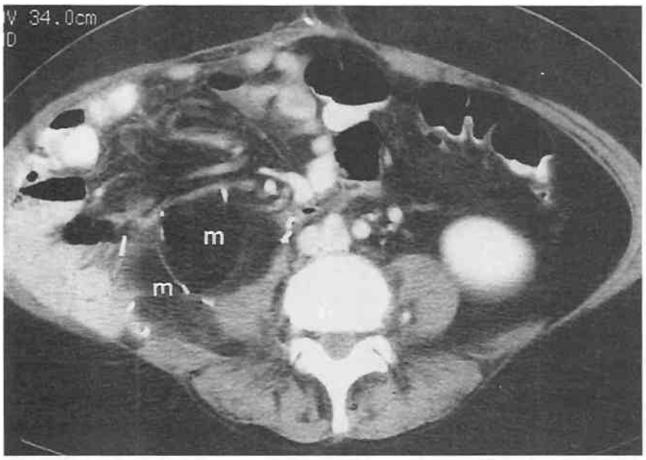

Figure 43–68. Recurrent liposarcoma. Contrast-enhanced CT scan demonstrates recurrences of a liposarcoma (m) in the right hemiabdomen of a 57-year-old woman 5 years after the initial resection. Surgical clips from the previous resection surround the tumors. The recurrent tumors have an attenuation similar to that of uninvolved adjacent retroperitoneal fat. When liposarcoma recurrences are small, they can be difficult to identify for this reason.

tion.[87] Detection of recurrent liposarcomas may also be a problem because it is occasionally difficult to distinguish normal retroperitoneal fat from fat in a recurrent tumor mass (Fig. 43–68).[87] In many instances, however, the fat in the recurrent tumor differs slightly in attenuation from normal, uninvolved fat.[87]

Retroperitoneal Fibrosis

Retroperitoneal fibrosis, a rare inflammatory and fibrotic process, most frequently involves the caudal aspect of retroperitoneum. The estimated prevalence is about 1 to 2 cases per 100,000 people each year.[4, 185] It usually affects middle-aged to elderly men but has also developed in women and children.[85, 257]

Pathology

Early retroperitoneal fibrosis is characterized by proliferation of fibroblasts, infiltration of acute inflammatory cells, and proliferation of capillaries, all of which are surrounded by collagen fibers.[219] Immunohistochemical studies of inflammatory tissue reveal the predominant cell type to be B lymphocytes and T-helper cells.[124, 199] Usually, a high fluid content characterizes the early stage.

Over time, the cellular activity in the retroperitoneal plaque diminishes substantially; fibrosis develops, and the collagen becomes hyalinized and much more tightly packed. Vascularity is decreased,[219] and fluid content becomes minimal.[4] On gross inspection, long-standing retroperitoneal fibrosis appears as a characteristic gray-white plaque of woody consistency that envelops the aorta and the IVC. Although in many patients the chronic phase of the disease is characterized by this fibrotic process, in some patients active inflammation may persist in addition to the fibrotic changes.

Etiology

In up to 70% of cases, retroperitoneal fibrosis is considered to be *idiopathic*. In most patients with the idiopathic form of disease, it is thought that the process develops as an immune response to atherosclerotic changes in the abdominal aorta.[4, 124] One substance thought to elicit this immune response is an insoluble lipid called *ceroid*, which is commonly detected in macrophages in the aortic adventitia or in periaortic lymph nodes. Indeed, immunoglobulin G has been found in ceroid.[124, 170, 198] Another substance that may also be able to elicit an antibody response is oxidized low-density lipoprotein.

Evidence that many cases of idiopathic retroperitoneal fibrosis might be caused by an anti-atherosclerotic immune response is supported by the fact that most of the patients are men in the fifth to seventh decades of life, individuals who tend to have atherosclerotic disease.[124] The nature of this autoimmune response, however, is unclear, because some patients are children without atherosclerotic disease. Furthermore, retroperitoneal fibrosis does not develop in all patients with atherosclerosis. Autoantibodies to ceroid have been identified in older patients with atherosclerosis and without retroperitoneal fibrosis.[124]

Retroperitoneal fibrosis may also develop around AAAs. This perianeurysmal fibrosis is also thought to represent an autoimmune reaction to the atherosclerotic changes in the dilated abdominal aorta, similar to that occurring around nondilated atherosclerotic aortas.

Of the many other known benign causes of retroperitoneal fibrosis, the most common is ingestion of one of a variety of medications, including methysergide, β blockers, methyldopa, hydralazine, antibiotics, and some analgesics. Benign diseases that may elicit retroperitoneal fibrosis include the following[4, 41, 144]:

1. Various systemic infections (e.g., tuberculosis, syphilis, actinomycosis, brucellosis, fungal infections).
2. Focal inflammatory or infectious conditions (e.g., diverticulosis, appendicitis, extravasation from the urinary tract).
3. Previous surgery or radiation treatment.
4. Trauma.
5. Retroperitoneal hemorrhage.
6. Marfan's disease.
7. Inflammatory bowel disease.

In a small minority of patients, malignant processes (primary neoplasms or metastatic disease) can provoke an extensive desmoplastic reaction in the retroperitoneum that cannot always be distinguished from benign retroperitoneal fibrosis. Tumors found to produce such a reaction include carcinoid and malignancies from the stomach, breast, ovary, and prostate gland.[157, 243]

Associated Processes

Associations have been reported between retroperitoneal fibrosis and a variety of inflammatory processes that can

occur elsewhere in the body, such as Riedel's thyroiditis, fibrosing mediastinitis, mesenteric fibrosis, and rheumatoid arthritis.[4, 193, 257]

Clinical Presentation

Patients with retroperitoneal fibrosis typically present with back pain and may have a history of fatigue and weight loss.[4] Symptoms or signs may be present that relate to compression of retroperitoneal structures, of which the ureters are the most commonly involved. Although ureteral obstruction is often clinically silent, some patients have flank pain or tenderness; others have oliguria or even anuria. Extrinsic narrowing of the IVC can cause lower extremity swelling with or without associated deep vein thrombophlebitis.

Occasionally, the distal abdominal aorta can be so severely compressed that vascular insufficiency may occur in the lower extremities, bowel, or kidneys.[4] Retroperitoneal fibrosis may be extensive and may spread into the perirenal space or pelvis. One patient with retroperitoneal fibrosis presented with a symptomatic, constricting mass involving the proximal rectum.[89]

Laboratory studies usually demonstrate significant elevation of the ESR. Blood urea nitrogen and creatinine levels may be elevated in patients with ureteral involvement.[4, 41, 144] Leukocytosis may also be present.

CT and MRI Technique

CT and MRI represent the two modalities of choice for imaging patients with known or suspected retroperineal fibrosis.

Computed Tomography

CT is best performed throughout the abdomen and pelvis at contiguous 7- to 10-mm intervals after administration of oral and IV contrast material; however, when renal function is compromised (usually because of the retroperitoneal fibrosis) or another contraindication to intravascular contrast material administration, unenhanced scans should be obtained.

The CT appearance of retroperitoneal fibrosis ranges from minimal periureteral stranding to large lobulated masses obliterating the fat planes between the aorta and the IVC (Fig. 43–69).[130] The classically described medial deviation of the ureters, with respect to the lumbar vertebral pedicles, is identified only in some patients with retroperitoneal fibrosis. Additionally, this finding can also be seen in a minority of normal patients.[224] Some studies have been unable to detect any difference in ureteral position in patients with retroperitoneal fibrosis when compared with normal patients.[4]

After IV contrast material administration, the fibrotic mass of retroperitoneal fibrosis typically demonstrates obvious enhancement. This enhancement can be seen with both benign and malignant causes of retroperitoneal fibrosis.[4]

In many instances, retroperitoneal fibrosis cannot be distinguished on CT scans of enlarged conglomerate lymph nodes in patients with metastatic disease (Fig. 43–70); however, several features have been identified that, when present, suggest retroperitoneal fibrosis as the most likely diagnosis. Metastases often have a masslike configuration. Retroperitoneal fibrosis tends to be located at the level of the L4 vertebral body and to be plaquelike and infiltrating rather than nodular.[29, 130, 219] Metastatic neoplasms often displace the aorta and IVC as well as the ureters. Conversely, retroperitoneal fibrosis usually surrounds (rather than displaces) the anterior and lateral aspects of the great

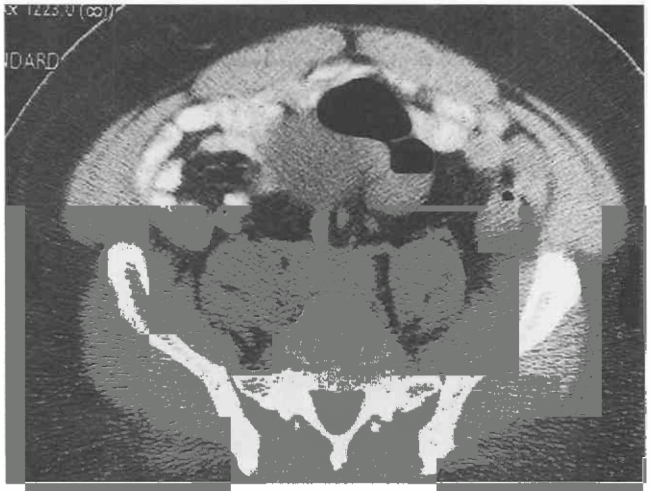

Figure 43–69. Retroperitoneal fibrosis. Contrast-enhanced CT scan shows a confluent, plaquelike, soft tissue attenuation mass surrounding the proximal common iliac arteries in a 49-year-old patient. The mass was later found to represent retroperitoneal fibrosis.

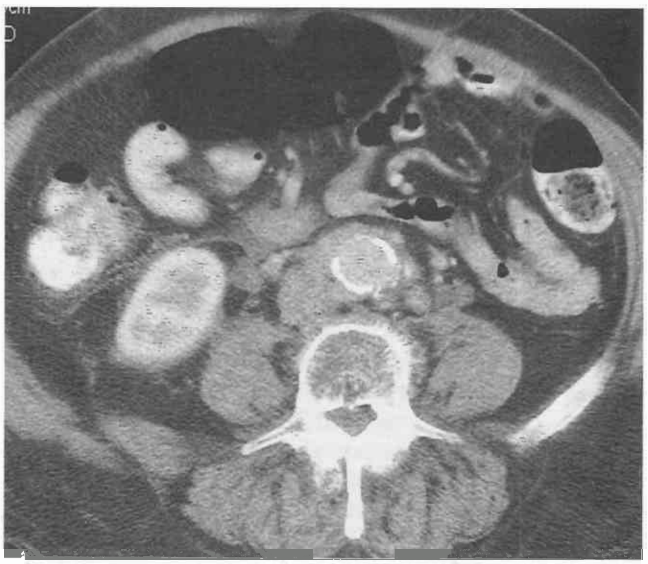

Figure 43–70. Retroperitoneal lymph node metastases mimicking retroperitoneal fibrosis. Contrast-enhanced CT scan demonstrates a conglomerate soft tissue mass of lymph nodes enlarged by tumor that surrounds the partially calcified abdominal aorta in a 75-year-old man with metastatic prostate cancer. The CT appearance is quite similar to that of retroperitoneal fibrosis.

vessels, although rarely, benign retroperitoneal fibrosis may cause anterior displacement of the aorta to a moderate extent.[53]

Other diseases with a CT appearance similar to that of retroperitoneal fibrosis include lymphoma, infection (with resultant lymph node enlargement), primary retroperitoneal neoplasms, amyloidosis, and hemorrhage.[4, 130] Occasionally, some of these processes demonstrate features suggesting a specific diagnosis. Enlarged lymph nodes from lymphoma are often centered more cephalad in the retroperitoneum and may be bulkiest at the level of the renal hila. Malignancies and infectious processes may invade and destroy adjacent bones or organs. Acute hemorrhage often shows high attenuation on unenhanced scans; it also infiltrates between the fascial planes in a characteristic fashion. Neoplasms may grow more quickly than retroperitoneal fibrosis, so that if a substantial increase in mass size is noted on sequential scans, malignant disease is much more likely.

Magnetic Resonance Imaging

MRI should be performed using at least three sequences. Both T1-weighted and T2-weighted spin-echo (or fast spin-echo) and gadolinium-enhanced images are recommended. MRI may be the study of choice for evaluating patients with suspected retroperitoneal fibrosis because it has two important advantages over CT.

The relationship of the mass to the great vessels is easily visualized on MRI. Whereas masses and vessels can have identical attenuation values on unenhanced CT, flow void in vessels on spin-echo MRI sequences allows for their identification even when they are surrounded by extensive tissue.

MRI can also be used in the coronal and sagittal planes, again facilitating evaluation of the relationship of retroperitoneal fibrosis to the retroperitoneal vasculature.

Additionally, MRI can sometimes suggest the specific diagnosis by detecting the low signal intensity of the mass on T2-weighted images. Since mature fibrosis contains much collagen and little cellularity and fluid, it is not surprising that long-standing retroperitoneal fibrosis commonly shows low signal intensity on T2-weighted images (Fig. 43–71).[4, 10, 141, 182, 278] Unfortunately, because acute benign retroperitoneal fibrosis, with its greater cellularity and fluid content, has intermediate or high signal intensity on T2-weighted sequences and because chronic retroperitoneal fibrosis with continuing active inflammation has intermediate or high signal intensity on T2-weighted sequences, the MRI characteristics may not be typical.[4, 182]

In summary, a specific diagnosis of benign retroperitoneal fibrosis can probably be offered for any patient who has a retroperitoneal mass that shows low signal intensity on both T1-weighted and T2-weighted images. High or intermediate signal intensity on either T1-weighted or T2-weighted images is not specific.

Percutaneous Biopsy

As can be seen, the definitive diagnosis of retroperitoneal fibrosis often cannot be made by any imaging study, and surgery may be required to determine with certainty whether this disease is present. Although CT-guided percutaneous biopsy is often technically feasible, a biopsy that does not result in detection of malignant cells is inconclusive. Tumor cells in patients with malignancy (with or

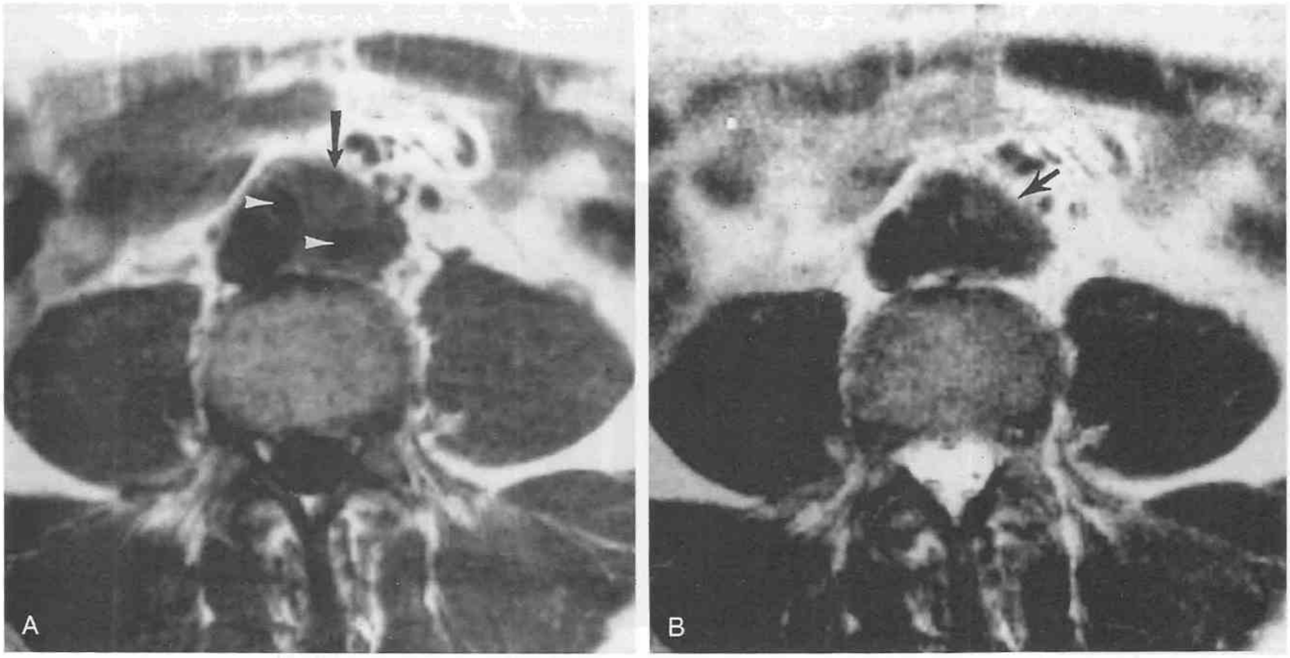

Figure 43–71. Retroperitoneal fibrosis. *A,* T1-weighted, spin-echo MR image demonstrates a low-signal-intensity, plaquelike mass *(arrow)* surrounding the proximal portions of both common iliac arteries *(arrowheads)* and the caudalmost aspect of the inferior vena cava. *B,* On the T2-weighted, spin-echo image, the mass *(arrow)* is again of very low signal intensity, a finding consistent with the presence of extensive fibrous tissue with little or no active inflammation.

without the malignant form of retroperitoneal fibrosis) may be sparse; therefore, sampling may not be successful when fine-needle aspiration or even a core biopsy is performed.

Obviously, performing surgery solely to make a diagnosis (rather than to treat) is undesirable. In some instances, patients whose clinical presentation and laboratory and imaging studies strongly suggest the diagnosis are now being treated medically, without a definitive surgical or histopathologic diagnosis, in an attempt to avoid surgery (and its attendant morbidity) solely for diagnosis.[71] If response to treatment is complete, surgery is never performed.

Treatment

Benign Disease

Treatment of benign idiopathic retroperitoneal fibrosis consists of administration of high doses of corticosteroids for long periods. For example, patients may be given up to 60 mg of prednisone per day until symptoms resolve.[71] The dose is tapered over several months and then maintained at a low level for 6 to 12 months. The chemotherapeutic agents azathioprine and cyclophosphamide have also been successfully employed, particularly for patients who have not responded to corticosteroids.[71]

In contrast, use of corticosteroids or other medications in patients with perianeurysmal fibrosis is not recommended because it is believed that resolution of the fibrotic process in these individuals places them at greater risk for aneurysm rupture. Instead, these patients should undergo elective AAA repair.

If the ureters are involved, patients may undergo open surgical or laparoscopic ureterolysis. At surgery, the ureters may be wrapped in omentum and mobilized and placed laterally over the psoas muscles or into the peritoneal cavity to remove them from the retroperitoneal inflammatory process. Alternatively, patients with ureteral involvement may respond successfully to medical treatment.[71]

Malignancy

Treatment of the malignant type of retroperitoneal fibrosis is palliative. Urinary diversion is recommended for patients with ureteral obstruction along with appropriate chemotherapy or radiation therapy.

Imaging after Treatment

In general, response to treatment is easily assessed by evaluating the patient for resolution of symptoms or by observing a reduced ESR or serum creatinine level (if there had been urinary tract obstruction). CT and MRI can be performed for follow-up, however, to confirm the clinical impression of response to treatment or to evaluate patients whose symptoms or laboratory results have not improved (Fig. 43–72).

In some instances, MRI may be more effective than CT in demonstrating a response to therapy, since the T2-weighted signal intensity of retroperitoneal fibrosis has been shown to decrease during treatment; this probably represents the disappearance of all active inflammation.[278] The change in signal intensity of a retroperitoneal mass might even precede regression of mass size. Although lack of mass regression or signal intensity change may merely indicate that the retroperitoneal fibrosis has not responded to treatment, other diagnostic alternatives, including malignancy, should be considered.

Prognosis

The prognosis in patients with benign retroperitoneal fibrosis is excellent; for those with the malignant form, it is usually poor. Most patients with benign retroperitoneal fibrosis respond to initial treatment; relapse is relatively uncommon. Most patients with malignant retroperitoneal fibrosis survive for only 3 to 6 months after diagnosis.[4, 244]

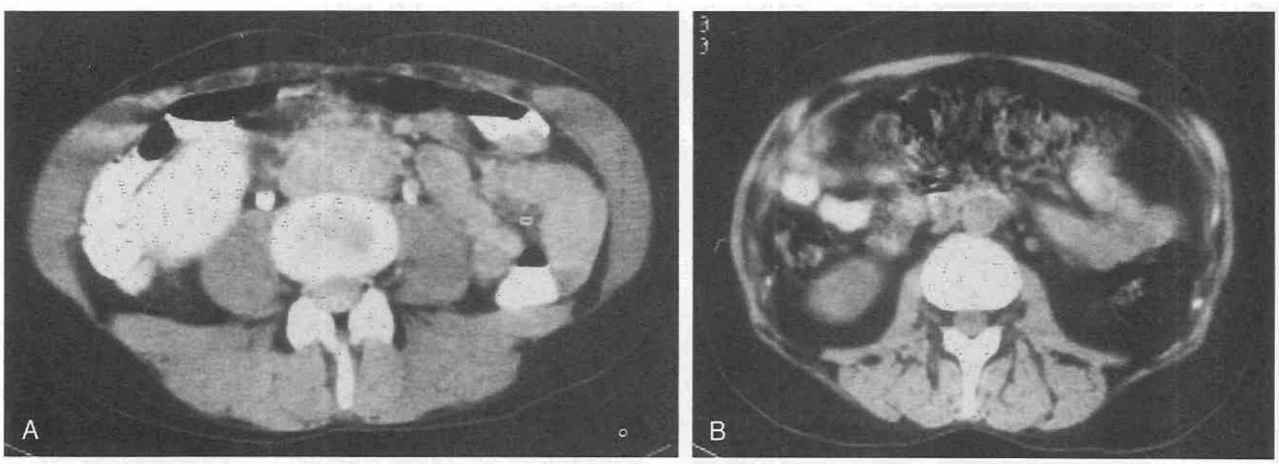

Figure 43–72. Retroperitoneal fibrosis. *A,* Nondynamically enhanced CT scan reveals a soft tissue mass enveloping the aorta and inferior vena cava. *B,* An unenhanced scan obtained after 3 months of corticosteroid therapy shows almost complete dissolution of the plaque. The increase in retroperitoneal fat is a result of corticosteroid use. (From Degesys GE, Dunnick NR, Silverman PM, et al: Retroperitoneal fibrosis: Use of CT in distinguishing among possible causes. Am J Roentgenol 146:57–60, copyright by American Roentgen Ray Society, 1986.)

Iliopsoas

Normal Anatomy

The psoas major muscles arise from the anterior and inferior surfaces of the transverse processes of the T12 and L1 to L5 vertebrae as well as from the adjacent vertebral bodies and intervertebral disks. They course inferiorly and fuse with the iliacus muscles before traversing under the inguinal ligament to insert onto the lesser trochanter of the femur. These bulky muscles are responsible for flexion of the thigh. When present, as is the case in 30% to 60% of individuals, the psoas minor muscles originate from the lateral aspects of T12 and L1 and travel caudad to insert onto the pectineal eminence of the ipsilateral iliac bone just anterior to the psoas major.

On routine abdominal and pelvic CT and MRI examinations, the psoas major muscles are easily visualized, lying immediately lateral to the lumbar vertebrae. Usually, the lateral aspect of the muscles is well defined by adjacent retroperitoneal fat. In children or cachectic adults, however, adjacent abdominal organs may obliterate the lateral margins of these muscles. The psoas major muscle reaches its largest cross-sectional size at the L3-L4 level. Subsequently, it thins as it fuses with the iliacus. The iliopsoas continues caudad into the thigh. It is easily visualized throughout its course.

The muscle is characterized by homogeneous attenuation, but a small linear zone of decreased density, representing fat surrounding branches of the lumbar plexus, may be identified in its lateral aspect. The psoas minor muscles may occasionally be identified as small soft tissue masses immediately anterior to the psoas major and, when observed, should not be confused with lymph nodes or retroperitoneal vessels (Fig. 43–73). The psoas minor muscles are often contiguous with the anterior aspects of the psoas major and therefore are not distinguishable as discrete structures.

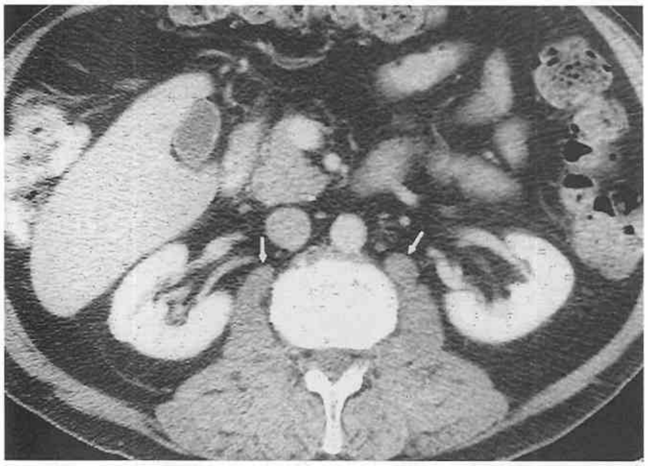

Figure 43–73. Psoas minor muscles. On this contrast-enhanced CT scan, the psoas minor muscles are identified as small masses *(arrows)* immediately anterior to the psoas major muscles. The right psoas minor is fused with the psoas major, which is the case in many patients. The left psoas minor muscle appears more discrete.

Abnormalities of the Iliopsoas Compartment

Abnormalities of the iliopsoas muscles usually result in asymmetrical enlargement; however, some patients with neurologic or muscular disorders may demonstrate atrophy of the iliopsoas muscles on the affected side. Causes of iliopsoas compartment disease include inflammation, neoplasms, hematomas, enlargement of iliopsoas bursae, aneurysms and pseudoaneurysms, and hernias. Inflammatory processes, neoplasms, and hemorrhage may all diffusely infiltrate the iliopsoas and involve the majority of or even the entire length of the muscle.

Iliopsoas compartment disease can be evaluated with CT or MRI. Although MRI may have some theoretical advantages over CT, including its ability to easily image patients in the coronal and sagittal planes, in many instances it is no more accurate than CT in identifying the cause of an iliopsoas mass.

Some authors[38, 275] have divided iliopsoas abnormalities into three categories based on the anatomic origin of the abnormality, as identified on cross-sectional imaging studies, in the hope that localization might help determine the cause:

1. Abnormalities intrinsic to the compartment.
2. Abnormalities extending from the spinal column, the sacroiliac joint, or hip joint.
3. Abnormalities extending from adjacent retroperitoneal structures.

Even with use of this classification, CT or MRI findings may not suggest the cause of an iliopsoas abnormality. In one study, for example, radiologists were only 48% accurate in diagnosing iliopsoas processes identified on CT when they had no knowledge of the clinical history.[143] In some instances, the diagnosis may not be possible even when imaging findings are correlated with the patient history and laboratory data.[66] Percutaneous biopsy, or occasionally even surgery, may be required for diagnosis.

Inflammatory Processes

Inflammatory processes of the iliopsoas muscles account for one third to two thirds of the psoas masses detected by CT or MRI.[51, 66, 195, 275] Patients with inflammatory iliopsoas masses commonly have abdominal or pelvic pain and fever, although symptoms may be absent. In the overwhelming majority of cases, myositis and frank abscess develop from spread of adjacent infection of the kidneys, aortic bed, spine, pancreas, or bowel (secondary to Crohn disease, diverticulitis, or perforated colonic neoplasm). Occasionally, iliopsoas infections are complications of abdominal surgery. Only rarely does iliopsoas myositis or abscess originate in the iliopsoas muscles, probably as a result of bacterial seeding during septicemia.[275]

Commonly encountered organisms responsible for pyogenic infections include *Staphylococcus aureus* (most frequent), *Enterococcus*, *Klebsiella pneumoniae*, *Pseudomonas aeruginosa*, *Escherichia coli*, and *Mycobacterium tuberculosis*. Psoas pyomyositis has also been reported to be caused by *Salmonella enteritidis* and *Salmonella*

typhi.[150, 271] The incidence of tuberculous spondylitis has dropped significantly over the past few decades.[66] Tuberculosis is still encountered in some patients, however, and should remain a consideration, particularly in populations at risk (i.e., people who are indigent, immunocompromised, or infected with HIV).[195]

On CT scans, iliopsoas inflammatory masses display a variety of appearances, ranging from diffuse homogeneous enlargement of the psoas muscles to discrete masses containing areas of low attenuation (usually representing fluid) (Fig. 43–74).[275] Punctate collections of gas are seen in only a minority of patients; when present, however, these are thought to be specific indicators of infection. In rare instances, however, air may be present in infected or even sterile necrotic tumors (either primary neoplasms or metastases).[66, 120, 268] Calcifications are occasionally detected in inflammatory masses, particularly in patients with tuberculosis.[66] Adjacent destruction of lumbar vertebrae, which usually represents spread into the iliopsoas muscle from adjacent tuberculous or pyogenic spondylitis, may also be encountered.

MRI may be the imaging modality of choice early in the development of the myositis. The increased signal intensity on T2-weighted images, indicating muscle edema, without evidence of a focal mass, suggests the diagnosis of myositis.[272] A correlative finding (of decreased muscle attenuation) is only occasionally detectable on CT. Other MRI features of inflammation, which are nonspecific, include asymmetrical muscle size and areas of low signal intensity on T1-weighted images and after gadolinium enhancement.[195]

The MRI appearance of an iliopsoas abscess is not specific. Once again, the affected muscle is enlarged. Areas of low signal intensity on T1-weighted images and of high signal intensity on T2-weighted images correspond to focal loculated fluid. Of course, any calcifications within an inflammatory mass are not directly visible on MRI studies.

CT or MRI evaluation of patients with iliopsoas infection must include scrutiny of surrounding abdominal organs for possible associated inflammatory changes. For example, associated bone destruction is easily identified.

Also, CT or MRI may be used to guide the percutaneous aspiration and placement of percutaneous drainage catheters for definitive treatment of iliopsoas abscess, thus obviating the need for surgery.[181] Because the CT appearances of iliopsoas phlegmon and iliopsoas abscess can be identical, it is not surprising that percutaneous aspiration of infected iliopsoas masses yields grossly purulent fluid in some instances but only solid tissue in others.[268] Percutaneous drainage is successful only when infected fluid can be drained from the iliopsoas mass. However, the underlying cause of the infection (e.g., renal disease, pancreatitis) must be adequately treated to ensure successful management of the iliopsoas disease.

Neoplasms

Neoplasms involving the iliopsoas represent one fourth to one half of iliopsoas masses detected by CT or MRI.[51, 66] These neoplasms most commonly result from direct invasion of adjacent primary or metastatic tumor masses. Primary retroperitoneal tumors, including liposarcomas, fibrosarcomas, and neurogenic neoplasms, can invade the iliopsoas muscle. Metastatic lymph nodes in patients with NHL, pelvic tumors, testicular tumors, renal malignancies, or malignant melanomas can invade the iliopsoas compartment. Other primary tumors that can produce metastases that invade the iliopsoas compartment are carcinomas of the cervix, ovary, colon, stomach, lung, and breast.[274] Primary iliopsoas neoplasms (usually sarcomas) are occasionally encountered. Only rarely do isolated metastases develop in the iliopsoas compartment, probably via hematogenous spread.

Iliopsoas compartment neoplasms frequently have a CT or an MRI appearance identical to that of other iliopsoas abnormalities. The affected muscle is usually enlarged. As with abscesses, CT iliopsoas tumors may have enhancing rims and low-attenuation centers (Fig. 43–75).[268] Calcification is unusual. Nonspecific MRI features include areas of low signal intensity on T1-weighted images, high signal intensity on T2-weighted images, and a reticulated texture.[274]

A specific diagnosis is possible only when a large

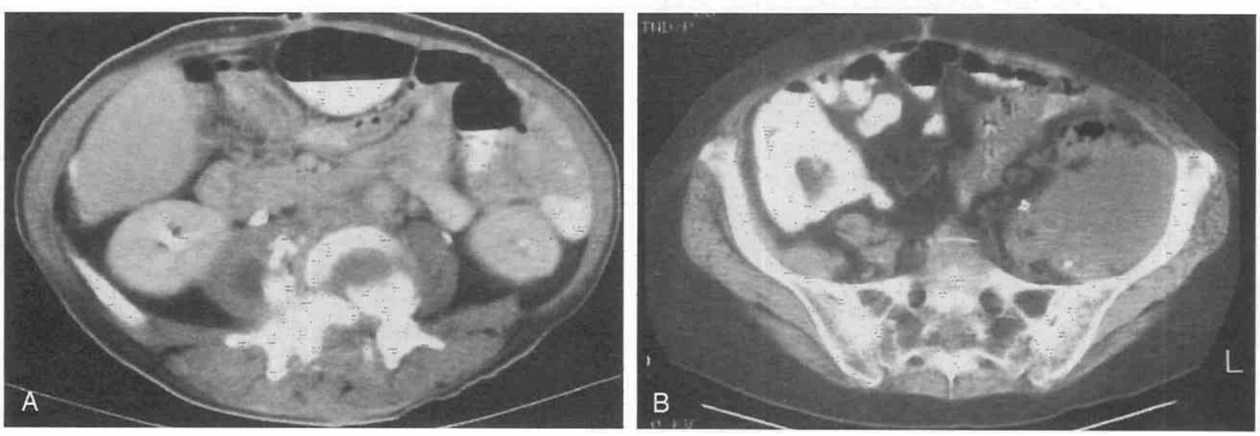

Figure 43–74. Iliopsoas abscesses. *A,* A nondynamically enhanced CT scan shows a low-attenuation mass within the right psoas muscle. At surgery, the mass contained purulent material. *B,* An unenhanced CT scan from another patient shows a large iliopsoas abscess on the left that was successfully managed by percutaneous drainage.

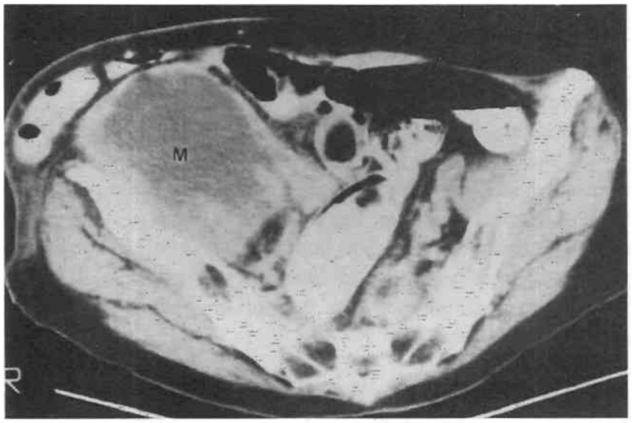

Figure 43–75. Malignant mass involving the iliopsoas muscles. Nondynamically enhanced CT scan shows a large, mildly heterogeneous mass (M) representing a colon cancer metastasis and infiltrating the right iliopsoas muscle. This mass would be difficult to distinguish from an abscess or a hematoma.

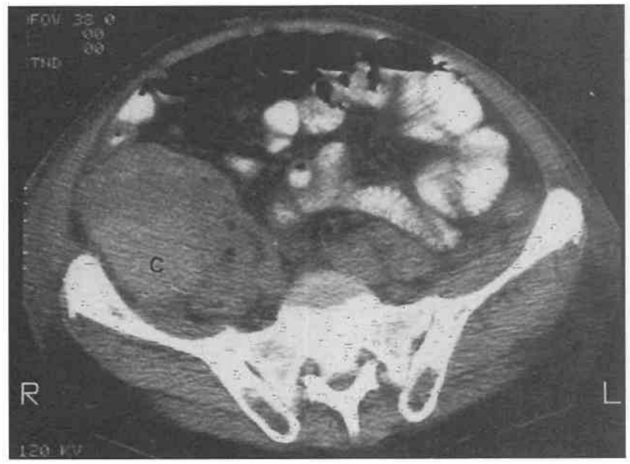

Figure 43–76. Spontaneous psoas hematoma in a patient receiving anticoagulant therapy. Unenhanced CT scan shows a retracting clot (C) with higher attenuation layering dependently.

amount of solid enhancing tissue is identified. Even more specific is the identification of fat within an iliopsoas mass, in which case a fatty tumor (usually a liposarcoma but occasionally a lipoma or teratoma) can be diagnosed.

Malignant iliopsoas masses are more likely to invade rather than respect fascial planes, which results in large, localized masses distorting only portions of the iliopsoas while spreading out to destroy adjacent bones and soft tissues.[143] Thus, in one study the most common CT findings were enlarged psoas muscle with irregular lesion margins and bone destruction.[275] Unfortunately, this finding was neither highly sensitive nor specific. Iliopsoas abscesses and hematomas may also produce localized masses, and bone destruction can result from infection. Conversely, occasionally iliopsoas neoplasms may diffusely infiltrate large portions of the iliopsoas.

Hemorrhage

Hemorrhage in and around the iliopsoas muscles is another cause of iliopsoas compartment disease.[51] Iliopsoas hematomas have been described in patients with hemophilia, von Willebrand's disease, thrombocytopenia, leaking AAAs or grafts, and traumatic injuries, and after femoral arteriography as well as in patients receiving anticoagulants.[66, 111]

If bleeding is acute, an unenhanced CT scan can demonstrate high-attenuation collections within enlarged iliopsoas muscles[214] (Fig. 43–76). Fluid-fluid levels, corresponding to layering of unclotted blood components, are typically seen in patients who have received anticoagulants and in those with bleeding diatheses. Over time, the hematoma often shows progressively lower attenuation, so that after several days it can have an appearance (on a noncontrast CT scan) identical to that of an inflammatory or a neoplastic mass. Old hematomas may undergo liquefaction and develop central components that show attenuation values near that of water.

The MRI features of hematomas tend to vary more dramatically over time than the CT features. Within the first few hours, hematomas have a nonspecific appearance on MRI examinations, demonstrating intermediate signal intensity on T1-weighted images and variable signal intensity on T2-weighted images.[63] Of all the iliopsoas masses, however, only hematomas can have high signal on both T1-weighted and T2-weighted sequences (within 24 to 48 hours of formation). Gradually, the T2-signal intensity begins to diminish first, so that subacute iliopsoas hematomas may have high-signal-intensity components on T1-weighted images and low signal intensity on T2-weighted images.[274]

Engelken and Ros noted that subacute hematomas may have three distinct components on T1-weighted MR images[63]:

1. A rim of low signal intensity.
2. More central but still peripheral areas of hyperintensity.
3. A medium-signal-intensity central region.

Finally, as the hematoma ages further, it tends to become smaller. A chronic hematoma, more than 2 weeks old, generally has areas that demonstrate low signal intensity on both T1-weighted and T2-weighted sequences because of its hemosiderin content.[63, 274]

Hematomas tend to spread between and not through fascial planes and may spread along the entire length of the iliopsoas compartment. Bone destruction is not present; thus, if bone abnormalities are identified, a diagnosis of hematoma without concomitant infection or neoplasm is unlikely. Although percutaneous biopsy is sometimes helpful in excluding other diagnoses, the clinical history and CT findings allow appropriate identification of iliopsoas hematomas in most patients.

Iliopsoas Bursitis

The iliopsoas synovial bursa lies between the musculotendinous junction of the iliopsoas muscle and the pelvic brim. When the bursa becomes inflamed, it may enlarge. Indeed, it has been suggested that enlargement of the ilio-

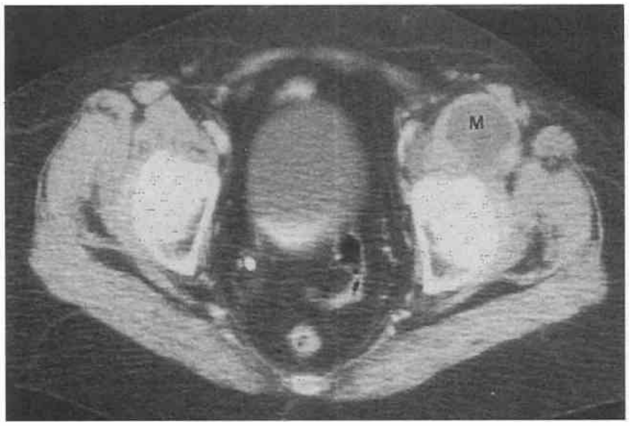

Figure 43–77. Enlarged iliopsoas bursa. Nondynamically enhanced CT scan shows an asymptomatic, low-attenuation groin mass (M) in a patient with rheumatoid arthritis. The mass represents an unusually prominent iliopsoas bursa.

psoas bursa should be included in the differential diagnosis of any groin mass.[49]

The three main causes of iliopsoas bursitis are rheumatoid arthritis, acute trauma, and overuse injury; trauma and overuse are the most common. In most instances, rheumatoid arthritis appears to involve the iliopsoas bursa as an extension from the hip, although communication with the hip joint space is seen in only 15% of cases when arthrography is performed.[119]

The most common presentation is anterior hip pain and a palpable or an audible snap on motion of the muscle, the latter occurring as a result of sudden movement of the iliopsoas tendon over an adjacent bony prominence, namely, the anterior inferior iliac spine, the iliopectineal eminence, or the bony ridge of the lesser trochanter.[119]

Iliopsoas bursitis/tendinitis, or the *iliopsoas syndrome*, can produce iliopsoas compartment abnormalities. On CT scans or MR images, the enlarged or inflamed iliopsoas bursa is usually identified as a fluid-containing structure within the iliopsoas muscle in the pelvis. Although generally rounded or ovoid in shape, it often has a slight invagination toward the hip joint (Fig. 43–77).

CT and MRI can also be used to identify a posteriorly malpositioned lesser trochanter, which can alter the course of the adjacent iliopsoas tendon and predispose patients to this condition.[119] MRI can be uniquely useful because it occasionally reveals signal intensity changes in the iliopsoas tendon, indicating that the inflammatory process involves this structure.

Aneurysms and Pseudoaneurysms

In rare instances, atherosclerotic aortic aneurysms and lumbar artery aneurysms or pseudoaneurysms may produce iliopsoas compartment masses.[107] On physical examination, many patients have a pulsatile mass and a bruit. The vascular nature of these abnormalities can be identified on CT scans only if IV contrast material has been administered (Fig. 43–78). A bolus injection of contrast material, followed by dynamic sequential imaging, is required and may demonstrate the abnormal vessel in the region of the psoas muscle.

On MR images, the vascular origin of these abnormalities is easily determined, even when contrast-enhanced studies are not performed. This is because flow void can be identified on spin-echo or fast spin-echo sequences; however, a flow-sensitive set of (limited flip-angle or gadolinium-enhanced) images should be obtained. It is clearly important to image the entire course of the aorta and the iliac vessels in such patients so that the extent of the aneurysm and the presence or absence of any additional aneurysms can be determined.

It is not possible to differentiate a true aneurysm from a pseudoaneurysm in any given case; however, true iliopsoas

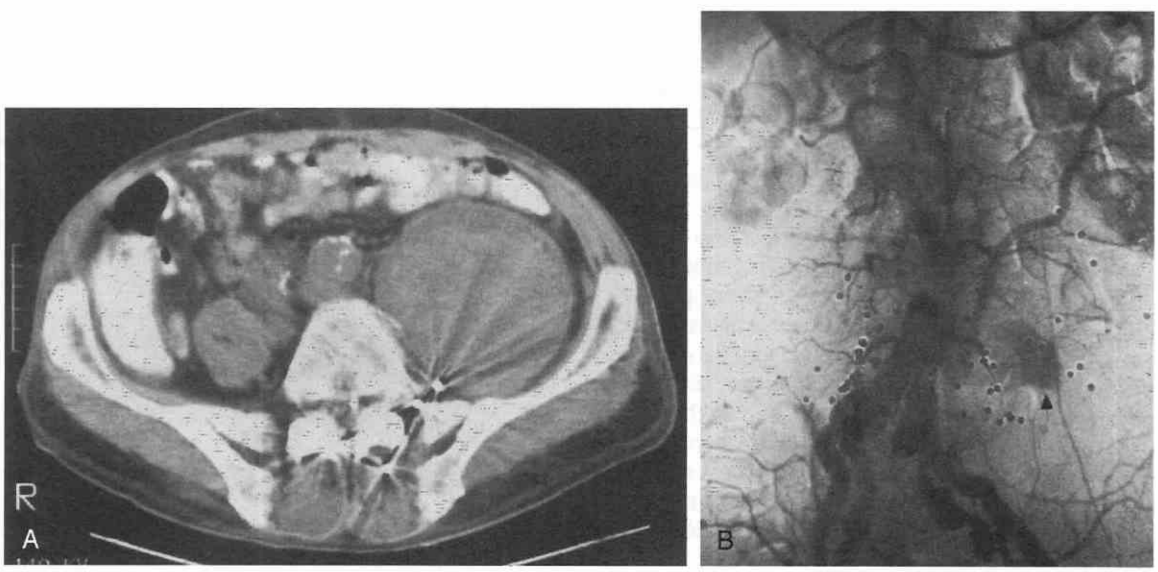

Figure 43–78. Lumbar artery pseudoaneurysm. *A,* Unenhanced scan shows a large left iliopsoas mass in a patient who had received a gunshot wound years previously. *B,* Arteriogram demonstrates contrast material in the center of the pseudoaneurysm *(arrow).*

aneurysms are extremely rare. Clinically, an atherosclerotic cause for an iliopsoas compartment aneurysm is suggested if a extensive atherosclerotic changes have occurred elsewhere in the abdomen. A pseudoaneurysm is suggested if a patient has a history of trauma or surgery, particularly if no atherosclerotic disease is seen elsewhere. Pseudoaneurysms tend to have an unusual shape.

Obviously, the possibility that an iliopsoas mass (or any visualized mass) represents an aneurysm or a pseudoaneurysm must be excluded before percutaneous biopsy is performed.

Hernias

Another rare cause of an iliopsoas compartment mass is a *retropsoas* hernia. This rare hernia occurs through a defect along the lateral border of the psoas muscle. When such a hernia is present and when bowel is involved, the bowel is noted to extend posteriorly and medially relative to the psoas muscle.

Although the diagnosis can be suspected on a small-bowel examination, CT and MRI can facilitate the diagnosis because they clearly demonstrate the abnormal posterior location of bowel.[22] Usually, the loop of bowel is appropriately identified. There is a risk of misdiagnosis, however: If, on cursory review of a CT scan, the herniated loop of bowel is not opacified with oral contrast material, the abnormally located air and fluid can be mistaken for an iliopsoas compartment abscess or other iliopsoas compartment abnormality.[22]

References

1. Aisen AM, Gross BH, Glazer GM, et al: Distribution of abdominal and pelvic Hodgkin disease: Implications for CT scanning. J Comput Assist Tomogr 9:463–465, 1985.
2. Akkersdijk GJ, van Bockel JH: Ruptured abdominal aortic aneurysm: Initial misdiagnosis and the effect on treatment. Eur J Surg 164:29–34, 1998.
3. Alvaranga JC, Ball ABS, Fisher C, et al: Limitations of surgery in the treatment of retroperitoneal sarcoma. Br J Surg 78:912–916, 1991.
4. Amis ES: Retroperitoneal fibrosis. AJR Am J Roentgenol 157: 321–329, 1991.
5. Amparo EG, Higgins CB, Hricak H, et al: Aortic dissection: Magnetic resonance imaging. Radiology 155:399–406, 1985.
6. Anagnostopolous CE, Prabhakar MJ, Kittle CF: Aortic dissections and dissecting aneurysms. Am J Cardiol 30:263–273, 1972.
7. Arita T, Matsunaga N, Takano K, et al: Abdominal aortic aneurysm: Rupture associated with the high-attenuating crescent sign. Radiology 204:765–768, 1997.
8. Armon MP, Whitaker SC, Gregson RHS, et al: Spiral CT angiography versus aortography in the assessment of aortoiliac length in patients undergoing endovascular abdominal aortic aneurysm repair. J Endovasc Surg 5:222–227, 1998.
9. Arrive L, Menu Y, Dessarts I, et al: Diagnosis of abdominal venous thrombosis by means of spin-echo and gradient echo MR imaging: Analysis with receiver operating characteristic curves. Radiology 181:661–668, 1991.
10. Ayuso JR, Garcia-Criado A, Caralt TM, et al: Atypical retroperitoneal fibrosis: MRI findings. Eur Radiol 9:937–939, 1999.
11. Bach DB, Vellet AD: Retroperitoneal sarcoidosis. AJR Am J Roentgenol 156:520–522, 1991.
12. Ballotta E, Da Giau GD, Bottio T, et al: Elective surgery for small abdominal aortic aneurysms. Cardiovasc Surg 7:484–490, 1999.
13. Barentsz JO: MR intervention in the pelvis: An overview and first experiences in MR-guided biopsy in nodal metastases in urinary bladder cancer. Abdom Imaging 22:524–530, 1997.
14. Barentsz JO, Jagr GJ, van Vierzen PBJ, et al: Staging urinary bladder cancer after transurethral biopsy: The value of fast dynamic contrast-enhanced MR imaging. Radiology 201:185–193, 1996.
15. Bass JC, Korobkin M, Cooper KD, et al: Cutaneous T-cell lymphoma: CT in evaluation and staging. Radiology 186:273–278, 1993.
16. Bass JC, Korobkin M, Francis IR, et al: Retroperitoneal plexiform neurofibroma: CT findings. AJR Am J Roentgenol 163:617–620, 1994.
17. Bastounis E, Papalambros E, Mermingas V, et al: Secondary aorto-duodenal fistulae. J Cardiovasc Surg 38:457–464, 1997.
18. Baum RA, Carpenter JP, Tuite CM, et al: Diagnosis and treatment of inferior mesenteric arterial endoleaks after endovascular repair of abdominal aortic aneurysms. Radiology 215:409–413, 2000.
19. Becquemin JP, Qvarfordt P, Kron KA, et al: Aortic graft infection: Is there a place for partial graft removal? Endovasc Surg 14:53–58, 1997.
20. Belair M, Soulez G, Oliva VL, et al: Aortic graft infection: The value of percutaneous drainage. AJR Am J Roentgenol 171:119–142, 1998.
21. Belville JS, Morgentaler A, Loughlin KR, et al: Spontaneous perinephric and subcapsular renal hemorrhage: Evaluation with CT, US, and angiography. Radiology 172:733–738, 1989.
22. Benson JE, Strauch ED: Retropsoas hernia as a cause of chronic abdominal pain: CT diagnosis. Pediatr Radiol 28:312–4, 1998.
23. Bevilacqua RG, Rgatko A, Hajdu SI, et al: Prognostic factors in primary retroperitoneal soft-tissue sarcomas. Arch Surg 126:328–334, 1991.
24. Blomlie V, Lien HH, Fossa SD, et al: CT in primary malignant germ cell tumors of the retroperitoneum. Acta Radiol 32:155–158, 1991.
25. Blum U, Wildanger G, Winfuhr M, et al: Preoperative CT and MR imaging of inferior vena cava leiomyosarcoma. Eur J Radiol 20: 23–27, 1995.
26. Bragg DG, Colby TV, Ward JH: New concepts in the non-Hodgkin lymphomas: Radiology implications. Radiology 159:289–304, 1986.
27. Brener BJ, Dorling RC, Frederuck PL, et al: Major venous anomalies complicating abdominal aortic surgery. Arch Surg 108:159–165, 1974.
28. Brown PM, Pattenden R, Gutelius JR: The selective management of small abdominal aortic aneurysms: The Kingston study. J Vasc Surg 125:21–27, 1992.
29. Brun B, Laursen K, Sorensen IN, et al: CT in retroperitoneal fibrosis. Am J Roentgenol 137:535–538, 1981.
30. Burger T, Meyer F, Tautenhahn J, et al: Ruptured infrarenal aortic aneurysm: A critical evaluation. Vasa 28:30–33, 1999.
31. Buss RW, Clagett GP, Fisher DF, et al: Emergency operation in patients with symptomatic abdominal aortic aneurysms. Am J Surg 156:470–473, 1988.
32. Carlsson-Farrelly E, Boquist L, Ljunberg B: Accuracy of clinical staging in nonseminomatous testicular cancer: A single centre experience of retroperitoneal lymph node dissection. Scand J Urol Nephrol 29:501–506, 1995.
33. Castellino RA, Marglin S, Blank N: Hodgkin disease, the non-Hodgkin lymphomas and the leukemias in the retroperitoneum. Semin Roentgenol 15:288–301, 1980.
34. Castellino RA, Hoppe RT, Blank N, et al: Computed tomography, lymphography, and staging laparotomy: Correlations in initial staging of Hodgkin disease. Am J Roentgenol 143:37–41, 1984.
35. Castellino RA: Hodgkin disease: Practical concepts for the diagnostic radiologist. Radiology 159:305–310, 1986.
36. Castellino RA: Lymph nodes of the posterior iliac crest: CT and lymphographic observations. Radiology 175:687–689, 1990.
37. Catton CN, O'Sullivan B, Kotwall C, et al: Outcome and prognosis in retroperitoneal soft tissue sarcoma. Int J Radiat Oncol Biol Phys 29:1005–1010, 1994.
38. Cheng TJ, Chien CT, Chiang HJ, et al: Iliopsoas compartment disorders: CT and MRI studies. Chin J Radiol 18:321–331, 1993.
39. Chin DP, Hopewell PC: Mycobacterial complications of HIV infection. Clin Chest Med 17:697–711, 1996.
40. Cho JS, Gloviczki P, Martelli E, et al: Long-term survival and late complications after repair of ruptured abdominal aortic aneurysms. J Vasc Surg 27:813–820, 1998.
41. Chong WK, Al-Kutoubi MA: Retroperitoneal fibrosis in Marfan's syndrome. Clin Radiol 44:386–388, 1991.
42. Churchill RJ, Wesbey G, Marsan RE, et al: Computed tomographic demonstration of anomalous inferior vena cava with azygos continuation. J Comput Assist Tomogr 4:398–402, 1980.

43. Cisternino SJ, Neiman HL, Malave SR Jr: Diagnosis of retroperitoneal hemorrhage by serial computed tomography. J Comput Assist Tomogr 3:686–688, 1979.
44. Cohan RH, Baker ME, Cooper C, et al: Computed tomography of primary retroperitoneal malignancies. J Comput Assist Tomogr 12: 804–810, 1988.
45. Cohan RH: Computed tomography of the abdominal aorta. Contemp Diagn Radiol 13:1–6, 1990.
46. Cohan RH, Siegel CL, Korobkin M, et al: Abdominal aortic aneurysms: CT evaluation of renal artery involvement. Radiology 194: 751–756, 1995.
47. Cohen MI, Gore RM, Vogelzang RL, et al: Accessory hemiazygos continuation of left inferior vena cava: CT demonstration. J Comput Assist Tomogr 8:777–779, 1984.
48. Collin J, Heather B, Walton W: Growth rates of subclinical abdominal aortic aneurysms: Implications for review and rescreening programmes. Eur J Vasc Surg 5:141–144, 1991.
49. Constant O, Mitchell RA: Case of the month: An unusual inguinal swelling. Br J Radiol 60:1139–1140, 1987.
50. Cooper JM, Silberzweig J, Mitty HA: Vena cava filters: Available devices and current practices. Mt Sinai J Med 63:273–81, 1996.
51. Daly BD, McPhillips M, Leung AW, et al: Ultrasound, computed tomography and magnetic resonance in the investigation of iliopsoas compartment disease. Australas Radiol 36:294–299, 1992.
52. Da Silva E, Rodrigues AJ, Castro de Tolosa EM, et al: Variation in infrarenal aortic diameter: A necropsy study. J Vasc Surg 29: 920–927, 1999.
53. Degesys GE, Dunnick NR, Silverman PM, et al: Retroperitoneal fibrosis: Use of CT in distinguishing among possible causes. Am J Roentgenol 146:57–60, 1986.
54. Delgado FG, Tjulandin SA, Garin AM: Long term results of treatment in patients with extragonadal germ cell tumours. Eur J Cancer 29:1002–1005, 1993.
55. Dennis JW, Littooy RN, Greisler HP, et al: Anastomotic pseudoaneurysms. Arch Surg 121:314–317, 1986.
56. Dimakakos PB, Kolokotronis L, Kehagias D, et al: Management of inflammatory abdominal aneurysms: Immediate and late results. Swiss Surg 5:18–22, 1999.
57. Di Marzo L, Sapienza P, Bernucci P, et al: Inflammatory aneurysm of the abdominal aorta: A prospective clinical study. J Cardiovasc Surg 40:407–412, 1999.
58. Dodd GD, Baron RL, Oliver JH, et al: Enlarged abdominal lymph nodes in end-stage cirrhosis: CT-histopathologic correlation in 507 patients. Radiology 203:127–130, 1997.
59. Dorfman RE, Alpern MB, Gross BH, et al: Upper abdominal lymph nodes: Criteria for normal size determined by CT. Radiology 180: 319–322, 1991.
60. Dudiak CM, Olson MC, Posniak HV: CT evaluation of congenital and acquired abnormalities of the azygos system. Radiographics 11: 233–246, 1991.
61. Einstein DM, Singer AA, Chilcote WA, et al: Abdominal lymphadenopathy: Spectrum of CT findings. Radiographics 11:457–472, 1991.
62. Ellis JH, Bies JR, Kopecky KK, et al: Comparison of NMR and CT imaging in the evaluation of metastatic retroperitoneal lymphadenopathy from testicular carcinoma. J Comput Assist Tomogr 8:709–719, 1984.
63. Engleken JD, Ros PR: Retroperitoneal MR imaging. Magn Reson Imaging Clin North Am 5:165–178, 1997.
64. Ernst CN: Abdominal aortic aneurysm. N Engl J Med 328:1167–1172, 1993.
65. Faggioli G, Stella A, Gargiulo M, et al: Early and long-term results in the surgical treatment of juxtarenal and pararenal aortic aneurysms. Eur J Endovasc Surg 15:205–211, 1998.
66. Feldberg MAM, Koehler PR, van Waes PFGM: Psoas compartment disease studied by computed tomography. Radiology 148:505–512, 1983.
67. Friedman AC, Pyatt RS, Hartman DS, et al: CT of benign cystic teratomas. Am J Roentgenol 138:659–665, 1982.
68. Garb M: The CT appearances of ruptured abdominal aortic aneurysms. Australas Radiol 33:154–156, 1989.
69. Gatewood OM, Fishman EK, Barrow CR, et al: Renal vein thrombosis in patients with nephrotic syndrome: CT diagnosis. Radiology 159:117–122, 1986.
70. Gehl HB, Bohndorf K, Klose KC: Inferior vena cava tumor thrombus: Demonstration by Gd-DTPA enhanced MR. J Comput Assist Tomogr 14:479–481, 1990.
71. Gilkeson GS, Allen NB: Retroperitoneal fibrosis: A true connective tissue disease. Rheum Dis Clin North Am 22:23–38, 1996.
72. Glajchen N, Shapiro RS, Stock RG, et al: CT findings after laparoscopic pelvic lymph node dissection and transperineal radioactive seed implantation for prostatic carcinoma. AJR Am J Roentgenol 166:1165–1168, 1996.
73. Glenn J, Sindelar WF, Kinsella T, et al: Results of multimodality therapy of resectable soft-tissue sarcomas of the retroperitoneum. Surgery 97:316–324, 1985.
74. Glynn TP, Kreipke DL, Irons JM: Amyloidosis: Diffuse involvement of the retroperitoneum. Radiology 170:726, 1989.
75. Godwin, JD, Korobkin M: Acute disease of the aorta: Diagnosis by computed tomography and ultrasonography. Radiol Clin North Am 21:551–554, 1983.
76. Goldman SM, Davidson AJ, Neal J: Retroperitoneal and pelvic hemangiopericytomas: Clinical, radiologic, and pathologic correlation. Radiology 168:13–17, 1988.
77. Golzarian J, Dussaussois L, Abada HT, et al: Helical CT of aorta after endoluminal stent-graft therapy: Value of biphasic acquisition. AJR Am J Roentgenol 171:329–331, 1998.
78. Golzarian J, Dussaussois L, Struyven J: Imaging of abdominal aortic aneurysms after endoluminal repair. Semin Ultrasound CT MR 20: 16–24, 1999.
79. Gore I, Hirst AE Jr: Atherosclerotic aneurysms of the abdominal aorta: A review. Prog Cardiovasc Dis 16:113–150, 1973.
80. Gorich J, Rilinger N, Sokiranski R, et al: Leakages after endovascular repair of aortic aneurysms: Classification based on findings at CT, angiography, and radiography. Radiology 213:767–772, 1999.
81. Gorich J, Rilinger N, Sokiranski R, et al: Treatment of leaks after endovascular repair of abdominal aortic aneurysms. Radiology 215: 414–420, 2000.
82. Gorski Y, Ricotta JJ: Weighting risks in abdominal aortic aneurysm: Best repaired in an elective, not an emergency, procedure. Postgrad Med 106:69–70, 75–80, 1999.
83. Gossios K, Nikolaides C, Fountzilas G: Widespread Castleman disease: CT findings. Eur Radiol 6:95–98, 1996.
84. Greatorex RA, Dixon AK, Flower CD, et al: Limitations of computed tomography in leaking abdominal aortic aneurysms. Br Med J 297:284–285, 1988.
85. Griebling TL, Hawtrey CE: Retroperitoneal fibrosis mimicking recurrent leukemia in a 7-year old boy. J Urol 159:229–230, 1998.
86. Guirguis EM, Barber GG: The natural history of abdominal aortic aneurysms. Am J Surg 162:481–483, 1991.
87. Gupta AK, Cohan RH, Francis IR, et al: Patterns of recurrent retroperitoneal sarcomas. AJR Am J Roentgenol 174:1025–1030, 2000.
88. Haaga JR, Baldwin GN, Reich NE, et al: CT detection of infected synthetic grafts: Preliminary report of a new sign. Am J Roentgenol 131:317–320, 1978.
89. Haciyanli M, Erkan N, Elverdi B, et al: Retroperitoneal fibrosis mimicking a rectal tumor: Report of a case. Dis Colon Rectum 41: 664–666, 1998.
90. Hadju SI, Hadju EO: Cytopathology of Sarcomas and Other Nonepithelial Malignant Tumors. Philadelphia, WB Saunders, 1976.
91. Hadju SI: Pathology of Soft Tissue Tumors. Philadelphia, Lea & Febiger, 1979.
92. Halliday KE, Al-Kutoubi A: Draped aorta: CT sign of contained leak of aortic aneurysms. Radiology 199:41–43, 1996.
93. Harisinghani MG: MR imaging of pelvic lymph nodes in primary pelvic carcinoma with ultrasmall superparamagnetic iron oxide (Combidex): Preliminary observations. J Magn Reson Imaging 7: 161–163, 1997.
94. Hartman DS: Retroperitoneal tumors and lymphadenopathy. Urol Radiol 12:132–134, 1990.
95. Hausegger KA, Tiesenhausen K, Karaic R, et al: Aortoduodenal fistula: A late complication of intraluminal exclusion of an infrarenal aortic aneurysm. J Vasc Interv Radiol 10:747–750, 1999.
96. Hawighorst H, Schoenberg SO, Knapstein PG, et al: Staging of invasive cervical carcinoma and of pelvic lymph nodes by high resolution MRI with a phased-array coil in comparison with pathologic findings. J Comput Assist Tomogr 22:75–81, 1998.
97. Hayasaka K, Tanaka Y, Soeda S, et al: MR findings in primary retroperitoneal schwannoma. Acta Radiol 40:78–82, 1999.
98. Hayes WS, Davidson AJ, Grimley PM, et al: Extraadrenal retroperitoneal paraganglioma: Clinical, pathologic, and CT findings. AJR Am J Roentgenol 155:1247–1150, 1990.

99. Heiberg E, Wolverson MK, Sundaram M, et al: CT characteristics of aortic atherosclerotic aneurysm versus aortic dissection. J Comput Assist Tomogr 9:78–83, 1985.
100. Hennessy OF, Ptasznik R, Chou ST, et al: Retroperitoneal xanthogranuloma: Report of two cases with a review of the literature. Australas Radiol 34:347–349, 1990.
101. Herts BR, Megibow AJ, Birnbaum BA, et al: High-attenuation lymphadenopathy in AIDS patients: Significance of findings at CT. Radiology 185:777–781, 1992.
102. Hirota S, Matsumoto S, Yoshikawa T, et al: Inferior vena cava filter placement for prevention of pulmonary tumor emboli of renal cancer with renal vein or vena caval tumor thrombus: Prophylactic usage prior to transcatheter arterial embolization. Radiat Med 16:335–339, 1998.
103. Hirst AE, Johns VJ, Kime SW Jr: Dissecting aneurysms of the aorta: A review of 505 cases. Medicine 37:217–279, 1958.
104. Hoane BR, Shields AF, Porter BA, et al: Comparison of initial lymphoma staging using computed tomography (CT) and magnetic resonance (MR) imaging. Am J Hematol 47:100–105, 1994.
105. Hopper KD, Sherman JL, Ghaed N: Aortic rupture into the retroperitoneum. Am J Roentgenol 145:435–437, 1985.
106. Hosono M, Kobayashi H, Fujimoto R, et al: Septum-like structures in lipoma and liposarcoma: MR imaging and pathologic correlation. Skeletal Radiol 26:150–154, 1997.
107. Hulnick DH, Naidich DP, Balthazar EJ, et al: Lumbar artery pseudoaneurysm: CT demonstration. J Comput Assist Tomogr 8:570–572, 1984.
108. Hulnick DH, Megibow AJ, Naidich DP, et al: Abdominal tuberculosis: CT evaluation. Radiology 157:199–204, 1985.
109. Huncharek M, Muscat M: Serum prostate-specific antigen as a predictor of staging abdominal/pelvic computed tomography in newly diagnosed prostate cancer. Abdom Imaging 21:364–367, 1996.
110. Husband JE, Robinson L, Thomas G: Contrast enhancing lymph nodes in bladder cancer: A potential pitfall on CT. Clin Radiol 45: 395–398, 1992.
111. Illescas FF, Baker ME, McCann R, et al: CT evaluation of retroperitoneal hemorrhage associated with femoral arteriography. Am J Roentgenol 146:1289–1292, 1986.
112. Jacobowitz GR, Rosen RJ, Riles TS: The significance and management of the leaking endograft. Semin Vasc Surg 12:199–206, 1999.
113. Jacoby WT, Cohan RH, Baker ME, et al: Ovarian vein thrombosis in oncology patients: CT detection and clinical significance. AJR Am J Roentgenol 155:291–294, 1990.
114. Jain KA, Jeffrey RB: Gonadal vein thrombosis in patients with acute gastrointestinal inflammation: Diagnosis with CT. Radiology 180: 111–113, 1991.
115. Jasinski RW, Yang CF, Rubin JM: Vena cava anomalies simulating adenopathy on computed tomography. J Comput Assist Tomogr 5: 921–924, 1981.
116. Jeffrey RB, Federle MP: The collapsed inferior vena cava: CT evidence of hypovolemia. AJR Am J Roentgenol 150:431–432, 1988.
117. Jing BS, Wallace S, Zornoza J: Metastases to retroperitoneal and pelvic lymph nodes: Computed tomography and lymphangiography. Radiol Clin North Am 20:511–530, 1982.
118. Johansen K, Kohler TR, Nicholls SC, et al: Ruptured abdominal aortic aneurysm: The Harborview experience. J Vasc Surg 13:240–247, 1991.
119. Johnston CA, Wiley JP, Lindsay DM, et al: Iliopsoas bursitis and tendinitis: A review. Sports Med 25:271–283, 1998.
120. Jones B, Hessel SJ, Weissman BN, et al: Psoas abscess: Fact and mimicry. Urol Radiol 2:73–79, 1980.
121. Kallman DA, King F, Hattery RR, et al: Renal vein and inferior vena cava tumor thrombus in renal cell carcinoma: CT, US, MRI and venacavography. J Comput Assist Tomogr 16:240–247, 1992.
122. Kalman PG, Rappaport DC, Merchant N, et al: The value of late computed tomographic scanning in identification of vascular abnormalities after abdominal aortic aneurysm repair. J Vasc Surg 29: 442–450, 1999.
123. Kazerooni EA, Bree RL, Williams DM: Penetrating atherosclerotic ulcers of the descending thoracic aorta: Evaluation with CT and distinction from aortic dissection. Radiology 183:759–765, 1992.
124. Keith DS, Larson TS: Idiopathic retroperitoneal fibrosis. J Am Soc Nephrol 3:1748–1752, 1993.
125. Kelekis NL, Semelka RC, Hill ML, et al: Malignant fibrous histiocytoma of the inferior vena cava: Appearances on contrast-enhanced spiral CT and MRI. Abdom Imaging 21:461–463, 1996.
126. Kim SH, Choi BI, Han ML, et al: Retroperitoneal neurilemoma: CT and MR findings. AJR Am J Roentgenol 159:1023–1026, 1992.
127. Kim T, Murakami T, Oi H, et al: CT and MR imaging of abdominal liposarcoma. AJR Am J Roentgenol 166:829–833, 1996.
128. Korobkin M: Computed tomography of retroperitoneal vasculature and lymph nodes. Semin Roentgenol 16:251–267, 1981.
129. Korobkin M, Silverman PM, Quint LE, et al: CT of the extraperitoneal space: Normal anatomy and fluid collections. AJR Am J Roentgenol 159:933–941, 1992.
130. Kottra JJ, Dunnick NR: Retroperitoneal fibrosis. Radiol Clin North Am 34:1259–1275, 1997.
131. Krug B, Heidenreich A, Dietlein M, et al: Lymphknotenstaging maligner testikularer Keimzelltumoren. Fortschr Rontgenstr 171: 87–94, 1999.
132. Kumar D, Kumar, S: Circumaortic left renal vein. J Comput Assist Tomogr 5:914–916, 1981.
133. Kvilekval KHV, Best IM, Mason RA, et al: The value of computed tomography in the management of symptomatic abdominal aortic aneurysms. J Vasc Surg 12:28–33, 1990.
134. Lane RH, Stephens DH, Reiman HM: Primary retroperitoneal neoplasms: CT findings in 90 cases with clinical and pathologic correlation. AJR Am J Roentgenol 152:83–89, 1989.
135. LaRoy LL, Cormier PJ, Matalon TA, et al: Imaging of abdominal aortic aneurysms. AJR Am J Roentgenol 152:785–792, 1989.
136. Lautin EM, Haramati N, Frager D, et al: CT diagnosis of circumcaval ureter. AJR Am J Roentgenol 150:591–594, 1988.
137. Lautin EM, Rosenblatt M, Friedman AC, et al: Calcification in non-Hodgkin lymphoma occurring before therapy: Identification on plain films and CT. AJR Am J Roentgenol 155:739–740, 1990.
138. Lederle FA, Wilson SE, Johnson GR, et al: Variability in measurement of abdominal aortic aneurysms. J Vasc Surg 21:945–952, 1995.
139. Lee JKT, Ling D, Heiken JP, et al: Magnetic resonance imaging of abdominal aortic aneurysms. Am J Roentgenol 143:1197–1202, 1984.
140. Lee JKT, Heiken JP, Ling D, et al: Magnetic resonance imaging of abdominal and pelvic lymphadenopathy. Radiology 153:181–188, 1984.
141. Lee JKT, Glazer HS: Controversy in the MR imaging appearance of fibrosis. Radiology 177:21–22, 1990.
142. Leibovitch I, Foster RS, Kopecky KK, et al: Improved accuracy of computerized tomography based clinical staging in low stage nonseminomatous germ cell cancer using size criteria of retroperitoneal lymph nodes. J Urol 154:1759–1763, 1995.
143. Lenchik L, Dovgan DJ, Kier R: CT of the iliopsoas compartment: Value in differentiating tumor, abscess, and hematoma. AJR Am J Roentgenol 162:83–86, 1994.
144. Lepor H, Walsh PC: Idiopathic retroperitoneal fibrosis. J Urol 122: 1–6, 1979.
145. Lewis E, Bernadino ME, Salvador PG, et al: Post-therapy CT-detected mass in lymphoma patients: Is it viable tissue? J Comput Assist Tomogr 6:792–795, 1982.
146. Lewis JJ, Leung D, Woodruff JM, et al: Retroperitoneal soft-tissue sarcoma: Analysis of 500 patients treated and followed at a single institution. Ann Surg 228:355–365, 1998.
147. Liebman CE, Messersmith RN, Levin DN, et al: MR imaging of inferior vena cava filters: Safety and artifacts. AJR Am J Roentgenol 150:1174–1176, 1988.
148. Limet R, Sakalihassan N, Adelin A: Determination of the expansion rate and incidence of rupture of abdominal aortic aneurysms. J Vasc Surg 14:540–548, 1991.
149. Lipson E, Polliak A, Bloom RA: Value of lymphography in the staging of Hodgkin lymphoma. Radiology 193:757–750, 1994.
150. Lortholary O, Jarrousse B, Attali P, et al: Psoas pyomyositis as a late complication of typhoid fever. Clin Infect Dis 21:1049–1050, 1995.
151. Low RN, Wall SD, Jeffrey RB, et al: Aortoenteric fistula and perigraft infection: Evaluation with CT. Radiology 175:157–162, 1990.
152. Lubat E, Megibow AJ, Balthazar EJ, et al: Extrapulmonary *Pneumocystis carinii* infection in AIDS: CT findings. Radiology 174:157–160, 1990.
153. Lucas DR, Nascimento AG, Sanjay BKS, et al: Well-differentiated liposarcoma: The Mayo Clinic experience with 58 cases. Am J Clin Pathol 102:677–683, 1994.

154. Machida K, Tasaka A: CT patterns of mural thrombus in aortic aneurysms. J Comput Assist Tomogr 4:840–842, 1980.
155. Mantello MT, Panaccione JL, Moriarty PE, et al: Impending rupture of nonaneurysmal bacterial aortitis: CT diagnosis. J Comput Assist Tomogr 14:950–953, 1990.
156. Marglin SI, Castellino RA: Selection of an imaging modality for staging abdominal involvement in malignant lymphomas: Lymphography or computed tomography. In Bennet JM (ed): Controversies in the Management of Lymphomas. Boston, Martinus Nijhoff, 1983.
157. Marinoni M, Boccasanta P, Venturi M, et al: Retroperitoneal fibrosis: Unusual localization. Hepatogastroenterology 5:73–77, 1998.
158. Martinez Garcia MA, Pastor A, Ferrando D, et al: Casual recognition of an azygous continuation of the inferior vena cava in a patient with lung cancer. Respiration 66:66–68, 1999.
159. May J, White GH, Waugh R, et al: Endovascular treatment of abdominal aortic aneurysms. Cardiovasc Surg 7:495–502, 1999.
160. May J, White GH, Waugh R, et al: Adverse events after endoluminal repair of abdominal aortic aneurysms: A comparison during two successive periods of time. J Vasc Surg 29:32–39, 1999.
161. Mayo J, Gray R, St. Louis E, et al: Anomalies of the inferior vena cava. Am J Roentgenol 140:339–345, 1983.
162. Mehard WB, Heiken JP, Sicard GA: High-attenuation crescent in abdominal aortic aneurysm wall at CT: Sign of acute or impending rupture. Radiology 163:359–362, 1994.
163. Menon KV, Insall RL, Ignotus PI: Inferior vena caval filters: An overview of current use. Hosp Med 59:224–225, 1998.
164. Meranze S, Coleman B, Arger P, et al: Retroperitoneal manifestations of sarcoidosis on computed tomography. J Comput Assist Tomogr 9:50–52, 1985.
165. Mii S, Mori A, Sakata H, et al: Para-anastomotic aneurysms: Incidence, risk factors, treatment and prognosis. J Cardiovasc Surg 39: 259–266, 1998.
166. Miller CL, Wechsler RJ: CT evaluation of Kimray-Greenfield filter complications. Am J Roentgenol 147:45–50, 1986.
167. Miller WT, Perez-Jaffe LA: Cross-sectional imaging of Kikuchi disease. J Comput Assist Tomogr 23:548–551, 1999.
168. Millward SF: Temporary and retrievable inferior vena cava filters: Current status. J Vasc Interv Radiol 9:381–387, 1998.
169. Mindell HJ, Mastromatteo JF, Dickey KW, et al: Anatomic communications between the three retroperitoneal spaces: Determination by CT-guided injections of contrast material. AJR Am J Roentgenol 164:1173–1178, 1995.
170. Mitchinson MJ, Hothersall DC, Brooks PN, et al: The distribution of ceroid in human atherosclerosis. J Pathol 145:177–183, 1985.
171. Molmenti EP, Balfe DM, Kanterman RY, et al: Anatomy of the retroperitoneum: Observations of the distribution of pathologic fluid collections. Radiology 200:95–103, 1996.
172. Moog F, Bangerter M, Diederichs CG, et al: Lymphoma: Role of whole-body 2-deoxy-(F-18) fluoro-D-glucose (FDG) PET in nodal staging. Radiology 203:795–800, 1997.
173. Moore WS, Kashyap VS, Vescera CL, et al: Abdominal aortic aneurysm: A 6-year comparison of endovascular versus transabdominal repair. Ann Surg 230:298–306, 1999.
174. Morehouse HT, Thornhill BA: Nodes or no nodes: CT of adenopathy. Crit Rev Diagn Imaging 25:177–207, 1986.
175. Morettin LB, Kumar R: Small renal carcinoma with large retroperitoneal hemorrhage: Diagnostic considerations. Urol Radiol 3:143–148, 1981.
176. Mori A, Sakata H, Kawazoe N: Para-anastomotic aneurysms: Incidence, risk-factors, treatment, and prognosis. J Cardiovasc Surg 39: 259–266, 1998.
177. Moriyama Y, Yamamoto H, Hisatomi K, et al: Penetrating atherosclerotic ulcers in an abdominal aortic aneurysm: Report of a case. Surg Today 28:105–107, 1998.
178. Moskowitz DM, Kahn RA, Marin ML, et al: Intraoperative rupture of an abdominal aortic aneurysm during an endovascular stent-graft procedure. Can J Anaesth 46:887–890, 1999.
179. Moul JW: Proper staging techniques in testicular cancer patients. Tech Urol 1:126–132, 1996.
180. Moulopoulos LA, Dimopoulos MA, Varma DG, et al: Waldenström macroglobulinemia: MR imaging of the spine and CT of the abdomen and pelvis. Radiology 188:669–673, 1993.
181. Mueller PR, Ferrucci JT, Wittenberg J, et al: Iliopsoas abscess: Treatment by CT-guided percutaneous catheter drainage. Am J Roentgenol 142:359–362, 1984.
182. Mulligan SA, Holley HC, Koehler RE, et al: CT and MR imaging in the evaluation of retroperitoneal fibrosis. J Comput Assist Tomogr 13:277–281, 1989.
183. Nasim A, Thompson MM, Sayers RD, et al: Role of magnetic resonance angiography for assessment of abdominal aortic aneurysm before endoluminal repair. Br J Surg 85:641–644, 1998.
184. Negendank WH, Al-Katib AM, Karanes C, et al: Lymphomas: MR imaging contrast characteristics with clinical-pathologic correlations. Radiology 177:209–216, 1990.
185. Netzer P, Binek J, Hammer B: Diffuse abdominal pain, nausea, and vomiting due to retroperitoneal fibrosis: A rare but often missed diagnosis. Eur J Gastroenterol Hepatol 9:1005–1008, 1997.
186. Nicholls SC, Gardner JB, Meissner MH, et al: Rupture in small abdominal aortic aneurysms. J Vasc Surg 28:884–888, 1998.
187. Nichols CR, Fox EP: Extragonadal and pediatric germ cell tumors. Hematol Oncol Clin North Am 5:1189–1209, 1991.
188. Nielsen PB: Retrocaval ureter: Report of a case. Acta Radiol 51: 179–188, 1959.
189. Nuzzo G, Lemmo G, Trischitta MMM, et al: Retroperitoneal cystic lymphangioma. J Surg Oncol 61:234–237, 1996.
190. O'Hara PJ, Borkowski GP, Hertzer NR, et al: Natural history of periprosthetic air on computerized axial tomographic examination of the abdomen following abdominal aortic aneurysm repair. J Vasc Surg 1:429–433, 1984.
191. Ohki T, Veith FJ, Sanchez LA, et al: Endovascular graft repair of ruptured aortoiliac aneurysms. J Am Coll Surg 189:102–112, 1999.
192. Oliver TW Jr, Bernadino ME, Sones PJ Jr: Monitoring the response of lymphoma patients to therapy: Correlation of abdominal CT findings with clinical course and histologic cell type. Radiology 149:219–224, 1983.
193. Oosterlinck W, Derie A: New data on diagnosis and medical treatment of retroperitoneal fibrosis. Acta Urol Belg 65:3–6, 1997.
194. Oyen RH, Van Poppel HP, Ameye FE, et al: Lymph node staging of localized prostatic carcinoma with CT and CT-guided fine needle aspiration biopsy: Prospective study of 285 patients. Radiology 190: 315–322, 1994.
195. Paley M, Sidhu PS, Evans RA, et al: Retroperitoneal collections: Etiology and radiological implications. Clin Radiol 52:290–294, 1997.
196. Pan X, Saida Y, Kurosaki Y, et al: Fatty mass in the inferior vena cava at CT: Lipoma or normal variant? Radiat Med 13:251–253, 1995.
197. Papanicolaou N, Yoder IC, Lee MJ: Primary retroperitoneal neoplasms: How close can we come in making the correct diagnosis? Urol Radiol 14:221–228, 1992.
198. Parums DV II, Chadwick DR, Mitchinson MJ: The localization of immunoglobulin in chronic periaortitis. Atherosclerosis 61:117–123, 1986.
199. Parums DV, Choudhury RP, Shields SA, et al: Characterization of inflammatory cells associated with idiopathic retroperitoneal fibrosis. Br J Urol 67:564–568, 1991.
200. Pena CS, Kaufman JA, Geller SC, et al: Gadopentetate dimeglumine: A possible alternative contrast agent for CT angiography of the aorta. J Comput Assist Tomogr 23:23–24, 1999.
201. Peterson MJ, Cambria RP, Kaufman JA, et al: Magnetic resonance angiography in the preoperative evaluation of abdominal aortic aneurysms. J Vasc Surg 21:891–899, 1995.
202. Picard E, Marty-Ane CH, Vernhet H, et al: Endovascular management of traumatic infrarenal abdominal aortic dissection. Ann Vasc Surg 12:515–521, 1998.
203. Pistolese GR, Ippoliti A, Tuccimei I, et al: Conservative treatment of aortic graft infection. Eur J Vasc Surg 14(Suppl A):47–52, 1997.
204. Pombo F, Rodriguez E, Caruncho MV, et al: CT attenuation values and enhancing characteristics of thoracoabdominal lymphomatous adenopathies. J Comput Assist Tomogr 18:59–62, 1994.
205. Pond GD, Castellino RA, Horning S, et al: Non-Hodgkin lymphoma: Influence of lymphography, CT, and bone marrow biopsy on staging and management. Radiology 170:159–164, 1989.
206. Prince MR: Gadolinium-enhanced MR aortography. Radiology 191: 155–164, 1994.
207. Prince MR, Narasimham DL, Stanley JC, et al: Gadolinium-enhanced magnetic resonance imaging angiography of abdominal aortic aneurysms. J Vasc Surg 21:656–669, 1995.
208. Radin R: Intraabdominal *Mycobacterium tuberculosis* vs *Mycobacterium avium-intracellulare* infections in patients with AIDS: Distinc-

tion based on CT findings. AJR Am J Roentgenol 156:487–491, 1991.
209. Radin R: HIV Infection: Analysis in 259 consecutive patients with abnormal CT findings. Radiology 197:712–722, 1995.
210. Raptopolous V, Kleinman PK, Marks S, et al: Renal fascial pathway: Posterior extension of pancreatic effusions within the anterior pararenal space. Radiology 158:367–374, 1986.
211. Raptopoulos V, Lei QF, Touliopoulos P, et al: Why perinephric disease does not extend into the pelvis: The importance of closure of the cone of the renal fasciae. AJR Am J Roentgenol 164:1170–1184, 1995.
212. Raptopoulos V, Touliopoulos P, Lei QF, et al: Medial border of the perirenal space: CT and anatomic correlation. Radiology 205: 777–784, 1997.
213. Rasmussen TE, Hallett JW: Inflammatory aortic aneurysms: A clinical review with new perspectives in pathogenesis. Ann Surg 225: 155–164, 1997.
214. Ray CE Jr, Wilbur AC: CT diagnosis of concurrent hematomas of the psoas muscle and rectus sheath: Case reports and review of anatomy, pathogenesis, and imaging. Clin Imaging 17:22–26, 1993.
215. Ray CE Jr, Kaufman JA: Complications of inferior vena cava filters. Abdom Imaging 21:368–374, 1996.
216. Rebner M, Gross BH, Korobkin M, et al: CT appearance of right gonadal vein. J Comput Assist Tomogr 13:460–462, 1989.
217. Reed MD, Friedman AC, Nealy P: Anomalies of the left renal vein: Analysis of 433 CT scans. J Comput Assist Tomogr 6:1124–1126, 1982.
218. Rodriguez M: Computed tomography, magnetic resonance imaging, and positron emission tomography in non Hodgkin's lymphoma. Acta Radiol 417(Suppl):1–36, 1998.
219. Rominger MB, Kenney PJ: Perirenal involvement by retroperitoneal fibrosis: The usefulness of MRI to establish diagnosis. Urol Radiol 13:173–176, 1992.
220. Ros PR, Viamonte M, Rywin AM: Malignant fibrous histiocytoma: Mesenchymal tumor of ubiquitous origin. Am J Roentgenol 142: 753–759, 1984.
221. Rosen A, Korobkin M, Silverman PM, et al: CT diagnosis of ruptured abdominal aortic aneurysm. Am J Roentgenol 143:265–268, 1984.
222. Rossi P, Arata FM, Salvatori FM, et al: Prosthetic graft infection: Diagnostic and therapeutic role of interventional radiology. J Vasc Interv Radiol 8:271–277, 1997.
223. Rubin GD, Silverman SG: Helical (spiral) CT of the retroperitoneum. Radiol Clin North Am 33:903–932, 1995.
224. Saldino RM, Palubinskas AJ: Medial placement of the ureter: A normal variant which may simulate retroperitoneal fibrosis. J Urol 107:582–585, 1972.
225. Sansom H, Seddon B, Padley SPG: Clinical utility of abdominal CT scanning in patient with HIV disease. Clin Radiol 52:698–703, 1997.
226. Sasai K, Sano A, Imanaka K, et al: Right periureteric venous ring detected by computed tomography. J Comput Assist Tomogr 10: 349–351, 1986.
227. Scatarige JC, Fishman EK, Kuhajola FP, et al: Low attenuation nodal metastases in testicular carcinoma. J Comput Assist Tomogr 7:682–687, 1983.
228. Scott RAP, Tisi PV, Ashton HA, et al: Abdominal aortic aneurysm rupture rates: A 7-year follow-up of the entire abdominal aortic aneurysm population detected by screening. J Vasc Surg 28:124–128, 1998.
229. Schmidt MH, Mitchell JR, Downey DB: Sonographic surveillance of abdominal aortic aneurysms: What is the smallest change in measured diameter that reliably reflects aneurysm growth? Can Assoc Radiol J 50:241–246, 1999.
230. Seeger JM, Back MR, Albright JL, et al: Influence of patient characteristics and treatment options on outcome of patients with prosthetic aortic graft infection. Ann Vasc Surg 13:413–420, 1999.
231. Segalov E, Gibson J, Joshua DE, et al: Primary amyloidosis copresenting with cervical and massive intra-abdominal lymphadenopathy. Leuk Lymphoma 19:519–520, 1995.
232. Siegel CL, Cohan RH, Korobkin M, et al: Abdominal aortic aneurysm morphology: CT features in patients with ruptured and nonruptured aneurysms. AJR Am J Roentgenol 163:1123–1129, 1994.
233. Siegel CL, Cohan RH: CT of abdominal aortic aneurysms. AJR Am J Roentgenol 163:17–29, 1994.
234. Silverman SG, Hillstrom MM, Doyle CJ, et al: Thrombophlebitic retroperitoneal collateral veins mimicking lymphadenopathy: MR and CT appearance. Abdom Imaging 20:474–476, 1995.
235. Singer S, Corson JM, Demetri GD, et al: Prognostic factors predictive of survival for truncal and retroperitoneal soft-tissue sarcoma. Ann Surg 221:185–195, 1995.
236. Sladen JG, Gerein AN, Miyagishima RT: Late rupture of prosthetic aortic grafts: Presentation and management. Am J Surg 153:453–458, 1987.
237. Smith PA, Heath DG, Fishman EK: Virtual angioscopy using spiral CT and real-time interactive volume-rendering techniques. J Comput Assist Tomogr 22:212–214, 1998.
238. Soler R, Rodriguez E, Lopez MF, et al: MR imaging in inferior vena cava thrombosis. Eur J Radiol 19:101–107, 1995.
239. Sondak VK, Robertson JM, Sussman JJ, et al: Preoperative idoxuridine and radiation for large soft tissue sarcomas: Clinical results with five-year follow-up. Ann Surg Oncol 5:106–112, 1998.
240. Soo CS, Bernadino ME, Chuang VP, et al: Pitfalls of CT findings in post-therapy testicular carcinoma. J Comput Assist Tomogr 5: 39–41, 1981.
241. Spencer JA, Smith MJ, Golding SJ: Lymphangioleiomyomatosis with unusual calcific retroperitoneal lymphangiomyoma: CT findings. Eur J Radiol 14:192–194, 1992.
242. Spritzer CE, Norconk JJ Jr, Sostman HD, et al: Detection of deep venous thrombosis by magnetic resonance imaging. Chest 104:54–60, 1993.
243. Srinvas V, Dow D: Retroperitoneal fibrosis with azotemia secondary to metastatic breast cancer. Br J Urol 58:231, 1986.
244. Stomper PL, Kalish LA, Garnick MB, et al: CT and pathologic predictive features of residual mass histologic findings after chemotherapy for non-seminomatous germ cell tumors: Can residual malignancy or teratoma be excluded? Radiology 180:711–714, 1991.
245. Sueyoshi E, Sakamoto I, Kawahara Y, et al: Infected abdominal aortic aneurysm: Early CT findings. Abdom Imaging 23:645–648, 1998.
246. Szilagyi DE, Elliott JP, Smitt RF, et al: A thirty-year survey of the reconstructive surgical treatment of aorto-iliac occlusive disease. J Vasc Surg 3:421–435, 1986.
247. Tai NR, Atwal AS, Hamilton G: Modern management of pulmonary embolism. Br J Surg 86:853–868, 1999.
248. Takasugi JE, Godwin JD: CT appearance of the retroaortic anastomoses of the azygos system. AJR Am J Roentgenol 154:41–44, 1990.
249. Teitelbaum GP, Bradley WG, Klei BD: MR imaging artifacts, ferromagnetism, and magnetic torque of intravascular filters, stents, and coils. Radiology 166:657–664, 1988.
250. Tennant WG, Hartnell GG, Baird RN, et al: Radiologic investigation of abdominal aortic aneurysm disease: Comparison of three modalities in staging and the detection of inflammatory change. J Vasc Surg 17:703–709, 1993.
251. Testini M, Catalano G, Macarini L, et al: Diagnosis and treatment of retroperitoneal tumours. Int Surg 81:88–93, 1996.
252. Thomas RV: Surgical implications of retroaortic left renal vein. Arch Surg 100:738–740, 1970.
253. Thompson MM, Smith JL, Bell PRF: Thromboembolic complications during endovascular aneurysm repair. Semin Vasc Surg 12: 215–219, 1999.
254. Tisnado J, Amendola MA, Vines FS, et al: Computed tomography of a double inferior vena cava: The "double cava" sign. Comput Tomogr 3:195–199, 1979.
255. Torsello GB, Klenk E, Kasprzak B, et al: Rupture of abdominal aortic aneurysm previously treated by endovascular stentgraft. J Vasc Surg 28:184–187, 1998.
256. Townsend RR: CT of AIDS-related lymphoma. AJR Am J Roentgenol 156:969–974, 1991.
257. Tsai TC, Chang PY, Chen BF, et al: Retroperitoneal fibrosis and juvenile rheumatoid arthritis. Pediatr Nephrol 10:208–209, 1996.
258. UK Small Aneurysm Trial participants: Mortality results for randomized controlled trial of early elective surgery or ultrasonographic surveillance for small abdominal aortic aneurysms. Lancet 352: 1649–1655, 1998.
259. Vardulaki KA, Prevost TC, Walker NM, et al: Growth rates and risk of rupture of abdominal aortic aneurysms. Br J Surg 85:1674–1680, 1998.
260. Varma DGK, Yoshimitsu K, Manning JT: Retroperitoneal granular cell tumor: Computed tomography findings with 5-year follow-up. Clin Imaging 20:279–281, 1996.

261. Vibits H, Wammen ES, Dunn PS: Recurrent benign retroperitoneal lipoma. Rev Med Chir 96:107–108, 1992.
262. Vinnicombe SJ, Norman AR, Nicolson V, et al: Normal pelvic lymph nodes: Evaluation with CT after bipedal lymphography. Radiology 194:349–355, 1995.
263. Warshauer DM, Dumbleton SA, Molina PL, et al: Abdominal CT findings in sarcoidosis: Radiologic and clinical correlation. Radiology 192:93–98, 1994.
264. Watanabe AT, Teitelbaum GP, Gomes AS, et al: MR imaging of the bird's nest filter. Radiology 177:578–579, 1990.
265. Weinerman PM, Arger PH, Coleman BG, et al: Pelvic adenopathy for bladder and prostate carcinoma: Detection by rapid-sequence computed tomography. Am J Roentgenol 140:95–99, 1983.
266. Weinstein ES, Cooper M, Hammond S, et al: The "stable" ruptured abdominal aortic aneurysm gives a false sense of security. Am J Surg 178:133–135, 1999.
267. Whitley NO, Brenner DE, Francis A, et al: Computed tomographic evaluation of carcinoma of the cervix. Radiology 142:439–446, 1982.
268. Williams MP: Non-tuberculous psoas abscess. Clin Radiol 37:253–256, 1986.
269. Williams MP, Olliff JFC: Case report: Computed tomography and magnetic resonance imaging of dilated lumbar lymphatic trunks. Clin Radiol 40:321–322, 1989.
270. Wilmink TBM, Quick CRG, Hubbard CS, et al: The influence of screening on the incidence of ruptured abdominal aortic aneurysms. J Vasc Surg 30:203–208, 1999.
271. Woodring JH, Howard RS, Johnson MV: Massive low-attenuation mediastinal, retroperitoneal, and pelvic lymphadenopathy on CT from lymphangioleiomyomatosis: Case report. Clin Imaging 18: 7–11, 1994.
272. Wysoki MG, Angeid-Backman E, Izes BA: Iliopsoas myositis mimicking appendicitis: MRI diagnosis. Skeletal Radiol 26:316–318, 1997.
273. Yamaguchi T, Naito H, Ohta M, et al: False lumens in type III aortic dissections: Progress CT study. Radiology 156:757–760, 1985.
274. Yang WT, Yeo W, Metreweli C: Imaging of iliopsoas metastases. Clin Radiol 54:85–89, 1999.
275. Yeh PH, Jaw WC, Wang TC, et al: Evaluation of iliopsoas compartment disorders by computed tomography. Chin Med J 55:172–179, 1995.
276. Young R, Friedman AC, Hartman DS: Computed tomography of leiomyosarcoma of the inferior vena cava. Radiology 145:99–103, 1982.
277. Young RM, Cherry KJ, Davis PM, et al: The results of in situ prosthetic replacement for infected aortic grafts. Am J Surg 178: 136–140, 1999.
278. Yuh WT, Barloon TJ, Sickels WJ, et al: Magnetic resonance imaging in the diagnosis and follow-up of idiopathic retroperitoneal fibrosis. J Urol 141:602–605, 1989.

44

Computed Tomography of the Pelvis

John A. Spencer, Sarah E. Swift

The principal clinical applications of computed tomography (CT) of the pelvis are in staging of pelvic cancers, assessment of major bony and soft tissue injury, and investigation of suspected postoperative and other post-treatment complications. Access to spiral CT technology is now widespread, and its strengths and weaknesses are well understood. The recent introduction of multislice technology promises reduced examination times with further refinements in contrast enhancement, volumetric, and multiplanar techniques. These developments suggest a bright future for pelvic CT, but there are few studies comparing multislice CT with conventional or spiral CT and with other competing modalities in key pelvic applications, such as cancer staging.

During the 1990s, pelvic CT has been challenged by developments in ultrasonographic and magnetic resonance imaging (MRI). The introduction of specialized endoluminal probes and endoluminal and pelvic surface coils, respectively, for ultrasound and MRI has improved the staging of small and confined pelvic cancers. Further, there are increasing concerns about the risk to patients with potentially curable cancers from ionizing radiation. For these reasons, ultrasonography and MRI have replaced CT in the initial assessment and follow-up of a number of pelvic cancers.

This chapter discusses current indications for pelvic CT in the initial staging and further management of pelvic cancers, in the assessment of major pelvic trauma, and in the characterization and management of pelvic masses and fluid collections. The appearances of pelvic lesions commonly encountered as incidental findings in body CT are also described.

Normal Anatomy

The pelvis is an osseous ring that consists of the innominate bones laterally and anteriorly, the sacrum and coccyx posteriorly. The sacrum lies between the two innominate bones, its alae supporting the psoas muscles, and the lumbosacral nerve trunks (Fig. 44–1). Each innominate bone is composed of three fused parts: the ilium, ischium, and pubis. Within the innominate bone is the acetabulum, which is contained within the inverted Y formed by the anterior (iliopubic) and posterior (ilioischial) columns. The triangular-shaped anterior and posterior columns are connected by the quadrilateral plate, which forms the medial acetabular wall (Fig. 44–2).

The pelvis is divided into the *true pelvis* and the *false pelvis*. The iliac wings bound the false pelvis and the iliac fossae, containing the ascending, descending, and sigmoid colon; small-bowel loops; the psoas and iliacus muscles; and the major neurovascular pedicles (see Fig. 44–1). The paired rectus abdominis muscles form the anterior border of the false pelvis. The true pelvis lies below the sacral promontory, contains the pelvic organs, and is separated inferiorly from the perineum by the urogenital diaphragm.

The pelvic muscles are normally symmetrical and are well visualized on CT. Psoas major passes caudally along the anterolateral border of the pelvis, tapering gradually to pass beneath the inguinal ligament anterior to the hip joint, and inserts onto the lesser trochanter of the femur (Figs. 44–3 and 44–4; see also Fig. 44–1). The iliacus is a fan-shaped muscle that fills the iliac fossa and narrows rapidly to insert on the lateral side of the psoas tendon and lesser trochanter (see Fig. 44–3). The femoral nerve lies in the fat plane between the psoas and iliacus muscles and passes caudally to lie under the inguinal ligament lateral to the femoral artery (see Fig. 44–3). The gluteus minimus, glu-

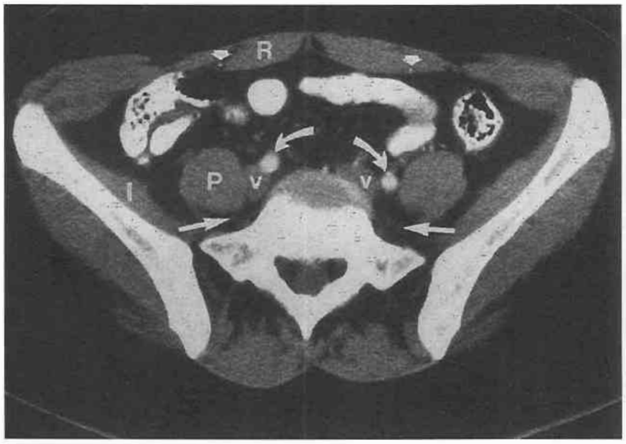

Figure 44–1. Normal anatomy. CT scan through contrast-filled ascending and descending colon in the iliac fossae shows the paired rectus abdominis (R), psoas (P), and iliacus (I) muscles. The common iliac arteries *(curved arrows)*, common iliac veins (v), and lumbosacral trunks *(straight arrows)* are located anterior to the ala of the sacrum. The inferior epigastric arteries *(arrowheads)* are related to the posterior rectus muscles.

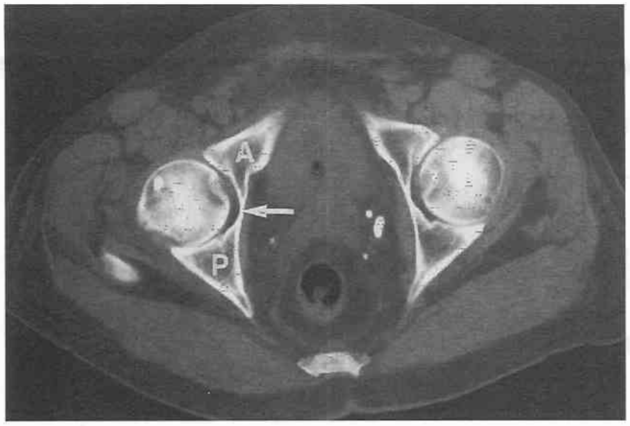

Figure 44–2. Normal anatomy. CT scan through the femoral heads shows anterior column (A), quadrilateral plate *(arrow)*, and posterior column (P) of the acetabulum.

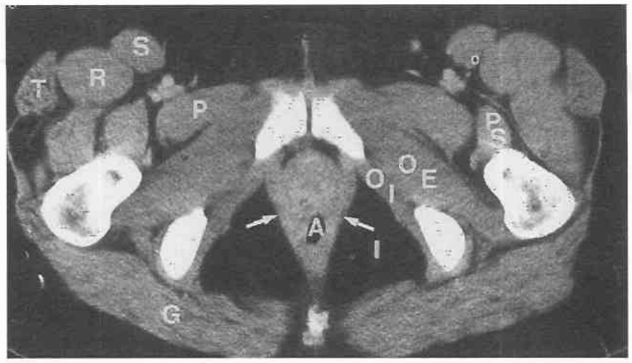

Figure 44–4. Normal anatomy. CT scan through the symphysis pubis shows the obturator internus muscle (OI) and obturator externus muscle (OE) on either side of the obturator foramen and the psoas muscle (PS) inserting on the lesser trochanter of the femur. Other muscles are the pectineus (P), sartorius (S), rectus femoris (R), tensor fasciae latae (T), and gluteus maximus (G) muscles. The pelvic diaphragm *(arrows)* separates the anus (A) from the ischiorectal fossae (I).

teus medius, and gluteus maximus muscles lie posterior to the innominate bones (see Fig. 44–3).[171]

The muscles within the pelvis are divided into two groups:

1. The true pelvis muscles: the levator ani and the coccygeus.
2. The muscles that originate within the pelvis and form part of the pelvic wall: the obturator internus and the piriformis.

The levator ani and coccygeus muscles compose the urogenital diaphragm, which is the floor of the pelvic cavity (see Fig. 44–4). This structure is pierced by the urethra, vagina, and anus. The piriformis and obturator internus muscles form most of the lateral sidewall of the true pelvis (Fig. 44–5). The obturator internus muscle also extends into the perineum to form the lateral boundary of the ischiorectal fossa (see Fig. 44–4). The greater sciatic foramen lies between the ischial spine and sacrum, and the sciatic nerve passes through it on the anterolateral aspect of the piriformis muscle (see Fig. 44–5).[50, 126]

The perineum is a diamond-shaped space below the urogenital diaphragm bounded anteriorly by pubic symphysis, laterally by the inferior pubic rami and ischial tuberosities, and posteriorly by the coccyx.[158] The triangular ischiorectal fossae are bordered laterally by obturator internus, medially by the pelvic diaphragm, and posteriorly by the gluteus maximus muscles (see Fig. 44–4).

The abdominal aorta divides to the left of the fourth lumbar vertebra into the common iliac arteries (see Fig. 44–1), which course laterally and caudally dividing opposite the L5–S1 disc space into the external and internal iliac arteries. Caudad to the aortic bifurcation, the inferior vena cava is formed by the confluence of the common iliac veins at the level of the fifth lumbar vertebra. The external iliac arteries pass along the anteromedial border of the iliopsoas muscles. The internal iliac arteries lie posteriorly

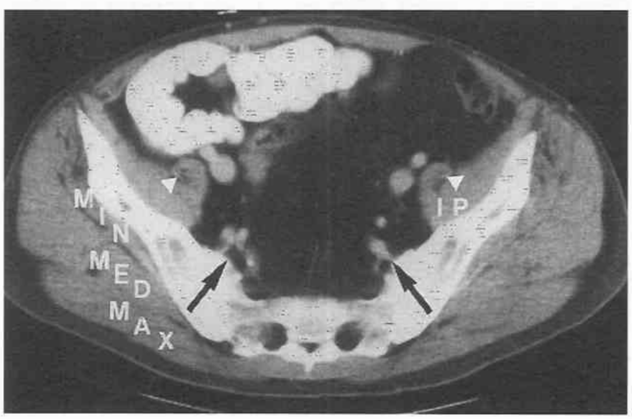

Figure 44–3. Normal anatomy. CT scan at the inferior sacroiliac joints shows the external iliac arteries and veins medial to the iliopsoas muscles (IP), which enclose the femoral nerves *(arrowheads)* and posterior dividing branches of the internal iliac arteries and veins *(arrows)*. The gluteus minimus (MIN), gluteus medius (MED), and gluteus maximus (MAX) muscles compose the buttocks.

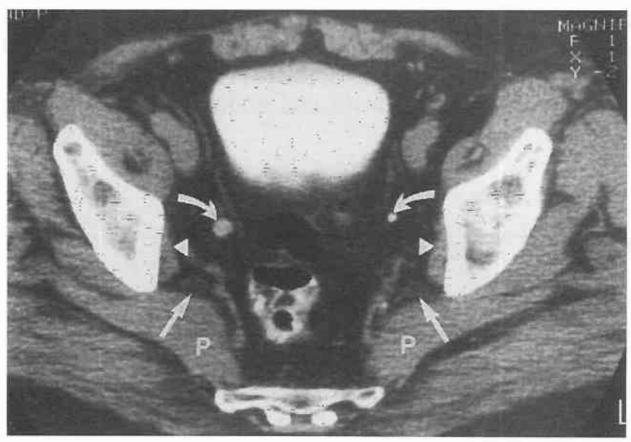

Figure 44–5. Normal anatomy. CT scan through the sciatic notch shows the sciatic nerves *(straight arrows)* anterior to the piriformis muscles (P) and the obturator internus muscles *(arrowheads)* along the pelvic sidewalls. The pelvic ureters *(curved arrows)* are immediately posterolateral to the pelvic peritoneal reflections.

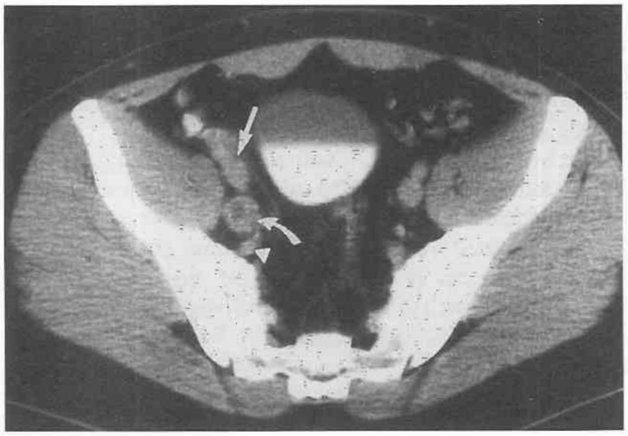

Figure 44–6. Pelvic lymph nodes. CT scan through the bifurcation of the external iliac artery and vein anteriorly *(straight arrow)* and the internal iliac vessels posteriorly *(arrowhead)* shows a classic right hypogastric lymph node metastasis *(curved arrow)* from cancer of the prostate gland.

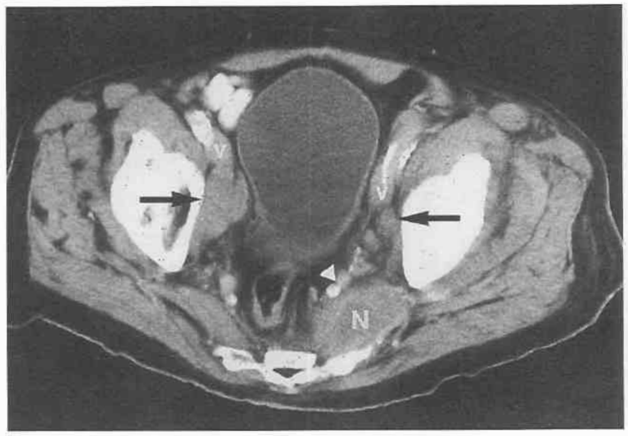

Figure 44–7. Pelvic lymph nodes. CT scan through the sciatic notch shows bilateral obturator lymph node metastases *(arrows)* from recurrent prostate cancer posterior to the external iliac veins (v) and a larger left internal iliac node metastasis (N) confluent with the piriformis muscle and posterior to the left internal iliac pedicle *(arrowheads)*.

on the lumbosacral plexus, course toward the greater sciatic foramen, and divide into multiple branches at the level of the inferior sacroiliac joints (see Fig. 44–3). Only the superior and inferior gluteal arteries are consistently seen on CT as they exit the sciatic notch. The external and internal iliac veins lie medial and posterior to the corresponding arteries.

Pelvic lymph nodes are classified according to accompanying vessels. The *common iliac lymph nodes* are located lateral and posterior to the arteries. The *hypogastric node* is situated at the bifurcation of the external and internal iliac vessels (Fig. 44–6). The *external iliac lymph nodes* are arranged in three chains:

1. The *lateral* chain on the lateral aspect of the external iliac artery.
2. The *middle* chain anterior and medial to the external iliac vein.
3. The *medial* chain posterior to the external iliac vein against the pelvic sidewall.

The obturator node is considered one of the medial external iliac nodes.[168] The most common internal iliac nodes identified on CT are located anterior to the piriformis muscle, around the inferior gluteal artery and vein (Fig. 44–7). The superficial inguinal lymph nodes lie distal to the inguinal ligament in the subcutaneous fat anterior and medial to the femoral artery and vein. A posterior iliac crest node has been reported to lie in the iliac fossa between the psoas and iliacus muscles.[26]

The pelvic ureters cross anterior to the common iliac artery bifurcation and course posterior to the peritoneal reflection (see Fig. 44–5). At the sciatic foramen, the ureters course medially toward the lateral angle of the bladder. In the male, they terminate anterior to the seminal vesicles (Fig. 44–8). In the female, the ureters lie lateral or posterior to the ovaries and then course 1 to 2 cm from the lateral border of the cervix, where they pass through the cardinal ligaments to enter the bladder (Fig. 44–9).

The urinary bladder is a midline structure. It indents the parietal peritoneum, which reflects over the dome, to form

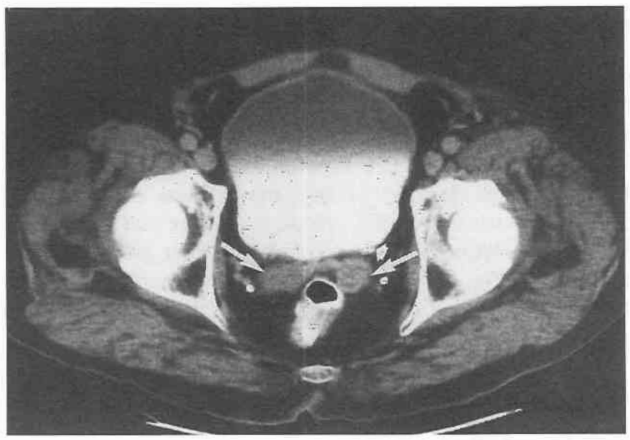

Figure 44–8. Normal anatomy. CT scan shows the seminal vesicles *(arrows)* between the bladder and rectum and the left pelvic ureter entering the bladder *(arrowhead)*.

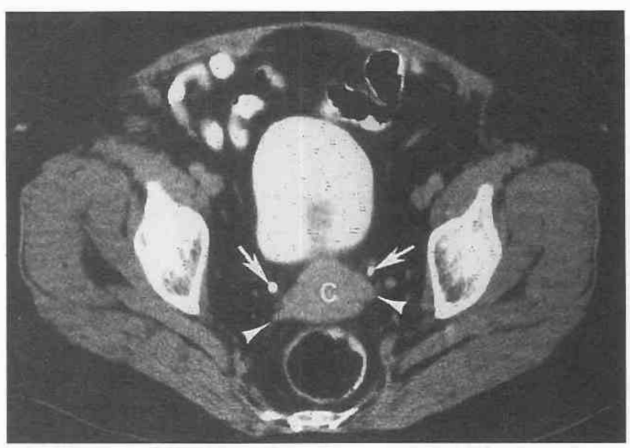

Figure 44–9. Normal anatomy. CT scan with delayed images through the cervix (C) shows triangular cardinal ligaments *(arrowheads)* tapering laterally and contrast-filled pelvic ureters *(arrows)* anteriorly.

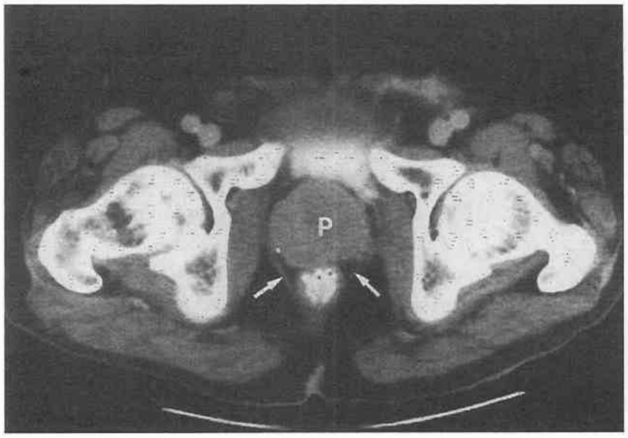

Figure 44–10. Normal anatomy. CT scan shows normal prostate gland (P) between bladder and rectum and pelvic diaphragm formed by the levator ani muscles *(arrows).*

the intraperitoneal paravesical fossae laterally. It is of variable shape and size, depending on the amount of urine present. Urine is of near-water attenuation on unenhanced images.[4]

The male internal genital organs are the prostate gland and the seminal vesicles. The seminal vesicles are two extraperitoneal lobulated pouches located superior to the prostate between the bladder and the rectum (see Fig. 44–8). They vary in size both in different patients and in the same individual on serial examinations. The prostate gland lies posterior to the symphysis pubis and anterior to the rectum, between the base of the bladder and the pelvic diaphragm (Fig. 44–10). It is of soft tissue attenuation, but the zonal anatomy cannot be reliably distinguished even after intravenous (IV) contrast enhancement.

The female genital organs are the ovaries, fallopian tubes, uterus, and vagina. The position of the ovaries is highly variable, but they are usually located posterolaterally at the level of the uterine fundus and round ligaments (Fig. 44–11). They lie in a shallow depression, the ovarian fossa, which is bounded by the external iliac vessels laterally and the ureter posteriorly.

In premenopausal women, normal ovaries are usually identified and their appearance may vary from soft tissue to more cystic attenuation, reflecting the presence of physiologic cysts or follicles. In postmenopausal women, the ovaries are often not identified.

The uterus appears as a soft tissue mass lying between the bladder and rectum. The myometrium shows intense contrast enhancement. A low-attenuation central area may be demonstrated reflecting fluid within the endometrial cavity. The uterus is divided into the *body (corpus)* (see Fig. 44–11), which has a triangular appearance on axial CT, and the *cervix* (see Fig. 44–9) which appears more ovoid. The cervix may also show contrast enhancement.

The broad ligaments are two fibrous sheets extending laterally from the uterus to the pelvic sidewall and covered on their anterior and posterior surfaces by peritoneum. They are not routinely seen on CT unless they are outlined by ascites. Between the leaves of the broad ligaments is the parametrium, which contains uterine and ovarian vessels (Fig. 44–12), fallopian tube, and round ligament. The round ligaments demarcate the superolateral border of the uterus and ascend anterolaterally over the external iliac vessels, pass through the inguinal canal, and insert in the labia majora (see Fig. 44–11). The triangular cardinal ligaments are located at the base of the broad ligament and fan out from their attachments at the cervix to insert on fascia covering the urogenital diaphragm (see Fig. 44–9).[165] The uterosacral ligaments arise in continuity with the cardinal ligaments and pass posterolaterally around the rectum to insert on the sacrum.

The proximal two thirds of the rectum is covered by peritoneum on its anterior and lateral sides, forming the pararectal fossae laterally. The distal one third of the rectum is covered only by anterior peritoneum, which reflects onto the seminal vesicles and bladder in the male to form the rectovesical pouch. In the female, the peritoneum covering the bladder and rectum is divided by the uterus and vagina into a shallow, anterior vesicouterine recess and a large, deep, posterior rectouterine fossa (pouch of Douglas

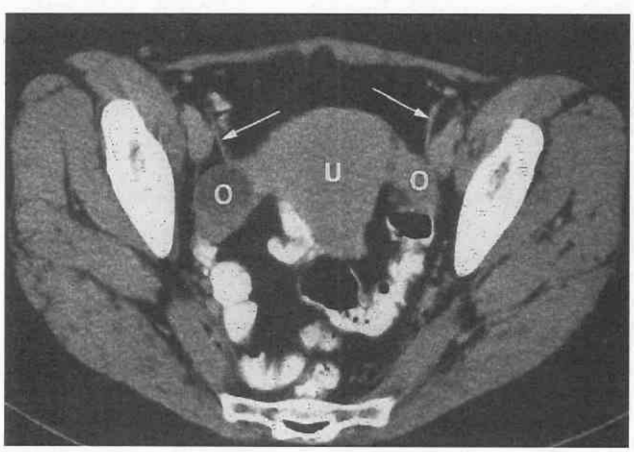

Figure 44–11. Normal anatomy. CT scan through the uterus (U) and ovaries (O) shows round ligaments *(arrows)* tapering anterolaterally over the external iliac vessels.

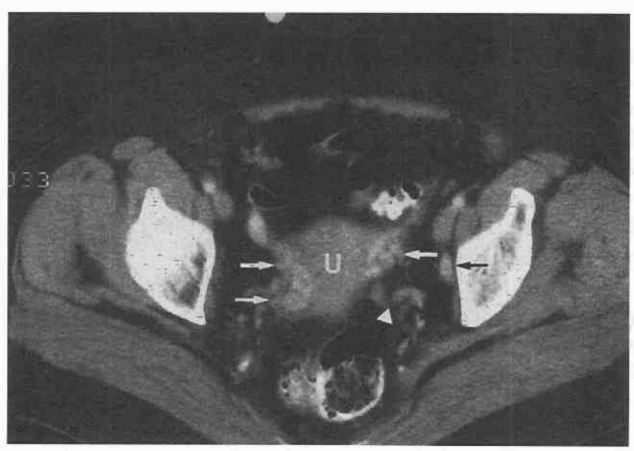

Figure 44–12. Normal anatomy. CT scan through the uterus (U) shows a tortuous left uterine artery and prominent vascular plexus *(white arrows)* running within the broad ligament. In the left obturator fossa a contrast-enhanced structure *(black arrow)* probably represents a pelvic varix.

or cul-de-sac). The cul-de-sac is continuous with the pararectal and ovarian fossae.[4]

The extraperitoneal spaces of the pelvis are complex. Anterior to the peritoneum and posterior to the transversalis fascia, the umbilicovesical fascia spreads inferiorly from the umbilicus to surround the urachus, obliterated umbilical arteries, and urinary bladder.[5] This fascia divides the anterior extraperitoneal fat into a perivesical space and a prevesical space. The bladder, umbilical arteries, and urachus lie within the confines of the umbilicovesical fascia in the small perivesical space. The large potential prevesical space lies anterior to the umbilicovesical fascia and includes the retropubic space or space of Retzius. The prevesical space has potential extensions into the anterior abdominal wall (rectus sheath), the parametria (round ligaments), the inguinal canal and scrotum, properitoneal fat, and the retroperitoneum.[5]

Examination Technique

Adequate opacification of small and large bowel by an oral contrast agent is essential for most CT examinations of the pelvis. Administration of 10 mL of a water-soluble iodine-based agent, such as diatrizoate meglumine (Gastrografin), diluted in 200 mL of water 6 to 12 hours before the study (or as an overnight preparation) ensures good colonic opacification. An additional 1 L of 3% solution given over 1 hour immediately before the CT study opacifies the small bowel. Some institutions use an additional 100 mL of dilute water-soluble contrast per rectum, especially when there is a previous history of pelvic malignancy. If bowel opacification remains suboptimal, delayed images following additional oral contrast agent or alteration of the patient into prone or decubitus positions may be useful. A vaginal tampon aids the identification of the vaginal canal and the level of the vault and may be helpful in women with gynecologic malignancy.

IV contrast enhancement is a major part of most CT examinations. It is used to delineate vessels, to help differentiate lymph nodes from vascular structures, to detect lesions, and to enhance solid components within tumors and other complex masses. We administer 100 to 150 mL, depending on patient size, of non-ionic 300 mg/mL of iodine concentration contrast material using a pump injector at a rate of 3 mL/second. Scanning the pelvis at approximately 35 to 40 seconds after the commencement of the injection allows enhancement of the bladder wall prior to filling of the bladder with excreted urinary contrast agent. This is important when bladder tumors are being imaged.

For many systems, the images obtained can be rapidly reviewed; when the distinction of lymph nodes from venous structures is uncertain, further study at 180 seconds shows venous enhancement. Use of delayed scans after 10 to 15 minutes allows injected contrast agent to opacify the ureters and the urinary bladder. This is particularly relevant when the scan is being performed in the context of trauma.

Scan parameters and technique can be varied according to the specific requirements of the individual study. When the pelvis is scanned alone in the context of an orthopedic examination, attention is paid to bony detail with narrow-slice collimation and overlapping reconstructions, which allow subsequent multiplanar reconstructions (MPRs) if required. Although oral and IV contrast agents are avoided and the radiation dose can be kept low, the trade-off is loss of soft tissue detail. For vascular applications dedicated to the aortoiliac segments, attention must be paid to the administration of IV contrast agent. Faster injection rates of up to 5 mL/second deliver the contrast agent as a compact bolus and early timing of image acquisition (e.g., at 30 to 35 seconds after the start of the injection) ensures an arterial-phase study. The use of automated-exposure devices, such as Smart Prep (General Electric) or a CARE bolus (Siemens), facilitates accurate timing of vascular examinations. Oral contrast agents again should be avoided because they may degrade images using postprocessing MPRs, multi-image projections (MIPs), and surface-shading techniques.

The pelvis is usually scanned as part of an abdominopelvic study in the setting of oncology, trauma, or suspected sepsis. Such studies are subject to competing requirements for information in terms of volume examined, detail provided, and timing relative to the contrast bolus. For example, the radiologist needs to obtain local detail regarding pelvic tumors as well as wider coverage of the liver and retroperitoneum for metastatic assessment.

Single-slice spiral CT offers the option to scan in either the craniocaudal or the caudocranial direction. In the latter the study is timed to reach the liver at approximately 60 seconds from the start of IV contrast injection. Two separate breath-hold volume acquisitions using different prescriptions for collimation and pitch, such as 8- to 10-mm collimation for the abdomen and 5- to 7-mm collimation for the pelvis, optimize information and coverage. An alternative approach might be to cover the whole area in a single acquisition; however, the cost is then extended pitch—and therefore helical stretch—and, consequently, decreased image quality.

New multislice technology offers the potential for wider flexibility, although the full range of its clinical applications has yet to be evaluated.[32] Because there is no dependence on spiral pitch and the reconstructed slice, width can be chosen retrospectively.[46] Faster acquisition times and finer collimation with multislice spiral CT reduce the trade-off between detail and coverage. The concurrent acquisition of multiple slices results in a reduction in scan time, allowing coverage of an entire anatomic region during optimal phase of enhancement while maintaining high spatial resolution. A twofold or threefold increase in volume acquisition rate with comparable image quality to a single-slice system has been shown to be obtainable.[68, 69] Scanning at speeds higher than this is possible, but there is some loss of image quality. This problem, however, may be acceptable in certain circumstances, such as with traumatized or uncooperative patients. In practical terms, the main advantage of the speed gain with multislice systems is the ability to obtain the required volume of information at high spatial resolution within a single breath-hold.

Depending on imaging requirements and patient cooperation, the focus of the examination can be ultra-high speed, intermediate speed, or high z-axis resolution (isotropic) imaging.[32] As an example, 2.5-mm collimation and a 3.2-mm effective slice thickness, with 50% overlapping reconstructions and a 1.6-mm reconstruction interval, result in

excellent quality MPRs for the pelvis. In the abdomen, 5-mm collimation, a 6.5-mm effective slice thickness, and 5-mm reconstruction interval offer an excellent compromise in speed, coverage, and spatial resolution.

Rapid reconstruction times are also important in view of the large amount of data and number of images generated. This capability to rapidly review an examination contributes to increased patient throughput. There are, however, concerns about the increasing radiation dose associated with diagnostic CT, and care should be taken to responsibly utilize the technique.[106]

Lymph Nodes

CT is used for evaluation of lymph node metastasis from a wide variety of primary pelvic tumors and in the staging of lymphoma. The major diagnostic criterion for CT evaluation is nodal size. During the 1990s, the upper limit of size considered "normal" for pelvic nodes has fallen from a diameter of 15 mm to 10 mm or less. As metastatic nodes enlarge, most become more rounded; thus, the maximum short-axis dimension (MSAD) is used in CT assessment. When staging pelvic cancers with spiral CT in the early vascular phase at 40 seconds after injection of contrast the pelvic veins are not opacified and it may be difficult to distinguish these from lymph nodes. A second phase of scanning at 180 seconds opacifies the pelvic veins.[48, 184]

The evidence supporting the use of smaller lymph node sizes comes principally from a unique study that correlated the size of normal pelvic lymph nodes on CT examinations before and after lymphangiography in men with stage I testicular cancer (i.e., with no likelihood of pelvic nodal metastasis). More than 98% of pelvic nodes had MSADs below 10 mm.[167] With the 99th percentile for MSAD used at individual pelvic sites, the upper limit of normal sizes varied between 7 and 10 mm (Table 44–1). For most pelvic cancer staging purposes, lymph nodes in the important obturator and internal iliac groups more than 8 mm in MSAD should be regarded as abnormal.[167] Support for these recommendations comes from a helical CT study of women with cervical cancer in which an MSAD of 8 mm was found to be optimal for evaluation of pelvic nodal metastases.[184]

In that study, CT and MRI were equivalent for nodal assessment. The overall accuracy of CT in this assessment using spiral CT was 89%.[184] Use of size thresholds as small as 5 mm has been described but with a reduced accuracy of 80%.[48] These data compare with older criteria for assessing lymphadenopathy for a combination of pelvic tumors, giving accuracies of 73% to 77%.[89, 168] There will always be a significant false-negative fraction owing to micrometastases in normal size lymph nodes, variously estimated at 15% to 40%.[89, 168] Conversely, there is a significant false-positive fraction because lymph node enlargement may result from benign causes such as chronic lymphadenitis, fatty replacement, and reactive hyperplasia.

Whatever size threshold is chosen to discriminate normal from metastatic lymph nodes, these two simple facts remain:

1. Lower thresholds are more sensitive to metastasis but result in more false-positive results and hence a lower specificity and positive predictive value.
2. Higher thresholds improve specificity but yield more false-negative results.

Use of a 5-mm threshold had a positive predictive value of only 43%; with a 10-mm threshold, however, the positive predictive value rises to 85%.[48, 184] Imaging strategies employing low threshold size may be combined with fine-needle lymph node biopsy to improve positive predictive value and specificity (Fig. 44–13).[122] High threshold sizes are appropriate when a therapy or intervention is withheld after a confident CT diagnosis of lymph node metastasis. In such circumstances, CT prevents unnecessary intervention in patients with unequivocally involved nodes, whereas patients with smaller nodes are sampled by staging lymphadenectomy.

A number of normal structures may be mistaken for pelvic lymph nodes, including unenhanced pelvic sidewall vessels, unopacified pelvic bowel loops, and the normal ovary (Fig. 44–14). Conversely, nodal metastases from some pelvic tumors may be confused with vascular structures. Enhancing lymph node metastases are seen with a number of pelvic cancers, notably bladder (Fig. 44–15).[71] Other abnormal appearances in metastatic lymph nodes include necrosis and calcification. Necrosis in lymph node deposits from squamous carcinoma may have a similar

Table 44–1. Upper Limit of Normal Size for Pelvic Lymph Nodes

Lymph Node Group	Maximum Short-Axis Dimension (MSAD)*
Internal iliac	7 mm
Obturator	8 mm
Common iliac	9 mm
External iliac	10 mm

* Using the 99th percentile for maximum short-axis dimension at individual pelvic sites.

Adapted from Vinnicombe S, Norman A, Nicolson V, Husband JE: Normal pelvic lymph nodes: Evaluation with CT after bipedal lymphangiography. Radiology 194: 349–355, 1995.

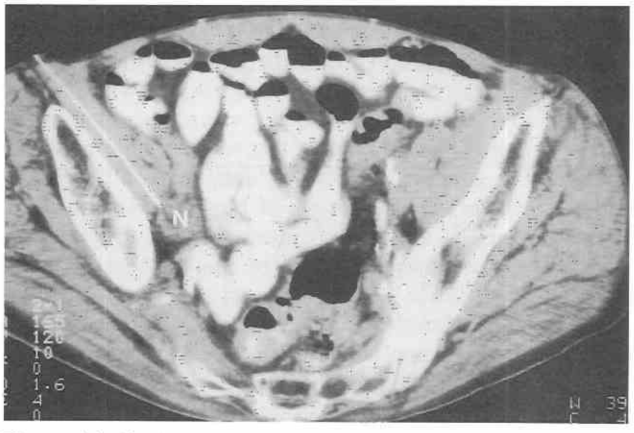

Figure 44–13. Lymph node biopsy. CT scan during fine-needle aspiration of right hypogastric nodal (N) metastasis from recurrent bladder cancer.

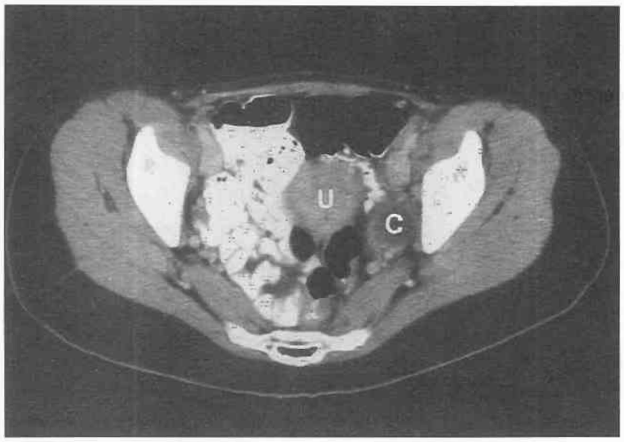

Figure 44–14. Ovary-mimicking metastasis. CT scan through the uterus (U) shows an unusual lateral position for an ovarian cyst (C) simulating a hypodense obturator lymph node metastasis.

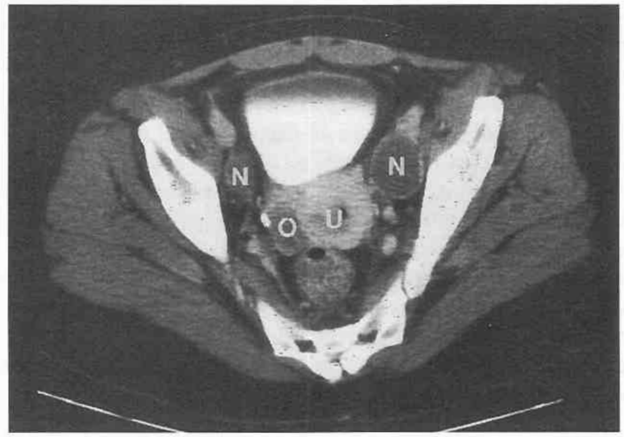

Figure 44–16. Metastatic cervical cancer. CT scan through the uterus (U) and right ovary (O) shows bilateral cystic/necrotic obturator lymph node metastases (N) from known cervical cancer.

appearance to simple cystic structures such as the ovary (Fig. 44–16). Ring enhancement in smaller necrotic nodal metastases may mimic venous thrombosis. Calcifications may be seen in metastases from papillary serous adenocarcinoma from a variety of sites in the female genital tract (Fig. 44–17).

Assessment of nodal metastasis from pelvic cancers remains a great challenge for CT, an imaging technique still largely relying on crude size criteria. Other factors to consider in assessment are lymph node site in relation to the primary tumor, the local tumor (T) stage, and the clinical context. For most pelvic cancers, the incidence of nodal metastasis increases with T stage, and there are predictable sites and patterns of lymph node metastasis for individual tumors discussed further in the relevant sections. Accurate nodal assessment is most important when management options are solely determined by CT findings. Technical factors and size thresholds chosen and the use of CT-guided biopsy thus vary with clinical indications and should reflect local clinical practice.

Bladder Cancer

Bladder cancer accounts for 4.5% of all malignant tumors and 2% of cancer deaths in the United States. About 80% of cases occur in men with the peak incidence in the 6th and 7th decades. Cigarette smoking is the most important recognized causative factor. Ninety percent of bladder tumors are transitional cell carcinomas. Some tumors express squamous cell differentiation, a feature that may predominate with chronic bladder irritation due to calculi and in areas of endemic schistosomiasis. Most bladder tumors are found around the trigone and posterolateral

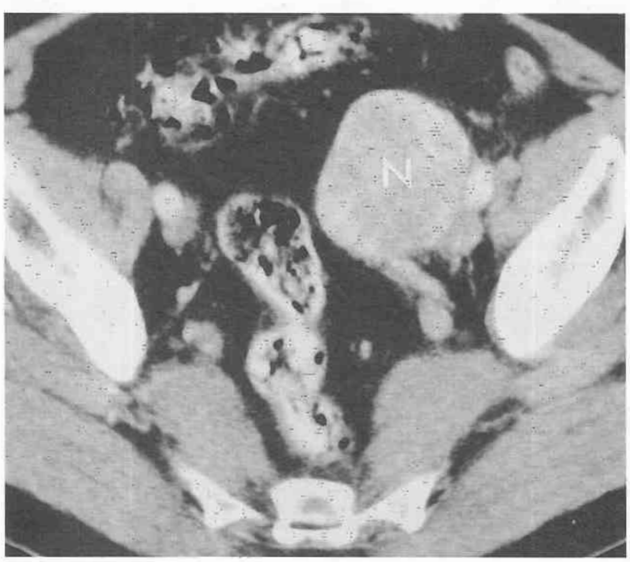

Figure 44–15. Lymph node metastasis. CT scan through the iliac vascular pedicles shows an enhancing left external iliac nodal metastasis (N) from newly diagnosed high-grade bladder cancer.

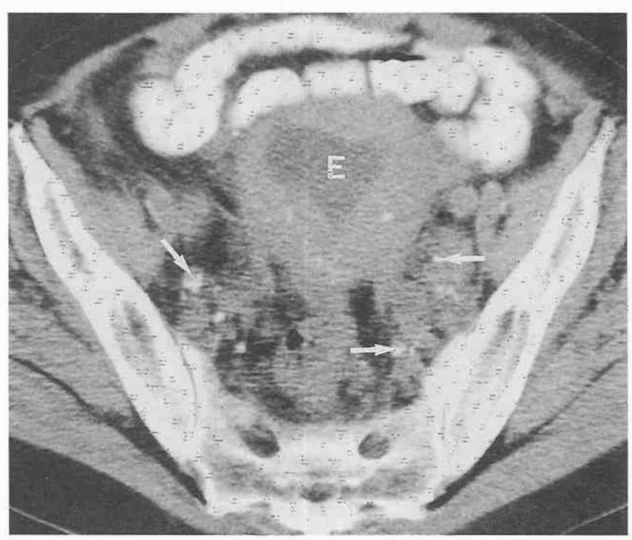

Figure 44–17. Calcified nodal metastases. CT scan through the uterus shows a distended endometrial cavity (E) and multiple nodal metastases *(arrows)* from a papillary serous adenocarcinoma of the endometrium.

walls of the bladder, and this proximity to the ureteric orifices results in hydronephrosis with some invasive tumors. About one third of patients have multifocal tumors.

Hematuria brings patients to medical attention early. The diagnosis of bladder cancer is usually made at cystoscopy, increasingly performed with a flexible endoscope. Most patients at diagnosis have early-stage superficial papillary disease. These patients require no further imaging and undergo cystoscopic follow-up. Formal transurethral resection is usually required to assess the depth of bladder wall (muscle) invasion. This is combined with bimanual examination under anesthesia (EUA) of the patient to evaluate perivesical extension. Examination under anesthesia is of limited value in determining perivesical tumor extension, and thus most patients with muscle invasive tumors undergo further imaging. In follow-up, superficial tumors may progress to muscle invasive tumors.

In the United States, clinical staging criteria are based on the Jewett-Strong-Marshall classification. Elsewhere in the world and particularly in Europe, the Tumor-Node-Metastasis (TNM) system predominates. The two schemes are compared in Table 44–2.

There are three principal options for management of bladder cancer:

1. Tumors without muscle invasion are managed by cystoscopic means (see earlier), with or without adjuvant intravesical therapies.
2. Muscle-invasive tumors, including those with minimal perivesical extension, may be managed by either cystectomy or radiation therapy.
3. Tumors with advanced perivesical extension or metastatic disease are usually managed with palliative chemotherapy or radiation therapy, although palliative cystectomy is used in selected cases for symptom control.

The key role of CT scanning is thus in staging of muscle-invasive tumors, as follows:

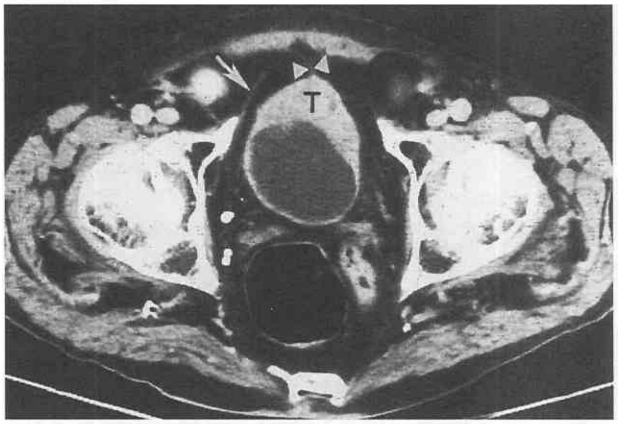

Figure 44–18. Confined bladder cancer. CT scan through bladder tumor (T), outlined by urine, of stage T2 or earlier on the anterior wall. Incidental note is made of the median *(arrowhead)* and medial *(arrow)* umbilical ligaments.

Stage B/T3a (or earlier) tumors are "confined" to the bladder, show no outer wall abnormality, but may produce a smooth focal contour bulge (Fig. 44–18).

Stage C/T3b tumors produce an irregular outer bladder wall or soft tissue infiltration into perivesical fat in the region of the tumor (Fig. 44–19). Either a soft tissue mass or stranding may project beyond the outer contour of the bladder.

Stage D1/T4a,b tumors extend locally to invade surrounding organs or to the pelvic sidewall musculature, principally the obturator internus and the pelvic diaphragm or the anterior abdominal wall for tumors arising at the dome.

Although cystoscopy is the best means of evaluating intravesical tumors, CT may be valuable when resection has been incomplete or has been limited by complications,

Table 44–2. Tumor-Node-Metastasis (TNM) Classification and Jewett-Strong Staging System of Urinary Bladder Cancer

Jewett-Strong Staging		TNM Histopathologic Findings
0	T0	No tumor
0	Tis	Carcinoma in situ
0	Ts	Papillary tumor, confined to epithelium (mucosa)
A	T1	Tumor invades subepithelial connective tissue (lamina propria)
B1	T2a	Tumor invades superficial muscle (inner half)
B2	T2b	Tumor invades deep muscle (outer half)
B2	T3a	Tumor with microscopic invasion of perivesical fat
C	T3b	Tumor with macroscopic invasion of perivesical fat
D1	T4a	Tumor invades surrounding organs
D1	T4b	Tumor invades pelvic or abdominal wall
D1	N1–3	Pelvic lymph node metastases
D2	M1	Distant metastases
D2	N4	Lymph node metastases above the bifurcation

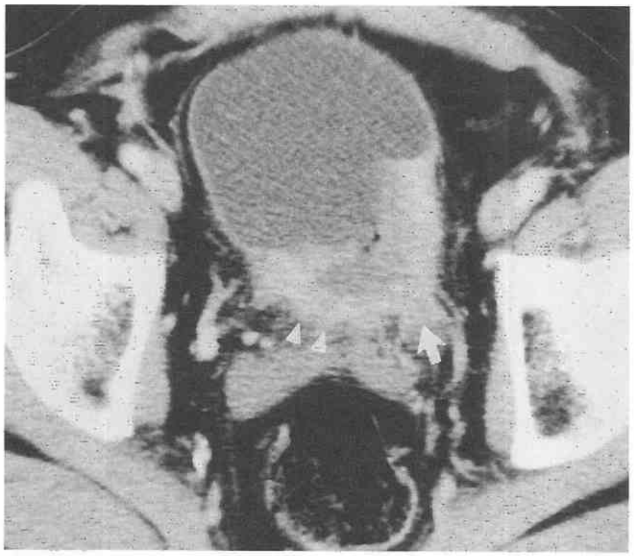

Figure 44–19. Stage T3b bladder cancer. CT scan through the trigone of the bladder shows an extensive enhancing tumor invading the perivesical fat *(arrowheads)* and extending up the left ureter *(arrow)*, which is dilated.

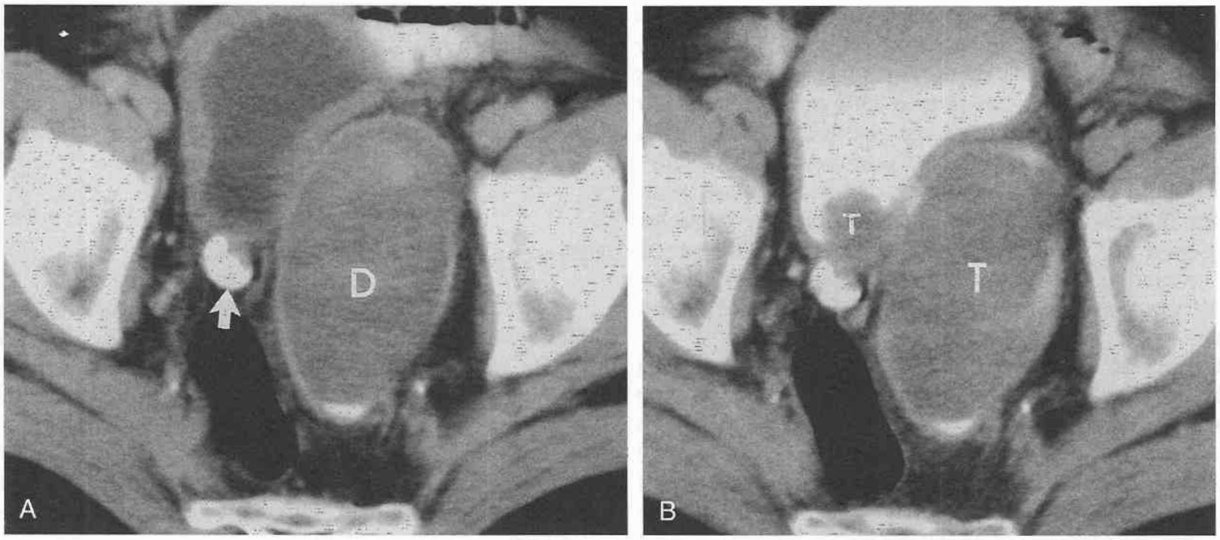

Figure 44–20. Bladder cancer in a diverticulum. CT scan through a thick-walled and trabeculated bladder with multiple diverticula. *A,* Early-phase image shows a calculus in the right-sided diverticulum *(arrow)* but possibly a tumor in the left-sided diverticulum (D). *B,* Delayed excretory-phase image shows tumor (T) both filling the diverticulum and intravesically at the same level.

such as bleeding, and when a tumor arises in a bladder diverticulum (Fig. 44–20). An intravesical tumor may manifest as a regular or irregular wall thickening, a sessile lesion, or a polypoid mural lesion. In extreme cases, an irregular tumor mass fills the bladder lumen (Fig. 44–21). Some tumors show a high-density cap. This usually reflects calcification but may be due to keratin from squamous carcinoma.[91]

Both the intraluminal and extraluminal components of the bladder cancer show IV contrast enhancement (see Fig. 44–18).[72] With contrast-enhanced spiral CT, the enhancing bladder wall is contrasted against unopacified urine (see Figs. 44–18 and 44–19) to outline the intravesical extent of the tumor. However, pseudotumors may result from swirling ureteric jets of contrast opacified urine.[120] Delayed images are occasionally required for clarification by outlining intravesical tumor against excreted urinary contrast material (see Figs. 44–20 and 44–21).

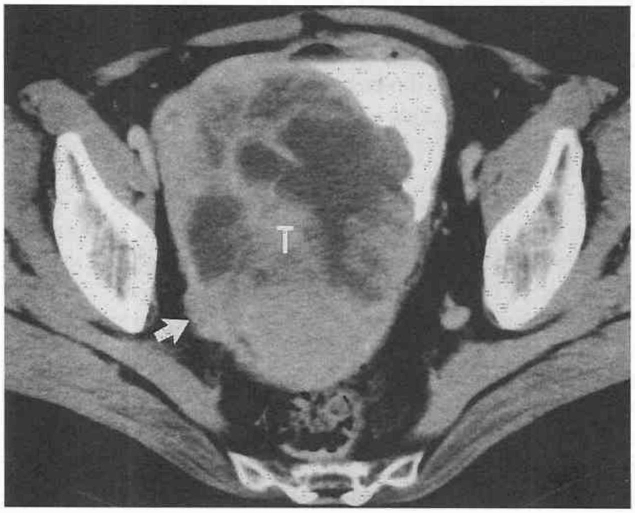

Figure 44–21. Bladder sarcoma. CT scan in the delayed excretory phase through the bladder shows a partially necrotic tumor (T), a high-grade sarcoma, filling most of the lumen, with an extravesical tumor on the right *(arrow).*

A number of other pitfalls exist. Caution is also required in interpretation of early postoperative CT examinations. There may be bladder wall thickening and perivesical fat "infiltration" from the mechanical or thermal trauma of resection, and perivesical extraperitoneal fluid collections may result from transmural extravasation of irrigation fluids. Chronic wall thickening may result after surgery or radiation therapy.[133] The bladder must be adequately distended, and when there is a urinary catheter in place, it should be clamped before the CT examination. However, overdistention of the bladder may result in underestimation of wall thickening and may obscure fat planes between the bladder and adjacent structures. Good opacification of pelvic small bowel loops is essential, and in cases of advanced local disease, additional rectal contrast administration may be valuable in delineating the rectosigmoid colon.

Spiral-CT data sets have been used to produce three-dimensional (3D) simulations of the bladder known as *virtual* cystoscopy.[110, 166] This technique has not had a wide impact on clinical practice.

The overall accuracy of CT for staging bladder cancer in various studies using nonspiral CT was between 64% and 81%.[74, 85, 141] For lymph node assessment, accuracy varied from 83% to 92%. The false-negative rate of 25% to 40% resulted from microscopic tumor deposits in normal-sized lymph nodes.[85, 117] The false-negative rate can be reduced by use of smaller nodal size criteria and by fine-needle aspiration biopsy of lymph nodes.[42] However, this approach is not widespread in the management of bladder cancer.

The other understaging CT error is failure to demonstrate microscopic invasion of the perivesical fat.[74, 117] This may not necessarily compromise outcome after cystectomy if the surgical margins are unaffected. CT overstaging

errors result from either mistaking absence of fat planes between pelvic organs as evidence of local invasion or misinterpreting normal structures abutting the bladder as perivesical tumor extension. Up to 27% of stage B/T3a or earlier tumors were overstaged because of loss of fat planes between the seminal vesicles and posterior bladder wall.[85] Overdistention should be avoided, and decubitus or post-voiding images may help separate the bladder from the pelvic sidewall. Additional oral contrast administration with delayed or decubitus images may be necessary to distinguish tumor from unopacified pelvic small-bowel loops.

Data on the accuracy of spiral CT for bladder staging are limited, and there have been few older comparative studies of dynamic incremental CT and MRI. Although there were no statistically significant differences in overall staging accuracy, there was a trend toward superiority of MRI over CT. MRI is helpful in delineating tumors at the dome and bladder base and in assessing invasion of the prostate gland.[2, 13, 72, 81]

CT is an excellent method for detecting recurrent bladder cancer after cystectomy.[37, 93, 121] The abdomen should also be examined because isolated abdominal metastases occur in recurrence of this disease.[37] CT findings include a mass in the cystectomy site, pelvic and retroperitoneal lymphadenopathy, and liver metastases.[37, 93, 121] Bony destruction may be seen with pelvic tumor recurrence (Fig. 44–22), and inspection of images on appropriate window settings may be necessary to detect lesser degrees of cortical erosion when tumor abuts bone.

Unusual bladder tumors include urachal carcinoma, small cell carcinoma, sarcoma, and metastasis. Eighty-five percent to 90% of urachal tumors are mucinous adenocarcinomas.[13] These are represented by either a mass at the bladder dome with a superior midline extravesical component or a mass anterosuperior to the bladder dome along the expected midline course of the urachus. The mass has low attenuation (because of mucin production) with peripheral or central calcification.[13] Small-cell carcinoma of the bladder tends to metastasize widely to the pelvic and retroperitoneal lymph nodes, the liver, the lungs, and even the brain.[11] An unusual histology should be suspected when a bulky endophytic or exophytic tumor is showing mixed enhancement patterns (see Fig. 44–21), although high-grade transitional cell cancers can result in similar appearances.

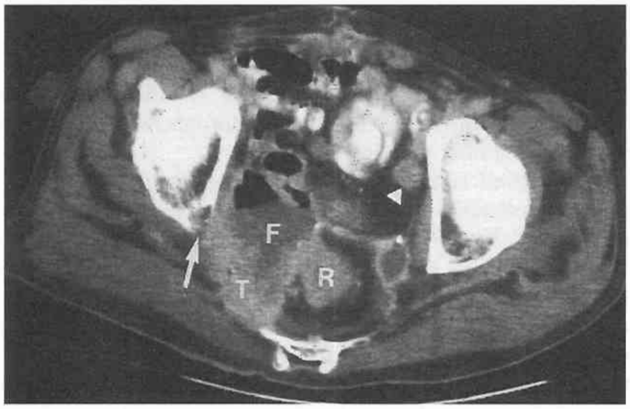

Figure 44–22. Recurrent bladder cancer. CT scan shows right posterior pelvic tumor recurrence (T) eroding the ischial spine *(arrow)* and associated with a gas-fluid collection (F) from a fistula to the rectum (R). There is also metastatic nodal disease in the left obturator group *(arrowhead)* in this patient with recurrence after cystectomy.

Prostate Cancer

Prostate cancer is the most common cancer in men in the United States and the second most common cause of cancer mortality in men. Prostate cancer occurs in about 20% of men, and for several years its incidence has been increasing. Most prostate cancers are adenocarcinomas and are graded according to the system of Gleason: a score of 1 up to 5 is given for each of two predominant histologic patterns in the tumor, giving a range of scores from 2 (indolent) up to 10 (highly aggressive).

Formerly, the diagnosis was confirmed mainly by digitally guided prostate biopsy or from the chippings of transurethral resection of the prostate gland. Now the diagnosis is commonly made by transrectal ultrasound–guided biopsy prompted by either an abnormal digital rectal examination or an elevated prostate-specific antigen (PSA) level. There is accumulating evidence that a patient's PSA level and the Gleason score of the tumor can be used to determine the need for a bone scan and cross-sectional imaging assessment of lymph node metastasis as part of initial staging.[124, 145] It is unlikely that CT will reveal evidence of lymph node metastasis in a man with a PSA level below 20 ng/mL and a Gleason score below 7.

In clinical practice, the TNM staging system is now more commonly used than the American Urological Association (AUA) staging system (Table 44–3). There is no consensus on treatment. Generally, patients with stage T2 or earlier, N0 (AUA stages A and B) prostate cancer, without extraprostatic extension or lymph node metastasis, are candidates for radical local therapy. This may involve radical prostatectomy or radiation therapy. Treatment selection is influenced by PSA level, tumor grade, patient age, and co-morbidity as well as patient and physician preference. For preoperative assessment MRI with pelvic surface or endorectal coils is now considered the most accurate staging technique, although early claims of accuracies exceeding 90% have not been realized in wider clinical practice.[9, 139, 156]

CT is not effective in differentiating stage T2 or earlier from stage T3 tumors and thus is not used for this purpose as a preoperative staging test. CT has reported overall accuracies of 64% in detecting periprostatic fat invasion (stage T3a disease) and only 58% in detecting seminal vesicle invasion (stage T3b).[128] Stranding in the periprostatic fat may represent minor degrees of tumor extension, but similar appearances arise from inflammation, infection, or biopsy and from normal vascular structures within the rich periprostatic venous plexus. Invasion of the seminal vesicles may occur without density changes and asymmetrical enlargement may occur without invasion.

CT remains valuable in evaluating locally advanced disease: bulky T3b disease replacing the seminal vesicles (Fig. 44–23), involving the rectum (stage T4a) (Fig. 44–

Table 44–3. Tumor-Node-Metastasis (TNM) Staging Classification for Prostate Cancer

T	**Primary tumor**
TX	Primary tumor cannot be assessed
T0	No evidence of primary tumor
T1	Clinically inapparent tumor not palpable or visible by imaging
	T1a Tumor incidental finding in 5% or less of tissue resected
	T1b Tumor incidental finding in more than 5% of tissue resected
	T1c Tumor identified by needle biopsy (e.g., because of elevated PSA)
	Tumor confined within prostate*
T2	T2a Tumor involves one lobe
	T2b Tumor involves both lobes
	Tumor extends through prostatic capsule
T3	T3a Extracapsular extension (unilateral or bilateral)
	T3b Tumor invades seminal vesicles
T4	Tumor is fixed or invades adjacent structures other than seminal vesicles: bladder neck, external sphincter, rectum, levator muscles, and/or pelvic wall
N	**Regional lymph nodes**
	NX Regional lymph nodes cannot be assessed
	N0 No regional lymph node metastasis
	N1 Regional lymph node metastasis
M	**Distant metastases**
	M0 No distant metastasis
	M1 Distant metastasis

* Tumor found in one or both lobes by needle biopsy, but not palpable or visible by imaging, is classified as stage T1c.
PSA, prostate-specific antigen.

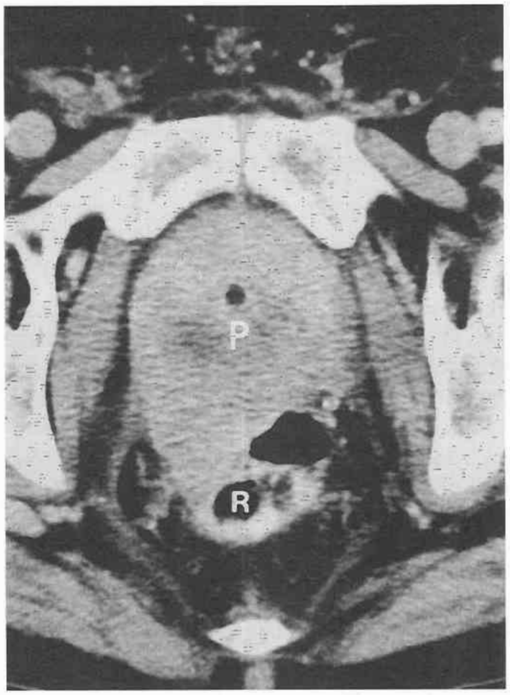

Figure 44–24. Stage T4a prostate cancer. CT scan through the prostate (P) shows direct invasion of the rectum (R).

24), or extending to the pelvic sidewall (stage T4b). CT may be used to confirm the findings of digital rectal examination with advanced disease and to plan palliative radiation therapy. Bulky T3a disease may cause asymmetrical thickening, irregularity and nodularity of the prostate contour, and obliteration of fat planes with adjacent structures, including the loss of the angle between the prostate and the seminal vesicle. In some cases, the tumor enhances and is of higher attenuation than the adjacent prostate gland

Figure 44–23. Stage T3b prostate cancer. CT scan through the seminal vesicles shows enhancing prostate tumor (T) extending out of the base and replacing most of the left vesicle.

(see Fig. 44–23), a feature that is accentuated with rapid spiral acquisition in the early enhancement phase.

The overall accuracy for detection of lymph node metastases in prostate cancer is 67% to 93%.[38, 95, 117, 172] This accuracy disguises a poor sensitivity. Results are dramatically improved when a threshold size of 6 mm for lymph node enlargement is used combined with an aggressive biopsy policy using fine-needle aspiration for enlarged nodes.[122] The clear advantages of MRI over CT for T-stage assessment compare with minimal reported improvements in lymph node staging because both use similar size criteria.[66] In newly diagnosed cases, lymph node metastases, as assessed by CT, extend in a predictable and stepwise fashion from the pelvis to the abdomen. In a retrospective CT series of 500 cases, only a single case of isolated retroperitoneal nodal enlargement was reported at presentation.[97] Thus, if there is no CT evidence of lymph node enlargement in the pelvis, there is no requirement to examine the abdomen for this purpose.[146] Prostate cancer spreads to the external and internal iliac chains with predilection for the obturator group lying on the obturator internus muscle, then to the common iliac group and the retroperitoneum. Lymph node metastases are more likely with increasing CT T stage, and with advanced disease, nodal metastases may be large and multiple.[146]

CT is also valuable in assessment of suspected soft tissue recurrent disease. Clinical presentations include back pain but a negative bone scan and lower limb swelling with negative sonovenographic findings. Patterns of disease differ from those at initial presentation. Retroperitoneal and upper abdominal disease may predominate, especially after pelvic radiation therapy.[148]

About 95% of prostate cancers are adenocarcinomas and are associated with elevated PSA levels. Uncommon

cancers include transitional carcinoma from the urethra and small-cell carcinoma. Metastatic disease is commonly present at diagnosis with both small-cell and anaplastic carcinoma variants of prostate cancer; unlike the situation with prostate adenocarcinoma, metastases develop in the face of normal or minimally elevated levels of PSA.[140]

Testicular Cancer

More than 95% of testicular cancers are germ cell tumors (GCTs), and these are the most common malignancy of men aged 15 to 34 years. The incidence is rising. However these are highly chemosensitive and radiosensitive tumors, and advances in therapy mean current prognosis is extremely good, especially in men with early-stage disease. Tumor stage, as assessed by imaging, is a key determinant of initial therapeutic options, and imaging has a major role in further management.

Malignant GCTs of the testis are divided into *seminomas* and *nonseminomatous germ cell tumors* (NSGCTs). Seminomas account for approximately 40% of GCTs and metastasize in a relatively predictable fashion via lymphatic channels. NSGCTs account for approximately 60% of testicular GCTs and have a more variable, hematogenous route of spread. Seminomas affect a slightly older population, with a mean age of 37 years, whereas NSGCTs occur in a group with a mean age of 27 years.

The serum tumor marker β-human chorionic gonadotropin (β-hCG) may be produced by both seminomas and NSGCTs, although usually only at low levels in the former. α-Fetoprotein (AFP) is elevated in up to 65% of NSGCTs but in fewer than 4% of those with seminoma. AFP is not specific to GCTs and may be elevated in patients with chronic liver disease, hepatoma, or other solid tumors. In men with tumor marker–positive NSGCTs, rising serum levels indicate metastatic disease and should prompt radiologic assessment of sites of relapse. In men with tumor marker–negative GCTs (most seminomas), radiologic examination has a key role in detection of recurrent disease.

In men with stage I NSGCTs, without adverse pathologic factors such as vascular and lymphatic invasion or greater than 50% embryonal carcinoma, a surveillance strategy is appropriate. At the other end of the spectrum, demonstration of factors known to predict poor outcome, such as para-aortic nodal disease greater than 5 cm in diameter (Fig. 44–25) or large and numerous pulmonary metastases, indicates the need for aggressive systemic therapy. The Royal Marsden Hospital staging system, widely used in the United Kingdom and Europe and adopted by the European Organization for Research and Treatment of Cancer (EORTC), takes into account both tumor volume and sites of spread (Table 44–4), as does the revised system used by both the American Joint Committee on Cancer (AJCC) and the International Union Against Cancer (Table 44–5).

CT is the most important and widely used imaging modality for staging testicular tumors. Nodal enlargement is the main criterion for assessing metastatic disease, and knowledge of patterns of spread helps with interpretation of equivocal findings. Right-sided GCTs drain primarily to the interaorticocaval, precaval, and paracaval nodes between L1 and L3 (Fig. 44–26), whereas left-sided tumors drain to the preaortic and para-aortic groups just below the left renal vascular pedicle (see Fig. 44–25).[33] Crossover does occur, particularly with right-sided tumors, but only in patients with more advanced disease and subsequent to ipsilateral nodal disease (see Fig. 44–26).[33] Pelvic nodal disease is uncommon in the absence of identifiable risk factors such as bulky abdominal disease (>5 cm), past history of maldescent or orchidopexy, other scrotal surgery, or invasion of tumor through the tunica vaginalis (Fig. 44–27).[174] Routine scanning of the pelvis in follow-up studies remains a contentious issue, but the evidence suggests that it is required only in men with the risk factors outlined earlier.[174, 182]

In patients with advanced seminoma, disease may

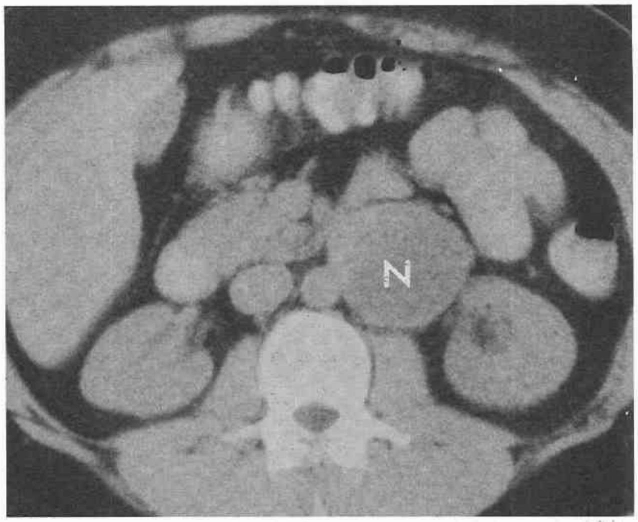

Figure 44–25. Metastatic testicular teratoma. CT scan through the retroperitoneum just below the left renal vein shows a large left para-aortic node metastasis (N) from a left-sided primary.

Table 44–4. Royal Marsden Hospital Staging Classification for Testicular Germ Cell Tumors

Stage	Definition
I	No evidence of metastases
IM	Rising serum markers with no other evidence of metastases
II	Abdominal node metastases
A	<2 cm in diameter
B	2–5 cm in diameter
C	>5 cm in diameter
III	Supradiaphragmatic node metastases
M	Mediastinal
N	Supraclavicular cervical axillary
O	No abdominal node metastases
ABC	Node size defined as in stage II
IV	Extralymphatic metastases
	Lung:
L1	≤3 metastases
L2	>3 metastases, all < 2 cm in diameter
L3	>3 metastases, one or more > 2 cm in diameter
H+	Liver metastases
Br+	Brain metastases
Bo+	Bone metastases

Table 44–5. Tumor-Node-Metastases (TNM) Staging Classification of Testicular Tumors—1997

Primary Tumor	
Extent of Primary Tumor Classified after Radical Orchiectomy (pT).	
pTX	Primary tumor cannot be assessed (if no radical orchiectomy has been performed, TX is used)
pT0	No evidence of primary tumor (e.g., histologic scar in testis)
pTis	Intratubular germ cell neoplasia (carcinoma in situ)
pT1	Tumor limited to testis and epididymis without vascular/lymphatic invasion; tumor may invade into the tunica albuginea but not tunica vaginalis
pT2	Tumor limited to testis and epididymis with vascular/lymphatic invasion, or tumor extending through tunica albuginea with involvement of tunica vaginalis
pT3	Tumor invades spermatic cord with or without vascular/lymphatic invasion
pT4	Tumor invades scrotum with or without vascular/lymphatic invasion
Regional Lymph Nodes	
Clinical Involvement	
NX	Regional nodes cannot be assessed
N0	No regional lymph node metastasis
N1	Metastasis with a lymph node mass ≤ 2 cm in greatest dimension or multiple lymph nodes none > 2 cm in greatest dimension
N2	Metastasis with a lymph node mass > 2 cm but ≤ 5 cm in greatest dimension
N3	Metastasis with a lymph node mass > 5 cm in greatest dimension
Pathologic Involvement	
pN0	No regional lymph node metastases
pN1	Metastasis with a lymph node mass ≤ 2 cm in greatest dimension and five or fewer positive nodes, none > 2 cm in greatest dimension
pN2	Metastasis with a lymph node mass > 2 cm but ≤ 5 cm in greatest dimension; or more than 5 nodes positive, none > 5 cm; or evidence of extranodal tumor
pN3	Metastasis with a lymph node mass > 5 cm in greatest dimension
Distant Metastasis	
MX	Distant metastasis cannot be assessed
M0	No distant metastasis
M1	Distant metastasis
M1a	Nonregional lymph node or pulmonary metastasis
M1b	Distant metastasis other than to nonregional lymph nodes and lungs

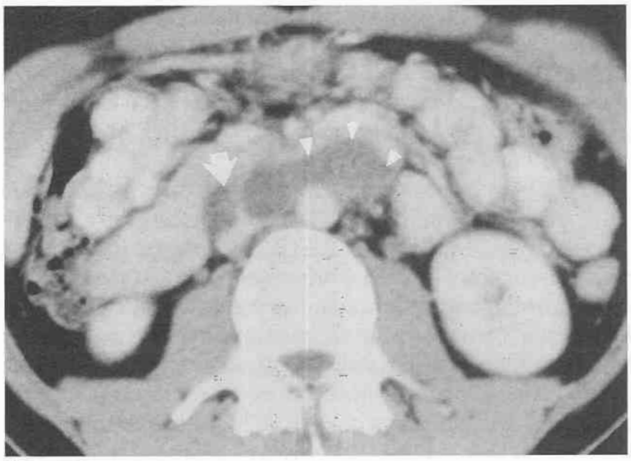

Figure 44–26. Metastatic testicular teratoma. CT scan through the retroperitoneum shows cystic nodal metastases from a right-sided primary. In addition to the precaval metastases *(arrow)*, there is crossover into left-sided preaortic and para-aortic nodes *(arrowheads)*.

spread to contiguous nodal groups in the mediastinum. Pulmonary metastases without such adenopathy are rare. Conversely, mediastinal disease from NSGCTs tends to be more unpredictable and lung metastases are relatively more common.[179, 181] Such patterns of disease spread have implications for follow-up and surveillance protocols involving the use of thoracic CT versus chest radiography.[173]

A continual challenge in radiology is to identify metastatic disease in nonenlarged nodes. Lymphangiography is the only modality that can demonstrate nodal internal architecture; however, it has its own inherent limitations, including an inability to demonstrate nodes above the level of the second lumbar vertebra or outside the retroperitoneal chain. The most lateral of the testicular drainage groups, the *echelon nodes*, are not opacified following pedal injections.[102] The extent of disease beyond the boundary of the node when capsular breach has been demonstrated can only be inferred, and its true extent cannot be assessed. Furthermore, the examinations are difficult to perform, time-consuming, and unpleasant for the patient. With continuing improvements in CT technology, the declining use of lymphangiography means that expertise is being lost and it is now rarely performed.

Size remains the only criterion for judging nodal involvement by GCTs, but familiarity with patterns of disease behavior allows radiologists to highlight nonenlarged nodes, which by virtue of their position in relation to other sites of disease should be regarded as suspicious for involvement. Appearance and attenuation values of nodes may also be helpful. Seminomatous metastases are generally of soft tissue density, whereas NSGCTs may be of low attenuation or frankly cystic (see Fig. 44–26).

Staging and follow-up examinations are generally carried out without IV contrast enhancement, and close attention to bowel opacification by oral contrast agent is re-

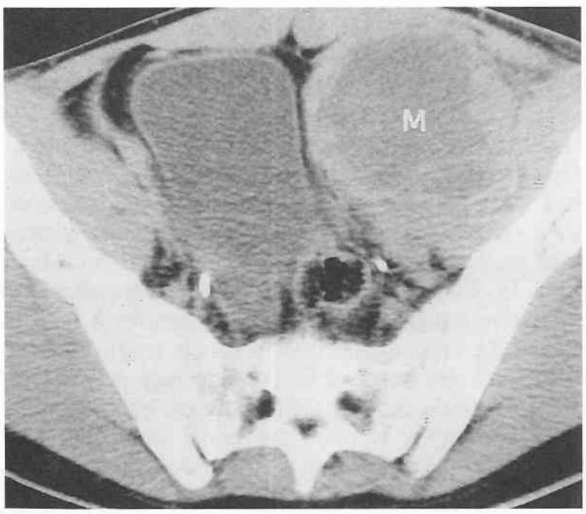

Figure 44–27. Tumor in an undescended testis. CT scan through the pelvis shows a large cystic-necrotic mass (M) invading the left iliopsoas muscles. Excision revealed testicular teratoma within a nodal mass.

quired to avoid overestimating abdominal disease. An IV contrast agent should be used for problem solving in the retroperitoneum when distinction of adenopathy from possible vascular anomalies of the inferior vena cava, renal vessels, or gonadal and lumbar veins is not readily apparent from the unenhanced images.

Residual masses are a relatively common finding in GCT patients treated initially with chemotherapy for advanced-stage disease. With NSGCTs, residual masses may be predominantly cystic and represent residual malignancy, mature or immature teratoma, or necrosis and fibrosis.[152] Enlarging retroperitoneal, mediastinal, or pulmonary masses in these patients with negative serum tumor markers after chemotherapy frequently represents mature teratoma.[98, 123] In patients with NSGCTs, because CT cannot reliably exclude malignancy, residual masses larger than 1 cm are resected.[62, 87]

Because many such retroperitoneal and mediastinal masses are intimately related to major vascular structures, preoperative limited, thin-section contrast-enhanced CT scans with MPR can aid surgical planning. The approach to seminomatous residual masses is not as clear-cut. Such abnormal areas often contain necrosis and fibrosis rather than viable tumor, and resection is often difficult and incomplete. The CT appearance alone may guide management strategy for seminoma, with the suggestion that residual masses smaller than 3 cm and poorly defined residua larger than 3 cm should undergo surveillance, whereas well-defined masses larger than 3 cm should be resected.[129] Gallium scanning in residual seminoma disease appears to be of minimal value.[170] However, there may be potential for FDG-PET (fluorodeoxyglucose–positron emission tomography) scanning in this area of clinical and radiologic uncertainty.

The Undescended Testis

The testis may be cryptorchid, lying anywhere along the path of normal descent between the renal hilum and scrotal sac. It may be retractile, ectopic, atrophic, or absent. Approximately 80% of impalpable testes lie in the inguinal canal and 20% are within the abdomen. Testicular absence occurs in about 4% of cases of impalpable testes. Complications of undescended testes include malignancy (see Fig. 44–27), infertility, torsion, sequelae associated with inguinal hernias, and the psychological impact on patients.

Orchidopexy is the desired treatment in patients older than 1 year of age because, until that age, spontaneous descent can occur. After puberty, because of the increased risk of malignant transformation, orchidectomy is performed. In children, surgery is usually performed and thus preoperative imaging is not routinely required. In adults, however, the cryptorchid testis warrants treatment, and in the 20% that are impalpable, imaging may play a role in locating the testis and in guiding surgical intervention.

Ultrasonography is often the initial investigative modality and can locate cryptorchid testes in the inguinal canal and between the external ring and scrotal neck. It can also detect an atrophic testis or an ectopic lie, such as in the superficial inguinal pouch or the contralateral hemiscrotum. Its limitation is in the assessment of testes that lie proximal to the internal inguinal ring.

The inherent soft tissue contrast of MRI and the lack of ionizing radiation make it the modality of choice for investigating patients with negative ultrasonographic findings.[45] The testis can be accurately located in the abdomen, pelvis, or inguinal region, and intratesticular lesions can be demonstrated within large cryptorchid testes that have become malignant.

CT demonstrates the undescended testis as an ovoid mass of soft tissue density, usually 2 cm or smaller in size, along the expected course of descent.[90, 180] Large masses should raise suspicion for malignant change (see Fig. 44–27).

For assessment of suspected intra-abdominal undescended testis, CT examination with full oral and IV contrast agents increases the ability to distinguish the testis from lymph nodes, vessels or bowel loops. Currently, laparoscopy is the preferred diagnostic and therapeutic procedure in adults.

Cervical Cancer

Invasive cervical cancer is the third most common gynecologic malignancy in the United Kingdom and the United States, with a peak incidence between ages 35 and 50 years. Most women present with vaginal bleeding. The clinical examination is frequently diagnostic, and colposcopy and biopsy establish the histologic diagnosis.

Most cervical tumors are of squamous cell type arising from the squamocolumnar junction near the external os. The remainder are adenocarcinomas or adenosquamous carcinomas. In older women, the external os migrates upward into the endocervical canal, and tumors arising here tend to expand the canal and extend upward into the uterine body. In younger women, tumors arising on the ectocervix tend to be more polypoidal and exophytic.

In most cases, cervical intraepithelial neoplasia (CIN) is known to precede invasive squamous disease, and detection of this condition and of early invasive disease by cervical screening programs has led to a reduction in overall mortality rates. CIN is radiologically occult, and therefore diagnostic imaging is reserved for histologically proven invasive disease.

Cervical cancer spreads locally into the parametrial tissues and the supporting ligaments around the uterus. Inferior spread onto the vagina occurs and with advancing disease involvement of the pelvic sidewalls, bladder, and rectum can be seen. Nodal spread initially is to parametrial, obturator, and presacral nodes, followed by internal, external, and common iliac groups. Later retroperitoneal and supraclavicular nodal disease may occur. Hematogenous involvement of liver, lung, and bone occurs in advanced disease.

Radical surgery and radiation therapy are treatment options for stages IA, IB, and IIA disease (Table 44–6); radiation therapy is the treatment of choice for more advanced stages IIB to IVB, with chemotherapy an option for those with distant metastases. The prognosis in cervical carcinoma is closely linked to tumor stage and volume.[64, 103] Although nodal status is not included in the International Federation of Obstetrics and Gynecology (FIGO) staging system, it has been found to have a significant prognostic

Table 44–6. International Federation of Obstetrics and Gynecology (FIGO) Staging of Carcinoma of the Uterine Cervix

Stage	Summary of FIGO Classification
0	Carcinoma in situ (preinvasive)
I	Carcinoma confined to the cervix; extension to corpus should be disregarded
IA	Preclinical carcinomas, i.e., those diagnosed only by microscopy
IA1	Stromal invasion ≤ 3.0 mm in depth and < 7.0 mm in horizontal spread
IA2	Lesions detected microscopically that can be measured. The upper limit of the measurement should not show a depth of invasion > 5 mm taken from the base of the epithelium, either surface or glandular, from which it originates, and a second dimension, the horizontal spread, must not exceed 7 mm. Larger lesions should be staged as IB
IB	Lesions of greater dimensions than stage IA2 whether seen clinically or not. Performed space involvement should not alter the staging but should be specifically recorded so as to determine whether it should affect treatment decisions in the future
IB1	Clinically visible lesion ≤ 4 cm in greatest dimension
IB2	Clinically visible lesion > 4 cm in greatest dimension
II	Carcinoma extending beyond the cervix but no extension onto the wall. The carcinoma involves the vagina but not the lower third
IIA	No obvious parametrial involvement
IIB	Obvious parametrial involvement
III	Carcinoma extension onto the pelvic wall. On rectal examination, there is no cancer-free space between the tumor and the pelvic wall. The tumor involves the lower third of the vagina. All cases with hydronephrosis or nonfunctioning kidney
IIIA	No extension to the pelvic wall
IIIB	Extension onto the pelvic wall and/or hydronephrosis or nonfunctioning kidney
IV	Carcinoma extension beyond the true pelvis or clinical involvement of the mucosa of the bladder or rectum. A bullous edema, as such, does not permit a case to be staged as stage IV
IVA	Spread of growth to adjacent organs
IVB	Spread to distant organs

impact on outcome in patients treated with radiation therapy.[159]

The aim of cross-sectional imaging is accurate local staging to identify patients who are candidates for radical surgery and to demonstrate the extent of disease in patients who are not. MRI is the modality of choice for local tumor staging. It is accurate and cost-effective in assessment of patients with invasive disease when it is used as an adjunct to clinical evaluation. It is not appropriate in patients with *stage IA* or obviously advanced disease. However, the inherent inaccuracy of clinical staging and the increased incidence of lymphadenopathy with increasing tumor bulk mean that it is recommended in those with suspected *stage IB* disease when the tumor is large (>2 cm) or within the endocervical canal and in patients with suspected parametrial extension.

MRI is significantly better than CT for local staging; therefore, the main role of CT is in more advanced disease.[153] The cervix may appear enlarged with an irregular contour, and enhancement may be inhomogeneous in the presence of areas of necrosis and ulceration. Uterine enlargement and fluid collections within the endometrial cavity are often seen when tumor obstructs the endocervical canal. Poorly defined lateral cervical margins, stranding of the parametrial fat, and an eccentric parametrial soft tissue mass have been described as CT criteria for parametrial invasion (Fig. 44–28). However, these are subject to considerable error and overstaging because hyperemia and parametritis can cause identical appearances. Effacement of fat planes around the ureter is a more reliable CT sign but is usually found only when gross parametrial extension has occurred.[67] Extension of abnormal tissue to or within a couple of millimeters of the pelvic sidewall characterizes stage IIIB disease. These cases often show associated renal tract compromise, and CT can elegantly demonstrate hydronephrosis and hydroureter. Secondary signs of renal obstruction, such as unilateral delayed renal cortical enhancement and cortical loss, can also be seen.

Although CT can demonstrate loss of local fat planes, bladder and rectal wall thickening, and frank intraluminal disease, the multiplanar ability and intrinsic soft tissue contrast of MRI make it more sensitive for detecting local organ invasion (stage IVA disease).[82] CT is widely used in a diagnostic capacity in both advanced primary and recurrent disease as described. However, another major role is that of therapy planning in those women who are to undergo radiation therapy either as primary treatment due to advanced stage disease or co-morbidity factors that preclude radical surgery, or as salvage treatment for recurrence. Information regarding nodal disease is vital for planning of radiation fields and for deciding between radical and palliative treatment.

One of the major roles of CT in the management of patients with clinically suspected advanced stage cervical carcinoma is assessment of lymphadenopathy. Knowledge of the probable pattern of disease spread aids in this task; however, size remains the only CT criterion available for predicting nodal involvement. Attenuation of nodes may also be helpful, as with testicular tumors. Nodal metastases from squamous cervical carcinomas may have low attenuation centers reflecting necrosis (Fig. 44–29).

In the detection of pelvic and retroperitoneal lymph node metastases, CT and MRI have a similar overall accuracy (~86%).[153] Lymphangiography is rarely performed now, but the use of ultra-small superparamagnetic iron oxide (SPIO) as an MR lymphangiographic contrast agent may be a useful tool in the future for further characterization of nodes that are indeterminate by size criterion alone.[58]

CT is widely used to investigate suspected recurrent disease (Fig. 44–30). In women treated initially with surgery, CT is accurate for demonstrating central pelvic recurrence, perineal disease, and nodal masses. When the primary treatment has been radical radiation therapy, recurrent masses and invasion of local structures as well as treatment complications such as fistulas can be assessed.

A persisting problem with CT is the differentiation of recurrent tumor from radiation therapy or postsurgical fibrosis.[80, 169] Although it had initially been hoped that MRI would be helpful in this situation, MRI also has its limitations, since the signal characteristics of radiation-induced fibrosis can be extremely variable and both recurrent disease and radiation fibrosis can show contrast en-

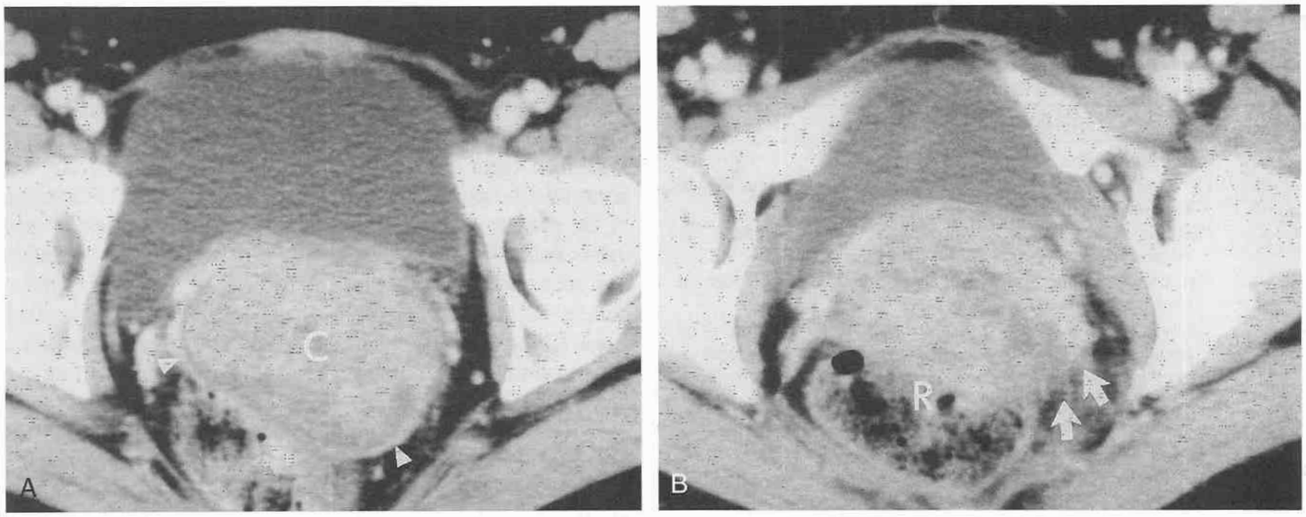

Figure 44–28. Stage T4 cervical cancer. CT scan through the cervix. *A,* The cervix (C) is expanded by a heterogeneous enhancing cancer that shows a thin, intact capsule *(arrowheads)*. *B,* At a lower level, invasion of the anterior wall of the rectum (R) and parametrial invasion *(arrows)* are seen.

hancement. The role of PET scanning in this situation is being assessed.[154]

The cervix is sometimes secondarily involved by non-Hodgkin's lymphoma (NHL) in the context of widely disseminated disease. However, primary lymphoma of the cervix is rare, accounting for approximately 1% of extranodal NHL. On CT scans, the cervix appears diffusely enlarged by an enhancing soft tissue mass (Fig. 44–31). Lymphadenopathy may be absent in primary cervical lymphoma, in contrast to secondary disease.[112] Internal heterogeneity may reflect areas of necrosis. The histologic diagnosis is vital in such cases because the treatment and prognosis of stage IE NHL are vastly different from those of cervical carcinoma.[84]

Uterine Tumors

Benign Uterine Tumors

Uterine leiomyomata are common benign uterine neoplasms, occurring in 20% to 40% of women. Often found incidentally on CT, they may present as a palpable abdominal mass, may be associated with pain or bleeding, or may cause symptoms of compression related to the bladder or rectum. They usually appear as homogeneous soft tissue attenuation masses causing uterine enlargement but often have a characteristic "whorled" appearance (Fig. 44–32). The presence of necrosis or degeneration can give a low attenuation appearance. Leiomyomata therefore may be hypodense, isodense, or hyperdense relative to normal myometrium on contrast-enhanced CT.

Calcification is not uncommon, occurring in approxi-

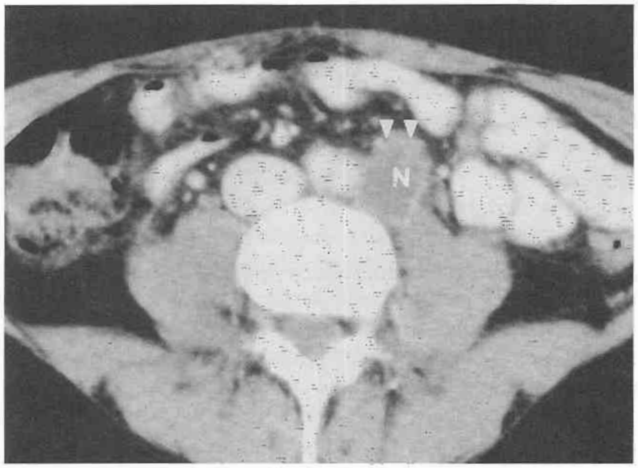

Figure 44–29. Metastatic cervical cancer. CT scan through the lower retroperitoneum shows a left para-aortic nodal metastasis (N) from cervical cancer having an irregular enhancing margin *(arrowheads)* and central necrosis. Such margins predict extranodal tumor extension.

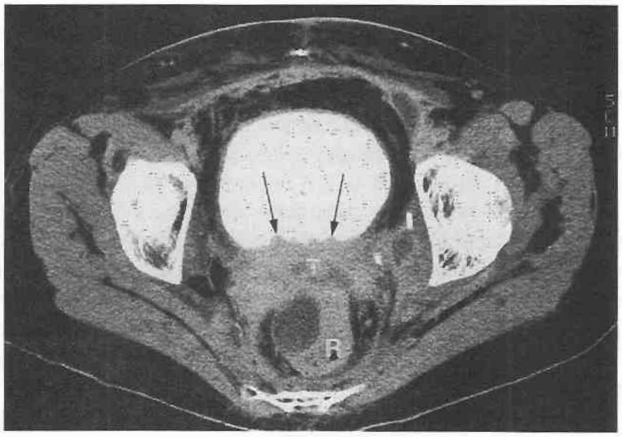

Figure 44–30. Recurrent cervical cancer. CT scan shows a central pelvic tumor (T) after hysterectomy involving the anterior rectum (R) and posterior bladder wall *(arrows)* and extending to both pelvic sidewalls on this delayed excretory-phase image. Note the lymphadenectomy clip in the left obturator fossa.

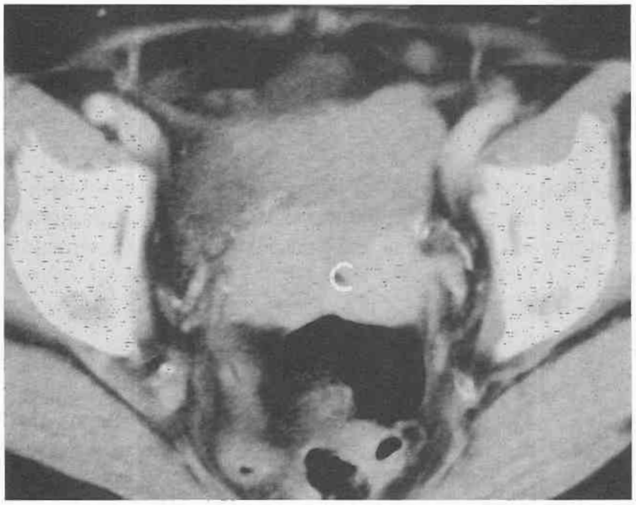

Figure 44–31. Cervical lymphoma. CT scan shows a homogeneous enhancing mass expanding the cervix (C).

mately 10%, and coarse dystrophic calcification is a relatively specific feature.[24, 78] Leiomyomata may lie in a subserosal location, causing a lobulated uterine contour or be submucosal, distorting the endometrial cavity and then becoming indistinguishable from endometrial tumors.[137] Some leiomyomata are pedunculated and mimic adnexal masses. It is not always possible to ascertain the organ of origin of such lesions, especially if noncalcified, and multiplanar MRI with its inherent tissue contrast showing zonal anatomy can help with such problem solving.

Uterine Cancer

Endometrial carcinoma is a common gynecologic malignancy that primarily affects postmenopausal women, who usually present with bleeding. Approximately 75% of patients have stage I disease at presentation (Table 44–7). Histologic type and grade of tumor, depth of myometrial invasion, cervical involvement, and the presence of nodal

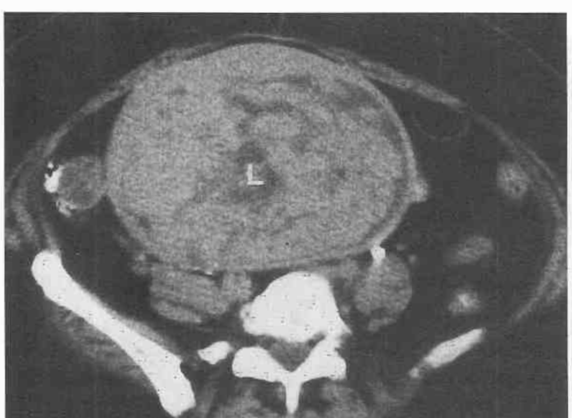

Figure 44–32. Large uterine leiomyoma. CT scan at the iliac crest shows a typical heterogeneous enhancement pattern of a giant leiomyoma (L) of the uterus.

Table 44–7. International Federation of Obstetrics and Gynecology (FIGO) Classification of Carcinoma of the Uterine Corpus

Stage	Summary of FIGO Classification
IA	Tumor confined to the endometrium
IB	Invasion of less than half of the depth of the myometrium
IC	Invasion of more than half of the depth of the myometrium
IIA	Extension to the cervix, endocervical glands only involved
IIB	Invasion of the cervical stroma
IIIA	Invasion of the uterine serosa, or adnexa, and/or positive peritoneal cytology
IIIB	Vaginal involvement (direct extension or metastasis)
IIIC	Pelvic and/or para-aortic lymph node metastases
IVA	Invasion of bladder and/or bowel mucosa
IVB	Distant metastases, including extrapelvic lymph node metastases

disease influence prognosis and treatment strategies. Surgery is the treatment of choice in patients with disease confined to the myometrium. Most endometrial cancers are well-differentiated adenocarcinomas, and surgical treatment for organ-confined disease has a 10-year survival of approximately 80%. Most of these patients are managed on clinical grounds alone without imaging other than transvaginal ultrasonography.

The prognosis is not as optimistic for clear cell and papillary serous carcinomas of the endometrium, and these tumor types correlate with higher incidence of lymph node metastases (see Fig. 44–17). The likelihood of nodal metastases also increases with depth of myometrial invasion.[12] Therefore, radiologic staging is appropriate in patients with high-grade or other adverse histology, clinical suspicion for advanced disease, or where co-morbidity factors make the patient a poor operative risk.

MRI, if available, is the imaging modality of choice for assessing depth of myometrial invasion and cervical involvement.[83, 142] Knowledge of such disease extent influences the type of hysterectomy and extent of lymphadenectomy performed. The presence of cervical involvement is important for planning brachytherapy. Demonstration of parametrial disease implies that nonoperative treatment is the appropriate management strategy.

When MRI is available, there is virtually no role for CT in the diagnosis and assessment of early-stage endometrial carcinoma.[28, 60] CT does, however, affect clinical management in women with more advanced-stage disease and is accurate for demonstrating disease extension to the pelvic sidewalls, pelvic and retroperitoneal nodal enlargement, and distant metastases to the liver and lungs.

Endometrial tumors appear as a hypodense or enhancing mass within the uterine cavity or within the myometrium on contrast-enhanced CT (Fig. 44–33). It may be difficult to distinguish tumor from coexistent leiomyomata and to assess disease in the atrophic postmenopausal uterus. Cervical involvement may cause a bulky cervix and a distended uterine cavity. In women with more advanced disease, the CT appearance of parametrial, adnexal, pelvic sidewall, and nodal involvement is similar to that seen with primary cervical carcinoma. Adnexal disease may also reflect coincident endometrioid ovarian cancer. The appearance and pattern of recurrent disease are similar to

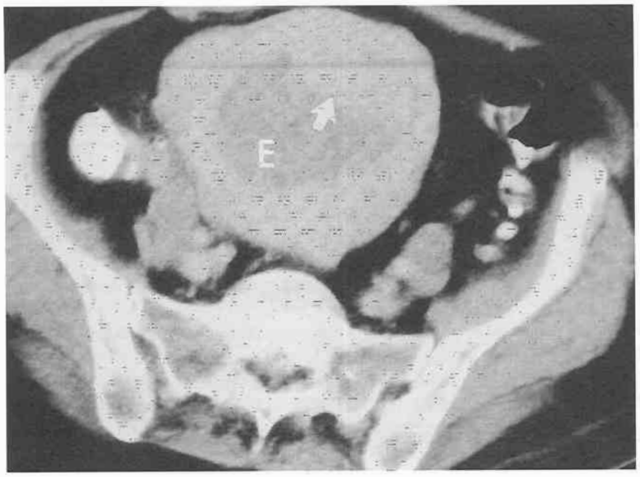

Figure 44–33. Endometrial cancer. CT scan through the uterus shows a distended endometrial cavity (E) containing enhancing tumor *(arrow)*.

those in advanced primary disease, but peritoneal recurrence may also be seen.

Gestational trophoblastic disease (GTD) results from abnormal proliferation of pregnancy-associated trophoblastic tissue and has a potential for malignant transformation. It includes benign partial and complete hydatidiform moles, malignant invasive moles, and choriocarcinoma. The clinical presentation is marked by vaginal bleeding, hypertension, hyperemesis, a large-for-dates uterus, and an inappropriately elevated serum β-hCG level. Ultrasonography demonstrates the characteristic appearance of a molar pregnancy with cystic and solid tissue filling the uterus. Ultrasonography can also identify the relatively rare occurrence of a molar pregnancy coexisting with a separate normal gestation. This is presumed to occur as a result of molar transformation in one of a twin gestation. Its main role, however, is to exclude a normal intrauterine pregnancy.

Hydatidiform moles are treated with dilatation and curettage (D&C). This is usually a curative procedure, and serum β-hCG levels subsequently return to normal. Persistent or recurrent disease occurs in 15% to 20%, and this diagnosis is confirmed by failure of serum markers to normalize. Invasive moles penetrate deep into the myometrium and may penetrate the parametria, broad ligaments, peritoneum, or vaginal vault. They are locally invasive but rarely metastasize.

Choriocarcinoma is a malignant tumor of the chorionic epithelium; absence of villous structures that give noninvasive and invasive moles their characteristic appearance is an important diagnostic feature. Metastatic disease occurs early with choriocarcinoma and is generally blood-borne. Pulmonary, hepatic, cerebral, and vaginal metastases are common.

Determining the serum β-hCG level is the most accurate way to detect persistent GTD and to monitor its treatment. Ultrasonography cannot always distinguish between noninvasive and invasive disease in the absence of gross tumor spread, and CT is used to image persistent local pelvic and metastatic GTD (Fig. 44–34).

Uterine invasive mole or choriocarcinoma typically appears as eccentric hypodense foci in the myometrium or endometrial cavity on contrast-enhanced CT.[54, 115, 135] CT can demonstrate disease that has invaded the broad ligament, parametria, and pelvic fascia and muscles.[31, 135] It can also evaluate hepatic, pulmonary, and cerebral metastases. Solid-organ secondary deposits are classically hypervascular (see Fig. 44–41). Theca-lutein cysts are sometimes found in patients with GTD and are thought to be due to overstimulation by the large amounts of β-hCG.[23] They are elegantly demonstrated by both CT and ultrasonography as multiloculated cysts that are often bilateral.

Leiomyosarcomas are rare uterine malignancies and may arise de novo or may occur as a result of malignant transformation. Distinction between degeneration and malignant change is not possible on morphologic grounds alone, and in the absence of any secondary signs of malignancy, imaging has a limited role in the assessment of such tumors. Mixed müllerian sarcomas are the more common uterine sarcoma. They tend to occur in postmenopausal women, have a more aggressive nature, and often present with a bulky, locally invasive primary and metastatic disease. The imaging appearance is not specific, but the size of the lesion may suggest its nature, and scanning the chest and abdomen allows assessment of distant disease spread.

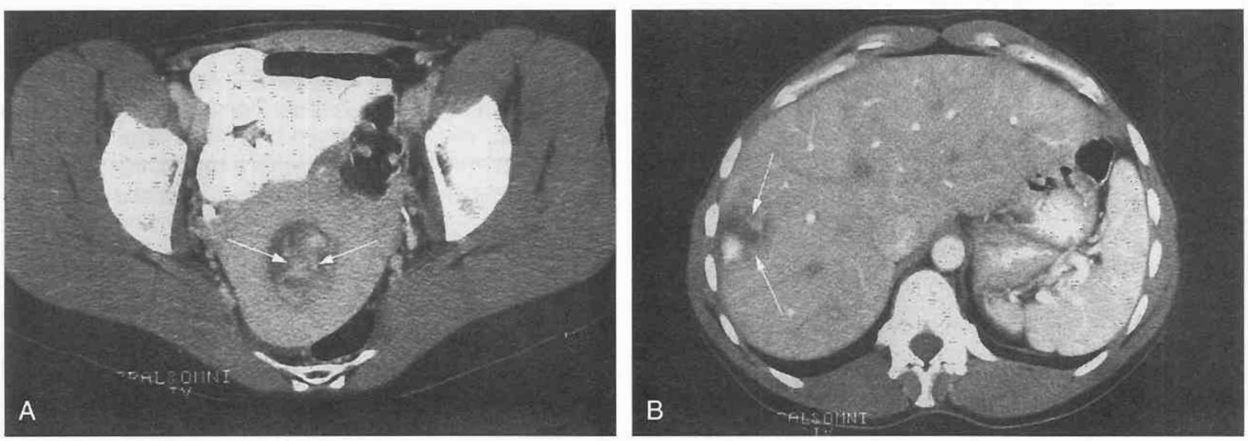

Figure 44–34. Gestational trophoblastic disease. *A,* CT scan through uterus shows a contrast-enhanced tumor *(arrows)* filling a dilated endometrial cavity and an intact myometrium. *B,* Dynamic CT scan through the liver shows a hypervascular metastasis *(arrows)*.

Ovarian Tumors

Ultrasonography is the investigative modality of choice in women when a pelvic mass is suspected. In most cases, ultrasonography can characterize the mass as either uterine or ovarian and suggests its malignant potential on the basis of morphologic features of the mass and the presence of ascites or visceral metastases. Symptomatic ovarian masses are usually removed. For a benign mass, excision alone suffices; for a malignant mass, major cytoreductive surgery may be required.

CT has a central role in the management of ovarian cancer but is infrequently used for assessment of benign gynecologic masses. It is essential, however, that the CT appearances of ovarian masses be recognized because these lesions may be discovered incidentally on pelvic CT assessment.[55, 137] Further, CT is increasingly being used to investigate the acute abdomen, and one needs to decide whether such a mass is relevant to the presenting complaint and, if not, whether further investigation is indicated.

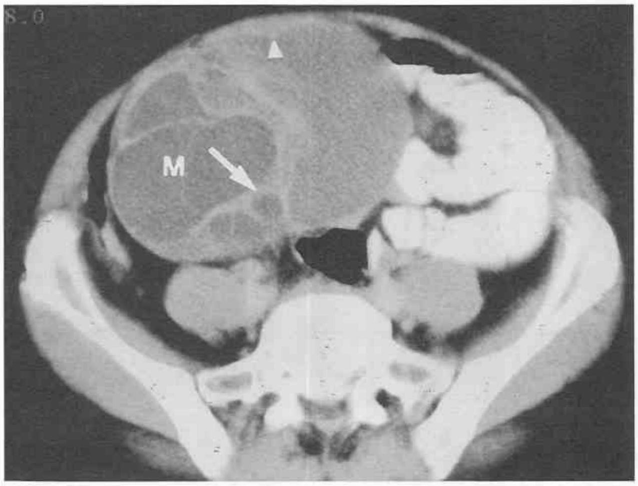

Figure 44–35. Borderline mucinous ovarian cancer. CT scan through a complex right ovarian mass (M) shows thick internal septa *(arrow)* and wall irregularities *(arrowhead)*.

Benign Ovarian Masses

The CT features of a simple ovarian cyst are those of a benign cyst at any site: a homogeneous, unilocular water-density mass with smooth, thin walls and no other internal contents.[55, 138] These are frequently functional cysts that usually resolve spontaneously and this can be confirmed by ultrasonographic follow-up after 2 to 3 months, without further exposure to ionizing radiation. Simple ovarian cysts are increasingly detected as incidental findings in postmenopausal women.

Criteria for diagnosis are a unilocular cyst with no internal components of no more than 5 cm in size in a woman without ascites.[53] Stability in such cysts should again be confirmed with follow-up ultrasonography. Congenital cysts of the lower urogenital tract and a variety of acquired fluid-containing structures can mimic a simple ovarian cyst, including unopacified bowel, bladder diverticulum, a peritoneal inclusion cyst, and focally entrapped fluid following pelvic inflammation or surgery.[63] A purely cystic ovarian cancer is rare.[47]

There is a wide differential diagnosis for a complex cystic adnexal mass, including a number of benign conditions: ovarian neoplasms such as cystadenoma and cystic teratoma and more common conditions, such as endometriosis and pelvic inflammatory disease with hydrosalpinx/pyosalpinx formation. CT criteria for complex adnexal masses include wall (mural) thickening and irregularity, heterogeneous density including calcifications, irregular or thick septa, internal or mural nodules, and outer contour irregularity. These are, unfortunately, common not only to the earlier benign conditions but also to borderline and invasive malignancies (Fig. 44–35). The presence of ascites suggests malignancy, but complicated benign disease can also result in ascites or localized fluid collections as a result of hemorrhage, infection, or torsion. After torsion, an ovarian mass may show poor contrast enhancement and irregular margins.

Although suspected endometriomas and tubo-ovarian abscesses are usually evaluated by ultrasonography, they may be detected on CT examinations performed to investigate pelvic pain and fever. These are lesions within the differential diagnosis for appendicitis and urinary colic, both of which are increasingly investigated by CT emergently. There are varying reports of the CT appearances of endometriomas, some indicating their nonspecific nature and others identifying small focal blood clots adjacent to the inner wall in 15% of endometriomas.[22, 40] Bilateral thick-walled, multilocular cysts or mixed cystic-solid masses may be present (Fig. 44–36). There may also be evidence of coincident adenomyosis with uterine enlargement. MRI may be diagnostic by showing contained blood products within suspected endometriomas.[114]

The acute tubo-ovarian abscess is the most severe complication of pelvic inflammatory disease. The CT features may reflect either or both of the two components: (1) a tubular fluid-density mass, the hydrosalpinx or pyosalpinx; or (2) the septated thick-walled adnexal cyst, the ovarian abscess (Fig. 44–37). Pelvic inflammatory changes may obscure the fat planes between pelvic organs and can result

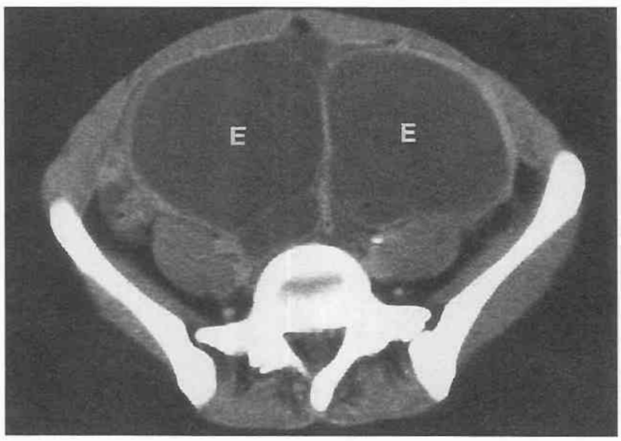

Figure 44–36. Endometriosis. CT scan through bilateral thick-walled giant ovarian endometriomas (E) in a 22-year-old woman with intermittent abdominal pain.

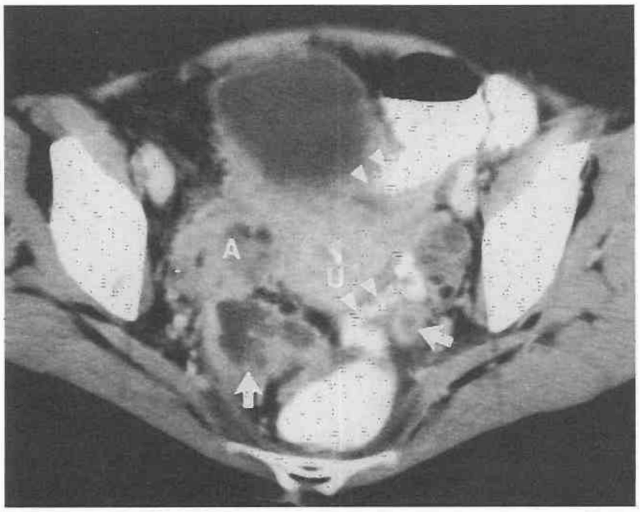

Figure 44–37. Pelvic inflammatory disease. CT scan through the pelvis shows a thick-walled multilocular right tubo-ovarian abscess (A). The uterus (U) contains a contraceptive device. Note also blurring of pelvic fat planes and loculi of pus *(arrows)*. There is narrowing of both the rectosigmoid junction and the pelvic small bowel *(arrowheads)*.

in thickened uterosacral ligaments and reactive pelvic and para-aortic lymphadenopathy. Other secondary effects include small-bowel and rectosigmoid involvement (see Fig. 44–37), ureteral dilatation, and gonadal vein thrombosis.[36, 178] Primary treatment is usually with antibiotic therapy, but intervention may be required and CT-guided abscess drainage offers a nonoperative option. CT drainage is associated with an 88% to 94% success rate.[25, 160]

Ovarian cystadenomas are usually serous or mucinous. They may occasionally be purely cystic and unilocular (Fig. 44–38), but more frequently cystadenomas are complex multilocular lesions showing varying degrees of mural abnormality and heterogeneous density, including calcifications and septation.[138] Mucinous cystadenomas may contain high-density loculi of mucin, but such high-density in cystadenomas may also result from hemorrhage. These high-density foci may mimic a solid tumor component. Complexity in mucinous cystadenomas may make distinction from a borderline or stage I malignant cystadenocarcinoma impossible (see Fig. 44–35).[21, 47]

Mature cystic teratoma *(dermoid tumor)* may have various CT appearances, depending on its contents. The diagnosis may be made incidentally on plain radiographs of the abdomen or pelvis or with ultrasonography. When the nature of an echogenic adnexal mass detected by ultrasonography is uncertain, either CT or MRI may be performed for a confident diagnosis.[151] CT findings include a mixture of low-density areas due to fat or oil, high density from dental elements or cartilaginous calcifications, a fat-fluid level, or a dermoid plug (Fig. 44–39).[20, 44] Alternatively, benign teratomas may appear as cystic lesions. Malignant teratomas are rare. The presence of an irregular solid component larger than 5 cm in diameter suggests malignancy (Fig. 44–40).[20]

Although the presence of a solid element is highly suggestive of malignancy, several benign solid tumors, including fibroma and fibrothecoma (Brenner's tumor), are uniformly solid and smoothly marginated.[138] Ovarian fibroma may be associated with large-volume ascites and pleural effusion *(Meig's syndrome)*. A pedunculated uterine leiomyoma may mimic a solid or cystic ovarian mass and may present as an emergency following torsion (Fig. 44–41).

Early studies have shown that CT was superior to ultrasonography in distinguishing between benign and malignant ovarian epithelial tumors and that CT and MRI had an equivalent overall accuracy in evaluating epithelial tumors of the ovary.[21, 52] The Radiology Diagnostic Oncology Group (RDOG) study, which compared CT with both Doppler ultrasonography and MRI in the assessment of pelvic masses, showed that MRI was slightly better than CT and significantly better than Doppler ultrasonography in assessment of the ovaries and adnexa.[88] All three modalities were equivalent in staging of malignant ovarian masses, given that ascites was indicative of peritoneal dissemination in most cases.

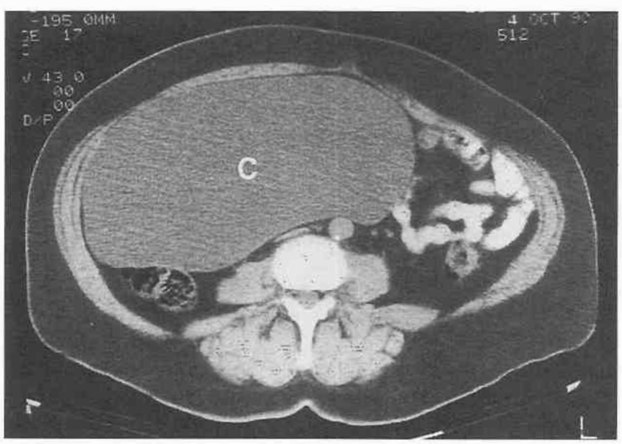

Figure 44–38. Mucinous cystadenoma of the ovary. CT scan through the purely cystic abdominal mass (C) in an asymptomatic 66-year-old woman with a palpable mass.

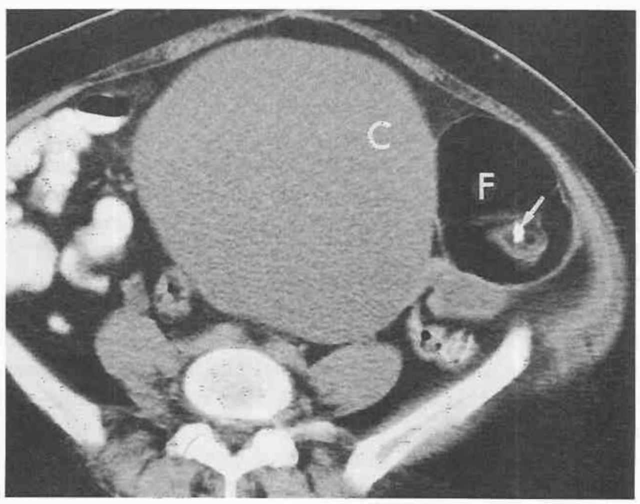

Figure 44–39. Bilateral benign teratomas. *Left,* CT scan shows a typical benign teratoma containing fat (F) and dental elements *(arrow)*. *Right,* A pure cystic teratoma (C) is seen.

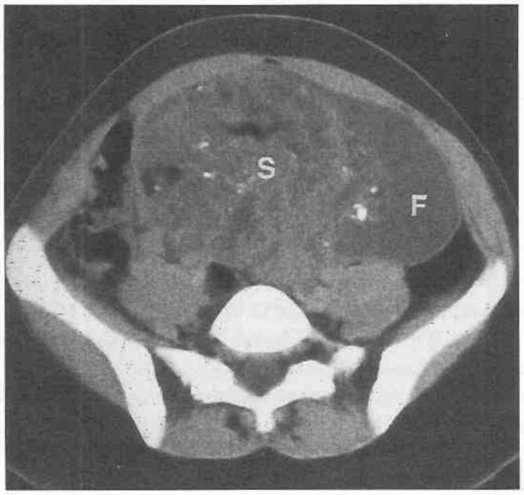

Figure 44–40. Malignant teratoma. CT scan through pelvic mass that contains fluid (F) and a complex solid component (S) that contains small areas of fat and calcification indicating malignancy.

Ovarian Cancer

Ovarian cancer is the leading cause of death from female genital tract malignancy and accounts for about 4% of all female cancers. Women with ovarian cancer typically present with advanced-stage disease, leading to elevation in the serum marker carcinoembryonic antigen 125 (CEA-125). Epithelial ovarian cancer (adenocarcinoma) is a disease of older women. In younger women, ovarian cancer is more commonly due to GCTs, which may produce elevated serum AFP and β-HCG, or to sex cord stromal tumors. Although there are various subtypes of ovarian adenocarcinoma, the prognosis is independent of these and is principally determined by stage at diagnosis (Table 44–8).

Management for all subtypes is similar, and the recommended initial treatment for epithelial ovarian cancer is debulking surgery. For the minority of women with disease apparently confined to the ovary, this may be curative. For the majority of women with peritoneal dissemination of tumor, treatment is with cytoreductive surgery, with the goal to leave deposits no more than 1 cm in diameter. The extent of residual disease is also a prognostic factor. Surgery is the definitive staging procedure. Biopsy specimens of peritoneal surfaces and lymph nodes are obtained, and the ovaries, uterus, and infracolic omentum are removed. For locally or distantly metastatic ovarian cancer, stages IC to IV, surgery is followed by chemotherapy.

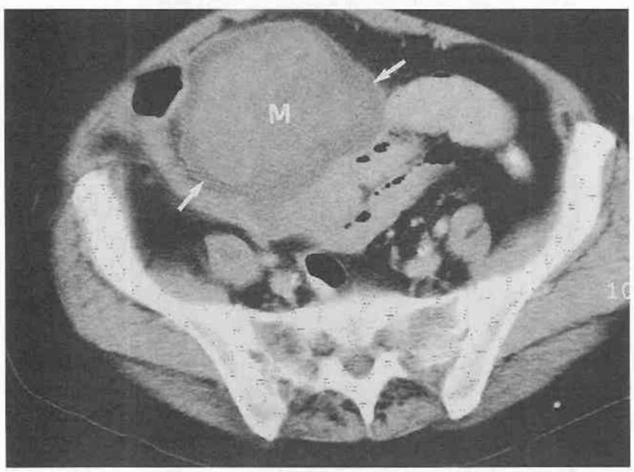

Figure 44–41. Solid adnexal mass. CT scan through the pelvis of a woman with acute abdominal pain and a lower abdominal solid mass (M). This image shows a rim of fluid *(arrows)* and a central solid element with lesser enhancement than muscle. At surgery, an infarcted pedunculated uterine leiomyoma was discovered.

Table 44–8. International Federation of Obstetrics and Gynecology (FIGO) Staging Classification for Ovarian Cancer

Stage	Characteristics
I	Growth limited to the ovaries
IA	Growth limited to one ovary; no malignant ascites; negative peritoneal cytology finding; no tumor on the external surface, capsule intact
IB	Growth limited to both ovaries; no malignant ascites; negative peritoneal cytology finding; no tumor on the external surface; capsule intact
IC	Tumor either stage IA or IB, but with tumor on the surface of one or both ovaries; or with capsule ruptured; or with ascites present containing malignant cells; or with positive peritoneal washings
II	Growth involving one or both ovaries with pelvic extension
IIA	Extension or metastasis to the uterus, tubes, or both
IIB	Extension to the pelvic tissues
IIC	Tumor either stage IIA or IIB, but with tumor on surface of one or both ovaries; or with capsule(s) ruptured; or with ascites present containing malignant cells; or with positive peritoneal washings
III	Tumor involving one or both ovaries with peritoneal implants outside the pelvis or a positive finding in retroperitoneal or inguinal glands; superficial liver metastases; tumor limited to the true pelvis but with histologically proven malignant extension to small bowel or omentum
IIIA	Tumor grossly limited to the true pelvis with unaffected nodes but with histologically confirmed microscopic seeding of abdominal peritoneal surfaces
IIIB	Tumor involving one or both ovaries with histologically confirmed implants on abdominoperitoneal surfaces, none > 2 cm in diameter, nodes unaffected
IIIC	Abdominal implants > 2 cm in diameter or unaffected retroperitoneal or inguinal nodes
IV	Growth involving one or both ovaries with distant metastases; if pleural effusion is present, there must be a positive cytology finding; parenchymal liver disease

When a suspected ovarian adenocarcinoma must be evaluated preoperatively, CT is the imaging modality of choice.[1, 76, 176] It can replace urography and barium studies for assessment of hollow organ involvement and in most cases accurately determines tumor extent. CT is inferior to surgical staging in detecting tiny peritoneal, omental, and mesenteric nodules, but this is not its role. Rather, in the presence of bulky disease, CT predicts the probable success of cytoreductive surgery.[111] CT also indicates when the gynecologist may require assistance from other surgical colleagues to achieve effective debulking (e.g, when the ureters, pelvic small bowel, or colon is involved). Bulky disease in the supracolic compartment around the spleen and stomach, suprarenal lymph nodes, subdiaphragmatic recesses, and parenchyma of the liver is usually beyond the scope of surgery.

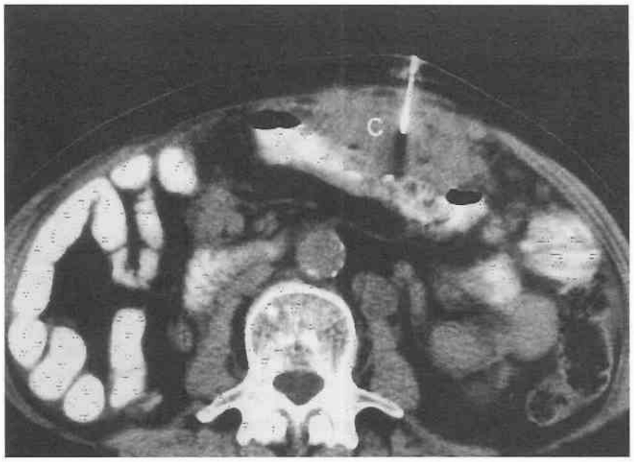

Figure 44–42. Omental biopsy. CT-guided biopsy of the omental cake (C) by means of an 18-gauge cutting needle. The patient had been considered unfit for primary surgery. Biopsy revealed serous papillary adenocarcinoma of müllerian type, consistent with ovarian cancer.

In one study, MRI was superior to CT in ovarian cancer staging in assessing pelvic disease but not abdominal disease.[43] In that study, CT was better at predicting nonresectability. CT-guided biopsy offers an alternative to surgery to provide a definitive histologic diagnosis in women with inoperable disease (Fig. 44–42).[149] There is current interest in neoadjuvant chemotherapy followed by interval debulking surgery for these women.

The CT features of epithelial ovarian cancer are those of the primary tumor and those of its metastatic spread. Several primary tumor patterns overlap with those of complex benign lesions: a multiloculated cyst with thick walls or septations and some solid components (see Fig. 44–35), a combined cystic and solid mass (Fig. 44–43), and a predominantly solid mass. Calcifications and contrast enhancement may be present in the cyst wall or within solid tumor components. There is an overlap in the CT features of the epithelial subtypes, but there are some more specific findings: serous cancers are the most common and may show heavy psammomatous calcification; ruptured or metastatic mucinous tumors result in a pseudomyxoma appearance; endometrioid cancers may coexist with uterine cancers (Fig. 44–44).

The CT appearance of ovarian metastases may be indistinguishable from that of primary ovarian cancer. Both conditions may produce bilateral masses. In further analysis of the RDOG study, the only factor favoring primary ovarian cancer was multilocularity, as shown by ultrasonography or MRI. This was not a significant feature for CT.[14] The stomach, colon, appendix, and pancreas are within the examination volume and should be inspected as potential primary cancer sites within the abdomen.[27, 107]

Breast cancer and ovarian cancer are now recognized to be linked genetically. In women with a history of a primary tumor whose metastases may exactly mimic primary ovarian cancer (e.g., breast and colon), a definite histologic diagnosis is required because debulking surgery is inappropriate for such metastatic disease and chemotherapeutic regimens differ. CT-guided peritoneal or adnexal biopsy suffices in this situation (see Fig. 44–42).[149]

Primary ovarian cancers are most frequently found in the adnexal region or pouch of Douglas (rectouterine recess), displacing the uterus, bladder, and rectum. The mass usually enlarges into the abdomen to lie above the bladder, displacing pelvic small bowel. Metastatic spread is predominantly via the peritoneal cavity, usually with ascites but also via lymphatics to the pelvic and para-aortic groups, and by hematogenous spread to the liver. Patterns of spread identified within the pelvis *(stage II)* by CT are involvement of small and large bowel, the pelvic sidewall with encasement of the iliac veins leading to thrombosis of the pelvic ureter with resultant hydronephrosis. However, hydronephrosis is more commonly due to simple mass effect on the pelvic ureter.

Metastatic spread to the abdomen *(stage III)* may manifest as peritoneal and mesenteric masses and omental

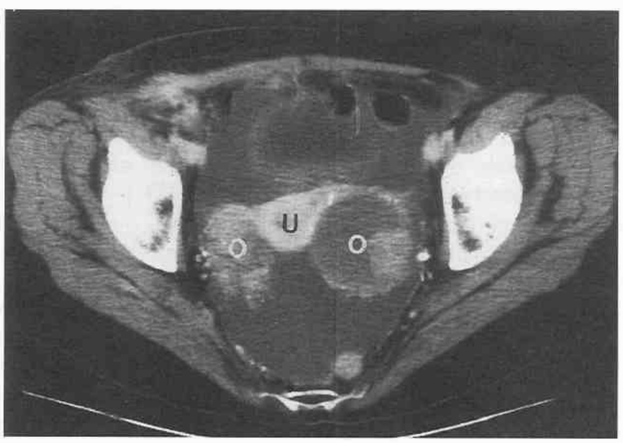

Figure 44–43. Bilateral ovarian cancers. CT scan through the uterus (U) shows solid right and cystic and solid left ovarian cancers (O) surrounded by ascites.

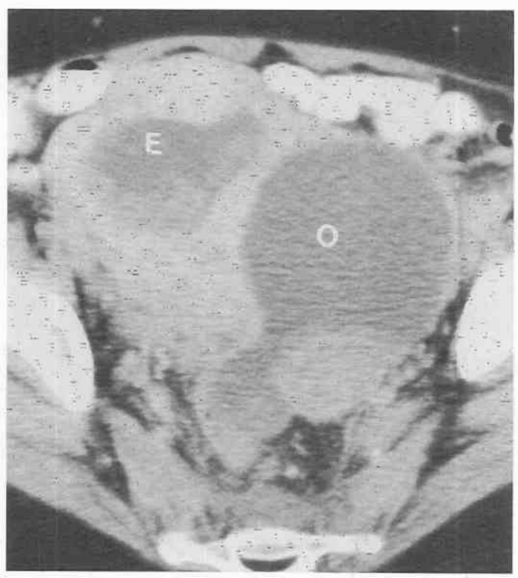

Figure 44–44. Endometrioid cancer. CT scan through the pelvis shows coincident tumors of the endometrium (E) and left ovary (O).

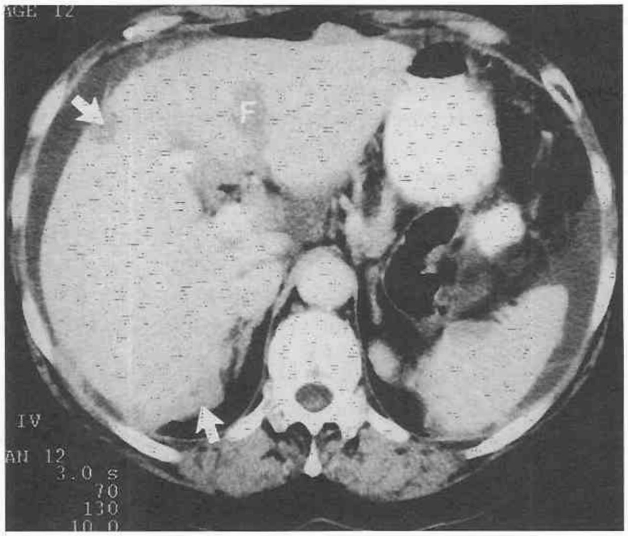

Figure 44–45. Stage IIIC ovarian cancer. CT scan through the liver and spleen shows multiple surface deposits *(arrows)*. A surface tumor within the cleft of the falciform ligament (F) mimics parenchymal metastasis.

cakes. Spread occurs to all peritoneal surfaces, recesses, and reflections and particularly the undersurfaces of the diaphragm. Involvement of the surface of the liver and spleen is classified as stage III (Fig. 44–45). Surface tumor within the cleft of the falciform ligament may mimic parenchymal metastasis (see Fig. 44–45).

Parenchymal deposits within the liver classify the patient as *stage IV*; parenchymal disease within the spleen appears to have a similar prognostic implication.[150]

Detection of peritoneal seedlings, especially en plaque tumor, is easier in the presence of ascites. However, CT can detect the calcified tumor implants containing psammoma bodies from serous cystadenocarcinoma of the ovary even in the absence of ascites.[113] Conversely, densely calcified tumor implants from serous tumors may be mistaken for bowel containing oral contrast agent (Fig. 44–46). This is an important cause of understaging of ovarian cancer. CT can detect 50% of implants that are 5 mm or more in

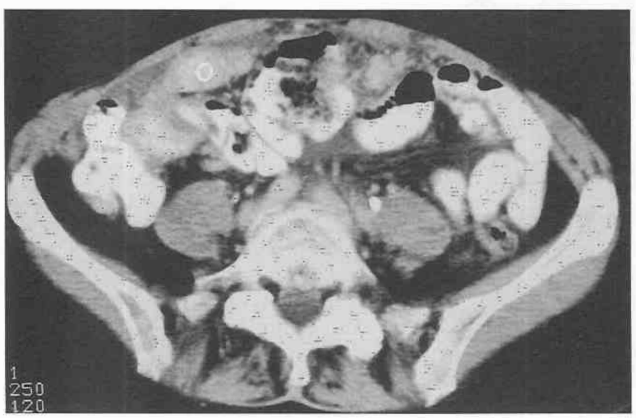

Figure 44–46. Calcified omental cake. CT scan through the upper pelvis shows omental metastasis (O) that mimics partially opacified small bowel.

diameter.[19] Detection of these and smaller peritoneal seedlings remains the province of surgery.

CT is also widely used to document tumor response during chemotherapy, to monitor persistent or residual disease after therapy, and to detect recurrent ovarian cancer.[108, 143] Before chemotherapy is begun, it is customary to obtain a baseline CT study and important to recognize postoperative findings that may lead to diagnostic confusion and, indeed, may mimic residual tumor.[130] There may be marked thickening at the vaginal vault, and fluid collections may be seen here as well as in a variety of other pelvic locations. Hematoma of the round ligament may mimic cystic tumor on the pelvic sidewall. Ovarian vein thrombosis may also occur, with most cases occurring on the right side. Characteristic CT findings are of a tubular retroperitoneal mass along the course of the vein from the pelvis to the infrarenal vena cava.[136]

In patients with recurrent ovarian cancer, CT findings may differ from findings at initial diagnosis. In the postoperative patient, the greater omentum is absent and thus omental cakes are rarely seen. Recurrent tumor may involve other peritoneal recesses and reflections, notably in the supracolic compartment around the spleen and stomach. Unopacified bowel loops may mimic recurrent peritoneal tumor. Meticulous CT technique with thinner sections and optimal bowel contrast opacification increases ability to detect recurrent disease.[131] Adhesions from previous surgery, radiation therapy, or tumor may impair bowel opacification, and it can be useful to compare findings with previous CT studies to identify fixed loops of bowel.

Pelvic recurrence of ovarian cancer may be central, at the vaginal vault, associated with vaginal bleeding and discharge, or may be lateral, involving the pelvic sidewall with venous thrombosis or ureteric obstruction. Ascites may become loculated with displacement of adjacent organs; encysted lesser sac ascites may compress the stomach.[147] Lymphadenopathy may be pelvic or retroperitoneal or may even involve the mediastinum or neck. With serous tumors, this may be heavily calcified and may be mistaken for granulomatous lymphadenopathy.[125] Women with previous stage IV disease may experience relapse with pleural effusion.

Although CT cannot exclude small peritoneal deposits and thus cannot confirm disease remission at the conclusion of chemotherapy, it is rare nowadays for gynecologists to perform second-look laparotomies in order to restage patients. Women believed to be in remission are kept under surveillance with clinical and CA-125 assessment, and CT is reserved to clarify the site and extent of suspected recurrent disease. There is no evidence that routine CT surveillance is of value in follow-up in women in clinical and biochemical remission.

Most cases of malignant ovarian cancer are primary epithelial or metastatic neoplasms. Other malignancies include mixed müllerian tumors (carcinosarcomas with variable solid components), GCTs, sex cord stromal tumors (principally granulosa cell tumors), and neuroendocrine tumors. Although some of these pathologic conditions may be associated with larger solid elements, there are few distinguishing features in the primary lesion, although there are differences in the patterns of metastasis and relapse. Lung and parenchymal liver metastases are seen with some

of the more aggressive lesions, such as carcinosarcoma. Granulosa cell tumors may recur after many years with only localized and easily resectable masses. There is some evidence that CT may help predict long-term outcome with granulosa cell tumor; that is, patients with masses smaller than 9 cm and no CT evidence of lymphatic, peritoneal, or liver metastasis achieved complete remission.[101]

Epithelial ovarian tumors of borderline or low malignant potential represent up to 15% of ovarian neoplasms (see Fig. 44–35). Compared with invasive malignancy, these tumors are associated with a much better prognosis. Most mucinous lesions are stage I at diagnosis, but 45% of serous lesions are stage III, and these are bilateral in one third of cases.[34] There is no role for CT in follow-up of completely resected stage I borderline malignancy. CT is useful for more advanced disease, especially when chemotherapy is given and for providing an objective baseline examination in the assessment of progression. Disseminated mucinous borderline malignancy is a cause of pseudomyxoma peritonei.

The Treated Pelvis

Pelvic cancers are treated with radical intent by surgery and radiation therapy and with palliative intent by these modalities, either in combination or with chemotherapy. Radical surgery alters anatomic relationships within the pelvis. All of these treatment modalities result in early and late side effects. They may alter the patterns of disease spread when compared with a lack of treatment. The challenge is to recognize these treatment effects, and central to this is distinction between post-treatment scar and residual or recurrent cancer. Some of these issues are addressed in the discussions of specific organ, but two situations are commonly encountered in pelvic CT imaging: the *postresection* pelvis and the *postradiation* pelvis.

The Postresection Pelvis

The vagina is rarely the primary organ of CT examination. It is an extraperitoneal structure but may be exposed to intraperitoneal processes after hysterectomy for benign or malignant disease. The vaginal vault is a common site for recurrent tumor within the pelvic "sump." After surgery, the vagina may become fixed to adjacent pelvic structures and may become secondarily involved by inflammatory or malignant conditions with development of enterovaginal or vesicovaginal fistulas. Fistulas are also recognized as late complications of radiation therapy. With a colovaginal or rectovaginal fistula, gas or feces may be present within the vaginal vault (Fig. 44–47). With a vesicovaginal fistula, contrast-opacified urine may be present within the vagina or may be soaked within the vaginal tampon. Delayed imaging with excreted contrast agent within the posterior bladder may be required to confirm the diagnosis (see Fig. 44–47).

Two cancer operations that result in gross distortion of the pelvic visceral anatomy are radical cystectomy and abdominoperineal resection of the rectum. After cystectomy, there is a pelvic void that becomes filled by pelvic small bowel and colon and, in women, by the gynecologic organs. An orthotopic ileal new bladder (conduit) is formed from loops of small bowel connecting the ureters with a urostomy on the lower abdominal wall, usually in the right iliac fossa. In men, the prostate gland and seminal vesicles are usually removed. The uterus, tubes, and ovaries may be retained and can assume unusual forms mimicking residual or recurrent tumor.

CT is useful in assessment of the postcystectomy patient.[37, 93] In the early postoperative period, complications may include hematoma, urinoma, and abscess. Later the concern is for recurrent bladder cancer, and the pelvis is the most common site (see Fig. 44–22).[37] If there are pelvic adhesions, loops of small bowel may be fixed, poorly filled with oral contrast agent, and difficult to distinguish from

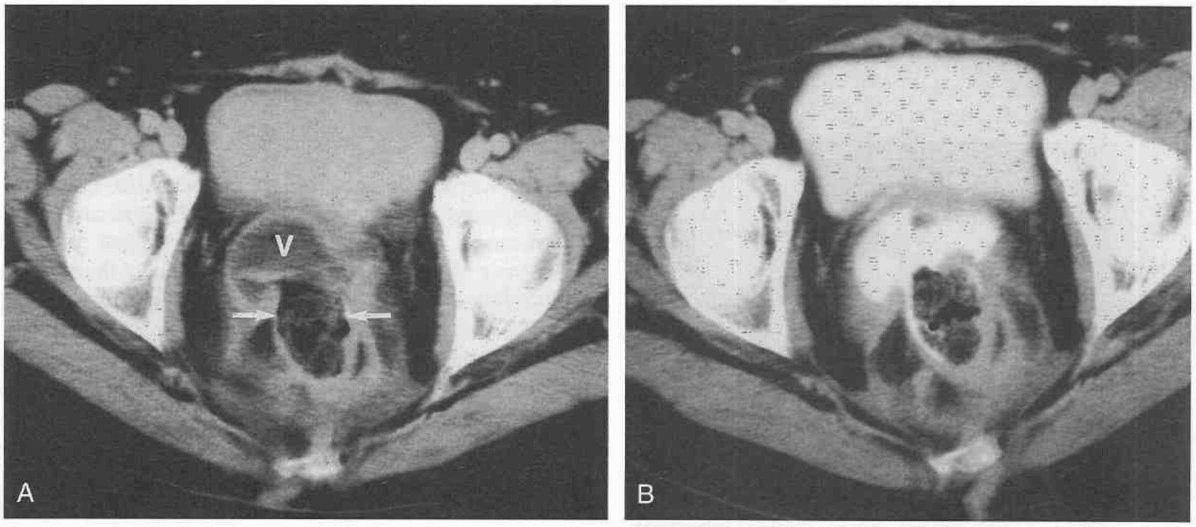

Figure 44–47. Radiation-induced fistulas. CT scan through the pelvis after radiation therapy for cancer of the cervix. *A,* Shown are fecal material *(arrows)* within a fistula between the rectum and the vagina (V) and a sliver of high-density contrast agent *(arrow)*. *B,* Delayed excretory-phase image with contrast-filled urine in the bladder shows filling of the vagina with contrast of similar density to that in the rectum.

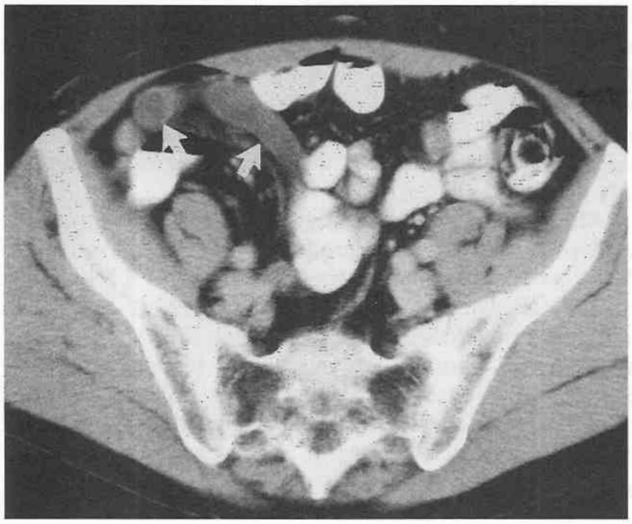

Figure 44–48. Postcystectomy appearances. CT scan through the pelvis in a patient with an ileal conduit mimicking unopacified small bowel *(arrows)*. On adjacent sections, the conduit was able to be followed to the urostomy site (not shown).

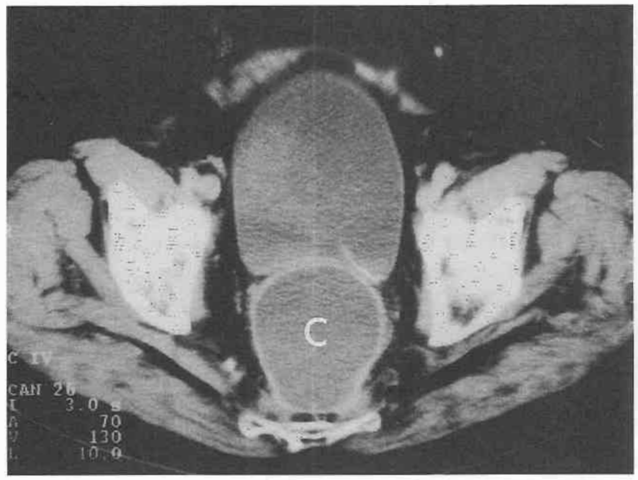

Figure 44–49. Postoperative hematoma. CT scan through the presacral space 3 months after abdominoperineal excision of the rectum. A thin-walled cyst (C) fills the excision site. Transperineal aspiration revealed altered blood.

recurrent disease without delayed or decubitus images. In one series,[61] recognition of the range of normal appearances was important in assessment of the postcystectomy abdomen; the conduit was not identified as such in one third of patients. With spiral CT, the conduit is typically unopacified by urinary contrast material and has the appearance of fluid-filled or collapsed small bowel; however, the conduit can be traced from the skin to the ureters, and identification is improved by good oral contrast opacification of the other normal pelvic small-bowel loops (Fig. 44–48). Alternatively, the conduit may be distinguished from a fluid collection or bowel loop with the use of delayed images to allow filling with the excreted urinary contrast agent.[61]

After abdominoperineal resection of the rectum, the anterior pelvic organs fall back into the void.[92] In men, the prostate gland and seminal vesicles fill the presacral space and the seminal vesicles may become distorted, mimicking residual or recurrent tumor. The trigone of the bladder may also become tethered into the void, resulting in an inverted, pear-shaped bladder. In women, the vagina, uterus, and adnexa fill the void. After surgery, the void may also be filled by hematoma and both sterile or infected fluid collections (Fig. 44–49).

These processes result in varying degrees of scar tissue and persistent mass lesions.[79] It is recommended that a baseline postoperative CT scan of the pelvis be obtained at 3 months against which future investigation of suspected recurrence can be compared.

The Postradiation Pelvis

Radiation therapy plays a major role in the radical and palliative treatment of pelvic cancers, historically for the prostate gland, bladder, and cervix but increasingly for the rectum. In addition to the desired treatment effects on the primary tumor, there are predictable effects on normal tissues. A variety of transient or progressive visceral complications occur and reflect the differing sensitivity of organs to radiation damage.[75] These include radiation enteritis and cystitis, stricture formation in the ureter, and, in severe cases, development of fistulas between pelvic organs, most commonly the bladder and vagina or bladder and bowel (see Fig. 44–47). The bowel is less tolerant than the urinary tract, and small-bowel loops are particularly susceptible to radiation effects if they are fixed within the pelvis by adhesions because the same loops are exposed to successive fractions of radiation. Late effects also include damage to bone with insufficiency fractures and radiation necrosis (Fig. 44–50).

In the first instance, symptomatic patients are usually investigated with cystoscopy, sigmoidoscopy, or contrast studies. Smooth, tapering strictures are typical of radiation damage but also occur with recurrent tumor, and CT has a role in excluding extramural masses and lymphadenopathy. After radiation therapy, the most frequent CT findings are thickening of the presacral space and perirectal tissues (Fig.

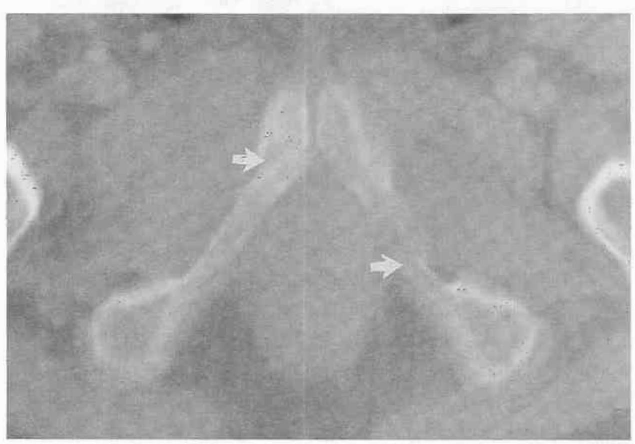

Figure 44–50. Insufficiency fractures. CT scan after radiation therapy for cancer of the cervix shows sclerotic and displaced bilateral pubic fractures *(arrows)*.

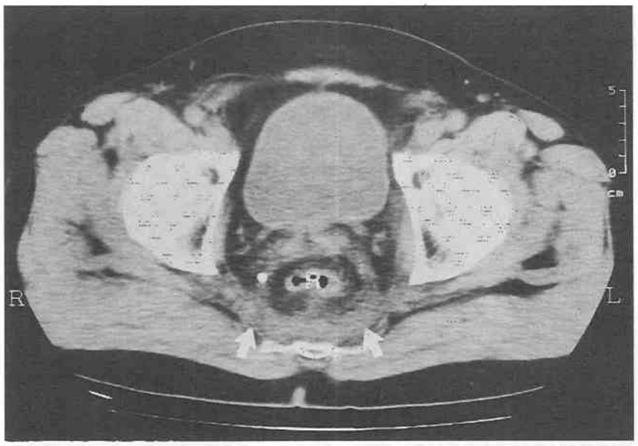

Figure 44–51. Postradiation changes. CT scan through the rectum (R) in a man who had previously undergone radiation therapy for prostate cancer. There is perirectal stranding and thickening of the presacral space *(arrows)*.

44–51). There may be atrophy and calcification of the prostate. Wall thickening, irregularity, and increased mucosal enhancement may be seen with acute injury to the bladder and bowel; more chronically, there is smooth thickening and matting of adjacent loops (Fig. 44–52).

The Post-treatment Mass

The differential diagnosis of a post-treatment mass includes postoperative change, postradiation scarring, and residual or recurrent tumor.[132] In the specific example of assessment following abdominoperineal excision of the rectum, the diagnosis of presacral tumor recurrence may be confirmed when there is bony erosion or destruction of the sacrum, with new or enlarging masses and in the presence of pelvic lymphadenopathy.[109] Masses larger than 4 cm that are globular and asymmetrical are probably due to recurrent tumor unless substantial postoperative bleeding or infection was present (see Fig. 44–49). This assessment emphasizes the importance of a baseline post-treatment study and highlights the limitations of CT, which relies on gross morphology and serial change.[73, 76]

Alternative imaging techniques to CT for assessment of equivocal masses in the previously treated pelvis include MRI, particularly using signal intensity on T2-weighted images and dynamic gadolinium enhancement techniques, and nuclear medicine studies, including PET and immunoscintigraphy. Ultimately, image-guided biopsy may be required; in this context, however, only a positive diagnosis of tumor is of value.[18] Endocavitary ultrasonography facilitates biopsy of masses deep in the central pelvis, but CT-guided biopsy may be required. This is most commonly undertaken from an anterolateral or trans-sciatic approach.

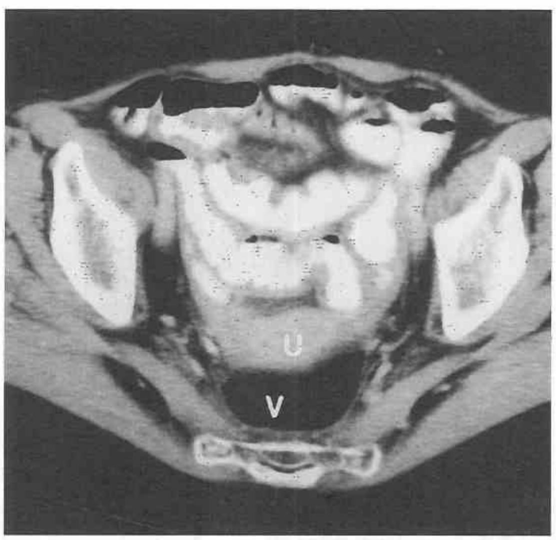

Figure 44–52. Postradiation enteritis. CT scan through the pelvic small bowel, diffusely thickened in a woman who had undergone radiation therapy for cancer of the rectum. The uterus (U) is displaced backward into the surgical void (V).

Fluid Collections

CT is widely used for the diagnosis and management of pelvic intraperitoneal and extraperitoneal abscesses, particularly in the postoperative setting. Although ultrasonography can identify most intraperitoneal fluid collections, diagnosis can be difficult in obese patients and in the postoperative setting with paralytic ileus caused by gas-filled bowel loops and when skin access is limited because of surgical dressings.

CT-guided abscess drainage may use a variety of approaches.[17, 47] The preferred route for pelvic abscess drainage is an *anterolateral* approach through the abdominal wall; with this technique, the radiologist can avoid the pelvic sidewall vessels, bowel, and bladder (Fig. 44–53). When intervening bowel limits this approach, decubitus positioning may displace bowel to allow access. Otherwise, drainage can be achieved with the *trans-sciatic* approach through the greater sciatic foramen (Fig. 44–54).[17] This technique is less popular. About 20% of patients experience pain during the procedure, and others subsequently find it extremely uncomfortable lying on the drainage tube.[17] There is a risk of damage to the sacral plexus and the inferior gluteal vessels. For these reasons, alternative methods should be considered for drainage of deep pelvic fluid collections, particularly those in the pouch of Douglas. Increasingly, such collections are drained via the transrectal route or the transvaginal route using ultrasonographic guidance, although transrectal drainage with CT guidance has also been described.[47, 163]

CT is used primarily for management of abscesses related to the gastrointestinal tract, particularly with acute diverticulitis (see Fig. 44–53) and appendicitis as a temporizing measure, with exacerbations of Crohn's disease (Fig. 44–55) and in the postoperative period. CT may also be used to facilitate drainage of large tubo-ovarian abscesses and, occasionally, in the management of complex pelvic urosepsis, but endocavitary ultrasonography is a preferred modality for drainage. Abscesses related to bowel disease may contain feces or thick pus, and large-bore drains are usually required to achieve effective drainage (see Fig. 44–53). Ultrasonography is of limited value in exclusion

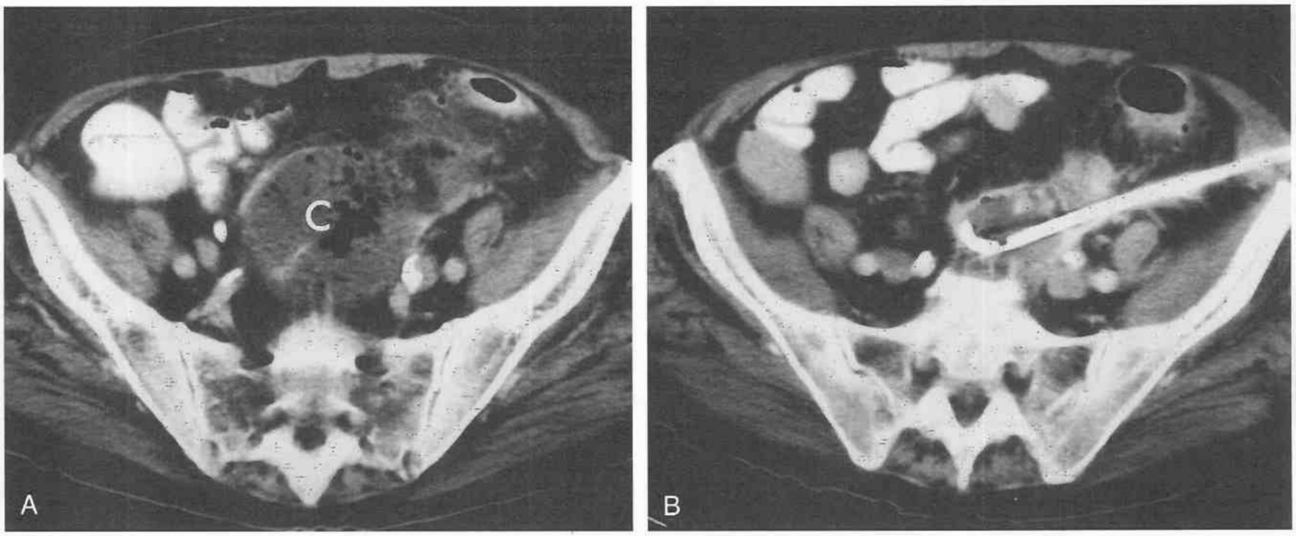

Figure 44–53. Diverticular abscess. CT scan through a pelvic abscess. *A,* A fluid- and gas-filled cavity (C) lies anterior to the sacrum in a patient with known diverticular disease. *B,* After placement of a large-bore drain via a left anterolateral approach.

of infection within the retroperitoneum, such as psoas abscess (see Fig. 44–55), and in assessment of buttock and hip muscle compartments and the deep extraperitoneal pelvic and perineal spaces. CT is valuable for assessment of these spaces, which may be affected by uncommon pelvic infections: gas-forming abscesses in diabetic and immunocompromised patients; collections related to osteomyelitis and orthopedic surgery; and other complex soft tissue infections, including pyomyositis (Fig. 44–56).[57]

After surgical procedures such as pelvic lymphadenectomy for cervical cancer and renal transplantation, a lymphocele may develop (Fig. 44–57). Typically, this type of fluid collection is discovered several weeks after surgery and must be distinguished from an infected collection or resolving hematoma. Lymphoceles contain fat globules and thus may have lower CT attenuation values than other collections, often less than 10 Hounsfield units (HU). A diagnostic needle aspiration may still be necessary; a lymphocele characteristically contains lymphocytes and fat globules. Lymphoceles often recur after aspiration, and thus percutaneous management requires either long-term catheter drainage or the use of sclerosing agents to obliterate the sac and its connections.[162, 175]

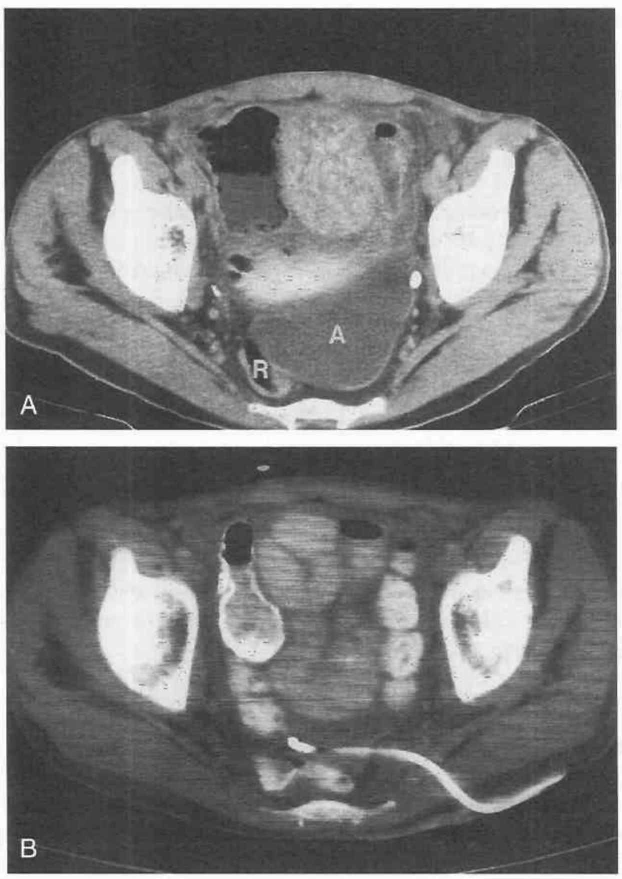

Figure 44–54. Pelvic abscess. *A,* CT scan shows a pelvic fluid collection (A) anterolateral to the rectum (R). *B,* CT scan shows successful catheter drainage through the left sciatic notch.

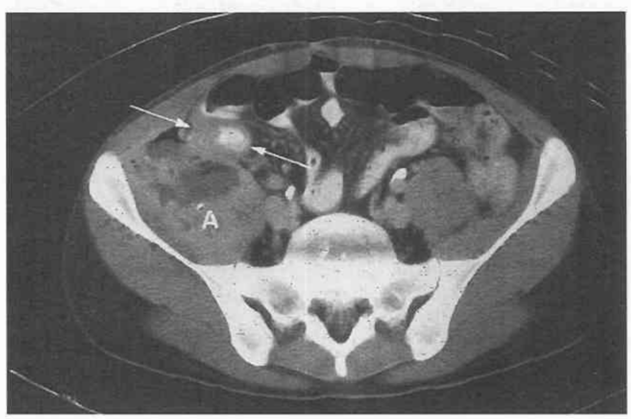

Figure 44–55. Abscess secondary to Crohn's disease. CT scan shows a right psoas muscle abscess (A) containing fluid and gas adjacent to a thick-walled small-bowel loop *(arrows).*

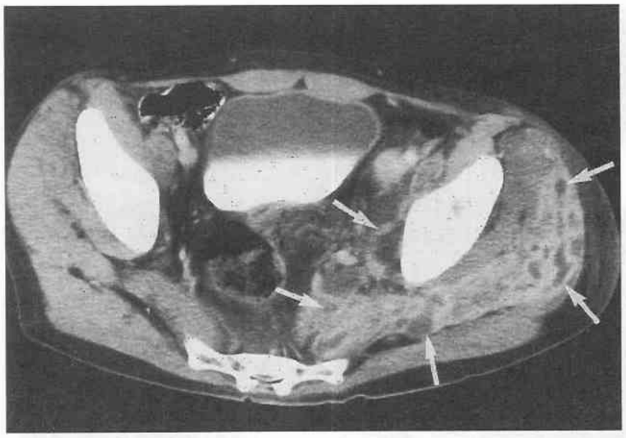

Figure 44–56. Pyomyositis in a diabetic patient caused by *Streptococcus pyogenes* infection. CT scan shows extensive fluid collections surrounded by intravenous contrast enhancement involving the left obturator internus, piriformis, and gluteus medius muscles *(arrows)*.

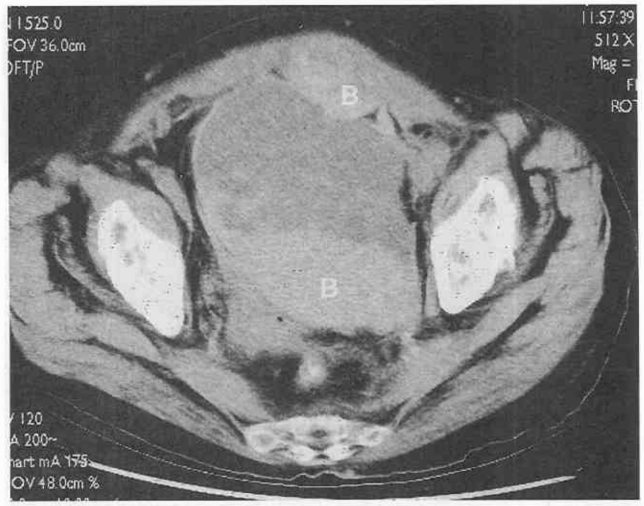

Figure 44–58. Pelvic hematomas. CT scan through the pelvis shows high-density blood (B) within the left rectus abdominis muscle and layering out in the left pelvis in an extraperitoneal location. This elderly patient had taken an overdose of anticoagulant therapy.

Lymphangiomas may have a similar CT appearance to that of lymphoceles but are more often multiloculated or composed of multiple adjacent locules. There may be calcifications. A variety of congenital and developmental anomalies may result in pelvic cystic collections, which may be incidentally discovered during CT examination. These include mesenteric and gastrointestinal tract duplication cysts and developmental cysts of the lower urogenital tract.

CT is a key modality for investigation of suspected pelvic hemorrhage. Trauma to the upper abdominal viscera may result in intraperitoneal hemorrhage, which collects in the pelvic sump. Hemorrhage may result in high-density fluid and in sedimentation with fluid-fluid levels (Fig. 44–58). Extraperitoneal hemorrhage is seen with pelvic bony or soft tissue injury. Other causes of pelvic and retroperitoneal bleeding include anticoagulant therapy (see Fig. 44–58), bleeding diatheses, and interventional procedures via the groin vessels. Hematomas within the psoas and rectus abdominis muscles are easily recognized in the acute phase in the appropriate clinical setting but may be more difficult to distinguish from abscess in the subacute and chronic phases.

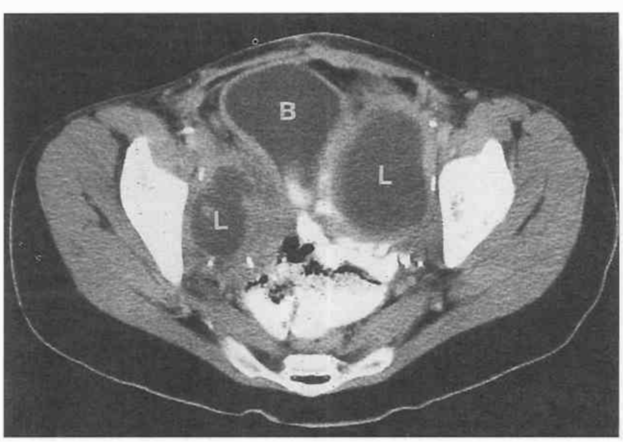

Figure 44–57. Lymphoceles. CT scan through bladder (B) shows bilateral large lymphoceles (L) surrounded by surgical clips from pelvic lymph node dissection.

Musculoskeletal Applications

MRI has replaced CT as the imaging technique of choice in the evaluation of pelvic soft tissue and bony tumors. It has superior soft tissue contrast and allows direct multiplanar imaging. A particular advantage is its ability to define the extent of bone marrow involvement, invasion of adjacent muscle compartments and neurovascular pedicles, and extension to joint surfaces.[30] When MRI is not available or when it is contraindicated, CT remains a useful imaging test for evaluating musculoskeletal tumors, and the volume acquisition of spiral CT allows MPRs, which may be valuable for planning reconstructive surgery.

Most patients with back pain or sciatica now undergo spinal MRI rather than CT. However, CT remains useful in assessing possible pelvic mass lesions compromising the lumbosacral plexus, particularly in patients with a history of pelvic cancer. MRI may be valuable after negative CT findings because it can detect a greater percentage of mass lesions involving the lumbosacral plexus.[8] Improved soft tissue contrast, particularly with gadolinium enhancement, and direct coronal imaging along the path of nerve roots are particular advantages of MRI.

Pelvic Fractures

The key musculoskeletal application of CT within the pelvis is the assessment of complex bony injury. Indications for CT of the bony pelvis include (1) all pelvic ring disruptions with suspected or potential instability, (2) patients in whom stability cannot be properly assessed, and (3) inconclusive plain radiographs. CT is particularly

valuable for assessment of sacral and sacroiliac joint injury, acetabular fracture, and hip dislocation.

Familiarity with the clinically important fracture classifications is important to achieve optimal planning and interpretation of CT findings and in dialogue with clinical colleagues. The most widely used classification of major pelvic fractures, described by Young and Burgess, relates fracture appearances to the force of injury.[185] Injury to the pelvis may result from (1) lateral compression invariably with fracture of the pubic rami and usually with sacral injury, (2) anteroposterior compression with opening of the anterior pelvis, (3) vertical shear with vertically oriented anterior and posterior fractures typically resulting from a precipitous fall, or (4) from combinations of these forces. Letournel and Judet classified acetabular fractures on the basis of plain radiographs.[94] CT classification is divided into three types[70]:

1. *Column* fractures split the acetabulum in a coronal plane into front and back halves.
2. *Transverse* fractures split the acetabulum in a sagittal plane into top (lateral) and bottom (medial) halves.
3. *Wall* fractures do not disrupt the load-bearing surface but may result in hip joint instability.

CT scans are superior to plain radiographs of the pelvis in the detection and classification of acetabular and sacral fractures.[59, 100, 104, 116] In comparison with CT, radiography cannot reveal 57% of acetabular fractures, 34% of vertical shear injuries, and 29% of sacroiliac joint injuries. CT provides an axial display of both the anterior and the posterior columns of the hip and the articular surface of the acetabulum. CT is particularly valuable in showing small intra-articular fragments and in revealing fractures of the posterior acetabulum (Fig. 44–59). CT detects such fragments missed by radiography in up to 40% of cases.

Developments in spiral CT have further enhanced the surface of volumetric rendering techniques described for 3D imaging of acetabular and other pelvic fractures and are now available as an on-line facility.[16, 41] Such images aid in planning the complex surgery for acetabular reconstruction by mapping fracture fragment position and displacement and by assessing the integrity of the acetabular dome and quadrilateral surface.[59, 100, 104] Sagittal and coronal reconstructions demonstrate the superior hip joint and acetabular dome with accurate definition of the acetabular surface.[104]

There are potential pitfalls with surface-shaded reconstructions, particularly the inability to show small intra-articular fragments and undisplaced fractures, although these images dramatically illustrate overall fracture orientation and are appreciated by clinicians (Fig. 44–60). It is possible to electronically disarticulate the femoral head to allow inspection of the acetabulum. For optimal imaging of acetabular fractures, the use of overlapping slices using collimation of no more than 3 mm is advised. The imaging volume should extend up to the limit of any iliac fracture line and down into the ischium to show the entire obturator ring.

Sacral injuries occur in 4% to 74% of patients with pelvic fractures[116] and are associated with neurologic and vascular injury and pelvic instability. CT is better than plain radiography in detecting sacral fractures and in demonstrating fracture pattern and extent.[116] CT is useful in evaluating sacral injuries, including sacroiliac diastasis, fractures abutting the sacroiliac joint, vertical shear fractures, and comminuted fractures. Pelvic fractures associated with bladder injury are those of the pubis, sacrum, and iliac bone, including diastasis of the pubic symphysis and sacroiliac joint. Isolated acetabular injuries are rarely associated with bladder injury.[118]

Insufficiency (stress) fractures may affect the sacrum and pubis after radiation therapy (see Fig. 44–50) or may result from osteoporosis. Radiation-related fractures were seen in 5 (2%) of 183 women who underwent radical treatment for cervical cancer, with identified risk factors being prior connective tissue disorder, steroid use, and older age.[10] Typically, these are vertical fractures of the sacral alae, parallel to the sacroiliac joints; however, they may be mistaken for metastatic disease. CT is an accurate means of displaying the fracture and excluding a destructive neoplastic process.[29]

Figure 44–59. Pelvic fracture. CT scan shows a vertical fracture through the right posterior column of the acetabulum *(arrow)* and a displaced fracture of the anterior column *(arrowhead)*. Only the anterior fracture was clearly shown by conventional radiography.

CT Pelvimetry

CT pelvimetry is performed when a vaginal delivery is contemplated with a breech presentation or if reduced pelvic dimensions are suspected, usually when difficulties have been encountered in a previous pregnancy. This technique is gradually replacing conventional radiographic pelvimetry because of the reduced radiation dose to the fetus.[6, 39] A survey of departments in the United Kingdom showed a trend away from conventional radiography to CT but with emergence of low-dose digital fluoroscopy and MR pelvimetry as alternative techniques.[157]

A variety of CT techniques have been described. The most extensive involve three views[39]:

1. An anteroposterior scanogram to measure the transverse pelvic inlet diameter.
2. A lateral scanogram to determine the anteroposterior pelvic inlet diameter between pubis and sacrococcyx.
3. A single axial CT scan at the level of the foveae of the

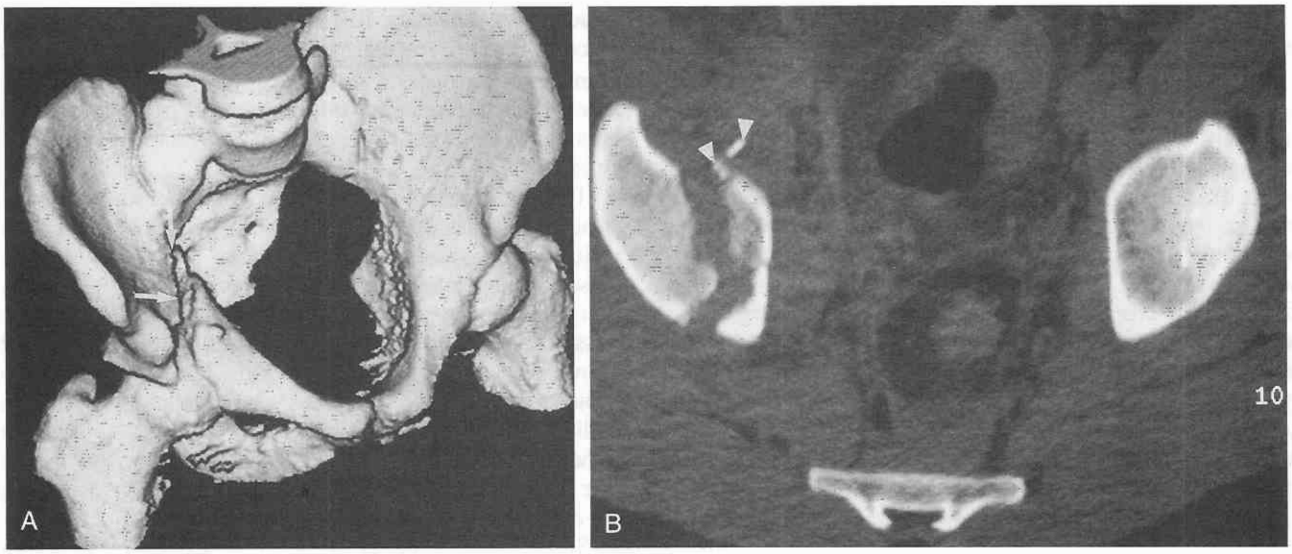

Figure 44–60. Acetabular fracture. Comminuted vertical fracture through the right acetabular roof. *A,* Surface-shaded 3D CT scan viewed obliquely from above shows the fracture line *(arrows)*. *B,* Axial section from the same examination volume shows fine detail of small fracture fragments *(arrowheads)* not appreciated on the 3D CT scan.

femoral heads to measure the distance between the ischial spines.

Increasingly, departments are using only a single view—the lateral scanogram—for assessment that achieves a 75% reduction in dose compared with conventional radiography.[157] There is a distinction to be made between pelvimetry in pregnant women, when a single view may be obtained, and in nonpregnant women, when three views may be obtained. The dose from three views increases fivefold over the single-view technique.[6]

There are a number of technical factors to consider, and various ploys are suggested to improve the accuracy of measurements.[144, 177] It is important to position the pelvis near the center of the CT gantry for accurate CT measurements.[39, 177] The ischial spines may lie up to 1 cm below the level of the foveae, leading to overestimation of the interspinous distance by about 1 cm.[3] The distance between the spines is the narrowest point in the midpelvis and the site of most cases of obstructed labor.[3] The lateral scanogram may better localize the level of the ischial spines for measurement with the axial CT section.

Lower Urinary Tract Trauma

Various bladder injuries may occur in patients with pelvic trauma, the most serious being intraperitoneal rupture, for which operative repair is required. Extraperitoneal rupture is four times more common and is usually managed nonoperatively with urinary catheter drainage. Distinguishing these two entities thus has major management significance. A few patients have combined space rupture. Bladder rupture occurs in about 10% of patients with pelvic fractures. Extraperitoneal rupture may be caused by bony fragments that directly contuse or rupture the bladder, with injury typically anterolaterally at the base. Intraperitoneal rupture usually results from a direct blow to the distended bladder, typically causing injury to the dome.

With each injury, there are predictable patterns of extravasation of contrast medium and urine into pelvic spaces. Extraperitoneal rupture involves the perivesical fat and obturator fossa (Fig. 44–61) but may extend to the anterior thigh and scrotum. Extravasation of opacified urine from the dome into the peritoneal spaces characterizes intraperitoneal rupture (Fig. 44–62).

Historically, conventional cystography has been the "gold standard" for evaluation of bladder trauma. Numerous studies have shown that CT cystography is as sensitive as cystography in detecting bladder injury.[77, 96, 127] It is logical to use CT rather than conventional cystography in patients who are to undergo CT evaluation for other aspects of trauma. In such patients, CT affords a "one-stop" facil-

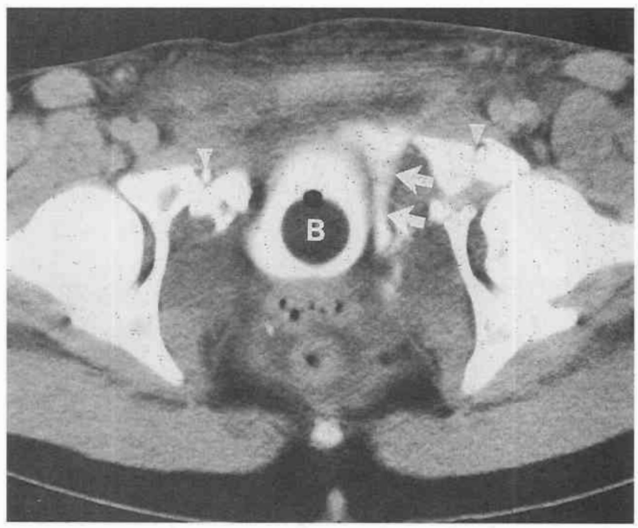

Figure 44–61. Extraperitoneal bladder rupture. CT cystogram via bladder catheter (B) shows extravasation of contrast agent into the left perivesical space *(arrows)*. Note the bilateral pubic fractures *(arrowheads)*.

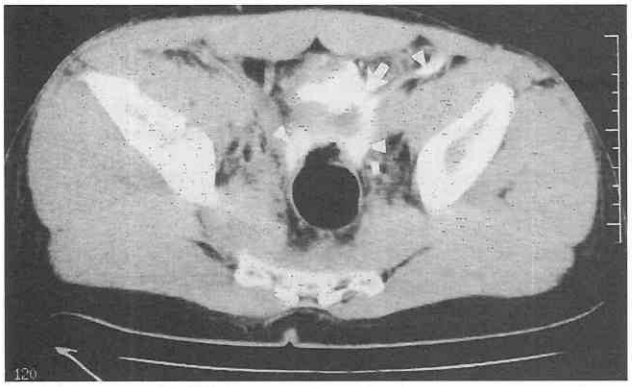

Figure 44–62. Intraperitoneal bladder rupture. CT cystogram shows left-sided bladder wall rupture *(arrow)* and free intraperitoneal contrast agent *(arrowheads)*. Note the presence of a right iliac blade fracture.

ity for differentiation of extraperitoneal from intraperitoneal fluid, identification and classification of associated pelvic fractures, and detection of other more life-threatening visceral injuries. The requirement for additional CT cystography is determined by a number of clinicoradiologic factors. In an unselected group of patients who underwent CT cystography for suspected bladder trauma, predictive features were pelvic fluid revealed on standard contrast-enhanced CT, gross hematuria, and pelvic fracture.[118]

With CT cystography, adequate bladder distention is required in order to detect contrast extravasation, and this is best achieved by retrograde instillation of 350 to 400 mL of 2% to 4% dilute contrast medium through an indwelling Foley catheter on the CT table after the standard CT study.[96] Alternatively, one may perform CT cystography by obtaining delayed CT images at 15 to 20 minutes through the bladder, relying on filling of the bladder with excreted urinary contrast material.[77] This method necessitates that the urinary catheter be clamped to achieve adequate bladder distention. There is greater variation in bladder filling and contrast opacification with this technique; consequently, the retrograde technique is preferred in most major trauma centers.

Vascular Applications

Internal Iliac Artery Aneurysm

Most internal iliac artery aneurysms occur in association with aortoiliac aneurysmal disease as a result of atherosclerosis. Isolated internal iliac artery aneurysms are rare and may present with a variety of clinical pictures as a result of their location and surrounding anatomic structures. They are potentially lethal lesions because their natural course is characterized by progressive expansion with relative lack of symptoms. Presentation may be misleading because of pressure effects on or erosion into adjacent structures, including the lower urinary tract, colon, pelvic vessels, and nerves or may be acute with rupture.[35, 99] CT can elegantly demonstrate the aneurysm and its local effects and complications (Fig. 44–63).[7, 105, 134] Some claim that it is more helpful than angiography in the evaluation of pelvic aneurysmal disease.[119]

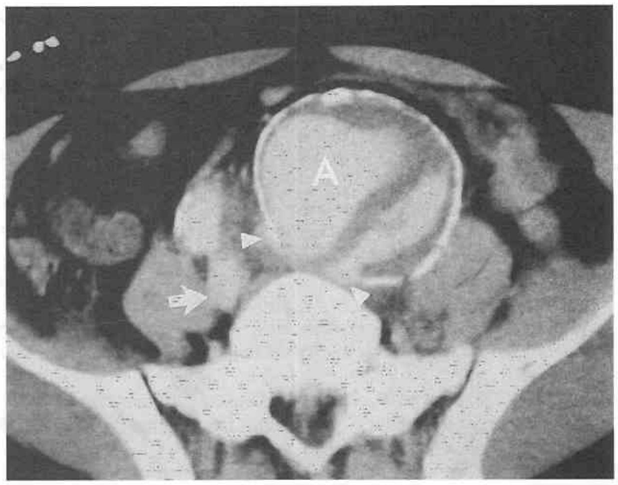

Figure 44–63. Arteriovenous fistula from ruptured iliac aneurysm. CT shows a large left iliac artery aneurysm (A) with complex internal channels. There was rupture *(arrowheads)* into the iliac vein with early venous contrast opacification *(arrow)* on this arterial-phase study.

Lower Limb Swelling

Leg edema may be unilateral or bilateral, acute or chronic. It can be due to systemic illness (e.g., heart failure or hypoproteinemia), to a compressive process within the pelvis or retroperitoneum, or to a primary lymphatic abnormality. CT is particularly useful in demonstrating or excluding a pelvic sidewall mass as a cause of unilateral limb swelling once deep venous thrombosis has been excluded. It may reveal a retroperitoneal lesion compressing the inferior vena cava when there is bilateral edema. With long-standing edema, CT may help in differentiating primary lymphedema from chronic venous obstruction by demonstrating the honeycomb pattern of the subcutaneous compartment of the lower limbs in the former condition.[56, 164]

Pelvic Lipomatosis

Pelvic lipomatosis is characterized by an abnormal deposition of adipose tissue within the pelvis surrounding the bladder, internal genital organs, and rectosigmoid colon. It is generally a benign condition with vague, nonspecific symptoms, but iliac vein obstruction and lower limb edema have been reported as a consequence.[161, 183] Elevation and compression of the bladder, giving a pear-shaped deformity, and widening of the presacral space with straightening and elongation of the rectosigmoid colon are characteristic radiologic findings. The use of CT nicely demonstrates the presence of excessive pelvic fat, excludes a mass lesion as the cause of the deformity, and thus precludes the need for surgery.[51, 86, 155]

References

1. Amendola MA, Walsh JW, Amendola BE, et al: Computed tomography in the evaluation of carcinoma of the ovary. J Comput Assist Tomog 5:179–186, 1981.
2. Amendola MA, Glazer GM, Grossman HB, et al: Staging of bladder

carcinoma: MRI-CT-surgical correlation. Am J Roentgenol 146: 1179–1183, 1986.

3. Aronson D, Kier R: CT pelvimetry: The foveae are not an accurate landmark for the level of the ischial spines. AJR Am J Roentgenol 156:527–530, 1991.
4. Auh YH, Rubenstein WA, Markisv JA, et al: Intraperitoneal paravesical spaces: CT delineation with US correlation. Radiology 159: 311–317, 1986.
5. Auh YH, Rubenstein WA, Schneider M, et al: Extraperitoneal paravesical spaces: CT delineation with US correlation. Radiology 159: 319–328, 1986.
6. Badr I, Thomas SM, Cotterill AD: X-ray pelvimetry: Which is the best technique? Clin Radiol 52:136–141, 1997.
7. Baron RL, Banner MP, Pollack HM: Isolated internal iliac artery aneurysms presenting as giant pelvic masses. Am J Roentgenol 140: 784–786, 1983.
8. Beatrous TE, Choyke PL, Frank JA: Diagnostic evaluation of cancer patients with pelvic pain: Comparison of scintigraphy, CT, and MR imaging. AJR Am J Roentgenol 155:85–88, 1990.
9. Bezzi M, Kressel HY, Allen KS, et al: Prostatic carcinoma: Staging with MR imaging at 1.5 T. Radiology 169:339–346, 1988.
10. Bliss P, Parsons CA, Blake PR: Incidence and possible aetiological factors in the development of pelvic insufficiency fractures following radical radiotherapy. Br J Radiol 69:548–554, 1996.
11. Blunt DM, Sansom HE, King DM: Imaging of small cell carcinoma of the male urogenital tract. Clin Radiol 51:724–727, 1996.
12. Boronow RC, Morrow CP, Creasman WT, et al: Surgical staging in endometrial cancer: Clinical-pathologic findings of a prospective study. Obstet Gynecol 63:825–832, 1984.
13. Brick SH, Friedman AC, Pollack HM, et al: Urachal carcinoma: CT findings. Radiology 169:377–381, 1988.
14. Brown DL, Zou KH, Tempany CM, et al: Primary versus secondary ovarian malignancy: Imaging findings of adnexal masses in the Radiology Diagnostic Oncology Group Study. Radiology 219:213–218, 2001.
15. Bryan PJ, Butler HE, LiPuma JP, et al: CT and MR imaging in staging bladder neoplasms. J Comput Assist Tomogr 11:96–101, 1987.
16. Burk DL Jr, Mears DC, Kennedy WH, et al: Three-dimensional computed tomography of acetabular fractures. Radiology 155:183–186, 1985.
17. Butch RJ, Mueller PR, Ferrucci JT Jr, et al: Drainage of pelvic abscesses through the greater sciatic foramen. Radiology 158:487–491, 1986.
18. Butch RJ, Wittenberg J, Mueller PR, et al: Presacral masses after abdominoperineal resection for colorectal carcinoma: The need for needle biopsy. Am J Roentgenol 144:309–312, 1985.
19. Buy JN, Moss AA, Ghossain MA, et al: Peritoneal implants from ovarian tumors: CT findings. Radiology 169:691–694, 1988.
20. Buy JN, Ghossain MA, Moss AA, et al: Cystic teratoma of the ovary: CT detection. Radiology 171:697–701, 1989.
21. Buy JN, Ghossain MA, Sciot C, et al: Epithelial tumors of the ovary: CT findings and correlation with US. Radiology 178:811–818, 1991.
22. Buy JN, Ghossain MA, Mark AS, et al: Focal hyperdense areas in endometriomas: A characteristic finding on CT. AJR Am J Roentgenol 159:769–771, 1992.
23. Callen PW: Ultrasound evaluation of gestational trophoblastic neoplasia. In Callen PW (ed): Ultrasonography in Obstetrics and Gynecology, 3rd ed. Philadelphia, WB Saunders, 1994, pp 615–623.
24. Casillas J, Joseph RC, Guerra JJ: CT appearance of uterine leiomyomas. Radiographics 10:999–1007, 1990.
25. Casola G, vanSonnenberg E, D'Agostino HB, et al: Percutaneous drainage of tubo-ovarian abscesses. Radiology 182:399–402, 1992.
26. Castellino RA: Lymph nodes of the posterior iliac crest: CT and lymphographic observations. Radiology 175:687–689, 1990.
27. Cho KC, Gold MB: Computed tomography of Krukenberg tumors. Am J Roentgenol 145:285–288, 1985.
28. Connor JP, Andrews JI, Anderson B, et al: Computed tomography in endometrial carcinoma. Obstet Gynecol 95:692–696, 2000.
29. Cooper KL, Beabout JW, Swee RG: Insufficiency fractures of the sacrum. Radiology 156:15–20, 1985.
30. Dalinka MK, Zlatkin MB, Chao P, et al: The use of magnetic resonance imaging in the evaluation of bone and soft-tissue tumors. Radiol Clin North Am 28:461–470, 1990.
31. Davis WK, McCarthy S, Moss AA, et al: Computed tomography of gestational trophoblastic disease. J Comput Assist Tomogr 8: 1136–1139, 1984.
32. Dawson P, Lees WR: Multislice technology in computed tomography. Clin Radiol 56:302–309, 2001.
33. Dixon AK, Ellis M, Sikora K: Computed tomography of testicular tumors: Distribution of abdominal lymphadenopathy. Clin Radiol 37:519–523, 1986.
34. Dobson M, Carrington BM, Radford JA, et al: The role of computed tomography in the management of ovarian tumors of borderline malignancy. Clin Radiol 52:280–283, 1997.
35. Dudeney S, O'Farrell D, Bouchier-Hayes D, et al: Extraspinal causes of sciatica: A case report. Spine 23:494–496, 1998.
36. Ellis JH, Francis IR, Rhodes M, et al: CT findings in tubo-ovarian abscess. J Comput Assist Tomogr 15:589–592, 1991.
37. Ellis JH, McCullough NB, Francis IR, et al: Transitional cell carcinoma of the bladder: Patterns of recurrence after cystectomy as determined by CT. AJR Am J Roentgenol 157:999–1002, 1991.
38. Emory TH, Reinke DB, Hill Al, et al: Use of CT to reduce understaging in prostatic cancer: Comparison with conventional staging techniques. Am J Roentgenol 141:351–354, 1983.
39. Federle MP, Cohen HA, Rosenwein MF, et al: Pelvimetry by digital radiography: A low-dose examination. Radiology 143:733–735, 1982.
40. Fishman EK, Scatarige JC, Saksouk FA, et al: Computed tomography of endometriosis. J Comput Assist Tomogr 7:257–264, 1983.
41. Fishman EK, Drebin B, Magid D, et al: Volumetric rendering techniques: Applications for three-dimensional imaging of the hip. Radiology 163:737–738, 1987.
42. Flanigan RC, Mohler JL, King CT, et al: Preoperative lymph node evaluation in prostatic cancer patients who are surgical candidates: The role of lymphangiography and computerized tomography scanning with directed fine-needle aspiration. J Urol 134:84–87, 1985.
43. Forstner R, Hricak H, Occhipinti KA, et al: Ovarian cancer: Staging with CT and MR imaging. Radiology 197:619–627, 1995.
44. Friedman AC, Pyatt RS, Hartman DS, et al: CT of benign cystic teratomas. Am J Roentgenol 138:659–665, 1982.
45. Fritzsche PJ, Hricak H, Kogan BA, et al: Undescended testis: Value of MR imaging. Radiology 164:169–173, 1987.
46. Fuchs TO, Kachelriess M, Kalender WA: System performance of multislice spiral computed tomography. IEEE Eng Med Biol Mag 19:63–70, 2000.
47. Fukuda TI, Keuchi M, Hashimoto H, et al: Computed tomography of ovarian masses. J Comput Assist Tomogr 10:990–996, 1986.
48. Fukuda H, Nakagawa T, Shibuya H, et al: Metastases to pelvic lymph nodes from carcinoma in the pelvic cavity: Diagnosis using thin-section CT. Clin Radiol 54:237–242, 1999.
49. Gazelle GS, Haaga JR, Stellato TA, et al: Pelvic abscesses: CT-guided transrectal drainage. Radiology 181:49–51, 1991.
50. Gebarski KS, Gebarski SS, Glazer GM, et al: The lumbosacral plexus: Anatomic-radiologic-pathologic correlation using CT. Radiographics 6:401–425, 1986.
51. Gerson ES, Gerzof SG, Robbins AH: CT confirmation of pelvic lipomatosis: Two cases. Am J Roentgenol 129:338–340, 1977.
52. Ghossain MA, Buy JN, Ligneres C, et al: Epithelial tumors of the ovary: Comparison of MR and CT findings. Radiology 181: 863–870, 1991.
53. Goldstein SR, Subramanyam B, Snyder JR, et al: The postmenopausal cystic adnexal mass: The potential role of ultrasound in conservative management. Obstet Gynecol 73:8–10, 1989.
54. Green CL, Angtuaco TL, Shah HR, et al: Gestational trophoblastic disease: A spectrum of radiologic diagnosis. Radiographics 16: 1371–1384, 1996.
55. Gross BH, Moss AA, Mihara K, et al: Computed tomography of gynecologic diseases. Am J Roentgenol 141:765–773, 1983.
56. Hadjis NS, Carr DH, Banks L, et al: The role of CT in the diagnosis of primary lymphoedema of the lower limb. Am J Roentgenol 144: 361–364, 1985.
57. Hall RL, Callaghan JJ, Moloney E, et al: Pyomyositis in a temperature climate. J Bone Joint Surg Am 72:1240–1244, 1990.
58. Harisinghani MG, et al: MR lymphangiography using ultrasmall superparamagnetic iron oxide in patients with primary abdominal and pelvic malignancies: Radiographic-pathologic correlation. AJR Am J Roentgenol 172:1347–1351, 1999.
59. Harley JD, Mack LA, Winquist RA: CT of acetabular fractures: Comparison with conventional radiography. Am J Roentgenol 138: 413–417, 1982.

60. Hardesty LA, Sumkin JH, Hakim C, et al: The ability of helical CT to preoperatively stage endometrial carcinoma. AJR Am J Roentgenol 176:603–606, 2001.
61. Heaney MD, Francis IR, Cohan RH, et al: Orthotopic neobladder reconstruction: Findings on excretory urography and CT. AJR Am J Roentgenol 172:1213–1220, 1999.
62. Hendry WF, A'Hern A, Hetherington JW, et al. Paraortic lymphadenectomy after chemotherapy for metastatic non-seminomatous germ cell tumors: Prognostic value and therapeutic benefit. Br J Urol 71: 208–213, 1993.
63. Hoffer FA, Kozakewich H, Colodny A, et al: Peritoneal inclusion cysts: Ovarian fluid in peritoneal adhesions. Radiology 169:189–191, 1988.
64. Hricak H, Quivey JM, Campos Z, et al: Carcinoma of the cervix: Predictive value of clinical and MR imaging assessment of prognostic factors. Int J Radiat Oncol Biol Phys 27:791–801, 1993.
65. Hricak H, Powell CB, Yu KK, et al: Invasive cervical carcinoma: Role of MR imaging in pre-treatment work-up: Cost minimization and diagnostic efficacy analysis. Radiology 198:403–409, 1996.
66. Hricak H, Dooms GC, Jeffrey RB, et al: Prostatic carcinoma: Staging by clinical assessment, CT and MR imaging. Radiology 162: 331–336, 1987.
67. Hricak H, Yu KK: Radiology of invasive cervical cancer. AJR Am J Roentgenol 167:1101–1108, 1996.
68. Hu H: Multi-slice helical CT: Scan and reconstruction. Med Phys 26:5–18, 1999.
69. Hu H, He HD, Foley WD, et al: Four multidetector-row helical CT: Image quality and volume coverage speed. Radiology 215: 55–62, 2000.
70. Hunter JC, Brandser EA, Tran KA: Pelvic and acetabular trauma. Radiol Clin North Am 35:559–590, 1997.
71. Husband JE, Robinson L, Thomas G: Contrast-enhancing lymph nodes in bladder cancer. Clin Radiol 45:395–398, 1992.
72. Husband JE, Olliff JF, Williams MP, et al: Bladder cancer: Staging with CT and MR imaging. Radiology 173:435–440, 1989.
73. Husband JE, Hodson NJ, Parsons CA: The use of computed tomography in recurrent rectal tumors. Radiology 134:677–682, 1980.
74. Jeffrey RB, Palubinskas AJ, Federle MP: CT evaluation of invasive lesions of the bladder. J Comput Assist Tomogr 5:22–26, 1981.
75. Johnson RJ, Carrington BM: Pelvic radiation disease. Clin Radiol 45:4–12, 1992.
76. Johnson RJ, Blackledge G, Eddleston B, et al: Abdomino-pelvic computed tomography in the management of ovarian carcinoma. Radiology 146:447–452, 1983.
77. Kane NM, Francis IR, Ellis JH: The value of CT in the detection of bladder and posterior urethral injuries. AJR Am J Roentgenol 153:1243–1246, 1989.
78. Karasick S, Lev-Toaff AS, Toaff ME: Imaging of uterine leiomyomas. AJR Am J Roentgenol 158:799–805, 1992.
79. Kelvin FM, Korobkin M, Heaston DK, et al: The pelvis after surgery for rectal carcinoma: Serial CT observations with emphasis on nonneoplastic features. Am J Roentgenol 141:959–964, 1983.
80. Kilcheski TS, Arger PH, Mulhern CB Jr, et al: Role of computed tomography in the presurgical evaluation of carcinoma of the cervix. J Comput Assist Tomogr 5:378–383, 1981.
81. Kim B, Semelka RC, Ascher SM, et al: Bladder tumor staging: Comparison of contrast-enhanced CT, T1- and T2-weighted MR imaging, dynamic gadolinium-enhanced imaging, and late gadolinium-enhanced imaging. Radiology 193:239–245, 1994.
82. Kim SH, Choi BI, Han JK, et al: Preoperative staging of uterine cervical carcinoma: Comparison of CT and MRI. J Comput Assist Tomogr 17:633–640, 1993.
83. Kinkel K, Kaji Y, Yu KK, et al: Radiologic staging in patients with endometrial cancer: A meta-analysis. Radiology 212:711–718, 1999.
84. Komaki R, Cox JD, Hansen RM, et al: Malignant lymphoma of the uterine cervix. Cancer 54:1699–1704, 1984.
85. Koss JC, Arger PH, Coleman BG, et al: CT staging of bladder carcinoma. Am J Roentgenol 137:359–362, 1981.
86. Krestin GP, Beyer D, Steinbrich W, et al: Computed tomography in the differential diagnosis of the enlarged retrorectal space. Gastrointest Radiol 11:364–369, 1986.
87. Kuczyk M, Machtens S, Stief C, et al: Management of the post-chemotherapy residual mass in patients with advanced stage non-seminomatous germ cell tumours (NSGCT). Int J Cancer 83:852–855, 1999.
88. Kurtz AB, Tsimikas JV, Tempany CMC, et al: Diagnosis and staging of ovarian cancer: Comparative values of Doppler and conventional US, CT, and MR imaging correlated with surgery and histopathologic analysis: Report of the Radiology Diagnostic Oncology Group. Radiology 212:19–27, 1999.
89. Lee JKT, Stanley RG, Sagel SS, et al: Accuracy of CT in detecting intraabdominal and pelvic lymph node metastases from pelvic cancers. Am J Roentgenol 131:675–679, 1978.
90. Lee JKT, McClennan BL, Stanley RJ, et al: Utility of computed tomography in the localization of the undescended testis. Radiology 135:121–125, 1980.
91. Lee JB, Kim KS, Choi YH, et al: Keratin material in squamous cell carcinoma of the urinary bladder: A rare cause of high CT density. AJR Am J Roentgenol 170:187–188, 1998.
92. Lee JKT, Stanley RJ, Sagel SS, et al: CT appearances of the pelvis after abdomino-perineal resection for rectal carcinoma. Radiology 141:737–741, 1981.
93. Lee JKT, McClennan BL, Stanley RJ, et al: Use of CT in evaluation of postcystectomy patients. Am J Roentgenol 136:483–487, 1981.
94. Letournel E, Judet R: Fractures of the Acetabulum, 2nd ed. New York, Springer-Verlag, 1993.
95. Levine MS, Arger PH, Coleman BG, et al: Detecting lymphatic metastases from prostatic carcinoma: Superiority of CT. Am J Roentgenol 137:207–211, 1981.
96. Lis LE, Cohen AJ: CT cystography in the evaluation of bladder trauma. J Comput Assist Tomogr 14:386–389, 1990.
97. Long MA, Husband JES: Features of unusual metastases from prostate cancer. Br J Radiol 72:933–941, 1999.
98. Lorigan JG, Eftekhari F, David CL, et al: The growing teratoma syndrome: An unusual manifestation of treated, nonseminomatous germ cell tumors of the testis. AJR Am J Roentgenol 151:325–329, 1988.
99. Lozano P, Julia J, Corominas C, et al: Ruptured aneurysms of the internal iliac artery: Report of two cases. J Cardiovasc Surg 36: 591–594, 1995.
100. Mack LA, Harley JD, Winquist RA: CT of acetabular fractures: Analysis of fracture patterns. Am J Roentgenol 138:407–412, 1982.
101. MacSweeney JE, King DM: Computed tomography, diagnosis, staging, and follow-up of pure granulosa cell tumour of the ovary. Clin Radiol 49:241–245, 1994.
102. MacVicar D: Staging of testicular germ cell tumours. Clin Radiol 47:149–158, 1993.
103. Magee BJ, Logue JP, Swindell R, et al: Tumour size as a prognostic factor in carcinoma of the cervix: Assessment by transrectal ultrasound. Br J Radiol 64:812–815, 1991.
104. Magid D, Fishman EK: Computed tomography of acetabular fractures. Semin Ultrasound CT MR 7:351–361, 1986.
105. Manaster BJ, Breenberg M, Rubin JM: Isolated internal iliac artery aneurysms. J Comput Assist Tomogr 6:845–846, 1982.
106. McCollough CH, Zink FE: Performance evaluation of a multi-slice CT system. Med Phys 26:2223–2230, 1999.
107. Megibow AJ, Hulnick DH, Bosniak MA, et al: Ovarian metastases: Computed tomographic appearances. Radiology 156:161–164, 1985.
108. Megibow AJ, Bosniak MA, Ho AG, et al: Accuracy of CT in detection of persistent or recurrent ovarian carcinoma: Correlation with second-look laparotomy. Radiology 166:341–345, 1988.
109. Mendez RJ, Rodriguez R, Kovacevich T, et al: CT in local recurrence of rectal carcinoma. J Comput Assist Tomogr 17:741–744, 1993.
110. Merkle EM, Wunderlich A, Aschoff AJ, et al: Virtual cystoscopy based on helical CT scan datasets: Perspectives and limitations. Br J Radiol 71:262–267, 1998.
111. Meyer JI, Kennedy AW, Friedman R, et al: Ovarian carcinoma: Value of CT in predicting success of debulking surgery. AJR Am J Roentgenol 165:875–878, 1995.
112. Miketic LM, Carroll R, Harris NL, et al: Computed tomography in the evaluation of lymphoma of the uterine cervix. J Comput Assist Tomogr 12:154–158, 1988.
113. Mitchell DG, Hill MC, Hill S, et al: Serous carcinoma of the ovary: CT identification of metastatic calcified implants. Radiology 158: 649–652, 1986.
114. Mitchell DG, Mintz MC, Spritzer CE, et al: Adnexal masses: MR imaging observations at 1.5T with US and CT correlation. Radiology 162:319–324, 1987.
115. Miyasaka Y, Hachiya J, Furuya Y, et al: CT evaluation of invasive trophoblastic disease. J Comput Assist Tomogr 9:459–462, 1985.

116. Montana MA, Richardson ML, Kilcoyne RF, et al: CT of sacral injury. Radiology 161:499–503, 1986.
117. Morgan CL, Calkins RF, Cavalcanti EJ: Computed tomography in the evaluation, staging, and therapy of carcinoma of the bladder and prostate. Radiology 140:751–761, 1981.
118. Morgan DE, Nallamala LK, Kenney PJ, et al: CT cystography: Radiographic and clinical predictors of bladder rupture. AJR Am J Roentgenol 174:89–95, 2000.
119. Nachbur BH, Inderbitzi RG, Bar W: Isolated iliac aneurysms. Eur J Vasc Surg 5:375–381, 1991.
120. Olcott EW, Nino-Murcia M, Rhee JS: Urinary bladder pseudolesions on contrast-enhanced helical CT: Frequency and clinical implications. AJR Am J Roentgenol 171:1349–1354, 1998.
121. Oliva L, Cariati M, Reggiani L, et al: CT evaluation of the pelvic cavity after cystectomy: Observation in 40 cases. J Comput Assist Tomogr 8:734–738, 1984.
122. Oyen RH, Van Poppel HHP, Ameye FE, et al: Lymph node staging of localised prostatic carcinoma with CT and CT-guided fine needle aspiration biopsy: Prospective study of 285 patients. Radiology 190: 315–322, 1994.
123. Panicek DM, Toner GC, Heelan RT, et al: Nonseminomatous germ cell tumours: Enlarging masses despite chemotherapy. Radiology 175:499–502, 1990.
124. Partin AW, Yoo J, Carter HB, et al: The use of prostate specific antigen, clinical stage, and Gleason score to predict pathological stage in men with localized prostate cancer. J Urol 150:110–115, 1993.
125. Patel SV, Spencer JA, Wilkinson N, et al: Supradiaphragmatic manifestations of papillary serous adenocarcinoma of the ovary. Clin Radiol 54:748–754, 1999.
126. Pech P, Haughton V: A correlative CT and anatomic study of the sciatic nerve. Am J Roentgenol 144:1037–1041, 1985.
127. Peng MY, Parisky YR, Cornwell EE III, et al: CT cystography versus conventional cystography in evaluation of bladder injury. AJR Am J Roentgenol 173:1269–1272, 1999.
128. Platt JF, Bree RL, Schwab RE: The accuracy of CT in the staging of carcinoma of the prostate. AJR Am J Roentgenol 149:315–318, 1987.
129. Ravi R, Ong J, Oliver RT, et al: The management of residual masses after chemotherapy in metastatic seminoma. BJU Int 83: 649–653, 1999.
130. Razzaq R, Carrington BM, Hulse PA, et al: Abdominopelvic CT scan findings after surgery for ovarian cancer. Clin Radiol 53: 820–824, 1998.
131. Reuter KL, Griffin T, Hunter RE: Comparison of abdominopelvic computed tomography results and findings at second-look laparotomy in ovarian carcinoma patients. Cancer 63:1123–1128, 1989.
132. Reznek RH, White FE, Young JWR, et al: The appearances on computed tomography after abdomino-perineal resection for carcinoma of the rectum: A comparison between the normal appearances and those of recurrence. Br J Radiol 56:237–240, 1983.
133. Sager EM, Talle K, Fossa S, et al: The role of CT in demonstrating perivesical tumor growth in the preoperative staging of carcinoma of the urinary bladder. Radiology 146:443–446, 1983.
134. Samuelsson L, Albrechtsson U: Ruptured aneurysm of the internal iliac artery. J Comput Assist Tomogr 6:842–844, 1982.
135. Sanders C, Rubin E: Malignant gestational trophoblastic disease: CT findings. AJR Am J Roentgenol 148:165–168, 1987.
136. Savader SJ, Otero RR, Savader BL: Puerperal ovarian vein thrombosis: Evaluation with CT, US, and MR imaging. Radiology 167: 637–639, 1988.
137. Sawyer RW, Walsh JW: CT in gynecologic pelvic diseases. Semin Ultrasound CT MR 9:122–142, 1988.
138. Sawyer RW, Vick CW, Walsh JW, et al: Computed tomography of benign ovarian masses. J Comput Assist Tomogr 9:784–789, 1985.
139. Schnall MD, Imai Y, Tomaszewski J, et al: Prostate cancer: Local staging with endorectal surface coil MR imaging. Radiology 178: 797–802, 1991.
140. Schwartz LH, La Trenta LR, Bonaccia E, et al: Small cell and anaplastic prostate cancer: Correlation between CT findings and prostate-specific antigen level. Radiology 208:735–738, 1998.
141. Seidelmann FE, Cohen WM, Bryan PJ, et al: Accuracy of CT staging of bladder neoplasms using the gas-filled method: Report of 21 patients with surgical confirmation. Am J Roentgenol 130: 735–739, 1978.
142. Seung Kim H, Kim HD, Song YS, et al: Detection of deep myometrial invasion in endometrial carcinoma: Comparison of transvaginal ultrasound, CT, and MRI. J Comput Assisr Tomogr 19:766–772, 1995.
143. Silverman PM, Osborne M, Dunnick NR, et al: CT prior to second-look operation in ovarian cancer. AJR Am J Roentgenol 150:829–832, 1988.
144. Smith RC, McCarthy S: Improving the accuracy of digital CT pelvimetry. J Comput Assist Tomogr 15:787–789, 1991.
145. Spencer JA, Chng WJ, Hudson E, et al: Prostate-specific antigen level and Gleason score in predicting the stage of newly diagnosed prostate cancer. Br J Radiol 71:1130–1135, 1998.
146. Spencer JA, Golding S: CT evaluation of lymph node status at presentation of prostatic carcinoma. Br J Radiol 65:199–201, 1992.
147. Spencer JA, Crosse BA, Mannion RA, et al: Gastroduodenal obstruction from ovarian cancer: Imaging features and clinical outcome. Clin Radiol 55:264–272, 2000.
148. Spencer JA, Golding S: Patterns of lymphatic metastases at recurrence of prostate cancer: CT findings. Clin Radiol 49:404–407, 1994.
149. Spencer JA, Swift SE, Wilkinson N, et al: Peritoneal carcinomatosis: Image-guided peritoneal core biopsy for tumor type and patient management. Radiology 221:173–177, 2001.
150. Spencer NJ, Spencer JA, Perren TJ, et al: CT appearances and prognostic significance of splenic metastases in ovarian cancer. Clin Radiol 53:417–421, 1998.
151. Stevens SK, Hricak H, Campos Z: Teratomas versus cystic hemorrhagic adnexal lesions: Differentiation with proton-selective fat-saturation MR imaging. Radiology 186:481–488, 1993.
152. Stomper PC, Kalish LA, Garnick MB, et al: CT and pathologic predictive features of residual mass histologic findings after chemotherapy for nonseminomatous germ cell tumors: Can residual malignancy or teratoma be excluded? Radiology 180:711–714, 1991.
153. Subak LL, Hricak H, Powell CB, et al: Cervical carcinoma: Computed tomography and magnetic resonance imaging for preoperative staging. Obstet Gynecol 86:43–50, 1995.
154. Sugawara Y, Eisbruch A, Kosuda S, et al: Evaluation of FDG PET in patients with cervical cancer. J Nucl Med 40:1125–1131, 1999.
155. Susmano DE, Dolin EH: Computed tomography in the diagnosis of pelvic lipomatosis. Urology 13:215–220, 1979.
156. Tempany CM, Rahmouni AD, Epstein JI, et al: Invasion of the neurovascular bundle by prostate cancer: Evaluation with MR imaging. Radiology 181:107–112, 1991.
157. Thomas SM, Bees NR, Adam EJ: Trends in the use of pelvimetry techniques. Clin Radiol 53:293–295, 1998.
158. Tisnado J, Nakano M, Higashi M, et al: Computed tomography of the perineum. Am J Roentgenol 136:475–481, 1981.
159. Toita T, et al: Prognostic value of cervical size and pelvic lymph node status assessed by computed tomography for patients with uterine cervical cancer treated by radical radiation therapy. Int J Radiat Oncol Biol Phys 33:843–949, 1995.
160. Tyrrel RT, Murphy FB, Bernardino ME: Tubo-ovarian abscesses: CT-guided percutaneous drainage. Radiology 175:87–89, 1990.
161. van Heurn LW, Varekamp AP: A rare case of iliac vein obstruction: Pelvic lipomatosis. Neth J Surg 42:58–60, 1990.
162. vanSonnenberg E, Wittich GR, Casola G, et al: Lymphoceles: Imaging characteristics and percutaneous management. Radiology 161: 593–596, 1986.
163. vanSonnenberg E, D'Agostino HB, Casola G, et al: US-guided transvaginal drainage of pelvic abscesses and fluid collections. Radiology 181:53–56, 1991.
164. Vaughan BF: CT of swollen legs. Clin Radiol 41:24–30, 1990.
165. Vick CW, Walsh JW, Wheelock JB, et al: CT of the normal and abnormal parametria in cervical cancer. Am J Roentgenol 143: 597–603, 1984.
166. Vining DJ, Zagoria RJ, Liu K, et al: CT Cystoscopy: An innovation in bladder imaging. AJR Am J Roentgenol 166:409–410, 1996.
167. Vinnicombe S, Norman A, Nicolson V, Husband JE: Normal pelvic lymph nodes: Evaluation with CT after bipedal lymphangiography. Radiology 194:349–355, 1995.
168. Walsh JW, Amendola MA, Konerding KF, et al: Computed tomographic detection of pelvic and inguinal lymph node metastases from primary and recurrent pelvic malignant disease. Radiology 137:157–166, 1980.
169. Walsh JW, Amendola MA, Hall DJ, et al: Recurrent carcinoma of the cervix: CT diagnosis. Am J Roentgenol 136:117–122, 1981.

170. Warren GP, Einhorn LH: Gallium scans in the evaluation of residual masses after chemotherapy for seminoma. J Clin Oncol 13:2784–2788, 1995.
171. Wechsler RJ, Schilling JF: CT of the gluteal region. Am J Roentgenol 144:185–190, 1985.
172. Weinerman PM, et al: Pelvic adenopathy from bladder and prostate carcinoma: Detection by rapid-sequence computed tomography. Am J Roentgenol 140:95–99, 1983.
173. White PM, Adamson DJ, Howard GC, et al: Imaging of the thorax in the management of germ cell testicular tumours. Clin Radiol 54:207–211, 1999.
174. White PM, Howard GC, Best JJ, et al: The role of computed tomographic examination of the pelvis in the management of testicular germ cell tumours. Clin Radiol 52:124–129, 1997.
175. White M, Mueller PR, Ferrucci JT Jr, et al: Percutaneous drainage of postoperative abdominal and pelvic lymphoceles. Am J Roentgenol 145:1065–1069, 1985.
176. Whitley N, Brenner D, Francis A, et al: Use of the computed tomographic whole-body scanner to stage and follow patients with advanced ovarian carcinoma. Invest Radiol 16:479–486, 1981.
177. Wiesen EJ, Crass JR, Bellon EM, et al: Improvement in CT pelvimetry. Radiology 178:259–262, 1991.
178. Wilbur AC, Aizenstein RI, Napp TE: CT findings in tuboovarian abscess. AJR Am J Roentgenol 158:575–579, 1992.
179. Williams MP, Husband JE, Heron CW, et al: Intrathoracic manifestations of metastatic testicular seminoma: A comparison of chest radiographic and CT findings. AJR Am J Roentgenol 149:473–475, 1987.
180. Wolverson MK, Jagannadharao B, Sundaram M, et al: CT in localization of impalpable cryptorchid testes. Am J Roentgenol 134:725–729, 1980.
181. Wood A, Robson N, Tung K, et al: Patterns of supradiaphragmatic metastases in testicular germ cell tumours. Clin Radiol 51:273–276, 1996.
182. Wright AR, White PM: Testicular cancer: Who needs surveillance pelvic CT? (letter). Clin Radiol 54:78, 1999.
183. Yamaguchi T, Shimizu Y, Ono N, et al: A case of pelvic lipomatosis presenting with oedema of the lower extremities. Jpn J Med 30:559–563, 1991.
184. Yang WT, Lam WW, Yu MY, et al: Comparison of dynamic helical CT and dynamic MR imaging in the evaluation of pelvic lymph nodes in cervical cancer. AJR Am J Roentgenol 175:759–766, 2000.
185. Young JWR, Burgess AR: Radiological Management of Pelvic Ring Fractures. Baltimore, Urban & Schwarzenburg, 1987.

45

Magnetic Resonance Imaging of the Pelvis

Eric K. Outwater

Since the first clinical reports of magnetic resonance imaging (MRI) of the pelvis, both the technical quality and range of applications of pelvic MRI have increased.[29, 42, 129] High cost, slow spread of technical expertise in the community, and the absence of unequivocal clinical indications have delayed its widespread acceptance as an important imaging technique in the pelvis. Nonetheless, MRI has some definite advantages over other techniques of pelvic imaging, and further technical advances will serve to expand the range of applications.

Early investigators realized four potential advantages of MRI over conventional imaging techniques in the pelvis:

1. It offered direct multiplanar imaging, which is essential for clear depiction of organ anatomy and tissue planes in the pelvis.
2. Intrinsic soft tissue contrast of pelvic organs appeared to be high with MRI because of the multiple parameters of tissue proton relaxation that contribute to the MR signal.
3. The unique characteristics of moving protons on MR images promised unequivocal identification of vessels without necessarily using intravascular contrast material.
4. MRI appeared to be safe in pregnant patients.

These basic observations have provided the impetus for further research into potential clinical applications of MRI in the pelvis.

The great challenge in pelvic imaging is to find a cross-sectional technique that combines very high resolution with high tissue contrast and tissue specificity, sufficient safety to apply to pregnant patients, and low enough cost to apply in common clinical situations. No other technique currently fulfills all these criteria across a broad spectrum of applications.

Ultrasonography is the current imaging procedure of choice for most pelvic disorders. Its safety is established, and it provides sufficient depiction of normal and pathologic anatomy for routine assessment of many gynecologic and almost all obstetric disorders. Endoluminal probes and color Doppler imaging further expand its applications in the pelvis. Nonetheless, pelvic ultrasonography has serious limitations; for example, it is generally not suitable for one of the largest potential clinical applications—tumor staging. Resolution and tissue contrast are not sufficient for accurate staging of any genitourinary malignancies in males or females. In addition, the accuracy of diagnosis of adnexal masses is not sufficient to obviate surgical diagnosis in many cases. Taking these limitations into account, cost-effectiveness of MRI has been suggested in several studies when ultrasound findings are equivocal, including for adnexal masses and scrotal imaging.[323, 335] Incorporating MRI appears to save money in the evaluation of patients with cervical carcinoma and prostate carcinoma.[138, 188, 189]

Computed tomography (CT) provides a more systematic examination of the pelvis than ultrasound, and it is better suited for defining bowel involvement in inflammatory and neoplastic disorders. CT is superior to ultrasound for depicting fat planes and adenopathy, which are important in staging malignancies. Aside from adipose tissue, however, soft tissue contrast is intrinsically poor on CT images of the pelvis. Zonal anatomy of the uterus or of the prostate is not demonstrated by CT, and depiction of perineal anatomy is limited. This poor tissue contrast, as well as the potential radiation risk in women of childbearing age, limits the general applicability of CT for the pelvis.

The risks of CT derive from the radiation dose and from the nephrotoxicity of intravenous (IV) contrast agents. Risks of radiation dose may be significant, particularly in younger patients. The probability of a radiation-induced cancer in a young adult undergoing CT of the abdomen and pelvis is about 1/2000 or greater.[124, 300, 306, 307] The cost of this one-time radiation dose has been estimated at $30 per millisievert, or $300 per abdominal CT.[306, 307] These considerations led one author to suggest that MRI in younger patients may be more cost-effective than CT on the basis of radiation risk alone.[306] Costs associated with irradiation of unsuspected pregnancies have not been assessed. Further costs derive from risks associated with iodinated contrast agents, and cost-effectiveness favors MRI over CT for patients at risk for nephrotoxicity.[193]

Important Imaging Techniques

The quality of MR images of the brain, spine, and musculoskeletal system exceeds that obtained in the chest, abdomen, and pelvis, primarily because of motion effects (respiratory, bowel peristalsis, and cardiac) and the lack of local receiver coils in the latter applications. Pelvic MR images are the least susceptible to motion effects but still suffer from suboptimal resolution because of the relatively large fields of view necessary to sustain a satisfactory signal-to-noise ratio (SNR). Two technical innovations—*multicoil (phased-array)* and *fast spin-echo* (FSE) sequences—can increase the SNR in pelvic images and shorten the acquisition time of long repetition time/echo time (TR/TE) pulse sequences. This time saving can be

used for higher-resolution matrices, acquisitions in multiple planes, or thinner sections, all of which are important in imaging the pelvis. In addition, improved methods of chemical shift imaging and vascular imaging allow added dimension to an overall examination of the pelvis.[246, 348, 349]

Surface Coils

Two strategies have been developed for imaging the pelvis with surface coils: (1) *endoluminal* surface coils and (2) multiple arrays of *external* surface coils. Both of these take advantage of the higher SNR achievable with small-diameter receiver coils to achieve smaller fields of view, and hence higher resolution, than that obtainable with the whole-volume body coils in the bore of the magnet system. These techniques are more widely applicable to pelvic imaging than the surface coil arrangements that have always been available, such as a single-loop anterior surface coil for imaging the scrotum.

Endoluminal surface coils increase the SNR achievable with small (10- to 12-cm) fields of view. The sensitivity profile of these small-diameter coils falls off steeply as distance from the coil increases; thus, they are suited only for perirectal structures and organs such as the prostate,[321] anal canal,[147] and rectum.[319] Endoluminal surface coils can also image the cervix with high resolution, showing cervical carcinoma that spreads into the parametria.[24, 228] These coils are less suited for imaging very bulky cervical tumors or other gynecologic neoplasms.

Multicoil (phased-array) arrangements have been designed for imaging the spine, abdomen, chest, and pelvis. Multiple separate receiver coils, preamplifiers, receiver channels, digitizers, and memory are used.[116, 301] The signal from each receiver is separately transformed into separate data sets, which are then reconstructed into a single composite image that uses an algorithm for the sum of the squares. Each coil is designed with a smaller effective diameter than would otherwise be used for a given volume of interest. The result is a composite image that can adequately include a larger area but with an SNR that is the same as or higher than that of a small-diameter coil.[116] In this chapter, most images use a four-coil multicoil arrangement with two 5-inch coils anteriorly and two coils posteriorly. For imaging the true pelvis, coils can be arranged either craniocaudad or transversely.

Multicoil arrays share the disadvantages of all surface coils. The primary disadvantage is an intense signal near the coil, with a steep gradient of signal loss away from it.[218] This near-field effect renders the image very susceptible to ghosting artifacts that arise along the phase-encoding axis from the motion of structures (Fig. 45–1).[218] These ghost artifacts may be ameliorated by judicious choice of phase-encoding direction, anterior saturation bands,[348] fat-suppression techniques, and physical restriction of the anterior pelvic wall. Multicoil arrays also impose additional burdens of increased memory demands and lengthened reconstruction times. Finally, the improvement in SNR of the multicoil over that of the body coil may be lost in particularly large patients, or in pregnant patients, because of the fall-off of sensitivity of the coils in the center of the imaging volume.[348]

Fast T2-Weighted Imaging

The development of FSE sequences was conceptually based on the RARE (rapid acquisition with relaxation en-

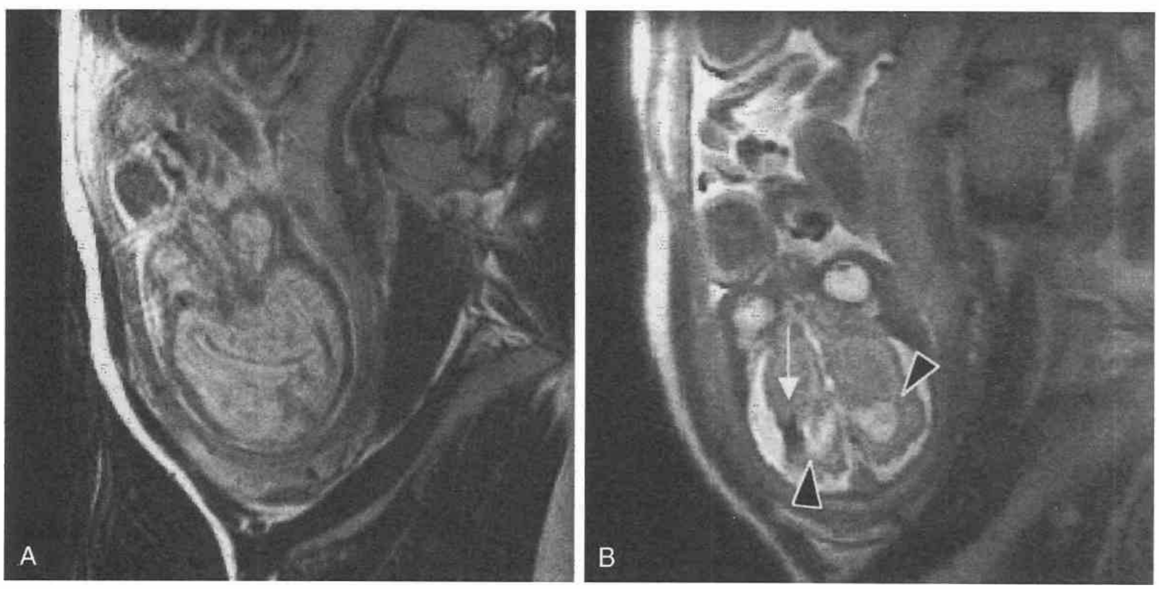

Figure 45–1. Comparison of conventional T2-weighted, fast spin-echo (FSE) images and single-shot FSE images for delineation of fetal anatomy. *A*, T2-weighted FSE image (TR = 2000 msec, TE_{eff} = 99 msec; two signal acquisitions) shows marked motion artifact related to fetal motion and maternal respiratory motion. Fetal anatomy is blurred and indistinct. *B*, Single-shot FSE image (TR = 16,000 msec, TE_{eff} = 96 msec, 0.5 half-Fourier acquisition) shows more discrete fetal anatomy with depiction of the cerebral lateral ventricles *(arrowheads)* and low-signal-intensity cerebral infarction *(white arrow)* in this patient with TORCH syndrome (toxoplasmosis, rubella, cytomegalovirus, herpes). TE_{eff}, effective echo time.

hancement) pulse sequence, first introduced by Hennig and colleagues.[120] Variants of these sequences—echo train spin echo, fast acquisition interleaved spin echo (FAISE), turbo spin echo (TSE), and gradient-recalled echo and spin echo (GRASE)—are grouped together under the term *fast spin echo* in this chapter.[1, 224, 225, 283] These sequences employ multiple, closely spaced, refocusing pulses, called an *echo train*, for every 90-degree pulse.

Conventional spin-echo (SE) imaging uses a single refocusing pulse and acquires only one phase-encoded step per 90-degree pulse. A typical FSE sequence with an echo train length of 16 refocusing pulses reduces the acquisition time 16-fold. This time saving allows larger acquisition matrices or a greater number of acquisitions. The drawback of FSE is that fewer sections can be obtained in multislice acquisitions because a greater portion of TR is devoted to the echo train. However, interslice gaps can be avoided if two contiguous, interleaved acquisitions are performed.

Contrast in FSE can be manipulated by the ordering of phase-encoding trajectories in k-space. The time between the 90-degree pulse and the *n*th signal that is assigned to the lowest-order, phase-encoding step in k-space determines the effective echo time (TE_{eff}). The low-order, phase-encoded signals are those with the weakest phase-encoding gradients. These low-order, phase-encoding steps determine the relative contrast, or *T2-weighting*, of the sequence.[69, 70, 198]

Three mechanisms assume the greatest importance in FSE tissue contrast in the pelvis: (1) modulation of J-coupling effects in lipids, (2) exaggeration of magnetization transfer effects, and (3) T2-dependent alteration of the point-spread function.[69, 70]

In conventional SE sequences, lipid protons *(spins)* undergo phase dispersion as a result of the different chemical shifts produced by spin-spin couplings (J-coupling) of the hydrocarbon chain protons. This results in a relative loss of signal from lipids. In FSE images, this phase dispersion is reduced by frequent refocusing, resulting in preservation of the lipid signal on FSE images.

The clinical situation determines whether the high-signal-intensity fat on T2-weighted sequences becomes a help or a hindrance in interpretation of the images. As a rule, use of a TE_{eff} longer than would be used in conventional T2-weighted SE sequences is preferable (Table 45–1).[256] This achieves more heavily T2-weighted images with correspondingly less fat signal intensity and relatively better conspicuity of edema and tumors, for example. For most applications, it is preferable to have high signal intensity of fat on T2-weighted images. Suppression of fat results in an obscuring of the muscularis layer of the bladder, rectum, and vagina, making tumor invasion of these structures difficult to appreciate.

FSE also shows increased magnetization transfer effects when compared with conventional SE imaging.[34] This results from the multiple 180-degree refocusing pulses causing off-resonance saturation on the nonselected slice. In general, this results in lower signal intensity of tissues that contain large numbers of macromolecules, such as tumor tissue and smooth muscle, and accentuation of structures that have no magnetization transfer, such as fat or fluid.[35]

Last, the effects of the point-spread function can work to alter edge definition of some objects in FSE images.[69, 70] FSE phase-encoded steps are acquired during the evolution of T2 decay. Just as contrast is determined by the position of the low spatial frequencies in k-space, the fidelity of edges is determined by the placement of high spatial frequencies. This can lead to an *edge enhancement* if the high spatial frequencies are collected at the early echoes (heavily T2-weighted) or to *edge blurring* if the high spatial frequencies are collected at the late echoes (intermediate weighting).[69, 70] Edge enhancement is more pronounced with longer-T2 structures, whereas structures with short T2 tend to be blurred.[198]

The practical result of these effects in pelvis imaging is a slight additional sharpness and conspicuity of cysts and other fluid collections in FSE images acquired with long TE_{eff} (>100 msec). This effect may combine with magnetization transfer effects to highlight small ovarian cysts and other small fluid collections.[246] This blurring of shorter T2 tissues is particularly pronounced with the single-shot FSE sequence, or HASTE (half-Fourier acquisition single-shot turbo spin echo). This effect limits the ability of the HASTE sequences to substitute for T2-weighted FSE images in the pelvis.[36]

For the pelvis, the FSE sequence is particularly well suited to heavily T2-weighted images with a TE_{eff} of 80 to 140 msec and a TR of 3000 to 4000 msec.[348, 349] A 256 × 256 acquisition matrix is used in conjunction with an 18- to 24-cm field of view, although finer matrices can be sustained in the pelvis (see Table 45–1). Respiratory gating and gradient moment nulling are usually unnecessary because respiratory motion artifacts are not usually a significant problem in pelvic MRI. Artifacts related to bowel

Table 45–1. MRI Protocol for the Female Pelvis*

Pulse Sequence	TR	TE	Matrix	Slice	SAT	NEX	FOV
†Cor FSE	4000	100	256 × 256	5 × 1	S, I	2	24 × 24
Sag FSE	3000	100	256 × 256	4 interl	S, I	2	20 × 20
Ax T1-SE	500	min	256 × 192	5 × 1	S, I	1	20 × 20
Ax FSE	4000	100	256 × 256	4 interl	S, I	2	20 × 20
AxFatSat GRE	~400	min	256 × 128	5 × 1	Fat, S, I	1	20 × 20
AxFatSat GRE	~400	min	256 × 128	5 × 1	Fat, S, I	1	20 × 20

*Technique: pelvic phased-array coil.
†Give glucagon 1.0 mg IM prior to study.
Ax, axial; Cor, coronal; Fat or FatSat, fat saturation; FOV, field of view; FSE, fast spin-echo; GRE, spoiled gradient-recalled echo; I, inferior; interl, interleaved; min, minimum; NEX, number of signal averages; S, superior; Sag, sagittal; SAT, saturation bands; T1-SE, T1-weighted spin echo; TE, echo time; TR, repetition time.

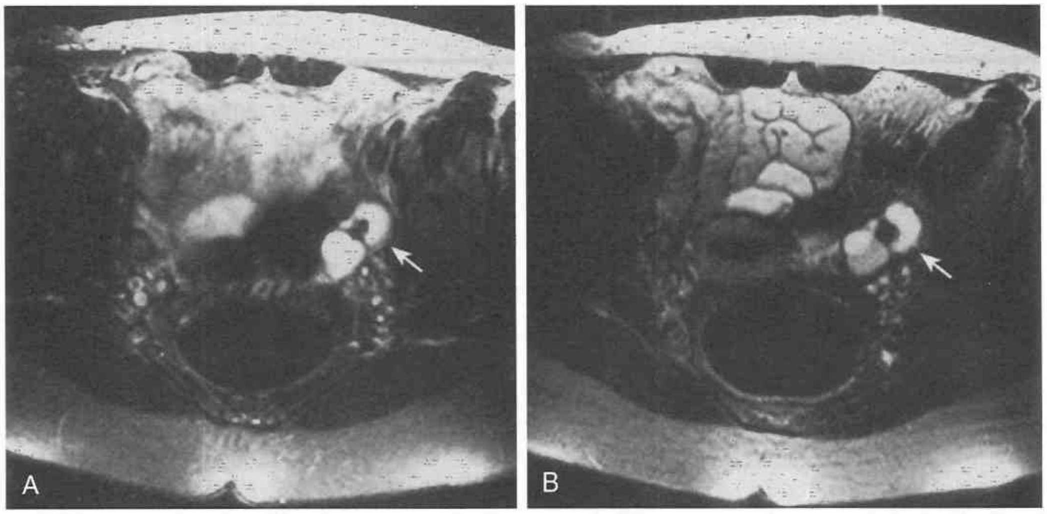

Figure 45–2. Use of glucagon to suppress motion artifact. Axial T2-weighted, fast spin-echo images (TR = 4000 msec, TE_{eff} = 12 msec) before *(A)* and after *(B)* intravenous administration of 0.1 mg glucagon. Glucagon improves the definition of the bowel wall and also results in fewer ghosting artifacts in the phase-encoding (right-to-left) axis. The septate high-signal-intensity left ovarian mass *(arrow)* with a central low-signal-intensity mural nodule proved to represent a cystadenofibroma. TE_{eff}, effective echo time.

motion can be suppressed with the use of glucagon (Fig. 45–2).

Single-Shot Fast Spin Echo

HASTE images were the first type of sequence to obtain high-quality T2-weighted SE-type images in a breath-holding period. HASTE sequences use a half-Fourier acquisition and a long echo-train FSE sequence to obtain all the data necessary to form k-space from a single acquisition, or a single shot.

Single-shot FSE sequences achieve relatively motion-free breath-hold images in the pelvis, with tissue contrast similar to that of more conventional T2-weighted FSE. For conventional pelvic imaging, they are advantageous in imaging the abdominal wall, mesenteric fat, and bowel without motion. The main disadvantage of these sequences is tissue blurring in the phase-encoding direction caused by alterations to the point-spread function (see FSE sequences earlier).

For certain specific applications, such as identification of fibroids, single-shot FSE sequences may be able to obtain a study in a shorter time.[180] Imaging of the bowel is better with single-shot FSE sequences for two reasons[25, 332]:

1. Imaging time is short enough that peristalsis-related motion artifacts are reduced.
2. The presence of any high-signal-intensity luminal contents causes the mucosal surfaces to be imaged with high resolution.

MR images of the fetus have always been susceptible to motion-induced artifact from respiratory-induced movement of the uterus and gross movements of the fetus itself.[211, 214] Motion of the fetus causes motion of the amniotic fluid around it, which generates a marked ghosting artifact and blurring. Traditionally, to scan for possible fetal abnormalities by conventional SE sequences or even FSE sequence, it was often necessary to paralyze the fetus. FSE sequences may be suitable for imaging the placenta and uterus but often yield poor-quality images of the fetus itself because of motion-induced artifact.

Single-shot sequences dramatically improved the potential for obtaining good MR images of the fetus.[7, 194] These images are acquired quickly (~1 second), before gross fetal motion has occurred. Although some images are degraded if fetal motion occurs during their acquisition, others are relatively free of motion artifact. Therefore, repeated acquisition of the sequences can be performed to obtain diagnostic images free of motion artifact. The blurring of soft tissue structures that HASTE sequences cause is of lesser importance in imaging the fetus because most structures are bordered by fluid and therefore result in sharp images.

Another approach to obtaining fetal scans is *echo-planar imaging*.[156] Like single-shot FSE, it can easily achieve images in less than a second; however, signal-to-noise considerations seem to favor single-shot FSE. Echo-planar imaging has been used to investigate aspects of lung and liver maturation.[87, 88]

Fat-Selective Methods

Various forms of fat-suppression techniques have been developed and have widespread clinical utility in imaging the pelvis,[169, 233] including:

- Chemical shift–sensitive methods, such as frequency-selective fat saturation[168]
- Dixon technique[80, 334, 363]
- Opposed-phase gradient-echo sequences[398]
- Short tau inversion recovery (STIR) technique

STIR suppresses all tissues with a T1 approximating that of fat. It is not chemical shift–specific and thus does not unequivocally identify fat-containing tissue.[233]

Frequency-selective fat saturation is the most widely available of the techniques performed at higher field strengths. It can be applied to T1-weighted or T2-weighted images to suppress signal from all aliphatic lipid protons in the volume. Fat and hemorrhage, both of which commonly show very high signal intensity on T1-weighted images, are distinguished by comparing fat-saturated T1-weighted images and T1-weighted images without fat saturation (Fig. 45–3). This technique is most often used in T1-weighted sequences after injection of IV contrast material to render enhancing structures more conspicuous relative to fat. In T2-weighted images, it permits reduced bandwidth technique to increase the SNR in the images and highlights pathologic conditions that may have T2 times approaching that of fat.[236] Like the Dixon technique, frequency-selective saturation is very sensitive to magnetic field inhomogeneities.[38, 414]

Opposed-phase images can be generated using SE (the *Dixon technique*) or *gradient-echo sequences*. Gradient-echo sequences do not use a refocusing radiofrequency pulse to rephase fat and water protons; therefore, the lipid signal cycles in and out of phase with the water signal during the TE period. Voxels containing lipids and water show higher signal intensity if the fat and water are in phase and additive than if they are out of phase and the fat and water signal cancel. At 1.5 Tesla, these resonances are in phase to yield maximal signal for voxels with lipid and fat at TEs that are a multiple of 4.4 msec and out of phase at TEs that are a multiple of 2.2 msec. Such opposed-phase images can be used to detect lipid in dermoids because the sebaceous lipid is generally mixed with water protons.[411]

Hybrid methods achieve maximal fat suppression by applying frequency-selective fat saturation to an opposed-phase image.[58, 362] When frequency-selective fat saturation is used, some significant amount of residual signal remains in adipose tissue. This is because of the presence of olefinic lipids with resonances near that of water and because of the steady-state effects of the fat-saturation pulse, which produce residual longitudinal magnetization of lipid protons. With the addition of opposed-phase imaging, these residual longitudinal magnetizations are out of phase at time TE, resulting in nearly complete loss of signal in adipose tissue (Fig. 45–4).[58] Hybrid techniques are the most reliable for fat suppression.[340] They aid in the diagnosis of masses that are mostly lipid, such as dermoids (see Fig. 45–4) and are also useful in contrast-enhanced images (see Table 45–1).

Magnetic Resonance Angiography

Magnetic resonance angiography (MRA) can be used in the pelvis for an overall evaluation of veins or arteries. Several modalities are available:

- Gadolinium-enhanced, three-dimensional (3D) MRA
- Two-dimensional (2D) time-of-flight (TOF) MRA
- Phase-contrast MRA

These three techniques have been used to image pelvic arteries, although the first is generally preferred. Phase-contrast angiography is sometimes used in special circumstances in the abdomen but is not discussed here.

Time-of-Flight 2D Imaging

Of the various MRA sequences available, TOF-MRA gradient-echo imaging was used most widely before the development of faster imaging methods. TOF-MRA can provide gross evaluation of the major arteries of the pelvis to determine vessel or graft patency, vessel displacement or encasement by masses, or stenoses.[11] A sequence that can yield good results in the pelvis uses a minimum TE with gradient moment nulling, a TR of 33 to 45 msec, a 30-cm field of view, a 2.5-mm slice thickness contiguously acquired, and a 128 × 256 acquisition matrix. A flip angle

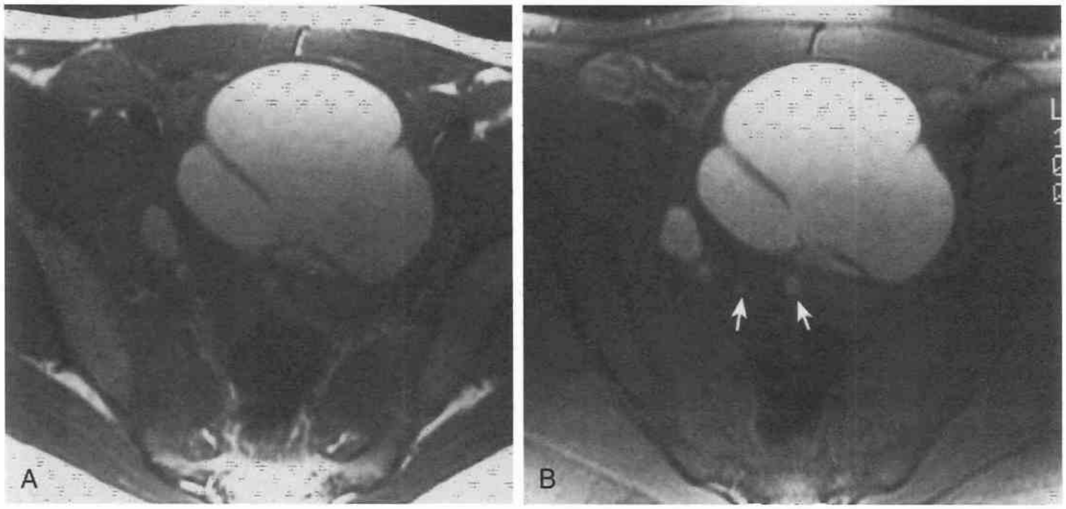

Figure 45–3. Endometriomas, chemical shift imaging. *A,* Axial spin-echo image (TR = 800 msec, TE_{eff} = 11 msec) demonstrates bilateral adnexal masses with signal intensity approaching that of fat. The left adnexal mass is partially septate. *B,* The same pulse sequence performed with frequency-selective presaturation of fat demonstrates that high signal intensity is not due to lipid. In addition, several small implants of endometriosis *(arrows)* are more easily seen. The subcutaneous fat signal is also suppressed. TE_{eff}, effective echo time.

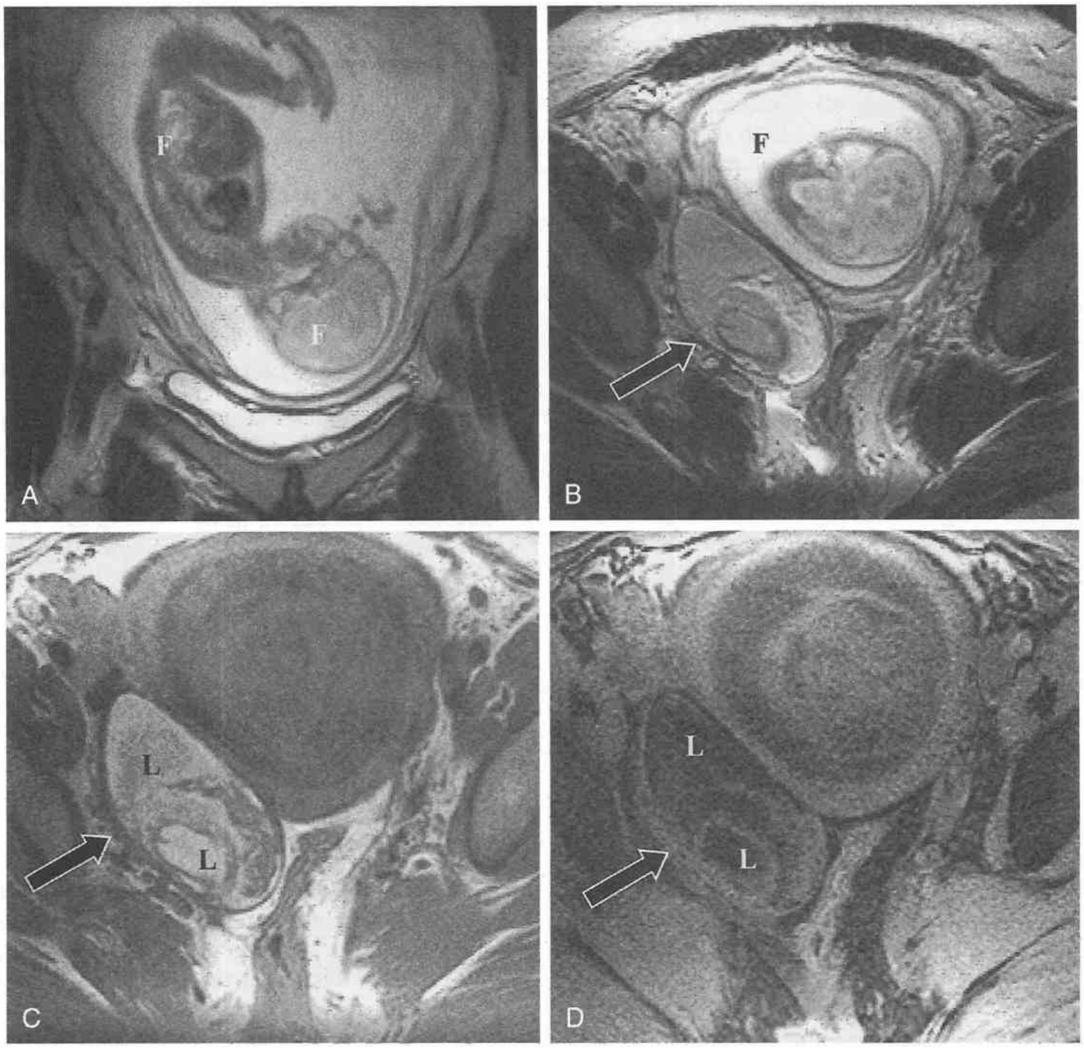

Figure 45–4. Mature cystic teratoma, chemical shift imaging. *A,* Coronal image shows normal fetal anatomy (F) at 22 weeks of gestation. *B,* T2-weighted image shows the gravid uterus (F) and a complex right adnexal mass *(arrow)*. The mass does not have the signal features of simple fluid. T1-weighted gradient-echo images with *(C)* and without *(D)* fat suppression show loss of signal of the lipid component (L) in the mass *(arrow)*, establishing the diagnosis of a mature cystic teratoma. (From Ascher SM, Outwater EK, Reinhold C: Adnexa. In Semelka RC, Ascher SM, Reinhold C [eds]: MRI of the Abdomen and Pelvis: A Text-Atlas. New York, Wiley-Liss, 1997, pp 661–715.[12])

of 60 degrees works well in most instances, although a lower flip angle may be used when prominent arterial pulsation artifact is present.[281, 367]

TOF-MRA imaging generally works well for imaging the pelvic veins, whereas the pelvic arteries have provided a greater challenge.[351] This is partly because prominent arterial pulsations are normally present in the pelvic arteries, leading to marked differences in flow-related enhancement from phase-encoding step to phase-encoding step. The changes in flow-related enhancement lead to prominent ghosting artifacts and resultant loss of signal intensity in the pelvic arteries.

Additionally, the pelvic arteries are frequently tortuous and thus susceptible to in-plane flow saturation on TOF images.

Finally, the pelvic arteries are vulnerable to magnetic susceptibility artifact resulting from neighboring colon. Because the pelvic arteries are of crucial importance for the imaging evaluation of patients with claudication or tissue loss, precise delineation of any stenoses is crucial. For these reasons, adequate imaging of the pelvic arteries awaited the development of fast imaging techniques with gadolinium enhancement.[351]

Gadolinium-Enhanced 3D Imaging

In overcoming the problems associated with TOF-MRA, 3D MRA with gadolinium proved to be a major advance. With the short echo time of this 3D MRA, magnetic susceptibility artifacts are not as noticeable. The dramatically shortened T1 of blood provided by gadolinium eliminates the in-plane flow saturation that was frequently seen in tortuous arteries. Finally, because the 3D MRA technique relies on imaging blood by virtue of its shortened T1 and not flow-related enhancement per se, this technique is not susceptible to the alterations in flow-related enhancement

that led to the view-to-view errors and pulsations of artifacts of the 2D TOF technique.

Details of gadolinium-enhanced, 3D gradient-echo imaging are presented elsewhere.[286] Briefly, this technique involves the use of a 3D gradient-echo acquisition to image a volume with thin sections amenable to 3D reconstruction and reformatting. This sort of sequence can be performed with more conventional gradient systems; however, the high performance gradients, with a higher gradient strength and slew rates, mean that the 3D sequence can be performed in a shorter time period. Acquisition of the 3D sequence in a shorter time means that timing the acquisition to the bolus is less problematic and the sequence can be performed with breath-holding to eliminate some sources of motion.

For imaging the pelvis, slab thickness and orientation must be chosen. This differs from the TOF-MRA technique, in which the pelvis is imaged in cross-section (axially) and final reconstructions are made in the anteroposterior projection. The coronal plane or slab is chosen to include the target vessels, and the section thickness determines the final resolution. The 3D gradient-echo sequence is obtained with minimum TE and TR. Because of the large number of phase-encoded steps involved in the acquisition, the minimum TR obtainable dramatically affects the total acquisition time. IV gadolinium is injected, and the plateau of arterial phase enhancement is timed to correspond to the center of k-space acquisition of the 3D gradient-echo scan. If the 3D sequence is a half-Fourier acquisition, the center of k-space may occur at the beginning of the acquisition rather than in the center. Saturation bands for suppression of venous in-flow are not possible, and selective imaging of the arterial systems depends on critical timing so that venous enhancement has not occurred (Fig. 45–5).

Several studies have shown greater accuracy with the 3D gadolinium-enhanced technique than with the 2D TOF technique.[2, 85, 287, 350–352] Pitfalls in the 3D technique are related primarily to technical problems with the performance of the examination. Because gadolinium dramatically shortens the T1 of the blood, selective in-flow saturation of venous vessels is far less effective with the gadolinium-enhanced technique than with the TOF technique.

Gadolinium-enhanced 3D sequences have been used in a number of applications in the pelvis.[99, 201] They provide more accurate identification of stenoses in the iliac arteries than conventional TOF sequences. Three-dimensional, gadolinium-enhanced MRA is particularly well suited for patients with complex arterial grafts in place (see Fig. 45–5). Imaging of femoral bypass grafts was particularly a problem with 2D TOF imaging because of the in-plane flow saturation. With 3D gadolinium-enhancement, the flow direction is irrelevant; therefore, flow in grafts running in any direction can be effectively imaged. Surgical clips may still cause artifactual stenosis with 3D gadolinium-enhanced sequences, but the problem is less profound than with 2D TOF imaging because the TE of the 3D sequence is much shorter.

Gadolinium-enhanced 3D sequences are useful in identifying stenosis and thrombosis affecting renal transplants, arteries, and veins.[155] Because of the short transient time of arterial blood through the kidneys, it is relatively simple to image both arteries and veins with this modality. These sequences can detect arterial lesions associated with impotence.[356] The potential of gadolinium-enhanced 3D sequences in delineating arterial supply in other pelvic disorders per se has not been explored.

Magnetic Resonance Venography

MR venography using TOF sequences reliably demonstrates the common femoral veins, the external and internal

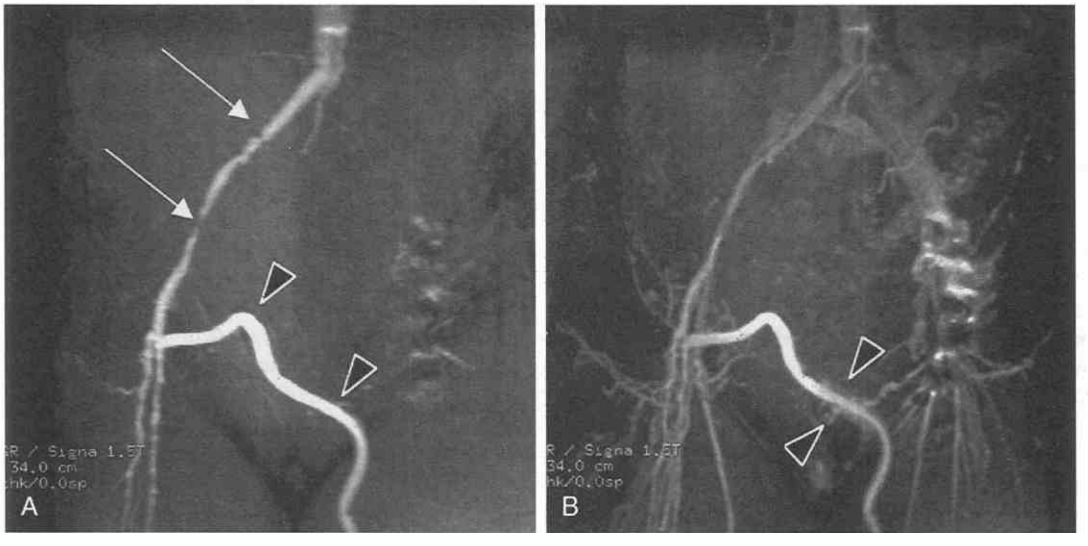

Figure 45–5. Infected femoral graft and venous thrombosis in a 73-year-old woman, shown by gadolinium-enhanced, 3D gradient-echo imaging. *A*, Projection reconstruction of a coronal slab from a gradient-echo sequence (TR = 13 msec, TE = 2.3 msec) shows a completely occluded left iliac arterial system. The right arterial system is severely diseased with multiple stenoses *(arrows)*. A patent cross-graft femoral-to-popliteal graft is seen *(arrowheads)*. *B*, Venous phase of the 3D technique shows focal enhancement around the graft *(arrowheads)*, which proved to represent infection in the graft. Numerous collateral veins from bilateral iliac venous occlusions can be seen. (From Outwater EK: Ultrafast MR imaging of the pelvis. Eur J Radiol 29:233–244, 1999.[255])

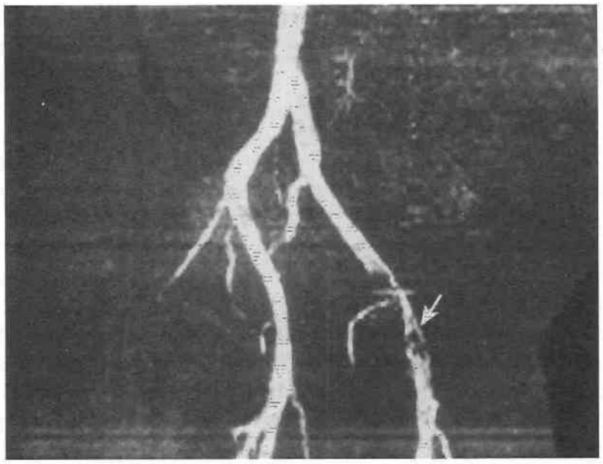

Figure 45–6. Diagnosis of thrombosis by MR venography. Reconstruction from axial 2D time-of-flight gradient-echo images (TR = 7.7 msec, TE = 45 msec, flip angle of 60 degrees, 120 slices of 2.5-mm thickness) shows filling defects in the left common femoral vein *(arrow)*. The presence of thrombosis was confirmed on venography.

iliac veins, and the inferior vena cava (Fig. 45–6).[355] MR venography is inferior to direct iliac or femoral injection contrast venography for demonstrating the iliac veins, but it is often superior to routine pedal injection for lower extremity venography. Venous occlusions due to thromboses or tumor encasement can be identified (see Fig. 45–6).[11, 355, 367] Gadolinium enhancement may increase the conspicuity of thrombi.[95] The presence of an apparent flow defect on the maximum intensity projection images must be compared to the axial gradient-echo or SE images to verify the presence of thrombus (Fig. 45–7). Venous compression and magnetic field inhomogeneity artifacts due to metal commonly result in an appearance similar to that of thrombus.

MRI Anatomy of the Pelvis

Male Pelvic System

Anatomic details of the male genital system are best appreciated with the highest possible resolution, which requires the use of surface coils to support smaller fields of view. For the scrotum, this is easily accomplished with a circular loop coil placed directly over the scrotum.[212, 295, 330] For the prostate, it is best achieved with a pelvic multicoil arrangement or the use of an endorectal coil. Body coil imaging with large fields does not permit the high resolution needed to identify important landmarks such as the prostatic capsule and the neurovascular bundles of the prostate.[134, 273, 318, 369] T2-weighted images display the zonal anatomy of the prostate and the testicular adnexa to best advantage; acquisition in the axial and coronal or oblique coronal planes is usually the most desirable.[134, 191, 273, 318, 369] T1-weighted images are important in assessment of the integrity of the periprostatic fat and neurovascular bundle and in identification of sites of hemorrhage.

Prostate Gland

The zonal anatomy of the prostate gland and its alteration, caused by *benign prostatic hyperplasia* (BPH), is somewhat complex. For imaging purposes, whether by ultrasound or MRI, the prostate gland usually displays three main regions: the central gland, the peripheral zone, and the anterior fibromuscular stroma (see Fig. 45–7).[134, 197, 280, 320]

The *central gland* in older men is usually involved, to some degree, by hyperplastic changes and shows lower signal intensity than the surrounding peripheral gland.[163, 274, 314] The central gland, as it appears on MR images, includes the anatomic designations of the central and transitional zones.[318, 320] The central and transitional zones are histologically and anatomically distinct,[15, 220] but the echogenicity on ultrasound and MR signal intensity characteristics are similar. In addition, the distinction between these becomes distorted and obscured by the development of hyperplasia.[320]

The *peripheral zone* shows higher signal intensity on T2-weighted images because of the presence of generally larger and more numerous glandular lumina than in the fibromuscular tissue of the central gland.[318] When the gland is affected by BPH, a thin, low-signal-intensity boundary usually appears between the central nodules and the peripheral gland.

The *anterior fibromuscular stroma* is a low-signal-intensity structure occupying the anterior edge of the prostate (Fig. 45–8).[134, 273]

The apex of the prostate, approximately the inferior 1.5 cm, is composed primarily of peripheral zone and urethra unless considerable BPH is present. Coronal T2-weighted images show the apex best (see Fig. 45–7). The central zone of the prostate extends from the verumontanum to the base of the gland, becoming progressively wider superiorly so that at the base it occupies most of the transverse area of the prostate. The lower signal intensity of this tissue is similar to that of a prostate carcinoma, rendering the base of the gland a more difficult area in which to identify carcinomas.

The prostatic capsule is not a true capsule but a thin fibromuscular band that blends with the prostatic stroma and, to a lesser extent, the periprostatic tissues. This band is incomplete at the apex.[15, 402] On T2-weighted images, the prostatic capsule appears as a thin, low-signal-intensity line at the margin of the prostate (see Fig. 45–7).[266, 318, 320] This band tends to have a signal intensity similar to that of tumors, rendering direct assessment of its integrity difficult when tumors abut the capsule. Posteriorly, the capsule blends with the prerectal fascia of Denonvilliers.[402] Nerves and vessels lie in the adjacent pericapsular fat. These are particularly prominent anterior to the apex (the anterior periprostatic plexus) and posterolateral to the peripheral zone (the neurovascular bundles). The neurovascular bundles are important structures to assess for nerve-sparing prostatectomy.[369] The venous plexus around the prostate shows high signal intensity on T2-weighted images (see Fig. 45–7).[279]

The seminal vesicles are easily identified on MR images as convoluted tubular structures coursing posterior and superior to the base of the prostate (Fig. 45–9). The seminal fluid within the lumina and glandular mucosa show high

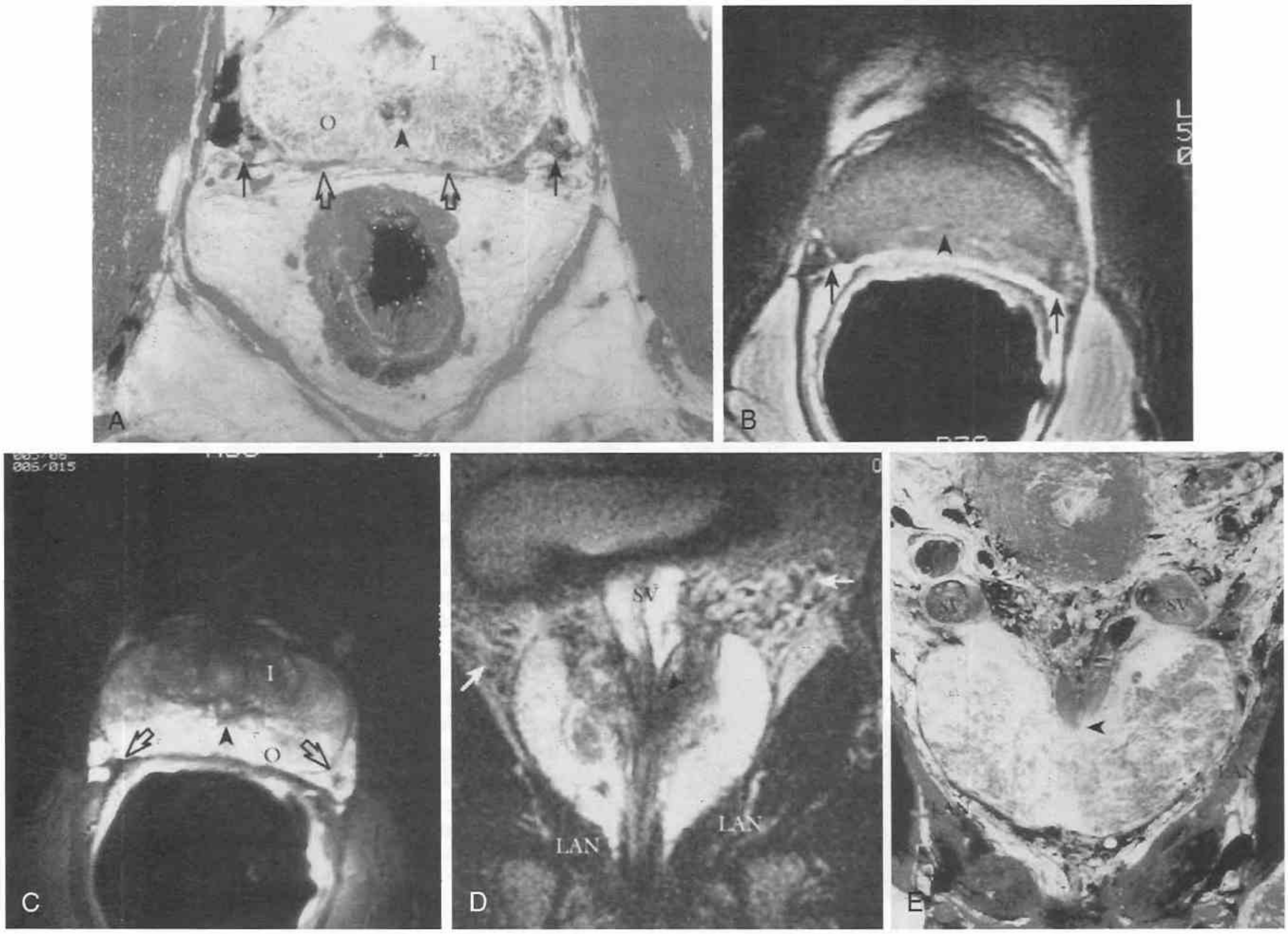

Figure 45–7. MRI anatomy of the prostate. Cadaveric sections (*A* and *E*) and MR images (*B* and *D*) demonstrate some of the anatomic features in the male pelvis.

A, Transverse section at the midprostate shows the inner gland (I) and the outer gland (O) of the prostate. The neurovascular bundles *(black arrows)* and the ejaculatory ducts *(black arrowhead)* are demonstrated. The prostatic capsule appears as a low-signal-intensity rim *(open arrows)*.

B, T1-weighted, spin-echo image shows little differentiation of central and peripheral gland. The neurovascular bundles are demonstrated laterally *(arrows)*. The *arrowhead* indicates the ejaculatory duct.

C, T2-weighted, fast spin-echo image is much better for differentiating between the inner (I) and the outer (O) prostate gland. Ejaculatory ducts *(arrowhead)* and neurovascular bundles and prostate capsule *(open arrows)* are shown.

D and *E*, Coronal T2-weighted *(D)* and cadaveric *(E)* images through the posterior prostate show the seminal vesicles and ejaculatory ducts *(arrowheads)*, seminal vesicles and ampulla of the vas deferens (SV), the periprostatic venous plexus *(black arrowheads)*, and the levator ani muscle (LAN).

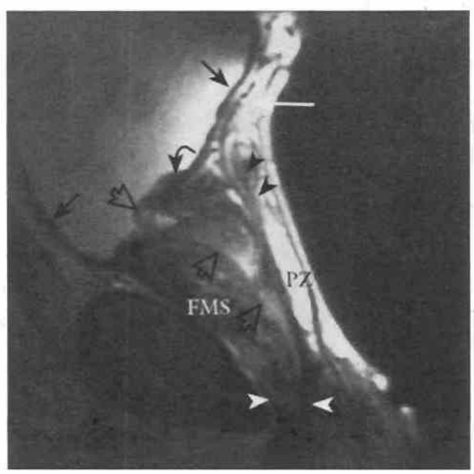

Figure 45–8. Sagittal midline, T2-weighted, fast spin-echo, endorectal coil imaging of the prostate gland. The seminal vesicles *(white arrow)*, ejaculatory ducts *(black arrowheads)*, bladder neck and prostatic urethra *(open arrows)*, membranous urethra *(white arrowheads)*, anterior fibromuscular stroma (FMS) and peripheral zone (PZ), and bladder wall *(black arrows)* are shown. Small nodules of benign prostatic hypertrophy can be seen bulging the trigone of the bladder *(curved arrow)*.

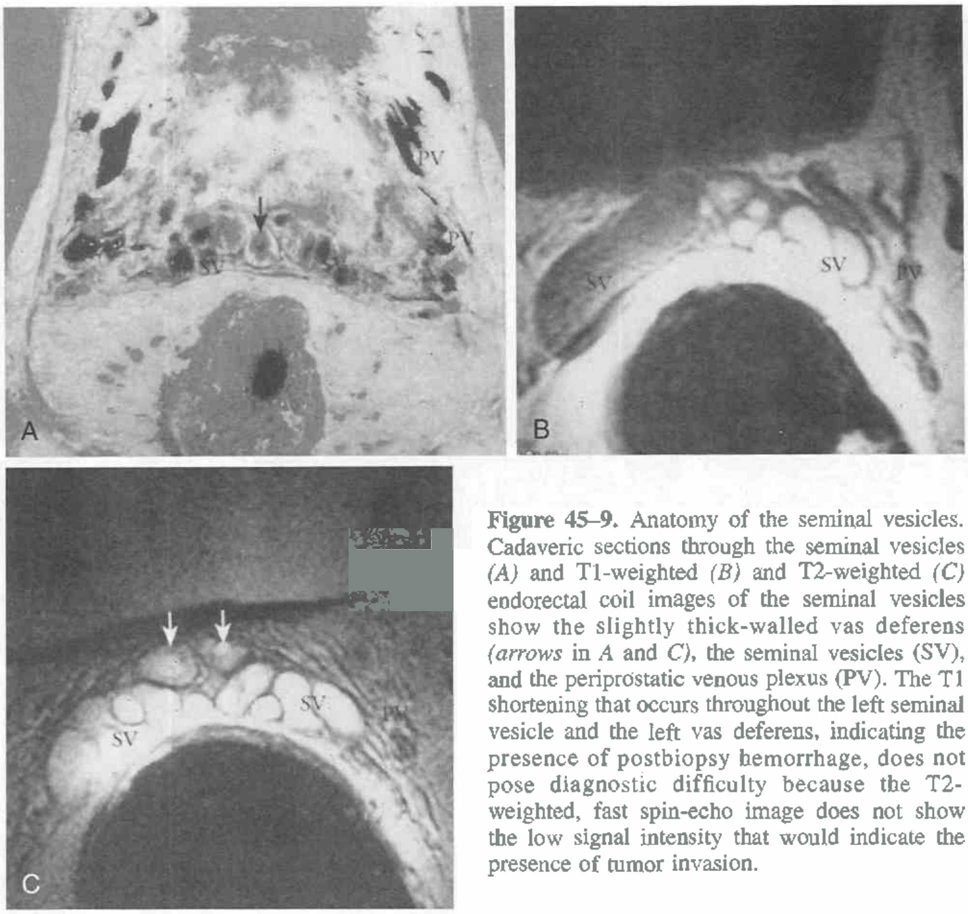

Figure 45–9. Anatomy of the seminal vesicles. Cadaveric sections through the seminal vesicles *(A)* and T1-weighted *(B)* and T2-weighted *(C)* endorectal coil images of the seminal vesicles show the slightly thick-walled vas deferens *(arrows* in *A* and *C)*, the seminal vesicles (SV), and the periprostatic venous plexus (PV). The T1 shortening that occurs throughout the left seminal vesicle and the left vas deferens, indicating the presence of postbiopsy hemorrhage, does not pose diagnostic difficulty because the T2-weighted, fast spin-echo image does not show the low signal intensity that would indicate the presence of tumor invasion.

signal intensity on T2-weighted images. The walls show low signal intensity.[266, 318, 320] The size of the seminal vesicles is highly variable. Because spread of tumor to the seminal vesicles occurs directly from the base of the gland or via the ejaculatory ducts,[402] it is important to image the inferior aspect of the seminal vesicles separately from the (low-signal-intensity) base of the gland with coronal or sagittal images. Medially, the vesicles terminate just posterolateral to the ampullae of the vas deferens, which demonstrate a thicker, low-signal-intensity wall (see Fig. 45–9).

The course of the vas deferens can be traced from the spermatic cord in the inguinal canal, laterally along the pelvic sidewall, and then medially to the base of the prostate gland. The distal few centimeters of each vas widens to form the ampulla, which contains the tortuous lumen and a thicker muscular wall (see Fig. 45–9). This thickening should not be confused with seminal vesicle invasion by prostatic carcinoma.

Scrotum

Scrotal MRI is usually performed to evaluate testicular abnormalities. The testis, like the peripheral zone of the prostate, demonstrates a fairly long T2 and, therefore, fairly high signal intensity on T2-weighted images.[19, 212, 295, 330] The signal intensity is homogeneous, except for faint, low-signal-intensity septa sometimes seen radiating from the low-signal-intensity mediastinum testis (Fig. 45–10).[212, 330]

The testis is invested in a thin, low-signal-intensity capsule, which represents the tunica albuginea and the tunica vaginalis.[19] The latter reflects over the bare area of the testis, thus serving to anchor the testis to the scrotal wall, and covers the interior of the scrotum as the parietal tunica vaginalis.[19] The epididymis demonstrates inhomogeneous intermediate signal intensity on T2-weighted images (see Fig. 45–10).[330] High-signal-intensity venous vessels of the pampiniform plexus surround the vas deferens in the spermatic cord and frequently obscure it.

Female Pelvic Anatomy

Female genital anatomy is best displayed on T2-weighted images. The sagittal plane is ideal for demonstrating the uterine zonal anatomy and vaginal anatomy and for showing the relationship of abnormalities of these organs to the bladder and rectum. Therefore, imaging in this plane and one other plane, usually axial, is important to adequately evaluate the female pelvis. T1-weighted images, offering information somewhat similar to that obtainable from CT scanning, show poor soft tissue contrast; however, these images are important for defining fat planes, adenopathy, and fat or hemorrhage in pathologic masses.

MRI provides striking depiction of the anatomy of the uterus, yielding information unavailable by other imaging techniques. The inner high-signal-intensity stripe, which represents the glandular tissue of the endometrium,[192, 215] is sharply demarcated from the very-low-signal-intensity deeper myometrium (the "junctional zone") (Fig. 45–11).

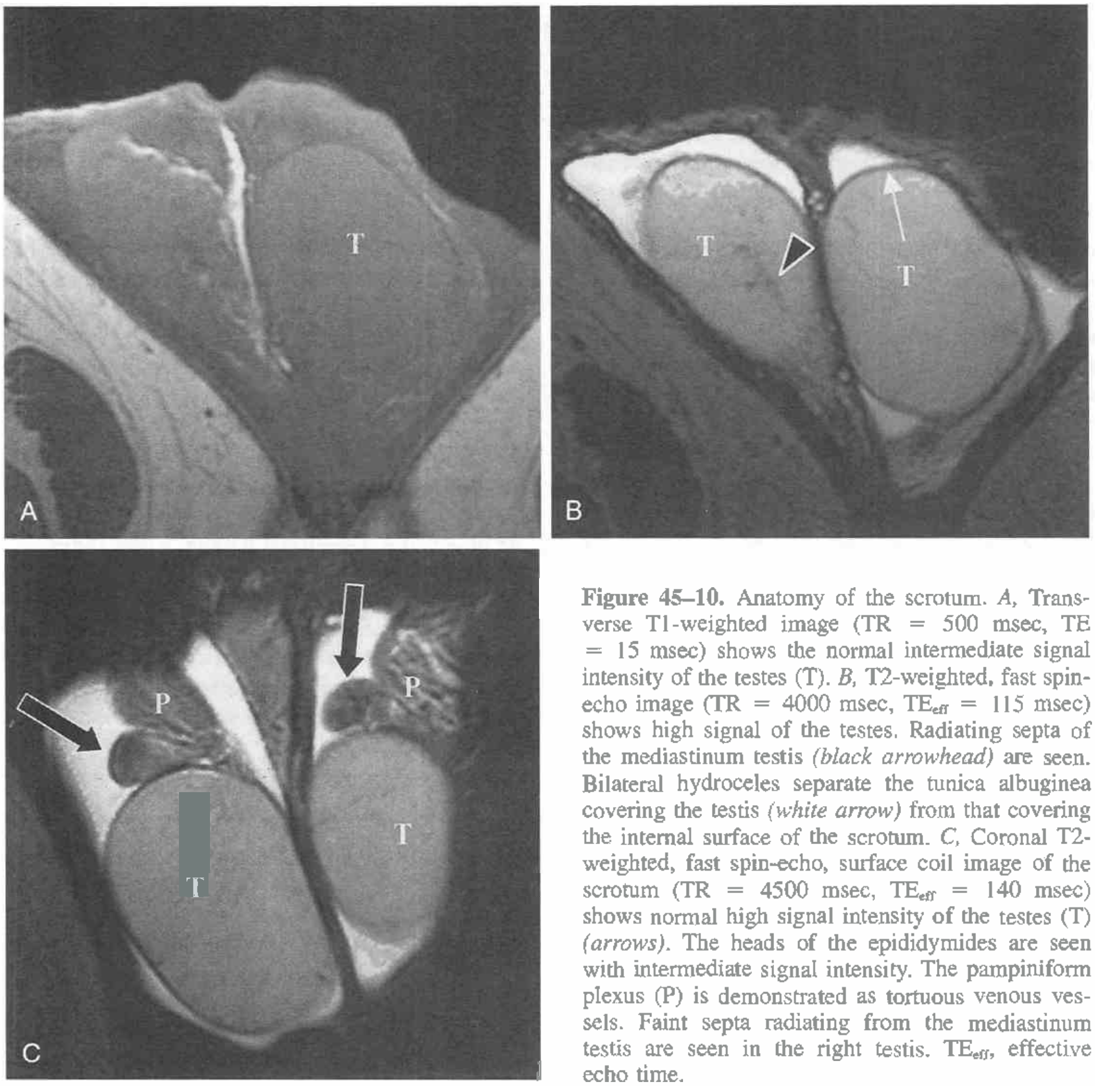

Figure 45–10. Anatomy of the scrotum. *A,* Transverse T1-weighted image (TR = 500 msec, TE = 15 msec) shows the normal intermediate signal intensity of the testes (T). *B,* T2-weighted, fast spin-echo image (TR = 4000 msec, TE_{eff} = 115 msec) shows high signal of the testes. Radiating septa of the mediastinum testis *(black arrowhead)* are seen. Bilateral hydroceles separate the tunica albuginea covering the testis *(white arrow)* from that covering the internal surface of the scrotum. *C,* Coronal T2-weighted, fast spin-echo, surface coil image of the scrotum (TR = 4500 msec, TE_{eff} = 140 msec) shows normal high signal intensity of the testes (T) *(arrows).* The heads of the epididymides are seen with intermediate signal intensity. The pampiniform plexus (P) is demonstrated as tortuous venous vessels. Faint septa radiating from the mediastinum testis are seen in the right testis. TE_{eff}, effective echo time.

Figure 45–11. Uterine anatomy as shown by sagittal imaging. T2-weighted, multicoil image (TR = 4000, TE_{eff} = 126) demonstrates the uterus with a normal-appearing junctional zone *(white arrowheads).* An anterior indentation of the endometrium can be seen at the site of a prior cesarean section *(white arrow).* The urethral wall *(open arrow)* and the normal bladder wall *(curved arrow)* are demonstrated. A tampon lies within the vagina (V). TE_{eff}, effective echo time.

This represents a compact, more cellular smooth muscle zone with a lower water content than the outer myometrium.[41, 216, 326] The bulk of the myometrium appears as intermediate-signal-intensity tissue with numerous high-signal-intensity small vessels running through it. To a variable degree, a thin, patchy subserosal low-signal-intensity layer may appear, also representing a smooth muscle zone similar to the junctional zone.[192, 215, 326]

The endometrium increases in thickness during the follicular phase of the cycle.[217] In women taking oral contraceptives, no such increase occurs; the endometrium is, in fact, thinner than normal throughout the cycle.[217] In addition, signal intensity on T2-weighted images is increased in these women.[217] Blood products with variable signal intensity on T1-weighted and T2-weighted images may appear in the uterine cavity during the menses and after dilatation and curettage.[13, 217] In postmenopausal women, the myometrium tends to lose signal and thus the contrast between the junctional zone and the outer myometrium decreases.

The cervix demonstrates a low-signal-intensity stroma that is continuous with the low signal intensity of the uterine corpus. This occupies a greater proportion of the cervical wall than the uterine body, with a correspondingly thinner outer myometrium.[328] The cervical mucosa and submucosa can be distinguished from cervical canal glandular secretions.[215] Depending on the level, the cervix is bordered externally by the lumen of the vaginal fornices (posteriorly and laterally); by the vesicovaginal septum (anteriorly); by the parametrial tissues, including cardinal ligaments, uterosacral ligaments, and paracervical venous plexus (laterally); and by the peritoneum of the cul-de-sac (posteriorly) (Fig. 45–12). These adjacent structures serve as important routes of invasion by cervical carcinoma.

High-resolution, T2-weighted images depict the normal ovaries as having an intermediate-signal-intensity central stroma with numerous high-signal-intensity follicular cysts and a low-signal-intensity cortex (Fig. 45–13).[257, 265] On high-resolution, long-TR/TE FSE images, these cysts may appear more numerous than is encountered with conventional body-coil SE techniques because of the higher resolution and contrast provided by heavily T2-weighted FSE sequences.[215, 348] This appearance should not be confused with polycystic ovarian disease, which shows innumerable cysts peripherally situated, with a fibrotic ovarian tunica (Fig. 45–14). The identification of ovarian follicular cysts by MRI is important in definitively identifying structures as ovaries. The presence of small follicular cysts splayed around an adnexal mass can help the radiologist to ascertain the ovarian origin of a mass (Fig. 45–15). Postmenopausal ovaries demonstrate fewer, smaller cysts or an absence of cysts (Fig. 45–16)[257, 265]

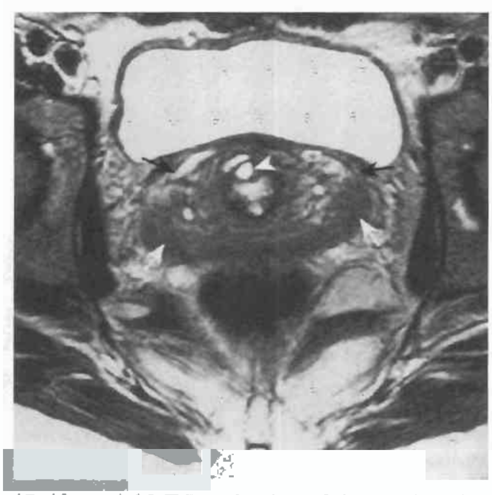

Figure 45–12. Axial MRI evaluation of the cervix. T2-weighted, fast spin-echo image through the cervix and vaginal fornices *(white arrows)* shows the low-signal-intensity cervical myometrium. Several small nabothian cysts *(white arrowhead)* are also seen. The perivaginal and pericervical plexus veins appear as high-signal-intensity structures in the parametrium *(black arrows)*.

Round ligaments are identified as low-signal-intensity structures coursing from the uterine cornua toward the inguinal canal. The peritoneal reflections of the broad ligament are not visualized except when bordered by ascites. The uterine arteries and veins within the broad ligaments, however, can be seen, and they serve as a landmark for the broad ligament (see Fig. 45–13). Normal fallopian tubes are usually not well depicted. Dilatation of the tubes by fluid or blood renders the tubes visible as serpentine, high-signal-intensity structures with a discrete low-signal-intensity muscularis.[260]

Bladder and Rectum

Four layers of the bladder wall are important for staging of bladder carcinoma: the mucosa, the lamina propria, and two muscular layers. Depending on the pulse sequence used, the degree of bladder distention, and any pathologic processes affecting the bladder, usually one or two of these layers can be seen on MR images.[90]

On T2-weighted images, the hypointense muscularis of the wall can always be discerned; high-resolution studies may depict more than one muscular layer. The inner muscularis layer shows very low signal intensity on T2-weighted images and the outer muscular layer shows intermediate signal intensity because of its looser muscle structure.[243] Inflamed submucosa or lamina propria may exhibit high signal intensity on T2-weighted images, similar to urine in the bladder.[122]

Intermediate-weighted images may depict this abnormal layer as high signal intensity contrasting with low-signal-intensity urine.[90, 91] Gadolinium-enhanced T1-weighted images can depict the mucosa as a thin, enhancing rim internal to the bladder wall.[245, 364]

The layered structure of the rectal wall is best depicted by high-resolution imaging with an endorectal coil.[147, 148] With this technique, the muscularis can be discerned and the mucosa and submucosa can be seen (Fig. 45–17).[57] High-resolution imaging of the rectal wall shows the low signal intensity of the mucosa and muscularis contrasted with the higher-signal-intensity submucosa on T2-weighted images.[148] No other technique can show the relationships of the rectum to important structures, such as the puborectalis and levator ani, with the multiplanar capability of MRI.[393]

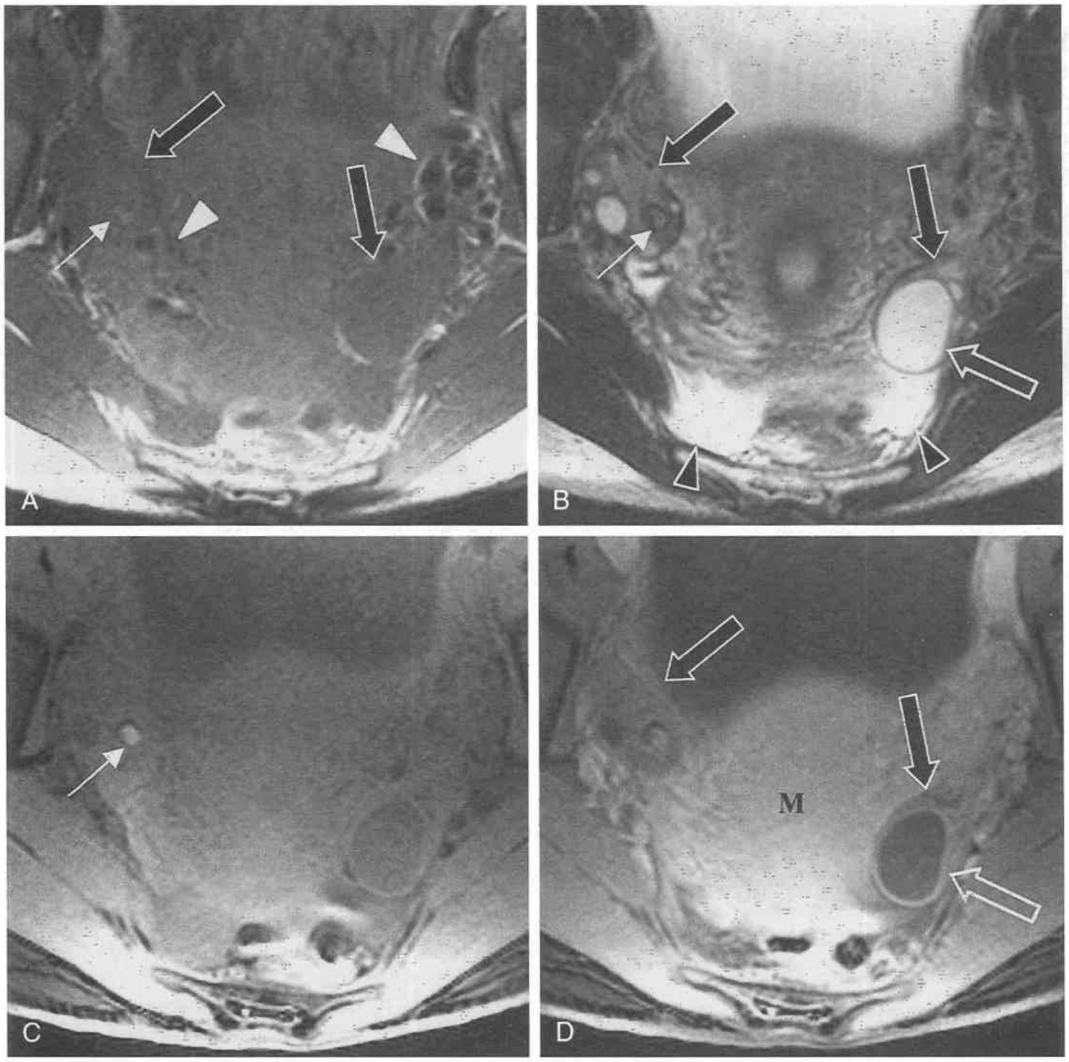

Figure 45–13. Normal ovaries in a 33-year-old woman.

A, T1-weighted, spin-echo image (TR = 617 msec, TE = 16 msec) shows the ovaries *(black arrows)* poorly differentiated from adjacent adnexal structures. Signal voids in the pelvic side wall and broad ligament vessels *(white arrowheads)* can be seen. A faint hyperintense focus is in the right ovary *(thin white arrow).*

B, Axial T2-weighted, fast spin-echo image (TR = 3817 msec, TE_{eff} = 119 msec) shows the right and left ovaries *(black arrows).* Multiple follicles are seen in the right ovary and a cyst is seen in the left ovary *(open arrow).* A normal amount of cul-de-sac fluid is identified *(black arrowheads).* The small endometriosis focus *(thin white arrow)* shows low signal intensity. TE_{eff}, effective echo time.

C, Fat-saturated, gradient-echo image (TR = 300 msec, TE = 2.9 msec), as in *A,* shows poor differentiation of the ovaries from the surrounding adnexa. The high-signal-intensity focus in *A* retains its high signal intensity *(arrow),* establishing that it is not fat.

D, Gadolinium-enhanced, fat-saturated, gradient-echo image (TR = 300 msec, TE = 2.9 msec) shows enhancement of both ovaries *(black arrows)* to a lesser degree than the myometrium (M). The rim of the corpus luteum cyst on the left *(open arrow)* enhances.

Evaluation of the Male Pelvis

Benign Disorders

The value of MRI for benign disease affecting the male pelvis has not been well defined. Because of cost considerations, availability, and the nature of the information needed, ultrasonography generally has proved most useful for imaging of the scrotum and penis. Clinical evaluation alone serves to identify most infectious diseases affecting the male genitalia, such as prostatitis and epididymitis. Transrectal sonography can be used to adequately visualize various developmental abnormalities affecting the prostate and seminal vesicles. MRI does not replace contrast radiography for evaluation of the urethra. Nonetheless, a number of applications for MRI have been described, and the technique may prove useful in selected cases when conventional evaluation is inadequate.

MRI may be of value as an alternative to CT in localizing undescended testes. A testis is undescended in about 3% of infants, but most of these descend by the age of 1 year. Cryptorchidism affects approximately 0.3% of the male population[207] and may be bilateral in 25% of cases.[207] Histologic changes in the malpositioned testis begin as early as 2 years of age and include tubular atrophy, fibrosis, small size, and a paucity of germ cells.[299] The undescended testis is subject to a 10-fold to 40-fold increased risk

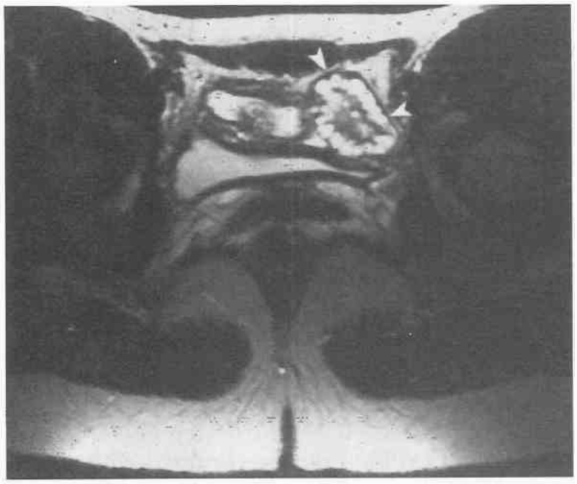

Figure 45–14. Polycystic ovarian syndrome in a 29-year-old woman. Axial T2-weighted, fast spin-echo image (TR = 4000 msec, TE_{eff} = 126 msec) shows a left ovary with innumerable high-signal-intensity peripheral cysts surrounded by a slightly thickened low-signal-intensity tunica *(arrowheads)*. TE_{eff}, effective echo time.

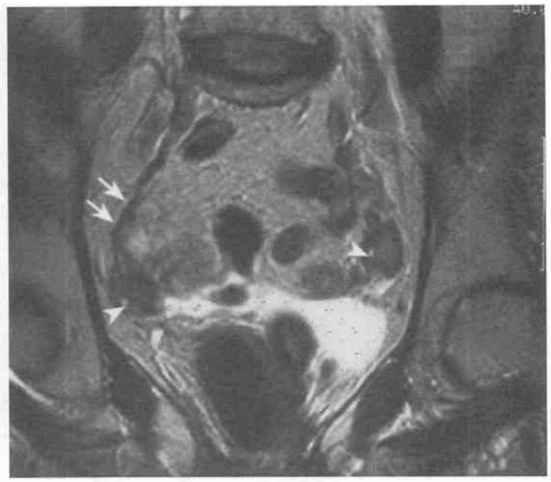

Figure 45–16. Normal postmenopausal ovaries. Coronal T2-weighted, fast spin-echo image (TR = 4000, TE_{eff} = 140 msec) demonstrates small, low-signal-intensity ovaries. The ovarian vessels leading to the right ovary *(arrows)* and the presence of a tiny follicular cyst in each ovary *(arrowheads)* identify these structures as ovaries. (For reference, a 5-cm scale is on right side of image). TE_{eff}, effective echo time.

of malignancy and an increased incidence of infertility; interestingly, there is an increased likelihood of both in the contralateral, normally descended testis as well.[207, 299] Almost 50% of occluding malignancies in malpositioned testes occur in intra-abdominal testes.[207]

The standard therapy for cryptorchidism is surgical, either orchiopexy for cases discovered early or orchiectomy for patients older than 10 years of age.[206, 207] Orchiopexy renders tumor surveillance easier and may decrease the incidence of malignancy.[206, 207]

Most patients with cryptorchidism do not require radiologic evaluation because the testis can be palpated in the inguinal canal. In approximately 4% of these patients, the testis cannot be palpated.[93] In these cases, radiologic evaluation with CT or MRI may be beneficial in localizing the testis. CT has been useful in this regard,[190] but high sensitivity (94%) with MRI in a small series has also been reported.[93] The undescended testis may have lower signal intensity and may be smaller on T2-weighted images than the normal testis.[93] The importance of not confusing lymph nodes or the remnant pars intravaginalis gubernaculi has been stressed.[303] MRI has also been used to identify polyorchidism on the basis of typical signal intensity and testicular morphology of the supernumerary testes.[20]

In most cases of epididymo-orchitis, diagnostic imaging is not needed because the condition can be adequately evaluated on clinical grounds. Patients not responding to antimicrobial therapy or whose clinical history and examination findings are compatible with those of tumor may require imaging to exclude an abscess or intratesticular mass.[383] The hallmark of intrascrotal infection is evidence of epididymal inflammation: increased size, increased signal on T2-weighted images, sympathetic hydrocele, and increased vascularity.[18, 383] The increased vascularity may manifest itself as increased numbers of vessels and signal voids seen in vessels that usually display slower flow.[18, 212, 383]

The testis often demonstrates evidence of orchitis as patchy areas of lower signal intensity, compared with the normally high signal intensity of testicular parenchyma (Fig. 45–18).[18, 212, 383] The fluid usually evident in the scrotal sac may outline the bare area of the testis. Visualization of this structure helps to exclude testicular torsion, which may be in the clinical differential diagnosis of subacute scrotal pain.[212, 383] If fluid within the hydrocele is other than simple fluid (i.e., has very long T1 and T2) the presence of hemorrhage or infection of the fluid is suggested. Gadolinium-enhanced images may be valuable in this regard to

Figure 45–15. Sertoli-Leydig cell tumor of the left ovary. T2-weighted, fast spin-echo image (TR = 4000 msec, TE_{eff} = 140 msec) through the cervix and left ovary depicts a solid mass arising within the left ovary *(arrow)*, displacing and deforming the small follicular cysts *(arrowheads)*. In this 17-year-old patient with virilization, the preoperative imaging diagnosis of ovarian stromal neoplasm was made. TE_{eff}, effective echo time.

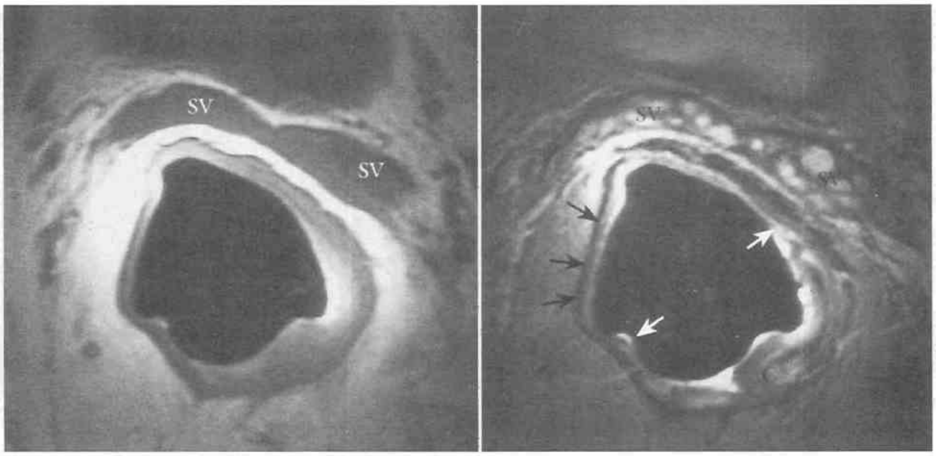

Figure 45–17. Endorectal coil imaging of superficial rectal tumor. *A*, Axial T1-weighted, spin-echo image (TR = 500 msec, TE = 14 msec) shows posterolateral rectal wall thickening. *B*, Axial fast spin-echo image (TR = 3800, TE_{eff} = 133 msec) shows the mucosal tumor (C). *Black arrows* indicate the low-signal-intensity rectal muscularis propria. Normal mucosa *(white arrows)* appears as a thin intermediate-signal-intensity stripe. SV, seminal vesicles; TE_{eff}, effective echo time.

demonstrate necrotic or infarcted areas of the testis as nonenhancing areas.

Testicular torsion is related to abnormally diminutive attachments of the testis to the scrotal wall (the so-called bell-clapper deformity), resulting in the capacity of the testis to rotate and twist about the spermatic cord.[383] Depending on the degree and duration of twist, this causes congestion and interstitial hemorrhage in the testis and progresses to hemorrhagic venous infarction due to venous occlusion.[299] Arterial occlusion producing complete infarction occurs late and infrequently. Spermatic cord torsion typically occurs in the second and third decades. Testicular torsion is an acute surgical condition. If the diagnosis can be made within 24 hours, detorsion and orchiopexy may save the testis.

Dynamic testicular scintigraphy is the most common means of assessing for testicular torsion and has generally high accuracy rates.[125] Color Doppler ultrasonography has also been used, with rates of 86% to 100% sensitivity and 100% specificity reported.[47, 227] It is unlikely that MRI can improve on these results because currently there is no way to definitively demonstrate flow or the absence of flow in the pampiniform plexus and testicular artery by MRI.

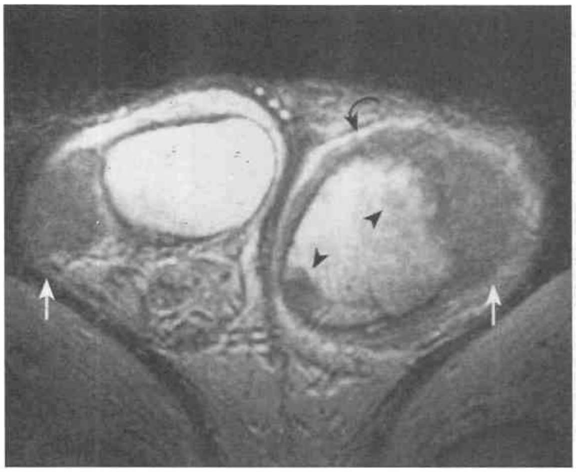

Figure 45–18. Chronic epididymo-orchitis in a 30-year-old man with pulmonary and scrotal sarcoidosis. The hallmarks of chronic epididymo-orchitis are present, including the marked enlargement at the epididymides *(white arrows)*, patchy low signal intensity in the testes *(black arrowheads)*, and hydrocele *(curved arrow)*.

MRI does reveal the parenchymal changes of torsion, however, showing hemorrhage and edema within the epididymis and testis. This produces lower than normal signal in the testicular parenchyma, often in a linear pattern radiating from the mediastinum.[371, 383] The affected testicle tends to be smaller than normal. The epididymis enlarges and demonstrates heterogeneous low signal intensity, in a pattern similar to that seen with epididymitis. A key finding, if it can be identified, is the twisted portion of the spermatic cord producing a vortex of helical low-signal-intensity structures surrounded by high-signal-intensity edematous cord.[383] In the absence of this torsion knot, it may be difficult to reliably distinguish torsion from inflammatory disorders of the testis. Torsion is typically not associated with the MRI evidence of increased vascularity seen in epididymo-orchitis.[383]

MRI with an endorectal coil has also been used in men with ejaculatory dysfunction to identify developmental abnormalities of the prostate and seminal vesicles.[322] Prostatic cysts along the course of the ejaculatory ducts (müllerian duct cysts),[111, 372] seminal vesicle cysts associated with ipsilateral seminal vesicle and renal agenesis, seminal vesicle calculi, and some cases of chronic inflammatory disease of the prostate and seminal vesicles can be identified (Fig. 45–19).[322] Evidence of hemorrhage is frequently seen in the seminal vesicles (short T1 of fluid) in men with hemospermia.

Acute or chronic prostatitis is frequently seen histologically and may mimic the MRI findings of carcinoma in the peripheral zone.[273] Prostatitis usually manifests as patchy, low-signal-intensity areas in the peripheral zone. Granulomatous prostatitis is indistinguishable from carcinoma by

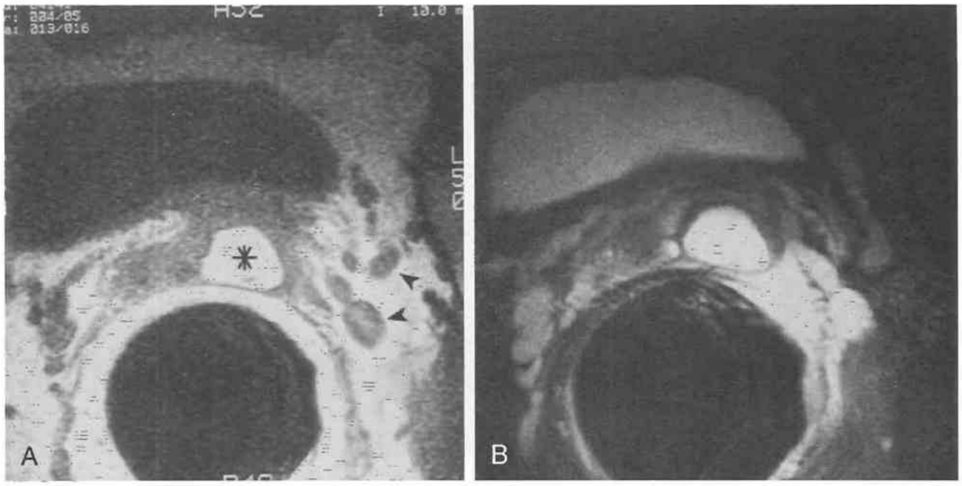

Figure 45–19. MRI evaluation of ejaculatory dysfunction. *A,* Axial T1-weighted, spin-echo, endorectal coil image shows high-signal-intensity cystic mass in the left seminal vesicle *(asterisk)*. Numerous periprostatic veins descend on the left *(arrowheads)*, but the seminal vesicle on the left is atrophic. *B,* T2-weighted, fast spin-echo image shows the cystic nature of the mass and again shows absence of the seminal vesicle on the left. The right seminal vesicle is normal and better demonstrated on other images. These findings are typical of a wolffian duct cyst with seminal vesicle aplasia, which was confirmed pathologically.

MRI, with discrete low-signal-intensity nodular lesions (Fig. 45–20), or generalized low signal intensity in the peripheral zone. Prostatic abscesses can easily be identified with MRI, and the multiplanar display may aid in the planning of surgical drainage (see Fig. 45–25).

Malignancies of the Male Pelvis

Testicular Carcinoma

Testicular malignancies are a leading cause of cancer and account for 8.8% of deaths in 15- to 34-year-old males.[118] Approximately 10% are associated with undescended testes.[206, 207] Important genetic differences in incidence are seen; the rate in Africans and African Americans is low. Testicular neoplasms are frequently misdiagnosed as epididymo-orchitis or other disorders on initial clinical examination.[268] Therefore, a role may exist for imaging to distinguish testicular masses from extratesticular processes (Fig. 45–21). Treatment and, to a certain extent, MRI features are dependent on the cell type and extent.[82, 126, 268]

Testicular neoplasms are broadly categorized into (1) germ cell tumors (~93%), (2) lymphomas (5%), and (3) sex cord–stromal tumors (2%). Sex cord–stromal cells are usually benign but capable of elaborating steroid hormones.

Germ cell tumors are further subdivided into *seminomatous tumors (seminomas)* and *nonseminomatous tumors*, an important distinction because of the different approaches to treatment of these two classes. In general, after orchiectomy and after the histologic type of tumor has been established, patients with seminomatous tumors receive radiation to the retroperitoneal lymph nodes, whereas pa-

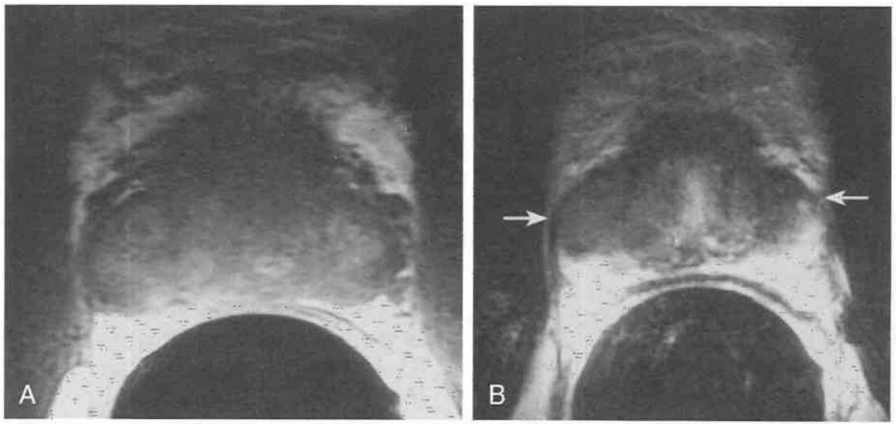

Figure 45–20. Granulomatous prostatitis. *A,* Axial T1-weighted, spin-echo image (TR = 400 msec, TE = 12 msec) shows slightly hyperintense nodules within the prostate but a normal overall prostatic morphology. *B,* Axial fast spin-echo image (TR = 4000 msec, TE_{eff} = 140 msec) shows hypoechoic nodules within the peripheral zone *(arrows)*. Pathologic examination of the cystoprostatectomy specimen in this patient, who had been treated with bacille Calmette-Guérin (BCG) therapy for a bladder carcinoma, showed only granulomatous prostatitis. The appearance of the low-signal-intensity nodules in the peripheral zone, however, is compatible with carcinoma. TE_{eff}, effective echo time.

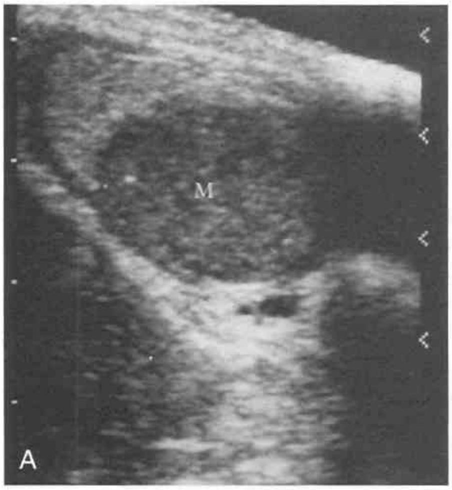

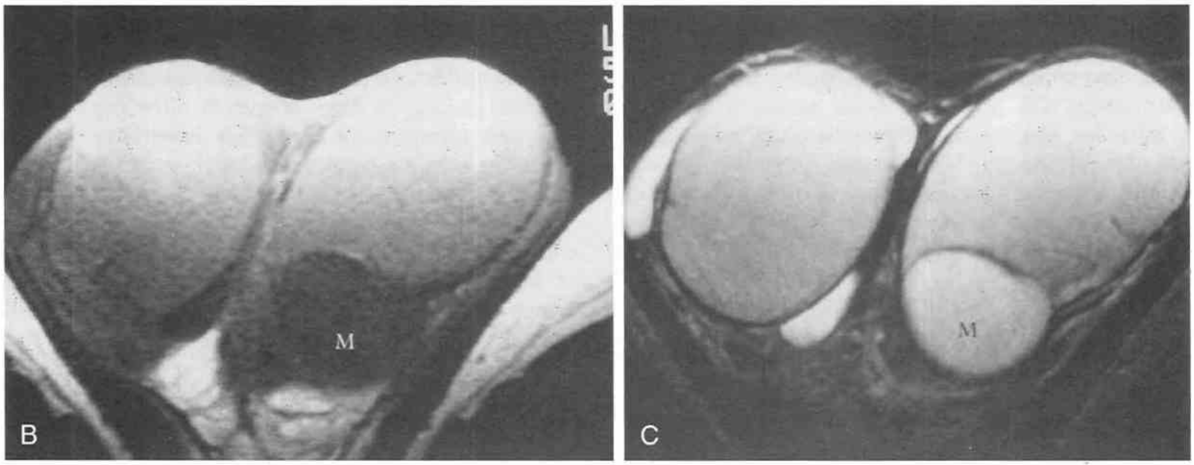

Figure 45–21. MRI differentiation of a palpable, left-sided testicular mass in a 24-year-old man. *A*, An ultrasound examination had demonstrated a left testicular mass (M) that showed diffuse moderate echogenicity and was thought to be a solid lesion. Increased through-transmission, however, can be noted. *B*, T1-weighted, spin-echo image (TR = 500 msec, TE = 15 msec), shows a well-circumscribed mass (M) of low signal intensity. *C*, T2-weighted, fast spin-echo image (TR = 4000 msec, TE_{eff} = 115 msec), shows the mass (M) to have very high signal intensity. The appearance of the mass in *B* and *C* is consistent with that of a cyst, and pathologic examination showed an intratesticular left-sided epidermoid cyst. A small right-sided hydrocele can be seen in *C*. TE_{eff}, effective echo time.

tients with nonseminomatous tumors usually undergo retroperitoneal lymphadenectomy and chemotherapy.[82, 126, 268] Approximately 30% of germ cell tumors appear to be of one cell type when combined criteria of histology and tumor markers are used.[299]

Seminomas are the most common type of germ cell tumor. The peak age of incidence is in the fourth and fifth decades, about one decade later than that of the nonseminomatous tumors. Pathologically, these tumors appear as solid, large masses without hemorrhage or necrosis, and they usually do not violate the tunica albuginea. On MR images, they appear as lobulated, more or less homogeneous intratesticular masses, and show predominantly intermediate signal on T2-weighted images, which contrasts with the high signal intensity of the remaining testicular tissue.[157] They are often large enough to replace the testicle entirely. Small associated hydroceles are common. Unlike the situation with epididymo-orchitis, the testicular adnexa, particularly the epididymis, appear normal when the testicular tumors are confined by the tunica albuginea (Fig. 45–22). Of course, more advanced tumors extend into the epididymis and enlarge it.

Nonseminomatous tumors include embryonal cell carcinomas, yolk sac tumors, teratomas, and choriocarcinomas, although most contain mixed elements. These tumors tend to be locally advanced, with a higher likelihood of metastases than is the case with seminomas. MRI demonstrates

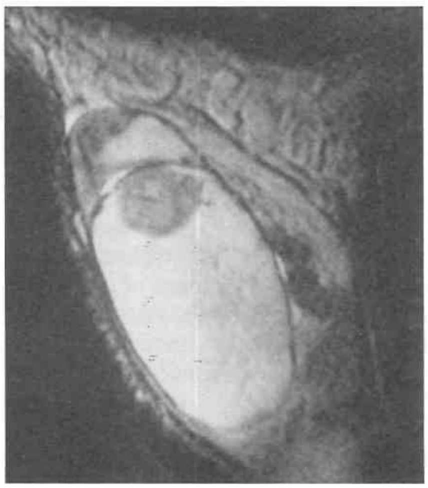

Figure 45–22. Clinically palpable abnormality of the testis in a 31-year-old man. Sagittal T2-weighted, fast spin-echo image (TR = 4500 msec, TE_{eff} = 140 msec) shows a low-signal-intensity mass in the superior pole of the testis without involvement of the overlying epididymis. The mass, which is confined by the tunica albuginea, proved to represent a Sertoli-Leydig cell tumor. TE_{eff}, effective echo time.

considerably more heterogeneity, compared with seminomas, and areas of high and low signal intensity on T2-weighted images.[157] A thin, low-signal-intensity capsule is a common finding.[157]

MRI, like ultrasonography, cannot distinguish benign from malignant intratesticular masses, except for simple lesions such as cysts (see Fig. 45–21) and hematomas.[212, 295, 330, 371] Therefore, orchiectomy is indicated for any solitary intratesticular mass. MRI may be more accurate than ultrasound in establishing the presence of diffuse infiltrating neoplasm involving the testis on the basis of diffusely decreased signal intensity.[371]

The role of pre-orchiectomy ultrasound or MRI for local staging of testicular neoplasms has not been defined. Initial studies have indicated poor accuracy of both ultrasound and MRI for this purpose.[371] Most attention has been focused on cross-sectional imaging of the retroperitoneum to determine lymph node metastases. Although MRI may be equally sensitive in detecting enlarged lymph nodes,[83] it cannot distinguish carcinomatous lymphadenopathy from benign lymphadenopathy. CT and MRI have accuracy rates of 75% to 80% for staging the retroperitoneum in patients with testicular carcinoma.[118, 277] Because lymphadenectomy can certainly improve these rates and is often believed to be therapeutic as well as diagnostic, it is preferred for initial management of low-stage disease.[82, 118, 277]

Prostate Carcinoma

Prostate carcinoma is the most common carcinoma discovered in men and the third leading cause of cancer mortality, with an estimated 39,000 deaths per year.[186] Studies of autopsies and prostatectomy specimens have demonstrated that clinically inapparent prostate carcinomas have a very high general prevalence in older men—an incidence of up to 80% in men older than 80 years of age.[324, 337] Most of these incidental carcinomas are low-volume, well-differentiated carcinomas with a good prognosis without treatment.[100, 154, 220, 324, 337, 357] Approximately 90% of these tumors remain undetected during the lifetime of the individual.[100] Relatively recent innovations, such as prostate-specific antigen (PSA) screening and ultrasound-guided biopsy, however, may considerably increase the number of carcinomas that are discovered.[56] There is evidence today that prostate carcinoma may be discovered at an earlier stage than previously.[272]

Clinicopathologic studies have revealed the major prognostic determinants of localized prostate carcinomas. Stage of disease, specifically the presence of capsular penetration and seminal vesicle invasion, was one of the first variables to be identified.[51] Capsular penetration and seminal vesicle invasion correlate with the presence of lymph node metastases, and with a poorer prognosis, and are generally considered a relative contraindication to prostatectomy.

The critical prognostic importance of cancer volume is also being realized. The incidence of lymph node metastases strongly correlates with the grade and volume of the tumor.[220, 395] These important determinants of cancer volume, grade, and local stage have provided part of the impetus for developing an imaging technique that can accurately depict the extent and volume of prostate carcinoma.[241] MRI demonstrates a higher accuracy for measurement of prostate volume than transrectal ultrasound.[290] This is especially important for calculating PSA corrections to distinguish patients with elevated PSA levels caused by BPH from those caused by carcinoma.[56, 250]

Approximately 5% to 10% of carcinomas arise in the central zone of the prostate. The remainder arise within the transitional zone of the gland, from which most benign prostatic hyperplasia nodules also arise, or from the peripheral zone. Most clinically significant prostate carcinomas arise in the peripheral zone. These distinctions are important because cancers largely confined to the central gland or within areas of BPH are generally not apparent with either ultrasonography or MRI.

Fortunately, most transitional zone tumors are low-volume, low-grade lesions that uncommonly extend outside the prostate gland or to the seminal vesicles.[105, 106, 220, 403] Incidental small foci of tumor discovered at transurethral resection of the prostate (TURP) may require no treatment; however, many stage A2 lesions may represent high-volume disease and may benefit from prostatectomy.[105, 337, 403, 421] Clinical staging of these lesions is often inaccurate,[421] and although tumor grade and PSA level may help stratify them, an accurate staging modality would be of benefit in managing the disease.[241, 337]

Prostate tumors spread by invasion through the prostatic capsule, by invasion of the seminal vesicles, by invasion of the bladder base, and by lymphatic spread to regional lymph nodes. Perineural invasion is a well-described feature of prostatic carcinoma, and although the presence of intraprostatic perineural spread is not itself a significant finding, the nerves serve as conduits to capsular transgression.[91, 147] Neural branches penetrate the capsule from the neurovascular bundle at the posterolateral edge of the prostate gland, at the superolateral margin, and at the apex.[220] These are the more common sites of capsular penetration (Fig. 45–23).

At the apex, such capsular penetration commonly results in positive surgical margins because of the difficulty of obtaining adequate margins around the prostate deep within the surgical field.[220, 221] In prostatectomy specimens (i.e., clinically stage B carcinomas), capsular penetration is often very shallow (<3 mm).[221] This fact highlights the need for high-resolution imaging for detection of capsular penetration.

Staging lymphadenectomy is generally performed before prostatectomy. The relative inaccuracy of lymphangiography and CT for determining spread to lymph nodes has led most urologists to sample nodes prior to prostatectomy. Spread typically occurs first to the hypogastric, obturator lymph nodes and, less commonly, to the external iliac chains.[219] Evaluation of these nodes with CT or MRI can obviate lymphadenectomy if the suspected nodes can be shown to contain metastasis by needle aspiration. The complication rate associated with lymphadenectomy is about 20% to 30%.[219]

The choice of treatment of prostatic carcinoma depends on many variables, including the clinical stage and grade of tumor, age of the patient, and concerns of the particular patient.[403] Options for treating early-stage disease range from no treatment to hormonal manipulation, radiation, and prostatectomy.[154, 347, 403] Stage A2 and stage B lesions show approximately equal survival rates with prostatectomy and

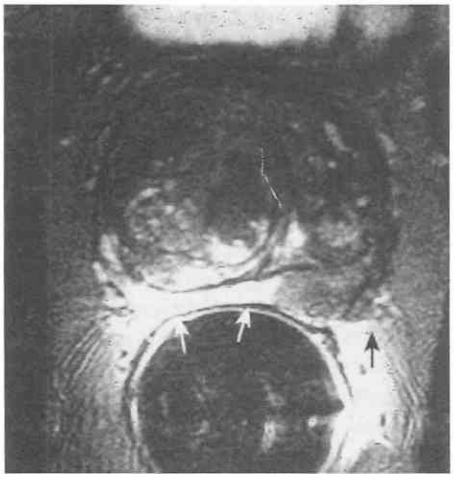

Figure 45–23. Invasion of the neurovascular bundle by prostate carcinoma. Axial T2-weighted fast spin-echo image (TR = 5000 msec, TE_{eff} = 140 msec) shows normal high-signal intensity to the right peripheral zone *(white arrows)*. A low-signal-intensity mass in the left posterolateral peripheral zone invades the left neurovascular bundle *(black arrow)* and invades through the capsule on the left side. The central gland is markedly enlarged and has the typical appearance of benign prostatic hyperplasia. TE_{eff}, effective echo time.

radiation therapy.[100, 403] However, rates of potency preservation above the approximately 50% level achievable with radiation therapy can be attained only with nerve-sparing prostatectomy or, possibly, with radioisotope implants.[100, 357]

The high levels of contrast between some carcinomas and the surrounding peripheral zone on MR images led to early enthusiasm for use of the technique in staging prostate cancer (Fig. 45–24; see Fig. 45–23).[127, 133, 274] Subsequent studies demonstrated fairly poor overall accuracy for MRI staging of prostate carcinoma, at least with the standard body receiver coil. Specifically, poor accuracy for staging results from an inability to assess capsular penetration and seminal vesicle invasion and frequently from an inability to even identify the tumor nodule.

Prostate tumors may not be correctly identified on MR images for several reasons:

1. Tumors may occur in the central gland, where contrast with the surrounding tissue is nil.
2. Tumors may infiltrate into the stroma of the peripheral zone without replacing glandular spaces so that no contrast in MRI signal intensity is apparent even though the tumor may be widespread.
3. Tumors may be imbedded in or surrounded by hemorrhage, prostatitis, or stromal fibrosis and thus may be obscured.

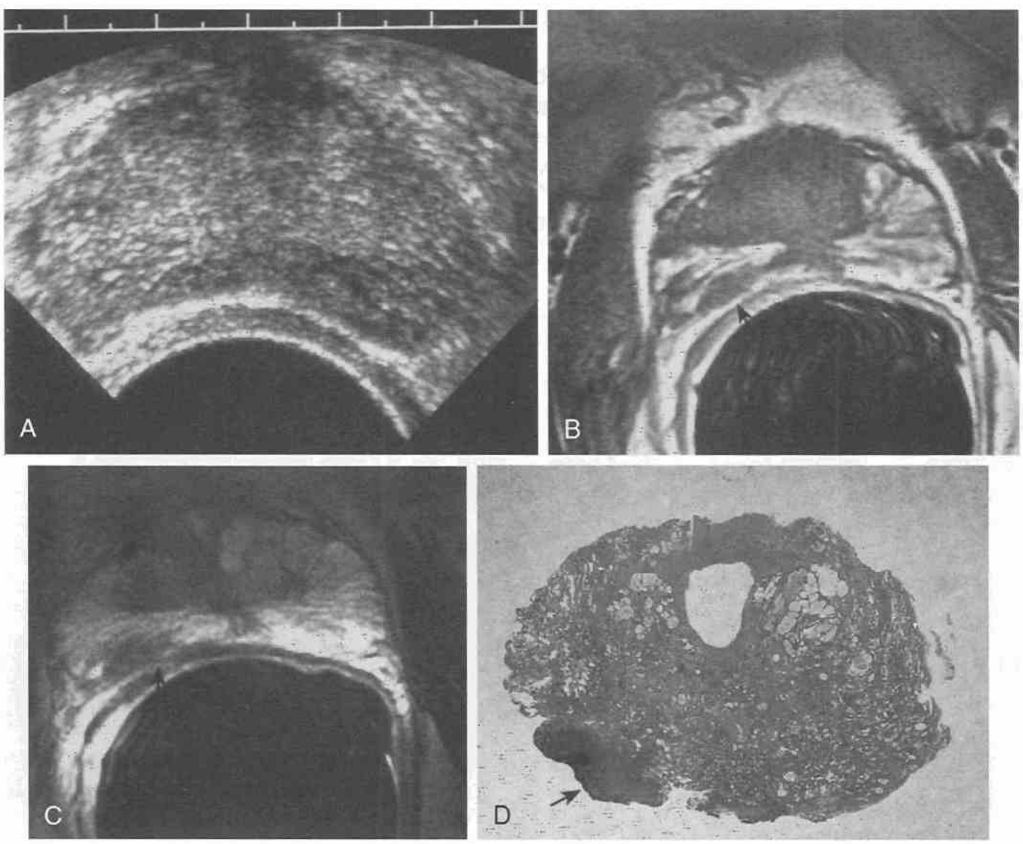

Figure 45–24. Peripheral zone prostate carcinoma. *A*, Trans[redacted]al ultrasonography shows a left-sided area of hypoechogenicity in the peripheral zone, the site of suspected carcinoma in this patient. Biopsy findings of the left side were negative, whereas biopsy results of the right peripheral zone were positive. *B*, Axial T1-weighted, endorectal coil image shows hemorrhage throughout the peripheral zone of the prostate. Hemorrhage does not enter a small focus in the right posterior peripheral zone *(arrow)*. *C*, T2-weighted, fast spin-echo image shows low signal intensity in the right peripheral zone *(arrow)*, indicating the site of the tumor. Signal intensity is similar to that in the central gland. *D*, Whole-mount section of the prostate shows the right-sided cancer *(arrow)* in the peripheral zone.

4. Other processes such as infection or fibrosis may mimic carcinoma by replacing glandular spaces with tissue.[55, 258]

The hallmark of prostate carcinoma on T2-weighted images is a relatively low-signal-intensity nodule in the high-signal-intensity peripheral zone (see Figs. 45–23 and 45–24). The signal intensity of the tissue within the prostate—whether fibrosis, tumor, or BPH—generally correlates with the number and size of glandular spaces.[288, 313] Specifically, the presence of larger and more numerous glandular fluid-filled spaces results in higher signal intensity on T2-weighted images.[288] The conspicuity of tumor nodules depends, to a large degree, on the replacement of the normal glandular spaces of the peripheral zone with more cellular tumor.

Normal variation in the amount of stromal tissue in the peripheral zone may result in areas of fibromuscular stroma that reflect low signal intensity within the peripheral zone.[54, 288] In some cases, prostate carcinoma may exhibit high signal intensity on T2-weighted images,[54, 253] rendering differentiation from the peripheral zone difficult. Variants of prostate carcinoma as well as other prostate neoplasms may show high signal intensity on T2-weighted images.[23, 79, 253]

Because MRI is usually performed for staging purposes after biopsy, hemorrhage within the gland is a common finding (see Fig. 45–24). High signal intensity on T1-weighted images persists for weeks or months after biopsy. It is difficult to locate tumor within an area of hemorrhage with certainty because hemorrhage may result in some low signal intensity on T2-weighted images.

Capsular penetration is most easily recognized on MR images when gross tumor is visualized outside the confines of the capsule (see Fig. 45–23). Unfortunately, tumor penetration of the capsule often occurs on a smaller scale, frequently apparent only on microscopic examination.[258] An indirect sign, such as bulging of the capsule or slight irregularity, may be of value in some cases (Figs. 45–25 and 45–26).[315, 369] Particular attention must be paid to the prostate apex and base, not only because these are frequent sites of capsular penetration but also because they may be particularly difficult areas to examine by MRI. Coronal images are important in evaluating tumor extension at the apex and base. In patients with prostate cancer, MRI has shown overall poor accuracy (55% to 69%) in identifying capsular penetration using the body coil.[298, 316] Higher accuracies (58% to 79%) are reported for the endorectal coil.[142, 271, 302, 308, 417] Select groups of patients with intermediate Gleason grades and PSA levels may show higher accuracies.[73]

Seminal vesicle invasion has been categorized into three types on the basis of pathologic studies of prostatectomy specimens[402]:

Type I invasion, the most common (40% of patients), involves extension along the ejaculatory ducts superiorly into the medial aspect of the seminal vesicles or ampullae of the vas deferens.

Type II invasion (30%) involves direct growth superiorly from the base of the prostate into the periprostatic tissue and then into the seminal vesicles.

Type III invasion (30%) involves foci of tumor within the seminal vesicles without evident connection to tumor in the prostate. These foci may represent metastases.

Capsular penetration is common with types I and II.[402]

The most reliable MRI sign of seminal vesicle invasion is gross replacement of the fluid-filled lumina by low-signal-intensity tumor (Fig. 45–27). As when identifying a tumor nodule in the peripheral zone, one must be aware that areas showing low signal intensity on T2-weighted images and high signal intensity on T1-weighted images usually represent hemorrhage.[231] Localized amyloid deposi-

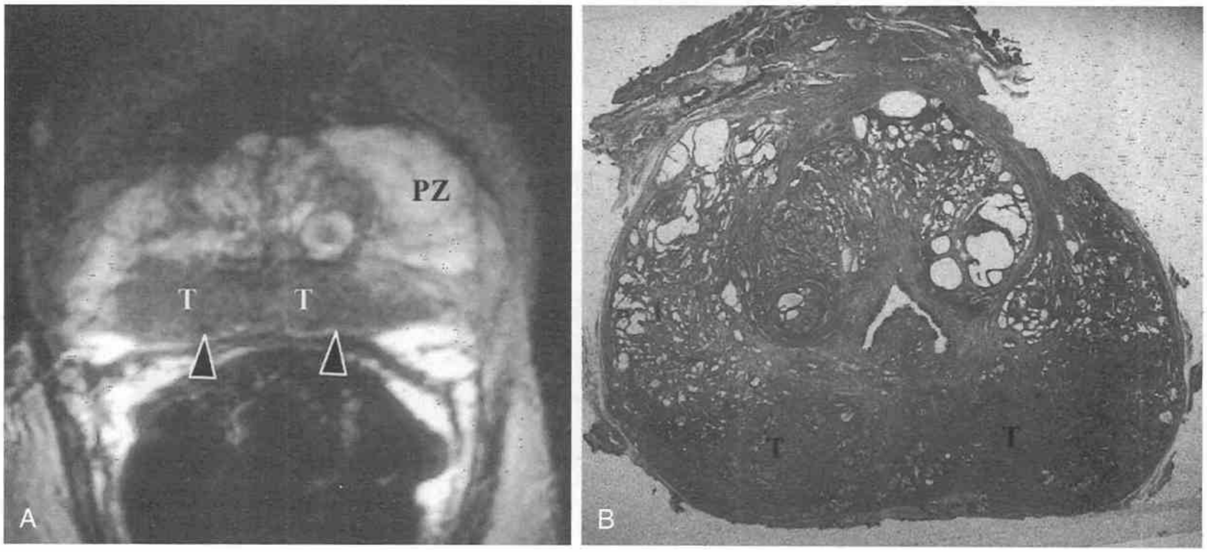

Figure 45–25. Capsular penetration by prostate carcinoma. *A,* T2-weighted, fast spin-echo, endorectal coil image shows the normal high-signal-intensity peripheral zone (PZ) laterally and the low-signal-intensity tumor (T) on both sides of the gland. The irregularity of the capsule can be noted posteriorly *(arrowheads)*. *B,* Whole-mount histologic sections show the darker-staining tumor (T) on both sides of the gland. Multifocal sites of capsular penetration occurred posteriorly. (From Outwater EK, Petersen RO, Siegelman ES, et al: Prostate carcinoma: Assessment of diagnostic criteria for capsular penetration on endorectal coil MR images. Radiology 193: 333–339, 1994.[258])

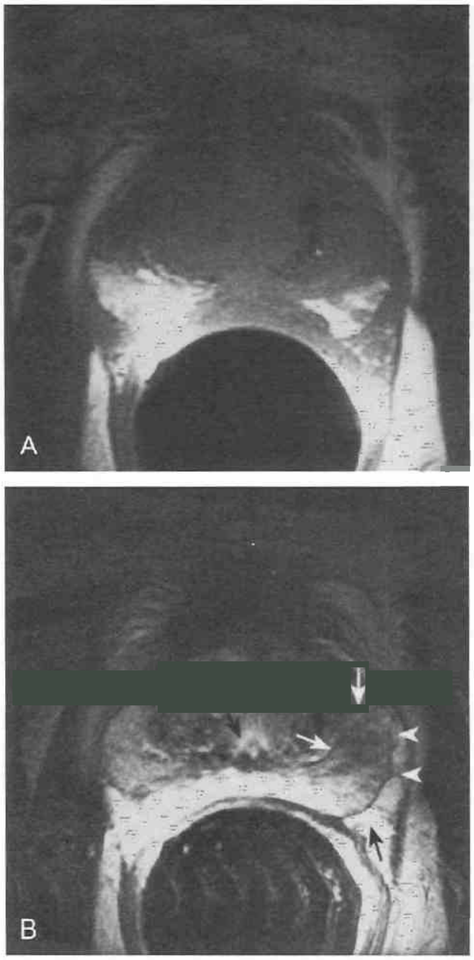

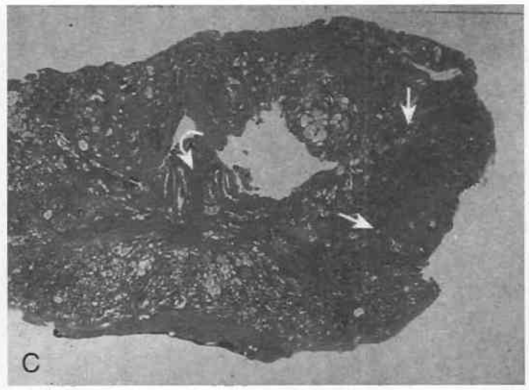

Figure 45–26. Capsular penetration by prostate carcinoma. Axial T1-weighted, fast spin-echo image *(A)*, T2-weighted, fast spin-echo image *(B)*, and whole-mount section *(C)* of the prostate show a left-sided peripheral zone tumor (*white arrows* on *B* and *C*). The subtle capsular bulging *(arrowheads)* evident in *B* corresponds to capsular penetration seen in *C*. Signal voids in *A* and *B* result from calcifications within the central gland, which also shows nodular changes indicative of benign prostatic hyperplasia. In *A*, the image shows evidence of high-signal-intensity methemoglobin in both the right and left sides of the peripheral zone, although it tends to be excluded from the tumor. The neurovascular bundle on the left *(black arrow)* is intact. The urethra (*curved arrows* in *B* and *C*) and the utricle can be visualized.

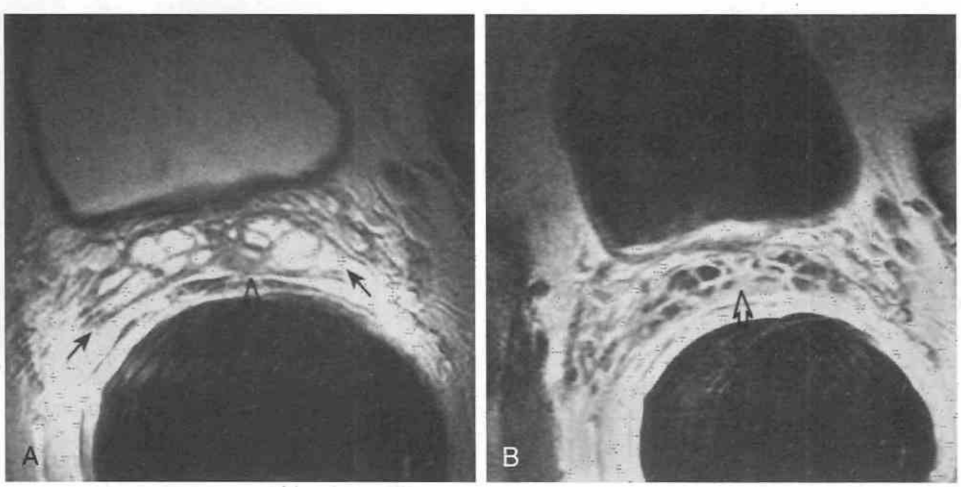

Figure 45–27. Early seminal vesicle invasion. *A*, Axial T2-weighted, fast spin-echo image of the seminal vesicles shows normal seminal vesicles laterally *(black arrows)*. Centrally, however, the abnormal low-signal-intensity tumor tissue *(open arrow)* lying along the left seminal vesicle and surrounding the vas deferens represents early tumor invasion of the seminal vesicle. *B*, On the gadolinium-enhanced, T1-weighted image, the abnormal low-signal-intensity area enhances *(open arrow)*, proving that it is solid tissue. The enhancement of the walls of the seminal vesicles is normal.

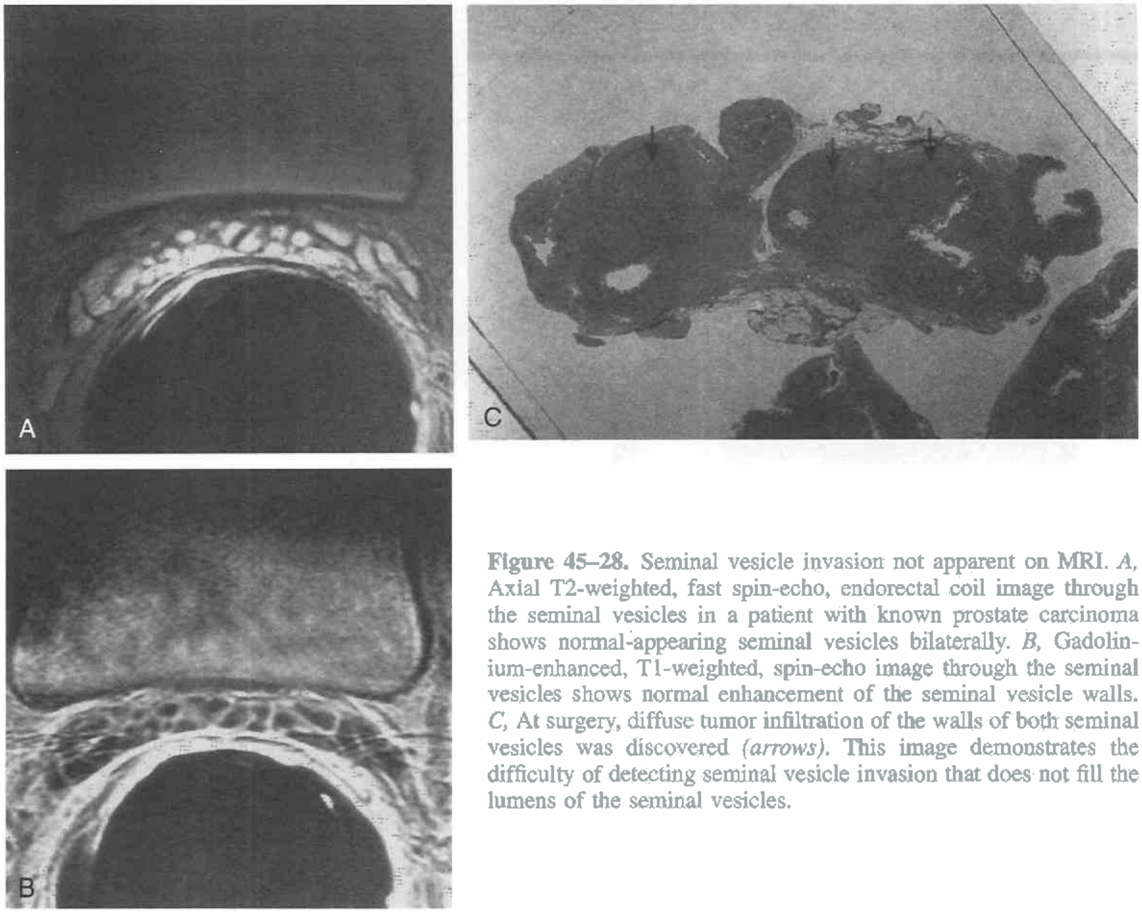

Figure 45–28. Seminal vesicle invasion not apparent on MRI. *A,* Axial T2-weighted, fast spin-echo, endorectal coil image through the seminal vesicles in a patient with known prostate carcinoma shows normal-appearing seminal vesicles bilaterally. *B,* Gadolinium-enhanced, T1-weighted, spin-echo image through the seminal vesicles shows normal enhancement of the seminal vesicle walls. *C,* At surgery, diffuse tumor infiltration of the walls of both seminal vesicles was discovered *(arrows)*. This image demonstrates the difficulty of detecting seminal vesicle invasion that does not fill the lumens of the seminal vesicles.

tion in the seminal vesicles, an uncommon but not rare occurrence, results in diffuse low signal intensity throughout the seminal vesicles.[164] Carcinoma often invades the seminal vesicles by invading through the walls, without replacement of the lumen with tumor. This form of spread is difficult to recognize on MR images (Fig. 45–28).

In most reports, the accuracy of MRI for staging prostate carcinoma has not been high. Endorectal coil imaging offers high-resolution imaging of the prostate; it is similar to intrarectal endosonography but offers better intraprostatic tissue contrast. Unfortunately, initial reports of high accuracy obtained with endorectal coil imaging were not supported by later studies.[66, 142, 266, 271, 302, 308, 318, 417] Staging of prostate cancer by endorectal coil imaging, however, does appear to be more accurate than clinical staging and therefore may be the preferred mode. Furthermore, some studies have shown a cost savings if MRI is used to stage this disease and to help determine whether the patient should undergo prostatectomy or radiation therapy.[188, 189] More recent research into the use of spectroscopy to identify the prostatic tumor has shown promise.[183, 312, 419] Endorectal coils have also been used to identify tumor in the surgical bed after prostatectomy (Fig. 45–29).

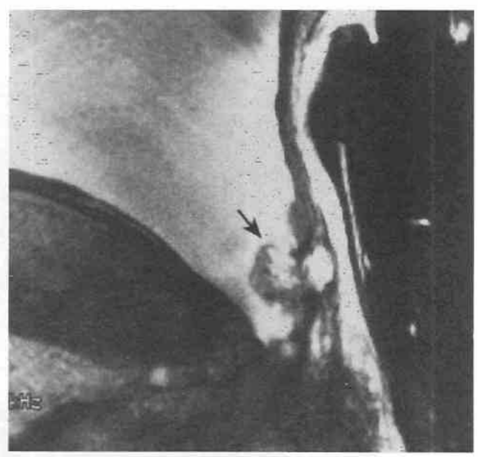

Figure 45–29. Endorectal coil evaluation of a patient after prostatectomy. Sagittal midline, T2-weighted, fast spin-echo image (TR = 4000 msec, TE_{eff} = 140 msec) shows the bladder wall as a low-signal-intensity structure. The wide bladder neck down to the membranous urethra represents the appearance after prostatectomy. In this patient with a rising prostate-specific antigen level, a large nodule was found at the anastomotic site *(arrow)*. Its appearance suggested recurrent tumor; at surgery, however, the diagnosis was recurrent benign prostatic hyperplasia. TE_{eff}, effective echo time.

Bladder and Rectum

Bladder Carcinoma

Bladder carcinoma is a very common tumor, the fourth most common tumor in men, and its incidence is rising.

Urothelial tumors demonstrate varying natural histories, depending on whether they are superficial or invasive. More than 70% of bladder cancer presents initially as a superficial (stage T1 or less) lesion.[289] Approximately 80% of these remain confined to the mucosa or submucosa through most of their natural history.[289, 293] Tumors that have invaded the muscle of the bladder wall at presentation, however, carry a worse prognosis, with a much higher incidence of pelvic lymph node metastases and a high rate of recurrence after resection.[122, 289, 353]

The treatment of bladder tumors depends on whether the lesion is superficial or invasive (Table 45–2). Superficial tumors are candidates for intravesical therapy: transurethral resection of the bladder (TURB), cautery, photodynamic therapy and intravesical chemotherapy, or bacille Calmette-Guérin therapy.[289, 353] Muscle-invasive tumors are generally treated with cystectomy, radiation therapy, or both.

For an imaging method to be useful as a staging tool, it must be able to distinguish T1 from T2 invasion.[289, 329] Staging by TURB is inaccurate, resulting in understaging in approximately 30% of patients.[122, 293, 329] Bimanual examination with the patient under anesthesia improves the accuracy of clinical staging, and some advocate this method to the exclusion of imaging for determining tumor stage.[109, 122, 353] The depth of muscle invasion is less important because differences are not reflected in different survival rates.[329] It is very important, however, to determine the spread of tumor into adjacent organs; this information may obviate the need for cystectomy.

On T1-weighted images, little or no contrast is evident between bladder tumors and the bladder wall (Fig. 45–30).[77, 91, 177] T1-weighted images do provide, however, sharp delineation of the external bladder wall and the surrounding perivesical fat. On T2-weighted images, the bladder muscularis is better demonstrated, and tumors show intermediate to high signal intensity (Fig. 45–31). Depending on the TE and TR used, contrast between tumor and urine may be poor.[77, 91, 177] In addition, differentiation between tumor and perivesical fat may be suboptimal on T2-weighted images (see Fig. 45–30).[177] Thus, the use of both T1-weighted and T2-weighted images, in multiple planes, is preferable for judging the extent of bladder tumors.[77, 91, 177]

Because of the inadequacy of either T1-weighted or T2-

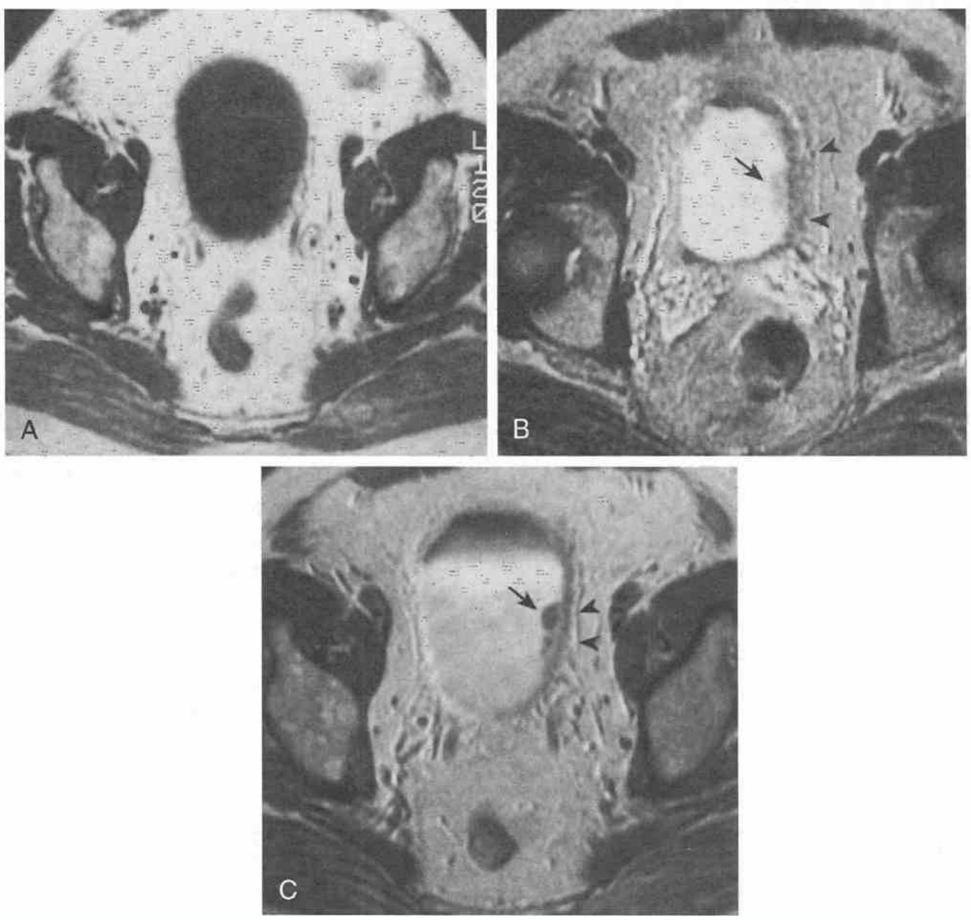

Figure 45–30. Superficial bladder carcinoma. *A,* Axial T1-weighted, spin-echo image (TR = 600 msec, TE = 18 msec) shows no evidence of spread of tumor into the perivesicular fat. The tumor itself as well as the bladder wall is poorly seen, however, because of the poor contrast between the urine and the tumor or the bladder wall. *B,* The T2-weighted, spin-echo image (TR = 2500 msec, TE = 80 msec) better demonstrates the tumor *(arrow).* Low-signal-intensity bladder muscularis *(arrowheads)* is seen underneath the polypoid tumor, indicating the superficial tumor. *C,* After administration of gadolinium, the axial T1-weighted spin-echo image shows the gadolinium within the urinary bladder outlining the tumor *(arrow).* The bladder wall enhances slightly and forms a continuous band *(arrowheads)* underneath the tumor, again verifying the superficial extent of the tumor.

Table 45–2. Local Staging of Bladder Cancer

TNM System	Modified Jewett	Pathologic Findings
TIS	CIS	Carcinoma in situ
Ta	O	Papillary tumor, noninvasive
T1	A	Invasion into lamina propria
T2	B1	Invasion into superficial muscle layer
T3a	B2	Invasion into deep muscle layer
T3b	C	Invasion into perivesical fat
T4a	D1	Invasion into prostate, uterus, vagina
T4b	D	Invasion into pelvic or abdominal wall

TNM, tumor-node-metastasis.

Figure 45–31. Bladder muscularis invasion. Fast spin-echo, multicoil image (TR = 5000 msec, TE_{eff} = 120 msec) reveals a low-signal-intensity tumor occupying most of the left posterolateral wall of the bladder. The tumor effaces the low-signal-intensity muscularis *(arrows)*, indicating deep invasion. TE_{eff}, effective echo time.

weighted images alone, gadolinium-enhanced imaging has been advocated for the evaluation of bladder tumors (see Fig. 45–30). Bladder tumors show enhancement similar to that shown by bladder mucosa/submucosa, which becomes visible as a thin, hyperintense lining of the bladder on contrast-enhanced, T1-weighted images.[244, 364] A number of investigators have claimed that the additional contrast between muscularis and tumor evident on gadolinium-enhanced, T1-weighted images facilitates staging.[245, 364, 366]

MRI has achieved overall staging accuracy of the primary tumor in 60% to 85% of patients.[5, 50, 245, 366] The accuracies for distinguishing tumors that have penetrated the bladder wall (T3b) from those that have not (T3a or less) range from 73% to 100% (Table 45–3). In various reports, MRI has been found to be equivalent[146, 294] or superior[5, 364, 366] to CT. In one report, it is suggested that MRI is superior to transurethral ultrasound as well.[364]

Rectal Carcinoma

Surgery is the major component of therapy for rectal carcinoma, and pathologic staging is the standard. The prognosis is closely tied to pathologic stage. Accurate preoperative staging of rectal carcinoma is increasingly important because the approach to treating these tumors is evolving. The surgical approach is determined, to some extent, by preoperative estimation of the stage but, more important, by the anatomic level of the rectal mass. The use of preoperative radiation therapy has increased the need, at least on a research level, for assessment of the extent of these tumors and their response to radiation. Sphincter-sparing operations, instead of either abdominoperineal resections for low rectal lesions or local resections for superficial lesions, requires more accurate determination of depth of invasion of the carcinoma.

Locoregional recurrence is a much more significant problem in rectal carcinoma than in colon carcinoma.[78] Reported incidences of local recurrence after attempts at cure range from 10% to 40%.[78, 204, 238] The risk of recurrence depends partly on the tumor level; the incidence of recurrence almost doubles in distal rectal tumors compared to the rate in higher rectal tumors.[204]

On T1-weighted images, rectal carcinoma appears as an intermediate-signal-intensity mass; its signal intensity is similar to that of the rectal wall (Fig. 45–32).[48] An intrarectal contrast agent, either insufflated air or a short-T1 liquid, aids in identifying the intraluminal tumor,[74] but it is not clear whether this is helpful for gauging transmural extent of the tumor. T1-weighted images provide excellent definition of the perirectal fat surrounding the rectal wall. With high resolution, fine stranding in the perirectal fat, radiating from the tumor, is discerned. This can occur in tumors confined by the wall and should not be interpreted as evidence of tumor spread.

On T2-weighted images, tumors have a variable appearance, reflecting their different histologic components.[48] Most tumors show intermediate signal intensity (see Fig. 45–32), but high-signal-intensity areas due to mucinous

Table 45–3. Accuracy of MRI for Staging Extravesicle Extension of Bladder Carcinoma

No.	Sensitivity (%)	Specificity (%)	Accuracy (%)	Comment	Reference
30	82	62	73	—	Husband et al[146]
23	—	—	96	—	Rholl et al[294]
40	67	100	85	—	Buy et al[50]
68	93	95	95	Gadolinium-enhanced	Neuerburg et al[245]
57	96	83	89	—	Tachibana et al[364]
28	100	100	100	Gadolinium-enhanced	Barentsz et al[22]
50	75	98	94	Gadolinium-enhanced	Narumi et al[243]

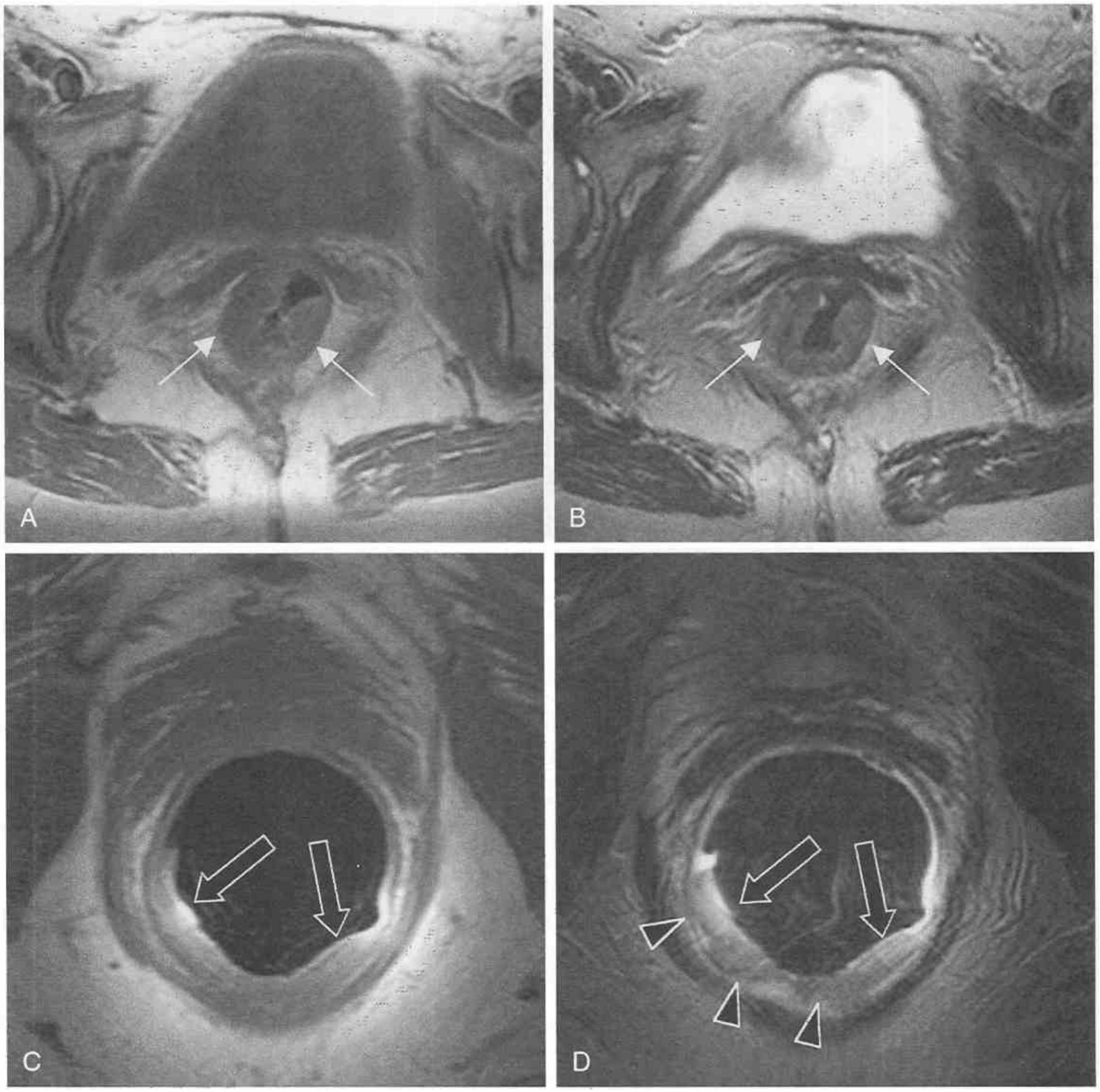

Figure 45–32. Pelvic and endorectal coil imaging of rectal carcinoma. *A,* T1-weighted, spin-echo multicoil image shows hemicircumferential thickening of the rectal wall *(arrows)*. *B,* T2-weighted, fast spin-echo image again demonstrates intermediate-signal-intensity thickening *(arrows)* compatible with tumor. The muscularis, however, is not well identified. *C,* T1-weighted, spin-echo, endorectal coil image shows the tumor in the right and left lateral walls of the rectum *(arrows)*. *D,* T2-weighted, spin-echo image shows the intermediate-signal-intensity tumor *(arrows)* and invasion of the muscularis underlying the tumor *(arrowheads)*.

areas and low-signal-intensity areas due to desmoplastic reaction are common. Complete disruption of the very-low-signal-intensity rectal muscularis propria is the key finding and indicates early transmural penetration (see Fig. 45–32).[57, 148] Gadolinium-enhanced, T1-weighted images, preferably obtained with fat saturation, may also be useful. The muscularis enhances very little, providing some contrast between the enhancing tumor and muscularis (Fig. 45–33).

Staging of rectal carcinoma by imaging methods is a complex issue that involves comparative assessment of imaging modalities for detection of hepatic metastases, lymphadenopathy, and depth of mural tumor invasion. Of the three modalities used for staging rectal carcinoma (transrectal ultrasound, CT, and MRI), only CT and MRI can provide a comprehensive evaluation of these areas. In a few published studies, MRI has achieved sensitivities of 75% to 100% and specificities of 66% to 100% for detection of transmural extension.[48, 74, 109]

As with staging of most malignancies by imaging, the lack of sensitivity and specificity for the detection of metastases to lymph nodes is a serious impediment to obtaining higher overall accuracy rates for staging rectal carcinoma.[72, 123] If special pathologic techniques are used to examine all lymph nodes (regardless of size) in the surgical specimen, very high rates of metastases to lymph nodes 1 to 3 mm in diameter are discovered.[123] In one study, 78% of all nodal metastases from rectal carcinoma occurred in nodes less than or equal to 5 mm in diameter.[123] This insight shows that determining the presence of nodal metastases on the basis of lymph node size is difficult at best.

Endorectal coil imaging achieves higher staging accuracy compared with body-coil studies. Accuracies of 79%

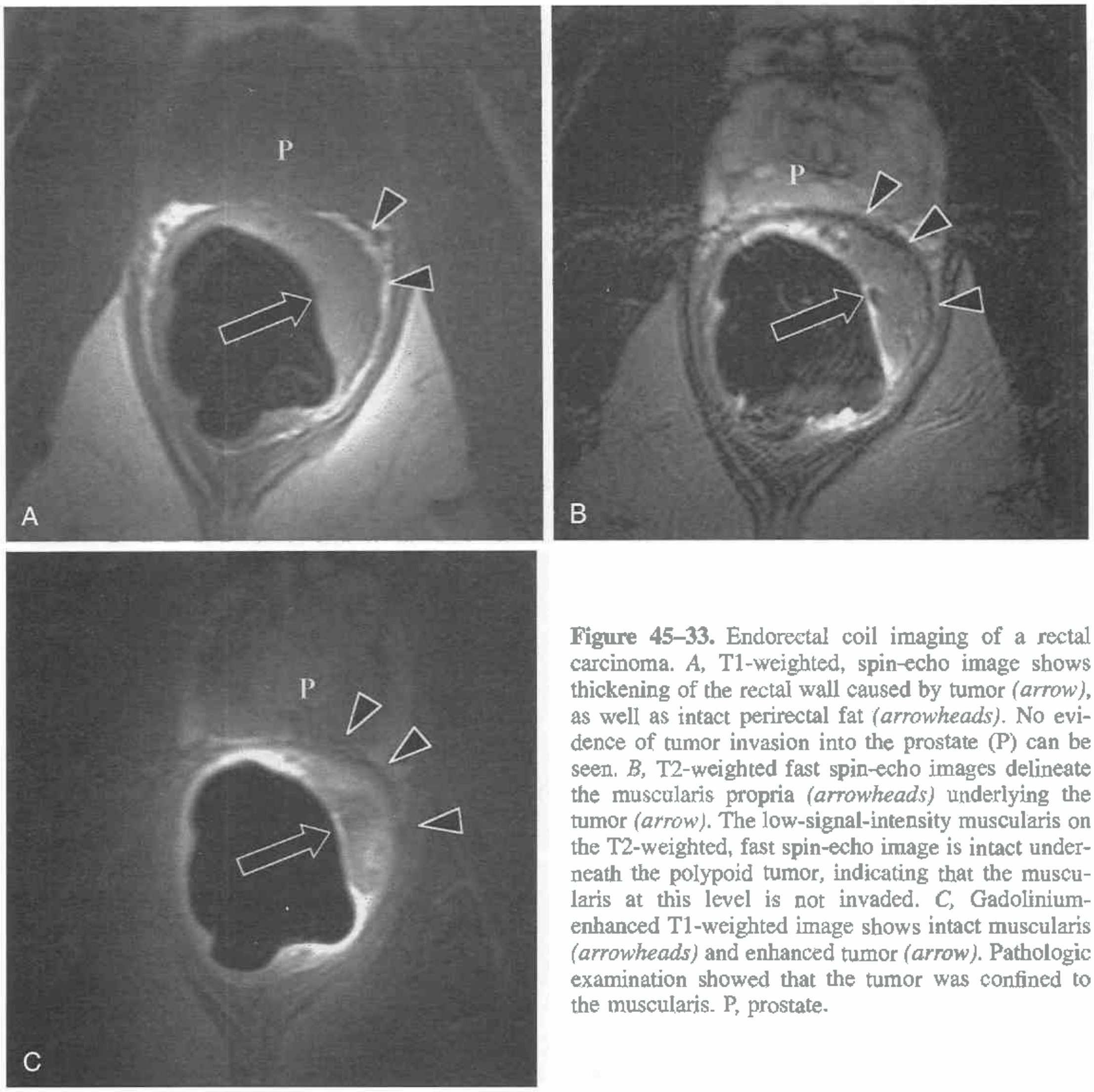

Figure 45–33. Endorectal coil imaging of a rectal carcinoma. *A,* T1-weighted, spin-echo image shows thickening of the rectal wall caused by tumor *(arrow),* as well as intact perirectal fat *(arrowheads).* No evidence of tumor invasion into the prostate (P) can be seen. *B,* T2-weighted fast spin-echo images delineate the muscularis propria *(arrowheads)* underlying the tumor *(arrow).* The low-signal-intensity muscularis on the T2-weighted, fast spin-echo image is intact underneath the polypoid tumor, indicating that the muscularis at this level is not invaded. *C,* Gadolinium-enhanced T1-weighted image shows intact muscularis *(arrowheads)* and enhanced tumor *(arrow).* Pathologic examination showed that the tumor was confined to the muscularis. P, prostate.

to 81% in diagnosis of transmural penetration of the muscularis are reported.[171, 226, 252] This imaging modality has been found to be as accurate as endoluminal ultrasound.[161, 171, 226, 368] Use of the endorectal coil is technically difficult, however, because placement is difficult or impossible with bulky or stenotic lesions, small lesions may be difficult to find, and long lesions may not be covered adequately with the coil. Furthermore, an additional study is required to assess the abdomen and pelvis for metastases.

Evaluation of the Female Pelvis

Because ultrasonography is usually the first modality used to image the female pelvis, MRI is restricted primarily for two indications[61, 112, 136, 232, 234, 375]:

1. Diagnosis of a uterine or an adnexal abnormality not adequately characterized by ultrasonography.
2. Staging of gynecologic malignancies.

As a result of cost and safety concerns, MRI has a small role in routine evaluation of pelvic complaints, in most obstetric disorders, or in the detection of malignancies.

Benign Conditions

Several studies have shown that MRI can be useful in identifying pelvic abnormalities that are poorly characterized or misdiagnosed on ultrasonography.[14, 136, 232, 296, 373, 400] Disorders that can be reliably identified by MRI include congenital uterine disorders, leiomyomas, adenomyosis, mature cystic teratomas, and, in some cases, endometriomas. The noninvasiveness of the technique is particularly important in pregnant patients. Accurate diagnosis of these masses requires attention to MRI technique, familiarity with diagnostic criteria, and good clinical judgment.

Uterus

Congenital Anomalies

The accuracy of MRI in classifying congenital deformities of the uterus is very high—75% to 100%.[53, 229, 269] Pellerito and colleagues[269] have reported that the accuracy of MRI exceeds that of hysterosalpingography and transvaginal ultrasonography, although the combination of these two probably correctly identifies the majority of uterine

anomalies.[292, 415] Unicornuate uteri are identified by the presence of a nonbifurcating endometrium within the horn in contiguity with the cervix. A rudimentary horn, if present, may contain endometrium, leading to hematometra (blood accumulation in the uterus). Didelphis anomaly is easily recognized by the presence of two unicornuate uteri and two cervices.

One of the more common distinctions to be made is between septate and bicornuate uteri. These two entities are treated differently; septations can be removed via hysteroscopy, whereas bicornuate uteri are repaired via laparotomy and metroplasty. Attempts to perform a septoplasty on what is actually a bicornuate uterus may lead to uterine perforation. Intervening tissue between the two cornua of bicornuate and septate uteri may resemble myometrium or fibrous tissue on T2-weighted images.[229, 269] A more useful finding is the external shape of the uterine fundus, which is notched in bicornuate uteri but typically convex or flat in septate uteri (Fig. 45–34).[269]

MRI can also be used to image uterine abnormalities associated with diethylstilbestrol exposure.[131, 389] Abnormalities include uterine hypoplasia, T-shaped uterus, constrictions of the endometrium, hydrosalpinges, and a shortened cervix.[131, 389]

Leiomyomas

Leiomyomas (fibroids) of the uterus are the most common gynecologic masses, but relatively few become symptomatic. Fibroids show various signal intensities on T2-weighted MR images, from homogeneously hypointense to heterogeneously hyperintense. Most leiomyomas, however, display a characteristic MRI appearance, either pedunculated or intramural, and are not confused with other uterine tumors.[136, 141, 375, 400] MRI is more sensitive and specific for the diagnosis of leiomyoma than an ultrasound study or a hysterosalpingogram.[86]

Leiomyomas show predominantly low signal intensity on long TR/TE images (Fig. 45–35).[141, 203, 382, 400] They appear well defined and sharply marginated from surrounding myometrium. MRI can be used to differentiate pedunculated fibroids from other adnexal masses and submucosal fibroids from endometrial lesions on the basis of this typical signal intensity and morphology (Fig. 45–36). Thin, hyperintense rims,[237] as well as internal signal heterogeneity caused by hyaline or myxoid degeneration,[136, 141, 382, 400] are sometimes seen, but these changes are usually not extensive enough to mimic a malignant adnexal neoplasm (Fig. 45–37). Only ovarian fibromas and thecomas commonly have signal intensity characteristics that match those of fibroids.

Leiomyomas may show intermediate signal intensity on T2-weighted images, similar to or slightly higher than the signal intensity of the normal outer myometrium. These changes are usually caused by the increased cellularity of the tumor.[141, 412] Increased cellularity indicates a separate histologic type of leiomyoma, reflecting those that are rapidly growing and more responsive to hormonal therapy than typical leiomyomas. The gadolinium-enhancement characteristics of fibroids are variable, but cellular lesions are usually hypervascular.

Adenomyosis

Adenomyosis, first described in 1860 by Rokitansky, is characterized by the presence of endometrial glands and

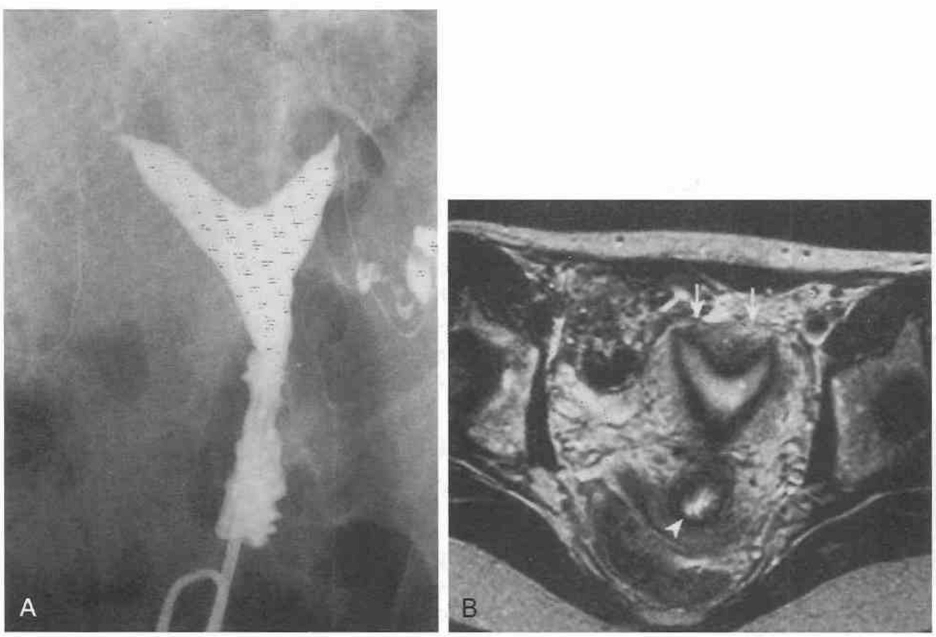

Figure 45–34. Septate uterus. *A*, Hysterosalpingogram in a 43-year-old patient with infertility. Bilateral tubal patency and uterine cornua with an angle of divergence of less than 90 degrees are seen. The appearance is consistent with bicornuate or septate uterus. *B*, T2-weighted fast spin-echo image in the axial plane (TR = 6200 msec, TE_{eff} = 102 msec) shows the divergent uterine cornua with a morphology similar to that seen in the hysterosalpingogram. The external surface of the uterine fundus is normal *(arrows)*. Thus, a bicornuate uterus is not present, and this uterus has a shallow uterine septum. *Arrowhead* indicates the uterine cervix. TE_{eff}, effective echo time.

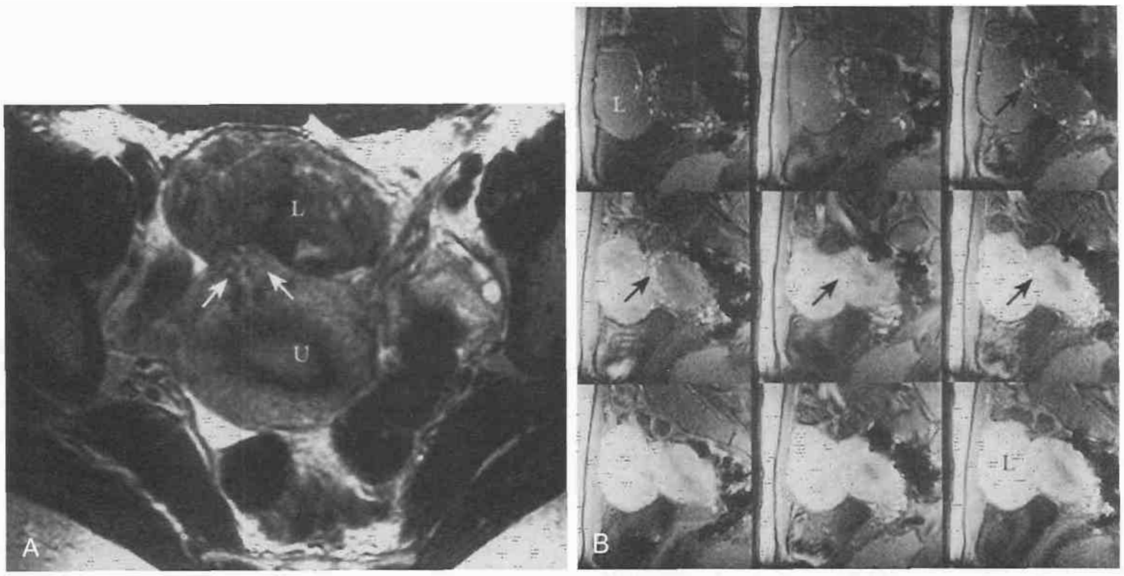

Figure 45–35. Pedunculated leiomyoma. *A,* Axial T2-weighted, fast spin-echo image through the uterine fundus shows a large, well-circumscribed, low-signal-intensity mass (L) anterior to the uterine fundus (U). The low signal intensity of this mass suggests leiomyoma. Vessels arising from the myometrium can be seen supplying the mass *(white arrows)*, confirming its myometrial origin. *B,* Dynamic gadolinium enhancement of a pedunculated leiomyoma shows a rapid enhancement of the leiomyoma (L) via vessels crossing from the myometrium *(arrows)*. The enhancement of the myometrium is similar to that of the leiomyoma, and the enhancement of the endometrium is less.

stroma deep within the myometrium.[16] Whorled hypertrophy of the myometrial smooth muscle occurs around the glands and results in low signal intensity of the lesion on MR images (Fig. 45–38). High-signal-intensity foci appearing within the nodules on T2-weighted images represent the glandular epithelium (see Fig. 45–47).[203, 378] These are occasionally hemorrhagic.[16, 378]

The prevalence of adenomyosis is high in the female population (~19% to 31% of women). Although adenomyosis is not usually symptomatic,[16] it is sometimes associated with menorrhagia and dysmenorrhea. The overall uterine size is enlarged in 60% to 80% of patients.[16, 382]

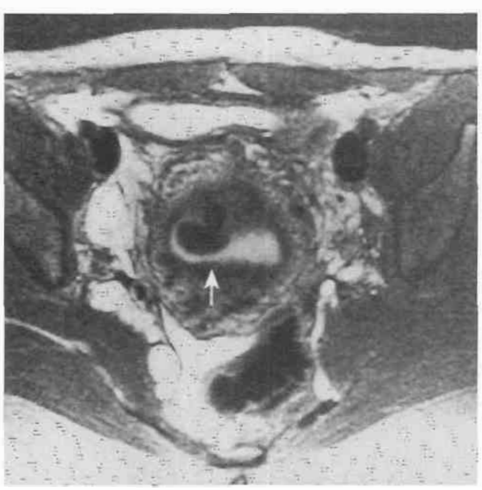

Figure 45–36. Submucosal leiomyoma in a patient with menorrhagia. Axial T2-weighted, fast spin-echo image (TR = 3500 msec, TE_{eff} = 80 msec) demonstrates a submucosal leiomyoma protruding into the endometrium *(arrow)*. Incidentally noted are plexiform neurofibromas along the sciatic nerve in this patient with neurofibromatosis. TE_{eff}, effective echo time.

Endometrial Polyps

Benign abnormalities, most commonly polyps, greatly outnumber cancers in patients screened by transvaginal ultrasound for a thickened endometrium.[187, 249, 338] Endometrial polyps, among the most common pathologic lesions of the uterine corpus,[342] are often found in patients taking tamoxifen.[317] These benign nodular protrusions of the endometrial surface consist of a stroma, composed of focally or diffusely dense fibrous or smooth muscle tissue, and irregularly distributed endometrial glands that frequently show cystic glandular hyperplasia.[299, 317, 342]

MRI features do not accurately distinguish endometrial polyps from cancer. On T2-weighted MR images, the fibrous core of the polyps appears as a central area of low signal intensity (Fig. 45–39); cysts within the polyp may appear as discrete structures or as peripheral areas of high signal intensity.

Uterine Adnexa

Ovarian Cysts

The morphology of functional ovarian cysts is as expected from the ultrasound appearance. Follicular cysts show a thin, smooth wall on MR images, and the cyst contents generally demonstrate the signal intensity of simple fluid (i.e., low signal intensity on T1-weighted images and very high signal intensity on T2-weighted images).

Corpus luteum cysts exhibit a thicker wall, which represents the luteinized lining (Fig. 45–40). This wall can demonstrate intense enhancement with gadolinium. MRI commonly reveals evidence of hemorrhage within corpus

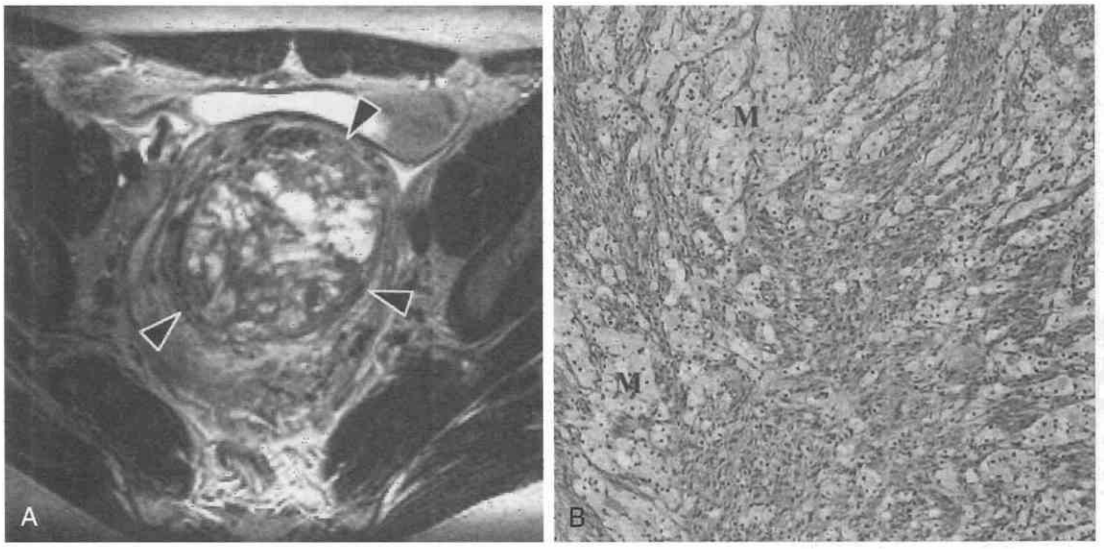

Figure 45–37. Myoma with myxoid degeneration. *A,* T2-weighted, fast spin-echo image shows a rounded mass *(arrowheads)* in the interior myometrium. Some low-signal-intensity components as well as patchy areas of very high signal intensity can be seen in this mass. *B,* Histologic section from an area of higher signal intensity shows abundant myxoid tissue (M) within the areas of whorled smooth muscle. (From Murase E, Siegelman ES, Outwater EK, et al: Uterine leiomyomas: Histopathologic features, MR imaging findings, differential diagnosis, and treatment. Radiographics 19:1179–1197, 1999.)

luteum cysts, with lower-signal-intensity blood or clot layering dependently in the cyst and shortened T1 and T2 of the cyst contents relative to simple fluid.[248]

Hemorrhagic cysts rarely exhibit the markedly shortened T1 and T2 commonly seen with endometriomas.[380] In contrast, some endometriomas overlap in signal intensity with corpus luteum cysts.[259] Small ovarian follicles normally stud the surface of ovaries of premenopausal women, and these are apparent on high-resolution MR images.[215, 348]

Endometriosis

Endometriomas, also known as endometriotic cysts, are manifestations of advanced-stage endometriosis.[401] They usually involve the ovaries and are bilateral in one third to one half of cases.[64, 96] The wall of these cysts is usually thick and fibrotic, but it may be thin and attenuated. The cyst contains altered blood that varies from the usual viscous "chocolate" material to the much less common watery fluid.[64] Dense adhesions often fix the endometrioma to surrounding pelvic structures.

Although MRI studies demonstrate that endometriomas are reliably detected,[11, 380, 420] MRI is insensitive, compared with laparoscopy, in overall detection and staging of endometriosis; it cannot accurately detect superficial implants and adhesions,[11] which are usually small and occur on peritoneal surfaces.

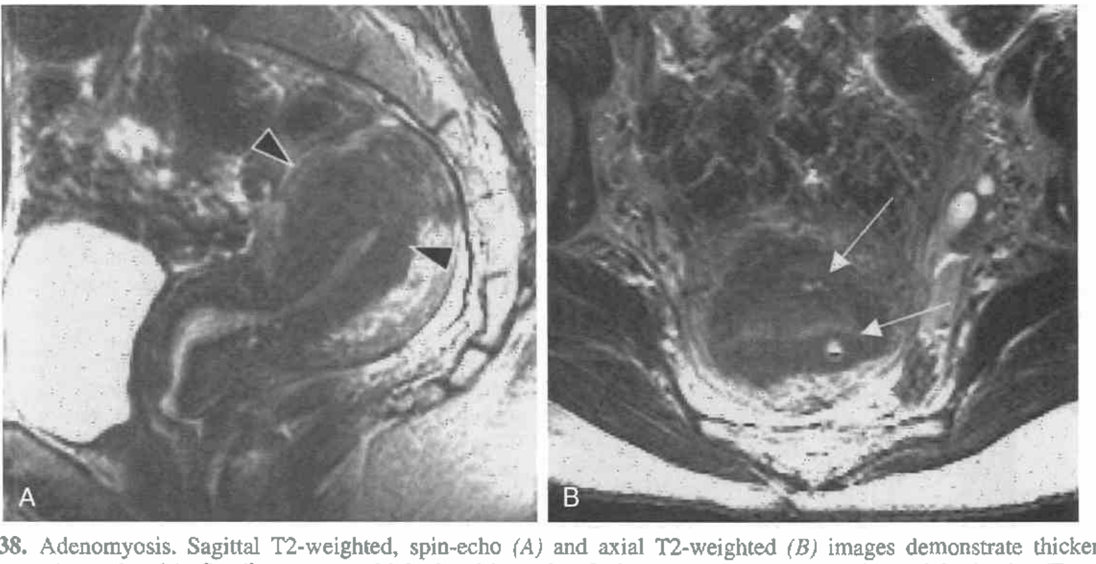

Figure 45–38. Adenomyosis. Sagittal T2-weighted, spin-echo *(A)* and axial T2-weighted *(B)* images demonstrate thickening of the junctional zone *(arrowheads)*. Small, punctate, high-signal-intensity foci *(arrows)* represent endometrial glands. (From Outwater EK, Siegelman ES, Van Deerlin V: Adenomyosis: Current concepts and imaging considerations. AJR Am J Roentgenol 170: 437–441, 1998.[263])

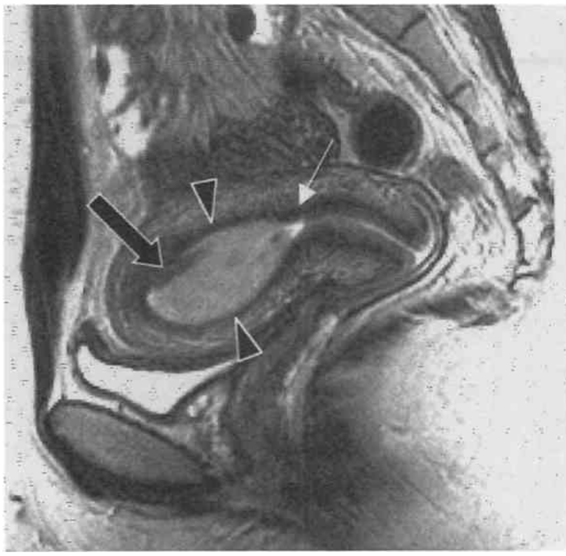

Figure 45–39. Endometrial polyp in a 31-year-old woman. Sagittal T2-weighted, fast spin-echo image shows the polyp *(arrowheads)* outlined by a small amount of fluid *(thin white arrow)*. The thin fibrous core of the polyp *(black arrow)* can be seen. The mass shows no evidence of invasion of the junctional zone.

MRI criteria can reliably distinguish endometriomas from most other ovarian masses, including ovarian malignancies.[375, 380] Endometriomas have variable appearances on T1-weighted and T2-weighted SE images, which differ, nonetheless, from simple (nonhemorrhagic) ovarian cysts.[420] On T1-weighted images, homogeneously very hyperintense cysts that become relatively hypointense on T2-weighted sequences, or multiple cysts that are entirely hyperintense on T1-weighted sequences, indicate endometriomas in the appropriate clinical setting (Fig. 45–41).[248, 380] MRI evidence of hemorrhage per se in a cystic mass is certainly not specific for a benign hemorrhagic cyst or endometrioma, since this feature is often seen in ovarian cystadenomas and carcinomas.[234, 235, 376]

Togashi and colleagues[380] listed MRI criteria that are helpful in the diagnosis of endometriomas, including:

1. A cystic lesion that is hyperintense on short TR/TE images and shows "shading," or relative hypointensity, on long TR/TE images.
2. The presence of multiple (more than two) hyperintense lesions on short TR/TE images.

Endometriomas may also be hyperintense on short TR/TE images and hyperintense without shading on long TR/TE images; however, this pattern of hyperintensity on T1-weighted and T2-weighted sequences is nonspecific and is

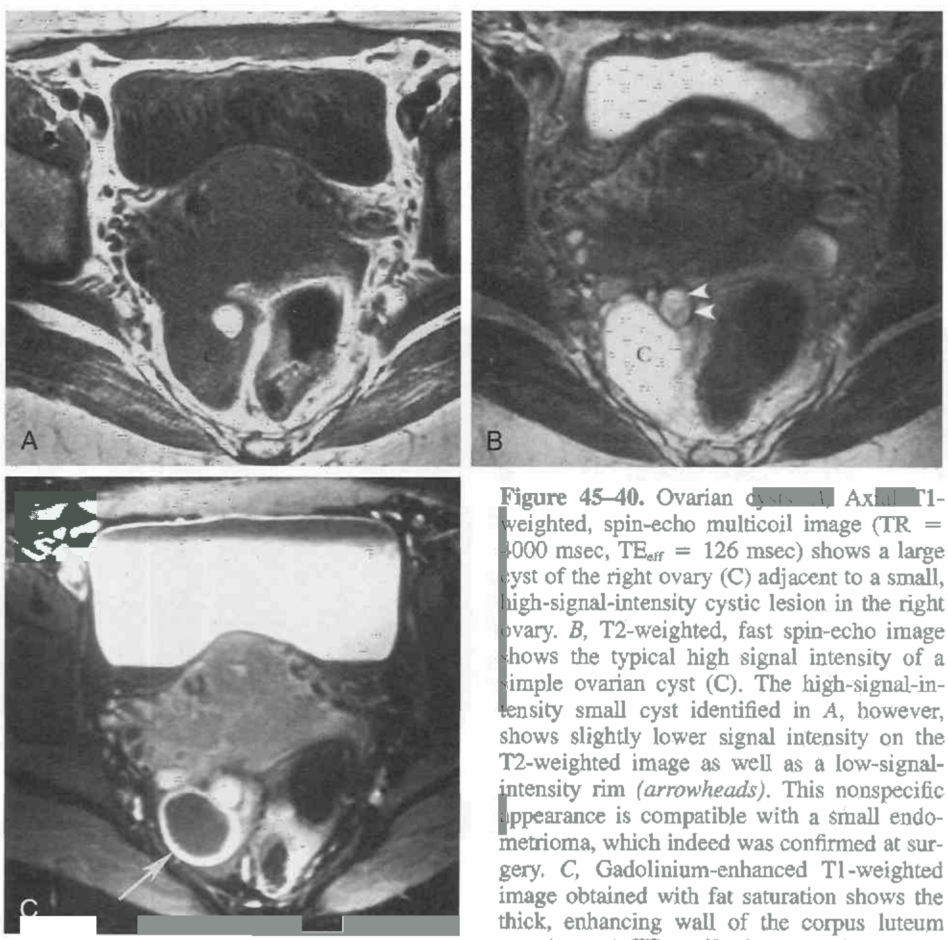

Figure 45–40. Ovarian cysts. *A,* Axial T1-weighted, spin-echo multicoil image (TR = 4000 msec, TE_{eff} = 126 msec) shows a large cyst of the right ovary (C) adjacent to a small, high-signal-intensity cystic lesion in the right ovary. *B,* T2-weighted, fast spin-echo image shows the typical high signal intensity of a simple ovarian cyst (C). The high-signal-intensity small cyst identified in *A*, however, shows slightly lower signal intensity on the T2-weighted image as well as a low-signal-intensity rim *(arrowheads)*. This nonspecific appearance is compatible with a small endometrioma, which indeed was confirmed at surgery. *C,* Gadolinium-enhanced T1-weighted image obtained with fat saturation shows the thick, enhancing wall of the corpus luteum cyst *(arrow)*. TE_{eff}, effective echo time.

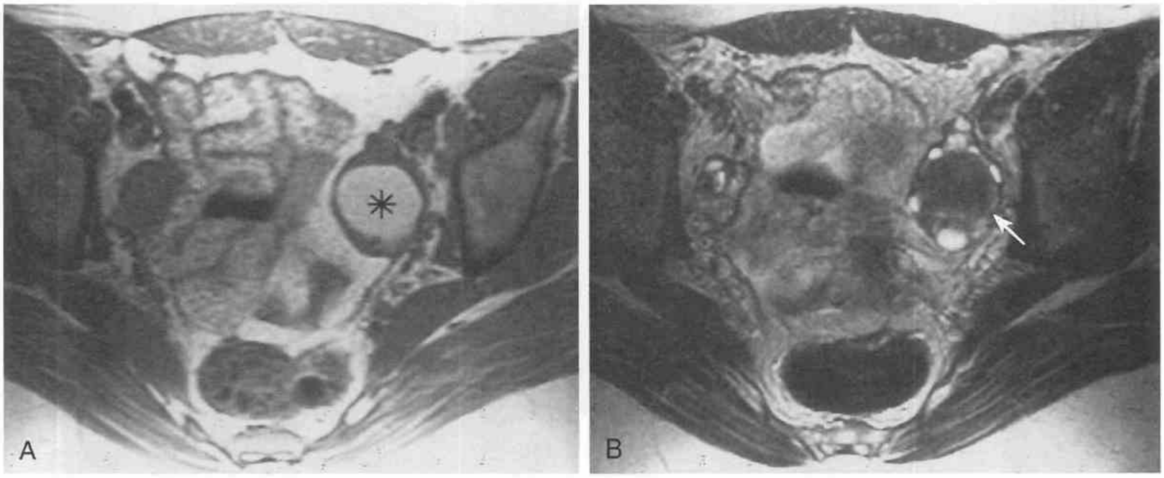

Figure 45–41. Ovarian endometrioma. *A*, Axial T1-weighted spin-echo image (TR = 600 msec, TE = 12 msec) through the ovaries show a high-signal-intensity mass of the left adnexa *(asterisk)*. *B*, T2-weighted fast spin-echo image (TR = 4000 msec, TE_{eff} = 140 msec; acquisition matrix = 256 × 256; field of view = 22 cm; slice thickness = 5 mm) shows marked low signal intensity *(shading)* within the mass *(arrow)*, characteristic of an endometrioma. Several high-signal-intensity ovarian follicular cysts surround the mass, indicating its location within the ovary. TE_{eff}, effective echo time.

commonly seen in hemorrhagic cysts as well.[259] These criteria exclude lesions with solid nodules, obvious septations, or very large size. Masses with signal intensity characteristics of hematomas are also excluded (see Fig. 45–51).

Applying these criteria in a prospective study, Togashi and coworkers[380] were able to identify endometrial cysts with 90% sensitivity, 98% specificity, and 96% accuracy. No malignancies were misdiagnosed as endometriomas.[380] Malignant transformation of endometriosis, although rare, may occur.[117] Ancillary findings that are commonly seen in endometriomas include low-signal-intensity rims, caused by the hemosiderin and fibrosis in the wall, and tethering to surrounding structures.[11]

Implants of endometriosis are sometimes seen on MR images.[30] These typically appear as nodules that show low signal intensity on T2-weighted images because of their dense fibrosis.[341] Punctate hemorrhage within them may be detected on fat-saturated, T1-weighted images.[365] Dilated fallopian tubes containing fluid that shows high signal intensity on T1-weighted images are sometimes seen in patients with endometriosis.[260]

Pelvic Inflammatory Disease

Tubo-ovarian abscess is a complication of pelvic inflammatory disease. In acute pyogenic salpingitis, pus emanating from the fallopian tube becomes confined by pelvic adhesions to form an abscess. This abscess usually lies near or involves the ovary. Such abscesses appear on MR images as unilocular or multilocular cystic masses, usually with a thicker wall than that seen in functional ovarian cysts (Fig. 45–42).[130] The abscess fluid shows variable signal intensity but usually has very high signal intensity on T2-weighted images and low signal intensity on T1-weighted images.[130, 235] Infiltration of pelvic fat surrounding the mass may be evident. Acute or chronic pelvic inflammatory disease is frequently accompanied by dilatation of the fallopian tube (see Fig. 45–52).[260, 386] Analysis of pyosalpinges or hydrosalpinges in more than one MRI plane may be necessary to recognize their tubal character.[260]

Puerperal ovarian vein thrombophlebitis is an uncommon complication of postpartum endometritis. The disorder usually presents in the puerperium with prolonged fever after an initial trial of antibiotic therapy for endometritis. Approximately 80% of cases occur on the right side, and the thrombus may extend into the inferior vena cava. Either CT or MRI may be used for diagnosis.[181, 310, 387] Typically, the thrombus is slightly hyperintense on T1-weighted images and hyperintense on T2-weighted images.[205, 310] Enlargement of the involved gonadal vein as well as surrounding inflammatory changes, seen as stranding, are typical.[181, 387] Gradient-echo techniques easily demonstrate the absence of flow in the involved veins.[181, 387]

Benign Ovarian Neoplasms

Mature cystic teratomas *(dermoid cysts)* are a common cause of adnexal masses, accounting for approximately 20% of all ovarian neoplasms. Almost all of these lesions have some component that demonstrates lipid characteristics on MR images (Fig. 45–43).[42, 379] This lipid represents the liquefied space within the cysts and may also represent adipose tissue in the wall or nodules of dermoid cysts. These areas show signal intensity characteristics that approximate (but do not necessarily coincide with) the signal intensity of adipose tissue.[379]

For definite identification of this lipid, a chemical shift–selective technique should be used to differentiate these lesions from hemorrhagic lesions that may have similar signal intensity characteristics (see Fig. 45–43).[108, 169, 358] The diagnosis of mature cystic teratomas may be confirmed when lipid structures are demonstrable within the mass.[108, 169, 358] and is easily performed with frequency-selective presaturation or chemical shift–selective techniques.[108, 169, 358] Although this finding is not absolutely specific for dermoid cysts, it virtually excludes a malignant tumor in a uterine or ovarian mass.[81]

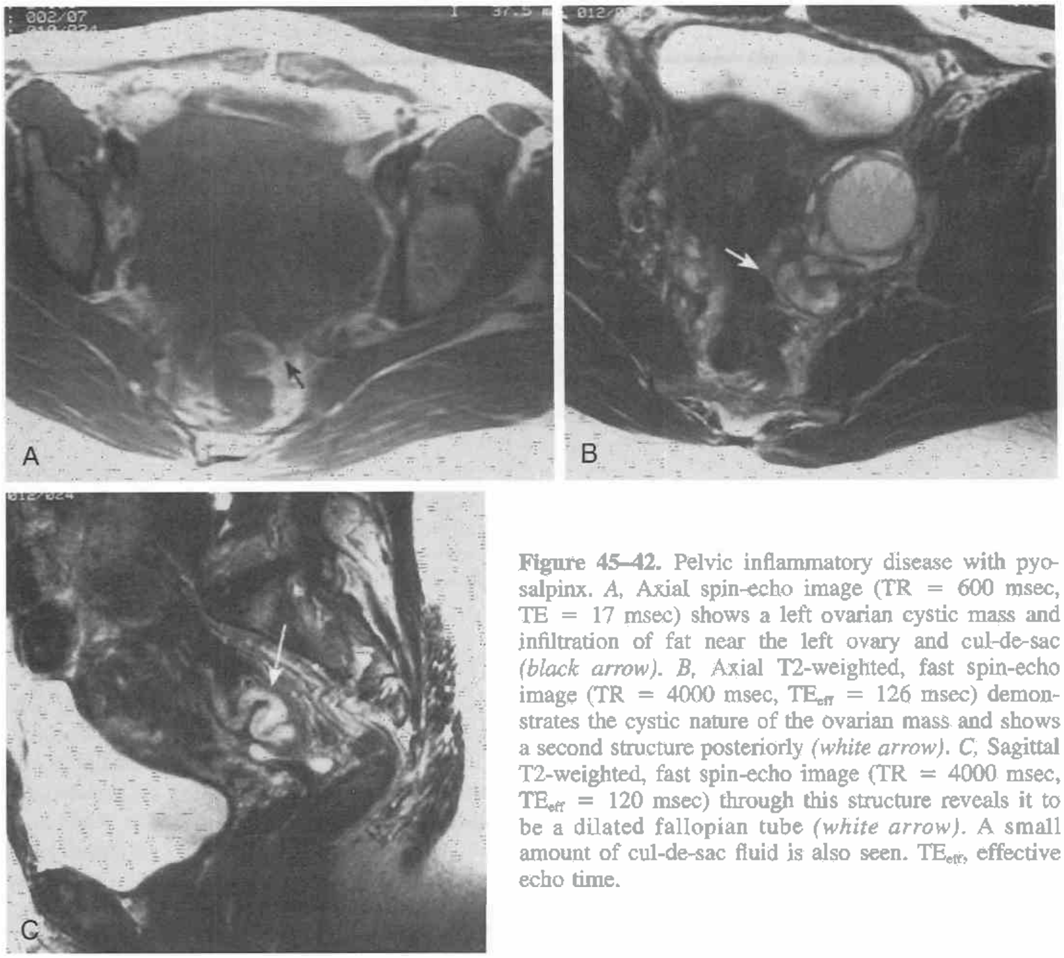

Figure 45–42. Pelvic inflammatory disease with pyosalpinx. *A,* Axial spin-echo image (TR = 600 msec, TE = 17 msec) shows a left ovarian cystic mass and infiltration of fat near the left ovary and cul-de-sac *(black arrow). B,* Axial T2-weighted, fast spin-echo image (TR = 4000 msec, TE_{eff} = 126 msec) demonstrates the cystic nature of the ovarian mass and shows a second structure posteriorly *(white arrow). C,* Sagittal T2-weighted, fast spin-echo image (TR = 4000 msec, TE_{eff} = 120 msec) through this structure reveals it to be a dilated fallopian tube *(white arrow).* A small amount of cul-de-sac fluid is also seen. TE_{eff}, effective echo time.

Accounting for approximately 4% of ovarian neoplasms are (1) fibromas, (2) thecomas, (3) fibrosed thecomas, and (4) fibrothecomas.

Ovarian fibromas are important from an imaging standpoint because they appear as solid masses and therefore mimic malignant neoplasms. They are associated with ascites in 40% of cases, particularly in larger lesions, and with pleural effusions in a small percentage (Meigs' syndrome).[6, 65] These tumors are composed of admixtures of fibrous tissue and theca cells with abundant lipid in the cytoplasm.

Fibromas show homogeneous intermediate to low signal intensity on T1-weighted MR images. On T2-weighted images, fibromas appear as well-circumscribed masses showing very low signal intensity with scattered high-signal-intensity areas that represent edema or cystic degeneration.[258, 259] The very low signal intensity results from the abundant collagen content of these tumors. Because of their predominantly low signal intensity on T2-weighted images, fibromas display a relatively specific appearance on MR images.[262, 384] *Brenner tumors,* another benign neoplasm, have a similar appearance because they have a dense fibrotic component.[261] Pedunculated leiomyomas also appear as low-signal-intensity masses (Fig. 45–44).

Benign forms of serous and mucinous tumor are common. Features more suggestive of benign cystic neoplasm include unilocularity of cysts, thin walls, minimal septations, and absence of papillary projections. Mucinous ovarian tumors represent 20% of all ovarian tumors.[261] They are generally cystic; unlike serous tumors, however, they may be very large and they tend to be multiloculated (see Fig. 45–14).[262] They often show variable signal intensity in the locules that results from proteinaceous or mucinous contents or hemorrhage.

In regard to cystadenofibromas, the fibrous component is part of the neoplasm, which is believed to be of epithelial and stromal origin, as are cystadenomas and cystadenocarcinomas.[256, 261] Cystadenofibromas usually appear as multilocular cystic masses with a solid portion, and the fibrotic component of these masses shows very low signal intensity on T2-weighted images (see Fig. 45–1).[258] These tumors are less likely to be borderline or malignant compared with other serous or mucinous tumors.

Obstetric Applications

MRI is ideally suited to the evaluation of pelvic masses in pregnant patients when ultrasound is nondiagnostic.[8, 100, 400] MRI is reliable in detecting benign ovarian masses and in identifying dermoids and leiomyomas (see Fig. 45–44), including those that may interfere with delivery.[8, 100, 400] Although adnexal masses are not uncommon in pregnant women, malignancies are rare. Ovarian carcinoma occurs

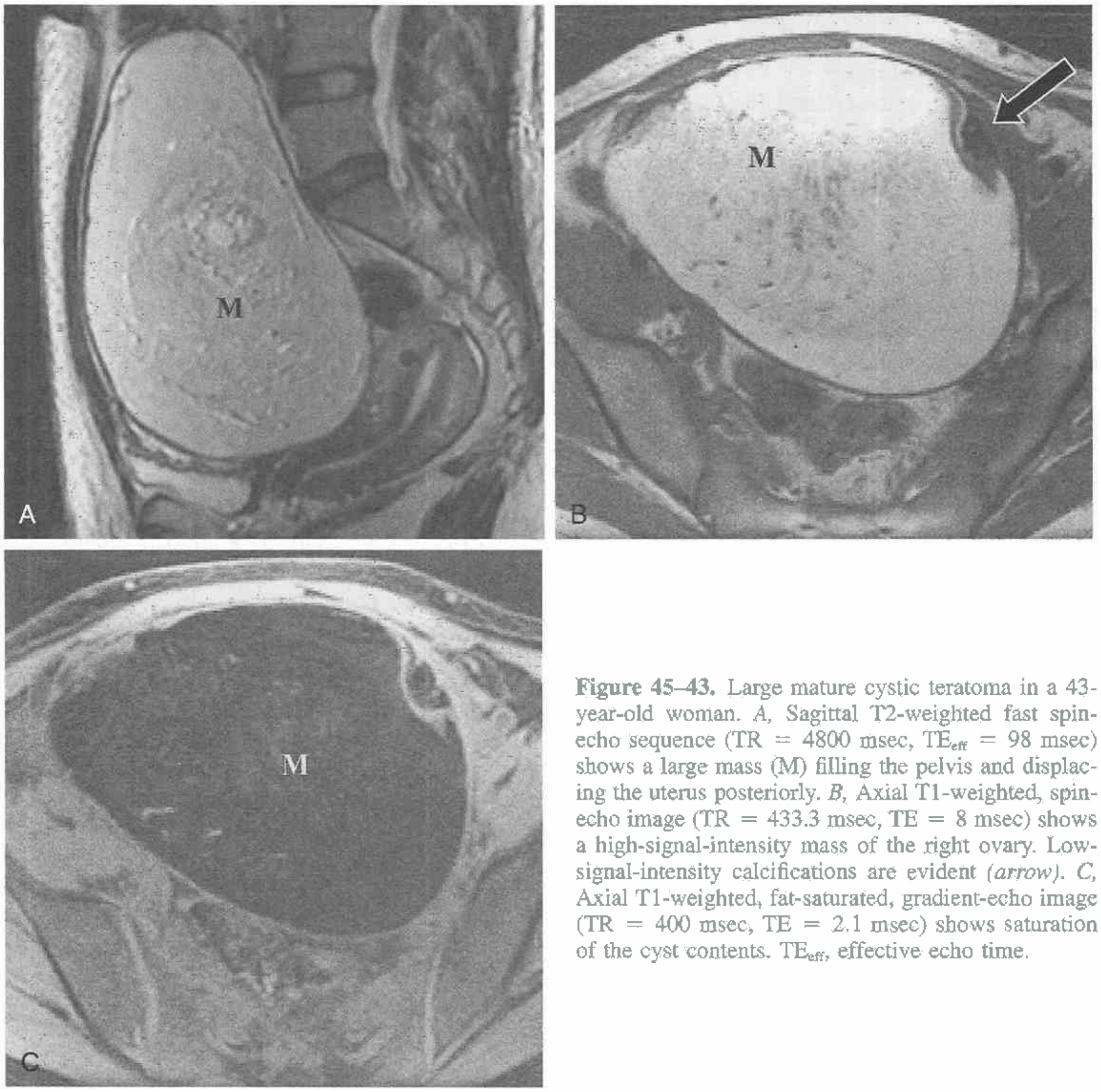

Figure 45–43. Large mature cystic teratoma in a 43-year-old woman. *A*, Sagittal T2-weighted fast spin-echo sequence (TR = 4800 msec, TE_{eff} = 98 msec) shows a large mass (M) filling the pelvis and displacing the uterus posteriorly. *B*, Axial T1-weighted, spin-echo image (TR = 433.3 msec, TE = 8 msec) shows a high-signal-intensity mass of the right ovary. Low-signal-intensity calcifications are evident *(arrow)*. *C*, Axial T1-weighted, fat-saturated, gradient-echo image (TR = 400 msec, TE = 2.1 msec) shows saturation of the cyst contents. TE_{eff}, effective echo time.

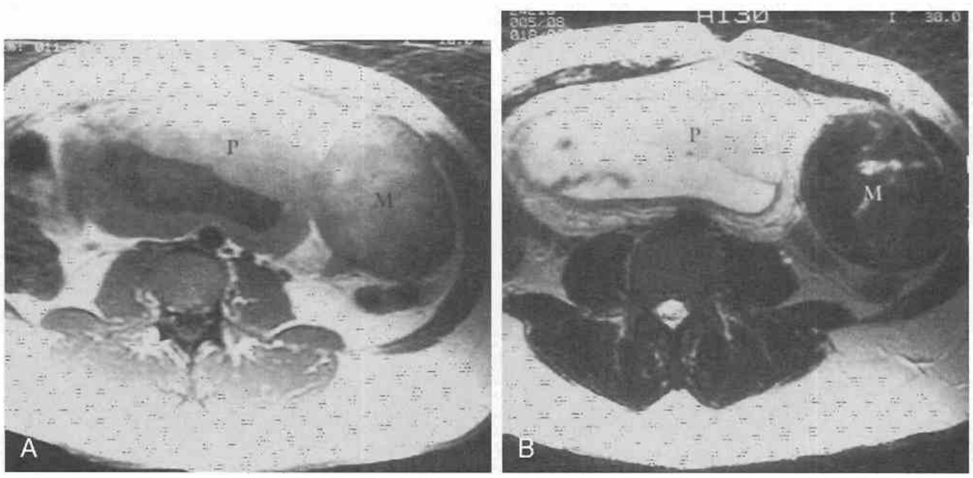

Figure 45–44. Adnexal mass in a pregnant patient. A previous ultrasound examination had shown a large, complex, partially solid mass. *A*, Axial spin-echo image (TR = 700 msec, TE = 12 msec) shows the placenta (P) and a mass in the left adnexa (M). *B*, Axial T2-weighted, fast spin-echo image (TR = 3800 msec, TE_{eff} = 126 msec) demonstrates the gravid uterus with the anterior placenta (P) as well as the left adnexal mass (M). The low signal intensity of the mass is consistent with a pedunculated leiomyoma. Small areas of hemorrhagic infarction are evident within the mass. TE_{eff}, effective echo time.

in only 1 of 17,000 to 38,000 pregnancies.[160] Ovarian tumors are one tenth as likely to be malignant in pregnant women as in nonpregnant women.[26]

Ultrasonography is the primary modality for evaluation of the gravid uterus. MRI may be useful in specific instances when ultrasound is equivocal, such as in cases of extrauterine pregnancy or in evaluation of placenta position.[8] Additional applications awaited the development of single-shot FSE (or HASTE) sequences, which permitted relatively motion-free images of the fetus. Before the advent of these sequences, fetal imaging required that pancuronium be administered to the fetus via an amniocentesis needle to alleviate motion artifacts. No known adverse fetal effects occur; however, large-scale studies showing the safety of MRI in pregnancy have not been performed.[166]

Single-shot FSE sequences are useful in imaging the fetus or placenta when ultrasound findings are equivocal. The display of fetal anatomy before 20 weeks of gestation is usually inferior to that of ultrasound because of the small size and motions of the fetus.[194, 195] Single-shot FSE images show particular advantages over ultrasound when ultrasound is limited (e.g., in the setting of oligohydramnios and in late third trimester). MRI can demonstrate additional findings in fetuses with neurologic abnormalities, such as germinal matrix hemorrhages and agenesis of the corpus callosum (Fig. 45–45).[176, 194, 195, 251, 291, 408] MRI is also useful in depicting the contents of diaphragmatic hernias and omphaloceles because the liver can easily be distinguished from the bowel.[144] Widespread use of single-shot FSE sequences for fetal imaging awaits research into the optimal indications for MRI in these patients.

Malignancies of the Female Pelvis

MRI has not yet achieved widespread use for staging of pelvic malignancies, partly because of its general unavailability and, more important, because of a lack of controlled clinical trials demonstrating efficacy in well-defined clinical situations in which additional staging information will affect the outcome for the patient. Nonetheless, MRI realizes fairly high staging accuracy for gynecologic malignancies, and persuasive arguments can be made for its increased clinical use.[61, 112, 136, 305]

Uterus

Cervical Carcinoma

Cervical epithelium can undergo a series of gradual histologic changes from progressively severe dysplasia to carcinoma in situ (CIS) and invasive carcinoma. The detection of this progress with screening and biopsy has led to marked reduction in the mortality rate from this disease in the last 50 years in the United States.[9, 36, 52, 276, 299] The incidence of CIS is greater than that of invasive carcinoma by a ratio of 4:1, and the highest incidence occurs around age 30 years, about 10 to 15 years earlier than that of invasive carcinoma.

Invasive carcinoma spreads by direct extension to adjacent organs, the vagina, the pelvic wall, and the bladder and rectum. Failure to achieve control of the disease when it is local is a major cause of treatment failure in advanced disease.[117, 151, 278, 404] Metastatic lymphadenopathy occurs commonly in the pelvic lymph nodes, but it also involves the periaortic chains in 17% to 29% of patients, including 5% to 27% of stage IB and IIA lesions.[3, 117, 119, 185, 276, 390] Locally advanced tumors may also disseminate along the peritoneum.[119]

The 5-year survival rate for invasive carcinoma is 80% to 90% for stage I, 75% for stage II, 35% for stage III, and 10% to 15% for stage IV.[121] The surgical approaches for early-stage carcinoma include total hysterectomy for stage IA and radical hysterectomy for stage IB and II, although

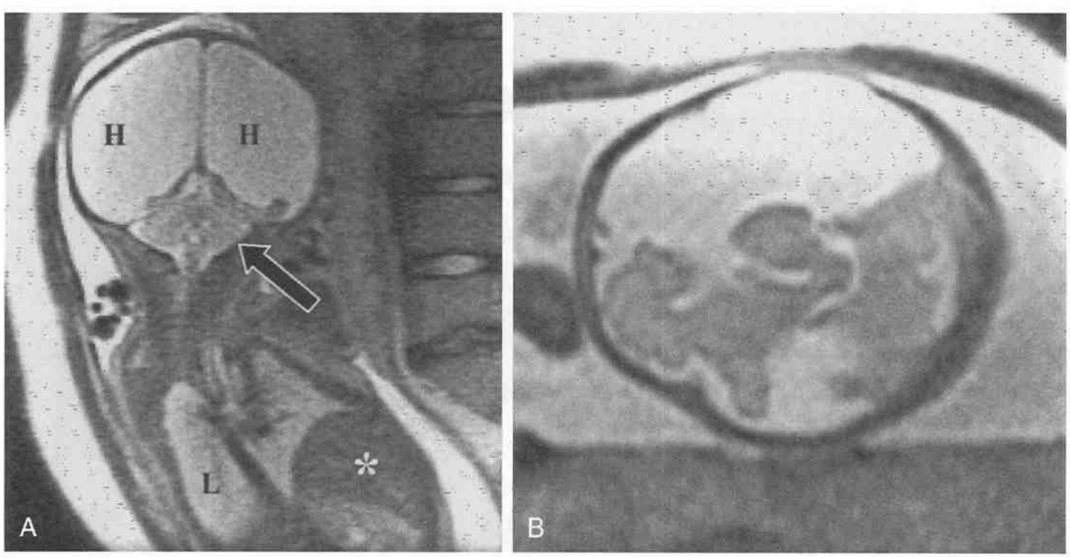

Figure 45–45. Single-shot, [redacted] imaging of a fetus to evaluate for severe hydrocephalus suspected on ultrasound. *A,* The image, in the sagittal plane relative to the mother but in the coronal plane relative to the fetus, demonstrates cerebrospinal fluid filling the right and left hemicrania (H). The cerebellum appears intact *(arrow).* The lungs (L) and liver *(asterisk)* are demonstrated. *B,* Preservation of some of the frontal lobe and temporal lobe on the right in a patchy distribution indicates hydranencephaly, not hydrocephalus. (From Outwater EK: Ultrafast MR imaging of the pelvis. Eur J Radiol 29:233–244, 1999.[255])

the National Institutes of Health (NIH) consensus panel suggests equal efficacy of radiation and surgery for this group. Radiation therapy is employed for bulky stage II, stage IIB, stage III, and stage IV disease.[121, 275, 276] Anterior or posterior exenteration may be indicated in some cases of stage IV disease with bladder or rectal involvement because of the risk of fistula formation after radiation treatment.[121]

The identification of cervical carcinoma on MRI is straightforward because the high-signal-intensity lesion contrasts with the very-low-signal-intensity cervical stroma on T2-weighted images (Fig. 45–46).[173, 405] Areas of coagulative necrosis may appear as small foci of lower signal intensity within the tumor mass.[343] The signal intensity of cervical carcinoma has a variable response to radiotherapy; tumors responding to therapy tend to lose signal intensity on T2-weighted images.[92, 309] T1-weighted images fail to reveal smaller lesions because of a lack of contrast between cervix and tumor. Hematometra is not uncommon in cervical carcinoma because of cervical obstruction or radiation-induced stenosis (Fig. 45–47).[39, 325]

An important potential role for accurate noninvasive staging of cervical carcinoma exists because staging based on clinical examination with the patient under anesthesia with cystoscopy and proctoscopy (Table 45–4) is inaccurate when compared with pathologic findings.[117, 119, 185, 278, 390] Surgical staging for clinical stages IIB to IV is not routinely performed, and it carries significant morbidity.[119, 185, 305] Intraoperative findings of advanced-stage tumors result in aborting plans for hysterectomy in up to 12% of patients with clinical stage I disease.[76, 185] Patients treated with radiotherapy alone may be understaged or overstaged, causing adverse effects on mortality.[117] Therefore, if sufficient accuracy can be established, MRI may become a desirable

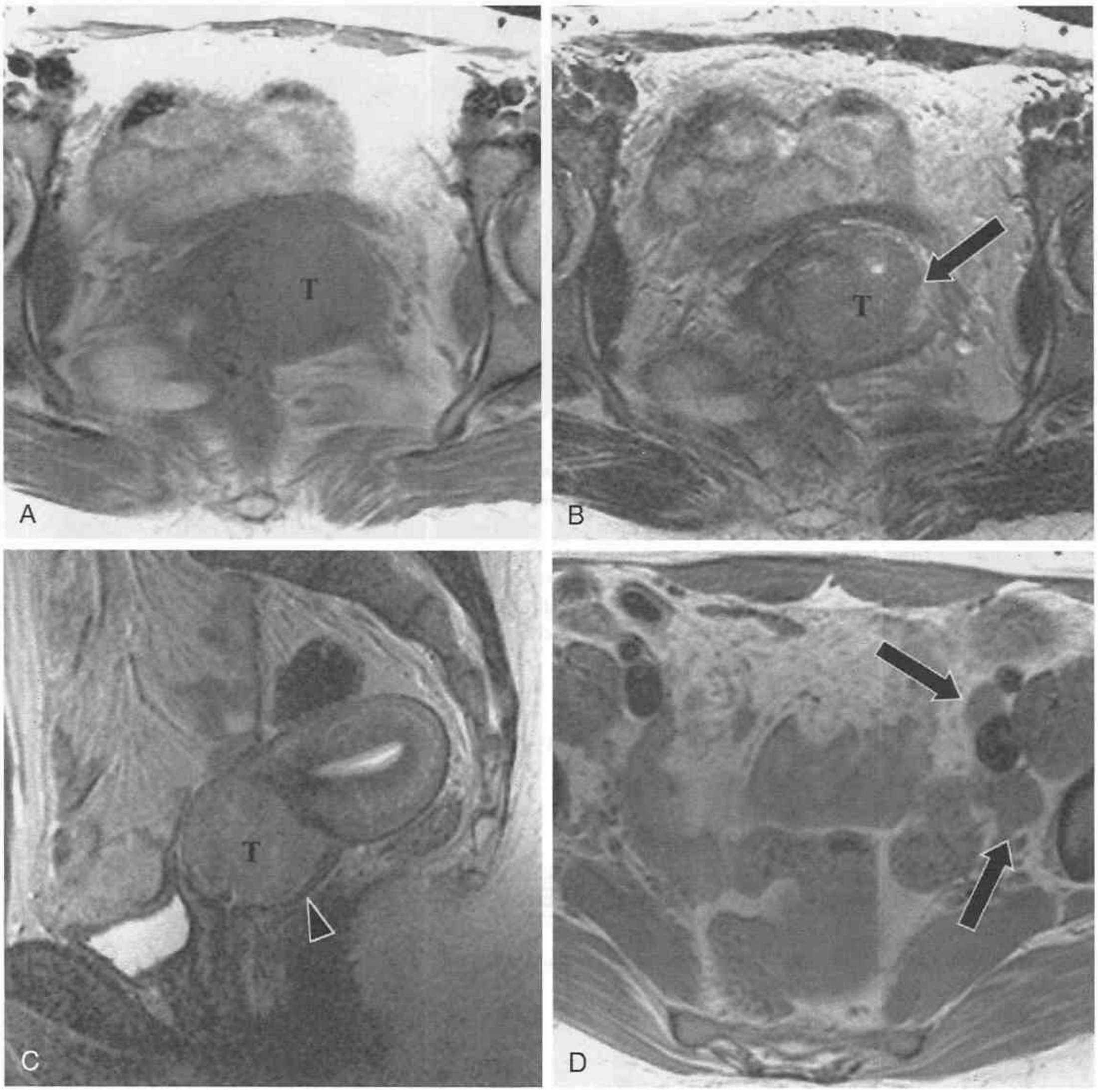

Figure 45–46. Cervical carcinoma, stage IIB. *A,* T1-weighted image shows cervical enlargement (T). No differentiation of tumor and cervical stroma is seen. *B,* Axial T2-weighted, fast spin-echo image shows high-signal-intensity tumor (T) arising from the left cervical lip and growing into the left parametrium *(arrow). C,* Sagittal T2-weighted, fast spin-echo image demonstrates the tumor (T) without invasion superiorly into the uterine corpus. The low-signal intensity of the posterior vaginal fornix *(arrowhead)* is identified. *D,* T1-weighted spin-echo axial image shows metastases to the left external iliac lymph nodes *(arrows).*

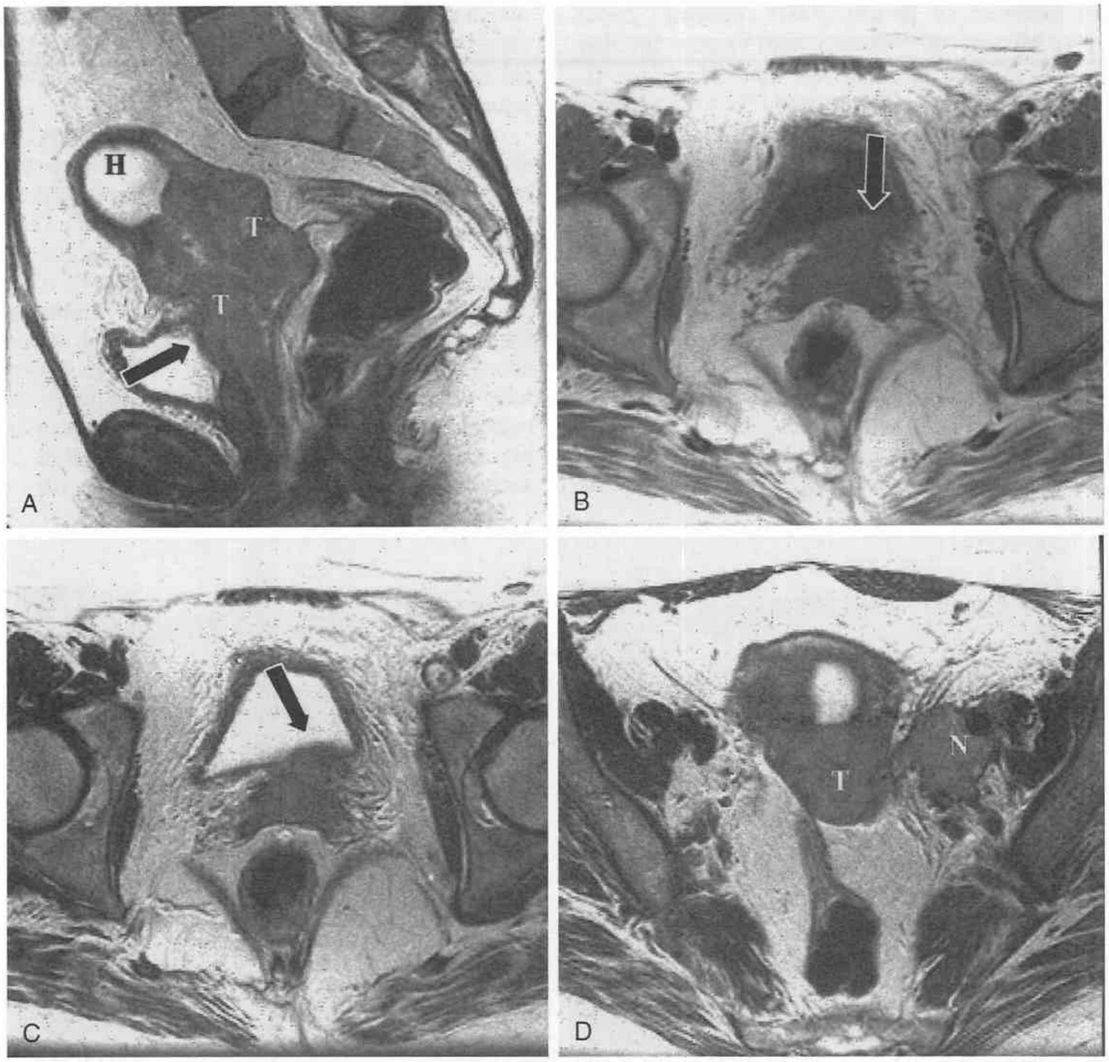

Figure 45–47. Vaginal and bladder invasion from cervical carcinoma.

A, T2-weighted, fast spin-echo image shows extensive tumor (T) infiltrating the cervix and lower uterine segment, with obstruction of the endocervical canal causing hematometra (H). Infiltration into the anterior vagina and the bladder wall *(arrow)* can be seen.

B, T1-weighted, spin-echo image at the level of the vagina shows tumor extending anterior to the bladder wall and producing effacement of the fat plane *(arrow)* between the vagina and the bladder.

C, T2-weighted, fast spin-echo image shows the infiltration of the normal lower-signal-intensity muscularis at the site of bladder invasion *(arrow)*.

D, T2-weighted image at the level of the myometrium shows the tumor (T) invading the uterine corpus. Nodal metastasis (N) produces obstruction of the left external iliac vein.

(From Outwater EK: Cervical carcinoma. In Mendelson E, Reuter K, Rubin E, Bohm-Velez M [eds]): Women's Imaging. St. Louis, Mosby, 2000.[254])

Table 45–4. Accuracy of MRI for Staging Parametrial Extension of Cervical Carcinoma

No.	Sensitivity (%)	Specificity (%)	Accuracy (%)	Reference
57	89	87	93	Hricak et al[137]
30	67	98	92	Kim et al[173]
66	76	94	89	Togashi et al[381]
25	100	80	88	Sironi et al[344]
46	71	87	85	Greco et al[104]
20	0	83	79	Waggenspack et al[396]
26	87	86	69	Hawighorst et al[115]
99	20	97	87	Kim et al[172]
79	100	94	94	Subak et al[360]
62	—	—	95	Yu et al[418]

substitute for clinical examination using anesthesia and may be cost-effective.[138, 143, 305, 416] Because small tumors tend to be limited to the cervix, it has been suggested that stage IB lesions greater than 2 cm may benefit from MRI but those smaller than 2 cm may not.[138, 416]

Consistently high rates of accuracy for MRI staging of cervical carcinoma (see Table 45–4) have been documented in several studies. Overall, rates of 76% to 90% accuracy are reported.[67, 104, 137, 172, 173, 381] MRI has no role in assessing most cases of cervical carcinoma (i.e., CIS and stage IA) because these lesions are not visible on the images.[173, 196, 381] In one prospective study, no stage 0 or IA lesions in 27 patients were detected.[381] Larger lesions are easily appreciated, and accurate measurement of tumor volumes can be obtained.[46, 196, 343] Tumor volume is an important prognostic predictor of failure after radiation therapy, although it does not directly affect clinical staging by the International Federation of Gynecology and Obstetrics (FIGO) system.[46, 151, 278, 343]

The detection of parametrial spread relies on visualization of tumor invading the paracervical venous plexus. Invasion into the paracervical tissues can be excluded if a low-signal-intensity rim of cervical stroma surrounds the tumor.[137, 173, 344, 381] If this rim becomes effaced, parametrial spread is likely.[137, 173, 294, 344, 377, 381]

Bulky stage I tumors may displace the plexus laterally without invading it.[60, 137, 228, 304, 344, 381] Tumors at the cervical lip that extend posterolaterally may protrude into the vaginal fornices; higher or anterior tumors extend directly into the parametria (see Fig. 45–46).[137] Advanced tumors grow along the sacrouterine ligaments and the cardinal ligaments to the pelvic sidewall.[228, 396, 397] These features are best seen with side-by-side comparison of T1-weighted and T2-weighted sequences for differentiation of tumor, paracervical venous plexus, and fat, since tumor and fat on T2-weighted sequences may exhibit little contrast.[344, 396, 397] Tumor invading the vaginal wall interrupts the thin, low-signal-intensity wall on T2-weighted sequences (see Fig. 45–47).[60, 67, 104, 137, 228, 377, 381] Similarly, if the low-signal-intensity muscularis of the bladder or rectum is focally disrupted, spread into these organs is likely (see Fig. 45–58).[67, 104, 137, 173]

The role of gadolinium enhancement in staging of cervical carcinoma is evolving. Preliminary studies have found similar information on enhanced T1-weighted images and T2-weighted images but an overall increase in staging accuracy with the enhanced images.[374] In other studies, however, staging was not improved with administration of contrast material (see Fig. 45–58).[110, 373, 385] Dynamic gadolinium-enhanced images show rapid enhancement of cervical tumors and may help in staging.[1, 115, 391, 409] Analysis of dynamic images may have prognostic value and aid in predicting response to radiation by identifying better-perfused tumors.[213] Finally, dynamic enhanced studies are useful for identifying recurrent cervical tumor.[114, 406]

A complete evaluation of patients with cervical carcinoma should include transverse T1-weighted images of the infrarenal periaortic and iliac lymph node chains to detect enlarged lymph nodes. Periaortic metastatic adenopathy increases the stage of the disease and indicates a poor prognosis (see Fig. 45–47).[3, 117, 278] The assessment of lymph nodes in cervical carcinoma is probably comparable to that obtained by CT.[83] Experience with CT, however, indicates that size criteria alone are not sufficiently specific or sensitive for metastases[117, 119, 210] and must be supplemented by needle aspiration to provide diagnostic information.[21, 112]

Endometrial Carcinoma

Endometrial carcinoma is a disease of menopausal or postmenopausal women, with a peak incidence at age 60 years.[200] Because in situ cervical carcinoma, detected by screening, has been largely eradicated, endometrial carcinoma has become the more common invasive tumor in the United States, with 36,000 cases in 1998.[71, 186] Many endometrial carcinomas, however, are surgically curable while confined to the uterus, and the mortality rate is lower than that of invasive cervical carcinoma.[186] Risk factors include diabetes, hypertension, and disorders associated with prolonged unopposed estrogen stimulation (i.e., obesity, nulliparity, infertility, estrogen-secreting tumors, and exogenous estrogen administration).[71, 299]

Endometrial carcinoma tends to proliferate within the endometrial cavity as a localized polypoid mass or as a diffuse tumor involving the entire endometrial surface.[299] Initially, invasion occurs through the myometrium or into the endocervical canal. Pelvic or periaortic lymph node metastases and peritoneal metastases ensue with advanced tumors,[37, 239, 299] although these can occur with stage I disease.[37, 299] Endometrial carcinoma mav metastasize to the adnexa or vagina, although frequently in microscopic deposits.[37, 239]

The most common MRI finding in patients with small endometrial carcinomas is widening of the endometrial cavity due to the tumor or associated hematometra (Fig. 45–48).[42, 130, 140, 369, 405] MRI scans are normal in 15% to 19% of patients with endometrial carcinoma because small superficial lesions blend in with the normal endome-

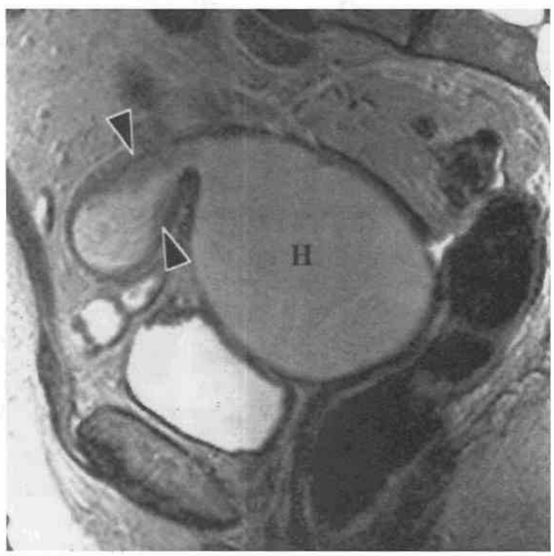

Figure 45–48. Endometrial carcinoma with hematometra. Sagittal T2-weighted image (TR = 5833 msec, TE_{eff} = 126 msec) shows the uterine and endocervical canals to be markedly distended with hemorrhagic fluid (H). The irregular tumor *(arrowheads)* lines the endometrial cavity. TE_{eff}, effective echo time.

trium.[139, 140] Masses of tumor within the endometrial cavity display variable signal intensity on T2-weighted images,[140, 405] but they exhibit higher intensity than the uterine junctional zone or myometrium (see Fig. 45–48).[103, 139, 140, 209, 285, 413] Considerable signal heterogeneity due to necrosis, hemorrhage, and endocervical canal obstruction by hematometra is evident with larger tumors on T2-weighted images.[130, 369, 376] Gadolinium enhancement easily distinguishes vascularized tumor from areas of nonenhanced necrosis or fluid accumulation.[110, 130, 376] Usually, tumor enhances somewhat less than myometrial tissue, although the tumor-myometrial interface is often obscured by gadolinium (Figs. 45–49 and 45–50).[135]

The clinical usefulness of preoperative radiologic staging of endometrial carcinoma is not established.[209, 240, 305] Endometrial carcinoma is definitively staged using the surgical FIGO system.[71, 394] Treatment decisions are made, in part, on the basis of lymph node sampling or an assessment of relative risk for occult lymph node metastases.[37, 44, 71, 165, 208, 239, 240] The risk factors for periaortic nodal metastases in stage I or II disease include depth of myometrial invasion, presence of adnexal metastases, tumor grade, and grossly positive lymph nodes, all of which may be determined intraoperatively.[37, 44, 71, 162, 165, 202, 208, 239, 247] Furthermore, lymphadenectomy may confer survival benefit.[170] The role of preoperative radiation (e.g., intracavitary treatments) is unclear, although less toxicity to bowel may ensue than with postoperative radiotherapy.[44, 202, 247] MRI may be useful to plan radiation treatment portals.[305]

Staging of endometrial carcinoma by MRI requires the following:

1. Demonstration of the tumor's relationship to the myometrium and cervix.
2. Clear demonstration of the boundaries between the uterus and the bladder, rectum, and vagina.
3. Assessment of lymph nodes from the level of the kidneys through the pelvis.

T2-weighted sagittal images display the uterine anatomy to best advantage and are considered most essential for showing intrauterine invasion. Transverse T1-weighted images are adequate for the evaluation of lymphadenopathy. The myometrium enhances intensely and rapidly on dynamically enhanced images, whereas endometrial adenocarcinomas enhance poorly. Differentiation between myometrium and invading tumor may be better in some cases on enhanced images than on T2-weighted images.

The depth of myometrial invasion is one of several pathologically defined risk factors that correlate with the surgical stage of disease, presence of lymph node metastases, and prognosis.[37, 44, 162, 202, 208, 239] The most reliable sign of myometrial invasion on MR images is focal discontinuity in an otherwise discrete junctional zone.[139, 140, 282, 285, 376, 413] A distinct junctional zone, however, is not always visualized in postmenopausal women.[327] Enhanced images, particularly dynamically enhanced images, may show better differentiation between myometrium and tumor in these patients than T2-weighted images (see Fig. 45–50).[331]

A second sign is focal thinning of the myometrium or irregularity of the tumor-myometrial interface (see Fig. 45–7).[140] Larger tumors and hematometra frequently thin the myometrium concentrically; therefore, this is a nonspecific finding.[140, 376]

The prospective accuracy of determination of invasion depth has been reported to be 74% to 94%.[27, 63, 103, 139, 140, 327, 369, 413] Studies suggest better accuracy with MRI for determination of myometrial invasion depth than with ultrasound or CT.[174, 175]

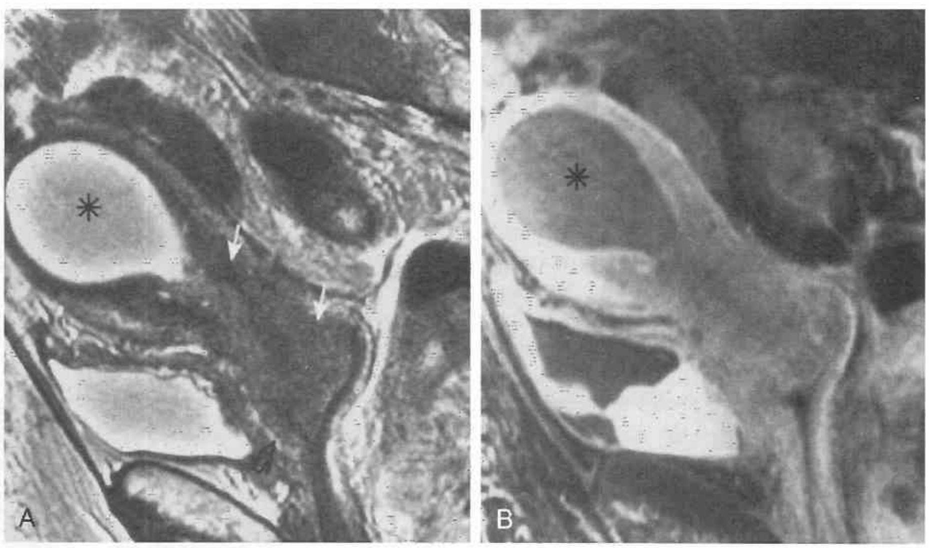

Figure 45–49. Obstructed uterus caused by endocervical adenocarcinoma. *A*, Sagittal T2-weighted, fast spin-echo (FSE) image (TR = 6000 msec, TE_{eff} = 119 msec) shows a hematometra *(asterisk)* caused by an irregular intermediate-signal-intensity tumor *(white arrows)* obstructing the end of the cervical canal. Because of tumor infiltration, the normal low signal intensity of the cervical stroma is entirely disrupted and the junctional zone in the low uterine segment is irregular and disrupted. The vaginal wall is irregularly thickened *(open arrow)*. *B*, Sagittal gadolinium-enhanced image corresponds to the same level as in *A*. The endocervical canal tumor enhances, although not as much as the normal myometrium, and the hematometra *(asterisk)* does not enhance. The thickened enhancing tissue along the anterior vaginal wall indicates vaginal wall invasion. TE_{eff}, effective echo time.

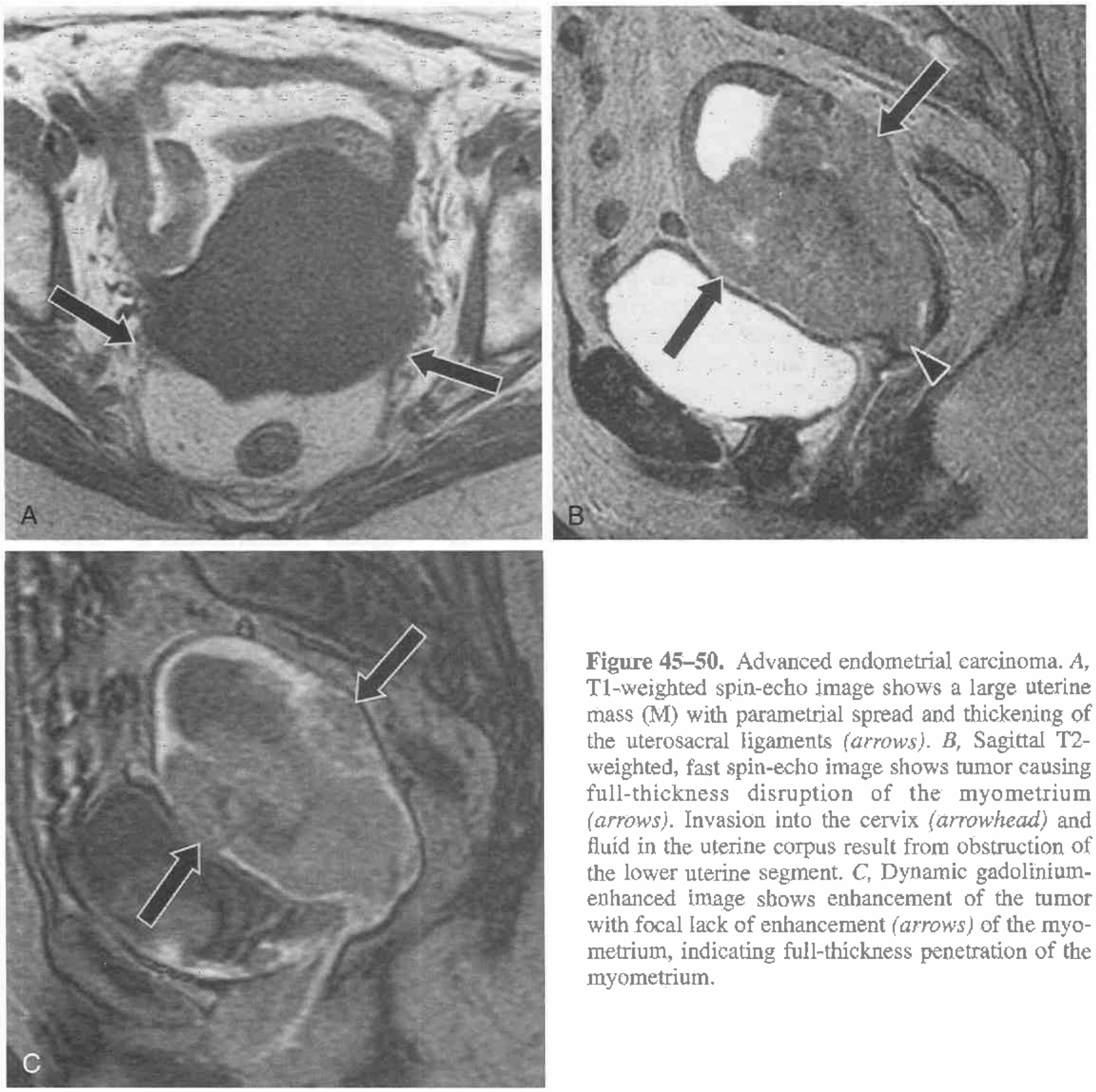

Figure 45–50. Advanced endometrial carcinoma. *A*, T1-weighted spin-echo image shows a large uterine mass (M) with parametrial spread and thickening of the uterosacral ligaments *(arrows)*. *B*, Sagittal T2-weighted, fast spin-echo image shows tumor causing full-thickness disruption of the myometrium *(arrows)*. Invasion into the cervix *(arrowhead)* and fluid in the uterine corpus result from obstruction of the lower uterine segment. *C*, Dynamic gadolinium-enhanced image shows enhancement of the tumor with focal lack of enhancement *(arrows)* of the myometrium, indicating full-thickness penetration of the myometrium.

Invasion of the cervix can be confirmed by MRI when high-signal-intensity tissue expands the endocervical canal or, more reliably, when tumor disrupts the low-signal-intensity cervical stroma (see Fig. 45–50).[27, 139, 140, 376] These findings are generally easily appreciated by MRI.[63, 140] Reported accuracies for the detection of cervical invasion are 85% to 90%.[27, 369]

Determination of stage III or IV disease requires assessment of the adnexa, uterine and cervical suspensory ligaments, pelvic lymph nodes, and bladder and rectal walls.[139, 140, 376] MRI findings indicative of advanced disease include transmural interruption of the myometrium, serosal irregularity, and disruption of the low-signal-intensity vaginal, bladder, or rectal muscularis.[63, 139, 140, 376] Adnexal metastases, which are not uncommon, may be confused with normal high-signal-intensity ovaries or other ovarian abnormalities.[63, 84]

In one prospective study, the sensitivity for the detection of stage III or IV disease by MRI was only 17% and the positive predictive value for findings suggestive of advanced tumor was only 50%.[139] The accuracy of MRI staging of endometrial carcinoma has been reported to be 85% overall.[139, 369] Gadolinium-enhanced images significantly improve accuracy.[159, 175, 311, 345, 407]

Uterine Sarcomas

In addition to arising from the endometrium, uterine malignancies may originate from endometrial stroma (stromal sarcoma), pluripotential mesoderm (müllerian mixed mesodermal tumors), and myometrial smooth muscle (leiomyosarcomas).[299] Unlike endometrial carcinoma, mesenchymal malignancies often remain undetected by screening techniques and tend to be in an advanced stage at diagnosis. Spread by either the lymphatic or the hematogenous route is more likely at presentation compared with endometrial carcinoma.[17, 59, 62, 336]

Müllerian mixed mesodermal tumors are aggressive malignancies with a propensity for advanced stage at diagnosis.[17, 31, 299] Their biologic behavior and MRI characteristics are otherwise similar to those of endometrial carcinoma.[336, 376]

Tumors derived from endometrial stromal tissues include benign stromal nodules, low-grade stromal sarcoma

(indistinguishable from benign nodules but with lymphatic invasion), and endometrial stromal sarcoma (Fig. 45–51).[17] These tumors show intermediate to high signal intensity and infiltrate into the myometrium or vessels, an appearance dissimilar from that of leiomyomas.[179]

Leiomyosarcomas arise from myometrial smooth muscle and usually occur in women between ages 40 and 60 years. Histologically, sarcomas are difficult to differentiate from leiomyomas; typical criteria include more than 10 mitoses per high-powered field or more than 5 mitoses with nuclear atypia per high-powered field.[17, 299] Given this subtle difference, it is unlikely that MRI will prove useful in differentiating between the two, although it serves to identify the myometrial origin of these tumors.[136, 152] A large size at presentation and heterogeneously increased signal on T2-weighted images distinguish sarcomas from most, but certainly not all, leiomyomas.[136, 152, 267, 354] MRI may prove useful in the unusual venoinvasive form of this sarcoma (intravenous leiomyomatosis) to demonstrate the extent of intravascular disease.[339]

Gestational Trophoblastic Disease

Gestational trophoblastic disease forms a spectrum of related conditions, which include molar pregnancy, invasive mole, and choriocarcinoma. After evacuation of a complete mole, persistent gestational trophoblastic disease develops in 20% of patients, and metastases occur in 5%.[28] Chemotherapy achieves a high rate of cure even when the tumor is widely metastasized.[28] The role of radiologic evaluation of patients with gestational trophoblastic disease lies primarily in the identification of metastases in the lung, brain, and liver.[28, 145]

MRI may be useful in demonstrating intrapelvic spread and tumor size. The signal intensity pattern of gestational trophoblastic disease is variable. Intratumoral hemorrhage frequently causes high-signal-intensity areas on T1-weighted sequences (Fig. 45–52).[132, 376] Heterogeneity on T2-weighted sequences results from necrosis, hemorrhage, and cyst formation.[61, 132, 230] Large uterine vessels supplying the tumor appear as peritumoral signal voids.[132, 230] Metastases to the vagina occur in 16% to 30% of cases.[28, 145] Theca lutein cysts, which are frequently hemorrhagic,[61] occur in 30% to 50% of cases.[28, 132]

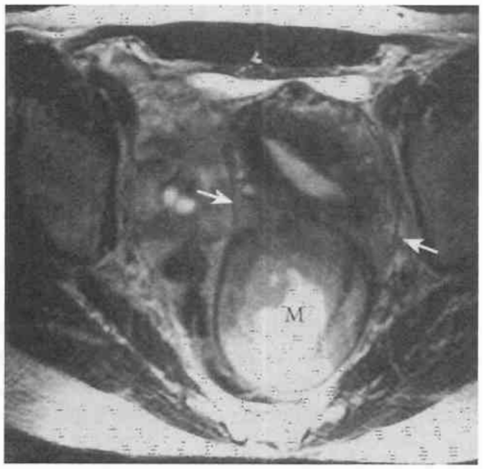

Figure 45–51. Uterine sarcoma. Axial T2-weighted, fast spin-echo multicoil image demonstrates heterogeneous intermediate signal intensity and a mass (M) arising from the posterior uterine wall. Continuity of the mass within the myometrium can be seen *(arrows)*. The mass has internal necrosis, and no part of it displays the usual low-signal-intensity areas of a uterine leiomyoma. Pathologic examination showed an endometrial stromal sarcoma.

Uterine Adnexa

Malignant Ovarian Neoplasms

Ovarian carcinoma causes more than twice as many deaths as any other pelvic gynecologic malignancy.[186] The incidence of epithelial ovarian carcinoma rises steadily between ages 30 and 70 years.[167]

More than 20 histologic types of tumors arise from the ovary. The origin of these neoplasms may be (1) surface ovarian epithelium, (2) germ cells, and (3) sex cord–stromal.[299]

Most malignant ovarian neoplasms in women are epithelial, including serous carcinomas, mucinous carcinomas, endometrioid carcinomas, and clear cell carcinomas.[299] These four neoplasms share similar clinical manifestations, frequency of bilaterality (20% to 40% of cases), propensity for intraperitoneal metastasis, and a poor prognosis.[167, 299] Low-grade forms, termed *borderline* or *low malignant potential tumors*, have a markedly better prognosis (>90% 5-year survival) than higher grades.[299] Endometrioid and clear cell carcinoma resemble endometrial carcinoma histologically and may coexist with endometriosis and synchronous endometrial carcinoma.[299] Clear cell carcinoma demonstrates a poorer prognosis and higher rates of lymphatic and hematogenous metastasis.[153] Epithelial carcinomas, indistinguishable from those of ovarian origin, may arise in the peritoneum without ovarian involvement.[4]

In MRI evaluation of an adnexal mass, the first step is to establish that the mass arises from the ovary. High-resolution, T2-weighted images are necessary to identify the ovaries and their relationship to the mass. Heavily T2-weighted FSE images identify small follicular cysts stretched around a mass, thus establishing an ovarian mass. Gynecologic masses of other origin (e.g., peritubal cysts, dermoid cysts, pedunculated fibroids, endometriomas, and hydrosalpinges) must be distinguished from malignancies.

Fairly high accuracy rates for distinguishing benign from malignant ovarian tumors by MRI have been reported, although it is unclear whether this is sufficient for clinical management in difficult cases. MRI features that suggest malignancy in an adnexal mass include the following (Fig. 45–53)[49, 346, 359, 373]:

- Size greater than 4 cm
- Irregular or large solid components in a cystic mass
- Thick (>3 mm) septations
- Evidence of peritoneal, lymphatic, or hematogenous spread or local invasion

Papillary projections within an ovarian mass establish that the mass is an ovarian neoplasm, although projections may also be seen in benign (uncommon), borderline (common), and higher-grade malignant lesions (Fig. 45–54; see Fig. 45–53). When these and other criteria described previously are used, accuracies of 60% to 93% for distinguishing benign from malignant masses have been reported for

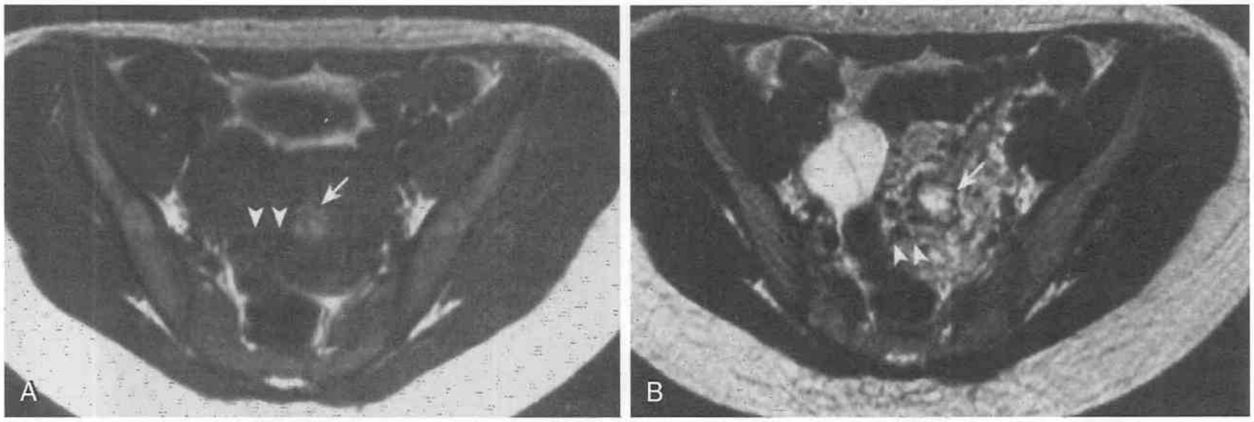

Figure 45–52. Gesta[redacted]al trophoblastic disease. T1-weighted *(A)* and T2-weighted *(B)* images show a high-signal-intensity mass embedded within the myometrium *(white arrows)* in a patient after evacuation of a complete mole. On the T2-weighted, spin-echo image in *B*, the punctation signal voids around the mass *(arrowheads)*. A multiseptate theca lutein cyst is present.

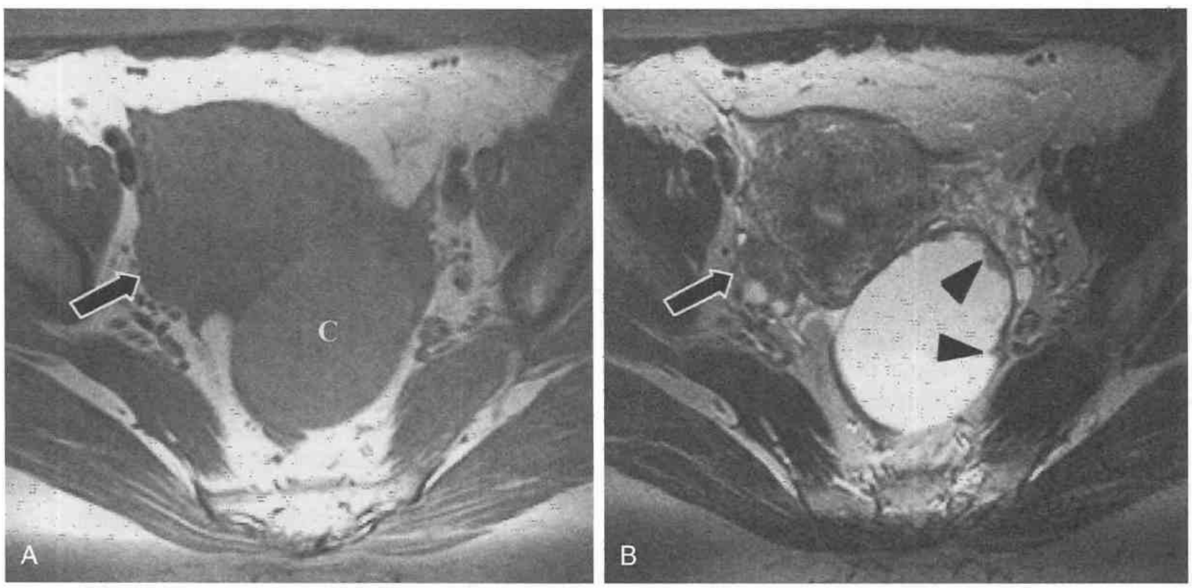

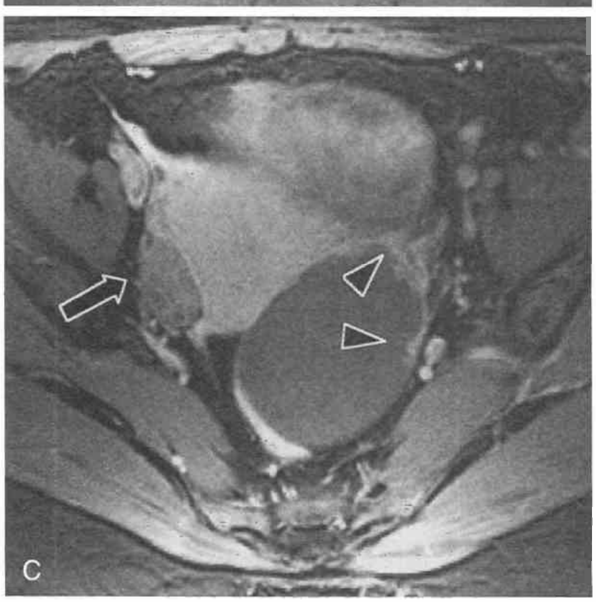

Figure 45–53. Borderline ovarian serous tumor in a 40-year-old woman.

A, T1-weighted, spin-echo image shows a left ovarian mass (C) with slightly high signal intensity of the cyst fluid. The normal right ovary *(arrow)* shows intermediate signal intensity, similar to that of the uterus.

B, T2-weighted, fast spin-echo image shows the normal right ovary *(arrow)* with small cystic follicles. The left serous tumor has the high signal intensity of the cyst fluid, with small papillary projections *(arrowheads)*.

C, Gadolinium-enhanced, T1-weighted, fat-suppressed gradient-echo image shows enhancement of the papillary projections *(arrowheads)*. The normal ovary *(arrow)* enhances less than the uterus.

(*A,* From Ascher SM, Outwater EK, Reinhold C: Adnexa. In Semelka RC, Ascher SM, Reinhold C [eds]: MRI of the Abdomen and Pelvis: A Text-Atlas. New York, Wiley-Liss, 1997, pp 661–715.[12] *B* and *C,* From Outwater EK, Mitchell DG: Normal ovaries and functional cysts: MR appearance. Radiology 198:397–402, 1996.[257])

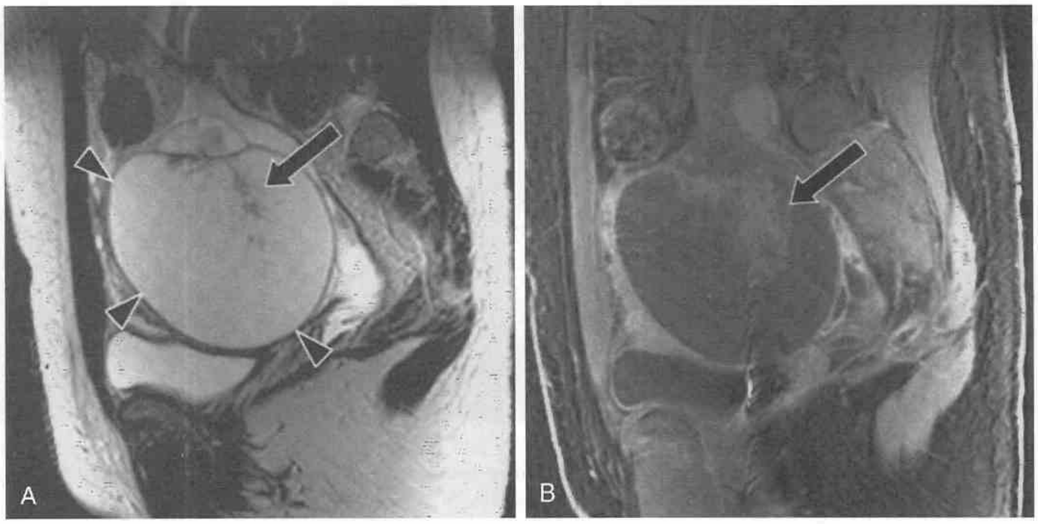

Figure 45–54. Papillary projections in a patient with a borderline ovarian serous tumor. *A,* Sagittal T2-weighted, fast spin-echo image ($TR = 6000$, $TE_{eff} = 119$) shows a multicystic left adnexal mass *(arrowheads)*. Within this mass is an ill-defined projection with a low-signal-intensity core *(arrow)*. *B,* Sagittal T2-weighted, fat-saturated, gradient-echo image ($TR = 250$, $TE = 2.9$) shows enhancement of the papillary projection *(arrow)*. Many of the papillary projections show very high signal intensity, blending in with the fluid within the cyst in *A*. TE_{eff}, effective echo time.

MRI,[346, 359] and higher accuracies have been reported with Gd-DTPA enhanced images.[359, 373] An accuracy rate of 86% has been described for distinguishing benign from malignant epithelial neoplasms.[98] These rates are comparable to those of 80% and 94%, respectively, reported for CT and ultrasound.[49] One comparative study established a higher accuracy rate for differentiating benign from malignant ovarian masses with MRI compared with transvaginal ultrasound and Doppler analysis (Table 45–5).[184]

The signal intensity of cystic components of ovarian neoplasms varies, especially in mucinous tumors.[98, 209, 234, 376] Specifically, the signal may be hyperintense on T1-weighted images and intermediate on T2-weighted images because of hemorrhage, mucin content, or cell debris (see Fig. 45–14).[98, 234, 235, 376, 380] Gd-DTPA can assist in defining nodules, fluid loculi, and septa in complex adnexal masses (Fig. 45–55; see Fig. 45–54).[98, 110, 359, 370]

Unlike endometrial and cervical carcinomas, ovarian carcinoma is usually diagnosed only after it is not surgically curable. About 30% of ovarian carcinoma (stage I and IIa disease) is surgically resectable by total hysterectomy and salpingo-oophorectomy. Optimal debulking of metastatic disease confers survival benefit.[35, 40, 284, 388]

Table 45–5. Accuracy of Transvaginal Ultrasound (TVUS) and MRI for Differentiating Benign from Malignant Adnexal Neoplasms

No.	TVUS	MRI	Reference
64	67	88*	Buist et al[45]
63	76	84	Hata et al[113]
32	83	70	Jain et al[150]
82	68	89	Komatsu et al[178]
72	88	95	Yamashita et al[410]
73	81	97	Medl et al[222]
280	78	91	Kurtz et al[184]

*Reader was more experienced.

Hysterectomy, salpingo-oophorectomy, omentectomy, and peritoneal inspection and washings constitute the definitive staging procedure for ovarian carcinoma.[43, 167, 297] Radiologic staging is inadequate primarily because of the high rates of microscopic peritoneal deposits throughout the abdomen.[43] Ascites is a nonspecific feature, and as few as 40% of patients with ascitic fluid exhibit positive findings in cytologic examinations of the peritoneum.[43] In second-look examinations, even laparotomy may have a 20% false-negative rate.[97] These observations limit the application of CT as a substitute for surgical staging or restaging of ovarian carcinoma.[107, 112, 158, 223] Similarly, MRI has no defined role in staging or in second-look evaluations during therapy. Preliminary results, however, suggest that accuracy rates of up to 75% may be achieved with contrast-enhanced MRI staging of ovarian carcinoma[359] and of 83% for detection of recurrent disease.[270]

In any case, recognizing macroscopic intra-abdominal spread of ovarian carcinoma is crucial during MRI evaluation of these patients. Solid or cystic peritoneal nodules can be identified in many cases;[98] in this regard, glucagon helps to suppress motion artifacts from bowel. The characteristic appearance of "omental cake" can be identified by its infiltrative margins and is distinguished from bowel by Gd-DTPA enhancement if necessary.[130] Gadolinium-enhanced, T1-weighted images with fat-suppression techniques may be particularly helpful in defining peritoneal spread (Fig. 45–56).[199, 264, 333]

Complications of Radiation and Surgery

MRI can demonstrate common postoperative complications in the pelvis. Hematomas, lymphoceles, abscesses, fistulas, and venous thromboses can be detected and charac-

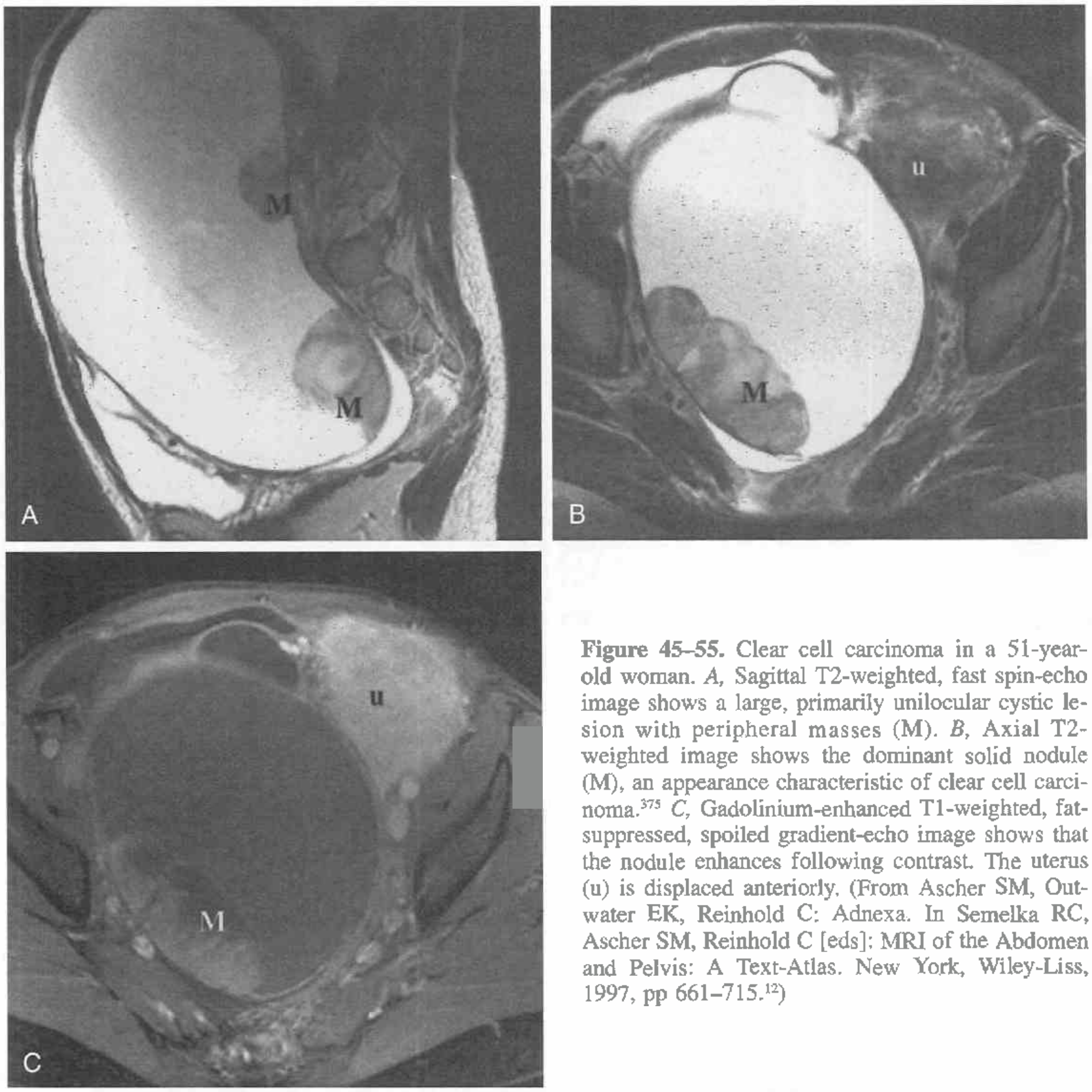

Figure 45–55. Clear cell carcinoma in a 51-year-old woman. *A,* Sagittal T2-weighted, fast spin-echo image shows a large, primarily unilocular cystic lesion with peripheral masses (M). *B,* Axial T2-weighted image shows the dominant solid nodule (M), an appearance characteristic of clear cell carcinoma.[375] *C,* Gadolinium-enhanced T1-weighted, fat-suppressed, spoiled gradient-echo image shows that the nodule enhances following contrast. The uterus (u) is displaced anteriorly. (From Ascher SM, Outwater EK, Reinhold C: Adnexa. In Semelka RC, Ascher SM, Reinhold C [eds]: MRI of the Abdomen and Pelvis: A Text-Atlas. New York, Wiley-Liss, 1997, pp 661–715.[12])

terized by MRI.[130] Fluid collections with peripheral hyperintense rims *(ring sign)* on T1-weighted images characterize hematomas.[130] Lymphoceles develop after lymphadenectomy; they manifest as sharply marginated cystic masses along the lymphatic chains and contain simple fluid.[130, 404] Gadolinium enhancement of a mass with central fluid signal intensity and infiltrative borders characterizes most abscesses in the postoperative period.[128, 130]

Fistulas are common complications after radiotherapy of larger gynecologic neoplasms and after surgery.[182] Enterovaginal and vesicovaginal fistulas are the most common types in this context.[182] Fistulous tracts on T2-weighted MR images appear as tracts of fluid signal intensity surrounded by lower-signal-intensity granulation tissue and fibrosis (Fig. 45–57).

External beam radiotherapy induces a number of changes in normal structures in the pelvis that are evident on MR images. Fascial and muscle edema; thickening of and edema in the walls of the rectum, bladder, and vagina; and fatty infiltration of bone marrow are all seen on MR images.[32–34, 361] Radiation effects depend on the radiation dose and the time elapsed since radiotherapy. Increased signal intensity on T2-weighted images usually reflects acute or subacute changes and does not persist indefinitely.[10, 89, 361] Increased signal intensity should not be confused with tumor recurrence.[10, 60] Bladder and rectal mucosal changes correlate, in part, with radiation cystitis and proctitis.[361]

The differentiation of recurrent pelvic carcinoma from postoperative fibrosis is a common clinical problem to which MRI has been applied. Recurrent tumor in the pelvis usually appears as nodules or masses with higher signal intensity than fibrosis on T2-weighted images (Fig. 45–58),[89, 101, 102, 149] although exceptions may occur.[75] Infiltrative recurrences without definable mass are not common.[89] Fibrotic scarring less than 6 months old shows slightly higher signal intensity than late fibrosis (>1 year) and overlaps in signal intensity with tumor recurrences.[89, 149] The surgical vaginal cuff and pelvic sidewall are common sites of recurrence of cervical and endometrial carcinoma[94, 151, 404]; the incidence varies with the type of radiation given.[151, 239, 404] An accuracy of 80%, with a sensitivity of 82% and a specificity of 78%, has been reported for the MRI determination of recurrent cervical carcinoma.[404]

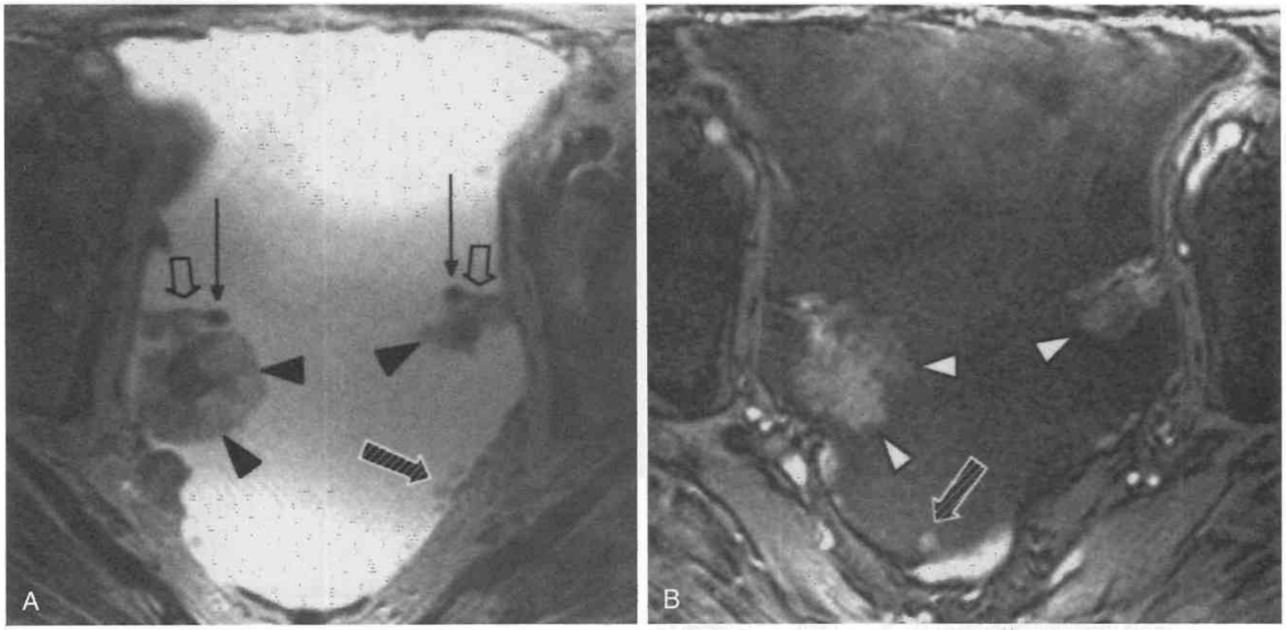

Figure 45–56. Marked ascites and bilateral ovarian surface implants of papillary serous carcinoma *(arrowheads). A,* T2-weighted, fast spin-echo image shows the normal fallopian tubes *(thin arrows)* attached to the broad ligaments *(open arrows)* by the thin mesosalpinges. *Arrowheads* point to implants of papillary ovarian cancer coating the surfaces above the ovaries. *Hatched arrow* points to nodular implants of papillary tumor in the cul-de-sac. *B,* Gadolinium-enhanced, T1-weighted, gradient-echo image demonstrates enhancement of the papillary tumor on the surface of the ovaries *(arrowheads)* and in the cul-de-sac *(hatched arrow).* (From Ascher SM, Outwater EK, Reinhold C: Adnexa. In Semelka RC, Ascher SM, Reinhold C [eds]: MRI of the Abdomen and Pelvis: A Text-Atlas. New York, Wiley-Liss, 1997, pp 661–715.[12])

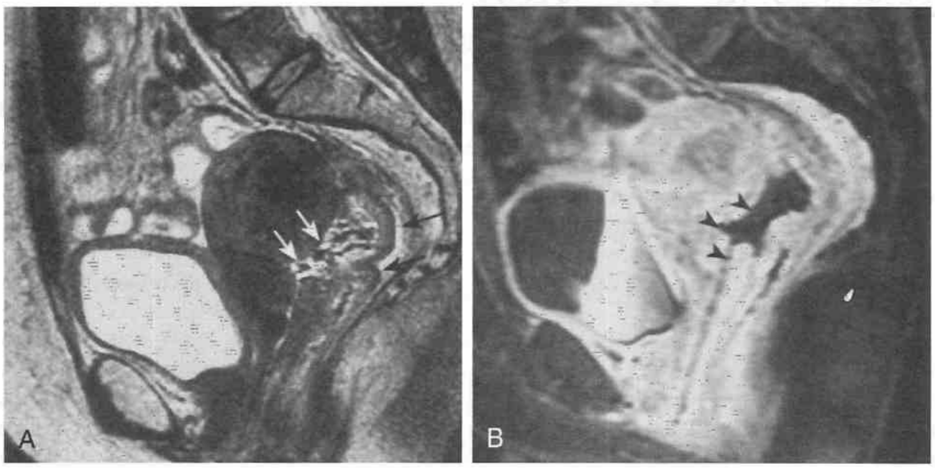

Figure 45–57. Rectovaginal fistula. Sagittal T2-weighted, fast spin-echo *(A)* and gadolinium-enhanced, fat-saturated *(B)* images in a patient after radiation for cervical carcinoma in whom fistula was not suspected at MRI. *A,* A high-signal-intensity tract *(white arrows)* extends from the rectum into the vaginal fornix. Although the posterior rectal wall is well delineated *(black arrows)*, a defect in the anterior rectal wall leads into the fistula. *B,* The tract is nonenhancing *(arrowheads)*. Incidentally noted are radiation changes in the spine and presacral space.

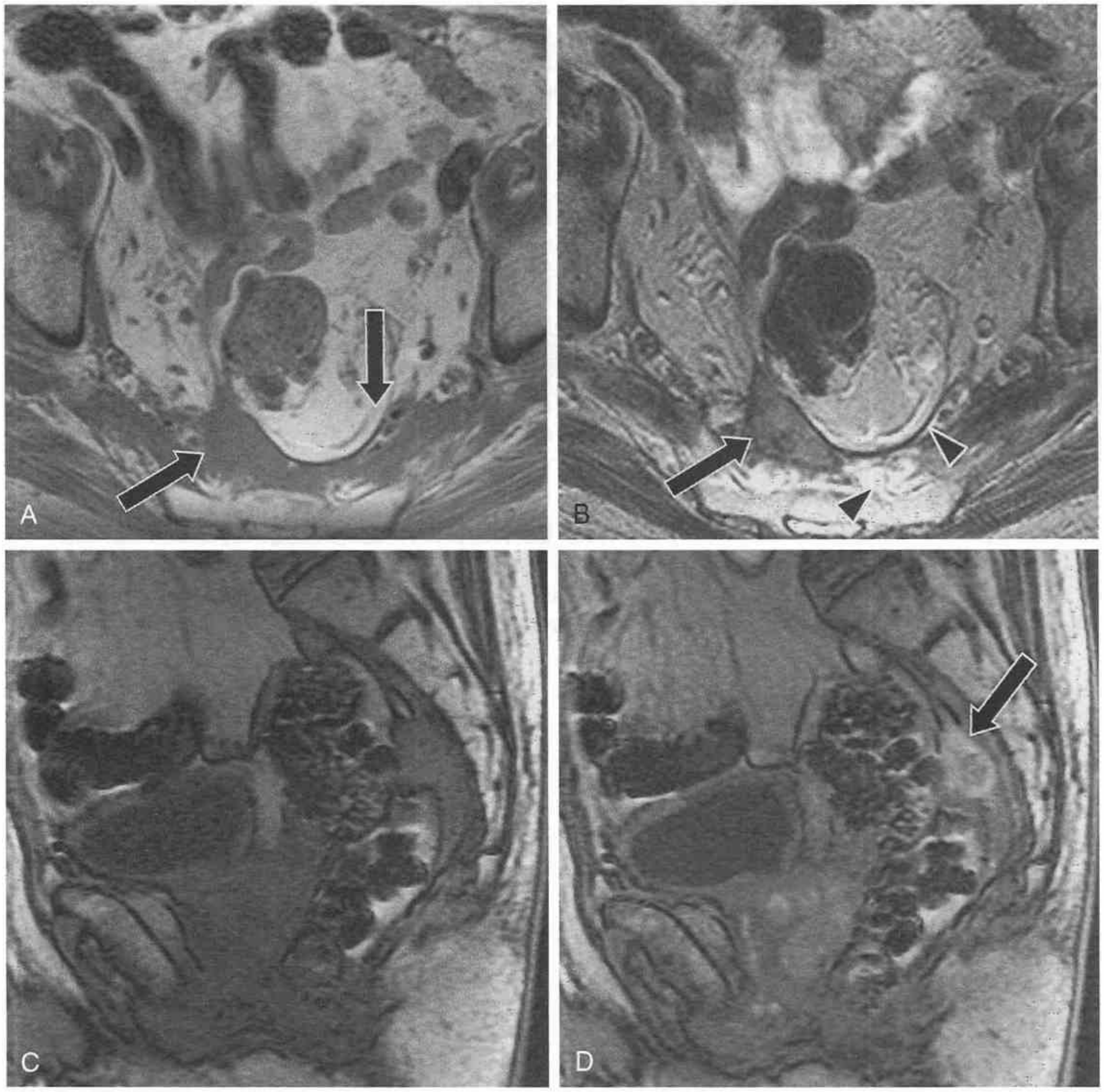

Figure 45–58. Tumor recurrence in a patient after proctectomy for rectal carcinoma. *A,* Axial T1-weighted image shows a presacral mass *(arrows)* with slightly more fullness on the right than on the left. *B,* Axial T2-weighted image shows an intermediate signal intensity to the fuller area on the right *(arrow)*, whereas some of the presacral tissue consists of edema and low-signal-intensity scarring *(arrowheads)*. Sagittal T1-weighted, fast spoiled gradient-echo images before *(C)* and after *(D)* administration of gadolinium show rapid enhancement of the nodular area *(arrow)*, indicating recurrent rectal tumor.

Disorders of pelvic floor relaxation from obstetric and other trauma can be evaluated with MRI. Focal defects in the levator can be identified (Fig. 45–59). Although MRI can easily identify cystoceles, rectoceles, and uterine prolapse, these disorders can be quantified clinically.[399] Enteroceles, however, are difficult to identify on clinical examination, and MRI easily identifies these. Dynamic imaging with straining can reveal organ prolapse not evident on static images.[68, 392]

Summary

MRI can delineate anatomy and pathology within the pelvis with higher intrinsic soft tissue contrast than ultrasound or CT, allowing better characterization of lesions and their relationship to surrounding organs. MRI has been useful in the diagnosis of some of the more common gynecologic pelvic masses, although in both the male and female pelvis most attention has focused on the potential for MRI to stage, rather than to diagnose, neoplasms. Currently, MRI has the greatest accuracy and potentially the greatest clinical usefulness in staging cervical carcinoma. MRI can also be used to stage endometrial carcinoma with reasonable accuracy, but the clinical indications for preoperative endometrial carcinoma staging are less clear. Initial experience with bladder and rectal carcinomas is encouraging, although MRI is not clearly better than CT for clinical staging. MRI has proved to be somewhat disappointing, however, for staging of prostate cancer.

Many of the problems inherent in staging of tumors by MRI are common to all staging modalities and arise from as yet suboptimal tumor tissue contrast, low image resolution, and an inability to distinguish benign from malignant lymphadenopathy. More recent techniques, such as surface

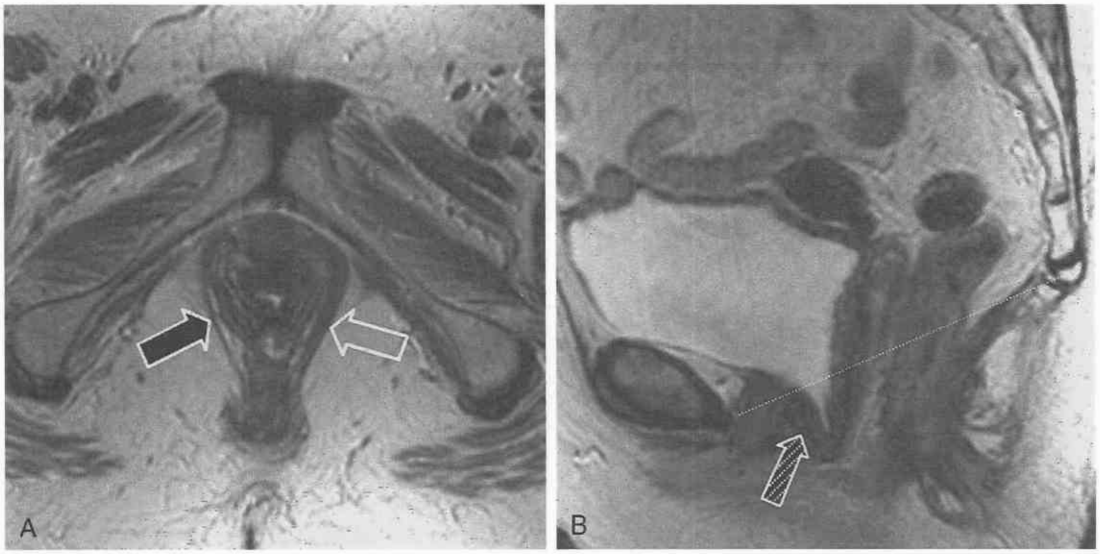

Figure 45–59. Pelvic floor relaxation in a 77-year-old woman with a history of obstetric trauma. *A,* T2-weighted, fast spin-echo image (TR = 4000, TE = 98) shows attenuation of the right puborectalis *(black arrow)* on the right compared to the left *(open arrow). B,* Sagittal T2-weighted image shows a cystocele *(hatched arrow)* projecting inferiorly below the pubococcygeal line *(dotted line).*

coil arrays, FSE sequences, endoluminal coils, and new contrast agents, are contributing to the rapid pace of technologic advancement in the field of MRI of the pelvis.

References

1. Abe Y, Yamashita Y, Namimoto T, et al: Carcinoma of the uterine cervix: High-resolution turbo spin-echo MR imaging with contrast-enhanced dynamic scanning and T2-weighting. Acta Radiol 39: 322–326, 1998.
2. Adamis MK, Li W, Wielopolski PA, et al: Dynamic contrast-enhanced subtraction MR angiography of the lower extremities: Initial evaluation with a multisection two-dimensional time-of-flight sequence. Radiology 196:689–695, 1995.
3. Alcock CJ, Toplis PJ: The influence of pelvic lymph node disease on survival for stage I and II carcinoma of the cervix. Clin Radiol 38:13–16, 1987.
4. Altaras MM, Aviram R, Cohen I, et al: Primary peritoneal papillary serous adenocarcinoma: Clinical and management aspects. Gynecol Oncol 40:230–236, 1991.
5. Amendola MA, Glazer GM, Grossman HB, et al: Staging of bladder carcinoma: MRI–CT–surgical correlation. Am J Roentgenol 146: 1179–1183, 1986.
6. Amin HK, Okagaki T, Richart RM: Classification of fibroma and thecoma of the ovary: An ultrastructural study. Cancer 27:438–446, 1971.
7. Amin RS, Nikolaidis P, Kawashima A, et al: Normal anatomy of the fetus at MR imaging. Radiographics 19:S201–S214, 1999.
8. Angtuaco TL, Shah HR, Mattison DR, et al: MR imaging in high-risk obstetric patients: A valuable complement to US. Radiographics 12:91–109; discussion, 12:110, 1992.
9. Anonymous: National Institutes of Health Consensus Development Conference statement on cervical cancer: April 1–3, 1996. Gynecol Oncol 66:351–361, 1997.
10. Arrive L, Chang YC, Hricak H, et al: Radiation-induced uterine changes: MR imaging. Radiology 170:55–58, 1989.
11. Arrive L, Hricak H, Martin MC: Pelvic endometriosis: MR imaging. Radiology 171:687–692, 1989.
12. Ascher SM, Outwater EK, Reinhold C: Adnexa. In Semelka RC, Ascher SM, Reinhold C (eds): MRI of the Abdomen and Pelvis: A Text-Atlas. New York, Wiley-Liss, 1997, pp 661–715.
13. Ascher SM, Scoutt LM, McCarthy SM, et al: Uterine changes after dilation and curettage: MR imaging findings. Radiology 180: 433–435, 1991.
14. Aubel S, Wozney P, Edwards RP: MRI of female uterine and juxta-uterine masses: Clinical application in 25 patients. Magn Reson Imaging 9:485–491, 1991.
15. Ayala AG, Ro JY, Babaian R, et al: The prostatic capsule: Does it exist? Its importance in the staging and treatment of prostatic carcinoma. Am J Surg Pathol 13:21–27, 1989.
16. Azziz R: Adenomyosis: Current perspectives. Obstet Gynecol Clin North Am 16:221–235, 1989.
17. Baggish MS: Mesenchymal tumors of the uterus. Clin Obstet Gynecol 17:51–85, 1974.
18. Baker LL, Hajek PC, Burkhard TK, et al: MR imaging of the scrotum: Pathologic conditions. Radiology 163:93–98, 1987.
19. Baker LL, Hajek PC, Burkhard TK, et al: MR imaging of the scrotum: Normal anatomy. Radiology 163:89–92, 1987.
20. Baker LL, Hajek PC, Burkhard TK, et al: Polyorchidism: Evaluation by MR. AJR Am J Roentgenol 148:305–306, 1987.
21. Bandy LC, Clarke-Pearson DL, Silverman PM, et al: Computed tomography in evaluation of extrapelvic lymphadenopathy in carcinoma of the cervix. Obstet Gynecol 65:73–76, 1985.
22. Barentsz JO, Jager G, Mugler JP 3rd, et al: Staging urinary bladder cancer: Value of T1-weighted three-dimensional magnetization prepared-rapid gradient-echo and two-dimensional spin-echo sequences. AJR Am J Roentgenol 164:109–115, 1995.
23. Bartolozzi C, Selli C, Olmastroni M, et al: Rhabdomyosarcoma of the prostate: MR findings. AJR Am J Roentgenol 150:1333–1334, 1988.
24. Baudouin CJ, Soutter WP, Gilderdale DJ, et al: Magnetic resonance imaging of the uterine cervix using an intravaginal coil. Magn Reson Med 24:196–203, 1992.
25. Beall DP, Regan F: MRI of bowel obstruction using the HASTE sequence. J Comput Assist Tomogr 20:823–825, 1996.
26. Beischer NA, Buttery BW, Fortune DW, et al: Growth and malignancy of ovarian tumours in pregnancy. Aust N Z J Obstet Gynaecol 11:208–220, 1971.
27. Belloni C, Vigano R, DelMaschio A, et al: Magnetic resonance imaging in endometrial carcinoma staging. Gynecol Oncol 37:172–177, 1990.
28. Berkowitz R, Goldstein D: Gestational trophoblastic disease. Semin Oncol 16:410–416, 1989.
29. Bies JR, Ellis JH, Kopecky KK, et al: Assessment of primary gynecologic malignancies: Comparison of 0.15-T resistive MRI with CT. Am J Roentgenol 143:1249–1257, 1984.
30. Bis KG, Vrachliotis TG, Agrawal R, et al: Pelvic endometriosis: MR imaging spectrum with laparoscopic correlation and diagnostic pitfalls. Radiographics 17:639–655, 1997.
31. Bitterman P, Chun B, Kurman RJ: The significance of epithelial differentiation in mixed mesodermal tumors of the uterus: A clinico-

pathologic and immunohistochemical study. Am J Surg Pathol 14: 317–328, 1990.
32. Blomlie V, Rofstad EK, Skjonsberg A, et al: Female pelvic bone marrow: Serial MR imaging before, during, and after radiation therapy. Radiology 194:537–543, 1995.
33. Blomlie V, Rofstad EK, Trope C, et al: Critical soft tissues of the female pelvis: Serial MR imaging before, during, and after radiation therapy. Radiology 203:391–397, 1997.
34. Blomlie V, Rofstad EK, Tvera K, et al: Noncritical soft tissues of the female pelvis: Serial MR imaging before, during, and after radiation therapy. Radiology 199:461–468, 1996.
35. Boente MP, Chi DS, Hoskins WJ: The role of surgery in the management of ovarian cancer: Primary and interval cytoreductive surgery. Semin Oncol 25:326–334, 1998.
36. Boring CC, Squires TS, Tong T, et al: Cancer statistics, 1994. CA Cancer J Clin 44:7–26, 1994.
37. Boronow R, Morrow C, Creasman W, et al: Surgical staging in endometrial cancer: Clinical-pathologic findings of a prospective study. Obstet Gynecol 63:825–830, 1984.
38. Borrello JA, Chenevert TL, Meyer CR, et al: Chemical shift-based true water and fat images: Regional phase correction of modified spin-echo MR images. Radiology 164:531–537, 1987.
39. Breckenridge JW, Kurtz AB, Ritchie WG, et al: Postmenopausal uterine fluid collection: Indicator of carcinoma. Am J Roentgenol 139:529–534, 1982.
40. Bristow RE, Lagasse LD, Karlan BY: Secondary surgical cytoreduction for advanced epithelial ovarian cancer: Patient selection and review of the literature. Cancer 78:2049–2062, 1996.
41. Brown HK, Stoll BS, Nicosia SV, et al: Uterine junctional zone: Correlation between histologic findings and MR imaging. Radiology 179:409–413, 1991.
42. Bryan PJ, Butler HE, LiPuma JP, et al: NMR scanning of the pelvis: Initial experience with a 0.3 T system. Am J Roentgenol 141: 1111–1118, 1983.
43. Buchsbaum HJ, Brady MF, Delgado G, et al: Surgical staging of carcinoma of the ovaries. Surg Gynecol Obstet 169:226–232, 1989.
44. Bucy GS, Mendenhall WM, Morgan LS, et al: Clinical stage I and II endometrial carcinoma treated with surgery and/or radiation therapy: Analysis of prognostic and treatment-related factors. Gynecol Oncol 33:290–295, 1989.
45. Buist MR, Golding RP, Burger CW, et al: Comparative evaluation of diagnostic methods in ovarian carcinoma with emphasis on CT and MRI. Gynecol Oncol 52:191–198, 1994.
46. Burghardt E, Hofmann HM, Ebner F, et al: Magnetic resonance imaging in cervical cancer: A basis for objective classification. Gynecol Oncol 33:61–67, 1989.
47. Burks DD, Markey BJ, Burkhard TK, et al: Suspected testicular torsion and ischemia: Evaluation with color Doppler sonography. Radiology 175:815–821, 1990.
48. Butch RJ, Stark DD, Wittenberg J, et al: Staging rectal cancer by MR and CT. Am J Roentgenol 146:1155–1160, 1986.
49. Buy JN, Ghossain MA, Sciot C, et al: Epithelial tumors of the ovary: CT findings and correlation with US. Radiology 178:811–818, 1991.
50. Buy JN, Moss AA, Guinet C, et al: MR staging of bladder carcinoma: Correlation with pathologic findings. Radiology 169:695–700, 1988.
51. Byar DP, Mostofi FK: Carcinoma of the prostate: Prognostic evaluation of certain pathologic features in 208 radical prostatectomies examined by the step-section technique. Cancer 30:5–13, 1972.
52. Cannistra SA, Niloff JM: Cancer of the uterine cervix. N Engl J Med 334:1030–1038, 1996.
53. Carrington BM, Hricak H, Nuruddin RN, et al: Mullerian duct anomalies: MR imaging evaluation. Radiology 176:715–720, 1990.
54. Carrol CL, Sommer FG, McNeal JE, et al: The abnormal prostate: MR imaging at 1.5 T with histopathologic correlation. Radiology 163:521–525, 1987.
55. Carter HB, Brem RF, Tempany CM, et al: Nonpalpable prostate cancer: Detection with MR imaging. Radiology 178:523–525, 1991.
56. Carter HB, Morrell CH, Pearson JD, et al: Estimation of prostatic growth using serial prostate-specific antigen measurements in men with and without prostate disease. Cancer Res 52:3323–3328, 1992.
57. Chan TW, Kressel HY, Milestone B, et al: Rectal carcinoma: Staging at MR imaging with endorectal surface coil: Work in progress. Radiology 181:461–467, 1991.
58. Chan TW, Listerud J, Kressel HY: Combined chemical-shift and phase-selective imaging for fat suppression: Theory and initial clinical experience. Radiology 181:41–47, 1991.
59. Chang KL, Crabtree GS, Lim-Tan SK, et al: Primary uterine endometrial stromal neoplasms: A clinicopathologic study of 117 cases. Am J Surg Pathol 14:415–438, 1990.
60. Chang Y, Hricak H, Thurnher S, et al: Vagina: Evaluation with MR imaging. Part II—Neoplasms. Radiology 169:175–179, 1988.
61. Chang YC, Hricak H: Current status of MR imaging of the female pelvis. Crit Rev Diagn Imaging 29:337–356, 1989.
62. Chen SS: Propensity of retroperitoneal lymph node metastasis in patients with stage I sarcoma of the uterus. Gynecol Oncol 32: 215–217, 1989.
63. Chen SS, Rumancik WM, Spiegel G: Magnetic resonance imaging in stage I endometrial carcinoma. Obstet Gynecol 75:274–277, 1990.
64. Clement PB: Pathology of endometriosis. Pathol Annu 25:245–295, 1994.
65. Clement PB, Young RH, Scully RE: Clinical syndromes associated with tumors of the female genital tract. Semin Diagn Pathol 8: 204–233, 1991.
66. Clements R, Griffiths GJ, Peeling WB: Staging prostatic cancer. Clin Radiol 46:225–231, 1992.
67. Cobby M, Browning J, Jones A, et al: Magnetic resonance imaging, computed tomography and endosonography in the local staging of carcinoma of the cervix. Br J Radiol 63:673–679, 1990.
68. Comiter CV, Vasavada SP, Barbaric ZL, et al: Grading pelvic prolapse and pelvic floor relaxation using dynamic magnetic resonance imaging. Urology 54:454–457, 1999.
69. Constable RT, Anderson AW, Zhong J, et al: Factors influencing contrast in fast spin-echo MR imaging. Magn Reson Imaging 10: 497–511, 1992.
70. Constable RT, Gore JC: The loss of small objects in variable TE imaging: Implications for FSE, RARE, and EPI. Magn Reson Med 28:9–24, 1992.
71. Creasman WT, Eddy GL: Recent advances in endometrial cancer. Semin Surg Oncol 6:339–342, 1990.
72. Crucitti F, Doglietto GB, Bellantone R, et al: Accurate specimen preparation and examination is mandatory to detect lymph nodes and avoid understaging in colorectal cancer. J Surg Oncol 51:153–157; discussion, 51:157–158, 1992.
73. D'Amico AV, Schnall M, Whittington R, et al: Endorectal coil magnetic resonance imaging identifies locally advanced prostate cancer in select patients with clinically localized disease. Urology 51:449–454, 1998.
74. de Lange EE, Fechner RE, Edge SB, et al: Preoperative staging of rectal carcinoma with MR imaging: Surgical and histopathologic correlation. Radiology 176:623–628, 1990.
75. de Lange EE, Fechner RE, Wanebo HJ: Suspected recurrent rectosigmoid carcinoma after abdominoperineal resection: MR imaging and histopathologic findings. Radiology 170:323–328, 1989.
76. Delgado G, Bundy BN, Fowler WC Jr, et al: A prospective surgical pathological study of stage I squamous carcinoma of the cervix: A Gynecologic Oncology Group study. Gynecol Oncol 35:314–320, 1989.
77. Dershaw DD, Panicek DM: Imaging of invasive bladder cancer. Semin Oncol 17:544–550, 1990.
78. Devesa JM, Morales V, Enriquez JM, et al: Colorectal cancer: The bases for a comprehensive follow-up. Dis Colon Rectum 31: 636–652, 1988.
79. Dhom G: Unusual prostatic carcinomas. Pathol Res Pract 186: 28–36, 1990.
80. Dixon WT: Simple proton spectroscopic imaging. Radiology 153: 189–194, 1984.
81. Dodd GD, Budzik RF: Lipomatous tumors of the pelvis in women: Spectrum of imaging findings. AJR Am J Roentgenol 155:317–322, 1990.
82. Donohue JP, Perez JM, Einhorn LH: Improved management of non-seminomatous testis tumors. J Urol 121:425–428, 1979.
83. Dooms GC, Hricak H, Crooks LE, et al: Magnetic resonance imaging of the lymph nodes: Comparison with CT. Radiology 153: 719–728, 1984.
84. Dooms GC, Hricak H, Tscholakoff D: Adnexal structures: MR imaging. Radiology 158:639–646, 1986.
85. Douek PC, Revel D, Chazel S, et al: Fast MR angiography of the aortoiliac arteries and arteries of the lower extremity: Value of bolus-enhanced, whole-volume subtraction technique. AJR Am J Roentgenol 165:431–437, 1995.

86. Dudiak CM, Turner DA, Patel SK, et al: Uterine leiomyomas in the infertile patient: Preoperative localization with MR imaging versus US and hysterosalpingography. Radiology 167:627–630, 1988.
87. Duncan K, Baker P, Johnson I: The complementary role of echoplanar magnetic resonance imaging and three-dimensional ultrasonography in fetal lung assessment [letter; comment]. Am J Obstet Gynecol 177:244–245, 1997.
88. Duncan KR, Baker PN, Gowland PA, et al: Demonstration of changes in fetal liver erythropoiesis using echo-planar magnetic resonance imaging. Am J Physiol 273:G965–967, 1997.
89. Ebner F, Kressel HY, Mintz MC, et al: Tumor recurrence versus fibrosis in the female pelvis: Differentiation with MR imaging at 1.5 T. Radiology 166:333–340, 1988.
90. Fisher MR, Hricak H, Crooks LE: Urinary bladder MR imaging: Part I—Normal and benign conditions. Radiology 157:467–470, 1985.
91. Fisher MR, Hricak H, Tanagho EA: Urinary bladder MR imaging: Part II—Neoplasm. Radiology 157:471–477, 1985.
92. Flueckiger F, Ebne RF, Poschauko H, et al: Cervical cancer: Serial MR imaging before and after primary radiation therapy: A 2-year follow-up study. Radiology 184:89–93, 1992.
93. Fritzsche PJ, Hricak H, Kogan BA, et al: Undescended testis: Value of MR imaging. Radiology 164:169–173, 1987.
94. Fu YS, Reagan JW: Pathology of the Uterine Cervix, Vagina, and Vulva. Philadelphia, WB Saunders, 1989, p 225.
95. Gehl HB, Bohndorf K, Klose KC: Inferior vena cava tumor thrombus: Demonstration by Gd-DTPA–enhanced MR. J Comput Assist Tomogr 14:479–481, 1990.
96. Gerbie AB, Merril JA: Pathology of endometriosis. Clin Obstet Gynecol 31:779–786, 1988.
97. Ghatage P, Krepart GV, Lotocki R: Factor analysis of false-negative second-look laparotomy. Gynecol Oncol 36:172–175, 1990.
98. Ghossain MA, Buy JN, Ligneres C, et al: Epithelial tumors of the ovary: Comparison of MR and CT findings. Radiology 181: 863–870, 1991.
99. Gilfeather M, Holland GA, Siegelman ES, et al: Gadolinium-enhanced ultrafast three-dimensional spoiled gradient-echo MR imaging of the abdominal aorta and visceral and iliac vessels [published erratum appears in Radiographics 17:804, 1997]. Radiographics 17:423–432, 1997.
100. Gittes RF: Carcinoma of the prostate. N Engl J Med 324:236–245, 1991.
101. Glazer HS, Lee JK, Levitt RG, et al: Radiation fibrosis: Differentiation from recurrent tumor by MR imaging. Radiology 156:721–726, 1985.
102. Gomberg JS, Friedman AC, Radecki PD, et al: MRI differentiation of recurrent colorectal carcinoma from postoperative fibrosis. Gastrointest Radiol 11:361–363, 1986.
103. Gordon AN, Fleisher AC, Dudley BS, et al: Preoperative assessment of myometrial invasion of endometrial adenocarcinoma by sonography (US) and magnetic resonance imaging (MRI). Gynecol Oncol 34:175–179, 1989.
104. Greco A, Mason P, Leung AW, et al: Staging of carcinoma of the uterine cervix: MRI-surgical correlation. Clin Radiol 40:401–405, 1989.
105. Greene DR, Fitzpatrick JM, Scardino PT: Anatomy of the prostate and distribution of early prostate cancer. Semin Surg Oncol 11: 9–22, 1995.
106. Greene DR, Wheeler TM, Egawa S, et al: A comparison of the morphological features of cancer arising in the transition zone and in the peripheral zone of the prostate. J Urol 146:1069–1076, 1991.
107. Guidozzi F, Sonnendecker EW: Evaluation of preoperative investigations in patients admitted for ovarian primary cytoreductive surgery. Gynecol Oncol 40:244–247, 1991.
108. Guinet C, Buy JN, Ghossain MA, et al: Fat suppression techniques in MR imaging of mature ovarian teratomas: Comparison with CT. Eur J Radiol 17:117–121, 1993.
109. Hall RR, Prout GR: Staging of bladder cancer: Is the tumor, node, metastasis system adequate? Semin Oncol 17:517–523, 1990.
110. Hamm B, Laniado M, Saini S: Contrast-enhanced magnetic resonance imaging of the abdomen and pelvis. Magn Reson Q 6:108–135, 1990.
111. Hamper UM, Epstein JI, Sheth S, et al: Cystic lesions of the prostate gland: A sonographic–pathologic correlation. J Ultrasound Med 9: 395–402, 1990.
112. Hann LE, Crivello MS: Imaging techniques in the staging of gynecologic malignancy. Clin Obstet Gynecol 29:715–727, 1986.
113. Hata K, Hata T, Manabe A, et al: A critical evaluation of transvaginal Doppler studies, transvaginal sonography, magnetic resonance imaging, and CA 125 in detecting ovarian cancer. Obstet Gynecol 80:922–926, 1992.
114. Hawighorst H, Knapstein PG, Schaeffer U, et al: Pelvic lesions in patients with treated cervical carcinoma: Efficacy of pharmacokinetic analysis of dynamic MR images in distinguishing recurrent tumors from benign conditions. AJR Am J Roentgenol 166:401–408, 1996.
115. Hawighorst H, Knapstein PG, Weikel W, et al: Cervical carcinoma: Comparison of standard and pharmacokinetic MR imaging. Radiology 201:531–539, 1996.
116. Hayes CE, Hattes N, Roemer PB: Volume imaging with MR phased arrays. Magn Reson Med 18:309, 1991.
117. Heaps JM, Berek JS: Surgical staging of cervical cancer. Clin Obstet Gynecol 33:852–862, 1990.
118. Heiken JP, Balfe DM, McClennan BL: Testicular tumors: Oncologic imaging and diagnosis. Int J Radiat Oncol Biol Phys 10:275–287, 1984.
119. Heller PB, Maletano JH, Bundy BN, et al: Clinical-pathologic study of stage IIB, III, and IVA carcinoma of the cervix: Extended diagnostic evaluation for paraaortic node metastasis—a Gynecologic Oncology Group study. Gynecol Oncol 38:425–430, 1990.
120. Hennig J, Nauerth A, Friedburg H: RARE imaging: A fast imaging method for clinical MR. Magn Reson Med 3:823–833, 1986.
121. Herbst AL, Ulfelder H, Hatch R: Gynecology. In Schwartz SI, Shires GT, Spencer FC, et al. (eds): Principles of Surgery. New York, McGraw-Hill, 1984.
122. Herr HW: Staging invasive bladder tumors. J Surg Oncol 51:217–220, 1992.
123. Herrera L, Villarreal JR: Incidence of metastases from rectal adenocarcinoma in small lymph nodes detected by a clearing technique. Dis Colon Rectum 35:783–788, 1992.
124. Hidajat N, Maurer J, Schroder RJ, et al: Relationships between physical dose quantities and patient dose in CT. Br J Radiol 72: 556–561, 1999.
125. Holder LE, Martire JR, Holmes ER, et al: Testicular radionuclide angiography and static imaging: Anatomy, scintigraphic interpretation, and clinical indications. Radiology 125:739–752, 1977.
126. Horwich A: Current controversies in the treatment of testicular cancer. Eur J Cancer 27:322–326, 1991.
127. Hricak H: Imaging prostate carcinoma. Radiology 169:569–571, 1988.
128. Hricak H: Postoperative and postradiation changes in the pelvis. Magn Reson Q 6:276–297, 1990.
129. Hricak H, Alpers C, Crooks LE, et al: Magnetic resonance imaging of the female pelvis: Initial experience. Am J Roentgenol 141: 1119–1128, 1983.
130. Hricak H, Carrington B: MRI of the Pelvis: A Text Atlas. Norwalk, Conn., Appleton and Lange, 1991.
131. Hricak H, Chang YC, Cann CE, et al: Cervical incompetence: Preliminary evaluation with MR imaging. Radiology 174:821–826, 1990.
132. Hricak H, Demas BE, Braga CA, et al: Gestational trophoblastic neoplasm of the uterus: MR assessment. Radiology 161:11–16, 1986.
133. Hricak H, Dooms GC, Jeffrey RB, et al: Prostatic carcinoma: Staging by clinical assessment, CT, and MR imaging. Radiology 162: 331–336, 1987.
134. Hricak H, Dooms GC, McNeal JE, et al: MR imaging of the prostate gland: Normal anatomy. AJR Am J Roentgenol 148:51–58, 1987.
135. Hricak H, Hamm B, Semelka RC, et al: Carcinoma of the uterus: Use of gadopentetate dimeglumine in MR imaging. Radiology 181: 95–106, 1991.
136. Hricak H, Lacey C, Schriock E, et al: Gynecologic masses: Value of magnetic resonance imaging. Am J Obstet Gynecol 153:31–37, 1985.
137. Hricak H, Lacey CG, Sandles LG, et al: Invasive cervical carcinoma: Comparison of MR imaging and surgical findings. Radiology 166: 623–631, 1988.
138. Hricak H, Powell CB, Yu KK, et al: Invasive cervical carcinoma: Role of MR imaging in pretreatment work-up—cost minimization and diagnostic efficacy analysis. Radiology 198:403–409, 1996.
139. Hricak H, Rubinstein LV, Gherman GM, et al: MR imaging evaluation of endometrial carcinoma: Results of an NCI cooperative study. Radiology 179:829–832, 1991.

140. Hricak H, Stern JL, Fisher MR, et al: Endometrial carcinoma staging by MR imaging. Radiology 162:297–305, 1987.
141. Hricak H, Tscholakoff D, Heinrichs L, et al: Uterine leiomyomas: Correlation of MR, histopathologic findings, and symptoms. Radiology 158:385–391, 1986.
142. Hricak H, White S, Vigneron D, et al: Carcinoma of the prostate gland: MR imaging with pelvic phased-array coils versus integrated endorectal—pelvic phased-array coils. Radiology 193:703–709, 1994.
143. Hricak H, Yu KK: Radiology in invasive cervical cancer. AJR Am J Roentgenol 167:1101–1108, 1996.
144. Hubbard AM, Adzick NS, Crombleholme TM, et al: Left-sided congenital diaphragmatic hernia: Value of prenatal MR imaging in preparation for fetal surgery. Radiology 203:636–640, 1997.
145. Hunter V, Raymond E, Christensen C, et al: Efficacy of the metastatic survey in the staging of gestational trophoblastic disease. Cancer 65:1647–1650, 1990.
146. Husband JE, Olliff JF, Williams MP, et al: Bladder cancer: Staging with CT and MR imaging. Radiology 173:435–440, 1989.
147. Hussain SM, Stoker J, Lameris JS: Anal sphincter complex: Endoanal MR imaging of normal anatomy. Radiology 197:671–677, 1995.
148. Imai Y, Kressel HY, Saul SH, et al: Colorectal tumors: An in vitro study of high-resolution MR imaging. Radiology 177:695–701, 1990.
149. Ito K, Kato T, Tadokoro M, et al: Recurrent rectal cancer and scar: Differentiation with PET and MR imaging. Radiology 182: 549–552, 1992.
150. Jain KA, Friedman DL, Pettinger TW, et al: Adnexal masses: Comparison of specificity of endovaginal US and pelvic MR imaging. Radiology 186:697–704, 1993.
151. Jampolis S, Andras EJ, Fletcher GH: Analysis of sites and causes of failures of irradiation in invasive squamous cell carcinoma of the intact uterine cervix. Radiology 115:681–685, 1975.
152. Janus C, White M, Dottino P, et al: Uterine leiomyosarcoma—magnetic resonance imaging. Gynecol Oncol 32: 79–81, 1989.
153. Jenison EL, Montag AG, Griffiths CT, et al: Clear cell adenocarcinoma of the ovary: A clinical analysis and comparison with serous carcinoma. Gynecol Oncol 32:65–71, 1989.
154. Johansson JE, Adami HO, Andersson SO, et al: High 10-year survival rate in patients with early, untreated prostatic cancer. JAMA 267:2191–2196, 1992.
155. Johnson DB, Lerner CA, Prince MR, et al: Gadolinium-enhanced magnetic resonance angiography of renal transplants. Magn Reson Imaging 15:13–20, 1997.
156. Johnson IR, Stehling MK, Blamire AM, et al: Study of internal structure of the human fetus in utero by echo-planar magnetic resonance imaging. Am J Obstet Gynecol 163:601–607, 1990.
157. Johnson JO, Mattrey RF, Phillipson J: Differentiation of seminomatous from nonseminomatous testicular tumors with MR imaging. AJR Am J Roentgenol 154:539–543, 1990.
158. Johnson RJ, Blackledge G, Eddleston B, et al: Abdomino-pelvic computed tomography in the management of ovarian carcinoma. Radiology 146:447–452, 1983.
159. Joja I, Asakawa M, Asakawa T, et al: Endometrial carcinoma: Dynamic MRI with turbo-FLASH technique. J Comput Assist Tomogr 20:878–887, 1996.
160. Jolles CJ: Gynecologic cancer associated with pregnancy. Semin Oncol 16:417–424, 1989.
161. Joosten FB, Jansen JB, Joosten HJ, et al: Staging of rectal carcinoma using MR double surface coil, MR endorectal coil, and intrarectal ultrasound: Correlation with histopathologic findings. J Comput Assist Tomogr 19:752–758, 1995.
162. Kadar N, Malfetano JH, Homesley HD: Determinants of survival of surgically staged patients with endometrial carcinoma histologically confined to the uterus: Implications for therapy. Obstet Gynecol 80: 655–659, 1992.
163. Kahn T, Burrig K, Schmitz-Drager B, et al: Prostatic carcinoma and benign prostatic hyperplasia: MR imaging with histopathologic correlation. Radiology 173:847–851, 1989.
164. Kaji Y, Sugimura K, Nagaoka S, et al: Amyloid deposition in seminal vesicles mimicking tumor invasion from bladder cancer: MR findings. J Comput Assist Tomogr 16:989–991, 1992.
165. Kamura T, Yahata H, Shigematsu T, et al: Predicting pelvic lymph node metastasis in endometrial carcinoma. Gynecol Oncol 72:387–391, 1999.
166. Kanal E: Pregnancy and the safety of magnetic resonance imaging. Magn Reson Clin North Am 2:309–317, 1994.
167. Katz ME, Schwartz PE, Kapp DS, et al: Epithelial carcinoma of the ovary: Current strategies. Ann Intern Med 95:98–111, 1981.
168. Keller PJ, Hunter WW, Schmalbrock P: Multisection fat-water imaging with chemical shift selective presaturation. Radiology 164: 539, 1987.
169. Kier R, Smith RC, McCarthy SM: Value of lipid- and water-suppression MR images in distinguishing between blood and lipid within ovarian masses. AJR Am J Roentgenol 158:321–325, 1992.
170. Kilgore LC, Partridge EE, Alvarez RD, et al: Adenocarcinoma of the endometrium: Survival comparisons of patients with and without pelvic node sampling. Gynecol Oncol 56:29–33, 1995.
171. Kim NK, Kim MJ, Yun SH, et al: Comparative study of transrectal ultrasonography, pelvic computerized tomography, and magnetic resonance imaging in preoperative staging of rectal cancer. Dis Colon Rectum 42:770–775, 1999.
172. Kim SH, Choi BI, Han JK, et al: Preoperative staging of uterine cervical carcinoma: Comparison of CT and MRI in 99 patients. J Comput Assist Tomogr 17:633–640, 1993.
173. Kim SH, Choi BI, Lee HP, et al: Uterine cervical carcinoma: Comparison of CT and MR findings. Radiology 175:45–51, 1990.
174. Kim SH, Kim HD, Song YS, et al: Detection of deep myometrial invasion in endometrial carcinoma: Comparison of transvaginal ultrasound, CT, and MRI. J Comput Assist Tomogr 19:766–772, 1995.
175. Kinkel K, Kaji Y, Yu KK, et al: Radiologic staging in patients with endometrial cancer: A meta-analysis. Radiology 212:711–718, 1999.
176. Kirkinen P, Partanen K, Ryynanen M, et al: Fetal intracranial hemorrhage: Imaging by ultrasound and magnetic resonance imaging. J Reprod Med 42:467–472, 1997.
177. Koelbel G, Schmiedl U, Griebel J, et al: MR imaging of urinary bladder neoplasms. J Comput Assist Tomogr 12:98–103, 1988.
178. Komatsu T, Konishi I, Mandai M, et al: Adnexal masses: Transvaginal US and gadolinium-enhanced MR imaging assessment of intratumoral structure. Radiology 198:109–115, 1996.
179. Koyama T, Togashi K, Konishi I, et al: MR imaging of endometrial stromal sarcoma: Correlation with pathologic findings. AJR Am J Roentgenol 173:767–772, 1999.
180. Krinsky G, DeCorato DR, Rofsky NM, et al: Rapid T2-weighted MR imaging of uterine leiomyoma and adenomyosis. Abdom Imaging 22:531–534, 1997.
181. Kubik-Huch RA, Hebisch G, Huch R, et al: Role of duplex color Doppler ultrasound, computed tomography, and MR angiography in the diagnosis of septic puerperal ovarian vein thrombosis. Abdom Imaging 24:85–91, 1999.
182. Kuhlman JE, Fishman EK: CT evaluation of enterovaginal and vesicovaginal fistulas. J Comput Assist Tomogr 14:390–394, 1990.
183. Kurhanewicz J, Vigneron DB, Nelson SJ, et al: Citrate as an in vivo marker to discriminate prostate cancer from benign prostatic hyperplasia and normal prostate peripheral zone: Detection via localized proton spectroscopy. Urology 45:459–466, 1995.
184. Kurtz AB, Tsimikas JV, Tempany CM, et al: Diagnosis and staging of ovarian cancer: Comparative values of Doppler and conventional US, CT, and MR imaging correlated with surgery and histopathologic analysis—report of the Radiology Diagnostic Oncology Group. Radiology 212:19–27, 1999.
185. Lagasse LD, Creasman WT, Shingleton HM, et al: Results and complications of operative staging in cervical cancer: Experience of the Gynecol Oncol Group. Gynecol Oncol 9:90–98, 1980.
186. Landis SH, Murray T, Bolden S, et al: Cancer statistics, 1998. CA Cancer J Clin 48:6–29, 1998.
187. Langer RD, Pierce JJ, O'Hanlan KA, et al: Transvaginal ultrasonography compared with endometrial biopsy for the detection of endometrial disease: Postmenopausal Estrogen/Progestin Interventions Trial. N Engl J Med 337:1792–1798, 1997.
188. Langlotz CP: Benefits and costs of MR imaging of prostate cancer. Magn Reson Clin North Am 4:533–544, 1996.
189. Langlotz CP, Schnall MD, Malkowicz SB, et al: Cost-effectiveness of endorectal magnetic resonance imaging for the staging of prostate cancer. Acad Radiol 3:S24–27, 1996.
190. Lee JK, McClennan BL, Stanley RJ, et al: Utility of computed tomography in the localization of the undescended testis. Radiology 135:121–125, 1980.
191. Lee JK, Rholl KS: MRI of the bladder and prostate. Am J Roentgenol 147:732–736, 1986.

192. Lee JKT, Gersell DJ, Balfe DM, et al: The uterus: In-vitro MR-anatomic correlation of normal and abnormal specimens. Radiology 157:175–179, 1985.
193. Lessler DS, Sullivan SD, Stergachis A: Cost-effectiveness of unenhanced MR imaging vs contrast-enhanced CT of the abdomen or pelvis. AJR Am J Roentgenol 163:5–9, 1994.
194. Levine D, Barnes PD, Sher S, et al: Fetal fast MR imaging: Reproducibility, technical quality, and conspicuity of anatomy. Radiology 206:549–554, 1998.
195. Levine D, Hatabu H, Gaa J, et al: Fetal anatomy revealed with fast MR sequences. AJR Am J Roentgenol 167:905–908, 1996.
196. Lien HH, Blomlie V, Kjorstad K, et al: Clinical stage I carcinoma of the cervix: Value of MR imaging in determining degree of invasiveness. AJR Am J Roentgenol 156:1191–1194, 1991.
197. Ling D, Lee JK, Heiken JP, et al: Prostatic carcinoma and benign prostatic hyperplasia: Inability of MR imaging to distinguish between the two diseases. Radiology 158:103–107, 1986.
198. Listerud J, Einstein S, Outwater EK, et al: First principles of fast spin echo. Magn Reson Q 8:199–244, 1993.
199. Low RN, Sigeti JS: MR imaging of peritoneal disease: Comparison of contrast-enhanced fast multiplanar spoiled gradient-recalled and spin-echo imaging. AJR Am J Roentgenol 163:1131–1140, 1994.
200. Lurain JR: Uterine cancer. In Berek JS, Adashi EY, Hillard PA (eds): Novak's Gynecology. Baltimore, Williams & Wilkins, 1996, pp 1057–1110.
201. Maki JH, Chenevert TL, Prince MR: Three-dimensional contrast-enhanced MR angiography. Top Magn Reson Imaging 8:322–344, 1996.
202. Mannel RS, Berman ML, Walker JL, et al: Management of endometrial cancer with suspected cervical involvement. Obstet Gynecol 75:1016–1022, 1990.
203. Mark AS, Hricak H, Heinrichs LW, et al: Adenomyosis and leiomyoma: Differential diagnosis with MR imaging. Radiology 163:527–529, 1987.
204. Marks G, Mohiuddin M, Masoni L: The reality of radical sphincter preservation surgery for cancer of the distal 3 cm of rectum following high-dose radiation. Int J Radiat Oncol Biol Phys 27:779–783, 1993.
205. Martin B, Mulopulos GP, Bryan PJ: MRI of puerperal ovarian-vein thrombosis (case report). Am J Roentgenol 147:291–292, 1986.
206. Martin DC: Germinal cell tumors of the testis after orchiopexy. J Urol 121:422–424, 1979.
207. Martin DC: Malignancy in the cryptorchid testis. Urol Clin North Am 9:371–376, 1982.
208. Marziale P, Atlante G, Pozzi M, et al: 426 cases of stage I endometrial carcinoma: A clinicopathological analysis. Gynecol Oncol 32: 278–281, 1989.
209. Masselot J, Buthiau D: Gynecology. In Vanel D, McNamara MT (eds): MRI of the Body. Paris, Springer-Verlag, 1989, p 223.
210. Matsukuma K, Tsukamoto N, Matsuyama T, et al: Preoperative CT study of lymph nodes in cervical cancer: Its correlation with histological findings. Gynecol Oncol 33:168–171, 1989.
211. Mattison DR, Kay HH, Miller RK, et al: Magnetic resonance imaging: A noninvasive tool for fetal and placental physiology. Biol Reprod 38:39–49, 1988.
212. Mattrey RF: Magnetic resonance imaging of the scrotum. Semin Ultrasound CT MR 12:95–108, 1991.
213. Mayr NA, Yuh WT, Zheng J, et al: Prediction of tumor control in patients with cervical cancer: Analysis of combined volume and dynamic enhancement pattern by MR imaging. AJR Am J Roentgenol 170:177–182, 1998.
214. McCarthy S: Magnetic resonance imaging in obstetrics and gynecology. Magn Reson Imaging 4:59–66, 1986.
215. McCarthy S: Magnetic resonance imaging of the normal female pelvis. Radiol Clin North Am 30:769–775, 1992.
216. McCarthy S, Scott G, Majumdar S, et al: Uterine junctional zone: MR study of water content and relaxation properties. Radiology 171:241–243, 1989.
217. McCarthy S, Tauber C, Gore J: Female pelvic anatomy: MR assessment of variations during the menstrual cycle and with use of oral contraceptives. Radiology 160:119–123, 1986.
218. McCauley TR, McCarthy S, Lange R: Pelvic phased array coil: Image quality assessment for spin-echo MR imaging. Magn Reson Imaging 10:513–522, 1992.
219. McDowell GC 2nd, Johnson JW, Tenney DM, et al: Pelvic lymphadenectomy for staging clinically localized prostate cancer: Indications, complications, and results in 217 cases. Urology 35:476–482, 1990.
220. McNeal JE: Cancer volume and site of origin of adenocarcinoma in the prostate: Relationship to local and distant spread. Hum Pathol 23:258–266, 1992.
221. McNeal JE, Villers AA, Redwine EA, et al: Capsular penetration in prostate cancer: Significance for natural history and treatment. Am J Surg Pathol 14:240–247, 1990.
222. Medl M, Kulenkampff KJ, Stiskal M, et al: Magnetic resonance imaging in the preoperative evaluation of suspected ovarian masses. Anticancer Res 15:1123–1125, 1995.
223. Megibow AJ, Bosniak MA, Ho AG, et al: Accuracy of CT in detection of persistent or recurrent ovarian carcinoma: Correlation with second-look laparotomy. Radiology 166:341–345, 1988.
224. Melki PS, Jolesz FA, Mulkern RV: Partial RF echo planar imaging with the FAISE method—I: Experimental and theoretical assessment of artifact. Magn Reson Med 26:328–341, 1992.
225. Melki PS, Mulkern RV, Panych LP, et al: Comparing the FAISE method with conventional dual-echo sequences. J Magn Reson Imaging 1:319–326, 1991.
226. Meyenberger C, Huch Boni RA, Bertschinger P, et al: Endoscopic ultrasound and endorectal magnetic resonance imaging: A prospective, comparative study for preoperative staging and follow-up of rectal cancer. Endoscopy 27:469–479, 1995.
227. Middleton WD, Siegel BA, Melson GL, et al: Acute scrotal disorders: Prospective comparison of color Doppler US and testicular scintigraphy. Radiology 177:177–181, 1990.
228. Milestone BN, Schnall MD, Lenkinski RE, et al: Cervical carcinoma: MR imaging with an endorectal surface coil. Radiology 180: 91–95, 1991.
229. Mintz MC, Thickman DI, Gussman D, et al: MR evaluation of uterine anomalies. AJR Am J Roentgenol 148:287–290, 1987.
230. Mirich DR, Hall JT, Kraft WL, et al: Metastatic adnexal trophoblastic neoplasm: Contribution of MR imaging. J Comput Assist Tomogr 12:1061–1067, 1988.
231. Mirowitz SA: Seminal vesicles: Biopsy-related hemorrhage simulating tumor invasion at endorectal MR imaging. Radiology 185: 373–376, 1992.
232. Mitchell DG: Benign disease of the uterus and ovaries. Radiol Clin North Am 30:777–787, 1992.
233. Mitchell DG: Chemical shift magnetic resonance imaging: Applications in the abdomen and pelvis. Top Magn Reson Imaging 4: 46–63, 1992.
234. Mitchell DG: Magnetic resonance imaging of the adnexa. Semin Ultrasound CT MR 9:143, 1988.
235. Mitchell DG, Mintz MC, Spritzer CE, et al: Adnexal masses: MR imaging observations at 1.5 T, with US and CT correlation. Radiology 162:319–324, 1987.
236. Mitchell DG, Vinitski S, Rifkin MD, et al: Sampling bandwidth and fat suppression: Effects on long TR/TE MR imaging of the abdomen and pelvis at 1.5 T. AJR Am J Roentgenol 153:419–425, 1989.
237. Mittl RL Jr, Yeh TT, Kressel HY: High-signal-intensity rim surrounding uterine leiomyomas on MR images: Pathologic correlation. Radiology 180:81–83, 1991.
238. Mohiuddin M, Marks G: Patterns of recurrence following high-dose preoperative radiation and sphincter-preserving surgery for cancer of the rectum. Dis Colon Rectum 36:117–126, 1993.
239. Morrow CP, Bundy BN, Kurman RJ, et al: Relationship between surgical-pathological risk factors and outcome in clinical stage I and II carcinoma of the endometrium: A Gynecologic Oncology Group study. Gynecol Oncol 40:55–65, 1991.
240. Morrow CP, Schlaerth JB: Surgical management of endometrial carcinoma. Clin Obstet Gynecol 25:81–92, 1982.
241. Mulholland SG: The impact of radiology on the management of prostatic disease: A clinician's perspective. Semin Ultrasound CT MR 9:335–338, 1988.
242. Murase E, Siegelman ES, Outwater EK, et al: Uterine leiomyomas: Histopathologic features, MR imaging findings, differential diagnosis, and treatment. Radiographics 19:1179–1197, 1999.
243. Narumi Y, Kadota T, Inoue E, et al: Bladder tumors: Staging with gadolinium-enhanced oblique MR imaging. Radiology 187:145–150, 1993.
244. Neuerburg JM, Bohndorf K, Sohn M, et al: Urinary bladder neoplasms: Evaluation with contrast-enhanced MR imaging. Radiology 172:739–743, 1989.

245. Neuerburg JM, Bohndorf K, Sohn M, et al: Staging of urinary bladder neoplasms with MR imaging: Is Gd-DTPA helpful? J Comput Assist Tomogr 15:780–786, 1991.
246. Nghiem HV, Herfkens RJ, Francis IR, et al: The pelvis: T2-weighted fast spin-echo MR imaging. Radiology 185:213–217, 1992.
247. Noren H, Granberg S, Friberg LG: Endometrial cancer stage II: 190 cases with different preoperative irradiation. Gynecol Oncol 41: 17–21, 1991.
248. Nyberg DA, Porter BA, Olds MO, et al: MR imaging of hemorrhagic adnexal masses. J Comput Assist Tomogr 11:664–669, 1987.
249. O'Connell LP, Fries MH, Zeringue E, et al: Triage of abnormal postmenopausal bleeding: A comparison of endometrial biopsy and transvaginal sonohysterography versus fractional curettage with hysteroscopy. Am J Obstet Gynecol 178:956–961, 1998.
250. Oesterling JE: Prostate-specific antigen: Improving its ability to diagnose early prostate cancer. JAMA 267:2236–2238, 1992.
251. Oi S, Honda Y, Hidaka M, et al: Intrauterine high-resolution magnetic resonance imaging in fetal hydrocephalus and prenatal estimation of postnatal outcomes with "perspective classification." J Neurosurg 88:685–694, 1998.
252. Okizuka H, Sugimura K, Ishida T: Preoperative local staging of rectal carcinoma with MR imaging and a rectal balloon. J Magn Reson Imaging 3:329–335, 1993.
253. Outwater E, Schiebler ML, Tomaszewski JE, et al: Mucinous carcinomas involving the prostate: Atypical findings at MR imaging. J Magn Reson Imaging 2:597–600, 1992.
254. Outwater EK: Cervical carcinoma. In Mendelson E, Reuter K, Rubin E, Bohm-Velez M (eds): Women's Imaging. St. Louis, Mosby, 2000.
255. Outwater EK: Ultrafast MR imaging of the pelvis. Eur J Radiol 29: 233–244, 1999.
256. Outwater EK, Mitchell DG: Magnetic resonance imaging techniques in the pelvis. Magn Reson Imaging Clin North Am 2:161–210, 1994.
257. Outwater EK, Mitchell DG: Normal ovaries and functional cysts: MR appearance. Radiology 198:397–402, 1996.
258. Outwater EK, Petersen RO, Siegelman ES, et al: Prostate carcinoma: Assessment of diagnostic criteria for capsular penetration on endorectal coil MR images. Radiology 193:333–339, 1994.
259. Outwater EK, Schiebler ML, Owen RS, et al: MRI characterization of hemorrhagic adnexal masses: A blinded reader study. Radiology 186:489–494, 1993.
260. Outwater EK, Siegelman ES, Chiowanich P, et al: Dilated fallopian tubes: MR imaging characteristics. Radiology 208:463–469, 1998.
261. Outwater EK, Siegelman ES, Kim B, et al: Ovarian Brenner tumors: MR imaging characteristics. Magn Reson Imaging 16:1147–1153, 1998.
262. Outwater EK, Siegelman ES, Talerman A, et al: Ovarian fibromas and cystadenofibromas: MRI features of the fibrous component. J Magn Reson Imaging 7:465–471, 1997.
263. Outwater EK, Siegelman ES, Van Deerlin V: Adenomyosis: Current concepts and imaging considerations. AJR Am J Roentgenol 170: 437–441, 1998.
264. Outwater EK, Siegelman ES, Wilson KM, et al: Benign and malignant gynecologic disease: Clinical importance of fluid and peritoneal enhancement in the pelvis at MR imaging. Radiology 200:483–488, 1996.
265. Outwater EK, Talerman A, Dunton C: Normal adnexa uteri specimens: Anatomic basis of MR imaging features. Radiology 201: 751–755, 1996.
266. Parivar F, Waluch V: Magnetic resonance imaging of prostate cancer. Hum Pathol 23:335–343, 1992.
267. Pattani SJ, Kier R, Deal R, et al: MRI of uterine leiomyosarcoma. Magn Reson Imaging 13:331–333, 1995.
268. Patton JF, Hewitt CB, Mallis N: Diagnosis and treatment of tumors of the testis. JAMA 171:2194–2198, 1959.
269. Pellerito JS, McCarthy SM, Doyle MB, et al: Diagnosis of uterine anomalies: Relative accuracy of MR imaging, endovaginal sonography, and hysterosalpingography. Radiology 183:795–800, 1992.
270. Perkins AC, Powell MC, Wastie ML, et al: A prospective evaluation of OC125 and magnetic resonance imaging in patients with ovarian carcinoma. Eur J Nucl Med 16:311–316, 1990.
271. Perrotti M, Kaufman RP Jr, Jennings TA, et al: Endo-rectal coil magnetic resonance imaging in clinically localized prostate cancer: Is it accurate? J Urology 156:106–109, 1996.
272. Petros JA, Catalona WJ: Lower incidence of unsuspected lymph node metastases in 521 consecutive patients with clinically localized prostate cancer. J Urol 147:1574–1575, 1992.
273. Phillips ME, Kressel HY, Spritzer CE, et al: Normal prostate and adjacent structures: MR imaging at 1.5 T [published erratum appears in Radiology 165:584, 1987]. Radiology 164:381–385, 1987.
274. Phillips ME, Kressel HY, Spritzer CE, et al: Prostatic disorders: MR imaging at 1.5 T. Radiology 164:386–392, 1987.
275. Photopulos GJ: Surgery or radiation for early cervical cancer. Clin Obstet Gynecol 33:872–882, 1990.
276. Piver MS: Invasive cervical cancer in the 1990s. Semin Surg Oncol 6:359–363, 1990.
277. Pizzocaro G, Nicolai N, Salvioni R, et al: Comparison between clinical and pathological staging in low stage nonseminomatous germ cell testicular tumors. J Urol 148:76–79, 1992.
278. Podczaski ES, Palombo C, Manetta A, et al: Assessment of pretreatment laparotomy in patients with cervical carcinoma prior to radiotherapy. Gynecol Oncol 33:71–75, 1989.
279. Poon PY, Bronskill MJ, Poon CS, et al: Identification of the periprostatic venous plexus by MR imaging. J Comput Assist Tomogr 15: 265–268, 1991.
280. Poon PY, McCallum RW, Henkelman MM, et al: Magnetic resonance imaging of the prostate. Radiology 154:143–149, 1985.
281. Pope CF, Dietz MJ, Ezekowitz MD, et al: Technical variables influencing the detection of acute deep vein thrombosis by magnetic resonance imaging. Magn Reson Imaging 9:379, 1991.
282. Posniak HV, Olson MC, Dudiak CM, et al: MR imaging of uterine carcinoma: Correlation with clinical and pathologic findings. Radiographics 10:15–27, 1990.
283. Postema S, Pattynama PM, van Rijswijk CS, et al: MR imaging of uterine cervical carcinoma: Comparison between fast spin-echo MRI and GRASE. Eur Radiol 8:45–49, 1998.
284. Potter ME, Partridge EE, Hatch KD, et al: Primary surgical therapy of ovarian cancer: How much and when. Gynecol Oncol 40:195–200, 1991.
285. Powell MC, Womack C, Buckley J, et al: Pre-operative magnetic resonance imaging of stage 1 endometrial adenocarcinoma. Br J Obstet Gynaecol 93:353–360, 1986.
286. Prince MR, Grist TM, Debatin JF: 3D contrast MR angiography. Berlin, Springer, 1997.
287. Quinn SF, Sheley RC, Szumowski J, et al: Evaluation of the iliac arteries: Comparison of two-dimensional time of flight magnetic resonance angiography with cardiac compensated fast gradient recalled echo and contrast-enhanced three-dimensional time of flight magnetic resonance angiography. J Magn Reson Imaging 7:197–203, 1997.
288. Quint LE, Van Erp JS, Bland PH, et al: Prostate cancer: Correlation of MR images with tissue optical density at pathologic examination. Radiology 179:837–842, 1991.
289. Raghavan D, Shipley WU, Garnick MB, et al: Biology and management of bladder cancer. N Engl J Med 322:1129–1138, 1990.
290. Rahmouni A, Yang A, Tempany CM, et al: Accuracy of in-vivo assessment of prostatic volume by MRI and transrectal ultrasonography. J Comput Assist Tomogr 16:935–940, 1992.
291. Reiss I, Gortner L, Moller J, et al: Fetal intracerebral hemorrhage in the second trimester: Diagnosis by sonography and magnetic resonance imaging. Ultrasound Obstet Gynecol 7:49–51, 1996.
292. Reuter KL, Daly DC, Cohen SM: Septate versus bicornuate uteri: Errors in imaging diagnosis. Radiology 172:749–752, 1989.
293. Reuter VE: Pathology of bladder cancer: Assessment of prognostic variables and response to therapy. Semin Oncol 17:524–532, 1990.
294. Rholl KS, Lee JK, Heiken JP, et al: Primary bladder carcinoma: Evaluation with MR imaging. Radiology 163:117–121, 1987.
295. Rholl KS, Lee JK, Ling D, et al: MR imaging of the scrotum with a high-resolution surface coil. Radiology 163:99–103, 1987.
296. Riccio TJ, Adams HG, Munzing DE, et al: Magnetic resonance imaging as an adjunct to sonography in the evaluation of the female pelvis. Magn Reson Imaging 8:699–704, 1990.
297. Richardson GS, Scully RE, Nikrui N, et al: Common epithelial cancer of the ovary (2). N Engl J Med 312:474–483, 1985.
298. Rifkin M: Comparison of magnetic resonance imaging and ultrasonography in staging early prostate cancer: Results of a multi-institutional cooperative trial. Invest Radiol 26:1024–1025, 1991.
299. Robbins SL, Cotran RS: Female genital tract. In Robbins SL, Cotran RS (eds): Pathologic Basis of Disease. Philadelphia, WB Saunders, 1979, p 1242.
300. Roebuck DJ, Metreweli C: Radiation risk in CT for acute abdominal pain [letter; comment]. Radiology 209:287–288, 1998.

301. Roemer PB, Edelstein WA, Hayes CE, et al: The NMR phased array. Magn Reson Med 16:192–225, 1990.
302. Rorvik J, Halvorsen OJ, Albrektsen G, et al: MRI with an endorectal coil for staging of clinically localised prostate cancer prior to radical prostatectomy. Eur Radiol 9:29–34, 1999.
303. Rosenfield AT, Blair DN, McCarthy S, et al: Society of Uroradiology Award paper: The pars infravaginalis gubernaculi—importance in the identification of the undescended testis. AJR Am J Roentgenol 153:775–778, 1989.
304. Rubens D, Thornbury JR, Angel C, et al: Stage IB cervical carcinoma: Comparison of clinical, MR, and pathologic staging. AJR Am J Roentgenol 150:135–138, 1988.
305. Russell AH, Anderson M, Walter J, et al: The integration of computed tomography and magnetic resonance imaging in treatment planning for gynecologic cancer. Clin Obstet Gynecol 35:55–72, 1992.
306. Russell JG, Fawcitt R: New risks, new doses [comment]. AJNR Am J Neuroradiol 13:850–852, 1992.
307. Russell JG, Webb GA: Valuing the man-sievert in x-ray diagnosis. Br J Radiol 60:681–684, 1987.
308. Sanchez-Chapado M, Angulo JC, Ibarburen C, et al: Comparison of digital rectal examination, transrectal ultrasonography, and multicoil magnetic resonance imaging for preoperative evaluation of prostate cancer. Eur Urol 32:140–149, 1997.
309. Santoni R, Bucciolini M, Cionini L, et al: Modifications of relaxation times induced by radiation therapy in cervical carcinoma: Preliminary results. Clin Radiol 38:569–573, 1987.
310. Savader SJ, Otero RR, Savader BL: Puerperal ovarian vein thrombosis: Evaluation with CT, US, and MR imaging. Radiology 167: 637–639, 1988.
311. Savci G, Ozyaman T, Tutar M, et al: Assessment of depth of myometrial invasion by endometrial carcinoma: Comparison of T2-weighted SE and contrast-enhanced dynamic GRE MR imaging. Eur Radiol 8:218–223, 1998.
312. Scheidler J, Hricak H, Vigneron DB, et al: Prostate cancer: Localization with three-dimensional proton MR spectroscopic imaging—clinicopathologic study. Radiology 213:473–480, 1999.
313. Schiebler ML, Schnall MD, Pollack HM, et al: Current role of MR imaging in the staging of adenocarcinoma of the prostate. Radiology 189:339–352, 1993.
314. Schiebler ML, Tomaszewski JE, Bezzi M, et al: Prostatic carcinoma and benign prostatic hyperplasia: Correlation of high-resolution MR and histopathologic findings. Radiology 172:131–137, 1989.
315. Schiebler ML, Yankaskas BC, Tempany C, et al: Efficacy of prostate-specific antigen and magnetic resonance imaging in staging stage C adenocarcinoma of the prostate. Invest Radiol 27:575–577, 1992.
316. Schiebler ML, Yankaskas BC, Tempany C, et al: MR imaging in adenocarcinoma of the prostate: Interobserver variation and efficacy for determining stage C disease. AJR Am J Roentgenol 158:559–562; discussion, 158:563–554, 1992.
317. Schlesinger C, Kamoi S, Ascher SM, et al: Endometrial polyps: A comparison study of patients receiving tamoxifen with two control groups. Int J Gynecol Pathol 17:302–311, 1998.
318. Schnall MD, Bezzi M, Pollack HM, et al: Magnetic resonance imaging of the prostate. Magn Reson Q 6:1–16, 1990.
319. Schnall MD, Furth EE, Rosato EF, et al: Rectal tumor stage: Correlation of endorectal MR imaging and pathologic findings. Radiology 190:709–714, 1994.
320. Schnall MD, Imai Y, Tomaszewski J, et al: Prostate cancer: Local staging with endorectal surface coil MR imaging. Radiology 178: 797–802, 1991.
321. Schnall MD, Lenkinski RE, Pollack HM, et al: Prostate: MR imaging with an endorectal surface coil. Radiology 172:570–574, 1989.
322. Schnall MD, Pollack HM, Van Arsdalen K, et al: The seminal tract in patients with ejaculatory dysfunction: MR imaging with an endorectal surface coil. AJR Am J Roentgenol 159:337–341, 1992.
323. Schwartz LB, Panageas E, Lange R, et al: Female pelvis: Impact of MR imaging on treatment decisions and net cost analysis. Radiology 192:55–60, 1994.
324. Scott R Jr, Mutchnik DL, Laskowski TZ, et al: Carcinoma of the prostate in elderly men: Incidence, growth characteristics and clinical significance. J Urol 101:602–607, 1969.
325. Scott WW Jr, Rosenshein NB, Siegelman SS, et al: The obstructed uterus. Radiology 141:767–770, 1981.
326. Scoutt LM, Flynn SD, Luthringer DJ, et al: Junctional zone of the uterus: Correlation of MR imaging and histologic examination of hysterectomy specimens. Radiology 179:403–407, 1991.
327. Scoutt LM, McCarthy SM, Flynn SD, et al: Clinical stage I endometrial carcinoma: Pitfalls in preoperative assessment with MR imaging—work in progress. Radiology 194:567–572, 1995.
328. Scoutt LM, McCauley TR, Flynn SD, et al: Zonal anatomy of the cervix: Correlation of MR imaging and histologic examination of hysterectomy specimens. Radiology 186:159–162, 1993.
329. See WA, Fuller JR: Staging of advanced bladder cancer: Current concepts and pitfalls. Urol Clin North Am 19:663–683, 1992.
330. Seidenwurm D, Smathers RL, Lo RK, et al: Testes and scrotum: MR imaging at 1.5 T. Radiology 164:393–398, 1987.
331. Seki H, Kimura M, Sakai K: Myometrial invasion of endometrial carcinoma: Assessment with dynamic MR and contrast-enhanced T1-weighted images. Clin Radiol 52:18–23, 1997.
332. Semelka RC, Kelekis NL, Thomasson D, et al: HASTE MR imaging: Description of technique and preliminary results in the abdomen. J Magn Reson Imaging 6:698–699, 1996.
333. Semelka RC, Lawrence PH, Shoenut JP, et al: Primary ovarian cancer: Prospective comparison of contrast-enhanced CT and pre- and postcontrast, fat-suppressed MR imaging, with histologic correlation. J Magn Reson Imaging 3:99–106, 1993.
334. Sepponen RE, Sipponen JT, Tanttu JE: A method for chemical shift imaging: Demonstration of bone marrow involvement with proton chemical shift imaging. J Comput Assist Tomogr 8:585–587, 1984.
335. Serra AD, Hricak H, Coakley FV, et al: Inconclusive clinical and ultrasound evaluation of the scrotum: Impact of magnetic resonance imaging on patient management and cost. Urology 51:1018–1021, 1998.
336. Shapeero LG, Hricak H: Mixed mullerian sarcoma of the uterus: MR imaging findings. AJR Am J Roentgenol 153:317–319, 1989.
337. Sheldon CA, Williams RD, Fraley EE: Incidental carcinoma of the prostate: A review of the literature and critical reappraisal of classification. J Urol 124:626–631, 1980.
338. Sheth S, Hamper UM, Kurman RJ: Thickened endometrium in the postmenopausal woman: Sonographic-pathologic correlation. Radiology 187:135–139, 1993.
339. Shida T, Yoshimura M, Chihara H, et al: Intravenous leiomyomatosis of the pelvis with reextension into the heart. Ann Thorac Surg 42: 104–106, 1986.
340. Siegelman ES, Outwater EK, Vinitski S, et al: Fat suppression by saturation/opposed-phase hybrid technique: Spin echo versus gradient echo imaging. Magn Reson Imaging 13:545–548, 1995.
341. Siegelman ES, Outwater EK, Wang T, et al: Solid enhancing masses in endometriosis: MR imaging observations. AJR Am J Roentgenol 163:357–361, 1994.
342. Silverberg SG, Kurman RJ: Tumors of the uterine corpus and gestational trophoblastic disease. In Rosai J, Aovin L (eds): Atlas of Tumor Pathology, vol 3. Washington, DC: Armed Forces Institute of Pathology, 1992, pp 113–151.
343. Sironi S, Belloni C, Taccagni G, et al: Invasive cervical carcinoma: MR imaging after preoperative chemotherapy. Radiology 180:719–722, 1991.
344. Sironi S, Belloni C, Taccagni GL, et al: Carcinoma of the cervix: Value of MR imaging in detecting parametrial involvement. AJR Am J Roentgenol 156:753–756, 1991.
345. Sironi S, Colombo E, Villa G, et al: Myometrial invasion by endometrial carcinoma: Assessment with plain and gadolinium-enhanced MR imaging. Radiology 185:207–212, 1992.
346. Smith FW, Cherryman GR, Bayliss AP, et al: A comparative study of the accuracy of ultrasound imaging, x-ray computerized tomography and low field MRI diagnosis of ovarian malignancy. Magn Reson Imaging 6:225–227, 1988.
347. Smith PH: The case for no initial treatment of localized prostate cancer. Urol Clin North Am 17:827–834, 1990.
348. Smith RC, Reinhold C, Lange RC, et al: Fast spin-echo MR imaging of the female pelvis: Part I—use of a whole-volume coil. Radiology 184:665–669, 1992.
349. Smith RC, Reinhold C, McCauley TR, et al: Multicoil high-resolution fast spin-echo MR imaging of the female pelvis [comment]. Radiology 184:671–675, 1992.
350. Snidow JJ, Aisen AM, Harris VJ, et al: Iliac artery MR angiography: Comparison of three-dimensional gadolinium-enhanced and two-dimensional time-of-flight techniques. Radiology 196:371–378, 1995.

351. Snidow JJ, Harris VJ, Johnson MS, et al: Iliac artery evaluation with two-dimensional time-of-flight MR angiography: Update. J Vasc Interv Radiol 7:213–220, 1996.
352. Snidow JJ, Johnson MS, Harris VJ, et al: Three-dimensional gadolinium-enhanced MR angiography for aortoiliac inflow assessment plus renal artery screening in a single breath hold. Radiology 198: 725–732, 1996.
353. Soloway MS: Invasive bladder cancer: Selection of primary treatment. Semin Oncol 17:551–554, 1990.
354. Soyer P, Riopel M, Bluemke DA, et al: Hepatic metastases from leiomyosarcoma: MR features with histopathologic correlation. Abdom Imaging 22:67–71, 1997.
355. Spritzer CE, Sostman HD, Wilkes DC, et al: Deep venous thrombosis: Experience with gradient-echo MR imaging in 66 patients. Radiology 177:235, 1990.
356. Stehling MK, Liu L, Laub G, et al: Gadolinium-enhanced magnetic resonance angiography of the pelvis in patients with erectile impotence. MAGMA 5:247–254, 1997.
357. Steinfeld AD: Questions regarding the treatment of localized prostate cancer. Radiology 184:593–598, 1992.
358. Stevens SK, Hricak H, Campos Z: Teratomas versus cystic hemorrhagic adnexal lesions: Differentiation with proton-selective fat-saturation MR imaging. Radiology 186:481–488, 1993.
359. Stevens SK, Hricak H, Stern JL: Ovarian lesions: Detection and characterization with gadolinium-enhanced MR imaging at 1.5 T. Radiology 181:481–488, 1991.
360. Subak LL, Hricak H, Powell CB, et al: Cervical carcinoma: Computed tomography and magnetic resonance imaging for preoperative staging. Obstet Gynecol 86:43–50, 1995.
361. Sugimura K, Carrington BM, Quivey JM, et al: Postirradiation changes in the pelvis: Assessment with MR imaging. Radiology 175:805–813, 1990.
362. Szumowski J, Eisen JK, Vinitski S, et al: Hybrid methods of chemical-shift imaging. Magn Reson Med 9:379–388, 1989.
363. Szumowski J, Plewes DB: Separation of lipid and water MR imaging signals by Chopper averaging in the time domain. Radiology 165: 247–250, 1987.
364. Tachibana M, Baba S, Deguchi N, et al: Efficacy of gadolinium-diethylenetriaminepentaacetic acid-enhanced magnetic resonance imaging for differentiation between superficial and muscle-invasive tumor of the bladder: A comparative study with computerized tomography and transurethral ultrasonography. J Urol 145:1169–1173, 1991.
365. Takahashi K, Okada M, Okada S, et al: Studies on the detection of small endometrial implants by magnetic resonance imaging using a fat saturation technique. Gynecol Obstet Invest 41:203–206, 1996.
366. Tanimoto A, Yuasa Y, Imai Y, et al: Bladder tumor staging: Comparison of conventional and gadolinium-enhanced dynamic MR imaging and CT. Radiology 185:741–747, 1992.
367. Teitelbaum GP, Ortega HV, Vinitski S, et al: Optimization of gradient-echo imaging parameters for intracaval filters and trapped thromboemboli. Radiology 174:1013, 1990.
368. Thaler W, Watzka S, Martin F, et al: Preoperative staging of rectal cancer by endoluminal ultrasound vs. magnetic resonance imaging: Preliminary results of a prospective, comparative study. Dis Colon Rectum 37:1189–1193, 1994.
369. Thorvinger B, Gudmundsson T, Horvath G, et al: Staging in local endometrial carcinoma: Assessment of magnetic resonance and ultrasound examinations. Acta Radiol 30:525–529, 1989.
370. Thurnher S, Hodler J, Baer S, et al: Gadolinium-DPTA enhanced MR imaging of adnexal tumors. J Comput Assist Tomogr 14:939–949, 1990.
371. Thurnher S, Hricak H, Carroll PR, et al: Imaging the testis: Comparison between MR imaging and US. Radiology 167:631–636, 1988.
372. Thurnher S, Hricak H, Tanagho EA: Mullerian duct cyst: Diagnosis with MR imaging. Radiology 168:25–28, 1988.
373. Thurnher SA: MR imaging of pelvic masses in women: Contrast-enhanced vs unenhanced images. AJR Am J Roentgenol 159:1243–1250, 1992.
374. Thurnher SA, von Schulthess GK, Marincek B: Staging of cervical carcinoma with contrast-enhanced MR imaging. San Francisco, Society for Magnetic Resonance in Medicine, 1991.
375. Togashi K: MRI of the Female Pelvis. Tokyo, Igaku-Shoin, 1993, pp 227–279.
376. Togashi K, Konishi J: Magnetic resonance imaging in the evaluation of gynecologic malignancy. Magn Reson Q 6:250–275, 1990.
377. Togashi K, Nishimura K, Itoh K, et al: Uterine cervical cancer: Assessment with high-field MR imaging. Radiology 160:431–435, 1986.
378. Togashi K, Nishimura K, Itoh K, et al: Adenomyosis: Diagnosis with MR imaging. 166:111–114, 1988.
379. Togashi K, Nishimura K, Itoh K, et al: Ovarian cystic teratomas: MR imaging. Radiology 162:669–673, 1987.
380. Togashi K, Nishimura K, Kimura I, et al: Endometrial cysts: Diagnosis with MR imaging. Radiology 180:73–78, 1991.
381. Togashi K, Nishimura K, Sagoh T, et al: Carcinoma of the cervix: Staging with MR imaging. Radiology 171:245–251, 1989.
382. Togashi K, Ozasa H, Konishi I, et al: Enlarged uterus: Differentiation between adenomyosis and leiomyoma with MR imaging. Radiology 171:531–534, 1989.
383. Trambert MA, Mattrey RF, Levine D, et al: Subacute scrotal pain: Evaluation of torsion versus epididymitis with MR imaging. Radiology 175:53–56, 1990.
384. Troiano RN, Lazzarini KM, Scoutt LM, et al: Fibroma and fibrothecoma of the ovary: MR imaging findings. Radiology 204:795–798, 1997.
385. Tsuda K, Murakami T, Kurachi H, et al: MR imaging of cervical carcinoma: Comparison among T2-weighted, dynamic, and postcontrast T1-weighted images with histopathological correlation. Abdom Imaging 22:103–107, 1997.
386. Tukeva TA, Aronen HJ, Karjalainen PT, et al: MR imaging in pelvic inflammatory disease: Comparison with laparoscopy and US. Radiology 210:209–216, 1999.
387. Twickler DM, Setiawan AT, Evans RS, et al: Imaging of puerperal septic thrombophlebitis: Prospective comparison of MR imaging, CT, and sonography. AJR Am J Roentgenol 169:1039–1043, 1997.
388. van der Burg MEL, van Lent M, Buyse M, et al: The effect of debulking surgery after induction chemotherapy on the prognosis in advanced epithelial ovarian cancer. N Engl J Med 332:629–634, 1995.
389. van Gils AP, Tham RT, Falke TH, et al: Abnormalities of the uterus and cervix after diethylstilbestrol exposure: Correlation of findings on MR and hysterosalpingography. AJR Am J Roentgenol 153: 1235–1238, 1989.
390. Van Nagell JR Jr, Roddick JW Jr, Lowin DM: The staging of cervical cancer: Inevitable discrepancies between clinical staging and pathologic findings. Am J Obstet Gynecol 110:973–978, 1971.
391. Van Vierzen PB, Massuger LF, Ruys SH, et al: Fast dynamic contrast enhanced MR imaging of cervical carcinoma. Clin Radiol 53:183–192, 1998.
392. Vanbeckevoort D, Van Hoe L, Oyen R, et al: Pelvic floor descent in females: Comparative study of colpocystodefecography and dynamic fast MR imaging. J Magn Reson Imaging 9:373–377, 1999.
393. Vanneuville G, Lenck LC, Garcier JM, et al: Contribution of imaging to the understanding of the female pelvic fasciae. Surg Radiol Anat 14:147–154, 1992.
394. Vardi JR, Tadros GH, Anselmo MT, et al: The value of exploratory laparotomy in patients with endometrial carcinoma according to the new International Federation of Gynecology and Obstetrics staging. Obstet Gynecol 80:204–208, 1992.
395. Villers A, McNeal JE, Freiha FS, et al: Multiple cancers in the prostate: Morphologic features of clinically recognized versus incidental tumors. Cancer 70:2313–2318, 1992.
396. Waggenspack GA, Amparo EG, Hannigan EV: MR imaging of uterine cervical carcinoma. J Comput Assist Tomogr 12:409–414, 1988.
397. Waggenspack GA, Amparo EG, Hannigan EV, et al: MRI of cervical carcinoma. Semin Ultrasound CT MRI 9:158–166, 1988.
398. Wehrli FW, Perkins TG, Shimakawa A, et al: Chemical-shift-induced amplitude modulations in images obtained with gradient refocusing. Magn Reson Imaging 5:157–158, 1987.
399. Weidner AC, Low VH: Imaging studies of the pelvic floor. Obstet Gynecol Clin North Am 25:825–848, 1998.
400. Weinreb JC, Brown CE, Lowe TW, et al: Pelvic masses in pregnant patients: MR and US imaging. Radiology 159:717–724, 1986.
401. Weitzman GA, Buttram VC Jr: Classification of endometriosis. Obstet Gynecol Clin North Am 16:61–77, 1989.
402. Wheeler TM: Anatomic considerations in carcinoma of the prostate. Urol Clin North Am 16:623–634, 1989.
403. Whitmore WF: Clinical management of prostatic cancer: An overview. Am J Clin Oncol 11:588–597, 1988.

404. Williams MP, Husband JE, Heron CW, et al: Magnetic resonance imaging in recurrent carcinoma of the cervix. Br J Radiol 62:544–550, 1989.
405. Worthington JL, Balfe DM, Lee JKT: Uterine neoplasms: MR imaging. Radiology 159:725–730, 1986.
406. Yamashita Y, Harada M, Torashima M, et al: Dynamic MR imaging of recurrent postoperative cervical cancer. J Magn Reson Imaging 6:167–171, 1996.
407. Yamashita Y, Mizutani H, Torashima M, et al: Assessment of myometrial invasion by endometrial carcinoma: Transvaginal sonography vs contrast-enhanced MR imaging. AJR Am J Roentgenol 161:595–599, 1993.
408. Yamashita Y, Namimoto T, Abe Y, et al: MR imaging of the fetus by a HASTE sequence. AJR Am J Roentgenol 168:513–519, 1997.
409. Yamashita Y, Takahashi M, Sawada T, et al: Carcinoma of the cervix: Dynamic MR imaging. Radiology 182:643–648, 1992.
410. Yamashita Y, Torashima M, Hatanaka Y, et al: Adnexal masses: Accuracy of characterization with transvaginal US and precontrast and postcontrast MR imaging. Radiology 194:557–565, 1995.
411. Yamashita Y, Torashima M, Hatanaka Y, et al: Value of phase-shift gradient-echo MR imaging in the differentiation of pelvic lesions with high signal intensity at T1-weighted imaging. Radiology 191:759–764, 1994.
412. Yamashita Y, Torashima M, Takahashi M, et al: Hyperintense uterine leiomyoma at T2-weighted MR imaging: Differentiation with dynamic enhanced MR imaging and clinical implications. Radiology 189:721–725, 1993.
413. Yazigi R, Cohen J, Munoz AK, et al: Magnetic resonance imaging determination of myometrial invasion in endometrial carcinoma. Gynecol Oncol 34:94–97, 1989.
414. Yeung HN, Kormos DW: Separation of true fat and water images by correcting magnetic field inhomogeneity in situ. Radiology 159:783–786, 1986.
415. Yoder IC: Diagnosis of uterine anomalies: Relative accuracy of MR imaging, endovaginal sonography, and hysterosalpingography. Radiology 185:343–344, 1992.
416. Yu KK, Forstner R, Hricak H: Cervical carcinoma: Role of imaging. Abdom Imaging 22:208–215, 1997.
417. Yu KK, Hricak H, Alagappan R, et al: Detection of extracapsular extension of prostate carcinoma with endorectal and phased-array coil MR imaging: Multivariate feature analysis. Radiology 202:697–702, 1997.
418. Yu KK, Hricak H, Subak LL, et al: Preoperative staging of cervical carcinoma: Phased array coil fast spin-echo versus body coil spin-echo T2-weighted MR imaging. AJR Am J Roentgenol 171:707–711, 1998.
419. Yu KK, Scheidler J, Hricak H, et al: Prostate cancer: Prediction of extracapsular extension with endorectal MR imaging and three-dimensional proton MR spectroscopic imaging. Radiology 213:481–488, 1999.
420. Zawin M, McCarthy S, Scoutt L, et al: Endometriosis: Appearance and detection at MR imaging. Radiology 171:693–696, 1989.
421. Zincke H, Blute ML, Fallen MJ, et al: Radical prostatectomy for stage A adenocarcinoma of the prostate: Staging errors and their implications for treatment recommendations and disease outcome. J Urol 146:1053–1058, 1991.

Part VII

Imaging of the Musculoskeletal System

Edited by
Mark Robbin

46 Musculoskeletal Tumors

Amilcare Gentili

Skeletal Tumors

Many imaging modalities are available for the evaluation of skeletal lesions. In most cases, standard radiographs are sufficient for detecting skeletal tumors[97]; when evaluated together with clinical data (e.g., age, sex, anatomic location, clinical presentation), radiographs are the best predictors of the histologic condition of the lesion. To fully characterize a tumor in an anatomically complex area, such as in the spine, scapula, or pelvis, or in a periarticular location, however, magnetic resonance imaging (MRI) or computed tomography (CT) is often necessary.

Bone scintigraphy is the modality of choice for screening for skeletal metastases. Although MRI is more sensitive than scintigraphy in detecting metastases, it is not an efficient technique for evaluating the entire skeleton.[32]

As stated, plain radiographs may be sufficient for diagnosis, but MRI and CT are fundamental in staging skeletal tumors. Optimal treatment of primary skeletal neoplasms in the absence of distant metastases includes complete surgical resection of the tumor. In the past, amputation was the treatment of choice. With improved surgical technique and aggressive chemotherapy, limb-sparing operations can be performed without affecting survival and with better functional results. In planning resection, accurate preoperative staging is essential. The initial CT or MRI procedures should be performed before biopsy because later it is often difficult to distinguish tumor from edema, hemorrhage, and granulation tissue.

Numerous studies have compared the usefulness of CT and MRI in the staging of musculoskeletal tumors.* MRI is superior for determining muscle compartment and vascular involvement because of the intrinsic contrast between tumor mass, muscle, and fat, without the need for enhancement with contrast medium. In addition, MRI is able to produce images in multiple planes, allowing easier assessment of intramedullary extent of tumor and intra-articular extension.[24] CT is superior for detecting subtle cortical invasion and periosteal and endosteal reaction and for depicting matrix calcification or ossification. Both MRI and CT are useful in evaluating the response to chemotherapy and radiation therapy.[42, 102] Signs of response to treatment are (1) decreased tumor size, (2) improved delineation of the mass, (3) reappearance of fat planes between muscle groups, and (4) calcification or ossification of the tumor.

* See References 1, 5, 9 to 12, 36, 76, 78, 96, 97, 108, and 113.

Technique

Computed Tomography

After a scout view, axial CT images are obtained with a slice thickness ranging from 1.5 to 10 mm, depending on the size and location of the tumor. Thin-section imaging should be used for small lesions. For evaluation of bone lesions, images are reconstructed using bone algorithms, images are reviewed using both bone and soft tissue window settings. Intravenous (IV) administration of a contrast agent aids in visualizing major vascular bundles and in assessing the vascularity of a lesion, and it may be helpful in distinguishing necrotic from viable tumor.

Magnetic Resonance Imaging

Numerous pulse sequences are available for the evaluation of musculoskeletal tumors, including (1) spin-echo and fast spin-echo, (2) inversion recovery, (3) gradient-echo, and (4) chemical shift sequences. My routine protocol for the evaluation of musculoskeletal masses includes images in at least two planes: usually (1) a T1-weighted sequence in the sagittal or coronal plane, followed by (2) either a double-echo (proton-density and T2-weighted), spin-echo sequence or a T2-weighted, fat-saturated, fast spin-echo sequence in the axial plane. A short tau inversion recovery (STIR) sequence is occasionally obtained to increase the conspicuity of a lesion.[94]

Whenever possible, imaging is performed with a *surface coil* for enhanced spatial resolution and an improved signal-to-noise ratio. *Body coils* are used when an entire bone or soft tissue region is to be evaluated for the detection of skip lesions or for surgical planning. The use of contrast-enhanced MRI for the characterization of musculoskeletal tumors has yielded controversial results[30, 83, 95] and is not routinely used in the musculoskeletal system.

Benign Skeletal Tumors

Enchondroma

An enchondroma is a common benign primary osseous tumor; its frequency follows only that of nonossifying fibromas and exostosis. There is no sex predilection, and approximately 50% of these tumors occur in the hands. They are asymptomatic unless they are undergoing malignant transformation or the bone is fractured, and they are often an incidental finding on radiographs.

Enchondromas are typically round or oval lesions with

well-defined, lobulated borders. The unmineralized matrix exhibits soft tissue attenuation on CT scans, and homogeneous high signal intensity appears on T2-weighted MR images. Calcification with a ring and arc appearance, which suggests a chondroid matrix,[2, 18] is best identified on plain radiography and CT. Calcifications are not consistently identified with MRI; when seen, however, they have low signal intensity on all sequences.

Benign and malignant chondroid lesions can have a similar appearance, making differentiation of an enchondroma from a low-grade chondrosarcoma difficult or impossible. The presence of a soft tissue mass or a cortical erosion or pain in the absence of fracture, however, increases the likelihood of malignancy.[24, 74]

Chondroblastoma

Chondroblastoma is a benign rare tumor of cartilaginous origin composed of chondroblasts. Its peak incidence is in individuals between 10 and 20 years of age. It is more common in males, with a male-to-female ratio of 2:1.

Chondroblastoma involves the epiphysis, the apophysis, or both but may extend into the metaphysis after destroying the growth plate.[43] CT accurately demonstrates the extent of the lesion as well as matrix calcifications and subtle cortical infractions. Extension through the growth plate, however, is best detected with conventional tomography or MRI because the growth plate is usually best visualized in the sagittal or coronal plane. Both T1-weighted and T2-weighted MR images demonstrate a peripheral rim of signal void that corresponds to the sclerotic margin of the lesion.[48] Abnormal signal intensity in large areas of bone marrow surrounding the lesion has been seen and probably represents bone marrow edema.[15, 40, 105, 110]

Osteochondroma

Osteochondromas (exostoses) are the second most common benign tumor of bone after nonossifying fibromas. The male-to-female ratio is 1.5:1 to 2:1. These are congenital lesions but are usually discovered between 10 and 20 years of age. Multiple exostoses are uncommon, occurring only one tenth as frequently as a solitary exostosis, but they manifest earlier, usually before 10 years of age.

Ninety percent of osteochondromas originate from a long bone close to the metaphysis. The most common locations are around the knee (distal femur and proximal tibia) and the proximal humerus. The morphology of an osteochondroma is more important than the signal intensity in diagnosis. The incidence of malignant transformation is approximately 1% for solitary osteochondromas and from 5% to 25% for hereditary multiple exostoses.

Both CT and MRI demonstrate the continuity of the cortex and medullary cavity of the osteochondroma with that of the parent bone (Fig. 46–1).[87] The perichondrium is well seen on T2-weighted MR images as an area of low signal intensity surrounding the outer surface of the high signal intensity of the cartilage cap.[59] MRI measurements of cartilage cap thickness are also accurate, whereas CT measurements of maximal cartilage thickness are often imprecise.[44] The thickness of this structure is important in distinguishing benign osteochondroma from an exostotic

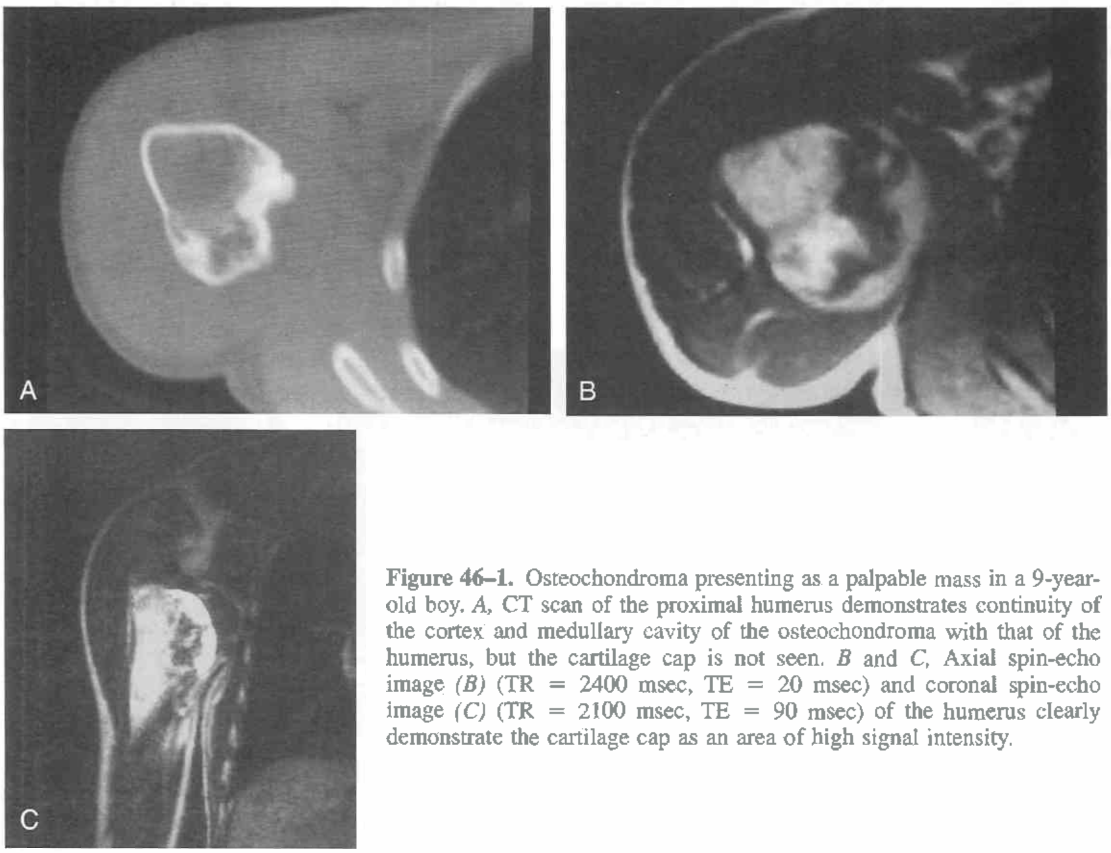

Figure 46–1. Osteochondroma presenting as a palpable mass in a 9-year-old boy. *A*, CT scan of the proximal humerus demonstrates continuity of the cortex and medullary cavity of the osteochondroma with that of the humerus, but the cartilage cap is not seen. *B* and *C*, Axial spin-echo image *(B)* (TR = 2400 msec, TE = 20 msec) and coronal spin-echo image *(C)* (TR = 2100 msec, TE = 90 msec) of the humerus clearly demonstrate the cartilage cap as an area of high signal intensity.

chondrosarcoma. According to most authors, the cartilage cap is usually thicker than 3 cm in a chondrosarcoma.[52]

Other complications of osteochondromas include nerve injuries, vascular injury, and bursa formation.[24, 68, 79] The formation of a bursa over an osteochondroma is common, and the bursa is usually asymptomatic; if it becomes inflamed and distended, it can be painful. On T2-weighted images, bursal fluid has high signal intensity similar to that of the cartilage cap, and it can be difficult to differentiate between the two. On gradient-echo sequences, cartilage has a lower signal intensity than that of fluid, and the diagnosis can be easily made. A rarer complication is the formation of a pseudoaneurysm adjacent to the exostosis.[81]

Chondromyxoid Fibroma

Chondromyxoid fibroma is composed of three principal elements: chondroid, fibrous, and myxoid tissue. It is the least common of the benign cartilaginous bone neoplasms. There is a male predominance, with a male-to-female ratio of 1.5 to 2:1. The tumor tends to occur around the knee joint but can involve any bone. The tumor is usually solid but may contain cystic or hemorrhagic areas. On MR images, signal intensities of this tumor vary with the proportions of chondroid, fibrous, and myxoid tissues present. CT may be better than MRI in delineating matrix calcification and sclerosis around the tumor.[109]

Osteoid Osteoma

Osteoid osteomas are relatively common, following only osteochondromas and fibrous cortical defects in prevalence. The male-to-female ratio is 3:1. They typically occur in teenagers and young adults and are rare before 5 and after 30 years of age. These tumors occur most frequently in the femur, tibia, and humerus and involve the diaphysis and, less commonly, the metaphysis. When the spine is involved, the posterior elements are typically affected. The main clinical symptom is pain relieved by aspirin.

CT is very accurate in detecting the nidus and is preferred to MRI for evaluating osteoid osteoma.[34, 56, 62] Occasionally, an osteoid osteoma can be confused with a stress fracture on MR images because of edema in the bone marrow. On a CT scan, the typical appearance of an osteoid osteoma is an area of sclerosis surrounding a small (<1 cm) radiolucent nidus (Fig. 46–2). Lesions larger than 1.5 cm are considered osteoblastomas.

The nidus may contain calcifications, the number of which can vary from none to enough to bring about almost complete calcification with only a thin peripheral rim of low density. For full evaluation of the nidus, thin-section CT with 2-mm slices is needed because the nidus is often less than 1 cm in diameter. The nidus enhances on dynamic CT scans, and depending on the degree of calcification, it has low signal intensity on T1-weighted MR images and variable intensity on T2-weighted images.

The surrounding bone marrow has low signal intensity on all pulse sequences in the presence of reactive sclerosis or high signal intensity on the T2-weighted images in the presence of edema (Fig. 46–3).[20, 28] Osteoid osteomas in younger patients tend to be associated with more extensive peritumoral edema.[28] When the osteoid osteoma is interarticular, an associated joint effusion may be detected.[88]

Osteoblastoma

Osteoblastoma is a rare benign tumor. It is at least four times less common than osteoid osteoma. There is a male predominance, with a male-to-female ratio of 2.5:1. Its peak incidence is in the second decade, and it is rare before 10 years of age and after 30 years of age. Its most common location is the spine, usually in the posterior elements. In the long bones, it is most often located in the metadiaphyseal region; in rare circumstances, it can extend into the epiphyses in the adult.

On CT scans, an osteoblastoma appears as an expansile lytic lesion, often with a mineralized matrix, surrounded by a thin bony shell. Dense sclerosis and periosteal reaction may occasionally be present. An osteoblastoma typically has low to intermediate signal intensity on T1-weighted MR images and high signal intensity on T2-weighted images. Edema in the surrounding soft tissues and in the bone marrow beyond the tumor margins is common.[5, 21, 58, 92]

Nonossifying Fibroma

Nonossifying fibroma and fibrous cortical defects share the same tissue appearance and differ only in size, the

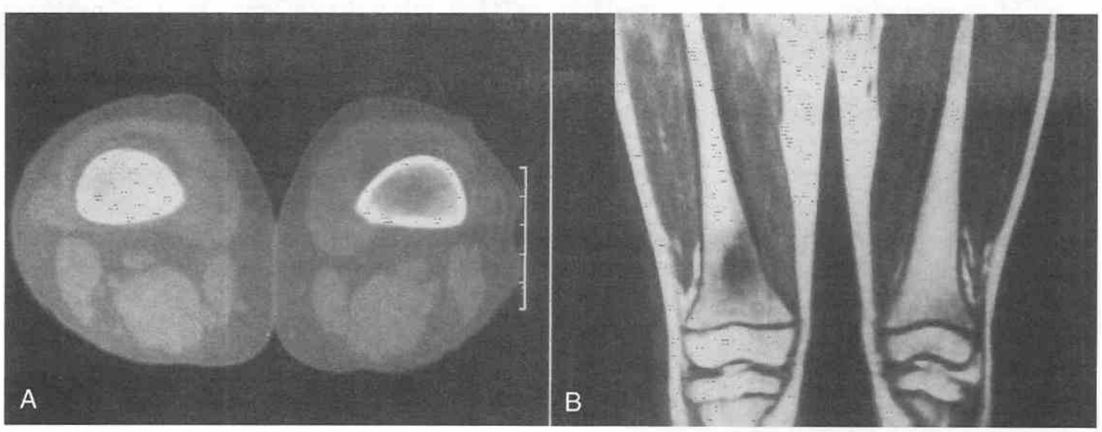

Figure 46–2. Intramedullary osteoid osteoma in a 9-year-old girl with knee pain. *A*, CT scan reveals an area (nidus) of sclerosis with a central lucency in the medullary cavity. *B*, Coronal T1-weighted spin-echo image (TR = 650 msec, TE = 20 msec) demonstrates an area of decreased signal intensity corresponding to the sclerosis seen in *A*; the nidus shows intermediate signal intensity.

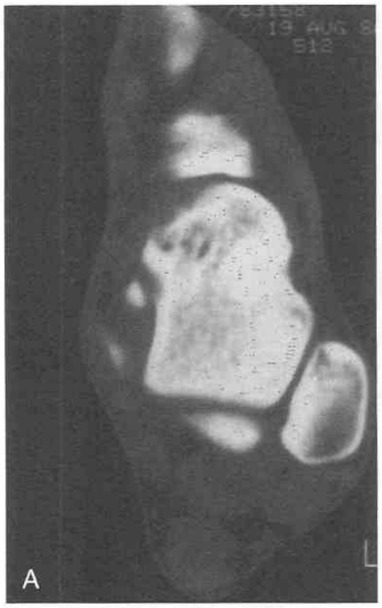

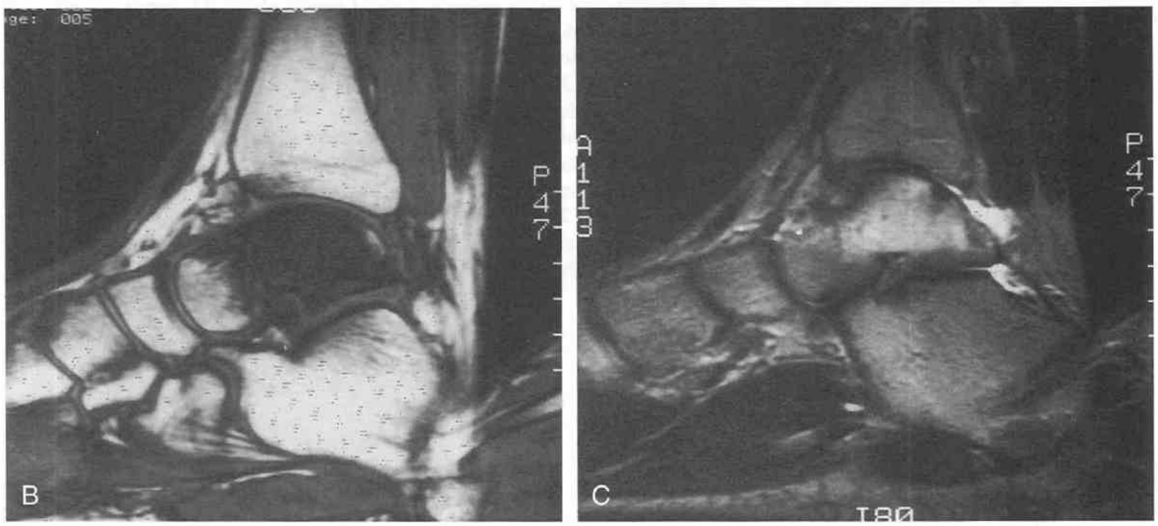

Figure 46–3. Osteoid osteoma. *A*, CT scan demonstrates an area (nidus) of sclerosis with a central lucency in the talus. Calcifications are present in the center of the nidus. *B*, Sagittal T1-weighted image shows decreased signal intensity in most of the talus, resulting from bone marrow edema. *C*, Sagittal T2-weighted image demonstrates high signal intensity in the bone marrow as a result of edema. The nidus also shows increased signal and is surrounded by a rim of low signal intensity that corresponds to the sclerosis seen in *A*.

fibrous cortical defects being smaller. They are sometimes called *fibroxanthomas* because they contain spindle-shaped fibroblasts and xanthoma (foam) cells. They are the most common benign lesion of bone and have been reported in 30% of normal children. Most of these non-neoplastic developmental aberrations are asymptomatic and disappear spontaneously. The male-to-female ratio is 1.5:1, and the peak incidence occurs around 10 years of age.

Nonossifying fibromas and fibrous cortical defects are usually localized to the metaphysis of a long bone and are most commonly found about the knee (distal femur and proximal tibia). They are uncommon in the upper extremities. Their radiographic appearance is often pathognomonic, and no additional studies are usually necessary. They are frequently seen as an incidental finding on MRI examinations of the knee and can have a varied MRI appearance (Fig. 46–4).

In the early stages, when the lesion is completely lytic on plain radiographs, it may have high signal intensity on T1-weighted images as a result of an abundance of xanthoma cells containing fat. Linear structures of low signal intensity are often present and represent fibrous septa or osseous pseudosepta. When the lesion starts healing, it has low signal intensity on both T1-weighted and T2-weighted images because of increased fibrous collagen, mineralization, and, possibly, hemosiderin deposits.[47, 84] The lesions are always well defined and are never surrounded by bone marrow edema.[54]

Simple Bone Cyst

The simple bone cyst is a benign cystic lesion of bone of unknown etiology. It arises in the metaphysis of the bone, but with growth it tends to move away from the growth plate toward the diaphysis. It is a common bone lesion, following only nonossifying fibromas and exostoses in prevalence. The male-to-female ratio is 2.5:1. It can be seen in any age group but is very rare before 5 years and after 20 years of age. The most common site is the proximal humerus, followed by the proximal femur. All other locations are rare.

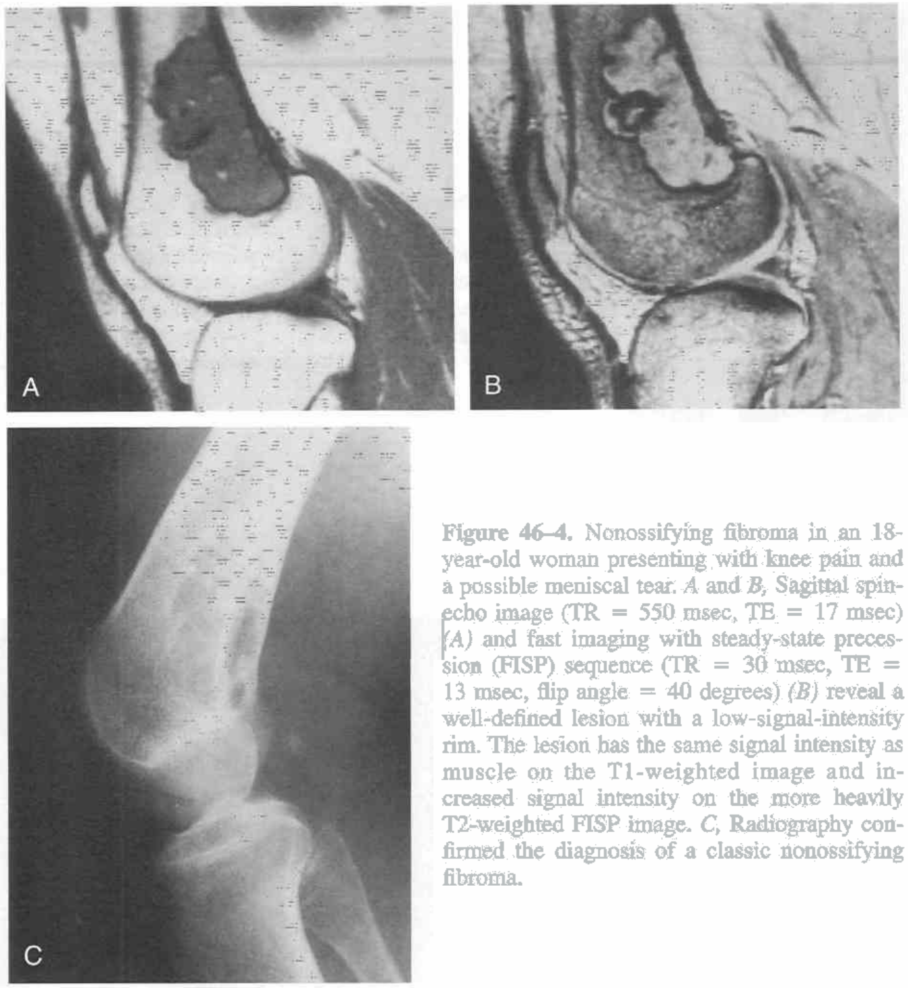

Figure 46–4. Nonossifying fibroma in an 18-year-old woman presenting with knee pain and a possible meniscal tear. *A* and *B*, Sagittal spin-echo image (TR = 550 msec, TE = 17 msec) *(A)* and fast imaging with steady-state precession (FISP) sequence (TR = 30 msec, TE = 13 msec, flip angle = 40 degrees) *(B)* reveal a well-defined lesion with a low-signal-intensity rim. The lesion has the same signal intensity as muscle on the T1-weighted image and increased signal intensity on the more heavily T2-weighted FISP image. *C*, Radiography confirmed the diagnosis of a classic nonossifying fibroma.

Simple cysts are central, lytic, expansile lesions. Their radiographic appearance is usually diagnostic, and neither MRI nor CT is usually necessary. They are well defined and have low signal intensity on T1-weighted images and high signal intensity on T2-weighted images as a result of their fluid content (Fig. 46–5). Typically, they are homogeneous on both T1-weighted and T2-weighted images unless hemorrhage has occurred. Peripheral low-signal-intensity borders represent reactive sclerosis. No edema is present in the surrounding bone marrow or muscle. CT is superior to MRI in detecting subtle infractions of the lesion.

Aneurysmal Bone Cyst

Aneurysmal bone cysts are expansile lytic lesions that contain thin-walled, cystic cavities; their cause is unknown. They can be seen at any age, although 75% are seen in patients younger than 20 years of age and they are rare after 30 years of age. There is a slight female predominance, with a male-to-female ratio of 1:1.5.

Aneurysmal bone cysts can occur in any bone but arise predominantly in the long bones and the spine. In the long bones, they are usually metaphyseal or metadiaphyseal. In the spine, they involve the posterior elements and may extend into the body, but involvement of the vertebral body alone is rare.

On CT scans, the cyst appears as an expansile lesion with a thin cortical shell (Fig. 46–6). Fluid-fluid levels may be seen and are thought to represent sedimentation of degraded blood cell products within the cystic cavity.[45] Fluid-fluid levels are best visualized if the patient is immobilized for some time before scanning. Fluid-fluid levels are a nonspecific finding and have also been described in giant cell tumors, chondroblastoma, and telangiectatic osteosarcomas.[100]

On both T1-weighted and T2-weighted MR images, an aneurysmal bone cyst appears as a well-defined, expansile mass with multiple internal septations, surrounded by a well-defined, low-signal-intensity rim of variable thickness.[4, 20, 46, 73, 112] The rim represents a bony shell. Fluid-fluid levels are often seen within well-defined cystic cavities.[46] On T1-weighted images, signal intensity in the cyst may be higher than that of muscle because of intracystic hemorrhage. One cavity may have signal intensity characteristics that are markedly different from those of an adjacent cavity. The different signal characteristics probably reflect intracystic hemorrhage of different ages. Edema may be present in the surrounding muscles. Septations within the lesion enhance after administration of gadolinium diethylenetriamine-penta-acetic acid, or pentetic acid (Gd-DTPA), but the cystic component does not enhance.

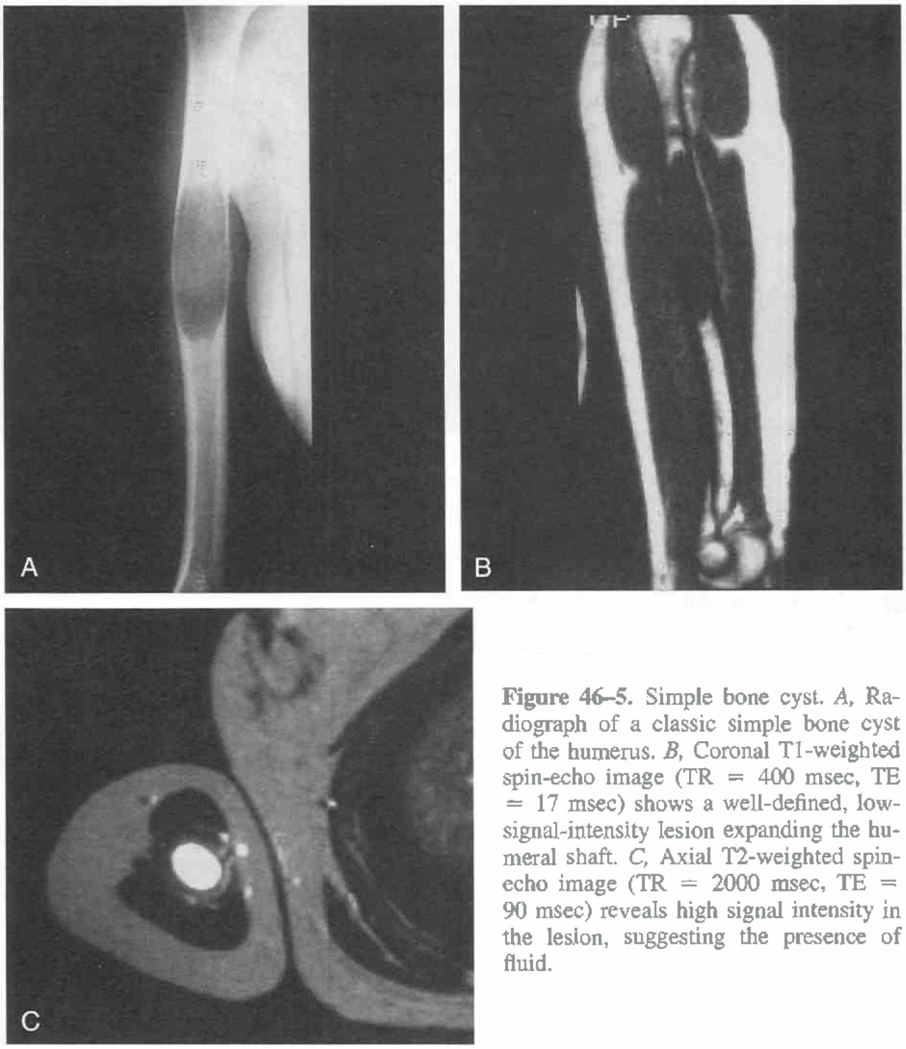

Figure 46–5. Simple bone cyst. *A,* Radiograph of a classic simple bone cyst of the humerus. *B,* Coronal T1-weighted spin-echo image (TR = 400 msec, TE = 17 msec) shows a well-defined, low-signal-intensity lesion expanding the humeral shaft. *C,* Axial T2-weighted spin-echo image (TR = 2000 msec, TE = 90 msec) reveals high signal intensity in the lesion, suggesting the presence of fluid.

Giant Cell Tumor

The giant cell tumor is found relatively frequently, but malignant transformation is rare, occurring in fewer than 10% of lesions. There is a slight female preponderance, and the peak incidence is between 20 and 49 years of age. It is rare before closure of the growth plate or after 50 years of age. This tumor is localized to the metaphysis.

Ninety percent of cases involve the long bones, where the lesion is localized to the metaepiphyseal region. More than 50% of giant cell tumors involve the knee (distal femur and proximal tibia metaepiphyseal region). Other bones that can be affected include, in order of frequency, the distal radius, sacrum, distal tibia, proximal humerus, pelvis, and proximal femur. Other sites are rarely affected.[23]

On CT scans, giant cell tumors appear as lytic lesions with thinning and erosion of the cortex (Fig. 46–7).[26] A sclerotic margin may be present between the tumor and the normal marrow cavity. On MR images, giant cell tumors are well defined with a low-signal-intensity rim or halo surrounding the tumor. On T1-weighted images, they have intermediate signal intensity and are usually homogeneous; on T2-weighted images, they have intermediate to high signal intensity and may be inhomogeneous.[14, 23, 41, 60, 71] Focal areas with increased signal intensity may be seen on both T1-weighted and T2-weighted images and represent hemorrhage. Fluid-fluid levels, often seen in aneurysmal bone cysts and telangiectatic osteosarcomas, are present only rarely in giant cell tumors.[100]

Both CT and MRI accurately demonstrate the intraosseous and soft tissue extension of the tumor; CT is better at showing cortical destruction, whereas MRI is better at demonstrating intra-articular involvement as a result of its multiplanar capability.[98]

Malignant Skeletal Tumors

Multiple Myeloma

Multiple myeloma is a multifocal malignant proliferation of plasma cells and is the most common primary malignant tumor of the skeleton. There is a male predominance, with a male-to-female ratio of 1.5:1. It is common after age 50 years and is rare before age 30 years. Because this neoplasm derives from bone marrow elements, it involves bones containing red marrow: the skull, ribs, sternum, pelvis, proximal humeral metaphysis, and proximal

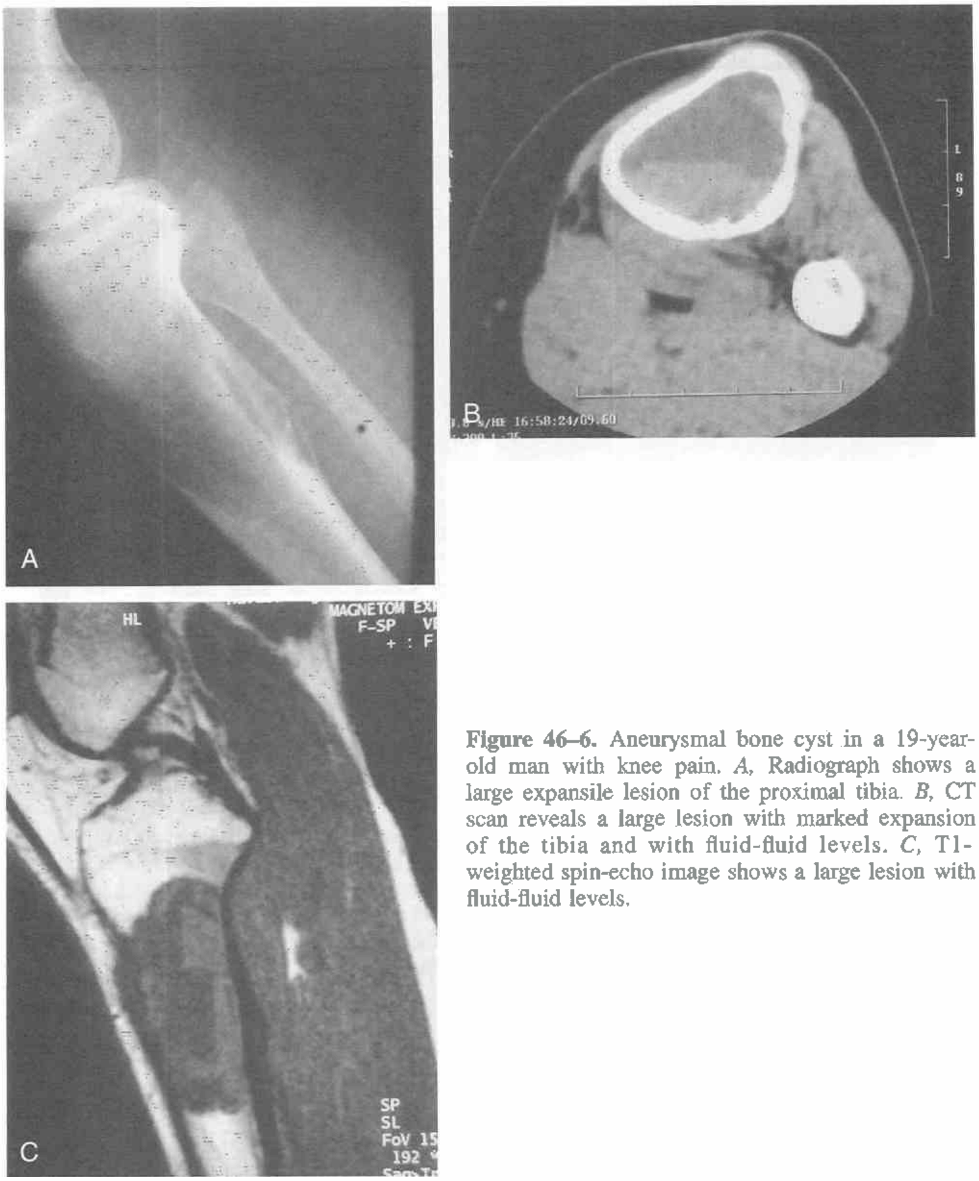

Figure 46–6. Aneurysmal bone cyst in a 19-year-old man with knee pain. *A,* Radiograph shows a large expansile lesion of the proximal tibia. *B,* CT scan reveals a large lesion with marked expansion of the tibia and with fluid-fluid levels. *C,* T1-weighted spin-echo image shows a large lesion with fluid-fluid levels.

femoral metaphysis. At the time of diagnosis, it is often disseminated throughout the red marrow of the axial skeleton.

Infiltration of bone marrow has two forms:

1. In the *diffuse* form, myeloma cells are mixed with hematopoietic cells. This form is difficult to image; the ouly MRI manifestation is an inhomogeneity of the bone marrow signal intensity that is difficult to quantitate and is subjective.[33, 72] CT, plain radiographs, and scintigraphy may result in negative findings.
2. In the *focal* form, normal bone marrow is displaced by nodules composed entirely of myeloma cells. Untreated myelomatous lesions reflect decreased signal intensity on T1-weighted images and increased signal intensity on T2-weighted images when compared with the surrounding bone marrow.[33, 72] CT demonstrates purely osteolytic lesions in the trabecular bone, which occasionally extend to involve the cortex (Fig. 46–8).[89] After irradiation, these lesions show low signal intensity on both T1-weighted and T2-weighted images, and a sclerotic border develops, as seen on CT.

Osteosarcoma

Osteosarcoma is a malignant neoplasm characterized by production of osteoid by the tumor cells. It is the second most common primary malignant tumor of bone after plasmocytoma. It is a rare tumor, representing only 0.2% of all malignant tumors. There is a male predominance, with a male-to-female ratio of 2:1. Its peak incidence is in the second decade, and it is rare before 10 and after 30 years of age.

Osteosarcoma can occur in any bone, but it has a strong predilection for the distal femur, proximal tibia, and proximal humerus. Two thirds of osteosarcomas are localized to the knee or shoulder.

Osteosarcomas can be divided into two categories: (1) *primary* osteosarcomas, which arise de novo, and (2) *secondary* osteosarcomas, which develop in abnormal bones.

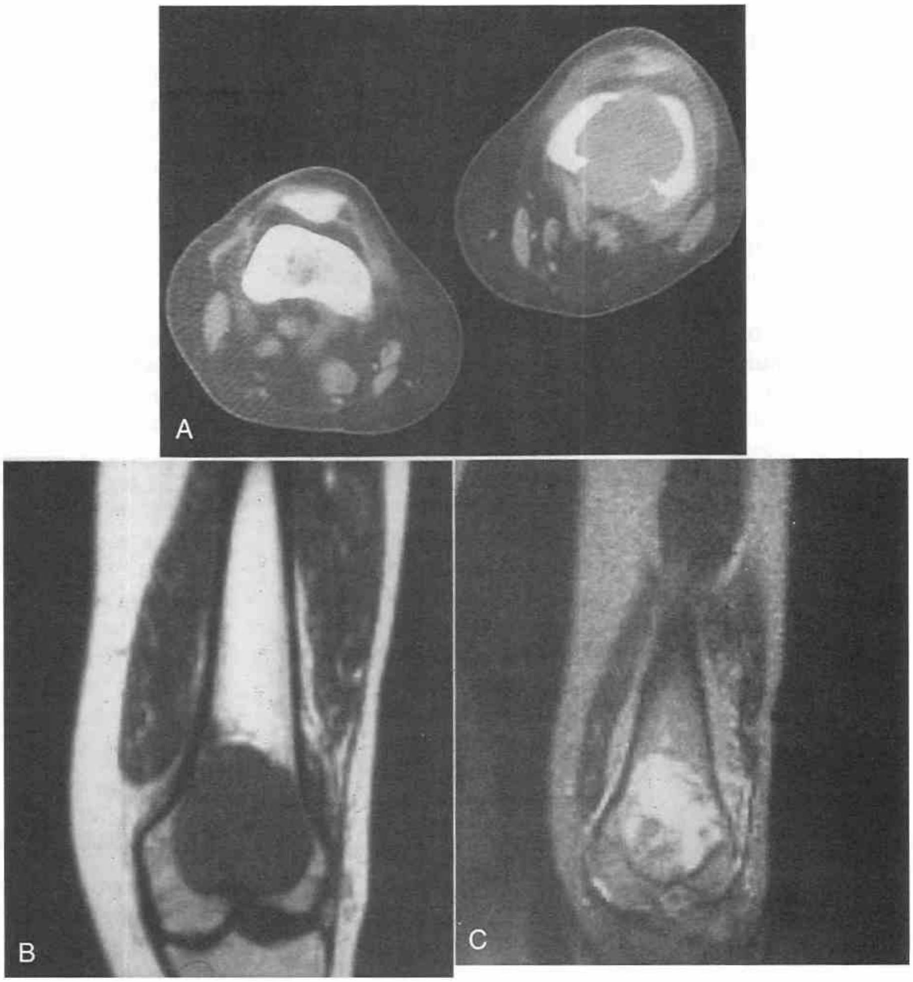

Figure 46–7. Giant cell tumor in a 16-year-old girl with knee pain. *A,* CT scan demonstrates a lytic lesion of the distal femur with marked expansion and thinning of the cortex both anteriorly and posteriorly. *B* and *C,* Coronal MR images show a well-defined lesion. The signal intensity is same as that of muscle on the T1-weighted, spin-echo image (TR = 600 msec, TE = 17 msec) *(B)* and higher than that of muscle on the T2-weighted, spin-echo image (TR = 2500 msec, TE = 90 msec) *(C).*

Underlying bone abnormalities include Paget's disease, complications of radiation therapy, multiple enchondromas, multiple osteochondromas, chronic osteomyelitis, fibrous dysplasia, or infarct. Secondary osteosarcomas, rather than primary osteosarcomas, usually affect older people.

MRI is useful for staging the tumor and for follow-up after treatment.[13, 31, 35, 75, 82, 90, 91, 113] The osteoblastic component of the tumor has low signal intensity on all sequences. The nonmineralized component has low signal intensity on T1-weighted images and high signal intensity on T2-weighted images. Bone marrow extension is best seen on T1-weighted images, where the loss of the high signal intensity of normal bone marrow can be appreciated. Soft tissue extension is best seen on T2-weighted images,

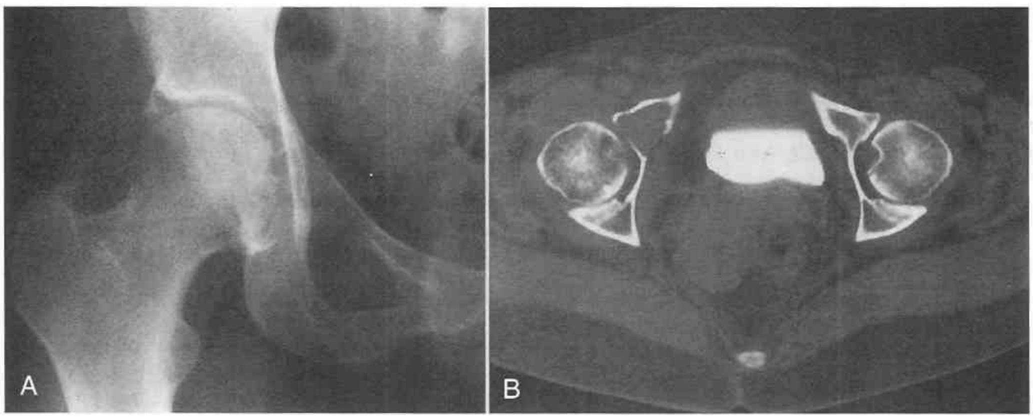

Figure 46–8. Multiple myeloma. *A,* Radiograph of the right hip demonstrates a lytic lesion of the superior pubic ramus. *B,* CT scan confirms the presence of a lytic lesion with destruction of the cortex posteriorly. No sclerotic borders are seen.

whereas tumor and muscle may have the same signal intensity on T1-weighted images. CT is better than MRI in demonstrating matrix mineralization but is less accurate in detecting skip lesions and bone marrow and soft tissue extension (Fig. 46–9).

Telangiectatic osteosarcomas contain large, cystic, blood-filled spaces with fluid-fluid levels that may mimic an aneurysmal bone cyst, but these tumors are usually less well defined than aneurysmal bone cysts.[100]

In the last two decades, the development of aggressive chemotherapy has significantly improved the survival of patients with osteosarcoma, and imaging studies are being used to evaluate the tumor's response to treatment. CT findings of a positive response to treatment include (1) marked decrease in size or complete disappearance of the soft tissue mass, (2) increased calcification of the mass, (3) improved delineation of the margins, and (4) formation of a peripheral rim of calcification.[67, 93]

Decreased signal intensity of the nonmineralized mass on T2-weighted MR images is thought to represent fibrosis or sclerosis of the tumor. Persistent high signal intensity may be a result of either nonresponding tumor or necrotic tumor, reactive granulation tissue, or hemorrhage.[31, 38, 63] Administration of gadolinium cannot help distinguish viable tumor from reactive inflammation, since both enhance, but a lack of enhancement indicates tumor necrosis.[91]

Chondrosarcoma

Chondrosarcoma is a malignant chondroid tumor. It is the fourth most common primary malignant bone tumor, after plasmocytoma, osteosarcoma, and Ewing's sarcoma. Its peak incidence is between 30 and 60 years of age.

According to their intraosseous location, chondrosarcomas may be divided into *central* and *peripheral* lesions. Most chondrosarcomas (~75%) are primary and arise de novo, but the remaining 25% are secondary and develop from malignant transformation of a benign lesion, such as an enchondroma or an osteochondroma (rarely a chondroblastoma). Central chondrosarcomas occur both in tubular bones (e.g., femur, proximal humerus, proximal tibia) and in flat bones (e.g., pelvis). Peripheral chondrosarcomas most commonly arise in flat bones (e.g., pelvis, ribs) and in the spine.

It is difficult to differentiate low-grade chondrosarcomas from benign chondroid lesions; however, the presence of pain in the absence of fracture and cortical destruction and the presence of a soft tissue mass are all signs suggestive of malignancy.[24, 74] On MR images, chondrosarcoma has a characteristic multilobular configuration. The lobules of hyaline cartilage have intermediate signal intensity, similar to that of muscle on T1-weighted images (Fig. 46–10), and homogeneous high signal intensity on T2-weighted images.[18, 38, 63, 104] The fibrous septa have low signal intensity on both T1-weighted and T2-weighted images, but they enhance after Gd-DTPA administration.[2, 35] Calcifications are common in low-grade chondrosarcoma and are best seen by conventional radiography and CT. Endosteal scalloping is also best depicted with CT and plain radiography.

Ewing's Sarcoma

Ewing's sarcoma is a malignant neoplasm that is probably of neuroectodermal origin. Among primary malignant neoplasms of bone, it follows plasmocytoma, osteosarcoma, and chondrosarcoma in frequency. There is a male predominance, with a male-to-female ratio of 2:1. Its peak incidence is in the second decade, with 90% of cases occurring between 5 and 25 years of age.

Ewing's sarcoma may involve any bone but has a predilection for the long bones and pelvis. In the long bones, it is localized to the diaphysis or metaphysis, and until the growth plate is open, it does not extend to the epiphysis.

MRI facilitates staging of Ewing's sarcoma and is better than CT for demonstrating bone marrow and soft tissue involvement.[37] MRI signal intensity characteristics of Ewing's sarcoma are not specific and are similar to those of other malignant neoplasms.[13, 31, 39] The tumor's signal intensity is lower than or equal to that of muscle on T1-weighted images and is higher on T2-weighted images (Fig. 46–11).

MRI and CT are helpful in evaluating response to treatment. If the tumor is sensitive to treatment, it decreases in size, the periosteal reaction matures, and the bone becomes sclerotic.[31, 42, 61] High signal intensity on T2-weighted images after treatment does not always indicate a poor response, since it may represent necrosis, reactive granulation tissue, or hemorrhage. Enhancement after Gd-DTPA does not aid in distinguishing reactive changes from residual tumor, but the lack of enhancement indicates tumor necrosis.[31, 42, 61]

Soft Tissue Tumors

CT has been widely used in detection and staging of soft tissue tumors,[106] but MRI is now the modality of choice in evaluation of these tumors because of its intrinsic high soft tissue contrast.[24, 25, 77, 97, 107] MRI offers improved accuracy in detecting and staging soft tissue masses and is more sensitive than CT in regard to the evaluation of these lesions.

On MR images, benign lesions tend to have well-defined margins, have homogeneous signal intensity, do not encase neurovascular bundles, and are not surrounded by peritumoral edema.[6] Conversely, malignant lesions typically have poorly defined margins, heterogeneous signal intensity, neurovascular bundle encasement, and peritumoral edema.[7, 8] Unfortunately, a large overlap exists between benign and malignant lesions, and the ability of MRI to differentiate benign from malignant soft tissue masses remains controversial.[22, 55]

Benign Soft Tissue Tumors

Lipoma

A lipoma is a benign tumor composed of mature adipose tissue. It is the most frequently occurring benign soft tissue tumor and is often asymptomatic. Superficial lipomas predominate in women, whereas deep lipomas are more common in men. The peak incidence of lipomas occurs between 40 and 60 years of age.

Superficial lipomas are usually localized to the subcutaneous tissue of the trunk and proximal extremities. Deep lipomas are usually in the retroperitoneum, chest wall, and deep soft tissue of the hands and feet.

Figure 46–9. Osteosarcoma in the femur of a 14-year-old boy. Radiograph *(A)* demonstrates a sclerotic lesion in the metaphysis, with medial destruction of the cortex and periosteal reaction. CT images using soft tissue window settings *(B)* and CT images using bone window settings *(C)* reveal a sclerotic lesion of the medial aspect of the femur with an associated soft tissue mass and a periosteal reaction. Four MR images were obtained: two axial spin-echo views (TR = 500 msec, TE = 15 msec) *(D)* and (TR = 2000 msec, TE = 70 msec) *(E)* and two coronal spin-echo views (TR = 600 msec, TE = 15 msec) *(F)* and (TR = 2000 msec, TE = 70 msec) *(G)*. The soft tissue component can be more easily visualized with MRI than with CT, but the periosteal reaction and soft tissue calcification are not as evident. An area of low signal intensity is present on both T1-weighted and T2-weighted images; it corresponds to the area of sclerosis seen on the CT scans.

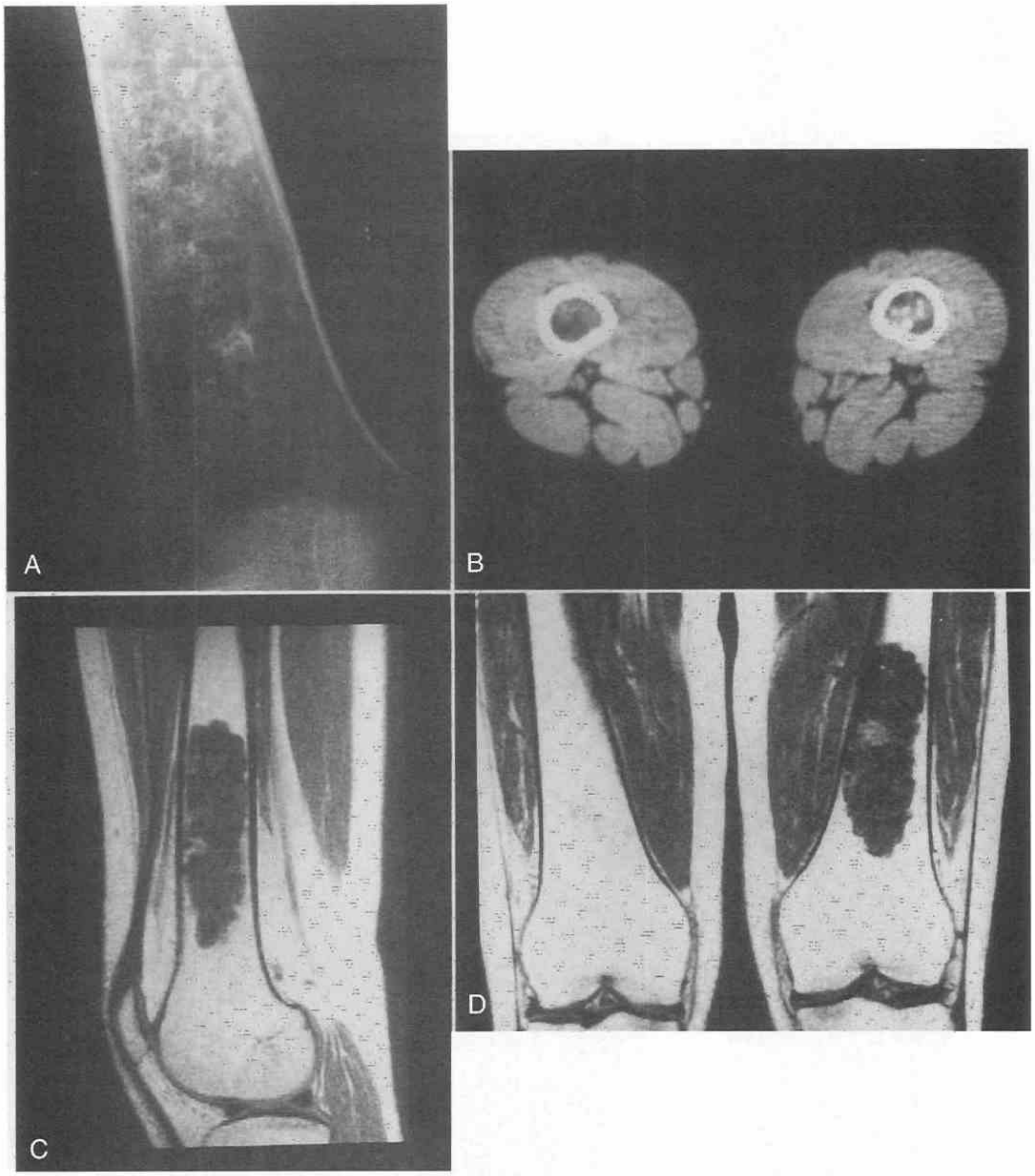

Figure 46–10. **Primary grade I chondrosarcoma in a 36-year-old woman.** *A,* Radiograph of the knee demonstrates a lesion with a cartilaginous matrix in the distal femur. *B,* CT scan shows the calcifications in the matrix of the lesion. *C* and *D,* Sagittal *(C)* and coronal *(D)* spin-echo images (TR = 500 msec, TE = 17 msec) demonstrate a lobulated lesion in the medullary cavity. The exact extension of the lesion is easily appreciated, but the matrix calcifications are poorly seen.

On CT scans, lipomas have a low attenuation coefficient, equal to that of subcutaneous fat, and they do not enhance after administration of contrast material. On MR images, they have the same signal intensity characteristics as subcutaneous fat on all imaging sequences (Fig. 46–12). On both CT and MR images, lipomas have a homogeneous appearance, although occasional thin fibrous septa can be present.[16, 57]

Vascular Anomalies

Vascular anomalies include hemangiomas, venous malformations, arteriovenous malformations, arteriovenous fistulas, and mixed lesions. The term *hemangioma* has also been used generically to describe all of these vascular anomalies.[51] Vascular anomalies are more common in females. They are usually congenital except for post-traumatic arteriovenous fistulas.

On MR images, hemangiomas have similar signal intensity as muscle with T1 weighting and high signal intensity with T2 weighting. The signal is usually heterogeneous with T2 weighting and may be either homogeneous or inhomogeneous with T1 weighting and may contain variable amounts of fat and vessels within the mass.[111]

Phleboliths are seen as focal areas of low signal intensity on all imaging sequences, but they are better identified on plain radiographs or CT scans (Fig. 46–13). Serpiginous areas of low signal intensity are occasionally seen and represent flow void in larger feeding arteries or draining veins.

On MR images, arteriovenous malformations and arte-

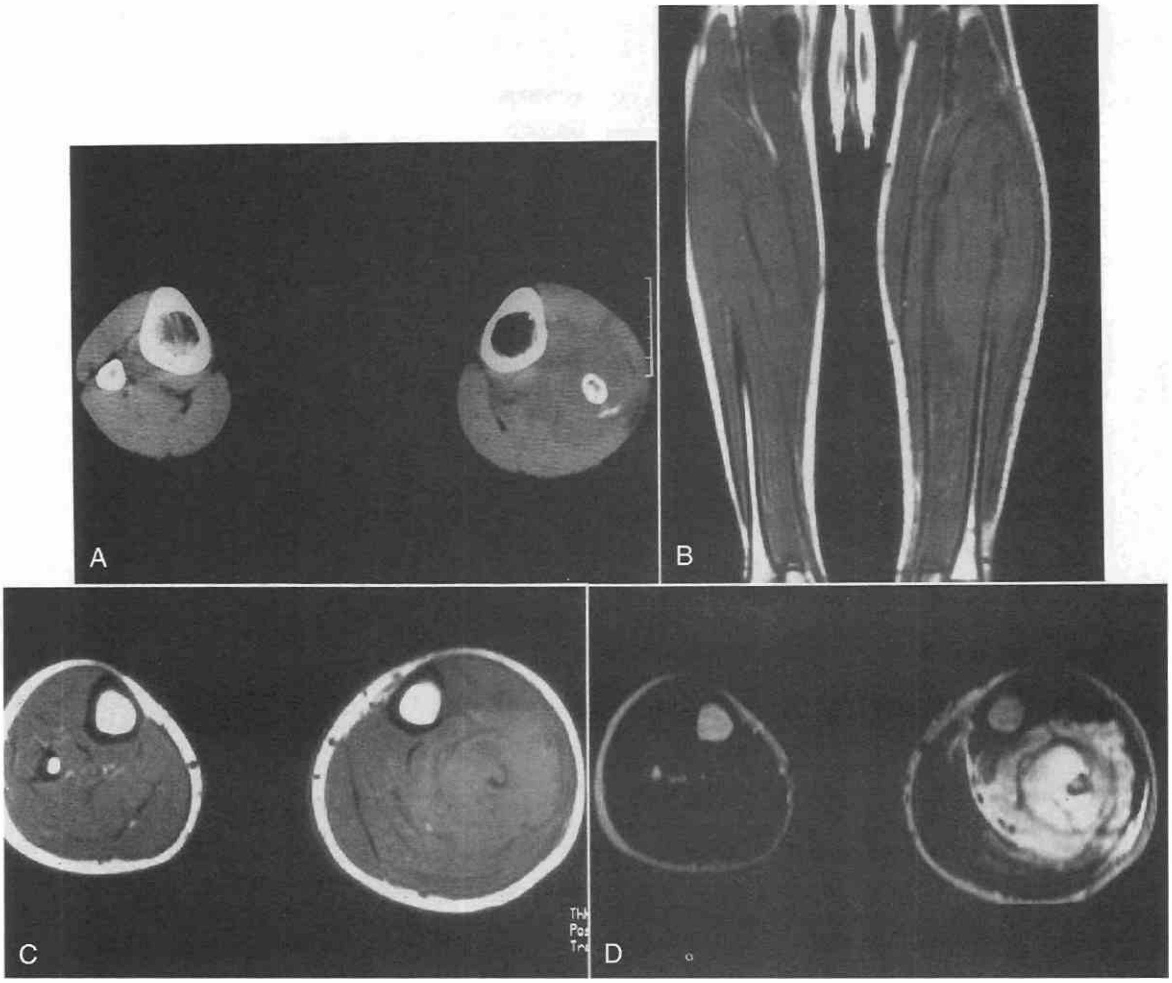

Figure 46–11. Ewing's sarcoma. *A,* CT scan reveals a large mass surrounding the left tibia. The mass reflects a density slightly lower than that of muscle. *B* and *C,* Coronal T1-weighted spin-echo image (TR = 700 msec, TE = 15 msec) *(B)* and axial T1-weighted spin-echo image (TR = 800 msec, TE = 15 msec) *(C)* demonstrate a large mass surrounding the fibula. This mass shows a signal intensity similar to that of muscle on the T1-weighted images in *B* and *C* and high signal intensity on an axial T2-weighted image (TR = 2500 msec, TE = 80 msec) *(D).*

riovenous fistulas have large tortuous vessels with flow void due to rapidly flowing blood. Feeding and draining vessels can be identified as vascular structures, but differentiation of veins and arteries is not always possible.[19, 69, 80]

Desmoid Tumor

A desmoid tumor is composed of fibroblasts. Histologically, the tumor is benign and does not metastasize, but it is locally aggressive, infiltrates contiguous structures, and tends to recur after resection. Desmoid tumors may occur at any age, but most often they are seen in the third and fourth decades.

On cross-sectional imaging, desmoids have well-defined borders two thirds of the time, but the rest of the time the margins are infiltrative and poorly defined. CT scans obtained without contrast enhancement show variable attenuation relative to muscle. After IV contrast administration, desmoid tumors may or may not enhance. Most are hyperdense or isodense with muscle on contrast-enhanced scans.

Desmoid tumors have a signal intensity lower than that of muscle on T1-weighted MR images, with variable signal intensity on T2-weighted images (Fig. 46–14).[101] They may have an aggressive appearance and be confused with a malignant tumor.[8, 21] The presence of areas of low signal intensity on both T1-weighted and T2-weighted images, resulting from fibrous tissue, is a clue to the correct diagnosis.[17, 29]

Intramuscular Myxoma

Intramuscular myxoma is a rare benign tumor that contains myxoid tissue. It occurs in older people between 40 and 70 years of age. Usually, it is solitary and has a slow growth rate. Multiple myxomas have been seen in patients with fibrous dysplasias. The tumor is usually localized in a large muscle of the thigh, shoulder, or hip.

The CT appearance is a well-defined, homogeneous mass with a density lower than that of muscle. The mass typically does not enhance after administration of contrast material. It has low signal intensity on T1-weighted MR images and high signal intensity on T2-weighted images.[99]

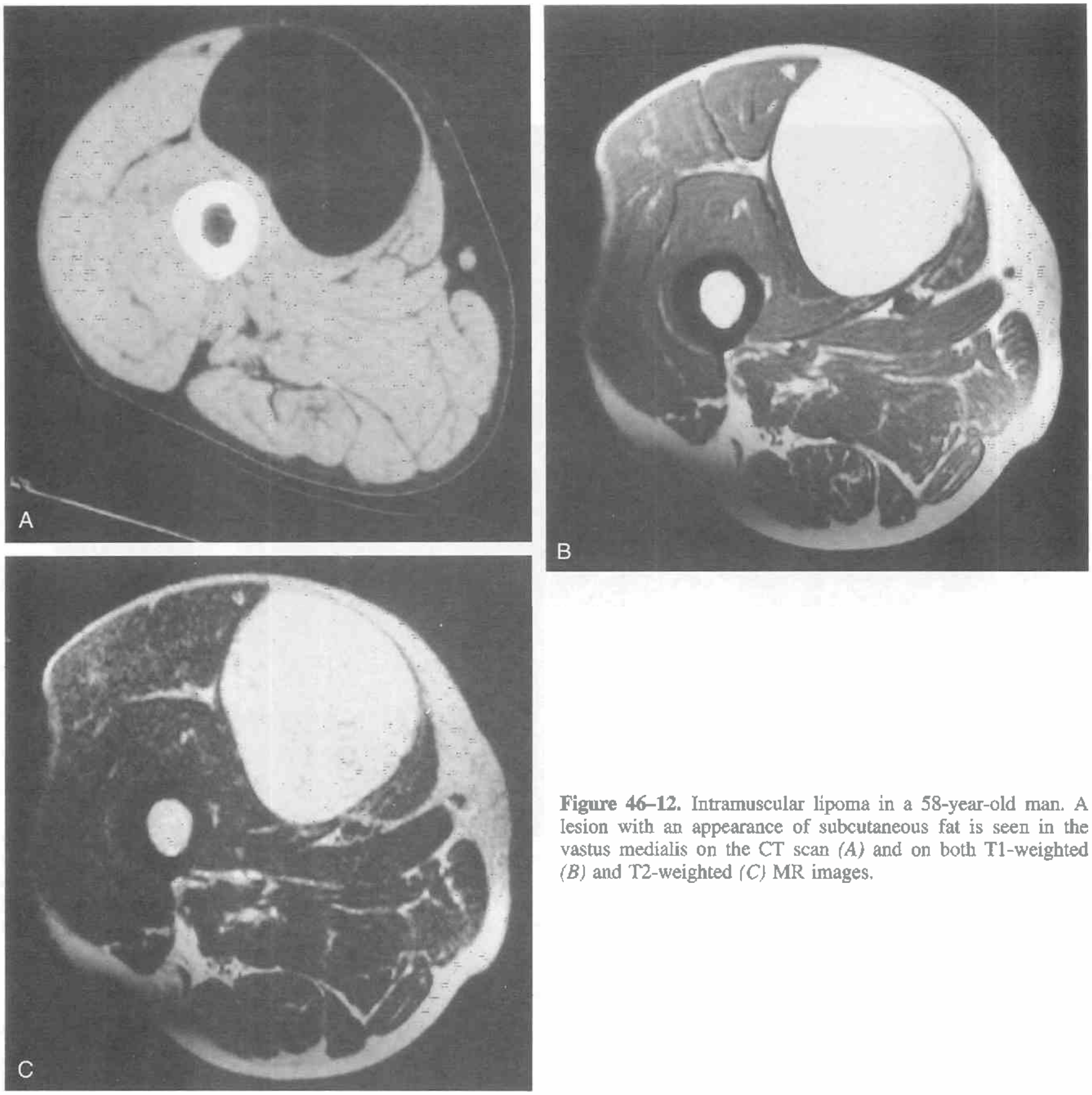

Figure 46–12. Intramuscular lipoma in a 58-year-old man. A lesion with an appearance of subcutaneous fat is seen in the vastus medialis on the CT scan *(A)* and on both T1-weighted *(B)* and T2-weighted *(C)* MR images.

Pigmented Villonodular Synovitis

Pigmented villonodular synovitis is a benign proliferative process of the synovial lining of a joint, bursa, or tendon sheath. The cause of this lesion is unknown. Repeated trauma, repeated intra-articular hemorrhage, and inflammation have been suggested.

There are two forms. The *focal* form (also called giant cell tumor of the tendon sheath) is more common and usually involves the tendon sheaths of the hands. The *diffuse* form involves large joints, especially the knee. There is no sex predilection. The peak incidence is between 20 and 40 years of age.

MRI characteristics are typical and often lead to the correct diagnosis. As a result of the deposition of hemosiderin within the tumor, the lesion has areas of low signal intensity on both T1-weighted and T2-weighted images (Fig. 46–15).[49, 53] The presence of bone erosion on both sides of the joint also suggests the diagnosis. Joint effusion may be present.

On CT scans, bone erosions have well-defined sclerotic borders. On non–contrast-enhanced scans, the soft tissue component may contain areas of high attenuation; these correspond to deposits of hemosiderin.[86]

Malignant Soft Tissue Sarcoma

Liposarcoma

A liposarcoma is a malignant soft tissue neoplasm that contains cells with lipoblastic or lipocytic differentiation.

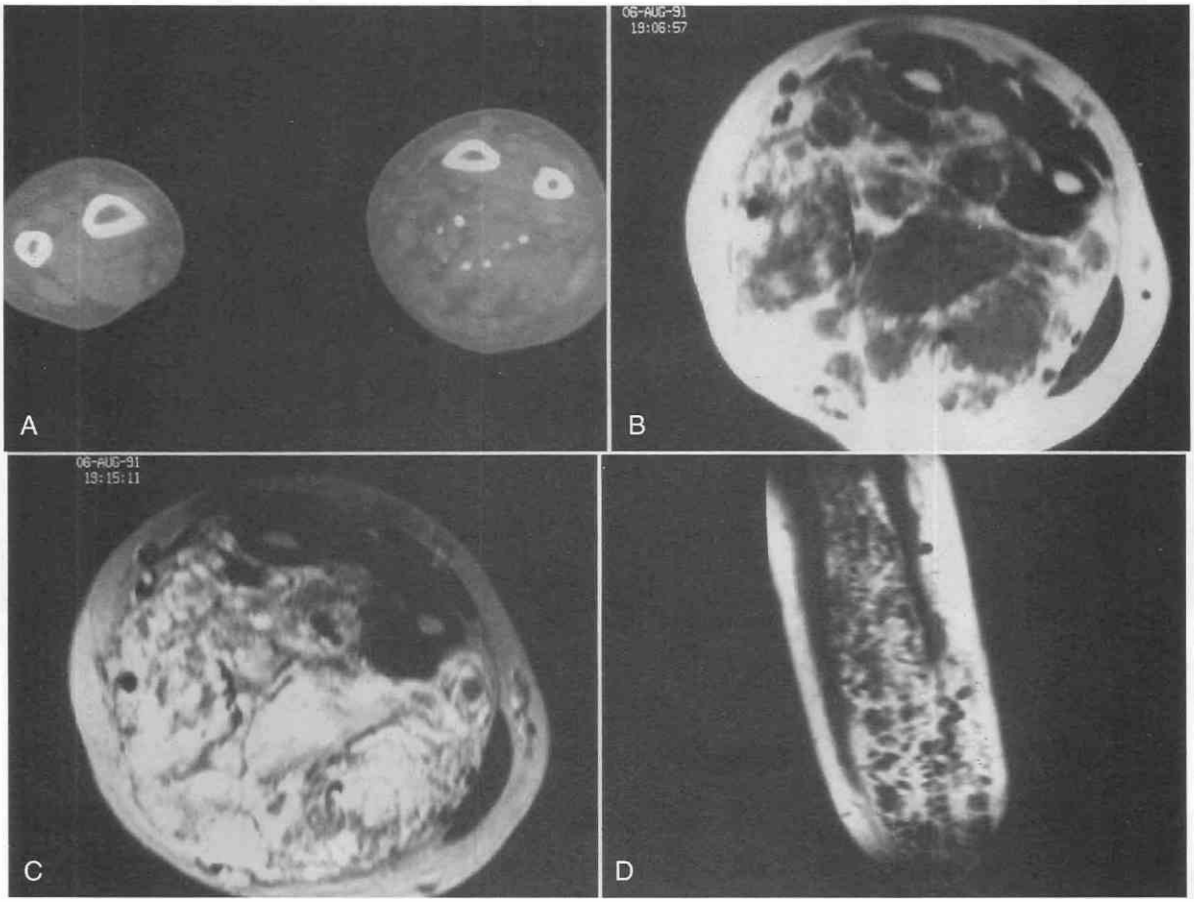

Figure 46–13. Hemangioma. *A,* CT scan shows multiple phleboliths in the forearm within a soft tissue mass. *B,* T1-weighted image shows the lesion to be isointense with muscle; an area that shows increased signal intensity corresponds to fat interposed between vascular elements. *C,* T2-weighted image shows vascular elements of high signal intensity. *D,* Coronal T1-weighted image shows large tortuous vessels with flow void caused by rapidly flowing blood.

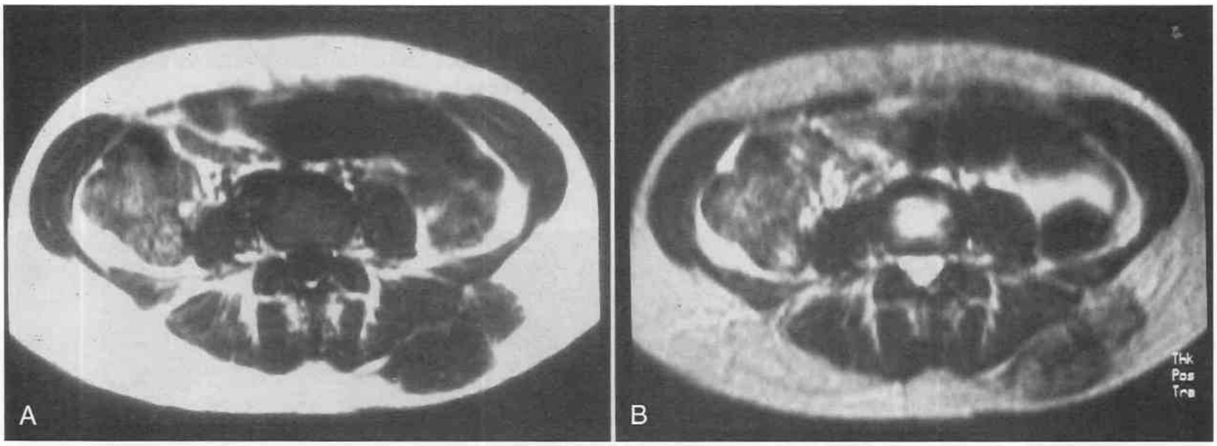

Figure 46–14. Desmoid tumor. Axial spin-echo images, T1-weighted axial spin echo *(A)* (TR = 540 msec, TE = 15 msec) and T2-weighted axial spin echo *(B)* (TR = 2000 msec, TE = 80 msec) demonstrate a lesion in the subcutaneous tissues of the back. The T1-weighted image *(A)* shows low signal intensity; the T2-weighted image *(B)* shows intermediate signal intensity and an area of low signal intensity. The low signal intensity seen on each sequence suggests fibrous tissue and aids in the diagnosis.

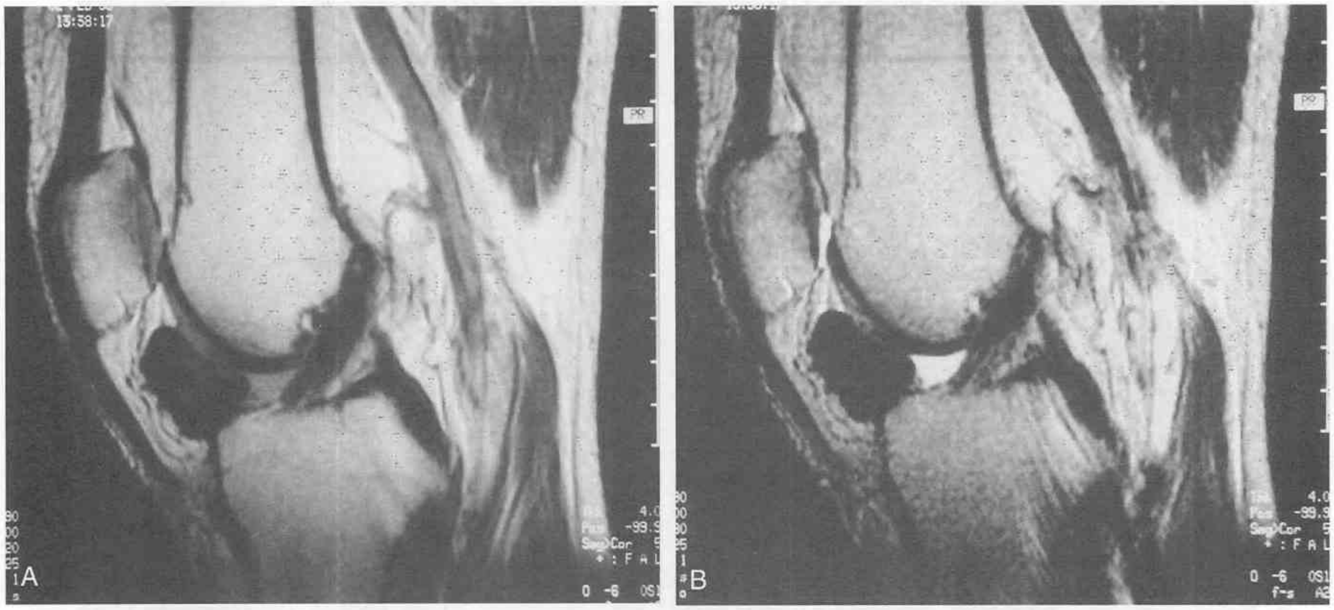

Figure 46–15. Pigm[redacted]ed v[redacted]odul[redacted]itis. Sag[redacted] spi[redacted]mages *(A)* (TR =[redacted]00 msec[redacted] 20 mse[redacted]TR = 2300 msec, TE = 80 msec) demonstrate a large, low-signal-intensity mass inferior to the patella in the Hoffa fat pad. Low signal intensity is the result of hemosiderin deposits in the tumor.

Figure 46–16. Low-grade liposarcoma. *A* and *B,* Coronal spin-echo image *(A)* (TR = 800 msec, TE = 17 msec) and axial spin-echo image *(B)* (TR = 800 msec, TE = 17 msec) demonstrate a large mass in the medial compartment of the thigh. A large part of the lesion shows the same signal intensity as fat; in some areas, however, the signal intensity is similar to that of muscle, making it possible to distinguish this lesion from a benign lipoma. *C,* Axial T2-weighted, spin-echo image (TR = 2500 msec, TE = 90 msec) shows the nonlipomatous portions of the tumor with a signal intensity higher than that of fat.

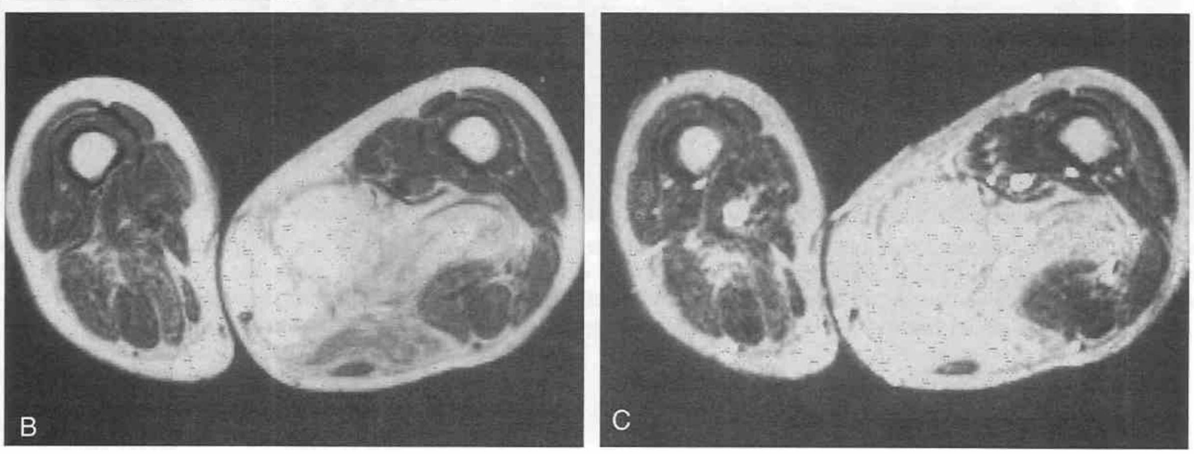

It is the second most common malignant soft tissue tumor after malignant fibrous histiocytoma. Its peak incidence is between 50 and 60 years of age, and it is rare before 20 years of age. Liposarcomas are most common in the extremities, especially the thigh, and in the retroperitoneum.

Liposarcomas can be divided into four groups on the basis of their histologic characteristics: (1) well-differentiated (2) myxoid, (3) round cell, and (4) pleomorphic.

The CT or MRI appearance depends on the degree of differentiation.[50, 57] The portions of the tumor that contain fat demonstrate a low attenuation coefficient on CT scans and have high signal intensity on T1-weighted MR images. The nonlipomatous portions of the tumor have a higher attenuation coefficient than fat on CT scans; their signal intensity is similar to that of muscle on T1-weighted MR images (Fig. 46–16) and is higher than that of fat on T2-weighted images.[64]

A well-differentiated liposarcoma and an atypical lipoma can share the same characteristics on both CT and MRI, making differentiation between these two entities difficult.[16] More aggressive liposarcomas may contain no fat that is detectable by either CT or MRI (Fig. 46–17). In these cases, the appearance of the tumor is indistinguishable from that of other malignant soft tissue tumors.

Malignant Fibrous Histiocytoma

Malignant fibrous histiocytoma is a tumor that develops from a primitive mesenchymal cell; it has markers of histiocytoid differentiation. It is the most common malignant neoplasm of soft tissues. It is seen more often in men, with a peak incidence between 50 and 70 years of age. Fifty percent are localized in the lower extremities, 20% in the upper extremities, and 20% in the abdominal cavity and retroperitoneum. Other locations are rare.

On MR images, malignant fibrous histiocytoma has low signal intensity with T1 weighting and heterogeneous high signal intensity with T2 weighting (Fig. 46–18)[27, 66] On CT scans, its density is the same as that of muscle and it frequently contains areas of lower attenuation that correspond to areas of necrosis.[85] MRI is better than CT in determining extent of tumor, but CT is superior in detecting bone involvement and calcifications within the tumor. Calcifications have been seen in up to 20% of malignant fibrous histiocytomas.[27]

Synovial Sarcoma

Synovial sarcoma is a malignant soft tissue tumor that develops from undifferentiated mesenchymal cells. It is relatively common, following malignant fibrous histiocytoma, liposarcoma, and rhabdomyosarcoma in prevalence. There is a slight male predilection and a peak incidence between 15 and 35 years of age.

Only 10% of synovial cell sarcomas are within a joint. Usually they are located adherent to a joint capsule, bursa, fascia, or tendon sheath. They are most common in the lower extremity.

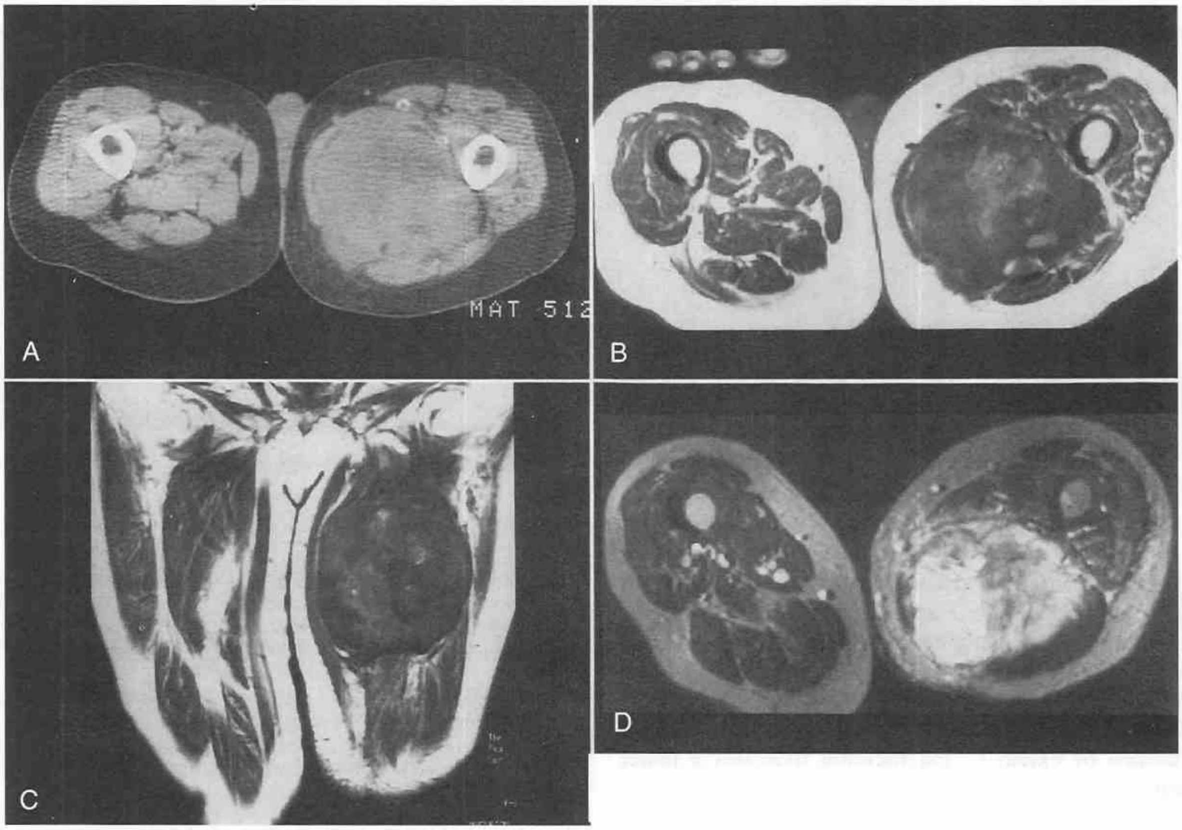

Figure 46–17. [redacted] liposarcoma. *A,* CT scan shows a large mass with heterogeneous density, suggesting that portions of this mass are necrotic, but fat density is not identified. *B* and *C,* Axial *(B)* and coronal *(C)* spin-echo images (TR = 600 msec, TE = 15 msec) show a large mass with heterogeneous signal; small foci with higher signal intensity may represent hemorrhage or fat within the tumor.

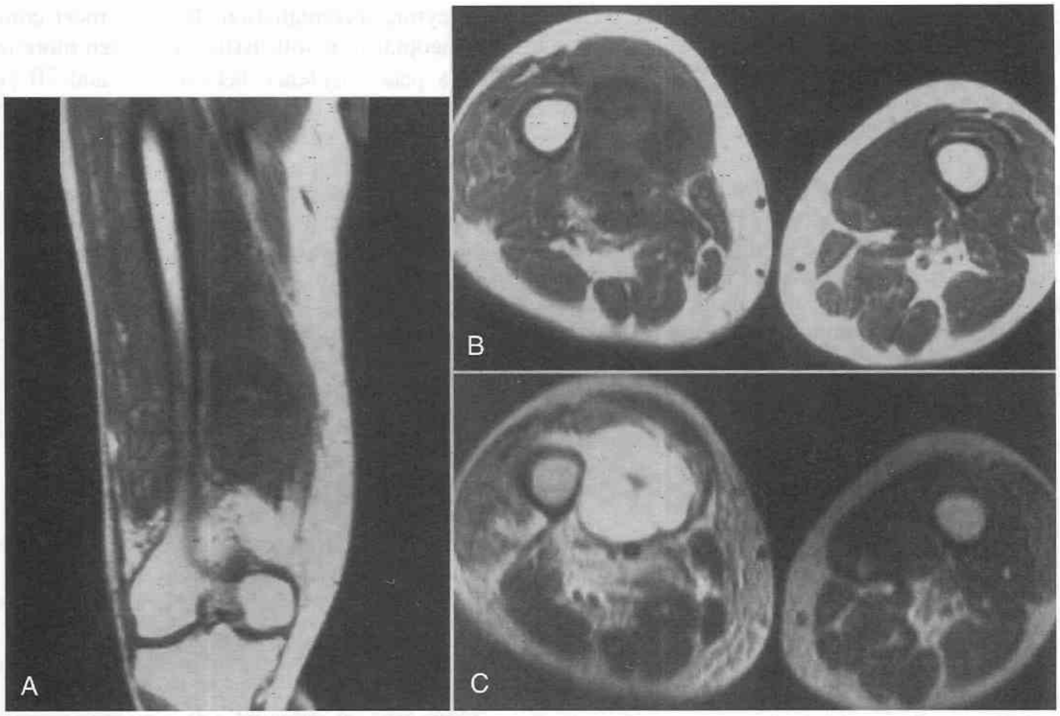

Figure 46–18. [redacted]t fibrous histiocytoma in [redacted]al compartment of the thigh. *A* and *B*, [redacted]ghte[redacted]n-echo image (TR = 600 msec, TE = 15 msec) *(A)* and axial T1-weighted spin-echo image (TR = 700 msec, TE = 15 msec) *(B)* reveal a large mass reflecting low signal intensity. *C*, Axial T2-weighted spin-echo image (TR = 2500 msec, TE = 80 msec) demonstrates that the mass has heterogeneous high signal intensity.

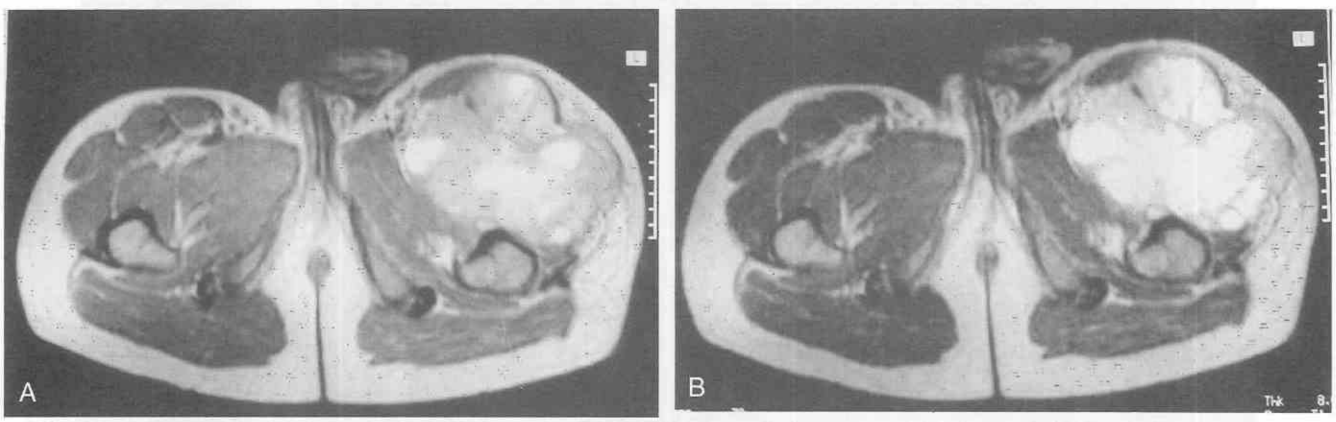

Figure 46–19. Synovial sarcoma. *A*, Axial proton-density image reveals intermediate to high signal intensity. *B*, Axial T2-weighted image reflects heterogeneous high signal intensity.

Synovial sarcoma has low to intermediate signal intensity on T1-weighted MR images and heterogeneous high signal intensity on T2-weighted images.[65, 70] This tumor is often multilocular with internal septation, and occasionally fluid-fluid levels are seen (Fig. 46–19).[100] Calcifications are present in 30% of the cases and are best seen on CT scans.[3] The presence of extensive calcification indicates a better prognosis.[103]

References

1. Aisen AM, Martel W, Braunstein EM, et al: MRI and CT evaluation of primary bone and soft tissue tumors. Am J Roentgenol 146: 749, 1986.
2. Aoki J, Sone S, Fujioka F, et al: MR of enchondroma and chondrosarcoma: Rings and arcs of Gd-DTPA enhancement. J Comput Assist Tomogr 15:1011, 1991.
3. Azouz EM, Vickar DB, Brown KLB: Computed tomography of the foot. J Can Assoc Radiol 34:85, 1984.
4. Beltran J, Simon DC, Levy M, et al: Aneurysmal bone cysts: MR imaging at 1.5 T. Radiology 158:689, 1986.
5. Beltran J, Noto AM, Chakeres DW, Christoforidis AJ: Tumors of the osseous spine: Staging with MR imaging versus CT. Radiology 162:565, 1987.
6. Beltran J, Simon DC, Katz W, Weis LD: Increased MR signal intensity in skeletal muscle adjacent to malignant tumors: Pathologic correlation and clinical relevance. Radiology 162:251, 1987.
7. Berquist TH: Magnetic resonance imaging of musculoskeletal neoplasms. Clin Orthop 244:101, 1989.
8. Berquist TH, Ehman RL, King BF, et al: Value of MR imaging in

differentiating benign from malignant soft-tissue masses: Study of 95 lesions. AJR Am J Roentgenol 155:1251, 1990.
9. Bloem JL, Falke TH, Taminiau AH, et al: Magnetic resonance imaging of primary malignant bone tumors. Radiographics 5:853, 1985.
10. Bloem JL, Bluemm RG, Taminiau AH, et al: Magnetic resonance imaging of primary malignant bone tumors. Radiographics 7:425, 1987.
11. Bloem JL, Taminiau AH, Eulderink F, et al: Radiologic staging of primary bone sarcoma: MR imaging, scintigraphy, angiography, and CT correlated with pathologic examination. Radiology 169:805, 1988.
12. Bohndorf K, Reiser M, Lochner B, et al: Magnetic resonance imaging of primary tumours and tumour-like lesions of bone. Skeletal Radiol 15:511, 1986.
13. Boyko OB, Cory DA, Cohen MD, et al: MR imaging of osteogenic and Ewing's sarcoma. AJR Am J Roentgenol 148:317, 1987.
14. Brady TJ, Gebhardt MC, Pykett IL, et al: NMR imaging of forearms in healthy volunteers and patients with giant-cell tumor of bone. Radiology 144:549, 1982.
15. Brower AC, Moser RP, Kransdorf MJ: The frequency and diagnostic significance of periostitis in chondroblastoma. AJR Am J Roentgenol 154:309, 1990.
16. Bush CH, Spanier SS, Gillespy T: Imaging of atypical lipomas of the extremities: A report of three cases. Skeletal Radiol 17: 472, 1988.
17. Casillas J, Sais GJ, Greve JL, et al: Imaging of intra- and extra-abdominal desmoid tumors. Radiographics 11:959, 1991.
18. Cohen EK, Kressel HY, Frank TS, et al: Hyaline cartilage: Origin of bone and soft tissue neoplasms—MR appearance and histologic correlation. Radiology 167:477, 1988.
19. Cohen JM, Weinreb JC, Redman HC: Arteriovenous malformation of the extremities: MR imaging. Radiology 158:475, 1986.
20. Cory DA, Fritsch SA, Cohen MD, et al: Aneurysmal bone cysts: Imaging findings and embolotherapy. AJR Am J Roentgenol 153: 269, 1989.
21. Crim JR, Mirra JM, Eckardt JJ, Seeger LL: Widespread inflammatory response to osteoblastoma: The flare phenomenon. Radiology 177:835, 1990.
22. Crim JR, Seeger LL, Yao L, et al: Diagnosis of soft-tissue masses with MR imaging: Can benign masses be differentiated from malignant ones? Radiology 185:581, 1992.
23. Dahlin DC: Giant cell tumor of bone: Highlight of 407 cases. Am J Roentgenol 111:966, 1985.
24. Dalinka MK, Zlatkin MB, Chao P, et al: The use of magnetic resonance imaging in the evaluation of bone and soft-tissue tumors. Radiol Clin North Am 28:461, 1990.
25. Demas BE, Heelan RT, Lane J, et al: Soft-tissue sarcomas of the extremities: Comparison of MR and CT in determining the extent of disease. AJR Am J Roentgenol 150:615, 1988.
26. DeSantos LA, Murray JA: Evaluation of giant cell tumors by computerized tomography. Skeletal Radiol 2:205, 1978.
27. Dorfman MD, Bhagavan BS: Malignant fibrous histiocytoma of the soft tissue with metaplastic bone and cartilage formation: A new radiologic sign. Skeletal Radiol 8:145, 1982.
28. Ehara S, Rosenthal DI, Aoki J, et al: Peritumoral edema in osteoid osteoma on magnetic resonance imaging. Skeletal Radiol 28:265, 1999.
29. Einstein DM, Tagliabue JR, Desai RK: Abdominal desmoids: CT findings in 25 patients. AJR Am J Roentgenol 157:275, 1991.
30. Erlemann R, Reiser MF, Peters PE, et al: Musculoskeletal neoplasms: Static and dynamic Gd-DTPA–enhanced MR imaging. Radiology 171:767, 1989.
31. Fletcher BD: Response of osteosarcoma and Ewing sarcoma to chemotherapy: Imaging evaluation. AJR Am J Roentgenol 157: 825, 1991.
32. Frank JA, Ling A, Patronas NJ, et al: Detection of malignant bone tumors: MR imaging vs scintigraphy. AJR Am J Roentgenol 155: 1043, 1990.
33. Fruehwald FX, Tscholakoff D, Schwaighofer B, et al: Magnetic resonance imaging of the lower vertebral column in patients with multiple myeloma. Invest Radiol 23:193, 1988.
34. Gamba JL, Martinez S, Apple J, et al: Computed tomography of axial skeletal osteoid osteomas. Am J Roentgenol 142:769, 1984.
35. Geirnaerdt MJ, Bloem JL, Eulderink F, et al: Cartilaginous tumors: Correlation of gadolinium-enhanced MR imaging and histopathologic findings. Radiology 186:813, 1993.
36. Gillespy T 3rd, Manfrini M, Ruggieri P, et al: Staging of intraosseous extent of osteosarcoma: Correlation of preoperative CT and MR imaging with pathologic macroslides. Radiology 167:765, 1988.
37. Ginaldi S, deSantos LA: Computed tomography in the evaluation of small round cell tumors of bone. Radiology 134:441, 1980.
38. Golfieri R, Baddeley H, Pringle JS, et al: Primary bone tumors: MR morphologic appearance correlated with pathologic examinations. Acta Radiol 32:290, 1991.
39. Hall TR, Kangarloo H: Magnetic resonance imaging of the musculoskeletal system in children. Clin Orthop 244:119, 1989.
40. Hayes CW, Conway WF, Sundaram M: Misleading aggressive MR imaging appearance of some benign musculoskeletal lesions. Radiographics 12:1119, 1992.
41. Herman SD, Mesgarzadeh M, Bonakdarpour A, Dalinka MK: The role of magnetic resonance imaging in giant cell tumor of bone. Skeletal Radiol 16:635, 1987.
42. Holscher HC, Bloem JL, Nooy MA, et al: The value of MR imaging in monitoring the effect of chemotherapy on bone sarcomas. AJR Am J Roentgenol 154:763, 1990.
43. Hudson TM, Hawkins IF: Radiologic evaluation of chondroblastoma. Radiology 139:1, 1981.
44. Hudson TM, Springfield DS, Spanier SS, et al: Benign exostoses and exostotic chondrosarcomas: Evaluation of cartilage thickness by CT. Radiology 152:595, 1984.
45. Hudson TM: Fluid levels in aneurysmal bone cysts: A CT feature. Am J Roentgenol 141:1001, 1984.
46. Hudson TM, Hamlin DJ, Fitzsimmons JR: Magnetic resonance imaging of fluid levels in an aneurysmal bone cyst and in anticoagulated human blood. Skeletal Radiol 13:267, 1985.
47. Jee WH, Choe BY, Kang HS, et al: Nonossifying fibroma: Characteristics at MR imaging with pathologic correlation. Radiology 209: 197, 1998.
48. Jee WH, Park YK, McCauley TR, et al: Chondroblastoma: MR characteristics with pathologic correlation. J Comput Assist Tomogr 23:721, 1999.
49. Jelinek JS, Kransdorf MJ, Utz JA, et al: Imaging of pigmented villonodular synovitis with emphasis on MR imaging. AJR Am J Roentgenol 152:337, 1989.
50. Jelinek JS, Kransdorf MJ, Shmookler BM, et al: Liposarcoma of the extremities: MR and CT findings in the histologic subtypes. Radiology 186:455, 1993.
51. Kaplan PA, Williams SM: Mucocutaneous and peripheral soft-tissue hemangioma: MR imaging. Radiology 163:163, 1987.
52. Kenney PJ, Gilula LA, Murphy WA: The use of computed tomography to distinguish osteochondroma and chondrosarcoma. Radiology 139:129, 1981.
53. Kottal RA, Vogler JB 3rd, Matamoros A, et al: Pigmented villonodular synovitis: A report of MR imaging in two cases. Radiology 163: 551, 1987.
54. Kransdorf MJ, Utz JA, Gilkey FW, Berrey BH: MR appearance of fibroxanthoma. J Comput Assist Tomogr 12:612, 1988.
55. Kransdorf MJ, Jelinek JS, Moser RP Jr, et al: Soft-tissue masses: Diagnosis using MR imaging. AJR Am J Roentgenol 153:541, 1989.
56. Kransdorf MJ, Stull MA, Gilkey FW, Moser RP Jr: Osteoid osteoma. Radiographics 11:671, 1991.
57. Kransdorf MJ, Moser RP Jr, Meis JM, Meyer CA: Fat-containing soft tissue masses of the extremities. Radiographics 11:81, 1991.
58. Kroon HM, Shurmans J: Osteoblastoma: Clinical and radiologic finding in 98 new cases. Radiology 175:783, 1990.
59. Lee JK, Yao L, Wirth CR: MR imaging of solitary osteochondromas: Report of eight cases. AJR Am J Roentgenol 149:557, 1987.
60. Lee MJ, Sallomi DF, Munk PL, et al: Pictorial review: Giant cell tumours of bone. Clin Radiol 53:481, 1998.
61. Lemmi MA, Fletcher BD, Marina NM, et al: Use of MR imaging to assess results of chemotherapy for Ewing sarcoma. AJR Am J Roentgenol 155:343, 1990.
62. Levine E, Neff JR: Dynamic computed tomography scanning of benign bone lesions: Preliminary results. Skeletal Radiol 9:238, 1983.
63. Lodwick GS: The radiologist's role in managing chondrosarcoma. Radiology 150:275, 1984.
64. London J, Kim EE, Wallace S, et al: MR imaging of liposarcomas: Correlation of MR features and histology. J Comput Assist Tomogr 15:832, 1989.

65. Mahajan H, Lorigan JG, Shirkhoda A: Synovial sarcoma: MR imaging. Magn Reson Imaging 7:211, 1989.
66. Mahajan H, Kim EE, Wallace S, et al: Magnetic resonance imaging of malignant fibrous histiocytoma. Magn Reson Imaging 7:283, 1989.
67. Mail JT, Cohen MD, Mirkin LD, Provisor AJ: Response of osteosarcoma to preoperative intravenous high-dose methotrexate chemotherapy: CT evaluation. Am J Roentgenol 144:89, 1985.
68. Mehta M, White LM, Knapp T, et al: MR imaging of symptomatic osteochondromas with pathological correlation. Skeletal Radiol 27: 427, 1998.
69. Meyer JS, Hoffer FA, Barnes PD, Mulliken JB: Biological classification of soft-tissue vascular anomalies: MR correlation. AJR Am J Roentgenol 157:559, 1991.
70. Morton MJ, Berquist TH, McLeod RA, et al: MR imaging of synovial sarcoma. AJR Am J Roentgenol 156:337, 1991.
71. Moser RP Jr, Kransdorf MJ, Gilkey FW, Manaster BJ: From the archives of the AFIP: Giant cell tumor of the upper extremity. Radiographics 10:83, 1990.
72. Moulopoulos LA, Varma DG, Dimopoulos MA, et al: Multiple myeloma: Spinal MR imaging in patients with untreated newly diagnosed disease. Radiology 185:833, 1992.
73. Munk PL, Helms CA, Holt RJ, et al: MR imaging of aneurysmal bone cysts. AJR Am J Roentgenol 153:99, 1989.
74. Murphey MD, Flemming DJ, Boyea SR, et al: Enchondroma versus chondrosarcoma in the appendicular skeleton: Differentiating features. Radiographics 18:1213; quiz, p 1244; 1998.
75. Pan G, Raymond AK, Carrasco CH, et al: Osteosarcoma: MR imaging after preoperative chemotherapy. Radiology 174:517, 1990.
76. Panicek DM, Gatsonis C, Rosenthal DI, et al: CT and MR imaging in the local staging of primary malignant musculoskeletal neoplasms: Report of the Radiology Diagnostic Oncology Group. Radiology 202:237, 1997.
77. Petasnick JP, Turner DA, Charters JR, et al: Soft-tissue masses of the locomotor system: Comparison of MR imaging with CT. Radiology 160:125, 1986.
78. Pettersson H, Gillespy T 3rd, Hamlin DJ, et al: Primary musculoskeletal tumors: Examination with MR imaging compared with conventional modalities. Radiology 164:237, 1987.
79. Prayer LM, Kropej DH, Wimberger DM, et al: High-resolution realtime sonography and MR imaging in assessment of osteocartilaginous exostoses. Acta Radiol 32:393, 1991.
80. Rak KM, Yakes WF, Ray RL, et al: MR imaging of symptomatic peripheral vascular malformations. AJR Am J Roentgenol 159:107, 1992.
81. Recht MP, Sachs PB, LiPuma J, Clampitt M: Popliteal artery pseudoaneurysm in a patient with hereditary multiple exostoses: MRI and MRA diagnosis. J Comput Assist Tomogr 17:300, 1993.
82. Redmond OM, Stack JP, Dervan PA, et al: Osteosarcoma: Use of MR imaging and MR spectroscopy in clinical decision making. Radiology 172:811, 1989.
83. Reuther G, Mutschler W: The value of CT and MRT in the diagnosis of cartilage-forming tumors [in German]. ROFO Fortschr Geb Rontgenstr Nuklearmed 151:647, 1989.
84. Ritshl P, Hajeck PC, Pechmann U: Fibrous metaphyseal defects: Magnetic resonance imaging appearance. Skeletal Radiol 18:253, 1989.
85. Ros PR, Viamonte M, Rywlin AM: Malignant fibrous histiocytoma: Mesenchymal tumor of ubiquitous origin. Am J Roentgenol 142: 753, 1984.
86. Rosenthal D, Aronow S, Murray WT: Iron content of pigmented villonodular synovitis detected by computed tomography. Radiology 133:409, 1979.
87. Rosenthal RE, Wozney P: Diagnostic value of gadopentetate dimeglumine for 1.5-T MR imaging of musculoskeletal masses: Comparison with unenhanced T1- and T2-weighted imaging. J Magn Reson Imaging 1:547, 1991.
88. Schlesinger AE, Hernandez RJ: Intracapsular osteoid osteoma of the proximal femur: Findings on plain film and CT. AJR Am J Roentgenol 154:1241, 1990.
89. Schreiman JS, McLeod R, Kyle RA, Beabout JW: Multiple myeloma: Evaluation by CT. Radiology 154:483, 1985.
90. Seeger LL, Eckardt JJ, Bassett LW: Cross-sectional imaging in the evaluation of osteogenic sarcoma: MRI and CT. Semin Roentgenol 24:174, 1989.
91. Seeger LL, Widoff BE, Bassett LW, et al: Preoperative evaluation of osteosarcoma: Value of gadopentetate dimeglumine-enhanced MR imaging. AJR Am J Roentgenol 157:347, 1991.
92. Shaikh MI, Saifuddin A, Pringle J, et al: Spinal osteoblastoma: CT and MR imaging with pathological correlation. Skeletal Radiol 28: 33, 1999.
93. Shirkhoda A, Jaffe N, Wallace S, et al: Computed tomography of osteosarcoma after intraarterial chemotherapy. Am J Roentgenol 144:95, 1985.
94. Shuman WP, Patton RM, Baron RL, et al: Comparison of STIR and spin-echo MR imaging at 1.5 T in 45 suspected extremity tumors: Lesion conspicuity and extent. Radiology 179:247, 1991.
95. Simon JH, Szumowski J: Chemical shift imaging with paramagnetic contrast material enhancement for improved lesion depiction. Radiology 171:539, 1989.
96. Sundaram M, McGuire MH: Computed tomography and magnetic resonance for evaluating the solitary tumor and tumor-like lesion of bone? Skeletal Radiol 17:393, 1988.
97. Sundaram M, McLeod RA: MR imaging of tumor and tumor like lesions of bone and soft tissue. AJR Am J Roentgenol 155:817, 1990.
98. Tehranzadeh J, Murphy BJ, Mnaymneh W: Giant cell tumor of the proximal tibia: MR and CT appearance. J Comput Assist Tomogr 13:282, 1989.
99. Totty WG, Murphy WA, Lee JKT: Soft tissue tumors: MR imaging. Radiology 160:135, 1986.
100. Tsai JC, Dalinka MK, Fallon MD, et al: Fluid-fluid level: A nonspecific finding in tumors of bone and soft tissue. Radiology 175: 779, 1990.
101. Vandevenne JE, De Schepper AM, De Beuckeleer L, et al: New concepts in understanding evolution of desmoid tumors: MR imaging of 30 lesions. Eur Radiol 7:1013, 1997.
102. Vanel D, Lacombe MJ, Couanet D, et al: Musculoskeletal tumors: Follow-up with MR imaging after treatment with surgery and radiation therapy. Radiology 164:243, 1987.
103. Varila-Duran J, Enzinger FM: Calcifying synovial sarcoma. Cancer 50:345, 1982.
104. Varma DGK, Ayala AG, Carrasco CH, et al. Chondrosarcoma: MR imaging with pathologic correlation. Radiographics 12:687, 1992.
105. Weatherall PT, Maale GE, Mendelsohn DB, et al: Chondroblastoma: Classic and confusing appearance at MR imaging. Radiology 190: 467, 1994.
106. Weekes RG, McLeod RA, Reiman HM, Pritchard DJ: CT of soft-tissue neoplasms. Am J Roentgenol 144:355, 1985.
107. Weekes RG, Berquist TH, McLeod RA, Zimmer WD: Magnetic resonance imaging of soft-tissue tumors: Comparison with computed tomography. Magn Reson Imaging 3:345, 1985.
108. Wetzel LH, Levine E, Murphey MD: A comparison of MR imaging and CT in the evaluation of musculoskeletal masses. Radiographics 7:851, 1987.
109. Wilson AJ, Kyriakos M, Acckerman LV: Chondromyxoid fibroma: Radiographic appearance in 38 cases and in review of the literature. Radiology 179:513, 1991.
110. Yamamura S, Sato K, Sugiura H, Iwata H: Inflammatory reaction in chondroblastoma. Skeletal Radiol 25:371, 1996.
111. Yuh WT, Kathol MH, Sein MA, et al: Hemangiomas of skeletal muscle: MR finding in five patients. AJR Am J Roentgenol 149: 765, 1987.
112. Zimmer WD, Berquist TH, Sim FH, et al: Magnetic resonance imaging of aneurysmal bone cyst. Mayo Clin Proc 59:633, 1984.
113. Zimmer WD, Berquist TH, McLeod RA, et al: Magnetic resonance imaging of osteosarcoma: Comparison with computed tomography. Clin Orthop 208:289, 1986.

47 Computed Tomography and Magnetic Resonance Imaging of the Foot and Ankle

Ken L. Schreibman

Overview

All imaging of the foot and ankle should begin with conventional radiographs. It is preferable that one obtain radiographs of the foot with the patient standing in order to visualize the bones in their weight-bearing alignment. The standard practice is to obtain anteroposterior (AP) and lateral views.[3] The oblique AP projection is a useful additional view, particularly to assess the alignment of the tarsal-metatarsal joints (Fig. 47–1). Ankle radiographs are typically obtained with the patient not bearing weight, and the standard series consists of three views[4]: (1) AP, (2) mortise, and (3) lateral (Fig. 47–2). The mortise view is similar to the AP view, with the leg internally rotated 15 degrees. This projection better profiles the ankle mortise.

Advanced imaging techniques are often employed when (1) radiographs cannot elucidate the cause of the symptoms, (2) better anatomic detail is required, or (3) the pathologic process primarily involves the soft tissues. Computed tomography (CT), magnetic resonance imaging (MRI), radionuclide scanning, and ultrasonography (US) each yield additional diagnostic information. Which advanced imaging study should be used depends on the findings on the initial radiograph and the clinical question being asked (Fig. 47–3).

A discussion of radionuclide scanning and ultrasonography of the foot and ankle, other than the brief reviews presented next, is beyond the scope of this chapter.

Computed Tomography

CT is best employed when the clinical or surgical question involves assessing the integrity of the cortex, particularly along articular surfaces. Most modern CT scanners have the ability to create two-dimensional (2D) reformatted images in any plane. This is particularly useful for examining joints that are difficult to profile radiographically, such as the subtalar joint. In the setting of trauma, CT is often used to reveal the pattern of calcaneal fractures as well as the extent of other intra-articular fractures. CT clearly demonstrates cortical fusion in cases of attempted arthrodesis and cortical irregularity in cases of osteoarthritis. CT is also our imaging modality of choice to evaluate tarsal coalitions, both solid and nonosseous. Example are demonstrated in the first half of this chapter.

Magnetic Resonance Imaging

MRI is used in most other situations. Soft tissue structures, particularly the ankle tendons, can be displayed with a high degree of anatomic and pathologic detail. The extent of abnormal soft tissue and osseous masses can be shown in multiple planes. MRI is also extremely sensitive in detecting radiographically occult bone lesions and osteochondral defects. Examples are presented in the second half of this chapter.

Nuclear Medicine

With the increasing use of MRI for the imaging of occult lesions of the foot and ankle, the role of nuclear medicine is diminishing in many imaging centers. Bone scans remain useful as a screening modality to detect the presence of bone disease. When one is screening for lesions in both feet or throughout the skeleton, a bone scan may be more practical than MRI. In patients with Charcot's arthropathy and advanced neuropathic deformity, the specificity of a bone scan, combined with a technetium-labeled white blood cell scan, can be higher than for MRI.

Ultrasonography

The role of ultrasound is somewhat limited in evaluation of the foot and ankle. In the hands of a skilled sonographer, ultrasonography can detect ankle tendon pathology. In certain clinical settings, ultrasonography can be helpful in determining the vascular or cystic nature of a soft tissue mass and in detecting nonradiopaque foreign bodies, such as a wooden splinter.

Computed Tomography

Technique and Anatomy

With modern CT scanners capable of rapidly acquiring many thin axial slices, the approach toward imaging an

Figure 47–1. Weight-bearing radiographic foot series in an asymptomatic 41-year-old male radiologist. *A,* Anteroposterior radiograph. *B,* Oblique radiograph. *C,* Lateral radiograph. The upward-pointing *white arrow* was placed by the technologist to indicate the patient was standing. The heel spur *(black arrow)* at the origin of the plantar fascia is of doubtful clinical significance in this normal volunteer, who has never had heel pain. *D,* In most radiology departments, the x-ray tube cannot be lowered to the floor. Weight-bearing lateral views can be obtained by having the patient stand on a wooden box. The central x-ray beam *(dashed arrow)* passes through the foot, from lateral to medial, striking the film cassette held upright between the feet.

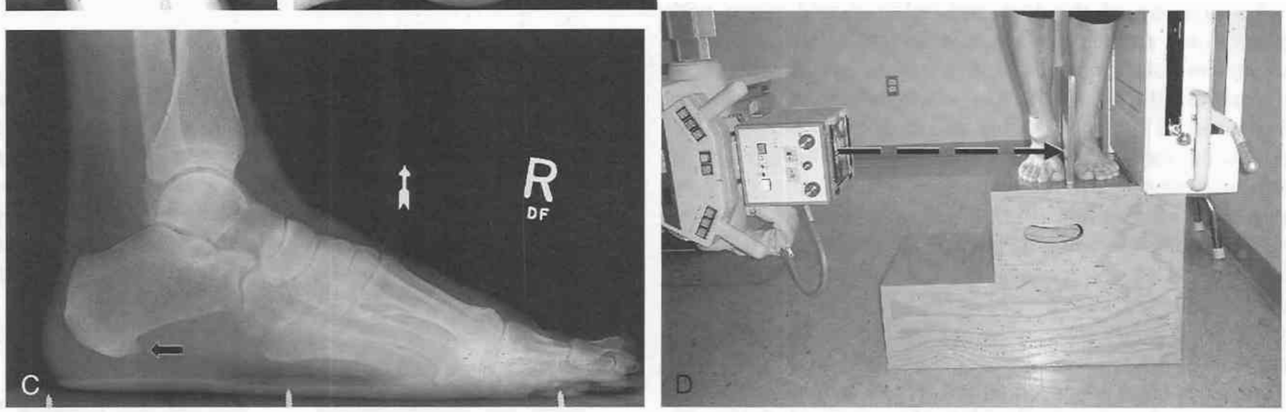

Figure 47–2. Non–weight-bearing radiographic ankle series in a 37-year-old man with lateral ankle pain following an acute inversion injury. *A,* Anteroposterior radiograph. *B,* Mortise radiograph. *C,* Lateral radiograph. The ankle joint and hindfoot are normal. The region outlined by the *dashed rectangle* in *C* is photographically magnified in *D. D,* Close inspection of the base of the fifth metatarsal on the lateral view of the ankle reveals a proximal diaphyseal fracture, a *Jones fracture (arrow).* Fractures of the base of the fifth metatarsal often present clinically as lateral ankle pain. The technologist must be careful to include the base of the fifth metatarsal on all lateral views of the ankle.

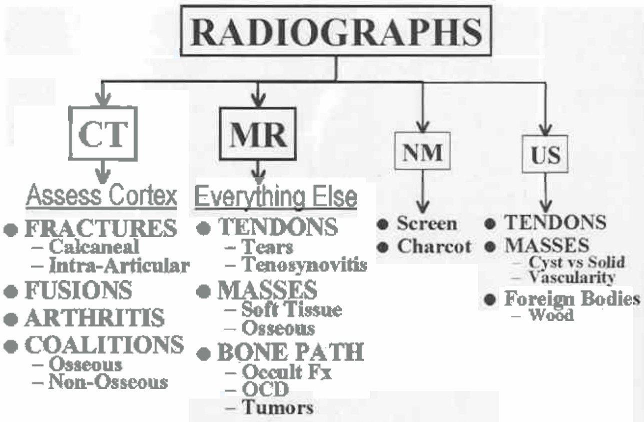

Figure 47–3. Flow chart for advanced imaging techniques (see text). Fx, fracture; OCD, osteochondritis dissecans.

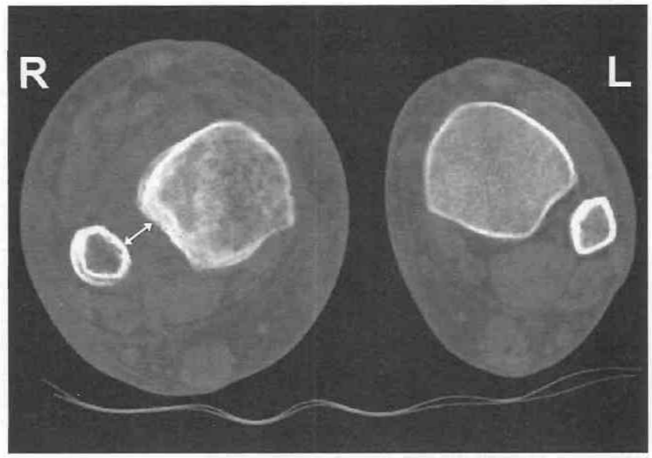

Figure 47–5. Asymmetrically wide syndesmosis on the right (*double-headed arrow*).

extremity has evolved. We are no longer limited to thinking of a CT scan as a series of individual images. Instead, the goal should be to obtain a solid volume of data and then create 2D reformatted images in planes optimized to illustrate the anatomic structures in question. When the ankle is being scanned, this solid acquisition volume should extend from above the syndesmosis (the distal tibia-fibula articulation) through the entire calcaneus (Fig. 47–4).

For a CT scan of the ankle, the field of view should be large enough to include the hindfoot (talus and calcaneus), the midfoot (navicular, cuboid, and the three cuneiforms), and at least the proximal bases of all five metatarsals. A scanning field of view between 18 and 22 cm is usually sufficient. Indeed, for many patients, it is possible to scan both ankles simultaneously within a 22-cm field of view, thus allowing a side-by-side comparison of the symptomatic ankle with the normal ankle. This can be helpful for evaluating asymmetry of joints such as the syndesmosis, which can be difficult to measure radiographically (Fig. 47–5).

For a CT scan of the foot, the field of view should be enlarged to encompass the entire forefoot (metatarsals and phalanges) as well as the hindfoot and midfoot.

When one is scanning the foot or ankle as a volume for subsequent multiplanar reconstruction, the exact position of the extremity within the scanning gantry is less important than ensuring that the limb is stable and will not move throughout the entire course of the scan. Taking a few extra seconds to check that the patient is comfortable and relaxed ensures that the patient will hold perfectly still during the several minutes it takes to obtain the scout images, prescribe the imaging protocol, and acquire the actual images. One way to help the patient hold still is to tape the two feet together. A cardboard or polystyrene plastic (Styrofoam) box can also be used to help keep the feet stable and provides uniformity in patient positioning (Fig. 47–6). Keeping the feet in the center of the gantry often allows for a "small" scanning field of view to be used.

It is not necessary to have a high-speed multislice scanner to obtain high-quality multiplanar reconstruction images. The key is to make the slices as thin as possible with no gap between the slices while the patient is holding perfectly still. In this chapter, all images were acquired using a single-slice helical scanner with 1-mm-thick collimation and a pitch of 1:1. It typically takes 90 to 120

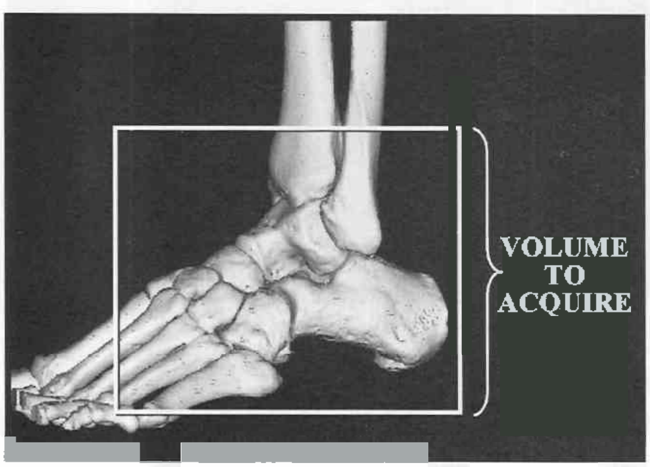

Figure 47–4. Acquisition volume for CT of the ankle.

Figure 47–6. Taping feet together to a box helps the patient hold still.

slices, 1 mm thick, to cover the ankle from above the syndesmosis to below the calcaneus.

CT of the foot and ankle allows for assessment of the congruity of articular surfaces in multiple planes. The choice of which planes to reconstruct depends upon which joints are desired to be seen.

The *direct axial plane* (Fig. 47–7*A*) is parallel to the plantar surface of the foot. It is the primary plane for assessing the ankle syndesmosis as well as the talonavicular, calcaneocuboid, and navicular-cuneiform joints. When scanning is performed with the patient's toes pointing straight up, the direct axial plane is acquired directly with the gantry straight up and reconstruction in this plane is not necessary. If the patient cannot be placed in this toes-up neutral position, it may be necessary to create reconstruction images in the direct axial plane.

The *oblique axial plane* (Fig. 47–7*B*) is parallel to the long axis of the metatarsals. It is the primary plane for assessing the tarsal-metatarsal joint and is useful in evaluation of a Lisfranc's fracture. This plane can be acquired directly by tilting the gantry 20 to 30 degrees so that the scanning plane is parallel to the metatarsals. Alternatively, oblique axial images can be reconstructed off a sagittal reference image, as in Figure 47–7*B*.

The *sagittal plane* divides the medial side of the foot and ankle from the lateral side. It is equivalent to the radiographic lateral projection of the foot and is created by reconstructing off a direct axial reference image (Fig. 47–7*C*). If the patient's foot was held in internal or external rotation at the time of scanning, the reconstruction slices should be angled accordingly. Sagittal images are often a good secondary plane by which to assess the integrity of the ankle and subtalar joints as well as the talonavicular, calcaneocuboid, navicular-cuneiform, and tarsal-metatarsal joints.

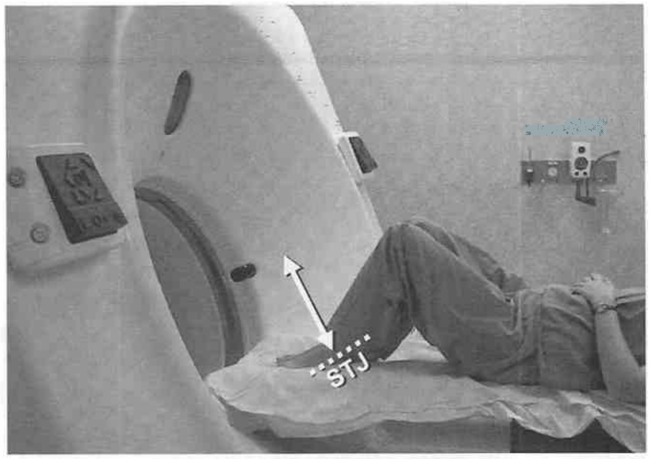

Figure 47–8. Direct acquisition in the oblique coronal plane. The *dotted line* indicates the orientation of the subtalar joint (STJ). The gantry is angled away from the patient, in a plane perpendicular to the subtalar joint, as indicated by the *double-headed arrow.*

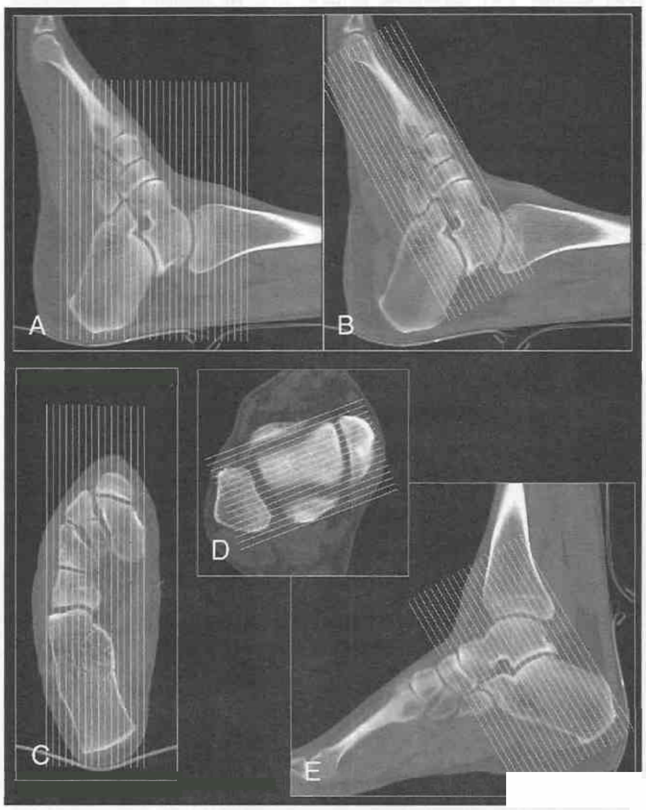

Figure 47–7. Reconstruction planes. *A*, Dire[redacted]xial plane. *B*, Oblique axial plane. *C*, Sagittal plane. *D*, Mortise coronal plane. *E*, Oblique coronal plane.

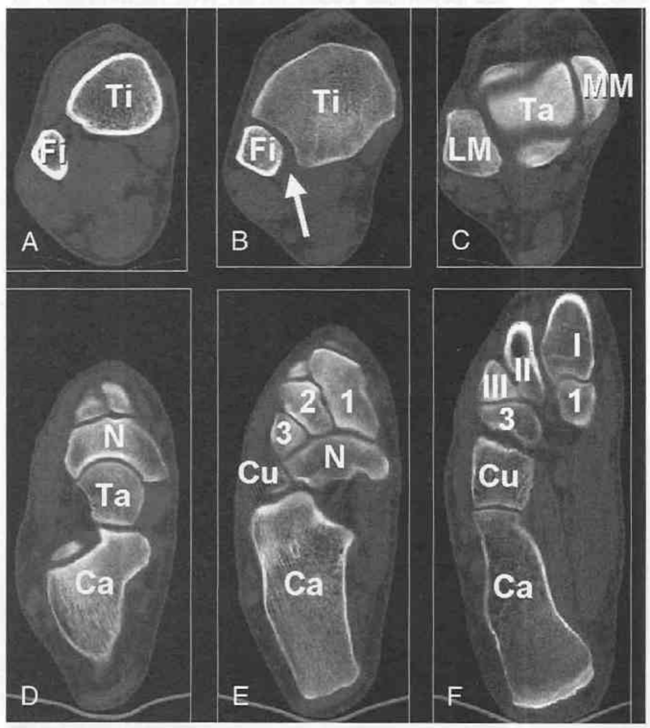

Figure 47–9. Normal anatomy: direct axial plane. *A*, Above the syndesmosis. *B*, Image obtained through the syndesmosis (*arrows* point to the syndesmosis). *C*, Image obtained through the ankle joint. *D*, Top of the calcaneus. *E*, Middle of the calcaneus. *F*, Bottom of the calcaneus. Ca, calcaneus; Cu, cuboid; Fi, fibula; LM, MM, lateral-medial malleolus; N, navicular; Ti, tibia; Ta, talus; 1, 2, and 3, cuneiforms; I, II, and III, metatarsals.

The *coronal plane* divides anterior from posterior structures and is equivalent to the AP radiographic projection of the ankle. This plane is customarily used to evaluate the ankle and subtalar joints, and the reconstruction planes can be optimized depending on which joint is in question. The ankle mortise can be clearly profiled via the *mortise coronal plane,* obtained by reconstructing off an axial reference image, along a line between the medial and lateral malleoli (Fig. 47–7*D*). The subtalar joint is best profiled via the *oblique coronal plane,* obtained by reconstructing off a sagittal reference image, perpendicular to the subtalar joint (Fig. 47–7*E*). When the oblique coronal images are angled correctly, the middle facet of the subtalar joint has a flat horizontal orientation (see Fig. 47–11*C*).

Oblique coronal images are of particular surgical importance in planning the management of calcaneal fractures. When technical constraints limit the ability to create satisfactory reconstruction images, or when the surgeon insists on it, images can be acquired directly in this coronal plane. As shown in Figure 47–8, the patient flexes the knees and places the feet flat on the scanning table. (This flexed-knee positioning may not be possible if the patient is in a long-leg cast or has other physical limitations.) Scout images are obtained, and the gantry is tipped with the top *away* from the patient so as to scan in a plane *perpendicular* to the subtalar joint, typically 20 to 30 degrees.

Figures 47–9 through 47–11 depict the anatomy of the tarsal bones and joints in the direct axial, sagittal, and oblique coronal planes, respectively.

Trauma

After conventional radiography, CT is the most useful modality for assessing the bones following trauma. With multiplanar reformatted images, CT clearly demonstrates the alignment of fracture fragments, intra-articular extent, and the presence of intra-articular loose bodies. Although a CT scan of the foot and ankle can certainly be obtained at the time of the acute trauma, in a multitrauma patient it is often prudent to attend to the most urgent clinical and imaging needs immediately and delay scanning the extremity until the patient is more stable and comfortable. The surgeon may elect to wait several days to a week for soft tissue swelling to decrease before repairing an ankle fracture. As such, a preoperative planning CT scan can be performed a day or two before the scheduled surgery.

Although it is not necessary to obtain a preoperative CT

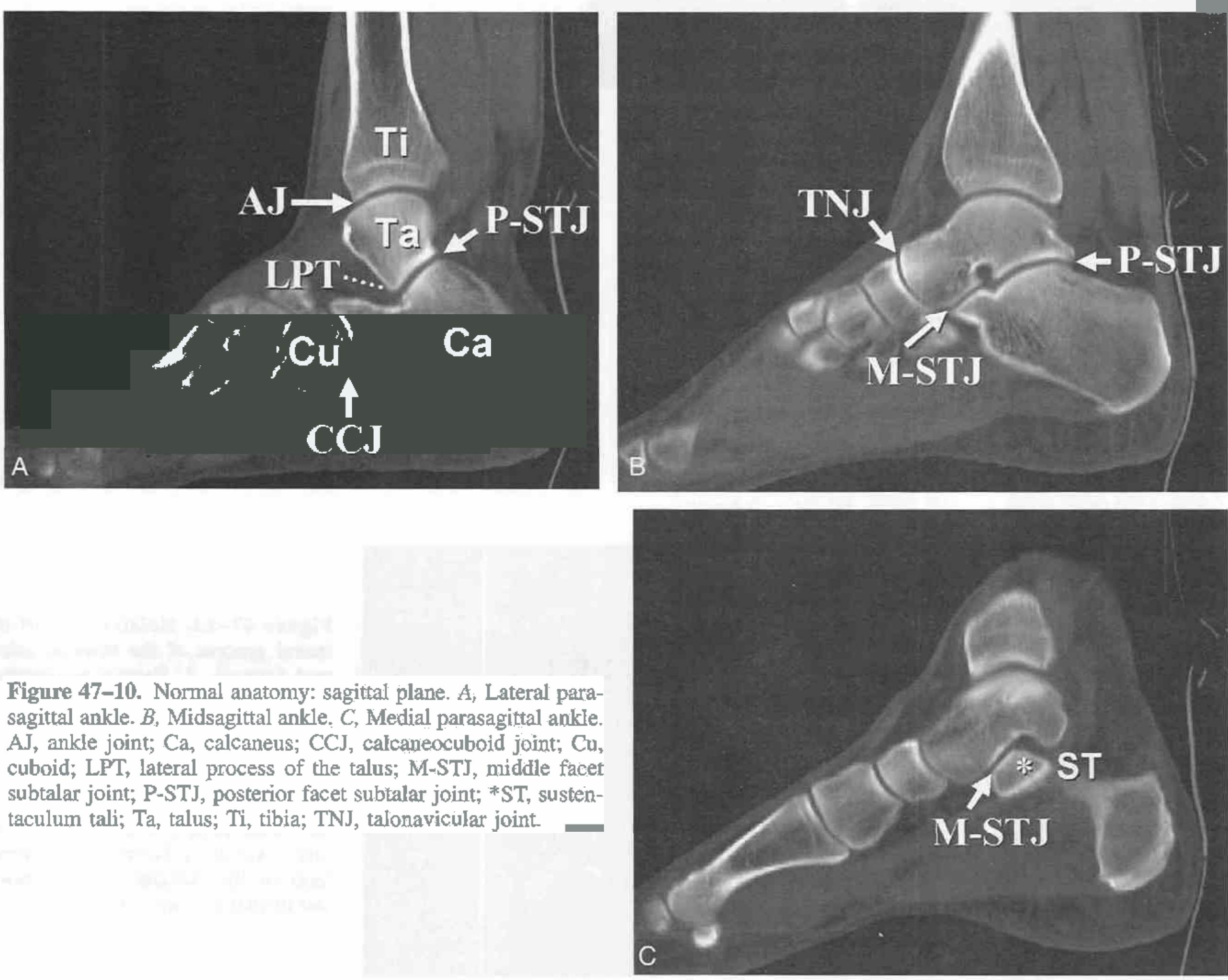

Figure 47–10. Normal anatomy: sagittal plane. *A,* Lateral parasagittal ankle. *B,* Midsagittal ankle. *C,* Medial parasagittal ankle. AJ, ankle joint; Ca, calcaneus; CCJ, calcaneocuboid joint; Cu, cuboid; LPT, lateral process of the talus; M-STJ, middle facet subtalar joint; P-STJ, posterior facet subtalar joint; *ST, sustentaculum tali; Ta, talus; Ti, tibia; TNJ, talonavicular joint.

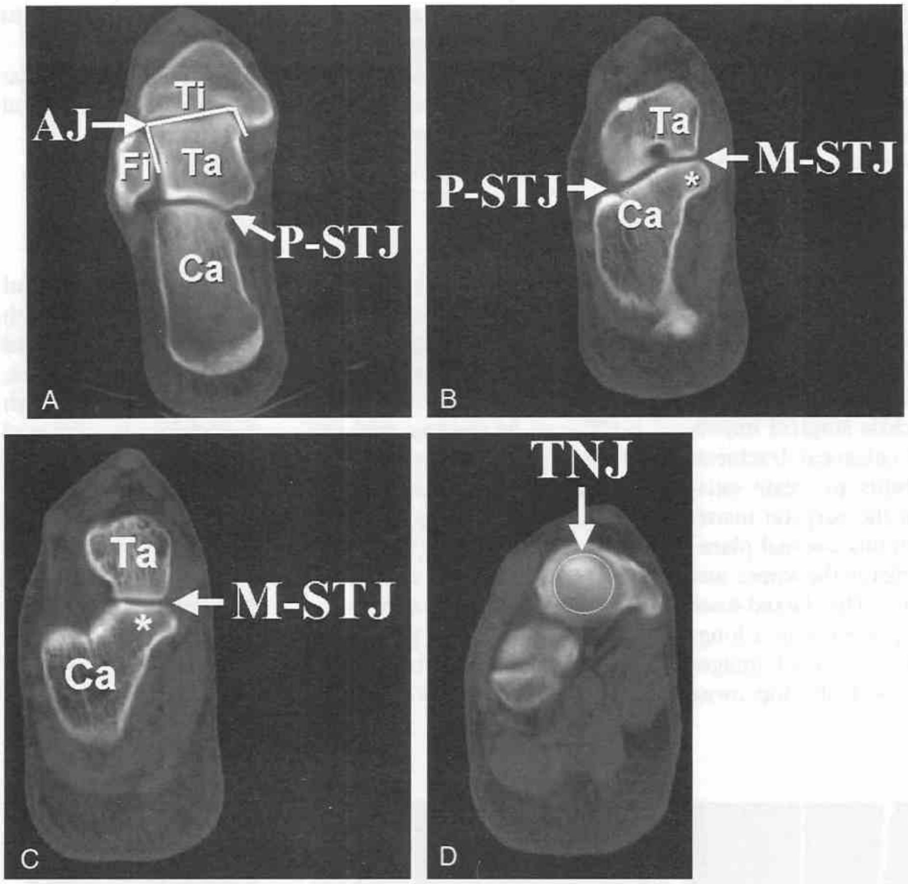

Figure 47–11. Normal anatomy: oblique coronal plane. *A,* Reconstructed image obtained through the ankle joint and back of the subtalar joint. *B,* Image obtained through the sustentaculum tali *(asterisk). C,* Image obtained through the sinus tarsi. *D,* Talonavicular joint. AJ, ankle joint; Ca, calcaneus; Fi, fibula; M-STJ, middle facet subtalar joint; P-STJ, posterior facet subtalar joint; Ta, talus; Ti, tibia; TNJ, talonavicular joint.

scan for each fracture of the foot or ankle, often the surgical approach to calcaneal fractures and many talar fractures, as well as complex fractures of the distal tibia, is dictated by the fracture pattern. If the fragments are severely displaced, the surgeon may request a 3D rendering of the CT scan to better visualize how the fragments should be realigned. In most cases, however, the multiplanar 2D reformatted images described earlier are sufficient for preoperative planning.

Calcaneal Fractures

The calcaneus is the most commonly fractured tarsal bone. Injury to this bone represents 60% of all tarsal fractures and 2% of all fractures.[38] The injuries are often disabling because of the slow healing time and symptomatic sequelae.[40] Calcaneal fractures are typically the result of axial loading, such as may occur when a person is jumping or falling from a height.

The calcaneus tends to fracture in a characteristic pattern. With axial loading, the wedge-shaped lateral process of the talus impacts into the calcaneus at the angle of Gissane. The fracture then propagates inferomedially (Fig. 47–12). Calcaneal fractures almost invariably extend into the posterior facet of the subtalar joint and may involve the sustentaculum tali and middle facet to a varying degree. For this reason, the oblique coronal plane, angled perpen-

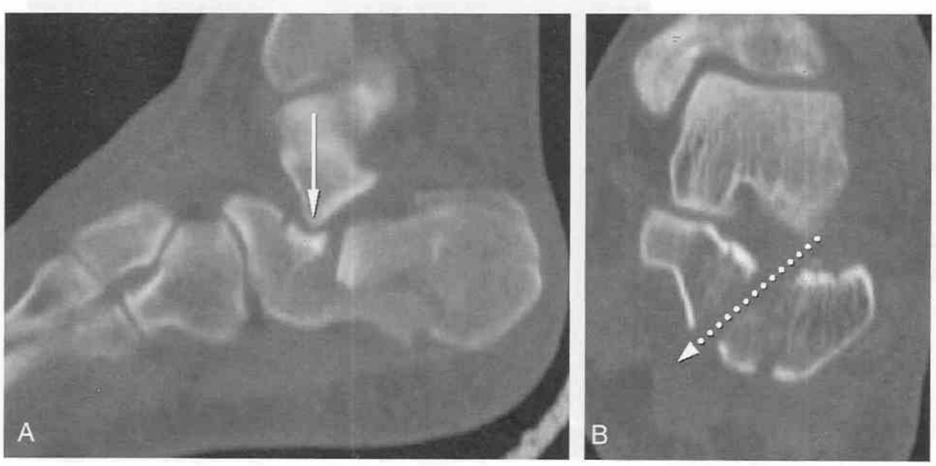

Figure 47–12. Relationship of the lateral process of the talus to calcaneal fracture. *A,* Sagittal reformatted image. With axial loading, the wedge-shaped lateral process of the talus *(arrow)* impacts into the calcaneus at the angle of Gissane. *B,* Oblique coronal reformatted image demonstrates the classic pattern of a calcaneal fracture, extending from the posterior facet of the subtalar joint inferiorly and medially *(dotted line).*

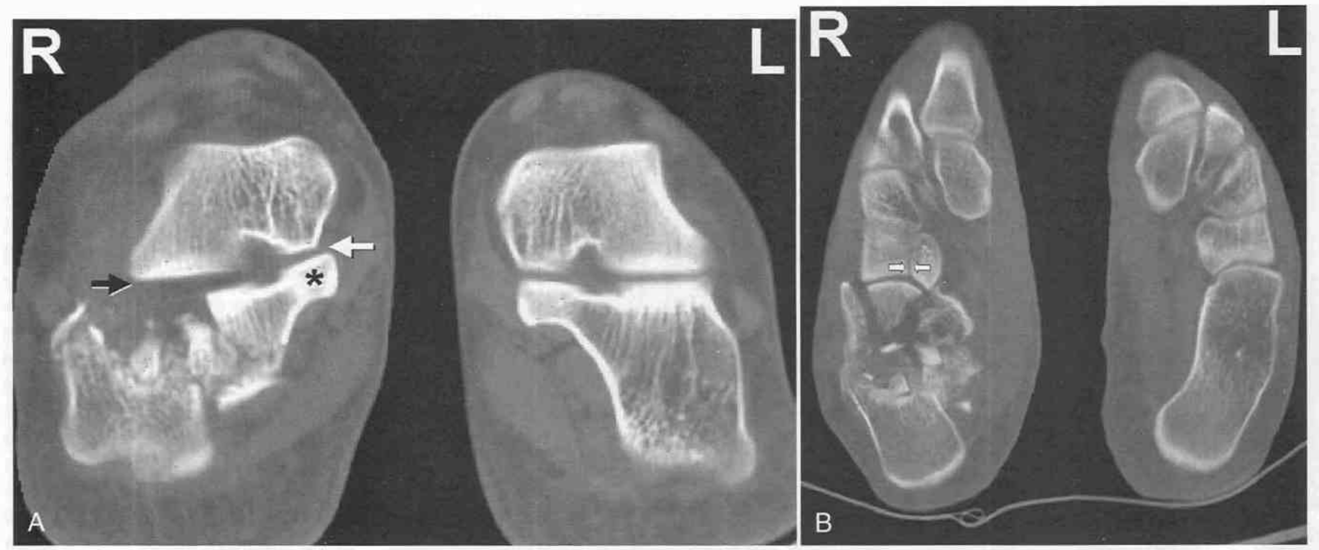

Figure 47–13. Calcaneal fracture. *A,* Oblique coronal reformatted image reveal the near-complete disruption of the posterior facet of the subtalar joint *(black arrow)*; however, this image also shows that the fracture does not extend into the sustentaculum tali *(asterisk)* and that the middle facet of the subtalar joint is maintained *(white arrow)*. By scanning through both hindfeet simultaneously, one may include the contralateral normal left subtalar joint for comparison. *B,* Direct axial image obtained through both hindfeet simultaneously demonstrates the severely comminuted fracture of the right calcaneus. There is also a nondisplaced longitudinal fracture through the cuboid *(arrows)*.

dicular to the subtalar joint, is the primary imaging plane in assessment of calcaneal fractures. Axial images should also be examined to determine whether the fracture extends into the calcaneocuboid joint or into the cuboid bone itself (Fig. 47–13).

Surgeons prefer to approach calcaneal fractures from the lateral side. This means that the sustentaculum tali and middle facet of the subtalar joint are not directly visualized. As such, surgeons rely on oblique coronal images to assess the integrity of these medial structures and to assess the relative size of the sustentaculum fragment.

Tibial Fractures

The common Weber-type inversion and eversion injuries of the ankle joint, resulting in fractures of the medial and lateral malleoli, typically do not require a CT scan for management decisions. For more complex distal tibial fracture patterns, however, a multiplanar CT scan may aid in surgical planning.

Comminuted (pilon) fractures involve the distal weight-bearing surface of the tibial (plafond). (*Pilon* is the French term for pestle, as in mortar and pestle.) In a pilon fracture, the articular surface of the tibial is shattered into multiple fragments. To acutely restore gross alignment of the ankle joint, the surgeon may choose to place an external fixation device and delay the more definitive internal fixation for several days. Obtaining a good-quality CT scan of the shattered articular surface while the external fixator is in place should not be a technical challenge. The longitudinal portion of the external stabilization rod tends to cause no appreciable beam-hardening streak artifacts to degrade the reconstruction images (Fig. 47–14). The metal brackets that connect the longitudinal rod to the transverse percutaneous pins are relatively dense and tend to cause artifacts. However, these artifacts are invariably proximal and distal to the fractured articular surface. As such, axial scanning can be limited to bones and joint structures between the levels of the percutaneous pins. Coronal and sagittal images should be reconstructed in planes optimized to show the surgeon the alignment of fragments within and around the ankle joint.

The distal tibial growth plate begins to fuse in the early teenage years, with the medial side fusing earlier than the lateral side. If a child of this age sustains a fracture through the distal tibial epiphysis, the fracture tends to extend through the lateral growth plate. This Salter-Harris type III fracture has been termed the *juvenile Tillaux fracture* and is well demonstrated with images in the coronal plane (Fig. 47–15).

Whereas the Salter-Harris type III fracture of the ankle follows the juvenile Tillaux pattern, a Salter-Harris type IV fracture occurs in a *triplane pattern* (Fig. 47–16). In a triplane fracture, as in the juvenile Tillaux fracture, the epiphyseal fracture occurs in the sagittal plane and the physeal fracture occurs in the axial plane. There is also a component of the fracture extending proximal to the growth plate, through the posterior metaphysis, which occurs in the coronal plane.

Arthritis

CT can be useful in assessing cortical integrity in the setting of chronic foot and ankle pain. Although arthritis is typically evaluated with conventional radiographs, the articular changes from osteoarthritis and erosive arthropathies are well shown with multiplanar CT. Particularly when a surgical fusion (arthrodesis) is being planned, the surgeon may wish to see inside the joints (e.g., ankle and subtalar joints), which are difficult to profile radiographically.

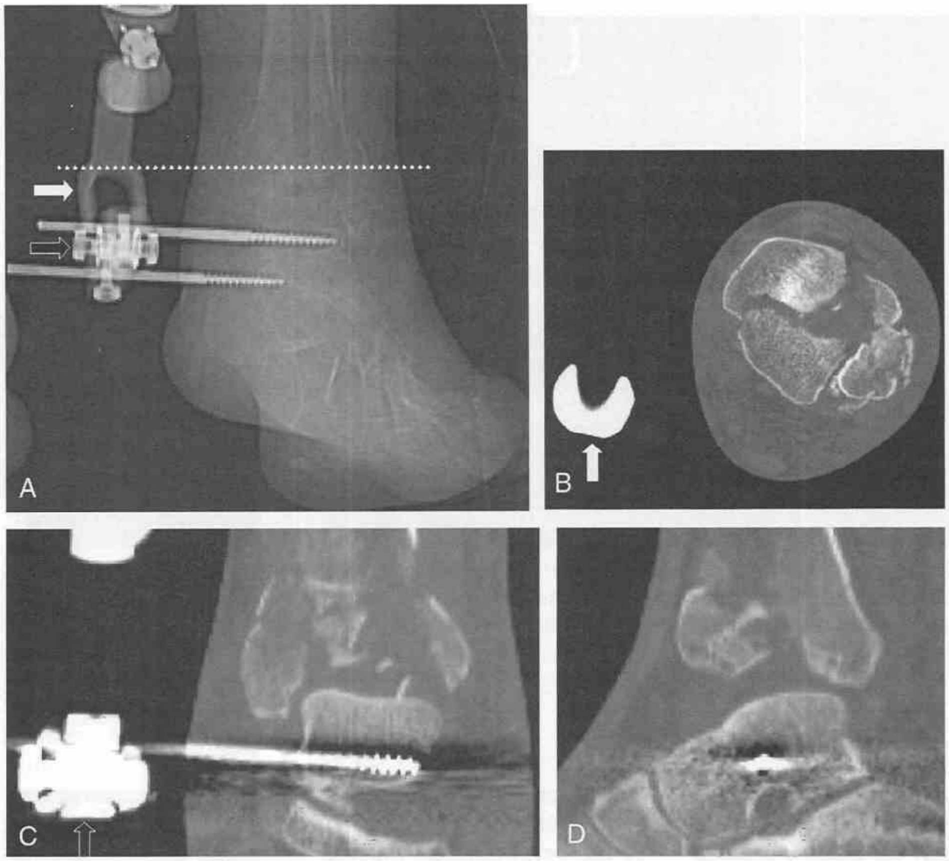

Figure 47–14. Pilon fracture. *A,* Anteroposterior scout image showing an external fixation device. The percutaneous pins are in the tibial diaphysis (above top on image) and in the hindfoot. The *black arrow* indicates the metal bracket that connects the transverse pins to the longitudinal rod, distal to the ankle joint. There is little hardware at the level of the ankle joint *(white arrow)*. The *dotted line* indicates the level of axial image *(B)*. *B,* Direct axial image obtained through a shattered tibial plafond. The *white arrow* indicates the external fixation rod. *C,* Coronal reconstruction image. Although there is a small amount of beam-hardening artifact at the level of the metal bracket *(arrow)*, this artifact is distal to the fractured tibial plafond. *D,* Sagittal reconstruction.

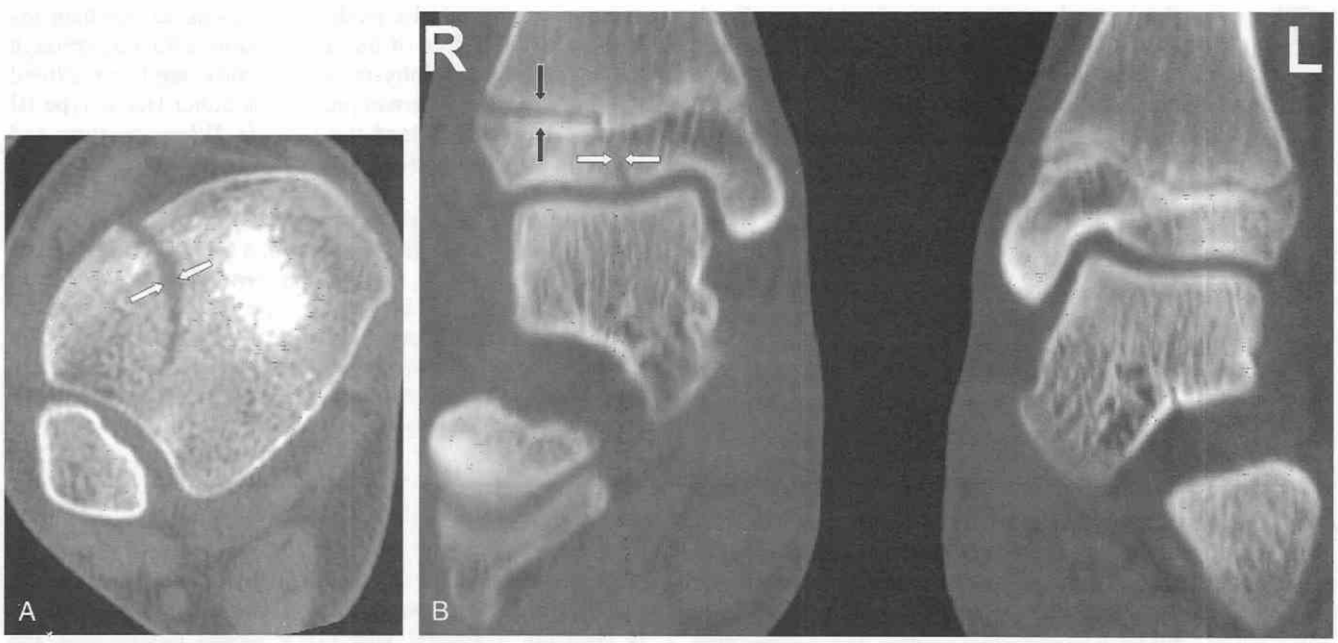

Figure 47–15. Juvenile Tillaux fracture. *A,* Direct axial image demonstrates the slightly displaced fracture through the anterolateral portion of the epiphysis *(white arrows)*. *B,* Coronal reconstruction image demonstrates not only the epiphyseal component of the fracture *(white arrows)* but also the slightly disrupted lateral physis *(black arrows)*. Because both ankles were scanned simultaneously, the normal left distal tibial growth plate is available for comparison.

Figure 47–16. Triplane fracture. *A,* Coronal reconstruction image. *B,* Sagittal reconstruction images. *White arrows* indicate the epiphyseal fracture in the sagittal plane. *Black arrows* indicate the physeal fracture in the axial plane. *White arrowheads* indicate the metaphyseal fracture in the coronal plane.

The four key features of osteoarthritis—nonuniform joint narrowing, subcortical sclerosis, subcortical cysts (geodes), and osteophyte formation—can all be demonstrated by CT (Fig. 47–17). Not infrequently, tiny intra-articular bodies accompany the arthritis; these are often radiographically subtle but can be demonstrated by CT. CT is also useful in detecting cortical erosions that may not be apparent on radiographs (Fig. 47–18).

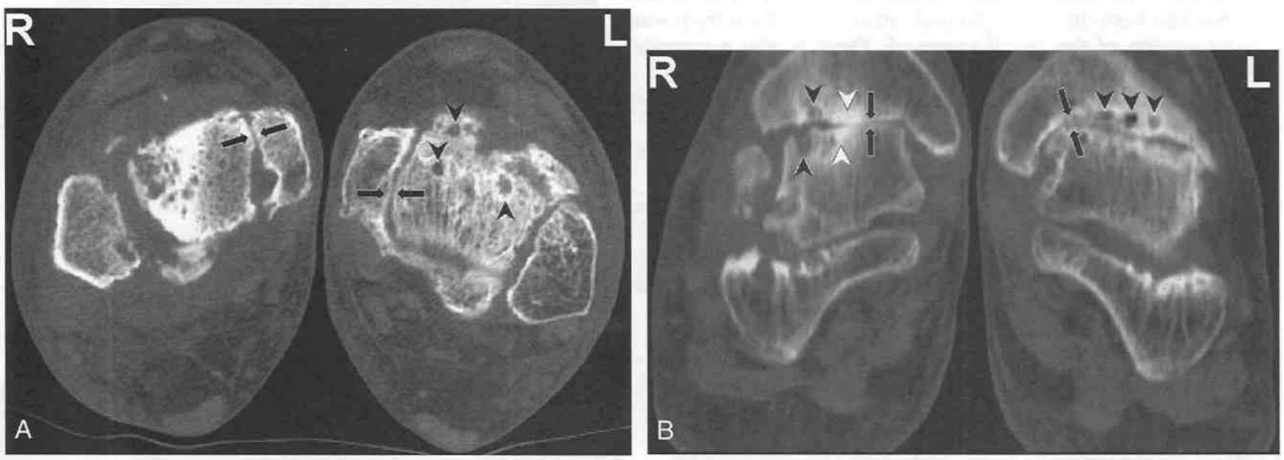

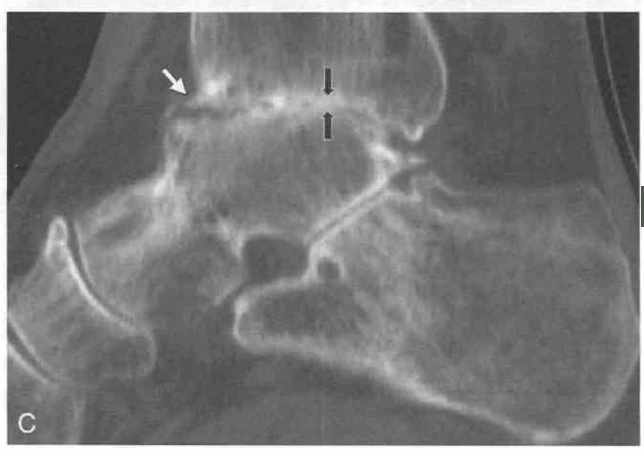

Figure 47–17. Osteoarthritis. *A,* Direct axial image demonstrates nonuniform narrowing of the medial ankle mortise *(black arrows).* Many geodes are also present *(black arrowheads). B,* Coronal reconstruction image demonstrates nonuniform narrowing *(black arrows)* and subcortical geodes *(black arrowheads)* as well as subcortical sclerosis *(white arrowheads). C,* Sagittal reconstruction image demonstrates nonuniform narrowing and subcortical sclerosis *(black arrows)* and a small anterior osteophyte *(white arrow).*

Figure 47–18. CT evaluation of a 34-year-old man who presented to the emergency department with acute onset of nontraumatic pain of his left great toe.

A, Oblique radiograph of the left foot. The region within the *dashed rectangle* is enlarged in *B.*

B, Close examination of the first metatarsal showed a th[redacted] white curved line just outside of the lateral diaphyseal cort[redacted] *(ellipse).* Initially, this was thought to represent a periosteal reaction from the first metatarsal rather than what it truly was: an erosion of the lateral sesamoid. There is also a marginal erosion of the medial first metatarsal head *(white arrow).*

C, Axial CT section obtained through the sesamoids of the great toes bilaterally demonstrates the lucent left lateral sesamoid *(circle).*

D, Coronal reconstruction CT image confirms the erosion in the left lateral sesamoid *(oval)* as well as in the adjacent lateral metatarsal head *(black arrow).*

E, An axial CT section proximal to *C* reveals the marginal erosion seen radiographically in the left medial metatarsal head *(white arrow)* and an erosion in the right second cuneiform (black arrow). This CT section nicely demonstrates that these two erosions both have well-defined, slightly sclerotic margins with sharp overhanging edges, characteristic of gout. Aspiration of the patient's left great toe metatarsophalangeal joint yielded uric acid crystals.

Osseous Fusion

When symptoms persist for months following trauma, CT can be used to determine the degree of fracture healing. Nonunion occurs in talar, navicular, and some distal tibial fractures but is rare following calcaneal fractures. When there is solid osseous fusion across the fracture line, CT may reveal other causes of the symptoms, such as an intra-articular fragment and secondary osteoarthritic changes. With calcaneal fractures in particular, osteoarthritis can develop in the large weight-bearing posterior facet of the subtalar joint if articular surfaces are not anatomically aligned (Fig. 47–19).

Arthrodesis (surgical fusion of a joint) is a common procedure for treating patients with symptomatic osteoarthritis of the ankle or foot. When symptoms persist beyond the expected postoperative recovery period, a CT scan with images obtained or reconstructed perpendicular to the joint in question can be useful to determine the degree, if any,

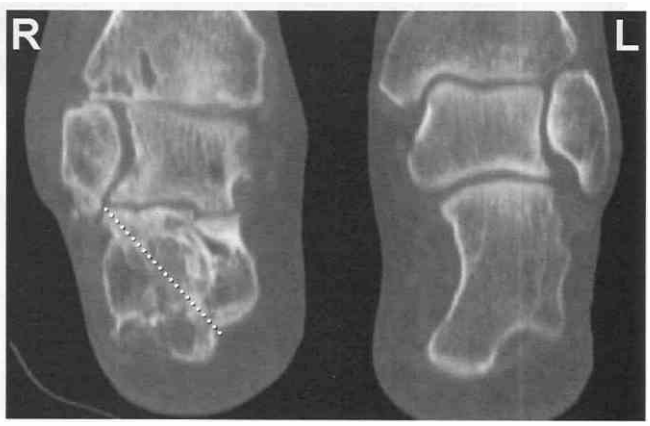

Figure 47–19. Coronal reconstruction CT image showing the healed right calcaneal fracture *(dotted line).* There is secondary osteoarthritis at the ankle and subtalar joints. The normal left hindfoot is included for comparison.

Figure 47–20. The patient is a 55-year-old man with persistent hindfoot pain after an attempted subtalar arthrodesis. Lateral radiograph of the ankle *(A)* and oblique radiograph of the foot *(B)* reveal a single lag screw across the subtalar joint. The degree of osseous fusion across the joint is unclear from these radiographic projections. Oblique coronal *(C)* and oblique sagittal *(D)* reconstruction images clearly reveal no solid cortical bridging across the subtalar joint *(white arrows)*. Subsequently, the arthrodesis was redone and a second screw was placed across the subtalar joint.

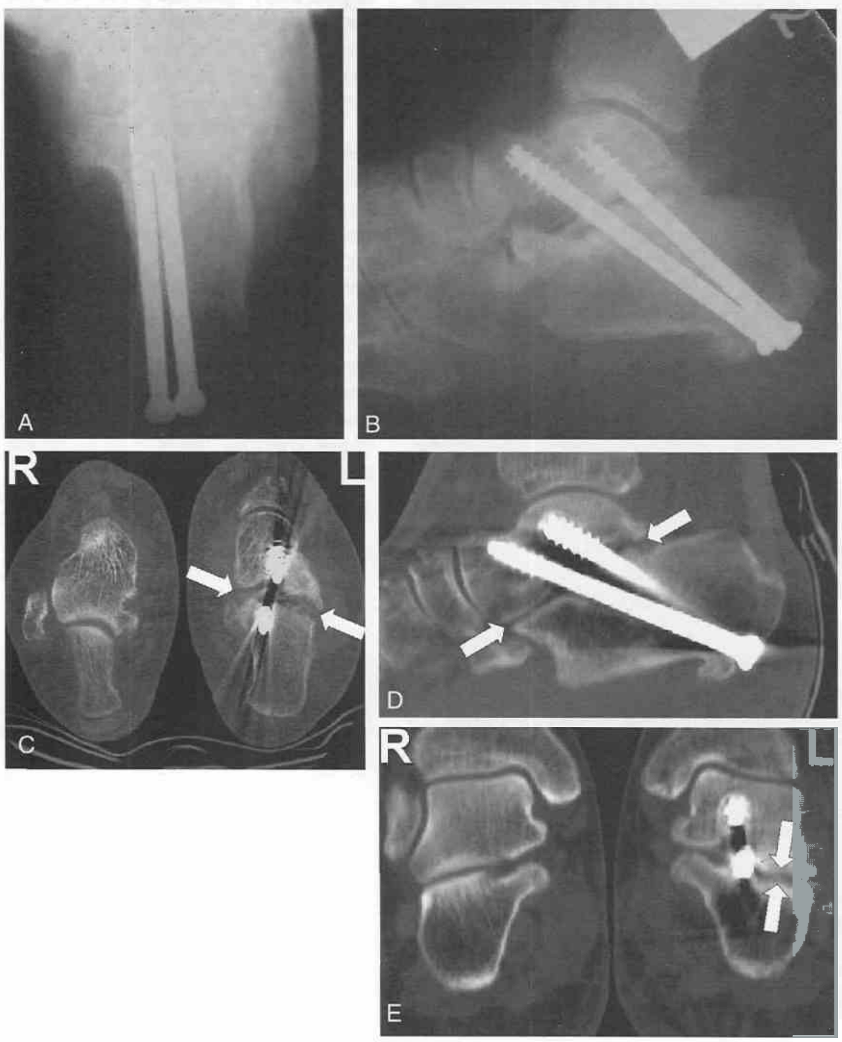

Figure 47–21. The patient is a 72-year-old woman with persistent hindfoot pain after an attempted subtalar arthrodesis with two lag screws. *A,* Harris radiographic axial view of the calcaneus. *B,* Lateral radiograph of the ankle. These two radiographic projections suggest that the subtalar joint is not fused. However, the surgeon was reticent to subject this patient to a second surgical procedure and requested a multiplanar CT scan to evaluate the subtalar joint. *C,* Direct axial CT image. *D,* Sagittal reformatted CT image. *E,* Oblique coronal reformatted CT image. Despite some beam-hardening artifacts between the two screws, all three planes clearly show no solid osseous fusion across the subtalar joint *(white arrows)*.

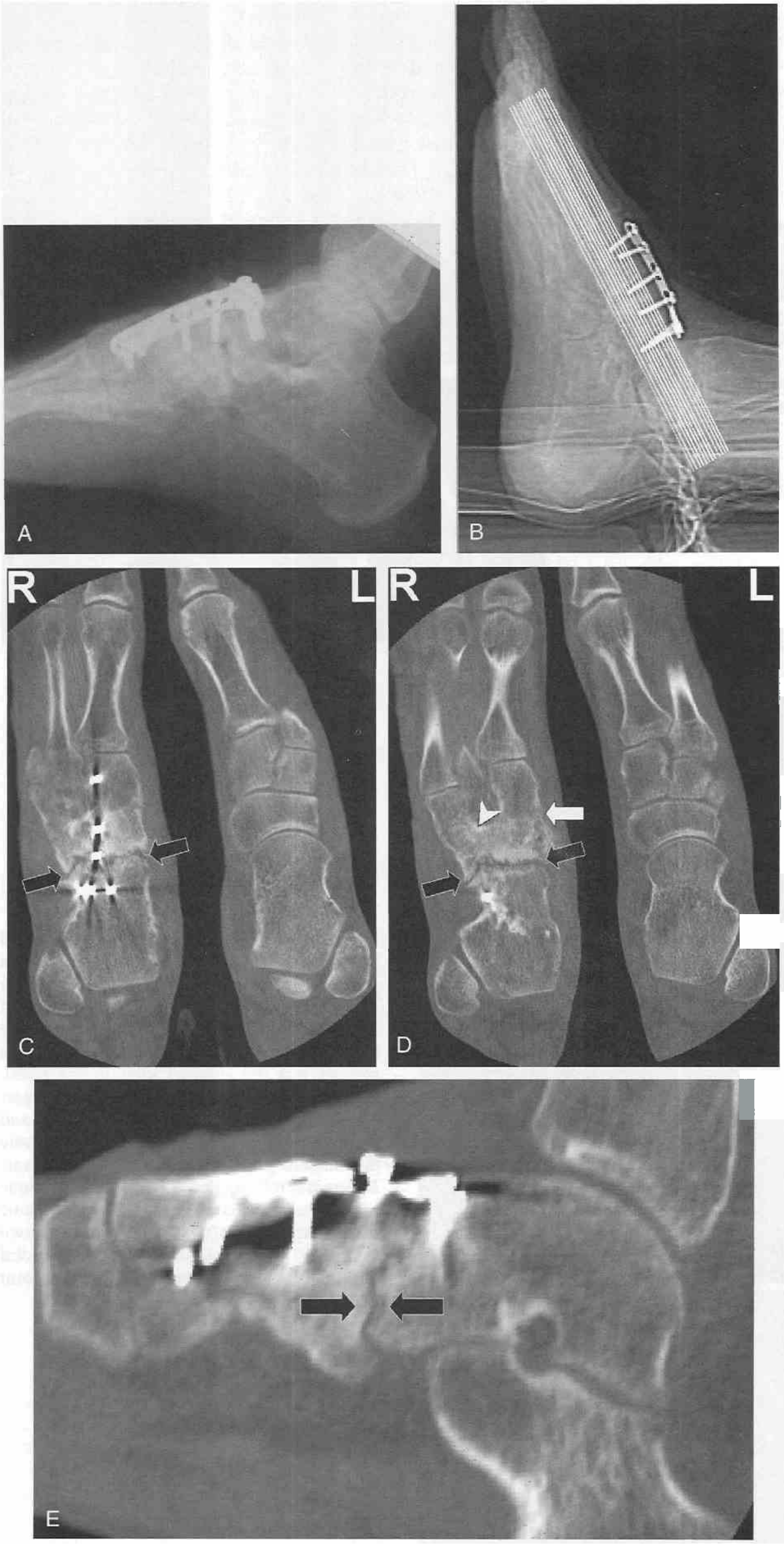

Figure 47–22. Attempted midfoot fusion in a 26-year-old man. *A,* Lateral radiograph demonstrates a dorsal plate with six screws extending across the talonavicular and navicular-cuneiform joints. *B,* Lateral scout projection for the CT scan. With the toes pointing up, the top of the gantry was angled away from the patient and the midfoot was scanned in the oblique axial plane *(white lines). C,* Oblique axial CT image. Even scanning through six screws, the streak artifact is minimal. No cortical bridging is seen across the talonavicular joint *(black arrows). D,* Oblique axial CT image, a few slices distal to *C.* At this level, the nonunion of the talonavicular joint is clearly demonstrated *(black arrows).* However, there is solid osseous fusion across the medial navicular cuneiform joint *(white arrow)* and partial fusion across the lateral navicular cuneiform joint *(arrowhead). E,* Sagittal reformatted CT image confirms the nonunion of the talonavicular joint *(black arrows).*

of osseous fusion across the attempted arthrodesis. The single cannulated lag screws used to fuse the subtalar joint typically cause no appreciable beam-hardening streak artifacts (Fig. 47–20). When more than one screw is present across the joint (Fig. 47–21) or when several small screws are used with a plate (Fig. 47–22), black streaks can occur in between the screws. However, by optimizing the scanning and reconstruction planes, we can still obtain useful information about cortical integrity.

Tarsal Coalitions

A *coalition* is an abnormal osseous, fibrous, or cartilaginous union between bones.[68] Tarsal coalitions occur in two characteristic sites: (1) between the anterior process of the calcaneus and the lateral pole of the navicular and (2) across the middle facet of the subtalar joint.

Coalitions result from failure of fetal primitive mesenchyme to segment by cleavage and thus produce the normal peritalar joint complex.[39] The reported incidence of tarsal coalition in the general population is less than 1%.[53, 82] However, before the advent of CT, many tarsal coalitions, particularly coalitions of the subtalar joint, went undiagnosed. The true incidence is probably considerably greater than 1%.[92] Approximately 60% of calcaneonavicular coalitions and 50% of talocalcaneal coalitions occur bilaterally.[60]

The subtalar joint complex consists of the subtalar joint,

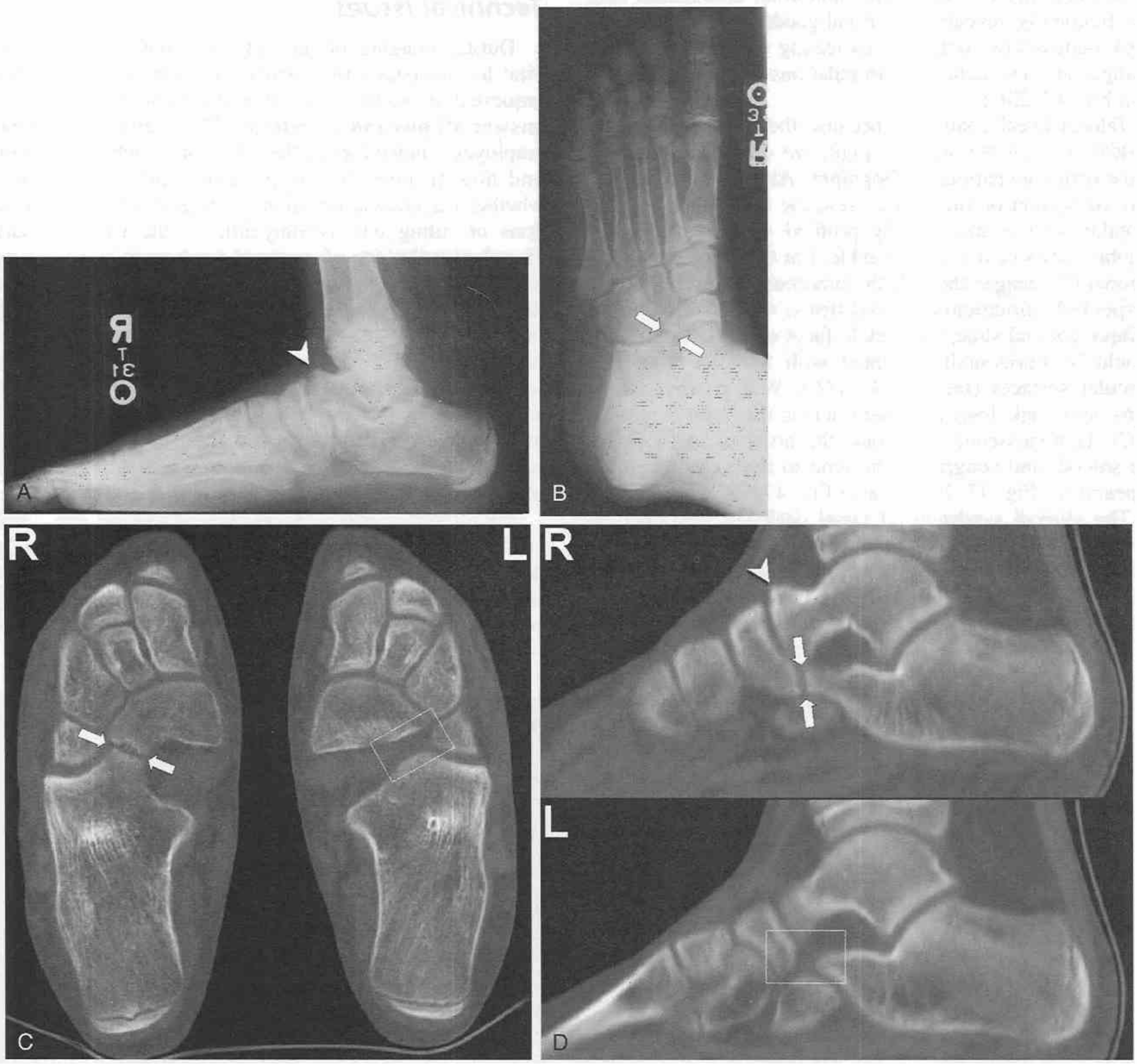

Figure 47–23. Nonosseous calcaneonavicular coalition in a 12-year-old boy. *A,* Lateral radiograph demonstrates a talar beak *(arrowhead). B,* Oblique radiograph shows the abnormal articulation *(arrows)* between the anterior process of the calcaneus and the lateral pole of the navicular. *C,* Axial CT image obtained through both feet clearly demonstrates the abnormal articulation *(arrows)* between the anterior process of the calcaneus and the lateral pole of the navicular on the right. Tiny subcortical geodes are present on each side of this abnormal articulation. The left foot has a normal gap between these bones *(rectangle). D,* Sagittal reformatted images through each foot. The image of the right shows the calcaneonavicular coalition *(arrows)* and the talar beak *(arrowhead).* The image of the left shows normal gap *(rectangle)* between calcaneus and navicular.

the calcaneocuboid joint, and the talonavicular joint. These joints function in unison during the gait cycle, and limitation of motion of any one of these joints limits the motion of the other joints.[15] The altered biomechanics across the talonavicular joint can result in a traction spur, or "beak," arising from the neck of the talus (Fig. 47–23*A*; see also Fig. 47–25*A*).[67] Talar beaks occur less frequently with nonosseous coalitions because some subtalar motion remains.[20]

Calcaneonavicular coalitions can be demonstrated radiographically with an oblique view of the foot (Fig. 47–23*B*). There is no normal joint between the calcaneus and the navicular. When adjacent cortical surfaces are present between the calcaneus and navicular, this represents a nonosseous coalition. CT shows this abnormal articulation and, less frequently, reveals subcortical geodes on either side of these nonosseous coalitions, indicating early osteoarthritic changes at these abnormal articulations (Fig. 47–24*B*; see also Fig. 47–23*C*).

Talocalcaneal coalitions, because they occur across the middle facet of the subtalar joint, are difficult to demonstrate with conventional radiographs. Although a talar beak may be present on the lateral view, the middle facet of the subtalar joint is not reliably profiled on standard radiographic views of the foot or ankle. For this reason, oblique coronal CT images through the hindfoot are invaluable for suspected talocalcaneal coalitions. On a well-angled oblique coronal slice, the middle facet of the subtalar joint should be horizontally oriented with flat and congruent articular surfaces (see Fig. 47–11*C*). With osseous coalitions, solid ankylosis is present across this joint (Fig. 47–25*C*). In nonosseous coalitions, the articular surfaces are not smooth and congruous and tend to have an overgrown appearance (Fig. 47–26; see also Fig. 47–25*C*).

The clinical syndrome of tarsal coalition, described in the 1920s,[1, 78] consists of pain, reduced or absent subtalar motion, pes planus, and peroneal muscle spasm (i.e., clonus on inversion stress). The exact cause of peroneal spasm is uncertain; however, peroneal muscle tightness is the result of tarsal coalition and not the cause. Other considerations in the differential diagnosis of peroneal muscle tightness include juvenile rheumatoid arthritis, osteochondral fracture, subtalar joint infection, and neoplasms. Symptoms usually manifest between 12 and 16 years of age and worsen with increasing age. Conservative treatment options include anti-inflammatory medication and a trial of reduced activity, cast immobilization, and molded orthotics. If conservative treatment fails, surgical options include resection of the coalition and arthrodesis if secondary osteoarthritis has developed.

Magnetic Resonance Imaging

Technical Issues

During imaging of the ankle or foot with MRI, it is vital to understand the clinical question the scan is being requested to address. No one standardized protocol can answer all possible questions. The scanning sequences employed—indeed, even the selection of which coil to use and how to position the patient—vary, depending on whether the clinical question is integrity of the ankle tendons or ruling out osteomyelitis of the toes. A marker placed over the site of maximal tenderness or near a nonhealing ulcer can be helpful to draw the attention of both the technologist acquiring the images and the radiologist interpreting the images. Such a marker needs to be conspicuous on all imaging sequences, including fat-suppressed sequences, and should be placed on the patient in such a way as to not deform the contour of the skin. Although markers are commercially available,[8, 42] generic capsules containing vitamin E or docusate sodium (Colace) also work well.

For protocol purposes, an MR image of the "foot" needs to be differentiated from that of the "ankle." Typically, an MR image of the ankle is ordered to evaluate the ankle joint, the bones of the hindfoot and midfoot, the ankle tendons, and the surrounding soft tissues. The field

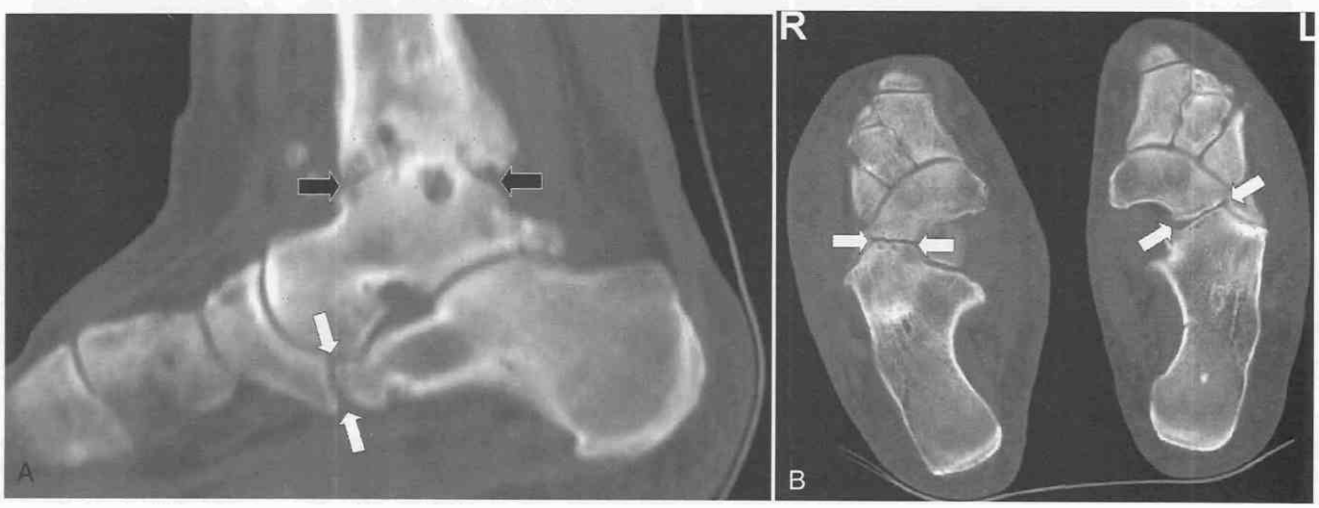

Figure 47–24. Evaluation of a 51-year-old woman for osteoarthritis of the ankle joint. *A*, Sagittal reconstruction image shows advanced osteoarthritic changes at the ankle joint *(black arrows)*, including narrowing, subcortical sclerosis, and geode formation. An incidental finding is a nonosseous calcaneonavicular coalition *(white arrows)*. *B*, Axial images obtained through both feet demonstrate bilateral calcaneonavicular coalitions *(white arrows)*. Tiny subcortical geodes are present on each side of these abnormal articulations.

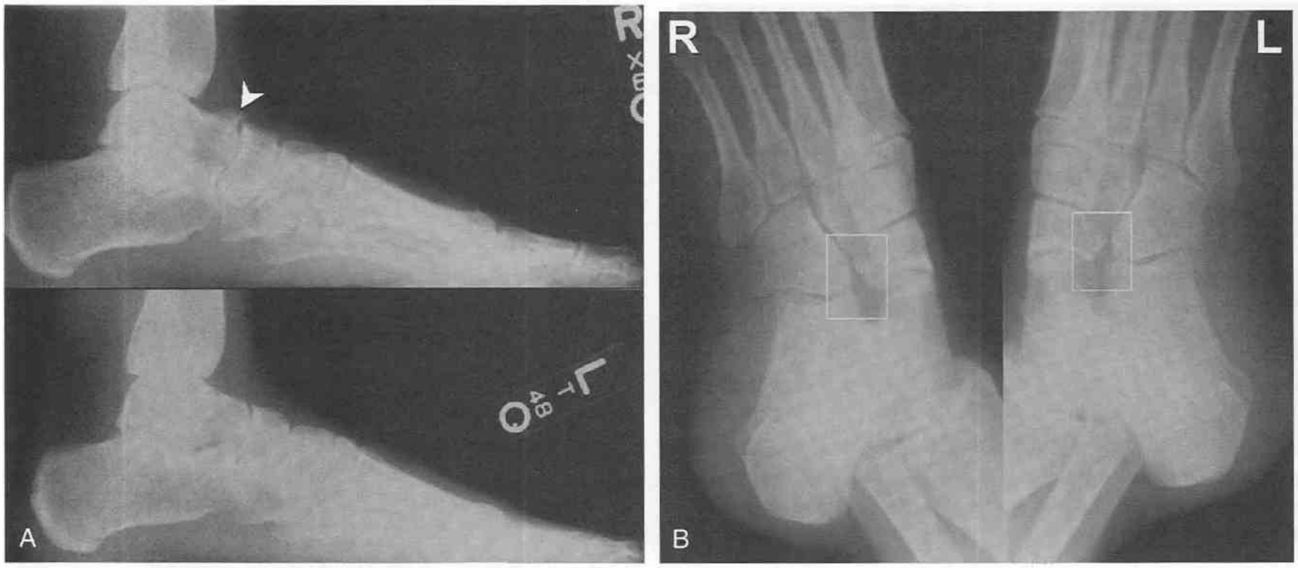

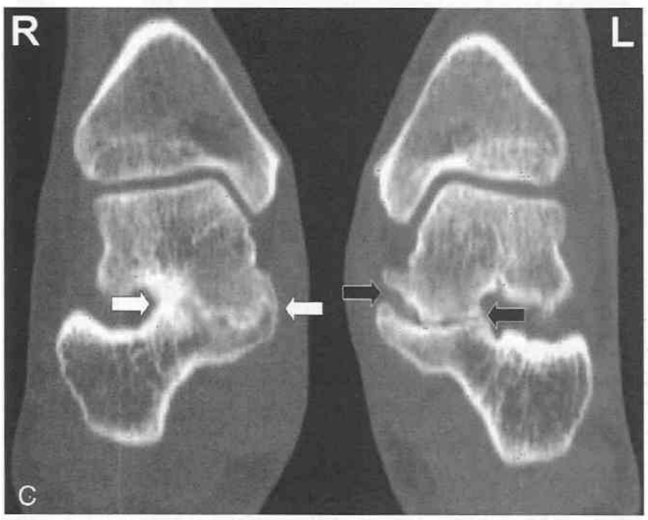

Figure 47–25. The patient is a 29-year-old radiology resident with a long history of bilateral foot pain. The pain had been worse on the right, was exacerbated by athletics, and was improved with custom orthotics. *A,* Lateral radiographs of both feet reveal a talar beak *(arrowhead)* on the right. *B,* Oblique radiographs show no calcaneonavicular coalition *(rectangles). C,* Coronal oblique reconstruction CT image demonstrates solid osseous coalition across the middle facet of the subtalar joint on the right *(white arrows).* There is also a nonosseous coalition of middle facet *(black arrows)* as manifested by a joint that is abnormally broad with irregular, noncongruent articular surfaces.

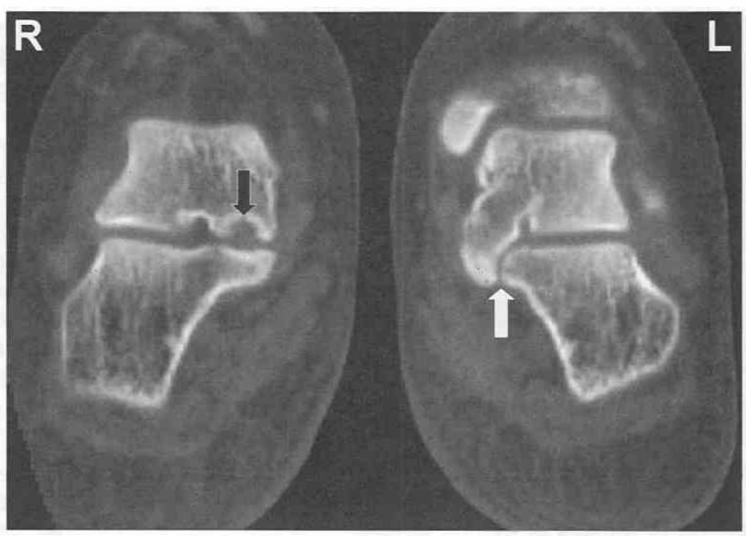

Figure 47–26. Nonosseous coalitions of the middle facet of the subtalar joint bilaterally in an 8-year-old girl. The left middle facet has an abnormal vertical orientation *(white arrow).* On the right, the talar-side middle facet has an abnormal rounded cortical surface *(black arrow).*

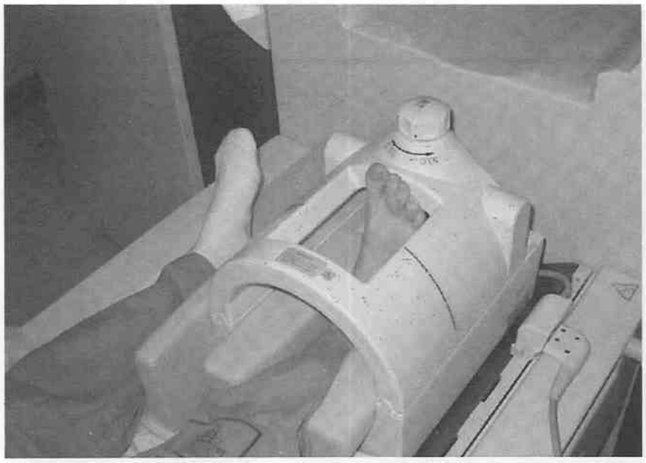

Figure 47–27. The open top on this knee coil for a Siemens scanner allows the toes to extend through the coil while the ankle/hindfoot is scanned.

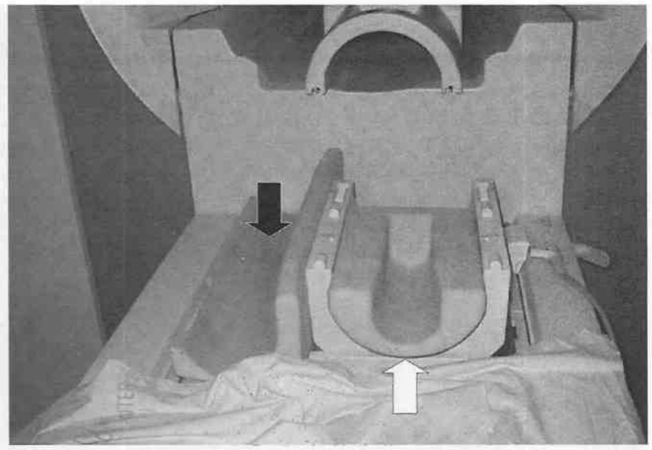

Figure 47–29. A foam pad within the coil *(white arrow)* helps to immobilize the hindfoot being scanned. A second pad next to the coil *(black arrow)* gives the contralateral foot a place to rest.

of view for an ankle MR image may incidentally include the metatarsal bases, but the phalanges are often excluded. An MR image of the foot, in contrast, should include the metatarsals and phalanges. Indications for MRI of a foot rather than an ankle would include suspected osteomyelitis or occult fracture of the forefoot, sesamoid disorders, and suspected Morton's neuroma.

Typically, when the ankle or foot is being scanned, the patient is positioned supine with the foot resting comfortably in a neutral position within the coil. It is not necessary to have a dedicated ankle coil to obtain high-quality images. Depending on the specific manufacturer's design, it may be possible to position the patient's ankle comfortably within a coil designed for the head or knee. For example, the top of the Siemens knee coil is open, allowing the toes to extend through it (Fig. 47–27). The General Electric foot coil includes a "chimney" that extends the field of view to include the toes (Fig. 47–28). Foam pads should be used to help immobilize the patient's hindfoot within the coil (Fig. 47–29). When it is necessary to scan the toes and the available coils do not easily accommodate the toes while the patient is supine, the patient can be positioned prone with the foot plantiflexed. The toes can then be centered within a knee coil, possibly even within a wrist coil.

To screen for osseous abnormalities, such as stress fractures or osteomyelitis, a sequence sensitive to bone marrow edema should always be performed. This can be a fat-suppressed, fast-spin-echo, T2-weighted sequence (TR $= \sim 4000$ msec, TE $= \sim 102$ msec, ETL $= 8$) or an inversion recovery sequence (TR $= \sim 3600$ msec, TE $= \sim 40$ msec, IT $= \sim 150$ to 160 msec, ETL $= 8$).* It is often desirable to have T1-weighted images (TR $= \sim 500$ msec, TE < 20 msec) to compare with the marrow-sensitive images.

The ankle tendons should be examined with a sequence that yields good contrast differentiation between the tendons and adjacent structures as well as with a sequence that is sensitive to fluid within the tendon sheaths. Both of these objectives can be obtained with a single spin-echo, double-echo sequence, with a TR in the range of 2150 to 2400 msec, the TE for the first echo about 20 msec, and the TE of the second echo about 80 msec. The first-echo proton-density–weighted images can then be compared side by side with second-echo T2-weighted images at the same slice positions.

As with most MR images, the double-echo sequence is acquired using 256 pixels in the frequency direction. When time permits, higher-resolution images can be obtained using more T1-weighted parameters (TR $= \sim 600$ msec, TE $= \sim 20$ msec) and a 512-pixel matrix.

Figure 47–30 is a side-by-side comparison of a T1-weighted image obtained by a high-resolution 512-pixel matrix, with proton-density–weighted and T2-weighted images obtained by a conventional 256-pixel matrix. The improved resolution is particularly noticeable in examinations of thin linear structures such as retinacular fibers. Such high-resolution T1-weighted images well illustrate

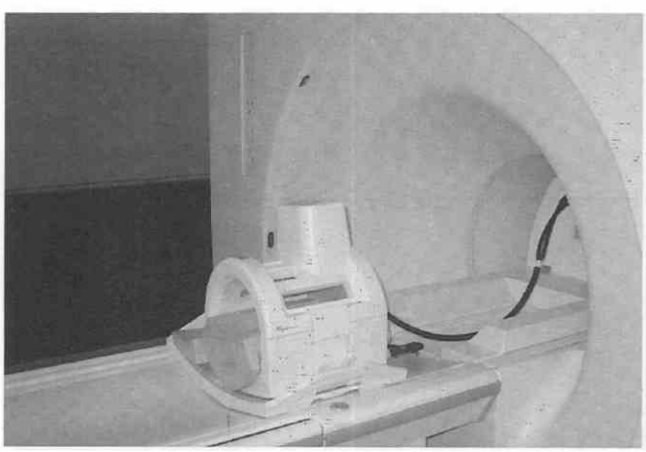

Figure 47–28. This dedicated ankle/foot coil for a General Electric scanner includes a chimney-like extension so that the phalanges can be included in the field of view.

*ETL = echo train length; IT = inversion time; TE = echo time; TR = repetition time.

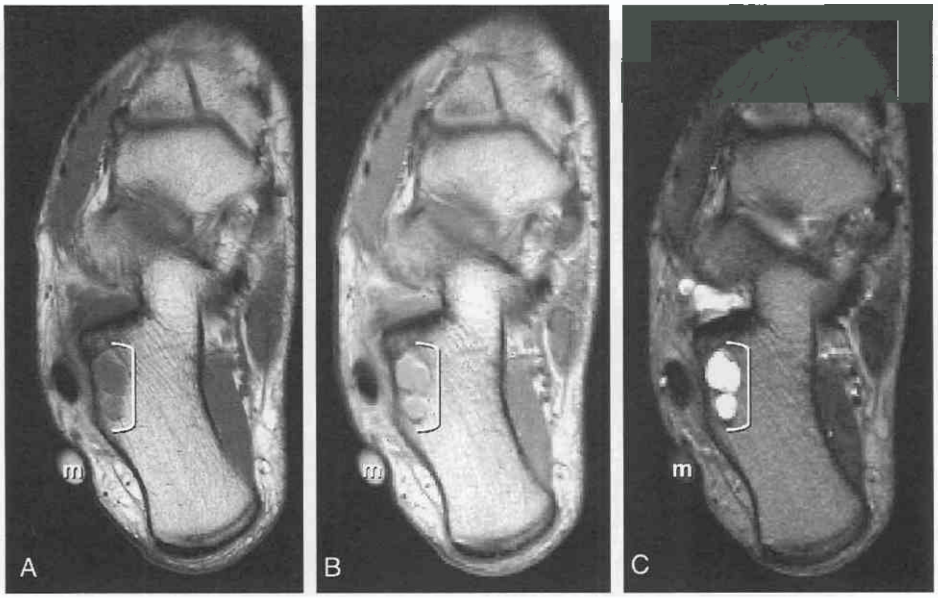

Figure 47–30. Comparison of T1-weighted, proton-density–weighted, and T2-weighted images at the same axial slice position. *A,* T1-weighted image obtained with a high-resolution 512-pixel matrix. *B,* Proton-density–weighted image obtained with a standard-resolution 256-pixel matrix. *C,* T2-weighted image obtained with a standard-resolution 256-pixel matrix. The marker (m), indicating the point of maximum symptoms, is a generic docusate sodium capsule and is visible on all three sequences. An incidental finding is an intraosseous ganglion *(bracket)* within the calcaneus.

normal anatomic structures (Figs. 47–31 and 47–32); however, they are rarely needed to determine the integrity of the ankle tendons.

Rectangular Field of View

Although the spin-echo, double-echo sequence yields images with good spatial and contrast resolution, it can take a long time to acquire. The three factors that determine acquisition time are (1) repetition time (TR), (2) the number of excitations (NEX), and (3) the number of phase encodes. Thus, even at a single excitation, acquiring a 256-pixel matrix with a TR of 2400 msec takes 614 seconds (10.24 minutes).

Although many patients can hold still for a 10-minute acquisition, particularly when the ankle is comfortably immobilized in the coil, some patients may not be able to cooperate for such a lengthy scan. Besides, in many imaging centers, scheduling constraints preclude the use of too many 10-minute sequences. In such instances, using a rectangular field of view can cut acquisition time in half, with no loss of resolution.

Figure 47–33*A* illustrates a typical axial slice through the hindfoot and midfoot using a conventional square field of view, 16 × 16 cm. If the image is mapped into a 256 × 256 pixel matrix, the resolution is 16 cm per 256 pixels = 0.6 mm per pixel.

One way to cut the acquisition time in half is to use half as many pixels in the phase direction (Fig. 47–33*B*). If we can decrease the number of phase encodes from 256 to 128, the time of acquisition is decreased from 10 to 5 minutes. However, this yields rectangular pixels with a resolution in the phase direction that is now 16 cm per 128 pixels = 1.2 mm per pixel, half the resolution in the frequency direction. Thus, although acquisition time is gained, resolution is sacrificed. This is a common tradeoff with MRI.

A true timesaving can be achieved if we realize that the foot/ankle is more than twice as long in AP length as in mediolateral (ML) width. A 50% rectangular field of view in the axial plane, measuring 16 cm in the AP direction and 8 cm in the mediolateral direction, covers the ankle and tarsal bones in all but the largest feet (Fig. 47–33*C*). This rectangular field of view can be divided into 256 pixels in the frequency direction, and 128 pixels in the phase direction. This yields square pixels with a resolution of 0.6 mm per pixel in both the phase and frequency directions (8 cm per 128 pixels = 16 cm per 256 pixels = 0.6 mm per pixel). Using a 50% rectangular field of view allows only 128 phase encodes to be performed, with only 5 minutes of acquisition time necessary, while still maintaining 0.6 mm per pixel resolution in both directions.

Potential problems with the rectangular field of view technique arise from anatomic structures *wrapping* in the phase direction (see Fig. 47–33*C*). Any structure extending beyond the lateral margin of the image in the phase direction is mapped onto the medial side of the image. This phase-wrapping problem is always present with MRI and can be overcome by using relatively large fields of view or *phase-oversampling* or *no-phase-wrap techniques*. The risk of phase wrapping with a rectangular field of view can be minimized if the technologist graphically prescribes the axial or coronal slices off a midline sagittal image. Some manufacturers include a second localizer on their scanning consoles, and this allows for easy visual determination for potential phase wrapping. Before starting a lengthy acquisition, the technologist should always confirm that the phase and frequency directions have not been inadvertently switched.

Ankle Tendons

The ankle tendons are best appreciated in cross-section in the direct axial plane (see Fig. 47–31). The oblique coronal plane (see Fig. 47–32) is a good secondary plane by which to observe the medial and lateral tendons as they course under the malleoli. Normal tendons should appear uniformly black on all imaging sequences and have a

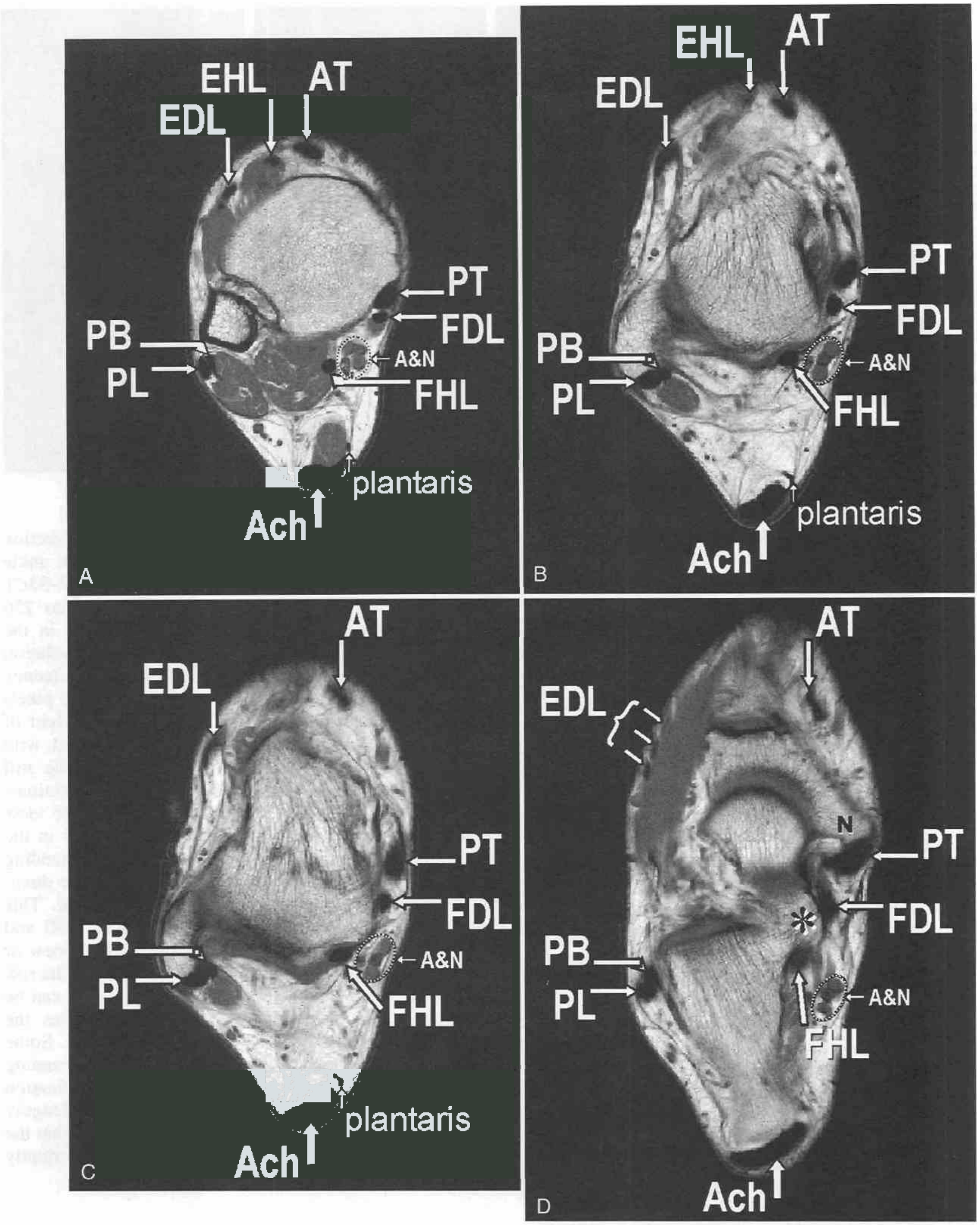

Figure 47–31. Normal ankle tendons shown on series of high-resolution T1-weighted MR images obtained in the direct axial plane. *A,* Image obtained through the top of the syndesmosis. *B,* Image obtained through the tip of the medial malleolus. *C,* One slice below *B*: this image demonstrates the normal loss of dark signal of the extensor hallucis longus tendon. *D,* Image obtained through the talonavicular joint demonstrates the posterior tibial tendon inserting into the navicular (N) and the flexor hallucis longus tendon passing under the sustentaculum tali *(asterisk)*. At this level, the extensor digitorum longus is dividing into separate tendon slips. A&N (artery and nerve) points to the *dotted circle* surrounding the neurovascular bundle that includes the posterior tibial artery and nerve. Ach, Achilles tendon; EDL, extensor digitorum longus tendon; EHL, extensor hallucis longus tendon; AT, anterior tibial tendon; FHL, flexor hallucis longus tendon; PB, peroneus brevis tendon; PL, peroneus longus tendon; PT, posterior tibial tendon; FDL, flexor digitorum longus tendon.

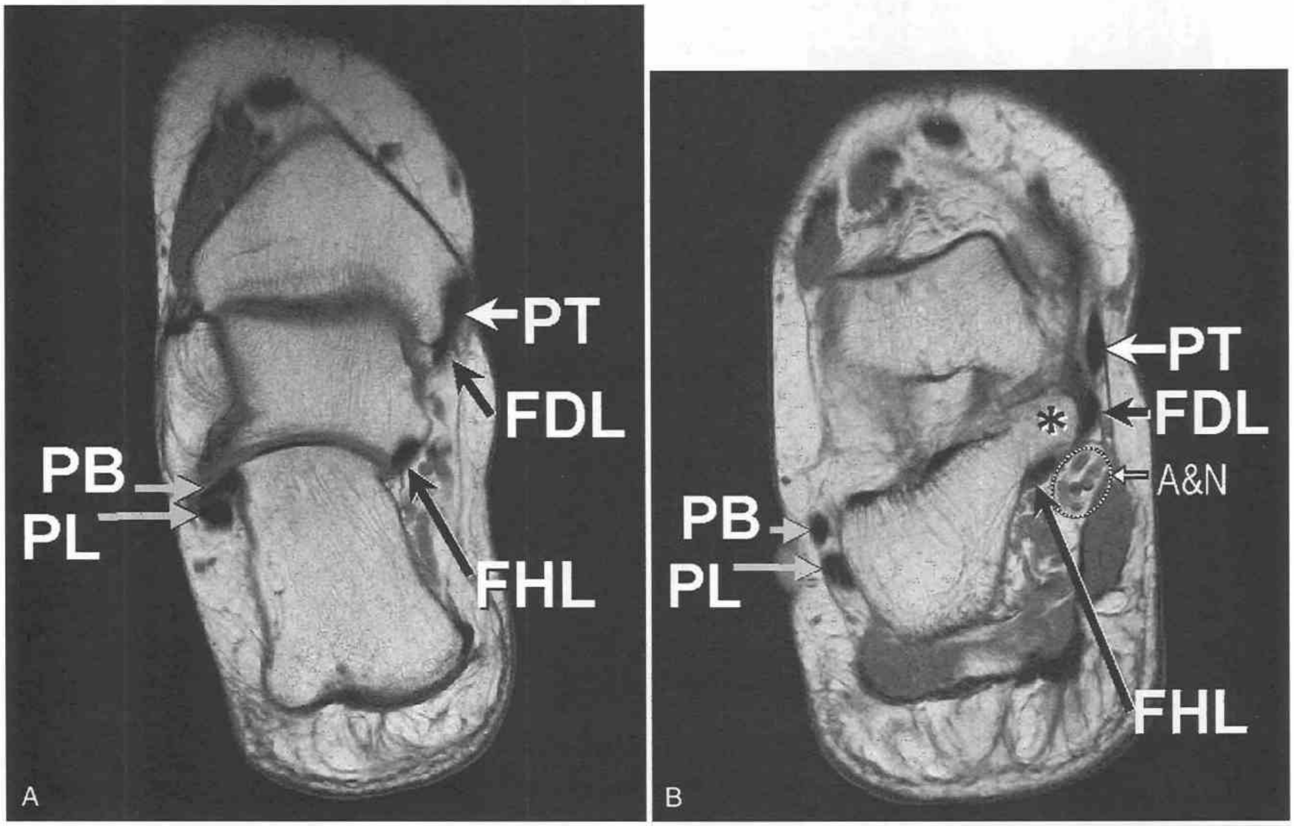

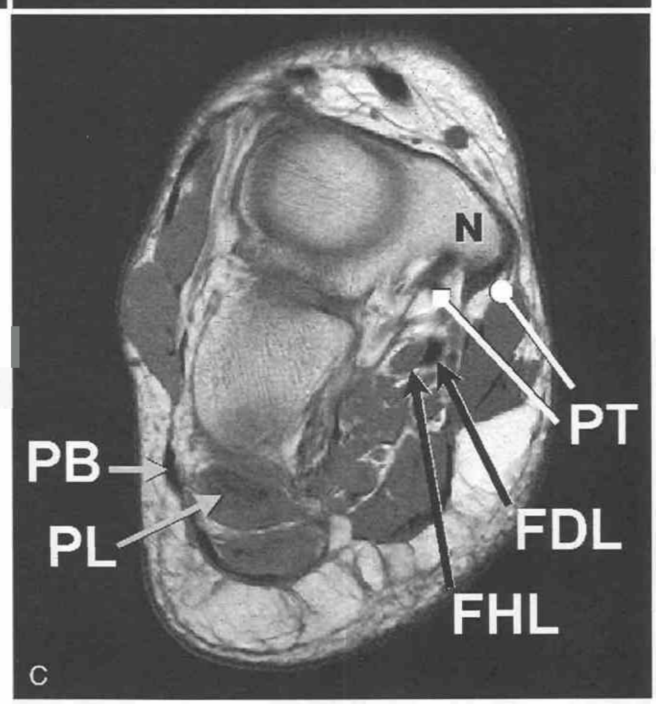

Figure 47–32. Normal ankle tendons shown on a series of high-resolution T1-weighted MR images obtained in the oblique coronal plane. *A,* Image obtained through the posterior facet of the subtalar joint. *B,* Image obtained through the middle facet of the subtalar joint. *C,* Image obtained through the talonavicular joint (same patient as in Fig. 47–55). At this level, the posterior tibial tendon has divided into two separate slips. The *white line with the round end* indicates the portion of the posterior tibial tendon inserts onto the navicular (N), and the *white line with the square end* indicates the portion that passes under the navicular. This patient has an os peroneum, which is why the peroneus longus tendon appears enlarged and gray at this level. A&N points to the *dotted circle* surrounding the neurovascular bundle that includes the posterior tibial artery and nerve. FDL, flexor digitorum longus tendon; FHL, flexor hallucis longus tendon; PB, peroneus brevis tendon; PL, peroneus longus tendon; PT, posterior tibial tendon.

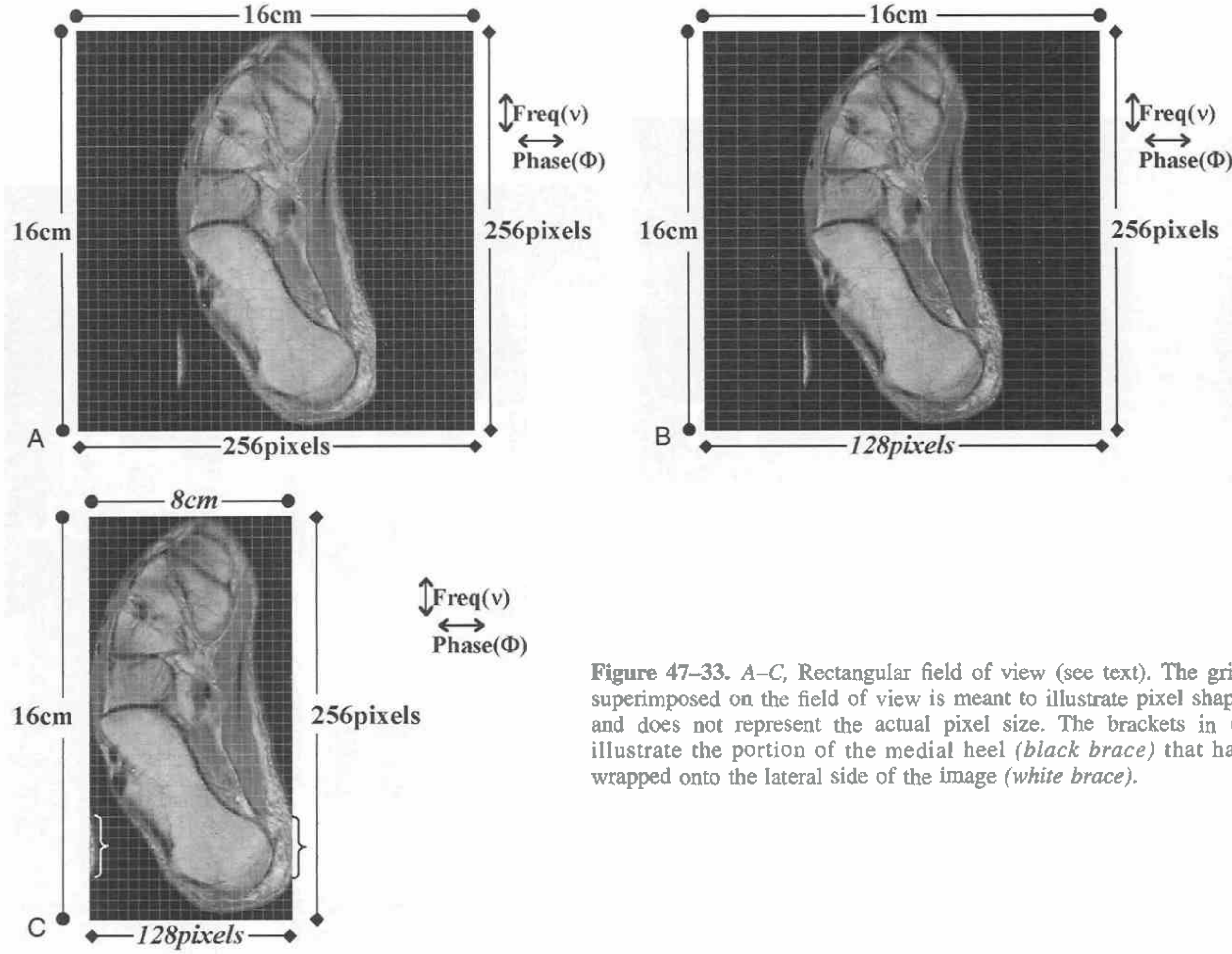

Figure 47–33. *A–C,* Rectangular field of view (see text). The grid superimposed on the field of view is meant to illustrate pixel shape and does not represent the actual pixel size. The brackets in *C* illustrate the portion of the medial heel *(black brace)* that has wrapped onto the lateral side of the image *(white brace).*

sharply defined interface between themselves and adjacent fatty soft tissues. Any increased signal within a tendon on a T2-weighted image indicates the presence of pathology, typically an intrasubstance tear. In addition, more than a trace amount of fluid around an ankle tendon is abnormal, indicating inflammation or some other pathologic process. The *exception* to this is the *flexor hallucis longus*, which may normally contain some fluid in its tendon sheath (Fig. 47–34*C*).

Typically, 10 tendons cross the ankle joint. These ten-

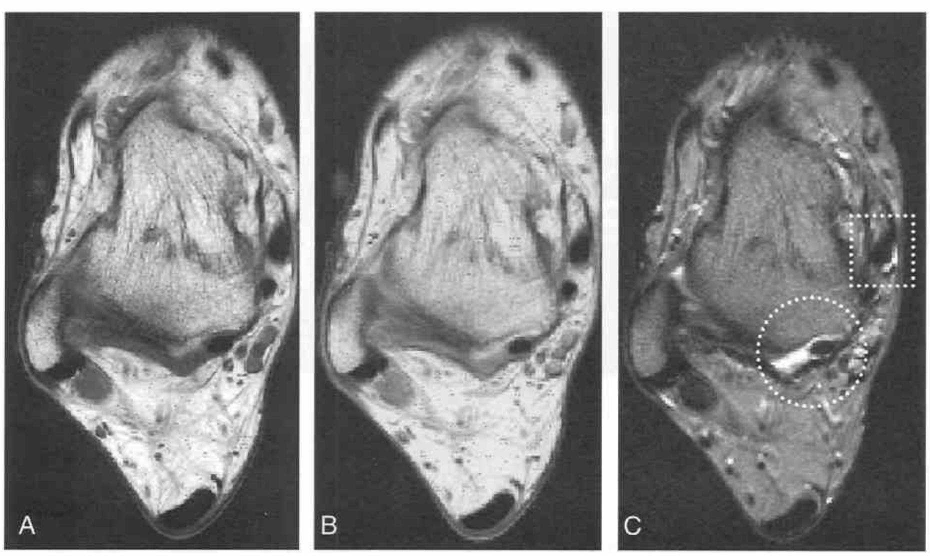

Figure 47–34. Comparison of T1-weighted, proton-density–weighted, and T2-weighted images at the same axial slice position. *A,* T1-weighted image obtained with a high-resolution 512-pixel matrix. *B,* Proton-density–weighted image obtained with a standard-resolution 256-pixel matrix. *C,* T2-weighted image obtained with a standard-resolution 256-pixel matrix. The *dotted circle* indicates a normal amount of fluid in the flexor hallucis longus tendon sheath. The *dotted square* indicates a slightly abnormal amount of fluid in the posterior tibial tendon sheath.

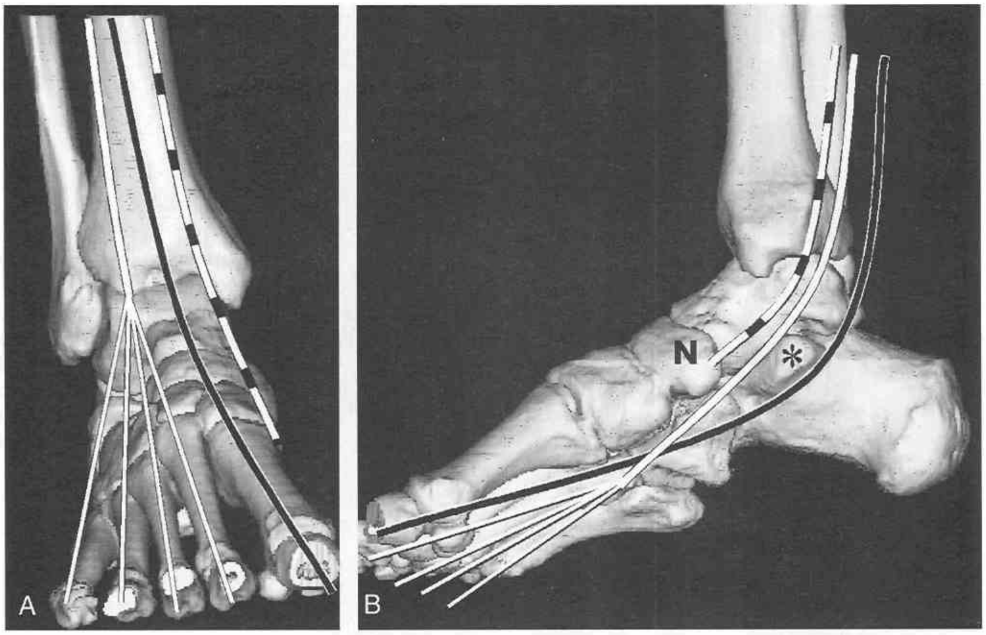

Figure 47–35. Ankle tendons, drawn on a three-dimensional reconstructed CT image. *A,* Anterior ankle tendons. *Dashed line,* anterior tibial tendon; *black line,* extensor hallucis longus tendon; *white line,* extensor digitorum longus tendon. *B,* Medial ankle tendons. *Dashed line,* posterior tibial tendon; *white line,* flexor digitorum longus tendon; *black line,* flexor hallucis longus tendon). N, navicular. *Asterisk* represents the sustentaculum tali.

dons can be clustered into four groups according to their anatomic locations. From an imaging standpoint, anteriorly are the anterior tibial tendon, the extensor hallucis longus tendon, and the extensor digitorum longus tendon (Fig. 47–35*A*). Posteriorly are the Achilles tendon and the plantaris tendon. Laterally, the peroneal longus and brevis tendons pass under the lateral malleolus. Medially, the posterior tibial tendon and the flexor digitorum longus tendon pass under the medial malleolus, whereas the flexor hallucis longus tendon passes under the sustentaculum tali (Fig. 47–35*B*).

Anterior Tendons

The anterior tendons are well visualized in the direct axial plane (see Fig. 47–31). They extend, uncrossed, across the ankle joint and midfoot. The anterior tibial tendon is the most medial of the three anterior tendons. It extends along the medial aspect of the great toe tarsal-metatarsal joint to insert on the plantar aspect of the base of the first metatarsal and the adjacent medial cuneiform bone.

The extensor hallucis longus tendon is the middle of the three anterior tendons, proceeding straight to its insertion at the dorsal base of the great toe distal phalanx. The most lateral of the three anterior ankle tendons is the extensor digitorum longus tendon; at the level of the midfoot, it fans out into four separate tendon slips, which, in turn, proceed along the forefoot to insert at the dorsal bases of second through fifth middle and distal phalanges.[46, 62]

Although the anterior tibial and extensor digitorum longus tendons can be followed over a series of axial images (see Fig. 47–31), it is common to lose visualization of the extensor hallucis longus tendon as it curves anterior to the midfoot (see Fig. 47–31*C*). This is due in part to magic-angle effects. It is important not to misinterpret this lack of visualization as a rupture of the extensor hallucis longus tendon, a condition that is exceedingly rare. The lack of edematous signal intensity along the course of the extensor hallucis longus on T2-weighted images should reassure the radiologist that there is no pathology.

Pathology of the anterior ankle tendons is rare. Indeed, if a patient indicates that the point of maximal tenderness is directly over the anterior tendons, it is prudent to search for other causes for pain, such as an unsuspected stress fracture (Fig. 47–36).

Certainly, ganglion cysts can arise from any synovium-lined structure, including the anterior ankle tendons. Figure 47–37 shows a synovial cyst arising from and partially enveloping the anterior tibial tendon.

The normal anterior tibial tendon serves as a useful internal standard against which to compare the size of the other ankle tendons. The anterior tibial is normally the largest tendon in axial cross-section (except, of course, the Achilles tendon).[74] Figure 47–38 illustrates a chronically swollen and scarred posterior tibial tendon, with its cross-sectional area greater than that of the normal anterior tibial tendon.

Posterior Tendons

For anatomic purposes, the Achilles and plantaris tendons together make up the posterior group, although for practical purposes the plantaris is seldom clinically relevant. The plantaris tendon can be very tiny and is generally difficult to find on MR images, particularly if a high-resolution matrix is not employed.

There is seldom confusion in interpreting MR images of the Achilles tendon. The Achilles tendon should appear uniformly straight and black on sagittal T1-weighted images (see Fig. 47–36*C*) and on fluid-sensitive images (see Fig. 47–36*D*). A normal retrocalcaneal bursa may be present just in front of the Achilles tendon (Fig. 47–36*D*, dotted circle). The normal retrocalcaneal bursa should measure less than 6 mm superior to inferior, 3 mm medial to lateral, and 2 mm anterior to posterior.[73]

In the axial plane, the Achilles tendon should appear

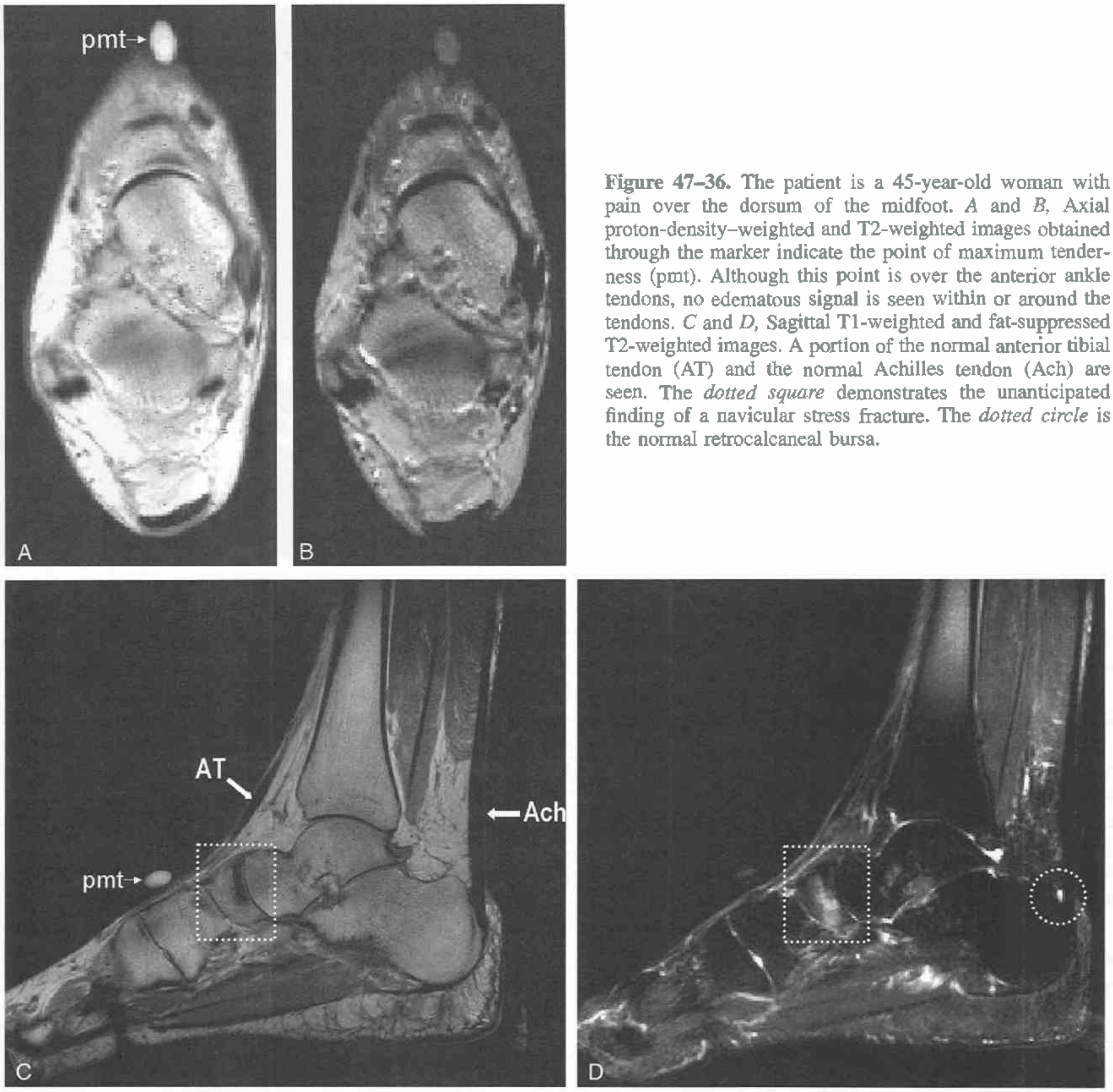

Figure 47–36. The patient is a 45-year-old woman with pain over the dorsum of the midfoot. *A* and *B,* Axial proton-density–weighted and T2-weighted images obtained through the marker indicate the point of maximum tenderness (pmt). Although this point is over the anterior ankle tendons, no edematous signal is seen within or around the tendons. *C* and *D,* Sagittal T1-weighted and fat-suppressed T2-weighted images. A portion of the normal anterior tibial tendon (AT) and the normal Achilles tendon (Ach) are seen. The *dotted square* demonstrates the unanticipated finding of a navicular stress fracture. The *dotted circle* is the normal retrocalcaneal bursa.

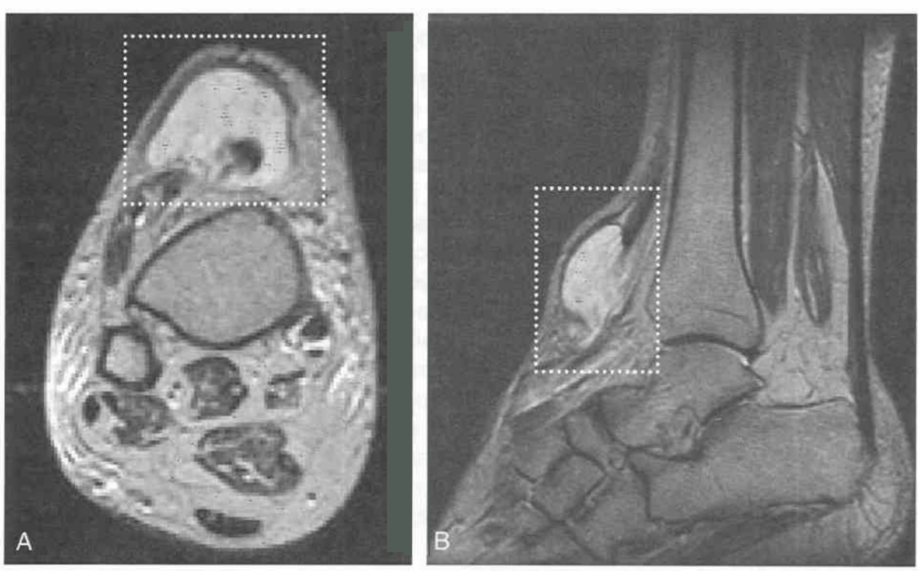

Figure 47–37. Swelling anterior to ankle joint in a 23-year-old woman. Axial *(A)* and sagittal *(B)* T2-weighted images of a synovial cyst *(dotted rectangle)* arising from and surrounding the anterior tibial tendon. The tendon itself is normal.

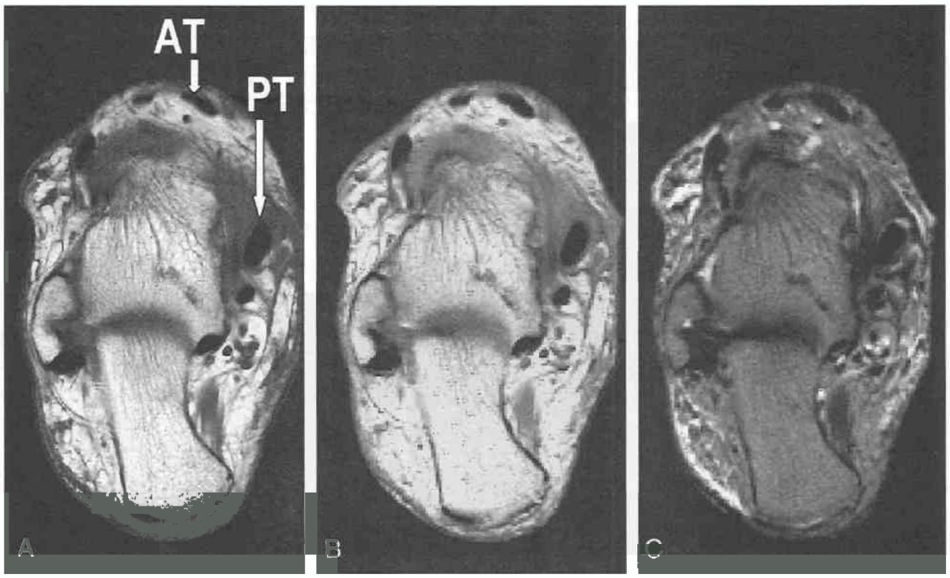

Figure 47–38. The patient is a 57-year-old woman with chronic medial ankle pain. *A,* T1-weighted image obtained with a high-resolution 512-pixel matrix. The chronically swollen and scarred posterior tibial tendon (PT) is larger in axial cross section than the normal anterior tibial tendon (AT). *B,* Proton-density–weighted image obtained with a standard-resolution 256-pixel matrix. There is loss of the normal sharp fat-tendon interface around PT. *C,* T2-weighted image obtained with a standard-resolution 256-pixel matrix. The relative lack of fluid in the tendon sheath is indicative of chronic scarring (stenosing tenosynovitis).

flattened in the AP direction. Distally, the ventral margin of the tendon becomes concave, with upturned corners resembling a smile (see Fig. 47–31*D*).

A complete tear of the Achilles tendon can be detected clinically and is often diagnosed by a skilled trainer or therapist. The patient can usually identify the exact instant in which the Achilles tendon has ruptured, describing the sensation as if "someone kicked me." The classic Achilles tendon rupture occurs with forced dorsiflexion of the planted foot, such as occurs in basketball or other jumping sports. The classic patient is a middle-aged "weekend warrior" who leads a sedentary life and then attempts to participate in sports (perhaps with younger players) without an adequate warm-up. Of all the tendons of the foot and ankle, the Achilles is the only one for which disorders have a male predominance.[73] When it is clinically apparent to all that the Achilles tendon is completely ruptured, confirmation with MRI is usually unnecessary.

Partial tears and the degree of healing of prior injuries of the Achilles tendon can be more difficult to assess by physical examination, thus rendering MRI particularly valuable. There are three types of Achilles tears (Fig. 47–39), similar to the pattern initially described in the posterior tibial tendon with CT scans[68]:

Type I. With this partial, intrasubstance tear (Fig. 47–40), the Achilles tendon is abnormally rounded in axial cross-section and T2-weighted images reveal increased internal signal intensity.

Type II. The Achilles tendon is attenuated, with a few remaining intact fibers (Fig. 47–41).

Type III. With this complete tear, no intact fibers can be identified in the sagittal or axial plane (Fig. 47–42). Classically, complete Achilles ruptures occur 3 to 5 cm proximal to the calcaneal insertion site[17] because this is a relatively hypovascular watershed region.[73]

On occasion, the Achilles tendon ruptures at the muscle-tendon junction. These unusual proximal tears sometimes require that the imaging coil be repositioned around the lower calf rather than around the ankle so that the torn and retracted proximal end can be visualized (Fig. 47–43).

An Achilles tendon that has undergone internal healing and scar formation from a prior tear tends to retain the thickened fusiform shape similar to that seen in a type I intrasubstance tear. Unlike a recent type I tear, however, a healed Achilles tendon does not contain increased internal signal intensity (Fig. 47–44).

Medial Tendons

The classic mnemonic "*T*om, *D*ick, and *H*arry" is useful for remembering the order of the medial ankle tendons:

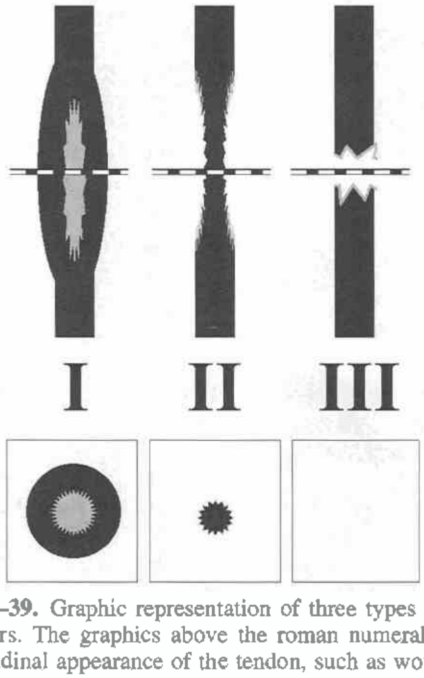

Figure 47–39. Graphic representation of three types of Achilles tendon tears. The graphics above the roman numerals represent the longitudinal appearance of the tendon, such as would be seen on a sagittal image. The graphics below the roman numerals are representations of an axial slice obtained through the tendon, taken at the level of the *dashed line*.

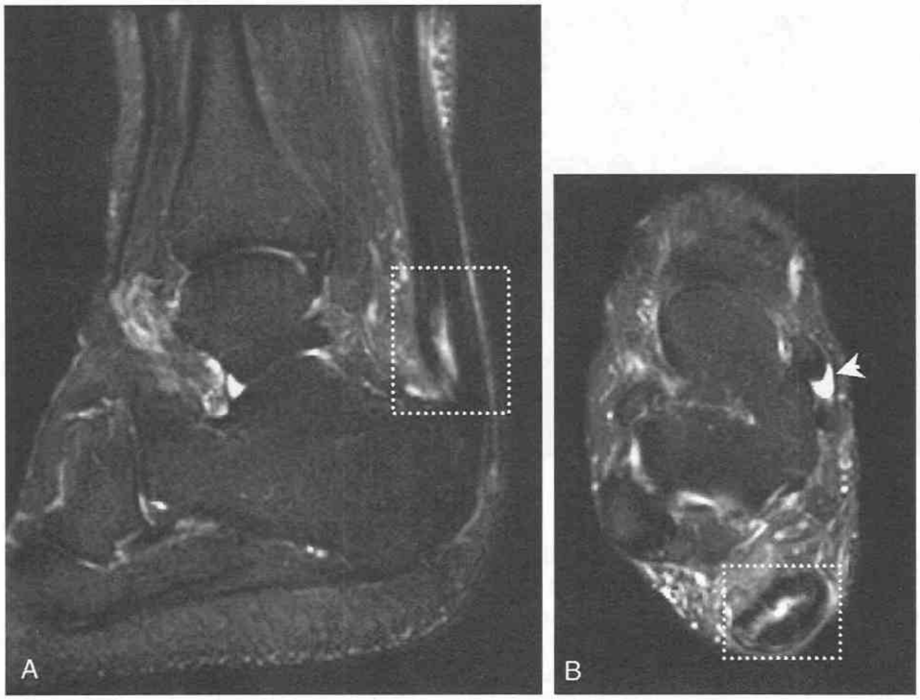

Figure 47–40. The patient is a 54-year-old woman with a history of rheumatoid arthritis and several months of persistent heel pain. Fat-suppressed T2-weighted images in the sagittal *(A)* and axial *(B)* planes reveal a type I partial intrasubstance tear of the Achilles tendon *(dotted rectangle)*. An incidental finding is an abnormal amount of fluid in the posterior tibial tendon sheath *(arrowhead)*.

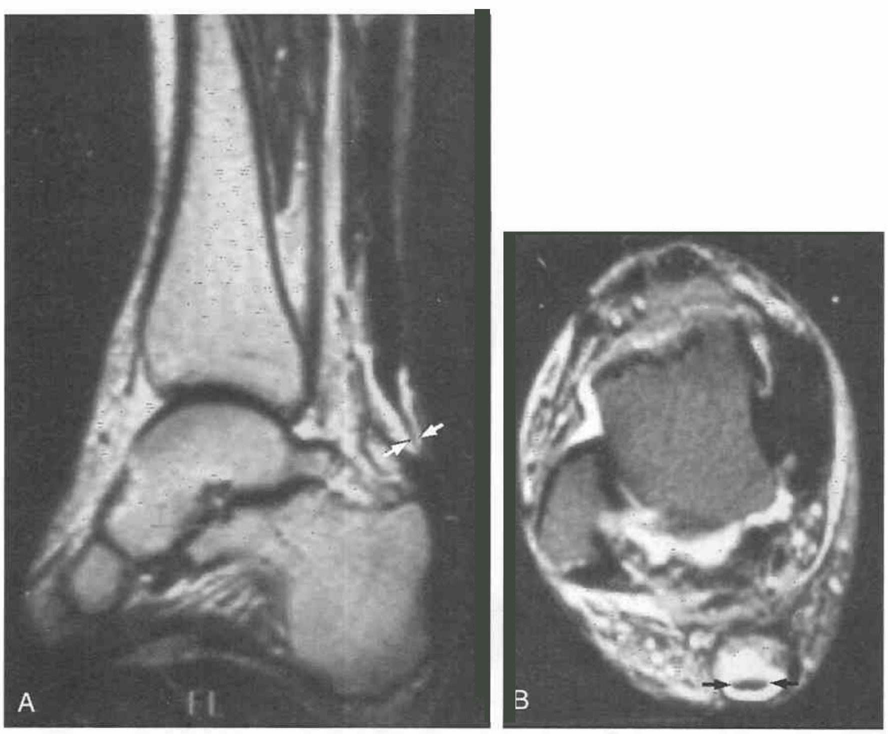

Figure 47–41. Type II partial tear of the Achilles tendon in a 74-year-old man. Sagittal *(A)* and axial *(B)* spin-echo T2-weighted images show a few intact Achilles fibers *(arrows)* surrounded by fluid.

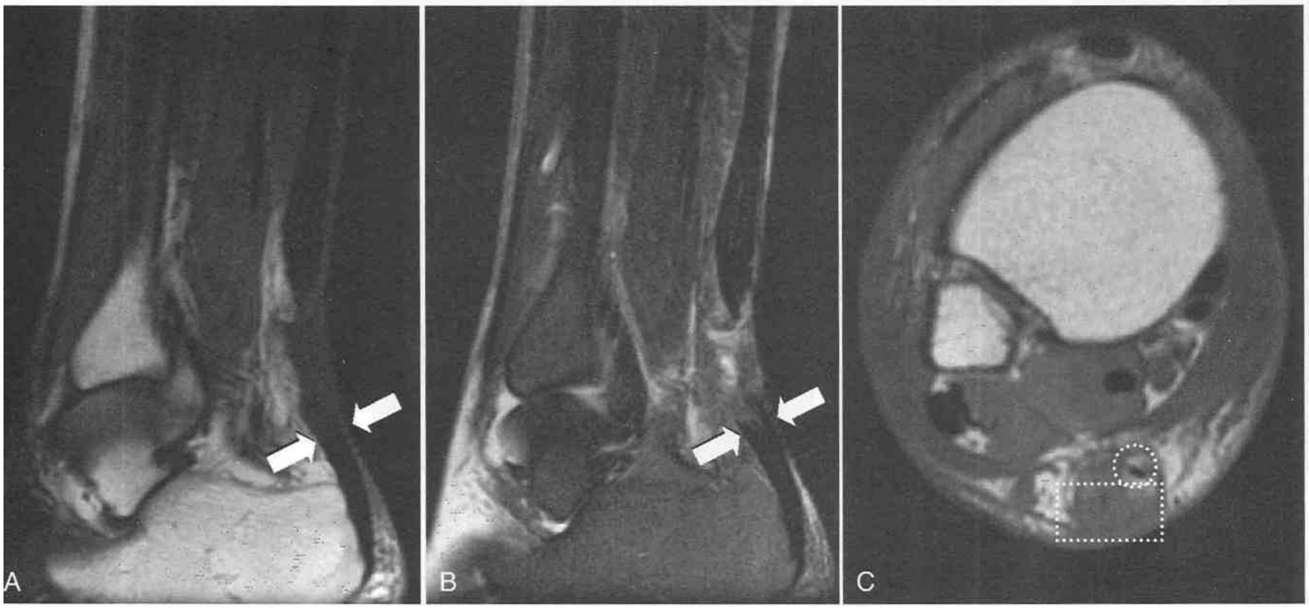

Figure 47–42. The patient is a 41-year-old woman with a history of renal transplantation and steroid use. She had experienced acute posterior ankle pain 5 days earlier when bending over while gardening. Sagittal T1-weighted *(A)* and fat-suppressed T2-weighted *(B)* images reveal a type III complete tear of the Achilles tendon at the "critical zone" *(arrows)* 2 cm proximal to the calcaneal insertion. An axial T1-weighted image *(C)* obtained through the tear reveals no intact Achilles fibers *(dotted rectangle)*. Incidentally noted is an intact plantaris tendon *(dotted circle)*.

Figure 47–43. Complete rupture of the Achilles tendon at the muscle-tendon junction in a 52-year-old man. *A*, Sagittal T1-weighted image with the coil centered on the calcaneus is too low to include the proximal side of the tear. *B*, Sagittal T1-weighted image with the coil repositioned above the ankle joint now includes the proximal side of the tear. The marker is at the palpable defect.

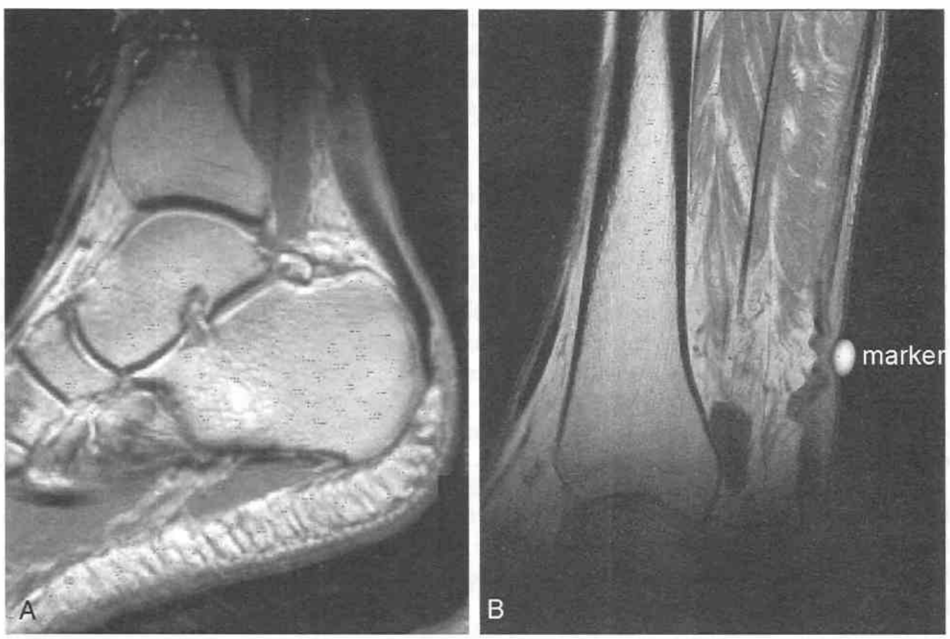

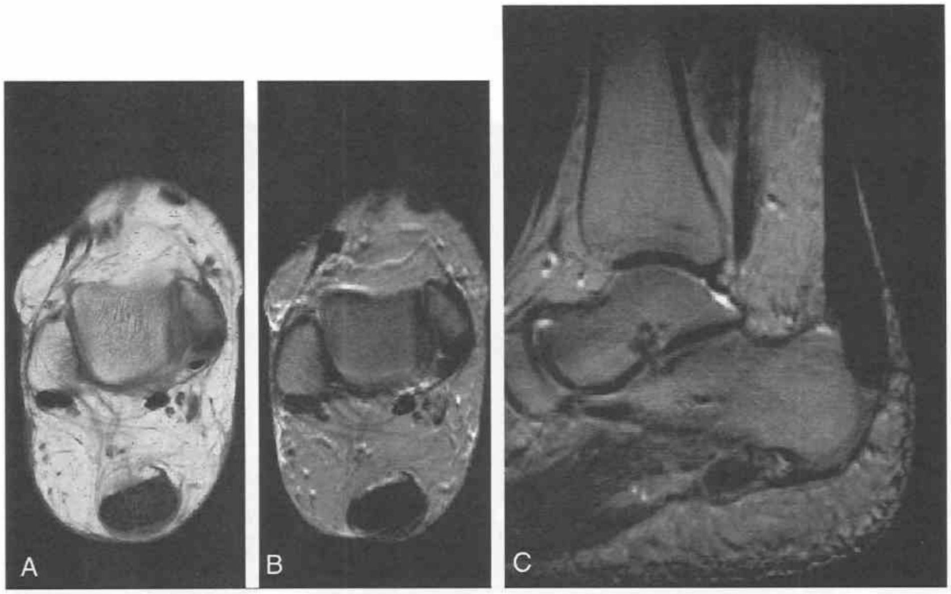

Figure 47–44. The patient is a 57-year-old woman with an Achilles tendon that has healed with chronic scarring. Axial T1-weighted *(A)*, axial T2-weighted *(B)*, and sagittal T2-weighted *(C)* images reveal that the distal Achilles is too round and thick but contains no increased signal.

"T" represents the posterior *t*ibial tendon; "D," the flexor *d*igitorum longus tendon; and "H," the flexor *h*allucis longus tendon. By changing the emphasis to "Tom, Dick, *AN*d Harry," with AN standing for the posterior tibial *a*rtery and *n*erve, it is easier to remember that the neurovascular bundle runs between the flexor digitorum longus and flexor hallucis longus tendons (see Figs. 47–31 and 47–32).

The posterior tibial tendon runs directly behind and under the medial malleolus, proceeds medial to the talus, and inserts on the medial pole of the navicular (see Fig. 47–31*D*). At this insertion site is a focal osseous prominence called the *navicular tubercle*. The bulk of the posterior tibial tendon inserts on this navicular tubercle, although smaller slips of tendon pass under the navicular (see Fig. 47–32*C*) to insert on the plantar aspect of all three cuneiforms as well as on the base of the second through fourth

The flexor digitorum longus tendon runs directly behind the posterior tibial tendon, although the two tendons maintain individual tendon sheaths. The flexor digitorum longus tendon extends plantar to the bones of the midfoot, crossing superficial to the flexor hallucis longus tendon. This crossover point has been called the "master knot of Henry,"[41] and the sheaths of these two flexor tendons communicate at this point. Distally, the flexor digitorum longus divides into separate tendon slips that insert on the plantar bases of the second through fifth distal phalanges.

The flexor hallucis longus muscle is a posterior structure that originates from the lower two thirds of the back of the fibula. The muscle-tendon junction extends distally to the level of the ankle joint, and the proximal end of the tendon passes through a groove along the posterior talus. Whereas the posterior tibial and flexor digitorum longus tendons pass under the medial malleolus, the flexor hallucis longus tendon passes under the sustentaculum tali. The flexor hallucis longus tendon then crosses deep to the flexor digitorum longus tendon and extends under the first metatarsal to insert on the plantar base of the great toe distal phalanx.

Of the three medial ankle tendons, the posterior tibial tendon is the most prone to tear, characteristically along the portion that curves around the medial malleolus. The posterior tibial tendon is relatively hypovascular in this region.[71] This region of the tendon is also susceptible to mechanical wear as the tendon rubs against the medial malleolus (Fig. 47–45). If the surrounding tendon sheath does not provide adequate lubrication, as in stenosing tenosynovitis or rheumatoid pannus formation, this frictional wear is increased. Perhaps because of these longitudinal frictional stresses, the posterior tibial tendon tends to tear with a longitudinal split rather than with the transverse rupture seen in Achilles tendon tears. When imaged in the axial plane, a longitudinal split in the posterior tibial tendon resembles two individual tendons. This longitudinally split posterior tibial tendon, when grouped with the flexor digitorum and hallucis longus tendons, has been called the *four-tendon sign* (Fig. 47–46).

Even when the posterior tibial tendon is intact, the tendon sheath and surrounding soft tissues should be carefully examined. An abnormal amount of fluid in the tendon sheath indicates active tenosynovitis (Fig. 47–47). Dark, fibrous tissue around the tendon suggests chronic scarring and/or stenosing tenosynovitis (Fig. 47–48). Rheumatoid pannus can also be demonstrated by MRI (Fig. 47–49) and should enhance if an intravenous contrast agent is administered. It has been suggested that these types of inflammatory conditions of the tendon sheath can be ameliorated via therapeutic tenography.[72]

Lateral Tendons

Laterally, the peroneus brevis and longus tendons share a common sheath as they pass under the lateral malleolus. Distal to the lateral malleolus, the tendons are enveloped with individual sheaths. The peroneal brevis tendon extends lateral to the midfoot and inserts on the tuberosity at the lateral base of the fifth metatarsal. The peroneal longus tendon passes through a groove in the plantar surface of the cuboid, crosses under the midfoot deep to the master

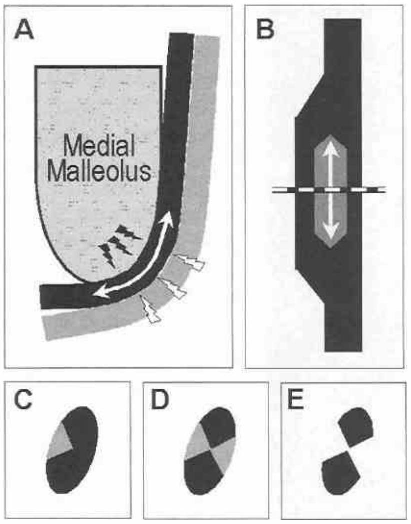

Figure 47–45. Graphic representation of posterior tibial tendon wear progressing to a tear.

A, The posterior tibial tendon *(thick black line)* is susceptible to mechanical wear ("lightning bolts") as it rubs back and forth *(double-headed arrow)* between the underlying medial malleolus and the overlying flexor digitorum longus tendon *(thick gray line).*

B, Graphic representation of a partially torn posterior tibial tendon as it might appear if it were laid flat. The tendon is thickened and "butterflied" open, with the gray region representing abnormal internal signal. *Dashed line* represents the location of cross-section for *C* to *E.*

C, Cross-sectional image obtained through *B.* The *gray wedge* represents abnormally increased signal along the inner aspect of the flattened posterior tibial tendon *(black ellipse).*

D, Same level as *C,* but the tendonopathy *(gray wedges)* now involves the outer and inner surfaces of the posterior tibial tendon.

E, Same level as *D,* but wedges of tendonopathy have progressed to a longitudinal tear, giving the appearance in cross-section that the posterior tibial tendon is two tendons.

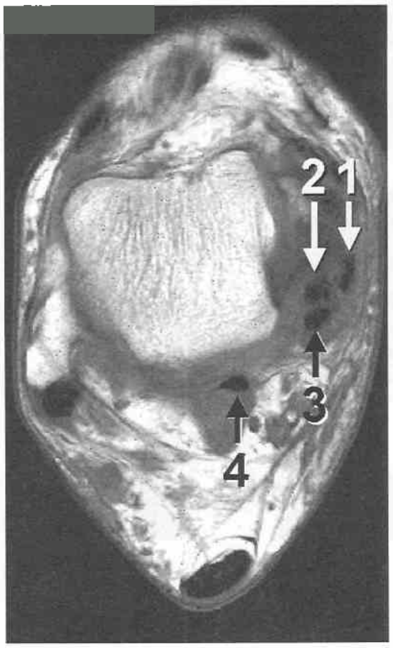

Figure 47–46. This partial longitudinal tear of the posterior tibial tendon in a 39-year-old woman shows the *four-tendon sign:* 1 and 2, torn posterior tibial tendon; 3 and 4, normal flexor digitorum and hallucis longus tendons.

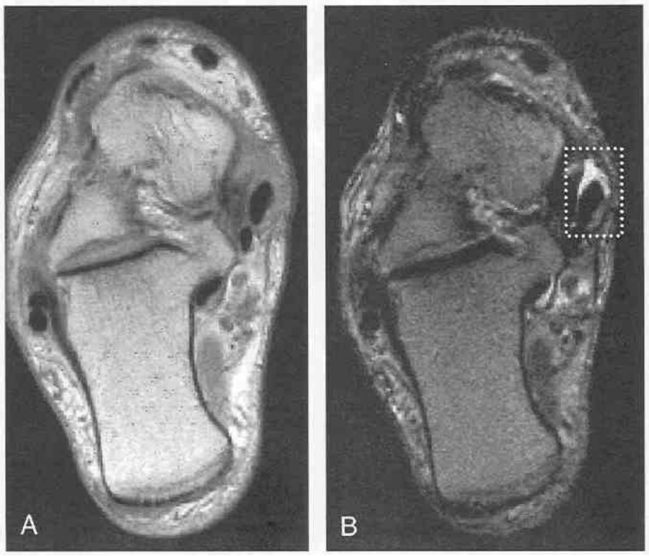

Figure 47–47. The patient is a 46-year-old woman with chronic pain in the distribution of the posterior tibial tendon. *A,* Axial proton-density–weighted image demonstrates that the posterior tibial tendon is intact and contains no abnormal internal signal. The tendon is slightly larger in cross-section than the anterior tibial tendon, with loss of the normal fat signal around the tendon. *B,* Axial T2-weighted image at the same level reveals an abnormal amount of fluid in the posterior tibial tendon sheath *(dotted rectangle),* indicating active tenosynovitis.

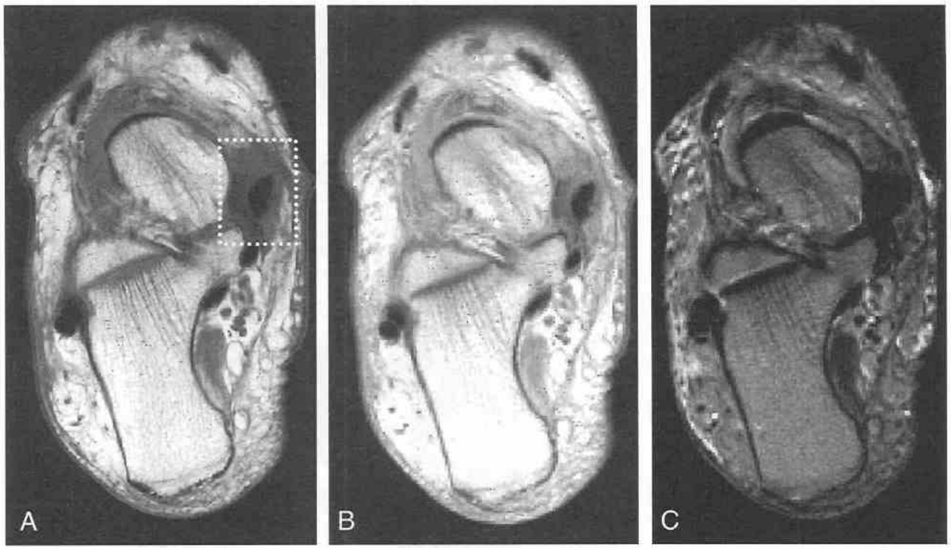

Figure 47–48. The patient (same as in Fig. 47–38) is a 57-year-old woman with chronic pain in the distribution of the posterior tibial tendon. *A*, Axial T1-weighted image shows abnormal dark signal rather than fat surrounding the posterior tibial tendon *(dotted rectangle)*. *B*, Axial proton-density–weighted image at the same level as *A*. *C*, Axial T2-weighted image at the same level as *A* and *B* reveals no fluid surrounding the posterior tibial tendon, indicating that this is chronic scarring (stenosing tenosynovitis).

knot of Henry, and extends medially to insert on the plantar aspect of the medial cuneiform and the base of the first metatarsal, just lateral to the anterior tibial tendon insertion site.

A trick for identifying the peroneal tendons is to think of the lateral malleolus as a race track (Fig. 47–50). The peroneal brevis, being the shortest, hugs the inside turn. The peroneal longus follows the outside of the curve, running posterior and inferior to the brevis.

Unlike the medial ankle tendons, which are normally round or oval in axial cross-section, the peroneal brevis can normally appear flattened as it passes around the lateral malleolus. The presence of increased signal intensity within the substance of the tendon or of fluid in the surrounding sheath aids in the diagnosis of pathology of the peroneal tendons. It is often helpful to examine the peroneal tendons over multiple slices by using several imaging planes and sequences (Fig. 47–51).

Peritendon Pathology

Tarsal Tunnel Syndrome

The tarsal tunnel in the ankle is analogous to the carpal tunnel in the wrist. Both are spaces confined by the underlying bones and overlying fibrous ligaments through which pass tendons, blood vessels, and nerves. The roof of the tarsal tunnel is the flexor retinaculum, a broad fibrous band extending between the medial malleolus and the medial tubercle of the calcaneus (Fig. 47–52*A*). These retinacular fibers help to prevent the medial tendons from becoming dislocated and can be identified on high-resolution axial

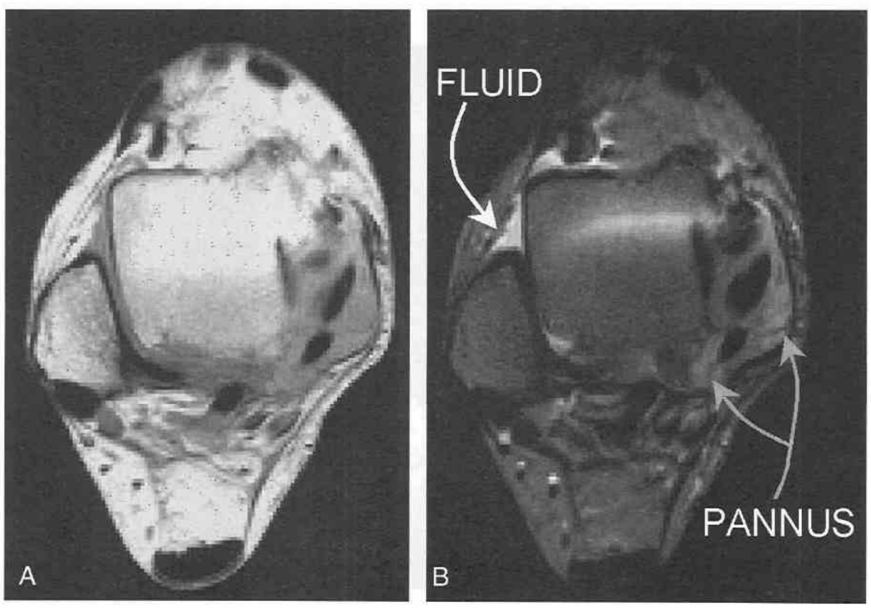

Figure 47–49. Rheumatoid arthritis and diffuse medial ankle pain in a 51-year-old woman. Axial proton-density–weighted *(A)* and T2-weighted *(B)* images reveal abnormal signal around both the posterior tibial and flexor digitorum longus tendons. However, this signal is not as bright as the normal fluid in the ankle joint *(white arrow)* and represents rheumatoid pannus *(gray arrows)*. The patient remained pain-free for 1 year following a therapeutic tenogram.

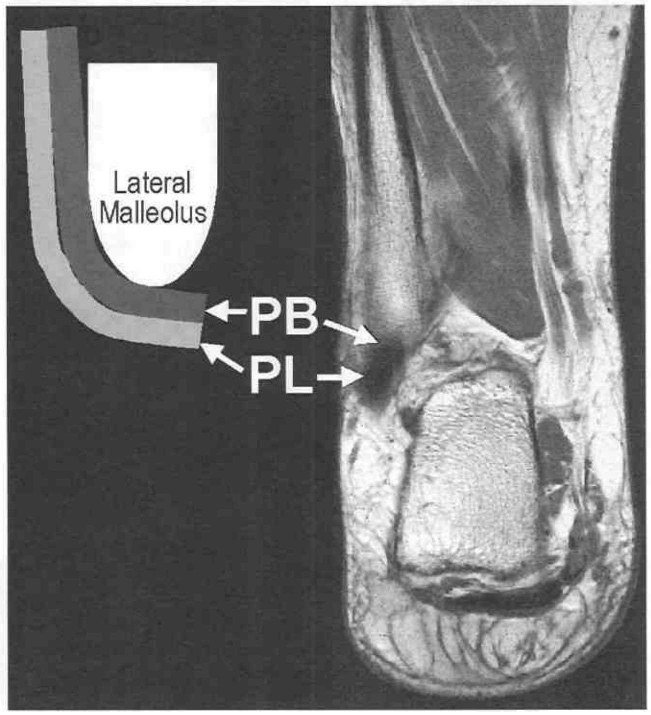

Figure 47–50. Graphic representation with coronal high-resolution T1-weighted image demonstrates the relationship of the peroneal tendons to the lateral malleolus. PB, peroneal brevis tendon; PL, peroneal longus tendon.

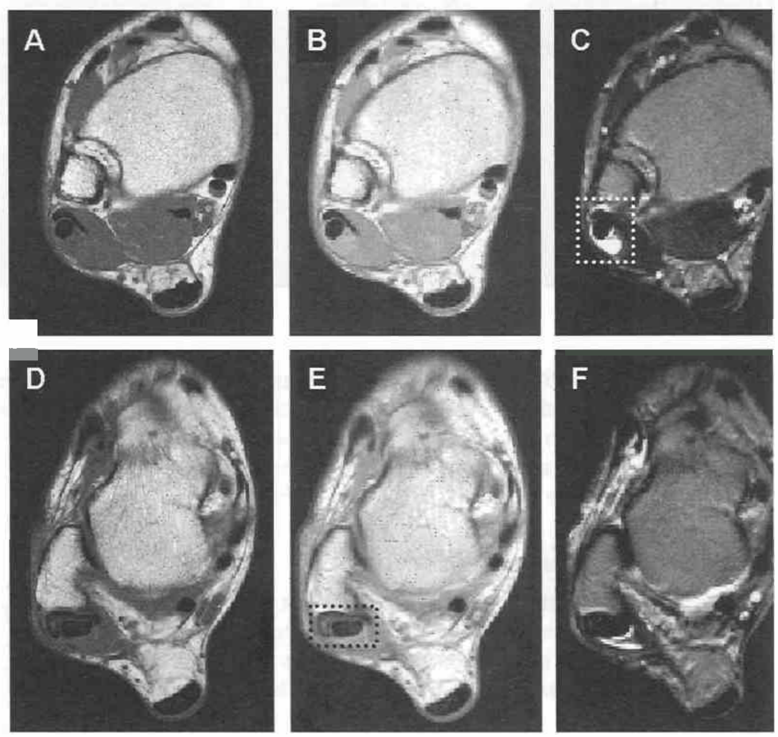

Figure 47–51. The patient is a 62-year-old woman with lateral ankle pain from a partial tear of the peroneal brevis tendon.

A–C, Axial T1-weighted, proton-density–weighted, and T2-weighted images at the level of the syndesmosis reveal an abnormal amount of fluid in the common peroneal tendon sheath *(white dotted rectangle).*

D–F, Axial T1-weighted, proton-density–weighted, and T2-weighted images at the level of the lateral malleolus reveal abnormal signal within the flattened peroneal brevis tendon *(black dotted rectangle).*

Illustration continued on following page

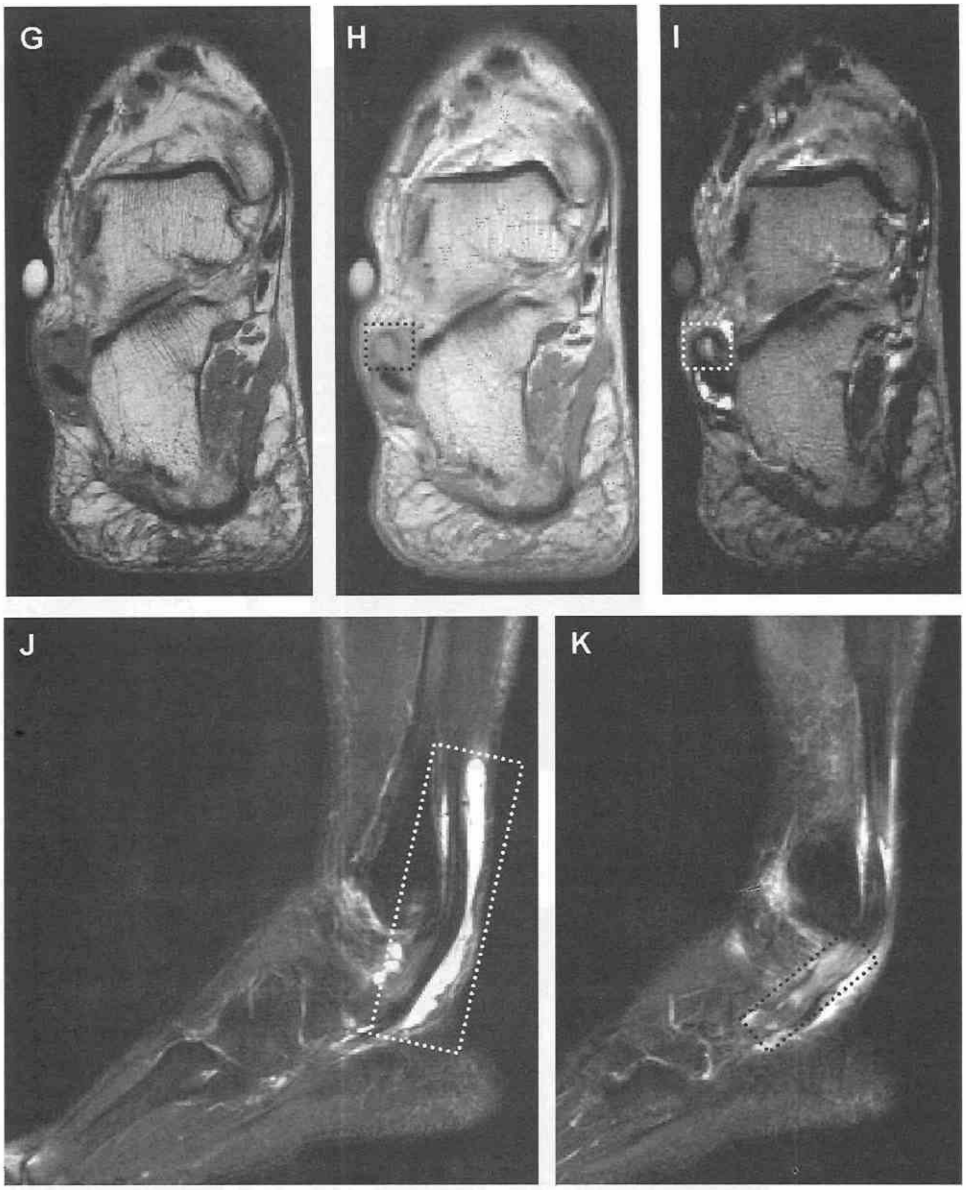

Figure 47–51 *Continued. G–I,* Coronal T1-weighted, proton-density–weighted, and T2-weighted images reveal abnormal signal within the substance of the peroneal brevis tendon *(dotted squares).* The marker is over the point of maximum tenderness.

J and *K,* Sagittal fat-suppressed T2-weighted images reveal abnormal fluid in the common peroneal tendon sheath *(white dotted rectangle)* as well as within the peroneal brevis tendon *(black dotted rectangle).*

images (Fig. 47–52*B*). Because the tarsal tunnel is a relatively tight space, otherwise innocuous volume-occupying lesions, such as synovial cysts, small nerve sheath tumors, focal synovitis, or rarely even varicose veins, can potentially impinge on the posterior tibial nerve (Fig. 47–53).[32]

Accessory Navicular Syndrome

The primary insertion site for the posterior tibial tendon is on the medial aspect of the navicular bone. The accessory navicular bone is an often seen normal variant ossicle just medial and proximal to the navicular bone.[44] If the accessory navicular bone is large enough, the posterior tibial tendon inserts upon it rather than on the navicular bone itself. Patients with this normal variation are typically asymptomatic unless there is a fracture through the normal fibrous synchondrosis between the navicular and accessory navicular bones.[51] MRI is useful in showing the presence of abnormal fluid between the navicular and accessory navicular bones (Fig. 47–54). A line of fluid indicates an abnormal pseudoarthrosis between these bones.

Os Peroneum Syndrome

The os peroneum is a common sesamoid bone, located within the peroneus longus tendon as it passes under the cuboid. In rare cases, this normal ossicle can become inflamed and painful.[80] Chronic inflammation can be suspected radiographically if the os peroneum is abnormally sclerotic (Fig. 47–55*A*), although this finding is subjective. A more objective finding of os peroneum syndrome is edema within and around the small ossicle, best shown with an edema-sensitive MRI sequence targeted to the lesion (Fig. 47–55*C*).

Ligament Injuries

Inversion injuries are the most common ankle injury and among the most common musculoskeletal complaints

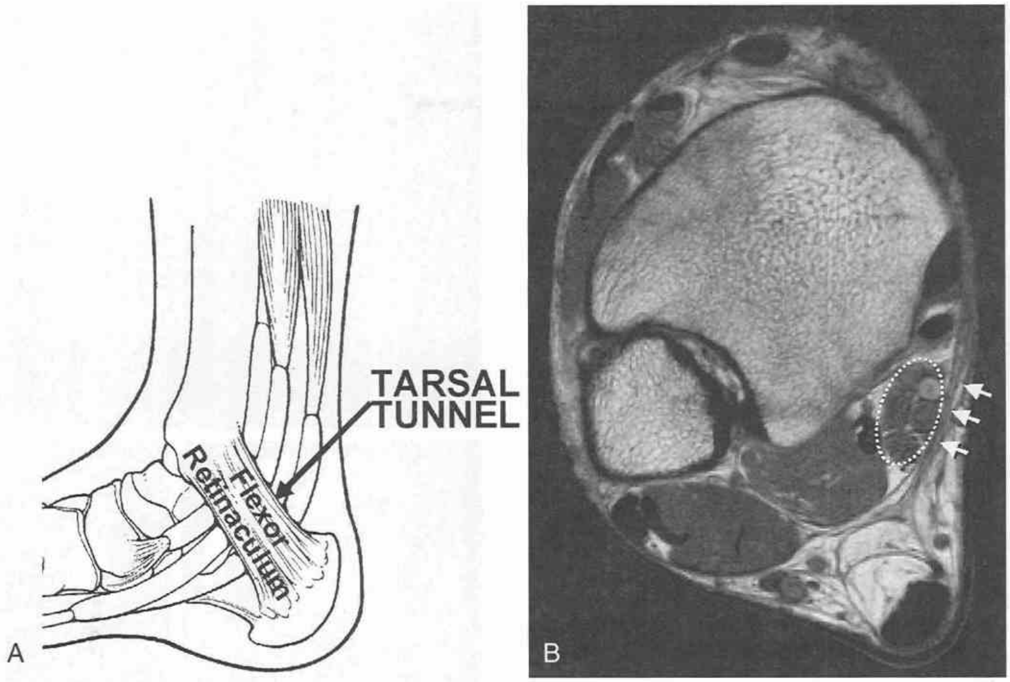

Figure 47–52. Tarsal tunnel. *A*, Location of the tarsal tunnel *(arrow)*, deep to the flexor retinaculum. (Illustrated by M. Schenk, M.S., C.M.I.) *B*, Axial high-resolution T1-weighted image shows the medial neurovascular bundle *(dotted ellipse)* deep to the flexor retinaculum *(arrows)*.

that bring patients to the emergency department. Most ankle sprains occur in 15- to 35-year-olds. It is estimated that on average an individual strains his or her ankle once every decade. These sprains account for 25% to 50% of injuries that occur in volleyball, soccer, and football.[14] Because the medial (deltoid) ligament is strong, osseous avulsions occur medially. The lateral ligamentous complex is the site of ankle ligament sprains. The laterally supporting ligamentous structures are the ankle and the hindfoot ligaments.[10] The anterior group consists of the anterior talofibular ligament and the calcaneal fibular ligament (lateral collateral ligament). The posterior talofibular is also part of the lateral collateral ligament, although it is injured only rarely.[14]

Supporting the hindfoot are the medial fibers of the inferior extensor retinaculum, the cervical ligament, and the interosseous talocalcaneal ligament. Acute ankle injuries typically affect the anterior talofibular ligament; the calcaneal fibular ligament is next most frequently affected. Acute injuries can be divided by grade or strain:

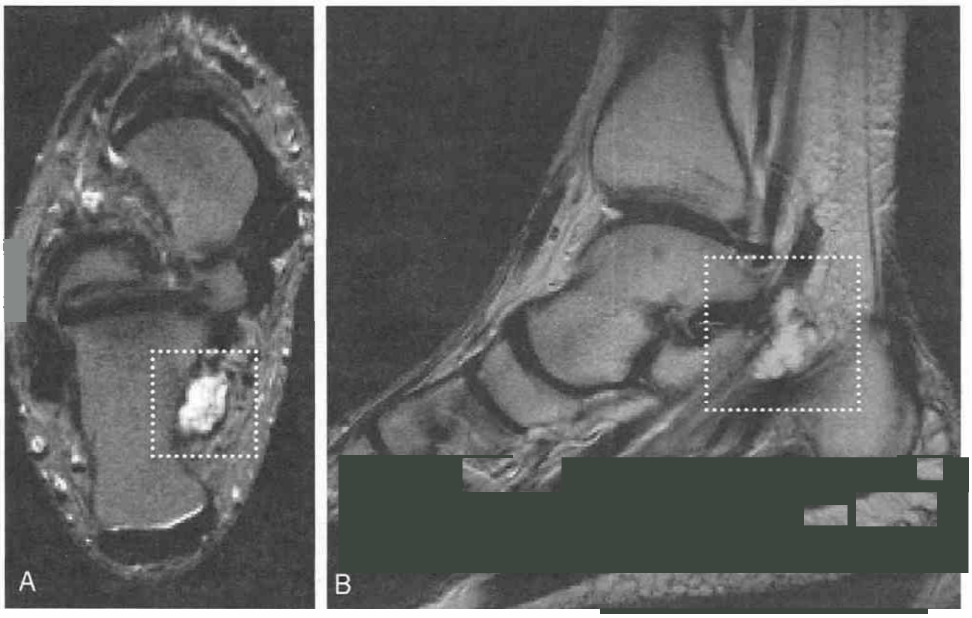

Figure 47–53. The patient is a 48-year-old man with medial pain in the distribution of the posterior tibial nerve. Axial *(A)* and sagittal *(B)* T2-weighted images reveal a ganglion *(dotted square)* within the tarsal tunnel, causing "tarsal tunnel syndrome."

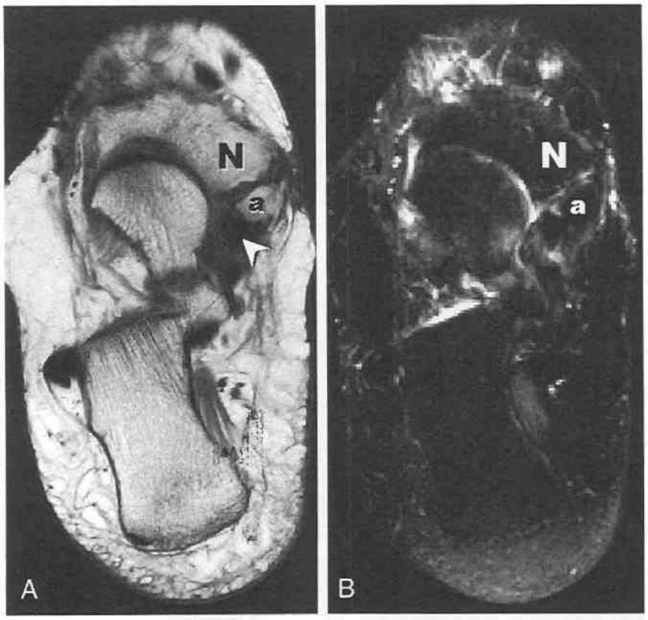

Figure 47–54. The patient is a 59-year-old woman with medial point tenderness. *A,* Axial T1-weighted image demonstrates an accessory navicular bone (a) separate from adjacent navicular (N). The posterior tibial tendon inserts on the accessory navicular *(arrowhead). B,* Axial fat-suppressed T2-weighted image at the same position as *A.* The line of fluid between the accessory navicular and the navicular indicates an abnormal joint between these two bones instead of a solid fibrous synchondrosis.

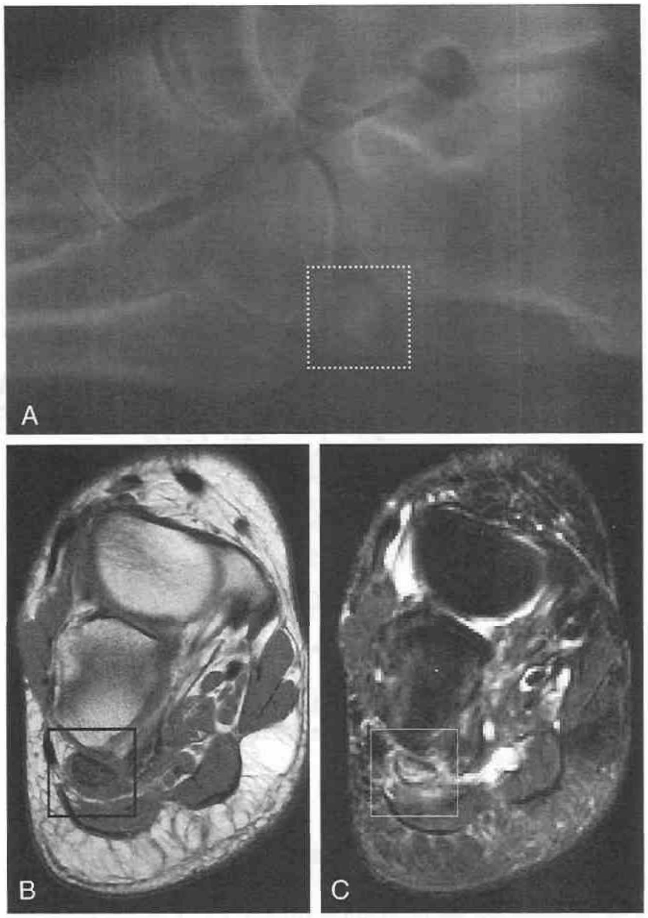

Figure 47–55. The patient is a 60-year-old woman with lateral point tenderness. *A,* Cone-down of a lateral radiograph of the midfoot. The os peroneum *(dotted square)* is perhaps slightly sclerotic, but this is a relatively subjective finding. *B,* Oblique coronal T1-weighted image demonstrates the os peroneum *(black square). C,* Fat-suppressed T2-weighted image, same position as *B.* Edema is present within and around the os peroneum *(white square),* indicative of "os peroneum syndrome."

Grade I is the stretching of and microscopic injury to the ligament.
Grade II is a partial tear.
Grade III is a complete tear.

Whether to treat these acute injuries surgically or conservatively is controversial. However, 10% to 20% of patients with lateral ankle ligament injuries experience chronic symptoms, and the severity of the initial injury does not correlate well with these long-term symptoms.[2] Most patients with chronic symptoms eventually require surgical intervention.[33]

The role of MRI, particularly in acute injuries, is currently unclear. Most MRI abnormalities are incidental or occur in patients with chronic, nonspecific symptoms. The anterior and posterior talofibular ligaments are seen best on axial MR images. The anterior ligament has an oblique course that is more anterior medially. The posterior talofibular ligament is horizontal.[30] The anterior ligament does not normally demonstrate internal signal intensity; it is usually half the thickness of the posterior ligament. The posterior ligament on high-resolution images gives the appearance of internal signal intensity secondary to the microanatomy of its fascicles.[64] The calcaneofibular ligament is best seen on coronal images. When the calcaneofibular ligament is injured, the anterior talofibular ligament is nearly always injured as well.

The anterior tibiofibular ligament is infrequently torn in isolation, but it may be avulsed off the tibia. Injury to this ligament may also demonstrate an osseous avulsion (Fig. 47–56) or, more commonly, joint fluid violation of its anterior boundary (Fig. 47–57). In acute ligament sprains, edema is seen in the adjacent subcutaneous fat. The ligament, when injured, may demonstrate internal signal intensity on any imaging sequence. The ligament may also appear widened with irregular margins. With chronic instability, the ligament may become scarred and thick and either demonstrate unusually low signal intensity on T2-weighted images or appear wavy.

The inferior extensor retinaculum inserts into the lateralmost aspect of sinus tarsi, where it is best seen on lateral sagittal images. The cervical ligament lies in the anterior sinus tarsi, extending from a tubercle on the inferior lateral talar neck to the dorsal calcaneus. It may be seen on coronal or sagittal MR images. The interosseous talocalcaneal ligament, seen just posterior to the cervical ligament, is a thicker band. Injuries to the lateral ligaments may therefore cause abnormally high signal intensity within the sinus tarsi.

The MRI differential diagnosis for this appearance is sinus tarsi syndrome, which may cause a similar appearance of high signal intensity. In sinus tarsi syndrome,

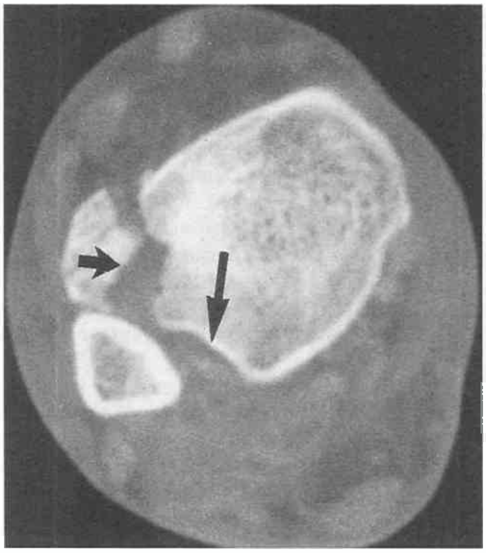

Figure 47–56. Axial CT image of the lower leg demonstrates disruption of the distal tibia fibular articulation with the fibular subluxated anteriorly out of its sulcus *(large arrow)*. A large avulsion fragment is seen at the tibial insertion of the anterior tibiofibular ligament *(small arrow)*. This avulsion represents an adult Tillaux fracture.

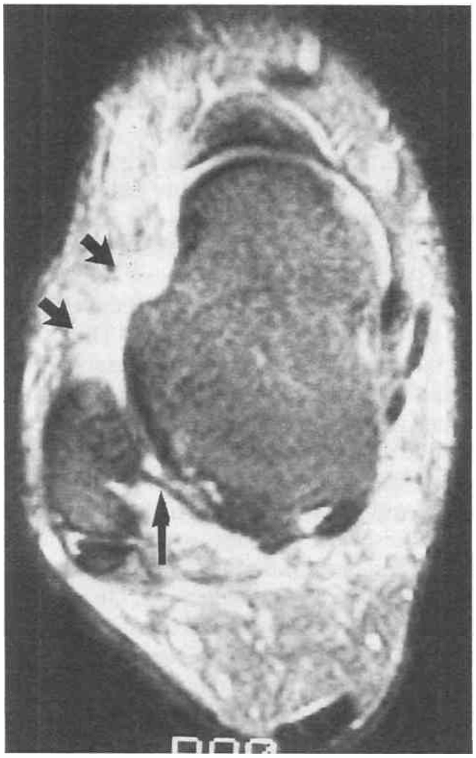

Figure 47–57. On an axial T2-weighted image, the posterior aspect of articular fluid is well marginated by the posterior talofibular ligament *(long arrow)*. The fluid extends too far anteriorly with an irregular margin secondary to a tear of the anterior talofibular ligament *(short arrows)*.

however, the morphologic integrity of the hindfoot ligaments is intact. Sinus tarsi syndrome may occur idiopathically, following ankle sprains, or in patients with rheumatoid arthritis or gout.

One additional complication, the anterolateral *ankle impingement syndrome*, may occur as a sequela of ankle sprain. In this syndrome, hypertrophic synovium develops in the lateral talofibular sulcus.[7] On MR images, the lateral aspect of the joint on axial image, particularly posterior to the anterior talofibular ligament, fills in, with pannus displacing fluid posteriorly.

Stress Reactions

Edema-sensitive inversion recovery and fat-suppressed T2-weighted images are extremely sensitive for the detection of bone marrow pathology, and such a sequence should be incorporated into every MRI study of the ankle or foot. When bone marrow edema is detected in one plane, typically the sagittal plane, it may be desirable to run a second edema-sensitive sequence in a secondary plane, such as the oblique axial plane (Fig. 47–58).

The term *stress fracture* can refer to any scenario in which a bone is subjected to excessive force of such a degree as to cause bone marrow edema but not a frank breach in the cortex. Stress fractures can be caused by excessive or repetitive forces on a normal bone or by relatively normal forces on an abnormally weakened bone. Stress fractures caused by repetitive abnormal forces are perhaps better termed *fatigue fractures*. Such fatigne fractures have been reported in characteristic locations, including the tibias of runners and the second metatarsals of military recruits *(march fracture)*. Fractures caused by relatively minor stresses on bones with preexisting abnormalities are known as *insufficiency fractures* and are common in patients with underlying osteoporosis.

Stress fractures of the tarsal bones can be radiographically occult[88] but are quite conspicuous when an edema-sensitive MRI sequence is employed (Figs. 47–59 and 47–60; see also Fig. 47–58). The differential diagnosis for bone marrow edema includes not only stress fracture but also arthritic changes, bone bruises, osteomyelitis, and rarely even neoplasms. These conditions can have somewhat similar appearances by MRI, and often the specific diagnosis is based not only on the imaging findings but also on the clinical history.

Plantar fasciitis is a stress reaction occurring at the origin of the plantar aponeurosis from the calcaneus, typically at the medial calcaneal tubercle. Degenerative changes from repetitive microtrauma in the origin of the plantar fascia cause traction periostitis and microtears, resulting in pain and inflammation.[69] Plantar fasciitis is the most common cause of pain in the inferior aspect of the heel,[77] and the diagnosis is typically confirmed by clinical symptoms and physical examination revealing tenderness along the medial calcaneal tuberosity. The relationship between plantar fasciitis and heel spurs has never been firmly established. A study of 90 heels in 45 patients found that although 75% of the painful heels had spurs, 63% of the painless heels also had spurs.[91]

Most patients with plantar fasciitis respond to conserva-

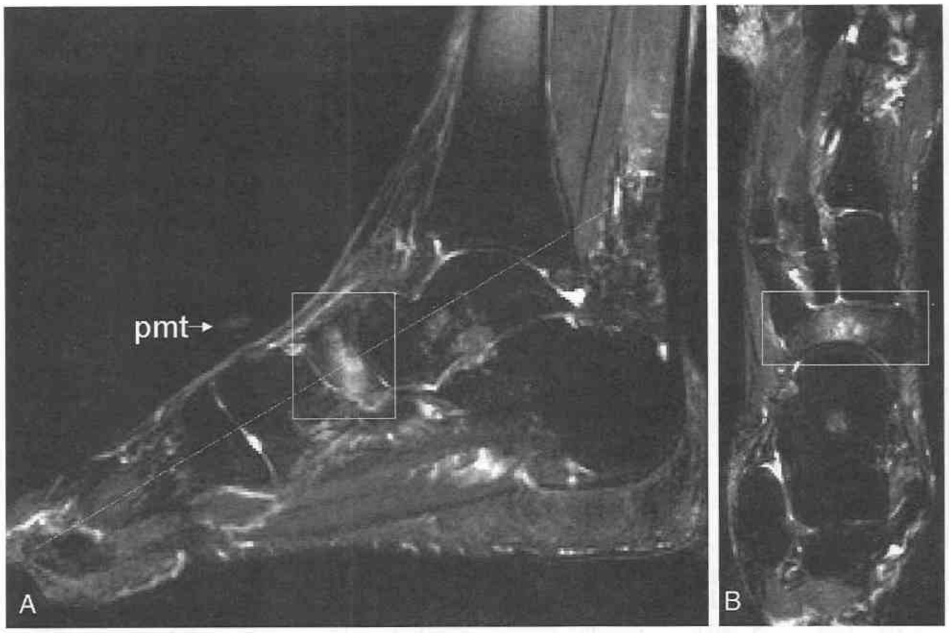

Figure 47–58. The patient (same as in Fig. 47–36) is a 45-year-old woman with pain over the dorsum of the midfoot. *A*, Sagittal fat-suppressed T2-weighted image. There is bone marrow edema within the navicular *(white rectangle)*. This stress fracture of the navicular corresponds to the point of maximal tenderness (pmt), as indicated by the capsule on the skin. The *dashed line* indicates the location of the oblique axial slice in *B*. *B*, Oblique axial fat-suppressed T2-weighted image. This secondary plane helps confirm the bone marrow edema within the navicular *(white rectangle)*.

tive treatments that include calf stretching, orthoses, nonsteroidal anti-inflammatory medication, and occasionally casting. Patients with atypical clinical presentations or who do not respond to conservative therapies may benefit from MRI to determine whether the pain is indeed related to the plantar fascia or to some other cause, such as a tarsal stress fracture. MRI scanning of plantar fasciitis reveals edema around the origin of the aponeurosis. The plantar fascia itself may be abnormally thickened, and edema may be present in the underlying calcaneal bone marrow (Fig. 47–61).

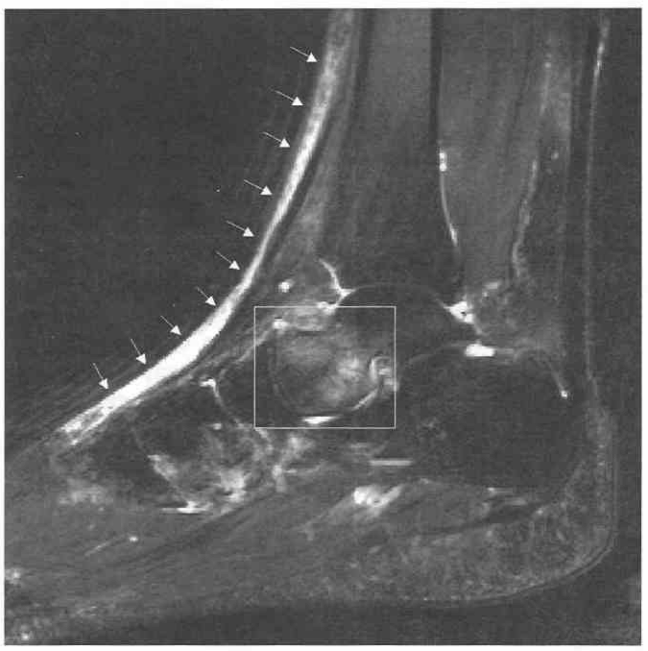

Figure 47–59. Sagittal fat-suppressed T2-weighted image with a stress fracture of the talar neck *(white rectangle)*. Incidentally noted is edema of the superficial soft tissues of the dorsum of the foot *(arrows)*.

Osteochondritis Dissecans

Osteochondritis dissecans (OCD) is a common disorder that may affect the femur, capitellum, or talus. It is more common in adolescents and young adults and usually affects men. *Osteochondral lesion* or *injury* is a better term for this disorder, with OCD best reserved for characteristic lesions in younger patients.

Although fracture was initially thought to be a *sequela* of bone necrosis, most authors now believe it to be the *cause* of this disorder, with necrosis the result. Talar OCD accounts for 1% of all fractures of the talus and 4% of all cases of OCD. OCD of talus, however, occurs in 6.5% of all ankle sprains.[75] OCD in locations in the foot and ankle other than the talus is exceedingly rare. The cause of this injury is a shear, rotatory, or even compressive (particularly medial talar OCD) force.

When the injury occurs early in life, the cartilage is resilient and it transmits the vector to the underlying bone. Because the bone is less elastic than cartilage is, the bone may fracture without a chondral fracture. However, shear injuries may displace cartilage even in young patients. With aging, cartilage elasticity is decreased; this leads to transchondral and osseous fractures at the time of injury. Even when the cartilage is not fractured, it is still traumatized, leading to premature degeneration.

Healing of OCD results from ingrowth of capillaries across a reduced immobile fragment. Any motion at the fracture site shears off the capillary buds.[11] Healing of this lesion thus depends on both the osseous stability of the fragment and the degree of intactness of the overlying cartilage because both of these factors affect the degree of immobilization. The imaging stage of the lesion, therefore, is the main determinant of prognosis.[65]

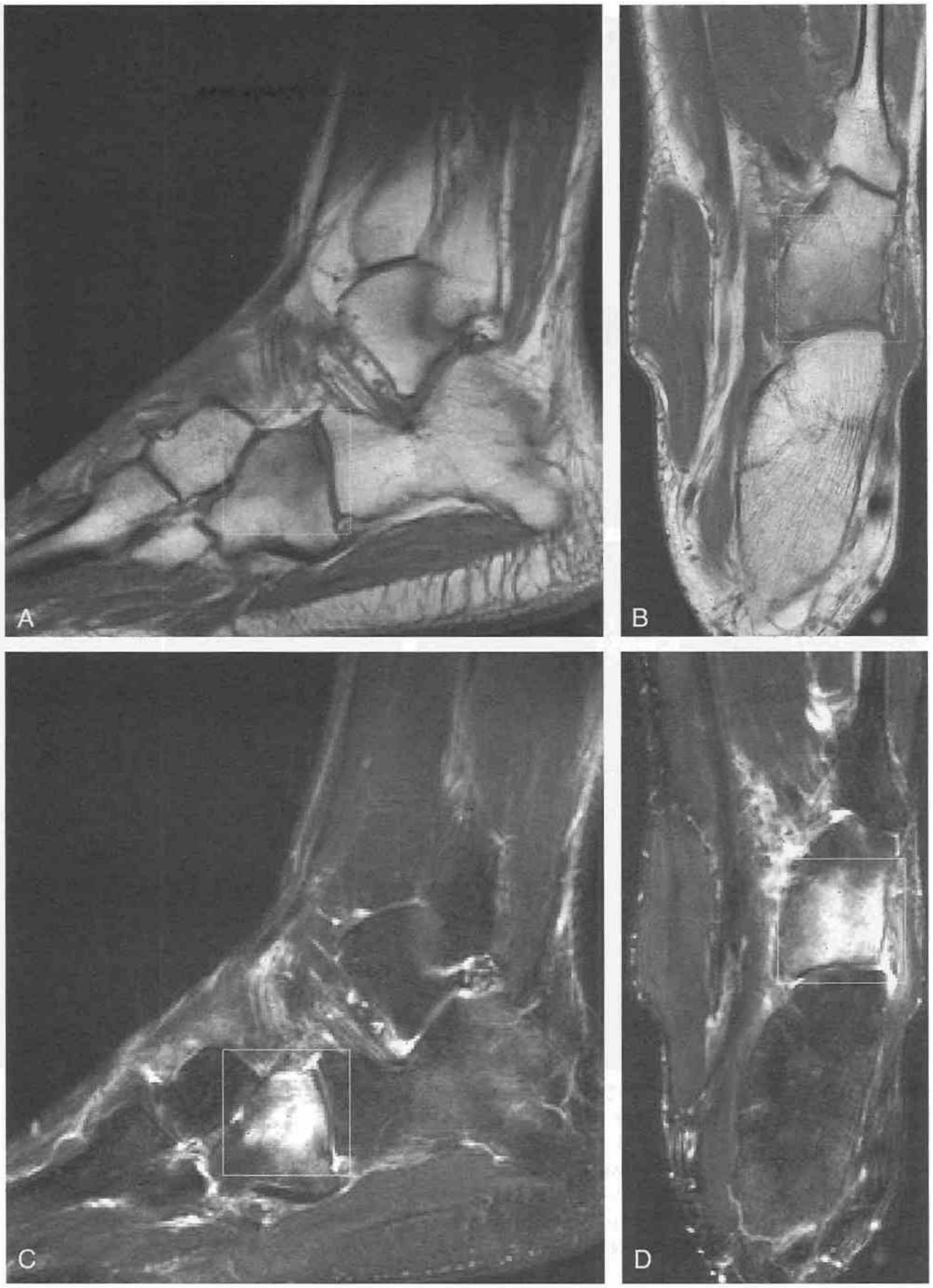

Figure 47–60. This stress fracture of the cuboid *(dotted squares)* is relatively subtle on the T1-weighted images obtained in the sagittal *(A)* and oblique axial *(B)* planes. On the more edema-sensitive, fat-suppressed T2-weighted images *(C* and *D)*, the bone marrow pathologic process is quite conspicuous ***(white squares)***.

Osteoarthritis occurs in up to 20% of patients with OCD but in up to 75% of patients with *loose* OCD. Loose fragments are surrounded by a high-signal-intensity interface around the fragment on T2-weighted or short tau inversion recovery (STIR) images. Any lesion with an underlying cyst is also invariably loose.[56] Irregular high signal intensity or incompletely circumferential high signal intensity is consistent with a partially loose fragment.[24] The fragment itself is of variable signal intensity; this fragment signal intensity is of no clinical significance. MRI can also be used to assess the intactness of the overlying cartilage with high-resolution techniques.[25] The cartilage may be fractured initially, may subsequently became fractured, or may become degenerated subsequently. The subset of OCD with an overlying cartilage defect is termed *loose in situ* (Fig. 47–62).

Most osteochondral lesions appear to be secondary to chronic stress rather than occurring as a single episode. The lateral talar OCD, however, is usually the sequela of a specific injury and is less frequently stable than medial talar OCD. Medial OCD, which is slightly more common, usually has cup-in-a-hole appearance, with lateral OCD more often seen as a horizontally oriented "wafer." Medial talar OCD, compared with lateral OCD, is also usually posterior. Anteromedial OCD-like lesions in the talus usually represent subchondral cysts *(geodes)* from osteoarthritis.

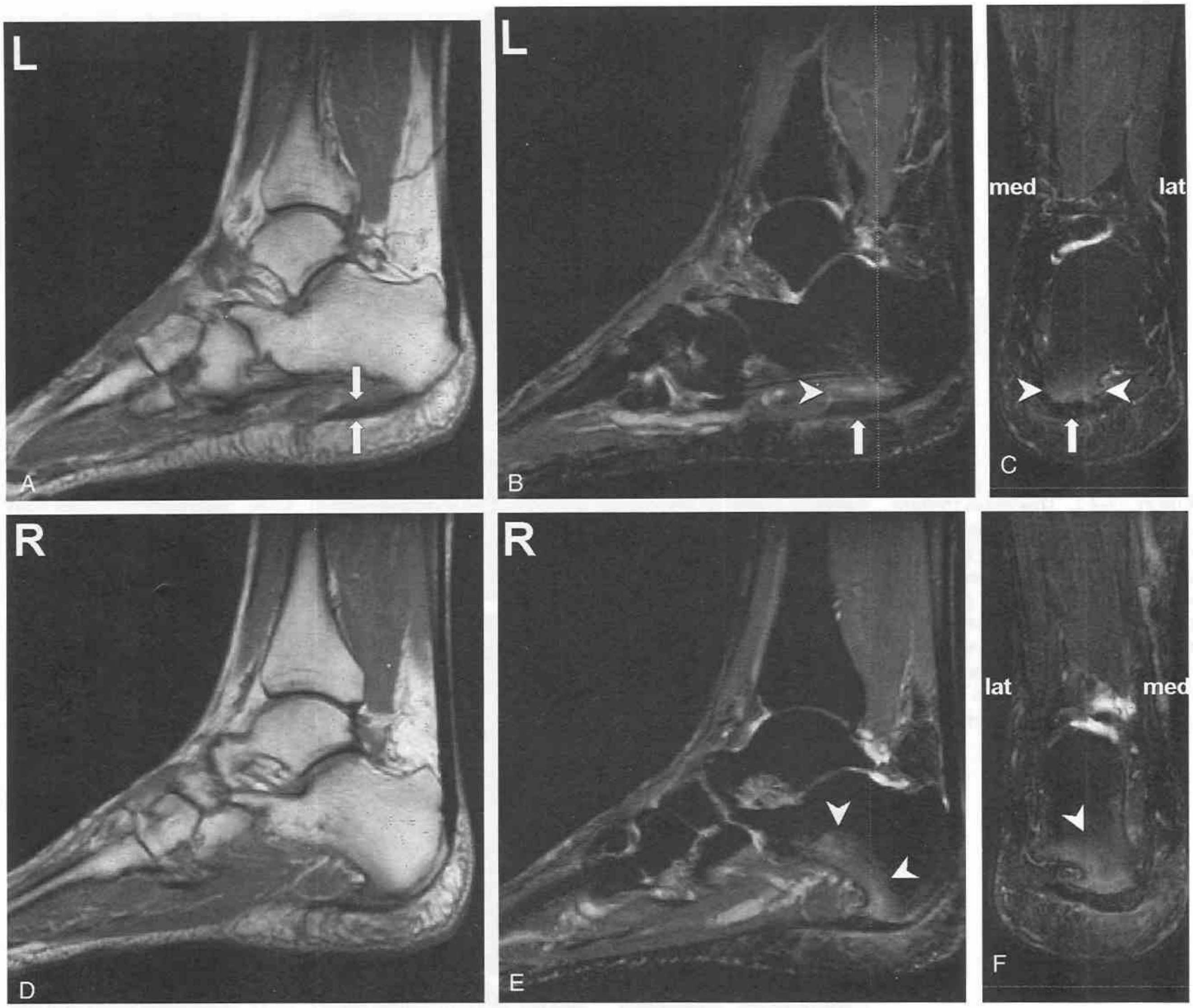

Figure 47–61. The patient is a 52-year-old woman with chronic bilateral heel pain.

A, Sagittal T1-weighted image obtained through the left hindfoot reveals thickening of the plantar fascia *(arrows).*

B, The corresponding sagittal inversion recovery–weighted image reveals edema *(arrowhead)* deep to the plantar fascia *(arrow). Dashed line* represents the position of coronal slice *(C).*

C, Coronal fat-suppressed T2-weighted image demonstrates bone marrow edema *(arrowheads)* deep to the origin of the plantar fascia *(arrow).* med, medial side of image; lat, lateral side of image.

D, Sagittal T1-weighted image of the contralateral right foot. The calcaneal bone marrow edema is less conspicuous than it is on more fluid-sensitive sequences.

E, Sagittal inversion recovery–weighted image corresponding to *D* reveals extensive bone marrow edema along the plantar portion of the calcaneus *(arrowheads). Dashed line* represents the position of coronal slice *(F).*

F, Coronal fat-suppressed T2-weighted image shows the bone marrow edema *(arrowhead)* radiating from the medial-plantar surface of the calcaneus.

Infection

Infection of the foot is common. Approximately 50% of all cases of cellulitis involve the lower extremity. Older patients are often affected because of risk factors such as venous disease, soft tissue edema, and decreased lymphatic drainage. Ulcers are seen in older patients, particularly in those who have diabetes. The rarer necrotizing infection that spares muscle is seen in younger patients.

Soft tissue infection, particularly in diabetes, may be indolent and can lead to abscesses. These abscesses usually involve the central compartment of the foot spreading along the flexor tendon sheaths. When the soft tissue infection spreads to bone, it usually involves the calcaneus, metatarsals, or talus.[94] Osteomyelitis that is spread hematogenously is rare in the foot, except in children. In diabetic patients, a complex interplay of infection, infarction, and sensory neuropathic conditions may result in a "neuropathic arthropathy."[6] The Lisfranc joint is most commonly affected, followed by the metatarsophalangeal and subtalar joints.

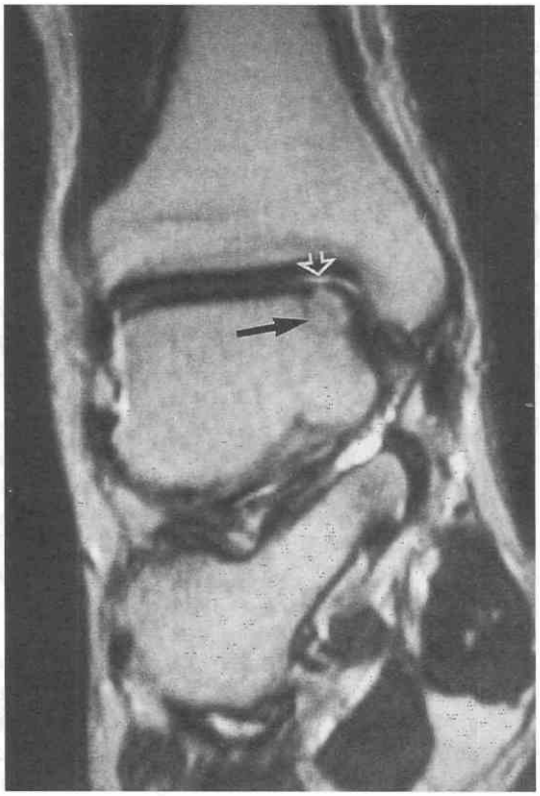

Figure 47–62. On this T2-weighted coronal image, an osteochondral defect is seen medially. The fragment is isointense to adjacent marrow, and no high signal rim is seen around it *(black arrow)*. Therefore, there is no definite evidence of loosening. Disruption of the articular cartilage *(open arrow)* is noted; the fragment is thus considered loose in situ.

Cellulitis, as seen with MRI, is manifested by subcutaneous and, less frequently, by deep muscle edema without mass effect. Diffuse high signal intensity on T2-weighted image, common in diabetic patients, typically affects the plantar soft tissue and muscles deep to the plantar aponeurosis. Soft tissue fluid collections, with or without enhancement after gadolinium administration, are also common in diabetic patients.[9, 58] These collections are typically, but not necessarily, seen near tissue ulcerations.

Osteomyelitis, as seen on MR images, is usually manifested by low signal intensity within the marrow on T1-weighted sequences and commonly by significantly increased intensity on T2-weighted sequences, particularly with fat suppression[55, 57, 87, 90] (Fig. 47–63). On STIR images, infection also shows high signal intensity, although false-positive STIR images may infrequently occur as a sympathetic response in cases of septic arthritis and in neuropathic disease (Fig. 47–64).[28] Intravenous gadolinium may be useful in complicated cases when marrow and soft tissue enhancement may help to differentiate postoperative and neuropathic changes from infection.[59] Neuroarthropathy may produce collapse of the midfoot. Neuropathic disease can show low signal intensity on most imaging sequences. More often, however, increased signal intensity is seen on T2-weighted images, even without infection.[37, 79] Variable enhancement with a contrast agent, however, is usually seen. Fluid in tendon sheaths is quite common in diabetes and is rarely of clinical significance; however, when tendon sheath enhancement is seen with gadolinium administration, soft tissue infection is almost always present.

Soft Tissue Masses

Benign soft tissue lesions commonly seen about the ankle and foot include ganglion cyst, lipomas, fibromatosis,

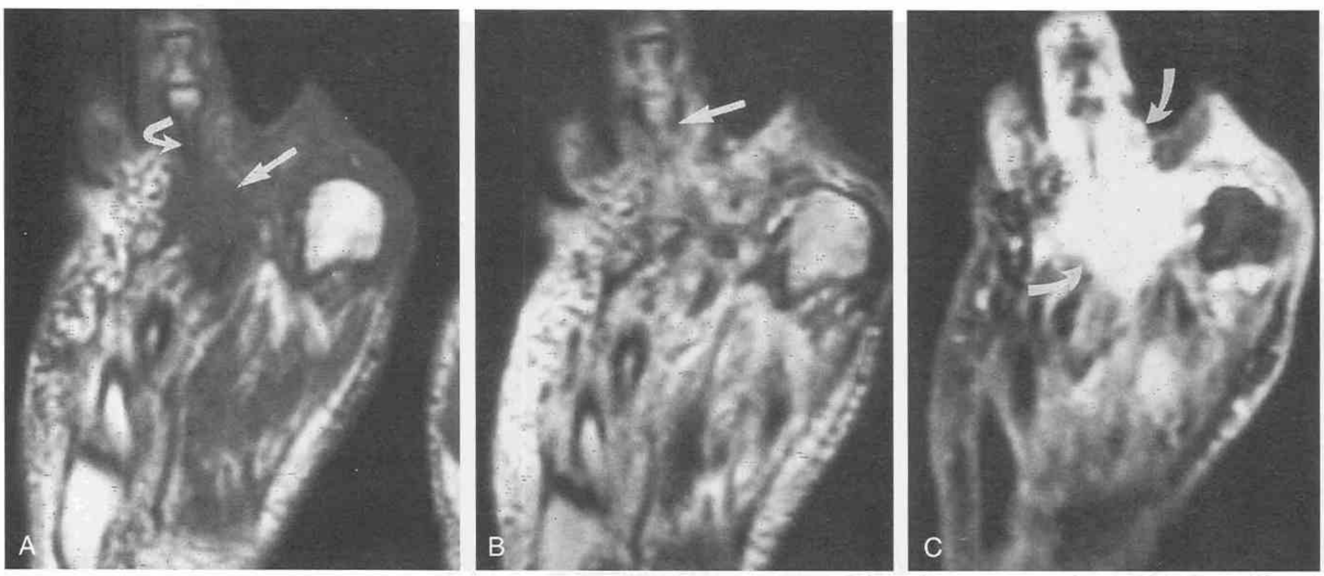

Figure 47–63. On a T1-weighted image *(A)*, low signal intensity is seen within the marrow of the second ray *(curved arrow)*. Adjacent soft tissue mass edema is seen *(straight arrow)*. The marrow increases in intensity on T2-weighted (fast spin-echo) images *(B) (arrow)* and enhances after gadolinium administration *(C)*; this is consistent with osteomyelitis. Extensive soft tissue enhancement is also seen *(arrows)*.

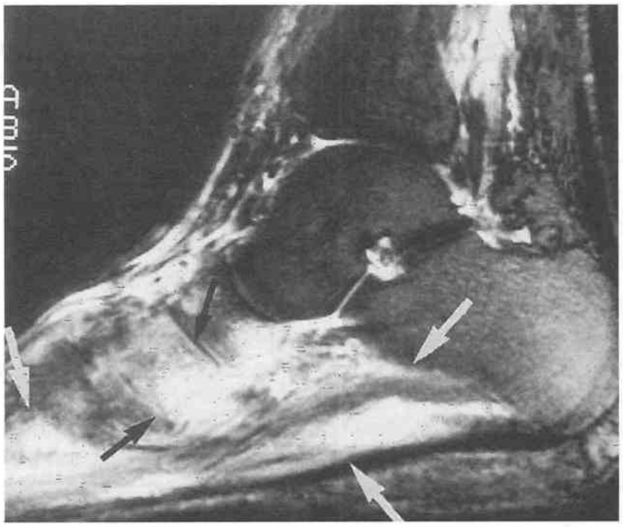

Figure 47–64. Extensive subcutaneous edema with a predominantly plantar distribution *(white arrows)* is seen in a patient with neuropathic disease. Sagittal short tau inversion recovery (STIR) image demonstrates high signal in the navicular and medial cuneiform *(black arrows).*

giant cell tumor or tendon sheath, hemangiomas, and neural tumors, e.g., neurofibroma, schwannoma, and Morton neuroma. The most common malignant soft tissue masses of the foot and ankle are synovial cell sarcoma and malignant fibrous histiocytoma (MFH). Synovial cell sarcomas are most common in teenagers and young adults, whereas MFH is most commonly seen in patients aged 40 years and older. Malignant peripheral nerve sheath tumors, clear cell sarcomas, and liposarcomas are seen less often.

Location is helpful in evaluation of lesions of the foot. Dorsally, most are ganglions or giant cell tumors of tendon sheath. In the nail bed, fibromas, glomus tumors, and pyogenic granulomas are most common. In the plantar aspect of the foot, they are usually fibromas, giant cell tumors of the tendon sheath, lipomas, or epidermal inclusion cysts. In the tarsal tunnel, neural tumors and ganglions are the most numerous.

MRI is much more useful than CT in the workup and surgical planning for soft tissue tumors. On CT, most tumors demonstrate soft tissue attenuation similar to that of muscle.[23] The peritumoral edema is difficult to distinguish from tumor on CT scans, and this limits detailed preoperative localization.[36] CT remains ideal for evaluation of soft tissue calcifications.

MRI is a significant advance over CT in revealing soft tissue tumors, and it offers more precise anatomic localization and potentially improved preoperative diagnoses.[23, 36] Most tumors, however, do not have specific signal characteristics.[49] Most tumors are characterized by low signal intensity on T1-weighted sequences and by increased signal intensity on T2-weighted sequences. Lipomas, however, demonstrate high T1-weighted and intermediate T2-weighted signal intensities, similar to the case of subcutaneous fat.[50] Other tumors that contain fat include liposarcomas and hemangiomas.[16, 19] Other causes of high signal intensity on a T1-weighted image include hemorrhage in aggressive necrotic tumors such as malignant fibrous histiocytomas or synovial cell sarcomas. Fibrous tumors such as aggressive fibromatosis,[48, 66] plantar fibromatosis, and some neurofibromas (only centrally[83]) demonstrate decreased signal on all sequences (except STIR in fibromatosis).

Schwannomas are identified in the region of a peripheral, but not a cutaneous, nerve. These tumors have high signal intensity on T2-weighted sequences, often with a central area of lower signal intensity. Fibromas (Fig. 47–

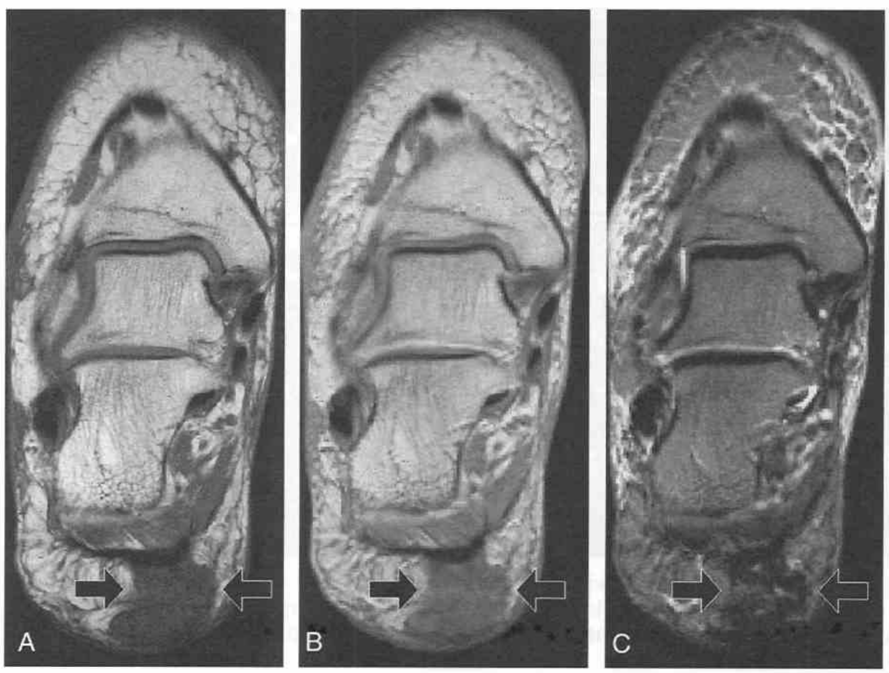

Figure 47–65. Plantar fibroma in a 44-year-old man. *A,* Coronal T1-weighted image. B, Coronal proton-density–weighted image. *C,* Coronal T2-weighted image. The large lesion *(arrows)* is of low signal intensity on all imaging sequences and is confined to the fat of the plantar heel pad.

65) have variable signal characteristics but are seen within the plantar fat adjacent to the aponeurosis, usually close to the calcaneus.[48, 66] Morton's neuromas are usually of low signal intensity on most imaging sequences[29] and can be quite subtle on the MR image (Fig. 47–66). Power Doppler ultrasound has been suggested as a sensitive imaging modality for Morton's neuromas.[47]

Pigmented villonodular synovitis shows areas of decreased signal intensity on both T1-weighted and T2-weighted images, secondary to hemosiderin deposition.[43, 81] A similar appearance may be seen with giant cell tumor of tendon sheath (Fig. 47–67), rheumatoid arthritis nodules (see Fig. 47–49), and fibromatosis.[5, 76]

Synovial cysts and ganglion cysts demonstrate fluid characteristics.[7, 31, 84] They are localized adjacent to joints, and ganglia are septate and have a connection to the joint. Because of the proteinaceous fluid they contain, they are isointense to muscle on T1-weighted images. The appearance of a synovial sarcoma may be remarkably similar to that of a simple synovial cyst, although a portion of its margin is often slightly irregular. Synovial cell sarcomas tend to have more aggressive growth patterns, and they can grow along a tendon sheath.[12] Single-intensity patterns are often heterogeneous on T1- and T2-weighted images, due to hemorrhage and calcification within the mass.

Hemangiomas have heterogeneous signal intensity on T1- and T2-weighted images owing to vascular channels and their signal voids, with areas of fat contained within the lesion. These tumors appear septate or lobulated and have infiltrative margins that routinely violate anatomic barriers. Calcifications in tumors are visualized as regions of signal void and may be difficult to distinguish from flow

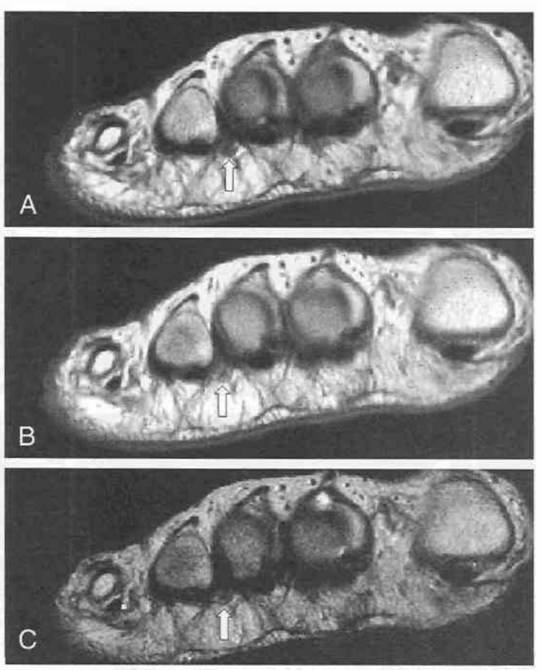

Figure 47–66. Morton's neuroma in a 51-year-old man. *A,* Coronal T1-weighted image. *B,* Coronal proton-density–weighted image. *C,* Coronal T2-weighted image. The small, inconspicuous lesion *(arrows)* between the third and fourth metatarsal heads is of low signal intensity on all imaging sequences.

voids in highly vascular tumors or from hemosiderin in necrotic tumors. Distinguishing tumor from surrounding edema may be difficult. Typically, the most prominent edema in soft tissue tumors is seen with malignant fibrous histiocytoma, which typically tracks up and down as a single muscle.[54] Either on STIR images or immediately following contrast administration, the tumor and its pseudocapsule can usually be distinguished from the edema.

The MRI appearance of a soft tumor is often nonspecific for evaluating its aggressiveness. Benign tumors tend to have smooth margins and relatively homogeneous signal intensity on MR imaging and often lack neurovascular and osseous involvement. However, these findings are nonspecific and can also be seen in aggressive malignant neoplasms such as synovial cell sarcoma. Malignant soft tissue tumors tend to be larger lesions that have infiltrative margins and heterogeneous signal intensity on MR imaging in addition to their rapid growth and neurovascular invasion. However, a benign lesion, such as aggressive fibromatosis, can also demonstrate these imaging characteristics. If the MR imaging appearance of a mass does not meet the specific criteria of a simple lipoma, synovial cyst, or hemangioma, biopsy should be performed.

Bone Tumors

Osseous tumors are much less common than soft tissue tumors of the foot and ankle. Osseous tumors continue to be initially evaluated by plain radiography. MRI, however, is useful in localizing tumors and in staging their extent. Most tumors have nonspecific signal characteristics. MRI is thus unable to render a specific preoperative diagnosis; however, signal characteristics may help narrow the differential diagnosis. The role of CT is limited to the evaluation of the degree of cortical involvement.

Primary bone tumors of the feet are rare, accounting for only 4% of all bone tumors and only 3% of resected foot malignancies. The staging system is based on both histologic grade (I = low; II = high; III = metastatic) and whether the tumor is intracompartmental or extracompartmental.[27]

In the foot, most bone neoplasms are primary. Benign bone neoplasms are more common than malignant ones. The most common benign tumors are enchondromas and osteoid osteomas. The most common primary malignant tumors are chondrosarcomas and Paget's sarcoma. Metastatic tumors are rare and usually occur as a result of colorectal, renal, or bladder primary tumors. Certain bone tumors have a propensity for a specific anatomic location in the feet. The calcaneus is the most common site of aneurysmal bone cysts and chondrosarcomas (Fig. 47–68). In the anterior calcaneus, intraosseous lipomas and unicameral bone cysts are most common. Chondromyxoid fibroma and fibrous dysplasia occur frequently in metatarsals. The talus is the usual location for osteoid osteoma and osteoblastoma. Enchondromas occur in the proximal and middle phalanges and metatarsals.

Osteosarcomas demonstrate low signal intensity on T1-weighted and high signal intensity on T2-weighted sequences.[34, 86] Matrix calcifications may be seen as areas of signal void. Cortical breakthrough, adjacent soft tissue

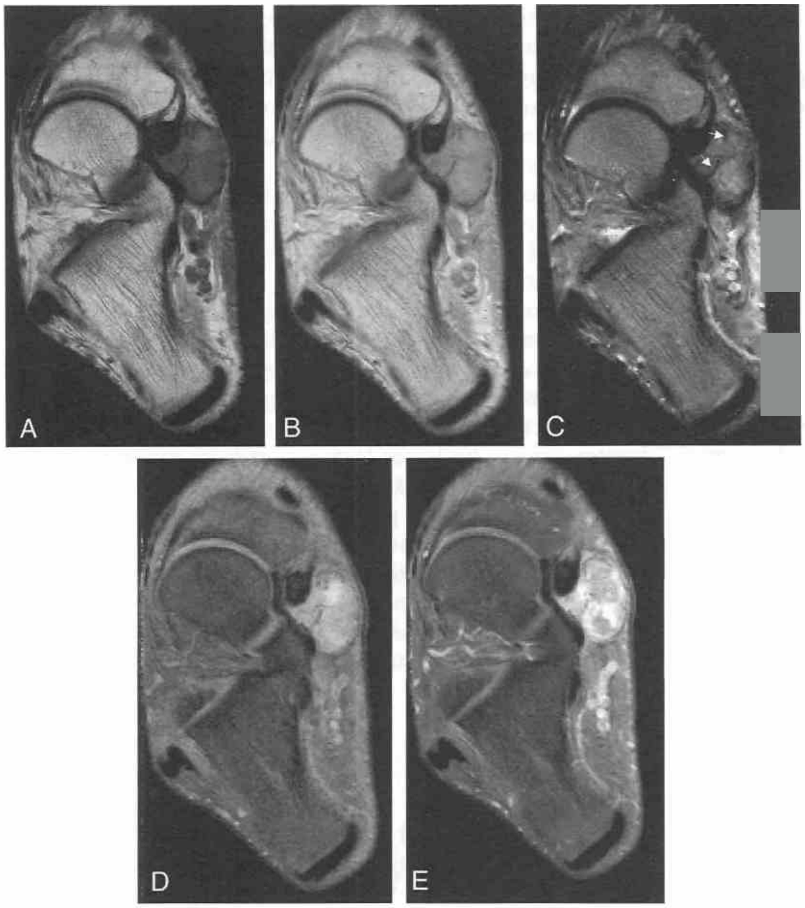

Figure 47–67. Giant cell tumor of the tendon sheath in a 19-year-old man. *A,* Axial T1-weighted image. *B,* Axial proton-density–weighted image. *C,* Axial T2-weighted image. The soft tissue mass adjacent to the posterior tibial tendon is relatively dark on the T1-weighted and T2-weighted images owing to the presence of hemosiderin. The mass is growing through the torn tendon sheath *(arrows)*. *D,* Axial precontrast fat-suppressed T1-weighted image. Some signal within the mass is brighter than the surrounding suppressed fat, suggesting the presence of proteinaceous fluid or methemoglobin. *E,* Axial postcontrast fat-suppressed, T1-weighted image demonstrates heterogeneous enhancement, indicative of the vascularity of such synovial proliferation.

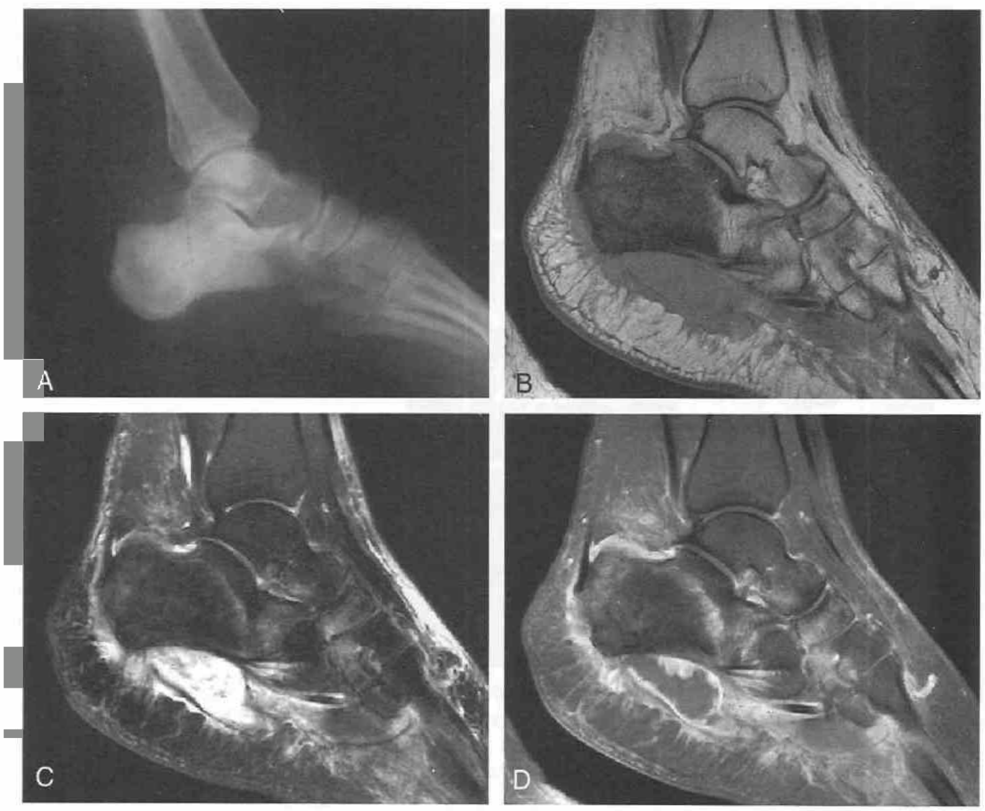

Figure 47–68. Chondrosarcoma arising from a calcaneal tuberosity in a 30-year-old woman. *A,* Lateral radiograph. The patient complained of heel pain for 10 months until the sclerosis within the calcaneus was recognized. *B,* Sagittal T1-weighted image shows diffusely decreased signal within the calcaneus corresponding to the radiographic sclerosis. *C,* Sagittal fat-suppressed T2-weighted image reveals marrow edema only at the periphery of the sclerotic region. Extensive bright signal, however, is present in the soft tissues immediately plantar to the calcaneus. *D,* Sagittal postcontrast fat-suppressed T1-weighted image demonstrates enhancement only at the periphery of the osseous and soft tissue masses. This enhancement pattern is a result of the relative hypovascularity of chondrosarcomas.

extension, and peritumoral edema may be noted. The signal characteristics are variable and may be affected by the tumor subtype. For example, telangiectatic osteosarcomas may show areas of increased signal intensity on both T1-weighted and T2-weighted sequences. Fluid levels may also be noted in telangiectatic osteosarcomas, but this is a nonspecific finding.[89] Osteoid osteomas show high signal intensity on T2-weighted sequences. The nidus may be visualized as an area of decreased signal intensity (Fig. 47–69).[35, 93] Intravenous gadolinium may aid in identifying the nidus, which significantly enhances. Extensive edema surrounding this tumor is also seen both in the marrow and in the adjacent musculature.[22] This extensive edema may also be seen in chondroblastomas (Fig. 47–70) and, less frequently and intensely, in osteoblastomas, eosinophilic granulomas, and aneurysmal bone cysts.

Usually, fibrous dysplasia demonstrates decreased signal intensity on T2-weighted sequences.[63] However, frequent islands of cartilage and cystic areas may be seen demonstrating increased T2 signal intensity. Nonossifying fibromas are cortically based lesions with decreased T2 signal intensity. A low-signal-intensity rim is seen with healing and increases in thickness with time. Occasional nonossifying fibromas demonstrate increased signal intensity on T2-weighted images.

Hyaline cartilage tumors, such as enchondromas, osteochondromas, and chondrosarcomas, show a lobulated high signal intensity on T2-weighted sequences.[18] Nonhyaline cartilage tumors, such as chondroblastomas, can show areas of decreased signal intensity on T2-weighted images, although there is a significant amount of overlap.[52]

Aneurysmal bone cysts demonstrate septations and fluid-fluid levels. The cystic areas may show varying signal intensity, depending on the stage of blood breakdown. Small diverticulum-type outpouchings have been described. A well-defined low-signal-intensity rim may also be noted. Internal high signal intensity on T1-weighted images is characteristic, as is susceptibility artifact on gradient-echo images.[21, 61]

Intraosseous lipomas have signal characteristics similar to those of subcutaneous fat, with high signal intensity on T1-weighted images and moderate signal intensity on T2-weighted images.[26] A central signal void corresponding to calcification and ossification noted on radiographs may be seen.

Although the previously described signal characteristics are useful in evaluating tumors, traditional criteria such as cortical breakthrough, soft tissue mass, and periosteal reaction remain optimal for determining the degree of a tumor's aggressiveness. Marrow-infiltrative tumors, such as lymphomas, leukemia, metastatic disease, and multiple myeloma, show a decrease in the normal high-signal-intensity marrow on T1-weighted sequences. On T2-weighted and STIR sequences, signal intensity increases. Adjacent soft

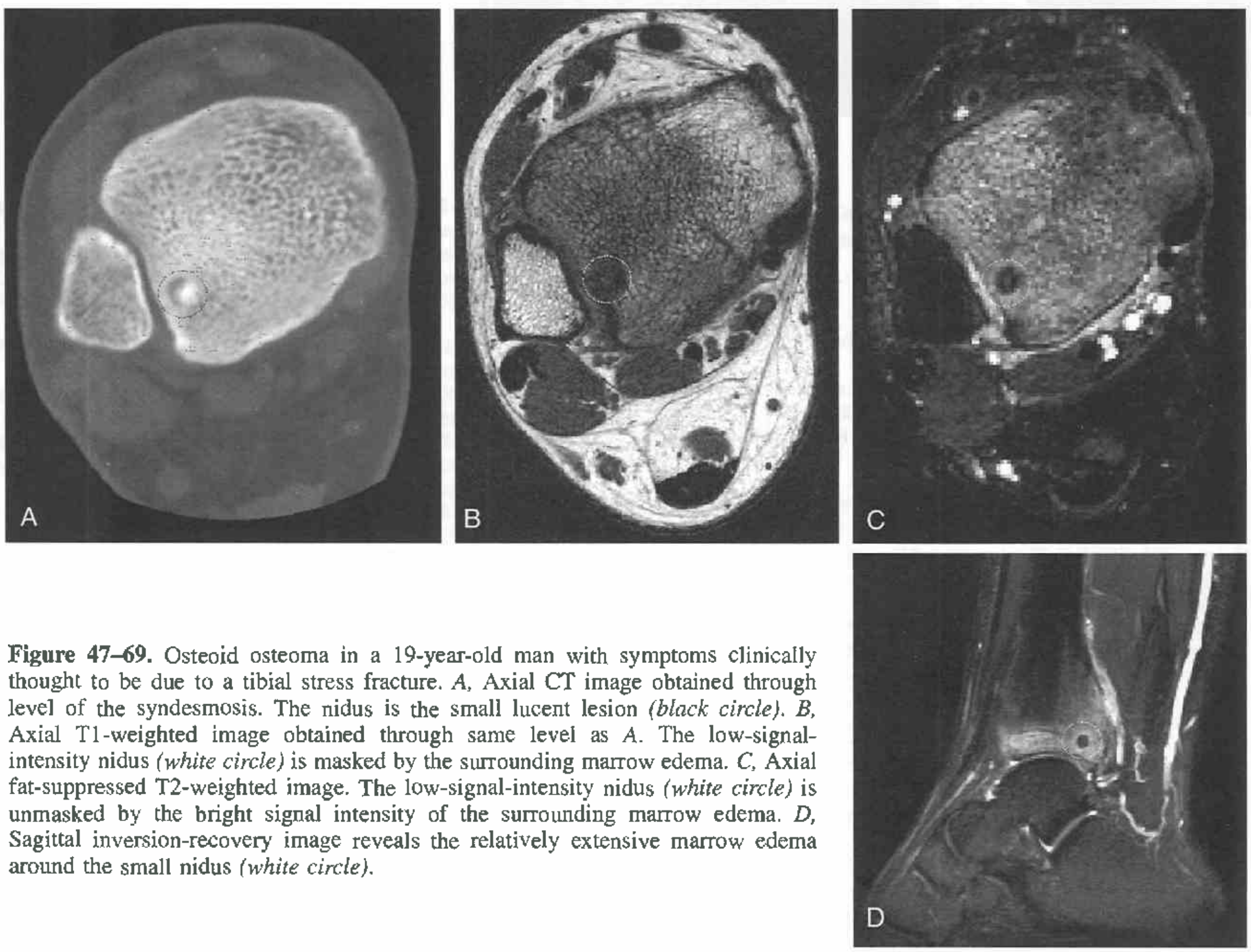

Figure 47–69. Osteoid osteoma in a 19-year-old man with symptoms clinically thought to be due to a tibial stress fracture. *A,* Axial CT image obtained through level of the syndesmosis. The nidus is the small lucent lesion *(black circle). B,* Axial T1-weighted image obtained through same level as *A.* The low-signal-intensity nidus *(white circle)* is masked by the surrounding marrow edema. *C,* Axial fat-suppressed T2-weighted image. The low-signal-intensity nidus *(white circle)* is unmasked by the bright signal intensity of the surrounding marrow edema. *D,* Sagittal inversion-recovery image reveals the relatively extensive marrow edema around the small nidus *(white circle).*

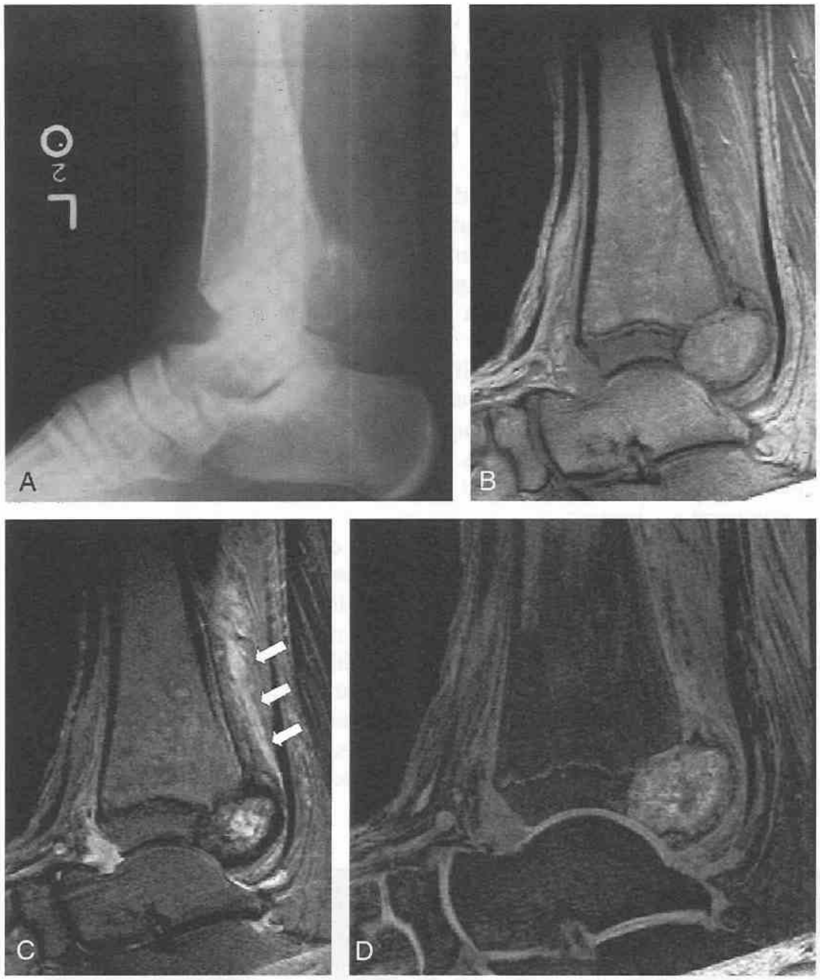

Figure 47–70. Chondroblastoma in a 16-year-old boy. *A,* Lateral radiograph demonstrates an expansile mass arising from the back of the tibia. *B,* Sagittal T1-weighted image shows that the mass is purely epiphyseal in this nearly skeletally mature patient. *C,* Sagittal T2-weighted image shows heterogeneous bright and isointense signal intensity within the mass as well as edema of the adjacent musculature *(arrows). D,* Sagittal cartilage-sensitive (fat-suppressed 3D gradient-echo) sequence yields signal intensity within this cartilage tumor that is nearly as bright as in the nearby articular hyaline cartilage.

tissue masses may be seen, most commonly in lymphoma and in aggressive subtypes of multiple myeloma.

References

1. Badgley CE: Coalition of the calcaneus and the navicular. Arch Surg 15:75–88, 1927.
2. Balduini FC, Vegso JJ, Torg JS, et al: Management and rehabilitation of ligamentous injuries to the ankle. Sports Med 4:364–380, 1987.
3. Ballinger PW, Frank ED: Merrill's Atlas of Radiographic Positions and Radiologic Procedures, 9th ed. St. Louis, Mosby, 1999, pp 254–256.
4. Ballinger PW, Frank ED: Merrill's Atlas of Radiographic Positions and Radiologic Procedures, 9th ed. St. Louis, Mosby, 1999.
5. Balsara ZN, Stainken BF, Martinez AJ: Case report: MR image of localized giant cell tumor of the tendon sheath involving the knee. J Comput Assist Tomogr 13:159–162, 1989.
6. Bamberger DM, Daus GP, Gerding DN: Osteomyelitis in the feet of diabetic patients: Long-term results, prognostic factors, and the role of antimicrobial and surgical therapy. Am J Med 86:653–666, 1987.
7. Bassett F, Gates H, Billys J, et al: Talor impingement by the anteroinferior tibiofibular ligament. J Bone Joint Surg 72A:55–59, 1990.
8. Contact Beekley MR-Spots, Beekley Corporation, 1 Prestige Lane, Bristol CT 06010; (860) 583–4700; *www.beekley.com.*
9. Beltran J, Campanni DS, Knight C, et al: The diabetic foot: Magnetic resonance imaging evaluation. Skeletal Radiol 19:37–41, 1990.
10. Beltran J, Munchow AM, Khabiri A, et al: Ligaments of the lateral aspect of the ankle and sinus tarsi: An MR imaging study. Radiology 177:455–458, 1990.
11. Berndt AL, Harty M: Transchondral fractures (osteochondritis dissecans) of the talus. J Bone Joint Surg 41A:988–1020, 1959.
12. Bernreuter WK, Sartoris DJ, Resnick D: Magnetic resonance imaging of synovial sarcoma. J Foot Surg 29:94–100, 1990.
13. Bloem JL, Taminiau AHM, Eulderink F, et al: Radiographic staging of primary bone sarcoma: MR imaging, scintigraphy, angiography, and CT correlated with pathologic examination. Radiology 169:805–810, 1988.
14. Boruta PM, Bishop JO, Braly WG, et al: Acute lateral ankle ligament injuries: A literature review. Foot Ankle 11:107–113, 1990.
15. Bower BL, Keyser CK, Gilula LA: Rigid subtalar joint: A radiographic spectrum. Skeletal Radiol 17:583–588, 1989.
16. Buetow PC, Kransdorf MJ, Moser RPJ, et al: Radiologic appearance of intramuscular hemangioma with emphasis on MR imaging. AJR Am J Roentgenol 154:563–567, 1990.
17. Chandnani VP, Bradley YC: Achilles tendon and miscellaneous tendon lesions. MRI Clin North Am 2:89–96, 1994.
18. Cohen EK, Kressel HY, Frank TS, et al: Hyaline cartilage-origin bone and soft tissue neoplasms: MR appearance and histologic correlation. Radiology 167:477–481, 1988.
19. Cohen EK, Kressel HY, Perosio T, et al: MR imaging of soft-tissue hemangiomas: Correlation with pathologic findings. AJR Am J Roentgenol 150:1079–1081, 1988.
20. Conway JJ, Coswell HR: Tarsal coalitions: Clinical significance and roentgenographic demonstration. Radiology 92:799, 1969.
21. Cory DA, Fritsch SA, Cohen MD, et al: Aneurysmal bone cysts: Imaging findings and embolotherapy. AJR Am J Roentgenol 153:369–373, 1989.
22. Crim JR, Mirra JM, Eckardt JJ, et al: Widespread inflammatory response to osteoblastoma: The flare phenomenon. Radiology 177:835–836, 1990.
23. Demas BE, Heelan RT, Lane J, et al: Soft-tissue sarcomas of the extremities: Comparison of MR and CT in determining the extent of disease. Am J Roentgenol 150:615–620, 1986.

24. DeSmet AA, Fisher DR, Burnstein MI, et al: Value of MR imaging in staging osteochondral lesions of the talus (osteochondritis dissecans). AJR Am J Roentgenol 154:555–558, 1990.
25. Dipaola D, Nelso DW, Colville MR: Characterizing osteochondral lesions by magnetic resonance imaging. Arthroscopy 7:101–104, 1991.
26. Dooms GC, Hricak H, Sollitto RA, et al: Lipomatous tumors and tumors with fatty component: MR imaging potential and comparison of MR and CT results. Radiology 157:479–483, 1985.
27. Enneking WF, Spanier SS, Goodman MA: A system for the surgical staging of musculoskeletal sarcoma. Clin Orthop 153:106–120, 1980.
28. Erdman WA, Tamburro F, Hayson HT, et al: Radiology 180:533–539, 1991.
29. Erickson SJ, Corale PB, Carrera GF, et al: Interdigital (Morton) neuroma: High-resolution MR imaging with a solenoid coil. Radiology 181:833, 1991.
30. Erickson SJ, Smith JW, Ruiz ME, et al: MR imaging of the lateral collateral ligament of the ankle. AJR Am J Roentgenol 156:131–136, 1991.
31. Feldman F, Singson RD, Staron RB: Magnetic resonance imaging of para-articular and ectopic ganglia. Skeletal Radiol 18:353–358, 1989.
32. Finkel JE, Tarsal tunnel syndrome. MRI Clin North Am 2: 67–78, 1994.
33. Freeman MAR, Dean MRE, Hanham IWF: The etiology and prevention of functional instability of the foot. J Bone Joint Surg 47B: 678–685, 1965.
34. Gillespy TI, Manfrini M, Ruggieri P, et al: Staging of intraosseous extent of osteosarcoma: Correlation of preoperative CT and MR imaging with pathologic macroslides. Radiology 167:765–767, 1988.
35. Glass RBJ, Poznanski AK, Fisher MR, et al: Case report: MR imaging of osteoid osteoma. J Comput Assist Tomogr 10:1065–1067, 1986.
36. Golfieri R, Baddeley H, Pringle JS, et al: MRI in primary bone tumors: Therapeutic implications. Eur J Radiol 12:201, 1991.
37. Gould N: Tenosynovitis of the flexor hallucis longus tendon at the great toe. Foot Ankle 2:46–48, 1981.
38. Guyer BH, Levinsohn EM, Fredrickson BE, et al: Computed tomography of calcaneal fractures: Anatomy, pathology, dosimetry, and clinical relevance. Am J Roentgenol 145:911, 1985.
39. Harris BJ: Anomalous structures in the developing human foot [abstract]. Anat Rec 121:399, 1955.
40. Heger L, Wulff K, Seddigi MSA: Computed tomography of calcaneal fractures. Am J Roentgenol 145:131–137, 1985.
41. Henry AK: Extensile Exposure, 2nd ed. Edinburgh, E & S Livingstone, 1957, p 304.
42. Contact IZI Multi-Modality Radiographic Markers, IZI Medical Products, 7020 Tudsbury Road, Baltimore MD 21244; (410) 594–9403; *www.izimed.com.*
43. Jelinek JS, Kransdorf MJ, Utz JA, et al: Imaging of pigmented villonodular synovitis with emphasis on MR imaging. AJR Am J Roentgenol 152:337–342, 1989.
44. Keats TE: Atlas of Normal Roentgen Variants That May Simulate Disease, 6th ed. St. Louis, Mosby, 1996, pp 656, 690–692.
45. Kirby EJ, Shereff MJ, Lewis MM: Soft-tissue tumors and tumor-like lesions of the foot. J Bone Joint Surg 71A:621–626, 1989.
46. Kirsch MD, Erickson SJ: Normal magnetic resonance imaging anatomy of the ankle and foot. MRI Clin North Am 2:1–21, 1994.
47. Kransdorf MJ, Murphy MD: Imaging of Soft Tissue Tumors. Philadelphia, WB Saunders, 1997, p 237.
48. Kransdorf MJ, Jelinek JS, Moser RPJ, et al: Magnetic resonance appearance of fibromatosis: A report of 14 cases and review of the literature. Skeletal Radiol 19:495–500, 1990.
49. Kransdorf MJ, Jelinek JS, Moser RPJ, et al: Soft-tissue masses: Diagnosis using MR imaging. AJR Am J Roentgenol 153:541–547, 1989.
50. Kransdorf MJ, Moser RPJ, Meis JM, et al: Fat-containing soft-tissue masses of the extremities. Radiographics 11:81–106, 1991.
51. Lawson JP: Clinically significant radiologic anatomic variants of the skeleton. AJR Am J Roentgenol 163:249–255, 1994.
52. Lee JK, Yao L, Wirth CR: MR imaging of solitary osteochondromas: Report of eight cases. AJR Am J Roentgenol 149:557–560, 1987.
53. Leonard MA: The inheritance of tarsal coalition and its relationship to spastic flat foot. J Bone Joint Surg 56B:520, 1974.
54. Mahajan H, Kim EE, Wallace S, et al: Magnetic resonance imaging of malignant fibrous histiocytoma. Magn Reson Imaging 7:283–288, 1989.
55. Mason MD, Zlatkin MB, Esterhai JL, et al: Chronic complicated osteomyelitis of the lower extremity: Evaluation with MR imaging. Radiology 173:355–359, 1989.
56. Mesgurzadeh M, Sapega AA, Bonakdarpour A, et al: Osteochondritis dissecans: Analysis of mechanical stability with radiography, scintigraphy, and MR imaging. Radiology 165:775–786, 1987.
57. Modic M, Feiglin D, Piraino D, et al: Vertebral osteomyelitis: Assessment using MR. Radiology 157:157–166, 1985.
58. Moore TE, Yuh WTC, Kathol MH, et al: Pictorial essay abnormalities of the foot in patients with diabetes mellitus: Findings on MR imaging. AJR Am J Roentgenol 157:813–817, 1991.
59. Morrison W, Schweitzer ME, Mitchell DG, et al: The utility of gadolinium-enhanced fat suppressed MRI in the diagnosis of osteomyelitis. Radiology 189:251–257, 1993.
60. Mosier KM, Asher M: Tarsal coalitions and peroneal spastic flat foot: A review. J Bone Joint Surg 66A:976–984, 1984.
61. Munk PL, Helms CA, Holt RG, et al: MR imaging of aneurysmal bone cysts. AJR Am J Roentgenol 153:99–101, 1989.
62. Netter FH: Bony attachments of muscles of leg. In Ciba Collection of Medical Illustration, vol 8, part 1. Summit, NJ, Ciba-Geigy, 1991, p 107.
63. Norris MA, Kaplan PA, Pathria MN, et al: Fibrous dysplasia: Magnetic resonance imaging. Clin Imaging 14:211, 1990.
64. Noto AM, Cheung Y, Rosenberg TS, et al: MR imaging of the ankle: Normal variants. Radiology 170:121–124, 1989.
65. Pritsch M, Horoshouski H, Farine J: Arthroscopic treatment of osteochrondral lesions of the talus. J Bone Joint Surg 68A:862–865, 1986.
66. Quinn SF, Erickson SJ, Dee PM, et al: MR imaging in fibromatosis: Results in 26 patients with pathologic correlation. AJR Am J Roentgenol 156:539–542, 1991.
67. Resnick D: Talar ridges, osteophytes, and beaks: A radiologic commentary. Radiology 151:329–332, 1984.
68. Richardson EG: Flatfoot in children and adults. In Coughlin MJ, Mann RA (eds): Surgery of the Foot and Ankle, vol 1, 7th ed. St. Louis, Mosby, 1999, p 718.
69. Richardson EG: Heel pain. In Coughlin MJ, Mann RA (eds): Surgery of the Foot and Ankle, vol 2, 7th ed. St. Louis, Mosby, 1999, p 862.
70. Roesnberg ZS, Jahss MH, Noto AM, et al: Rupture of the posterior tibial tendon: CT and surgical findings. Radiology 167:489–493, 1988.
71. Rosenberg ZS: Chronic rupture of the posterior tibial tendon. MRI Clin North Am 2:79–87, 1994.
72. Schreibman KL, Gilula LA: Ankle tenography: A therapeutic imaging modality. Radiol Clin North Am 36:739–756, 1998.
73. Schweitzer ME, Karasick D: MR imaging of disorders of the Achilles tendon. AJR Am J Roentgenol 175:613–625, 2000.
74. Schweitzer ME, Karasick D: MR imaging of disorders of the posterior tibialis tendon. AJR Am J Roentgenol 175:627–635, 2000.
75. Shea MP, Manoli A: Osteochondral lesions of the talar dome. Foot Ankle 14:48–55, 1993.
76. Sherry CS, Harmes SE: MR evaluation of giant cell tumors of the tendon sheath. Magn Reson Imaging 7:195–201, 1989.
77. Shikoff MD, Figura MA, Postar SE: A retrospective study of 195 patients with heel pain. J Am Podiatr Med Assoc 78:194–197, 1988.
78. Slomann HC: On coalition calcaneo-navicularis. J Orthop Surg 3: 586, 1921.
79. Sobel M, Geppert MJ, Olsen EJ, et al: The dynamics of peroneus brevis tendon splits: A proposed mechanism, technique of diagnosis, and classification of injury. Foot Ankle 73:413–422, 1992.
80. Sobel M, Pavlov H, Geppert MJ, et al: Painful os peroneum syndrome: A spectrum of conditions responsible for plantar lateral foot pain. Foot Ankle 15:112–124, 1994.
81. Spritzer CE, Dalinka MK, Kressel HY: Magnetic resonance imaging of pigmented villonodular synovitis: A report of two cases. Skeletal Radiol 16:316–319, 1987.
82. Stormont DM, Peterson HA: The relative incidence of tarsal coalition. Clin Orthop 181:28–36, 1983.
83. Stull MA, Moser RPJ, Kransdorf MJ, et al: Magnetic resonance appearance of peripheral nerve sheath tumors. Skeletal Radiol 20: 9–14, 1991.
84. Sundaram M, McGuire MH, Fletcher J, et al: Magnetic resonance imaging of lesions of synovial origin. Skeletal Radiol 15:110–116, 1986.
85. Sundaram M, McGuire MH, Herbold DR: Magnetic resonance imaging of soft tissue masses: An evaluation of fifty-three histologically proven tumors. Magn Reson Imaging 6:237–248, 1988.

86. Sundaram M, McGuire MH, Herbold DR: Magnetic resonance imaging of osteosarcoma. Skeletal Radiol 16:23–29, 1987.
87. Tang JS, Gold RH, Bassett LW, et al: Musculoskeletal infection of the extremities: Evaluation with MR imaging. Radiology 166: 205–209, 1988.
88. Torg JS, Pavlov H, Cooley LH, et al: Stress fractures of the tarsal navicular: A retrospective review of twenty-one cases. J Bone Joint Surg 63A:700–712, 1982.
89. Tsai JC, Dalinka MK, Fallon MD, et al: Fluid-fluid level: A nonspecific finding in tumors of bone and soft tissue. Radiology 175: 779–782, 1990.
90. Unger EC, Moldofsky PJ, Gatenby RA, et al: Diagnosis of osteomyelitis by MR imaging. AJR Am J Roentgenol 150:605–610, 1988.
91. Williams PL, Smibert JG, Cox R, et al: Imaging study of the painful heel syndrome. Foot Ankle 7:345–349, 1987.
92. Wynne-Davies R: Heritable disorders in orthopedics. Orthop Clin North Am 9:3, 1978.
93. Yeager BA, Schiebler ML, Wertheim SB, et al: Case report: MR imaging of osteoid osteoma of the talus. J Comput Assist Tomogr 11:916–917, 1987.
94. Zlatkin MB, Pathria M, Sartoris DJ, et al: The diabetic foot. Radiol Clin North Am 25:1095–1105, 1987.

48 The Knee

Steven Shankman, Javier Beltran

Magnetic resonance imaging (MRI) has revolutionized our ability to picture the soft tissue structures of the musculoskeletal system. Increased soft tissue contrast coupled with multiplanar slice capability allows visualization of muscles, tendons, ligaments, cartilage, and bone marrow in a way that is unprecedented. Although the knee is a common site for all disorders occurring in and about the joints, most cases requiring MRI are traumatic in nature. The role of computed tomography (CT) in the evaluation of internal derangement of the knee has always been limited because of its inability to depict normal and abnormal soft tissue anatomy accurately. CT remains the modality of choice, however, in certain situations, such as tibial plateau fracture. This chapter emphasizes standard spin-echo MRI of the traumatized knee. Normal anatomy is discussed, and other disorders affecting the knee joint are included.

Technical Considerations

MRI of the knee is performed using a transmit-receive, general-purpose extremity surface coil, available from most companies that manufacture imaging equipment. Quadrature and phase-array coils are also available. Increased spatial resolution and decreased signal-to-noise (S/N) ratio are important advantages of these coils. The knee is placed in full extension in a neutral position. In general, a small field of view of 14 to 16 cm and a 3-mm slice thickness are recommended.

Different institutions use different pulse sequences for knee imaging. When spin-echo, two-dimensional Fourier transform (2D FT) techniques are used, three planes of section (axial, sagittal, and coronal) are obtained. It is convenient to obtain a proton-density–weighted and a T2-weighted set of images in one plane (e.g., repetition time/echo time [TR/TE], 2000/20–80), frequently the sagittal. Proton-density images are probably the most sensitive for detection of meniscal tears. The axial plane can be imaged using T1-weighted pulse sequences (e.g., TR/TE, 500/20) or, alternatively, T2*-weighted, gradient-echo techniques, which allow good visualization of the articular cartilage (e.g., TR/TE/flip angle, 400/9/75). The same T2* sequence can be used in the coronal plane. Coronal proton-density, fat-supressed, high-resolution images provide high sensitivity for bone marrow lesions in addition to meniscal tears.

An alternative for articular cartilage imaging is the use of fat-suppressed, spoiled gradient-echo technique; more recently, fast spin-echo T2-weighted images have demonstrated high accuracy for detection of cartilage lesions. Software developments allow fast spin-echo techniques that produce similar contrast in a fraction of the time it takes to obtain classic spin-echo sequences (e.g., TR/TE, 3600/20–80).

Alternatively, radial imaging can be used, with multiple oblique planes oriented in a radial fashion and centered over each side of the tibial plateau, with extra sections oriented along the axis of the anterior cruciate ligament (ACL). This technique can be used also with 2D FT gradient-echo pulse sequences and provides images similar to those obtained with conventional arthrography.

Three-dimensional Fourier transform (3D FT) volume-acquisition techniques are becoming more popular as a result of software improvements and availability of workstations. These techniques are performed using gradient-echo pulse sequences with short TR/TE (e.g., TR/TE/flip angle, 18/9/30). The advantages of 3D FT data acquisition include improved S/N ratio and reconstruction of true contiguous slices of about 1 mm in infinite planes of section with minimal distortion.

Finally, for kinematic studies of the femoropatellar joint for patellar tracking abnormalities, multiple images can be obtained with ultrafast gradient-echo techniques in the axial plane during active flexion and extension of the knee within the gantry.

Menisci

Anatomy

The menisci of the knee are two semilunar, C-shaped fibrocartilaginous disks that sit on the peripheral margins of the essentially flat tibial plateau. The upper surfaces of both menisci are concave, and they articulate with the convex femoral condyles. Both menisci measure approximately 4 to 7 mm in height at the periphery and 1 mm or less at the free edge. The peripheral one third contains neurovascular structures, whereas the remaining two thirds is strictly fibrocartilaginous.

The lateral meniscus has the same width throughout, approximately 7 to 10 mm. It is shaped like a three-quarter circle, with its anterior and posterior horns attached to the tibia immediately in front of and behind the intercondylar eminence. The central attachment sites are narrower. The peripheral margin of the lateral meniscus is attached to the capsule except posterolaterally, where the popliteal tendon crosses it, and more posteriorly and centrally near the central attachment site, where the capsule does not extend anteriorly into the joint.

The medial meniscus is shaped more like a half-circle. Although its posterior horn is attached to the tibia just posterior to the posterior lateral meniscal attachment, its anterior horn attaches far anteriorly, approximately 10 to

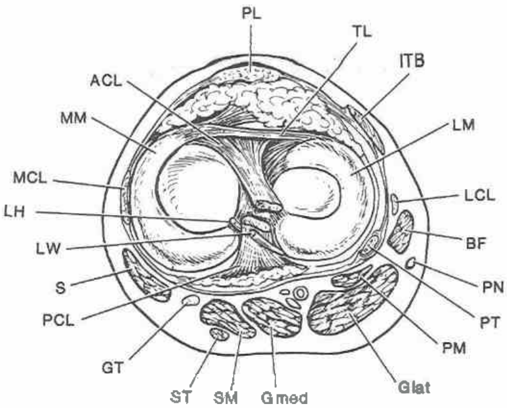

Figure 48–1. Normal anatomy. ACL, anterior cruciate ligament; BF, biceps femoris; Glat, gastrocnemius lateral head; Gmed, gastrocnemius medial head; GT, gracilis tendon; ITB, iliotibial band; LCL, lateral collateral ligament; LH, ligament of Humphrey; LM, lateral meniscus; LW, ligament of Wrisberg; MCL, medial collateral ligament; MM, medial meniscus; PCL, posterior cruciate ligament; PL, patellar ligament; PM, plantaris muscle; PN, peroneal nerve; PT, popliteus tendon; S, sartorius; SM, semimembranosus; ST, semitendinosus; TL, transverse ligament.

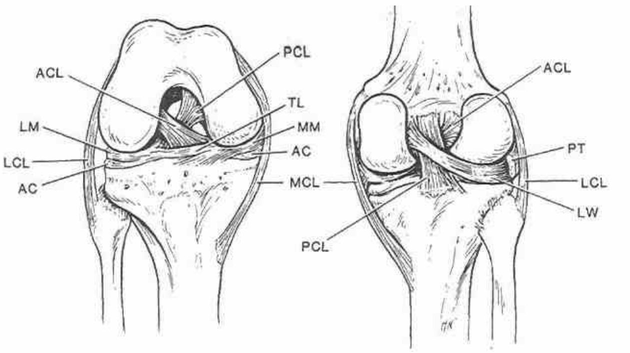

Figure 48–2. Normal anatomy. AC, articular cartilage; ACL, anterior cruciate ligament; LCL, lateral collateral ligament; LM, lateral meniscus; LW, ligament of Wrisberg; MCL, medial collateral ligament; MM, medial meniscus; PCL, posterior cruciate ligament; PT, popliteus tendon; TL, transverse ligament.

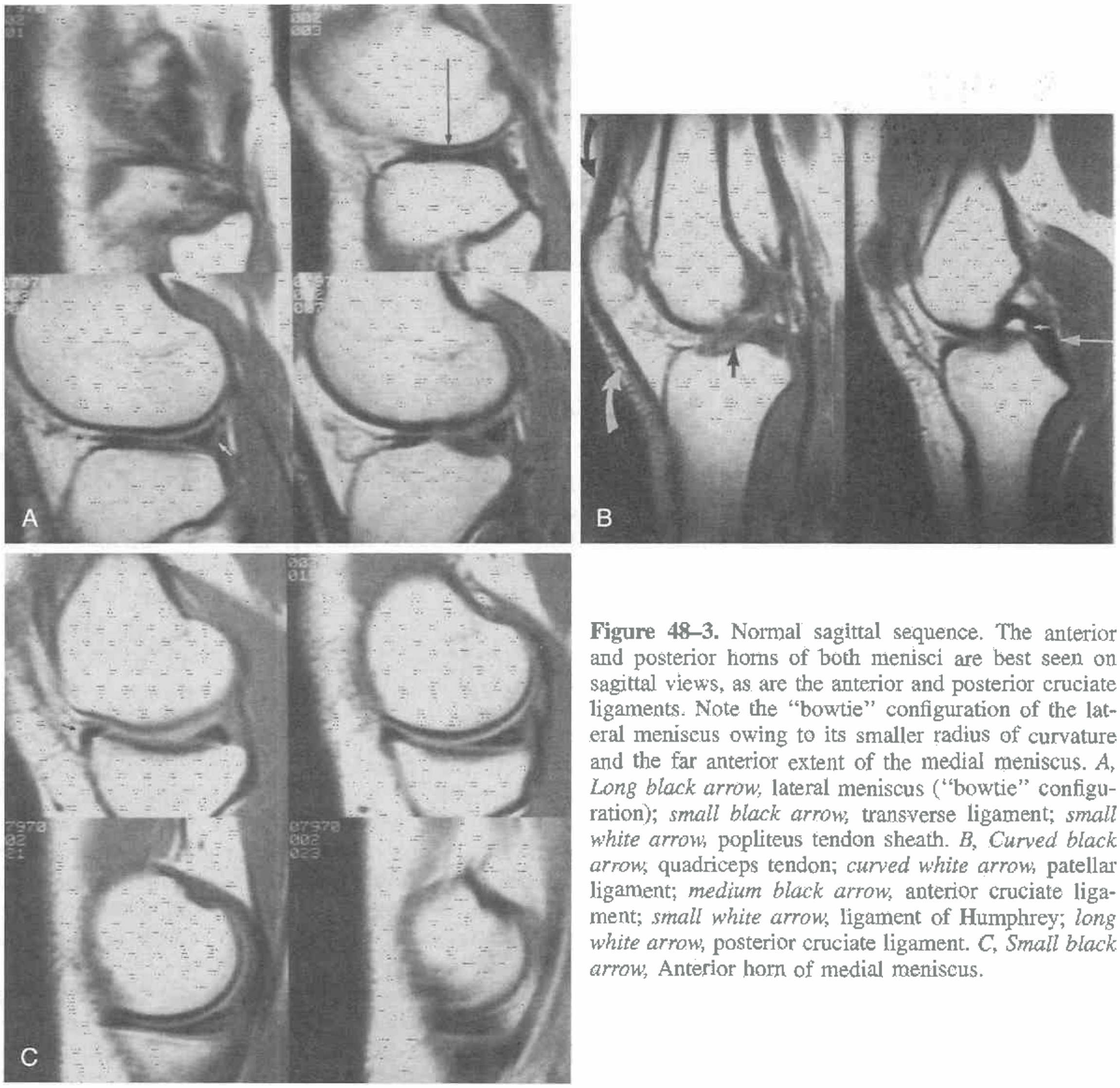

Figure 48–3. Normal sagittal sequence. The anterior and posterior horns of both menisci are best seen on sagittal views, as are the anterior and posterior cruciate ligaments. Note the "bowtie" configuration of the lateral meniscus owing to its smaller radius of curvature and the far anterior extent of the medial meniscus. *A, Long black arrow,* lateral meniscus ("bowtie" configuration); *small black arrow,* transverse ligament; *small white arrow,* popliteus tendon sheath. *B, Curved black arrow,* quadriceps tendon; *curved white arrow,* patellar ligament; *medium black arrow,* anterior cruciate ligament; *small white arrow,* ligament of Humphrey; *long white arrow,* posterior cruciate ligament. *C, Small black arrow,* Anterior horn of medial meniscus.

14 mm anterior to the anterior horn of the lateral meniscus. The width of the medial meniscus, in contrast to the lateral meniscus, gradually tapers from posterior to anterior. The peripheral margin of the medial meniscus is more firmly attached to the joint capsule and to the tibial plateau itself, the latter via the coronary ligament. As on the lateral side, the capsule does not extend anteriorly into the joint near the posterior central attachment site.

The transverse ligament connects the anterior horns of both menisci. Its thickness varies from 1 to 4 mm. It arises at the most anterior-superior portion of the lateral meniscus and crosses in front of the ACL tibial attachment, merging with the superior portion of the posterior aspect of the anterior horn of the medial meniscus.

The meniscofemoral ligaments are inconstant, 3- to 4-mm fibrous bands arising from the posterior horn of the lateral meniscus and attaching to the lateral aspect of the medial femoral condyle. The ligaments of Humphrey and Wrisberg arise together, the former coursing anterior to the posterior cruciate ligament (PCL) and the latter coursing posterior to the PCL (Figs. 48–1 and 48–2).

MRI Appearance

In general, sagittal images best show the anterior and posterior horns of the medial and lateral menisci. Coronal images best show the meniscal bodies (Figs. 48–3 and 48–4).

Sagittal cross-sections show the posterior horn of the medial meniscus as an isosceles triangle, with the sides nearly twice as long as the base. The neurovascular portion of the posterior horn of the medial meniscus is extensive, sometimes measuring 4 to 6 mm in width (Fig. 48–5).

The anterior horn of the medial meniscus is about one-half the width of the posterior horn, appearing more like an equilateral triangle. It may vary in its appearance, sometimes seeming almost rounded. It sits on the extreme edge of the anterior tibia, the transverse ligament joining it more superiorly and somewhat posteriorly. This junction may create an arrowhead appearance, pointing posteriorly. The lower portion represents the anterior horn attachment site, and the upper portion represents the transverse ligament junction (Fig. 48–6).

On the lateral side, the transverse ligament attaches to the most anterior-superior aspect of the anterior horn. It may appear as a round dot anterior to the meniscus and should not be confused with a tear (Figs. 48–7 to 48–9).[18] The anterior horn of the lateral meniscus is, in fact, the uncommon site of a meniscal tear. The anterior horn of the lateral meniscus may also demonstrate a striated or speckled, increased-signal-intensity pattern on proton-density images. This normal variation may represent dense collaginous fibers of the anterior cruciate ligament intertwined with the fibrocartilage of the meniscus itself (Fig. 48–10).[46] The anterior and posterior horns of the lateral meniscus are about equal in size, although the anterior is slightly smaller; both resemble isosceles triangles.

The posterior horn of the lateral meniscus differs from the medial, in that its attachment to the capsule is interrupted by the popliteal tendon, and this should not be mistaken for a tear (Fig. 48–11).[18] The ligament of Wrisberg is usually seen at its origin at the superior margin of the posterior horn. It may appear as a round dot adjacent to the superior aspect of the posterior horn and should not be confused with a tear (Fig. 48–12).[55]

The more peripheral sagittal images show the bodies of the medial and lateral menisci, although not optimally. On both sides, the menisci appear as flat bands. On the lateral side, because of the smaller radius of the curvature, more central slices show a "bowtie" configuration. Volume averaging of the capsule and menisci on slices at the extreme

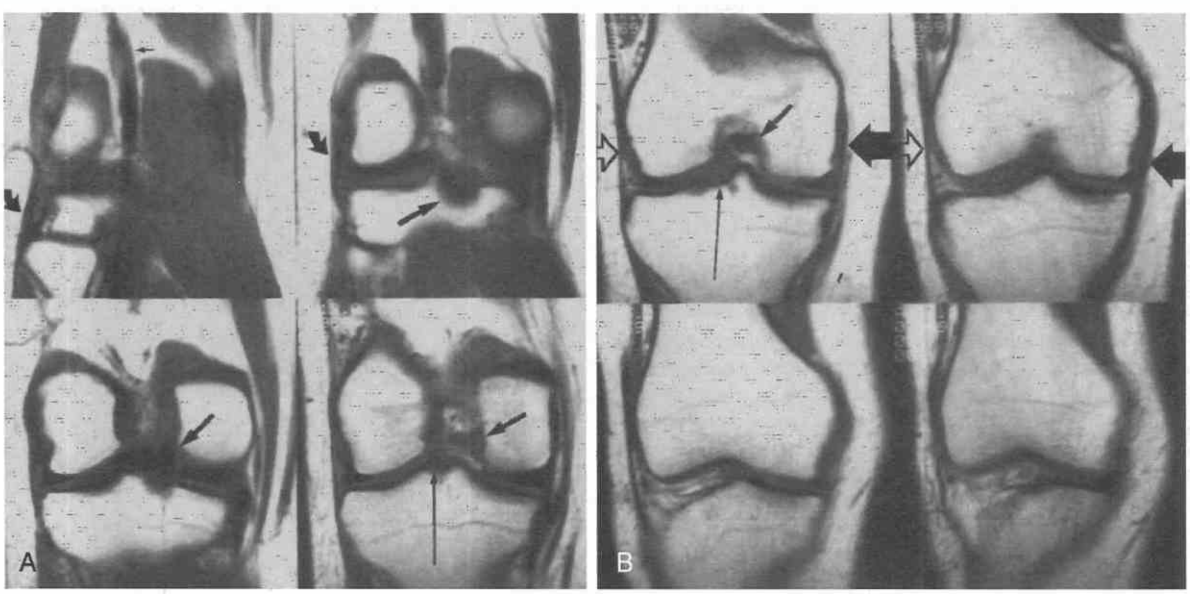

Figure 48–4. Eight coronal images of the right knee extending from posterior (*A*) to anterior (*B*). Normal coronal sequence. The bodies of both menisci are seen best on coronal views, as are the medial and lateral collateral ligaments. Note the decreasing width of the medial meniscus as it courses anteriorly where it attaches at the anterior margin of the tibial plateau. *Smallest arrow,* popliteal artery; *curved arrow;* lateral collateral ligament; *short arrow,* posterior cruciate ligament; *long arrow,* anterior cruciate ligament; *hollow arrow,* iliotibial band; *thick arrow,* medial collateral ligament.

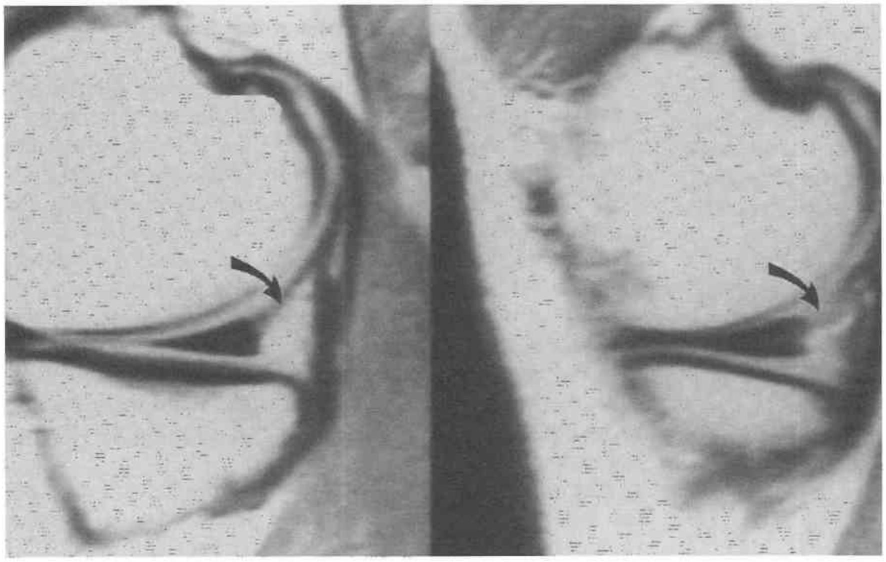

Figure 48–5. Normal peripheral third of the meniscus. Sagittal T1-weighted images reveal normal increased signal intensity at the periphery of the posterior horn of the medial meniscus where neurovascular structures and fatty tissue are present (*arrow*). This may be quite prominent, sometimes measuring 4 to 6 mm in width.

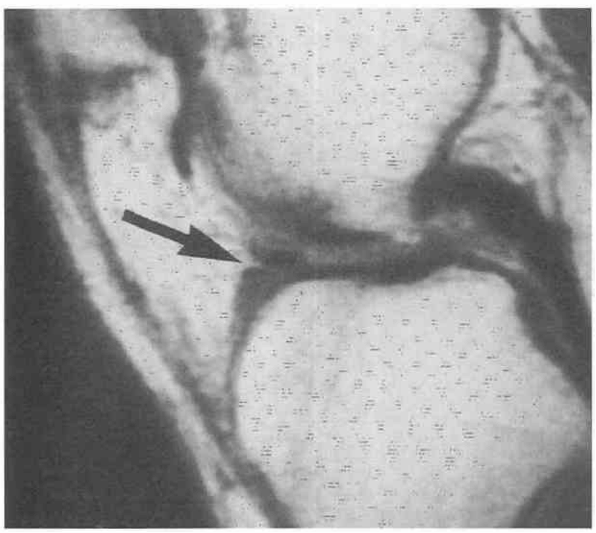

Figure 48–6. Normal anterior horn of the medial meniscus. Sagittal T1-weighted image shows the "arrowhead" configuration of the anterior horn of the medial meniscus. The "arrowhead" points posteriorly, with the lowermost anterior portion representing the anterior horn of the medial meniscus and the higher portion representing the transverse ligament attachment. The cleft in between should not be confused with a tear (*arrow*).

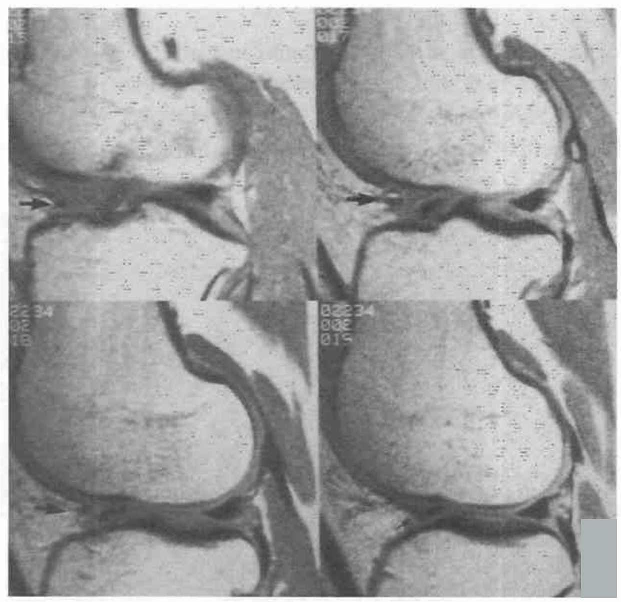

Figure 48–7. Transverse ligament. Sagittal T1-weighted images show the transverse ligament (*arrow*) joining the anterior horn lateral meniscus. The junction (*small arrow*) should not be confused with a tear.

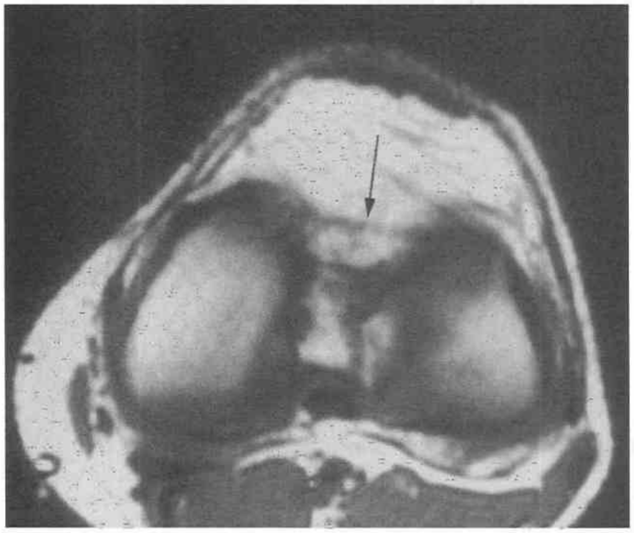

Figure 48–8. Transverse ligament. Axial T1-weighted image shows the transverse ligament extending from the medial joint compartment to the lateral joint compartment (*arrow*).

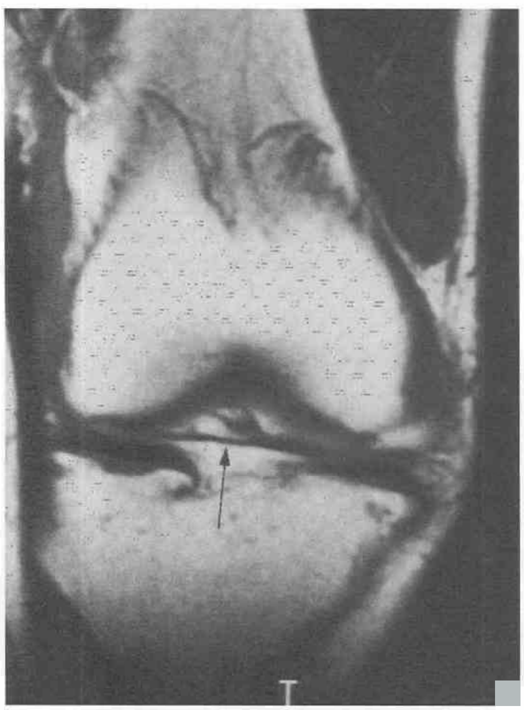

Figure 48–9. Transverse ligament. Coronal T1-weighted image, far anteriorly, shows the transverse ligament extending from the medial to the lateral compartments of the knee (*arrow*).

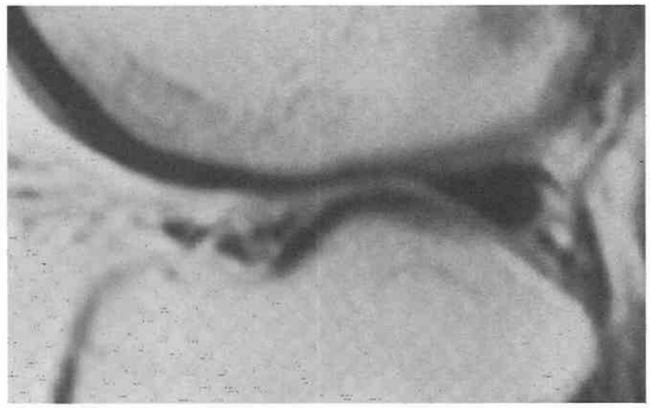

Figure 48–10. Sagittal proton-density image shows a speckled or striated increased-signal-intensity pattern at the anterior horn of the lateral meniscus near its central attachment site.

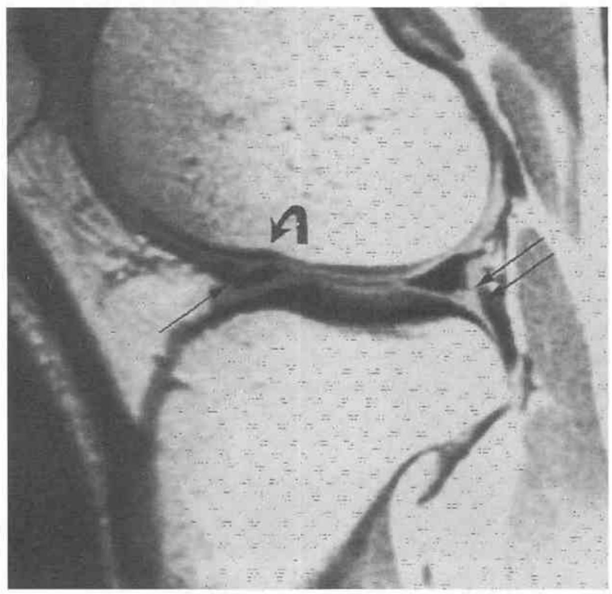

Figure 48–11. Popliteus tendon sagittal view. Sagittal T1-weighted image shows the normal high signal intensity of the popliteus tendon sheath at the posterior horn of the lateral meniscus (*double arrow*). Also, note the transverse ligament attachment to the anterior horn of the lateral meniscus. The plane between them should not be mistaken for a tear (*arrow*). The normal indentation of the lateral condylar surface representing the junction of its tibial and patellar articular surfaces should not be confused with an osteochondral fracture. The cartilage and subchondral cortex are intact (*curved arrow*).

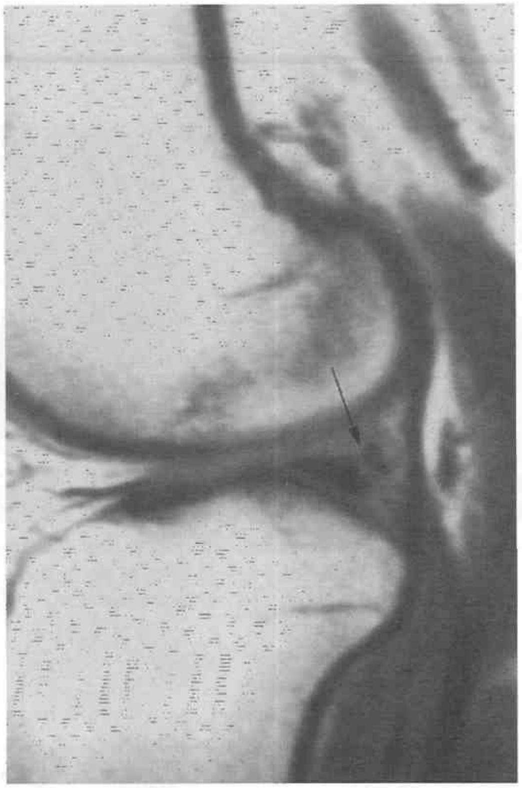

Figure 48–12. Pseudotear posterior horn of the lateral meniscus. Sagittal T1-weighted image shows the takeoff of the ligament of Wrisberg at the posterior horn of the lateral meniscus. The signal between the ligament of Wrisberg and the lateral meniscus itself (*arrow*) should not be confused with a tear.

periphery may be confused with a tear of the meniscal body (Fig. 48–13).[18] This normal increased signal may also represent truncation artifact. Parallel signal lines are produced in the phase-encoding direction at edges where there is a large, abrupt transition in tissue signal intensity.

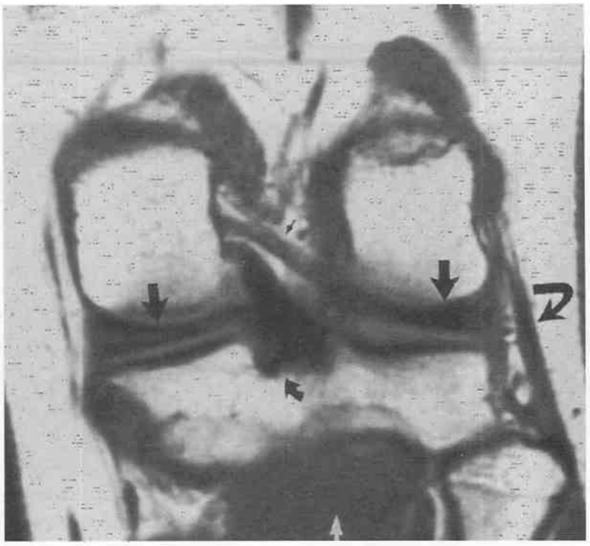

Figure 48–14. Posterior coronal view. Coronal T1-weighted image shows the posterior horns of both menisci as rather large flat bands that should not be confused with discoid menisci (*large black arrows*). Of note are the posterior cruciate ligament (*small curved arrow*), ligament of Wrisberg (*small black arrow*), fibular collateral ligament (*large curved arrow*), and popliteus muscle belly (*white arrow*).

Coronal cross-sections at the midportion of the knee best show the bodies of both menisci. They appear triangular in shape, the lateral slightly larger than the medial. The capsular attachment on the medial side is incorporated into the tibial or medial collateral ligament. A small amount of fat may be interposed between the body of the medial meniscus and the capsule.

Posteriorly, coronal cross-sections show the posterior horns as flat bands. On the lateral side, the popliteal tendon courses upward and laterally at 45 degrees (Figs. 48–14 and 48–15). Synovium extends superiorly and inferiorly

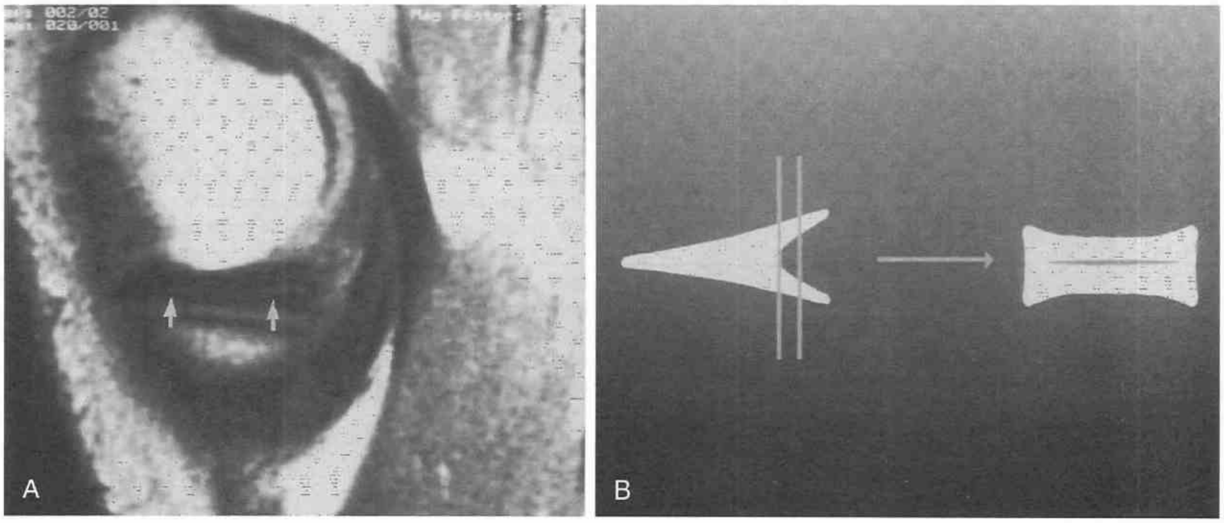

Figure 48–13. Far peripheral sagittal pseudotear. Far sagittal T1-weighted image of the medial joint compartment shows normal linear high signal intensity representing volume averaging of the joint capsule, concave surface of the meniscus periphery, and normal fat in between (*arrows*). This may represent truncation artifact as well.

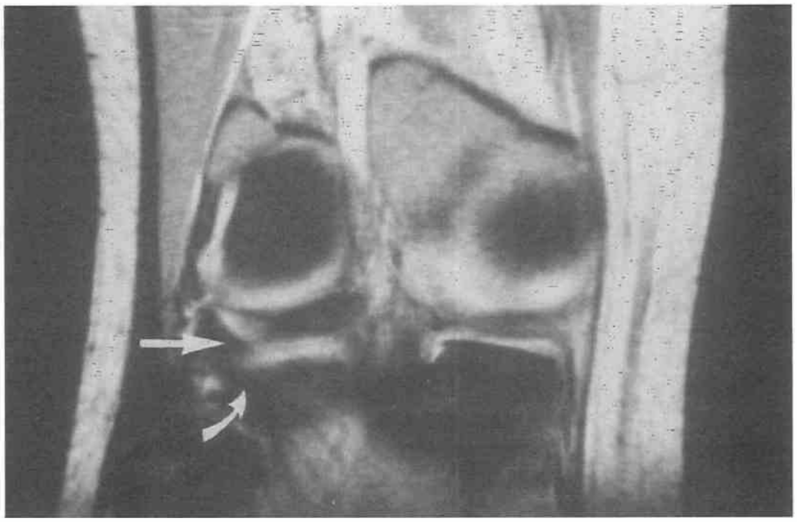

Figure 48–15. Popliteus tendon, coronal view. Coronal T1-weighted image, far posteriorly, shows the popliteus muscle belly extending laterally (*curved arrow*) and the popliteus tendon itself (*straight arrow*) crossing through the posterior horn of the lateral meniscus.

about the tendon through the opening in the capsule. It appears as increased signal intensity and is linear in nature. This is seen on both sagittal and coronal images as medium signal intensity on T1-weighted and spin-density images and as high signal intensity on T2-weighted images.

More anteriorly, coronal images show the anterior horn of the lateral meniscus as bandlike. The anterior horn of the medial meniscus is quite small and extends more anteriorly than the lateral.

The avascular portions of the normal menisci and the transverse and meniscofemoral ligaments appear dark, without signal on all pulse sequences. The peripheral vascular zones are of low to medium signal intensity on T1-weighted and spin-density images and are of medium to high signal intensity on T2-weighted images. This is most prominent at the posterior horn of the medial meniscus and is seen best on sagittal images. With increasing age, degeneration leads to indistinct focal areas of medium to high signal intensity in the avascular portion of the menisci.[19]

Meniscal Trauma

Traumatic meniscal tears are usually longitudinal, produced when the femoral condyle compresses the meniscus, usually superiorly to inferiorly, posteriorly to anteriorly, and from outside inward. These tears may extend along the radius of the meniscus or may be localized to one segment, usually the posterior horn, and are often referred to as radial or "parrot beak" tears. An extensive tear with central displacement of the free edge is referred to as a "bucket-handle" tear, the handle representing the displaced free margin. Tears with displacement of a portion of meniscal tissue are referred to as *flap tears*. Incomplete partial-thickness tears are usually seen at the posterior horn and extend to an articular surface, usually the inferior one.

Meniscal tears may result in abnormal signal within the meniscus, abnormal size and shape of the meniscus, and abnormal position of meniscal fragments.

Increased signal intensity representing a torn meniscus is best seen on T1-weighted and proton-density images and may not be seen on T2-weighted images. These T2-weighted images are more helpful when synovial fluid insinuates itself within the tear. Such signal changes represent a torn meniscus only when the signal extends to the superior or inferior articular surface (Figs. 48–16 and 48–17). The periphery of the meniscus does not represent such a surface. Such findings may be seen on only one image or in only one plane. Altering the gray scale of an image should be done cautiously, because false-positive images result from exaggeration of intrameniscal signal. When it is not clear whether signal extends to the articular surface, a true tear is probably not present. Controversy exists about whether intrameniscal signal, globular or linear, represents degeneration, since many such cases are seen to have resolved at follow-up examination. Of note, however, is the "meniscus-within-a-meniscus" appearance, in which increased signal is seen throughout the meniscus cross-section. This represents a meniscal tear approximately 50% of the time (Fig. 48–18).

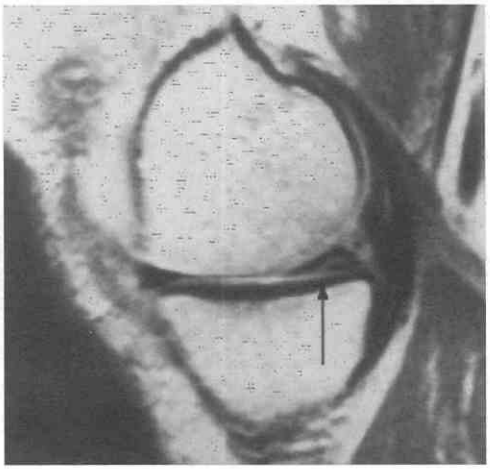

Figure 48–16. Nondisplaced meniscal tears. Sagittal T1-weighted image shows high signal intensity at the posterior horn of the medial meniscus extending to the inferior articular surface (*arrow*).

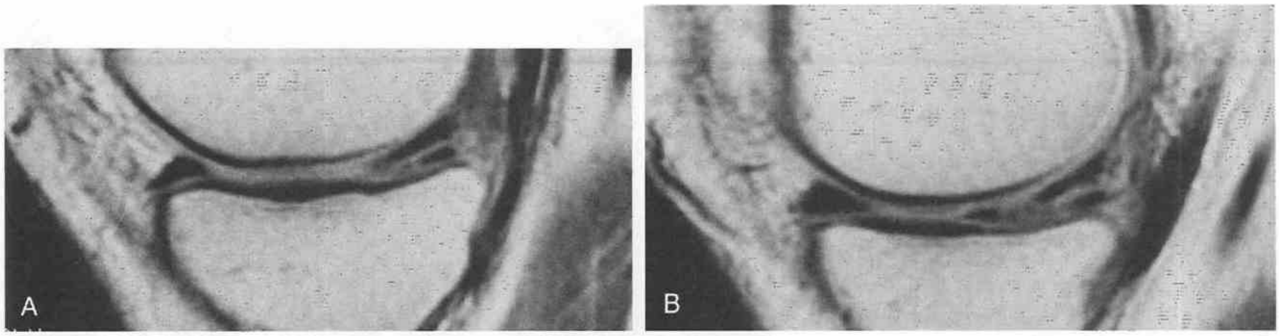

Figure 48–17. *A* and *B*, Sagittal proton-density images show curvilinear increased signal at the posterior horn of the medial meniscus extending to the articular surfaces, indicative of a tear.

Nondisplaced peripheral separations may be difficult to detect. The most specific finding is irregular, jagged, increased signal intensity at the periphery that brightens on T2-weighted images (Fig. 48–19).

More extensive tears may alter the size, shape, and position of the meniscus. When a portion of the free margin of the meniscus is detached (a bucket-handle tear), the remaining peripheral portion appears small and often truncated. The displaced portion usually lies in the intercondylar notch beneath the ACL or the PCL (Figs. 48–20 and 48–21). Occasionally, it may flip anteriorly above the anterior horn (Fig. 48–22). Coronal views are helpful in further identifying such displaced fragments, which should not be confused with the central attachment sites of posterior meniscal horns.

Small radial tears of the free edge, almost always seen laterally (as parrot beak tears), are best seen on coronal images. On sagittal views, the "bowtie" configuration of the lateral meniscus may be disrupted centrally (Fig. 48–23).[4, 13, 35, 36, 53]

Thin-section CT of the menisci after air-contrast arthrography has been used for evaluation of tears. This technique has had limited acceptance, with conventional arthrography favored until the advent of MRI.

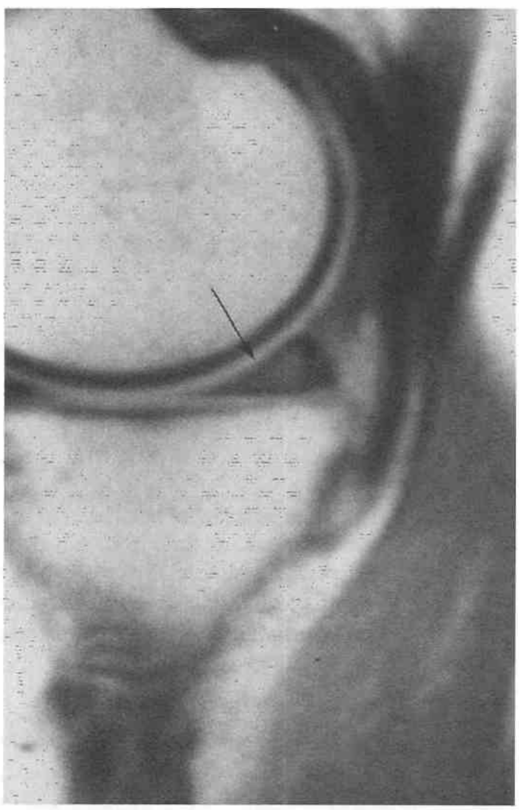

Figure 48–18. Meniscus-within-a-meniscus appearance. Sagittal T1-weighted image shows increased signal intensity throughout the confines of the posterior horn of the medial meniscus. Although signal does not extend to the articular surface, a true tear is seen at arthroscopy 50% of the time.

Postoperative Appearance

The MRI appearance of the postsurgical meniscus depends on the nature of the surgical intervention. After partial meniscectomy, it can be quite difficult to evaluate tearing of the meniscal remnant or incomplete meniscal resection. The MRI appearance of the arthroscopically nor-

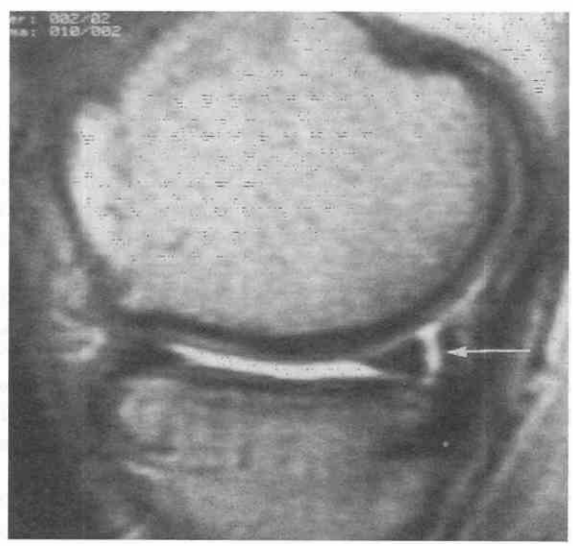

Figure 48–19. Peripheral tear. Sagittal T2-weighted images show high signal intensity at the periphery of the posterior horn of the medial meniscus (*arrow*). A joint effusion is present.

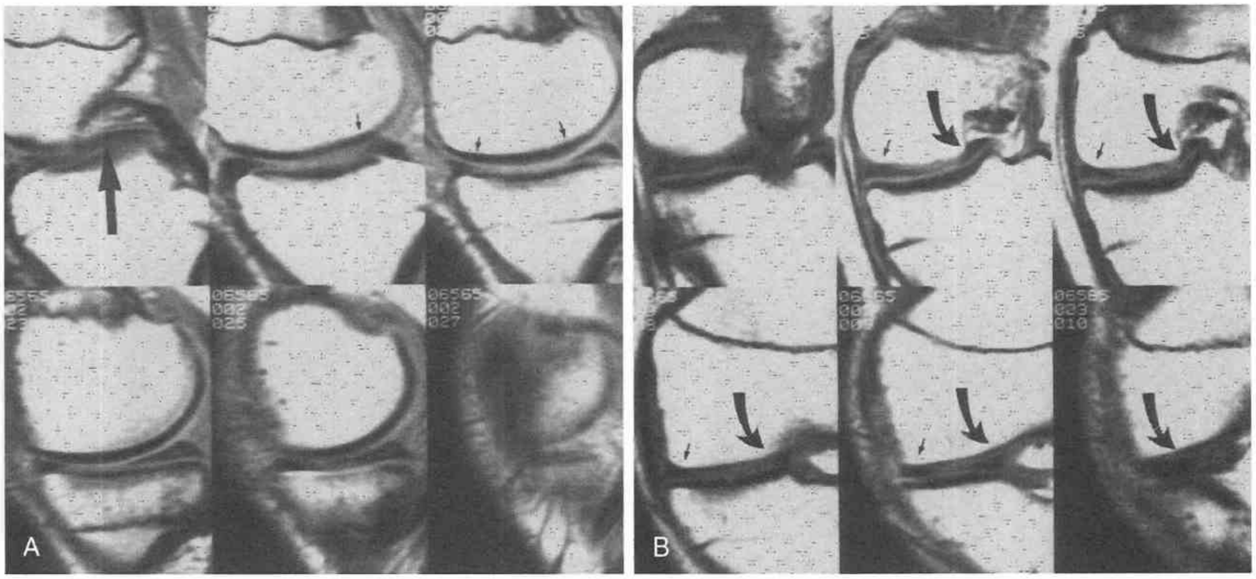

Figure 48–20. Bucket-handle tear. *A,* Sagittal T1-weighted images show a bucket-handle tear of the medial meniscus. The central portion is displaced into the intercondylar notch (*large arrow*). Note the distorted size and shape of the peripheral portion (*small arrows*). *B,* Coronal T1-weighted images show the irregular periphery (*small arrows*) and the displaced central portion (*curved arrows*).

mal meniscal stump varies. The contour may be smooth with homogeneous signal intensity. Standard MRI criteria for meniscal tears are useful only in this situation. Other such "normal" stumps may demonstrate an irregular surface contour with inhomogeneous signal intensity; in fact, such a postoperative appearance represents a normal meniscal remnant most of the time. In such a setting, however, it is nearly impossible to delineate true pathology (Fig. 48–24).[49]

Peripheral meniscal tears are often treated conservatively or with arthroscopic repair. In either situation, in patients who have become asymptomatic and presumably healed, persistently increased signal intensity at the periphery of the meniscus remains unchanged from that seen on preoperative studies. The presence of such signal, therefore, should not be misinterpreted as a meniscal re-tear. In this regard, some cases of false-positive MRI findings may actually represent older injuries that have healed by the time arthroscopic examination is performed.[11]

MR arthrography of the knee is recommended when there has been prior meniscectomy or arthroscopic repair of a peripheral tear. Diluted gadolinium can be injected into the knee joint directly or intravenously, with imaging performed after 10 to 15 minutes of moderate exercise.

Figure 48–21. *A* and *B,* Sagittal proton-density images show displaced meniscal tissue at the intercondylar notch indicative of the bucket-handle tear. Meniscal tissue beneath the posterior cruciate ligament is known as the PCL sign.

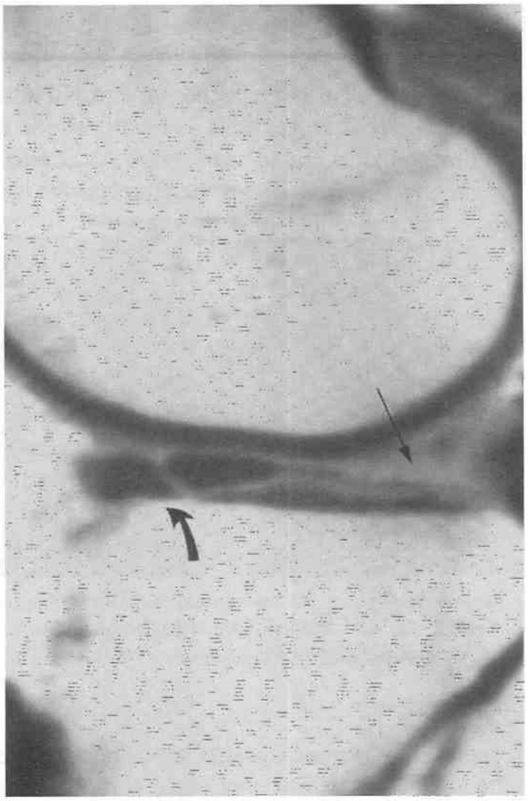

Figure 48–22. Displaced meniscal tear. Sagittal T1-weighted image shows virtual absence of the posterior horn of the lateral meniscus (*straight arrow*). The displaced fragment (*curved arrow*) has flipped anterior to the anterior horn of the lateral meniscus.

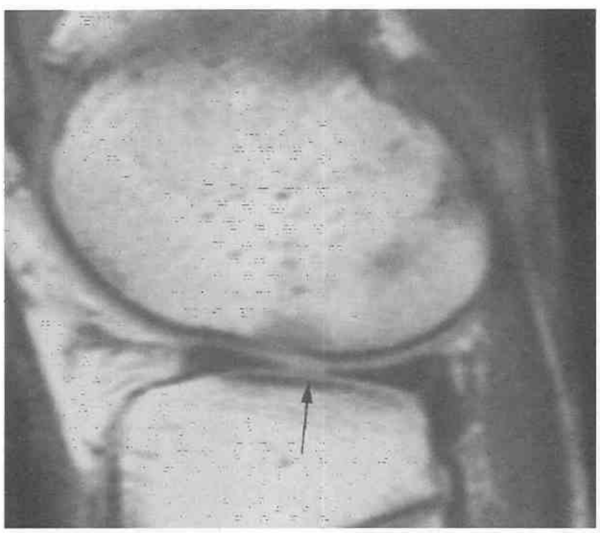

Figure 48–23. Parrot beak tear. Sagittal T1-w[redacted]ted [redacted]ge shows increased signal intensity interrupting the [redacted]wtie"[redacted]figuration of the lateral meniscus (*arrow*) indicative of a parrot beak tear.

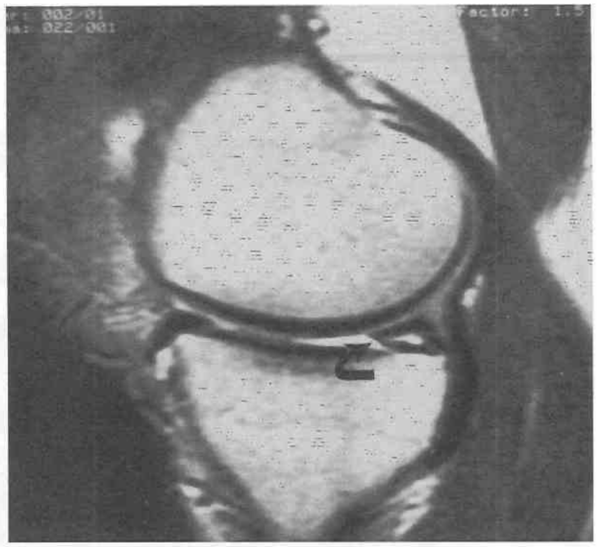

Figure 48–24.[redacted]tial resection of the meniscus. Sagittal proton-density image shows partial resection of the posterior horn of the medial meniscus. Note the marked increase in signal within a clinically "normal" stump (*arrow*).

Contrast insinuates itself into true tears and does not extend into areas of healing (Fig. 48–25). T1-weighted imaging with fat suppression is recommended following the intra-articular injection of a gadolinium saline solution. If a joint effusion is present, a routine MR image of the knee may be diagnostic. Fluid, like contrast, may insinuate itself into a true tear.[2, 28]

Discoid Meniscus

A *discoid* meniscus refers to a meniscus, almost always the lateral one, that is not C-shaped but disklike; it covers most of the tibial plateau to varying degrees rather than just its periphery. It is prone to tearing and is usually seen in children and adolescents, in whom it may be asymptomatic and noted incidentally. Although the discoid meniscus is seen in youngsters, it is believed to be more developmental than congenital, because the fetal meniscus never assumes such a shape. MRI shows the signal void of the meniscus extending toward the intercondylar notch. Although much has been said about the increased number of routine sagittal images on which the discoid meniscal body is seen (Fig. 48–26), it is simpler to judge such an enlarged meniscus on the coronal view (Fig. 48–27).[48]

Anterior Cruciate Ligament

Anatomy

The ACL extends from its semicircular attachment at the posterior aspect of the medial surface of the lateral femoral condyle to the anterior intercondylar region of the tibia, just medial to the midline, just lateral and anterior to the anterior tibial spine. This attachment is therefore several millimeters posterior to the anterior tibial margin. It is just posterior to the transverse ligament and just anterior

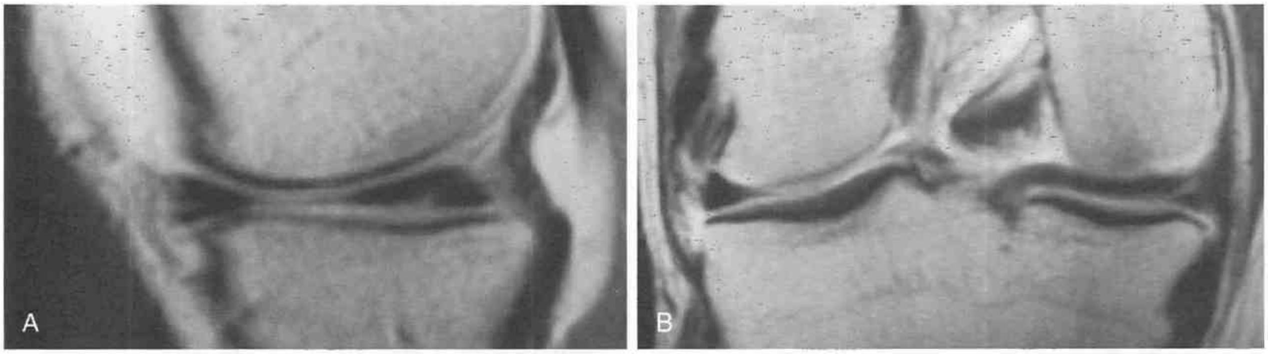

Figure 48–25. Sagittal (*A*) and coronal (*B*) T1-weighted images of the knee following the intra-articular injection of a gadolinium saline solution show contrast material within the posterior horn of the medial meniscus, after partial meniscectomy, indicative of a recurrent tear.

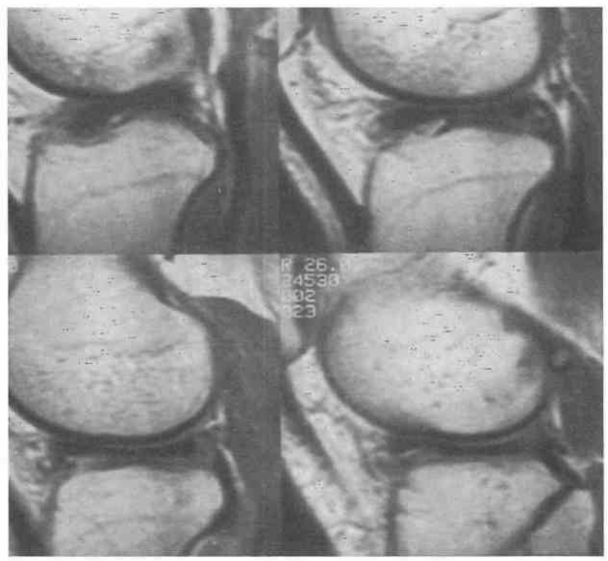

Figure 48–26. Discoid meniscus, sagittal views. Sagittal T2-weighted images show the lateral meniscus extending too far centrally, consistent with a discoid meniscus.

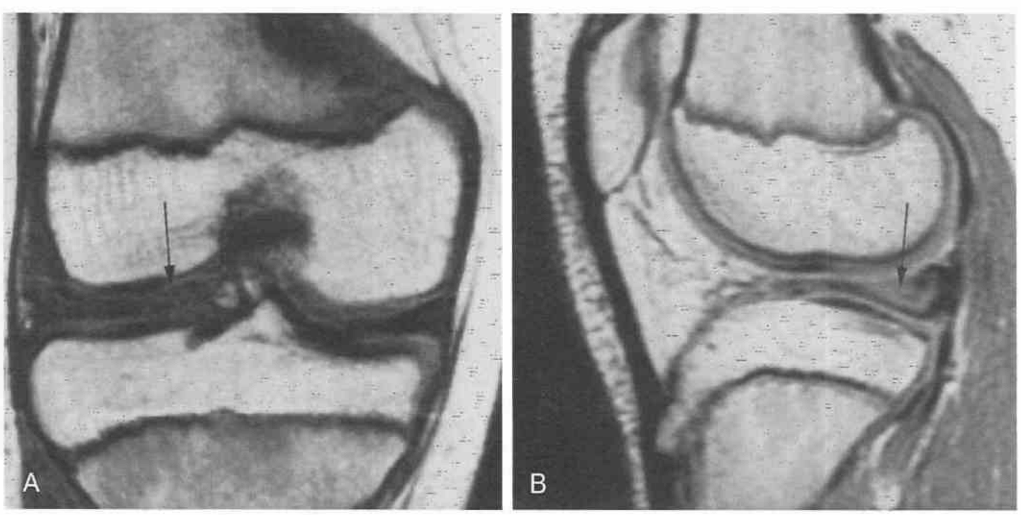

Figure 48–27. Discoid meniscus. *A*, Coronal T1-weighted image shows a large, discoid lateral meniscus extending to the intercondylar notch with internal high signal areas (*arrow*). *B*, Sagittal proton density–weighted image better shows the tear present (*arrow*).

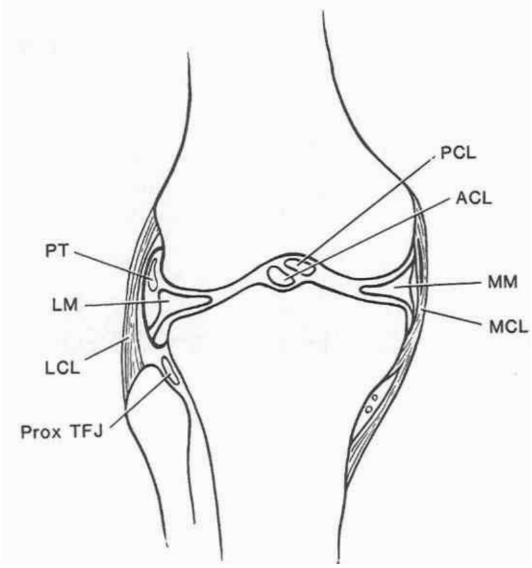

Figure 48–28. Normal anatomy. ACL, anterior cruciate ligament; LCL, lateral collateral ligament; LM, lateral meniscus; MCL, medial collateral ligament; MM, medial meniscus; PCL, posterior cruciate ligament; Prox TFJ, proximal tibial-fibular joint; PT, popliteus tendon.

Figure 48–30. Normal anterior cruciate ligament (ACL). Sagittal T1-weighted image shows a normal low-signal-intensity ACL (*arrow*). Slight increased signal intensity at the tibial attachment site is normal.

to the central attachment of the anterior horn of the lateral meniscus where some fibers mix. The tibial attachment is larger than the femoral and fanlike in shape.

The ligament measures approximately 4 × 1 cm (Figs. 48–28 and 48–29; see Figs. 48–1 and 48–2). It may consist of two or more distinct bundles separated by loose connective tissue and fat, more prominent at the mid- and distal portions. Two distinct bands, the smaller anteromedial and the larger posterolateral, have been identified. The former is taut in flexion, and the latter is taut in extension. Synovium covers the entire anterior surface of the ACL.

MRI Appearance

The ACL is best seen on sagittal oblique images with slices parallel to the cortex of the lateral femoral condyle. The knee is usually extended during the examination, and the ligament therefore should appear taut, angled about 60 degrees to the tibial plateau. If the knee is flexed more than 5 degrees, it may appear lax. In general, the ACL may appear as a solid low-signal-intensity band or as three

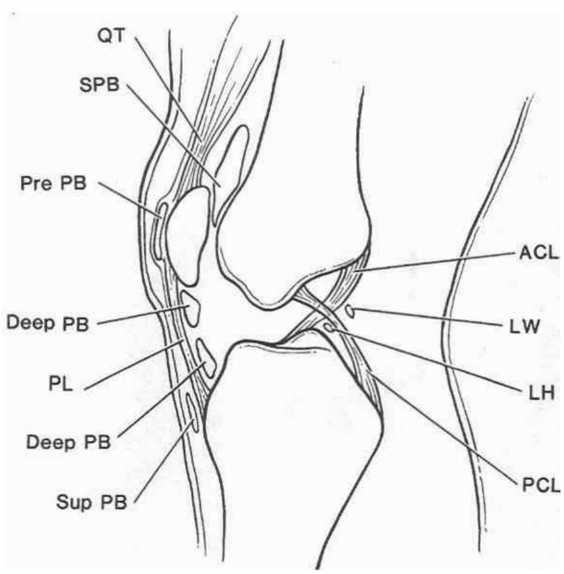

Figure 48–29. Normal anatomy. ACL, anterior cruciate ligament; deep PB, deep patellar bursa; LH, ligament of Humphrey; LW, ligament of Wrisberg; PCL, posterior cruciate ligament; PL, patellar ligament; Pre PB, prepatellar bursa; QT, quadriceps tendon; SPB, suprapatellar bursa; Sup PB, superficial patellar bursa.

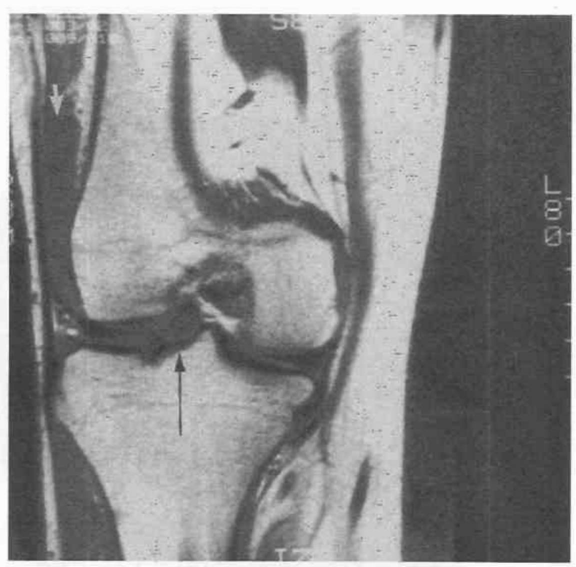

Figure 48–31. Anterior cruciate ligament (ACL), coronal view. Coronal T1-weighted image shows the fanlike ACL insertion (*black arrow*). Joint fluid is evident at the suprapatellar gutters (*white arrow*).

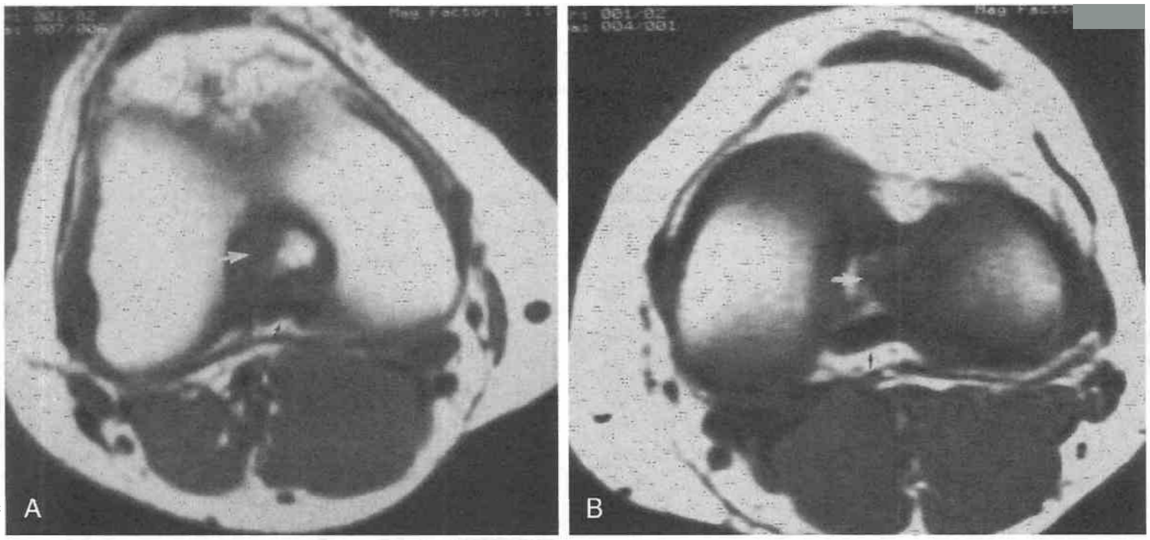

Figure 48–32. Anterior cruciate ligament (ACL)–posterior cruciate ligament (PCL) on the axial view. Axial T1-weighted images show the normal ACL flattened against the lateral femoral condyle (*white arrows*). The PCL is always better seen as a low-signal-intensity structure coursing posteriorly and laterally (*black arrows*).

or four separate low-signal-intensity bundles. The tibial attachment is usually better seen than the femoral attachment because of partial-volume averaging of the proximal ligament with the lateral femoral condyle. Normally, increased signal intensity on T1-weighted and spin-density images at the tibial insertion may be seen, presumably the result of the decreased density of the ligament itself or interposed fat (Fig. 48–30).

Coronal and axial images are also useful in evaluating the ACL. Coronal images show the ACL as a curvilinear fanlike structure adjacent to the horizontal segment of the PCL, near the medial surface of the lateral femoral condyle (Fig. 48–31). Proximally, the signal intensity is uniformly low, whereas distally it may be slightly increased. Axial images proximally show the ACL as a low-signal-intensity band flattened against the medial surface of the lateral femoral condyle (Fig. 48–32). Distally, the ligament is not as well seen (Figs. 48–32 and 48–33).

All imaging sequences demonstrate fat at the intercondylar notch, adjacent to the ACL origin.

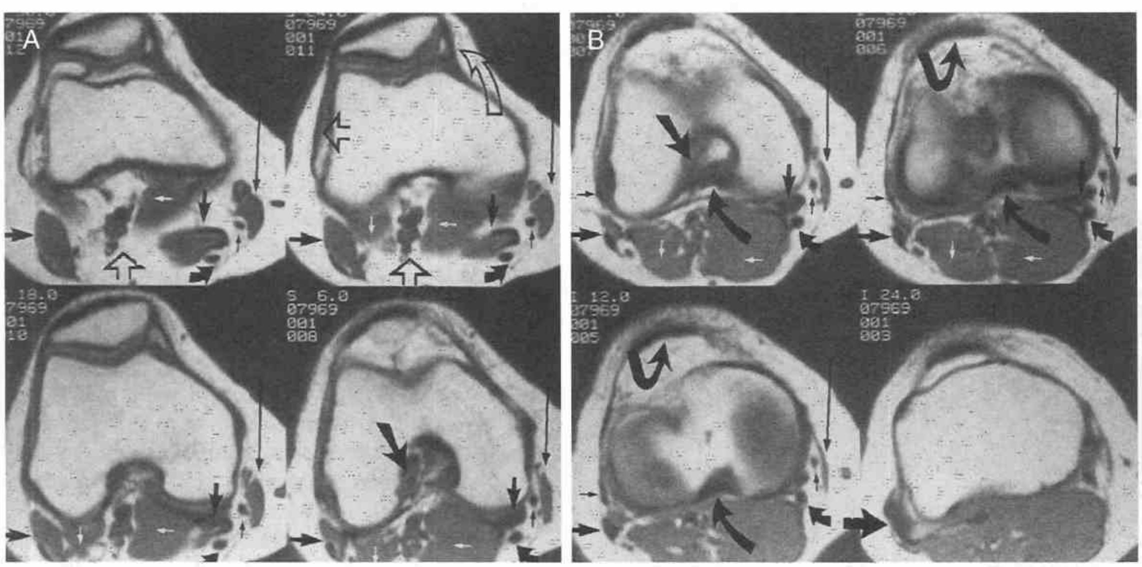

Figure 48–33. Normal axial images. *Horizontal medium black arrow,* biceps femoris muscle and tendon; *horizontal small black arrow,* fibular collateral ligament; *horizontal large black arrow,* conjoined tendon; *vertical long black arrow*; sartorius muscle and tendon; *vertical small black arrow,* gracilis tendon; *vertical medium black arrow,* semimembranosus muscle and tendon; *small curved black arrow,* semitendinosus tendon; *large curved black arrow,* posterior cruciate ligament; *looped black arrow,* patellar ligament; *vertical white arrow,* gastrocnemius muscle, lateral head; *horizontal white arrow,* gastrocnemius muscle, medial head; *horizontal hollow arrow,* lateral patellar retinaculum; *vertical hollow arrow,* popliteal artery and vein; *curved hollow arrow,* medial patellar retinaculum; *oblique black arrow,* anterior cruciate ligament.

Trauma

Tears of the ACL occur more commonly at its proximal portion. Complete or partial avulsions occur more commonly at the femoral origin, whereas avulsion fractures are more common at the tibial insertion (Fig. 48–34).

The MRI appearance of an ACL tear varies according to the extent and chronicity of the injury. The more common acute, complete, interstitial tear appears as a fairly diffuse mass of reactive edema and hemorrhage rather than as a discrete structure with a tear within (Fig. 48–35). With time, usually 6 to 8 weeks, and subsequent resolution, the ligament itself may be seen as bowed (Fig. 48–36) or dropped within the intercondylar notch (Fig. 48–37). At times, such a ligament may scar near its origin and appear virtually normal and yet be insufficient. Smaller tears may cause no contour abnormalities but may lead to obscuration of the fasciculi within the ligament.

Indirect or secondary signs of ACL tear include buckling of the PCL, anterior translation of the tibia relative to the femur (Fig. 48–38), posterior displacement of the lateral meniscus from the tibial plateau, indentation of the anterior margin of the medial femoral condyle, and fairly specific combinations of bone contusions (described later). These, in fact, are manifestations of abnormal bony contact at the time of injury and subsequent instability.[8, 14, 32, 44, 55]

Chronic incomplete tears of the ACL may cause laxity. Diffuse, nonhomogeneous, moderately increased signal intensity may be present on the T1-weighted and spin-density images. The ligament itself may have an indistinct margin or may not be seen at all. Occasionally, a chronic tear may demonstrate a normal MRI appearance as a result of scar formation.

It should be stressed that the normal ACL may not be seen well on routine sagittal oblique images. The ligament may, at times, be seen best on coronal and axial images. Correlation of the different imaging planes is always essential (Fig. 48–39).[20, 31, 43, 56]

Figure 48–34. Sagittal T2-weighted image shows avulsion fracture at the anterior cruciate ligament (ACL) tibial insertion. The ACL is retracted, not taut, but intact.

Figure 48–35. Sagittal proton-density image shows a complete interstitial tear of the anterior cruciate ligament manifest as fullness (edema or hemorrhage) at the intercondylar notch.

Repair

Most ACL repairs are intra-articular and consist of arthroscopic ACL reconstruction with patellar bone central-third patellar tendon tibial bone autografts. MRI demonstrates a well-defined, intact, low-signal-intensity autograft in clinically stable postoperative knees. Revascularization, which takes place 4 to 9 months postoperatively, may increase the signal intensity of the graft, leading to isointensity with the intra-articular space. This may account for apparent discrepancies in graft size. In this regard, focal and diffuse signal changes may be physiologic. Therefore, the object of postoperative evaluation in the first year following surgery is to identify continuity of the graft itself rather than contour deformities or abnormal signal patterns (Fig. 48–40).[39] After the first year, graft impingement may appear as increased signal intensity. Impingement precedes graft disruption and is usually secondary to anterior placement of the tibial tunnel.

Localized anterior arthrofibrosis may result from such impingement or from debris raised by drilling the tibial tunnel. Because of its headlike appearance on arthroscopy and its characteristic focal reddish blue discoloration that resembles the eye of Cyclops, it is often referred to as the *Cyclops lesion.* It usually appears as a low-signal-intensity mass surrounded by fluid.[41]

Other complications of ACL reconstruction include pa-

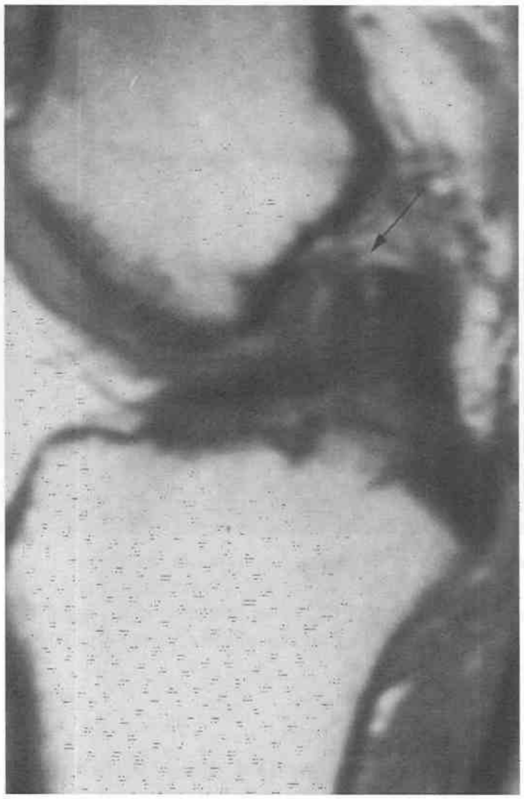

Figure 48–36. Anterior cruciate ligament (ACL) tear. Sagittal T1-weighted image shows buckling of the ACL, with increased signal intensity at its proximal portion, consistent with a tear (*arrow*).

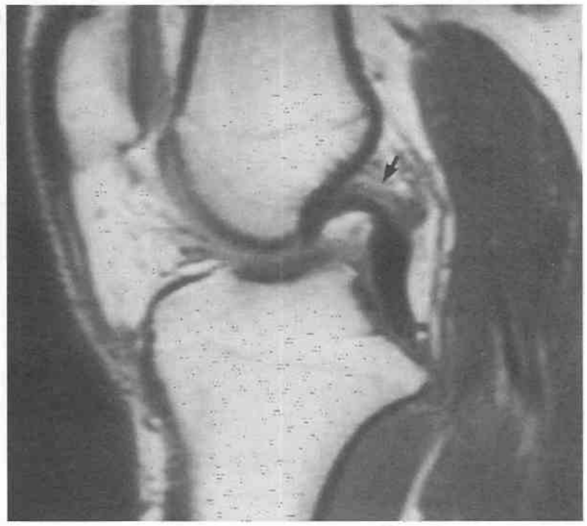

Figure 48–38. Buckling of the posterior cruciate ligament (PCL). Sagittal T1-weighted image shows buckling of the PCL (*arrow*). This is an indirect sign of the anterior cruciate ligament tear present in this patient. Also note anterior subluxation of the tibia.

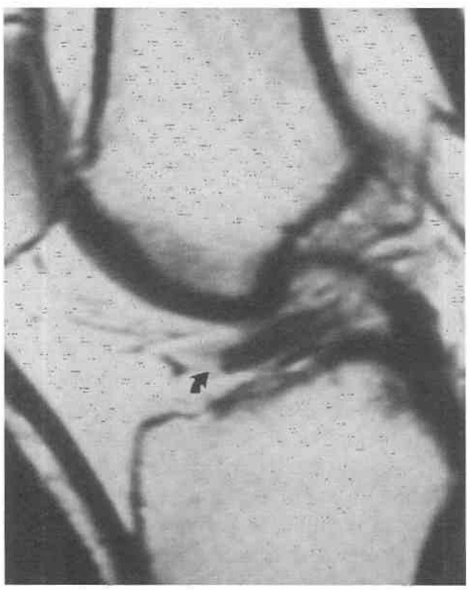

Figure 48–37. Anterior cruciate ligament (ACL) tear. Sagittal T1-weighted image shows a complete tear of the ACL, which is lying nearly horizontal within the intercondylar notch (*arrow*).

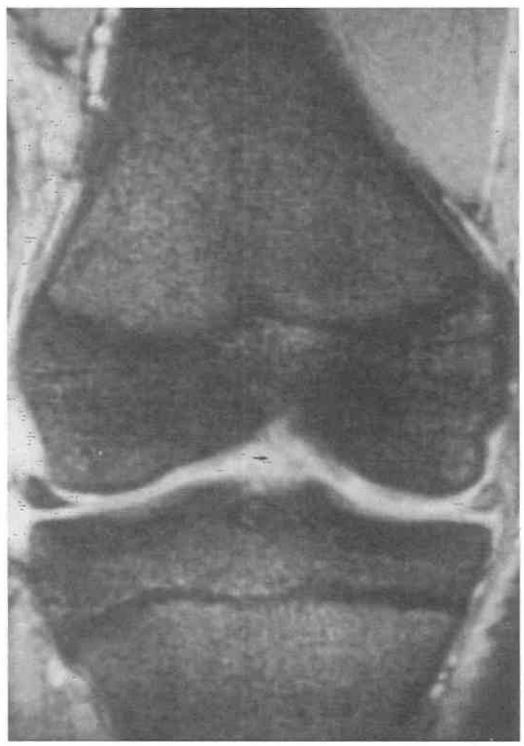

Figure 48–39. Anterior cruciate ligament (ACL) tear on the coronal view. Coronal gradient-echo image shows no identifiable ACL at the intercondylar notch (*small arrow*), indicative of a tear.

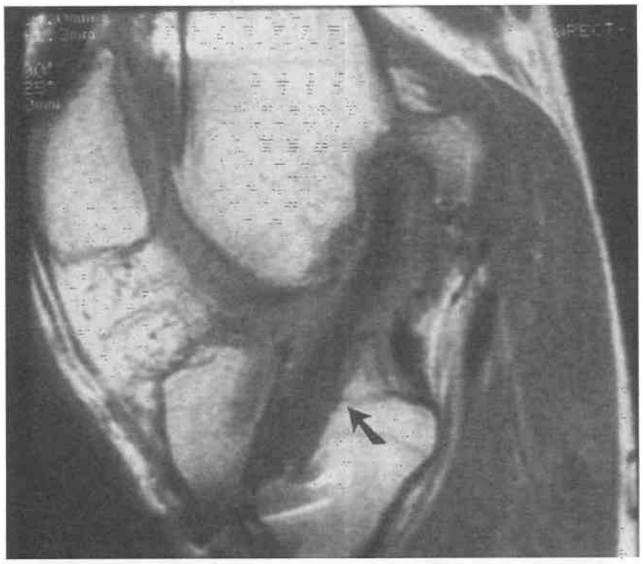

Figure 48–40. Anterior cruciate ligament (ACL) reconstruction. Sagittal T2-weighted image shows a normal-appearing ACL repair with patella tendon autograph (*arrow*). (Photograph courtesy of Dr. Padron, Madrid, Spain.)

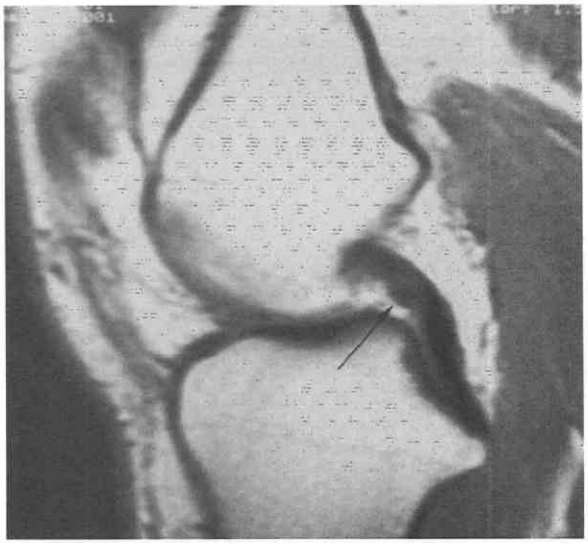

Figure 48–41. Normal posterior cruciate ligament (PCL) with the ligament of Humphrey. Sagittal T1-weighted image shows the normal course of the PCL. The anterior low-signal-intensity "dot" represents the ligament of Humphrey in cross-section (*arrow*).

tellar fracture and dislodged hardware. The patellar ligament itself may remain thickened.[4, 40]

Posterior Cruciate Ligament

Anatomy

The PCL arises at the lateral surface of the medial femoral condyle and extends to the posterior surface of the intercondylar region, below the level of the articular tibial plateau. It is wider and thicker than the ACL. It is arcuate in shape when the knee is extended or slightly flexed, and it becomes taut with increasing flexion (see Figs. 48–1, 48–2, 48–28, and 48–29).

MRI Appearance

Sagittal images best show the PCL; it appears as a uniformly low-signal-intensity structure with a nearly horizontal takeoff at the femoral origin and then an abrupt descent at about 45 degrees to the tibia. This angled portion of the ligament is normally directed toward the femur; it is not posterior to it unless the knee is hyperextended. In 20% to 25% of cases, the meniscofemoral ligaments of Humphrey and Wrisberg are seen as low-signal-intensity dots anterior and posterior to the PCL and should not be mistaken for displaced meniscal fragments (Fig. 48–41).

Trauma

Tears of the PCL are uncommon. Perhaps 50 ACL tears are imaged for each PCL tear. Most are incomplete and occur in the midportion of the ligament. Others involve the tibial insertion, where avulsion fracture may be present. In about 30% of patients, the PCL injury is isolated. In the remaining patients, it is associated with other abnormalities.

Tears of the PCL are best seen on sagittal images. Acute intrasubstance tears produce zones of increased signal intensity secondary to edema and hemorrhage (Fig. 48–42). With disruption or detachment of the ligament, similar signal changes are seen and the ligament itself may appear redundant.[15, 51, 52] Trauma to the PCL can be seen on axial and coronal images as well (Fig. 48–43).

Medial Collateral Ligament

Anatomy

The medial collateral ligament (MCL) consists of three functional units. The superficial or tibial collateral ligament is a broad, flat band, 2 cm in width and 2 to 4 mm in thickness. The superficial fibers extend from the medial epicondyle of the femur to the tibia, attaching about 2 cm below the joint line and then extending 3 to 4 cm more, distally across the medial concavity of the proximal tibia, where fat and blood vessels are normally present.

The deep fibers, which function as the joint capsule, attach loosely to the periphery of the body of the medial meniscus, where a small bursa or a small amount of fat may intervene. The superior portion constitutes the meniscofemoral ligament. The firmer attachment to the tibia just below the joint line forms the coronary ligament. A small amount of fat may be present between the superficial and deep fibers of the MCL. In addition, numerous bursae may be present between the MCL and bone and between the MCL and the pes anserinus (Figs. 48–44 to 48–46).

The third unit is composed of the posterior oblique fibers, which blend into the posterior capsule of the knee.

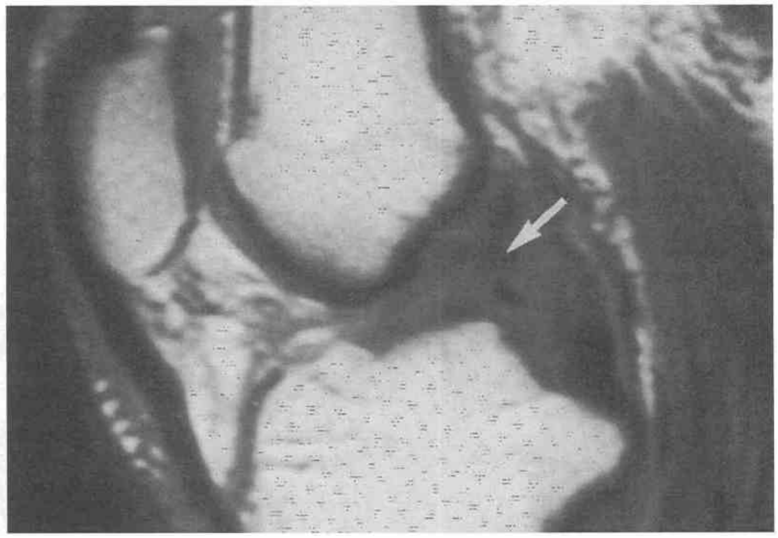

Figure 48–42. Posterior cruciate ligament (PCL) tear. Sagittal T1-weighted image shows no identifiable PCL configuration. Hemorrhage and edema replace the region of a complete tear (*arrow*).

MRI Appearance

The tibial collateral ligament is the portion best seen on coronal images, where it appears as a homogeneously low-signal-intensity structure on all pulse sequences. Moderately increased signal intensity may be seen between the superficial and deep fibers and below the superficial fibers at the distal tibial attachment site, where fat is normally interposed (see Fig. 48–4).

Trauma

Traumatic injuries of the MCL are common and range from *intrasubstance* tears (grade 1 sprain) to *incomplete* tears (grade 2 sprain) to *complete disruption* (grade 3 sprain). These are best seen on coronal images.

A *grade 1* sprain appears as increased signal intensity within the ligament secondary to intrasubstance edema. Fluid may be seen on both sides of the ligament as well. All of these changes are best noted on spin-density and T2-weighted images. When internal signal extends to the superficial or deep surface, a *grade 2* sprain is diagnosed (Fig. 48–47). A *grade 3* sprain is seen as complete disruption of the low-signal-intensity band with redundancy of its proximal and distal portions. The ligament may be stripped from its femoral and tibial attachments, in which case hemorrhage and edema are seen as increased signal

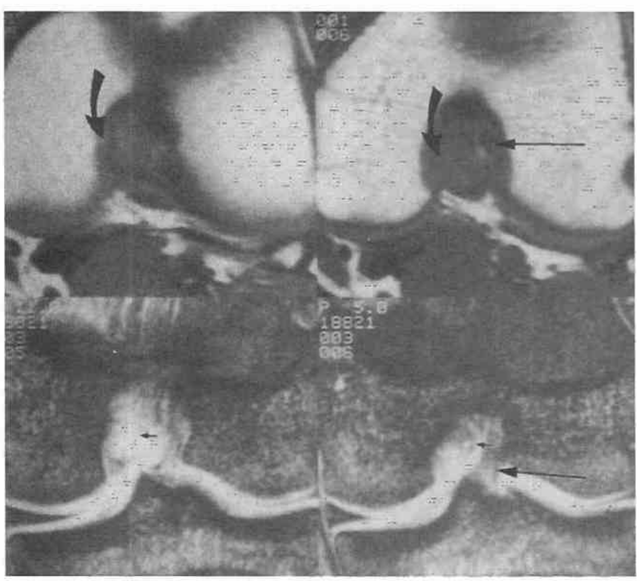

Figure 48–43. Tear of the poster[redacted]ruciate ligament (PCL) on axial and coronal views. Axial T1-weighted images show no identifiable PCL at its origin (*curved arrows*). Gradient-echo coronal images show no identifiable PCL at the intercondylar notch (*small arrows*). The normal anterior cruciate ligament is well defined (*large arrow*).

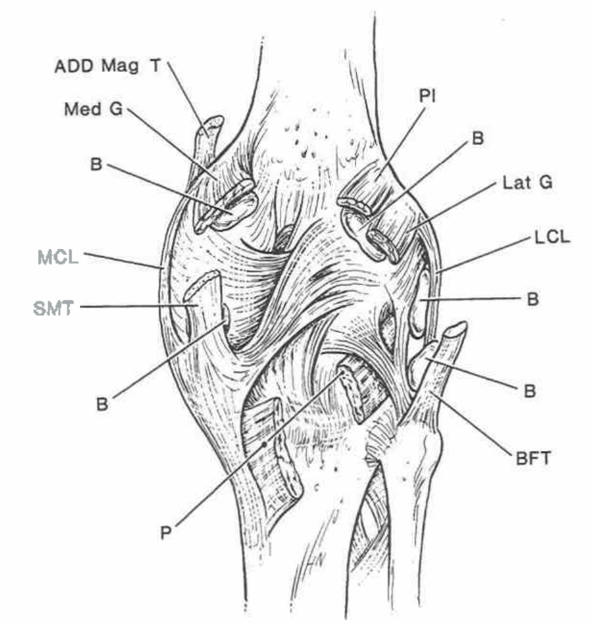

Figure 48–44. Normal anatomy. ADD Mag T, adductor magnus tendon; B, bursa; BFT, biceps femoris tendon; Lat G, lateral head gastrocnemius; LCL, lateral collateral ligament; MCL, medial collateral ligament; Med G, medial head gastrocnemius; P, popliteus; PI, plantaris; SMT, semimembranosus tendon.

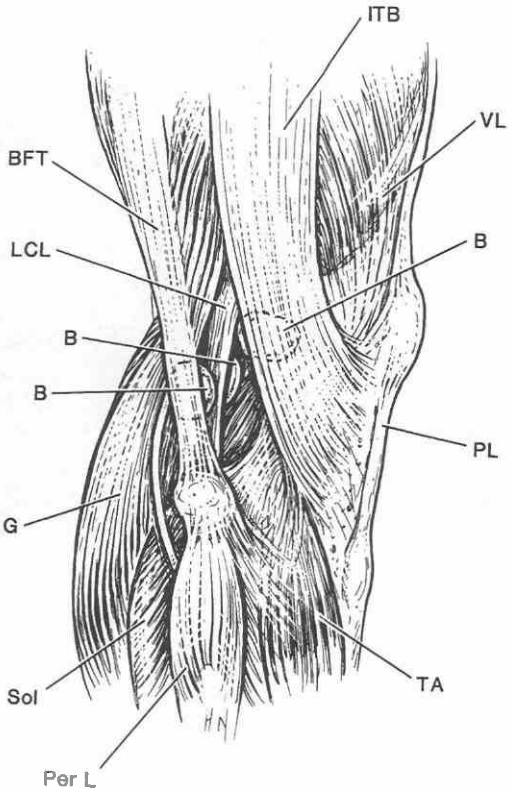

Figure 48–45. Normal anatomy. B, bursa; BFT, biceps femoris tendon; G, gastrocnemius; ITB, iliotibial band; LCL, lateral collateral ligament; Per L, peroneus longus; PL, patellar ligament; Sol, soleus, TA, tibialis anterior; VL, vastus lateralis.

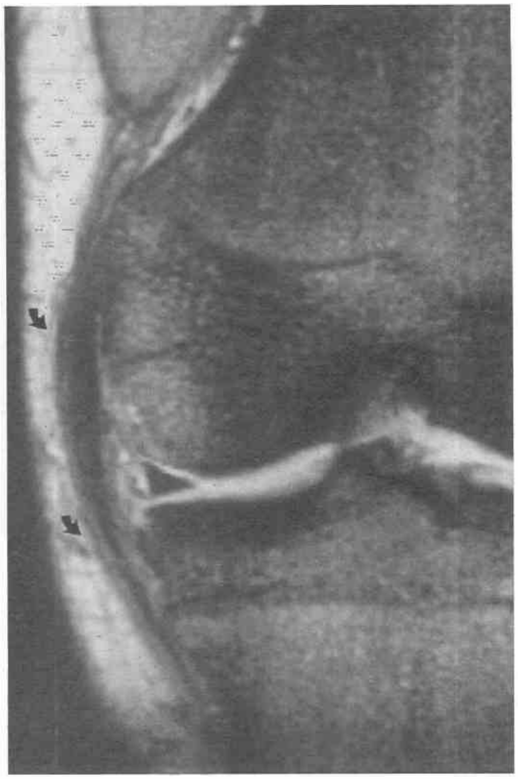

Figure 48–47. Medial collateral ligament tear. Coronal gradient-echo image shows thickening of the medial collateral ligament with increased signal intensity (*curved arrow*). This represents a grade 2 sprain with signal extending to the superficial and deep surfaces.

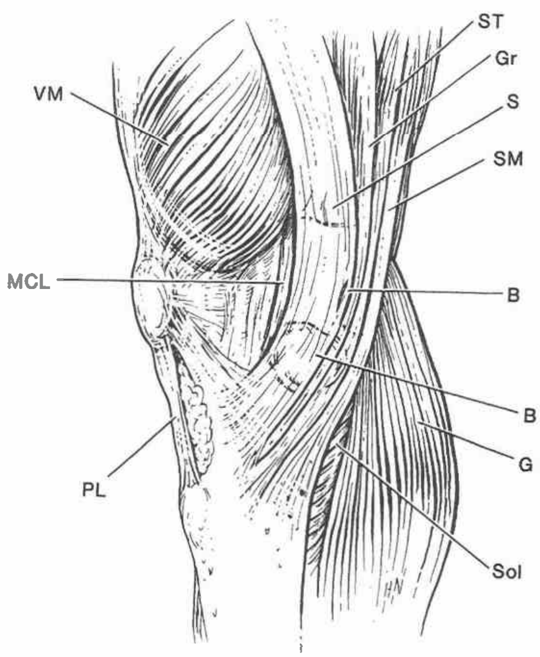

Figure 48–46. Normal anatomy. B, bursa; G, gastrocnemius; Gr, gracilis; MCL, medial collateral ligament; PL, patellar ligament; S, sartorius; SM, semimembranosus; Sol, soleus; ST, semitendonosus; VM, vastus medialis.

intensity medial to the ligament (Figs. 48–48 and 48–49). This should be distinguished from fluid in the gutters of the suprapatellar bursa.

Bone bruise adjacent to the MCL attachments may be another manifestation of MCL injury, representing microavulsions.[4, 13, 36, 44]

Lateral Collateral Ligament

Anatomy

The lateral or fibular collateral ligament is a tubular cord arising at the lateral epicondyle of the femur above the popliteal groove, and extending inferiorly and posteriorly to the fibular head, where it joins with the biceps femoris insertion, the conjoined tendon (Fig. 48–50). In contrast to the MCL, the lateral collateral ligament is separate and apart from the lateral joint capsule, with the lateral geniculate veins and arteries interposed (see Figs. 48–1, 48–2, 48–28, and 48–44 to 48–46).

Numerous other structures at the lateral aspect of the knee contribute to its stability, including the iliotibial band, the biceps femoris tendon, the fabellofibular ligament, the arcuate ligament, and the popliteal muscle and tendon.[61]

MRI Appearance

The lateral collateral ligament is best seen on coronal images, where it appears as a uniformly low-signal-intensity cord on all pulse sequences (see Figs. 48–4 and 48–49).

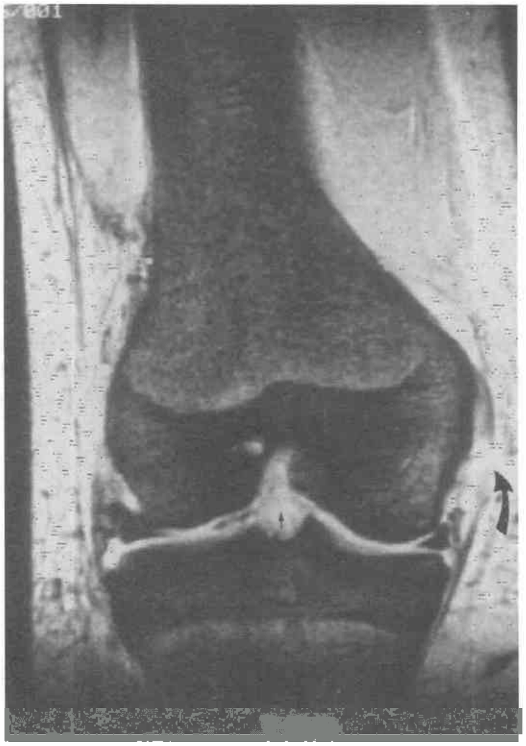

Figure 48–48. Medial collateral ligament tear, grade 3. Coronal gradient-echo image shows complete disruption of the medial collateral ligament (*curved arrow*). In addition, a normal anterior cruciate ligament is not seen at the intercondylar region and is therefore torn (*small arrow*).

Figure 48–49. Medial collateral ligament tear, grade 3. Coronal T1-weighted image shows complete disruption of the medial collateral ligament (*large arrow*). Edema and hemorrhage surround the ligament. Also, note the origins of the anterior cruciate ligament (*small curved arrow*) and posterior cruciate ligament (*large curved arrow*). Portions of the fibular collateral ligament are seen (*small arrow*).

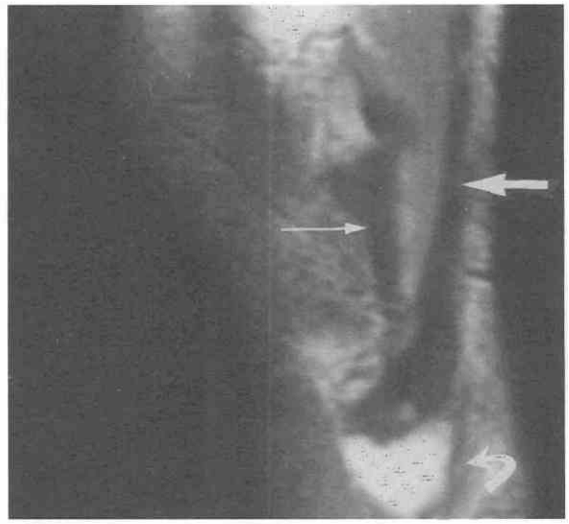

Figure 48–50. Conjoined tendon. Sagittal T1-weighted image, far lateral, shows the tendon of the biceps femoris (*thick arrow*) inserting with the fibular collateral ligament (*thin arrow*) as the conjoined tendon at the fibular head (*curved arrow*).

Trauma

Injuries to the fibular collateral ligament are usually the result of severe trauma involving varus force. Hemorrhage and edema with or without disruption of the ligament may be present. Signal intensity changes, as expected, reflect the edema present (Figs. 48–51 and 48–52).[4, 13, 36] Avulsion of the lateral capsule at its tibial insertion is often associated and is referred to as a *Segond fracture,* the lateral capsular sign.[58]

CT of the cruciate and collateral ligaments is never routinely performed.

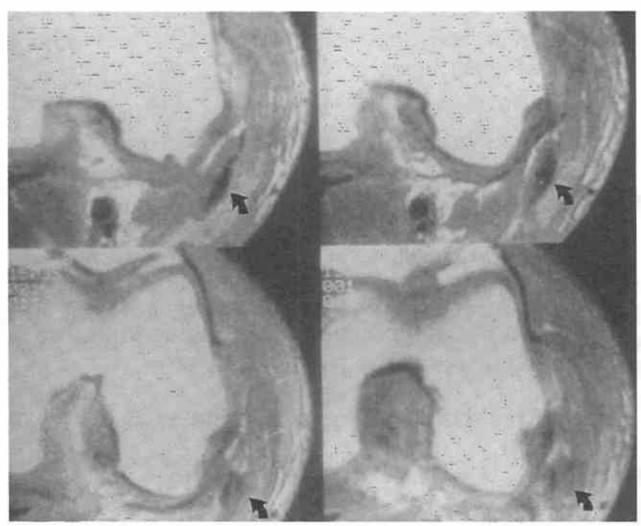

Figure 48–51. Tear of the lateral collateral ligament complex. Axial T1-weighted images show no identifiable fibular collateral ligament. The biceps femoris tendon is irregular proximally and completely torn distally (*curved arrows*). In addition, no identifiable anterior cruciate ligament or posterior cruciate ligament is seen at the intercondylar notch.

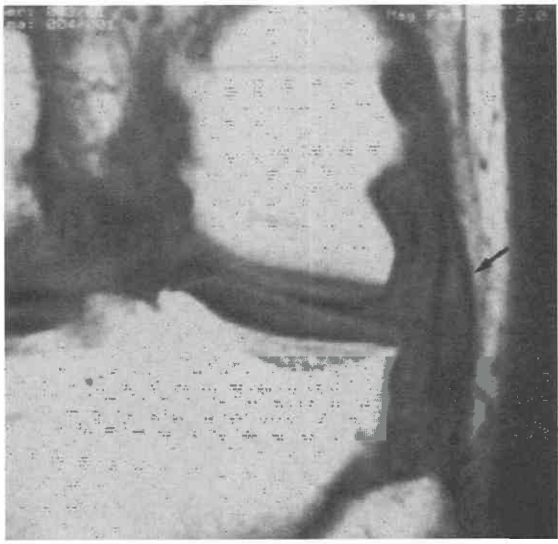

Figure 48–52. Lateral collateral ligament tear. Coronal T1-weighted image shows intermediate-signal-intensity replacement of the lateral collateral ligament, which is split, redundant, and discontinuous (*arrow*).

Pitfalls in Diagnosis

Transverse Ligament

The attachment sites of the transverse ligament to the anterior horns of the medial and lateral menisci may mimic a tear on sagittal views (see Figs. 48–3 and 48–7).

Meniscofemoral Ligaments

The takeoff of the ligament of Wrisberg at the posterior horn of the lateral meniscus may mimic a meniscal tear on sagittal views. When seen on end at its midportion, it may mimic a joint body posterior to the PCL. Similarly, a thick or low-lying ligament of Humphrey may appear as a displaced meniscal fragment (see Fig. 48–12).

Popliteal Tendon

The popliteal tendon and synovium cross the posterolateral aspect of the posterior horn of the lateral meniscus. The oblique region of increased signal intensity that results should not be confused with a meniscal tear (see Figs. 48–3, 48–4, 48–11, and 48–15).

Central Attachment Sites of the Posterior Menisci

The posterior horns of both menisci at the central attachment sites are not attached to the joint capsule and therefore may appear irregular on sagittal views. The posterior horns are seen on coronal views as flat bands that should not be confused with discoid menisci (see Fig. 48–14).

Meniscocapsular Junction

Far peripheral sagittal sections may show increased signal intensity at the bodies of both menisci because of volume averaging of the normal concavity of the meniscal body periphery with the joint capsule. Coronal images are normal (see Fig. 48–13).

Peripheral Meniscus

Increased signal intensity at the periphery of the meniscus represents the normal neurovascular portion, which can be quite prominent, especially at the posterior horn of the medial meniscus (see Fig. 48–5).

Origin of the Anterior Cruciate Ligament

Sagittal images may demonstrate volume averaging of the ACL and its origin at the lateral femoral condyle. This may mimic a proximal tear. Brightening on T2-weighted images, however, is not seen.

Anterior Horn of the Lateral Meniscus

The anterior horn of the lateral meniscus at its central attachment site often shows a speckled or striated, increased-signal-intensity pattern on proton-density images (see Fig. 48–10), which should not be confused with a tear. This pattern may represent dense collagen fibers of the ACL intertwined with the fibrocartilaginous meniscus. Isolated tears of the anterior horn of the lateral meniscus are less common than this normal variation.

Bone and Bone Marrow

The cortical bone of the distal femur, proximal tibia, and patella is of low signal intensity on all pulse sequences.

The signal intensity of the medullary canal reflects the changing amounts of hematopoietic and fatty bone marrow with age; the fatty marrow increases with time. Older patients may have residual islands of hematopoietic marrow, which should not be confused with infiltrative disease. The epiphyseal portions of the distal femur and the proximal tibia, and the epiphysoid patella always contain predominantly fatty marrow. The sensitivity of MRI to bone marrow alterations makes it ideal for detecting traumatic injuries.

Essentially four types of bone injury occur about the knee:

- Bone bruise or contusion
- Osteochondral fracture
- Stress fracture
- Obvious fractures of the femoral shaft, tibial plateau, and patella.

Some of these are occult; others are not (Fig. 48–53).

Figure 48–53. Sagittal proton-density image shows curvilinear low signal intensity at the proximal tibial epiphysis, indicative of nondisplaced fracture.

Bone Bruises

A bone bruise represents an acute, occult microfracture of subchondral trabecular bone with subsequent hemorrhage and edema. The cortex and articular cartilage are intact. They may be secondary to direct trauma or associated with twisting injuries and internal derangement of the knee; they resolve in 6 to 8 weeks. These injuries, which were not apparent before MRI became available, appear as ill-defined, subchondral, reticulated or stellate regions of low signal intensity on T1-weighted images and high signal intensity on T2-weighted images (Fig. 48–54).[29, 34, 60]

Osteochondral Fractures

An *acute* osteochondral fracture may be displaced or impacted:

1. *Displaced* osteochondral fragments are best seen on T2-weighted images, especially if a joint effusion is present. These are often seen at the medial patellar facet and the anterolateral femoral condyle secondary to patellar femoral dislocation (Fig. 48–55).
2. *Impacted* osteochondral lesions are commonly seen at the anterolateral femoral condyle. Decreased signal intensity is seen on T1-weighted images at the impaction site; increased signal intensity is seen about the impaction site on T2-weighted images as a result of edema. The overlying cartilage may be intact (Fig. 48–56).[29, 34, 57]

Chronic osteochondral fractures (osteochondritis dissecans) are well visualized with MRI. Some believe that increased signal intensity at the base of the osteochondral fracture on T2-weighted images represents a loose or unstable fragment.[10] Evaluation by MRI of the overlying cartilage, however, remains less reliable (Figs. 48–57 and 48–58).[29,57]

CT arthrography may delineate acute and chronic osteochondral defects, but it is also unreliable.

Stress Fracture

Stress fractures may be occult. They appear as linear, low-signal-intensity bands, away from the joint on T1-weighted and T2-weighted images. Increased signal intensity may be seen about the impacted fracture site on T2-

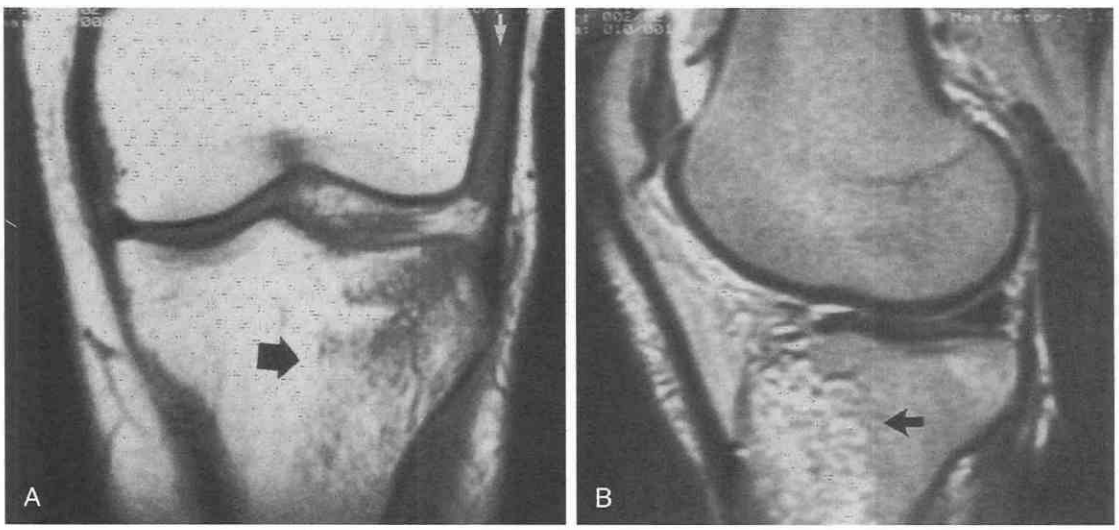

Figure 48–54. Bone bruise. *A,* Coronal T1-weighted image shows an ill-defined, subchondral, reticulated or stellate region of low signal intensity beneath the lateral tibial plateau (*black arrow*). Fluid is seen at the suprapatellar bursa, at the lateral gutter (*white arrow*). *B,* Sagittal T2-weighted image shows increased signal intensity indicative of edema or hemorrhage (*arrow*).

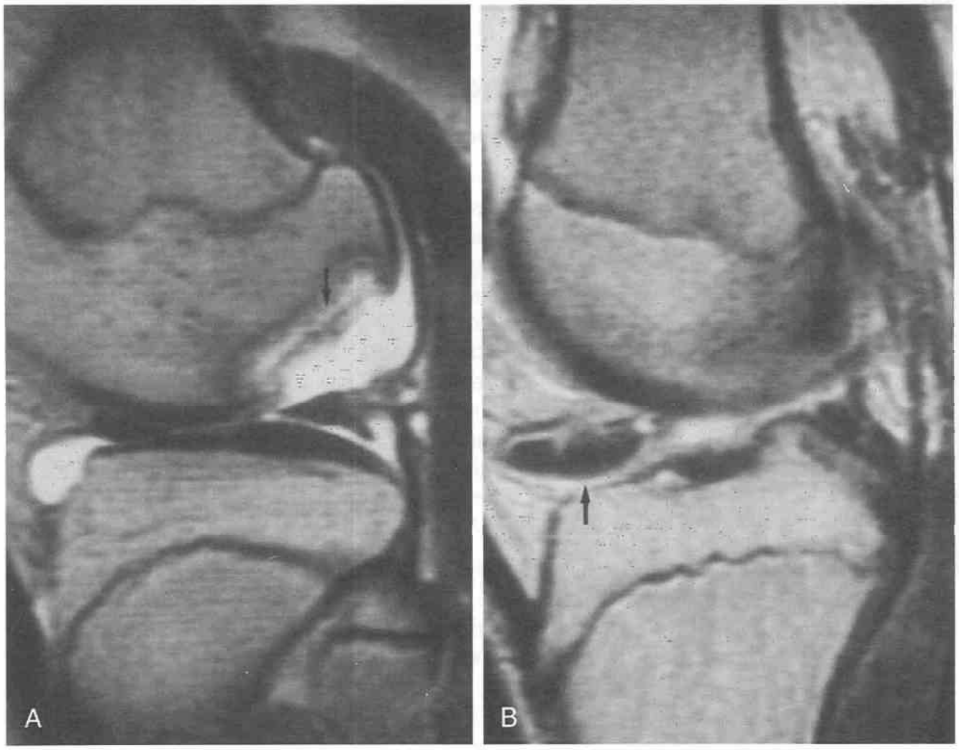

Figure 48–55. Displaced osteochondral fracture. *A,* Sagittal T2-weighted image shows a large osteochondral defect at the posterior aspect of the lateral femoral condyle (*arrow*). A large joint effusion is present. *B,* Sagittal T2-weighted image more centrally shows the detached bony fragment anteriorly (*arrow*). The low signal intensity of the fragment is suggestive of secondary osteonecrosis.

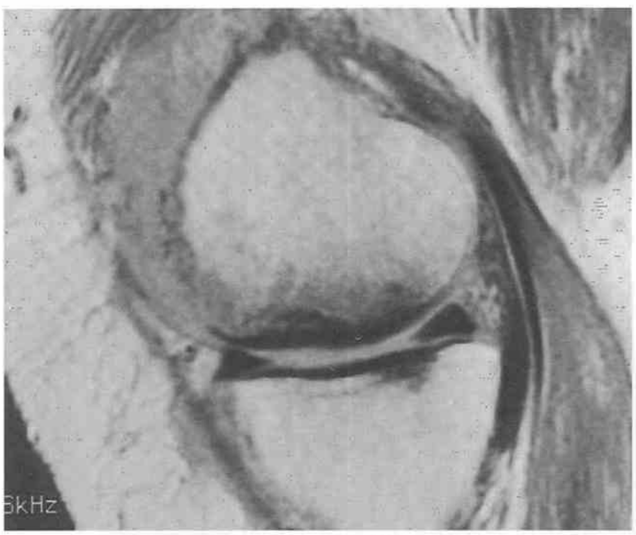

Figure 48–56. Impacted osteochondral fracture. Sagittal proton-density image shows a small, impacted osteochondral fracture at the medial femoral condyle. Edema surrounds the impacted cortex. Of note is the torn posterior horn of the medial meniscus. Joint effusion is present at the suprapatellar bursa.

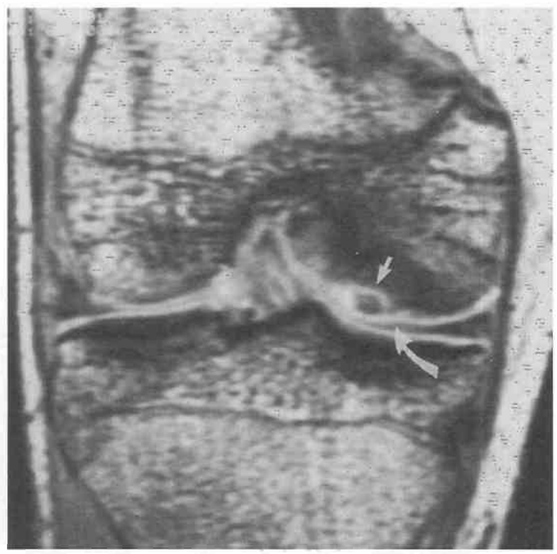

Figure 48–57. Osteochondritis dissecans. Coronal gradient-echo image shows an osteochondral defect at the notch aspect of the medial femoral condyle (*arrow*). A defect is seen at the adjacent articular cartilage (*curved arrow*). High signal intensity surrounds the osteochondral fragment. There is controversy as to whether this represents a loose fragment or a healing one. Of note is the fanlike insertion of the anterior cruciate ligament. Also, note the medial collateral ligament and iliotibial band.

Figure 48–58. Osteochondritis dissecans. Sagittal proton-density-weighted and T2-weighted images show an osteochondral defect (*arrow*) at the notch aspect of the medial femoral condyle. The overlying cortex appears intact. High signal intensity at the base of the defect may represent granulation tissue or may suggest loosening.

weighted images, reflecting the associated edema (Fig. 48–59).[26]

CT may detect stress fractures, especially those that are longitudinal (Fig. 48–60).[1]

Tibial Plateau Fractures

Tibial plateau fractures result from extreme valgus force at the knee and represent a common type of knee injury. Both CT and MRI can define the fracture and the degree of depression. Because osseous detail is better seen with CT, tibial plateau fractures are often best studied in this manner, complemented with 2D and 3D reconstructions. Fracture fragmentation, displacement, and depression may be seen more clearly (Fig. 48–61).[3, 24, 33, 38] MRI, of course, allows visualization of the cruciate and collateral ligaments and menisci.

Patterns of Injury

Although the structures of the knee and their injuries have been discussed separately, most traumatic injuries to the knee result in patterns of injury involving multiple structures.

The ACL principally resists anterior translation of the tibia and secondarily resists internal tibial rotation. This explains why twisting injuries of the ACL occur without direct trauma. Such injuries usually involve valgus stress as well. As a result, tearing of the ACL may be associated with distractive forces at the medial joint compartment and compressive forces at the lateral joint compartment. Distraction may produce injuries to the peripheral medial meniscus and the MCL. Compressive forces may produce lateral meniscus tears, bone contusion, or osteochondral fracture at the lateral femoral condyle and posterior-lateral tibia. These two articular surfaces are in contact only after an ACL tear and internal rotation of the tibia. Bony injury at the posterior-lateral tibia always occurs in these situations, whereas the lateral femoral condyle may be spared. Therefore, the pattern of posterior-lateral tibial injury with or without lateral femoral injury suggests an ACL tear (Fig. 48–62).[54]

A less common mechanism of ACL tear involves hyperextension without rotation. This mechanism allows impaction at the anterior femoral condyle and anterior tibia without injury to the menisci or collateral ligaments. Hence, this pattern of "kissing" contusions suggests an isolated ACL tear.

The least common mechanism of ACL injury involves varus stress and external rotation of the tibia. As expected, distractive forces result at the lateral joint compartment, and compressive forces are seen medially. Typically, there is disruption of the lateral collateral ligament complex. Avulsion fracture of the lateral capsnle at the tibia (a Segond fracture) is associated with an ACL tear more than 90% of the time. MRI may not show the fracture fragment itself, but edematous changes at the lateral tibial rim are always present and suggest the presence of an ACL tear.[22, 37, 42]

The PCL resists posterior translation of the tibia. Car accidents and sports activity are the two most common causes of PCL injury. A direct blow to the anterior tibia when the knee is flexed forcefully displaces the tibia posteriorly, causing a midsubstance tear of the PCL. A fall on the hyperflexed knee may also drive the tibia posteriorly. Bone contusion may result at the anterior tibial plateau and the posterior femoral condyles.[51, 52]

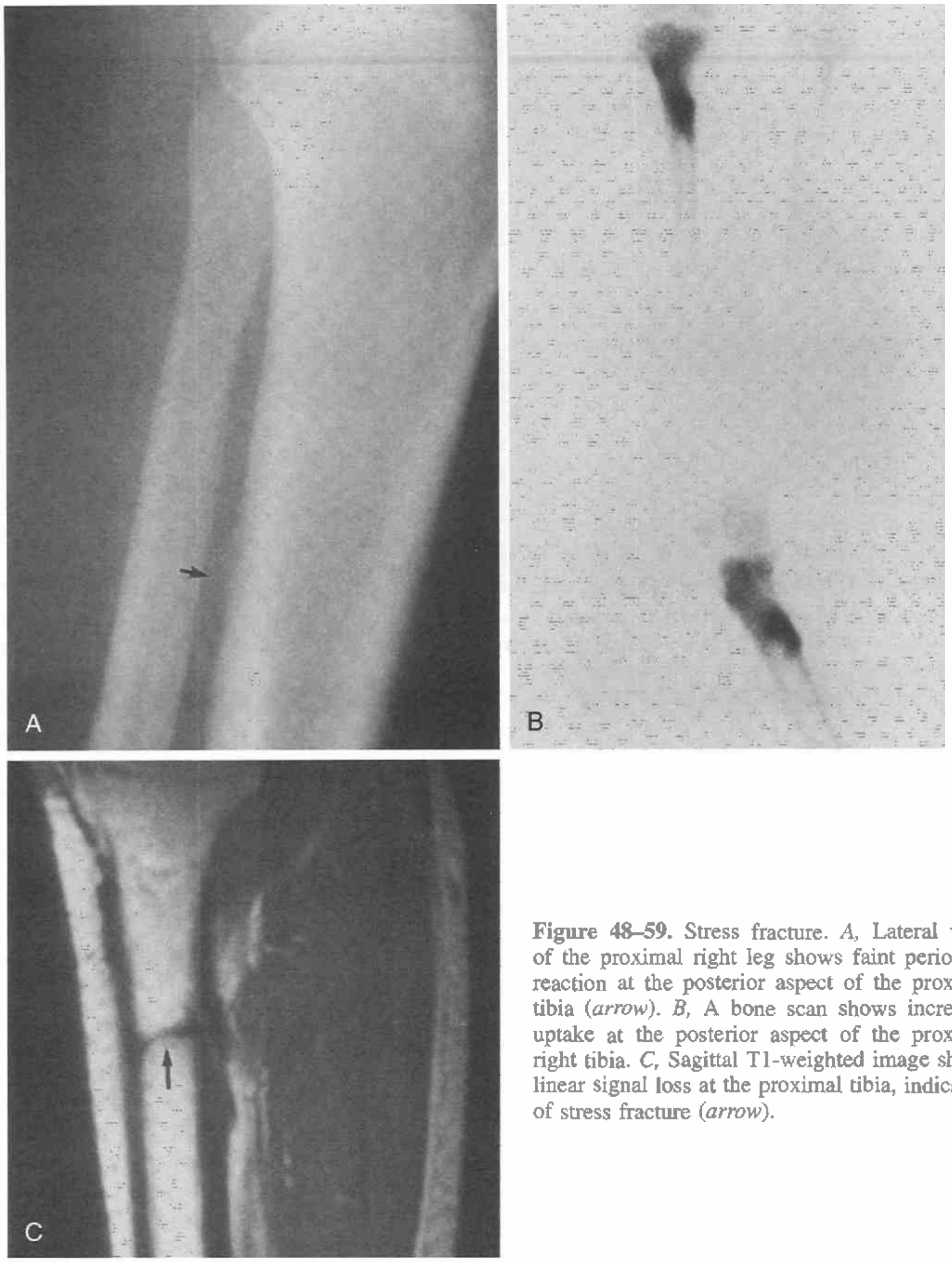

Figure 48–59. Stress fracture. *A,* Lateral view of the proximal right leg shows faint periosteal reaction at the posterior aspect of the proximal tibia (*arrow*). *B,* A bone scan shows increased uptake at the posterior aspect of the proximal right tibia. *C,* Sagittal T1-weighted image shows linear signal loss at the proximal tibia, indicative of stress fracture (*arrow*).

Muscles and Tendons

Ten muscles and their respective tendons cross the knee joint. The anterior quadriceps represents the rectus femoris, the vastus medialis, the vastus intermedius, and the vastus lateralis, which insert on the proximal pole of the patella. The anterolateral tensor fasciae latae and its iliotibial band insert at Gerdy's tubercle at the anterolateral tibia. The posterior-lateral biceps femoris inserts with the fibular collateral ligament as the conjoined tendon at the fibular head. The posterior-medial sartorius, gracilis, and semitendinosus insert at the posterior-medial tibia, proximally at the pes anserinus. The posterior-medial semimembranosus inserts separately, slightly more posteriorly. The medial and lateral heads of the gastrocnemius arise at the posterior supracondylar region of the femur. The popliteal muscle belly rests at the posterior proximal tibia, its tendon coursing intra-articularly through the posterior horn of the lateral meniscus, toward the popliteal groove of the femur. The plantaris muscle originates at the posterior-lateral supracondylar femur, and its tendon, the longest in the body, courses toward the ankle (Fig. 48–63; see Figs. 48–1, 48–29, 48–44 to 48–46, and 48–62).

Extensor Mechanism

The extensor mechanism of the knee includes the quadriceps muscle and tendon, the patellar ligament, and the components of the patellofemoral joint.

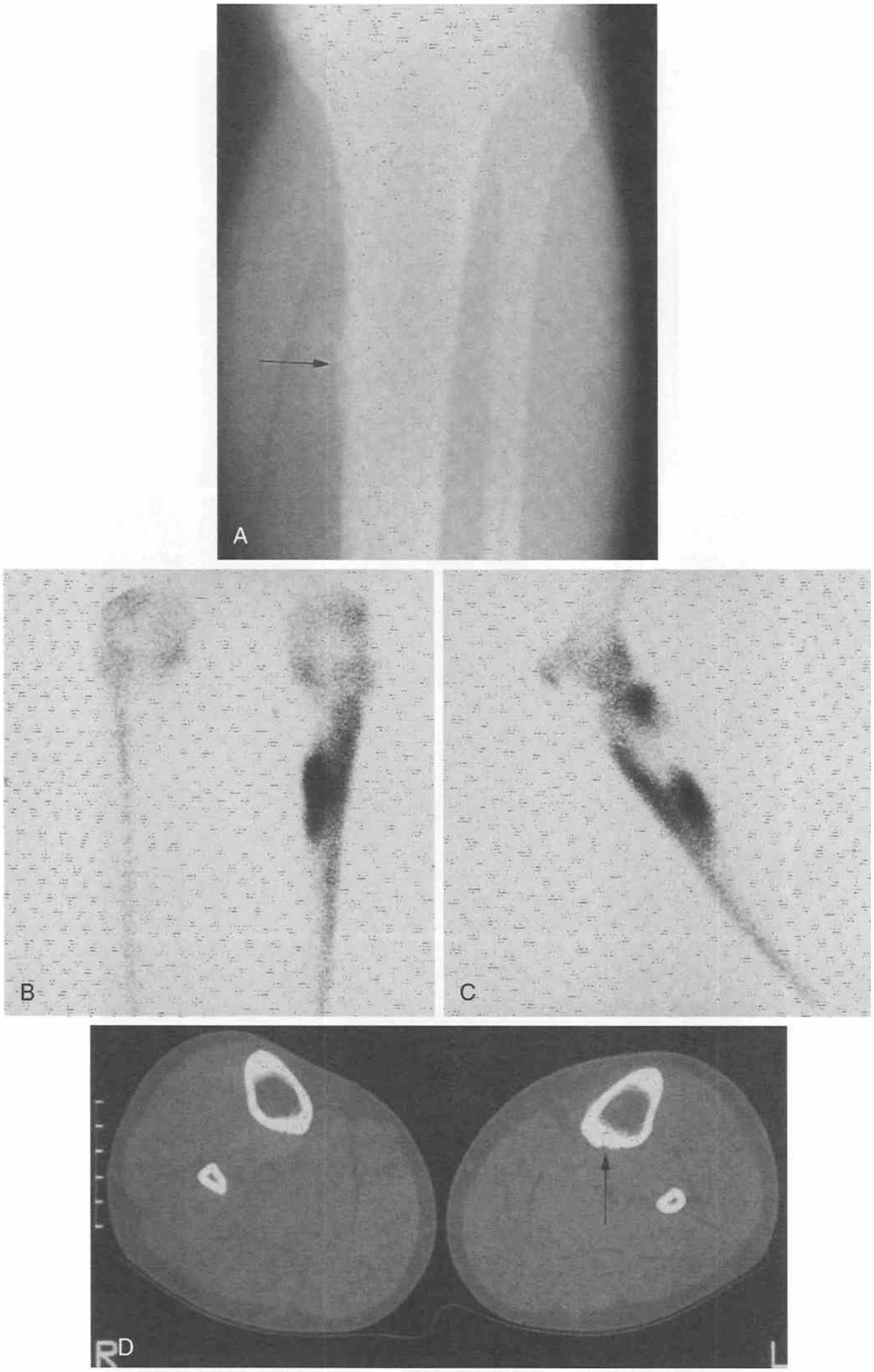

Figure 48–60. CT scan of stress fracture. *A*, An anteroposterior radiograph of the proximal left leg shows faint periosteal reaction at the medial proximal tibia (*arrow*). *B* and *C*, Frontal and lateral bone scan shows uptake at the posteromedial proximal tibia. *D*, CT scan shows a linear cleft at the posteromedial cortex of the left tibia (*arrow*), indicative of a fatigue fracture in this marathon runner.

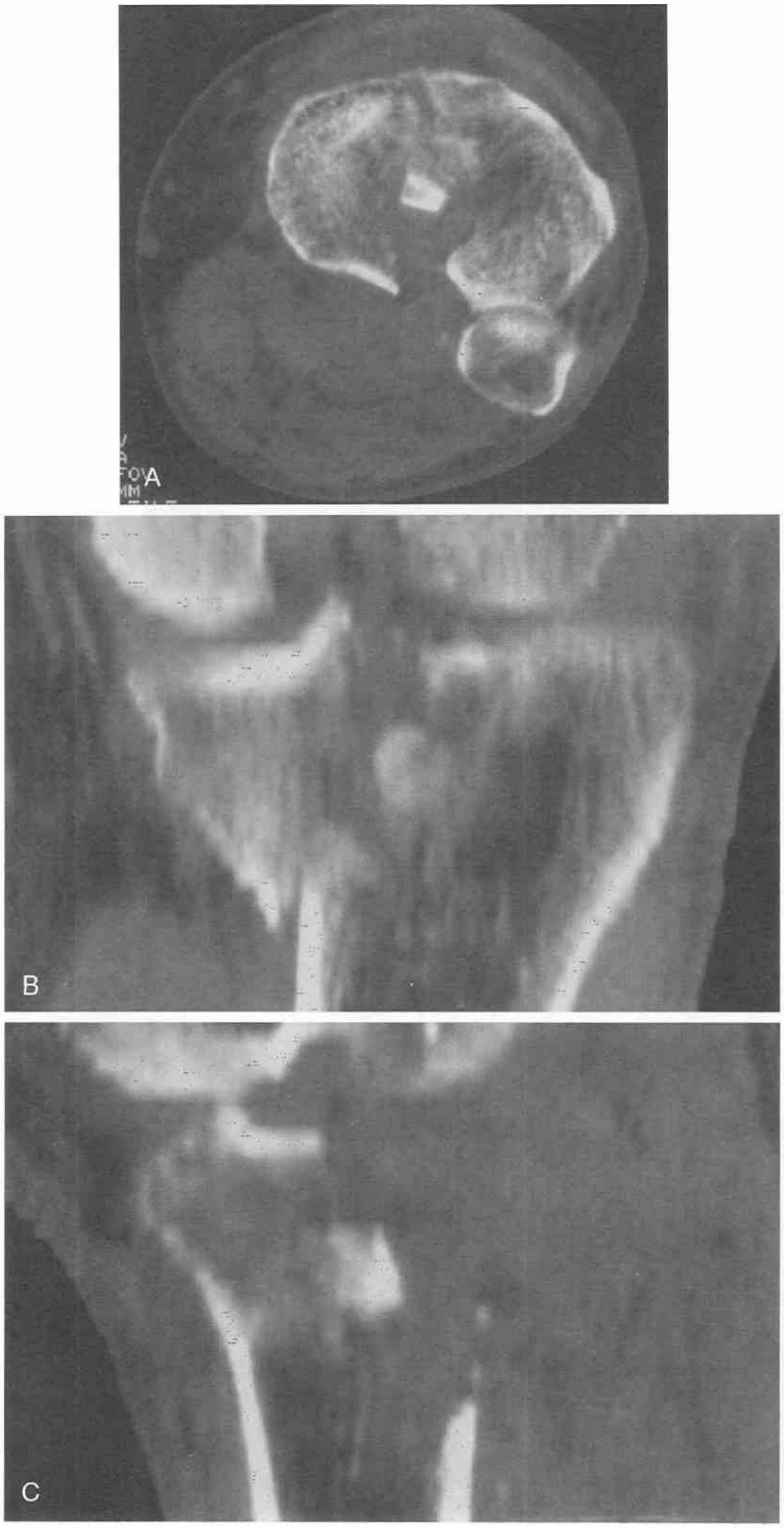

Figure 48–61. Tibial plateau fracture. Axial CT image with sagittal and coronal reconstructions shows the degree of comminution of the tibial plateau fracture. The central depressed fracture is well visualized and appears rotated.

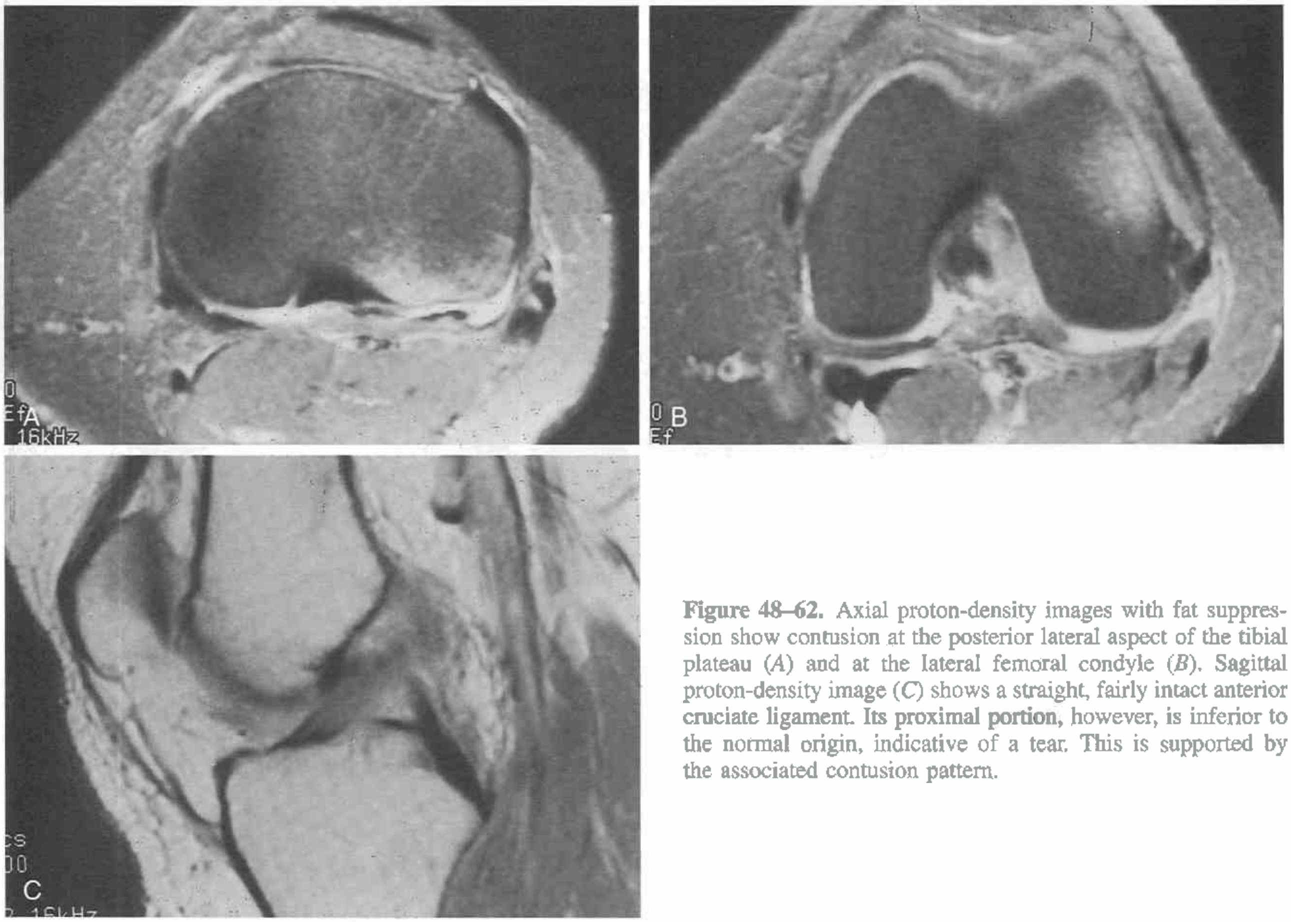

Figure 48–62. Axial proton-density images with fat suppression show contusion at the posterior lateral aspect of the tibial plateau (*A*) and at the lateral femoral condyle (*B*). Sagittal proton-density image (*C*) shows a straight, fairly intact anterior cruciate ligament. Its proximal portion, however, is inferior to the normal origin, indicative of a tear. This is supported by the associated contusion pattern.

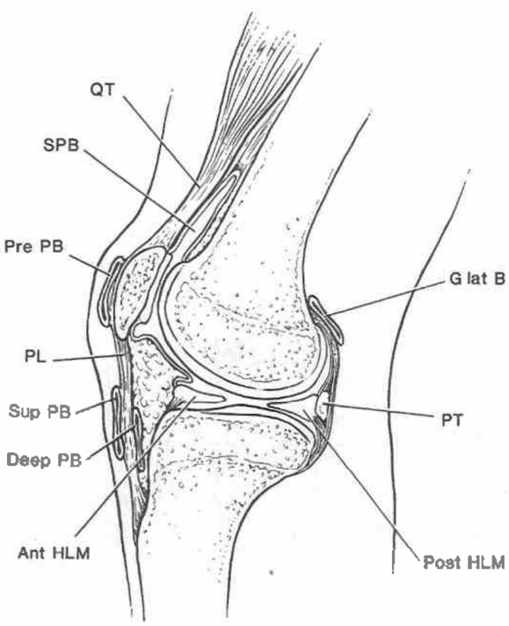

Figure 48–63. Normal anatomy. Ant HLM, anterior horn lateral meniscus; deep PB, deep patellar bursa; G lat B, gastrocnemius lateral head bursa; PL, patellar ligament; post HLM, posterior horn lateral meniscus; pre PB, prepatellar bursa; PT, popliteus tendon; QT, quadriceps tendon; SPB, suprapatellar bursa; sup PB, superficial patellar bursa.

Quadriceps Tendon

The rectus femoris, vastus intermedius, vastus medialis, and vastus lateralis muscles converge to insert as the quadriceps tendon at the superior pole of the patella. The fasciae of these four individual muscles combine to varying degrees to form a multilayered structure. The overall thickness of the quadriceps tendon is 8 ± 2 mm. The transverse width of the tendon averages 35 ± 7 mm. Usually, the vastus medialis and the vastus lateralis merge, producing a three-layered quadriceps tendon, with the fascia from the rectus femoris seen anteriorly and the fascia from the vastus intermedius seen posteriorly. It is also common for the fasciae of the vastus medialis and lateralis muscles to combine with each other and with the fascia of either the rectus femoris or the vastus intermedius muscle, producing a two-layered tendon. This laminar structure can easily be seen on axial and sagittal MRI scans. Attention to these layers is paramount because partial ruptures of the quadriceps tendon tend to involve one of these fascial groups. This may be difficult to detect clinically (Fig. 48–64). Full-thickness tears are more obvious (Fig. 48–65).[62]

Patellar Ligament

The patellar ligament extends from the distal pole of the patella to the anterior tibial tubercle. Its sagittal dimension is 3.7 ± 1.2 mm proximally, 4.3 ± 1.1 mm at the

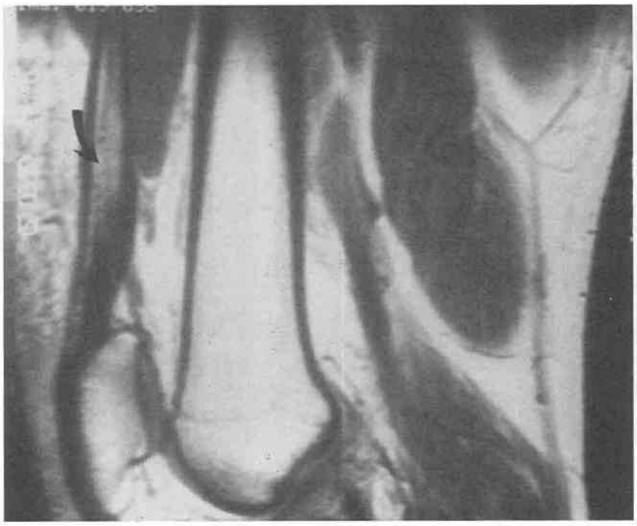

Figure 48–64. Partial tear of the quadriceps tendon. Sagittal T1-weighted image shows increased signal intensity at the proximal portion of the quadriceps tendon indicative of partial tearing (*arrow*). The fasciae from the vastus medialis and vastus lateralis are involved with sparing of the fasciae from the rectus femoris and vastus intermedius muscles.

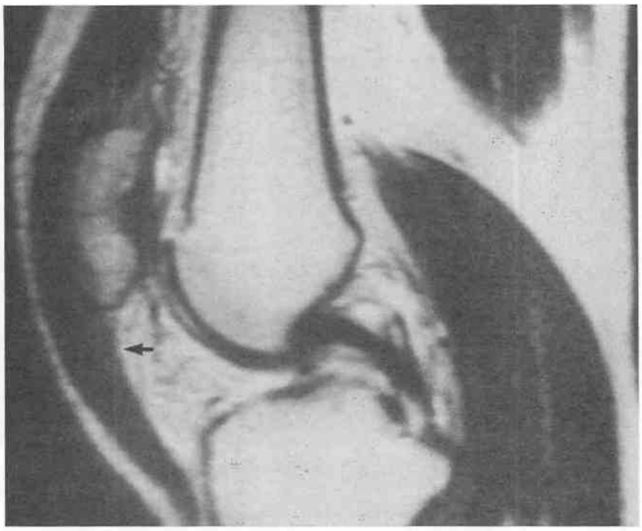

Figure 48–66. Patellar tendinitis. Sagittal T1-weighted image shows thickening of the patellar ligament proximally (*arrow*).

midportion, and 5.6 ± 1 mm distally. It is a fairly uniformly low-signal-intensity structure seen best on sagittal images. The syndrome of patellar tendinitis represents partial tearing and degeneration, usually of the proximal portion with secondary inflammation. Increased thickness of the proximal part, thicker than 7 mm, is the greatest indication of disease in symptomatic patients (Fig. 48–66). Other findings include an indistinct margin with increased signal changes.[12] It has been shown, however, that these same changes can be seen in asymptomatic individuals.[45] Complete rupture leads to discontinuity, redundancy, and retraction of the ligament.

Damage to the quadriceps tendon and patellar ligament may be caused by trauma or chronic overuse or may be secondary to underlying systemic illness, such as diabetes, hyperparathyroidism, gout, and rheumatic diseases. Damage to the patellofemoral articulation may be secondary to malalignment and tracking problems.

Patellofemoral Joint

Patellar tracking abnormalities can be imaged with axial CT or MRI of the patellofemoral joints performed during incremental knee flexion. Both modalities show the relationship of the patella to the femoral trochlear sulcus during the initial 30 degrees of flexion when most pathology is evident. MRI better defines the medial and lateral retinacula, although CT may image these structures as well. The patellar cartilage itself is better seen with MRI. CT arthrography may be helpful in evaluating gross cartilage defects.

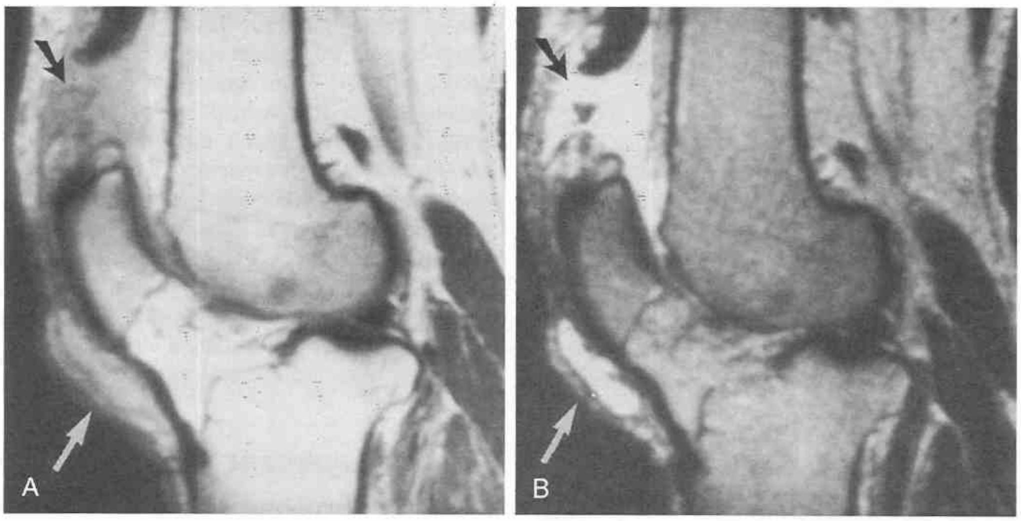

Figure 48–65. Quadriceps tendon rupture. Sagittal proton-density-weighted and T2-weighted images show complete disruption of the quadriceps tendon (*black arrow*). Incidentally noted is a prepatellar bursitis (*white arrow*).

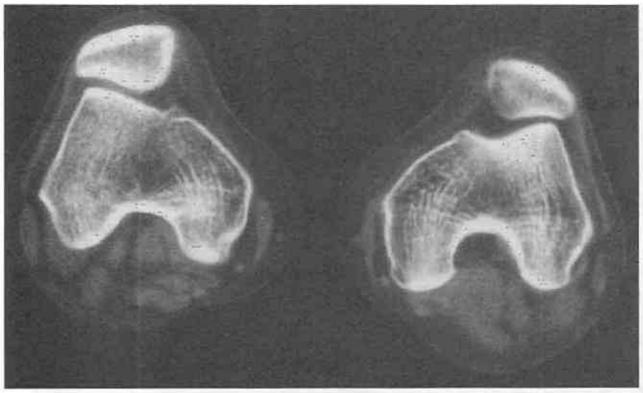

Figure 48–67. Patellofemoral instability. Axial CT images of the patellar femoral joints show bilateral patellofemoral subluxation. Note the medial and lateral retinacula, neither of which appears taut.

Figure 48–69. Patellofemoral dislocation. Axial CT scan of the right knee in this patient with cerebral palsy shows chronic patellofemoral dislocation. The femoral trochlear sulcus is hypoplastic.

At 0 degrees of flexion, the patellofemoral joint is not congruent with the patella laterally displaced. With increasing flexion, the medial and lateral retinacula tighten and the patella descends toward the midline. Eventually, congruence of the patella and the trochlea is reached. In a normal knee, this state of patellofemoral congruence is reached with a lesser degree of flexion than in an abnormal knee. There remains then a wide range of what is considered normal. Additional factors contributing to patellofemoral malalignment include structural abnormalities, such as misshapen patella, hypoplastic femoral trochlear sulcus, and abnormally high position of the patella itself (Figs. 48–67 to 48–69).[47, 50]

Transient lateral patellofemoral dislocation may often be diagnosed from a constellation of findings associated with the injury. These include disruption of the medial patellar retinaculum and the capsule as the capsule is drawn laterally, and contusion at the medial patella and lateral femoral condyle as the patella reduces. Osteochondral lesions and loose joint bodies may result. These most frequently arise at the medial patellar facet (Fig. 48–70).[50]

Articular Cartilage

Because degeneration of the patellar cartilage is such a common problem in young and older individuals, it has been extensively studied. The term *chondromalacia patella* has been used for both actual cartilage softening and the clinical syndrome of patellofemoral pain in adolescents and young adults.

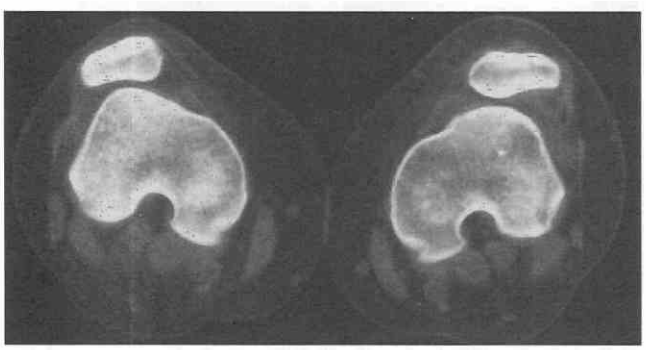

Figure 48–68. Patellofemoral instability. Axial CT scan shows bilateral patellar femoral subluxation. The femoral trochlea grooves are shallow. A joint effusion is noted on the left.

The degree to which standard spin-echo sequences predict the stages of patellar cartilage degeneration, however, remains controversial. On the basis of these routine protocols for evaluating internal derangement of the knee, certain conclusions can be drawn:

1. The articular cartilage is of uniformly low-to-intermediate signal intensity on T1-weighted, spin-density, and T2-weighted images.
2. Focal signal intensity changes appear to represent localized cartilaginous defects, especially when multiple pulse sequences are used.
3. Spin-density images alone are relatively insensitive to cartilage abnormalities. Normal-appearing cartilage may underestimate the degree of disease present.

These conclusions can apparently be applied to evaluation of the femoral and tibial cartilage as well. Although the consensus is that MRI is best suited for the evaluation of articular cartilage, different pulse sequences may be required.[9, 16, 17, 21, 31]

Fat-suppressed 3D spoiled gradient-echo MRI is currently in favor. Even here, however, early morphologic defects and cartilage softening are not seen with high sensitivity.[30]

Inversion recovery sequences, chemical shift selective techniques, and numerous gradient-echo sequences have been proposed. MR arthrography using a dilute gadolinium solution has been investigated. A less invasive technique involving intravenous gadolinium injection followed by diffusion of the agent across the synovium into preexisting joint effusion appears to produce an arthrographic effect within 15 minutes.

Known pitfalls in the evaluation of articular cartilage include the chemical shift and volume-averaging artifacts. The spatial misrepresentation of the interface of predomi-

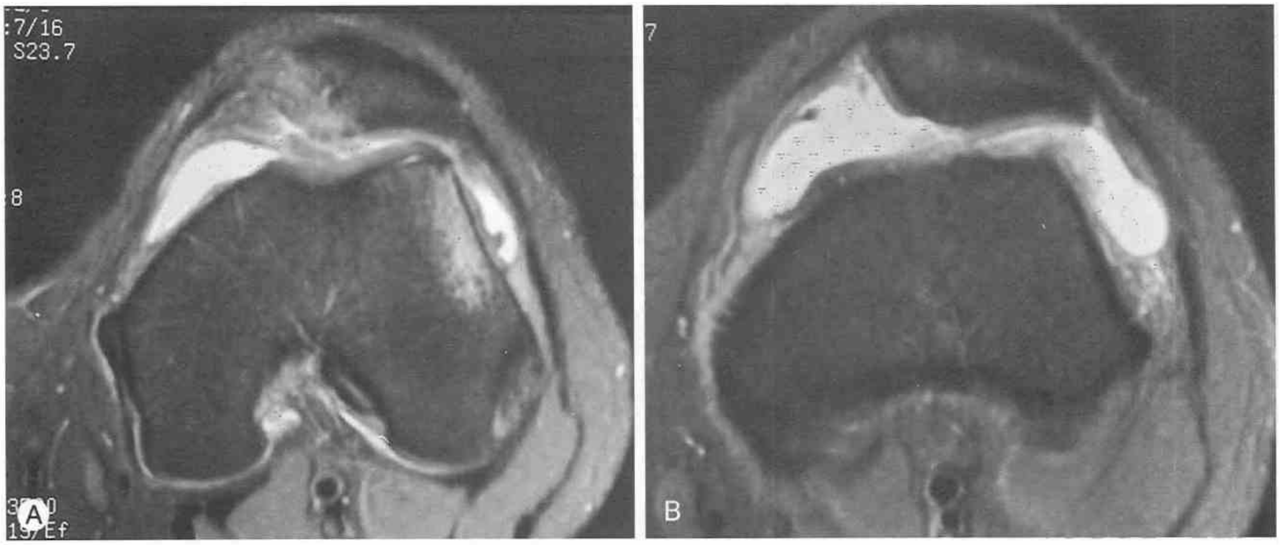

Figure 48–70. *A* and *B*, Axial proton-density images with fat suppression show contusion at the lateral femoral condyle and a chondral fracture at patella apex, after patellofemoral dislocation.

nantly water-containing and fat-containing tissues occurs in the frequency-encoding direction. Therefore, cartilage whose surface is perpendicular to the frequency-encoding axis appears thicker or thinner than it actually is. This artifact may be reduced by decreasing the field of view or by repeating the imaging sequence after rotating the frequency and phase-encoding gradients.

Volume averaging occurs whenever the imaged interface is not perpendicular to the imaging plane. The curved surfaces of the patella and femoral condylar cartilage are thus prone to such artifacts. Imaging in at least two planes may be necessary. Also, the femoral and tibial cartilage is thinner than the patellar cartilage and hence more susceptible to volume averaging.

Bursae

Numerous bursae are present about the knee joint. Anteriorly, two superficial bursae sit anterior to the extensor mechanism, and the prepatellar bursa is anterior to the patellar ligament. One or two deep patellar bursae sit posterior to the patellar ligament (see Figs. 48–29 and 48–63).

Posteriorly, a bursa resides beneath both the medial and lateral heads of the gastrocnemius. The bursa beneath the medial head is adjacent to and usually connected with the semimembranosus bursa. This gastrocnemius-semimembranosus bursa commonly communicates with the joint itself and represents the so-called popliteal cyst (Fig. 48–71; see Fig. 48–44).

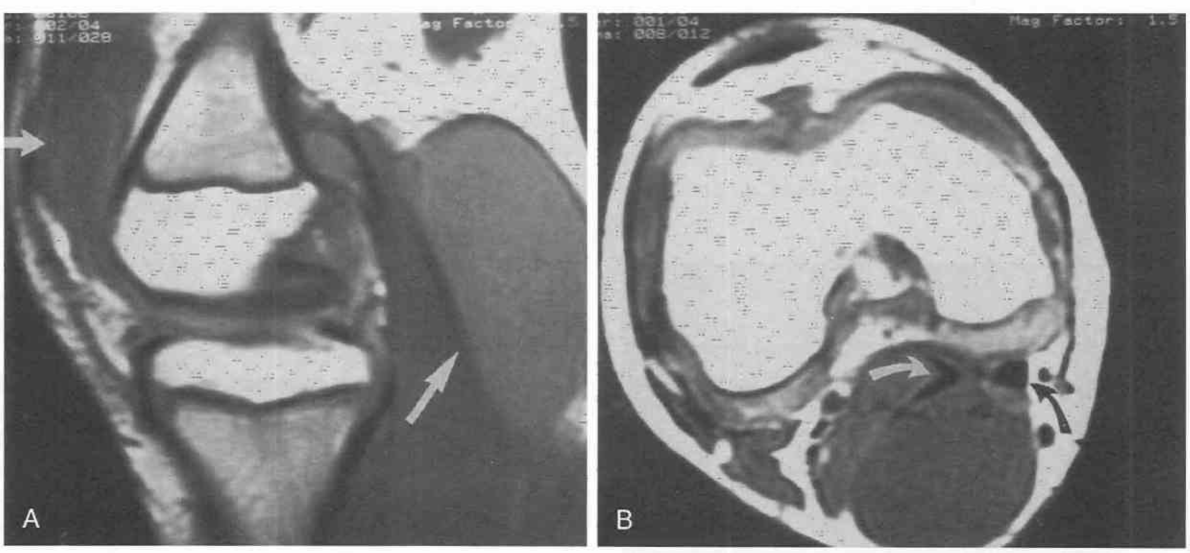

Figure 48–71. Popliteal cyst. Sagittal and coronal T1-weighted images show fluid in the knee joint and popliteal cyst, the latter representing a distended, communicating semimembranosus–medial gastrocnemius bursa. *A,* The sagittal image shows low-signal-intensity fluid at the "cyst" and suprapatellar bursa (*small arrow*). Normal high-signal-intensity fatty marrow is seen at the epiphyses. *B,* The axial images show the fluid-filled bursa and its relationship to the semimembranosus tendon (*curved black arrow*) and the medial gastrocnemius tendon (*curved white arrow*).

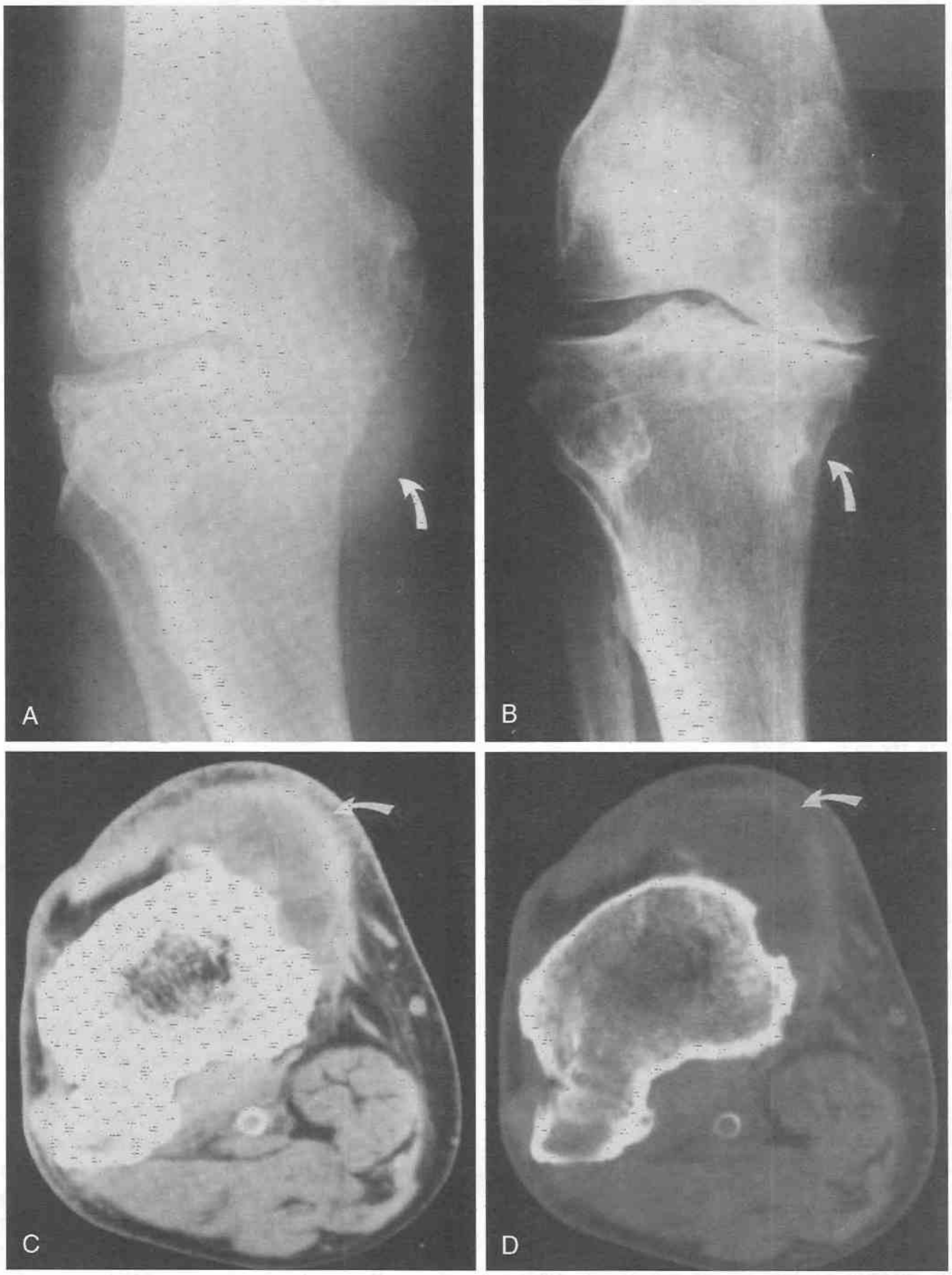

Figure 48–72. Meniscal cyst. *A* and *B*, Anteroposterior radiographs of the right knee show osteoarthritis with a soft tissue mass medially causing pressure erosion of the proximal medial tibia (*arrow*). *C* and *D*, CT scan shows a fluid-filled mass eroding the adjacent tibia (*arrow*).

Illustration continued on following page

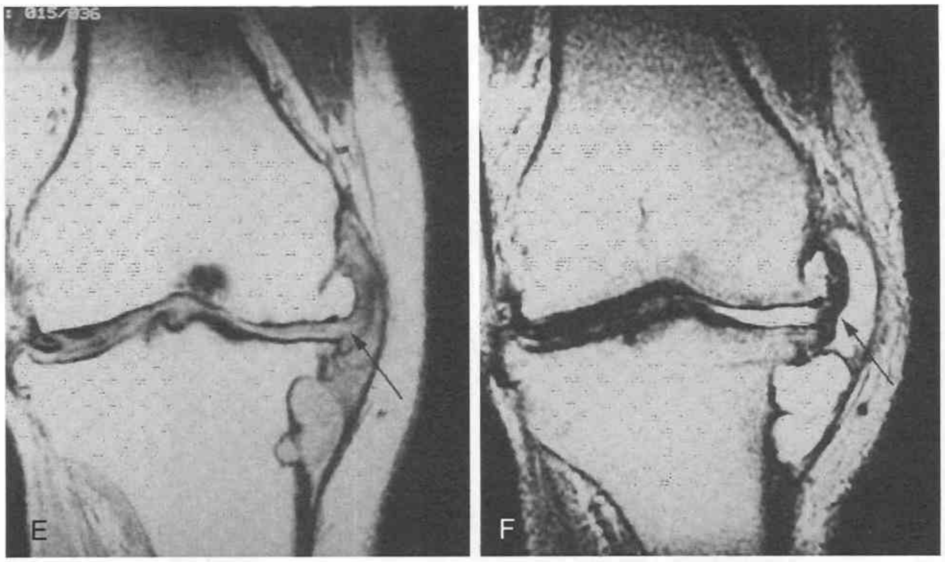

Figure 48–72. *Continued. E* and *F,* Coronal proton-density-weighted and T2-weighted images show the cystic structure communicating with the osteoarthritic joint. The lateral meniscus is degenerated, and what remains of the medial meniscus has been displaced beyond the joint margins (*arrow*). A meniscal cyst was found at surgery.

Numerous bursae are present at the lateral and medial aspects of the knee joint. Laterally, one bursa resides between the fibular collateral ligament and the joint capsule, a second between the biceps femoris and the fibular collateral ligament, and a third beneath the iliotibial tract. Medially, bursae reside beneath the tibial collateral ligament and the pes anserinus. A bursa may be present between the superficial and deep fibers of the tibial collateral ligament as well (see Figs. 48–45 and 48–46).

Joint Capsule

The knee is the largest, most complex joint in the body. Its fibrous capsule is just as complex. Anteriorly, the aponeurosis of the vastus medialis and lateralis extends from the medial and lateral margins of the quadriceps tendon, patella, and patellar ligament, posteriorly to the respective tibial and fibular collateral ligaments and the tibial plateau. This anterior portion of the capsule is referred to as the medial and lateral patellar retinacula.

Medially, the fibrous capsule attaches at the femoral condyle just above the articular cartilage and at the tibia just below the plateau. The medial meniscus attaches to the capsule and the tibial collateral ligament complex. The coronary ligament refers to that portion of the capsule that attaches the inferior margin of the peripheral medial meniscus to the tibia.

Laterally, the fibrous capsule attaches at the femoral condyle just above the popliteus tendon groove and at the tibia just below the plateau. The lateral meniscus attaches to the lateral capsule, more loosely than the medial, along its periphery except posteriorly, where the popliteus muscle and tendon interpose. The synovial membrane extends through an opening in the capsule posterolaterally between the popliteal tendon and the meniscus and more inferiorly between the tendon and the tibial cortex, often referred to as the subpopliteal recess.

Nontraumatic Disorders

Nontraumatic conditions affecting the knee joint include (1) the development of cystic masses, (2) proliferative disorders of the synovium, (3) osteonecrosis, (4) inflammatory arthritis, (5) osteoarthritis, and (6) hematopoietic and neoplastic diseases.

Cystic Masses and the Knee

Synovial cysts about the knee represent distended bursae, which may or may not be inflamed. The most commonly encountered is the popliteal cyst, which usually communicates with the joint (see Fig. 48–71). Isolated bursitis is also seen, pes anserinus bursitis representing such an entity. Other cystic masses about the knee include ganglion cysts and meniscal cysts.

Meniscal cysts occur at the joint line and are invariably associated with a degenerative horizontal cleavage tear of the meniscus. Ganglion cysts may or may not have a definable communication with the joint and may occur in atypical locations, attached to tendon sheaths, within muscles, or near the proximal tibiofibular joint.

Before any resection, the cystic nature of such a knee mass must be ascertained. The relationship to the joint must be evaluated, and associated intra-articular disease must be sought. MRI is most suited to study these issues. Generally, cystic lesions on MRI are well circumscribed with smooth walls. Because ganglion and meniscal cysts may contain a gelatinous substance high in protein content, short TR/TE images may not show lower signal intensity.

Meniscal cysts are probably secondary to degenerative tears of the menisci. Synovial fluid is forced through the tear and accumulates at the meniscal capsular junction. The large cysts are seen posteromedially, where they may enlarge without restraint if they are posterior to the tibial collateral ligament (Fig. 48–72). They may be mistaken for popliteal cysts. Laterally, cysts appear to be more contained by the fibular collateral ligament and the iliotibial band and

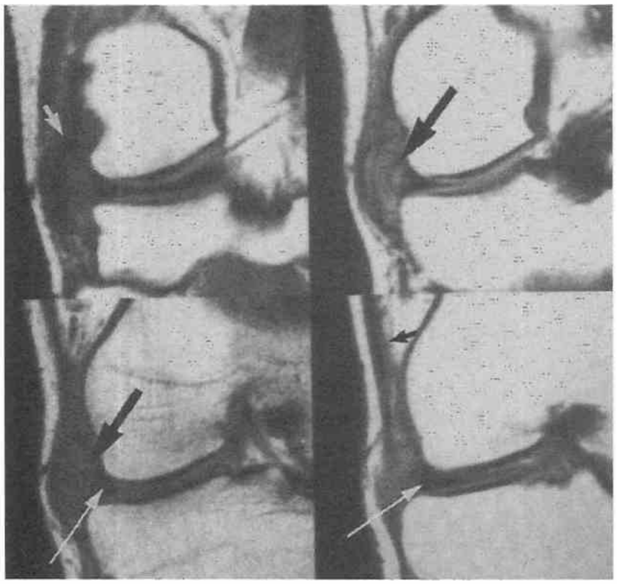

Figure 48–73. Lateral meniscal cyst. Coronal T1-weighted images show a small lateral meniscal cyst (*large black arrow*) and an associated meniscal tear (*large white arrow*). Note the relative containment by the fibular collateral ligament (*small white arrow*) and the iliotibial band (*small black arrow*).

therefore are usually smaller (Fig. 48–73). The detection of the meniscal tear is essential in that treatment of only the cyst itself results in recurrence.

Ganglion cysts are not associated with meniscal tears but may or may not show communication with the joint capsule. Multiple components may be present. More common locations include the proximal tibiofibular joint and adjacent to the suprapatellar pouch (Fig. 48–74).[7] Ganglion cysts also occur about the cruciate ligaments and may be related to prior ligament sprain (Fig. 48–75).

Although CT may show fluid-containing structures about the knee, communication with the joint and meniscal tears is not demonstrated.[27]

Pigmented Villonodular Synovitis

Pigmented villonodular synovits (PVNS) is a rare monoarticular proliferative disorder of the synovium that occurs in adults. The most common site of involvement is the knee. Although conventional radiographs may show associated pressure erosions of the underlying bone, most cases involving the knee demonstrate normal osseous structures at the time of clinical presentation. Soft tissue masses within the knee joint may be appreciated on plain films.

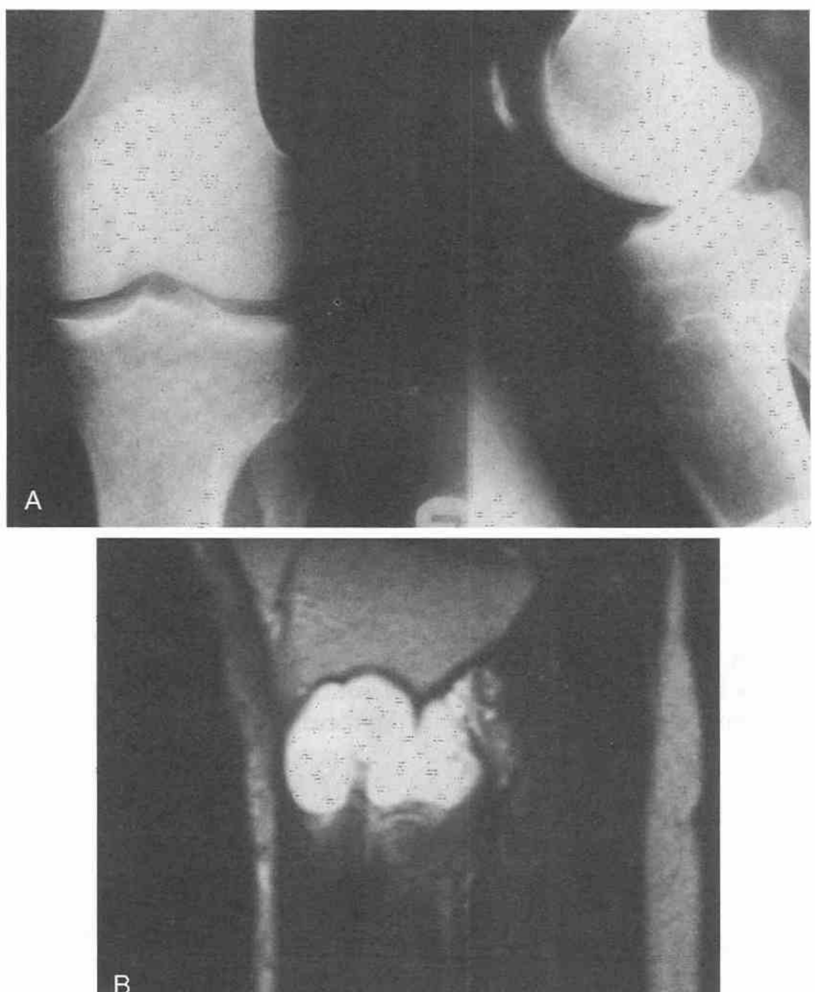

Figure 48–74. Ganglion cyst. *A*, Anteroposterior and lateral radiographs of the left knee reveal osseous erosion at the lateral aspect of the proximal left tibia. *B*, Sagittal T2-weighted image shows a high-signal-intensity mass at the lateral aspect of the proximal left tibia near the proximal tibial-fibular joint. A ganglion cyst was removed surgically.

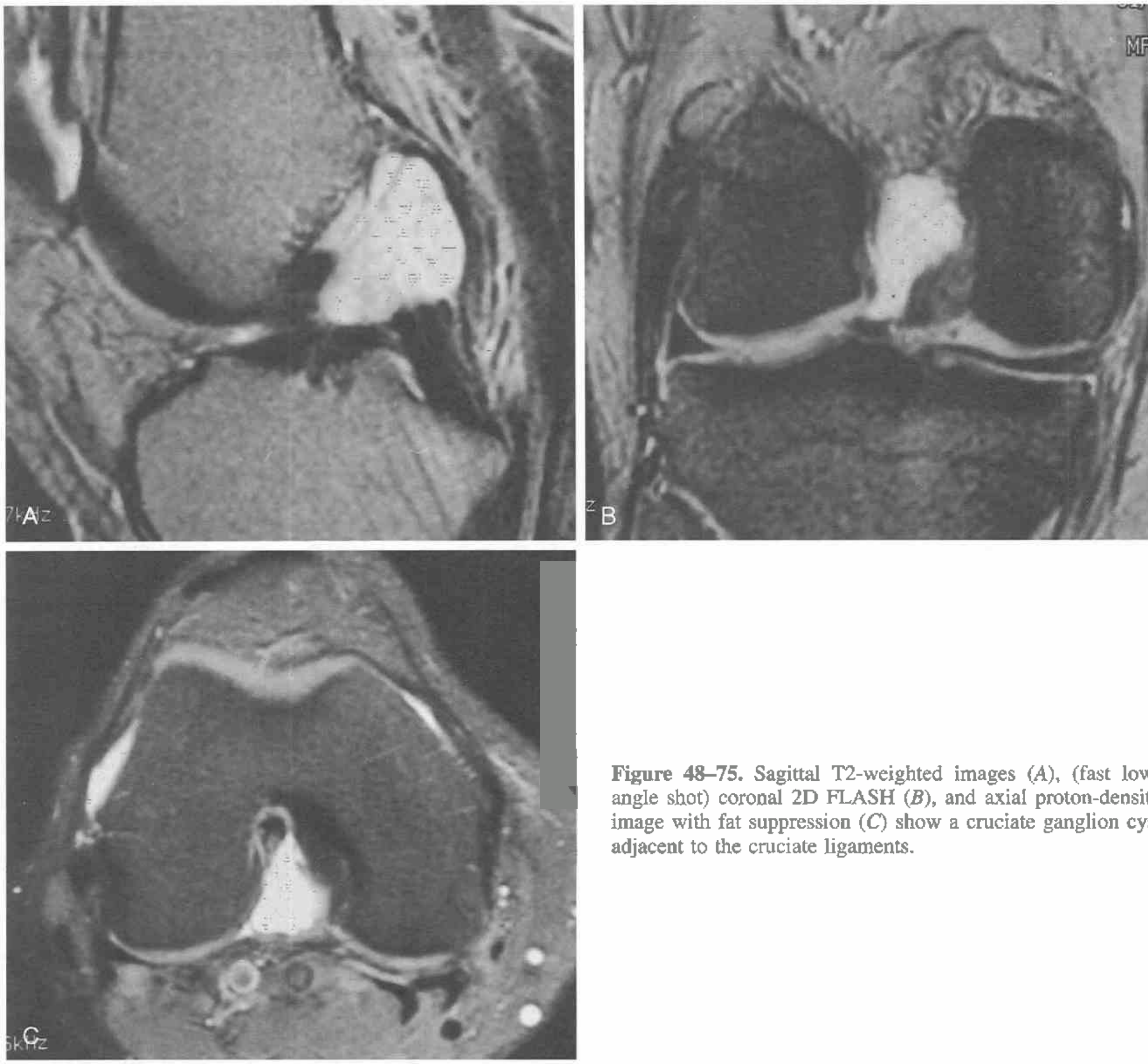

Figure 48–75. Sagittal T2-weighted images (*A*), (fast low-angle shot) coronal 2D FLASH (*B*), and axial proton-density image with fat suppression (*C*) show a cruciate ganglion cyst adjacent to the cruciate ligaments.

MRI reveals the proliferative synovial mass throughout the confines of the joint capsule. The signal intensity characteristics may vary as a result of the presence of abundant hemosiderin, inflamed synovium, and joint effusion. Certainly, the presence of multiple areas of low signal intensity on all pulse sequences, especially at the periphery, is a clue to the abundant hemorrhage present (Figs. 48–76 and 48–77). The differential diagnosis, however, includes other disorders that may be accompanied by hemarthrosis, such as hemophilia, synovial hemangioma, and inflammatory arthritis.

CT arthrography shows nonspecific nodular proliferation of the synovium. Osseous erosions are demonstrated.

Synovial Chondromatosis

Synovial chondromatosis represents the other major proliferative disorder of the synovium. Like PVNS, it is a rare monoarticular disease that is seen principally in adults. Cartilaginous metaplasia of the synovium leads to the production of multiple cartilaginous bodies within the confines of the joint. The knee is most commonly involved. As in PVNS, osseous erosions may be present. Although PVNS virtually never calcifies, cartilaginous bodies are prone to such calcification and ossification. The radiographic appearance of multiple calcified and ossified bodies of similar sizes distributed throughout the confines of the joint capsules is diagnostic of the disorder. When these bodies are not calcified, MRI detects them and is often diagnostic.

CT arthrography shows multiple bodies in the joint as well. Plain CT may detect calcification not apparent on radiographs and thus may differentiate synovial chondromatosis from PVNS.

Osteonecrosis

Spontaneous osteonecrosis of the knee is an idiopathic disorder of middle-aged and older adults that usually af-

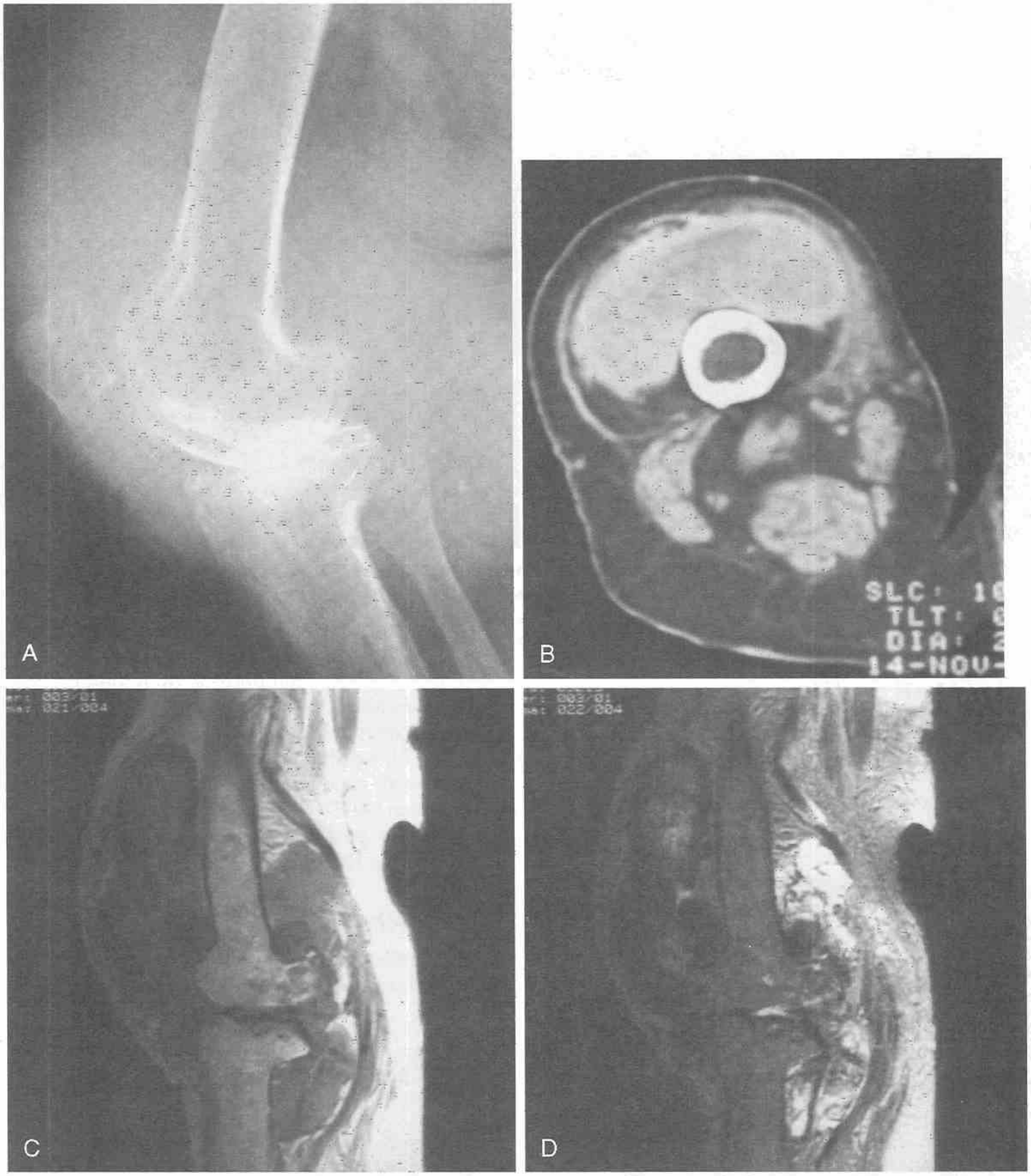

Figure 48–76. Pigmented villonodular synovitis (PVNS). *A,* Lateral radiograph shows marked soft tissue prominence within the joint capsule associated with osseus erosions. *B,* Axial CT scan shows mixed attenuation fullness at the suprapatellar bursa. *C* and *D,* Sagittal proton-density-weighted images and T2-weighted images show the extent of the mixed-signal mass within the joint. Persistent low signal areas on both sequences, especially those at the capsular margins, indicate extensive hemosiderin deposition and a probable diagnosis of PVNS.

fects the weight-bearing portion of the medial femoral condyle; it less frequently affects the medial tibial plateau, lateral femoral condyle, and lateral tibial plateau. Its onset is heralded by acute pain. X-ray films are normal for approximately 4 to 6 weeks. MRI, however, usually demonstrates a poorly defined zone of decreased signal intensity on T1-weighted images; a poorly defined ring of moderately high signal intensity may be noted about the lesion (Fig. 48–78). Associated osteoarthritis and degenerative tearing of the medial meniscus may be present. Such meniscal tears precede the necrotic event.[6] Of course, degenerative cleavage tears are common in the population susceptible to osteonecrosis of the knee.

Eventually, bone necrosis progresses to fracture and collapse of the subchondral bone with fragmentation of the articular cartilage. Osteoarthritis then may be secondary to the necrosis or may exist coincidentally before the necrotic event.[5] Current studies suggest that spontaneous osteonecrosis of the knee actually represents a subchondral insufficiency fracture.[59]

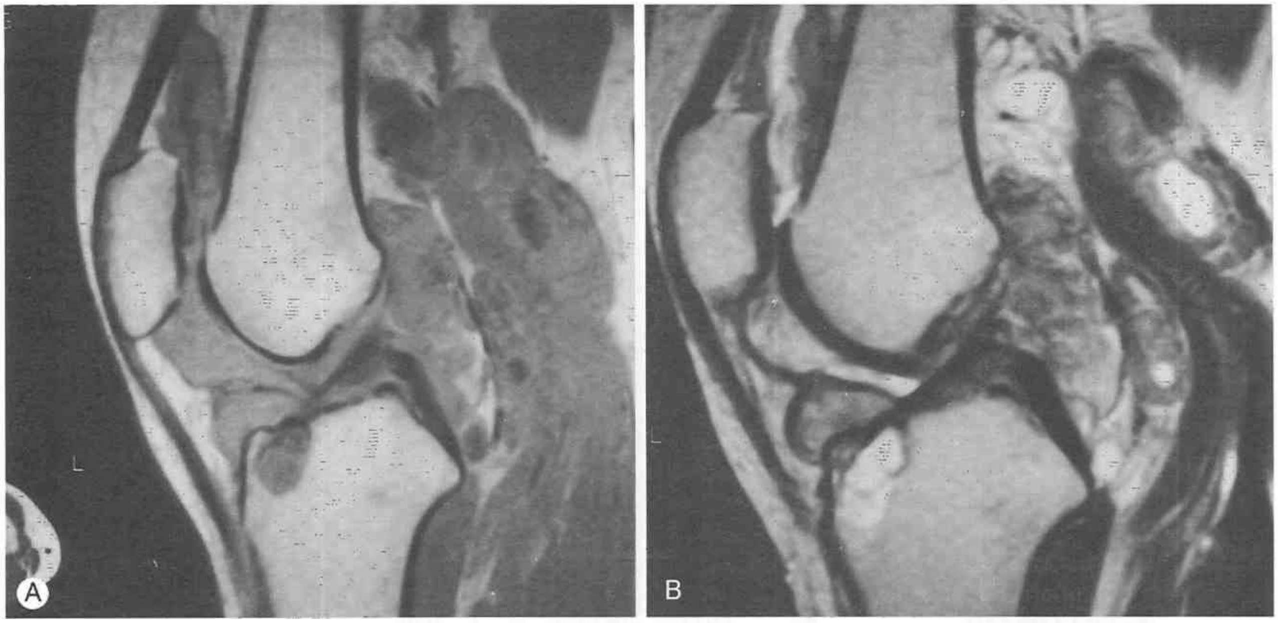

Figure 48–77. Pigmented villonodular synovitis. Sagittal proton-density (*A*) and T2-weighted (*B*) images show a mixed-signal-intensity mass throughout the joint capsule. Low signal intensity is seen at the periphery on both sequences.

Inflammatory Arthritis

The role of MRI in the care of patients with inflammatory arthritis is controversial. Certainly, MRI can show early erosions. With the aid of gadolinium, it can also differentiate among joint effusion, active pannus formation and chronic pannus, and fibrosis. Both joint fluid and active pannus brighten on T2-weighted images, but only active pannus significantly enhances after gadolinium administration on T1-weighted images. Fibrotic pannus does not enhance with gadolinium on T1-weighted images and does not brighten on T2-weighted images. These distinctions are important to patient management in some, but not all, centers at this time (Fig. 48–79).[25]

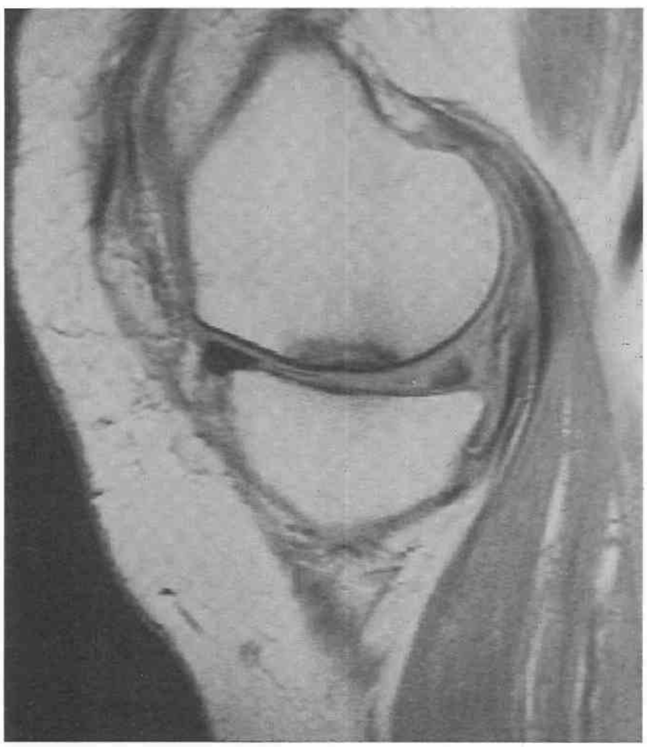

Figure 48–78. Sagittal proton-density image shows a curvilinear margin at the region of osteonecrosis at the medial femoral condyle.

Osteoarthritis

Osteoarthritis may be present coincidentally when other disorders are sought. Osteophyte formation, subchondral

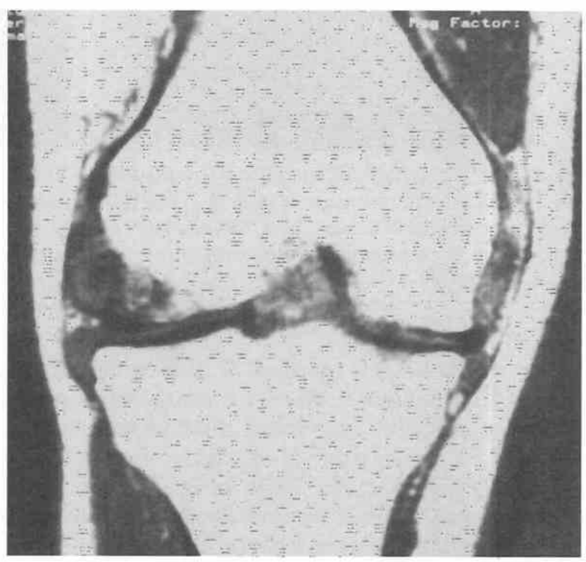

Figure 48–79. Rheumatoid arthritis. Coronal T1-weighted image shows mixed-signal-intensity pannus within the joint capsule leading to osseous erosions.

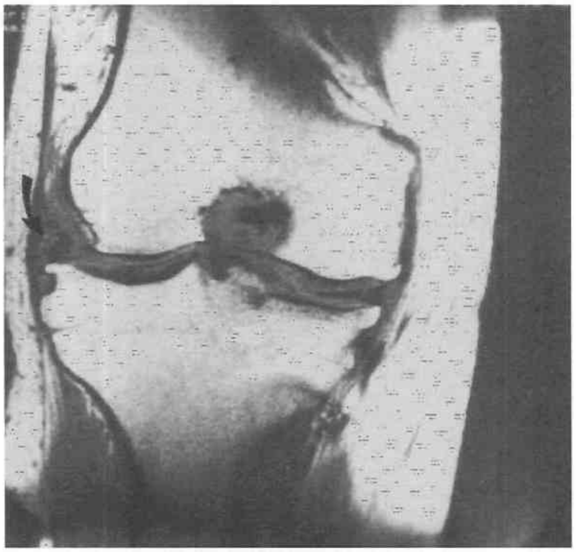

Figure 48–80. Osteoarthritis. Coronal T1-weighted image shows marked lateral compartment narrowing, osteophyte formation, and lateral subluxation of the tibia. The lateral meniscus is degenerated, and what remains rests beyond the margin of the joint (*arrow*).

sclerosis, subchondral cyst formation, and cartilage loss can all be appreciated.

Degeneration of the menisci is independent of degeneration of the femorotibial compartments. It usually precedes the development of osteoarthritis, although it may accelerate the process. Therefore, associated degenerative horizontal cleavage tears of the menisci may be seen. These represent the extension of internal meniscal disruption to the free edge, inferior articular surface, or capsular margin. The development of meniscal cysts has already been discussed.

With advancing osteoarthritis, what remains of the menisci may become adherent to the marginal osteophytes and eventually extruded beyond the margins of the joint. As the femorotibial compartments narrow, the meniscus may be forced between the joint capsule and underlying bone, often to a point above or below the level of the joint itself (Fig. 48–80).

Hematopoietic and Neoplastic Diseases

As mentioned, MRI is exquisitely sensitive to changes in bone marrow, and hence myeloproliferative disorders, neoplasm, marrow reconversion, and marrow failure are all well visualized. Processes affecting the marrow itself can be imaged long before trabecular bony changes are seen (Fig. 48–81). Such changes are necessary before CT can be of value.

It becomes clear that MRI has become the primary imaging modality of the knee. CT, however, remains helpful in evaluating any lesion characterized by calcification or ossification. As discussed earlier, both CT and MRI are also useful in evaluation of patellofemoral instability and tibial plateau fractures.

Osteoid osteoma remains one bone lesion that is best identified with thin-section CT scanning, often after localization with bone scans (Figs. 48–82 and 48–83).[23] It more clearly defines the tiny nidus, whereas MRI may reveal a more vague region of bone marrow edema. Detection of

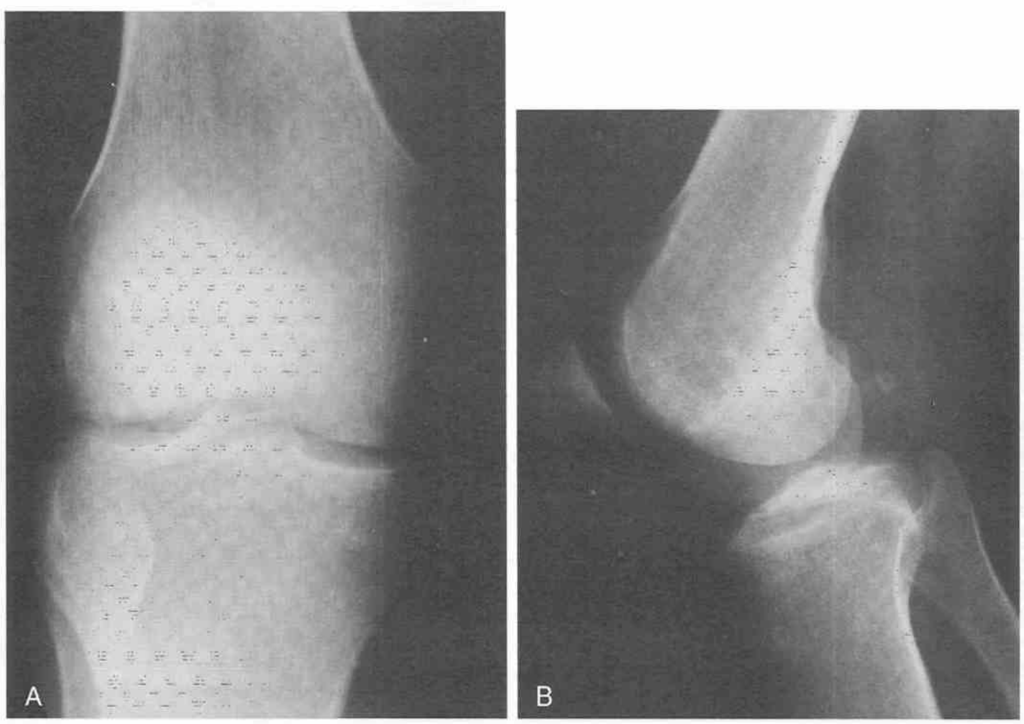

Figure 48–81. Lymphoma. *A* and *B*, Anteroposterior and lateral radiographs of the right knee are normal.

Illustration continued on following page

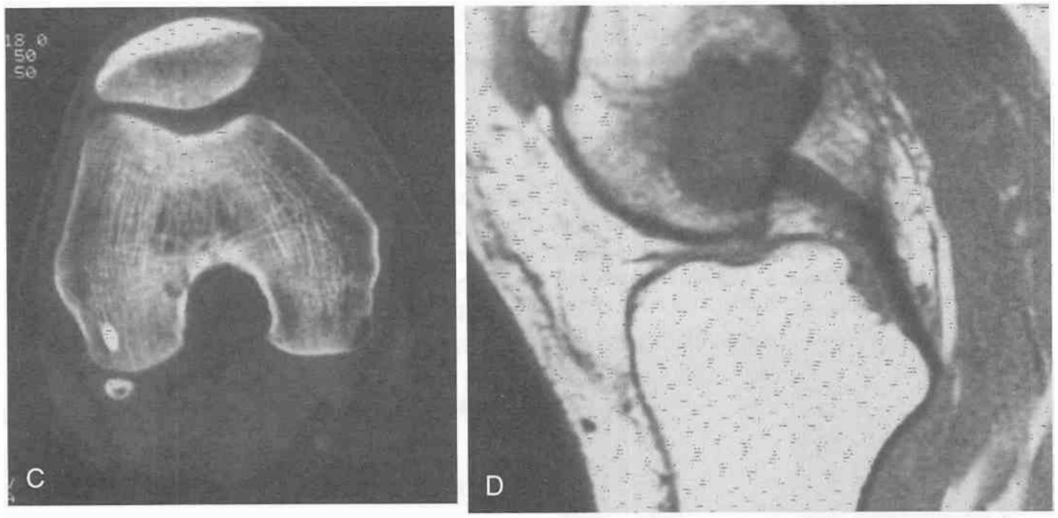

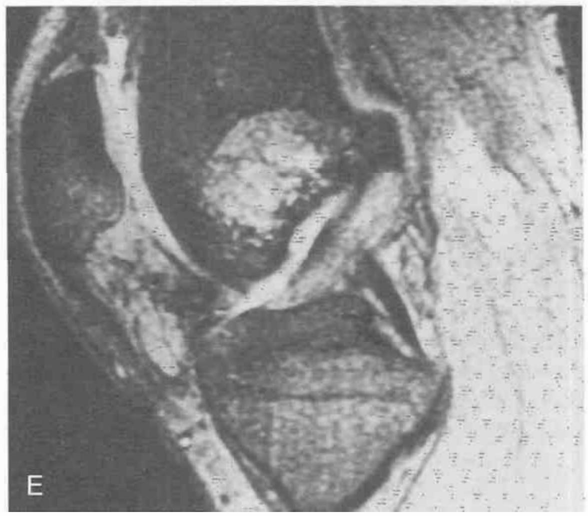

Figure 48–81. *Continued. C,* CT scan of the condylar region shows vague rarefaction. *D* and *E,* Sagittal T1-weighted and gradient-echo images show a focal abnormality at the condylar region, which represents non-Hodgkin's lymphoma before gross trabecular destruction.

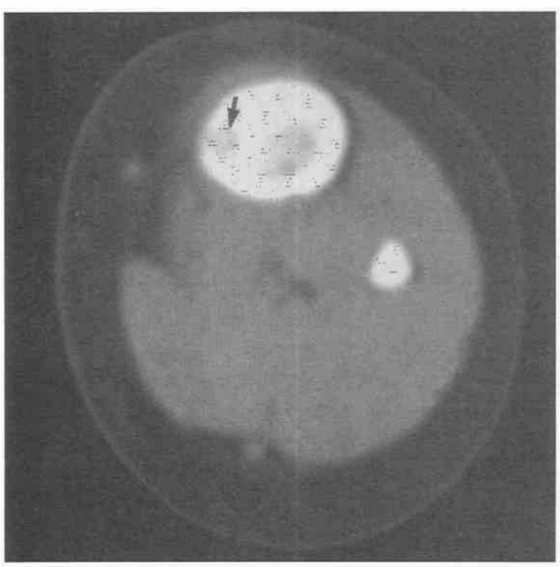

Figure 48–82. Osteoid osteoma. CT scan of the proximal left leg shows the nidus with central mineralization (*arrow*).

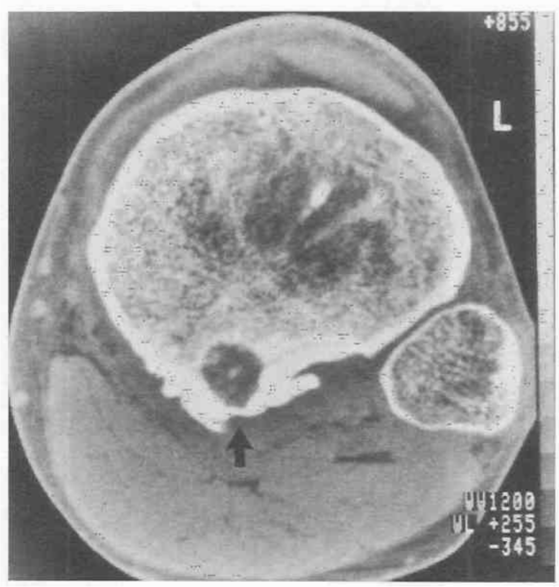

Figure 48–83. Osteoid osteoma. CT scan of the proximal left leg shows a well-defined nidus with central mineralization and associated periosteal reaction at the posterior aspect of the proximal left tibia (*arrow*).

tumor calcification or ossification is also more clearly seen with CT scanning and may be missed altogether with MRI. This is particularly useful in the evaluation of other bone-forming tumors and cartilage tumors.

References

1. Allen GJ: Longitudinal stress fractures of the tibia: Diagnosis with CT. Radiology 167:799–801, 1988.
2. Applegate GR, Flannigan BD, Tolin BS, et al: MR diagnosis of recurrent tears in the knee: Value of intraarticular contrast material. AJR Am J Roentgenol 161:821–825, 1993.
3. Barrow BA, Fajman WA, Parker LM, et al: Tibial plateau fractures: Evaluation with MR imaging. Radiographics 14:553–559, 1994.
4. Beltran J: MRI Musculoskeletal System, 1st ed. New York, Gower Medical, 1990.
5. Bjorkengren AG, Al Rowaih A, Lindstrand A, et al: Spontaneous osteonecrosis of the knee: Value of MR imaging in determining prognosis. AJR Am J Roentgenol 154:331–336, 1990.
6. Brahme SK, Fox JM, Ferkel RD, et al: Osteonecrosis of the knee after arthroscopic surgery: Diagnosis with MR imaging. Radiology 178:851–853, 1991.
7. Burk DL Jr, Dalinka MK, Kanal E, et al: Meniscal and ganglion cysts of the knee: MR evaluation. AJR Am J Roentgenol 150:331–336, 1988.
8. Chan WP, Peterfly C, Fritz RC, Genant HK: MR diagnosis of complete tears of the anterior cruciate ligament of the knee: Importance of anterior subluxation of the tibia. AJR Am J Roentgenol 162: 355–360, 1994.
9. Chandnani VP, Ho C, Chu P, et al: Knee hyaline cartilage evaluated with MR imaging: A cadaveric study involving multiple imaging sequences and intraarticular injection of gadolinium and saline solution. Radiology 178:557–561, 1991.
10. DeSmet AA, Fisher DR, Graf BK, Lange RH: Osteochondritis dissecans of the knee: Value of MR imaging in determining lesion stability and the presence of articular cartilage defects. AJR Am J Roentgenol 155:549–553, 1990.
11. Deutch AL, Mink JH, Fox JM, et al: Peripheral meniscal tears: MR findings after conservative treatment or arthroscopic repair. Radiology 176:485–488, 1990.
12. El-Khoury GY, Wira RL, Berbaum KS, et al: MR imaging of patellar tendinitis. Radiology 184:849–854, 1992.
13. Firooznia HF, Gollimbu C, Rafil N, et al: MRI and CT of the Musculoskeletal System. St. Louis, Mosby–Year Book, 1992.
14. Gentili A, Seeger LL, Yao L, Do HM. Anterior cruciate ligament tear: Indirect signs at MR imaging. Radiology 193:835–840, 1994.
15. Grover JS, Bassett LW, Gross ML, et al: Posterior cruciate ligament: MR imaging. Radiology 174:527–530, 1990.
16. Hayes CW, Conway WF: Evaluation of articular cartilage: Radiographic and cross-sectional imaging techniques. Radiographics 12: 409–428, 1992.
17. Hayes CW, Conway RW, Conway WF: Patellar cartilage lesions: In vitro detection and staging with MR imaging and staging with MR imaging and pathologic correlation. Radiology 176:479–483, 1990.
18. Herman LJ, Beltran J: Pitfalls in MR imaging of the knee. Radiology 167:775–781, 1988.
19. Hodler J, Haghighi P, Pathria MN, et al: Meniscal changes in the elderly: Correlation of MR imaging and histologic findings. Radiology 184:221–225, 1992.
20. Hodler J, Haghighi P, Trudell D, Resnick D: The cruciate ligaments of the knee: Correlation between MR appearance and gross and histologic findings in cadaveric specimens. AJR Am J Roentgenol 159:357–360, 1992.
21. Hodler J, Resnick D: Chondromalacia patellae. AJR Am J Roentgenol 158:106–107, 1992.
22. Kaplan PA, Walker CW, Kilcoyne RF, et al: Occult fracture patterns of the knee associated with anterior cruciate ligament tears: Assessment with MR imaging. Radiology 183:8355, 1992.
23. Klein MH, Shankman S: Osteoid osteoma: Radiologic and pathologic correction. Skeletal Radiol 21:23–31, 1992.
24. Kode L, Lieberman JM, Motta AO, et al: Evaluation of tibial plateau fractures: Efficacy of MR imaging compared with CT. AJR Am J Roentgenol 163:141–147, 1994.
25. Konig H, Sieper J, Wolf KJ: Rheumatoid arthritis: Evaluation of hypervascular and fibrous pannus with dynamic MR imaging enhanced with Gd-DTPA. Radiology 176:473–477, 1990.
26. Lee JK, Yao L: Stress fractures: MR imaging. Radiology 169:217–220, 1988.
27. Lee R, Cox G, Neff J, et al: Cystic masses of the knee: Arthrographic and CT evaluation. AJR Am J Roentgenol 148:329–335, 1987.
28. Lim PS, Schweitzer ME, Bhatia M, et al: Repeat tear of postoperative meniscus: Potential MR imaging signs. Radiology 210:183–188, 1999.
29. Lynch TCP, Crues JV III, Morgan FW, et al: Bone abnormalities of the knee: Prevalence and significance at MR imaging. Radiology 171: 761–766, 1989.
30. McCauley TR, Disler DG: MR imaging of articular cartilage. Radiology 209:629–640, 1998.
31. McCauley TR, Kier R, Lynch KJ, Okl P: Chondromalacia patellae: Diagnosis with MR imaging. AJR Am J Roentgenol 158:101–105, 1992.
32. McCauley TR, Moses M, Kier R, et al: MR diagnosis of tears of anterior cruciate ligament of the knee: Importance of ancillary findings. AJR Am J Roentgenol 162:115–119, 1994.
33. McEnery KW, Wilson AJ, Pilgram TK, et al: Fractures of the tibial plateau: Value of spiral CT coronal plane reconstructions for detecting displacement in vitro. AJR Am J Roentgenol 163:1177–1181, 1994.
34. Mink JH, Deutsch AL: Occult cartilage and bone injuries of the knee: Detection, classification, and assessment with MR imaging. Radiology 170:823–829, 1989.
35. Mink JH, Levy T, Crues JV III: Tears of the anterior cruciate ligament and menisci of the knee: MR imaging evaluation. Radiology 167: 769–774, 1988.
36. Mink JH, Reicher MA, Crues JV III. Magnetic Resonance Imaging of the Knee, 1st ed. New York, Raven Press, 1987.
37. Murphy BJ, Smith RL, Uribe JW, et al: Bone signal abnormalities in the posterolateral tibia and lateral femoral condyle in complete tears of the anterior cruciate ligament: A specific sign. Radiology 182: 221–224, 1992.
38. Rafii M, Firooznia H, Golimbu C, et al: Computed tomography of tibial plateau fractures. AJR Am J Roentgenol 142:1181–1185, 1984.
39. Rak KM, Gillogly SD, Schaefer RA, et al: Anterior cruciate ligament reconstruction: Evaluation with MR imaging. Radiology 178:553–556, 1991.
40. Recht MP, Piraino DW, Applegate G, et al: Complications after anterior cruciate ligament reconstruction: Radiographic and MR findings. AJR Am J Roentgenol 167:705–710, 1996.
41. Recht MP, Piraino SW, Cohen MAH, et al: Localized anterior arthrofibrosis (Cyclops lesion) after reconstruction of the anterior cruciate ligament: MR imaging findings. AJR Am J Roentgenol 165: 383–385, 1995.
42. Remer EM, Fitzgerald SW, Friedman H, et al: Anterior cruciate ligament injury: MR imaging diagnosis and patterns of injury. Radiographics 12:901–915, 1992.
43. Robertson PL, Schweitzer ME, Bartolozzi AR: Anterior cruciate ligament tears: Evaluation of multiple signs with MR imaging. Radiology 193:829–834, 1994.
44. Schweitzer ME, Tran D, Deely DM, Hume E: Medial collateral ligament injuries: Evaluation of multiple signs, prevalence and location of associated bone bruises, and assessment with MR imaging. Radiology 194:825–829, 1995.
45. Schweitzer ME, Mitchell DG: MR imaging of the patella tendon: Buckling and other normal variants [Abstract]. Presented at Radiological Society of North America, 1992.
46. Shankman S, Beltran J, Melamed E, Rosenberg ZS: Anterior horn of the lateral meniscus: Another potential pitfall in MR imaging of the knee. Radiology 204:181–184, 1997.
47. Shellock FG, Mink JH, Deutsch AL, Fox JM: Patellar tracking abnormalities: Clinical experience with kinematic MR imaging in 130 patients. Radiology 172:799–804, 1989.
48. Silverman JM, Mink JH, Deutsch AL: Discoid menisci of the knee: MR imaging appearance. Radiology 173:351–354, 1989.
49. Smith DK, Totty WG: The knee after partial meniscectomy: MR imaging features. Radiology 176:141–144, 1990.
50. Sonin AH, Fitzgerald SW, Bresler ME, et al: MR imaging appearance of the extensor mechanism of the knee: Functional anatomy and injury patterns. Radiographics 15:367–382, 1995.
51. Sonin AH, Fitzgerald SW, Friedman H, et al: Posterior cruciate ligament injury: MR imaging diagnosis and patterns of injury. Radiology 190:455–458, 1994.

52. Sonin AH, Fitzgerald SW, Hoff F, et al: MR imaging of the posterior cruciate ligament: Normal abnormal, and associated injury patterns. Radiographics 15:551–561, 1995.
53. Stoller DW, Martin C, Crues JV III, et al: Meniscal tears: Pathologic correlation with MR imaging. Radiology 163:731–735, 1987.
54. Tung GA, Davis LM, Wiggins ME, Fadale PD: Tears of the anterior cruciate ligament: Primary and secondary signs at MR imaging. Radiology 188:661–667, 1993.
55. Vahey TN, Bennett HT, Arrington LE, et al: MR imaging of the knee: Pseudotear of the lateral meniscus caused by the meniscofemoral ligament. AJR Am J Roentgenol 154:1237–1239, 1990.
56. Vahey TN, Broome DR, Kayes KJ, Shelbourne KD: Acute and chronic tears of the anterior cruciate ligament: Differential features at MR imaging. Radiology 181:251–253, 1991.
57. Vellet AD, Marks PH, Fowler PJ, Munro TG: Occult posttraumatic osteochondral lesions of the knee: Prevalence, classification, and short-term sequelae evaluated with MR imaging. Radiology 178: 271–276, 1991.
58. Weber WN, Neuman CH, Barakos JA, et al: Lateral tibial rim (Segond) fractures: MR imaging characteristics. Radiology 180:731–734, 1991.
59. Yamamoto T, Bullough PG: Subchondral insufficiency fracture of the femoral head and medial femoral condyle. Skeletal Radiol 29: 40–44, 2000.
60. Yao L, Lee JK: Occult intraosseous fracture: Detection with MR imaging. Radiology 167:749–751, 1988.
61. Yu JS, Salonen DC, Hodler J, et al: Posterolateral aspect of the knee: Improved MR imaging with a coronal oblique technique. Radiology 198:199–204, 1996.
62. Zeiss J, Saddemi SR, Ebraheim NA: MR imaging of the quadriceps tendon: Normal layered configuration and its importance in cases of tendon rupture. AJR Am J Roentgenol 159:1031–1034, 1992.

49 The Hip

Mark D. Murphey, Cheryl A. Petersilge

The hip joint is a large and complex articulation that can be involved by numerous pathologic conditions. These include abnormalities resulting from trauma, infection, avascular necrosis, neoplastic involvement, and synovial-based processes. In addition, manifestations of congenital and developmental anomalies are not infrequently recognized in the hip.

Although radiographs remain the initial imaging technique in most instances, computed tomography (CT) and/or magnetic resonance imaging (MRI) is often the next most valuable radiologic method of evaluation. CT and MRI have two advantages: Both eliminate overlying osseous structures that can restrict assessment with radiographs, and both clearly demonstrate the surrounding soft tissue structures as a result of improved contrast resolution. Unfortunately, clinical evaluation of, and distinction between, the various causes of hip pain usually yields nonspecific and, ultimately, unrewarding results. It is therefore important that we, as radiologists, be aware of the disease manifestations that commonly occur about the hip, as seen on CT scans and MR images. In this chapter, we discuss and illustrate the application of CT and MRI to assessment of pathologic conditions involving the hip joint.

Congenital and Developmental Abnormalities

Developmental Hip Dysplasia

Developmental dysplasia of the hip (DDH), previously termed *congenital hip dysplasia* (CHD), is most often evaluated radiologically by ultrasonography and radiographs. MRI, however, can also be used to evaluate DDH; as with ultrasonography, MRI does not expose these patients to radiation. MRI can be particularly helpful in evaluating patients after unsuccessful initial treatment and in evaluating older children after ossification of the capital femoral epiphysis, a situation in which ultrasonography can be difficult to perform.[87, 96, 112]

Axial and coronal MR images are most useful, and small surface coils with high spatial resolution are necessary to best evaluate the changes of DDH.[87] Coronal images allow assessment of the shape of the acetabulum and femoral head coverage. MR images also improve evaluation of surrounding soft tissue structures, including the labrum, iliopsoas tendon, capsular tissue, ligamentum teres, transverse acetabular ligament, and associated fibrofatty pulvinar (Fig. 49–1).[112]

Ligamentous structures may invaginate into the joint, not allowing reduction of the articulation.[29, 112, 195] Normally, the acetabular labrum is a triangular area of fibrocartilage superolaterally. It can also insinuate into the joint and make nonoperative reduction impossible.[29, 87] The ligaments and labrum have low signal intensity on all pulse sequences and are often accentuated by surrounding joint fluid on long repetition time (TR) images. Capsular tissue has intermediate signal intensity on all pulse sequences.

CT is most useful in evaluation of DDH after intraoperative reduction. Injection of contrast medium into the joint is also often performed at intraoperative reduction. The performance of CT as soon as possible after intraoperative arthrography allows contrast material surrounding the non-ossified femoral head to be identified to help assess alignment and its relationship to the acetabulum.[5, 29, 93, 115, 153, 161, 195] The adequacy of reduction can then be well evaluated by CT.[87, 112, 119, 120] The overlying cast, typically present, does not create artifact on CT and helps to limit patient motion.

Conversion Defects (Herniation Pits)

Conversion defects (herniation pits) result from an abrasive effect of the anterior hip capsule in an area of the anterosuperior subcapital region of the femoral neck. This phenomenon is common, affecting 4% to 5% of adults, and occurs in an area where there are often normal cortical defects.[7, 156, 162] The medullary canal is exposed to erosion from the overlying soft tissue and synovium, which creates a subcortical pit.[7] This developmental alteration, increasingly recognized on CT scans and MR images, is important to recognize as an incidental finding and typically is not a cause of hip pain. In addition, conversion defects must be distinguished from other pathologic conditions (including osteoid osteoma, avascular necrosis, chronic abscess, and intraosseous ganglion) with which they may be confused.

CT scans and radiographs reveal a subchondral area of soft tissue attenuation replacing the marrow or radiolucency, respectively, with surrounding sclerosis in the anterior subcortical region of the superolateral femoral neck (Fig. 49–2*A* and *B*).[162] On MR images, herniation pits show marrow replacement in this subcapital region with a rim of low signal intensity on all pulse sequences corresponding to the area of sclerosis (Fig. 49–2*C* and *D*). This appearance is seen best on axial and coronal MR images. Internally, the lesions are composed primarily of fibrocollagenous tissue and cystic components. Lesions show low to intermediate signal intensity on T1-weighted MR images and are of variable appearance on T2-weighted images. (Fig. 49–2*D* and *E*).

The opinions and assertions contained herein are the private views of the authors and are not to be construed as official or as reflecting the views of the Departments of the Navy, Army, or Defense.

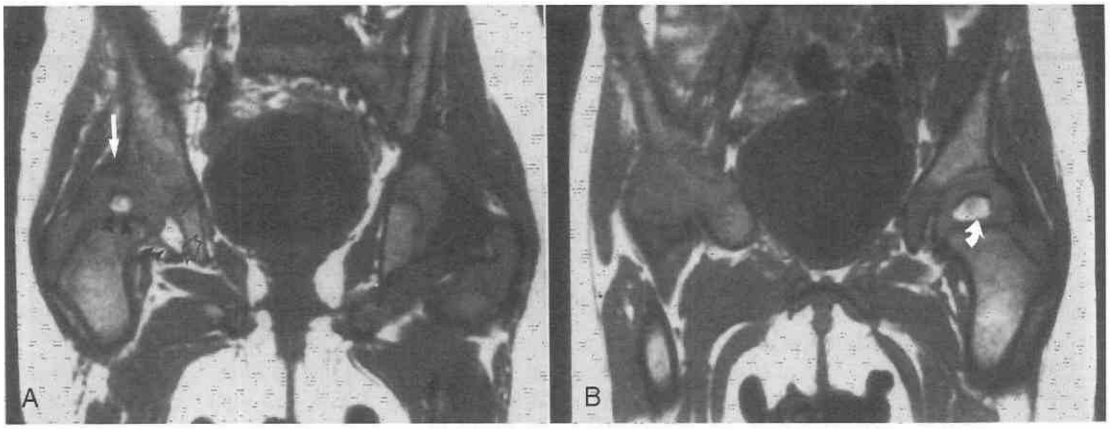

Figure 49–1. Developmental dysplasia of the right hip in a [redacted]month-old girl. *A* and *B*, Coronal T1-weighted MR images show delayed ossification of right capital femoral epiphysis *(large arrowheads)* compared with left side *(curved arrow)* and displacement superolaterally. Thickening of the fibrofatty pulvinar *(open arrow)*, transverse acetabular ligament *(small arrowheads)*, and ligamentum teres *(small arrows)* on the right has limited reduction of the hip; however, the acetabular labrum is not infolded *(large arrow)* to block reduction. (Courtesy of Edgar Colon, M.D.)

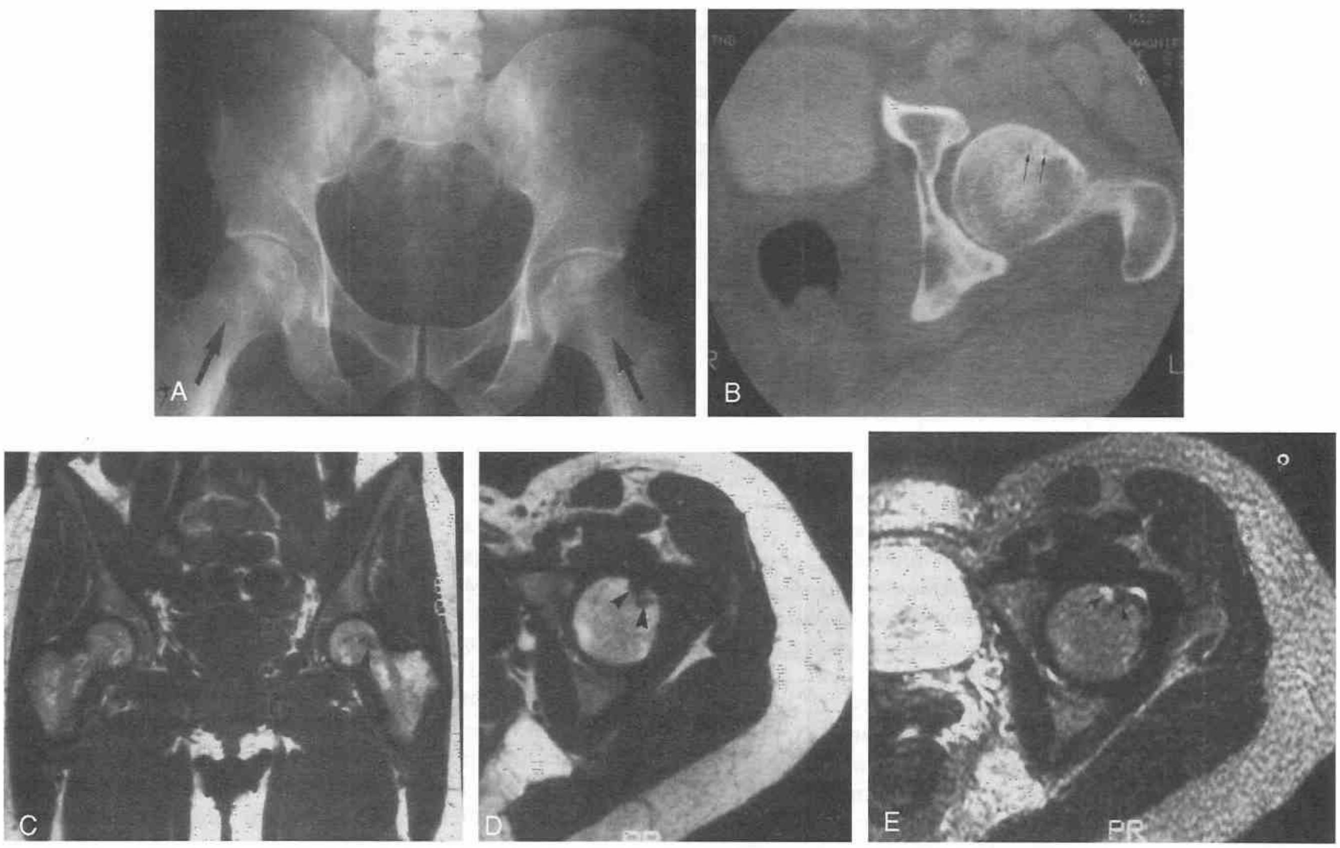

Figure 49–2. Conversion defects in asymptomatic patients. *A,* Pelvic radiograph shows large conversion defects bilaterally seen as subcapital lucencies with surrounding sclerosis *(large arrows)*. *B,* CT scan shows a small herniation pit in the anterior subchondral region *(small arrows)* with vertical extension toward the cortex. *C* and *D* T1-weighted MR images in the coronal *(C)* and axial *(D)* planes reveal herniation pits as focal areas of marrow replacement *(large arrowheads)*. This region reveals a channel-like appearance that extends toward the anterior cortex in the axial plane. *E,* Axial T2-weighted MR image reveals heterogeneous signal intensity in the conversion defect *(small arrowheads)*, consistent with both fluid and fibrocollagenous tissue.

Herniation pits, composed predominantly of fibrous tissue, remain low in signal intensity on all MR pulse sequences, whereas those with prominently fluid components show high signal intensity on T2-weighted MR images (see Fig. 49–2*E*).[156] The connection to the cortex can usually be detected by both CT and MRI (optimally seen in the axial plane) with a linear or channel-like appearance.

Herniation pits range in size from 5 mm to several centimeters and can enlarge over time.[162] The lesion's location and imaging characteristics should allow distinction from other pathologic considerations. Daenen and colleagues studied several patients with symptomatic herniation pits and noted this association with lesions larger than 1 cm in runners.[48] They postulated that the movement of the iliopsoas muscle may cause progressive invagination of soft tissue and may lead to symptoms in a small percentage of patients.

Proximal Femoral Focal Deficiency

Proximal femoral focal deficiency (PFFD) represents a congenital partial absence of the upper femur with resultant shortening.[173] The degree of deficiency of the proximal femur is extremely variable and can be difficult to assess adequately on radiographs.

Only limited use of CT and MRI in evaluating PFFD has been reported in the literature.[205] However, assessment is important in presurgical planning to guide orthopedic reconstruction because of the wide variation in the degree of the gap between the femoral head and subtrochanteric femur. This gap may be small with pseudarthrosis, or it may be filled with fibro-osseous tissue or devoid of connecting tissue.[173] MRI or CT can be used to assess this osseous gap and the femoral head, which is delayed in ossification (Fig. 49–3). These structures and the resultant coxa varus deformity cannot be adequately evaluated with radiographs because the gap is radiolucent, whether it is filled with fibro-osseous tissue or a tissue void.

CT shows the nonossified areas as soft tissue attenuation, although these areas can be difficult to distinguish from surrounding muscle. MRI is more valuable because of improved contrast resolution and multiplanar imaging capability. On MR images, the femoral head, if present, shows intensity of yellow marrow, whereas fibrous tissue is low in signal intensity on all pulse sequences (Fig.

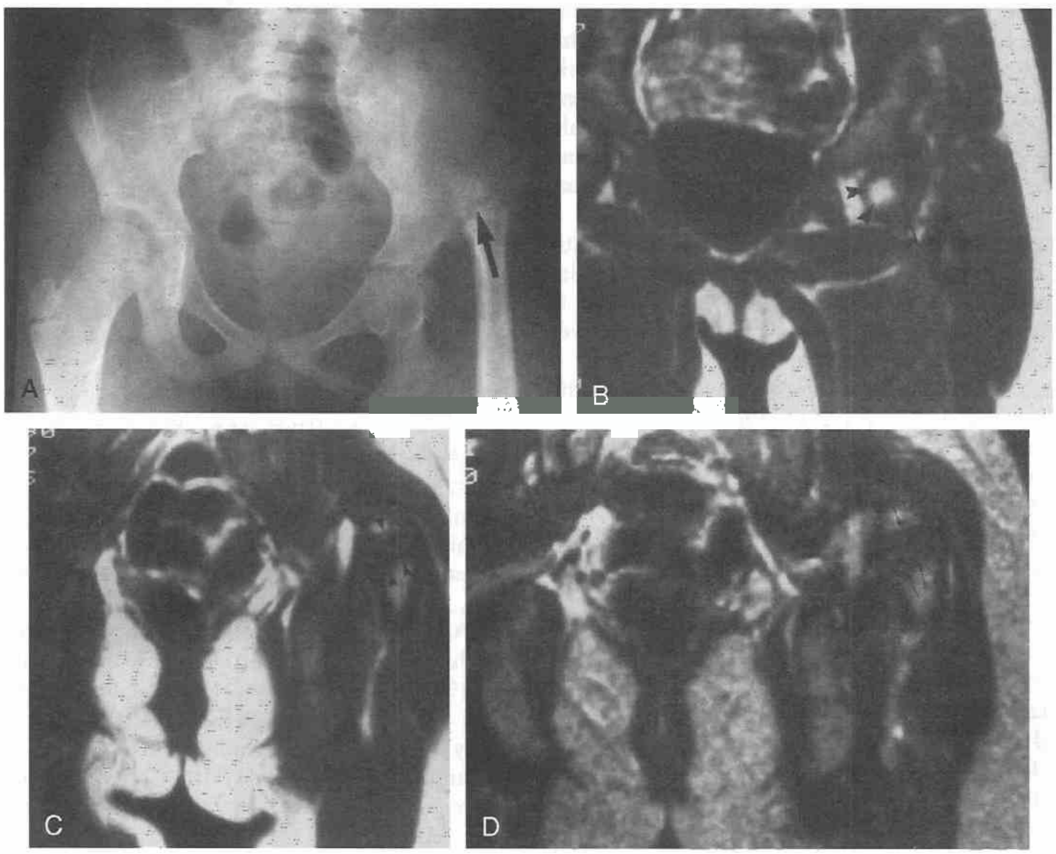

Figure 49–3. Proximal femoral focal deficiency in a 6-year-old child. *A,* Pelvic radiograph shows deficiency of the proximal femur with lucent cleft in upper portion of remaining femur *(large arrow)*. *B,* Coronal T1-weighted MRI was performed to evaluate for possible surgical reconstruction. The image shows a capital femoral epiphysis, seen as high signal intensity (fatty marrow) not well visualized on the radiograph *(large arrowheads)*. The femoral head, however, is not connected to the remainder of the femur, where there is intervening tissue *(open arrow)*, and thus cannot be used for reconstruction. *C,* More posteriorly, a coronal T1-weighted MR image shows the upper femur with a low-signal-intensity gap at its upper extent *(small arrowheads)*. *D,* T2-weighted coronal MR image shows that this area maintains low signal intensity, consistent with fibrous tissue *(small arrows)* rather than pseudoarthrosis, which may show high signal intensity.

49–3*B*, *C*, and *D*). Pseudarthrosis may show linear or bandlike high-intensity fluid on long TR images.[173] Evaluation of PFFD is often best accomplished with coronal images.

Rotation and Version Deformities

Abnormalities of rotation and version (degree of hip anteversion) may be congenital; more often, however, they are a result of trauma. CT and, more recently, MRI have been used to evaluate both types of abnormalities.[5, 6, 80, 93, 115, 145, 161, 180] Axial images obtained through the femoral head and neck and additional images of the distal femoral condyles are needed. From these images, measurements are obtained of both femoral eversion and rotational abnormalities. These deformities may require orthopedic correction with the use of osteotomies, and imaging is necessary to direct surgical management.

Labral Abnormalities

Historically, labral abnormalities as a cause of internal hip derangement have been difficult to evaluate both clinically and by imaging. With the advancement of hip arthroscopy, however, labral pathology as a cause of radiographically occult hip pain is not uncommon. In fact, this association was identified in 55% of 94 patients in one study.[83, 143] Detection of labral tears is important not only to identify the cause of symptoms but also to direct arthroscopic repair to prevent development of secondary osteoarthritis.[4, 66, 68, 91, 103, 155, 182, 209]

The normal acetabular labrum represents a fibrocartilaginous rim of tissue about the acetabulum. It is triangular in cross-section, arises directly from the acetabulum, is thickest posteriorly, and covers a 5- to 18-degree arc over the superior aspect of the femoral head.[44, 46, 88, 100, 107]

Two normal focal cartilage defects are seen about the hip: (1) the acetabular notch and (2) the fovea capitis of the femur. The notch is spanned by the transverse ligament, and the labrum blends with this structure. The ligamentum teres lies in the fovea capitis (Fig. 49–4). Several ligaments(i.e., iliofemoral, ischiofemoral, and pubofemoral) reinforce the hip joint capsule. The capsule inserts at the base of the labrum anteriorly and posteriorly, creating small perilabral recesses (see Fig. 49–4). However, the capsule attaches above the labrum superiorly, creating a larger recess is this region.[59, 101, 160, 224]

The normal labrum is triangular in cross-section and low in signal intensity on all MR pulse sequences. As with the shoulder, however, numerous normal variations in labral appearance may simulate pathology. In two studies, the labra of asymptomatic patients were triangular (in 66% to 80%), rounded (in 11% to 13%), flat (in 9%), or irregular (in 7%).[1, 121] In addition, both studies showed a reduction in a triangular shaped labrum in older patients, suggesting that this may represent a degenerative phenomenon (from 79%–96% to 41%–62%).[1, 121]

Absent labra have been described in 1% to 14% of individuals, although the significance of this finding (normal variation versus pathology) is uncertain.[1, 101, 121] Labra

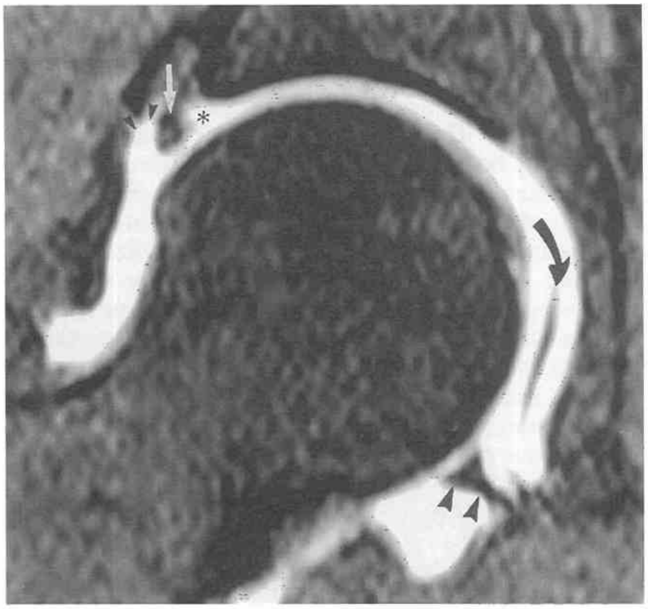

Figure 49–4. Partial superior labral detachment in a 40-year-old man. Coronal T1-weighted MRI arthrogram shows the superior labrum *(arrow)* with contrast at the acetabular junction *(asterisk)* representing partial labral detachment. Small perilabral recess *(small arrowheads)*, ligamentum teres *(curved arrow)*, and transverse ligament *(large arrowheads)* are also seen.

may have intermediate signal foci on T1-weighted and spin density–weighted MR images in 42% to 58% of patients.[1, 101, 121] Intermediate and high signal intensity may be seen in 37% and 13% of labra on T2-weighted MR images, respectively.[101] These areas may be linear, globular, or curvilinear and may extend to the labral margins.[101, 121] This increased signal intensity is more common in men, in the superior labrum, and with increasing patient age, suggesting a degenerative process.

Labral pathology is most frequently a tear or detachment, with the latter being the more common (see Fig. 49–4).[46, 47, 55, 68, 125] The superior and anterior labra are most often affected, while posterior involvement is more common in younger patients.[46, 47, 68, 144, 160, 182] As with meniscal tears, the defects may be classified as radial in orientation, degenerative, bucket-handle, horizontal cleavage, and peripheral longitudinal.[125, 158, 160, 169]

Although a description of technique is beyond the scope of this chapter, MR arthrography has increased the sensitivity (90%) and accuracy (91%) in detection of labral pathology versus standard MRI (30% sensitivity, 36% accuracy).[46, 47] This is primarily a result of the ability to distinguish true pathology from a normal variation. Labral tears are diagnosed by the presence of contrast material in the substance of the labrum. Labral detachment shows contrast material separating a portion of the labrum with or without displacement.

Staging of labral pathology has been described by Czerny and colleagues[46, 47]:

Stage 0 labra are normal with homogeneous low signal intensity, a triangular shape, and an unremarkable acetabular-labral interface and perilabral sulcus.

Stage 1 labra demonstrate an intralabral signal that does not extend to the labral margin.
Stage 2 labra show contrast material on MR arthrography extending into the labra.
Stage 3 labra reveal detachment.

These stages are further subdivided into A and B, with B showing hypertrophy and obliteration of the perilabral sulcus.

The significance of an abnormal labral shape is more difficult to assess. Absence of the labrum should be considered abnormal except anterosuperiorly. Irregular labral margins may represent degenerative fraying.[101, 160] Labral hypertrophy is abnormal and may be related to altered mechanics secondary to tear or detachment.

A sulcus between the labrum and underlying acetabulum may be a normal variation and is not uncommon on MR arthrography.[46, 47, 160, 220] Perilabral cysts are commonly associated with labral pathology, particularly detachments.[133, 185] These cysts (previously referred to as *ganglia*) may extrinsically erode the adjacent acetabulum, suggesting a more aggressive process on radiographs. There is an increased incidence of perilabral cysts in patients with DDH.[55, 81, 117, 142] Articular cartilage defects are also commonly associated with labral pathology, although the reliability of MRI in this assessment is uncertain.

Synovial Abnormalities

Abnormalities primarily involving the cartilage and synovium of the hip are common. These include (1) *arthritis* (osteoarthritis, inflammatory arthropathy) and (2) the more infiltrative disorders, such as *pigmented villonodular synovitis* (PVNS), *synovial chondromatosis*, and *amyloidosis*.

Arthropathy

Radiography remains the primary modality by which arthropathy of the hip is evaluated. However, CT and MRI can provide valuable information about the extent of disease, visualization of the surrounding soft tissue involvement, and a means of identifying other causes of hip pain. Detection of hyaline cartilage thinning and focal defects in osteoarthritis continues to challenge the contrast and spatial resolution capabilities of MRI. The clinical use of the CT and MRI in evaluation of osteoarthritis of the hip continues to be relatively limited.[28, 127] Rarely, hip osteoarthritis can be rapidly progressive (coxarthrosis), simulating infection or neuropathic disease.[176]

Involvement of the hip by inflammatory arthritis, both rheumatoid arthritis and the seronegative spondyloarthropathies, is not infrequent. Because the hip is a relatively noncapacious joint space, radiographs demonstrate erosions relatively early in the disease. MRI and, to a much lesser degree, CT can detect the extent of synovial hypertrophy *(pannus)* that is common to all inflammatory arthritides but not evident on radiographs (Fig. 49–5).[172, 189, 231]

Pannus generally shows low signal intensity on T1-weighted MR images and high signal intensity on T2-weighted MR images. Pannus can be difficult to differenti-

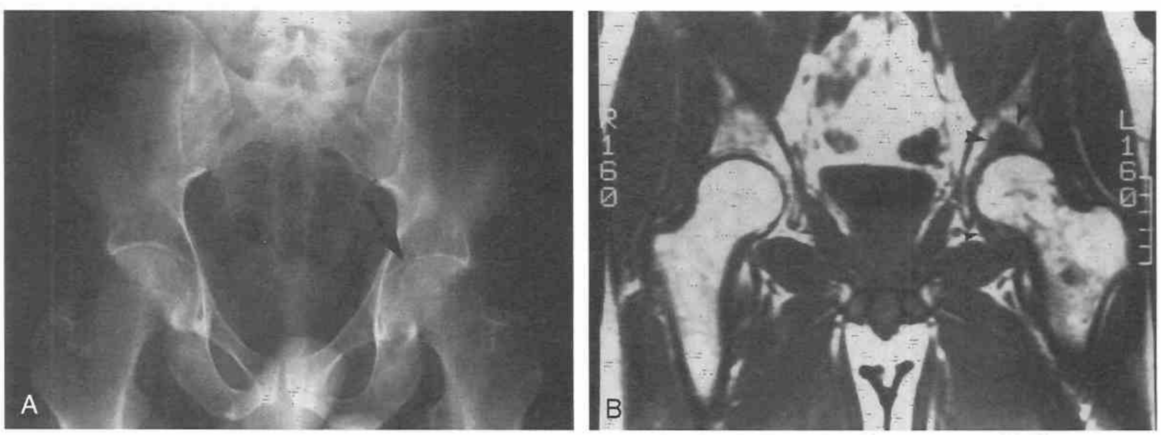

Figure 49–5. Monoarticular left hip pain of 6 months' duration in a 29-year-old man. *A,* Radiograph of the pelvis shows mild axial narrowing of the hip without erosions *(large arrow)*. *B,* Coronal T1-weighted MR image shows soft tissue thickening (synovitis) about the hip of intermediate intensity *(small arrowheads)* and acetabular erosion (*large arrowheads*). *C,* On the T2-weighted coronal MR image, synovitis reveals increased intensity *(small arrowheads)* and heterogeneous signal intensity in the acetabular erosion *(large arrowheads),* suggesting a fibrous component to the tissue. Erosion was not visible by CT (not shown), and low-grade infection could not be excluded. The patient had a history of psoriasis with subsequent development of polyarticular disease, typical of psoriatic arthritis in other joints.

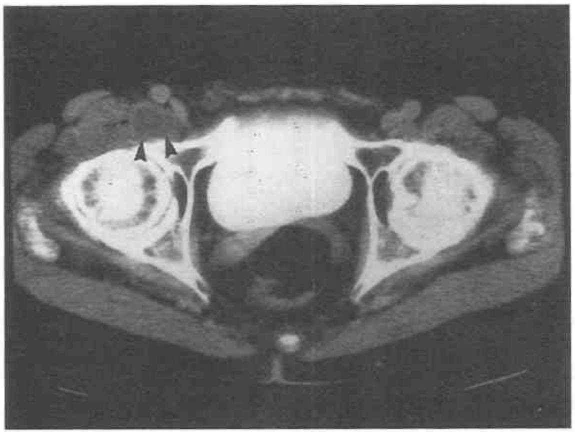

Figure 49–6. CT scan shows an iliopsoas bursal fluid collection *(arrowheads)* with a higher-attenuation fibrous wall *(arrows)* resulting from iliopsoas bursitis.

ate from synovial fluid, which is also frequently present with involvement of the hip by inflammatory arthritis. Subtle differences between pannus and synovial fluid may be apparent on both T1-weighted and T2-weighted images. Pannus, compared with synovial fluid, usually shows a slightly higher signal intensity on short TR images and has more heterogeneous and mildly lower signal intensity on long TR images (Fig. 49–5*B* and *C*). Intravenous (IV) gadolinium injection can facilitate the distinction.[172] Areas of synovitis and pannus formation enhance dramatically and diffusely after gadolinium injection, whereas synovial fluid shows only peripheral contrast enhancement.[2, 24, 106] Imaging should be performed early after contrast injection because synovial fluid also shows enhancement by diffusion on delayed images.[114, 171, 173]

Compared with radiography, both CT and MRI demonstrate osseous erosions more clearly because of improved delineation of exposed cortical surfaces.[172, 232] In addition, MRI provides multiplanar imaging capabilities. Bursal extensions from the hip joint (Fig. 49–6) can also be detected by CT and MRI and are not infrequently seen in patients with inflammatory arthritis, particularly rheumatoid arthritis.[131, 132] Pannus may occasionally retain relatively low signal on T2-weighted MR images (Fig. 49–5*C*). This phenomenon may be the result of hemorrhage and deposition of hemosiderin (paramagnetic effect shortening T2 relaxation time) or fibrosis in more chronic areas of inflammation.[2, 24] Fibrotic components in pannus are often more prominent in the seronegative spondyloarthropathies and may reflect more inactive disease or therapeutic effect.

Overall, MRI of inflammatory arthritis of the hip can be very useful. It allows determination of the extent of pannus formation as well as the degree of bone erosion and articular cartilage thinning. Knowledge of these factors is important in patient management. MRI can also be used to monitor the effects of therapy by quantitating the volume of pannus.[171, 173]

Infiltrative Disorders

Pigmented Villonodular Synovitis

PVNS represents benign synovial hypertrophy with a variable degree of histologic components, including villous or nodular synovial hypertrophy as well as pigment deposition of hemosiderin. PVNS occurs in 2 to 11 individuals per million, with relatively equal incidence in men and women.[56, 62, 76, 173] It is almost always a monoarticular disease and usually affects individuals in their second to fourth decades of life.

There are two basic forms of PVNS:

1. The *localized* form often involves the fingers and accounts for approximately 75% of cases.[14, 94, 98] Also referred to as *giant cell tumor of the tendon sheath* (GCTTS), it may involve tenosynovial tissues about the hip.
2. The *diffuse* form frequently affects larger joints.[56] The knee is most commonly involved, and the hip joint is the second most frequently affected articulation.

The pathogenesis of PVNS is unknown; possible causes include neoplasia, sequelae from a synovial hemangioma, disorders of lipid metabolism, repetitive trauma, and the most commonly supported theory of an inflammatory process. Patients with PVNS often complain of long-standing joint pain and decreased range of motion.

Radiographic changes are more frequently seen with PVNS of the hip than of the knee. This is a result of the relative nondistensibility of the hip joint, with synovial thickening causing early extrinsic pressure erosions in most cases (90% to 95%).[76] These extrinsic erosions on both sides of the joint are well visualized by both CT and MRI (Fig. 49–7).

Coronal and axial MR images often demonstrate the erosive changes and their relationship to the hip joint to best advantage. CT and MRI reveal nodular synovial masses, and there is associated joint effusion in nearly 80% of cases.[173] This effusion, when aspirated, is a xanthochromic to brownish-stained bloody fluid. On CT scans, there is soft tissue thickening about the hip, and the synovial-based masses often have higher attenuation than the surrounding muscle because of hemosiderin deposition.[35, 51] These areas of focal synovial masses are usually associated with localized pockets of joint effusion that may extend into the iliopsoas and obturator bursae. Injection of dilute contrast medium, followed by CT examination, reveals nodular filling defects and synovial thickening identical to the findings at arthrography (Fig. 49–7*B*).

MRI of the diffuse form of PVNS is usually characteristic.[21, 95, 108, 132] Synovial thickening with nodular excrescences arising from the joint surface is well delineated on MRI. These areas are of heterogeneous signal intensity on all pulse sequences, with prominent low signal intensity on long TR images (Fig. 49–7*C* and *D*). The hypointensity is caused by hemosiderin deposition. Specifically, the unpaired electrons of iron in the ferric state (Fe^{+3}) interact with adjacent water molecules, which results in the shortening of the T2 relaxation time.[95, 132, 193] These effects are directly related to the square of the magnetic field and are thus accentuated with high-field-strength MR units.[95, 132, 193] Focal areas of synovial fluid, low intensity on T1-weighted images and high intensity on T2-weighted images, are also usually present within the hip joint involved by PVNS. Typically, these fluid collections in PVNS are surrounded by a peripheral rind of low-intensity hemosiderin-laden tissue on T2-weighted MR images. The areas of synovial

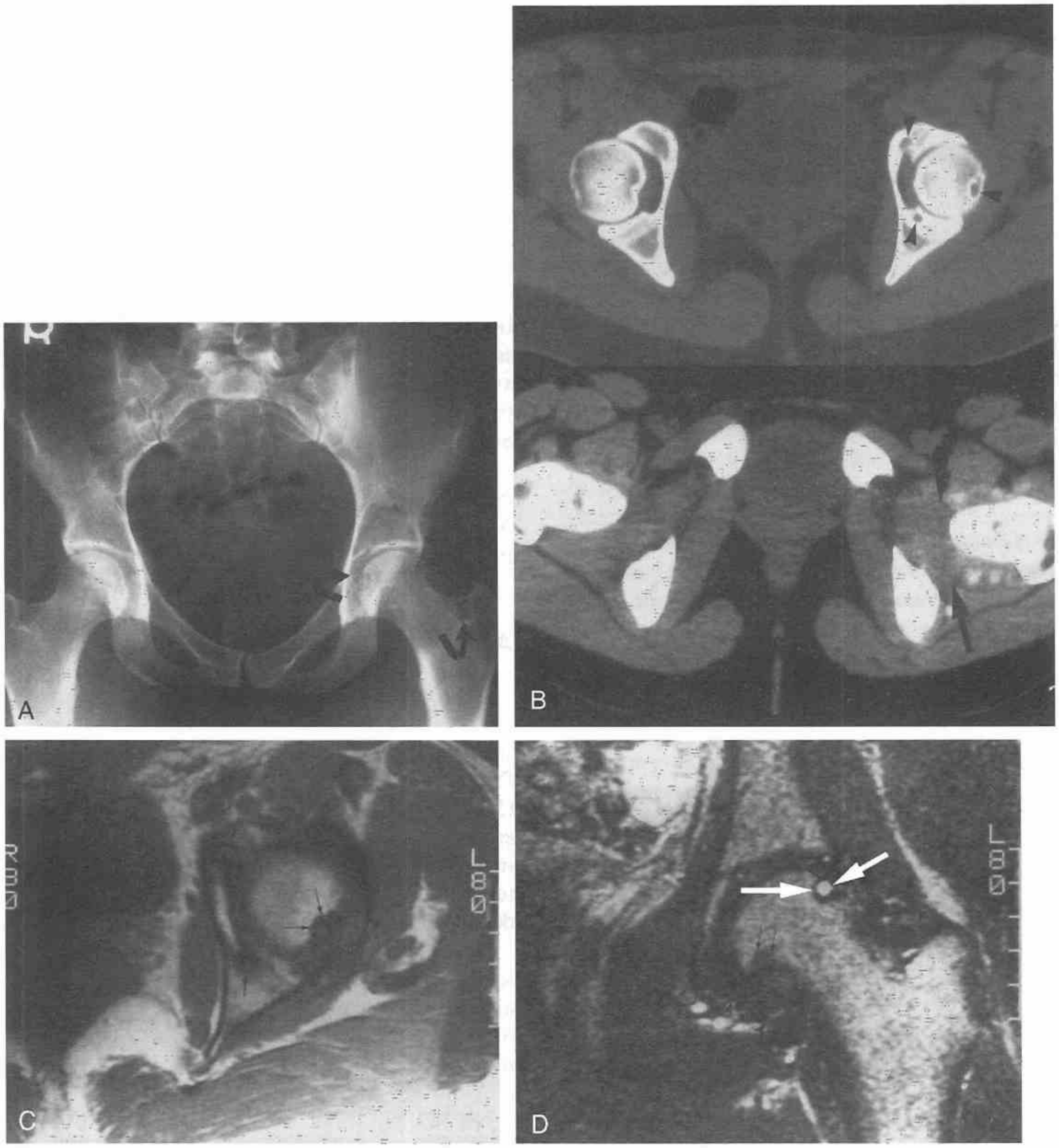

Figure 49–7. The patient is a 27-year-old woman with a 5-year history of left hip pain. *A,* Pelvic radiograph shows extrinsic erosive changes *(curved arrows)* on both sides of the joint. *B,* CT scans before *(B, top)* and after intra-articular contrast injection *(B, bottom)* also reveal extrinsic erosions of acetabulum and femur *(large arrowheads)* and soft tissue thickening displacing the contrast *(large arrows)*. *C* and *D,* Axial T1-weighted *(C)* and coronal T2-weighted *(D)* MR images reveal extensive thickening about the hip *(small arrowheads)*, causing extrinsic osseous erosions seen as areas of marrow replacement *(small arrows)*. Most of this material maintains low signal intensity on the long TR/TE image, although pockets of high-signal-intensity fluid are seen on the T2-weighted image. This appearance is due to hemosiderin in this patient with pigmented villonodular synovitis, confirmed at surgical synovectomy.

proliferation are hypervascular and may show significant enhancement after IV contrast injection using either CT or MRI.

The localized form of PVNS infrequently involves the tenosynovial tissues about the hip. GCTTS is more variable in the degree of hemosiderin deposition. CT or MRI may show characteristics similar to those of diffuse PVNS with low signal intensity on T1-weighted and T2-weighted images in cases with extensive hemosiderin.[14, 94, 98] MRI, however, may be less distinctive in cases of GCTTS by showing significant intermediate to high signal intensity within a mass adjacent to the hip on long TR images resulting from cases with limited hemosiderin.[14, 98]

MRI and CT are important in follow-up of patients with PVNS to detect recurrences, which are common. Synovectomy is the usual initial treatment; however, because of the difficulty in removing all synovial tissue, estimates of recurrence are as high as 40% to 50% with the diffuse form.[69] External radiation therapy and injection of a beta-emitting agent into the joint tagged to radiocolloid, producing a nonsurgical synovectomy, may be used as adjuvant treatment methods.[173] Recurrent disease is identical in ap-

pearance to the initial characteristics previously described on both CT and MRI.

Synovial Chondromatosis

Synovial chondromatosis is caused by the occurrence of cartilage metaplasia within the synovial membrane.[146, 219] Although many authors consider this a neoplastic disorder, inflammatory and traumatic etiologies have also been postulated.[92] The disease is usually seen in those between ages 20 and 50 years and is twice as frequent in men. Typical clinical symptoms include joint pain of long duration and locking with limitation of range of motion.

Cartilage metaplasia within the hyperplastic synovium is seen pathologically in synovial chondromatosis.[146, 219] These villous nodules often become detached from the synovium and are then free intra-articular bodies. The intra-articular fragments of cartilage may grow, deriving nourishment from synovial fluid, or reattach to the synovial lining, where they may grow or may be reabsorbed. The cartilage fragments may undergo endochondral ossification, at which point the term *synovial osteochondromatosis* is appropriate. The synovial tissue of the tendons or bursa about the hip may also be involved by an identical process termed *tenosynovial* or *bursal chondromatosis*, respectively.[99]

In 70% to 95% of cases of synovial chondromatosis, the cartilage fragments calcify. These areas often have a diagnostic ring-type appearance on radiographs (Fig. 49–8).[173] CT is often the optimal examination for detecting, characterizing, and localizing these chondroid bodies (Fig. 49–8*B*).[25, 30] Smaller chondroid bodies are often solidly calcified on CT scans. CT may reveal ossification of the cartilaginous bodies with a cortical rim and trabecular bone centrally containing yellow marrow. A target appearance may be demonstrated because at times there is a central dot of chondroid tissue with calcification.

The MRI appearance of synovial chondromatosis is variable, depending on the degree of cartilage, calcification, and ossification.[33, 34, 43] Because hyaline cartilage is composed of 75% to 80% water, noncalcified cartilaginous tissue shows low to intermediate signal intensity on T1-weighted images and very high signal intensity on T2-weighted images.[111] Calcified intra-articular bodies show low signal intensity on all MR pulse sequences (Fig. 49–8*C*); however, smaller fragments are better detected by CT or radiographs.[33, 34, 43] The MRI appearance of ossification is low signal intensity on all pulse sequences if it is composed of cortical bone; if it is composed of trabecular bone, it has the intensity of fat (high signal intensity on T1-weighted images, intermediate signal intensity on T2-weighted images).

A target appearance corresponding to the osteochondral bodies on MRI may also be apparent. MRI and CT may reveal an associated joint effusion. Soft tissue thickening about the hip in the noncalcified areas of cartilage metaplasia reveals attenuation similar to or less than that of muscle on CT scans. On MR images, synovial chondromatosis may show low-signal-intensity areas (corresponding to calcified chondral bodies) on all pulse sequences surrounded by high-signal-intensity fluid or noncalcified cartilage metaplasia on T2-weighted images, an appearance exactly opposite of that of PVNS (see Fig. 49–7 and Fig. 49–8). On long TR images, low-signal-intensity fibrous septation may be present within the synovial metaplasia. CT and MRI may show extrinsic erosion and secondary osteoarthritis, a finding more common when synovial chondromatosis involves the hip, as opposed to larger joints such as the knee, because of the hip's relative lack of distensibility.[157, 195, 198]

In rare circumstances, synovial chondromatosis may undergo malignant degeneration to chondrosarcoma.[173] Identification by CT or MRI of osseous invasion or destruction should suggest this complication.

Multiple intra-articular osteochondral bodies may also be apparent after involvement of the hip joint by infection, trauma, or arthritis. This process, often termed *secondary synovial chondromatosis*, should be distinguished from the primary type by associated changes about the hip joint. In addition, the osteochondral bodies are fewer in number, are more varied in size, and show multiple rings of growth with calcification and ossification, creating an appearance of lamination. This multiple ring appearance is not seen in primary synovial chondromatosis.[146, 219]

Amyloidosis

Amyloid deposition within the tenosynovial tissue and osseous structures about the hip occurs more commonly with secondary amyloidosis than with primary amyloidosis. Primary amyloidosis is associated with multiple myeloma (5% to 10% of patients) and chronic inflammatory diseases.[11, 37, 130, 173] Patients with chronic renal failure receiving long-term hemodialysis are being increasingly reported to show a unique form of secondary amyloidosis with deposition of β_2-microglobulin.[15, 37, 40, 72]

Camacho and coworkers reported an incidence of amyloidosis of 35% in a group of 88 patients receiving hemodialysis longer than 4 years.[36] In the future, however, use of newer membranes in hemodialysis to better filter β_2-microglobulin may decrease the incidence. All forms of amyloidosis appear to have some proclivity for deposition about the hip, both within bone and within tenosynovial tissue. Osseous lesions usually have a punched-out appearance, are eccentric, or occur from extrinsic erosion, and they reveal a thin sclerotic margin on radiographs and CT scans. MR images show marrow replacement on T1-weighting (Fig. 49–9*A*).

Femoral lesions often predispose to pathologic fracture. Both CT and MR images reveal diffuse thickening about the joint with intra-articular deposition of amyloid. This thickening has an appearance on CT scans and a signal intensity on T1-weighted MR images similar to those of muscle attenuation. Interestingly, T2-weighted MR images show that the signal intensity within the amyloid deposition remains low to intermediate, although high signal intensity from focal fluid collection is also often present (Fig. 49–9*B*).[132, 178] Pathologically, this low signal intensity is probably related to the fibrillar, collagen-like composition of amyloid. Injection of IV contrast material may reveal enhancement of the synovial thickening on CT and MR images (Fig. 49–9*C*). The MR and CT appearance is similar to that of PVNS; in contrast to monoarticular disease in PVNS, however, amyloidosis is typically polyarticular

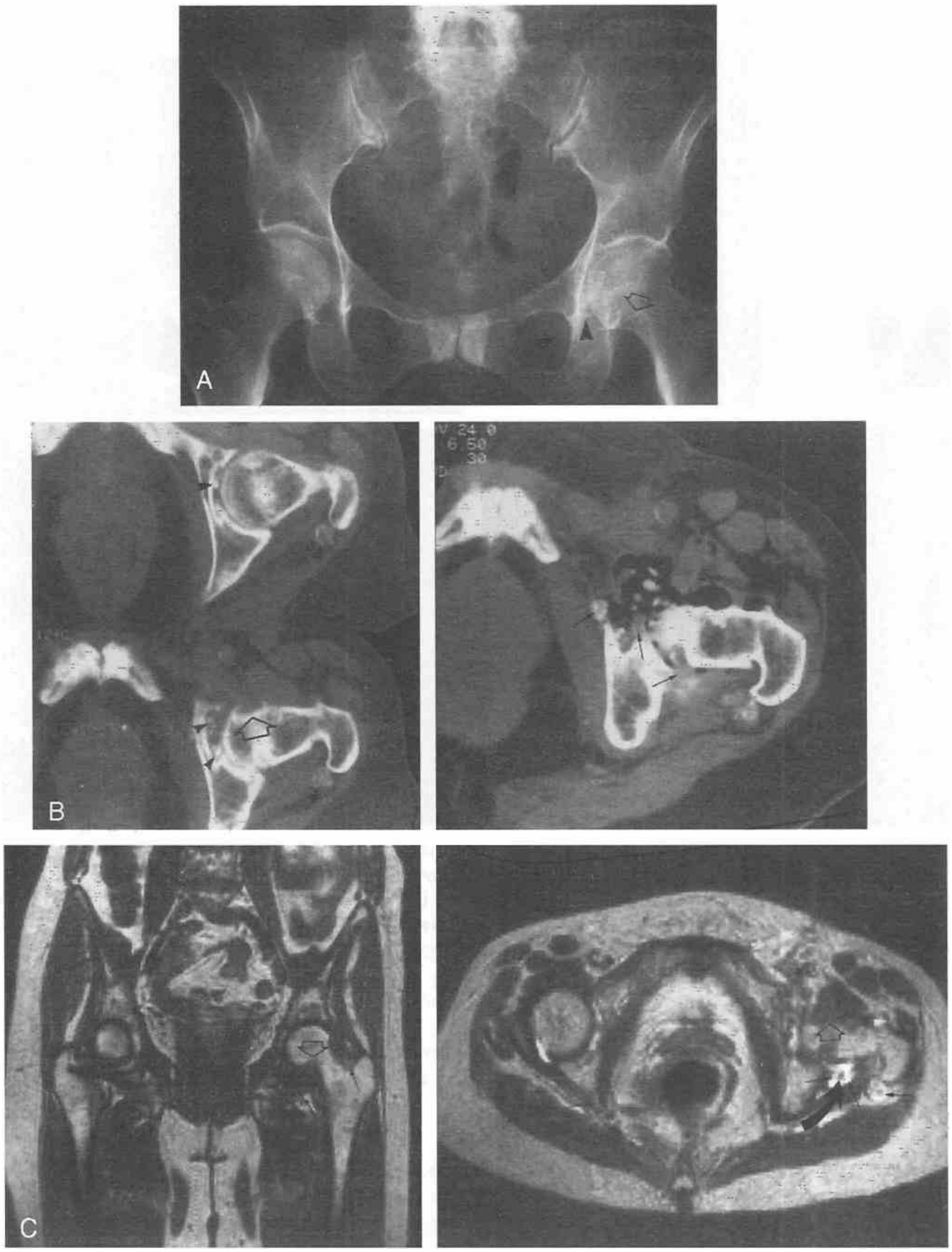

Figure 49–8. The patient is a 67-year-old woman with a 2-year history of left hip pain caused by synovial chondromatosis. *A,* Pelvic radiograph shows subtle multifocal areas of calcification about the hip *(large arrowheads)* with extrinsic erosion *(open arrow). B,* CT scans, before *(left)* and after *(right)* intra-articular air injection reveal calcifications *(small arrowheads),* some of which have a typical ringlike appearance of cartilage and extrinsic erosion of bone *(open arrow).* After intra-articular injection, nodular soft tissue areas of synovial metaplasia and calcification *(small arrows)* are surrounded by air. *C,* Coronal T1-weighted *(left)* and axial T2-weighted *(right)* MR images show thickening about the hip *(small arrows)* and extrinsic erosion *(open arrow).* High signal intensity on the T2-weighted image represents fluid and synovial metaplasia *(small arrows),* with a filling defect representing a calcified fragment *(curved arrow).*

with bilateral hip involvement reflecting that it is a systemic process.[173]

Hemophilia, an X-linked recessive genetic disorder caused by deficiency of clotting factor, is associated with repetitive, intra-articular, intramuscular, and intraosseous episodes of bleeding.[173] With each bleeding episode, hemosiderin is progressively deposited within the synovial membrane, ultimately resulting in synovial hypertrophy and pannus formation. Although hip involvement is not frequent, the hip may show progressive joint destruction and spontaneous dislocation. MRI and CT reveal synovial thickening, and on long TR images the hemosiderin-laden synovial tissue stays low to intermediate in signal intensity, as with PVNS.[113, 225, 231]

Synovectomy can be helpful in patient treatment; however, it must be performed before cartilage destruction

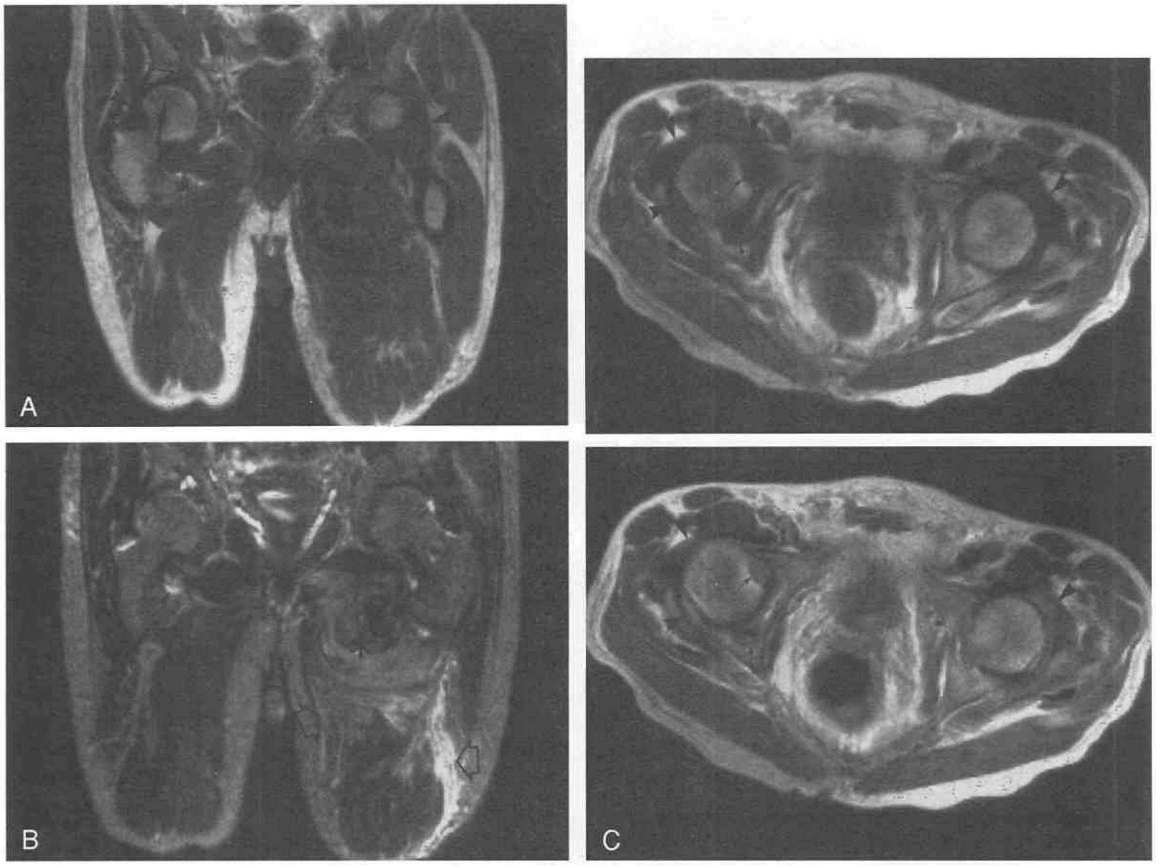

Figure 49–9. Renal failure in a 43-year-old man undergoing chronic hemodialysis. *A* and *B*, Coronal T1-weighted *(A)* and T2-weighted *(B)* MR images show thickening of the tissues about both hips *(large arrowheads)* with marrow replacement from acetabular erosions *(small arrow)*. The image in *B* reveals that much of this tissue remains low in signal intensity, although pockets of high intensity fluid *(small arrowheads)* are present. There is a focus of decreased marrow signal from avascular necrosis on the right *(large arrow)*. Histologic evaluation of this tissue revealed amyloid deposition. The large mass in the left medial thigh *(asterisk)* in *A* and *B* represents a spontaneous hemorrhage resulting from heparin administration during dialysis. The hematoma has areas of high signal intensity on T1-weighted and T2-weighted images with heterogeneity. There is marked associated edema *(open arrows)* on the long TR images owing to hemorrhage dissecting throughout the surrounding tissues. *C*, Axial T1-weighted preintravenous *(top)* and postintravenous (*bottom*) gadolinium injection also shows extrinsic erosions *(small arrows)* and thickening about the soft tissue of the hip, which enhances with contrast *(large arrowheads)*. The changes about the hips are related to amyloid deposition.

occurs. MRI can also be useful in this determination.[86] In patients with hemophilia, areas of soft tissue or intraosseous hemorrhage also occur about the hips.

Hermann and colleagues described soft tissue hemorrhage on MRI with acute hematoma (1 to 6 days) having an appearance similar to that of muscle on T1-weighted images and having low signal intensity on long TR images.[86] Beyond 1 week after hemorrhage, signal intensity increases on both T1-weighted and T2-weighted images. These hematomas may subsequently ossify (myositis ossificans or heterotropic bone formation) with cortical bone peripherally and trabecular bone with yellow marrow centrally. This zonal pattern of ossification, beginning peripherally, is distinctive and is best detected in its earliest phases by CT.

Infection

Infection of the bone or soft tissue about the hip or septic arthritis is often very difficult to detect on initial radiographs. Osseous manifestation of osteomyelitis, such as bone destruction and periosteal reaction, may not be apparent on radiographs for 10 to 14 days after the onset of infection.[173] The metaphysis of the proximal femur is intra-articular because the hip capsule attaches in the intertrochanteric region. Infection localized to this region, a common pattern in children because of the normal vascular supply, may thus gain rapid access to the joint if the process extends through the osseous cortex.[74] Bacterial infection of the hip joint can then lead to rapid and irreparable cartilage damage and joint destruction.

Early recognition of osteomyelitis, septic arthritis, and soft tissue abscess about the hip is thus imperative in order to prevent these dire sequelae and to improve clinical outcome. CT and MRI help to distinguish inflammation, such as cellulitis, from abscess formation.[151]

Osteomyelitis

Osteomyelitis about the hip is most commonly caused by hematogenous seeding; however, other sources of spread

include a contiguous soft tissue infection, direct implantation, such as from a puncture wound, or after surgery.[173] Although CT and MRI findings in osteomyelitis may be nonspecific, both modalities are sensitive indicators of infection of the marrow space in the appropriate clinical setting (Fig. 49–10).[151]

CT changes indicative of osteomyelitis are cortical destruction (particularly with osteomyelitis arising from contiguous spread), periosteal reaction, and increased attenuation within the marrow space.[12, 74] Inflammation in the surrounding soft tissues is also often visualized on CT, seen as muscle and skin thickening, and soft tissue stranding in the subcutaneous fat.

MRI is superior to CT in identifying acute osteomyelitis, primarily because of its improved contrast resolution.[16, 20, 74, 151] Acute osteomyelitis reveals replacement of fatty marrow with low to intermediate signal intensity on T1-weighted and with high signal intensity on T2-weighted images.[63, 151, 200] These changes represent inflammatory and edematous tissue and usually demonstrate ill-defined margins with similar changes in the surrounding soft tissues. The sensitivity of MRI in detecting osteomyelitis has been reported by Erdman and colleagues to be up to 98%; however, specificity was lower at 82%.[63] Both sensitivity and specificity of MRI are superior to those of CT and scintigraphy.[61, 63, 74]

The degree of activity in sites of chronic osteomyelitis often creates a clinical dilemma. Identification of new bone destruction, as well as the presence of irregular periosteal reaction and *sequestra* (small sclerotic avascular bone fragments surrounded by granulation tissue), suggests active osteomyelitis. CT can be valuable in detecting these findings, particularly sequestra (Fig. 49–10*B*).[12, 74] Although by definition sequestra are not infected, they provide an ideal milieu for organisms and must be considered foci of residual infection in the appropriate clinical setting. It is our belief that because of improved spatial resolution, CT is better to detect sequestra; overall, however, MRI may be superior to all other methods (including indium white blood cell scanning) in identifying active areas of osteomyelitis.[139]

On T1-weighted MR images, marrow replacement is

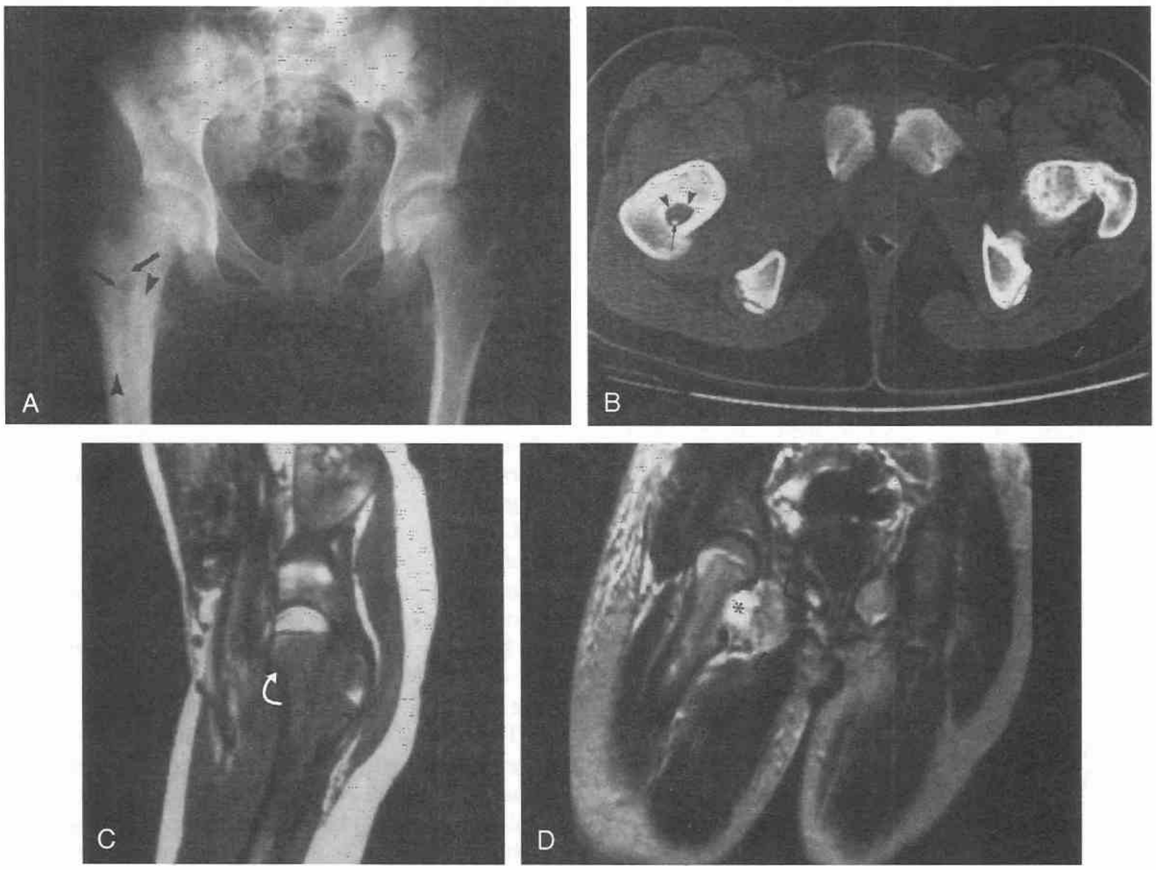

Figure 49–10. The patient is a 13-year-old girl with a 1-year history of intermittent right hip pain, now worsening with fever and clinical signs of sepsis. The patient had a history of bladder infection caused by *Staphylococcus aureus* 1 year earlier.
A, Pelvic radiograph shows channel-like lucency *(large arrows)* with associated sclerosis *(large arrowheads)* in the proximal femur.
B, CT shows a Brodie abscess *(small arrowheads)* with sequestra *(small arrow)*. There is soft tissue thickening posteriorly, although focal fluid is not seen. *C,* Sagittal T1-weighted MR image reveals marrow replacement in the proximal femur *(curved arrow)* with a channel-like abscess *(small arrowheads)*. *D,* Coronal T2-weighted MR image shows soft tissue changes of focal abscess *(asterisk)* and more diffuse edema *(open arrows)* posteromedially. The intraosseous abscess had extended into the soft tissues, causing the patient's acute symptoms. Both soft tissue and an intraosseous abscess were drained at surgery; culture revealed *S. aureus* as the causative organism. Soft tissue abscess was larger on a more posterior coronal T2-weighted MR image (not shown).

seen in chronic osteomyelitis because of fibrosis and osseous sclerosis regardless of the activity of the infection. On T2-weighted MR images, however, active foci of infection show high signal intensity.[41, 43, 131, 137, 139, 200]

On T1-weighted and T2-weighted images, sequestra have low signal intensity; on long TR images, however, the surrounding inflammatory tissue shows a high-intensity halo. Subacute osteomyelitis, such as a Brodie abscess, can be identified on CT and MRI as a focal, intraosseous fluid collection, often lobulated or showing focal areas of elongation or channel-like extensions with surrounding sclerosis (Fig. 49–10*B, C,* and *D*).[131, 137] The fluid may be complex and, compared with simple fluid, may have higher attenuation or signal intensity on T1-weighted MR images. The surrounding sclerosis has low signal intensity on all MR images.

Soft Tissue Infection

Soft tissue infection about the hips can involve the joint or surrounding muscles. In the appropriate clinical setting localized fluid collection usually requires fluid drainage for adequate treatment. CT and MRI are helpful because of their ability to identify anatomically localized fluid collections. CT and MRI changes suggesting an infected fluid collection are internal debris or septations and a thick wall (best seen on postcontrast images with enhancement).[50] The abscess wall often has intermediate signal intensity on T1-weighted images, perhaps as a result of increased protein content.

MRI, again because of its improved contrast resolution, is superior to CT in detecting fluid collections (see Fig. 49–10*D*). CT should be performed with IV contrast material when the possibility of an abscess is considered.[12, 74] The absence of focal fluid collections by imaging essentially excludes localized soft tissue infection.

The location of the fluid collection about the hip determines the infected site: septic joint, bursitis, tenosynovitis, soft tissue abscess, or sinus tract or fistula (see Fig. 49–10*D*). Septic bacterial arthritis involving the hip joint is a surgical emergency (see earlier) because of the rapid cartilage destruction that can result.

Hip joint infection is common in infancy and childhood. CT and MRI show nonspecific joint fluid. MRI, in addition, can reveal early cartilage destruction indicative of infection. More indolent infections, including tuberculous and fungal forms, often result in a prominent synovitis, and the MRI appearance may simulate a noninfectious inflammatory arthritis. However, any case of monoarticular arthritis should be considered infectious until proved otherwise.

Osteomyelitis is frequently associated with septic arthritis of the hip because of both joint anatomy and cartilage loss, which expose underlying bone to infection. Tendons involved by infection reveal fluid within the sheath. This fluid surrounds the tendon, which has high attenuation on CT and low signal intensity on all MR pulse sequences. Soft tissue abscess may be superficial or deep focal fluid collections. Cellulitis has an appearance of inflammation or edema, with muscle and skin thickening and soft tissue stranding in the subcutaneous tissue on CT as well as diffuse heterogeneous linear high signal intensity seen on T2-weighted MR images.[16, 20, 200]

CT and MRI allow distinction of the nonlocalized changes of cellulitis from the focal fluid collection of a soft tissue abscess (see Fig. 49–10*D*). This determination is vital to guide patient management because cellulitis is treated medically, whereas abscess is treated with drainage. MRI often reveals slightly higher signal intensity with T1-weighting about infected focal fluid collections (bone or soft tissue).

Sinus and fistula tracts are more common in adults and are seen as linear tracts on CT and MR images. On CT scans, these tracts have high-attenuation walls; on long TR images, high signal intensity often represents fluid in the tracts. Sinus tracts are not unusual sequelae of osteomyelitis of the ischial tuberosities in paraplegic patients with chronic decubitus ulcers (Fig. 49–11). These sinus tracts may seed the hip joints, causing septic arthritis, osteomyelitis, and joint destruction.

Trauma

Trauma about the hip is common. The two most frequent types of fractures involve the acetabulum and the proximal femoral neck.

Acetabular *fractures* and fracture dislocations are usually caused by motor vehicle accidents, and the complex anatomy and fracture patterns frequently require additional imaging beyond radiographs. *Femoral neck fractures* are often easily diagnosed on radiographs, although some injuries are quite subtle, requiring additional imaging.

Acetabular Fractures

Acetabular fractures constitute between 20% and 25% of all pelvic fractures in adults.[188] These fractures have a high association with concomitant injuries to the genitourinary system and vascular structures. Radiographs with oblique (Judet) views are often difficult to evaluate in determining the extent of involvement for presurgical planning.[97, 124]

CT is the modality of choice for evaluation of these injuries.[78, 82] Axial images should be performed with contiguous slices not thicker than 3 mm. Sagittal and coronal reconstructions and three-dimensional (3D) images are often helpful for the radiologist, and—more importantly—for the orthopedic surgeon, to conceptualize the fracture pattern before surgery.[52, 67, 124, 138, 181]

The normal acetabulum is formed by two columns, one *anterior* (iliopubic) and the other *posterior* (ilioischial); these unite superiorly in the shape of an inverted Y. Medially, the bone between the anterior and posterior columns is the quadrilateral plate, and the acetabular socket is completed superiorly by the weight-bearing surface, called the *roof.*[191] Acetabular fractures can be divided into five basic or elementary patterns:

- Posterior wall
- Posterior column
- Transverse
- Anterior column
- Anterior wall

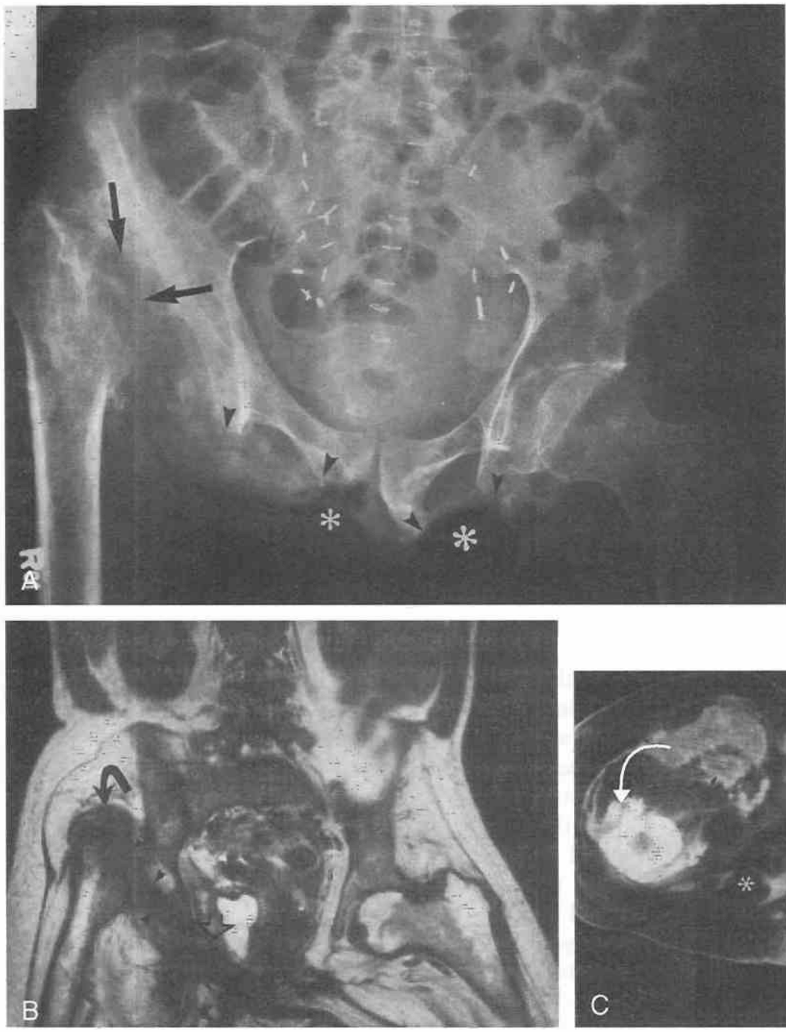

Figure 49–11. The patient is a paraplegic 35-year-old man with chronic decubitus ulcers and fever. *A*, Pelvic radiograph shows bone destruction and production about the ischial tuberosities *(large arrowheads)* from chronic osteomyelitis and subcutaneous air related to the decubitus ulcers *(asterisks)*. There is also chronic destruction of the right femoral head *(large arrows)*. *B*, Coronal T1-weighted MR image reveals sinus tract *(small arrowheads)* extending from the ischial area of osteomyelitis *(open arrow)* that seeded the right hip joint, resulting in an additional site of pyarthrosis and osteomyelitis *(curved arrow)*. *C*, CT scan shows bone destruction about the right hip *(curved arrow)*. A large fluid collection anteriorly represents abscess *(small arrows)* and subcutaneous air *(asterisk)*.

In addition, complex fractures occur with various combinations of the elementary components.[97, 159, 188]

Posterior column or *posterior wall fractures* account for nearly 30% of all acetabular fractures.[174] These fractures are most common and are often a result of posterior hip dislocation (Fig. 49–12). The extent of posterior wall defect is well evaluated on CT and is important in determining both hip stability after reduction and the need for operative fixation.

Posterior dislocation is the most common type of hip dislocation (85% to 90% of cases) (see Fig. 49–12).[174] CT allows identification of associated intra-articular fragments (see Fig. 49–12) and impaction fractures or shearing osteochondral fractures of the femoral head, which are common sequelae of this injury.[174, 202] Impaction fractures (seen in 13% to 61% of posterior hip dislocations) involve the anterior surface of the femoral head and are due to compression of the femur on the posterior acetabulum during dislocation. Large portions of the femoral head can be sheared (seen in 7% to 10% of posterior hip dislocations) from the remainder of the femur during dislocation (Fig. 49–13). These can be difficult to detect on radiographs, and CT is helpful in directing surgical fixation.

Fairbairn and colleagues have described focal areas of

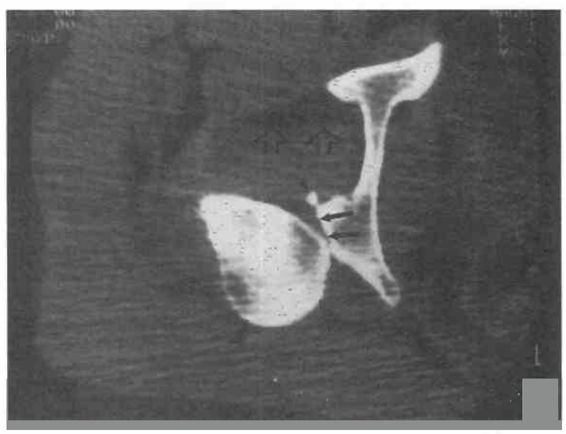

Figure 49–12. Posterior column fracture with dislocation in a 30-year-old man after a motor vehicle accident. CT scan shows the femoral head posteriorly dislocated *(large arrowheads)*, with small intra-articular fragment *(small arrowhead)*, fractured posterior column *(large arrows)*, and lipohemarthrosis in the joint *(open arrows)*.

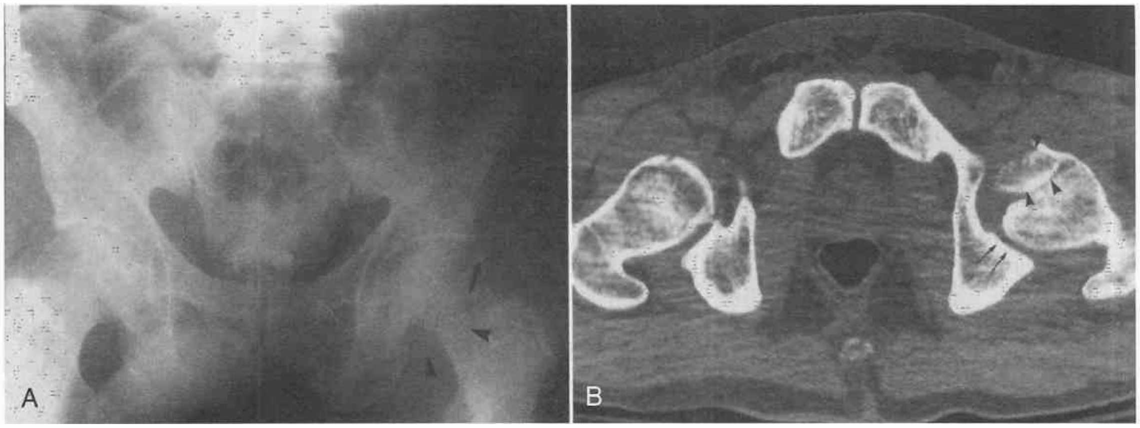

Figure 49–13. Shearing femoral head osteochondral fracture resulting from posterior hip dislocation in a 39-year-old man after a motor vehicle accident. *A*, Pelvic radiograph after reduction shows a small fragment superolateral to the left hip *(large arrow)*; however, large osteochondral femoral head fragment is only vaguely visible *(large arrowheads)*. *B*, CT at the lower extent of the acetabulum shows a large osteochondral femoral head fragment *(small arrowheads)* that is rotated 180 degrees, with its articular surface facing the remainder of the femur. The posterior column of the acetabulum is largely intact *(small arrows)*. Subcutaneous air is seen anteriorly from associated soft tissue injury.

air in the hip joint as a sign of posterior hip dislocation (even if spontaneous or surgically reduced) resulting from *vacuum phenomenon* within the joint.[65] This finding should emphasize the need to search for associated osteochondral fragments in the joint arising from the femoral head or acetabulum.

Posterior column fractures are associated with central dislocations, and the fracture is directed obliquely across the posterior inferior acetabular fossa and inferior pubic ramus. This type of fracture separates the posterior column from the remainder of the iliac bone.

Transverse fractures (8% to 10% of acetabular fractures) are axially oriented injuries involving both columns (Fig. 49–14).[188, 191] These fractures separate the innominate bone into superior and inferior fragments, usually at the level of the acetabular roof. They are often associated with central fracture dislocations.

Anterior column and *anterior wall fractures* account for only 6% to 7% of acetabular fractures and may be associated with anterior hip dislocation.[188, 191] Analogous to posterior column fractures, anterior column injuries divide this area from the remainder of the innominate bone. Anterior wall fractures only involve a portion of the anterior column. Anterior hip dislocations account for 10% to 15% of all hip dislocations.[188, 191] Associated impaction fractures of the femoral head are not uncommon and may be detected only on CT as a cortical indentation along the posterolateral femoral head.

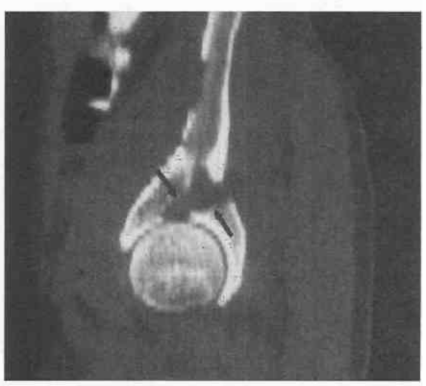

Figure 49–14. The patient is a 25-year-old man who sustained a transverse acetabular fracture in an automobile accident. Sagittal CT reconstruction shows the axially oriented fracture *(arrows)* involving both columns at the level of the acetabular roof, dividing the innominate bone into superior and inferior fragments.

Complex acetabular fractures combining two or more elementary fracture components are common. Frequently observed patterns combining two or more elementary components include transverse and posterior wall fractures (associated with posterior and central hip dislocation), fractures of both columns, and T-shaped fractures.[78, 82, 188, 191] The T-shaped injury combines a transverse fracture with a vertical component usually extending into and dividing the obturator ring.

CT, in addition to initially evaluating acetabular fractures, can be used to assess both the adequacy of reduction after fixation and the position of metallic devices (particularly to exclude intra-articular location).[13] Some artifact is produced by the orthopedic fixation; however, these devices are relatively small in the acetabulum, and the use of bone windows and reconstructions usually allows adequate evaluation by CT.

Femoral Neck Fractures

Femoral neck fractures are common, with more than 250,000 subcapital fractures occurring annually in the United States at a cost exceeding $9 billion in direct medical and indirect morbidity expenses.[186] Most of these fractures are well evaluated with radiographs. With the relatively recent advent of MRI, however, occult femoral neck fractures have become more often reported in older patients. Scintigraphic results may be falsely negative in these older osteoporotic patients for up to 4 or 5 days.[126]

MRI can be helpful in these patients, and only coronal T1-weighted images are needed to detect an abnormality.

If the marrow signal is normal, a fracture is immediately excluded. Fractures often have a linear or bandlike oblique or horizontal marrow replacement pattern seen on T1-weighted images (Fig. 49–15*A*).[19, 167] On T2-weighted or inversion recovery MR images, areas around the fracture line show increased intensity caused by hemorrhage and edema; however, the fracture line often retains low signal intensity (Fig. 49–15*B*).[175, 230] This low signal intensity on long TR images may not be apparent in all cases, particularly before callus formation begins.

On MR images, *stress fractures* have a similar appearance; these are frequent in the pubic rami and supra-acetabular region in older patients (insufficiency fracture) and in the medial femoral neck in young patients (fatigue fracture).[122]

Subchondral fractures of the femoral head have been reported with a linear band of low signal intensity on T1-weighted MR images simulating avascular necrosis (AVN).[229] Pubic rami and femoral neck insufficiency fractures (normal stress on bone of deficient elastic resistance) in elderly patients with osteoporosis occasionally simulate pathologic fractures. This is caused by post-traumatic osteolysis simulating an osteolytic lesion or callus formation, subacutely suggesting a chondroid- or osteoid-producing neoplasm.[173] This appearance can be particularly confusing when previous radiographs, at the time of the acute fracture, are not available for review. In these cases, CT is often useful to define the linear fracture plane and sur-

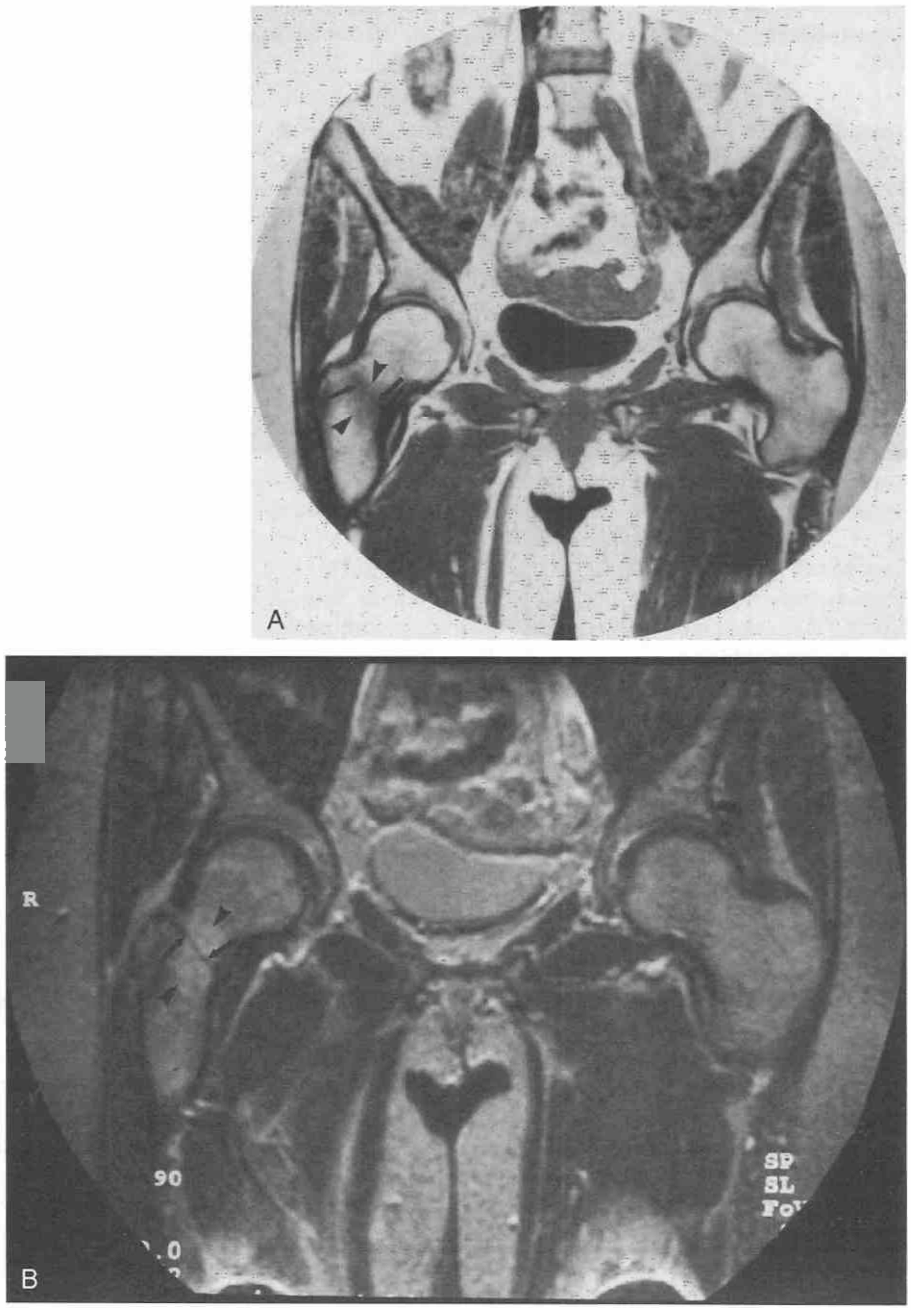

Figure 49–15. Occult femoral neck fracture in a middle-aged woman with hip pain. *A,* Coronal T1-weighted MR image shows a linear band of low intensity in the basicervical region of the right femoral neck *(arrows)* representing the fracture with surrounding marrow replacement from edema and hemorrhage *(arrowheads)*. *B,* Coronal T2-weighted MR image shows a linear low signal intensity band representing the fracture line *(arrows)* and surrounding high signal intensity resulting from marrow edema *(arrowheads)*. A radiograph (not shown) revealed vague sclerosis in this area of the femoral neck, retrospectively. (Courtesy of Harold Campbell, M.D.)

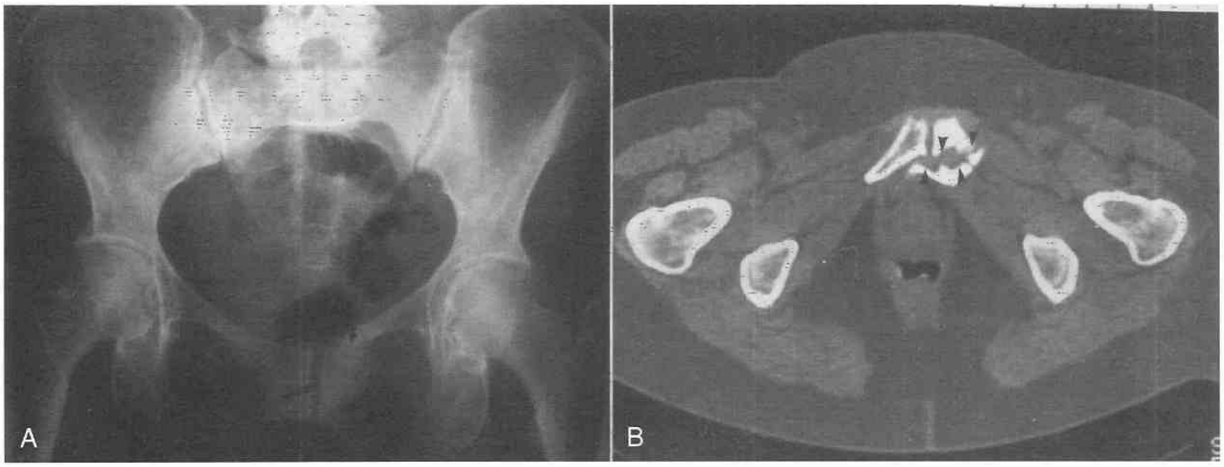

Figure 49–16. Pubic insufficiency fracture simulating a neoplasm in a 61-year-old woman. *A,* Pelvic radiograph shows changes in the symphysis on the left with sclerosis, suggesting a chondroid- or osteoid-producing lesion *(arrows)*. *B,* CT reveals linear fracture plane and surrounding callus *(arrowheads)* resulting from the healing fracture and no evidence of a soft tissue mass.

rounding callus and to confirm no evidence of soft tissue mass (although muscle thickening may be present) (Fig. 49–16). These factors exclude neoplastic involvement as a reasonable consideration.

MRI can also be used to evaluate muscle tears and hemorrhage about the hip[54]; these most frequently involve the rectus femoris muscle anteriorly and the hamstrings posteriorly. In 1999, tears of the abductor muscle's attachment to the greater trochanter (rotator cuff tear of the hip) were described.[102]

The appearance of intramuscular hemorrhage is somewhat inconsistent; however, the most characteristic pattern is increased signal intensity on T1-weighted and T2-weighted images, with the area of involvement being much larger on long TR images (see Fig. 49–9*A* and *B*).[54, 179, 225] Chronically low-signal-intensity areas on all pulse sequences may be apparent because of hemosiderin and fibrosis. The area involved on MR images is frequently irregular and infiltrative, representing blood dissecting between muscle bundles, and surrounds the low-signal-intensity intramuscular component of the tendon. The multiplanar imaging capability of MRI is also helpful in assessing the degree of muscle disruption and in directing intervention when tears are complete.

Neoplasia

Neoplastic involvement about the hip, both benign and malignant, can involve either the osseous structures or soft tissues. CT and MRI can provide localization and characterization of these neoplastic lesions, factors that are invaluable in staging and preoperative planning. Advantages of MRI include (1) multiplanar imaging, (2) superior contrast resolution, and (3) lack of ionizing radiation.

Although MRI has supplanted CT as the modality of choice in evaluation of many musculoskeletal masses, CT can still play an important role. Osseous neoplasms that produce mineralized matrix not adequately assessed on radiographs are often better evaluated by CT.[201, 222] CT allows improved detection and characterization of the matrix, particularly important when this is subtle, to determine whether the lesion is of osteoid or chondroid derivation.

Numerous primary osseous neoplasms occur about the hip; however, commonly encountered lesions include (1) osteoid osteoma, (2) chondroblastoma, and (3) chondrosarcoma.

Symptoms usually include nonspecific pain. Radiography should be the initial imaging in any case of suspected osseous neoplasms. The radiographs are of primary importance to identify the lesion, to characterize its margin and aggressiveness, to detect any mineralized matrix formation, and to provide a reasonable differential diagnosis. CT, MRI, or both may then be performed to further characterize the lesion and to delineate its extent.

Osteoid Osteoma

Osteoid osteoma is common, accounting for 10% to 12% of primary benign skeletal neoplasms.[104, 110] These lesions are seldom larger than 1.5 to 2.0 cm in diameter and are classified by their location as (1) *cortical* (75%), (2) *cancellous* (25%), or (3) *subperiosteal* (rare).

Cortical lesions are the most common type in long bones, such as the tibia and femur, and are usually easily identified as a small, radiolucent nidus with extensive surrounding reactive sclerosis and cortical thickening.

Cancellous lesions are most common about the hip, with the proximal femur involved more frequently than the acetabulum. These lesions are often difficult to detect on radiographs because of their small size and lack of prominent reactive sclerosis resulting from limited periosteal tissue in the region.[38]

Patients' clinical findings may suggest inflammatory synovitis, and the classic history of night pain relieved by aspirin may not be apparent. Patients are usually between 10 and 20 years of age, and males are affected about two to three times as frequently as females.[104, 110] Radiographs of the hip may be nonspecific, showing only disuse osteopenia. Periosteal reaction may be seen only inferior to

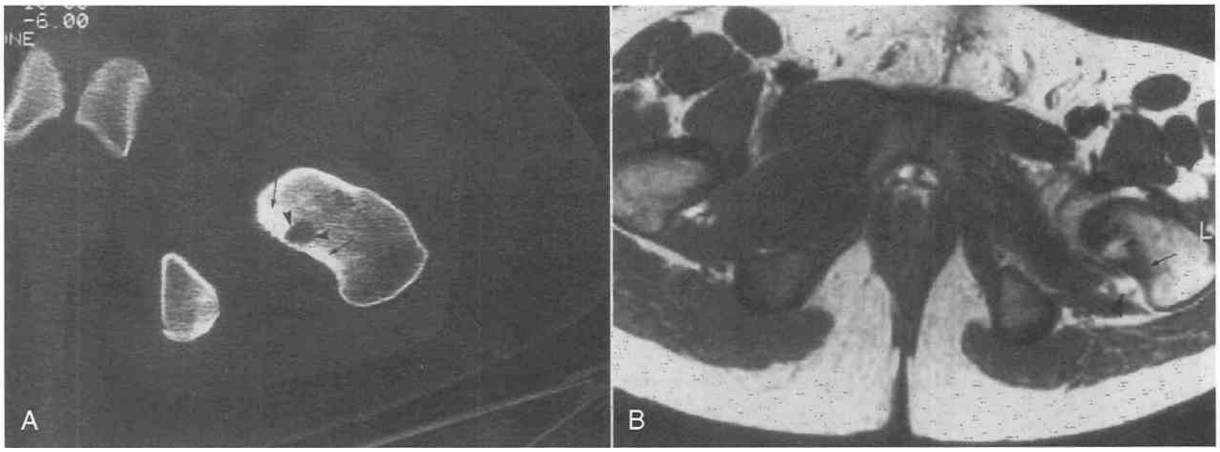

Figure 49–17. Intra-articular osteoid osteoma in a 16-year-old boy with hip and knee pain. *A*, CT scan shows a focal low-attenuation nidus *(small arrowheads)* in the endosteal region of the femoral neck medially with mild associated reactive sclerosis *(arrows)*. ***B***, Proton-density axial MR image reveals osteoid osteoma nidus of intermediate intensity *(small arrowheads)* with reactive sclerosis showing low signal intensity *(arrows)*. Reactive joint effusion resulting from lymphofollicular synovitis is also seen *(large arrowheads)*.

the joint capsule attachment, in the subtrochanteric region.[77]

Because of these difficulties, CT is often valuable in identifying these lesions and is usually preferable to MRI. On CT scans, the nidus is a well-defined area of decreased attenuation with a variable degree of surrounding reactive sclerosis (Fig. 49–17*A*). The nidus, which is composed of osteoid and woven bone, may show mineralization on CT in approximately 50% of cases.[92, 104, 184] This mineralization is usually a solitary central focus within the nidus but may be ringlike or multifocal; rarely, the entire nidus is ossified.

MRI is usually not necessary to detect these lesions, and the appearance has been reported to be quite variable, depending on the degree of mineralization. The nidus may show low to intermediate signal intensity on T2-weighted images if it is mineralized, or its signal intensity may be similar to that of fat or higher if it is nonmineralized (Fig. 49–17*B*).[92, 104, 110] This situation can create a target appearance, with the low-signal-intensity rim representing sclerosis. On long TR images, extensive marrow edema surrounding the nidus may obscure the lesion.

Both CT and MRI may show an associated joint effusion resulting from a lymphofollicular synovitis as well as contrast enhancement from the vascular nidus (see Fig. 49–17*B*). A reactive soft tissue mass with osteoid osteoma has been reported on MR images,[22, 227] although this should not be surprising or confused with a more aggressive process. It represents another manifestation of associated inflammatory response seen with these lesions, as opposed to a true "mass." CT is invaluable for localizing the nidus for the orthopedic surgeon before open resection and can also be used to direct needle placement before surgical removal.[105, 194] In addition, CT can be used to treat osteoid osteoma by guiding core needle or electrode placement for percutaneous removal (Fig. 49–18) or radiofrequency ablation, respectively, while the patient is on the CT table.[10, 57, 141, 177]

Chondroblastoma

Chondroblastoma, a benign chondroid neoplasm, involves primarily the epiphysis of young patients between 10 and 20 years of age.[140] One of the most common sites, the proximal femur, is involved in 16% of cases; less frequently involved is the iliac bone, in the area of the triradiate cartilage.[27, 140] The lesion is usually seen on radiographs as a radiolucency within the epiphysis eccentrically (Fig. 49–19*A*) that may extend into the metaphysis (55% of cases).[173] There is usually a rim of surrounding sclerosis.

Thick periosteal reaction may be seen in 50% of patients with proximal femoral lesions.[32] The periosteal reaction is distal to the lesion about the femoral neck and subtrochanteric region (see Fig. 49–19*A*). The differential diagnosis of epiphyseal lesions in the proximal femur includes Langerhans cell histiocytosis and infection.

CT can be helpful in detecting distinctive chondroid calcification (a ring and arc appearance), which is present in up to 60% of cases of chondroblastoma and which can be difficult to identify on radiographs (Fig. 49–19*B*).[27] On T1-weighted images, MRI shows marrow replacement. In our experience, most chondroblastomas retain low to intermediate signal intensity on long TR images (solid components), a feature that is unusual for most osseous neoplasms, particularly cartilage tumors (Fig. 49–19*C* and *D*). This MRI appearance is probably related to high cellularity, fibrosis, or areas of chondroid mineralization. Cystic (aneurysmal bone cyst) elements may also be seen. As with osteoid osteomas, MRI may show hip joint effusion and extensive surrounding edema with chondroblastoma (see Fig. 49–19*C* and *D*).

Many different primary and metastatic osseous malignancies occur about the hip. Multiple myeloma and metastatic foci are well evaluated by MRI and typically show marrow replacement on T1-weighted images and high signal intensity on long TR images (Fig. 49–20).[168, 170] Myelomatous areas of involvement, diffuse or focal, occasionally retain low signal intensity on T2-weighted MR images (see Fig. 49–20).[75, 129, 152, 173, 204] Osteoblastic metastases often show significant areas of low signal intensity corresponding to the sclerosis on T2-weighted images and high attenuation on CT scans. The size, extent, and presence of associated soft tissue mass are well evaluated on MRI; this information can be important in patient management.

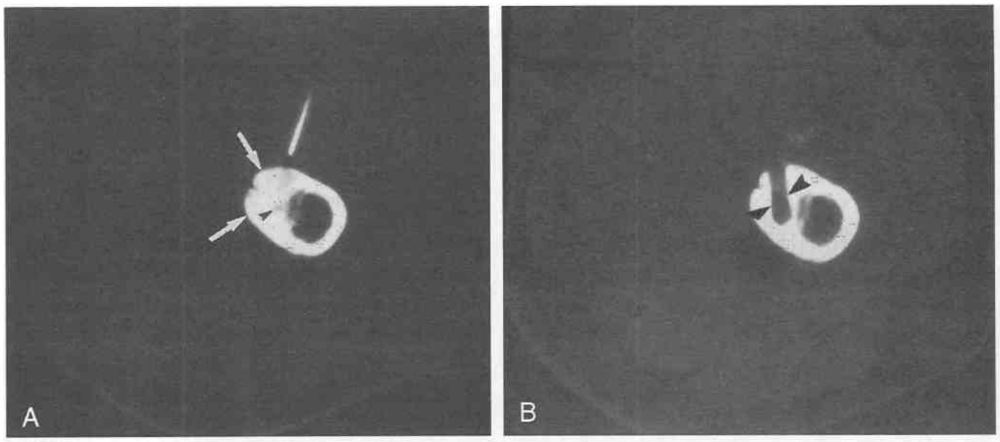

Figure 49–18. The patient is a 22-year-old man who underwe[redacted]ercutaneous removal of a proximal femur cortical osteoid osteoma under general anesthesia. CT scan shows initial localizing needle placement *(A)* directed toward the low-attenuation nidus *(arrowhead)*. Marked reactive cortical thickening is present *(arrows)*. Craig needle apparatus was then used to remove a core of bone, including the nidus. The core tract *(B)* is seen *(arrowheads)* with removal of the low-attenuation nidus. The patient was discharged from the hospital within 23 hours of this procedure.

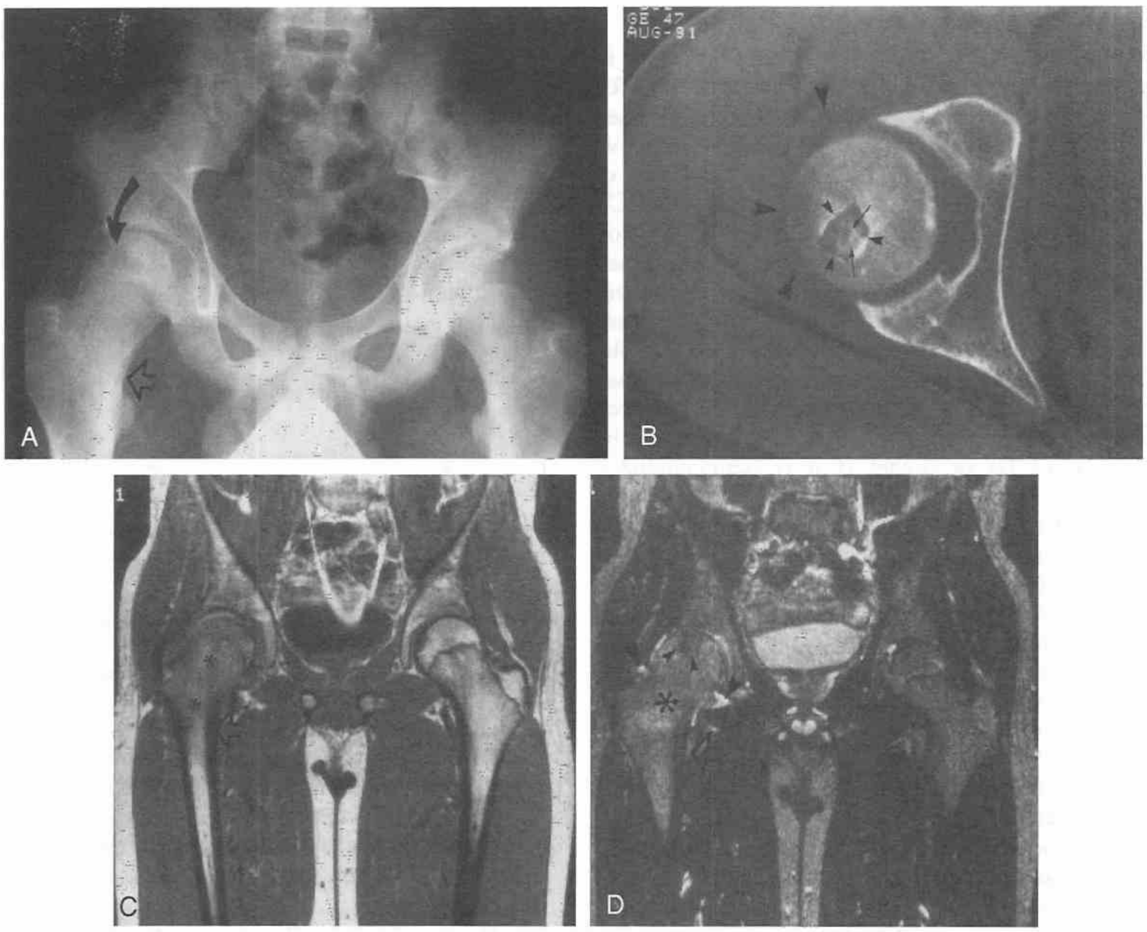

Figure 49–19. Chondroblastoma of the right femoral head in a 14-year-old boy after several months of hip pain. *A,* Pelvic radiograph shows deformity of the right femoral head with a periosteal reaction in the medial femoral neck *(open arrow)*. The lytic lesion *(curved arrow)* is difficult to detect. *B,* CT scan reveals the lytic lesion *(small arrowheads)* with surrounding sclerosis and chondroid matrix within the chondroblastoma *(arrows)*. Joint effusion is also identified *(large arrowheads)*. *C,* Coronal T1-weighted MR image reveals diffuse marrow replacement in the right proximal femur *(asterisks)* with the chondroblastoma difficult to distinguish as a focal lesion. Periosteal reaction is seen as increased signal intensity within the medial femoral neck cortex *(open arrow)*. *D,* Coronal T2-weighted MR image shows diffuse, mildly increased marrow signal intensity in the right femur from edema *(asterisk)*. The chondroblastoma shows low signal intensity *(small arrowheads)* resulting from chondroid matrix and high cellularity (confirmed by pathologic examination). Associated high-signal-intensity joint effusion *(large arrowheads)* and periosteal reaction *(open arrow)* are also seen.

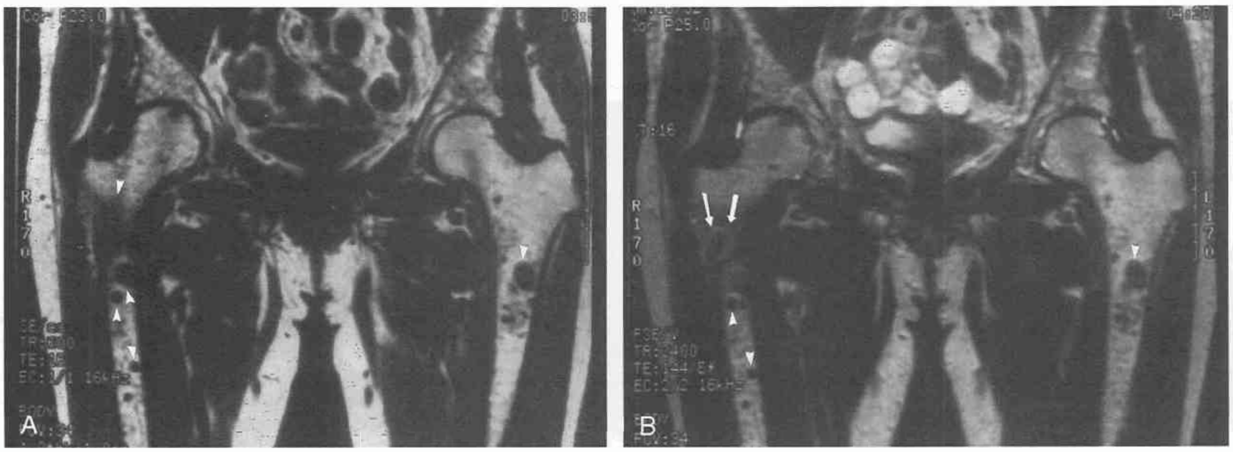

Figure 49–20. Multiple myeloma involvement of the proximal femoral heads in a 65-year-old woman. Coronal T1-weighted *(A)* and T2-weighted *(B)* MR images reveal multiple focal areas of marrow replacement *(arrowheads)* resulting from myelomatous involvement. In *B*, most of these lesions retain low signal intensity, although in the right femur the largest lesion shows mild increased intensity *(arrows)*. The size of this lesion suggests impending pathologic fracture, and the right femur was prophylactically internally fixed with an intramedullary rod.

CT shows myeloma and lytic metastatic lesions as areas of higher attenuation replacing the normally fatty marrow space, and the degree of cortical involvement is easily assessed. CT and MRI are helpful in evaluating metastatic and myelomatous lesions to determine impending pathologic fracture of the proximal femur (a high risk if the lesion is larger than 2 to 3 cm in size, if greater than 50% of the cortex is involved or if the patient has postradiation pain) and to guide the need for prophylactic fixation and radiation therapy (see Fig. 49–20).[75, 192]

Chondrosarcoma

Chondrosarcoma is one of the more frequently occurring primary bone malignancies to involve the osseous structures about the hip. Approximately 25% of all chondrosarcomas involve the pelvis, with many occurring about the proximal femur (particularly the clear cell variety) and acetabulum in the region of the triradiate cartilage (Fig. 49–21).[165, 173]

CT is effective in identifying and characterizing the chondroid matrix, which appears as rings and arcs of calcification, when radiographs are not adequate because of lack of contrast resolution or complex pelvic anatomy (Fig. 49–21*B*).[8, 45, 170] CT also allows identification of any soft tissue mass, which is common in higher-grade chondrosarcomas (up to 50% of cases).[173, 218]

MRI is superior to CT in demonstrating the extent of marrow and soft tissue involvement in chondrosarcoma or other osseous neoplasms about the hip. Marrow replacement is as seen on T1-weighted images, and relative high intensity is seen on T2-weighted images. Mineralization is of low signal intensity on all pulse sequences; however, it is not as well characterized by MRI as by CT.[218] The multiplanar imaging capability of MRI is important in assessing osseous neoplasms about the hip for surgical planning. Detection of hip joint invasion is particularly important because resection of structures on both sides of the joint is then required. Involvement of the joint is usually best shown on coronal and sagittal images with soft tissue mass within the articulation and with associated effusion (Fig. 49–21*C* and *D*). In our experience, the absence of a joint effusion in cases of osseous malignancy about the hip essentially excludes joint involvement.

Soft tissue masses about the hip, both benign and malignant, are not uncommon.[62, 109] MRI has largely supplanted CT as the modality of choice in evaluation of these masses.[192, 196, 201, 221, 222] A specific histologic diagnosis by MRI is apparent in only approximately 25% to 40% of cases (lipoma, hemangioma); however, the contrast resolution of MRI allows exquisite distinction of tumor from surrounding soft tissue and osseous structures.[109, 132] Staging of soft tissue neoplasm for presurgical planning is also aided by the multiplanar imaging capability of MRI.[192, 196]

MRI is also important in assessing the effects of chemotherapy and radiation therapy on tumor size and extent, for both osseous and soft tissue components of musculoskeletal neoplasms.[64, 212, 213] In general, a decreased intensity on T1-weighted images and an increased intensity on long TR images suggest a response to therapy with necrosis and edema. MRI is also vital in postoperative evaluation to detect early soft tissue recurrence. Edema resulting from surgery and radiation results in irregular, nonlocalized, often linear areas of high signal intensity on long TR images that do not disrupt the normal muscle texture pattern on T1-weighted images.[23, 212, 213] However, any nodular regions not characteristic of fluid (seroma or lymphocele) that disrupt the muscle texture on T1-weighted images should be considered residual or recurrent tumor.[23] Recurrent osseous neoplasm is seen as new areas of marrow replacement.

After IV injection of gadolinium, MRI is useful for distinguishing vascular tissue (neoplasm, granulation tissue, inflammation) from nonvascular components (hemorrhage, necrosis, seroma, lymphocele, abscess) following surgery.[64, 212] By using dynamic contrast-enhanced subtraction MRI, Vanel and coworkers have suggested that tumor recurrence can be distinguished from other tissues.[213] Neoplastic tissue shows enhancement in the early stages (the

Figure 49–21. Chondrosarcoma of the left acetabulum in a 30-year-old man with vague hip pain of several months' duration. *A*, Radiograph of the pelvis shows subtle aggressive bone destruction of the medial left acetabulum with permeation of the iliopectineal line *(curved arrows)*. *B*, CT scans show bone destruction with chondroid matrix formation *(large arrowheads)* and an associated soft tissue mass *(asterisk)*. *C* and *D*, Coronal T1-weighted MR image *(C)* and axial T2-weighted MR images *(D)* reveal marrow replacement *(small arrowheads)* and soft tissue mass *(asterisk)*, which becomes high signal intensity on the long TR/TE image *(D)*. The soft tissue mass has invaded the hip joint, as evidenced by the fact that the soft mass abuts the femoral head *(arrows)*.

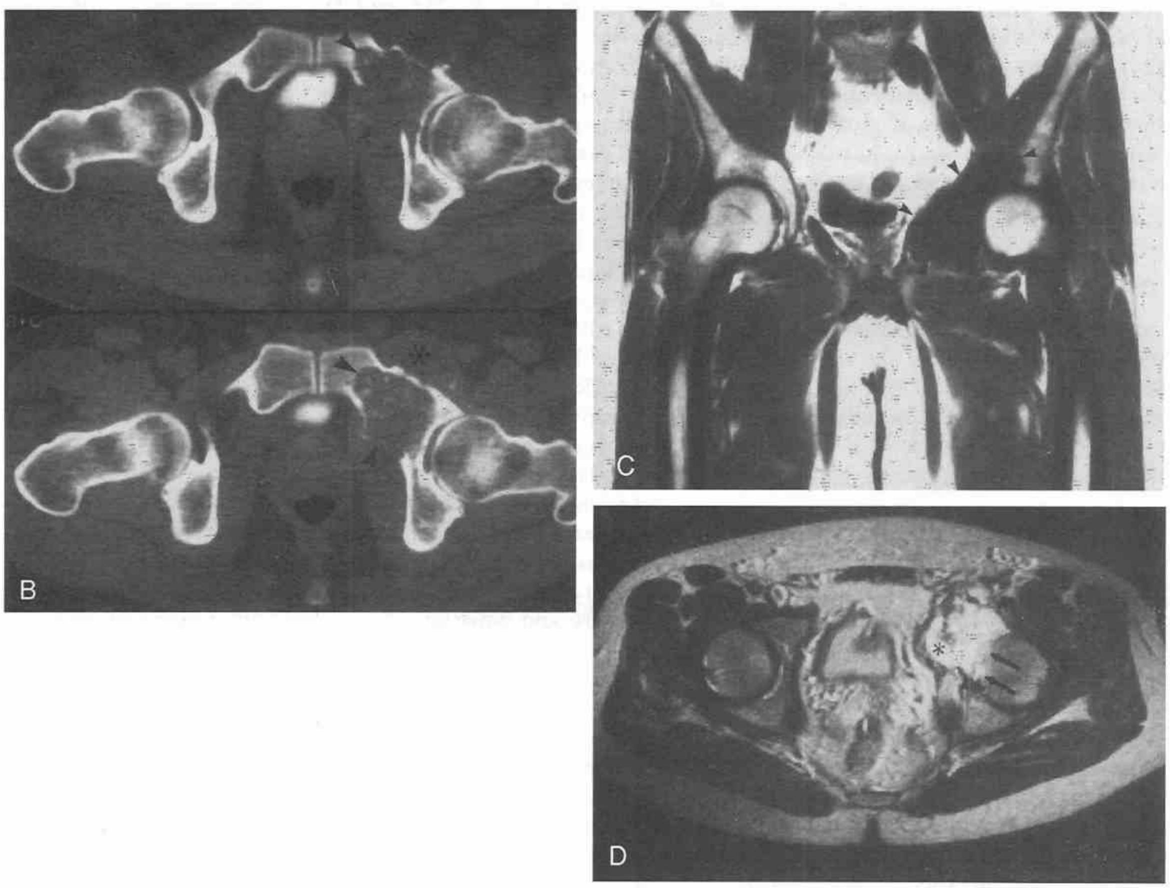

first 2 minutes), in contrast to non-neoplastic tissue, which enhances at a later time.[213]

Avascular Necrosis and Transient Osteoporosis

Avascular Necrosis

Osteonecrosis of the hip is caused by an insufficient vascular supply to the femoral head. AVN of the femoral head results from numerous abnormalities, including trauma, steroids, collagen vascular disease, alcoholism, pancreatitis, hemoglobinopathies, and Gaucher disease.[39, 70, 173] AVN may also be idiopathic in both adults and children (Legg-Calvé-Perthes disease). Trauma is the most frequent known cause of AVN, usually related to femoral neck fracture or hip dislocation, with an increasing incidence associated with the degree of displacement and delay in reduction.[70] AVN related to trauma is usually unilateral, whereas nontraumatic osteonecrosis is bilateral in up to 70% of patients.[70]

The common sequelae of AVN are collapse and joint deformity with subsequent osteoarthritis and pain; these often lead to orthopedic intervention and account for 10% of all total joint replacements in the United States.[70] Numerous treatment modalities are available, including a variety of joint replacements, joint fusion, or joint-preserving surgery such as core decompression or osteotomy. The use and success of core decompression, which reduces the intramedullary pressure thought to be the underlying cause of AVN, are controversial in the orthopedic literature.[17, 43] However, most experts agree that this procedure, if used, must be performed at the earliest stages of AVN to be of significant benefit.

Various staging systems have been used to assess femoral head AVN. The most commonly used classification is that developed by Ficat and Arlet.[9] This system is based on radiographs:

Stage 0 disease. Patients are asymptomatic, as shown by normal radiographs and bone scan; only biopsy reveals changes of AVN.

Stage 1 disease. Patients have pain, a decreased range of motion, an abnormal bone scan, and a normal radiographic appearance.

Stage 2 disease. Radiographs show femoral head osteoporosis with areas of cystic lucency and sclerosis.

Stage 3 disease. There is progression to subchondral collapse *(crescent sign).*

Stage 4 disease. There is progressive segmental femoral head collapse with a normal hip joint space and acetabulum.

Stage 5 disease. Secondary osteoarthritic changes are seen on both the femoral and acetabular sides of the joint with narrowing.

MRI is clearly the most sensitive and specific radiologic modality available for detecting the early changes of AVN of the femoral head.[31, 42, 71, 73, 203] The sensitivity of MRI in detecting AVN in symptomatic patients has ranged from 88% to 100% in studies of Markisz and Beltran and their coworkers[17, 136]; sensitivity was 10% to 20% more than with bone scintigraphy. However, there is some delay between the histologic changes and development of MRI abnormalities of AVN; the extent of this gap remains unclear.[71, 73, 199, 203] In animal studies, changes have been seen as early as 1 week.

On MR images, the typical marrow pattern seen with AVN is variably sized areas of decreased intensity on T1-weighted images, usually in the anterosuperior subchondral aspect of the femoral head laterally (Figs. 49–22 and 49–23). This area may be homogeneous or heterogeneous with band, ring, wedge, or crescentic configuration and regions of higher signal intensity centrally.[207] In the study by Mitchell and coworkers,[149] this defect was present in 96% of patients, with the rim remaining low intensity on both T1-

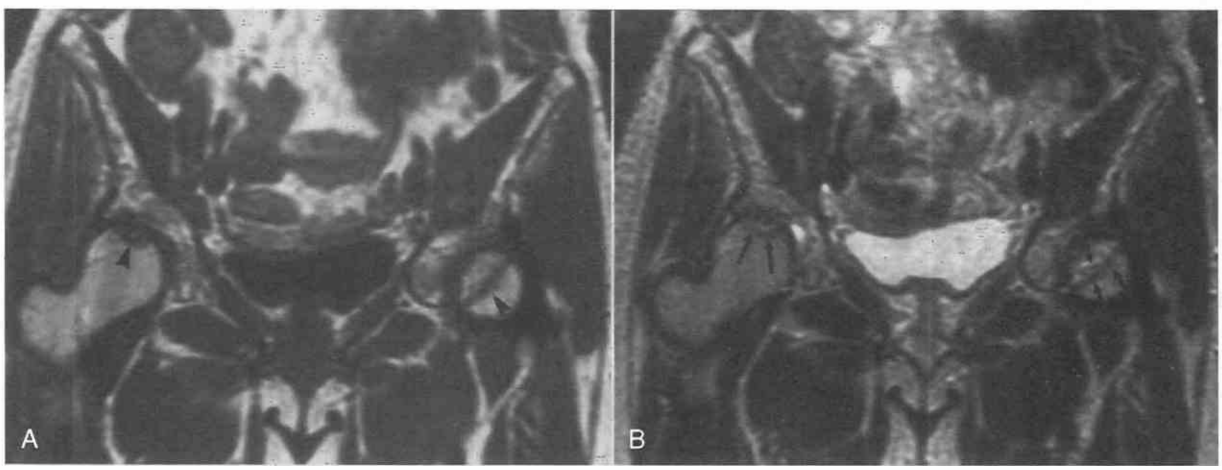

Figure 49–22. Avascular necrosis (AVN) of both femoral heads in a 41-year-old patient receiving steroids for long-standing systemic lupus erythematosus. *A,* Coronal T1-weighted MR image shows focal crescentic areas of decreased marrow signal typical of AVN in both femoral heads *(arrowheads). B,* Coronal T2-weighted MR image shows linear high signal intensity band *(small arrows)* with a persistent low-signal-intensity rim *(large arrows),* consistent with the *double line sign,* characteristic of AVN on the right. The area of AVN on the left has fat-like signal intensity typical of class A changes, and predominantly low signal intensity on the right (fibrous tissue), typical of class D changes.

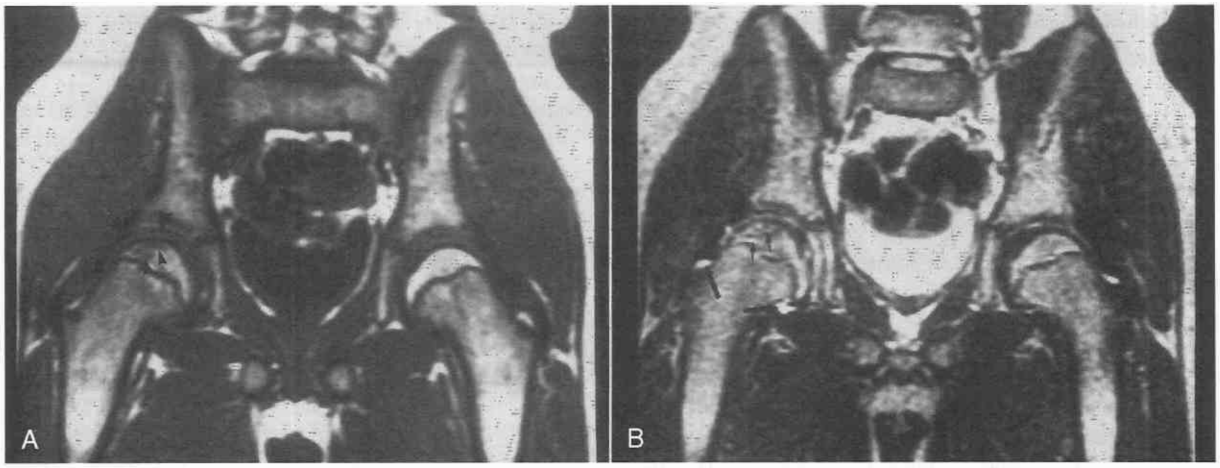

Figure 49–23. Legg-Calvé-Perthes disease in a 7-year-old boy with recent onset of right hip pain. Pelvic radiographs (not shown) were normal. *A,* Coronal T1-weighted MR image shows bandlike areas of marrow replacement in the superolateral aspect of the right femoral head *(small arrowheads)*. Overlying cartilage *(large arrowheads)* appears intact, and the femoral head is well covered by the acetabulum. *B,* Coronal T2-weighted image reveals the areas of avascular necrosis to be largely high signal intensity *(small arrows)*, consistent with class C changes (fluid-like). Minimal associated joint effusion is also present *(large arrows)*.

weighted images (94% of cases) and long TR/TE sequences (86% of cases) (see Fig. 49–22).

The appearance of AVN on long TR/TE MR images is more variable but often adds specificity. A high-signal-intensity line within the low-intensity rim *(double line sign)* has been described in 80% of patients with AVN in one series (Fig. 49–22*B*).[108–110]

Mitchell and coworkers have developed an MRI classification scheme based on the appearance of the central region.[147–149] This area may simulate the following:

1. *Fat, class A.* High signal intensity on short TR/TE images, and intermediate signal intensity on T2-weighted images (see Fig. 49–22).
2. *Blood, class B.* High signal intensity on short and long TR/TE images.
3. *Fluid, class C.* Low signal intensity on short TR/TE images and high signal intensity on long TR/TE images (see Fig. 49–23).
4. *Fibrous tissue, class D.* Low signal intensity on all images (see Fig. 49–22).

Class A and B changes appear to correspond to early stages 1 and 2 of AVN, whereas class C and D changes correlate with the later stages of 3 and 4.[147–149] In addition, clinical symptoms are usually most severe with class D changes and least prominent with class A findings.

MRI findings correspond to the histologic changes seen with AVN. Areas of low signal intensity on all sequences correspond to fibrosis or sclerosis, whereas regions of low signal intensity on short TR/TE images that become high signal intensity on long TR/TE images represent granulation tissue attempting to repair avascular regions. Marrow with residual high signal intensity on short TR/TE images represents necrotic tissue that is not invaded by granulation tissue.

The manifestations of AVN are usually best evaluated on coronal MR images; however, sagittal and axial sequences can be helpful in assessing regions of collapse.[90] MRI may also be useful in the assessment of patients with AVN after core decompression to evaluate for revascularization, further collapse, and any change in the volume of tissue involved.[18, 154, 195, 206, 215]

It is vital to emphasize that long-term symptoms of AVN are related to collapse and the ensuing mechanical alterations. If collapse does not occur or if it is minimal, clinical symptoms are also typically not substantial, reflecting the fact that "dead bone is as strong as live bone." It is therefore important to identify radiologic features that are correlated to AVN that is more likely to lead to collapse and, perhaps, to provide earlier and more aggressive treatment for these patients.

Iida and colleagues suggested that the presence of bone marrow edema is a significant marker (85% of their 13 patients had this finding) for potential progression.[90] An additional feature increasing the likelihood of subsequent collapse is the volume of femoral head affected by AVN. Specifically, involvement of more than 25% of the femoral head diameter (and at least 67% of weight-bearing area) was associated with collapse by 32 months in the study by Shimizu and associates.[190]

MRI findings of AVN may occasionally be nonspecific and may show only diffuse marrow edema without focal defects, as described in six patients by Turner and colleagues.[208] This pattern can also be seen with transient osteoporosis of the hip. Use of IV contrast medium may help in this distinction and in earlier recognition of AVN. Areas of contrast enhancement are seen in regions of viable marrow and granulation tissue, whereas avascular regions lack enhancement.[128, 207] Additional associated MRI features of AVN are small hip joint effusion and premature conversion of hematopoietic marrow to fatty marrow. This premature conversion was seen in more than 60% of patients with AVN in the study by Mitchell and coworkers and may be caused by ischemia.[147]

MR images of Legg-Calvé-Perthes disease show identical changes as in other causes of AVN (see Fig. 49–23).

The capital femoral epiphysis often reveals necrosis centrally, with peripheral portions of viable epiphysis.[60, 61] Peripheral portions of viable epiphysis may also develop or may increase in size with revascularization and healing.[60, 187] This is important in treatment because viability of the lateral aspect of the epiphysis corresponds to a reduced risk of further deformity or to an extension of AVN.[187] In these patients, bracing can be discontinued and the patient can begin weight bearing.

MRI can also assess the shape of the cartilaginous portions of the femoral head and the degree of containment by the acetabulum. Dynamic MRI has now been used on open configuration MRI units to assess containment and to detect hinge abduction (blocking of a flattened femoral head against the lateral acetabulum). These determinations are vital in identifying children who require treatment by an osteotomy (25% of patients). Previously, this information had to be obtained by arthrography.[60]

CT is less sensitive than MRI in detecting AVN. The earliest CT sign of AVN is alteration of the asterisk, a starlike condensation of trabeculae in the normal femoral head.[53] Changes in the asterisk in early AVN have been described as central or peripheral clumping or sclerosis (Fig. 49–24). CT is probably superior to MRI in evaluation of long-standing AVN to delineate structural deformities of the femoral head, such as subchondral fracture, collapse, and calcified intra-articular fragments. When osteotomy is planned as a temporizing procedure, CT is often useful in determining which femoral surface is best preserved.[134, 135, 183] This information guides the surgeon in determining the feasibility and type of osteotomy to perform.[135]

Transient Osteoporosis

Transient osteoporosis of the hip, as originally described in women, almost exclusively involved the left hip in the third trimester of pregnancy.[61, 173, 228] It is now recognized

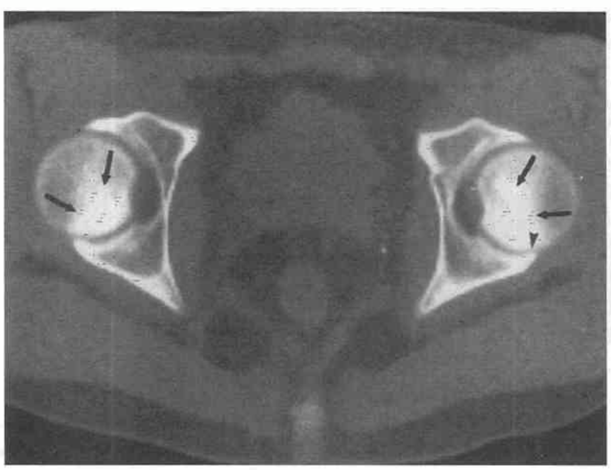

Figure 49–24. Bilateral avascular necrosis (AVN) of the femoral heads in a 22-year-old man receiving steroid therapy for Crohn disease. CT scan shows focal sclerosis in both femoral heads posteriorly *(arrows)*, typical of AVN with minimal cortical collapse *(arrowhead)* on the left.

as actually being more common in middle-aged men and affecting either hip. Symptoms include severe hip pain and decreased range of motion that resolves spontaneously in 6 to 12 months.[214]

The etiology is poorly understood, and the disease has been associated with a type of reflex sympathetic dystrophy syndrome. It may be migratory, with subsequent involvement of the opposite hip or an adjacent joint. Radiologic changes may simulate indolent infection, osteonecrosis, or infiltrative neoplasm. The underlying pathologic condition appears to be bone marrow reaction or edema.[58, 79, 163, 228] Current terminology may refer to this entity as *transient bone marrow edema syndrome*.[223]

Radiographs usually show osteopenia, and bone scan reveals intense activity focally within the femoral head—unlike AVN, which often displays central photopenia.

MRI demonstrates diffuse marrow abnormalities that usually extend from the subchondral femoral head to the intertrochanteric and subtrochanteric regions. There is low signal intensity on T1-weighted MR images and high signal intensity on T2-weighted sequences (Fig. 49–25).[3, 26, 84, 85, 164] These MRI changes reflect the nonspecific marrow reaction or edema that is present. Focal marrow defects in the subchondral region or subtle femoral head flattening should be searched for diligently on MR images; unlike the case with AVN, these defects are usually absent in transient osteoporosis.

In 1999, Vande Berg and coworkers described small subchondral areas of low signal intensity in 30% of patients with bone marrow edema syndrome.[214] Lesions that were less than 4 mm thick or 12.5 mm long *(reversible)* returned to normal as opposed to those that were larger *(irreversible)* that continued onto collapse, probably representing progression to AVN.[214] IV gadolinium injection may also be useful in these patients to help distinguish AVN from transient osteoporosis.[89, 216]

In transient osteoporosis, diffuse, homogeneous enhancement of the marrow space and edema are seen on postinjection T1-weighted images to a greater extent than that seen in contralateral normal femoral marrow (Fig. 49–26). This is in contradistinction to AVN, in which contrast enhancement is heterogeneous, with avascular foci showing persistent low signal intensity resulting from lack of enhancement. According to Bloem,[26] MR images gradually improve in transient osteoporosis of the hip without residual defects in a 6- to 10-month time frame and return to normal marrow signal intensity (Fig. 49–25*C*).[116, 118] These MRI findings lag behind clinical improvement.

Although the relationship between transient osteoporosis of the hip and AVN is unclear, some researchers now believe that the entities are related, with marrow reaction (increased fibrovascular tissue) being the important common pathologic feature.[79, 163, 228] Transient osteoporosis of the hip might thus represent a forme fruste of AVN, with ischemia and resultant marrow reaction that, for some reason, does not progress to focal necrosis. Turner and colleagues have reported six patients with a bone marrow pattern seen on MRI without focal defects that showed AVN at biopsy.[208] Studies with larger numbers of patients are required to further investigate the relationship between these two conditions. Recently, the importance of associ-

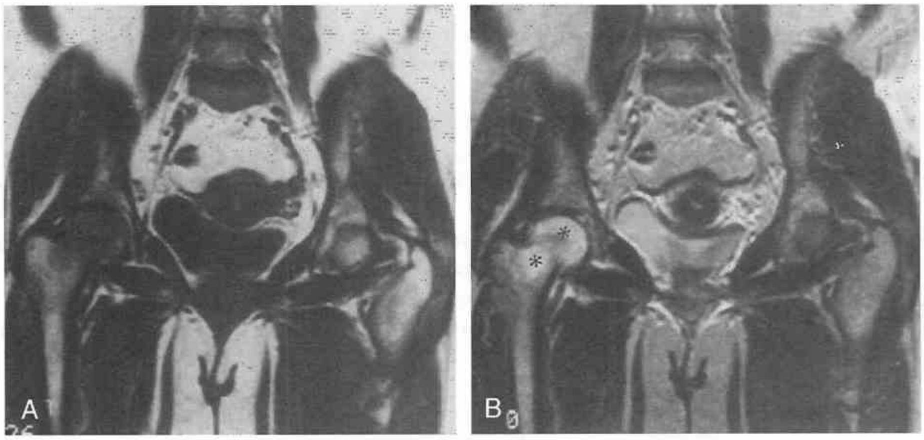

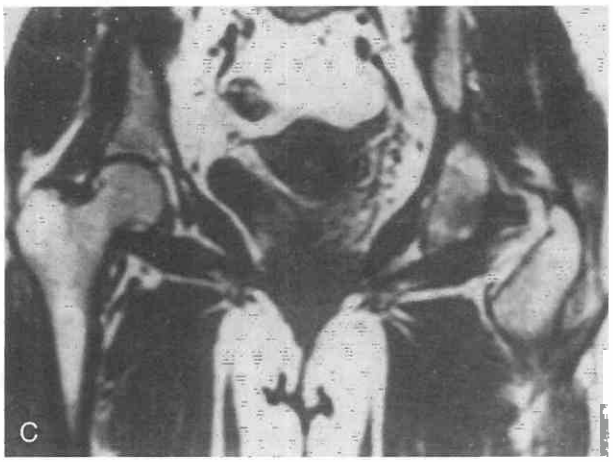

Figure 49–25. *A–C,* Transient osteoporosis of the hip in a 47-year-old woman with right hip pain of several months' duration. Pelvic radiograph and bone scan (not shown) revealed osteopenia of the right proximal femur and diffuse marked increased activity about the right femoral head, respectively. Coronal T1-weighted MR image *(A)* and T2-weighted MR image *(B)* show marrow replacement in the right femoral head and neck that becomes high signal intensity on the long TR image *(asterisks),* consistent with marrow edema. Three months later, symptoms resolved and the T1-weighted coronal MR image *(C)* shows a return to normal marrow signal intensity. No focal subchondral areas of marrow replacement were seen on any image to suggest avascular necrosis.

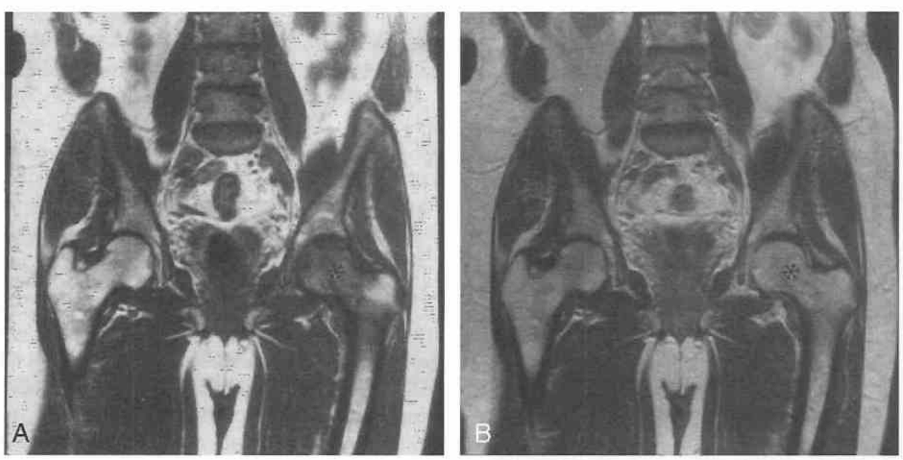

Figure 49–26. Transient osteoporosis of the hip in a 77-year-old man with a 3-month history of left hip pain. Coronal T1-weighted MR images before *(A)* and after *(B)* intravenous gadolinium injection show marrow replacement diffusely in the left femoral head and neck *(asterisk),* which enhances with contrast material to become isointense to normal marrow *(asterisk),* respectively. No focal nonenhancing areas are seen, as would be expected with avascular necrosis. Long-repetition-time (TR) MR images (not shown) revealed increased intensity in the left femoral head and neck, consistent with edema and small joint effusion. Patient symptoms and MRI changes resolved over the next 3 months without treatment.

ated subchondral fracture in transient osteoporosis of the hip has been suggested.[150]

Summary

Joint pain is a frequent presenting clinical symptom for a variety of pathologic conditions that can involve the hip. Radiographs should be the initial radiologic study performed to assess these patients. Although radiographs may sometimes provide diagnostic information, in many instances further imaging is necessary. CT, and more recently MRI, are the radiologic modalities of choice to provide this additional assessment.

In this chapter, we have attempted to describe and illustrate the CT and MRI appearances of commonly encountered pathologic conditions of the hip. Recognition of these characteristics, as seen on CT scan and MR images, is important to provide our clinical colleagues with specific information that often allows diagnosis and directs patient management.

References

1. Abe I, Harada Y, Oinuma K, et al: Acetabular labrum: Abnormal findings at MR imaging in asymptomatic hips. Radiology 216: 576, 2000.
2. Adam G, Dammer M, Bohndorf K, et al: Rheumatoid arthritis of the knee: Value of gadopentetate dimeglumine–enhanced MR imaging. AJR Am J Roentgenol 156:125, 1991.
3. Alarcon GS, Sanders C, Daniel WW: Transient osteoporosis of the hip: Magnetic resonance imaging. J Rheumatol 14:1184, 1987.
4. Altenberg AR: Acetabular labrum tears: A cause of hip pain and degenerative arthritis. South Med J 70:174, 1977.
5. Anda S, Terjesen T, Kvistad KA: Computed tomography measurements of the acetabulum in adult dysplastic hips: Which level is appropriate? Skeletal Radiol 20:267, 1991.
6. Anda S, Terjesen T, Kvistad KA, et al: Acetabular angles and femoral anteversion in dysplastic hips in adults. J Comput Assist Tomogr 15:115, 1991.
7. Angel JL: The reaction area of the femoral neck. Clin Orthop 32: 130, 1964.
8. Aoki J, Sone S, Fujioka F, et al: MR of enchondroma and chondrosarcoma: Rings and arcs of Gd-DTPA enhancement. J Comput Assist Tomogr 15:1011, 1991.
9. Arlet J, Ficat RP: Diagnostic de l'osteo-necrose femoro-capitale primitive au stade 1. Rev Chir Orthop 54:637, 1968.
10. Assoun J, Railhac JJ, Bonnevialle P, et al: Osteoid osteoma: Percutaneous resection with CT guidance. Radiology 188:541, 1993.
11. Athanasou NA, Ayers D, Rainey AJ, et al: Joint and systemic distribution of dialysis amyloid. Q J Med 78:205, 1991.
12. Azouz EM: Computed tomography in bone and joint infections. J Can Assoc Radiol 32:102, 1981.
13. Baird RA, Scobert WE, Pais MJ, et al: Radiographic identification of loose bodies in the traumatized hip joint. Radiology 145:661, 1982.
14. Balsara AN, Stainken BF, Martinez AJ: MR image of localized giant cell tumor of the tendon sheath involving the knee. J Comp Assist Tomogr 13:159, 1989.
15. Bardin T, Kuntz D, Zingraff J, et al: Synovial amyloidosis in patients undergoing long-term hemodialysis. Arthritis Rheum 28:1052, 1985.
16. Beltran J, Noto Am, McGhee RB, et al: Infections of the musculoskeletal system: High-field-strength MR imaging. Radiology 164: 449, 1987.
17. Beltran J, Herman LJ, Burk JM, et al: Femoral head avascular necrosis: MR imaging with clinical-pathologic and radionuclide correlation. Radiology 166:215, 1988.
18. Beltran J, Knight CT, Zuelzer WA, et al: Core decompression for avascular necrosis of the femoral head: Correlation between long-term results and preoperative MR staging. Radiology 175:533, 1990.
19. Berger PE, Ofstein RA, Jackson DW, et al: MRI demonstration of radiographically occult fractures: What we have been missing? Radiographics 9:407, 1989.
20. Berquist TH, Brown ML, Fitzgerald RH Jr, et al: Magnetic resonance imaging: Application in musculoskeletal infection. Magn Reson Imaging 3:219, 1985.
21. Bessette PR, Cooley PA, Johnson RP, et al: Gadolinium-enhanced MRI of pigmented villonodular synovitis of the knee. J Comput Assist Tomogr 16:992, 1992.
22. Biebuyck J-C, Katz LD, McCauley TR: Soft-tissue edema in osteoid osteoma. Skeletal Radiol 22:37, 1993.
23. Biondetti PR, Ehman RL: Soft-tissue sarcomas: Use of textural patterns in skeletal muscle as a diagnostic feature in postoperative MR imaging. Radiology 183:845, 1992.
24. Bjorkengren AG, Geborek P, Rydholm U, et al: MR imaging of the knee in acute rheumatoid arthritis: Synovial uptake of gadolinium-DOTA. AJR Am J Roentgenol 155:329, 1990.
25. Blacksin MF, Ghelman B, Freiberger RH, et al: Synovial chondromatosis of the hip: Evaluation with air computed arthrotomography. Clin Imaging 14:315, 1990.
26. Bloem JL: Transient osteoporosis of the hip: MR imaging. Radiology 167:753, 1988.
27. Bloom JL, Mulder JD: Chondroblastoma: Clinical and radiological study of 104 cases (abstract). Radiology 157:851, 1985.
28. Bongartz G, Bock E, Horbach T, et al: Degenerative cartilage lesions of the hip: Magnetic resonance evaluation. Magn Reson Imaging 7: 179, 1989.
29. Bos CF, Bloem JL, Obermann WR, et al: Magnetic resonance imaging in congenital dislocation of the hip. J Bone Joint Surg Br 48:1413, 1988.
30. Brody AS, Ball WS Jr, Towbin RB: Computed arthrotomography as an adjunct to pediatric arthrography. Radiology 170:99, 1989.
31. Brody AS, Strong M, Babikian G, et al: John Caffey Award paper: Avascular necrosis: Early MR imaging and histologic findings in a canine model. AJR Am J Roentgenol 154:341, 1991.
32. Brower AC, Kransdorf MJ, Moser RP: Frequency and diagnostic significance of periostitis in chondroblastoma. AJR Am J Roentgenol 154:309, 1990.
33. Brower AC, Kransdorf MJ: Imaging of hip disorders. Radiol Clin North Am 28:955, 1990.
34. Burnstein MI, Fisher DR, Yandow DR, et al: Case Report 502: Intra-articular synovial chondromatosis of shoulder with extra-articular extension. Skeletal Radiol 17:458, 1988.
35. Butt YP, Hardy G, Ostlere SJ: Pigmented villonodular synovitis of the knee: Computed tomographic appearances. Skeletal Radiol 19: 191, 1990.
36. Camacho CR, Melendez AT, Valenzuela A, et al: Radiological findings of amyloid arthropathy in long-term hemodialysis. Eur Radiol 2:305, 1992.
37. Casey TT, Stone WJ, DiRaimondo CR, et al: Tumoral amyloidosis of bone of beta-2 microglobulin origin in association with long-term hemodialysis: A new type of amyloid disease. Hum Pathol 17: 731, 1986.
38. Cassar-Pullicino VN, McCall IW, Wan S: Intra-articular osteoid osteoma. Clin Radiol 45:153, 1992.
39. Chan TW, Dalinka MK, Steinberg ME, Kressel HY. MRI appearance of femoral head osteonecrosis following core decompression and bone grafting. Skeletal Radiol 20:103, 1991.
40. Cobby MJ, Adler RS, Swartz R, et al: Dialysis-related amyloid arthropathy: MR findings in four patients. AJR Am J Roentgenol 157:1023, 1991.
41. Cohen MD, Cory DA, Kleiman M, et al: Magnetic resonance differentiation of acute and chronic osteomyelitis in children. Clin Radiol 41:53, 1990.
42. Coleman BG, Kressel HY, Dalinka MK, et al: Radiographically negative avascular necrosis: Detection with MR imaging. Radiology 168:525, 1988.
43. Conway WF, Totty WG, McEnery KW: CT and MR imaging of the hip. Radiology 198:297, 1996.
44. Cotten A, Boutry N, Demondion X, et al: Acetabular labrum: MRI in asymptomatic volunteers. J Comput Assist Tomogr 22:1, 1998.
45. Crim JR, Seeger LL: Diagnosis of low-grade chondrosarcoma. Radiology 189:504, 1993.
46. Czerny C, Hofmann S, Urban M, et al: MR arthrography of the adult acetabular-labral complex: Correlation with surgery and anatomy. AJR Am J Roentgenol 173:345, 1999.
47. Czerny C, Hofmann S, Neuhold A, et al: Lesions of the acetabular labrum: Accuracy of MR imaging and MR arthrography in detection and staging. Radiology 200:225, 1996.

48. Daenen B, Preidler KW, Padmanabhan S, et al: Symptomatic herniation pits of the femoral neck: Anatomic and clinical study. AJR Am J Roentgenol 168:149, 1997.
49. Dameron TB: Bucket-handle tear of acetabular labrum accompanying posterior dislocation of the hip. J Bone Joint Surg Am 41: 131, 1959.
50. Dangman BC, Hoffer FA, Rand FF, et al: Osteomyelitis in children: Gadolinium-enhanced MR imaging. Radiology 182:743, 1992.
51. Darrason R, Quentin Y, Chance P, et al: Role of arteriography and x-ray computed tomography in the current evaluation system of pigmented villonodular synovitis. J Radiol 69:645, 1988.
52. Deutsch AL, Mink JH, Waxman AD: Occult fractures of the proximal femur: MR imaging. Radiology 170:113, 1989.
53. Dihlmann W: CT analysis of the upper end of the femur: The asterisk sign and the ischemic bone necrosis of the femoral head. Skeletal Radiol 8:251, 1982.
54. Dooms GC, Fisher MR, Hricak H, et al: MR imaging of intramuscular hemorrhage. J Comput Assist Tomogr 9:908, 1986.
55. Dorrell JH, Catterall A: The torn acetabular labrum. J Bone Joint Surg Br 68:400, 1986.
56. Dorwart RH, Genant HK, Johnston WH, et al: Pigmented villonodular synovitis of synovial joints: Clinical, pathologic, and radiologic features. AJR Am J Roentgenol 143:877, 1984.
57. Doyle T, King K: Percutaneous removal of osteoid osteomas using CT control. Clin Radiol 40:514, 1989.
58. Dunstan CR, Evans RA, Somers NM: Bone death in transient regional osteoporosis. Bone 13:161, 1992.
59. Edwards DJ, Lomas D, Villar RH: Diagnosis of the painful hip by magnetic resonance imaging and arthroscopy. J Bone Joint Surg Br 77:374, 1995.
60. Egund N, Wingstrand H: Legg-Calvé-Perthes disease: Imaging with MR. Radiology 179:89, 1991.
61. Ensign MF: Magnetic resonance imaging of hip disorders. Semin Ultrasound CT MR 11:288, 1990.
62. Enzinger FM, Weiss SW: Soft-Tissue Tumors, 4th ed. St. Louis, Mosby, 2001.
63. Erdman WA, Tamburro F, Jayson HT, et al: Osteomyelitis characteristics and pitfalls diagnosis with MR imaging. Radiology 180:533, 1991.
64. Erlemann R, Reiser MF, Peters PE, et al: Musculoskeletal neoplasms: Static and dynamic Gd-DTPA–enhanced MR imaging. Radiology 171:767, 1989.
65. Fairbairn KJ, Mulligan ME, Murphey MD, Resnik CS: Gas bubbles in the hip joint on CT: Indication of recent dislocation. AJR Am J Roentgenol 164:931, 1995.
66. Fargo LA, Glick JM, Sampson TG: Hip arthroscopy for acetabular labral tears. Arthroscopy 15:132,1999.
67. Fishman EK, Magid D, Drebin RA, et al: Advanced three-dimensional evaluation of acetabular trauma: Volunteric image processing. J Trauma 29:214, 1989.
68. Fitzgerald RH: Acetabular labrum tears: Diagnosis and management. Clin Orthop 311:60, 1995.
69. Flandry F, Hughston JC: Current concepts review pigmented villonodular synovitis. J Bone Joint Surg Am 69:942, 1987.
70. Froberg PK, Braunstein EM, Buckwalter KA: Osteonecrosis, transient osteoporosis, and transient bone marrow edema: Current concepts. Radiol Clin North Am 34:273, 1996.
71. Genez BM, Wilson MR, Houk RW, et al: Early osteonecrosis of the femoral head: Detection in high-risk patients with MR imaging. Radiology 168:521, 1988.
72. Gielen JL, van Holsbeeck MT, Hauglustaine D, et al: Growing bone cysts in long-term hemodialysis. Skeletal Radiol 19:43, 1990.
73. Glickstein MF, Burk DL Jr, Schiebler ML, et al: Avascular necrosis versus other diseases of the hip: Sensitivity of MR imaging. Radiology 169:213, 1988.
74. Gold RH, Hawkins RA, Katz RD: Bacterial osteomyelitis: Findings on plain radiography, CT, MR, and scintigraphy. AJR Am J Roentgenol 157:365, 1991.
75. Gold RI, Seeger LL, Bassett LW, et al: An integrated approach to the evaluation of metastatic bone disease. Radiol Clin North Am 28:471, 1990.
76. Goldman AB, DiCarlo EF: Pigmented villonodular synovitis: Diagnosis and differential diagnosis. Radiol Clin North Am 26:1327, 1988.
77. Goldman AB, Schneider R, Pavlov H: Osteoid osteomas of the femoral neck: Report of four cases evaluated with isotopic bone scanning. CT and MR imaging. Radiology 186:227, 1993.
78. Griffiths HJ, Standertskjold-Nordenstan CG, Burke J, et al: Computed tomography in the management of acetabular fractures. Skeletal Radiol 11:22, 1984.
79. Grimm J, Higer HP, Benning R, et al: MRI of transient osteoporosis of the hip. Arch Orthop Trauma Surg 110:98, 1991.
80. Guenther KP, Tomczak R, Kessler S, et al: Measurement of femoral anteversion by magnetic resonance imaging: Evaluation of a new technique in children and adolescents. Eur J Radiol 1:47, 1995.
81. Haller J, Resnick D, Greenway G, et al: Juxtaacetabular ganglionic (or synovial) cysts: CT and MR features. J Comp Assist Tomogr 13:976, 1989.
82. Harley JD, Mack LA, Winquist RA: CT of acetabular fractures: Comparison with conventional radiography. AJR Am J Roentgenol 138:413, 1982.
83. Hase T, Ueo T: Acetabular labral tear: Arthroscopic diagnosis and treatment. Arthroscopy 15:138, 1999.
84. Hauzeur JP, Hanqunet S, Gevenois PA, et al: Study of magnetic resonance imaging in transient osteoporosis of the hip. J Rheumatol 18:1211, 1991.
85. Hayes CW, Conway WF, Daniel WW: MR imaging of bone marrow edema pattern: Transient osteoporosis, transient bone marrow syndrome, or osteonecrosis. Radiographics 13:1001, 1993.
86. Hermann G, Gilbert MS, Abdelwahab IF: Hemophilia: Evaluation of musculoskeletal involvement with CT, sonography, and MR imaging. AJR Am J Roentgenol 158:119, 1992.
87. Hernandez RJ: Evaluation of congenital hip dysplasia and tibial torsion by computed tomography. J Comput Assist Tomogr 7:101, 1983.
88. Hodler J, Yu JS, Goodwin D, et al: MR arthrography of the hip: Improved imaging of the acetabular labrum with histologic correlation. AJR Am J Roentgenol 165:887, 1995.
89. Hofmann S, Kramer J, Schneider W, et al: Transient osteoporosis may represent a reversible early form of avascular necrosis of the hip joint. Curr Orthop 11:164, 1997.
90. Iida S, Harada Y, Shimizu K, et al: Correlation between bone marrow edema and collapse of the femoral head in steroid-induced osteonecrosis. AJR Am J Roentgenol 174:735, 2000.
91. Ikeda T, Awaya G, Suzuki S, et al: Torn acetabular labrum in young patients. J Bone Joint Surg Br 70:13, 1988.
92. Jaffe HL: Synovial chondromatosis and other articular tumors. In Tumors and Tumorous Conditions of the Bones and Joints. Philadelphia, Lea & Febiger, 1958.
93. Janzen DL, Hippersbach SE, Munk PL, et al: Three-dimensional CT measurement of adult acetabular dysplasia: Technique, preliminary results in normal subjects, and potential applications. Skeletal Radiol 27:352, 1998.
94. Jelinek JS, Kransdorf MJ, Shmookler BM, et al: Giant cell tumor of the tendon sheath: MR findings in nine cases. AJR Am J Roentgenol 162:919, 1994.
95. Jelinek JS, Kransdorf MJ, Utz JA, et al: Imaging of pigmented villonodular synovitis with emphasis on MR imaging. AJR Am J Roentgenol 152:127, 1989.
96. Johnson ND, Wood BP, Noh KS, et al: MR imaging anatomy of the infant hip. AJR Am J Roentgenol 153:127, 1989.
97. Judet R, Judet J, Letournel E: Fractures of the acetabulum: Classification and surgical approaches for open reduction. J Bone Joint Surg Am 46:1615, 1964.
98. Karasick D, Karasick S: Giant cell tumor of tendon sheath: Spectrum of radiologic findings. Skeletal Radiol 21:219, 1992.
99. Karlin CA, De Smet AA, Neff J, et al: The variable manifestations of extraarticular synovial chondromatosis. AJR Am J Roentgenol 137:731, 1981.
100. Keene GS, Villar RN: Arthroscopic anatomy of the hip: An in vivo study. Arthroscopy 10:329,1994.
101. Kim YT, Azuma H: The nerve endings of the acetabular labrum. Clin Orthop 320:176, 1995.
102. Kingzett-Taylor A, Tirman PFJ, Feller J, et al: Tendinosis and tears of gluteus medius and minimus muscles as a cause of hip pain: MR imaging findings. AJR Am J Roentgenol 173:1123, 1999.
103. Klaue K, Durnin CW, Ganz R: The acetabular rim syndrome. J Bone Joint Surg Br 73:423, 1991.
104. Klein MH, Shankman S: Osteoid osteoma: Radiologic and pathologic correlation. Skeletal Radiol 21:23, 1992.

105. Kneisl JS, Simon MA: Medical management compared with operative treatment for osteoid-osteoma (abstract). Radiology 185:294, 1992.
106. Konig H, Sieper J, Wolf K: Rheumatoid arthritis: Evaluation of hypervascular and fibrous pannus with dynamic MR imaging enhanced with Gd-DTPA. Radiology 176:473, 1990.
107. Konrath GA, Hamel AJ, Olson SA, Sharkey NA: The role of the acetabular labrum and the transverse acetabular ligament in load transmission in the hip. J Bone Joint Surg 80:1781, 1998.
108. Kottal RA, Vogler JB 3rd, Matamoros A, et al: Pigmented villonodular synovitis: A report of MR imaging in two cases. Radiology 163: 551, 1987.
109. Kransdorf MJ, Jelinek JS, Moser RP Jr, et al: Soft-tissue masses: Diagnosis using MR images. AJR Am J Roentgenol 153:541, 1989.
110. Kransdorf MJ, Stull MA, Gilkey FW, Moser RP Jr.: Osteoid osteoma. Radiographics 11:671, 1991. Review.
111. Kransdorf MJ, Meis JM: From the archives of the AFIP: Extraskeletal osseous and cartilaginous tumors of the extremities. Radiographics 13:853, 1993.
112. Krasny R, Prescher A, Botschek A, et al: MR anatomy of infants: Comparison to anatomical preparations. Pediatr Radiol 21:211, 1991.
113. Kulkarni MV, Drolshagen LF, Kaye JJ, et al: MR imaging of hemophiliac arthropathy. J Comput Assist Tomogr 10:445, 1986.
114. Kursunoglu-Brahme S, Riccio T, Weisman MH, et al: Rheumatoid knee: Role of gadopentetate-enhanced MR imaging. Radiology 176: 831, 1990.
115. Lafferty CM, Sartoris DJ, Tyson R et al: Acetabular alterations in untreated congenital dysplasia of the hip: Computed tomography with multiplanar reformation and three-dimensional analysis. J Comput Assist Tomogr 10:84, 1986.
116. Laffourgue P, Dahan E, Chagnaud C, et al: Early-stage avascular necrosis of the femoral head: MR imaging for prognosis in 31 cases with at least 2 years of follow-up. Radiology 187:199, 1993.
117. Lagier R, Seigne JM, Mbakop A: Juxta-acetabular mucoid cyst in a patient with osteoarthritis of the hip secondary to dysplasia. Int Orthop 8:19, 1984.
118. Lakhanpal S, Ginsburg WW, Luthra HS, et al: Transient regional osteoporosis: A study of 56 cases and review of the literature. Ann Intern Med 106:444, 1987.
119. Lang P, Steiger P, Genant HK, et al: Three-dimensional CT and MR imaging in congenital dislocation of the hip: Clinical and technical considerations. J Comput Assist Tomogr 12:459, 1988.
120. Lang P, Genant HK, Jergesen HE, et al: Imaging of the hip joint: Computed tomography versus magnetic resonance imaging. Clin Orthop 274:135, 1992.
121. Lecouvet FE, Vande Berg BC, Malghem J, et al: MR imaging of the acetabular labrum: Variations in 200 asymptomatic hips. AJR Am J Roentgenol 167:1025–1028, 1996.
122. Lee JK, Yao L: Stress fracture: MR imaging. Radiology 169:217, 1988.
123. Leonidas JC: MR imaging of transient osteoporosis. Radiology 170: 281, 1989.
124. Letournel E: Acetabulum fractures: Classification and management. Clin Orthop 151:81, 1980.
125. Leunig M, Werlen S, Ungersbock A, et al: Evaluation of the acetabular labrum by MR arthrography. Br J Bone Joint Surg 79:230, 1997.
126. Lewis SL, et al: Pitfalls of bone scintigraphy in suspected hip fractures. Br J Radiol 64:403, 1991.
127. Li KC, et al: MRI in osteoarthritis of the hip: Gradations of severity. Magn Reson Imaging 6:229, 1988.
128. Li KCP, Hiette P: Contrast-enhanced fat saturation magnetic resonance imaging for studying the pathophysiology of osteonecrosis of the hips. Skeletal Radiol 21:375, 1992.
129. Libshitz HI, et al: Multiple myeloma: Appearance at MR imaging. Radiology 182:833, 1992.
130. Liu S-K, Moroff S: Case report 753. Skeletal Radiol 22:50, 1993.
131. MacDougall L, Conway WF: Controversies in magnetic resonance imaging of the hip. Top Magn Reson Imaging 8:44, 1996.
132. Madewell JE, Sweet DE: Tumors and tumor-like lesions in or about joints. In Resnick D, Niwayama G (eds): Diagnosis of Bone and Joint Disorders, 2nd ed. Philadelphia, WB Saunders, 1988, pp 3889–3943.
133. Magee T, Hinson G: Association of paralabral cysts with acetabular disorders. AJR Am J Roentgenol 174:1381, 2000.
134. Magid D, et al: Femoral head avascular necrosis: CT assessment with multiplanar reconstruction. Radiology 157:751, 1985.
135. Maistrelli G, et al: Osteonecrosis of the hip treated by intertrochanteric osteotomy: A 4- to 15-year follow-up (abstract). Radiology 172:294, 1989.
136. Markisz JA, et al: Segmental patterns of avascular necrosis of the femoral heads: Early detection with MR imaging. Radiology 162: 717, 1987.
137. Marti-Bonmati L, et al: Brodie abscess: MR imaging appearance in 10 patients. J Magn Reson Imaging 3:543, 1993.
138. Martinez CR, et al: Evaluation of acetabular fractures with two- and three-dimensional CT. Radiographics 12:227, 1992.
139. Mason MD, et al: Chronic complicated osteomyelitis of the lower extremity: Evaluation with MR imaging. Radiology 173:355, 1989.
140. Matsuno T, Hasegawa I, Masuda T: Chondroblastoma arising in the triadiate cartilage: Report of two cases with review of the literature. Skeletal Radiol 16:216, 1987.
141. Mazoyer J-F, Kohler R, Bossard D: Osteoid osteoma: CT-guided percutaneous treatment. Radiology 161:199, 1986.
142. McBeath AA, Neidhart DA: Acetabular cyst with communicating ganglion. J Bone Joint Surg Am 58:267, 1976.
143. McCarthy JC, Busconi B: The role of hip arthroscopy in the diagnosis and treatment of hip disease. Orthopedics 18:753, 1995.
144. McCarthy JC, Day B, Busconi B: Hip arthroscopy: Applications and technique. J Am Acad Orthop Surg 3:115, 1995.
145. Mesgarzadeh M, Revesz G, Bonakdarpour A: Femoral neck torsion angle measurement by computed tomography. J Comput Assist Tomogr 5:799, 1987.
146. Milgram JW: Synovial osteochondromatosis: A histopathological study of thirty cases. J Bone Joint Surg 59:792, 1977.
147. Mitchell DG, et al: Hematopoietic and fatty bone marrow distribution in the normal and ischemic hip: New observations with 1.5 T MR imaging. Radiology 161:199, 1986.
148. Mitchell DG, et al: Femoral head avascular necrosis: Correlation with MR imaging, radiographic staging, radionuclide imaging, and clinical findings. Radiology 162:709, 1987.
149. Mitchell DG, et al: Avascular necrosis of the femoral head: Morphologic assessment of MR imaging with CT correlation. Radiology 161:739, 1986.
150. Miyanishi K, et al: Subchondral changes in transient osteoporosis of the hip. Skeletal Radiol 30:255, 2001.
151. Modic MT, et al: Magnetic resonance imaging of musculoskeletal infections. Radiol Clin North Am 24:247, 1986.
152. Moulopoulos LA, et al: Multiple myeloma: Spinal MR imaging in patients with untreated newly diagnosed disease. Radiology 185: 833, 1992.
153. Murphy SB, et al: Acetabular dysplasia in the adolescent and young adult. Clin Orthop 261:214, 1990.
154. Neuhold A, et al: Bone marrow edema of the hip: MR findings after core decompression. J Comput Assist Tomogr 16:951, 1992.
155. Nishina T, Saito S, Ohzono K, et al: Chiari pelvic osteotomy for osteoarthritis: The influence of the torn and detached acetabular labrum. J Bone Joint Surg Br 72:765, 1990.
156. Nokes SR, et al: Herniation pits of the femoral neck: Appearance at MR imaging. Radiology 172:231, 1989.
157. Norman A, Steiner GC: Bone erosion in synovial chondromatosis. Radiology 161:749, 1986.
158. Paterson I: The torn acetabular labrum. J Bone Joint Surg Br 39: 306, 1957.
159. Pennal GF, et al: Pelvis disruption: Assessment and classification. Clin Orthop 151:12, 1980.
160. Petersilge CA, Haque MA, Petersilge WJ, et al: Acetabular labral tears: Evaluation with MR arthrography. Radiology 1996; 200:231.
161. Peterson HA, et al: The use of computerized tomography in dislocation of the hip and femoral neck anteversion in children. J Bone Joint Surg Br 63:198, 1981.
162. Pitt MJ, et al: Herniation pit of the femoral neck. AJR Am J Roentgenol 138:1115, 1982.
163. Plenk H, et al: Histomorphology and bone morphometry of the bone marrow edema syndrome of the hip. Clin Orthop 334:73, 1997.
164. Potter H, et al: Magnetic resonance imaging in diagnosis of transient osteoporosis of the hip. Clin Orthop 280:223, 1992.
165. Present D, et al: Clear cell chondrosarcoma of bone: A report of 8 cases. Skeletal Radiol 20:187, 1991.
166. Pritchard RS, et al: MR and CT appearances of iliopsoas bursal distention secondary to diseased hips. J Comput Assist Tomogr 14: 797, 1990.

167. Quinn SF, McCarthy JL: Prospective evaluation of patients with suspected hip fracture and indeterminate radiographs: Use of T1-weighted MR images. Radiology 187:469, 1993.
168. Rahmouni A, et al: MR appearance of multiple myeloma of the spine before and after treatment. AJR Am J Roentgenol 160:1053, 1993.
169. Rashleigh-Belcher HJC, Cannon SR: Recurrent dislocation of the hip with a 'Bankart-type' lesion. J Bone Joint Surg Br 68:398, 1986.
170. Reinus WR, et al: Plasma cell tumors with calcified amyloid deposition mistaken for chondrosarcoma. Radiology 189:505, 1993.
171. Reiser MF, Naegele M: Inflammatory joint disease: Static and dynamic gadolinium-enhanced MR imaging. J Magn Reson Imaging 3:307, 1993.
172. Reiser MF, et al: Gadolinium-DTPA in rheumatoid arthritis and related diseases: First results with dynamic magnetic resonance imaging. Skeletal Radiol 18:591, 1989.
173. Resnick D, Niwayana G: Diagnosis of Bone and Joint Disorders, 3rd ed. Philadelphia, WB Saunders, 1995.
174. Richardson P, Young JWR, Porter D: CT detection of cortical fracture of the femoral head associated with posterior hip dislocation. AJR Am J Roentgenol 155:93, 1990.
175. Rizzo PF, et al: Diagnosis of occult fractures hip: Magnetic resonance imaging compared with bone-scanning (abstract). Radiology 189:295, 1993.
176. Rosenberg ZS, Shankman S, Steiner GC, et al: Rapid destruction osteoarthritis: Clinical, radiographic, and pathologic features. Radiology 182:213, 1992.
177. Rosenthal D, et al: Ablation of osteoid osteomas with a percutaneously placed electrode: A new procedure. Radiology 183:29, 1992.
178. Ross LV, et al: Hemodialysis-related amyloidomas of bone. Radiology 178:263, 1991.
179. Rubin JL, et al: High-field MR imaging of extracranial hematomas. AJR Am J Roentgenol 148:813, 1987.
180. Ruwe PA, et al: Clinical determination of femoral anteversion: A comparison with established techniques. J Bone Joint Surg Am 6: 820, 1992.
181. Saks BJ: Normal acetabular anatomy for acetabular fracture assessment: CT and plain film correlation. Radiology 159:139, 1986.
182. Santori N, Villar RN: Acetabular labral tears: Result of arthroscopic partial limbectomy. Arthroscopy 16:11, 2000.
183. Sartoris DJ, et al: Computed tomography with multiplanar reformation and three-dimensional analysis in the preoperative evaluation of ischemic necrosis of the femoral head. J Rheumatol 13:153, 1986.
184. Schlesinger AE, Hernandez RJ: Intracapsular osteoid osteoma of the proximal femur: Findings on plain film and CT. AJR Am J Roentgenol 154:1241, 1990.
185. Schnarkowski P, Steinbach LS, Tirman PF, et al: Magnetic resonance imaging of labral cysts of the hip. Skeletal Radiol 25:733, 1996.
186. Schwappach JR, et al: Subcapital fractures of the femoral neck: Prevalence and cause of radiographic appearance simulating pathologic fracture. AJR Am J Roentgenol 162: 651, 1994.
187. Scoles PV, et al: Nuclear magnetic resonance imaging in Legg-Calvé-Perthes disease. J Bone Joint Surg Am 66:1357, 1984.
188. Scott WW Jr, Fishman EK, Magid D: Acetabular fractures: Optimal imaging. Radiology 165:537, 1987.
189. Senac MO Jr, et al: MR imaging in juvenile rheumatoid arthritis. AJR Am J Roentgenol 150:873, 1988.
190. Shimizu K, Moriya H, Akita T: Prediction of collapse with magnetic resonance imaging of avascular necrosis of the femoral head. J Bone Joint Surg Am 76:215, 1994.
191. Shirkoda A, Brashear R, Staab EV: Computed tomography of acetabular fractures. Radiology 134:683, 1980.
192. Shuman WP, et al: Comparison of STIR and spin-echo MR imaging at 1.5 T in 45 suspected extremity tumors: Lesion conspicuity and extent. Radiology 179:247, 1991.
193. Spritzer CE, Dalinka MK, Kressel HY: Magnetic resonance imaging of pigmented villonodular synovitis: A report of two cases. Skeletal Radiol 16:316, 1987.
194. Steinberg GC, Coumas JM, Breen T: Preoperative localization of osteoid osteoma: A new technique that uses CT. AJR Am J Roentgenol 155:883, 1990.
195. Stutley JE, Conway WF: Magnetic resonance imaging of the pelvis and hips. Orthopedics 17:1053, 1994.
196. Sundaram M, McGuire MH, Herbold DR: Magnetic resonance imaging of soft-tissue masses: An evaluation of fifty-three histologically proven tumors. Magn Reson Imaging 6:237, 1988.
197. Suzuki S, Awaya G, Okada Y, et al: Arthroscopic diagnosis of ruptured acetabular labrum. Acta Orthop Scand 57:513, 1986.
198. Szpryt P, et al: Synovial chondromatosis of the hip joint presenting as a pathological fracture. Br J Radiol 59:399, 1986.
199. Takatori Y, et al: Avascular necrosis of the femoral head: Natural history and magnetic resonance imaging. J Bone Joint Surg Br 75: 217, 1993.
200. Tang JSH, et al: Musculoskeletal infection of the extremities: Evaluation with MR imaging. Radiology 166:205, 1988.
201. Tehranzadeh J, et al: Comparison of CT and MR imaging in musculoskeletal neoplasms. J Comput Assist Tomogr 13:466, 1989.
202. Tehranzadeh J, Vanarthos W, Pais MJ: Osteochondral impaction of the femoral head associated with hip dislocation: CT study in 35 patients. AJR Am J Roentgenol 155:1049, 1990.
203. Tervonen O, et al: Clinically occult avascular necrosis of the hip prevalence in an asymptomatic population at risk. Radiology 182: 845, 1992.
204. Thrall JH, Ellis BI: Skeletal metastases. Radiol Clin North Am 25: 1155, 1987.
205. Toby EB, Koman LA, Bechtold RE: Magnetic resonance imaging of pediatric disease. J Pediatr Orthop 5:665, 1985.
206. Tooke SM, et al: Results of core decompression for femoral head osteonecrosis. Clin Orthop 226:99, 1986.
207. Totty WG, et al: Magnetic resonance imaging of the normal and ischemic femoral head. AJR Am J Roentgenol 143:1273, 1984.
208. Turner DA, et al: Femoral capital osteonecrosis: MR findings of diffuse marrow abnormalities without focal lesions. Radiology 171: 135, 1989.
209. Ueo T, Suzuki S, Iwasake R, Yosikawa J: Rupture of the labra acetabularis as a cause of hip pain detected arthroscopically, and partial limbectomy for successful pain relief. Arthroscopy 6:48, 1990.
210. Unger EC, et al: Diagnosis of osteomyelitis by MR imaging. AJR Am J Roentgenol 150:605, 1988.
211. Unger EC, et al: MRI of extracranial hematomas: Preliminary observations. AJR Am J Roentgenol 146:403, 1986.
212. Vanel D, et al: Musculoskeletal tumors: Follow-up with MR imaging after treatment with surgery and radiation therapy. Radiology 164: 243, 1987.
213. Vanel D, et al: Dynamic contrast-enhanced subtraction MR imaging in follow-up of aggressive soft-tissue tumors: A prospective study of 74 patients. Radiology 189(P):205, 1993.
214. Vande Berg BE, et al: Idiopathic bone marrow edema lesions of the femoral head: Predictive value of MR imaging findings. Radiology 212:527, 1999.
215. Vande Berg BE, et al: MR imaging of avascular necrosis and transient marrow edema of the femoral head. Radiographics 13: 501, 1993.
216. Vande Berg BE, et al: Avascular necrosis of the hip: Comparison of contrast-enhanced and nonenhanced MR imaging with histologic correlation. Radiology 182:445, 1992.
217. Varma DGK, et al: MR appearance of the distended iliopsoas bursa. AJR Am J Roentgenol 156:1025, 1991.
218. Varma DGK, et al: Chondrosarcoma: MR imaging with pathologic correlation. Radiographics 12:687, 1992.
219. Villacin AB, Brigham LN, Bullough PG: Primary and secondary synovial chondrometaplasia: Histopathologic and clinicoradiologic differences. Hum Pathol 10:439, 1979.
220. Walker JM: Histological study of the fetal development of the human acetabulum and labrum: Significance in congenital hip disease. Yale J Biol Med 54:255, 1981.
221. Weekes RG, et al: CT of soft-tissue neoplasms. AJR Am J Roentgenol 144:355, 1985.
222. Wetzel LH, Levine E, Murphey MD: A comparison of MR imaging and CT in the evaluation of musculoskeletal masses. Radiographics 7:851, 1987.
223. Wilson AJ, et al: Transient osteoporosis: Transient bone marrow edema? Radiology 167:757, 1988.
224. Williams PL, Warwick R (eds): Arthrology: The joints of the lower limb: The hip (coxal) joint. In Gray's Anatomy, 36th ed. Philadelphia, WB Saunders, 1980, pp 477–482.
225. Wilson DA, Prince JR: Imaging of hemophilic pseudotumors. AJR Am J Roentgenol 150:349, 1988.

226. Wing VW, et al: Chronic osteomyelitis examined by CT. Radiology 154:171, 1985.
227. Woods ER, et al: Reactive soft-tissue mass associated with osteoid osteoma: Correlation of MR imaging features with pathologic findings. Radiology 186:221, 1993.
228. Yamamoto T, et al: A clinicopathologic study of transient osteoporosis of the hip. Skeletal Radiol 28:621, 1999.
229. Yamamoto T, Schneider R, Bullough PG: Subchondral insufficiency fracture of the femoral head: Histopathologic correlation with MRI. Skeletal Radiol 30:247, 2001.
230. Yao L, Lee JK: Occult intraosseous fracture: Detection with MR imaging. Radiology 167:749, 1988.
231. Yulish BS, et al: Hemophilic arthropathy: Assessment with MR imaging. Radiology 164:759, 1987.
232. Yulish BS, et al: Juvenile rheumatoid arthritis: Assessment with MR imaging. Radiology 165:149, 1987.

50 The Shoulder

Tamara Miner Haygood,
Kathleen Gallagher Oxner,
J. Bruce Kneeland, and Murray K. Dalinka

In 1993, when the first version of this chapter was drafted, hundreds of articles and one book[220] had already been devoted to shoulder imaging. Since that time, published sources have increased greatly in number, with many new journal articles and another book.[190] Magnetic resonance (MR) arthrography, still a new technique of uncertain potential in 1993, has become accepted and is commonly performed in both academic and private practice settings. Orthopedists have revised their collective opinion of the cause and treatment of some shoulder disorders.

To accommodate this new material and yet confine the discussion to a reasonable length, disorders occurring in locations other than the shoulder are covered more succinctly than in our previous offering. Tumors, in fact, have been dropped entirely. SLAP (superior labrum, anterior and posterior) lesions are now included with other labral tears in the section on instability rather than separately. As we said last time, no scheme will please everyone, but we hope this arrangement will be satisfactory to most.

Anatomy

For purposes of this chapter, the shoulder is considered to include the glenohumeral joint, the acromioclavicular joint, and related soft tissues. The glenohumeral joint is relatively shallow, with the humeral head large in comparison to the glenoid fossa. This configuration grants mobility at the expense of stability. The labrum is a meniscus-like, fibrous or fibrocartilaginous structure that runs about the edge of the glenoid. It serves to increase the depth of the glenoid, providing more contact area and thus more stability for the glenohumeral joint. A recess lined with synovium may be interposed between the labrum and origin of the long head of the biceps brachii muscle. Anterior to this muscle origin and extending to the midglenoid, the labrum may be absent or unattached, with a smooth foramen between itself and the glenoid rim. A recess may also be present in this area.[25, 95, 123, 157, 185, 197]

Surrounding the glenohumeral joint is the joint capsule, which attaches to both the anatomic neck of the humerus and the scapula. Its scapular attachment is variable, particularly at the midpoint of the glenoid. In this area, the capsule may attach to the anterior labrum, to the glenoid just medial to the labrum, or farther medially along the glenoid.[123, 132]

Compared with the capsules of other joints, the glenohumeral joint capsule is relatively loose and allows maximal movement of the joint. There are three normal extensions of the joint capsule where joint fluid may be seen at imaging in patients with an effusion. The first is a communication with the sheath of the long head of the biceps as it runs through the intertubercular groove. The second reaches under the coracoid process to communicate with the subscapular recess. The third is the axillary recess or axillary pouch, a loose fold of thickened capsule at the caudal extent of the joint that tightens when the arm is abducted. Normally, joint fluid is restricted to a thin film, with no distention of these recesses.[121, 173]

Three glenohumeral ligaments are seen as thickened areas of the joint capsule:

1. The *superior* glenohumeral ligament arises from the superior glenoid within a centimeter anterior to the biceps origin and runs to the fovea capitis of the humerus. It is the most consistent of the three in its course and is often identified at cross-sectional imaging.[26, 47, 147]
2. The *middle* glenohumeral ligament is the most variable of the three in its course and thickness. It often arises in common with the superior glenohumeral ligament and runs anteriorly in an inferolateral direction to the lesser tuberosity of the humerus.[26, 47, 147]
3. The *inferior* glenohumeral ligament complex consists of distinct anterior and posterior bands separated by the axillary pouch. It runs from a broad-based origin along the mid to inferior labrum to the humeral neck. This complex is the most important ligamentous stabilizer, guarding against both anterior and posterior dislocations.[142, 147]

A number of other ligaments also help stabilize the shoulder. The *coracoacromial* ligament passes deep to the deltoid and superficial to the subacromial-subdeltoid bursa. It supports the shoulder against upward pressure.[121]

The *coracohumeral* ligament runs from the lateral aspect of the base of the coracoid to insert on the humerus adjacent to the greater tuberosity, where its fibers blend at its insertion site with those of the joint capsule. It passively supports the humerus when the arm hangs at the side. It is also a major stabilizer of the biceps tendon in its groove.[121]

The *coracoclavicular* ligament is made up of two parts, the trapezoid ligament and the conoid ligament. The former runs from the coracoid process to the undersurface of the distal clavicle, and the latter runs from the coracoid to the more medially located conoid tubercle of the clavicle.[121]

The *acromioclavicular* ligament strengthens the superior portion of the tight-fitting acromioclavicular joint capsule. Both it and the coracoclavicular ligament stabilize the acromioclavicular joint.[121, 170]

Four muscles (supraspinatus, infraspinatus, teres minor,

subscapularis), together with their tendons, form the *rotator cuff*. All originate on the scapula and insert on the humerus. They are responsible for abduction and internal and external rotation of the glenohumeral joint. Of these muscles, the supraspinatus is the one injured most often. It arches superiorly over the humerus to insert superolaterally on the greater tuberosity. The infraspinatus and teres minor also insert on the greater tuberosity, each a little more inferiorly and posteriorly. The subscapularis has a broad origin on the anterior scapula and inserts with multiple tendon slips onto the lesser tuberosity.

The large deltoid muscle extends from a very broad origin on the distal clavicle and acromion to insert into the deltoid tubercle of the lateral aspect of the proximal humeral diaphysis. Occasionally, a proximal tendon slip of the deltoid arises from the undersurface of the clavicle or acromion, where it may mimic a spur. The deltoid muscle is external to the rotator cuff and is separated from it by the subacromial-subdeltoid bursa and its associated extrasynovial fat pad. The subacromial-subdeltoid bursa does not normally communicate with the glenohumeral joint. The peribursal fat pad has a rather variable appearance. At MRI, part of this fat pad may not be visible, either in normal shoulders or in shoulders with rotator cuff pathology.[33, 82, 118, 133] The subcoracoid bursa lies caudal to the coracoid process and anterior to the subscapularis muscle. It communicates with the subacromial-subdeltoid bursa about half the time.[172]

Between the greater and lesser tuberosities lies the bicipital groove, also called the intertubercular sulcus. This depression cradles the tendon of the long head of the biceps brachii, which originates from the superior glenoid tubercle and superior labrum. Its proximal tendon passes anteriorly over the humeral head through the rotator interval, a ligament-cloaked space separating the supraspinatus and subscapularis muscles. It then passes through the bicipital groove to the muscle belly. The tendon is secured in its groove superiorly by the coracohumeral ligament, its most important stabilizer, and by the transverse humeral ligament, to which the subscapularis tendon may lend some fibers. More distally, the tendon of the pectoralis major also contributes to stabilization of the biceps tendon in its groove.[41]

The coracoacromial ligament forms part of the coracoacromial arch, which consists of the coracoacromial ligament and the structures it connects—the coracoid process of the scapula and the anterior acromion. This relatively immobile complex not only provides support to the shoulder but may also impinge on the tendon of the supraspinatus muscle, causing tendinitis and contributing to an eventual tear.

Three different configurations of the acromion have been described. *Type I* is flat inferiorly. *Type II* curves smoothly. In *type III*, the most anterior portion of the acromion has a hooked shape.[9] The acromion may also be convex along its inferior surface.[46] The inferior margins of the acromion and distal clavicle usually lie at approximately the same level in the coronal plane.

Three neurovascular structures are important to the imaging anatomy of the shoulder. Running on the posterior aspect of the scapula are the suprascapular nerve and artery. The nerve arises from the upper trunk of the brachial plexus (C5 and C6) and passes through the suprascapular notch. It then runs deep to the supraspinatus muscle. When it emerges from beneath the supraspinatus muscle, it passes through the spinoglenoid notch. It carries both sensory and motor fibers and supplies motor innervation to the supraspinatus and infraspinatus muscles.[52, 121]

The anterolateral branch of the anterior circumflex humeral artery runs for a short distance next to the tendon of the long head of the biceps within the bicipital groove. This small vessel can be mistaken for a bicipital tendon disorder, particularly on gradient-echo sequences in which arterial flow appears bright.[121]

Cross-Sectional Anatomy

The following paragraphs describe the anatomy of the shoulder from the viewpoint of cross-sectional imaging in the four planes often obtained with MRI:

- Axial
- Coronal oblique
- Sagittal oblique
- Abduction, external rotation (ABER)

The descriptions are complemented by Figures 50–1 to 50–4.

Axial Projection (Fig. 50–1)

At the level of the acromioclavicular joint, seen in part *A* of Figure 50–1, the acromion curves in on the lateral side of the shoulder to meet the distal end of the clavicle. It is not unusual for the ends of the bones to be oriented at slightly different angles.

Part *B* shows the level of the top of the humeral head. The supraspinatus muscle arches across the humerus from posteromedial to anterolateral and may appear to surround the humeral head. A large, principal tendon arises from the anterior, fusiform portion of the muscle. Small individual tendon slips arise from the posterior supraspinatus muscle, which morphologically resembles a strap muscle. The course of the main tendon is at a slightly different angle from that of the muscle.[204, 205] The deltoid forms a thick semicircle of muscle external to the supraspinatus. The scapular spine can be noted posteriorly as it runs laterally and superiorly to form the acromion.

In part *C*, at the level of the top of the coracoid process of the scapula, the humeral head normally has a round shape. The top of the glenoid is usually seen here, but it is not uncommon for the labrum to be inapparent. The supraspinatus muscle projects between the glenoid and the inferior extension of the scapular spine. The infraspinatus tendon emerges anteriorly to attach to the greater tuberosity. Running from posterior to anterior is the superior glenohumeral ligament.

In part *D*, closer to the base of the coracoid, the superior labrum becomes identifiable. A Hill-Sachs deformity, if present, can be identified at this level or higher.

In part *E*, the normal posterior labrum has a relatively constant blunt triangular shape. The anterior labrum may vary considerably in shape. It may appear either round or

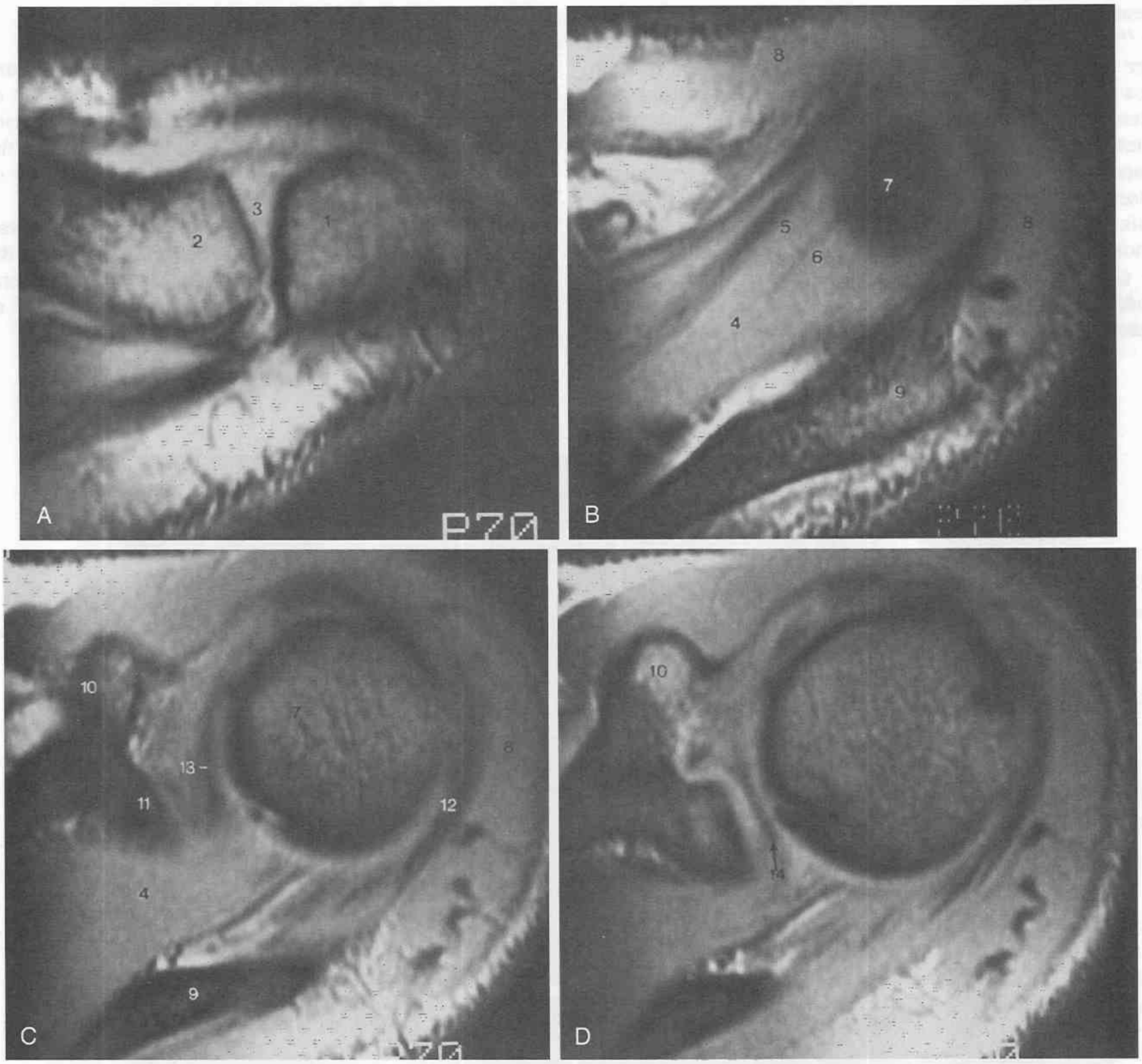

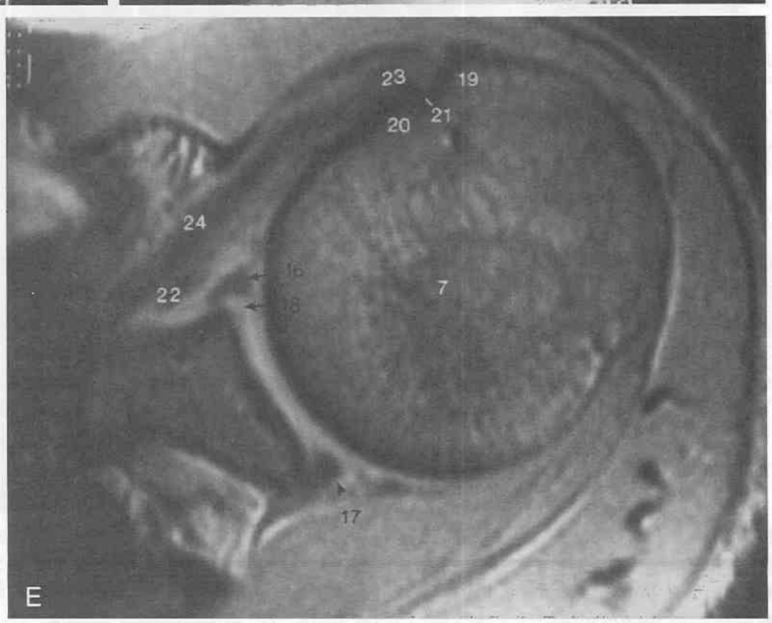

Figure 50–1. *A–E,* MRI axial views of the shoulder (see text for details). 1, acromion; 2, clavicle; 3, acromioclavicular joint; 4, supraspinatus muscle; 5, anterior main tendon; 6, posterior tendon slip; 7, humeral head; 8, deltoid muscle; 9, scapular spine; 10, coracoid process; 11, glenoid; 12, infraspinatus muscle/tendon; 13, superior glenohumeral ligament; 14, superior labrum; 15, coracohumeral ligament; 16, anterior labrum; 17, posterior labrum; 18, glenoid articular cartilage; 19, greater tuberosity; 20, lesser tuberosity; 21, bicipital groove; 22, middle glenohumeral ligament; 23, bicipital tendon; 24, subscapularis muscle and tendon.

pointed and may exhibit longitudinal or transverse clefts.[73, 109, 114, 132] Both anteriorly and posteriorly, the articular cartilage comes to the edge of the glenoid, and this forms an area of increased signal intensity that burrows beneath the internal edge of the labrum and must not be mistaken for a tear.[99] At this level, the humeral head has an oblong shape with two indentations. Anteriorly, the greater and lesser tuberosities surround the bicipital groove, in which rests the tendon of the long head of the biceps. Posteriorly, a normal, small concavity or flattening of the humerus can be seen.[175] Other structures routinely visualized here include the anterior joint capsule, the middle glenohumeral ligament, and the subscapularis muscle and tendon.

Coronal Oblique Projection (Fig. 50–2)

In part *A* of Figure 50–2, the subscapularis muscle runs anterior to the scapular blade and just beneath the base of the coracoid to attach to the lesser tuberosity. Inferior to this are the flow voids of axillary vessels within the quadrilateral space. Superiorly, the anteriormost extent of the clavicle is the origin of a portion of the deltoid.

In part *B*, more posteriorly, the anterior humeral head may be seen with the greater and lesser tuberosities and the dark bicipital tendon within its groove. The coracohumeral ligament runs at an angle with respect to this plane of imaging, but portions of it may be seen.

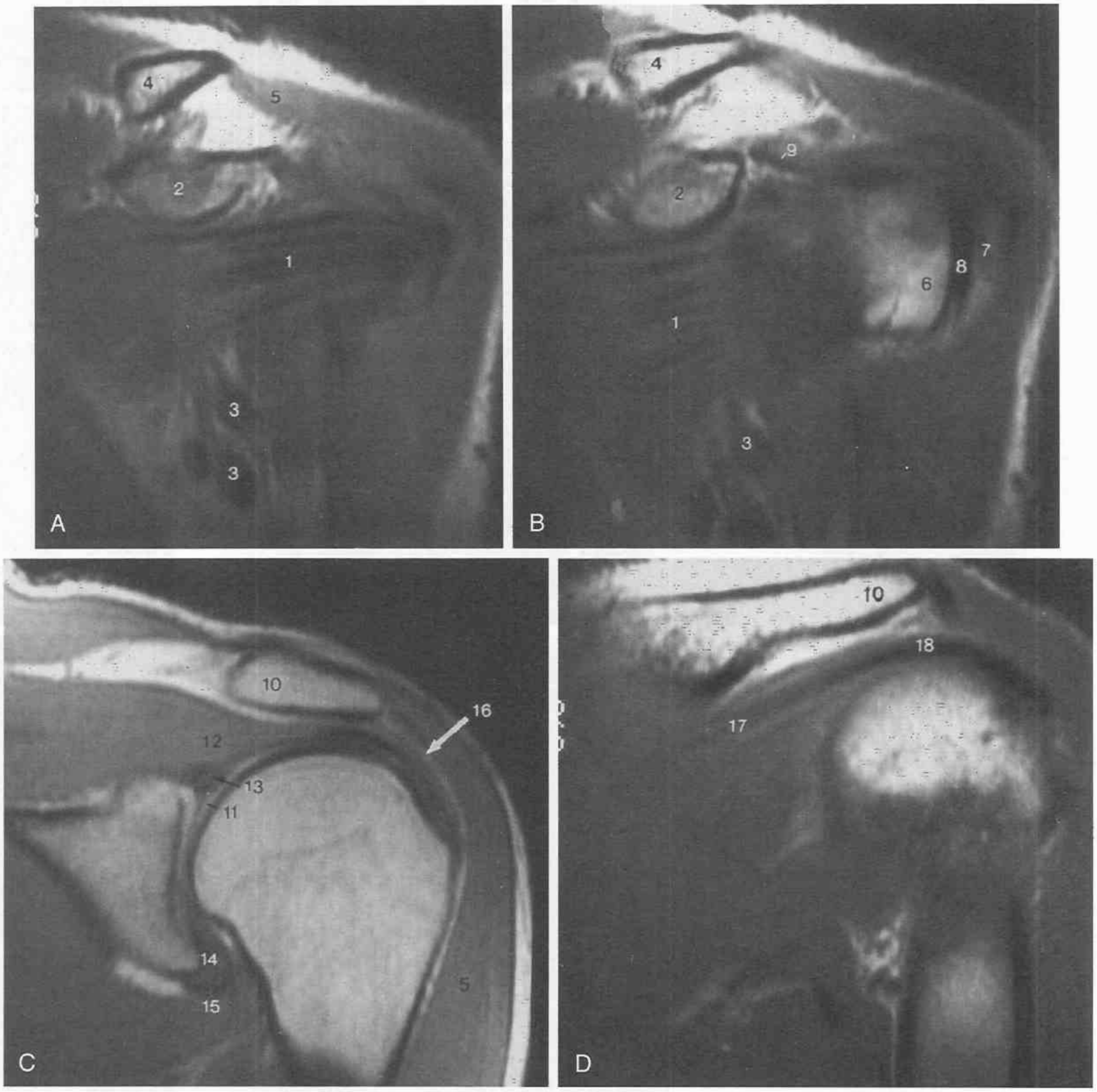

Figure 50–2. *A–D,* MRI coronal oblique views of the shoulder (see text for details). 1, subscapularis muscle; 2, coracoid process; 3, axillary vessels; 4, clavicle; 5, deltoid; 6, lesser tuberosity; 7, greater tuberosity; 8, bicipital tendon; 9, coracohumeral ligament; 10, acromion; 11, humeral articular cartilage; 12, supraspinatus muscle and tendon; 13, superior labrum; 14, inferior labrum; 15, inferior glenohumeral ligament/axillary recess; 16, fat stripe; 17, infraspinatus muscle; 18, infraspinatus tendon.

In part *C*, at the midglenoid, the glenohumeral articulation is well seen. It is best visualized in the coronal projection at the point at which the glenoid is most prominent. Also well seen at this level is the tendon of the supraspinatus and the peribursal fat stripe. A portion of the inferior glenohumeral ligament is seen below the inferior labrum. Although it is not evident here, a thin, crescentic band of preserved red marrow may be seen in the humeral epiphysis, running parallel to the articular cortex.[164]

In part *D*, far posterior in the shoulder, the infraspinatus muscle and tendon pass under the acromion to insert on the greater tuberosity. Depending on the degree of internal or external rotation, this attachment site may not always be visualized in the same plane as the muscle. It may be quite difficult in an individual patient to decide where the supraspinatus muscle ends and the infraspinatus begins.

Sagittal Oblique Projection (Fig. 50–3)

In part *A* of Figure 50–3, the four rotator cuff tendons blend at their insertion sites into a fibrous band that appears on magnetic resonance imaging (MRI) as a solid arc of dark signal draped across the humeral head. The deltoid muscle projects external to the rotator cuff. The physeal scar is often visible in adults. To distinguish anterior from posterior in the sagittal projection, note that a supine patient's arm usually tilts backward a bit from the shoulder, so as a first approximation the direction the distal humerus points may be taken as posterior.

In part *B*, at the level of the medial humeral head, the rotator cuff muscles are separate from one another. (The infraspinatus and teres minor, however, may be inseparable both anatomically and tomographically.) The biceps tendon is seen close to the humeral head in the rotator interval between the subscapularis and the supraspinatus. The coracoacromial ligament is the dark structure arching anteriorly and inferiorly from the inferior margin of this slightly hooked acromion.

In part *C*, slightly more medial, the lateral aspect of the coracoid process becomes visible. The coracoid is a reliable marker for anterior.

In part *D*, farther medial, the coracoid process arises from its base on the scapula. One of the coracoclavicular ligaments projects between the coracoid and the clavicle.

In part *E*, at the level of the scapular "Y," the suprascapular artery and nerve are seen running beneath the body of the supraspinatus muscle and through the spinoglenoid notch.

Abduction, External Rotation (ABER) Positioning (Fig. 50–4)

In part *A* of Figure 50–4, a coronal scout image allows sections to be obtained parallel to the humeral shaft and perpendicular to the glenohumeral joint, running in this case from the inferior to the superior glenoid.

In part *B*, at the level of the inferior labrum, the posterior joint space balloons outward as the anterior capsule is placed under tension by this positioning technique.

In part *C*, as in other externally rotated sequences, the anterior labrum assumes a pointed, triangular shape. The posterior labrum becomes rounded and globular. As the humerus rotates up into position, the medial aspect of the bone now faces anteriorly. The concave shape of the metaphysis is typical of the medial, upper humerus.

In part *D*, at approximately the midglenoid, the anterior band of the inferior glenohumeral ligament is visible.

In part *E*, at the level of the superior glenoid, the course of the tendon of the long head of the biceps brachii is displayed, almost in its entirety in this patient.

Technique

In evaluation of bony trauma, noncontrast computed tomography (CT) of the shoulder is often useful. Contiguous 5-mm sections in the axial plane beginning at the acromioclavicular joint are sufficient to find or exclude fractures. The scan should extend a few centimeters below the most inferior fracture line. If coronal, sagittal, or three-dimensional (3D) reconstruction is desired, thinner cuts will provide smoother reconstructed images. Overlapped 3-mm sections obtained at 2-mm increments, for example, may improve the quality of reconstructed images. A bone algorithm should be employed.[30] Helical CT has proved useful in the skeletal system, allowing fast imaging with excellent reconstruction in additional planes at the cost of slight loss of resolution in the plane of primary acquisition.[181]

CT arthrography is useful for evaluation of the joint capsule and intracapsular structures and for finding loose bodies within the joint. For the double-contrast technique, 0.5 to 3.0 mL of contrast material and approximately 10 mL of room air are introduced into the glenohumeral joint. Contiguous slices are obtained at 3- to 4-mm intervals from a level just above the acromioclavicular joint to below the glenoid fossa.[30, 34, 159, 180, 183, 184, 213] Single-contrast technique may also be employed.[66, 91, 166]

CT arthrography has been largely overtaken by MRI as the preferred technique for evaluation of intracapsular structures. MRI allows better concurrent evaluation of extracapsular structures, such as the rotator cuff, and is noninvasive. It does have disadvantages, however. MRI is contraindicated in patients with intraorbital metal, pacemakers, defibrillators, and incompatible intracranial surgical clips. It may ruin such a large number of electronic devices, including implanted drug infusion ports, bone stimulator devices, and hearing aids, that a complete discussion of safety in MRI is beyond the scope of this chapter. Ferromagnetic metallic surgical devices in the region being scanned may ruin the images. (This, of course, may also be a problem with CT.) Claustrophobic patients who find it difficult to tolerate the confinement of a cylindrical superconducting magnet may better tolerate scanning in a low-field-strength open system. Relatively little research has been done to evaluate the diagnostic accuracy of the open scanners.[115]

MRI depiction of intracapsular structures, the capsule itself, and the undersurface of the rotator cuff is greatly enhanced by a joint effusion, which is sometimes conveniently present concomitantly with disease, particularly in young persons. When an effusion is not present, however,

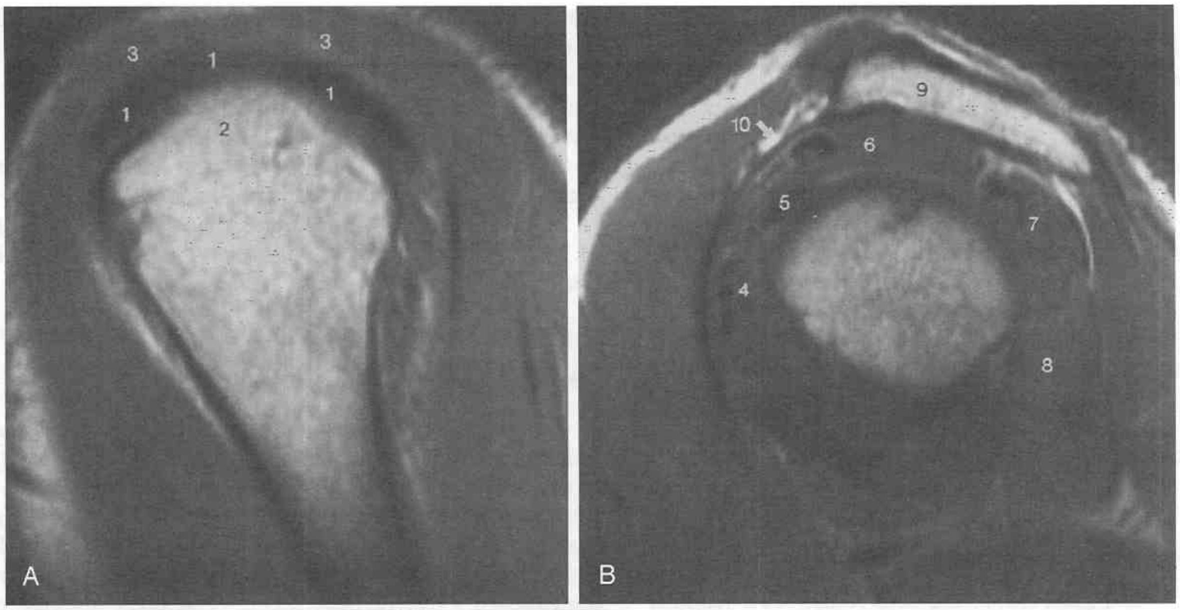

Figure 50–3. *A–E,* MRI sagittal oblique views of the shoulder (see text for details). 1, rotator cuff; 2, humeral head; 3, deltoid muscle; 4, subscapularis; 5, bicipital tendon; 6, supraspinatus; 7, infraspinatus; 8, teres minor; 9, acromion; 10, coracoacromial ligament; 11, conjoined tendon of short head of biceps brachii and coracobrachialis; 12, coracoid process; 13, clavicle; 14, acromioclavicular joint; 15, acromioclavicular ligament; 16, coracoclavicular ligament; 17, scapular spine (root of acromion); 18, suprascapular nerve and artery.

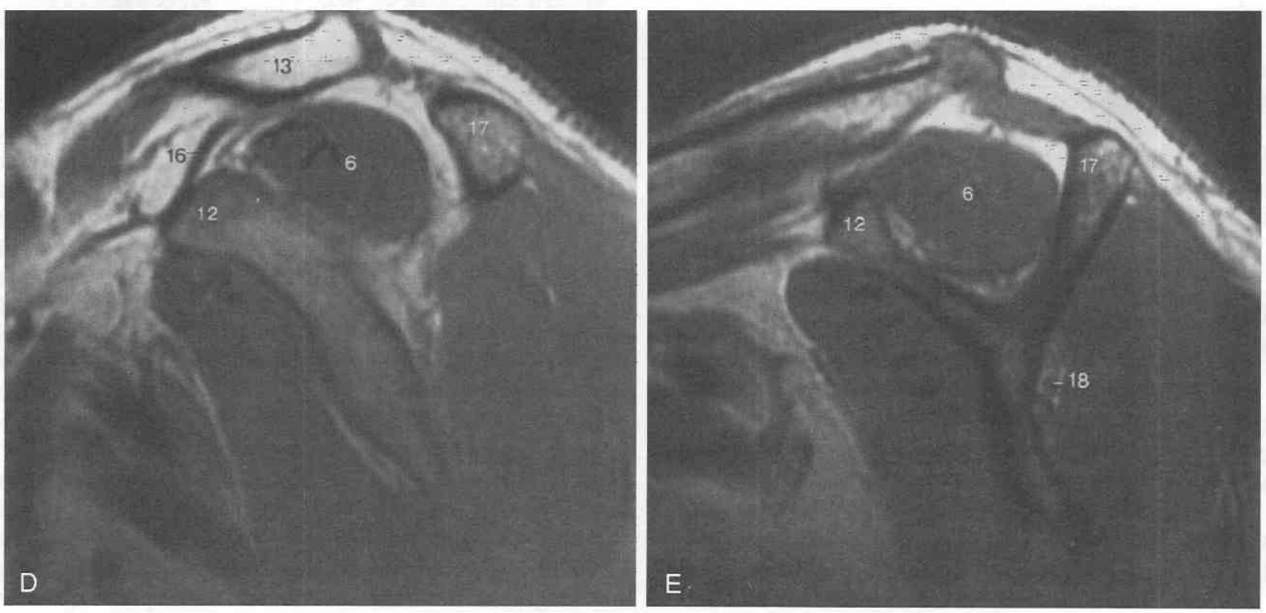

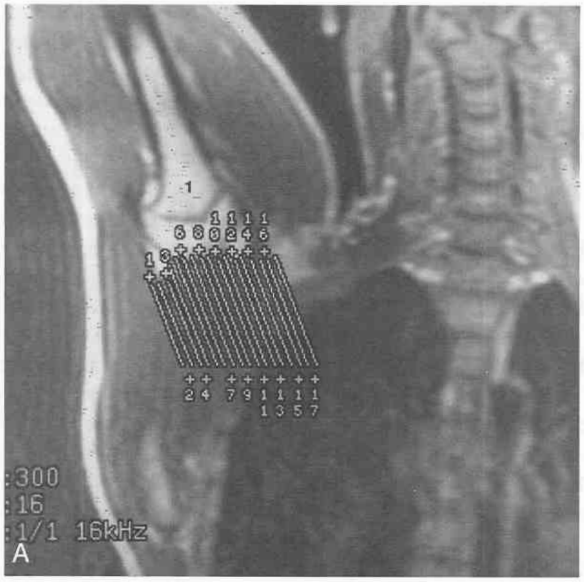

Figure 50–4. *A–E,* Abduction, external rotation (ABER) oblique axial views of the shoulder. 1, humeral shaft; 2, humeral epiphysis; 3, glenoid; 4, redundant posterior capsule; 5, taut anterior capsule; 6, anterior humeral cortex; 7, anterior labrum; 8, posterior labrum; 9, posterior rotator cuff; 10, inferior glenohumeral ligament; 11 (and *arrowheads*), biceps tendon, long head.

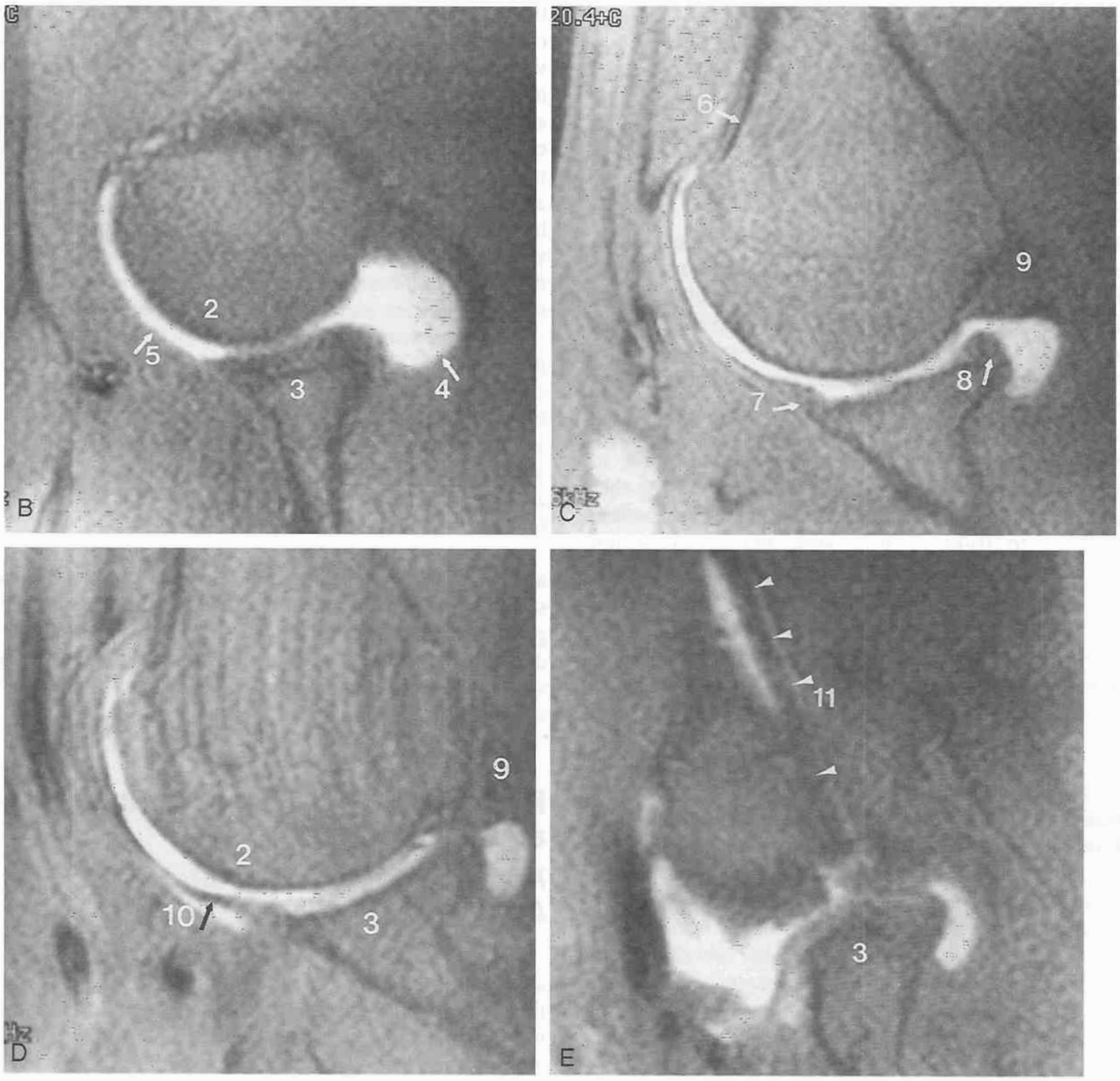

these structures become more difficult to interpret. To obtain the effect of an effusion, intra-articular gadolinium-diethylenetriamine-penta-acetic acid (Gd-DTPA) can be used. Gd-DTPA, diluted approximately 1:250 with normal saline, is injected into the glenohumeral joint.[91]

Palmer and colleagues suggested a solution obtained by mixing 2 mL of gadopentetate dimeglumine (Magnevist, Berlex Laboratories, Wayne, NJ) in 250 mL of normal saline. They mixed 10 mL of this solution with 5 mL of iodinated contrast (60% meglumine diatrizoate), 5 mL of 1% lidocaine, and 0.3 mL of 1:1000 epinephrine.[147]

Beltran and coworkers have used 1 to 5 mL of iodinated contrast to confirm intra-articular needle placement fluoroscopically; they then injected a solution obtained by diluting 0.1 mL of gadopentetate dimeglumine in 20 mL of normal saline and mixing with 0.3 mL of 1:1000 epinephrine.[5]

Each of these methods assumes needle placement at fluoroscopy. Palmer's technique allows performance of a single-contrast arthrogram at the time of injection, as may Beltran's, depending on how much iodinated contrast has been used. Some radiologists prefer to achieve intra-articular needle placement sonographically, with MRI guidance, or without imaging guidance, using anatomic landmarks.[32, 155, 206] In those circumstances, nothing would be gained by injection of iodinated contrast. An alternative procedure is the intra-articular injection of normal saline with acquisition of T2-weighted sequences.[209]

Diagnostic MRI images of the shoulder depend on a number of technical considerations. The proliferation of varied imaging platforms by numerous manufacturers during the 1990s has made it difficult to generalize about technique and increases the need for all radiologists to become familiar with the capabilities and limitations of their own machines. Recommendations given here are colored by experience with the General Electric (G.E.) Signa 1.5 Tesla systems and must be adapted as appropriate to other magnets. Small field-of-view (FOV) images with thin sections are essential to obtain sufficient spatial resolution. We use a 14- to 16-cm field of view and a 3- to 4-mm section thickness with a 0.5- to 1-mm intersection gap in all projections and for all pulse sequences. The larger field of view, section thickness, and intersection gap are used for larger patients. Local or surface radiofrequency coils, including quadrature coils, provide a sufficient signal-to-noise ratio to support the necessary resolution.

One final technical point that is often overlooked is the importance of stabilizing the shoulder to reduce motion artifact. Motion arises from a combination of respiratory and small voluntary movements by the subject. When the coil allows it, this small amount of motion may be effectively suppressed by placing a sandbag on the shoulder. It is important to be sure of the contents of the sandbag before bringing it into the MRI scanning room. Some "sand" bags actually contain ferromagnetic metallic shot.

There is no uniform agreement concerning the ideal pulse sequences for imaging the shoulder. For evaluation of the rotator cuff, most radiologists use a long repetition time (TR), double-echo sequence obtained in an oblique coronal plane chosen to be parallel to the supraspinatus muscle or perpendicular to the glenoid fossa. Using the same pulse sequence, we also obtain a second set of images in an oblique sagittal plane perpendicular to the coronal set.

Most published experience with T2-weighted technique is based on the use of spin-echo images, but beginning around 1995, results with fast spin-echo have suggested that it is equally diagnostic.[3, 17, 169, 182, 187, 219] At least one group of investigators has used T2-weighted gradient-echo images with success.[169] Some radiologists prefer a short TR/TE (echo time) sequence for the sagittal oblique plane, which has the advantage of shorter acquisition time but the disadvantage of lower sensitivity to rotator cuff disease.

For long TR/TE spin-echo sequences, we also recommend that those working on G.E. Signa systems use the "classic" option with frequency centered on the water peak. This provides some fat suppression on the second echo. We do not routinely use other fat-suppression techniques, although they may be useful, particularly when fast spin-echo is preferred to spin-echo imaging.[3, 148, 158, 162, 182]

For evaluation of glenohumeral instability and the glenoid labrum, we image in the axial plane and use either the long TR, double-echo sequences previously described or a two-dimensional (2D) gradient-echo sequence obtained with a TR of 400 to 600 msec, a TE of 10 msec, and a flip angle of 20 degrees. We prefer to position the patient's shoulder in slight external rotation. Keeping the patient's elbow extended, we rotate the hand so that the palm faces medially and upward, making approximately a 45-degree angle with the tabletop. Placing a wedge cushion under the hand and sandbags across the palm maintains this position without active muscular effort, thus increasing comfort and decreasing motion artifact. Greater external rotation may slightly increase sensitivity to anterior labral tears.[201]

When performing gadolinium MRI shoulder arthrography, we use T1-weighted spin-echo or gradient-echo axial, coronal oblique, and sagittal oblique images with fat saturation. It is important to include at least one set of T2-weighted images, usually in the coronal oblique plane. This allows identification of intrasubstance rotator cuff disease and fluid collections not in communication with the glenohumeral joint.

A fourth imaging plane that may be helpful with MR arthrography is the oblique axial plane, with the patient's shoulder in abduction and external rotation.[29, 96, 196] If the patient places the hand under the head, palm up, the shoulder will be appropriately positioned. A coronal localizing sequence then allows images to be obtained parallel to the shaft of the humerus.

Rotator Cuff Disease, Impingement, and Instability

Pathophysiology of Rotator Cuff Disease and Impingement

Rotator cuff disease is a common cause of shoulder pain and disability. It is linked with impingement, glenohumeral instability, and bicipital tendon disorders in a complex web of associations. It is impossible to speak or write comprehensively of one without bringing up the others, for whatever one may believe of the causal relationship of these disorders, patients with any one of them have an

increased incidence of the others compared with individuals not so affected.[80, 129, 136]

In 1991, Fu and coworkers drew on the work of many authors to propose a unifying theory linking rotator cuff disease to impingement and glenohumeral instability.[53] *Intrinsic* and *extrinsic* factors, acting together or separately, result in a common endpoint.

Intrinsic factors lead to degenerative changes within the substance of the rotator cuff with increasing age.[24, 143, 146] The degeneration may result from relative ischemia within the distal portion of the supraspinatus tendon near its insertion site on the greater tuberosity. This zone of relative ischemia, called the *critical zone*, corresponds to the most common site of rotator cuff disease, although its exact location and size vary from one patient to another.[87, 100, 122, 161] Rotator cuff degeneration may incite secondary proliferative bony changes on the undersurface of the acromion. These changes, in turn, may lead to further cuff degeneration and, ultimately, to a cuff tear.[146]

Extrinsic causes of rotator cuff disease relate to mechanical impingement by surrounding structures. The impingement can lead to inflammatory and degenerative change in the underlying tendons. The causes of impingement can be further divided into *primary* and *secondary* types.[53]

Primary impingement results from contact between the coracoacromial arch or acromioclavicular joint and the underlying tendons.[9, 53, 129] The coracoacromial arch (consisting of the coracoid process, the coracoacromial ligament, and the undersurface of the anterior third of the acromion), the acromioclavicular joint, and both the rotator cuff tendons and the tendon of the long head of the biceps have a very close anatomic relationship. The supraspinatus tendon passes between the coracoacromial arch superiorly and the humeral head inferiorly to reach its insertion site on the greater tuberosity. The bicipital tendon passes through the same area, coming only slightly more anteriorly. Mechanical compression of these tendons is particularly likely when the shoulder is flexed and internally rotated, as during a tennis serve. Overuse in sports or work accelerates tendon degeneration resulting from either impingement or intrinsic degeneration.[8, 9, 53, 129, 131, 136]

Neer divides the impingement syndrome into three stages:[126, 128, 131]

Stage I is characterized by edema and hemorrhage within the distal supraspinatus tendon and is usually reversible with conservative treatment.

In *stage II* impingement syndrome, there are tendinitis and thickening and fibrosis of the subacromial-subdeltoid bursa. The bursal changes compound the problem by decreasing the subacromial space available to the tendons.

In *stage III* disease, a partial or a full-thickness tear of the rotator cuff or biceps tendon occurs, along with osseous changes including anterior acromial osteophyte formation and degenerative changes in the greater tuberosity.

Stage III lesions usually occur in patients older than 40 years of age, whereas stage I and II lesions are found in younger adults. Long-standing rotator cuff tears may lead, furthermore, to erosions of the humerus and to glenohumeral destruction, termed *rotator cuff arthropathy*.[126, 128, 131]

Whereas primary impingement syndrome is caused by the effects of the coracoacromial arch and acromioclavicular joint on the rotator cuff in a normally positioned and functioning glenohumeral joint, *secondary impingement syndrome* is related to glenohumeral instability. Secondary impingement usually occurs in young athletic individuals involved in sports that demand overhead arm movement. Repetitive external rotation in abduction, as during the cocking phase of a baseball pitch, may lead to laxity of the capsule and mild instability. This is initially compensated for by an increase in the tone of the rotator cuff, which pulls the humeral head into the glenoid and enhances stability. With continued vigorous activity, however, the rotator cuff loses its ability to compensate, and the humeral head subluxates. The subluxation results in secondary impingement.[53, 79, 94] This atraumatic form of instability is often multidirectional and may damage different portions of the labrum or rotator cuff, depending on individual circumstances.[166]

Patients with impingement syndrome present with a "painful arc" consisting of pain over the anterolateral humeral head exacerbated by flexion and abduction, particularly in the 70-degree to 120-degree portion of the arc. Orthopedic surgeons test for impingement by injecting lidocaine into the subacromial region. If the condition is present, this temporarily relieves the pain.

Differentiating primary from secondary impingement may be clinically difficult. Patients with secondary impingement are usually younger than those with primary impingement, and they may relate the pain to a very specific activity. A baseball pitcher with pain restricted to the late cocking or early acceleration phase of throwing is a typical example.

At physical examination, a relocation maneuver may reveal the subtle instability found in these patients. With the patient supine and the shoulder abducted and externally rotated, posteriorly directed force is applied to the anterior, proximal humerus. As the humerus is reduced posteriorly, the patient's pain is alleviated.[78, 94]

It is important to differentiate primary from secondary impingement because the treatments differ significantly. Patients with primary impingement are usually treated with an anterior acromioplasty, with appropriate attention to the rotator cuff and biceps tendon. In patients with secondary impingement, treatment is aimed at the instability.[79, 80, 106, 107, 129, 131]

Coracoid Impingement

A distinct subtype of impingement, occurring with the shoulder flexed, internally rotated, and adducted, is associated with impingement of the coracoid process upon the lesser tuberosity. This rare cause of anterior shoulder pain may be associated with an unusually long and medially oriented coracoid process. It may also follow a Bristow procedure, in which the tip of the coracoid process is moved further medially along the glenoid neck to correct anterior instability, or an osteotomy of the glenoid neck to correct posterior instability. Patients without an iatrogenic risk factor often engage repeatedly in occupational or recreational activities requiring overhead motion in internal rotation.[8, 36, 56]

Imaging of Rotator Cuff Disease

After retrospective studies of Kneeland and colleagues in 1986[90] and 1987[89] indicated that MRI had potential for

Table 50–1. Performance of MRI in Diagnosis of Rotator Cuff Tears

Brief Citation	Reference No.	No. of Patients	Full-Thickness Tears: Sensitivity/Specificity/ Accuracy (%)*	Partial-Thickness Tears: Sensitivity/Specificity/ Accuracy (%)*	Comment
Evancho, 1988	44	31	80/94/89	—	—
Burk, 1989	14	38	92/100/94	—	—
Rafii, 1990	160	80	97/94/95	89/84/85	—
Hodler, 1992	71a	36 (13 with partial tears, 4 with full tears)	Combined full and partial tears a. MRI: 41/79/61 b. MR arthrography with gadolinium: 71/84/70		Accuracy improved with MR arthrography
Traughber, 1992	199	28	100/100/100	5 of 9 partial tears diagnosed with MRI	—
Palmer, 1993	148	36	100/100/100	100/100/100	Tested use of fat saturation; performance was lower without fat saturation (90%, 75%, and 84% for combined full and partial tears)
Flannigan, 1994	49	23	—	—	Improved performance of MR arthrography over MRI
Quinn, 1995	158	100	85/99/96	82/99/97	Tested use of fat saturation
Reinus, 1995	162	80	80/87–92/–(spin-echo without fat saturation) 100/77–87/–(spin-echo with fat saturation)	10–20/83–93/–(spin-echo without fat saturation) 24–45/93–97/–(spin-echo with fat saturation)	Performance of MRI improved by using fat saturation
Robertson, 1995	165	82	81–100/89–98/–	19–57/85–93/–	Compared 4 readers
Singson, 1996	182	43	100/–/–	92/–/–With fat saturation 67/–/–Without fat saturation	
Sonin, 1996	187	26	89/94/92	—	Compared conventional and turbo spin echo and found them equivalent
Balich, 1997	3	222	84–96/94–98/92–97	35–44/85–97/77–87	Evaluated scans from 1989 to 1995, during which time technique changed from spin-echo to fast spin-echo with fat suppression
Sahin-Akyar, 1998	169	39	83–100/–/–		Found that T2-weighted gradient echo and fast spin echo with fat saturation both gave acceptable results

*As given in the original article; not recalculated or derived from data with the article.
MRI, magnetic resonance imaging.

identifying rotator cuff pathologic conditions, MRI quickly became established as an accurate, noninvasive means of diagnosing rotator cuff tears.[43, 221] Reported sensitivities for full-thickness rotator cuff tears have ranged from 80% to 100%, and specificities from 94% to 100%. Arriving at a diagnosis of partial-thickness tears is more problematic. Sensitivities of 10% to 92% have been reported, with specificities of 83% to 100% (Table 50–1).

MRI Appearance

MRI can depict the continuum between rotator cuff degeneration or tendinopathy and partial or full-thickness rotator cuff tears. Intrinsic cuff degeneration or tendinopathy is seen as increased signal intensity within the distal tendon on proton-density images; this persists but does not intensify on T2-weighted images.

Partial tears of the tendon may be intratendinous in location or may occur on either the bursal or the articular side of the tendon. They are most common along the articular surface of the cuff.[199] On MRI, partial tears are depicted as focal areas of increased signal intensity on short TE images; these areas increase in relative signal intensity on long TE images but need not match the signal intensity of joint fluid (Figs. 50–5 and 50–6). The abnormal focus does not extend through the entire thickness of the tendon. There may be increased fluid within the glenohumeral joint, particularly if the partial tear is on the articular side. Alternatively, fluid may be seen within the subacromial-subdeltoid bursa if the partial tear lies on the bursal side of the tendon.

In a full-thickness rotator cuff tear, the tendon is interrupted by an abnormal focus of bright signal intensity extending across its complete superior to inferior extent on at least one image. The signal intensity within the tendon gap is usually notably bright on T2-weighted images, pre-

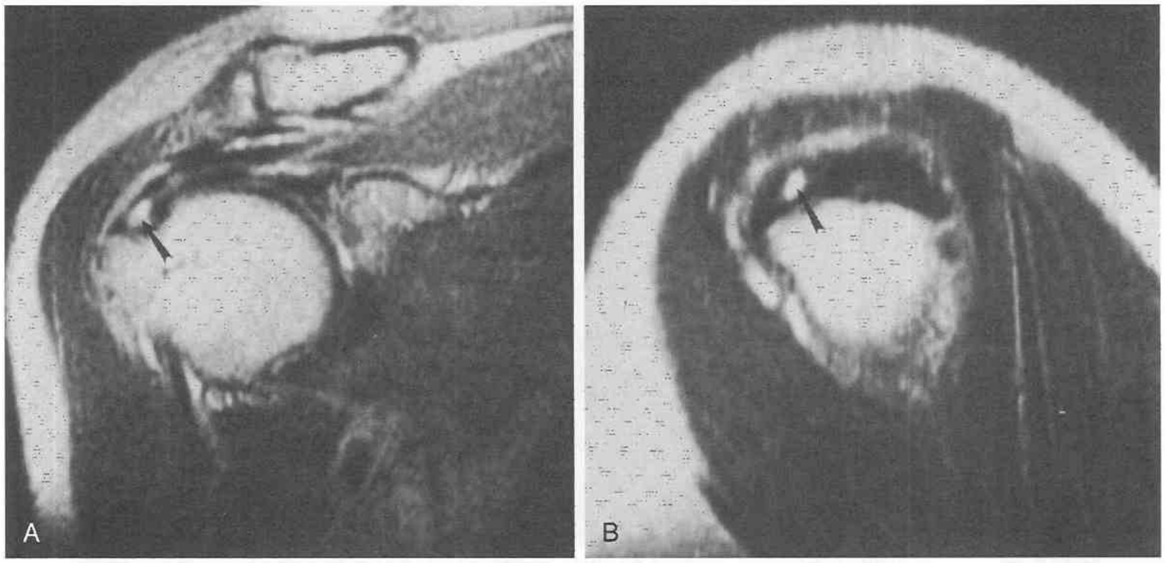

Figure 50–5. Articular side partial tear. *A,* T2-weighted (TR = 2500 msec, TE = 70 msec) coronal oblique image. *B,* T2-weighted (TR = 2500 msec, TE = 70 msec) sagittal oblique image. On the articular side of the supraspinatus tendon is a bright gap *(arrow)* covered on the bursal side with a thin layer of remaining tendon. Increased joint fluid is present, and some fluid is present in the subdeltoid bursa.

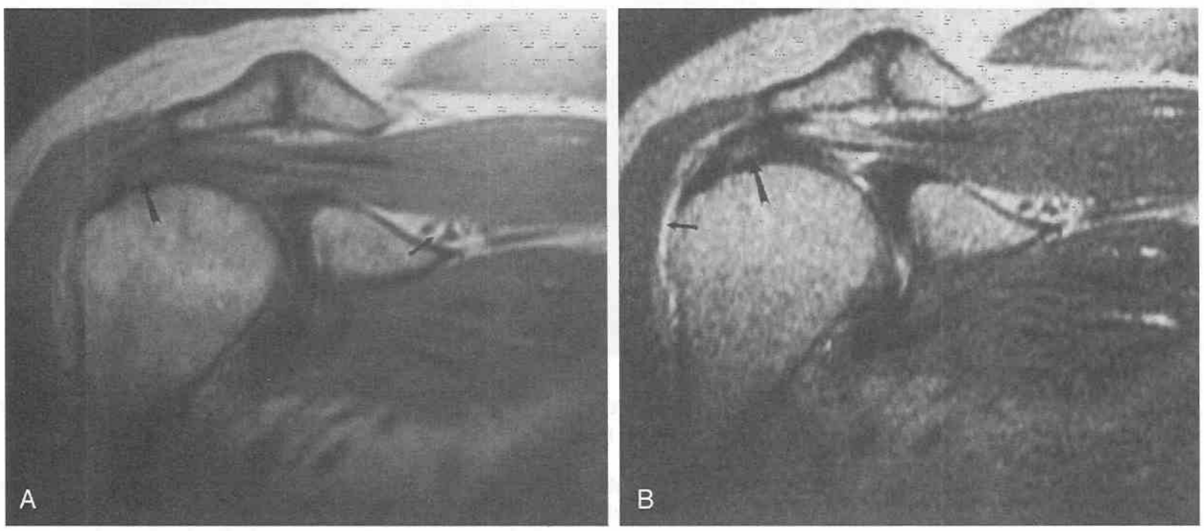

Figure 50–6. Possible tendinopathy, tendinitis, or partial tear.

A, Proton-density–weighted (TR = 2500 msec, TE = 14 msec) coronal oblique image. The central tendon of the supraspinatus muscle is interrupted by an ill-defined area of increased signal in the critical zone near its attachment site *(arrow).* Note the suprascapular neurovascular structures in the suprascapular notch *(small arrow).*

B, T2-weighted (TR = 2500 msec, TE = 70 msec) coronal oblique image. The small area of increased signal in the supraspinatus tendon *(arrow)* has become relatively brighter with T2 weighting, and it is quite focal. This probably represents a partial tear of the supraspinatus tendon. Fluid can be seen in the subdeltoid bursa *(small arrow).*

C, T2-weighted (TR = 2500 msec, TE = 70 msec) sagittal oblique image. This section is farther medial than the partial tear, yet a tiny bright spot is present near the anterior edge of the supraspinatus muscle *(arrow).* This is probably joint fluid in the biceps interval that can be mistaken for a rotator cuff tear. Fluid in the subacromial-subdeltoid bursa is also visible.

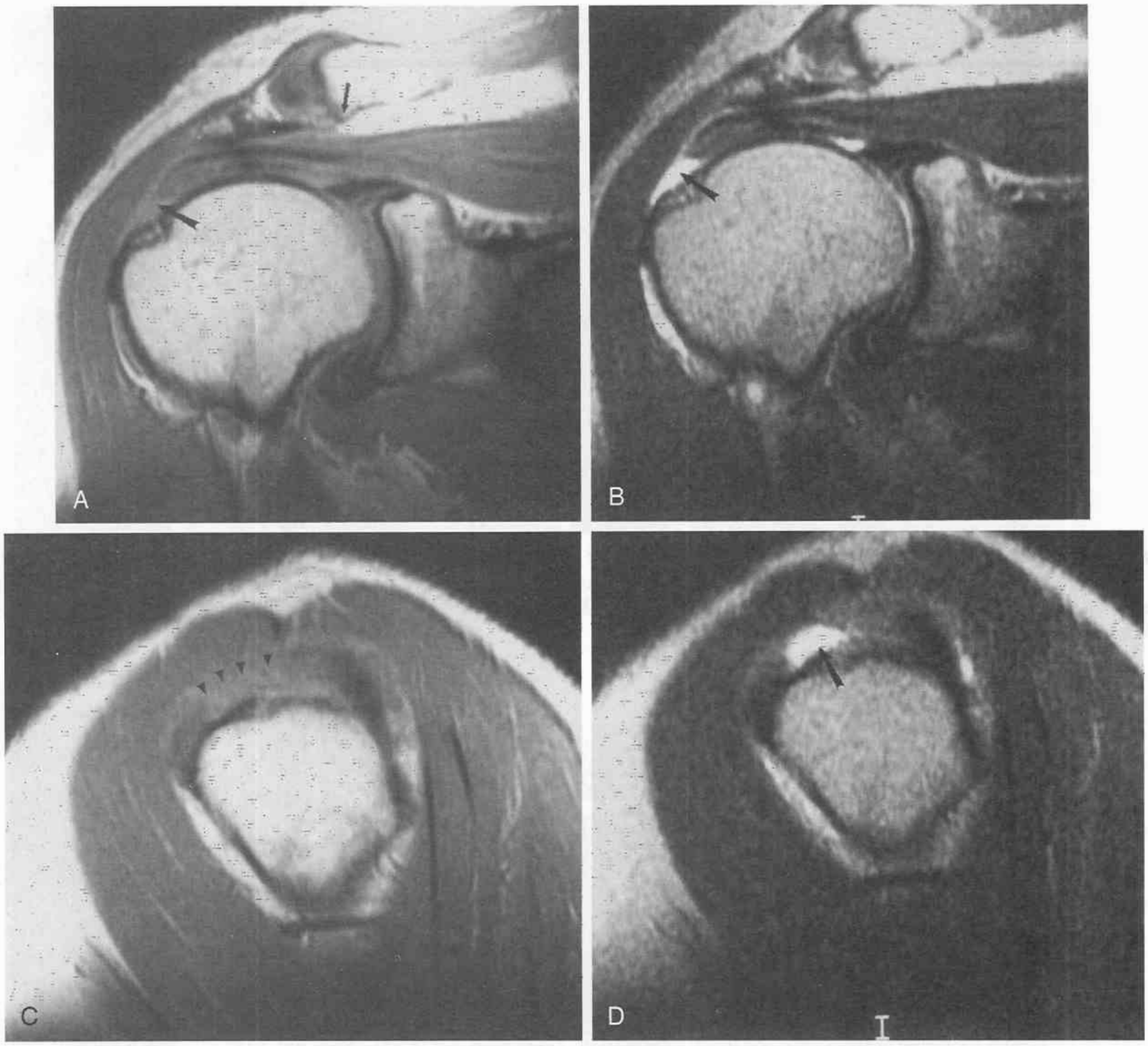

Figure 50–7. Full-thickness tear.

A, Proton-density–weighted (TR = 2500 msec, TE = 14 msec) coronal oblique image. A gap is present in the supraspinatus tendon near its insertion site *(arrow)*. Some proliferative changes affect the acromioclavicular joint, including a small, downward-pointing spur *(small arrow)*.

B, T2-weighted (TR = 2500 msec, TE = 70 msec) coronal oblique image. The tendon gap is very bright *(arrow)* and is most likely filled with fluid. No intact tendon exists above or below the abnormal area.

C, Proton-density–weighted (TR = 2500 msec, TE = 14 msec) sagittal oblique image. Anterosuperiorly, the normal dark band of the rotator cuff is interrupted by a fuzzy area of relatively increased signal *(arrowheads)*.

D, T2-weighted (TR = 2500 msec, TE = 70 msec) sagittal oblique image. The anterior part of this area becomes very bright *(arrow)*. The remainder brightens only slightly. Often a tear is adjacent to or surrounded by an area of tendinopathy.

sumably as a result of fluid (Figs. 50–7 to 50–9). Fluid within the subacromial-subdeltoid bursa is a common finding in full-thickness tears, although it may occasionally be present without a tear when the patient has bursitis.[45, 72] Some full-thickness tears lack fluid-intensity signal because of a paucity of fluid within the joint or because the tendon gap is filled with scar.[160] Other useful signs include tendon retraction and atrophy of the involved muscles with associated fatty infiltration. Tendon retraction becomes more obvious as the size of the tear increases, and it may be inapparent in small tears.[160] Fatty infiltration of the muscle is expected only in relatively chronic tears (Fig. 50–10).

Large tears may be surprisingly subtle if there is little fluid in the joint to communicate with the tendon gap or subacromial bursa. Occasionally, tendon retraction may bring the amputated stump to rest along the medial surface of the humeral head so that the humeral cortex resembles a smooth continuation of the tendon. In these cases, cephalad migration of the humeral head may be the most obvious sign of tearing (Fig. 50–11).

Another occasional accompanying sign is irregularity of the bony elements of the glenohumeral joint as a result of rotator cuff arthropathy (Fig. 50–12). An irregular greater tuberosity has been shown to correlate with rotator cuff

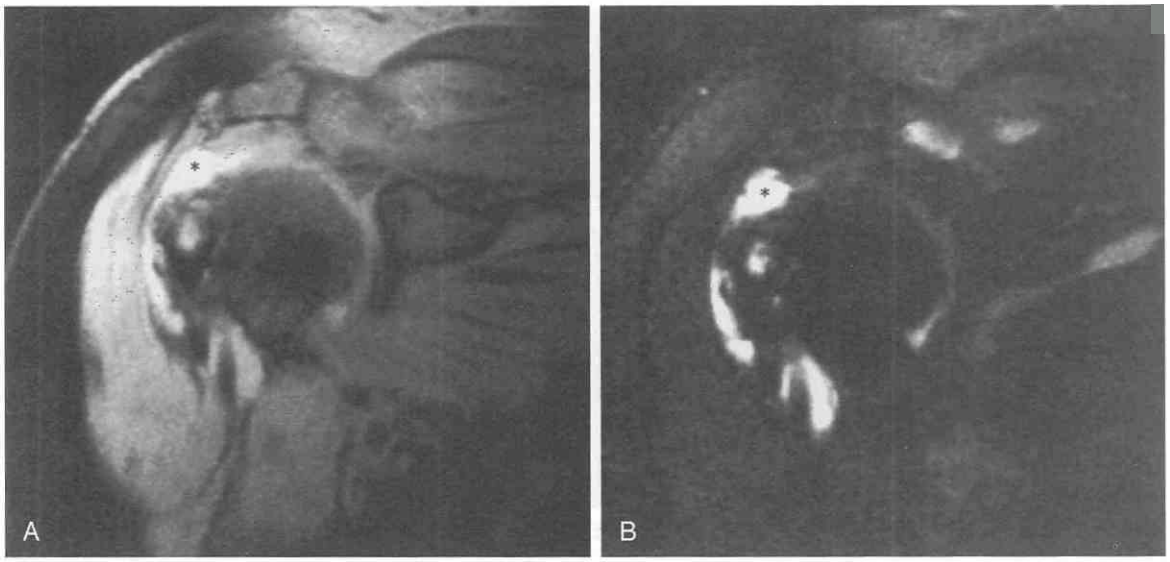

Figure 50–8. Fat-suppression technique. *A,* Proton-density–weighted (TR = 2000 msec, TE = 15 msec) coron[redacted]blique image. *B,* T2-weighted (TR = 2000 msec, TE = 90 msec) coronal oblique image. Fat-suppression techniques may increase [redacted] conspicuity of a rotator cuff tear *(asterisks)* as well as that of a small cystlike defect in the humeral head, but less detail may be discernible elsewhere. (Courtesy of Thomas Hedrick, M.D., Houston.)

tears at sonography.[214] To our knowledge, this has not been tested with MRI. Cystlike lesions of the humeral head have a modest correlation with the presence of rotator cuff disease but are also common in asymptomatic individuals.[74, 125]

Rotator Interval Tears

Rotator cuff tears most commonly begin in the supraspinatus tendon, usually near its anterior edge. As the tear enlarges, it may extend completely across the anterior to posterior dimension of the supraspinatus muscle and tendon, to involve parts or all of the infraspinatus and subscapularis. When the tear occurs at the critical zone of the supraspinatus muscle and spreads anteriorly into the subscapularis, it crosses and involves the intervening rotator interval. Isolated tears of the rotator interval also occur, although uncommonly. They are usually the result of an anterior dislocation. Synovium may herniate from the glenohumeral joint into the rotator interval. With MRI, it can be difficnlt, if not impossible, to distinguish an isolated rotator interval tear from herniated synovium, especially

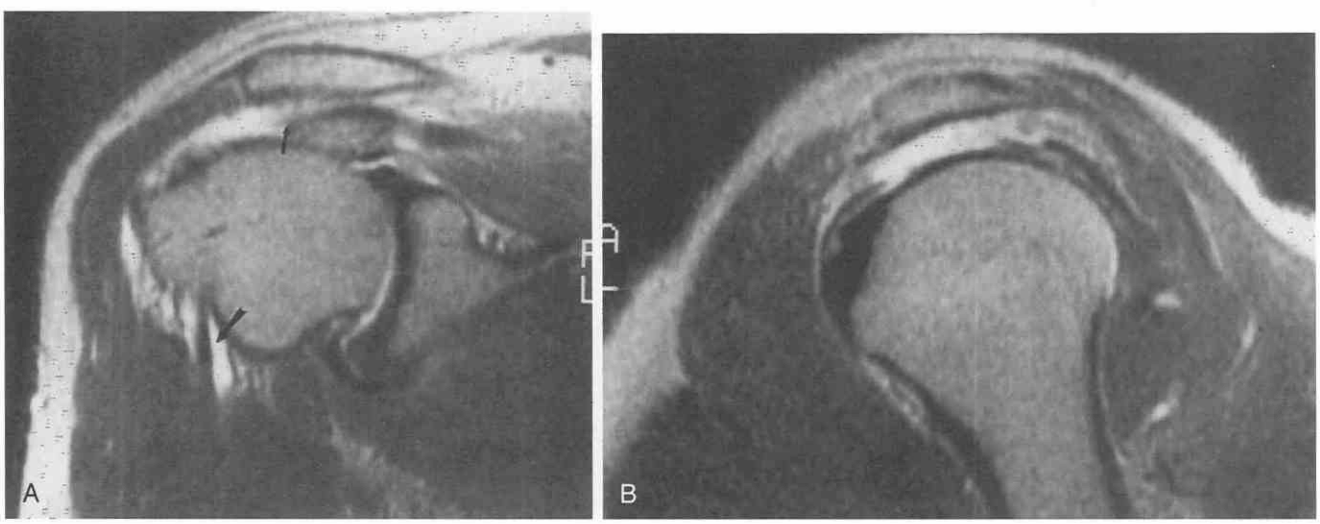

Figure 50–9. Large cuff tear. *A,* T2-weighted (TR = 2500 msec, TE = 70 msec) coronal obliqu[redacted]age. Bright-signal fluid spills from the glenohumeral joint through a large rent in the rotator cuff into the subacromial-sub[redacted]oid [redacted]. Joint f[redacted]ks d[redacted] the sheath of the long head of the biceps brachii muscle *(arrow).* The supraspinatus tendon is retracted *(small arrow). B.* T2-weighted (TR = 2500 msec, TE = 70 msec) sagittal oblique image. The large size of this tear may be best appreciated on this sagittal image. At surgery, the tear included all of the supraspinatus, most of the infraspinatus, and the superior part of the subscapularis.

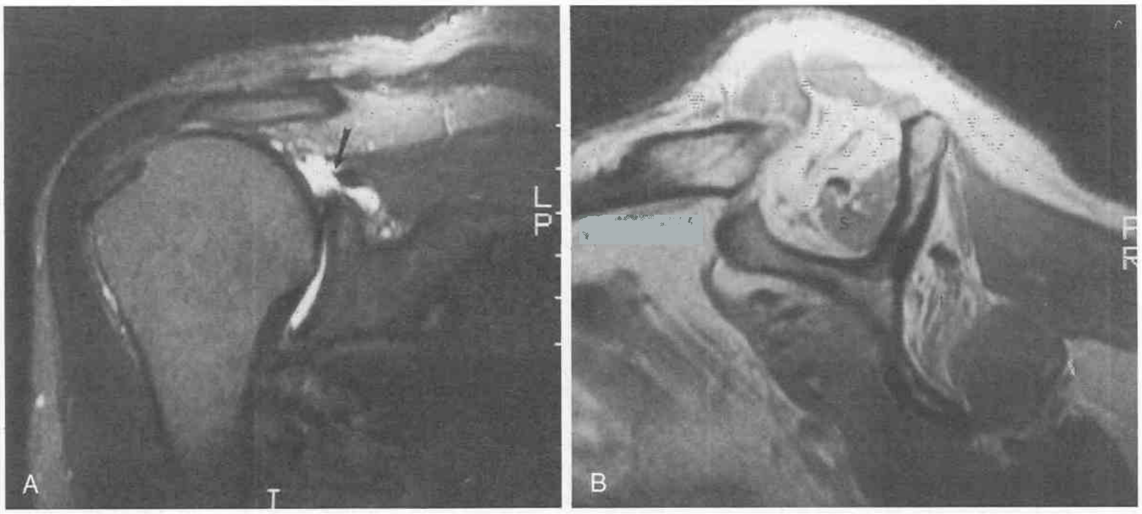

Figure 50–10. Atrophy. *A,* T2-weighted (TR = 2500 msec, TE = 70 msec) coronal oblique image. The supraspinatus muscle and tendon are retracted to the glenoid *(arrow)*, and the humeral head contacts the acromion. *B,* Proton-density–weighted (TR = 2500 msec, TE = 14 msec) sagittal oblique image. The supraspinatus (S) and infraspinatus (I) muscles are markedly atrophied and infiltrated with fat.

without administration of intra-articular contrast medium.[140, 177]

Isolated Subscapularis Tears

Isolated tears of the subscapularis tendon are rare. Deutsch and coworkers studied these tears in 13 patients and found that all were caused by a definable traumatic incident, usually forced hyperextension or external rotation of an abducted shoulder.[35] At MRI, subscapularis tendon injuries are evident in all three usual imaging planes—axial, coronal oblique, and sagittal oblique—although they may be most obvious on axial images. An area of disorganized tendon morphology is identified with increased signal intensity on T2-weighted images.[152, 219]

Pitfalls in Diagnosis

To avoid overcalling rotator cuff pathologic findings, one must be aware of a normal area of increased signal intensity in the distal supraspinatus tendon. It is located approximately 1 cm proximal to the insertion site of the tendon. It has been described by some authors as isointense with muscle.[82, 117] Others refer to it merely as increased in signal intensity without providing a point of reference. Although most authors have noted it on short TE technique, Kaplan and colleagues[82] found it to be most apparent on gradient-echo images, and Mirowitz[117] also noted it in some T2-weighted images. It has been identified in asymptomatic individuals and does not necessarily represent a pathologic finding. Attention to tendon morphology may help distin-

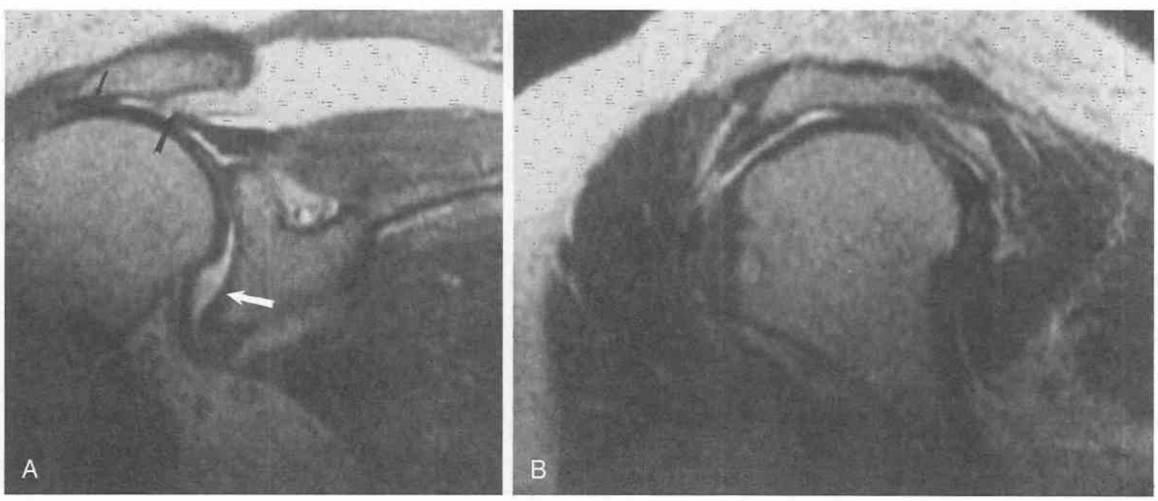

Figure 50–11[redacted]arge chronic cuff tear. *A,* [redacted]-weighted (TR = [redacted]00 msec, TE = 70 mse[redacted]oronal oblique image. Relatively little joint fluid is present. The supraspinatus tendon is retracted nearly to the glenoid *(black arrow)*, and the humeral head has translated superiorly and contacts the acromion *(small black arrow)*. Migration of the humeral head, leaving a partially empty glenoid fossa *(white arrow)*, is one of the most obvious signs of rotator cuff tearing in this patient. *B,* T2-weighted (TR = 2500 msec, TE = 70 msec) sagittal oblique image. The acromion has a hooked shape. Note again the close apposition of the acromion and the humeral head.

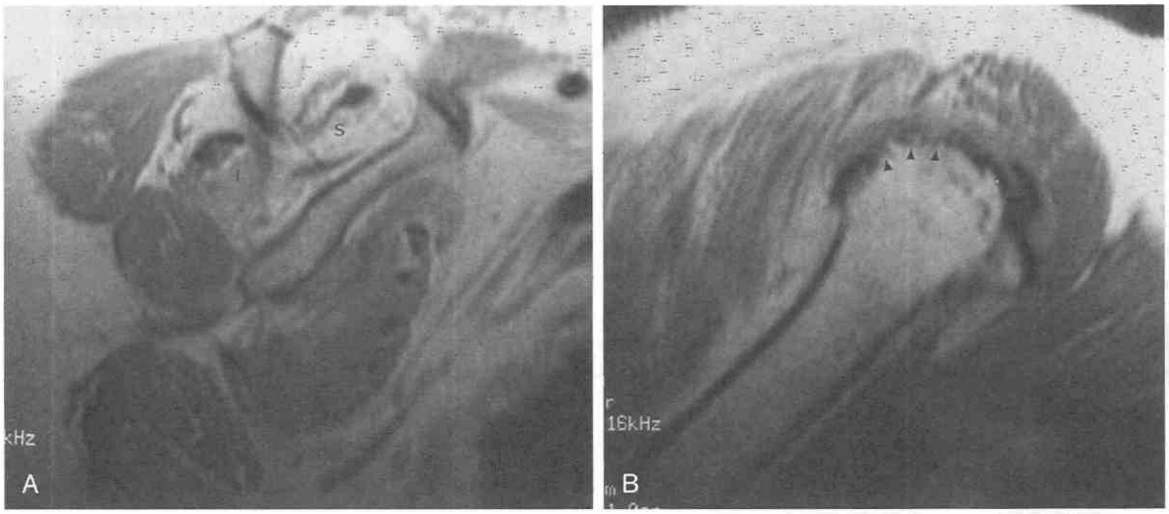

Figure 50–12. Cuff arthropathy. *A*, Proton-density–weighted (TR = 2500 msec, TE = 14 msec) sagittal oblique image. Atrophy of the supraspinatus (S) and infraspinatus (I) muscles attests to long-standing rotator cuff tear. *B*, Proton-density–weighted (TR = 2500 msec, TE = 14 msec) sagittal oblique image. Jagged, irregular humeral cortex *(arrowheads)* is typical of cuff arthropathy. On this film, the anterior part of the shoulder is to the right.

guish normal from pathologic increases in signal intensity. A normal tendon should taper smoothly from the musculotendinous junction to the insertion site.

Several theories have been proposed to explain this area of increased signal intensity. It may represent subclinical degenerative change within the tendon.[117, 160, 222] Erickson and coworkers noted increased signal intensity on T1-weighted images that they attributed to the "magic angle phenomenon," in which an artifactual focus of increased signal intensity may occur on short TE images of a tendon oriented 55 degrees to the constant magnetic field.[42] They postulated that such increased signal intensity may also be expected on intermediate-weighted images but not on long TE images. Timins and colleagues, including Erickson, bolstered this suggestion in 1995 by showing that the area of increased signal intensity changed position within the tendon with changes in patient position.[193]

Another possible explanation concerns positioning of the shoulder. If the arm is internally rotated, the distal supraspinatus and infraspinatus tendons move anteriorly. This carries the distal infraspinatus tendon and small posterior supraspinatus tendon slips forward into the plane of the main supraspinatus tendon on oblique coronal images. The infraspinatus muscle routinely has multiple tendon slips with muscle interposed between them.

The supraspinatus tendon may be divided into two structures—the anterior main tendon and smaller posterior slips. In addition, there are bits of fatty connective tissue between the supraspinatus and infraspinatus muscles. This fatty tissue, along with the muscle interdigitated between slips of infraspinatus tendon or between the principal anterior supraspinatus tendon and the smaller posterior tendon slips, may result in an apparent area of increased signal intensity on short TE images that fades on T2-weighted images. One may reach the correct conclusion by following the intact tendons on oblique sagittal images.[31, 99, 133, 204]

Rotator cuff tears may be diagnosed by CT or MR arthrography using essentially the same diagnostic criteria employed with conventional arthrography and conventional MRI. One simply searches for extravasation of contrast from the glenohumeral joint into the substance of a tendon or through the cuff into the subacromial-subdeltoid bursa. One also looks for evidence of intrasubstance high signal intensity on T2-weighted images. Nonarthrographic MRI of the shoulder already has a high degree of accuracy, particularly for full-thickness tears, so any substantial gain in accuracy with MR arthrography is likely to be in the diagnosis of partial tears (Fig. 50–13).

Postsurgical Imaging

MRI may be helpful in assessment of the rotator cuff after surgery. Results, however, must be cautiously coordi-

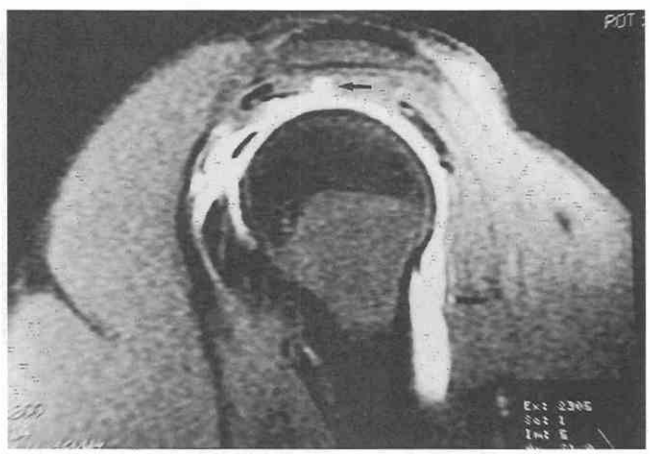

Figure 50–13. Partial tear of the supraspinatus muscle. T1-weighted (TR = 500 msec, TE = 14 msec), sagittal oblique image with fat saturation obtained after intra-articular injection of dilute gadolinium. Gadolinium fills a partial tear of the undersurface of the belly of the supraspinatus muscle *(arrow)*. No bright signal is present in the subacromial-subdeltoid bursa, thus effectively excluding a full-thickness cuff tear.

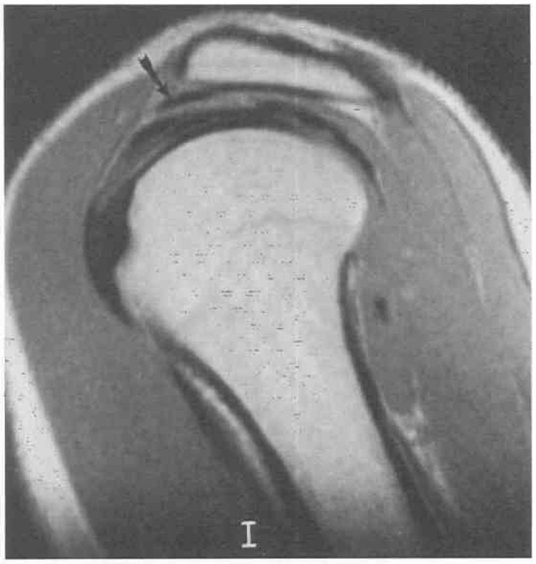

Figure 50–14. Flat acromion. Proton-density–weighted (TR = 2500 msec, TE = 14 msec) sagittal oblique image. The undersurface of the acromion has a perfectly straight, flat shape. The *arrow* indicates the coracoacromial ligament.

nated with clinical status. In a majority of patients, repaired rotator cuff tears exhibit increased signal intensity on T2-weighted images.[145, 188] Recurrent cuff tears may enable the diagnosis with a high degree of accuracy on the basis of the presence of distinct, fluid-intensity signal within the tendons on T2-weighted images, but the significance of the finding is not always clear.[103, 145] Spielmann and colleagues, studying the supraspinatus and infraspinatus tendons of a group of 15 asymptomatic patients after rotator cuff repair, found MRI evidence of rotator cuff tear in 11 (37%) of the 30 tendons. They also found subacromial-subdeltoid effusions, joint effusions, and bone marrow edema to be common in their patients.[188]

Imaging of Primary Impingement

MRI can be quite useful in the assessment of patients with primary impingement. These patients frequently have narrowing of the space between the acromion and the superior surface of the humeral head that is well delineated on MR images in either the sagittal oblique or the coronal oblique projection.[85, 176] This narrowing may be related to the configuration of the anterior acromion or the acromioclavicular joint.

Bigliani and coworkers described an association between the shape of the undersurface of the anterior acromion and the likelihood of rotator cuff tear.[9] They established three categories of acromial shape; *type I* is flat (Fig. 50–14), *type II* is curved, and *type III* is hooked anteriorly. Despite some debate about the nature of the hook, it seems likely that most arise as enthesophytes at the origin of the coracoacromial ligament.[38, 57]

Bigliani and coworkers found an increasing incidence of rotator cuff tears with type II and particularly with type III acromia.[9] The association of hooked acromia and rotator cuff tears has been confirmed by others.[40, 143] However, the practical application of the work of Bigliani and colleagues to interpretation of shoulder MRI is somewhat problematic. They performed their investigation using conventional radiography, and with this modality, the eye perceives a summation shadow composed of the entire acromion. MRI, of course, demonstrates acromial shape tomographically. On MR images, it is not unusual for the shape of the acromion to change from section to section. Thus, for example, an acromion with a flat configuration in one oblique sagittal section may have a curved shape in another (Fig. 50–15). Slight variations in positioning for the conventional radiographic outlet view may also change the apparent shape of the acromion. These factors contribute to considerable interobserver variability in classification of acromial shape.[68, 153]

In practice, the authors habitually include an assessment

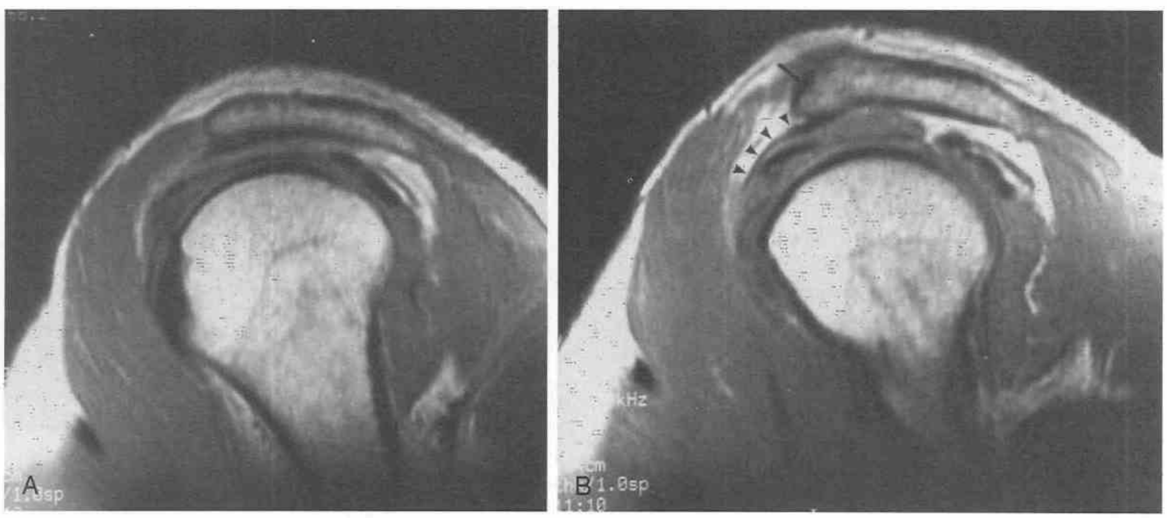

Figure 50–15. Acromial variation. *A,* Proton-density–weighted (TR = 2500 msec, TE = 14 msec) sagittal oblique image. This relatively laterally placed section demonstrates an acromion with a smoothly curved undersurface. *B,* Proton-density–weighted (TR = 2500 msec, TE = 14 msec) sagittal oblique image. More medially, the same acromion has a hooked shape (*arrow* at hook). *Arrowheads* indicate the coracoacromial ligament.

of acromial morphology in interpretation of shoulder MRI (or supraspinatus outlet views) but add modifying adverbs such as "gently curved" or "sharply hooked" to help the reader form a mental image of the acromial shape. As an alternative, measurement of the acromial angle gives a numeric assessment of acromial shape with acceptably low interobserver variability, although this has been tested only on outlet views of the shoulder and not on MR or CT images.[200] The acromial angle should probably not be used in interpretations without a prior common understanding with referring physicians.

A low-lying acromion has also been implicated as a cause of impingement. The acromion is considered to be low if its inferior border is lower than that of the clavicle at the acromioclavicular joint. Unfortunately, there are no criteria for distinguishing a low-lying acromion from a high-riding clavicle (such as may result from a previous acromioclavicular joint separation).[83]

An os acromiale occurs as a normal variant in approximately 8% of people. Since the 1930s, it has been considered to result from a failure of fusion of one of three ossification centers of the acromion. A study of 270 scapulae in 1993 found no support for this venerable theory and instead suggested a single site of occurrence, with the free fragment approximating one-third the length of the acromion.[39] There appears to be an association between the presence of an os acromiale and development of impingement syndrome and rotator cuff tear.[39, 124, 151] An os acromiale may be identified on axial and sagittal oblique images as a linear interruption of the marrow of the acromion (Fig. 50–16).[151]

Degenerative changes at or near the acromioclavicular joint are variously considered either a cause or a result of impingement and rotator cuff disease. These include hypertrophic changes involving soft tissue within the joint capsule as well as osteophytes that may project inferiorly from the acromion or clavicle and enthesophytes at the origin of the coracoacromial ligament. Spurs may visibly distort the supraspinatus muscle as it passes below them. At times, it may be difficult to distinguish a spur from a tendinous or ligamentous attachment site, particularly because spurs may develop at such sites (Figs. 50–17 and 50–18). Some authors believe that spurs always contain marrow and thus match other marrow-containing bones in signal intensity.[82] Our experience and that of others suggest that this is generally, but not invariably, true.[58]

Thickening of the acromial origin of the coracoacromial ligament is associated with impingement syndrome even without enthesophyte formation.[54] It may be identified on sagittal oblique MR images.

Although an association exists between these configurations of the coracoacromial arch and impingement syndrome, any of these findings may also be seen in asymptomatic individuals. A patient may, in fact, have visible indentation of the tendon by a portion of the coracoacromial arch and have no symptoms, much as an asymptomatic person may have a herniated lumbar disk. At the same time, a patient may have no visible indentation of the cuff yet clinically have impingement syndrome. This is partly because impingement is generally positional. Open MRI units may allow greater freedom of positioning, so that the patient can be imaged in the position in which

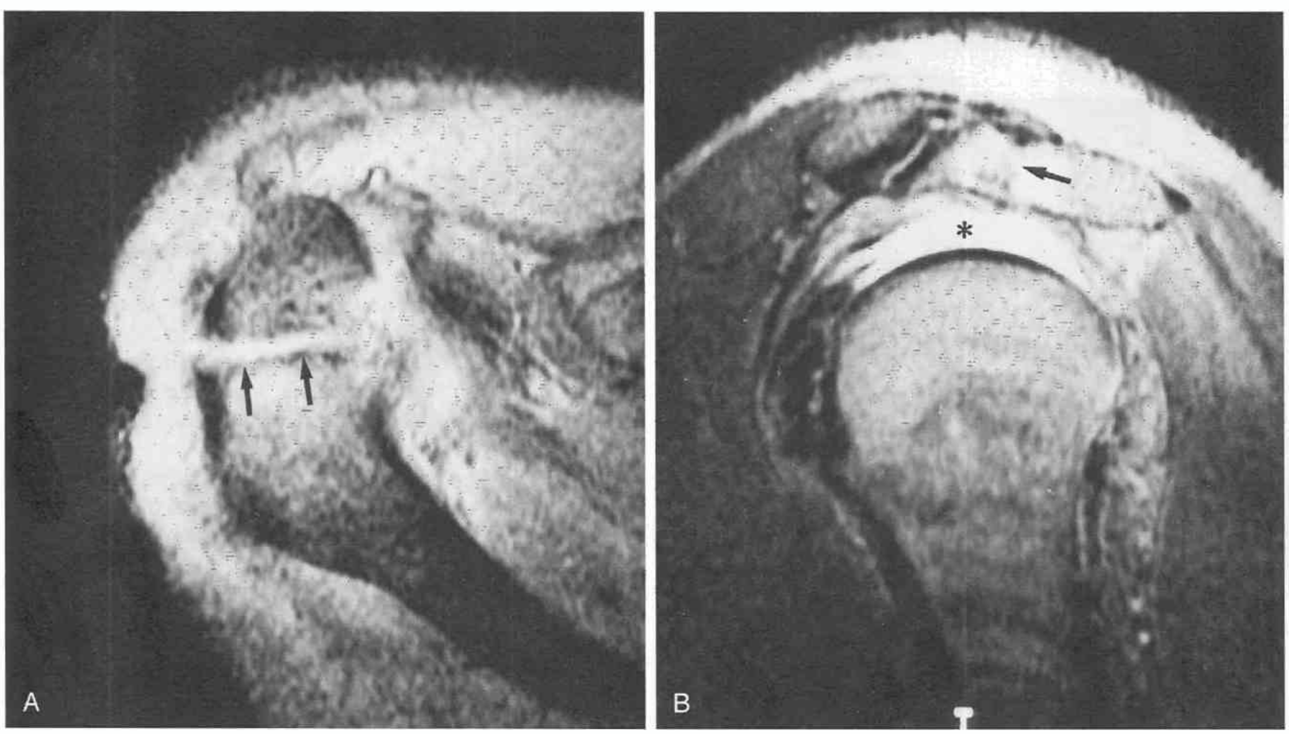

Figure 50–16. Os acromiale. *A,* T2-weighted gradient-echo (TR = 700 msec, TE = 10 msec, flip angle = 20 degrees) axial image. A high-signal-intensity line *(arrows)* runs through the acromion and demarcates the division between the anterior os acromiale and the remainder of the acromion. *B,* T2-weighted (TR = 2500 msec, TE = 70 msec) sagittal oblique image also demonstrates a dividing line crossing the acromion *(arrow).* A large, full-thickness rotator cuff tear is visible as well *(asterisk).*

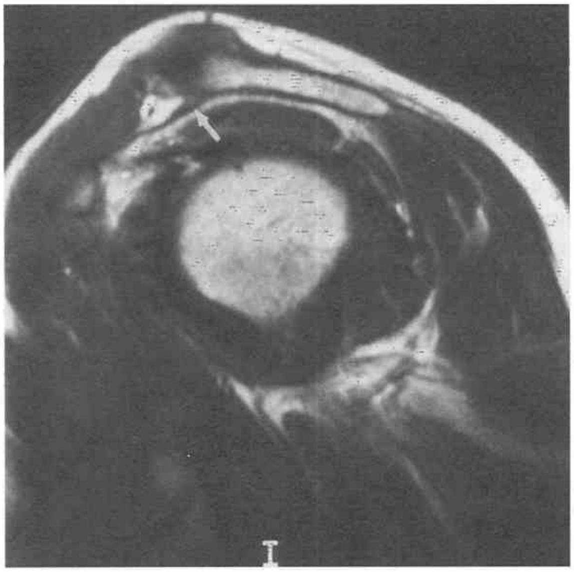

Figure 50–17. Spur. Fast spin-echo, T2-weighted sagittal oblique image. A spur containing marrow projects from the undersurface of the otherwise flat acromion at the attachment site of the coracoacromial ligament *(arrow)*. The conjoined tendons of the short head of the biceps brachii muscle and the coracobrachialis are seen originating from the coracoid process.

difficulties occur, thus increasing the chance of catching the guilty anatomic feature in action.[13, 51, 59–61] Because of imperfect correlation between impingement and the anatomic features associated with it, impingement syndrome remains a clinical diagnosis. These findings may, however, reasonably be taken as support of clinically suspected impingement or may form a basis for suggestion of the diagnosis.

Figure 50–18. Spurious spur. Proton-density–weighted (TR = 2500 msec, TE = 14 msec) coronal oblique image. A slender, black structure projects from the undersurface of the lateral acromion *(small arrow)*. It represents a slip of deltoid tendon or a portion of the coracoacromial ligament (or both, as their fibers may fuse), but it may be mistaken for a spur. A small area of decreased signal *(arrow)* in the greater tuberosity or, in other cases, a small cyst is a common finding and may be associated with rotator cuff disease.

Pathophysiology of Glenohumeral Instability

Glenohumeral joint stability depends on the supporting and restraining effect of the glenoid labrum, the joint capsule including the glenohumeral ligaments, and the rotator cuff. With failure of these structures, the glenohumeral joint becomes unstable. Instability may present clinically and anatomically as either subluxation or frank dislocation and may manifest chronically, recurrently, or as an isolated episode. Shoulder dislocations, which most commonly occur in an anterior and subcoracoid location, are usually the result of acute trauma. During an initial episode of dislocation, the glenoid labrum and anterior capsule may become damaged, and an impaction fracture of the posterolateral humeral head, or Hill-Sachs deformity, may occur. These lesions predispose to recurrent dislocation, often after minimal or no trauma. Recurrent dislocations are common in young patients but become progressively less common with advancing age; they are relatively rare after age 40 years.[4, 33, 107, 150, 198] Some patients can, and do, dislocate the shoulder voluntarily.[168]

Atraumatic instability has been considered less common than traumatic instability.[107] Concern is growing in the orthopedic community, however, about atraumatic instability as a cause of both labral abnormalities and rotator cuff disease due to secondary impingement. A typical patient is a young athlete involved in sports requiring repetitive overhead motion; the stereotypical example is a baseball pitcher. During overhead motion (the late cocking and early acceleration phases of a baseball pitch), the humeral head may come in contact with the posterior-superior glenoid labrum, pressing it, in turn, into the adjacent posterior rotator cuff.

Theoretically, this contact becomes pathologic in some people because of overuse, particularly in the context of inadequate conditioning of the supporting muscles and resulting microinstability. Contact leads to tearing of the posterior-superior glenoid labrum and the adjacent rotator cuff. Anterior instability may occur during the deceleration phase of throwing and may be accompanied by anterior labral tears.[78, 94, 166] Labral tears beginning posteriorly and superiorly may propagate farther along the labrum, producing SLAP lesions.

In 1990, Snyder and colleagues[186] divided SLAP lesions into four types, depending on the nature of the labral injury and whether there is associated biceps tendon damage:

In *type I* lesions, the labrum is frayed, but it and the biceps tendon are not torn from the glenoid.

In *type II* lesions, the labrum is stripped from the glenoid with the biceps tendon.

In *type III* lesions, there is a bucket-handle tear of the labrum.

In *type IV* lesions, the bucket-handle tear extends into the biceps tendon.

In 1995, Maffet and coworkers expanded the classifica-

tion of Snyder and colleagues to account for additional injury patterns[102]:

In *type V* lesions the tear involves the labrum from the anterior-inferior position to the posterior-superior position.

In *type VI* lesions one finds an unstable flap tear of the labrum and separation of the biceps tendon from its anchor.

In *type VII* lesions, the labral tear extends anteriorly beneath the middle glenohumeral ligament.

Not all SLAP injuries are the result of instability. They may also be caused by sudden, violent traction on the arm, as occurs when catching a heavy object, or by falling on an outstretched arm.[62, 66, 78, 94, 102]

Imaging of Glenohumeral Instability

Labral Tears

MRI, CT arthrography, and MR arthrography can often demonstrate the anatomic residua of prior episodes of instability. Identification of the stigmata of instability, however, does not indicate whether the problem is ongoing, because (1) anatomic changes may occur at a single episode of dislocation and (2) it is rare to identify actual displacement of the humeral head at the time of imaging. The imaging signs of instability include labral and glenoid rim abnormalities, capsular stripping, and deformities of the humeral head. Although practically any combination of injuries may occur in an individual patient, certain groupings of anatomic abnormalities occur repeatedly (Table 50–2).

Tears of the glenoid labrum are identified by either complete absence of a portion of the labrum, displacement of the labrum from the glenoid rim, or abnormal linear areas of increased signal intensity within the labrum at MRI (Table 50–3).[55, 63, 84, 97, 174, 220] Similar diagnostic criteria are used at CT or MR arthrography (Figs. 50–19 and 50–20). In addition, contrast entering the labrum or tracking beneath the labrum to the external surface of the joint is consistent with a tear. When the tear has formed a displaced bucket handle, the fragment creates at double-contrast CT arthrography a characteristic rounded area of attenuation that is less than that of normal labral tissue but greater than that of gas, termed the "cheerio sign."[75] The bucket-handle fragment may also be identified at MRI or MR arthrography as a low-signal-intensity intra-articular body.[120]

Good results in diagnosis of labral tears have been reported for MRI, CT arthrography, and MR arthrography, albeit somewhat less consistently for the first two than for MR arthrography (see Table 50–3). Relatively few studies have directly compared their performances. In 1993, Chandnani and coworkers compared MRI, MR arthrography, and CT arthrography and found MR arthrography to be the most sensitive in detecting labral tears (96%); it also offered the best evaluation of the inferior labrum and inferior glenohumeral ligament.[22] In 1999, Roger and colleagues compared conventional arthrography, CT arthrography, and MR arthrography in 17 throwing athletes and discovered that MR arthrography was both more sensitive and more specific than the other modalities, not only for labral abnormalities but also for rotator cuff lesions.[166]

Pitfalls and Variants in Diagnosis of Labral Tears

The appearance of the labrum has many normal variations. The CT arthrographic configuration of the posterior labrum is rounded, and the MRI appearance has been described as usually triangular. The configuration of the anterior labrum may vary considerably from one individual to another, and in the same person labral shape changes with rotation of the humerus.[123, 174] With internal rotation,

Table 50–2. "Alphabet Soup" of Glenohumoral Instability and Glenoid Lesions

Acronym	Stands for	Description	Brief Citation	Reference No.
SLAP	Superior labrum, anterior to posterior	Labral tear stretching across superior portion of labrum, crossing origin of long head of biceps brachii muscle	Andrews, 1985	2
			Legan, 1991	97
			Cartland, 1992	18
			Grauer, 1992	62
			Hodler, 1992	71
			Hunter, 1992	75
			Monu, 1994	120
			Maffet, 1995	102
			Handelberg, 1998	66
HAGL	Humeral avulsion of the glenohumeral ligament	Detachment of capsule and inferior glenohumeral ligament from their anterior humeral attachment site; uncommon lesion first described in 1942	Nicola, 1992	139
			Wolf, 1995	215
			Tirman, 1996	195
			Bokor, 1999	12
GLAD	Glenolabral articular disruption	Tear of anterior-inferior glenoid labrum with associated injury to glenoid articular cartilage; lesion is caused not by instability but by an impaction injury	Neviaser, 1993	135
			Sanders, 1999	171
ALPSA	Anterior labroligamentous periosteal sleeve avulsion lesion	Periosteum of the anterior-inferior glenoid remains intact, whereas labrum is displaced medially and rotated inferiorly	Neviaser, 1993	134

Table 50–3. Performance of CT Arthrography, MRI, and MR Arthrography in Diagnosis of Labral Tears

Brief Citation	Reference No.	No. of Patients	Labral Tears: Sensitivity/ Specificity/Accuracy (%)*	Comment
			CT Arthrography	
Deutsch, 1984	34	44	96/–/86	—
Callaghan, 1988	16	30	66/100/96 (SLAP lesions) 100/100/100 (posterior labrum) 90/73/83 (anterior labrum)	—
Chandnani, 1993	22	28	73/–/–	Compared MRI, MR arthrography, and CT arthrography and found MR arthrography to be the most sensitive modality
			MRI	
Garneau, 1991	55	24	44–77/67/–	Concluded that axial MR imaging was relatively inaccurate for labral evaluation
Chandnani, 1993	22	30	93/–/–	—
Tuite, 1995	201	24	36–50/90/55–67	Compared 2 readers' performances with axial MR images obtained in neutral and externally rotated positions
Gusmer, 1996	63	103	89/97/95	Argued that technical advances in MRI have allowed better evaluation of the labrum than was possible previously; used both gradient-echo and proton-density–weighted, fast spin-echo axial sequences to obtain the reported level of accuracy
			MR Arthrography	
Chandnani, 1993	22	30	96/–/–	—
Palmer, 1994	147	48	91/93/92	—
Palmer, 1995	149	121	92/92/92	—
Cvitanic, 1997	29	92	96/97/–	Tested ABER position and found better performance with combined ABER and axial images than with either alone (44% sensitivity, 92% specificity for axial images alone)
Willemsen, 1998	212	44	93/80/89 (Bankart lesions) 89/89/89 (SLAP lesions)	Used intra-articular saline solution
Bencardino, 2000	7	52	89/91/90 (SLAP lesions)	Found 76% of SLAP lesions correctly graded by MR arthrography

*As given in the original article; not recalculated or derived from data within the article.
ABER, abduction, external rotation; CT, computed tomography; MRI, magnetic resonance imaging; SLAP, superior labrum, anterior and posterior.

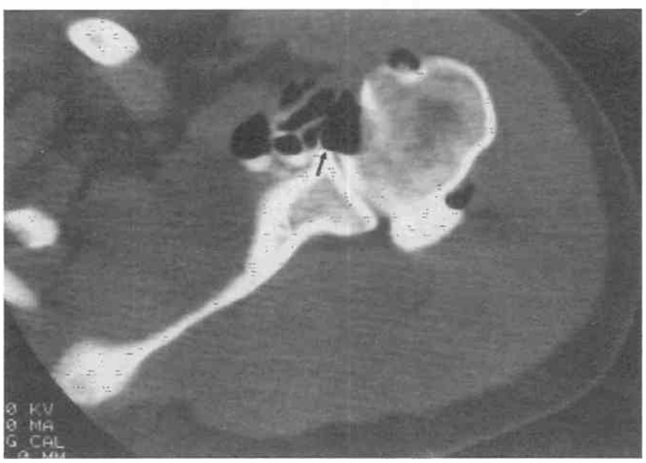

Figure 50–19. Labral damage, as shown on a double-contrast CT arthrogram. Gas within the joint capsule projects immediately adjacent to the glenoid cortex *(arrow)*. The anterior labrum is missing.

the anterior labrum assumes a large, globular configuration; with external rotation, it is attenuated and pointed (Fig. 50–21; see Fig. 50–4). The anterior aspect of the labrum may exhibit horizontal clefts or vertical notches. If this pattern is seen posteriorly, however, it suggests a tear. With gradient-echo imaging, an area of smooth, linear high signal intensity within the anterior labrum may occasionally be seen. This finding alone does not indicate a tear; however, its cause has not been ascertained.[73, 109, 114, 132]

Some normal structures may be misinterpreted as labral tears. The hyaline articular cartilage of the glenoid extends under the base of the labrum.[99, 175] At MRI, this produces a line of bright signal intensity that may resemble a tear. At the level of the subscapularis tendon, the middle glenohumeral ligament runs parallel to the anterior labrum and also shows low signal intensity. The space between the ligament and the labrum may mimic a tear along the outer border of the labrum, but its true nature is usually revealed when one follows the ligament along its normal course on sequential images (Fig. 50–22).

Superiorly, the sublabral recess or foramen can mimic a labral tear, particularly when intra-articular contrast material enters the recess.[95] A collection paralleling the shape

Figure 50–20. Anterior labral avulsion and periosteal stripping. T1-weighted (TR = 500 msec, TE = 14 msec), fat-saturated, axial oblique MR arthrogram image in abduction and external rotation. The anterior labrum has been avulsed from the glenoid rim with a short segment of periosteum, allowing the intra-articular gadolinium solution *(arrow)* to flow between these structures and the glenoid.

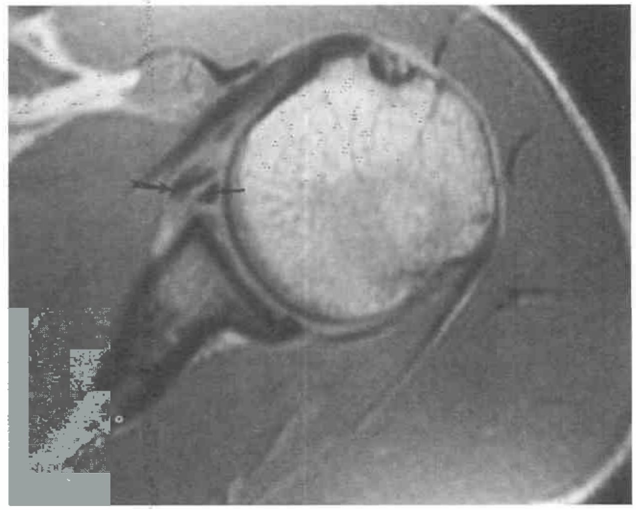

Figure 50–22. Labral pitfalls in diagnosis. Proton-density–weighted (TR = 2000 msec, TE = 14 msec) axial image. The anterior labrum and capsule proved to be normal at surgery. The labrum *(small arrow)* is separated from the glenoid rim by an unusually thick and easily seen layer of articular cartilage. The middle glenohumeral ligament *(arrow)* runs parallel to the labrum, separated from it by a bright line of connective tissue that might be interpreted as a tear.

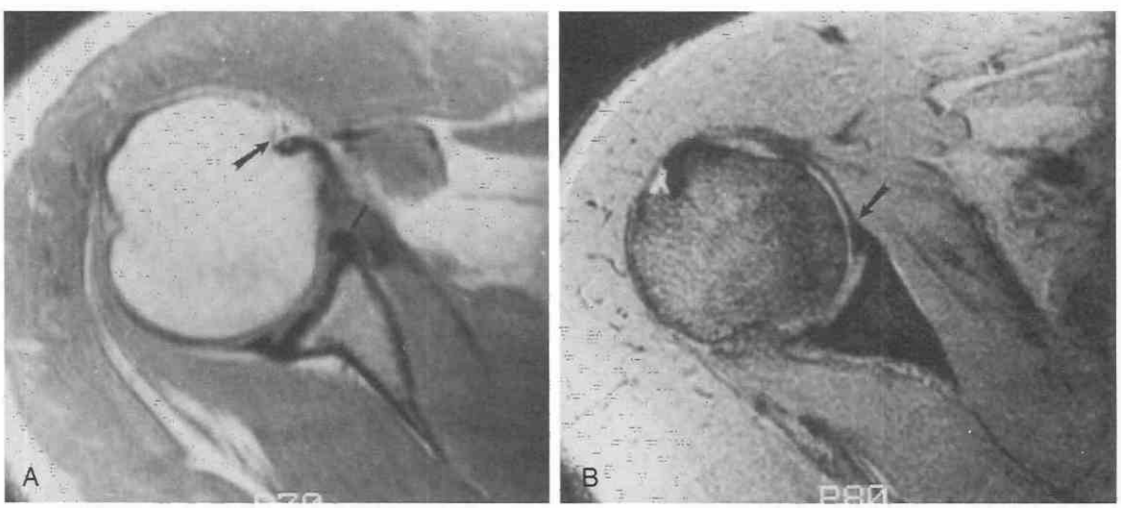

Figure 50–21. Effect of rotation. *A,* Proton-density–weighted (TR = 2500 msec, TE = 14 msec) axial image. With the humeral head in internal rotation (*arrow* indicates the position of the bicipital groove), the anterior labrum has a rounded configuration *(small arrow)*. *B,* Gradient-echo axial image. With external rotation, the same anterior labrum assumes a pointed, triangular configuration *(arrow)*. The attachment of the joint capsule to the tip of the labrum can be appreciated.

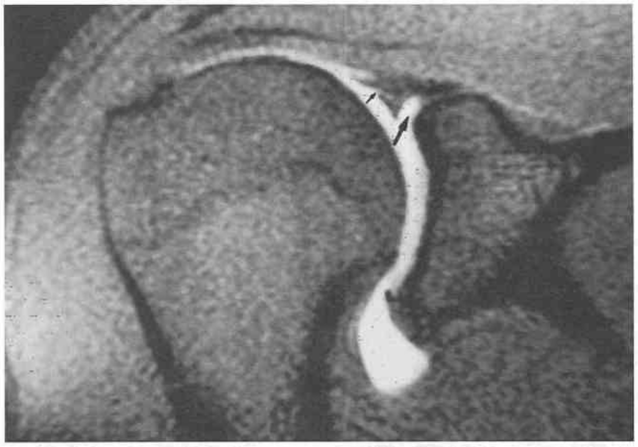

Figure 50–23. Sublabral recess. T1-weighted (TR = 500 msec, TE = 14 msec), fat-saturated, coronal oblique MR arthrogram image. A smooth-bordered collection of gadolinium *(arrow)* parallels the cortex of the superior glenoid. A small amount of signal also enters the articular surface of the superior labrum in a fashion typical of a type I SLAP (superior labrum, anterior and posterior) lesion *(small arrow)*.

of the bony glenoid is probably a normal structure, whereas a collection that turns in a lateral direction into the substance of the labrum is most likely a tear (Figs. 50–23 and 50–24).[7, 202] The exact location of the fluid collection may also provide a hint, as a normal recess or foramen should not extend posterior to the biceps origin, whereas a labral tear often (but not invariably) does.[185, 202] An absence of the anterior-superior glenoid labrum may be paired with a thick, cordlike middle glenohumeral ligament, a combination called the *Buford complex*.[197]

Interpretation of labral images may be particularly difficult in elderly patients because of the considerable overlap between pathologic labral changes and changes associated with normal aging. Intrasubstance degenerative changes are noted in individuals after age 30 years and become increasingly evident with advancing age.[33, 157] On proton-density or gradient-echo images, these may produce globular increased signal intensity within the labrum.[109, 132] The labrum may also appear small in older adults.

Other Structures

The anterior joint capsule and glenohumeral ligaments are also important in maintaining shoulder stability.[198] In abduction and external rotation, the glenohumeral ligaments restrain the humeral head and prevent anterior instability. Because of the capsular tension produced by fluid in the joint, capsular abnormalities may be most easily diagnosed with arthrographic technique and either CT or MRI (Figs. 50–25 and 50–26). The anterior capsule may arise from various positions on the neck or edge of the glenoid or from the labrum.[34, 123] The origin is easily demonstrated by these techniques, but a suspected association between a more medial capsular origin and glenohumeral instability has not been substantiated.[26, 149]

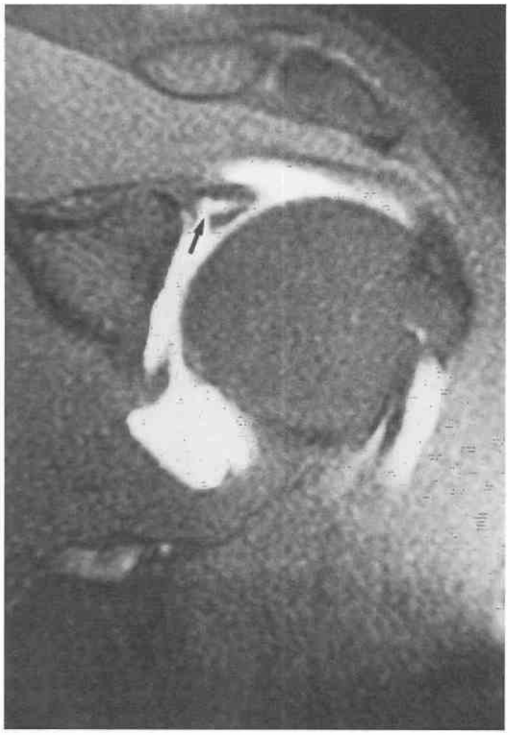

Figure 50–24. SLAP (superior labrum, anterior and posterior) lesion. T1-weighted (TR = 500 msec, TE = 14 msec), fat-saturated coronal oblique MR arthrogram image. Gadolinium *(arrow)* enters the substance of the labrum and turns laterally, away from the glenoid. In this case, the high signal continues to the anterior edge of the labrum, suggesting a bucket-handle tear or type III SLAP lesion.

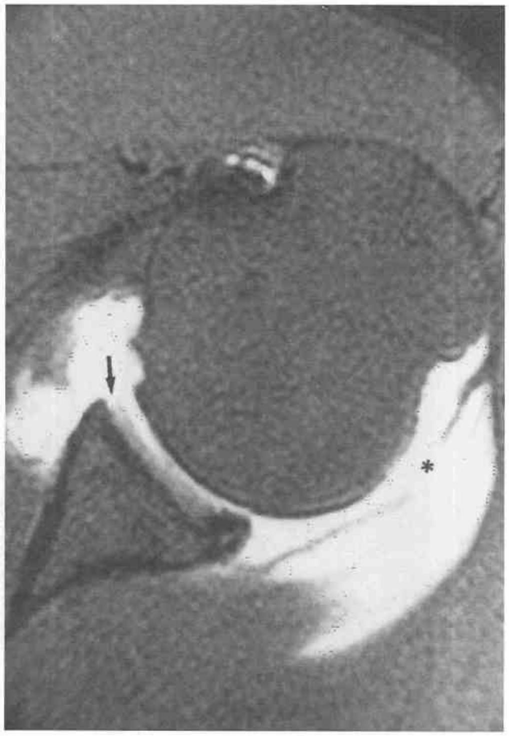

Figure 50–25. Posterior capsular tear. T1-weighted (TR = 500 msec, TE = 14 msec), fat-saturated, axial MR arthrogram image. A tear in the posterior joint capsule *(asterisk)* allows gadolinium to escape into the adjacent soft tissues. The anterior labrum has been avulsed as well *(arrow)*.

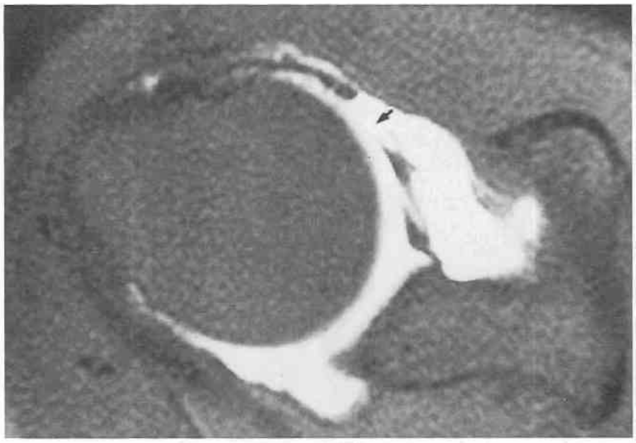

Figure 50–26. Humeral avulsion of the glenohumeral ligaments (HAGL lesion). T1-weighted (TR = 500 msec, TE = 14 msec), fat-saturated axial MR arthrogram image. A tear in the anterior capsuloligamentous complex is clearly visible *(arrow)* near its insertion on the humerus. Whether the tear is close enough to the humerus to constitute a true HAGL lesion is debatable.

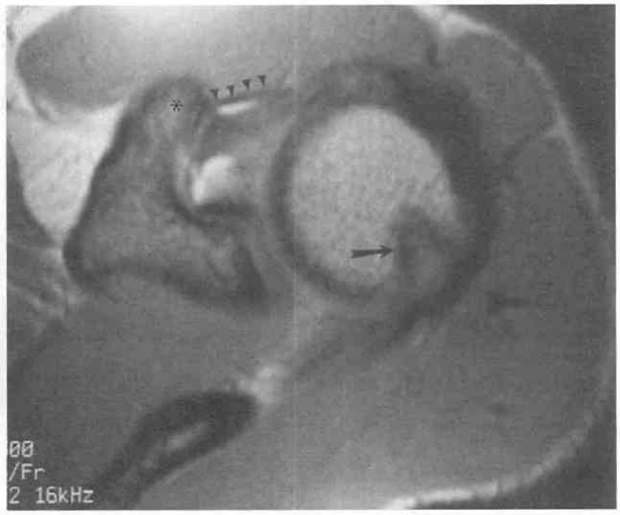

Figure 50–27. Hill-Sachs deformity. Proton-density–weighted (TR = 2500 msec, TE = 14 msec) axial image. At the level of the coracoid process *(asterisk)*, a notch-shaped defect in the posterolateral humeral head *(arrow)* is typical of a Hill-Sachs defect. The patient had a history of recurrent anterior dislocation. *Arrowheads* indicate the coracohumeral ligament.

Glenohumeral dislocation can result in bony abnormalities that are sometimes visible on plain films but are clearly identified on either CT scans or MR images. As the humeral head dislocates anteriorly, it impacts on the anterior glenoid rim, producing a bony Bankart lesion (anterior glenoid rim fracture) or a Hill-Sachs deformity. On axial images, Hill-Sachs lesions are visualized in the posterolateral border of the humeral head at or superior to the base of the coracoid process. They must not be confused with the normal flattening of the humeral head, which is usually visualized more posteriorly and inferiorly but which may be found at the level of the coracoid in a patient with a large rotator cuff defect and superior translation of the humerus (Fig. 50–27).[84, 163, 175, 216] In patients who have had a posterior dislocation, a "reverse" Hill-Sachs or trough lesion may be identified on the anteromedial margin of the head of the humerus in association with a posterior glenoid or labral abnormality.

Choice of Imaging Modality

MRI, CT arthrography, and MR arthrography all have roles to play in diagnosis of rotator cuff disease, impingement syndrome, and instability as well as other causes of shoulder pain. Furthermore, although not the topic of this chapter, conventional radiography, ultrasound, and conventional arthrography are also useful. Choosing the proper tool for each patient can be a daunting task, with no single, absolutely correct solution. We suggest that, in all patients, plain films of the shoulder should be the first imaging step. They may be sufficient. In young patients, they may reveal a fracture; in older patients they may disclose, with low sensitivity but as much as 98% specificity, a large rotator cuff tear.[81] Spurs and other bony morphology associated with impingement syndrome may be appreciated. Conventional radiography can reveal calcific tendinitis and the erosions of rheumatoid arthritis.

Questions often remain after conventional radiographs are obtained. The nature of the question and the age of the patient help guide the next choice.[191] For instance, in a patient age 40 or older, in whom primary impingement syndrome and rotator cuff disease are suspected, MRI without intra-articular contrast is likely to provide accurate evaluation of the rotator cuff and a useful assessment of the labrum. In experienced hands, ultrasound may also assess the rotator cuff accurately and for less expense than MRI.

In a patient younger than 40 years of age, in whom instability is more likely to be a problem, either overtly or as a cause of impingement, it may be worth the extra expense and risk to use MR arthrography because of its improved depiction of the labrum. CT arthrography should probably be reserved for patients with contraindications for MRI.

Abnormalities of the Biceps Tendon

Bicipital Tendinopathy or Rupture

Most cases of bicipital tendinopathy are the result of mechanical impingement that occurs with rotator cuff disease in middle-aged or older patients. With flexion of the shoulder, the tendon of the long head of the biceps may become closely approximated to the coracoacromial ligament and the anterior acromion, particularly in the presence of a rotator cuff defect, and may be compressed between these structures and the humeral head.[33, 136, 154] This impingement eventually results in tendinopathy, with flattening and thinning of the tendon that may lead to complete rupture.[128, 218] Bicipital tendinopathy can also occur in patients who have glenohumeral instability, particularly in the presence of pathologic conditions involving the superior labrum.

Early bicipital tendinopathy is often undetected on im-

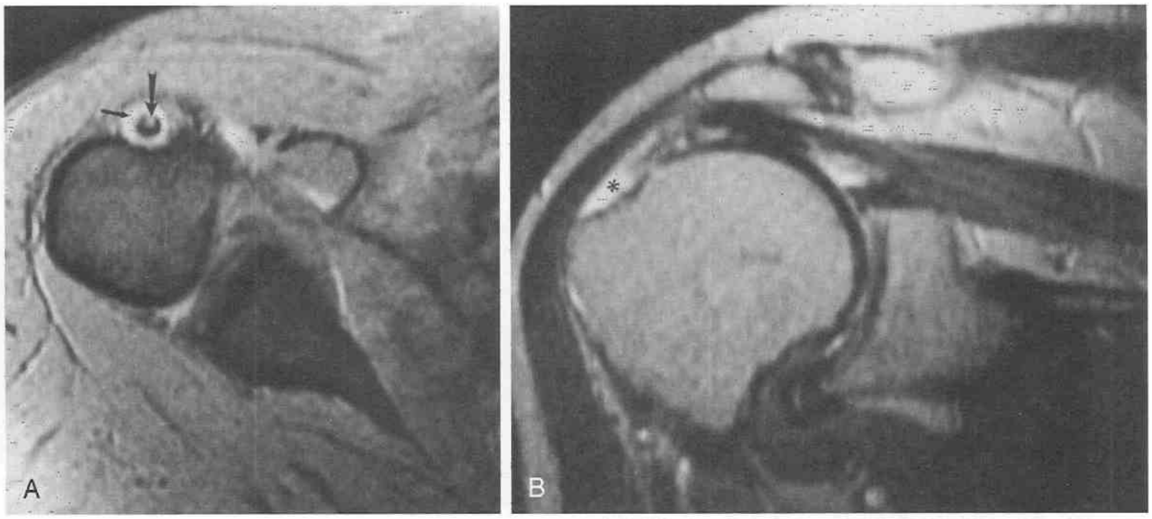

Figure 50–28. Bicipital tendinopathy. *A,* T2-weighted axial image. Fluid surrounds the bicipital tendon within the groove. In addition, an abnormal focus of high signal intensity is present within the tendon *(arrow).* The anterolateral branch of the anterior circumflex humeral artery may be identified *(small arrow). B,* T2-weighted coronal oblique image. In this patient, as is commonly the case, biceps tendinopathy is associated with rotator cuff disease. A large tendon gap *(asterisk)* marks the location of a full-thickness tear of the supraspinatus muscle and tendon. (Courtesy of Timothy Greenan, M.D., Washington, DC.)

aging studies. Increased signal intensity within the abnormal tendon is rarely visualized on MR images (Fig. 50–28), but as in the rotator cuff tendon, it may be a result of the magic angle effect.[42]

Morphologic abnormalities (e.g., fraying, flattening, absence of the tendon) may sometimes be identified, particularly within the bicipital groove. Fluid within the bicipital tendon sheath helps to delineate tendon morphology. The presence of fluid does not necessarily indicate bicipital tendon disease, however, because any fluid present often comes from the glenohumeral joint. Rarely, a disproportionately large amount of fluid is found within the biceps sheath compared with the amount within the joint; this should suggest bicipital abnormality.

Bicipital Tendon Dislocation

Bicipital tendon dislocation usually occurs in conjunction with large, long-standing tears of the rotator cuff that have extended to include the subscapularis tendon (Fig. 50–29). The tendon dislocation may be overlooked clinically because the symptoms are masked by the associated cuff tear. Other lesions necessary for bicipital tendon dislocation to occur include disruption of both the strong coracohumeral ligament, an important stabilizer of the biceps tendon,[105] and the weak transverse humeral ligament. In this setting, the tendon of the long head of the biceps dislocates medially, moving posterior to the subscapularis tendon and muscle and into the glenohumeral joint, where it may be mistaken for a detached anterior labrum. In rare circumstances, when the subscapularis tendon remains intact yet the coracohumeral and transverse humeral ligaments are disrupted, the biceps tendon displaces extra-articularly and anterior to the subscapularis muscle. Occasionally, the biceps tendon lodges within the fibers of the distal subscapularis tendon (Fig. 50–30).[20, 21, 156]

Besides allowing identification of the displaced biceps tendon, both CT and MRI show an empty bicipital groove. On axial MR images, particularly those using gradient-echo sequences, tiny bony spicules projecting into the bicipital groove may mimic the biceps tendon. They may be distinguished from it, however, because they are probably not present on all the axial images where the biceps tendon would be expected to be seen. In addition, the far anterior coronal images also show an empty bicipital groove. Scar tissue within the bicipital groove may also resemble the tendon and mask a dislocation or tear.[207]

Surgery is usually performed in the young or middle-aged patient with dislocation of the biceps tendon. The tendon is replaced in the bicipital groove, and the fibrous

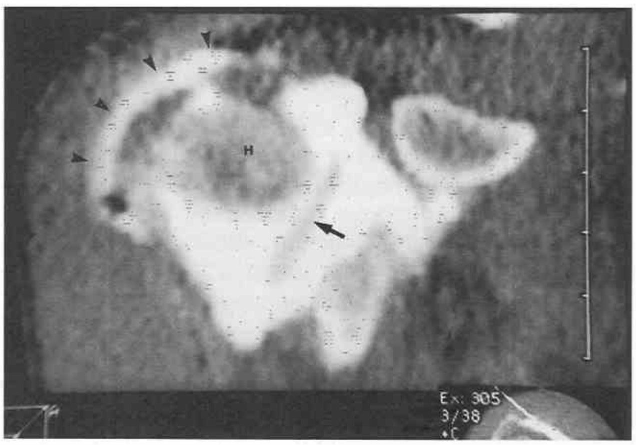

Figure 50–29. Bicipital tendon dislocation. Coronal reconstruction of an axial single-contrast CT arthrogram. The bicipital tendon *(arrow)* projects medial to the humeral head (H) in an intra-articular location. Contrast material extends through a gap in the supraspinatus tendon to outline the subacromial-subdeltoid bursa *(arrowheads).*

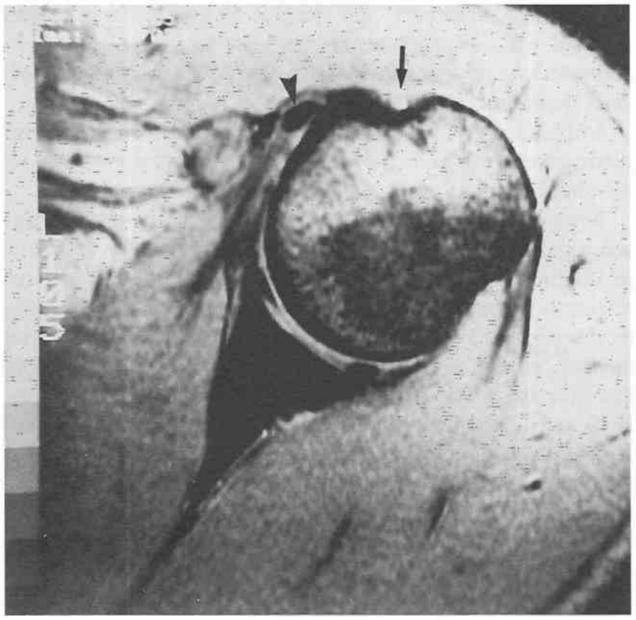

Figure 50–30. Bicipital tendon dislocation. Gradient-echo (TR = 600 msec, TE = 15 msec, flip angle = 70 degrees) axial MR image. The intertubercular groove is empty *(arrow)*. The bicipital tendon is dislocated medially and lodged within the fibers of the subscapularis muscle and tendon *(arrowhead)*.

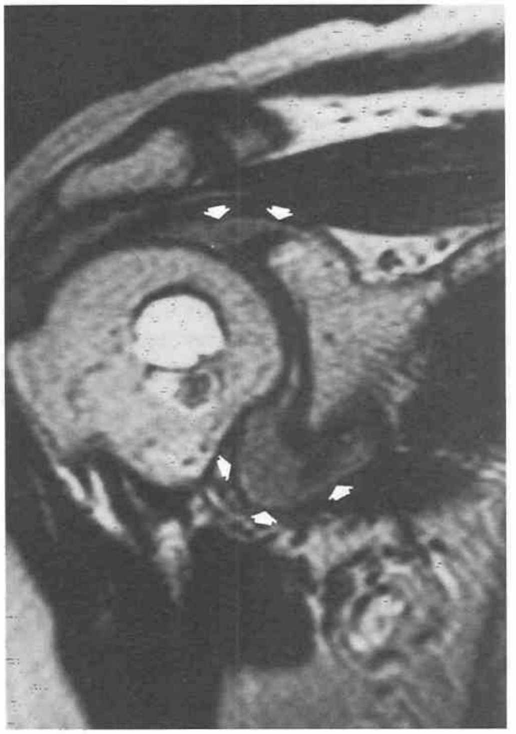

Figure 50–31. Rheumatoid arthritis. T2-weighted (TR = 2500 msec, TE = 80 msec) coronal oblique MR image. High-signal-intensity and mixed-signal-intensity lesions in the humeral head contact the articular surface in other sections and probably represent deep erosions. Pannus at the periphery of the joint *(short arrows)* is lower in signal than the usual joint fluid and is slightly heterogeneous in signal.

roof is reconstructed. Tenodesis is not necessary unless the tendon is severely attenuated. Acromioplasty as well as rotator cuff arthroplasty can be performed. In older patients, the treatment is usually directed to the rotator cuff disorder; the biceps tendon dislocation is considered secondary.

Calcium Deposition Diseases

Hydroxyapatite deposition disease, including its manifestations as (1) calcific tendinitis or bursitis, (2) idiopathic destructive arthritis ("Milwaukee shoulder syndrome"), and (3) tumoral calcinosis, may all occur in the shoulder.

Calcific Tendinitis

Calcific tendinitis can involve most tendons, but it most commonly involves the supraspinatus tendon. Patients are typically in middle age, although the disease has been reported in a child as young as 3 years. Women are affected more commonly than men. The dominant shoulder is more likely to be affected. The cause is unknown, but calcific tendinitis is believed by some to be the result of calcification of metaplastic cartilage in the relatively ischemic distal supraspinatus tendon. The deposits may also extrude from the tendon into a bursa, usually the subacromial-subdeltoid bursa, producing calcific bursitis. The deposits may erode bone. Pain is the presenting complaint and seems to be correlated with fluffy, ill-defined deposits occurring with resorption rather than with the well-defined deposits more commonly seen in asymptomatic patients.[112, 141, 203, 208]

Plain films are generally sufficient for the diagnosis. The calcium deposits are also readily apparent on CT scans. If an MRI study is obtained, a small calcium deposit may be inapparent. Larger ones may appear dark because of immobile protons in calcium. If ossification has occurred and marrow is present in the deposit, the signal intensity matches that of other marrow. Bursal deposits have the same appearance as those in the tendons but are often accompanied by bursal fluid (Fig. 50–31).

Idiopathic Destructive Arthritis

Idiopathic destructive arthritis of the shoulder, or Milwaukee shoulder syndrome (named for the city where it was first described), is another calcium crystal–related abnormality. It is most often seen in elderly women. It is characterized by large, blood-tinged effusions containing calcium hydroxyapatite and by extensive destruction of cartilage and bone. It is often accompanied by derangement of the rotator cuff or the proximal tendon of the long head of the biceps brachii. The calcium-containing effusions distinguish it from simple rotator cuff arthropathy as does a tendency toward bilateral involvement and involvement of other joints, particularly the hips and knees.

The diagnosis of Milwaukee shoulder syndrome is generally made clinically. CT and MRI studies, if obtained, demonstrate the effusions and destruction of articular sur-

faces. CT may also demonstrate calcium deposition on synovial surfaces.[64, 65, 108, 138]

Tumoral Calcinosis

In patients with tumoral calcinosis, amorphous, often liquid, deposits of calcium form near the joints, particularly the shoulder, hip, and elbow. The idiopathic form of the disease usually occurs in otherwise healthy young persons. There is a genetic component to this disease. It has been reported concurrently in siblings and has a predilection for blacks. The same term is often used for similar chalky deposits occurring in conjunction with systemic disease, usually chronic renal failure.

The diagnosis may be made by plain radiography along with history, physical examination, and laboratory studies. Neither CT nor MRI is usually necessary. Occasionally, however, the plain film appearance of such masses may be confusing and CT may help distinguish them from other calcified masses, such as chondrosarcoma and osteosarcoma.[10, 23, 101, 116, 137] MRI, however, may be preferred for evaluating less intensely calcified masses.[27, 43]

Rheumatoid Arthritis

Rheumatoid arthritis is a common disease with a predilection for women of middle age. The glenohumeral joint, the acromioclavicular joint, or both may be involved, but it is unusual for the disease to present in the shoulder before it has manifested elsewhere.[28, 113]

In the glenohumeral joint, as elsewhere, rheumatoid arthritis is characterized by osteopenia, effusions, progressive loss of joint space, and osseous erosions. The effusions may cause outpouchings of the synovium; when very large they are termed giant synovial cysts. Acromioclavicular involvement has a similar appearance, except that the scapula and clavicle are held in their respective locations by surrounding structures and do not migrate closer to one another with destruction of the joint surfaces. Thus, the acromioclavicular joint space widens rather than narrows with rheumatic involvement.[28, 113]

Inflammatory arthritides, especially rheumatoid arthritis, predispose the patient to tendon and ligament ruptures. In the shoulder, they may lead to rotator cuff tears.

Rheumatoid arthritis may be identified by clinical and serologic means. Radiographic techniques are less useful in diagnosis than in plotting progression of disease and response to therapy. MRI is more sensitive than plain films to the presence of effusions and small erosions and may directly depict pannus (Fig. 50–32). Use of intravenous gadolinium helps to distinguish pannus from effusions. Both may appear low in signal intensity on unenhanced T1-weighted images and high in signal intensity on T2-weighted images, but pannus enhances. Therefore, MRI may have a role in evaluating therapeutic response. Most likely, however, the hands and wrists will be a more fruitful site of evaluation than will the shoulder.[6, 50, 167, 211]

Pigmented Villonodular Synovitis

Pigmented villonodular synovitis (PVNS) is an uncommon disorder of unknown cause. It usually affects young adults and is typically monoarticular, with most frequent involvement of the knee. It is rare in the shoulder.[37, 48, 179] Histologically, PVNS demonstrates fatty areas together with hemosiderin deposition. This results in a heterogenous appearance on both CT scans and MR images. On MR images, the hemosiderin creates areas of decreased signal intensity on intermediate weighting. The signal intensity decrease becomes more prominent on T2 weighting. On gradient-echo imaging, the paramagnetic affect of hemosiderin causes even more dramatic signal loss. Effusions may be present.[15, 77, 88, 92, 104, 189] One case that involved the shoulder is reported to have had very little hemosiderin on histologic study and to have demonstrated on MR images

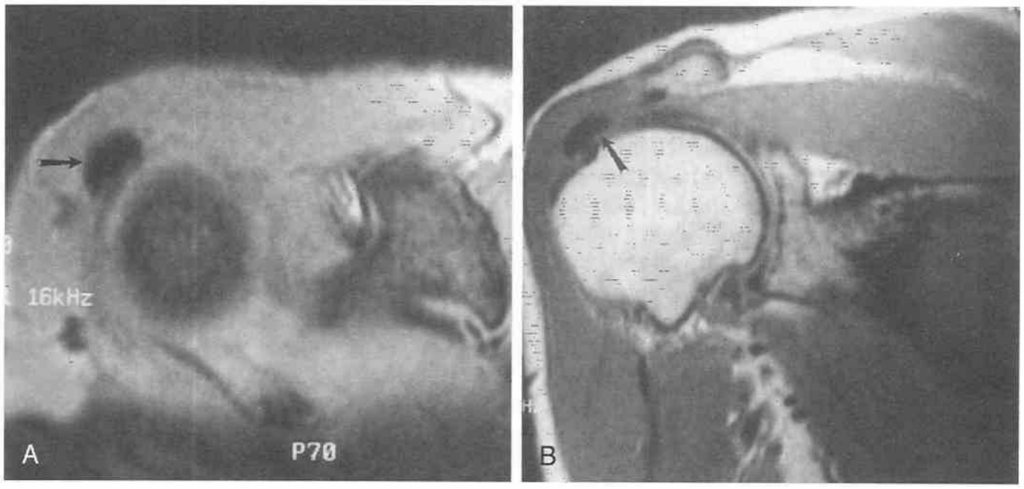

Figure 50–32. Calcific tendinitis. *A*, Gradient-echo axial image. A large area of signal void *(arrow)* is present near the attachment site of the supraspinatus tendon. *B*, Proton-density–weighted (TR = 2500 msec, TE = 14 msec) coronal oblique image. Signal void is present in the relatively avascular area of the supraspinatus tendon *(arrow)*. This area was also dark on T2-weighted images. Calcium was apparent by plain films (not shown).

Figure 50–33. Spinoglenoid notch lipoma. T1-weighted (TR = 500 msec, TE = 14 msec) sagittal oblique image. A homogenous mass *(asterisk)* of fatty signal intensity in the spinoglenoid notch is typical of a lipoma. Its signal parallels that of fat on other pulse sequences as well.

none of the signal dropout usually ascribed to hemosiderin.[179]

Neurogenic Shoulder Disfunction

Suprascapular Nerve

Pressure on the suprascapular nerve as it courses across the posterior scapula is an uncommon cause of shoulder pain. Any mass that arises in an appropriate location can produce suprascapular nerve entrapment; reported causes include neoplasms and hematoma (Fig. 50–33). The most common cause, however, is a ganglion cyst. These cysts usually occur in young men. They typically arise from a labral tear in much the same fashion that a meniscal cyst arises from a torn meniscus.[194, 209] Ganglion cysts may occur at various sites about the shoulder, but those causing suprascapular nerve compression usually occur at the spinoglenoid notch. They may extend superiorly into the supraspinatus fossa or inferiorly into the infraspinatus fossa. They may produce muscle paralysis and atrophy as well as pain. The infraspinatus muscle is most often affected, but the supraspinatus muscle may be involved as well.

Ganglia may be detected as a water-density mass by CT. On MR images, they are approximately isointense with muscle on short TE images and very bright on T2-weighted images. If intravenous Gd-DTPA is administered, the cysts may enhance about their rim. They often appear septate. Muscle atrophy, if it has ensued, may also be apparent on the MR image; the earliest sign of denervation atrophy is increased signal intensity on T2-weighted images within the involved muscle. In three reported cases, CT-guided aspiration yielded relief. In other cases, patients have successfully undergone surgery, and occasionally such cysts have resolved spontaneously (Fig. 50–34).[52, 144] When the cyst arises from a labral tear, the tear must be addressed.[194, 209]

Suprascapular nerve dysfunction may also be caused by direct injury to the nerve. One reported case was associated with a previous clavicular fracture. MRI assisted in the diagnosis by demonstrating abnormally high signal intensity on T2-weighted images in the belly of the supraspinatus and infraspinatus muscles.[217]

Acute Brachial Neuritis

Acute brachial neuritis, or *Parsonage-Turner syndrome*, presents with a sudden onset of intense, burning shoulder

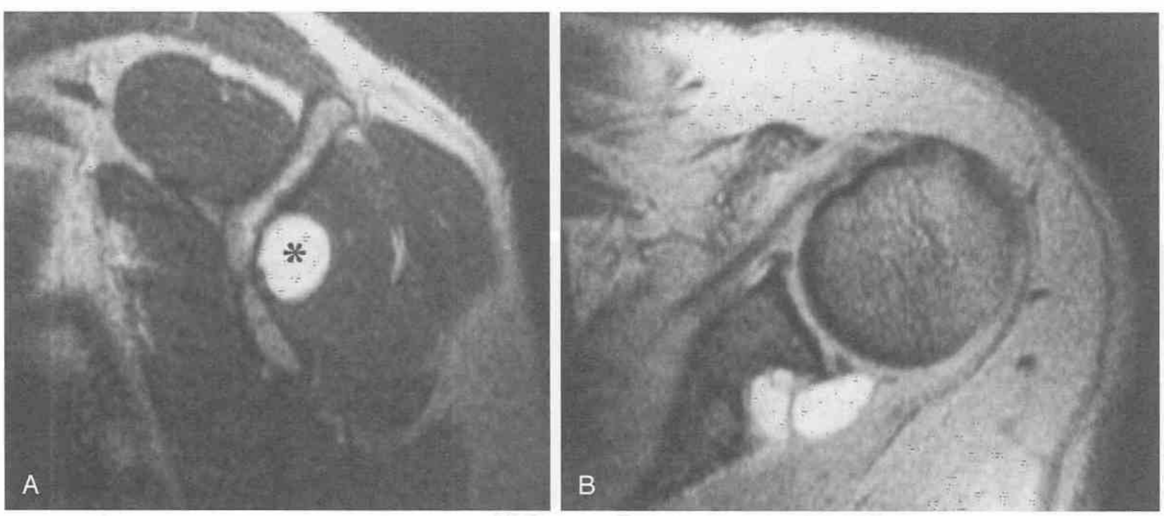

Figure 50–34. Spinoglenoid notch ganglion. *A*, T2-weighted (TR = 2500 msec, TE = 70 msec) sagittal oblique image. A single, rounded, hyperintense mass *(asterisk)* is present in the spinoglenoid notch of this young man who presented with shoulder pain. *B*, Gradient-echo axial image. At this level, the lesion is composed of multiple smaller masses. On proton-density images, this mass was intermediate in signal, approximately isointense with muscle. This location and appearance are typical of a spinoglenoid notch ganglion.

pain and muscle weakness, most commonly involving the supraspinatus and infraspinatus muscles, although other shoulder muscles may be involved as well. The patients are most typically young to middle-aged adults. There is a marked male predominance. This is a self-limited disease, with resolution first of the pain. Muscle weakness may last years but usually resolves in 2 to 3 months. MRI may reveal increased signal intensity in the involved muscles on T2 weighting. Later in the course of the disease, muscle wasting without fatty infiltration may be evident. MRI is chiefly useful in excluding other causes of shoulder pain and dysfunction, particularly compressive masses in the spinoglenoid notch.[69]

Quadrilateral Space Syndrome

Another cause of shoulder pain and dysfunction is quadrilateral space syndrome, in which the axillary nerve is compressed by fibrous bands as it traverses the quadrilateral space. This space is bounded by the teres minor and teres major muscles, the long head of the triceps muscle, and the surgical neck of the humerus. It manifests clinically with poorly localized shoulder pain, lateral shoulder and posterior upper arm paresthesias, and weakness and atrophy of the teres minor and/or deltoid muscles. MRI does not show the actual entrapment but may demonstrate denervation atrophy of the appropriate muscles and exclude other causes of shoulder pain.[98]

Angiography has been used to confirm the diagnosis on the basis of occlusion of the posterior humeral circumflex artery with the arm in abduction. In 1994, Mochizuki and coworkers cast doubt upon the usefulness of this approach or, more specifically, of using MR angiography in place of conventional contrast angiography, when they found that MR angiography demonstrated occlusion of 80% of the posterior humeral circumflex arteries of six asymptomatic volunteers with abduction.[119]

Trauma

Most fractures about the shoulder are adequately evaluated with plain radiography. In cases of complex fractures of the proximal humerus, CT may be helpful for pretreatment planning. Treatment of these fractures varies considerably, depending on their position in the widely used classification scheme of Neer.[127] This scheme is based on the degree of separation or rotation of the four possible major fracture fragments (shaft, head, greater tuberosity, and lesser tuberosity). A fragment is considered displaced if it is distracted 1 cm or more from its neighbors or if it is angulated 45 degrees or more from its proper location.[127]

Fractures without displacement are commonly treated with early mobilization, whereas those involving displace-

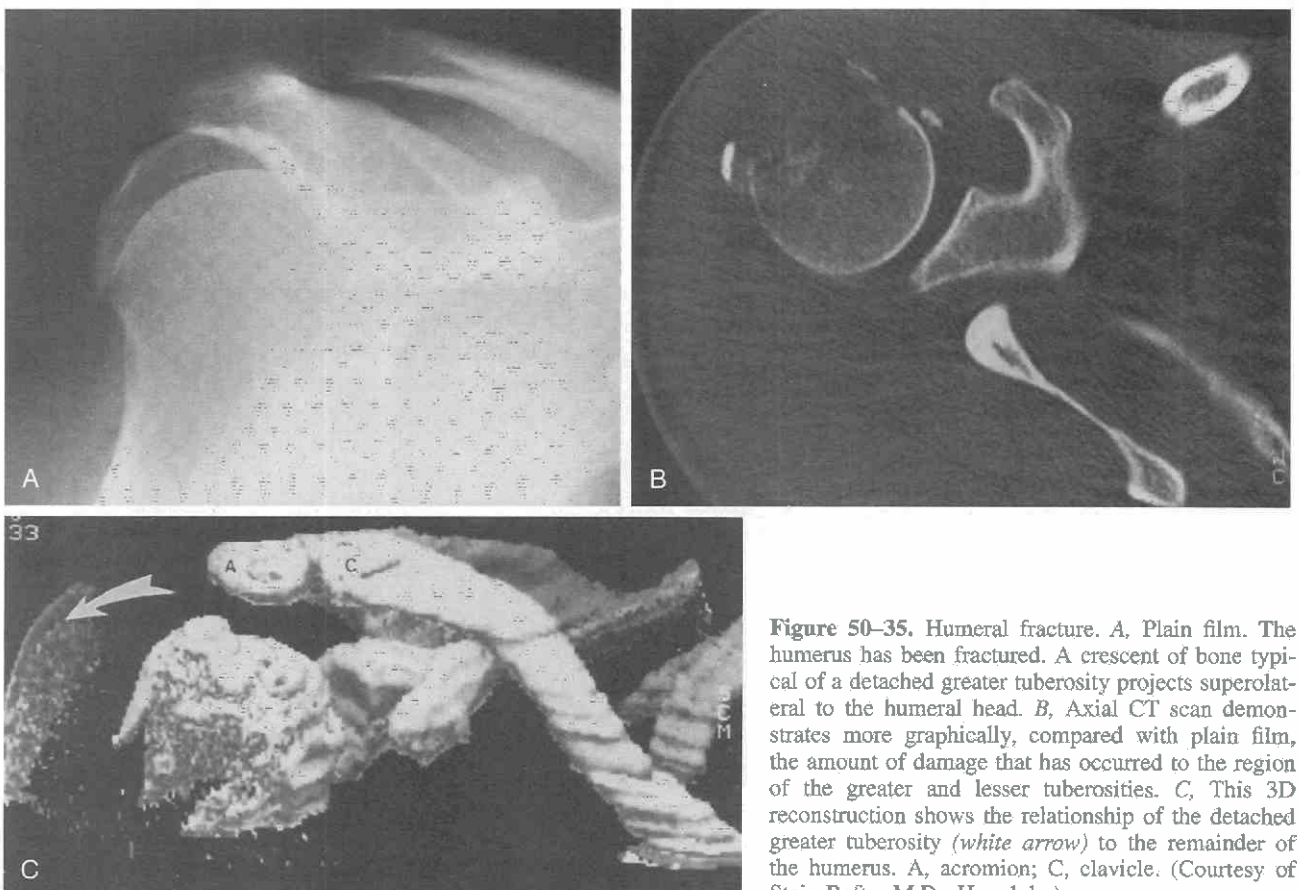

Figure 50–35. Humeral fracture. *A,* Plain film. The humerus has been fractured. A crescent of bone typical of a detached greater tuberosity projects superolateral to the humeral head. *B,* Axial CT scan demonstrates more graphically, compared with plain film, the amount of damage that has occurred to the region of the greater and lesser tuberosities. *C,* This 3D reconstruction shows the relationship of the detached greater tuberosity *(white arrow)* to the remainder of the humerus. A, acromion; C, clavicle. (Courtesy of Stein Rafto, M.D., Honolulu.)

ment of one of the tuberosities often require open reduction. It is important, therefore, to determine accurately the position of all fragments before definitive treatment is carried out. This may be difficult with plain radiographs alone.

Castagno and colleagues found that in 12 cases of acute fractures and five cases of persistent limitation of motion after treatment of fracture, CT provided useful information that was not evident on plain film.[19] Even when the information is available on the plain films, evaluation of fragment location may be difficult, as evidenced by reports of high interobserver variability in classifying humeral fractures according to Neer's scheme. Furthermore, CT may be useful because it can provide a much more graphic depiction of fragments, particularly when 3D reconstruction is available. In addition to localizing major fracture fragments, CT can locate smaller ones; this is particularly useful for intra-articular fragments. Loose bodies of nontraumatic origin may also be located with CT, of course (Fig. 50–35).[19, 70, 86, 93, 130]

CT may be used to detect complex scapular fractures. These are rare injuries, usually seen in patients who have sustained multiple injuries as a result of direct, blunt trauma, often an automobile accident. These fractures may be missed on initial plain radiography, particularly on the portable chest films often obtained on patients who have sustained severe trauma. When a suspected scapular fracture has not been revealed on such a film, it may be easier as well as more diagnostically rewarding to obtain a CT study rather than plain films of the shoulder.[1, 67, 110, 192]

CT may also be useful in evaluation of scapular fractures. Treatment of scapular fractures is less well established than treatment of humeral fractures. Some surgeons believe that displaced fractures of the glenoid and scapular spine should receive internal fixation; others suggest that these injuries, like other scapular fractures, may be satisfactorily treated by immobilization, followed by range-of-motion exercises shortly thereafter. In addition, the patient's other injuries may preclude surgical intervention. When treatment hinges on the site of the fracture and the degree of displacement, however, CT may be more easily obtained and more revealing than plain films (Fig. 50–36).[1, 111]

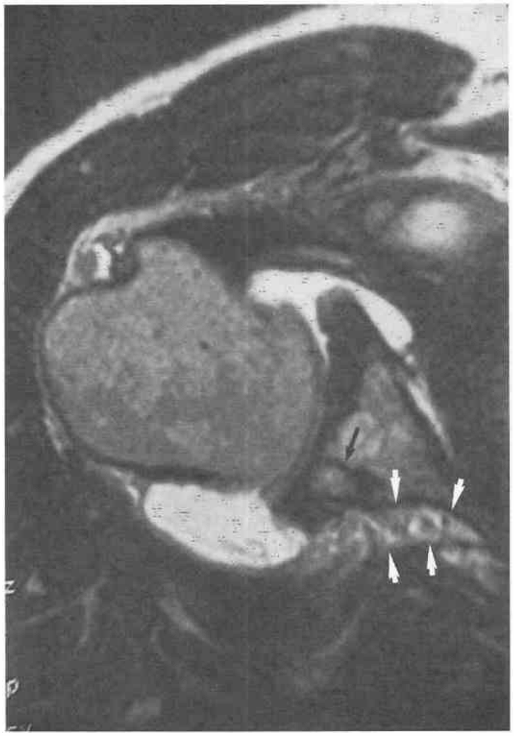

Figure 50–37. Occult fracture. Gradient-echo axial image. The low-signal-intensity line oriented perpendicular to the articular surface of the glenoid *(arrow)* is a fracture line and represents a reverse bony Bankart lesion. The patient had a history of posterior dislocation. The posterior capsule has also been stripped from the glenoid neck, leaving an inhomogenous collection of subperiosteal hematoma and/or granulation tissue *(arrowheads)*.

MRI may reveal occult fractures, which appear as a line of abnormal signal intensity extending through cancellous bone to reach a cortical surface (Fig. 50–37). MRI may demonstrate the anterior-inferior labral tear and associated

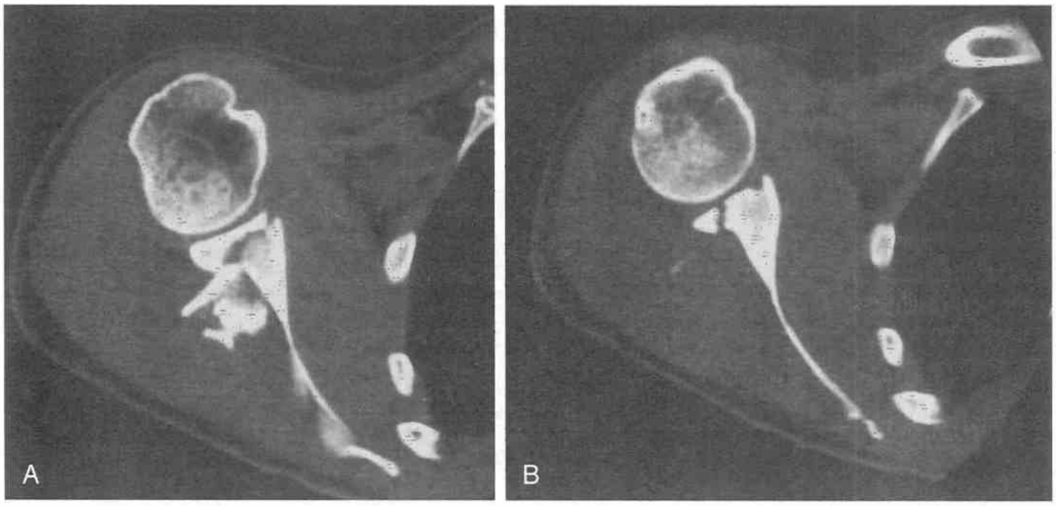

Figure 50–36. Glenoid fracture. *A* and *B,* Axial CT scans. Extension of this fracture to the articular surface of the glenoid is easily appreciated at CT.

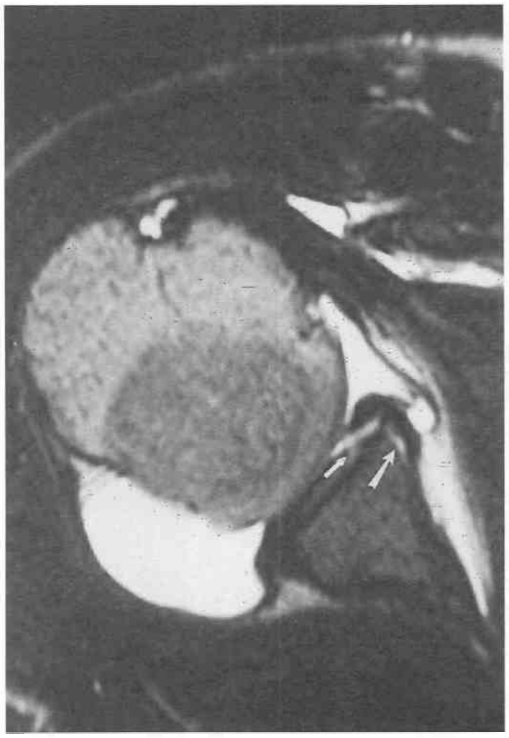

Figure 50–38. GLAD (glenolabral articular disruption) lesion. Gradient-echo axial MR arthrogram. Gadolinium tracks between the anterior labrum and the glenoid and extends medially to the neck of the glenoid, indicating an avulsion of the anterior-inferior labrum *(arrow)*. Abnormally increased signal is also present in the articular cartilage, indicating the cartilaginous injury found in this constellation of associated abnormalities *(small arrow)*.

articular cartilaginous injury typical of the *glenolabral articular disruption* (GLAD) lesion. This combination of injuries is not associated with dislocation or instability; rather, it is an impaction injury caused by the humerus being driven forcefully into the glenoid (Fig. 50–38). Acute trauma may also cause a rotator cuff tear, particularly when superimposed on preexisting degeneration. The tear may be evaluated on MRI using the same criteria discussed previously for tears not related to trauma.

Summary

There is little doubt that CT, MRI, and CT and MR arthrography accurately reveal anatomic defects in the shoulder. Less research has focused on the usefulness of the information. Blanchard and colleagues in 1996 found that MRI led to new diagnoses in 20 (34%) of 59 patients. For 25 of the 52 unchanged diagnoses (some patients had more than one diagnosis), MRI increased the referring physician's confidence in the diagnosis.[11]

For any of these modalities to be maximally effective in a patient's care, however, there must be careful correlation between clinical presentation and imaging results, a task that largely rests on the shoulders of the referring physician. In 1995, Sher and coworkers discovered a 34% prevalence of MRI findings of rotator cuff tear in asymptomatic individuals. The frequency of these presumed tears increased with age.[178] To optimize imaging for individual patients, it is also important to remember the contributions that can be made by plain films, arthrography, and ultrasound.

Acknowledgments

We would like to thank Kim Slonaker for her patient and precise word processing and Cheryl Bost for photography.

References

1. ADA JR, Miller ME: Scapular fractures. Clin Orthopia 269:174–180, 1991.
2. Andrews JR, Carson WG JR, McLeod WD: Glenoid labrum tears related to the long head of the biceps. Am J Sports Med 13: 337–341, 1985.
3. Balich SM, Shelly RC, Brown TR, et al: MR imaging of the rotator cuff tendon: Interobserver agreement and analysis of interpretive errors. Radiology 204:191–194, 1997.
4. Bankart ASB: The pathology and treatment of recurrent dislocation of the shoulder-joint. Br J Surg 26:23–29, 1938.
5. Beltran J, Rosenberg ZS, Chandnani VP, et al: Glenohumeral instability: Evaluation with MR arthrography. Radiographics 17:657–673, 1997.
6. Beltran J, Caudill JL, Herman LA, et al: Rheumatoid arthritis: MR imaging manifestations. Radiology 165:153–157, 1987.
7. Bencardino JT, Beltran J, Rosenberg ZS, et al: Superior labrum anterior-posterior lesions: Diagnosis with MR arthrography of the shoulder. Radiology 214:267–271, 2000.
8. Bigliani LU, Levine WN: Current concepts review: Subacromial impingement syndrome. J Bone Joint Surg Am 79:1854–1867, 1997.
9. Bigliani LU, Morrison DS, April EW: The morphology of the acromion and its relationship to rotator cuff tears. American Shoulder and Elbow Surgeons. Orthop Trans 10:228, 1986.
10. Bishop AF, Destouet JM, Murphy WA, et al: Tumoral calcinosis: Case report and review. Skeletal Radiol 8:269–274, 1982.
11. Blanchard TK, Mackenzie R, Bearcroft PW, et al: Magnetic resonance imaging of the shoulder: Assessment of effectiveness. Clin Radiol 52:363–368, 1997.
12. Bokor DJ, Conboy VB, Olson C: Anterior instability of the glenohumeral joint with humeral avulsion of the glenohumeral ligament. J Bone Joint Surg Br 81:93–96, 1999.
13. Brossman J, Preidler KW, Pedowitz RA, et al: Shoulder impingement syndrome: Influence of shoulder position on rotator cuff impingement—an anatomic study. AJR Am J Roentgenol 167:1511–1515, 1996.
14. Burk DL Jr, Karasick D, Kurtz AB, et al: Rotator cuff tears: Prospective comparison of MR imaging with arthrography, sonography, and surgery. AJR Am J Roentgenol 153:87–92, 1989.
15. Butt WP, Hardy G, Ostlere SJ: Pigmented villonodular synovitis of the knee: Computed tomographic appearances. Skeletal Radiol 19: 191–196, 1990.
16. Callaghan JJ, McNiesh LM, DeHaven JP, et al: A prospective comparison study of double contrast computed tomography (CT) arthrography and arthroscopy of the shoulder. Am J Sports Med 16: 13–20, 1988.
17. Carrino JA, McCauley TR, Katz LD, et al: Rotator cuff: Evaluation with fast spin-echo versus conventional spin-echo MR imaging. Radiology 202:533–539, 1997.
18. Cartland JP, Crues JV 3rd, Stauffer A, et al: MR imaging in the evaluation of SLAP injuries of the shoulder: Findings in 10 patients. AJR Am J Roentgenol 159:787–792, 1992.
19. Castagno AA, Shuman WP, Kilcoyne RF, et al: Complex fractures of the proximal humerus: Role of CT in treatment. Radiology 165: 759–762, 1987.
20. Cervilla V, Schweitzer ME, Ho C, et al: Medial dislocation of the biceps brachii tendon: Appearance at MR imaging. Radiology 180: 523–526, 1991.
21. Chan TW, Dalinka MK, Kneeland JB, et al: Biceps tendon dislocation: Evaluation with MR imaging. Radiology 179:649–652, 1991.
22. Chandnani VP, Yeager TD, DeBerardino T, et al: Glenoid labral tears: Prospective evaluation with MR imaging, MR arthrography, and CT arthrography. AJR Am J Roentgenol 161:1229–1235, 1993.
23. Chew FS, Crenshaw WB: Idiopathic tumoral calcinosis. AJR Am J Roentgenol 158:330, 1992.

24. Codman EA: The classic rupture of the supraspinatus tendon. Clin Orthop 254:3–26, 1990.
25. Cooper DE, Arnoczky SP, O'Brien SJ, et al: Anatomy, histology, and vascularity of the glenoid labrum. J Bone Joint Surg Am 74: 46–52, 1992.
26. Coumas JM, Waite RJ, Goss TP, et al: CT and MR evaluation of the labral capsular ligamentous complex of the shoulder. AJR Am J Roentgenol 158:591–597, 1992.
27. Crim JR, Seeger LL, Yao L, et al: Diagnosis of soft-tissue masses with MR imaging: Can benign masses be differentiated from malignant ones? Radiology 185:581–586, 1992.
28. Cruess RL: Rheumatoid arthritis of the shoulder. Orthop Clin North Am 11:333–342, 1980.
29. Cvitanic O, Tirman PF, Feller JF, et al: Using abduction and external rotation of the shoulder to increase the sensitivity of MR arthrography in revealing tears of the anterior glenoid labrum. AJR Am J Roentgenol 169:837–844, 1997.
30. Dalinka MK, Boorstein JM, Zlatkin MB: Computed tomography of musculoskeletal trauma. Radiol Clin North Am 27:933–944, 1989.
31. Davis SJ, Teresi LM, Bradley WG, et al: Effect of arm rotation on MR imaging of the rotator cuff. Radiology 181:265–268, 1991.
32. DeMouy EH, Menendez CV, Bodin CJ: Palpation-directed (non-fluoroscopically guided) saline-enhanced MR arthrography of the shoulder. AJR Am J Roentgenol 169:229–231, 1997.
33. DePalma AF: Surgery of the Shoulder. Philadelphia, JB Lippincott, 1950.
34. Deutsch AL, Resnick D, Mink JH, et al: Computed and conventional arthrotomography of the glenohumeral joint: Normal anatomy and clinical experience. Radiology 153:603–609, 1984.
35. Deutsch A, Altchek DW, Veltri DM, et al: Traumatic tears of the subscapularis tendon: Clinical diagnosis, magnetic resonance imaging findings, and operative treatment. Am J Sports Med 25: 13–22, 1997.
36. Dines DM, Warren RF, Inglis AE, et al: The coracoid impingement syndrome. J Bone Joint Surg Br 72:314–316, 1990.
37. Dorwart RH, Genant HK, Johnston WH, et al: Pigmented villonodular synovitis of the shoulder: Radiologic-pathologic assessment. Am J Roentgenol 143:886–888, 1984.
38. Edelson JG: The "hooked" acromion revisited. J Bone Joint Surg Br 77:284–287, 1995.
39. Edelson JG, Zuckerman J, Hershkovitz I: Os acromiale: Anatomy and surgical implications. J Bone Joint Surg Br 75:551–555, 1993.
40. Epstein RE, Schweitzer ME, Frieman BG, et al: Hooked acromion: Prevalence on MR images of painful shoulders. Radiology 187: 479–481, 1993.
41. Erickson SJ, Cox IH, Hyde JS, et al: Effect of tendon orientation on MR imaging signal intensity: A manifestation of the "magic angle" phenomenon. Radiology 181:389–392, 1991.
42. Erickson SJ, Fitzgerald SW, Quinn SF, et al: Long bicipital tendon of the shoulder: Normal anatomy and pathologic findings on MR imaging. AJR Am J Roentgenol 158:1091–1096, 1992.
43. Erlemann R, Reiser MF, Peters PE, et al: Musculoskeletal neoplasms: Static and dynamic Gd-DTPA–enhanced MR imaging. Radiology 171:767–773, 1989.
44. Evancho AM, et al: MR imaging diagnosis of rotator cuff tears. AJR Am J Roentgenol 151:751–754, 1988.
45. Farley TE, Neumann CH, Steinbach LS, et al: Full-thickness tears of the rotator cuff of the shoulder: Diagnosis with MR imaging. AJR Am J Roentgenol 158:347–351, 1992.
46. Farley TE, Neumann CH, Steinbach LS, et al: The coracoacromial arch: MR evaluation and correlation with rotator cuff pathology. Skeletal Radiol 23:641–645, 1994.
47. Ferrari DA: Capsular ligaments of the shoulder. Am J Sports Med 18:20–24, 1990.
48. Flandry F, Norwood LA: Pigmented villonodular synovitis of the shoulder. Orthopedics 12:715–718, 1989.
49. Flannigan B, Kursunoglu-Brahme S, Snyder S, et al: MR arthrography of the shoulder: Comparison with conventional MR imaging. AJR Am J Roentgenol 155:829–832, 1990.
50. Foley-Nolan D, Stack JP, Ryan M, et al: Magnetic resonance imaging in the assessment of rheumatoid arthritis: A comparison with plain film radiographs. Br J Rheumatol 30:101–106, 1991.
51. Friedman RJ, Bonutti PM, Genez B: Cine magnetic resonance imaging of the subcoracoid region. Orthopedics 21:545–548, 1998.
52. Fritz RC, Helms CA, Steinbach LS, et al: Suprascapular nerve entrapment: Evaluation with MR imaging. Radiology 182:437–444, 1992.
53. Fu FH, Harner CD, Klein AH: Shoulder impingement syndrome. Clin Orthop 269:162–173, 1991.
54. Gagey N, Ravaud E, Lassau JP: Anatomy of the acromial arch: Correlation of anatomy and magnetic resonance imaging. Surg Radiol Anat 15:63–70, 1993.
55. Garneau RA, Renfrew DL, Moore TE, et al: Glenoid labrum: Evaluation with MR imaging. Radiology 179:519–522, 1991.
56. Gerber C, Terrier F, Ganz R: The role of the coracoid process in the chronic impingement syndrome. J Bone Joint Surg Br 67: 703–708, 1985.
57. Getz JD, Renfrew DL, Moore TE, et al: Acromial morphology: Relation to sex, age, symmetry, and subacromial enthesophytes. Radiology 199:737–742, 1996.
58. Gold RH, Seeger LL, Yao L: Imaging shoulder impingement. Skeletal Radiol 22:555–561, 1993.
59. Graichen H, Bonel H, Stammberger T, et al: A technique for determining the spatial relationship between the rotator cuff and the subacromial space in arm abduction using MRI and 3-D image processing. Magn Reson Med 40:640–643, 1998.
60. Graichen H, Bonel H, Stammberger T, et al: Subacromial space width changes during abduction and rotation: A 3-D MR imaging study. Surg Radiol Anat 21:59–64, 1999.
61. Graichen H, Bonel H, Stammberger T, et al: Three-dimensional analysis of the width of the subacromial space in healthy subjects and patients with impingement syndrome. AJR Am J Roentgenol 172:1081–1086, 1999.
62. Grauer JD, Paulos LE, Smutz WP: Biceps tendon and superior labral injuries. Arthroscopy 8:488–497, 1992.
63. Gusmer PB, Potter HG, Schatz JA, et al: Labral injuries: Accuracy of detection with unenhanced MR imaging of the shoulder. Radiology 200:519–524, 1996.
64. Halverson PB, McCarty DJ, Cheung HS, et al: Milwaukee shoulder syndrome: Eleven additional cases with involvement of the knee in seven (basic calcium phosphate crystal deposition disease). Semin Arthritis Rheum 14:36–44, 1984.
65. Halverson PB, Carrera GF, McCarty DJ, et al: Milwaukee shoulder syndrome: Fifteen additional cases and a description of contributing factors. Arch Intern Med 150:677–682, 1990.
66. Handelberg F, Willems S, Shahabpour M, et al: SLAP lesions: A retrospective multicenter study. Arthroscopy 14:856–862, 1998.
67. Harris RD, Harris JH Jr: The prevalence and significance of missed scapular fractures in blunt chest trauma. AJR Am J Roentgenol 151: 747–750, 1988.
68. Haygood TM, Langlotz CP, Kneeland JB, et al: Categorization of acromial shape: Interobserver variability with MR imaging and conventional radiography. AJR Am J Roentgenol 162:1377–1382, 1994.
69. Helms CA, Martinez S, Speer KP: Acute brachial neuritis (Parsonage-Turner syndrome): MR imaging appearance—report of three cases. Radiology 207:255–259, 1998.
70. Heppenstall RB: Fractures of the proximal humerus. Orthop Clin North Am 6:467–475, 1975.
71. Hodler J, Kursunoglu-Brahme S, Flannigan B, et al: Injuries of the superior portion of the glenoid labrum involving the insertion of the biceps tendon: MR imaging findings in nine cases. AJR Am J Roentgenol 159:565–568, 1992.
71a. Hodler J, Kursunoglu-Brahme S, Snyder SJ, et al: Rotator cuff disease: Assessment with MR arthrography versus standard MR Imaging in 36 patients with arthroscopic confirmation. Radiology 182:431–436, 1992.
72. Hollister MS, Mack LA, Patten RM, et al: Association of sonographically detected subacromial/subdeltoid bursal effusion and intra-articular fluid with rotator cuff tear. AJR Am J Roentgenol 165: 605–608, 1995.
73. Holt RG, Helms CA, Steinbach L, et al: Magnetic resonance imaging of the shoulder: Rationale and current applications. Skeletal Radiol 19:5–14, 1990.
74. Huang LF, Rubin DA, Britton CA: Greater tuberosity changes as revealed by radiography: Lack of clinical usefulness in patients with rotator cuff disease. AJR Am J Roentgenol 172:1381–1388, 1999.
75. Hunter JC, Blatz DJ, Escobedo EM: SLAP lesions of the glenoid labrum: CT arthrographic and arthroscopic correlation. Radiology 184:513–518, 1992.

76. Iannotti JP, Zlatkin MB, Esterhai JL, et al: Magnetic resonance imaging of the shoulder: Sensitivity, specificity, and predictive value. J Bone Joint Surg Am 73:17–29, 1991.
77. Jelinek JS, Kransdorf MJ, Utz JA, et al: Imaging of pigmented villonodular synovitis with emphasis on MR imaging. AJR Am J Roentgenol 152:337–342, 1989.
78. Jobe CM: Superior glenoid impingement. Clin Orthop 330:98–107, 1996.
79. Jobe FW, Giangarra CE, Kvitne RS, Glousman RE: Anterior capsulolabral reconstruction of the shoulder in athletes in overhand sports. Am J Sports Med 19:428–434, 1991.
80. Jobe FW, Bradley JP: Rotator cuff injuries in baseball. Sports Med 6:378–387, 1988.
81. Kaneko K, De Mouy EH, Brunet ME: Massive rotator cuff tears: Screening by routine radiographs. Clin Imaging 19:8–11, 1995.
82. Kaplan PA, Bryans KC, Davick JP, et al: MR imaging of the normal shoulder: Variants and pitfalls. Radiology 184:519–524, 1992.
83. Keats TE, Pope TL: The acromioclavicular joint: Normal variation and the diagnosis of dislocation. Skeletal Radiol 17:159–162, 1988.
84. Kieft GJ, Bloem JL, Rozing PM, Obermann WR: MR imaging of recurrent anterior dislocation of the shoulder: Comparison with CT arthrography. AJR Am J Roentgenol 150:1083–1087, 1988.
85. Kieft GJ, Bloem JL, Rozing PM, Obermann WR: Rotator cuff impingement syndrome: MR imaging. Radiology 166:211–214, 1988.
86. Kilcoyne RF, Shuman WP, Matsen FA 3rd, et al: The Neer classification of displaced proximal humeral fractures: Spectrum of findings on plain radiographs and CT scans. AJR Am J Roentgenol 154:1029–1033, 1990.
87. Kjellin I, Ho CP, Cervilla V, et al: Alterations in the supraspinatus tendon at MR imaging: Correlation with histopathologic findings in cadavers. Radiology 181:837–841, 1991.
88. Klompmaker J, Veth RP, Robinson PH, et al: Pigmented villonodular synovitis. Arch Orthop Trauma Surg 109:205–210, 1990.
89. Kneeland JB, Middleton WD, Carrera GF, et al: MR imaging of the shoulder: Diagnosis of rotator cuff tears. AJR Am J Roentgenol 149:333–337, 1987.
90. Kneeland JB, Carrera GF, Middleton WD, et al: Rotator cuff tears: Preliminary application of high-resolution MR imaging with counter rotating current loop-gap resonators. Radiology 160:695–699, 1986.
91. Kopka L, Funke M, Fischer U, et al: MR arthrography of the shoulder with gadopentetate dimeglumine: Influence of concentration, iodinated contrast material, and time on signal intensity. AJR Am J Roentgenol 163:621–623, 1994.
92. Kottal RA, Vogler JB 3rd, Matamoros A, et al: Pigmented villonodular synovitis: A report of MR imaging in two cases. Radiology 163:551–553, 1987.
93. Kristiansen B, Andersen UL, Olsen CA, Varmarken JE: The Neer classification of fractures of the proximal humerus: An assessment of interobserver variation. Skeletal Radiol 17:420–422, 1988.
94. Kvitne RS, Jobe FW, Jobe CM: Shoulder instability in the overhand or throwing athlete. Clin Sports Med 14:917–935, 1995.
95. Kwak SM, Brown RR, Resnick D, et al: Anatomy, anatomic variations, and pathology of the 11- to 3-o'clock position of the glenoid labrum: Findings on MR arthrography and anatomic sections. AJR Am J Roentgenol 171:235–238, 1998.
96. Kwak SM, Brown RR, Trudell D, Resnick D: Glenohumeral joint: Comparison of shoulder positions at MR arthrography. Radiology 208:375–380, 1998.
97. Legan JM, Burkhard TK, Goff WB 2nd, et al: Tears of the glenoid labrum: MR imaging of 88 arthroscopically confirmed cases. Radiology 179:241–246, 1991.
98. Linker CS, Helms CA, Fritz RC: Quadrilateral space syndrome: Findings at MR imaging. Radiology 188:675–676, 1993.
99. Liou JT, Wilson AJ, Totty WG, Brown JJ: The normal shoulder: Common variations that simulate pathologic conditions at MR imaging. Radiology 186:435–441, 1993.
100. Lohr JF, Uhthoff HK: The microvascular pattern of the supraspinatus tendon. Clin Orthop 254:35–38, 1990.
101. Longacre AM, Sheer AL: Tumoral calcinosis: Case presentation and review of 55 cases in the literature. J Fla Med Assoc 61:221–225, 1974.
102. Maffet MW, Gartsman GM, Moseley B: Superior labrum-biceps tendon complex lesions of the shoulder. Am J Sports Med 23:93–98, 1995.
103. Magee TH, Gaenslen ES, Seitz R, et al: MR imaging of the shoulder after surgery. AJR Am J Roentgenol 168:925–928, 1997.
104. Mandelbaum BR, Grant TT, Hartzman S, et al: The use of MRI to assist in diagnosis of pigmented villonodular synovitis of the knee joint. Clin Orthop 231:135–139, 1988.
105. Matsen FA III, Arntz CT: Rotator cuff tendon failure. In Rockwood CA Jr, Matsen FA III (eds): The Shoulder. Philadelphia, WB Saunders, 1990.
106. Matsen FA III, Arntz CT: Subacromial impingement. In Rockwood CA Jr, Matsen FA III (eds): The Shoulder. Philadelphia, WB Saunders, 1990.
107. Matsen FA III, Thomas SC, Rockwood CA Jr: Glenohumeral instability. In Rockwood CA Jr, Matsen FA III (eds): The Shoulder. Philadelphia, WB Saunders, 1990.
108. McCarty DJ, Halverson PB, Carrera GF, et al: "Milwaukee shoulder": Association of microspheroids containing hydroxyapatite crystals, active collagenase, and neutral protease with rotator cuff defects. Arthritis Rheum 24:464–473, 1981.
109. McCauley TR, Pope CF, Jokl P: Normal and abnormal glenoid labrum: Assessment with multiplanar gradient-echo MR imaging. Radiology 183:35–37, 1992.
110. McGahan JP, Rab GT, Dublin A: Fractures of the scapula. J Trauma 20:880–883, 1980.
111. McGinnis M, Denton JR: Fractures of the scapula: A retrospective study of 40 fractured scapulae. J Trauma 29:1488–1493, 1989.
112. McKendry RJR, Uhthoff HK, Sarkar K, Hyslop PS: Calcifying tendinitis of the shoulder: Prognostic value of clinical, histologic, and radiologic features in 57 surgically treated cases. J Rheumatol 9:75–80, 1982.
113. McNair MM, Boyle JA, Buchanan WW, Davidson JK: A clinical and radiological study of rheumatoid arthritis with a note on the findings in osteoarthrosis: I. The shoulder joint. Clin Radiol 20:269–277, 1969.
114. McNiesh LM, Callaghan JJ: CT arthrography of the shoulder: Variations of the glenoid labrum. AJR Am J Roentgenol 149:963–966, 1987.
115. Merl T, Scholz M, Gerhardt P, et al: Results of a prospective multicenter study for evaluation of the diagnostic quality of an open whole-body low-field MRI unit. A comparison with high-field MRI measured by the applicable gold standard. Eur J Radiol 30:43–53, 1999.
116. Metzker A, Eisenstein B, Oren J, Samuel R: Tumoral calcinosis revisited: Common and uncommon features. Eur J Pediatr 147:128–132, 1988.
117. Mirowitz SA: Normal rotator cuff: MR imaging with conventional and fat-suppression techniques. Radiology 180:735–740, 1991.
118. Mitchell MJ, Causey G, Berthoty DP, et al: Peribursal fat plane of the shoulder: Anatomic study and clinical experience. Radiology 168:699–704, 1988.
119. Mochizuki T, Isoda H, Masui T, et al: Occlusion of the posterior humeral circumflex artery: Detection with MR angiography in healthy volunteers and in a patient with quadrilateral space syndrome. AJR Am J Roentgenol 163:625–627, 1994.
120. Monu JU, Pope TL Jr, Chabon SJ, Vanarthos WJ: MR diagnosis of superior labral anterior posterior (SLAP) injuries of the glenoid labrum: Value of routine imaging without intraarticular injection of contrast material. AJR Am J Roentgenol 163:1425–1429, 1994.
121. Moore KL: Clinically Oriented Anatomy. Baltimore, Williams & Wilkins, 1980.
122. Moseley HF, Goldie I: The arterial pattern of the rotator cuff of the shoulder. J Bone Joint Surg Br 45:780–789, 1963.
123. Moseley HF, Övergaard B: The anterior capsular mechanism in recurrent anterior dislocation of the shoulder. J Bone Joint Surg Br 44:913–927, 1962.
124. Mudge MK, Wood VE, Frykman GK: Rotator cuff tears associated with os acromiale. J Bone Joint Surg 66:427–429, 1984.
125. Needell SD, Zlatkin MB, Sher JS, et al: MR imaging of the rotator cuff: Peritendinous and bone abnormalities in an asymptomatic population. AJR Am J Roentgenol 166:863–867, 1996.
126. Neer CS: Anterior acromioplasty for the chronic impingement syndrome in the shoulder. J Bone Joint Surg Am 54:41–50, 1972.
127. Neer CS: Displaced proximal humeral fractures: Part I. Classification and evaluation. J Bone Joint Surg Am 52:1077–1089,1970.
128. Neer CS: Impingement lesions. Clin Orthop 173:70–77, 1983.
129. Neer CS, Craig EV, Fukuda H: Cuff-tear arthropathy. J Bone Joint Surg Am 65:1232–1244, 1983.

130. Neer CS, Foster CR: Inferior capsular shift for involuntary inferior and multidirectional instability of the shoulder. J Bone Joint Surg Am 62:897–908, 1980.
131. Neer CS, Welsh RP: The shoulder in sports. Orthop Clin North Am 8:583–591, 1977.
132. Neumann CH, Holt RG, Steinbach LS, et al: MR imaging of the shoulder: Appearance of the supraspinatus tendon in asymptomatic volunteers. AJR Am J Roentgenol 158:1281–1287, 1992.
133. Neumann CH, Petersen SA, Jahnke AH: MR imaging of the labral-capsular complex: Normal variations. AJR Am J Roentgenol 157: 1015–1021, 1991.
134. Neviaser TJ: The anterior labroligamentous periosteal sleeve avulsion lesion: A cause of anterior instability of the shoulder. Arthroscopy 9:17–21, 1993.
135. Neviaser TJ: The GLAD lesion: Another cause of anterior shoulder pain. Arthroscopy 9:22–23, 1993.
136. Neviaser TJ, Neviaser RJ, Neviaser JS, Neviaser JS: The four-in-one arthroplasty for the painful arc syndrome. Clin Orthop 163: 107–112, 1982.
137. Nguyen VD, Nguyen KD: "Idiopathic destructive arthritis" of the shoulder: A still fascinating enigma. Comput Med Imaging Graph 14:249–255, 1990.
138. Nguyen VD, Nguyen KD, Kamath V: Unusual feature of soft-tissue calcification in chronic renal failure: Tumoral calcification. Comput Med Imaging Graph 15:397–402, 1991.
139. Nicola T: Anterior dislocation of the shoulder: The role of the articular capsule. J Bone Joint Surg 24:614–616, 1942.
140. Nobuhara K, Ikeda H: Rotator interval lesion. Clin Orthop 223: 44–50, 1987.
141. Nutton RW, Stothard J: Acute calcific supraspinatus tendinitis in a three-year-old child. J Bone Joint Surg Br 69:148, 1987.
142. O'Brien SJ, Neves MC, Arnoczky SP, et al: The anatomy and histology of the inferior glenohumeral ligament complex of the shoulder. Am J Sports Med 18:449–456, 1990.
143. Ogata S, Uhthoff HK: Acromial enthesopathy and rotator cuff tear. Clin Orthop 254:39–48, 1990.
144. Ogino T, Minami A, Kato H, et al: Entrapment neuropathy of the suprascapular nerve by a ganglion. J Bone Joint Surg Am 73: 141–147, 1991.
145. Owen RS, Dalinka MK, Deren JA, et al: Shoulder after surgery: MR imaging with surgical validation. Radiology 186:443–447, 1993.
146. Ozaki J, Fujimoto S, Nakagawa Y, et al: Tears of the rotator cuff of the shoulder associated with pathological changes in the acromion. J Bone Joint Surg Am 70:1224–1230, 1988.
147. Palmer WE, Brown JH, Rosenthal DI: Labral-ligamentous complex of the shoulder: Evaluation with MR arthrography. Radiology 190: 645–651, 1994.
148. Palmer WE, Brown JH, Rosenthal DI: Rotator cuff: Evaluation with fat-suppressed MR arthrography. Radiology 188:683–687, 1993.
149. Palmer WE, Caslowitz PL: Anterior shoulder instability: Diagnostic criteria determined from prospective analysis of 121 MR arthrograms. Radiology 197:819–825, 1995.
150. Pappas AM, Goss TP, Kleinman PK: Symptomatic shoulder instability due to lesions of the glenoid labrum. Am J Sports Med 11: 279–288, 1983.
151. Park JG, Lee JK, Phelps CT: Os acromiale associated with rotator cuff impingement: MR imaging of the shoulder. Radiology 193: 255–257, 1994.
152. Patten RM: Tears of the anterior portion of the rotator cuff (the subscapularis tendon): MR imaging findings. AJR Am J Roentgenol 162:351–354, 1994.
153. Peh WCG, Farmer THR, Totty WG: Acromial arch shape: Assessment with MR imaging. Radiology 195:501–505, 1995.
154. Penny JN, Welsh RP: Shoulder impingement syndromes in athletes and their surgical management. Am J Sports Med 9:11–15, 1981.
155. Petersilge CA, Lewin JS, Duerk JL, Hatem SF: MR arthrography of the shoulder: Rethinking traditional imaging procedures to meet the technical requirements of MR imaging guidance. AJR Am J Roentgenol 169:1453–1457, 1997.
156. Petersson CJ: Spontaneous medial dislocation of the tendon of the long biceps brachii. Clin Orthop 211:224–227, 1986.
157. Prodromos CC, Ferry JA, Schiller AL, Zarins B: Histological studies of the glenoid labrum from fetal life to old age. J Bone Joint Surg Am 74:1344–1348, 1990.
158. Quinn SF, Sheley RC, Demlow TA, Szumowski J: Rotator cuff tendon tears: Evaluation with fat-suppressed MR imaging with arthroscopic correlation in 100 patients. Radiology 195:497–501, 1995.
159. Rafii M, Firooznia H, Golimbu C, et al: CT arthrography of capsular structures of the shoulder. Am J Roentgenol 146:361–367, 1986.
160. Rafii M, Firooznia H, Sherman O, et al: Rotator cuff lesions: Signal patterns at MR imaging. Radiology 177:817–823, 1990.
161. Rathbun JB, Macnab I: The microvascular pattern of the rotator cuff. J Bone Joint Surg Br 52:540–553, 1970.
162. Reinus WR, Shady KL, Mirowitz SA, Totty WG: MR diagnosis of rotator cuff tears of the shoulder: Value of using T2-weighted fat-saturated images. AJR Am J Roentgenol 164:1451–1455, 1995.
163. Richards RD, Sartoris DJ, Pathria MN, Resnick D: Hill-Sachs lesion and normal humeral groove: MR imaging features allowing their differentiation. Radiology 190:665–668, 1994.
164. Richardson ML, Patten RM: Age-related changes in marrow distribution in the shoulder: MR imaging findings. Radiology 192:209–215, 1994.
165. Robertson PL, Schweitzer ME, Mitchell DG, et al: Rotator cuff disorders: Interobserver and intraobserver variation in diagnosis with MR imaging. Radiology 194:831–835, 1995.
166. Roger B, Skaf A, Hooper AW, et al: Imaging findings in the dominant shoulder of throwing athletes: Comparison of radiography, arthrography, CT arthrography, and MR arthrography with arthroscopic correlation. AJR Am J Roentgenol 172:1371–1380, 1999.
167. Rominger MB, Bernreuter WK, Kenney PJ, et al: MR imaging of the hands in early rheumatoid arthritis: Preliminary results. Radiographics 13:37–46, 1993.
168. Rowe CR, Pierce DS, Clarke JG: Voluntary dislocation of the shoulder. J Bone Joint Surg Am 55:445–460, 1973.
169. Sahin-Akyar G, Miller TT, Staron RB, et al: Gradient-echo versus fat-suppressed fast spin-echo MR imaging of rotator cuff tears. AJR Am J Roentgenol 171:223–227, 1998.
170. Salter EG, Nasca RJ, Shelley BS: Anatomical observations on the acromioclavicular joint and supporting ligaments. Am J Sports Med 15:199–206, 1987.
171. Sanders TG, Tirman PF, Linares R, et al: The glenolabral articular disruption lesion: MR arthrography with arthroscopic correlation. AJR Am J Roentgenol 172:171–175, 1999.
172. Schraner AB, Major NM: MR imaging of the subcoracoid bursa. AJR Am J Roentgenol 172:1567–1571, 1999.
173. Schweitzer ME, Magbalon MJ, Fenlin JM, et al: Effusion criteria and clinical importance of glenohumeral joint fluid: MR imaging evaluation. Radiology 194:821–824, 1995.
174. Seeger LL, Ruszkowski JT, Bassett LW, et al: MR imaging of the normal shoulder: Anatomic correlation. AJR Am J Roentgenol 148: 83–91, 1987.
175. Seeger LL, Gold RH, Bassett LW, Ellman H: Shoulder impingement syndrome: MR findings in 53 shoulders. AJR Am J Roentgenol 150: 343–347, 1988.
176. Seeger LL, Gold RH, Bassett LW: Shoulder instability: Evaluation with MR imaging. Radiology 168:695–697, 1988.
177. Seeger LL, Lubowitz J, Thomas BJ: Case report 815. Skeletal Radiol 22:615–617, 1993.
178. Sher JS, Uribe JW, Posada A, et al: Abnormal findings on magnetic resonance images of asymptomatic shoulders. J Bone Joint Surg Am 77:10–15, 1995.
179. Sher M, Lorigan JG, Ayala AG, Libshitz HI: Case report 578: Pigmented villonodular synovitis of the shoulder. Skeletal Radiol 19:131–133, 1990.
180. Shuman WP, Kilcoyne RF, Matsen FA, et al: Double-contrast computed tomography of the glenoid labrum. Am J Roentgenol 141: 581–584, 1983.
181. Silverman PM: Helical (Spiral) Computed Tomography: A Practical Approach to Clinical Protocols. Philadelphia, Lippincott-Raven, 1998.
182. Singson RD, Hoang T, Dan S, Friedman M: MR evaluation of rotator cuff pathology using T2-weighted fast spin-echo technique with and without fat suppression. AJR Am J Roentgenol 166: 1061–1065, 1996.
183. Singson RD, Feldman F, Bigliani LU, Rosenberg ZS: Recurrent shoulder dislocation after surgical repair: Double-contrast CT arthrography. Radiology 164:425–428, 1987.
184. Singson RD, Feldman F, Bigliani L: CT arthrographic patterns in recurrent glenohumeral instability. AJR Am J Roentgenol 149: 749–753, 1987.

185. Smith DK, Chopp TM, Aufdemorte TB, et al: Sublabral recess of the superior glenoid labrum: Study of cadavers with conventional nonenhanced MR imaging, MR arthrography, anatomic dissection, and limited histologic examination. Radiology 201:251–256, 1996.
186. Snyder SJ, Karzel RP, Del Pizzo W, et al: SLAP lesions of the shoulder. Arthroscopy 6:274–279, 1990.
187. Sonin AH, Peduto AJ, Fitzgerald SW, et al: MR imaging of the rotator cuff mechanism: Comparison of spin-echo and turbo spin-echo sequences. AJR Am J Roentgenol 167:333–338, 1996.
188. Spielmann AL, Forster BB, Kokan P, et al: Shoulder after rotator cuff repair: MR imaging findings in asymptomatic individuals—initial experience. Radiology 213:705–708, 1999.
189. Steinbach LS, Neumann CH, Stoller DW, et al: MRI of the knee in diffuse pigmented villonodular synovitis. Clin Imaging 13:305–316, 1989.
190. Steinbach LS, Tirman PFJ, Peterfy CG, et al (eds): Shoulder Magnetic Resonance Imaging. Philadelphia, Lippincott-Raven, 1998.
191. Stiles RG, Otte MT: Imaging of the shoulder. Radiology 188:603–613, 1993.
192. Thompson DA, Flynn TC, Miller PW, Fischer RP: The significance of scapular fractures. J Trauma 25:974–977, 1985.
193. Timins ME, Erickson SJ, Estkowski LD, et al: Increased signal in the normal supraspinatus tendon on MR imaging: Diagnostic pitfall caused by the magic-angle effect. AJR Am J Roentgenol 164:109–114, 1995.
194. Tirman PFJ, Feller JF, Janzen DL, et al: Association of glenoid labral cysts with labral tears and glenohumeral instability: Radiologic findings and clinical significance. Radiology 190:653–658, 1994.
195. Tirman PFJ, Steinbach LS, Feller JF, Stauffer AE: Humeral avulsion of the anterior shoulder stabilizing structures after anterior shoulder dislocation: Demonstration by MRI and MR arthrography. Skeletal Radiol 25:743–748, 1996.
196. Tirman PFJ, Bost FW, Steinbach LS, et al: MR arthrographic depiction of tears of the rotator cuff: Benefit of abduction and external rotation of the arm. Radiology 192:851–856, 1994.
197. Tirman PFJ, Feller JF, Palmer WE, et al: The Buford complex—variation of normal shoulder anatomy: MR arthrographic imaging features. AJR Am J Roentgenol 166:869–873, 1996.
198. Townley CO: The capsular mechanism in recurrent dislocation of the shoulder. J Bone Joint Surg Am 32:370–380, 1950.
199. Traughber PD, Goodwin TE: Shoulder MRI: Arthroscopic correlation with emphasis on partial tears. J Comput Assist Tomogr 16:129–133, 1992.
200. Tuite MJ, Feller JF, Palmer WE, et al: Acromial angle on radiographs of the shoulder: Correlation with the impingement syndrome and rotator cuff tears. AJR Am J Roentgenol 165:609–613, 1995.
201. Tuite MJ, De Smet AA, Norris MA, Orwin JF: MR diagnosis of labral tears of the shoulder: Value of T2*-weighted gradient-recalled echo images made in external rotation. AJR Am J Roentgenol 164:941–944, 1995.
202. Tuite MJ, Cirillo RL, De Smet AA, Orwin JF: Superior labrum anterior-posterior (SLAP) tears: Evaluation of three MR signs on T2-weighted images. Radiology 215:841–845, 2000.
203. Uhthoff HK, Sarkar K: Calcifying tendinitis: Its pathogenetic mechanism and a rationale for its treatment. Int Orthop 2:187–193, 1978.
204. Vahlensieck M, Pollack M, Lang P, et al: Two segments of the supraspinous muscle: Cause of high signal intensity at MR imaging? Radiology 186:449–454, 1993.
205. Vahlensieck M, Haack K, Schmidt HM: Two portions of the supraspinatus muscle: A new finding about the muscles macroscopy by dissection and magnetic resonance imaging. Surg Radiol Anat 16:101–102, 1994.
206. Valls R, Melloni P: Sonographic guidance of needle position for MR arthrography of the shoulder. AJR Am J Roentgenol 169:845–847, 1997.
207. Van Leersum M, Schweitzer ME: Magnetic resonance imaging of the biceps complex. Magn Reson Imaging Clin North Am 1:77–86, 1993.
208. Vebostad A: Calcific tendinitis in the shoulder region. Acta Orthop Scand 46:205–210, 1975.
209. Wang DH, Koehler SM: Isolated infraspinatus atrophy in a collegiate volleyball player. Clin J Sport Med 6:255–258, 1996.
210. Weiss JJ, Good A, Schumacher HR: Four cases of "Milwaukee shoulder," with a description of clinical presentation and long-term treatment. J Am Geriatr Soc 33:202–205, 1985.
211. Whitten CG, Moore TE, Yuh WT, et al: The use of intravenous gadopentetate dimeglumine in magnetic resonance imaging of synovial lesions. Skeletal Radiol 21:215–218, 1992.
212. Willemsen UF, Wiedemann E, Brunner U, et al: Prospective evaluation of MR arthrography performed with high-volume intraarticular saline enhancement in patients with recurrent anterior dislocations of the shoulder. AJR Am J Roentgenol 170:79–84, 1998.
213. Wilson AJ, Totty WG, Murphy WA, Hardy DC: Shoulder joint: Arthrographic CT and long-term follow-up, with surgical correlation. Radiology 173:329–333, 1989.
214. Wohlwend JR, van Holsbeeck M, Craig J, et al: The association between irregular greater tuberosities and rotator cuff tears: A sonographic study. AJR Am J Roentgenol 171:229–233, 1998.
215. Wolf EM, Cheng JC, Dickson K: Humeral avulsion of glenohumeral ligaments as a cause of anterior shoulder instability. Arthroscopy 11:600–607, 1995.
216. Workman TL, Burkhard TK, Resnick D, et al: Hill-Sachs lesion: Comparison of detection with MR imaging, radiography, and arthroscopy. Radiology 185:847–852, 1992.
217. Yu JS, Fischer RA: Clinical image: Denervation atrophy caused by suprascapular nerve injury—MR findings. J Comput Assist Tomogr 21:302–303, 1997.
218. Zanetti M, Weishaupt D, Gerber C, Hodler J: Tendinopathy and rupture of the tendon of the long head of the biceps brachii muscle: Evaluation with MR arthrography. AJR Am J Roentgenol 170:1557–1561, 1998.
219. Zanetti M, Weishaupt D, Jost B: MR imaging for traumatic tears of the rotator cuff: High prevalence of greater tuberosity fractures and subscapularis tendon tears. AJR Am J Roentgenol 172:463–467, 1999.
220. Zlatkin MB: MRI of the Shoulder. New York, Raven Press, 1991.
221. Zlatkin MB, Iannotti JP, Roberts MC, et al: Rotator cuff tears: Diagnostic performance of MR imaging. Radiology 172:223–229, 1989.
222. Zlatkin MB, Reicher MA, Kellerhouse LE, et al: The painful shoulder: MR imaging of the glenohumeral joint. J Comput Assist Tomogr 12:995–1001, 1988.

Part VIII

Pediatric Radiology

Edited by
Carlos J. Sivit

51

Computed Tomography and Magnetic Resonance Imaging in the Pediatric Patient: Special Considerations

Donald P. Frush

Children present unique challenges for computed tomography (CT) and magnetic resonance imaging (MRI). Although it is well recognized that the type and frequency of disorders differ between children and adults, it is less often apparent that there are also important considerations for performing CT and MRI.[23] These technical considerations are a critical component of the examination, as adequate (and preferably optimal) images are requisite for interpretation.

This chapter focuses on technical aspects of CT and MRI when used for neonates, infants, and children, especially on those features that are common to both modalities. Emphasis is placed on technical aspects that either differ from or are not addressed in the chapters on adult CT and MRI. Aspects that differ between modalities are covered in other chapters.

General Technical Considerations

CT and MRI examinations of children share several technical issues, including the need for sedation, the potential for movement artifacts, and the smaller anatomy. In addition, the wide range of sizes in the pediatric population, from under 1.0 kg to the weight of a large adult, requires the radiologist to be familiar with a greater variety of technical modifications than those needed in the adult population. For this reason, the concept of protocols is less applicable in children than in adults. Although protocol imaging can be performed at times, the radiologist should realize that alterations in scan preparation and parameters may be necessary.

The first issue to address in cross-sectional imaging is the indication of the study. It may be that another imaging technique, such as sonography, would give sufficient information, obviating the use of greater resources (e.g., sedation, intravenous [IV] or oral contrast material), scheduling difficulties, and expense. Once it has been determined that either CT or MRI is appropriate, attention can be directed to the technical considerations.

Reduction of anxiety (for both children and parents) is an important aspect of pediatric imaging.[8, 22] In a number of centers, child-friendly environments both inside and outside the scanning area provide a more pleasant experience. Examination preparation includes instructions about nil per os (NPO) instructions if sedatives are to be used. This prevents having to reschedule the examination, which can be a great inconvenience for the family. At the time of the examination, written material, videotapes, or digital media explaining the procedure can reduce anxiety and uncertainty. Discussion with the technologist (or other radiology staff) gives family members an opportunity to ask questions about the procedure. Because the parent is usually essential in helping a child adjust to a potentially threatening environment in the CT or MRI suite, this pre-examination preparation is extremely important. Some centers have found success with models of scanners, which allow the child to become familiar with the appearance of the scanners and aspects of the physical environment.

One of the most important technical facets in cross-sectional imaging modalities is sedation. Several comprehensive reviews on the sedation of children for diagnostic radiology are available.[8, 14, 20–22] The following text emphasizes the salient aspects.

Although both CT and MRI examination times have decreased with the advent of newer technology, sedation remains an unavoidable aspect in imaging children. The general principles and guidelines for pediatric sedation were published several years ago[2, 10, 28] and have resulted in a substantial change in the way in which sedation for diagnostic imaging is performed.[20, 22, 42] The basic tenet is to protect the welfare of the child. To do this, it is vital to adhere to a minimal set of standards,[10, 28] which include:

- Presedation evaluation (i.e., history and physical examination)
- Selection of agents from a standard compendium of agents used in diagnostic imaging (Table 51–1)
- Procedural monitoring
- Adherence to strict discharge criteria

Various agents have been used successfully and safely for sedation in infants and children (see Table 51–1). Although multiple sedatives and combinations of agents are available, a successful sedation program makes use of a relatively small subset of proven agents with which the radiologists is familiar. Used as part of an appropriate sedation program, these agents should provide successful sedation in more than 95% of children.[14, 22] Sedatives are not always safe, and their administration does not guarantee success. To this end, newer agents continue to be introduced (e.g., propofol, ketamine), and new combinations of agents are promoted for use in diagnostic imaging.

No single agent or combination of agents is perfect. Sedation in pediatric imaging will become an insignificant issue only when imaging is nearly instantaneous, such as with radiography. Faster MR sequences have not had the same impact on sedation that the faster technology of helical and multislice helical CT scanning has had. The rate of sedation for children dropped from about 18% to 10% as helical CT replaced the incremental slice-by-slice scanning.[30, 44] Multislice helical CT technology has further reduced the rate of sedation to about 3% in children younger than 6 years of age.[34] Alternatives to sedatives include feeding young infants immediately prior to examination, reduction of anxiety in older children and adolescents, and pain management.[8, 22]

Choral hydrate and sodium pentobarbital are two of the most commonly employed sedatives in pediatric diagnostic imaging.[14, 22] Choral hydrate is generally given orally in doses of 50 to 100 mg/kg of body weight (maximum dose, 2.0 g). This dose is most successful in infants younger than 1 year of age. IV sodium pentobarbital is another very successful agent and is safe when used appropriately. The dose is given in titrated amounts of 1.0 to 3.0 mg/kg to a total dose of 6.0 to 8.0 mg/kg (maximum dose, 200 mg).

Occasionally, fentanyl citrate in titrated doses of 1.0 μg/kg (maximum dose, 4.0 μg/kg) can be used in conjunction with pentobarbital in children who are more difficult to sedate or need some analgesia in addition to sedation. For CT-guided or MRI-guided interventional procedures, midazolam 0.02 to 0.05 mg/kg (maximum initial dose, 1.0 mg; subsequent doses titrated to effect) is useful in conjunction with fentanyl. The combination of fentanyl citrate and sodium pentobarbital is usually more successful in children younger than 8 years of age for CT interventional procedures.

Specific Technical Considerations

Computed Tomography

Technical parameters to be considered in designing appropriate CT examinations for children include breathing techniques, oral or IV contrast agents, and the scanning parameters, such as tube current and factors affecting pitch. Attention to these specific parameters is imperative in order to perform an optimal examination while minimizing potential risk to the child. Such risks include (1) excessive radiation exposure (e.g., from rescanning because of poor technique), (2) the need for additional IV contrast media, and (3) inappropriate use of oral contrast materials. General recommendations for parameters in chest, abdomen, and pelvis helical CT scanning are presented in Tables 51–2 and 51–3.

Breathing Strategies

Breathing strategies, usually standard for adult helical CT scanning, depend on the age of the child. After a child is about 8 years old, scan durations of 20 to 30 seconds can be performed during a breath-hold. Before that time, the ability to breath-hold remains relatively limited, although it is worth attempting a trial. However, trials may be unreliable because of the potential unpleasant sensations of IV contrast administration, noise, and movement of the table and scan gantry during the procedure. During CT of the chest and abdomen and during CT angiography, it is often best to simply have the young child breathe quietly to avoid the risk of nonperiodic respiratory motion, which would diminish scan quality. Breath-holding is not necessary during pelvic scanning.

Oral Contrast Material

Gastrointestinal (GI) contrast material can be given in several ways. Oral administration generally refers to methods of giving contrast media by mouth or through tubes into the upper GI tract. Rectal administration via a rectal tube can also be useful but is not routine. Although GI contrast material is often considered routine for adults, administration in children can be more difficult, can pose risks (although rarely) and either may be unnecessary or may adversely affect diagnosis.

Recommended amounts of oral contrast material for children of different ages are listed in Table 51–4. Agents usually consist of water-soluble contrast diluted with a clear liquid beverage, such as a fruit drink or a carbonated soft drink. Barium solutions are also available. Other oral contrast agents should be considered for pediatric CT. For example, water is sometimes helpful in opacification of the upper GI tract (Fig. 51–1). Air may be a sufficient intrinsic luminal contrast agent in the setting of an ileus, or fluid and air, in the case of an obstruction. In one review of CT techniques, whole milk has been suggested as an agent because the fat is thought to slow bowel peristalsis.[19]

The advantage of orally administered contrast agents is primarily opacification of the hollow viscus, which provides information on course, caliber, lumen and wall, and separation from subjacent structures; however, contrast material is not always necessary. For example, evaluations of the liver, adrenal glands, and kidneys do not mandate opacification of bowel.

There are also disadvantages with these agents. It can be difficult to get young children to drink. Taking fluid by mouth prior to sedation increases the risk of aspiration in children who need sedation for a CT scan.[2, 22] Oral contrast material can be considered an important component of a CT scan and is not contraindicated in this setting.[20, 22] GI

Table 51–1. Sedative Agents for Pediatric Imaging

Agent	Class	Effect	Dose	Route*	Onset	Duration†
Chloral hydrate‡	NA	Sedative	50–100 mg/kg, up to 120 mg/kg reported, max single dose 2 g	PO (PR)	20–30 min (rarely, up to 60 min)	30–90 min
Sodium pentobarbital	Barbiturate	Sedative	2–3 mg/kg doses titrated q 5–7 min until sedated or max cumulative amount of 8 mg/kg, not to exceed 200 mg	IV (PO, IM)	5–10 min	40–60 min
Fentanyl citrate	Narcotic	Analgesic with sedative properties	1 μg/kg slowly IV q 5–7 min, adult-sized patients 25–50 μg per dose, max cumulative dose 4.0 μg/kg	IV	1–2 min	30–60 min for analgesia; sedation may be shorter
Midazolam	Benzodiazepine	Sedative, anxiolytic, amnestic	0.02–0.05 mg/kg IV, titrate using ½ original dose (2–4 min) based on effect and oxygen saturation, max bolus dose 1.0 mg	IV (PO)	1–5 min (IV)	20–30 min
Diazepam	Benzodiazepine	Sedative, anxiolytic, amnestic	0.05–0.1 mg/kg IV, max cumulative dose 5.0 mg; 0.2–0.3 mg/kg PO, max cumulative dose 10 mg	IV (PO)	5–15 min (IV)	30–120 min
Methohexital	Barbiturate	Sedative	20 mg/kg in 10% solution	PR	10–15 min	45 min
Morphine	Narcotic	Analgesic with sedative properties	0.1–0.2 mg/kg, max dose 3–4 mg	IV (IM)	3–5 min	Analgesia up to 4 hr; sedation is variable but shorter
Meperidine	Narcotic	Analgesic with sedative properties	1–2 mg/kg, max dose 100 mg	IV (IM)	5–10 min	Analgesia 1–2 hr; sedation is variable but shorter
Naloxone hydrochloride	NA	Narcotic antagonist	0.01–0.1 mg/kg (lower antagonist dose for infant); repeat 2–3 min; titrate to reversal, max dose 2 mg	IV	1–2 min	Max to 20–30 min
Flumazenil	NA	Benzodiazepine antagonist	0.01 mg/kg, max dose (adult) 0.2 mg, max cumulative dose 1 mg	IV	1–3 min; peak effect 6–10 min	Max 60 min but usually <30 min depending on benzodiazepine dose

IM, intramuscular; max, maximum; NA, not applicable; PO, per os (orally); PR, per rectum.
*Preferred route listed first, with alternate routes in parentheses.
†Duration of sedative effect for imaging purposes. Drowsiness, ataxia, and other effects may have variable durations depending on the agent, dose, and route of administration.
‡Thioridazine or hydroxyzine have been reported as adjuncts in children difficult to sedate with chloral hydrate alone.
From Frush D: Pediatric sedation in radiology: The practice of safe sleep. Am J Roentgenol 167:1383, 1996.

Table 51–2. Recommendations for Pediatric Chest Helical CT Scanning

	≤4 yr	5–8 yr	9–12 yr	>12 yr
Scan Parameters				
kVp	120–140	120–140	120–140	120–140
mAs (suggested)*	25–100	50–125	50–150	50–175
Collimation (mm)	3–5	5	5–7	5–7
Table speed (mm/rotation)†	1.5 × collimation	1.5 × collimation	1.5 × collimation	1.5 × collimation
Reconstruction Parameters				
Interval (mm)‡	3–5	5	5–7	5–7
Contrast Parameters				
IV contrast§	+	+	+	+
Amount (mL/kg)‖	1.5*	1.5	1.5	1.5
Rate (mL/sec)	1.0–2.0	2.0	2.0	2.0
Delay after injection completion (sec)	0–10	0–10	0–10	0–10

For reconstructions for airway evaluation, use narrow (1–3 mm) collimation through region of interest.
*Use higher range with scan indication of mediastinal pathology, lower range with pulmonary parenchymal evaluation.
†Gantry rotation speed, 0.6–1.0 sec.
‡Decrease by up to 50% for small-lesion evaluation (e.g., rule out metastases).
§IV contrast for mediastinal evaluation, cardiovascular or CT angiography applications.
‖Power injector whenever possible. Can use up to 3.0 mL/kg for CT angiography.
kVp, kilovolt peak; mAs, milliampere-second.

Table 51–3. Recommendations for Pediatric Abdominal Helical CT Scanning (up to 45 kg)

	General Abdomen Survey	Liver	Pancreas	Kidney
Contrast Parameters				
Oral contrast	+	+	+	+
IV contrast	+	+	+	+
Amount (mL/kg)*	2.0	2.0	1.5–2.0	2.0
Rate	1.0–3.0 mL/sec	1.0–3.0 mL/sec	1.0–3.0 mL/sec	1.0–3.0 mL/sec
Delay (following contrast)	15–20 sec	15–20 sec	0–10 sec; follow with general abdomen protocol	0–10 sec: arterial 15–20 sec: medullary 2–4 min: excretory
Scan Parameters				
kVp	120–140	120–140	120–140	120–140
mAs (suggested)	100–160	100–160	120–180	100–160
Collimation	4–8 mm	4–8 mm	2–4 mm	2–8 mm
Table speed	6–12 mm/sec (pitch 1.5)	6–12 mm/sec (pitch 1.5)	3–6 mm/sec (pitch 1–1.5)	4–12 mm/sec (pitch 1–1.5)
Reconstruction Parameters				
Interval†	4–8 mm	4–8 mm	1–4 mm	2–8 mm
Additional Comments	Selective use of oral contrast in trauma	—	—	For stone evaluation, no oral or IV contrast

*Power injector whenever possible
†For most applications, reconstruction interval equals collimation.
From Frush DP: Helical CT in the pediatric abdomen: Techniques and applications. Special Course in Pediatric Radiology: Current Concepts in Body Imaging at the Millennium. Radiologic Society of North America, 1999, p 18.

Table 51–4. Oral Contrast for Abdominal and Pelvic CT in Infants and Children*

Age	Amount†
1–6 mo	60–120 mL (2–4 oz)
6–12 mo	120–180 mL (4–6 oz)
1–4 yr	180–270 mL (6–9 oz)
4–8 yr	270–360 mL (9–12 oz)
8–12 yr	360–480 mL (12–16 oz)
12–16 yr	480–600 mL (16–20 oz)
>16 yr	Adult volume

*45–90 minutes before examination.

†1.5%–3.0% solution; consider giving an additional amount equal to one half of original volume 15 minutes before scanning.

From Frush DP: Pediatric helical CT: Techniques and applications. Med Imaging Int 9:12–18, 1999.

tract contrast material may mask subtle mucosal enhancement (e.g., in inflammatory, infiltrative, or ischemic bowel disease), may mask an intraluminal or submucosal hematoma (e.g., in the setting of trauma or bleeding diathesis),[12] or may hinder three-dimensional (3D) reconstructions used for CT angiography. Although oral contrast for trauma patients is generally safe,[16, 32] the risk of aspiration needs to be considered.[13]

Oral iodinated media and barium are other contrast agents. A similar concentration of iodine as given orally can be given via a rectal tube and is generally tolerated in young infants (who are not sedated) and in children older than about 4 years of age. For children between infancy and 4 years of age, enemas often cause agitation and can arouse a sedated child. Rectal contrast administration should be used as a problem-solving tool when one is evaluating unclear processes adjacent to the colon or in the lower abdomen or pelvis. In particular, retrograde colon opacification may help in the definition of bowel from an adjacent inflammatory process such as an abscess (Fig. 51–2).

Intravenous Contrast Material

A critical aspect of chest, abdomen, and pelvis CT scanning in children is administration of IV contrast material. Among the many challenging variables in pediatric scanning are the small contrast volumes, the location and caliber of IV catheters, the method of injection, and the unpredictable physiologic factors.[26] Despite these challenges, attention to each facet of IV contrast technique can result in excellent contrast-enhanced CT scans in almost every instance.

In general, although low-osmolar, nonionic agents are recommended for scanning in children,[9] choices must be made on the basis of pertinent practice standards. The dose of contrast material is generally 2.0 mL/kg (up to an adult dose of about 150 mL), although higher amounts, up to 3.0 mL/kg,[38] have been advocated. Smaller amounts have been advocated in adults[18, 40] but have not been systematically tested in children. However, because organ and vessel enhancement depends on the amount of iodine delivered, there is a threshold amount at which opacification is suboptimal. One study has shown sufficient although significantly reduced enhancement of the liver in children with a dose of 1.5 mL/kg of iodinated contrast material at an iodine concentration of 300 mg/mL.[25]

For chest scanning, in which opacification of vascular structures (not organ enhancement) is the goal of IV contrast material, doses of about 1.5 mL/kg can be used successfully.[23, 45] For CT angiography in children, doses vary from about 1.5 to 3.0 mL/kg.[24]

The rate of contrast administration varies with the caliber of the angiocatheter and the method. Rates of about 2.0 mL/second are recommended for overall scanning. Higher rates can be used in adolescents (e.g., 3.0 mL/second). Rates as low as 1.0 mL/second have provided good enhancement of abdomen viscera.[26]

Manual administration of contrast medium results in an unpredictable rate. In general, the rates of manual administration vary between about 1.0 and 3.0 mL/second, with an average in most injections of about 2.0 mL/second.[24] Power injectors have been used with increasing frequency in the pediatric population.[23] Suggested rates are 1.0 to 1.5 mL/second for 24-gauge angiocatheters and 1.5 to 2.0 mL/second for 22-gauge angiocatheters.[23]

The complication rate with power injection of contrast material does not differ from that with manual administration when the angiocatheter functions well and the site is

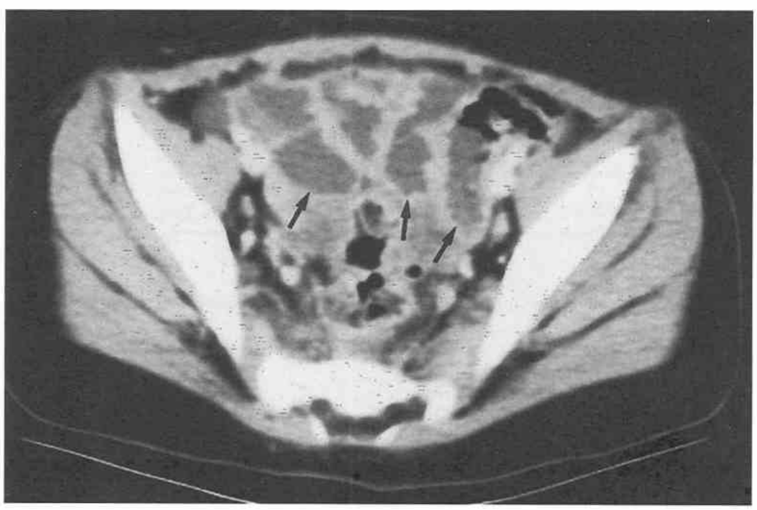

Figure 51–1. Malignant sacrococcygeal germ cell tumor in a 1-year-old girl. Surveillance CT examination was performed to evaluate for metastatic disease. Because the child refused to drink contrast media, a fruit-flavored clear liquid was administered in place of iodinated contrast material. Note the excellent delineation of the small-bowel loop *(arrows)* in the pelvis. The small bowel and the large bowel were also well visualized in the upper abdomen (not shown) as a result of a combination of intraluminal fluid and gas.

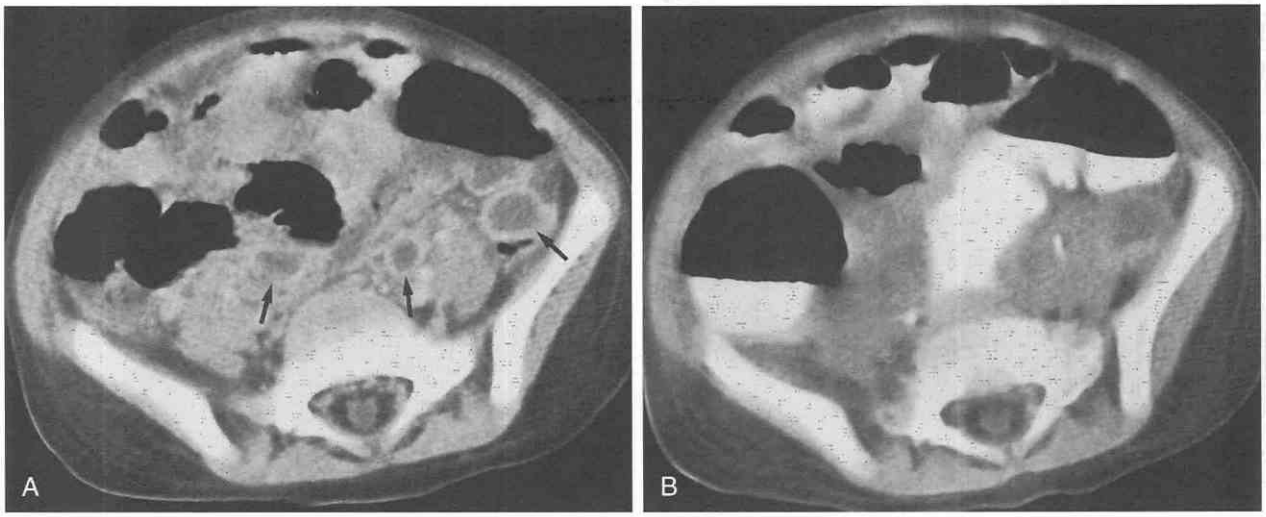

Figure 51–2. Complicated appendicitis in a 3-year-old girl. *A,* Axial CT scan at the level of the upper pelvis following administration of oral and intravenous contrast material. There are several interloop abscesses *(arrows).* More anteriorly, it was difficult to distinguish intestine from inflammatory change. *B,* After administration of 360 mL of rectal contrast material, it is clear that colon occupied the region in question. There were no abscesses that were amenable to percutaneous drainage.

monitored during injection. The use of contrast power injectors with central venous catheters is more controversial, although the reported rate of complications is also low.[29] The practice of power injection of contrast material through central lines is probably more common than reported in the literature.[23]

With the advent of helical CT, techniques for the initiation of contrast-enhanced scanning have changed. With conventional or incremental abdomen scanning, imaging was initiated after approximately half of the bolus was administered, and it continued throughout the remainder of the scanning of the liver. With helical CT scanning, nearly all investigators recommend that scanning of the abdomen should begin after the administration of contrast material is complete (Table 51–5).

Recommendations for the delay from the end of contrast administration to the beginning of scanning vary from about 3 to 30 seconds. With multislice technology, image acquisition is many times faster than with a standard helical scanner, and new demands are placed on the technique of administration. If scanning is initiated too early, all imaging would be completed before optimal or desired enhancement is obtained. Recent work with multislice scanners has indicated that a delay of 20 seconds,[25] in line with delays recommended in some previous studies[26, 40] for the helical CT scanner, results in excellent enhancement of intra-abdominal structures in children.

In addition to the empirical delays just noted, a number of CT manufacturers offer bolus-tracking technology. With bolus tracking, serial low-dose, isolevel slices are obtained rapidly and sequential enhancement is displayed (Fig. 51–3). When the desired organ or vessel enhancement is obtained, diagnostic scanning is initiated. In this way, scanning can be individualized. This technology can be useful when pediatric scanning is infrequent and empirical methods for initiating the scan are less familiar or in complex cases when the time until optimal enhancement is uncertain.[26] In particular, CT angiography in young infants can achieve excellent results using bolus-tracking technology.[24]

In addition to GI and IV contrast administration, a variety of other parameters must be thoughtfully selected for pediatric CT, including tube current (in mA) (Fig. 51–4), kilovoltage, collimation, table speed, and reconstruction interval. Recommendations for collimation and pitch are listed in Tables 51–2 and 51–3.

In general, most routine chest, abdomen, and pelvis scans can be obtained at a pitch of 1.5. Pitches up to 2.0 may be used to study, for example, abscesses, small-bowel obstruction, or follow-up examinations for trauma. With new multislice technology, the concept of pitch is more

Table 51–5. Pediatric Contrast-Enhanced Abdominal Helical CT: Recommendations for Initiation of Diagnostic Scanning

Investigator	Injection	Rate	Delay*
White[43]	Manual	—	10–20 sec
Luker et al[33]	Power	1.2 mL/sec	130% of injection duration
Roche et al[36]	Power	1.7–2.0 mL/kg/min	60–70 sec from onset of contrast injection
Ruess et al[38]	Power	2.0 mL/sec	10–12 sec
Frush et al[26]	Manual	0.3–3.5 mL/sec	Mean, 29 sec

*Delay from end of contrast injection unless stated otherwise.

From Frush DP: Pediatric helical CT: Techniques and applications. Med Imaging Int 9:12–18, 1999.

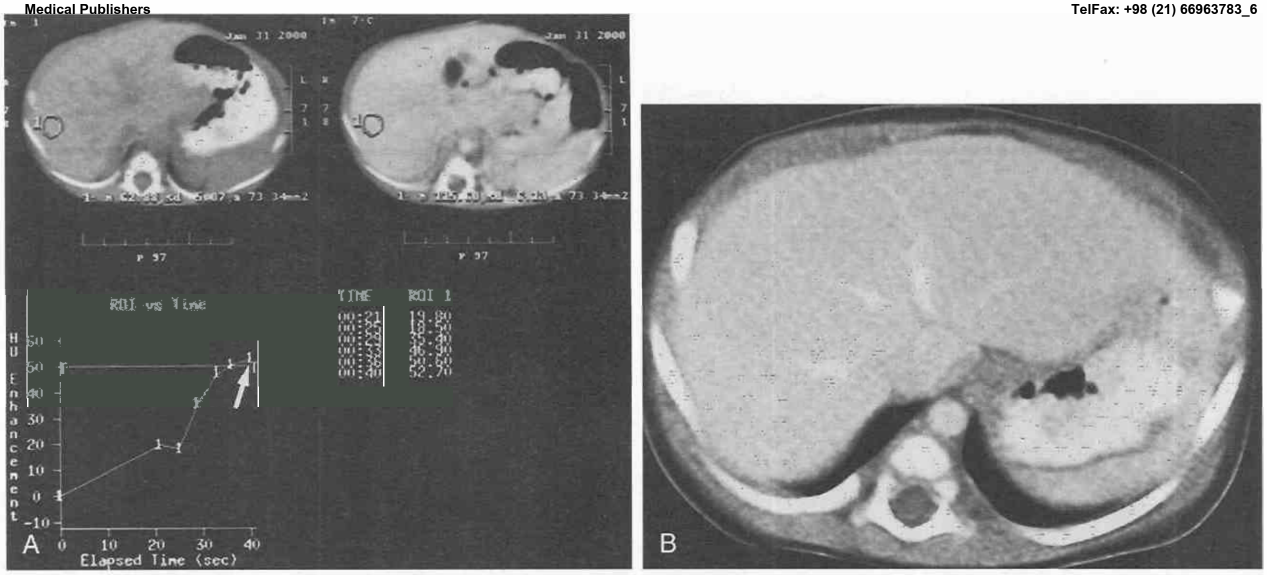

Figure 51–3. Value of bolus-tracking technology in a 14-day-old male infant. The rate of contrast administration (manual injection via a 24-gauge angiocatheter in the hand) was 0.25 mL/sec. *A*, Bolus-tracking technology displayed on the CT monitor includes the baseline unenhanced image of the liver *(upper left)*, final image in the series *(upper right)*, and graphic *(lower left)* and tabular *(lower right)* display of actual hepatic enhancement. A region-of-interest cursor was placed on the liver. Diagnostic scanning was initiated once hepatic enhancement surpassed 50 Hounsfield units *(arrow)*. Each of the seven images obtained during bolus tracking (one baseline precontrast image and six postcontrast monitoring images) was obtained at 8 mA. *B*, Axial contrast-enhanced CT scan near the level of the confluence of the hepatic veins demonstrates excellent enhancement of the liver parenchyma, hepatic veins, and aorta.

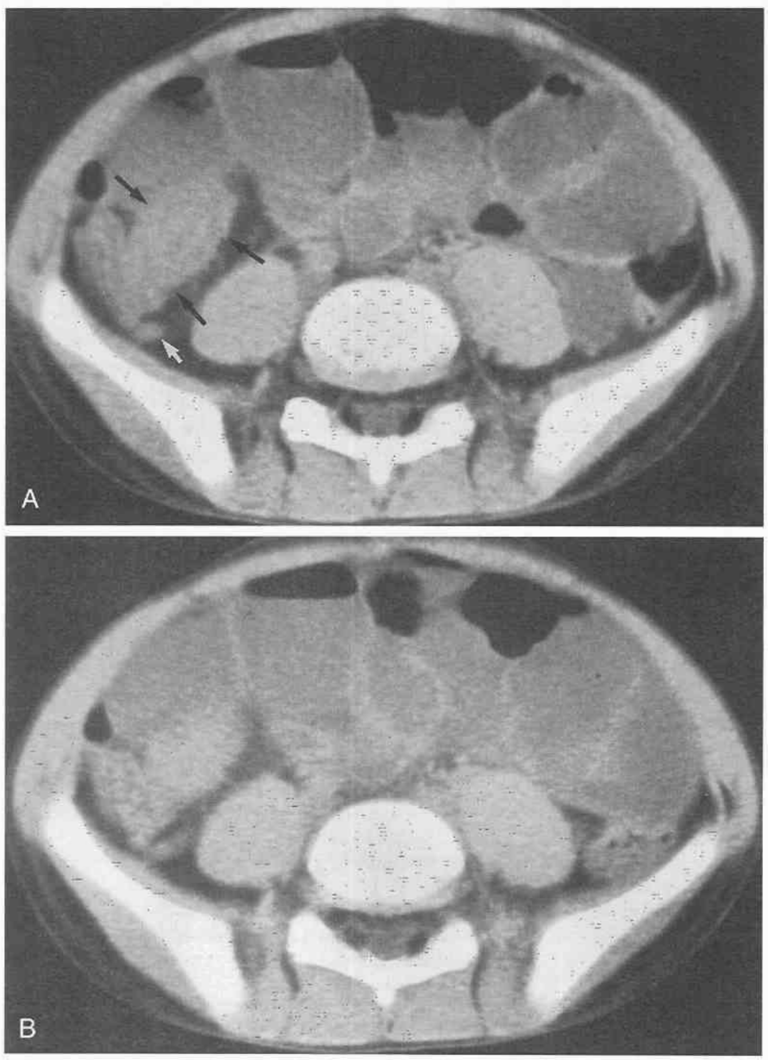

Figure 51–4. Low-dose CT scanning in an 8-year-old boy seen in the emergency department for possible appendicitis. *A*, Axial CT scan obtained through the pelvis without oral or intravenous contrast material was obtained initially at 100 mA. These are multiple fluid-filled loops of small bowel in addition to thickening of the terminal ileum *(arrow)* due to Crohn's disease. The appendix *(small arrow)* was normal. *B*, Subsequent CT images were obtained through the pelvis because an artifact was present in the initial series. The image from a level similar to that in *A* but obtained at 30 mA shows no substantial difference in diagnostic information. (Courtesy of Ithaca Center for Postgraduate Medical Education, Ithaca, NY, 2001.)

complex. Depending on the detector array, higher pitches (e.g., 6.0) are now possible, with even faster scanning on the horizon as a greater number of detectors become available.

Increasing tube current provides increased spatial resolution because of an increased signal-to-noise ratio, but a higher radiation dose results. The optimal range of tube currents has not been determined for body scanning in infants and children, but probably much of pediatric helical CT is performed using too great a tube current. For example, one review of 55 CT scans from a variety of practices revealed that the mean dose for body CT in children was nearly 200 mA,[34a] more than is recommended for children[23, 45] and occasionally for adults.[45] Some data on chest scanning in both adults[11] and children[1, 37] have shown that low tube current in the range of 25 to 50 mA yields acceptable diagnostic quality. In addition to lower tube current, the use of higher pitches (1.5 to 2.0) imparts less radiation than a pitch of 1.0 (when all other parameters are kept constant), with no loss in diagnostic quality.[41] Therefore, until definitive recommendations are available, it is prudent to consider lower tube currents and higher pitches for pediatric CT (see Tables 51–2 and 51–3).

Pediatric CT angiography has only recently been addressed in children.[24] The technique is difficult because of the need for rapid scanning during peak vascular enhancement. Again, small patient size and smaller total dose, small-gauge angiocatheters, relatively remote locations (i.e., hands and feet), uncertain injection rates with manual injection, and small vessel anatomy make CT angiography in children challenging. Nevertheless, adequate pediatric CT angiography can be performed (Tables 51–6 and 51–7).

Table 51–6. Pediatric CT Angiography: Technical Problems and Potential Solutions

Problem	Solution
Small patient size (small contrast volume)	Increase dose up to 3.0 mL/kg Dilute contrast (e.g., 3:1 with normal saline) Faster scanners (dual and multiple detector row)
Large area of coverage	Increase dose up to 3.0 mL/kg Dilute contrast (e.g., 3:1 with normal saline) Increase table speed Faster scanners (dual and multiple detector row)
Unable to breath-hold	Quiet respiration General anesthesia with suspended respiration Faster scanners (dual and multiple detector row)
Small-caliber IV	Power injector at rates 1.2–2.0 mL/kg (24 gauge); 1.2–2.5 mL/kg (22 gauge)
Scan initiation	Bolus tracking Test bolus in larger children Empirical delay of 5–20 sec after beginning of contrast administration (the shorter delay for young children, or central venous catheters); longer delays may be necessary for foot angiocatheters
Small-vessel anatomy	Narrow collimation and reconstruction interval
Unable to hold still	Sedation

Table 51–7. Steps for Pediatric CT Angiography

1. Determine or estimate breath-holding ability (generally 5–30 seconds).
2. Determine length of coverage.
3. Calculate table speed for which scan can be completed during breath-hold (length of coverage/breath-hold duration) or peak vessel enhancement (less than duration of injection—see below), whichever is shorter. Use the minimum collimation that gives appropriate pitch (e.g., 1.5–2.0 with single-array detector scanner).
4. Peak vessel enhancement.
   a. Select IV contrast material dose (2.0–3.0 mL/kg).
   b. Select rate of contrast administration (power injector 1.2–4.0 mL/sec); manual injection rate needs to be estimated (range, 1.0–2.5 mL/sec).
   c. Calculate (or estimate if manual injection) duration of injection (IV contrast is started prior to diagnostic scanning and should finish before scanning is completed).
   d. Adjust rate, volume (e.g., consider dilution or increasing total dose), or table speed so that contrast administration is completed shortly before the end of scanning.
   e. Scan onset. Use test bolus (larger children), bolus tracking, or empirical delay. Empirical scan onset determined by adjusting table speed, collimation, rate, and volume such that scanning begins with a minimum delay of 5 to 20 seconds after beginning contrast (short delays with small total volumes of contrast, central venous catheters; long delays with lower extremity venous access).

Magnetic Resonance Imaging

Some technical aspects of pediatric MRI differ from those of CT scanning. Moreover, the types of sequences performed and the parameters for each sequence vary to a greater degree (and are evolving more rapidly) than in CT scanning. For these reasons, a more general discussion of MRI techniques is appropriate (see other chapters that discuss MRI for organ systems and specific disease processes in adults and children). The text here addresses general techniques that apply to MRI across organ systems and that are unique to pediatric MRI.

The greatest technical hurdle in children is motion artifact, which is caused either by periodic or physiologic motion (cardiovascular pulsation, respiration) or by random motion (including peristalsis and musculoskeletal movement). Periodic motion causes ghosting artifact, whereas image blurring results from random motion.

Several useful strategies can minimize or prevent the artifacts associated with random motion in children. Sedation has already been discussed. Because of longer MRI times, children require sedation more often than they do for CT,[5] but children older than 7 years do not routinely need sedation. Children younger than 7 years may not need to be sedated; however, it is better to anticipate the possibility by ensuring that they have nothing to eat or drink for several hours before the procedure and that they be accompanied by someone who can give consent for sedation.

Because of the more limited visual contact in the bore of the scanner, monitoring is more difficult with MRI than CT.[5] When this is a substantial issue, an alternative to a sedated MRI examination, such as CT or involvement of an anesthesiologist or anesthetist, should be considered.

The pulse sequences in the MRI study must be priori-

tized for sedated and young children so that the initial pulse sequences and the selected planes provide the greatest amount of information. For the sedated child, the range of scanning opportunity is between 30 minutes and 1 hour.[22] Beginning at about 1 hour, the infant or child is much more likely to wake up. This can happen very quickly as well. Occasionally, additional doses of sodium pentobarbital or fentanyl citrate (see earlier) can provide a longer period of sedation. Additional doses of chloral hydrate are not recommended. The sleepy child is at increased risk of aspiration of the oral sedative, and the length of time before the sedative takes effect is long and unpredictable.[22]

For MRI, an initial amount at the top of the dose range of chloral hydrate (80 to 100 mg/kg) is recommended. Although additional amounts of IV sedative should be attempted if the maximum total dose has not been reached, this attempt may be unsuccessful and it is best to complete scanning within the suggested time.

If scanning time might exceed about 1.5 hours, use of an anesthetic agent should be considered. Usually an anesthesiologist or an intensive care specialist would be involved, requiring additional scheduling considerations.

Even when sedation is not required, young children have a limited ability to hold still. The length of the examination, the examination noises, and the enclosure (when the parent is not in visual contact) all contribute to this. For these children too, it is important to prioritize pulse sequences and planes. In addition to sedation, faster MRI sequences, such as fast spin echo, T2-weighting, and gradient sequences, and signal averaging[35] can help minimize the impact of random motion.

Blurring from bowel peristalsis can severely degrade abdominal MR images. Use of IV glucagon can reduce artifact, but it is unreliable, requires an injection, and is not routine for pediatric MRI. Negative-contrast MRI agents for the GI tract can improve the quality of abdominal images in children,[6] but their use is not routine.

Several strategies can reduce artifact caused by periodic motion. Because most sequences in pediatric MRI are obtained during breathing, respiratory artifact is a concern,[31] as it is for adults. Respiratory ordered-phase encoding is useful in older children, but it is less successful in infants and small children, in whom the transducer may not detect the smaller chest wall excursion. Fat suppression or saturation bands placed along chest or abdominal fat can be helpful, particularly in obese children. Respiratory artifact can be reduced with breath-holding, when possible, and with gradient imaging. Signal averaging can also reduce respiratory artifact, although at the expense of increased imaging time. When motion artifact is evident or anticipated, careful selection of a few sequences with more excitations (longer imaging time per sequence) may provide better quality than more sequences with less signal averaging.

The increased availability of a greater selection of coils during the 1990s resulted in excellent MRI quality across a wide range of pediatric ages. This includes specifically designed pediatric body and surface coils and adult coils modified for children. For example, excellent examinations of the torso can be obtained using a knee coil in a neonate and a head coil in an infant.[3, 7] As with any MRI study, the coil should be selected that provides the best signal-to-noise ratio for spatial resolution, as well as penetration, while minimizing the sequence duration.[35]

The use of IV contrast material that includes paramagnetic gadolinium chelate in MRI is similar to the use of iodinated material in CT. For single-dose applications, a dose of 0.1 to 0.2 mmol/kg is used.[15, 27, 39] When dynamic scanning is indicated, such as in magnetic resonance angiography (MRA) or hepatic or renal imaging, a power injector can be used. Although injection protocols are not as developed for MRI as for CT, the rate of administration is generally lower with IV MRI contrast agents.[27] For nondynamic imaging, a hand bolus is usually sufficient. Bolus-tracking technology is also available on some MRI scanners,[17] although it has not been applied in pediatric body MRI as commonly as in pediatric CT.

Contrast material for the GI tract is also available for pediatric scanning.[4] Agents are classified as either positive (e.g., infant formula)[22] or negative.[6] Use of GI contrast agents in pediatric MRI is not routine.

Summary

The cross-sectional imaging modalities of CT and MRI are invaluable for pediatric imaging. The diagnostic potential of these modalities depends on obtaining optimal image quality. However, unique and often challenging technical demands can make scan optimization in children difficult. Nevertheless, excellent-quality images can be obtained in even the most complex circumstances when the radiologist applies strategies using appropriate scanning techniques.

References

1. Ambrosino MM, Genieser NB, Roche KJ, et al: Feasibility of high-resolution, low-dose chest CT in evaluating the pediatric chest. Pediatr Radiol 24:6, 1994.
2. American Society of Anesthesiologists Task Force: Practice guidelines for sedation and analgesia by non-anesthesiologist: A report by the American Society of Anesthesiologists. Anesthesiology 84: 459, 1996.
3. Barkovich AJ: Techniques and methods in pediatric magnetic resonance imaging. Semin Ultrasound CT MR 9:186, 1988.
4. Bisset GS III: Evaluation of potential practical oral contrast agents for pediatric magnetic resonance imaging. Pediatr Radiol 20:61, 1989.
5. Bisset GS, Ball WS: Preparation, sedation, and monitoring of the pediatric patient in the magnetic resonance suite. Semin Ultrasound CT MR 12:376, 1991.
6. Bisset GS, Emery KH, Meza MP, et al: Perflubron as a gastrointestinal MR imaging contrast agent in the pediatric population. Pediatr Radiol 26:409, 1996.
7. Boechat MI, Kangarloo H: MR imaging of the abdomen in children. AJR Am J Roentgenol 152:1245, 1989.
8. Boyer RS: Sedation in pediatric neuroimaging: The sciences and the art. AJNR Am J Neuroradiol 13:777, 1992.
9. Cohen MD, Smith JA: Intravenous use of ionic and nonionic contrast agents in children. Radiology 191:793, 1994.
10. Committee on Drugs, American Academy of Pediatrics: Guidelines for monitoring and management of pediatric patients during and after sedation for diagnostic and therapeutic procedures. Pediatrics 89: 1110, 1992.
11. Diederich S, Lenzen H, Windmann R, et al: Pulmonary nodules: Experimental and clinical studies at low-dose CT. Radiology 213: 289, 1999.
12. Donnelly LF: Commentary: Oral contrast medium administration for abdominal CT: Reevaluating the benefits and disadvantages in the pediatric patient. Pediatr Radiol 27:770, 1997.
13. Donnelly LF, Frush DP, Frush KS: Aspirated contrast material contributing to respiratory arrest in a pediatric trauma patient. AJR Am J Roentgenol 171:471, 1998.
14. Egelhoff JC, Ball WS, Koch BL, et al: Safety and efficacy of sedation

in children using a structured sedation program. AJR Am J Roentgenol 168:1259, 1997.
15. Fagan SJ, Byrd SE: Normal anatomy and development of the brain. In Cohen MD, Edwards MK (eds): Magnetic Resonance Imaging of Children. Philadelphia, BC Decker, 1990, p 97.
16. Federle MP, Yagan N, Peitzman AB, et al: Abdominal trauma: Use of oral contrast material for CT is safe. Radiology 205:91, 1997.
17. Foo TK, Saranathan M, Prince MR, Chenevert TL: Automated detection of bolus arrival and initiation of data acquisition in fast, three-dimensional, gadolinium-enhanced MR angiography. Radiology 203: 275, 1997.
18. Freeney PC, Gardner JC, von Ingersleben G, et al: Hepatic helical CT: Effect of reduction of iodine dose of intravenous contrast material on hepatic contrast enhancement. Radiology 197:89, 1995.
19. Frush DP: Helical CT in the pediatric abdomen: Techniques and applications. Special Course in Pediatric Radiology: Current Concepts in Body Imaging at the Millennium. Radiologic Society of North America, 1999, Chicago.
20. Frush DP, Bisset GS. Sedation of children for emergency imaging. Radiol Clin North Am 35:789, 1997.
21. Frush DP, Bisset GS: Sedation of children in radiology: Time to wake up. AJR Am J Roentgenol 165:912, 1995.
22. Frush DP, Bisset GS, Hall SC: Pediatric sedation: The practice of safe sleep. AJR Am J Roentgenol 167:1381, 1996.
23. Frush DP, Donnelly LF: State of the art: Helical CT—technical considerations and body applications. Radiology 209:37, 1998.
24. Frush DF, Donnelly LF, Spencer EB, Bisset GS III: Pediatric CT angiography: Large problems in little people. Paper presented at the 41st Annual Meeting, Society for Pediatric Radiology, May 4–9, 1998, Tucson, Arizona.
25. Frush DP, Donnelly LF, Zheng J, Bisset GS III: Multiarray-detector helical CT in children: Effects of intravenous contrast material dose and timing variations on hepatic enhancement. Paper presented at the 42nd Annual Meeting, Society for Pediatric Radiology, May 1999, Vancouver, BC.
26. Frush DP, Spencer EB, Donnelly LF, et al: Optimizing contrast-enhanced abdominal CT in infants and children using bolus tracking. AJR Am J Roentgenol 172:1007, 1999.
27. Haliloglu M, Hoffer FA, Gronemeyer SA, et al: Applications of 3D contrast-enhanced MR angiography in pediatric oncology. Pediatr Radiol 29:863, 1999.
28. Joint Commission on Accreditation of Health Care Organizations: 1995 Comprehensive Accreditation Manuals for Hospitals. Oakbrook Terrace, Ill, 1995.
29. Kaste SC, Young CW: Safe use of power injectors with central and peripheral venous access devices for pediatric CT. Pediatr Radiol 26: 499, 1996.
30. Kaste SC, Young CW, Holmes TP, et al: Effect of helical CT on the frequency of sedation in pediatric patients. AJR Am J Roentgenol 168:1001, 1997.
31. Lam WW, Lam TP, Saing H, et al: MR cholangiography and CT cholangiography of pediatric patients with choledochal cysts. AJR Am J Roentgenol 173:401, 1999.
32. Lim-Dunham JE, Narra J, Benya EC, et al: Aspiration after administration of oral contrast material in children undergoing abdominal CT for trauma. AJR Am J Roentgenol 169:1015, 1997.
33. Luker GD, Siegel MJ, Bradley DA, et al: Hepatic spiral CT in children: Scan delay time-enhanced analysis. Pediatr Radiol 26:337, 1996.
34. Pappas JN, Donnelly LF, Frush DP: Marked reduction in the frequency of sedation of children using new multislice helical CT. Radiology 215:897, 2000.
34a. Paterson A, Frush DP, Donnelly LF: Helical CT of the body: Are settings adjusted for pediatric patients? AJR Am J Roentgenol 176: 297, 2001.
35. Rawson JV, Siegel MJ: Techniques and strategies in pediatric body MR imaging. Magn Reson Imaging Clin North Am 4:589–598, 1996.
36. Roche KJ, Genieser NB, Ambrosino MM: Pediatric hepatic CT: An injection protocol. Pediatr Radiol 26:502, 1996.
37. Rogalla P, Stover B, Scheer I, et al: Low-dose spiral CT: Applicability to paediatric chest imaging. Pediatr Radiol 28:565, 1998.
38. Ruess L, Bulas DI, Kushner DC: Peak enhancement of the liver in children using power injection and helical CT. AJR Am J Roentgenol 170:677, 1998.
39. Shellock FG, Kanal E: Safety of magnetic resonance imaging contrast agents. J Magn Reson Imaging 10:477, 1999.
40. Tello R, Seltzer SE, Polger M, et al: A contrast agent delivery nomogram for hepatic spiral CT. J Comput Assist Tomogr 21:236, 1997.
41. Vade A, Demos TC, Olson MC, et al: Evaluation of image quality using 1:1 pitch and 1.5:1 pitch helical CT in children: A comparative study. Pediatr Radiol 26:891, 1996.
42. Vade A, Sykhani R, Dolenga M, et al: Chloral hydrate sedation of children undergoing CT and MR imaging: Safety as judged by American Academy of Pediatrics guidelines. AJR Am J Roentgenol 165: 905, 1995.
43. White KS: Invited article: Helical/spiral CT scanning: A pediatric radiology perspective. Pediatr Radiol 26:5, 1996.
44. White KS: Reduced need for sedation in patients undergoing helical CT of the chest and abdomen. Pediatr Radiol 25:344, 1995.
45. Zeman RK, Baron RL, Jeffery RB Jr, et al: Helical body CT: Evolution of scanning protocols. AJR Am J Roentgenol 170:1427, 1998.

52 Heart and Great Vessels

Sheila C. Berlin

The past two decades have seen major advances in pediatric cardiac imaging. Echocardiography has become the primary modality for imaging most forms of congenital heart disease. It provides high-resolution real-time images, the quality of which further improved with the introduction of new sonographic techniques such as tissue harmonics. Cardiologists have historically relied on the combination of echocardiography and cardiac catheterization for a comprehensive evaluation of patients with congenital heart disease. However, both modalities have important limitations; both are inconsistent in their ability to measure blood flow and quantify regional myocardial function. Echocardiographic access may be limited in older children, and the examination may be technically difficult in postoperative patients who have a wound or scarring. Cardiac catheterization is a costly, invasive examination, exposing children to radiation and complications. Furthermore, this two-dimensional (2D) technique sometimes necessitates difficult and inconclusive mental three-dimensional (3D) image reconstruction. Overcoming many of these limitations, magnetic resonance imaging (MRI) and helical computed tomography (CT) now offer excellent imaging alternatives in both infants and children with congenital heart disease.

During the 1990s, MRI emerged as an important, if not the premier, imaging modality in pediatric cardiac imaging. Since its introduction in the early 1980s,[44, 73] cardiac MRI has evolved from a solid technique for anatomic description of the heart and great vessels and for information about nonquantifiable flow disturbances, to a study capable of providing accurate physiologic data and detailed 3D cardiovascular anatomy. In centers with state-of-the art equipment, MRI serves an integral role in providing unique functional and morphologic information for a cost of only about 20% more than that of an echocardiogram.

MRI can now quantify volumes and masses of cardiac chambers, ejection fraction, stroke volumes, regurgitant volume and fraction, and regional biventricular myocardial function. This is particularly important for the right side of the heart, a focus of great concern in patients with congenital heart disease. Volumetric measurements of blood flow, which are difficult to obtain with other techniques, are potentially useful for quantitative evaluation of pulmonary artery flow, collateral flow, shunt lesions, valvular regurgitation, and ventricular filling.

Established applications for which MRI is well suited include evaluation of the aorta and its branches, pulmonary arteries, pulmonary venous connections, systemic veins, tetralogy of Fallot, heterotaxy syndrome, postoperative cardiac baffles and conduits, pericardial and cardiac masses, and arrhythmogenic right ventricular dysplasia.

Helical CT generates similar high-quality images of the extracardiac vascularity in infants and children. Advantages of CT include the following:

1. Its relative ease of accessibility, particularly for critically ill patients traveling with life-support devices.
2. Its speed and the related limited sedation requirements.
3. Its increased spatial resolution relative to MRI.

Helical CT angiography allows the collection of volumetric data for 3D image reconstruction. It is an established technique for evaluation of aortic dissection and aneurysm[63, 86] as well as for pulmonary embolism[8, 39, 82] and vascular compression of the airway.[49, 58] More recently, helical CT has proved a reliable means of evaluating branch pulmonary arteries, anomalous pulmonary veins, aortopulmonary collateral vessels, and postoperative shunts, conduits, and complicating thromboses.[12] Cine helical CT offers the added functional data for measuring chamber volume and for the direct calculation (without using geometric assumptions) of ejection fractions and cardiac output.

Techniques

Magnetic Resonance Imaging

Sedation

The average pediatric cardiovascular MRI examination takes 30 to 45 minutes. Because tolerance of this procedure varies widely among pediatric patients, anticipation of sedation requirements is essential.

Newborns can occasionally be scanned without sedation if feeding is withheld for 3 hours before the examination and then given immediately before scanning. Infants and young children can be safely and effectively sedated with intravenous (IV) sodium pentobarbital in an average total dose of 5 mg/kg. The drug is given in two parts, with the first delivered slowly over 30 seconds and additional medication given as needed. Scanning can usually be initiated within 10 minutes of delivery.

Older children with claustrophobia or anxiety can be sedated with 2 to 10 mg of (IV) diazepam. Resuscitation supplies and personnel trained in pediatric advanced life support must be available in the event of cardiorespiratory arrest.

In the case of significant cyanotic heart disease or other

risks for complication related to anesthesia, the patient should be sedated by a pediatric anesthesiologist.

Electrocardiographic Gating

Almost all pulse sequences designed for cardiovascular MRI require electrocardiographic (ECG) gating. To achieve high-quality images, the gating signal should be strong and free of artifact. Electrodes can be placed on the anterior or posterior chest. Anterior electrode placement generally returns a stronger signal, whereas posterior placement generates fewer artifacts.[27] Recent advances in gating technology promise quicker and easier methods.[11, 20]

Pulse Sequences

Practical pediatric cardiovascular MR imaging requires appropriate selection among the many available pulse sequences and fine-tuning of individual sequence parameters. In general, anatomic imaging sequences fall into either one of two categories:

1. *Black-blood* sequences are most commonly used for anatomic description. They include conventional spin-echo (CSE) sequences and double or triple inversion recovery fast spin-echo (IRFSE) sequences.
2. *White-blood* sequences helpful in morphologic assessment include cine fast gradient-echo and gadolinium-enhanced 3D magnetic resonance angiography (3D MRA).

Four sequences are commonly used for collecting physiologic and functional information: (1) gradient-echo or general cine techniques, (2) myocardial tissue tagging, (3) blood or bolus tagging, and (4) phase-encoded velocity mapping.

Morphologic Assessment

Conventional Spin Echo. The standard initial anatomic evaluation begins with a non–breath-hold CSE sequence. This sequence is performed over an area of interest set up from the short, non–ECG-gated, fast gradient-recalled echo (GRE) localizers. With good ECG gating, high-resolution images with excellent signal-to-noise ratios (SNRs) are possible in most infants and children. The repetition time (TR) is set to the RR interval, and the echo time (TE) is approximately 20 msec; bandwidth is 16 kHz. Slice thickness varies from 2 to 7 mm with a minimum skip. Signal averages run from 2 to 5 with a matrix of 256 to 512 × 192. Limitations include a relatively long imaging time, sensitivity to motion artifact, and static-only images. Typically, a CSE is the first sequence run to define the morphology of vessel wall and airway or to characterize tissues such as in right ventricular dysplasia and cardiac masses.

Inversion Recovery Fast Spin Echo. The second black-blood sequence is the newer IRFSE designed for breath-hold imaging.[92] Depending on the heart rate and sequence parameters, imaging times range from 10 to 20 seconds. A clear advantage over CSE is that IRFSE sequences generate quicker high-quality anatomic images in cooperative children. The TR is usually 2 RR intervals, TE about 40 msec, echo train length 32, and bandwidth 62.5 kHz. The slice thickness is 5 to 10 mm, and skip is usually minimal. The matrix is 256 × 152 to 256, and the number of signal averages is usually 1. Limitations include image acquisition only during the end-diastolic phase of the cardiac cycle, and reduced SNR compared to CSE images.

Gradient-Recalled Echo. The white-blood, fast gradient-echo sequence with segmented k-space filling is a very useful sequence that allows multiphase imaging in a short period of time. The sequence can be run with breath-holding using one signal average or without breath-holding using multiple averages. Imaging time for the former is approximately 2 to 5 minutes and for the latter, approximately 30 to 60 seconds per location. Images can be viewed in cine format at a workstation. Parameters include a minimum TR and TE, flip angle of 30 degrees, bandwidth of 32 Hz, slice thickness of 4 to 10 mm with minimal skip, matrix of 256 × 128, and four signal averages. Disadvantages of this sequence are reduced SNR and spatial resolution. As with all gradient-echo sequences, there is a greater sensitivity to susceptibility artifacts from metallic clips, stents, and wires.

Contrast-Enhanced 3D Magnetic Resonance Angiography. A newer white-blood sequence is the 3D fast spoiled gradient-echo sequence with IV administration of gadolinium-based contrast agent. A 3D data set that can be analyzed using postprocessing techniques, such as multiplanar reformatting and maximum intensity projection, is acquired. A 3D MRA sequence, which typically requires about 20 seconds per acquisition, is useful for demonstrating extracardiac vascular anatomy. In particular, the vessels of interest can be isolated from the full data set (Fig. 52–1) and displayed in multiple angiographic projections.

The circulation time of contrast medium varies with the size of the child, the injection site, intracardiac shunting, and the degree of impaired cardiac function. Timing of imaging relative to the contrast bolus can be determined using a test bolus technique[41, 48] or an automated method such as SmartPrep.[34] Parameters include a minimum TR and TE (5/2), a flip angle of 25 to 45 degrees, a slice thickness of 2 mm, no gap, a 128 × 256 matrix, bandwidth of 62 kHz, and a single average of signal. A bolus dose of gadolinium (0.1 to 0.25 mmol/kg body weight) is followed by a 15-mL saline flush.

An injection rate of 0.3 to 0.8 mL/second is obtained with a power injector. An automated injector is recommended for small volumes of contrast material and short circulation times.[48] Limitations of 3D MRA are its inability to resolve intracardiac anatomy, dependence on breath-holding, and the need for satisfactory timing of image acquisition relative to contrast administration.

Physiologic and Functional Assessment

General Cine Gradient Echo. General cine GRE MRI, which is useful for both anatomic and functional assessment, has been discussed earlier. Acquisition of images at various phases in the cardiac cycle allows calculation of cardiac index, examination of wall motion, blood flow (e.g., shunts, stenoses, anastomoses), and valvular compe-

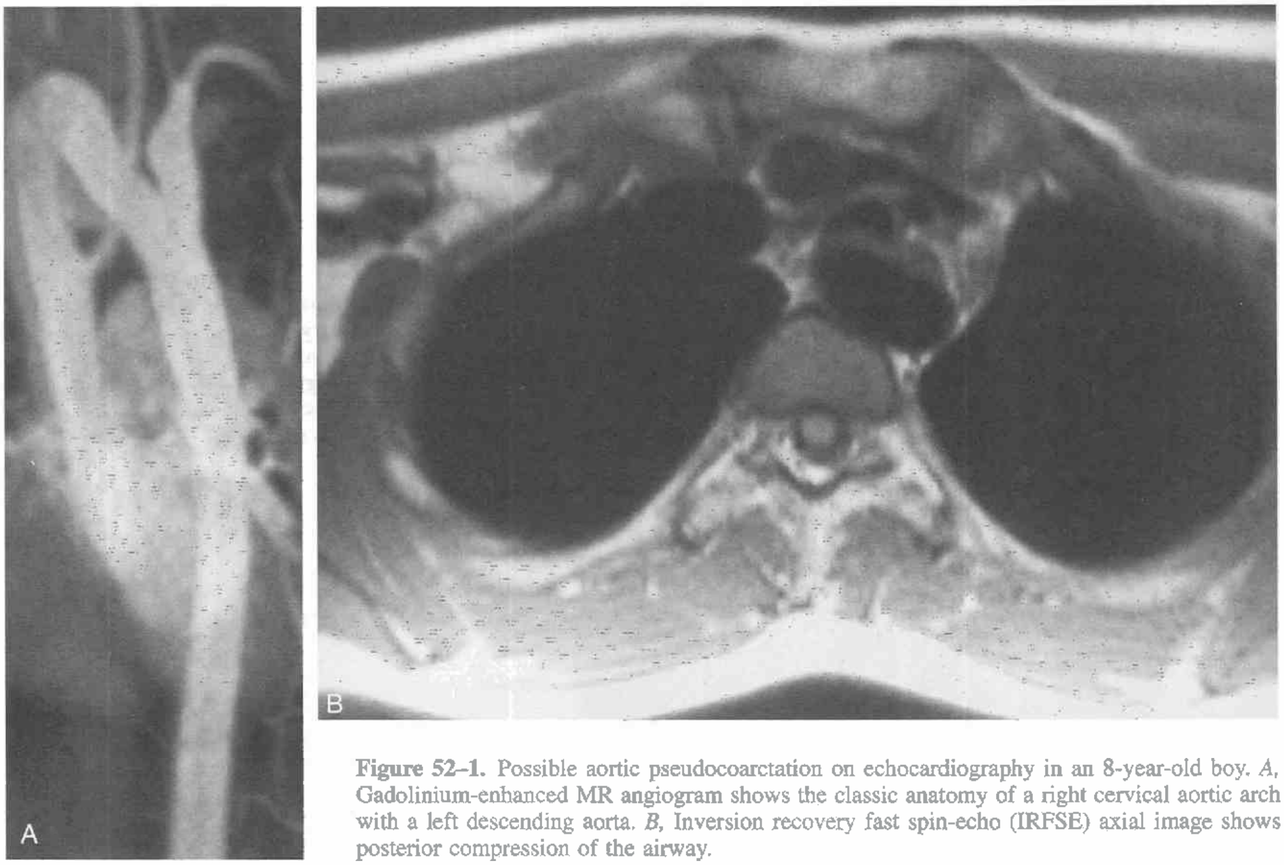

Figure 52–1. Possible aortic pseudocoarctation on echocardiography in an 8-year-old boy. *A*, Gadolinium-enhanced MR angiogram shows the classic anatomy of a right cervical aortic arch with a left descending aorta. *B*, Inversion recovery fast spin-echo (IRFSE) axial image shows posterior compression of the airway.

tence. A set of 16 frames is generally sufficient to evaluate the entire cardiac cycle. Images are usually obtained either parallel to the long axis of the heart (horizontal and vertical long-axis planes) or perpendicular to the long axis (short-axis planes).

Ventricular time-volume curves obtained with multisection cine GRE imaging can be used to assess systolic and diastolic function. In addition, static GRE images obtained at various levels (multislice, single phase) can "label" vessels with high signal intensity. This application is useful in detecting aortic collateral vessels in a patient with cyanotic heart disease.

GRE sequences readily identify turbulent flow (Fig. 52–2) as an area of signal void,[89] a property useful in detecting valvular or blood vessel stenosis and valvular regurgitation. The appearance of high-velocity flow and turbulence depends on technical factors, including display parameters (window width and level), flip angle, and TE. With long TE sequences (12 msec), the flow void is well demonstrated; with short TE sequences (<7 msec), it tends to disappear.

Myocardial Tissue Tagging. MRI is unique among imaging modalities in its ability to magnetically "tag" tissue. Tagging is achieved using a cine sequence in combination with a special sequence that destroys all the spins in a given plane, thus creating a line of signal void. The spatial modulation of magnetization (SPAMM) sequence[1, 2, 112] is an example of such a technique. This sequence uses multiple radiofrequency pulses of 130 degrees, separated in time, and a series of gradient radiofrequency pulses to produce saturated spins. Subsequently, a standard cine sequence divides the cardiac wall into cubes of magnetization.

Observing the translation, rotation, and deformation of the cubes allows assessment of wall motion, regional wall thickening, and strain. Tracking is performed in both 2D and 3D, in systole and diastole and as frequently as every 20 msec. Either manual or semiautomatic tracking of grid intersections on the image can be performed through the cardiac phases of interest.

Blood (Bolus) Tagging. The same concept that allows myocardial tissue tagging also allows tagging blood flow. Blood tagging is performed with a gradient-echo sequence that uses radiofrequency pulses to produce saturated spins along a line designated by the imager across a blood vessel. A saturation pulse precedes each acquisition.[32, 33] Blood flow then displaces this band of saturation while stationary structures keep the band's original position. The displacement of the saturation band allows the calculation of velocity because the time between band placement and image acquisition is measurable.

Phase-Encoded Velocity Mapping. Velocity mapping in MRI is used for quantitative assessment of hemodynamics. The basic principle of the phase-encoding technique[72, 78] is that magnetic spins of intravascular protons flowing along a magnetic field gradient acquire a phase shift that is proportional to the flow velocity. Measuring phase from

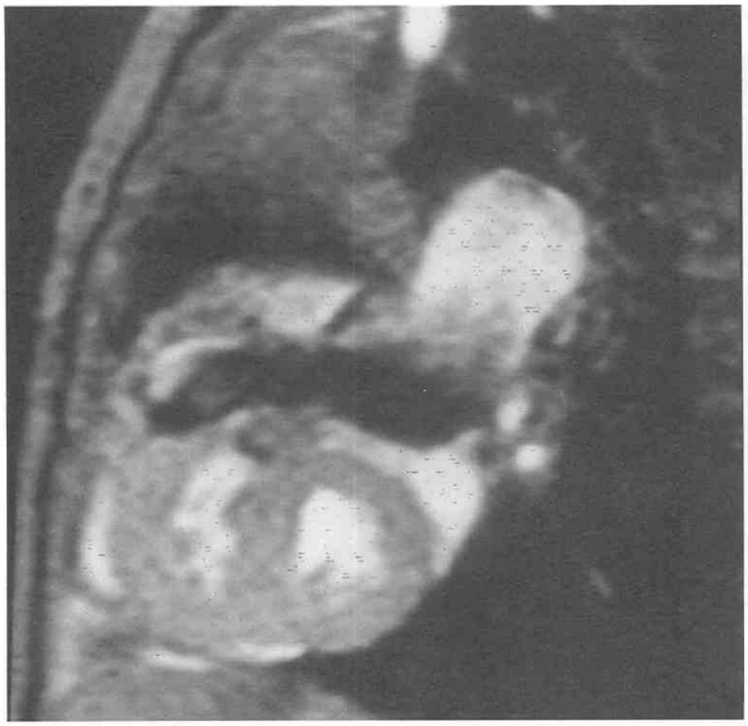

Figure 52–2. Respiratory distress and tetralogy of Fallot with absent pulmonary valve in a 3-week-old infant. Single-phase image of a cine gradient-recalled echo (GRE) sequence through the long axis of the pulmonary outflow tract shows the turbulent flow across the rudimentary pulmonic valve.

signal amplitude allows calculation of velocity (Fig. 52–3), which can be done both parallel and perpendicular to the flow. Pressure gradients can be estimated from peak blood flow velocities (using the Bernoulli equation) in stenotic pulmonary arteries or surgical conduits.

Because flow volume can be measured, pulmonary artery flow, valvular regurgitation, left-to-right shunts, and ventricular filling can all be quantified. This technique provides accurate information on pulmonary flow volume and velocity after Fontan surgery[79] and on pulmonary regurgitation late after tetralogy of Fallot repair.[77]

A limitation of this sequence is aliasing artifact, which occurs when the flow velocity in a vessel is underestimated. Velocities exceeding the expected range are displayed as flow in the opposite direction. Aliasing is easily corrected during postprocessing techniques.

Limitations

MRI can provide excellent images of both intracardiac and extracardiac anatomy. High-quality images, however, depend on a stable, cooperative patient who can breath-hold for at least several seconds. In addition, diagnostic images may be limited by difficult or impossible cardiac gating in patients with arrhythmia. Metallic clips and stents cause signal drop-off on MR images, which is more problematic than the beam-hardening artifact seen in CT. Signal loss is also caused by strong acceleration and turbulence, as at a site of severe stenosis.

The total setup and examination time for a cardiac MRI examination, even without sedation, is usually 30 to 45 minutes. Infants and small children usually require sedation for this duration. The cost at Rainbow Babies and Children's Hospital is about 20% more than for an echocardiogram and 30% more than for a contrast-enhanced 3D CT scan. Although many cardiac lesions can be fully characterized by MRI or a combination of MRI and echocardiography, cardiac catheterization will be necessary in the foreseeable future to accurately measure pulmonary pressure and resistance in those being considered for the Fontan procedure. Finally, patients who have had pacemakers, pumps, or stent placement for less than 6 weeks are not candidates for MRI.

Computed Tomography

Sedation

Most infants and children do not require sedation for helical cardiac CT imaging. Total scanning time usually does not exceed 20 seconds, a duration short enough for most patients to tolerate gentle wrapping, restraint, and coaching. Light sedation, typically with choral hydrate, can be given to older infants and small, uncooperative children.

Electrocardiographic Gating

Newer, multirow, multidetector scanners offer both prospective and retrospective cardiac gating. A robust ECG signal allows gating as effective as that obtained with MRI.

Imaging Parameters

Delivery of Contrast Material

In most children, 2 mL of nonionic iodinated contrast material per kilogram of body weight can be administered by a power injector into the largest available extremity vein. An angiocatheter of 22 gauge or larger is recommended.

For the newborn or small infant, increasing the contrast

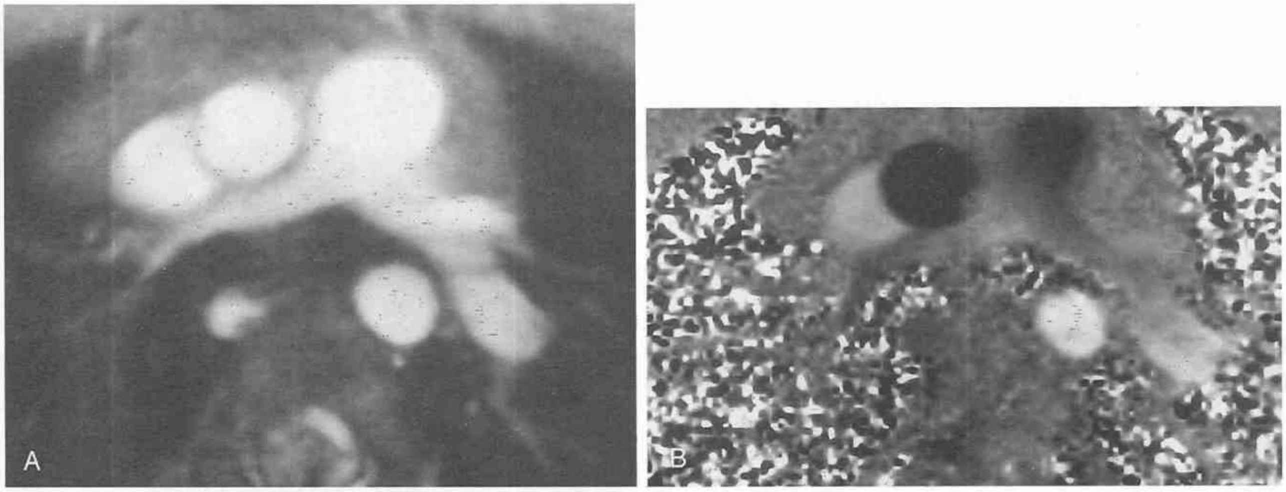

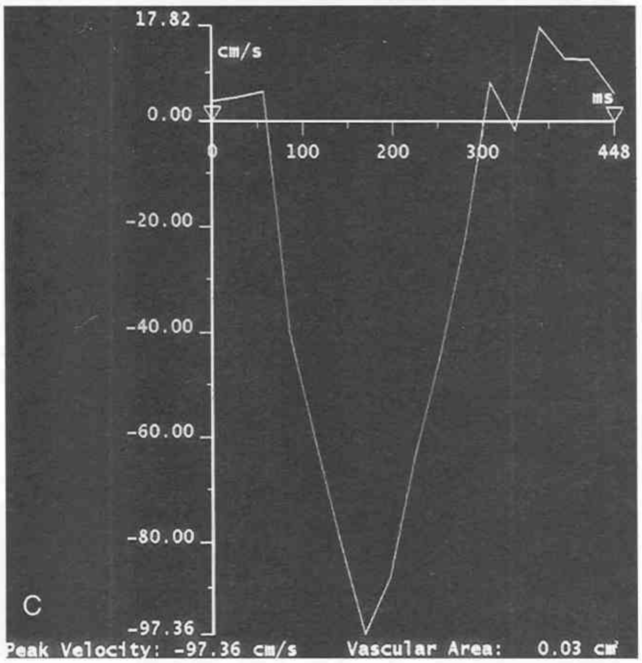

Figure 52–3. Magnitude *(A)* and phase *(B)* images of the phase-encoded velocity-mapping technique. Images are obtained perpendicular to flow to map the velocity in the descending aorta. Graphic display *(C)* of maximum velocity through a single cardiac cycle.

dose to 2.5 to 3 mL/kg and delivering the dose by hand are acceptable. Scanning can be started approximately 15 seconds after initiation of the bolus. This should allow time for opacification of all chambers and great vessels. When hand-injection is used, scanning should begin after approximately 60% of the contrast medium has been delivered. This scanning delay period is shorter than that used in adults because of the shorter circulation time and higher heart rate in infants.

An injection rate of 2.5 to 3.0 mL/second is appropriate with adequate IV access. The bolus is followed with a 10-mL bolus of saline to minimize the venous inflow streak artifact and to maximize the dose of contrast material, particularly when the allowable dose is small.

Scan Technique

An initial scout image of the chest and upper abdomen maps the longitudinal field of view of the helical scan. The transverse field of view can be adapted to the patient's body size. Selection of collimation and table motion depends on the likelihood of motion artifact from respiration or lack of cooperation.

In breath-holding or quietly breathing older children, narrow collimation (1.5 mm) and a pitch of 0.875 to 1.0 can be used. In the rapidly breathing, uncooperative patient, collimation can be widened to 3 mm and the pitch increased to 2.0. Scanning of the heart and great vessels proceeds in an inferior-to-superior direction for an upper extremity vein injection and the reverse for a lower extremity injection. Scanning parameters of 90 to 120 (kVp) and 125 to 260 mAs are appropriate for most pediatric patients. Postprocessing techniques include both maximum intensity projection and multiplanar reformatting for display of 3D images.

Limitations

Helical CT exposes children to ionizing radiation and the small risk of an adverse reaction to contrast material.

This technique is also sensitive to miscalculation of the peak opacification of the cardiac chambers and great vessels. If the contrast bolus arrives either too early or too late with respect to scanning time, images may not be diagnostic. If an unsedated child moves during the scan, the bolus will be lost and cannot be readministered immediately because of recommended contrast limits. CT images are degraded by beam-hardening artifact of metallic wires, clips, and coils, although the effect here is not as great as the susceptibility artifact in MRI.

Applications

Aortic Arch Anomalies

Anomalies of the aorta, such as coarctation, supravalvular stenosis, interrupted aortic arch, cervical aortic arch, double aortic arch, and aberrant subclavian artery, can be accurately diagnosed with MRI.[37, 102]

Coarctation

Coarctation of the aorta is the most common symptomatic congenital lesion of the aortic arch. The focal narrowing present in the proximal thoracic aorta, typically in the juxtaductal region, is classified as either "focal" or "diffuse." A bicuspid valve is reported in 75% to 85% of cases, and there is an association with other congenital lesions of the left side of the heart, including tubular hypoplasia of the arch.[6]

Accurate assessment of the site and severity of the aortic lesion, as well as any involvement of the brachiocephalic vessels, is important for preoperative planning. For evaluation of coarctation of the aorta, IRFSE black-blood imaging in the axial and steep left antero-oblique planes clearly delineate the anatomy (Fig. 52–4) in most patients.

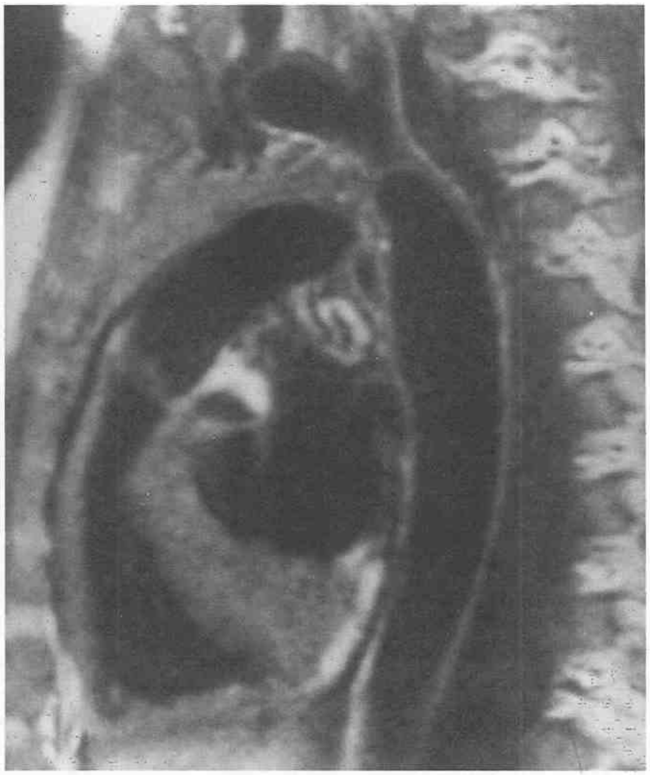

Figure 52–4. Pressure gradient measured by echocardiography after repair of a focal aortic coarctation in a 10-year-old boy. Cross-sectional echocardiographic image in the left anterior oblique plane shows a residual narrowing at the coarctation site.

In infants and very small children, more time-consuming CSE images with multiple averages may be necessary to define the anatomy. Cine GRE shows turbulent flow at and beyond the site of coarctation (Fig. 52–5), or within, above, or below the aortic valve. Gadolinium-enhanced MRA best displays the 3D anatomy of the aorta and brachiocephalic vessels. Phase-contrast images acquired just beyond the coarctation site determine the maximum velocity and allow for calculation of a pressure gradient.[98]

Figure 52–5. Single phase of a cine gradient-recalled echo sequence, left anterior oblique projection, shows a poststenotic jet just beyond the coarctation site.

Other Anomalies

Thoracic arch anomalies are common, occurring in 0.5% to 3% of the population. These arch anomalies may be associated with congenital heart disease, may form a vascular ring, or may be isolated findings and asymptomatic. A double aortic arch, present in about 0.3% of autopsies, is the most common vascular ring as well as the most common ring to be symptomatic.[29] The right arch is generally higher in position and larger in size than the left arch, and it passes posterior to the trachea and esophagus to join the descending aorta that is characteristically left-sided. Less frequently, however, the left arch can be the same size as or larger than the right arch. Alternatively, a portion of the smaller arch may exist only as a fibrous cord. In cases of partial left arch atresia, the descending aorta is typically right-sided.

Arch variants, such as double aortic arch and right arch with aberrant left subclavian artery, are well visualized

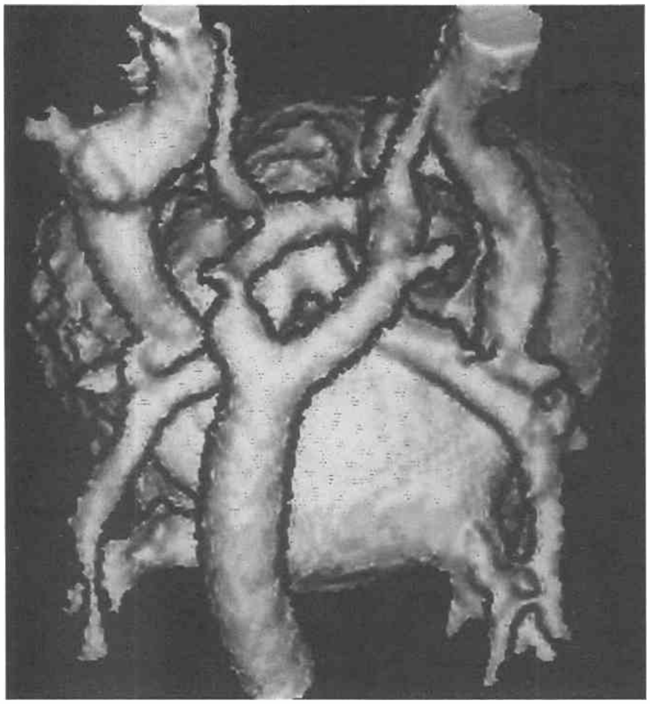

Figure 52–6. Stridor in a 2-month-old infant. A double aortic arch is seen in the 3D CT angiogram.

with either MRI[53, 67] or CT.[49, 58] Although the black-blood technique IRFSE is usually adequate, smaller patients may require CSE images acquired with multiple signal averages to achieve a high-enough SNR. The diagnosis is generally obvious on the individual axial images of helical CT, but 3D reconstruction (Fig. 52–6) is a simpler means of projecting the global anatomy (including the airway) to referring clinicians and surgeons.

Pulmonary Arteries

The pulmonary arteries are commonly involved in congenital heart lesions, particularly in cases of right ventricular outflow tract obstruction. Identification and precise description of the pulmonary arteries is critical in treatment planning and assessing patient risk.[74]

Pulmonary artery confluence/nonconfluence, stenoses, and the presence of aorticopulmonary collaterals can alter the approach to medical and surgical management. Measurement of pulmonary artery size on angiocardiography, the longtime reference standard, is inaccurate because of magnification. Also, angiocardiography may fail to demonstrate central pulmonary arteries identified at surgery or autopsy.[96] In some cases, it is impossible to accurately delineate the pulmonary artery anatomy in one angiographic study because of contrast volume limits. Echocardiography may be unsuccessful in demonstrating the morphology of the distal main pulmonary arteries (particularly the left[38]), largely because of interposition of lung tissue.

MRI has shown promising results in evaluation of presence, size, and distribution of central pulmonary arteries.[16, 38, 42, 46, 80, 99, 105] Coronal and oblique-coronal CSE images, obtained parallel to the long axis of the vessel, provide accurate visualization up to the first or second hilar branch.[42] Other factors contributing to treatment planning, such as the status of the pulmonary artery confluence and the presence of aorticopulmonary collaterals, are also reliably evaluated with MRI.

More recently, both electron beam and volumetric helical CT angiography have shown high-quality pulmonary artery anatomy.[108, 109] In a 1999 study,[108] helical CT angiography with 3D reconstruction was superior to echocardiography for the noninvasive assessment of pulmonary artery anatomy in patients with complex congenital heart disease. Helical CT was as accurate as angiocardiography in revealing stenotic or nonconfluent central pulmonary arteries and aorticopulmonary collaterals.

Aberrant origin of the left pulmonary artery (pulmonary sling) can be clearly imaged with either MRI (Fig. 52–7) or helical CT (Fig. 52–8). Associated airway anomalies such as tracheal rings or bronchus suis (Fig. 52–9) are also demonstrated with either MR CSE sequences or 3D reconstruction of the airway on helical CT. Absent pulmonary valve is another lesion well evaluated by MRI. CSE MR images clearly define the dilated pulmonary arteries (Fig. 52–10) and their relationship to the airway, whereas cine GRE images display flow disturbances typical at the pulmonary valve region. Phase-contrast images can measure regurgitant volume into the right ventricle.

Pulmonary Venous Connections

Echocardiographic evaluation of the pulmonary veins is limited because of poor far-field resolution, overlying lung and bronchi, and a generally small field of view. Without accurate echocardiographic information, poor levophase images of the pulmonary veins and selective pulmonary venograms may result in misdiagnosis of pulmonary venous connections at angiocardiography. MRI can depict pulmonary venous connection anomalies such as partial and total anomalous connections and cor triatriatum.[21, 71, 104] In a large study evaluating 56 patients with congenital heart disease with normal pulmonary venous connection and 22 patients with anomalous pulmonary venous return, the venous connections were correctly identified on axial MR images in 88% and 95% of patients, respectively.[71] In a small number of surgically proven cases, the accuracy of MRI in the diagnosis of total anomalous pulmonary venous connections was 100%, better than that of angiocardiography (25%) or echocardiography (57%).[21]

The typical findings of total anomalous pulmonary venous connection on MR images include (1) a venous structure posterior to the left atrium, (2) a small left atrium and ventricle, (3) an atrial septal defect (in most cases), and (4) a vertical vein (in some cases).[21] Axial CSE and gadolinium-enhanced MRA are the preferred modalities for showing the anatomy (Fig. 52–11).

Heterotaxy Syndrome

MRI is well suited for the "segmental analysis"[102] of heterotaxy syndrome. The segmental approach requires documentation of the following anatomy: (1) positions of

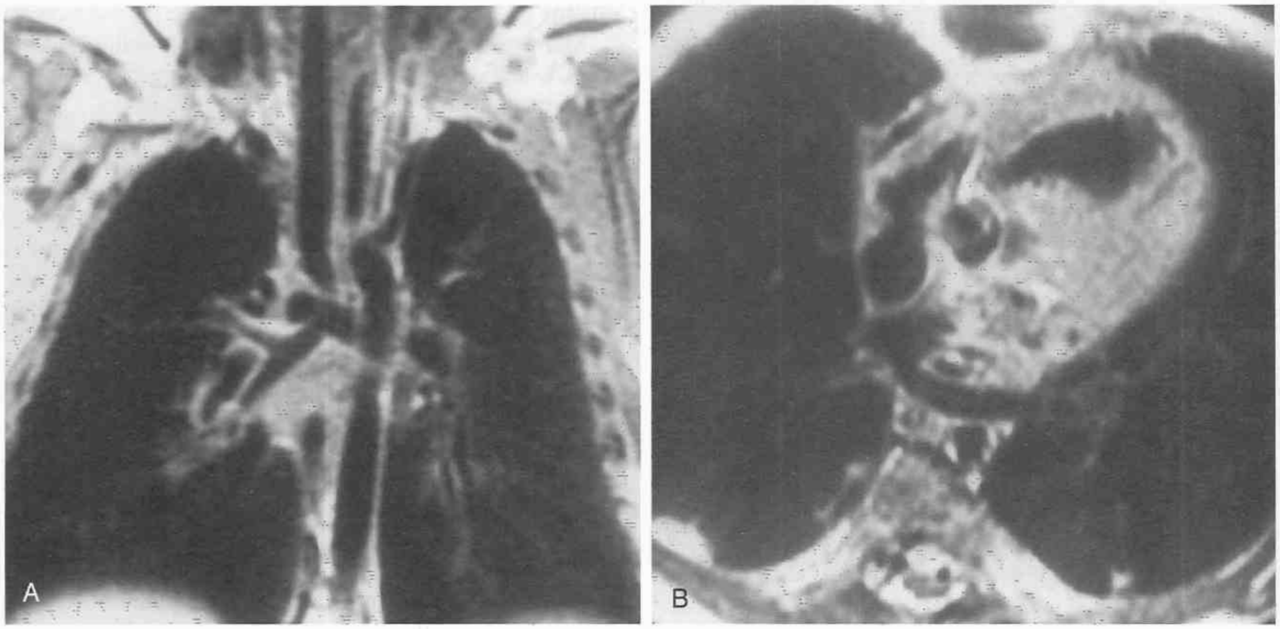

Figure 52–7. Respiratory distress in a 1-month-old infant. Coronal *(A)* and axial *(B)* cross-sectional echocardiographic images show the aberrant origin of the left pulmonary artery from the right. Airway narrowing is also noted.

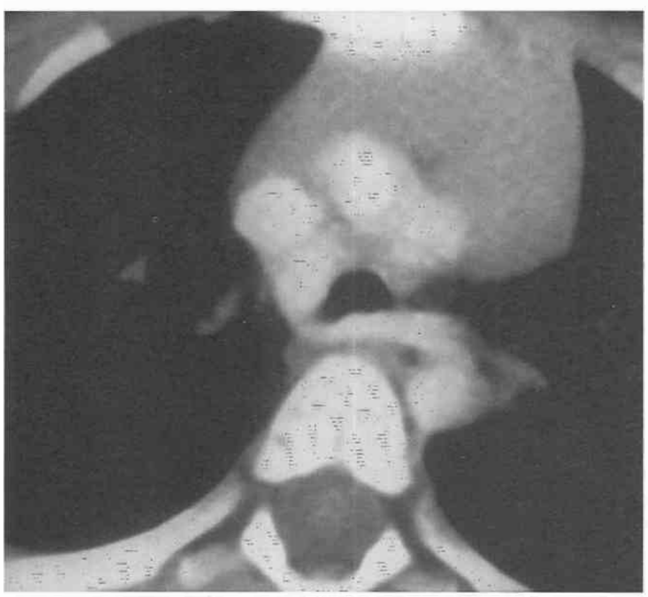

Figure 52–8. Failure to thrive and respiratory distress in a 2-month-old infant. Axial CT image shows the left pulmonary artery as it courses behind the trachea and anterior to the esophagus.

Figure 52–9. Respiratory distress in a 1-month-old infant. Coronal cross-sectional echocardiographic image through the trachea shows a bronchus suis.

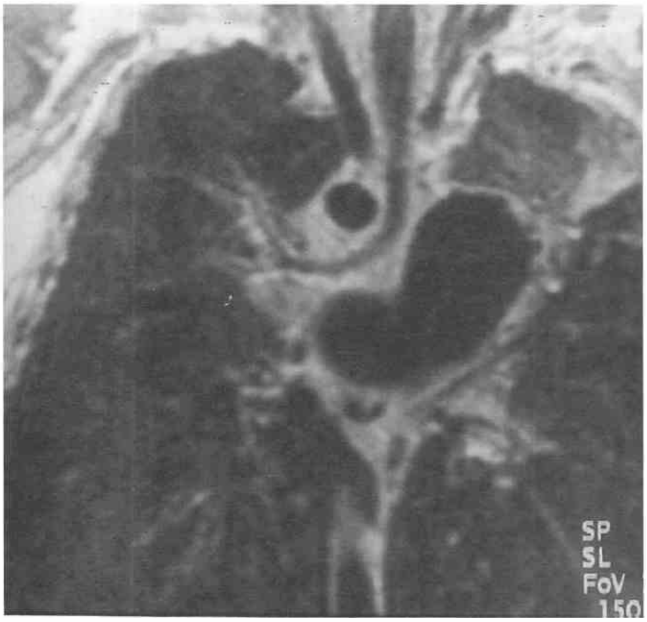

Figure 52–10. Tetralogy of Fallot and absent pulmonary valve in a 2-week-old infant. Coronal cross-sectional echocardiographic image shows aneurysmal dilatation of the pulmonary arteries and uplifting of the right main bronchus.

the atria, main bronchi, and ventricles; (2) atrioventricular relationships; (3) great vessel morphology; and (4) other intracardiac and extracardiac anomalies, such as polysplenia and a midline liver. In a 1994 prospective study, the value of MRI in preoperative planning for the heterotaxy syndrome was compared with that of echocardiography and cardiac catheterization.[36] MRI provided excellent anatomic and functional information not available from either echocardiography or cardiac catheterization in some patients.

In most cases of visceroatrial situs abnormalities, the situs of the atria can be determined by the MR appearance of the appendages. The morphologic right atrial appendage has a broad junction with the atrial chamber and a prominent terminal crest and pectinate muscles. The morphologic left atrial appendage has a narrow junction with the atrial chamber and no terminal crest. Bronchial situs is best seen on coronal images in plane with the carina.

Postoperative Cardiac Baffles and Conduits

Visualization of intracardiac and extracardiac conduits by echocardiography and angiocardiography has been inconsistent. Limited echocardiographic access usually prohibits visualization of the full course of a conduit. Maximum contrast dosage and prolonged radiation may influence the number of angiographic runs performed, thereby limiting visualization of conduits.

MRI visualizes the anatomy of extracardiac conduits in their entirety more often than angiocardiography or echocardiography.[12, 60] MRI has an unlimited number of viewing planes, thus avoiding the overlap of structures seen with angiocardiography. Furthermore, 3D MRA images can be rotated 360 degrees and defines the spatial interrelations of vascular and nonvascular structures.

Baffles, shunts, and conduits can be delineated by IR-FSE or CSE images (Fig. 52–12), GRE (Fig. 52–13) or MRA techniques. The anatomy of the Rastelli and Jantene procedures is depicted on axial and sagittal images. The results of the Senning and Damus procedures are best visualized in the sagittal or coronal planes. The modified Blalock-Taussig shunt is best depicted on sagittal or coronal images (Fig. 52–14) and cavopulmonary shunts on oblique-coronal images.

Pericardial and Cardiac Masses

As image acquisition with CT and MRI has become faster, these modalities have played an increasingly important role in the evaluation of cardiac neoplasms.[3, 23, 66, 69, 90, 113] Although spatial and temporal resolution is lower than with echocardiography, the soft tissue contrast of

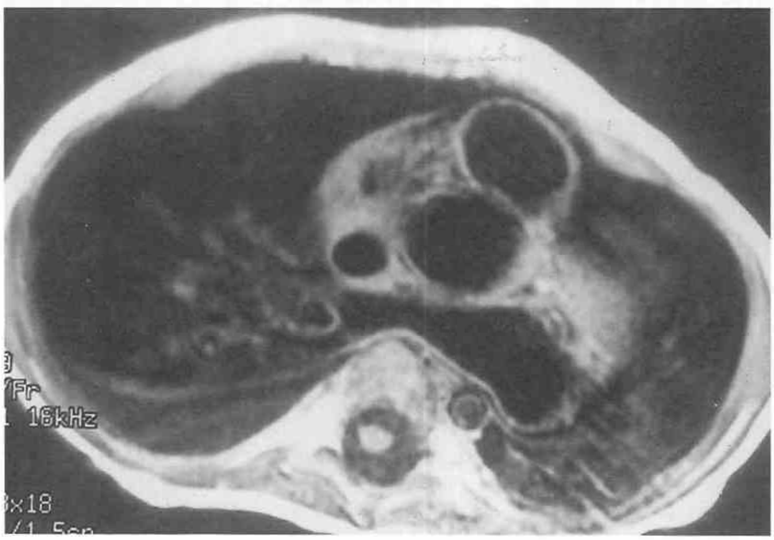

Figure 52–11. Marfan syndrome in an 8-month-old infant. Cross-sectional echocardiographic axial image shows both the dilated aortic root and the absent left pulmonary veins.

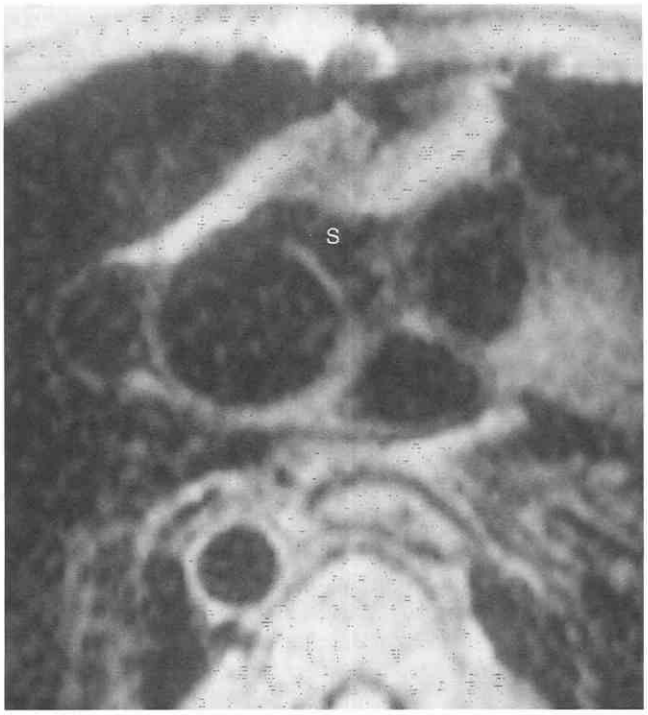

Figure 52–12. Central shunt in a 2-month-old infant with pulmonary atresia. Axial cross-sectional echocardiographic image shows flow void in the patent central shunt (S), which courses from the anterior ascending aorta to the pulmonary artery.

both CT and MRI is superior to that of echocardiography. Furthermore, both modalities allow imaging of the entire mediastinum and evaluation of the extracardiac extent of disease. CT can detect calcification, an important variable in the differential diagnosis of cardiac neoplasms. In addition, CT is faster and easier to perform, and it generally produces more reliable image quality. MRI has better soft tissue contrast than CT and offers greater flexibility in selection of imaging planes.

MRI examination for a cardiac mass should include a CSE sequence for anatomy, supplemented by a cine GRE sequence to assess for flow disturbance at the valve level or effect on myocardial contractility. Fat-saturated sequences are helpful in the diagnosis of a lipoma. Gadolinium is helpful in distinguishing between thrombus and soft tissue mass (Fig. 52–15) because thrombus does not enhance.

Teratomas and pericardial cysts are the most common pericardial lesions in children. Cardiac masses seen in the pediatric population include myxoma (7% occur in setting of Carney complex), fibroma, lymphangioma, lipoma, and rhabdomyoma.

Myxomas associated with the Carney complex are more likely to occur outside the left atrium, to be multifocal, and to recur after resection.[17, 76, 83] Because of their gelatinous nature, myxomas usually show heterogeneous low attenuation on CT scans. Calcification is a frequent finding on CT. Prolapse across cardiac valves may be seen with CT or MRI. Markedly increased signal intensity on T2-weighted images is typical of a myxoma, although scattered foci of decreased signal from calcification or hemosiderin may be present.

Cardiac fibroma is the second most common benign primary cardiac tumor in children after rhabdomyoma.[15] Most cases are detected in infants or in utero.[7, 15] The prevalence of cardiac fibroma is increased in Gorlin's syndrome.[15] This tumor arises in the myocardial wall, almost always in the ventricles. It is large, with a mean diameter of about 5 cm,[15] often obliterating the ventricular cavity (Fig. 52–16). On CT studies, fibromas typically show uniform soft tissue attenuation, often with calcification. The dense, fibrous tissue of these tumors shows hypointensity on T2-weighted images and isointensity relative to muscle on T1-weighted images. Little or no enhancement with gadolinium is the most common presentation;[107] however, the enhancement pattern is truly variable with both homogeneous and heterogeneous patterns of enhancement reported.[14]

Figure 52–13. After a Mustard procedure for transposition of the great arteries in a 14-year-old patient, cine gradient-recalled echo (GRE) was performed to determine whether there was a baffle obstruction. A single phase from the GRE sequence shows patent baffle flow without turbulence.

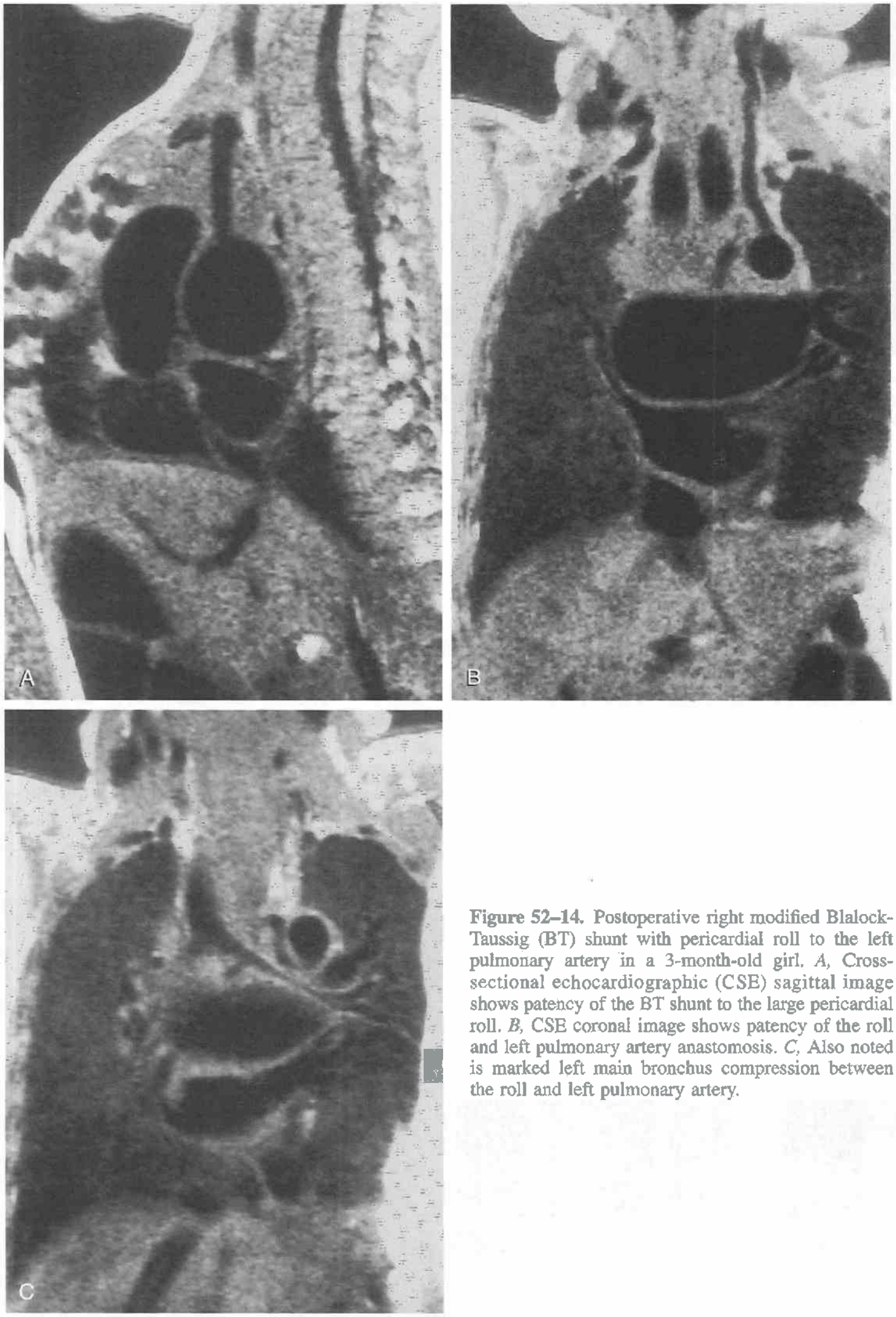

Figure 52–14. Postoperative right modified Blalock-Taussig (BT) shunt with pericardial roll to the left pulmonary artery in a 3-month-old girl. *A,* Cross-sectional echocardiographic (CSE) sagittal image shows patency of the BT shunt to the large pericardial roll. *B,* CSE coronal image shows patency of the roll and left pulmonary artery anastomosis. *C,* Also noted is marked left main bronchus compression between the roll and left pulmonary artery.

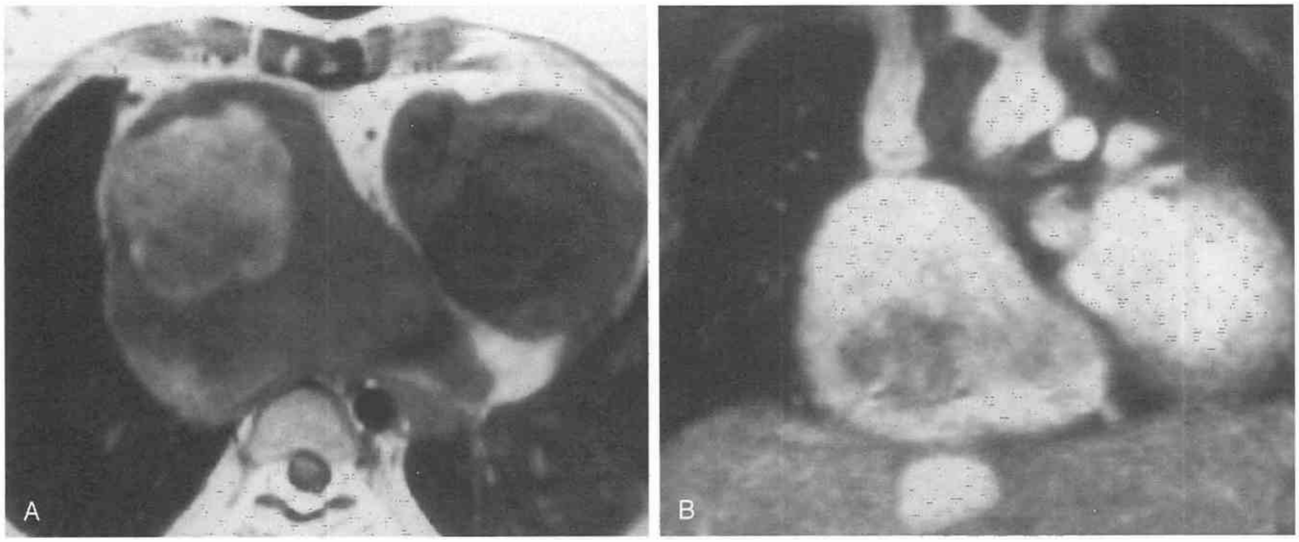

Figure 52–15. Tricuspid atresia and right atrial mass after a Fontan procedure in a 13-year-old girl. *A,* Unenhanced cross-sectional echocardiographic axial image shows a bright signal thrombus surrounded by slow flow. *B,* Coronal gradient-recalled echocardiographic image shows flow around the thrombus.

In infants, the primary differential diagnosis of an intramural mass is a cardiac rhabdomyoma, accounting for more than 50% of pediatric intracardiac masses. If there are multiple masses or other signs of tuberous sclerosis, rhabdomyoma can be diagnosed with confidence.[7] If the tumor is solitary, ventricular, and calcified, the diagnosis of fibroma is confirmed.

Rhabdomyosarcoma, a rare malignant tumor, occurs much less commonly in children than in adults. It occurs with equal frequency in all cardiac chambers and does not calcify.[4] Often cystic or necrotic, it may invade pulmonary veins, the pericardial space, or other adjacent structures.[4]

Summary

Extraordinary technical advances over the past decade have paved the way for less invasive diagnostic tests in cardiac imaging such as MRI and CT. These studies not only render the same diagnostic information as cardiac catheterization but also offer more accurate quantitative information, such as about the volume and mass of cardiac chambers. We are currently on the threshold of a revolutionary change in the way we diagnose and treat cardiovascular disease. The current limitations in temporal resolution will be soon be overcome by "real-time" sequences.[59, 81, 103, 111]

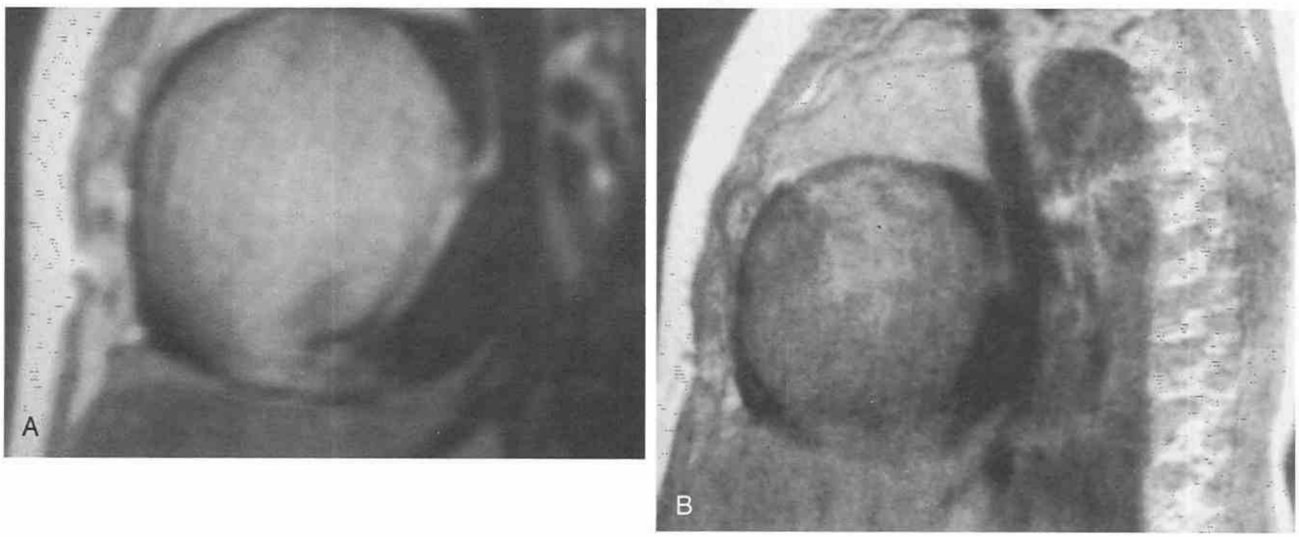

Figure 52–16. Cardiac fibroma in a 5-week-old infant who has had a murmur since birth. Sagittal cross-sectional echocardiographic unenhanced T1-weighted *(A)* and T2-weighted *(B)* images show a large, well-circumscribed soft tissue mass arising from the free wall of the right ventricle. Intermediate signal of the mass is noted on both sequences.

MRI-guided interventional cardiology[65] is in the earliest stages of development, but it is a promising new approach just on the horizon.

One of the major barriers to widespread utilization of cardiac CT or MRI is the question of who should perform and interpret these studies—radiologists or cardiologists. Few radiologists are experts in pediatric cardiac disease, and few cardiologists are experts in CT and MRI. Therefore, the current solution will involve an interdisciplinary effort to fully realize the possibilities of this remarkable revolution.

References

1. Amparo EG, Higgins CB, Farmer D, et al: Gated MRI of cardiac and paracardiac masses: Initial experience. Am J Roentgenol 143: 1151–1156, 1984.
2. Araoz PA, Eklund HE, Welch TJ, Breen JF: CT and MR imaging of primary cardiac malignancies. Radiographics 19:1421–1434, 1999.
3. Axel L, Dougherty L: Heart wall motion: Improved method of spatial modulation of magnetization of MR imaging. Radiology 172: 349–350, 1989.
4. Axel L, Dougherty L: MR imaging of motion with spatial modulation of magnetization. Radiology 171:841–845, 1989.
5. Araoz PA, Mulvagh SL, Tazelaar HD, et al: CT and MR imaging of benign primary cardiac neoplasms with echocardiographic correlation. Radiographics 20:1303–1319, 2000.
6. Becker AE, Becker MJ, Edwards JE: Anomalies associated with coarctation of the aorta: Particular reference to infants. Circulation 41:1067–1075, 1970.
7. Beghetti M, Gow RM, Haney I, et al: Pediatric primary benign cardiac tumors: A fifteen year review. Am Heart J 134:1107–1114, 1997.
8. Blachere H, Latrabe V, Montaudon M, et al: Pulmonary embolism revealed on helical CT angiography: Comparison with ventilation-perfusion radionuclide lung scanning. Am J Roentgenol 174:1041–1047, 2000.
9. Blake LM, Scheinmann MM, Higgins CB: MR features of arrhythmogenic right ventricular dysplasia. AJR Am J Roentgenol 162: 809–812, 1994.
10. Bleiweis MS, Mao SS, Brundage BH: Total biventricular and total left ventricular volume by ultrafast computed tomography: Prediction of left ventricular mass. Am Heart J 127:667–673, 1994.
11. Bloomgarden DC, Morris GR, Valentine J, et al: Improved ECG triggering with the T-wave terminator. Proc Int Soc Magn Reson Med 7:1995, 1999.
12. Bornemeier RA, Weinberg PM, Fogel MA: Angiographic, echocardiographic, and three dimensional magnetic resonance imaging of extracardiac conduits in congenital heart disease. Am J Cardiol 78: 713–717, 1996.
13. Boxt LM, Katz J: Magnetic resonance imaging for quantification of right ventricular volume in patients with pulmonary hypertension. J Thorac Imaging 8:92–97, 1993.
14. Burke AP, Rosado-de-Christenson M, Templeton PA, et al: Cardiac fibroma: Clinicopathologic correlates and surgical treatment. J Thorac Cardiovasc Surg 108:862–870, 1994.
15. Burke A, Virmani R: Tumors of the heart and great vessels. In Atlas of Tumor Pathology, Fascicle 16, Series 3. Washington, DC, Armed Forces Institute of Pathology, 1996, pp 1–98.
16. Canter CE, Gutierrez FR, Mirowitz SA, et al: Evaluation of pulmonary arterial morphology in cyanotic congenital heart disease. Am Heart J 118:347–354, 1989.
17. Casey M, Mah C, Merlis AD, et al: Identification of a novel genetic locus for familial cardiac myxomas and Carney complex. Circulation 98:2560–2566, 1998.
18. Chen JC, Lue HC: Three-dimensional reconstruction of abnormal ventriculoarterial relationship by electron beam CT. J Comput Assist Tomogr 22:560–568, 1998.
19. Chen SJ, Li YW, Wang LK, et al: Three dimensional reconstruction of abnormal ventriculoarterial relationship by electron beam CT. J Comput Assist Tomogr 22:560–568, 1998.
20. Chia JM, Fischer SE, Wickline SA, et al: Clinical application of vectorcardiographic triggered MR imaging. Proc Int Soc Magn Reson Med 7:1303, 1999.
21. Choe YH, Lee HJ, Kim HS, et al: MRI of total anomalous pulmonary venous connections. J Comput Assist Tomogr 18:243–249, 1994.
22. Choyke PL, Kressel HY, Reichek N, et al: Nongated cardiac magnetic resonance imaging preliminary experience at 0.12 T. Am J Roentgenol 143:1143–1150, 1984.
23. Conces DJ, Vix VA, Klatte EC: Gated MR imaging of left atrial myxomas. Radiology 156:445–447, 1985.
24. Culham JA, Vince DJ: Cardiac output by MR imaging: An experimental study comparing right ventricle and left ventricle with thermodilution. Can Assoc Radiol J 39:247–249, 1988.
25. Dell'Italia LJ, Blackwell GG, Pearce DJ, et al: Assessment of ventricular volumes using cine magnetic resonance imaging in the intact dog. A comparison of measurement methods. Invest Radiol 29:162–167, 1994.
26. Didier D, Ratib O, Lerch R, et al: Detection and quantification of valvular heart disease with dynamic cardiac MR imaging. Radiographics 20:1279–1299, 2000.
27. Dimick RN, Hedlund LW, Herfkens RJ, et al: Optimizing electrocardiograph electrode placement for cardiac-gated magnetic resonance imaging. Invest Radiol 22:17–22, 1987.
28. Domingo ML, Marti-Bonmati L, Dosda R, et al: Interobserver agreement in the diagnosis of pulmonary embolism with helical CT. Eur J Radiol 34:136–140, 2000.
29. Ekstrom G, Sandblom P: Double aortic arch. Acta Chir Scand 102: 183, 1951.
30. Eldredge WJ, Flicker S: Evaluation of congenital heart disease using cine-CT. Am J Card Imaging 1:38–50, 1987.
31. Fogel MA, Weinberg PM, Chin AJ, et al: Late ventricular geometry and performance changes of functional single ventricle throughout staged Fontan reconstruction assessed by magnetic resonance imaging. J Am Coll Cardiol 28:212–221, 1996.
32. Fogel MA, Weinberg PM, Hoydu A, et al: Effect of surgical reconstruction on flow profiles in the aorta using magnetic resonance blood tagging. Ann Thorac Surg 63:1691–1700, 1997.
33. Fogel MA, Weinberg PM, Hoydu A, et al: The nature of flow in the systemic venous pathway in Fontan patients utilizing magnetic resonance blood tagging. J Thorac Cardiovasc Surg 114:1032–1041, 1997.
34. Foo TKF, Saranathan M, Price MR, et al: An automated method for detecting the bolus arrival time and initiating data acquisition in fast 3D gadolinium-enhanced MRA. Radiology 203:275–280, 1997.
35. Furusho H, Nagai H, Takamura M, et al: Three-dimensional computed tomography of corrected transposition of the great arteries. Circulation 96:4115, 1997.
36. Geva T, Vick W, Wendt RE, et al: Role of spin echo and cine magnetic resonance imaging in presurgical planning of heterotaxy syndrome. Circulation 90:348–356, 1994.
37. Gomes AS, Lois JF, George B, et al: Congenital abnormalities of the aortic arch. Radiology 165:691–695, 1987.
38. Gomes A, Lois JR, Williams RG: Pulmonary arteries: MR imaging in patients with congenital obstruction of the right ventricular outflow tract. Radiology 174:51–57, 1990.
39. Goodman LR, Lipchik RJ, Kuzo RS, et al: Subsequent pulmonary embolism: Risk after a negative helical CT pulmonary angiogram: Prospective comparison with scintigraphy. Radiology 215:535–542, 2000.
40. Gross RE: Arterial malformations which cause compression of the trachea or esophagus. 11:124–130, 1955.
41. Haliloglu M, Hoffer FA, Gronemeyer SA: Applications of three-dimensional gadolinium-enhanced MR angiography in children. Proc Int Soc Magn Reson Med 7:1222, 1999.
42. Hayes AM, Baker EJ, Parsons J, et al: Evaluation of pulmonary artery anatomy using magnetic resonance: The importance of multiplanar and oblique imaging. Pediatr Cardiol 15:8–13, 1994.
43. Heiken JP, Brink JA, Vannier MW: Spiral (helical) CT. Radiology 189:647–656, 1993.
44. Herfkens RJ, Higgins CB, Hricak H, et al: Nuclear magnetic resonance imaging of the cardiovascular system: Normal and pathologic findings. Radiology 147:749–759, 1983.
45. Hernandez RJ, Aisen AM, Foo TKF, et al: Thoracic cardiovascular anomalies in children: Evaluation with a fast gradient-recalled-echo sequence with cardiac-triggered segmented acquisition. Radiology 188:755–780, 1993.

46. Hernandez RJ, Bank ER, Shaffer EM, et al: Comparative evaluation of the pulmonary arteries in patients with right ventricular outflow tract obstructive lesions. AJR Am J Roentgenol 148:1189–1194, 1987.
47. Holland P, Fitzpatrick JD: Case report: Magnetic resonance imaging of a right-sided cervical aortic arch with a congenital aneurysm. Clin Radiol 43:352–355, 1991.
48. Holmqvist C, Larsson E-M, Stahlberg F, et al: Contrast-enhanced thoracic 3D-MR angiography in infants and children. Proc Int Soc Magn Reson Med 7:1219–1223, 1999.
49. Hopkins KL, Patrick LE, Simoneaux F, et al: Pediatric great vessel anomalies: Initial clinical experience with spiral CT angiography. Radiology 200:811–815, 1996.
50. Husayni T: Ultrafast computed tomographic imaging in congenital heart disease. In Stanford W, Rumberger JA (eds): Ultrafast Computed Tomography in Cardiac Imaging: Principles and Practice. Mount Kisco, NY, Futura Publishing, 1992, pp 311–336.
51. Husayni TS: Computed tomography. In Moss AJ, Adams FH (eds): Heart Disease in Infants, Children, and Adolescents. Baltimore, Md, Williams & Wilkins, 1995, pp 190–206.
52. Jacobstein MD, Fletcher BD, Nelson AD: Magnetic resonance imaging: Evaluation of palliative systemic-pulmonary artery shunt. Circulation 70:650–656, 1984.
53. Jaffe RB: Magnetic resonance imaging of vascular rings. Semin Ultrasound CT MR 11:206–220, 1990.
54. Jerewski A, Steendijk P, Peter MT, et al: Simultaneous right and left ventricular pressure-volume relationships assessed with echo-planar magnetic resonance imaging: Differential response to β-adrenergic stimulation. Circulation 96:1–514, 1997.
55. Johnson PT, Health DG, Bliss DF, et al: Three-dimensional CT: Real-time interactive volume rendering. AJR Am J Roentgenol 167: 581–583, 1996.
56. Julsrud PR, Ehman RI, Hagler DJ, et al: Extracardiac vasculature in candidate for Fontan surgery: MR imaging. Radiology 173:503–506, 1989.
57. Katz J, Milliken MC, Stray-Gundersen J, et al: Estimation of human myocardial mass with MR imaging. Radiology 169:495–498, 1988.
58. Katz M, Konen E, Rozenman J, et al: Spiral CT and 3D image reconstruction of vascular ring and associated tracheobronchial anomalies. J Comput Assist Tomogr 19:564–568, 1995.
59. Kerr AB, Pauly JM, Nishimura DG: Partial k-space acquisitions for real-time MR imaging. Proc Int Soc Magn Reson Imaging 3: 1945, 1998.
60. Kersting-Sommerhoff BA, Seelos KC, Hardy C, et al: Evaluation of surgical procedures for cyanotic congenital heart disease by using MR imaging. AJR Am J Roentgenol 155:259–266, 1990.
61. Kilner PJ, Firmin DN, Rees RS, et al: Valve and great vessel stenosis: Assessment with MR jet velocity mapping. Radiology 178: 229–235, 1991.
62. Kilner PJ, Manzara CC, Mohiaddin RH, et al: Magnetic resonance jet velocity mapping in mitral and aortic valve stenosis. Circulation 87:1239–1248, 1993.
63. Kimura F, Shen Y, Date S, et al: Thoracic aortic aneurysm and aortic dissection: New endoscopic mode for three dimensional CT display of aorta. Radiology 198:573–578, 1996.
64. Koelling TM, Poncelet BP, Schmidt CJ, et al: Oxygen-sensitive magnetic resonance imaging: Assessment of myocardial perfusion reserve in swine. Circulation 96:1–304, 1997.
65. Lardo AC, McVeigh ER, Atalar E, et al: Magnetic resonance guided radiofrequency ablation: Visualization and temporal characterization of thermal lesions. Circulation 98:3385, 1998.
66. Levine RA, Weyman AE, Dinsmore RE, et al: Noninvasive tissue characterization: Diagnosis of lipomatous hypertrophy of the atrial septum by nuclear magnetic resonance imaging. J Am Coll Cardiol 7:688–692, 1986.
67. Link KM, Lesko NM: Magnetic resonance imaging in the evaluation of congenital heart disease. Magn Reson Q 7:173–190, 1991.
68. Lorenz CH, Walker ES, Morgan VL, et al: Normal human right and left ventricular mass, systolic function and gender differences by cine magnetic resonance imaging. J Cardiovasc Magn Reson 1: 7–22, 1999.
69. Lund JT, Ehman RL, Julsrud PR, et al: Cardiac masses: Assessment by MR imaging. AJR Am J Roentgenol 152:469–473, 1989.
70. Maddahi J, Crues J, Berman DS, et al: Noninvasive quantification of left ventricular myocardial muscle mass by gated proton nuclear magnetic resonance imaging. J Am Coll Cardiol 10:681–692, 1987.
71. Masui T, Seelos KC, Kersting-Sommerhoff BA, et al: Abnormalities of the pulmonary veins: Evaluation with MR imaging and comparison with cardiac angiography and echocardiography. Radiology 181: 645–649, 1991.
72. Meier D, Meier S, Boseger P: Quantitative flow measurements on phantoms and on blood vessels with MR. Magn Reson Med 8: 25–34, 1988.
73. McNamara MT, Higgins CB: Cardiovascular applications of magnetic resonance imaging. Magn Reson Imaging 2:2167–2186, 1984.
74. Permut LC, Laks H: Surgical management of pulmonary atresia with ventricular septal defect and multiple aortopulmonary collaterals. Adv Card Surg 5:75–95, 1994.
75. Prince M, Yucel E, Kaufman J: Dynamic gadolinium-enhanced three-dimensional abdominal MR arteriography. J Magn Reson Imaging 3:877–881, 1993.
76. Radin R, Kempf RA: Carney complex: Report of three cases. Radiology 196:383–386, 1995.
77. Rebergen SA, Chin JG, Ottenkamp J, et al: Pulmonary regurgitation in the late postoperative follow-up of tetralogy of Fallot: Volumetric quantification by MR velocity mapping. Circulation 88:2257–2266, 1993.
78. Rebergen SA, Niezen RA, Helbing WA, et al: Cine gradient-echo MR imaging and MR velocity mapping in the evaluation of congenital heart disease. Radiographics 16:467–481, 1996.
79. Rebergen SA, Ottenkamp J, Doornbos J, et al: Postoperative pulmonary flow dynamics after Fontan surgery: Assessment with nuclear magnetic resonance velocity mapping. J Am Coll Cardiol 21:123–131, 1993.
80. Rees RSO, Sommerville J, Underwood SR, et al: Magnetic resonance imaging of the pulmonary arteries and their systemic connections in pulmonary atresia: Comparison with angiographic and surgical findings. Br Heart J 58:621–626, 1987.
81. Reeder SB, Atalar E, Faranesh AZ, McVeigh ER: Multiecho segmented k-space imaging: An optimized hybrid sequence for ultrafast cardiac imaging. Magn Reson Med 41:375–385, 1999.
82. Remy-Jardin M, Remy J, Baghaie F, et al: Clinical value of thin collimation in the diagnostic workup of pulmonary embolism. AJR Am J Roentgenol 175:407–411, 2000.
83. Reyen K: Cardiac myxomas. N Engl J Med 333:1610–1617, 1995.
84. Robergen SA, Niezen RA, Helbing WA, et al: Cine gradient echo MR imaging and MR velocity mapping in the evaluation of congenital heart disease. Radiographics 16:467–481, 1996.
85. Rozenman KM, Szeinberg A, Itzchack Y: Spiral CT and 3D image reconstruction of vascular rings and associated tracheobronchial anomalies. J Comput Assist Tomogr 19:564–568, 1995.
86. Rubin GD, Beaulieu CF, Argiro V, et al: Perspective volume rendering of CT and MR images: Applications for endoscopic imaging. Radiology 199:321–330, 1996.
87. Rubin GD, Dake MD, Napel SA, et al: Three-dimensional spiral CT angiography of the abdomen: Initial clinical experience. Radiology 186:147–152, 1993.
88. Rubin GD, Napel S, Leung AN: Volumetric analysis of volumetric data: Achieving a paradigm shift. Radiology 200:312–317, 1996.
89. Sechtem U, Pflugfelder PW, White RD, et al: Cine MRI: Potential for the evaluation of cardiovascular function. Am J Roentgenol 148: 239–246, 1987.
90. Sechtem U, Tscholakoff D, Higgins CB: MRI of the abnormal pericardium. Am J Roentgenol 147:245–252, 1986.
91. Sehgal M, Hirose K, Reed JE, et al: Regional left ventricular wall thickness and systolic function during the first year after index anterior wall myocardial infarction: Serial effects of ventricular remodeling. Int J Cardiol 53:45–64, 1996.
92. Simonetti OP, Finn JP, White RD, et al: "Black blood" T2-weighted inversion-recovery MR imaging of the heart. Radiology 199:49–57, 1996.
93. Sodickson DK, Stuber M, Botnar RM, et al: SMASH real-time cardiac MR imaging at echocardiographic frame rates. Proc Int Soc Magn Reson Med 7:387, 1999.
94. Sondergaard L, Thomsen C, Stahlberg F, et al: Mitral and aortic valvular flow: Quantification with MR phase mapping. J Magn Reson Imaging 2:295–302, 1992.
95. Sondheimer HM, Oliphant M, Schneider B, et al: Computerized axial tomography of the chest for visualization of "absent" pulmonary arteries. Circulation 65:1020–1025, 1982.
96. Sotomora RF, Edwards JE: Anatomic identification of so-called absent pulmonary artery. Circulation 57:624–633, 1978.

97. Stark DD, Higgins CB, Lanzer P, et al: Magnetic resonance imaging of the pericardium: Normal and pathologic findings. Radiology 150: 469–474, 1984.
98. Steffens JC, Bourne MW, Sakuma H, et al: Quantification of collateral blood flow in coarctation of the aorta by velocity-encoded cine magnetic resonance imaging. Circulation 90:937–943, 1994.
99. Strouse PJ, Hernandez RJ, Beckman RH: Assessment of central pulmonary arteries in patients with obstructive lesions of the right ventricle: Comparison of MR imaging and cineangiography. AJR Am J Roentgenol 167:1175–1183, 1996.
100. Taneja K, Sharma S, Kumar K, et al: Comparison of computed tomography and cineangiography in the demonstration of central pulmonary arteries in cyanotic congenital heart disease. Cardiovasc Intervent Radiol 19:97–100, 1996.
101. Tran BQ, Hoffman EA: Role of pleural pressure on left ventricular volume assessed via high speed magnetic resonance imaging. Circulation 96:1–514, 1997.
102. Van Praagh R: The sequential segmental approach to diagnosis in congenital heart disease. Birth Defects 8:4–23, 1972.
103. Van Vaals JJ, Brummer ME, Dixon WT, et al: "Key-hole" method for accelerating imaging of contrast agent uptake. J Magn Reson Imaging 3:671–675, 1993.
104. Vesely TM, Julsrud PR, Brown JJ, et al: MR imaging of partial anomalous pulmonary venous connections. J Comput Assist Tomogr 15:752–756, 1991.
105. Vick GW III, Rockey R, Huhta JC, et al: Nuclear magnetic resonance imaging of the pulmonary arteries, subpulmonic region, and aorticopulmonary shunts: A comparative study with echocardiography and angiography. Am Heart J 119:1103–1110, 1990.
106. Von Schulthess GK, Higashino SM, Higgins SS, et al: Coarctation of the aorta: MR imaging. Radiology 158:469–474, 1986.
107. Weekly clinicopathological exercises: A 33-year-old man with wide complex tachycardia and a left ventricular mass: Case 31-1999. N Engl J Med 341:1217–1224, 1999.
108. Westra SJ, Hill JA, Alejos JC, et al: Three-dimensional helical CT of pulmonary arteries in infants and children with congenital heart disease. AJR Am J Roentgenol 173:109–115, 1999.
109. Westra SJ, Hurteau J, Galindo A, et al: Cardiac electron-beam CT in children undergoing surgical repair for pulmonary atresia. Radiology 213:502–512, 1999.
110. Yamada T, Harada J, Tada S: Complex congenital cardiovascular anomalies evaluated by continuous-rotation computed tomography in children. Pediatr Cardiol 10:65–74, 1989.
111. Yang PC, Kerr AB, Liu AC, et al: New real-time interactive cardiac magnetic resonance imaging system complements echocardiography. J Am Coll Cardiol 32:2049–2056, 1998.
112. Young AA, Axel L, Dougherty L, et al: Validation of tagging with MR imaging to estimate material deformation. Radiology 188: 101–108, 1993.
113. Zeitler E, Kaiser W, Schuierer G, et al: Magnetic resonance imaging of aneurysms and thrombi. Cardiovasc Intervent Radiol 8:321–328, 1986.

53 Chest

Lane F. Donnelly

There are many similarities and differences in the use of cross-sectional imaging methods—computed tomography (CT) and magnetic resonance imaging (MRI)—for imaging the chest of a child compared with that of an adult. In many clinical scenarios, such as the evaluation of pulmonary metastatic disease (one of the more common indications for CT scanning of the chest), there are more similarities than differences. This chapter focuses on the clinical issues for which there are significant differences in the uses of cross-sectional imaging of the chest in children and in adults and serves as a complement to other chapters covering issues concerning CT and MRI of the chest in adults.

The chapter discusses the lung, mediastinum, and chest wall. Concerning CT and MRI, CT has a more dominant role in the imaging of most diseases of the pediatric chest and is emphasized here. Several of the areas in which MRI is used with more frequency, such as cardiac imaging and evaluation of vascular rings, are covered in Chapter 52 and are not repeated. For areas in which MRI is advantageous, compared with CT, the emphasis is on MRI. In addition, adaptation of techniques and protocols for CT and MRI in pediatric imaging is discussed in Chapter 52 and is not repeated here.

Special Considerations in the Pediatric Lung

There are several scenarios in which either the disease processes that are present or the use of CT in the evaluation of these diseases differs in children. These scenarios include (1) the use of CT in the evaluation of pediatric lung masses, (2) suppurative complications of pneumonia, (3) the immunocompromised child with potential pneumonia, (4) pulmonary trauma, and (5) cystic fibrosis.

Focal Pediatric Lung Masses or Lesions

Issues pertaining to the evaluation of metastatic lung lesions are similar in children and in adults. In contrast to the situation with adults, in whom a large percentage of lung masses represent bronchogenic carcinoma, primary lung neoplasms, such as pulmonary blastoma, are exceedingly rare in children. More commonly, focal lung masses in children are related to congenital lung lesions, including such entities as congenital cystic adenomatoid malformation (CCAM), sequestration, bronchogenic cyst, and congenital lobar emphysema. Such masses can present during childhood or, less commonly, adulthood; most often, these lesions present during early childhood.

When a suspected congenital lung lesion is encountered on radiographs of the chest, CT scans are usually obtained to further characterize the lesion and to define its extent. These lesions may present as respiratory distress in the newborn or as recurrent pneumonia. Some are identified in utero with sonography.

When encountered in the neonatal period, the differential for a focal lung lesion can be separated on the basis of whether the lesion appears lucent or solid on the chest radiograph.[9] Most likely considerations for a lucent chest lesion in a newborn include congenital lobar emphysema, CCAM, persistent pulmonary interstitial emphysema, and congenital diaphragmatic hernia. CT may be helpful in differentiating these lesions by demonstrating whether the abnormal lucency is related to air in distended alveoli or the interstitium or within abnormal cystic structures[9] (Figs. 53–1 to 53–4). Lesions that typically appear solid and nonlucent during the neonatal period include sequestration and bronchogenic cysts.

Congenital Cystic Adenomatoid Malformation

CCAM is a congenital adenomatoid proliferation that replaces normal alveoli. The majority involve only one lobe, and unlike congenital lobar emphysema, there is no lobar predilection. CCAMs are divided into three types on the basis of how large the cysts appear on imaging or at pathology[26, 35]:

Type 1 lesions (50%) have one or more large (2- to 10-cm) cysts (see Fig. 53–1).

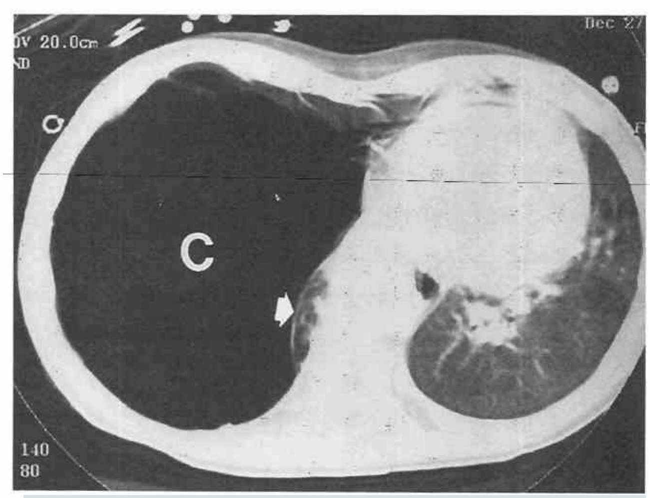

Figure 53–1. Type 1 congenital cystic adenomatoid malformation in a 16-month-old boy. CT scan shows large air-filled cyst (C) occupying most the right hemithorax. The right lower lobe is compressed *(arrow)*, and there is leftward mediastinal shift.

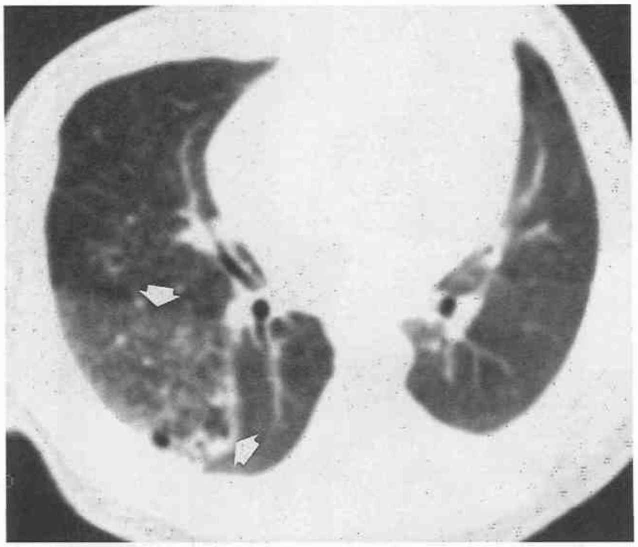

Figure 53–2. Type 2 congenital cystic adenomatoid malformation in a 2-day-old boy. CT scan shows abnormal density and lucency within the right lower lobe *(arrows)*. The diameters of the small air-filled cystic structures within the mass are smaller than the spaces between normal interstitial markings, differentiating this congenital cystic adenomatoid malformation from congenital lobar emphysema.

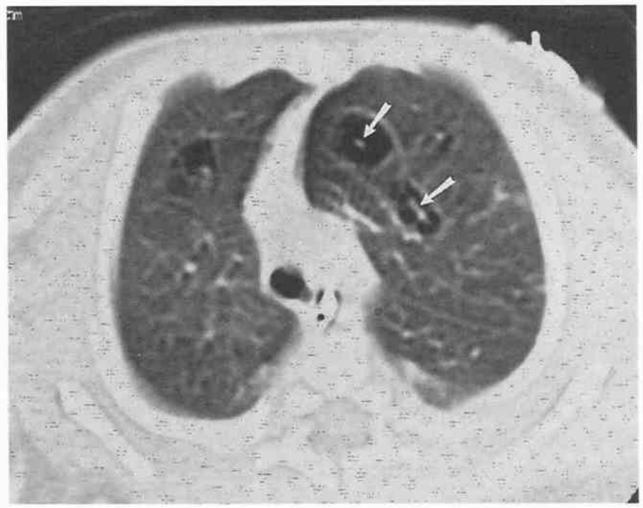

Figure 53–4. Persistent pulmonary interstitial emphysema in a 9-day-old girl. CT scan shows areas of lucency with central nodular and linear opacities (interstitial vascular structures) *(arrows)*, documenting that the abnormal gas collection is within the interstitial space. (From Donnelly LF, Frush DP: Localized lucent chest lesions in neonates: Causes and differentiation. AJR Am J Roentgenol 172:1651, 1999.)

Type 2 lesions (40%) have numerous small cysts of uniform size (see Fig. 53–2).

Type 3 lesions (10%) appear solid on gross inspection and imaging but have microscopic cysts.

The classification system has no clinical relevance except that it is a reminder that CCAMs can have multiple imaging appearances.

The imaging appearance reflects the type. CCAMs communicate with the bronchial tree at birth and therefore fill with air within the first hours to days of life[9, 26, 35] (see Figs. 53–1 and 53–2). On radiography and CT, a completely cystic mass, mixed cystic and solid mass, or solid mass is seen, depending on the number and size of cysts and on whether those cysts contain air or fluid.[9, 26, 35] The management of symptomatic CCAMs consists of surgical resection. The management of asymptomatic CCAMs is somewhat controversial, but most advocate elective resection because these lesions are at an increased risk of infection and, although rare, rhabdomyosarcoma can develop.

An increasingly encountered scenario is a prenatally diagnosed lung mass that becomes less prominent on serial prenatal ultrasounds and demonstrates only subtle findings or is not detected on a chest radiograph obtained soon after birth.[42] Almost all such lesions are type 2 CCAMs and demonstrate abnormalities on CT even when chest radiographic findings are normal.[42]

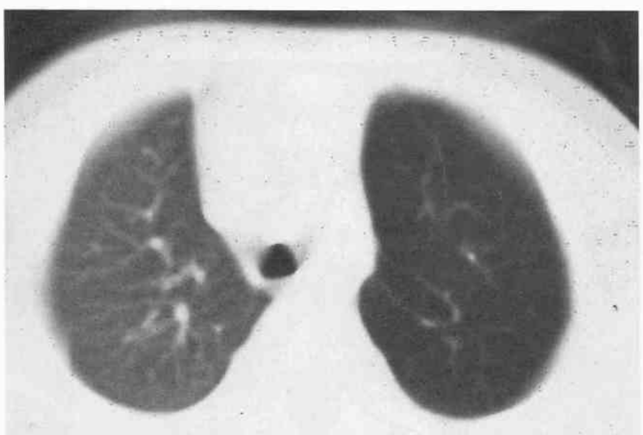

Figure 53–3. Congenital lobar emphysema in a 23-month-old girl. CT scan shows asymmetrical low attenuation within the left upper lobe. The pulmonary vessels are attenuated compared with those on the right, and the spaces between the vessels are greater on the left than those on the right.

Congenital Lobar Emphysema

Congenital lobar emphysema is related to overexpansion of the alveoli. The cause is debated. There can be associated anomalies, usually cardiac, but this occurs in the minority of patients. There is a lobar predilection, with the most common site being the left upper lobe (43%), followed by the right middle lobe (32%) and right lower lobe (20%).[38]

On chest radiography, a hyperlucent, hyperexpanded lobe is seen. On initial radiographs, the lesion may appear of soft tissue density related to retained fetal lung fluid. This density resolves and is replaced by progressive hyperlucency.[9]

On CT, air is in the alveoli, and the interstitial septa and bronchovascular bundles are thus at the periphery (not the center) of the lucency. The air spaces are larger than the adjacent normal lung, and pulmonary vessels appear attenuated[9, 38] (see Fig. 53–3). The treatment is lobectomy.

Persistent Pulmonary Interstitial Emphysema

Most commonly, pulmonary interstitial emphysema is a transient phenomenon related to air leak in premature neonates as a result of barotrauma. Its significance lies in that it is a warning sign of another potential air-block complication, such as pneumothorax or pneumomediastinum. Occasionally, pulmonary interstitial emphysema can persist and develop into an expansive, multicystic mass.[9, 24] The air cysts can become sufficiently large to cause mediastinal shift and compromise pulmonary function.

The primary therapy for persistent pulmonary interstitial emphysema is nonsurgical, including selective intubation of the opposite lung or decubitus positioning. Therefore, differentiation from other air-filled cystic masses that are treated surgically, such as CCAMs, is important. On CT scans, the air cysts are in the interstitial space, with the bronchovascular bundles positioned within the center of the air cysts.[9, 24] They appear as linear or nodular densities in the center of the cysts[9, 24] (see Fig. 53–4).

Sequestration

Pulmonary sequestration refers to a congenital area of abnormal pulmonary tissue that does not have a normal connection to the bronchial tree. The characteristic feature of sequestration is the demonstration of anomalous arterial supply to the abnormal lung via a systemic artery that arises from the aorta. All modalities that can demonstrate this abnormal systemic arterial supply, including MRI, helical CT, sonography, and arteriography, have been advocated in making the diagnosis of sequestration. Helical CT is the imaging modality of choice because it both visualizes the systemic arterial supply when a sequestration is present and further characterizes the lung abnormality if a sequestration is not present.[22]

On CT scans, the sequestration appears as soft tissue attenuation with the affected lung. The systemic arterial feeder is identified as an enhancing vessel that arises from the descending aorta and extends to the sequestration[22] (Fig. 53–5). The systemic arterial arteries can vary in size, from several millimeters in diameter to very large arterial structures. Because sequestrations do not communicate with the bronchial tree unless they become infected, in the neonatal period sequestrations appear as a radiopaque mass.[9] After infection has occurred, air may be introduced and sequestrations may appear as multiloculated cystic masses.[22] The most common location is within the left lower lobe.

Much debate has focused on differentiation of *intralobar* and *extralobar* sequestrations. Extralobar sequestrations are characterized by a separate pleural covering; intralobar sequestrations, which are more common, are not. Extralobar sequestrations are associated with other abnormalities in 65% of cases; intralobar sequestrations are not. Differences in venous drainage patterns have been emphasized, but they vary with both types. The differentiation between intralobar and extralobar sequestration cannot be made at imaging and does not affect surgical management.[22] Visualization of the supplying systemic artery is the characteristic finding and the documentation that the surgeons are looking for before surgical removal of the lesion.

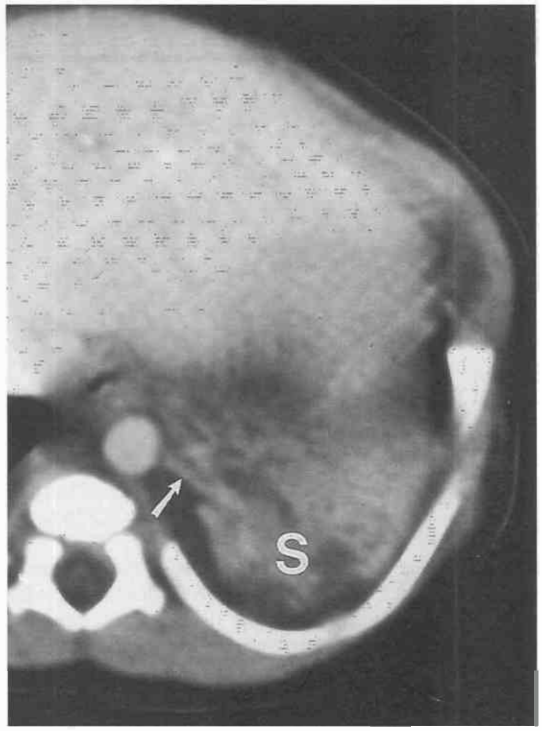

Figure 53–5. Sequestration in a 1-day-old boy. CT scan shows abnormal opacity (S) within the left lower lobe. An enhancing systemic artery *(arrow)* is seen arising from the aorta and leading into the lung opacity.

Bronchogenic Cysts

Bronchogenic cysts occur secondary to abnormal budding of the tracheobronchial tree during development and occur in the lung parenchyma and mediastinum with equal frequency.[23] Like sequestrations, they do not contain air until they become infected and thus may appear as well-defined soft tissue attenuation or cystic air-fluid–containing masses.[23] They can be quite large. They appear as well-defined cystic structures on images (Fig. 53–6). When they

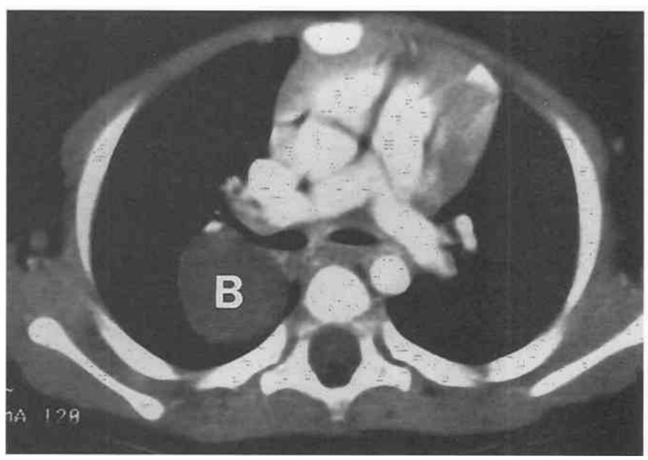

Figure 53–6. Bronchogenic cyst in a 10-month-old boy. CT scan shows well-defined, nonenhancing mass (B) within the right parahilar region.

occur within the lung, the most common location for a bronchogenic cyst is central within the perihilar areas.

Imaging of Suppurative Complications of Pneumonia

Respiratory tract infection is the most common cause of illness in children and continues to be a significant cause of complications and death.[4] Because of its frequency, an understanding of the appropriate roles of imaging in these children is important.

The roles of imaging in the evaluation of immunocompetent children with community-acquired pneumonia are multiple: (1) confirmation or exclusion of pneumonia, (2) characterization and prediction of the infectious agent, (3) exclusion of other causes of the symptoms, (4) evaluation when there is failure to resolve, and (5) evaluation of related complications.[6] Radiography of the chest remains the primary imaging modality in most of these scenarios, and CT plays a secondary role in most of these respects.

Concerning the confirmation or exclusion of pneumonia, CT usually plays no role in making the diagnosis of pneumonia and, consequently, in treatment determination and patient disposition. This is accomplished with radiography of the chest.[6] Also, characterization of a lower respiratory tract infection as probably viral or bacterial pneumonia is accomplished through a combination of clinical examination and radiography of the chest.[6] CT plays no role.

CT sometimes has a role in the child who has pneumonia that is recurrent or fails to resolve. Unlike the case with adults, in whom postobstructive pneumonia secondary to bronchogenic carcinoma is a concern, follow-up radiography to ensure resolution of radiographic findings is not routinely necessary in an otherwise healthy child who has had pneumonia. Causes of failure of suspected pneumonia to resolve include infected developmental lesions (as discussed previously), bronchial obstruction, gastroesophageal reflux and aspiration, and underlying systemic disorders.

Complications

The evaluation of complications related to community-acquired pneumonia can be divided into two clinical scenarios: (1) primary evaluation of parapneumonic effusions and (2) evaluation of the child who has persistent or progressive symptoms despite medical or surgical therapy.

Primary Evaluation of Parapneumonic Effusions

Parapneumonic effusions occur commonly in patients with bacterial pneumonia. There are differences in opinion between many pediatric surgeons and pediatric pulmonologists regarding the timing and aggressiveness of the management of parapneumonic effusions. Many investigators advocate the use of antibiotics, drainage tube placement, and thrombolytic therapy.[6] Other investigators advocate early intervention with thoracoscopy and débridement.[6] The indications for imaging these effusions reflect the patterns of management at specific institutions. Traditionally, the aggressiveness of therapy has been based on categorization of parapneumonic effusions as *empyema* or *transudative effusion* on the basis of aspiration and analysis of pleural fluid.[27] Multiple attempts have been made to use imaging criteria to differentiate empyema from transudative effusion so that every child with a parapneumonic effusion does not have to undergo diagnostic thoracentesis.

In the past, CT was advocated in the differentiation between empyema and transudative parapneumonic effusion.[31, 39] CT findings of enhancement and thickening of the parietal and visceral pleura, thickening of the extrapleural subcostal tissues, and increased attenuation of the extrapleural subcostal fat were described as highly accurate in differentiating empyema from transudate[31, 39] and should be used to influence therapeutic decisions in the management of parapneumonic effusions. Later studies, however, have shown these findings to be inaccurate in determining which parapneumonic effusions meet the laboratory criteria for empyema in children and that the presence or absence of such CT findings should not influence therapeutic decisions concerning the management of parapneumonic effusions.[14]

A study[34] advocated the use of sonography to aid in making therapeutic decisions regarding parapneumonic effusions. In this study, parapneumonic effusions were categorized as low grade (anechoic fluid without internal heterogeneous echogenic structures) or high grade (fibrinopurulent organization demonstrated by the presence of fronds, septations, or loculations). In children with high-grade effusions, length of hospitalization was reduced by nearly 50% when surgical intervention was performed.[34] Length of hospitalization in children with low-grade effusions was not affected by surgical intervention.[34] Therefore, sonography may play a more useful role than CT in the early evaluation of parapneumonic effusions.

Evaluation of Persistent or Progressive Symptoms

When children exhibit persistent or progressive symptoms (e.g., fever, respiratory distress, sepsis) despite appropriate medical management of pneumonia, there often is an underlying suppurative complication.[13] Potential suppurative complications include parapneumonic effusions such as empyema, other inadequately drained effusions, and malpositioned chest tubes. Parenchymal complications (e.g., cavitary necrosis, lung abscess) and purulent pericarditis are also possibilities.[6, 13]

Although chest radiography is the primary imaging modality for detecting such complications, a significant percentage of these complications are not demonstrated on radiography.[6, 13] Contrast-enhanced CT is useful in detecting clinically significant suppurative complications.[6, 12, 13, 15] CT can help to differentiate whether the persistent illness is pleural or related to lung parenchyma, directing therapy in the appropriate direction.[13] The intravenous administration of contrast medium is vital in maximizing the detection and characterization of both lung parenchymal and pleural complications.[12, 13, 15] This is one of the few indications for the use of intravenous contrast medium when chest CT is performed primarily to image lung disease.

Lung Parenchymal Complications

On contrast-enhanced CT, noncompromised lung parenchyma consolidated with pneumonia enhances diffusely.[15] This enhancement is not surprising, given the degree of

inflammation associated with pneumonia. Large areas of decreased or absent enhancement are indicative of underlying parenchymal ischemia or impending infarction.[15] In one study,[15] the presence of decreased enhancement was associated with a significantly increased rate of admission to the intensive care unit, increased length of hospitalization, and increased incidence of the development of cavitary necrosis. Therefore, the detection of the presence of decreased lung enhancement in this setting yields important prognostic information.

Suppurative lung parenchymal complications represent a spectrum of abnormalities, including cavitary necrosis, lung abscess, pneumatocele, bronchopleural fistula, and pulmonary gangrene.[15] The name given to the suppurative process depends on several factors, including the severity and distribution of the process, the condition of the adjacent lung parenchyma, and the temporal relationship with disease resolution.[15, 32]

Lung abscess represents a dominant focus of suppuration surrounded by a well-formed fibrous wall.[15, 32] On contrast-enhanced CT scans, lung abscesses appear as fluid-filled or air-filled cavities with definable, enhancing walls.[15, 32] Typically, there is no evidence of necrosis in the surrounding lung. *Pneumatocele* is a term given to thin-walled cysts seen on imaging and may represent a later or less severe stage of resolving or healing necrosis[6] (Fig. 53–7). On CT scans, a thin-walled cyst containing air with or without fluid is identified. The wall does not enhance. The surrounding lung may be opacified but does not demonstrate findings of necrosis. Bronchopleural fistulas are identified on CT when a direct communication is visualized between the air spaces of the lung and the pleural space.[6, 13]

Cavitary necrosis represents a dominant area of necrosis of a consolidated lobe associated with a varying number of thin-walled cysts.[12, 15] The mechanism of necrosis complicating pneumonia is related to thrombotic occlusion of alveolar capillaries associated with adjacent inflammation, resulting in ischemia and eventually necrosis of the lung

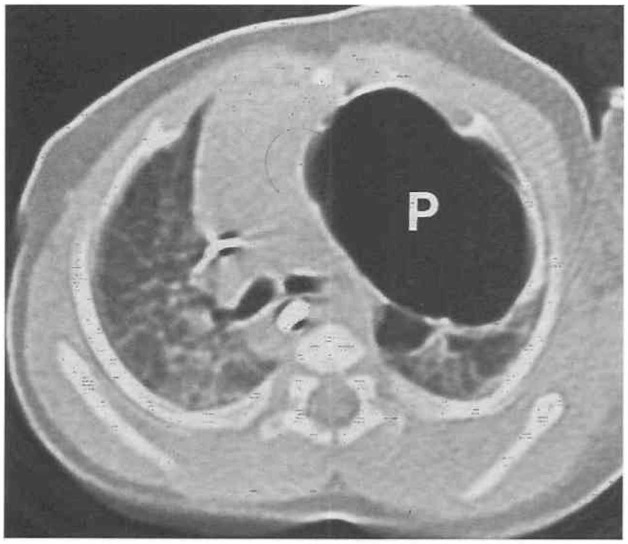

Figure 53–7. Pneumatocele in a 3-month-old boy. CT scan shows large air-filled cavity (P) with thin walls in the left upper lobe. The surrounding lung parenchyma demonstrates no evidence of necrosis.

parenchyma. The characteristic CT findings of cavitary necrosis include loss of normal lung architecture, decreased parenchymal enhancement, loss of the lung-pleural margin, and multiple thin-walled cavities that contain air or fluid and lack an enhancing border[12, 15] (Fig. 53–8).

Historically, cavitary necrosis has been described as uncommon and usually associated with staphylococcal pneumonias. However, cavitary necrosis is most commonly encountered in children with *Streptococcus pneumoniae* infection.[6, 12, 15] Only 41% of cases of cavitary necrosis identified on CT are seen on chest radiography.[12] Most children with cavitary necrosis are severely ill.[12, 15] However, unlike in adults, in whom the mortality rate for cavitary necrosis is high and early surgical removal of the affected lung has been advocated,[12, 15] the long-term outcome of children with cavitary necrosis is favorable with medical management alone[12] (see Fig. 53–8). Amazingly, in children with cavitary necrosis, follow-up radiographs obtained later than 40 days after the acute illness are most often normal, lacking any evidence of chronic scarring, persistent cavity formation, or other sequelae.[12]

Pleural Complications

The cause of persistent sepsis in a child who is being treated for pneumonia may also be related to a pleural complication. This is most often the unrecognized cause of sepsis, when previous intervention has been performed to treat a parapneumonic effusion. CT yields helpful information regarding the management of parapneumonic effusions, such as depicting a loculated pleural collection not in communication with a indwelling chest tube, poor chest tube placement, or failure of lung reexpansion.[13] All of these findings suggest a need for a change in drainage strategy.

Finally, on chest radiography, it often is difficult to determine how much of an opacity is due to pleural effusion and how much is due to consolidated lung when each is present. Accurate determination by CT of the amount of pleural fluid also affects therapeutic decisions regarding drainage.[13]

CT Evaluation of Immunocompromised Children with Suspected Pneumonia

Children can be immunocompromised for a variety of reasons, including cancer therapy, bone marrow transplantation, solid organ transplantation, primary immunodeficiency, and acquired immune deficiency syndrome (AIDS). They represent a population who continue to increase in number. At most tertiary children's medical centers, the number of CT examinations of the chest performed in immunocompromised children far outnumber those performed in immunocompetent children.

Acute pulmonary processes are a common cause of complications and death in immunocompromised children.[5, 41, 43] Because of the fragile condition of these patients, prompt diagnosis and treatment of pulmonary infections are imperative. When a pulmonary process is suspected on the basis of imaging, invasive diagnostic procedures such as bronchoscopy are performed or new therapies are empirically started.

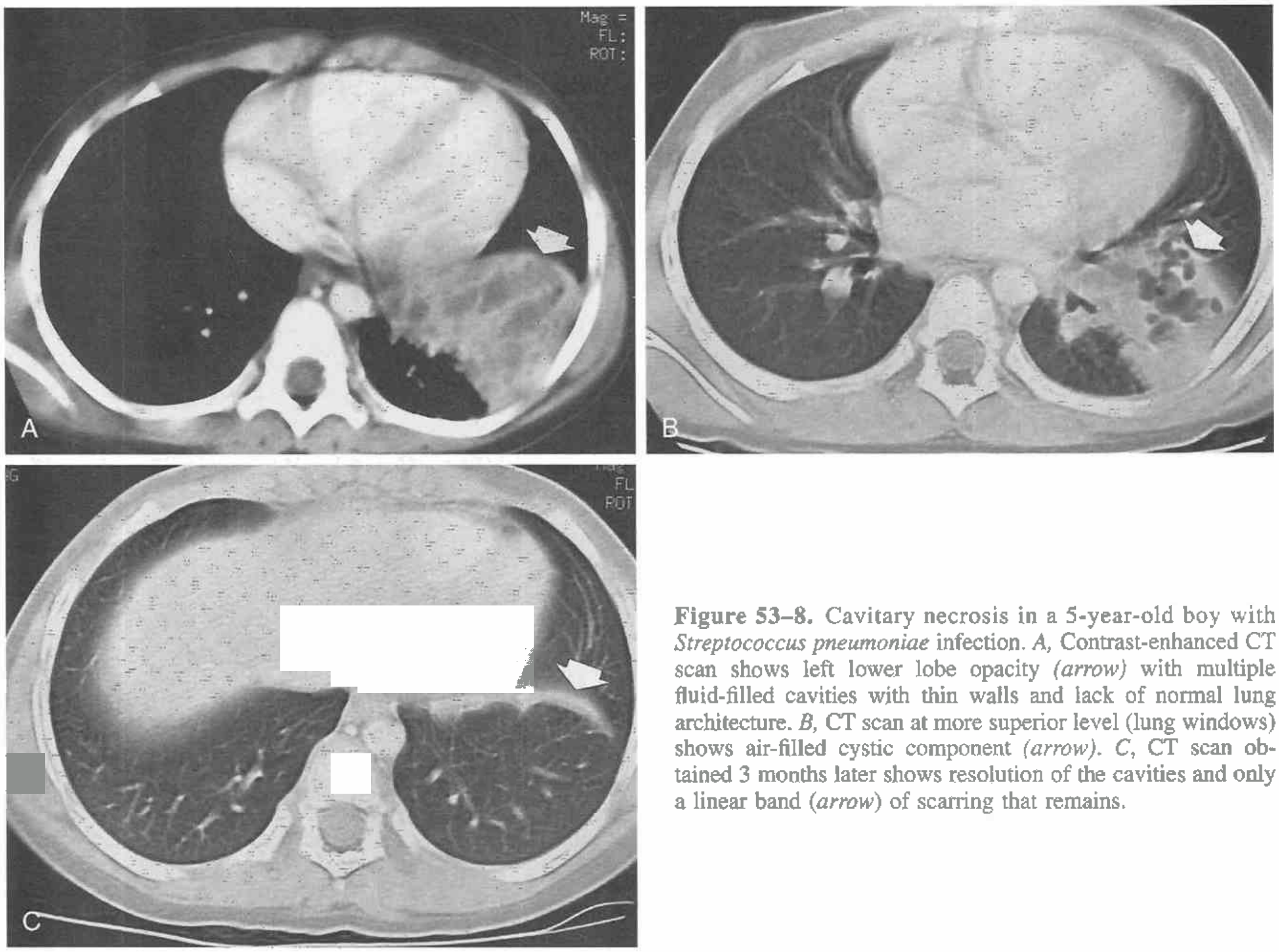

Figure 53–8. Cavitary necrosis in a 5-year-old boy with *Streptococcus pneumoniae* infection. *A,* Contrast-enhanced CT scan shows left lower lobe opacity *(arrow)* with multiple fluid-filled cavities with thin walls and lack of normal lung architecture. *B,* CT scan at more superior level (lung windows) shows air-filled cystic component *(arrow)*. *C,* CT scan obtained 3 months later shows resolution of the cavities and only a linear band *(arrow)* of scarring that remains.

Regarding confirmation or exclusion of pneumonia, as in immunocompetent patients, chest radiography is the primary imaging modality. However, because of the poor condition of many of these patients and the risk associated with exposure to multiple persons, radiographic evaluation of these patients is often performed with portable equipment. Often these patients are not able to take deep breaths, rendering low lung volume radiographic examinations. The negative predictive value of such radiographs is low compared with frontal and lateral radiographs obtained at full inspiration.

Because of these factors, CT plays a greater role in detecting and excluding pulmonary infection. The detection of pulmonary abnormalities with CT is excellent.[41] CT localizes high-yield areas for diagnostic procedures such as bronchoscopy and needle aspiration.

In immunocompetent children, the primary characterization of pulmonary infections is determining whether the infectious agent is bacterial or viral. In immunocompromised hosts, the issue is more complex. The array of agents that can cause aggressive infections is great and includes fungal infections such as *Aspergillus* and *Candida*, viral infections such as cytomegalovirus infection, and *Pneumocystis carinii*.[5, 41, 43]

In addition, a variety of noninfectious pulmonary processes can present with acute or subacute clinical findings that mimic pulmonary infection,[5] including alveolar hemorrhage, pulmonary edema, drug reaction, idiopathic pneumonia, lymphoid interstitial pneumonitis, bronchiolitis obliterans, bronchiolitis obliterans with organizing pneumonia, and chronic graft-versus-host disease.[5, 41, 43] The CT findings of many of these entities are nonspecific, with overlap of the findings seen between different causes. However, the combination of certain CT findings, in conjunction with clinical findings, can be very suggestive of a specific diagnosis.

The exclusion of fungal infection is often the clinical indication for CT in these patients. The hallmark CT finding that is associated with possible fungal infection is the presence of nodules.[3, 5, 30, 41, 43] These nodules are often clustered and can demonstrate any of the following associated findings: poorly defined margins, cavitation, or a surrounding halo of ground-glass opacity[3, 5, 30, 41, 43] (Fig. 53–9). Pathologically, the central nodular density on CT represents the actual fungal infection, and the surrounding halo represents hemorrhagic infarction caused by thrombosis secondary to vascular invasion by the fungus.[30] These findings are, however, nonspecific and can be seen with nonfungal infections such as cytomegalovirus infection.[3, 5, 30, 41, 43]

CT Evaluation of Pulmonary Trauma

Trauma is the leading cause of death in children older than 1 year,[5] with chest injury responsible for 25% of

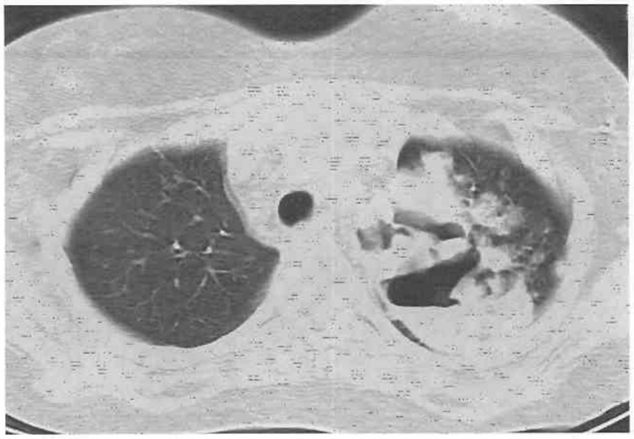

Figure 53–9. Fungal pneumonia in a 17-year-old liver and kidney transplant recipient. CT scan shows large cavitary process containing an air-fluid level in the left upper lobe. Multiple clustered nodules are adjacent to the cavity.

pediatric trauma deaths.[37] There are a number of causes of lung consolidation in children who have undergone traumatic injury, including contusion, laceration, aspiration, atelectasis, and preexisting lung opacification as occurs from pneumonia.[16, 28, 37]

The primary imaging modality in the evaluation of chest trauma is radiography. CT is uncommonly performed for the primary purpose of evaluating pulmonary trauma. However, when CT is being performed to evaluate traumatic injury to either the abdominal contents or the mediastinum, it is important to evaluate for lung contusion or other trauma-related lung opacity.

Lung contusion is defined as hemorrhage and edema formation in the alveoli and interstitium secondary to blunt chest trauma, without accompanying parenchymal laceration.[16, 28, 37] The presence of lung contusion has been reported to be associated with an adverse effect on patient outcome.[37] In one study,[37] the mortality rate was 1.3% for pediatric trauma victims without lung contusions and 10.8% for those with contusions. Accurate identification of lung contusion and differentiation from other causes of lung opacification is helpful in planning the management of pediatric trauma patients.

On CT, lung contusions are characteristically nonsegmental in distribution and do not follow segmental or lobar anatomic boundaries[16, 37] (Fig. 53–10). Contusions are usually located posteriorly (85%), have a crescentic (50%) or an amorphous (45%) shape, and are of mixed confluent and nodular quality (70%).[16] The lung contusions of children may also demonstrate a 1- to 2-mm region of uniformly nonopacified subpleural lung that separates the area of lung consolidation from the adjacent chest wall[16] (see Fig. 53–10). This finding is referred to as *subpleural sparing*; it is seen with many lung contusions and is not seen with other causes of airspace opacification and therefore is helpful in identifying contusions.[16] The larger the lung contusion, the less likely subpleural sparing is to be present.[16]

Pulmonary laceration differs from pulmonary contusion; with a laceration, there is a frank tear within the lung parenchyma. The characteristic CT finding of pulmonary

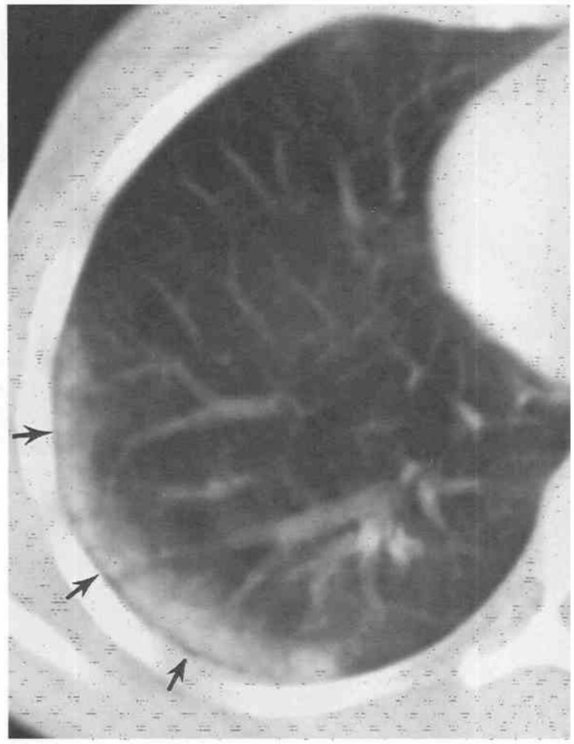

Figure 53–10. Pulmonary contusion in a 12-year-old girl after a motor vehicle accident. CT scan shows characteristic findings of contusion, including posterior location, cresentic shape, nonsegmental distribution, and subpleural sparing *(arrows).*

laceration is the presence of an air-filled or a fluid-filled cavity[28, 37] (Fig. 53–11). CT findings of atelectasis include a triangular shape, segmental distribution, and obvious signs of volume loss.[16, 37]

Cystic Fibrosis

Image scoring systems have been used clinically and as a research tool to objectively evaluate the progression of

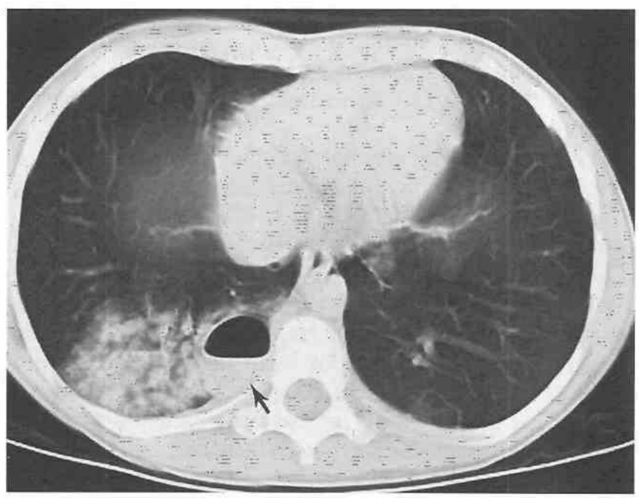

Figure 53–11. Pulmonary laceration in a 10-year-old girl who fell out of a tree. CT scan shows consolidation within the posterior right lower lobe with an associated parenchymal cavity *(arrow)* containing an air-fluid level.

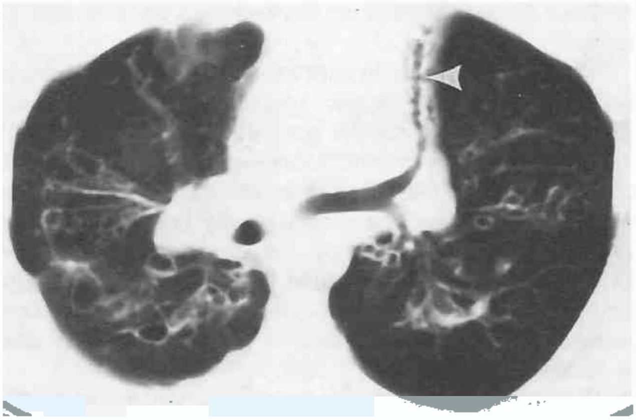

Figure 53–12. High-resolution CT scan of patient with cystic fibrosis shows multiple sites of bronchiectasis and bronchial wall thickening. There is volume loss within the left upper lobe, demonstrated by medial displacement of the upper lobe bronchus (*arrowhead*).

lung disease in patients with cystic fibrosis.[1, 2, 11, 33] The goal is to facilitate objective evaluation of existing and newly developed therapeutic regimens, such as gene therapy and mucolytic agents.[1, 2, 11, 33]

Options in the pulmonary evaluation of patients with cystic fibrosis include chest radiography and high-resolution CT (HRCT).[1, 2, 11, 33] HRCT and chest radiography are used to evaluate morphologic changes of cystic fibrosis to determine the severity of disease. Multiple studies have suggested that HRCT is superior to chest radiography in the evaluation of lung disease, such as bronchiectasis, peribronchial thickening, mucus plugging, and emphysema, in patients with cystic fibrosis[1, 2, 11, 33] (Fig. 53–12). Other uses of CT in the evaluation of the patient with cystic fibrosis include evaluation for pulmonary abscess in patients not responding appropriately to antibiotic therapy and evaluation before lung transplantation.

There has been concern that the morphologic changes seen on HRCT and chest radiography may not reflect early functional pulmonary disease.[11, 17] Functional imaging may offer a more sensitive way to detect early changes of cystic fibrosis in patients with minimal disease.[11, 17] Some authors have advocated the use of hyperpolarized helium 3–enhanced MRI in the evaluation of both functional ventilation and morphologic information[17] (Fig. 53–13). However, results are preliminary.

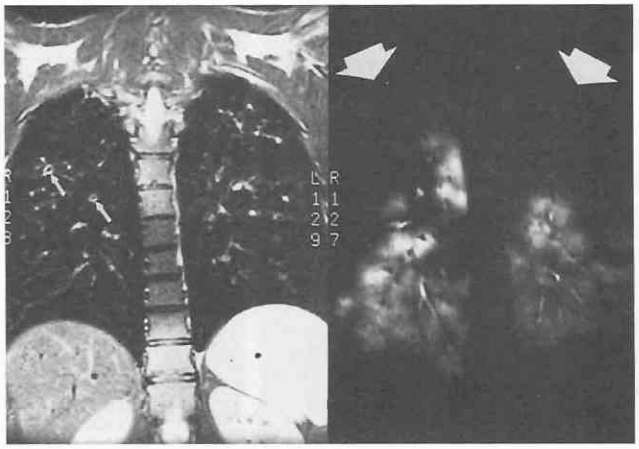

Figure 53–13. Hyperpolarized helium 3–enhanced MR image of the lungs in a patient with cystic fibrosis. *Left*, A fast spin-echo (TR, 2857; TE, 80) coronal image through the posterior lung shows minimal peribronchial thickening demonstrated as linear high-signal areas (*small arrows*). No other morphologic changes of cystic fibrosis are present. *Right*, MR image obtained after the patient was ventilated with a single breath of hyperpolarized helium 3 demonstrates the absence of ventilation throughout the majority of the upper lobes (*arrows*). High-signal areas represent ventilated lung. The high signal intensity on the left should be distributed throughout the lung.

Special Considerations in the Pediatric Mediastinum

Mediastinal Masses

The mediastinum is the most common location of primary thoracic masses in children. In addition, most mediastinal masses occur in children, not adults. As in adults, characterization of the location of the mass as anterior, middle, or posterior can focus the differential diagnosis of mediastinal masses (see Chapter 29).

By far, the mostly commonly encountered imaging issues in the anterior mediastinum are the normal thymus, which should not be mistaken for a mass, and lymphoma.[29] There are a large number of other potential but much less common causes of anterior mediastinal masses in children, including teratoma (and other germ cell tumors), thymoma, and multilocular thymic cysts seen in association with AIDS.[29]

Middle mediastinal masses are less common than anterior or posterior mediastinal masses and are usually related to either lymphadenopathy or duplication cysts.[29]

Lymphadenopathy can be inflammatory, most often secondary to granulomatous diseases such as tuberculosis or fungal infection, or neoplastic, secondary to metastatic disease or lymphoma.

Duplication cysts can be bronchogenic, enteric, or neurenteric. These appear as well-defined masses that are cystic on cross-sectional imaging.

Neurenteric cysts, by definition, have associated vertebral anomalies.

Pathologic processes related to the esophagus can also cause middle mediastinal abnormalities. Foreign bodies can erode from the esophagus on a chronic basis and cause a middle mediastinal mass. A dilated esophagus caused by achalasia or a hiatal hernia may also appear as a middle mediastinal mass on chest radiographs.

There are a number of causes of posterior mediastinal masses in children, including neural crest tumors, neurofibromas, lateral meningocele, diskitis, hematoma, and extramedullary hematopoiesis.[29] However, similar to how anterior mediastinal masses in older children are considered to be lymphoma, the working diagnosis for posterior mediastinal masses in young children is neuroblastoma until proven otherwise.

Two issues specific to the mediastinum of children re-

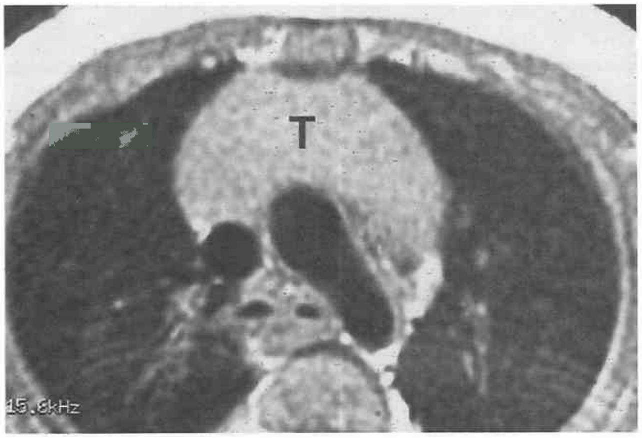

Figure 53–14. Normal thymus in a 6-month-old girl. Axial, T1-weighted MR image shows thymus (T) to be homogeneous in signal and to have convex margins.

quire further discussion: the normal thymus and neuroblastoma.

Normal Thymus

One of the most common areas of confusion in the imaging of children is related to differentiation of the normal thymus from pathologic processes. This confusion led to "thymic radiation" therapy in the first half of the 1990s and continues to cause diagnostic problems for those who infrequently image children.[25] The thymus has a variable appearance in both size and shape in children. In children younger than age 5 years, and particularly in infants, the thymus can appear very large. The thymus also has a variable configuration. Between 5 and 10 years of age, the thymus becomes less prominent radiographically, related to the decreased growth of the thymus in relationship to the growth of the remainder of the body. During the second decade of life, the thymus should not be visualized as a discrete anterior mediastinal mass on chest radiography.[21]

Abnormality of the thymus (or anterior mediastinum) is suspected when the thymic silhouette has an abnormal shape or abnormal size for patient age. Displacement of the airway or other structures suggests an abnormality. On CT or MRI, the normal thymus should appear homogeneous in attenuation or signal, typically is quadrilateral in shape, and may have slightly convex margins[21] (Fig. 53–14). Heterogeneity, calcification, and displacement of the airway or vascular structures indicate an abnormality. True pathologic masses of the thymus are actually quite rare in children.

Thymic rebound is another source of confusion concerning normal thymic tissue. After a patient has ceased receiving chemotherapy for a malignancy, it is normal for the thymus to "grow back" on serial CT examinations. This interval increase in soft tissue attenuation in the anterior mediastinum (Fig. 53–15) should not be considered abnormal when encountered on cross-sectional imaging.

Neuroblastoma

Neurogenic tumors (neuroblastoma, ganglioneuroblastoma, ganglioneuroma) are the most common mediastinal masses of childhood. Approximately 15% of neuroblastomas occur in the posterior mediastinum, most before 2 years of age.[36]

Most neuroblastomas are visible on frontal radiographs of the chest as a posterior opacity. Erosion or destruction of the adjacent ribs is common. Calcifications are reported to be visible on chest radiography up to 25% of the time, although in my experience they have occurred less often.[36] Cross-sectional imaging with CT or MRI confirms the presence of the tumor and evaluates the extent of disease, particularly whether there is intraspinal extension.[36] Thoracic neuroblastomas carry a better prognosis compared with abdominal neuroblastomas (Fig. 53–16).

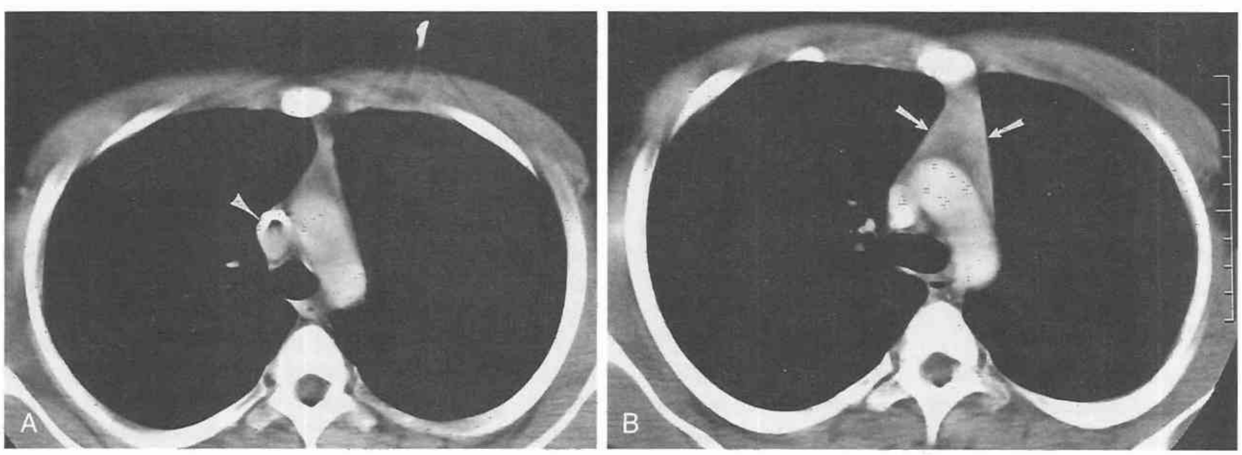

Figure 53–15. Thymic rebound in a 12-year-old boy treated with chemotherapy. *A*, CT scan at level of aortic arch obtained while the patient was on chemotherapy demonstrates a lack of soft tissue in the prevascular space. The central line is in place *(arrowhead)*. *B*, CT scan at the same level obtained 3 months later, when the patient is no longer receiving chemotherapy, demonstrates an interval increase in the soft tissue *(arrows)* in the prevascular space. The rebounded thymus has a triangular configuration, and the central line is no longer present.

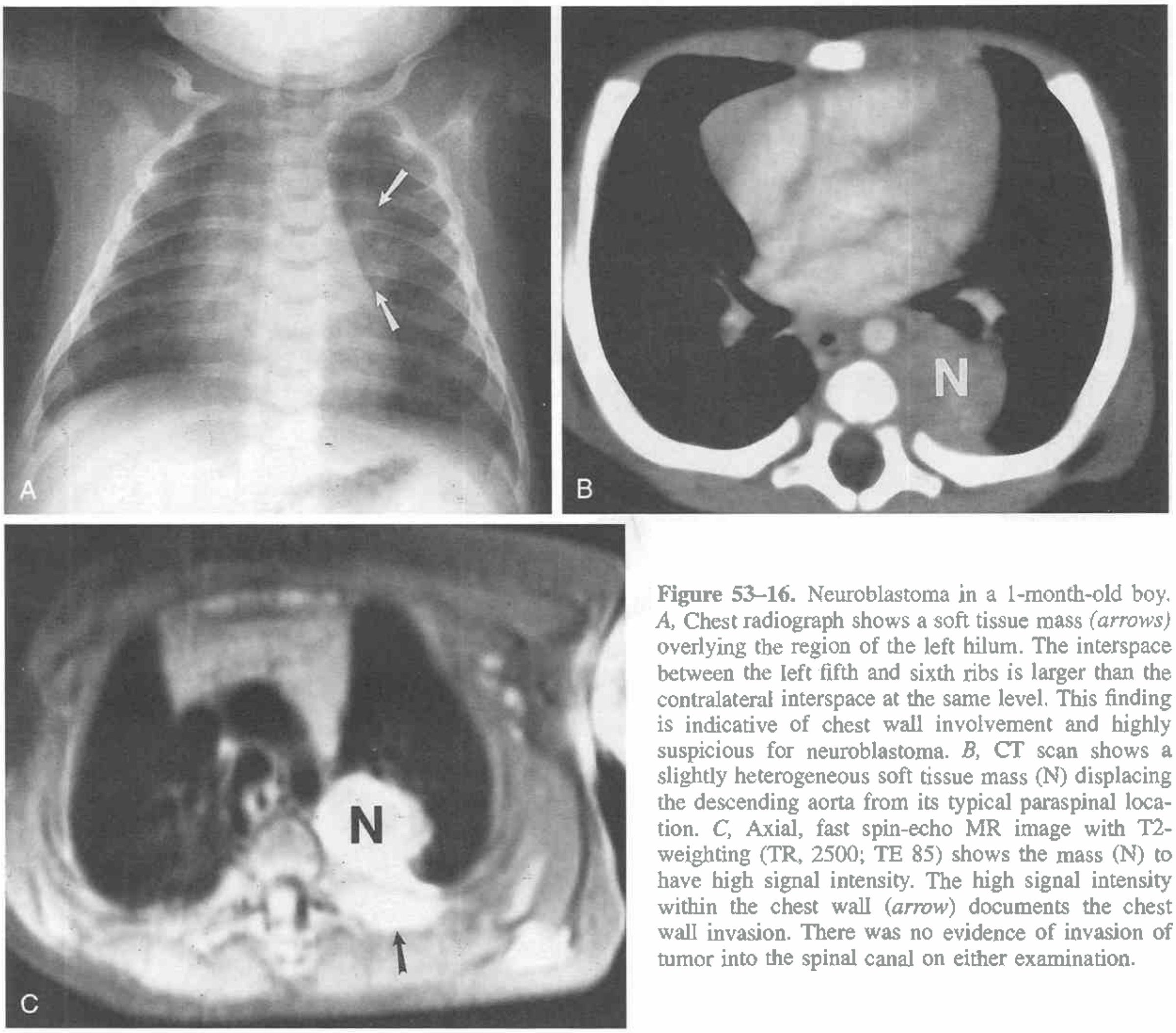

Figure 53–16. Neuroblastoma in a 1-month-old boy. *A,* Chest radiograph shows a soft tissue mass *(arrows)* overlying the region of the left hilum. The interspace between the left fifth and sixth ribs is larger than the contralateral interspace at the same level. This finding is indicative of chest wall involvement and highly suspicious for neuroblastoma. *B,* CT scan shows a slightly heterogeneous soft tissue mass (N) displacing the descending aorta from its typical paraspinal location. *C,* Axial, fast spin-echo MR image with T2-weighting (TR, 2500; TE 85) shows the mass (N) to have high signal intensity. The high signal intensity within the chest wall *(arrow)* documents the chest wall invasion. There was no evidence of invasion of tumor into the spinal canal on either examination.

Special Considerations in the Pediatric Chest Wall

The chest wall has a number of functions that, when altered, can result in a variety of pathologic processes. In children, the chest wall is unique in that it is primarily cartilaginous. This makes several issues different in imaging of the pediatric chest wall.

Normal Anatomic Variations

There is a great deal of variation in the configuration of the anterior chest wall in children.[10, 18] One study[10] showed that one third of children have some variation in the anterior chest wall, including asymmetry such as a tilted sternum, prominent convexity of an anterior rib or costal cartilage, prominent asymmetrical costal cartilage, parachondral nodules, or mild degrees of pectus excavatum or carinatum[10, 18] (Fig. 53–17). The importance of recognizing these variations is that they not be mistaken for serious abnormalities on imaging studies. Familiarity with these variations and their frequency may obviate the need for costly imaging.

For example, when one of these variations is palpated by a parent or physician, the concern of malignancy can be raised and cross-sectional imaging requested.[10, 18] In a previous study that reviewed CT or MRI examinations performed to evaluate children thought to have a chest wall mass, all of the palpable lesions that were asymptomatic were related to normal anatomic variations.[18] Knowledge of the high frequency of such variations should be communicated to referring physicians and parents when imaging is being contemplated in a child with an asymptomatic chest wall "lump."

Abnormalities of Chest Wall Configuration

The bony thorax provides a structural framework on which the function of the pulmonary system depends.[7] The association between deformity of the thorax and the development of respiratory dysfunction is well described.[40] Abnormal configuration of the thorax can also cause obstructive airway disease.[7] The space in the superior mediastinum is normally limited, confined by the manubrium and sternum superiorly and the vertebral column posteriorly.

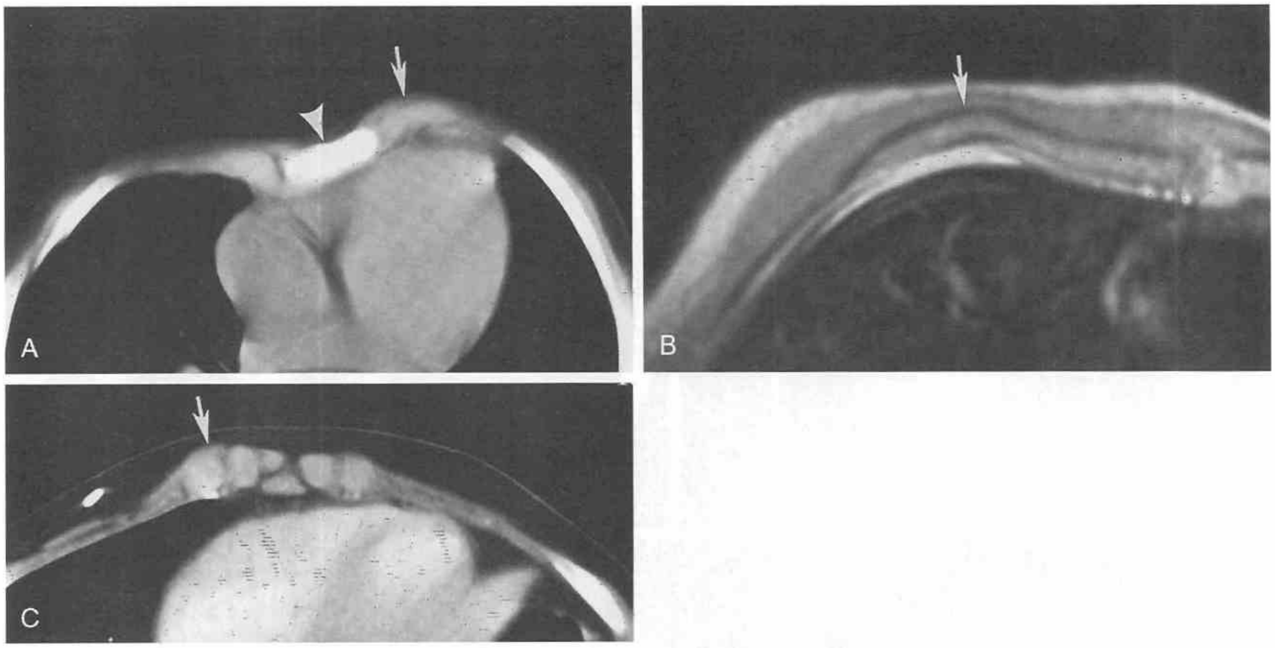

Figure 53–17. Normal variation of the anterior chest wall, which may present as palpable, nontender lumps on physical examination and be referred for cross-sectional imaging to exclude a mass. *A,* Tilted sternum *(arrowhead)* with associated asymmetrical anterior convex left rib (*arrow*) is shown in a 5-year-old girl. *B,* Anterior convex rib *(arrow)* is shown on T1-weighted image (TR, 740; TE, 15) of a 7-year-old boy. *C,* Asymmetry size of right costal cartilage *(arrow)* is shown on CT scan of a 13-year-old boy. (From Donnelly LF, Frush DP: Abnormalities of the chest wall in pediatric patients. AJR Am J Roentgenol 173:1595–1601, 1999.)

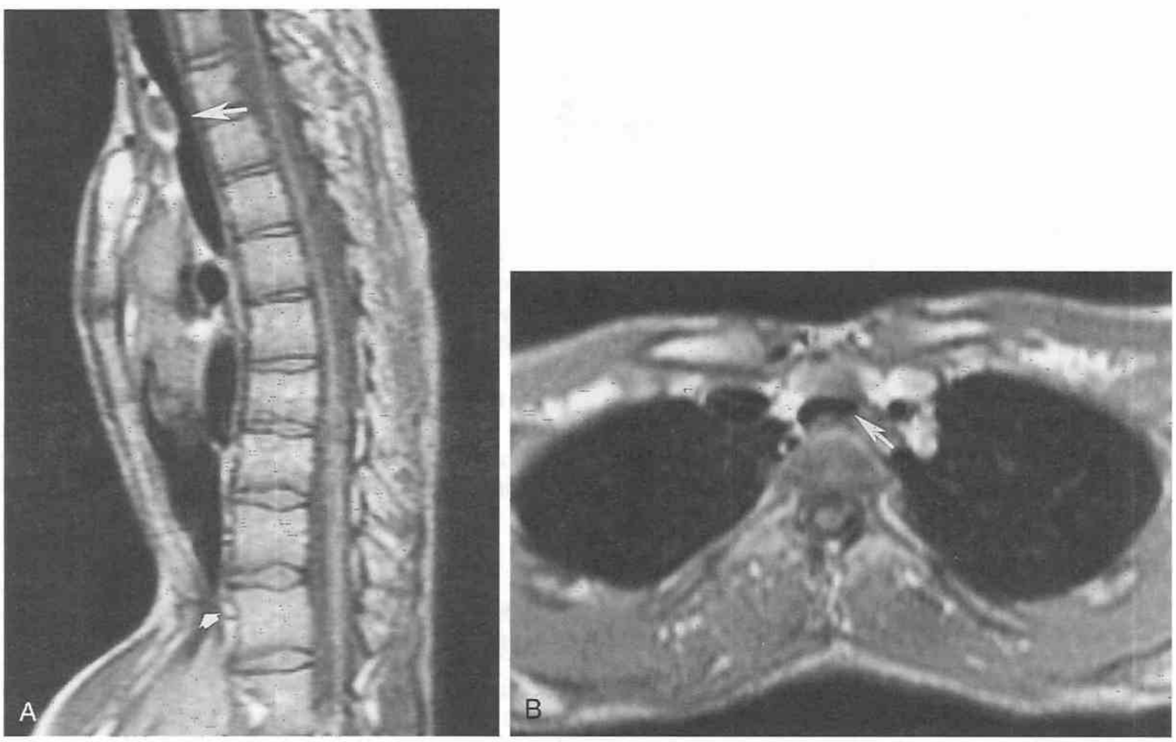

Figure 53–18. Tracheal compression and severe pectus deformity are shown on T1-weighted MR images (TR, 830; TE, 11) of a 16-year-old boy with Marfan's syndrome. *A,* Sagittal image shows loss of normal thoracic lordosis and pectus excavatum, which is so severe that the xiphoid *(arrowhead)* abuts anterior aspect of spine. Compression of the trachea *(arrow)* at the thoracic inlet is caused by a narrow anteroposterior diameter. *B,* Axial image at the level of the thoracic inlet shows severe tracheal compression *(arrow)* between the manubrium and spine. (From Donnelly LF, Frush DP: Abnormalities of the chest wall in pediatric patients. AJR Am J Roentgenol 173:1595–1601, 1999.)

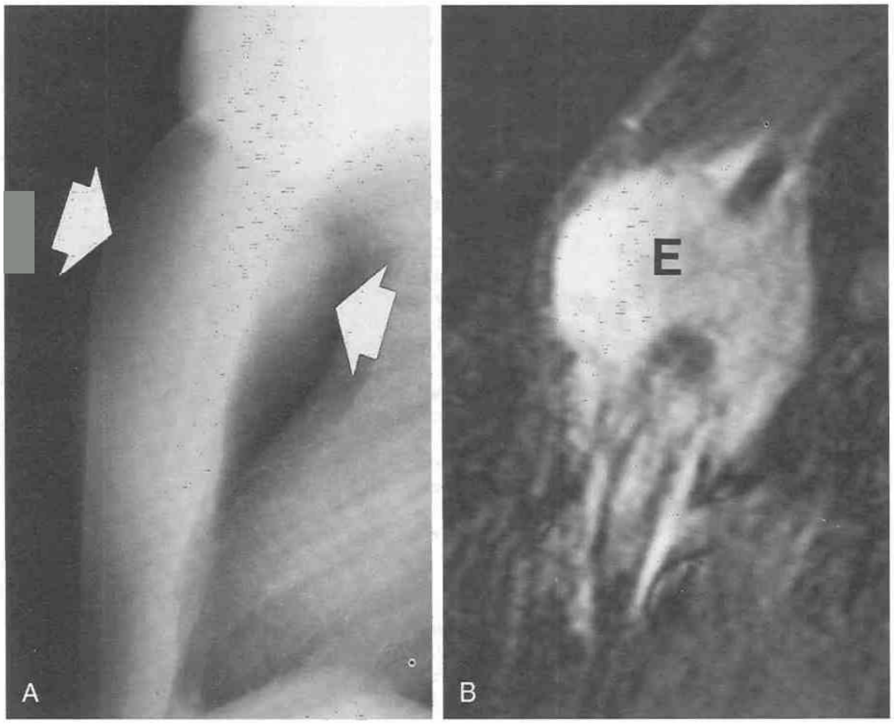

Figure 53–19. Ewing's sarcoma of the sternum in a 16-year-old boy. *A*, Lateral radiograph shows soft tissue mass *(arrows)* and permeative appearance and periosteal reaction of underlying sternum. *B*, Sagittal T2-weighted fast spin-echo MR image (TR, 2000; TE, 60) shows high-signal-intensity soft tissue mass (E) arising from and destroying the sternum. (From Donnelly LF, Frush DP: Abnormalities of the chest wall in pediatric patients. AJR Am J Roentgenol 173: 1595–1601, 1999.)

Abnormal thoracic configuration can result in further reduction in the volume of this space or in alteration in the anatomic relationship between the trachea and adjacent structures, resulting in compression of the trachea or main bronchi (Fig. 53–18). The most common locations of such airway compression include the trachea at the level of the thoracic inlet and the left main bronchus.[7]

Two of the most common abnormalities of chest wall configuration are pectus excavatum and pectus carinatum. Although the majority of problems resulting from these deformities are cosmetic, pectus deformities can cause chest pain, fatigability, dyspnea on exertion, palpitations, and restrictive lung disease.[19] When the deformities are severe, surgical repair is often performed. Although the diagnosis is made visually and does not involve imaging, cross-sectional imaging with CT or MRI has been useful in demonstrating the anatomy of severe deformities (see Fig. 53–18) and in evaluating possible complications after surgical repair.[19]

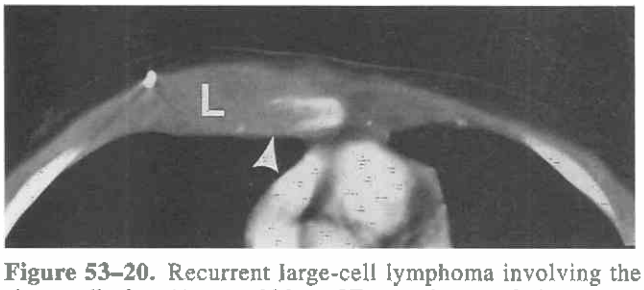

Figure 53–20. Recurrent large-cell lymphoma involving the chest wall of an 11-year-old boy. CT scan shows soft tissue mass (L) arising from the sternum *(arrowhead)* with associated bony destruction.

Aggressive Focal Processes

The chest wall can be involved in a number of aggressive neoplastic and inflammatory processes in children. The most common malignant primary bone tumors that involve the chest wall are Ewing's sarcoma (Fig. 53–19) and Askin's tumor (primitive neuroectodermal tumor of the chest wall).[8, 20] Other primary bone tumors, such as mesenchymal chondrosarcoma, fibrosarcoma (Fig. 53–20), and osteosarcoma, infrequently involve the chest wall.[8, 20] Metastatic involvement by neuroblastoma, lymphoma (see Fig. 53–10), or leukemia is more common.[8, 20]

On CT or MRI scans, all of these malignancies typically appear as nonspecific aggressive lesions. Other lesions that can present with aggressive appearing focal masses in the chest wall include osteomyelitis and Langerhans' cell histiocytosis. Vascular malformations such as venous malformations and lymphangiomas can also involve the chest wall. The appearance of vascular malformations on studies such as MRI is variable and depends on the composition of the malformation and on whether the lesions are of high or low flow.[8]

References

1. Bhalla M, Turcios N, Aponte V, et al: Cystic fibrosis: Scoring system with thin section CT. Radiology 179:783–788, 1991.
2. Brasfield D, Hicks G, Soong SJ, et al: Evaluation of scoring system of the chest radiograph in cystic fibrosis: A Collaborative Study. Am J Roentgenol 134:1195–1198, 1980.
3. Brown MJ, Miller RR, Muller NL: Acute lung disease in the immunocompromised host: CT and pathologic examination findings. Radiology 190:247–254, 1994.
4. Condon VR: Pneumonia in children. J Thorac Imaging 6:31–44, 1991.
5. Donnelly LF: CT of acute lung disease: Infection and trauma. In Seigel MJ (ed): RSNA Special Course in Pediatric Radiology: Current Concepts in Body Imaging at the Millennium. Oakbrook, Ill, RSNA Publications, 1999, pp 69–81.

6. Donnelly LF: Maximizing the usefulness of imaging in children with community-acquired pneumonia. AJR Am J Roentgenol 172: 505–512, 1999.
7. Donnelly LF, Bisset GS III: Airway compression in children with abnormal thoracic configuration. Radiology 206:323–326, 1998.
8. Donnelly LF, Frush DP: Abnormalities of the chest wall in pediatric patients. AJR Am J Roentgenol 173:1595–1601, 1999.
9. Donnelly LF, Frush DP: Localized lucent chest lesions in neonates: Causes and differentiation. AJR Am J Roentgenol 172:1651–1658, 1999.
10. Donnelly LF, Frush DP, Foss JN, et al: Anterior chest wall: Frequency of anatomic variations in children. Radiology 212:837–840, 1999.
11. Donnelly LF, Gelfand MJ, Brody AS, Wilmontt RW: Comparison between morphologic changes seen on high-resolution CT and regional pulmonary perfusion seen on SPECT in patients with cystic fibrosis. Pediatr Radiol 27:920–925, 1997.
12. Donnelly LF, Klosterman LA: Cavitary necrosis complicating pneumonia in children: Sequential findings on chest radiography. AJR Am J Roentgenol 171:253–256, 1998.
13. Donnelly LF, Klosterman LA: The yield of CT of children who have complicated pneumonia and noncontributory chest radiography. AJR Am J Roentgenol 170:1627–1631, 1998.
14. Donnelly LF, Klosterman LA: CT appearance of parapneumonic effusions in children: Findings are not specific for empyema. AJR Am J Roentgenol 169:179–182, 1997.
15. Donnelly LF, Klosterman LA: Pneumonia in children: Decreased parenchymal contrast enhancement—CT sign of intense illness and impending cavitary necrosis. Radiology 205:817–820, 1997.
16. Donnelly LF, Klosterman LA: Subpleural sparing: A CT finding of lung contusion in children. Radiology 204:385–387, 1997.
17. Donnelly LF, MacFall JR, McAdams HP, et al: Combined hyperpolarized He-3 enhanced and conventional proton MR imaging of the lung in patients with cystic fibrosis: Preliminary observations. Radiology 212:885–889, 1999.
18. Donnelly LF, Taylor CNR, Emery KH, Brody AS: Asymptomatic, palpable, anterior chest wall lesions in children: Is cross-sectional imaging necessary? Radiology 202:829–831, 1997.
19. Ellis DG: Chest wall deformities in children. Pediatr Ann 18:161–165, 1989.
20. Faro SH, Mahroubi S, Ortega W: CT diagnosis of rib anomalies, tumors, and infection in children. Clin Imaging 17:1–7, 1993.
21. Francis IR, Glazer GM, Bookstein FL, Gross BH: The thymus: Reexamination of age-related size and shape. Am J Roentgenol 145: 249–254, 1985.
22. Frush DP, Donnelly LF: Pulmonary sequestration spectrum: A new spin with spiral CT. AJR Am J Roentgenol 169:679–682, 1997.
23. Hernanz-Schulman M: Cysts and cystlike lesions of the lung. Radiol Clin North Am 31:631–649, 1993.
24. Jabra AA, Fishman EK, Shehata BM, Perlman EJ: Localized persistent pulmonary interstitial emphysema: CT findings with radiographic-pathologic correlation. AJR Am J Roentgenol 169:1381–1384, 1997.
25. Jacobs MT, Frush DP, Donnelly LF: The right place at the wrong time: Historical perspective of the thymus in pediatric radiology. Radiology 210:11–16, 1999.
26. Kim WS, Lee KS, Kim IO, et al: Congenital cystic adenomatoid malformation of the lung: CT-pathologic correlation. AJR Am J Roentgenol 168:47–53, 1997.
27. Light RW: Parapneumonic effusions and empyema. Clin Chest Med 6:55–62, 1985.
28. Manson D, Babyn PS, Palder S, Bergman K: CT of blunt chest trauma in children. Pediatr Radiol 23:1–5, 1993.
29. Merten DF: Diagnostic imaging of mediastinal masses in children. AJR Am J Roentgenol 158:825–832, 1992.
30. Mori M, Galvin JR, Barloon TJ, et al: Fungal pulmonary infections after bone marrow transplantation: Evaluation with radiography and CT. Radiology 178:721–726, 1991.
31. Muller NL: Imaging of the pleura. Radiology 186:297–309, 1993.
32. Naidich DP, Zerhouni EA, Siegelman SS: Computed Tomography and Magnetic Resonance of the Thorax, 2nd ed. New York, Raven Press, 1991, pp 423–426.
33. Nathanson I, Conboy K, Murphy S, et al: Ultrafast computerized tomography of the chest in cystic fibrosis: A new scoring system. Pediatr Pulmonol 11:81–86, 1991.
34. Ramnath RR, Heller RM, Ben-Ami T, et al: Implications of early sonographic evaluation of parapneumonic effusions in children with pneumonia. Pediatrics 101:68–71, 1998.
35. Rosado-de-Christenson ML, Stocker JT: From the archives of the AFIP: Congenital cystic adenomatoid malformation. Radiographics 11:865–886, 1991.
36. Siegel MJ, Jamroz GA, Glazer HS, Abramson CL: MR imaging of intraspinal extension of neuroblastoma. J Comput Assist Tomogr 10: 593–595, 1986.
37. Sivit CJ, Taylor GA, Eichelberger MR: Chest injury in children with blunt abdominal trauma: Evaluation with CT. Radiology 171: 815–818, 1989.
38. Stigers KB, Woodring JH, Kanga JF: The clinical and imaging spectrum of findings in patients with congenital lobar emphysema. Pediatr Pulmonol 14:160–170, 1992.
39. Waite RJ, Carbonneau RJ, Balikian JP, et al: Parietal pleural changes in empyema: Appearance at CT. Radiology 175:145–150, 1990.
40. Weber B, Smith JP, Briscoe WA: Pulmonary function in asymptomatic adolescents with idiopathic scoliosis. Am Rev Respir Dis 111:389–393, 1975.
41. Winer-Muram HT, Rubin SA, Fletcher BD, et al: Childhood leukemia: Diagnostic accuracy of bedside chest radiography for severe pulmonary complications. Radiology 193:127–133, 1994.
42. Winters WD, Effmann EL, Nghiem HV, Nyberg DA: Disappearing fetal lung masses: Importance of postnatal imaging studies. Pediatr Radiol 27:535–539, 1997.
43. Worthy SA, Flint JD, Muller NL: Pulmonary complications after bone marrow transplantation: High-resolution CT and pathologic findings. Radiographics 17:1359–1357, 1997.

54 Hepatobiliary System

Ellen C. Benya

Computed Tomography

This chapter discusses the computed tomography (CT) and magnetic resonance imaging (MRI) appearances of pediatric diseases of the liver and biliary tree. CT is commonly used to evaluate the liver and biliary system in children. Routine CT imaging of the pediatric liver is performed after administration of intravenous (IV) contrast material, with precontrast imaging performed only in selected cases.

Many, but not all, centers exclusively use low-osmolality, nonionic IV contrast material for CT imaging in children. The volume administered for CT imaging is typically 2 to 3 mL/kg (up to 150 mL maximal volume).[29, 44] Rapid injection to achieve peak hepatic enhancement during CT imaging can be safely performed with power injectors in children when secure IV access with a 24-gauge or larger-bore peripheral or central venous catheter is present.[21, 29, 41] Prior to use, the catheter or central venous line should always be checked, with a rapid hand infusion of saline, for blood return through the line and for patency. Additionally, optimal positioning of the access device should be assured in all cases before use. The rate of contrast administration using a power injector varies from 0.5 to 2.0 mL/sec depending on the luminal diameter, length, and type of the catheter.[21, 29, 43]

Imaging of the liver on helical CT scanners is timed to coincide with expected peak hepatic enhancement: either imaging is performed immediately after injection of contrast material[29] or a tracking device is used to trigger imaging when a threshold attenuation value has been reached in the liver.[44, 52] Multiple helical CT images can be obtained during shallow breathing in the infant or sedated child or with breath-holding in the older child. Slice thickness ranges from 5 to 10 mm depending on patient size, with a pitch of 1:1 to 2:1.[29, 41, 52] The advent of rapid imaging on helical CT scanners has significantly diminished the need to sedate children undergoing CT examination.

Magnetic Resonance Imaging

The use of magnetic resonance imaging (MRI) in the evaluation of the pediatric hepatobiliary system is increasing. In almost all children younger than 8 years, sedation is required to obtain motion-free MR images. Although sedation protocols vary from institution to institution, many utilize oral chloral hydrate for children younger than 2 years, and IV pentobarbital alone or in conjunction with other intravenously administered sedatives for children older than 2 years of age.[15]

The MRI sequences chosen for pediatric hepatic imaging are generally tailored to the individual patient. Routinely, T1 and T2 or fast spin-echo T2 with fat saturation sequences are performed to evaluate the liver. Following gadolinium contrast administration, additional T1-weighted images may be obtained. Although the likelihood of allergic reaction to gadolinium contrast medium is low, adequate venous access is required to eliminate the risk of contrast extravasation.

In addition to standard T1 and T2 sequences, gradient-recalled echo sequences and MR angiography and venography can supplement the assessment of the hepatic vasculature,[16, 51] and MR cholangiography can yield diagnostic information about the biliary system.[25, 35]

Developmental Anomalies of the Liver

Abnormal Position

Variations in hepatic development, including agenesis of a hepatic lobe and accessory hepatic lobes, are infrequently encountered. The location of the liver is normally below the right hemidiaphragm in the right upper abdomen. Alterations in hepatic position may occur in children with visceroatrial situs abnormalities, situs inversus, and polysplenia and asplenia; in these children, the liver may be left-sided or horizontally positioned. Abnormal hepatic fixation leading to hepatic mobility, or a "wandering liver," has been reported.[1] Additionally, in children with diaphragmatic defects or eventration, a portion of the liver may reside in the right or left hemithorax.

Hepatic Cysts

Simple hepatic cysts are focal parenchymal lesions that are considered to be a congenital developmental anomaly. These cysts may be unilocular or multilocular and are typically lined with biliary epithelium.[34] They are usually small lesions detected incidentally during the course of abdominal imaging. Rarely, they become large and result in a palpable abdominal mass. Computed tomography reveals unilocular or multilocular low-attenuation lesions (usually less than 20 Hounsfield units), with internal septa when multilocular but without other peripheral or internal enhancement (Fig. 54–1).[34] On MRI examination, hepatic cysts may show low or high signal intensity on T1 sequences, depending on the character of their internal contents, and they typically show high signal intensity on T2-weighted images.[31]

Importantly, differentiation of simple hepatic cysts from

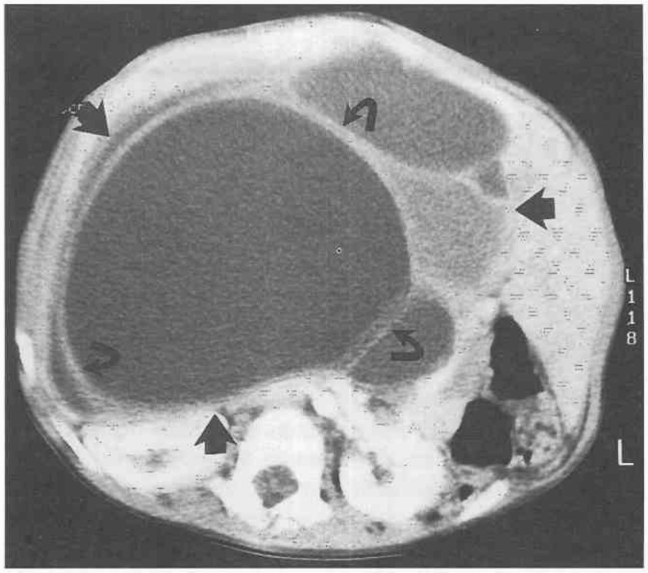

Figure 54–1. Hepatic cyst. CT image after administration of intravenous contrast material, revealing a large multiloculated hepatic cyst. The cyst has central low attenuation *(arrow)* with thin enhancing septations *(curved arrows)*.

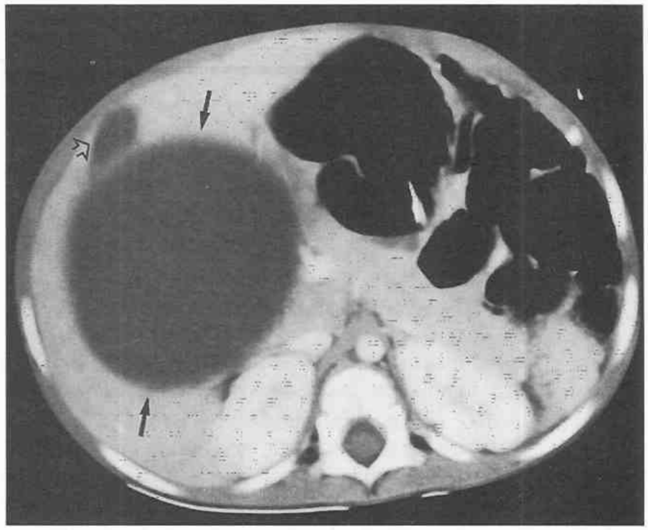

Figure 54–2. Choledochal cyst. CT of the upper abdomen reveals a large low-attenuation choledochal cyst *(arrows)* in the portal hilum of the liver. The gallbladder, visualized anteriorly, is displaced by the large choledochal cyst *(open arrow)*.

other cystic hepatic lesions, such as echinococcal cysts, bilomas, resolving hematomas, and mesenchymal hamartomas, is not always possible on CT and MRI.[18, 34] When multiple cysts are discovered in the liver, an associated condition, such as polycystic kidney disease, von Hippel–Lindau disease, biliary atresia, Byler's disease, or Caroli's disease, should be considered.[6, 17, 19]

Choledochal Cysts and Caroli's Disease

Choledochal cysts are a developmental malformation of the biliary tree with resultant focal or diffuse dilatation of the extrahepatic biliary system. The most common type of choledochal cyst is a fusiform dilatation of the extrahepatic common bile duct. Occasionally, extension of the dilatation into the right and left common hepatic ducts may occur.[18]

Children with choledochal cysts may present with a palpable abdominal mass, pain, and/or jaundice, or with a cystic mass detected on prenatal sonogram. Diagnostic workup usually consists of sonography and nuclear hepatobiliary scintigraphy. A CT examination, although not routinely used to assess choledochal cysts, if performed shows a low-attenuation, fluid-filled cystic lesion in the region of the porta hepatis (Fig. 54–2).[18]

Caroli's disease is a developmental biliary abnormality with focal or diffuse intrahepatic biliary duct dilatation; it may occur alone or in conjunction with congenital hepatic fibrosis. Numerous rounded and/or tubular low-attenuation foci in the liver and the region of the portal hilum on contrast-enhanced CT examination correspond to the abnormally dilated intrahepatic biliary ducts. An eccentrically positioned enhancing nodule, the fibrovascular bundle, may be detected in the dilated bile duct.[32]

Congenital hepatic fibrosis related to autosomal recessive polycystic kidney disease (ARPKD) consists of portal tract fibrosis and biliary ductal plate malformation with an otherwise normal hepatic parenchyma.[27] There is considerable variability in the phenotypic expression of this inherited disease, with the severity of the hepatic component of this genetic disease often inversely related to the degree of renal disease present. On CT, the liver may appear macroscopically normal, or mild to severely dilated intrahepatic biliary ducts may be identified.[27] If dilated intrahepatic biliary ducts are present, the corresponding MRI scan reveals low-signal-intensity bile ducts or bile lakes on T1-weighted images, and these show high signal intensity on T2-weighted images (Fig. 54–3). The use of MR cholangiography to detect intrahepatic biliary dilatation in congenital hepatic fibrosis due to ARPKD has recently been described.[19]

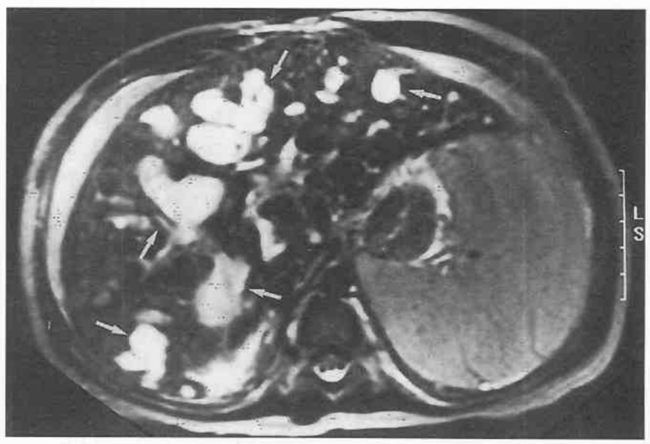

Figure 54–3. Biliary dilatation related to congenital hepatic fibrosis associated with autosomal recessive polycystic kidney disease. T2-weighted MR image of the liver demonstrates numerous large, high-signal-intensity regions of biliary dilatation *(arrows)*. (Courtesy of Dr. Cynthia K. Rigsby, Children's Memorial Hospital, Chicago.)

Hepatic Infection

Pyogenic Abscesses

The liver parenchyma may become infected with a variety of pathogens. The imaging appearance varies depending on the type of infecting organism. Pyogenic abscesses in the liver are rare, occurring more commonly in children with underlying immunodeficiency syndromes and less commonly in immunocompetent children with indwelling umbilical venous lines, penetrating or nonpenetrating trauma, or sepsis.[20, 48] CT imaging to evaluate for intrahepatic abscesses requires the use of IV contrast material. Precontrast CT images are not routinely obtained.

Abscesses have a low-attenuation, central collection of fluid on contrast-enhanced CT; a peripheral rim of enhancement or septations may be present (Fig. 54–4).[18] MRI of the liver is not typically performed for pyogenic abscesses.

Fungal Infections

Children with congenital or acquired immunodeficiency syndromes or those who are receiving immunosuppressive medications are at increased risk for hepatic fungal infections. Disseminated fungal infections may result in numerous microabscesses in the liver, with associated microabscesses frequently detected simultaneously in the spleen and kidneys. *Candida* and *Aspergillus* are the most frequent fungal organisms that cause hepatic microabscesses. On CT, these microabscesses are typically small (smaller than 1 cm) foci in the liver; peripheral enhancement may or may not be detected (Fig. 54–5).[14, 49]

Viral Hepatitis

A diffuse hepatic infection can occur with a variety of viral agents including, but not limited to, hepatitis A, hepatitis B, hepatitis C, and non-A, non-B hepatitis. A contrast-enhanced CT examination performed on a child with acute viral hepatitis may appear normal or may reveal a nonspecific, mottled, heterogeneous pattern of hepatic enhancement, and thickening of the gallbladder wall.[49] With progression to chronic liver disease and cirrhosis, a small liver with nodularity and varices secondary to portal hypertension may be detected.

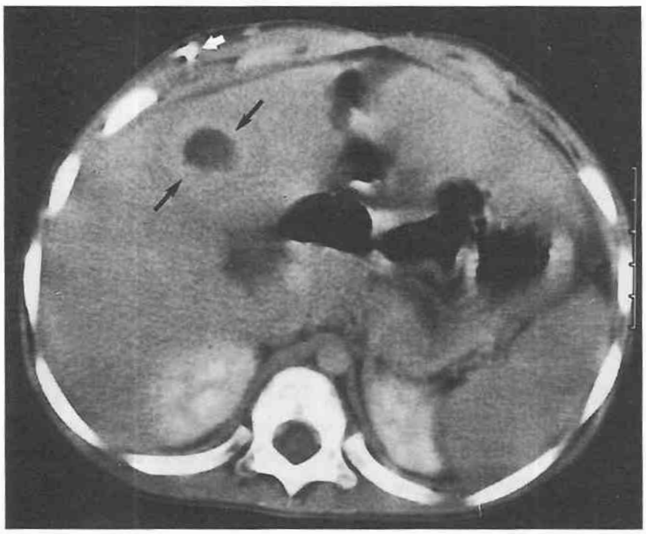

Figure 54–4. Pyogenic abscess. Contrast-enhanced CT image shows a low-attenuation abscess in the left lobe of the liver with peripheral rim enhancement *(arrows)*. Incidentally noted is a ventriculoperitoneal shunt tube *(open arrow)* in the subcutaneous tissues of the anterior abdominal wall.

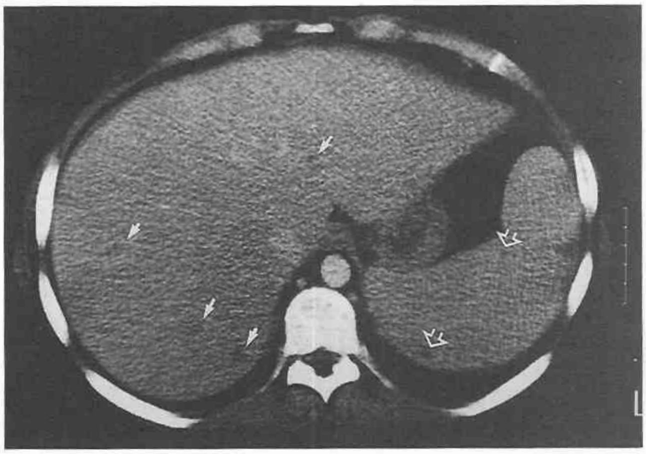

Figure 54–5. Candidal abscesses. CT image in an immunosuppressed child reveals multiple small low-attenuation microabscesses *(arrows)* in the liver, with associated microabscesses in the spleen *(open arrows)*.

Cat-Scratch Disease

Unusual hepatic infections are occasionally encountered in the pediatric population, such as cat-scratch disease. In children with cat-scratch disease, CT reveals multiple low-attenuation foci in the liver, corresponding to necrotizing granulomas.[38]

Benign Hepatic Neoplasms

Infantile Hemangioendotheliomas

Infantile hemangioendotheliomas are the most frequent hepatic neoplasm discovered in the young child, usually infants younger than 6 months of age.[12, 23, 28] Infants with this benign vascular neoplasm may be asymptomatic or present with a palpable abdominal mass, high output congestive heart failure, coagulopathy secondary to platelet consumption, or liver dysfunction. Associated cutaneous hemangiomas may be detected in up to 45% of children with hepatic hemangioendotheliomas.[12]

On CT and MRI, the spectrum of imaging appearances varies from a single lesion to multiple hepatic lesions that may diffusely involve the liver. On precontrast CT images, hemangioendotheliomas are lower in attenuation than the adjacent normal liver parenchyma, and foci of calcification are seen in approximately 50% of lesions.[23]

When the CT examination is performed with rapid bolus administration of IV contrast material, a pattern of early peripheral enhancement with subsequent central enhance-

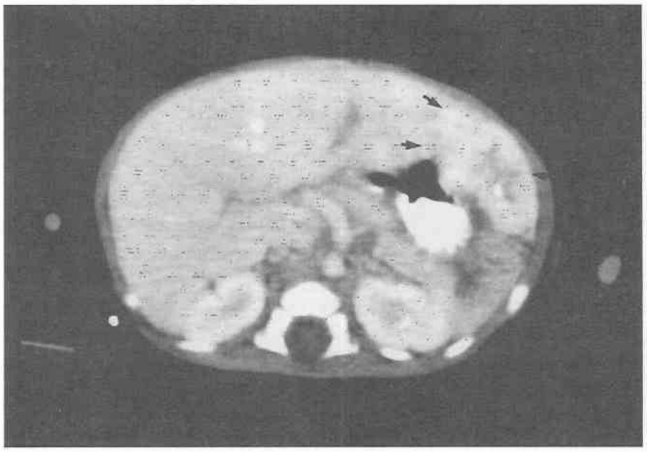

Figure 54–6. Hemangioendothelioma. CT of the upper abdomen demonstrates a lesion in the left lobe of the liver *(arrows)* with peripheral enhancement and central low attenuation due to hemorrhage or necrosis within the hemangioendothelioma.

ment detected on delayed images is often seen.[12, 23, 28] With larger lesions, an area of central necrosis or hemorrhage that remains low in attenuation is frequently observed (Fig. 54–6). Because of the high degree of vascular shunting through hemangioendotheliomas, it is common to see a significant diminution in size of the infrahepatic aorta, with a corresponding large caliber to the draining hepatic veins (Fig. 54–7).[28]

On MRI examination, the lesions are typically hypointense with respect to adjacent liver parenchyma on T1-weighted images and hyperintense on T2-weighted images (Fig. 54–8).[23, 26] When intratumoral hemorrhage has occurred within the hemangioendothelioma, high-signal-intensity foci may be detected on T1-weighted MR images. Gadolinium contrast enhancement on MRI examination mirrors the centripetal pattern seen on CT examination, with early peripheral enhancement followed by central and more uniform enhancement of the lesion.[33]

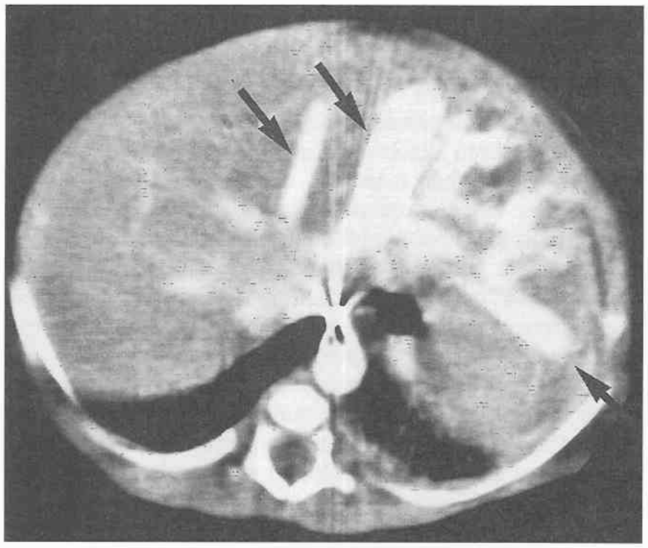

Figure 54–7. Hemangioendothelioma. CT of the liver shows the enlarged draining hepatic veins *(arrows)* in this infant with hemangioendothelioma.

Cross-sectional imaging with CT and/or MRI is utilized to assess location and extent of the lesion if surgical resection of the hemangioendothelioma is being considered in the symptomatic infant.[7] Additional modes of treatment for this condition include the medical therapies, steroids or interferon, and embolization.[40] Occasionally, hemangioendotheliomas may regress without treatment.[12]

A vascular hepatic mass lesion to consider in the young infant besides hemangioendothelioma is an arteriovenous malformation of the liver. This may also be a cause of congestive heart failure, neonatal hepatomegaly, or anemia.[8]

Mesenchymal Hamartomas

Recent pathologic evidence suggests that mesenchymal hamartoma of the liver, once considered a developmental liver lesion,[42] may in fact be a benign hepatic neoplasm.[36] Histologically, these lesions are composed of a mixture of bile ducts and mesenchymal tissue. Mesenchymal hamartomas are usually detected in children younger than 2 years who present with a palpable abdominal mass.[42] Although most mesenchymal hamartomas are complex cystic lesions in the liver, those with a large stromal (mesenchymal) component can be partially or completely solid lesions.[39] Exophytic growth of mesenchymal hamartomas from the liver may occur.

On CT, the more common cystic form of mesenchymal hamartoma appears as a low-attenuation mass; enhancing septa may be seen (Fig. 54–9).[42, 47] Lesions that are predominantly stromal have regions of enhancing solid tissue.

On MRI examination, the appearance of mesenchymal hamartomas depends on the composition of the lesion. Cystic mesenchymal hamartomas may show low or high signal intensity on T1-weighted images, depending on the amount of protein content in the cystic portion, and they usually appear as high-signal-intensity lesions on T2-weighted images.[14] Septations are frequently detected as low signal intensity bands on T2-weighted MR images. Stroma-predominant lesions commonly show low signal intensity on both T1-weighted and T2-weighted images.[39] Treatment of mesenchymal hamartoma is usually surgical resection of the lesion, although some have advocated assessment by serial imaging after biopsy without removal.[4]

Focal Nodular Hyperplasia

Focal nodular hyperplasia (FNH) is a benign hepatic neoplasm that is not often seen in the pediatric population.[11, 31] The typical clinical presentation is detection of an asymptomatic, palpable abdominal mass.[3, 11] Pathologically, FNH is composed of nodules of hyperplastic hepatocytes and proliferating bile ductules surrounding a scar.[11] There is a broad spectrum of CT and MRI appearances for FNH in children, and the central scar is not always identified on images.[11]

On contrast-enhanced CT images, FNH significantly

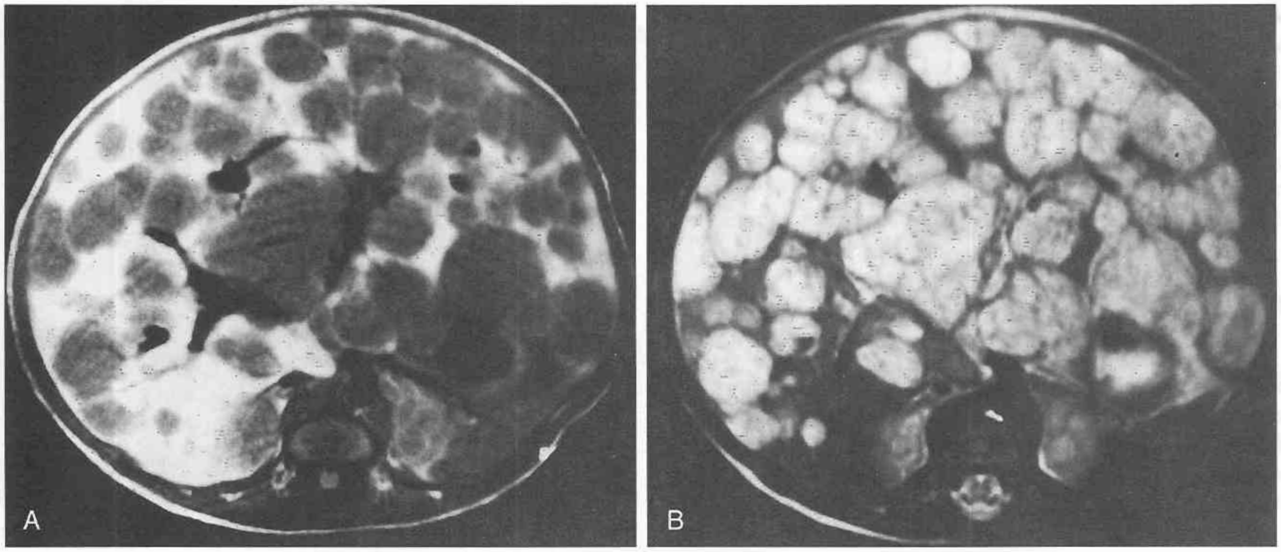

Figure 54–8. Hemangioendothelioma. *A,* T1-weighted MR image in an infant with multifocal hemangioendothelioma in the liver. Numerous hypointense foci are seen throughout the liver. *B,* On a T2-weighted MR image, these same foci are hyperintense.

enhances during the arterial phase of contrast administration; the degree of enhancement diminishes in attenuation during the venous phase, resulting in a lesion whose attenuation is similar to that of the adjacent normal liver parenchyma.[11] When visible, the central scar remains a linear or ovoid region of low attenuation on contrast-enhanced CT (Fig. 54–10).[3, 11]

On MRI examination, FNH has been described as a hypointense to isointense lesion on T1-weighted and as an isointense to mildly hyperintense lesion on T2-weighted images.[31, 39] The region of the scar is typically hypointense on T1-weighted images and hyperintense lesion on T2-weighted images; however, significant variability exists, and this appearance is not always present.[11]

Adenoma

Hepatic adenoma is another benign hepatic mass lesion that is rarely detected in the pediatric population. Those children and adolescents with glycogen storage disorder type 1, those taking oral contraceptives, and those receiving androgen therapy for Fanconi's anemia are most likely to develop hepatic adenomas.[14]

The CT imaging appearance is nonspecific. On contrast-enhanced CT, a low-attenuation lesion can typically be identified.[37] However, because hemorrhage may occur and lead to presentation with symptoms of abdominal pain and/or hypotension, a heterogeneous attenuation of the mass

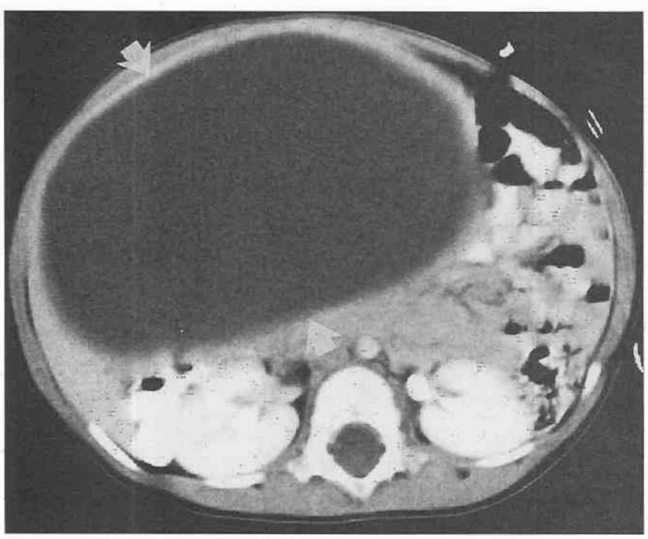

Figure 54–9. Mesenchymal hamartoma. Contrast-enhanced CT image of the liver demonstrates a large low-attenuation lesion *(arrows).*

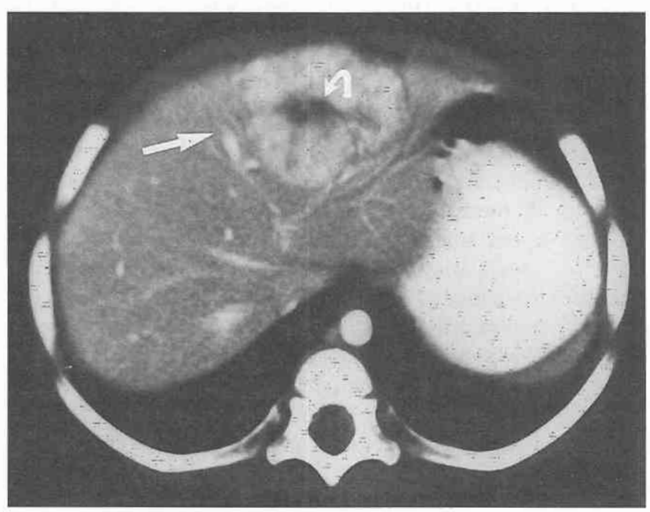

Figure 54–10. Focal nodular hyperplasia. CT of the liver obtained during the early arterial phase of intravenous contrast administration reveals an enhancing mass in the left lobe of the liver *(arrows)* with a visible central scar of low attenuation *(curved arrow).*

and/or perihepatic or intraperitoneal fluid may be detected on CT.

On MRI, the appearance of hepatic adenomas is quite variable and nonspecific. More than half of hepatic adenomas have heterogeneously hyperintense signal on T1-weighted images, related to hemorrhagic necrosis, and a peripheral hypointense rim corresponding to the pseudocapsule of the adenoma may be seen in a third of patients.[2]

Malignant Hepatic Masses

The most common primary pediatric liver tumor identified is hepatoblastoma. Other malignant hepatic tumors that may occur in children include hepatocellular carcinoma (HCC), undifferentiated embryonal sarcoma, and biliary rhabdomyosarcoma. Primary malignant liver tumors occur less commonly in children than metastatic Wilms' tumor or neuroblastoma.

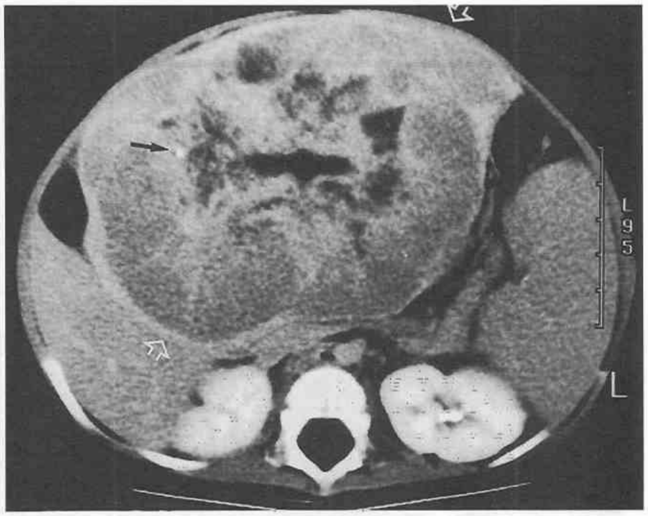

Figure 54–11. Hepatoblastoma. CT of a large unifocal hepatoblastoma shows a focus of calcification *(arrow)* in the heterogeneously low-attenuation mass *(open arrows)*.

Hepatoblastoma

Hepatoblastoma usually produces a palpable mass in the child younger than 3 years. Abdominal pain and anemia are occasionally present. Children with Beckwith-Wiedemann syndrome and hemihypertrophy are known to have an increased risk for development of hepatoblastoma and other abdominal tumors, and they should have periodic screening abdominal ultrasound examinations.[37, 40] When a hepatic mass is detected on physical examination and/or abdominal ultrasound, abdominal CT is performed to further characterize and stage the extent of liver involvement, and chest CT is performed to evaluate for the presence of pulmonary metastases. In up to 90% of children with hepatoblastoma, an elevated α-fetoprotein level is found, and thus serial testing of the α-fetoprotein level is useful for tumor surveillance.[40]

CT reveals hepatoblastomas as unifocal or multifocal low-attenuation masses, with calcification present in up to 40% (Fig. 54–11). Tumor thrombus, when present, can be appreciated extending into the portal vein, the hepatic veins, or the inferior vena cava on contrast-enhanced CT (Fig. 54–12).

On MRI, hepatoblastomas usually demonstrate decreased signal intensity on T1-weighted sequences and heterogeneously increased signal on T2-weighted sequences. If there is intratumoral hemorrhage, foci of increased signal intensity on T1-weighted images may be seen.[13, 14] MRI may help confirm or exclude suspected venous extension of the tumor. Cross-sectional imaging with CT and/or MRI is used to assess location and extent of the lesion; this can help determine the feasibility of surgical resection of the hepatoblastoma both prior to and after chemotherapy.[7, 24] Curative treatment includes surgical resection if hepatic lobectomy or trisegmentectomy can be performed.

Hepatocellular Carcinoma

Hepatocellular carcinoma does not commonly occur in the pediatric population. The average age at diagnosis is 12 years, and underlying chronic liver disease is present in up to 50% of these children.[14] HCC may be detected as solitary or multifocal low-attenuation masses on contrast-enhanced CT images (Fig. 54–13); changes caused by coexistent cirrhotic disease may be appreciated. On MRI, T1-weighted sequences show low-signal-intensity lesions and T2-weighted sequences typically show heterogeneously high-signal-intensity foci. In the subtype of fibrolamellar HCC, a central scar may be identified on cross-sectional imaging. This is, however, a nonspecific finding, as FNH and hemangiomas may also have central scars.

Undifferentiated Embryonal Sarcoma

Undifferentiated embryonal cell sarcoma is a rare tumor most often detected in older children or adolescents. Pre-

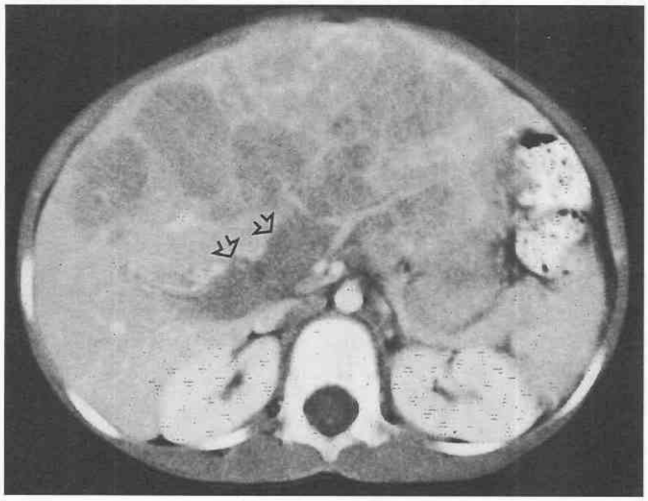

Figure 54–12. Hepatoblastoma. CT of the liver reveals multifocal hepatoblastoma with extension of tumor thrombus into the portal vein *(open arrows)*.

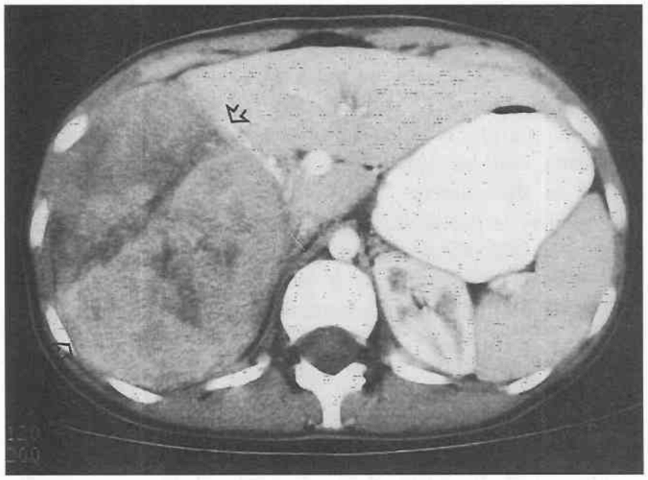

Figure 54–13. Hepatocellular carcinoma. CT of a large unifocal hepatocellular carcinoma shows a large heterogeneous low-attenuation mass *(open arrows)* in the right lobe of the liver.

sentation usually occurs after discovery of a large, palpable abdominal mass. These tumors occur more commonly in the right than in the left hepatic lobe.

On CT, these malignant mesenchymal tumors are low-attenuation lesions that frequently have cystic-appearing components with regions of enhancing solid tissue (Fig. 54–14).[9] On MRI, they may show low or high signal intensity on T1-weighted sequences, and they usually show heterogeneously high signal intensity on T2-weighted sequences.[39] Gadolinium enhancement of solid tissue is detected on T1-weighted sequences.[9]

Biliary Rhabdomyosarcomas

Rhabdomyosarcomas of the liver in children are rare malignant tumors arising in the biliary tree. These are low-attenuation lesions on CT and may occur in any segment

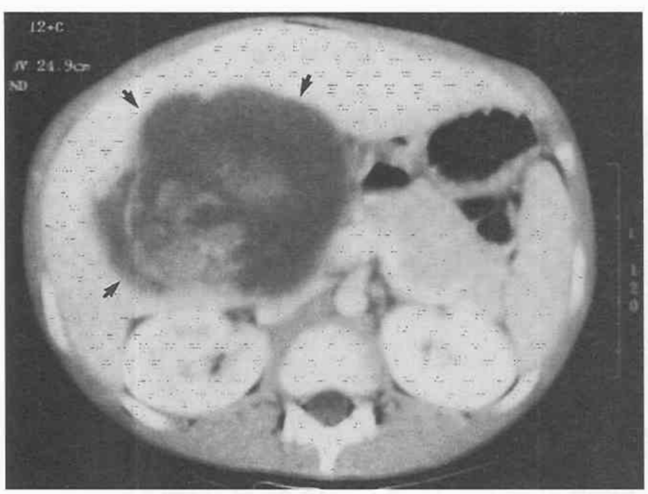

Figure 54–14. Undifferentiated embryonal sarcoma. Contrast-enhanced CT image of the liver demonstrates a large lesion in the right lobe of the liver *(arrows)* with heterogeneous low attenuation centrally and peripheral nodules of enhancing tissue.

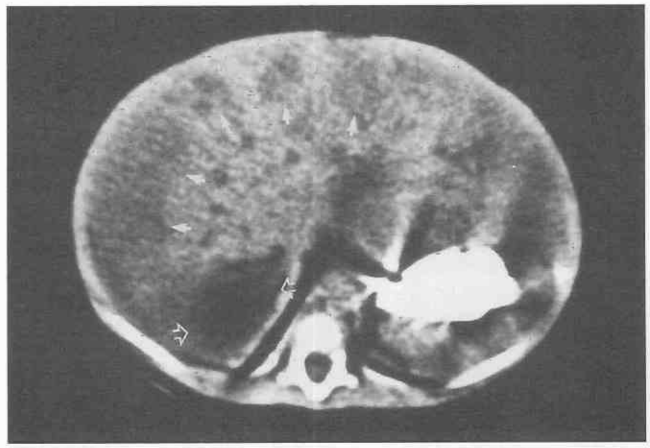

Figure 54–15. Hepatic metastases secondary to neuroblastoma. Contrast-enhanced CT shows numerous low-attenuation hepatic metastases *(arrows)* in a child with neuroblastoma *(open arrows)*.

of the liver. Biliary dilation or obstruction may be identified distal to the tumor.[18] The MRI appearance of hepatic rhabdomyosarcoma has not yet been described.

Metastatic Disease

Secondary or metastatic lesions to the liver occur frequently in children with Wilms' tumor and neuroblastoma. On contrast-enhanced CT images, the primary Wilms' tumor or neuroblastoma (arising in the abdomen) is usually easily identified, with metastatic disease to the liver detected as multiple low-attenuation lesions of varying sizes (Fig. 54–15). Lymphoma and leukemia and other neoplastic processes can also lead to metastatic foci in the liver.

Hepatic Trauma

Liver injuries from blunt abdominal trauma in the hemodynamically stable child are best evaluated with contrast-enhanced CT examinations.[22, 49] Currently, MRI plays no role in the detection of acute abdominal injury.

The CT appearance of hepatic injuries in children mirrors that seen in adults: hematomas appear as rounded foci of heterogeneous low attenuation on contrast-enhanced CT examination, and liver lacerations appear as simple or complex linear low-attenuation foci (Fig. 54–16). Subcapsular hematomas are detected as crescentic low-attenuation fluid collections adjacent to the liver parenchyma in a subcapsular location. Associated hemoperitoneum may be identified in the peritoneal cavity or retroperitoneal space.[50]

The CT appearance of healing hepatic injuries and the time course for their resolution have been described.[10] Delayed complications of hepatic injury in children, such as pseudoaneurysms, delayed hemorrhage, abscesses, bilomas, and biliary strictures, are rare.[10, 45, 46]

Hepatic Vascular Disease

Portal Vein Thrombosis

Portal vein thrombosis in children may be associated with a history of indwelling umbilical venous lines, phlebi-

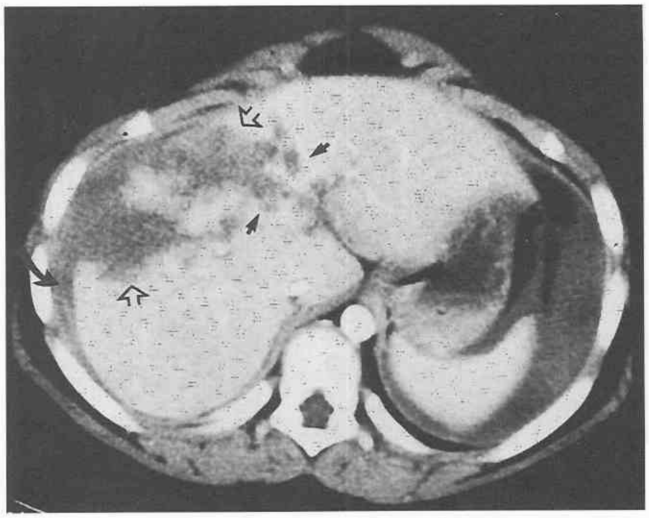

Figure 54–16. Hepatic injury. Contrast-enhanced CT image reveals a complex laceration *(arrows)* and hematoma *(open arrows)* in the liver, with an associated subcapsular hematoma *(curved arrows)*. Hemoperitoneum is visible in the left upper abdomen adjacent to the spleen.

tis secondary to intra-abdominal infection, hypercoagulable conditions, or tumor extension, or it may be idiopathic.[49] Following portal vein occlusion, numerous venous collaterals may develop in the portal hilum as alternate routes of venous blood supply to the liver. This phenomenon is referred to as cavernous transformation of the portal vein.

CT reveals the characteristic appearance of cavernous transformation of the portal vein as a tangle of small, enhancing vessels in the region of the porta hepatis, and no normally enhancing portal vein is visualized.[30] The clinical sequela of portal vein occlusion is the development of varices, which may hemorrhage. MRI and MR venography can be used to further clarify the venous anatomy both outside and within the liver of the child with cavernous transformation of the portal vein (Fig. 54–17).

Budd-Chiari Syndrome

Budd-Chiari syndrome is a rare hepatic vascular disease that is occasionally detected in children. It is caused by obstruction of the hepatic veins or the suprahepatic inferior vena cava by a web, stricture, or thrombus.

The CT appearance varies depending on the etiology. The enhancement pattern of the liver is mottled, with frequent sparing of the caudate lobe.[49] When present, a thrombus can be identified as a low-attenuation filling defect in the inferior vena cava or hepatic veins. MR venography is particularly well suited for detection of hepatic vein and inferior vena cava abnormalities leading to Budd-Chiari syndrome, as it is a noninvasive diagnostic technique that precludes the need for a conventional venogram.

Biliary Obstruction

The common causes of biliary obstruction in the pediatric population change with the age of the child. In the neonate or infant, obstruction of the biliary system may be caused by bile plugging, choledochal cysts, or biliary atresia. Ultrasound, rather than CT or MRI, is the cross-sectional imaging modality of choice in this population.[14]

In the older child or adolescent, biliary obstruction may be caused by calculi, previously unrecognized choledochal cysts, sclerosing cholangitis, adenopathy, or a pancreatic mass. In these children, CT or MRI may be performed after an ultrasound examination to further define obstructing neoplastic adenopathy or pancreatic masses.

Pediatric Liver Transplantation

Pretransplant Evaluation

Liver transplantation has become an accepted form of treatment of end-stage liver disease in children as well as in adults. In children, common causes of liver failure that result in a need for liver transplantation include biliary atresia, severe hepatitis, and metabolic disorders. In certain situations, hepatic neoplasms may be treated by liver transplantation. Size considerations and limited availability of organs may require children to receive whole or segmental liver transplants from cadaveric donors or segmental liver transplants from living related donors.[5] A pretransplant

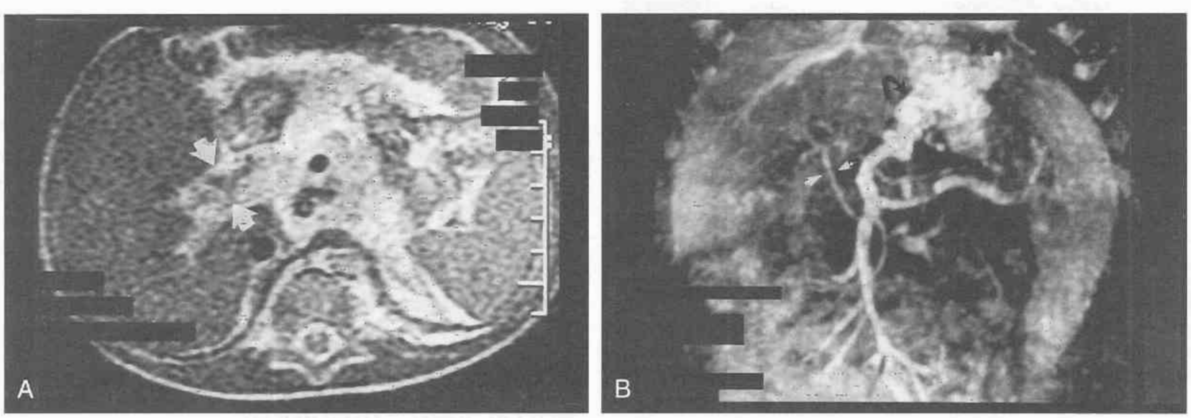

Figure 54–17. Cavernous transformation of the portal vein. *A,* Axial MR image reveals numerous small collateral veins in the portal hilum *(arrows)* with no normal portal vein visible. *B,* MRI venogram shows absence of the main portal vein. The hepatic artery *(arrows)* alone is visible entering the liver hilum. Large gastric varices *(curved arrows)* are present.

imaging workup is usually performed with ultrasound; it is performed less often with CT or MRI, unless liver transplantation is being considered in a child with a malignant hepatic neoplasm.

Post-transplant Complications

After liver transplantation, CT examinations are often used to evaluate for associated complications. Infection is common in this pediatric population and CT is the imaging modality of choice to assess for intrahepatic and extrahepatic abscesses. There may be multiple fluid-filled bowel loops related to the Roux-en-Y biliary anastomosis in the right upper quadrant that may not opacify after administration of oral contrast material and that can cause difficulty in the assessment of abscesses or bilomas in this region.[5] After a segmental liver transplant, there may be a postsurgical change at the cut edge of the liver with subsequent calcification of the region with time.[5]

Vascular complications following liver transplantation are better assessed with Doppler sonography. However, if focal hepatic necrosis has occurred as a result of vascular compromise, a contrast-enhanced CT may reveal areas of diminished enhancement within the liver.

Biliary complications of hepatic transplantation include leaks and obstruction.[25] Biliary leaks or disruption at the anastomotic site occur more commonly in the early post-transplant period. On contrast-enhanced CT examination, a low-attenuation bile collection may be detected in the region of the biliary-bowel anastomosis following bile duct leak (Fig. 54–18). Biliary necrosis, frequently seen secondary to occlusion or compromise of the hepatic artery, may also lead to breakdown of the bile ducts, with formation of intrahepatic bilomas or bile lakes that appear as low-attenuation collections within the hepatic parenchyma.

Biliary obstruction is typically a later complication of hepatic transplantation. Stricture formation may occur at the anastomosis, with subsequent dilatation of the intrahepatic bile ducts, which may be identified on CT as tubular low-attenuation structures adjacent to the enhancing portal veins (Fig. 54–19). MRI cholangiography may further define the biliary anatomy and sites of obstruction in the pediatric liver-transplant patient.[25, 35]

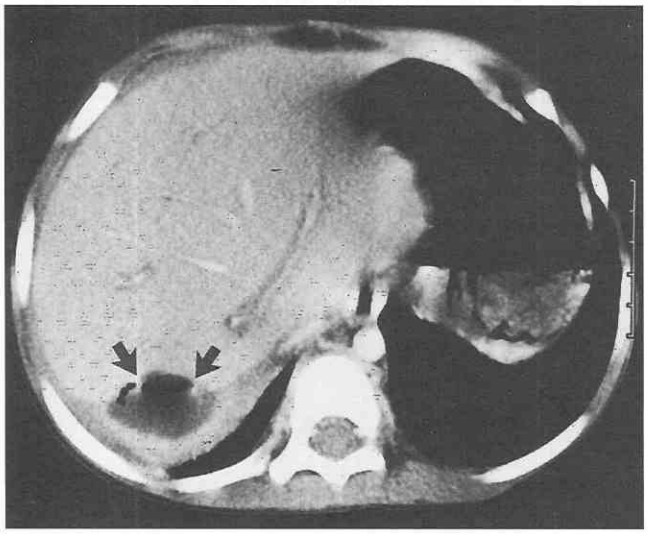

Figure 54–18. Bile leak following segmental liver transplantation. Contrast-enhanced CT image in a child with a segmental liver transplant reveals an irregular, low-attenuation collection of bile *(arrows)* with foci of air following anastomotic leak at the biliary-bowel anastomosis.

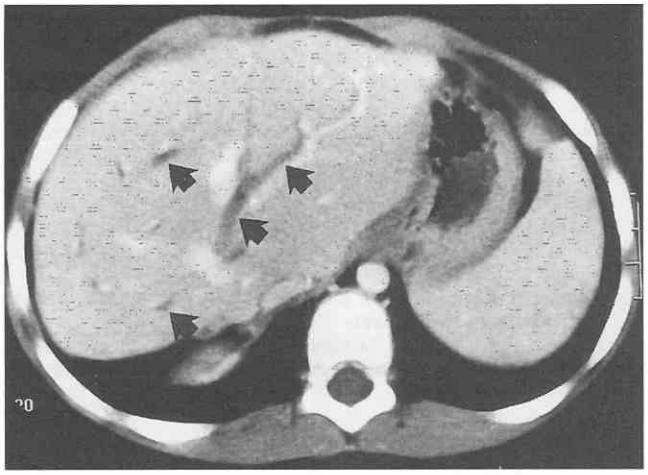

Figure 54–19. Biliary stricture following segmental liver transplantation. Contrast-enhanced CT image in a child who has developed a focal anastomotic stricture at the biliary-to-bowel anastomosis. Tubular low-attenuation structures *(arrows)* correspond to dilated intrahepatic biliary ducts. (Courtesy of Dr. Cynthia K. Rigsby, Children's Memorial Hospital, Chicago.)

Post-transplant lymphoproliferative disorder (PTLD) associated with Epstein-Barr virus infection and immunosuppression may occur following liver transplantation. Macroscopic evidence of PTLD may not be visible on CT imaging. When such evidence is visible, it includes low-attenuation mass lesions in the liver[14] and/or intraperitoneal and retroperitoneal adenopathy and pulmonary nodules.

References

1. Al-Ali F, Macpherson RI, Othersen HB, et al: A "wandering liver" in an infant. Pediatr Radiol 27:287, 1997.
2. Arrivé L, Fléjou, JF, Vilgrain V, et al: Hepatic adenoma: MR findings in 51 pathologically proved lesions. Radiology 193:507–512, 1994.
3. Atkinson GO Jr, Kodroff M, Sones PJ, et al: Focal nodular hyperplasia of the liver in children: A report of three new cases. Radiology 137:171–174, 1980.
4. Barnhart DC, Hirschl RB, Garver KA, et al: Conservative management of mesenchymal hamartoma of the liver. J Pediatr Surg 32: 1495–1498, 1997.
5. Ben-Ami TE, Martich V, Yousefzadeh DK, et al: Anatomic features of reduced-size liver transplant: Postsurgical imaging characteristics. Radiology 187:165–170, 1993.
6. Betz BW, Bisset III GS, Johnson ND, et al: MR imaging of biliary cysts in children with biliary atresia: Clinical associations and pathologic correlation. AJR Am J Roentgenol 162:167–171, 1994.
7. Boechat MI, Kangarloo H, Ortega J, et al: Primary liver tumors in children: Comparison of CT and MR imaging. Radiology 169: 727–732, 1988.
8. Boon LM, Burrows PE, Paltiel HJ, et al: Hepatic vascular anomalies in infancy: A twenty-seven-year experience. J Pediatr 129:346–354, 1996.
9. Buetow PC, Buck JL, Pantongrag-Brown L, et al: Undifferentiated (embryonal) sarcoma of the liver: Pathologic basis of imaging findings in 28 cases. Radiology 203:779–783, 1997.
10. Bulas DI, Eichelberger MR, Sivit CJ, et al: Hepatic injury from

blunt trauma in children: Follow-up evaluation with CT. AJR Am J Roentgenol 160:347–351, 1993.
11. Cheon J-E, Kim WS, Kim I-O, et al: Radiological features of focal nodular hyperplasia of the liver in children. Pediatr Radiol 28:878–883, 1998.
12. Dachman AH, Lichtenstein JE, Friedman AC, et al: Infantile hemangioendothelioma of the liver: A radiologic-pathologic-clinical correlation. Am J Roentgenol 140:1091–1096, 1983.
13. Dachman AH, Pakter RL, Ros PR, et al: Hepatoblastoma: Radiologic-pathologic correlation in 50 cases. Radiology 164:15–19, 1987.
14. Donnelly LF, Bisset GS III: Pediatric hepatic imaging. Radiol Clin North Am 36:413–427, 1998.
15. Hoffer FA: MR imaging of pediatric abdominal and pelvic tumors. Appl Radiol 29:23–29, 2000.
16. Hubbard AM, Meyer JS, Mahboubi S: Diagnosis of liver disease in children: Value of MR angiography. AJR Am J Roentgenol 159: 617–621, 1992.
17. Itai Y, Ebihara R, Eguchi N, et al: Hepatobiliary cysts in patients with autosomal dominant polycystic kidney disease: Prevalence and CT findings. AJR Am J Roentgenol 164:339–342, 1995.
18. Jabra AA, Fishman EK, Taylor GA: Hepatic masses in infants and children: CT evaluation. AJR Am J Roentgenol 158:143–149, 1992.
19. Jung G, Benz-Bohm G, Kugel H, et al: MR cholangiography in children with autosomal recessive polycystic kidney disease. Pediatr Radiol 29:463–466, 1999.
20. Kaplan SL: Pyogenic liver abscess. In Feigin RD, Cherry JS (eds): Textbook of Pediatric Infectious Diseases, 4th ed. Philadelphia, WB Saunders, 1998, pp 655–658.
21. Kaste SC, Young CW: Safe use of power injectors with central and peripheral venous access devices for pediatric CT. Pediatr Radiol 26: 499–501, 1996.
22. Kaufman RA, Towbin R, Babcock DS, et al: Upper abdominal trauma in children: Imaging evaluation. Am J Roentgenol 142:449–460, 1984.
23. Keslar, PJ, Buck JL, Selby DM: Infantile hemangioendothelioma of the liver revisited. Radiographics 13:657–670, 1993.
24. King SJ, Babyn PS, Greenberg ML, et al: Value of CT in determining the resectability of hepatoblastoma before and after chemotherapy. AJR Am J Roentgenol 160:793–798, 1993.
25. Laor T, Hoffer FA, Vacanti JP, et al: MR cholangiography in children after liver transplantation from living related donors. AJR Am J Roentgenol 170:683–687, 1998.
26. Leary DL, Weiskittel DA, Blane CE, et al: Follow-up imaging of benign pediatric liver tumors. Pediatr Radiol 19:234–236, 1989.
27. Lonergan GJ, Rice RR, Suarez ES: Autosomal recessive polycystic kidney disease: Radiologic-pathologic correlation. Radiographics 20: 837–855, 2000.
28. Lucaya J, Enriquez G, Amat L, et al: Computed tomography of infantile hepatic hemangioendothelioma. Am J Roentgenol 144:821–826, 1985.
29. Luker GD, Siegel MJ, Bradley DA, et al: Hepatic spiral CT in children: Scan delay time-enhancement analysis. Pediatr Radiol 26: 337–340, 1996.
30. Marn CS, Francis IR: CT of portal venous occlusion. AJR Am J Roentgenol 159:717–726, 1992.
31. Mergo PJ, Ros PR: Benign lesions of the liver. Radiol Clin North Am 36:319–331, 1988.
32. Miller WJ, Sechtin AG, Campbell WL, et al: Imaging findings in Caroli's disease. AJR Am J Roentgenol 165:333–337, 1995.
33. Mortele KJ, Mergo PJ, Urrutia M, et al: Dynamic gadolinium-enhanced MR findings in infantile hepatic hemangioendothelioma. J Comp Assist Tomogr 22:714–717, 1998.
34. Murphy BJ, Casillas J, Ros PR, et al: The CT appearance of cystic masses of the liver. Radiographics 9:307–322, 1989.
35. Norton KI, Glass RBJ, Kogan D, et al: MR cholangiography in children and young adults with biliary disease. AJR Am J Roentgenol 172:1239–1244, 1999.
36. Otal TM, Hendricks JB, Pharis P, et al: Mesenchymal hamartoma of the liver: DNA flow cytometric analysis of eight cases. Cancer 74: 1237–1242, 1994.
37. Pobiel RS, Bisset GS III: Pictorial essay: Imaging of liver tumors in infant and child. Pediatr Radiol 25:495–506, 1995.
38. Port J, Leonidas JC: Granulomatous hepatitis in cat-scratch disease. Pediatr Radiol 21:598–599, 1991.
39. Powers C, Ros PR, Stoupis C, et al: Primary liver neoplasms: MR imaging with pathologic correlation. Radiographics 14:459–482, 1994.
40. Reynolds M: Pediatric liver tumors. Semin Surg Oncol 16:159–172, 1999.
41. Roche KJ, Genieser NB, Ambrosino MM: Pediatric hepatic CT: An injection protocol. Pediatr Radiol 26:502–507, 1996.
42. Ros PR, Goodman ZD, Ishak KG, et al: Mesenchymal hamartoma of the liver: Radiologic-pathologic correlation. Radiology 158:619–624, 1986.
43. Ruess L, Bulas DI, Rivera O, et al: In-line pressures generated in small-bore central venous catheters during power injection of CT contrast media. Radiology 203:625–629, 1997.
44. Ruess L, Bulas DI, Kushner DC, et al: Peak enhancement of the liver in children using power injection and helical CT. AJR Am J Roentgenol 170:677–681, 1998.
45. Shilyansky J, Navarro O, Superina RA, et al: Delayed hemorrhage after nonoperative management of blunt hepatic trauma in children: A rare but significant event. J Pediatr Surg 34:60–64, 1999.
46. Sidhu MK, Shaw DWW, Daly CP, et al: Post-traumatic hepatic pseudoaneurysms in children. Pediatr Radiol 29:46–52, 1999.
47. Stanley P, Hall TR, Woolley MM, et al: Mesenchymal hamartomas of the liver in childhood: Sonographic and CT findings. Am J Roentgenol 147:1035–1039, 1986.
48. Stringer DA: The liver. In Stringer DA (ed): Pediatric Gastrointestinal Imaging, 1st ed. Toronto, BC Decker, 1989, pp 506–509.
49. Taylor GA: Acute hepatic disease. Radiol Clin North Am 35:799–813, 1997.
50. Taylor GA, Sivit CJ: Computed tomography imaging of abdominal trauma in children. Semin Pediatr Surg 1:253–259, 1992.
51. Teo EHJ, Strouse PJ, Prince MR: Applications of magnetic resonance imaging and magnetic resonance angiography to evaluate the hepatic vasculature in the pediatric patient. Pediatr Radiol 29:238–243, 1999.
52. Vade A, Olson MC, Vittore CP, et al: Hepatic enhancement analysis in children using Smart Prep monitoring for 2:1 pitch helical scanning. Pediatr Radiol 29:689–693, 1999.

55 Pediatric Spleen

Kimberly E. Applegate

Helical computed tomography (CT) is commonly used to investigate the spleen for injury, infection, infarction, and tumor and to determine spleen size and position.[33, 34, 43, 50] Both the normal and the abnormal spleen are optimally imaged at CT using intravenous (IV) contrast (Fig. 55–1). There is a growing interest in using CT imaging guidance in the spleen for interventional procedures, including tumor biopsy, needle aspiration of cysts and infection, and abscess drainage.[36] The role of magnetic resonance imaging (MRI) in spleen disorders is not well defined, although there is some evidence of its use in the detection of fungal infection, systemic iron overload, tumor, and the heterotaxy syndromes.[2, 9, 12, 13]

The normal spleen may demonstrate heterogeneous enhancement following IV contrast administration if there is a short scan delay time, a rapid injection rate, or severe cardiac or hepatic dysfunction. This appearance has been described as serpentine, cordlike enhancement.[58] IV contrast medium is hypothesized to enhance the white and red pulp of the spleen at different rates (Fig. 55–2).[14]

Normal Anatomy and Variants

Beginning in the 5th week of embryogenesis, the spleen develops as a mesenchymal mass within the dorsal gastric mesentery. It is the only alimentary tract organ that does not develop directly from the gut.[11] The spleen is a hematopoietic organ in the fetus and retains the potential for hematopoiesis in the child and adult. For example, in chronic anemic conditions, the spleen may act as a hematopoietic organ similar to the liver. After birth, the spleen normally functions as a filter for abnormal red and white blood cells.[43] From 10% to 30% of humans have accessory spleens, usually located in the splenic hilum and typically measuring 1 cm.[29]

The spleen has a number of mesenteric attachments, including the splenorenal, phrenicosplenic, and gastrosplenic ligaments. When these mesenteric attachments are either absent or more lax than usual, the spleen has the ability to move within the abdominal cavity. This rare entity, called "wandering spleen," may be asymptomatic, may produce intermittent abdominal pain, or may present with acute abdominal pain when torsion occurs.[4, 25, 32, 41, 42, 46, 48] The spleen may move from the left upper quadrant to the lower left or right side of the abdomen (Fig. 55–3). Torsion is more likely to occur in these cases, and children may present with acute abdominal pain and splenic infarction (Fig. 55–4). When infarction has occurred, the treatment is splenectomy; when symptoms are more chronic, splenopexy may be performed.[21]

Another rare congenital anomaly of the spleen, called *splenogonadal fusion*, occurs during the first trimester in utero, when the spleen fuses with the left gonad prior to normal ovarian or testicular descent at 9 weeks.[11] Some of the developing splenic tissue may migrate with the gonad into the pelvis or scrotum. In boys, cryptorchidism may be an associated finding. Because children with splenogonadal

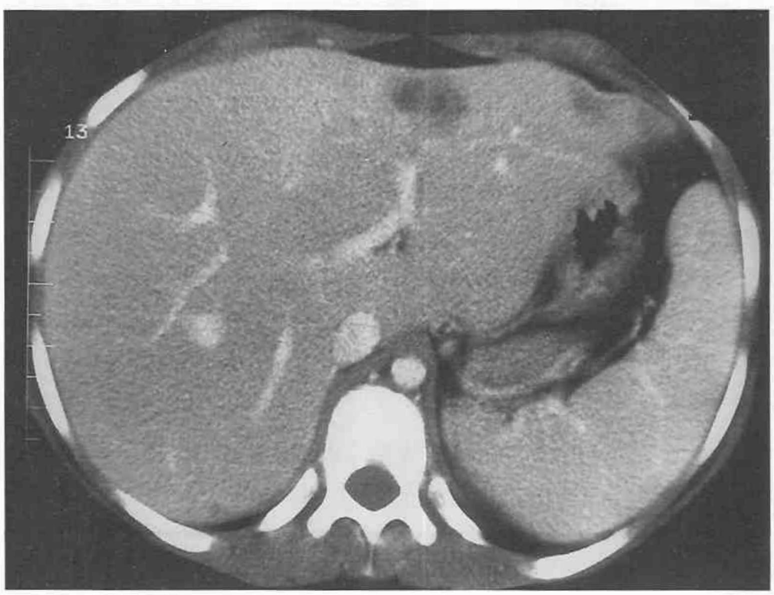

Figure 55–1. Normal, homogeneous enhancement of the spleen. This helical CT image shows mild splenomegaly in a 12-year-old girl with a fever after bone marrow transplant. The two low-density lesions in her liver are the result of a fungal infection.

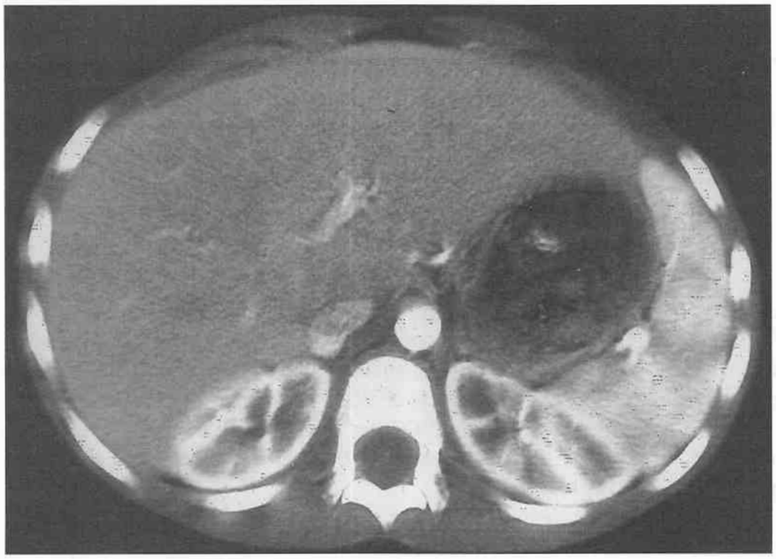

Figure 55–2. Heterogeneous enhancement of the normal spleen. Helical CT in a 10-year-old boy performed to evaluate for possible trauma shows the layered heterogeneous effect of short scan delay times. It is hypothesized that this appearance is caused by the difference in early contrast enhancement of the white and red pulp in the spleen.

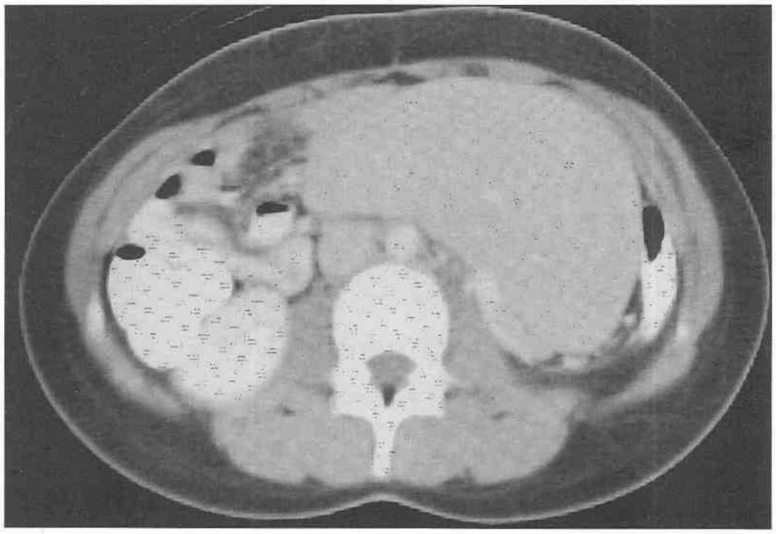

Figure 55–3. Wandering spleen in an 18-year-old girl who presented with an abdominal mass. Helical CT image of the lower abdomen shows the ectopic position of the spleen on the left. The spleen is homogeneously enlarged from a mononucleosis infection. (Courtesy of Lynn A. Fordham, M.D., Chapel Hill, N.C.)

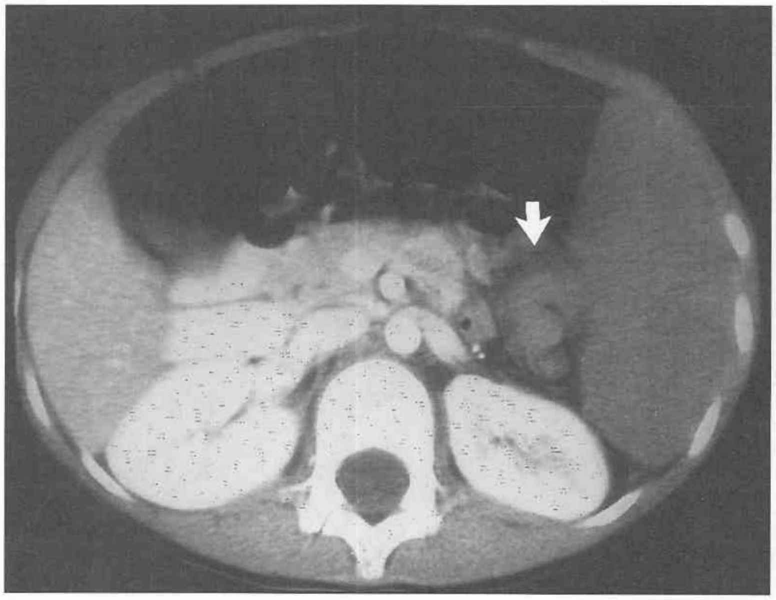

Figure 55–4. Acute infarction from torsion of the spleen in an 8-year-old girl with a 2-day history of left upper quadrant abdominal pain. Helical CT image shows complete lack of contrast enhancement of the enlarged, low-density spleen. Mesenteric edema and fat stranding can be visualized around the splenic vein *(arrow)*.

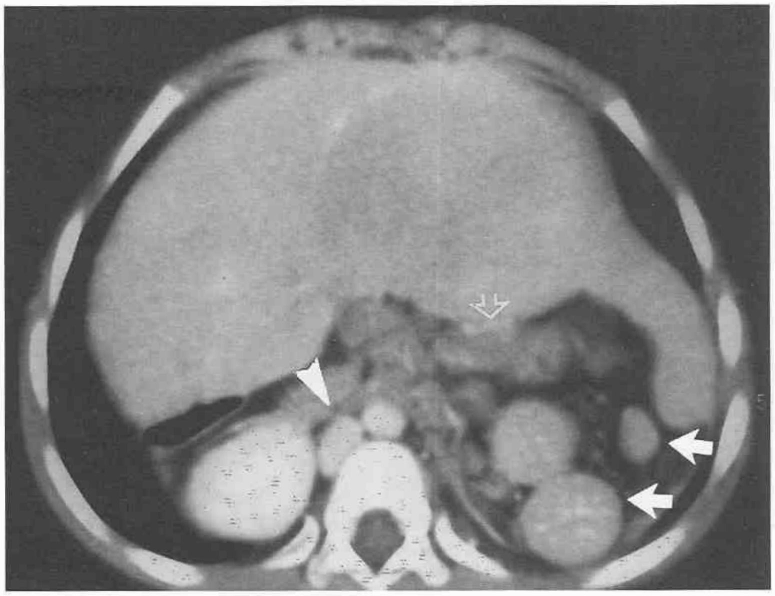

Figure 55–5. Polysplenia in a 6-year-old girl with congenital heart disease. Three small spleens *(arrows)* are located in the left upper quadrant, and the two larger spleens contain multiple, tiny calcifications of uncertain etiology. Note the azygous continuation of the inferior vena cava *(arrowhead)* on the right, the bridging liver, and the left-sided stomach location *(open arrow)* ipsilateral to the spleens.

fusion are often asymptomatic, splenogonadal fusion is not discovered unless a mass is palpated in the scrotum or until it is incidentally identified at surgery.

The spleen is *always* located on the same side of the abdomen as the stomach regardless of abdominal situs. In situs solitus, the stomach and spleen are located in the left upper quadrant; in situs inversus, they are located in the right upper quadrant. In situs ambiguus, in which the thoracoabdominal organs may be disordered, the location of the stomach air bubble on the plain radiograph defines the expected location of the spleen if it is present. Children with ambiguous position of the abdominal and chest organs may have a normal spleen, multiple small spleens (Fig. 55–5), or absence of the spleen.

Polysplenia and asplenia comprise the heterotaxy syndromes, an overlapping spectrum of abnormalities with situs ambiguus.[2, 60, 61] Typically, associated congenital heart disease, vascular anomalies, a bridging liver, and intestinal malrotation are present.[10, 22, 35] Asplenia occurs more frequently in boys and as for boys more severe congenital cardiac and vascular anomalies. Polysplenia occurs more commonly in girls and is associated with less severe cardiac disease, azygous continuation of the inferior vena cava, and, rarely, biliary atresia.

Splenomegaly

The ranges of normal spleen size throughout infancy and childhood have been established.[38] As a rule, the maximum spleen length is 6 cm plus one third times the child's age in years and should not exceed 12 cm.[56] When the spleen is enlarged, the normally pointed tips become rounded or bulbous (see Figs. 55–1, 55–3, and 55–4), and the inferior margin may extend below the inferior pole of the left kidney.

There are many causes of splenomegaly, but the most common in children are chronic liver disease and the leukemias/lymphomas.[56] Other causes include viral infections such as mononucleosis,[24] cat-scratch disease,[37] storage disorders such as Gaucher's disease,[23] collagen vascular diseases, inflammatory bowel disease, Langerhans' cell histiocytosis, and hemolytic anemias. Infants undergoing therapy sequester blood, producing splenic enlargement.[26] More commonly, children with sickle cell anemia may have splenomegaly in early childhood when there is splenic sequestration but later may undergo "autosplenectomy," leaving a small, densely calcified spleen (see Fig. 55–9).[27, 57]

Splenic vein thrombosis and splenomegaly may develop in children with pancreatitis, but this occurrence is less common than in adults.[56] In developing societies, splenomegaly may be caused by parasitic infection, particularly hydatid disease.

Trauma

After blunt trauma to the abdomen, the spleen and liver are the most commonly injured organs in children.[45, 51, 52, 54] Splenic injuries are similar to liver injuries and include a range of abnormalities from subcapsular hematoma to intrasplenic hematoma, laceration (Fig. 55–6), and devascularizing injury (Fig. 55–7). Contrast-enhanced CT imaging is highly accurate in identifying these injuries and remains the imaging modality of choice.[51–55] Typically, CT imaging demonstrates single or multiple low-density regions that result from lack of normal enhancement.

To estimate the severity of injury, the Organ Injury Scale Committee of the American Association for the Surgery of Trauma has classified the CT appearance of splenic injuries.[28] The five grades are as follows:

1. Capsular tears less than 1 cm parenchymal depth, or subcapsular hematoma less than 10% surface area.
2. Capsular tears 1 to 3 cm parenchymal depth, subcapsular hematoma 10% to 50% surface area, or intraparenchymal hematoma less than 2 cm in diameter.
3. Capsular tears greater than 3 cm parenchymal depth, subcapsular hematoma more than 50% surface area,

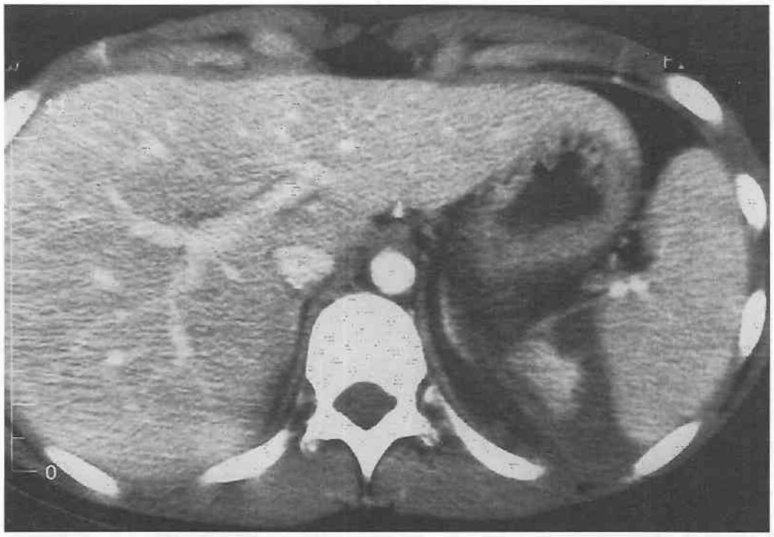

Figure 55–6. Splenic trauma, a result of a motor vehicle accident, in a 16-year-old girl. Helical CT image of the spleen shows the laceration of the posterior aspect associated with decreased enhancement. There is some low-density fluid around the injured portion of the spleen.

or intraparenchymal hematoma greater than 5 cm in diameter.
4. Hilar laceration with more than 25% splenic devascularization.
5. Completely shattered spleen or hilar laceration with complete devascularization.

Although grading systems based on extent of injury at CT have been developed to predict clinical outcomes and the need for operative intervention,[28, 53] CT grading of splenic injury does not correlate with the need for operative intervention.[17, 18] Most children with splenic injuries do not require operative management. In contradistinction, when the CT study is normal, there is strong predictive value that the child will not need surgical intervention later.[40, 55]

Hemorrhage is frequently associated with splenic injury and appears as low-density, perisplenic fluid or free fluid in the dependent portions of the abdomen and pelvis. A small proportion of children with splenic injury have extraperitoneal hemorrhage into the anterior pararenal space.[44] The presence of free fluid at CT is associated with more severe splenic injury but does not predict the need for operative intervention or the need for transfusion.[39, 40, 55]

Most small splenic injuries resolve at follow-up imaging in 2 to 4 months, but larger injuries may take up to 1 year.[3] In one report, 30% of splenic injuries of all grades resolved at follow-up CT.[5] Abnormal splenic findings at follow-up CT included clefts, small cysts, and segmental infarctions. The role of follow-up CT after splenic trauma remains unclear.[15]

Infarction

Spleen infarction results either from arterial or venous occlusion. The arteries supplying the spleen are end-arteries, leaving the spleen without an alternative blood supply if arterial thrombosis, thromboembolism, or injury occurs.[43, 59] Single or multiple, wedge-shaped, low-density lesions in the spleen periphery are well demonstrated by

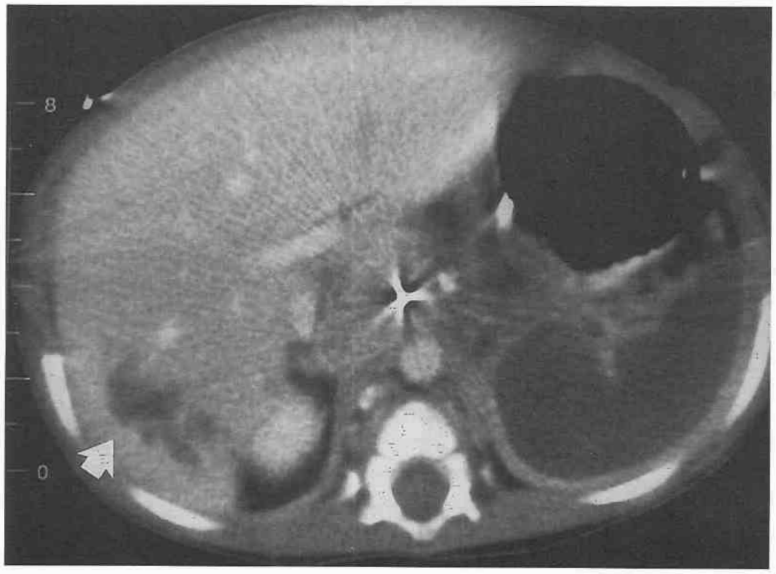

Figure 55–7. Iatrogenic injury resulting in complete splenic infarction. This CT image is from an 8-month-old boy who underwent surgical resection of a large neuroblastoma in the left upper quadrant. Helical CT image reveals no contrast enhancement of the spleen except for its rim, because of capsular artery supply. A liver hematoma can be visualized in the posterior right lobe *(arrow)*.

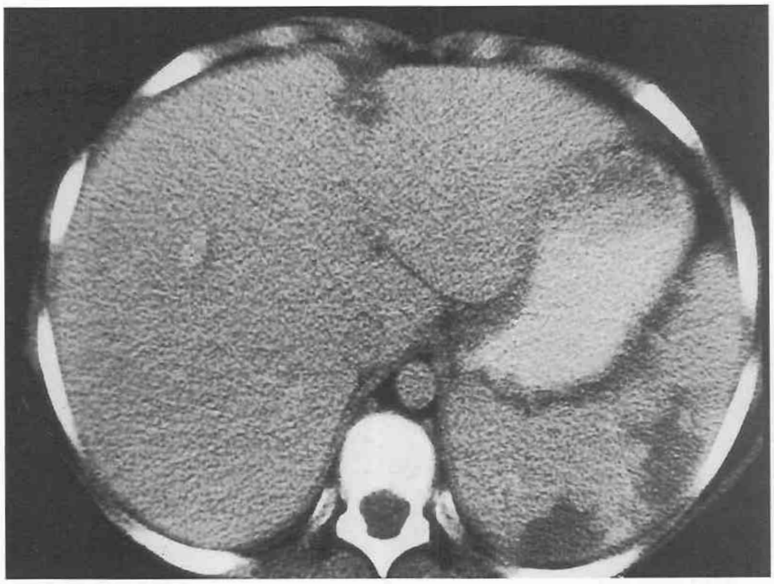

Figure 55–8. Multiple splenic infarcts in a 13-year-old girl after bone marrow transplant for treatment of a desmoplastic round cell tumor of the abdomen. Helical CT image demonstrates the typical wedge-shaped, low-density areas of infarction in the spleen.

CT (Fig. 55–8). Global infarction may be characterized by a rim sign on a contrast-enhanced CT scan (see Fig. 55–7). It may be difficult to distinguish an infarct from an abscess at CT imaging.[56, 58] On MRI scans, the appearance of splenic infarction is variable, depending on both the age and the degree of hemorrhage within it.[1, 59] Remote splenic infarction has a variable appearance at CT. It may not be visible, it may show scarring with contour irregularity, or it may result in cyst formation. Global infarction may result in a small, densely calcified spleen (Fig. 55–9).

Infection

Abscesses in the spleen are unusual but can be seen after splenic trauma, as a result of septic embolism, and in immunocompromised children. Splenic abscesses are usually of low density and variable size at CT. In immunocompromised children, systemic candidiasis sometimes produces multiple, tiny, round, low-density abscesses in the spleen, liver, and, less commonly, the kidneys (Fig. 55–10).[16] Children undergoing chemotherapy for leukemia or children with acquired immunodeficiency syndrome (AIDS) are most commonly affected by multiple fungal abscesses. Children with AIDS are also at increased risk for mycobacterial abscesses in the spleen.

CT imaging may reveal multiple punctate calcifications in the spleen and liver in asymptomatic children (Fig. 55–11). These calcifications are usually caused by granulomatous disease such as chronic granulomatous disease, tuberculosis, histoplasmosis, or cat-scratch disease.[8, 37, 49]

Cysts and Neoplasms

Splenic masses are rare—even the most common one in children, the cyst. Cysts may be either true epithelium-lined cysts or pseudocysts, which occur after infection, infarction, or trauma (Fig. 55–12).[6, 7, 16, 19, 31] After IV contrast administration, cysts have a low density relative to

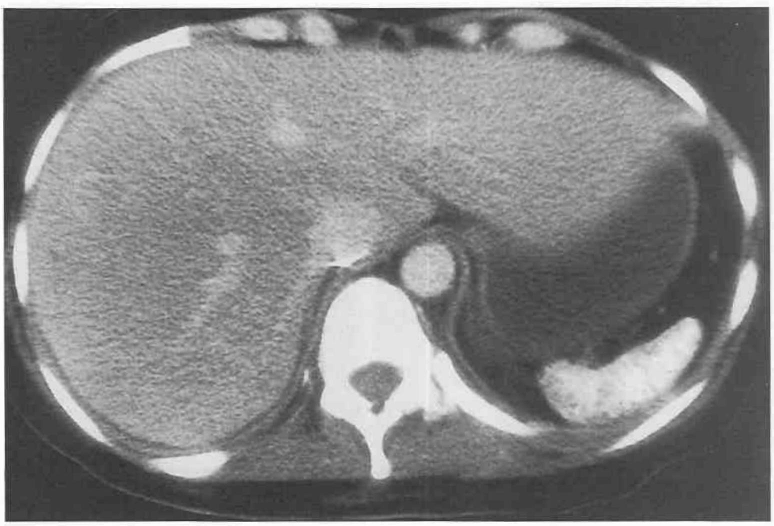

Figure 55–9. Remote infarction of the spleen in a 12-year-old girl after meningococcal sepsis. She had a remote history of bone marrow transplant for chronic myelogenous leukemia. Helical CT image reveals a diminutive, densely calcified spleen.

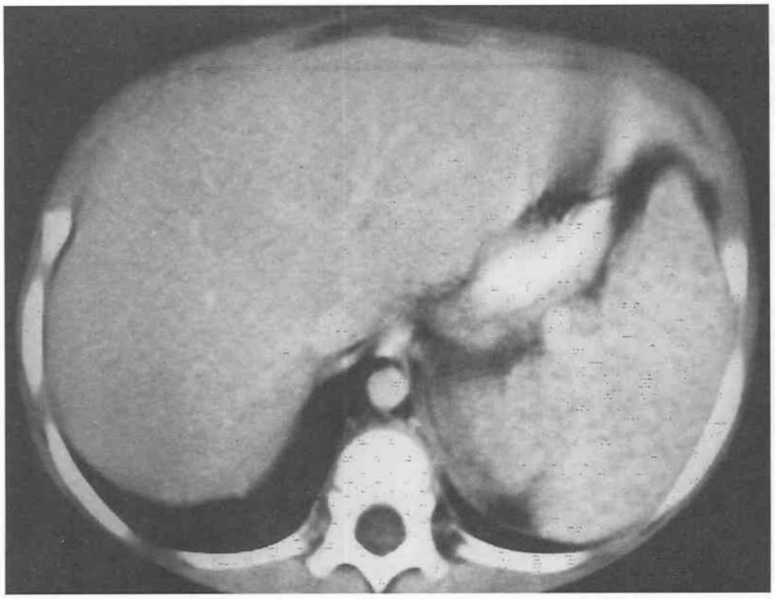

Figure 55–10. Candidiasis of the spleen in a 2-year-old boy with acute myelogenous leukemia undergoing chemotherapy. Helical CT image reveals the typical low-density appearance of numerous small abscesses in the spleen due to *Candida albicans* infection. Although the liver is typically coinfected in candidiasis, there were no abscesses seen in this child's liver at CT examination. Multiple abscesses, however, were also seen in both kidneys at CT.

Figure 55–11. Granulomatous disease of the liver and spleen in a 10-year-old girl. Helical CT image reveals scattered punctate calcifications within the liver and spleen. The cause of the granulomatous disease was not known.

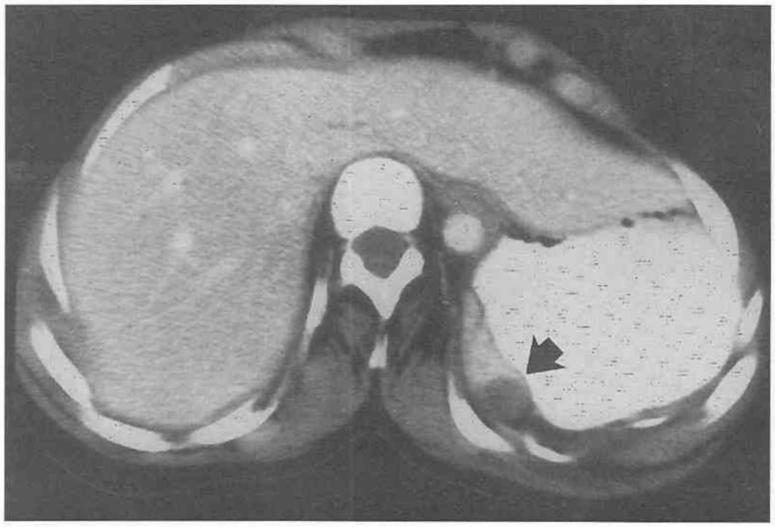

Figure 55–12. Incidental splenic cyst in a child with Crouzon's syndrome. Helical CT image shows a small, low-density, round cyst in the spleen *(arrow)*. The cause of the cyst was unknown, and there is no known association with Crouzon's syndrome. The child also has a marked scoliosis deformity.

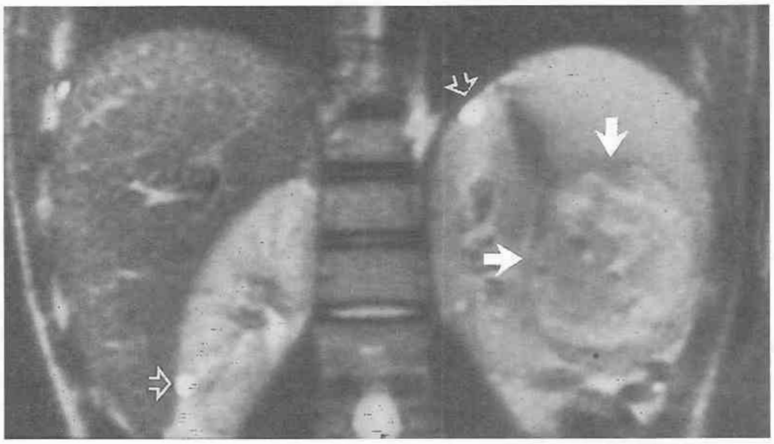

Figure 55–13. Hamartoma of the spleen in a 17-year-old boy with tuberous sclerosis. Coronal T2-weighted MR image of the abdomen shows a large heterogeneous-signal-intensity mass in the lower portion of the spleen in the left upper quadrant *(arrows)*. Note the high signal intensity of a small renal cyst in each of the patient's kidneys *(open arrows)*.

normal spleen. The most common infectious type is the hydatid cyst, caused by *Echinococcus* tapeworm infection. This cyst may be unilocular or multilocular and commonly affects children in developing societies.[59]

Primary splenic tumors are exceedingly rare in children and are usually benign.[20] The most common benign tumor in children is the hamartoma (Fig. 55–13), followed by the hemangioma. Both are often asymptomatic. The hamartoma is usually a solid, solitary lesion of low or mixed low and high density, although it may appear partially cystic. The imaging appearance of the hemangioma in the spleen is similar to that in the liver. It is hypodense or isodense to the spleen without contrast material; after administration of IV contrast, it enhances homogeneously, appearing hyperdense, compared with the normal spleen appearance. Hemangiomas may be solitary or multiple. In rare instances, they are associated with a consumptive coagulopathy called the Kasabach-Merritt syndrome. Vascular and lymphatic malformations can occur in the spleen either in isolation or in association with similar lesions at other body sites. Lymphatic malformations may appear as either unilocular or multilocular cysts.[30]

Lymphoma and leukemia are the most common malignant tumors to involve the spleen in children. Unfortunately, CT cannot distinguish spleen involvement from noninvolvement. The involved spleen may be of normal size and show an enhancement pattern. When abnormal, the spleen most commonly shows homogeneous enlargement without masses. Four CT patterns of lymphomatous involvement have been described:

1. Homogeneous enlargement.
2. Miliary masses.
3. Macroscopic masses.
4. A large solitary mass.[16, 47]

Typically, the masses are of low density compared with the normal spleen appearance, as visualized with contrast-enhanced CT (Fig. 55–14).

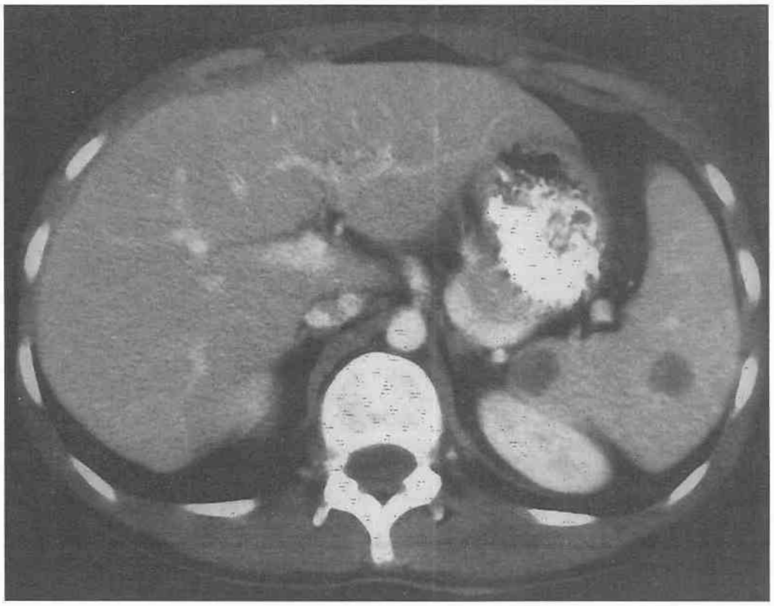

Figure 55–14. Lymphomatous involvement of the spleen in a 15-year-old boy. Helical CT image reveals two low-density lesions in the patient's spleen, which is mildly enlarged. The patient also had several low-density lesions in his right kidney (not shown) at presentation. Two weeks after institution of chemotherapy, the low-density lesions resolved completely and spleen size reverted to normal.

References

1. Adler DD, Glazer GM, Aisen AM: MRI of the spleen: Normal appearance and findings in sickle-cell anemia. Am J Roentgenol 147: 843, 1986.
2. Applegate KE, Goske M, Pierce G, et al: Situs revisited: Imaging of the heterotaxy syndrome. Radiographics 19:837–852, 1999.
3. Benya EC, Bulas DI, Eichelberger MR, Sivit CJ: Splenic injury from blunt abdominal trauma in children: Follow-up evaluation with CT. Radiology 195:685–688, 1985.
4. Berkenblit RG, Mohan S, Bhatt GM, et al: Wandering spleen with torsion: Appearance on CT and ultrasound. Abdom Imaging 19: 459–460, 1994.
5. Blane CE, Strouse PJ, Teitelbaum DH, et al: CT appearance of the spleen following conservative management of traumatic injury. Emerg Radiol 6:157–159, 1999.
6. Dachman AH, Ros PR, Murari JP, et al: Nonparasitic splenic cysts: A report of 52 cases with radiologic pathologic correlation. Am J Roentgenol 147:537, 1986.
7. Daneman A, Martin DJ: Congenital epithelial splenic cysts in children: Emphasis on sonographic appearances and some unusual features. Pediatr Radiol 12:119–125, 1982.
8. Dangman BC, Albanese BA, Kacica MA, et al: Cat-scratch disease in two children presenting with fever of unknown origin: Imaging features and association with a new causative agent, *Rochalimaea henselae*. Pediatrics 95:767–771, 1995.
9. De Roos A: Invited commentary. Radiographics 19:853–854, 1999.
10. Ditchfield MR, Hutson JM: Intestinal rotational abnormalities inpolysplenia and asplenia syndromes. Pediatr Radiol 28:303–306,1998.
11. Dodds WJ, Taylor AJ, Erickson SJ, et al: Radiologic imaging of splenic anomalies. AJR Am J Roentgenol 155:805–810, 1990.
12. Donnelly LF, Bisset GS 3rd: Dark spleens and liver on MRI after chemotherapy: Is it really iron overload? Pediatr Radiol 28:486, 1998.
13. Donnelly LF, Emery KH, Bove KE, et al: Normal changes in the MR appearance of the spleen during early childhood. AJR Am J Roentgenol 166:635–639; 1996.
14. Donnelly LF, Foss JN, Frush DP, et al: Heterogeneous splenic enhancement patterns on spiral CT images in children: Minimizing misinterpretation. Radiology 10:493–497, 1999.
15. Federle MP: Splenic trauma: Is follow-up CT of value? Radiology 194:23–24, 1995.
16. Freeman JL, Jafri SZH, Roberts JL, et al: CT of congenital and acquired abnormalities of the spleen. Radiographics 13:597–610, 1993.
17. Frumiento C, Sartorelli K, Vane D: Complications of splenic injuries: Expansion of the nonoperative theorem. J Pediatr Surg 35:788–791, 2000.
18. Gavant ML, Schurr M, Flick PA, et al: Predicting clinical outcome of nonsurgical management of blunt splenic injury: Using CT to reveal abnormalities of splenic vasculature. AJR Am J Roentgenol 168:207–212, 1997.
19. Griscom NT, Hargreaves HK, Schwartz MZ, et al: Huge splenic cyst in a newborn: Comparison with 10 cases in later childhood and adolescence. Am J Roentgenol 129:889–891, 1977.
20. Hahn PF, Weissleder R, Stark DD, et al: MR imaging of focal splenic tumors. AJR Am J Roentgenol 150:823–827, 1988.
21. Herman TE, Siegel MJ: CT of acute splenic torsion in children with wandering spleen. AJR Am J Roentgenol 156:151–153, 1991.
22. Hernanz-Schulman M, Ambrosino MM, Genieser NB, et al: Pictorial essay. Current evaluation of the patient with abnormal visceroatrial situs. AJR Am J Roentgenol 154:797–802, 1990.
23. Hill SC, Damaska BM, Ling A, et al: Gaucher disease: Abdominal MR imaging findings in 46 patients. Radiology 184:561–566, 1992.
24. Johnson MA, Cooperberg PL, Boisvert J, et al: Spontaneous splenic rupture in infectious mononucleosis: Sonographic diagnosis and follow-up. Am J Roentgenol 136:111–114, 1981.
25. Kanthan R, Radhi JM: The "true" splenic wanderer. Gastroenterology 13:169–171, 1999.
26. Klippenstein DL, Zerin JM, Hirschl RB, Donn SM: Splenic enlargement in neonates during ECMO. Radiology 190:411–412, 1994.
27. Magid D, Fishman EK, Siegelman SS: Computed tomography of the spleen and liver in sickle cell disease. Am J Roentgenol 143: 245–249, 1984.
28. Moore EE, Cogbill TH, Jurkovich GJ, et al: Organ injury scaling: Spleen and liver (1994 revision). J Trauma 38:323–324, 1995.
29. Moore KL: The digestive system. In Moore KL (ed): The Developing Human: Clinically Oriented Embryology, 3rd ed. Philadelphia, WB Saunders, 1982, pp 228–239.
30. Morgenstern L, Bello JM, Fisher BL, Verham RP: The clinical spectrum of lymphangiomas and lymphangiomatosis of the spleen. Am Surg 58:599–603, 1992.
31. Musy PA, Roche B, Belli D, et al: Splenic cysts in pediatric patients: A report on 8 cases and review of the literature. Eur J Pediatr Surg 2:137–140, 1992.
32. Nemcek AA Jr, Miller FH, Fitzgerald SW: Acute torsion of a wandering spleen: Diagnosis by CT and duplex Doppler and color flow sonography. AJR Am J Roentgenol 157:307–309, 1991.
33. Olutola PO, Daneman A, Martin DJ, et al: Unusual renal distortion and displacement due to the spleen. Pediatr Radiol 12:185–189,1982.
34. Paterson A, Frush DP, Donnelly LF, et al: A pattern-oriented approach to splenic imaging in infants and children. Radiographics 19:1465–1485, 1999.
35. Peoples WM, Moller JH, Edwards JE: Polysplenia: A review of 146 cases. Pediatr Cardiol 4:129–137, 1983.
36. Quinn SF, van Sonnenberg E, Casola G, et al: Interventional radiology in the spleen. Radiology 161:289–291, 1986.
37. Rappaport DC, Cumming WA, Ros PR: Disseminated hepatic and splenic lesions in cat-scratch disease: Imaging features. AJR Am J Roentgenol 156:1227–1228, 1991.
38. Rosenberg HK, Markowitz RI, Kolberg H, et al: Normal splenic size in infants and children: Sonographic measurements. AJR Am J Roentgenol 157:119–121, 1991.
39. Ruess L, Sivit CJ, Eichelberger MR, et al: Blunt hepatic and splenic trauma in children: Correlation of a CT injury severity scale with clinical outcome. Pediatr Radiol 25:321–325, 1995.
40. Ruess L, Sivit CJ, Eichelberger MR, et al: Blunt abdominal trauma in children: Impact of CT on operative and nonoperative management. AJR Am J Roentgenol 169:1011–1014, 1997.
41. Seo T, Ito T, Watanabe Y, Umeda T: Torsion of an accessory spleen presenting as an acute abdomen with an inflammatory mass: US, CT, and MRI findings. Pediatr Radiol 24:532–534, 1994.
42. Shiels WE II, Johnson JF, Stephenson SR, et al: Chronic torsion of the wandering spleen. Pediatr Radiol 19:465, 1989.
43. Siegel MJ: Spleen, peritoneum, and abdominal wall. In Siegel MJ (ed): Pediatric Body CT. Philadelphia, Lippincott Williams & Wilkins, 1999, pp 175–200.
44. Sivit CJ, Frazier AA, Eichelberger MR: Prevalence and distribution of extraperitoneal hemorrhage associated with splenic injury in infants and children. AJR Am J Roentgenol 172:1015–1017, 1999.
45. Sivit CJ, Taylor GA, Eichelberger MR: Visceral injury in battered children: A changing perspective. Radiology 173:659–661, 1989.
46. Spector JM, Chappell J: Gastric volvulus associated with wandering spleen in a child. J Pediatr Surg 35:641–642, 2000.
47. Strijk SP, Wagener DJ, Bogman MJ, et al: The spleen in Hodgkin disease: Diagnostic value of CT. Radiology 154:753, 1985.
48. Swischuk LE, Williams JB, John SD: Torsion of wandering spleen: The whorled appearance of the splenic pedicle on CT. Pediatr Radiol 23:476–477, 1993.
49. Talenti E, Cesaro S, Scapinello A, et al: Disseminated hepatic and splenic calcifications following cat-scratch disease. Pediatr Radiol 24: 324–343, 1994.
50. Taylor AJ, Dodds WJ, Erickson SJ: CT of acquired abnormalities of the spleen. AJR Am J Roentgenol 157:1213–1219, 1991.
51. Taylor GA, Eichelberger MR, O'Donnell R, et al: Indications for computed tomography in children with blunt abdominal trauma. Ann Surg 213:212–218, 1991.
52. Taylor GA, Fallat ME, Potter BM, et al: The role of computed tomography in blunt abdominal trauma in children. J Trauma 28: 1660–1664, 1988.
53. Taylor G, O'Donnell R, Sivit C, et al: Abdominal injury score: A clinical score for the assignment of risk in children after blunt trauma. Radiology 190:689–694, 1994.
54. Taylor GA, Sivit CJ: Computed tomography imaging of abdominal trauma in children. Semin Pediatr Surg 1:253–259, 1992.
55. Taylor GA, Sivit CJ: Posttraumatic peritoneal fluid: Is it a reliable indicator of intraabdominal injury in children? J Pediatr Surg 30: 1644–1648, 1995.

56. Teele RL, Share JC: The spleen. In Teele RL, Share JC (eds): Ultrasonography of Infants and Children. Philadelphia, WB Saunders, 1991, pp 405–415.
57. Topley JM, Rogers DW, Stevens MCG, Serjeant GR: Acute splenic sequestration and hypersplenism in the first five years in homozygous sickle cell disease. Arch Dis Child 56:765–769, 1981.
58. Urban BA, Fishman EK: Helical CT of the spleen. AJR Am J Roentgenol 179:997–1003, 1998.
59. Urrutia M, Mergo PJ, Ros LH, et al: Cystic masses of the spleen: Radiologic-pathologic correlation. Radiographics 16:107–129, 1996.
60. Van Praagh R, Vlad P: Dextrocardia, mesocardia, and levocardia: The segmental approach to diagnosis in congenital heart disease. In Keith JD, Rowe RD, Vlad P (eds): Heart Disease in Infancy and Childhood. New York, Macmillan, 1978, pp 638–695.
61. Winer-Muram HT, Tonkin ILD: The spectrum of heterotaxic syndromes. Radiol Clin North Am 27:1147–1170, 1989.

56 Pancreas

Carlos J. Sivit

Computed tomography (CT) has a primary role in the assessment of suspected pancreatic pathology in children. It is the modality of choice for evaluating suspected pancreatic neoplasms, trauma, or complications of pancreatitis. The use of helical CT scanning with thin collimation has allowed for the more precise delineation of many pancreatic conditions. In addition, magnetic resonance imaging (MRI) is being increasingly used to assess the pancreas in children, particularly in the evaluation of developmental or traumatic abnormalities of the pancreatic duct.

Normal Anatomy

The pancreas is located in the *anterior pararenal space*. Other anatomic structures in the same retroperitoneal anatomic compartment include the *duodenum*, the *ascending colon*, and *descending colon*. The pancreatic tail is in close proximity to the *splenic hilum*, which is peritoneal in location. The spleen contains a covering layer of peritoneum that is limited medially at the hilum, resulting in a bare area.[21] This results in a potential two-way communication between the retroperitoneum and the greater peritoneal cavity. Thus, inflammatory or traumatic pancreatic conditions may be associated with the spread of fluid or inflammation into the peritoneal cavity, whereas splenic trauma that extends into the hilum may result in extension of blood into the anterior pararenal space that surrounds the pancreas.

Anterior to the anterior pararenal space that surrounds the pancreas is the *lesser sac*. This normally is a potential space that is an extension of the greater peritoneal cavity. The lesser sac connects to the greater peritoneal cavity through the foramen of Winslow. The boundaries of the lesser sac include the liver and stomach anteriorly, peritoneal reflections posteriorly, and the hilum of the spleen to the left.

Additional important anatomic structures in relation to the pancreas include the duodenum, which lies adjacent to the pancreatic head; the *inferior vena cava*, which lies posterior to the pancreatic head; the *portal vein* origin at the confluence of superior mesenteric vein and splenic vein, which lies posterior to the pancreatic neck; the *common bile duct*, which courses through the pancreatic head; and the *splenic vein* and the *splenic artery*, which run posterior to the pancreatic body and tail.

Developmental Abnormalities

Pancreas Divisum

Pancreas divisum is the most clinically important and common developmental abnormality of the pancreas. In patients with this condition, the two pancreatic ducts (Wirsung and Santorini) are separate throughout their course. Normally, these fuse during development, with the main pancreatic duct of Wirsung forming from the ventral pancreatic duct and the distal portion of the dorsal duct. Pancreas divisum is associated with an increased incidence of pancreatitis.[4] This is thought to arise secondary to partial obstruction to the passage of pancreatic exocrine secretions from the pancreas due to a narrowed orifice at the duodenum, resulting in the leak of pancreatic secretions into pancreatic tissue.

Magnetic resonance (MR) pancreatography is highly accurate in depicting the pancreatic ductal abnormalities in pancreas divisum.[6, 8] The multiplanar capability of MR pancreatography allows visualization of the isolated ventral and dorsal ducts and of their entrance into the major and minor ampullae.

Annular Pancreas

An annular pancreas consists of an abnormal ring of pancreatic tissue surrounding the second portion of the duodenum. It is thought to be an abnormality in pancreatic development secondary to duodenal atresia. Thus, the primary abnormality is in the abnormal development of the duodenum. CT shows pancreatic tissue surrounding the second portion of the duodenum.[10]

Hereditary Diseases

Cystic Fibrosis

Cystic fibrosis is an autosomal recessive disease in which the majority of patients have severe exocrine pancreatic insufficiency. Pancreatic disease in these patients results from pancreatic ductal obstruction by inspissated secretions that leads to acinar and ductal dilatation and atrophy of acinar tissue.[10, 24, 26] With the progression of fibrosis, there is eventual fatty replacement of the gland in many patients; less severe fibrosis may not result in fatty replacement. A correlation exists between the degree of fatty infiltration of the pancreas and the extent of pancreatic exocrine dysfunction present in these patients.[24]

The CT appearance after fatty replacement of the pancreas includes a reduction in size of the pancreas with low-attenuation values equal to the fat noted within the gland[10, 24, 26] (Fig. 56–1). Dystrophic parenchymal calcifications and cysts also may be noted.[10, 11, 24, 26] Rarely, there can be complete replacement of the pancreas by macroscopic cysts, a condition described as *pancreatic cystosis*.[11]

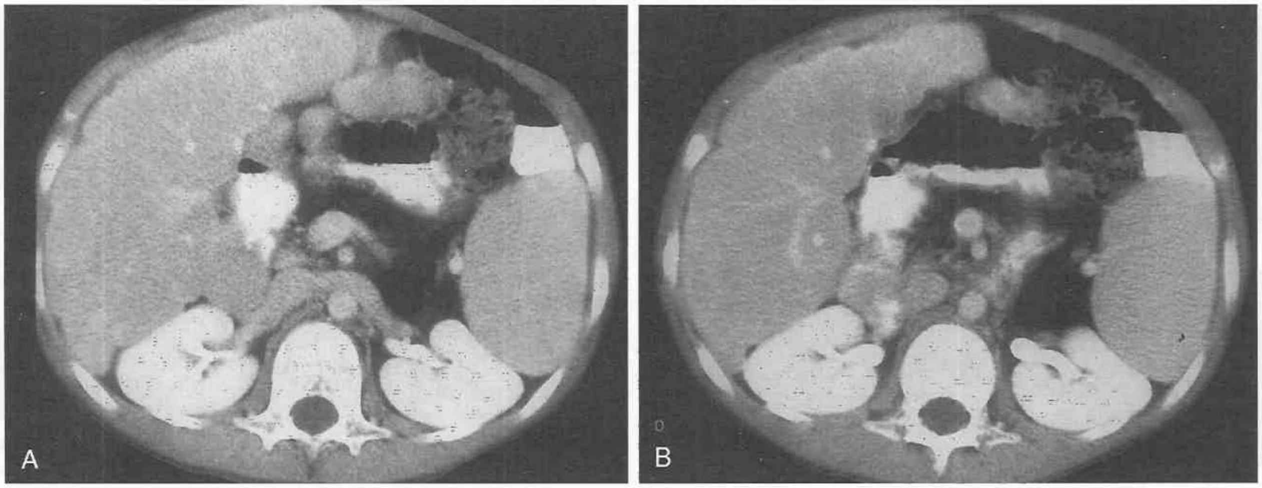

Figure 56–1. Fatty replacement of the pancreas in cystic fibrosis. CT scans through the body and tail of the pancreas *(A)* and through the head of the pancreas *(B)* in a patient with cystic fibrosis demonstrate diffuse low attenuation of the pancreas indicative of diffuse fatty infiltration.

Shwachman (Shwachman-Diamond) Syndrome

This is a rare congenital syndrome characterized by metaphyseal chondrodysplasia, short stature, bone marrow dysfunction, and pancreatic insufficiency. On CT scans, the pancreas is characterized by fatty replacement of the gland, similar to the changes seen in cystic fibrosis. With increasing fat replacement of the pancreas, a decrease in gland size is noted.

Von Hippel–Lindau Disease

Von Hippel–Lindau disease is an autosomal dominant disease characterized by retinal angiomatosis, cerebellar hemangioblastoma, and cysts in various organs, including the pancreas.[10] Multiple pancreatic cysts are usually noted, which range widely in size. The cysts are seen primarily in the pancreatic body and tail. Occasionally, the cyst walls may calcify.

Infectious and Inflammatory Conditions

Acute Pancreatitis

Acute pancreatitis in children is most commonly seen after blunt abdominal trauma. Nontraumatic causes of acute pancreatitis include infection, drug toxicity, developmental anomalies, and hereditary pancreatitis. Acute pancreatitis can involve surrounding soft tissues and remote organs. The disease is classified as mild or severe on the basis of pathologic and clinical findings.

Mild acute pancreatitis is characterized pathologically by interstitial edema and rarely by microscopic foci of acinar cell necrosis.[20] Clinically, these patients may have abdominal pain and tenderness but few systemic signs. They generally demonstrate an improvement in clinical signs and symptoms within 48 to 72 hours after the onset of illness.

Severe acute pancreatitis is characterized pathologically by fat necrosis, parenchymal hemorrhage, and pancreatic ductal disruption.[20] Patients may have severe clinical findings, including prolonged severe abdominal pain, gastrointestinal bleeding, disseminated intravascular coagulation, shock, and pulmonary insufficiency.

Acute pancreatitis may be associated with a number of complications, such as pancreatic necrosis, which consists of focal or diffuse zones of liquefied, nonviable pancreatic parenchyma; peripancreatic inflammation, consisting of soft tissue inflammation that surrounds the pancreas; acute focal or free extrapancreatic fluid collections; and pseudocysts, which represent focal fluid collections surrounded by a well-defined capsule of fibrous tissue.

Pancreatic necrosis tends to occur early in the course of the disease. The presence of pancreatic necrosis is predictive of severe pancreatitis and is the single greatest determinant of complications and death in patients with acute pancreatitis.[2] Focal fluid collections associated with acute pancreatitis may develop in the first few days after the onset of illness. These fluid collections may spontaneously resolve or evolve into pseudocysts.

A *pseudocyst* is a more mature fluid collection that characteristically takes at least 4 to 6 weeks to develop. Pseudocysts do not have an epithelial lining and hence are not true cysts.

Many cases of acute pancreatitis are successfully managed without the need for imaging. CT is commonly used in the evaluation of complications associated with severe acute pancreatitis because it is useful in diagnosing pancreatic necrosis and pseudocyst formation and in defining complex extrapancreatic spread of the inflammatory process.[1, 2, 10, 13, 20, 26] Thin-collimation scanning is essential in the CT evaluation of the pancreas. The collimation should be between 2 and 4 mm, depending on patient size.

Optimization of intravenous contrast enhancement is also critical, with higher injection rates and dual arterial phase and venous phase scanning useful in detection of

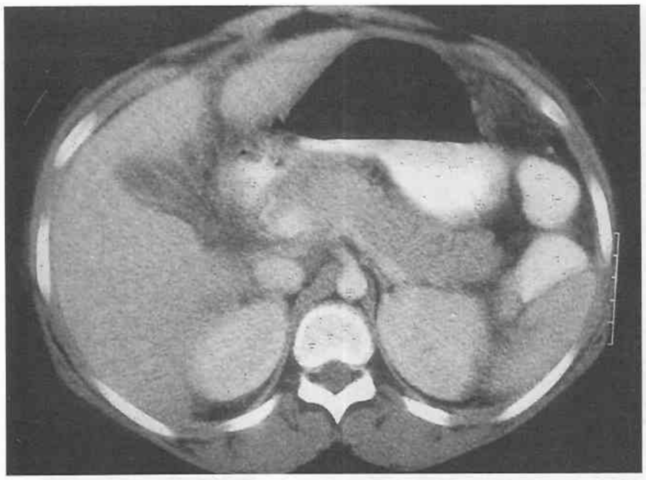

Figure 56–2. Acute pancreatitis with pancreatic enlargement and ill-defined borders. CT scan through the pancreas in a patient with acute pancreatitis demonstrates diffuse pancreatic enlargement. There are ill-defined pancreatic margins secondary to peripancreatic inflammation.

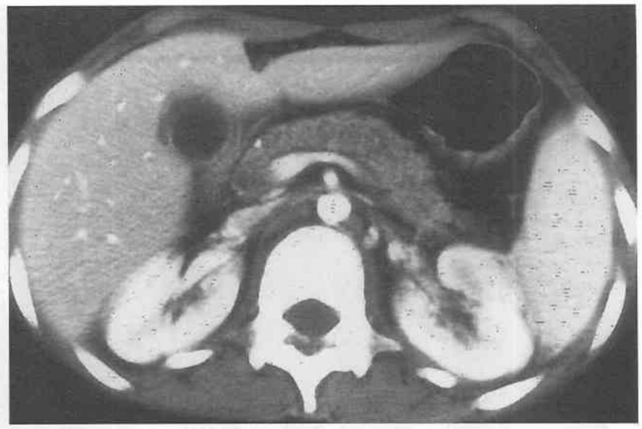

Figure 56–4. Acute pancreatitis with fluid in the anterior pararenal space. CT scan through the pancreas in a patient with recurrent episodes of acute pancreatitis demonstrates fluid in the anterior pararenal space. There is a punctate parenchymal calcification in the head of the pancreas, likely secondary to prior inflammatory episodes.

hemorrhage or necrosis. Oral contrast opacification is also important not only for delineating the duodenum-pancreas interface but also because the spread of pancreatic inflammation may involve the small bowel mesentery as well.

CT findings associated with uncomplicated acute pancreatitis range from a normal appearing pancreas to diffuse gland enlargement[13, 20, 24] (Fig. 56–2). The pancreas is reported to appear normal on CT in as many as 50% of all patients with acute pancreatitis.[13, 20, 24] The pancreatic contour is usually smooth in mild pancreatitis and becomes more ill defined with increased severity of disease as the inflammatory process extends to involve the peripancreatic soft tissues (see Fig. 56–2). The gland demonstrates normal, homogeneous contrast enhancement in mild pancreatitis (see Fig. 56–2). Areas of decreased parenchymal enhancement are seen in severe pancreatitis associated with pancreatic necrosis.

The CT appearance of pancreatic necrosis consists of areas of nonenhancing pancreatic parenchyma that involve 30% or more of the pancreatic volume[5, 17, 25] (Fig. 56–3). As the devitalized tissue undergoes liquefaction, it gradually appears as an intrapancreatic fluid collection[17] (see Fig. 56–3). Pancreatic necrosis may be complicated by infection. On CT scans, infected necrosis is characterized by air collections within nonenhancing or heterogeneous enhancing pancreas or adjacent soft tissues.

Acute fluid collections associated with acute pancreatitis may be seen on CT. Because these fluid collections are unencapsulated, they take the shape of the anatomic space in which they are located. These collections may be intrapancreatic or extrapancreatic. Extrapancreatic fluid collections occur more frequently than intrapancreatic collections. They may be seen in the retroperitoneum (Fig. 56–4), peritoneal cavity (Fig. 56–5), or mesentery.[5, 13, 17, 18, 20, 25] The most common location of these fluid collections is the anterior pararenal space that surrounds the pancreas[13, 25] (see Fig. 56–4).

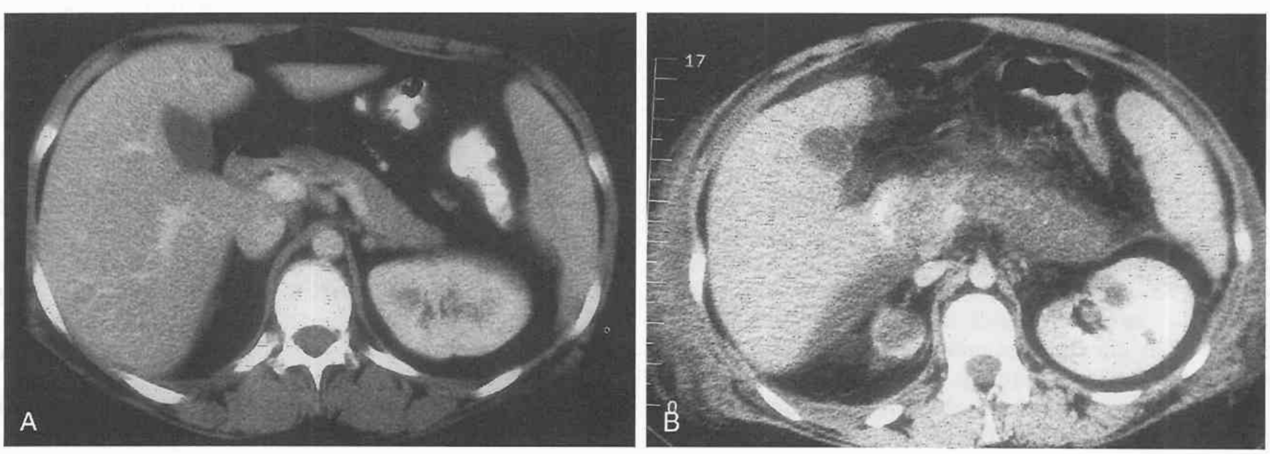

Figure 56–3. Acute pancreatitis with pancreatic necrosis. *A,* CT scan through the pancreas in a patient with acute pancreatitis demonstrates a normal-appearing pancreas. *B,* Follow-up CT scan through the pancreas 48 hours later after clinical deterioration shows the absence of parenchymal enhancement in the body and tail of the pancreas, indicative of areas of pancreatic necrosis.

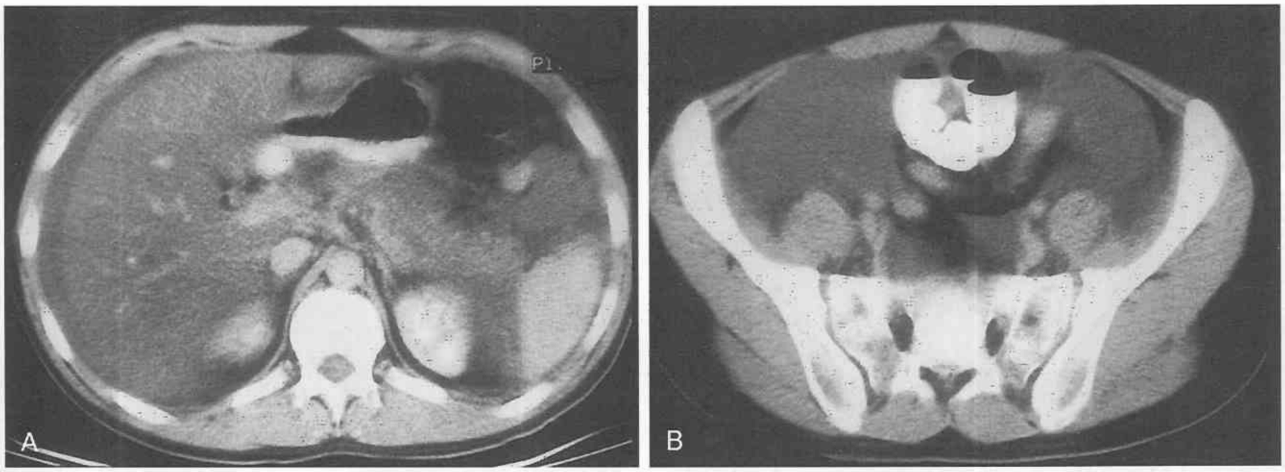

Figure 56–5. Acute pancreatitis with free peritoneal fluid. *A*, CT scan through the upper abdomen in a patient with acute pancreatitis demonstrates ill definition of the pancreatic margins and fluid in the anterior pararenal space. *B*, CT scan through the pelvis in the same patient demonstrates a large amount of free peritoneal fluid.

With extrapancreatic spread of the inflammatory process in severe pancreatitis, extensive inflammatory changes can be seen on CT throughout the abdomen and pelvis. In addition to the fluid collections described here, infiltration of peripancreatic and mesenteric fat may be noted. On CT, this appears as areas of stranding in the normally homogeneous low-attenuation fat (Fig. 56–6).

CT is useful in the follow-up of patients with acute pancreatitis to assess the development of pseudocysts. Pancreatic pseudocysts are round or oval on CT (Fig. 56–7). They are homogeneous in appearance, demonstrating fluid attenuation[25] (see Fig. 56–7). The pseudocyst wall ranges from barely perceptible to thick. Pseudocysts may be intrapancreatic (see Fig. 56–7) or extrapancreatic (Fig. 56–8) in location. Extrapancreatic pseudocysts develop more frequently in a retroperitoneal location in close proximity to the pancreas, but they may be seen anywhere in the abdomen or pelvis. Approximately 50% of all pseudocysts resolve spontaneously. Pseudocysts may be complicated by hemorrhage, infection, or rupture. Internal septations within the pseudocyst usually indicate prior hemorrhage (Fig. 56–9). The treatment of choice for persistent pseudocysts is percutaneous drainage.

Chronic Pancreatitis

Chronic pancreatitis is rare in childhood. The condition is characterized by irreversible damage to the pancreas from persistent or recurrent inflammation followed by fibrosis. In childhood, the most common cause of chronic pancreatitis is hereditary pancreatitis, a rare familial disorder.[10, 26] Other causes include hyperlipidemia, hypercalcemia, sclerosing cholangitis, and trauma. The most common CT findings associated with chronic pancreatitis include pancreatic atrophy (Fig. 56–10) and parenchymal calcifica-

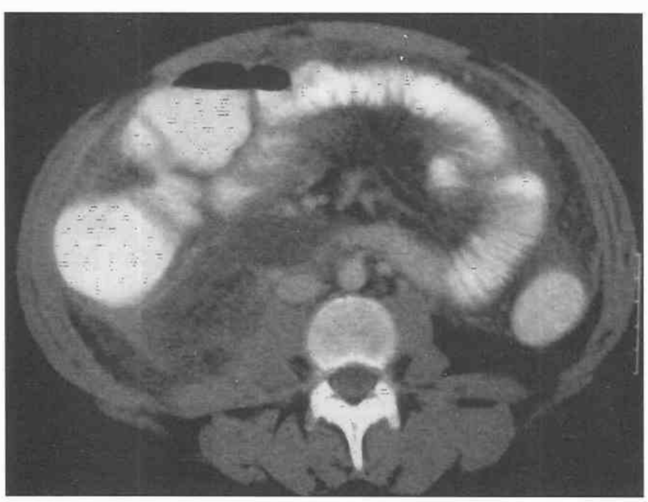

Figure 56–6. Acute pancreatitis with stranding of the mesenteric fat. CT scan through the midabdomen in a patient with acute pancreatitis shows diffuse infiltration of mesenteric fat.

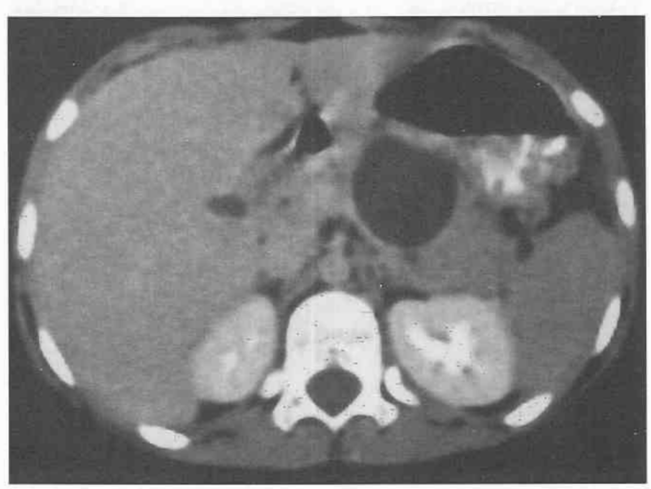

Figure 56–7. Intrapancreatic pseudocyst. CT scan at the level of the pancreas in a patient with acute pancreatitis demonstrates a large pseudocyst originating within the body of the pancreas.

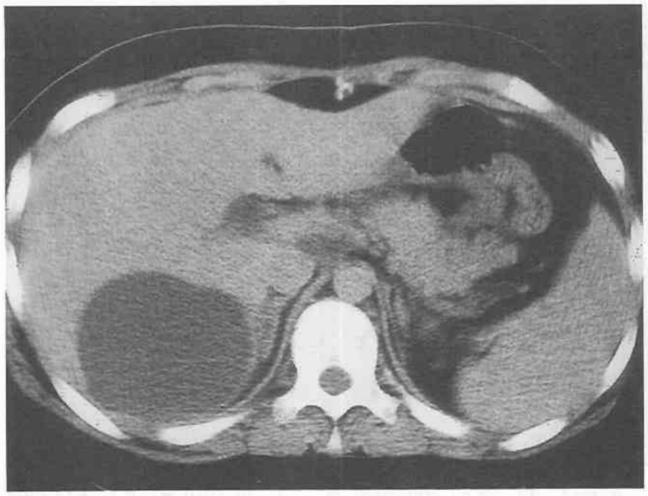

Figure 56–8. Extrapancreatic pseudocyst. CT scan through the upper abdomen in a patient with acute pancreatitis demonstrates an intraperitoneal pseudocyst posterior to the right lobe of the liver.

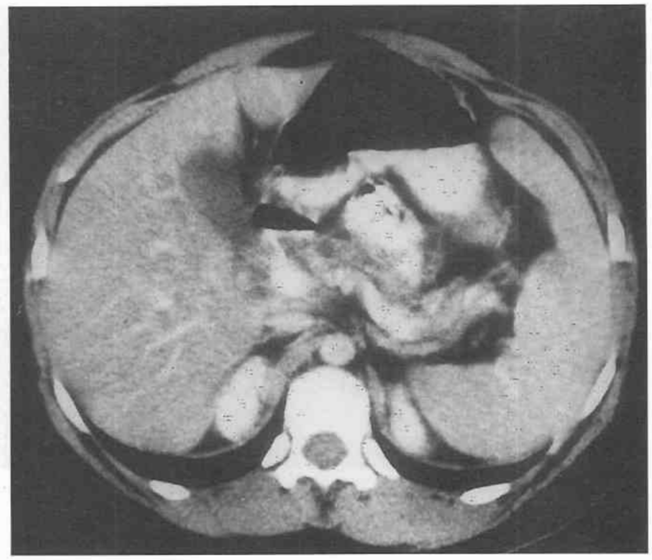

Figure 56–10. Chronic pancreatitis. CT scan through the pancreas in a patient with chronic pancreatitis demonstrates a small, atrophic pancreas.

tions[10, 26] (see Fig. 56–4). Pseudocysts are noted in approximately 5% of patients with chronic pancreatitis.

Trauma

Pancreatic injury is uncommon in children, accounting for approximately 6% of all solid viscus injury.[22] Pancreatic injury is the most common cause of acute pancreatitis in childhood. Blunt force trauma is a more common mechanism of pancreatic injury than is perforating injury. The most common mechanism of injury is compression of the pancreas against the vertebral column.

The early clinical diagnosis of pancreatic injury may be difficult. Typically, there are few specific clinical symptoms, and laboratory data also are not helpful in the early diagnosis. Serum amylase and lipase levels may not rise for 24 hours or longer after the injury. In addition, elevated serum amylase and lipase levels are commonly noted after blunt trauma in the absence of pancreatic injury.

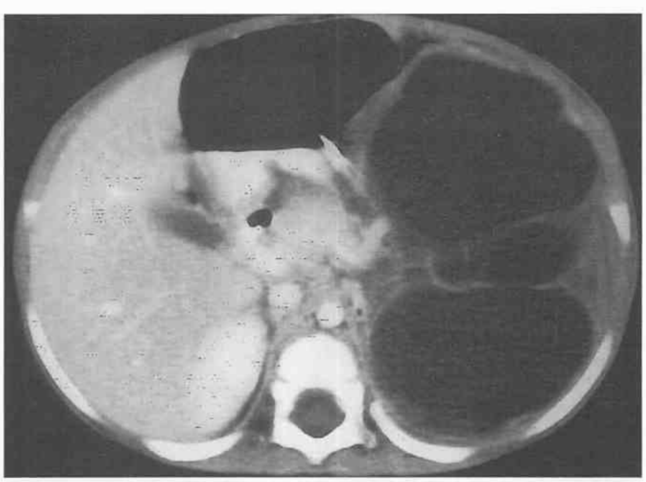

Figure 56–9. Pancreatic pseudocyst with internal septations. CT scan through the upper abdomen in a patient with acute pancreatitis shows a large multiseptated pseudocyst in the left upper abdomen.

The surgical classification of pancreatic injury is based on the extent of parenchymal injury and ductal disruption. The most widely used classification system is from the American Association for the Surgery of Trauma[16] (Table 56–1). The main determinant of outcome severity is whether the main pancreatic duct is intact. Ductal disruption is associated with an increased prevalence of severe pancreatitis, pancreatic necrosis, hemorrhage, pseudocyst formation, and sepsis.

CT is the primary modality for the initial evaluation of suspected pancreatic injury in children. The CT-aided diagnosis of pancreatic injury can be difficult. The diagnosis is missed at CT in approximately one third of children with such injury.[22] The difficulty involved in the CT scan diagnosis of pancreatic injury has several causes. Injuries may be missed because the pancreas is a small organ, and in children there is a relative paucity of surrounding retroperitoneal fat. Thus, delineation of the pancreatic margins and separation from surrounding bowel loops may be difficult. Also, when a pancreatic injury is present, there may be little separation of the fractured fragments secondary to organ elasticity (Fig. 56–11).

CT findings of acute pancreatic injury include direct visualization of low-attenuation laceration or fracture traversing the gland (Fig. 56–12), fluid in the anterior pararenal

Table 56–1. Pancreatic Injury Severity Scale

Grade	Description of Injury
I	Minor contusion or superficial laceration without duct injury
II	Major contusion or laceration without duct injury or tissue loss
III	Distal transection or parenchymal injury with duct injury
IV	Proximal transection or parenchymal injury involving the ampulla
V	Massive disruption of the pancreatic head

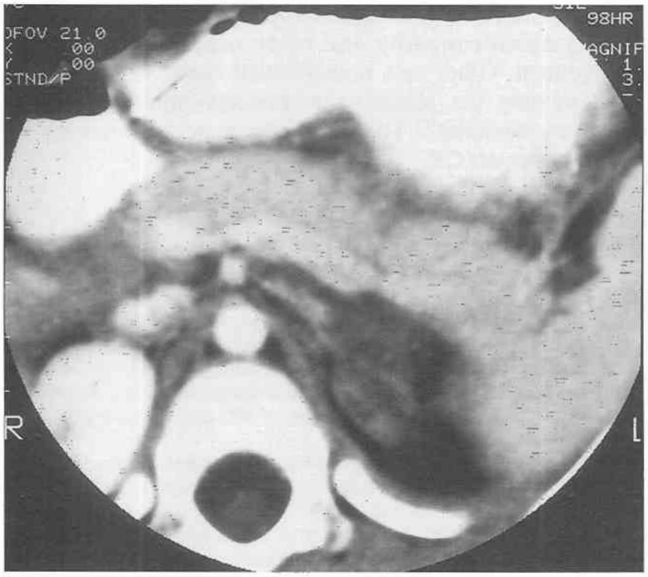

Figure 56–11. Pancreatic laceration with minimal separation of fracture fragments. Magnified CT scan through the pancreas of a patient injured in a motor vehicle accident shows a laceration through the body of the pancreas with minimal separation of the fracture fragments.

space (Fig. 56–13), fluid in the lesser sac, free peritoneal fluid, and thickening of the anterior renal fascia.[7, 14, 22, 23] The best indicator of pancreatic injury on CT is unexplained peripancreatic fluid (fluid in the anterior pararenal space or lesser sac in the absence of visceral injury[22] (see Fig. 56–13). Fluid in the anterior pararenal space may also dissect the pancreas and splenic vein, because the vein is only partially imbedded in the organ[14, 23] (see Fig. 56–13).

Changes related to the development of acute pancreatitis after pancreatic injury, including gland enlargement, contour irregularity, and peripancreatic inflammatory changes, may be noted on follow-up examination. However, these changes are not present immediately after the injury. Posttraumatic pancreatitis may be complicated by all of the conditions listed in the discussion of acute pancreatitis.

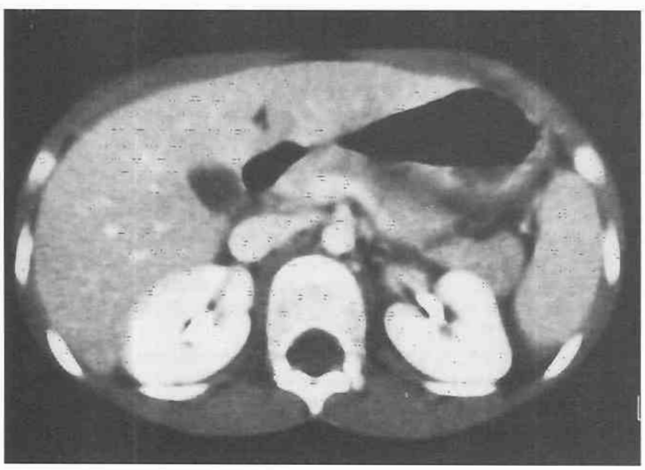

Figure 56–12. Pancreatic laceration. CT scan through the pancreas in a patient who was assaulted shows a laceration through the tail of the pancreas.

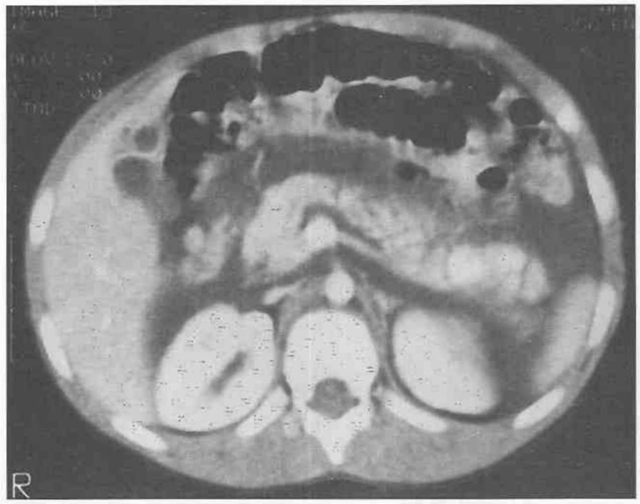

Figure 56–13. Pancreatic injury with fluid in the anterior pararenal space. CT scan through the pancreas of a patient injured in a motor vehicle accident demonstrates peripancreatic fluid in the anterior pararenal space and fluid between the splenic vein and pancreas. No pancreatic laceration was visible on CT; at surgery, a pancreatic laceration was noted.

Neoplasms

Pancreatic neoplasms are rare in childhood. They are usually of epithelial origin and rarely of mesenchymal origin.[9, 10, 26]

Epithelial Tumors

Epithelial pancreatic tumors may originate from endocrine or nonendocrine tissue. Most nonendocrine tumors are malignant, including pancreaticoblastoma, solid and papillary neoplasm, and adenocarcinoma. Although these are all rare tumors, pancreaticoblastoma is the most common of the three in childhood. It is typically seen in younger children. The CT appearance is that of a large, well-circumscribed, solid mass.[10, 15, 26] There often is anterior extension of the tumor into the lesser sac.

The solid and papillary epithelial neoplasm is an uncommon low-grade malignancy. Metastases are rare. It is usually seen in young women, presenting most frequently in the second to third decades of life and thus may occur in adolescents. On CT, the appearance is that of a large, well-circumscribed, solid mass that typically originates from the pancreatic tail[3, 10, 26] (Fig. 56–14).

Adenocarcinoma of the pancreas is extremely rare in children.[19] The tumor is usually large at presentation and metastasizes aggressively. On CT, the tumor has a complex appearance with solid and cystic areas.[19] Calcifications are occasionally noted within the tumor.

The epithelial tumors that originate from endocrine tissue are the islet cell tumors. They may be benign or malignant. Most are functioning tumors and include insulinoma, gastrinoma, vasoactive intestinal polypeptide (VIP)–secreting tumor, glucagonoma, and somatostatinoma.[26] These tumors often are not visualized on CT. If they are visible on a CT scan, their appearance is that of a

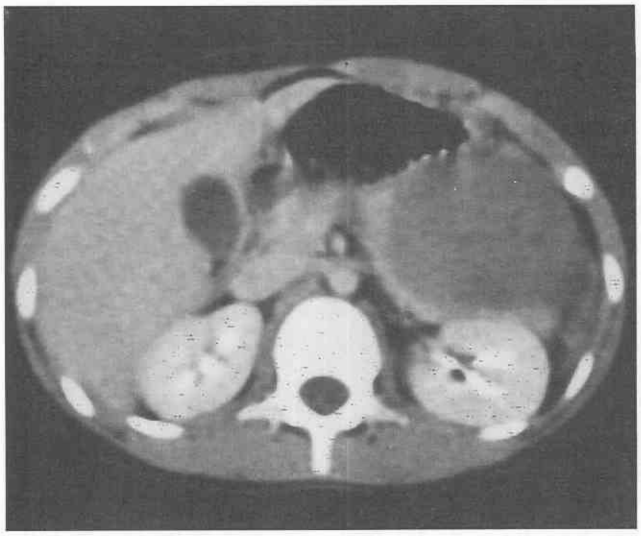

Figure 56–14. Solid and papillary epithelial neoplasm of the pancreas. CT scan through the pancreas demonstrates a large mass originating in the tail of the pancreas. The mass demonstrates decreased attenuation relative to the pancreatic body and tail.

small, enhancing, hyperdense mass. They usually measure less than 2 cm in diameter. In malignant islet cell tumors, lymphadenopathy and hepatic metastases may be present even if the primary tumor cannot be identified on CT.

Nonepithelial Tumors

Nonepithelial tumors may be primary to the pancreas or may secondarily involve the pancreas. The most common nonepithelial tumor of the pancreas is children is non-Hodgkin's lymphoma. The CT appearance of non-Hodgkin's lymphoma includes the presence of a focal intrapancreatic mass or diffuse gland enlargement[26] (Fig. 56–15).

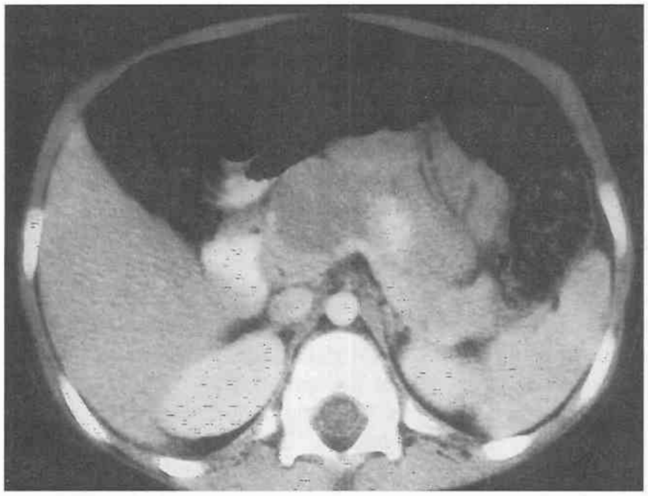

Figure 56–15. Pancreatic lymphoma. CT scan through the pancreas in a patient with non-Hodgkin's lymphoma demonstrates a rounded, low-attenuation, solid mass in the head of the pancreas.

Typically, there is associated retroperitoneal and/or mesenteric lymphadenopathy and often other solid visceral involvement. Other rare nonepithelial tumors of the pancreas include the primitive neuroectodermal tumor and rhabdomyosarcoma.[12] They also appear as solid masses of varying sizes on CT.

References

1. Balthazar EJ, Freeny PC, Van Sonnenberg E: Imaging and intervention in acute pancreatitis. Radiology 193:297–306, 1994.
2. Balthazar EJ, Robinson DL, Megibow AJ, et al: Acute pancreatitis: Value of CT in establishing prognosis. Radiology 174:331–336, 1990.
3. Balthazar EJ, Subramanyam BR, Lefleur RS, et al: Solid and papillary epithelial neoplasm of the pancreas. Radiology 150:39–40, 1984.
4. Bernard JP, Sahel J, Giovanni M, et al: Pancreas divisum is a probable cause of acute pancreatitis: A report of 137 cases. Pancreas 5:248–254, 1990.
5. Bradley E: A clinically based classification system for acute pancreatitis: Summary of the International Symposium on Acute Pancreatitis. Arch Surg 128:586–590, 1993.
6. Bret PM, Reinhold C, Taourel P, et al: Pancreas divisum: Evaluation with MR cholangiopancreatography. Radiology 199:99–103, 1996.
7. Dodds WJ, Taylor AJ, Erickson SC, et al: Traumatic fracture of the pancreas: CT characteristics. J Comput Assist Tomogr 14:375–378, 1990.
8. Fulcher AS, Turner MA: MR pancreatography: A useful tool for evaluating pancreatic disorders. Radiographics 19:5–24, 1999.
9. Grosfeld JL, Vane DW, Rescoria FJ, et al: Pancreatic tumors in childhood. J Pediatr Surg 25:1057–1062, 1990.
10. Herman TE, Siegel MJ: CT of the pancreas in children. AJR Am J Roentgenol 157:375–379, 1991.
11. Hernanz-Schulman M, Teele RL, Perez-Atayde A, et al: Pancreatic cystosis in cystic fibrosis. Radiology 158:629–631, 1986.
12. Ibarburen C, Haberman JJ, Zerhouni EA: Peripheral primitive neuroectodermal tumors: CT and MRI evaluation. Eur J Radiol 21:225–232, 1996.
13. King LR, Siegel MJ, Balfe DM: Acute pancreatitis in children: CT findings of intra- and extrapancreatic fluid collections. Radiology 195:196–200, 1995.
14. Lane MJ, Mindelzun RE, Sandhu JS, et al: CT diagnosis of blunt pancreatic trauma: Importance of detecting fluid between the pancreas and the splenic vein. AJR Am J Roentgenol 163:833–835, 1994.
15. Lee JY, Kim I, Kim WS, et al: CT and US findings of pancreatoblastoma. J Comput Assist Tomogr 20:370–374, 1996.
16. Moore EE, Cogbill TH, Malangoni MA, et al: Organ injury scaling: Pancreas, duodenum, small bowel, colon and rectum. J Trauma 30:1427–1429, 1990.
17. Paulson EK, Vitellas KM, Keogan MT, et al: Acute pancreatitis complicated by gland necrosis: Spectrum of findings on contrast-enhanced CT. AJR Am J Roentgenol 172:609–613, 1999.
18. Raptopoulos V, Kleinman PK, Marks S, et al: Renal fascial pathway: Posterior extension of pancreatic effusions within the anterior pararenal space. Radiology 158:367–374, 1986.
19. Robey G, Daneman A, Martin DJ: Pancreatic carcinoma in a neonate. Pediatr Radiol 13:284–286, 1983.
20. Siegel MJ, Sivit CJ: Pancreatic emergencies. Radiol Clin North Am 35:815–830, 1997.
21. Sivit CJ: CT scan of mesentery-omentum peritoneum. Radiol Clin North Am 34:863–884, 1996.
22. Sivit CJ, Eichelberger MR, Taylor GA, et al: Blunt pancreatic trauma in children: CT diagnosis. AJR Am J Roentgenol 158:1097–1100, 1992.
23. Sivit CJ, Frazier AA, Eichelberger MR: Prevalence and distribution of hemorrhage associated with splenic injury in children. AJR Am J Roentgenol 172:1015–1017, 1999.
24. Soyer P, Spelle L, Pelage JP: Cystic fibrosis in adolescents and adults: Fatty replacement of the pancreas—CT evaluation and functional correlation. Radiology 210:611–615, 1999.
25. Urban BA, Curry CA, Fishman EK: Complications of acute pancreatitis: Helical CT evaluation. Emerg Radiol 6:113–120, 1999.
26. Vaughn DD, Jabra AA, Fishman EK: Pancreatic disease in children and young adults: Evaluation with CT. Radiology 18:1171–1187, 1998.

57

Kidneys and Adrenal Glands

J. Michael Zerin

Kidneys

Normal Anatomy

Both computed tomography (CT) and magnetic resonance imaging (MRI) generally provide excellent visualization of the kidneys, even in infants and younger children in whom there is relatively little perirenal fat. The kidneys lie within the retroperitoneum anterior to the psoas muscles. In infants and younger children, the longitudinal axes of the kidneys are roughly parallel to the spine. As the child grows, the psoas muscles enlarge and displace the lower renal poles anteriorly and laterally. As a result, the kidneys come to lie more obliquely in relation to the spine in the adolescent and adult. Anteriorly, the perirenal fat is bounded by Gerota's fascia, posteriorly by the fascia of Zuckerkandl, and laterally by the lateral conal fascia.

Computed Tomography

Renal parenchymal attenuation on nonenhanced CT scans is normally very homogeneous (32 to 60 Hounsfield units) with no visible corticomedullary differentiation.[33, 40] The renal hilum and pelvis are usually visible; however, nondilated calices and infundibula are only occasionally visualized as subtle regions of fluid attenuation within the parenchyma. In older children and adults, the main renal vessels are often visible, even on nonenhanced studies, but it may not be possible to distinguish them from the renal pelvis in infants and younger children without contrast enhancement.

On postcontrast studies, renal parenchymal attenuation varies with (1) state of renal function, (2) dose of contrast material and rate of administration, and (3) timing of imaging in relation to administration of the contrast bolus.[33, 40] After rapid administration of contrast material as a single intravenous (IV) bolus, the aorta and renal arteries are normally opacified first, followed by the renal veins and inferior vena cava. Renal cortical enhancement follows.

Corticomedullary differentiation is maximal during this phase, with the cortex appearing as 4- to 6-mm-thick peripheral bands of higher attenuation surrounding lower-attenuation medullary pyramids that are not yet enhanced. Thereafter, corticomedullary differentiation declines as medullary enhancement progresses and cortical enhancement wanes, until the renal parenchymal attenuation becomes more homogeneous. Once contrast material appears in the collecting system, renal parenchymal attenuation gradually declines.

Magnetic Resonance Imaging

On MR spin-echo T1-weighted images, the cortex has higher signal intensity than the medullary pyramids, and corticomedullary differentiation is, therefore, readily visualized. Corticomedullary differentiation on spin-echo T1-weighted MR images is most pronounced early in life and decreases with age.[45, 81, 101] Corticomedullary differentiation is also more conspicuous on inversion recovery sequences and can be influenced by the patient's state of hydration. On very heavily T1-weighted images, however, the signal intensity of both the cortex and the medulla is lower and corticomedullary differentiation is thus reduced.[17] Because infants and young children generally have less hilar fat than adults, the renal hilum is lower in signal intensity and less conspicuous early in life. By early adolescence, the appearance is similar to that in adults.[17, 45] The renal artery and vein normally have very low signal intensity because of rapid blood flow in and out of the kidney[81, 101]; when flow is slower, however, an intraluminal signal can occasionally be identified. This artifact can also be caused by flow-related enhancement when the vessels are imaged in cross-section.[21] The collecting system and ureter have low signal intensity on spin-echo sequences because of the long T1 relaxation time of urine.[45, 81]

The renal cortex and medulla both have increased signal intensity on T2-weighted sequences; however, the cortex is only slightly higher in signal intensity than the medulla. As a result, corticomedullary differentiation is less well visualized.[45, 71] Perirenal fat appears bright on T2-weighted sequences, although somewhat less so than on spin-echo T1. Gerota's fascia appears as a low-intensity line separating the perirenal and pararenal spaces. A chemical shift misregistration artifact at the interface between the kidney and the adjacent perirenal fat occasionally produces the appearance of a low-signal-intensity line along one side of the kidney with a symmetrical high-signal-intensity line along the opposite side.[147] This artifact should not be misinterpreted as calcification.

Renal Anomalies

Most congenital renal malformations, including renal agenesis, renal ectopia, congenital obstructive uropathy, and multicystic dysplastic kidney, are fully evaluated with the following: (1) ultrasonography, (2) diuretic (MAG3) and cortical (DMSA) renal scintigraphy, and (3) voiding cystourethrography. The roles of CT and MRI in these disorders are generally restricted to more complex situa-

tions in which these modalities can provide clinically useful information that cannot be obtained noninvasively by other means. At CT, IV contrast material should be administered unless renal function is impaired sufficiently to contraindicate it.

MR T1-weighted images provide excellent visualization of most renal malformations.[33, 46] Imaging in the axial plane with either CT or MRI is usually sufficient. In fact, the site of fusion in horseshoe kidney or crossed-fused ectopia is often best visualized on axial images; however, direct coronal MRI imaging allows rapid evaluation of large areas of the abdomen and pelvis and can be particularly useful for identifying small, poorly functioning or nonfunctioning kidneys.

Ectopic Kidneys

Most ectopic kidneys lie caudal to the normal renal fossa—either lumbar or pelvic. In patients who have anterior abdominal wall defects (e.g., gastroschisis, omphalocele), the kidneys are occasionally located above the normal renal fossa. In patients with congenital diaphragmatic hernia, the ipsilateral kidney can be intrathoracic. In horseshoe kidney, both kidneys are low in position, with their lower poles joined by an "isthmus" composed of functioning parenchyma and fibrous tissue in variable proportions. In crossed renal ectopia, the ectopic kidney lies caudal and medial to the contralateral kidney, which is the normal position. The crossed ectopic kidney is usually fused to the lower pole of the contralateral kidney; however, crossed ectopic kidneys can also be unfused. In either case, the ureter draining the ectopic kidney crosses the midline to insert on its proper side on the trigone (Fig. 57–1).

Renal Agenesis

In girls, unilateral renal agenesis is frequently associated with uterovaginal anomalies, such as agenesis, duplication, or atresia.[156] In boys, unilateral renal agenesis can be associated with an ipsilateral seminal vesicle cyst.[91] The ipsilateral vas deferens and testis can also be absent, and testicular abnormalities, such as absence, cryptorchidism, and cystic dysplasia, can also be associated.[19] Occasionally, CT or MRI reveals a small, poorly functioning or nonfunctioning kidney in a child who appears to have unilateral renal agenesis at ultrasound, IV urography, or renal scintigraphy. In such cases, the small kidney probably represents the remnant of an involuted multicystic dysplastic kidney, and a single ectopic ureter is typically present.[79] This appearance is not specific, however. In the absence of associated lower genitourinary anomalies, definitive information in the history, or previous imaging studies, differentiation from other causes of severe renal atrophy, such as renal infarction or reflux nephropathy, is not possible by imaging.

Upper-Pole and Single Ectopic Ureters in Girls with Incontinence

When a girl presents with incontinence characterized by persistent and incessant dampness, the most likely cause of

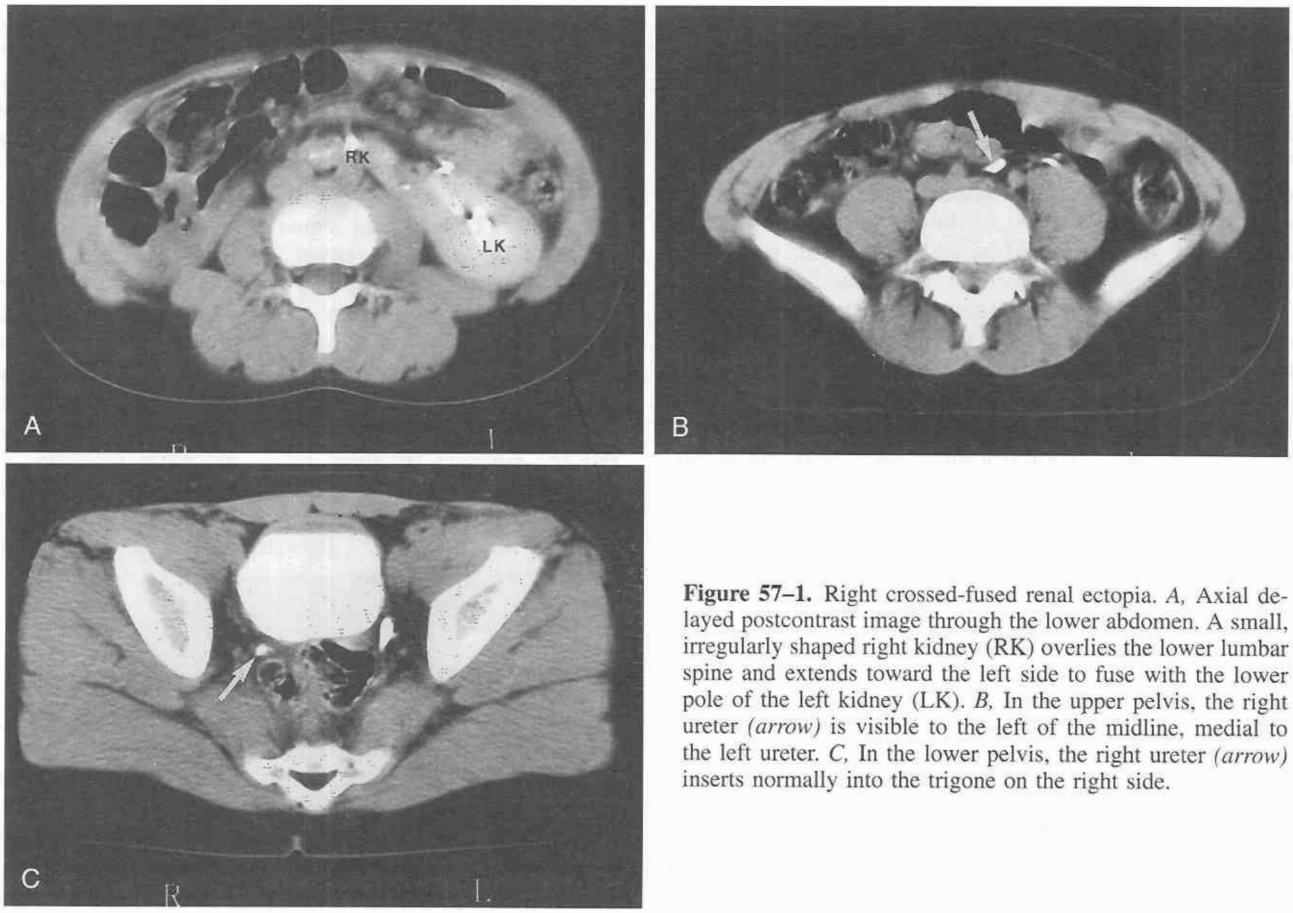

Figure 57–1. Right crossed-fused renal ectopia. *A,* Axial delayed postcontrast image through the lower abdomen. A small, irregularly shaped right kidney (RK) overlies the lower lumbar spine and extends toward the left side to fuse with the lower pole of the left kidney (LK). *B,* In the upper pelvis, the right ureter *(arrow)* is visible to the left of the midline, medial to the left ureter. *C,* In the lower pelvis, the right ureter *(arrow)* inserts normally into the trigone on the right side.

her wetting is an extravesical, ectopic ureter that inserts into the urethra, into the vagina, or onto the perineum. In most cases, the ectopic ureter drains the upper pole of a completely duplicated collecting system[23]; however, the same clinical syndrome can also occur in a girl with a nonduplicated collecting system and ureter that drain to an ectopic orifice.[66, 128] In boys, ectopic ureters do not cause incontinence because the ectopic ureter always inserts proximal to the urethral sphincter.[164]

Despite the distinctive pattern of the incontinence in girls with this disorder, the diagnosis of ectopic ureter is, unfortunately, often not suspected, or the diagnosis is missed because the wrong imaging studies are requested or results are misinterpreted.[28] Because the upper pole that is drained by an ectopic ureter is often not dilated, it may not be visible on ultrasound examination. IV urography is usually diagnostic, but the findings can be subtle, especially when the offending upper pole functions poorly and cannot be directly visualized.[151] When the ectopic ureter drains a nonduplicated collecting system, the kidney is small and dysplastic and functions very poorly, if at all. In this situation, the appearances at both ultrasound and IV urography are indistinguishable from unilateral renal agenesis. Arriving at a diagnosis can be even more difficult when the kidney itself is ectopic.[66] Delayed contrast-enhanced CT with thin sections through the kidneys, coronal T1-weighted MRI, and MR urography are the most sensitive modalities for identifying an occult ectopic ureter[23, 28, 66] (Fig. 57–2).

Renal Infections

Acute Pyelonephritis and Renal Scarring

It is often difficult to differentiate upper from lower urinary tract infection in children on the basis of clinical and laboratory parameters alone.[108, 124] The imaging diagnosis of acute pyelonephritis relies on the identification of anatomic changes secondary to inflammatory edema as well as segmental or lobar reduction in renal parenchymal perfusion and excretory function. Technetium 99m dimercaptosuccinic acid (DMSA) renal cortical scintigraphy, power Doppler ultrasonography, CT, and MRI have all been used to identify acute pyelonephritis in children who have fever and bacteriuria.[37, 38, 104, 107, 135] All of these modalities are more sensitive than either conventional gray scale ultrasound or IV urography for the diagnosis of acute pyelonephritis.

On IV contrast–enhanced CT scans, acute pyelonephritis appears as one or multiple wedge-shaped or triangular areas of decreased parenchymal enhancement.[100, 131] The anatomic distribution of the lesions is characteristically segmental, with a predilection for the renal poles[80, 93] (Fig. 57–3). The affected areas appear edematous, with convex, rounded margins. Bulging areas of pyelonephritis that distort the renal contour can occasionally mimic intrarenal masses. When the infection is extensive, the kidney appears globally enlarged, although usually still reniform, with patchy enhancement of the less involved areas. Acute pyelonephritis is more difficult to diagnose on nonenhanced

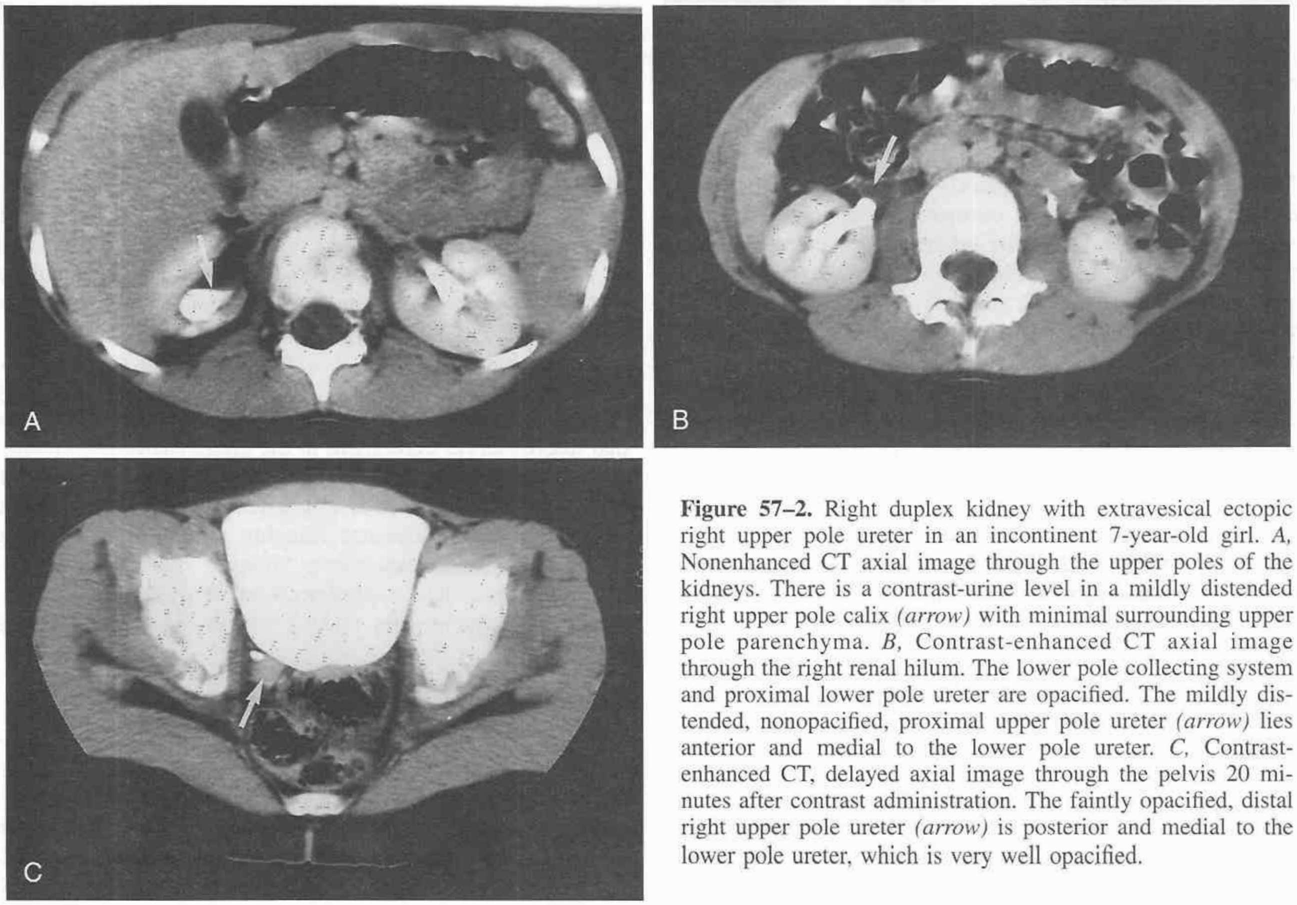

Figure 57–2. Right duplex kidney with extravesical ectopic right upper pole ureter in an incontinent 7-year-old girl. *A,* Nonenhanced CT axial image through the upper poles of the kidneys. There is a contrast-urine level in a mildly distended right upper pole calix *(arrow)* with minimal surrounding upper pole parenchyma. *B,* Contrast-enhanced CT axial image through the right renal hilum. The lower pole collecting system and proximal lower pole ureter are opacified. The mildly distended, nonopacified, proximal upper pole ureter *(arrow)* lies anterior and medial to the lower pole ureter. *C,* Contrast-enhanced CT, delayed axial image through the pelvis 20 minutes after contrast administration. The faintly opacified, distal right upper pole ureter *(arrow)* is posterior and medial to the lower pole ureter, which is very well opacified.

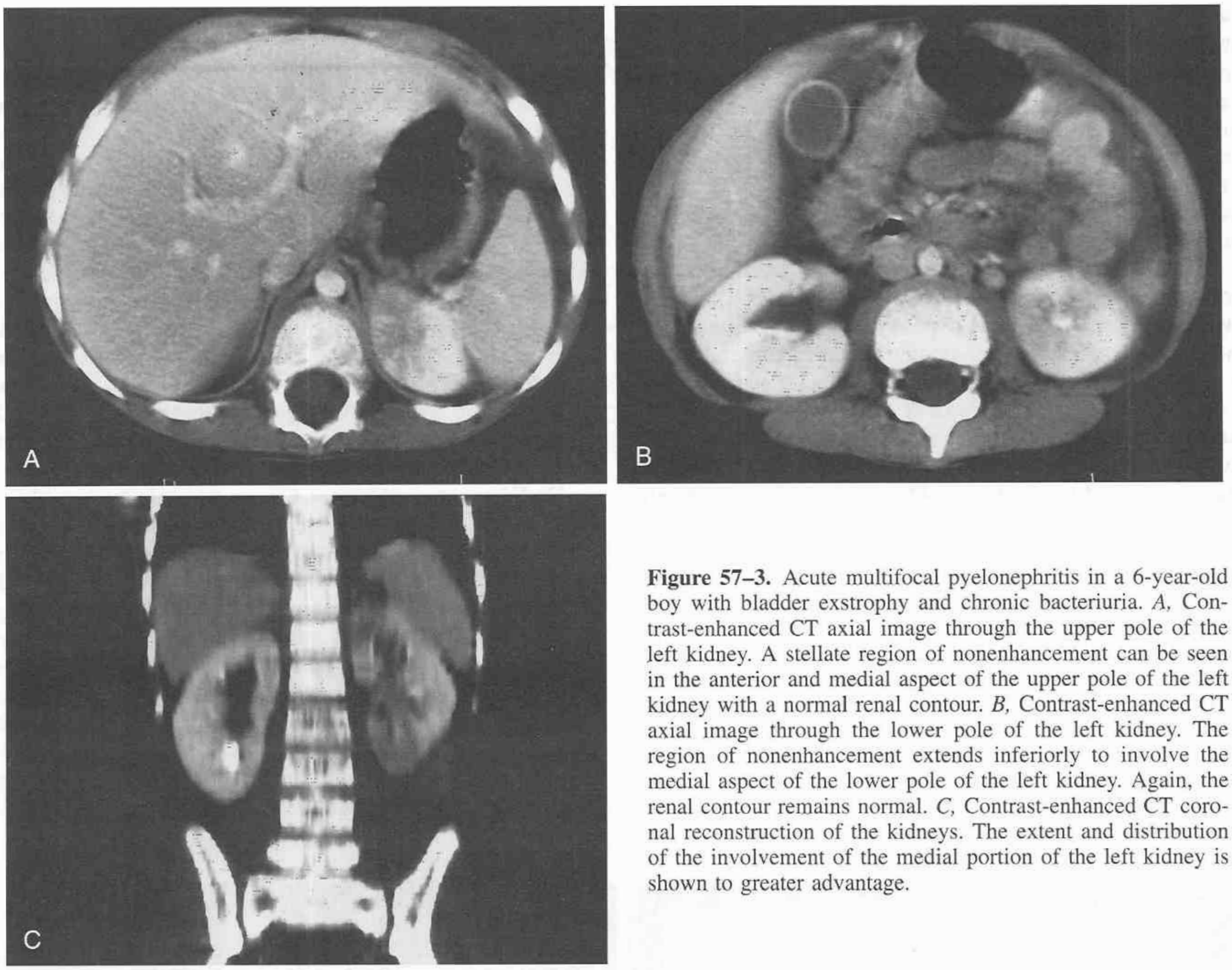

Figure 57–3. Acute multifocal pyelonephritis in a 6-year-old boy with bladder exstrophy and chronic bacteriuria. *A,* Contrast-enhanced CT axial image through the upper pole of the left kidney. A stellate region of nonenhancement can be seen in the anterior and medial aspect of the upper pole of the left kidney with a normal renal contour. *B,* Contrast-enhanced CT axial image through the lower pole of the left kidney. The region of nonenhancement extends inferiorly to involve the medial aspect of the lower pole of the left kidney. Again, the renal contour remains normal. *C,* Contrast-enhanced CT coronal reconstruction of the kidneys. The extent and distribution of the involvement of the medial portion of the left kidney is shown to greater advantage.

CT because the infected segments are usually isodense or only slightly hypodense in comparison to adjacent uninvolved parenchyma.[131] On the other hand, localized parenchymal hemorrhage secondary to segmental venous obstruction (Fig. 57–4) occasionally produces increased attenuation within an area of acute pyelonephritis on nonenhanced CT.

The appearance of acute pyelonephritis at CT is not microbiologically specific.[168] The abnormal pattern of enhancement in the infected areas can persist for weeks or even several months after completion of antibiotic therapy, before resolving or progressing to scar formation.[150] The sensitivity of CT in acute pyelonephritis is comparable with that of DMSA and superior to that of combined power Doppler and conventional gray scale ultrasound. The ability of CT to differentiate between scars and areas of acute infection in the absence of a previous examination is a significant advantage over conventional DMSA. Because of the axial plane of imaging, however, milder degrees of asymmetrical reduction in renal parenchymal volume can be difficult to detect unless coronal reformatting is done.

The use of MRI for the diagnosis of acute pyelonephritis and renal cortical scarring has been studied in both piglets and humans.[30, 104, 107, 123] On gadolinium-enhanced, fast spin-echo T2 and inversion recovery sequences, normally enhancing renal parenchyma has a much reduced signal intensity because of shortening of both the T1 and T2 relaxation times by the gadolinium. As a result, nonenhancing areas of acute pyelonephritis remain very bright in comparison with the lower signal intensity of normal renal parenchyma (Fig. 57–5). The sensitivity of MRI using fat-saturated T1-weighted and enhanced fast spin-echo sequences is comparable with that of planar DMSA renal cortical scintigraphy in detecting renal scarring. Suggestions in the literature that interobserver agreement in the diagnosis of both pyelonephritis and cortical scarring is better with MRI than with DMSA[28, 104] remain to be confirmed. MRI does offer the advantages of multiplanar imaging and lack of ionizing radiation. Nonetheless, many younger children who undergo this procedure require sedation or even general anesthesia; consequently its routine use in infants and young children is limited.

Complicated Renal Infections

Renal abscesses and other serious acute complications of pyelonephritis, fortunately, are very rare in otherwise healthy children with acute ascending pyelonephritis.[167] These abscesses are more often encountered in children who have hematogenous pyelonephritis or who are immunocompromised or when the infection occurs in an ob-

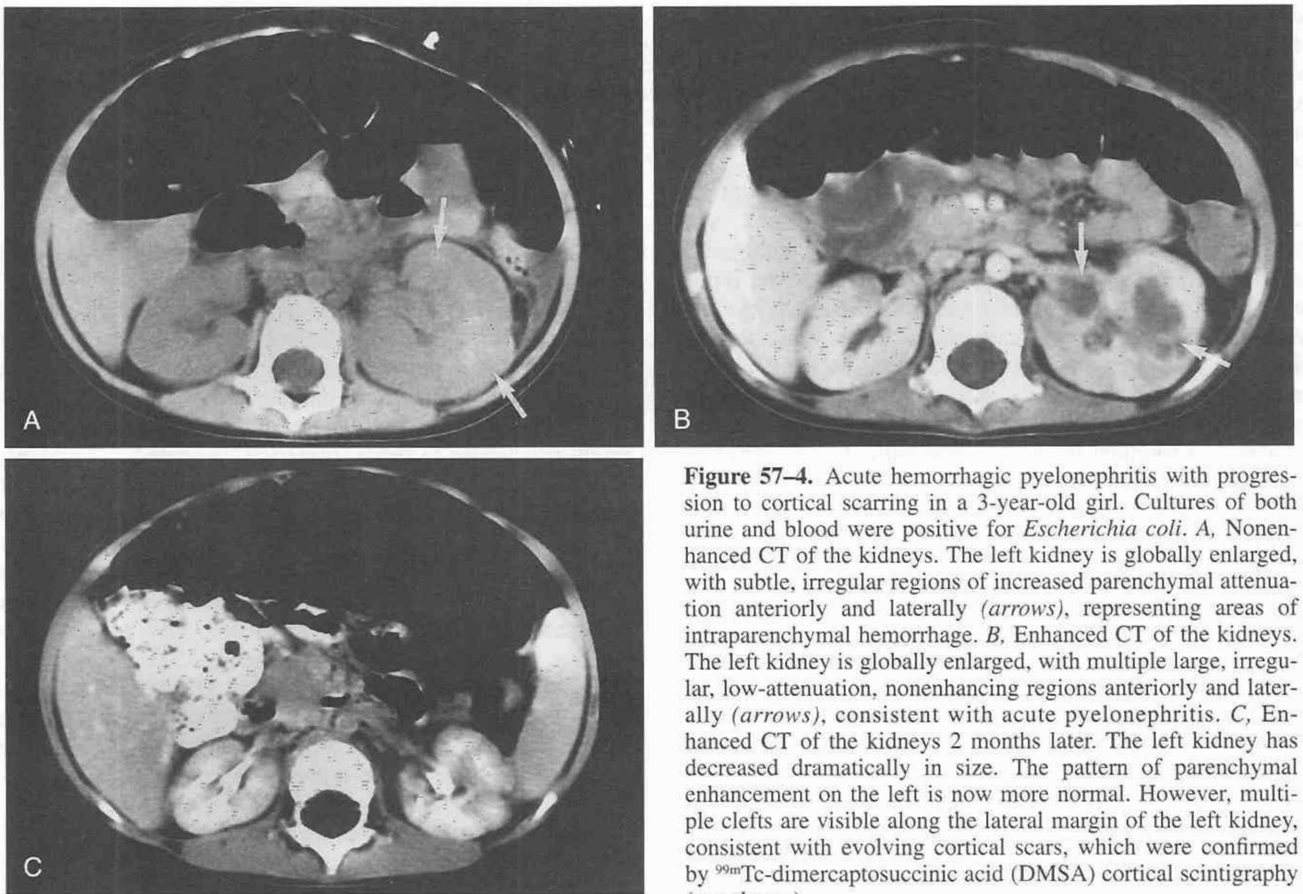

Figure 57–4. Acute hemorrhagic pyelonephritis with progression to cortical scarring in a 3-year-old girl. Cultures of both urine and blood were positive for *Escherichia coli*. *A,* Nonenhanced CT of the kidneys. The left kidney is globally enlarged, with subtle, irregular regions of increased parenchymal attenuation anteriorly and laterally *(arrows)*, representing areas of intraparenchymal hemorrhage. *B,* Enhanced CT of the kidneys. The left kidney is globally enlarged, with multiple large, irregular, low-attenuation, nonenhancing regions anteriorly and laterally *(arrows)*, consistent with acute pyelonephritis. *C,* Enhanced CT of the kidneys 2 months later. The left kidney has decreased dramatically in size. The pattern of parenchymal enhancement on the left is now more normal. However, multiple clefts are visible along the lateral margin of the left kidney, consistent with evolving cortical scars, which were confirmed by ^{99m}Tc-dimercaptosuccinic acid (DMSA) cortical scintigraphy (not shown).

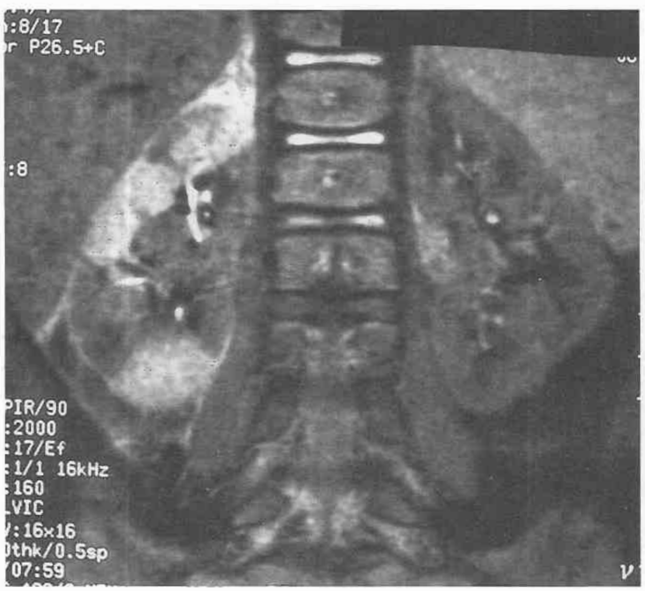

Figure 57–5. Right acute multifocal pyelonephritis. Gadolinium-enhanced coronal inversion recovery image through the kidneys. Multiple segmental zones of abnormally increased signal intensity are visible throughout the right kidney. The left kidney appears normal.

structed collecting system. Such serious complications are best evaluated with CT, which demonstrates both the intrarenal and extrarenal extent of the infectious process.[111, 149, 150, 168] Abscesses can be either intraparenchymal or perirenal, and they usually appear as a central, low-density, nonenhancing cystic area surrounded by an enhancing wall. The distinction between uncomplicated acute pyelonephritis and abscess is important. The former is treated with antibiotics alone, whereas an abscess usually calls for drainage.[149]

Renal Vein Thrombosis

In neonates and younger infants, renal vein thrombosis is usually associated with severe dehydration, hypotension, sepsis, or asphyxia.[13, 40, 84] Premature infants and infants of diabetic mothers are at particular risk. In neonates with left adrenal hemorrhage, extension of thrombus from the left adrenal vein into the renal vein can lead to ipsilateral renal vein thrombosis. This is less common on the right, because the right adrenal vein drains directly into the inferior vena cava.

In neonates, renal vein thrombosis primarily involves smaller intrarenal veins, whereas the main renal vein and inferior cava frequently remain patent. In children with nephrotic syndrome, thrombosis can also arise primarily in the main renal vein or inferior vena cava, as in adults. In

patients with renal vein thrombosis, the affected kidney is enlarged and usually palpable in the flank. Gross hematuria is usually present, and hypertension is common. Renal vein thrombosis is usually unilateral; however, bilateral thrombosis does occur and results in severe acute renal insufficiency.

The diagnosis is usually made at sonography.[112] In the acute phase, the kidney is enlarged and edematous, with poor corticomedullary differentiation. Linear, echogenic bands radiating peripherally within the parenchyma represent thrombus in the interlobar and intralobular renal veins with surrounding perivascular hemorrhage. Occasionally, thrombus is also visible in the ipsilateral main renal vein and the inferior vena cava. Renal scintigraphy reveals markedly reduced or absent function. On follow-up, renal atrophy is a frequent but not an invariable result. Punctate, linear, or branching calcifications can appear over time within the thrombosed veins.[84, 112] In cases of prenatal renal vein thrombosis, branching intrarenal calcifications and renal atrophy can be seen in the neonatal period. Alternatively, an older infant or child with severe renal infarction secondary to previously unrecognized neonatal renal vein thrombosis can present with the appearance of a small, echogenic, poorly functioning kidney that is sonographically indistinguishable from renal dysplasia.

The findings at CT closely correspond to those noted at sonography and scintigraphy.[40] Acutely, the affected kidney is enlarged and appears edematous. Perfusion is markedly reduced with inhomogeneous parenchymal attenuation and reduced or no function. If infarction results, areas of necrosis can progress to cyst formation. During the subacute and chronic phases, calcification within the thrombus and parenchymal atrophy can be seen.[13, 40, 84]

In children with upper abdominal or lower thoracic neoplasms, renal parenchymal injury or infarction can occur secondary to the direct effects of the primary or metastatic tumor; from surgical trauma, chemotherapy, or radiation therapy; or from any combination of the two[2, 42] (Fig. 57–6). In some cases, the impact on the kidney can be dramatic and devastating, resulting in obvious renal infarction or necessitating nephrectomy. More subtle parenchymal injuries may be manifested by impairment of renal growth or by more insidious renal atrophy.

Nephrocalcinosis and Nephrolithiasis

IV urography has long served as the primary imaging modality in patients with suspected acute urinary colic.[127] This modality is successful in precisely identifying the location of the offending calculus and in assessing the severity of the obstruction and its functional impact on the kidney. It is also useful in diagnosing preexisting obstructive uropathy and renal and ureteral malformations that might predispose to stone formation. Despite the simplicity and accuracy of IV urography, however, many calculi are not identifiable on plain radiographs. In addition, patients with ureteral colic frequently have severe pain, and the marked reduction in renal function caused by the acute obstruction can result in considerable prolongation of the study in some patients. There is also the potential for adverse reactions to the contrast material.

In recent years, noncontrast spiral CT has increasingly been used in place of the IV urography to investigate suspected urolithiasis.[60, 144–146, 148] Noncontrast CT can be performed rapidly, and interpretation is usually straightforward. Reported sensitivity and specificity exceed 90%. Interobserver and intraobserver agreement in the interpretation of noncontrast CT is also reported to be very high.[65] Several reports have suggested that this modality is also effective in children.[143, 155] Because the use of IV contrast material is avoided, the examination poses little risk of complication. CT also has the potential to provide useful diagnostic information even when the patient's pain turns out not to be caused by a calculus. The greater cost of CT, compared with that of IV urography, however, remains a challenge in many locations.

The study is performed without oral or IV contrast

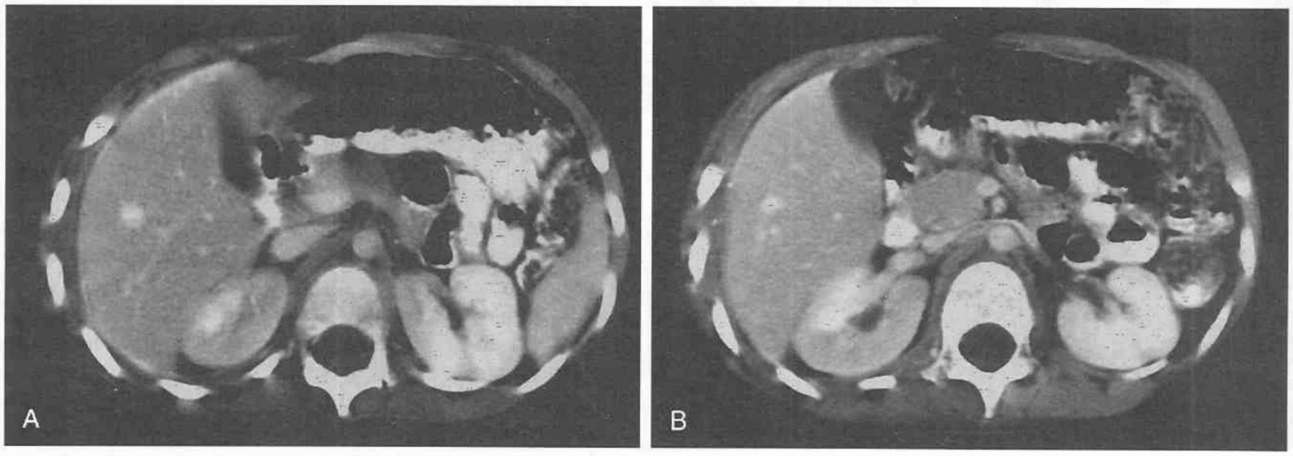

Figure 57–6. Subacute radiation nephritis in a 5-year-old girl who had recent radiation therapy for an undifferentiated sarcoma of the posterior right eleventh rib. Contrast-enhanced CT axial images through the upper poles *(A)* and hila *(B)* of the kidneys. A very sharply defined, nonsegmental, homogeneously low-attenuation band of nonenhancement extends through most of the upper pole of the right kidney and the medial portion of the upper pole of the left kidney. There is also thickening of the soft tissues of the right lateral chest wall and over the lateral margin of the liver.

material. Contiguous 4- to 5-mm-thick axial images are obtained from the top of the kidneys to the symphysis pubis during a single breath-hold. In some very tall individuals, it may be necessary to obtain a second acquisition through the pelvis, but this is generally not required in children. Diagnosis relies principally on direct identification of the offending calculus within the ureter. Edema of ureteral wall—the "tissue rim sign"—and of the fat surrounding the ureter at the level of the impacted stone suggests the presence of a localized inflammatory reaction to the calculus.[60, 90, 144] Edema of the ureterovesical junction can similarly be seen with calculi that are impacted within the submucosal tunnel. Perinephric stranding is an important observation indicative of obstruction, even in the absence of associated hydronephrosis or hydroureter proximal to the stone. After passage of a previously impacted stone, transient persistence of any or all of these findings occasionally provides an indirect clue to the diagnosis.[60]

Abdominal radiographs and ultrasound are usually sufficient for the diagnosis of renal calculi, but non–contrast-enhanced CT can be very helpful in some patients whose kidneys are difficult to examine with ultrasound.[40] For example, in older patients with myelomeningocele or spinal cord injuries, visualization of the kidneys at sonography can be impeded by scoliosis or interfering bowel gas. Multiple, small calculi in ectopic kidneys, in horseshoe kidneys, or in severely hydronephrotic kidneys can be precisely localized with CT. Small calculi that fail to produce a posterior acoustic shadow at sonography are also readily identified at CT.

Renal Tumors

Wilms' Tumor

Wilms' tumor represents 95% of malignant genitourinary neoplasms in children and is the most common primary solid neoplasm in the pediatric abdomen.[24, 165] The peak age at presentation ranges from 1 to 4 years. More than 90% of cases are diagnosed before age 8 years. Wilms' tumor is, however, rare in the first year of life.[24, 46]

Most children present with a palpable abdominal mass. Other common findings include hematuria, fever, abdominal pain, and hypertension. Children with hemihypertrophy, sporadic aniridia, and Beckwith-Wiedemann syndrome are predisposed to developing Wilms' tumor, but they represent less than 5% of all patients with Wilms' tumor. Other more rare disorders associated with Wilms' tumor include Drash's syndrome and Perlman's syndrome. The risk of Wilms' tumor is also slightly increased in children who have genitourinary malformations such as hypospadias and ectopic or horseshoe kidney.[9, 24, 43, 114]

Wilms' tumor is a malignant neoplasm arising from primitive, embryonal renal tissue.[7, 35, 36] Most are solitary and can occur anywhere in the kidney. Multiple tumors occur in 5% of patients and are strongly associated with nephroblastomatosis. Bilateral tumors are usually synchronous; however, metachronous contralateral tumors can also occur, even many years after the original presentation.[8, 9, 24, 35, 36, 132] Wilms' tumors grow rapidly and are usually very large at presentation. The mass is usually surrounded by a well-defined pseudocapsule composed of compressed tissue.

Histologically, Wilms' tumors are classified as either "favorable histology" (>90% of cases) or "anaplastic." Wilms' tumors with favorable histology present a "triphasic" appearance, with epithelial (tubular or glomerular), blastemal (small round cells), and stromal (spindle or myxoid) components in variable proportions and variable degrees of differentiation. Anaplastic Wilms' tumors occur at a slightly older age and have both a greater tendency for extending locally beyond the renal capsule into adjacent structures and a higher frequency of distant metastases. Hematogenous metastatic spread is most common to the lungs, liver, and central nervous system. Skeletal metastases are rare. Lymphatic spread to renal hilar and para-aortic lymph nodes can also occur. Intravascular extension into the renal vein and inferior vena cava occurs in 4% of children, and in 1% the tumor thrombus propagates into the right atrium[35, 36, 115] (Fig. 57–7).

Usually, ultrasound is the first imaging study performed in an infant or young child who presents with an abdominal mass. As a result, the diagnosis of Wilms' tumor is initially made upon ultrasound examination in most cases. Wilms' tumor appears as a hyperechoic, solid, intrarenal mass. The mass is often large, and it is usually predominantly solid, although it can contain cystic areas of necrosis and hemorrhage as well. Primarily cystic Wilms' tumors are rare.

On CT scanning, Wilms' tumor appears as a low-attenuation renal mass on nonenhanced scans. Postcontrast scans show a more inhomogeneous appearance, with variable enhancement of the solid components and no enhancement in areas of necrosis and cystic change. Calcification is unusual. Wilms' tumors containing small amounts of fat have been reported but are quite rare.[62, 122]

On MRI scans, the mass typically appears inhomogeneous with relatively low signal intensity on T1-weighted sequences and bright signal on T2-weighted sequences. Solid areas enhance moderately after administration of gadolinium but much less so than normal renal cortex.[12, 15, 17, 63, 88] Calcifications within the tumor appear as very-low-signal foci, and they are more difficult to recognize by MRI than by either CT or ultrasound.[11, 14]

CT and MRI generally provide similar information regarding local tumor extent and regional adenopathy. Both modalities are superior to ultrasound for precisely defining tumor extent and staging[35, 129] (Table 57–1). Direct,

Table 57–1. National Wilms' Tumor Study Committee Staging System

Stage I	Tumor confined to the kidney with complete surgical resection
Stage II	Tumor outside the kidney with complete surgical resection
Stage III	Residual tumor below the diaphragm, or previous massive intraperitoneal spillage with no hematogenous metastasis
Stage IV	Distant hematogenous metastasis
Stage V	Bilateral renal involvement at the time of diagnosis

From D'Angio GJ, Beckwith JB, Breslow N, et al: Wilms tumor. Status report, 1990: By the National Wilms Tumor Study Committee. J Clin Oncol 9:877–887, 1991; and D'Angio GJ, Breslow N, Beckwith JB, et al: Treatment of Wilms tumor: Results of the Third National Wilms' Tumor Study. Cancer 64:349–360, 1989.

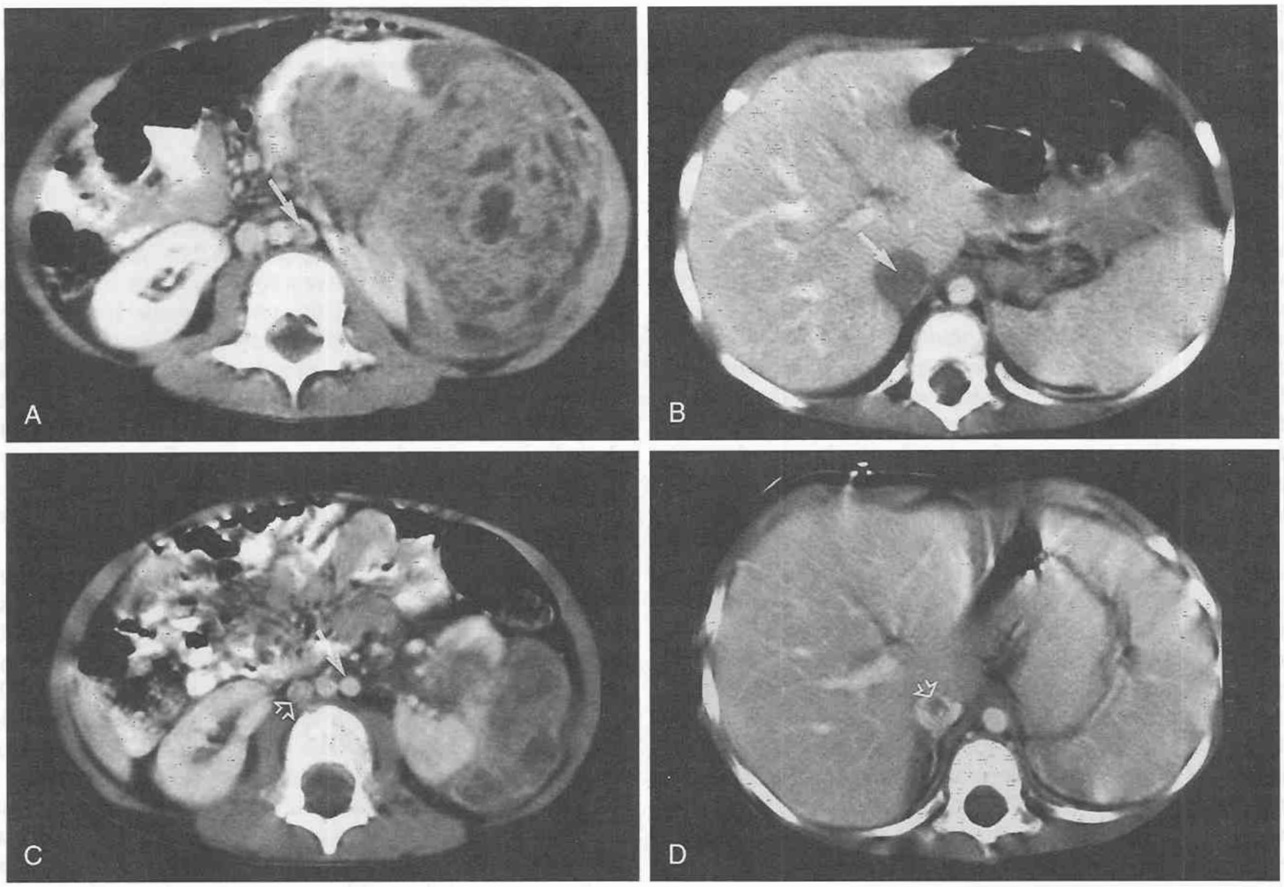

Figure 57–7. Left Wilms' tumor with intravascular extension in a 2½-year-old girl who responded dramatically to 6 weeks of chemotherapy before nephrectomy.

A, Contrast-enhanced CT axial image through the kidneys. A large, predominantly solid, nonenhancing, left renal mass with enhancing parenchyma splayed around its periphery anteriorly and medially can be seen. Multiple small areas of focal necrosis are visible within the mass. A filling defect in the left gonadal vein *(arrow)* represents tumor thrombus.

B, Contrast-enhanced CT axial image through the liver. The intrahepatic portion of the inferior vena cava is distended with low-attenuation, nonenhancing tumor thrombus *(arrow).*

C, Contrast-enhanced CT axial image through the kidneys after 2 months of chemotherapy. The left renal mass is much smaller. The left gonadal vein *(arrow)* is well opacified and contains no residual visible tumor thrombus. Residual thrombus can be visualized in the inferior vena cava, however, and it enhances more inhomogeneously *(open arrow).*

D, Contrast-enhanced CT axial image through the liver after 2 months of chemotherapy. The intrahepatic portion of the inferior vena cava is now patent, and a small central filling defect represents residual thrombus *(open arrow).*

multiplanar imaging with MRI occasionally provides more detailed information when direct invasion of adjacent structures is difficult to confirm at CT.[12, 76]

Careful evaluation of the contralateral kidney for tumor or nephroblastomatosis is mandatory. Unfortunately, nearly one third of synchronous contralateral tumors are not detected preoperatively. Although some authors have challenged the practice,[94] intraoperative inspection and palpation of the contralateral kidney are the generally accepted surgical standard, even when preoperative imaging studies show no abnormality in the contralateral kidney.[35, 132]

Because of the propensity of Wilms' tumor to grow into the renal vein and inferior vena cava, these structures should be carefully evaluated for evidence of tumor thrombus (see Fig. 57–7). Identification of the cranial extent of the thrombus is critical in presurgical planning.[35, 117, 159, 162] Intravascular extension can be more difficult to detect in some tumors that arise in the right kidney, particularly when they are very large, because the right renal vein is very short. In addition, right renal masses frequently compress the inferior vena cava. Congenital variations in left renal vein anatomy—either retroaortic or circumaortic—can also cause difficulty in patients who have left renal tumors. Flow-related artifacts in the inferior vena on contrast-enhanced CT[69] and axial gradient-echo MRI[21, 51, 140] should not be mistaken for tumor thrombus.

Because of its low cost and its availability, and because the patient does not need to be exposed to ionizing radiation or iodinated contrast material, ultrasound is typically used for continued postnephrectomy surveillance; however, CT or MRI should be performed without hesitation if there is any question of recurrent or contralateral tumor.[22]

Nephroblastomatosis

Nephroblastomatosis is the persistence of nonfunctioning, primitive, nephrogenic blastema in the kidney after

birth.[7] Nephrogenesis is completed by the 34th to the 35th week after conception. No macroscopic blastemal remnants normally remain after this point, but microscopic blastemal remnants, or *nephrogenic rests*, are present in 1% of autopsies of newborns.

Anatomically, nephrogenic rests can be described as unifocal, multifocal, or diffuse.[7, 163] Histologically, nephrogenic rests are described as perilobar or intralobar. Perilobar nephrogenic rests, which are located at the boundaries between the renal lobes, are more common than intralobar rests, which lie deep within the cortex or medulla. Perilobar and intralobar rests often coexist. Panlobar nephroblastomatosis is a rare condition in which both kidneys are nearly entirely replaced by nephrogenic rest tissue (Fig. 57–8).

The clinical importance of nephroblastomatosis lies in the potential for malignant transformation into Wilms' tumor.[7, 121, 163] Microscopic rests can remain dormant for long periods and then mature, sclerose, or enlarge to become macroscopic, hyperplastic, or neoplastic nodules. Hyperplastic nephrogenic rests can be difficult to distinguish from Wilms' tumor histologically. Although intralobar rests statistically have a much higher association with neoplastic transformation, malignancy can develop within perilobar rests as well. Histologically, 41% of patients with unilateral Wilms' tumor have nephroblastomatosis, compared with 99% of patients with bilateral Wilms' tumor.

Macroscopic nephrogenic rests appear hypoechoic at ultrasound and have low attenuation at CT.[133, 163] A nodular, undulating renal contour may suggest nephroblastomatosis in at-risk patients even when discrete nodules are not identifiable. CT is generally more sensitive than ultrasound in detecting nephroblastomatosis, although some lesions that are visible at ultrasound are not seen at CT, and vice

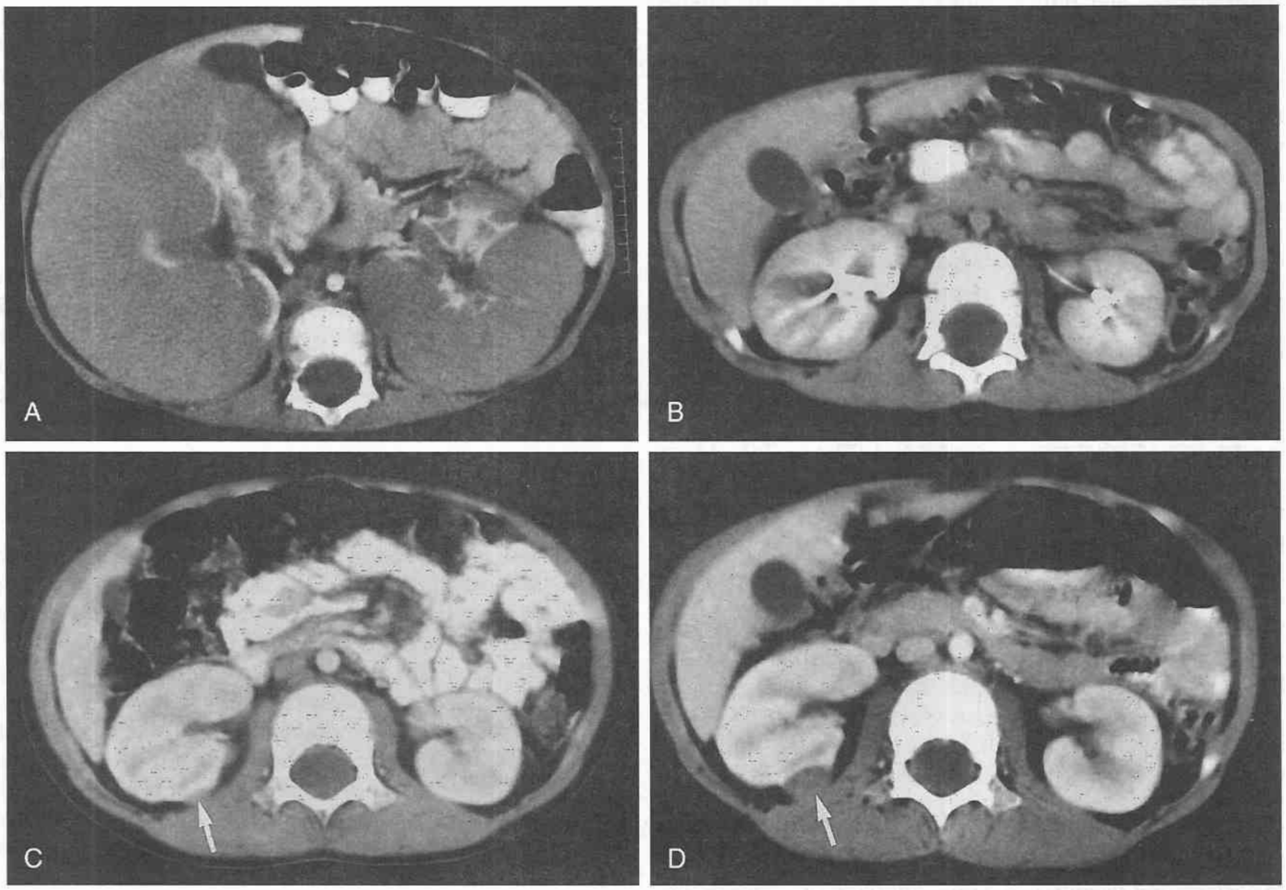

Figure 57–8. Panlobar nephroblastomatosis with chemotherapy-induced remission and later recurrence with malignant degeneration into Wilms' tumor. The patient is a boy who presented at 15 months of age with marked abdominal distention.

A, Contrast-enhanced CT axial image through the kidneys at the level of the renal hila at the initial presentation. Both kidneys are markedly enlarged and almost entirely replaced by low-attenuation, nonenhancing, solid masses. Scattered strands of residual enhancing renal parenchyma are visible interspersed between the masses.

B, Contrast-enhanced CT axial image through the kidneys at the level of the renal hila 9 months later (after completion of chemotherapy). No residual tumor is visible. The kidneys appear normal.

C, Contrast-enhanced CT axial image through the kidneys at the level of the renal hila 20 months later. A small, low-attenuation, nonenhancing, solid peripheral nodule *(arrow)* measuring just less than 1 cm in diameter is now visible posteriorly in the mid right kidney.

D, Contrast-enhanced CT axial image of the kidneys at the level of the renal hila 1 year later. The peripheral nodule posteriorly in the mid right kidney has enlarged and now measures 2 cm in diameter *(arrow)*. The nodule was resected and histologic examination confirmed malignant degeneration into Wilms' tumor.

versa.[58, 72] Foci of nephroblastomatosis that sclerose and involute occasionally appear cystic. At MRI, nephrogenic rests do not enhance; they appear homogeneously hypointense, compared with the cortex, and isointense, compared with the medulla, on both T1-weighted and T2-weighted sequences.[72, 133, 163]

In patients with Wilms' tumor, all visible macroscopic foci of nephroblastomatosis should be carefully identified on the prenephrectomy imaging studies and followed on subsequent examinations because these can indicate an increased risk of later contralateral tumor. Although some nephrogenic rests can be identified during intraoperative inspection and by palpation of the kidneys at the time of nephrectomy, many perilobar rests and most intralobar rests are not detectable in this fashion, including some that are visible at CT or MRI.[34] Microscopic foci of nephroblastomatosis are not detectable with any currently available imaging modality.

Patients with syndromes that are associated with nephroblastomatosis and Wilms' tumor[9, 24, 43, 114] (e.g., hemihypertrophy, sporadic aniridia, Beckwith-Wiedemann syndrome) are screened with ultrasound during infancy and childhood. The frequency and duration of screening vary among institutions. We observe and follow patients every 3 to 6 months until the patient is 10 years of age, gradually lengthening the interval between studies as the child gets older.[3] CT is used to evaluate suspected lesions that are identified at ultrasound. The expanded use of CT in screening children who are at risk for development of Wilms' tumor has increased the frequency of detection of smaller tumors.[102]

Clear Cell Sarcoma

Once described as a Wilms' tumor variant, clear cell sarcoma is now accepted to be a separate disease, accounting for 5% of renal tumors in children. The peak incidence is between 3 and 5 years of age. As with Wilms' tumor, most children with clear cell sarcoma also present with a palpable abdominal mass. Clear cell sarcoma is distinguished from Wilms' tumor by its greater tendency for early hematogenous metastases, particularly to bone (rare in Wilms' tumor), and its generally much poorer prognosis.[8, 97, 116] Clear cell sarcoma is not associated with nephroblastomatosis, hemihypertrophy, or aniridia.

Ultrasound, CT, and MRI reveal a predominantly solid, although frequently complex, renal mass with imaging features that are usually indistinguishable from Wilms' tumor.[68] Well-defined areas of cystic necrosis are frequent. Skeletal metastases are suggestive of clear cell sarcoma and can be present at diagnosis or appear later.[97] Skeletal metastases are usually osteolytic, although osteoblastic metastases do occur. On bone scans, both hot and cold defects occur.

Malignant Rhabdoid Tumor

Malignant rhabdoid tumor is the least common and the most uniformly deadly of the primary malignant renal tumors that occur during childhood.[158, 159] Rhabdoid tumor occurs at a younger age than Wilms' tumor, with most cases presenting during the first year of life. A distinctive feature of this tumor is its association with synchronous or asynchronous primary tumors of the central nervous system.[20] These tumors, which are histopathologically diverse, include primitive neuroectodermal tumor, ependymoma, and astrocytoma. Malignant rhabdoid tumor can metastasize to the central nervous system. Skeletal metastases also occur.

Ultrasound, CT, and MRI show a large, infiltrating, solid mass. The mass often arises centrally within or adjacent to the renal hilum[142] and expands in a lobular fashion invading and compressing the surrounding parenchyma. Calcification is common and is usually linear. In some cases, the calcification outlines distinct tumor lobules. Crescentic subcapsular fluid collections around the periphery of the mass are considered to be suggestive of this disease and frequently indicate extrarenal extension. Because of its association with both primary and metastatic brain tumors, CT or MRI of the brain should be performed whenever the diagnosis of malignant rhabdoid tumor is suspected.

Renal Cell Carcinoma

Fewer than 0.5% of renal cell carcinomas occur in people under 20 years of age. The mean age at presentation for children with renal cell carcinoma is 11 to 12 years, which is considerably older than is typically the case with Wilms' tumor. Children with renal cell carcinoma that is limited to the kidney and that is completely resected have a relatively good prognosis; however, if the primary resection is incomplete or there is distant metastatic spread, the prognosis is poor.

The histopathologic and imaging features of renal cell carcinoma in children are similar to those in adults[87] (Fig. 57–9). The tumor usually appears hyperechoic at ultrasound and hyperdense at CT, although tumor enhancement after contrast is frequently less intense in children. Calcification is present in 5% to 10%.

Leukemia, Lymphoma, and Lymphoproliferative Diseases

Although infiltration of the kidneys is evident histologically in most children who die with leukemia or lymphoma, clinical or radiographic evidence of renal involvement is uncommon during life.[4] Renal involvement is usually detected incidentally during staging or follow-up imaging studies in patients with disease elsewhere in the abdomen. Much less often, renal involvement precedes other manifestations of the disease, in which case the patient presents with a palpable mass, hematuria, or reduced renal function. Renal involvement in both leukemia and lymphoma is almost invariably bilateral, although it can be asymmetrical.

Renal lymphoma is usually of the non-Hodgkin type—Burkitt's lymphoma is most common—and associated with disease arising outside the urinary tract.[4, 138, 160] Primary lymphoma of the kidney is rare. Early in the disease, tumor involves primarily the interstitium, sparing the nephrons themselves, and gross renal morphology is usually preserved. Later, as the neoplastic cells coalesce to form larger, expansile masses, irreversible nephron damage ensues and the renal architecture becomes disrupted.

Leukemic infiltration of the kidneys is usually characterized by diffuse bilateral renal enlargement. The normal reniform shapes of the kidneys are usually preserved, al-

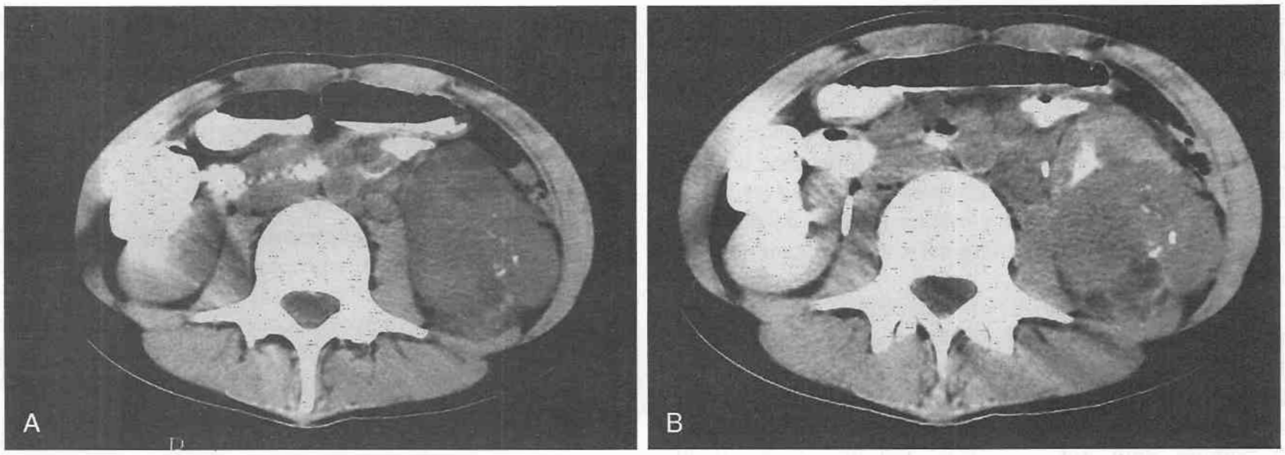

Figure 57–9. Renal cell carcinoma of the left kidney in a 13-year-old girl. *A,* Nonenhanced CT axial image through the kidneys. A 6-cm solid mass arises from the lower pole of the left kidney. Numerous punctate and stippled calcifications are visible within the mass. *B,* Contrast-enhanced CT axial image through the kidneys. The mass in the lower pole of the left kidney is better demarcated from adjacent uninvolved renal parenchyma after contrast administration. The multiple small calcifications within the mass are again visible.

though the normal corticomedullary architecture is disrupted. Bilateral, focal masses that distort the collecting system and renal contours are more common in lymphoma, but both patterns can be seen in either leukemia or lymphoma. CT is superior to ultrasound for detecting renal involvement with lymphoma in children.[138, 160] At ultrasound, the involved portions of the kidneys appear slightly hypoechoic, with diminished or absent corticomedullary differentiation. At CT, the involved areas are homogeneously low in attenuation and do not enhance (Fig. 57–10). Perirenal extension and renal hilar and retroperitoneal lymph node involvement also can be demonstrated.

Lymphoproliferative disorders represent an important group of potentially life-threatening conditions that occur in patients with severely impaired or suppressed T-lymphocyte–mediated immunity. These disorders can occur as a complication of immunosuppressive therapy for organ transplantation,[49, 118, 126] in patients who have primary immunodeficiencies,[49] and in patients who have acquired immunodeficiency syndrome (AIDS).[168] Regardless of the underlying cause of the immunodeficiency, Epstein-Barr virus–mediated induction of polyclonal B-lymphocyte proliferation is critical in the pathogenesis of this disorder.[103, 118]

Lymphoproliferative disorders are associated with lymphadenopathy, focal parenchymal masses, and diffuse infiltration of solid organs. The disease can be focal, multifocal, or widely disseminated, and any organ or body space can be involved. The gastrointestinal tract, solid abdominal organs, and abdominal lymph nodes are most often affected. Renal involvement occurs in 17% to 20% of cases.

Mesoblastic Nephroma

Congenital mesoblastic nephroma, or congenital fetal renal hamartoma, occurs almost exclusively in the first year

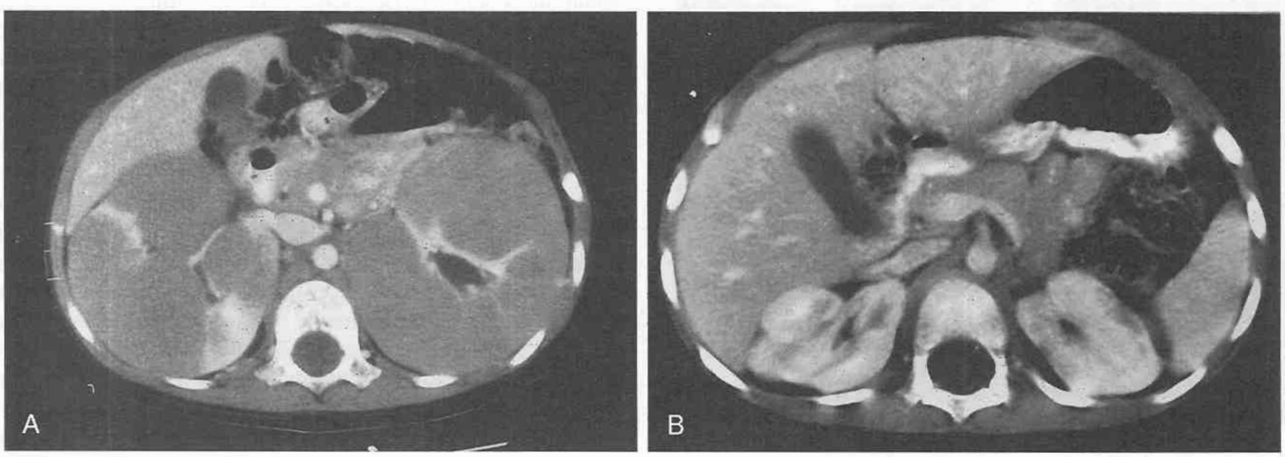

Figure 57–10. Burkitt's lymphoma with renal involvement in a 3-year-old boy. *A,* Contrast-enhanced CT axial image through the kidneys. Both kidneys are massively enlarged and almost completely replaced by multiple, low-attenuation, nonenhancing solid masses. *B,* Contrast-enhanced CT axial image through the kidneys 8 months later. The renal masses are no longer present and the kidneys are now normal in size. However, the renal margins are now irregular and somewhat lobular.

of life, and it is the most common solid renal tumor in the newborn.[18, 29, 75] Most patients present with a palpable abdominal mass. Hematuria, hypercalcemia, abdominal pain, and hypertension also occur. The tumor is occasionally discovered prenatally. Once believed to be a congenital variant of Wilms' tumor, mesoblastic nephroma is distinguished by its occurrence at an earlier age, its generally benign course and limited growth potential, its derivation from predominantly mesenchymal derivatives, and its lack of a malignant epithelium.

The "typical" form of mesoblastic nephroma—representing approximately 60% of cases—appears as a firm to hard, pale yellow to gray solid tumor with no cysts or areas of hemorrhage or necrosis.[18, 29, 75] Histologic examination reveals uniform spindle-shaped cells arranged in bundles with low cellularity and no cellular atypia. Although the renal capsule is frequently penetrated by strands of tumor extending radially into the perirenal fat, adjacent organs are not involved.

The "atypical" form of mesoblastic nephroma tends to be larger and more cellular, with a disorganized histologic appearance. Macroscopic areas of hemorrhage and necrosis produce a multicystic appearance. The tumor can invade adjacent organs and encase the inferior vena cava and renal vessels, but it is distinct from Wilms' tumor in that intravascular extension does not occur. Local recurrence after nephrectomy is unusual and is generally limited to tumors with "atypical" histology. Several well-documented cases of atypical mesoblastic nephroma metastasizing to lung and brain have been reported, but this is undoubtedly very rare.[137] Chemotherapy is indicated only when the surgical resection is incomplete or there is metastatic disease, regardless of the histologic appearance.

At ultrasound, mesoblastic nephroma appears as a large, solid renal mass that often replaces much of the renal parenchyma[18, 29, 75] (Fig. 57–11). The mass can be either homogeneous or complex. Cysts are present in 60%, and small, scattered foci of calcification are occasionally present.[59] Tumors that obstruct the renal pelvis produce hydronephrosis.

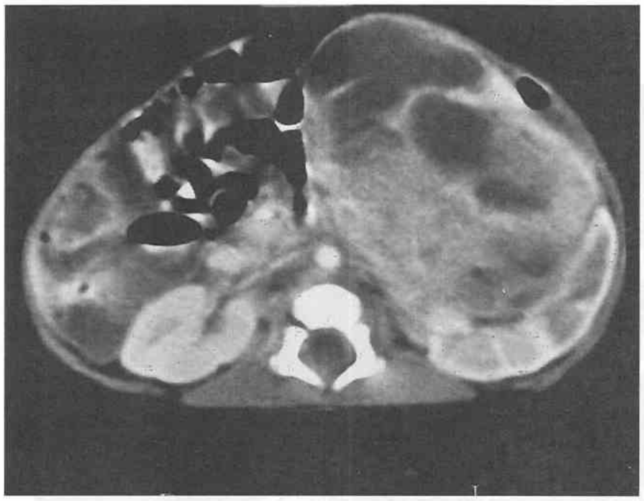

Figure 57–11. Congenital mesoblastic nephroma in a 1-day-old male infant. Contrast-enhanced CT axial image through the kidneys. Enhancing renal parenchyma is visible splayed around the posterior and inferior margins of a very large, partially necrotic mass arising from the upper pole of the left kidney.

On CT scans, the tumor presents as a nonenhancing, low-attenuation mass within which scattered islands of enhancing residual normal parenchyma may be seen.[29, 75]

Multilocular Cystic Nephroma

Multilocular cystic nephroma is a benign, cystic tumor of the kidney that occurs primarily in infant boys between 3 months and 4 years of age and in middle-aged women.[5, 86, 106] The tumor is frequently palpable. Hematuria, flank pain, and hypertension are also common findings. The tumor is usually solitary, but multiple synchronous tumors can also occur.

The tumor can involve part or all of the kidney. Grossly, it is composed of multiple, noncommunicating cysts of varying size, with intervening septa consisting of a mixture of fibrous tissue, tubular elements, and immature blastemal tissue. Rarely, rests of cells that are histologically similar to Wilms' tumor—so-called Wilms' tumorlets—are identified in the walls of the cysts; however, multilocular cystic nephroma appears to have no potential for malignant transformation. Nephrectomy usually results in cure, and local recurrence is rare after complete resection.

The imaging appearance of multilocular cystic nephroma is distinctive.[47, 106] The tumor appears as a complex, multicystic mass. The septa between the cysts are characteristically thin and can enhance in some cases. The septa are frequently demonstrated to greater advantage with ultrasound than with CT. Thicker septations with irregular, solid areas of nodular thickening should suggest another diagnosis, such as cystic Wilms' tumor.[86] Curvilinear septal calcifications are occasionally present in adults. At MRI, the capsule surrounding the cystic mass appears relatively hypointense, with the signal intensity of the fluid within the locules reflecting differences in their hemorrhagic and proteinaceous composition.[47]

Angiomyolipoma and Other Renal Manifestations of Tuberous Sclerosis

Angiomyolipoma is a benign, nonencapsulated, hamartomatous lesion of the kidney that is composed of blood vessels, smooth muscle, and fat in variable proportions.[10, 119, 154] The tumor can arise in the cortex or the medulla. In children, angiomyolipoma is frequently multiple and bilateral, and it is almost invariably a manifestation of tuberous sclerosis. Renal cysts also occur in patients with tuberous sclerosis and can mimic familial polycystic kidney disease[10, 115, 119, 154] (Fig. 57–12). Occasionally, angiomyolipomas or renal cysts are detected in a child with undiagnosed tuberous sclerosis who presents with a palpable mass or hematuria. More often, other features typical of this syndrome are already known, such as adenoma sebaceum, subungual fibroma, mental retardation, seizure disorder, cardiac rhabdomyoma, and the central nervous system tubers, tumors, and heterotopias.

Demonstration of fat within a renal mass in a child is suggestive of angiomyolipoma. Rarely, however, the tumor has more vascular and muscular elements and contains little or no visible fat.[10, 119, 154]

On ultrasound examination, angiomyolipomas are usu-

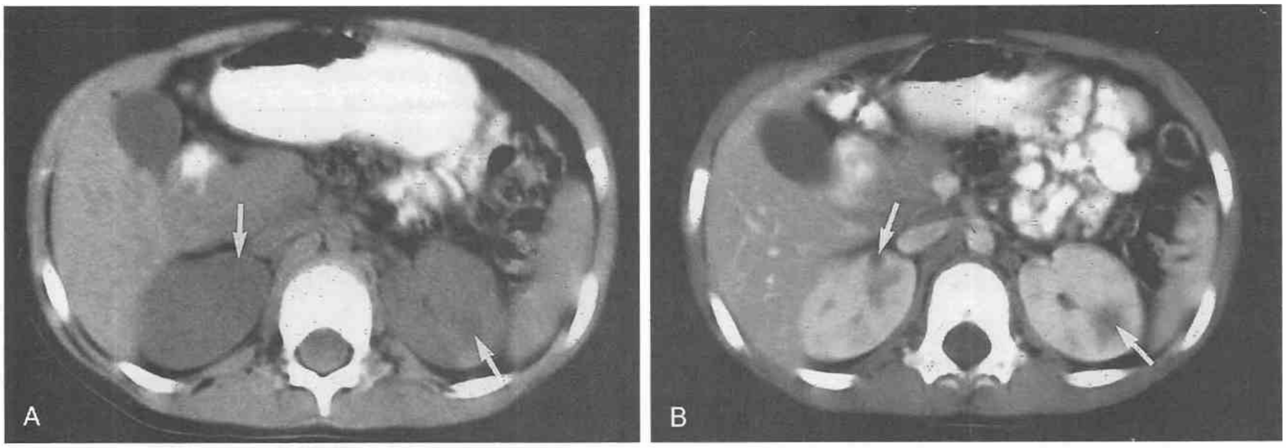

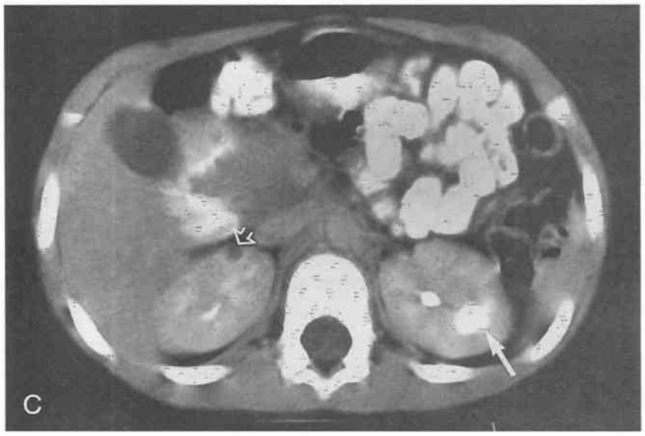

Figure 57–12. Left renal angiomyolipoma and right simple renal cyst in a 5-year-old boy with tuberous sclerosis.

A, Nonenhanced CT axial view through the kidneys just below the renal hila. Subtle, low-attenuation foci are visible in the mid right kidney anteriorly and in the mid left kidney posteriorly *(arrows).*

B, Contrast-enhanced CT axial view through the kidneys just below the renal hila during the corticomedullary phase. The lesions anteriorly in the right kidney and posteriorly in the left kidney are seen much more clearly than on the nonenhanced study. Both lesions again appear very low in attenuation *(arrows)* compared with the surrounding enhancing renal parenchyma. The small anterior lesion in the right kidney is nearly circular and is sharply defined compared with the lesion on the left, which is larger with less well defined margins.

C, Contrast-enhanced CT axial view through the kidneys just below the renal hila during the excretion phase. Delayed images show that the lesion on the right does not enhance, consistent with a simple cyst *(open arrow).* The lesion on the left, on the other hand, enhances very intensely, consistent with an angiomyolipoma *(arrow).*

ally brightly echogenic. At CT, the same areas have very low attenuation on nonenhanced scans, with an appearance similar to that of perirenal fat. Detection of the fat composition of very small angiomyolipomas can be facilitated by using single-voxel region-of-interest measurements of attenuation.[96]

At MRI, the tumors are hyperintense on both T1-weighted and T2-weighted images. Because angiomyolipomas are usually very hypervascular, they enhance intensely at both CT and MRI. Larger angiomyolipomas also tend to bleed, often abruptly and profusely, resulting in areas of hemorrhage within the tumor as well as hemorrhage beneath the renal capsule and into the perirenal space; however, less vascular, smaller lesions can sometimes be difficult to distinguish from cysts. Calcification is generally absent in angiomyolipoma.

Lymphangioma and Related Disorders

Isolated renal lymphangioma is a rare, benign, cystic tumor of the kidney that can be radiographically difficult to distinguish from multilocular cystic nephroma.[99, 125] Extensive renal lymphangiomatosis is quite rare; it produces massive, bilateral nephromegaly with residual functioning islands of renal parenchyma that appear as irregular bands separating the cystic masses. Renal lymphangiomatosis may be isolated, but more often it occurs in association with retroperitoneal lymphangiomatosis.[41] Cystic pulmonary lesions may also coexist.[73]

Lipoblastomatosis is a benign tumor of fetal adipose tissue that occurs mainly before the age of 3 years. Lobules of immature fat are present, together with a myxoid stroma separated by vascular connective tissue septa. The fat density is easily appreciated at CT, with denser areas that represent the myxoid tissue.[61]

Renal Cystic Diseases

Ultrasound is used for the primary evaluation of renal cystic diseases. In general, the role of CT and MRI is limited to cases in which the sonographic appearances are confusing or when a complication such as cyst rupture, hemorrhage, or neoplasia is suspected.[45, 77]

Isolated simple renal cysts are uncommon in children. For this reason, polycystic kidney disease should be suspected when even a single cyst is identified in an otherwise normal-appearing kidney in a child. In fact, most cystic renal lesions that are identified upon ultrasound examination in children are not cysts in the strict sense. Caliceal diverticula, hydrocalices, and even very prominent and

hypoechoic medullary pyramids are often misinterpreted as cysts.

On CT and MRI scans, simple cysts appear as homogeneous, well-defined, fluid-filled, spherical or fusiform masses with clearly defined, thin walls. In uncomplicated cysts, the fluid is of homogeneously low attenuation at CT and has low signal intensity on spin-echo and inversion recovery T1-weighted images.[45, 46, 81, 101] On spin-echo T2-weighted images, the signal intensity of the fluid increases and the wall of the cyst and the fluid may not be distinguishable.

At MRI, hemorrhagic cysts vary widely in signal intensity. In general, the signal intensity in hemorrhagic cysts is brighter and more inhomogeneous on both T1-weighted and T2-weighted images.[31, 46, 78, 81, 101, 109] At CT, larger clots can often be identified within cysts but differences in fluid composition and small particulate debris within the cyst fluid are more readily identified at MRI than with CT.

Calcification in the wall of the cysts is more commonly seen in adults and is rare in children. Although larger calcifications are sometimes visible as regions of signal void within the wall of the cyst at MRI, mural calcifications are better evaluated at CT or ultrasound.

Caliceal Diverticulum ("Congenital Caliceal Cyst")

A caliceal diverticulum represents a congenital malformation of the collecting system.[77] At ultrasound, caliceal diverticula appear as solitary or multiple cystic lesions within the renal parenchyma. These diverticula are usually centrally located within the kidney, adjacent to the pyramids and collecting system. Although most caliceal diverticula are small (<1 cm), occasionally they can be quite large and can vary somewhat in size and shape, depending on the degree of distention of the collecting system.

Many caliceal diverticula communicate freely with the collecting system and become opacified during either antegrade or retrograde urography as well as during CT. Occasionally, however, the neck of the diverticulum is stenotic, in which case the diverticulum becomes only faintly opacified or, in some cases, not at all. Detection of faint opacification of a caliceal diverticulum at CT can be assisted by comparing the attenuation within the "cyst" on delayed imaging sequences with the patient first supine and then prone.

Autosomal Recessive Polycystic Kidney Disease

Autosomal recessive polycystic disease is manifested by severe dilatation and ectasia of the collecting tubules. Because most patients with this disorder present very early in life, it is also called "infantile polycystic disease," but presentations later in childhood or adolescence are not unusual.[77]

Very young patients with recessive polycystic disease have markedly enlarged kidneys. On cross-section, the dilated and ectatic collecting tubules appear as fusiform cystic structures within the enlarged medullary pyramids (Fig. 57–13). With increasingly severe involvement, the tubular ectasia extends beyond the collecting tubules in the medulla to involve the convoluted tubules. In its most severe expression, the cystic changes extend to the surface of the kidney, with innumerable cysts erupting beneath the renal capsule.

Liver disease may also occur in patients with recessive polycystic disease. Histopathologically, the spectrum of severity of the hepatic disease varies widely—from mild biliary proliferation and dilatation to biliary atresia with severe periportal fibrosis, to portal hypertension with varices and upper gastrointestinal hemorrhage. In general, patients with more severe liver involvement have less severe renal disease and usually present at a somewhat older age.[77]

Recessive polycystic kidney disease is generally evaluated with ultrasonography. The kidneys are typically very

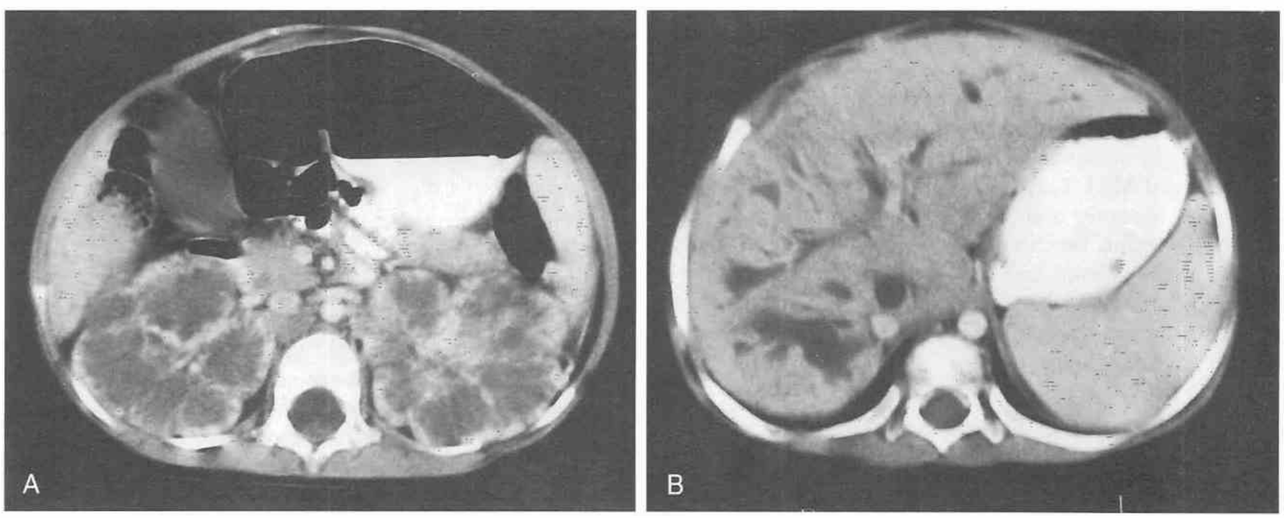

Figure 57–13. Autosomal recessive polycystic kidney disease with hepatic fibrosis in a 3-year-old girl who presented with severe hypertension. *A*, Contrast-enhanced CT axial image through the kidneys. Both kidneys are very enlarged. Dilated and ectatic collecting tubules appear as fusiform cystic structures within the very enlarged medullary pyramids. At the periphery of the kidney, the cortex is thinned and enhances inhomogeneously. *B*, Contrast-enhanced CT axial image through the liver. The intrahepatic bile ducts are diffusely dilated and ectatic.

enlarged and inhomogeneously echogenic. The echogenic appearance of the parenchyma results from the abnormally increased reflectivity of the walls of the distended and ectatic collecting tubules and distal convoluted tubules. Macrocysts, when present, are usually located peripherally, producing a hypoechoic marginal halo around the kidney and occasionally even around individual renal lobes.

Autosomal Dominant Polycystic Kidney Disease

Autosomal dominant polycystic disease occasionally presents in childhood. The cysts are usually small and few in number early in life. In neonates, the kidneys appear large and contain multiple small cysts mimicking the appearance of the recessive form of the disease.[56] As the child becomes older, the cysts increase in size and number. Eggshell mural calcification is seen only rarely in children (Fig. 57–14). Complications such as hemorrhage within a cyst can be visualized either at CT or MRI. MRI often shows striking differences in the signal intensity of the fluid in the cysts, reflecting differences in protein content of the fluid.

Multicystic Dysplastic Kidney

Atresia of the ureteral bud at or below the ureteropelvic junction results in a severely dysplastic, nonfunctioning, cystic kidney.[57, 74, 77] The diagnosis is usually easily established on the basis of characteristic imaging findings at ultrasound and renal diuretic or cortical scintigraphy of a nonfunctioning kidney that is replaced by multiple noncommunicating cysts with no residual normal-appearing parenchyma. At CT and MRI, the kidney is shown to be entirely replaced by multiple cysts of different sizes that are separated by a small amount of nonfunctioning, dysplastic parenchyma.

In the hydronephrotic variant of multicystic dysplasia, the kidney is nonfunctioning and contains one or more smaller peripheral cysts, with a large central cyst representing the dilated, dysmorphic collecting system.[57] In the segmental multicystic dysplastic kidney, the anomaly affects only one moiety of a partially or completely duplicated collecting system.[85] Bilateral multicystic renal dysplasia is incompatible with extrauterine life and is accompanied by severe oligohydramnios, pulmonary hypoplasia, and the other features of Potter's syndrome.

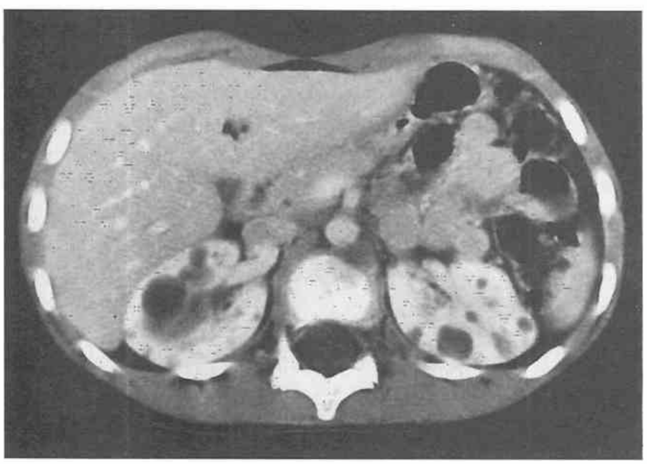

Figure 57–14. Autosomal dominant polycystic kidney disease in an 8-year-old girl. Contrast-enhanced CT axial image through the kidneys. Innumerable cysts are present throughout both kidneys, surrounded by normally enhancing renal parenchyma.

In most patients with a multicystic dysplastic kidney, the fluid within the cysts is gradually absorbed and the kidney progressively decreases in size until it is no longer identifiable at ultrasound. This process of involution of a multicystic dysplastic kidney results in an appearance that is indistinguishable from unilateral renal agenesis. Because the dysplastic renal remnant has no function, it is not identifiable at renal scintigraphy. In patients who have severe hypertension or other signs or symptoms suggestive of an occult, dysplastic kidney, MRI has been used to identify the tiny offending dysplastic remnant.

Renal Trauma

CT is commonly used to evaluate patients with suspected renal trauma. It provides excellent anatomic and functional information that correlates very closely with surgical findings. It is superior to either urography or ultrasonography in patients who have traumatic renal injuries. In addition, with CT, the entire abdomen and pelvis can be rapidly surveyed, permitting immediate diagnosis of associated injuries to other viscera.[25, 55, 89, 98, 136]

Renal injuries range from isolated parenchymal contusions with no associated subcapsular or perirenal hemorrhage (grade I) to superficial parenchymal lacerations that do not involve the collecting system (grade II), to deeper parenchymal lacerations that are associated with urinary extravasation (grade III), to extensive disruption and fragmentation of the kidney (grade IV) (Table 57–2). Grades I and II injuries account for more than half of all injuries in children.[89, 139] The possibility of a preexisting renal abnormality should always be considered. Kidneys that are abnormally large, hydronephrotic, or ectopic, or that contain masses or cysts, are more prone to injury[67, 130] (Fig. 57–15).

Function is commonly decreased or absent in the area of the injury as a result of venous thrombosis and vascular compression by adjacent edematous parenchyma or clot. With more minor injuries, function often returns with healing; however, in patients with extensive parenchymal fractures, infarction of completely devascularized renal fragments is not associated with recovery of function. Disruption or thrombotic occlusion of polar arterial

Table 57–2. CT Grading of Renal Trauma

Grade I	Small parenchymal injury No subcapsular or perirenal fluid Uninjured anomaly
Grade II	Incomplete renal laceration Subcapsular or small amount of perirenal fluid
Grade III	Extensive laceration or fracture
Grade IV	Multiple fragments (shattered)
Grade V	Vascular injury

From Karp MP, Jewett TC, Kuhn JP, et al: The impact of computed tomography scanning on the child with renal trauma. J Pediatr Surg 21:617–623, 1986.

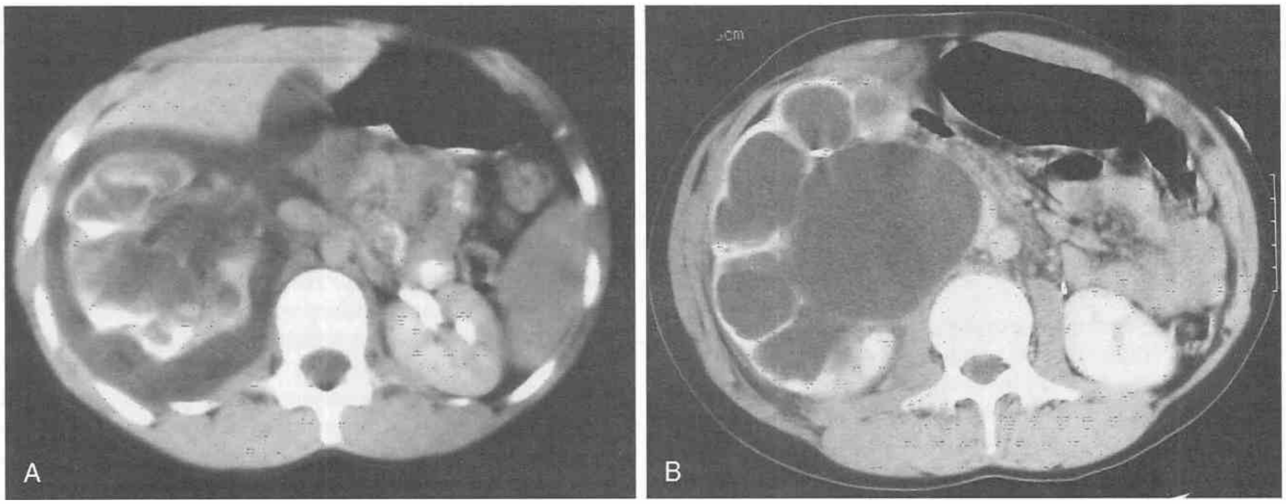

Figure 57–15. Rupture of the right renal collecting system and right perinephric urinoma in an 11-year-old boy with preexisting severe ureteropelvic junction obstruction. The patient presented with gross hematuria and abdominal pain after a skiing accident.

A, Contrast-enhanced CT axial image through the kidneys performed several hours after the injury. There is moderate right hydronephrosis with severe, diffuse, cortical thinning consistent with long-standing obstructive uropathy. A large right perinephric fluid collection is also present.

B, Contrast-enhanced CT axial image through the kidneys 6 weeks after the injury. The right hydronephrosis has considerably increased and the collecting system appears more tense. The cortex is diffusely and severely thinned; it appears as enhancing crescents surrounding the dilated calices that are filled with nonopacified urine. The perinephric fluid collection has resolved.

branches can also lead to segmental parenchymal infarcts.[136, 139]

Subcapsular and perirenal hemorrhages often accompany superficial and deeper parenchymal lacerations.[89, 139] Subcapsular fluid collections closely conform to the renal contour and are separated from Gerota's fascia by the perirenal fat. On the other hand, perirenal blood extends to Gerota's fascia. On nonenhanced images obtained early after the injury, subcapsular and perirenal blood appears higher in attenuation than the adjacent renal parenchyma. After contrast material is given, the renal parenchyma enhances and the adjacent, nonenhancing clot appears relatively lower in attenuation. As the clot matures and liquefies, its attenuation gradually decreases. Urinomas resulting from disruption of the walls of the collecting system or proximal ureter appear as masses of fluid attenuation. If the leakage is still active during the study, the mass will contain opacified urine and the site of the extravasation from the collecting system can occasionally be directly identified (Fig. 57–16).

An injury to the renal vascular pedicle should be suspected when there is complete loss of flow and function in the kidney. This a critical point, because renal pedicle injury is one of the few absolute indications for emergent surgical intervention. Collateral flow through capsular vessels frequently results in a rim of enhancement at the periphery of the kidney.[70, 120] Severe renal vascular compromise can result from subendothelial hemorrhage or dissection within the wall of the renal artery, from direct laceration of the vessel, or from extrinsic compression of the renal vascular pedicle by adjacent hematoma in the perirenal space.

Surgical intervention is usually limited to those patients who are hemodynamically unstable and those who are thought to have injuries to the renal vascular pedicle.[6, 89] Early CT permits rapid and accurate diagnosis of the nature and severity of the child's injuries. Although ultrasound generally has no role in the acute investigation of the child with suspected blunt renal injury, it is ideally suited for follow-up of abnormalities that have been previously demonstrated by CT. With conservative management, the rate of renal salvage is high. Hypertension is the most common long-term clinical complication.[1, 6, 110]

Adrenal Glands

Although the adrenal glands are generally easily visualized by ultrasonography in neonates and infants, the reliability of this modality diminishes with age and CT and MRI are more sensitive in diagnosing and characterizing adrenal disease in older children. Nonetheless, ultrasound is still used as the primary screening modality in most forms of adrenal disease because it does not expose the patient to ionizing radiation and it is widely available; however, when adrenal pathology is strongly suspected clinically, either MRI or CT or both should be performed, even when ultrasonographic findings are negative.

Normal Anatomy

At CT, the adrenal glands appear as triangular or crescentic soft tissue structures draped over the upper poles of the kidneys immediately anterolateral to the crura of the diaphragm. The two limbs of each adrenal gland appear as thin strands that join superiorly. At MRI, the normal adrenal glands appear on T1-weighted images as triangular or crescentic suprarenal structures of medium signal intensity, with the two limbs of each gland outlined by the high-

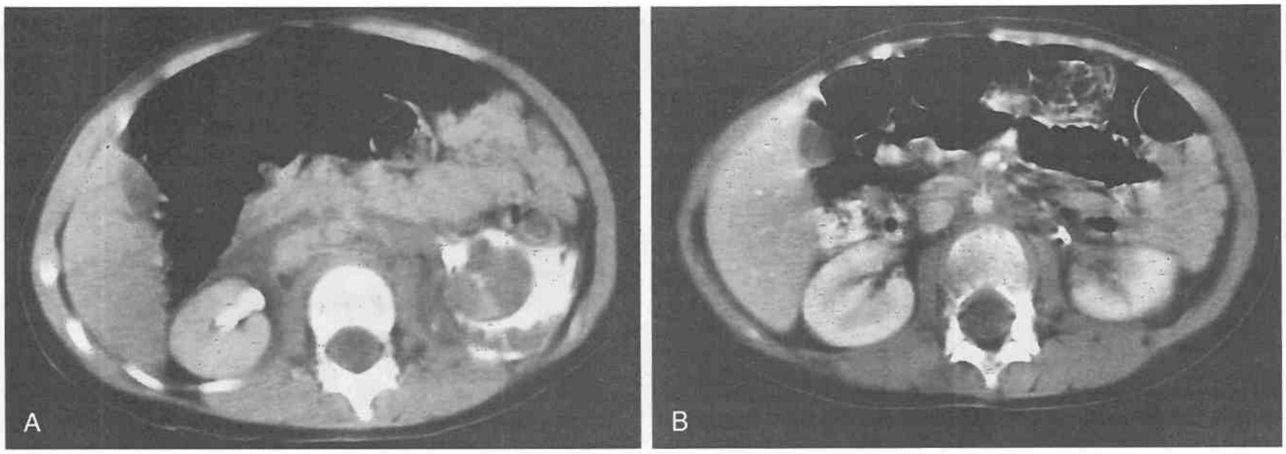

Figure 57–16. Left renal fracture with laceration of the collecting system and lower pole infarction in a 5-year-old girl who was run over by a bulldozer. *A*, Contrast-enhanced CT axial image through the lower poles of the kidneys several hours after the injury. The lower pole of the left kidney enhances very poorly, especially the lateral half. Perinephric extravasation of contrast material secondary to laceration of the collecting system has resulted in a large, opacified perinephric fluid collection surrounding the lower pole of the left kidney. The lower pole of the right kidney appears normal. *B*, Contrast-enhanced CT axial image through the lower poles of the kidneys 2 months later. The contour of the lower pole of the left kidney appears somewhat irregular. The medial portion of the lower pole still enhances poorly. The perinephric urinoma has resolved.

signal-intensity perirenal fat.[27, 81] On T2-weighted images, the adrenals have slightly greater signal intensity but still show less intensity than the surrounding fat.

The normal triangular, "arrowhead" configuration of the adrenal gland results from elevation of the two adrenal limbs by the upper pole of the subjacent kidney. For this reason, when a kidney is absent or ectopic, the ipsilateral adrenal gland assumes an elongated, linear, or discoid configuration and occupies more of the renal fossa than normal.[141] On axial images, the elongation of the adrenal gland in this situation is often difficult to recognize; on coronal MRI images, the discoid adrenal gland appears as an elongated linear structure and should not be mistaken for a small hypoplastic or dysplastic kidney.

Adrenal Hemorrhage

Adrenal hemorrhage occurs in fetuses and neonates secondary to a variety of perinatal insults, including hypoxemia, metabolic acidosis, septicemia, renal vein thrombosis, coagulation disorders, and birth trauma.[27, 53, 113, 161] Anemia and jaundice are common. Larger hemorrhages may appear with hypovolemic shock, profound anemia, and a palpable mass. In some patients, the hemorrhage is asymptomatic and is discovered incidentally during abdominal or renal sonography performed for an unrelated reason.

Ultrasonography is the modality of choice both for the initial evaluation and for follow-up of neonates thought to be having adrenal hemorrhage. Imaging with other modalities, such as CT or MRI, is unnecessary except when there is concern that the hemorrhage might be masking an underlying adrenal neoplasm, such as neuroblastoma. Even in this case, serial sonography and a "tincture of time"[157] are usually the optimal approach because adrenal hemorrhage will liquefy and contract in size over several weeks. Given the generally excellent prognosis in neonatal neuroblastoma, aggressive multimodality imaging is not warranted unless a subsequent sonogram shows an enlarging mass or evidence of regional nodal or liver metastases.

Chunky or speckled calcification within the mass also suggests neuroblastoma. Calcification is not present early in the course of adrenal hemorrhage, although the hematoma can calcify later, usually beginning at the periphery. More often, neither MRI nor CT can clarify the situation, because both yield findings of a complex, hemorrhagic adrenal mass.[27, 53, 113, 161] Acutely, adrenal hemorrhage has low signal intensity on T1-weighted images. Subacute hemorrhage has very bright signal on both T1-weighted and T2-weighted images.

Adrenal Tumors

Neuroblastoma

Neuroblastoma is the most common primary extracranial solid tumor in childhood.[26, 27, 44, 113] It can occur anywhere along the sympathetic chain from the neck to the pelvis; 75% are in the abdomen, and two thirds of these (50% of the total) are in the adrenal gland. Twenty percent of neuroblastomas occur in the chest and neck. Most children with neuroblastoma are between 1 and 5 years of age.

Symptoms are related to the primary tumor and to metastases, which are present at initial diagnosis in more than half of patients. A mass is frequently palpable. Pain is common, both from the primary tumor and from metastases, and the child appears ill and irritable. Large paraspinal tumors can lead to paraplegia and urinary and fecal retention or incontinence secondary to involvement of the spinal cord and lumbosacral nerve roots. The most common sites of metastases are regional and distant lymph nodes, cortical bone, bone marrow, skin, and liver. Lung metastases are rare. In patients with extensive marrow involvement, profound anemia and thrombocytopenia can mimic primary reticuloendothelial disease.

Symptoms related to secretion of neurotransmitters are

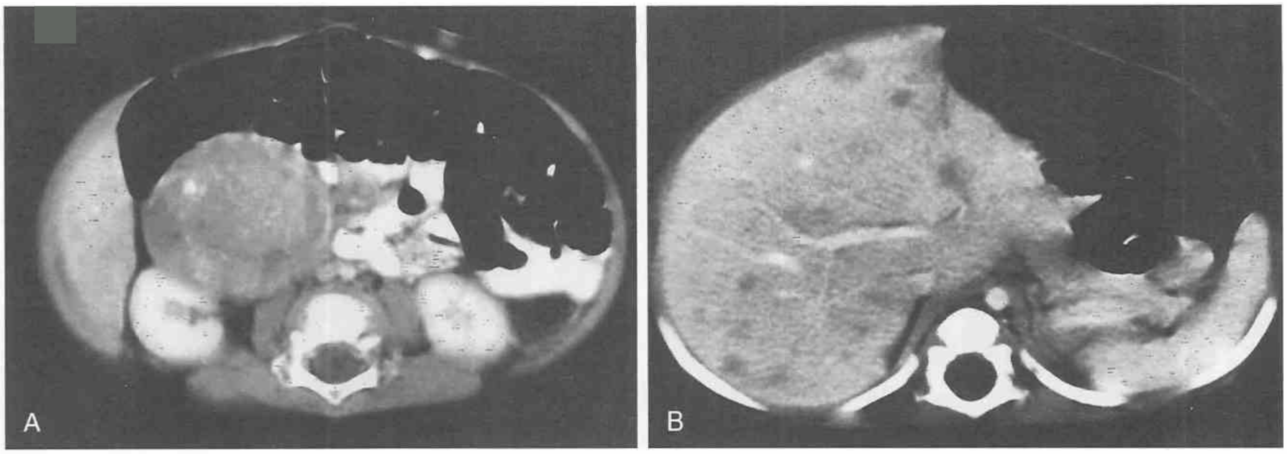

Figure 57–17. Stage IV-S right adrenal neuroblastoma with liver metastases in a 4-month-old boy who presented with multiple nodular skin metastases on physical examination. *A*, Contrast-enhanced CT axial image through the upper abdomen. A 5-cm, solid, right suprarenal mass exhibits a somewhat inhomogeneous attenuation and indents the anterior surface of the upper pole of the right kidney. Scattered mottled calcifications are visible within the mass. *B*, Contrast-enhanced CT axial image through the liver. Multiple low-attenuation, nonenhancing lesions are visible throughout the liver, consistent with metastases.

common, and hypertension is present in 5%. Opsomyoclonus is a rare clinical syndrome that occurs in 2% of children with neuroblastoma. Opsomyoclonus is characterized by chaotic, disconjugate eye movement. Myoclonic jerks and cerebellar ataxia are also frequently present.[48, 54] Half the children with opsomyoclonus have neuroblastoma. Because these tumors are often small and may not produce catecholamines, CT or MRI screening is performed to identify nonpalpable neuroblastomas in this group of patients. The neurologic signs and symptoms often improve with removal of the tumor.

At CT, abdominal neuroblastoma appears as an irregular, lobulated, suprarenal or paraspinal mass[105, 152] (Fig. 57–17). Areas of hemorrhage, necrosis, and cyst formation are common. Chunky or speckled calcification is visible within the mass at CT in 80% of patients. Unlike Wilms' tumor, which typically has a well-defined pseudocapsule, neuroblastoma frequently invades adjacent structures and encases the aorta and its branches early in the course of the disease. Neuroblastoma frequently spreads to retroperitoneal lymph nodes, and retrocrural lymphadenopathy is specific for neuroblastoma.

Encasement of the aorta and its main branches is more important in guiding management and determining prognosis than the conventional staging system, which uses the midline as a landmark between stage II and stage III disease (Table 57–3). Although neuroblastomas that cross the midline but do not encase major vessels technically represent stage III disease, they are usually still surgically resectable even when they are very large or involve regional lymph nodes.[16]

Paraspinal neuroblastomas that extend directly through the neural foramina to involve the spinal cord and roots are best evaluated with MRI. The appearance of a "dumbbell" mass centered at one or more foramina is characteristic of paraspinal neuroblastoma.

On T1-weighted images, the signal intensity of neuroblastoma is similar to that of the renal medulla and slightly lower than that of liver or renal cortex. The signal intensity of the mass increases on T2-weighted images and appears similar to that of kidney.[44] Marrow involvement is best demonstrated on T1-weighted images, with the normally high-signal-intensity marrow fat replaced by lower-signal-intensity tumor. On T2-weighted images, the tumor is more similar in signal intensity to marrow and less easily identified. Calcifications are not usually visible on MRI scans unless they are large, in which case they appear as very-low-signal areas within the mass on both T1-weighted and T2-weighted images. When neuroblastoma invades the adjacent kidney, it can mimic a primary intrarenal mass,[105, 134] but tumor calcification, retroperitoneal lymphadenopathy, and encasement of the aorta and inferior vena cava are far more likely in neuroblastoma than in Wilms' tumor.

After treatment, CT scanning offers the most sensitive method of detecting tumor recurrence.[153] Both CT and MRI scanning can identify tumor recurrence in the retroperito-

Table 57–3. Staging of Neuroblastoma

Stage I	Tumor confined to organ or structure of origin and completely resected
Stage II	Tumor extending in continuity beyond the organ or structure of origin, but not crossing the midline. Regional lymph nodes on the ipsilateral side may be involved.*
Stage III	Tumors extending in continuity beyond the midline. Regional nodes bilaterally may be involved.
Stage IV	Remote disease involving skeleton, parenchymatous organs, soft tissues, or distant lymph node groups (see stage IV-S).
Stage IV-S	Disease that would otherwise be stage I or II but is remote and confined to one or more of the following sites: liver, skin, or bone marrow, without radiographic evidence of cortical bone metastases on complete skeletal survey.

*All "dumbbell" tumors are classified as stage II unless the abdominal or thoracic portion crosses the midline.

From Stark DD, Brasch RC, Moss AA, et al: Recurrent neuroblastoma: The role of CT and alternative imaging tests. Radiology 148:101–105, 1983.

neum, liver, cranium, mediastinum, lymph nodes, and skeleton.

Adrenal Cortical Tumors

Adrenal cortical tumors are quite rare during childhood but tend to be highly malignant and locally invasive.[39, 92, 166] Carcinoma is three times as common as adenoma in children, compared with the much higher proportion of adenomas in adults.[64] The tumors are usually unilateral and are hormonally active in most cases. Excess androgens produce virilization in girls and pseudoprecocious puberty in boys. Cushing's syndrome, feminization, and hyperaldosteronism are less common findings.

At CT, adrenal cortical tumors are seen as an inhomogeneous, complex solid mass with internal areas of necrosis and hemorrhage.[39] Calcification is occasionally present. Tumors larger than 5 cm in diameter are more likely to be carcinomas. Carcinomas also tend to have more irregular margins, and they demonstrate a somewhat higher signal intensity at MRI than adenomas do[64]; however, an adenoma cannot be reliably differentiated from carcinoma at either CT or MRI[27, 64, 113] except when local invasion or distant metastases are identified. Carcinomas commonly extend into the adrenal vein and inferior vena cava (Fig. 57–18). CT of the lungs should be performed in all cases to exclude metastases.

Pheochromocytoma and Paraganglioma

Pheochromocytomas are rare in childhood. They can occur wherever chromaffin tissue is found.[14, 46, 50, 52, 113] Eighty percent arise in the adrenal gland. Extra-adrenal tumors, referred to as paragangliomas, can occur in a variety of locations, including the organ of Zuckerkandl, sympathetic ganglia, nerve plexuses, and nerves.

Patients with von Hippel–Lindau disease, multiple endocrine neoplasia syndrome, and familial pheochromocytoma are at increased risk for development of pheochromocytomas; however, most occur sporadically. Multiple tumors are present in one third of patients and are more common in those patients who have one of these syndromes. Fewer than 10% of tumors are malignant. The most common sites of metastases are bone, liver, lymph nodes, and lung, and rarely, the central nervous system.

Symptoms are secondary to secretion by the tumor of epinephrine or norepinephrine or both, and occasionally dopamine. Seventy percent to 80% of patients have hypertension, which is often severe. Less common manifestations include headache, sweating, palpitations, anxiety, tremor, nausea, vomiting, abdominal and chest pain, and visual disturbances. The clinical diagnosis of pheochromocytoma can usually be confirmed in patients who have sustained hypertension by documenting elevated levels of catecholamines and their metabolites in plasma and 24-hour urine collections.[113] Biochemical diagnosis is more difficult in patients who have only episodic symptoms or who are asymptomatic.

Once the clinical diagnosis has been established, CT or MRI can be used to localize the tumor for surgical resection. At MRI, pheochromocytomas have slightly lower signal intensity than liver on T1-weighted sequences and very high signal intensity on T2-weighted images.[14, 67] In some cases, the very bright signal intensity of the tumor on T2-weighted images can mimic that of a cyst.[32] After gadolinium administration, tumor enhancement is marked even during the early phase.[14, 82, 83, 95] Smaller tumors are typically more homogeneous than larger masses, which often contain areas of cystic degeneration and necrosis. CT and MRI are equally sensitive in detecting adrenal pheochromocytomas.[52] Direct coronal imaging with MRI permits rapid screening of large sections of the body and is somewhat more sensitive than CT for identifying extra-adrenal tumors. Neither modality can distinguish between benign and malignant pheochromocytomas unless metastases are visible.[32]

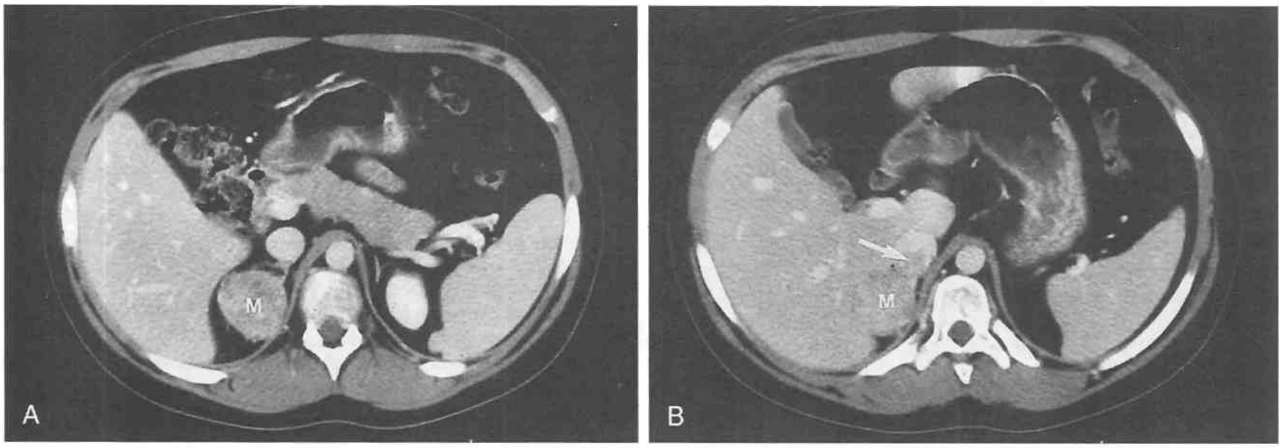

Figure 57–18. Right adrenal cortical carcinoma with intracaval extension in a 9-[redacted]-old girl with Cushing's syndrome. *A,* Contrast-enhanced CT axial image through the upper abdomen shows a 3-cm, solid, right adrenal mass of inhomogeneous attenuation. The mass has slightly irregular margins with thin strands extending into the pararenal fat posteriorly. The inferior vena cava enhances homogeneously at this level. *B,* Contrast-enhanced CT axial image through the upper abdomen. The right adrenal mass is difficult to separate from the overlying liver. Thin strands are again visible extending from the mass into the pararenal fat adjacent to the right diaphragmatic crux. In addition, there is an irregular intraluminal filling defect within the inferior vena cava, consistent with intravascular extension of the adrenal tumor.

References

1. Amparo EG, Fagan CJ: Page kidney. J Comput Assist Tomogr 6: 839–841, 1982.
2. Andersen BL, Lauver JW, Ross P, Fitzgerald RH: Demonstration of radiation nephritis by computed tomography. Comput Radiol 6: 187–91, 1982.
3. Andrews MW, Amparo EG: Wilms' tumor in a patient with Beckwith-Wiedemann syndrome: Onset detected with 3-month serial sonography. AJR Am J Roentgenol 160:139–140, 1993.
4. Araki T: Leukemic involvement of the kidney in children: CT features. J Comput Assist Tomogr 6:781–784, 1982.
5. Banner MP, Pollack HM, Chatten J, Witzleben C: Multilocular renal cysts: Radiologic-pathologic correlation. Am J Roentgenol 136:239–247, 1981.
6. Bauman L, Greenfield SP, Aker J, et al: Nonoperative management of major blunt renal trauma in children: In-hospital morbidity and long-term follow-up. J Urol 148:691–693, 1992.
7. Beckwith JB, Kiviat NB, Bonadio JF: Nephrogenic rests, nephroblastomatosis, and the pathogenesis of Wilms' tumor. Pediatr Pathol 10:1–36, 1990.
8. Beckwith JB, Palmer NF: Histopathology and prognosis of Wilms' tumor: Results from the First National Wilms' Tumor Study. Cancer 41:1937–1948, 1978.
9. Beckwith JB: Children at increased risk for Wilms tumor: Monitoring issues. J Pediatr 132:377–379, 1998.
10. Bell DGT, King BF, Hattery RR, et al: Imaging characteristics of tuberous sclerosis. AJR Am J Roentgenol 156:1081–1086, 1991.
11. Bellin M, Maidenberg M, Raveau V, et al: MR imaging of adult Wilms' tumor: Correlation with US, CT, and pathology. Urol Radiol 12:148–150, 1990.
12. Belt TG, Cohen MD, Smith JA, et al: MRI of Wilms' tumor: Promise as the primary imaging method. Am J Roentgenol 146: 955–961, 1986.
13. Bennett WG, Wood BP: Radiological case of the month: Renal vein thrombosis. Am J Dis Child 145:1299–1300, 1991.
14. Bilal MM, Brown JJ: MR imaging of renal and adrenal masses in children. Magn Reson Imaging Clin North Am 5:179–197, 1997.
15. Boechat MI, Kangarloo H: MR imaging of the abdomen in children. AJR Am J Roentgenol 152:1245–1250, 1989.
16. Boechat MI, Ortega J, Hoffman AD, et al: Computed tomography in stage III neuroblastoma. Am J Roentgenol 145:1283–1287, 1985.
17. Boechat MI: Magnetic resonance imaging of abdominal and pelvic masses in children. Top Magn Reson Imaging 3:25–41, 1990.
18. Bolande RP: Congenital mesoblastic nephroma of infancy. Perspec Pediatr Pathol 1:227–250, 1973.
19. Bonnet JP, Aigrain Y, Ferkadji L: Cystic dysplasia of the testis with ipsilateral renal agenesis: A case report and review of the literature. Eur J Pediatr Surg 7:57–59, 1997.
20. Bonnin JM, Rubinstein LJ, Palmer NF, Beckwith JB: The association of embryonal tumors originating in the kidney and in the brain: A report of seven cases. Cancer 54:2137–2146, 1984.
21. Bradley, Waluch V: Blood flow: Magnetic resonance imaging. Radiology 154:443–450, 1985.
22. Brasch RC, Randel SB, Gould RG: Follow-up of Wilms' tumor: Comparison of CT with other imaging procedures. Am J Roentgenol 137:1005–1009, 1981.
23. Braverman RM, Lebowitz RL: Occult ectopic ureter in girls with urinary incontinence: Diagnosis by using CT. AJR Am J Roentgenol 156:365–366, 1991.
24. Breslow NR, Beckwith JB: Epidemiological features of Wilms' tumor: Results of the National Wilms' Tumor Study. J Natl Cancer Inst 68:429–436, 1982.
25. Bretan PN Jr, McAninch JW, Federle MP, Jeffrey RB: Computerized tomographic staging of renal trauma: 85 consecutive cases. J Urol 136:561–565, 1986.
26. Brodeur AE, Brodeur GM: Abdominal masses in children: Neuroblastoma, Wilms tumor, and other considerations. Pediatr Rev 12: 196–206, 1991.
27. Caron KH: Magnetic resonance imaging of the pediatric abdomen. Semin Ultrasound CT MR 12:448–474, 1991.
28. Carrico C, Lebowitz RL: Incontinence due to an infrasphincteric ectopic ureter: Why the delay in diagnosis and what can the radiologist do about it? Pediatr Radiol 28:942–949, 1998.
29. Chan HSL, Cheng M-Y, Mancer K, et al: Congenital mesoblastic nephroma: A clinicoradiologic study of 17 cases representing the pathologic spectrum of the disease. J Pediatr 111:64–70, 1987.
30. Chan Y-L, Chan K-W, Yeung C-K, et al: Potential utility of MRI in the evaluation of children at risk of renal scarring. Pediatr Radiol 29:856–862, 1999.
31. Choyke PL, Kressel NY, Pollack NM, et al: Focal renal masses: Magnetic resonance imaging. Radiology 152:471–477, 1984.
32. Cohen MD: Reticuloendothelial and endocrine systems. In Cohen MD, Edwards MK (eds): Magnetic Resonance Imaging of Children. Philadelphia, BC Decker, 1990, pp 679–723.
33. Cohen MD: Kidneys. In Siegel MJ (ed): Pediatric Body CT. New York, Churchill Livingstone, 1988, pp 135–175.
34. Cormier PS, Donaldson JS, Gonzalez-Crussi F: Nephroblastomatosis: Missed diagnosis. Radiology 169:737–738, 1988.
35. D'Angio GJ, Beckwith JB, Breslow N, et al: Wilms tumor: Status report, 1990: By the National Wilms Tumor Study Committee. J Clin Oncol 9:877–887, 1991.
36. D'Angio GJ, Breslow N, Beckwith JB, et al: Treatment of Wilms tumor: Results of the Third National Wilms' Tumor Study. Cancer 64:349–360, 1989.
37. Dacher JN, Boillot B, Eurin D, et al: Rational use of CT in acute pyelonephritis: Findings and relationship with reflux. Pediatr Radiol 23:281–285, 1993.
38. Dacher JN, Pfister C, Monroc M, et al: Power Doppler sonographic pattern of acute pyelonephritis in children: Comparison with CT. AJR Am J Roentgenol 166:1451–1455, 1996.
39. Daneman A, Cahn HSL, Martin J: Adrenal carcinoma and adenoma in children: A review of 17 patients. Pediatr Radiol 13:11–18, 1983.
40. Daneman A: Kidneys. In Daneman A (ed): Pediatric Body CT. New York, Springer-Verlag, 1987, pp 145–171.
41. Davidson AJ, Hartman DS: Lymphangioma of the retroperitoneum: CT and sonographic characteristics. Radiology 175:507–510, 1990.
42. Day DL, Johnson RT, Odrezin GT, et al: Renal atrophy or infarction in children with neuroblastoma. Radiology 180:493–495, 1991.
43. DeBaun MR, Tucker MA: Risk of cancer during the first four years of life in children from the Beckwith-Wiedemann Syndrome Registry. J Pediatr 132:398–400, 1998.
44. Dietrich RB, Kangarloo H, Lenarsky C, Feig SA: Neuroblastoma: The role of MR imaging. Am J Roentgenol 148:937–942, 1987.
45. Dietrich RB, Kangarloo H: Kidneys in infants and children: Evaluation with MR. Radiology 158:313–317, 1986.
46. Dietrich RB: Genitourinary system. In Cohen MD, Edwards MK (eds): Magnetic Resonance Imaging of Children. Philadelphia, BC Decker, 1990, pp 679–723.
47. Dikengil A, Benson M, Sanders L, Newhouse JH: MRI of multilocular cystic nephroma. Urol Radiol 10:95–99, 1988.
48. Donaldson JS, Gilsanz V, Miller JH: CT scanning in patients with opsomyoclonus: Importance of nonenhanced scan. Am J Roentgenol 146:781–783, 1986.
49. Donnelly LF, Frush DP, Marshall KW, White KS: Lymphoproliferative disorders: CT findings in immunocompromised children. AJR Am J Roentgenol 171:725–731, 1998.
50. Doppman JL, Reinig JW, Dwyer AJ, et al: Differentiation of adrenal masses by magnetic resonance imaging. Surgery 102:1018–1026, 1987.
51. Edelman RR, Mattle HP, Atkinson DJ, Hoogewoud HM: MR angiography. AJR Am J Roentgenol 154:937–946, 1990.
52. Egglin TK, Hahn PF, Stark DD: MRI of the adrenal glands. Semin Roentgenol 23:280–287, 1988.
53. Eklof O, Mortensson W, Sandstedt B: Suprarenal haematoma versus neuroblastoma complicated by haemorrhage: A diagnostic dilemma in the newborn. Acta Radiol Diagn 27:3–10, 1986.
54. Farrelly C, Daneman A, Chan HSL, Martin DJ: Occult neuroblastoma presenting with opsomyoclonus: Utility of computed tomography. Am J Roentgenol 142:807–810, 1984.
55. Federle MP, Kaiser JA, McAninch JW, et al: Computerized tomography in renal trauma. Radiology 141:455–460, 1981.
56. Fellows RA, Leonidas JC, Beatty EC Jr: Radiologic features of "adult type" polycystic disease in the neonate. Pediatr Radiol 4: 87–92, 1976.
57. Felson B, Cussen LJ: The hydronephrotic type of congenital multicystic disease of the kidney. Semin Roentgenol 10:113–123, 1975.
58. Fernbach SK, Feinstein KA, Donaldson JS, Baum ES: Nephroblastomatosis: Comparison of CT with US and urography. Radiology 166:153–156, 1988.
59. Fernbach SK, Schlesinger AE, Gonzalez-Crussi F: Calcification and

ossification in congenital mesoblastic nephroma. Urol Radiol 7: 165–167, 1985.

60. Fielding JR, Silverman SG, Rubin GD: Helical CT of the urinary tract. AJR Am J Roentgenol 172:1199–1206, 1999.
61. Fisher MF, Fletcher BD, Dahms BB, et al: Abdominal lipoblastomatosis: Radiographic, echographic, and computed tomographic findings. Radiology 138:593–596, 1981.
62. Fishman EK, Hartman DS, Goldman SM, Siegelman SS: The CT appearance of Wilms' tumor. J Comput Assist Tomogr 7:659–665, 1983.
63. Forman HP, Leonidas JC, Berdon WE, et al: Congenital neuroblastoma: Evaluation with multimodality imaging. Radiology 175: 365–368, 1900.
64. Francis IR, Gross MD, Shapiro B, et al: Integrated imaging of adrenal disease. Radiology 184:1–13, 1992.
65. Freed KS, Paulson EK, Frederick MG, et al: Interobserver variability in the interpretation of unenhanced helical CT for the diagnosis of ureteral stone disease. J Comput Assist Tomogr 22:732–737, 1998.
66. Gharagozloo AM, Lebowitz RL: Detection of a poorly functioning malpositioned kidney with single ectopic ureter in girls with urinary dribbling: Imaging evaluation in five patients. AJR Am J Roentgenol 164:957–961, 1995.
67. Giayanani VL, Gerlock AJ Jr, Grozinger KT, et al: Trauma of occult hydronephrotic kidney. Urology 25:8–12, 1985.
68. Glass RBJ, Davidson AJ, Fernbach SK: Clear cell sarcoma of the kidney: CT, sonographic, and pathologic correlation. Radiology 180: 715–717, 1991.
69. Glazer GM, Callen PW, Parker JJ: CT diagnosis of tumor thrombus in the inferior vena cava: Avoiding the false-positive diagnosis. Am J Roentgenol 137:1265–1267, 1981.
70. Glazer GM, Francis IR, Brady TM, Teng SS: Computed tomography of renal infarction: Clinical and experimental observations. Am J Roentgenol 140:721–727, 1983.
71. Glazer GM: MR imaging of the liver, kidneys, and adrenal glands. Radiology 166:303–312, 1988.
72. Glylys-Morin VM, Hoffer FA, Kozkewich H, Shamberger RC: Wilms tumor and nephroblastomatosis: Imaging characteristics. Radiology 188:517–521, 1993.
73. Graham JM Jr, Boyle B, Troxell J, et al: Cystic hamartomata of lung and kidney: A spectrum of developmental abnormalities. Am J Med Genet 27:45–49, 1976.
74. Griscom NT, Vawter FG, Fellers FX: Pelvoinfundibular atresia: The usual form of multicystic kidney: 44 unilateral and two bilateral cases. Semin Roentgenol 10:125–131, 1975.
75. Hartman DS, Lesar MSL, Madewell JE, et al: Mesoblastic nephroma: Radiologic-pathologic correlation in 20 cases. Am J Roentgenol 136:69–74, 1981.
76. Hausegger KA, Fotterr R, Flückiger F, Sorantin E: Can MR contribute to the diagnosis of nephroblastomatosis? Pediatr Radiol 21: 533–535, 1991.
77. Hayden CK Jr, Swischuk LE, Smith TH, Armstrong EA: Renal cystic disease in childhood. Radiographics 6:97–116, 1986.
78. Hilpert PL, Friedman AC, Radecki PD, et al: MRI of hemorrhagic cysts in polycystic kidney disease. Am J Roentgenol 146:1167–1172, 1986.
79. Hitchcock R, Burge DM: Renal agenesis: An acquired condition? J Pediatr Surg 29:454–455, 1994.
80. Hodson CJ, Maling TM, McManamon PJ, Lewis MG: The pathogenesis of reflux nephropathy (chronic atrophic pyelonephritis). Br J Radiol 1975(suppl 13):1, 1975.
81. Hricak H, Crooks L, Sheldon P, Kaufman L: Nuclear magnetic resonance imaging of the kidney. Radiology 146:425–432, 1983.
82. Ishikawa T, Fujimoto H, Murakami K, et al: Extraadrenal pheochromocytoma: Dynamic demonstration at 0.5 Tesla. Clin Imaging 16: 187–189, 1992.
83. Ishikawa T, Ohtomo K, Uchiyama G, et al: Contrast-enhanced dynamic MRI of adrenal masses: Classification of characteristic enhancement patterns. Clin Radiol 50:295–300, 1995.
84. Jayogapal S, Cohen HL, Brill PW, et al: Calcified renal vein thrombosis demonstration by CT and US. Pediatric Radiol 20:160–162, 1990.
85. Jeon A, Cramer BC, Walsh E, Pushpanathan C: A spectrum of segmental multicystic renal dysplasia. Pediatr Radiol 29:309–315, 1999.
86. Joshi VV, Beckwith JB: Multilocular cyst of the kidney (cystic nephroma) and cystic, partially differentiated nephroblastoma: Terminology and criteria for diagnosis. Cancer 64:466–479, 1989.
87. Kabala JE, Shield J, Duncan A: Renal cell carcinoma in childhood. Pediatr Radiol 22:203–205, 1992.
88. Kangarloo H, Dietrich RB, Ehrlich RM, et al: Magnetic resonance imaging of Wilms' tumor. Urology 28:203–207, 1986.
89. Karp MP, Jewett TC, Kuhn JP, et al: The impact of computed tomography scanning on the child with renal trauma. J Pediatr Surg 21:617–623, 1986.
90. Katz DS, Lane MJ, Sommer FG: Unenhanced helical CT of ureteral stones: Incidence of associated urinary tract findings. AJR Am J Roentgenol 166:1319–1322, 1996.
91. King BF, Hattery RR, Lieber MM, et al: Congenital cystic disease of the seminal vesicle. Radiology 178:207–211, 1991.
92. King DR, Lack EE: Adrenal cortical carcinoma: A clinical and pathological study of 49 cases. Cancer 44:239–244, 1979.
93. Klar A, Hurvitz H, Berkun Y, et al: Focal bacterial nephritis (lobar nephronia) in children. J Pediatr 128:850–853, 1996.
94. Koo AS, Koyle MA, Hurwitz RS, et al: The necessity of contralateral surgical exploration in Wilms tumor with modern noninvasive imaging technique: A reassessment. J Urol 144:416–417, 1990.
95. Krestin GP, Steinbrich W, Friedmann G: Adrenal masses: Evaluation with fast gradient echo MRI and Gd-DTPA enhancement: Dynamic study. Radiology 171:675–680, 1989.
96. Kurosaki Y, Tanaka Y, Kuramoto K, Itai Y: Improved CT fat detection in small kidney angiomyolipomas using thin sections and single voxel measurements. J Comput Assist Tomogr 17:745–748, 1993.
97. Lamego CMB, Zerbini MCN: Bone-metastasizing primary renal tumors in children. Radiology 147:449–454, 1983.
98. Lang EK, Sullivan J, Frentz G: Renal trauma: Radiological studies: Comparison of urography, computed tomography, angiography, and radionuclide studies. Radiology 154:1–6, 1985.
99. Laurent F, Joullie M, Biset JM, et al: Cystic lymphangioma of the kidney: A rare cause of multiloculated renal masses. Eur J Radiol 12:67–68, 1991.
100. Lee JK, McClennan BL, Melson GL, Stanley RJ: Acute focal bacterial nephritis: Emphasis on gray scale sonography and computed tomography. Am J Roentgenol 135:87–92, 1980.
101. Leung AWL, Bydder GM, Steiner RE, et al: Magnetic resonance imaging of the kidneys. Am J Roentgenol 143:1215–1227, 1984.
102. Levine C, Levine E: Small pediatric renal neoplasms detected by CT. J Comput Assist Tomogr 14:615–618, 1990.
103. List AF, Greco FA, Vogler LB: Lymphoproliferative diseases in immunocompromised hosts: The role of Epstein-Barr virus. J Clin Oncol 5:1673–1689, 1987.
104. Lonergan GJ, Pennington DJ, Morrison JC, et al: Childhood pyelonephritis: Comparison of gadolinium-enhanced MR imaging and renal cortical scintigraphy for diagnosis. Radiology 207:377–384, 1998.
105. Lowe RC, Cohen MD: Computed tomographic evaluation of Wilms' tumor and neuroblastoma. Radiographics 4:915–928, 1984.
106. Madewell JE, Goldman SM, Davis CJ Jr, et al: Multilocular cystic nephroma: A radiographic-pathologic correlation of 58 patients. Radiology 146:309–321, 1983.
107. Majd M, Shalaby-Rana E, Blask A, et al: Comparison of ^{99m}Tc DMSA SPECT, spiral CT, MRI, and power Doppler sonography [abstract]. Paper presented at the 83rd Scientific Assembly and Annual Meeting of the Radiological Society of North America, November 30–December 5, 1997, Chicago.
108. Majd M, Rushton HG, Jantausch B, Wiedermann BL: Relationship among vesicoureteral reflux, P-fimbriated *Escherichia coli*, and acute pyelonephritis in children with febrile urinary tract infection. J Pediatr 119:578–585, 1991.
109. Marotti M, Hricak N, Fritzche P, et al: Complex and simple renal cysts: Comparative evaluation with MR imaging. Radiology 162: 679–684, 1987.
110. Marshall WH Jr, Castellino RA: Hypertension produced by constricting capsular renal lesions ("Page" kidney). Radiology 191: 561–565, 1971.
111. Mendez G Jr, Ishikoff MB, Morillo G: The role of computed tomography in the diagnosis of renal and perirenal abscesses. J Urol 122: 582–586, 1979.
112. Metreweli C, Pearson R: Echographic diagnosis of neonatal renal venous thrombosis. Pediatr Radiol 14:105–108, 1984.
113. Meyer JS: Retroperitoneal MR imaging in children. Magn Reson Imaging Clin North Am 4:657–678, 1996.

114. Miller RW, Fraumeni JF Jr, Manning MD: Association of Wilms' tumor with aniridia, hemihypertrophy, and other congenital malformations. N Engl J Med 270:922–927, 1964.
115. Mitnick JS, Bosniak MA, Hilton S, et al: Cystic renal disease in tuberous sclerosis. Radiology 147:85–87, 1983.
116. Morgan E, Kidd JM: Undifferentiated sarcoma of the kidney: A tumor of childhood with histopathologic and clinical characteristics distinct from Wilms' tumor. Cancer 42:1916–1921, 1978.
117. Nakayama DK, DeLorimier AA, O'Neill JA, et al: Intracardiac extension of Wilms' tumor. Ann Surg 204:693–697, 1986.
118. Nalesnik MA, Makowka L, Starzl TE: The diagnosis and treatment of posttransplant lymphoproliferative disorders. Curr Probl Surg 25: 370–472, 1988.
119. Narla LD, Slovis RL, Watts FB, Nigro M: The renal lesions of tuberosclerosis (cysts and angiomyolipoma): Screening with sonography and computerized tomography. Pediatr Radiol 18:205–209, 1988.
120. Nunez D Jr, Becerra JL, Fuentes D, Pagson S: Traumatic occlusion of the renal artery: Helical CT diagnosis. AJR Am J Roentgenol 167:777–780, 1996.
121. Papadopoulou E, Efremidis SC, Gombakis N, et al: Nephroblastomatosis: The whole spectrum of abnormalities in one case. Pediatr Radiol 22:598–599, 1992.
122. Parvey LS, Warner RM, Callihan TR, Magill HL: CT demonstration of fat tissue in malignant renal neoplasms: Atypical Wilms' tumors. J Comput Assist Tomogr 5:851–854, 1981.
123. Pennington DJ, Lonergan GJ, Flack CE, et al: Experimental pyelonephritis in piglets: Diagnosis with MR imaging. Radiology 201: 199–205, 1996.
124. Pennington DJ, Zerin JM: Imaging of the urinary tract in children. Ann Pediatr 28:678–686, 1999.
125. Pickering SP, Fletcher BD, Bryan PJ, Abramowsky CR: Renal lymphangioma: A cause of neonatal nephromegaly. Pediatr Radiol 14:445–448, 1984.
126. Pickhardt PJ, Siegel MJ: Posttransplantation lymphoproliferative disorder of the abdomen: CT evaluation in 51 patients. Radiology 213:73–78, 1999.
127. Pollack HM, Banner MP: Current status of excretory urography: A premature epitaph? Urol Clin North Am 12:585–601, 1985.
128. Prewitt LH Jr, Lebowitz RL: The single ectopic ureter. Am J Roentgenol 127:941–948, 1976.
129. Reiman TAH, Siegel MJ, Shackelford GD: Wilms' tumor in children: Abdominal CT and US evaluation. Radiology 160:501–505, 1986.
130. Rhyner P, Federle MP, Jeffrey RB: CT of trauma to the abnormal kidney. Am J Roentgenol 142:747–750, 1984.
131. Rigsby CM, Rosenfield AT, Glickman MG, Hodson J: Hemorrhagic focal bacterial nephritis: Findings on gray-scale sonography and CT. Am J Roentgenol 146:1173–1177, 1986.
132. Ritchey ML, Green DM, Breslow NB, et al: Accuracy of current imaging modalities in the diagnosis of synchronous bilateral Wilms' tumor. Cancer 75:600–604, 1995.
133. Rohrscheider WK, Weirch AM, Rieden K, et al: US, CT and MR imaging characteristics of nephroblastomatosis. Pediatr Radiol 28: 435–443, 1998.
134. Rosenfield NS, Leonidas JC, Barwick KW: Aggressive neuroblastoma simulating Wilms' tumor. Radiology 166:165–167, 1988.
135. Rushton HG: The evaluation of acute pyelonephritis and renal scarring with technetium 99m-dimercaptosuccinic acid renal scintigraphy: Evolving concepts and future directions. Pediatr Nephrol 11: 108–120, 1997.
136. Sandler CM, Toombs BD: Computed tomographic evaluation of blunt renal injuries. Radiology 141:461–466, 1981.
137. Schlesinger AE, Rosenfield NS, Castle VP, Jasty R: Congenital mesoblastic nephroma metastatic to brain: A report of two cases. Pediatr Radiol 25:S73–75, 1995.
138. Sheeran SR, Sussman SK: Renal lymphoma: Spectrum of CT findings and potential mimics. AJR Am J Roentgenol 171:1067–1072, 1998.
139. Siegel MJ, Balfe DM: Blunt renal and ureteral trauma in childhood: CT patterns of fluid collections. AJR Am J Roentgenol 152:1043–1047, 1989.
140. Siegel MJ: MR imaging of the pediatric abdomen. Magn Reson Imaging Clin North Am 3:161–182, 1995.
141. Silverman PM, Carroll BA, Moskowitz PS: Adrenal sonography in renal agenesis and dysplasia. Am J Roentgenol 134:600–602, 1980.
142. Sisler CL, Siegel MJ: Malignant rhabdoid tumor of the kidney: Radiologic features. Radiology 172:211–212, 1989.
143. Smergel EM, Greenberg SB, Crisci KL, et al: Secondary signs of obstruction with ureteral calculi: Children are different from adults. Paper presented at the 43rd Annual Meeting of the Society for Pediatric Radiology, May 2, 2000, Naples, Fla.
144. Smith RC, Rosenfield AT, Choe KA, et al: Acute flank pain: Comparison of non-contrast-enhanced CT and intravenous urography. Radiology 194:789–794, 1995.
145. Smith RC, Verga M, Dalrymple N, et al: Acute ureteral obstruction: Value of secondary signs on helical unenhanced CT. AJR Am J Roentgenol 167:1109–1113, 1996.
146. Smith RC, Verga M, McCarthy S, Rosenfield AT: Diagnosis of acute flank pain: Value of unenhanced helical CT. AJR Am J Roentgenol 166:97–101, 1996.
147. Soila KP, Viamonte M Jr, Starewicz PM: Chemical shift misregistration effect in magnetic resonance imaging. Radiology 153:819–820, 1984.
148. Sommer FG, Jeffrey RB Jr, Napel S, et al: Detection of ureteral calculi in patients with suspected renal colic: Value of reformatted noncontrast helical CT. AJR Am J Roentgenol 165:509–513, 1995.
149. Soulen MC, Fishman EK, Goldman SM, Gatewood OMB: Bacterial renal infection: Role of CT. Radiology 171:703–707, 1989.
150. Soulen MC, Fishman EK, Goldman SM: Sequelae of acute renal infections: CT evaluation. Radiology 173:423–426, 1989.
151. Stannard MW, Lebowitz RL: Urography in the child who wets. Am J Roentgenol 130:959–962, 1978.
152. Stark DD, Brasch RC, Moss AA, et al: Recurrent neuroblastoma: The role of CT and alternative imaging tests. Radiology 148:101–105, 1983.
153. Stark DD, Moss AA, Brasch RC, et al: Neuroblastoma: Diagnostic imaging and staging. Radiology 148:101–105, 1983.
154. Stillwell TJ, Gomez MR, Kelalis PP: Renal lesions in tuberous sclerosis. J Urol 138:477–481, 1987.
155. Strouse PJ, Bloom DA, Bates DG: Renal stone protocol CT in children. Paper presented at the 43rd Annual Meeting of the Society for Pediatric Radiology, May 2, 2000, Naples, Fla.
156. Tanaka YO, Kurosaki Y, Kobayashi T, et al: Uterus didelphys associated with obstructed hemivagina and ipsilateral renal agenesis: MR findings in seven cases. Abdom Imaging 23:437–441, 1998.
157. Teele RL, Share JC: The abdominal mass in the neonate. Semin Roentgenol 23:175–184, 1988.
158. Weeks DA, Beckwith JB, Mierau GW, Luckey DW: Rhabdoid tumor of kidney: A report of 111 cases from the National Wilms' Tumor Study Pathology Center. Am J Surg Pathol 13:439–458, 1989.
159. Weese DL, Appelbaum H, Taber P: Mapping intravascular extension of Wilms' tumor with magnetic resonance imaging. J Pediatr Surg 26:64–67, 1991.
160. Weinberger E, Rosenbaum DM, Pendergrass TW: Renal involvement in children with lymphoma: A comparison of CT with sonography. AJR Am J Roentgenol 155:347–349, 1990.
161. Westra SJ, Zaninovic AC, Hall TR, et al: Imaging of the adrenal gland in children. Radiographics 14:1323–1340, 1994.
162. White KS, Grossman H: Wilms' and associated renal tumors of childhood. Pediatr Radiol 21:S81–88, 1991.
163. White KS, Kirks DR, Bove KE: Imaging of nephroblastomatosis: An overview. Radiology 182:1–5, 1992.
164. Williams DI, Royle M: Ectopic ureter in the male child. Br J Urol 41:421–427, 1969.
165. Young JL, Miller RW: Incidence of malignant tumors in U.S. children. J Pediatr 86:254–258, 1975.
166. Zaitoon MM, Mackie GG: Adrenal cortical tumors in children. Urology 12:645–649, 1978.
167. Zerin JM: Uroradiologic emergencies in infants and children. Radiol Clin North Am 35:897–919, 1997.
168. Zinn HL, Haller JO: Renal manifestations of AIDS in children. Pediatr Radiol 29:558–561, 1999.

58

Gastrointestinal Tract, Peritoneal Cavity, and Mesentery

Carlos J. Sivit

Gastrointestinal Tract

Computed tomography (CT) is commonly used in the assessment of children with suspected gastrointestinal (GI) tract pathology. Recent advances in CT scanning have substantially altered the imaging evaluation of many common GI tract conditions, many of which present a diagnostic challenge to caregivers. An accurate diagnosis is essential for triage, or separation of children who require surgery from those who can be managed nonoperatively.

Infectious and Inflammatory Conditions

Acute Appendicitis

Acute appendicitis is the most common condition requiring emergency abdominal surgery in childhood.[19] It is typically seen in older children and adolescents. Although the diagnosis has traditionally been based on clinical criteria, the clinical diagnosis is not always straightforward, and approximately one third of patients with the disease have an uncertain preoperative diagnosis.[24, 44] This in turn may result in a delay in surgery with resultant increased morbidity, including perforation, abscess formation, and peritonitis.

CT is becoming the principal imaging modality for the evaluation of suspected acute appendicitis in childhood. It is a highly sensitive and specific modality for such diagnosis. CT has been shown to have a higher diagnostic accuracy than graded-compression sonography for such diagnosis.[14, 22] A variety of techniques have been used in the performance of appendiceal CT, including:

1. Full abdominopelvic scanning after intravenous and oral administration of contrast material.[3]
2. Imaging limited to the lower abdomen and upper pelvis without any contrast material.[23, 27]
3. Imaging of the lower abdomen and upper pelvis with thin (4-mm) collimation and only rectal contrast material.[14, 35]

The use of rectal contrast in conjunction with thin collimation has yielded the highest reported diagnostic accuracy.[14, 35] Rectal contrast in children with suspected acute appendicitis is typically well tolerated. A 3% diatrizoate solution is administered intracolonically through a rectal catheter. The administered fluid volume ranges from 500 mL in small children to 1000 mL in teenagers.

At CT, signs of acute appendicitis include a distended (>7 mm) and unopacified appendix (Fig. 58–1), appendiceal wall thickening and enhancement (see Fig. 58–1), an appendicolith (Fig. 58–2), cecal apical thickening (see Fig. 58–1), deformity of the cecal tip (arrowhead sign) (Fig. 58–3), pericecal fat stranding (see Fig. 58–1), mesenteric lymphadenopathy, and peritoneal fluid. Secondary changes, including cecal apical changes and stranding of pericecal fat, can be quite useful when the appendiceal diameter measurement is borderline. After rupture, the appendix is usually not visualized. Findings at CT following ruptured appendicitis include the presence of abdominal or pelvic phlegmon or abscess (Fig. 58–4).

Inflammatory Bowel Disease

Inflammatory bowel disease is commonly encountered in older children and adolescents. The principal conditions are Crohn's disease and ulcerative colitis, which are both idiopathic inflammatory conditions.

Crohn's disease, the most common chronic inflammatory GI tract condition in childhood (and thus seen more frequently than ulcerative colitis), most often affects the terminal ileum (Fig. 58–5) but can involve any region of the GI tract. It is characterized by skip areas of involvement, whereas the lesions in ulcerative colitis tend to be continuous.

Crohn's disease is a transmural process associated with severe complications, including ulceration, strictures, fistula formation, and perforation with abscess formation. Ulcerative colitis is characterized by superficial inflammatory changes typically confined to the mucosa and submucosa. Therefore, the serious complications seen in Crohn's disease are uncommon in ulcerative colitis, although an

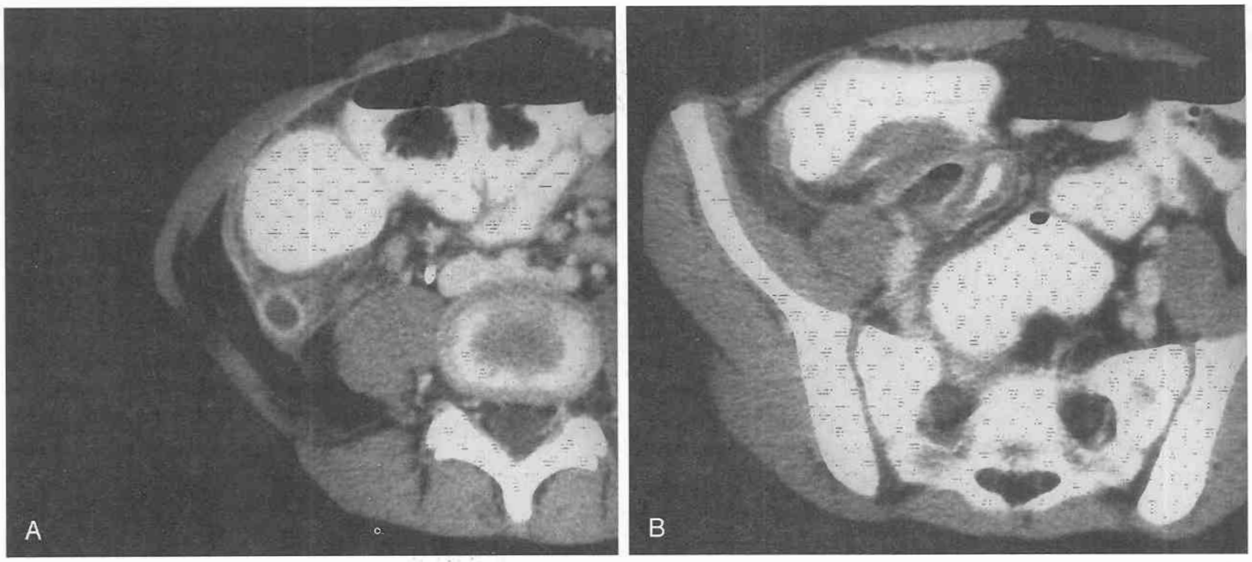

Figure 58–1. Acute appendicitis. *A,* CT scan through the lower abdomen in a patient with appendicitis demonstrates an enlarged, thick-walled appendix with wall enhancement and an associated infiltration of surrounding fat. *B,* CT scan through the upper pelvis in the same patient demonstrates cecal apical thickening.

association exists between ulcerative colitis and the later development of carcinoma of the colon.

CT is frequently used in the evaluation of children with inflammatory bowel disease, although many of the findings are nonspecific and may also be seen with infectious, ischemic, or radiation-induced enteritis or colitis; vasculitis; or graft-versus-host disease. Predominant involvement of the distal small bowel and right colon is more common in Crohn's disease (see Fig. 58–5), whereas involvement of the rectum and sigmoid colon is more common in ulcerative colitis (Fig. 58–6).

One rather specific CT finding in patients with Crohn's disease is the presence of fibrofatty proliferation of the mesentery surrounding the involved colon (Fig. 58–7).[32] Additionally, bowel wall thickening tends to be more pronounced in Crohn's disease than in ulcerative colitis.[18] Extensive bowel fibrosis is often present in advanced cases of Crohn's disease, resulting in marked luminal narrowing. CT plays an important role in the evaluation of children thought to have complications such as bowel obstruction, bowel perforation, and abscess, phlegmon, and fistula for-

Figure 58–2. Appendicolith. CT scan through the upper pelvis of a patient with appendicitis shows an enlarged appendix containing an appendicolith.

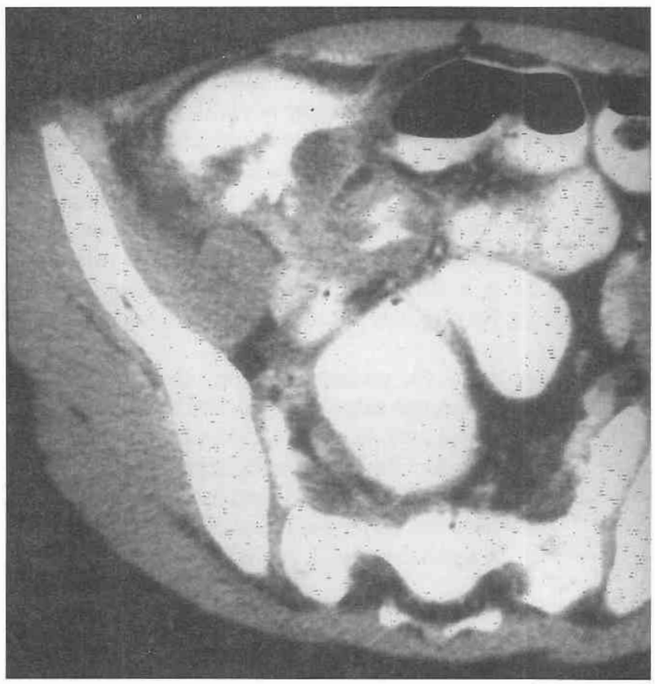

Figure 58–3. Acute appendicitis. CT scan through the lower abdomen in a child with appendicitis demonstrates the "arrowhead sign" consisting of a triangle-shaped contrast collection between the thickened cecal apical walls.

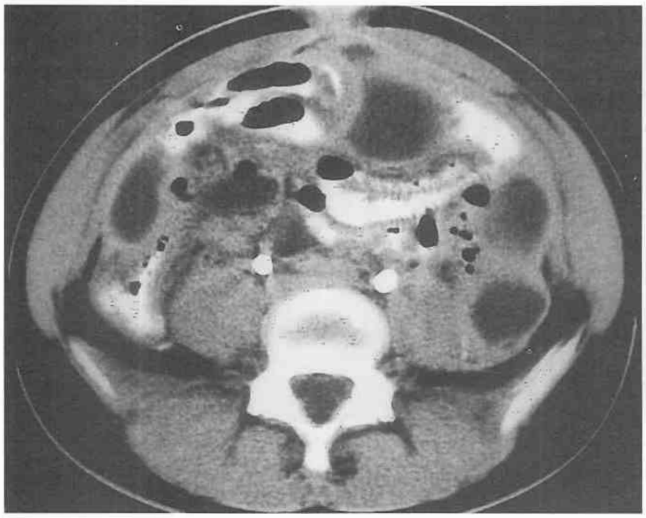

Figure 58–4. Ruptured appendix. CT scan through the lower abdomen in a patient with a ruptured appendix demonstrates multiple rounded, low-attenuation interloop collections representing multiple abscesses.

mation (Fig. 58–8).[15, 18, 32] Bowel perforation and abscess formation occur more commonly in Crohn's disease than in ulcerative colitis.

Pseudomembranous Colitis

Pseudomembranous colitis is an iatrogenic disease that is almost exclusively related to an alteration of colonic microflora by antibiotic that facilitates colonization by *Clostridium difficile*.[8] An occasional case is associated with *Staphylococcus* infection. The spectrum of severity is wide, and the disease is occasionally fatal. The diagnosis is established by endoscopic demonstration of characteristic yellow plaques (pseudomembranes) on colonic mucosa, or by laboratory documentation of the *C. difficile* enterotoxin. The condition is managed conservatively, with cessation of the implicated antibiotic, institution of appropriate antibiotic therapy, and maintenance of fluid and electrolyte balance.

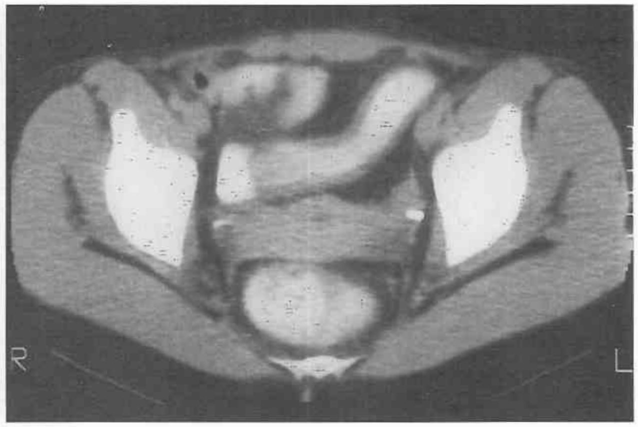

Figure 58–6. Ulcerative colitis. CT scan through the pelvis in a patient with ulcerative colitis demonstrates mild thickening of the sigmoid colon.

CT is usually obtained in patients with suspected pseudomembranous colitis to assess for possible complications, including bowel obstruction and perforation with abscess formation. CT findings associated with pseudomembranous colitis are nonspecific and may be seen with any severe infectious or ischemic colitis. For example, contrast material trapped between thickened haustral folds, referred to as the accordion sign (Fig. 58–9),[12, 26, 36] may be noted in a variety of other infectious and inflammatory conditions that involve the colon.[26] The thickened colonic wall in pseudomembranous colitis typically has a low attenuation value (Fig. 58–10). Colonic involvement may be diffuse or segmental[7, 26, 36]; the diffuse form is more common. Because the appearance of pseudomembranous colitis is normal in nearly 40% of patients at CT,[7] this is not a sensitive method of establishing the diagnosis.

Neutropenic Typhlitis

Neutropenic typhlitis is a necrotizing enteropathy of the right colon that develops in the setting of neutropenia. It probably begins secondary to a cytotoxic drug–induced

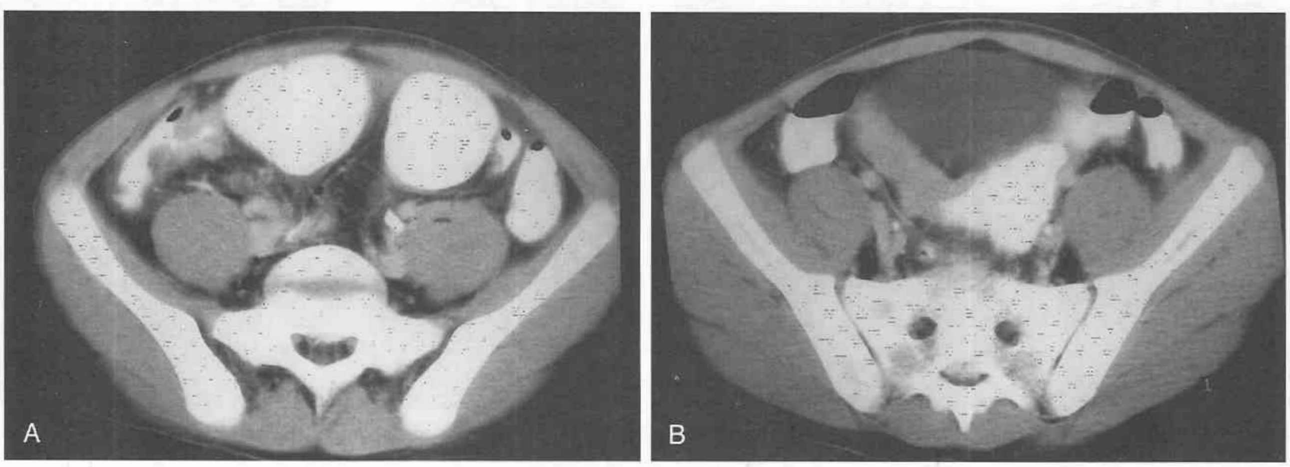

Figure 58–5. Crohn's disease. *A*, CT scan through the lower abdomen in a patient with Crohn's disease demonstrates thickening of the distal ileum. *B*, CT scan in the same patient 2 cm below *A* shows marked thickening of the distal ileum.

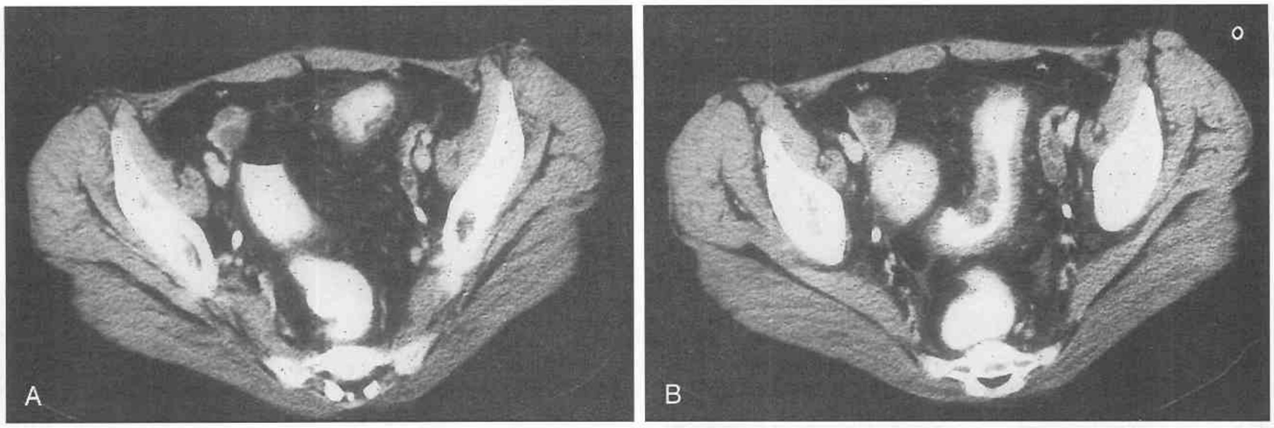

Figure 58–7. Crohn's disease. *A,* CT scan through the midpelvis in a patient with Crohn's disease demonstrates marked fibrofatty mesenteric proliferation. *B,* CT scan in same patient 2 cm below *A* demonstrates thickening of the sigmoid colon.

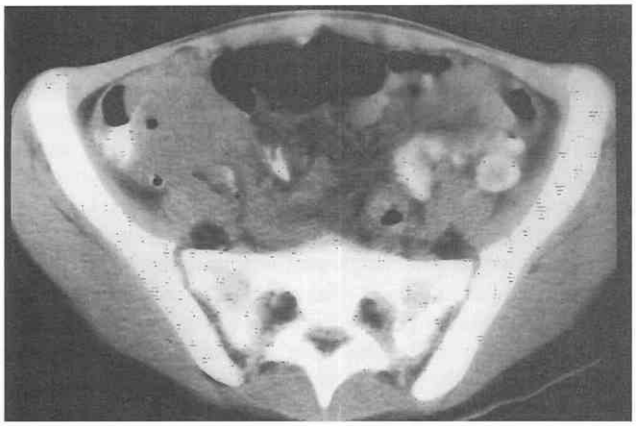

Figure 58–8. Crohn's disease complicated by perforation and phlegmon formation. CT scan through the upper pelvis in a patient with Crohn's disease demonstrates a phlegmon in the right iliac fossa.

ileus, and it may become complicated by secondary bacterial invasion. Mucosal ulceration is seen early, and it can progress to mucosal and submucosal necrosis accompanied by intramural edema and hemorrhage. The condition is usually restricted to the cecum, ascending colon, appendix, and terminal ileum. Neutropenic typhlitis occurs most commonly in children with leukemia.[51] The spectrum of clinical disease is wide, and perforation is a rare complication.

CT is useful in the assessment of children believed to have neutropenic typhlitis, particularly if complications such as bowel obstruction and perforation are suspected. The examination should be performed following a delay of at least 2 hours after the administration of oral contrast material to allow the contrast to reach the colon. Rectal contrast is contraindicated in these patients, who are at increased risk for perforation. CT findings in patients with neutropenic typhlitis include colonic, distal ileal, and appendiceal wall thickening (Fig. 58–11).[6, 10] The ascending and transverse colon may also be affected. Associated stranding of pericecal fat is often visualized, and pneumatosis intestinalis is occasionally involved. Follow-up ex-

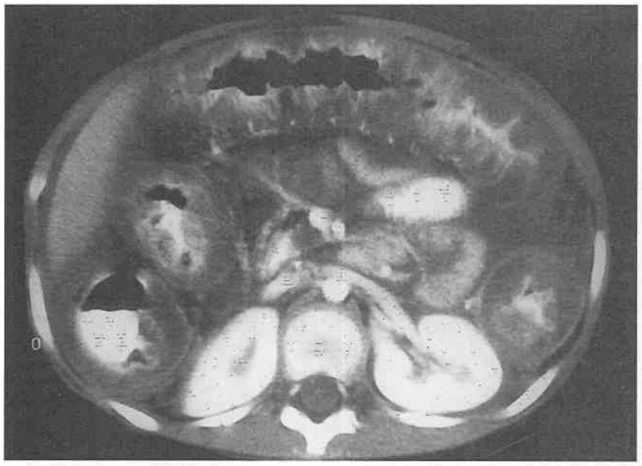

Figure 58–9. Pseudomembranous colitis. CT scan through the midabdomen in a patient with pseudomembranous colitis shows contrast material trapped between thickened haustral folds, a finding that has been labeled the "accordion sign."

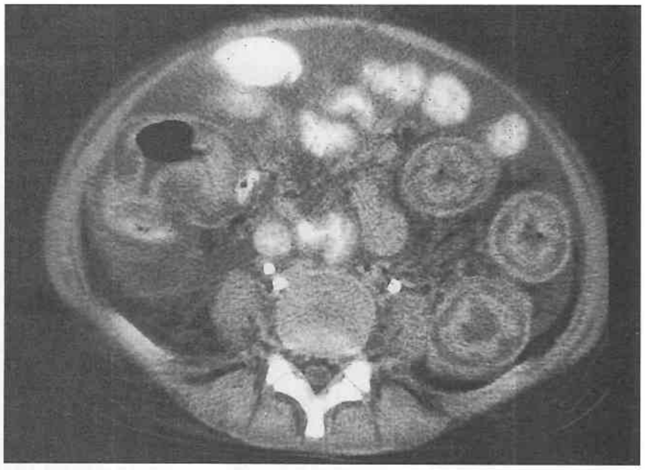

Figure 58–10. Pseudomembranous colitis. CT scan through the lower abdomen in a patient with pseudomembranous colitis demonstrates diffuse colonic wall thickening. The wall has a homogenous, low-attenuation appearance.

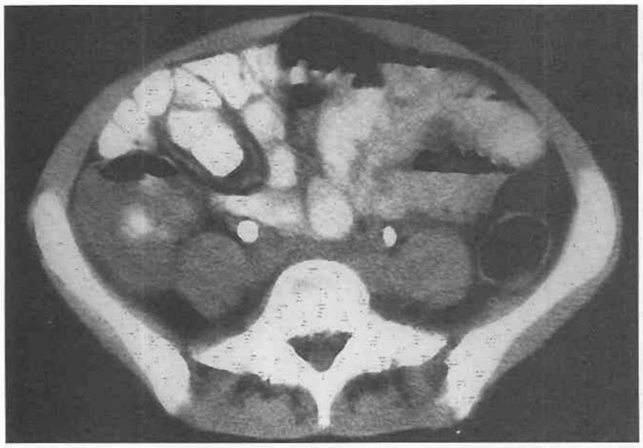

Figure 58–11. Neutropenic typhlitis. CT scan through the lower abdomen in a patient with leukemia and neutropenic typhlitis demonstrates cecal thickening.

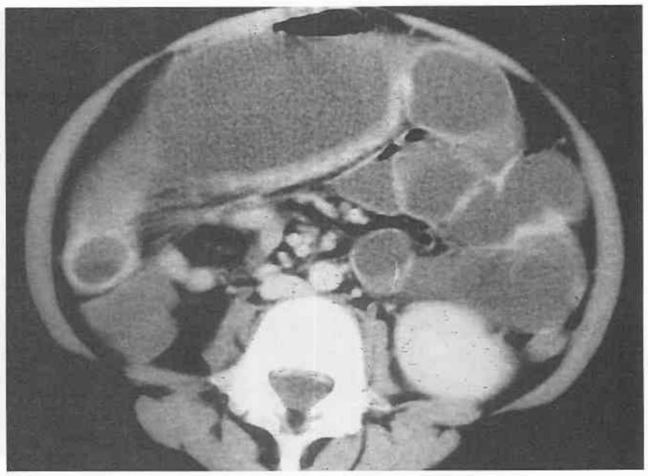

Figure 58–12. Graft-versus-host disease complicated by small bowel obstruction. CT scan through the midabdomen in a patient with prior graft-versus-host disease demonstrates diffuse small bowel dilatation indicative of a small-bowel obstruction. At surgery, a stricture was identified.

aminations with CT typically show decreasing bowel wall diameters corresponding to clinical improvement.

Graft-versus-Host Disease

Graft-versus-host disease is specific to allogeneic bone marrow transplantation. It is initiated by immunocompetent donor T cells that react with the host cells. The disease is considered acute if it occurs in the first 100 days following transplantation and chronic if it develops after 100 days. The disease is characterized by crypt cell necrosis and diffuse mucosal destruction throughout the small and large intestines. Clinical grading of the acute form is based on the degree of damage to the skin, GI tract, and liver.

The CT appearance of graft-versus-host disease is similar in the acute and chronic forms and includes segmental or diffuse bowel wall thickening; fluid-filled, dilated bowel loops; abnormally intense bowel wall enhancement; and infiltration of mesenteric fat.[6, 10] Bowel wall thickening may involve the small or large bowel, and it is typically less severe than that observed in neutropenic typhlitis or pseudomembranous colitis. Stricture formation with subsequent small-bowel obstruction has been reported as an uncommon sequela (Fig. 58–12).[6]

Ischemic Colitis

Ischemic colitis in children is rare. It is typically associated with multisystem disease, colonic obstruction, or vasculitis. It encompasses a wide spectrum of severity ranging from mild reversible disease to bowel infarction and perforation. Ischemic colitis is usually characterized by mucosal necrosis and ulcerations, submucosal edema, and hemorrhage that may progress to infarction.[1, 4]

Colonic involvement may be segmental or diffuse. The segmental form, which is more common,[1] often involves "watershed areas" at sites between different vascular supplies. These include the ascending colon near the splenic flexure (at the junction between the superior and inferior mesenteric arterial blood supplies) and the rectosigmoid junction (between the inferior mesenteric and hypogastric arterial blood supplies).[1] Thickened bowel wall associated with bowel ischemia may have a variable appearance at CT, ranging from homogeneous to heterogeneous attenuation (Fig. 58–13). Intramural air (pneumatosis intestinalis) is also occasionally associated.

Neoplasms

Lymphoma is the primary neoplasm involving the GI tract in children and adolescents. Rarely, carcinoma of the colon may be noted in adolescents. Adenocarcinoma is the most common histologic type of colon carcinoma.

Lymphoma

The GI tract is the most commonly involved extranodal site of lymphoma. GI tract involvement is seen more frequently in non-Hodgkin's than in Hodgkin's lymphoma.[52] The mesentery is typically also involved.

CT findings of GI tract lymphoma include segmental or multifocal thickening of the stomach and of the small or large bowel (Fig. 58–14).[13, 38, 52] The stomach is the most frequent site, followed by the small intestine.[13] The bowel wall thickening may become quite bulky and masslike; however, because associated luminal narrowing is uncommon, bowel obstruction is rare unless an intussusception occurs as a complication (Fig. 58–15).[52] Ulceration may occur, resulting in perforation and abscess formation. Associated mesenteric lymph node enlargement and mesenteric masses are commonly noted.[13]

Colon Carcinoma

Carcinoma of the colon is rarely noted in adolescents with familial polyposis syndromes and in children who have undergone a urinary diversion procedure in which the ureters are diverted into the sigmoid colon. Even when associated with those conditions, however, carcinoma of the colon is more likely seen in adulthood; fewer than 1% of cases are seen in patients under 25 years of age. The

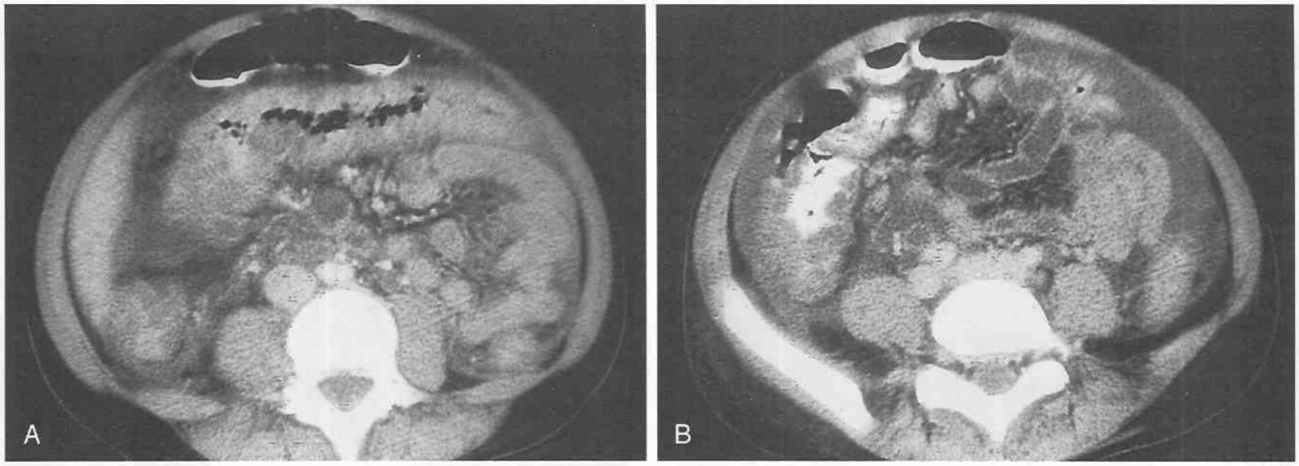

Figure 58–13. Ischemic colitis. *A,* CT scan through the midabdomen demonstrates bowel wall thickening in the transverse colon. *B,* CT scan in same patient 3 cm below *A* demonstrates bowel wall thickening involving the ascending colon. The thickened colonic wall has a diffuse, low-attenuation appearance. The patient was noted to have ishemic colitis with perforation at surgery.

CT appearance of colonic carcinoma at CT includes an irregular mass originating in the wall of the large bowel (Fig. 58–16), usually with associated luminal narrowing. Associated mesenteric and retroperitoneal lymphadenopathies are common.

Trauma

Bowel Injury

Most bowel injuries in children result from motor vehicle crashes in which they were wearing lap belts. These children demonstrate lap-belt ecchymoses, which are linear and located in the lower abdomen or flank.[49] Bowel injury can be a partial-thickness tear, resulting in an intramural hematoma, or a full-thickness tear, resulting in bowel rupture.

The most common location of an intramural bowel hematoma is the duodenum.[54, 57] Intramural hematomas result in eccentric bowel wall thickening at CT. Large hematomas appear dumbbell-shaped at CT (Fig. 58–17) and may result in a proximal small-bowel obstruction. These injuries can typically be managed nonoperatively, although gastric decompression may be required for a week or more.

Bowel rupture occurs most commonly in the mid to distal jejunum.[43] The most common findings at CT include moderate to large "unexplained" peritoneal fluid collections (peritoneal fluid in the absence of solid viscus injury or pelvic fracture) and intense bowel wall enhancement (Fig. 58–18).[16, 29, 43, 54, 57] Extraluminal air is noted in only approximately one third of patients.[43] Additional CT find-

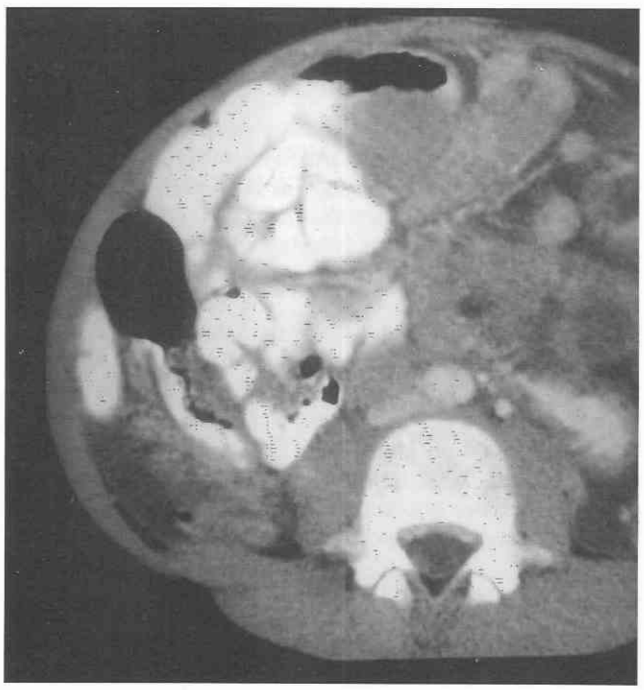

Figure 58–14. Non-Hodgkin's lymphoma involving the distal small bowel. CT scan through the lower abdomen in a patient with non-Hodgkin's lymphoma demonstrates bowel wall thickening involving the distal ileum. Note the associated mesenteric masses.

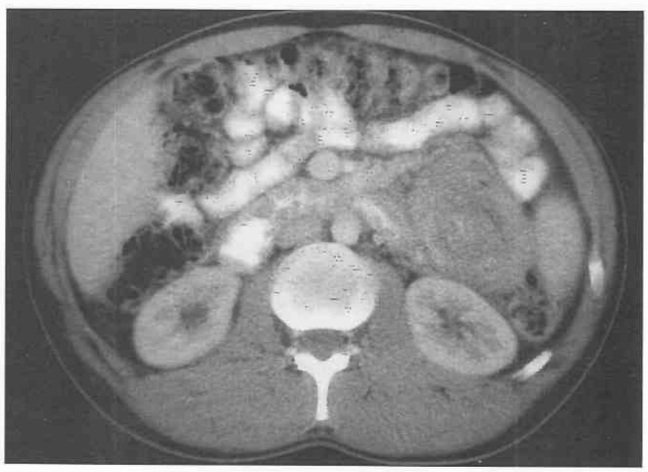

Figure 58–15. Small bowel intussusception. CT scan through the upper abdomen in a patient with lymphoma shows a small bowel intussusception.

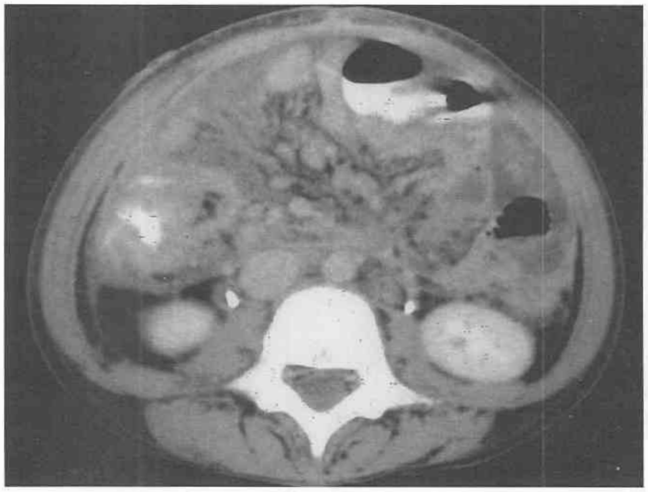

Figure 58–16. Adenocarcinoma of the colon. CT scan through the lower abdomen of an adolescent patient demonstrates irregular thickening of the ascending colon with luminal narrowing and associated mesenteric lymphadenopathy. At surgery, adenocarcinoma of the colon was noted.

ings associated with bowel rupture include bowel dilatation, bowel wall thickening, and, rarely, extravasation of oral contrast.[16, 29, 43, 54, 57]

Hypoperfusion Complex

A characteristic hypoperfusion complex associated with hypovolemic shock may be seen at CT in severely injured young children.[47, 55] This topic is included here because many of the CT findings associated with the complex involve the GI tract. Most children with the hypoperfusion complex have arterial hypotension on admission, indicating uncompensated shock.[47] The hypoperfusion may be transiently corrected, and the children may be thought to be hemodynamically stable enough to undergo CT; however, rapid hemodynamic decompensation may develop subsequently.

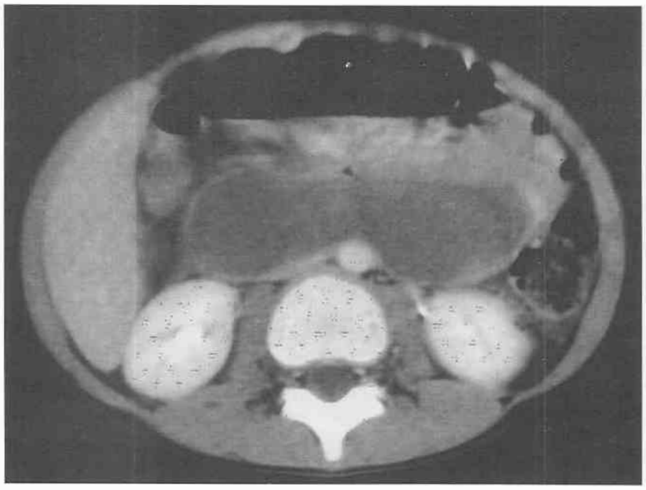

Figure 58–17. Intramural duodenal hematoma. CT scan through the upper abdomen in a patient following blunt abdominal trauma demonstrates a large, dumbbell-shaped duodenal hematoma.

CT findings in all children with the hypoperfusion complex include diffuse intestinal dilatation with fluid; abnormally intense contrast enhancement of bowel wall, mesentery, kidneys, aorta, and inferior vena cava; and diminished caliber of the aorta and inferior vena cava (Fig. 58–19).[47, 55] Variable findings associated with systemic hypoperfusion include intense contrast enhancement of the adrenal glands, decreased pancreatic and splenic enhancement, periportal low-attenuation zones, and peritoneal and retroperitoneal fluid.

The hypoperfusion complex, a strong predictor of a poor outcome, is associated with a high mortality rate.[47, 55] There is great overlap of observed findings at CT in the hypoperfusion complex and in bowel rupture.[43] Both conditions demonstrate intense bowel wall enhancement, bowel dilatation, bowel wall thickening, and moderate to large amounts of "unexplained" peritoneal fluid.

Peritoneal Cavity

Although primary abnormalities of the peritoneal cavity and its specialized folds (the mesentery and omentum) are rare, these sites are often involved in infectious, neoplastic, and traumatic conditions that originate at other sites in the abdomen or pelvis. Therefore, knowledge of the spectrum of disease processes that involve these sites is essential to optimize the value of CT in the evaluation of a variety of complex abdominal and pelvic conditions.

The peritoneum is composed of a serous membrane extending from the abdomen to the pelvis. It consists of two portions: a parietal and a visceral peritoneum. The term *parietal peritoneum* is used to describe the portions that cover the abdominal wall, and the term *visceral peritoneum* refers to the portions that cover viscera. The peritoneal cavity lies between these two layers. In nonpathologic states, it is largely a potential space containing minimal fluid.

The peritoneal cavity is divided into various spaces by ligaments, which are folds of peritoneum. The mesentery and omenta are specialized folds of peritoneum. The mesentery is a broad, fan-shaped fold composed of a double layer of serous membrane. It encloses the jejunum, ileum, and transverse and sigmoid colons. The mesentery also connects those segments of bowel to the posterior abdominal wall.

The major divisions of the peritoneal cavity are made by the transverse mesocolon, which separates the supramesocolic and inframesocolic compartments. The supramesocolic compartment is further divided into perihepatic and perisplenic spaces. Morison's pouch is a posterior extension of the perihepatic space. It is the most dependent recess in the upper abdomen. The inframesocolic compartment is subdivided into the right and left paracolic spaces located lateral to the ascending and descending colons, the lateral paravesical recesses, and the midline pouch of Douglas. The pouch of Douglas, which is located posterior to the bladder and anterior to the rectosigmoid colon, is the most dependent portion of this compartment and of the greater peritoneal cavity.

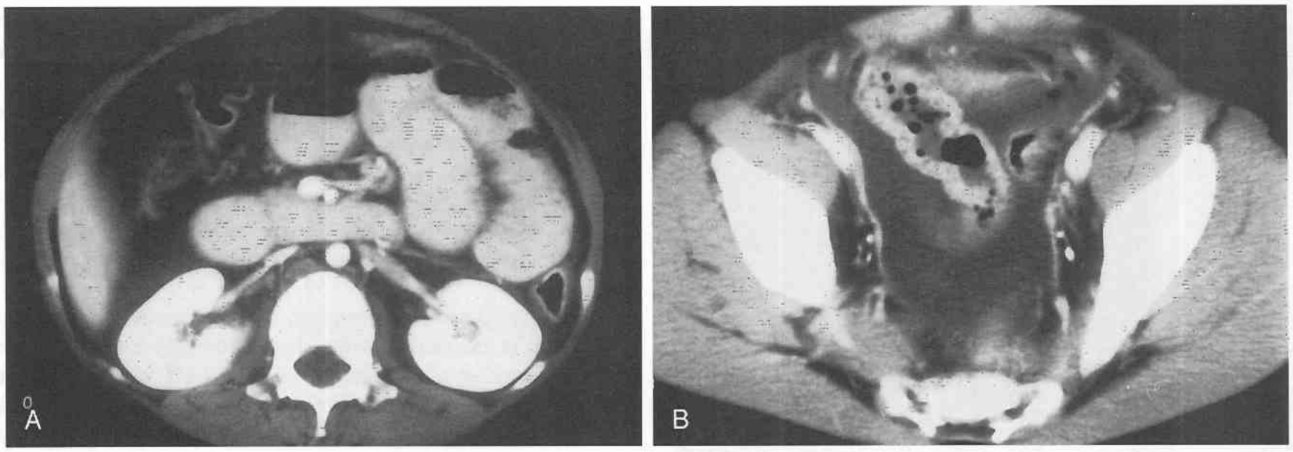

Figure 58–18. Jejunal rupture. *A,* CT scan through the upper abdomen of a patient injured in a motor vehicle crash shows free peritoneal fluid in Morison's pouch. *B,* CT scan through the pelvis in the same patient shows a large amount of peritoneal fluid. No solid viscus injury was identified. At surgery, a jejunal rupture was noted.

Infectious and Inflammatory Conditions

Peritoneal Abscess

Peritoneal cavity infection may be localized (peritoneal abscess) or generalized (peritonitis). The spread of an abscess within the peritoneal cavity has been well described by Meyers.[28] Factors that affect such spread are the primary site of infection, gravity, mesenteric partitions, peritoneal recesses, and pressure gradients.[28] In the inframesocolic compartment, the site of initial accumulation is the pouch of Douglas, which is the most dependent site (Fig. 58–20). From the pouch of Douglas, the infectious process preferentially ascends into the right paracolic recess and drains into Morison's pouch.

The most common source of a peritoneal abscess in children is a ruptured appendix. A periappendiceal abscess is more commonly found in the pouch of Douglas or in the perihepatic space than in its expected location in the right iliac fossa because of the typical spread of infection in the peritoneal cavity.

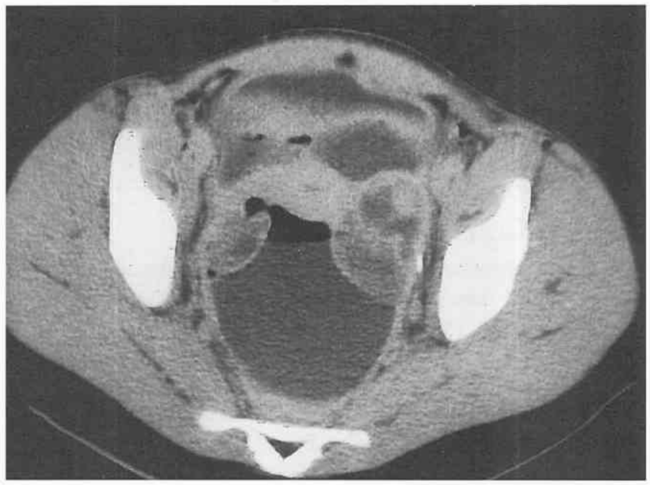

Figure 58–20. Peritoneal abscess in the pouch of Douglas. CT scan through the pelvis of a patient with a ruptured appendix shows a peritoneal abscess in the pouch of Douglas.

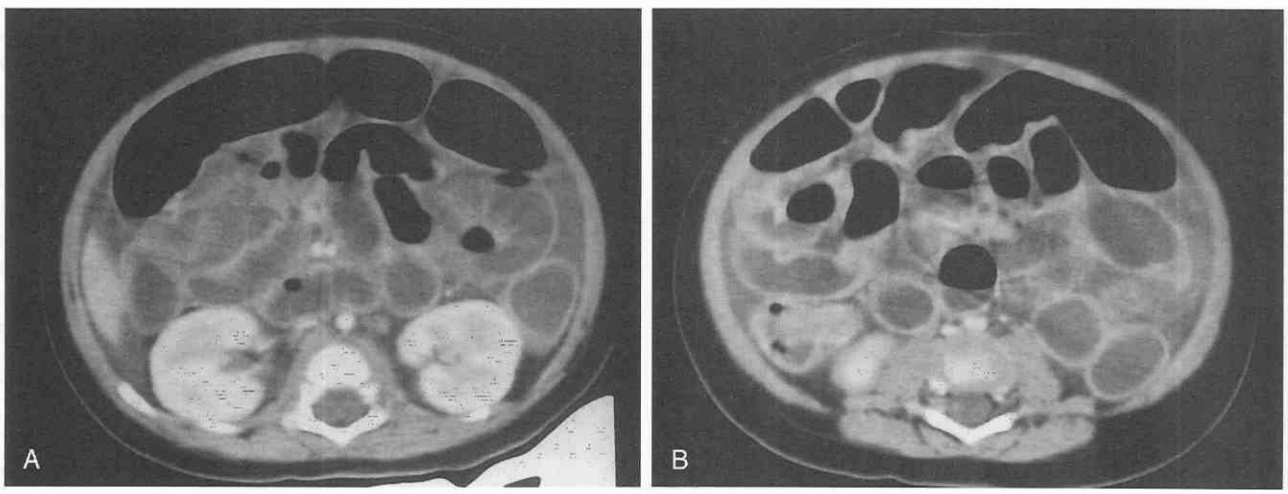

Figure 58–19. Hypoperfusion complex. CT scans through the upper abdomen *(A)* and the midabdomen *(B)* in a patient following blunt trauma demonstrate diffuse intestinal dilatation with fluid; intense contrast enhancement of bowel wall, kidneys, and great vessels; and diminished caliber of great vessels, consistent with the hypoperfusion complex.

The CT appearance of a peritoneal abscess varies. It is typically well circumscribed and has a mass effect, displacing adjacent bowel loops (see Fig. 58–4).[20, 21] The walls of the lesion are usually thick and may enhance. Variable attenuation is noted within the lesion, ranging from that of water to that of a solid or complex mass (see Fig. 58–20). Air may occasionally be noted within the abscess.

Peritonitis

Peritonitis may be primary (when the origin is outside the peritoneal cavity) or secondary (when it extends from a peritoneal source). Primary peritonitis usually spreads by blood or lymph. Secondary peritonitis can develop after extension from an intraperitoneal abscess or rupture of a hollow viscus. On a CT scan, the principal finding is peritoneal fluid of high attenuation (Fig. 58–21). Septations may be noted within the fluid. Nodularity and irregularity of the peritoneum may also be noted.

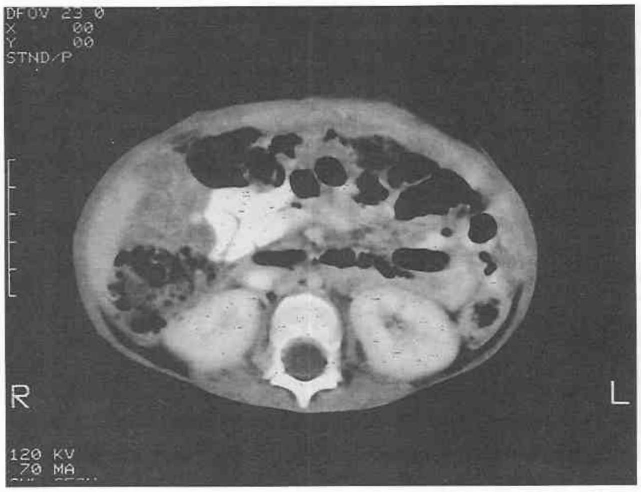

Figure 58–22. Peritoneal implant. CT scan through the upper abdomen demonstrates a peritoneal implant in Morison's pouch.

Neoplasms

Intraperitoneal neoplasms are usually secondary to metastatic disease. Primary neoplasms of the peritoneal cavity, which are rare in childhood, include cystic mesothelioma, yolk sac tumor, immature teratoma, and papillary cystadenoma.[9, 30, 40, 53]

Peritoneal Metastases

Neoplasms involving the peritoneal cavity are usually metastases from the GI or genitourinary tract. The more common extraperitoneal neoplasms reported to metastasize to the peritoneal cavity include ovarian germ cell tumors, neuroblastoma, Wilms' tumor, and lymphoma.[9, 50] Peritoneal invasion usually occurs after the neoplasm breaks through the organ capsule or spills at the time of surgery and spreads along the visceral peritoneum. Intraperitoneal metastases of intracranial tumors in children with ventriculoperitoneal shunts have also been described.[9] The spread of a neoplasm along the peritoneal cavity follows a pattern similar to that described for infection.

CT findings of peritoneal metastases include nodularity and irregularity of the peritoneum secondary to implants (Fig. 58–22), drop metastases into the pouch of Douglas (Fig. 58–23), and high-attenuation peritoneal fluid.[9, 50, 58] Associated mesenteric and omental masses are also typically seen.

Cystic Mesothelioma

Cystic mesothelioma is a rare primary neoplasm of the peritoneal cavity in children. It is not related to asbestos exposure. It originates in the serous lining of the peritoneal space and shows predilection for the surfaces of the pelvic viscera.[9, 30, 40] The CT scan appearance is that of a large, multiseptated cystic mass (Fig. 58–24). The neoplasm does not metastasize, but if it is not completely removed, it often recurs locally.

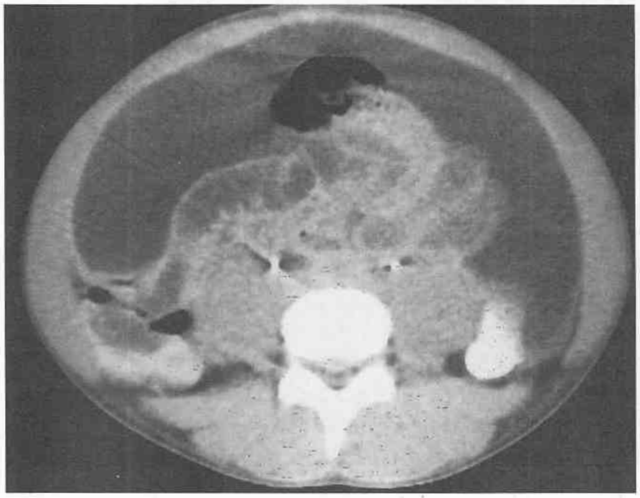

Figure 58–21. Peritonitis. CT scan through the midabdomen of a patient with peritonitis shows a large amount of peritoneal fluid. The fluid demonstrates a mass effect on the bowel and mesentery.

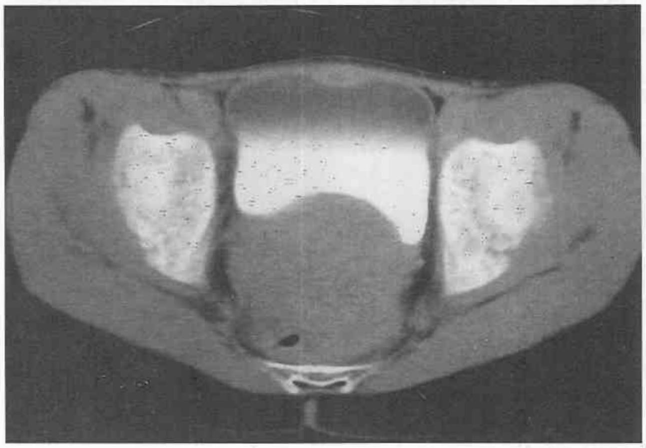

Figure 58–23. Drop metastasis into the pouch of Douglas. CT scan through the pelvis shows a large drop metastasis in the pouch of Douglas.

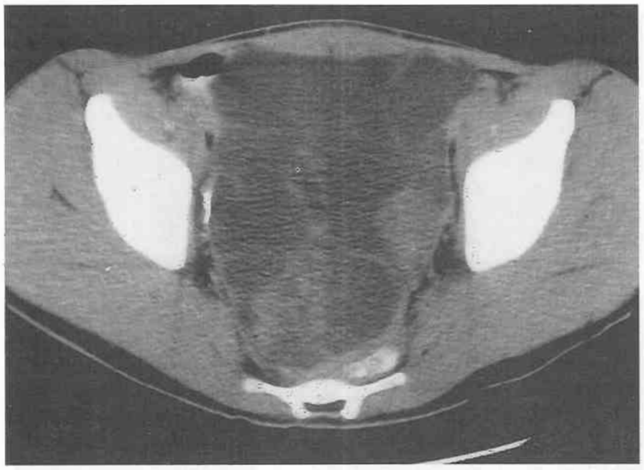

Figure 58–24. Peritoneal cystic mesothelioma. CT scan through the pelvis shows a large, multiseptated, cystic mass. At surgery, a cystic peritoneal mesothelioma was noted.

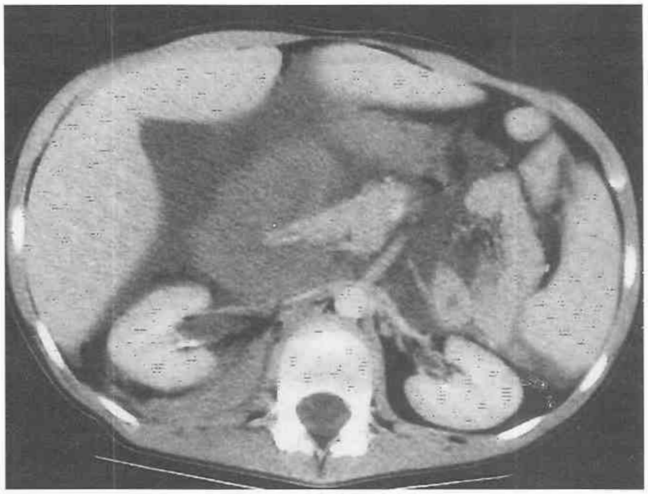

Figure 58–26. Clotted blood (sentinel clot). CT scan through the midabdomen in a patient following blunt abdominal trauma shows a well-circumscribed mesenteric hematoma. The hematoma has higher attenuation than free hemoperitoneum.

Trauma

Hemoperitoneum

Post-traumatic peritoneal fluid may represent blood, urine, third-space fluid losses, or bowel contents.[11, 48] Peritoneal blood, or hemoperitoneum, is seen in association with approximately two thirds of all intraperitoneal solid-organ injuries.[48] Hemoperitoneum may not be present if the injury does not extend to the organ surface or if there is no capsular disruption.

The attenuation values of blood in the peritoneal cavity vary widely, depending on whether it is unclotted blood, clotted blood, or active hemorrhage. Unclotted hemoperitoneum has attenuation values of less than 60 Hounsfield units (HU) (Fig. 58–25). Clotted blood has higher attenuation values than unclotted hemoperitoneum because of its greater density and hemoglobin content (Fig. 58–26). Because clotted blood is typically seen adjacent to the site of injury, the presence of focal higher-attenuation clotted blood (the sentinel clot sign) is a marker for the principal site of hemorrhage.[31] Active hemorrhage is characterized by focal or diffuse, high-attenuation areas (>90 HU) following vascular enhancement (Fig. 58–27). It depends on the presence of brisk extravasation of contrast-enhanced blood.[46, 56]

The amount of hemoperitoneum noted at CT is not a measure of ongoing hemorrhage but, instead, reflects the amount of blood that accumulated between the time of injury and the time the CT was obtained.[48] The peritoneal blood seen at CT may have accumulated in the first few minutes after the injury, or it may be continuing to accumulate. The only sign of active hemorrhage at CT is focal or diffuse, high-attenuation areas measuring over 90 HU and

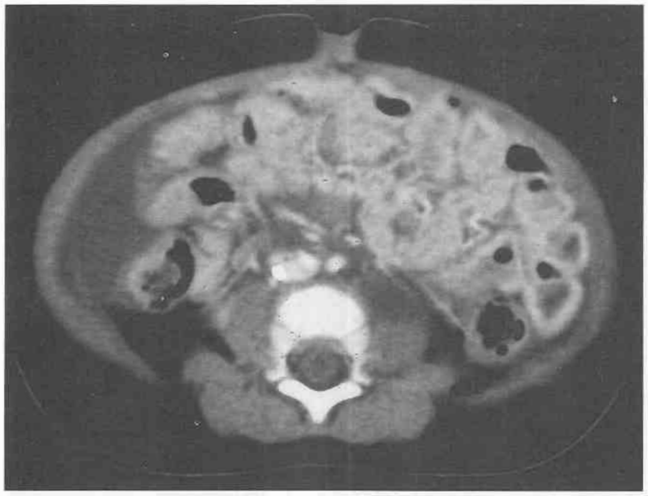

Figure 58–25. Unclotted hemoperitoneum. CT scan through the midabdomen of a patient with hepatic injury following blunt abdominal trauma demonstrates low-attenuation, free hemoperitoneum in the right paracolic recess.

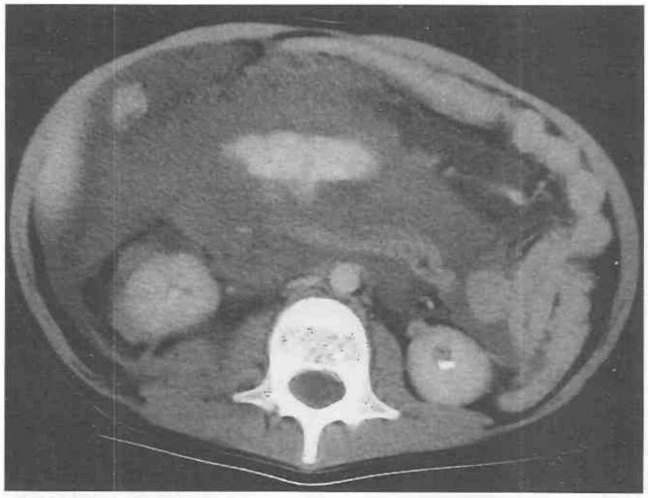

Figure 58–27. Active hemorrhage. CT scan through the midabdomen demonstrates a focal area of high-attenuation fluid representing active hemorrhage from a torn mesenteric vessel. The surrounding intermediate-attenuation clotted blood can be seen.

representing extravasated intravascular contrast media mixed with blood (see Fig. 58–27).[46, 56]

Mesentery and Omentum

Developmental Abnormalities

Midgut Malrotation

Malrotation of the small-bowel mesentery around the superior mesenteric artery occurs when the normal process of gut development is arrested during fetal development. In the first trimester, the duodenum fuses to the posterior body wall and becomes retroperitoneal, whereas the remainder of the small bowel and its mesentery herniates into the umbilical cord and undergoes a counterclockwise rotation about the superior mesenteric artery. The result is that the normal jejunoileal mesentery extends obliquely from the duodenal-jejunal junction in the left upper quadrant to the ileocecal valve in the right lower quadrant.

Arrest of this process leads to malrotation, which may result in intestinal obstruction secondary to remnant peritoneal folds (Ladd's bands) that cross the duodenum, or in twisting of the shortened mesentery with subsequent midgut volvulus. The most direct imaging technique for identifying midgut malrotation is a barium upper GI tract examination; however, the diagnosis can be strongly suggested at cross-sectional imaging. CT scan findings in midgut volvulus include reversal of the normal relationship between the superior mesenteric artery and vein (Fig. 58–28), and twisting of the mesentery around the artery, which creates a whirlpool appearance (Fig. 58–29).[60]

Figure 58–29. Midgut malrotation. CT scan through the midabdomen of a patient with midgut malrotation and volvulus demonstrates twisting of the small-bowel mesentery around the superior mesenteric artery.

Mesenteric Lymphangioma

A mesenteric lymphangioma, or mesenteric cyst, is a contiguous mass of dilated lymphatics. It occurs secondary to failure of lymphatic tissue within the mesentery and omentum to establish normal communication with the remainder of the lymphatic system during fetal development.[37] Lymphangiomas arise within the small bowel mesentery, the mesocolon, or peritoneal reflections. The mass can become large, but because it is soft, it rarely results in bowel obstruction. Most patients present with a palpable mass.

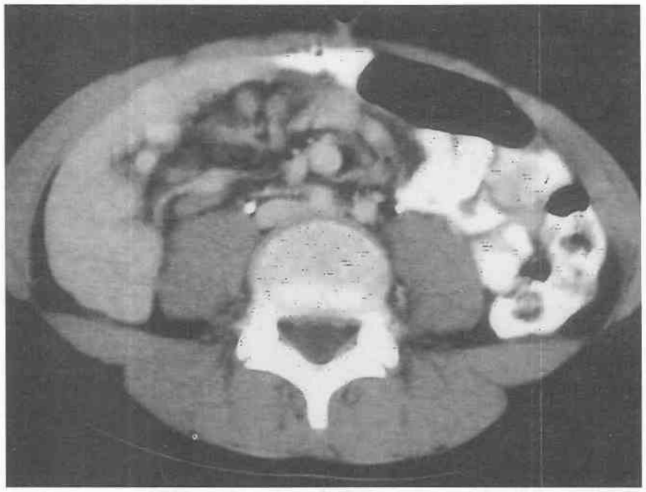

Figure 58–28. Midgut malrotation. CT scan through the midabdomen in a patient with midgut malrotation demonstrates inversion of the superior mesenteric vessels, with the superior mesenteric vein positioned to the left of the superior mesenteric artery.

The typical CT appearance of lymphangioma is that of a large, thin-walled, multiseptate cystic mass (Fig. 58–30).[37] The walls are occasionally thick and irregular, and calcifications may be noted in them. The internal fluid contents are usually homogeneous, and the attenuation varies from that of water to that of fat. Mesenteric lymphangiomas occasionally rupture, resulting in the presence of associated free peritoneal fluid.

Infection and Inflammation

Mesenteric Lymphadenopathy

Mesenteric lymph nodes are located adjacent to bowel wall along the ileal and jejunal arteries and superior mesen-

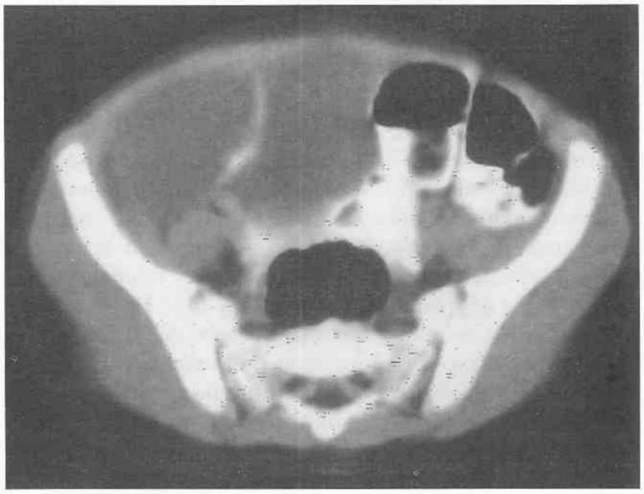

Figure 58–30. Mesenteric lymphangioma. CT scan through the pelvis shows a thin-walled, septate cystic mass.

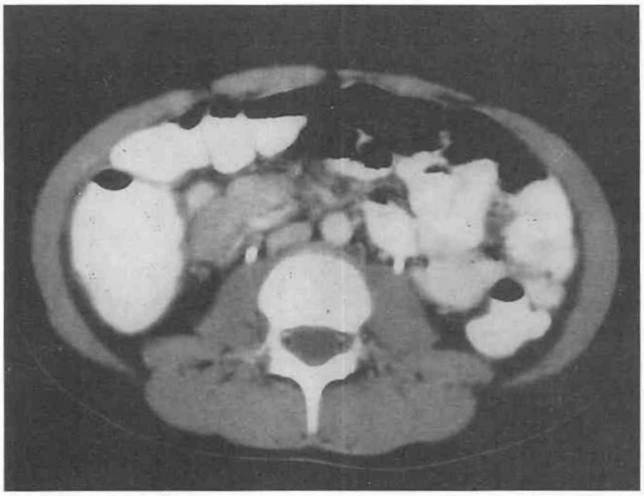

Figure 58–31. Mesenteric lymphadenopathy. CT scan through the lower abdomen shows enlarged mesenteric lymph nodes in the right lower quadrant.

teric vein. Mesenteric lymphadenopathy is a nonspecific finding associated with a variety of abdominal or pelvic infectious, inflammatory, and neoplastic conditons.[34, 45] The clinical syndrome of mesenteric lymphadenitis, which includes acute right lower quadrant pain and tenderness, fever, and leukocytosis, may mimic an acute abdomen. In several series, mesenteric lymphadenitis was the most frequent alternative diagnosis in children who underwent surgery because of suspected acute appendicitis.

Enlarged mesenteric lymph nodes measure greater than 5 mm in maximal diameter on the CT scan.[34, 39] The lymph nodes are oval, homogeneous in attenuation, and generally seen in clusters (Fig. 58–31). The most common location is the right iliac fossa. Enlarged mesenteric lymph nodes may be noted as an isolated finding at CT or in conjunction with other pathology. The most frequent associated finding is small-bowel thickening related to an enteritis. Although enlarged mesenteric lymph nodes are generally considered to be simply a secondary finding and themselves insignificant, associated complications may be noted occasionally. These include abscess formation (suppurative mesenteric lymphadenitis) (Fig. 58–32), peritonitis, and mesenteric venous thrombosis.[2]

Segmental Omental Infarction

Segmental omental infarction is an uncommon condition that may present with the clinical signs and symptoms of an acute abdomen. The condition is generally managed nonoperatively. Proposed underlying causes of segmental omental infarction include omental torsion, trauma, thromboembolism, and prior surgery. It may also be idiopathic. The condition is more frequently right-sided.[33] The CT appearance of segmental omental infarction includes a focal area of well-circumscribed infiltration of omental fat with heterogeneous areas of increased attenuation (Fig. 58–33).[33] The range of the abnormality extends from anterior to the liver, inferiorly to the lower abdomen. Associated mass effect is often present on adjacent structures, including liver and bowel loops.

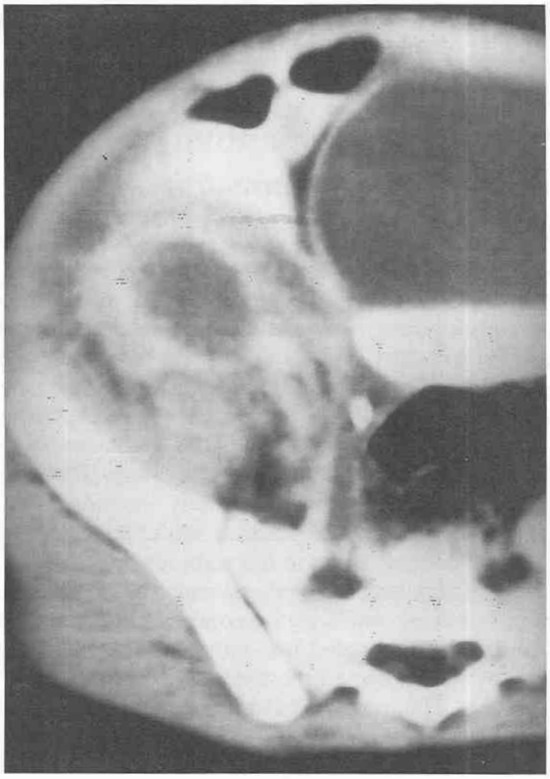

Figure 58–32. Suppurative mesenteric lymphadenopathy. CT scan through the lower abdomen shows a rounded, low-attenuation lesion with a thick, enhancing wall. At surgery, suppurative mesenteric lymphadenopathy was noted.

Neoplasms

The most common neoplasms that involve the mesentery and omentum in children are lymphoma, usually in the disseminated form, and metastases.

Lymphoma

Mesenteric involvement is more common in non-Hodgkin's lymphoma than in Hodgkin's disease. When mesen-

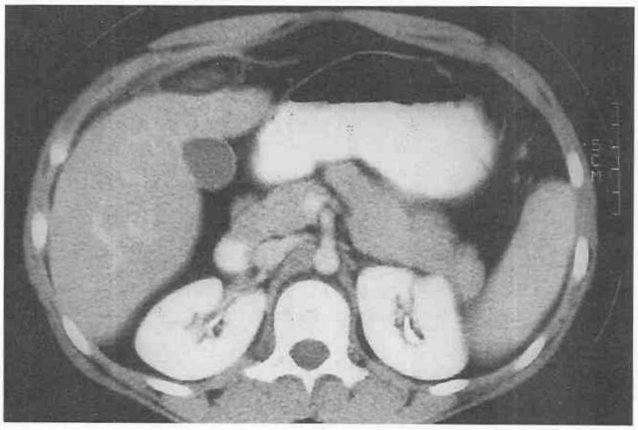

Figure 58–33. Segmental omental infarction. CT scan through the upper abdomen demonstrates well-circumscribed, focal infiltration of right-sided omental fat.

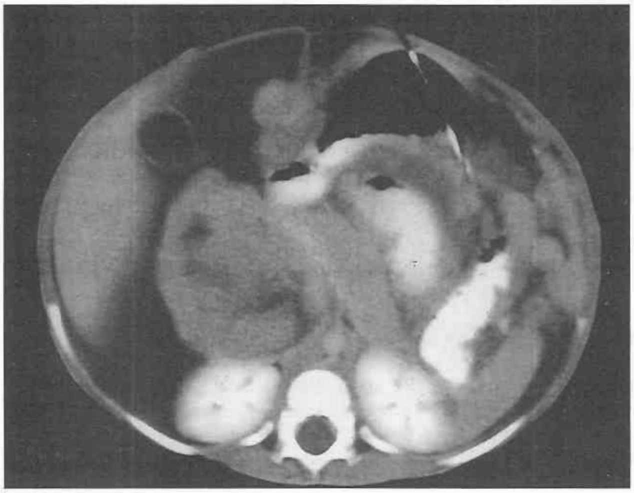

Figure 58–34. Rounded omental metastasis. CT scan through the upper abdomen demonstrates a rounded, heterogeneous mass in the lesser omentum, representing metastatic disease.

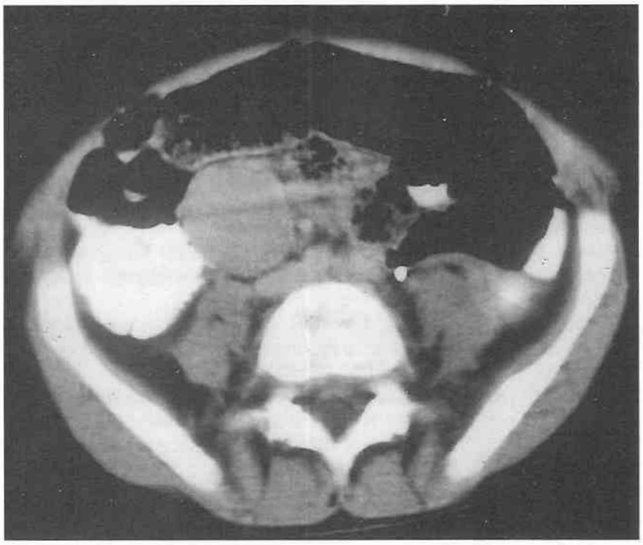

Figure 58–35. Castleman's disease of the mesentery. CT scan through the lower abdomen demonstrates a large, solid mass in the mesentery. At surgery, this was noted to be Castleman's disease.

teric lymphadenopathy is observed in children with lymphoma, retroperitoneal lymph nodes are usually enlarged. The CT scan of metastatic disease in the mesentery and omentum varies from discrete masses that may be cakelike or rounded (Fig. 58–34), to ill-defined masses.[9, 59] Infiltration of surrounding mesenteric fat may also be seen.

Primary Neoplasms

Primary mesenteric and omental neoplasms are rare. Those reported include fibroma, lipoma, lipoblastoma, desmoid tumor, Castleman's tumor, and yolk sac tumor.[5, 9, 17, 25, 42] Fibroma, the most common primary mesenteric neoplasm, is typically well circumscribed, with homogeneous soft tissue attenuation at CT scan. The mesenteric lipoma is well circumscribed and homogeneous, with fat attenuation. Lipoblastoma has a heterogeneous appearance, with areas of soft tissue attenuation seen within a focal fatty mass. Desmoid tumors, which typically occur in postcolectomy patients with Gardner's syndrome,[5] are large and highly infiltrative.

Castleman's disease, also known as giant lymph node hyperplasia or angiofollicular lymph node hyperplasia, is a rare benign condition (Fig. 58–35).[17] It is most commonly noted in the mediastinum but in rare instances arises in extrathoracic sites containing lymphoid tissue, including the mesentery. The yolk sac tumor is a highly malignant entity that occasionally arises in the mesentery.[25]

Trauma

Mesenteric Injury

Mesenteric injury may occur following blunt or penetrating trauma. It is often associated with bowel injury. Associated CT findings include mesenteric hematoma, infiltration of mesenteric fat, bowel wall enhancement, and unexplained peritoneal fluid (see Fig. 58–26).[54, 57] It may be difficult to differentiate isolated mesenteric injury from bowel rupture with CT because similar findings may be noted in both entities. A late complication of mesenteric injury is intestinal stricture, probably resulting from associated bowel ischemia following the injury that heals by means of fibrosis, thus narrowing the intestinal lumen.[41]

References

1. Alpern MB, Glazer GM, Francis IR: Ischemic or infarcted bowel: CT findings. Radiology 166:149–152, 1988.
2. Asch MJ, Amoury RA, Touloukian RJ, et al: Suppurative mesenteric lymphadenitis. Am J Surg 115:570–573, 1968.
3. Balthazar EJ, Birnbaum RA, Yee J, et al: Acute appendicitis: CT and US correlation in 100 patients. Radiology 190:31–35, 1994.
4. Balthazar EJ, Yen BC, Gordon RB: Ischemic colitis: CT evaluation in 54 cases. Radiology 211:381–388, 1999.
5. Baron RL, Lee JKT: Mesenteric desmoid tumors. Radiology 140: 777–779, 1981.
6. Benya EC, Sivit CJ, Quinones RR: Abdominal complications after bone marrow transplantation in children: Sonographic and CT findings. AJR Am J Roentgenol 161:1023–1027, 1993.
7. Boland GW, Lee MJ, Cats AM, et al: Antibiotic-induced diarrhea: Specificity of abdominal CT for the diagnosis of *Clostridium difficile* disease. Radiology 191:103–106, 1994.
8. Bolton RP, Thomas DF: Pseudomembranous colitis in children and adults. Br J Hosp Med 35:37–42, 1986.
9. Chung CJ, Bui V, Fordham LA, et al: Malignant intraperitoneal neoplasms of childhood. Pediatr Radiol 28:317–321, 1998.
10. Donnelly LF: CT imaging of immunocompromised children with acute abdominal symptoms. AJR Am J Roentgenol 167:909–913, 1996.
11. Federle MP, Jeffrey RB: Hemoperitoneum studied by computed tomography. Radiology 148:187–192, 1993.
12. Fishman EK, Kavuru M, Jones B, et al: Pseudomembranous colitis: CT evaluation in 26 cases. Radiology 180:57–60, 1991.
13. Fishman EK, Kuhlman JE, Jones RJ: CT of lymphoma: Spectrum of disease. Radiographics 11:647–669, 1991.
14. Garcia Pena BM, Mandl KD, Kraus SJ, et al: Ultrasonography and limited computed tomography in the diagnosis and management of appendicitis in children. JAMA 282:1041–1046, 1999.
15. Gore RM: CT of inflammatory bowel disease. Radiol Clin North Am 27:717–729, 1989.
16. Hara H, Babyn PS, Bourgeois D: Significance of bowel wall enhancement on CT following blunt abdominal trauma in childhood. J Comput Assist Tomogr 13:430–432, 1989.

17. Iida E, Kohno A, Mikami T, et al: Mesenteric Castleman tumor. J Comput Assist Tomogr 7:338–340, 1983.
18. Jabra AA, Fishman EK, Taylor GA: CT findings in inflammatory bowel disease in children. AJR Am J Roentgenol 162:975–979, 1994.
19. Janik JS, Firor HV: Pediatric appendicitis: A 20-year study of 1,640 children at Cook County (Illinois) Hospital. Arch Surg 114:717–719, 1979.
20. Jeffrey RB, Federle MP, Tolentino CS: Periappendiceal inflammatory masses: CT-directed management and clinical outcome in 70 patients. Radiology 167:13–16, 1988.
21. Jones B, Fishman EK, Siegelman SS: Computed tomography and appendiceal abscess: Special applicability in the elderly. J Comput Assist Tomogr 7:434–438, 1983.
22. Karakas SP, Guelguat M, Leonidas JC, et al: Acute appendicitis in children: Comparison of clinical diagnosis with ultrasound and CT imaging. Pediatr Radiol 30:94–98, 2000.
23. Lane MJ, Katz DS, Ross BA, et al: Unenhanced helical CT for suspected appendicitis. AJR Am J Roentgenol 168:405–409, 1997.
24. Lau W, Fan J, Viu T, et al: Negative findings at appendectomy. Am J Surg 148:375–378, 1984.
25. Lev MH, Blickman JG: Extragonadal yolk sac tumor: Sonographic and CT findings. AJR Am J Roentgenol 160:370–373, 1993.
26. Macari M, Balthazar EJ, Megibow AJ: The accordion sign at CT: A nonspecific finding in patients with colonic edema. Radiology 211: 743–746, 1999.
27. Malone AJ, Wolf CR, Malmed AS, et al: Diagnosis of acute appendicitis: Value of unenhanced CT. AJR Am J Roentgenol 160:763–766, 1993.
28. Meyers MA: Intraperitoneal spread of infections. In Meyers MA (ed): Dynamic Radiology of the Abdomen: Normal and Pathologic Anatomy. New York, Springer-Verlag, 1994.
29. Mirvis SE, Gens DR, Shanmuganathan K: Rupture of the bowel after blunt trauma: Diagnosis with CT. AJR Am J Roentgenol 159: 1217–1221, 1992.
30. O'Neil JD, Ros PR, Storm BL, et al: Cystic mesothelioma of the peritoneum. Radiology 170:333–337, 1989.
31. Orwig D, Federle MP: Localized clotted blood as evidence of visceral trauma at CT: The sentinel clot sign. AJR Am J Roentgenol 153: 747–749, 1989.
32. Philpotts LE, Heiken JP, Westcott MA, et al: Colitis: Use of CT findings in differential diagnosis. Radiology 190:445–449, 1994.
33. Puylaert JBCM: Right-sided segmental infarction of the omentum: Clinical, US, and CT findings. Radiology 185:169–172, 1992.
34. Rao PM, Rhea JR, Novelline RA: CT diagnosis of mesenteric adenitis. Radiology 202:145–149, 1997.
35. Rao PM, Rhea JT, Novelline RA, et al: Helical CT combined with contrast material administered only through the colon for imaging of suspected appendicitis. AJR Am J Roentgenol 169:1275–1280, 1997.
36. Ros PR, Buetow PC, Pantograg-Brown L, et al: Pseudomembranous colitis. Radiology 198:1–9, 1996.
37. Ros PR, Olmstead WW, Moser RP, et al: Mesenteric and omental cysts: Histologic classification with imaging correlation. Radiology 164:327–332, 1987.
38. Rubesin SE, Gilchrist AM, Bronner M, et al: Non-Hodgkin lymphoma of the small intestine. Radiographics 10:985–998, 1990.
39. Ruess L, Frazier AA, Sivit CJ: CT of the mesentery, omentum, and peritoneum in children. Radiographics 15:89–104, 1995.
40. Schneider JA, Zelnick EJ: Benign cystic peritoneal mesothelioma. J Clin Ultrasound 13:190–192, 1985.
41. Shalaby-Rana E, Eichelberger M, Kerzner B, et al: Intestinal stricture due to lap-belt injury. AJR Am J Roentgenol 158:63–64, 1992.
42. Sivit CJ: CT scan of the mesentery-omentum peritoneum. Radiol Clin North Am 34:863–884, 1996.
43. Sivit CJ, Eichelberger MR, Taylor GA: CT in children with rupture of the bowel following blunt trauma: Diagnostic efficacy and comparison with hypoperfusion complex. AJR Am J Roentgenol 163:1195–1198, 1994.
44. Sivit CJ, Newman KD, Boenning DA, et al: Appendicitis: Usefulness of US in a pediatric population. Radiology 185:549–552, 1992.
45. Sivit CJ, Newman KD, Chandra RS: Visualization of enlarged mesenteric lymph nodes at US examination: Clinical significance. Pediatr Radiol 23:471–475, 1993.
46. Sivit CJ, Peclet MH, Taylor GA: Life threatening intraperitoneal bleeding: Demonstration with CT. Radiology 171:430, 1989.
47. Sivit CJ, Taylor GA, Bulas DI, et al: Post traumatic shock in children: CT findings associated with hemodynamic instability. Radiology 182: 723–726, 1992.
48. Sivit CJ, Taylor GA, Bulas DI, et al: Blunt trauma in children: Significance of peritoneal fluid. Radiology 178:185–188, 1991.
49. Sivit CJ, Taylor GA, Newman KD, et al: Safety-belt injuries in children with lap-belt ecchymosis: CT findings in 61 patients. AJR Am J Roentgenol 157:111–114, 1991.
50. Slasky BS, Bar-Ziv J, Freeman AI, et al: CT appearances of involvement of the peritoneum, mesentery and omentum in Wilms' tumor. Pediatr Radiol 27:14–17, 1997.
51. Sloas MM, Flynn PM, Kaste SC: Typhlitis in children with cancer: A 30-year experience. Clin Infect Dis 17:484–490, 1993.
52. Smith C, Kubicka RA, Thomas CR: Non-Hodgkin lymphoma of the gastrointestinal tract. Radiographics 12:887–889, 1992.
53. Spurney RF, McCormack KM: Immature omental teratoma. Arch Pathol Lab Med 111:762–764, 1987.
54. Strouse PJ, Close BJ, Marshall KW, et al: CT of bowel and mesenteric trauma in children. Radiographics 19:1237–1250, 1999.
55. Taylor GA, Fallat ME, Eichelberger MR: Hypovolemic shock in children: Abdominal CT manifestations. Radiology 164:479–481, 1987.
56. Taylor GA, Kaufman RA, Sivit CJ: Active hemorrhage in children after thoracoabdominal trauma: Clinical and CT features. AJR Am J Roentgenol 162:401–404, 1994.
57. Vu Nghiem H, Jeffrey RB, Mindelzun RE, et al: CT of blunt trauma of the bowel and mesentery. AJR Am J Roentgenol 160:53–58, 1993.
58. Walkey MM, Friedman AC, Sohotra P, et al: CT manifestations of peritoneal carcinomatosis. AJR Am J Roentgenol 150:1035–1041, 1988.
59. Whitley NO, Bohlman ME, Baker LP: CT patterns of mesenteric disease. J Comput Assist Tomogr 6:490–495, 1982.
60. Zerin JM, DiPietro MA: Mesenteric vascular anatomy at CT: Normal and abnormal appearances. Radiology 179:739–742, 1991.

59 Pediatric and Adolescent Pelvis

Marilyn J. Siegel

Computed tomography (CT) and magnetic resonance imaging (MRI) provide a useful adjunct to sonography in the evaluation of the pediatric and adolescent pelvis. Sonography remains the imaging study of choice for the initial assessment of suspected pelvic lesions, whereas CT and MRI are helpful in establishing the origin of a mass when the results of sonography are equivocal, to delineate the full extent of neoplastic or inflammatory lesions, and to characterize further müllerian malformations.[4, 6, 16, 57–63, 65, 67] This chapter reviews the CT and MRI findings of the most common pelvic abnormalities in children. In particular, lesions of the genital tract, bladder, and pelvic soft tissues are addressed.

Patient Preparation: Technical Considerations

Computed Tomography

Oral Contrast Material

Oral contrast medium is routinely administered for pelvic CT examinations in order to opacify loops of small bowel lest they be mistaken for a mass lesion or abnormal fluid collection.[60] This is usually achieved by giving the patient a dilute contrast agent by mouth or through a nasogastric tube at least 1 hour before the start of the study. To increase patient compliance, the contrast agent can be mixed with fruit juice. The volume of contrast medium varies with the age of the patient (Table 59–1).

Despite the administration of a relatively large amount of contrast medium, the descending and rectosigmoid colon often remain unopacified. Although these segments can be recognized by their relatively fixed location and fecal contents, their opacification is sometimes desirable. Opacification of the distal colon can be achieved by administering additional oral contrast medium and then rescanning the patent after a suitable delay to allow the contrast agent to pass distally. Alternatively, a contrast enema can be administered to expedite opacification of these segments.

Table 59–1. Oral Contrast Doses Versus Patient Age

Age	Minimum Amount Given at Least 1 Hour Before Scanning
<1 mo	2–3 oz (60–90 mL)
1 mo to 1 yr	4–8 oz (120–240 mL)
1–5 yr	8–16 oz (240–480 mL)
6–12 yr	16–24 oz (480–720 mL)
≥13 yr	24–36 oz (720–1000 mL)

Intravenous Contrast Material

Differentiation of the pelvic vessels from enlarged lymph nodes is facilitated by the use of intravenous (IV) contrast medium.[60] The recommended dose of contrast is 2 mL/kg, not to exceed a total of 4 mL/kg or 100 mL (whichever is the lesser amount). Contrast medium may be administered by hand injection or via a mechanical injector. The latter type of administration is preferred if a 22-gauge or larger angiocatheter can be placed in an antecubital vein. A flow rate of 1.2 to 1.5 mL/sec is acceptable for a 22-gauge angiocatheter, whereas a rate of 2.0 mL/sec is recommended for 20-gauge catheters. Hand injection is preferred for smaller-caliber needles in the antecubital region and for needles positioned in the hand.

The initiation of scanning should be delayed until 60 to 75 seconds after the start of the contrast medium bolus to ensure opacification of pelvic vessels. Because the initial scans are obtained before significant contrast medium excretion has occurred, the ureters and bladder are not usually opacified. Delayed scanning at 3 to 5 minutes allows contrast medium to accumulate in the bladder, facilitating the recognition of pelvic fluid collections and bladder pathology.

Imaging Technique

For routine pelvic studies, contiguous 5- to 8-mm scans usually suffice. Decreased collimation (2 to 4 mm) is reserved for infants and very small children, for areas of maximum interest, and for detailed examinations of smaller structures. If the patient is cooperative, CT sections are obtained with breath-holding at suspended inspiration. If the patient is sedated or unable to suspend respiration, CT sections are obtained at resting lung volume.

Magnetic Resonance Imaging

The pelvis also can be successfully evaluated with MRI. Unlike the procedure in CT, oral contrast medium is not routinely administered for MRI examinations.

Coil Selection

For optimal signal-to-noise ratio and spatial resolution, MRI examinations of the pelvis should be performed with the smallest receiver coil that fits tightly around the body part being studied. A head coil or phased-array coil is used in most infants and small children, whereas a phased-array or whole-body coil is the receiver coil of choice for imaging larger children and adolescents. Phased-array coils

are preferred over body coils for imaging of the pelvis because they provide better anatomic resolution.

Slice Thickness and Matrix

Slice thickness varies with patient size and the area of interest. A slice thickness of 4 to 8 mm obtained at 5- to 10-mm intervals is usually adequate for a general survey of the pelvis and larger lesions. Thinner slices obtained at 4 mm are particularly useful for evaluating small lesions and through areas of maximum interest. A 128 or 192 matrix and one or two signal acquisitions generally are used in pediatric MRI examinations to shorten imaging time, although a 286 × 286 matrix may be needed in areas where more anatomic detail is desired.

Pulse Sequences

Both T1-weighted and T2-weighted sequences are required to image the pelvis. *T1-weighted sequences* (short repetition time [TR], short echo time [TE]) exploit the contrast differences between soft tissue structures and fat and are used to increase lesion detection and to characterize hemorrhagic and fatty components of pelvic masses.

T2-weighted sequences (long TR, long TE) provide excellent contrast between tumor and adjacent soft tissues and are useful for tissue characterization. Fast spin-echo techniques have virtually replaced conventional T2-weighted sequences. The fast spin-echo techniques substantially reduce imaging time, although they may result in slight loss of contrast between fat and other similarly intense fluid and tissues. To increase the contrast range of nonfatty tissue and to reduce or minimize ghost and chemical shift artifacts, the T2-weighted fast spin-echo sequences should be performed with fat-suppression techniques.

Fat-suppressed sequences are useful to increase contrast between normal and pathologic tissue on T2-weighted images and to improve lesion conspicuity. Fat suppression can be accomplished with either short tau inversion recovery (STIR) or radiofrequency presaturation of the lipid peak (fat saturation). Signal from fat is made null on STIR and fat-saturated images, whereas pathologic lesions have prolonged T1 and T2 values secondary to increased free water and are bright on the fat-suppressed sequences.

Optional imaging sequences include the *gradient-echo* technique and *contrast-enhanced imaging*. The gradient-echo sequence results in high signal in flowing blood and is useful in evaluating the patency of blood vessels and in differentiating vessels and lymph nodes.[55] The relatively short acquisition time required for gradient-echo images also allows serial dynamic imaging immediately after IV administration of a gadolinium (Gd) chelate agent. The Gd-enhanced images can provide additional information about the character of neoplasms and the relationship of neoplasms to adjacent pelvic structures.

Imaging Planes

Transaxial images are routinely obtained in pelvic MRI examinations. These images are useful for displaying the contour and anatomy of the bladder, uterus, and prostate and for assessing tumor extension to the pelvic side walls. In most instances, additional images are obtained in either the coronal or sagittal planes. Coronal images are useful for defining the relationship of the uterus and prostate to adjacent vessels, viscera, and pelvic floor and for demonstrating pelvic side wall invasion and lymphadenopathy. Sagittal images are best for evaluating the uterine fundus, vagina, rectum, spine, and presacral soft tissues.

Normal Anatomy

Female Pelvis

Ovaries

The ovaries descend from the upper abdomen into the pelvis during fetal life. With activation of the hypothalamic-pituitary-ovarian axis at the time of puberty, the ovaries move deeper into the pelvis, reaching their adult position posterolateral to the body of the uterus, although not necessarily at the same horizontal level. In some individuals, descent is incomplete, and the ovaries remain high in the pelvis, lying dorsal or cephalad to the uterus. They may be seen posterior to the uterus if ligamentous attachments are lax.

On both CT and MRI, the ovaries and uterus are identified more often in menarchal girls than in prepubertal girls. Cystic structures, representing follicles, can be seen in more than 70% of girls, regardless of age[53] (Fig. 59–1). In premenarchal girls, these cysts represent unstimulated (primordial) follicles; in menarchal girls, they may represent either unstimulated or stimulated (graafian or corpus luteum) follicles.[53] Unstimulated follicles usually have a diameter of less than 9 mm (Fig. 59–1*A* and *B*). Developing graafian or corpus luteum follicles range between 9 mm and 3 cm in diameter (Fig. 59–1*C*). A cystic mass larger than 3 cm in diameter is considered pathologic and usually represents a stimulated follicle that failed to involute.

Mean ovarian volumes on CT range between 0.4 and 0.8 cm^3 in girls younger than 8 years and between 2.1 and 6.9 cm^3 in girls 9 years of age or older.[53]

On T1-weighted MR images, the normal ovaries have a low to medium signal intensity and are isointense relative to uterine myometrium and to skeletal muscle. On T2-weighted images, the follicles increase in signal intensity and are hyperintense to fat, whereas the ovarian stroma becomes isointense or hyperintense to myometrium (Fig. 59–2).

Uterus and Vagina

Computed Tomography

The neonatal uterus is relatively large because of in utero stimulation by maternal hormones. During the first month of life, the uterus decreases in size as the level of exogenous hormones declines. In prepubertal girls, the uterus appears as a homogeneous, oval soft tissue structure posterior to the bladder; zonal anatomy is not evident (Fig. 59–3). As puberty approaches, the uterus begins to increase in size, with the corpus becoming thicker and larger than the cervix, producing the adult pear-shaped uterus. In the postmenarchal girl, the uterus is seen as an oval or a triangular soft tissue structure. Zonal anatomy may be recognized after the IV administration of contrast medium. On contrast-enhanced scans, the myometrium and endometrium show intense enhancement, and although they cannot be differentiated from each other, they can be differentiated

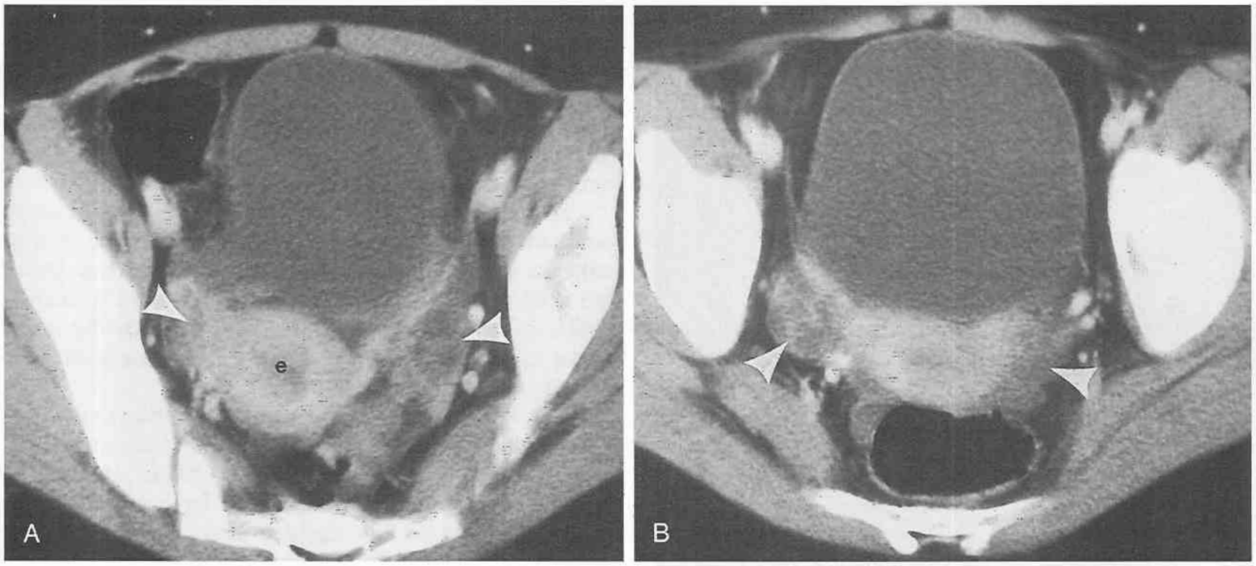

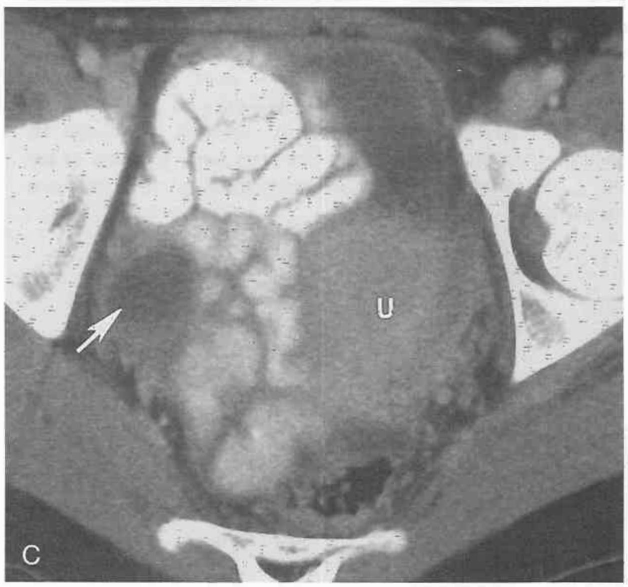

Figure 59–1. Normal postmenarchal female pelvis. *A* and *B*, Contrast-enhanced CT scans of a 15-year-old girl show low-attenuation ovaries *(arrowheads)* and an oval uterine fundus that demonstrates zonal differentiation. The higher-attenuation myometrium and endometrium can be differentiated from the lower-attenuation endometrial canal (e), but they cannot be differentiated from each other. *C*, CT scan of a different 15-year-old girl on day 12 of the menstrual cycle demonstrates a cystic structure *(arrow)* in the right ovary, representing a developing follicle. The diameter of the cyst is 2.0 cm. U, uterus.

from the lower-attenuation endometrial cavity (see Fig. 59–1*A* and *B*). The hypodensity centrally reflects the presence of secretions or blood.

The mean uterine volumes reported on CT examinations of pediatric patients range between 0.5 and 1.3 cm^3 in girls younger than 8 years of age and between 4.1 and 37.3 cm^3 in older girls.[53]

Although there are no clear-cut planes between the cervix and vagina, they usually can be distinguished by their shape. The cervix has a rounded appearance, whereas the vagina usually appears as a flat rectangular structure. On contrast-enhanced CT scans, the central portions of the cervix and vagina enhance, reflecting their mucosal lining.

Magnetic Resonance Imaging

On MRI scans, the uterus, cervix, and vagina of the premenarchal girl have a relatively low to medium signal intensity and indistinct zonal anatomy. In pubertal girls, the uterus has a homogeneous medium signal intensity on T1-weighted images. The characteristic zonal anatomy usually can be seen on T2-weighted images.[40, 41] The central high-signal-intensity zone represents the endometrium, the adjacent low-signal-intensity layer corresponds to the inner myometrium, and the peripheral intermediate-signal-intensity layer corresponds to the outer myometrium (see Fig. 59–2). Endometrial width normally varies during the menstrual cycle; it is thinnest immediately after menses and is thickest at midcycle.

The cervix has a homogeneous low to intermediate signal intensity on T1-weighted images. Three zones are seen on T2-weighted images: the high signal intensity central canal, an adjacent low signal intensity layer, and an outermost medium signal intensity layer. Like the uterus and cervix, the vagina also has an intermediate signal intensity on T1-weighted images. Two zones are seen on T2-weighted images: the central high-signal-intensity canal and the intermediate-signal-intensity wall.[40]

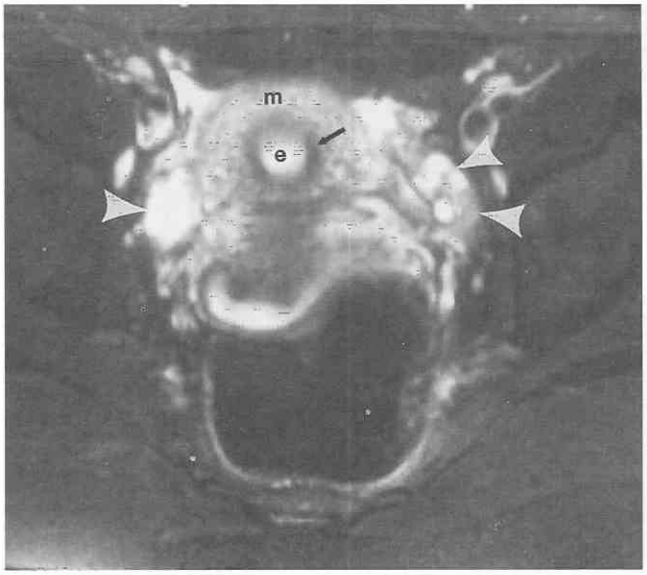

Figure 59–2. Normal postmenarchal female pelvis. T2-weighted fat-saturated (3500/98/180 degrees) MR image of a 14-year-old girl demonstrates that both ovaries have relatively high signal intensity *(arrowheads)*, reflecting the presence of multiple follicles. Some intermediate-signal-intensity stromal tissue can be noted in the left ovary posteriorly. Note the zonal anatomy of the uterus. e, endometrial canal; m, myometrium. *Arrow* indicates junctional zone.

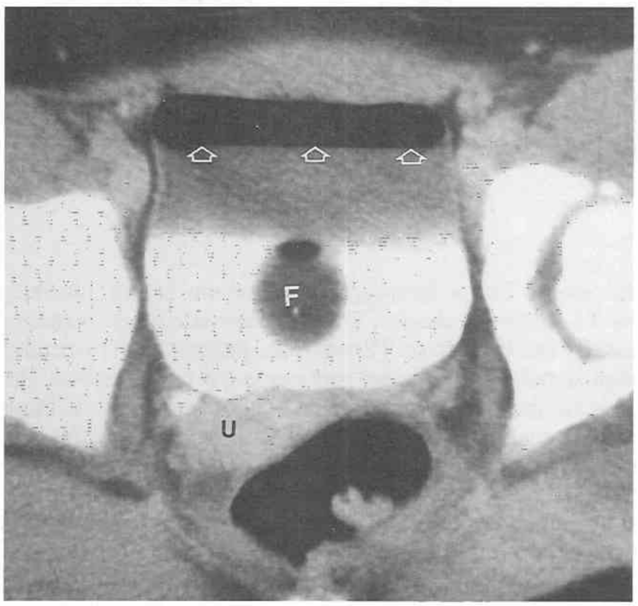

Figure 59–3. Normal prepubertal female pelvis. CT scan of a 7-year-old girl. The uterus (U) appears as a homogeneous, oval soft tissue structure posterior to the bladder. The endometrial cavity is indistinguishable from the myometrium. Neither ovary is visualized. The normal bladder wall is thin. On this contrast-enhanced scan, the opacified urine occupies the dependent portion of the bladder and unopacified urine layers are above it. A Foley catheter (F) is present, accounting for the air-fluid level *(open arrows)*.

Male Pelvis

The prostate gland and seminal vesicles are usually too small to be appreciated on routine pelvic CT or MRI studies in infants and young boys. Because these structures increase in size at the time of puberty, they are easier to recognize on routine examinations.

The prostate gland lies posterior to the symphysis pubis and anterior to the rectum. In prepubertal boys, it usually appears as a homogeneous soft tissue attenuation structure on both noncontrast and contrast-enhanced CT scans and MRI. In pubertal boys, zonal anatomy may be seen on some contrast-enhanced CT and MRI examinations (Fig. 59–4).

The seminal vesicles are located posterior to the urinary bladder, cephalic to the prostate gland, and anterior to the rectum. They are seen on CT as soft tissue structures with oval or bow-tie configurations. They have a low to medium signal intensity on T1-weighted images and a high signal intensity on T2-weighted images. The spermatic cords are found anterolateral to the symphysis pubis and medial to the femoral veins. They appear either as oval or round homogeneous soft tissue structures or as thin-walled, ring-like structures containing fat, vessels, and the vas deferens.

Urinary Bladder

The urinary bladder is a midline structure with varying size and configuration depending on the degree of distention. The bladder wall has an attenuation value or signal intensity equal to that of soft tissue, whereas the urine has an attenuation value or signal intensity near that of water.

Other Structures

The pelvic muscles (psoas, iliacus, obturator internus, pyriformis, and levator ani) are symmetrical in size and

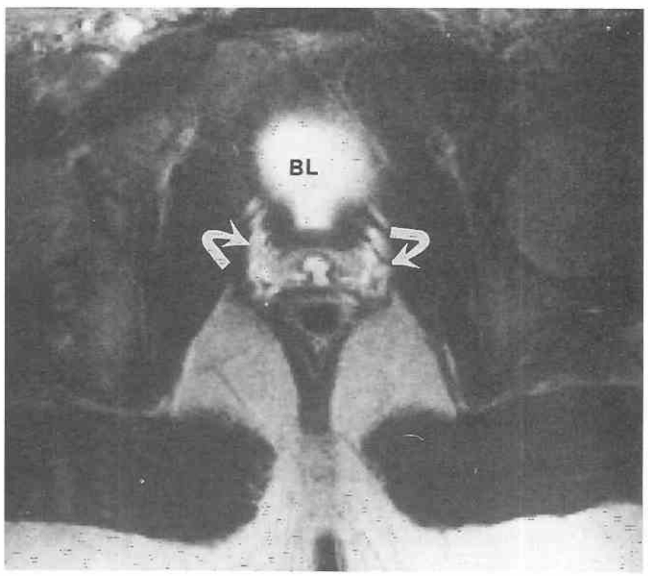

Figure 59–4. Normal male pelvis. Transaxial T2-weighted fast spin-echo MR image (2500/90) through the pubic symphysis in a 14-year-old boy shows the high-signal-intensity peripheral zone *(curved arrows)* of the prostate and the lower-signal-intensity central gland. BL, bladder.

shape in normal individuals. Small-bowel loops and the rectum, ascending, descending, and sigmoid colon are easily seen, especially on CT when the bowel lumen is distended with contrast medium. Normal pelvic lymph nodes are not routinely recognized on CT or MRI examinations in children.

Congenital Anomalies

Imaging Approach

Ultrasonography and MRI have both been shown to be useful methods of evaluating patients with suspected uterine or vaginal anomalies.[11, 20, 30, 31, 40, 42, 43, 52, 59] Hysterosalpingography also is a well-established technique for evaluating uterine anomalies, but since the advent of MRI, it is not usually needed for diagnosis. CT can be used to detect and differentiate congenital anomalies, although it is not performed as routinely as MRI because it uses ionizing radiation and has suboptimal soft tissue contrast compared with MRI.

Ultrasonography, especially transvaginal sonography, probably is the best initial examination in the evaluation of patients with suspected uterine anomalies because it is widely available and relatively lower in cost than MRI.[31] If the results of sonography are indeterminate or if additional information is needed to characterize an anomaly seen on sonography, MRI is indicated. In one series that compared transvaginal sonography, MRI, and hysterosalpingography, the accuracy of MRI for diagnosis of uterine anomalies was 100%, 90% for sonography, and 30% for hysterosalpingography.[48]

MRI Techniques

The MRI examination of suspected müllerian anomalies should include the following[31]:

1. A T1-weighted coronal image of the abdomen to show the size, shape, and position of the kidneys.
2. T1-weighted axial and sagittal images of the pelvis to show the relationship of the obstructed uterus to the vagina and the presence of subacute blood products.
3. A T2-weighted fast spin-echo sagittal scan to show the length and contour of the vaginal canal and uterine zonal anatomy.
4. A T2-weighted fast spin-echo axial image to show communication between the two parts of a unicornuate, bicornuate, or didelphys uterus and the location of the ovaries.
5. An off-axis coronal scan to show the contour of the fundus.

Imaging of the upper urinary tract is important because 20% to 25% of all patients with uterine anomalies have concomitant urinary tract anomalies.[28, 42]

Uterine Anomalies

Classification

The prevalence of uterine malformations is 0.1% to 0.5%.[11, 40, 42, 43] The spectrum of anomalies includes agenesis, hypoplasia, and duplication. Although a number of systems have been proposed for classifying müllerian anomalies, the system most widely in use today is the one presented by the American Fertility Society.[1] This classification, based on the degree of failure of normal development, has seven major subgroups:

- I, segmental agenesis or hypoplasia (cervical, fundal, tubal, or combined anomalies)
- II, unicornuate uterus
- III, didelphys uterus
- IV, bicornuate uterus
- V, septate uterus
- VI, arcuate uterus
- VII, diethylstilbestrol (DES)-related uterine hypoplasia with luminal changes

The most common abnormalities, which include agenesis/hypoplasia, unicornuate uterus, and the duplication anomalies (didelphys, bicornuate, and septate), are discussed later.

Embryology

The uterus, fallopian tubes, cervix, and upper part of the vagina develop from the paired müllerian ducts. The ducts descend into the pelvis from the upper abdomen, migrate into the midline, and fuse medially at about the 10th week of fetal life.[25, 31] The union of the two müllerian ducts begins in the lower half of the uterus and extends cephalocaudally. The septum between the two uterine bodies involutes and usually disappears by the 20th week of fetal life, leaving behind the fully developed fallopian tubes, uterus, and proximal vagina. Developmental anomalies result when there is failure of ductal fusion or incomplete septal regression.

The lower two thirds of the vaginal canal forms from the sinovaginal bulb. The distal and proximal parts of the vagina ultimately communicate when a cell cord between the two dissolves. Failure of normal development can result in vaginal hypoplasia or agenesis or a septum within the vaginal canal.

Specific Anomalies

Uterine Agenesis and Hypoplasia

Uterine agenesis and hypoplasia are the result of arrested development of the müllerian ducts bilaterally. This can be an isolated finding, or it may occur in association with the *Mayer-Rokitansky-Küster-Hauser syndrome*. Patients with arrested development of the müllerian ducts most commonly present with primary amenorrhea.[52]

The Mayer-Rokitansky-Küster-Hauser syndrome is characterized by vaginal atresia and a spectrum of uterine anomalies, including absence, hypoplasia, and duplication.[19, 52] Patients have a normal female karyotype, external genitalia, and secondary sexual development and normal ovaries and fallopian tubes. Renal anomalies, usually agenesis and rarely ectopia or hydronephrosis, occur in about 50% of patients, and skeletal anomalies occur in about 15% of patients.

MRI is particularly well suited to show uterine size, the degree of zonal differentiation, and the absence of the vaginal stripe. In addition to its small size, the hypoplastic

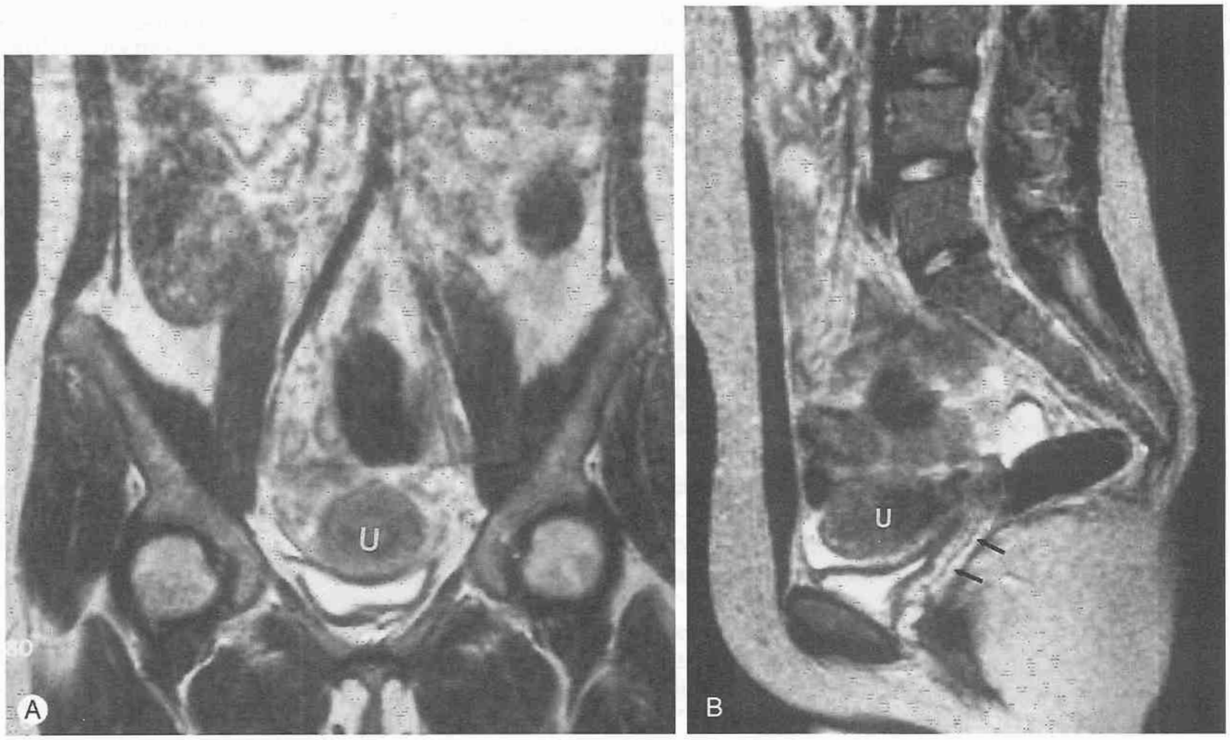

Figure 59–5. Mayer-Rokitansky-Küster-Hauser syndrome in a 16-year-old girl with amenorrhea. *A,* Coronal T1-weighted image (600/30) shows a low-signal-intensity uterus (U). *B,* Sagittal T2-weighted image (2500/90) shows absence of the vaginal canal and a hypoplastic uterus (U) with absent zonal differentiation. This patient has normal ovaries and no associated renal anomalies. *Arrows* indicate the urethra.

uterus exhibits poorly differentiated zonal anatomy, abnormally low signal intensity of the myometrium on T2-weighted sequence, and reduced endometrial and myometrial width[11] (Fig. 59–5).

Possible diagnoses to be considered in patients with this syndrome include primary vaginal atresia with a patent endometrial canal and cervix (see later) and congenital disorders of sexual differentiation, such as Turner's syndrome (45 XO karyotype, streak ovaries), true hermaphroditism, and the testicular feminization syndrome.[52] The latter syndrome results from the absence of testosterone receptors and is characterized by a male karyotype, testes that may be maldescended, female external genitalia, a blind-ending vagina that may be shortened, and an absent uterus. The role of MRI in these patients is to depict the pelvic anatomy and to identify abnormally developed or positioned gonads.

Unicornuate Uterus

The unicornuate uterus results from failure of development of one of the two müllerian ducts. The affected hemiuterus may have a communicating rudimentary horn or a noncommunicating rudimentary horn (Fig. 59–6), or it may be absent.[11] The rudimentary horn, communication between the two horns, and size of the endometrial cavity are best appreciated on T2-weighted images. Renal anomalies occur in about 25% of cases. Unicornuate uterus is not usually treated surgically.[31]

Uterus Didelphys

The anomaly known as uterus didelphys is characterized by complete duplication of the uterine body and cervix resulting from nonfusion of the müllerian ducts. Patients are usually asymptomatic unless an associated vaginal septum is causing hematocolpos. MRI shows two separate normal-sized uterine bodies, two cervices, and in many cases an upper longitudinal vaginal septum.[11] The uterine

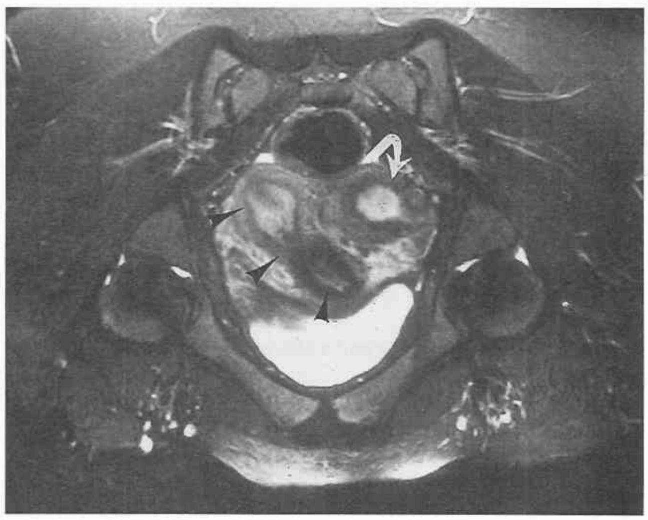

Figure 59–6. Unicornuate uterus with a noncommunicating rudimentary horn. An off-axis (oblique) T2-weighted fat-saturated image (TR 3500/TE 90/180 degrees) shows a hypoplastic left uterine horn *(curved arrow)* that does not communicate with the normal right uterine horn *(arrowheads).* Both uterine horns are deviated laterally.

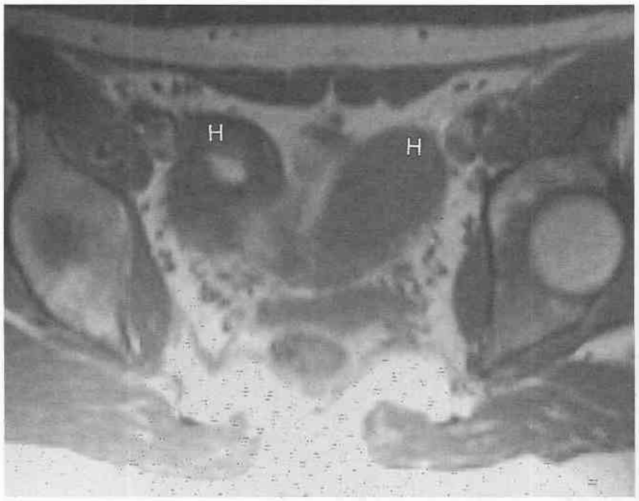

Figure 59–7. Uterus didelphys. Axial T1-weighted (600/15) MR image demonstrates duplicated uterine horns (H) with a widened intercornual distance. Fatty tissue is noted between the two horns. The high-signal-intensity focus within the right endometrial cavity represents blood. (From Siegel MJ: Pediatric applications. In Lee KRL, Sagel SS, Stanley RJ, Heiken JP [eds]: Computed Body Tomography with MRI Correlation. Philadelphia, Lippincott-Raven, 1998, p 1549.)

horns are widely divergent with an intercornual angle of more than 75 degrees (Fig. 59–7). Each horn has a fusiform shape, convex lateral margins, and a central endometrial cavity surrounded by a junctional zone. In each uterus, the endometrial-myometrial width and ratio are preserved.[11] There is no effective surgical repair for uterus didelphys.

Bicornuate Uterus

The anomaly known as bicornuate uterus is due to a lack of fusion of the uterine corpus; there is a single cervix (Fig. 59–8). MRI features of a bicornuate uterus are a concave fundal contour (instead of the normal outward fundal convexity) and a deep cleft (>1 cm) between the two uterine bodies.[11, 28, 43] The tissue between the two horns is composed of myometrium and thus typically enhances on CT (see Fig. 59–8); it has an intermediate signal intensity on T1-weighted images and a higher signal intensity on T2-weighted images. The endometrial-myometrial ratio and width are normal.[11] The bicornuate uterus is treated with transabdominal surgical resection of the muscular division between the two sides of the uterus to fuse the two horns (metroplasty).

Septate Uterus

The septate uterus is the most common müllerian anomaly. It is characterized by a single uterus, cervix, and vagina with a septum that divides the uterus into two compartments. The anomaly results from partial or complete failure of resorption of the midline septum. On MRI scans, there is a single uterine fundus with a normal convex fundal contour or minimal (>1 cm) concavity and a normal intercornual distance.[11] Signal intensity of the septum depends on the relative amounts of fibrous tissue or myometrium. A fibrous septum has a relatively low signal intensity

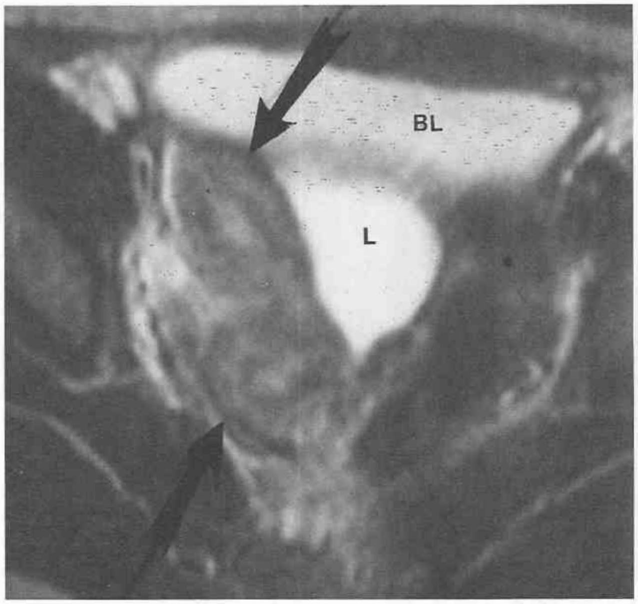

Figure 59–8. Bicornuate uterus. T2-weighted (2500/90) MR image shows two uterine bodies *(arrows)* separated by intermediate-signal-intensity myometrium. The fundal contour is concave, and there is a deep cleft between the two uterine horns. The uterine horns are of a similar size and have differentiated zonal anatomy. The high-signal-intensity fluid collection to the left of the duplicated uterus represents a lymphocele (L). BL, bladder.

on both T1-weighted and T2-weighted sequences, whereas myometrium has a bright signal on T2-weighted images (Fig. 59–9). The treatment of the septate uterus is hysteroscopic metroplasty.[11]

Vaginal Anomalies

Congenital Vaginal Obstruction

Congenital anomalies of the vagina can be classified into two groups: those in which the vagina is absent and those in which the vagina is obstructed because of transverse membranes or septa. Vaginal atresia is the result of arrested development of the sinovaginal bulb or primitive vagina, whereas the development of transverse vaginal membranes or septa is secondary to errors in canalization.

Vaginal obstruction can be encountered in the neonatal period or at menarche. In the neonate, vaginal obstruction is caused by vaginal or cervical atresia, high-grade stenosis, a transverse septum, or an imperforate membrane. In adolescent girls, vaginal obstruction is most often the result of a simple imperforate membrane or septum. Affected neonates present with a palpable pelvic or abdominal mass resulting from the production and excessive accumulation of vaginal and/or uterine secretions in utero secondary to maternal hormone stimulation. Adolescent patients present with cyclic lower abdominal pain or a mass and a history of absent menses. There is an increased association of congenital anomalies (e.g., imperforate anus, esophageal or duodenal atresia, congenital heart disease, and renal abnormalities) in neonates with vaginal atresia but not in patients with imperforate hymen.

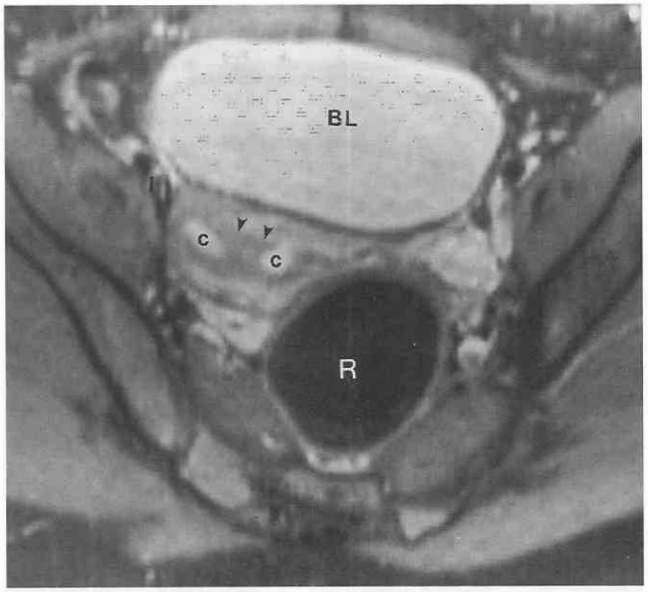

Figure 59–9. Septate uterus in a 15-year-old girl. T2-weighted (2500/90) MR image shows duplicated uterine cavities (c). The uterine contour *(arrowheads)* is normal. The septum has an intermediate signal intensity because it contains some myometrial tissue. The rectum (R) is dilated because of rectal stenosis related to repair of imperforate anus. The diagnosis of septate uterus is best made on the basis of demonstration of a normal or minimally concave fundus. BL, bladder. (From Siegel MJ: Pediatric applications. In Lee KRL, Sagel SS, Stanley RJ, Heiken JP [eds]: Computed Body Tomography with MRI Correlation. Philadelphia, Lippincott-Raven, 1998, p 1549.)

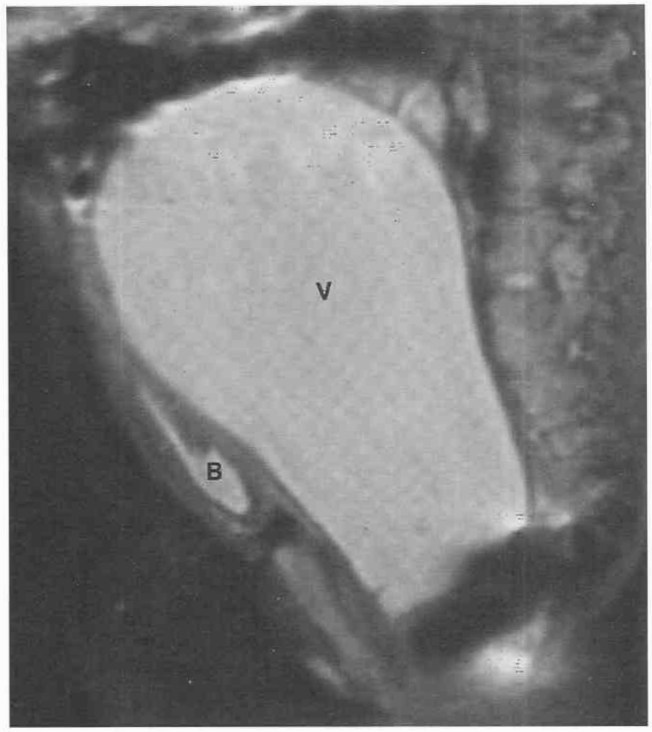

Figure 59–10. Hydrocolpos in a young girl with a large pelvic mass after resection of a sacrococcygeal teratoma. Sagittal T2-weighted fat-saturated (5000/120/180 degrees) image shows high-signal-intensity fluid in the dilated vaginal canal (V) posterior to the bladder (B). The hypointense band overlying the distal vagina represents a susceptibility artifact from a metallic clip.

The CT findings of *hydrocolpos* (dilated vagina) or *hydrometrocolpos* (dilated vagina and uterus) are those of a tubular, fluid-filled, midline mass between the bladder and rectum. The distended vagina has a thin, barely perceptible wall, whereas the uterus has a thicker muscular wall that enhances after IV administration of contrast medium. The MRI appearance of hydrocolpos and hydrometrocolpos varies with the nature of the vaginal contents. Serous fluid has a low signal intensity on T1-weighted images and a high signal intensity on T2-weighted images (Fig. 59–10). The signal intensity increases on T1-weighted images if the contents are hemorrhagic.[30] Additional findings on CT and MRI include hydrosalpinx or hematosalpinx, ureterectasis, and hydronephrosis.

Pelvic Masses

Masses within the osseous pelvis may arise in the anterior pelvis and be of gynecologic, nodal, or lower urinary tract origin, or they may arise in the presacral space. The latter tumors are neurogenic or embryonic in origin. When a pelvic mass is detected on physical examination or another radiologic study, further characterization of the mass and delineation of its cause and extent are possible with ultrasonography, CT, and MRI.[57–63, 65, 67]

Ultrasonography is used initially in the evaluation of most children with a suspected pelvic mass because it is easy to perform and ionizing radiation is not required. It is accurate in the diagnosis of gynecologic disease, but it is not as useful in determining the extent of gynecologic disease or in identifying presacral masses. Both CT and MRI can delineate the size and character of a mass and its relationship to adjacent pelvic viscera and soft tissue structures. In general, CT is more sensitive than MRI in demonstrating bone involvement, calcifications, and gas bubbles, whereas MRI is superior in detecting soft tissue invasion and bone marrow alterations and in displaying the extent of a presacral mass. CT is recommended for staging patients with gynecologic malignancies; MRI is preferred in patients with presacral mass lesions.

Ovarian Masses

Ovarian Cysts

Follicular and Corpus Luteum Cysts

Non-neoplastic cysts account for 25% to 35% of ovarian masses in children, of which half are follicular and half are luteal or paraovarian cysts.[50] Follicular and corpus luteum cysts result when a follicle continues to grow after failed ovulation or fails to collapse after ovulation occurs. The cysts can vary in size from 3 to 20 cm, but most are usually between 3 and 5 cm.[59] *Follicular cysts* contain clear serous fluid. *Corpus luteal cysts* can contain serous or hemorrhagic fluid. Both types of cysts may be discovered incidentally by pelvic ultrasonography, CT, or MRI, or they

may present as lower abdominal or pelvic pain secondary to mass effect, hemorrhage, or torsion.

CT is not usually needed for diagnosis, but recognition of the appearance of ovarian cysts is important because they are often unsuspected findings on CT studies obtained for other clinical indications. In patients with large ovarian cysts, CT may be requested as a primary study to document the exact location or extent of the cyst before aspiration or surgery.

Uncomplicated ovarian cysts appear as well-circumscribed, low-attenuation (<20 Hounsfield units) unilocular masses with thin walls that do not enhance after IV contrast administration (Fig. 59–11). A fluid-debris level, septa, or thick walls should raise the suspicion of a hemorrhagic cyst or adnexal torsion with the cyst acting as a fulcrum (Fig. 59–12). On MRI, the cysts demonstrate a low signal intensity on T1-weighted images and a high signal intensity on T2-weighted sequences.[45, 78] Follicular and corpus luteal cysts cannot be differentiated on the basis of the CT findings alone. Both types of cysts usually involute spontaneously.

Multiple Ovarian Cysts

The differential diagnosis of the ovary with multiple follicles includes theca-lutein cysts and the spectrum of polycystic ovary disease.

Theca-lutein cysts are believed to represent hyperstimulated follicles and are most often seen in adolescent girls or women who have gestational trophoblastic disease or who are taking drugs to stimulate ovulation. In patients with theca-lutein cysts, both ovaries are enlarged and contain multiple cysts. Other ancillary findings are those related to the molar pregnancy, which include an enlarged, thick-walled uterus and dilated parametrial vessels.

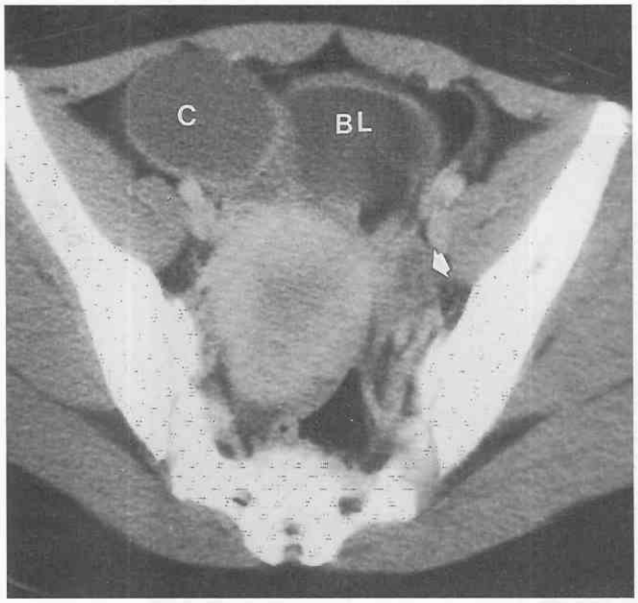

Figure 59–11. Benign ovarian cyst. Contrast-enhanced CT scan of a 14-year-old girl with pelvic pain and a mass shows a well-circumscribed, round, nonenhancing mass of near-water attenuation arising from the right ovary consistent with a cyst (C). The cyst measures 5 × 4 cm. Note the normal uterus and left ovary (*arrow*). BL, bladder.

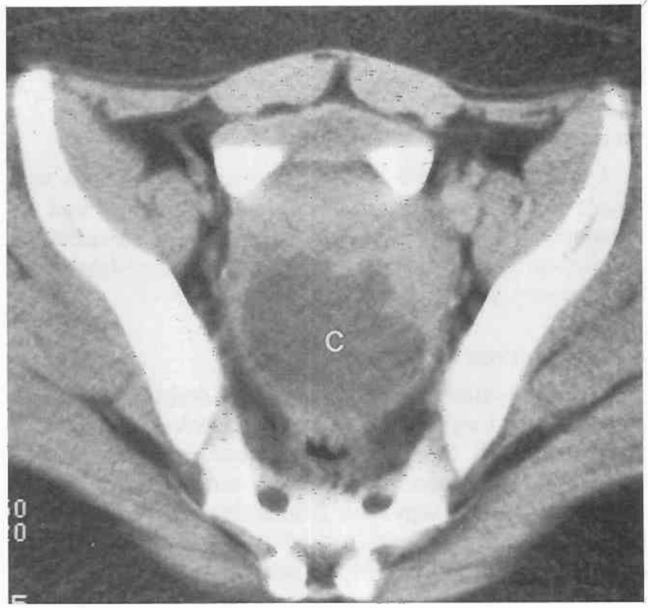

Figure 59–12. Atypical ovarian cyst secondary to torsion. Contrast-enhanced CT scan in a 13-year-old girl shows a cystic mass (C) with thick enhancing walls posterior to the urinary bladder. A torsed right ovary containing a hemorrhagic corpus lutein cyst was found at surgery.

Polycystic ovary disease, also known as the *Stein-Leventhal syndrome*, is characterized by amenorrhea, obesity, hirsutism, and chronic anovulation. Consistent pathologic features are hyperstimulated ovarian stroma and an increased number of immature and atretic follicles.

The characteristic CT findings of gestational trophoblastic disease and polycystic ovary disease are bilaterally enlarged ovaries that contain multiple small cysts.[15, 44] In some patients with cystic ovary disease, the ovaries may be of normal size or the cysts may be too small to be recognized on CT or MRI, and the diagnosis can be made only with biopsy.

Hemorrhagic Cysts

Hemorrhagic cysts develop when blood vessels within a follicular or corpus luteal cyst rupture. Patients may present with the sudden onset of pelvic pain. The appearance of hemorrhagic cysts on CT and MRI depends on the age of the clot. On CT scan, acute hemorrhage has a high attenuation value; old blood has an attenuation value near that of water density. On MRI, subacute blood is typically bright on both T1-weighted and T2-weighted images, related to the formation of methemoglobin.[45, 78] Acute blood that contains intact red blood cells can have a high signal on T1-weighted images but a low signal intensity on T2-weighted or gradient-echo images. The high signal intensity of subacute blood on T1-weighted images can mimic the appearance of fat.

Fat-suppressed and gradient-echo images can help to differentiate between hemorrhagic cysts and fat-containing tumors, such as teratomas. Serial imaging, usually with sonography, also can be useful to exclude neoplasm. Most

hemorrhagic ovarian cysts resolve in one or two menstrual cycles, whereas tumor remains unchanged or increases in size.

Ovarian Tumors

Approximately 65% to 80% of ovarian tumors are true neoplasms, of which approximately 65% are benign and the remainder are malignant.[8, 17, 50] The most common benign ovarian tumor is a *cystic teratoma*. *Cystadenomas* occur less frequently.

Cystic Teratoma

Ovarian teratomas (cystic teratomas, dermoid cysts) are congenital lesions that contain tissue derivatives from all three germ cell layers (endoderm, ectoderm, and mesoderm). On pathologic examination, teratomas are subdivided into mature, immature (containing embryonic neural elements), and malignant types.[8, 13] The first subtype accounts for more than 90% of ovarian germ cell tumors. Ovarian teratomas usually present as a pelvic or an abdominal mass, but they may produce pain if the tumor undergoes torsion, rupture, or hemorrhage. They usually range in diameter from 5 to 10 cm and are bilateral in 25% of cases.

On CT scans, the benign teratoma appears typically as a well-circumscribed, predominantly cystic mass (i.e., <50% soft tissue elements) that has smooth walls (2 to 5 mm thick). A specific diagnosis of a benign ovarian teratoma can be made on CT or MRI when fatty elements or a combination of fatty and calcific elements are identified within a predominantly cystic mass[9, 51, 56] (Fig. 59–13). In one series of 43 cystic teratomas (41 benign and 2 malignant) imaged with CT, fat was seen in 93%, Rokitansky protuberances in 81%, teeth or calcific elements in 56%, and a fat-fluid level in 12% of lesions.[9] Calcific elements and fat are usually located in the Rokitansky protuberance or dermoid plug arising from the cyst wall. Occasionally, the intracystic fat is mobile and shifts position.[46]

Typically, benign teratomas are predominantly hypointense on T1-weighted images and markedly hyperintense on T2-weighted images, indicating that the cystic cavity contains aqueous fluid.[45, 70, 77] Foci of fatty tissue have a high signal intensity on both T1-weighted and T2-weighted images, whereas calcifications, teeth, bone, hair, and fibrous tissue show low signal intensity on both pulse sequences. Gradient-echo and fat-suppression techniques are the best sequences to confirm the presence of lipid contents.[66] Other MRI findings of cystic teratomas include fat-fluid levels and gravity-dependent or floating debris.[70]

Malignant Neoplasms

Ovarian tumors account for 1% to 2% of malignant neoplasms in girls younger than age 17 years.[8, 12, 13, 50] Germ cell tumors (dysgerminoma, immature or malignant teratoma, endodermal sinus tumor, embryonal carcinoma, and choriocarcinoma) account for 60% to 90% of malignant neoplasms; stromal tumors (Sertoli-Leydig cell, granulosa-theca cell, and undifferentiated neoplasms) have a 10% to 13% incidence; and epithelial carcinomas account for 5% to 11% of malignant ovarian lesions.[8, 13, 17, 50]

Most ovarian neoplasms present in adolescent girls as asymptomatic pelvic or abdominal masses. Isosexual precocity may be a presenting sign in patients with granulosa-theca cell tumors, whereas virilization may be observed in patients with Sertoli-Leydig cell tumors.[12, 13] Levels of alpha-fetoprotein can be elevated in patients with endodermal sinus tumors, whereas levels of beta-human choriogonadotropin levels increase in patients with embryonal carcinoma and choriocarcinoma.[50] Treatment is by complete resection when possible. Otherwise, surgical debulking or biopsy is performed, followed by chemotherapy and definitive resection.

In general, malignant ovarian lesions appear as large, solid masses (>50% soft tissue elements) with thick, irregular walls.[7, 10] Other common findings include focal low-

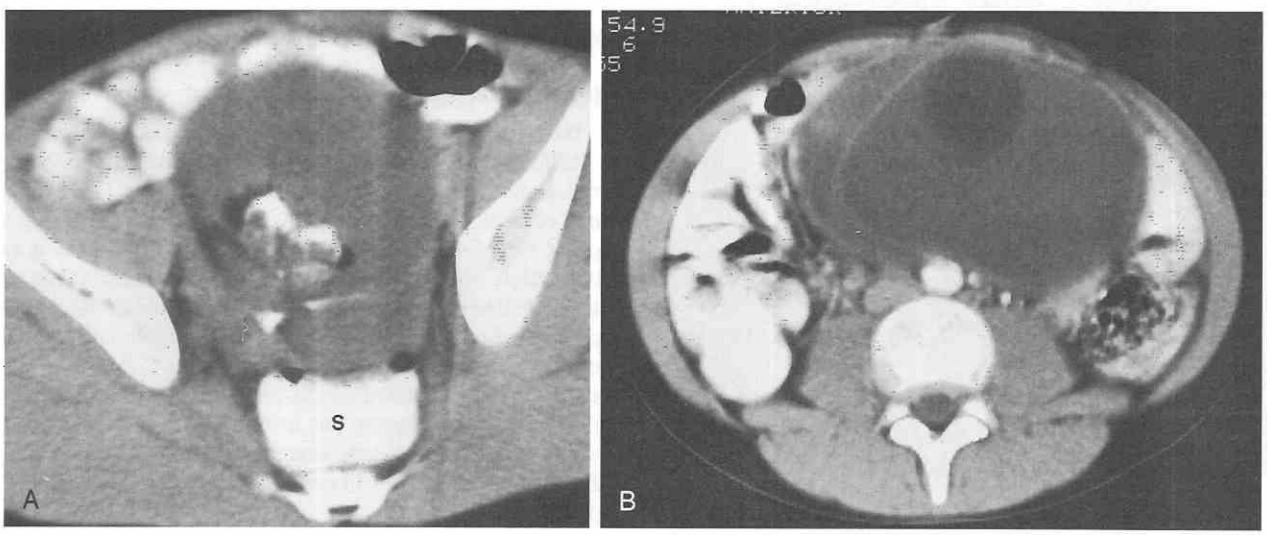

Figure 59–13. Benign ovarian teratoma in 15-year-old girl with pelvic pain. *A*, Contrast-enhanced CT shows a well-defined, low-attenuation mass anterior to the sigmoid (S) colon. Toothlike calcifications and fatty tissue are seen within the mass. On pathologic section, the teratoma contained predominantly sebaceous fluid and small amounts of hair, bone, and fat within several mural nodules. *B*, CT scan in another patient shows a low-attenuation mass with a septation and an intracystic fat ball.

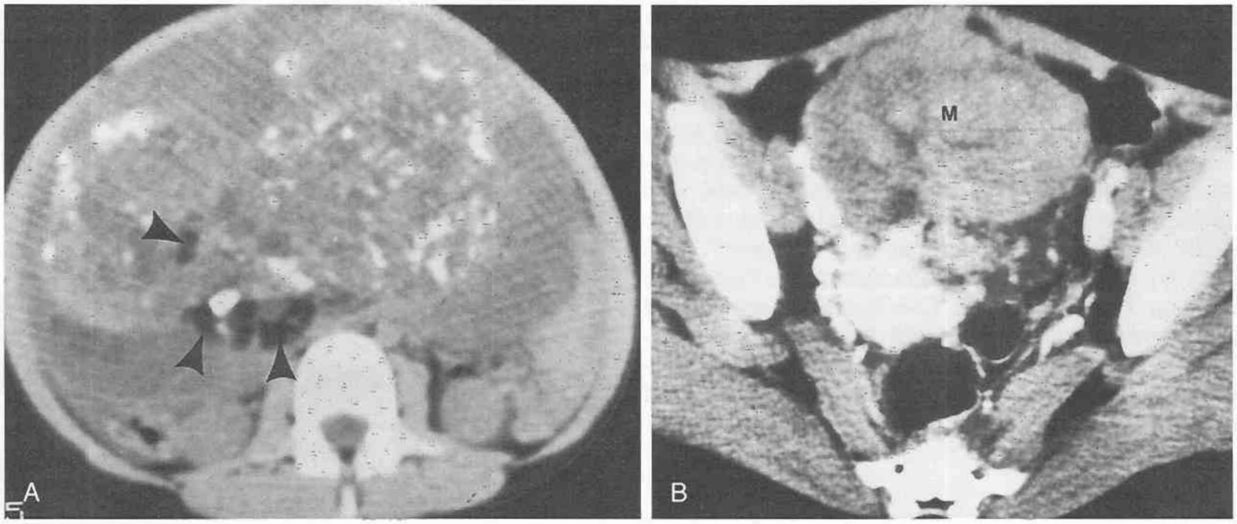

Figure 59–14. Malignant ovarian germ cell tumors. *A,* Teratocarcinoma in a 11-year-old girl. CT scan shows a large solid mass with large amounts of calcification and scattered areas of fatty tissue *(arrowheads). B,* Dysgerminoma in a 13-year-old girl. Contrast-enhanced CT demonstrates a bulky, slightly heterogeneous mass (M) of soft tissue attenuation in the anterior pelvis.

attenuation areas due to necrosis or hemorrhage, calcifications, thick septa, and papillary projections[7, 10, 51] (Fig. 59–14). On MRI, malignant ovarian neoplasms have a low to intermediate signal intensity on T1-weighted images and intermediate or high signal intensity on T2-weighted images.[24]

The malignant germ cell and stromal neoplasms spread by contiguous extension, by lymphogenous spread to regional or distant lymph nodes, or by hematogenous dissemination to lungs or liver. Ovarian carcinomas tend to spread by seeding the peritoneal or omental surfaces. Peritoneal tumor implants are seen as soft tissue nodules on the lateral peritoneal surfaces or in the ligaments and mesenteries of the abdomen on CT and as medium signal intensity nodules on MRI.[24] Omental implants appear as discrete nodules or as conglomerate soft tissue masses ("omental cake") beneath the anterior abdominal wall. They have a soft tissue attenuation on CT (Fig. 59–15) and a medium signal intensity on MRI. Peritoneal and omental implants may enhance after IV contrast medium administration.

Other Adnexal Masses

Adnexal Torsion

Adnexal torsion is most commonly encountered after menarche. Patients present with acute or recurrent pelvic pain. Torsion results from rotation of the ovary or fallopian tube on its vascular pedicle, which causes compromise of lymphatic, venous, and arterial flow, and, ultimately, infarction. Torsion can occur in the presence of normal adnexa or in association with an underlying mass, most often a teratoma or ovarian cyst, which acts as a fulcrum. The diagnosis usually is suggested by ultrasonography,[64] but CT or MRI may be useful when a sonogram is indeterminate.

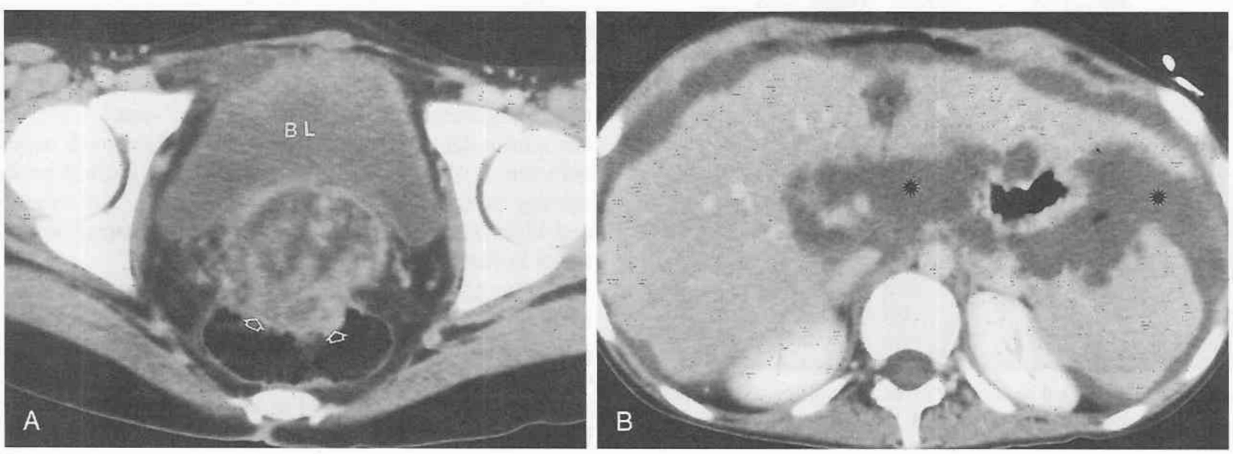

Figure 59–15. Mucinous ovarian carcinoma. *A,* Contrast-enhanced CT scan of a 14-year-old girl with abdominal distention and weight loss shows a complex cystic and solid mass behind the bladder (BL). The tumor has invaded the rectum *(open arrows)* and extended into the parametrial fat. *B,* At a more superior level, there is a soft tissue omental mass ("omental cake") anterior to the liver and the mesenteric implants *(asterisks).*

On both CT and MRI, the edematous and usually hemorrhagic ovary is enlarged and may contain multiple, peripheral cystic structures that represent dilated follicles[5] (Fig. 59–16). The involved ovary also may assume a midline position, either behind the bladder or cephalad to the uterus. Other findings include engorgement of blood vessels on the affected side, a thickened fallopian tube with hemorrhage, a small amount of ascites, obliteration of the pelvic fat planes, and an underlying cyst or tumor.[23, 34] On MRI, the enlarged ovary usually demonstrates a high signal intensity on T1-weighted and T2-weighted images related to the presence of subacute hemorrhage and edema.[34] Viable ovarian tissue demonstrates some degree of enhancement on CT and MRI. The lack of enhancement of mural nodules or septa appears to be diagnostic of infarction.[34]

Tubo-ovarian Abscess

Pelvic inflammatory disease affects girls of reproductive age and is usually due to *Neisseria gonorrhoeae* or *Chlamydia trachomatis*.[26] The inflammatory process begins in the vagina and cervix and then ascends to the endometrium and fallopian tubes, where it can spread to the ovaries, parametrium, and peritoneal cavity. The diagnosis is usually made clinically. Sonography is used to identify complications such as pyosalpinx, tubo-ovarian abscess, and cul-de-sac abscess and to assess the response to treatment. CT has a role in evaluating the extent of adnexal and peritoneal abscesses.

The CT appearance of an tubo-ovarian abscess is a round, thick-walled, fluid density mass in an adnexal location[18, 74] (Fig. 59–17). Internal septations are common, and

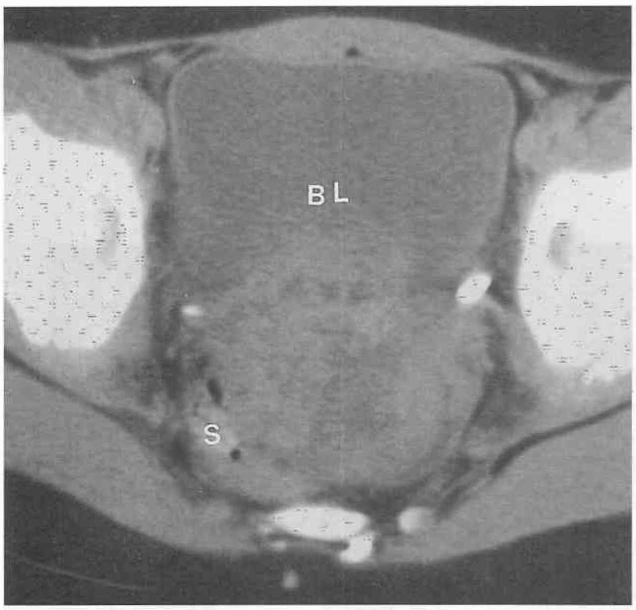

Figure 59–16. Adnexal torsion in a 14-year-old girl with acute pelvic pain suspected to be caused by appendicitis. Contrast-enhanced CT shows an enlarged, nonenhancing mass of soft tissue density posterior to the urinary bladder (BL), corresponding to the left ovary. The low-attenuation areas *(arrows)* within the mass represent dilated follicles. An infarcted left ovary was confirmed surgically. S, sigmoid colon.

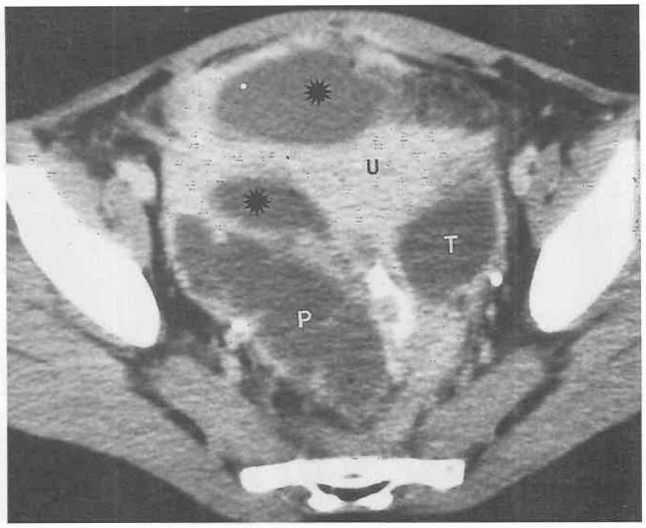

Figure 59–17. Pelvic inflammatory disease. Contrast-enhanced CT scan in a 17-year-old girl reveals a dilated right fallopian tube consistent with pyosalpinx (P), a round fluid-filled mass in the left adnexal region consistent with a tubo-ovarian abscess (T), and two pelvic abscesses (*asterisks*). Both lesions were confirmed surgically. The pelvic fat planes are obliterated. U, uterus.

air or an air-liquid level also may be noted. Pyosalpinx should be considered when a tubular fluid-filled adnexal mass is seen[74] (see Fig. 59–17). Loss of the fat planes that interface with the uterus, ureterosacral ligament thickening, increased density in the pelvic fat, narrowing or irregularity of the rectosigmoid colon, bilateral or unilateral hydronephrosis and hydroureter, and lymphadenopathy are additional evidence for pelvic inflammatory disease.[74] In selected patients, CT may be used to guide percutaneous drainage of pelvic abscesses.

MRI is not usually indicated for the evaluation of tubo-ovarian abscess.

Prostate and Vagina

Rhabdomyosarcoma is the most common tumor of the genitourinary tract in children, accounting for 5% to 15% of all malignant solid tumors in patients younger than 15 years.[38, 73] The median age of presentation of children with rhabdomyosarcoma is approximately 7 years.[2] The tumor has a bimodal age distribution, with the first peak occurring between 2 and 6 years of age and the second peak occurring between 14 and 18 years of age. The embryonal and botryoid subtypes are the predominant histologic subtypes in the genitourinary tract.

In the genitourinary tract, rhabdomyosarcoma can arise in the prostate, bladder, and vagina. Most patients with prostatic or bladder rhabdomyosarcoma present with signs of urinary retention. Females with gynecologic rhabdomyosarcoma come to clinical attention because of vaginal bleeding or a mass that prolapses into the introitus or onto the perineum. Rhabdomyosarcoma spreads via direct extension to contiguous structures or via hematogenous or lymphatic dissemination to lymph nodes, lungs, bone, bone marrow, or liver.[2, 38, 50, 73] Between 10% and 20% of all

patients with rhabdomyosarcoma have metastases at the time of diagnosis. The overall 3-year survival rate is between 73% and 89%.[2]

Whenever possible, surgical excision is the initial treatment of choice. In patients with bulky nonresectable tumor, the initial treatment is chemotherapy followed by excision of residual disease. Radiation is added if there is still residual tumor. The goal of treatment is to minimize radical surgery and to preserve the major pelvic organs.

Imaging Findings

On CT scans, prostatic rhabdomyosarcoma is manifested as a bulky soft tissue mass that may elevate the bladder base and elongate the prostatic urethra (Fig. 59–18*A*). Vaginal rhabdomyosarcoma results in a soft tissue mass that enlarges the vaginal lumen[3, 69] (Fig. 59–19). Secondary findings include uterine enlargement and fluid collections in the endometrial cavity when there is obstruction of the

Figure 59–18. Prostatic rhabdomyosarcoma in a 3-year-old boy with urinary retention. *A,* CT scan shows an enlarged prostate gland (P) between the rectum (R) and the bladder. The planes between the mass and obturator internus muscles (pelvic side walls) are obliterated. *Open arrow* indicates bladder catheter. Coronal T1-weighted (*B*) (400/15) and T2-weighted fat-saturated (*C*) (TR 2500/TE 90/180 degrees) images show a large prostatic mass (P) extending laterally to the pelvic side walls. There are enlarged iliac lymph nodes *(arrows)*. Invasion of pelvic side walls and lymph nodes was confirmed at surgery.

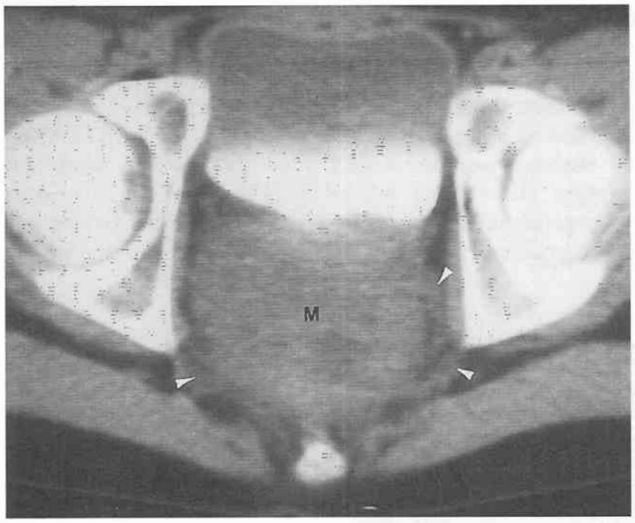

Figure 59–19. Vaginal rhabdomyosarcoma in a 13-year-old girl with vaginal bleeding. CT scan shows a bulky, soft tissue mass (M) that expands the vagina and infiltrates the pelvic fat *(arrowheads)*.

cervix by the tumor. Both prostatic and vaginal tumors may invade the bladder base or obstruct the ureters, leading to hydronephrosis.

On MRI, rhabdomyosarcoma demonstrates a low signal intensity on T1-weighted sequences and a high signal intensity on T2-weighted MRI images[21] (Fig. 59–18*B* and *C*). Tumor heterogeneity secondary to necrosis and calcification are common. The tumor typically shows enhancement at MRI and CT after IV contrast medium administration.

The presence of fat planes between the neoplasm and adjacent structures militates against gross invasion, but the absence of fat planes may be normal or due to adherence or invasion. When the loss of fat planes is associated with an eccentric soft tissue mass, a confident diagnosis of extravaginal or prostatic extension can be made. CT is useful in determining the extent of both regional and retroperitoneal lymph node enlargement and is the study of choice for the detection of pulmonary metastases. Lymphadenopathy has a spectrum of appearances, ranging from small discrete nodules to large conglomerate masses (Fig. 59–18*C*).

Other Vaginal and Uterine Neoplasms

Adenocarcinoma is a rare neoplasm of the vagina in childhood. The imaging features are similar to those of rhabdomyosarcoma.

Gestational trophoblastic disease can be a cause of an intrauterine mass in an adolescent girl. It represents a spectrum of tumors varying from the benign hydatidiform mole to the more malignant invasive mole and choriocarcinoma.[27, 54, 71] The clinical features of trophoblastic disease are vaginal bleeding and elevated levels of serum human chorionic gonadotrophin.

CT and MRI are more useful than sonography in the evaluation of molar disease by better defining tumor extent. On CT, the uterus often is enlarged and shows heterogeneous contrast enhancement with central areas of lower attenuation or hypoattenuating foci in the myometrium.[27, 54, 71] On MRI, the trophoblastic neoplasm appears as a heterogeneous mass of low signal intensity on T1-weighted images and of high signal intensity on T2-weighted images.[27, 71] Numerous cystic spaces are usually present within the mass. Other findings on CT and MRI examinations include a gestational sac, with or without a small fetal pole or immature fetus; tortuous dilated parametrial vessels; and enlarged ovaries that contain multiple theca-lutein cysts. Local invasion is suggested by the presence of parametrial extension. Distant metastases to the liver and lung are seen in *choriocarcinoma*.

Urinary Bladder

Bladder Neoplasms

Malignant Tumors

Rhabdomyosarcoma is the most common bladder tumor in childhood. The pathology and staging systems for rhabdomyosarcoma are similar to those described for vaginal and prostatic rhabdomyosarcoma. Symptoms of bladder rhabdomyosarcoma include a palpable pelvic mass, hematuria, increased frequency, and urinary retention.[73]

On CT and MRI, bladder rhabdomyosarcoma appears as a sessile or polypoid soft tissue mass that deforms the bladder base. It often projects into the bladder lumen (botryoid, or "bunch of grapes" appearance). Central necrosis and hemorrhage are other common findings. With MRI, rhabdomyosarcoma shows low signal intensity on T1-weighted images and intermediate or high signal intensity on T2-weighted images. The tumor enhances after the IV administration of iodinated contrast medium or Gd-chelate compounds. Transitional cell carcinoma and leiomyosarcoma are rare bladder neoplasms in childhood. On CT and MRI, they produce focal or diffuse wall thickening or a sessile or polypoid mass.

Benign Tumors

Hemangioma, neurofibroma, pheochromocytoma, and leiomyoma of the bladder are rare neoplasms of the urinary bladder. In general, the CT and MRI features of these tumors are similar and include a sessile or polypoid mass that arises within the bladder wall and projects into the bladder lumen. If the tumor shows intense contrast enhancement, the diagnosis of hemangioma and pheochromocytoma should be considered. Tumor distribution along the neurovascular bundles is a finding of neurofibromatosis.

Urachal Anomalies

Embryologically, the anterior bladder wall and umbilicus communicate with each other via a tubular channel (i.e., the urachus). This channel closes before birth. Failed obliteration of the urachal lumen results in four major types of anomalies:

1. The patent urachus, a persistent fistula between the bladder and umbilicus.
2. The urachal sinus, persistence of the urachus at its umbilical end.

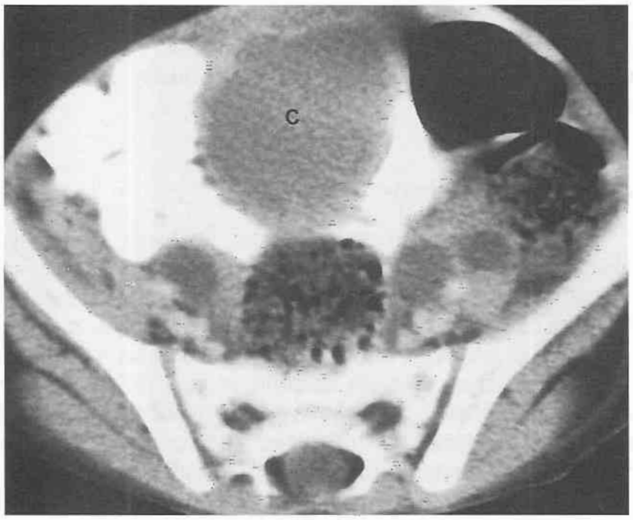

Figure 59–20. Urachal cyst. Contrast-enhanced CT scan shows a round, midline fluid-filled cyst (C) with thin, smooth walls just beneath the rectus abdominis muscles. The cyst did not communicate with either the bladder or the umbilicus.

3. The urachal diverticulum, persistence of the urachus at its bladder end.
4. The urachal cyst, an encapsulation of fluid within a portion of the urachus that is closed at both the cranial and caudal ends.

The persistent urachus and the urachal sinus are small-caliber tubular structures that are best evaluated with fistulography.[47] The urachal cyst and diverticulum are closed fluid-filled spaces that can be easily identified with sonography and CT.

On CT, the urachal diverticulum has a wide communication with the bladder dome and empties when the bladder is emptied. The urachal cyst appears as a midline thin-walled, fluid-filled mass beneath the rectus abdominis muscle (Fig. 59–20). Increased density or heterogeneous fluid contents and cyst wall thickening may be seen with infection (pyourachus) or hemorrhage. Additional findings of pyourachus include bladder wall thickening, increased attenuation of the subcutaneous or mesenteric fat, rectus muscle thickening (Fig. 59–21), intraperitoneal abscess, and a small amount of ascites.[29]

Other Pelvic Masses

Pelvic lymph node enlargement, abscess, hematoma, and urinoma are additional causes of a pelvic mass. CT can help establish the true nature of these abnormalities when sonography is indeterminate or suboptimal because of abundant intestinal gas, obesity, or overlying dressings or drainage tubes that impede sound transmission. MRI does not have a major role in evaluation of these lesions.

Pelvic lymph nodes are found along the course of the internal and external iliac veins and the femoral veins. The CT appearance of lymphadenopathy varies from a small number of discretely enlarged lymph nodes to a large conglomerate mass, in which individual nodes are no longer recognizable, obscuring the contours of normal surrounding structures (Fig. 59–22).

A mature abscess usually has a soft tissue rim that enhances after IV contrast medium administration and a fluid-filled center that may contain fluid or fluid mixed with gas, in the form of either small bubbles or an air-fluid level. The diagnosis of an abscess can be made with confidence if gas bubbles are demonstrated within an extraintestinal mass. In the absence of gas bubbles, an abscess may be indistinguishable from a urinoma or seroma. The latter masses should be considered when CT scans show a near-water-attenuation mass with thin or

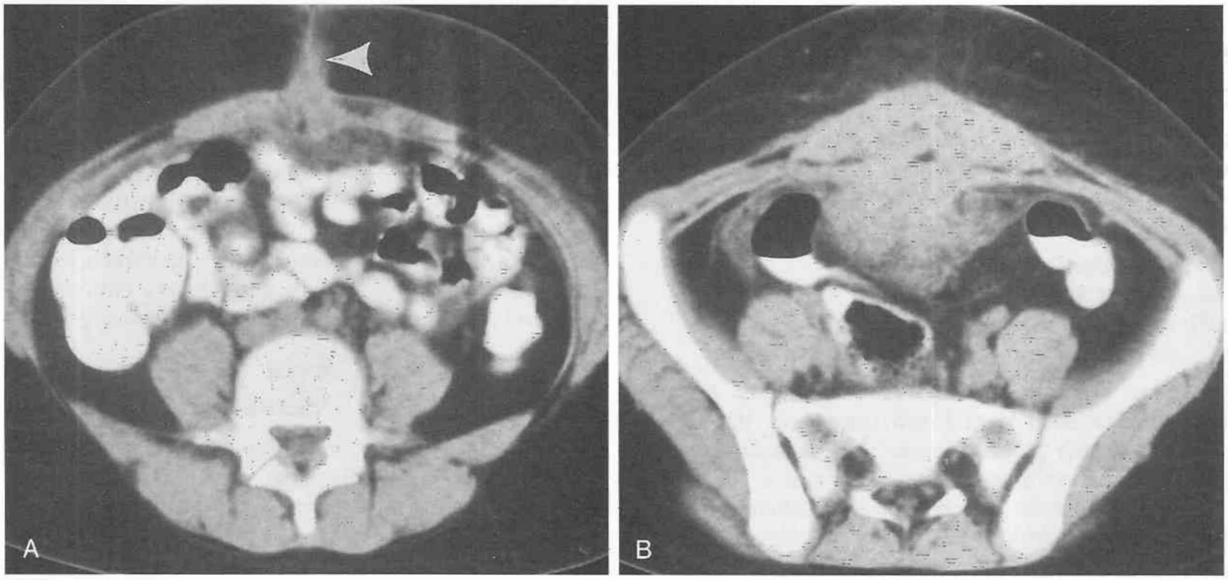

Figure 59–21. Pyourachus on serial CT scans. *A,* CT scan just below the level of the umbilicus shows a thickened fistulous tract *(arrowhead)* between the anterior abdominal wall and the rectus abdominis muscles. *B,* A more inferior CT scan shows inflammatory infiltration of the abdominal wall as well as a large heterogeneous midline mass deep to the rectus muscles.

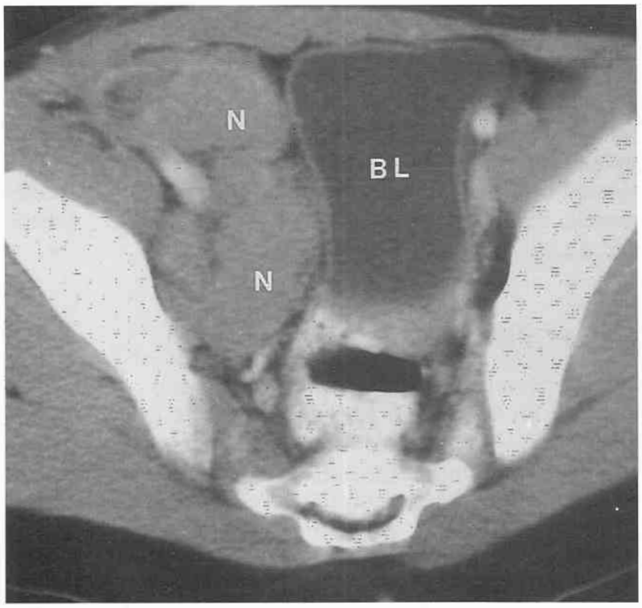

Figure 59–22. Lymphadenopathy secondary to Hodgkin's disease in a 13-year-old girl. Enlarged pelvic lymph nodes (N) cause compression and displacement of the urinary bladder (BL).

barely perceptible walls. Correlation with clinical history and physical examination and sometimes biopsy of the lesion will be required for diagnosis.

On CT, a hematoma appears as an abnormal soft-tissue mass, enlarging, obliterating, or displacing normal structures. The location and attenuation characteristics depend on the source of the hemorrhage and the age of the extravasated blood. Acute hematoma has an attenuation value that is equal to or greater than that of pelvic muscle, due to the high hemoglobin content.[68] As the hematoma matures, the red blood cells lyse and the attenuation value decreases. A chronic hematoma appears as a well-circumscribed, low-attenuation mass with a higher attenuation rim.

Presacral Tumors

Sacrococcygeal Teratomas

Sacrococcygeal teratomas are the most common tumor of the presacral space in children.[12] Four types of sacrococcygeal teratomas have been described based on the relative amounts of internal and external tumor[13, 72]:

Type I, predominantly external (47%)
Type II, external and intrapelvic (34%)
Type III, external, pelvic, and abdominal (9%)
Type IV, purely presacral (10%)

More than 90% of sacrococcygeal teratomas are detected in the neonatal period and present as large soft-tissue masses in the gluteal region. The diagnosis is often delayed if the tumors are small and confined to the presacral area. These latter patients usually present in later childhood or adolescence with a history of chronic constipation. The incidence of malignant components varies with the extent of the tumor (38% in type IV versus 8% in type I) and patient age at diagnosis. The older the patient at the time of diagnosis, the greater the likelihood of malignant transformation in the tumor. About 20% of all sacrococcygeal teratomas exhibit malignant elements.[13, 72] Malignant tumors metastasize to lung and occasionally to liver or lymph nodes.

Imaging Findings

The diagnosis of sacrococcygeal teratoma is usually obvious when a patient presents with a large pelvic or gluteal mass, but imaging is warranted to determine the full extent of tumor. Both CT and MRI can be used to characterize and stage sacrococcygeal teratomas. Like teratomas elsewhere, benign sacrococcygeal teratomas are mainly fluid-filled[33, 72] and have an attenuation value equal to or slightly above that of water. They contain less than 50% solid elements, in the form of fat, calcification, bone, or teeth. The solid components may appear as a rounded mass that protrudes from a cyst wall, as a bridge or band that crosses the cyst, or as a thickened segment of cyst wall. Calcifications may be amorphous, punctate, or spiculated, or they may resemble bone formation.[72] Although sacrococcygeal teratomas arise from the coccyx, abnormalities of the spine are uncommon.

Benign teratomas typically appear as low-signal-intensity masses on T1-weighted images and as high-signal-intensity masses on T2-weighted images, reflecting their aqueous or sebaceous contents. The signal intensity can be higher than that of simple fluid on T1-weighted images when the cyst contents are proteinaceous or hemorrhagic (Fig. 59–23). Fat appears as a high-signal-intensity focus on T1-weighted and T2-weighted images; calcification, bone, and hair appear as low-signal-intensity foci on both T1-weighted and T2-weighted images.

Similar to teratomas elsewhere in the body, malignant teratomas are predominantly solid masses[33, 51, 72] (Fig. 59–24). Calcifications, common in benign teratomas, are less frequent in the malignant forms. Signs of local extension include intraspinal involvement, soft tissue stranding, or an eccentric soft tissue mass. The tumor metastasizes to the lung and occasionally to the liver or retroperitoneal lymph nodes.

CT suffices for the diagnosis and determination of the extent of benign sacrococcygeal tumors. Because of its superb soft tissue contrast, MRI is the imaging study of choice to determine the extent of a malignant sacrococcygeal teratoma. MRI is superior to CT in the detection of invasion of pelvic soft tissue structures and in the identification of intraspinal involvement.[32] After treatment, malignant sacrococcygeal tumors may regress entirely, leave a small fibrotic mass, or may convert to a mature teratoma.[14]

Other Presacral Masses

Neurogenic tumors, including neuroblastoma and neurofibroma, anterior meningocele, rectal duplication cyst, and lymphoma, are other causes of presacral masses in childhood.

Approximately 5% of neuroblastomas arise in the pelvis. On CT and MRI, pelvic neuroblastomas appear as heterogeneous soft tissue masses with areas of necrosis and amorphous, coarse calcifications (Fig. 59–25). Benign neu-

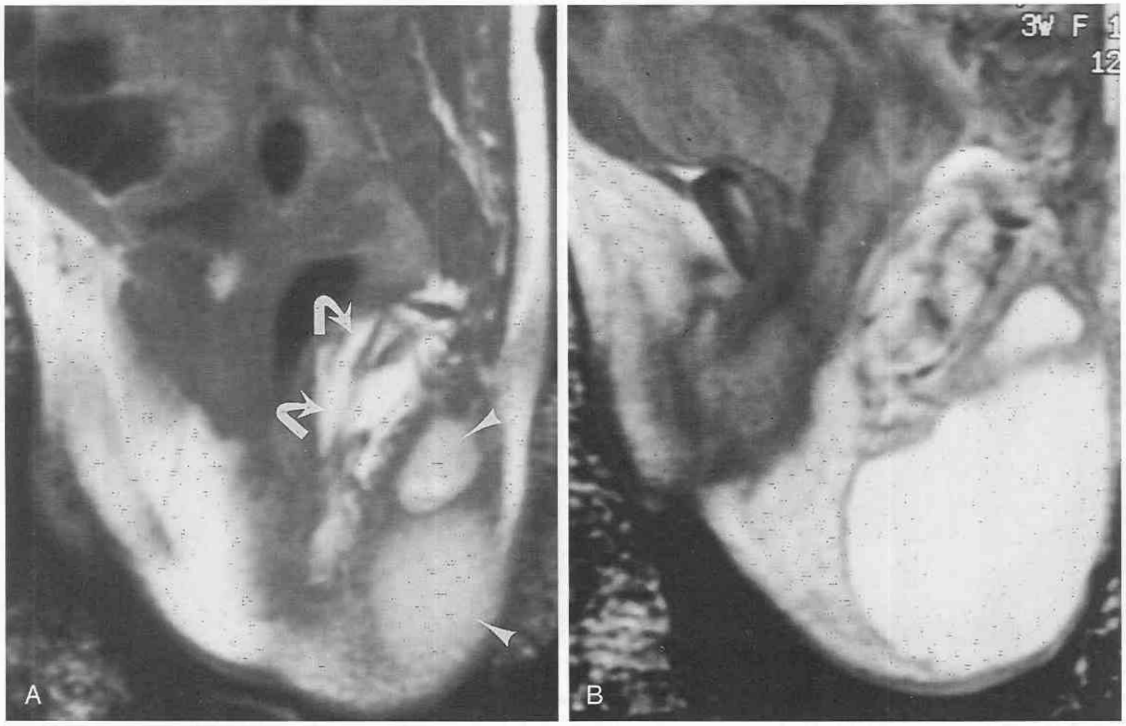

Figure 59–23. Benign sacrococcygeal teratoma. *A,* T1-weighted (500/16) image shows a large pelvic mass with external and presacral components. The presacral components *(curved arrows)* have a high signal intensity similar to that of subcutaneous fat. The larger posterior portion of the mass *(arrowheads)* extending into the gluteal muscles has an intermediate signal intensity. *B,* On a T2-weighted (2500/90) image, the presacral mass again has an intensity equal to that of subcutaneous fat. The extrapelvic portion of the tumor has a signal intensity higher than that of fat, consistent with fluid. A predominantly cystic mass with fat and few soft tissue elements is characteristic of a benign teratoma. (Courtesy of Andrew Landes, M.D., Hollywood, Fla.)

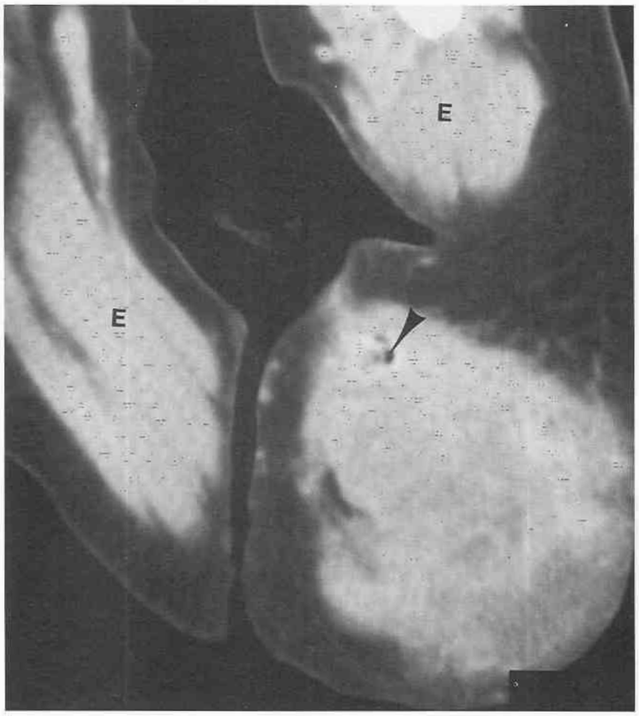

Figure 59–24. Malignant presacral teratoma in a newborn girl with a gluteal mass. CT scan demonstrates a large heterogeneous mass of soft tissue density displacing the gas-filled rectum *(arrowhead)* anteriorly. E, lower extremities.

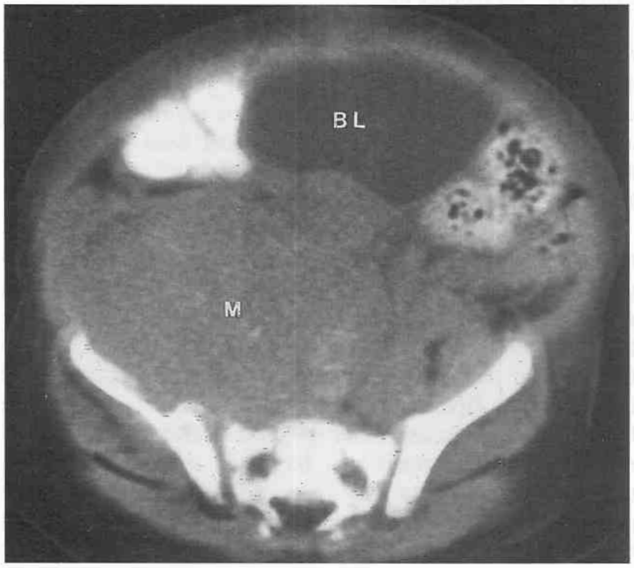

Figure 59–25. Presacral neuroblastoma. Nonenhanced CT shows a large mass (M) of soft tissue attenuation anterior to the sacrum (S) and posterior to the bladder (BL). The tumor has invaded the right sacroiliac joint and the right iliac wing.

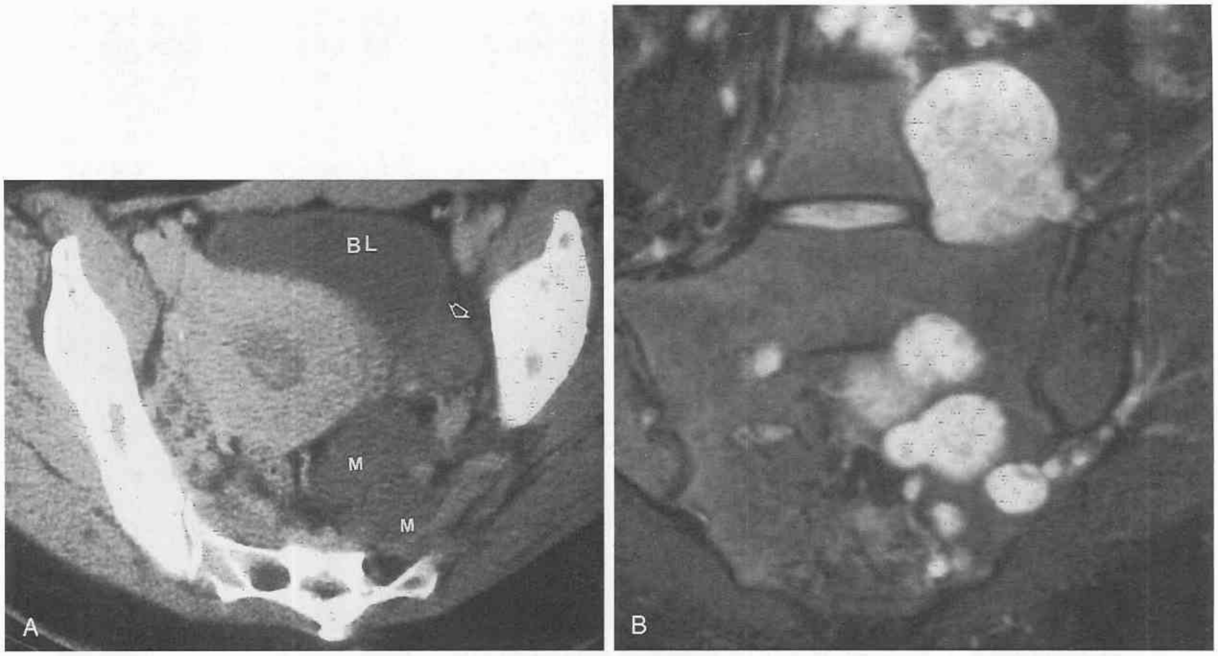

Figure 59–26. Neurofibromatosis. *A,* CT scan of a 18-year-old girl shows low-attenuation masses (M) with a density less than that of myometrium and muscle in the left hemipelvis. BL, bladder. *Open arrow* indicates the left ovary. *B,* Transaxial T2-weighted fast spin-echo (TR 3000/TE 54/180 degrees) image shows high-signal-intensity neurofibromas in the left paraspinal area and involving the sacral foramen.

rofibromas usually have a homogeneous appearance and a low attenuation value on CT that is slightly higher than that of water but much lower than that of paraspinal muscle, a low or intermediate signal intensity on T1-weighted images, and a high signal intensity on T2-weighted images (Fig. 59–26). The low-attenuation value in benign lesions may reflect the presence of cystic degeneration, hypocellularity, or xanthomatous (fatty) tissue. Because of their neural origin, neuroblastomas and neurofibromas can invade the spinal canal. MRI is superior to CT in delineating the extent of intraspinal disease.

The anterior meningocele herniates through a congenital defect in the vertebral body. It is most common in the sacral region and at the lumbosacral junction. When the contents of the herniated sac contain neural elements in addition to meninges and cerebrospinal fluid, the mass is termed a *myelomeningocele*; when fat and cerebrospinal fluid are present, the mass is termed a *lipomeningocele*.

The diagnosis of an anterior meningocele or myelomeningocele can be strongly suspected on conventional radiographs when a presacral mass is seen in association with a scimitar- or crescent-shaped sacrum. CT can demonstrate the fluid-filled sac of the meningocele, the bony defect in the lumbar vertebra or sacrum, the low-attenuation fatty elements of a lipomeningocele, and the relationship of the lesion to the spine and other structures of the pelvic cavity. Although the diagnosis can be made with CT, the soft tissue contents of the herniated spinal sac, especially the presence of a tethered cord and the communication between the meningocele and the thecal sac, are demonstrated best with MRI.

Rectal duplication cysts account for about 10% of all gastrointestinal duplications.[39] They usually appear as thin-walled, fluid-filled, round or oval masses attached to the rectum (Fig. 59–27). The attenuation value and MR signal characteristics of the cyst contents are usually similar to those of water. However, the attenuation value and signal intensity on T1-weighted images can be higher if the cyst contains blood or mucinous material. On occasion, duplication cysts communicate with the true colon.

Lymphomas and chordomas are rare presacral tumors in children. On CT and MRI, presacral lymphoma appears as a homogeneous soft tissue mass. CT and MRI examination of chordomas reveals a soft tissue mass with amorphous cartilaginous calcifications. Chordomas typically produce destruction of the sacrum and coccyx.

Figure 59–27. Rectal duplication cyst in a 4-year-old girl with chronic constipation. A nonenhanced CT scan shows a well-circumscribed ovoid cyst (C) of water attenuation in the presacral region displacing the rectum (R) anteriorly.

Localization of Undescended Testes

The prevalence of undescended testis *(cryptorchidism)* is 3.5% at birth and decreases to 0.8% by 1 year, because many testes descend spontaneously.[22] Identification of an undescended testis or cryptorchidism is important because of the increased incidence of infertility and neoplasm if the testis remains undescended. Early surgery, either orchiopexy in younger patients or orchiectomy in postpubertal patients, minimizes but does not eliminate those risks.[22, 49]

The testis develops from the embryonic gonad, which arises ventral to the mesonephric ridge. It migrates from its abdominal position to the scrotal sac during the late portion of gestation.[49] Arrest of this migratory process produces an ectopically positioned testis. Ultrasonography can reliably detect an undescended testis when it is intracanalicular, which occurs in about 90% of cases. Ultrasonography, however, is not usually reliable in detecting the undescended testis located higher in the pelvis or in the abdomen. If sonographic findings are equivocal or negative and preoperative localization of the testis is desired, either CT or MRI can be performed. A disadvantage of MRI in children, compared with CT, is the lack of a contrast agent to opacify bowel loops, which makes detection of the atrophic testis more difficult.

The CT features of an undescended testis are an oval, soft tissue mass located anywhere along the pathway of testicular descent, from the lower pole of the kidney down to the external inguinal ring.[22, 35, 36] The undescended testis is usually smaller than the normally descended testis. The demonstration of an undescended testis that is unusually large or heterogeneous should suggest malignant transformation.[37] The accuracy of CT for localization of nonpalpable testes exceeds 90%.[35, 75, 76] Unless it is atrophic or ischemic, the undescended testis has an intermediate signal intensity equal to that of muscle on T1-weighted images (Fig. 59–28) and higher than that of subcutaneous fat on T2-weighted images. Undescended testes that are atrophic or ischemic may have a signal intensity lower than that of the normal testis.

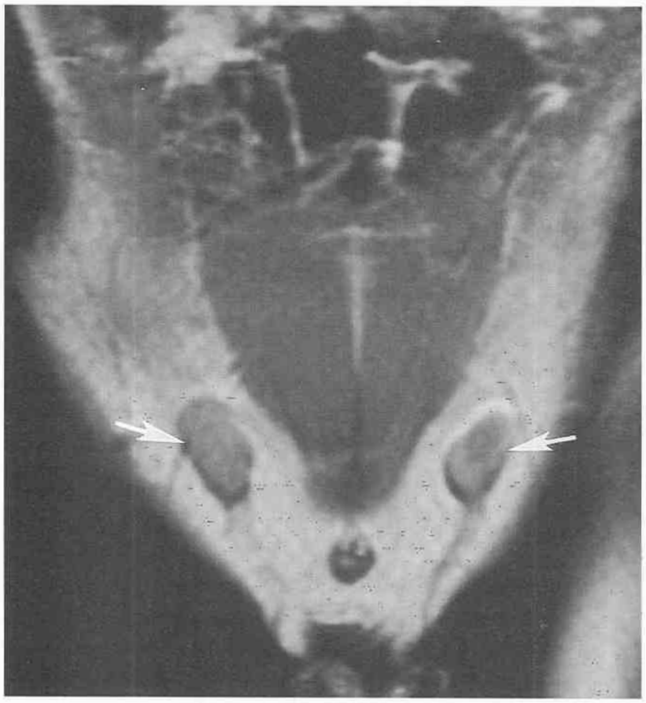

Figure 59–28. Undescended testes in a 7-year-old boy. Coronal T1-weighted MR image (600/17) demonstrates intermediate-signal-intensity ovoid structures *(arrows)* in the inguinal canals bilaterally, representing the undescended testes. (From Siegel MJ: Pediatric applications. In Lee KRL, Sagel SS, Stanley RJ, Heiken JP [eds]: Computed Body Tomography with MRI Correlation. Philadelphia, Lippincott-Raven, 1998, p 1550.)

References

1. American Fertility Society: Classification of adnexal adhesions, distal tubal occlusion, tubal occlusion secondary to tubal ligation, tubal pregnancies, müllerian anomalies, and intrauterine adhesions. Fertil Steril 49:944–955, 1988.
2. Argons GA, Wagner BJ, Lonergan GJ, et al: Genitourinary rhabdomyosarcoma in children: Radiologic-pathologic correlation. Radiographics 17:919–937, 1997.
3. Baker ME, Silverman PM, Korobkin M: Computed tomography of prostatic and bladder rhabdomyosarcomas. J Comput Assist Tomogr 9:780–783, 1985.
4. Barr LL, Cohen HL: Ultrasonography of the pediatric and adolescent pelvis. In Anderson JC (ed): Gynecologic Imaging. London, Churchill Livingstone, 1999, pp 397–410.
5. Bellah RD, Griscom NT: Torsion of normal uterine adnexa before menarche: CT appearance. AJR Am J Roentgenol 152:123–124, 1989.
6. Boechat IN: MR imaging of the pediatric pelvis. MRI Clin North Am 4:679–697, 1996.
7. Brammer HM, Buck JL, Hayes WS, et al: Malignant germ cell tumors of the ovary: Radiologic-pathologic correlation. Radiographics 10: 715–724, 1990.
8. Breen JL, Bonamo JF, Maxson WS: Genital tract tumors in children. Pediatr Clin North Am 28:355–367, 1981.
9. Buy J-N, Ghossain MA, Moss AA, et al: Cystic teratoma of the ovary: CT detection. Radiology 171:697–701, 1989.
10. Buy JN, Ghossain MA, Sciot C, et al: Epithelial tumors of the ovary: CT findings and correlation with US. Radiology 178:811–818, 1991.
11. Carrington BM, Hricak H, Nuruddin RN, et al: Müllerian duct anomalies: MR imaging evaluation. Radiology 176:715–720, 1990.
12. Castleberry RP, Cushing B, Perlman E, Hawkins EP: Germ cell tumors. In Pizzo PA, Poplack DG (eds): Principles and Practice of Pediatric Oncology. Philadelphia, Lippincott-Raven, 1997, pp 921–945.
13. Castleberry RP, Kelly DR, Joseph DB, Cain WS: Gonadal and extragonadal germ cell tumors. In Fernbach DJ, Vietti TJ (eds): Clinical Pediatric Oncology, 4th ed. St. Louis, Mosby–Year Book, 1991, pp 577–594.
14. Cranston PE, Smith EE, Hamrick-Turner J: Emergence of mature teratoma following treatment of sacrococcygeal endodermal sinus tumor: CT and MR imaging with pathological correlation. Pediatr Radiol 24:239–240, 1994.
15. Davis WK, McCarthy S, Moss AA, Braga C: Computed tomography of gestational trophoblastic disease. J Comput Assist Tomogr 8: 1136–1139, 1984.
16. Dietrich RB, Kangarloo H: Pelvic abnormalities in children: Assessment with MR imaging. Radiology 163:367–372, 1987.
17. Ehren IM, Mahour GH, Isaacs H: Benign and malignant ovarian tumors in children and adolescents. Am J Surg 147:339–344, 1984.
18. Ellis JH, Francis IR, Rhodes M, et al: CT findings in tubo-ovarian abscess. J Comput Assist Tomogr 15:589–592, 1991.
19. Fedele L, Dorta M, Brioschi D, et al: Magnetic resonance imaging in Mayer-Rokitansky-Küster-Hauser syndrome. Obstet Gynecol 76: 593–596, 1990.
20. Fielding JR: MR imaging of müllerian anomalies: Impact on therapy. AJR Am J Roentgenol 167:1491–1495, 1996.
21. Fletcher BD, Kaste SC: Magnetic resonance imaging for diagnosis and follow-up of genitourinary, pelvic, and perineal rhabdomyosarcoma. Urol Radiol 14:262–272, 1992.
22. Friedland GW, Chang P: The role of imaging in the management

of the impalpable undescended testis. AJR Am J Roentgenol 151: 1107–1111, 1988.
23. Ghossain MA, Buy NJ, Bazot M, et al: CT in adnexal torsion with emphasis on tubal findings: Correlation with US. J Comput Assist Tomogr 18:619–625, 1994.
24. Ghossain MA, Buy NJ, Ligneres C, et al: Epithelial tumors of the ovary: Comparison of MR and CT findings. Radiology 181:863–870, 1991.
25. Golan A, Langer R, Bukovsky I, Caspi E: Congenital anomalies of the müllerian system. Fertil Steril 51:747–755, 1989.
26. Golden N, Neuhoff S, Cohen H: Pelvic inflammatory disease in adolescents. J Pediatr 114:138–143, 1989.
27. Green CL, Angtuaco TL, Shah HR, Pamley TH: Gestational trophoblastic disease: A spectrum of radiologic diagnosis. Radiographics 16:1371–1384, 1996.
28. Hamlin DJ, Pettersson H, Ramey SL, Moazam F: Magnetic resonance imaging of bicornuate uterus with unilateral hematometrosalpinx and ipsilateral renal agenesis. Urol Radiol 8:52–55, 1986.
29. Herman TE, Shackelford GD: Pyourachus: CT manifestations. J Comput Assist Tomogr 19:440–443, 1995.
30. Hricak H, Chang YCF, Thurnher S: Vagina: Evaluation with MR imaging: Part I. Normal anatomy and congenital anomalies. Radiology 169:169–174, 1988.
31. Javitt MC: Magnetic resonance imaging in the diagnosis of congenital uterine anomalies. In Fleischer AC, Javitt MC, Jeffrey RB, Jones HW III (eds): Clinical Gynecologic Imaging. Philadelphia, Lippincott-Raven, 1997, pp 299–310.
32. Kaste SC, Bridges JO, Marina NM: Sacrococcygeal yolk sac carcinoma: Imaging findings during treatment. Pediatr Radiol 26:212–219, 1996.
33. Kesslar PJ, Buck JL, Suarez ES: Germ cell tumors of the sacrococcygeal region: Radiologic-pathologic correlation. Radiographics 14:607–620, 1994.
34. Kimura I, Togashi K, Kawakami S, et al: Ovarian torsion: CT and MR imaging appearances. Radiology 190:337–341, 1994.
35. Lee JKT, Glazer HS: Computed tomography in the localization of the nonpalpable testis. Urol Clin North Am 9:397–404, 1982.
36. Lee JKT, McClennan BL, Stanley RJ, Sagel SS: Utility of computed tomography in the localization of the undescended testis. Radiology 135:121–125, 1980.
37. Lorigan JG, Shirkoda A, Dexeus FH: CT and MR imaging of malignant germ cell tumor of the undescended testis. Urol Radiol 11: 113–117, 1989.
38. Maurer HM, Ragab A: Rhabdomyosarcoma. In Fernbach DJ, Vietti TJ (eds): Clinical Pediatric Oncology, 4th ed. St. Louis, Mosby–Year Book, 1991, pp 491–515.
39. Macpherson RI: Gastrointestinal tract duplications: Clinical, pathologic, etiologic, and radiologic considerations. Radiographics 13: 1063–1080, 1993.
40. McCarthy S, Hricak H: The uterus and vagina. In Higgins CB, Hricak H, Helms CA (eds): Magnetic Resonance Imaging of the Body, 3rd ed. Philadelphia, Lippincott-Raven, 1997, pp 761–814.
41. McCarthy S, Scott G, Majumdar S, et al: Uterine junctional zone: MR study of water content and relaxation properties. Radiology 171: 241–243, 1989.
42. Mintz MC, Grumbach K: Imaging of congenial uterine anomalies. Semin Ultrasound CT MR 9:167–174, 1988.
43. Mintz MC, Thickman DI, Gussman D, Kressel HY: MR evaluation of uterine anomalies. Am J Roentgenol 148:287–290, 1987.
44. Mitchell DG, Gefter WB, Spritzer CE, et al: Polycystic ovaries: MR imaging. Radiology 160:425–429, 1986.
45. Mitchell DG, Outwater EK: Benign gynecologic disease: Applications of magnetic resonance imaging. Top Magnet Reson Imaging 7:26–43, 1995.
46. Muramatsu Y, Moriyama N, Takayasu K, et al: CT and MR imaging of cystic ovarian teratoma with intracystic fat balls. J Comput Assist Tomogr 15:528–529, 1991.
47. Nagasaki A, Handa N, Kawanami T: Diagnosis of urachal anomalies in infancy and childhood by contrast fistulography, ultrasound and CT. Pediatr Radiol 21:321–323, 1991.
48. Pellerito JS, McCarthy SM, Doyle MB, et al: Diagnosis of uterine anomalies: Relative accuracy of MR imaging, endovaginal sonography, and hysterosalpingography. Radiology 183:795–800, 1992.
49. Pinch L, Aceto T Jr, Meyer-Bahlburg HFL: Cryptorchidism. Urol Clin North Am 1:573–592, 1974.
50. Pizzo PA, Poplack DG, Horowitz ME, et al: Solid tumors of childhood. In DeVita VT, Hellman S, Rosenberg SA (eds): Cancer: Principles and Practice of Oncology, 4th ed. Philadelphia, JB Lippincott, 1993, pp 1738–1791.
51. Quillin SP, Siegel MJ: CT features of benign and malignant teratomas in children. J Comput Assist Tomogr 16:722–726, 1992.
52. Reinhold C, Hricak J, Forstner, et al: Primary amenorrhea: Evaluation with MR imaging. Radiology 203:383–390, 1997.
53. Rigsby CK, Siegel MJ: CT appearance of pediatric ovaries and uterus. J Comput Assist Tomogr 18:72–76, 1994.
54. Sanders C, Rubin E: Malignant gestational trophoblastic disease: CT findings. Am J Roentgenol 148:165–168, 1987.
55. Shady KL, Siegel MJ, Brown JJ: Preoperative evaluation of intra-abdominal tumors in children: Gradient-recalled echo vs spin-echo MR imaging. AJR Am J Roentgenol 161:843–847, 1993.
56. Sheth S, Fishman EK, Buck JL, et al: The variable sonographic appearances of ovarian teratomas: Correlation with CT. AJR Am J Roentgenol 151:331–334, 1988.
57. Siegel MJ: Magnetic resonance imaging of the pediatric pelvis. Semin Ultrasound CT MR 12:475–505, 1991.
58. Siegel MJ, Surratt JT: Pediatric gynecologic imaging. Obstet Gynecol Clin North Am 19:103–127, 1992.
59. Siegel MJ: Female pelvis. In Siegel MJ (ed): Pediatric Sonography. New York, Raven Press, 1995, pp 437–477.
60. Siegel MJ: Pediatric applications. In Lee KRL, Sagel SS, Stanley RJ, Heiken JP (eds): Computed Body Tomography with MRI Correlation. Philadelphia, Lippincott-Raven, 1998, p 1493.
61. Siegel MJ: Pelvic tumors. Radiol Clin North Am 35:1455–1475, 1997.
62. Siegel MJ: Pelvic organs and soft tissues. In Siegel MJ (ed): Pediatric Body CT. Philadelphia, Lippincott Williams & Wilkins, 1999.
63. Siegel MJ: Computed tomography and magnetic resonance imaging of the pediatric and adolescent pelvis. In Anderson JC (ed): Gynecologic Imaging. London, Churchill Livingstone, 1999, pp 397–410.
64. Stark JE, Siegel MJ: Ovarian torsion in prepubertal and pubertal girls: Sonographic findings. AJR Am J Roentgenol 163:1479–1482, 1994.
65. States LJ, Bellah RD: Imaging of the pediatric female pelvis. Semin Roentgenol 31:312–329, 1996.
66. Stevens SK, Hricak H, Campos Z: Teratomas versus cystic hemorrhagic adnexal lesions: Differentiation with proton-selective fat-saturation MR imaging. Radiology 186:481–488, 1993.
67. Surrattt JT, Siegel MJ: Imaging of pediatric ovarian masses. Radiographics 11:533–548, 1991.
68. Swensen SJ, McLeod RA, Stephens DH: CT of extracranial hemorrhage and hematomas. Am J Roentgenol 143:907–912, 1984.
69. Tannous WN, Azouz EM, Homsy YL, et al: CT and ultrasound imaging of pelvic rhabdomyosarcoma in children: A review of 56 patients. Pediatr Radiol 19:530–534, 1989.
70. Togashi K, Nishimura I, Itoh K, et al: Ovarian cystic teratomas: MR imaging. Radiology 162:669–673, 1987.
71. Wagner BJ, Woodward PH, Dickey GE: Gestational trophoblastic disease: Radiologic-pathologic correlation. Radiographics 16:131–148, 1996.
72. Wells RG, Sty JR: Imaging of sacrococcygeal germ cell tumors. Radiographics 10:701–713, 1990.
73. Wexler LH, Helman LJ: Rhabdomyosarcoma and the undifferentiated sarcomas. In Pizzo PA, Poplack DG (eds): Principles and Practice of Pediatric Oncology. Philadelphia, Lippincott-Raven, 1997, pp 799–829.
74. Wilbur AC, Aizenstein RI, Napp TE: CT findings in tubo-ovarian abscess. AJR Am J Roentgenol 158:575–579, 1992.
75. Wolverson MK, Jagannadharao B, Sundaram M, et al: CT in localization of impalpable cryptorchid testes. Am J Roentgenol 134:725–729, 1980.
76. Wolverson MK, Houttuin E, Heiberg E, et al: Comparison of computed tomography with high-resolution real-time ultrasound in the localization of the impalpable undescended testis. Radiology 146: 133–136, 1983.
77. Yamashita Y, Hatanka Y, Torashima M, et al: Mature cystic teratomas of the ovary without fat in the cystic cavity: MR features in 12 cases. AJR Am J Roentgenol 163:613–616, 1994.
78. Yu KK, Hricak H: The adnexa. In Higgins CB, Hricak H, Helms CA (eds): Magnetic Resonance Imaging of the Body, 3rd ed. Philadelphia, Lippincott-Raven, 1997, pp 815–844.

60 Musculoskeletal System

Peter J. Strouse

Tumors of Bone

Imaging of pediatric bone tumors begins with conventional radiography. Radiographs may characterize a lesion such that a specific diagnosis can be made or a narrow differential diagnosis constructed. Radiographs serve to guide the planning of subsequent magnetic resonance imaging (MRI) and computed tomography (CT) examinations.

MRI delineates the intramedullary extent, cortical violation, and extraosseous extension of bone tumors. In children, MRI is the best method to demonstrate the relationship of a tumor to the growth plate, epiphysis, and articular surface. A drawback of MRI is its inability to demonstrate calcification. Tumor matrix and periosteal new bone formation are thus not well assessed. The MRI examination should always be interpreted with correlative radiographs, which provide information on tumor matrix, periosteal new bone formation, and lesion margins. MR images should also be assessed for metastases, including skip lesions and lymph node disease. MRI demonstration of neurovascular encasement may alter therapy.

The approach to an MRI protocol for a bone tumor should be based on information obtained from preceding history, physical examination, and plain radiographs. If a nonaggressive process is suspected, the examination can be targeted to the area of interest from the start. If the process is thought to be aggressive, such as osteosarcoma or Ewing's sarcoma, it is wise to start with a broader field of view (Fig. 60–1). Imaging is often started in a body coil to image the full length of the affected bone. Coronal T1-weighted images and sagittal inversion recovery images suffice. Once skip lesions have been excluded and the longitudinal extent of the tumor is defined, a smaller coil is used to target the area of interest with higher resolution.

With their focus on the tumor, axial T1-weighted images with and without fat saturation, and axial T2-weighted images are obtained. After the administration of gadolinium (0.1 mmol/kg), axial and coronal T1-weighted fat saturation images are obtained. Imaging planes may vary on the basis of tumor location. Pregadolinium T1-weighted fat saturation images can be omitted to shorten examination time, but they are often helpful in characterizing and defining the extent of enhancement on the postgadolinium images. If there is a possibility of vascular encasement or if the tumor itself is potentially vascular in nature, time-of-flight images can be added.

The enhancement pattern of musculoskeletal neoplasms is an area of active research. Several investigators have studied temporal enhancement patterns as a method of distinguishing different types of tumors, differentiating tumor from peritumoral edema, assessing tumor response to therapy, and identifying viable residual tumor.[21, 24, 52, 53]

Malignant Bone Tumors

Osteosarcoma

Any sarcoma that produces bone is, by definition, an osteosarcoma. Osteosarcoma is the most common malignant bone tumor of childhood. It most often presents in the second decade of life but is occasionally seen in children younger than 10 years of age and not infrequently in the young adult. Patients usually present with pain or a painful mass. Although osteosarcoma can develop in any bone, most of the tumors are seen in metaphyses of long bones.

On plain radiographs, osteosarcomas are varied in appearance. Most commonly, radiographs show an aggressive lytic lesion with osteoid production, aggressive periosteal reaction ("hair-on-end," "onion-skin," Codman's triangle), and a soft tissue mass. Less commonly, lesions are predominantly sclerotic. Rarely, an osteosarcoma produces a well-defined, lytic lesion that might be mistaken for a nonaggressive lesion. Plain radiographs often allow the specific diagnosis of osteosarcoma.

MRI is performed in patients with suspected osteosarcoma to confirm the diagnosis and, more often, to assess the extent of disease (see Fig. 60–1).[28, 69, 70, 72, 77] Like most neoplasms, osteosarcoma is of low signal intensity on T1-weighted images and of high signal intensity on T2-weighted images. Areas of osteoid production may be seen as low signal (Fig. 60–2). MRI shows the extent of intramedullary and extraosseous tumor. Edema is seen at the margins of the tumor, within bone and adjacent soft tissues. A sharp margin of the lesion allows its differentiation from an inflammatory condition (i.e., osteomyelitis). The mass enhances with gadolinium administration. There may be extensive areas of necrosis.

Occasionally, fluid-fluid levels are seen. These are common with telangiectatic osteosarcoma, or they may indicate a secondary aneurysmal bone cyst. The presence of a fluid-fluid level is not indicative of a benign lesion.[92]

Parosteal Osteosarcoma

Parosteal osteosarcoma presents most often in young adults but occasionally in the second decade. The dorsal surface of the distal femur is a common location. Parosteal osteosarcomas are often heavily ossified for their size. A cleavage plane may be seen between the tumor and the

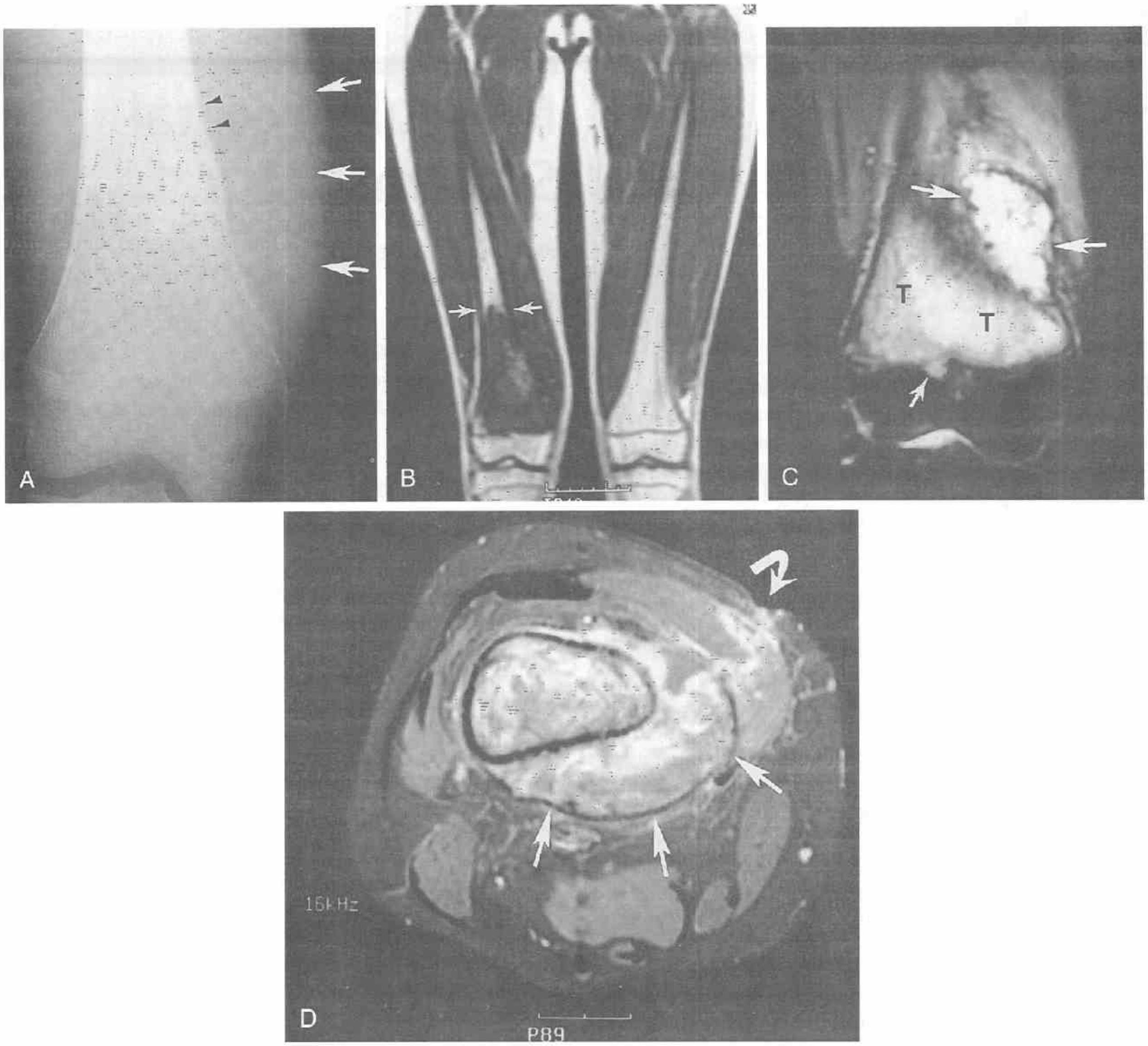

Figure 60–1. Osteosarcoma of the distal femur in a 13-year-old girl.

A, A plain radiograph is diagnostic. An aggressive lesion is seen within the distal femoral metaphysis. The mass effect can be visualized medially *(arrows)*, with faint osteoid production and periosteal new bone *(arrowheads)*.

B, The MRI examination begins in the body coil with T1-weighted images (TR = 300 msec, TE = 14 msec) covering the entire femur to exclude skip lesions and determine the proximal extent of tumor *(arrows)*. Subsequently, an extremity coil is used to better define the tumor.

C, Coronal inversion recovery image (TR = 4000 msec, TE = 30 msec, TI = 165 msec) shows the tumor (T) as having a high signal within the distal femoral metaphysis. A portion of the soft tissue mass, which is of fluid signal intensity due to necrosis, is seen medially *(long arrows)*. Note a small extension of the tumor across the distal femoral growth plate into the epiphysis *(small arrow)*.

D, Postgadolinium axial T1-weighted image (TR = 716 msec, TE = 14 msec) with fat saturation shows the extent of the soft tissue mass *(arrows)*. The *curved arrow* marks a tract from the preceding biopsy. The patient eventually underwent a limb salvage procedure with a total knee arthroplasty with a long-stem femoral component.

underlying cortex.[63] CT helps to differentiate parosteal osteosarcoma from osteochondroma and myositis ossificans (Fig. 60–3).[39] MRI better defines the degree of intraosseous extension.

Periosteal Osteosarcoma

Periosteal osteosarcoma is extremely rare, particularly in childhood. These lesions are frequently diaphyseal and involve the lower extremities. The tumor is closely apposed to the cortex of the underlying bone. A juxtacortical mass with hair-on-end periosteal new bone is characteristic.[63]

Ewing's Sarcoma

Ewing's sarcoma is the second most common malignant bone tumor of childhood. It is rare in infancy but otherwise presents throughout childhood and occasionally in early adulthood. As with osteosarcoma, the most common presentations are pain or a painful mass. In younger children,

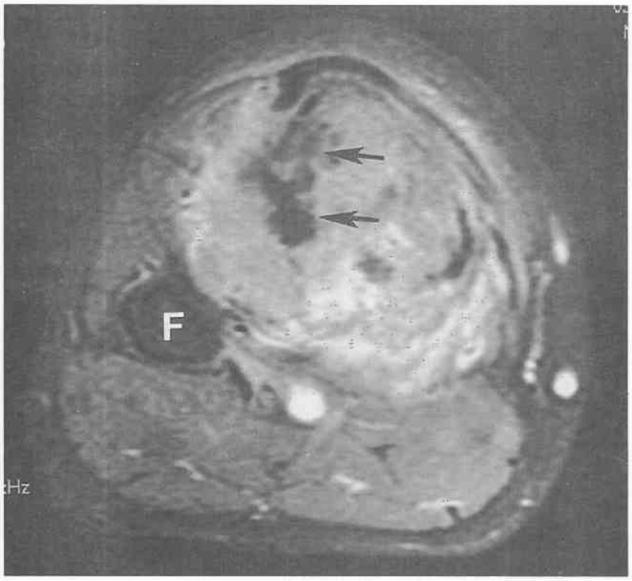

Figure 60–2. Osteosarcoma in a 15-year-old boy. Postgadolinium axial T1-weighted image (TR = 550 msec, TE = 8 msec) with fat saturation shows enhancing soft tissue of an osteosarcoma replacing the proximal tibial metaphysis. The cortex is largely destroyed. An area of low signal intensity *(arrows)* represents osteoid formation. F, fibula.

Ewing's sarcoma most commonly presents in the diaphyses of the long bones. In older children, Ewing's sarcoma tends to occur in bones of the axial skeleton, such as within the pelvis. Ewing's sarcoma is an aggressive neoplasm. Metastatic disease is common at presentation.

On plain radiographs, Ewing's sarcoma is usually seen as a permeative lesion of bone. The tumor does not produce osteoid matrix; however, there may be abundant periosteal new bone formation. Onion-skin periosteal new bone is characteristic (Fig. 60–4). The extraosseous soft tissue component may be large, particularly with pelvic or chest wall tumors. Rarely, Ewing's sarcoma can arise primarily within soft tissue ("extraosseous"). The radiographic findings in Ewing's sarcoma are less specific than in osteosarcoma. In particular, osteomyelitis can mimic Ewing's sarcoma in the long bones. The clinical presentations overlap as well. In the axial skeleton, other neoplasms, such as primitive neuroectodermal tumor (PNET) and rhabdomyosarcoma, mimic Ewing's sarcoma.

Figure 60–3. Parosteal osteosarcoma of the distal femur in a 15-year-old girl. CT shows central ossification within the lesion and involvement of the medullary space *(arrows)*.

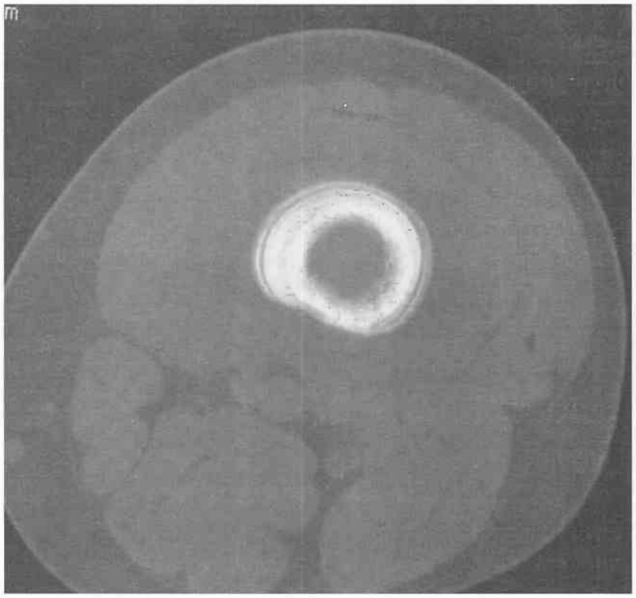

Figure 60–4. Ewing's sarcoma of the distal femur in a 15-year-old boy. The CT image at the bone window shows characteristic "onion skin" periosteal new bone formation.

As with osteosarcoma, MRI shows the extent of neoplasm within the medullary space, extension through the cortex, and associated soft tissue mass (Figs. 60–5 and 60–6).[28, 29] Peritumoral edema may render margins of the tumor indistinct on some imaging sequences. Usually, the tumor has well-defined margins on at least one sequence, which is often conventional T1-weighted, helping to differentiate it from infection.

Primitive Neuroectodermal Tumor

PNET can originate in bone or soft tissue. This aggressive tumor is seen throughout childhood. In the skeleton, PNET is seen as a destructive tumor with associated soft tissue mass, indistinguishable from Ewing's sarcoma (Fig. 60–7). Metastases are common at the time of presentation. PNET is most commonly seen in the pelvis and chest wall. Tumors at the latter location are known as *Askin's tumors*.

Lymphoma

Focal osseous involvement of lymphoma occurs in only a small percentage of pediatric patients with lymphoma. On radiographs and MRI, lymphoma in bone appears similar

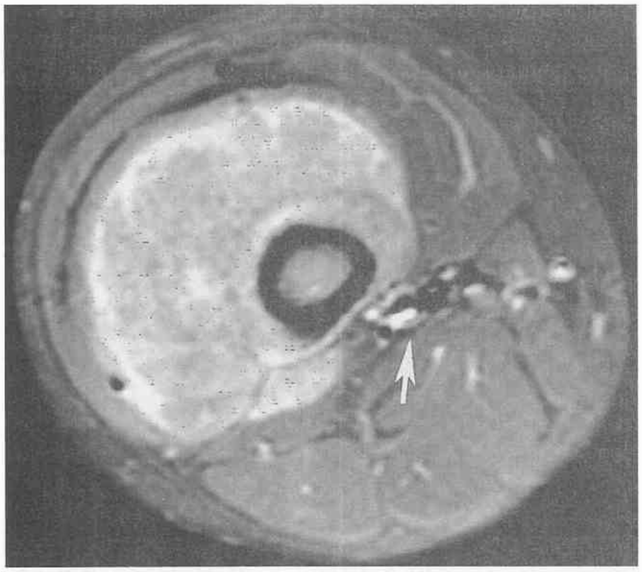

Figure 60–5. Ewing's sarcoma of the distal femur in a 5-year-old girl. Postgadolinium axial T1-weighted image (TR = 550 msec, TE = 11 msec) with fat saturation shows an eccentric mass enveloping the distal femur. Anterior thigh musculature is displaced. Enhancing tumor is also seen in the medullary space. The neurovascular bundle *(arrow)* is not involved.

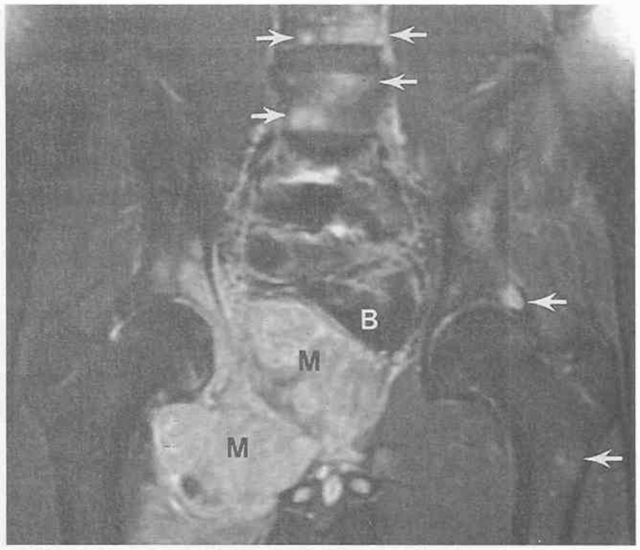

Figure 60–7. Primitive neuroectodermal tumor arising from the right hemipelvis in a 14-year-old boy. Postgadolinium coronal T1-weighted image (TR = 700 msec, TE = 14 msec) with fat saturation shows the mass (M) to extend into proximal thigh and to displace the bladder (B). The medial right acetabulum is destroyed. Metastatic lesions can be seen within the lower spine, left ilium, and left proximal femur *(arrows)*.

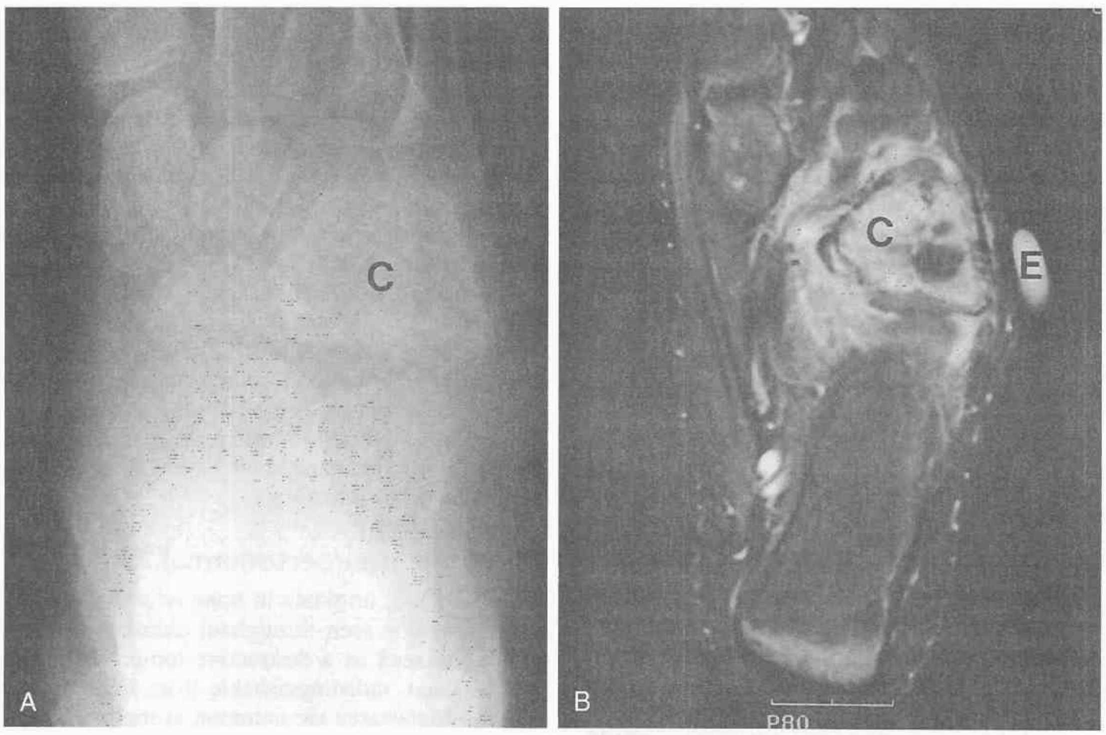

Figure 60–6. Ewing's sarcoma of the cuboid bone in an 8-year-old boy. *A,* Radiograph shows a lytic expansile lesion of the cuboid bone (C). *B,* Postgadolinium axial T1-weighted image (TR = 716 msec, TE = 14 msec) with fat saturation shows enhancing soft tissue replacing the cuboid (C). Areas of necrosis are seen as low signal intensity. The cortex of the cuboid is partially destroyed. Enhancement is seen within adjacent soft tissues as a result of peritumoral edema. E, vitamin E capsule.

to other malignant lesions. Bone destruction, aggressive periosteal new bone, and soft tissue mass are seen along with a permeative pattern of destruction. Both long bones and flat bones are affected. Involvement of vertebral bodies is not uncommon.

Giant Cell Tumor

Giant cell tumors are not encountered until late in childhood, after the growth plates are fused. This tumor is characterized on plain radiographs as a well-defined lesion, bridging the growth plate and abutting the articular surface. Fluid-fluid levels may be seen on CT and MR. Typically, no extraosseous soft tissue component is seen.

Leukemia

Leukemia can produce focal destructive masses anywhere in the skeleton. More commonly, lesions are confined to the metaphyses of growing bones. Early in the disease, leukemic infiltration is confined to within the medullary space. If treatment is delayed, osseous destruction can progress to the extent of pathologic fracture. Large extraosseous soft tissue masses may appear identical to osteosarcoma by MRI (Fig. 60–8). Involvement of multiple bones suggests the diagnosis. Plain films may show characteristic lucent metaphyseal bands.

Metastases

Metastases to bone are much less common in children than in adults. Pediatric neoplasms metastasizing to bone include neuroblastoma, PNET, Wilms' tumor, hepatoblastoma, and osteosarcoma. Neuroblastoma is most common. A metastasis can mimic a primary neoplasm of bone on radiography or MRI.

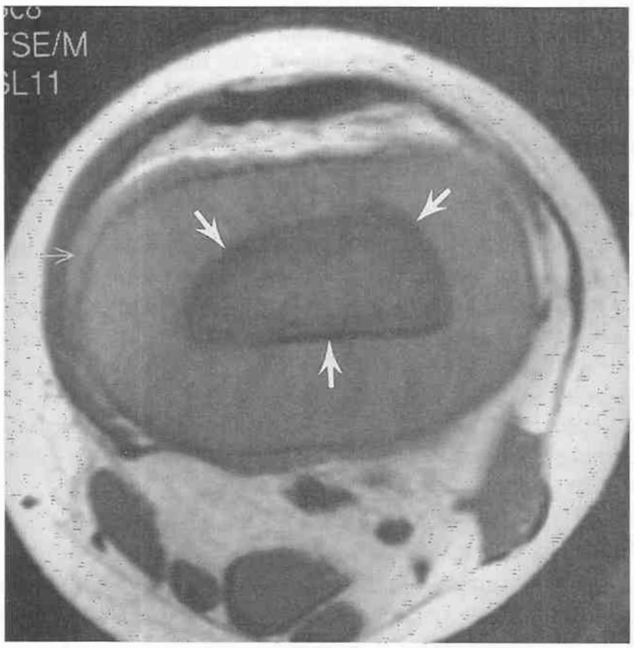

Figure 60–8. Focal distal left femoral mass due to acute lymphocytic leukemia in a 4-year-old girl. The patient initially presented with distal thigh pain and was thought to have a primary bone neoplasm of the distal femur. Axial T1-weighted image (TR = 689 msec, TE = 13 msec) shows a circumferential soft tissue mass encasing the distal femur. The underlying femoral cortex is nearly absent *(arrows)*. Lesser abnormality was present within the other metaphyses of both knees. Plain films showed destructive changes in the distal left femur with characteristic leukemic lucent bands in the other metaphyses.

Figure 60–9. Unicameral bone cyst of the left proximal femur and resultant pathologic fracture in a 3-year-old girl. The lesion is mildly expansile and thins the overlying cortex. Note the fallen fragment within the cyst from the fracture *(arrow)*.

Benign Bone Tumors

Plain films often suffice in the characterization of nonaggressive, benign bone lesions. MRI is thus indicated less often for these lesions than it is for aggressive, malignant lesions. CT is occasionally helpful in characterizing benign lesions on the basis of their effect on the host bone.

Simple (Unicameral) Bone Cyst

Simple bone cysts are seen as well-defined oval metaphyseal lesions without aggressive characteristics on plain radiographs. Neither MRI nor CT is indicated unless atypical features suggest a more aggressive lesion. Not infrequently, bone cysts present as a result of a pathologic fracture. CT may be helpful in demonstrating a "fallen fragment," indicative of a simple bone cyst (Fig. 60–9).

Aneurysmal Bone Cyst

Aneurysmal bone cysts are well-defined, multiloculated, expansile lesions. The overlying cortex is thinned but present. These cysts can occur anywhere within the skeleton, although locations in the long bones are most common. Presentation is usually the result of a pathologic fracture or pain. A few aneurysmal bone cysts form secondary to underlying lesions, including malignancies such as osteosarcoma. Images must be carefully inspected for evidence of an underlying lesion. On MRI and CT, an aneurysmal bone cyst is seen as a multilocular lesion.[4, 38] Larger loculi show fluid–fluid levels (Fig. 60–10).[38] Septations and margins of the lesion enhance. Any soft tissue component should raise suspicion for an underlying malignancy. Pathologic confirmation of benignity is recommended for all lesions.

Fibrous Cortical Defect/Nonossifying Fibroma

Fibrous cortical defects and nonossifying fibromas are very common benign lesions of bone whose appearance on

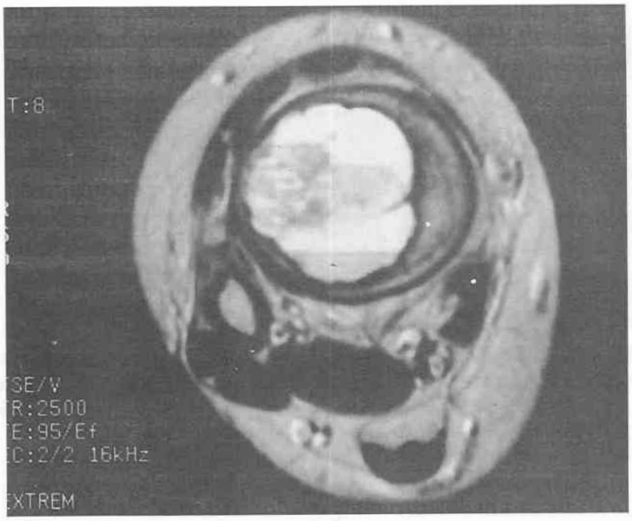

Figure 60–10. Aneurysmal bone cyst of the distal femur in a 10-year-old boy. Axial T2-weighted image (TR = 2500, TE = 95) without fat saturation shows multiple fluid–fluid levels within the lesion.

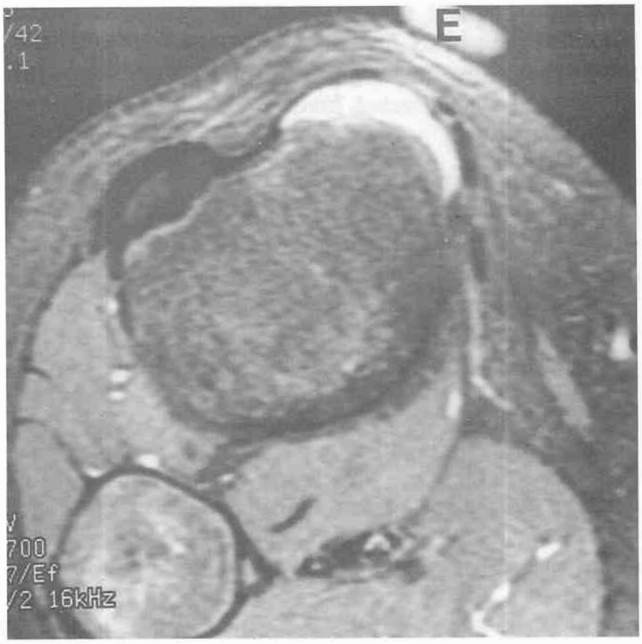

Figure 60–11. Osteochondroma of the proximal tibia in a 12-year-old boy. A vitamin E capsule (E) was placed on the palpable abnormality prior to scanning and overlies the lesion. The cartilaginous cap is well defined and of high signal intensity on this proton-density image (TR = 2700 msec, TE = 17 msec) with fat saturation.

radiographs is diagnostic. These lesions are asymptomatic unless they are large enough to cause a pathologic fracture. Fibrous cortical defects are smaller than 2 cm, and nonossifying fibromas are larger than 2 cm. Atypical lesions may warrant evaluation with MRI or CT for characterization. Lesions are detected incidentally on studies performed for other indications. The lesions are metaphyseal in location, moving away from the growth plate with time and involuting by skeletal maturation.

On radiographs and CT, a well-defined cortical lesion with a sclerotic margin is seen.[100] On MRI, lesions are well defined, with a low signal intensity on T1-weighted images and a high signal intensity on T2-weighted images. No adjacent edema is seen. Radiographs should be reviewed or obtained for confirmation.

Osteochondroma

Osteochondroma *(exostosis)* is a nonaggressive, benign lesion with a characteristic radiographic appearance. The lesion is corticated with a medullary space contiguous with that of the underlying metaphyseal bone. Lesions may be sessile or pedunculated. Pedunculated lesions are directed away from the end of the bone. Most osteochondromas are asymptomatic unless they are located so as to cause stress irritation of an overlying muscle or tendon, or mass effect. Although malignant degeneration is rare, pain in a previously asymptomatic osteochondroma or growth after skeletal maturity should raise concern for malignant degeneration.

CT is occasionally performed to define the three-dimensional anatomy of an osteochondroma. On MRI, the cartilaginous cap parallels articular cartilage in signal intensity and is well defined (Fig. 60–11).[43, 63] Irregularity or thickness greater than 2 cm should raise concern for malignancy.[63] Patients with the syndrome of multiple hereditary exostoses have numerous osteochondromas throughout the skeleton.

In patients with Trevor's disease (dysplasia epiphysealis hemimelica), osteochondroma-like lesions of the epiphyses develop. Classically, the lesions involve one side of the bone. Adjacent bones or joints within the same extremity may be involved. Deformity may interfere with bone growth and joint function. CT, MRI, and arthrography have been used to delineate the abnormality.

Enchondroma

Enchondromas are diagnosed infrequently in children. These lesions are well defined and typically metaphyseal in location. Punctate calcification ("arcs and rings") may be evident on plain radiography or CT. On MRI, lesions are well defined and of high signal intensity on cartilage sequences (Fig. 60–12). Irregularity, soft tissue mass, or clinical symptoms should raise concern for chondrosarcoma, which can have an imaging appearance very similar to that of enchrondroma.[30]

Osteoid Osteoma

Osteoid osteomas present throughout childhood and into early adulthood. The classic history is that of pain, particularly at night, relieved by aspirin. Most osteoid osteomas are cortical. The lesion produces sclerosis, cortical thickening, and exuberant smooth periosteal new bone. The osteoid osteoma is seen as a lucent nidus centered within the sclerotic region. A punctate opacity may be seen with the lucent nidus. The nidus may be identified by radiography; however, CT is performed to confirm the diagnosis and localize the nidus (Fig. 60–13).[60] At some institutions, curative biopsies are performed under CT guidance.[91]

Osteoid osteomas within the joints produce little reactive

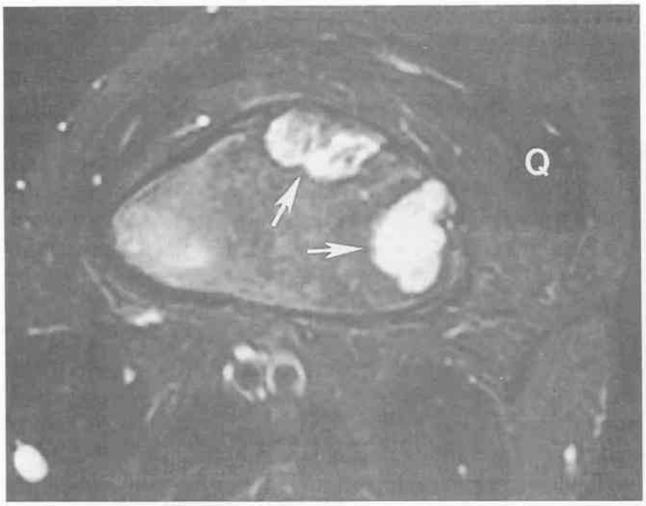

Figure 60–12. Multiple enchondromatosis in a 12-year-old boy. Axial T2-weighted image (TR = 3500 msec, TE = 105 msec) shows the enchondromas as well-defined high-signal-intensity lesions *(arrows)* with no adjacent edema. The quadriceps tendon (Q) is medially displaced as a result of deformity of the distal femur (not illustrated).

Figure 60–14. Osteoid osteoma of the proximal femur in an 8-year-old boy. Postgadolinium axial T1-weighted image (TR = 750 msec, TE = 12 msec) with fat saturation shows the nidus at the inner margin of the medial cortex *(arrow)*. Marked enhancement is seen within the adjacent medullary cavity and extraosseous soft tissues.

bone.[78] Intramedullary osteoid osteomas also produce little periosteal new bone or cortical thickening. Intramedullary lesions may mimic osteosarcoma or stress fractures in their radiographic appearance. CT suggests the diagnosis by showing a radiolucent nidus within an area of medullary sclerosis.[1]

On MRI, osteoid osteoma produces an amount of edema that is disproportionately large relative to the size of the lesion, thus simulating a more aggressive lesion (Fig. 60–14). Edema extends into the adjacent soft tissues. The nidus can occasionally be identified centrally within the lesion.[1] Correlation with plain radiographs is imperative.

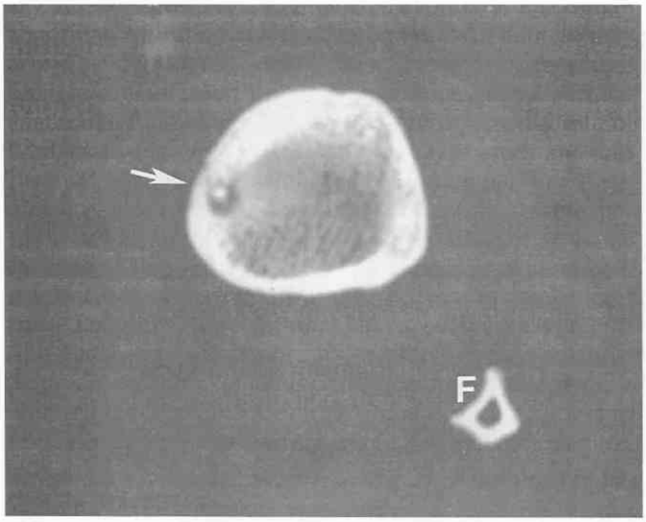

Figure 60–13. Osteoid osteoma of the proximal tibia in an 8-year-old girl. A punctate sequestrum is seen within the lucent nidus *(arrow)*. Note the diffuse cortical thickening. F, fibula.

Chondroblastoma

Chondroblastoma most commonly presents in the second decade of life. These lesions may produce pain, typically localized near a joint because of the epiphyseal and apophyseal location of the lesions. Radiographically, a well-defined round lesion is identified within an epiphysis or apophysis. The lesion may abut the articular surface. MRI or CT can be performed to further characterize the lesion and delineate its relationship to the articular surface and growth plate (Fig. 60–15).[71, 94] On CT, cartilaginous matrix may be evident. On MRI, the lesion is well defined and parallels cartilage in signal intensity. The differential diagnosis includes osteochondritis dissecans, epiphyseal osteomyelitis, and eosinophilic granuloma.

Fibrous Dysplasia

Fibrous dysplasia may present as a solitary lesion or as a multifocal abnormality. In McCune-Albright syndrome, children present with precocious puberty, café-au-lait spots, and polyostotic fibrous dysplasia. The radiographic and CT appearance of fibrous dysplasia is varied.[48] Focal lesions are well defined and expansile. A "ground glass" appearance of the medullary space may be seen (Fig. 60–16). On MRI, lesions vary in signal intensity on T2-weighted images.[25, 97]

Langerhans' Cell Histiocytosis

Langerhans' cell histiocytosis represents a spectrum of abnormality, ranging from a solitary bone lesion to a dif-

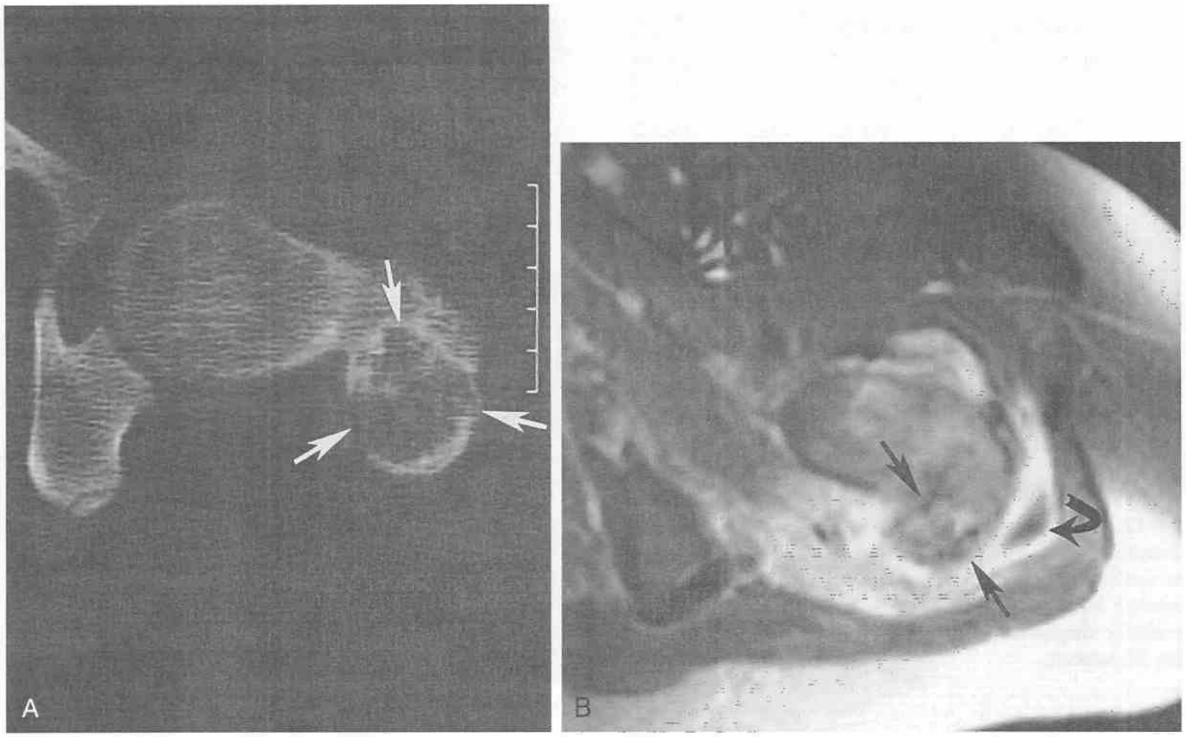

Figure 60–15. Chondroblastoma of the greater trochanter of the femur in a 14-year-old boy. *A,* CT shows a relatively well defined lucent expansile lesion with a few punctate internal calcifications *(arrows). B,* Axial postgadolinium T1-weighted image (TR = 550 msec, TE = 18 msec) with fat saturation shows marked enhancement within the adjacent soft tissues as a result of irritation. The lesion *(arrows)* enhances minimally. A small bursa is evident *(curved arrow).*

fuse process with skeletal and visceral involvement. Solitary lesions are still commonly referred to as eosinophilic granuloma. Langerhans' cell histiocytosis can have virtually any radiographic appearance; however, lesions typically do not show markedly aggressive features. Classic lesions are well defined on plain radiographs, with minimal sclerosis or periosteal reaction. Exceptions to this are common. Eosinophilic granuloma can affect any bone at any location, including the epiphyses. On MRI scans, lesions show a nonspecific low signal on T1-weighted images and a high signal on T2-weighted images, and they enhance briskly (Fig. 60–17).[27] There may be extraosseous extension of soft tissue.[86]

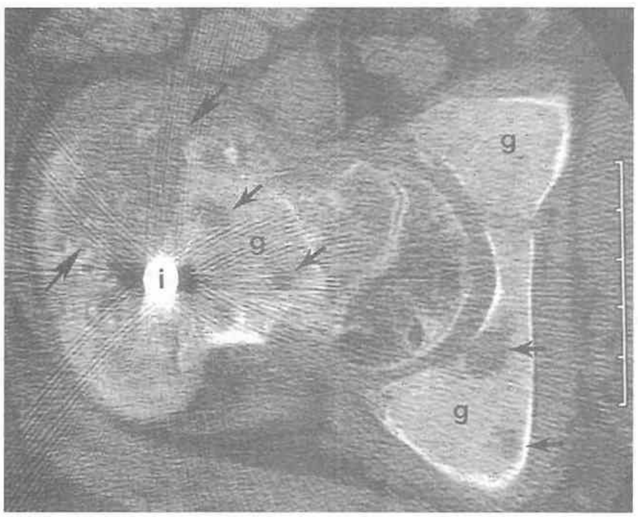

Figure 60–16. Polyostotic fibrous dysplasia in a 12-year-old boy. A CT image through the right hip shows a spectrum of appearances including "ground glass" abnormality (g), lucent, expansile change with punctate calcification *(large arrows),* and smaller lucent lesions *(small arrows).* An intramedullary rod (i) is present.

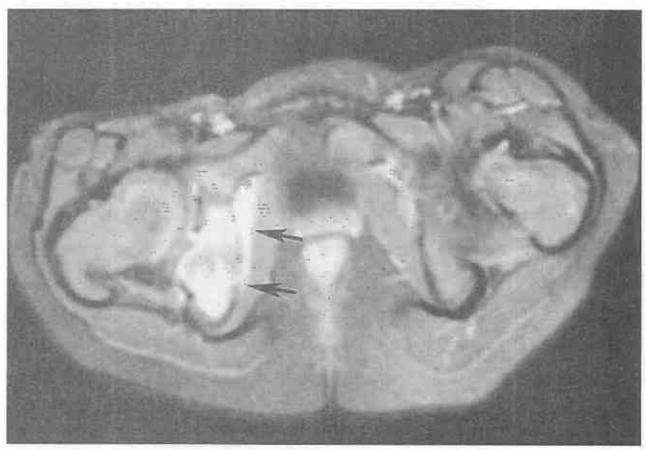

Figure 60–17. Focal Langerhans' cell histiocytosis of the right ischium in a 3-year-old girl. Postgadolinium axial T1-weighted image (TR = 600 msec, TE = 18 msec) with fat saturation shows marked, but slightly inhomogeneous, enhancement within the lesion *(arrows).* The medial ischial cortex is destroyed.

Soft Tissue Masses

Imaging of soft tissue masses in children begins with radiography. Radiographs exclude the bony origin of the mass. The presence of calcification (e.g., phleboliths) or ossification (as in myositis ossificans) may suggest a particular diagnosis or may serve to guide subsequent imaging.

Most soft tissue tumors are similar in attenuation and enhancement to skeletal muscle and are thus poorly delineated by CT. Because of its greater tissue contrast and multiplanar capability, MRI is the preferred method for delineation of soft tissue tumors. The MRI imaging sequences used to evaluate soft tissue tumors are similar to the protocol previously outlined for bone tumors. Precontrast T1-weighted images with fat saturation are helpful in differentiating high signal caused by hemorrhage from that caused by enhancement. Time-of-flight images are helpful in assessing vascular soft tissue masses.

Malignant Soft Tissue Masses

Rhabdomyosarcoma

Rhabdomyosarcoma is the most common malignant soft tissue mass of childhood. It presents throughout childhood and may originate in any muscle. On T1-weighted images, the lesion is similar in signal intensity to skeletal muscle and is thus difficult to detect and define. On proton-density, T2-weighted, inversion recovery, and postgadolinium images, rhabdomyosarcoma shows increased signal intensity relative to muscle and is well visualized. Tumor margination varies. Rhabdomyosarcoma is indistinguishable from other malignant soft tissue masses. Lymph node metastases parallel the primary tumor in signal intensity on all sequences.

Synovial Sarcoma

Synovial sarcoma is a relatively uncommon soft tissue mass that arises from mesenchyme. In children, this tumor is most common in the second decade and usually arises near tendon sheaths, not joints. Calcifications may be present on plain radiographs, suggesting the diagnosis. MRI reveals a nonspecific soft tissue mass (Fig. 60–18).[65]

Other Malignant Soft Tissue Masses

Liposarcoma, fibrosarcoma, angiosarcoma, and malignant fibrous histiocytoma are all extremely rare in childhood. Fibrosarcoma may be congenital.[57] Liposarcoma is seen as an aggressive mass containing both soft tissue and fatty components. Otherwise, these tumors have a nonspecific presentation and appearance.

Benign Soft Tissue Masses

Lipoma

Lipomas are relatively uncommon in children but the incidence increases with age. Lesions present as a painless lump or area of fullness. On CT or MRI, the lesion has a homogeneous appearance consistent with fat. No soft tissue component is seen.

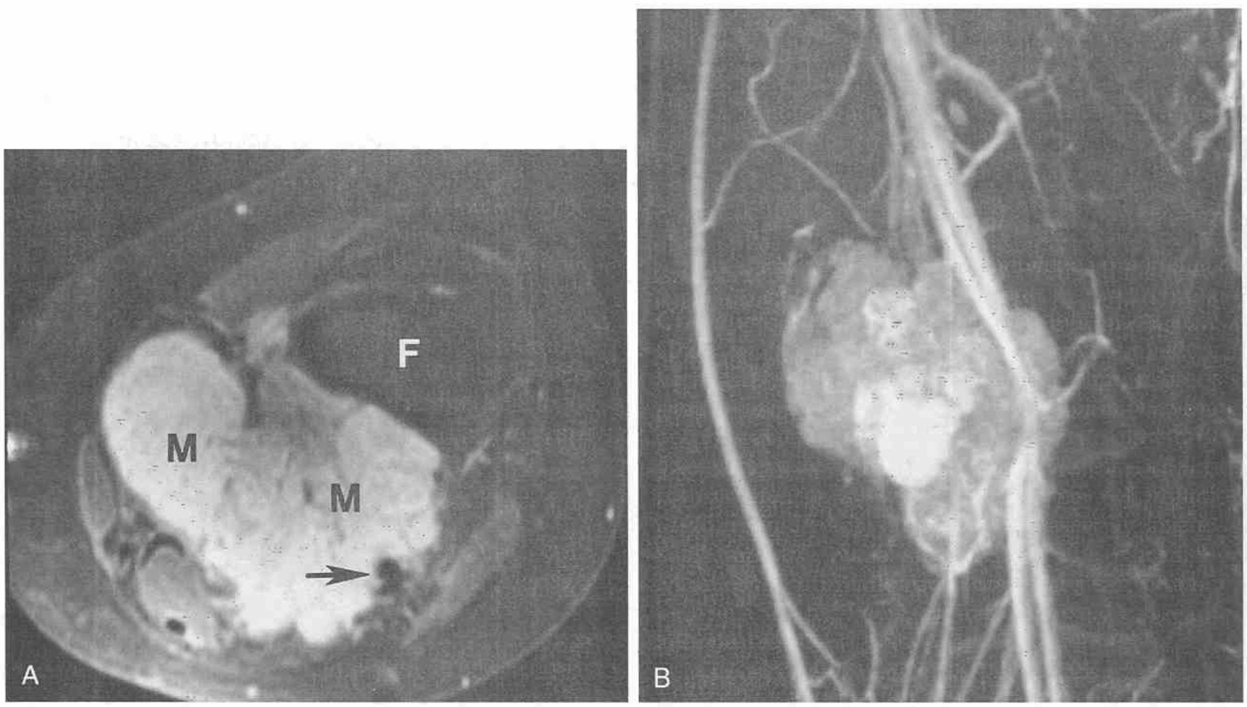

Figure 60–18. Synovial sarcoma of the popliteal fossa in a 7-year-old girl. *A,* Postgadolinium axial T1-weighted image (TR = 500 msec, TE = 8 msec) with fat saturation shows a multilobular mass (M) abutting the posterior margin of the femur and partially encasing the neurovascular bundle *(arrow)*. *B,* Coronal maximum intensity projection time-of-flight image (TR = 7.8 msec, TE = 2.4 msec, flip angle = 45 degrees) showing the three-dimensional relationship of the mass to the vasculature. Imaging was performed after gadolinium enhancement, which accounts for the increased signal intensity of the mass.

Lipoblastoma

Lipoblastoma is a rare neoplasm, typically presenting in children younger than 5 years of age. Although it is a benign tumor, lesions can be locally aggressive and may recur repeatedly if they are not completely excised.[10] Some lesions reportedly mature to stable, benign lipomas. Both the extremities and the trunk can be affected. In most patients, the lesion is solitary. The term *lipoblastomatosis* refers to the presence of multiple lesions.[10]

The various appearances of lipoblastomas on CT and MRI correspond to their varied histologic features (Fig. 60–19).[44, 49] Portions of the tumor with homogeneous fatty tissue on histologic examination have an appearance on CT and MRI that parallels normal body fat. Portions of the tumor with mucoid degeneration have an appearance on CT and MRI that is more congruent with soft tissue.

Fibromatous Lesions

A variety of fibromatous lesions may be seen in the pediatric age group. Lesions may be solitary or multifocal, and they may be indolent and nonaggressive or frankly aggressive.[22, 59, 74] Aggressive lesions may be characterized as fibrosarcoma. Contrary to the common expectation that fibrous lesions are of low signal intensity on all sequences, fibromatous lesions of childhood may show high signal intensity on T2-weighted and inversion recovery images.[22, 46, 59, 74] Margins may be well defined or infiltrative. Enhancement with gadolinium is variable (Fig. 60–20).

Neurofibroma

Neurofibromas may be solitary or multiple. Patients with neurofibromatosis may have multiple lesions or large

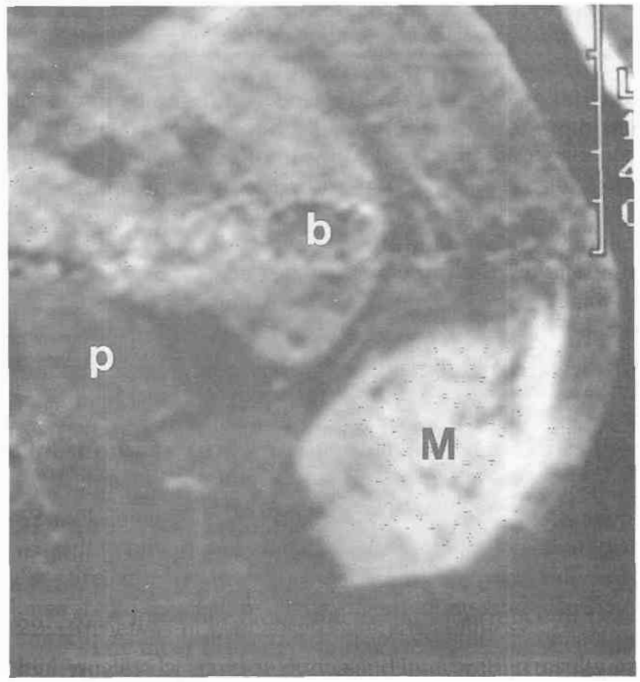

Figure 60–20. Aggressive fibromatosis of the posterolateral abdominal wall musculature in a 12-year-old boy. Axial postgadolinium T1-weighted image (TR = 700 msec, TE = 10 msec) with fat saturation shows marked enhancement of the mass (M). Lesion margins are irregular. b, bowel; p, psoas muscle.

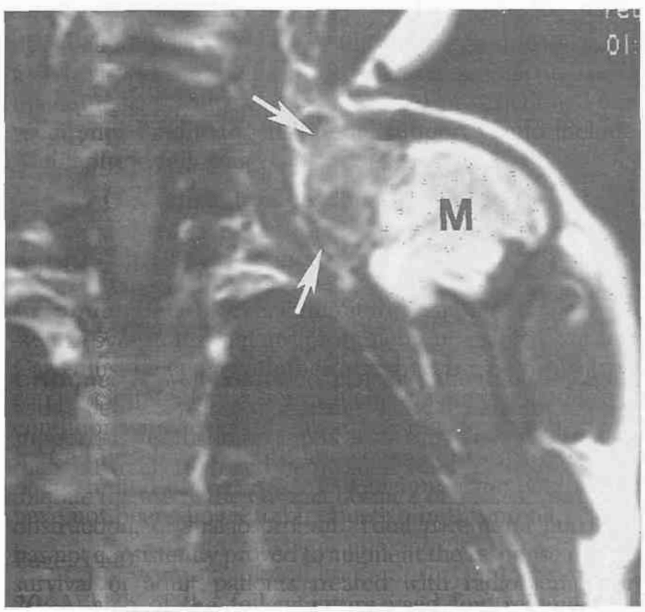

Figure 60–19. Lipoblastoma of the left supraclavicular soft tissues in a 17-month-old girl. Coronal T1-weighted image (TR = 550 msec, TE = 14 msec) shows a predominantly high-signal-intensity mass (M). The mass paralleled subcutaneous fat on all imaging sequences. An area of lower signal intensity *(arrows)* represents myxoid degeneration of a portion of the tumor.

Figure 60–21. Neurofibromatosis in a 4-year-old boy. Coronal inversion recovery image (TR = 4000 msec, TE = 30 msec, TI = 150 msec) shows a large plexiform neurofibroma. The multilobular appearance, central low signal intensity with lobules ("target sign") *(arrows)*, and plexiform course of the mass following the expected anatomic location of a nerve and its branches are characteristic findings.

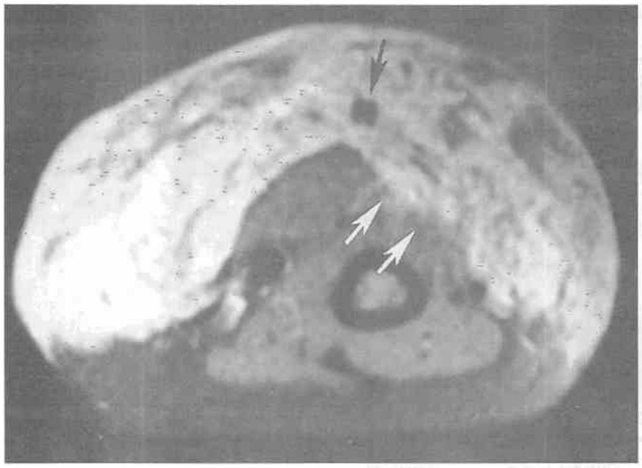

Figure 60–22. Hemangioma of the arm in a 2-year-old girl. Axial proton-density image (TR = 3700 msec, TE = 21 msec) with fat saturation shows a large, high-signal-intensity mass within the volar subcutaneous tissues. An indistinct plane with muscle anterolaterally *(white arrows)* suggests possible muscular involvement. Vasculature within the lesion produces small areas of signal void *(black arrow)*.

plexiform masses, typically following the course of a peripheral nerve. A characteristic finding is the "target sign" of central low signal intensity and peripheral high signal intensity within tumor lobules (Fig. 60–21).[5] A dominant mass within the lesion without this sign should raise concern about malignancy.[5]

Vascular Masses of Soft Tissue

Vascular lesions of the soft tissues[17, 54, 61, 66] constitute a diagnostic challenge because of their substantial overlap in appearance. A single lesion may contain components of different histologic lesions.

Hemangioma

Hemangioma is the most common benign soft tissue mass of childhood. Lesions present at birth or shortly thereafter, grow disproportionately to the child in infancy, and involute in later childhood. Histologically, hemangiomas are composed of solid tissue.

MRI reveals a characteristic appearance (Fig. 60–22). The lesions are of strikingly high signal intensity on T2-weighted images and inversion recovery images. An enhancing soft tissue component is seen after gadolinium administration. Blood vessels within the lesion produce flow voids on spin-echo sequences and high signal on gradient-echo sequences because of fast flow. Involuting hemangiomas may have a "feathery" appearance from interspersed fat. Occasionally, enlarged blood vessels are seen supplying the lesion.

Lymphangioma

Lymphangiomas are composed of anomalous lymphatic channels and cystic spaces filled with fluid. On MRI, these lesions may produce an appearance similar to hemangiomas on T2-weighted images; unlike hemangiomas, however, they do not enhance homogeneously after gadolinium enhancement (Fig. 60–23). Cystic areas enhance only at

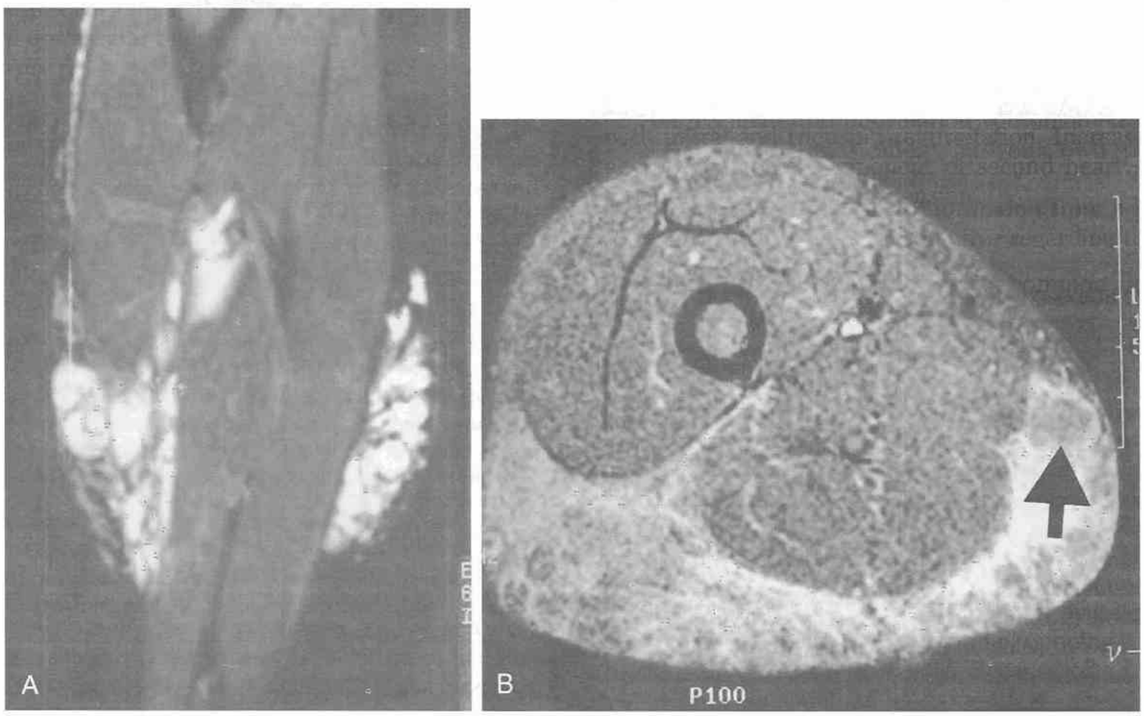

Figure 60–23. Lymphangioma of the thigh in a 7-year-old boy. *A,* Coronal inversion recovery image (TR = 4000 msec, TE = 25 msec, TI = 150 msec) shows a diffuse, multilobular, high-signal-intensity lesion principally within subcutaneous tissues. *B,* Postgadolinium axial T1-weighted image (TR = 650 msec, TE = 19 msec) with fat saturation shows minimal enhancement within interstices of the subcutaneous tissue. No soft tissue mass is defined. The fluid-containing cystic spaces do not enhance, but they do show peripheral enhancement *(arrow)*.

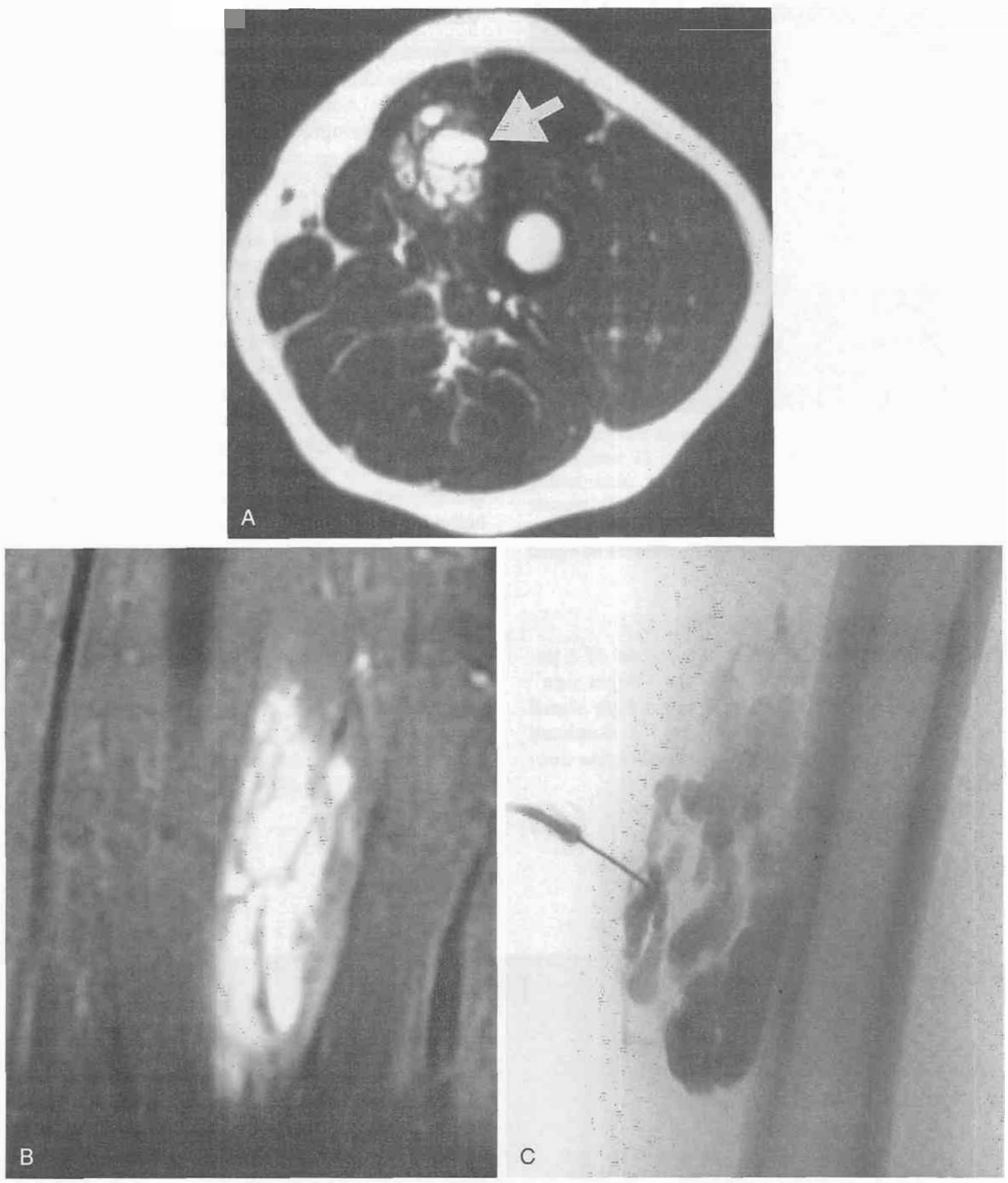

Figure 60–24. Venous malformation of the leg in an 11-year-old boy. *A,* Axial T2-weighted image (TR = 4000 msec, TE = 85 msec) shows a high-signal-intensity multilobulated mass *(arrow)* deep within the musculature. *B,* Sagittal postgadolinium T1-weighted image (TR = 500 msec, TE = 16 msec) with fat saturation shows diffuse enhancement of the lesion. Note the vertically oriented venous channels within the lesion. *C,* Correlative fluoroscopic spot image of the lesion obtained after direct contrast injection into the lesion in preparation for sclerotherapy.

their periphery. No enlarged blood vessels are identified within or supplying the lesion.

Vascular Malformation

Venous malformations arise from abnormal development of veins. Phleboliths are commonly present on radiographs. On MRI, lesions are of intermediate signal intensity on T1-weighted images and of high signal intensity on T2-weighted images (Fig. 60–24). Flow within venous malformation is stagnant; therefore, flow voids and bright gradient-echo signal are absent. MRI defines the extent of involvement of underlying muscle. Lesions enhance but without a soft tissue component.

Arteriovenous Malformation

Arteriovenous malformations represent a combined maldevelopment of arteries and veins with resultant shunting.

Figure 60–25. Myositis ossificans in a 9-year-old boy. *A*, Coronal T1-weighted image (TR = 600 msec, TE = 14 msec) with fat saturation shows an enhancing mass *(arrows)* within the proximal thigh. Enhancement is also seen within the adjacent soft tissues. *B*, The corresponding radiograph shows peripheral ossification within the lesion *(arrows)*.

MRI shows a tangle of blood vessels with evidence of high flow and no soft tissue component.

Post-traumatic Soft Tissue Masses

Hematoma

Hematoma produces a high signal on T1-weighted images, suggestive of blood products. Ring enhancement is seen after gadolinium administration. In boys with hemophilia, hemophilic pseudotumors may develop as a result of repeated hemorrhage. Over time, these pseudotumors can cause remodeling of adjacent bone.

Myositis Ossificans

Myositis ossificans may produce an aggressive-appearing lesion on MRI, quite similar in appearance to malignant soft tissue lesions.[47] These masses are bright on T2-weighted images and inversion recovery and enhance markedly with contrast (Fig. 60–25). If the clinical history of preceding trauma is not obtained, the cause of the mass may not be suspected. Plain radiographs and occasionally, if necessary, CT demonstrate a characteristic peripheral distribution of ossification within the lesion, suggestive of the diagnosis. The CT appearance differentiates the lesion from a surface osteosarcoma.

Bone Marrow

Normal Appearance and Physiologic Conversion

To diagnose abnormalities of bone marrow in children, it is imperative to understand the normal appearance on MRI and the changes that occur with age.[13, 64, 73, 80, 88, 89] Hematopoietic marrow is of low signal intensity on T1-weighted images and is isointense to muscle on T2-weighted and inversion recovery images. Fatty marrow is of high signal intensity on both T1-weighted and T2-weighted images. With fat saturation or on inversion recovery images, fatty marrow is of low signal relative to hematopoietic marrow.

With gadolinium administration, there is a mild enhancement of hematopoietic marrow that lessens with age.[3, 19] Fatty marrow does not enhance. Processes that replace normal marrow usually lower marrow signal on T1-weighted images, increase marrow signal on T2-weighted and inversion recovery images, and enhance with gadolinium.[3, 62] Substantial marrow enhancement usually indicates a pathologic process. For MRI evaluation of marrow, images of the lower lumbar spine (sagittal plane) and pelvis and proximal femurs (axial and coronal planes) are obtained.

At birth, hematopoietic marrow is present throughout the skeleton (Fig. 60–26). The epiphyseal and apophyseal ossification centers convert to fatty marrow within a few months after ossification. Next, the diaphyses of the long bones convert, followed by the distal metaphyses and later the proximal metaphyses. In teenagers and adults, residual hematopoietic marrow persists within the axial skeleton. In older children, streaks of hematopoietic marrow create an inhomogeneous appearance of the metaphyses, particularly in the proximal humeri and femora (Fig. 60–27). Disease processes that stress the marrow, such as anemia, cause reconversion of marrow from fatty marrow to hematopoietic marrow. Reconversion occurs in the inverse order of the physiologic conversion caused by aging.

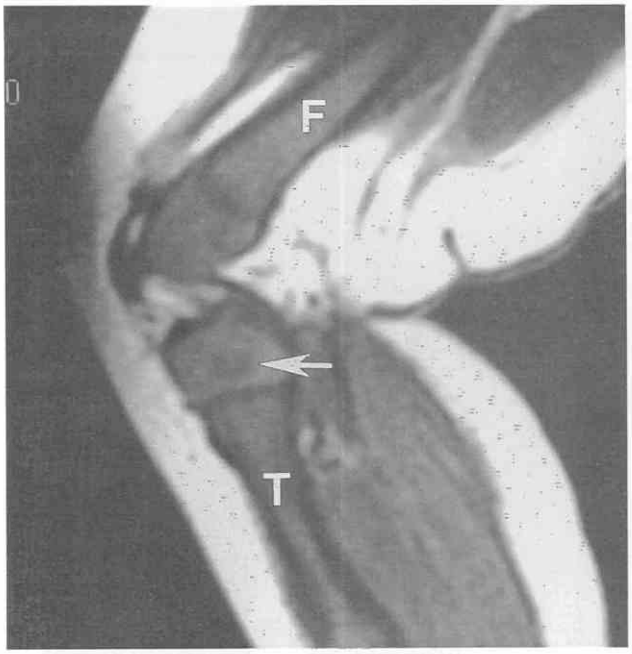

Figure 60–26. Normal bone marrow in a 9-week-old boy. Sagittal T1-weighted image (TR = 350 msec, TE = 16 msec) of the knee shows diffuse low signal intensity within metaphyseal and diaphyseal marrow, consistent with hematopoietic marrow. The proximal tibial ossification center is faintly visible *(arrow)*. F, femur; T, tibia.

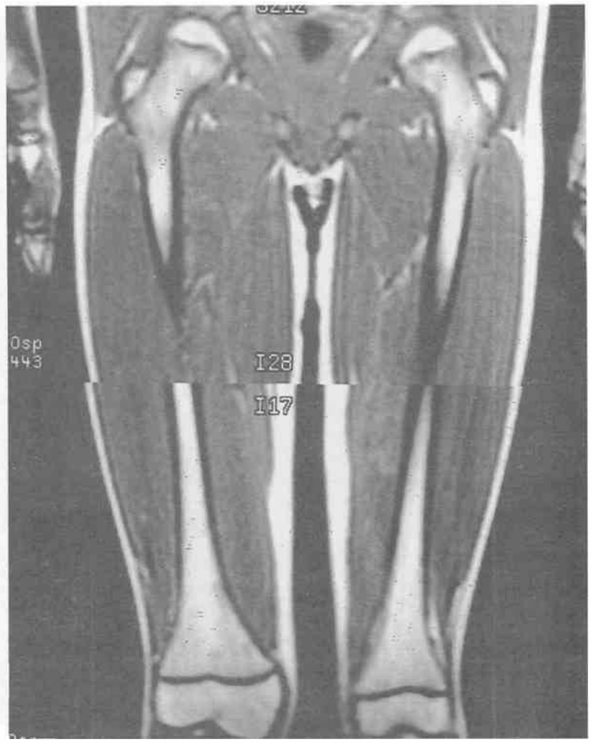

Figure 60–27. Normal bone marrow in an 11-year-old boy. Coronal T1-weighted images (TR = 500 msec, TE = 10 msec) of the distal and proximal femurs. Slight inhomogeneous decreased signal within the metaphyses is caused by normal residual hematopoietic marrow, more prominent in the proximal metaphyses than distal metaphyses. The epiphyses and diaphyses of the femurs are completely converted to fatty marrow.

Bone Marrow Edema

Bone marrow edema is produced by traumatic injury, inflammatory processes, and tumors. Edema within the marrow space decreases the signal intensity of fatty marrow on T1-weighted images and produces high signal on T2-weighted images and inversion recovery. Margins are ill defined. Enhancement is seen beyond the confines of the underlying infection or tumor.

Hematopoietic Malignancy

Hematopoietic malignancies, namely leukemia and lymphoma, infiltrate and proliferate within the marrow space. Normal marrow is replaced by neoplastic cells. Diffuse decreased signal is seen on T1-weighted images. Increased signal is seen on T2-weighted and inversion recovery images. Enhancement with gadolinium may be subtle and is usually seen diffusely (Fig. 60–28).[3] Marrow involvement with leukemia tends to be diffuse, but occasionally it is multifocal; however, marrow involvement with lymphoma tends to be multifocal but occasionally is diffuse. Metastatic disease may be multifocal or diffuse (see Fig. 60–7).[90]

Effects of Therapy

Chemotherapy causes a depletion of hematopoietic marrow, causing fatty replacement. Marrow reconversion is seen during the recovery stage. Granulocyte colony-stimulating factor stimulates stem cell proliferation and hence reconversion (Fig. 60–29).[26, 76] Described MRI findings after bone marrow transplant include hypointense peripheral bands in vertebral bodies, and diffuse homogeneous marrow hypointensity.[7, 84] Both findings are thought to represent engrafting marrow. Radiation therapy causes bone marrow edema acutely, with subsequent marrow depletion with fatty replacement within the radiation field.[85, 87]

Other Bone Marrow Disorders

In aplastic anemia, the marrow loses the ability to produce blood cells. There is diffuse and accelerated fatty replacement of hematopoietic marrow. In myelofibrosis, the marrow space is replaced by fibrotic tissue, yielding low signal on all MRI sequences. Disorders of hemoglobin synthesis and anemias, such as sickle cell disease, thalassemia, and spherocytosis, cause hyperplasia of hematopoietic marrow, which affects the entire skeleton. Hypertransfusion therapy may cause iron deposition within marrow. In these patients, marrow signal is strikingly low on all sequences (Fig. 60–30).[58]

Bone Marrow Infarction

Bone marrow infarction is seen most commonly in children with disorders of hemoglobin production, such as

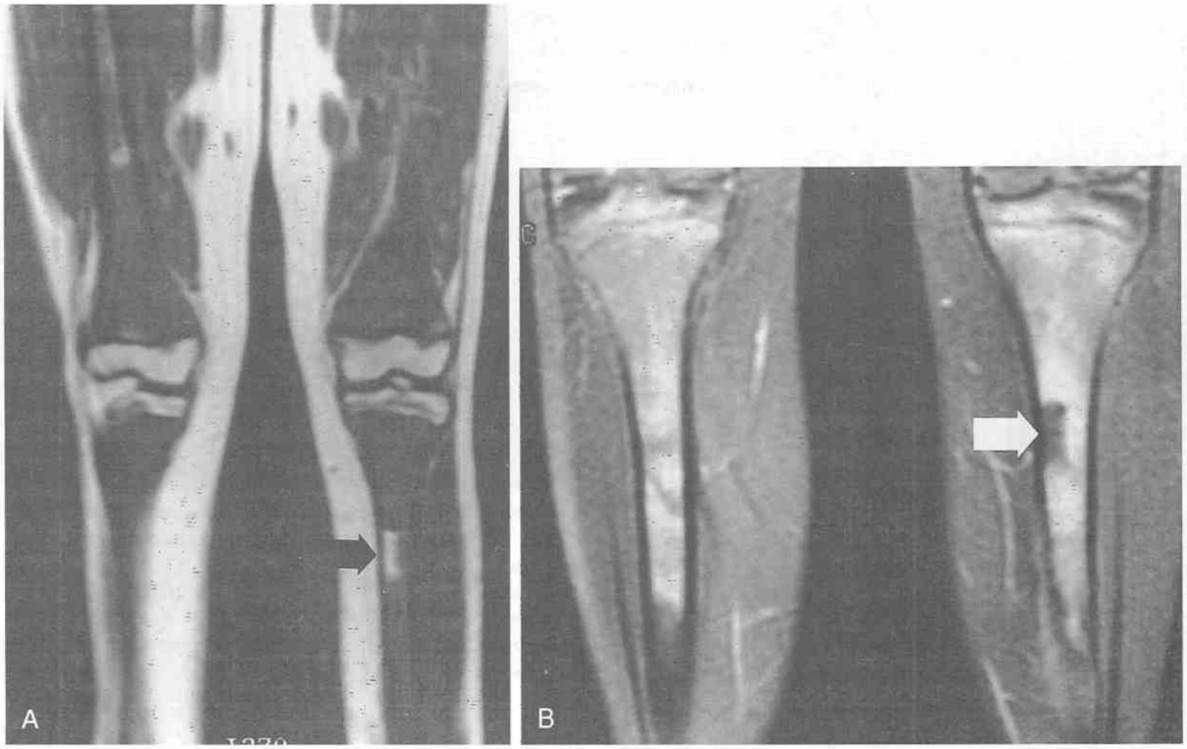

Figure 60–28. Acute lymphocytic leukemia in an 8-year-old girl. The patient initially presented with a 6-week history of knee pain and an elevated erythrocyte sedimentation rate and was thought clinically to have juvenile rheumatoid arthritis. *A,* Coronal T1-weighted image (TR = 700 msec, TE = 16 msec) shows diffuse low-signal-intensity abnormality within the metaphyses and diaphyses of the distal femurs and proximal tibias. A small area of normal marrow is seen in the left tibial diaphysis *(arrow)*. Lesser abnormality can be seen within the epiphyses. *B,* Postgadolinium coronal T1-weighted image (TR = 650 msec, TE = 10 msec) shows increased diffuse enhancement of the abnormal marrow. The residual area of normal marrow *(arrow)* does not enhance.

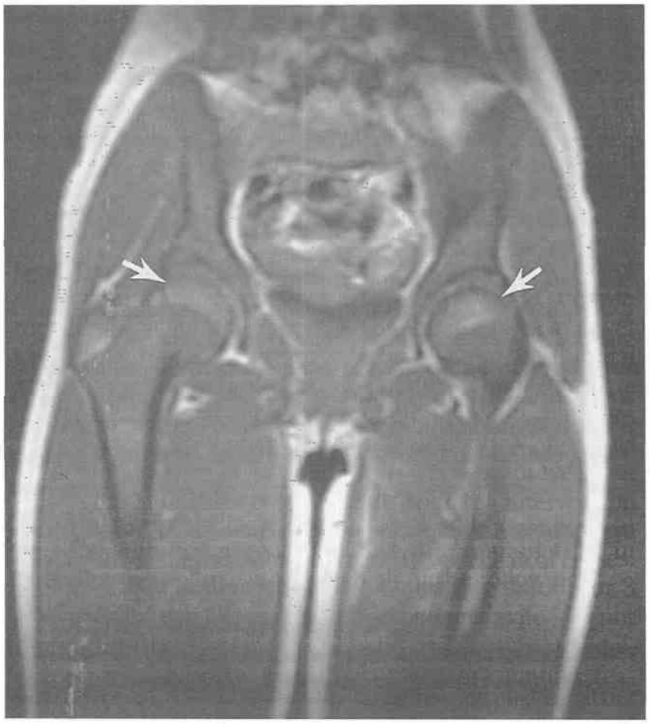

Figure 60–29. Pelvis and proximal femurs of a 10-year-old girl receiving chemotherapy and granulocyte colony-stimulating factor. Coronal T1-weighted (TR = 300 msec, TE = 9 msec) image shows pelvic and femoral metaphyseal and diaphyseal bone marrow of low signal intensity, consistent with reconversion. The marrow of the proximal femoral epiphyses *(arrows)* is slightly decreased in signal because of early reconversion.

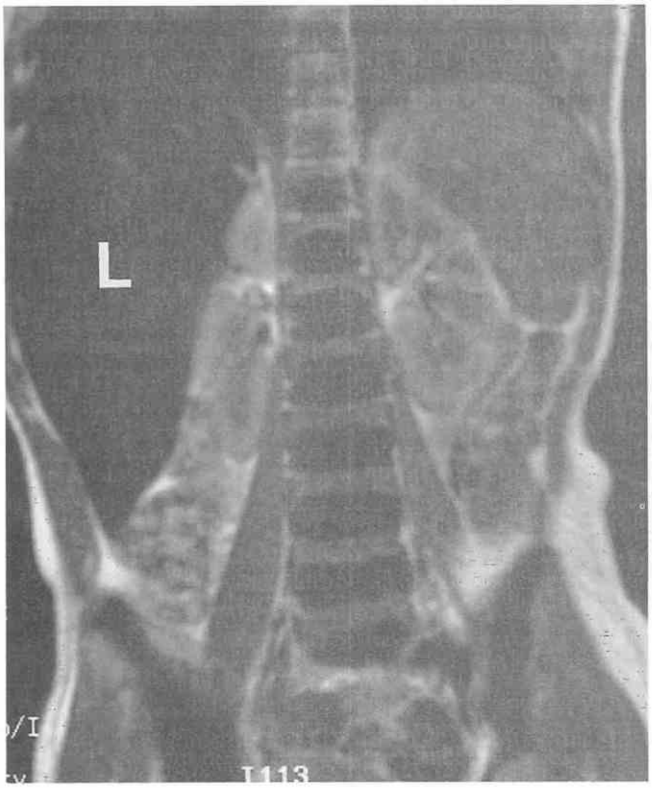

Figure 60–30. Thalassemia in a 3-year-old boy. A T1-weighted image (TR = 300 msec, TE = 16 msec) shows diffuse low signal intensity in vertebral and pelvic bone marrow caused by iron deposition. The low signal intensity within the liver (L) is also caused by iron deposition.

sickle cell disease, and in children taking steroids for various maladies. Bone marrow infarcts are of decreased signal intensity on T1-weighted images and of increased signal intensity on T2-weighted images. Enhancement may be seen on T1-weighted postgadolinium images. Differentiation between infarct and osteomyelitis may be difficult.[6] Infarcts are typically metaphyseal or metadiaphyseal and have well-defined serpiginous margins. Osteomyelitis is less well defined.

Avascular Necrosis

General Considerations

Idiopathic avascular necrosis can affect a number of sites throughout the skeleton. Commonly affected sites include the capital femoral epiphysis (Legg-Calvé-Perthes disease), the capitellum (Panner's disease), and the tarsal navicular bone (Köhler's disease). Post-traumatic avascular necrosis is most common at the scaphoid, talar dome, and capital femoral epiphysis. When symmetrical or multifocal, an underlying disease process (e.g., sickle cell disease) or therapy (e.g., steroids) may be the cause.

Plain radiographs are often diagnostic of avascular necrosis; however, early in the disease process plain radiographs appear normal or minimally abnormal. Bone scintigraphy may show a "cold spot" in acute infarction. In the reparative stages, the scintigrams become less specific. On

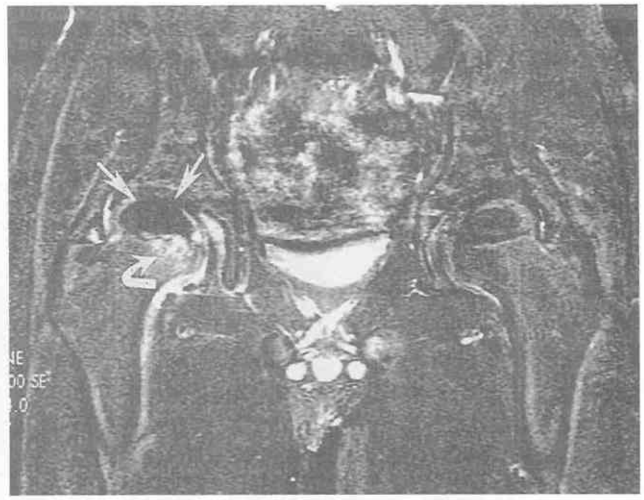

Figure 60–31. Idiopathic avascular necrosis of the right femoral head in a 9-year-old boy. Postgadolinium coronal T1-weighted subtraction image (TR = 400 msec, TE = 14 msec) with fat saturation shows low signal intensity in the right femoral head *(arrows)*, indicative of lack of normal enhancement. Some enhancement can be seen within the right femoral neck *(curved arrow)*.

MRI, infarcted bone is of low signal intensity on T1-weighted images and high signal intensity on T2-weighted images.[81] Devascularized portions of bone show a lack of enhancement after gadolinium administration (Fig. 60–31).

Legg-Calvé-Perthes Disease

Legg-Calvé-Perthes disease occurs most commonly in children from 4 to 8 years of age. Bilateral disease develops in 10% to 20% of patients; however, it is uncommon for both hips to show the same stage and degree of abnormality. If the abnormality is symmetrical, one should consider an underlying systemic disease process that may be predisposing the patient to avascular necrosis or to a skeletal dysplasia (e.g., Meyer's, epiphyseal, or spondyloepiphyseal dysplasia). MRI of avascular necrosis is most valuable early in the disease process when the diagnosis is in doubt.[31, 51] Some investigators have used MRI during the treatment phase of disease.[93] Prognostic schemes have been proposed on the basis of the MRI findings.[9, 18]

Infection and Inflammatory Processes

Osteomyelitis

Acute Osteomyelitis

Acute osteomyelitis in children is usually metaphyseal in location. Slow flow within sinusoidal end vessels at the metaphysis and decreased phagocytosis foster the deposition and growth of bacteria. In the axial skeleton, acute osteomyelitis has a propensity for sites equivalent to a metaphyseal area, such as adjacent to the triradiate cartilage or the vertebral end plates.

The initial imaging approach to suspected osteomyelitis is radiography. In a child with clinical signs and symptoms

of osteomyelitis and with radiographic findings consistent with the diagnosis, no further imaging may be necessary. More often, patients present with pain and fever early in the disease process, before bone destruction or periosteal new bone formation is evident on radiography. Traditionally, nuclear scintigraphy has been the next step in evaluation. Nuclear medicine is most valuable in patients when symptoms are poorly localized, when the site of disease is unknown, or when multifocal disease is suspected.

MRI for osteomyelitis is most productive when symptoms are localized so that a focused examination can be performed. MRI is indicated specifically when physeal or epiphyseal involvement is suspected, when the patient is thought to have spine or pelvic osteomyelitis, or when there is no response to therapy.[41] In the latter instance, MRI can identify fluid collections or devascularized bone.

At MRI examination, acute osteomyelitis produces low signal intensity on T1-weighted images and high signal intensity on T2-weighted images and inversion recovery because of infiltration of the marrow space with inflammatory cells and edema (Fig. 60–32). Enhancement is seen after gadolinium administration.[12] Margins of the lesion are ill defined, helping to distinguish infection from tumor, which may produce a sharp margin. Edema may extend into adjacent soft tissues. The presence of a subperiosteal fluid collection or abscess confirms the diagnosis of osteomyelitis and heralds the need for surgical drainage (Fig. 60–33).

Epiphyseal Osteomyelitis

Osteomyelitis may also be epiphyseal, resulting in a well-defined, rounded lesion. Either CT or MRI can be performed to characterize the lesion and to define its precise anatomic location.[2]

Subacute Osteomyelitis (Brodie's Abscess)

Subacute osteomyelitis represents a walled-off focus of less aggressive infection. Lesions are typically metaphyseal. A track leading to the adjacent physis is characteristic. The abnormality is well visualized on CT, particularly with the advent of longitudinal reconstructions (Fig. 60–34).

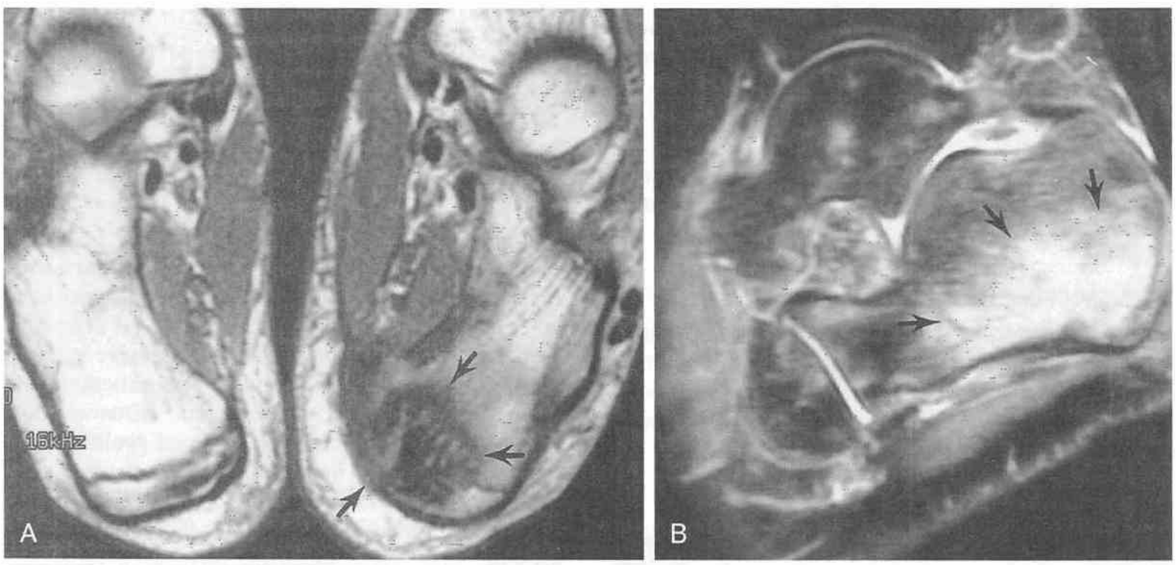

Figure 60–32. Acute osteomyelitis of the calcaneus in a 13-year-old. *A,* Axial T1-weighted image (TR = 600 msec, TE = 15 msec) shows low signal intensity in the posterior calcaneal body and adjacent apophysis *(arrows)*. *B,* Sagittal inversion recovery image (TR = 4000 msec, TE = 29 msec, TI = 165 msec) shows increased signal in the same region *(arrows)*. *C,* Coronal postgadolinium T1-weighted image (TR = 500 msec, TE = 17 msec) shows enhancement *(arrows)*. Findings are not specific; however, no focal mass is identified to suggest a neoplasm.

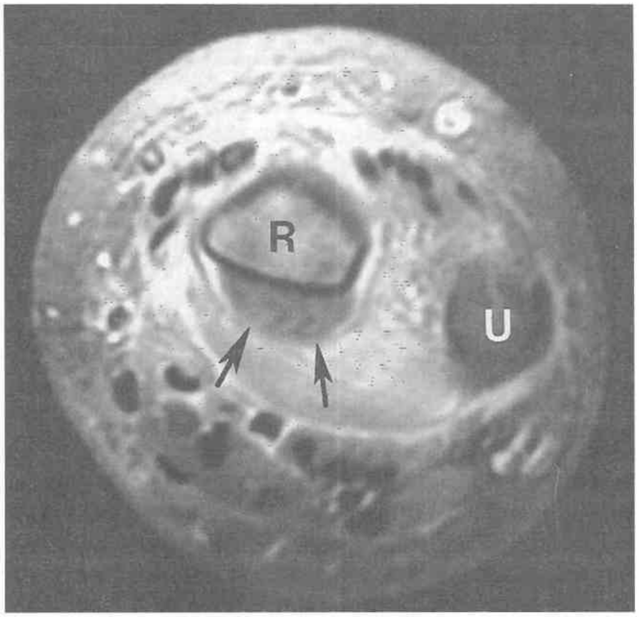

Figure 60–33. Acute osteomyelitis of the distal radius (R) in an 8-year-old girl. Axial postgadolinium T1-weighted image (TR = 500 msec, TE = 14 msec) with fat saturation shows a subperiosteal abscess *(arrows)*. Marrow of the radius enhances relative to the marrow of the ulna (U). Enhancement is also seen in adjacent soft tissues.

MRI demonstrates a layered appearance, which represents the layers of peripheral edema, sclerosis, and granulation tissue.

Chronic Osteomyelitis

Chronic osteomyelitis is the sequela of inadequately treated acute osteomyelitis. Chronic osteomyelitis is characterized by bony sclerosis, destruction, necrotic bone fragments (sequestra), cloaks of periosteal new bone containing the infection (involucra), and draining sinuses (cloaca). CT can delineate the bony abnormality and can specifically identify small sequestra that are poorly visualized by MRI.[33, 96] MRI can be performed to identify the extent of inflammatory tissue and to identify fluid collections to be drained.

Figure 60–34. Subacute osteomyelitis in a 6-year-old boy. Sagittal CT reformat image shows a well-defined lucent lesion *(arrows)* bridging the distal tibial growth plate.

Septic Arthritis

Most cases of septic arthritis of childhood are of hematogenous origin. Septic arthritis is most prevalent in the first decade of life. The hip and knee are most commonly affected. In the second decade of life, axial joints, particularly the sacroiliac joint, show greater involvement. For most joints, CT and MRI are not primary diagnostic modalities for joint infection[41]; nevertheless, for some children with joint infection, these techniques are used occasionally.

Infection produces a joint effusion. The synovium is inflamed and enhances briskly with contrast. Increased signal and enhancement may be seen in adjacent soft tissues. Some signal change and enhancement may be seen within the adjacent bone, even in the absence of infection. The MRI features of septic arthritis are nonspecific; other inflammatory joint conditions may have a similar appearance.

Juvenile Rheumatoid Arthritis, Hemophilia, and Pigmented Villonodular Synovitis

Juvenile rheumatoid arthritis (JRA), hemophilia, and pigmented villonodular synovitis (PVNS) have overlapping MRI imaging characteristics. All three processes are characterized by the presence of effusion and synovitis.[32, 42, 67]

Patients with JRA may show extensive pannus formation. This is seen as enhancing periarticular soft tissue, often with associated bone erosion.[37] Erosive changes can also be seen because of the synovial proliferation seen in PVNS. PVNS and hemophilia are both characterized by iron deposition within the synovium resulting from repeated hemarthrosis (Fig. 60–35).[42, 67] Occasionally, PVNS presents in a more localized form as a focal soft tissue mass.

Dermatomyositis

Dermatomyositis is an autoimmune condition not infrequently presenting in childhood. The disease process is characterized by muscle weakness and elevated blood levels of muscle enzymes and inflammatory markers. Skin disease may be minimal. Proximal muscles, particularly in the pelvis and proximal lower extremities, are affected in symmetrical fashion.

MRI can be used to confirm the diagnosis, delineate the extent of involvement, guide biopsy, and assess response to therapy.[34] In the acute stage of the disease, involved muscles have increased signal intensity on T2-weighted images and inversion recovery (Fig. 60–36). Strands of fluid are seen within septations between muscle bundles. The abnormality is occult on T1-weighted images. Gadolin-

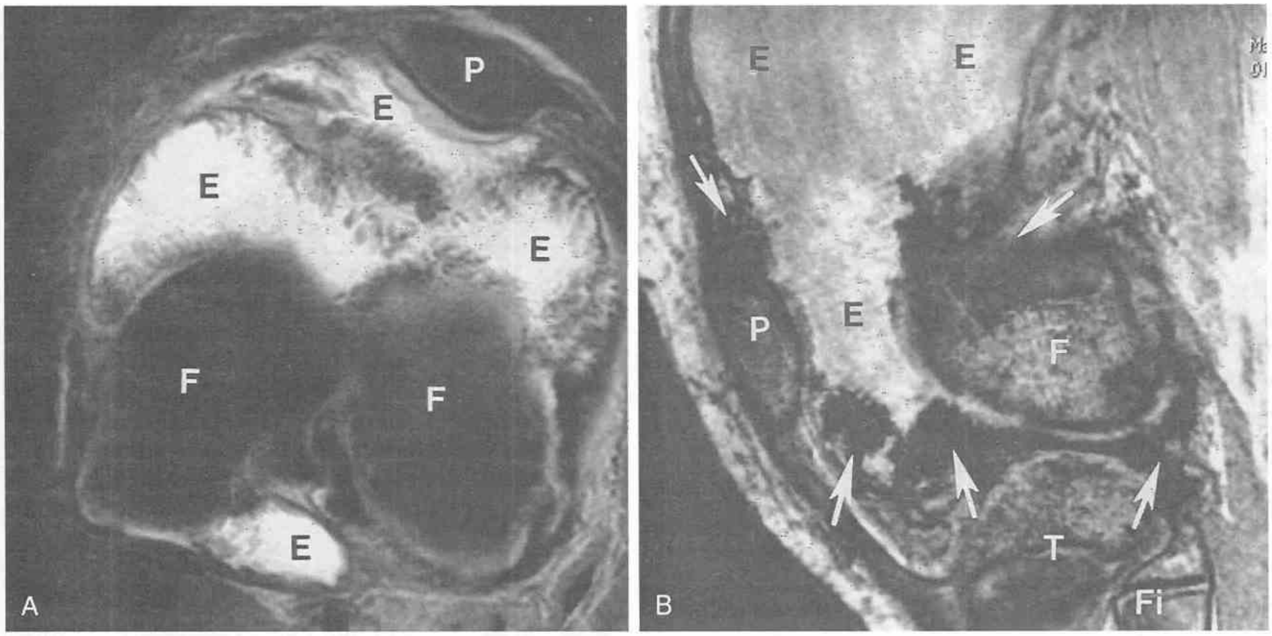

Figure 60–35. Persistent knee joint effusion in a 12-year-old boy with hemophilia. *A,* Axial proton-density image (TR = 4000 msec, TE = 15 msec) with fat saturation shows a large effusion (E) with marked synovial proliferative changes. *B,* Sagittal gradient-echo image (TR = 31 msec, TE = 15 msec, flip angle = 30 degrees) shows low-signal-intensity artifact from chronic hemosiderin deposition *(arrows).* F, femur; Fi, fibula; P, patella; T, tibia.

ium is not required. In advanced disease, fatty infiltration of the involved muscle may be seen.

Pyomyositis

A focus of infection within muscle is defined as pyomyositis. Pyomyositis can be solitary or multifocal. If multifocal, an underlying source, such as endocarditis, should be sought. Early in the disease process, an ill-defined increased signal within the involved muscle can be visualized. This progresses to the formation of an abscess within the muscle (Fig. 60–37). At this stage, MRI can identify a focal fluid collection with an enhancing rim within the muscle. The abnormality usually appears larger on T2-weighted fat saturation and inversion recovery images than on gadolinium-enhanced images because of the adjacent edema.

Necrotizing Fasciitis

Necrotizing fasciitis is an infection of the fascial planes of soft tissue. The infection can spread rapidly, subjecting the patient to substantial tissue loss and even death. MRI can be performed to help confirm the diagnosis and to define the extent of abnormality as a guide to therapy. MR images show edematous changes infiltrating deep fascial planes with fluid collections and enhancement after contrast

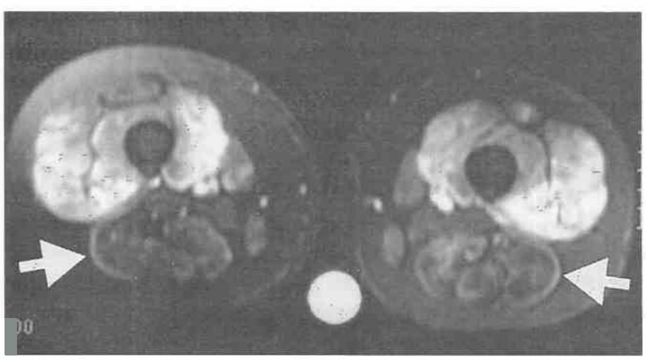

Figure 60–36. Dermatomyositis in a 13-year-old girl. Axial T2-weighted image (TR = 2500 msec, TE = 80 msec) with fat saturation shows symmetrical increased signal intensity within anterior thigh musculature. The relative sparing of the hamstring muscles posteriorly *(arrows)* is characteristic.

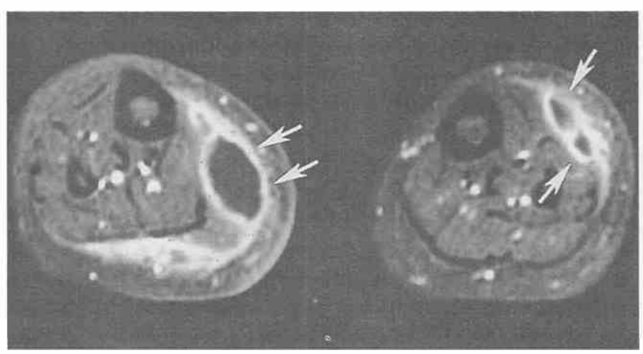

Figure 60–37. Pyomyositis in an 11-year-old girl. Axial postgadolinium T1-weighted image (TR = 417 msec, TE = 12 msec) with fat saturation shows intramuscular abscesses *(arrows)* within both legs. Multiple additional abscesses were present within both legs. No source was identified. A drain was placed in the right calf abscess under sonographic guidance.

administration.[79] In contradistinction, in cellulitis the inflammatory changes involve subcutaneous tissues and superficial fascia. An aggressive cellulitis may simulate necrotizing fasciitis on MRI.[79]

Trauma

Fracture

Radiographs delineate most fractures adequately such that further imaging is not usually necessary. CT is commonly used to delineate fractures of the axial skeleton that are incompletely shown by radiographs. Within the appendicular skeleton, CT is less often needed. In the pediatric population, CT is used to assess juvenile Tillaux and triplane fractures of the distal tibia, with specific reference to distraction or offset of fragments at the articular surface (Fig. 60–38).[23] CT is occasionally used to assess the adequacy of reduction of growth plate fractures in younger children, particularly Salter IV fractures, in which the incidence of premature fusion is increased by malalignment of the fracture fragments at the growth plate.

MRI identifies a fracture as a linear abnormality of low signal intensity on T1-weighted images and high signal intensity on T2-weighted images. It is also adept at demonstrating fractures of the growth plate, which may be occult to other imaging modalities.[40] In the infant who lacks ossification, MRI can define fractures that pass through the cartilaginous model of a growth center or through the adjacent growth plate. In older children, fractures involving the growth plate can occasionally be subtle on plain radiography. MRI demonstrates increased signal intensity within the fractured portion of the growth plate, accompanying metaphyseal or epiphyseal fracture lines, bone marrow edema, periosteal elevation or disruption, associated soft tissue edema, and joint effusion (Fig. 60–39).

Acute scaphoid fractures can be occult on radiographs. When there is a strong clinical suspicion but initial radiographs are negative or equivocal, the patient can be immobilized and follow-up films obtained. Alternatively, either CT or MRI can be performed.[11] MRI should be performed in a dedicated wrist coil. CT images are obtained with narrow collimation to allow reconstruction in other planes. Positioning the long axis of the scaphoid parallel to the CT scanner gantry (radial deviation) improves resolution of a fracture. In follow-up, CT is helpful to assess the nonunion of a scaphoid fracture and bony collapse. Both CT and MRI can be used to assess for proximal pole avascular necrosis caused by disruption of its recurrent blood supply. Acutely, no abnormality is seen on CT. More advanced avascular necrosis produces a sclerotic appearance of the proximal pole. On MRI, the avascular segment demonstrates low signal intensity on T1-weighted images because of edema acutely or sclerosis later.[11] On a T2-weighted scan, the avascular segment has high signal intensity. If gadolinium is administered, the avascular segment fails to enhance.

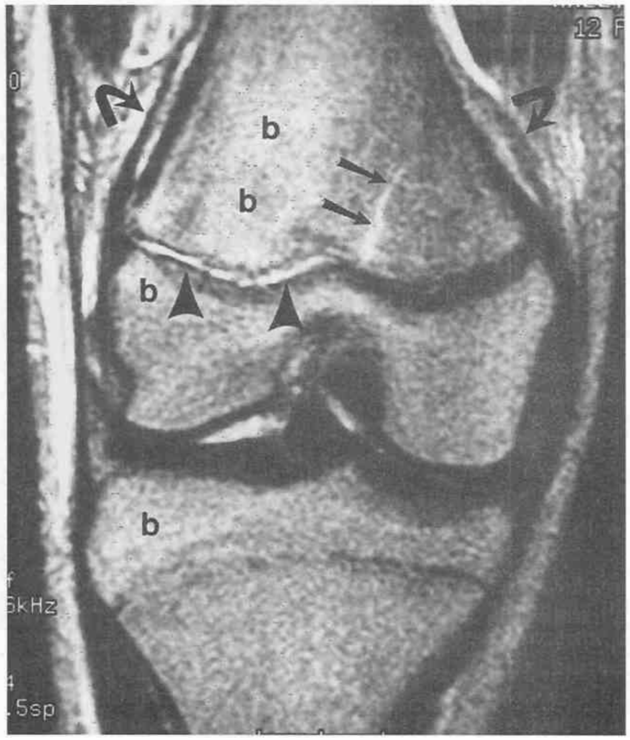

Figure 60–39. Salter II fracture of the distal femur in a 12-year-old girl. Coronal T2-weighted image (TR = 4200 msec, TE = 120 msec) delineates the fracture as a high-signal line in the metaphysis *(arrows)* and increased signal within the lateral growth plate *(arrowheads)*. b, bone marrow edema. Periosteal elevation is indicated by *curved arrows*.

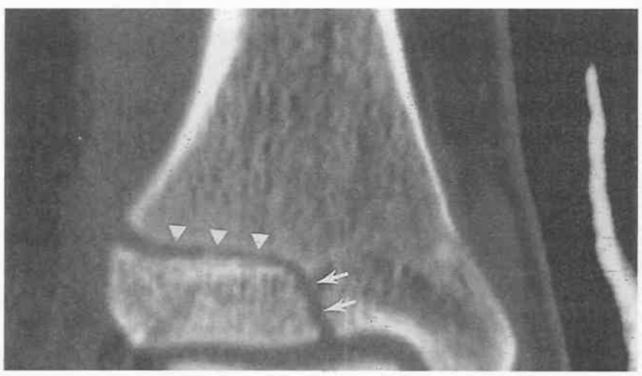

Figure 60–38. A juvenile Tillaux fracture of the distal tibia in a 14-year-old boy. Coronal CT reformat image delineates the transverse fracture line through the lateral growth plate *(arrowheads)* and the sagittal fracture line through the epiphysis *(arrow)*. The width and alignment of the fracture at the articular surface can be well visualized.

Stress Fracture

Children tend to experience stress fractures at a variety of locations throughout the body. The lower extremities are affected most frequently. The clinical history and physical examination are usually suggestive. Plain films may suffice for diagnosis. Bone scintigraphy, CT, or MRI may be performed when the diagnosis is unclear.[56, 99]

CT shows evidence of nonaggressive periosteal new bone formation.[99] On MRI, the affected bone shows decreased signal intensity on T1-weighted images and increased signal on T2-weighted and inversion recovery im-

Figure 60–40. A stress fracture of the distal femur in a 14-year-old boy. The patient had a remote history of Wilms' tumor but was also a cross-country runner who had recently increased his training. Coronal T2-weighted image (TR = 4800 msec, TE = 60 msec) shows increased signal within the distal femoral metaphysis and adjacent soft tissues. A transverse band of decreased signal corresponds to a band sclerosis *(arrows)* seen on subsequent radiographs.

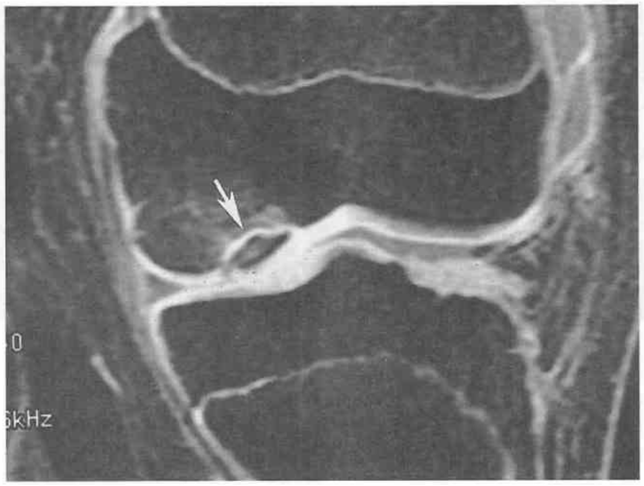

Figure 60–41. Osteochondritis dissecans in a 14-year-old girl. The 3D-gradient-echo image (TR = 60 msec, TE = 7 msec, flip angle = 40 degrees) with fat saturation shows a nondisplaced fragment within a defect within the medial femoral condyle *(arrow)*. The overlying cartilage appears to be intact.

ages.[56] Both CT and MRI may show cortical thickening. Edema is seen within adjacent soft tissues; however, no associated soft tissue mass is identified. In advanced cases of stress fracture, a distinct fracture line may be identified (Fig. 60–40). The MRI findings of stress fracture may be nonspecific and difficult to separate from infection or tumor. Correlation with plain radiographs is imperative.

Osteochondritis Dissecans

Osteochondritis dissecans is probably a sequela of trauma. Although the femoral condyles are the most common location, osteochondral injury is also seen at the talus, patella, and capitellum.[14, 16, 68] At the knee, the classic location is the lateral aspect of the medial femoral condyle. Patients present with joint pain and swelling.

The prognosis and treatment of osteochondral injuries depend on the size of the lesion and its stability. It is important to determine whether there is a bone fragment within the defect, whether the bone fragment is affixed to the underlying bone, and whether the overlying cartilage is intact.[15] CT is occasionally performed to characterize the defect and identify the bone fragments. Without intra-articular contrast, CT cannot define cartilage integrity. CT arthrography can be used to identify loose bodies within the joint, with precontrast images to assess for osseous fragments and postcontrast images to assess for cartilaginous fragments.

MRI is excellent for assessing osteochondral injury (Fig. 60–41).[14–1[illegible]] The size of the defect and the presence of a fragment within the defect are readily confirmed. High signal intensity at the interface between the fragment and the underlying bone suggests that the fragment is unstable.[15] Cartilage sequences can usually define the integrity of the overlying cartilage. Intra-articular gadolinium can also be used to assess cartilaginous integrity as well as to define the stability of a fragment. Gadolinium seen between the fragment and the underlying bone suggests an unstable fragment. MRI does have some limitations in assessing for intra-articular loose bodies. The presence of a joint effusion makes identification of loose bodies easier.

Soft Tissue Injury

As in adults, MRI in children is adept at identifying and defining injuries of muscle, tendons, and ligaments.[45, 101] Ligamentous injury is relatively uncommon in the young

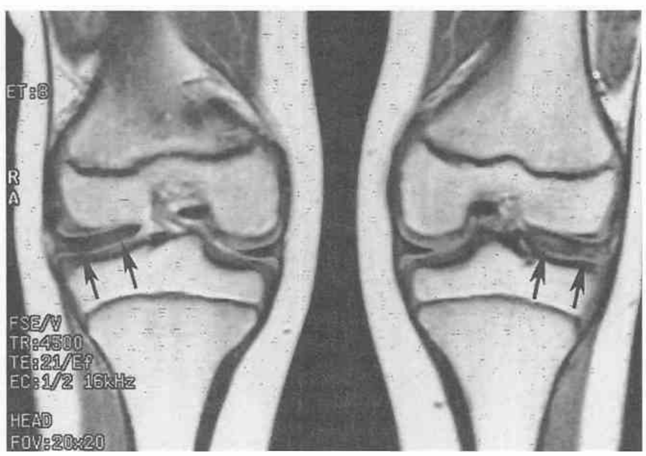

Figure 60–42. Bilateral discoid lateral menisci in a 9-year-old boy who complained of "clicking" within both knees. Coronal proton-density image (TR = 4500 msec, TE = 21 msec) shows abnormally large lateral menisci *(arrows)*. Increased signal within the substance of the menisci may represent early degeneration, although no tear is identified.

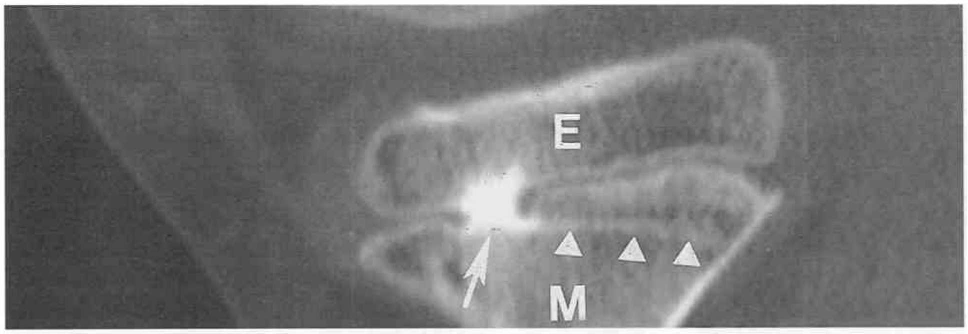

Figure 60–43. Post-traumatic growth arrest of the proximal tibia in an 11-year-old boy. A coronal CT reformat image from 1-mm collimation helical source images shows a focal bony bar *(arrow)* joining metaphysis (M) to epiphysis (E) across the growth plate. A growth line *(arrowheads)* is tethered by the bony bar. This bar was resected.

child because the growth plates are not yet fused and thus represent a site of relative weakness. Some degree of inherent ligamentous laxity in children also contributes to the lower incidence of ligamentous injury. Lateral compartment contusions, usually indicative of an anterior cruciate ligament (ACL) tear in adults, may be seen in children with an intact ACL.[83] Once the growth plates have fused, the adolescent is prone to many of the same ligament and tendon injuries seen in young adults. These injuries are detailed in Chapter 48, The Knee.

A few particular sites of injury warrant specific comment. The ACL is rarely injured prior to fusion of the physes; however, the presence of open physes and the diagnosis of physeal fracture do not necessarily exclude the presence of ACL injury. Avulsions of the tibial spines, and hence the ACL, are not infrequent in children. Discoid menisci should be suspected in younger children with meniscal injuries, particularly if the lateral meniscus is involved (Fig. 60–42).[82]

Foreign Body

Although sonography is preferred at superficial locations, both CT and MRI have been employed to confirm the presence of soft tissue foreign bodies and to delineate their location.

Growth Plate Arrest

The most common cause of premature growth plate fusion is trauma. Other causes include infection, thermal injury, and frostbite. Radiographs are often sufficient to make the diagnosis. Both CT and MRI have been employed to confirm premature growth plate fusion and to delineate its extent for planning operative therapy.

Growth plate fusion is assessed by CT with narrow collimation axial source images and reconstructions in the coronal and sagittal planes. Areas of premature fusion are

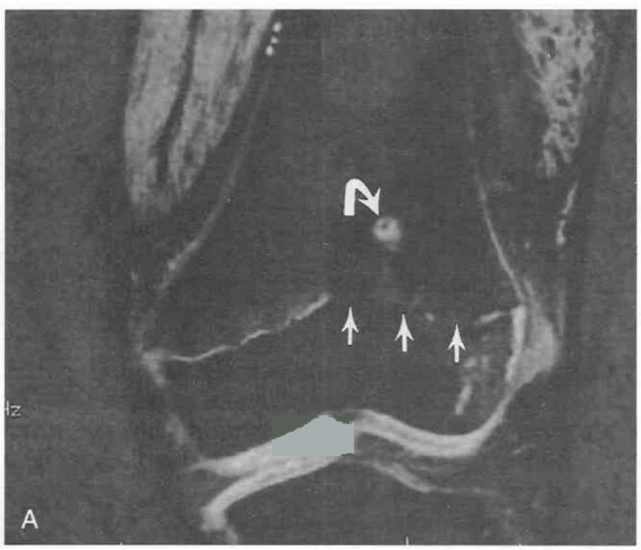

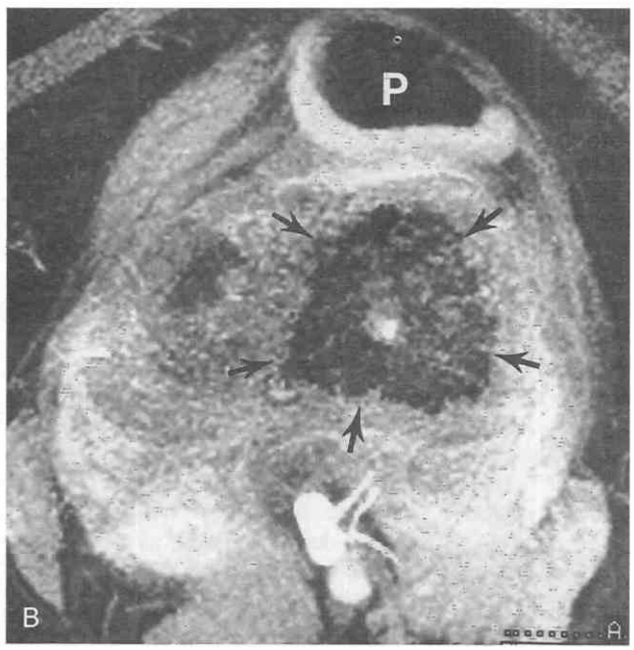

Figure 60–44. Post-traumatic growth arrest of the distal femur in an 11-year-old boy. *A,* Coronal gradient-echo image (TR = 500 msec, TE = 12 msec, flip angle = 60 degrees) with fat saturation shows an extensive area of fusion *(arrows)* within the lateral aspect of the distal femoral growth plate. A small cartilaginous inclusion in the metaphysis is indicated by the *curved arrow. B,* Axial maximum intensity projection image obtained from 3D-gradient-echo images maps the area of growth plate fusion *(arrows).* Because the area of fusion was extensive, resection was not attempted. The patient subsequently underwent an Ilizarov limb-lengthening procedure. P, patella.

seen as sclerotic bridges of bone crossing the growth plate (Fig. 60–43).[98] Larger areas of fusion may lead to medullary continuity between metaphysis and epiphysis. Growth lines may be seen within the adjacent metaphysis, tethered to the physis by the site of fusion. Premature physeal fusion can also be assessed by MRI with cartilage-sensitive gradient-echo images or proton-density images with fat saturation.[8] Areas of premature fusion are seen as low-signal-intensity defects within the high-signal-intensity physis. Maximum intensity projection images in the axial plane map the extent of fusion (Fig. 60–44).[8]

Developmental Abnormalities

Congenital Limb Anomalies

In children with congenital limb-reduction anomalies, MRI may be used to delineate the cartilaginous model of bone before ossification.[55] MRI is particularly valuable in cases of proximal focal femoral deficiency in determining whether there is continuity of the femur (Fig. 60–45).

Developmental Dysplasia of the Hip

CT can be used to determine the relationship of the femoral head to the acetabulum during treatment of developmental dysplasia of the hip.[20, 32] CT is particularly valuable after operative reduction, when an overlying cast diminishes the value of plain radiographs (Fig. 60–46).

Targeted axial images are centered at the level of the hips. A reduced milliampere-second (mAs) setting can be employed. If concentrically positioned, the femoral head is located immediately over the triradiate cartilage. Prior to ossification, the position of the femoral head is less well delineated; however, its position may be inferred from the position of the proximal femoral metaphysis. In cases of

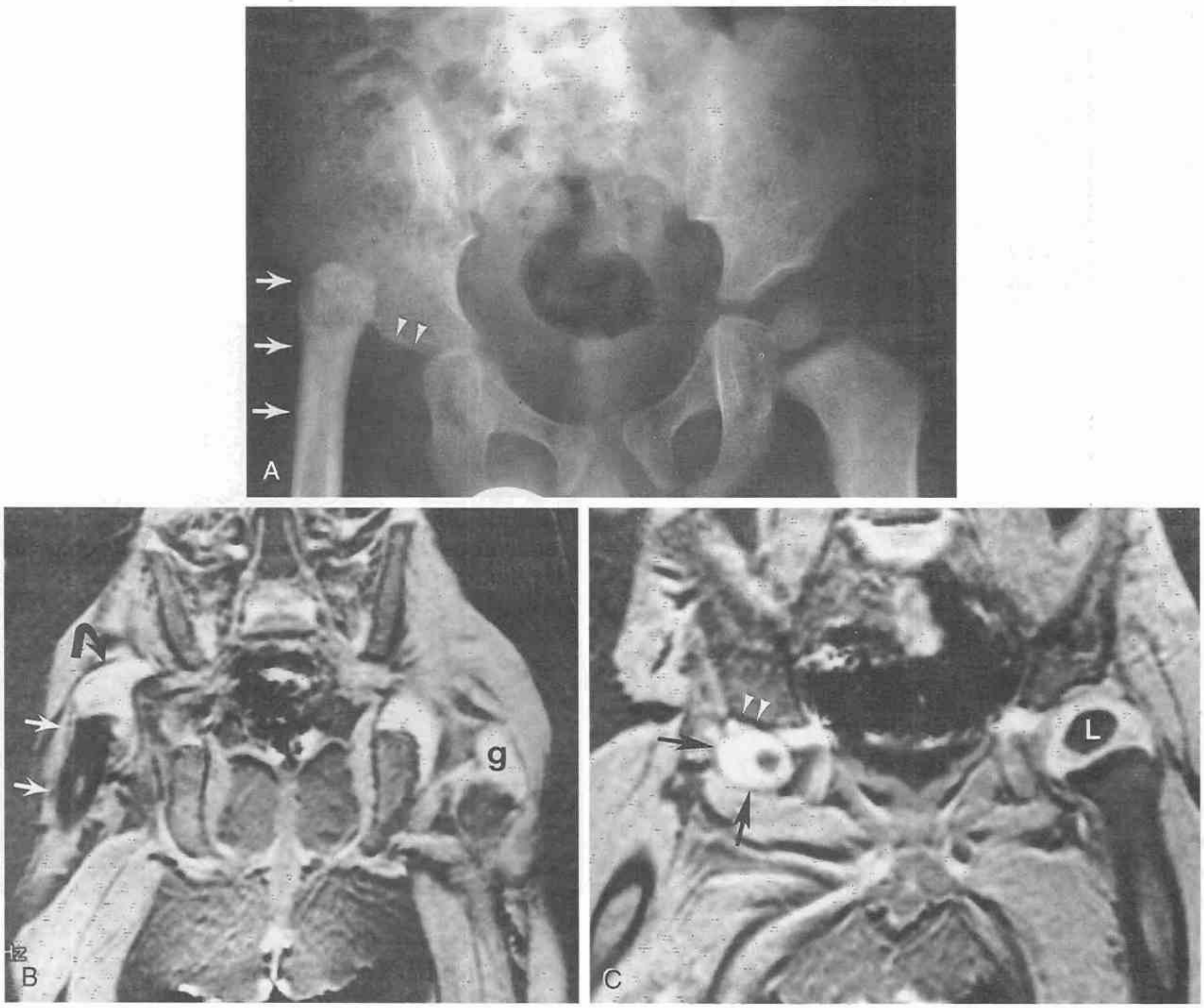

Figure 60–45. Proximal focal femoral deficiency in a 19-month-old boy. *A*, Radiograph shows no oss[redacted] right femor[redacted]ead. The proximal femur is diminutive and displaced superolaterally. A relatively well formed right acetabulum *(arrowheads)* suggests the presence of a right femoral head. The left hip and femur appear normal. *B* and *C*, Coronal gradient-echo images (TR = 60 msec, TE = 7 msec, flip angle = 40 degrees) show displacement of the proximal right femur *(short arrows)* with a cartilaginous greater trochanter growth center at its cephalad aspect *(curved arrow)*. A separate femoral head *(long arrows)* with a small early ossification center is seen within a relatively well formed right acetabulum *(arrowheads)*. g, greater trochanter; L, left proximal femoral epiphysis.

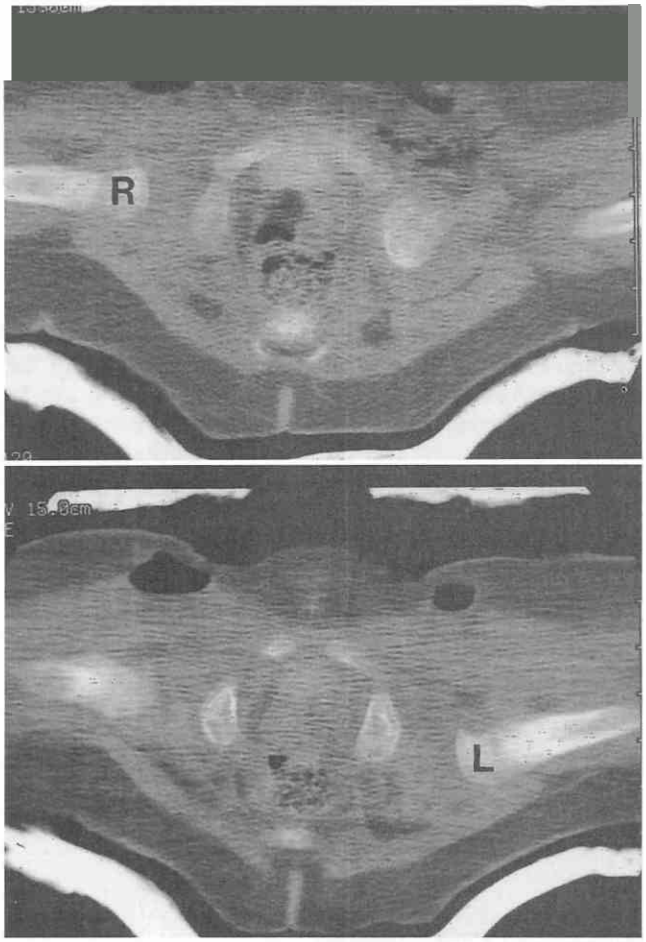

Figure 60–46. Bilateral developmental dysplasia of the hips in a 2-month-old infant wearing a spica cast. Apart from the scout topogram, these two axial images constituted the entire CT examination. The images were obtained with 40 milliampere-seconds (mAs). Neither femoral head is ossified. *Top,* Right hip reduced, with the femoral metaphysis (R) in correct alignment with the right acetabulum. *Bottom,* persistent posterior dislocation of the left hip (L).

failed reduction, CT may identify tissue (pulvinar) or iliopsoas tendon interposed between the femoral head and the acetabulum.[35]

Femoral Anteversion/Tibial Torsion

Rotational anomalies of the femur or tibia may produce in-toeing, genu valgum, and gait abnormalities. Femoral anteversion refers to the anteriorly directed angle the femoral neck makes relative to the femoral shaft. Tibial torsion refers to the rotation of the proximal tibia relative to the distal tibia. Although rough assessments of femoral anteversion and tibial torsion can be obtained through physical examination, CT provides a more precise delineation.[36]

To measure femoral anteversion, limited axial images are obtained through the femoral neck and femoral condyles (Fig. 60–47). The difference in angulation between the axis of the femoral neck and the femoral condyles determines femoral anteversion. The normal measurement decreases with age, from an average of 32 degrees at birth to 16 degrees at 16 years of age.[36, 75] Tibial torsion is measured by a similar method.[50]

Tarsal Coalition

Calcaneonavicular and talocalcaneal are the most common forms of tarsal coalition. Patients most commonly present in the second decade of life with foot pain and flatfoot deformity. Early in childhood, coalitions are not evident on CT or plain radiographs, since they are cartilaginous or fibrous. With maturation, the coalitions increase in symptoms and radiologic conspicuity.

Calcaneonavicular coalitions form between the anterior process of the calcaneus and the posterolateral aspect of the navicular bone. Calcaneonavicular coalitions are well seen on oblique radiographs of the foot. CT is not usually required. Talocalcaneal coalitions form at the middle facet joint and involve the sustentaculum tali of the calcaneus. Talocalcaneal coalitions may be suspected on the basis of plain radiographs; however, they are better seen with CT.[95] Coronal images demonstrate osseous continuity of the talus and calcaneus or, in the case of fibrous union, close apposition of the bones with lack of the normal joint space and deformity, suggesting union (Fig. 60–48). Images can be obtained directly in the coronal plane or reconstructed from an axial acquisition. MRI has also been used to assess for tarsal coalition and is particularly helpful in nonosseous coalition.[95]

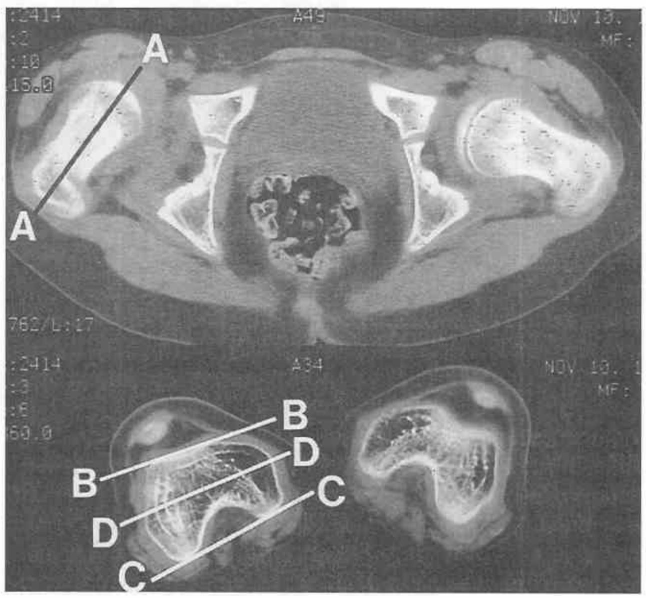

Figure 60–47. Recurrent right hip dislocation in a 9-year-old girl with cerebral palsy. Axial CT images obtained at the levels of the femoral necks *(top)* and the femoral condyles *(bottom)* are used to measure anteversion. The difference in angulation between the axis of the femoral neck (line A) and the transcondylar axis (line D) gives the angle of anteversion. The transcondylar axis is determined by bisecting the angle formed by tangent lines along the anterior (line B) and posterior (line C) aspects of the femoral condyles. The subluxated right femur is anteverted compared to the left femur.

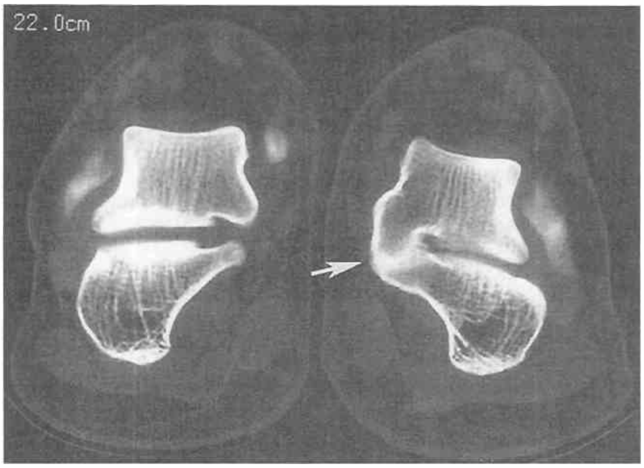

Figure 60–48. Tarsal coalition in a 15-year-old boy. The direct coronal CT image shows osseous continuity of the left talus and calcaneus at the middle talocalcaneal joint *(arrow)*. The right side is normal.

References

1. Assoun J, Richardi G, Railhac J, et al: Osteoid osteoma: MR imaging versus CT. Radiology 191:217, 1994.
2. Azouz EM, Greenspan A, Marton D: CT evaluation of primary epiphyseal bone abscesses. Skeletal Radiol 22:17, 1993.
3. Baur A, Stabler A, Bartl R, et al: MRI gadolinium enhancement of bone marrow: Age-related changes in normals and in diffuse neoplastic infiltration. Skeletal Radiol 26:414, 1997.
4. Beltran J, Simon DC, Levy M, et al: Aneurysmal bone cysts: MR imaging at 1.5 T. Radiology 158:689, 1986.
5. Bhargava R, Parham DM, Lasater OE, et al: MR imaging differentiation of benign and malignant peripheral nerve sheath tumors: Use of the target sign. Pediatr Radiol 27:124, 1997.
6. Bonnerot V, Sebag G, de Montalembert M, et al: Gadolinium-DOTA enhanced MRI of painful osseous crises in children with sickle cell anemia. Pediatr Radiol 24:92, 1994.
7. Boothroyd AE, Sebag G, Brunelle F: MR appearances of bone marrow transplantation. Pediatr Radiol 21:291, 1991.
8. Borsa JJ, Peterson HA, Ehman RL: MR imaging of physeal bars. Radiology 199:683, 1996.
9. Bos CFA, Bloem JL, Bloem RM: Sequential magnetic resonance imaging in Perthes' disease. J Bone Joint Surg Br 73:219, 1991.
10. Chung EB, Enzinger FM: Benign lipoblastomatosis: An analysis of 35 cases. Cancer 32:482, 1973.
11. Cook PA, Yu JS, Wiand W, et al: Suspected scaphoid fractures in skeletally immature patients: Application of MRI. J Comput Assist Tomogr 21:511, 1997.
12. Dangman BC, Hoffer FA, Rand FF, et al: Osteomyelitis in children: Gadolinium-enhanced MR imaging. Radiology 182:743, 1992.
13. Dawson KL, Moore SG, Rowland JM: Age-related marrow changes in the pelvis: MR and anatomic findings. Radiology 183:47, 1992.
14. DeSmet A, Fisher D, Burnstein M, et al: Value of MR imaging in staging osteochondral lesions of the talus (osteochondritis dissecans): Results in 14 patients. AJR Am J Roentgenol 154:555, 1990.
15. DeSmet AA, Fisher DA, Graf BK, et al: Osteochondritis dissecans of the knee: Value of MR imaging in determining lesion stability and the presence of articular cartilage defects. AJR Am J Roentgenol 155:549, 1990.
16. De Smet AA, Ilahi OA, Graf BK: Untreated osteochondritis dissecans of the femoral condyles: Prediction of patient outcome using radiographic and MR findings. Skeletal Radiol 26:463, 1997.
17. Dubois J, Garel L: Imaging and therapeutic approach of hemangiomas and vascular malformations in the pediatric age group. Pediatr Radiol 29:879, 1999.
18. Ducou le Pointe H, Haddad S, Silberman B, et al: Legg-Calvé-Perthes disease: Staging by MRI using gadolinium. Pediatr Radiol 24:88, 1994.
19. Dwek J, Shapiro F, Laor T, et al: Normal gadolinium-enhanced MR images of the developing appendicular skeleton: Part 2. Epiphyseal and metaphyseal marrow. AJR Am J Roentgenol 169:191, 1997.
20. Eggli KD, King SH, Boal DKB, et al: Low-dose CT of developmental dysplasia of the hip after reduction: Diagnostic accuracy and dosimetry. AJR Am J Roentgenol 163:1441, 1994.
21. Erlemann R, Reiser MF, Peters PE, et al: Musculoskeletal neoplasms: Static and dynamic Gd-DTPA-enhanced MR imaging. Radiology 171:767, 1989.
22. Feld R, Burk DL, McCue P, et al: MRI of aggressive fibromatosis: Frequent appearance of high signal intensity of T2 weighted images. Magn Reson Imaging 8:583, 1990.
23. Feldman F, Singson RD, Rosenberg ZS, et al: Distal tibial triplane fractures: Diagnosis with CT. Radiology 164:429, 1987.
24. Fletcher BD: Response of osteosarcoma and Ewing sarcoma to chemotherapy: Imaging evaluation. AJR Am J Roentgenol 157:825, 1991.
25. Fletcher BD, Hanna SL: Pediatric musculoskeletal lesions simulating neoplasms. Magn Reson Imaging Clin North Am 4:721, 1996.
26. Fletcher BD, Wall JE, Hanna SL: Effect of hematopoietic growth factors on MR images of bone marrow in children undergoing chemotherapy. Radiology 189:745, 1993.
27. George JC, Buckwalter KA, Cohen MD, et al: Langerhans cell histiocytosis of bone: MR imaging. Pediatr Radiol 24:29, 1994.
28. Gronemeyer SA, Kauffman WM, Rocha MS, et al: Fat-saturated contrast-enhanced T1-weighted MRI in evaluation of osteosarcoma and Ewing sarcoma. J Magn Reson Imaging 7:585, 1997.
29. Hanna SL, Fletcher BD, Kaste SC, et al: Increased confidence of diagnosis of Ewing sarcoma using T2-weighted MR images. Magn Reson Imaging 12:559, 1994.
30. Hanna LS, Magill HL, Parham DM, et al: Childhood chondrosarcoma: MR imaging with Gd-DTPA. Magn Reson Imaging 8:669, 1990.
31. Henderson RC, Renner JB, Sturdivant MC, et al: Evaluation of magnetic resonance imaging in Legg-Calvé-Perthes disease: A prospective, blinded study. J Pediatr Orthop 10:289, 1990.
32. Hernandez RJ: Concentric reduction of the dislocated hip. Computed-tomographic evaluation. Radiology 150:266, 1984.
33. Hernandez RJ: Visualization of small sequestra by computerized tomography: Report of 6 cases. Pediatr Radiol 15:238, 1985.
34. Hernandez RJ, Sullivan DB, Chenevert TL, et al: MR imaging in children with dermatomyositis: Musculoskeletal findings and correlation with clinical and laboratory findings. AJR Am J Roentgenol 161:359, 1993.
35. Hernandez RJ, Tachdjian MO, Dias LS: Hip CT in congenital dislocation: Appearance of tight iliopsoas tendon and pulvinar hypertrophy. Am J Roentgenol 139:335, 1982.
36. Hernandez RJ, Tachdjian MO, Poznanski AK, et al: CT determination of femoral torsion. Am J Roentgenol 137:97, 1981.
37. Hervé-Somma CMP, Sebag GH, Prieur A-M, et al: Juvenile rheumatoid arthritis of the knee: MR evaluation with Gd-DOTA. Radiology 182:93, 1992.
38. Hudson TM: Fluid levels in aneurysmal bone cysts: A CT feature. Am J Roentgenol 141:1001, 1984.
39. Hudson TM, Springfield DS, Benjamin M, et al: Computed tomography of parosteal osteosarcoma. Am J Roentgenol 144:961, 1985.
40. Jaramillo D, Hoffer F, Shapiro F, et al: MR imaging of fractures of the growth plate. AJR Am J Roentgenol 155:1261, 1990.
41. Jaramillo D, Treves ST, Kasser JR, et al: Osteomyelitis and septic arthritis in children: Appropriate use of imaging to guide treatment. AJR Am J Roentgenol 165:399, 1995.
42. Jelinek JS, Kransdorf MJ, Utz JA, et al: Imaging of pigmented villonodular synovitis with emphasis on MR imaging. AJR Am J Roentgenol 152:337, 1989.
43. Karasick D, Schweitzer ME, Eschelman DJ: Symptomatic osteochondromas: Imaging features. AJR Am J Roentgenol 168:1507, 1997.
44. Katz DS, Merchant N, Beaulieu CF, et al: Lipoblastoma of the thigh: MR appearance. J Comput Assist Tomogr 20:1002, 1996.
45. King SJ, Carty HM, Brady O: Magnetic resonance imaging of knee injuries in children. Pediatr Radiol 26:287, 1996.
46. Kransdorf MJ, Jelinek JS, Moser RP, et al: Magnetic resonance appearance of fibromatosis. A report of 14 cases and review of the literature. Skeletal Radiol 19:495, 1990.
47. Kransdorf MJ, Meis JM, Jelinek JS: Myositis ossificans: MR appearance with radiologic-pathologic correlation. AJR Am J Roentgenol 157:1243, 1991.

48. Kransdorf MJ, Moser RP Jr, Gilkey FW: Fibrous dysplasia. Radiographics 10:519, 1990.
49. Kransdorf MJ, Moser RP, Meis JM, et al: Fat-containing soft-tissue masses of the extremities. Radiographics 11:81, 1991.
50. Laasonen EM, Jokio P, Lindholm TS: Tibial torsion measured by computed tomography. Acta Radiol Diagn (Stockh) 25:325, 1984.
51. Lahdes-Vasama T, Lamminen A, Merikanto J, et al: The value of MRI in early Perthes' disease: An MRI study with a 2-year follow-up. Pediatr Radiol 27:517, 1997.
52. Lang P, Honda G, Roberts T, et al: Musculoskeletal neoplasm: Perineoplastic edema versus tumor on dynamic postcontrast MR images with spatial mapping of instantaneous enhancement rates. Radiology 197:831, 1995.
53. Lang P, Wendland MFW, Saeed M, et al: Osteogenic sarcoma: Non-invasive in-vivo assessment of tumor necrosis using diffusion-weighted MR imaging. Radiology 206:227, 1998.
54. Laor T, Burrows PE, Hoffer FA: Magnetic resonance venography of congenital vascular malformations of the extremities. Pediatr Radiol 26:371, 1996.
55. Laor T, Jaramillo D, Hoffer FA, et al: MR imaging in congenital lower limb deficiencies. Pediatr Radiol 26:381, 1996.
56. Lee JK, Yao L: Stress fractures: MR imaging. Radiology 169: 217, 1988.
57. Lee MJ, Carins RA, Munk PL, et al: Congenital-infantile fibrosarcoma: Magnetic resonance imaging findings. Can Assoc Radiol J 47:121, 1996.
58. Levin TL, Sheth SS, Hurlet A, et al: MR marrow signs of iron overload in transfusion-dependent patients with sickle cell disease. Pediatr Radiol 25:614, 1995.
59. Liu P, Thorner P: MRI of fibromatosis: With pathologic correlation. Pediatr Radiol 22:587, 1992.
60. Mahboubi S: CT appearance of nidus in osteoid osteoma. J Comput Assist Tomogr 10:457, 1986.
61. Meyer JS, Hoffer FA, Barnes PD, et al: Biological classification of soft-tissue vascular anomalies: MR correlation. AJR Am J Roentgenol 157:559, 1991.
62. Mirowitz SA, Apicella P, Reinus WR: MR imaging of bone marrow lesions: Relative conspicuousness on T1-weighted, fat-suppressed T2-weighted, and STIR images. AJR Am J Roentgenol 162:215, 1994.
63. Mirra JM: Parosteal tumors. In Mirra JM (ed): Bone Tumors: Clinical, Radiologic, and Pathologic Correlations. Philadelphia, Lea & Febiger, 1989, pp 1587–1753.
64. Moore SG, Dawson KL: Red and yellow marrow in the femur: Age-related changes in appearance at MR imaging. Radiology 175: 219, 1990.
65. Morton MJ, Berquist TH, McLeod RA, et al: MR imaging of synovial sarcoma. AJR Am J Roentgenol 156:337, 1991.
66. Mulliken JB, Glowacki J: Hemangiomas and vascular malformations in infants and children: A classification based on endothelial characteristics. Plast Reconstr Surg 69:412, 1982.
67. Nagele M, Bruning R, Kunze V, et al: Hemophilic arthropathy of the knee joint: Static and dynamic Gd-DTPA–enhanced MRI. Eur Radiol 5:547, 1995.
68. Nelson D, DiPaola J, Colville M, et al: Osteochondritis dissecans of the talus and knee: Prospective comparison of MR and arthroscopic classification. J Comput Assist Tomogr 15:804, 1990.
69. Norton KI, Hermann G, Abdelwahab IF, et al: Epiphyseal involvement in osteosarcoma. Radiology 180:813, 1991.
70. Onikul E, Fletcher BD, Parham DM, et al: Accuracy of MR imaging for estimating intraosseous extent of osteosarcoma. AJR Am J Roentgenol 167:1211, 1996.
71. Oxtoby JW, Davies AM: MRI characteristics of chondroblastoma. Clin Radiol 51:22, 1996.
72. Panuel M, Gentet JC, Scheiner C, et al: Physeal and epiphyseal extent of primary malignant bone tumors in childhood: Correlation of preoperative MRI and the pathologic examination. Pediatr Radiol 23:421, 1993.
73. Ricci C, Cova M, Kang YS, et al: Normal age-related patterns of cellular and fatty bone marrow distribution in the axial skeleton: MR imaging study. Radiology 177:83, 1990.
74. Romero JA, Kim EE, Kim CG, et al: Different biologic features of desmoid tumors in adult and juvenile patients: MR demonstration. J Comput Assist Tomogr 19:782, 1995.
75. Ruby L, Mital MA, O'Connor J, et al: Anteversion of the femoral neck. J Bone Joint Surg Am 61:46, 1979.
76. Ryan SP, Weinberger E, White KS, et al: MR imaging of bone marrow in children with osteosarcoma: Effect of granulocyte-colony-stimulating factor. AJR Am J Roentgenol 165:915, 1995.
77. Schima W, Amann G, Stiglbauer R, et al: Preoperative staging of osteosarcoma: Efficacy of MR imaging in detecting joint involvement. AJR Am J Roentgenol 163:1171, 1995.
78. Schlesinger AE, Hernandez RJ: Intracapsular osteoid osteoma of the proximal femur: Findings on plain film and CT. AJR Am J Roentgenol 154:1241, 1990.
79. Schmid MR, Kossmann T, Duewell S: Differentiation of necrotizing fasciitis and cellulitis using MR imaging. AJR Am J Roentgenol 170:615, 1998.
80. Sebag GH, Dubois J, Tabet M: Pediatric spinal bone marrow: Assessment of normal age-related changes in the MRI appearance. Pediatr Radiol 23:515, 1993.
81. Sebag G, Ducou le Pointe H, Klein I, et al: Dynamic gadolinium-enhanced subtraction MR imaging—a simple technique for the early diagnosis of Legg-Calvé-Perthes disease: Preliminary results. Pediatr Radiol 27:216, 1997.
82. Silverman JM, Mink JH, Deutsh AL: Discoid menisci of the knee: MR imaging appearance. Radiology 173:351, 1989.
83. Snearly WN, Kaplan PA, Dussault RG: Lateral-compartment bone contusions in adolescents with intact anterior cruciate ligaments. Radiology 198:205, 1996.
84. Stevens SK, Moore SG, Amylon MD: Repopulation of marrow after transplantation: MR imaging with pathologic correlation. Radiology 175:213, 1990.
85. Stevens SK, Moore SG, Kaplan ID: Early and late bone-marrow changes after irradiation: MR evaluation. AJR Am J Roentgenol 154:745, 1990.
86. Stull MA, Kransdorf MJ, Devaney KO: Langerhans cell histiocytosis of bone. Radiographics 12:801, 1992.
87. Sugimura H, Kisanuki A, Tamura S, et al: Magnetic resonance imaging of bone marrow changes after irradiation. Invest Radiol 29: 35, 1994.
88. Taccone A, Oddone M, Dell'Acqua AD, et al: MRI "road-map" of normal age-related bone marrow: II. Thorax, pelvis and extremities. Pediatr Radiol 25:596, 1995.
89. Taccone A, Oddone M, Occhi M, et al: MRI "road-map" of normal age-related bone marrow: I. Cranial bone and spine. Pediatr Radiol 25:588, 1995.
90. Tanabe M, Takahashi H, Ohnuma N, et al: Evaluation of bone marrow metastasis of neuroblastoma and changes after chemotherapy of MRI. Med Pediatr Oncol 21:54, 1993.
91. Towbin R, Kaye R, Meza MP, et al: Osteoid osteoma: Percutaneous excision using a CT-guided coaxial technique. AJR Am J Roentgenol 164:945, 1995.
92. Tsai JC, Dalinka MK, Fallon MD, et al: Fluid–fluid level: A nonspecific finding in tumors of bone and soft tissue. Radiology 175: 779, 1990.
93. Uno A, Hattori T, Noritake K, et al: Legg-Calvé-Perthes disease in its evolutionary period: Comparison of MRI with bone scintigraphy. J Pediatr Orthop 15:362, 1995.
94. Weatherall PT, Maale GE, Mendelsohn DB, et al: Chondroblastoma: Classic and confusing appearance of MR imaging. Radiology 190: 467, 1994.
95. Wechsler RJ, Schweitzer ME, Deely DM, et al: Tarsal coalition: Depiction and characterization with CT and MR imaging. Radiology 193:447, 1994.
96. Wing VW, Jeffrey RB Jr, Federle MP, et al: Chronic osteomyelitis examined by CT. Radiology 154:171, 1985.
97. Yao L, Eckardt JJ, Seeger LL: Fibrous dysplasia associated with cortical bony destruction: CT and MR findings. J Comput Assist Tomogr 18:91, 1994.
98. Young JWR, Bright RW, Whitley NO: Computed tomography in the evaluation of partial growth plate arrest in children. Skeletal Radiol 15:530, 1986.
99. Yousem D, Magid D, Fishman EK, et al: Computed tomography of stress fractures. J Comput Assist Tomogr 10:92, 1986.
100. Zeanah WR, Hudson TM, Springfield DS: Computed tomography of ossifying fibroma of the tibia. J Comput Assist Tomogr 7:688, 1983.
101. Zobel MS, Borrello JA, Siegel MJ, et al: Pediatric knee MR imaging: Pattern of injuries in the immature skeleton. Radiology 190: 397, 1994.

Part IX

Special Considerations

61 Image-Guided Micro Procedures: CT and MRI Interventional Procedures

John R. Haaga

Image-Guided Microsurgery—New Name, Topics, and Innovations

Since I performed the first CT-guided procedure in 1975 (Fig. 61–1), this field has progressed remarkably. Nonvascular interventions have finally gained their appropriate role in medical practice today and stand on an equal par with vascular interventions The use of CT and MRI procedures has become ubiquitous in every hospital in the country, if not the world. Even tiny hospitals with census of five or six patients have occasional CT-guided procedures and in fact demand that such services be provided. The scope and sophistication of these procedures continue to increase.

It is my very strong opinion that radiologists will maintain control over the field of imaging only if they continue to master and develop these image-guided procedures. Multislice scanners and sophisticated MRI devices display anatomy and pathology so well that other clinical groups can learn the major facets of our field. The procedures set us apart from the other physician groups and represent a unique skill set that is not easily mastered by casual observation. It is critical that we continue development and refinement of these valuable methods. Those who develop, use, and refine these interventional techniques will control the field of imaging. Furthermore, it is imperative that we begin to better describe our field so it develops a distinct identity among the public and other physicians. Assigning a new name to these valuable procedures will go a long way in establishing this identity.

The old term of *interventional radiology* does not communicate the essential elements of our methods. We basically use imaging to guide our procedures, and we use instruments smaller than those of the minimally invasive techniques of the surgeons. For both ease of communication and better identification of our art, I believe we should call these techniques *image-guided microsurgery.*

New Topics and Information

When textbooks have had numerous editions, the authors run the risk of repeating major portions of earlier work and readers run the risk of purchasing a book that is partially outdated and presents little new information. For these reasons I feel compelled to mention in the beginning of the chapter the major changes that have occurred.

The historical sections have changed to reflect the remarkable refinements in the field of image-guided microsurgery. Knowledge of the historical evolution of these methods minimizes the possibility that authors might retrace old pathways. The old adage about human history is of course applicable to interventional procedures: "Those who do not know history are condemned to repeat it."

The main body of this chapter has been totally rewritten. Older material has been deleted and new information provided. The highlights of the chapter are the new approaches to needle techniques and the discussion of new assistance methods for interventional approaches. New methods of anatomic approach are included in the areas such as the middle mediastinum, hemostasis in coagulopathic patients, and use of chemical agents and drugs to improve the treatment of infections and tumors.

Diagnostic Imaging Versus Procedures

Some radiologists have looked at procedures as time consuming and not an important part of their practice. Nothing could be farther from the truth. Diagnostic imaging studies are important, but interventional procedures are even more critical for patient care, the preservation of radiology, and advances in medicine at large. Despite the most remarkable development and evolution of imaging modalities, definitive diagnosis and treatment of patients are still dependent on examination of tissue samples. Such tissue samples are even more critical now because current and future therapy is dependent on definitive characterization of the many tissue factors such as specific cell type, enzyme content, DNA profile, proteonic character, and other physiologic parameters. Surgical methods for obtaining such samples have been largely supplanted by image-guided procedures that are more accurate and cost-effective and have much lower morbidity and mortality.

Of even more importance than the diagnostic biopsies is the development of therapeutic techniques for the treatment of infections and tumors. Current treatment modalities

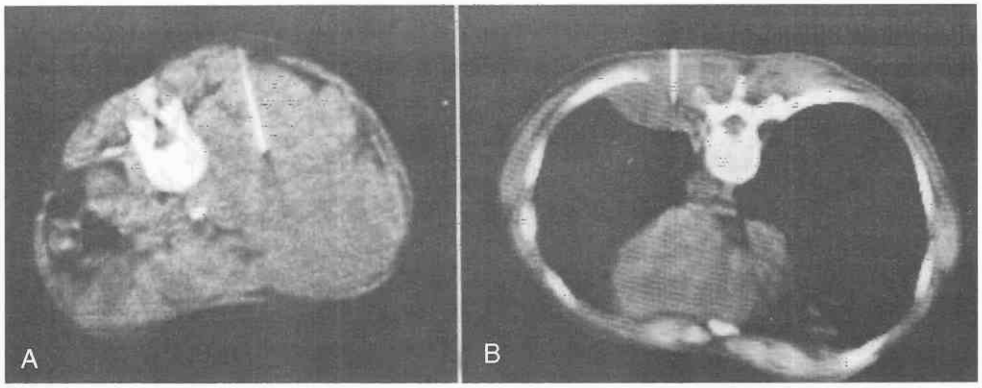

Figure 61–1. *A*, First CT guided biopsy was of a retroperitoneal mass (by the author). Even though the results of this biopsy were negative, the merits of CT guidance were obvious. *B*, First CT-guided procedure of the lung in 1975 (by the author).

include catheter drainages for abscesses, lymphoceles, hydronephrosis, gallbladders, and even loops of bowel. The treatment of tumors is a major part of percutaneous procedures by local chemical injection, local radiofrequency treatment of tumors, and, in the near future, direct deposition of chemotherapeutics, DNA transfer agents, RNA agents, peptides, or other compounds.

This chapter is somewhat longer than others because of my intense interest and extensive experience. I performed the first CT biopsy and drainage procedures in 1975 and 1976 and have continued to perform such cases on a daily basis (see Fig. 61–1). We also developed the "longitudinal scan" in 1976 (Fig. 61–2), which was the precursor to all of the current localization scans. The basic principle of performing axial procedures is demonstrated in Figure 61–3*A*. It is fascinating to note the progress to date, wherein we are beginning to use robots to assist in such procedures (Fig. 61–3*B*, *C*). The usefulness of MRI scans for revealing subtle pathology was evident in the beginning, but the advantage of clear instrument visualization by CT has always been apparent (Fig. 61–4).

Guided MRI procedures have become an integral part of the interventional methods, and I am proud to say, have been refined and perfected by several of my colleagues.[240] MRI procedures have yet to play a major role in the daily routine of most departments, but major refinements and developments in the field of MRI interventions continue.

Although many different techniques and methods have been reported and are unquestionably effective, I am confident that our techniques developed over many years and after literally thousands of procedures are valuable and compare favorably to other proposed methods.

History of Percutaneous Procedures

Reviewing the historical perspective of interventional CT procedures can be somewhat confusing if one takes a narrow viewpoint and assumes that their evolution in the past 50 years has been along a single pathway. If one takes an objective, global viewpoint, however, one can see that the development of percutaneous procedures has been quite varied and has involved four separate disciplines: instrument development, clinical techniques, pathologic and cytopathologic techniques, and guidance methods.

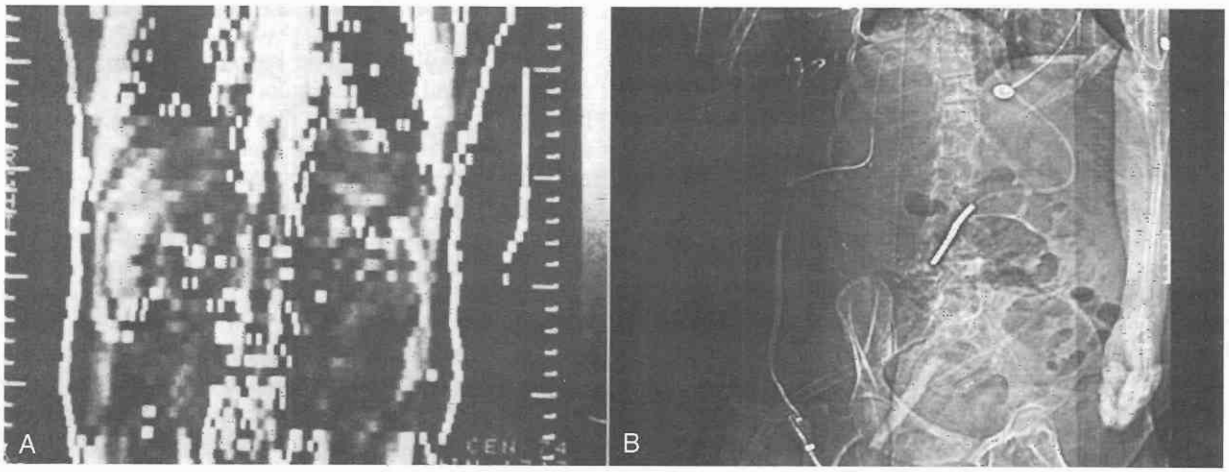

Figure 61–2. *A*, First, CT radiographic image ever produced or reported. One of its original purposes was to aid with interventional procedures (see later portion of chapter on catheter insertions). This primitive scan shows the lower chest and upper abdomen. This preceded all of the current commercial images including the Topogram, Scoutview, Synerview, etc. The originator (J.R. Haaga) reported and published this figure, but he was not clever enough to obtain patents at the time! *B*, Modern image showing the remarkable detail of current images. The image of this patient shows the abdominal anatomy and several catheters, wires, and monitoring devices. (*A*, From Haagal JR. et al: CT longitudinal scan. AJR 127:1059–1060, 1976.)

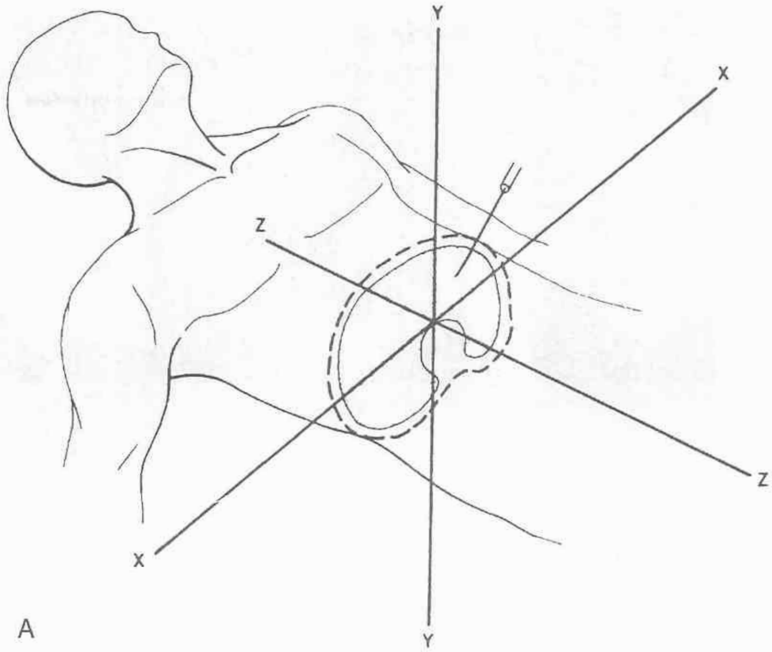

Figure 61–3. *A,* Placement of a biopsy needle within an anatomic location. The relationship of the needle to both the plane of the z axis and the plane of the *x-y* axis is illustrated. *B, C,* Current approaches have evolved far beyond earlier methods and even initiated developmental work with robotic assistance. *B,* CT scanner with robot mounted on the side of the table, placing the instrument in a swine model. *C,* CT scan taken after insertion of the needle by the robot, to a site adjacent to aorta. This corresponds to the celiac plexus. With the positive results of these tests, I am convinced robotics will be used in future devices. See section on assisted guidance. (*A,* From Haaga JR et al: CT-guided biopsy. Cleve Clin Q 44:27–33, 1977.)

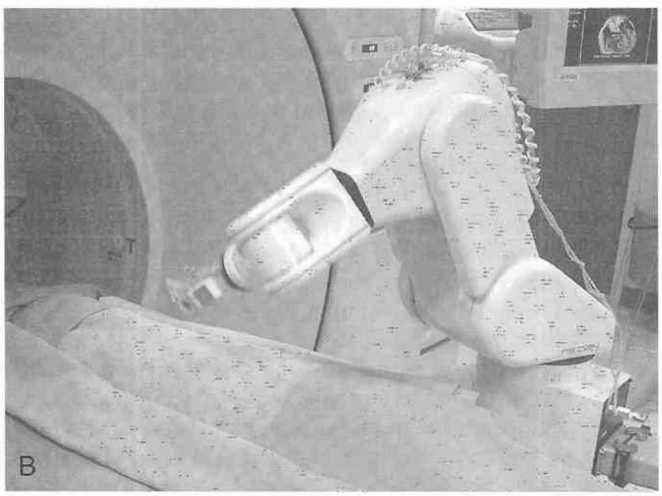

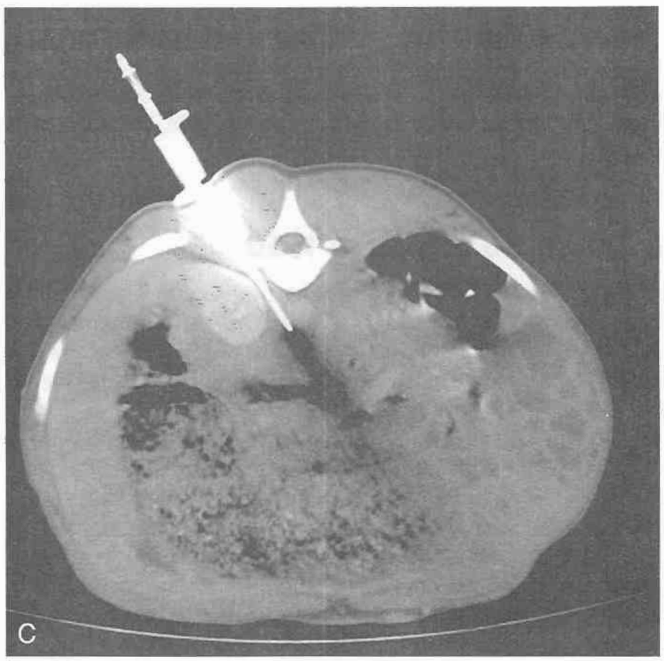

The advances in these four areas have at times occurred concurrently, and it is difficult to appreciate the overall perspective if one selectively reads the literature. Furthermore, as one reads the various reports in the literature, one must be aware of individual bias relative to data interpretation and reference sources. When authors look to the literature to support the thesis of their report, they have a natural tendency to use only the information that supports their viewpoint. For this reason it is most important that in some cases the informed reader consult the primary reference source rather than relying strictly on the author's interpretation (this applies even to the reading of this chapter).

The best way to demonstrate this complex premise is to explore the example of the small-caliber, or "skinny," needle. In many reports authors refer to the experience of Lundquist to support the accuracy of the ultrasonic-guided skinny-needle biopsy, despite the fact that Lundquist performed only "blind" biopsies with the skinny needle.[255,256] In addition, Lundquist is frequently quoted in attempts to prove the safety of the skinny needle compared to the large cutting or Menghini-type needle. If readers take a more comprehensive approach to the literature, however, they will find that in his final dissertation, Lundquist noted a favorable result with large needles as well as with the skinny needle. Using the skinny needle first to probe the pathway for the large needle, Lundquist had performed more than 1000 procedures with the Menghini needle with

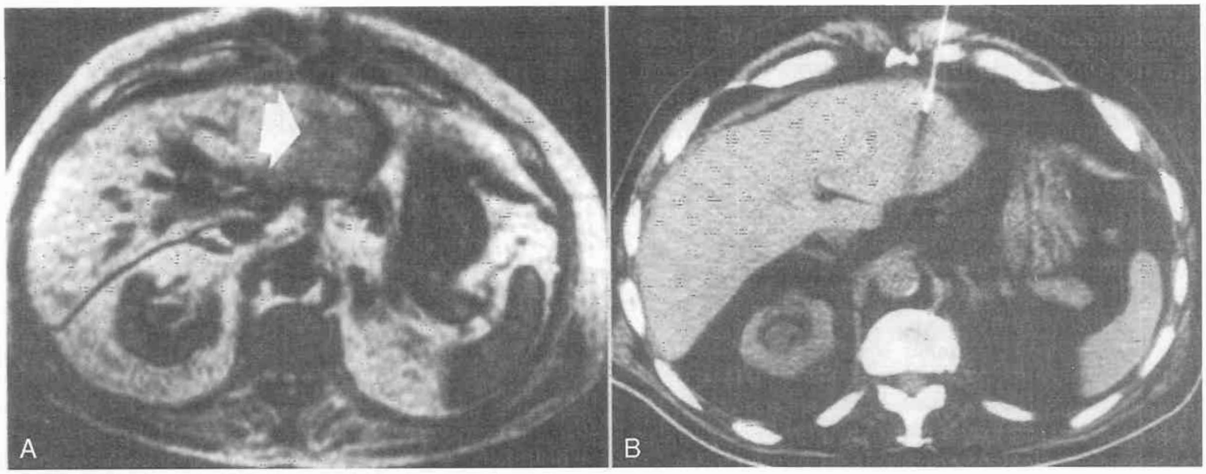

Figure 61–4. These scans show an MR-guided procedure and a CT-guided procedure of a liver lesion. *A,* This MR scan shows the low-intensity mass within the left lobe much more clearly than does the CT scan. The needle *(arrow)* is difficult to see. *B,* This CT scan taken at the same level shows the visualization of the needle in the same mass. With current technology, the best result in such cases is to correlate the location on the MRI scan with the CT during biopsy.

"no complications" (of 2611 cases involving the use of the skinny needle, he reported one hematoma). His data are valid within the complete context of his work and the literature, but one may draw incorrect conclusions if only selected sources of information are used.

Progress from 1930 to 1960

From 1930 to 1960 most progress in percutaneous biopsies was made in the area of unguided clinical methods and instrument development. There was very little progress in the development of pathologic techniques or guidance by imaging.

Two important clinical points concerning liver biopsy were discovered during this period. First, for blind procedures, the inercostal approach was found safer than the anterior subcostal approach (if the liver was not massively enlarged). Second, the liver biopsy was proved safer when performed while the patient suspended respiration and motion. The importance of this latter clinical procedure was emphasized by Menghini,[272] who introduced his "1-second" technique. Menghini's real contribution was his recommended method of having the patient suspend respiration while the biopsy is quickly performed. Motion by the patient was thus avoided and possible injury to the liver was minimized. This "breath-holding" maneuver, and not the needle that bears his name, was his significant innovation.

Instrument development during this time was confined to the various types of cutting needles. Instruments introduced included the end-cutting needles, the Vim-Silverman needle, and the Tru-Cut needle. A number of general review articles were published about the incidence and cause of the complications associated with blind, large-needle liver biopsy. These complications included hemorrhage, bile peritonitis, and gallbladder perforation. The major causes of hemorrhage were abnormal prothrombin time, severe liver disease, and abnormal vessels. Although it now seems astonishing, biopsies were performed on patients who had very abnormal prothrombin times. The major cause of bile peritonitis was caused by penetration of dilated bile ducts with obstructive jaundice or perforation of the gallbladder (most frequent with an anterior subcostal approach).

These review articles about the complications of large-needle biopsy are especially interesting to note because these very old articles are typically quoted in the radiology literature to discourage the use of the larger cutting needles. Obviously, comparisons of today's guided techniques with the results of the old articles are completely invalid. Current methods of patient selection, detection of coagulopathy, local anesthesia, and patient sedation are remarkably different from those of the early authors. Furthermore, modern CT techniques eliminate almost all potential causes of complications with the large needles.

Biopsies of the liver and/or lung were performed either blind or with the assistance of "red goggle" fluoroscopy. Blind localization for these procedures required either palpation, percussion, or approximated localization from plain radiographs. Fluoroscopic guidance using direct visualization or a phosphored glass screen (no image intensification on television) required that the radiologist localize the abnormality for the clinician. After localization by direct fluoroscopy in a darkened room, the biopsy procedure was performed by a clinical physician with the lights on. The radiologists donned their red goggles so that their eyes could remain accommodated for the dark, direct fluoroscopy (black images on green phosphor). Biopsies were not a radiologic procedure during this era.

Progress from 1960 to 1970

Development during the 1960s included comparison data about the various large cutting needles, introduction of cytopathologic methods, introduction of the skinny nee-

dle for blind biopsies, and the first "break-through" with guided biopsies: image intensification fluoroscopy.

Qualities of the different cutting needles were compared by Parker et al.[321] Their comparison of the Vim-Silverman needle with the Menghini needle showed that the latter was superior for sample recovery. The adequacy of sample was 94% for the Menghini needle compared with 77% for the Vim-Silverman needle. They also noted the higher incidence of complications with the Vim-Silverman needle. The advantages of the Menghini method using the end-hole needle were its simplicity, the short time required for the procedure, and lack of patient respiratory motion.

During this period the development of cytopathologic techniques revolutionized percutaneous procedures. Although earlier authors such as Martin[264] used a cytologic method, Soderstrom[204] in 1958 and 1966 developed and reported the first well-defined method of needle aspiration and cytopathologic evaluation. Several of his protegés, including Lundquist[255,256] and Nordenstrom,[304] continued this work and reported extensively on the clinical application of these techniques (discussed later).

Aside from these workers, other authors evaluated the usefulness of the cytopathologic techniques on material obtained from cutting needles rather than on the aspirates from the skinny needle. Grossman et al,[129] using tissue and fluid from Menghini biopsy of the liver, performed cytopathologic studies of the fluid and "touch preps" of the tissue on slides. They found that their diagnostic accuracy for malignancy improved by an additional 15%, compared with the histologic results of the tissue core. Later work by Atterbury et al[71] confirmed their observations, but these results were not quite as remarkable. From their study they found that in their series of 29 malignancies, the yield improved only by 3% (one patient).

These articles, which were very frequently misquoted during the 1980s, show the added benefit of the cytologic techniques on the samples obtained with larger cutting needles (in addition to the traditional histologic methods) for the detection of malignant cells. These articles were not comparisons between the skinny needles and the large needles (discussed later).

After the positive results reported by these authors and the experience of Soderstrom,[361] other authors began clinical trials using a small-caliber, or skinny, needle for unguided procedures to obtain liver samples for cytologic examination. One of the largest series about skinny-needle biopsy of the liver was Lundquist's study in 1970 about unguided or blind biopsies of the liver. In his first report[255] about a series of 1748 liver biopsies, he correctly made the diagnosis of cancer in 74% of patients (50 of 74) with no complications. No mention is made concerning the diagnosis of benign disease in the remaining 1674 cases. In this series of malignant cases the authors were able to make the prospective specific diagnosis in only 2 metastatic lesions and 5 of 10 hepatomas. Lundquist's intent was to develop a safe screening method for detection of tumor that would permit a wide latitude of technique error without significantly endangering the patient.[255] He did not refute the advantage of the larger needles to make a more definitive diagnosis. In Lundquist's later report of a larger series,[256] he reported an equivalent diagnostic accuracy with one serious complication of bleeding. In this paper he also related his experience of 1000 large-needle biopsies with no complications. The important point of avoiding complications, he believed, was the evaluation of the chosen entrance site by probing with a skinny needle before using the large needle. In this fashion he could avoid bowel, lung, gallbladder, vessels, or excessively vascular tumors (current CT methods provide the same information and advantage).

One of the few comparison studies of different needles during this time was by Johansen et al,[195] who compared the use of a skinny needle with a Menghini needle in blind liver biopsy. These authors found identical results for the detection of malignancy; both needles were correct for 6 of 12 cases. There were no complications.

With this initial experience and the development of image intensification television as a background, radiologists began to evaluate the merits of the skinny needle for sampling the lung with fluoroscopic guidance. In 1966 Dahlgren and Nordenstrom[66] began using image-intensified fluoroscopy to guide the skinny needle for biopsy of lung masses. Their result showed a high accuracy and a low complication rate.

These early workers clearly established the usefulness of the skinny needle for obtaining samples from epithelial tumors such as adenocarcinoma and squamous cell carcinomas. Such tumors lack the cellular organization or "cement" to bind them together. Therefore, the nontraumatic skinny needle can recover such loosely adherent cells. They also noted that when other than epithelial tumors were biopsied by these methods, the results were good but diagnoses were not as specific. This was especially true when architecture was important, such as in cases of lymphoma, benign tumors, or neurogenic tumors.

Television image intensification has made a remarkable contribution to the performance of biopsy procedures. With red goggle fluoroscopy, radiologists could not turn room light on and off during a procedure because of eye accommodation. With the direct fluoroscopy, radiologists had to enhance their visualization of the dark fluoroscopy by preceding their examinations with a period of wearing the red goggles to accommodate their eyes. With image intensification, which improved light output by a factor of 1000, radiologists could turn lights on and off and thereby assume direct responsibility for the procedures.

Progress from 1970 to the 1980s

During the period of the 1970s and 1980s, more progress was made with percutaneous procedures than during any of the previous periods. Progress was rapid because of the excellent groundwork by earlier workers and because of the remarkable technologic advances. Some refinement was made in the cytopathologic area, but remarkable progress was made in the areas of clinical experience, instrument evaluation, and imaging guidance.

Before outlining the progress made with the skinny needle and the various imaging systems, some comments about clinical work with the cutting needles are appropriate. First, a prospective series in 1978 by Perrault et al[327] showed no complication difference among the Vim-Silverman, Menghini, and Tru-Cut needles. This is fascinat-

ing, considering the significant difference in both the calibers and cutting actions. One might conclude that, if there are any basic differences in complications due to needle configuration, good clinical technique and experience can compensate, so that complication rates are equivalent. To further support this point, Bateson's comparison[21] in 1980 of the Tru-Cut needle and the Menghini needle showed no diagnostic or other complications, although the physical integrity of the sample was more consistently intact with the Tru-Cut needle, especially with cirrhotic livers.

The two other significant events that occurred in the 1970s were the introductions of ultrasound[22] and CT as guidance modalities. Ultrasound was introduced as a biopsy guidance system by Holmes et al[178,179] in 1975. CT guidance was introduced by Haaga et al[138] in 1976.[77] As noted later, both of these later imaging systems have developed into valuable tools for sampling different areas.

The 1980s

In the early 1980s, the cutting needles, both side-cutting and end-cutting, came into their prime.[137,146,150] With the advent of the automated needles, many radiologists now use these devices almost routinely. Other major advances undoubtedly would be made during the 1990s, the seminal work appearing in the literature clearly indicating the directions.

With further development of biopsy devices, I am confident that a hemostatic biopsy device will be developed and introduced. The first indication of the potential of such a device was reported by Gazelle et al.[49] In this initial work by our group, a hemostatic sheath, which could be deposited at the site of the biopsy procedure, was developed. In animal models using anticoagulated pigs, it was shown that such a device could prevent significant bleeding in the liver. It is probable that a recent modification of this device could reach the market in the next several years and potentially result in a "risk-free" biopsy.

More sophisticated ancillary guidance devices are being designed; these will simplify the performance of CT-, ultrasound-, and MRI-guided procedures (see Fig. 61–7). One device recently introduced by Magnusson et al[259] shows great promise for the future. Other mechanical and light-guided devices are being developed.

Additional new techniques will be developed and refined for the percutaneous treatments of tumors and also insertion of physiologic monitoring or activating devices. The first examples of in vivo tumor treatment using ethanol injections have been reported; these are described in this chapter. Physiologic monitoring devices such as thermisters for hyperthermia and pressure transducers for tumor treatment will follow in the near future. Also, it is probable that insertion of electrodes for stimulation of various muscles will come into common usage.

The 1990s

Several significant changes occurred in the 1990s in routine procedures, relative to devices used and new approaches to assist in percutaneous procedures. In the type of needles used, the cutting needle has become ubiguitous and used in virtually all circumstances. It is somewhat strange, looking back at the early days of interventional, that it took two intense years of reviews and negotiations to get our first paper on lung biopsies and cutting needles by Goralnic et al[120] published, and now such procedures are extremely commonplace. Relative to cutting needles in general, a recent survey by Mayoral and Lewis showed that 95% of liver biopsies were performed by cutting needle "guns."[266]

The treatment of tumors has progressed rapidly. While in the earlier edition of this text, the first cases of alcohol treatment were just being performed, these procedures have become common and are performed everywhere. Ironically, this area has progressed so rapidly that the technique came into vogue, was developed and refined, and now is relegated into a secondary role already by radiofrequency ablation. We are now in the rapid phase of refining those methods and have progressed from simple radiofrequency ablation to that of combined therapy, which is described in that section.

Methods of instrument localization and guidance have been refined and have progressed remarkably. Our lament in our earlier editions about the lack of attention to the interventions by vendors has now been answered. Numerous improvements in equipment have occurred to simplify and facilitate CT- and MRI-guided procedures. These have ranged from special changes in the equipment to provide faster scans, scans on demand with the operator in the room, new localization devices, and even early experiments into robotic-assisted procedures.

Hemostasis control has also progressed, as discussed in the appropriate sections. New methods and devices have been developed and introduced.

Historical Perspective of Organ Procedures

Lung

The first experience using skinny needles with image-intensification guidance in the lung was reported by Dahlgren[66] and Nordenstrom[304] in 1965. After their report, their results were confirmed by a number of authors using a variety of guidance methods and small-caliber needles. Another early group, Sargeant et al,[347] performed biopsies without image intensification with good results. Once image intensification became standard, many authors, including Lauby,[232] Lalli,[226] Westcott,[402] and Sinner[356] reported their series. Many important observations were made about different factors that alter diagnostic accuracy and complications, which will be discussed in the following section on lung procedures.

One fascinating fact that is apparent from reports of these authors is that many different calibers of needles have been called "skinny" needles. Regardless of the caliber of the needle used by the authors (e.g., Lalli et al[226] used an 18-gauge needle, and Zornoza[420] used a 23-gauge needle, the diagnostic accuracy was quite good, and the complication rate was quite acceptable.

In the recent literature, the most important article of which is the one by Khouri et al,[214] it is clear that needle caliber has almost no impact on pneumothorax rate but has a definite impact on hemoptysis. The incidence of pneumothorax is almost identical with all sizes of needles but Khouri et al[214] reported that the incidence of hemoptysis is greater with needles larger than 20 gauge than the rate of 20 gauge or less.

Further progress for sampling the lung and mediastinum occurred with the introduction of CT procedures in 1976 by my group.[137] While fluoroscopy has continued to be the main modality for biopsy of the peripheral, well-defined lung nodule, CT provided new advantages for the lung and mediastinum. With CT it became possible to biopsy more difficult lung lesions, to biopsy the mediastinum, and to use the cutting needle safely in selected cases.

Liver

Although Lundquist showed the usefulness of blind skinny-needle biopsies, guided biopsy of the liver with the skinny needle was infrequent until the introduction of ultrasound and CT scanning. The first ultrasound biopsy of the liver was performed by Rasmussen et al.[336] Their study noted the increased diagnostic yield of ultrasound-guided skinny needle biopsy of liver masses, compared with blind Menghini biopsy. The improved yield was of course secondary to the accurate targeting provided by ultrasound. This article is sometimes mistakenly quoted as showing the superiority of the ultrasound-guided skinny needle over the larger cutting needle guided by CT. This article does not even include CT-guided procedures, so any comparison or inference is not valid. Many other authors[353] later confirmed the high accuracy of both the skinny-needle procedure of the liver and the ultrasound guidance. These are noted in the liver section.

After the first CT biopsy of the liver by our group, a large body of experience with both the skinny needle and larger cutting needles has accumulated. Haaga et al,[144,145] and Ferrucci et al,[87,89] among others, confirmed that CT-guided skinny needle procedures are quite effective for the diagnosis of many primary and metastatic malignancies. During direct comparisons of the skinny needles and cutting needles, our group confirmed the usefulness of the skinny needle and also noted additional advantages with the larger cutting needles. Currently both ultrasound and CT are used for the performance of biopsies using large cutting needles. For easily visualized lesions, ultrasound guidance is more than adequate, but for more difficult or complicated cases CT is still the modality of choice because of advantages associated with guidance and diagnostic scanning (see later section on liver biopsy).

During this time another researcher, Pagani,[316] investigated the significance of needle caliber on the diagnostic yield and complication rate of aspiration biopsy of liver masses. With CT techniques he found there was an increased diagnostic yield with the larger needle and no difference in complication rate (see section on needle selection).

Pancreas

Percutaneous skinny-needle biopsy of the pancreas also developed quickly. Before the guided skinny-needle biopsies of the pancreas, some authors evaluated skinny-needle aspirations under direct visualization at surgery. Christoferson[53] used the skinny needle in the surgical suite to show that the diagnosis of malignancy could be made with the skinny needle. Forsgren et al[93] then used percutaneous skinny-needle aspiration for diagnosis of palpable pancreatic tumors.

With this favorable experience, guided percutaneous pancreatic biopsies of the pancreas were quickly accepted. The first guided percutaneous pancreatic biopsy was performed in 1972 by Oscarson et al,[314] who used fluoroscopy in conjunction with angiography to localize the needle placement. Although other authors such as Tylen[382] used fluoroscopy with contrast studies, the widespread acceptance occurred after the introduction of ultrasound and CT guidance.

Ultrasonic biopsy was first pioneered by Holm et al[178,179] in 1975. CT-guided biopsy of the pancreas was introduced in 1976 by Haaga and Alfidi.[138] Both guidance systems have been used successfully, but there are some differences in the methods, accuracy, and complication rates (discussed later).

Impact of Experience

It appears that complication rates with the large or skinny needles are higher with inexperienced persons and lower with experienced ones. If one looks at the reports in the literature, one usually finds an improvement in the authors' results as their reported experience accumulates. Although the skinny needle has a better tolerance for error and inexperienced individuals can use it with few problems, even the complication rates improve. The improvement of diagnostic accuracy with experience was documented by Evander,[81] Zornoza,[424] and Hopper.[255]

CT and MRI Procedures

CT Advantages

CT uses a beam of radiation to penetrate virtually all natural and artificial materials within the human body. Information concerning attenuation of these substances can be measured, and an image can be reconstructed. Because of the wide latitude of imaging capabilities, an extremely low-density material such as gas can be imaged as well as high-density materials such as metal, bone, or synthetic catheters (Fig. 61–5). In addition, CT is sensitive enough to detect subtle abnormalities such as fluid densities, cysts, or small pockets of gas.[156,157]

The ability to image high-density material accurately offers wide versatility, so that any type of instrument (i.e., needle, drainage tube, or other device) may be used in a procedure. Moreover, contrast material can be injected when vascularity, an anatomic space, or an abnormal cavity needs further delineation. For example, an abscess can have unpredictable serpiginous tracts or communicating

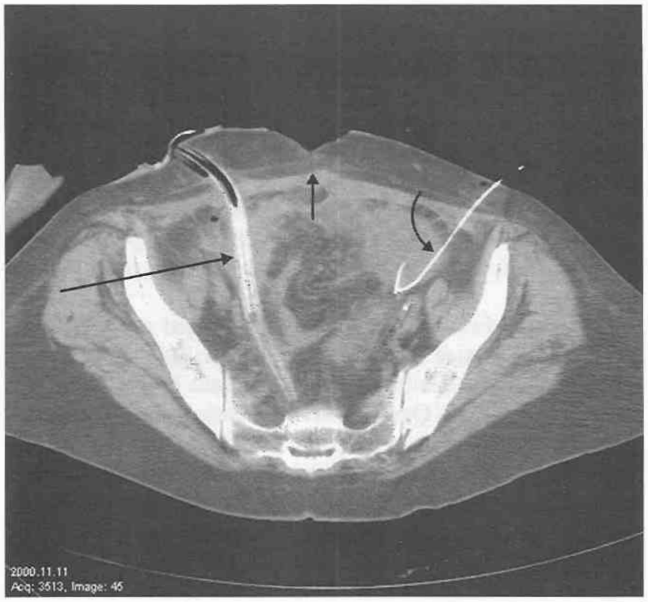

Figure 61–5. Patients with drainage catheters, high-density metallic material, and surface wounds are still suited for CT procedures. This scan shows aspiraton of an abscess in a patient with surgical drains *(long arrow)* and skin defects *(small arrow).* Although the scan is not of superior quality, the visualization of the wire *(curved arrow)* used to insert a drain in the abcess is quite easily accomplished.

channels that can be difficult to perceive unless contrast material is used, (Fig. 61–6).

Because the CT unit uses an air interface, it consistently provides a detailed and complete image in virtually all patients. In patients who have draining sinuses, wounds, ileostomies, scars, or other unusual surface problems, the examination can be performed without difficulty.

Another advantage is that the longitudinal scan (Topogram, Scoutview) that I originated[152] is now available on all CT scanners, making it possible to obtain conventional radiographs of the anatomy and to visualize instruments or catheters during insertion or manipulation.

MRI Advantages

MRI advantages relate to its superior ability to image and display subtle qualities related to molecular characteristics. In its earliest and current iterations, it essentially means that proton characteristics are demonstrated within the context of anatomy. This is quite unique because CT shows solely the density or electron density of tissues. MRI is incapable of showing subtle variations within tissues, which may reflect slight variations in tissue characteristics such as viable tumor, slight inflammation, or differences in tissue relaxation that may reflect intralesional detail not detected by CT.

The concrete examples of these properties are the ability of MRI to visualize some subtle pathologies in disease processes (Fig. 61–7). Those details are found in those specific chapters, but several areas are worthy of mentioning in this chapter. In the pancreas, MRI is remarkably superior to CT for the detection of subtle islet cell tumors and the details of some cystic tumors of the pancreas. From an anatomic resolution perspective CT is superior, but with these tumors molecular qualities related to their molecular properties make MRI superior for detection or characterization. It is not illogical to assume that in the future, these qualities will be exploited by future interventional strategies, most likely therapeutic approaches.

Also because of these qualities MRI is well-suited to follow the progress of the treatment procedures. It has been well-documented that MRI is the most accurate for displaying the tissue changes from radiofrequency treatment. Experimentally it has even been able to display characteristics correlating with absolute tissue temperature. With the current emphasis on treatment, it may also be possible with higher field magnets with broadband capabilities to visualize drugs in situ as they circulate within the tissues and the target molecular sites.

Another advantage of MRI imaging is its ability to image blood vessels and also to assess vascularity as it relates to general blood flow. MRI during standard pulsing sequences shows vessels even without contrast material. Moderate-size vessels are clearly seen as a flow void.

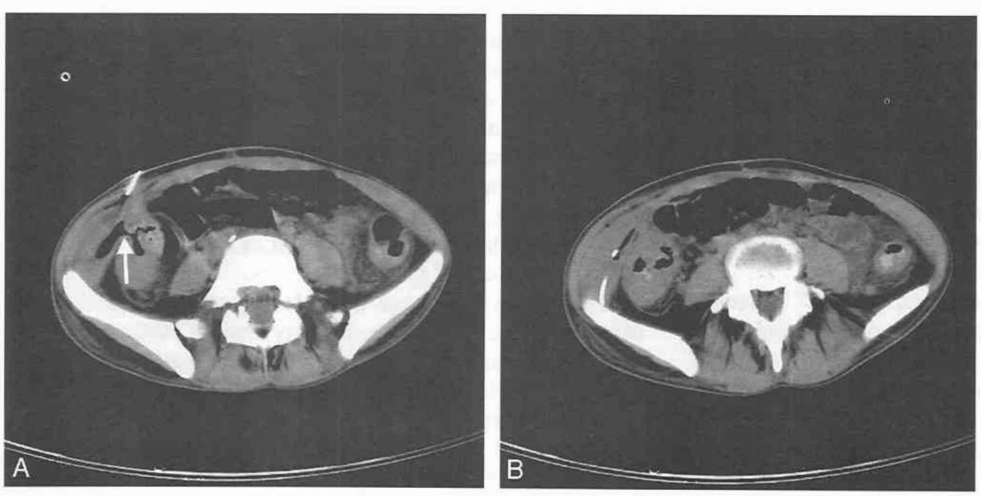

Figure 61–6. *A,* Patient with Crohn's disease and abscess. Scan shows a needle being inserted in the abdominal wall abscess as well as a subtle air-filled fistula between the colon and the abscess. Visualization permited placement of the catheter adjacent to the fistula to improve drainage and resolution. *B,* Repeat scan shows a catheter close to the fistula into the bowel.

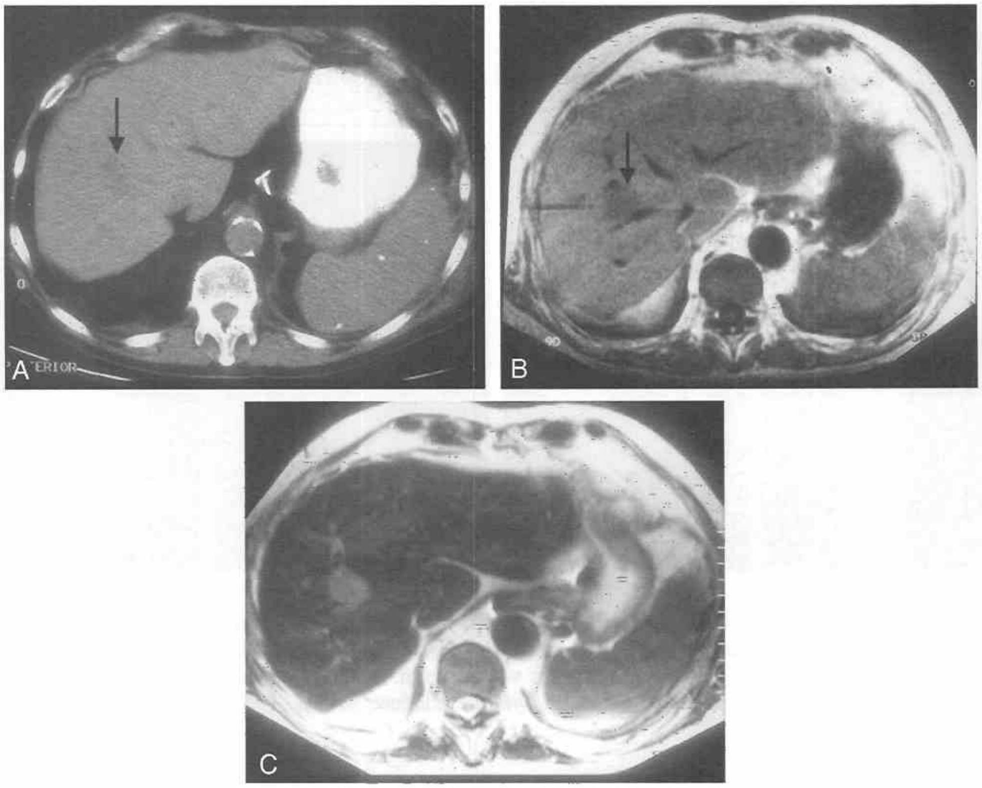

Figure 61–7. *A,* CT scan shows a very subtle lesion on an unenhanced scan. Because of the proximity of vessels and poor visibility, it was decided to biopsy the mass under MRI. *B,* T1-weighted scan shows a subtle mass in the mid-right lobe of the liver. *C,* T2-weighted scan shows increased signal in the lesion, which was biopsied under MR guidance and proved to be metastatic cholangiocarcinoma.

Although the anatomic spatial resolution of MRI is less than CT, it can also display general tissue blood flow as one might see in hemangiomas but administering gadolinium as a bolus injection. An indirect advantage is also that gadolinium, unlike iodinated contrast material, has a much lower idiosyncratic rate, so that patients who are allergic to traditional contrast material used with CT can be imaged and evaluated by MRI flow studies.

CT Accuracy of Localization

The potential accuracy of the CT-guided method can best be appreciated by examining a schematic drawing of a cross-sectional image (see Fig. 61–3). If the instrument is placed within an anatomic area and the CT scan shows the needle in that area, then the needle must lie within the 10-mm section of the abdomen corresponding to the CT section. Location of an instrument in this plane is limited by the section thickness, which is 10 mm; therefore the resolution in the z axis is $+5$ mm. If one uses narrower slices, such as 5 mm, the accuracy in the y-z plane is $+2.5$ mm. Resolution of the CT system in the x-y plane is less than 1 mm with modern scanners. The precision required in determining the position of such an instrument is less limited by the imaging equipment than it is by the degree of the operator's accuracy, as determined by manual dexterity and by the degree of accuracy of the guidance system rather than the imaging equipment.

The ability to localize the needle tip consistently and accurately in an axial plane is a distinct advantage of CT over fluoroscopy or ultrasound. Although fluoroscopy can provide multiplanar visualization of a needle or instrument, it is not capable of directly visualizing soft tissue abnormalities, except in the chest. Fluoroscopic localization of instruments depend on indirect information obtained from displacement of contrast-filled structures (e.g., bowel, biliary).

The special advantage of CT guidance is that visualization of the needle is an absolute forgone conclusion and does not require special technical approaches or concerted efforts to visualize the needle. These simple facts make this technique adaptable to virtually any environment so that even radiologists without special MR skills can master this guidance method. Unfortunately, MRI procedures require special expertise and also low-field magnets to effectively perform invasive procedures. Talented MRI physicians are adept and skillful at the use of MRI, but the average physician has some difficulty (see MR section). Fluoroscopy is ill suited because it does not provide three-dimensional relationships required for most accurate procedures.

MRI Accuracy of Localization

The accuracy of MRI localization is somewhat more complicated to discuss than CT localization. MRI is very

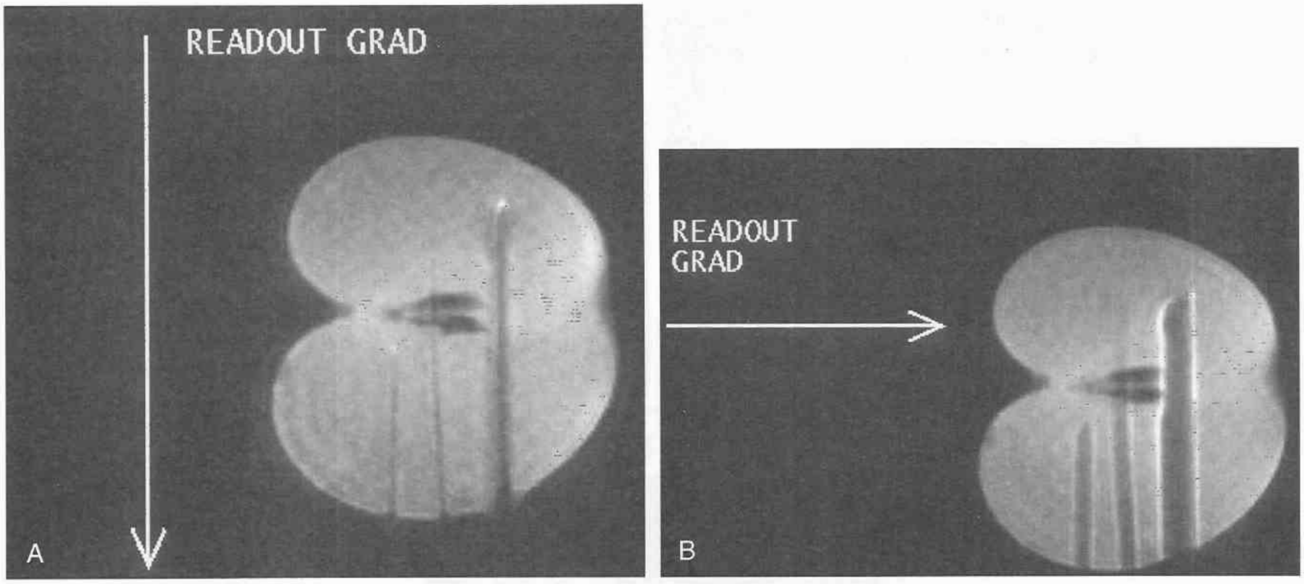

Figure 61–8. *A,* These two sets of images show the importance of properly orienting the readout gradient to the alignment of the needles. This image shows various size needles within an apple with the gradient parallel to the needles. Note how visualization of the needles is lessened by the apparent thin diameters of the needles. *B,* This set of images of the same needles in the same apple shows the diameter of the needles as being very large, enhancing their visualization. With the gradient perpendicular to the orientation of the needles, the localization of the needle tip is more accurate than with the gradient parallel. This was well demonstrated by Lewin et al.[240]

accurate at displaying general anatomy and precise molecular proton qualities. This makes it suitable to see pathology well, but displaying the needle or instrument is more involved. In selected cases MRI is indicated because the lesions are more clearly visualized on MRI than CT (Fig. 61–8).

Because most instruments are made of a metal that is a major component of steel, the ferromagnetic properties dictated that special materials be used for such procedures. One should use instruments specifically designed for MR usage, because standard needles can become mobile within the magnetic field.

Low-field magnets with open access are required for optimal performance of such procedures. Seminal work by Lewin et al[240] evaluated the merits of high- and low-field magnets for procedures and determined quite definitively that low-field magnets were best suited. In this paper, Lewin et al[240] reported the importance of using frequency encoding axis perpendicular to the needle shaft. This provides the most accurate visualization of the needle because it artifacturally widens the image of the needle, making it more visible in the tissues and more accurately displaying the needle tip (see Fig. 61–8). Gradient-echo imaging is the preferred pulsing sequence because it increases the apparent width of the needle, improving its visualization but not large enough to preclude accurate needle-tip localization. Because of the rapid scan times of the gradient-echo sequences, they almost permit near real-time monitoring during needle insertion.

Ultrasound is useful for the diagnosis and visualization of soft tissue abnormalities, and in some cases it can provide localization of instruments.[58,178] It is somewhat less flexible for such procedures because visualization can be impaired by overlying gas and bone and thus requires "windows" for accurate imaging. Because of the reflective properties of a needle, it can be seen "breaking" the beam and providing some general localization; precise localization of the tip, however, is not always easy. This is not a significant problem because one can wiggle the needle and improve its visualization by movement of the tissues. The visualization can be optimized if the needle can be inserted at a right angle to the beam, but this is not always convenient or appropriate in many patients.

There are several innovations with ultrasound[309] that may potentially improve the visualization of the needle tip. One company has recently introduced a needle that transmits an ultrasound signal audible to the transducer. Others have suggested that with the exquisite sensitivity of color-flow Doppler for motion, better visualization of the needle is possible.

Recently, several authors introduced the possibility of using MRI to perform biopsies. Mueller et al[294] have done some promising preliminary work with various types of stainless steel instruments. Although in theory MRI-guided biopsies are appealing, there are technical problems because of the physical configuration of current devices, spatial fidelity of current devices and the difficulty in the clinical monitoring of such patients.

Although almost all reports confirm the advantages of CT, there is still occasional controversy on occasion concerning which modality should be used in which circumstance. In practical terms the individual radiologist must determine the degree of accuracy, confidence level, and role for CT, ultrasound, and MRI.

Versatility

Versatility is still one of the most valuable advantages of CT-guided procedures. Since the skin is unimpeded,

no "holding" devices are required. There is significant versatility in selecting the entry point for the biopsies because of the completeness of the CT image: A full 360-degree view of the patient is provided. All organs, including the bowel, are visualized, so that a variety of needle pathways can be chosen. It is possible to choose appropriate pathways to avoid specific organs or the bowel, if clinically indicated. Changing the body position of the patient may be advantageous for opening windows for instruments because of organ shifting or patient comfort (changing positions creates no adverse effect on image quality). Finally, a wide variety of instruments can be used, ranging in size from a 23-gauge Chiba needle to a 14-gauge Tru-Cut needle. Of all of the advantages of CT procedures, versatility is the one that is least recognized.

Versatility in being able to approach the patient in any angle or body position is extremely useful. As noted in the later clinical sections, three major benefits are derived. First, if patients are going to cooperate during a procedure, it is critical that they are comfortable on the table. Patients with back pain or localized discomfort in the flank can be induced to remain still during a procedure if they can become comfortable by shifting their position. Permitting the patient to lie in a prone, lateral, or oblique position can go a long way to improving patient comfort, cooperation, and therefore success of the procedure. The second benefit of moving patients into different positions is that the internal anatomy shifts accordingly and permits better and safer trajectory planning and execution. In the abdomen, bowel and organs shift sufficiently to permit a safer sampling procedure. In the chest, lesions in the anterior mediastinum can be more safely sampled because laying them on their side may shift the anterior junction line sufficiently to permit a pathway avoiding the lung parenchyma (Fig. 61–9). Third, in some cases when a patient has control taking consistent breaths and the lesion is quite mobile, placing the patient in a lateral or oblique position can be helpful in limiting the movement of the lesion. When the ipsilateral side of the patient is dependent, the weight of the viscera partially immobilizes the diaphragm and limits the movement of the lesion.

It is indeed perplexing that some radiologists do not change the patient position or trajectory of the needle to avoid uninvolved structures. For example, instead of approaching retroperitoneal lesions posteriorly through the flank, they use only a direct anterior approach to traverse bowel or other organs. As noted in the sections on organs, especially adrenal, pancreas, and others, traversing an uninvolved organ can produce significant complications.

MRI is also versatile based mainly on its ability to display coronal and sagittal planes in quick scanning sequences. This permits more convenient angulation of devices and trajectory planning when lesions are high under the diaphragm. Also, because of the flow void phenomenon, blood vessels are easily visualized as structures void of signal. There are some limitations related to the short distance between the coils in an interventional device. This creates some problems with long instruments, but they can usually be resolved by patient positioning and approaches unless the very largest patients are encountered.

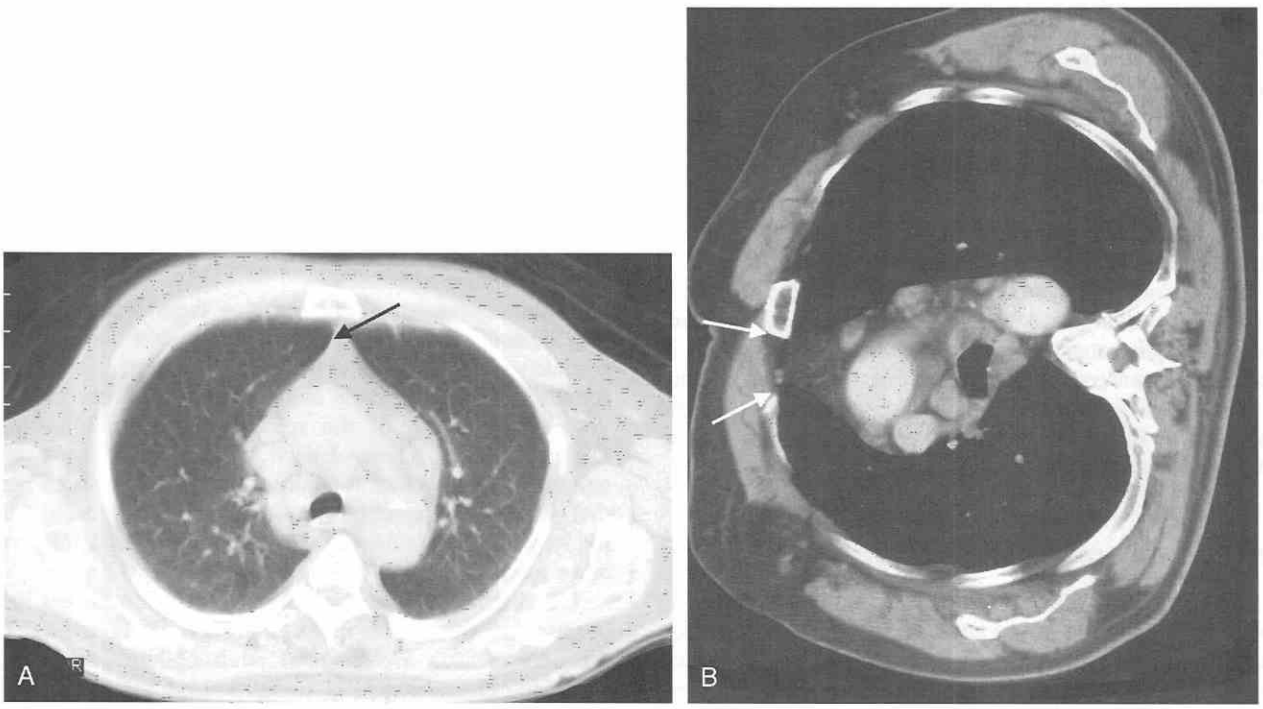

Figure 61–9. *A,* Scan shows a subtle mass in the anterior mediastinum, thought to be thymus, but the clinical situation dictated that a biopsy be performed. The anterior junction line is concealed behind the sternum. The only possible biopsy approach would be a very lateral one traversing much lung parenchyma. *B,* With the patient lying on the right side, the mediastinum shifted so that a clear access to the mass without crossing the lung was provided.

Disadvantages of CT Guidance

CT guidance has a number of apparent disadvantages that are quite minimal in comparison to its advantages. Those to be considered include cost, radiation, and availability of equipment.

Although it is true that the cost is greater than for other examinations, the cost savings of a CT biopsy compared to alternative costs of surgery and/or hospitalization are remarkable. Mitty et al[281] calculated a savings for CT-guided pancreatic biopsies of more than $3000 per case. Considering that more than half of all such biopsies are performed on an outpatient basis, the savings is actually more than that amount. By comparison, ultrasound is much cheaper but MRI is much more expensive.

The CT scan obviously uses radiation for generation of the scans, but the dose delivered to the patient is much less than other specialized studies such as angiography. With modern scanning devices, doses for individual scans can be calibrated to lessen these exposures.

In the recent generation of scanning devices, as a result of increased awareness about radiation safety, vendors are finally producing "photo-timed" CT scanners. The detector systems are being utilized in conjunction with the computers to measure the dosage "on the fly" so that optimization of dosage occurs even within the context of a specific scan. I cannot avoid the opportunity to say "I told you so and it's about time," noting this was proposed many years ago in our second edition of the textbook.

Disadvantages of MRI Guidance

The major disadvantage of MRI guidance is that visualization of instruments and anatomy is dependent on operator technical skills. Small-field magnets are required to ensure access to the patient so the appropriate technical sequences of the device are critical as well as the experience of the radiologists. In practical terms, interventionalists must be experts in the field of MRI so that they can alter the sequences during the procedure to maximize lesion resolution and minimize artifacts of the instrument visualization. An average radiologist does not have the skills to routinely perform such procedures.

A practical disadvantage that results from these facts is that MRI procedures are seldom time-efficient. Procedures typically require considerably longer than an hour. Even in experienced centers, seldom are more than three or four procedures performed during an 8-hour period. On the other hand it is not uncommon for experienced CT sites to perform four to nine procedures per 8-hour day.

Future of Combined-Modality Imaging

In recent years, devices have been built that combine positron-emission tomography (PET) and CT devices within the same piece of hardware. As one might expect, these devices offer great potential for enhancement of interventional procedures. The functional aspects of PET should permit better visualization of active pathology within the immediate context and milieu of the interventional procedures.

One must recall, however, that these devices are not designed for enhanced patient throughput. PET scans still require considerable time for collection of data to ensure appropriate signal-to-noise ratio.

It must also be noted that modern computer techniques permit fusion of functional PET images with CT images. These techniques use standard imaging devices already in existence, and clinical practice can answer most queries related to activity and anatomy.

For the devices to become widely accepted, their role with interventional procedures must be better defined and developed. There is little question that the emphasis on image-guided local treatment of neoplasm will continue to improve and evolve.

It is my opinion that within this context, these new devices will come into wide usage only if their role with interventions can be developed and defined.

Indications for CT-Guided Procedures

The indications for CT-guided procedures vary from institution to institution, depending on the expertise of the radiologists and the available imaging modalities. Generally, the important factors to consider are the visibility of the lesion on CT as compared to other modalities, the type of pathologic sample required, and the location of the lesion.

Considering that the prime function of the guidance modality is to direct the needle to the lesion, visibility of the lesion is the most obvious factor. Plainly stated, if one cannot see the lesion, one cannot biopsy the lesion. Therefore, if a lesion is seen only on CT or much better on CT, then CT is the modality of choice. Likewise, if a lesion is seen only on ultrasound or MRI, then they are the preferred guidance methods.

When an aspiration type of biopsy is clinically indicated, a variety of factors should be considered. As a rule, the simplest modality that satisfactorily shows the abnormality, pathway of the instrument, and adjacent anatomic information should be used. Generally, anatomic areas such as the retroperitoneum and pelvis are in most instances best suited for CT guidance. Specific consideration of each anatomic area are discussed later.

When lesions are small (ranging from 3 to 5 cm) and are located in critical areas, CT is again the preferred modality (Figs. 61–10 and 61–11). Critical areas best suited for CT punctures include abnormalities adjacent to major vessels, the hilum of the spleen, and the mediastinum. Certainly, visualization of such small lesions may be first attempted using other modalities (but most authors agree that successful punctures on the first attempt are more likely with CT guidance). Any procedure that fails with other modalities should be attempted using CT.

CT should be used when avoidance of intestinal loops or vascular structures is important (Figs. 61–11 and 61–12). We believe such avoidance is advisable in several situations. In immunologically compromised patients, we believe that CT procedures should be used to avoid penetration of the bowel and possible contamination (even with the skinny needle). Even in immunocompetent patients, if the abnormality to be punctured is a fluid density, we

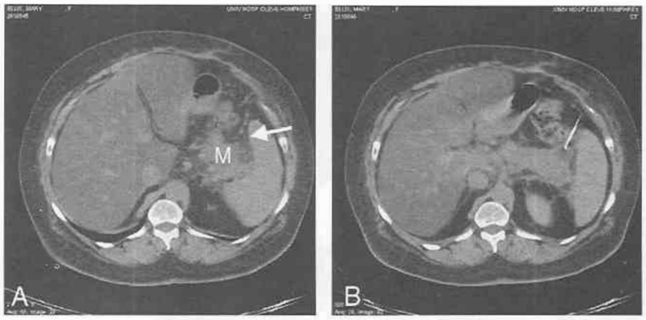

Figure 61–10. *A,* Scans adjacent to a mass (M) in the tail of the pancreas shows the close proximity of varices *(arrows)* in the gastrosplenic ligament. *B,* With the patient in an oblique position and angled approached, aspiration needle biopsy *(arrow)* of pancreatic mass avoiding the colon, spleen, and varices was accomplished. Unlike other authors who commend traversing uninvolved organs, I recommend at least an attempt at avoiding them. In most cases, penetration can be avoided. Over a large series of procedures, the absolute number of complications will be less because at least a relatively smaller number of inadvertent penetrations will occur.

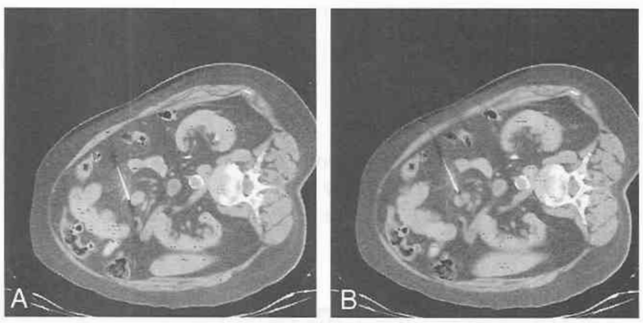

Figure 61–11. *A,* Small lesions in deep locations can only be sampled using CT. Scan shows a tiny mass in the root of the mesentery. This first pass shows the needle *(arrow)* deflecting past the mass. Note that the patient was positioned obliquely, which permitted the bowel to float away slightly, thereby clearing a pathway for the needle. *B,* Repositioning of the needle and using the bevel of the needle to prevent deflection, the mass was sampled adequately. See section on needle deflection.

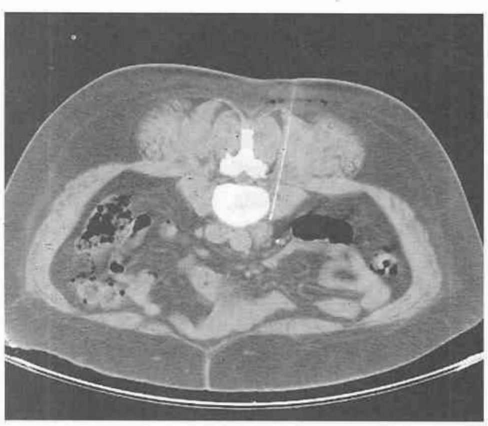

Figure 61–12. Lymph nodes adjacent to aorta are only suited for CT guidance because of the accuracy required.

believe penetration of the bowel should be avoided (see section on pyogenic contamination). A variety of approaches can be used to avoid bowel because the bowel can be seen and patient position can be varied (see Fig. 61–11). A recent advance (discussed later) has been the use of carbon dioxide or other gas to move various loops of bowel.

When a large cutting-needle biopsy is clinically indicated, CT is usually the modality of choice. Even though fluoroscopy or ultrasound can be used safely in many cases, CT is the best guidance modality because it eliminates the two most likely errors: (1) inappropriate biopsy of uninvolved organs (e.g., gallbladder, vessels) and (2) inappropriate biopsy of abnormalities with increased vascularity. The accurate display of abnormalities as well as any normal structures that may be displaced prevents inadvertent puncture. Bolus dynamic scanning is accepted by virtually all authors as being highly accurate for the assessment of vascularity (Fig. 61–13), whether in the liver or other areas. It is as accurate as digital subtraction because both use the same detector principles and computer enhancement.

CT may also be a modality of choice when some type of contrast agent such as urographic contrast or air is to be injected. Such contrast can provide additional information about cysts, abscess, pseudocysts, or dissemination of medication.

Indications for MRI Procedures

The primary indications for MR procedures are basically (1) superior visualization of abnormalities on MRI and (2) the need to watch tissue changes during ablative procedures, either chemical or radiofrequency heating. Some subtle abnormalities in the liver or kidney are not well seen with CT or ultrasound and are best seen on MRI. Depending on the lesion being ablated, it may be critical to follow the heating changes to ensure that complete destruction of the lesion occurs or to monitor potential inadvertent damage to uninvolved structures.

General Complications of Procedures

A number of possible complications are specific to the various organ systems, but some general concepts are relevant to all areas. Because of the advantages of CT procedures the possibilities of complications are significantly reduced. If proper CT techniques are used, the major causes of complications are limited to poor technique, lack of patient cooperation, undetected coagulopathy, or undiagnosed obstructive or diffuse interstitial processes in the lung.

Before discussing in detail how one can avoid certain problems, several comments should be made concerning complications as they relate to the two major categories of instruments: the aspirating, or skinny needle and the large cutting needles. Contrary to the opinions of others, severe complications may occur with any needle (including the skinny needle, manual cutting needles, or the automated biopsy guns) unless one exercises caution, common sense, and meticulous technique.

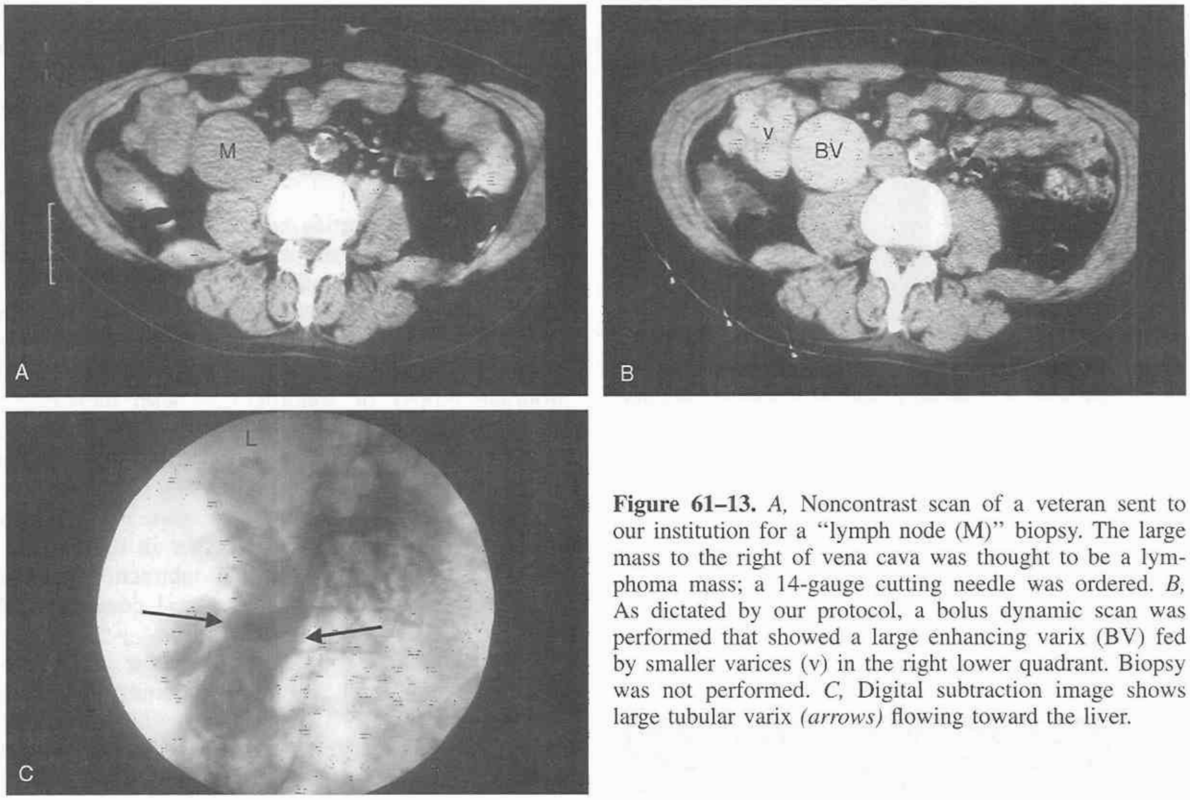

Figure 61–13. *A,* Noncontrast scan of a veteran sent to our institution for a "lymph node (M)" biopsy. The large mass to the right of vena cava was thought to be a lymphoma mass; a 14-gauge cutting needle was ordered. *B,* As dictated by our protocol, a bolus dynamic scan was performed that showed a large enhancing varix (BV) fed by smaller varices (v) in the right lower quadrant. Biopsy was not performed. *C,* Digital subtraction image shows large tubular varix *(arrows)* flowing toward the liver.

Skinny-Needle Complications

There is no question that the skinny needle is the safest instrument available, but even this needle can produce complications in selected circumstances. For example, one can find in a careful review of reports of skinny-needle biopsies of the pancreas instances of pancreatitis, pancreatic fistula, cholangitis, needle-tract seeding, significant hemorrhage, abscess formation, and fatal pancreatitis. An awareness of these potential problems should not be a deterrent to performing such procedures but instead should be an incentive to eliminate complications, even with the skinny needle.

Most complications have occurred with skinny needles when lesions have been highly vascular or numerous needle passes have been made. The reported fatalities from liver and adrenal hemorrhage occurred with apparently vascular hemangioma and pheochromocytoma. One can see in reviewing the literature that most complications have occurred in those cases with four or five needle passes.

This viewpoint about limiting the number of passes and minimizing risks even with skinny needles is shared by another expert interventionist, Dr. Ed Smith of the University of Massachusetts.[390] Dr. Smith, in his recent chapter on the risk of fine-needle biopsy, reported on the results of a survey mailed to 100 university hospitals and every fifth hospital with more than 200 beds. In this survey he noted the occurrence of 4 deaths, 27 cases of hemorrhage, 3 occurrences of needle-tract seeding, and 16 cases of generalized infections (nonfatal). In his conclusion Dr. Smith made a statement with which I concur completely.

> It is logical to assume that the number of complications should be related to the number of needle passes made during the biopsy procedure. However, serious and even fatal complications, although rare, can and do occur and it is important to be aware of the possibility and take all the appropriate precautions in order to reduce their incidence.

Cutting-Needle Complications

With large needles one obviously has a greater probability of incurring possible complications because a large "hole" is being produced. It is quite apparent however, that by using meticulous technique, the potential risks of these needles can be offset and very low complication rates can be achieved.

A recent alarming trend in regard to the large needles is that some authors who advocate their use have become somewhat "cavalier" about potential complications. One must pay careful attention to meticulous technique or serious and even fatal complications will result. Indeed, it is likely that in the near future, unnecessary and serious complications related to the large needles will be reported. It is my hope that individuals who are now starting to use these needles will seriously adhere to the cautionary advice of experienced interventionists.

It is especially important to note that the new automated cutting devices are no safer than the standard Tru-Cut needle that has been used for many years. The speed of cutting has no effect on the local damage produced to tissue and thereby the potential risk from such a procedure. In the first report about the biopsy gun, the authors described a serious hemorrhagic complication following a liver biopsy. Potential problems are minimized by CT guidance and a careful, meticulous technique such as I have

described. These measures can eliminate many potential causes of complications (e.g., hemorrhage or inadvertent penetration of an uninvolved organ) and can result in excellent accuracy with few problems.

Avoidance of Uninvolved Structures

A major determinant of complications is the penetration of uninvolved structures. With the spectacular imaging characteristic of CT, intentional penetration of adjacent structures is inexcusable if other clear pathways are readily available. There are numerous articles in the literature that proselytize using a trajectory through an adjacent structure such as pancreas or liver during an adrenal biopsy, bowel during a pancreas biopsy, aorta or vena cava for pancreatic procedures, spleen during pancreas biopsy, and pleura during an abdominal procedure. The facts are such advocates are promoting sloppy, ill-advised techniques.

It is of course unavoidable that penetration of such structures may occur during an attempt of a meticulous and appropriately planned technique. The point is that complications may occur on a statistical basis. The fewer times one penetrates an avoidable structure, the lower the long-term complication rate. For example, if one chooses to penetrate the aorta or venous structure during a celiac nerve block, there will be a well-defined rate of complication. It may be the rate will be less than 5% of 100 cases. If one intentionally uses this approach, the operator will have five complications when they have accumulated 100 cases. If one tries to avoid these vessels, inadvertent penetration may occur in 10 of 100. It may be that the involved radiologists might never have the five complications, because it statistically will take a total number of 1000 cases before 100 penetrations occur.

The reasons to avoid such approaches are for legal reasons and also the future of the field. Legally the more complications, the greater the chance of lawsuit and monetary damages. The other reason is that we should develop meticulous techniques to advance the field. The average radiologists who read this chapter may think the procedures I show are not possible for them to learn. The fact is that every time operators perform a meticulous technique avoiding other structures, they are learning the methods to advance their skills, such as we are demonstrating in the mediastinum, pancreas, and other organs.

"Crap Happens"

It is quite obvious that complications may occur even if no error was made (Fig. 61–14). This was the subject of the article published by Dr. Yohan and our group called "Complications of No Biopsy."[413] Recognizing these can occur randomly on occasion, we should avoid approaches with a higher incidence of complications.

Hemorrhage

The most likely potential risk during any biopsy procedure is the occurrence of bleeding. The vascularity of the pathologic lesion as well as the anatomy, occurrence rate, and risk of bleeding are specific for each organ system, these factors are discussed in relation to each organ system. For example, highly vascular lesions of the liver such as hepatomas, sarcomas or hemangiomas[173] potentially have a high incidence of serious hemorrhage unless meticulous methods are used. Generalized statistics that combine rates for multiple organ systems (e.g., liver, pancreas, lung) are not relevant to the modern approach to biopsies.

Obviously, to avoid complications one must ensure that a patient does not have any bleeding coagulopathy and the laboratory values are within acceptable ranges. Several animal studies by our group[102,104,105] evaluated the effect of needle caliber, type, prothrombin time, and platelet counts. In those studies platelet function appeared to be even a more important factor than prothrombin time. With either abnormal platelets or prothrombin time, it was shown that there was a considerable difference between needles smaller than 16 gauge and those larger than 16 gauge. I prefer that the prothrombin time be within 2 seconds of normal, with the partial prothrombin time within 25% of normal, and the platelet count be greater than 50,000. In some critical clinical circumstances exceptions can be made, but with such variances the potential risk is greater. The attendant risks and associated precautions should be understood by all involved (patient and physicians) and appropriate contingencies made.

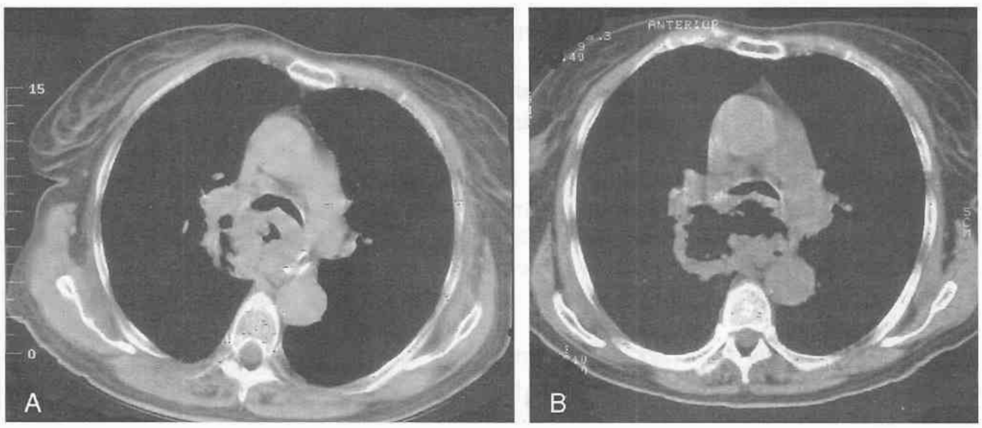

Figure 61–14. *A,* Scan shows thickening of the gastric pull through segment, believed to represent tumor. Based on this study, I scheduled the patient for a biopsy procedure. *B,* Repeat scan on the day of the procedure shows a normal-appearing stomach, so the procedure was canceled. There was no skin preparation or local anesthetic. The patient was admitted to a local hospital the next day with life-threatening hemoptysis. She ultimately died from bleeding. See section on "Crap Happens."

Patient Cooperation

One cause of complications common to all procedures and not eliminated by CT is lack of patient cooperation. If a patient moves or cannot suspend respiration at the appropriate time, difficulties may arise. The most critical factor to enhance patient cooperation is adequate local anesthesia in the area of the biopsy. Local anesthesia should be administered down to the serosal surface of the organ (e.g., pleura, capsule). If this area is not anesthetized, the patient may "jerk" at the time of insertion and produce a tear, bleed, or pneumothorax.

The other factor that has been alluded to and is critical is patient comfort on the table. The patient should be positioned in whatever position is the most comfortable within the context of the anatomic trajectory. This must be specific to the patient and may include pillows under the knees, shoulders, and so forth. If patients must lie immobile, they may fidget if they are uncomfortable.

For those patients who are emotionally upset, administration of an appropriate hypnotic or sedative can be quite helpful. Dosages of such drugs vary widely, and local sedation policies should be followed.

Pyogenic Contamination

Contamination of sterile areas is possible from either a cutaneous source or, if a loop of bowel is penetrated, an enteric source. If Betadine is used for preparation of the skin, cutaneous contamination is improbable. Contamination from bowel can occur, depending on the immune status of the patient, the nature of the abnormality, the size of the pyogenic inoculum, and the virulence of the pathogens. Interventionists who advocate traversing bowel with impunity should be regarded with a slight amount of skepticism.

It is true that an immunocompetent patient can tolerate spillage of a small amount of bacteria within the peritoneum, but the clearance of bacteria is impaired in certain circumstances. If bacteria are introduced into a fluid space, experimental data shows that the effectiveness of bacterial "killing" is impaired because (1) opsonization of pyogens by antibodies and complement is less efficient in a fluid space, and (2) phagocyte-clearing activity is impaired in a fluid space based on physical spatial considerations and the probabilities of random particle encounters.[409] Moreover, an immunocompromised patient is obviously at a greater risk from pyogenic organisms because of the reduced number or function of immunologic cells.[226]

This concern about bacterial contamination from percutaneous procedures is well-founded. A number of secondary infections have occurred and been reported in the literature. One reported case of peritonitis was produced in an elderly woman after penetration of the colon by a skinny needle during a lymph node biopsy.[358] In his survey Smith accumulated 16 cases of generalized bacteremia occurring from aspiration biopsy in the survey that were treated by antibiotics.[358]

For these reasons I modify my technique in several circumstances to eliminate or lessen any potential risk of bacterial contamination. If the mass is solid in an immunocompetent patient, I will accept a trajectory crossing bowel; a small inoculum of bacteria is no match for the normal immune system. (Practically speaking, it is difficult to penetrate bowel unless one tries because it will move away from the needle). If the lesion being sampled is cystic, I insist on avoidance of bowel for the reasons stated earlier. Passage through bowel also would be counterproductive for the culture of cystic masses because of possible spurious results from contamination.

If the patient is known to be immunocompromised, I will avoid traversing colon or small bowel in all cases. In such cases I usually prefer to cancel the procedure rather than to put the patient at risk.

Avoidance of bowel in any of the cases noted earlier can usually be achieved by changing the position of the patient, which may result in "shifting" of the bowel that may open clear pathways for needle insertion (see Fig. 61–11). In other cases, injection of carbon dioxide may be used to move bowel loops (see section on tissue retraction and movement).

Vasovagal and Hysterical Reactions

Interventionists not familiar with vasovagal or hysterical reactions cannot diagnose or properly treat them. Both of these events, which are relatively common, must be dealt with properly and expeditiously to prevent physiologic sequelae or inappropriate iatrogenic intervention.

The vasovagal reaction is a sudden discharge of the parasympathetic vagal nerve, resulting in bradycardia, vasodilation, and hypotension. Such patients appear pale and ashen gray and may be partially responsive or unresponsive. The appearance is not unlike that of a patient who has had a cardiopulmonary arrest. Close inspection of the patient will show the presence of bradycardia, diaphoresis, dilated pupils, and hypotension. Treatment of this event should be tailored to the severity of the situation. The patient should first be put in a Trendelenburg position to enhance venous return to the heart and cerebral blood flow. Do not sit the patient upright—the hypotension will be worsened. If the patient improves within 1 to 2 minutes, no other action need be taken.

However, if the patient does not improve quickly, oxygen should be administered by nasal cannula and an appropriate dose of atropine, either intramuscularly or intravenously, should be administered. Before administration of the drug, a quick review of the patient's clinical notes is appropriate, patients with cardiac arrhythmias may be quite sensitive to the drug. A single intravenous dose of 0.5 or 1 mg will usually restore the normal heart rate. If the patient's condition persists (i.e., if the atropine does not improve the situation), urgent consultation with a resuscitation team is appropriate. Such patients, especially the elderly, can develop a complete heart block, vascular collapse, and cardiac arrest if not properly treated.

The other event, which is more spectacular but fortunately less dangerous, is a hysterical reaction. Such patients appear agitated, tremulous, and may be crying. Close inspection of the patient may demonstrate tachycardia and systolic hypertension, the pupils will be normal size or smaller. Such patients may be breathing fast and complain

of subjective shortness of breath. After auscultation of the chest confirms good air exchange, the best treatment of such patients is to have them breathe into their hands or into a bag to prevent hyperventilation and subsequent fainting. If hyperventilation occurs, the patient may become alkalotic and faint because of constriction of the cerebral vessels. The next step is to give the patient gentle but firm reassurance; if there is no response, the patient should be removed from the biopsy suite. Before any repeat attempt, the patient should receive an appropriate sedative. Careful assessment of all biopsy patients during the informed consent period usually indicates those who need sedation, thereby preventing any such hysterical reactions.

Tumor Recurrence in Needle Pathway

Growth of residual tumor cells tracked through needle pathways has been a minimal problem in the past but potentially will be a larger problem in the future. The potential for more problems stems from the fact that more procedures are being performed throughout the world, so the absolute numbers will increase even if the relative occurrence remains low. A guidance cannula in the skin stops tracking in the skin, but of course this does not stop any deeper seeding beyond the tip of the cannula. In reality, most tumors are inoperative when they are biopsied, but if there is a possibility of curative resection, a trajectory should be chosen that will permit resection of the needle track by the surgeon.

Although the exact reason why tumor implants occur is not known, it is clear there are two main factors affecting the outcome: type of tumor and the implant site milieu. The best example to appreciate this is with breast cancer. This is ideally suited because I personally have not been involved with breast procedures and have no bias to bring to this topic. Several authors, Diaz et al[72] and Stolier et al,[372] have reported on the frequency of tumor cell displacement occurring in tissues after large-needle biopsies and provide significant insights into tumor seeding. Diaz et al[72] studied a series of 352 cases and looked at the occurrence of tumor cell displacement in specimens that were resected. Diaz et al[72] found that a greater number of tumor cells were present in a short period after the biopsies than at a later time. This suggests that tumor cells do not survive displacement in usual circumstances in the breast. In the group resected in less than 15 days, 42% had displaced tumor cells present. In the group resected more than 28 days, only 15% had displaced tumor cells. The reason a few residual cells may survive to cause low seeding or recurrence is likely dependent on the type of tumor, general differentiation, immune system of the person, antigenicity of the tumor, and local milieu such as vascular characteristics.

There are five organ systems that should be discussed: lung, kidney, pancreas, musculoskeletal tumors, and liver. In the first four systems, implantation and seeding have not been a problem, but numerous incidents with liver are being reported.

In the lung the question of tracking in the tract is often raised, but occurrences are rate. Indeed, only a few cases of seeding have been reported. Considering the thousands

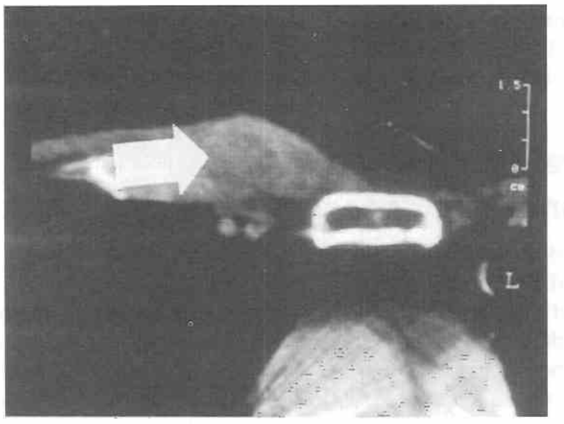

Figure 61–15. Enlarged view of the chest wall shows a tumor implant (*arrow*) to the left of the sternum from a previous lung biopsy from an outside hospital. (Courtesy of Dr. Julie Clayman, Cleveland, OH.)

of such procedures performed, the incidence, as noted by Wolinsky,[408] is very low. We have never encountered a tumor implant in any of our cases, but we have observed one from an outside institution (Fig. 61–15).

Needle tracking of renal tumors is a frequently mentioned potential problem by some colleagues in urology, but it is a very low rate of occurrence. However, I am familiar with only one case of needle tract seeding, reported from the Mason Clinic following aspiration with an 18-gauge needle. However, there is overwhelming evidence that seeding is not a problem with such a tumor. Von Schreeb et al[395] reported a controlled series of about 150 cases of proved renal cell carcinoma used to study the impact of needle aspiration. One half of these cases were aspirated and one half were not. There were no instances of needle tract seeding. Furthermore, the difference in recurrence, morbidity, and survival was actually better in the biopsy group.

The pancreas has had a surprisingly frequent rate of tumor seeding compared with the kidney or lung. There have been two reported cases[88,335] of skin seeding with this pancreas tumor. Considering that there have been only several hundred cases reported in the literature, this is a relatively high frequency compared to the frequency associated with the lung or kidney. Tumor seeding in patients with pancreatic cancer is not a significant clinical problem because they are invariably incurable.

The fourth group of cases that have a possible incidence of seeding is musculoskeletal tumors. Until more experience is gained with percutaneous biopsy of these tumors, one must exercise caution and make a special selection of entry point in collaboration with the orthopedic surgeon. In my practice, I contact the referring orthopedic physician for each procedure to choose an entry point so that the needle pathway can be resected at the time of surgery.

Finally, in recent years a large number of incidental cases of tumor seeding has occurred in patients with hepatocellular carcinoma. Multiple authors (Soyer et al,[366] Llovet et al,[249] Sato et al,[349] Kim et al[216]) have reported this in relation to needle biopsy, tumor ablation, biliary drainage, and even laparoscopic procedures. The increase in reports

is undoubtedly due to the increased frequency of image-guided microsurgery use and minimally invasive surgery as well as the nature of hepatocellular carcinoma.

Preprocedural Steps

Patient History and Consent

Before the procedure and any administration of any medication, it is important to discuss the procedure in depth with the patient. All details, including the rationale, medical alternatives, method of the procedure, sensations to be felt by the patient, and the postprocedural routine, should be mentioned. After this discussion the patient may sign the informed consent form and help confer about the need for any sedation.

During this time, also inquire about any medication that may alter coagulation or platelet function. The latter is especially important because platelet inhibitors are widely used and not described to patients as "blood thinners." Routine coagulation studies do not detect the presence or activity of platelet inhibitors. Laboratory work performed by our group has confirmed the serious alteration and risk of the coagulation status in patients on aspirin-like compounds.

Two of the most troublesome situations are those patients who are being treated with low-molecular-weight heparin and also patients with systemic lupus erythematosus. There is widespread use of low-molecular-weight heparin because it has a much lower incidence of over-anticoagulation than traditional heparin. The problem with this agent from the perspective of interventional procedures is that the methods for assessing the degree of anticoagulation are not readily available at many hospitals. Furthermore, few clinicians are aware of the required test, which is an assessment of factor X inhibitor. Within our community several catastrophic events have occurred in association with this new agent.

The other troublesome clinical scenario has been in those patients with lupus erythematosus. With lupus, there is a high incidence of patients who have spuriously elevated coagulation tests due to unknown circulating antibodies. The dilemma that arises is when such tests are positive, one cannot be sure if the patient will clot normally.

Both of these situations are fraught with difficulty because the attending radiologist, not the referring clinician, bears the brunt of the legal consequences if bleeding occurs. The best approach in these situations or others that might arise is to rely on an older coagulation study—the bleeding test—when available. This test evaluates the time required for a standard puncture site to stop bleeding; as such it actually takes into account all factors, including the intrinsic, extrinsic, and the capillary properties. A substitute for this test for the interventionalist to become accustomed is to carefully observe a small stab wound made at the entrance site for the procedure. A rule of thumb that I use is that the site should not continue bleeding after gentle pressure for several seconds. If the blood continues to flow, one should inspect the site and review the history. Although this is rather arbitrary, this observation is worthwhile and can avoid catastrophe if one becomes accustomed to making this observation.

Sedation and Analgesia

Because of the powerful but effective sedative and analgesic agents now available, one must be conversant with basic life support resuscitation and also the sedation protocols of the home institution. Most institutions now require some type of basic proficiency for sedation administration, so the operators must make sure they comply with institutional, state, and federal guidelines and certification.

Two types of medication may be given to patients: one for sedation and anxiety and another for analgesia. For anxiety, a mild sedative such as midazolam (Versed) should be given. In most average-size adult patients, 1 mg intravenously can be given at the onset and then titrate the needs of the patient during the procedure. As a rule it is probably better to err on the side of giving medication, but if there is no apparent need by the history or from clinical observations of the patient, one should withhold the drugs.

Laboratory Studies

For routine aspiration procedures on a patient with no history of coagulopathy or medication, I request partial thromboplastin time, prothrombin time, and platelet count. If it were not for the litigious environment, I would not even obtain these studies for aspiration biopsies. For patients who are to have cutting biopsies I prefer the platelet count above 50,000, prothrombin time within 2 seconds of normal, and a partial thromboplastin time within 25%. If there is any suspicion of anemia, I order a hematocrit study. I perform aspiration at almost any hematocrit level if the coagulation is normal, but I insist on a value of 32% for any type of cutting biopsy. Because of the demonstrated safety of CT-guided procedures, I no longer type and cross-match a patient for any blood products unless there is some unusual clinical circumstance.

Bedside Assessment of Bleeding Diathesis

Over the years I have developed great confidence in the use of a bedside method for evaluating bleeding propensity as follows. Hemostasis is a complicated process dependent on platelets, blood proteins, capillary fragility, and circulating inhibitors or antibodies. It is well-recognized that the best way to assess clinical bleeding is to use the traditional bleeding test. This consists of making a standard stab wound and measuring the time interval required for local hemostasis. This test is seldom used in modern hospitals because of all of the specific laboratory tests that reflect specific coagulation causes. We do not order this test but use a different permutation at the bedside that I believe is helpful for avoiding possible catastrophe.

After the skin is prepared, I always make a small stab wound at the entrance site of the needle. One can use this site as a "bleeding test." Although I do not time the event, I pay careful attention to the clotting of blood from this site. If bleeding continues to "stream" from the site despite several minutes and "blotting" with gauze, I am always concerned about a bleeding diathesis. In the past I have

been able to recognize patients who have had incorrect laboratory values, inappropriate administration of anticoagulants, and other problems. In such cases I would rather terminate the procedure than create a problem; in such cases the laboratory tests, history, and so forth are reviewed. It is a tragedy that the quality of health care has become so degraded, but the facts of the matter are that physicians and professionals are pressured every day to work faster so that oversights are not an uncommon event.

Coagulopathy

With the wider use of image-guided microsurgery, more patients with suboptimal coagulation status are being sampled and treated with these methods. There are a limited number of clinical articles that deal with this topic. Most authors depend on the standard laboratory values that measure the clotting mechanism. Those most commonly used are prothrombin time, INR, and platelet count.

As most radiologists recognize, there are two different pathways that affect the formation of a clot: the intrinsic and the extrinsic pathways. The purpose of both pathways is to ultimately generate a firm clot containing fibrin at the site of injury, either intravascularly (intrinsic) or extravascularly (extrinsic). The common mechanism is the production of thrombin at the site of injury that causes the polymerization of fibrinogen to fibrin.

Within the vascular system (intrinsic), platelets agglutinate onto any site of injury and release platelet tissue thromboplastin, which begins the thrombosis cascade within the blood, ultimately changing prothrombin to thrombin. Extravascularly, tissue thromboplastin is released by injured tissue, that reacts with plasma proteins to again convert prothrombin to thrombin.

It is important to seek the proper remedy to the demonstrated coagulation problem before performing a procedure. The assumption is that the radiologist has the luxury of time to correct the problem. When a patient has an abnormal prothrombin time, it is most appropriate to give vitamin K and wait several days for the prothrombin to correct itself. When time does not permit waiting for this correction or the correction does not work, then administration of blood products will be required (discussed later).

For an impaired platelet function or low platelet count, two possible approaches can be taken: platelet replacement or the infusion of desmopressin (DDAVP). The dosage and regimen for infusions should be obtained from the local pharmacy. Although the exact mechanism of action is not known, it has been demonstrated over many years that the administration of this medication will improve the adhesiveness of platelets and thereby minimize the probability of hemorrhage. The exact mechanism is not understood, but it is recognized that the medication is typically most effective on the first administration and is less effective when later doses are administered.

Traditional Infusion Replacement

The traditional approach for correction of coagulopathy is to administer intravenous platelets or fresh frozen plasma over the course of many hours to obtain a systemic improvement of these factors. Replacement platelets restore a sufficient circulating number so that platelet agglutination occurs (>50,000 is required). Fresh frozen plasma is administered to restore the prothrombin time to within 2 seconds of normal. Fresh plasma permits this because it replenishes a number of factors such as prothrombin and factors VII, IX, and X, which are produced by the liver and are deficient when liver function is impaired.

The difficulties with the traditional method are several. The most difficult issues are related to obtaining the blood, administering the blood, rechecking the tests, and transporting the patient to the imaging site to perform the procedure. Regardless of the institution, any where in the world, there are always logistical problems.

The problem typically encountered is incomplete correction of the laboratory tests to the desired levels. The causes are quite numerous and can be related to acquisition of blood samples for testing or acquisition of the blood product, administration of the products, repeat laboratory testing, and transport of the patient. If correction has not occurred, then additional blood products must be administered and more delays ensue. With such delays, the patient is seldom ready for the procedure until late in the day or at night, when availability of support staff is least.

To make this approach work, one must be aggressive in ordering the tests and products and keep close oversight of the time issues. Depending on the level of impairment, the exact amount used will vary, but in most cases I use the following protocol: Order a four-pack of fresh frozen plasma, administer three units over several hours. I request a repeat lab test after the third unit but continue to administer the fourth unit following the procedure. In most cases the fourth unit will have been given to the patient when the lab report returns. From the results one can determine if the correction is proceeding as expected or not; if the results are appropriate the patient is transported, if they are not the test is deferred.

The traditional method has obviously been accepted over the many years, but there are some problems with this approach. If patients have cardiovascular compromise, then the multiple units infused may cause cardiac overload and decompensation. In some patients, there may be antibodies or unknown reasons why such products will not correct deficiencies.

Local Infusion of Blood Products

Since the last edition of this textbook was published, we have developed a new technique that has proven worthwhile in a select number of patients. First, one must realize that this is not a Food and Drug Administration (FDA)-approved use of blood products, but under current legal guidelines, a physician can act on the best behalf of a patient in unusual circumstances. If a product is approved for human usage, a licensed physician can use that product for other uses when the benefit to the patient seems to outweigh the risks. Under these guidelines, a physician can use the technique described later in this section, but they take on any associated ethical or legal risks.

The history of this technique is as follows. Several years

ago a colleague unfortunately had a patient with refractory leukemia that would not respond as well as chronic thrombocytopenia. He even had antibodies to platelets so that any platelets that were administered were consumed quickly. After he refused thoracic surgery for chest drainage, he was sent to us for a possible procedure. At the time I reasoned that one might be able to use platelets with local administration as an alternate method. Because there was no other alternative, we tried the method and it worked. Since then we have used local injection of platelets and fresh frozen plasma in patients who have an abnormal prothrombin time or low platelet count to partially solve the problem.

If attempts at correcting the problem by systemic administration fail, we use the technique as follows. After preparation of the site with Betadine and local anesthetic, approximately 5 to 10 mL of blood product is injected into the expected trajectory of the needle through the skin, the subcutaneous tissue, and the surface of the organ and target (Fig. 61–16). The procedure is then performed in the routine fashion.

We have reserved this method for aspiration procedures at this time, believing that other steps should be taken if a cutting needle is used. In such cases, one should use a method that includes a guidance cannula and some plugging material such as Gelfoam or angiographic coils (see later).

The rationale for this technique is as follows. First, experience has shown that local infiltration of blood products does not create any problem except local swelling. Everyone of course reflects on previous patients they have observed who have had local infiltration of blood products. No problems occur from the agents themselves. Second, we believe the local injection creates a local "seroma" of the missing product so that if any adjacent vessel is inadvertently punctured, the local elevated concentrate of the blood product provides material for an effective blood clot. With fresh frozen plasma, the seroma concept is appropriate. With platelets, the platelets probably undergo immediate activation, which provides overabundant amounts of thromboplastin to initiate the thrombosis cascade. A clot formed after the restoration of local or systemic coagulation factors is of better quality than one formed when an imbalance of coagulation factors exists. When a "balanced" clot occurs, this is more effective because studies have shown that the strength of a clot is half due to the platelet agglutination and half to the serum proteins.

Occlusive Hemostatic Methods for Cutting Needles

If there is a severe coagulopathy that cannot be corrected completely, there are hemostatic methods that can be employed to prevent bleeding after a biopsy. The first can be used only when a diffuse liver biopsy is being performed and is not suitable for a guided procedure. The second coaxial method can be used with either a guided procedure of a mass or a diffuse sample of the liver (Figs. 61–17 to 61–19).

Years ago, authors reported the use of a long transvenous (usually jugular access) needle to biopsy the liver through the hepatic venous system. The rationale used is that if one performs a biopsy of the liver from a vessel within the liver, any bleeding would simply occur back into the liver system and not the peritoneum. The risk of such procedures is somewhat less except when the liver is quite small and there is a risk of perforating the liver capsule into the peritoneum. The first versions of this approach were large-bevel, Chiba types of needles that did not work well because only minimal diagnostic tissue was recovered. In years, a side-cutting needle similar to the Tru-Cut design was introduced, which has proven very effective. The other practice that has enhanced this approach is the common usage of a transhepatic decompression procedure for relief of portal hypertension. With a

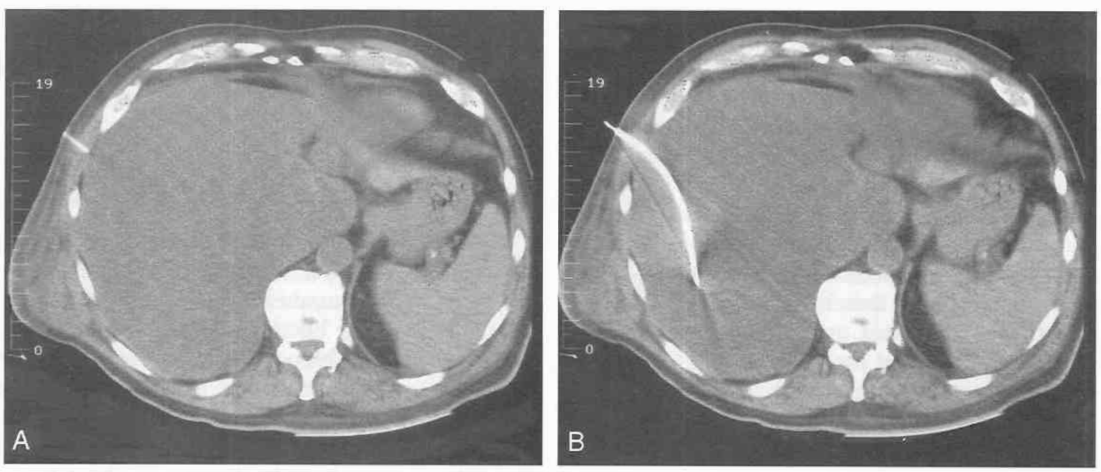

Figure 61–16. *A,* CT scan of a former friend (an interventional radiologist) showing a large hematoma in the right chest. Because the patient had refractory leukemia and antibodies to platelets, the platelet level could never be elevated above a total value of 0 to 5. Other clinical services refused to attempt drainage to permit expansion of the lung. A small needle is used along the pathway to infiltrate platelets. (This is not an FDA-approved technique, but it is legal under FDA guidelines.) *B,* Subsequent scan shows placement of a large catheter in the hemothorax, which was successful and allowed drainage without problems.

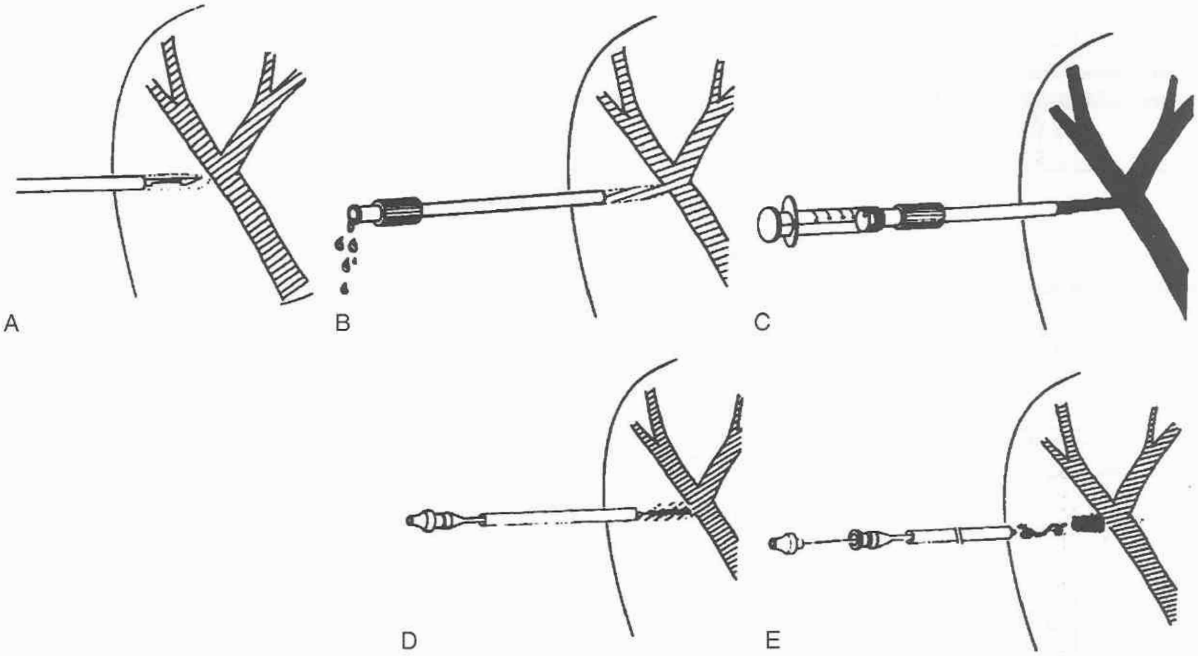

Figure 61–17. Schematic picture shows use of a cannula with a biopsy needle to prevent bleeding in a high-risk patient. In *A*, a plastic cannula is placed over a biopsy needle and a sample is obtained. As noted in *B*, the biopsy needle is removed but the cannula is left as a conduit to deliver a hemostatic coil. Contrast material may be used as in *C* to demonstrate the vascular system. Finally, as can be seen in *D* and *E*, the conduit is used to deliver hemostatic coils into the biopsy site.

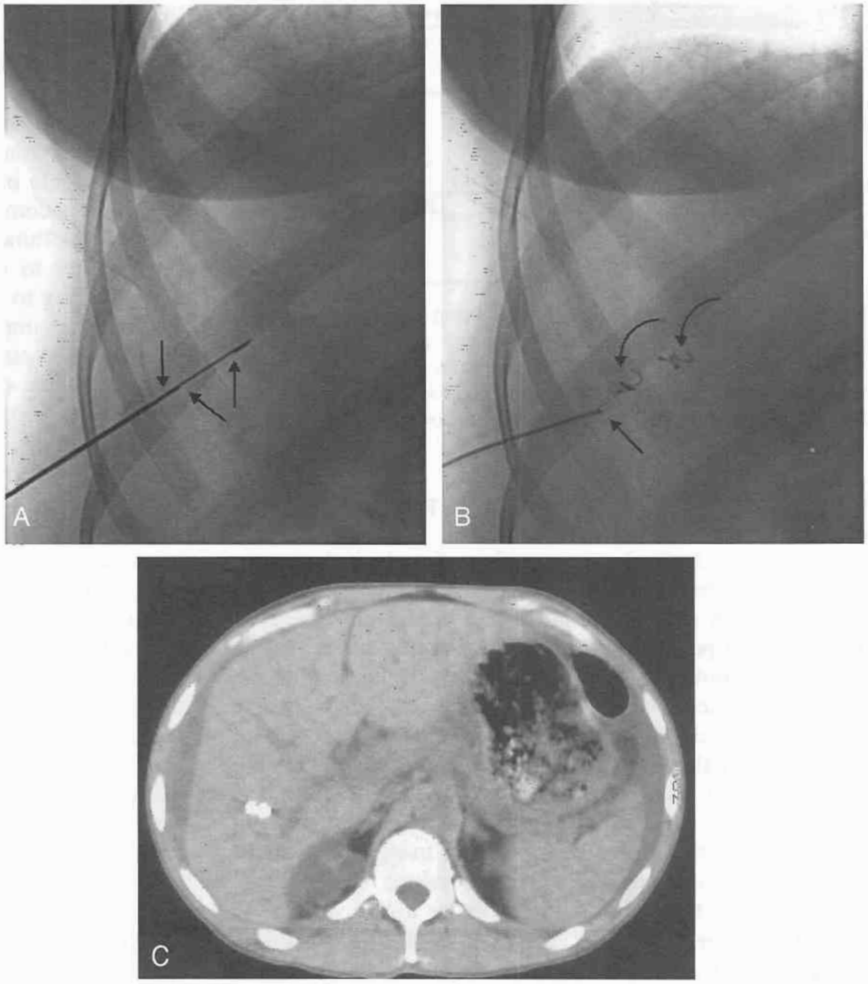

Figure 61–18. *A*, Radiograph shows fluoroscopically guided placement of coil. The guidance cannula *(long arrow)* is noted proximally, and the "gap" *(small arrows)* of the cutting needle is noted distal to the cannula. *B*, Follow-up image shows the cannula containing an angiographic wire, after pushing the two steel coils into the liver *(curved arrows)*. *C*, Follow-up CT scan shows the coil in the liver.

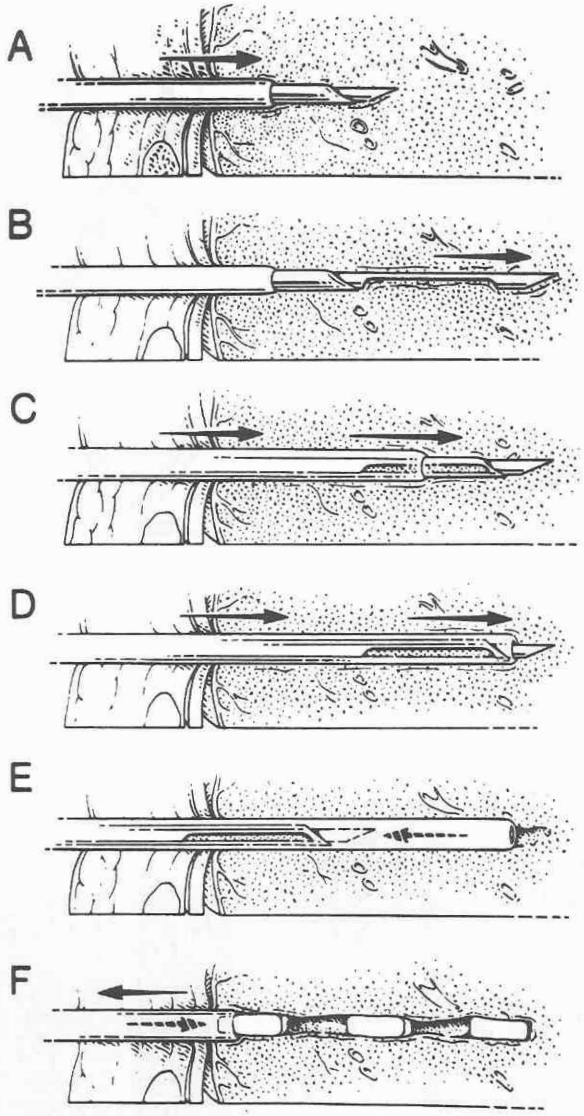

Figure 61–19. Schematic diagram showing a similar technique with Gelfoam. In *A* through *D,* the biopsy needle is introduced with a plastic cannula around it. As noted in *E,* the biopsy needle is removed and the cannula left in place. As seen in *F,* the cannula is used to introduce Gelfoam material to provide hemostasis.

common familiarity of the transjugular pathway, such procedures are commonplace.

The second method is a coaxial one in which the procedure is performed percutaneously. With this method, a coaxial system is used to introduce a needle into the liver. The biopsy is performed through the cannula and the tissue sample is removed with the cannula left in place. Through the cannula, occlusive material is placed into the biopsy site to provide local thrombosis and occlusion. The occlusive material typically used is Gelfoam or angiographic coil, which may or may not be soaked in thrombin before insertion (Figs. 61–17 and 61–18). It is pushed through the cannula with an angiographic wire using the standard Seldinger technique. After the procedure, the patients should lie quietly for 30 minutes to let a clot secure the occlusive material in place. If patients get up too quickly, the device may dislodge into the peritoneum if they happen to cough or exert themselves; there is no direct harm to the peritoneum except for possible bleeding from the site. This may be used in the liver or other sites as needed.

This method is a rather complicated and difficult procedure unless one is experienced with angiographic methods. With current trends in imaging with vascular surgeons and cardiologists making inroads into taking over angiography, we must continue our development of a nonangiographic method. Even in the best of hands, this older method is fraught with difficulty because of the numerous steps.

In most cases it is better to perform such procedures under fluoroscopic guidance so that the insertion of the coil and material can be followed in real time (Figs. 61–17 to 61–19). With experience such procedures can be performed at the bedside with CT or ultrasound, but this requires extensive experience because with this approach the procedure is essentially "blind" (Fig. 61–20).

Although theoretically this procedure is quite simple, it can be difficult to have consistent results because of the many steps involved. If the patient is uncooperative or moves inadvertently, the occlusive material can be accidentally misplaced. Even under the best of circumstances, the material may dislodge itself. Because of these difficulties we are developing a more simplified introduction device for quickly and accurately introducing the occlusive material.

Patient Positioning

Patient positioning is important for three reasons: patient comfort, anatomic approach for trajectory planning, and producing immobility of a mass in cases where the target may be partially mobile.

Realizing that movement of the patient during a procedure can be troublesome, one should ensure that a patient is on the table in a stable position that is comfortable. If a patient is uncomfortable, it may result in a movement at a most inopportune time or increase the patients' anxiety and their ability to cooperate. This generally affects the patients' ability to control their respirations and so forth.

The other important aspect of patient positioning is that by having the patient lie in different positions, the anatomic access may be easier if internal shift of anatomy occurs. This is true in the abdomen and the chest as follows. On some occasions, it may not be possible to biopsy a mediastinal mass when the patient is in the supine position, but by positioning the patient on the side, access through the anterior junction line may be possible (see earlier section on versatility, Fig. 61–9).

As noted earlier, if a lesion being sampled appears to be quite mobile due to respiratory variation, placing the ipsilateral side down can be helpful to limit the motion of the mass. In such cases, the weight of the viscera partially immobilizes the ipsilateral diaphragm and thereby limits the motion during quiet respiration (see Fig. 61–22)

If a patient is somewhat uncooperative or if the lesion being sampled is small, place the patient in the ipsilateral decubitus or oblique position (not at the compromise of the entrance site, of course). The weight of the abdominal viscera partially immobilizes the diaphragm and limits the respiratory motion of the diaphragm (see Fig. 61–22). This is especially important for lung, kidney, adrenal, or liver lesions.

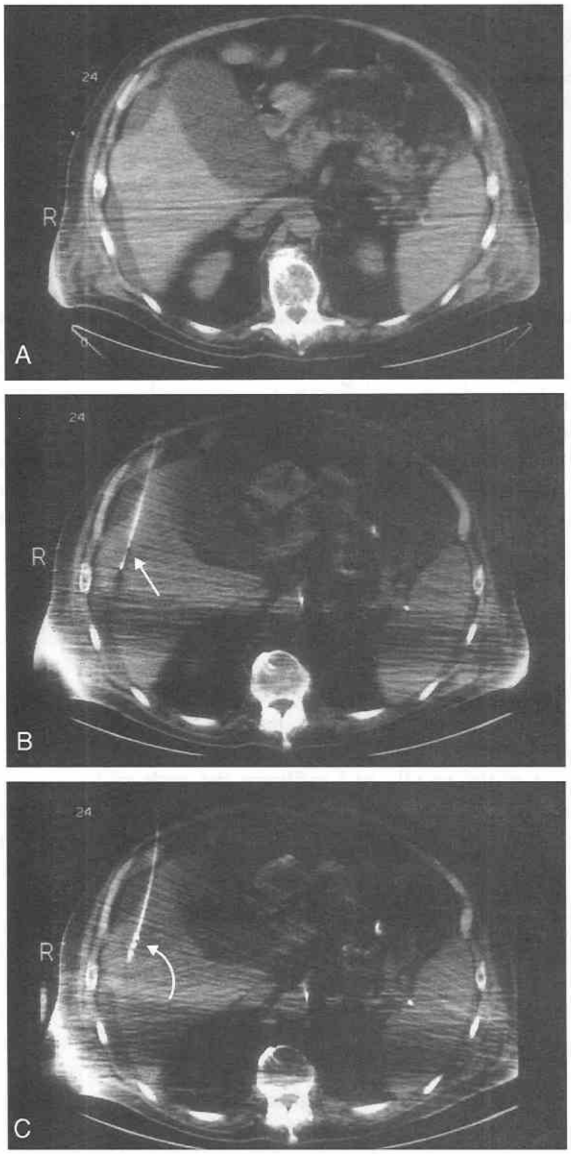

Figure 61–20. *A,* CT scan shows a mass in the lateral portion of the right lobe of the liver. *B,* Cannula with cutting needle is located in the liver; *arrow* points to gap. *C,* Scan shows the coil at the end of the cannula being inserted into the liver.

Entrance Site and Trajectory

Site and trajectory planning should be made after a review of the diagnostic scans. The entire procedure can be greatly expedited if one notes the location of the mass, plans the anatomic approach of the trajectory, and decides on the type of needle to be used before putting the patient on the table. In my opinion, a great amount of time is wasted because physicians do not plan ahead for each case but "make it up" as they go.

After the previous diagnostic scan has been reviewed and an appropriate slice has been selected, localization to that slice can be made from the longitudinal type of scan (e.g., Scoutview, Topogram, Synerview). These scans are referenced to the axial slices, making relocalization after quite easy. (Some groups have advocated the use of catheter mats or commercial products to aid localization and have found them useful.)

Several general comments about site selection and pathway are appropriate. It is important to decide on a pathway that traverses the least amount of uninvolved tissue and that is also the least precarious relative to possible complications. The concept of using a shortest line to the trajectory is valid; the less liver, lung, or other noninvolved organ crossed, the less the possibility for a problem.

We prefer to avoid pathways that include major nerves or muscles. Involving such structures is painful when traversed and makes it difficult for a patient to cooperate. Common sense dictates that potential problem areas such as arteries and veins should be avoided. Muscles can be a nuisance, because they are highly vascular and can bleed locally. Also, when penetrated, the muscles can be tightened purposely or unintentionally by the patient and cause difficulty with needle placement. The trajectory of a needle can be changed by a muscle contraction. If a powerful muscle group such as the erector spinal or gluteal muscles contracts, a needle can be physically bent (Fig. 61–21). The most notable areas where this can be a problem are pathways through the sciatic notch and the retroperitoneum.

If an oblique or angled approach is to be used, it may be helpful to place the patient in a lateral or oblique position. However, do not put the patient in an awkward position that cannot be held for a prolonged period.

In choosing the trajectory, one must decide whether to perform the procedure within the axis of the slice or outside the axis as an angled approach. If one is a neophyte, it is best to develop experience by choosing the entrance site in the same axial slices as the abnormality.

Skin Preparation

Once the entrance site has been chosen, the skin is prepared with Betadine and a local anesthesic agent such as lidocaine is administered. At the time of lidocaine administration, it is important to palpate the tissue carefully to ascertain the location of the ribs, cartilages, processes, and so forth, so that they can be avoided. This is true especially next to ribs, the sacrum, the scapula, or other bony structures that have a tapered edge or traverse the scan obliquely. Such structures produce a partial volume error in the CT scan that results in a discrepancy between their apparent location on the scan and their actual anatomic location.

When infiltrating local anesthetic, completely infiltrate the pathway in two steps. In the first step, infiltrate the skin, the subcutaneous tissue, and the superficial muscles. After that point is reached, have the patient suspend respiration and then infiltrate the local anesthetic down to and including the pleura, peritoneum, or the capsule of the organ (e.g., kidney or liver) (Fig. 61–22). Such infiltrations should be made as the patient suspends respiration. If the capsule is not adequately anesthetized, the patient may "jerk" the diaphragm during the procedure. It is my opinion that inadequate administration of local anesthesia is the most common cause of poor patient cooperation. If a needle is inserted without anesthesia of the capsule, a "spinal level reflex" occurs; this moves the organ and produces a potential lacerating effect. Adequate anesthesia is also most

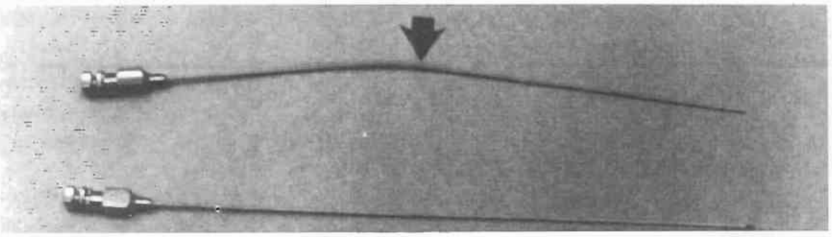

Figure 61–21. Picture of a needle *(arrow)* that was bent by the erector spinae muscle in an uncooperative patient. Compare to the normal needle.

important with anxious patients because they will not cooperate well if they feel pain.

Another important method I have learned and instituted over the past 5 or 6 years has been two new aspects of administering local anesthetic (lidocaine) as follows. The first important point relates to changing the chemical nature of the lidocaine before administering it to the patient, as noted later. The second is the simple methodology for instilling the lidocaine into the injection site itself.

First, it should be recognized that the discomfort associated with the administration of lidocaine is due to the "burning" produced by the acid nature of the lidocaine preservative. One can mix a small amount of sodium bicarbonate into the lidocaine vial that will reverse the acidity. Each day, a nurse should premix the lidocaine vial to be used with 5 mL of sodium bicarbonate into a 50-mL vial of lidocaine. This will neutralize the acid character. This premixed lidocaine can be used only during the day of the mixing and should be discarded the following day.

Painless Local Anesthesia

The second important point is the method of injecting the lidocaine into the projected needle pathway. The traditional method of injecting local anesthetic that we have been taught in medical school is actually an antiquated method based on old approaches and antiquated local anesthetic agents.

The traditional method, which I now believe is obsolete, was based on the use of procainamide, which was a useful local anesthetic and an effective cardiac antiarrhythmic. The traditional teaching is that one should make multiple insertions and injections in the following fashion. One inserts the needle a small distance, pulls back on the syringe plunger to see if blood is aspirated, and then injects the anesthetic. This process is repeated numerous times until the entire pathway is infiltrated with medication. I believe this is similar to the old torture method of the Middle Ages called "death by a thousand cuts."

My method of administration is as follows. Once the first skin wheal is raised with local injection of lidocaine, I gradually infiltrate the site in the following fashion. I start continuously infiltrating the lidocaine at a very low rate as I slowly move the needle into and through the pathway. In effect, a small boundary of anesthesia precedes the tip of the needle as I infiltrate the path with the needle. The same amount of lidocaine is used during injection during the entire path. Although this requires some practice, the results are spectacular: patients literally feel nothing.

To understand the safety of my method of administration, one must recall how commonly lidocaine is used as an antiarrhythmic agent and how large doses of many milligrams are given intravenously. The probability of having the small-caliber needle cannulate a vessel is astronomically small, and even if a small vessel were penetrated, the potential effects of injecting a small volume of lidocaine are virtually nonexistent. In the past 6 years, I have personally injected hundreds if not thousands of patients. I

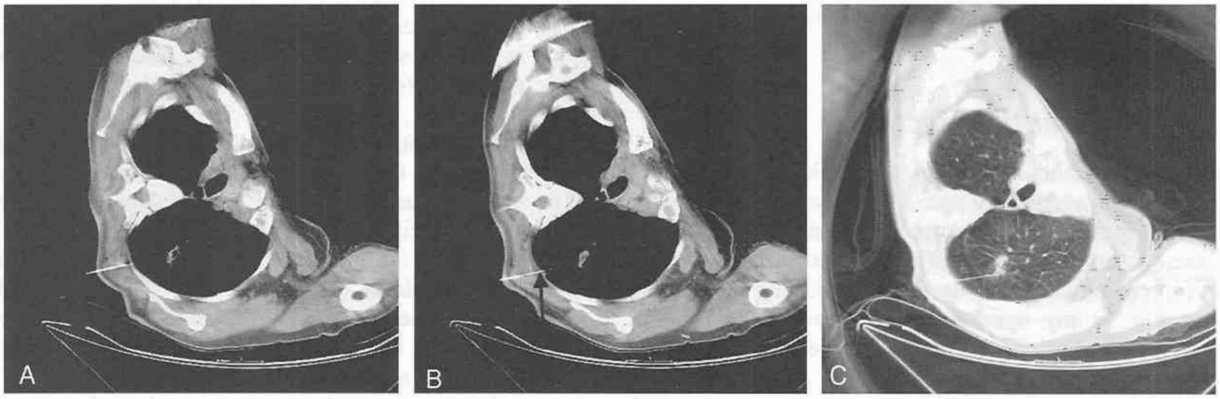

Figure 61–22. Small lesions may be difficult if the patient has any variation in respiration. These three images show the methodology for immobilizing the lesion and a method of providing a pain-free procedure for the patient. *A,* This scan shows the patient in a decubitus position with the lesion side down. In such cases one must be sure access is possible anteriorly or posteriorly. On this scan the needle is on the margin of the rib, where lidocaine is infiltrated. *B,* This scan shows infiltration with a small amount of lidocaine in the pleura *(arrow)*, not the raised pleura from the injection. *C,* This scan documents the placement of the needle in the margin of the lesion.

would hope to someday perform a sophisticated study looking at the systemic concentrations of the lidocaine, but the chances of this getting funded are minuscule.

Needle Selection

General selection of the needle should be made before any preparation of the skin and site. Based on the history, appearance of the mass, and the trajectory, one can select the appropriate needle, either aspiration of cytology or cutting needle for tissue sampling.

Since the last edition of this text, there has been widespread acceptance of the principles previously defined. More complete discussion follows in a later section preceding the specific sections on the different organs.

In general if the patient has a known malignancy and the purpose of the procedure is to simply confirm the presence of recurrence or metastasis, then an aspiration needle is the only type required. If the patient presents with unknown disease, possible change of cell type, previously failed aspiration, or suspected benign disease, then a cutting-needle biopsy should be performed. If one looks at a recent survey of patients undergoing liver biopsy, it is quite clear that automated side-cutting needles have become the norm, as we have previously suggested.

A clinical decision about the biopsy must first be made according to the type of information sought by the attending physician from the pathologic sample. Generally, if a patient has a known malignancy and only a confirmation of metastases or recurrence is desired, an aspiration biopsy with a skinny needle is all that is required. If a patient has an unknown problem or if a question of a second malignancy exists, a large cutting-needle biopsy is indicated (assuming laboratory, clinical, or anatomic information does not preclude a safe procedure). Only a sample with such a needle can accurately establish the diagnosis of a lymphoma, benign tumor, or an unusual tumor.

If a clinical decision is made to use a large needle, consideration of clinical, laboratory, anatomic, and dynamic scan information should be made. Clinically, there must be no history of a coagulopathy and the patient must not be on any type of medication that would impair coagulation or platelet function (see section on patient preparation).

Careful consideration of the anatomy, from a recent or current baseline CT obtained during the planning of the procedure, is appropriate. A large needle can be used if clear access is available to the organ of the abnormality (i.e., no intervening uninvolved structure or close proximity of the aorta, vena cava, portal vein, or bowel). As experience is gained, skill increases and one's safety tolerance relative to anatomy improves. For example, although a novice might be fearful of performing a biopsy of a node several centimeters from the aorta, an experienced person will be quite comfortable biopsying some lesions that abut the aorta.

Comparison of Aspiration and Cutting Needles

From a historical perspective, it is important to briefly review previous information about the prior controversy. Before experience with appropriate cutting needles became common, there were some individuals who advocated the use of aspiration needles (cytologic samples) over those of cutting needles. This was based on a reputed accuracy of diagnostic outcome and increased safety. The fallacy of this position was shown by older literature by Lundquist[255,256] and Ha.[136] These articles clearly show the superiority of cutting needles over the aspiration needles.

Domestic and international authors have reconfirmed in recent reports the advantage of diagnostic accuracy with little difference in complications.[23,217,223,412] Suffice it to say there is no longer a controversy, and virtually all workers concur that cutting needles are superior to aspiration needles. The choice between the two types of needles is dependent only on anatomic factors, slight differences in accuracy and complications, vascular characteristics, and coagulation status. The relative differences in tissue recovery can be appreciated by looking at the material recovered by different types and sizes of needles (Fig. 61–23).

Selection of Aspiration Needle for Cytology

The selection of aspiration needles is quite simple because there is clear laboratory and clinical information that indicates the best types of aspiration needles to use. These points were clearly demonstrated by historical articles and have been reconfirmed over the years without controversy. In the earliest laboratory study by Andriole et al,[10] our group showed that the best sample with the least amount of artifact was the small-angle bevel needle tip and the largest caliber needle (Table 61–1). This was later confirmed by Dahnert et al.[68]

In the direct clinical comparisons, these results were reconfirmed. Pagani et al[316] showed with aspiration biopsies of adrenal glands that an 18-gauge aspiration needle was better than a 22-gauge. In the lung, there has been no definite benefit shown with large aspiration needles, but there was a larger incidence of hemoptysis shown by Khouri et al.[214] In the pancreas, Dickey et al[73] of our group showed the diagnostic return for a 20-gauge needle compared to a 22-gauge needle, with no difference in complication. Most recently reporting on the prostate, Norbert et al[302] showed increased diagnostic yield of the 0.9-mm needle (20 gauge) over the 0.8- (22 gauge) or 0.7-mm aspiration needles.

With our prior experience and the numerous reports as noted earlier, we have consolidated the needle choices in our institution to use the 20-gauge Chiba needle in all organs. It is suitable for all organs and has an acceptable complication rate relative to all organs sampled.

Selection of Cutting Needle

Before one selects a cutting needle, a number of factors need to be considered, including the site, trajectory, and local anatomy (see earlier sections on site preparation). The other critical factor to evaluate is the local vascularity of the tumor lesion. The reason there is little information about the different calibers of needles is the fact that needle caliber is a minor determinant of bleeding. The numerous

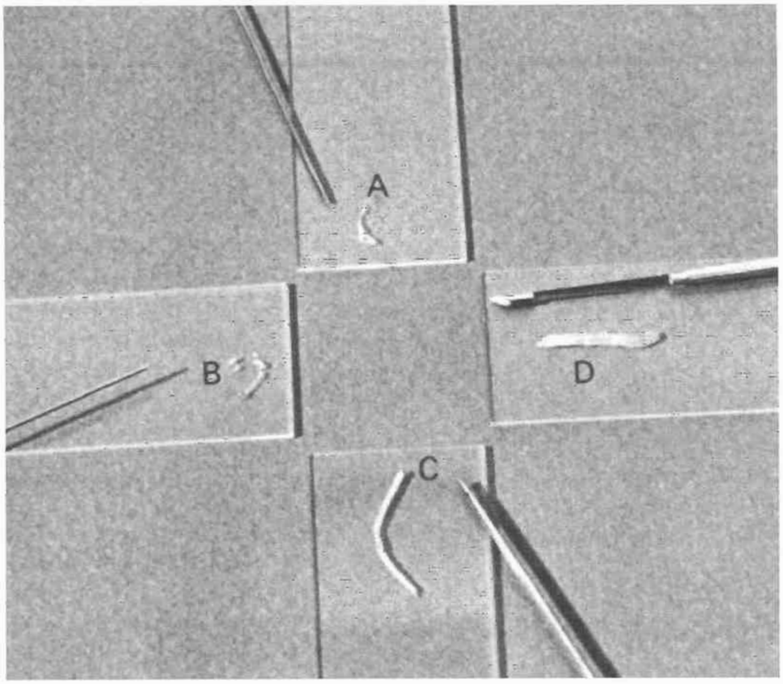

Figure 61–23. The type and relative size of specimens obtained with four different needles. Specimen **A** was obtained with three passes of the 22-gauge skinny-core needle using 30 mL of suction and a 2-cm insertion of the needle. Specimen **B** was obtained in one pass of an 18-gauge bevel-end needle using 30-mL of suction and a 2-cm insertion of the needle. Specimen **C** was obtained with an 18-gauge Menghini needle using 30 mL of suction and a 2-cm insertion of the needle. Specimen **D** was obtained with the Tru-Cut needle and no suction.

Table 61–1. Comprehensive Quantitative Comparison*

Needles	Type of Needle	Average Weight of Sample (mg)
22-gauge	Chiba	4.1 ± 0.1 SD
	30-degree bevel	4.0 ± 0.1 SD
	45-degree bevel	3.3 ± 0.1 SD
	90-degree bevel	2.8 ± 0.2 SD
	Franseen	5.0 ± 0.2 SD
	CSI fine lung	5.4 ± 0.4 SD
21-gauge	90-degree bevel	5.7 ± 0.3 SD
20-gauge	30-degree bevel	7.6 ± 0.2 SD
	45-degree bevel	7.0 ± 0.2 SD
	90-degree bevel	5.8 ± 0.2 SD
	Franseen	10.4 ± 0.6 SD
	CSI fine lung	10.3 ± 0.4 SD
19-gauge	30-degree bevel	12.5 ± 0.6 SD
	90-degree bevel	10.8 ± 0.2 SD
18-gauge	30-degree bevel	16.2 ± 1.3 SD
	30-degree bevel†	16.0 ± 0.3 SD
	45-degree bevel	14.8 ± 0.2 SD
	45-degree bevel†	15.1 ± 0.8 SD
	60-degree bevel	15.3 ± 0.3 SD
	90-degree bevel	14.6 ± 0.5 SD
	90-degree bevel†	14.3 ± 0.1 SD
	Franseen	20.0 ± 0.9 SD
	Lee	19.3 ± 0.4 SD
17-gauge	45-degree bevel	17.9 ± 1.0 SD
16-gauge	30-degree bevel	37.3 ± 2.4 SD
	45-degree bevel	37.6 ± 1.2 SD
	60-degree bevel	39.1 ± 3.1 SD
	Franseen	39.0 ± 0.2 SD
Rotex		1.9 ± 0.6 SD
Travenol Tru-Cut		59.4 ± 3.7 SD

* Three samples were taken from the same liver specimen with each needle.
† Modified Menghini needle.

technical factors and anatomic factors discussed are important, but the other important factors are the approach (discussed in the various sections on the body organs) and the vascularity of the lesion.

The first point that should be clarified is the predominance of the biopsy gun over manual needles. When we first introduced the concept of using the side-cutting needles, one manual Tru-Cut needle was available. Radiologists were not comfortable using the manual device. Other vendors were able to manufacture the device because of patent restrictions. Once the original patents expired on the cutting tips, automated guns were introduced and radiologists overwhelming accepted the concept of cutting needles. A recent survey by Mayoral and Lewis showed over 90% of radiologists doing liver biopsies use these devices; the only variabilities are the vendor and caliber of the needle.[266]

In every case when a tumor is to be biopsied, one must have an imaging procedure that demonstrates the blood flow. This can be done by a basic visual technique or a more sophisticated computer program now available on many scanning devices. The importance of the basic vascularity on the incidence of biopsy can be appreciated by noting the incidence of complications in the liver when bolus scans are used to biopsy the liver and those series of cases where no such assessment occurs. Bret et al[37] reported a series of biopsies on hepatoma patients using 22-gauge aspiration needles and had a hemorrhagic complication rate of almost 5%. In our 12-year experience of liver biopsies using 14-gauge needles, we reported a hemorrhagic complication rate of 0.5% in a group of 200 patients (see liver section).

In general one must decide which caliber of cutting needle is optimal for achieving the appropriate diagnostic sample with the acceptable amount of risk of complication. There is some information in the clinical literature that will

indicate what the proper choice of needle caliber is for specific patients, but there has been some laboratory work performed by our group that sheds considerable light on the tradeoff between needle sizes as they affect recoverable sample and bleeding. In a paper by Plecha et al,[328a] our group studied the outcome in an animal model using 20-gauge, 18-gauge, and 14-gauge needles. In the study, the authors evaluated the amount of diagnostic information compared to the amount of bleeding by weighing the amount of DNA (nuclear material) and blood in the tissue sample. They noted that the larger the amount of tissue required for the diagnostic information, the more efficient it was to use a large-caliber needle.

A number of clinical articles have studied the histologic information obtained from tissue samples for kidney and other organs. Hopper et al[181] showed that sufficient diagnostic tissue could be obtained from the kidney with an 18-gauge needle in the pediatric age group. Haage et al[160] found in a comparison of 18-gauge and 14-gauge needles that the diagnosis was equivalent for both devices. A recent survey among gastroenterologists and radiologists showed that most physicians use an automated side-cutting needle in the range of 18-gauge.[266]

While the use of the 18-gauge needle is the norm in the United States, there is good reason for radiologists to begin using even large-caliber needles within the general body area. In recent years, new methodologies have been developed at our institution in conjunction with the National Cancer Institute that portend to enhance the development of new cancer agents and drugs by using samples from 14-gauge needles.[75,125a] The traditional method for drug development over the years has been to locate patient tumors by imaging and enter them into a protocol of periodic diagnostic examinations. The drug trials would indirectly monitor the effects of the drugs on the tumors by watching the change or lack thereof based on the imaging appearance. The trials would run for long periods with little accurate information about the real effect of the drug on the target site of the end organ. By the use of the large needles and microchemistry techniques, the histologic samples recovered are used to assay the specific target site of the cytolytic or modulatory agent. It is believed that adoption of our methods by other cancer centers would bring about more rapid drug development at a lower cost. From the work of our institution, the agency has actually coined a new phrase for the goal of pharmokinetics and dosage determination of drugs. Instead of trying to find the MTD (maximum tolerable dose, i.e., maximum dose used before unacceptable complications occur), the goal of the new program is to find the BMD (biochemical modulatory dose, based on end target site in the tissues from tumors).[368]

Needle Choices in Coagulopathic Patients

There is little indication in the literature that needle caliber has any significant impact on bleeding if the patient has normal coagulation and the proper careful technique has been used. In our experience with normal patients recently reported by Dowaloti et al,[75] we had a 0.5% bleeding rate with 14-gauge cutting needles in the liver, in a series of 200 patients.

Table 61–2. Separation of Means of Biopsy Blood Loss Data by Needle Gauges

Target Organ	Groupings of Needle Gauges	*P* Value
Liver		
No warfarin	(14) (16) (18, 20, 22)	<0.01
Warfarin	(14) (16) (18, 20, 22)	<0.01
Kidney		
No warfarin	(18, 20, 22)	NS
Warfarin	(18, 20) (22)	<0.05

Note: Groupings within a single set of parentheses taken are equal, versus those grouped those in other parentheses.

NS = not significant.

From Gazelle GS, Haaga JR, Rowland DY: Effect of needle gauge, level of anticoagulation, and target organ on bleeding associated with aspiration biopsy. Radiology 183:509–513, 1992.

In coagulopathic patients, one assumes there must be a difference in the bleeding rate with different caliber of needles, but it would be difficult to design a clinical study from an ethical perspective that would shed light on this question. In a previous laboratory model from our institution, Gazelle et al[102] from our group reported on the effect of anticoagulation on blood loss in two organs: the liver and the kidney. Using aspiration needles, they found that there were absolute differences in local bleeding with various calibers of needles, as shown in Tables 61–2 and 61–3. We also showed that by using a occlusive hemostatic device, the amount of bleeding was acceptably limited.[102] From these data, we believe that the development of a simple, effective hemostatic method will encourage more widespread use of larger cutting needles.

Needle Techniques

Since the prior edition, the needle techniques have matured so the only two general approaches now used are the single-needle or coaxial-needle method.

The *single-needle technique* is simple because it uses the primary instrument as the device primarily localized. This is typically used when one anticipates taking only a single sample. The most usual clinical scenarios differ with the aspiration needle and the cutting needle. With a Chiba

Table 61–3. Summary Statistics Based on Raw Data

Needle Configuration	Drug Treatment	No. of Procedures	Mean Blood Loss (g) ± SD
Tru-Cut only	None	32	2.46 ± 1.37
	Venopirin	30	4.60 ± 1.71
PPS	None	21	0.31 ± 0.15
	Venopirin	27	0.61 ± 0.28
Thrombin-coated PPS	None	14	0.11 ± 0.06
	Venopirin	24	0.23 ± 0.14

Note: The statistics are based on raw data for blood loss caused by liver biopsy performed with differently configured biopsy needles in pigs, with or without venopirin treatment.

From Gazelle GS, Haaga JR, Halpern EF: Hemostatic protein polymer sheath: Improvement in hemostasis are percutaneous biopsy in the setting of platelet dysfunction. Radiology 187:269–272, 1993.

needle and a lesion that is fairly large and accessible, it is easy to perform several procedures as needed without concern about repeat positioning of the needle. With large cutting needles, it is usually when a 14-gauge needle is used to obtain a sample; seldom are multiple samples needed in such a circumstance.

Coaxial methods are now commonly used and offer significant advantages. In the prior edition we made a distinction between a short cannula and a long cannula. Essentially that terminology is irrelevant because vendors now market coaxial systems, with a cannula that is medium length. This permits one to use it superficially or as a deep cannula. In the superficial mode, it permits repetitive sampling of moderate or small lesions without repeat localization. In the deep mode, it can be helpful for minimizing several possible adverse outcomes from procedures.

Using a deep cannula, one can ensure precise placement of a sampling needle into a small site with the flexibility of taking multiple samples or changing instruments without repetitive positioning efforts. The second benefit of the cannula is that it prevents seeding of either infectious material or tumor cells along the pathway, which can have adverse effects. As noted later in the liver section, with the increased interventional activity, more cases of needle tract seeding have occurred. The use of a cannula potentially permits a multitude of procedures with the access provided. Multiple procedures with different needles or instruments are possible. Finally, the cannula can also be used as a conduit for the deposition of occlusive material as needed should some type of bleeding occur, as discussed earlier in the section on hemostatic methods.

The only place where the use of the coaxial cannula is of some question is in the lung. One must be careful when dealing with the lung to not puncture the pleura and cause a pneumothorax. I personally do not use the coaxial system in the lung for this reason. In the mediastinum its use is quite helpful (see later).

Basic Sampling Method for Aspiration and Cutting Biopsy

Aspiration Technique

The standard aspiration procedure is quite simple but can be broken down into three individual steps as follows: (1) application of suction, (2) movement of the needle, and (3) delivery of the sample to the appropriate medium for evaluation (Fig. 61–24).

As noted earlier, the best device to use for aspiration sample is the 20-gauge Chiba needle, which can be used in virtually every organ. Once the tip of the needle is correctly positioned in the area of the lesion, the following steps are taken. Some type of device for achieving vacuum is applied to the hub of the needle.

The best technique is to use a one-person approach to apply suction to the hub using a syringe. The amount of suction to apply has been evaluated by our group and others.[84,184,222] Both our group and Kreula[222] had similar findings. In a laboratory model, we found that displacing the syringe barrel by 5 mL produced about 84% of obtainable sample and that displacement of the barrel by 10 mL produced 94% of the obtainable sample (see Fig. 61–24). There was an "apparent" slight discrepancy between Kreula's data[222] and ours, but there is a simple explanation. Kreula found a straight-line relationship between the sample and the vacuum, but the fact is they only measured the effects between 0 and 5 mL of displacement.

Several other points merit discussion. To maximize the vacuum during the movement of the barrel, it is important to make sure all of the air has been expressed from the syringe before hooking it up to the hub. Even a small amount of air dilutes the vacuum when the barrel is moved.

During the removal of the needle, it is important to maintain the suction to retain any fragments in the lumen of the cannula. The in vitro study our group performed documented the small but definite benefit of this process (Fig. 61–25).

Historically, some groups advocated the use of no suction during the sample acquisition. This "capillary" method works with very necrotic tissue like squamous cell tumor but not with most tumors. Some authors have asserted that the application of suction pulls too much extraneous material, especially blood, into the needle, but a recent study by Ha et al[136] showed that such degradation only occurred in 6% of cases; this slight tradeoff is minimal compared to the improvement of the sample. Furthermore, depending on the fixative chosen, the red blood cells can be lysed by certain additives to the fixative material and thereby eliminate the problem.

Number of Needle Passes

With appropriately planned procedures, one can minimize the number of needle passes and thereby save time and reduce the risk to the patient. It is quite clear from our experience[73] that equivalent diagnostic accuracy can be obtained from two well-positioned, meticulously performed aspirations. Our results compared favorably with other authors who recommended four or five needle passes.

The incidence of complications increases accordingly with the number of needle passes. Numerous reporting authors[89,219–221] support the association of passes with complication frequency. One important article by Smith[358] who described sampling the pancreas with four or five passes, stated that there was a direct relationship between passes and complications.

The emphasis on taking many needle passes has evolved incorrectly from misinterpretation of an article by Ferucci et al[87,89] (Table 61–4). These authors took a sample of 20 cases, proven positive by cytologic results, and looked at the incidence of positivity with each needle pass. At first glance one would belief 100% accuracy could be achieved with many needle passes, but this is not true. Of course 100% of this group had positive results because they were selected as positive at the onset. In the same study the unselected group had only an 82% accuracy despite their protocol of five passes on every patient.

Sample Preparation

After a sample has been taken, it is critical that it is properly handled. Perform the smear quickly in close proximity to the fixative to prevent drying, which can occur quite quickly. Always flush the syringe and needle with fixative and send the fluid for tissue cell block or cytocen-

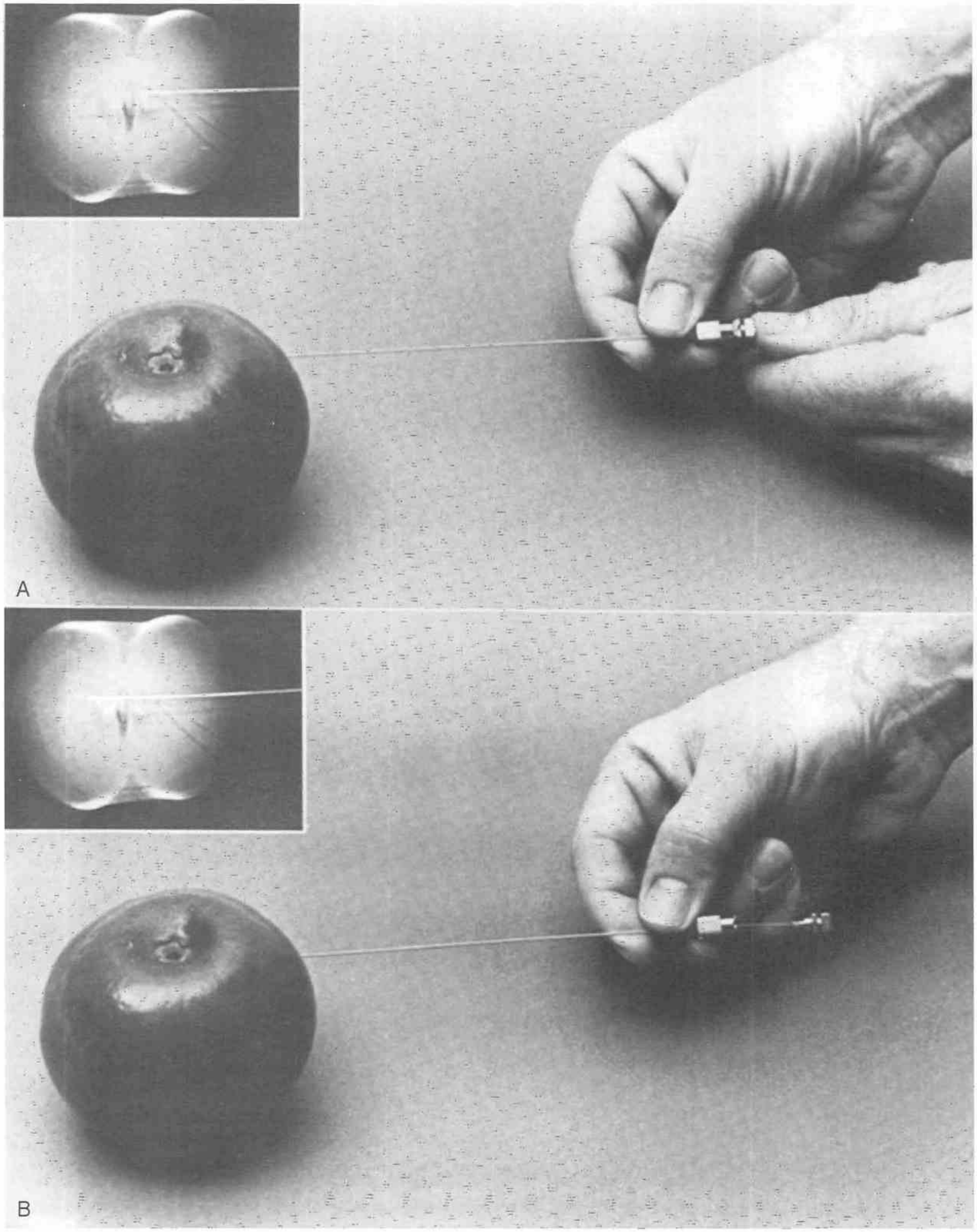

Figure 61–24. The five steps in obtaining an aspiration specimen. *A,* Insert the needle adjacent to the lesion, represented by the "core." *B,* Retract the stylet several centimeters and make several in-and-out motions and rotations of the needle to "free" up some cells. *(figure continues)*

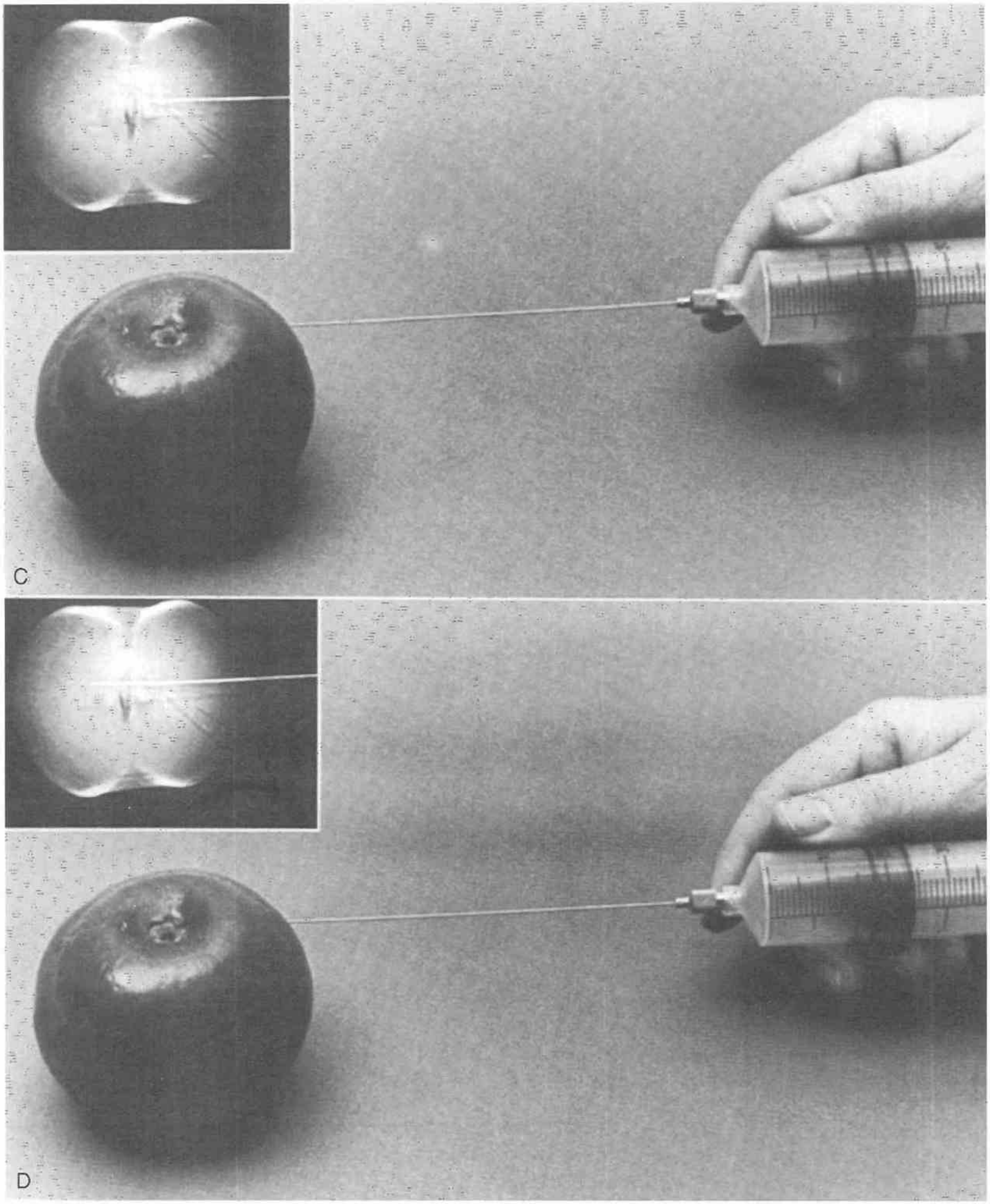

Figure 61–24. *Continued. C* and *D,* Attach a syringe and apply suction while making several in-and-out excursions to obtain more tissue. Release the suction while removing the needle. Eject the specimen onto the slides or into fluid for histologic examination when possible.

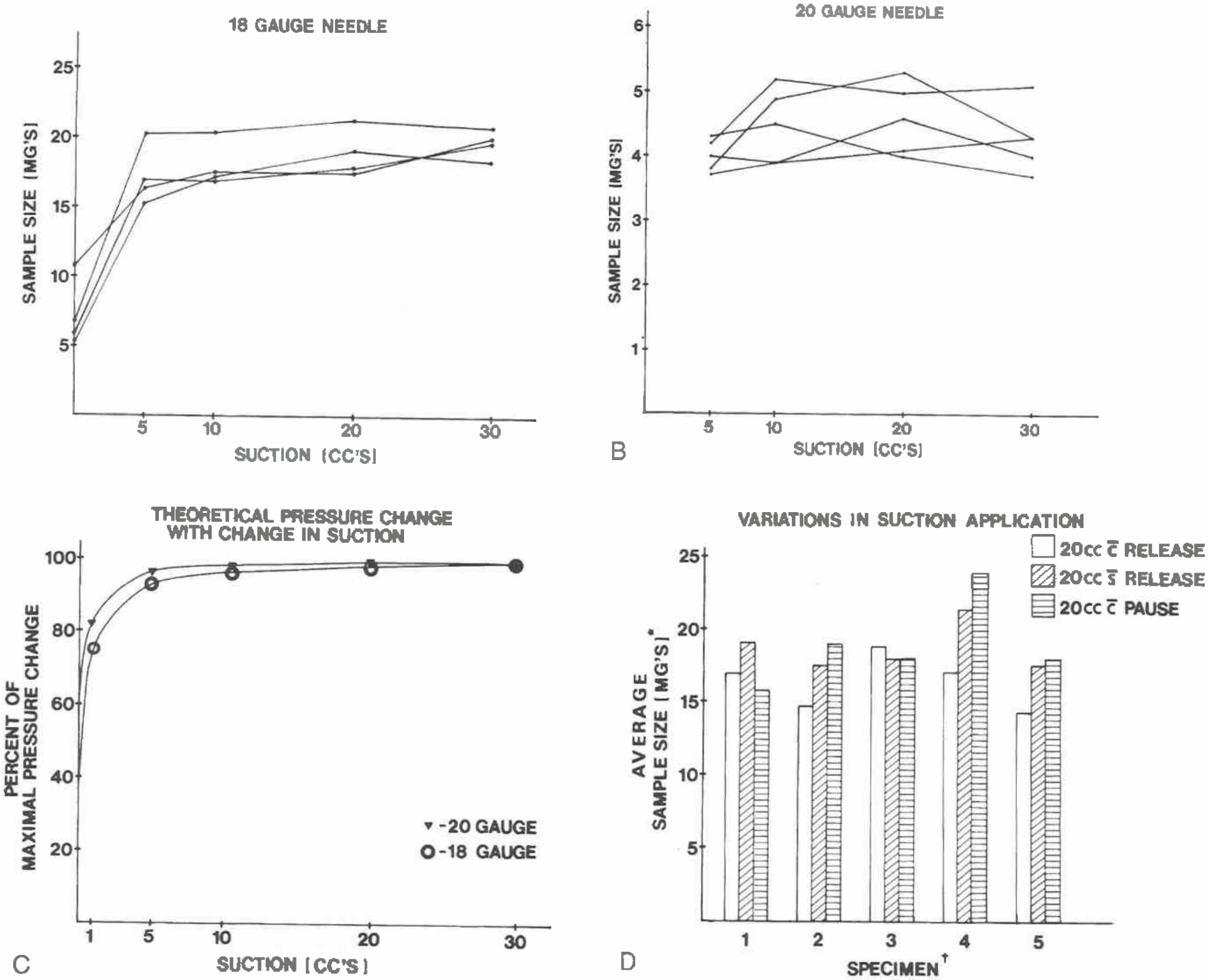

Figure 61–25. *A,* Sample size versus suction, 18-gauge needle. Each point equals average of five samples. *B,* Sample size versus suction, 20-gauge needle. Each point equals average of five samples. *C,* Theoretical pressure change as calculated by Poiseuille's law for noncompressible fluids ($Q = \tau 8(Pa^4/l)n$. Q = volume of fluid through cylinder, P = pressure difference at ends of cylinder, a = radius of cylinder, l = length, n = viscosity of fluid) and Boyle's law for ideal gases (PV = PV at constant temperature, P = initial pressure, V = initial volume, P = final pressure, V = final volume). *D,* Specimens 1 to 4, average of 5 human samples, specimen 5, average of 10 bovine samples; c = with s = without. (*D,* From Hueftle MG, Haaga JR: Effect of suction on biopsy sample size, AJR 147:1014–1016, 1986.)

trifuge, whatever the routine approach is at your institution. This can increase the diagnostic yield by several percentage points. One author[207] has reported that heparinizing the needle and syringe is helpful, but no other workers have confirmed this. Others have measured the carcinoembryonic antigen in the cytologic samples and found this test useful.[231]

Side-Cutting Needles

The type of cutting needle used throughout the world is based on the original side action cutting Tru-Cut design. This manual device demonstrated in Figures 61–26 and 61–27 is the prototype of virtually all cutting needles used today. The percentage of end-cutting needles originally represented by the Menghini needle is used in only a small percentage of cases. Rather than delete the images used in the prior editions, I have retained them because they show in individual frames the action of this needle that are now used almost solely in an automated spring-loaded variety. By understanding the basic action, one can better appreciate any future permutation of this classic design.

The chief benefits of this needle are several-fold. By numerous in vitro tests by ourselves and Hopper,[181] this design provides the most complete and preserved samples of all needle types. Also, because the location of the biopsy is confined to the "gap" of the needle, one can carefully localize the site of the biopsy. The action of the needle is so precisely predicted that it can be used in close proximity to other structures.

Another advantage of this needle is that the tissue gap

Table 61–4. Fine-Needle Aspiration Biopsy: Number of Passes Required to Establish Diagnosis in 20 Positive Cases

	Needle Aspirate Number*			
Anatomic Location	*1*	*2*	*3*	*4*
Pancreas	(+)	+	–	+
Retroperitoneum	(+)	+	+	–
Liver	–	–	–	(+)
Retroperitoneum	(+)	+	+	+
Pelvis	–	–	(+)	+
Lymph node	(+)	+	–	–
Liver	(+)	–	–	–
Pancreas	(+)	+	+	+
Liver	(+)	+	+	+
Porta hepatis	–	(+)	–	+
Porta hepatis	(+)	+	+	+
Ovary	(+)	+	+	+
Pancreas	(+)	+	+	+
Liver	(+)	+	+	+
Liver	–	(+)	[illegible]	+
Pancreas	(+)	+		+
Porta hepatis	–	(+)		+
Liver	(+)	+		–
Retroperitoneum	(+)	+	+	+
Retroperitoneum	(+)	+	+	+
Total	(15)	(3)	(1)	(1)

* Parentheses denote first positive aspirate.

From Ferrucci JT, et al: Diagnosis of abdominal malignancy by radiologic fine-needle aspiration biopsy. AJR 134:323–330, 1980.

can be moved or adjusted as needed without any adverse effects on the tissue. The cutting action takes place only when the outer cannula is advanced forward either manually or by the spring device.

Relative to use of the needle, there are several points that will improve the diagnostic yield and minimize the possibility of complication. To improve the diagnostic yield, two factors should be kept in mind. When spring-driven devices push the stylet forward, there is actually a backward recoil of the device. Because of this motion, the device should be held firmly. In a study by Kellermeyer,[209] he found that holding the needle firmly would improve the yield by reducing the recoil. In his unpublished data, there was a 14% improvement of the yield. Another anecdotal factor is that one should hold the device exactly as explained in the instructions. If an operator holds such a device casually without the fingers in the correct location, the movement of the actions may be impeded and the sample less than optimal.

There is one word of caution about these needles, relative to bending. These needles should not be used for very hard tumors or bone. The thick waist of these needles can bend if too much force is applied, even if the needle is closed (Fig. 61–28).

Assessing Vascularity

Before sampling any abnormality with any type of needle, either aspiration or cutting type, one should have an

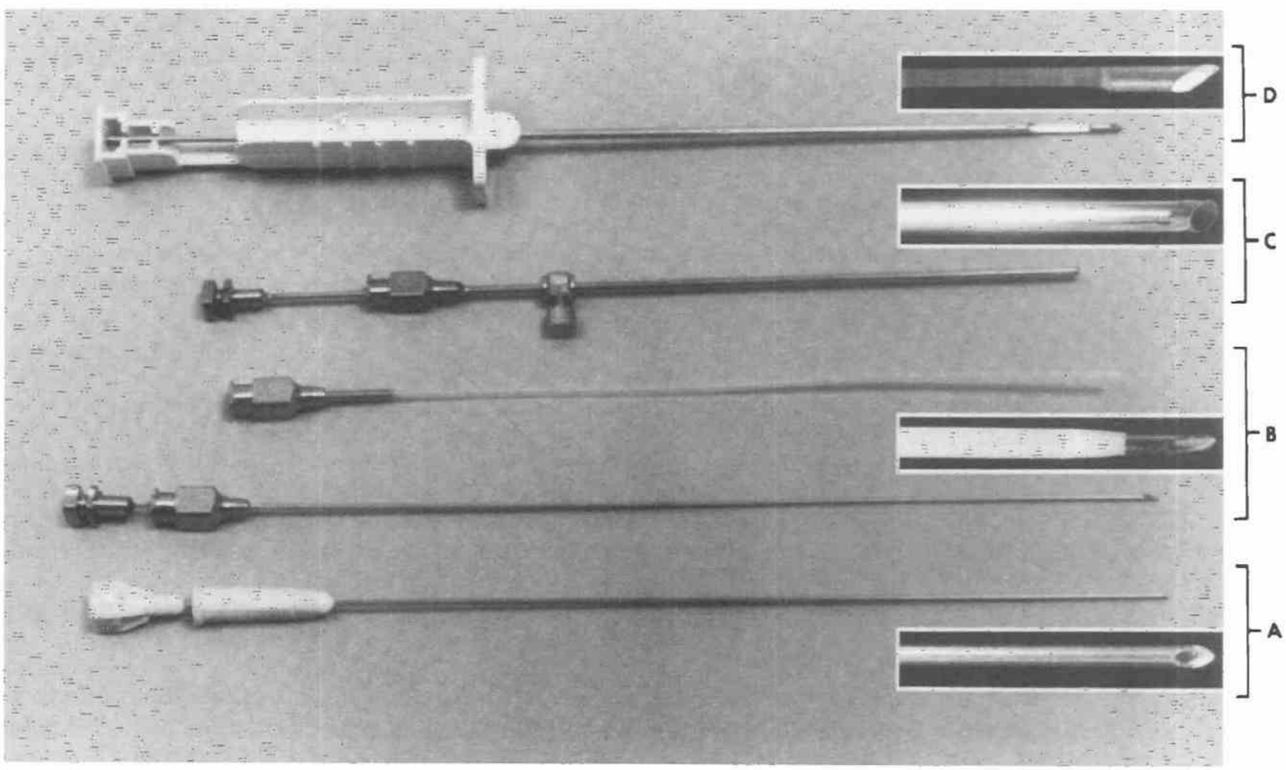

Figure 61–26. Picture of the four needles used. Insets show the needle tip of each instrument. The 20-gauge Chiba needle (A) is used for aspiration biopsies. The 19-gauge needle with the 18-gauge sheath (B) is used for aspiration of fluid collections. The Menghini-type needle (C) is used for cutting biopsies of "hard" lesions. The 14-gauge Tru-Cut needle (D) is used for biopsy of most tumors.

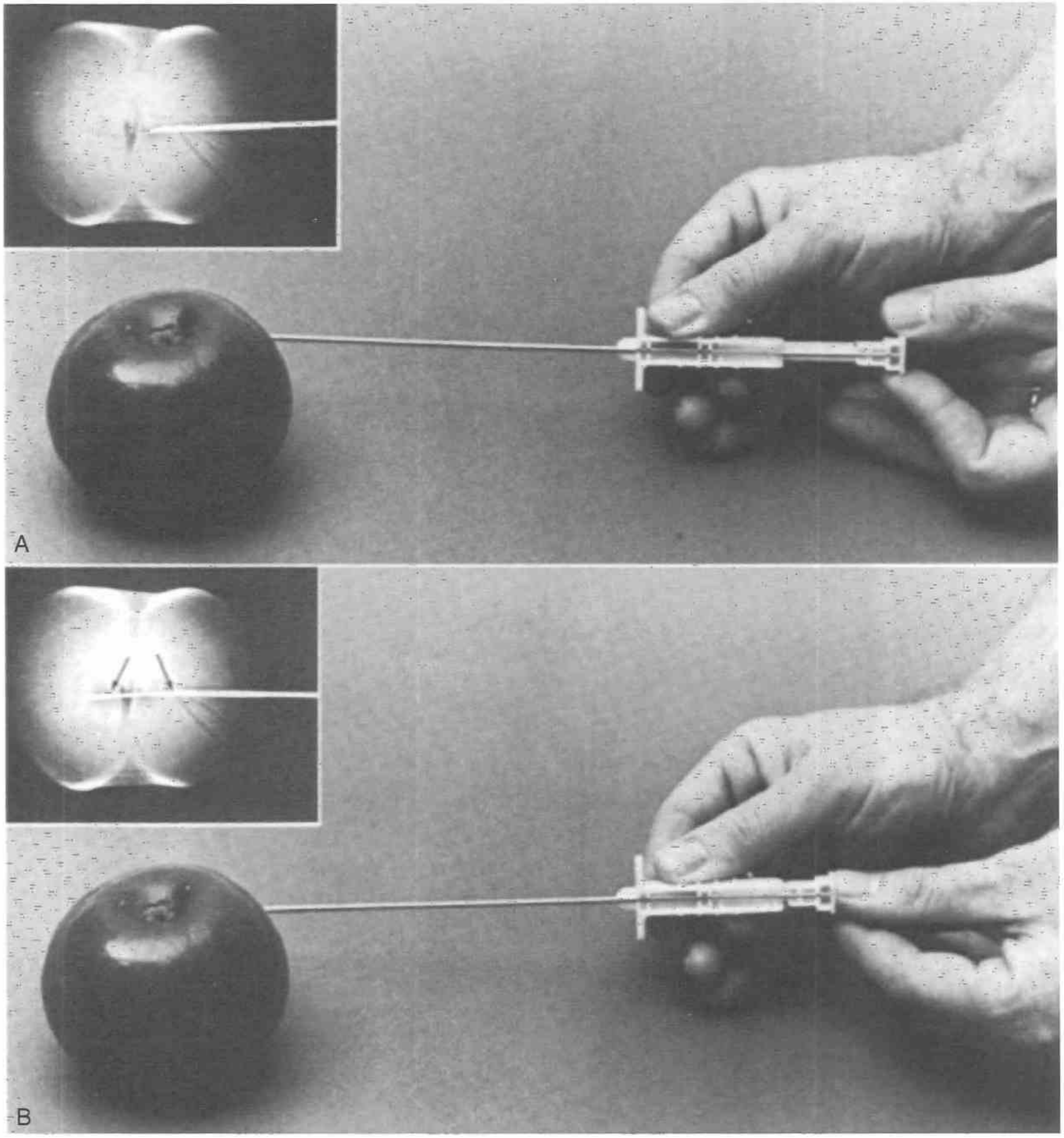

Figure 61–27. "Core" biopsy of an apple using the Tru-Cut needle. *A*, Insert the needle in the closed position to the margin of the lesion. *B*, Insert the inner stylet with the "gap" (*arrows*) briskly through the area of the lesion. (If the needle is improperly positioned, it can be withdrawn in this position; a specimen will not be cut unless the outer needle is advanced over the gap.) *(figure continues)*

assessment of the vascularity. From my experience and review of the literature, the nature of the abnormality is a major determinant of bleeding complication. One can note that high bleeding rates occur even with 22-gauge needles when vascular tumors such as hepatomas are biopsied.[51] On the other extreme, such as in our latest series of 200 liver biopsies in which we use a bolus injection to assess vascularity, the complication rate with a 14-gauge needle is 0.5%.[75]

In most instances, the vascular character of the lesion is apparent from a prior contrast-enhanced study. If not, one should perform a bolus of contrast material with repetitive scans at the site of the biopsy to evaluate the vascularity.

Needle Positioning

Axial Slice

Positioning a needle in the same *xy* plane of an abnormality is the simplest approach, if at all possible. In these cases, with the needle in the superficial tissues, the angle of the needle is adjusted with repetitive scans until angled

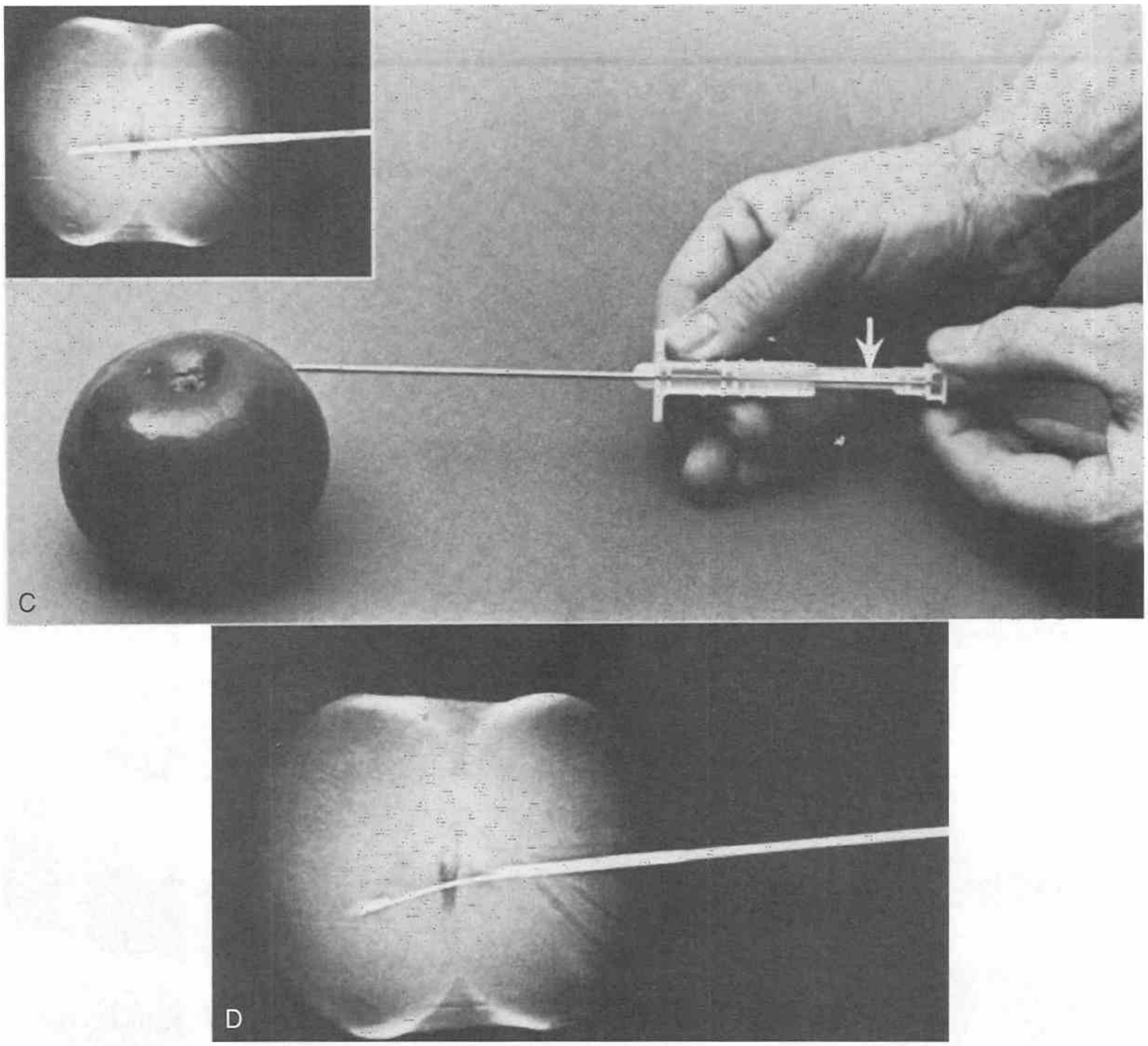

Figure 61–27. *Continued. C,* With the inner stylet (*arrow*) held stationary, advance the outer needle rapidly over the gap. (The outer needle cuts the specimen into the gap.) *D,* A hard material such as bone (in this case, an apple seed) can deflect the thin portion of the needle. This has never been a problem with soft tissue tumors, but the Tru-Cut needle is not suitable for lesions in or against bone for this reason.

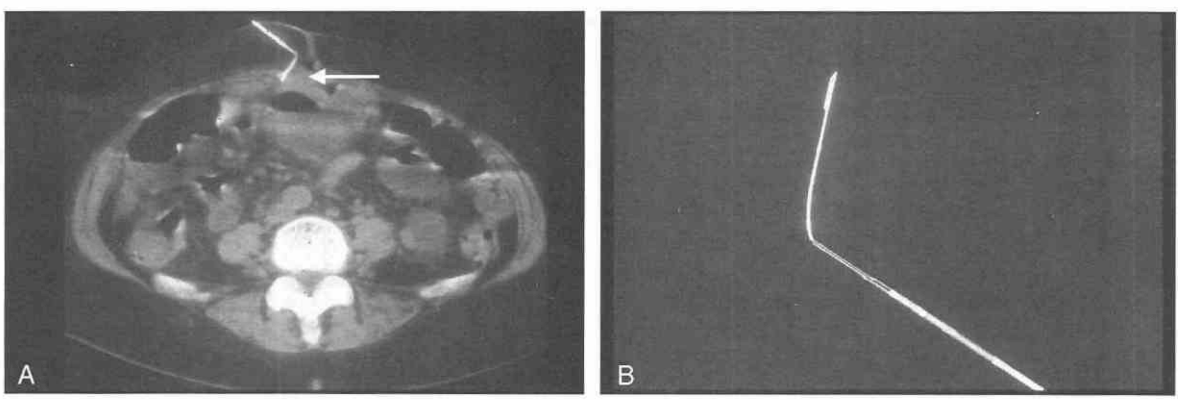

Figure 61–28. *A,* Scan shows a bend in the middle of the gap, [redacted]le in a patient. The fibrous material was so hard it bent the needle. *B,* Scan shows the bent needle after it was extracted.

correctly. Once the correct angle is achieved, the device is inserted to the desired depth with either incremental adjustments and repeat scans or to a premeasured distance. Subtle adjustments using the deflection principles or cannula manipulations noted in the following sections may have to be employed for small final adjustments close to the mass.

Angled or Out-of-Slice Targeting

When a needle must be inserted into a lesion located at a different *z* axis position, different approaches must be taken. There are three approaches that can be taken: (1) free hand, (2) angle estimated, or (3) device assistance.

Free-Hand Method

With the free-hand approach it is best to consider the approach to the lesion as a three-dimensional system. The final vector or angle of the needle to the lesion will be a combined angle consisting of the *xy* angle and the *yz* angle. When doing this it is best to establish the *xy* angle in the superficial tissues of the lowest slice before attempting the *z* angulation. Once the *xy* angle is proper, one can consciously hold that angle constant while moving the needle into the *z* axis (Fig. 61–29).

When the needle is close to the target site, one makes numerous scans over the path of the needle to judge the position in the three dimensions. If a minor adjustment needs to be made, one should then use the tip deflection method described later. Using this technique after the first major angulation has been accomplished saves time and makes success more likely.

Angle-Estimate Method

The angle-estimate method is really just a permutation of the free-hand method, but more care is given to trying to calculate or simulate the angle more precisely. Most simply this is done by using a calculation of the Pythagorean angle from the scans to arrive at a numerical angle in the different planes (Fig. 61–30). The execution of the instrument insertion is performed by the free-hand method or by using a manual angulation device.

Assisted Devices

There are now available two assisted devices for guiding biopsy procedures: articulated arm device and localization device by electronic means. The articulated arm device (marketed by Phillips) consists of a software package integrated with the image files on the computer. The position and angulation of the device are calibrated so that a "virtual" needle presents itself on the monitor to serve as a guide for the needle. The articulate arm is quite accurate and duplicates the pathway of the virtual needle that has been chosen by the operator.

The other device used for CT localization consists of sound- or light-emitting holding devices that secure the needle. A receiver coupled with a computer localizes the needle in the three-dimensional space and displays it on the monitor. This has proven effective and has gained significant popularity in the marketplace. Rather than discuss such products, the reader is referred to the commercial realm for evaluation of available products.

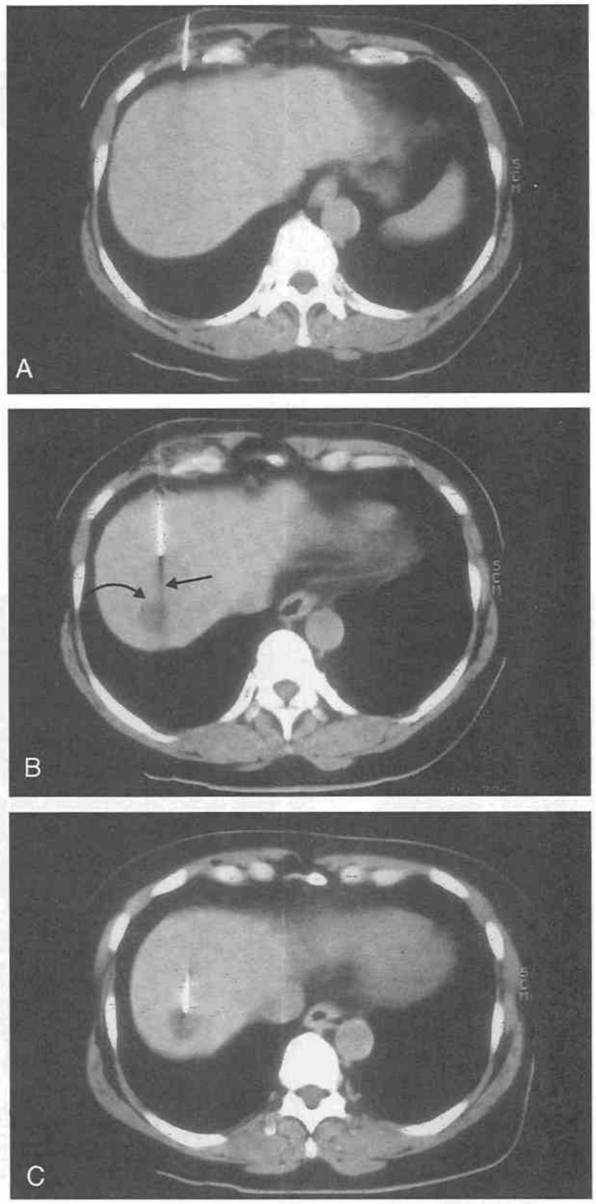

Figure 61–29. *A*, An entrance site below the mass is chosen so that the needle is introduced below the diaphragmatic insertions. The XY angle is approximated and needle inserted partially. *B*, Higher scan at the level of the cyst (*curved arrow*) shows that the trajectory of the needle *(arrow)* is slightly too medial for puncture. The needle was withdrawn slightly and the bevel rotated, as demonstrated in later scans, so that the point is directed laterally and the needle is pushed slowly to facilitate the subtle bending. *C*, Final scan shows the needle centrally in the cyst. Fluid confirmed the simple nature.

Robotics

Everyone is aware of the classic childhood story of "Paul Bunyon and the Steam Machine," where the machine provides more rapid "logging" than even the great lumberjack legend. With the resolution and computers in recent years, there is no question that in the near future robot-assisted procedures will become available.

To be realistic, there will always be the need for the caring physician/radiologist to be on site to use the robotic

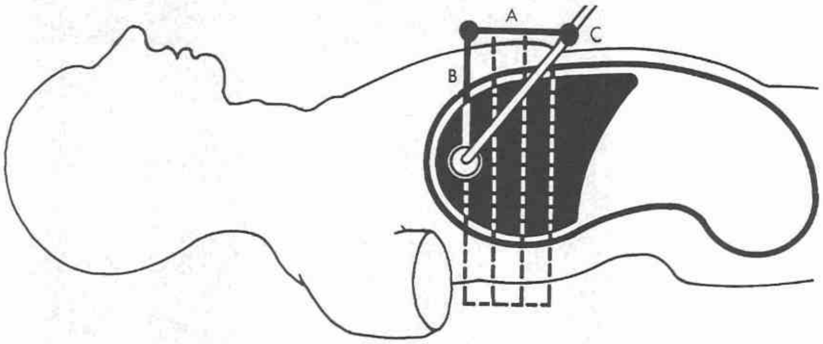

Figure 61–30. Calculation of the distance to the lesion and angle of entry when the entrance point to the skin and the target lesion is not in the same CT section. When the entrance point C and distances A and B are known, the distance to the lesion and the angle of insertion can be calculated. Although theoretically this method has merit, pragmatically its use is limited because of the difficulty in duplicating the angle "freehand." We prefer to estimate the angle with such lesions and take a series of sequential scans or use the longitudinal scan method.

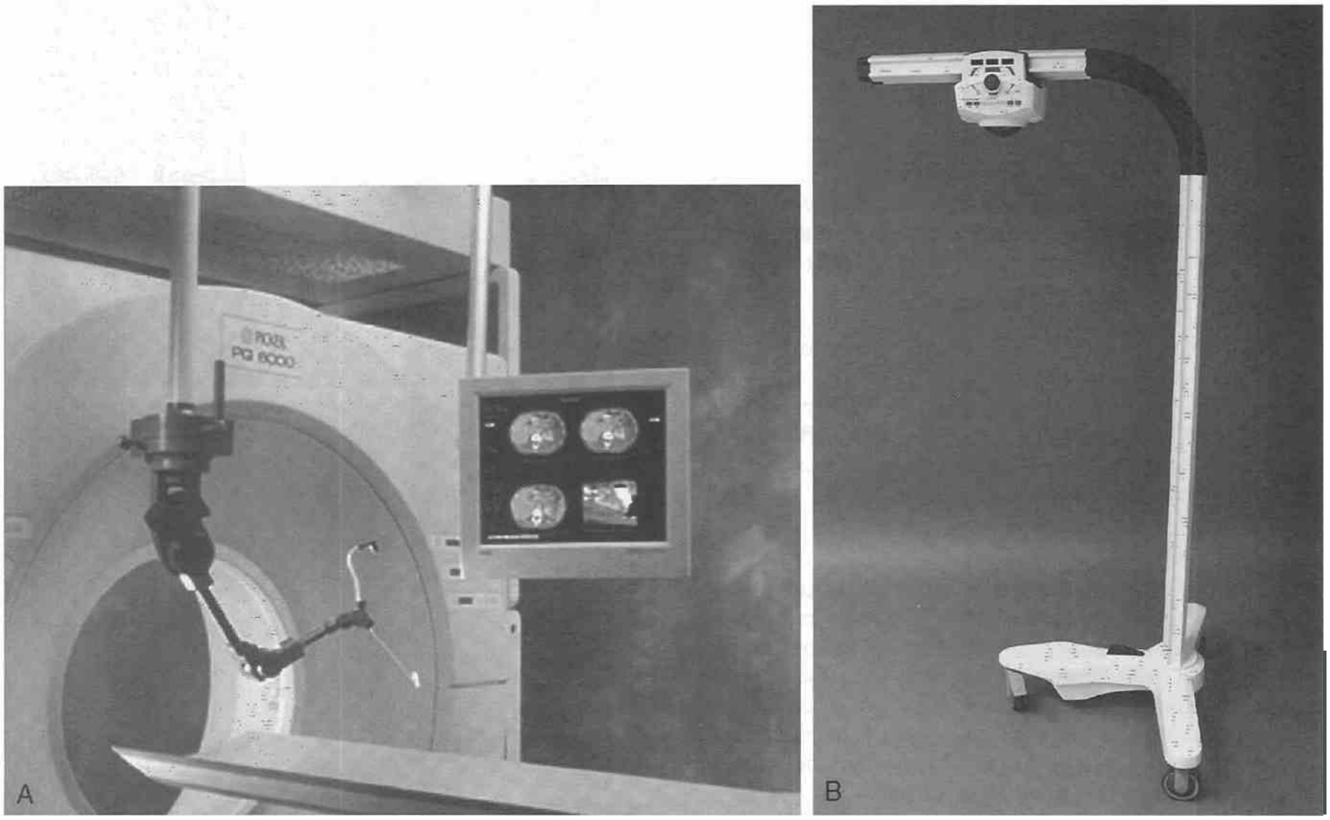

Figure 61–31. *A, B,* Pin point product has an articulated arm that provides coordinate information on image screen. The localization device provides accurate measurement and guidance for placement of the needle at the surface of a patient.

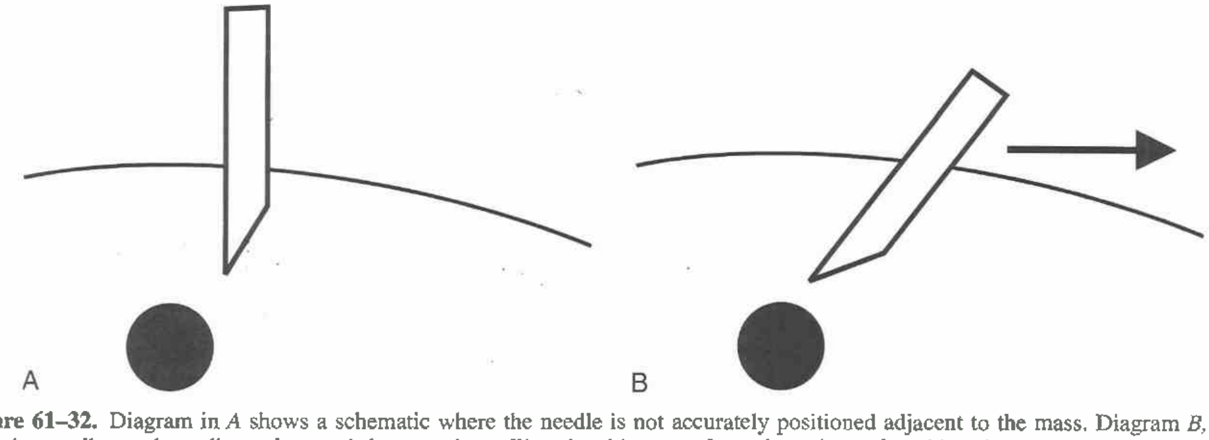

Figure 61–32. Diagram in *A* shows a schematic where the needle is not accurately positioned adjacent to the mass. Diagram *B,* shows how the needle can be redirected toward the mass by pulling the skin away from the point and pushing the needle slowly.

assistances, monitor the procedure, and manage the patient, but targeting lesions will be much easier. We have performed some initial testing using a standard industrial robot and have found it to be quite interesting (Fig. 61–31).

In a swine model, we tested a robot for the execution of a celiac nerve block. Much to my surprise, the execution of the procedure was faster and more precise than I ever imagined. Unlike manually performed procedures during which needle adjustments are made below the skin surface to account for small errors during the insertion, the robot executed the insertion quickly without error.

The final configuration and type of robot have yet to be determined, but I expect to personally continue research on robots in the future.

Needle Deflection

With a bevel needle, the needle will move either straight or deflect depending on the hardness of the mass, the angle of the needle, and the speed of insertion. If a needle is pushed quickly, it tends to go straighter. If it is pushed slowly, it is more likely to move toward the point away from the flatter part of the needle. Depending on the consistency of the target, the movement may or may not be enhanced. In very soft materials or fluids, no deflection can occur. In moderate-density material, controlled deflection is possible. This typically corresponds to the texture of normal solid organs. Pathology tends to be harder. With hard material, deflection is the rule, not the exception.

Intentional Deflection

A useful technique that can be of benefit for the final positioning of a needle is the needle deflection technique using bevel needles. Intended deflection can be enhanced to change the angle of the needle at the latest stage of adjustment before striking the mass. This is best accomplished by rotating the needle so the flat side of the bevel is facing the area one wishes to avoid and the point is directed more toward the target direction. The skin adjacent to the needle is pulled away from the point. This changes the fulcrum of the needle so that it is more angled toward the target (Fig. 61–32). The needle is then pushed slowly.

With this method, one can change direction of a needle when it is located in a patient below the surface of the skin. By using the proper method, one can change the direction of the needle by 10 to 15 degrees and prevent the need for a major readjustment or reinsertion of the needle (Fig. 61–33). This technique can be used for needles 18 gauge or less. It can even be used with the stylet of a cutting needle (Fig. 61–34). This will work with needles 18 gauge or less in caliber.

Avoiding Unintended Deflection

Unintended deflection may occur when masses are very hard. The methods to compensate for unintended deflection or intended deflection are as follows. With hard masses, a beveled device, either needle or stylet, is more likely to enter the mass if the needle is pushed quickly. For very hard masses, deflection cannot be avoided unless one continuously rotates the needle during insertion or a stiff guidance cannula greater than 18 gauge is used. This is a very rare circumstance, but it can be perplexing when it occurs.

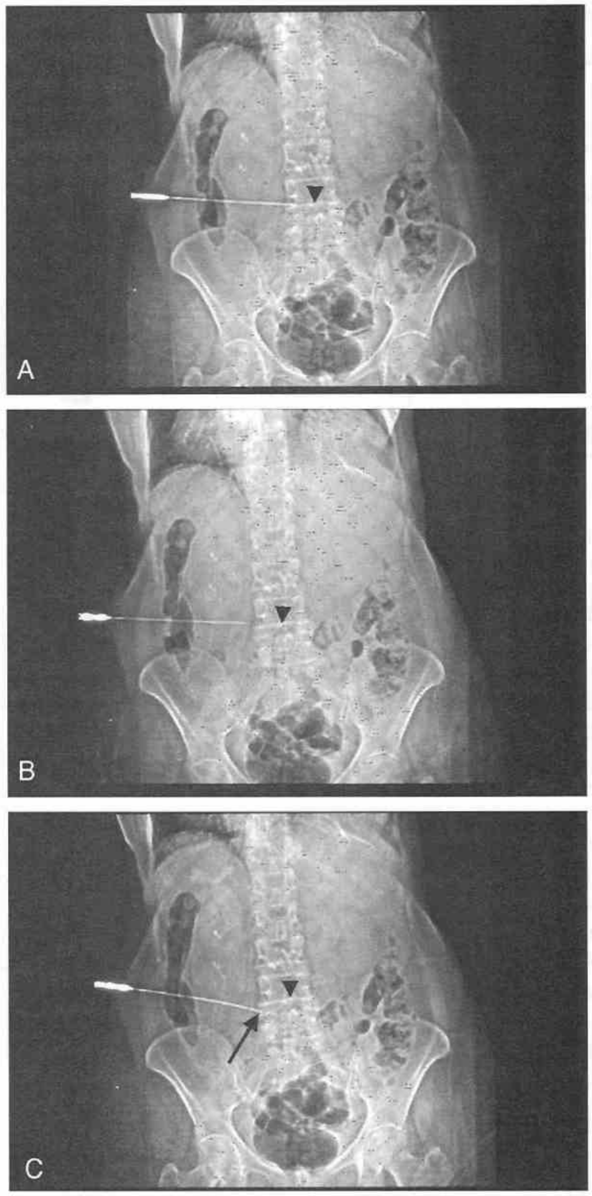

Figure 61–33. These three radiographs (*A* to *C*) show the position of a needle tip that is moved by the deflection method (see text). Note in the first radiograph *(A)* the needle tip is adjacent to the lower end plate of the L4 body. In *B*, the needle has been retracted back slightly before the deflection maneuver. The skin was retracted and the bevel rotated cephalad as noted above and the needle was pushed forward. In *C*, one can see that the needle tip *(arrow)* was deflected caudally almost 10 mm to the top of the L5 end plate.

Coaxial Cannula Manipulation

Because the coaxial approach has such benefits as described earlier, one should consider the possibilities with the guidance cannula. Because the guidance cannula is

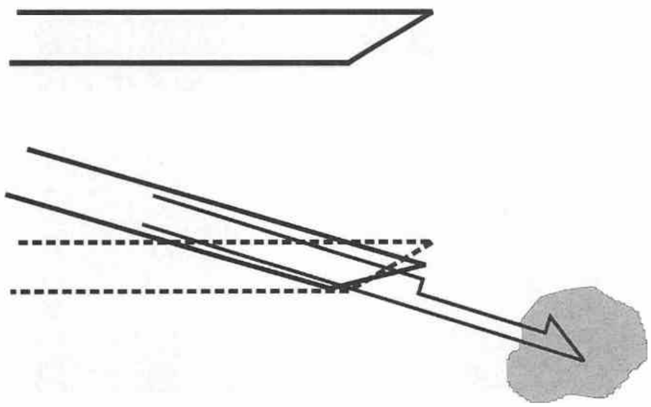

Figure 61–34. Diagram shows the same result of deflecting the needle tip with a side-cutting needle. By pushing the needle at an angle and then slowly pushing out the stylet, the bevel of the stylet can direct the needle into a mass when there is a slight trajectory error.

stiffer than the basic needle, it can be used to torque the needle. This is done by simply angling the cannula in the desired direction. One must be aware that such devices are stiff, and moving such a device can potentially produce shearing.

It is true that the intended deflection noted earlier will and can occur with a coaxial cannula. Another technique to move a needle into a difficult area can be used that combines the benefits of a Chiba needle with a cannula. For lack of a better term, I have called this a *cannula slide maneuver* (see Fig. 61–90*A–C*). If one wishes to use a cutting needle beyond a vital structure, one can advance the cannula in the following fashion. Through the cannula one pushes a bevel Chiba needle beyond the vessel. Then one advances the cannula forward over the small-caliber needle. When the cannula is distal to the vital structure, one can safely use the cutting needle.

Rotation of Cutting Needle to Optimize Sampling

In some cases when a biopsy is being attempted with a side-cutting needle, the placement is not completely opti-

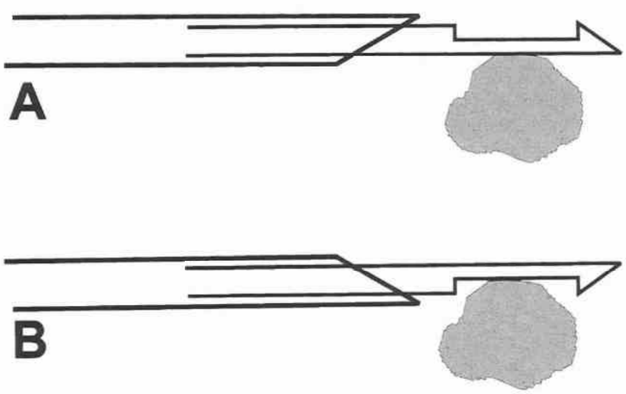

Figure 61–35. In some circumstances, the "gap" of a cutting needle is close to the edge and one cannot be completely certain the cutting side will obtain a suitable sample. In such cases, one can optimize this possibility by rotating the needle 180 degrees so that the gap faces the tumor.

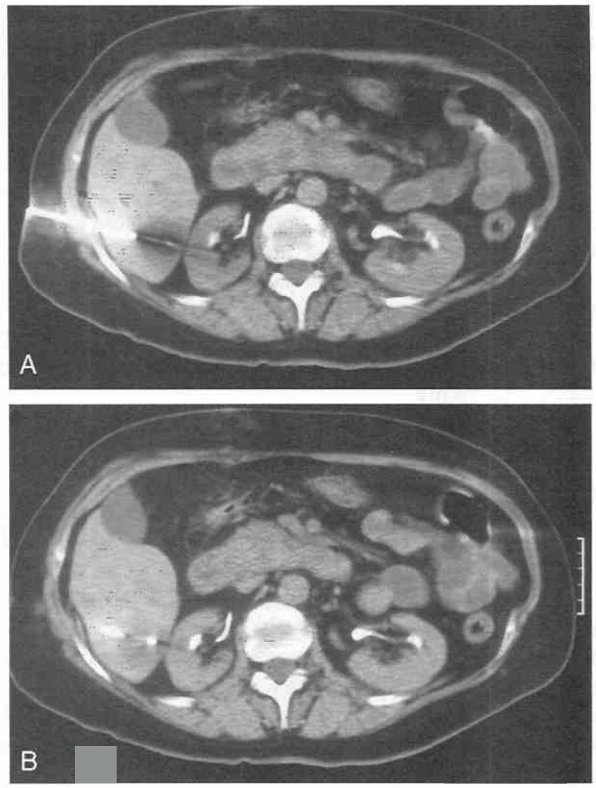

Figure 61–36. *A,* Scan through the liver shows the gap of the needle faintly visible in the lesion. *B,* By rotating the needle, the gap is turned so the cutting edge is toward the mass. There is a greater probability that an adequate sample will be obtained.

mal because the "needle gap" misses the mass slightly. In such cases, one can increase the probability of getting an adequate sample by rotating the needle so the gap is oriented toward the center of the mass (Figs. 61–35 and 61–36).

Localization of the Needle Tip

After insertion of the needle, one may occasionally have some difficulty in localizing the tip. There are several methods that can be used to solve this problem. The simplest method is to take a longitudinal scan and take an axial slice at the end. This is virtually foolproof and is the most expeditious. Another method that can be used if the angle of the needle is slight involves simply taking multiple scans in one direction until the end of the needle is reached (Fig. 61–37). Some of the new scanners have a cluster scan feature consisting of three or more scans, which is well-suited for this purpose. When the end of the needle is found, it will appear to have a square end and may have an artifact from the end. On occasion the end of the needle will not be "square" in appearance, but the end is easily appreciated by noting when the end is no longer seen on sequential scans.

Respiratory Variation

For the routine circumstances, one can encourage the patient to take consistent breaths by using the following approach. Most patients become confused and frustrated if

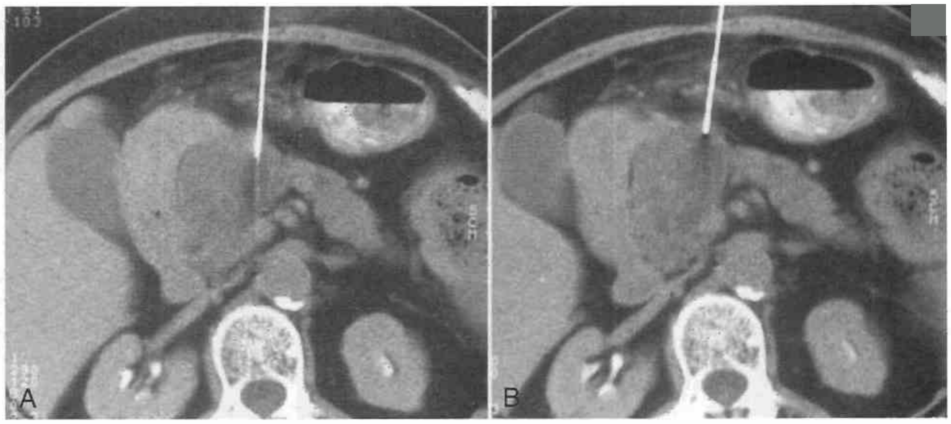

Figure 61–37. Localization of the needle tip may be problematic at times. When the needle is "tapered," as seen in *A,* it means that a variable number of pixels is being occupied along the length of the needle and thus the end may not be seen. When the end is "square," as in *B,* the tip is being accurately localized.

one tells a patient to "take a deep breath" or to "blow your air out and hold it." The best approach is to simply remind the patient to take a normal breath and hold it.

When patients are anxious and not cooperative, their respiratory efforts may vary in depth. In such cases the best opportunity to lessen the movement is to use the lateral positioning as described earlier (p. 2144).

Percutaneous Tissue Retraction

When only a skinny needle is used, it is permissible to penetrate certain loops of bowel and organs. If one is using either a cutting needle or catheter or dealing with an immunocompromised patient, one should not penetrate or traverse any intervening structure. Two methods have been used for dealing with this problem: the injection of carbon dioxide and the injection of saline.

We have reported[159] that carbon dioxide insufflation can be used to move bowel and the bladder a short distance; in this fashion a pathway for such a procedure can be opened. However, this gas will not move solid organs such as kidneys.

The procedure is easily performed as follows. After the trajectory is planned, decide from the scans the proper location of the carbon dioxide. Then insert a needle and inject by hand 50 to 100 cc of carbon dioxide (Fig. 61–38). If the intended loop of structure does not move, attempt to reposition the needle or repeat the injection of carbon dioxide. Although this requires some practice, generally try to get it in a location such that the gas will move the bowel perpendicularly away.

Although there are some theoretical objections, the use of carbon dioxide is quite safe. This gas has been used for all types of in vivo procedures, including peritoneoscopy, mediastinal insufflation, and even intravascular use, without any difficulty. The gas is absorbed very quickly because carbon dioxide is quite soluble in body fat.

Other authors[131] have proposed the use of injected saline to increase the size of pathways through which one can insert a needle. This has been used predominantly in the chest for widening the paraspinal space, but potentially it could be used in other localizations (see later section on biopsy of middle mediastinal tumors) (Fig. 61–39).

Both of these methods have a similar problem. Depending on the location of connective tissue, either the gas or fluid may dissect cephalad or caudad and not substantially produce enlargement in the axial plane. Nevertheless, both of the methods can work in selected cases.

Langen et al[228] studied the efficiency of carbon dioxide

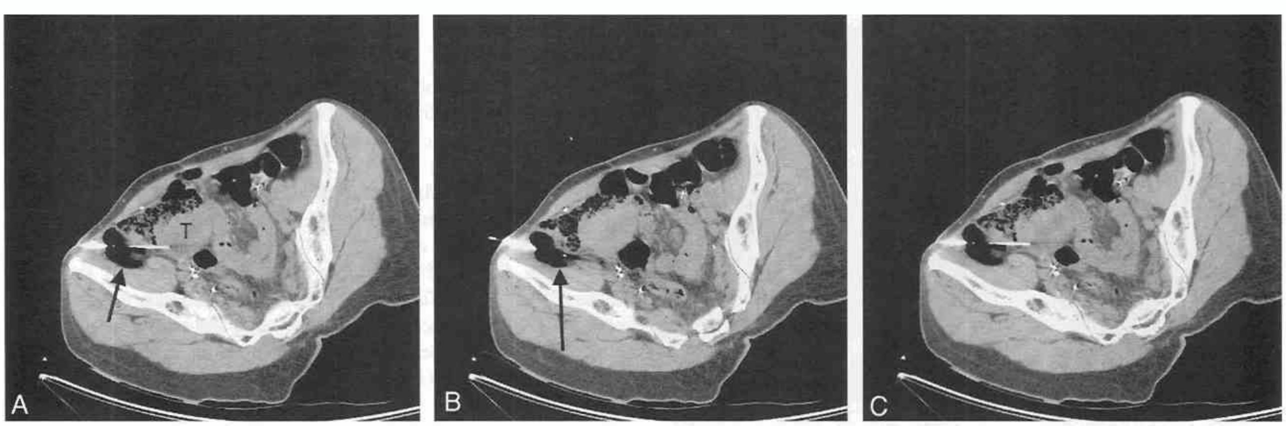

Figure 61–38. *A,* Scan [redacted] a tumor (T) in the right lower quadrant. The needle (*arrow*[redacted] inserted adjacent to the bowel. to be moved. *B,* Air (10 to 15 sc) is injected quickly to push the bowel away. The gas with the needle is noted adjacent to the bowel (*arrow*). The metal needle shaft is not well seen because of the partial volume of air with the metal needle. *C,* With the bowel moved away, the needle could be inserted into the mass.

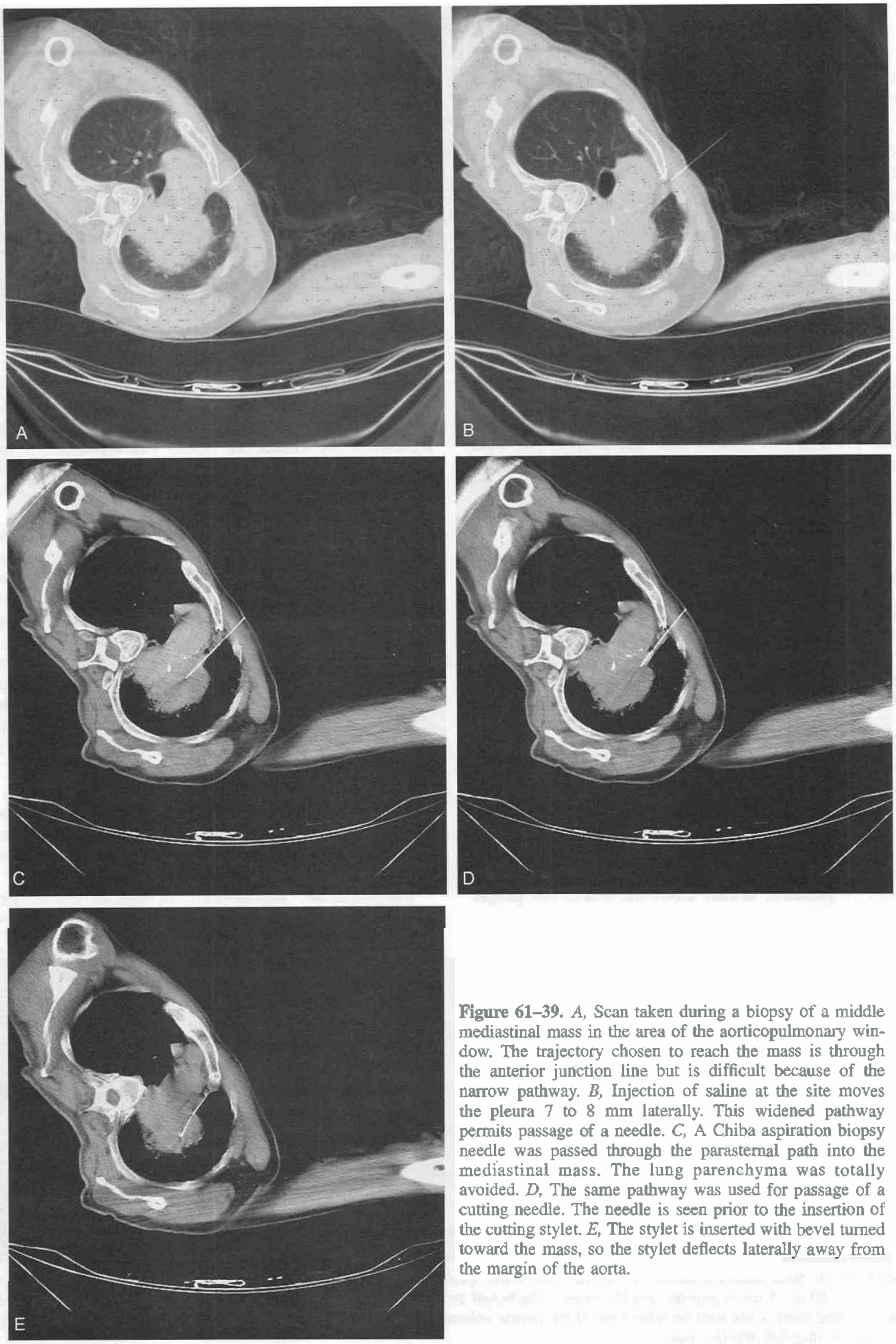

Figure 61–39. *A*, Scan taken during a biopsy of a middle mediastinal mass in the area of the aorticopulmonary window. The trajectory chosen to reach the mass is through the anterior junction line but is difficult because of the narrow pathway. *B*, Injection of saline at the site moves the pleura 7 to 8 mm laterally. This widened pathway permits passage of a needle. *C*, A Chiba aspiration biopsy needle was passed through the parasternal path into the mediastinal mass. The lung parenchyma was totally avoided. *D*, The same pathway was used for passage of a cutting needle. The needle is seen prior to the insertion of the cutting stylet. *E*, The stylet is inserted with bevel turned toward the mass, so the stylet deflects laterally away from the margin of the aorta.

and saline in an animal model to move structures from a needle trajectory pathway. With equivalent amounts of gas or saline, they found the saline produced substantially more movement of organs than carbon dioxide. The maximum distance was slightly greater than 1 cm. The caveats for saline injection include patient discomfort, decrease in target-lesion conspicuity, and adverse effects of absorbed fluid in patients with kidney or heart disease.

The optimal methods for carbon dioxide injection have yet to be defined experimentally. One caveat that should be mentioned is the effect of severe inflammation or tumor invasion. If either of these are present around the structure being pushed by the saline or carbon dioxide, the structures will not move effectively.

If a patient is somewhat uncooperative or if the lesion being sampled is small, place the patient in the ipsilateral decubitus or oblique position (not at the compromise of the entrance site, of course). The weight of the abdominal viscera partially immobilizes the diaphragm and limits the respiratory motion of the diaphragm (see Fig. 61–22). This is especially important for lung, kidney, adrenal, or liver lesions.

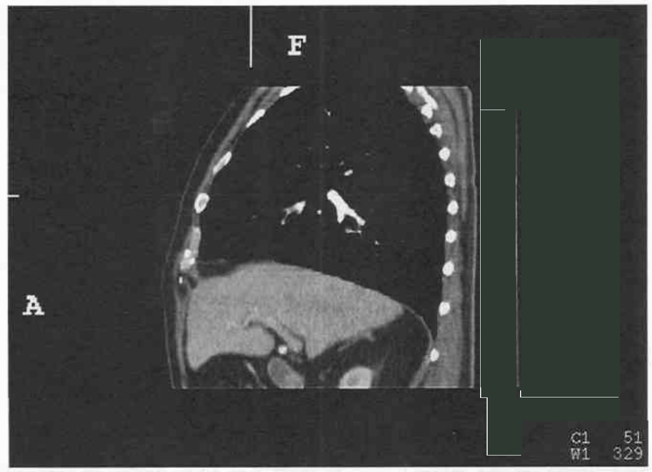

Figure 61–40. Sagittal scan close to the central chest shows the relationship of the various ribs. Anteriorly, there is fusion of several costal cartilages (*vertical arrow*). Posteriorly, one can see the ribs are much closer than anteriorly. In addition, the narrowing size of the ribs as they approach the apex shows how the interspaces become more narrow owing to the close proximity of the ribs (*curved arrow*).

Lungs and Mediastinum

For the routine well-defined pulmonary nodule, fluoroscopy and CT are now the modalities of choice. Since the first edition of this text,[145] our experience with CT biopsies of the lung has been considerable, and CT has surprisingly developed a much larger role than anticipated.[55] In fact, almost all lung biopsies are now done under CT guidance. This is true for two reasons. First, there has been such a refinement and development of CT procedures that almost any lung nodule can be biopsied with CT guidance.[329] Second, the availability of sophisticated fluoroscopy equipment is limited because of its use for many current vascular procedures.

If CT expertise and/or the appropriate equipment is not available, one can use either fluoroscopy or ultrasound.[116] The primary role of ultrasound is still the aspiration of pleural fluid; its minor role is the sampling of pleural-based nodules.

Indications

The clinical situations that justify the performance of a biopsy include sampling of nodules for neoplasm or sampling of infiltrate for infectious agents. One can justify performing a biopsy of a suspected primary nodule for two reasons. First, aspiration biopsy can distinguish small cell tumors from non-small cell tumors.[356] Many oncologists believe that small cell tumors should be treated medically rather than surgically. Second, Sinner et al[356] stated that percutaneous biopsy can expedite surgical treatment. Obviously, confirmation of malignancy in cases of metastatic or recurrent tumors is important. In cases of pulmonary infiltrate when the causative organism is unknown diagnostic aspiration can obtain material for culture that can distinguish among pyogenic, fungal, or opportunistic organisms.

CT is indicated for the biopsy of a variety of lesions not well-suited for fluoroscopy or ultrasound because of their locations as well as other factors. Lesions in the apices (Figs. 61–40 to 61–42), the costophrenic angles, the costovertebral angles (Fig. 61–43), the pleura, the hila (Fig. 61–44), and those obscured by fluid and mediastinum are best suited for CT because they are not well seen with fluoroscopic imaging. The dynamic-bolus CT scan is an important adjunct for the mediastinum and hila because major vessels can be opacified and delineated, making separation from masses in these areas quite easy.

Parenchymal lesions well-suited for CT biopsy also include those lesions with ill-defined edges, as well as other lesions poorly visualized by fluoroscopy. These latter lesions are better seen because of the better contrast resolution and the tomographic nature of CT scans.

Figure 61–41. Lesion in anterior apex adjacent to the mediastinum. Needle (*arrow*) can be noted anteriorly entering the mass without traversing any intervening lung. In such cases one must be careful to avoid the subclavian vein, which was at a level slightly higher.

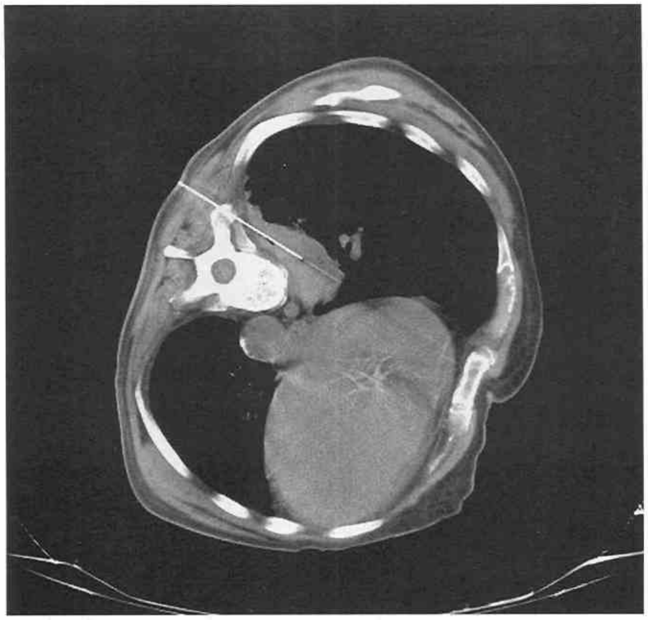

Figure 61–42. Mass in the posterior paraspinal region can be approached without traversing lung parenchyma.

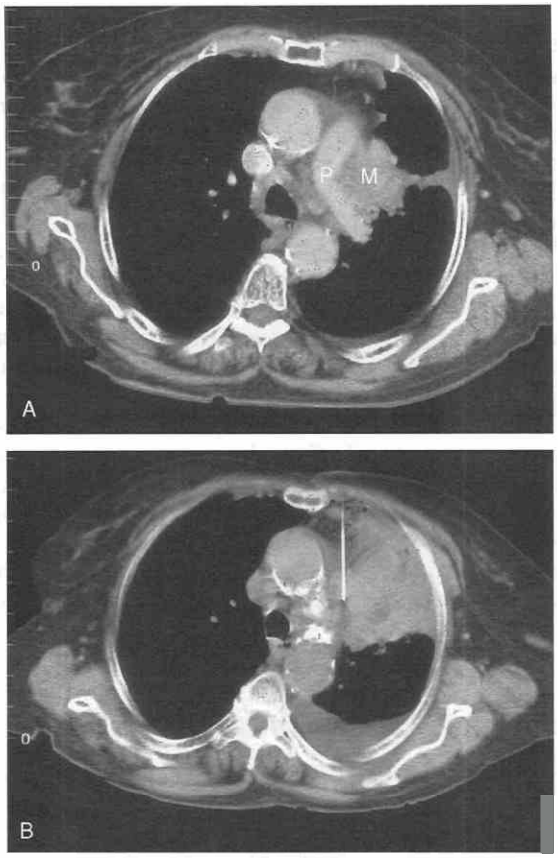

Figure 61–44. *A,* When a large mass (M) is adjacent to the hilum, a bolus injection should be performed to localize the pulmonary artery (P). *B,* This scan shows the needle biopsy of the central mass, at a level above the artery. The distal lung is atelectatic.

Peripheral nodules in patients with severe parenchymal disease are well-suited to CT. Blebs are also more easily avoided with CT by careful planning of the trajectory (Fig. 61–45). In such cases if one takes thin scan sections, one can sometimes find a pleural attachment that permits a "risk-free" access, thus avoiding penetration of the lung.

Contraindications

With the further refinement of techniques, the number and significance of contraindications have lessened. There are several absolute contraindications that include uncorrectable coagulopathy, severe pulmonary hypertension, uncontrollable coughing, possible *Echinococcus* infection, and an uncooperative patient insufficiently controlled by anesthetics.

The levels of the coagulopathy that I find acceptable are a prothrombin time within normal range, INR of 1.0, and a platelet count of at least 50,000. Virtually normal values are important because the air-filled lung cannot tamponade bleeding, which would result in serious bleeding. Uncon-

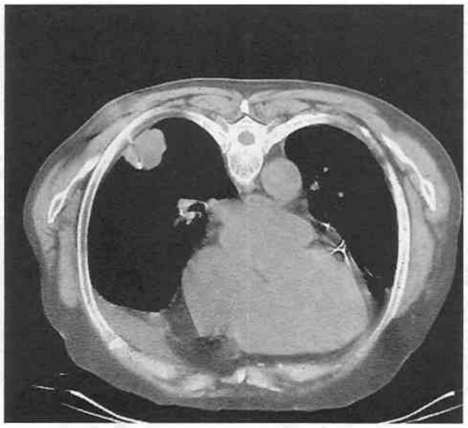

Figure 61–43. Biopsy of pleural-based masses can be easily and safely accomplished with cutting needles, if the gap (*arrows*) of the needle is confined to the mass. Note the thin fat line of retracted pleura adjacent to the mass, indicating adherence.

Figure 61–45. This scan shows the approach of a mass in the right apex. The needle is positioned to traverse the "fibrous band" *(arrow)* traversing to the pleura. This approach minimizes the possibility of a pneumothorax.

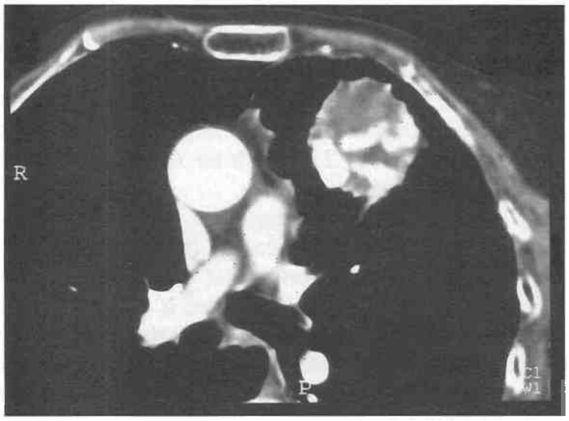

Figure 61–46. Because a cutting needle was being considered, this bolus injection was performed. Note the remarkable vascularity in the mass, later proved to be an angiosarcoma. If a biopsy had been performed, it surely would have been catastrophic.

trollable coughing and a patient with an uncooperative nature are important because movement of the lung during a procedure may cause a tear of the lung by the needle that might cause air embolism, pneumothorax, or bleeding.

Techniques for Lung Biopsy

There are several important techniques used for chest biopsy that relate to both the preparation of the entry site and the needle technique. Appropriate choice and preparation of the entrance site are important to ensure a painless and successful biopsy procedure.

Although it has not been traditional in the past, I now believe it is important to perform a bolus injection for lung biopsy in a number of circumstances. First, if the patient has any history of bruit on auscultation of the chest, a bolus should probably be performed (Figs. 61–46 and 61–47). The other circumstance would be in those instances when there is no clear history of smoking or other risk factors for a tumor. A bolus is *absolutely indicated* if any consideration of a cutting needle is being made.

After one has selected a tentative entrance point from the CT scan, one should carefully inspect the chest at the entrance site for several problems. First, if there are any obvious superficial veins noted, the site should be moved accordingly. Second, one should palpate deeply for the intercostal space between the margins of the ribs. It is important to note that the interspace between the ribs is greater the more anterior the location and less posteriorly (Fig. 61–40). The ribs become smaller as they approach the apex, making posterior approaches the most difficult in that area because of the narrow spaces and angle. Palpation of the ribs is necessary because the location of the intercostal space as seen on the CT scan is not reliable. The tapered margin of the rib and the oblique orientation of the rib as it traverses the imaging section produce considerable partial volume effect and discrepancy regarding the actual location of the intercostal space on the scan. The problem of identifying the location of the ribs is especially relevant to the anterior chest wall where the ribs are mostly cartilaginous and fuse together in an unpredictable pattern. Although it is true that one can use a needle or a guidance cannula to "drill" through a cartilaginous rib, I do not recommend this with CT guidance because if one drills through the cartilage, the pathway of the needle is fixed, thereby preventing corrective angulation. Also, the fixed needle cannot move with respiration, thereby making a small tear more likely if the patient moves the lung while breathing. In the lung as in other areas, the needle should be permitted to "swing" freely with respiration. Any time the needle is adjusted the patient should be asked to suspend respiration temporarily during the manipulation of the needle or removal of the stylet to prevent tearing of the parenchyma or a pneumothorax.

Another structure that should be carefully noted is the scapula. When approaching a lesion from the posterior chest wall, at any location, one should carefully palpate for the scapula. Although on first consideration one might think this would not typically interfere with a procedure, the tip of the scapula is tapered in two directions so the location of the tip of the scapula is "averaged out" so that what is seen on the scan does not correspond to the palpable tip on the patient. In some cases, the needle is deflected without the operator being aware of the problem. Also, in some cases the patient will slightly move the scapula into the path of the needle and deflect it sufficiently to preclude a successful needle placement.

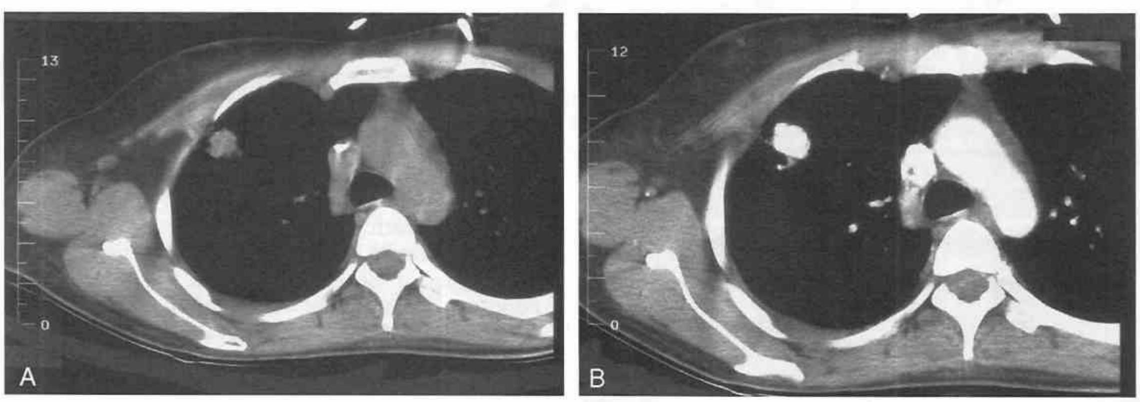

Figure 61–47. *A,* This small lesion was being considered for a cutting needle technique because of the close proximity to the pleura. *B,* Bolus scan shows enhancement of an arteriovenous malformation.

Another important point is related to the infiltration of the local anesthetic at the entrance sight. When the area is anesthesized, it is important to infiltrate anesthetic through the subcutaneous tissues and down to and including the pleura. Adequate anesthesia of the pleura makes the procedure virtually pain-free and permits insertion of the needle without the patient moving because of pain. So important is this step of anesthetizing the pleura that as I perform the actual insertion of the needle, I stop the needle tip at the pleura to inject a small amount of anesthetic at the pleura and to check the final angle of needle insertion before entering the lung (Fig. 61–48). If a rib is inadvertently hit during the initial anesthetic administration, I give a small bolus of lidocaine on the rib; this prevents any recurrence of pain if that area is struck again during the procedure.

There are two methods one can use for a needle aspiration of the lung: a single-needle method or a coaxial method. With the single needle, the needle is started into the superficial tissues and a scan is obtained to verify its angulation. Once the correct angle is determined, the needle is inserted to the correct depth. The other method that should be used for deep or small lesions is the coaxial, short-guidance cannula method as follows: The guidance cannula is inserted into the chest wall and adjusted until it is directed toward the lesion. The Chiba needle is inserted to the correct depth, and sample is obtained (see earlier discussion on coaxial method).

Aspiration Needle

Because aspiration needles have been used for many years by numerous authors, one can reliably make a number of valid conclusions regarding their use. First, the needle caliber size appears to have little effect on the success rate of the procedures. Equivalent successes have been reported with a wide range of needle calibers, from 23 to 18 gauge. The pneumothorax rate has little relationship to the needle caliber, but the hemoptysis rate is directly related to the needle caliber. When needles smaller than 20 gauge are used, the hemoptysis rate is quite low. This was confirmed by Khouri et al,[214] who noted in his series that the hemoptysis rate was 21% with an 18 gauge needle but only 5% with a 20-gauge needle.

Several early reports by Sargent et al[347] and Stevens et al described the effects of increasing the number of needle passes. Stevens et al[371a] reported that a second needle pass increased diagnostic yield by 10% and a third needle pass increased it by 1.5%. Sargent et al reported that a second needle pass increased the diagnostic yield by an additional 5% and that the third needle pass increased the diagnostic yield by another 3%. Stevens et al reported that the pneumothorax rate more than doubled with two passes.

From the above data, one can understand how we arrived at our current method when I use a 20-gauge Chiba needle for an aspiration biopsy and routinely only take a single needle pass. I prefer to defer a second needle pass until after the results of the first pass are known, unless there has been a break in the technique. If the cytologist is available for a rapid stain interpretation, the patient will remain in the department until the results are known. If this service is not available, I still prefer to wait for the results instead of taking a second pass, because the 24-hour delay is a small trade-off considering the high success rate. If a technical error has been made or the final position of the needle placement is not satisfactory, then a second needle pass will be made at once.

Cutting Needles

In recent years, there has been a remarkable change in the acceptance of cutting needles, especially in the chest. Whereas there was remarkable controversy and conflict

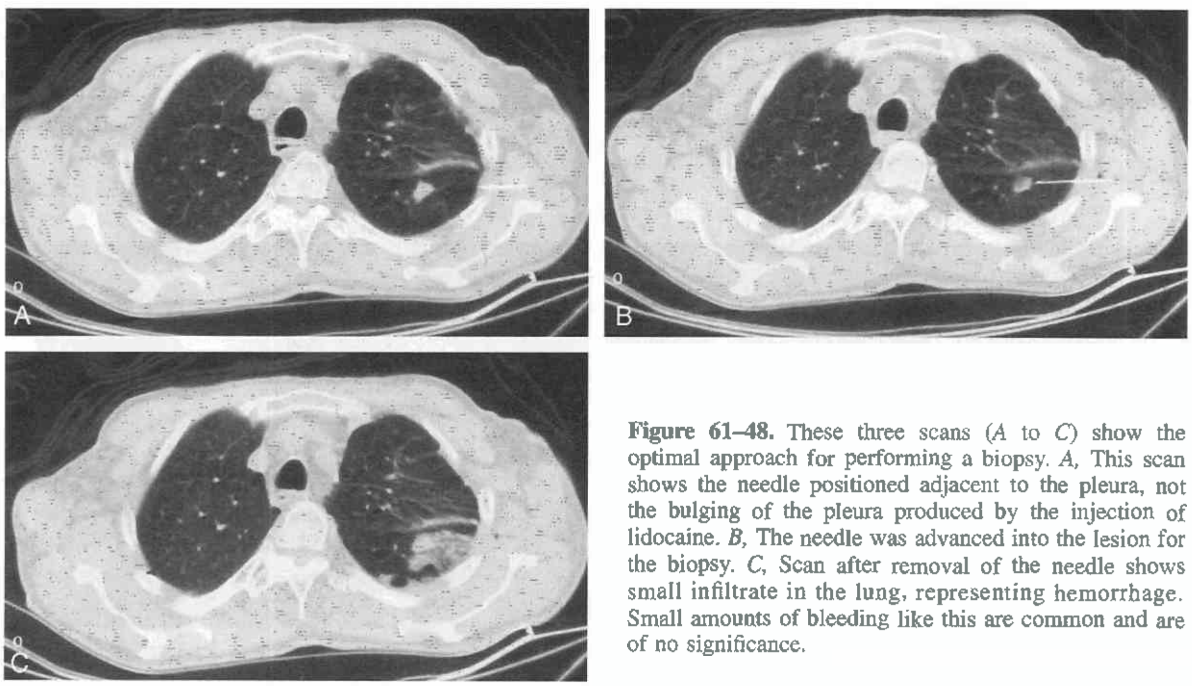

Figure 61–48. These three scans (*A* to *C*) show the optimal approach for performing a biopsy. *A*, This scan shows the needle positioned adjacent to the pleura, not the bulging of the pleura produced by the injection of lidocaine. *B*, The needle was advanced into the lesion for the biopsy. *C*, Scan after removal of the needle shows small infiltrate in the lung, representing hemorrhage. Small amounts of bleeding like this are common and are of no significance.

when our group[120] published the first use of cutting needles in the chest, they have been extensively assimilated as a routine consideration for lung biopsy.

As strange as it may seem, I believe that the usage of cutting needles has actually extended too far relative to procedures of the lung. Some groups seem to prefer cutting needles in all cases of lung biopsy, but I still believe they should be selected when appropriate to ensure the greatest safety and accuracy.

The basic tenet of all biopsy procedures is to use the most appropriate device to achieve success and a low complication rate. In most cases, a solitary lung tumor is of only three cell types: adenocarcinoma, squamous cell, or small cell. Aspiration biopsy with the 20-gauge needle as noted earlier is appropriate.

When a mass is accessible and in the appropriate location, a cutting needle may be used judiciously. The most critical factor with any cutting needle procedure is that a bolus injection be performed prior to the procedure. Although infrequent, vascular lesions such as arteriovenous malformations or vascular sarcomas may occur and catrastrophe can be avoided by aborting the procedure (Figs. 61–46 and 61–47).

If a lesion within the parenchyma is accessible and of sufficient size, then a 20-gauge cutting needle may be considered because the risk is no different than an aspiration needle. This assumes the size and location of the mass are adequate to permit complete placement of the cutting area within the lesion (see Fig. 61–43). In such case, the intervening lung has no additional trauma than a Chiba needle because there is no caliber difference or exposure of the traumatic tip to the lung.

One must be prepared to compensate for deflection and bending of the needle when the stylet is inserted. Benign lesions tend to be very hard and the surrounding lung does not provide much resistance. Such lesions may bend the stylet or deflect to the side (Fig. 61–49).

If a mass abuts against the chest wall, as was true in our first report, larger needles such as an 18 or 14 gauge may be used. Because no lung is traversed, there is no additional risk.

The cutting needle is clearly indicated, as we have previously noted, if there has been a failed aspiration procedure or suspicion of lymphoma or thymoma. Mesotheliomas are quite difficult to diagnose even with a large cutting needle because the morphology varies little between benign and malignant lesions.

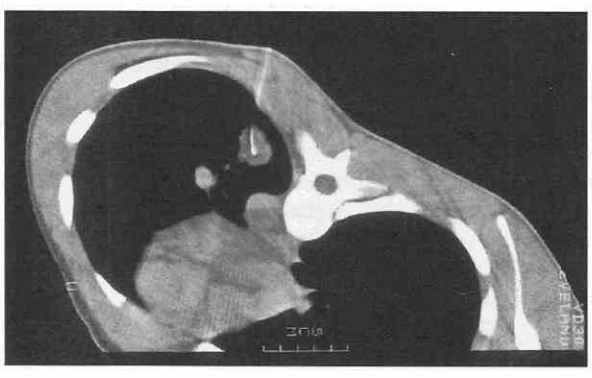

Figure 61–49. Scan of a cutting biopsy of granuloma. Note the bend in the needle produced by the hard character of the mass.

Important Planning Factors

Common sense dictates that several precautions be taken when planning the trajectory. These include avoidance of vessels, bronchi, and blebs. Although there are no data to support the following statement, it is quite clear that avoidance of vessels and bronchi, in addition to using a 20-gauge needle or less, has definitely decreased the incidence of hemoptysis. In my practice the incidence of hemoptysis decreased from about 20% to less than 1% with CT procedures. Penetration of a bronchi may produce a spasm of coughing, which in turn can produce uncontrollable lung movement and predispose the patient to pneumothorax, bleeding, or air embolism (see complication section). Penetration of blebs will obviously predispose the patient to an immediate severe pneumothorax; avoidance is therefore prudent.

Minimizing Pneumothoraces

In many cases one can minimize the possibility of a complication by looking carefully for a "safe pathway" through the lung to the nodule being biopsied. In such cases one might locate the attachment to the pleura or an area of fibrosis that can be traversed by the needle. By planning the trajectory through such an area, only a minimal amount of parenchyma is traversed and/or the fibrosis can serve to keep the layers of the pleura attached and thereby avoid a pneumothorax. By looking for a small amount of "fat" that may be tented at the pleura, one can usually distinguish between a mass that is simply adjacent to the pleura and one that has a fibrous extension. This type of approach is especially important in high-risk patients with pulmonary hypertension, severe restrictive disease, or other serious underlying pulmonary problems.

Two other factors that can minimize the incidence of pneumothorax are minimizing the pathway of lung crossed (Fig. 61–50) and using a pathway of through nonaerated lung. One of my colleagues, Dr. Locke,[250] studied a series of 235 cases from our center and looked at the incidence of pneumothorax as compared with the distance of the lung traversed. The distances crossed with the corresponding incidence of symptomatic pneumothorax were 1 cm, 3.7%; 1 to 2 cm, 10.7%; 3 to 4 cm, 19%; and 5 to 6 cm, 44.4%. Because these measurements were taken from CT scans, they were quite accurate without errors in magnification; other authors who have not supported this relationship made their measurements from radiographs, which are more subject to error.

Since our last edition was published, other authors[98,208,234] have confirmed the importance of lesion depth. All three of these groups indicated that lesion depth was the prime determinant of pneumothorax for CT procedures.

Our previous claim that traversing nonaerated lung would diminish pneumothorax has been documented. Recently, Haramati and Austin[166] showed quite convincingly that if aerated lung was avoided, the pneumothorax rate decreased significantly. They found that the pneumothorax incidence through aerated lung was 46% as compared with

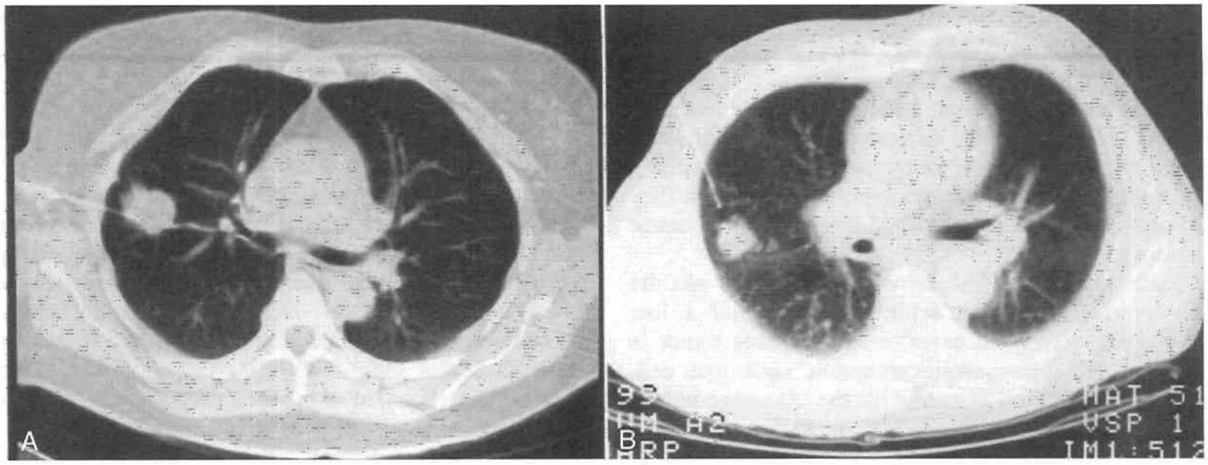

Figure 61–50. *A,* This shows the difference in approach for two lesions that are almost identical. This scan shows a direct lateral approach, with the distance of lung being crossed of almost half of that in *B*. *B,* This biopsy approach traverses almost twice the distance of lung and increases the potential risk by almost a factor of 3, according to new data (see text).

0% through nonaerated lung Stated differently, if there is an area of infiltrate adjacent to a nodule, one should intentionally traverse the consolidated area (Fig. 61–44).

Target Lesion Sampling

Choice of the target site is self-evident, but several points are worthy of emphasis relative to biopsy of nodules. If the nodule being sampled contains a small amount of calcification, the calcified area should be avoided and the adjacent soft tissue density targeted. If the nodule is cavitated, appears necrotic, or is quite large, the central portion should be avoided in preference to the peripheral area (Fig. 61–51). Some caution should be exercised in such a case to limit the penetration into the cavity portion as well as the vigor with which the sample is obtained. Early authors have claimed such cases are more likely to result in pneumothorax and severe bleeding; this has not been our experience.

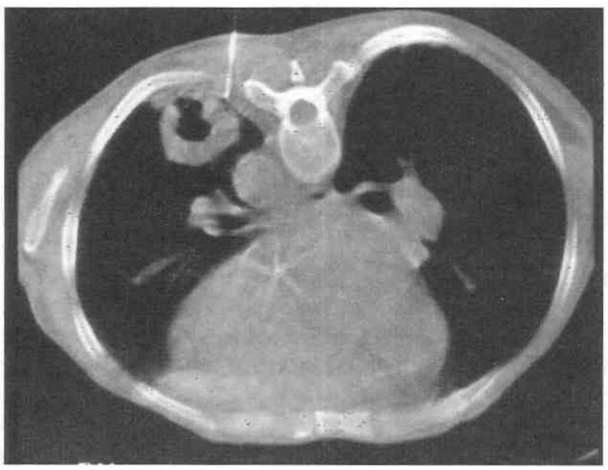

Figure 61–51. CT scan shows biopsy of a large cavitated nodule. The periphery of the mass is targeted for best results. Some authors have suggested that in such cases a higher incidence of pneumothorax and hemorrhage exists.

Patient Position

In most instances it is simplest to have the patient lie in the prone or supine position, but other positions might also be considered (see Fig. 61–22). As noted earlier, there might be an optimal choice of pathway taking into account the factors described. In such cases, access to the appropriate entrance site might be facilitated by placing the patient in the prone, oblique, or decubitus position.

If the lesion is small and moves with respiratory motion, it may be wise to put the patient in an ipsilateral decubitus position and insert the needle through a direct anterior or posterior approach. This position minimizes the motion of the ipsilateral diaphragm because of the weight of the abdominal organs against the diaphragm. This restriction of motion minimizes movement of the lesion and thereby simplifies the performance of the procedure.

Hilar Lesions

Hilar lesions are best sampled by bronchoscopy and should be percutaneously biopsied only as a second choice. The success rate for bronchoscopy is better and the complication rate lower than for percutaneous procedures. With percutaneous procedures, the length of the lung to be crossed and the proximity of vessels make the incidence of pneumothorax and hemoptysis more likely. If a bronchoscopy has been attempted unsuccessfully, a percutaneous procedure will be performed with the following guidelines.

Before the procedure, intense contrast enhancement of the vasculature should be performed to highlight the location of the anterior, lateral, or posterior approach to be taken. Unquestionably, with such lesions a coaxial short-cannula method should be used. This method is especially helpful because, as noted earlier, before the biopsy needle is inserted the guidance cannula predetermines the angle. With a long distance from the pleura to the hilum, a few

degrees in error will result in a large localization error centrally.

Apical Lesions

Careful planning for apical lesions is important because of the unique anatomy of the upper chest. Anteriorly, the brachicephalic vessels, mediastinal vessels, clavicle, and axillary vessels make the approach more difficult. Posteriorly, the scapula covers a substantial portion of the posterior chest. Avoidance is best accomplished by having the patient fully abduct the shoulder so that the scapula moves laterally. Careful palpation usually reveals the margin of the scapula. Another anatomic factor making the approach more difficult is that the ribs become smaller as one progresses from the midchest cephalad to the apex. It is usually easier to plan the entrance site so that the angle is also slightly caudal, which makes penetration of the intercostal space easier (Fig. 61–41).

Several final points should be made about unusual masses in the apex. Neurogenic tumors and lateral meningocele may occur in the posterior mediastinum adjacent to the neural foramina (Fig. 61–52). Neurogenic tumors are hard and painful in biopsy[67]; only seldom can a diagnostic sample be obtained. Puncture of a lateral meningocele will yield clear fluid consistent with spinal fluid.

Pleural Lesions

Pleural lesion biopsies are difficult to perform fluoroscopically because as the lesion is turned perpendicularly to the fluoroscope, it becomes en face and more difficult to see. With CT, sampling of such lesions is quite easy and actually provides considerable flexibility for needle selection. Of course, an aspiration needle can be used at any time; in those cases in which it is indicated, a cutting needle can actually be used for a more adequate tissue sample. Goralnik et al[120] reported that these cutting needles could be used safely for pleural lesions. She recommended their use when either lymphomas or unusual tumors such as mesotheliomas were suspected. Any of the automated biopsy devices can also be used if the size of the lesion is large enough to accommodate the length of the needle action.

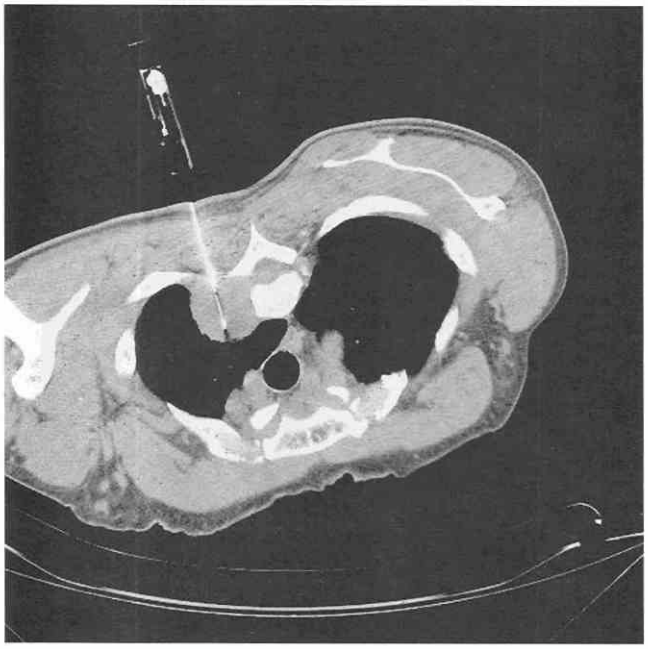

Figure 61–52. Rounded masses such as this by the neural foramina are likely to be of neurogenic origin. Lateral meningoceles yield cerebrospinal fluid on aspiration. Schwannomas such as this one yield diagnostic tissue when sampled by cutting needle, as noted here, but are painful during biopsy because they are attached to the nerve roots.

Mediastinal Lesions

Before the use of CT only a few authors ventured to perform biopsy of the mediastinum using fluoroscopic guidance. With the refinement of CT techniques, however, CT is now the modality of choice and is commonly used for this area.[3]

Several limited studies by Lauby et al,[232] Jereb and Krasovec,[194] and Rosenberger[341] and Adler[3] demonstrated the feasibility of mediastinal biopsies with fine needles guided by fluoroscopy. Weisbrod[396] and Westcott[402] confirmed the benefits of fluoroscopic procedures but also noted some of the disadvantages and potential hazards. The most extensive series consisting of 100 patients was reported by Westcott. Although the results showed a 96% correct answer, there were 10 patients with vascular aneurysms that created some difficulty. Five of the patients were excluded from a biopsy because of a difficulty in evaluating the mediastinum. In another five cases, inadvertent puncture of aortic aneurysms occurred; in one patient a hemomediastinum developed.

Weisbrod et al[396] also reported several important observations. In their series they noted that although aspiration needles were satisfactory for metastatic disease, the needles were less than optimal for lymphomas (see later section). They also reported one case of cardiac tamponade, which was successfully treated.

Since these reports, Adler et al[3] and our own group have reported the preference for CT in guiding such procedures, which can be quite effective and safe if the appropriate guidelines are used. Anatomic approach for the mediastinum is slightly different, depending on the space being sampled and the approach used.

Mediastinal Anatomy and Approaches

The mediastinum is an exciting area for the application of procedures because in the early development of these techniques they were considered off limits for several reasons. With the evolution of imaging and its corresponding procedures, radiologists and clinicians have become confident of mediastinal anatomy and pathology. The reliability of anatomic display and refinement of the interventional techniques are such that finally procedures of the mediastinum are now commonplace. However, these procedures require considerable skill and should only be performed by the most skillful radiologists, who are well versed in anatomy and procedures.

As one would expect, performing procedures in the mediastinum is contingent on comprehensive and complete knowledge of the mediastinal anatomy. One must be familiar with virtually all variations so that inadvertent puncture of a vascular structure does not occur. Aberrant subclavian vessels, left-sided vena cava, and prominent azygos veins are the most likely variations to occur. Furthermore, appropriate use of bolus dynamic scanning is critical to ensure all vascular structures are well-defined. Although it is seldom that tumors are vascular and represent a bleeding risk, it is not uncommon for vascular anomalies, aneurysms, or pseudoaneurysms to exist (Fig. 61–53).

Procedures of the different portions of the mediastinum (superior, anterior, middle or posterior) require uniquely different approaches for such procedures. Successful and safe procedures in these areas require careful attention to the subtle techniques used to guide and manipulate instruments in these areas.

Superior Mediastinum

The superior mediastinum consists of the space above the aortic arch and contains the various brachiocephlic vessels (venous and arterial). This is the most common area for congenital variations because arteries emanating from the arch and venous variations are quite common.

This space requires an anterior insertion in virtually all cases and usually results in an approach through the suprasternal notch or the parasternal region (Fig. 61–54). In all cases a good vascular study with bolus injection is critical to clearly define the carotids, jugulars, and small vessels (Fig. 61–53). In most cases the lower portion of the thyroid gland and the trachea must be dealt with to approach such masses. As a matter of course it is always critical to identify clearly the lobes of the thyroid, because it is common for substernal or low-lying thyroid to be mistaken for a mass in the upper mediastinum. If the ipsilateral lobe of the gland is not identified, one should always consider the possibility that the observed mass might be the lobe of the thyroid.

The methods for choosing the correct entrance site and pathway are essentially the same as the other areas. As the needle is inserted, the pathway and tip of the needle are carefully monitored with incremental adjustments. Use of the bevel to slide past the different structures is important to provide clearance around the vessels. As noted in the earlier technical section, the bevel is turned toward the structure to be avoided and the point is rotated so that it is directed toward the intended target. Also as noted in earlier sections, successful maneuvering of the needle around a vessel or structure is best accomplished by pushing the instrument slowly, which facilitates the deflection of the needle.

Anterior Mediastinum

Lesions in the anterior mediastinum are in the anterior space behind the sternum or anterior to the aortic arch. In the vast majority of cases, one can access these lesions by using an insertion site just lateral to either side of the sternum. One must be cautious to not sample the internal mammary artery or vein. With these lesions one can use either an aspiration or cutting needle as in other portions of the mediastinum. Careful localization of the cutting

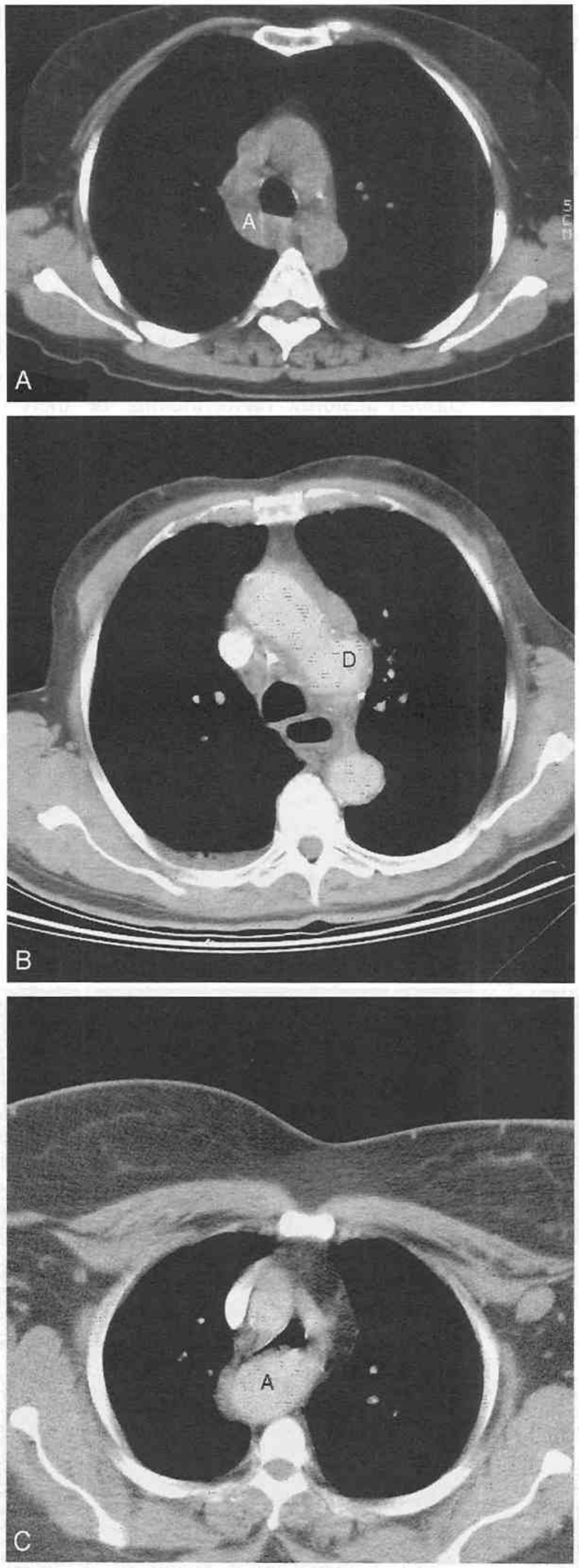

Figure 61–53. Common vascular variations are noted in these three images, which of course should not be mistaken for tumors; distinction is quite easy with contrast material. *A,* This scan shows a very prominent azygos vein. *B,* Scan at the level of the arch shows a small aneurysm, at the ductus region (D). *C,* Scan of the upper mediastinum shows an enhancing mass behind the trachea, which represents an aberrant subclavian artery.

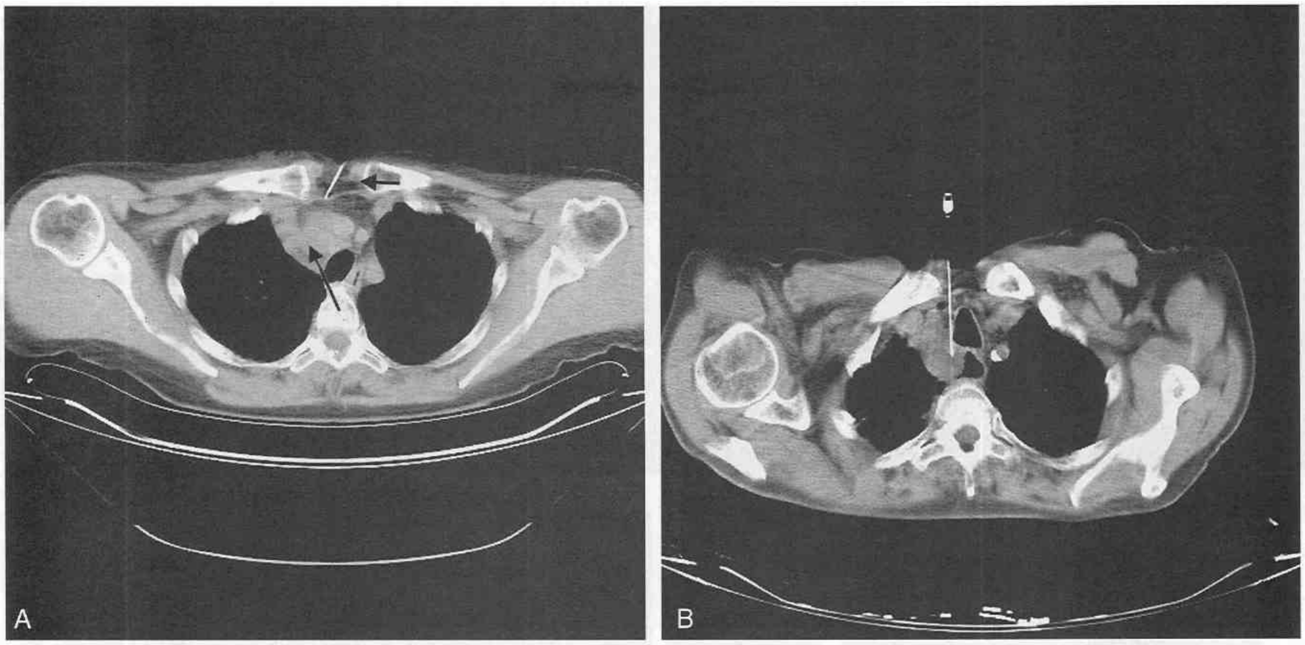

Figure 61–54. *A,* The most cephalad portion of the superior mediastinum includes the brachiocephalic vessels. This shows a mass (*long arrow*) adjacent to the subclavian artery. A needle (*horizontal arrow*) is inserted through the suprasternal notch and carefully advanced into the mass. In such cases it is best to keep the bevel directed toward the vessel so it will skim over the surface of the vessel. *B,* A different patient with a small mass posteriorly, adjacent to the esophagus and trachea. A needle is noted passing by the trachea. The bevel of the needle was directed toward the trachea.

needle gap is critical in such cases (Figs. 61–55 and 61–56) because cutting of the major vessels would certainly be catastrophic. As noted in the earlier section, placing a patient in a lateral position can shift the anterior junction line to make such procedures simpler. Gupta et al[133] have proposed using a trans-sternal approach with a coaxial system; these authors advocate using a coaxial cannula to penetrate the sternum and use a needle through the cannula. I have not found the need for this approach and have preferred to use the methods discussed here.

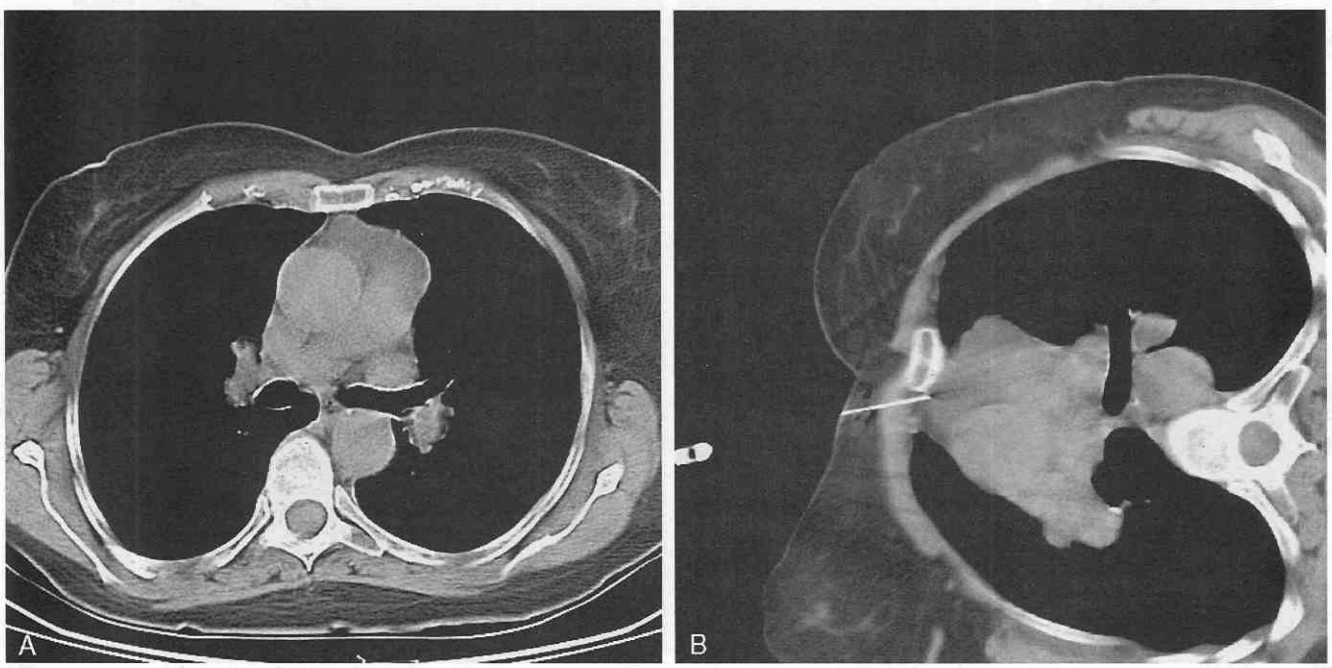

Figure 61–55. *A,* CT scan shows an ill-defined mass in the anterior mediastinum, [redacted]d to be subtle n[redacted] in thym[redacted] With the patient in the prone position, access to the mass cannot be obtained without crossing the lung. *B,* When the patient is positioned on the side the mediastinal structures shift, permitting access for needle placement into the mediastinum.

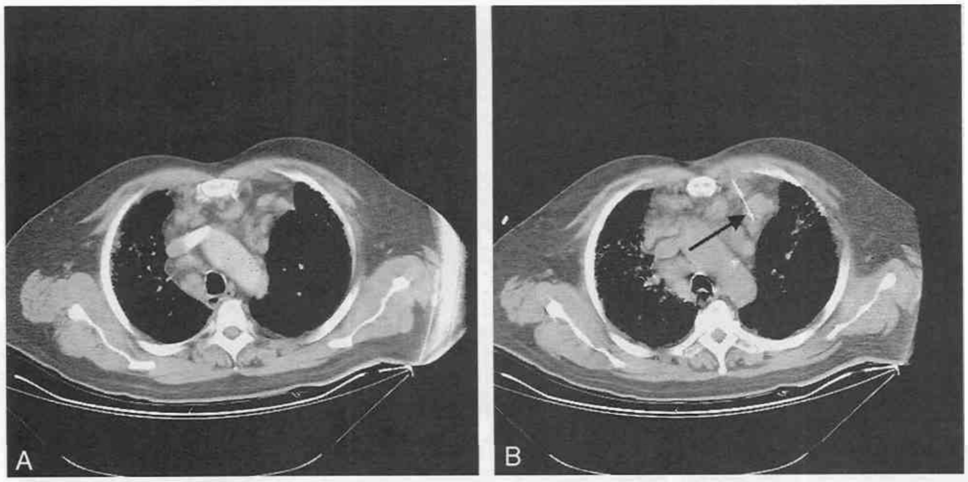

Figure 61–56. *A,* Biopsy of anterior mediastinal lesions can be safely performed if the edge of the anterior space abuts the pleura and there is sufficient space to avoid the lung. Also, as noted here, it is critical to perform a bolus injection to distinguish opacified vessels from lymph nodes. *B,* Lymph node biopsies can be safely performed if the cutting needle "gap" can be confined to the node *(arrow).*

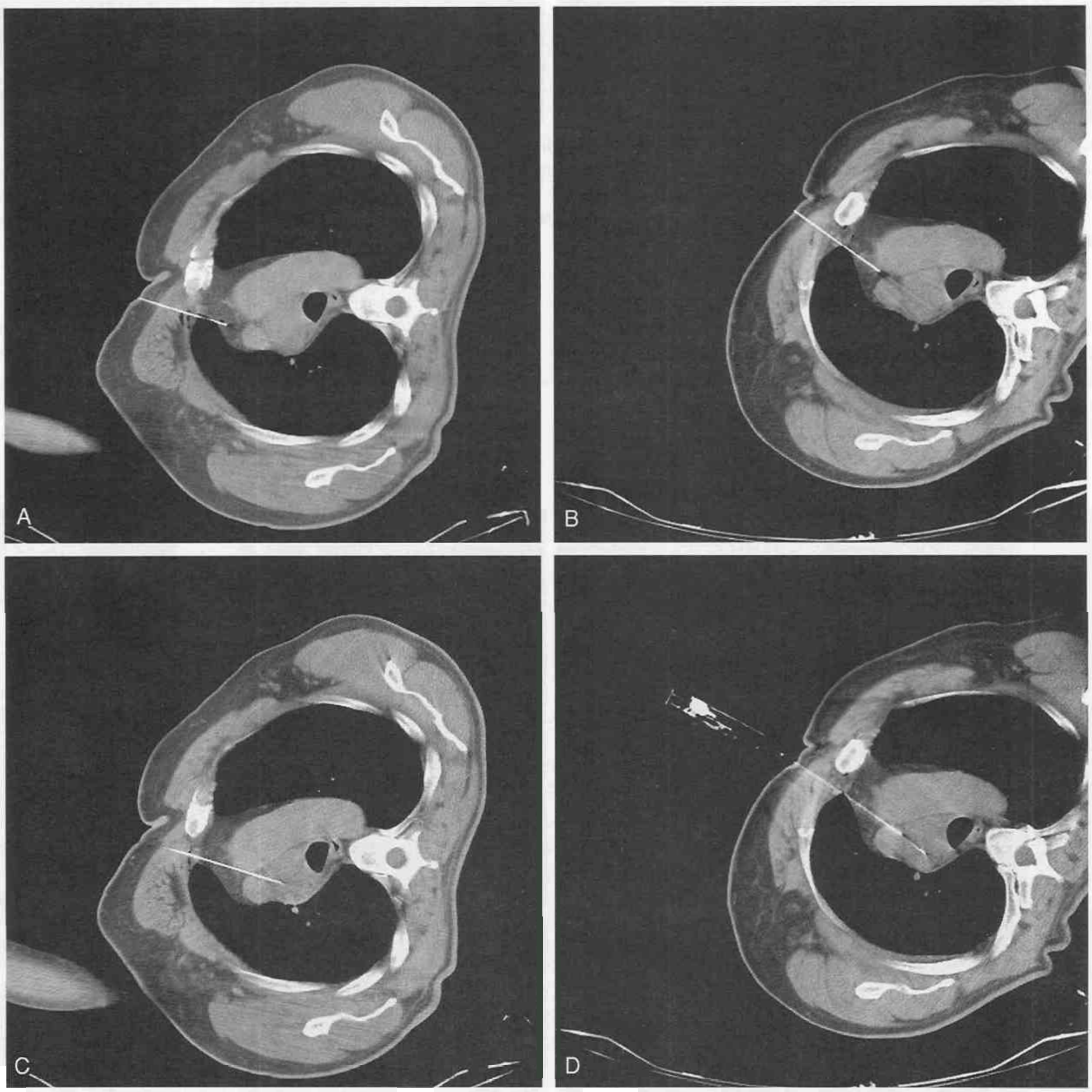

Figure 61–57. *A,* A mass (m) located in the azygous region shows tumor posterior to the cava and aorta. Initial positioning of needle required slight direc[redacted]medially. *B,* A Chiba needle, within the coaxial cannula, is pushed past the vesse[redacted]with the bevel[redacted]ected toward the vena cava. *C,* Through the cannula, a Chiba needle aspiration was performed. *D,* After removal of the Chiba needle, a cutting needle (20 gauge) procedure was performed.

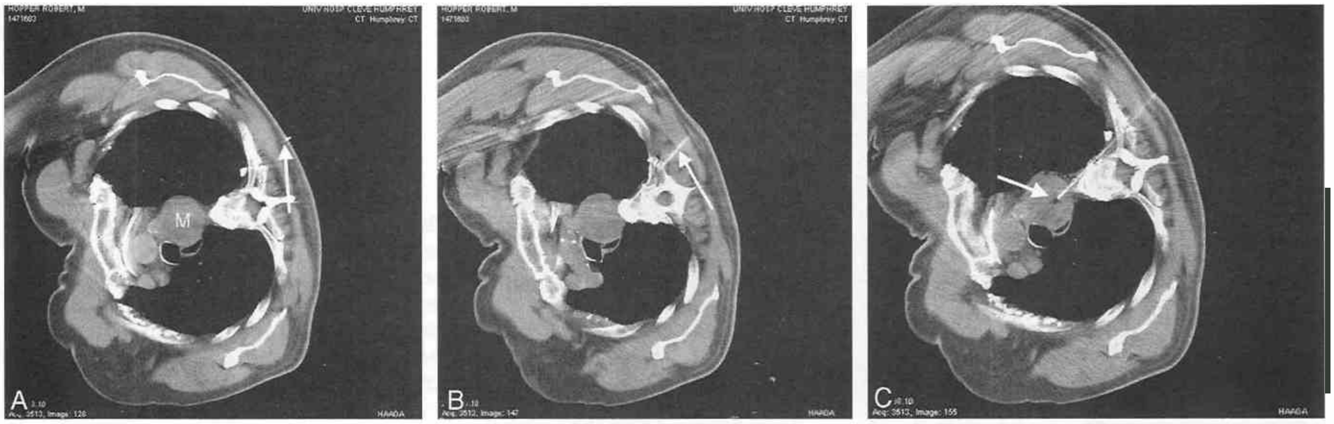

Figure 61–58. *A,* A mass (M) is located lateral to [redacted]rachea. Note the marker on the skin surface *(arrow)* used to choose the entrance site. *B,* The pathway for the needle *(arrow)* is most [redacted]ropriate when it traverses the juncture point between the transverse process and the rib. *C,* By using ample local anesthetic along the ribs and paraspinal path, the needle *(arrow)* can slide along the vertebral body and enter the mass.

Middle Mediastinum

The middle mediastinum is a rather large space below the arch and encompasses the azygous node (Fig. 61–57), peritracheal region (Fig. 61–58), aortic pulmonary window (Figs. 61–59 and 61–60), subcarinal region (Fig. 61–61), and the periesophageal region (Fig. 61–62). The peritracheal regions and the aortic pulmonary windows are typically best approached by an anterior approach through the anterior junction line while avoiding the lung parenchyma and other structures. It is worthwhile to recall that the internal mammary vessels should be identified prior to any procedure so that the entrance and pathway can be planned appropriately to avoid these structures.

The anterior approach may be performed if the patient has a wide anterior junction region, but in many cases it is helpful to place the patient in a lateral position, either on the right or left side. By doing this, the anatomy may shift so that a clear pathway through the anterior fat space may be possible, thereby preventing any possible pneumothorax

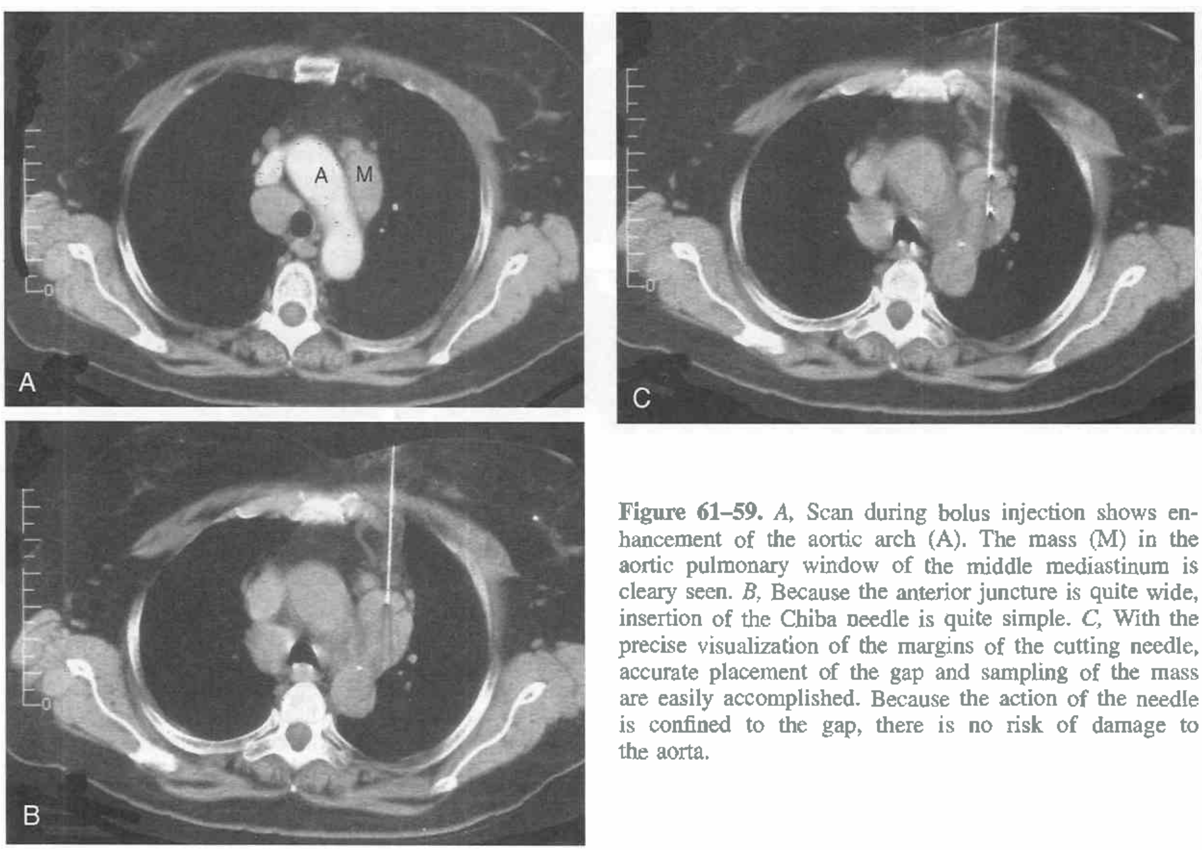

Figure 61–59. *A,* Scan during bolus injection shows enhancement of the aortic arch (A). The mass (M) in the aortic pulmonary window of the middle mediastinum is cleary seen. *B,* Because the anterior juncture is quite wide, insertion of the Chiba needle is quite simple. *C,* With the precise visualization of the margins of the cutting needle, accurate placement of the gap and sampling of the mass are easily accomplished. Because the action of the needle is confined to the gap, there is no risk of damage to the aorta.

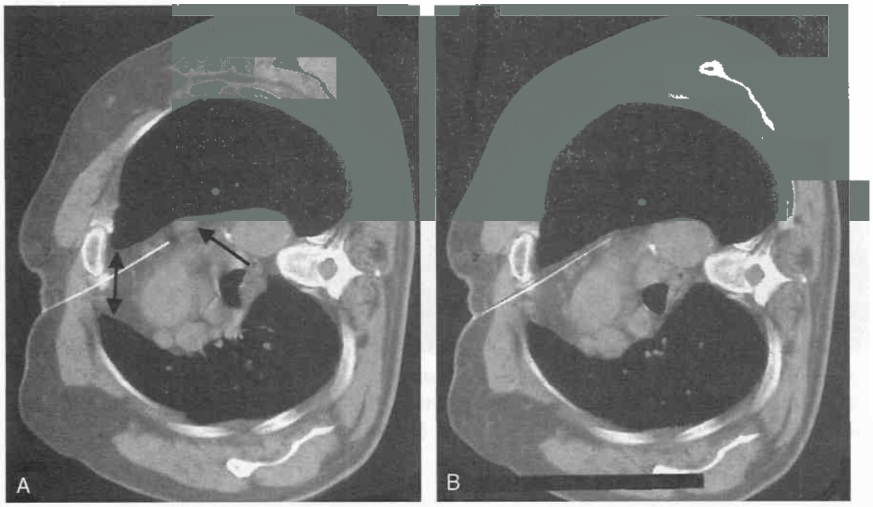

Figure 61–60. *A,* Access for this biopsy was not present when the patient was lying supine (see Figure 61–9*A* and *B*). The path of the needle was not appropriate for sampling a small lymph node (*arrow*). *B,* The needle was redirected using the deflection method described and demonstrated earlier. The node was sampled without removal of the needle and redirection.

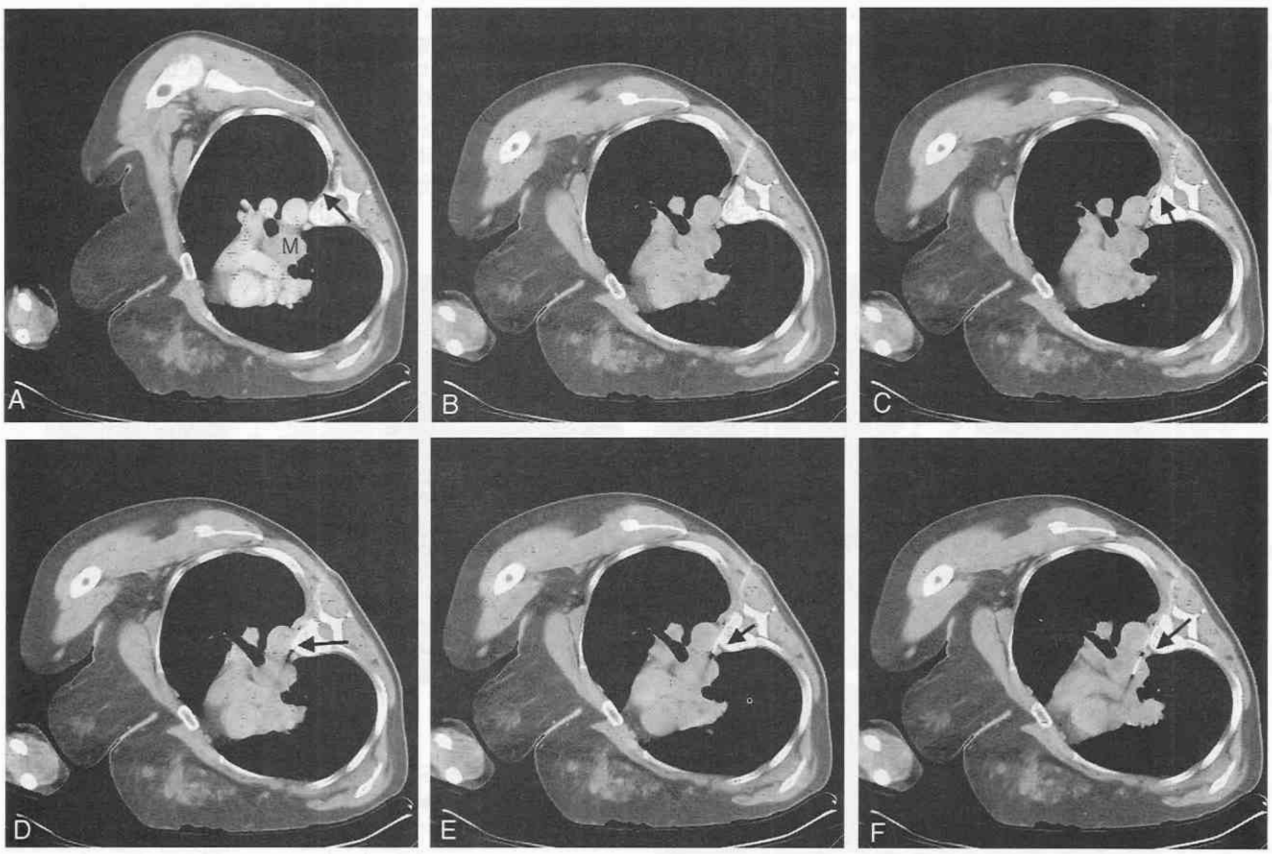

Figure 61–61. *A*[redacted]e middle medistinum shows a mass (M) clearly distinguished from the opacified vessels. The method shown here is effective for c[redacted]tently sampling such masses. *B,* The needle is inserted at a point where the trajectory crosses the junction between the transverse process and the rib. Saline is injected into the paraspinal tissues, moving the pleura more laterally, facilitating easy passage of the needle. *C,* This scan shows the next step in the procedure, which consists of positioning the needle against the anterior lateral margin of the vertebral body. The bevel of the needle is directed toward the body; the needle is pushed forward close to the aorta. *D,* When the needle is against the aorta, the bevel is turned toward the aorta and pushed forward past the aorta. *E,* At this point, the bevel of the needle is turned toward the azygos vein and pushed forward. *F,* The final positioning of the needle is within the mass.

Figure 61–62. *A,* A patient with a history of hepatoma shows a mass (M) in the middle mediastinum lateral to the esophagus. The lidocaine needle is used to inject saline in the paraspinal space, enlarging the pathway; compare to the opposite paraspinal space *(arrow). B,* An aspiration needle biopsy is performed. Performing such aspiration needle biopsies prior to cutting needle permits assessment of pathway clearance and cooperation of the patient. *C,* The cutting needle has been inserted after aspiration biopsy and the stylet inserted. Note that the gap is rather medial, and it was considered too close to the esophagus. The stylet was retracted and the needle rotated 180 degrees. *D,* Using the deflection of the bevel of the stylet, the gap is more laterally positioned so that the sample could be taken without a major readjustment of the needle. Note the position of the gap compared to that in *C.*

that could occur if the lung were traversed (see Fig. 61–59). In such cases injection of saline or gas may be helpful to slightly enlarge the potential pathway (see Fig. 61–60). The widening of the pathway is typically quite small because these materials disperse along the long axis of tissues as well as the cross-sectional areas, so the change in the anatomy is usually minimal. Maneuvering the instruments past corresponding vessels is a critical part of the procedure.

Paratracheal or azygous lymph nodes can be approached by traversing the anterior mediastinum and the space between the superior vena cava and the ascending aorta. The level of entrance is below the origins of the brachiocephalic vessels and the subclavian veins. When using this ap-

proach, it is critical to choose the correct entrance site and trajectory to ensure uneventful passage of the needle past the vessels. Traversing the space between the cava and aorta is simpler if the process has slightly widened the space. In those cases when the vessels have not been separated in this fashion, the successful placement can be accomplished by using a coaxial system as follows. With the newly designed devices, blunt or rounded stylets are available so that the walls can be pushed slightly and penetration avoided. In other cases, one might choose to use a small-caliber bevel needle to slide between the two structures, and the coaxial cannula can then be advanced over the Chiba needle (see Fig. 61–57).

The subcarinal area is best approached through a posterior paraspinal approach from either the right or left side depending on the location of the mass. Surprisingly, the left approach between the aorta and the vertebral body is usually the best approach because there is more space compared to the paraspinal region on the right side (Figs. 61–61 and 61–62). As one reviews the provided figures, the approach seems almost unbelievable but the truth is that I have consistently performed this approach for 15 years with no complications. From my perspective, it would be gratifying to believe I was the only one capable of doing this, but the facts are that the approach and methodology are valid and most experienced and motivated interventional radiologists can learn to perform this procedure.

Choice of the correct pathway and entrance site is critical to the success of the procedure. The most suitable trajectory from which an entrance site must be chosen is a pathway that includes the margin of the transverse process/rib junction, the margin of the vertebral body, and the mass itself. The trajectory path should not include any vessel. A small amount of lung parenchyma in the path is acceptable but not preferable.

Selection of any other pathway more medial than this will not be successful for the following reasons. The contiguous overlap of the transverse process and the rib articulation provides an almost impenetrable "shield" that is painful and traps the needle so that no angulation or adjustment is possible.

When this technique is executed, ample use of local anesthetic is important in not only the skin but also at the site of the transverse process and the vertebral body. These two additional sites are painful because of the periosteum unless adequately anesthetized.

The various steps of the procedure are as follows. The site is prepared and the needle is advanced just to the margin of the transverse process. At this level, local anesthesia is infiltrated on the periosteum. The needle is rotated so the bevel is turned against the body and the needle pushed slowly. The tip of the needle is located closely to the margin of the vertebral body and local anesthesia is injected. The needle is adjusted if needed so that the bevel of the needle is against the edge of the vertebral body and pushed slowly several millimeters. The bevel is then rotated so the bevel is toward the aorta and pushed forward 4 to 5 mm to pass the aorta. If the hemiazygos vein or esophagus is close, the bevel may also be adjusted to pass by those structures. Once positioned in the mass, the sample is acquired as appropriate with either the aspiration or cutting needle.

The sequence of events in this procedure will typically proceed predictably, but it can be aborted any time at the judgment of the operator. As one begins to learn this technique, each succeeding attempt provides additional confidence that enhances eventual success and comfort with the procedure. One almost insurmountable difficulty is the presence of a large osteophyte that may occur at the edge of the vertebral body. When a large spur is present, one might not even choose to attempt the procedure. If the procedure is being performed and an obstruction occurs at the edge of the vertebral body, minor adjustments of the needle can be made to determine if passage is possible. Persisting beyond several attempts is seldom beneficial.

Posterior Mediastinum

Sampling abnormalities in the posterior mediastinum is much easier than either the anterior or middle mediastinum. The posterior mediastinum represents the space adjacent to the vertebral body and the pleura region. In most cases, there is clear access to the mass without crossing the lung parenchyma. In such circumstances it is usually most expeditious to perform a quick sample with an aspiration needle and then follow it with a cutting needle. Performing the aspiration first permits one to ascertain the effectiveness of the local anesthesia and the cooperation of the patient prior to using the cutting needle (see Fig. 61–42).

Pneumonias and Infiltrates

Recovery of samples for culture and identification of infectious processes has become more popular in recent years. The results have been somewhat variable for the routine pyogenic infections, so we have seldom been asked to sample such problems. The opportunistic infections in immunocompromised patients have become a more significant diagnostic dilemma, and thus the occasion may arise in which sampling is more critical.

In our experience the diagnosis of fungal infection with cavitation or fungus ball by needle aspiration is quite reliable and easy to perform. In such cases, the procedure is performed in a standard fashion, except that the sample is sent for appropriate stains and culture.

When a more difficult pathogen such as *Pneumocystis carinii* is suspected, simple aspiration may not suffice. Although some authors have inferred that recovery of diagnostic tissue is quite easy, we have found that it is not. In many cases one may require a small cutting sample that can provide more ample material for evaluation. When the infiltrate abuts the pleural membrane, we have employed a small cutting 20-gauge needle with considerable success and no morbidity. Our experience is quite limited (to perhaps 10 cases), but we are optimistic for this technique.

Results: Success and Complications

The success rate of lung biopsies has varied widely among the many reports of fluoroscopic and CT-guided procedures. These rates have ranged as low as 60% and as high as 95%.

In our experience, the success rate is about 75% with a single pass and overall 85% with a second pass as required. These results are exclusive of lymphoma and mesothelioma cases, which are very difficult to diagnose with aspiration biopsies. Weisbrod et al[396] noted that in about 67% of cases the diagnosis of lymphoma can be suggested, but not the definitive subtype. Goralnik et al[120] found that the specific subtype could be diagnosed using a large cutting needle for suspected lymphoma lesions.

Although it is true that the outcome may vary from one institution to the next depending on the selection criteria for patients, favorable results can be obtained with the careful attention to detail and technique as noted in this chapter.

Reliability of Aspiration and Cutting Needle Results

Several reports by Sinner et al,[356] Thornbury et al,[380] and Greene[124] have documented that the results of aspiration biopsies correlate well with histologic results. Green et al[124] found the correlation to be 92.3% for adenocarcinomas, 100% for squamous cell, 88.9% for large cell undifferentiated, and 100% for small cell undifferentiated. Taft et al[345] found an interobserver error to be only 6% with 94% overall consistency.

The consistency for diagnosing lymphomas is much less. Weisbrod et al[396] and Westcott et al[400] have shown that aspiration biopsies are capable of suggesting the diagnosis of lymphoma, but Goralnik et al[120] showed that only a cutting needle biopsy was capable of providing the definitive subtype of lymphoma.

Cutting Needles

Since the prior edition of this book, there has been considerable data presented about the use of cutting needles for lung biopsies. The concensus supports our previous position on the use of aspiration and cutting needles. In the vast majority of patients with common neoplasms of the lung, the cutting needle offers no definite benefit. In those cases when a failed aspiration biopsy has been performed, suspicion of a benign or unusual tumor such as thymoma or lymphoma is suspected, a cutting needle appropriately used provides considerable benefit.

Numerous authors, including Kushihashi et al,[223] Laurent et al,[233] Rotte,[343] Greif et al,[127] and Klein et al,[217] have verified the usefulness of the cutting needles but confirm the role of aspiration needles. Klein et al found little difference in the diagnosis of malignant lesions but great superiority for benign disorders. The correct diagnosis with benign lesions was 44% with aspiration needles and 100% for cutting needles. Greif et al found little difference in the diagnostic accuracy for malignant lesions but considerable benefit for benign disease. With peripheral lung nodules, Greif et al reported an accuracy of 81% for benign lesions compared to 16% for aspiration needles.

For the unusual malignant and benign tumors, multiple authors have shown the improved results with cutting needles. Carruthers et al[47] reported the usefulness of cutting needles for diagnosing Wegener's granulomatosis. Greif et al[127] reported that in the mediastinum, the cutting needles could diagnose lymphoma, thymoma, and bronchogenic carcinoma accurately. Zinzani et al[419] reported on a series of 83 patients, in which the accurate diagnosis of lymphoma was achieved in 81%. Lopez et al[251] reported a 93% accuracy for the diagnosis of benign lesions.

Mesotheliomas are also quite difficult to diagnose with any type of needle. In our experience with about eight such cases, the diagnosis of mesothelioma can be suggested, but the differentiation of benign versus malignant cannot be made even with cutting needles.

The most difficult question to be resolved relative to these procedures is the significance of a negative or benign diagnosis. Some authors have suggested that because they obtained a "negative" aspiration for malignancy from a benign lesion, the correct diagnosis could be inferred. This is obviously not the case, for one must always be suspicious of a negative aspiration unless other information is available. It is difficult to accept that authors correctly made the diagnosis of granulomas, sequestration, and other unusual benign lesions based solely on aspiration biopsy. As Westcott noted, it is appropriate to accept a specific result that states a diagnosis (e.g., hamartoma, infarct), but claims of the recovery of histiocytes, leukocytes, and other nonspecific cells should be regarded with skepticism.

It is only after several repeat biopsies that yield nonspecific material that one can consider following such a lesion. If there is a strong history of family disease or smoking, it is appropriate to have surgical removal of such a lesion regardless of the results.

In patients without risk factors, one may choose to follow such cases at 3-month intervals, for a total of 9 months. If such a lesion is benign, it will usually shrink or calcify during this period. If there is any increase in size, then surgery should be performed immediately. At the end of 9 months, if there has been no change, it is appropriate to re-evaluate the case.

Success Factors

A number of factors improve the probability of a positive biopsy. These factors include the operator's experience and technique; pathology; needle type; and character, size, and location of the lesion. Experience of the cytologists and pathologists is important. The greater the experience, the more consistent the results of the procedure. Proper technique includes choice of appropriate needle and maintenance of proper vacuum.

It is always important to include the routine slide smears as well as a saline rinse of the needle and syringe for submission to pathology; a cytocentrifuge and cell block preparation will increase the diagnostic yield of such samples. Pathologic results depend on the cell type of the tumor as noted in the results section; the common primary lung tumors are easily diagnosed, whereas others are not.

The size and location of a mass affect the probability of a positive diagnostic aspiration. Bergquist et al[30] noted that the diagnostic accuracy was higher for larger lesions and for more peripheral lesions. For example, a 1-cm nodule was successfully biopsied in 58% of cases when it was central; it was successfully biopsied in 85% of cases when it was peripheral. More recently, two additional authors, Li et al[241] and Miller et al[278], have confirmed the improved diagnostic recovery from large lesions compared to smaller ones.

Postprocedure Care

The postprocedure care of these patients is quite simple and consists of observing them for severe hemoptysis and pneumothorax. Immediately after completion of the procedure, I prefer to have the patient lie still for 5 to 10 minutes to let the puncture site seal. Moore et al[286] have shown that if the patient is positioned with the puncture site down after the procedure, the incidence of pneumothorax is reduced. The pneumothorax rate for patients placed in this position was 17.9%, whereas the rate was 33.6% for those not so positioned. Chest tube rate was 9.8% for those who were correctly positioned, compared with 0.4% for those who were not.

Before removing the patient from the table, I take a repeat scan to evaluate for postprocedural problems. Miller et al[279] have shown that CT is as reliable for detecting pneumothorax as is a plain radiograph. A small pneumothorax is of little significance, as noted later. Some bleeding in the parenchyma in the area of the needle tract is quite frequent, but it is of no significance. If there is any question of the patient's stability, oxygen should be administered and appropriate treatment given, as noted later.

Postprocedure chest films should be taken at 1-, 4-, and 8-hour intervals. Perlmutt et al[326] showed that pneumothoraces could be detected in the following percentages at the noted timed delays: 89% immediately after procedure, 9% after 1 hour, and only 2% after 4 hours.

The most frequent complication is pneumothorax, which can be easily treated with a small-caliber tube and a one-way valve. The decision to insert a chest tube is dependent on patient symptoms, patient attitude and attending service, and patient reliability. In the best of circumstances, the chest tube is inserted only if the patient is symptomatic. Even a 50% pneumothorax does not require treatment unless the patient is symptomatic. If there is any question of the patient's symptoms, reliability, or housing status, the chest tube should be inserted.

Chest Tube Insertion

It is best for the inexperienced operator to insert the chest tube under fluoroscopy or at the table side, depending on the experience of the interventionist and the distress of the patient.[325,337] The placement of the chest tube is quite simple and can be accomplished in the following fashion. One should use an entrance site in the anterior second or third intercostal space on the side of the pneumothorax. After preparation of the site with antiseptic solution, one should thoroughly anesthetize the site down to and including the pleura. One can estimate the depth required for the tube insertion by using the anesthetic needle to aspirate air at the site (Fig. 61–63).

After administration of the anesthetic, a nick in the skin is made with a scalpel to provide ample space for the tube. As one pushes the tube through the chest wall, a "give" is noted; this indicates passage through the pleura. The tube is kept perpendicular relative to the axial plane until it passes into the pleural space. It is then angled slightly cephalad so the tube will lie in the apical lateral region. This location is optimal because in this position it will evacuate "rising" air when the patient is either lying down or standing up.

After placement of the tube, one should always reconfirm the proper location of the tube, even if the placement was optimal. This can be done by checking the tube position with oblique or lateral films. Another method one can use is to place the end of the valve close to one's ear and listen for the escape of air through the valve.

After the placement of the tube, patients will usually experience some pain as the lung reexpands against the

Figure 61–63. *A,* Disposable chest tube trays such as this are available. These are complete and provide all necessary equipment, including the instruments, tube, and Heimlich valve. *B,* This chest film shows the chest tube in the left upper lobe. Whenever the tube is positioned, one should clinically check for the egress of air to ensure proper function.

tube. A mild analgesic will relieve the discomfort; repeat analgesics are seldom necessary.

At this point a complete explanation should be provided to the patient and nursing staff to prevent inappropriate or premature closure of the tube.

If the lung is reinflated for 10 to 12 hours, the tube can be removed. The tube should be clamped for several hours and a repeat film taken. If the lung remains expanded, it can be removed. If not, the valve should be reopened for 24 hours and the procedure repeated at a later time. If severe primary lung disease is present, expansion could take as long as 2 to 3 days.

Complications and Causative Factors

Pneumothorax

The pneumothorax rate reported for CT procedures varies widely among patient groups. The asymptomatic rate varies between 17.5% and 72%. The symptomatic rate, requiring chest tube, varies between 6% and 18%. Our rates using the single-needle method and the coaxial, short-cannula method are 17.5% for asymptomatic and 6% for symptomatic pneumothoraces. The higher rates reported by other authors are probably the result of the prolonged time of the procedures and the multiple needle punctures associated with the tandem-needle technique.

Some authors attribute the high pneumothorax rate to the prolonged length of the procedure. They reported the average period for the needle to be within the lung parenchyma as 15 to 20 minutes. This compares to the average of 6 minutes we tabulated in our department. The difference we believe is related to patient selection, preplanning, proper needle selection, and technique.

The risk of a pneumothorax also depends on many other factors, including status of the lung, number of needle passes, and length of pathway through aerated lung penetrated. Fish et al[91] and Miller et al[279] showed a definite relationship of pneumothorax to lung disease. Fish et al evaluated chest films and spirometry to determine the presence of chronic obstructive pulmonary disease (COPD) and found that normal patients had a pneumothorax rate lower than those with COPD. With spirometry measurements the ratio for pneumothorax was 45% for COPD patients, compared with 25% for normal patients. Using the chest x-ray examination as the standard, the rate was 42% for COPD compared with 25% for normal patients (see earlier section on minimizing pneumothoraces).

Hemoptysis

The rate of hemoptysis is quite low with all types of techniques and appears to be dependent only on needle size. In a series by Khouri et al,[214] the hemoptysis rate for 20-gauge needles was only 5%, compared with 21% for 18-gauge needles.

The other factors affecting hemoptysis are the depth of lesions, coagulation status, and presence of congestive failure. Deep lesions or hilar lesions are at greatest risk because of the long pathway and proximity of blood vessel. Those patients with coagulopathies, pulmonary hypertension, or congestive heart failure are at greatest risk for hemoptysis and even endobronchial bleeding (as noted later) and should be biopsied without correction of the basic problem. Commonly, localized hemorrhage in the parenchyma may occur following a biopsy, but it is of no significance.

Fatalities

As seen in the original articles describing fatalities, the two causes are endobronchial bleeding and air embolism. I have been able to locate nine reported deaths in the literature—five from endobronchial bleeding and four from air embolism.

Endobronchial bleeding is a rare event. In my opinion its occurrence is based on the nature of the abnormality being sampled as well as on needle caliber.[280,305] Although deaths have occurred with both 22-gauge and 18-gauge needles, it is quite clear that the rate of hemoptysis is less with small-caliber needles. The cases reported in the literature were associated with ill-defined masses adjacent to the hila. Also, however, one must remember the importance of bolus studies in selected patients (Figs. 61–46 and 61–47).

Those cases of air embolism were associated with coughing paroxysms. Several authors[381,400] hypothesized that the air embolism is a result of the elevated intrabronchial pressure that occurs with coughing; the high-pressure air follows along the needle track into the blood vessels. One should avoid the temptation to "counsel" the patient not to cough. To avoid such problems, one should immediately remove the needle if a patient starts to cough during a procedure. Patients with a propensity to cough should be treated with codeine before attempting a biopsy.

Blood-Patch Technique

Several authors have reported on the blood-patch technique, which is used to reduce the possibility of a pneumothorax.[35, 172,267] With this method a coaxial needle method is used and a blood clot is injected through the long cannula during its removal from the lung. The results of this method are variable, and Bourgouin et al[35] reported no difference in outcome when it was evaluated in a randomized prospective fashion.

Liver Biopsy

Liver biopsy is a common procedure* because the liver is commonly involved with malignant processes and benign disorders that can mimic malignancy. Because specific differentiation of these various processes is not possible by imaging methods, definitive diagnosis by biopsy is necessary for planning proper patient management and avoiding unnecessary surgical procedures. A new era of treating disease focally has also begun (discussed later).[76]

Indications

The indications are quite broad considering the diagnostic and guidance accuracy of both ultrasound and CT. Any

*References 258, 265, 369, 370, 398, 404.

patient with a focal hepatic mass or unusual anatomic configuration should have a guided rather than a blind procedure.

Diffuse processes of the liver are probably best performed by the blind method at the bedside, but any blind procedure that has failed is an indication for a guided procedure. Those associated with large amounts of ascites are best served by a guided procedure because the presence of fluid makes percussion of the liver edge quite difficult, so bedside procedures are compromised. The other indication for CT guidance is the need for the use of a 14-gauge cutting needle. Although the use of smaller cutting needles such as a 20 or 18 gauge is somewhat commonplace with ultrasound, the large size of the 14 gauge dictates the use of CT. CT is the best modality for characterization of lesions and visualization of the anatomy and the needle. When a radiologist becomes experienced, one can perform biopsies on a routine basis with considerable success and low complication rate[75] (see section on new cancer initiatives).

Biopsy of patients with abnormal coagulopathy should be performed under a combined guidance procedure, both imaging and fluoroscopy, so that special hemostatic techniques as described later can be used.

The choice between ultrasound, MRI, or CT must be made by the individual physician, but in general, CT is still considered the gold standard. Difficult anatomic location, poor visualization under ultrasound, or concern about increased vascularity is a clear indication for CT guidance. In some cases, lesion may be only visible on MRI, so the modality of choice is probably MRI.

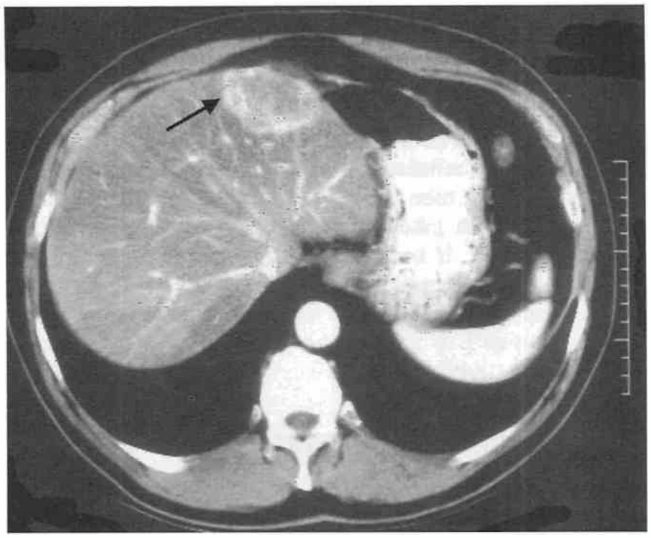

Figure 61–64. Diagnostic scan on patient with colon cancer shows a highly vascular lesion in the left lobe of the liver. This lesion is so vascular that no biopsy should be performed with standard methods (aspiration or cutting).

The larger cutting needles, either 18 or 14 gauge, can and should be used if a lesion is unknown, accessible, and avascular with a contrast enhancement. When an abnormality is unknown, only the sample obtained with the cutting needle can provide the type of histologic detail for the definitive diagnosis of virtually all benign and malignant lesions (see later sections on results).

Selection of Needle

For the liver, I use either a 20-gauge Chiba needle for an aspiration cytologic sample or a Tru-Cut needle of 18- or 14-gauge caliber. Selection of a needle is based on clinical factors, anatomic characteristics, and bolus contrast enhancement.

From a clinical perspective, a previous history of a malignancy is sufficient evidence to consider using only an aspiration needle. In the vast majority of cases the cytologic sample is quite adequate to confirm a previously diagnosed tumor.

A number of anatomic factors dictate the need for an aspiration biopsy. Unusually close proximity to various structures such as the vena cava, hepatic vein, portal vein, gallbladder, pleura, or diaphragm indicates the need for an aspiration biopsy.

Concern about a possible hemorrhagic complication is also an indication for an aspiration procedure. Such concern is typically raised if a coagulation problem exists or if a lesion is suspected of being vascular. A small abnormality in the coagulation studies is sufficient to justify the use of an aspiration needle. Bolus contrast enhancement is useful for assessing the vascularity of lesions. Those lesions that are slightly vascular should be sampled by an aspiration needle because it is safer than a cutting needle. If a lesion is highly vascular, one probably should not even use an aspiration needle (see later section on hepatoma) (Fig. 61–64).

New Cancer Initiatives

In recent years with the development of new sophisticated treatments for cancer, a new approach for cancer drug development and treatment has evolved based on acquisition of biopsy tissue. These initiatives have focused on the ability to measure molecules and microchemistries of tissue samples to assess the end-target effectiveness. The protocols that have been used for limited early drug development will be expanded to enhance new treatment approaches to include DNA, RNA, peptides, cytokines, and so forth. It is likely that these approaches will enter everyday clinical practice and that tissue sampling and testing will become the mainstay for drug selection and determination of efficacy.

The protocol for drug development has been that a large-caliber (14-gauge) needle is used to sample target tumor tissue prior to drug administration and at selected times following drug administration. From the tissue samples, microassays are performed to determine the presence and effectiveness of the administered drug. Using these methods, remarkable findings have occurred that have revolutionized the outcome of such studies. Probably the greatest testimony to this trend is the change in the vernacular for cancer therapy. Whereas previously researchers would talk about the maximum tolerable dose (MTD), they now talk about optimal modulatory dose (OMD) of the chosen drug or modulating agent.

In the future it is very likely that cancer patients will

receive repetitive biopsies over the course of their treatment to assay drug, change drug therapy, and modulate treatment based on such samples. The approach will not be dissimilar to that of sampling and treatment of infectious agents that occur in abscesses or blood cultures.

The reason this topic is discussed in this section is that the success of this new approach is contingent on obtaining sufficient tissue for assays, which depends on the use of larger needles such as the 14 gauge. These approaches are clearly the direction of the future, so it is imperative that radiologists learn the best techniques for performing such procedures. Because of our experience over the past 25 years, we are confident that our approach can provide a sound basis for further expansion of these methods.

Contraindications

There are several contraindications to liver biopsy. Severe uncorrectable coagulopathy is the most common contraindication; if an abnormal baseline exists and it can be corrected with fresh frozen plasma or platelets, the procedure can be performed without additional precautions. If an abnormal baseline cannot be corrected, other steps must be taken as described later in the section on hemostatic techniques.

Lack of patient cooperation is a relative contraindication. If a patient cannot cooperate with sedatives, then general anesthesia might be considered.

Another contraindication is the presence of increased vascularity or prominent vascular collaterals as noted with contrast enhancement. Those lesions, which may be vascular, include focal nodular hyperplasia, hepatomas, hemangiomas, sarcomas, and metastases (Figs. 61–64 to 61–66).

Aspiration Biopsy

For aspiration biopsy, either the single-needle or coaxial method using the 20-gauge Chiba needle should be used. A number of factors should be considered regarding entrance site selection and preparation, trajectory planning, target selection, and follow-up.

Entrance site selection is based on the location of the lesion. Generally, the shortest pathway that avoids the portal venous system, gallbladder, bowel, and diaphragm should be chosen. To avoid the pleural space, one should choose a site below the insertion of the diaphragm. If the lesion is somewhat high, this can be most practically accomplished by choosing a site no more posterior than the midaxillary line. When the lesion is high in the liver above the insertion of the diaphragm, an angled approach is necessary. The anterior diaphragm is much higher than the posterior portion, and lesions are more easily approached without crossing lung.

If the lesion is mobile, the patient can be placed in either a decubitus or oblique position to help immobilize the lesion.

Careful palpation of the site and preparation are important. Avoidance of ribs can be accomplished by palpation. To make the procedure completely pain-free, the pathway should be anesthetized from the skin down to the capsule of the liver.

For the best results, the pathway should include a cuff of normal liver. This cuff can help prevent leakage of blood or tumor cells into the peritoneum (Fig. 61–67).

Target selection is fairly straightforward. One should choose the lowest lesion that is easily approachable. If the lesion appears quite necrotic, one should attempt to position the needle within the periphery where one would expect more viable tissue.

The needle procedure is the standard aspiration procedure as previously described. We use the standard application of suction and reciprocating motion and two passes.

After the procedure, minimal follow-up is required. For patients who have not had a complicated procedure, we typically undertake an observation period of 1 to 2 hours.

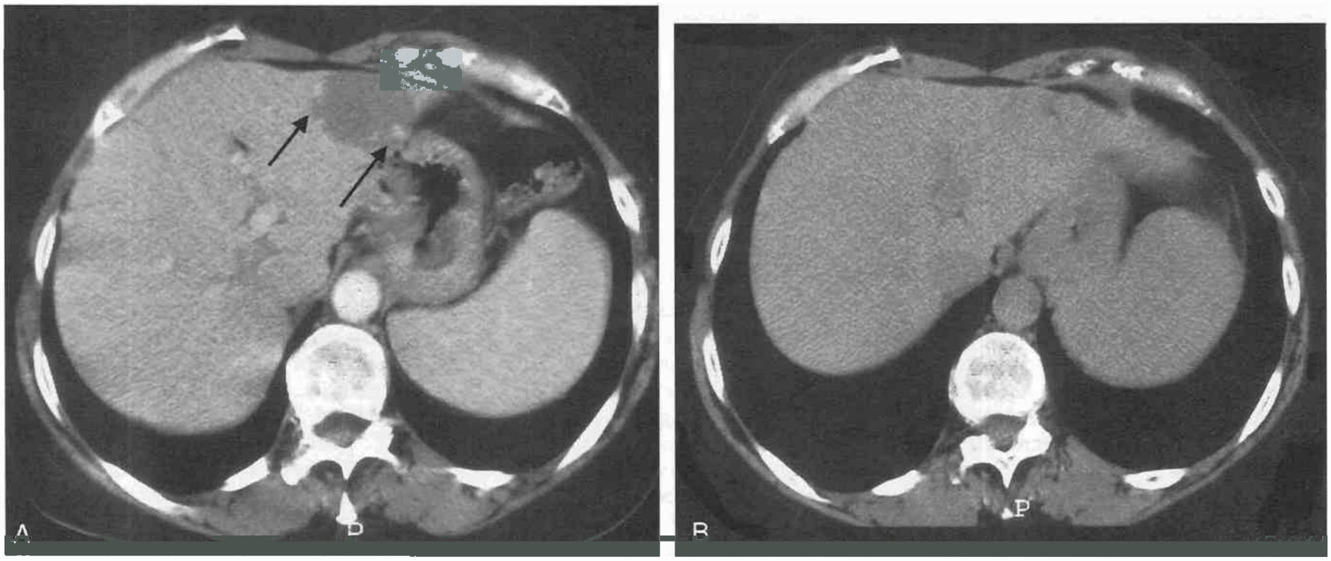

Figure 61–65. Hemangioma is a fairly common benign problem that has the potential for catastrophic bleeding. *A,* This scan was taken during the contrast phase and shows the characteristics of feeding vessels in the wall of the lesion. *B,* Late-phase scan shows the mass to be completely homogeneous in the delayed phase. These qualities are pathognomonic, and no procedure should be performed.

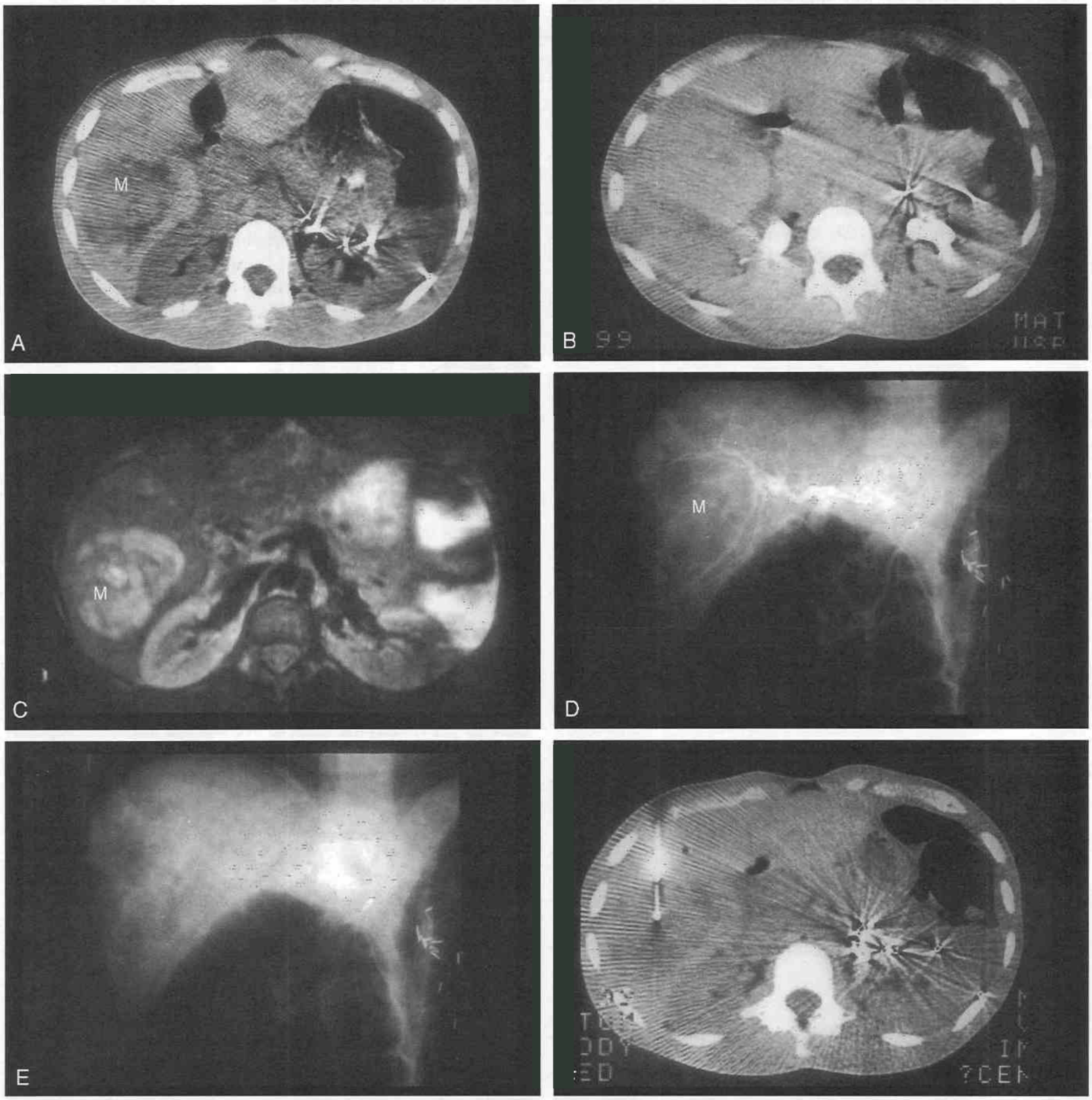

Figure 61–66. T[redacted] of [redacted]dem[redacted] highly unusual case. This series of sca[redacted]hem[redacted]ow[redacted]ties. Suc[redacted] partially thrombosed and have very small capillaries so there is no significant increased blood flow perceptible. *A,* This scan shows a low-density mass (M) in the right lobe of the liver. *B,* Later scans did not show typical enhancement but did show homogeneous appearance in the late phase. *C,* T2-weighted image shows a large image with inhomogenous intensity, not completely characteristic with hemangioma. *D,* Because there was still concern about hemangioma, an angiogram was performed. This early-phase image shows hepatic vasculature but no increased vascularity. *E,* Late-phase angiogram shows no evidence of "puddling," said to be characteristic of hemangioma. *F,* A 14-gauge biopsy of the lesion shows a gap centrally in the lesion. Pathology reports showed hemangioma. The point is not that biopsy should not be performed in hemangiomas but rather that the bolus study is so sensitive to blood flow that if a lesion is avascular with this method, one can perform a biopsy of an unknown mass with confidence that there will be no bleeding. Rarely, such avascular masses will ultimately prove to be atypical hemangiomas.

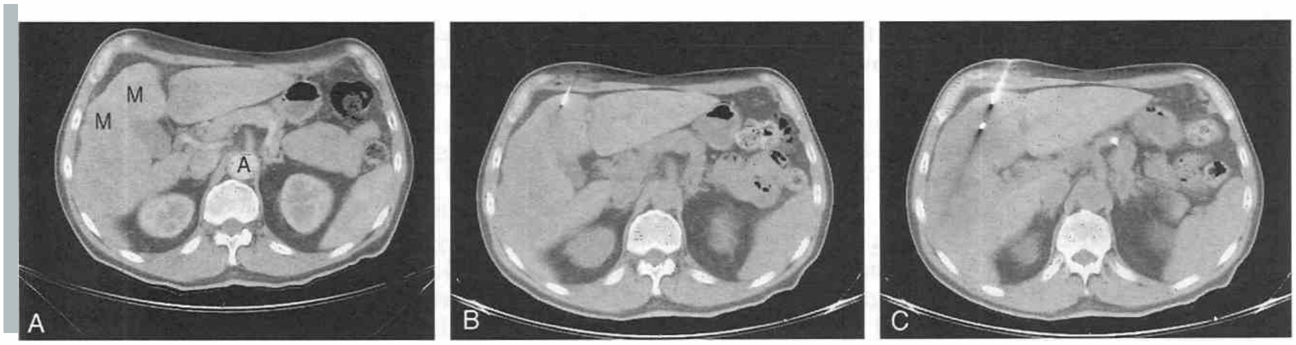

Figure 61–67. This figure demonstrates the typical approach for a liver biopsy. *A,* This image was taken during a bolus injection and shows the masses (M) in the liver that are not vascular. (*A* marks the aorta). *B,* Scan shows the preliminary insertion of a small-caliber needle, which was used to anesthetize the capsule of the liver as well as provide an aspiration sample from the mass. This quick needle aspiration provides useful information about the status of the anesthetic and the cooperation of the patient. *C,* This final scan shows the cutting needle localized to the mass; the gap is clearly visible.

Cutting-Needle Biopsy

Cutting-needle biopsy is performed using the single-needle technique and the techniques described previously. The most commonly used needle is the 14-gauge Tru-Cut type, but occasionally we use an 18- or 20-gauge Tru-Cut needle. Most commonly I use the manual Tru-Cut needle, but in some circumstances I use the automated biopsy gun.

Routinely, I prefer a single pass of a 14-gauge needle rather than multiple passes with smaller-gauge cutting needles. A quandary always exists concerning the amount of tissue required for a specific diagnosis, relative to the size of the needle being used. Although the larger needle cuts a large surface area within the liver, multiple needle passes increases the probability of randomly striking a small blood vessel. As noted in the complication section, the relative risk of taking multiple samples versus a single large sample has yet to be determined.

The same criteria and considerations are used for selection of the entrance site, trajectory, and target as were noted with the aspiration needle, except for some differences with target selection. When the abnormality is quite small, it is best to plan the procedure so that the entire width of the abnormality will be sampled. When the lesion is large, it is best to choose a target so that a small portion of the normal liver as well as the abnormality are sampled (Fig. 61–68).

If one uses a cutting needle, it is reasonable to perform a small-needle aspiration before the cutting-needle biopsy. Using the small needle first is valuable for several reasons. By performing the biopsy first with a small needle, the operator and the patient can practice the procedure and determine the cooperation of patient and sufficiency of the local anesthetic. If the procedure goes well, the large-needle biopsy may proceed. If the procedure entails problems, adjustments can be made in regard to entrance site, target, trajectory, sedation, and local anesthetic.

Automated Biopsies

Automated biopsies have become popular because they minimize technical inconsistencies from one procedure to the next. A recent survey by Mayoral and Lewis,[266] revealed that almost 90% of radiologists use an automated cutting device for liver biopsy. The choice of such a device is subject to personal preference, but the smaller spring-loaded devices are easier to use and are reliable.

There are two substantive benefits of the automated gun relative to body size and the physical nature of a tumor. When a patient is quite large and the lesion is somewhat deep, it is difficult to move the outer cutting cannula of the manual Tru-Cut effectively because of the "drag" put on the cannula. Considerable resistance and "drag" on the cannula that make the manual device difficult to use also occur when the abnormality being sampled is quite fibrotic or hard.

Regarding technique, also note that with the movement of the needle, "recoil" occurs. One of our colleagues has

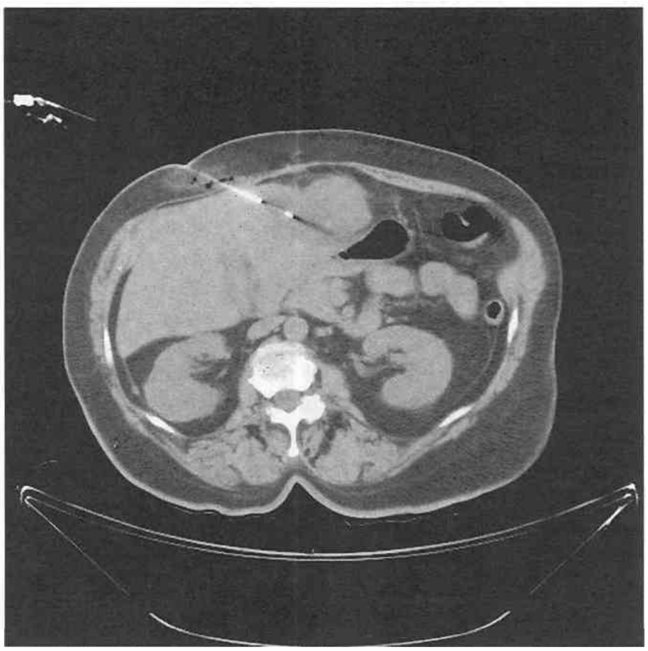

Figure 61–68. Scan shows biopsy of mass in left lobe, with cutting needle trajectory planned to cross the normal liver. This provides a protective cuff to minimize bleeding or tearing of tumor surface. A trajectory directly into the left lobe was avoided.

shown than if one holds such a device firmly rather than loosely with one hand, there is an improvement in sample size by about 14%.

Additional Caveat

When sampling an abnormality in the upper liver, there are several factors to consider in avoiding the pleura and the diaphragm. First, the normal diaphragm is much higher anteriorly than posteriorly; thus, a lateral approach is safer than a posterior one, and an anterior one is safer than a lateral one. As long as one does not see aerated lung, a pneumothorax will not occur during liver biopsy. Ample local anesthesia is critical to avoid undue patient discomfort and movement of the diaphragm, which might cause a complication during insertion of the needle.

One group has provided their experience with transdiaphragmatic biopsies. It is my opinion that although this may be true for small-caliber needles and reportedly is safe in their experience, the concept "flies in the face of common sense." Widespread application of this method will surely have a higher incidence of complications. If it is ever used, it surely would involve only small-caliber aspiration needles.

Factors Affecting Accuracy

One of the most important factors to consider when evaluating the outcome of various techniques is the extent of disease present at the time of the biopsy. The greater the number and the larger the lesions within the liver, the greater the probability of a positive biopsy. Conn et al[57] studied this with a series of blind biopsies performed on cadaver livers at autopsy. They graded the degree of involvement of the liver by the number of lesions and found the following recovery accuracy. Grade I, 1 to 3 lesions had a 16% success rate; Grade II, 4 to 25 lesions had a 27% success rate; Grade III, 25 to 50 lesions had a 45% success rate; and Grade IV, with over 50% involvement by weight had a 86% success rate. This finding is important to consider whenever a new method, technique, or type of needle is first being reported in the literature.

It is quite clear that historically, guided biopsy procedures are superior to blind or unguided biopsy procedures. One of the first articles in diagnostic aspiration by Lundquist[255] reported a high success rate in about 70% of cases using only manual palpation of the abdomen. In his series, the only cases sampled were those involving palpable nodules that would correspond to the Grade IV types of lesions as noted earlier.

Rasmussen et al[336] reported the first series on ultrasound biopsy using a 22-gauge needle with multiple passes. They recovered positive tissue in 70% of cases with ultrasound guidance, compared with an anticipated rate of 23% for blind biopsies (extrapolating Conn's[57] classification of his cases as described in the report). Subsequent reports showed similar results with success rates varying between 66% and 94%. Despite the advantages of the small needle, authors such as Ho noted the disadvantages of the aspiration types of biopsy:

> Based on our study and the literature, the information obtained by fine-needle aspiration on the general state of the liver is not as comprehensive as from a tissue sample taken by the Menghini technique.

These data clearly indicate that several simple and obvious factors affect the results: (1) the appropriate technique must be used with each needle (see the earlier sections on methods of biopsy for both aspiration and cutting needles) and (2) diagnostic yield depends on accurate localization of the instrument. Meticulous placement of the device is critical regardless of the guidance modality used. As technology evolves and devices change, operator preferences may change as well. The effect of needle size on diagnostic success has been well documented for aspiration needles in both in vitro and in vivo studies. Andriole et al[10] studied the yield in liver biopsy of various aspiration needles and found that in vitro there was a definite increase in the diagnostic material with the larger-caliber needles. In a series of liver biopsies Pagani et al[316,317] reported the results of using both 18-gauge and 22-gauge needles. They found a significant benefit 85% versus 98%, respectively, without any difference in the complication rate. In our own institution the diagnostic yield and complication rates of various aspiration needles have been determined and compared with cutting needles; these rates were reported by Martino et al[265] and Ha et al.[136] With a single pass with aspiration needles and providing samples for both slide smears and cell block material, the diagnostic yield for malignant disease with a 22-gauge needle was 60.9%, compared with the 20-gauge needle at 77.6%. It is important to note that Pagani's data were based on the performance of multiple passes, and that our data involved single passes, which explains their higher yields.

From these data and those of Ferrucci et al[88,89] it is clear that the more needle passes taken, the higher the diagnostic accuracy. In their series they selected 20 cases that were positive and looked at the diagnostic yield for each needle pass. The yield was 75% with one pass and 90% with two passes. (One can never expect 100% yield even with five passes.) In the same article, Ferrucci's overall yield was 82%. Even with blind biopsies the diagnostic yield increases appreciably with multiple passes. Grossman et al[130] noted an increase in the diagnostic yield from 41% to 54% with two passes and Conn and Yesner[57] noted that the yield increased from 47% to 58% with two passes.

All of the comparison articles concerning diagnostic yield from aspiration and cutting needles (single passes) have shown that cutting needles are superior to aspiration needles. The two comparison articles using a single pass were reported by our group. Martino et al[265] showed that the diagnostic yield of Menghini and Tru-Cut biopsy needles was 88.1%, compared with 60.9% for 22-gauge aspiration needles. Our more recent experience reported by Ha et al[136] showed the 14-gauge Tru-Cut needle to be superior to the 20-gauge aspiration needle, with yields of 90.2% as compared with 77.6%. A comparison article by Jacobsen et al[190] showed a slightly greater accuracy with a skinny needle; however, their comparison was flawed by the fact that they took three passes with the skinny needle and only one with the cutting needle.

For benign disease, all reporting authors have shown a clear advantage for the cutting types of needles relative to

determining specific disease processes. In our most recent experience reported by Ha et al,[136] the cutting needles provided a specific diagnosis in 88.5% compared to 39.4% for aspiration needles; nonspecific diagnosis was provided in 11.5% by the cutting and 48.8% for the aspiration needle.

The combination of slide smears and histology can provide an added increment of positivity for the results. Numerous authors, including ourselves, attest to the benefit of combining aspirate samples with cell block histology. In our most recent study, the addition of cell block histology increased our diagnostic yield from 54.8% to 77.4%. Other authors including Sherlock et al,[353] Grossman et al,[129,130] Carney et al,[46] and Atterbury et al[12] have noted that producing a cellular smear by "rolling" the sample on a slide adds some additional accuracy. These authors showed an increase in positivity of between 3% and 17% by performing this technique. The only plausible explanation for this result is that the needle passes through the tumor during its incursion but no tissue is "cut." The cells are located in the side of the tissue core and can therefore be "smeared" onto the slide.

The automated cutting needles have added a new dimension to procedures. Prior to their introduction, cutting needles were seldom used for biopsies. In a recent survey, more than 90% of radiologists performing liver biopsies use the automated devices. Strangely enough, Hopper et al[180] in the evaluation of numerous automated devices, noted that the gold standard device to which all devices should be compared and the one as yet unsurpassed is the 14-gauge manual Tru-Cut device.

The success of percutaneous liver biopsy by CT guidance depends on the various important factors noted earlier. In our experience, the success rate for malignancy and benign disease has varied according to the type of needle used and the abnormality being sought. The success rate for sampling all malignant disease with aspiration needles is 77.6% and for cutting needles, 90.2%. The success rate for benign disease is 39.4% with aspiration needles and 88.5% for cutting needles.

Complications

As experience with guided biopsy procedures has accumulated, the same types and spectrum of complications have occurred with guided biopsies as have occurred with unguided procedures. These include biliary peritonitis, tumor seeding,[311] hepatic infarction, pneumothorax, inadvertent puncture of bowel, abscess, and hemorrhage.[416]

In regard to complications, the logical differences between aspiration and cutting needles must be made clear. In view of the wide variety of devices used and reported, some general as well as specific comments should be made.

From our experience there is little question that there is a slight difference in complication rate between the cutting needles and the aspiration needles. It is also true with experience and refinement of techniques that there can be improvement in these rates. In reporting our various series, we have shown a decrease in the complication rate with minimal improvements as we have refined our techniques. In our second report in reference to aspiration needles, Martino et al[265] reported a complication rate of 0.83% for serious complications, and in our most recent study by Ha et al[136] we reported a complication rate of 0%. Relative to cutting needles, Martino et al[265] reported a complication rate of 1.44% and in our recent report by Ha et al,[136] the complication rate was 1.1%. In our most recent assessment of complications, the complication rate for cutting needles was 0.5% in 200 cases. Our experience indicates that complication rates can be quite low and acceptable for all needles if appropriate techniques are used.

The more obvious factors that affect complications include coagulation status, lesion characteristics, characteristics of the needle, and the number of needle passes[379,416] The presence of ascites is not a contraindication for biopsy of the liver. A review of our cases and several reports by other authors confirm this. Bernadino et al[27] and Little et al[243] showed that ascites had no impact on complications. Furthermore, from a common-sense perspective, one can understand this quite easily. If one assumes that local pressure on a biopsy site might tamponade bleeding, the presence of intraperitoneal fluid actually increases intra-abdominal pressure and surely would not have an adverse effect on hemostasis. If there is any relationship, it would be because the most common cause of ascites is cirrhosis, which can be associated with compromise of coagulation factors. Hence, if coagulation studies are normal, ascites should be irrelevant.

Coagulation Status

One obvious factor that affects complications is the coagulation status of the patient. For biopsy using either an aspiration or cutting type of needle, we prefer to have the platelet count greater than 50,000, the INR less than 1.2, and the prothrombin time less than 14 seconds. If either value is not within the desired range, corrective action should be taken as needed (either platelet transfusion or administration of fresh frozen plasma). (See the general section on coagulopathy under general preprocedural items for new method to correct coagulopathy.) Patients should also not be on any anticoagulating drugs such as aspirin or warfarin (see section on contraindications). Unusual problems such as hemophilia, Christmas disease, lupus, or renal failure must be addressed individually. If there is any question of an unusual coagulation status, a bleeding time should be measured. This is the most accurate method of determining bleeding status because it is an in vivo test that takes into account all factors including the coagulation factor cascade, capillary fragility, and platelet function. An abnormal bleeding test warrants a consultation with the hematologist to preclude any major problems.

Lesion Vascularity

The other factor that is seldom discussed and is actually quite important is the vascular nature of the abnormality being biopsied. We have encountered bleeding problems in patients with vascular lesions such as hemangiomas and metastatic renal carcinoma. Several others have reported serious problems with vascular bleeding. Bret et al[37,38] reported a small series of hepatomas biopsied using a 22-gauge needle for aspiration and some serious hemorrhagic complications. One of the patients required transfusion,

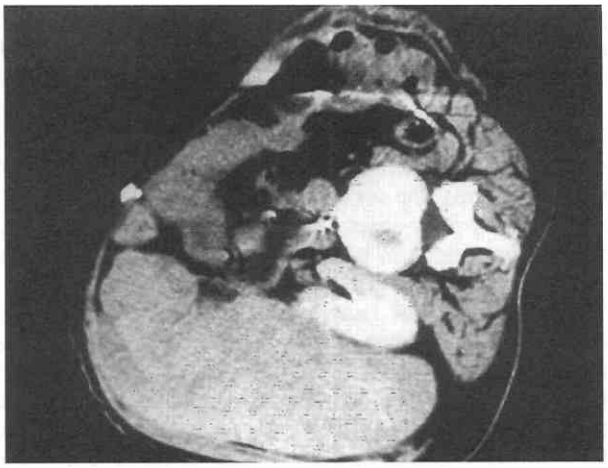

Figure 61–69. Significant hemorrhage can occur as a result of numerous factors. This scan shows a large hematoma outlining the capsule of the liver in the lower portion of the abdomen caused by a single pass of a 20-gauge Chiba needle (performed by the author). The patient has diffuse metastatic renal cell carcinoma to the liver that was very vascular.

two required corrective surgery, and one died. Considering the small caliber of the needle and the experience level of the authors, the only explanation for these problems is that hepatomas and other tumors that are inherently vascular are predisposed to bleeding (Fig. 61–69).

There is also a case report of a bleeding death from a 22-gauge needle biopsy of a cavernous hemangioma. The authors did not mention assessment of vascularity using a dynamic study, nor did they choose a trajectory through a small cuff of normal liver.

Smith et al[360] also reported that one cannot prevent complications by using a fine needle. From a mail survey they determined that in a series of 63,000 reported cases there were 27 cases of significant hemorrhage requiring transfusion, and 3 deaths.

Needle Traits

Regarding the needles used in cases of reported complications, several points must be made. First, as stated, there is a difference in the overall complication rate between cutting needles and aspiration needles. Second, there is no definite difference in the complication rates among the various caliber needles of the aspiration type. Pagani et al[316] reported no difference in the complication rate between 18-gauge and 22-gauge needles. In our two sequential series, our complication rates actually dropped when we switched from a 22-gauge to a 20-gauge needle. One cannot necessarily infer that the reduction in the rate was due to the needles; the reduced rate is most likely a result of experience and technique that naturally overcomes any minimal difference among the aspiration needles. In a laboratory study on animals by our group (see Table 61–2), there were only minimal differences among any of the needles less than 18 gauge, but there was significant difference between these and the larger-gauge needle.

Different Calibers of Cutting Needles

The key question recently answered is the relative risk of bleeding among the various Tru-Cut types of needles of different calibers. A recent laboratory study by Plecha et al compared the amount of diagnostic tissue obtained to amount of local bleeding with various calibers of Tru-Cut needles (Tables 61–5 and 61–6).[328a] They found that per unit of tissue, there was slightly more bleeding with the larger needle (14-gauge) as compared with the 20-gauge needle. The data further showed, however, that if one looks at the relative tissue yield (reflected by the quantity of DNA) compared to the blood loss, there is relatively no difference among the various caliber of needles (20, 18, and 14 gauge). In theory, if one was required to obtain a finite amount of tissue, the efficiency and risk of using a 14-gauge needle may well be theoretically less. As noted earlier, the amount of bleeding per unit of diagnostic tissue is no different among the needles. The second factor to recall is that significant bleeding is usually the result of inadvertently striking a small artery. This is essentially a random event so that if multiple passes with a small-caliber needle are required, there is a statistically greater chance of bleeding. It may be that three to four passes with a 20-gauge needle are less safe than one pass of a 14-gauge needle. That is, it has not been clinically determined whether multiple small-caliber Tru-Cut needles

Table 61–5. Blood Loss and Amount of DNA after Biopsy

A: Blood Loss

Needle Size	*No. of Samples*	*Unadjusted Blood Loss (g)**
14 gauge	64	1.69 (2.22)
18 gauge	63	0.74 (0.89)
20 gauge	63	0.32 (0.50)

B: Amount of DNA

Needle Size	*No. of Samples*	*Amount of DNA per Sample (μg)**
14 gauge	17	40.38 (10.29)
18 gauge	16	12.18 (3.84)
20 gauge	16	5.86 (1.58)

* Data are means. Numbers in parentheses are 1 SD.

Table 61–6. Statistical Results for Each Outcome Measure

Comparison	Blood Loss	Blood Loss with Amount of DNA per Sample	Blood Loss with Needle Chamber Volume	Blood Loss with Amount of DNA per Sample and with Needle Chamber Volume
14 vs. 18 gauge	.025*	.24	.14	.0002†
18 vs. 20 gauge	.059	.76	.42	.025*
14 vs. 20 gauge	<.001†	.47	.07	.0007†

Note: Data are P values. Blood loss was measured in grams. Amount of DNA per sample was measured in micrograms. Needle chamber volume was measured in cubic millimeters.

* Difference was statistically significant ($P < .05$).

† Difference was statistically significant ($P < .001$).

are safer to use than a single pass with a large needle. In our practice we have actually had a major complication with the use of a 20-gauge Tru-Cut, which resulted in a major hemorrhage and required a surgical procedure.

Needle Passes

Although multiple needle passes increase the diagnostic outcome, they introduce a higher incidence of complication with all needles, including small aspiration types. In our experience we limit our needle passes to two in virtually all cases. The expected yield should be about 75% to 85%. If the procedure is not a successful one, a repeat two-pass biopsy is warranted, after which one should choose either a cutting needle or a surgical procedure. The adverse effect of numerous needle passes was best documented in a survey by Smith.[360] We concur with his opinion that the number of needle passes even with a small needle should be limited to as few as possible. As is seen in reports in the literature, serious complications occurred in cases involving four or five needle passes, and none occurred in those involving two or less passes.

Coagulopathy

Patients with coagulopathy should have the appropriate treatment as indicated to improve coagulation. Patients with low platelet count should receive several units of platelets. Considering the time delays required with laboratory studies and the life expectancy of platelets, I manage the administration as follows. If I intend to give six units of platelets, I will send a blood sample for platelet count after the first two units; if the observed effect in the repeat count is what I anticipate as compared with the baseline value, I will then proceed with the procedure immediately following the fourth unit. The last two units are given after the biopsy. The same type of laboratory and administration schedule is used with fresh frozen plasma for an elevated prothrombin time. Patients requiring factor VIII are treated in a more routine fashion.

Patients with impaired platelet function on the basis of either medication such as aspirin or renal failure can be handled in the following manner. Although the effects of aspirin are long-lasting, I consider a passage of 7 days after the last aspirin an acceptable period after which the biopsy can be performed. For renal failure patients, one can administer DDAVP in appropriate doses to lessen the complication risk for biopsies.

If the coagulation state cannot be returned to normal, one should use special hemostatic techniques as described earlier under coagulopathy and later under high-risk procedures. These have been proved effective for the prevention of bleeding.

Special Pathologic Entities

Hemangiomas. Although cavernous hemangioma is said to be the most common hepatic tumor, it has received little attention until recently because it is benign and seldom causes spontaneous problems. Attention has focused on these benign masses in recent years because as imaging technology has become more refined, commonly detected lesions can be mistaken for more serious problems. Correct diagnosis is important to prevent unnecessary surgery and errors in cancer staging. If inappropriate imaging studies are performed or incorrectly interpreted, a patient may present for a biopsy procedure (see the chapter on liver diagnosis for details).

In most instances, hemangiomas typical on imaging will be correctly diagnosed but occasionally an atypical one will present for biopsy. Surprisingly, once the typical vascular hemangiomas are excluded there is little risk of a significant complication from the atypical variety. The reason for this is that the pathologic features that make their imaging appearance atypical also preclude the potential for bleeding complication. Stated differently, the increased vascularity of hemangiomas is what gives the typical appearance on such imaging modalities as CT enhancement, isotope pooling, etc. When the increased vascularity is not present because of thrombosis, fibrosis, or hyalinization, the lesion is unlikely to bleed with a biopsy.

Clinically the reported experience has supported this concept.[356] As we have noted in our previous editions, the only complication we have had with hemangiomas occurred before the development of bolus dynamic scanning. Since the appropriate use of contrast material, we have had no problems with hemangiomas. We have inadvertently biopsied numerous atypical hemangiomas with 14-gauge cutting needles under the assumption that they were lesions other than hemangiomas. Other authors including Spamer et al,[367] Cronan et al,[62] and Solbiatic et al,[362] have reported the safe biopsy of atypical hemangiomas. These authors have also noted the difficulty in diagnosing hemangiomas with small aspiration needles; they note also that hemangiomas can inconsistently be diagnosed with special-purpose needles and consistently diagnosed with the standard cutting needles.

Cirrhosis. The issues surrounding the biopsy of cirrhotic livers are only two, one concerning the possibility of complications and the other concerning intactness of tissue samples. The cirrhosis itself does not predispose to problems, but associated changes may. One must always be aware of possible prothrombin elevations and the pathologic changes of cirrhosis, which increases the hepatic concentration of small arteries and venous collaterals. We have experienced a case of life-threatening hemorrhage in such a patient, reported by Nachamoto et al.[299] If one chooses a needle to sample cirrhosis, the side-cutting Tru-Cut needle has been shown to be better than the Menghini type of needle in preventing fragmentation of a fibrotic, cirrhotic liver sample.

Fatty Metamorphosis. Since the introduction of CT scanning, it has become apparent that fatty change can be quite focal and can perfectly simulate a neoplastic lesion. Although many times the geographic appearance will betray its true identity, biopsy of such lesions is quite common. A cutting type of needle is superior to aspiration types for diagnosing this entity.

Cystic Abnormalities. With these abnormalities, one important point should be made. The fluid obtained from such lesions may not be diagnostic and one should always endeavor to sample the wall of such lesions. If one is using an aspiration needle, one should send two samples as

follows. The first sample of fluid should be aspirated and sent for cytology. A second cellular sample should be obtained from the opposite wall of the cyst by "reciprocating" the needle against the opposite wall.

Endocrine Tumors. Biopsy of nonfunctional[9] endocrine tumors is straightforward. When functional tumors are to be biopsied, one should be both cautious and prepared to treat any symptoms if a hormone release occurs. It is important to note that a death has been reported after biopsy of metastatic carcinoid in the liver.[32] Generally, biopsy of functional tumors is discouraged.

Echinococcus. Several series of percutaneous treatment of *Echinococcus* are reported in the literature. While it is true that anaphylaxis is not as likely as previously thought, percutaneous puncture for diagnosis is discouraged because the imaging appearance of daughter cysts is characteristic and a serum test can accurately confirm the diagnosis. The major concern in such patients is to prevent spillage of daughter cysts into the peritoneum or other spaces. If therapy is considered, special precautions should be taken; those are discussed under the therapeutic section.

Hepatoma. Primary tumors warrant a separate discussion because they have some unique traits from several perspectives.[376] Clinically, the specific nature can usually be suspected by an elevation of the serum alpha-fetoprotein level. Differentiation from other entities may be difficult from an imaging perspective; recent data, however, suggests that MRI can differentiate between regenerating nodules and hepatomas. Hepatomas tend to have a higher T2 intensity than do regenerating nodules. If such a lesion were only visible on MRI, it would be appropriate to perform an MRI-guided procedure.

Biopsy of hepatomas has variable results, depending on the technique used. Successful diagnosis may be difficult with small needles because differentiating normal hepatocytes from well-differentiated tumors can be difficult with small aspiration samples. This problem can be overcome by taking numerous aspiration samples or by using a larger needle. The trade-off is in the form of a potentially higher complication rate. It is well-documented that hepatomas have an increased vascularity and therefore predispose to a higher complication rate. Wittenberg et al[406] reported a significant bleed requiring a two-unit transfusion after skinny-needle aspiration of a hepatoma. More recently Bret et al[38] reported successful diagnosis in 63 of 69 hepatomas with a 22-gauge needle and multiple passes, but numerous complications resulted. In their series they had four major complications in the 69 patients; these consisted of one death and three hemorrhages, two treated by surgery and one by transfusion alone.

Complications reported by other authors have included the full gamut of problems, including infarction, infection, and tumor seeding within the needle tract. With the ubiquitous use of procedures numerous cases of tumor implants have occurred with hepatomas. This can be avoided by use of a coaxial method. The outer cannula prevented implantation of cells.

Pancreas

Percutaneous procedures of the pancreas have become widely accepted as the method of choice for the diagnosis of various pancreatic problems. In major medical institutions it is routine practice for a percutaneous aspiration procedure to be used in lieu of exploratory laparotomy for diagnosis and treatment of tumors and inflammatory processes.*

Tumor Indications

The indications for using percutaneous procedures for pancreas are quite broad and relate to diagnosis of tumors, pseudocysts, or infectious processes. Relative to the diagnosis of tumors, I believe the threshold for biopsying any mass is quite low because of both the high success rate and the low incidence of significant complications. Any suspected solid tumors of the pancreas should be biopsied very early in the course of patient treatment for two reasons. For those patients with large inoperable tumors, a biopsy should be performed at the earliest time to make the definitive diagnosis and to eliminate the need for more expensive or complicated procedure such as surgery or endoscopic procedures. For subtle cases, this offers the best opportunity for early diagnosis and surgical treatment.

Indications for Cystic Tumors

The indications for sampling cystic tumors are somewhat different than other problems. With these tumors there are really two objectives. The first one is to differentiate cystic tumors from pseudocysts of the pancreas. By imaging alone, it is virtually impossible to distinguish between a pseudocyst and a cystic tumor. In such cases the goal is to aspirate fluid from a fluid-density mass so that an assay of amylase can be performed to diagnose a pseudocyst; very high levels are indicative of a pseudocyst. When the amylase content is low, one cannot distinguish between a cystic tumor and a "burned-out" pseudocyst. Such cases typically go to surgery for definitive treatment. The other purpose of aspirating such tumors is to distinguish among mucinous, mucinous cystadenocarcinoma, and serous cystadenomas. My personal experience with these is limited, so I must depend on the literature. The outcome with these lesions is not completely clear, as discussed later under pathologic results and accuracy.

Other Indications

In cases of severe inflammatory processes, CT-guided aspirations are indicated to obtain fluid for diagnosis of infected processes. The presence of infection is a critical determinant for overall outcome of severe pancreatitis, as noted in the pancreas chapter.

If one is careful, meticulous, and judicious in technique, one can even justify aspiration of unusual fusion anomalies of the gland if there is any question of tumor.

Contraindications

There are only a limited number of contraindications that are primarily related to the presence of vascularity

*References 25, 70, 73, 119, 144, 164, 175, 257.

and anatomic approach. In some rare circumstances, the vascularity of tumors will be so great or collateral vessels so numerous that no type of aspiration or biopsy procedure should be performed. The presence of a large pseudoaneurysm should also be a contraindication for a procedure (Fig. 61–70).

A relative contraindication is the presence of a large number of varices. When pancreatic tumor obstructs the splenic vein, many venous collaterals will be created. When there are a large number, one must decide if a clear anatomic pathway exists or not and thereby proceed or defer the procedure.

If patients are immunocompromised, fluid-density masses should not be aspirated while traversing bowel; if no pathway is available, such procedures should be avoided.

Needle Selection and Technique

Sampling of the pancreas can be performed by either aspiration or cutting needles. In most cases, a 20-gauge aspiration needle is appropriate to obtain a cytologic specimen. The diagnostic yield is typically quite good and there is a low incidence.

In certain circumstances one can perform biopsy of the pancreas with a cutting needle as large as 18 gauge. The key to success with these devices is to carefully target the pathologic areas of the gland so that when a biopsy is taken, there is minimal trauma to the functioning glandular tissue. Elvin et al[52] reported a series of 47 patients in which cutting needles were successful. Cutting needles have also been used successfully for biopsy also of pancreatic transplants by Aideyan et al[4] with few complications.

Complications occur when an uninvolved structure such as a vessel, pseudoaneurysm, or functioning glandular tissue is damaged (see later section). Such complications have been reported with both small-caliber aspiration and cutting needles.

General Technique and Anatomic Approach

The choice of imaging technique for diagnosing and localizing pancreatic masses is important. A good contrast-enhanced study is critical for several reasons in planning a biopsy procedure. The success of the biopsy depends on accurate localization of the tumor and display of the vascularity of the area. If a tumor is avascular, then the margins of the tumor can be defined more clearly and accurately targeted for the aspiration needle. Although one group has noted that many pancreatic tumors are diffuse, it has been our experience that well-defined margins can usually be found if careful technique is used.

If the pancreatic tumor is an unusual one with increased vascularity, the enhanced vascularity can be noted and advisability of the procedure can be reconsidered or the planning simplified. Hypervascular tumors include nonfunctioning islet cell tumors, islet cell tumors, and certain metastatic lesions such as renal cell carcinoma (see Fig. 61–69).

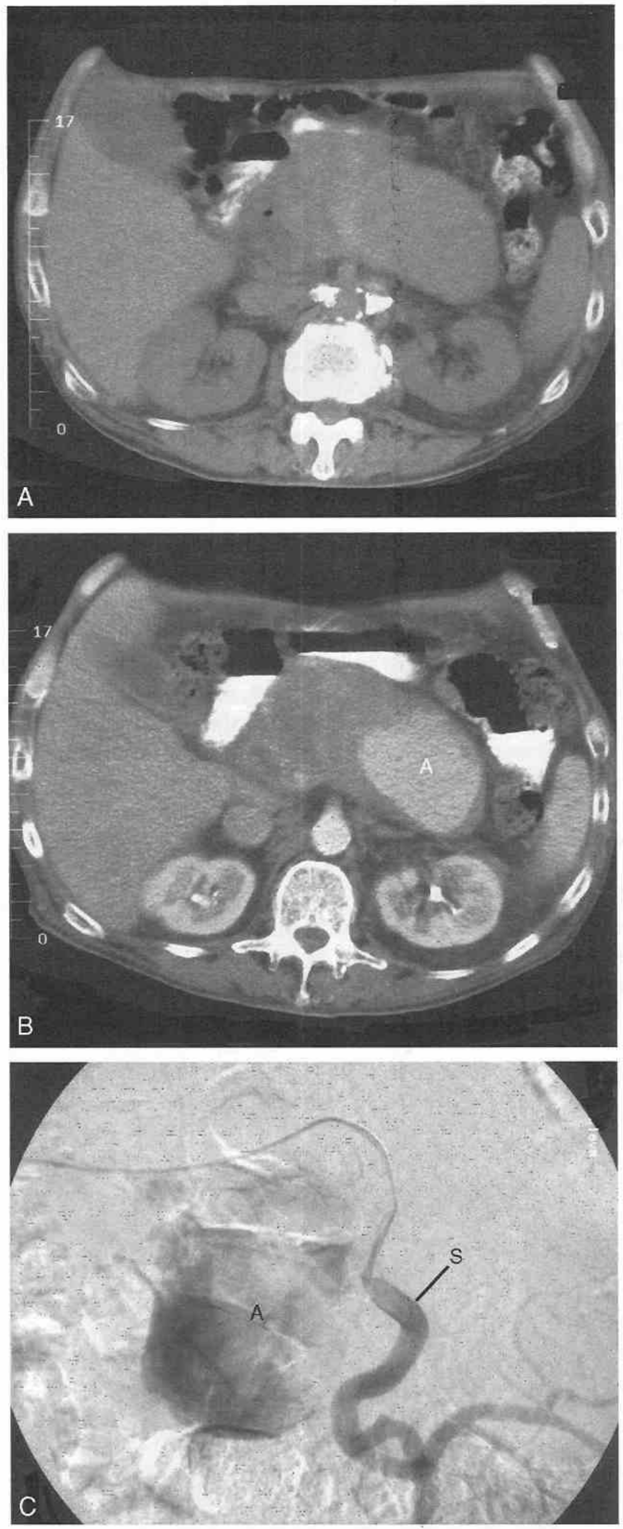

Figure 61–70. These images (*A* to *C*) demonstrate the importance of performing a dynamic bolus injection study for every pancreas biopsy. *A*, This image shows what appears to be a large mass in the body of the pancreas with no indication of any prior history. Biopsy was planned. There was a prior history of contrast allergy, so no contrast study was available. *B*, At the time the patient was on the table, a bolus injection was performed. Note the very large enhancing pseudoaneurysm (A). *C*, Angiogram was performed in the course of embolizing the aneurysm (A). Note the origin is from the splenic artery (S).

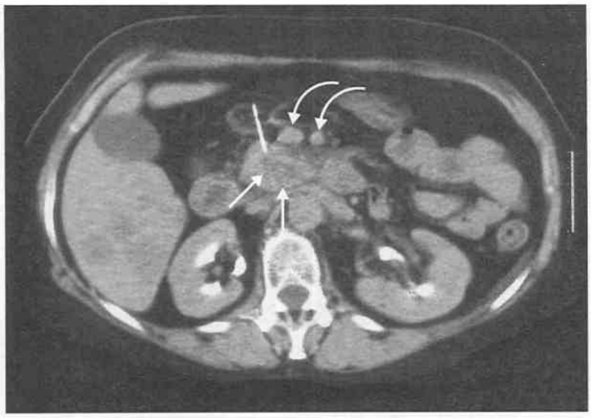

Figure 61–71. Biopsy of the pancreas performed from an anterior approach. The needle is positioned in the low-density area (*arrows*) of the tumor. Note the trajectory was planned to avoid the superior mesenteric vein and smaller veins, *(curved arrows).*

The proper vascular enhancement can also demonstrate any collateral vessel formation or vascular abnormalities that can produce a multitude of small and large venous and arterial collaterals, all of which should be avoided. The most common entities creating confusion include pseudoaneurysms, varices, and cavernous transformation of the portal vein (see pancreas chapter).

When planning the trajectory, I choose the target in the pancreas that is well-defined but does not appear necrotic. If the anatomy is optimal and one's experience is extensive, all structures should be avoided, except the fat of the mesentery and the pancreas. If anatomy is less than optimal or one is less experienced with angled procedures, then penetration of certain structures can be tolerated (Figs. 61–71 to 61–73).

If one considers penetrating a loop of colon, possible adverse outcomes should be considered, and careful judgment should be exercised. It is my judgment that penetration of colon should be avoided in all cases because it contains many pathogenic organisms. Avoiding loops of bowel is a good thing to do if at all possible because although it is commonly done, there is always a finite probability of leakage. We at least make an attempt to plan a pathway that avoids such loops using several techniques. First, one plans the trajectory accordingly, and then can use several maneuvers to accomplish this (Fig. 61–74).

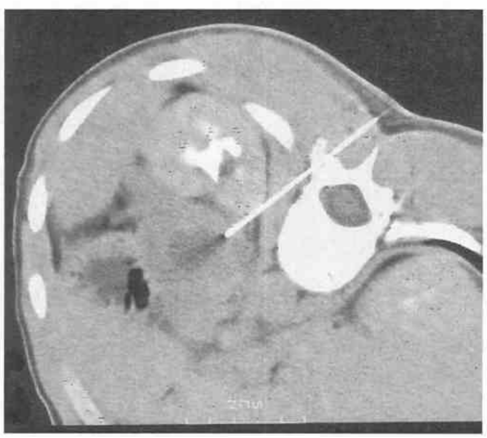

Figure 61–72. Posterior approach for biopsy of low-density tumor of pancreas. The mass proved to be a neuroendocrine tumor, with no clinical function noted. Posterior approaches are satisfactory, but one must be careful to avoid pertinent structures and vessels; penetration of vessels is not advisable because long-term complications are likely to occur. The small series reported are not valid in recommending a transvascular approach routinely.

Certain anatomic structures I absolutely avoid, but others I will accept the possibility of traversing during an aspiration procedure. I definitely prefer to avoid traversing any major artery or vein, as well as the spleen, to preclude the risk of bleeding. I accept penetration of the stomach or liver if it is absolutely necessary, in the belief that the risk is minimal (Fig. 61–75).

Small bowel can be penetrated safely if a necrotic tumor or cyst is present and the tumor mass is not cystic. I think avoidance is important for two reasons. In our studies we have confirmed that a small inoculum of bacteria can be carried from the bowel by a skinny needle. If that inoculum is carried into a solid tumor or structure, there is little possibility for bacterial growth. If it is carried into a fluid collection, however, the body's immune system has difficulty in eliminating the inoculum. The fluid space acts as a culture medium in which, at the time of contamination, the phagocytes' and antibodies' functions are impaired (Fig. 61–76).

In the immunocompromised patient, the avoidance of all bowel is important because with the severe compromise produced by chemotherapy, transplant treatment, or chronic conditions, even the smallest inoculum of virulent pathogens can create a serious problem. The nature of the bacterial contents can vary in disease states, especially those associated with abnormal or altered peristalsis. The amount and type of various bacteria depend partially on the enteric peristalsis. As an obstruction occurs, there can be ascent of the colon flora retrograde into the small bowel and stomach so that the flora in those viscera may include many gram-negative species. Although some authors have implied or stated that concerns about secondary infections are excessive, there are several reports of serious complications from such infections.

Another precaution to be taken is avoiding possible penetration of a dilated bile or pancreatic duct. Damage to these structures could result in leakage, peritonitis, or fistula formation.

Although it is true that one could probably penetrate any and all structures routinely and not have a problem for a long time, most likely the statistical probabilities will catch up with the interventionists if too many cases are performed with disregard for potential problems. One must remember the numerous case reports of complications and deaths following percutaneous pancreatic instrumentation.

Recently an approach has been proposed for pancreatic tumors that I consider inappropriate until further data are accumulated. Gupta et al[135] reported a small series of patients in which they intentionally traversed the vena cava from a posterior approach. I fully support making a posterior approach in some patients when no other clear access is available, but I think it is appropriate to try to avoid major vessels such as the aorta or vena cava. If during those attempts one inadvertently traverses either of those

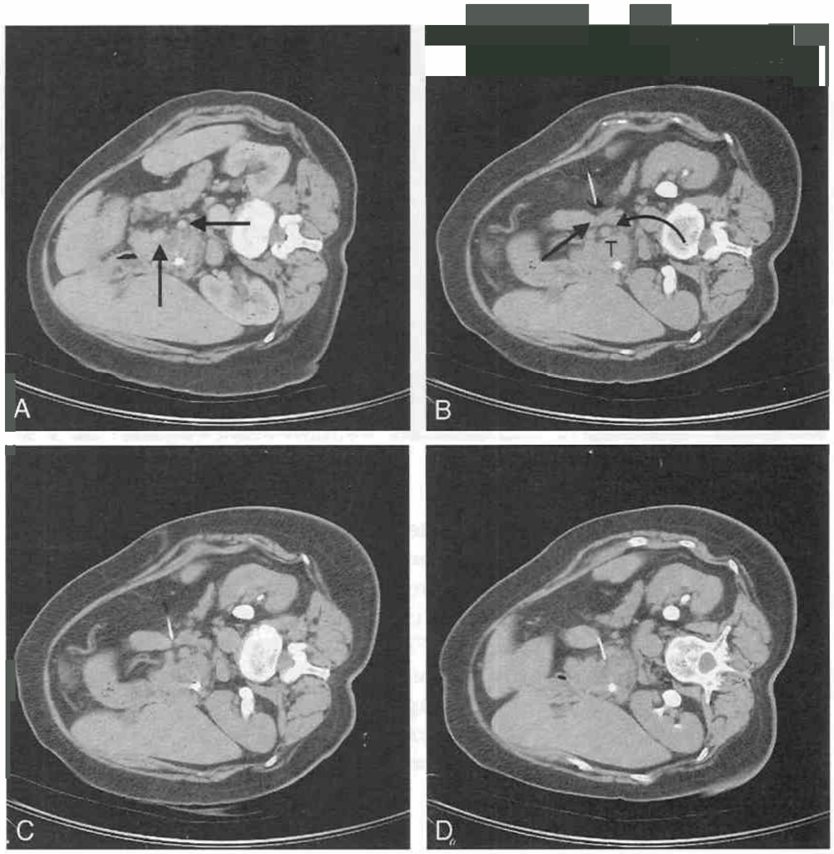

Figure 61–73. *A,* Dynamic bolus scan shows a low-density mass in the pancreas. The superior mesenteric artery *(horizontal arrow)* and superior mesenteric vein *(vertical arrow)* are noted. The patient was positioned in the lateral position to move the "bowel" out of the way. *B,* Initial approach shows a loop of small bowel *(arrow)* intervening in the pathway; also, the direction is such that the needle might strike the superior mesenteric artery *(arrow).* Tumor (T) is noted. *C,* Readjustment of the needle is made so the needle is directed toward the mass and partially compressing loop of small bowel. By turning the needle so the bowel is caudad toward the bowel and pushing slowly, the needle can be pushed by. Small bowel will typically push aside by peristalsis. *D,* Final image shows placement of the needle in the pancreatic mass.

vessels, then it is comforting to know that a bad result is unlikely. There is no question that if this method is adopted, more complications will result.

New Methods for Cutting Needles

Since the last edition, the usage of cutting needles has grown remarkably. With the increased usage, refinement of techniques, and improvement of imaging equipment, these needles have now become used commonly even in the pancreas.

To effectively and safely use these needles, several basic tenets must be followed. Every case should have a high-quality vascular study with CT bolus. In many cases, a good vascular study will have been performed during the routine diagnostic examination. In such cases one can quite

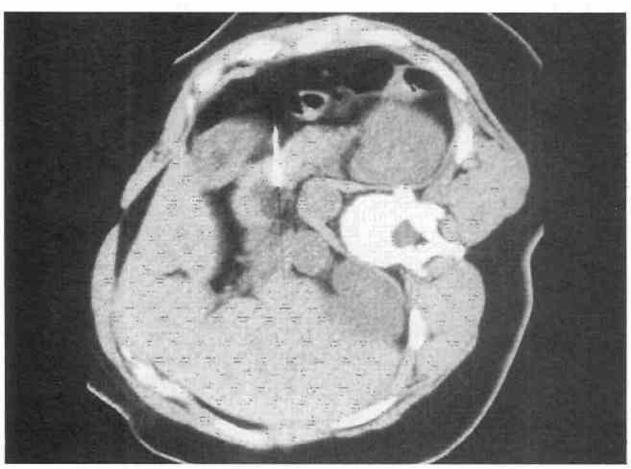

Figure 61–74. Guided aspirations of pancreatic pseudocysts are critical to the differentiation from cystic tumors. This scan shows aspiration of a small cystic mass adjacent to but behind the pancreas. Because of the high amylase content, the concern about a cystic tumor was eliminated.

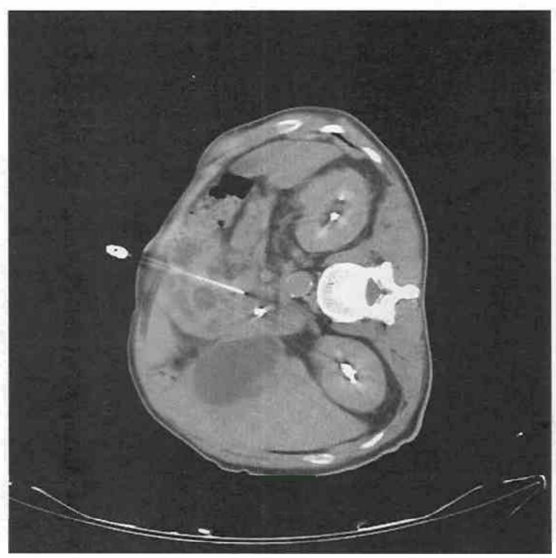

Figure 61–75. A large mass *(arrows)* in the body of the pancreas extends into the submucosa of the stomach. A transgastric approach was used to sample the mass.

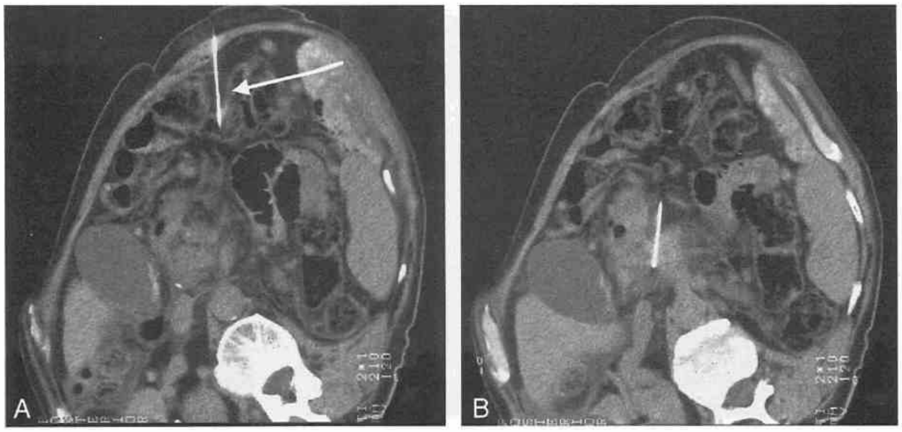

Figure 61–76. Avoidance of colon is very important if at all possible, because of high bacterial count in colon. *A,* The approach used was to insert the needle from a lower origin, to traverse below the transverse colon. At this level, the needle is pushing by the lower edge of the colon and is directed cephalad. *B,* Slightly higher scan shows the needle entering the pancreatic mass. Such attempts are worthwhile, and occasionally one may penetrate the bowel. At least over a long experience, the probability of a complication is less likely the fewer penetrations are made.

clearly see the normal vessels, collateral vessels, and any tumor vascularity. Avoidance of these vascular structures is absolutely critical to prevent bleeding. Furthermore, clear delineation of the target structure is critical to careful positioning of the gap into the mass (Fig. 61–77). One must avoid cutting a hole in normal-functioning parenchyma and also any ductal structures. Damaging the normal parenchyma may result in severe pancreatitis. Damaging the ductal system may result in bile peritonitis or pancreatic ascites.

Implications for Surgery

In recent years, our surgical colleagues have become more aggressive in approaching the resection of pancreatic cancer, because new imaging methods can better define anatomy and screen patients for surgery. Several recurring questions are raised that can be answered by reviewing certain reports. First, the accuracy of percutaneous image-guided procedures was shown by Savarino et al[350] to be equivalent to those biopsies performed during laparotomy.

Another common question raised is whether or not percutaneous biopsy "seeds" the peritoneum and thereby affects the ultimate outcome. Johnson et al[196] confirmed two important principles. These authors studied the presence of tumor cells in the peritoneum at the time of laparotomy in two groups of patients. They found viable tumor cells in both groups, biopsied and nonbiopsied, with no statistical difference between the two groups. Second, they found the ultimate survival was no different between the groups. Balen et al[15] also confirmed that biopsy produced no adverse effect on the survival of patients.

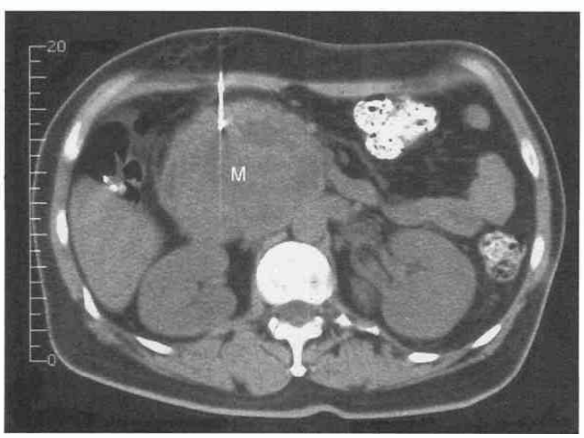

Figure 61–77. A large mass (M) in the pancreas was believed to be lymphoma. A cutting needle sample revealed lymphoma.

Accuracy of Various Tumor Diagnoses

Many articles have now appeared about the accuracy for diagnosing pancreatic tumors. It is generally accepted that the larger the needles, the better the accuracy. In our series by Dickey et al[48] we showed the benefit of using 20-gauge rather than 22-gauge aspiration needles for diagnosing typical adenocarcinoma.

With aspiration biopsies virtually every tumor type has been successfully diagnosed using modern cytopathologic methods. Iselin et al[187] reported a small series in which cytology was able to distinguish mucinous and serous tumors. Gupta and al Ansare[133] reported success in diagnosing four cases of mucinous cystadenoma of the pancreas. Acinar tumors diagnosed by aspiration were reported by Samuel and Frierson.[345] Papillary tumor was diagnosed by Suarez et al[373] and Mandrekar et al.[261] Islet cell tumors can be diagnosed by cytology according to Collins and Cramer.[56] As noted later under specific entities, I am still of the opinion that one should not biopsy functioning tumors because an endocrine release and possible hormonal crisis may result.

Complications

Although most authors infer that percutaneous pancreatic biopsy is without risk, a number of mild complications and a number of serious complications have been reported. The mild complications reported by Smith,[360] Goldman,[118] and McLoughlin[271] included transient rectal or colonic bleeding, probably because of trauma to the transverse colon. Ohto[309] reported one case of transient hematemesis following a biopsy. Other mild complications also included four cases of mild pancreatitis that resolved; these were reported by Evans and McLoughlin.[271]

The serious complications related to tumor sampling (pseudocysts are reported later) have included hemorrhage, fatal pancreatitis,[82,296] sepsis, cholangitis, fistula, and needle-tract seeding. Fataar[85, 86] reported two cases of hemorrhage, one that required cardiopulmonary resuscitation and two units of blood, and one that resulted in a 6.5-cm hematoma in the mesocolon. Evans et al[82] and Levin et al[238] have reported cases of fatal pancreatitis following ultrasonic biopsies. Phillips et al[328] reported one case of cholangitis and pancreatic fistula, as well as severe vasovagal reaction. Ferrucci et al[89] had a case of cystadenoma of the pancreas that resulted in generalized sepsis. Two authors, Rashleigh-Belcher[335] and Ferrucci,[88] reported separate cases of needle-tract seeding from pancreatic carcinoma.

Based on our experience and a review of the literature, it is my belief that risks are directly related to inaccurate targeting and the number of passes made with the needle. This premise has also been recently stated by Smith[358,360] (see earlier general section on complications).

With our conservative method and techniques, such as trajectory, number of passes, etc. that minimize all possible risk factors, pancreatic biopsy is safe and effective. As a routine, the risks are minimal enough that percutaneous pancreatic biopsy is considered an outpatient procedure. In our reported experience with 96 biopsies, including patients with 40 neoplasms and other abnormalities,[73] we had only one patient who had a transient elevation of the amylase (without clinical pancreatitis). Since that time we have encountered one patient who developed an acute abdomen following aspiration of a pancreatic abscess; as a result, surgical exploration was required.

Other Important Points

When the results are cytologically positive for malignancy, the disposition is obvious. If the cytologic results are negative, I place importance on the texture of the gland felt during the needle aspiration. If the gland is "hard" or the mass is large, surgical biopsy is indicated. If the gland is "soft" during aspiration of a subtle mass, no further investigation is needed. Surprisingly, many times normal acinar cells can be recovered in such cases. One may consider performing a small-caliber cutting needle with a 20-gauge needle if clinical circumstances dictate this as a preference over surgical exploration.

It is our belief that biopsy of a functioning endocrine tumor should not be performed. The definition of "functioning" is made on clinical information about these patients that includes specific symptoms associated with the released hormone (see Chapter 29). One author reported the successful but uneventful biopsy of a pancreatic insulinoma.[191] Experience with a single case, however, should not be accepted as establishing the principle of safety; further experience is required before endocrine tumor biopsy can be generally recommended.

Specific Entities

Adenocarcinoma is the most common entity biopsied. There is nothing unique about this tumor beyond what has been discussed earlier. Meticulous evaluation, trajectory planning, and good aspiration technique should be used as described earlier.

Acinar cell carcinoma is a rare tumor, so it is doubtful there will ever be accumulation of any significant number of cases. As predicted in our last edition, it has now been demonstrated that diagnosis can be made by aspiration biopsy; several cases were reported by Samuel and Frierson.[345]

Cystic Tumors

As noted in the pancreas chapter, cystic tumors of the pancreas are unusual entities that include both a benign and a premalignant variety. Differentiation of these tumors by imaging is not possible; it would therefore be convenient if one could differentiate the two by needle aspiration. Because one of the tumors is reported to produce glycogen and the other does not, it would also seem convenient if one could stain for this material. Practically speaking, it has not been possible to accomplish this in our laboratory. Authors who have reported have appropriately noted that there may be considerable sampling error and that the recovery of benign cells from one component may not exclude malignancy in another region. Several authors (Iselin et al[187] and Gupta and al Ansare[133]) report success in differentiating the mucinous/serous cystic tumors as well as diagnosing cystadenocarcinoma. Most authors agree that it is not the results of the aspiration but rather the demographics of the patient that provides the best predictors of outcome and the need for surgery.[100,199,392]

Endocrine Tumors

The biopsy of endocrine tumors that are nonfunctional (and thus are obscure as to their nature) is appropriate, but biopsy of a functional lesion is not. Although there is a case report of a biopsy of a pancreatic insulinoma,[330] I believe the biopsy is inappropriate because of the possibility of a hormonal release. Because some endocrine tumors do not secrete active hormone, this stipulation applies to only functioning tumors. Nonfunctioning endocrine tumors ocassionally are diagnosed by cytologic sampling, after it has been performed under the presumptive diagnosed as a routine neoplasm.

Pseudocyst Aspiration

Aspiration of pseudocyst fluid or inflammatory fluid is important for the exclusion of cystic tumors (as noted earlier) or the diagnosis of an abscess. Laboratory analysis of fluid from a pseudocyst will show a high amylase content, while that of a cystic tumor will not (see Fig. 61–74). Aspiration of any suspicious fluid collection in patients with pancreatitis should be performed to exclude pyogenic infection. When such procedures are being performed, one should be sure bowel loops are not being traversed to exclude the possibility of contaminating a fluid collection or recovering spurious culture results. Good evidence for this cautionary approach was provided by Smith who collected 16 cases of generalized sepsis from a physician survey.[360]

Cavernous Transformation of Portal Vein

Interestingly, in some cases cavernous transformation of the portal vein may produce a mass that will be recommended for a biopsy. In most cases when the vascular channels are large, the portal cavernomas can be recognized with a bolus dynamic scan. If a cavernous transformation of the portal vein does not have large vascular channels or rapid flow, such masses may not enhance with a bolus dynamic scan. In such cases, if a biopsy is inadvertently performed in a patient, a complication is most unlikely because the vascular channels are very small. Unaware of their pathologic identity, I have biopsied three such cases without difficulty.

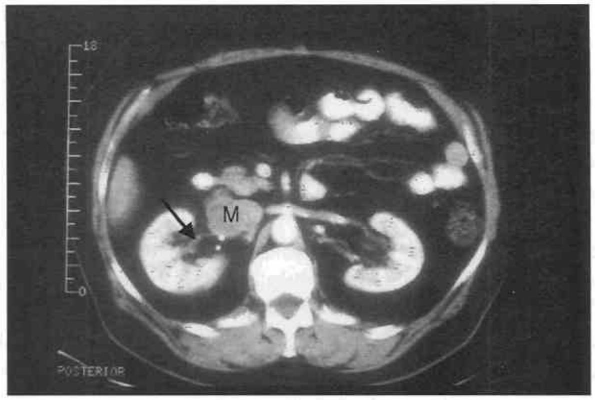

Figure 61–79. For all retroperitoneal biopsies, it is prudent to perform a dynamic bolus scan. This scan shows a mass in the hilum *(arrow)* of the right kidney; note the numerous small vessels around the mass (M). A small-needle aspiration biopsy might be possible, but in cases such as this when lymphoma is more likely, such samples are not helpful. Even though the risk of a problem is small, the probability of success is very low.

Retroperitoneum

CT procedures in the retroperitoneum prove valuable because even though ultrasound and fluoroscopy have been used in the past, CT provides the best visualization of pathosis and instruments in this area. Only CT can visualize precise location of tumors in relationship to the aorta and vena cava.[76,121,218,322]

Indications

The indication for procedures within the retroperitoneum are similar to those for other areas, it is usually the presence of a mass in a patient suspected of having some type of a malignancy or an inflammatory process.

Instruments

As in the other organ systems, we use our general guidelines for the selection of instruments. For a mass in a patient with suspected metastatic malignancy, I use a 20-gauge aspiration needle for a cytologic sample (Figs. 61–78 and 61–79). For unknown or undiagnosed tumors or for lymphomas we use the side-cutting Tru-Cut needle (Fig. 61–80) or automated Tru-Cut.

In most instances the Tru-Cut needle is the needle of choice because it provides the largest well-preserved sample. Also, this instrument is the most carefully controlled because the cutting gap can be well seen on the CT scan and the cutting action occurs only at the gap. There is no possibility of "overshoot" during the procedure such as may occur with the end-cutting Menghini type of needle.

Even the beginning interventionist can biopsy fairly large masses in the retroperitoneum with this needle. With experience, even very small lymph nodes immediately adjacent to the major vessels can be sampled if the proper technique and attention to detail are observed.

Anatomic Approach

The approach used is typically posterior, adjusted according to the location of the kidney, major vessels, colon, small bowel, and psoas muscle.

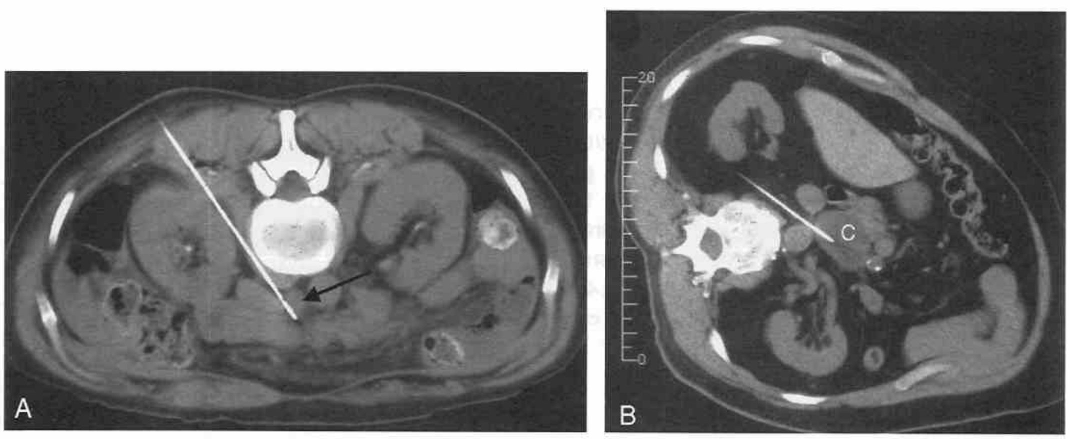

Figure 61–78. *A,* Scan shows a small mass *(arrow)* between the vena cava and aorta. After a bolus injection, the needle was inserted between the vessels for cytologic sampling. *B,* The accuracy of needle placement is so precise, one can even "thread" a needle between the vessels and sample structures (C) slightly anterior. When passing needles by such vessels, it is always important to have the bevel directed toward the vessel.

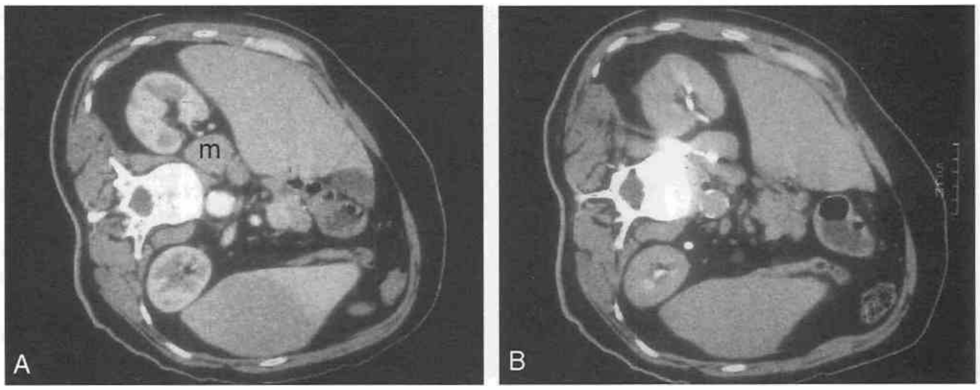

Figure 61–80. *A,* A patient with a mass (M) adjacent to the kidney. This is more posterior than noted in the prior case (Fig. 61–79), and the vessels are located anteriorly. *B,* Cutting needle biopsy provided definitive information for lymphoma.

The posterior approach for such procedures is obviously easier with the patient lying in a lateral, anterior oblique, or prone position. If an aspiration needle is used, an anterior or posterior approach can be taken, but if a cutting needle is used, a posterior approach is necessary.

Most lesions are in the periaortic region, and in such cases the anatomy should be carefully examined and the aorta and vena cava traced through the entire expanse of the abdomen. As with the other areas, the bolus injection is important to define the location of vessels and the presence of any tumor vascularity (see Figs. 61–79 to 61–81). Carefully note other vessels such as the renal pedicle, the splenic vein, the left gonadal vein, and the inferior mesenteric vein (which runs in the left periaortic area). Also, note the location of the ureters on both sides after the administration of intravenous contrast material.

If the vena cava cannot be identified, perform an injection of the foot vein to get better opacification. If the gonadal, inferior mesenteric vein or the ureter is not seen because of the surrounding tumor, do not search for them. In such cases they are so encased and infiltrated with tumor that they are nonfunctional. In over 25 years I have never penetrated or cut any of these structures inadvertently when they were not seen.

Several specific areas warrant special mention. The areas that are difficult to biopsy safely are the retropancreatic region and the area of the aortic bifurcations. In these areas there are multiple vessels branching and converging that make exact delineation difficult. In these areas I usually perform only an aspiration biopsy to avoid the possibility of injuring one of the vessels.

Although the approaches noted here seem rather risky to the neophyte, it is quite clear that the average radiologist can develop sufficient skill with experience. Although I do not recommend several articles that report the safety of penetrating the aorta or vena cava during the course of a pancreatic procedure, one can appreciate that surely an inadvertent penetration while attempting these procedures is probably a low-risk situation. Again, I do not recommend traversing vessels, but one should surely develop the techniques to pass by such structures, knowing that a penetration would probably not be catastrophic.

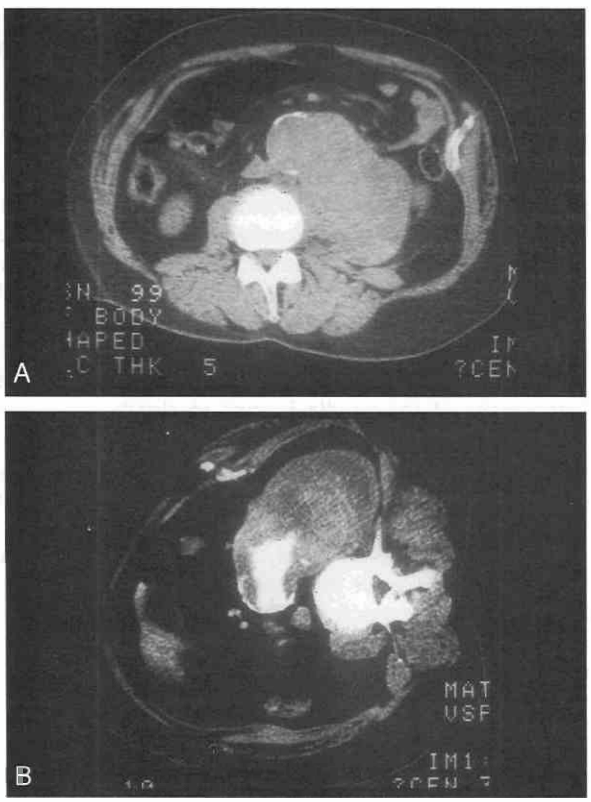

Figure 61–81. *A,* Potential biopsy showed a large mass in the retroperitoneum on the left of the aorta. *B,* Scan with the patient on the right side was performed with bolus. The mass proved to be a large hematoma in a contained rupture of the aorta. No biopsy was done.

Results

The biopsy of lymphoma was previously controversial but is no longer. Using a 14-gauge cutting needle, one can diagnose not only specific lymphomas successfully but unusual entities such as atypical *Mycobacterium,* retroperitoneal fibrosis (Fig. 61–82), and even sarcoidosis. If clinically indicated, one can get ample tissue for electron microscopy, gene studies, or chemical assays. Quinn et al[334] reported a series of 43 cases in which cutting needles correctly diagnosed lymphoma in 84%. The authors recommended that image-guided biopsy be performed as a first procedure in all cases of suspected lymphoma.

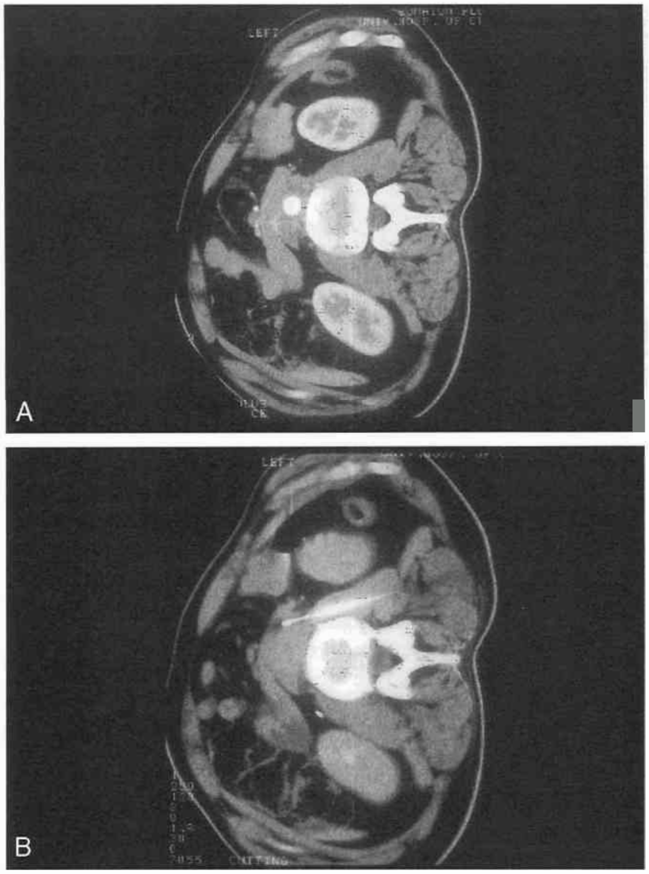

Figure 61–82. *A,* Scan shows a poorly defined mass around the aorta, enhanced by contrast medium. *B,* Scan during the biopsy shows a mass adjacent to the aorta, which proved to be retroperitoneal fibrosis. Tissue samples with a 14-gauge needle are ample enough to diagnose unusual processes.

Complications

Only limited data are available on the retroperitoneum.[420,421] In our preliminary study comparing large and small needles, only one complication occurred.[218] A small asymptomatic hematoma appeared on the CT scan during the small-needle aspiration before the large-needle biopsy. The diagnostic accuracy was high for both metastatic disease and lymphoma. Bernardino et al[27] have also reported a good success rate for diagnosing lymphoma.

Kidney

Two types of CT biopsies are performed on the kidney, one for evaluation of masses and another for the sampling of diffuse parenchymal disease. In many instances CT is the second-choice modality if the problem is well seen by other methods. If the lesion is best seen by CT, then CT is the modality of choice.

Indications

With renal masses virtually all authors agree that there is no indication for biopsy of a simple renal cyst that is unequivocal on either CT or ultrasound. The basic indication is the presence as an indeterminant mass in which distinction between a benign and malignant mass is important. In most cases only an aspiration needle is indicated. In some cases when the cytologic sample does not provide adequate histologic data (assuming the bolus dynamic scan shows the mass to be avascular), a cutting needle should be used.

In most such patients the approach is directly posterior, with the trajectory chosen to avoid the erector spinae muscle if possible (this muscle can be painful and it can deflect or bend the needle). As in other areas it is important to anesthetize the renal capsule locally.

Cystic Masses

Several points should be made about aspiration of the renal cyst. Following aspiration of fluid, either diluted urographic contrast material or air may be injected (Fig. 61–83) to define the thickness of the wall. When there is a central mass or wall thickening within a cystic mass, try to sample the irregular wall or solid portion of the mass. In such cases the fluid may be cytologically negative, yet a sample from the mass may be positive.

Solid Masses

Sampling of the solid renal mass is similar to that of masses in other organs. A bolus dynamic scan must be performed to assess vascularity. In most cases if the mass has a slight increased vascularity, aspiration is quite safe (Fig. 61–84). An avascular mass can be biopsied with a large cutting needle if clinically indicated and a specific tissue type is

Other Tips

Several technical points may be helpful. First, when approaching a small mass, perform the procedure in two steps. The first step is to carefully position the needle immediately adjacent to the area being sampled. Several initial approaches may be needed in this way because the kidney is mobile, and with variable respirations a small mass may move in and out of the slice. After the needle has been confirmed adjacent to the mass, "pop" the needle into the mass. If the needle is pushed slowly toward the mass, it may deflect because the bevel of the needle may slide over its curved surface. (I have seen a simple cyst deflect an 18-gauge needle 15 or 20 degrees if pushed slowly.)

Second, when a small renal mass is quite mobile with respiratory motion, place the patient in an ipsilateral decubitus position and approach the mass posteriorly. The weight of the viscera will partially immobilize the diaphragm and the mass.

Results

The accuracy rate for diagnostic aspiration of renal mass is almost 100%. The results of CT aspirations are not much different from results appearing in the older literature on fluoroscopic aspirations except, because simple renal cysts are easy to diagnose by imaging, the number of diagnostic

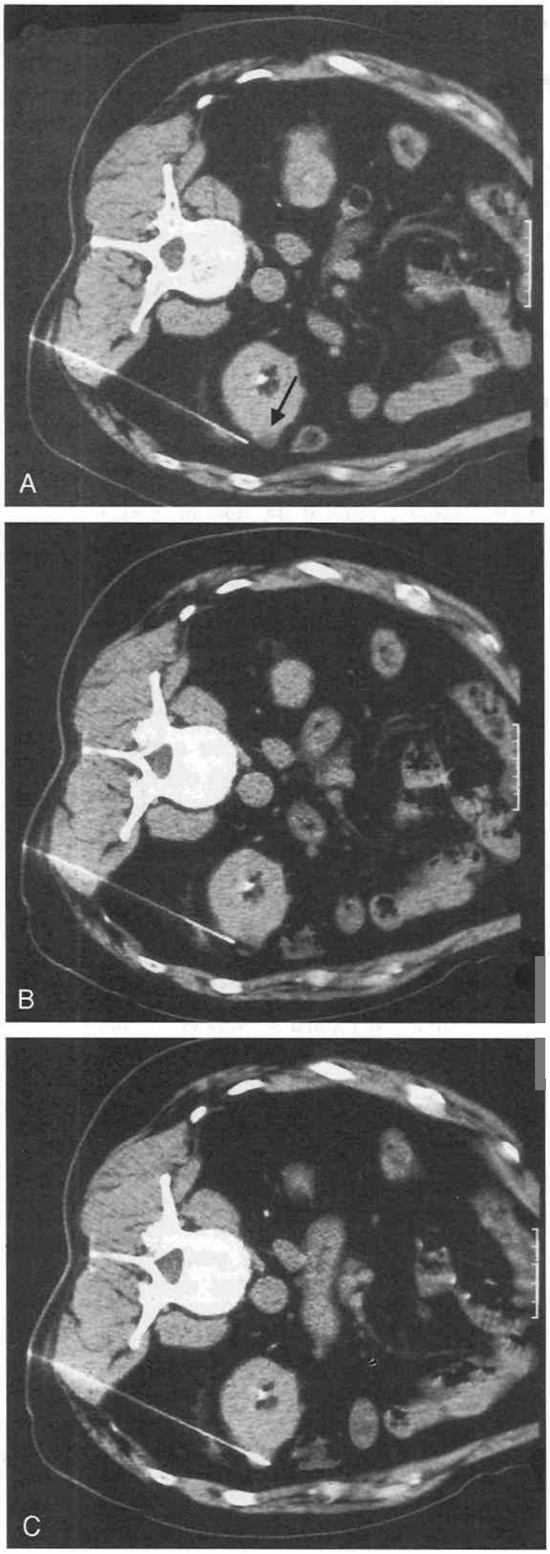

Figure 61–83. *A*, A patient with a small cystic mass on the left kidney (*arrow*) was scanned with the left side down. The weight of the abdominal viscera partially impairs movement of the diaphragm, making such masses more immobile. During this initial approach, the needle deflected from the cyst. *B*, Scan shows repositioning with needle "poised" adjacent to the mass. The bevel was turned downward to deflect the needle up. *C*, Puncture of cyst was successful, and clear fluid was extracted.

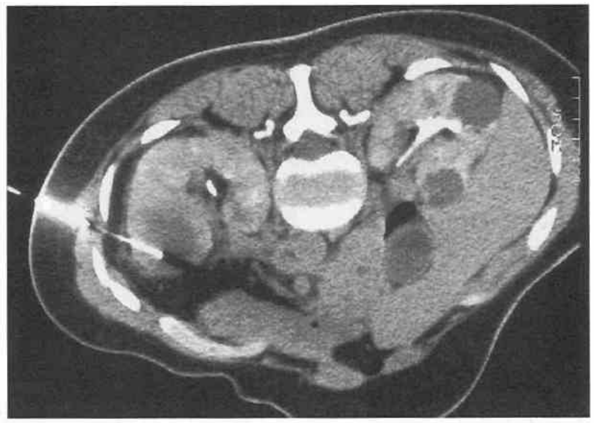

Figure 61–84. Solid tumors of the kidney are occasionally aspirated. The needle is accura[redacted]tioned into the mass.

aspirations is fewer and the percentage of solid tumors is higher.

A comment about aspiration of small adenomas is appropriate. As with the adrenal gland, normal-appearing cells can be recovered from a renal adenoma, but the significance is remarkably different. In the kidney, some believe the adenoma is the precursor to renal cell carcinoma. Consequently, unlike with adrenal adenomas, the recovery for renal tubular cells from a mass indicates a need for surgical removal.

Complications

The complications related to such procedures are quite low, and I have had two. One hematoma occurred during the biopsy of a renal mass close to the hilum, suspected of being a focal lymphoma. In this case a cutting needle was used, and the sample was very close to the segmental arteries. A hematoma developed that required neither surgical intervention nor the administration of blood.

A potential complication mentioned by clinicians is the possible occurrence of needle-tract seeding, for which I can find only one reported case in the literature. However, a carefully controlled study by Von Schreeb[391] compared the outcome and complications in two groups of patients with proven renal carcinoma. There was no difference in the complication rates, the morbidity rates, or the mortality rates between the groups (and no needle-tract seeding in 75 cases of carcinoma that were sampled).

Renal Parenchymal Biopsy

Renal parenchymal biopsies should be performed only in those cases that preclude the use of ultrasound guidance. In these cases the Tru-Cut needle should be used, but unlike for other areas, no bolus injection is needed. Choose an entrance site and trajectory to avoid the erector spinal muscle for reasons noted earlier in the retroperitoneum section. Unlike in the blind renal biopsy, it is not necessary to "target" the lower pole of the kidney. A good-quality sample avoiding the segmental vessels may be obtained

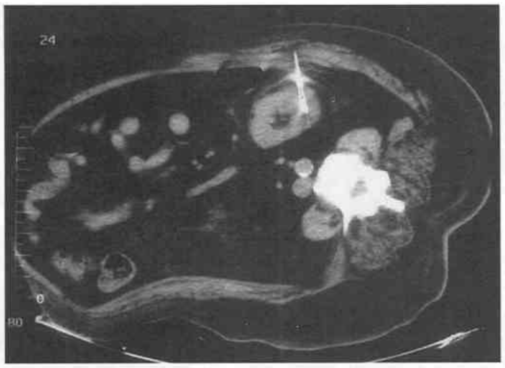

Figure 61–85. Because the goal of parenchymal biopsy is to recover glomeruli and not produce bleeding, one tries to sample the most peripheral cortex. This scan shows the gap of needle in the most peripheral cortex for sample. The central area should be avoided to prevent inadvertent injury to segmental arteries.

(with more cortex and glomeruli) by choosing an oblique placement within the cortex (Fig. 61–85). In this fashion the medullary region of the kidney, which contains the renal vessels, can be avoided.

The bleeding complication rate from parenchymal biopsies is fairly high, varying in some reports between 5.2% and 8.8%. Sateriale and Cronan[348] reported a number of risk factors related to renal biopsies, including hemodialysis, sex, site of biopsy, and treatment with DDAVP (Table 61–7). There is no question that biopsy of renal parenchyma is more dangerous than other procedures; even if the best device and technique are used, serious complications can occur.

There is some controversy among authors about what size needle is most effective for the diagnosis of diffuse renal disease. Although some authors have claimed that an 18-gauge needle is sufficient for assessment of renal pathology, most agree that a larger-caliber needle is better. Mostbeck et al[289] compared 18- and 16-gauge needles and

Table 61–7. Factors Affecting Hemorrhagic Complication Rates after Renal Biopsy

Factor	Hemorrhagic Complication Rate (%)*	Increased Risk of Hemorrhagic Complications	P Value†
Hemodialysis			
No	5.9 (13/220)	—	
Yes	24.0 (5/21)	×4.1	<0.025
Patient sex			
Male	4.5 (7/156)	—	
Female	13.0 (11/85)	×2.9	<0.01
Side of biopsy			
Right	5.2 (8/155)	—	
Left	14.0 (12/86)	×2.7	<0.01
Pretreatment With DDAVP			
No	6.4 (15/236)	—	
Yes	60.0 (3/5)	×9.4	<0.001

* Numbers in parentheses are actual number of patients with hemorrhagic complications per total number of patients in each subgroup.

† P values indicate the significance of the difference in complication rates for each set of paired values.

From Sateriale M, Cronan JJ, Savadier LD: A 5-year experience with 307 CT-guided renal biopsies: Results and complications. JVIR 2:401–407, 1991.

found the 16-gauge needle to be more effective. In our hospital, the pathologists and nephrologists report that a 14-gauge Tru-Cut needle is superior to other devices.

Adrenal Biopsy

Adrenal biopsy by CT guidance is easy, and the indications vary among different institutions. Either an aspiration or cutting biopsy can be performed using different approaches as described. A number of authors have reported on CT-guided biopsies of adrenal masses.[24,29,69,168,169,171]

Indications

If a patient with a malignant or infectious process has an adrenal mass and if confirmation of the process will change the management of the patient, a biopsy should be performed. Although most adrenal masses that are 3 cm or less are benign nonfunctioning adenomas, there is no method other than cytologic or histologic sampling that can prove this.

These principles have been confirmed by numerous authors, including Candel et al,[45] Lumachi et al,[254] Silverman et al,[355] and Welch et al.[399] Candel et al[45] showed clearly that lesions greater than 3 cm have a high probability of malignancy. Even those less than 3 cm had a 13% chance of malignancy. In the setting of a patient with even a small adrenal mass and a lung cancer, biopsy should be performed.

Contraindications

The contraindications for the adrenal gland are the same as for other areas in regard to access or increased vascularity, except for one addition. I believe that a pheochromocytoma or other functioning tumor should not be biopsied. It is well-documented that manual manipulation can initiate a hypertensive crisis; therefore, it seems logical to assume that needling such a tumor might create a similar problem. Thus if a patient has any clinical symptoms of a functioning adrenal tumor, a biopsy should not be done until a laboratory test for catecholamines is performed to exclude a functioning tumor. Despite several uneventful aspirations (unreported from other institutions), two deaths have been reported in the literature (one pheochromocytoma and one hemangioma).[268]

As an additional precaution against a potential problem it is prudent to have an intravenous alpha blocker available in the department for use should such a lesion be inadvertently sampled and a hypertensive crisis develop.

The validity of sampling even the most subtle mass in a patient with a malignancy is best emphasized by the experience of Pagani.[317] In his series of patients with small cell lung tumors, he sampled normal-appearing glands and actually recovered malignant cells in a significant number.

Needle Selection

The choice of needles for this organ is the same as for other areas, but commonly an aspiration type must be used

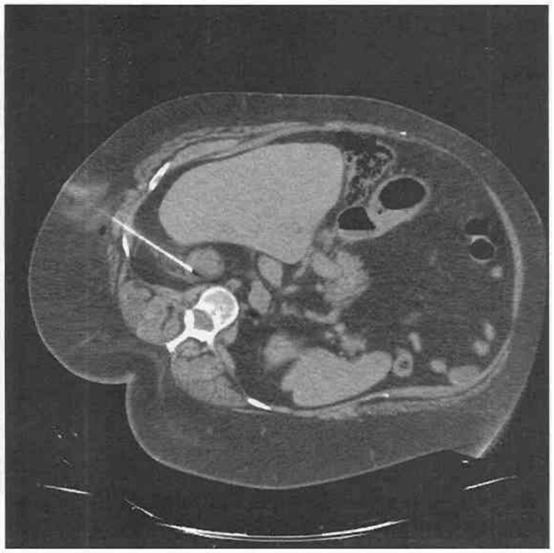

Figure 61–86. Oblique biopsy of the adrenal gland can be performed if the mass is large enough and the anatomic structure is suitable. This scan shows a mass in the right adrenal gland, which can be approached by a retroperitoneal approach without traversing liver or kidney.

because of the anatomy. In many cases an aspiration needle will be required because either another organ must be penetrated or the trajectory is too close to other structures. In unknown disease if a safe access is available and other factors are appropriate, I will use a large cutting needle.

Approach

There are four different anatomic approaches in biopsying an adrenal mass: an oblique-angled approach, a direct posterior paraspinal approach, a transrenal route, and a transhepatic approach. The first and most desirable approach uses an oblique angled pathway that avoids all intervening structures (Fig. 61–86). This approach is ideally suited for either cutting or aspiration needles because all structures are avoided and it can be used on either the right or left side. However, this approach is technically difficult and requires an entrance site below the level of the lesion. On the right side the angled pathway is between the right lobe of the liver and the kidney, and on the left side the pathway transverses the retroperitoneum behind the tail of the pancreas, medial to the spleen and anterior to the kidney. Sometimes, having the patient in an oblique position expedites this approach. This approach, as well as the next, is suited to aspiration- and cutting-needle procedures.

The second most desirable approach, which is probably the easiest to execute, is a posterior paraspinal route that traverses the crura. This is a straightforward method usable by almost all interventionists because it does not require an angled approach. If a paraspinal approach is taken, an aspiration or a cutting needle can be used (Fig. 61–87).

The next most desirable approach, which is limited to an aspiration needle, is the transrenal approach. This approach is quite direct (Fig. 61–88). It is appealing for several reasons. Literally thousands of aspiration procedures have been performed on renal cysts in kidneys without significant problems, so a transrenal approach for the adrenal is equally safe. If a complication occurs, it is confined to the retroperitoneum, making diagnosis and treatment easier than if a pathway crossing the peritoneum and retroperitoneum is used.

The last approach for the right adrenal gland is a transhepatic approach, which has been proposed by several authors.[333] This approach can be used with the patient in a supine or oblique position. If the transhepatic approach is chosen, I prefer to perform the procedure with the patient in the decubitus position. By doing this, the liver shifts anteriorly and a shorter pathway through the liver is possible. Theoretically, this should present fewer problems than if a long path through the liver is taken with the patient supine. On the left side, transpancreatic or transplenic routes should be avoided because of the high risk of complications.

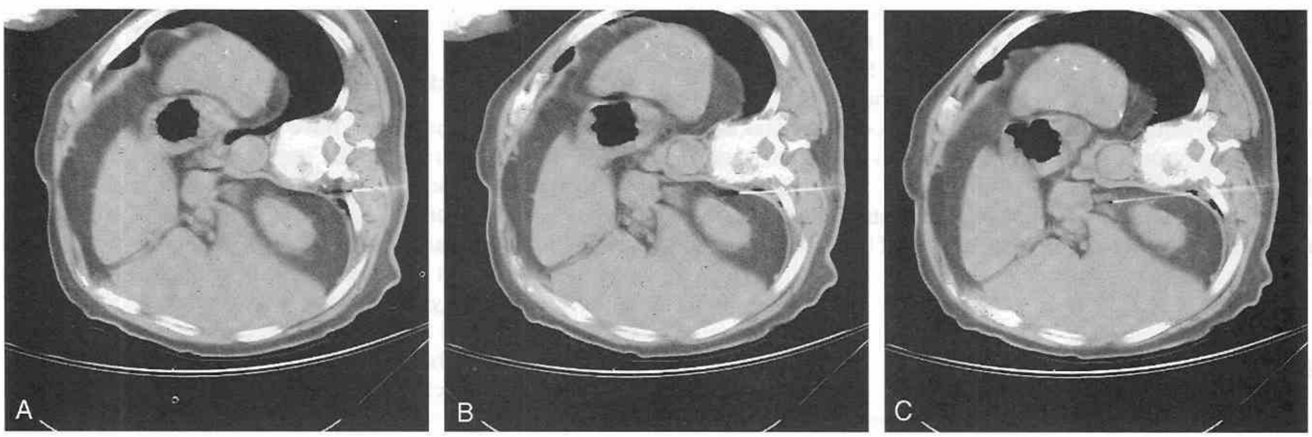

Figure 61–87. *A,* Sampling of adrenal masses can be accomplished best by placing the patient in ipsilateral sidedown position to immobilize the mass. The entrance site should be at the junction of the transverse process and the rib. The local anesthetic should be amply applied. *B,* At the level of the diaphragmatic slip, more local anesthetic should be given because movement would move the needle. *C,* Final placement of the needle tip into the gland. Final adjustments can be made by turning the bevel as previously described.

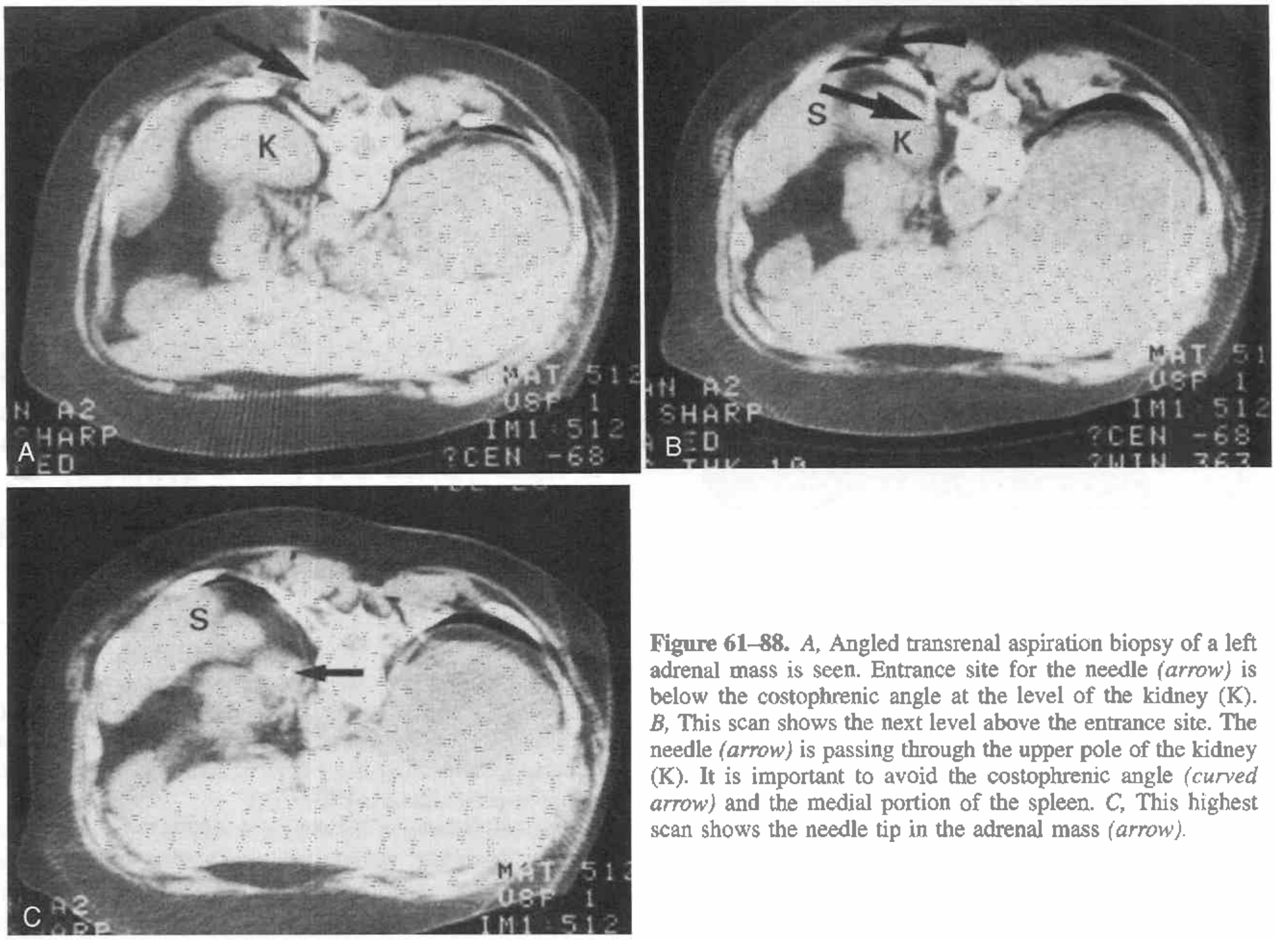

Figure 61–88. *A,* Angled transrenal aspiration biopsy of a left adrenal mass is seen. Entrance site for the needle *(arrow)* is below the costophrenic angle at the level of the kidney (K). *B,* This scan shows the next level above the entrance site. The needle *(arrow)* is passing through the upper pole of the kidney (K). It is important to avoid the costophrenic angle *(curved arrow)* and the medial portion of the spleen. *C,* This highest scan shows the needle tip in the adrenal mass *(arrow).*

Asymptomatic Adrenal Masses

One question frequently asked is how a mass 3 cm or smaller should be managed,[205] with the knowledge that in most cases such masses are benign nonfunctioning adenomas. In my opinion such lesions should be observed or sampled based on the clinical situation. If a patient is asymptomatic without proven malignant or inflammatory disease, no biopsy is needed. If a patient has a proven pathologic problem and involvement of the adrenal gland changes the patient's management, I believe a biopsy should be taken. According to our experience and others,[69] a cytologic sample will show the presence of normal adrenal cells in nonfunctioning adenomas or hyperplasia, thereby excluding the possibility of a malignant or inflammatory disease. If the cytologic interpretation raises any question about the benign nature of the adrenal cells, further exploration is needed.

Accuracy

The accuracy of CT sampling of adrenal masses is quite high. Heaston et al[168] reported a series of 14 cases and had correct results in 18 patients without complications. Bernadino[25–29] reported a series of 50 cases with an accuracy rate of 83%. They had an 11% complication rate overall, with serious complications requiring blood transfusions in 3.5% of cases. Silverman et al[355] reported a positive predictive accuracy of 96% and a negative predictive accuracy of 91%. Obtaining benign tissue was a high indicator of benignity. Lumachi et al[254] in 2001 reported definitive diagnosis in 97%. The authors discounted the risk of sampling pheochromocytomas, to which I strongly object (see earlier section on contraindications).

Complications

A number of problems have been reported. Bernadino et al,[25–29] using a transhepatic approach in a reported series of 50 patients, had an overall complication rate of 11%, with a serious complication rate of 3.5%. Two patients required blood transfusions. Pagani[317] reported a case of pneumothorax that required chest tube placement. Heaston et al[169] and our group, using an indirect approach that attempted to avoid other structures, had no significant complications. There have been two deaths reported (see section on contraindications).

More recently, other authors have reported their experience with complications. Kane et al[201] reported a 6% incidence of severe pancreatitis when the left adrenal gland was sampled with aspiration needles, using an anterior transpancreatic approach. Mesurolle et al[274] reported 6

cases of pneumothorax in a series of 44 patients. Mody et al[282] reported an overall series of 44 patients, in which complications occurred in 8.4%. These authors reported 7 cases of complications (2 pneumothoraces, 2 severe pain, 3 hematomas, and 1 needle tract metastasis). It was also noted that 5 of the 7 complications occurred with a 22-gauge needle.

In view of the large number of reported complications, I believe our conservative approach is warranted. To date we have had no complications from adrenal biopsies, except two pneumothoraces, over the past 25 years. After the adoption of the transcrural, paravertebral approach, no pneumothoraces have occurred.

Mesenteric Mass

Our approach for mesenteric masses is similar to that for all other areas, and the results have been equally successful and safe.

As in other areas, if there is a possibility of penetrating a loop of bowel, a small aspirating needle (20 gauge) is used. If the mass can be approached without penetrating a bowel loop and the other criteria are met, a 14-gauge Tru-Cut needle can be used. Of course, a bolus injection should be used to assess the vascularity of the lesion before the biopsy (Fig. 61–89).

When using the cutting needle, both oral and intravenous contrast material can be helpful in opacifying the normal bowel so that it can be avoided. In addition, try to have the entire gap within the mass that is being biopsied. If a part of the cutting needle overlaps within the peritoneum, some of the abundant small vascular network of the mesentery or omentum may be cut, causing a hemorrhage.

Spleen

The spleen is an area that represents uncharted territory because of the lack of experience and the significant problems other physicians have had with inadvertent injury to the spleen. From surgical and clinical information, it is obvious that the spleen is very vascular and can be easily severely injured. Because of these previous experiences I believe a larger body of information should be collected before the sampling of the organ can be recommended on a routine basis.

Figure 61–89. Biopsy of small, mobile masses in the peritoneum is possible, but one must adjust the bevel of the needle as required and insert it quickly to prevent movement of the mass.

Over the last 12 years I have sampled a number of lesions in the spleen, both cystic and solid, without complication. I have not published or presented the information because I am not convinced that the benefit sufficiently outweighs the potential risks for widespread application. This is one of the few areas I think should be left to academic centers until more information is obtained.

Recently an additional report on splenic biopsy was reported by Keogan et al.[211] In their series of 18 patients they performed 20 biopsies. They used a variety of needles and achieved an accuracy of 88.9%. Although the authors conclude that this is a safe procedure, I believe the experience is not sufficiently large to recommend it as a routine procedure.

Pelvis

The pelvis is a frequent site for biopsy with CT guidance because of the frequency of gynecologic, urologic, and colonic pathosis.[43,408] All of the general principles for clinical indications—needle selection, bolus dynamic scan, and anatomic considerations—apply in this area, with some qualifications.

Indications

Indications for the pelvis are varied; some are well-defined and others are somewhat nebulous. Clearly defined entities that should be sampled include metastatic tumors from the colon, bladder, prostate, or other organs. The safety and benefit of sampling primary tumors in these areas have not been documented, so generally I do not biopsy primary ovarian tumors unless the patient is considered incurable. One would not want to potentially "seed" the peritoneum in an operable patient.

Approach

The approach to be used depends on the location of the abnormality (i.e., whether it is high in the pelvis, at the level of the iliac crests, or low in the pelvis near the pelvic floor).

Anterolateral Approach

When abnormalities are in the upper portion of the pelvis, an anterior or anterolateral approach may be used. At this level, it is not possible to pass a needle posteriorly because the bony structures are intact posteriorly. When a mass is large enough to push anteriorly, access is quite easy because the bowel has been pushed laterally. When masses are obscured anteriorly by bowel, having the patient lie on either side will allow the bowel to move, permitting

access for a needle placement. When a loop of bowel is partially obscuring a pathway, one can push the needle slowly and the loop of bowel will typically be pushed aside.

Sometimes in the pelvis an injection of carbon dioxide may be useful to displace loops of bowel away from the iliac vessels and psoas muscle. When such procedures are performed, the needle is placed in the small space between the loop of bowel being moved and the lateral structures (see earlier section on tissue retraction) (see Fig. 61–38).

Lateral masses can be approached with a pathway parallel to the iliac crest, with the needle directed either medially or laterally to the iliac vessels and femoral nerve. The vessels can be identified by injecting contrast material for opacification. The femoral nerve lies in the small "notch" at the margin of the psoas and iliac muscle.

When significant expertise is developed, one can sample masses or nodes even closer to the vessels. It is always important to recall the importance of using the bevel of a needle to pass by a vessel. In some circumstances, one can even pass a needle between the artery and vein to reach a subtle mass (Fig. 61–90).

Posterior Approach

The posterior approach through either sciatic notch is suitable for the sampling of any presacral mass[42,318] (Figs. 61–91 and 61–92). See Fig. 61–38, which shows technique for movement of bowel. As with other regions a guidance cannula can be quite helpful to expedite the procedure and ensure precision of needle placement. When performing the procedure through the notch, be careful to avoid the sciatic nerve and the margins of the bone. Inadvertent needle puncture of these areas can be quite uncomfortable.

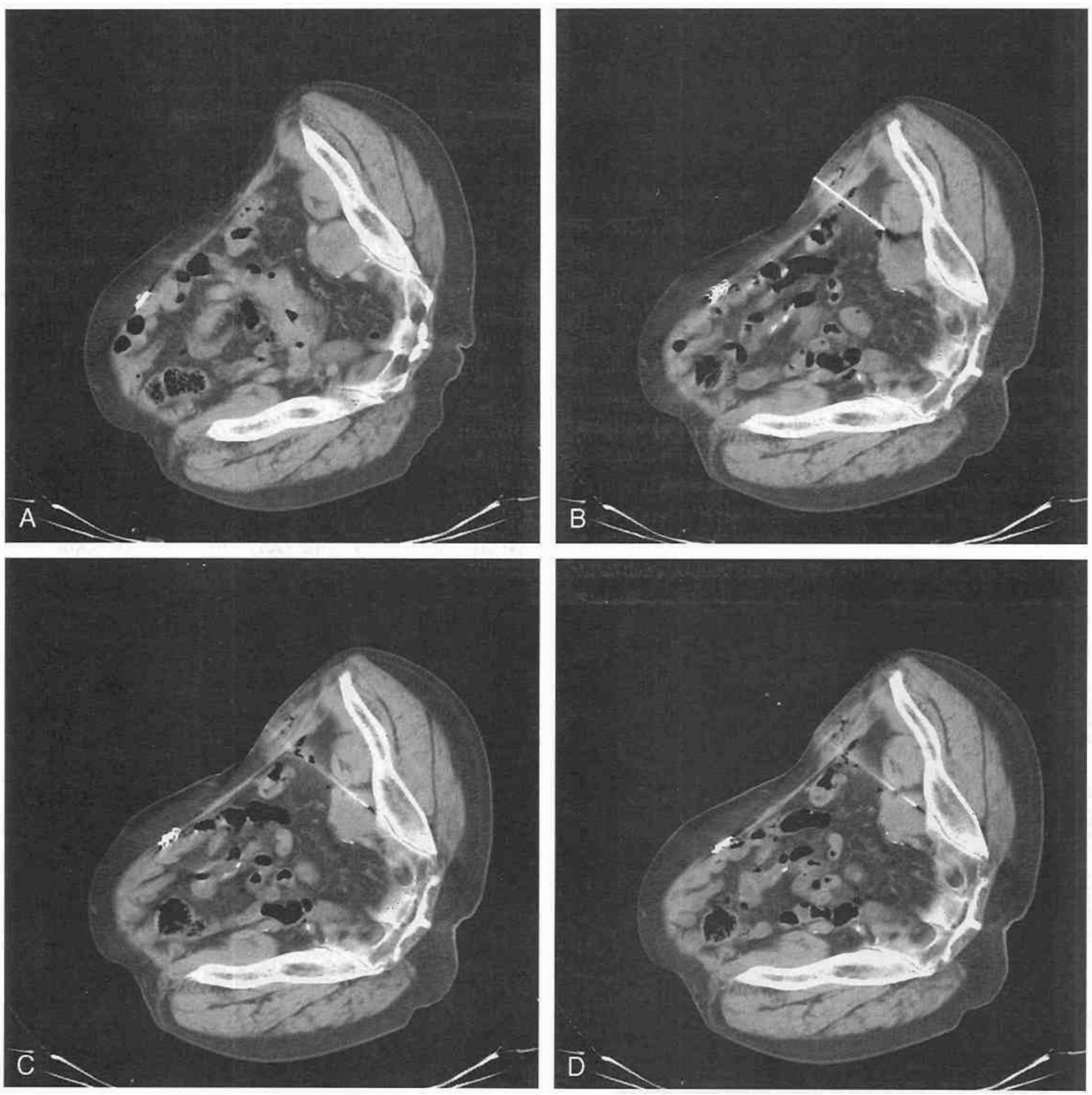

Figure 61–90. *A,* A mass [redacted] is located posterior to artery and vein, making approach rather difficult. *B,* A cannula of coaxial system and Chiba needle is noted anteriorly to the space between the iliac artery and the psoas muscle. The bevel was turned toward the artery to permit safe passage of both instruments past the artery. *C,* The Chiba needle was inserted beyond the cannula and a sample was taken. *D,* The Chiba needle was replaced with a small-caliber cutting needle (Temno). This could be safely performed because the cutting gap was beyond the vessels with the Chiba needle and cutting needle inserted.

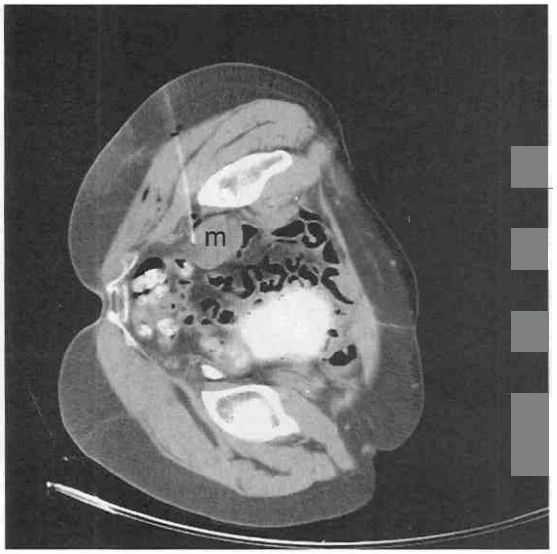

Figure 61–91. Pelvic biopsy of a patient with deep mass (M). In this case there is a large mass located posteriorly. This was approached through the sciatic notch. I consider this approach less optimal than the anterior lateral approach because of the pain associated with the margin of the notch and the nerve. If the patient experiences pain down the sciatic nerve, the needle should be moved.

Also avoid the area of the gluteal and hemorrhoidal vessels if collateral blood flow has produced pathologic enlargement.

Choice of entrance point is important to avoid impingement against the sacrum because there is a discrepancy between the apparent location of the sacrum as seen on the CT image and its real location. Since the anterior posterior and the lateral margins of the sacrum are tapered, there is a significant partial volume error created on the CT image of the sacrum. Carefully palpate the sciatic notch before any needle insertion because the margin of the bone is more lateral and caudad than would appear on the CT image. With the information from the palpation of the notch, the location of the notch can be anticipated better and the discomfort associated with the procedure can be minimized.

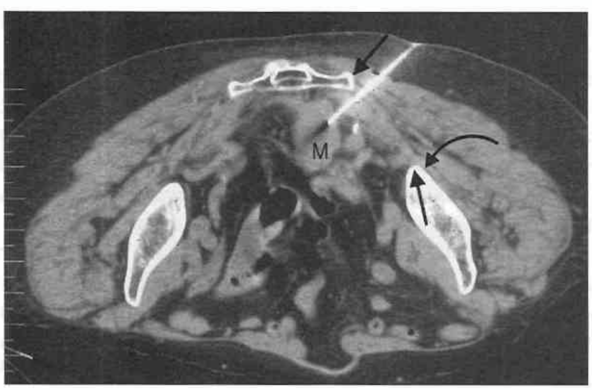

Figure 61–92. Biopsy of a presacral mass (M). Note that the position of the lateral margin of the sacrum *(arrow)* can be deceptive. Because of the tapered edges, the margin is more lateral than one might expect. Careful palpation of the site should be performed to prevent any undue discomfort. The sciatic nerve *(curved arrow)* should always be avoided if possible.

Accuracy

There are several articles from two perspectives in the literature about the accuracy of CT-guided procedures in this area. The first article on this topic from my group examined the accuracy of percutaneous procedures relative to surgical biopsies. We[415] found that in patients percutaneous procedures were more successful than was the surgical approach (either perineal or peritoneal). Butch et al[34] reported a series of CT-guided procedures evaluating the overall diagnostic accuracy, correctly diagnosing 15 of 19 cases of neoplasm.

Complications

No complications have been reported to date. The only difficulty has been some pain associated with inappropriate placement of needles through the sciatic nerve or local trauma to the sacrum.

Therapeutic Procedures

CT can be used quite readily for performing a number of aspirations and drainages in different portions of the body. By far the greatest number of drainages that will be performed are those on abscesses, but occasionally cysts, lymphoceles, pseudocysts, bilomas, or other fluid collections may be drained.

Lymphoceles

Lymphoceles are collections of lymph fluid, usually caused by the local disruption of lymphatic vessels after surgery. The appearance of these lymphoceles is indistinguishable from abscesses appearing as well-delineated fluid collections (Fig. 61–93). These fluid collections spontaneously resolve without any type of therapy intervention when new lymphatic channels open.

There are only two valid indications for intervening when such a fluid collection is found. If a clinical suspicion of an infection exists, a diagnostic aspiration is indicated. There is no rationalization for catheter insertion in such cases unless purulent material is present. Inserting a catheter may cause secondary infection, but in most cases the cavity will close after the infection has resolved. The second indication is when the lymphocele is producing obstruction of the urinary tract or gastrointestinal tract. In such cases needle puncture and catheter insertion are the same as for the other fluid collections. Another point to be made is that a lymphocele will persist in draining fluid until the lymphatics open new channels, whether a catheter is present or not. Removal of the tube will result in reaccumulation of lymph fluid, if such channels have not formed.

When a lymphocele has been drained for one of these

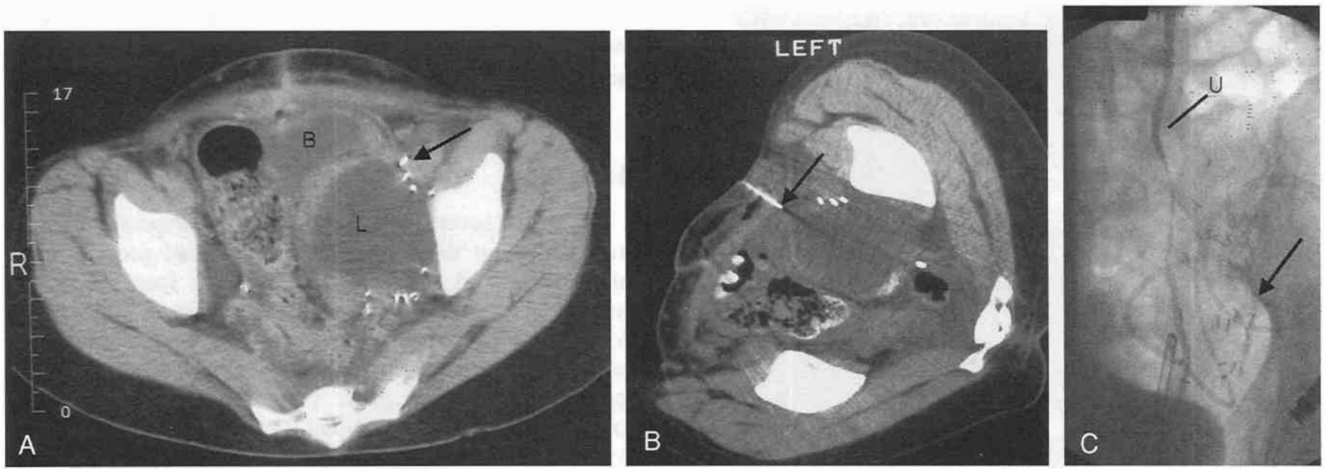

Figure 61–93. *A,* A large lymphocele (L) is noted in the left side of pelvis following kidney transplant. Access to the collection is impaired because of the proximity of bladder (B) and the clips from surgery. *B,* Positioning of the patient with the right side down increases the space for the needle trajectory (*arrow*) so the cyst can be punctured without penetration of the bowel or bladder, which could potentially introduce infectious agents. *C,* Radiograph shows the catheter in the lymphocele (*arrow*) and the ureter (U).

reasons, some radiologists have instilled sclerosing material such as tetracycline to speed resolution. In recent years, numerous authors have reported the use of a variety of agents that sclerose lymphoceles. These have included doxycycline (Caliendo et al[44]), bleomycin (Kerlan et al[212]), ethanol (Zuckerman and Yeager[425]), and Betadine (Gilliland et al[112] and Montalvo et al).[284]

The results of such sclerosing procedures have been variable and in many cases, surgeons will default to internal drainage. Laparoscopic procedures have been reported by Gruessner et al[132] and Hamilton and Winfield.[163]

Renal and Liver Cysts

Deciding to Sclerose

The decision to sclerose a large cyst in the kidney or the liver is not an easy one for several reasons. First, any procedure—no matter how benign—can have adverse side effects, and the use of these sclerosing agents are not without their danger. Second, it is an unusual circumstance when a cyst produces physical discomfort, so I am highly selective. To make sure a patient with a cyst is experiencing symptoms and not just having psychological overlay from "knowing" a cyst is there, I do the following intermediate step: On the patient's first presentation, I will only aspirate the cyst without sclerosing agent. The instructions to the patient and the purpose in this is as follows. In some cases a cyst will not come back, so if it does not and the patient is not symptomatic, the patient will not return. If the patient comes back and the repeat scan shows no recurrence of the cyst, then there is no reason to do anything, and one can be confident that the symptoms are not related to the cyst. If the patient comes back and the cyst is back, then this proves the symptoms are from the cyst and worthy of sclerosis.

True cysts with endothelial linings can occur in many organs, including the kidney, liver, pancreas, and spleen. They all have similar appearances and are seldom punctured for diagnosis or drained, unless they are producing symptoms or are suspected of being either infected or neoplastic. The mere presence of a cyst in an organ is no reason for sclerosis, but in some cases cyst size may be so great as to impair respiration, produce pain, obstruct the portal structures, or obstruct the renal collecting system.

The diagnostic puncture of such cystic cavities is quite easy and is performed in the routine fashion using either the 20-gauge needle or the Teflon-sheathed 18-gauge needle. The trajectory should be planned so that a "cuff" of tissue is included in the pathway of the puncture. If this is not done, the risk of rupturing the cystic cavity into an adjacent space exists because the walls can be quite tense and can tear. Obviously, if this were a simple cyst, ill effects would not be a concern. However, if the cystic lesion is an abscess or a tumor, a complication could result. Avoiding leakage is also important if alcohol sclerosis is to be performed to prevent back-leakage of alcohol into the peritoneum.

If the decision is made to drain the cyst and prevent reaccumulation, simple aspiration will usually not suffice because the endothelial lining that produced the fluid will continue to fill the cyst. The only way to stop this from recurring or growing is to inject a sclerosing agent such as tetracycline or ethyl alcohol. Our choice is alcohol because it is a potent local irritant, it has no idiosyncratic effects, and it is easily metabolized. Since surgeons have attempted for years to eliminate these by simple injections with varying success, I expect that this simple injection method will have equal success as a radiologic procedure.

Our approach has been different from that of other authors who have simply evacuated a portion of the fluid, injected alcohol equivalent to 25% of the volume, and then repeated the injection several times. I object to this method for two reasons. The alcohol is diluted significantly; this limits its local effect of destroying the endothelial lining. Because large volumes of alcohol may be needed in large cysts, there is the possibility of administering a large systemic dose. My approach begins with the insertion of a small 5-French pigtail catheter as a conduit (Fig. 61–94). Before any further manipulation of the cavity, a contrast

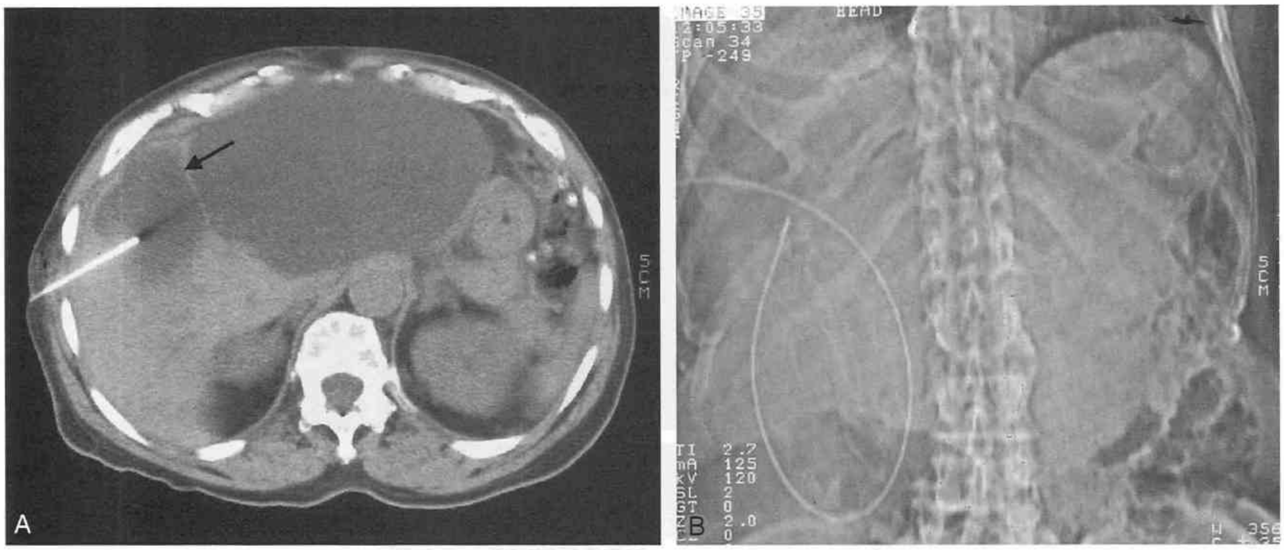

Figure 61–94. *A*, Scan shows two large cysts that are separated by a septum (*arrow*). The needle was inserted to permit puncture of both cysts. Note that the path was chosen to provide a cuff of normal liver to prevent the spillage of either cyst fluid and alcohol when it is injected at a later time. *B*, Radiograph shows the insertion of wire and catheter into the cyst cavity. The cyst is left to drain for several hours before the instillation of alcohol (see text).

injection is performed to ensure that there is no communication with the biliary or urinary system. If the system communicates, the procedure must be aborted, because injection of alcohol would sclerose the system. I then evacuate all of the fluid and apply suction until the walls are opposed.

Following this I make multiple injections of small amounts of alcohol as follows. I inject an initial volume of 15 mL of alcohol and leave it in place for 5 to 10 minutes. During this time I have the patient rotated into various positions, lateral and prone, to ensure that the alcohol bathes all surfaces of the cyst. After 10 minutes I attempt to recover the alcohol injected. If the alcohol cannot be recovered, I will inject an additional 10 mL and pull the catheter. If the alcohol can be recovered, I aspirate out as much of the alcohol as possible and then reinject 15 mL and repeat the process. The alcohol is removed a second time and a third aliquot of 15 mL of alcohol is injected and left in place. The alcohol that is removed will show a remarkable change when it is removed. The color changes from crystal clear to very cloudy, turbid, and pink. The change is due to the sloughing of cells into the fluid as it damages the inner surface of the cyst (Fig. 61–95).

After this procedure there is really no need for repeat studies because if the patient remains asymptomatic, the cyst is resolved. If the cyst returns, the patient will return with symptoms and the procedure can be repeated with slightly larger amounts of alcohol if desired.

I believe this conservative method is better than the large-volume methods used by other authors. Such large volumes invariably result in some intoxication of the patient and can actually put other portions of the liver at risk because of the local toxicity of the alcohol. When the readers go to a conference, they will be amazed at how cases being demonstrated using the high-volume method will show destruction of other liver lobes; the lecturers seldom make note of that in their presentation.

Another approach has been offered by Cellier et al.[50] In a group of five patients, the authors performed the following technique. The cyst was punctured and half of the cyst content was aspirated. A single dose of 100 to 500 mg of minocycline hydrochloride was injected and left in place. At follow-up four of the five cysts had resolved.

Pancreatic Pseudocysts

Pseudocysts of the pancreas are collections of necrotic debris, inflammatory material, and digestive enzymes that require treatment because they are associated with a number of complications. The optimal time to drain these is after 6 weeks and before 13 weeks. Approximately 6 weeks should elapse before any procedure because a high percentage (≥25%) may actually disappear spontaneously. With those that have gone untreated longer than 13 weeks, some authors have reported a high incidence of infection, rupture, or bleeding, all of which can be catastrophic. To prevent such complications, as well as the symptoms associated with these problems, effective treatment is indicated. An important point is that only fluid collections, and not poorly defined phlegmons or edema collections, should be drained.[131,150]

Surgical Versus Radiologic Methods

If one carefully reviews the literature, there are numerous articles that discuss the merits of surgical approaches versus radiologic ones (discussed later). In general, the antagonists and protagonists of each position tend to emphasize several points on either side of the argument. Generally, the percutaneous procedures tend to require a longer time for resolution than surgical ones but radiologic procedures tend to have fewer complications and lower morbidity. One of the largest series reported in the surgical literature was by Heider et al.[170] In their retrospective study

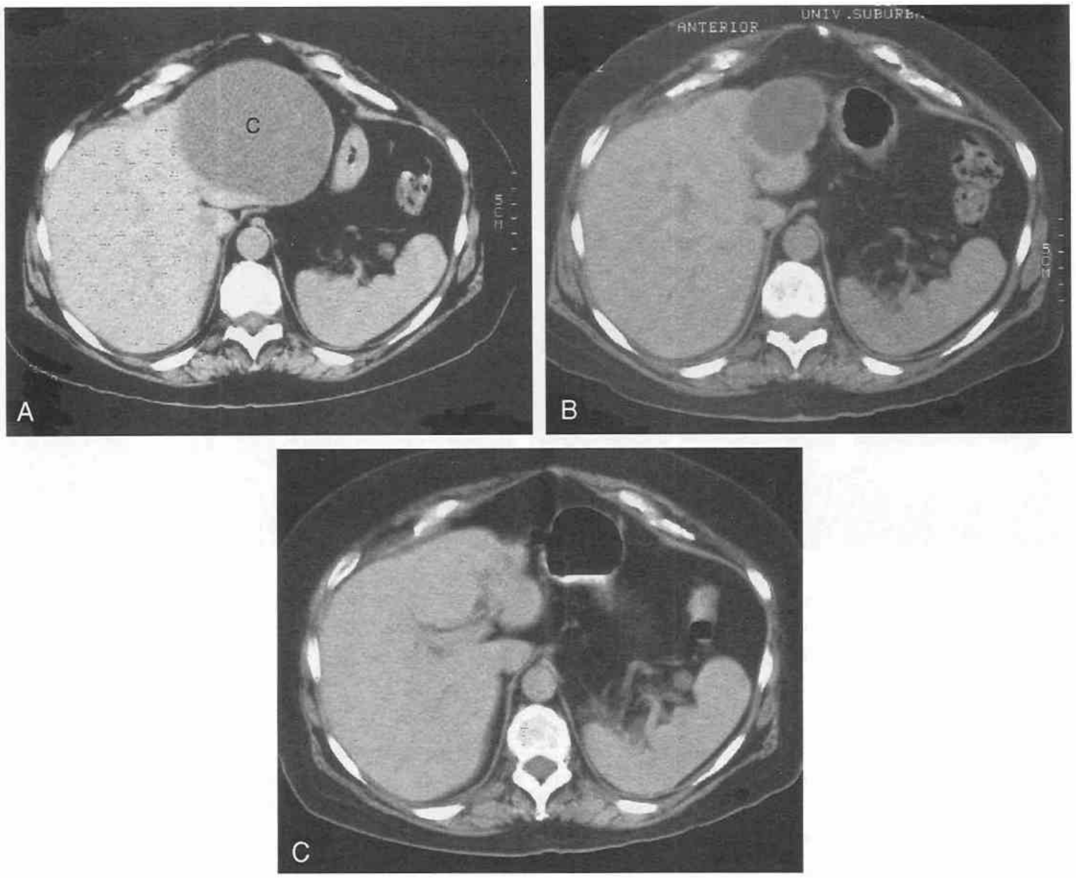

Figure 61–95. These three images (*A* to *C*) show the gradual reduction in the size of a cyst (C) that has been sclerosed with alcohol. The reduction in the cyst occurs over many weeks.

of 173 patients, percutaneous methods were inferior to surgical treatment. They reported successful treatment in only 42% for percutaneous and 88% for surgical treatment. The other factors were worse outcome for percutaneous methods with mortality 16% versus 0%, complications 64% versus 27%, and longer hospital stay 45 days versus 18 days. In my opinion the merits of various methods depend on the individual physicians at each site and the selection criteria for the methods. The best examples of this controversy can be appreciated by noting two articles from the same institution in the same year by Adams and Anderson[2] and Criado et al.[60a] The two groups from the same institution seem to contradict one another in their support of surgical or radiologic methods.

Suffice it to say that each institution tends to have its own idiosyncracies, and the skill levels of each group probably differs from one center to the next. Depending on the local talent and experience produces a preference for surgery or radiology.

Three methods of treatment have been reported, and after a number of years of development the advantages and disadvantages of each are well known.[13,77] These methods, in chronology of development, are aspiration, external drainage, and internal drainage. None of the reports in the radiology literature reveals the deficiencies of the methods. An impression is given that each method has solved the problem. In my extensive experience with the different treatments of pseudocysts I have formed personal opinions of their various roles, and I have found each method to have some merit but also some shortcomings. With each succeeding method the results have been better, but there remains a subset of patients who are not "cured" by our percutaneous methods and who therefore require surgical treatment. Each of the methods are described, and the benefits and disadvantages are noted from our perspective.

CT is ideally suited for any of the methods. It is the best modality for visualization of the anatomy and instruments so that avoidance of uninvolved structures is possible. Avoidance of small bowel and colon is important because secondary contamination can occur. Furthermore, with CT, pseudoaneurysms can be accurately diagnosed and avoided. Life-threatening hemorrhage has occurred when these structures were inappropriately penetrated.

Observation

When a pseudocyst is first detected by imaging, it is probably reasonable to observe the pseudocyst for a period because a significant number spontaneously resolve. Sanfey et al[346] reported that in their series of 97 cases of inflammatory pseudocysts, 32% resolved spontaneously. If the patient is asymptomatic, then observation for 4 to 5 weeks before attempting treatment is probably appropriate.

Aspiration

Simple aspiration of a pseudocyst appears to work in slightly less than 25% of cases, but it is advantageous

because of its simplicity. This procedure can be performed with the standard methods described previously and with little or no risk (assuming one avoids bowel loops and vascular structures). The procedure is so simple that most can be performed on an outpatient basis, as noted earlier. Some have recommended that several aspirations may be required over a period of weeks or months. The subset of pseudocysts most likely to be cured by this method is that occurring after a localized and minor leakage from the pancreas after a surgical procedure.

External Drainage

This type of drainage is analogous to the external drainage performed for abscesses. With this method various structures are avoided, and a catheter that drains to the external environment is put in place. Some authors have reported good results using this method, but in our experience a fairly high percentage will persist or recur. The risk of a permanent fistula or secondary infection also exists. Although the literature on this problem does not indicate significant recurrences, we have performed such procedures for more than 20 years (Fig. 61–96) and found the recurrence rate to be similar to the aspiration method. Indeed, if this method were so effective, the transgastric method would not have been developed.

Two subsets of pseudocysts have responded quite well to this mode or the aspiration mode of therapy. Well-defined pseudocysts that are secondarily injected are well suited for percutaneous external drainage.[97,388,389] In those patients who have a pseudocyst secondary to external or surgical injury, the pseudocyst can easily be treated by aspiration or external drainage.[14,20,34] In most of the cases I have treated and in those reported in the literature, such drainages are uniformly successful without any sequela or recurrence.

Transgastric Drainage

The most promising method for draining such pseudocysts is a transgastric approach as described by Nunez,[307] Bilbao,[31] Bernadino et al,[28] and Ho.[175] With this method a trajectory is chosen that includes the walls of the stomach and the pseudocyst in the lesser sac. The catheter provides internal and external drainage until such time as the pseudocyst resolves.[31]

In the largest series by Nunez,[308] eight pseudocysts in seven patients were successfully drained. The length of drainage was 3 weeks in six cases and 6 weeks in two cases. No recurrences were noted, but the length of follow-up was not mentioned.

Modified PEG Drainage

We have stopped using Nunez' method because of clinicians' concern about possible gastric spillage into the peritoneum. We have devised a modification of this method that eliminates this potential problem and that has been well received by the clinical physicians. After the decision has been made to drain the pseudocyst, we have the endoscopist insert a percutaneous endoscopic gastrostomy (PEG). The tube used differs slightly in that the end of the gastrostomy tube is cut off. With this PEG securing the stomach wall to the abdominal wall, we use it as a conduit through the gastric space into the pseudocyst (Fig. 61–97). A Teflon-sheathed needle is inserted through the gastrostomy through the posterior stomach wall into the pseudocyst. This has worked well because the entrance point is secure and there is no risk for peritoneal soilage. The trajectory is easy because the gastrostomy site in the skin serves as a fulcrum and one can angle the needle to any point on the posterior stomach wall. The distance is short, and angulation is simple. Once the pseudocyst has been successfully punctured, a catheter is inserted using the Seldinger technique. Because a 20-French gastrostomy tube can be inserted, angiographic catheters as large as 9- or 10-French can be used to penetrate the pseudocyst.

In our experience the short-term results of the transgastric method are quite good. Unfortunately, in the long term (up to a year after the removal of the tube), some will recur. It has been our experience that leaving the tube in for about 6 to 8 weeks is sufficient. If the cyst remains or recurs after this, then surgical treatment is probably needed.

There are two advantages of the transgastric method.

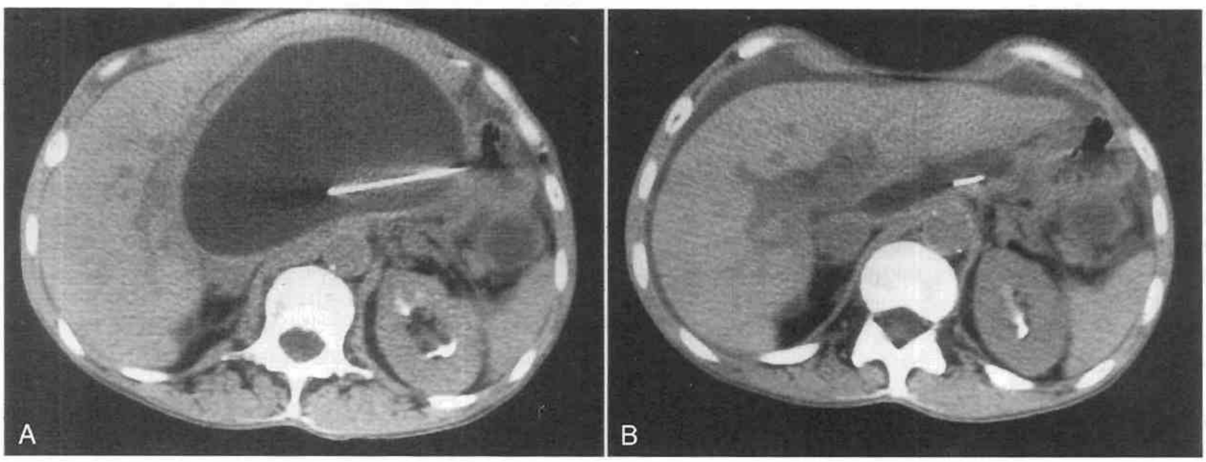

Figure 61–96. Percutaneous transgastric drainage of pseudocyst is a viable option for drainage. *A,* This scan shows the needle trajectory through the stomach into a large retrogastric pseudocyst. *B,* Later scan with a catheter in place shows remarkable resolution of the pseudocyst.

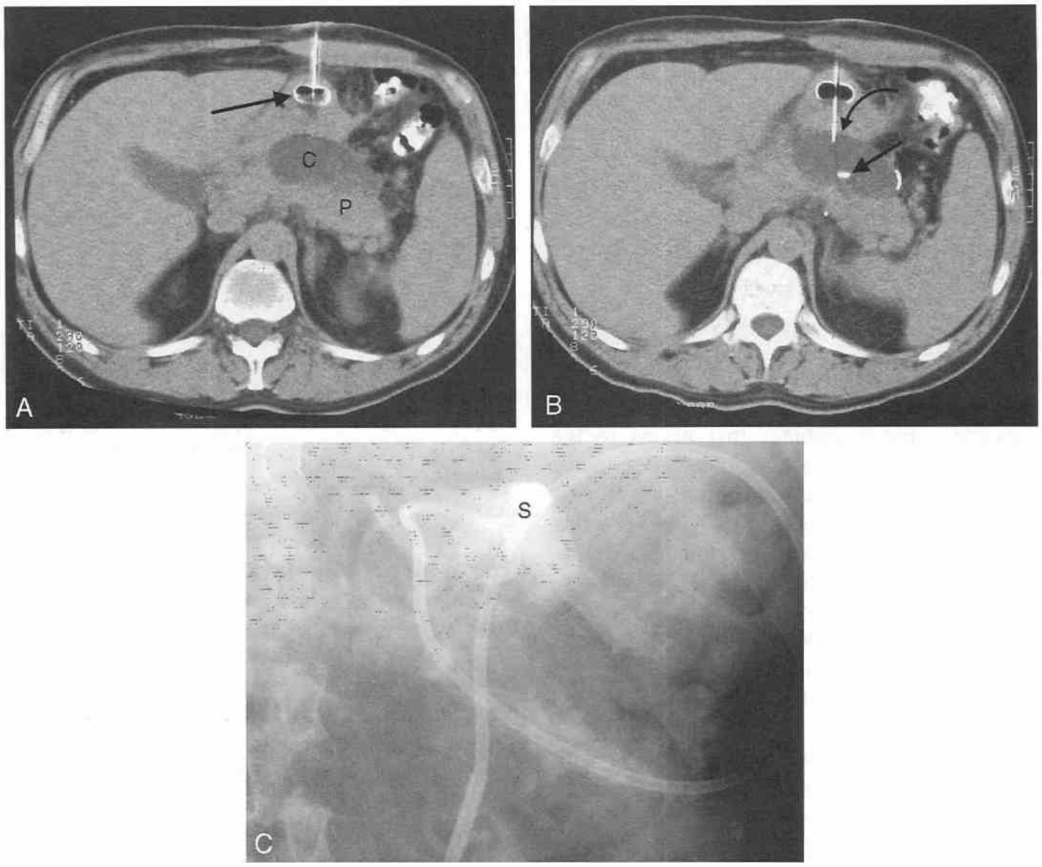

Figure 61–97. *A,* Scan shows pseudocyst (C) anterior to the pancreas (P). Note the percutaneous endoscopic gastrostomy *(arrow)* anteriorly in the stomach. *B,* Scan shows the needle *(curved arrow)* penetrating the end of the tube into the cyst, and the wire *(arrow)* looped in the pseudocyst. *C,* Radiograph shows a large tube traversing the stomach and located in pseudocyst; contrast medium defines the stomach (S).

First, residual or leaking pancreatic juice can exit into the stomach, thereby preventing a fistula. Second, the enteric flora can colonize the pseudocyst, thus permitting inflammatory reaction and better closure of the cavity.

Pancreatic Fistula

Rarely, a pancreatic fistula may result after tube drainage of a pseudocyst. Of the several approaches that might be used, only one has been reported. First, some authors have used the hormone somatostatin to decrease the exocrine output of the gland.[287] The results have been variable, however, and the medication is quite expensive. Another method, proposed by Haaga and Stout, is the use of a biologic glue such as "fibrin glue" to seal such a pathway from a pseudocyst or the pancreatic duct.

A number of authors have evaluated factors that might be indicators of likely success for percutaneous methods. Duvnjak et al[51] reported that pseudocysts with a high amylase content were unlikely to respond to percutaneous methods. These findings may be an indirect observation based on communication with the pancreatic duct; those pseudocysts having direct communication with the duct are more likely to have high levels of amylase. Barthet et al[19] noted that percutaneous methods were less likely to be successful if there was communication with the pancreatic duct.

Other Proposed Adjunctive Management

Morgan et al[288] advocated the use of MRI to evaluate fluid collections to assess the presence of large pieces of necrotic debris within fluid collections to determine if percutaneous methods are suitable. Such collections were judged to be not drainable if the material measures more than 1 cm in size.

D'Agostino et al[65] reported the use of the hormone octreotide to lessen pancreatic secretion and flow during percutaneous drainage. The drug was given in recommended doses and appeared to be beneficial in four of eight cases.

Abscess Aspiration

Percutaneous aspiration and percutaneous drainages guided by CT represent the most significant advance in the care of acutely ill patients since the development of surgical drainage and the discovery of antibiotics. Since the first CT-guided aspiration and drainage (Fig. 61–98) that I performed in 1975 and reported in 1976,[153] the use of this technique has grown rapidly.* This growth has occurred

*References 111, 158, 191, 210, 300, 319, 322, 383, 390.

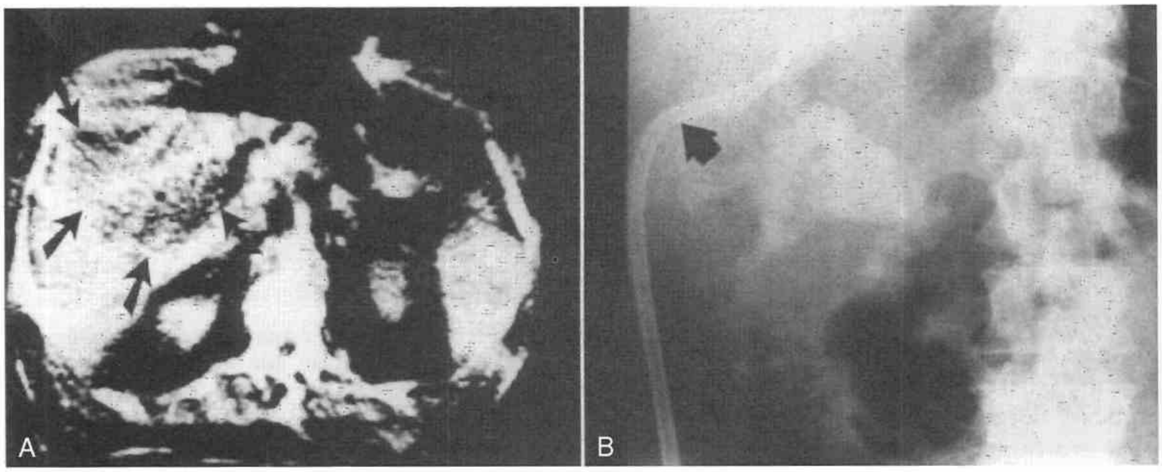

Figure 61–98. *A,* First CT-guided drainage of an abscess *(arrow)* performed in 1975 by the author. *B,* Plain radiograph of the abdomen shows a drainage tube in place (*arrow*). The patient recovered uneventfully. (*B,* From Haaga JR, et al: Definitive treatment of a large pyogenic liver abscess with CT guidance. Cleve Clin Q 43:85–88, 1976.)

because of the increased number of scanners available, the excellent accuracy of CT for the detection of any fluid collection, the high accuracy for guidance, and the popularization of the technique by enthusiasts such as Haaga,[147,153,155] Gerzof,[106–111] and Van Sonenberg.[384,386–390]

Diagnostic Aspirations

Because patients with infectious fluid collections may or may not manifest the typical signs of infection, I believe that if there is even the slightest clinical concern about an abscess, a diagnostic aspiration should be performed. This aggressive diagnostic approach is justified because with careful technique, including avoidance of bowel, a sample can be successfully recovered in almost 100% of cases with little or no risk. In my experience with CT guidance over the last 27 years, I have aspirated more than 500 cases with no secondary infection and with only one hematoma that occurred as a complication.

The diagnostic sampling of fluid collections requires the same planning as that of all of the other lesions we have discussed, but several factors must be kept in mind. The material being obtained may contain viable pathogenic material and can disseminate infection if it is inappropriately spilled or contaminated into sterile spaces. Even though modern potent antibiotics can eradicate any minor spillage of purulent material, great care should be taken not to contaminate sterile areas. Patients may develop serious peritonitis or bacteremia if the inoculum is larger or the organism virulent (or if the patient is immunocompromised by any cause).

A question occasionally arises concerning the interpretation of culture results—that is, how culture results should be interpreted when only a limited number of colonies grow. It is my opinion that any number of colonies involving organisms other than *Staphylococcus* should be considered an infection at least warranting antibiotic therapy based on the culture sensitivities. Depending on the number of bacteria within a fluid collection or the presence of antibiotics, the possibility always exists for a sampling error that can result in a negative culture or possibly growth of a limited number of pathogens.

Finally, during the aspiration of fluid densities, it is important to avoid traversing gastrointestinal loops. First, a sample taken through bowel may provide spurious culture results. Of course, some claim that presence of mixed flora and absence of a "pure" culture of a single organism can distinguish an abscess from gastrointestinal colonization. However, as has been well documented in the radiology literature, many abscesses are caused by a gastrointestinal fistula that contains many types of organisms. Second, the function of humoral cellular defenses is lessened in a fluid space, so that clearing of bacteria by phagocytes is impaired and a secondary infection might occur if a small inoculum is introduced into a fluid collection.

Mycotic Aneurysms or Infected Vascular Prostheses

Because of the difficult treatment required for infected vessels or synthetic aortic prostheses, it is my firm belief that any patient with such a suspected infection should have a diagnostic aspiration at the earliest time. With both infected prostheses and primary mycotic infections in the infected prostheses we have encountered, the cultures have been positive and reliable. In each of these cases the culture results were critical and helped initiate the expeditious treatment of the problem. With prompt treatment most of these patients survived the surgical therapy. In another group of 10 patients with uninfected grafts, the results were negative. There have been no complications associated with the needle procedures (Figs. 61–99 and 61–100).

Such cases should be approached from the flank, and a pathway should be chosen to avoid the kidney and major vessels. In most instances a clearly defined fluid collection will be seen either adjacent to the graft or between the wall of the aneurysm and the graft. As with other procedures performed from this approach, we try to avoid the psoas muscle, erector muscles of the spine, and the spinal elements to prevent patient discomfort.

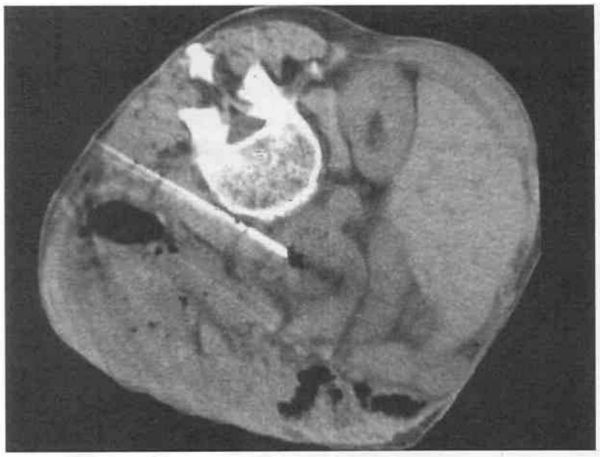

Figure 61–99. Diagnostic aspiration of air collection around a prosthetic graft. CT scan shows the patient lying prone. Note the needle penetrating the wall of the aneurysm, which encloses air collection next to the graft.

In such cases, if there is any question about the location of the vessel or prosthetic wall, a bolus dynamic CT scan should be performed. Dynamic CT is highly effective for the demonstration of a vascular problem, even better than Doppler ultrasound and angiography. In one patient with a clotted mycotic aneurysm, only CT correctly showed the vascular nature of the lesion.

Some individuals have raised concerns about possible injury to such an infected vessel, but in our experience this is not a problem. In the more than 20 suspected cases we have aspirated, there have been no complications.

The need for such aggressive expeditious procedures is clear. The mortality rate of untreated prosthesis infection is high, almost 100%. Corrective treatment and surgery can be effective only if initiated early. In some instances, percutaneous drainage of infected prostheses may be effective[229] if the infection involves only the midportion and not the anastomotic ends (Fig. 61–101).

Other authors such as Rossi et al[342] have also proposed an aggressive approach to the diagnosis and management of these difficult infections. These authors have also advocated percutaneous aspiration for diagnosis of infectious agents as well as palliating the infection with preoperative catheter drainage. We have effectively cured a patient with graft infection using local catheter drainage.

Abscess Drainage

Before CT, percutaneous abscess drainage (PAD) was occasionally performed, but with the advent of CT assistance it has become a routine procedure. CT has been especially useful because it has a high detection accuracy for abscesses and allows accurate determination of the anatomic location and extent of the lesion. Because CT is not impeded by gas or bone, any involvement of peritoneal spaces or anatomic areas can be clearly delineated. This information is absolutely necessary if one is to determine whether an abscess can be drained by a percutaneous method.

Although there was some controversy in the early literature concerning the merits of different guidance systems for drainage, there now appears to be a consensus that CT guidance is the best method available.[147,230,389]

Perspectives on Abscess Drainages

With a global perspective toward abscess drainage, it is clear that the intent of interventional percutaneous procedures is to at least duplicate the excellent treatment results established by our surgical colleagues. The benefit of percutaneous procedures lies in their simplicity, lower complication rates, and presumably lower overall expense. Recent publications in the surgical literature have illuminated some of the factors that relate to the outcome of both percutaneous and surgical procedures.[16]

The benefits of improved detection and localization of

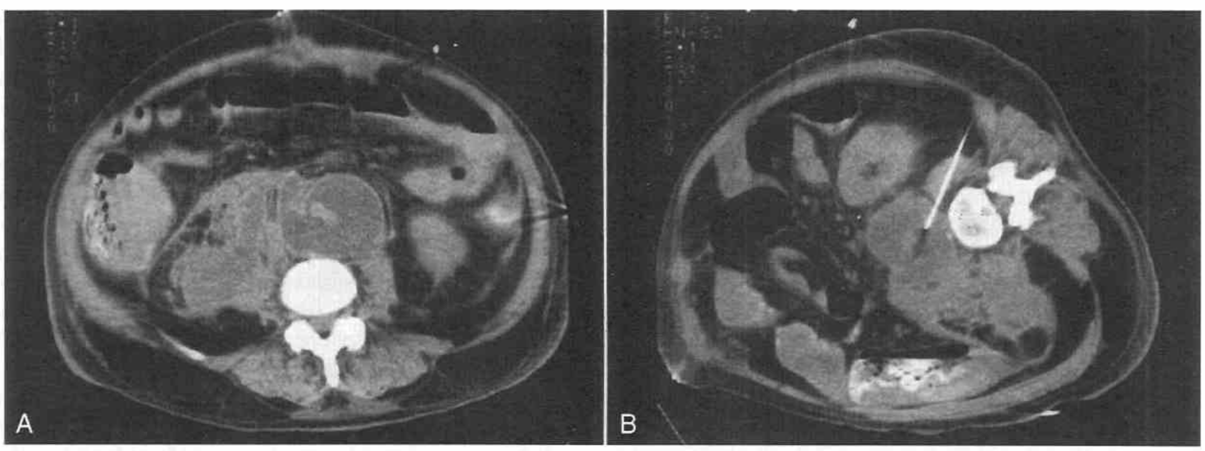

Figure 61–100. *A,* This scan shows postoperative fluid collections around the graft material within the old aneurysm bed as well as in the right flank. *B,* With the patient in the left decubitus position, percutaneous aspiration of fluid around graft was performed. Because *Staphylococcus* is the most common organism, such aspirations may be necessary even if gas is not present. Aspiration of the opposite right fluid collection was performed independently using a different pathway to avoid possible cross-contamination of the spaces, if one space happened to be sterile and one happened to be infected.

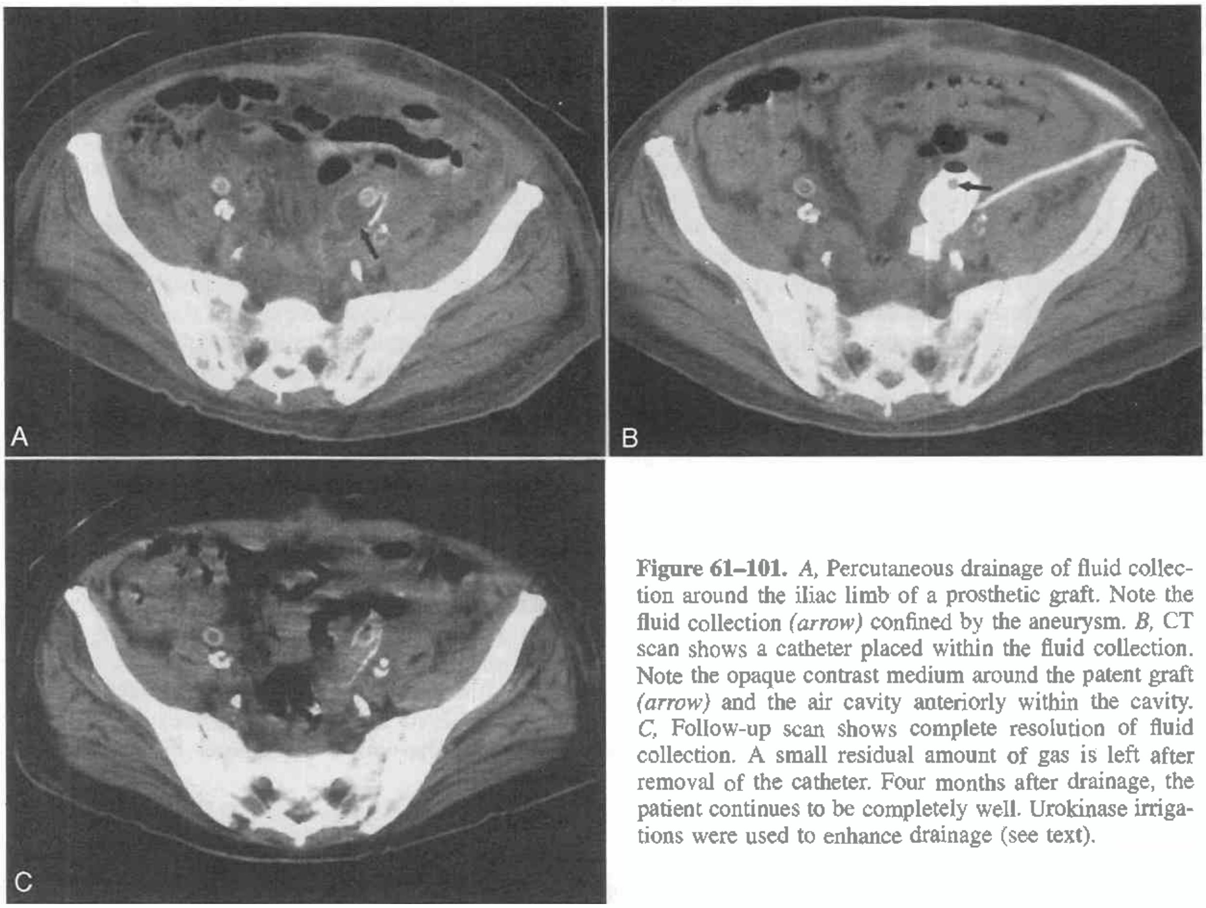

Figure 61–101. *A,* Percutaneous drainage of fluid collection around the iliac limb of a prosthetic graft. Note the fluid collection *(arrow)* confined by the aneurysm. *B,* CT scan shows a catheter placed within the fluid collection. Note the opaque contrast medium around the patent graft *(arrow)* and the air cavity anteriorly within the cavity. *C,* Follow-up scan shows complete resolution of fluid collection. A small residual amount of gas is left after removal of the catheter. Four months after drainage, the patient continues to be completely well. Urokinase irrigations were used to enhance drainage (see text).

abscess have been documented by Deveney et al,[71] who showed conclusively that the improved localization and intensive care methods have resulted in a greater percentage of drainage success as well as decreased mortality resulting from organ failure. These authors, in a veteran population, studied two 5-year periods (1973 to 1978 and 1981 to 1986) and noted the following. The mortality of the two groups was 39% and 21%, respectively. The successful initial drainage was 55% compared with 74%. Organ failure rate decreased from 52% to 23%. The surgical success rate was 76%, compared with the percutaneous success rate of 72%. The authors concluded that accurate localization and early drainage are the most important factors and that there is no difference in outcome between the surgical and percutaneous methods.

The importance of overall patient status has also been documented by Levison et al.[239] These authors used the APACHE II system to grade patients and follow their outcome. The final results were that mortality was directly related to the APACHE score. Of those with a score less than 15, the mortality was 1.7%, compared with a mortality of 78% when the score was greater than 15. There was no significant statistical difference in outcome between percutaneous and surgical drainages. (One is cautioned not to quote this finding out of context, because the authors subjectively maintain that surgical drainage was better by *absolute* numbers. The finding was *not* statistically significant, however.)

The importance of the immune system has been emphasized throughout this discussion on intervention. Lambiase et al[229] have documented how critical this factor is as it relates to abscess drainage. These authors considered the following states as immunocompromised: absolute neutropenia, human immunodeficiency viral infection, cancer with distant spread, chemotherapy, radiation therapy, lymphoproliferative disorders, diabetes requiring treatment, chronic renal dialysis, splenectomy, and severe alcoholism. They found that with percutaneous abscess drainage the overall cure rate for immunocompromised patients was 53.1% compared with the normal rate of 72.6%.

Patient Selection

In recent years the indication for percutaneous methods has expanded significantly.[39,48] Unlike most new techniques and procedures in which there is an initial period of enthusiasm followed by either a moderation or a restriction of the method, percutaneous drainage guided by CT has continued to expand its role. The results of percutaneous procedures have been so positive and so widely accepted that the indications and applications have continued to find new application.

To maintain a proper clinical perspective, it is important that the proper patients be selected for curative or palliative PAD procedures[384,386] and for surgical procedures. Simplis-

tically, one could try PAD for palliation in every patients, but it is not logical to expand its use for patients with certain surgical problems.[39] On a practical level, although the role and the indications for percutaneous procedures have expanded greatly, there are still clear indications for surgical drainages.

To anticipate a curative percutaneous procedure, certain clinical and anatomic facts must be confirmed. Patients who have an abscess or abscesses that appear well-defined are suitable candidates if a clear anatomic pathway is available. In the early experience procedures were restricted to those abscesses with only a few cavities. The results with septated abscess has been variable; some drain quite well and others do not (Fig. 61–102). The most plausible explanation for this is that fibrin septa in such cavities may be complete or incomplete: when they are complete, drainage is poor and when they communicate and are incomplete, curative drainage can occur. We have studied the use of fibrinolytic agents in the former cases and have found them quite effective for improving drainage (see later discussion on fibrinolytic agents). Also, the multiplicity of abscesses is no longer considered a contraindication to percutaneous drainage because each site is treated independently.

For the choice of anatomic pathways, we still prefer a clear pathway into the abscess cavity without traversing an uninvolved space or organ. I believe that a routine penetration through an uninvolved organ is inappropriate because of possible seeding of pyogenic organisms into the organ. Although with the potent antibiotics of today most such procedures appear feasible, I believe that when larger series are collected, the success and complication rate will favor avoidance of uninvolved organs and spaces.

Another important factor to consider is the viscosity of the material in the abscess. If the entire cavity can be evacuated easily after aspiration, percutaneous drainage will probably work. If the material appears to be quite viscous, techniques should be adjusted appropriately (i.e., special attention given to catheter size, catheter placement, and use of an appropriate irrigant). These are discussed in the section on catheter management.

Choosing PAD for palliation is most appropriate. Adequate palliative drainage will reduce the "toxic load" resulting from drainage of purulent material and will usually produce considerable improvement in such patients. Remarkably, some will be cured, but even those who are not will benefit from an improved physiologic state that makes them better surgical candidates.

The appropriateness of percutaneous drainages for abscess associated with entities requiring surgical treatment is an area of significant controversy (discussed later). In the final analysis, however, one must weigh the palliative benefits of PAD against the final curative benefits of surgery.[397] Similar views are shared by Dr. Claude Welsh

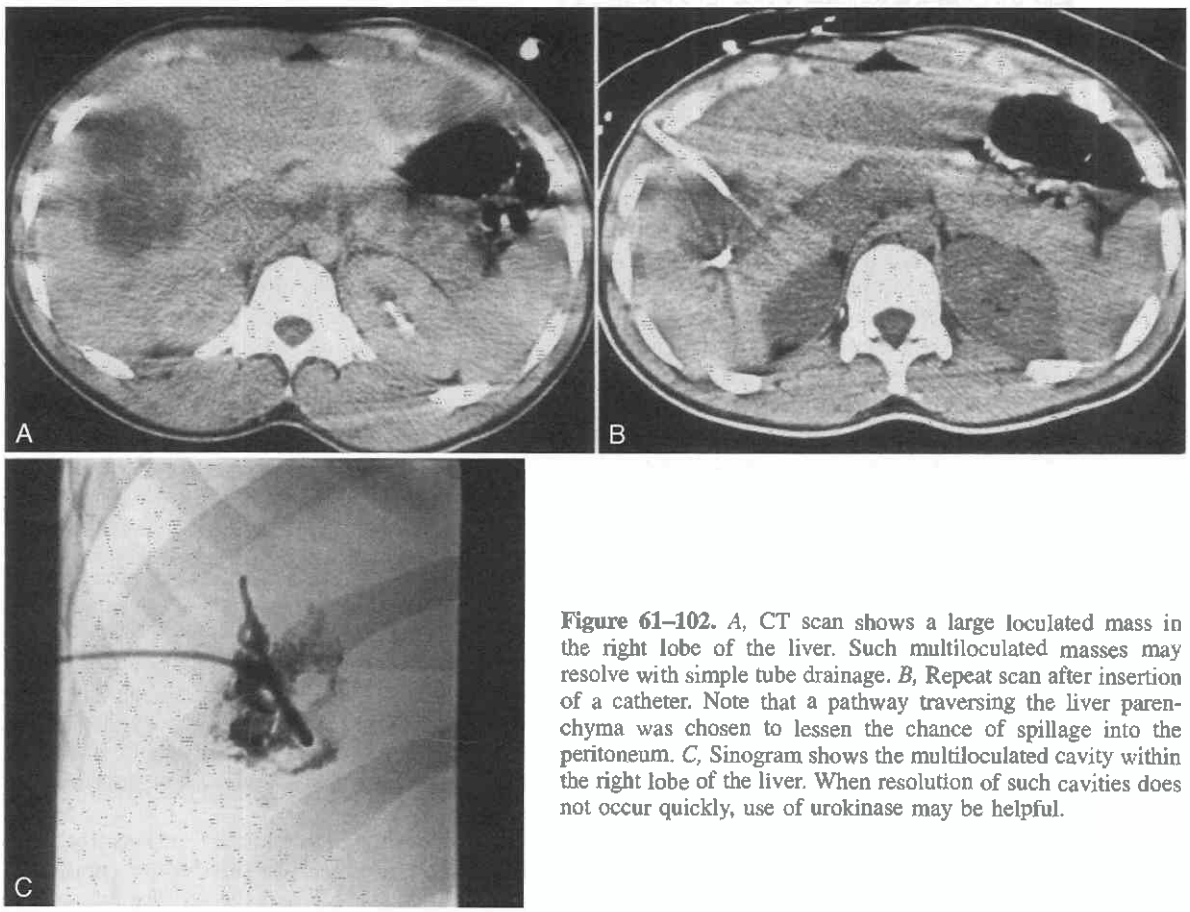

Figure 61–102. *A,* CT scan shows a large loculated mass in the right lobe of the liver. Such multiloculated masses may resolve with simple tube drainage. *B,* Repeat scan after insertion of a catheter. Note that a pathway traversing the liver parenchyma was chosen to lessen the chance of spillage into the peritoneum. *C,* Sinogram shows the multiloculated cavity within the right lobe of the liver. When resolution of such cavities does not occur quickly, use of urokinase may be helpful.

of Massachusetts General Hospital,[397] who noted in an editorial:

> Unfortunately, abscesses vary so greatly in many ways that studies with proper, randomized controls would be very difficult to establish. It is far more likely that further experience will lead to greater concurrence between radiologists and surgeons. Thus the letter by Haaga et al. outlines conclusions that appear to be quite closely in accord with our own studies in the Massachusetts General Hospital. *Since Haaga and his co-workers originated the radiologic method, their opinion must be given great respect.*

Indications for Surgery

Some patients are not good candidates for percutaneous procedures and are better suited for surgical drainage. This group consists of patients with fungal infections,[410] infected hematomas, echinococcal disease, surgical disease requiring correction, most pancreatic abscesses, and failed percutaneous drainages.

Patients with fungal abscesses require surgical drainage because there is extensive tissue invasion, necrosis, and mycotic plaque formation with the wall of the cavity. Our experience with several such cases and reports in the literature show that surgical drainage or resection is best for adequate débridement.

Infected hematomas do not drain well because of the extensive amount of fibrin deposition and the protective effects of fibrin on bacteria. Again, as shown from our early experience and from reports in the literature, it is clear that such hematomas have uniformly failed by percutaneous drainage. In our more recent experience, fibrinolytic agents used as a catheter irrigant can improve the drainage of infected hematomas.

Echinococcal disease requires a special approach to prevent spread of the daughter cysts into the peritoneum or other areas. The issues related to anaphylaxis are essentially minimial with appropriate technique, and many authors have now reported on the technique of percutaneous drainage. The specific approach is discussed at the end of the section on abscess drainage.

Finally, for those patients who have had a failed percutaneous procedure, surgical drainage is appropriate. Because of the difference in philosophy among surgeons, radiologists, and institutions, the definition of a failed procedure can be determined only at the local level and not in this text.

Treatment of Abscesses by Aspiration Alone

In recent years there has been introduction of a new approach for abscesses that is somewhat avant garde and may have a role in the future. These techniques have been based on single or multiple aspiration procedures on abscesses, in lieu of drainage tube placement. It is difficult to understand the origin of such techniques, but usually it was based on two factors: (1) lack of safe access to permit catheter insertion and (2) small size preventing catheter placement.

The techniques published recently were by McFadzian et al,[268a] Giorgio et al,[114,115] Saluja et al,[344] Ch Yu S et al,[51] Wroblicka and Kuligowska.[411] The specific details of each author differed slightly, but most reported single or multiple aspirations of the abscess cavity while systemic antibiotics were given. Wroblicka and Kuligowska[411] reported irrigating the cavities with saline. McFadzian et al[268a] and Giorgio et al[114,115] also injected intracavitary antibiotics. The authors all claimed high success rates. It should be noted that the authors also reported numerous failures and complications, including transient sepsis, death by sepsis, failure because of enteric fistula, and peritonitis.

Several important points from these papers should be noted. The selection of patients is not consistent, so widespread application of this technique is not appropriate at this time. I disagree with an editorial comment by Miller et al,[277] who stated that this might be the biggest advance for abscess treatment in 80 years. The biggest advance was surely the use of CT and drainage methods for treatment. When the first such diagnosis and procedure were made in 1975, patients were literally dying from undiagnosed and ineffectively treated abscesses; current techniques provide remarkable diagnosis and cure, so any major change should be made only when appropriate study has been made. On the other hand, if other authors report similar experience as Giorgio et al,[114,115] then perhaps this new drainage approach will become a more widely accepted and used method.

It is my belief that these techniques offer a good second-line treatment for abscesses if drainage is not possible. My opinion, however, is that if radiologists use the techniques described in this work and others, the occasion when a catheter cannot be placed is rare indeed. When such cases do arise, the best approach would be to combine the best of all details in these articles. When catheter placement is not possible on the basis of access or size of the abscess, the following technique should be used: (1) aspiration of purulent contents, (2) lavage with saline, and (3) injection of a small dose of antibiotic. The antibiotic chosen should be the one selected from cultures and sensitivies (if available from fluid or blood cultures). Because there are few guidelines, one should probably use close to a single IM or IV dose, and that quantity should be deducted from any daily limit stipulated by the manufacturer or the FDA. It is also important to pay attention to the volume required because one must not inject volumes too large for the cavity. For typical pyogens, when routine broad-spectrum antibiotics are used, the volume will not be an issue. With fungal abscesses, the volume of the dilute drug may be too high, so the dosage will need to be reduced.

Sequential Steps for Drainage

The technique of abscess drainage can be divided into the following steps:

1. Abscess detection
2. Trajectory planning
3. Selection of the guidance modality
4. Diagnostic aspiration
5. Catheter selection and insertion
6. Sinogram and catheter adjustment
7. Catheter management and irrigation
8. Follow-up diagnostic evaluation
9. Catheter removal

Abscess Detection

Detection of an abscess can be accomplished in selected cases by any modality, but CT plays the most critical role. CT is the preferred examination because it is the most accurate of all imaging systems for abscess detection. Not only can CT confirm or exclude the presence of drainable fluid, but it can also diagnose the causative or associated problem. CT can provide valuable information about diverticulitis, tumors, appendicitis, fistulae, infarcts, cellulitis, phlegmons, inflammatory bowel disease, bowel obstructions, or other problems.

If an abscess has been detected by either plain radiography, gallium, or ultrasound, a CT scan should be performed to determine the complete extent of the abscess. The geographic location and degree of involvement are essential factors in choosing the trajectory, determining the number of catheters required, and anticipating possible difficulties. Although some authors were initially reluctant to accept not only the advantages but the critical role of CT in defining the nature of an abscess, virtually all authors now agree that CT is the modality of choice for the detection, staging, and planning of a drainage procedure. The criteria for drainage have been expanded to include many patients, so the need for accurate detection and staging is even greater.

Trajectory Planning

Trajectory planning is best accomplished by CT, regardless of the imaging modality chosen for guidance. Although as most authors agree it is best to choose the shortest

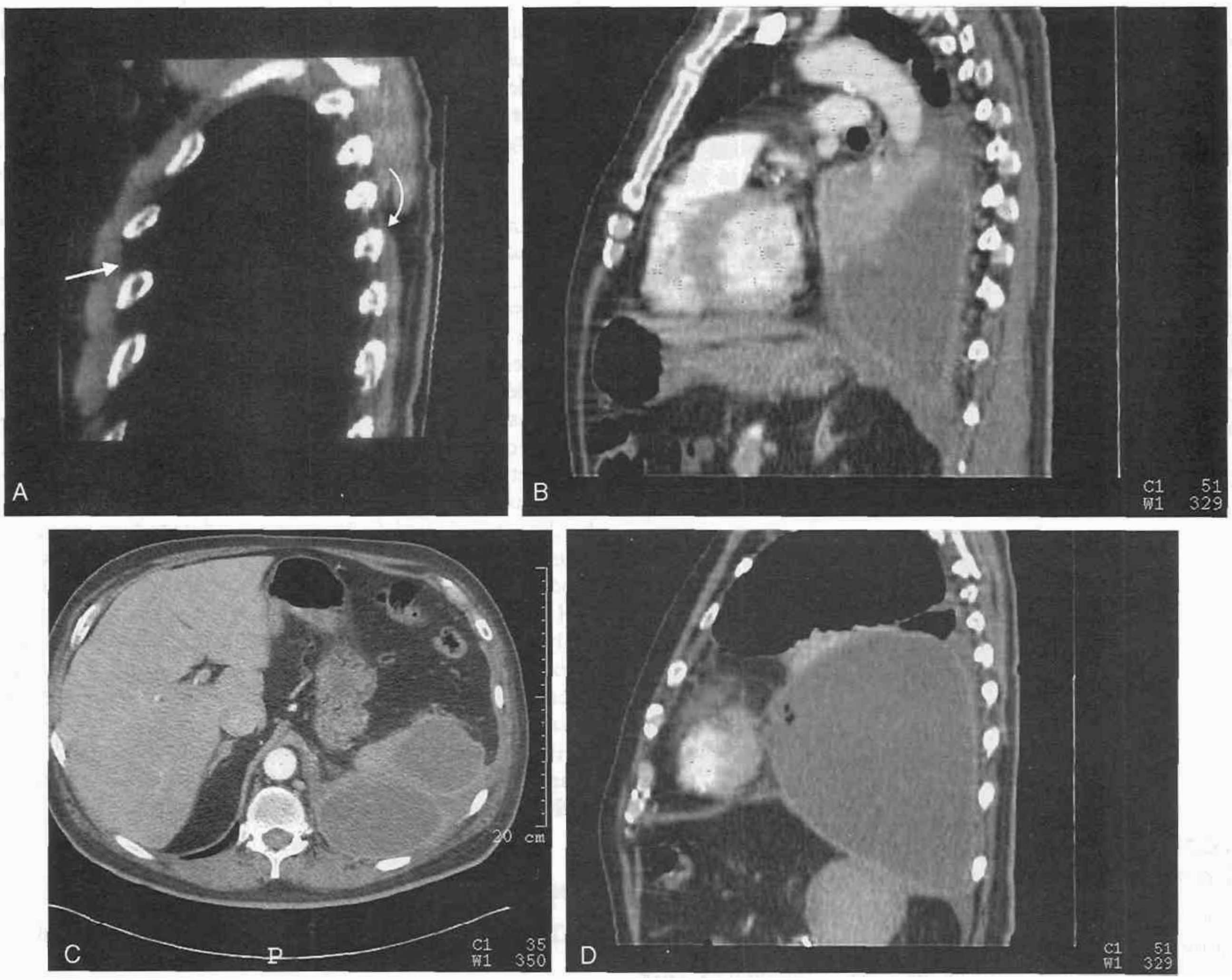

Figure 61–103. Sagittal reconstruction taken through the lateral portion of the chest, about 3 cm lateral to the midclavicular line. *A,* This scan shows quite clearly the widened space between the anterior ribs compared to the posterior ribs (*arrow*). Furthermore, you can appreciate how the structure of the ribs actually enhances the cephalad direction of the needle or catheter—there is an upward slope of the ribs. This permits remarkable flexibility in angling the device when inserted through the ribs. *B,* Sagittal reconstruction through the left side of the chest. Note that the anterior diaphragm is much higher than the posterior portion and therefore the muscle slips are much higher anteriorly. *C,* Relationships of the diaphragm can also be appreciated by noting the position of the diaphragm in a patient with an inverted diaphragm. This scan shows what would apparently be a left subdiaphragmatic collection. Examination of contiguous slices suggests its true nature. *D,* Sagittal scan shows how large pleural fluid collection pushes down and forwards the posterior portion of the diaphragm. Note how the anterior portion is virtually stationary because it is higher and less mobile; more anterior approaches are less variable and less prone to motion during the procedure.

pathway, it is also optimal to avoid uninvolved organs and noncontiguous peritoneal spaces.

One of the most problematic areas typically involved includes the supracolic spaces above the mesocolon and below the diaphragm (see peritoneal chapter). The most common are the right subphrenic, left subphrenic, and lesser bursa (sac). To plan the trajectory in these areas, it is critical to understand and appreciate the spaces as they relate to the diaphragm and rib cage.

These relationships can be best understood by noting the spaces between the ribs (Figs. 61–103 and 61–104). The subphrenic collections can be typically punctured and drained without traversing the pleura as suggested by some authors if one uses an angled approach and chooses a trajectory as anterior and lateral as possible. One should never choose an entrance pathway that traverses the pleura; quite candidly, I have never encountered an abscess that required such an approach. Improved delineation of anatomy and access to these spaces can be optimized by having the patients in variable positions as discussed in the peritoneal chapter. One should never have an entrance point more posterior than the mid-axillary line—if a collection is small, it would be better to traverse an organ. On the right, one can penetrate the liver to approach such collections. I think this is preferable because with the liver abuting any such collections there are bacteria circulating through the liver anyway.

The left subphrenic space is demonstrated at this point; discussion of the right side is provided later under specific anatomic areas. When an abscess is present, it is best to choose one of the lowest levels of the abscess and to choose a point in the mid-axillary line (Fig. 61–105). The instrument is angled cephalad, the puncture made, and the wire advanced cephalad. Note how the wire naturally moves cephalad and follows a line parallel to the intercostal spaces.

Several points should be made concerning the configuration and nature of the abscess collection. If an abscess collection is long, plan the trajectory of the puncture so that when the catheter is inserted it will lie throughout the length of the cavity. Two approaches may be used. First, one can choose an entrance site at the upper or lower end of the cavity (Fig. 61–105) so that the catheter will traverse the entire length or width. The alternative is to make two punctures at the center point, one directed cephalad and one directed caudad to permit positioning of a catheter at the top and bottom of the cavity (see section on catheterization) (Fig. 61–106). If such an abscess is elongated in a transverse direction, catheters should be similarly placed in that plane. If multiple septations are seen within a cavity, it is reasonable to plan the trajectory so that the maximum number of cavities will be traversed. Although best surgical results are obtained if an extraperitoneal approach is used, this is not true with percutaneous procedures. With surgery, a peritoneal approach is disadvantageous because it opens the possibility of "soiling" sterile portions of the peritoneum. A percutaneous puncture and drainage expose only the pathway to contamination rather than the wide surface of the peritoneum. Potential contamination is minimal if meticulous technique and methods are used.

Neither we nor other authors have found any indications that a peritoneal approach differs in outcome from an extraperitoneal approach with percutaneous drainage. In our experience, planning the trajectory to provide dependent drainage is not required. Purulent material follows the line of least resistance, which is the catheter tract. In fact, for subphrenic collections I prefer a more mid-axillary approach to a posterior one, to avoid the pleura.

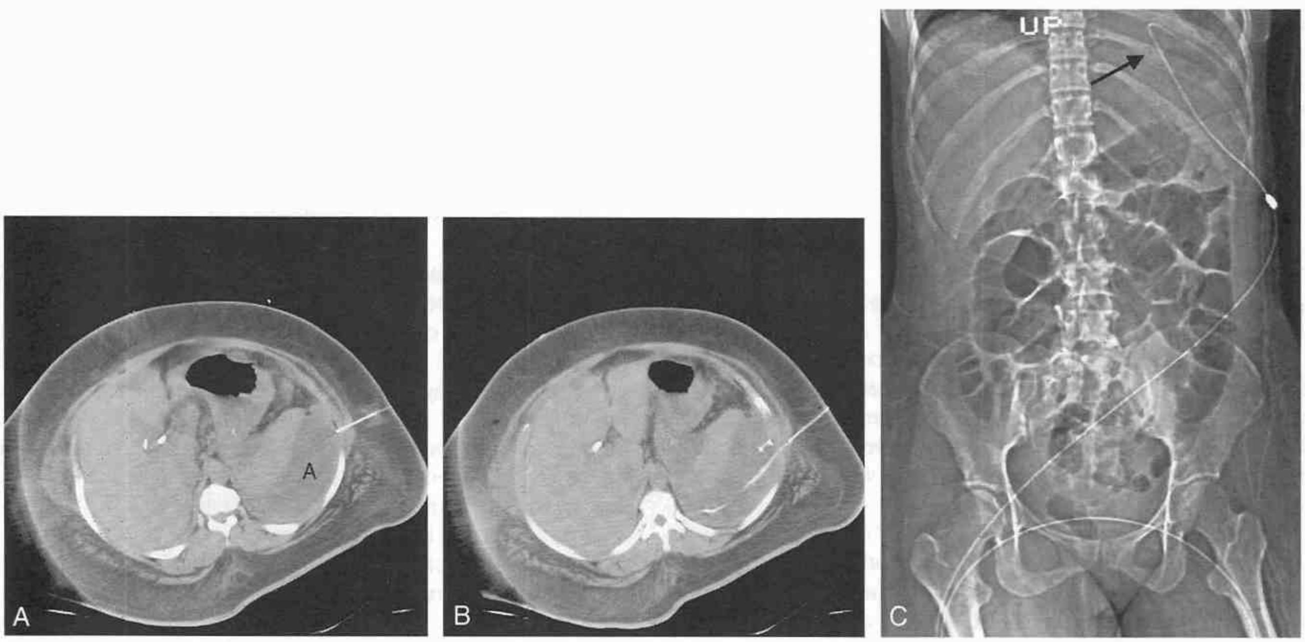

Figure 61–104. *A,* CT scan shows fluid collection around the spleen. The needle is directed posteriorly and cephalad. *B,* With insertion of wire, the wire moves posterior and cephalad. *C,* With a digital radiograph, the cephalad positioning of the wire at the highest level of the abscess *(arrow)* below the diaphragm can be appreciated. There is no need to traverse the pleura to drain these very high collections.

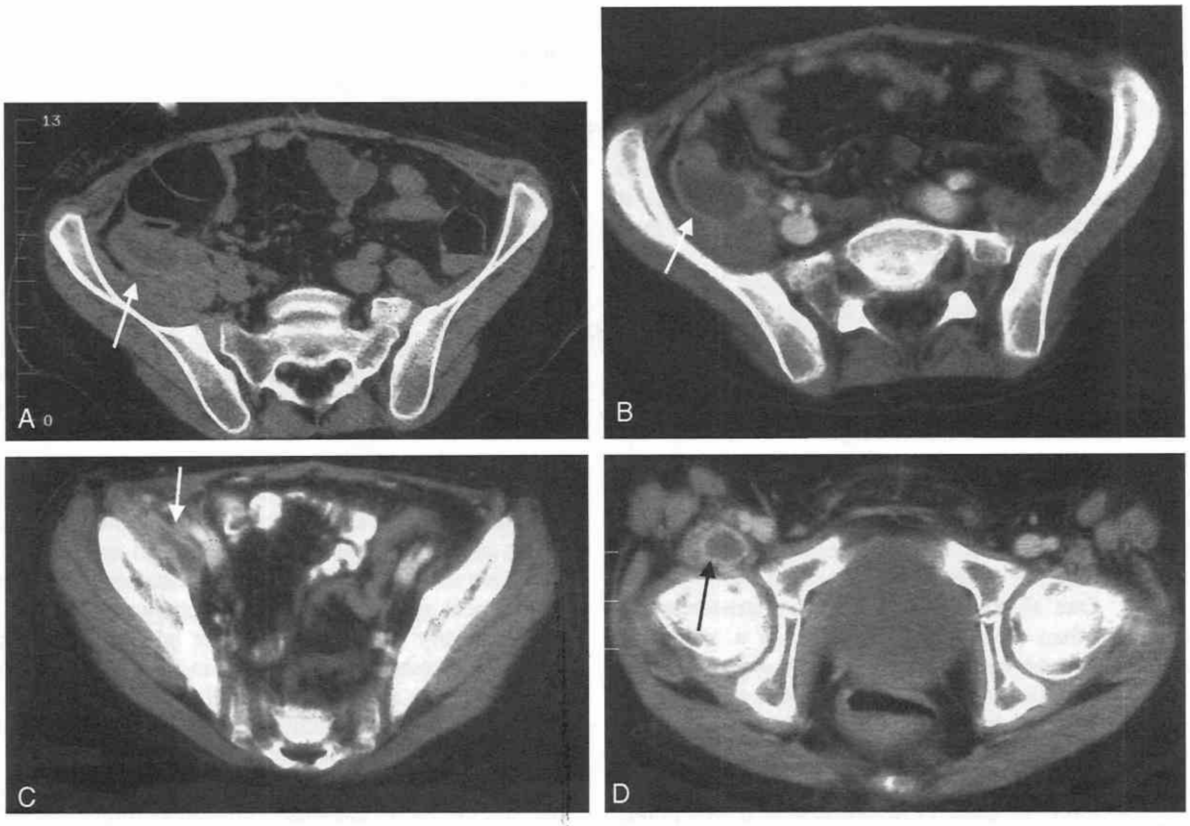

Figure 61–105. *A* to *D*, The four scans taken before the drainage procedures show a long abscess in a child who had perforation of the duodenum secondary to a vasculitis. The abscess designated by the *arrow* is seen in the iliacus in *A*, the iliopsoas in *B*, the psoas in *C*, and the distal psoas in *D*. Others had attempted percutaneous drainage by only draining the fluid in *D*.

Selection of Modality

Once a trajectory has been planned, choose the guidance modality most suitable for the procedure. Fluoroscopy, ultrasound,[193, 200,208] or CT can be used, but CT is the preferred method in almost all cases.[111,147,192,203,389] The larger and more superficial fluid collections can be punctured by using fluoroscopy or ultrasound.[338,359] The more difficult the abscess, that is, the deeper, smaller, or more critically located it is, the more likely it is that CT guidance can be used.

Diagnostic Aspiration

Before catheter or trocar placement, perform a diagnostic aspiration to confirm the presence of an abscess. There are two reasons I use an 18-gauge needle to perform diagnostic aspirations. First, the larger needle permits aspiration of even the thickest purulent material. Second, if at the time of aspiration the fluid appears purulent, the sheath permits insertion of an angiographic wire and catheter without a second puncture.

The actual puncture and placement of the needle are performed in the same manner as any other needle procedure. Try to plan the procedure so that the tip of the needle is placed in a more posterior or dependent location so that the anterior wall will not be retracted away from the needle as the fluid is aspirated and the wall partially collapses.

I take two steps to minimize the risk of contamination along the pathway. First, when draining abscesses in a solid organ, I choose the path to include a "cuff" of normal parenchyma to lessen the chance of tearing the thin wall of an abscess. Second, at the time the puncture is made I aspirate a sufficient amount of material to lessen the "back pressure." There is one reported case of spillage into the peritoneum that produced peritonitis, as well as a case of dissemination into the subphrenic area (Fig. 61–107) reported by Johnsen et al.[197] One must always strive for meticulous technique. If the catheter is in the area of the spillage, no further treatment is necessary, but if it is not, another catheter should be inserted in the area (Fig. 61–108).

If purulent material is aspirated, a sample of 10 to 20 mL is aspirated before catheter insertion and sent for culture. If the flow of purulent material is quite fast, I will remove 25 to 75 mL to relieve any back pressure and prevent any spillage or tracking during catheter insertion. After removal of this purulent material, I inject a small amount of urographic contrast material to facilitate the fluoroscopically guided catheter insertion. Also, if the wire and needle become inadvertently displaced, the contrast material permits a clear "target" for a puncture under fluoroscopy. Be careful not to inject too large a volume, which might overdistend the cavity and cause spillage of purulent material. After this step, insert an angiography wire into the cavity to stabilize the sheath if the patient is being transported to fluoroscopy. At times one may simply choose to insert the catheter on the CT, using the topogram as the method for confirming the catheter location or

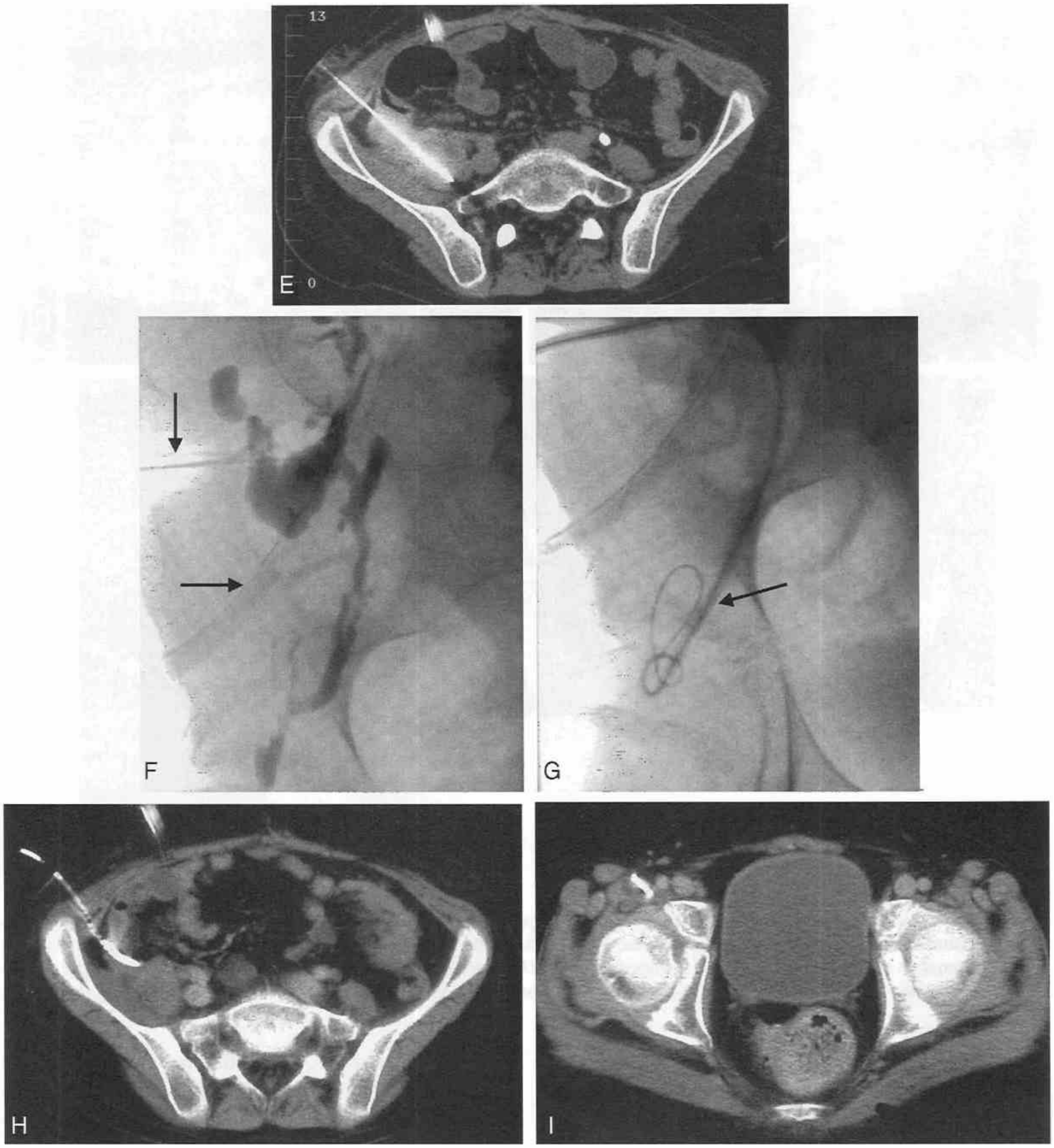

Figure 61–105. *E* to *I*, The five images show the proper procedure with positioning of the catheter. In *E*, the needle puncture through the widest extent of the abscess was made. In *F*, the CT catheter *(vertical arrow)* is seen as it is used to perform a sonogram of the cavity that flows down through the psoas over the femoral head. The *horizontal arrow* shows the surgical catheter previously placed, which did not drain the abscess. In *G*, the wire and catheter were manipulated to follow the entire length of the cavity. In *H* and *I*, the axial scans show the upper and lower extent of the catheter in all portions of the abscess.

blindly using a sense of "feel." Availability of a portable fluoroscopy device or an attached fluoroscope is helpful.

If the material is not obviously purulent, I aspirate only a small amount of fluid and send it for culture. In the event that a repeat puncture and drainage might be required, I try not to aspirate the fluid collection "dry"; if such a cavity is aspirated dry, there will be no well-defined lesion to target should a drainage be required later. I do not insert a catheter when the fluid is not obviously infected, because if such a collection is sterile, an indwelling catheter might introduce pyogens and cause a secondary infection. In patients with tumors in the area, a cytologic sample should be sent to determine if there is a necrotic neoplasm or secondarily infected tumor giving toxic symptoms similar to abscesses (discussed later). Catheter drainage may provide some palliation for such tumors or secondarily infected tumors.

Catheter Selection and Insertion

There are two types of catheters available for drainage: drainage catheters inserted by the Seldinger method and

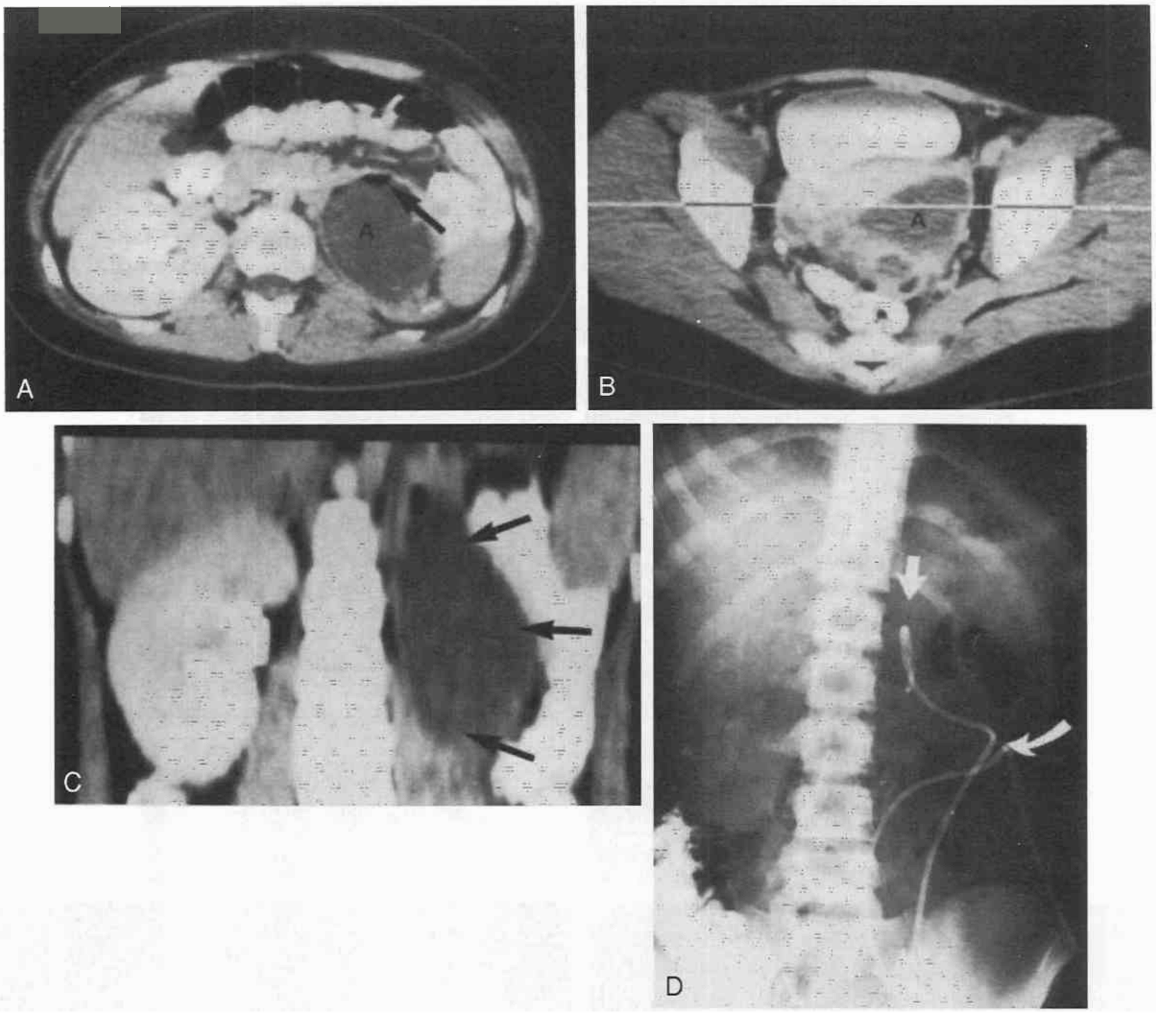

Figure 61–106. *A,* CT scan through the midabdomen shows a large abscess (A) in the retroperitoneum, containing some gas *(arrow). B,* The lowest portion of the abscess (A) extends into the pelvis behind the left adenexa of the uterus. *C,* Coronal reconstruction shows a long abscess *(arrows)* extending through the retroperitoneum. *D,* Plain film shows placement of two catheters entering from the middle of the cavity *(curved arrow),* extending to the top and bottom of the cavity *(arrows).*

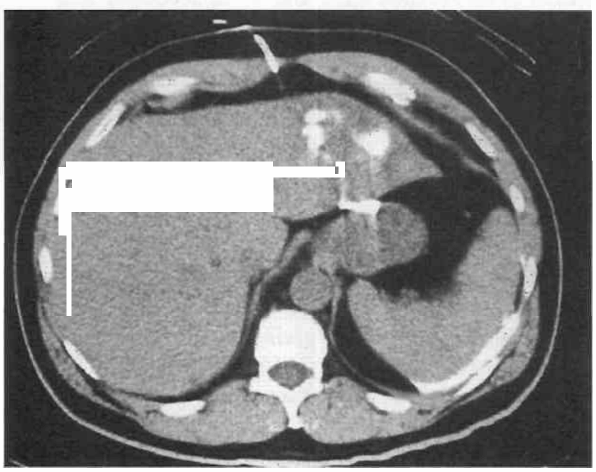

Figure 61–107. CT scan shows an abscess in the left lobe filled with contrast material. The drainage catheter has penetrated the posterior surface of the liver; no repositioning was made because the catheter tracted through the cavity.

single-step catheters.[128,143] Either may be chosen, depending on the specific nature of each case. The configuration of the tip and location of the holes vary among those available.

The size of the catheter and the size of the pigtail shape to be used should be matched to the size of the abscess cavity, so that the entire curved end is in the cavity. As a rule it is important to use the largest catheter possible from the beginning; if the procedure becomes technically difficult, one can settle for almost any size of catheter and upgrade it later. Larger catheters do permit faster drainage of material. It is important not to have holes outside the cavity. If holes are outside, leakage into a sterile space or organ can occur. Conversely, if a cavity is large, it may be important to cut additional side holes in the catheter if needed.

Two options are available for insertion of large abscess catheters. The trocar catheters now commercially available from many different companies can be used. I have found that these trocar catheters are useful for large, superficial abscesses but not so suitable for most of the small or critically located abscesses.

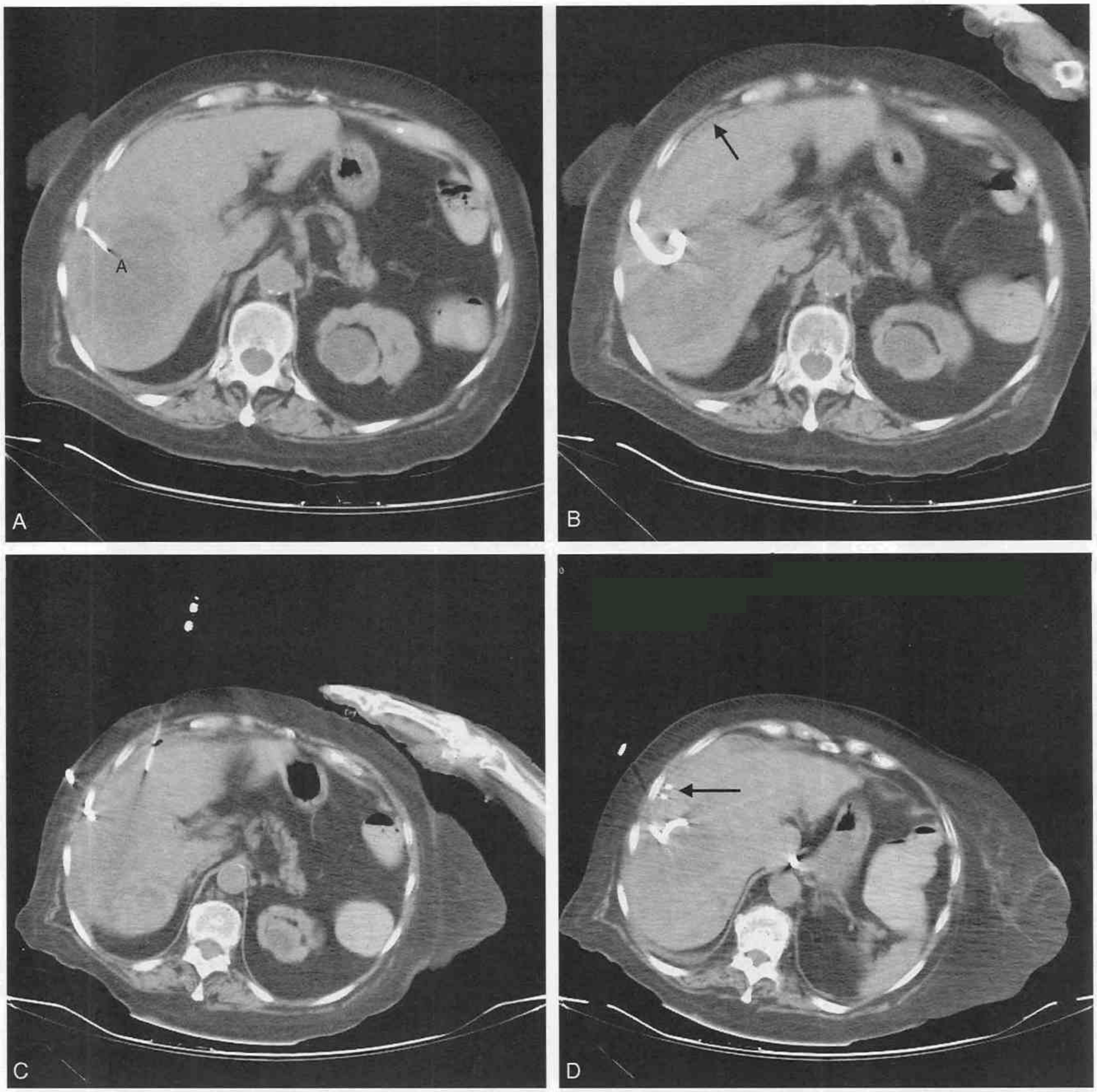

Figure 61–108. *A,* CT scan shows puncture of intrahepatic abscess (A) through a midaxillary line location. Because a cuff of normal liver was used, no leakage occurred at this time. *B,* After insertion of the large catheter *(arrow),* it was noted that a leakage of purulent material occurred into the subphrenic space *(arrow). C,* Puncture of the small subphrenic fluid was performed. When such punctures are attempted, they should be planned obliquely and so that the needle penetrates beyond the space. The instrument is withdrawn while suction is applied; the location of the tip in the space is heralded by aspiration of fluid. The wire and catheter are then inserted. *D,* Because of the small space, repeat scan is important to confirm the location of the catheter in the space *(arrow).*

The second option I also like to use is a two-step procedure. In the first step an angiographic catheter is inserted on the first day of the puncture and in the second step the catheter is upgraded in size on the second or third day as needed after the sinogram.

The chosen catheter can be inserted in one of two ways. First, if one has only limited experience, the best way is to transport the patient to a fluoroscopic unit for catheter insertion and positioning. If one has a fluoroscopic device with the CT scanner, as afforded by many companies, placement of this catheter is quite easy. As a rule, I always adjust the catheter position to ensure that it traverses the entire length of the cavity and that there are no kinks. Also, if the cavity is small or if the catheter has a large number of holes, be certain that none of the holes are outside the cavity. If holes are outside the cavity, then dissemination can occur through the side hole with drainage or irrigation. The second choice is to put the catheter in by "feel" and to observe the location with the Topogram or the Scoutview. If one is quite experienced, this second

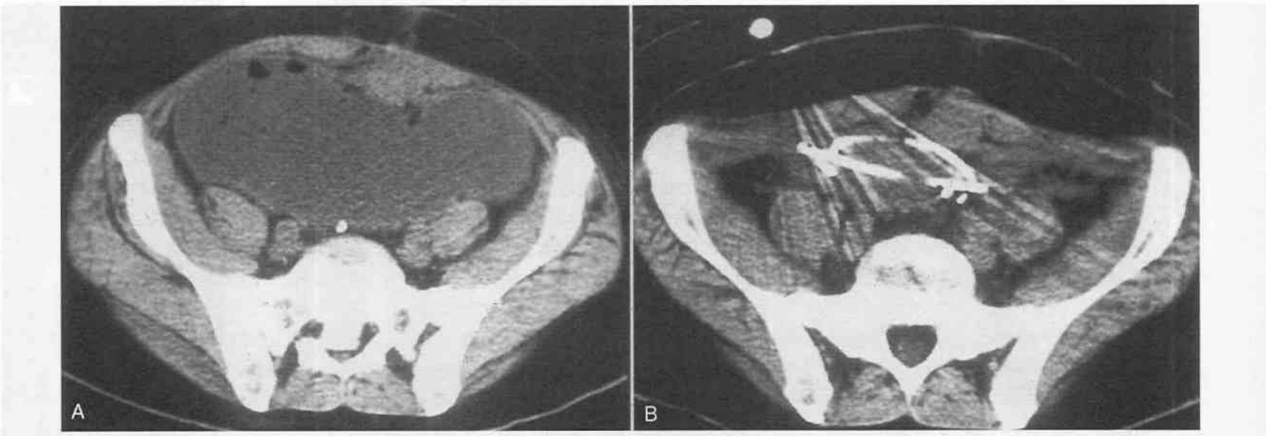

Figure 61–109. *A,* This scan shows a very large abscess, which is very wide across the entire abdomen. To ensure adequate drainage, a catheter was inserted from each side and crossed in the midline. *B,* This follow-up scan shows total evacuation of the cavity and the catheters in the midline.

method will suffice, and any necessary adjustment in catheter position can be done on the second or third day during the sinogram.

To ensure that the entire length of a cavity is covered, there are two possible approaches. One can start at either the highest or lowest end and then insert the catheter throughout the length. Alternatively, one can insert two separate catheters in the middle and cross them so that each one is directed toward the upper or lower extreme (Fig. 61–109). Cavities with multiple loculations may drain spontaneously, or the effective drainage can be improved with a fibrinolytic material as noted later. If there is any question about communication among the different spaces, one must not hesitate to use multiple catheters (Fig. 61–110).

With the catheter in place, I gently evacuate all of the purulent material from the cavity until the cavity is empty, unless several liters of material are present. In such cases it is probably prudent to remove no more than 1 L of fluid by aspiration and then to permit the remainder to drain more slowly through the catheter. This prevents potential fluid shifts between various compartments. I adopted this approach after we had one patient who suffered a hypotensive collapse after the acute removal of 6 L of purulent material (Fig. 61–111). At this time I use saline irrigations to flush the cavity until the returning material is almost clear. If the fluid becomes blood tinged during the irrigation, I stop the irrigation and send the patient back to let the material drain slowly. Besides these steps of positioning and irrigation, I perform no other manipulation at the time of the first insertion to avoid bacteremia.

Some authors have recommended the use of a wire at this point to disrupt any septations or adhesions. This appears to be imprudent because use of a wire traumatizes the wall and may cause a significant bacteremia or hemorrhage from the granulation tissue.

Sinogram and Catheter Adjustment

Sinograms are performed somewhere between 48 and 72 hours subsequent to the procedure to check the position

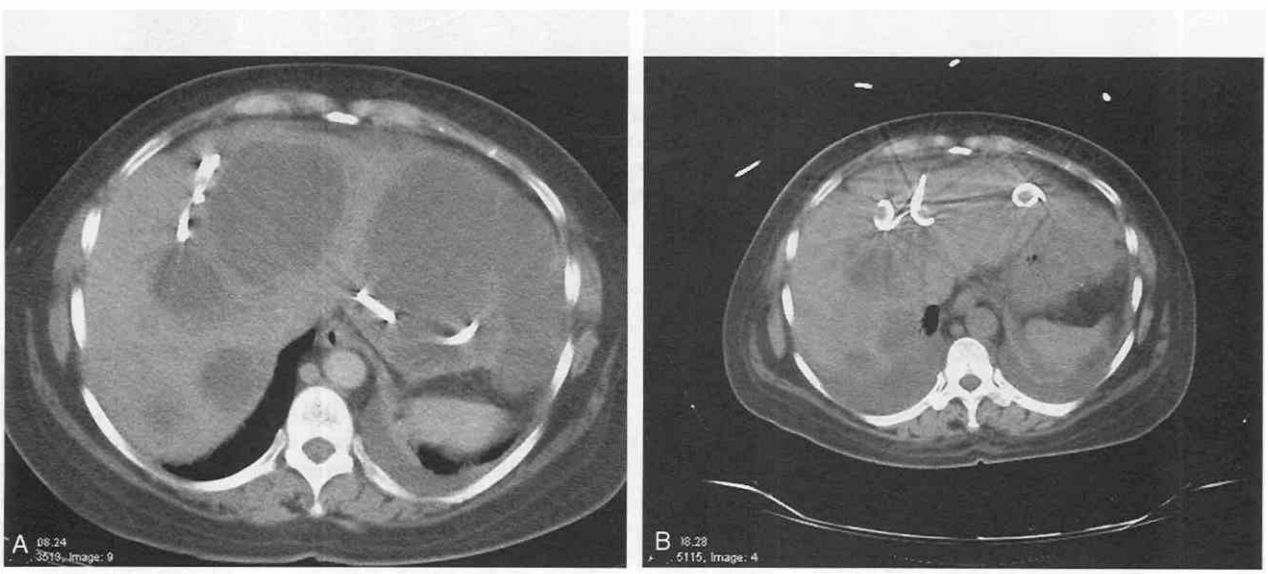

Figure 61–110. *A,* Scan shows multiple, large abscess cavities in the liver. Because of the large number, only the two largest cavities were drained. *B,* Follow-up scan shows reduced size of two drained cavities as well as the other smaller cavities.

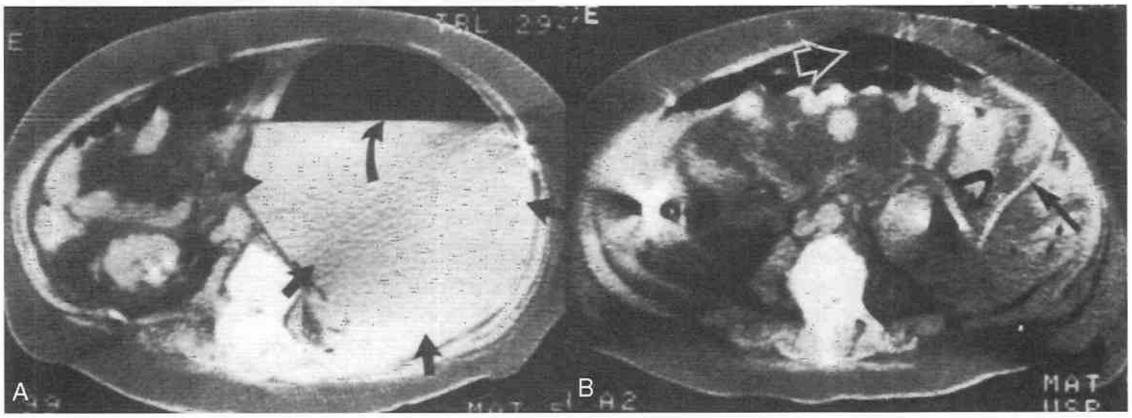

Figure 61–111. *A*, Large abscess cavity *(arrows)* with air-fluid level *(curved arrow)* is located in the left side of the abdomen. After the acute removal of 6 L of purulent material, this patient suffered a severe hypotensive crisis. *B*, Scan of the same patient after several days shows incorrect placement of the catheter *(arrow)* through the anterior wall of the abscess. The wall of the abscess *(curved arrow)* receded past the catheter so that holes in the catheter permitted air *(open arrow)* and material to flow into the peritoneum.

of the catheter and every 4 to 5 days after to assess the progress of healing. During the first sinogram one evaluates whether the catheter placed is still in correct position and is of adequate size for the evacuation of any residual purulent material. As the cavity is evacuated, the contour may change and shift the location of the catheter, requiring adjustment of the position. If there is considerable purulent material left, one may choose to increase the size of the catheter. At this time, sequential dilation may be performed safely. I discourage extensive dilation at the first procedure because of concerns about either spillage of bacteremia or bleeding. Furthermore, if the material is thick or loculations are present, one might institute catheter irrigation with fibrinolytic agents at this time, if it was not used initially.

If one chooses subsequent sinograms, they are used to assess the size of the cavity and the possible presence of fistula. Assessing the size of the cavity is important to determine the time of catheter removal. As healing occurs with the ingrowth of granulation tissue, the cavity size reduces. The catheter should be left in place until the cavity almost disappears. Fistulae are seldom seen except in the later sinograms as the inflammation recedes. Most fistulae close spontaneously (see later) (Fig. 61–112).

Catheter Management and Irrigation

Once the catheter is in place, a few guidelines must be followed to ensure a successful drainage. It has been my

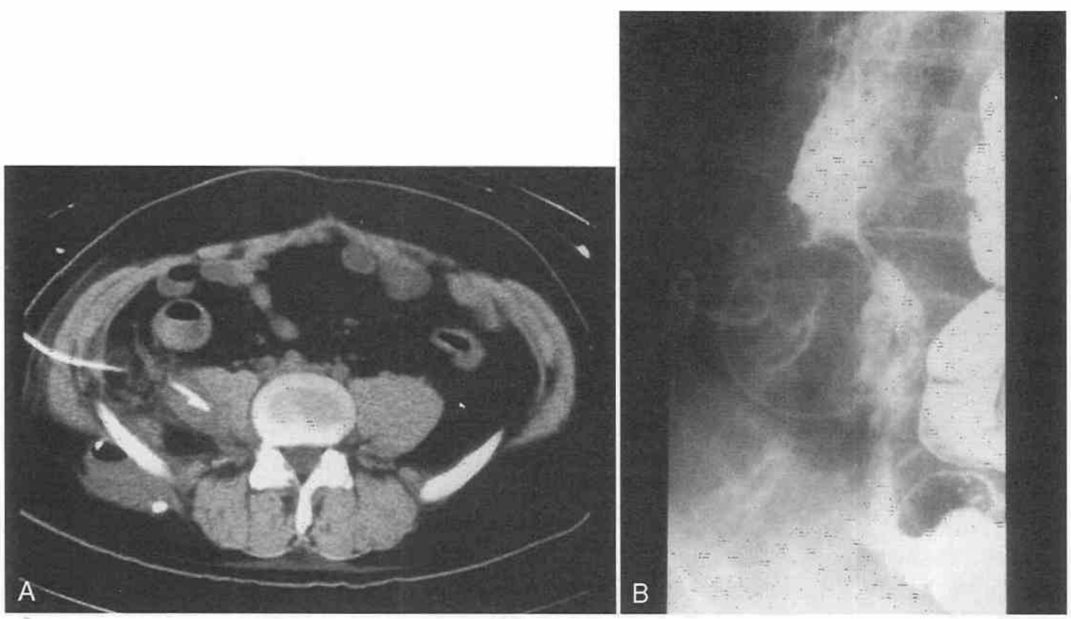

Figure 61–112. *A*, CT scan shows two abscess cavities in the right side: one in the psoas muscle and one in the gluteus muscle behind the iliac crest. The high-density objects are cross-sections of two different catheters that were used to drain the abscesses. *B*, A sinogram taken later in the course of the patient's recovery shows communication of the long cavity in the psoas muscle with the small bowel. Total resolution without surgery followed (see text).

routine to leave a catheter only to gravity drainage. My concern about application of high suction is that the holes may be occluded by tissue and loculations can accumulate peripherally.

The one circumstance in which active suction is best is when there is free communication with either a fistula or biliary system (see Fig. 61–115).

Catheter irrigation should be performed with either one or two agents, as follows. The two agents we use to facilitate drainage are saline and tissue plasminogen activator (tPA). If the material being drained is quite thin and there are no definite septations noted on imaging studies, we inject saline. Saline in the amount of 10 to 15 mL should be injected every 6 to 8 hours to keep the catheter lumen clear. If the material being drained is quite thick or there are septations in the abscess, urokinase should be injected in amounts as follows, depending on the size of the cavity: 0 to 3 cm, 12,500 units; 3 to 5 cm, 25,000 units; 5 to 10 cm, 50,000 units; and greater than 10 cm, 100,000 units. After the urokinase has been injected, a small amount of saline should be used to clear the catheter of the urokinase. The catheter should be clamped for 5 minutes and then left to gravity drainage. The irrigations are continued for 3 to 4 days.

The effectiveness and safety of urokinase has been documented by our group[8] in the literature (Fig. 61–113). Park et al[320] showed that in vitro, the urokinase as compared with saline definitely decreased the viscosity of the purulent material (Fig. 61–114). The safety of urokinase in vivo was proved by Lahorra et al,[224] who demonstrated that intracavitary urokinase produced no systemic effects. A later article by Haaga et al demonstrated considerable benefit for using urokinase compared to saline (Tables 61–8 to 61–10).

The action of urokinase is similar to tPA, which is why we now recommend using that agent. Both of these fibrinolytic agents change the substrate plasminogen to the active fibrinolytic agent plasmin. There is no reason to suspect that its activity should be any different than urokinase. If one reviews the tables of information from the urokinase study, it can be seen that it improved the clinical factors of the patient and shortened the drainage time and hospital stay. This is an "off-label" use of the drug and so a patient must be notified of that, but it is legal for a physician to use the product in this fashion. In fact, we are now in the midst of an FDA-reviewed trial in which the FDA ruled there was no need for a new IND application. At this time the agent is not approved for usage, but individual physicians can use such drugs because they are approved for other uses.

Table 61–8. Other Abscess Parameters

Abscess Parameters	Urokinase	Saline
Abscess diameter (cm)		
0–3	1	1
3–3	6	8
5–10	8	7
>10	4	3
Location[a]		
Peritoneal	7	9
Retroperitoneal	3	6
Parenchymal	9	3
Infected hematoma	2	3
Catheter size		
>10 French	3	5
<10 French	16	14
Suction		
Gravity	19	18
Not specified	0	1

[a] Total for each category is 18. Each group had one designated site.
From AJR 174, June 2000, p. 1683.

Constant Irrigation

In some cases when especially thick material is present or there is injury to the vascular supply, placement of several catheters for irrigation may be beneficial. In such

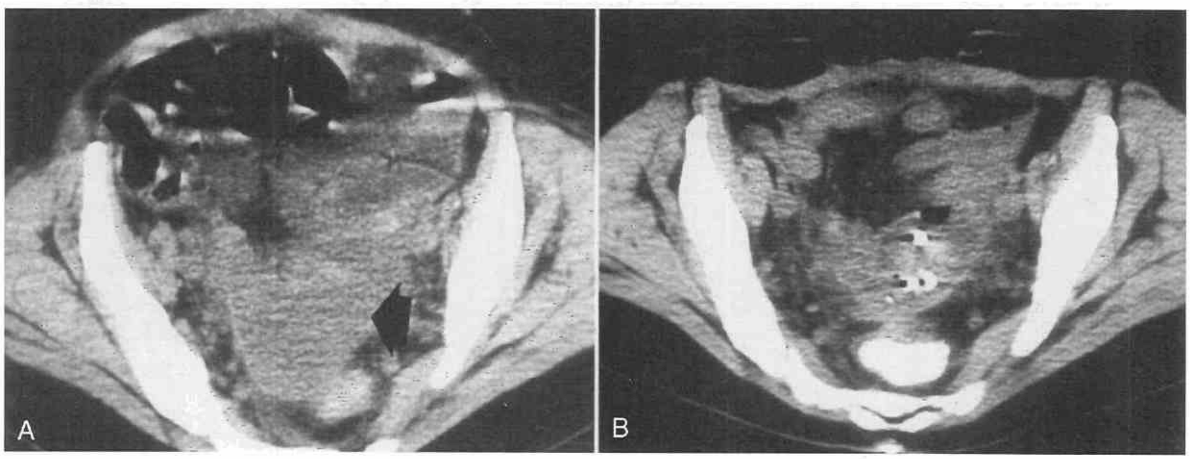

Figure 61–113. *A*, CT scan shows large high-density mass *(arrow)* in the posterior pelvis. The mass proved to be an infected hematoma following hysterectomy. The patient had systemic lupus and was on high doses of systemic steroids. Even with these complicating factors, the patient was cured by percutaneous drainage enhanced by urokinase irrigations. *B*, Follow-up scan shows reduction in size of cavity with a high-density catheter in place. There was ultimately total resolution without surgical treatment.

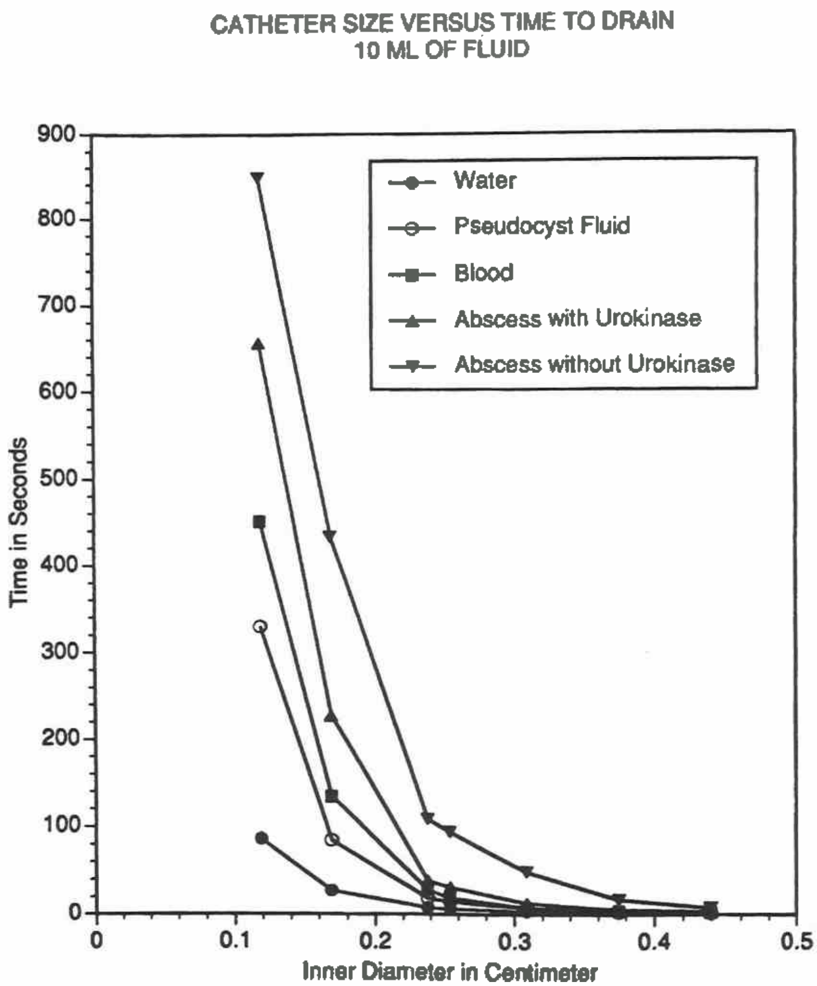

Figure 61–114. An in vitro experiment was performed evaluating different parameters including urokinase treatment. The graph shows the drainage time of various fluid types through various sizes of catheters. The upper two lines show how urokinase improves the drainage of purulent material. (Data from Park JK, Kraus FC, Haaga JR: Fluid flow during percutaneous drainage procedures: An in vitro study of the effects of fluid viscosity, catheter size, and adjunctive urokinase. AJR Am J Roentgenol 160:165–169, 1993.)

cases one should make sure that fluid is moving freely between the catheters so there is no buildup of fluid (see later section on hepatic abscess drainage).

Follow-up Evaluation

Before final removal of the catheter in a routine case, perform a final CT scan to ensure that all areas of the abscess are drained. An abscess that is completely resolved should show virtually complete obliteration of the cavity (but one may see a small amount of residual fluid and air) or decreased density in the liver. If a considerable amount of fluid remains, it is best to wait until the cavity has more completely resolved and has been reduced in size by granulation tissue. If a patient is doing well clinically, he or she may be discharged and managed as an outpatient during the time it takes for the cavity to granulate closed.

The last question to be considered during this final evaluation is whether the primary cause of the abscess and any important sequelae have been found. In most instances an abscess is the result of a surgical procedure or other intervention, but if there is no known cause, other diagnostic studies should be performed until all possible causes have been excluded (e.g., ulcer, diverticula). If a surgical problems exists, the appropriate therapy is instituted. In most instances a sinogram will have demonstrated a fistula to a loop of bowel, and management as described later is appropriate.

Table 61–9. Results of Student's Test for Length of Stay, Treatment Cost, Days of Elevated WBC Febrile Course and Days of Drainage

Test for	Group	Mean	t	df	p[a]
Length of stay (days)	Saline	29.00 ± 17.2	3.56	24	0.0025
	Urokinase	13.11 ± 9.5			
Treatment cost ($)	Saline	62,102.11 ± 42,844	3.49	22.3	0.0021
	Urokinase	24,178.00 ± 17,871			
Febrile course (days)	Saline	4.00 ± 6.25	1.63	18.1	0.1202
	Urokinase	1.45 ± 1.73			
WBC elevation (days)	Saline	9.12 ± 8.79	1.41	25.7	0.1710
	Urokinase	5.62 ± 5.04			
Drainage (days)	Saline	14.88 ± 20.5	1.57	17.5	0.1361
	Urokinase	6.93 ± 4.2			

Note:—df = degrees of freedom.
[a] Separate variance t test used.
From AJR 174, June 2000, p. 1682.

Catheter Removal

When a drainage procedure has gone well, the patient will respond quickly and show dramatic clinical improvement. In such patients the fever will defervesce, the white

Table 61–10. Effect of Loculation on Length of Stay and Hospital Costs

Loculation	Test	Group	Mean	*t*	*df*	*p*[a]
No	Length of stay (days)	Saline	27.09 ± 17.8	2.81	11.5	0.0168
		Urokinase	11.04 ± 4.72			
No	Treatment cost ($)	Saline	58,023.33 ± 44,075	2.81	11.8	0.0169
		Urokinase	21,567.40 ± 7,797			
Yes	Length of stay (days)	Saline	32.50 ± 17.0	2.13	9	0.0617
		Urokinase	13.20 ± 11.81			
Yes	Treatment cost ($)	Saline	70,259.66 ± 42,981	2.97	5.3	0.031
		Urokinase	17,315.60 ± 6,760			

Note:—$\chi^2 = 1.57$, $df = 17.5$, $p = 0.8933$, df = degrees of freedom.
[a] Separate variance *t* test used.
From AJR:174, June 2000, p. 1682.

blood cell count will drop, and sweating episodes will stop. The progress of the drainage can also be assessed by following the sequential changes in the physical appearance of the fluid. Initially, the material will be cloudy and turbid; it will then change to a serosanguineous appearance, and finally it will change to a clear serous material. Cultures of the fluid will also change sequentially so that when the abscess has resolved, drainage fluid will be sterile. After this clinical response and the change in character of the material, the catheter can be removed.

If the fluid from the catheter does not change as expected but drains bile or enteric contents, a repeat sinogram is necessary to evaluate for a fistula. Many times fistulae may not be seen with an early sinogram, since they will be closed because of edema and inflammation.

The decision to remove the catheter is quite easy if the course of the drainage (i.e., clinical response, evolution of fluid changes, and appearance of the sinograms) is as expected. Before removal of a catheter, a final scan should be obtained to ensure that the cavity has closed completely. If this has occurred and there is no continued drainage, the catheter can be removed. The patient's antibiotics should be continued for several days after removal of the catheter.

Fistulae

Gastrointestinal fistulae commonly occur with intra-abdominal abscesses; some probably are causative in nature, and some are sequelae. Management depends on the amount of flow, whether it is of low or high output.[213,229,292] Low-output fistulae (320 mL per day) usually close spontaneously without additional therapy (see Fig. 61–103). High-output fistulae require treatment. High suction on the catheter should be maintained, and the bowel should be put at rest. This usually means insertion of a nasogastric tube. Hyperalimentation may also be needed for several weeks in some severe cases. Failure of these methods indicates a need for surgery.

Drainage Issues

Drainage Errors

Relative to placement of the catheter, it is important that the largest catheter possible be inserted to permit reasonably rapid drainage of the fluid but also to provide ample diameter should some purulent material become inspissated on the inner wall of the catheter. This does not mean that a massive catheter is required, but least a 10- to 12-French should be used. Also the catheter should be placed in the most remote site of the cavity so that loculations do not occur distal to the placement of the catheter.

The administration of antibiotics is absolutely mandatory. Historically, it has been widely recognized that drainage is even more critical than administration of antibiotics, but the facts are that abscesses resolve quicker and lessen the possibility of generalized sepsis, which is always possible.

Proper maintenance of the catheter includes irrigation of the catheter adequately with either saline or a fibrinolytic material. Purulent material tends to become encrusted within the lumen so the functional diameter is reduced. Catheters should be irrigated three times a day with saline, with a volume to clear the entire catheter volume. In many cases, a fibrinolytic should be used. Our study with a fibrinolytic clearly showed remarkable improvement in the resolution of abscesses using this agent. Septations and loculations are also cleared by such a fibinolytic agent.

Although the routine abscess does not require suction, in some circumstances drainage is improved by its use. If a sinogram demonstrates a fistula to the biliary system or a loop of bowel, application of suction is mandatory. In these cases resolution will not occur unless suction is maintained to ensure the cavity and fistula are devoid of excess material (Fig. 61–115).

Finally, if an abscess does not resolve with drainage or even increases in size, one should suspect a fungal infection or even spontaneous bleeding. It is frequently observed that the infectious agent in an abscess may change based on elimination of sensitive organisms and selection of resistant organisms. *Candida* commonly becomes the dominant organism in a patient with multiorganism infection who is treated with broad-spectrum antibiotics selected for bacterial pyogens. In several cases, we have encountered an abscess that appeared to increase in size and developed an elevated density. In such cases, localized bleeding had occurred due to the infectious injury to local blood vessels (Fig. 61–116).

Errors associated with abscess drainages have been documented by numerous authors.[109,111,140,141,225] Perhaps the most common error made is the improper choice of trajectory, which can cause either a portion of the pleura to be crossed when draining a subphrenic abscess or a solid

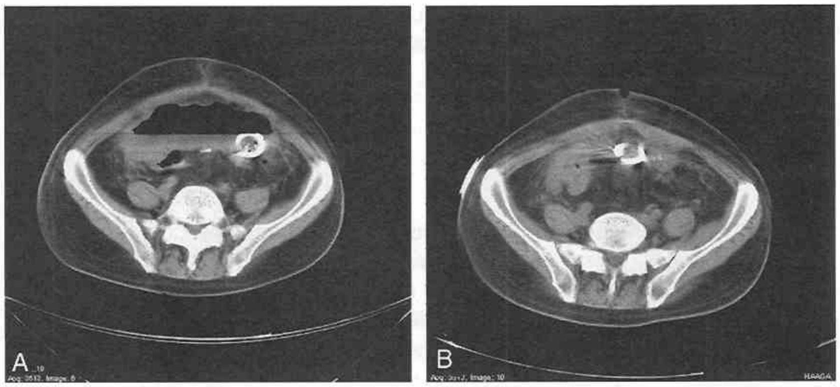

Figure 61–115. *A*, Scan shows a large abscess in anterior lower abdomen, with an air-fluid level *(arrow)* that did not resolve with siphon drainage. *B*, Application of suction was required, which resulted in total resolution. Note that the air-fluid level is resolved and no residual material is noted around the catheter.

organ to be traversed. Although with today's potent antibiotics dissemination of an infection is infrequent, it can occur and produce significant difficulty.

Other errors include selecting inappropriate cases—attempting to drain either an inflamed area that is not liquefied, an infected tumor, a fungal infection, or an infected hematoma. Infected hematomas cannot be drained using routine methods with saline or a catheter irrigant.

Several other common errors occur late in management. Inadvertent or early removal of the catheter results in recurrence of the abscess. Failure to either identify or correct the cause results in a recurrence such as fistula or ulcer. If a final CT scan is not obtained, a recurrent or undrained abscess can be present.

Unusual Clinical Circumstances

A number of unusual clinical circumstances are encountered in daily practice that are worthwhile to note specifically. These include patients with Crohn's disease, critically ill patients in intensive care, and infections caused by antibiotic-resistant organisms.

Relative to Crohn's disease, Garcia et al[99] reported on the outcome of medical/percutaneous drainage versus surgical treatment. In their series of 51 patients, fewer recurrent abscesses developed in postoperative patients than in those treated by the more conservative method (12% vs. 56%).

Schurawitzki et al[352] noted the superiority of CT guidance over ultrasound in the intensive care setting. With ultrasound there were a high number of equivocal studies that prevented adequate evaluation and/or performance of a drainage procedure.

Antibiotic-resistant organisms are becoming more prevalent in the environment, so the question of drainage effectiveness is raised. Catalano et al[49] reported a series of 21 patients with vancomycin-resistant enterococci abscesses.

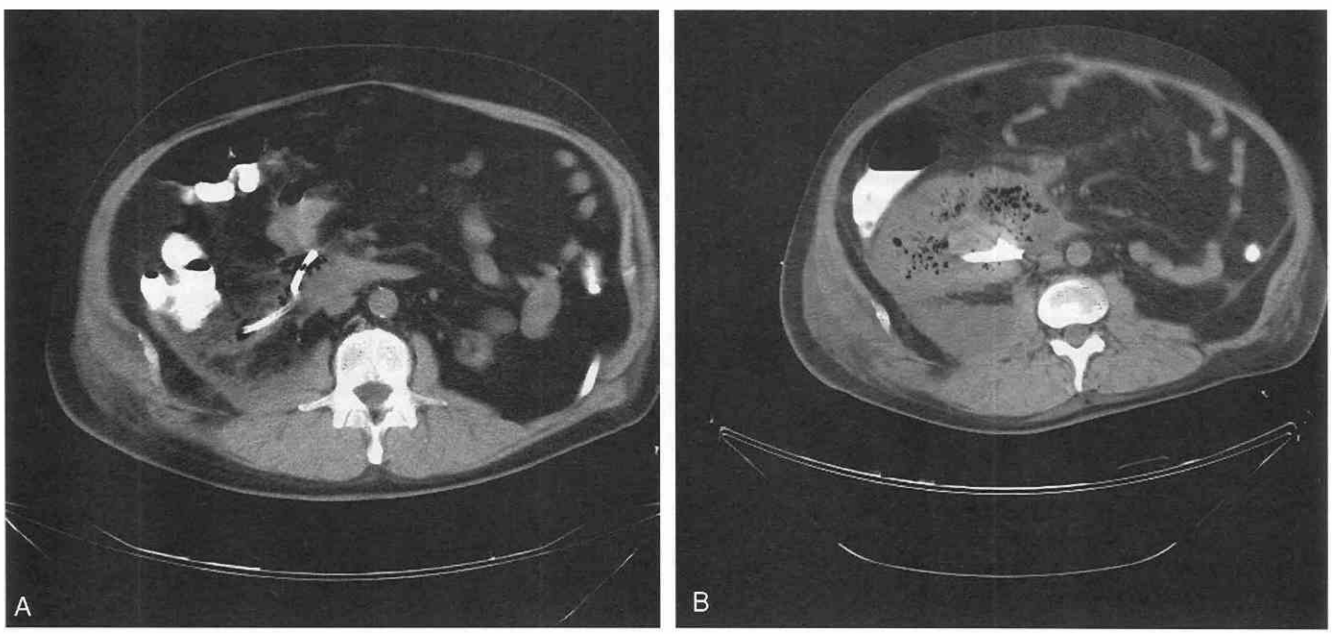

Figure 61–116. *A*, Scan shows an abscess that appears to be draining appropriately. *B*, Subsequent scan shows enlargement of the abscess cavity *(arrow)* with increased density secondary to local bleeding.

In this group, 71% were drained successfully using standard guidance methods and systemic antibiotics.

Success Rates

Since the introduction and development of percutaneous abscess drainages, there has been controversy among the various groups about the achievable success rate, which overall has varied between 62% and 90%. The differences in success rates undoubtedly depend on numerous factors, including selection criteria, drainage techniques and catheters, and final criteria for outcome determination (i.e., definition of cure, palliation, etc).

A number of authors have studied the factors that affect the outcome of the drainage procedures. Several major determinants have been found, including the status of the immune system, the overall severity of the patient's illness, and the accuracy of abscess localization.

Lambiase[229] recently reported a large series of patients treated with PAD and noted a significant difference in the outcomes of his patients (see earlier section on immune system). He found that those patients who were immunocompetent had a successful outcome in 72.6%, compared with those immunocompromised patients with a success rate of 53.4%.

Levison et al[239] correlated the APACHE II score with drainage techniques and outcomes. He found that those patients with scores less than 15 had a mortality rate of 1.7% and those with scores greater than 15 had a mortality rate of 78%. There was no benefit of one method—surgical or percutaneous drainage—over the other.

Deveney et al[71] studied the outcome of abscess drainage in two periods: the first in the 1970s and the second in the 1980s. The difference in mortality in the two periods was 39% compared with 21%, respectively. There was no difference in outcome between patients treated with surgical or those treated with percutaneous methods. The authors concluded that the improvement in localization had a major impact on the treatment of abscesses.

There are a number of reasons for the failures reported. These include premature withdrawal of the catheter, presence of a gastrointestinal fistula, pleural contamination, hemorrhage, and the errors of selecting cases as noted earlier.

Laing et al[225] reported a series of 136 patients with a failure of 29 of 119 attempted curative procedures. With infected pancreatic processes the authors were successful in 11 of 22 cases. In their series they had 17 patients with identified gastrointestinal fistula; 9 resolved spontaneously, and 8 required surgical management. Failure to document the complete obliteration of abscesses by CT resulted in failure in 7 cases. The authors had two cases of hemorrhage associated with inappropriate placement of catheters in phlegmonous areas. The most common misdiagnosis was failure to identify loculated or residual cavities. Premature withdrawal was made in a number of cases because of the cessation of drainage fluid. The authors recommended that a repeat CT scan be performed before the removal of the catheter.

Complications

The incidence of complications varies widely, depending on technique, types of abscess being drained, and the various authors' experience. The reported rates vary between 5% and 9.8%. In regard to possible abscess locations, the complication rate varies between 1.4% and 30%. The lowest complication rate is associated with the liver and the highest with the spleen (see later section on specific location).

The most common complication in all series is that of sepsis immediately after the catheter insertion. According to our review of the literature, this occurred in about 6% of all cases; as seen in the recent review article by Lambiase,[230] it occurred in about 4.2% of cases.

Other less frequent complications included spontaneous hemorrhage, spillage of infected material, and fistula formation.

Anatomic Approaches

The various anatomic areas involved by abscesses have unique characteristics as discussed in the earlier chapter on the peritoneum. Information unique to the technical approach and outcomes in each area will be discussed in the following sections.

Subphrenic Abscesses

With a subphrenic abscess, one must always look at the contiguous anatomic areas to see if there are any extensions of the abscess into these areas. Contiguous spaces that may require drainage include the right subhepatic and right pericolonic space with right subphrenic abscesses. With left subphrenic abscesses, extension into the right subphrenic, left subhepatic, and the left pericolonic space may also occur. Traditionally, such extension is not expected, but because of anatomic variability some peritoneal margins do not serve as effective barriers to the spread of infection.

When performing drainage procedures of the subphrenic spaces, several anatomic points should be kept in mind. To best avoid the pleural space, remember the attachment of the diaphragm. The slips of the diaphragm attach more cephalad anteriorly and more caudad posteriorly. Because of these relationships the entrance point for a drainage should not be more posterior than the midaxillary line (Figs. 61–117 and 61–118). The trajectory for such procedures should be from a caudad-to-cephalad angle. The target for entrance of the needle should be the lowest portion of the abscess. This permits positioning of the catheter throughout the enteric length and keeps the trajectory as far away from the diaphragm as possible, ensuring avoidance of the pleural space.

Obviously, when performing such a procedure, always visualize and avoid the pleural space, gallbladder, and hepatic flexure of colon when planning the trajectory. If there is any problem with localizing a subphrenic abscess or separating hepatic flexure of colon from the liver, place the patient in the left decubitus position.

The rate of cure for subphrenic collections varies be-

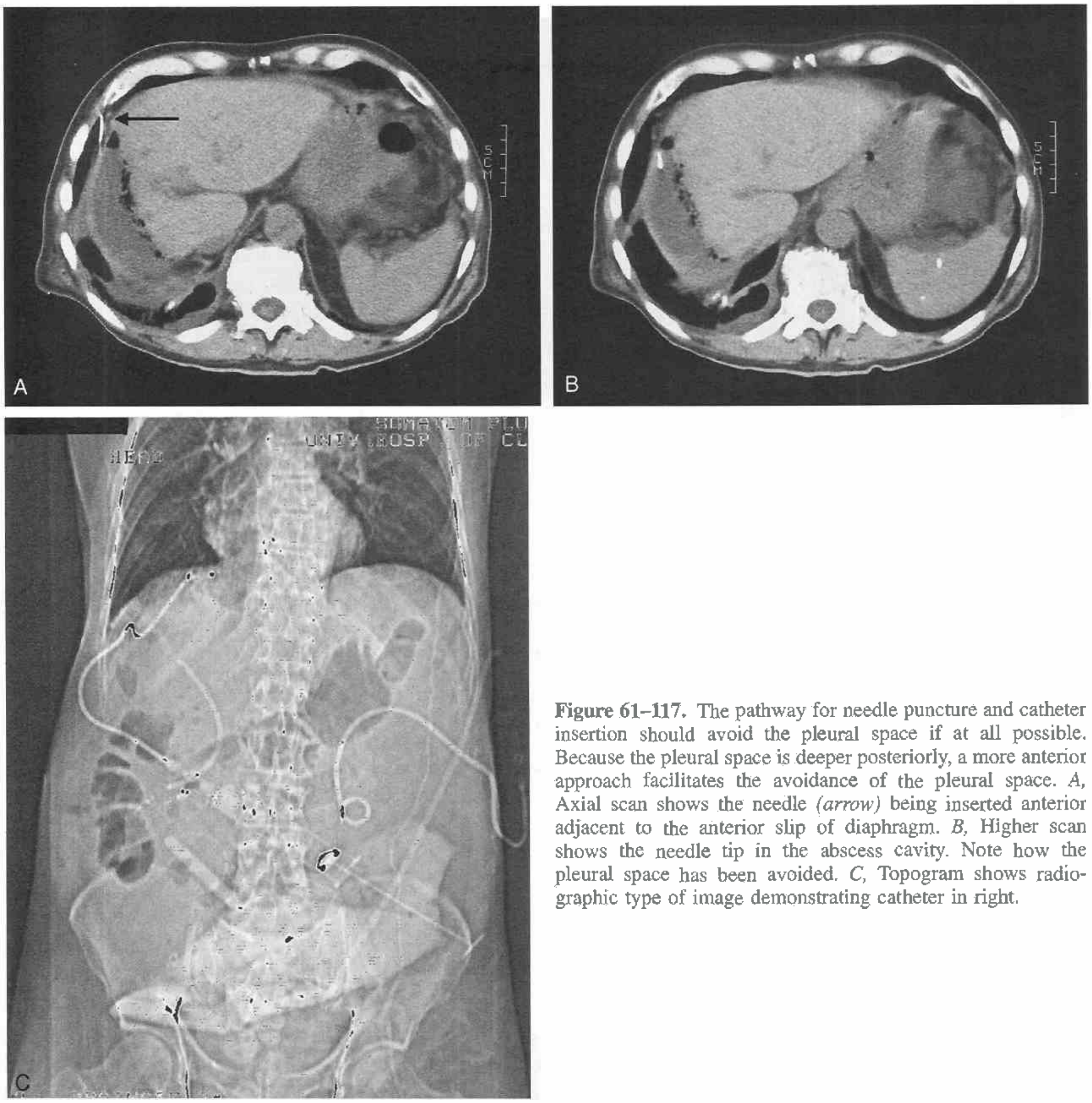

Figure 61–117. The pathway for needle puncture and catheter insertion should avoid the pleural space if at all possible. Because the pleural space is deeper posteriorly, a more anterior approach facilitates the avoidance of the pleural space. *A,* Axial scan shows the needle *(arrow)* being inserted anterior adjacent to the anterior slip of diaphragm. *B,* Higher scan shows the needle tip in the abscess cavity. Note how the pleural space has been avoided. *C,* Topogram shows radiographic type of image demonstrating catheter in right.

tween 79% and 81%. Complications include empyema and sepsis, the incidence of which is 2%.[111,147,230,295]

Right Subhepatic Abscess

An abscess in the right subhepatic space can be easily approached either laterally or posterolaterally. Penetration of any adjacent structure such as the colon, gallbladder, or duodenum can be easily avoided. In some cases a left decubitus position can also be helpful in moving the hepatic flexure of the colon to simplify a puncture (Fig. 61–119). In cases when clear access is not available, it is reasonable to traverse a portion of the liver. Obviously, the liver in such cases is clearly exposed to the pyogens because of close proximity so there is minimal risk with this alternative trajectory.

Left Subhepatic Abscess

This abscess, located in the anterior subphrenic space below the left lobe of the liver, appears between the liver and the stomach on axial CT scan. The administration of oral contrast is important for confirmation of the stomach location. The optimal approach for this area is a directly anterior approach that avoids liver and stomach (Fig. 61–120).

Omental Bursa

Drainage of the omental bursa can be approached from several directions. Fluid collections in the inferior recess of the lesser sac can be approached anteriorly beneath the lower margin of the stomach if a fluid collection is large enough. If the fluid collection is in the splenic portion

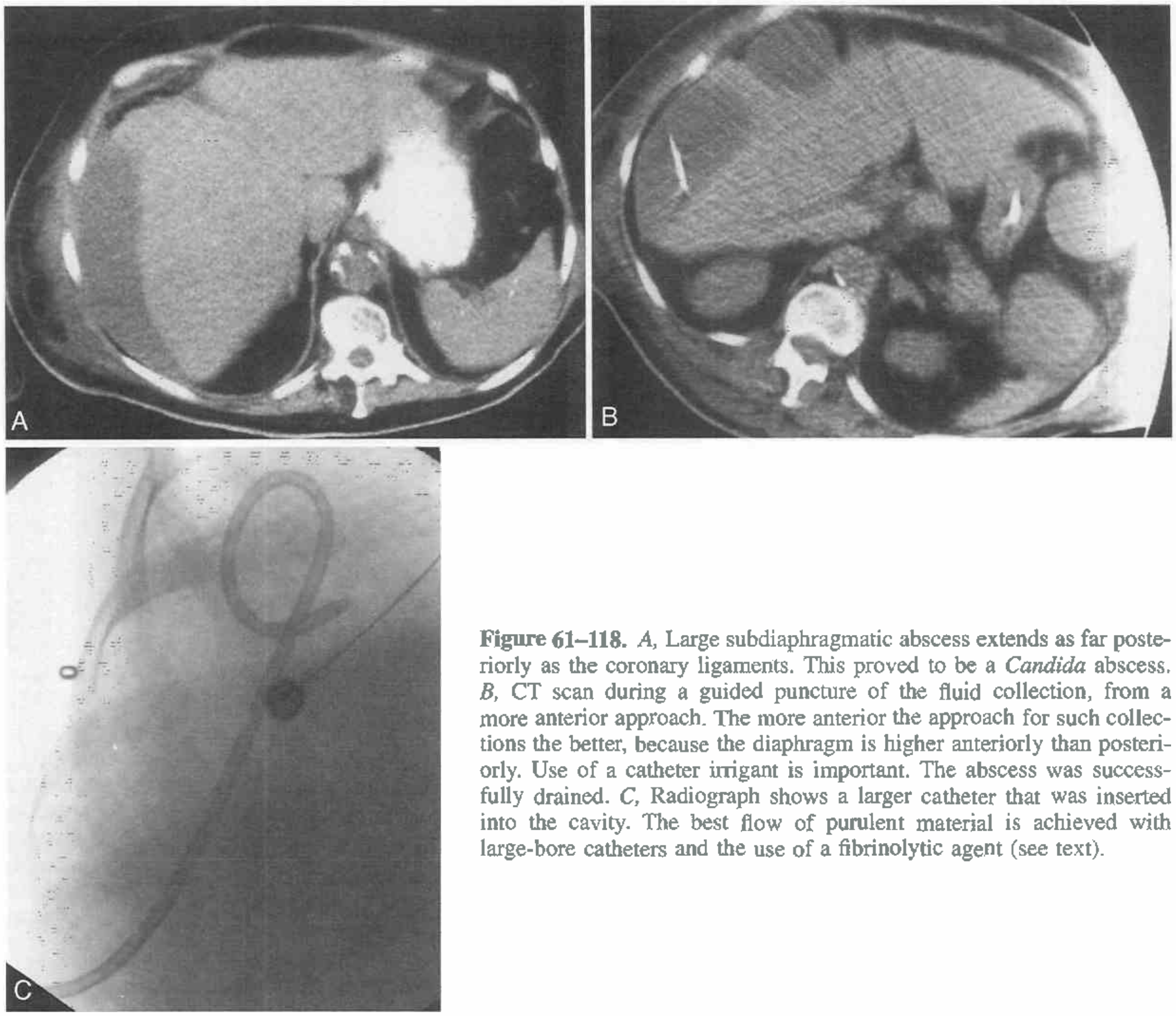

Figure 61–118. *A,* Large subdiaphragmatic abscess extends as far posteriorly as the coronary ligaments. This proved to be a *Candida* abscess. *B,* CT scan during a guided puncture of the fluid collection, from a more anterior approach. The more anterior the approach for such collections the better, because the diaphragm is higher anteriorly than posteriorly. Use of a catheter irrigant is important. The abscess was successfully drained. *C,* Radiograph shows a larger catheter that was inserted into the cavity. The best flow of purulent material is achieved with large-bore catheters and the use of a fibrinolytic agent (see text).

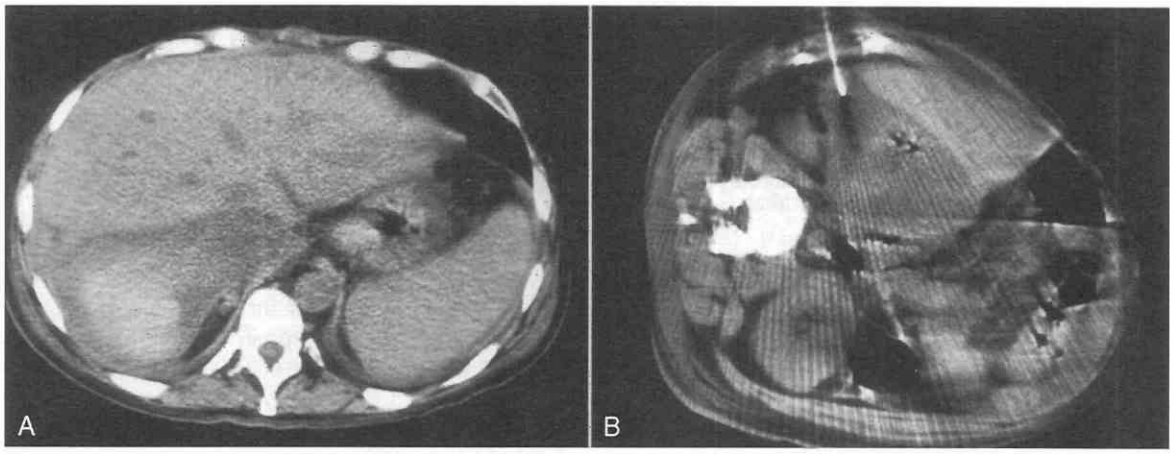

Figure 61–119. *A,* CT scan of a patient in the supine position shows a high-density fluid collection in the right subhepatic space. *B,* When the patient is positioned on the left side, the fluid remains in the same location and does not shift. Note the drainage needle in the right flank.

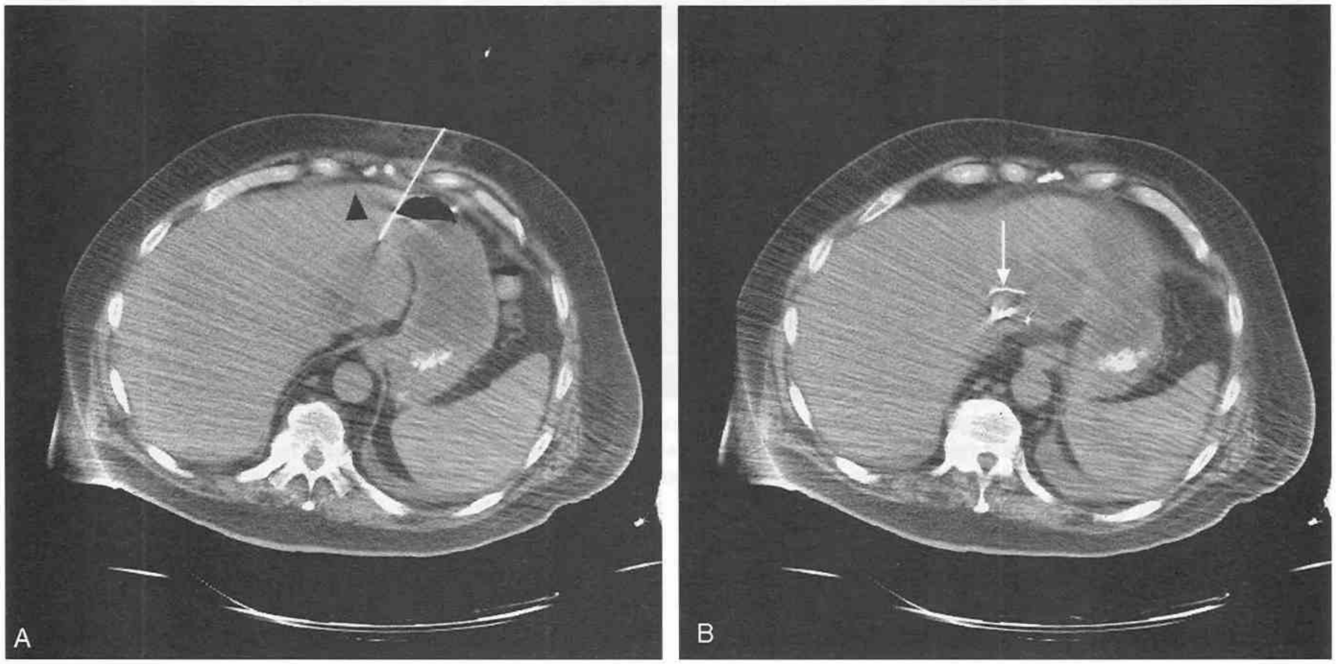

Figure 61–120. Collections in the left subhepatic space are best approached through the gastrohepatic space. The needle *(arrow)* will usually avoid liver and stomach; if inadvertent puncture occurs on occasion, it is certainly better than intentionally penetrating these structures in every case. *B,* Scan shows wire and catheter *(arrow)* coiled in abscess.

of the inferior recess, the best approach is through the gastrosplenic ligament. This approach is best accomplished when the patient is in a right decubitus position to permit the stomach to shift anteriorly. Obviously, in such cases one must be careful to avoid the splenic flexure of the colon, looking carefully for varices in the gastrosplenic ligament to avoid penetration of any such vessels (Figs. 61–121 and 61–122).

If the approach through the gastrosplenic ligament is not available, two other approaches are possible. For a

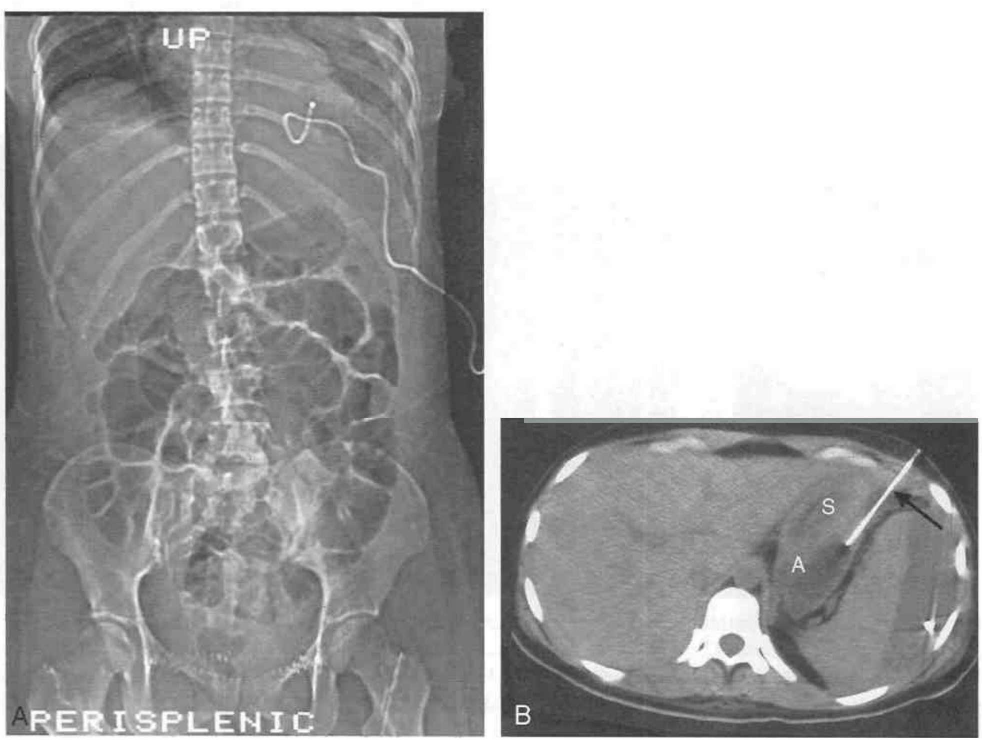

Figure 61–121. *A,* Scan shows the standard approach for drainage of the superior recess of less sac behind the stomach (S). The space is wide enough between the stomach and spleen to permit easy access. *B,* Radiograph shows catheter in splenic recess of lesser sac.

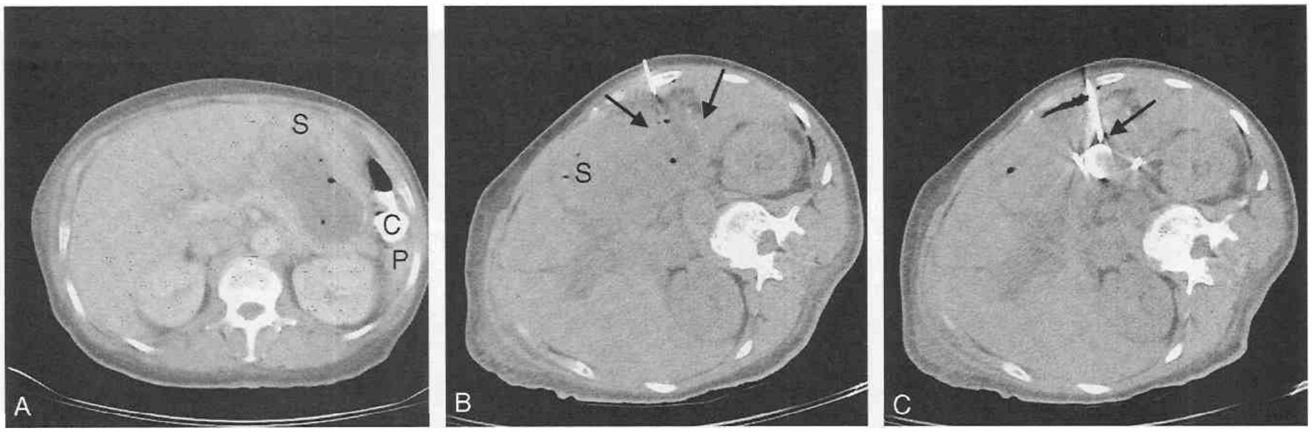

Figure 61–122. *A,* Drainage of the splenic recess of the lesser bursa, behind the stomach (S) was not possible with the patient in the supine position. *B,* With the patient lying in the right decubitus position, the stomach (S) moved anteriorly, providing a wide pathway between the spleen and stomach *(arrows). C,* Insertion of the catheter *(arrow)* through the space was easily accomplished.

second choice I would use a transgastric approach, ideally through a PEG as described earlier for pseudocysts. Another approach is a transhepatic approach through the left lobe of the liver (other authors recommend this as a primary approach).[293] I dislike this approach because of possible injury or pyogenic dissemination into the left biliary or portal system.

Inferior Recess of Lesser Bursa and Porta Region

With the mastery of these techniques it is now possible to approach drainage of deep areas, which can provide remarkable benefit. These deep areas are difficult to drain by inexperienced operators, but with experience and knowledge of the techniques described in this chapter, drainage of very deep areas is possible. To successfully accomplish these procedures one must take advantage of patient positioning and also needle deflection as described in earlier sections (Figs. 61–123 and 61–124).

Pericolonic Spaces

The pericolonic spaces are easily approached laterally. One should always look for extension of an abscess into the pelvis or either subphrenic space. Contrary to traditional teaching, an abscess in the left pericolonic space may extend into the left subphrenic space unimpeded by the phrenicolic ligament.

When draining an abscess in these spaces, always make sure the catheter traverses the entire length of the cavity. To do this it is always best to enter either the upper or lower end of the cavity. Another option is to insert two catheters at the midportion of the cavity, with one extending cephalad and one extending caudad.

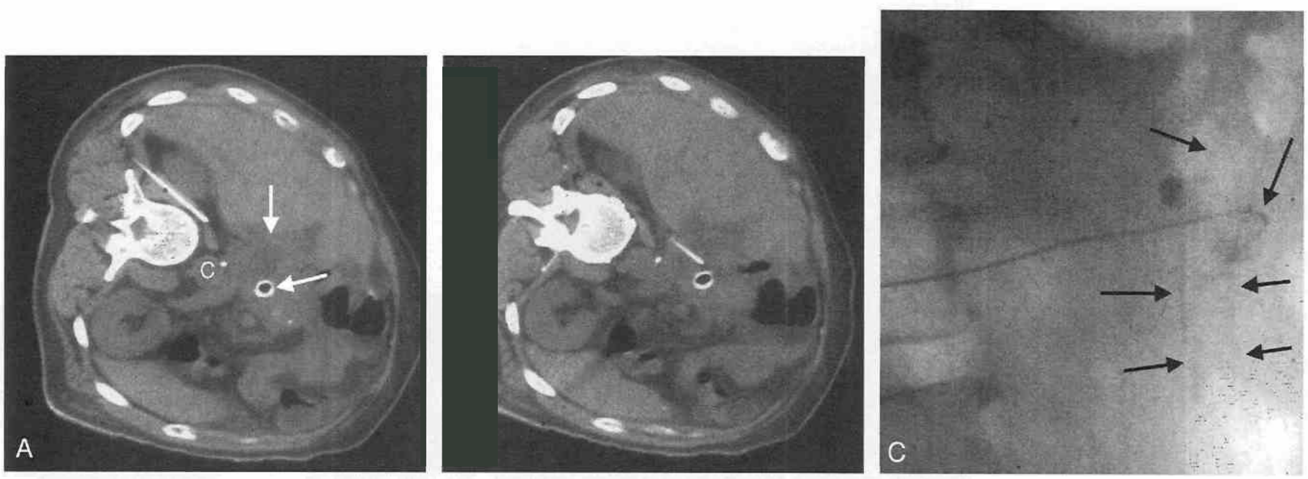

Figure 61–123. *A,* A patient with a small abscess *(vertical arrow)* beside a metallic stent in the biliary system *(horizontal arrow)* anterior to the vena cava (C). An anterior approach would be impossible, so a posterior approach was chosen. For the needle to clear the vena cava, the bevel was rotated toward the left (vena cava) and pushed slowly to permit deflection. *B,* Placement of the needle precisely in the abscess was accomplished. *C,* Final placement of the catheter *(arrow)* next to the stent *(small arrows)* was accomplished. Patient defervesced and survived, without surgical drainage.

Figure 61–124. *A,* The patient was positioned in the lateral position to permit access through the lateral abdomen to reach the small abscess *(arrow)* beside the opaque biliary stent. The needle was advanced past the kidney by turning the bevel toward the kidney and pushing slowly. *B,* Scan shows placement of the needle in the cavity with contrast injection *(arrow). C,* Final scan before catheter removal shows resolution of the abscess. The abscess was caused by a small diverticular abscess.

Empyema and Pleural Effusions

Drainage of empyemas is quite straightforward, and the same methods are used as other areas. The most important point relative to empyemas is to use a more lateral or anterior approach in preference to a posterior approach. If a catheter is inserted posteriorly, it is uncomfortable for the patient, and the tube is likely to kink and limit the drainage. Because such abscesses have a significant amount of inflammatory reaction, vacuum on the catheter is required not to keep the lung re-expanded but rather to improve removal of the material.

If a pleural effusion is being drained, it is best to have the catheter put to a water-seal vacuum drainage to prevent a pneumothorax from forming.

Liver Abscesses

Abscesses in the liver should be approached by the shortest trajectory available, with an entrance point on the anterior or lateral surface. When a lateral entrance site is used, do not go more posterior than the midaxillary line, to avoid traversing the pleura.

When puncturing and draining hepatic abscess, avoid any visible hepatic vessel as well as the gallbladder and pleura. Also, when planning the trajectory for hepatic abscesses, always include a cuff of normal tissue to prevent inadvertent spillage of material into the peritoneum.

Many hepatic abscesses may appear to be multiseptated,[74,76,197] but experience has shown that many clear completely with one drainage tube. A variety of explanations have been proposed, including (1) they intercommunicate, (2) they drain spontaneously into the drained cavity, and (3) antibiotics clear the different cavities. A repeat scan is important to ensure that all such cavities eventually clear because separate cavities that persist occasionally require drainage (Figs. 61–110 and 61–125).

The success rate for hepatic abscesses varies between 69% and 89%.[177,197] The complication rate varies between 1.7% and 7.3%. The complications include sepsis, contamination of peritoneum, and production of an empyema.

Renal Abscesses

Such abscesses are best approached posteriorly through a path avoiding erector spinal muscles, colon, liver, and spleen. The puncture and drainage of most such abscesses can be performed with ultrasound or CT guidance. When the upper pole is involved, CT is indicated to avoid inadvertent trauma to the spleen, splenic pedicle, or pancreas. Success rate varies (Fig. 61–126).

Splenic Abscess

Drainage of splenic abscess is quite controversial for several reasons. Some early investigators reported favorably on drainage of splenic abscesses, but if one carefully reviews their reports, there was a high incidence of emer-

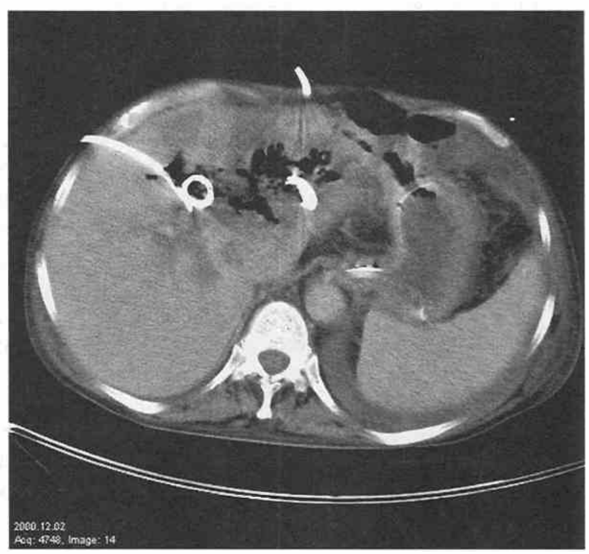

Figure 61–125. Two large abscesses in a patient with liver transplant. Because the portal vein was occluded, the tissue was necrotic and effective drainage was difficult. Two catheters were inserted, with one providing inflow and the second providing exit flow from the communicating cavities.

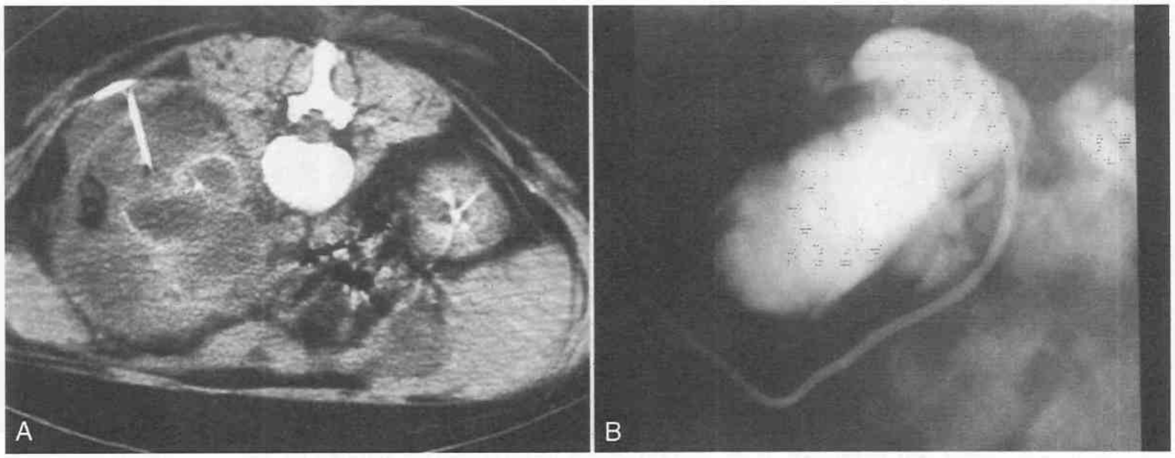

Figure 61–126. *A,* CT scan shows a large abscess around the left kidney and severe pyohydronephrosis. The needle trajectory was planned to cross both abscess collections. *B,* Catheter injection shows opacification of the collecting system and some extravasation of contrast material into the perinephric space.

gent splenectomy. Having never been an advocate of such procedures on a routine basis, we have waited for additional experience to be accumulated before recommending this approach.

Unfortunately the recent information has remained inconsistent. Liu et al[244] reported a 90% success rate, whereas Green[123] reported a 25% success rate. These reports come from different areas of the world, and there may well be differences in selection of the patients as well as geographic and ethnic differences among the patients.

Because the incidence of splenic abscesses worldwide is increasing due to the increasing number of immunocompromised patients, I believe the procedure be used but only in very selected patients. Because the spleen is so vascular, one should probably drain only those abscesses that are very close to the surface of the spleen. Realizing this procedure has not proven to be safe in controlled studies, one must always have close communication with surgeons to make sure an emergent splenectomy is possible.

Perirenal and Pararenal Spaces

The anterior and posterior pararenal spaces are frequent sites of abscess and can be approached safely; however, certain facts must be remembered. These spaces extend from the pelvis to the diaphragm and are long. Unless a catheter or catheters are positioned throughout the entire length of the cavity, drainage may not be successful (Fig. 61–127). It is especially important to use CT for follow-up of such cases because the abscesses may spread toward the diaphragm or pelvis. Examination of these areas may be difficult with ultrasound.

The success rate for these abscesses varies between 68% and 81%. The complication rate varies between 3% and 6%, with sepsis and hemorrhage being the most common.[227,230]

Pelvic Abscesses

The procedure for drainage of pelvic abscesses is quite similar to that of other areas. The most significant controversy involves the choice of drainage pathways. It is our opinion that the best pathways are an anterior, lateral, or transrectal one (Figs. 61–128 and 61–129).

When such abscess cavities are close to the rectum, a transrectal approach is indicated[103] (Figs. 61–130 and 61–131). To perform this procedure, a series of baseline scans are taken over the pelvis to demonstrate the collection. A short plastic tube (with Betadine ointment) is then inserted into the rectum. A plastic sheath needle is inserted into the tube and a series of repeat scans are taken over the pelvis. Once the needle is aligned properly, the puncture into the fluid collection is made. The needle is removed, but the plastic tube is left in place to serve as a conduit for catheter insertion. The tube prevents buckling of the wire or catheter in the rectum during the insertion.

The last choice for draining pelvic abscesses is through the sciatic notch (Fig. 61–132). This pathway is satisfactory for biopsy procedures, but long-term drainage catheters are not recommended, for two reasons. The use of this pathway can produce a lot of pain, and there have been reports of abscess tracking into the gluteal muscles, of sciatic neuritis, and of pseudoaneurysm formation in the iliac vessels.

Controversial Areas

Treatment Without Catheter Drainage

Several authors have reported on the concept of treating abscesses with only aspiration and lavage of an abscess cavity and intravenous antibiotics. The largest series reported by Wroblicka and Kuligowska[411] involved 82 nonconsecutive patients. These authors used a single-step procedure in which they used an 18-gauge needle to puncture, aspirate purulent material, and irrigate with saline. They claim a 90% cure rate in unilocular abscess and a 85% cure rate in multiloculated abscesses.

When reviewing these articles, it must be noted these were not well-designed studies. They did not have well-defined selection criteria, were nonconsecutive, and had no control groups. The data are subject to remarkable bias because of selection of patients.

From my perspective, I have no intention of using this

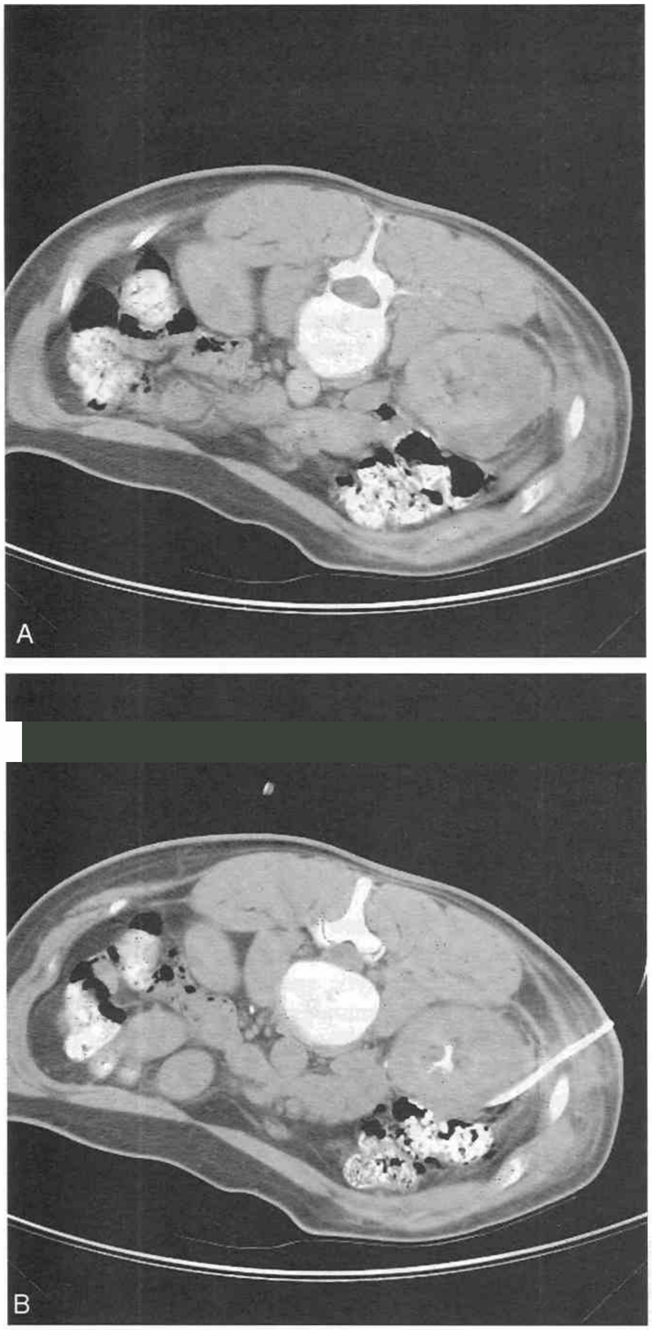

Figure 61–127. *A,* Scan shows a fluid collection around the left kidney, representing a perinephric abscess. *B,* Placement of the catheter into the abscess was performed through the posterior flank.

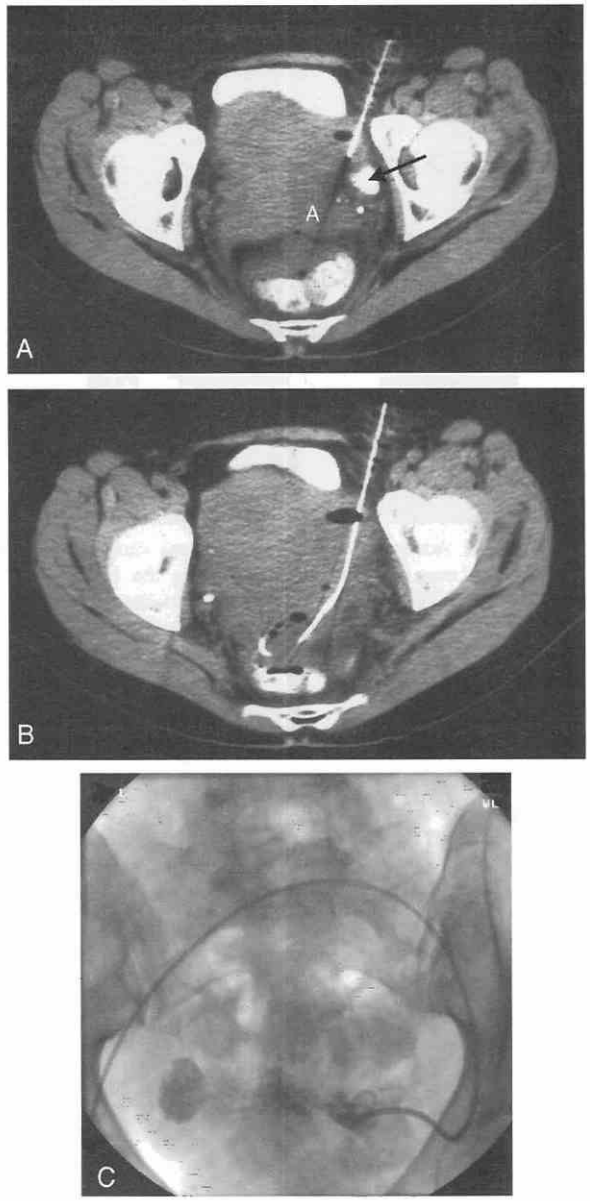

Figure 61–128. *A,* Scan shows an approach to an abscess (A) posterior to the bladder and adjacent to sigmoid colon *(arrow)* from diverticular abscess. *B,* Scan shows insertion of a wire throughout the length of the cavity. *C,* Radiograph shows the injection of contrast material, demonstrating a fistula to diverticulum of colon.

approach until further controlled studies are performed. I do find the concept interesting and believe there may be some limited role in the future if the method can be better defined and results proven. In the future such an approach might be effective if a long-acting antibiotic could be deposited in the abscess cavity.

Catheters

Some authors use angiographic catheters, whereas others use large catheters and trocars. In most areas either type of catheter works well, except in the case of certain pancreatic abscesses (see later section). In pertinent drainage literature, a report by Park et al[320] showed there was little difference in drainage success rates regardless of whether small or large catheters were used. This is probably the result of selection of catheters by operators (i.e., small catheters for thin material and large catheters for thick material). Controversy exists about whether gravity (siphon) drainage, sump drainage, or irrigation drainage (multiple catheters) is the most effective. There is no clear advantage to any of these methods appearing in the surgical and radiologic literature, so any individual preference can be followed.

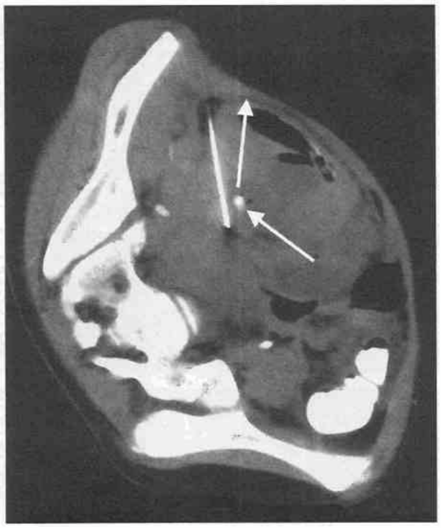

Figure 61–129. Access *(arrow)* to an abscess caused by a ruptured appendix was possible by positioning the patient in the oblique position. The needle was targeted to the appendicolith *(oblique arrow)* in case extraction of calculus was indicated.

Sinograms

Some authors[147,225,230] have performed sinograms to follow abscess cavities, whereas others[111] have not. We use sinograms in many cases to follow the progress of granulation tissue that closes the cavity. Sinograms are not intended to see "undrained" areas. By definition, if these areas are not drained and do not communicate, one will not see them. Sinograms are used to see the size of the cavity as it heals from granulation or to detect fistulae. CT scanning is used to see undrained areas. With this in mind, one must not overinject cavities during sinograms to maximum distention, because this can cause spillage or bacteria into anatomic spaces or into blood or other portions of the organ.

Antibiotics

It is my belief that all patients who have a percutaneous procedure should have systemic antibiotics before[100] and during the course of abscess drainage.

With antibiotics, patients have quicker resolution of the abscess and fewer local complications. I have noted that some patients not receiving antibiotics may develop a localized cellulitis around the site of catheter insertion; administration of antibiotics resolves or prevents this. If antibiotics are not given, septicemia is more likely to occur after or during instrument manipulation.

In our opinion the only valid controversy is whether the antibiotics should be started before or after the diagnostic aspiration. Starting antibiotics when a patient initially develops septic symptoms can be justified to prevent further deterioration. On the other hand, it can be argued that unless the patient is not receiving antibiotics, a valid culture cannot be obtained. It appears that either philosophy is sound; I usually accept the preference expressed by my clinical colleagues attending the patient.

Mucolytic Agents

There have been several suggestions in the literature about using materials to try to enhance drainage from abscesses. One author[391] has proposed the use of acetylcysteine (Mucomyst) to decrease the viscosity of purulent material; most workers do not accept this material as being effective.

Fibrinolytic Agents

Extensive work has been performed using urokinase, but unfortunately that agent has been taken from the marketplace. Because fibrinolytic agents all work by the same pathway, converting plasminogen to plasmin, the newer agents, prourokinase and tPA, should both be useful in a similar fashion. Because no work has yet been done on those agents, one would need to calculate equivalent doses of these agents if a fibrinolytic is needed. Reviewing the

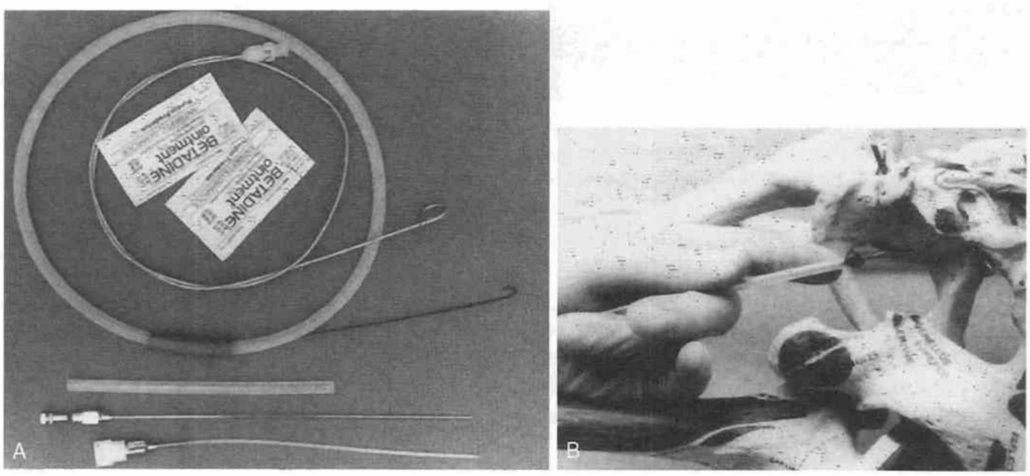

Figure 61–130. *A,* The various devices used for a transrectal approach include the plastic sheath needle, plastic cannula, angiographic wire, and catheter. *B,* Simulated procedure using the bony pelvis of a skeleton and the equipment as noted in *A.* This shows the plastic sheath along the side of the finger. The needle is within the sheath (protecting both the rectum and the operator's finger), and Betadine ointment occludes the end of the plastic sheath.

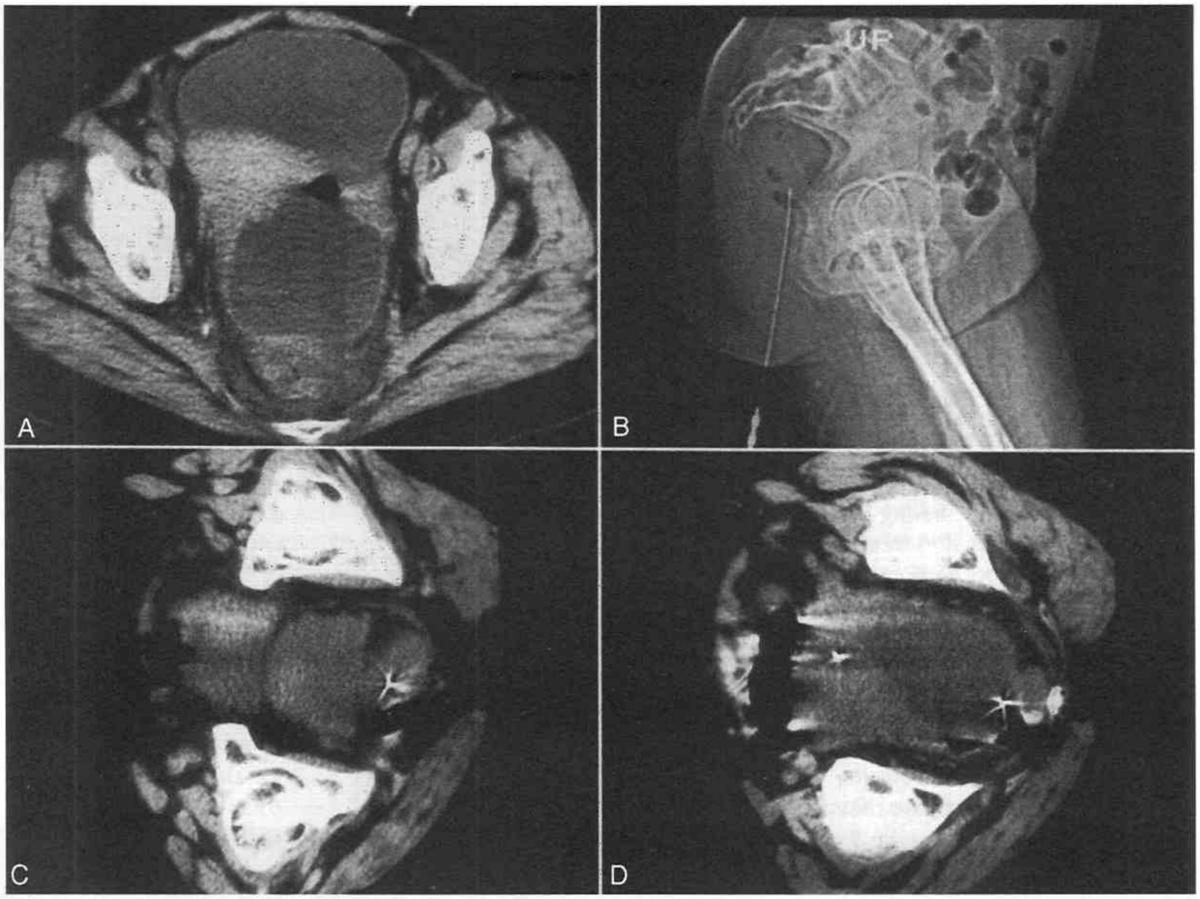

Figure 61–131. *A,* CT scan shows a large abscess between the uterus and rectum, which was drained by a transrectal drainage. *B,* Topogram shows a needle being inserted by means of the rectum, through the plastic tube as noted in Figure 61–131. *C,* CT scan over the lower pelvis shows the needle in the rectum. Compared with the first image in *A,* the needle was correctly angled to enter the cavity. *D,* Lowest CT scan over the pelvis shows the needle entering the abscess cavity. With the use of the topogram, the angiographic wire and catheter were inserted.

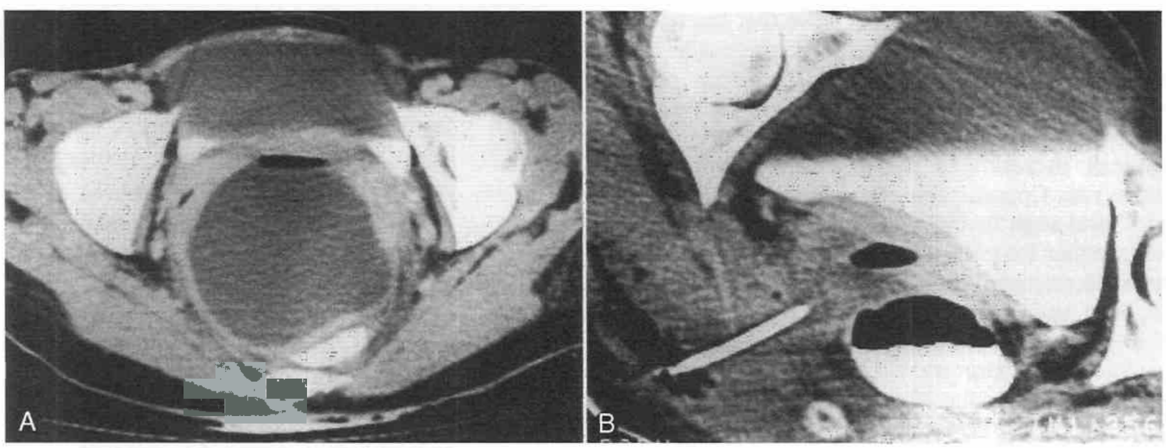

Figure 61–132. *A,* CT scan of the pelvis shows a large abscess posterior to the bladder and anterior to the rectum. *B,* Follow-up scan shows catheter drainage through the sciatic notch. Note that the cavity is much smaller, but there is also an abscess that has tracked posteriorly into the gluteal muscle.

clinical data on urokinase is helpful in this regard.[224,235,320] In an article by our group, Park et al[320] showed that in vitro urokinase decreased the viscosity of purulent material by 23%. Increased flow through various catheters was observed, and this was most significant with small-caliber catheters.

In another report by our group, Lahorra et al[224] showed the safety of administering urokinase through drainage catheters into abscess cavities. In this study all abscesses with loculations were successfully drained, as well as three infected hematomas, one fungal abscess, and one recurrent abscess. Based on this initial experience, we now routinely use fibrinolytics in any abscess that contains thick material or infected hematoma (Fig. 61–133). See the previous section on fibrinolytics, under "Catheter Management." Our most recent article on urokinase showed its use improved treatment of abscesses. Its use produced improvement of clinical parameters earlier and shortened hospital stay. Other fibrinolytics are now being evaluated as irrigant for catheters.

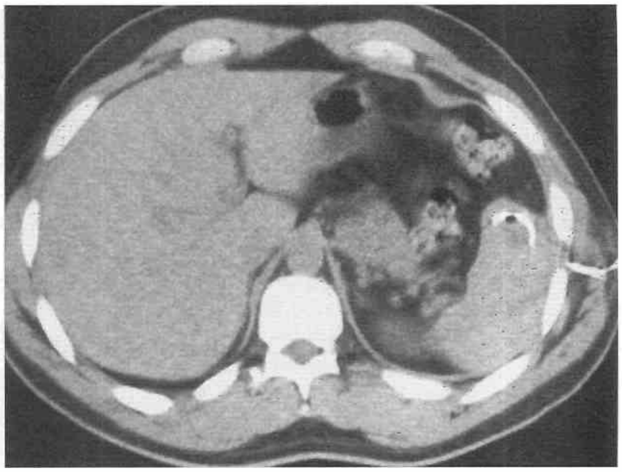

Figure 61–133. Small splenic abscess in the anterior spleen caused by *Salmonella*. This abscess, despite having been previously aspirated, drained by catheter, and treated with antibiotics, continued to recur. Catheter drainage of the abscess was performed because it had been done before without difficulty and because the patient refused surgery. Redrainage with urokinase as an irrigant produced total resolution.

Palliative Procedures

A number of authors have advocated palliative drainage procedures in different areas. PAD in each of these areas has been tried with varying success (each area is described in the following sections).

Drainage of Splenic Abscesses. Percutaneous drainage of splenic abscess is a questionable procedure because of surgical experience and the reported data in the literature. The spleen is a large vascular organ, and any manipulation presents a potential risk. Even with the current surgical trends favoring preservation of the spleen in traumatic injury, most surgeons perform a splenectomy rather than attempt a catheter drainage. In the accumulated literature about percutaneous abscess drainage of the spleen, a high failure rate, as well as high complication and mortality rates are reported. I believe that surgery is the most acceptable treatment for a splenic abscess, except in extraordinary cases (Fig. 61–133).

Drainage of Pancreatic Abscesses. Drainage of pancreatic abscess by PAD is a complex issue that has not yet been resolved, but certain comments can be made. The issue is complex because there is a discrepancy in the literature about the objective results, recommendations, and the experience of various authors.

The overall success rate is 57%, with a fairly high complication rate. Complications have been both short- and long-term. Short-term complications have been related to hemorrhage, either for pseudoaneurysms or for inappropriately attempted drainage of poorly defined phlegmons. Initial attempts to drain pancreatic abscesses were somewhat nonselective, and the methods were not clearly defined. Recent personal communications have reported that better selection criteria and more clearly defined methods are being used (see Fig. 61–134).

Most workers differentiate between necrotic, ill-defined pancreatitis with superimposed infection versus well-delineated, low-density fluid collections, which more closely resemble infected pseudocysts.

The latter types of infections, the well-defined fluid

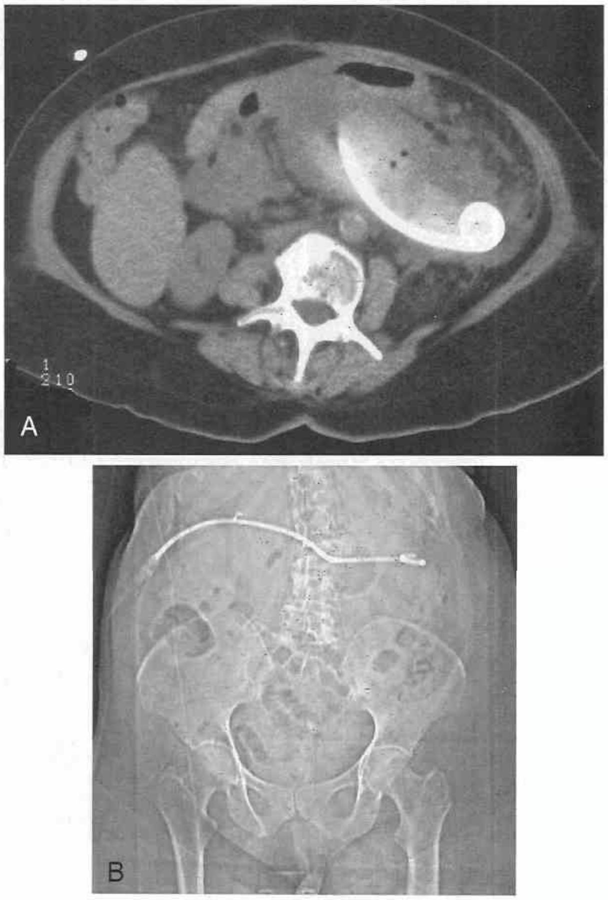

Figure 61–134. *A*, CT scan shows a large catheter in the large pancreatic abscess. *B*, Radiograph shows a catheter inserted into the abscess.

density collections, are those that are best suited for percutaneous drainage. The standard methods using the Seldinger technique or the trocar methods provide good results. Freeny[95,96] reported a high success rate with such methods. In his group of 21 patients, the success rate was 85%. Von Sonnenberg[384,386–390] also claimed a high success rate of 69%. They encountered 13 fistulae, 10 of which closed spontaneously. Most recently, Lambiase[229–231] reported successful drainage of 2 of 2 infected pseudocysts as compared with 1 of 7 cures in a group of patients with abscesses exclusive of pseudocysts.

The only worker attempting drainage of necrotic pancreatitis is Dr. Eric Martin.[263] Employing what I would call extraordinary methods, he uses 20- to 30-French catheters, which are capable of draining large amounts of necrotic tissue. With these methods, he has success, complication, and mortality rates comparable to surgical results. In his group of 20 cases Martin had a cure rate of 65%, a mortality rate of 25%, and fistulae in 10% of cases. Although these values seem high, one should remember this is treatment of infected necrotic pancreatitis, not well-defined fluid collections.

Regardless of the primary approach taken for drainage of pancreatic abscesses, the successful resolution of the problem depends on diligent, repetitive clinical and imaging evaluation of the patient. Close cooperation between surgeon and radiologist is quite essential because of the recurring and unpredictable nature of the disease. Many times, a radiologic procedure is needed after an operative drainage or vice versa to produce complete resolution of the problem. As has been indicated by Martin and others,[264] regardless of optimal care a high percentage of such patients will die.

In my experience, the technique and approach used depend on the appearance and location of the pancreatic fluid collections. For well-defined collections, I am quite willing to perform percutaneous drainage because of the high success rate. Those collections representing infected necrotic tissue or poorly defined multiple collections are best drained surgically. If a patient has had a surgical drainage and develops a collection postoperatively, I will attempt percutaneous drainage regardless of the appearance, knowing that the infection is most likely well-confined and that a second surgical procedure would be quite difficult.

I use either an anatomic approach that avoids all adjacent organs or a transgastric approach. If one is attempting to avoid bowel or solid organs, the approach often must be retroperiteonal, anterior to the kidney or directly anterior. I use such a direct anterior approach only if there is a "window" between the various loops of bowel. If there is any problem with access, I choose a transgastric approach using the same method I have described for pseudocyst drainage, with a gastrostomy as a conduit for entry (see earlier section).

Diverticular Abscesses. Percutaneous drainage of diverticular abscesses is a technically simple procedure for which the indications are limited. The indications for this procedure are limited because in most patients with diverticular abscesses, a colonic diverticular fistula will result after successful drainage of the abscess. I concur with Mueller et al,[292] who reported that the primary purpose in performing this procedure is to change a potential two-stage procedure into a one-stage procedure. Specifically, most cases of small diverticular abscesses can be treated with a single surgical procedure consisting of an en bloc resection of a segment of the sigmoid colon and a confined abscess. The entire problem is resolved with a single procedure. In those cases in which the abscess is so large that this cannot be accomplished, surgical treatment would require two procedures: one to drain the abscess and divert the bowel and a second to reanastomose the bowel. In such cases percutaneous drainage can remove the infectious material and a single surgical procedure can be performed to remove the offending segment of sigmoid colon (Fig. 61–128).

I try to approach such lesions from an angle not traversing bowel; I believe that including the bowel within the pathway increases the possibility of fistulae.

Neff reported a series of 16 patients with diverticular abscesses.[301] According to the author, all responded. In this group, 11 patients required sigmoid resection after the drainage and 1 patient had a three-stage procedure. There were 10 fistulae resulting; 2 required surgical treatment.

Infected Neoplasms. Although experience has shown that percutaneous drainage of infected neoplasms will not be curative,[297,407] there has been some recent interest in using percutaneous drainage as a palliative procedure. Using the standard technique as described, Zeman[417] has had some positive experience with palliation. In 12 patients with infected tumors, those authors had noted improvement in all cases, with favorable response in 50%; no complications occurred.

Echinococcal Drainage

A number of authors (Bosanac and Lisanin,[33] Sayek and Onat,[351] Giorgio et al,[115] Ormeci et al[313] and Khuroo et al[215]) have reported on the percutaneous drainage of echinococcal cysts. The method is quite simple and consists of the typical percutaneous puncture and aspiration using ultrasound or CT. With the Seldinger technique, catheters between 12 and 20 French are inserted. The cavity is then irrigated with alcohol and Betadine and left in site for 30 minutes. The catheter is left to drainage until fluid ceases. Concurrent treatment with albendazole is also important, in the appropriate doses and duration. Anaphylactoid reactions did occur in several cases but were not fatal.

Amebic Abscess

Typically amebic abscesses respond to systemic treatment with amebicidal therapy; however in some cases the abscesses are resistant to drug therapy. Akgun et al,[5] Tandon et al,[377] and Hanna et al[165] reported on the use of aspiration and drainage in conjunction with aspiration and drainage. It was the concensus that percutaneous aspiration and drainage may expedite therapy and provide a cure when there is resistance to medical therapy.

Percutaneous Nephrostomy

The same advantages for CT procedures are applicable to nephrostomy placements, but several different points

should be emphasized. CT has been successful in a high percentage of cases; in one early report we completed 12 of 13 attempts.[148] Barbaric et al[17] reported a series of 148 procedures using CT and fluoroscopy. Their success rate was 97% and there were no major complications. Authors such as Hagspiel et al[161] and Merkle et al[273] have used MRI for placement of nephrostomy tubes.

The indication for CT guidance is limited, but I believe that most nephrostomies can be performed easily using either fluoroscopic or ultrasonic guidance. Those cases for which we use CT guidance are renal transplants, unilateral kidney, high-risk patients, or a kidney with a urinoma associated with the hydronephrosis.

Renal transplants are well suited for CT nephrostomies. Transplants represent high-risk patients who are immunosuppressed, and therefore a higher margin of safety is needed. The transplants are somewhat mobile and the axis is unpredictable. CT may be needed to ensure proper placement of the catheter through the parenchyma. Unilateral kidneys should be performed with CT because these cases present a high-risk situation. Potential damage or complications in such cases must be minimized.

When a collecting system with hydronephrosis has ruptured and produced an adjacent urinoma, CT is better than other methods for several reasons. First, if the urinoma is displacing the axis of the kidney, the orientation can be appreciated. Second, if there is active excretion of contrast material, the perinephric space may fill with contrast material, making it difficult to visualize the collection system under fluoroscopy. This is not the case with CT (Fig. 61–135).

The technique is similar to that described for abscess punctures. Prepare the skin with the standard antiseptic preparation and administer a local anesthetic. Use an 18-gauge plastic-sheathed needle to puncture the renal pelvis. Insert an angiographic wire, remove the plastic sheath, and follow with the chosen nephrostomy catheter. The longitudinal type of scan or fluoroscopy may be used after the puncture to insert the catheter.

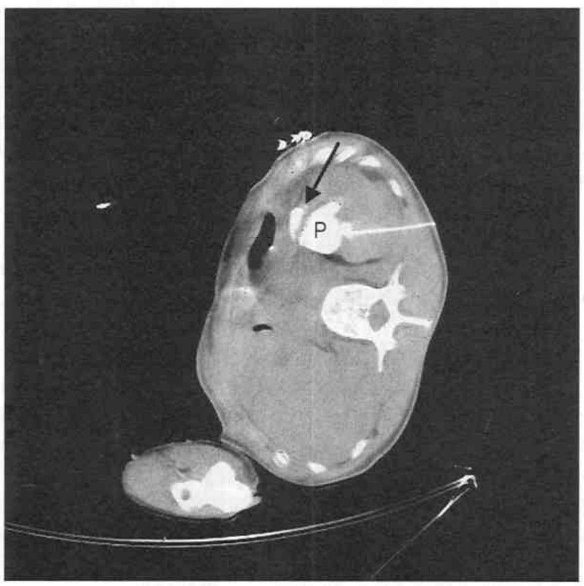

Figure 61–135. Scan shows percutaneous nephrostomy of a unilateral kidney. The needle is positioned in the dilated, contrast-filled pelvis (P). Note the small amount of contrast material that extravasated anteriorly from a small penetration of the anterior wall during the adjustment of the needle. Such small leaks are of no consequence if the collecting system is adequately drained.

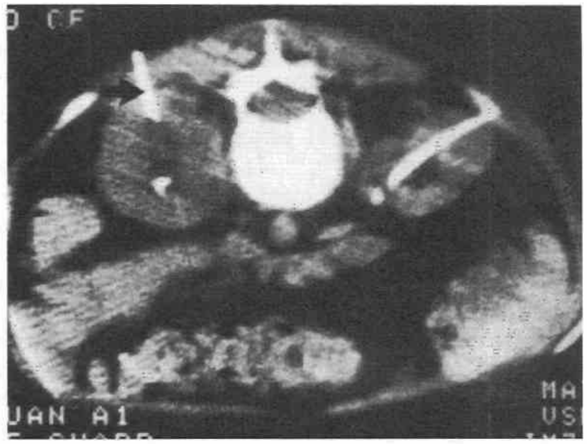

Figure 61–136. CT-guided procedure of the author's daughter (see Dedication), who had multiple renal calculi. There is one catheter in the right kidney, and this shows puncture of the left kidney with the needle *(arrow)*. Such special cases warrant the best method available.

When the nephrostomy is performed under CT, several technical maneuvers are important. Once the collecting system has been penetrated, a small sample of fluid should be aspirated for culture and then a small amount of contrast material should be immediately injected. This injected contrast material permits direct visualization under fluoroscopy when the catheter is being inserted. In addition, I recommended the 18-gauge Teflon-sheathed needle so that with successful puncture the angiographic wire can be inserted into the collecting system without additional manipulation (Fig. 61–136). The patient can then be transported to the fluoroscopy area without concern about displacement of the sheath or wire. In some cases the final positioning of the catheter should be made under fluoroscopy, but in many cases adjustments can be made with localizing scans. If one has access to a fluoroscope attached to a CT scanner, this step is simplified.

Nerve Blocks

One of the newest and most exciting areas of interventional radiology is CT-guided nerve blocks. The same types of nerve blocks that were previously performed blindly or by fluoroscopy can be better performed with CT guidance.*

Celiac Nerve Blocks

It is important to review the rationale behind celiac nerve blocks to gain a better understanding of the process, side effects, and possible complications.

The sensory nerve fibers transmitting pain sensation

*References 43, 139, 151, 156, 158, 242, 285, 290.

from the bowel, mesentery, capsule of the liver, and some portions of the retroperitoneum around the major vessels pass through a major neural plexus adjacent to the celiac artery called the *celiac plexus*. This large plexus contains ganglia from the sympathetic, parasympathetic, and sensory nerves. Once the sensory fibers pass through this area, they converge to form the right and left splanchnic nerves through the retroperitoneum and the mediastinum toward the central nervous system.

Interruption of these sensory fibers prevents pain stimuli from being carried back to the brain, thereby eliminating pain. Numerous methods have been used to interrupt these pathways, including surgical ablation, unguided percutaneous neurolysis, and guided percutaneous neurolysis.

Before CT guidance, authors had tried fluoroscopic guidance and ultrasonic guidance, but most procedures were performed blind. These guidance methods have various supporters, depending on the experience at various institutions and the expertise of the individuals. These factors are of course quite variable; thus, some centers have excellent results and others have poor results with a high incidence of complications.

Unfortunately, because the different nerves cannot be separated from one another, ablation of the sensory fibers in turn produces ablation of both the sympathetic and parasympathetic fibers. This results in the two commonly observed side effects:

1. Short-term orthostatic hypotension produced by splanchnic pooling of blood, caused by interruption of the sympathetic fibers
2. Diarrhea from interruption of the parasympathetic fibers

Different Approaches

Three general methods have traditionally been used, a transcrural approach, a retrocrural approach, or an anterior approach. The retrocrural approach attempts to interrupt the pathway after the splanchnic nerves have formed and as the nerves course in the posterior mediastinum. The transcrural approach interrupts the pathway at the plexus before formation of the nerves. With our method I approach the plexus directly and use an angled trajectory so that the entire needle pathway is beneath the diaphragm. This lessens possible complications caused by tracking of medication into the chest or abdomen. Other authors have used an anterior approach to destroy the plexus.[255,340]

Recommended Method

As with most CT procedures, my experience is quite extensive and dates back to the first such CT procedure in 1977[156] (Fig. 61–137). Since then I have evolved the technique to its current state.

The major elements of my technique are the following:

1. Use of a 19-gauge needle with 18-gauge Teflon sheath
2. Substitution of air instead of urographic contrast as a marker
3. Using a local anesthesia for a test block
4. Injection of 90% ethyl alcohol on the left side or bilaterally (Fig. 61–138), if needed

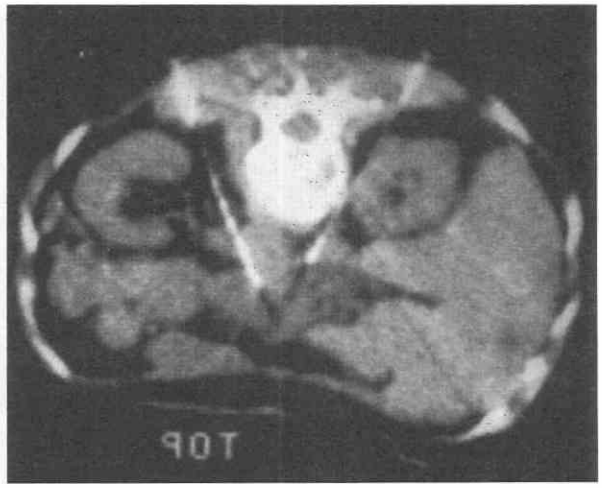

Figure 61–137. This CT procedure, which took place in 1976, shows the placement of two skinny needles for performance of a celiac nerve block (see text).

The early procedures reported by my group and Buy et al[43] used the 22-gauge skinny needles for the instruments and urographic contrast material mixed with alcohol for a marker. I have discarded the use of the skinny needles because they required too much pressure for injection. Since the pressure for injection is so high, any tissue resistance during injection cannot be manually perceived. According to the anesthesia literature, this ability to feel this pressure is important, because if excessive pressure is required, the needle may be inappropriately within the fascia of a vessel or organ.

In addition, the small-caliber needle that was previously used does not always permit free backflow of blood from a small vessel (as does the larger caliber 18-gauge sheath). Inappropriate injection into an artery can cause serious side effects, ranging from loss of an organ to paraplegia.

The injection of the local anesthetic is worthwhile for several reasons. First, there can be congenital variation in the location of the plexus. Depending on the relief of the abdominal pain with the local anesthetic, one can confirm that the pain sensed by the patient is carried by fibers through the plexus. If the pain is not relieved, it does not make sense to inject the alcohol, which can have significant complications.

Finally, instead of mixing contrast material with alcohol, we substitute 4 cc of ambient air to serve as a marker for injection. Because air works as well as contrast material, I decided that we should avoid any possible idiosyncratic contrast reactions or volume dilution of the alcohol.

Anatomic Approach

I use a posterior angled transcrural approach, which avoids virtually all anatomic structures. I do not penetrate the kidney, bowel, or other organs, because I believe that the terrible complications previously reported by the blind method were the result of inadvertent injection of a neurolytic agent into such structures. I attempt to interrupt the nerve fibers in the plexus itself primarily by placing the needles and the medication anterior to the aorta between

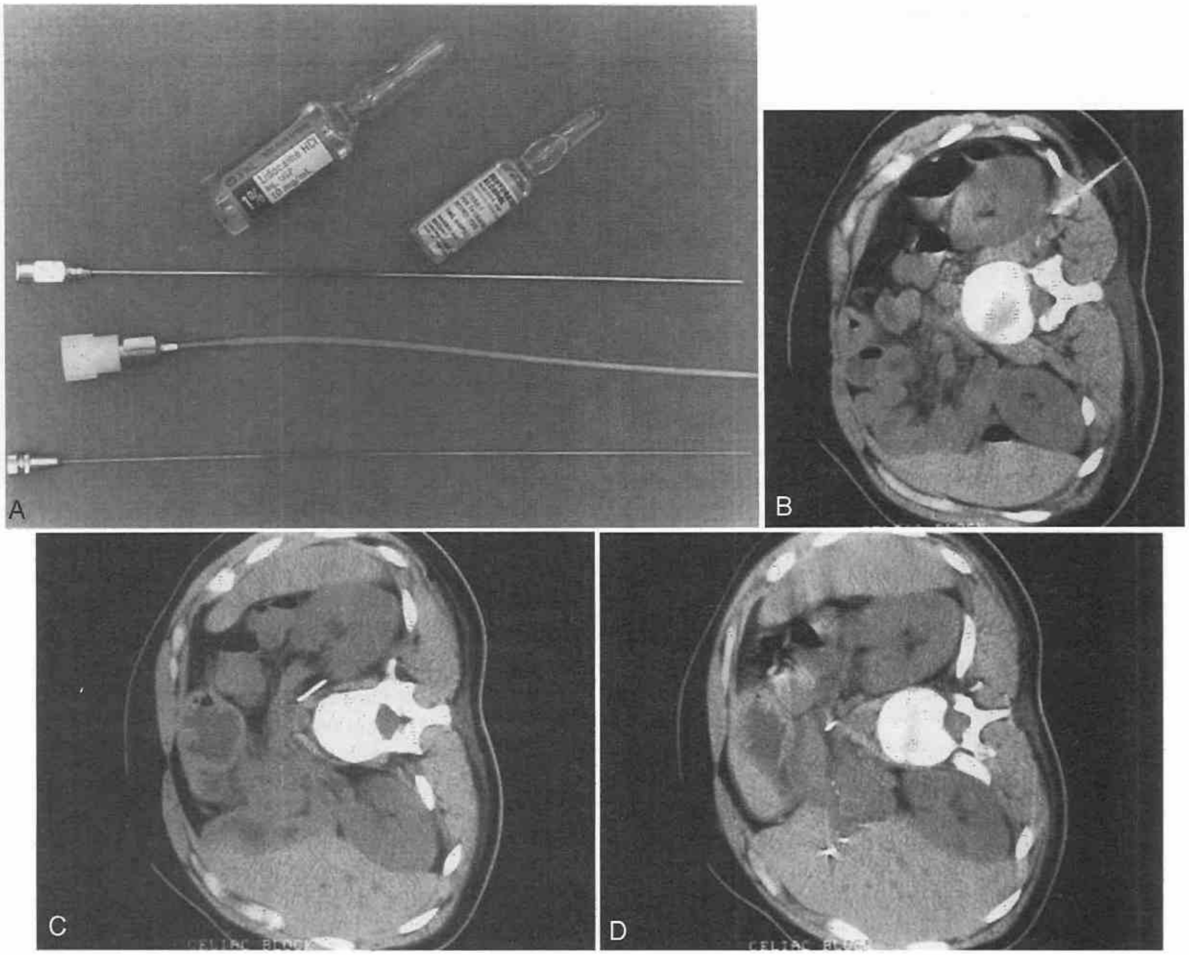

Figure 61–138. *A,* The equipment used for nerve blocks include a plastic sheath needle (sheath, needle, and stylet are disassembled), lidocaine anesthesia, and ethanol. *B,* This and the subsequent CT scan shows the appropriate positioning for a celiac nerve block. This scan shows the introduction of the needle into the retroperitoneum on the left. *C,* With cephalad angulation, the needle is passed behind the renal pedicle and then passed beside the aorta. *D,* This scan shows final placement of the needle tip beside the superior mesenteric artery behind the pancreas. One should note that even if inadvertant penetration of the vessels should occur, any adverse developments are unlikely (see text under other methods as proposed by Lieberman).

the superior mesenteric artery and the celiac artery. On some occasions interruption of the splanchnic nerves in the more peripheral areas must be accepted if the needles and medication are to be safely placed only posterior and lateral to the vessels.

I have not used the anterior approach or transaortic approach proposed by some because of concern about potential damage to the portal vein, hepatic artery, or pancreas.[255,340]

Technique

The technique that we use is essentially a four-step procedure: a diagnostic scan, placement of the needles and sheaths, a temporary test block, and a neurolytic alcohol ablation.

Diagnostic Scan

During a routine diagnostic scan, I look for any signs of an active process that should not be blocked. Under this category I have diagnosed and deferred patients with emphysematous pancreatitis, small bowel obstruction, or disease so extensive that a block would not be of any benefit. In the last category I exclude patients who have disease so extensive that the tumor is invading the musculoskeletal portions of the retroperitoneum. The pain will be carried by somatic sensory fibers; a celiac block will not significantly ablate the pain in such patients.

Before insertion of the needles, I ask the patient to grade their pain on a scale of 0 to 10, 0 being normal and 10 being unbearable. This scale is used for a reference value after the test block to help decide if the alcohol should be injected. To facilitate this, I ask that the patient not have pain medication the morning of the procedure so the pain level can be used as a guide during the procedure.

Placement of Needles

We position the patient in the left decubitus position (i.e., right side up and the left side down) if a unilateral block is to be used, or prone if a bilateral is used. One can thus easily approach the left side from almost a straight

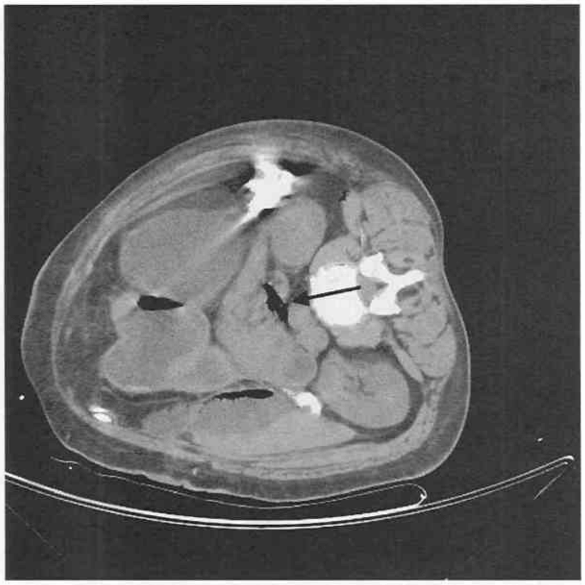

Figure 61–139. Scan of a patient in the right decubitus position after injection of air into the retroperitoneum. The air *(arrow)* crosses from left to right in the plexus area.

angle and the right side with a more oblique approach (Figs. 61–138 to 61–140, if a bilateral block is required.

The trajectory chosen is slightly angled, with the entrance point at the level of the renal vein and the target area just above the superior mesenteric artery, which is easily seen. The needle is angled slightly so that the final placement will be adjacent to the side of the aorta at a level between the celiac and the mesenteric artery.

If an appropriate placement of a single needle is made, the block can be accomplished with a single needle placement (Fig. 61–139). Injection of gas shows the gas crossing the midline, which indicates the injected alcohol will cross from left to right and ablate the major portion of the plexus. If the gas does not cross sufficiently from the left side, a placement of a second needle from the right side should be performed (Fig. 61–140).

Test Dose

Once successful placement of a left side needle has been made, a test injection is performed. I inject 15 mL of 2% lidocaine on the left side and 3 to 4 cc of ambient room air. I then repeat the CT scan over the area of the needles to assess the distribution of the air in the abdomen. If the air crosses from left to right, covering the entire area, a unilateral block is performed. If the air does not cross, a bilateral block is performed.

I let the medication permeate for 10 minutes and then ask the patient to grade the pain. If there is a remarkable improvement in their grading scale (i.e., a reduction from 8 or 9 to 0 or 3) and if the air has not tracked into an inappropriate area, the final block is performed. In some cases when the patient has a tumor and the patient requests it, I will inject the alcohol despite a poor response because this may be the last resort. If a bilateral block is required, we typically finish the left-sided procedure completely and then insert the needle on the right side.

Neurolytic Alcohol Ablation

The alcohol for the final block is not injected if there is no relief of pain or if there is an inappropriate tracking of the air. The tracking of the air is a good indicator of where the alcohol will go. A radiologist who did not follow this guideline produced a severe case of posterior mediastinitis because the alcohol tracked into the chest; the test study showed air tracking into the mediastinum, but he disregarded it. If the air tracks posteriorly adjacent into the nerve area behind the psoas muscle or the mediastinum area, I do not inject the alcohol on that side because of possible nerve damage. The "marker" of gas is a worthwhile portion of the examination. Fluoroscopy and ultrasound cannot evaluate this effectively, and catastrophes may result.

Also, if there is a return of blood from the needles, do not inject the alcohol. If a vessel is injected with alcohol, destruction of the end organ (e.g., kidney, spinal cord) will result.

At this time the alcohol is injected very slowly into the unilateral or bilateral needles. Because of the effective outcome of our procedures, we have reduced the volume of alcohol injected (since our prior edition) from 25 mL to 15 mL of alcohol. If a unilateral block is performed, a single dose of 15 mL is injected. If a bilateral block is performed, 15 mL is injected on each side. (Plastic syringes must be used because with glass syringes the evaporation of alcohol is so rapid that the barrels will "lock up.")

Since the previous edition of this book, I have learned a valuable lesson from my anesthesia colleague Dr. Mark Boswell,[34] who has shown me that if one injects the alcohol very slowly, the discomfort is minimal to the patient. In the previous edition we reported rapid injection of alcohol, which produces intense pain that has been described as the sensation of being "kicked" in the abdomen.

In some cases the pain may involve the diaphragm, chest, or back because of referral pathways. The distribution can be anticipated by noting the distribution of the "air marker."

Follow-up

After the procedure, the patient is returned to his or her room on a stretcher and kept at bedrest for 8 hours. This time permits resolution of the potential orthostatic hypotension. This routine is important to follow; testing for orthostatic hypotension is inadvisable. One patient in our institution was made unconscious three times by three different resident physicians who wanted to test her orthostatic hypotension by taking her blood pressure in an upright position. She had a very bad headache after these "tests" but did fine after the appropriate bedrest.

Side Effects

Two side effects—temporary orthostatic hypotension and bowel irregularity—can occur. Interruption of the sym-

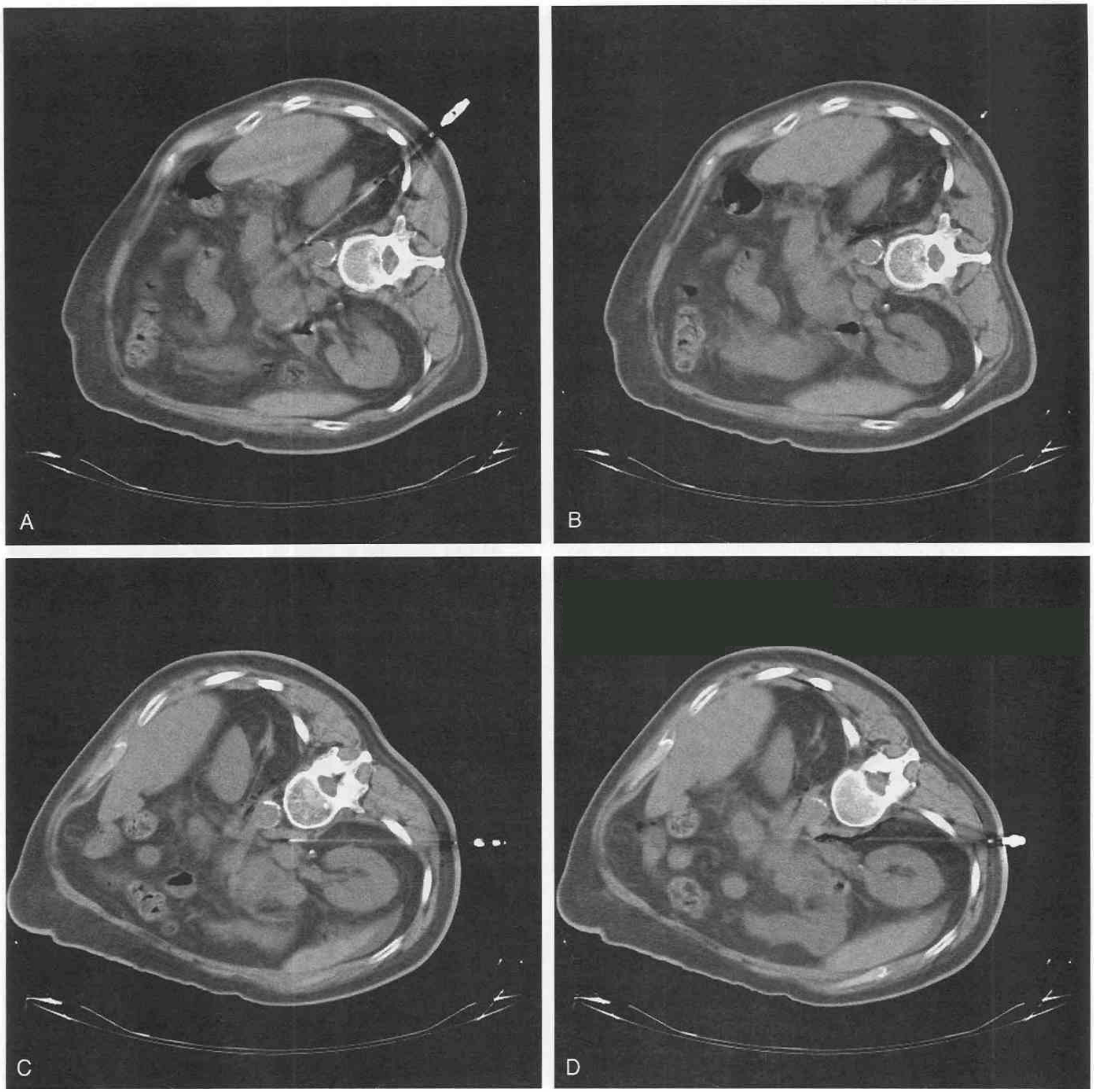

Figure 61–140. *A*, Scan with the patient in the right decubitus position shows a needle adjacent to the superior mesenteric artery. Note the small amount of tumor encasing the anterior portion of the vessel. *B*, Injection of air shows the gas localized by the artery. It does not cross the midline, indicating that coverage of the right side will not occur and the need for right-sided treatment. *C*, Placement of a right-sided needle is performed. The tip is between the crus of the diaphragm and the vena cava. *D*, Injection of air shows gas distributing only on the right side.

pathetic fibers stops the physiologic vascular tone in the splanchnic vessels, resulting in their dilation. The dilation produces pooling of blood; therefore if patients attempt to stand after a completed block, they will lose consciousness. If patients remain at bedrest for 8 to 10 hours, the problem resolves spontaneously. They should be gradually raised to the sitting and upright positions after the period of bedrest.

With interruption of the parasympathetic fibers, motility of the bowel changes so that some patients have diarrhea and some inexplicably complain of constipation, which is manageable with over-the-counter stimulants if needed.

Complications

In the past 27 years I have had only two transient complications. One patient had hematuria for 2 days, and one developed a small subcapsular renal hematoma. Com-

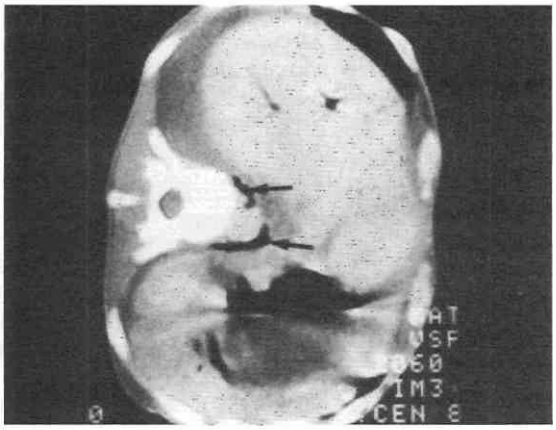

Figure 61–141. CT scan of a patient shows the air "marker" tracking into the chest (*arrows*) behind the crura. Injection should not be made in such cases, or mediastinitis may develop.

plications from the blind or other guidance methods are many and severe, including death, paraplegia, loss of kidneys or liver, hemorrhage, and mediastinitis (Figs. 61–141 and 61–142).

Briefly, there have been two other distinctly different methods reported in the literature: a transaortic method and an anterior approach.

Lieberman and Waldman[242] reported a transaortic approach in which the authors planned a trajectory to traverse the aorta. Once penetration of both walls of the aorta was accomplished, the alcohol was injected. Two groups have reported on a direct anterior needle approach with penetration of anterior structures such as liver and pancreas. Once the needles are in place, the appropriate medications are injected.

I do not favor either of these approaches because of possible problems associated with tracking of the alcohol and potential complications. If additional reports confirm the beneficial results and safety of those reports, one might consider these as alternative methods to the preferred one reported earlier.

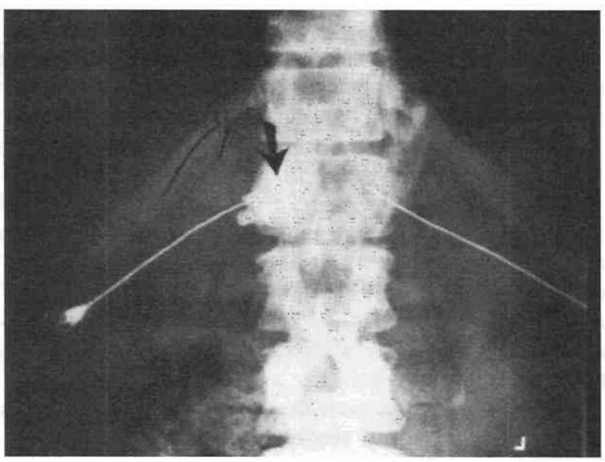

Figure 61–142. Radiograph of a patient with fluoroscopic localization for a celiac nerve block shows injection of contrast material (*arrow*). Permanent paraplegia developed after the procedure, despite the interventionist's considerable fluoroscopic experience and meticulous fluoroscopic technique.

Unfortunately, there is a tendency not to report complications with such invasive procedures, so it is difficult to assess the complication rates with the different approaches. However, Fitzgibbons et al[92] reported a case of superior mesenteric vein occclusion associated with injection of alcohol from an anterior approach.

There have been three large international series reported by Prasanna,[332] Marra et al,[262] and Gimenez et al.[113] Prasanna reported on 200 cases with good results for reduction of pain using a posterior unilateral left-sided block. Marra et al[262] and Gimenez et al[113] used an identical anterior approach using a 22-gauge needle with injection of alcohol and reported significant difference in the outcome. Marra et al[262] reported that 21% were pain free at 15 days and Gimenez et al[113] reported 61% pain free at 6 months.

Factors Affecting Pain Relief and a New Approach

Looking at the available results indicates that the exact anatomic approach used, needle size, or guidance modality is not a critical factor if adequate alcohol is delivered appropriately to the area of the celiac plexus. To ensure there is proper delivery of the alcohol it is prudent to use some type of marking agent (contrast material or air) prior to the injection of the alcohol to make sure no subtle adjustment of the needle tip is required. If the distribution of the contract marker is not satisfactory, the needle should be moved and the contrast marker injection repeated. When the contrast marker spreads throughout the plexus area to the right and left, it is appropriate to inject the alcohol. Individual results observed in the various studies probably depends on how meticulous the operator is with the needle placement and contrast injection. Mixing contrast material with the alcohol is not useful because it simply documents the placement of the alcohol after injection. It does not permit assessment of needle position so that it can be adjusted. Another step we know is helpful is to inject local anesthetic into the celiac area prior to the alcohol to see if pain relief is relieved. If complete relief results, one can be confident that the alcohol will diffuse in a similar fashion. Also relative to pain control during the alcohol injection, the local anesthetic will make the process of alcohol less uncomfortable. The alcohol should be injected very slowly to minimize intense pain.

Another factor that strongly affects the outcome of celiac nerve blocks is the degree of tumor invasion or involvement of the plexus area by fibrosis. Akhan et al[6] have shown that when tumor has invaded the plexus, alcohol will not distribute and may not ablate the nerve tissues. To further improve the results of plexus blocks, we have introduced a new technique that we believe offers great promise for the future of pain relief and perhaps even treatment of pancreatic cancer.

Radiofrequency Ablation of Celiac Plexus

Even though this method is just being developed, I want to introduce this new approach because it seems promising. If one reviews the subsequent section on tumor ablation,

one can reaffirm that ablation of tumor or tissues has been dependent on uniform and effective distribution of the ablative liquid agent into the target area. When a liquid is injected into solid tissue, whether it be tumor or the retroperitoneum with tumor, the liquid follows pathways of least resistance. When tumor is blocking the pathway for the alcohol, it may spread to unanticipated areas and can potentially cause complications. The use of liquid ablative agents has generally been replaced by radiofrequency heat coagulation because of this problem. Recognizing the benefits of radiofrequency for solid tumor ablation outside the pancreas, I decided to try judicious use of radiofrequency in a pilot group of patients who were not suitable for alcohol ablation of the celiac plexus. Although this might initially raise some safety concerns in the area of the pancreas where there are many vessels, it is an indisputable fact that large blood vessels act as heat sinks and are resistant to injury. The flowing blood carries the heat away from the area acting as a "radiation." For these reasons, it seems that radiofrequency might be an ideal methodology for ablating the plexus.

In a group of eight patients with intractable pain not suitable for alcohol block, we used radiofrequency to ablate the plexus. These patients had tumors in the peripancreatic area that we believed would impair the diffusion of alcohol into the plexus area.

Using a posterior or lateral approach, we inserted the radiofrequency probe with a 2-cm heating segment into the plexus area. The active portion of the probe could be visualized on the CT scan so that it could be carefully positioned next to the plexus area. The area was heated at 90°C for 10 minutes (Fig. 61–143). Realizing that this was the first such procedures performed, we were pleased with favorable results in six patients; two patients did not have good pain relief. The cause for failure was due to incorrect positioning of the probe in one patient and inadequate heating in the second. We are now in the process of performing a Phase I study to determine the safety of this method in a larger series of patients.

Figure 61–143. CT scan of patient during radiofrequency treatment of celiac plexus. Because the tumor had invaded into the plexus, successful treatment with alcohol was unlikely.

Because we had no complications from these procedures, we are also contemplating the possibility that radiofrequency may be used in the future to palliate or treat pancreatic cancers themselves.

Percutaneous Cholecystostomy

Percutaneous cholecystostomy is accepted as a viable alternative to surgical cholecystostomy in cases of cholecystitis-producing sepsis. Although it is true that any guidance method may be used for performing the puncture of the gallbladder, all authors agree that puncture of the gallbladder through the hepatic "bare" side is important to prevent leakage and proper tract formation.

As one might imagine, CT is superior for such guidance and should be used when a high confidence level is desired. Selection of tubes is dependent on the operator's own bias, but in our hospital we have relied on a small-caliber pigtail to effect emergency drainage. If stone removal or other manipulation is intended, sequential dilation can be performed as needed (Fig. 61–144).

Many reports have appeared in the literature about percutaneous cholecystostomy that have highlighted the benefits and the difficulties.

Among the authors reporting (Van Sonnenberg et al,[385] Hatjidakis et al,[167] Granlund et al,[122] and England et al[80]) there is consistent agreement that these procedures are effective and provide effective palliation for acute cholecystitis. Complications are quite varied and include bile peritonitis, bleeding, vagal reactions, hypotension, and acute respiratory distress. Rates vary between 4% and 10%.

All authors agree that the procedure, when optimally performed, uses a transhepatic pathway rather than a transperitoneal approach. Because of this uniform principle, I believe such procedures should be performed under CT guidance. In the past 15 years, we have never had a complication when the cases were performed and catheter positioned under CT guidance, compared to the 4% to 10% reported above.

Tumor Ablation

Radiologic ablation of tumors began in recent years with the acceptance of the surgical principles and outcomes that showed that removal of primary and metastatic lesions from the liver resulted in improved morbidity and survival rates of patients. The literature is replete with information by a number of authors who have devoted considerable effort and time to develop, introduce clinically, and refine these methods. The most notable of these are Gazelle,[101] Goldberg,[117] Solbiati,[363–365] Lewin,[240] Livrahi,[247] Curley,[63] and others. The publications have been so numerous and rapid that it is difficult to properly reference all of those who have made contributions.

The enthusiasm for local treatment originated from the seminal work of several surgeons who performed meticulous resection of multiple nodules throughout the liver. These authors, most notably Minton, showed increased survival of these patients. Although this approach was considered remarkably controversial at the time, it represents the base under the current philosophy. Another cate-

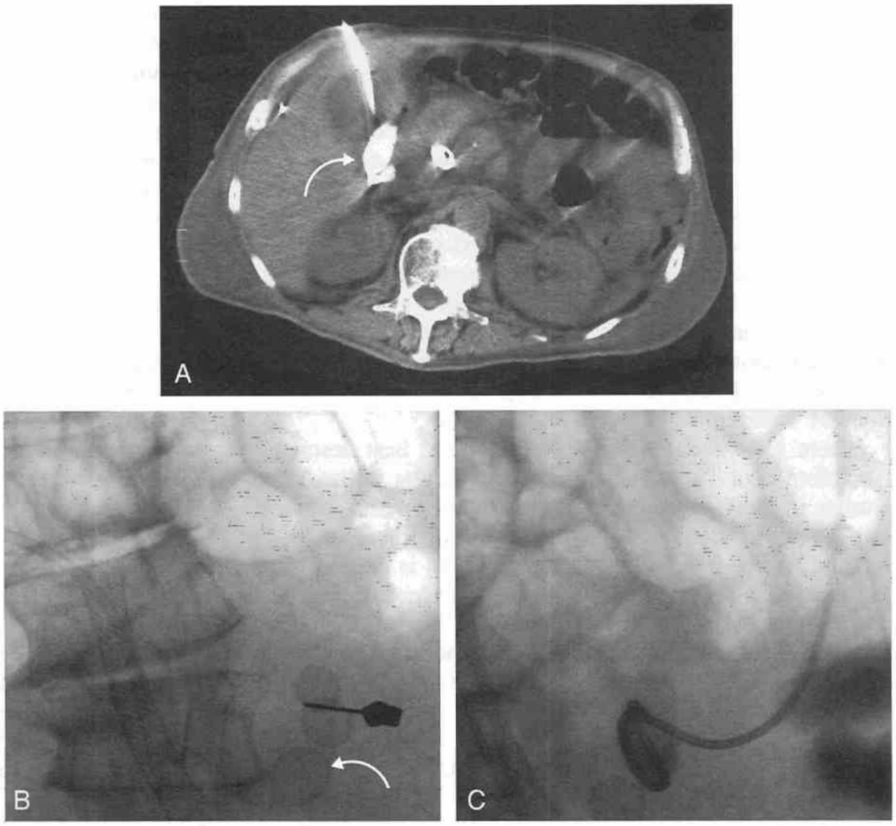

Figure 61–144. *A,* Scan shows a needle puncture of the gallbladder through a cuff of liver *(arrow).* The needle was intentionally directed toward the gallstones *(arrow).* This was done in case there was a need for percutaneous removal of the stones later. *B,* Radiograph shows the needle in place adjacent to the gallstones *(curved arrow).* Theoretically, one could consider performing this study under fluoroscopy, but the margin of the liver could not be visualized in this manner. *C,* Radiograph shows insertion of the catheter in the gallbladder with contrast injection.

gory of patients who became recognized as amenable to the local destruction were those patients with hepatocellular carcinoma. Surgery is curative for those patients suitable for resection, but a significant number are not surgical candidates because of the size of lesions, proximity to vital structures, compromised status of the liver (cannot endure loss of functioning liver parenchyma associated with lobar liver resection), or generally poor health (Curley et al[63]).

Surgical literature has definitely shown an increase in the survival rate of patients with metastatic colorectal and breast cancer. Taylor et al,[378] Hugh et al, and Yoon and Tanabe[414] have shown survival rates at 5 years of 25% to 40%. With breast cancer, improved survival of 18% to 20% at 5 years was reported by Elias et al and Raab et al.

As a result of the general acceptance of the surgical principles, the methodologies appropriately evolved to simpler means of surgical treatment (cryoablation and heat ablation at open laparotomy) and ultimately to percutaneous application of the same methods. The trend is to further refine the percutaneous approaches knowing that the low morbidity and cost of percutaneous procedures will drive these simpler approaches. Even the surgical literature (Bowles et al,[36] Curley et al[63]) confirms that the radiofrequency cumulative survival outcomes parallel the surgical results.

There are three major methodologies that have developed and are being refined by many centers. These consist of (1) application of various energy forms—freezing or cryoablation, heat application (including laser, microwave or radiofrequency); (2) injection of destructive liquid agents (alcohol, acetic acid, hot saline); (3) delivery of chemotherapeutic agents directly into the tumor (angiographic injection is different); and (4) delivery of other sophisticated products such as DNA vectors, polypeptides, and hormones.

Cryoablation has been available for many years, but the instruments were so large that the methodologies were confined to surgical methods at open laparotomy. This method depends on repetitive freezing that produced death of tumor cells by creating ice crystals within the cells. Two freezing cycles were required to ensure reliable death of tumor cells. The advantage of this approach is that large tumors could be treated. The disadvantages were that there is a likelihood that large cracks in the liver can occur and result in a surgical repair. Another adverse outcome was that there was a systemic reduction in platelets, which would be problematic. Recently, smaller percutaneous probes have become available, but the issues related to liver cracking persist, and some results indicate that cell death by freezing is not as reliable as heat coagulation.

The development of heat application and injection of chemical agents evolved at about the same period, with the chemical agents becoming accepted quickly because of their simplicity and heat coagulation becoming more popular as the relevant technology evolved.

Alcohol and Other Chemical Agents

Percutaneous chemical ablation, typically with alcohol, is the most common minimally invasive method for treating hepatocellular carcinoma and metastatic lesions. It is low tech, economical, and available to any center in the world.

In recent years, it has been shown to be less effective than radiofrequency ablation for general metastatic disease and hepatocellular carcinoma (HCC) but it still remains an effective method for the treatment of HCC.

The effects of alcohol are caused by cytoplasmic dehydration, which causes coagulation necrosis, endothelial damage, platelet aggregation, local tissue ischemia, and ultimately fibrous reaction. Its advantages are that it is only locally destructive, can be metabolized readily, and does not typically cross major anatomic boundaries. It is effective for HCC because it typically has well-defined borders that confine and restrict the spread and localize the effects. Metastatic lesions are less well suited because the margins are less well defined and ethanol spreads in a more unpredictable fashion.

There have been two reported methods, best described by Shiina et al[354] and Livraghi et al.[246,248] The methods are similar in their approach for the injection of the material but differ in the quantity and intervals of injection. Both methods use a small-caliber needle, which is inserted into the most distal portion of the lesion and then is reinserted during injection of the alcohol to the lateral, posterior, caudad, cranial, and anterior walls of the mass. Shiina et al[354] calculated the amount of alcohol to be used by using a volumetric calculation of a sphere:

$$\text{Volume} = 4/3\ \pi\ (R + 0.5)^3$$

The volume is in cubic centimeters and R is the radius of the lesion. An additional 0.5 cm is added to account for spread into the margin of the lesion with the normal liver with anticipation that this may produce a chemical margin of the lesion. The injection is made over 10 to 20 minutes with some modification based on the patient's compliance. Typically a second treatment was performed several months later.

Livraghi et al[248] used ultrasound to monitor the injection of alcohol with no precalculated volume specified. Their procedures were performed under general anesthesia to permit better pain control and management of ventilation. With their method the lesion was monitored with ultrasound and the injection was continued as long as the "flow" from the end of the needle continued without undue injection pressure. With their method they carefully infiltrated all walls as well as the central portion of the lesion. Repetitive injections were performed over several months if repeat imaging studies showed evidence of nonresponse or recurrence.

Follow-up was consistent in several perspectives. There was invariably a transient rise in the liver enzyme profiles, which returned to normal within 10 days. Blood alcohol levels were elevated postprocedure, and Shiina et al[354] noted mild intoxication in 25% of patients. Successful treatment of confined or encapsulated tumors showed significant reduction in the alpha-fetoprotein levels.

Complications were not infrequent (Livraghi et al[248] and Shiina et al[354]). The most common adverse effect was localized pain during and following the procedure. Pain persisted for several days with upper abdominal discomfort, enhanced by palpation, but this was easily controlled by analgesics. Patients may have spread of alcohol to uninvolved areas of the liver and produce necrosis of normal tissue. Both authors reported intraperitoneal bleeding when a normal "cuff" of normal liver did not exist below the capsule.

Barnett and Curley[18] and Livraghi et al[247] summarized the general results of alcohol ablation as follows. For HCC, the success depends on the size of the lesions. With lesions less than 5 cm, ethanol injection was successful in 75% of lesions that underwent subsequent resection. With lesions between 5 and 8 cm, the ablation rate is 60%. Livraghi et al[247] reported a 1-year survival rate of 90% and a 3-year survival rate of 63% (Figs. 61–145 and 61–146).

A comparison study of alcohol injection and radiofrequency ablation was performed by Livraghi et al[247] and Ikeda et al.[186] Livraghi et al reported better results with HCC tumors less than 3 cm for radiofrequency than alcohol injection; however, there were higher complication rates with radiofrequency. Ikeda et al[186] studied small HCC lesions and found almost identical results of success and complications but favored radiofrequency because it required fewer treatment episodes.

Ethanol injection has much less effect for metastatic lesions and therefore is seldom used, in favor of radiofrequency treatment (Solbiati et al[363,364,365]). The recommendation by most authors is to use alcohol injection when lesions are in an opportune site for radiofrequency or when lesions are greater than 3 to 4 cm.

As a final comment, other agents have been injected such as acetic acid (Ohnishi et al) and gel cisplatin (Engelmann et al[79]), but the techniques still show the disadvantages of irregular distribution and therefore nonuniform response.

Heat Coagulation by Radiofrequency

Application of heat effectively kills tumor cells in two methods depending on the temperature. At 42°C tumor cells may die in preference to normal cells because of the induction of hypermetabolism from increased temperature. Because tumor cells lack the normal homeostatic controls of normal cells, they typically die a metabolic death over many minutes. With temperatures at 45° to 60°C intracellular proteins denature and bilipid membranes melt, resulting in cell death. With temperatures above this level (80° to

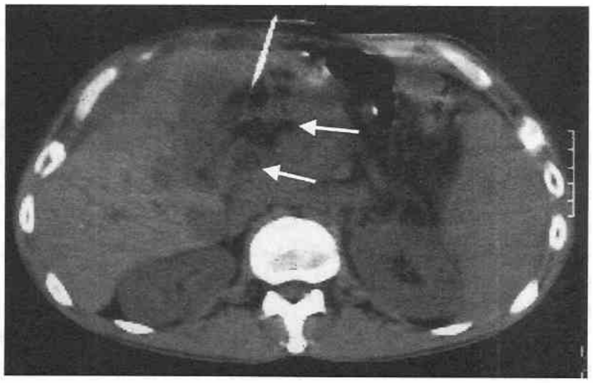

Figure 61–145. CT scan shows injection of alcohol into a large mass in the epigastrium. Note the distribution of alcohol is irregular (*arrows*). Because the distribution is so irregular, effective treatment of large tumors is difficult.

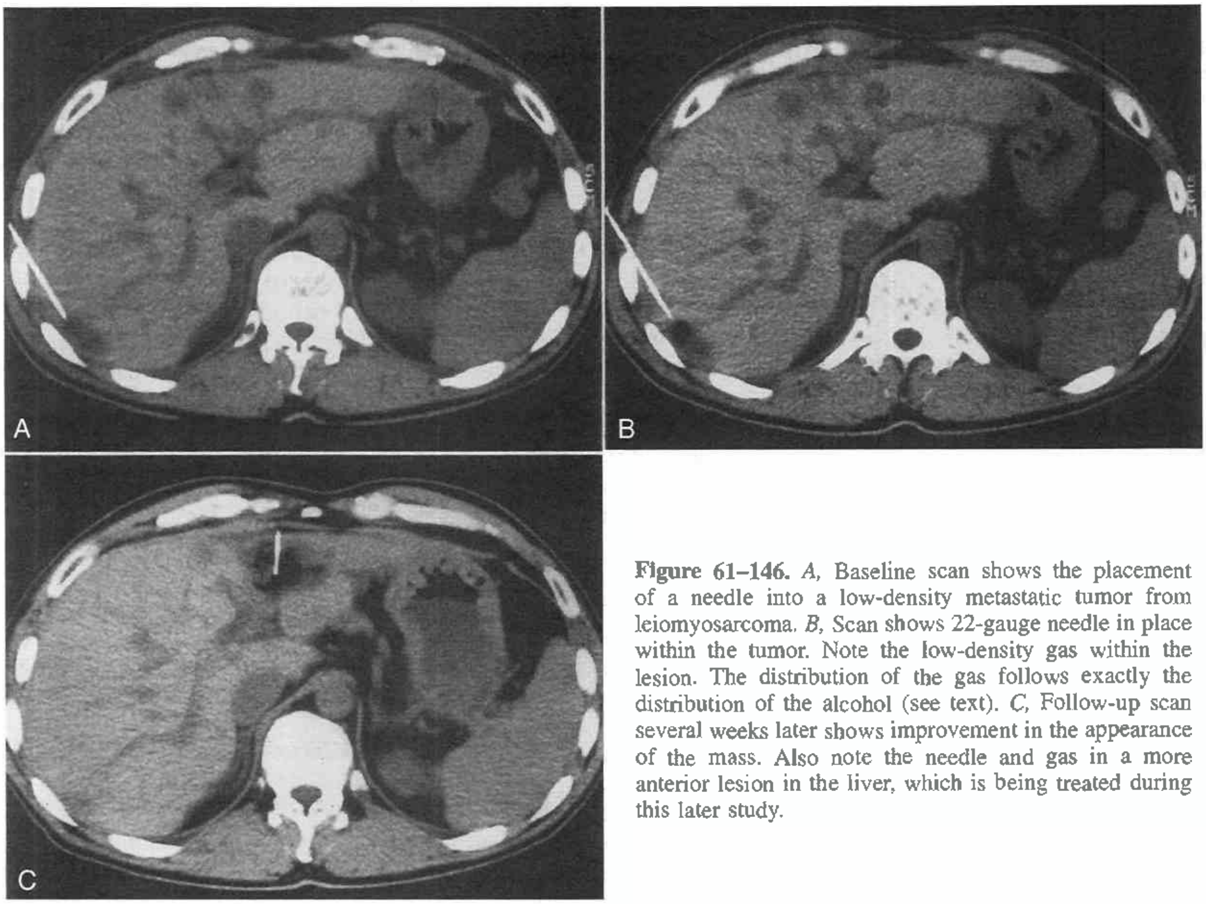

Figure 61–146. *A,* Baseline scan shows the placement of a needle into a low-density metastatic tumor from leiomyosarcoma. *B,* Scan shows 22-gauge needle in place within the tumor. Note the low-density gas within the lesion. The distribution of the gas follows exactly the distribution of the alcohol (see text). *C,* Follow-up scan several weeks later shows improvement in the appearance of the mass. Also note the needle and gas in a more anterior lesion in the liver, which is being treated during this later study.

110°C) heat coagulation necrosis occurs for all tissues. The temperature levels and effects reported by different authors vary slightly, but this is probably due to minor differences in the basic models studied and differences in cell types.

One critical factor that must be mentioned is the influence of blood flow both microscopically and macroscopically on the effect on local tissues and the survivability of normal and tumorous cells. Flowing blood acts as a heat sink or radiator effect so that heat is moved away from the immediate site of the treatment region. This result is helpful because one wishes to preserve normal vessels in close proximity to the tumor, but it has a negative effect on the survival of tumor cells in immediate proximity to the vessels. The residual tumor cells within tumors or especially at the margins of the treated areas are the cause of local recurrences (Curley et al,[63] and Sobiati et al[363–365]).

Relative to the methods of heat application, radiofrequency heat coagulation remains the preeminent method for heat coagulation. Laser, microwave, and ultrasound heating have been attempted and are being refined, but there is little indication they will provide heat deposition superior to that of radiofrequency.

Radiofrequency Devices

There are two major types of radiofrequency devices used for these treatments. One is a single probe and the other type is a spoke device, shaped somewhat like an umbrella. The single-probe device is our preferred one because placement of the device is more easily achieved and has a better definition of the probe into the tissues, because it has a simpler configuration. I cannot comment on the efficiency of the other type of device because I do not have the experience.

General Technique and Placement of the Radiofrequency Probe

Preprocedural Steps

Patient selection criteria have varied among the various authors. Considering the motivation of cancer patients, there is little question that one could select almost any patient, but the most rational and human approach is to select only those patients who are likely to derive a direct benefit in survival or symptoms. The presence of multifocal disease in widely spread sites is a relative contraindication. In most cases patients being considered will be those with liver metastasis. It has been well established that the successful treatment of tumors is closely related to size because of the difficulty in treating patients with larger lesions. Solbiati et al,[363, 364] Lewin et al,[240] and Livraghi et al[247] have shown that lesions smaller than 3 cm are likely to have a good outcome. Livraghi et al in a multi-institutional study involving metastases showed that lesions less than 2 cm were cured, lesions between 2 and 3 cm had a cure rate of 70% (recurrence rate of 30%), and lesions

greater than 3 cm had a cure rate of 58% (recurrence rate of 42%). The success and recurrence rate with HCC is similar. HCC lesions less than 2.5 cm are effectively destroyed while large lesions are prone to recur (Curley et al,[63] Bowles et al[36]).

Assessment of lesions prior to the procedure relative to vascularity is important. Patients with lesions that are highly vascular as demonstrated by CT or MRI flow studies are less than optimal candidates. Patients with metastatic lesions from colon and breast are considered good candidates.

Exclusion criteria include the presence of severe coagulopathy, renal failure, jaundice, or anatomic issues related to proximity. It has been shown that if lesions are too close to the gallbladder, hilum, or bowel wall, injury may occur. A distance of 1 cm from these structures is considered adequate to prevent severe damage. Likewise, close proximity to major vessels is considered a relative contraindication because such vessels reduce the efficiency of heating and thereby reduce the local coagulation benefit.

Procedure Steps

Before the insertion of the probe, several important items must be addressed. If the lesions are in the liver, one should decide whether to give a dose of antibiotics. Solbiati[363–365] recommends 2 g of ceftriaxone; in view of the occasional issues raised with infection, this seems a rational approach.

The grounding pads must be attached to the skin to enable good conduction of the current from the electrode to ground. The skin should be shaved to permit good contact. The pads should be attached with the long side of the pads perpendicular to the long axis. Lack of good ground can result in local burns.

Anesthesia for these procedures can be deep sedation or general anesthesia. When one begins performing such procedures, it is appropriate to visit a center where such procedures are performed. Also during the initial cases, general anesthesia is helpful to ensure patient comfort. After the procedural steps are mastered, procedures can be performed under local anesthesia and intravenous medications consisting of fentanyl and midazolam. In all cases one should plan the procedure to ensure optimal heating and treatment of all segments of the lesion. In each case this means planning single or multiple insertions to cover the area of the lesion.

Depending on which probe is used, one plans appropriately. Available devices have automatic feedback mechanisms that modulate the current appropriately. With the device made by radionics, the heating period should be 12 minutes, but final heating depends on the final temperature after treatment. If the final temperature after turning off the probe does not measure at least 60°C, additional heating is appropriate. In each case one should follow the recommendations of the equipment manufacturer. Multiple insertions require repetitive heating periods for each geographic site. The size and degree of the thermal lesion are dependent on the temperature achieved and the duration of the heat application.

The therapeutic response can be assessed in several ways: from imaging and from monitoring of changes in the tissue impedance measurements. Any of three imaging devices can be used to monitor visually the change in tissue appearance that indirectly reflects tissue coagulation. Ultrasound shows a change of increased echogenicity when tissue coagulates. MRI shows change in tissue signal during coagulation of protein, changing the T2 appearance (Figs. 61–147 and 61–148). CT only shows imaging changes with injection of contrast material. It is not clear that any of these modalities offer great advantage one over the other so the choice of the modality is left to the reader, depending on their own experience and knowledge base (Figs. 61–149 to 61–151). The intent of monitoring the lesions under imaging is to produce necrosis of a "cuff" of tumor free area by necrosing 10 mm of adjacent normal liver.

When tumor has undergone heat coagulation, the impedance (or conductivity) increases; if the change has increased by 20 Ohms there is usually complete necrosis. Goldberg et al[117] compared the amount of tissue necrosis produced by constant current flow over a finite period and variable current flow adjusted according to impedance chances. If the impedance rises too quickly (or electrical conductivity decreases) due to local tissue charring, con-

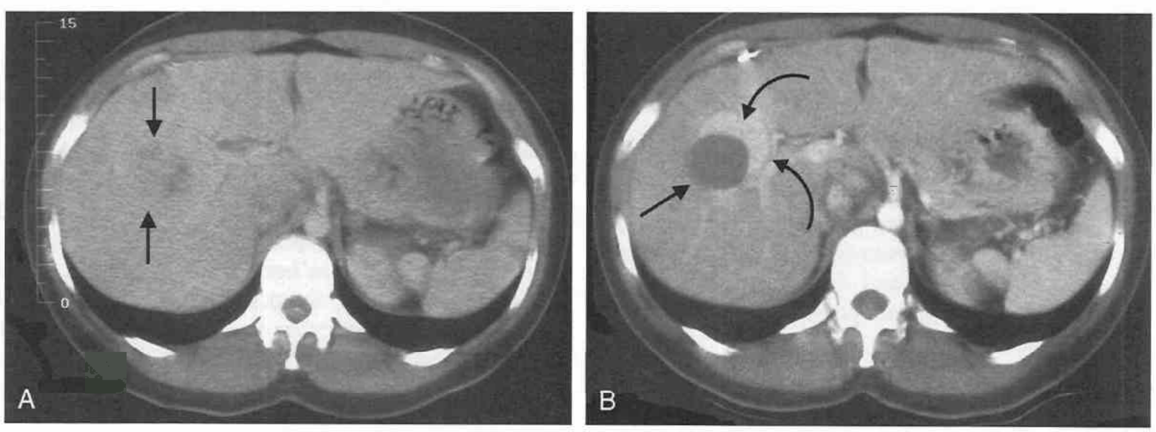

Figure 61–147. CT scan shows a large mass in the porta region of the liver *(arrows)*. This was treated under MRI by radiofrequency treatment. *B*, Follow-up scan shows a low-density mass *(arrow)* representing the necrotic treated area. The large enhancing rim (*curved arrows*) represents recurrent tumor.

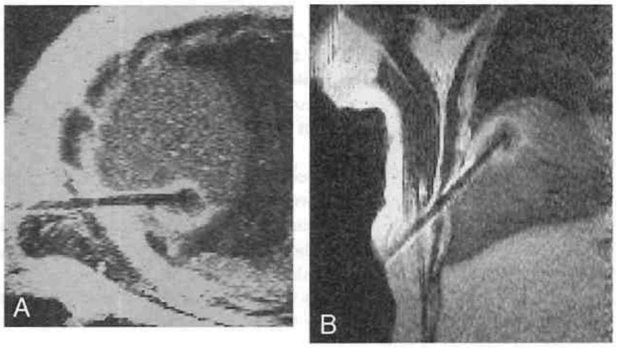

Figure 61–148. Turbo spin-echo T2-weighted oblique axial *(A)* and coronal *(B)* images obtained during MRI-guided radiofrequency (RF) thermal ablation. During the ablation session, T2-weighted and STIR images allow assessment of the developing zone of tissue damage, seen as a hypointense region surrounded by a bright ring of edema at the tip of the RF electrode. These images are intermittently acquired during the ablation session to ensure ablation of the entire tumor and thin rim of surrounding normal tissue.

duction of heat is not efficient. They found that if the current was reduced for 15 seconds after rapid rise of impedance, a greater volume of tissue was treated. This algorithm is the basis for the automated treatment mode of the single-probe device.

Follow-up after Therapy

For follow-up, CT or MRI is suitable for assessment of treatment but not ultrasound. Solbiati et al[363–365] demonstrated that acute appearance of ultrasound changes cannot predict ultimate tumor necrosis. MRI shows hypointense areas of unenhanced T1 and T2 images, which do not enhance with gadolinium injection. With CT scanning, necrosis of tissue can be appreciated only with the intravenous injection of contrast material. Size change can also be used. Those lesions that reduce in size or remain stable are considered necrotic. Those that increase are classified as progressing. Any appearance of recurrence indicates a need for retreatment if clinically relevant.

The major shortcoming with any of the radiofrequency methods (also shared by cryoablation) is the survival of viable residual tumor cells within the lesions or at the periphery of the lesions (see Fig. 61–147). Virtually all authors note that the most common site of recurrence is at the margin of the lesions. Despite the fact that the intent is

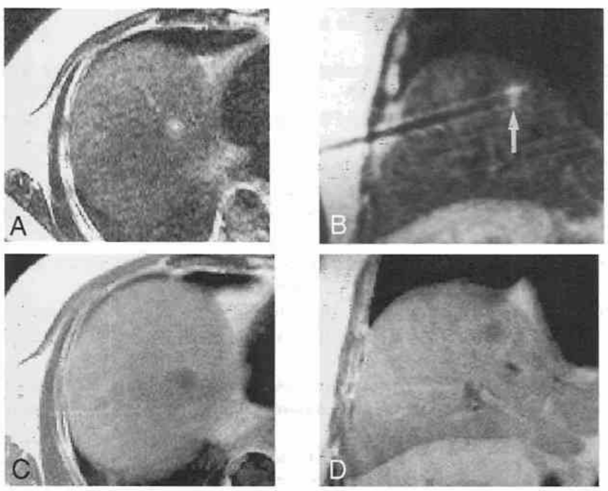

Figure 61–149. *A*, Turbo spin-echo T2-weighted axial image demonstrates a 1-cm metastasis near the dome of the liver. *B*, Turbo spin-echo T2-weighted coronal image demonstrates the radiofrequency electrode, placed under MRI guidance, with its tip centered within the tumor nodule. Axial *(C)* and coronal *(D)* contrast-enhanced T1-weighted images at the end of the ablation session demonstrate a hypointense zone corresponding to the treated metastasis. The lesion was treated to ensure complete ablation of the tumor plus a thin surrounding margin of normal tissue.

Figure 61–150. Scan through the chest shows a mass in the posterior mediastinum, containing calcium. The probe is located in the mass for ablation. Especially in the lung, it is critical to localize the treatment portion of the probe completely in the mass so that no contiguous tissues are damaged.

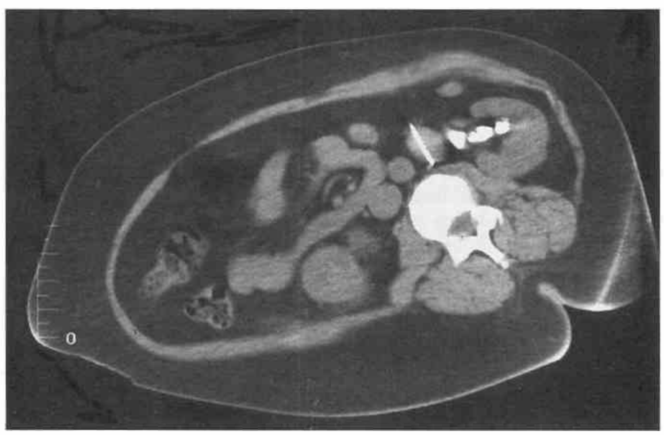

Figure 61–151. CT-guided ablation of a retroperitoneal lymph node. An approach through the anterior abdominal wall was used because this was the shortest unimpeded pathway.

to create a margin of tumor-free tissue, this is problematic. None of the imaging devices can accurately display small tumor rests at the margin of the lesions, so improvement will come only when further advances are made, probably with some method of multimodality treatment.

Multimodality Approaches

Combination with multiple other materials or agents have been evaluated in a preliminary fashion to enhance or increase the effects of radiofrequency. Several authors (Curley[63] and Hamilton[163] and Goldberg et al,[117]) have injected saline in different volumes and concentration and found that the resulting coagulation area was increased.

Goldberg et al,[117] studied the benefits of combining radiofrequency ablation with ethanol injection and doxorubicin injection into the tumor site with animal models. With ethanol injection, they found increased area of coagulation when the ethanol was injected prior to the radiofrequency heating but no improvement when ethanol was injected following the radiofrequency ablation. The size of the lesion increased from 6.7 mm from ablation alone to 10.1 mm with the ethanol combination. Increase in the tissue impedance was found after the alcohol injection. This group also injected the chemotherapeutic agent doxorubicin into the tumor before and after radiofrequency ablation. The authors found that doxorubicin improved tumor coagulation when it followed the ablation but not before. The increase in the ablation site changed from 6.7 mm in the ablation site alone to 11.1 mm with the combination therapy.

Percutaneous Enteric Stoma

A logical extension of the percutaneous puncture and catheter insertions is the development of percutaneous methods for insertion of catheters into bowel loops.

Percutaneous gastrostomies and other enterostomas may be performed by fluoroscopy; they are not discussed in this chapter. Catheter insertion into the colon, however, is quite different and may require the use of CT for optimal placement of the entrance site.[142] CT is well suited to ensure that the entrance site is on the retroperitoneal side of the colon so that peritoneal spillage will not occur. One author has used this for treatment of Ogilvie's syndrome.[61] I have used it for catheter-instilled antibiotics in a case of toxic megacolon.[142]

References

1. Acunas B, et al: Purely cystic hydatid disease of the liver: treatment with percutaneous aspiration and injection of hypertronic saline. Radiology 182:541–543, 1992.
2. Adams DB, Anderson MC: Percutaneous catheter drainage compared with internal drainage in the management of pancreatic pseudocyst. Ann Surg 215:571–576, 1992 (discussion, pp 576–578).
3. Adler O: Personal communication, 1987.
4. Aideyan OA, Schmidt AJ, Trenkner SW, et al: CT-guided percutaneous biopsy of pancreas transplants. Radiology 201:825–828, 1996.
5. Akgun Y, Tacyildiz IH, Celik Y: Amebic liver abscess: Changing trends over 20 years. World J Surg 12:1316, 1999.
6. Akhan O, Altinok D, Ozmen MN, et al: Correlation between the grade of tumoral invasion and pain relief in patients with celiac ganglia block. AJR 168:1565–1567, 1997.
7. Alexander JW, Korelitz J, Alexander NS: Prevention of wound infections: A case for closed suction drainage to remove wound fluids deficient in opsonic proteins. Am J Surg 132:59–64, 1976.
8. Alexander MC: Unpublished data, 1986.
9. Andersson T, et al: Percutaneous ultrasonography-guided cutting biopsy from liver metastases of endocrine gastrointestinal tumors. Ann Surg 206:728–732, 1987.
10. Andriole JG, et al: Biopsy needle characteristics assessed in the laboratory. Radiology 148:659–662, 1983.
11. Arakawa H, Nakajima Y, Kurihara Y, et al: CT-guided transthoracic needle biopsy: A comparison between automated biopsy gun and fine-needle aspirations. Clin Radiol 51:503–506, 1996.
12. Atterbury CE, et al: Comparison of the histologic and cytologic diagnosis of liver biopsies in hepatic cancer. Gastroenterology 76: 1352–1357, 1979.
13. Aurell Y, et al: Percutaneous puncture and drainage of pancreatic pseudocysts: A retrospective study. Acta Radiol 31:177–180, 1990.
14. Axel L: Simple method for performing oblique CT-guided needle biopsies. AJR 143:341, 1984.
15. Balen FG, Little A, Smith AC, et al: Biopsy of inoperable pancreatic tumors does not adversely influence patient survival time. Radiology 193:753–755, 1994.
16. Ball WS, Bisset GS, Towbin RB: Percutaneous drainage of chest abscess in children. Radiology 171:431–434, 1989.
17. Barbaric ZL, Hall, T, Cochran ST, et al: Percutaneous nephrostomy: Placement under CT and fluoroscopy guidance. AJR 169:151–155, 1997.
18. Barnett CC, Curley SA: Ablative techniques for hepatocellular carcinoma. Semin Oncol 28:487–496, 2001.
19. Barthet M, Bugallo M, Moreira LS, et al: Management of cysts and pseudocysts complicating chronic pancreatitis: A retrospective study of 143 patients. Gastroenterol Clin Biol 17:270–276, 1993.
20. Bass J, Di Lorenzo M, Desjardins JG, et al: Blunt percutaneous injuries in children: The role of percutaneous external drainage in the treatment of pancreatic pseudocysts. J Pediatr Surg 23:721–724, 1988.
21. Bateson MC, et al: A comparative trial of liver biopsy needles. J Clin Pathol 33:131–133, 1980.
22. Becker JA, et al: Needle aspiration and B-mode scanning. Invest Radiol 10:173–175, 1975.
23. Berger H, Permanetter W, Steiner W: Percutaneous biopsy technic: Aspiration fine-needle cutting biopsy cannula in an experimental comparison. Ultraschall Med 9:128–131, 1988.
24. Berkman WS, et al: Computed tomography guided adrenal biopsy: An alternative to surgery in adrenal mass diagnosis. Radiology 155: 858, 1984.
25. Bernardino M, et al: Pancreatic transplants: CT-guided biopsy. Radiology 177:709–711, 1990.
26. Bernardino ME: Automated biopsy devices: Significance and safety. Radiology 176:615–616, 1990.
27. Bernardino ME: Percutaneous biopsy. AJR 142:41, 1984.
28. Bernardino ME, Amerson JR: Percutaneous gastrocystostomy: A new approach to pancreatic pseudocyst drainage. AJR 143:1096, 1984.
29. Bernardino ME, et al: CT-guided adrenal biopsy: Accuracy, safety, and indications. AJR 144:67, 1985.
30. Berquist TH, et al: Transthoracic needle biopsy: Accuracy and complications in relation to location and type of lesion. Mayo Clin Proc 55:475–481, 1980.
31. Bilbao JR, et al: Pancreatic pseudocyst in a gastrectomized patient: Treatment with internalized endoprosthesis. Gastrointest Radiol 16: 70–72, 1991.
32. Bissonnette RT, et al: Fatal carcinoid crisis after percutaneous fine-needle biopsy of hepatic mestastasis: Case report and literature review. Radiology 174:751–752, 1990.
33. Bosanac ZB, Lisanin L: Percutaneous drainage of hydatid cyst in the liver as a primary treatment: Review of 52 consecutive cases with long-term follow-up. Clin Radiol 55:839–848, 2000.
34. Boswell M: University Hospitals of Cleveland, Personal Communication 1996.
35. Bourgouin PM, et al: Transthoracic needle aspiration biopsy: Evaluation of the blood patch technique. Radiology 166:93–95, 1988.
36. Bowles BJ, Machi J, Whitney M, et al: Safety and efficacy of radiofrequency thermal ablation in advanced liver tumors. Arch Surg 136:864–868, 2001.

37. Bret PM, et al: Abdominal lesions: Prospective study of clinical efficacy of percutaneous fine-needle biopsy. Radiology 159:345, 1986.
38. Bret PM, et al: Ultrasonically guided fine-needle biopsy in focal intrahepatic lesions: Six years' experience. J Can Assoc Radiol 37: 5, 1986.
39. Brolin RE, et al: Percutaneous catheter versus open surgical drainage in the treatment of abdominal abscesses. Am Surg 50:102–108, 1984.
40. Browning PD, McGahan JP, Gerscovich EO: Percutaneous cholecystostomy for suspected acute cholecystitis in the hospitalized patient. J Vas Interv Radiol 4:531–537, 1993.
41. Bungay HK, Berger J, Traill ZC, Gleeson FV: Pneumothorax post CT-guided lung biopsy: A comparison between detection on chest radiographs and CT. Br J Radiol 72:1160–1163, 1999.
42. Butch RJ, et al: Presacral masses after abdominal resection for colorectal carcinoma: The need for needle biopsy. AJR 144:309–312, 1985.
43. Buy JN, Moss AA, Singler RC: CT-guided celiac plexus and splanchnic nerve neurolysis. J Comput Assist Tomogr 6:315–319, 1982.
44. Caliendo MV, Lee DE, Queiroz R, Waldman DL: Sclerotherapy with use of doxycycline after percutaneous drainage of postoperative lymphoceles. J Vasc Interv Radiol 12:73–77, 2001.
45. Candel AG, Gattuso P, Reyes CV, et al: Fine-needle aspiration biopsy of adrenal masses in patients with extraadrenal malignancy. Surgery 114:1132–1136, 1993 (discussion, pp 1136–1137).
46. Carney CH: Clinical cytology of the liver. Acta Cytol 19:244–250, 1975.
47. Carruthers DM, Connor S, Howie AJ: Percutaneous image-guided biopsy of lung nodules in the assessment of disease activity in "Wegener" granulomatosis. Rheumatology (Oxford) 39:776–782, 2000.
48. Casola G, et al: Percutaneous drainage of tubo-ovarian abscesses. Radiology 182:399–402, 1992.
49. Catalano OA, Hahn PF, Hooper DC, Mueller PR: Efficacy of percutaneous abscess drainage in patients with vancomycin-resistant enterococci. AJR 175:533–536, 2000.
50. Cellier C, Cuenod CA, Deslandes P: Symptomatic hepatic cysts: Treatment with single-shot injection of minocycline hydrochloride. Radiology 206:205–209, 1998.
51. Ch Yu S, Hg Lo R, Kan PS, Metreweli C: Pyogenic liver abscess: Treatment with needle aspiration. Clin Radiol 52:912–916, 1997.
52. Chesmar JL, et al: Liver transplant biopsies with a biopsy gun. Radiology 179:447–448, 1991.
53. Christopherson P, et al: Preoperative pancreas aspiration biopsies. Acta Pathol Microbiol Scand 112:28–33, 1970.
54. Civardi G, Filice C, Caremani M, Giorgio A, et al: Clinical efficacy of ultrasound-guided percutaneous drainage of abscesses in patients with leukaemia and lymphoma. Eur J Cancer 34:580–583, 1998.
55. Cohan RH, et al: CT assistance for fluoroscopically guided transthoracic needle aspiration biopsy. J Comput Assist Tomogr 8:1093, 1984.
56. Collins BT, Cramer HM: Fine-needle aspiration cytology of islet cell tumors. Diagn Cytopathol 15:37–45, 1996.
57. Conn HO, Yesner R: A re-evaluation of needle biopsy in the diagnosis of metastatic cancer of the liver. Ann Intern Med 59:53–61, 1963.
58. Conrad MR, Sanders RC, Mascardo AD: Perinephric abscess aspiration using ultrasound guidance. AJR 128:459–464, 1977.
59. Copeland PM: Diagnosis and treatment: the incidentally discovered mass. Ann Intern Med 98:940–945, 1983.
60. Corr P, Beningfield SJ, Davey N: Transjugular liver biopsy: A review of 200 biopsies. Clin Radiol 45:238–239, 1992.
60a. Criado E, De Stefano AA, Weiner TM, Jaques PF: Long term results of percutaneous catheter drainage of pancreatic pseudocysts. Surg Gynecol Obstet 175(4):293–298, 1992.
61. Crass JR, et al: Percutaneous decompression of the colon using CT guidance in Ogilvie syndrome. AJR 144:475, 1985.
62. Cronan JJ, et al: Cavernous hemangioma of the liver: Role of percutaneous biopsy. Radiology 116:135–138, 1998.
63. Curley SA, Izzo F, Ellis LM, et al: Radiofrequency ablation of hepatocellular cancer in 110 patients with cirrhosis. Ann Surg 232: 381–391, 2000.
64. Cwikiel W: Percutaneous drainage of abscess in psoas compartment and epidural spaces: Case report and review of the literature. Acta Radiol 32:159–161, 1991.
65. D'Agostino HB, vanSonnenberg E, Sanchez RB, et al: Treatment of pancreatic pseudocysts with percutaneous drainage and octreotide. Radiology 187:685–688, 1993.
66. Dohlgren SE, Nordenstrom B: Transthoracic Needle Biopsy. Stockholm, Almquist & Wiksell/Bebers, Forlag AB, 1966.
67. Dahlgren SE, Ovenfors CO: Aspiration biopsy diagnosis of neurogenous mediastinal tumours. Acta Radiol [Diagn] (Stockh) 10:289–298, 1970.
68. Dahnert WF, et al: Fine-needle aspiration biopsy of abdominal lesions: Diagnostic yield for different needle tip configurations. Radiology 185:263–268, 1992.
69. DeBlois GG, DeMay KM: Adrenal myelolipoma diagnosis by computed tomography–guided fine-needle aspiration: A case report. Radiology 156:569, 1985.
70. DelMaschio A, et al: Pancreatic cancer versus chronic pancreatitis: Diagnosis with CA 19-9 assessment, US, CT, and CT-guided fine needle biopsy. Radiology 178:95–99, 1991.
71. Deveney CW, Lurie K, Deveney KE: Improved treatment of intra-abdominal abscess: A result of improved localization, drainage, and patient care, not technique. Arch Surg 123:1126–1130, 1988.
72. Diaz LK, Wiley EL, Venta LA: Are malignant cells displaced by large-gauge needle core biopsy of the breast? AJR 173:1303–1313, 1999.
73. Dickey JE, et al: Evaluation of CT-guided percutaneous biopsies of the pancreas. Surg Gynecol Obstet 163:497–503, 1986.
74. Dondelinger RF, Kurdziel JC, Gathy C: Percutaneous treatment of pyrogenic liver abscess: A critical analysis of results. Cardiovasc Intervent Radiol 13:174–182, 1990.
75. Dowlati A, Haaga JR, Remick SC, et al: Sequential tumor biopsies in early phase clinical trials of anticancer agents for pharmacodynamic evaluation. Clin Cancer Res 7:2917–2976, 2001.
76. Dunnick NR, et al: Percutaneous aspiration of retroperitoneal lymph nodes in ovarian cancer. AJR 135:109–113, 1980.
77. Duvnjak M, et al: Assessment of value of pancreatic pseudocyst amylase concentration in the treatment of pancreatic pseudocysts by percutaneous evacuation. J Clin Ultrasound 20:183–186, 1992.
78. Elvin A, et al: Biopsy of the pancreas with a biopsy gun. Radiology 176:677–679, 1990.
79. Engelmann K, Mack MG, Straub R, et al: CT-guided percutaneous intratumoral chemotherapy with a novel cisplatin/epinephrine injectable gel for the treatment of inoperative malignant liver tumors. Rofo Fortschr Geb Rontgenstr Neuen Bildgeb Verfahr 173:1020–1027, 2000.
80. England RE, McDermott VG, Smith TP, et al. Percutaneous cholecystostomy: Who responds? AJR 168:1247–1251, 1997.
81. Evander A: Percutaneous cytodiagnosis of carcinoma of the pancreas and bile duct. Ann Surg 188:90–92, 1978.
82. Evans WK, et al: Fatal necrotizing pancreatitis following fine-needle aspiration biopsy of the pancreas. Radiology 141:61–62, 1981.
83. Elvin A, et al: Biopsy of the pancreas with a biopsy gun. Radiology 176:677–679, 1990.
84. Fagelman D, Chess Q: Nonaspiration fine-needle cytology of the liver: A new technique for obtaining diagnostic samples. AJR 155: 1217–1219, 1990.
85. Fataar S: Percutaneous drainage of pancreatic pseudocysts: Technique and problems. Australas Radiol 34:334–338, 1990.
86. Fataar S, et al: Fine-needle aspiration biopsy of malignant tumours of the abdomen. S Afr Med J 62:638–641, 1982.
87. Ferrucci JT, Wittenberg J: CT biopsy of abdominal tumors: Aids for lesion localization. Radiology 129:739–744, 1978.
88. Ferrucci JT, et al: Malignant seeding of needle tract after thin-needle aspiration biopsy: A previously unrecorded complication. Radiology 130:345, 1979.
89. Ferrucci JT, et al: Diagnosis of abdominal malignancy by radiologic fine-needle aspiration biopsy. AJR 134:323–330, 1980.
90. Filice C, et al: Parasitologic findings in percutaneous drainage of hyman hydatid liver cysts. J Infect Dis 161:1290–1295, 1990.
91. Fish GD, et al: Postbiopsy pneumothorax: estimating the risk by chest radiography and pulmonary function tests. AJR 150:71–74, 1988.
92. Fitzgibbon DR, Schmiedl UP, Sinanan MN: Computed tomography–guided neurolytic celiac plexus block with alcohol complicated by superior mesenteric venous thrombosis. Pain 92:307–310, 2001.
93. Forsgren L, et al: Aspiration cytology in carcinoma of the pancreas. Surgery 73:38–42, 1973.

94. Frederick PR, et al: Light-guidance system to be used for CT-guided biopsy. Radiology 154:535, 1985.
95. Freeny PC, Lewis GP, Marks WM: Percutaneous catheter drainage of infected pancreatic fluid collections and abscesses. RSNA Meeting, 1986.
96. Freeny PC, et al: Infected pancreatic fluid collections: Percutaneous catheter drainage. Radiology 167:435–441, 1988.
97. Fugazzola C, et al: Cystic tumors of the pancreas: Evaluation by ultrasonography and computed tomography. Gastrointest Radiol 16: 53–61, 1991.
98. Fukushima A, Ashizawa K, Aso N, et al: CT-guided needle biopsy of the lung: Factors affecting risk of complications. Nippon Igaku Hoshasen Gakkai Zasshi 61:96–99, 2001.
99. Garcia JC, Persky SE, Bonis PA, Topazian M: Abscesses in Crohn's disease: Outcome of medical versus surgical treatment. J Clin Gastroenterol 32:409–412, 2001.
100. Gazelle GS, Haaga JR: Guided percutaneous biopsy of intraabdominal lesions. AJR 153:929, 1989.
101. Gazelle GS, Haaga JR, Neuhauser D: Hemostatic protein-polymer sheath: New method to enhance hemostasis at percutaneous biopsy. Radiology 175:671–674, 1990.
102. Gazelle GS, Haaga JR, Rowland DY: Effect of needle gauge, level of anticoagulation, and target organ on bleeding associated with aspiration biopsy. Radiology 183:509–513, 1992.
103. Gazelle GS, et al: Pelvic abscesses: CT-guided transrectal drainage. Radiology 181:49–51, 1991.
104. Gazelle SG, Haaga JR: Biopsy needle characteristics. Cardiovasc Intervent Radiol 14:13–16, 1991.
105. Gazelle SG, Haaga JR, Rowland DY: Bleeding due to needle biopsy: Effect of venopirin in an animal model and implications for humans. JVIR 4:305–310, 1993.
106. Gerzof SG, Spira R, Robbins AH: Percutaneous abscess drainage. Semin Roentgenol 16:62–71, 1981.
107. Gerzof SG, et al: Percutaneous drainage of infected pancreatic pseudocysts. Radiology 155:275, 1985.
108. Gerzof SG, et al: Percutaneous catheter drainage of abdominal abscesses guided by ultrasound and computed tomography. AJR 133:1–8, 1979.
109. Gerzof SG, et al: Percutaneous catheter drainage of abdominal abscesses: A five-year experience. N Engl J Med 305:653–657, 1981.
110. Gerzof SG, et al: Percutaneous drainage of infected pancreatic pseudocysts. Arch Surg 119:888–893, 1984.
111. Gerzof SG, et al: Expanded criteria for percutaneous abscess drainage. Arch Surg 120:227–232, 1985.
112. Gilliland JD, Spies JB, Brown SB, et al: Lymphoceles: Percutaneous treatment with povidone-iodine sclerosis. Radiology 171:227–229, 1989.
113. Gimenez A, Martinez-Noguera A, Donoso L, et al: Percutaneous neurolysis of the celiac plexus via the anterior approach with sonographic guidance. AJR 161:1061–1063, 1993.
114. Giorgio A, Tarantino L, deStefano G, et al: Hydatid liver cyst: An 11-year experience of treatment with percutaneous aspiration and ethanol injection. J Ultrasound Med 20:729–738, 2001.
115. Giorgio A, Tarantino L, Mariniello N, et al: Pyogenic liver abscesses: 13 years of experience in percutaneous needle aspiration with US guidance. Radiology 195:122–124, 1995.
116. Gobien RP, et al: Thoracic biopsy: CT guidance of thin-needle aspiration. AJR 142:827, 1984.
117. Goldberg SN: Radiofrequency tumor ablation: Principles and techniques. Eur J Ultrasound 13:129–147, 2001.
118. Goldman ML, et al: Preoperative diagnosis of pancreatic carcinoma by percutaneous aspiration biopsy. Dig Dis Sci 22:1076–1082, 1977.
119. Goldstein HM, et al: Percutaneous fine-needle aspiration biopsy of pancreatic and other abdominal masses. Radiology 123:319–322, 1977.
120. Goralnik CH, O'Connell DM, El Yousef SJ, Haaga JR: CT-guided cutting-needle biopsies of selected chest lesions. AJR 151:903–907, 1988.
121. Gothlin JH: Post-lymphographic percutaneous fine-needle biopsy of lymph nodes guided by fluoroscopy. Radiology 120:205–207, 1976.
122. Granlund A, Karlson BM, Elvin A, Rasmussen I: Ultrasound-guided percutaneous cholecystostomy in high-risk surgical patients. Langenbecks Arch Surg 386:212–217, 2001.
123. Green BT: Splenic abscess: Report of six cases and review of the literature. Am Surg 67:80–85, 2001.
124. Greene R, et al: Supplementary tissue-core histology from fine-needle transthoracic aspiration biopsy. AJR 144:787–792, 1985.
125. Greif J, Marmur S, et al: Percutaneous core cutting-needle biopsy compared with fine-needle aspiration in the diagnosis of peripheral lung malignant lesions: Results in 156 patients. Cancer 84:144–147, 1998.
126. Greif J, Marmor S, et al: Percutaneous core needle biopsy vs. fine-needle aspiration in diagnosing benign lung lesions. Acta Cytol 43: 756–760, 1999.
127. Greif J, Staroselsky AN, Gernjac M, et al: Percutaneous core needle biopsy in the diagnosis of mediastinal tumor. Lung Cancer 25: 169–173, 1999.
128. Gronvall J, Gronvall S, Hegedus V: Ultrasound-guided drainage of fluid-containing masses using angiographic catheterization techniques. AJR 129:997–1002, 1977.
129. Grossman E, et al: Liver physiology and disease: Cytological examination as an adjunct to liver biopsy in the diagnosis of hepatic metastases. Gastroenterology 62:56–60, 1972.
130. Grossman M, et al: Percutaneous treatment (including pseudocystogastrostomy) of 74 pancreatic pseudocysts. Radiology 173:493–497, 1989.
131. Gronemeyer DH: Thorax Biopsy. Oxford, Blackwell Scientific, 1990.
132. Gruessner RW, Fasola C, Benedetti E, et al: Laparascopic drainage of lymphoceles after kidney transplantation: Indications and limitations. Surgery 1173:288–295, 1995.
133. Gupta RK, al Ansari AG: Needle aspiration cytology in the diagnosis of mucinous cystadenocarcinoma of pancreas: A study of five cases with an emphasis on utility and differential diagnosis. Int J Pancreatol 15:149–153, 1994.
134. Gupta S, Ahrar K, Morella FA Jr, et al: Masses in or around the pancreatic head: CT-guided coaxial fine-needle aspiration biopsy with a posterior transcaval approach. Radiology 222:63–69, 2002.
135. Gupta S, Wallace MJ, Morella FA Jr, et al: CT-guided percutaneous needle biopsy of intrathoracic lesions by using the transsternal approach: Experience in 37 patients. Radiology 222:57–62, 2002.
136. Ha HK, Sachs PB, Haaga JR, et al: CT-guided liver biopsy: An update. Clin Imaging 15:99–104, 1991.
137. Haaga JR: New techniques for CT-guided biopsies. AJR 133:633–641, 1979.
138. Haaga JR, Alfidi RJ: Precise biopsy localization by computed tomography. Radiology 118:603–607, 1976.
139. Haaga JR, Alfidi RJ: Interventional CT. In Margulis A, Burhenne S (eds): Alimentary Tract Roentgenology, vol 3. St. Louis, CV Mosby, 1979.
140. Haaga JR, Alfidi RJ, Weinstein A: Percutaneous catheter drainage of abdominal abscesses (letter). N Engl J Med 306:106–108, 1982.
141. Haaga JR, Alfidi RJ: Peritoneal abscesses and other disorders. In Haaga JR, Alfidi RJ (eds): Computed Tomography of the Whole Body. St. Louis, CV Mosby, 1983.
142. Haaga JR, Beale S: Use of CO_2 to move structures as an aid to percutaneous procedures. Radiology 161:j829–830, 1986.
143. Haaga JR, Bick RJ, Zollinger RM Jr: CT-guided percutaneous catheter cecostomy. Gastrointest Radiol 12:166–168, 1987.
144. Haaga JR, LiPuma JP, Eckhauser ML: A piggyback technique for percutaneous insertion of large catheters. AJR 136:1245–1246, 1981.
145. Haaga JR, Reich NE: Computed Tomography of Abdominal Abnormalities. St. Louis, CV Mosby, 1978.
146. Haaga JR, Vanek J: Computed tomographic–guided liver biopsy using the Menghini needle. Radiology 133:405–408, 1979.
147. Haaga JR, Weinstein AJ: CT-guided percutaneous aspiration and drainage of abscesses. AJR 135:1187–1194, 1980.
148. Haaga JR, Zelch MG, Alfidi RJ: CT-guided antegrade pyelography and percutaneous nephrostomy. AJR 128:621–624, 1977.
149. Haaga JR, et al: CT-guided interstitial therapy of pancreatic carcinoma. J Comput Assist Tomogr 11:1077–1078, 1987.
150. Haaga JR, et al: Clinical comparison of small-caliber cutting needle with large-caliber needles. Radiology 146:665–667, 1983.
151. Haaga JR, et al: Improved technique for CT-guided celiac ganglia block. AJR 142:1201–1204, 1984.
152. Haaga JR, et al: CT longitudinal scan. AJR 127:1059–1060, 1976.
153. Haaga JR, et al: Definitive treatment of a large pyogenic liver abscess with CT guidance. Cleve Clin Q 43:85–88, 1976.
154. Haaga JR, et al: CT detection and aspiration of abdominal abscesses. AJR 128:465–474, 1977.

155. Haaga JR, et al: CT-guided biopsy. Cleve Clin Q 44:27–33, 1977.
156. Haaga JR, et al: Interventional CT scanning. Radiol Clin North Am 15:449–456, 1977.
157. Haaga JR, et al: Computed tomography: Guided biopsy overview. J Comput Assist Tomogr 2:25–30, 1978.
158. Haaga JR, et al: New interventional techniques in the diagnosis and management of inflammatory disease within the abdomen. Radiol Clin North Am 17:485–513, 1979.
159. Haaga JR, et al: Percutaneous CT-guided pancreatography and pseudocystography. AJR 132:829–830, 1979.
160. Haage P, Piroth W, Statz G, et al: CT-guided percutaneous biopsies for the classification of focal liver lesions: A comparison between 14G and 18G puncture biopsy needles. Rofo Fortschr Geb Rontgenstr Neuen Bildgeb Verfahr 171:44–48, 1999.
161. Hagspiel KD, Kandarpa K, Silverman SG: Interactive MR-guided percutaneous nephrostomy. J Magn Reson Imaging 8:1319–1322, 1998.
162. Hall-Craggs MA, Leew WRP: Fine-needle aspiration biopsy: Pancreatic and biliary tumors. AJR 147:399, 1986.
163. Hamilton BD, Winfield HN: Laparoscopic marsupialization of pelvic lymphoceles. Tech Urol 2:220–224, 1996.
164. Hancke S, Holm HH, Koch F: Ultrasonically guided percutaneous fine-needle biopsy of the pancreas. Surg Gynecol Obstet 140:361–364, 1975.
165. Hanna RM, Dahniya MH, Badr SS, El-Betagy A: Percutaneous catheter drainage in drug-resistant amoebic liver abscess. Trop Med Int Health 5:578–581, 2000.
166. Haramati LB, Austin JH: Complications after CT-guided biopsy through aerated vs. nonaerated lung. Radiology 101:778, 1991.
167. Hatjidakis AA, Karampekios S, Prassopoulos P, et al: Maturation of the tract after percutaneous cholecystostomy with regard to the access route. Cardiovasc Intervent Radiol 21:36–40, 1998.
168. Heaston DK, et al: Narrow-gauge needle aspiration of solid adrenal masses. AJR 141:169, 1983.
169. Heaston DK, et al: Narrow-gauge needle aspiration of solid adrenal masses. AJR 188:1143–1148, 1982.
170. Heider R, Meyer AA, Galanko JA, Behrus KE: Percutaneous drainage of pancreatic pseudocysts is associated with a higher failure rate than surgical treatment in unselected patients. Ann Surg 229: 781–787, 1999.
171. Heilberg E, Wolverson MK: Ipsilateral decubitus position for percutaneous CT-guided adrenal biopsy. J Comput Assist Tomogr 9: 217–218, 1985.
172. Herman SJ, Weisbrod GL: Usefulness of the blood patch technique after transthoracic needle aspiration biopsy. Radiology 176:395–397, 1990.
173. Hertzanu Y, et al: Massive bleeding after fine-needle aspiration of liver angiosarcoma. Gastrointest Radiol 15:43–46, 1990.
174. Ho CS, Taylor B: Percutaneous transgastric drainage for pancreatic pseudocyst. AJR 143:623, 1984.
175. Ho CS, et al: Percutaneous fine-needle aspiration biopsy of the pancreas following endoscopic retrograde cholangiopancreatography. Radiology 125:351–353, 1977.
176. Ho CS, et al: Guided percutaneous fine-needle aspiration biopsy of the liver. Cancer 47:1781–1785, 1981.
177. Hochbergs P, Forsberg L, Hederstrom E, et al: Diagnosis and percutaneous treatment of pyogenic hepatic abscesses. Acta Radiol 31: 351–353, 1990.
178. Holm HH, Rasmussen SN, Kristensen JR: Ultrasonically guided percutaneous puncture technique. J Clin Ultrasound 1:27–31, 1973.
179. Holm HH, et al: Ultrasonically guided percutaneous puncture. Radiol Clin North Am 13:493–503, 1975.
180. Hopper KD, et al: Automated biopsy devices: A blinded evaluation. Radiology 187:653–660, 1993.
181. Hopper KD, et al: Fine-needle aspiration biopsy for cytopathologic analysis: Utility of syringe handles, automated guns, and the nonsuction method. Radiology 185:819–824, 1992.
182. Hopper KD, et al: Efficacy of automated biopsy guns versus conventional biopsy needles in the pygmy pig. Radiology 176:671–676, 1990.
183. Hsu WH, Chiang CD, Hsu JY, et al: Ultrasonically guided needle biopsy of anterior mediastinal masses: Comparison of carcinomatous and non-carcinomatous masses. J Clin Ultrasound 23:349–356, 1995.
184. Hueftle MG, Haaga JR: Effect of suction on biopsy sample size. AJR 147:1014–1016, 1986.
185. Husband JE, Golding SJ: Role of computed tomography–guided needle biopsy in an oncology service. Radiology 150:296, 1984.
186. Ikeda M, Okada S, Ueno H, et al: Radiofrequency ablation and percutaneous ethanol injection in patients with small hepatocellular carcinoma: A comparative study. Jpn J Clin Oncol 31:322–326, 2001.
187. Iselin CE, Meyer P, Hauser H, et al: Computed tomography and fine-needle aspiration cytology for preoperative evaluation of cystic tumours of the pancreas. Br J Surg 80:1166–1169, 1993.
188. Isler RJ, et al: Tissue core biopsy of abdominal tumors with a 22-gauge cutting needle. AJR 136:725–728, 1981.
189. Isobe H, Fukai T, Iwamoto H, et al: Liver abscess complicating intratumor ethanol injection therapy for HCC. Am J Gastroenterol 85:1646–1648, 1990.
190. Jacobsen GK, Gammelgaard J, Fuglo M: Coarse-needle biopsy in suspected hepatic malignancy. Acta Cytol 27:152–156, 1983.
191. Jaques P, et al: CT features of intra-abdominal abscesses: Prediction of successful percutaneous drainage. AJR 146:1041–1045, 1986.
192. Jeffrey RB: Personal communication.
193. Jeffrey RB Jr, Wing VW, Laing FC: Real-time sonographic monitoring of percutaneous abscess drainage. AJR 144:469–470, 1985.
194. Jereb M, Us-Krasovec M: Transthoracic needle biopsy of mediastinal and hilar lesions. Cancer 40:1354–1357, 1977.
195. Johansen S, Myren J: Fine-needle aspiration biopsy smears in the diagnosis of liver diseases. Scand J Gastroenterol 6:583–588, 1971.
196. Johnson DE, Pendurthi TK, Balshem, et al: Implications of fine-needle aspiration in patients with resectable pancreatic cancer. Am Surg 63:675–679, 1997 (discussion, pp. 679–680).
197. Johnson RD, et al: Percutaneous drainage of pyogenic liver abscesses. AJR 144:463–467, 1985.
198. Johnson WC, et al: Treatment of abdominal abscesses: Comparative evaluation of operative drainage versus percutaneous catheter drainage guided by computed tomography or ultrasound. Ann Surg 194: 510–520, 1981.
199. Jones EC, et al: Fine-needle aspiration cytology of neoplastic cysts of the pancreas. Diagn Cytopathol 3:238–243, 1987.
200. Juul N, Sztuk FJS, Torp-Pedersen S, et al: Ultrasonically guided percutaneous treatment of liver abscesses. Acta Radiol 31:275–277, 1991.
201. Kane NM, Korobkin M, Francis IR, et al: Percutaneous biopsy of left adrenal masses: Prevalence of pancreatitis after anterior approach. AJR Am J Roentgenol 157:777–780, 1991.
202. Karayalcin K, Besim H, Sonisik M, et al: Effect of hypertonic saline and alcohol on viability of daughter cysts in hepatic hydatid disease. Eur J Surg 165:1043–1044, 1995.
203. Karlson KB, et al: Percutaneous drainage of pancreatic pseudocysts and abscesses. Radiology 142:619–624, 1982.
204. Karlsson S, Persons PH: Angiography, ultrasound, and fine-needle aspiration biopsy in evaluation of gynecologic tumors (abstract). Radiology 134:285, 1980.
205. Karstaedt N, et al: Computed tomography of the adrenal gland. Radiology 129:723–730, 1978.
206. Karstrup S, Nolsoe C, Brabrand K, et al: Ultrasonically guided percutaneous drainage of breast abscesses. Acta Radiol 31:157–159, 1990.
207. Kasugai H, et al: Value of heparinized fine-needle aspiration biopsy in liver malignancy. AJR 144:243, 1985.
208. Kazerooni EA, Lim FT, Mikhail A, Martinez FJ: Risk of pneumothorax in CT-guided transthoracic needle aspiration biopsy of the lung. Radiology 198:371–375, 1996.
209. Kellermeyer Scott: Personal communication. Cleveland, Ohio, 1993.
210. Ken J, et al: Perforated amebic liver abscesses: Successful percutaneous treatment. Radiology 170:195–197, 1989.
211. Keogan MT, Freed KS, Paulson EK, et al: Imaging-guided percutaneous biopsy of focal splenic lesions: Update on safety and effectiveness. AJR 172:933–937, 1999.
212. Kerlan RK Jr, LaBerge JM, Gordon RL, Ring EJ: Bleomycin sclerosis of pelvic lymphoceles. J Vasc Interv Radiol 8:885–887, 1997.
213. Kerlan RK, Jr, et al: Radiologic management of abdominal abscesses. AJR 144:149, 1985.
214. Khouri NF, Stitik FP, Erozan YS: Transthoracic needle aspiration biopsy of benign and malignant lung lesions. AJR 144:281–288, 1985.
215. Khuroo MS, Wani NA, Javid G, et al: Percutaneous drainage compared with surgery for hepatic hydatid cysts. N Engl J Med 337: 881–887, 1997.

216. Kim SH, Lim HK, Lee WJ, et al: Needle-tract implantation in hepatocellular carcinoma: Frequency and CT findings after biopsy with a 19.5-gauge automated biopsy gun. Abdom Imaging 25:246–250, 2000.
217. Klein JS, Salomon G, Stewart EA: Transthoracic needle biopsy with a coaxially placed 20-gauge automated cutting needle: Results in 122 patients. Radiology 198:715–720, 1996.
218. Knelson, Haaga JR, Lazarus H, et al: CT-guided retroperitoneal biopsies. J Clin Oncol 7:1169–1173, 1989.
219. Koehler PR, Feldberg MAM, van Waes PFGM: Preoperative staging of rectal cancer with computerized tomography, accuracy, efficacy, and effect on patient management. Cancer 54:512–516, 1984.
220. Kreula J: Effect of sampling technique on specimen size in fine-needle aspiration. Invest Radiol 25:1294–1299, 1990.
221. Kreula J: A new method for investigating the sampling technique of fine-needle aspiration biopsy. Invest Radiol 25:245–249, 1990.
222. Kreula J, Virkkunen P, Bondestam S: Effect of suction on specimen size in fine-needle aspiration biopsy. Invest Radiol 25:1175–1181, 1990.
223. Kushihashi T, Munechika H, Otsuki N, et al: CT-guided percutaneous lung biopsy using a cutting needle and an automated biopsy gun: Comparison with lung biopsy using a manual aspiration needle. Nippon Igaku Hoshasen Gakkai Zasshi 52:191–198, 1992.
224. Lahorra JM, et al: Safety of intracavitary urokinase with percutaneous abscess drainage. AJR 160:171–174, 1993.
225. Laing EK, et al: Abdominal abscess drainage under radiologic guidance: causes of failure. Radiology 159:329–336, 1986.
226. Lalli AF, et al: Aspiration biopsies of chest lesions. Radiology 127: 35–40, 1978.
227. Lang EK: Renal, perirenal, and pararenal abscesses: Percutaneous drainage. Radiology 174:109–113, 1990.
228. Langen HJ, Jochims M, Gunther RW: Artificial displacement of kidneys, spleen, and colon by injection of physiologic saline and CO_2 as an aid to percutaneous procedures: Experimental results. J Vasc Interv Radiol 6:411–416, 1995.
229. Lambiase RE, Dorfman GS, Cronan JJ: Percutaneous management of abscesses that involve native arteries or synthetic arterial grafts. Radiology 173:815–818, 1989.
230. Lambiase RE, et al: Percutaneous drainage of 335 consecutive abscesses: Results of primary drainage with 1-year follow up. Radiology 184:167–179, 1992.
231. Lambiase RE, et al: Postoperative abscesses and enteric communication: Percutaneous treatment. Radiology 171:497–500, 1989.
232. Lauby RW, et al: Value and risk of biopsy of pulmonary lesions by needle aspiration: Twenty-one years' experience. J Thorac Cardiovasc Surg 1:159–172, 1965.
233. Laurent F, Latrabe V, Bergier B, Michel P: Percutaneous CT-guided biopsy of the lung: Comparison between aspiration and automated cutting needles using a coaxial technique. Cardiovasc Intervent Radiol 23:266–272, 2000.
234. Laurent F, Michel P, Latrabe V, et al: Pneumothoraces and chest tube placement after CT-guided transthoracic lung biopsy using a coaxial technique: Incidence and risk factors. AJR 172:1049–1053, 1999.
235. Lee KS, et al: Treatment of thoracic multiloculated empyemas with intracavitary urokinase: A prospective study. Radiology 179:771–775, 1991.
236. Lee MJ, et al: Measurement of tissue carcinoembryonic antigen levels from fine-needle biopsy specimens: Technique and clinical usefulness. Radiology 184:717–720, 1992.
237. Lerma E, Musulen E, Cuatrecasas M, et al: Fine-needle aspiration cytology in pancreatic pathology. Acta Cytol 40:683–686, 1996.
238. Levin DP, Bret PM: Percutaneous fine-needle aspiration biopsy of the pancreas resulting in death. Gastrointest Radiol 16:67–69, 1991.
239. Levison MA, Ziegler D: Correlation of Apache II score, drainage technique and outcome in postoperative intra-abdominal abscess. Surg Gynecol Obstet 172:89–94, 1991.
240. Lewin J, Duerk J, Jain V, et al: Needle localization in MR-guided biopsy and aspiration: Effects of field strength, sequence design, and magnetic field orientation. AJR 166:1337–1345, 1996.
241. Li H, Boiselle PM, Shepard JO, et al: Diagnostic accuracy and safety of CT-guided percutaneous needle aspiration biopsy of the lung: Comparison of small and large pulmonary nodules. AJR 167: 105–109, 1996.
242. Lieberman RP, Waldman SD: Celiac plexus neurolysis with the modified transaortic approach. Radiology 175:274–276, 1990.
243. Little AF, Ferris JV, Dodd GD III, Baron RL: Image-guided percutaneous hepatic biopsy: Effect of ascites on the complication rate. Radiology 199:79–83, 1996.
244. Liu KY, Shyr YM, Su CH, et al: Splenic abscess—a changing trend in treatment. S Afr J Surg 38:55–57, 2000.
245. Livraghi T: Guidelines for treatment of liver cancer. Eur J Ultrasound 13:167–176, 2001.
246. Livraghi T, Bolondi L, Lazzaroni S, et al: Percutaneous ethanol injection in the treatment of hepatocellular carcinoma in cirrhosis: A study of 207 patients. Cancer 69:925–929, 1992.
247. Livraghi T, Lazzaroni S, Meloni F: Radiofrequency thermal ablation of hepatocellular carcinoma. Eur J Ultrasound 13:159–166, 2001.
248. Livraghi T, Lazzaroni S, Pellicano S, et al: Percutaneous ethanol injection of hepatic tumors: Single-session therapy with general anesthesia. AJR 161:1065–1069, 1993.
249. Llovet JM, Vilana R, Bru C, et al: Increased risk of tumor seeding after percutaneous radiofrequency ablation for single hepatocellular carcinoma. Hepatology 33:1124–1129, 2001.
250. Locke John: Unpublished data.
251. Lopez Hanninen E, Vogl TJ, Ricke J, Felix R: CT-guided percutaneous core biopsies of pulmonary lesions: Diagnostic accuracy, complications, and therapeutic impact. Acta Radiol 42:151–155, 2001.
252. Lublin M, Danforth DN: Iatrogenic gallbladder perforation: Conservative management by percutaneous drainage and cholecystomy. Am Surg 67:760–763, 2001.
253. Lufkin R, Layfield L: Coaxial needle system of MR- and CT-guided aspiration cytology. J Comput Assist Tomogr 13:1105–1107, 1989.
254. Lumachi F, Borsato S, Brandes AA: Fine-needle aspiration cytology of adrenal masses in noncancer patients: Clinicoradiologic and histologic correlations in functioning and nonfunctioning tumors. Cancer 93:323–329, 2001.
255. Lundquist A: Fine-needle aspiration biopsy for cytodiagnosis of malignant tumor in the liver. Acta Med Scand 188:465–470, 1970.
256. Lundquist A: Fine-needle aspiration biopsy of the liver. Acta Med Scand 520:1–28, 1971.
257. Luning M, et al: CT-guided percutaneous fine-needle biopsy of the pancreas. Radiology 158:567, 1986.
258. Luning M, et al: Percutaneous biopsy of the liver. Cardiovasc Intervent Radiol 14:40–42, 1991.
259. Magnusson A, Akerfeldt D: CT-guided core biopsy using a new guidance device. Acta Radiol 32:83–85, 1991.
260. Malden ES, Picus D: Hemorrhagic complication of transgluteal pelvic abscess drainage: Successful percutaneous treatment. JVIR 3: 323–328, 1992.
261. Mandrekar SR, Pinto RG, Patil R, et al: Solid and papillary epithelial neoplasm of the pancreas: Report of a case with diagnosis by fine-needle aspiration cytology. Acta Cytol 4:1823–1827, 1997.
262. Marra V, Debernardi F, Frigerio A, et al: Neurolytic block of the celiac plexus and splanchnic nerves with computed tomography: The experience in 150 cases and an optimization of the technic. Radiol Med (Torino) 98:183–188, 1999.
263. Martin E: Personal communication, 1988.
264. Martin HE, et al: The advantages and limitations of aspiration biopsy. AJR 35:54, 1936.
265. Martino CR, et al: CT-guided liver biopsies: Eight years' experience. Radiology 152:755, 1984.
266. Mayoral W, Lewis JH: Percutaneous liver biopsy: What is the current approach? Results of a questionnaire survey. Dig Dis Sci 46:118–127, 2001.
267. McCartney R, Tait D, Stilson M, et al: A technique for the prevention of pneumothorax in pulmonary aspiration biopsy. AJR 120: 872–875, 1974.
268. McCorkell S, Niles NL: Fine-needle aspiration of catecholamine-producing adrenal masses: A possibly fatal mistake. AJR 145:113–114, 1985.
268a. McFadzien A, Chang K, Wong C: Solitary pyogenic abscess treated by closed aspiration and antibiotics. Fourteen consecutive cases with recovery. Br J Surg 41:141–152, 1953.
269. McGill DB, Rakela J, Zinsmeister AR, et al: (abstract). Gastroenterology 99:1936–1400, 1990.
270. McLoughlin MJ, Tao LC, Ho CS: Computed tomography biopsy of abdominal tumors (letter). Radiology 131:800, 1979.
271. McLoughlin MJ, et al: Fine-needle aspiration biopsy of malignant lesions in and around the pancreas. Cancer 41:2413–2419, 1978.
272. Menghini G: One second biopsy of the liver. N Engl J Med 282: 582–585, 1970.

273. Merkle EM, Hashim M, Wendt M, Lewin JS: MR-guided percutaneous nephrostomy of the nondilated upper urinary tract in a porcine model. AJR 172:1221–1225, 1999.
274. Mesurolle B, Ariche-Cohen M, Tardivon A, et al: Retrospective analysis of 44 adrenal puncture biopsies under x-ray computed tomographic guidance. J Radiol 77:17–21, 1996.
275. Meyer JE, Ferrucci JT, Janower ML: Fatal complications of percutaneous lung biopsy: Review of the literature and report of a case. Radiology 96:47–48, 1970.
276. Miki K, Makuuchi M, Takayama T, et al: Peritoneal seeding of hepatocellular carcinoma after ethanol injection therapy. Hepatogastroenterology 47:1428–1430, 2000.
277. Miller FJ, Ahola DT, Bretzman PA, Fillmore DJ: Percutaneous management of hepatic abscess: A perspective by interventional radiologists. JVIR 8:241–247, 1997.
278. Miller JA, Pramanik BK, Lavenhar MA: Predicting the rates of success and complications of computed tomography–guided percutaneous core-needle biopsies of the thorax from the findings of the preprocedure chest computed tomography scan. J Thorac Imaging 13:7–13, 1998.
279. Miller KS, et al: Prediction of pneumothorax rate in percutaneous needle aspiration of the lung. Chest 93:742–745, 1988.
280. Milner LB, Ryan K, Gullo J: Fatal intrathoracic hemorrhage after percutaneous aspiration lung biopsy. AJR 132:280–281, 1979.
281. Mitty HA, Efremidis SC, Yeh HC: Impact of fine-needle biopsy on management of patient with carcinoma of the pancreas. AJR 137: 1119–1121, 1981.
282. Mody MK, Kazerooni EA, Korobkin M: Percutaneous CT-guided biopsy of adrenal masses: Immediate and delayed complications. J Comput Assist Tomogr 19:434–439, 1995.
283. Montali G, et al: Sonographically guided fine-needle aspiration biopsy of adrenal masses. AJR 143:1081, 1984.
284. Montalvo BM, Yrizarry JM, Casillas VJ, et al: Percutaneous sclerotherapy of lymphoceles related to renal transplantation. J Vasc Interv Radiol 7:117–123, 1996.
285. Moore DC, Bush W, Burnett L: Computed axial tomography: The most accurate method of performing alcohol celiac plex block (abstract). Proceedings of the Fifth Annual Meeting of the American Society of Anesthesiologists, San Francisco, March 1980.
286. Moore EH, et al: Effect of patient positioning after needle aspiration lung biopsy. Radiology 181:385–387, 1991.
287. Morali GA, et al: Successful treatment of pancreatic pseudocyst with a somatostatin analogue and catheter drainage. Am J Gastroenterol 86:515–518, 1991.
288. Morgan DE, Baron TH, Smith JK, et al: Pancreatic fluid collections prior to intervention: Evaluation with MR imaging compared with CT and US. Radiology 203:773–778, 1997.
289. Mostbeck GH, et al: Optimal needle size for renal biopsy: In vitro and in vivo evaluation. Radiology 173:819–822, 1989.
290. Muchle C, et al: Radiographically guided alcohol block of the celiac ganglion. Semin Int Radiol 4:195–199, 1987.
291. Mueller PR, et al: Hepatic echinococcal cyst: Successful percutaneous drainage. Radiology 155:627–628, 1985.
292. Mueller PR, et al: Inadvertent percutaneous catheter gastroenterostomy during abscess drainage: Significance and management. AJR 145:387–391, 1985.
293. Mueller PR, et al: Lesser sac abscesses and fluid collections: Drainage by transhepatic approach. Radiology 155:615–618, 1985.
294. Mueller PR, et al: MR-guided aspiration biopsy: Needle design and clinical trials. Radiology 161:605, 1986.
295. Mueller PR, et al: Percutaneous drainage of subphrenic abscesses: A review of 62 patients. AJR 147:1237–1240, 1986.
296. Mueller PR, et al: Severe acute pancreatitis after percutaneous biopsy of the pancreas. AJR 151:493–494, 1988.
297. Mueller PR, et al: Infected abdominal tumors: Percutaneous catheter drainage. Radiology 173:627–629, 1989.
298. Nakaizumi A, et al: Diagnosis of hepatic cavernous hemangioma by fine-needle aspiration biopsy under ultrasonic guidance. Gastrointest Radiol 15:39–42, 1990.
299. Nakamato D: University Hospitals of Cleveland, personal communication.
300. Neff CC, et al: CT follow-up of empyemas: Pleural peels resolve after percutaneous catheter drainage. Radiology 176:195–197, 1990.
301. Neff CC, et al: Diverticular abscesses: Percutaneous drainage. Radiology 163:15, 1987.
302. Norberg M, Busch C, Stavinoha J, et al: Transrectal ultrasound-guided core biopsies of the prostate: A comparison between the standard 1.2 mm needle and three thinner needles. Acta Radiol 35: 463–467, 1994.
303. Nordenstrom B: New instruments for biopsy. Radiology 117:474–475, 1975.
304. Nordenstrom B: A new technique for transthoracic biopsy of lung changes. Br J Radiol 38:550–553, 1965.
305. Norenberg R, Claxton CP, Takaro T: Percutaneous needle biopsy of the lung: Report of two fatal complications. Chest 66:216–218, 1974.
306. Nosher JL, Plafker J: Fine-needle aspiration of the liver with ultrasound guidance. Radiology 136:177–180, 1980.
307. Nunez D Jr, et al: Transgastric drainage of pancreatic fluid collections. AJR 145:815, 1985.
308. Nunez D Jr, et al: Renal cell carcinoma complicating long-term dialysis: Computed tomography–guided aspiration cytology. CT 10: 61, 1986.
309. Ohto M, et al: Ultrasonically guided percutaneous contrast medium injection and aspiration biopsy using a real-time puncture transducer. Radiology 136:171–176, 1980.
310. Onik G, et al: CT body stereotaxis: Aid for CT-guided biopsies. AJR 146:163, 1986.
311. Onodera H, Oikawa M, Abe M, et al: Cutaneous seeding of hepatocellular carcinomna after fine-needle aspiration biopsy. J Ultrasound Med 6:273–275, 1987.
312. Ooi LL, Leong SS: Splenic abscesses from 1987 to 1995. Am J Surg 174:87–93, 1997.
313. Ormeci N, Soykan I, Bektas A, et al: A new percutaneous approach for the treatment of hydatid cysts of the liver. Am J Gastroenterol 96:2225–2230, 2001.
314. Oscarson J, Stormby N, Sundgren R: Selective angiography in fine-needle aspiration cytodiagnosis of gastric and pancreatic tumours. Acta Radiol [Diagn] (Stockh) 12:737–749, 1972.
315. Otto RC: Indications for real-time ultrasound-controlled fine-needle punctures under permanent view. Radiology 151:275, 1984.
316. Pagani JJ: Biopsy of focal hepatic lesions: Comparison of 18- and 22-gauge needles. Radiology 147:673–675, 1983.
317. Pagani JJ: Non-small cell lung carcinoma adrenal metastases, computed tomography and percutaneous needle biopsy in their diagnosis. Cancer 53:1058–1060, 1984.
318. Pardes JG, et al: Percutaneous needle biopsy of deep pelvic masses: Posterior approach. Cardiovasc Intervent Radiol 9:65, 1986.
319. Parfrey NA: Improved diagnosis and prognosis of mucomycosis: A clinicopathologic study of 33 cases. Medicine 65:113–123, 1986.
320. Park JK, Kraus FC, Haaga JR: Fluid flow during percutaneous drainage procedures: An in vitro study of the effects of fluid viscosity, catheter size, and adjunctive urokinase. AJR 160:165–169, 1993.
321. Parker JG, et al: Needle liver biopsy in benign and malignant disease: Comparison of the Menghini and Vim-Silverman techniques. Am J Digest Dis 7:687–698, 1962.
322. Peer A, Strauss S: Percutaneous drainage of postappendectomy abscesses complicated by enteric communication. Cardiovasc Intervent Radiol 14:106–108, 1991.
323. Pelaez V, Kugler C, del Carpio M, et al: Treatment of hepatic hydatid cysts by percutaneous aspiration and hypertonic saline injection: Results of a cooperative work. Bol Chil Parasitol 54:63–69, 1999.
324. Pereiras RV, et al: Fluoroscopically guided thin-needle aspiration biopsy of the abdomen and retroperitoneum. AJR 131:197–202, 1978.
325. Perlmutt LM, Braun SD, Newman GE, et al: Transthoracic needle aspiration: Use of a small chest tube to treat pneumothorax. AJR 148:849–851, 1987.
326. Perlmutt LM, et al: Timing of chest film follow-up after transthoracic needle aspiration. AJR 146:1049–1050, 1986.
327. Perrault J, et al: Liver biopsy: Complications in 1,000 in-patients and out-patients. Gastroenterology 74:103–106, 1978.
328. Phillips VM, et al: Percutaneous biopsy of pancreatic masses. Gastroenterology 7:506–510, 1985.
328a. Plecha DM, Goodwin D, Rowland DY, et al: Effect of needle size on bleeding and tissue recovery. Radiology 204:101–104, 1997.
329. Plunkett MB, et al: Peripheral pulmonary nodules: Preoperative percutaneous needle localizations with CT guidance. Radiology 185: 274–276, 1992.

330. Pogany AC, et al: Cystic insulinoma. AJR 142:951–952, 1984.
331. Prando AC, et al: Lymphangiography in staging of carcinoma of the prostate: Potential value of percutaneous lymph node biopsy. Radiology 131:641–656, 1979.
332. Prasanna A: Unilateral celiac plexus block. J Pain Symptom Manage 11:154–157, 1996.
333. Price RB, et al: Biopsy of the right adrenal gland by the transhepatic approach. Radiology 148:566, 1983.
334. Quinn SF, Sheley RC, Nelson HA, et al: The role of percutaneous needle biopsies in the original diagnosis of lymphoma: A prospective evaluation. J Vasc Interv Radiol 6:947–952, 1995.
335. Rashleigh-Belcher HJC, Russell RCG, Lees WR: Cutaneous seeding of pancreatic carcinoma of fine-needle aspiration biopsy. Br J Radiol 59:182–183, 1986.
336. Rasmussen SN, et al: Ultrasonically guided liver biopsy. Br Med J 2:500–502, 1972.
337. Rescorla FJ, et al: Failure of percutaneous drainage in children with traumatic pancreatic pseudocysts. J Pediatr Surg 25:1038–1042, 1990.
338. Reuvers GB, et al: Ultrasound-guided percutaneous drainage of 25 abscesses. Acta Chir Scand 149:161–164, 1983.
339. Rhim H, Dodd GD III: Radiofrequency thermal ablation of liver tumors. J Clin Ultrasound 5:221–229, 1999.
340. Romanelli DF, Beckmann CF, Heiss FW: Celiac plexus block: Efficacy and safety of the anterior approach. AJR 160:497–500, 1993.
341. Rosenberger A, Adler O: Fine-needle aspiration biopsy in the diagnosis of mediastinal lesions. AJR 131:239–242, 1978.
342. Rossi P, Arata FM, Salvatori FM: Prosthetic graft infection: Diagnostic and therapeutic role of interventional radiology. J Vasc Interv Radiol 8:271–277, 1997.
343. Rotte KH: CT-assisted needle biopsy in pulmonary and mediastinal space-occupying lesions: The effect of spiral CT and various biopsy needles on results. Aktuelle Radiol 5:136–139, 1995.
344. Saluja S, Fields JM, Schwartz DS, et al: Percutaneous needle aspiration of small interloop abscesses in children. Pediatr Surg Int 13: 528–530, 1998.
345. Samuel LH, Frierson HF Jr: Fine-needle aspiration cytology of acinar cell carcinoma of the pancreas: A report of two cases. Acta Cytol 40:585–591, 1996.
346. Sanfey H, Aguilar M, Jones RS: Pseudocysts of the pancreas: A review of 97 cases. Am Surg 60:661–668, 1994.
347. Sargent EN, et al: Percutaneous pulmonary needle biopsy: Report of 350 patients. J Thorac Cardiovasc Surg 122:758–768, 1974.
348. Sateriale M, Cronan JJ, Savadier LD: A five year experience with 307 CT guided renal biopsies: results and complications. JVIR 2: 401–407, 1991.
349. Sato M, Tokui K, Watanabe Y, et al: Generalized intraperitoneal seeding of hepatocellular carcinoma after microwave coagulation therapy: A case report. Hepatogastroenterology 46:2561–2564, 1999.
350. Savarino V, Ceppa P, Biggi E, et al: Comparative study of percutaneous and peroperative fine-needle aspirations in the diagnosis of pancreatic cancer. Hepatogastroenterology 33:75–78, 1986.
351. Sayek I, Onat D: Diagnosis and treatment of uncomplicated hydatid cyst of the liver. World J Surg 25:21–27, 2001.
352. Schurawitzki H, Karnel F, Stiglbauer R: CT-guided percutaneous drainage and fluid aspiration in intensive care patients. Acta Radiol 33:131–136, 1992.
353. Sherlock P, Kim YS, Koss LG: Cytologic diagnosis of cancer from aspirated material obtained at liver biopsy. Am J Dig Dis 12: 396–402, 1967.
354. Shiina S, Tagawa K, Niwa Y, et al: Percutaneous ethanol injection therapy for hepatocellular carcinoma: Results in 146 patients. AJR 160:1023–1028, 1993.
355. Silverman SG, Mueller PR, Pinkney LP, et al: Predictive value of image-guided adrenal biopsy: Analysis of results of 101 biopsies. Radiology 187:715–718, 1993.
356. Sinner WN: Transthoracic needle biopsy of small peripheral malignant lung lesions. Invest Radiol 8:305–314, 1973.
357. Skamel HJ, Hanusch A, Mathias K: CT-guided punctures: Fine-needle biopsy vs. automated co-axial cutting biopsy. Aktuelle Radiol 8:273–277, 1998.
358. Smith EH: Fine-needle aspiration biopsy: Are there any risks? In Holm HH, Kristensen JK (eds): Interventional Ultrasound. New York, Thieme, 1985.
359. Smith EH, Bartrum RJ: Ultrasonically guided percutaneous aspiration of abscesses. AJR 122:308–312, 1974.
360. Smith EH: Complications of percutaneous abdominal fine-needle biopsy. Radiology 178:253–258, 1986.
361. Soderstrom N: Fine-Needle Aspiration Biopsy. New York, Grune & Stratton, 1966.
362. Solbiati L, et al: Fine-needle biopsy of hepatic hemangioma with sonographic guidance. AJR 144:471, 1985.
363. Solbiati L, Goldberg SN, Ierace T, et al: Hepatic metastases: Percutaneous radiofrequency ablation with cooled-tip electrodes. Radiology 205:367–373, 1997.
364. Solbiati L, Goldberg SN, Ierace T, et al: Percutaneous US-guided RF tissue ablation of liver metastases: Long-term follow-up. Radiology 202:195–203, 1997.
365. Solbiati L, Ierace T, Tonolini M, et al: Radiofrequency thermal ablation of hepatic metastases. Eur J Ultrasound 13:149–158, 2001.
366. Soyer P, Pelage JP, Dufresne AC: CT of abdominal wall implantation metastases after abdominal percutaneous procedures. J Comput Assist Tomogr 22:889–893, 1998.
367. Spamer C, et al: Benign circumscribed lesions of the liver diagnosed by ultrasonically guided fine-needle biopsy. JCUI 14:83, 1986.
368. Spiro TP, Gerson SL, Liu L, et al: 06-Benzylguanine: A clinical trial establishing the bicohemical modulatory dose in tumor tissue for alkytransferase-directed DNA repair. Cancer Res 59:2402–2410, 1999.
369. Staab EV, Jacques PF, Partain CL: Percutaneous biopsy in the management of solid intra-abdominal masses of unknown etiology. Radiol Clin North Am 17:435–459, 1979.
370. Stephens D: Personal communication, November 1982.
371. Stephenson TF, et al: Evaluation of contrast markers for CT aspiration biopsy. AJR 133:1097, 1979.
372. Stolier A, Skinner J, Levine EA: A prospective study of seeding of the skin after core biopsy of the breast. Am J Surg 180:104–107, 2000.
373. Suarez JF, De Teresa J, Gonzalez A, et al: Papillary tumor of the pancreas diagnosed by fine-needle aspiration. Rev Esp Enferm Dig 88:53–55, 1996.
374. Taavitsainen M, et al: Fine-needle aspiration biopsy of liver hemangioma. Acta Radiol 31:69–71, 1990.
375. Taft PD, Szyfelbein WM, Greene R: A study of variability in cytologic diagnoses based on pulmonary aspiration specimens. Am J Clin Pathol 73:36–40, 1980.
376. Tanaka S, et al: Early diagnosis of hepatocellular carcinoma: Usefulness of ultrasonically guided fine-needle aspiration biopsy. JCU 14:11, 1986.
377. Tandon A, Jain AK, Dixit VK, et al: Needle aspiration in large amoebic liver abscess. Trop Gastroenterol 18:19–21, 1997.
378. Taylor M, Forster J, Langer B, et al: A study of prognostic factors for hepatic resection for colorectal metastases. Am J Surg 173: 467–471, 1997.
379. Terry R: Risks of needle biopsy of liver. Br Med J 1102–1103, 1951.
380. Thornbury JR, Burke DP, Naylor B: Transthoracic needle aspiration biopsy: Accuracy of cytologic typing of malignant neoplasms. AJR 136:719–724, 1981.
381. Tolly TL, Feldmeier JE, Czarnecki D: Air embolism complicating percutaneous lung biopsy. AJR 150:555–556, 1988.
382. Tylen U, et al: A percutaneous biopsy of carcinoma of the pancreas guided by angiography. Surg Gynecol Obstet 142:737–739, 1976.
383. Tyrrel RT, Murphy FB, Bernardino ME: Tubo-ovarian abscesses: CT-guided percutaneous drainage. Radiology 175:87–89, 1990.
384. Van Sonnenberg E, et al: Percutaneous drainage of abscesses and fluid collection: Technique, results, and applications. Radiology 142: 1–10, 1982.
385. Van Sonnenberg E, D'Agostino HB, Goodacre BW, et al: Percutaneous gallbladder puncture and cholecystostomy: Results, complications, and caveats for safety. Radiology 183:167–170, 1992.
386. Van Sonnenberg E, et al: Temporizing effect of percutaneous drainage of complicated abscesses in critically ill patients. AJR 142: 821–826, 1984.
387. Van Sonnenberg E, et al: Complicated pancreatic inflammatory disease: Diagnostic and therapeutic role of interventional radiology. Radiology 155:335, 1985.
388. Van Sonnenberg E, et al: Percutaneous drainage of infected and noninfected pancreatic pseudocysts: Experience in 101 cases. Radiology 170:757–761, 1989.
389. Van Sonnenberg E, et al: Percutaneous abscess drainage: Current concepts. Radiology 181:617–626, 1991.

390. Van Sonnenberg E, et al: Percutaneous abscess drainage: Editorial comments. Radiology 184:27–29, 1992.
391. Van Waes PF, et al: Management of abscesses that are difficult to drain: A new approach. Radiology 147:57–63, 1983.
392. Vellet D, et al: Fine-needle aspiration cytology of mucinous cystadenocarcinoma of the pancreas: Further observations. Acta Cytol 32: 43–48, 1988.
393. Vergier B, Latrabe V, Belleannee G, et al: Transthoracic aspiration: Evaluation of cytologic and histologic diagnosis in a pulmonary nodule by retrospective comparison of 2 series of 267 cytoaspirations and 292 coaxial needle aspirations. Ann Pathol 19:463–471, 1999.
394. Vogl T, Muller PK, Mack MG, et al: Liver metastases: Interventional therapeutic techniques and results, state of the art. Eur Radiol 9: 675–684, 1999.
395. von Schreeb T, et al: Renal adenocarcinoma: Is there a risk of spreading tumor cells in diagnostic puncture? Scand J Urol Nephrol 1:270, 1967.
396. Weisbrod GL, Lyons DJ, Tao LC, et al: Percutaneous fine-needle aspiration biopsy of mediastinal lesions. AJR 143:525–529, 1984.
397. Welch CE: Percutaneous catheter drainage of abdominal abscesses (letter to the editor). N Engl J Med 306:108, 1982.
398. Welch TJ, et al: CT-guided biopsy: prospective analysis of 1,000 procedures. Radiology 171:493–496, 1989.
399. Welch TJ, Sheedy PFII, Stephens DH, et al: Percutaneous adrenal biopsy: Review of a 10-year experience. Radiology 193:341–344, 1994.
400. Westcott JL: Air embolism complication: Percutaneous needle biopsy of the lung. Chest 63:108–110, 1973.
401. Westcott JL: Direct percutaneous needle aspiration of localized pulmonary lesions: Results in 422 patients. Radiology 137:31–35, 1980.
402. Westcott JL: Percutaneous needle aspiration of hilar and mediastinal masses. Radiology 141:323–329, 1981.
403. Westcott JL: Percutaneous transthoracic needle biopsy. Radiology 169:593–601, 1988.
404. Whitmire LF, et al: Imaging guided percutaneous hepatic biopsy: Diagnostic accuracy and safety. J Clin Gastroenterol 7:511–515, 1985.
405. Wilson SR, Rosen IE: Abdominal biopsy with ultrasound guidance (abstract). Radiology 136:580, 1980.
406. Wittenberg J, et al: Core biopsy of abdominal tumors using a 22-gauge needle. Paper presented at the Sixty-Seventh Scientific Assembly and Annual Meeting, Radiological Society of North America, Chicago, Nov. 15–20, 1981.
407. Wittenberg J, et al: Nonfocal enlargement of pancreatic carcinoma. Radiology 144:131, 1982.
408. Wolinsky H, et al: Needle tract inplantation of tumor after percutaneous lung biopsy. Ann Intern Med 21:359–362, 1969.
409. Wood WB, et al: Studies on the cellular immunology of acute cytosis. J Exp Med 94:521–540, 1951.
410. Wright RN, et al: Pulmonary mucormycosis (phycomycetes) successfully treated by resection. Ann Thorac Surg 29:166–169, 1980.
411. Wroblicka JT, Kuligowska E: One-step needle aspiration and lavage for the treatment of abdominal and pelvic abscesses. AJR 170: 1197–1203, 1998.
412. Yang PC, Lee YC, Yu CJ, et al: Ultrasonographically guided biopsy of thoracic tumors: A comparison of large-bore cutting biopsy with fine-needle aspiration. Cancer 69:2553–2560, 1992.
413. Yohann MM, Haaga JR: Complications of no biopsy. AJR 172: 1475–1476, 1999.
414. Yoon SS, Tanabe KK: Surgical treatment and other regional treatments for colorectal cancer liver metastases. Oncologist 4:197–208, 1999.
415. Zalas P, et al: The diagnosis by percutaneous biopsy with computed tomography of a recurrence of carcinoma of the rectum in the pelvis. Surg Gynecol Obstet 151:525–527, 1980.
416. Zamchek N: Liver biopsy: II. The risk of needle biopsy. N Engl J Med 299:1062–1069, 1953.
417. Zeman R, et al: Personal communication, 1987.
418. Zins M, et al: US-guided percutaneous liver biopsy with plugging of the needle track: A prospective study in 71 high-risk patients. Radiology 184:841–843, 1992.
419. Zinzani PL, Corneli G, Cancellieri A: Core needle biopsy is effective in the initial diagnosis of mediastinal lymphoma. Haematologica 84: 600–603, 1999.
420. Zornoza J: Aspiration biopsy of discrete pulmonary lesions using a new thin needle. Radiology 123:519–520, 1977.
421. Zornoza J, et al: Fine-needle aspiration biopsy of retroperitoneal lymph nodes and abdominal masses: An updated report. Radiology 125:87–88, 1977.
422. Zornoza J, et al: Transperitoneal percutaneous retroperitoneal lymph node aspiration biopsy. Radiology 122:111–115, 1977.
423. Zornoza J, et al: Fine-needle aspiration biopsy of the liver. AJR 134:331–334, 1980.
424. Zornoza J, et al: Percutaneous needle biopsy in abdominal lymphoma. AJR 136:97–103, 1981.
425. Zuckerman DA, Yeager TD: Percutaneous ethanol sclerotherapy of postoperative lymphoceles. AJR 169:433–437, 1997.

62 Multislice Helical Computed Tomography: Clinical Applications

Kenyon K. Kopecky, Jonas Rydberg,
Thorsten R. Fleiter, Kenneth A. Buckwalter

Applied Principles

Multislice helical computed tomography (MSH CT) is superior to *single-slice* helical CT (SSH CT) for all clinical applications. The principal technical advance brought forth with this new generation of CT scanners is increased speed. The new "quad slice" scanners simultaneously acquire four "slices," or "channels," of contiguous spatial information. In addition, the gantry rotates at up to two revolutions per second (0.5 second per 360-degree rotation). Because most SSH CT scanners acquire one slice of data per rotation at a rotation speed of one revolution per second, the new MSH CT scanners are up to eight times faster. The increased speed provides many benefits, including:

1. *Improved patient tolerance*. Because the examination can be performed very quickly, the patients are in the CT suite for only a few minutes, which may help save the lives of unstable, critically ill patients. Patients who are in pain and those who experience severe claustrophobia also benefit.
2. *Improved temporal resolution*. Faster scanning decreases motion artifacts in the CT images, which result from voluntary and involuntary movements. Voluntary movement arising from skeletal muscle activity may occur when patients are unable or unwilling to lie still or suspend respirations during the examination. Involuntary movement results from cardiac pulsations, respiratory motion, intestinal peristalsis, and so on. All motion artifacts are reduced with faster data acquisition. In addition, new techniques are being used to synchronize scanning with the heart to minimize artifacts from cardiac motion.
3. *Improved spatial resolution*. Some of the improved temporal resolution can be traded for improved spatial resolution by selecting a thinner slice width for data acquisition. With thinner slices, the spatial resolution along the longitudinal (z) axis of the patient is improved. This reduces partial volume artifacts and increases diagnostic accuracy.
4. *Improved contrast medium use*. Iodinated contrast medium is administered intravenously (IV) at higher rates, resulting in higher peak enhancement values, which occur sooner after the start of injection. This improved *contrast resolution* increases the conspicuity of both normal and diseased tissues. Because scanning is completed rapidly, a shorter period of enhancement is needed; thus, for certain examinations, the dose of contrast medium may be reduced.
5. *Improved image quality*. The x-ray tube current (milliamperes [mA]) may be increased without risk of overheating because the scan is completed rapidly. Increasing the current decreases image noise and improves image quality, which is especially important when scanning very large patients and when using very thin slices.
6. *Increasing patient throughput*. Because scanning is completed more rapidly, more patients can be scanned per hour. This decreases the cost of the examination, which is especially important as reimbursements for medical care decline.
7. *Improved use of the x-ray tube*. Because imaging is completed more quickly, heating of the x-ray tube is diminished, which decreases or eliminates the need to wait for tube cooling between scans. In addition, many more images are created during the lifetime of a tube installed in a multislice scanner compared with that in a single-slice scanner, decreasing glassware costs and downtime.

Not all of the benefits of faster scanning described here can be realized simultaneously in each patient. The operator must choose faster speed, thinner slices, or lower noise or some compromise, permitting modest improvements in some of these factors.

In addition to these improvements, there is another innovation with multislice technology: the ability to use slice widths of less than 1 mm. Because of the large penumbra encountered when the x-ray beam is collimated to less than 1 mm, the radiation dose to the patient is unacceptably high with submillimeter SSH CT. With MSH CT, slices thinner than 1 mm can be created while the overall beam collimation remains at 1 mm or larger. This allows for high-resolution, *isotropic* imaging (i.e., imaging with equal spatial resolution in all three orthogonal planes, resulting in a cube-shaped voxel). The main advantage of isotropic

imaging is that reformation of the image data into any inclined plane results in the same resolution and image quality as the originally acquired slices. When a small x-ray focal spot is used, the pixel size in the scanned plane is approximately 0.5 × 0.5 mm. To achieve isotropic, high-resolution imaging, the slice width must be 0.5 mm, which is possible only with multislice CT.

MSH CT creates larger data sets, which present new challenges for the radiologists, technologists, network administrators, and medical equipment vendors. A chest CT examination performed with a slice width of 2.5 mm may generate more than 200 slices. A multiphase examination of the abdomen and pelvis or a CT arteriogram may generate more than 1000 slices. These huge volumes of image data result in increased image reconstruction time, increased transfer time, increased archival costs (the Picture Archival and Communication System [PACS] or film), and challenges for image review and interpretation. MSH CT scanners also cost more than SSH CT scanners and require more powerful workstations. Image interpretation requires the increased use of auxiliary display techniques such as (1) workstation review of source images in leaf (scrolling) mode, (2) multiplanar reformatting, (3) maximum and minimum intensity projections, (4) volume rendering, (5) virtual endoscopy, and (6) three-dimensional (3D) shaded-surface display.

Because of the advantages described here, MSH CT is superior to SSH CT for nearly all clinical applications. In addition, new applications of CT scanning are arising that had been previously impossible with SSH CT. As a result of its spectacular diagnostic power, MSH CT replaces more costly or more invasive medical diagnostic procedures, leading to earlier and more accurate diagnoses with reduced costs. This chapter highlights some of the indications for which MSH CT promises to have a major impact in patient care and clinical outcomes and is divided into sections based on organ systems: neurologic, cardiovascular, thoracic, abdominal, and skeletal. Because many organ systems may be examined in a matter of seconds with MSH CT, a discussion of multiorgan systems is added.

The information presented in this chapter cannot replace that covered in depth in other chapters of this text. Clinical materials were chosen that illustrate applications of CT that either are greatly improved by the multislice technique or were impossible before the introduction of the technology. The applications illustrated here represent only a few examples of the usefulness of MSH CT and not a comprehensive catalog of clinical indications. All CT scans reported in this chapter were performed on the MX 8000 scanner (Marconi Medical Systems, Inc., Cleveland, Ohio), and all postprocessing work was performed on the MX View workstation (Marconi Medical Systems). For this chapter, we used the definition of pitch suggested by McCollough and Zink,[4] which applies equally well to SSH CT and MSH CT:

$$\text{pitch} = \frac{\text{table travel per gantry rotation}}{\text{total nominal scan width}}$$

Clinical Applications

Neurologic Imaging

High-resolution, thin-section direct axial and coronal nonhelical CT used to be the standard technique for temporal bone imaging. A study[1] comparing the previous standard technique with MSH CT using isotropic voxels (0.5 mm) found MSH CT to be superior for visualization of the anatomy. Coronal views were created from the source images using multiplanar reformatting software. In addition, the MSH CT examination is much faster and more comfortable for the patient because it eliminates the hanging head position for direct coronal scanning. The radiation dose is lower in MSH CT because direct coronal scanning is eliminated (Fig. 62–1).

Surgical planning for the treatment of aneurysms of the circle of Willis requires superb visualization of the aneurysm and its relationship with arterial branch vessels and surrounding structures. Conventional angiography offers excellent spatial resolution, but the procedure is invasive and expensive and in rare cases may cause significant neurologic complications. In addition, only a limited number of views are possible because each projection requires a separate injection of contrast medium and a series of radiographic exposures. MSH CT angiography with isotropic 0.5-mm voxels offers high-resolution, minimal invasiveness without the risk of neurologic complications, a much lower cost, and an infinite choice of viewing projections (Fig. 62–2).

At our institutions, the neurosurgeons come to the workstation before surgery to rotate the 3D images with the track ball to ensure that they understand the anatomy from

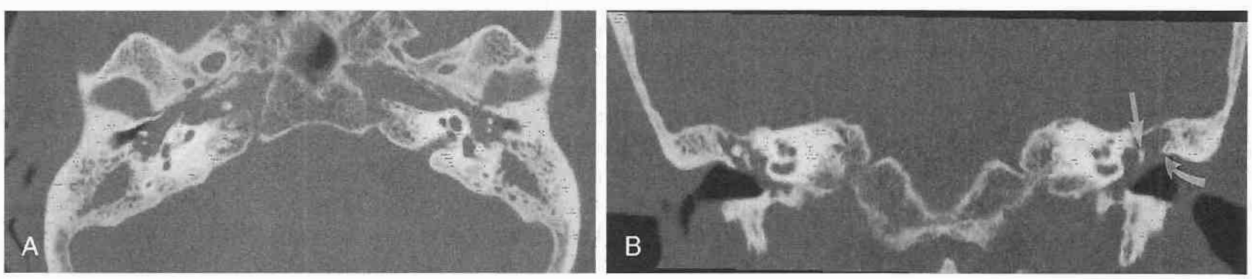

Figure 62–1. Bilateral chronic otitis media and cholesteatoma. Isotropic multislice helical CT was performed with 0.5-mm slice width. *A,* Axial image shows opacification of both middle ear cavities, mastoid antrum, and mastoid air cells as a result of chronic otitis. *B,* Coronal reformat provides excellent spatial resolution and depicts the cholesteatoma with erosion of the ossicles *(straight arrow)* and scutum *(curved arrow).*

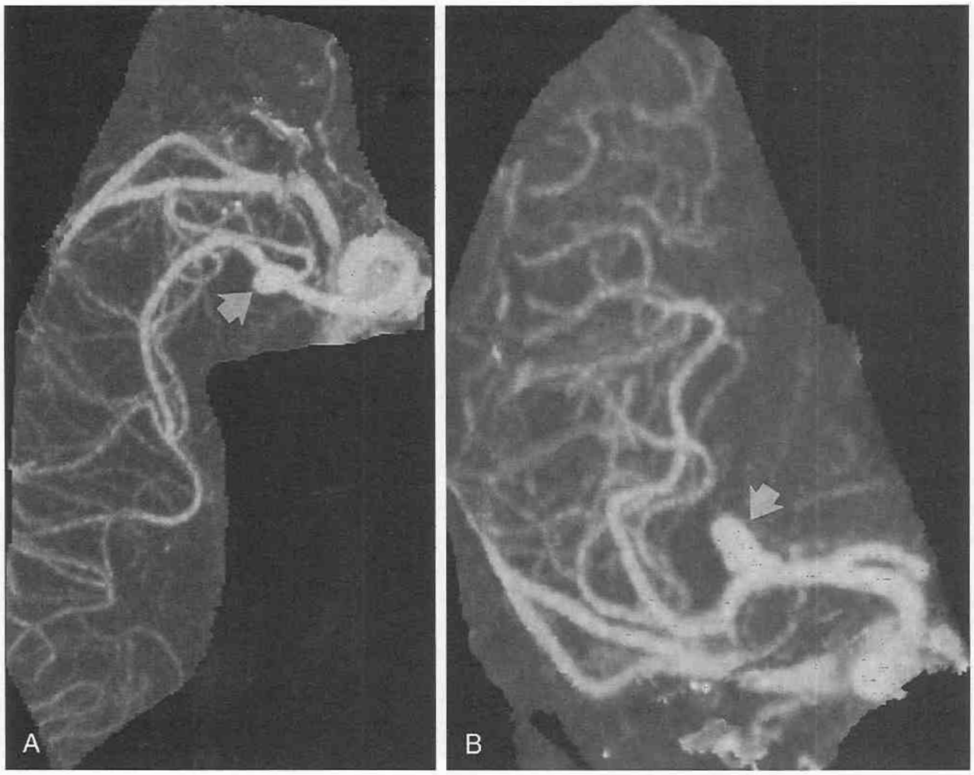

Figure 62–2. Middle cerebral artery aneurysm in a 60-year-old man who presented with headaches. Multislice helical CT was performed with a slice width of 0.5 mm and a reconstruction increment of 0.2 mm. Maximum-intensity projection axial *(A)* and oblique *(B)* images show a middle cerebral artery aneurysm *(arrows)*.

all projections. In addition, because of its higher spatial resolution, MSH CT angiography is preferred to magnetic resonance angiography (MRA) in the preoperative evaluation of cerebral aneurysms, although both techniques are powerful and have different strengths and weaknesses.

Perfusion imaging is used clinically in magnetic resonance imaging (MRI) to evaluate stroke patients. The advent of MSH CT improves the capability of CT for the measurement of blood flow in tissue. Before scanning begins, the tabletop is locked in a predefined position to cover the region of interest (usually the middle cerebral artery and its distribution). Fifty milliliters of contrast medium is injected at a rate of 5 to 10 mL/sec into an antecubital vein, and scans are obtained every 2 seconds for about 30 seconds. The computer records the density in every pixel in every image, beginning before the contrast medium reaches the organ of interest and continuing until after the bolus has passed. The computer then measures the rate at which the brain tissue density increases with time. The maximum rate of increase is normalized to the arterial peak enhancement to obtain a blood perfusion value for each pixel.

In addition, the computer calculates time to peak enhancement and the mean transit time of the bolus through the brain. Color maps of the different functions are created and displayed (Fig. 62–3). The information gleaned from this test may help distinguish areas of reversible from irreversible ischemia.[3] The disadvantages of this technique relative to MRI are (1) the limitation on the volume of brain tissue that can be studied (width of detector array) and (2) the inability to perform diffusion imaging.

During the 1990s, MRI became the principal imaging modality for evaluating the spinal canal and surrounding structures. Some surgeons, however, preferred to use CT in conjunction with myelography because of CT's ability to depict the bony structures in fine detail. With MSH CT, a wide anatomic zone of the spine can be scanned with the thin-slice technique. For example, the cervical spine can be scanned with 1-mm slice thickness in 30 seconds or less, providing isotropic, 1-mm resolution in all planes (Fig. 62–4). Another indication may be radiculopathy, in which IV contrast-enhanced MSH CT may be used to distinguish soft from hard disc disease.

Cardiovascular Imaging

CT angiography is possible with single-slice helical technology, but it is severely limited by the acquisition of only one slice of data at a time. Thus, either the volume of anatomic coverage must be very limited, or the image quality must be compromised by the choice of thick slices (poor z-axis resolution) or high pitch (high noise, more artifacts). With the advent of MSH CT, CT angiography has become a powerful clinical diagnostic tool for the evaluation of a wide variety of vascular diseases, supplanting other imaging modalities, including conventional angiography.

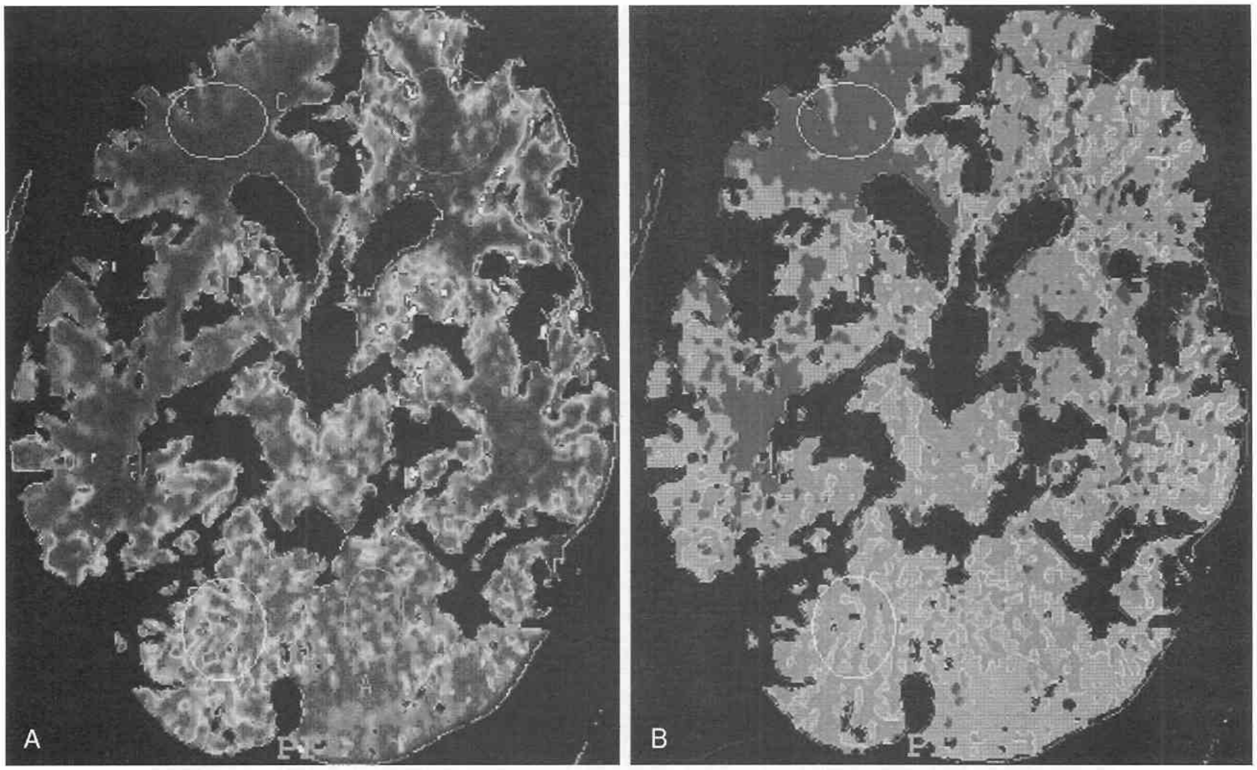

Figure 62–3. Brain perfusion study in a 64-year-old woman who presented with acute left hemiplegia caused by acute right internal carotid occlusion. The unenhanced CT was normal. Perfusion study was performed with 4 × 5-mm dynamic axial scans every 2 seconds through a single brain location. Density curves that are proportional to contrast concentration were generated from brain parenchyma, an arterial input vessel, and dural sinus. These curves were used to generate the cerebral blood flow (CBF) *(A)* and time-to-peak (TTP)*(B)* maps, demonstrating decreased cerebral blood flow (blue) and increased time to peak (red) within the right cerebral hemisphere.

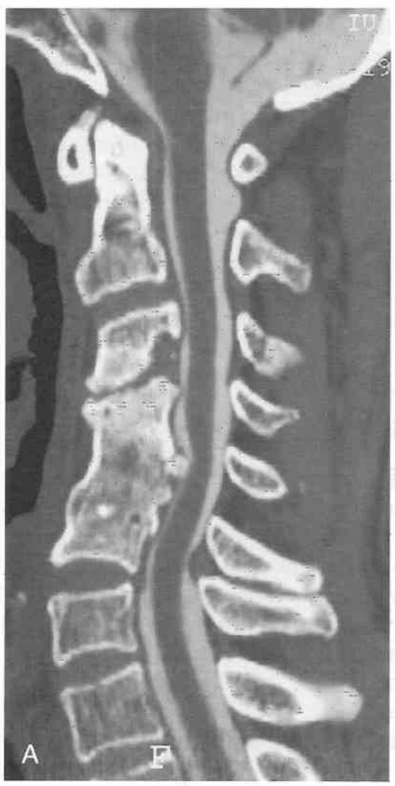

Figure 62–4. CT myelogram of a 67-year-old man with a history of cervical and lumbar fusion. The patient had presented with neck and back pain. The cervical scan was performed with a 1-mm slice width, rotation time of 0.75 second, pitch of 1, and scan time of 44 seconds. Sagittal *(A)* and axial *(B)* images show fused vertebra with osteophytes that impinge on the spinal cord.

Concurrent with the development of less invasive diagnostic imaging techniques has been the development of less invasive surgical techniques. One example of the marriage of less invasive imaging with less invasive surgery is the use of MSH CT angiography with endoluminal repair of aortic aneurysms using stent-grafts. At many institutions, MSH CT has completely supplanted conventional angiography in preoperative and postoperative evaluations of patients with aortic aneurysms (Fig. 62–5). MSH CT not only is less invasive and less expensive but also provides more information. Accurate measurements of the aneurysm and its relationship to branch vessels are made on the preoperative study, which are used to determine whether a patient is a candidate for endoluminal therapy. If the patient is a candidate, the proper diameters and lengths of the modular graft components are selected using the CT data. Postoperatively, MSH CT is used to assess patency of the endograft and to detect complications such as endoleaks.

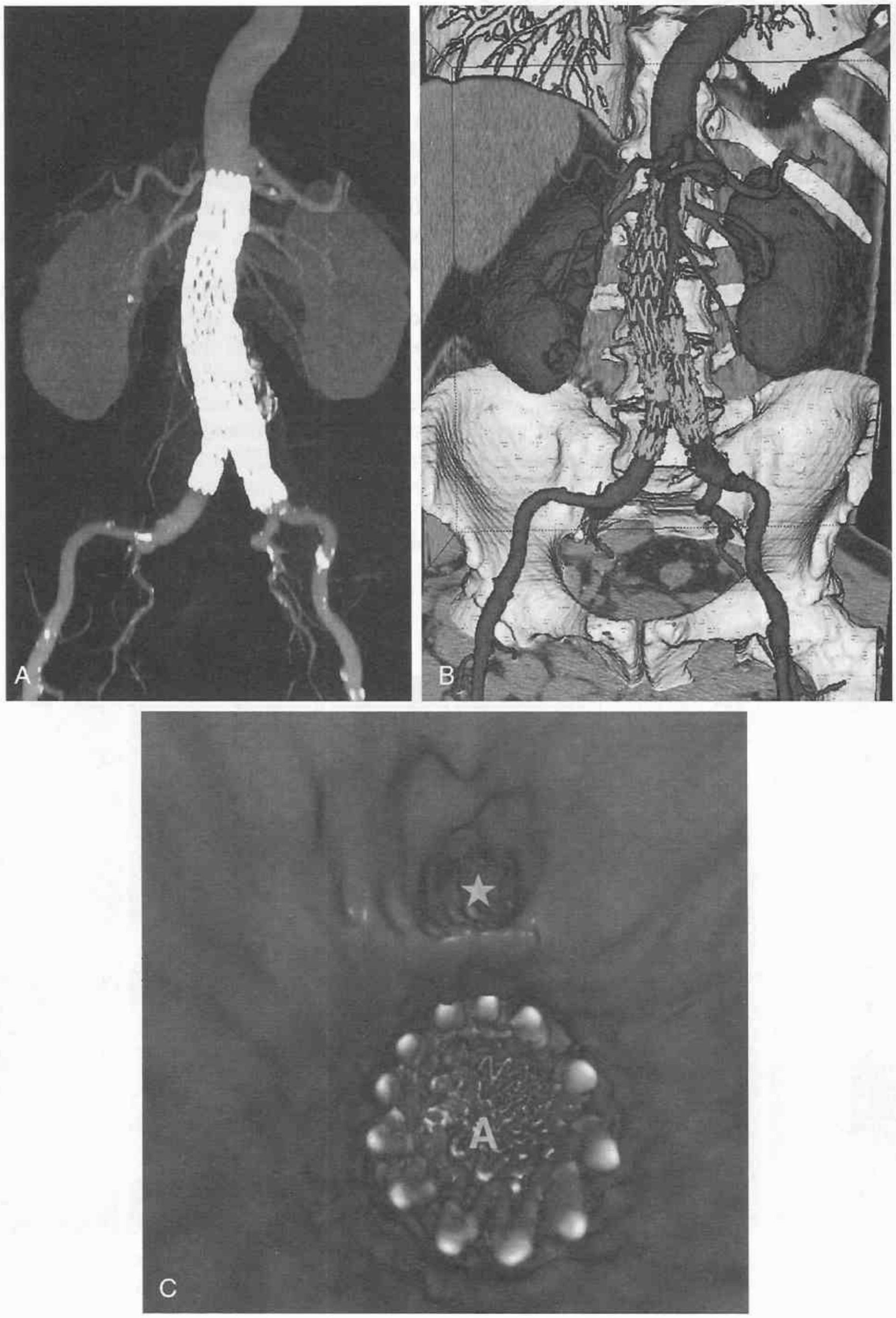

Figure 62–5. Aortic stent-graft in a 69-year-old man who underwent endoluminal repair of an abdominal aortic aneurysm. Postoperative multislice helical CT demonstrated graft patency and absence of an endoleak. Anteroposterior maximum-intensity projection *(A),* 3D surface-shaded display *(B),* and virtual arterioscopy *(C)* images show the wire frame of the stent-graft within the aorta. *C,* View from the superior portion of the abdominal aorta looking caudally into the celiac trunk *(asterisk)* and the main aortic lumen (A).

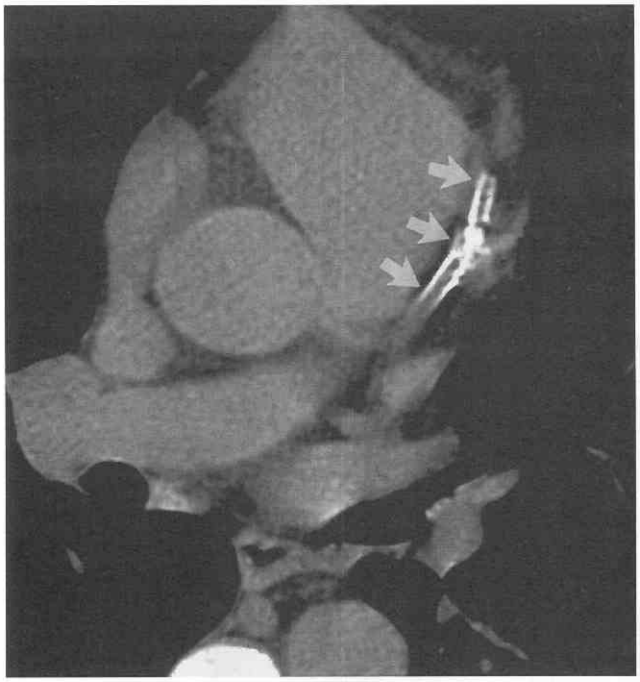

Figure 62–6. Coronary calcium scoring. Multislice CT was performed in nonhelical mode using prospective electrocardiographic triggering, 0.5-second rotation time, 180-degree interpolation, and 0.3-second image acquisition time. The image acquired during diastole shows heavy calcifications *(arrows)* in the left anterior descending coronary artery and no visible motion artifact.

Imaging of the heart with helical CT had been limited by the rapid motion of the heart relative to the slow data acquisition times of CT. With the advent of multislice technology, some cardiac imaging applications have become more feasible. The simplest of these is *cardiac calcium scoring*, which refers to the quantitative measurement of calcium within atherosclerotic plaques in the walls of the coronary arteries (Fig. 62–6). The fastest multislice scanners acquire four slices within 0.3 second using a 0.5-second rotation time and a 180-degree reconstruction algorithm.

There are two ways to synchronize the CT data acquisition to the heart motion: (1) *prospective* electrocardiographic (ECG) triggering and (2) *retrospective* ECG gating.

Prospective triggering is used in a nonhelical mode, and it permits the x-ray beam to be turned on and off as the tube rotates around the patient. Some patients are not candidates for triggered imaging because of irregular cardiac rhythms. For calcium scoring, the x-rays are turned on during diastole, when the ventricles are relatively motionless.

Prospective triggering provides a lower radiation dose to the patient than retrospective gating because the x-ray beam is turned off during systole. With a slice width of 2.5 mm, the coronary arteries are imaged during suspended respirations in 15 seconds or less. The images have very little motion artifact, and future research will determine whether MSH CT is as accurate and reproducible as electron beam CT for calcium scoring.

MSH CT performed with retrospective ECG gating is being investigated for several uses:

1. Coronary CT angiography (Fig. 62–7).

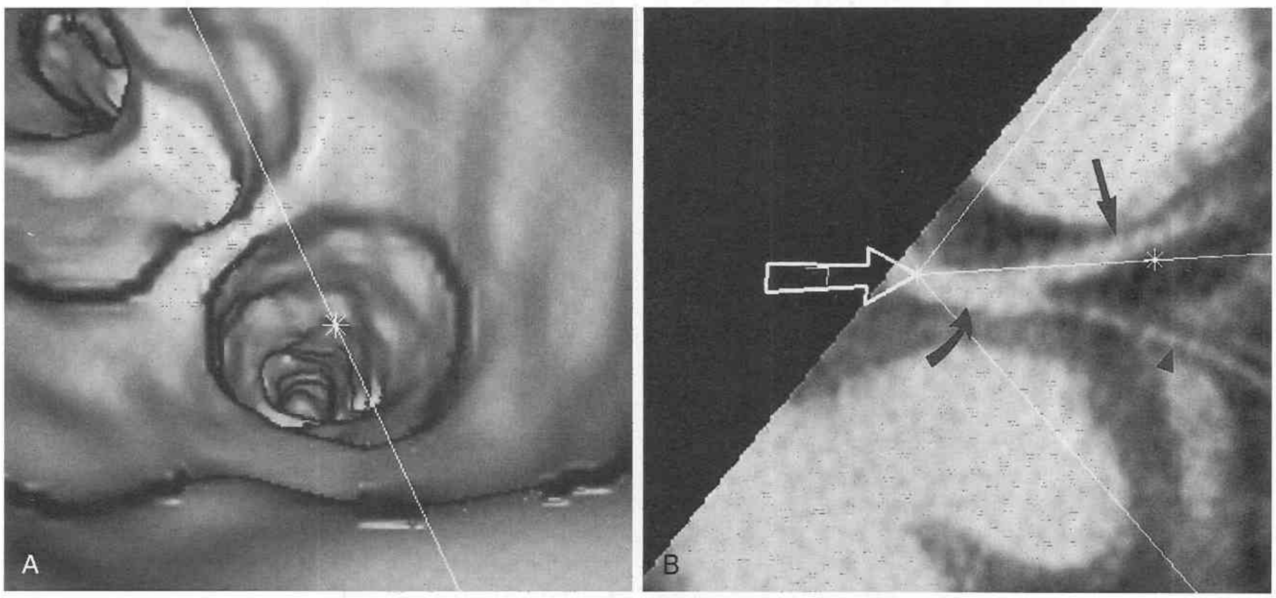

Figure 62–7. Coronary CT arteriography. Multislice helical CT was performed during intravenous administration of contrast medium with 1-mm slice width and retrospective electrocardiographic gating. *A,* In the virtual arterioscopy image, the viewer is positioned within the left main coronary artery looking distally. In the direction of the *asterisk*, on the *dotted line*, the lumen of the anterior descending coronary artery is seen. *Upper left,* Proximal circumflex artery. For orientation purposes, the virtual endoscopy images are accompanied by a reformatted planar image *(B)* that displays the position of the viewer and the viewing direction *(open arrow)*. The *asterisk* positions in *A* and *B* are identical. *B,* Visualization of left main artery *(curved arrow)*, left anterior descending coronary artery (*straight arrow*), and circumflex artery *(arrowhead)*. (Courtesy of Robert C. Gilkeson, M.D., University Hospitals of Cleveland.)

2. Assessment of ventricular ejection fraction.
3. Evaluation of ventricular wall motion.
4. Evaluation of ventricular perfusion.

To use helical CT with retrospective gating, the operator must choose a pitch of 0.5 or less to provide sufficient data throughout the cardiac cycle. If the operator chooses a nominal slice width of 1 mm, a rotation time of 0.5 second, and a pitch of 0.5, the time required to cover the entire heart is 30 to 40 seconds, which is longer than many patients can suspend respirations. Retrospective gating is less sensitive to cardiac rhythm irregularities than prospective triggering. The clinical acceptance of MSH CT for some of these applications may have to await further advances in CT, which promise to deliver rotation times of less than 0.5 second and more than four slices per rotation. There will be formidable competition from MRI for these same clinical applications.

Perfusion imaging with multislice CT, as mentioned, is being studied as a diagnostic tool in stroke patients. This technique can be used to evaluate blood flow in other organs, such as the kidney (Fig. 62–8). Perfusion CT may prove complementary to CT angiography in the evaluation of arterial inflow obstructive disease. The anatomic information about renal artery stenosis, coupled with the functional information about renal perfusion, may prove more useful than either one alone.

Thoracic Imaging

Pulmonary embolism is a common cause of death, and until now, the methods of establishing the diagnosis have had significant drawbacks. The nuclear medicine ventilation-perfusion scan has low accuracy. Pulmonary arteriography, although accurate, is invasive, expensive, and not widely available. SSH CT has been used to evaluate patients with suspected acute pulmonary embolism, but the accuracy, relative to arteriography, is not sufficiently high. A prospective blinded multireader study revealed a sensitivity and specificity of 60% and 81%, respectively, for SSH CT, compared with arteriography.[2] MSH CT has the potential to replace ventilation-perfusion scanning and arteriography and to improve the diagnosis and outcome of

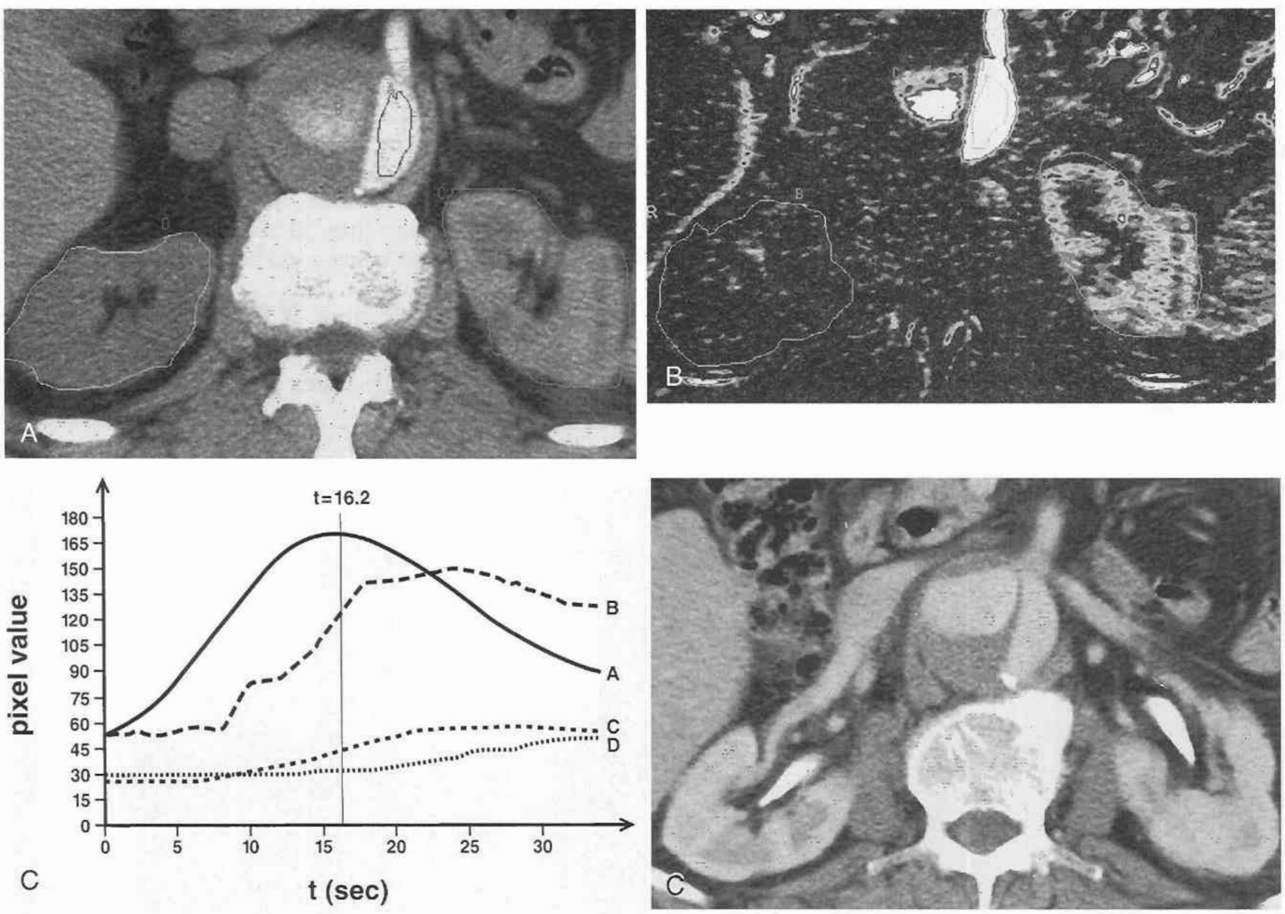

Figure 62–8. Aortic dissection. A CT perfusion study was performed through the midportions of the kidneys during intravenous administration of 30 mL of contrast medium at 10 mL/sec in a man with known aortic dissection. Axial images were obtained at 2-second intervals for 35 seconds. *A,* CT scan from the late arterial phase shows bright enhancement of the true lumen and lesser enhancement of the false lumen. *B,* Perfusion scan shows severe impairment of right renal blood flow (supplied via the false lumen) compared with the left. *C,* Graph of CT density versus time illustrates perfusion in the true lumen (A), false lumen (B), left kidney (C), and right kidney (D). CT arteriography followed the perfusion study (not shown). *D,* On a venous phase CT scan, enhancement of the kidneys appears equal, illustrating the limitations of conventional CT in the evaluation of perfusion.

Table 62–1. Multislice Helical Computed Tomography Technique for Acute Chest Pain and Dyspnea

IV Contrast Medium Administration	
Catheter size	≥20 gauge
Catheter location	Right antecubital vein
Medium type	Nonionic
Concentration	300 mg iodine/mL
Volume	1.5–2.0 mL/kg, up to 150 mL
Rate	4–5 mL/sec
Delay time	17–24 sec
Scanning Technique	
Channels/rotation	4
Nominal slice width	2.5 mm
Pitch	1.0
Rotation time	0.5 sec
Focal spot	Large
kVp	120
mAs	230
Scan time	10–15 sec
Direction	Base to apex of lungs
Reconstruction Technique	
Reconstruction field of view	To include lungs, excluding chest wall
Filter (algorithm)	Medium body
Reconstruction increment	1.0–1.3 mm
Matrix	512 × 512 pixels
Edge enhancement	0%

IV, intravenous; kVp, kilovolt peak; mAs, milliampere-second.

patients with pulmonary embolism. Clinical trials are under way to determine the accuracy of MSH CT relative to arteriography.

MSH CT is powerful because it also can be used to diagnose many diseases that clinically mimic pulmonary emboli, such as pneumonia, pulmonary edema, aortic dissection, pericarditis, pleuritis, carcinoma that obstructs pulmonary arteries, bronchial obstruction, and esophageal rupture. The technique that we use to evaluate patients with acute chest pain or dyspnea is shown in Table 62–1. It is possible to follow the chest CT with CT scans of the abdomen, pelvis, and legs to detect possible deep venous thrombosis, all with the use of just one injection of iodinated contrast medium (Fig. 62–9).

Abdominal Imaging

Multiphase examinations of the liver, pancreas, and kidneys are ideally suited to MSH CT because multiple scans with thin slices are needed in rapid succession, which is impossible with SSH CT. Multiphase examinations of the liver commonly are required for patients with hepatitis or cirrhosis to evaluate for hepatomas (hypervascular tumors are best seen during the arterial phase) (Fig. 62–10) and patency of the hepatic and mesenteric arteries and veins.

Multiphase examinations of the pancreas are usually performed to assess islet cell tumors, which are best seen in the pancreatic phase of contrast medium administration (Fig. 62–11). The onset and duration of the *arterial*, *pancreatic*, and *portal venous* phases depend on the rate and duration (volume) of contrast medium administration.

Tublin and colleagues[6] compared the enhancement of the pancreas and the liver using two different contrast medium injection rates: 2.5 and 5.0 mL/sec. They found that the peak enhancement was higher and that the time to peak occurred sooner with the higher injection rate for both the pancreas and the liver (Fig. 62–12).

To take advantage of the increased enhancement associated with the higher injection rate, MSH CT must be used to complete the scans rapidly with thin slices. Ideally (in patients with normal cardiac output), the pancreatic phase images should begin at 40 seconds from the start of injection and last no more than 15 seconds; the portal venous phase images should begin at 65 seconds and last no more than 20 seconds.

Multiphase examinations of the kidney are performed for a number of indications, including the following:

1. Evaluation of renal masses to distinguish benign from malignant.

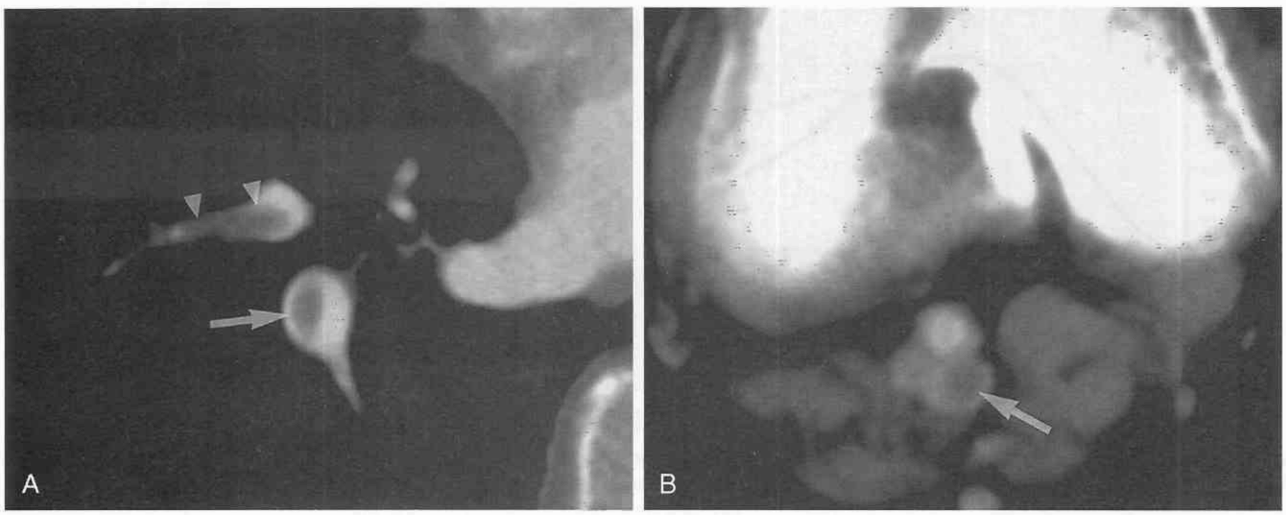

Figure 62–9. Pulmonary emboli and deep venous thrombosis. *A,* Multislice helical CT of the chest was completed in 15 seconds with 2.5-mm slice width. Emboli are seen within two segmental arteries: one oriented in the cephalocaudal direction *(arrow)* and the other in the transverse direction *(arrowheads)*. *B,* The pelvis and legs were scanned beginning 2.5 minutes after the start of contrast medium injection; popliteal venous thrombosis *(arrow)* is seen.

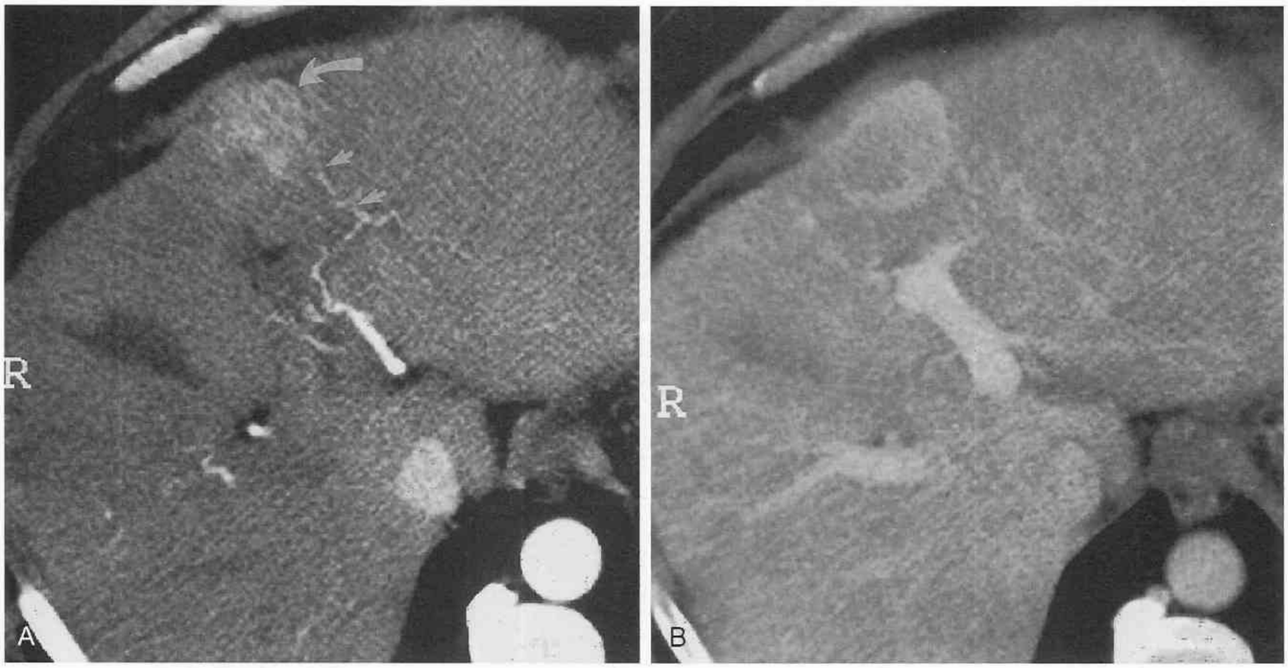

Figure 62–10. Hepatoma. Dual-phase multislice helical CT was performed in a man with hepatitis C and cirrhosis. *A,* The arterial phase scan depicts an enhancing neoplasm *(curved arrow)* and its feeding artery *(straight arrows)*. *B,* The hepatoma is also seen in the portal venous phase.

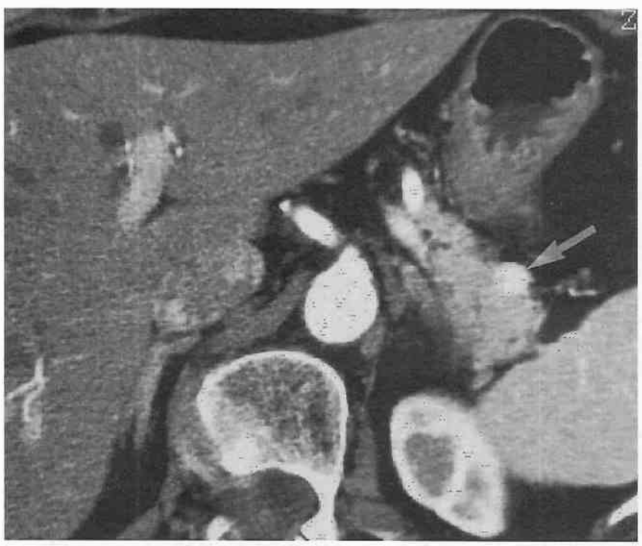

Figure 62–11. Insulinoma. A patient with symptomatic hypoglycemia was scanned in the pancreatic and portal venous phases. This pancreatic phase image shows an 8-mm hypervascular neoplasm in the tail *(arrow)*.

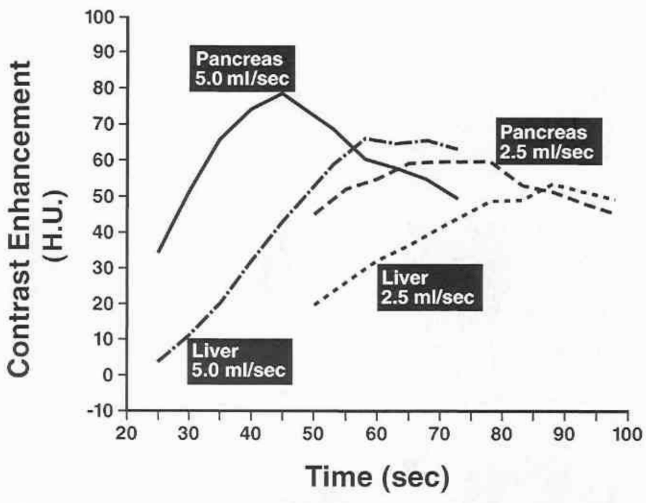

Figure 62–12. Pancreatic and hepatic enhancement showing a comparison of two contrast medium injection rates. Compared with the slower rate (2.5 mL/sec), the faster injection rate (5.0 mL/sec) provided an earlier rise in parenchymal enhancement and higher peak enhancement. Multislice helical CT is ideally suited to take advantage of the superior enhancement afforded by the faster injection rate for dual-phase scanning of the pancreas and liver. (Adapted from Tublin ME, Tessler FN, Cheng SL, et al: Effect of injection rate of contrast medium on pancreatic and hepatic helical CT. Radiology 210:97–101, 1999.)

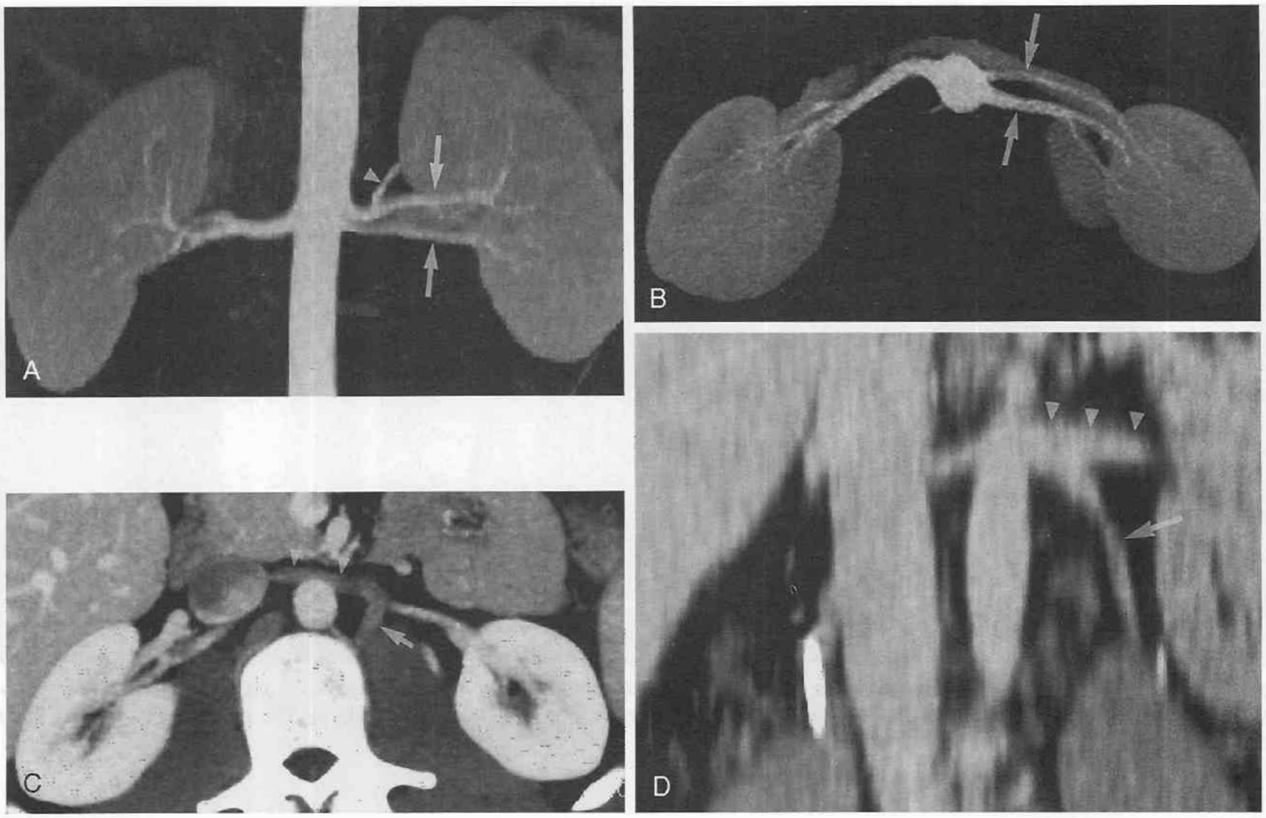

Figure 62–13. Renal donor evaluation. The multislice helical CT examination has three or more phases. In this potential donor, the arterial phase coronal *(A)* and axial *(B)* maximum-intensity projection images demonstrate two left renal arteries *(arrows)* and an early branching artery to the upper pole *(arrowhead)*. *C,* The nephrographic phase disclosed a lumbar vein *(arrow)* merging with the left renal vein *(arrowheads)* as shown on an axial maximum-intensity projection image. *D*, On an oblique multiplanar reformat, a left gonadal vein *(arrow)* is shown merging with the left renal vein *(arrowheads)*.

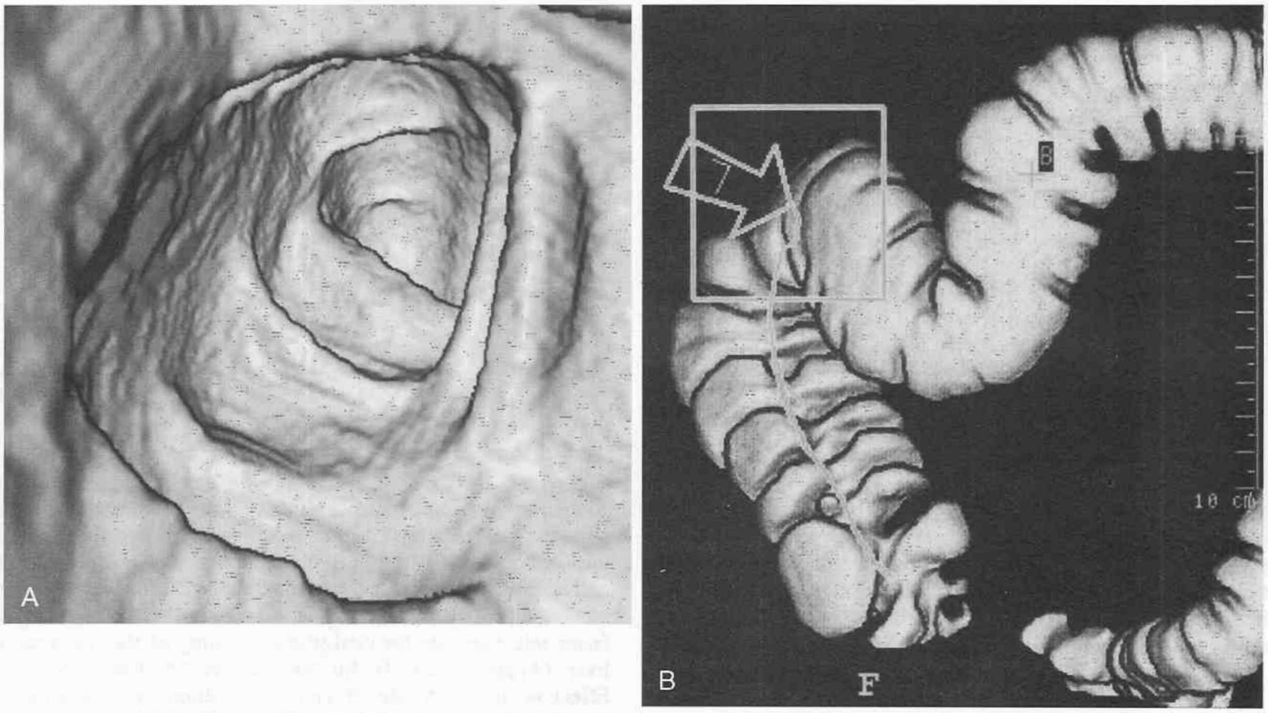

Figure 62–14. Virtual colonoscopy. Multislice helical CT was performed with 2.5-mm slice width after rectal insufflation of 2 L of carbon dioxide. *A,* This normal virtual endoscopy image was taken from the top of the hepatic flexure looking down into the proximal transverse colon. *B,* The overview image shows the viewer's position *(open arrow)* in *A*.

Figure 62–15. Calcaneal fracture of a 35-year-old man who sustained comminuted fractures of the right calcaneus and femur. Multislice helical CT was performed in the axial scan plane with 1-mm slice thickness. Sagittal *(A)* and coronal *(B)* reformats show fracture extent, number, and size of fracture fragments and violation of joint surface *(arrow)*.

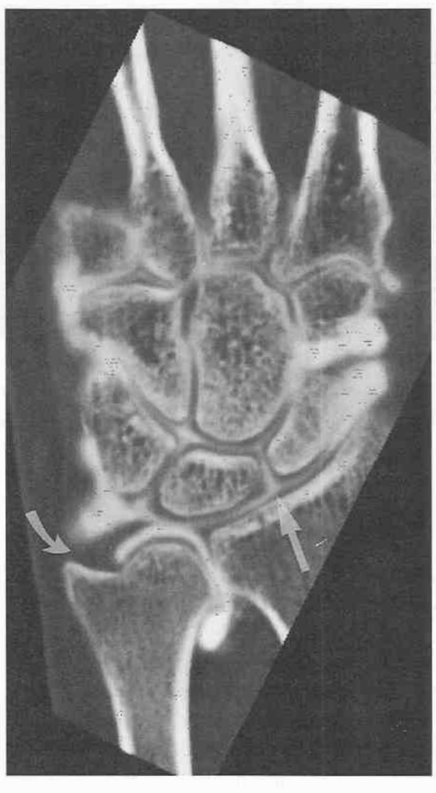

Figure 62–16. Wrist CT arthrography of a man who complained of wrist pain after playing golf. Multislice helical CT was performed (slice thickness of 0.5 mm, reconstruction increment of 0.2 mm) after contrast medium injection into the midcarpal and radioulnar joint spaces. The coronal reformatted image shows complete tear of the scapholunate ligament *(long arrow)*, enabling communication between the normally separate midcarpal and radiocarpal joint spaces. The triangular fibrocartilage *(curved arrow)* is intact.

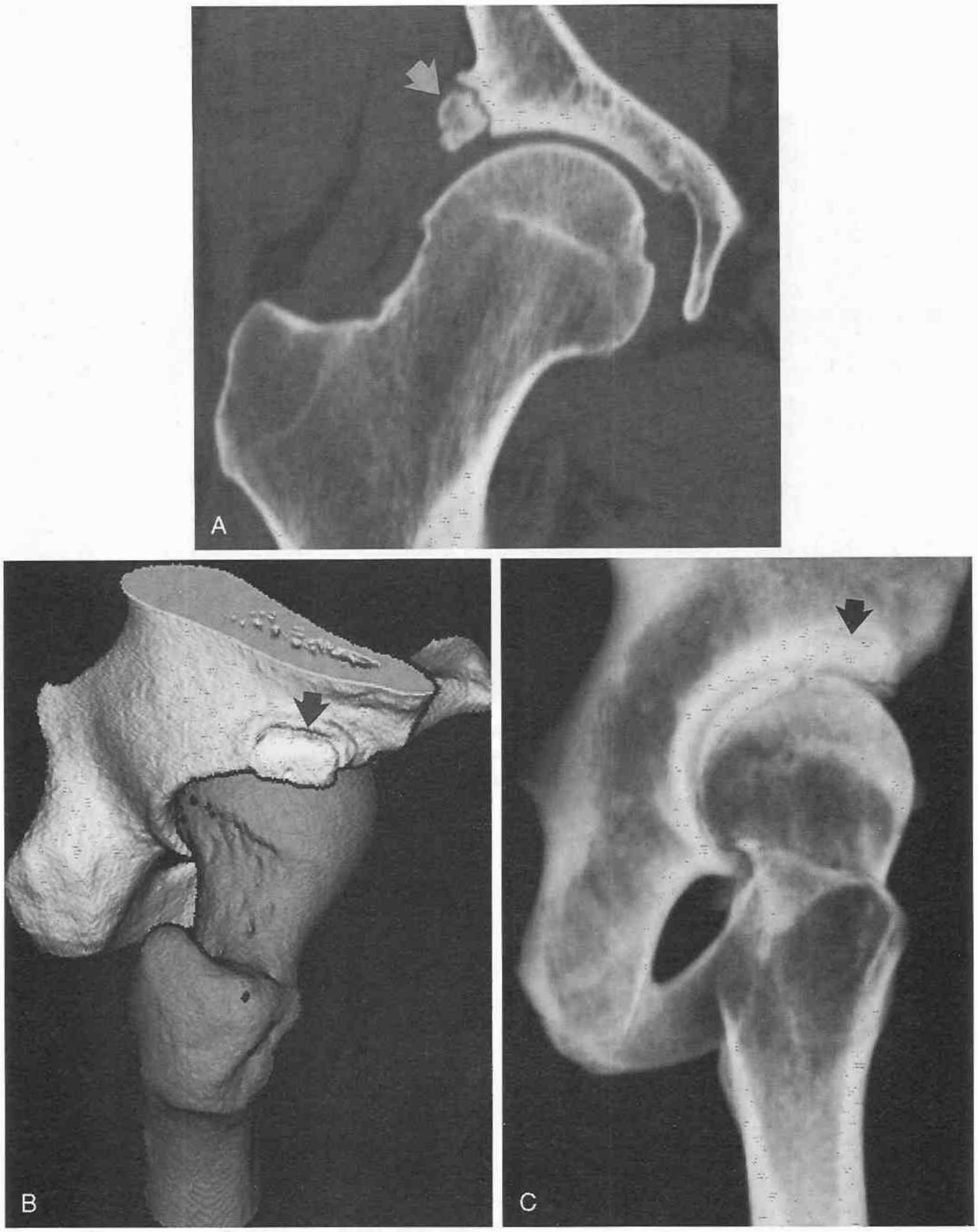

Figure 62–17. Os acetabuli of a 24-year-old man who complained of right hip pain. Multislice helical CT was performed with 1.0-mm slice thickness. An accessory ossicle *(arrow)* with sclerotic margins is shown on coronal reformat image *(A)*, 3D surface shaded display image *(B)*, and volume-rendered image *(C)*. The volume rendering is performed with a high degree of transparency, emulating plain radiography.

2. Evaluation of urolithiasis and its complications.
3. Evaluation of potential renal donors.

Traditionally, the evaluation of potential renal donors included excretory urography (IV pyelography) and conventional arteriography. Now these two examinations have been replaced at some centers by MSH CT, and this single examination provides more information than the traditional examinations with less invasiveness and at a lower cost.

The less invasive MSH CT examination is perfectly suited to complement the new less invasive surgery: laparoscopic donor nephrectomy. To perform a laparoscopic nephrectomy, the surgeon must have detailed anatomic information before surgery because he or she operates through a small umbilical incision with limited visibility and surgical exposure. All arteries, veins, and ureters must be identified before surgery to minimize the chance of surgical complications.

The MSH CT examination has three (or more) phases: (1) noncontrast, (2) arterial, and (3) nephrographic, plus an immediate post-CT plain radiograph.

The *noncontrast* (precontrast) phase is used to evaluate for urolithiasis and to provide baseline CT density measurements for any mass lesions that may be detected.

The *arterial* phase is used to identify all renal arteries, including accessory arteries, and to create three-dimensional images of the arterial anatomy.

The *nephrographic* phase is used to identify all renal veins, including anomalous veins, and communications between the renal veins, the gonadal veins, and the lumbar or azygos veins (Fig. 62–13). It is also used to identify any renal masses and to provide density measurements, which are compared with density measurements on the precontrast images. The plain radiograph of the abdomen and pelvis obtained after the CT scan is used to identify any abnormalities of the collecting system such as medullary sponge kidney disease and ureteral duplication.

Virtual colonoscopy (CT colography or colonography) is being investigated as a method of detecting colonic polyps. The examination is performed after a bowel-cleansing regimen. Air or carbon dioxide is administered per rectum, and the abdomen and pelvis are scanned without contrast materials. Some authors conclude that helical CT colonography, performed with a 5-mm slice width, is not adequate as a colorectal cancer screening test.[5] With MSH CT, the entire colon and rectum can be examined using 2.5-mm slice width, pitch 1, in 25 seconds or less. Superior image quality is achieved with this technique (Fig. 62–14), and research is under way to compare it with conventional colonoscopy.

Skeletal Imaging

MSH CT is well suited for musculoskeletal imaging because (1) submillimeter slice thickness makes isotropic imaging possible and (2) the use of multiple detectors allows for greater coverage of regional anatomy with thinner slices, higher milliamperes, and lower noise.

High-resolution (small focal spot), isotropic imaging can be used for smaller regions of interest such as the hand, wrist, foot, and ankle. In scanning a traumatized extremity, the need for multiple scanning planes is eliminated. The limb is placed in a position that is comfortable for the patient. From the acquired volume of image data, any viewing plane can be reformatted (Fig. 62–15). MSH CT may be used in conjunction with arthrography to better visualize the joint spaces and articular surfaces (Fig. 62–16).

Skeletal MSH CT can be performed in the torso (shoulders, spine, pelvis, hips) using the large focal spot, creating 1-mm, isotropic voxels. Imaging of the hips may be performed with a slice width of 1 mm, a rotation time of 1 second or more, and a pitch of 1 or less, providing high-quality images with low noise levels (Fig. 62–17). These techniques are possible only with MSH CT because of the improved use of the x-ray tube output.

Multisystem Imaging

There are several clinical indications for imaging large portions of patients, including multiorgan systems, at one setting, such as the neck, the chest, the abdomen, and the pelvis. These indications include multiple trauma, diagnosis and staging of cancer, and evaluation of sepsis (Fig. 62–18). These indications are sufficiently common and sufficiently important for all large medical centers to provide MSH CT capabilities.

Figure 62–18. Thymic rebound after chemotherapy in a 7-year-old boy with lymphoma who had completed chemotherapy 4 months earlier. CT was requested to assess for residual or recurrent disease. The neck, chest, abdomen, and pelvis were scanned (2.5-mm slice width) in 24 seconds with a single contrast medium injection. Coronal *(A)*, sagittal *(B)*, and axial *(C)* images show excellent intravascular and tissue enhancement and high spatial resolution. Multislice helical CT showed no evidence of lymphoma. The thymus *(arrows)* had grown in size over the previous 4 months, typical of rebound phenomenon after cessation of stress (i.e., chemotherapy).

Summary

The evolution of helical CT has made a great leap forward with the development of multislice technology. This advance is facilitating earlier and more accurate diagnoses, saving lives, and reducing the cost of health care. Future advancements will result in even faster, higher-resolution instruments, which will improve on present capabilities and add new clinical applications.

References

1. Caldemeyer KS, Sandrasegaran K, Shinaver CN, et al: Temporal bone: Comparison of isotropic helical CT and conventional direct axial and coronal CT. AJR Am J Roentgenol 172:1675–1682, 1999.
2. Drucker EA, Rivitz SM, Shepart JO, et al: Acute pulmonary embolism: Assessment of helical CT for diagnosis. Radiology 209:235–241, 1998.
3. Klotz E, Konig M: Perfusion measurements of the brain: Using dynamic CT for the quantitative assessment of cerebral ischemia in acute stroke. Eur J Radiol 30:170–184, 1999.
4. McCollough CH, Zink FE: Performance evaluation of a multislice CT system. Med Phys 26:2223–2230, 1999.
5. Rex DK, Vining D, Kopecky KK: An initial experience with screening for colon polyps using spiral CT with and without CT colography (virtual colonoscopy). Gastrointest Endosc 50:309–313, 1999.
6. Tublin ME, Tessler FN, Cheng SL, et al: Effect of injection rate of contrast medium on pancreatic and hepatic helical CT. Radiology 210: 97–101, 1999.

Index

Note: Page numbers followed by f indicate figures; those followed by t, tables; and those by b, boxes.